# Advances in Civil and Industrial Engineering IV

Edited by
Guangfan Li, Chaohe Chen,
Bifeng Jiang and Qizhong Shen

TRANS TECH PUBLICATIONS

# Advances in Civil and Industrial Engineering IV

Edited by
Guangfan Li
Chaohe Chen
Bifeng Jiang
Qizhong Shen

# Advances in Civil and Industrial Engineering IV

Selected, peer reviewed papers from the
the 4th International Conference on
Civil Engineering, Architecture and Building Materials
(CEABM 2014),
May 24-25, 2014, Haikou, China

*Edited by*

**Guangfan Li, Chaohe Chen,**
**Bifeng Jiang and Qizhong Shen**

TTP

**Copyright** © 2014 Trans Tech Publications Ltd, Switzerland

All rights reserved. No part of the contents of this publication may be reproduced or transmitted in any form or by any means without the written permission of the publisher.

Trans Tech Publications Ltd
Churerstrasse 20
CH-8808 Pfaffikon
Switzerland
http://www.ttp.net

Volumes 580-583 of
*Applied Mechanics and Materials*
*ISSN print 1660-9336*
*ISSN cd 1660-9336*
*ISSN web 1662-7482*

Full text available online at *http://www.scientific.net*

***Distributed** worldwide by*

Trans Tech Publications Ltd
Churerstrasse 20
CH-8808 Pfaffikon
Switzerland

Fax: +41 (44) 922 10 33
e-mail: sales@ttp.net

*and in the Americas by*

Trans Tech Publications Inc.
PO Box 699, May Street
Enfield, NH 03748
USA

Phone: +1 (603) 632-7377
Fax: +1 (603) 632-5611
e-mail: sales-usa@ttp.net

# Preface

The International Conference on Civil Engineering, Architecture and Building Materials provides a forum for accessing to the most up-to-date and authoritative knowledge from both industrial and academic worlds, sharing best practice in this exciting field of Civil Engineering, Architecture and Building Materials. The first CEABM was successfully taken place in Haikou, China, June 18-20, 2011, the second CEABM was in held in Yantai, China, from May 25 to 27, 2012 and the third in Jinan, from May 24 to 26, 2013. After the very successful previous issues, the 4th CEABM was successfully held in Haikou, China, from May 24 to 25, 2014.

All papers included in this collection had undergone the careful peer-review by the experts of international and domestic of China before it is selected for publications. This book covers the subject areas of Geotechnical Engineering, Geological Engineering, Tunnel, Subway and Underground Facilities, Seismic Engineering, Hydraulic Engineering, Water Resources and Hydrology, Coastal Engineering, Construction Technology, Water Supply and Drainage Engineering, Heating, Gas Supply, Ventilation, Air Conditioning Works and Daylighting Design, Oil, Gas and Mineral Exploration, Disaster Prevention and Mitigation, Cartography and Geographic Information System, Surveying Engineering, Applied and Computational Mechanics, CAD/CAE/Computer Technology, etc. We hope that this collection of papers will contribute in stimulating debate among scholars, researchers and academicians and we aspire that you find them interesting and thought-provoking.

We would like to thank the authors for their valuable contribution and we are grateful to our general chairs, session chairs and the reviewers for having read and commented on the papers. Our most sincere thanks go to all keynote speakers who shared with us their expertise and knowledge. We are grateful to all the sponsors for their technical and financial support. We would also like to express our gratitude to all the members of the Organizing Committee for the efforts they have made before and during the conference.

We look forward to meeting you all in the next CEABM conference.

*The Organizing Committee of CEABM 2014*

The 4th International Conference on

Civil Engineering, Architecture and Building Materials

(CEABM 2014)

### Organized by:

College of Civil Engineering and Architecture, Hainan University

Hainan Society of Theoretical and Applied Mechanics

# Conference Organization

### Chairman

Prof. Hongnan Li, Dalian University of Technology, China

### Co-Chairman

Prof. Chaohe Chen, South China University of Technology, China

### International Scientific Committee

Prof. J. H. Bungey, University of Liverpool, Liverpool, UK

Prof. K. J. Bathe, Massachusetts Institute of Technology, USA

Prof. Lawrence C. Bank, University of Wisconsin-Madison, USA

Prof. Longsheng Bao, Shenyang Jianzhu University, China

Prof. Tai Bao, Guizhou University, China

Prof. Wenbo Bao, Shenyang University of Technology, China

Prof. Chaohe Chen, Hainan University, China

Prof. Jian-Fei Chen, the University of Edinburgh, UK

Prof. Changyu Cui, Harbin Institute of Technology, China

Prof. Zhiheng Deng, Guangxi University, China

Prof. Shengguo Ding, Guizhou University, China

Prof. Yongfeng Du, Lanzhou University of Technology, China

Prof. Xiuli Du, Beijing University of Technology, China

Prof. Ping Feng, Tianjing University, China

Prof. Luciano Feo, University of Salerno, Italy

Prof. Yaojun Ge, Tongji University, China

Prof. Han-Bin Ge, Meiju University, Japan

Prof.Zong Woo Geem, iGlobal University, USA

Prof. I. E. Harik, University of Kentucky, USA

Prof. David Hui, University of New Orleans, USA

Prof. Yong Huang, Guizhou University, China

Prof. Zhihong Huang, Guizhou University, China

Prof. Tan Kiang Hwee, National University of Singapore

Prof. Tim Ibell, University of Bath, UK

Prof. Weiliang Jin, Zhejiang University, China

Dr.Tianjian Ji, The University of Manchester, UK

Prof. A. Kaveh, Iran University of Science & Technology, Iran

Prof. Kang Seok Lee, Chonnam National University, South Korea

Prof. Marcus M.K. Lee, the University of Southampton, UK

Prof. Zhuguo Li, Yamaguchi University, Japan

Prof. Hongnan Li, Dalian University of Technology, China

Prof. Zhengliang Li, Chongqing University, China

Prof. Zhengnong Li, Hunan University, China

Prof. Qiusheng Li, Hong Kong City University, Hong Kong

Prof. Aiqun Li, Southeast University, China

Prof. Hui Li, Harbin Institute of Technology, China

Prof. Shirong Li, Yangzhou University, China

Prof. Guangfan Li, Hainan University, China

Prof. Feng Liu, Guangdong University of Technology

Prof. Lijuan Li, Guangdong University of Technology

Prof. Tianqing Ling, Chongqing Jiaotong University, China

Prof. Ayman Mosallam, Univ of California Irvine, USA

Prof. Aftab Mufti, University of Manitoba, Canada

Prof. Antoine E. Naaman, University of Michigan, USA

Prof. Jianguo Nie,Tsing Hua University, China

Academician Prof. Wei Sun, Southeast University, China

Prof. Hamid Ronagh, The University of Queensland, Australia

Prof. R. Sri Ravindra rajah, University of Technology, Australia

Prof. Yaozong Shi, Highway Survey and Design Institute of Hainan Province

Prof. Ramiro Sofronie, University of Bucharest, Romania

Dr. Scott T. SMITH, Hong Kong University, Hong Kong

Prof. M. N. Soutsos, University of Liverpool, Liverpool, UK

Prof. Mark G Stewart, The University of Newcastle, Australia

Prof. J-G. Teng, Hong Kong Polytechnic University, Hong Kong

Prof. B. H. V. Topping, Heriot-Watt University, Edinburgh, UK

Prof. Tamon UEDA, Hokkaido University, Japan

Prof. Jinfeng Wang, Huaqiao University, China

Prof. Zhi-Shen Wu, Ibaraki University, Japan

Prof. Bo Wu, South China University of Technology, China

Prof. Hong Wang, Guizhou University, China

Prof. Yan Xiao, Hunan University, China

Prof. Shilang Xu, Zhejiang University, China

Senior Engineer. Jianxin Xu, China Communications Water Transportation Planning and Design Institute Co.,Ltd

Prof. Shanhua Xu,Xi'An Univ. of Architecture and Tech., China

Prof. Tao Xie, Guizhou University, China

Prof. Zhixin Yan, Lanzhou University, China

Prof. Jiru Zhang, Wuhan University of Technology, China

Prof. Chuangbin Zhou, Wuhan University, China

Prof. Lau Hieng Ho, Curtin University of Technology, Malaysia

Prof.Junan Shen, Georgia Southern University, USA

Prof. Mohammad Arif Kamal, Integral University, India

## Conference Secretary

Prof. Guangfan Li, Hainan University, China

# Table of Contents

**Preface and Conference Organiztaion**

## Chapter 1: Geotechnical Engineering

**3D Finite Element Analysis on Behaviour of Piled Raft Foundations**
A. Vu, D. Pham, T. Nguyen and Y. He 3

**A Modified Method to Fit Probability Distributions of Geotechnical Parameters Using Stochastic Weighted Entropy Principle**
S.J. Zhang, Z.J. Xu, L. Zhong and Z.R. Xiao 9

**A Research on Elastoplastic Theory Based on Full State Function**
Z.H. Wei, M.S. Wang and D.L. Zhang 17

**Affect of Large Deep Foundation Pit Dewatering on the Neighboring Buildings**
K.W. Ding, F. Zhao and X.Z. Zhang 24

**Analysis of Monitoring Results of a Deep Foundation Pit with Pile-Anchor Retaining Structure**
X.H. Yang, F.W. Wu, T. Chen and X. Liu 28

**Analysis on Strengthening of Plant to Slope Soil under Orthogonal States**
J.B. Gu 34

**Centrifuge Model Study of High Strength Piles Composite Foundation Settlement & Instability under Embankment in Different Kind Soils by Different Pile Spacing**
Q.J. Wang, S.J. Zhang, C. Guo and Z.R. Lu 38

**Comparative Experimental Research of Soil Freezing with Pressure and Non-Pressure**
S.Y. Zhang 48

**Discussion on Treatment Technology of Reinforcement Pile in Karst Area**
C.B. Zheng and J. Xu 52

**Effect of Variable Permeability Coefficient on Consolidation of Ultra-Soft Ground under Vacuum Preloading**
B.B. Xu, A.H. Liang and M.Y. Li 56

**Experimental Application of Fractal Theory into Selection of Subgrade Filling Materials**
X.G. Wang 61

**Experimental Study of Static Disintegration on Unsaturated Soil**
N.Q. Wang, Q.T. Wang, Q. Xue and X.L. Liu 68

**Experimental Study on Bubble Curtain Technology Applied in Underwater Blasting Damping**
H.Y. Hu, Y.C. Zhang, Z.M. Huang and C.X. Peng 73

**Experimental Study on the Position of Balanced Point of Large-Tonnage Pile with Self-Balanced Load Method in the Northwest Region**
Y. Xin, F. Yue, P. Li and G.S. Wang 78

**Finite Element Simulation and Stability Analysis of Composite Soil Nailing**
J. Zhao and L.L. Wang 83

**Fuzzy Mathematical Method of Slope Reliability Analysis in Surface Mine under Seepage Conditions**
K. Yang, H.X. Li and H. Han 89

**Influence of Density on Mechanical Properties for Coarse-Grained Soil Based on Percolation Theory**
Y.D. Huang, L.K. Yao and J. Wang 93

**Justification for Determination of the Depth of an Active Zone Based on the II Group of Limiting States**
N.L. Maksotovna and B.A. Nikolaevich 98

**Mechanics Analysis of Semi-Rigid Subgrade Pavement Structure**
L.Y. Su 105

**Model Test Study of Squeezed Branch Pile under Horizontal Vibration Load**
B. Lv and X.J. Gao 109

**Model Tests of Foundation Bearing Capacity of Sandy Soil and Pile Foundation Bearing Capacity**
S.J. Lu, H.D. Chen, W. Chen, T. Xiang and X.F. Hong 113

**Numerical Simulation of Load Transfer Mechanism of T-Shaped Soil-Cement Deep Mixing Column**
P.S. Xi, X.T. Zhang and B. Liu 118

**One-Dimensional Consolidation Modelling for Unlayered Soil**
I. Hanafi, F. Dimane, F. Mata Cabrera and J. Tejero Manzanares 123

**Practical and Experimental Study of Grouting Anchor in Slope Reinforcement Engineering**
G.R. Lu, L.W. Zhang and H.B. Wang 129

**Reliability Analysis on the Foundation Bearing Capacity in Ningbo Rail Transit Engineering**
J.F. Zhu, G.B. Liu and J.N. Ye 135

**Research on the Anchorage Technology of Steep Slope in Sanitary Landfill**
P. Li, H. Wang and Y. Xin 143

**Study on Graphic Method for the Stability of High Loess Slopes Based on MATLAB**
J.C. Hu, J.Y. Gao and Y.X. Chen 148

**Analysis about Stability of a Slope**
Y.J. Yin, G.H. Xu and Y.M. Qian 152

**Analysis of Micro-Seismic Monitoring Vibration on the Adjacent Buried Pipeline Affected by Impacting of Punching Pile Construction**
Y.H. She 156

**Consolidation of Unsaturated Soils due to Dissipation of Pore-Air Pressure**
H.F. Xu, W.J. Wang and Z.X. Zha 160

**Determine the Shear Strength of Aeolian Sand and Bearing Capacity**
Y.Z. Yin and Y.L. Wang 165

**Dynamic Response of Two-Dimensional Fluid-Saturated Porous Beam**
F.X. Zhou and Q. Ma 169

**Process Simulation and Formation Mechanism of Shear Band in Soil**
S.W. Hou, J.H. Qu, Y.F. Zhang and X.L. Du 175

**Research of the Shear Strength Test of the Soil on the Surface of Lop Nor Gobi**
L. Yin, S. Qiu, W.J. Li, H. Hu and Z.K. Chen 180

**Study of Soil Structural Parameters Based on the Gunary Model**
X.F. Huang, Y. Kong, B.S. Yang and P.F. Zhen 185

**Study on Static Strength of Aeolian Sand before and after Cyclic Loading**
D.P. Liu, X.H. Yang, J. Wang and Z.J. Mao 191

**Study on the Development of Plastic Zone Based on Strain Expressed Mohr- Coulomb Yield Condition**
C. Yang and T.G. Feng 195

**Testing Study on the Effects of Water Content on Permeability for Coal**
C.H. Zhang and X.P. Xu 201

**The Application of Cubic Spline Interpolation Function in Determining Rock Rheological Long-Term Strength**
M.L. Zhao and Q.Y. Zhang 205

**The Application of Vacuum Preloading Method in Soft Soil Foundation Underwater**
Y.Q. Feng and L. Zhang 209

**The Microstructure Formation Process Research in Loading Condition of Dredger Fill**
J. Wang and P.L. Cai 213

**The Research on Mean Spacing of Rock Fracture**
L. Jiang and Y.S. Zhang 219

**The Research Review of Underground Continuous Wall on Deformation Characteristic**
S.M. Zhang, T.K. Yuan, Y.K. Zhou, D.H. Li and K.H. Zhuo 224

**The Rheological Properties and Yield Stress Model of High-Density Slurry Added with Coarse Sands**
X.X. Zhang and D.P. Qiao 231

**3-D Numerical Study of Mechanical Behaviors of Pile-Anchor System**
R.C. Liu, B.S. Xu, B. Li and Y.J. Jiang 238

**A General Criterion for Complex Rocks and Soils and its Application**
H.N. Ruan, M.L. Luo, D. Wang and J.W. Ju 243

**A Method to Determine GSI Value by Using P-Velocity and its Application in Engineering**
Y. Zhao, L.Q. Wang, P. Zhou, Y. Han and G.R. Chen 250

**Analysis of Engineering Characteristics of Cement Soil with Low Mix Additions**
A.M. Liu 256

**Energy Characteristics of Brittle Rock in Failure Process**
A.J. Tang, C.G. Shi, Y. Wang and J.H. Wang 260

**Estimation Study on Shear Wave Velocity of Seabed Using GRNN**
S.J. Di, Z.G. Shan and X.Y. Xu 264

**P-Wave Attenuation Mechanism of Calcareous Sand under Explosion**
X.Y. Xu, S.J. Di, W.Q. Cheng, W. Li and W.B. Du 268

**Response of Non-Homogeneous Saturated Soils and Free-Field to Incident Plane SH Wave**
F.X. Zhou and R.X. Song 273

**Study of Key Parameters in the Process of Aeolian Sand Compactibility**
Y.Z. Yin and Y.L. Wang 278

**Construction Techniques and Mechanism of Pre-Anchoring Fissured Stope Hangingwall by Fully-Grouted Cable Bolts**
F.L. Zhan and P. Ye 283

**Numerical Analysis of the Bearing Behavior of Single Pile under Horizontal Load**
D.F. Ma, G.J. Guo, X. Yang and Z.D. Zhou 287

**Simplified Bishop Method Homogeneous Soil Slope Stability Analysis Based on the C# Language**
H.B. Wei, Q. Zhang and J.H. Zhao 291

**Study on Engineering Behavior of Non-Embedded Pile-Board Structure Crossing Over-Shallow-Embedded Metro**
C.B. Zhou, Q. Su, H. Bai, Y. He and W.H. Zhao 296

**The Analysis on Bearing Characteristic of Residue Pile Composite Foundation Formed by DDC**
Z.R. Liu, Q.J. Sun and Z.F. Yan 302

**The Explanation of Yield Surface Rotation of Sands by Principle of Thermodynamics with Internal Variables**
J.Y. Chen and Y. Hai 308

**The Studies of Rock Damage Softening Statistical Constitutive Model under True Triaxial Stress State**
H.M. Zhang, X.M. Xie and G.S. Yang 312

**A New Algorithm for Computing Threshold Value Used to Image Segmentation**
G.Y. Chen, D.Q. Liang, Y. Zhang and H.Y. Xie 316

**Comparison Analysis of Buildings Settlement, Calculated in Accordance with Rheological Properties of Soils (Based on the Geotechnical Conditions of St. Petersburg)**
A. Ekaterina 320

**Stability Analysis of Jinghua Gypsum Mine Golf in Jingmen City**
C.X. Chen, K.Z. Xia, Y.B. Dong, X.M. Liu and P.L. Huang 324

**Study on Deformation Property of Coarse Particles (Sulfate) Saline Soil with Field Test**
P. Yang, Y.F. Liu, H.Z. Mi and Y.P. Zhu 329

**Study on the Value Range of Horizontal Ground Stress in Initial Geostress Field Based on the Generalized Hoek - Brown Criterion**
Z. Ou, C.X. Chen, H. Fu and Y.C. Zhou 334

**Analysis of Long-Term Deformation of Reinforced Retaining Wall Using Optical Fiber Sensor Geotextile**
L. Lu, Z.J. Wang, H. Feng and K. Arai 338

**Analysis of Platform on Piles Application on Deformation Control of Underground Pipe in Reclamation Areas**
D.N. Zhou, Q. Shang and B. Xiao 344

**Research on Water Temperature Change of Hot Dry Rock Fracture Storage Layer in Shenyang**
J.B. Zhao, H.D. Song, D. Li and Z. Zhang 349

**Studies about Creep Characteristic of Silty Clay on Triaxial Drained Creep Test**
Y.F. Wang, Z.G. Zhou and Z.Y. Cai 355

**Test Study on Effects of Temperature, Sand Mix Ratios and Dry Density on Soil Water Characteristic Curves of Bentonite-Sand Mixtures**
X.W. Fang, C.N. Shen, C.H. Li and L. Wang 359

**The Prediction of Northern Slope Deformation and Failure Caused by the Transformation of Open-Pit to Underground Mining in the Yanqianshan Iron Mine**
A.L. Shao and H.L. Feng 364

**The Study on the Engineering Properties of Squeezed Branch Piles under Combined Load**
W.F. Han, B.B. Feng, J. Zhou and C.Y. Lu 371

**Triaxial Test Study on Marine Sediments Sample with Simulated Combustible Ice**
X.L. Wang, G.F. Li and J. Du 376

**Weak Form Quadrature Element Analysis of Diaphragm Walls**
Y. Li and H.Z. Zhong 380

**A Chemo-Elasto-Plastic Coupling Model for Sandstone Considering pH Effect**
X.H. Li, W. Wang, Z.Y. Tian and W.Y. Xu 386

**A Critical-Line-Based Predictive Model for Landslides**
G.T.C. Kung and Y.G. Tang 391

**Analysis and Process Control of the Deformation for Deep Excavation in Soft Clay**
H. Liu, W.B. Li and H.T. Liu 395

**Analysis of the Interaction of Foundation Pit Supporting Structure and Soil**
Y.Q. Feng and C.X. Liu 401

**Calculation for Earth Pressure of Cavity Expansion Considering Displacement**
W.M. Zhang and X. Huang 405

**Experimental Study on Shear Strength of Different Types of Soil**
H.M. Chen, F.H. Guo and X.Q. Zhou 409

**Failure Mechanism of Strip Footing on Geotextile-Reinforced Soil**
Z.J. Wang, L. Lu and B. Zheng 415

**Horizontal Displacement of GFRP Bars and PC Strand Combination of Technology Supporting Piles**
X.H. Li, Y.Y. Gao, C.X. Yue and C.Q. Hu 420

**Numerical Analysis of Stabilization of Slopes Overlying Bedrock Using Piles and Effect of Socketed Length of Pile on Stability**
M. Bakri, Y.Y. Xia and H.B. Wang 424

**Numerical Simulation Analysis of Bearing Characteristics on Super-Large Diameter Rock Socketed Pile**
C.Z. Gong, C.L. He and M.X. Zhu 432

**Prediction of Displacement Time Series Based on Support Vector Machines-Markov Chain**
F. Xu, W.X. Xu and K. Wang 436

**Project Design of Dewatering for Deep Foundation Pit in Dalian**
B.L. Guo and H.B. Liu 440

**Reinforcement and Characteristic Analysis of Bolt Technology Applied in Bedding Rock Slope**
E.H. Wang, Z.D. Wang, L.M. Jiang, L. Hao and A. Ran 445

**Analysis on Influencing Factors of Cement Stabilized Macadam Base of Compressive Strength in Shenyang Area**
Y. Xu, C.Z. Bai, Y.F. Zhang, X. Liu and D. Li 450

**Experimental Study on Dynamic Characteristics of Tailings**
J.B. Zhao, Y.C. Ji, X. Liu and D. Li 455

**Experimental Study on Engineering Characteristics of Basalt Residual Soil on High Slope**
K. Cui and Y. Yang 460

**Influences of Cross Section Parameters on Bending Resistance of TSC Pile**
X.Q. Wang, S.M. Zhang, J. Liao and Y.S. Huang 464

**Roadbed Treatment Research in Expansive Soil Area**
Z. Feng, C.J. Li and X.L. Gao 469

**Simplified Method for Estimating the Inner Support and Internal Force through Stand Column Uplift of Foundation Pit in Soft Soil**
Y. Liu, J.Y. Liu and T. Liu 474

**Slope Early Warning System Design and Preliminary Practice**
F. Xu, W.X. Xu and K. Wang 481

**Slope Stability Evaluation Based on PSO-PP**
K. Wang and F. Xu 486

**Stability Analysis of Tower Foundation for Transmission Line**
Z. Chen 490

**Study on Sheltering Effect of Underground Building to Horizontal Displacement of Retaining Wall of Foundation Pit**
Y. Liu, J.Y. Liu and S.B. Cai 494

**Study on the Stress and Strain of EPS Silt Light-Weight Soil by Laboratory Test**
Y. Feng and Y.B. Pei 499

**The Analys of Stability of Composite Soil Nail**
Y. Zeng 503

**The Application of Origin Software in the Data Processing of Rock Creep Experiment**
C.Y. Gao, J.G. Niu and Q.C. Gao 509

**The Experimental Study of the Influence of the Matric Suction on the Unsaturated Soil Strength**
C.R. Liu 514

**The Settlement Analysis of the Cement Fly-Ash Gravel Pile Composite Foundation of Baotou**
J. Li, Y. Xu and J. Yin 518

**Three-Dimensional Numerical Analyses of Pile Response due to Braceded Excavation-Induced Lateral Soil Movement**
L. Li, X.X. Hu, G.H. Dong and J. Liu 524

**3D Finite Element Numerical Analysis for Stability Calculation of High Steep Rock Slope**
X.F. Xie, Y.L. Liu, J.Y. Han and L. Xing 532

**A Certain Foundation Pit Support Design and Construction in Baotou**
X.K. Bao and M.H. Que 539

**A Study on Micro Pile Reinforcement Technology for the Accumulative Landslide of Expansive Soil**
H. He, Y. Xu, Z.Z. Huang and Z. Li 544

**Analyses of Anti-Seepage Measure for Expansive Soil Subgrade in Hefei**
Y. Wei, W.Z. Xing and Y. Shao 552

**Analysis on Deformation and Support Technology of Deep Soft Rock Roadway**
Y.S. Liu, W. Liu and X.Y. Dong 556

**Analytical Solution for Contaminant Extraction Using Well Injection Depth Extraction Technology Considering the Effect of Smear Zone**
H.Y. Wang, X.W. Tang and P.L. Gan 560

**Application of Fuzzy Set Theory to Evaluate the Stability of Slopes**
T. Mohamed and A. Kasa 566

**Application Research on Distributed Optical Fiber Monitoring Technology in Static Load Test of Large Diameter and Post-Grouting Filling Pile**
J.X. Chen, T.H. Zhou and Y.C. Guo 572

**Coaction Analysis on Pile-Net-Cushion-Soil**
R.F. Wang and K.Y. Wang 579

**Cone Penetration Test Study of Ultra Soft Soil after Vacuum Preloading**
J.Q. Yu, H.W. Li and W.S. Wang 585

**Defects Discrimination and Error Analysis of Wharf Bored Piles Detected by Low Strain Reflection Wave Method**
T. Li, Q.C. Qiu and J. Wang 589

**Double-Row Composite Anchor Bolt Design and Construction Monitoring Analysis of Green Building**
H.X. Li, Y.W. Wang and G.K. Fang 596

**Experiment Research of Rock Anchor Foundation on Sandstone Ground in Transmission Line**
Y. Zhang and W.F. Zheng 601

**Experimental Studies on Acoustic Emission of Different Damaged Concrete**
H.G. Ji, X.R. Li and C.L. Song 606

**Experimental Study on Post-Peak Failure Behavior of Rock Masses with Persistent Joint**
L. Wang, J. Yu and X. Hua 610

**Explanation of Phenomenological Characteristics in Seepage Force Concept System**
Y. Shen and W.H. Du 614

**Finite Element Analysis of Rock Bolt Foundation in Metallurgical Industrial Plant**
M.X. Tan and H.B. Liu 619

**Laboratory Studies on Acoustic Emission Characteristics to Coal Dynamic Response under Variable Accelerative Load**
X.H. Liu, C.X. Liu, S. Zhuang, L. Wang and S.S. Lin 623

**Mechanical Model of Pile-Soil Work Together**
S.J. Zhang 628

**Mechanics Analysis of Flexible Base Pavement Structure**
L.Y. Su 632

**Monitoring Analysis and Safety Evaluation of Deep Foundation Pit under Complex Conditions**
X.T. Zhang, Q.Y. Zhang, C. Wang and Y.F. Wang 636

**Analysis of Coral Reef Rock Mass Integrity Based on RMDI Method**
J.C. Wang, C.Y. Wang and Z.Q. Han 641

**Application of Curve Model Fitting Methods to Settlement Prediction**
M. Wu and J.L. Niu 651

**Effect of Overload on Bearing Capacity of FRP Reinforced Ground**
C.X. Bai, X.Y. Shao and Q.P. Wang 655

**Influence of Density on the Hydraulic and Mechanical Properties of Sands**
O. de Freitas Neto, O. Santos Jr and R. Severo 659

**Numerical Simulation of Failure Process on Soil Slope with Different Support Measures**
Y.W. Zhang, L.X. Tang, D.C. Bai and P. Zhou 665

**Prediction of Composite Foundation Settlement Based on Multi-Variable Gray Model**
Y. Wang and G. Yang 669

**Preparation of a New Type of Joint Filler and Study on Adhesion Performance**
X.W. Li and C. Sha 674

**Probability Statistical Model and Network Simulation Technology of Random Fractured Rock Mass**
C.X. Han, D.H. Zhou, W.Y. Liao, X. Chen, L.Q. Li and K.C. Yao 679

**Pullout Test Research on Interfacial Interaction of Reinforced Band and Gravelly Soil**
Y.L. Wang, Z.L. Cheng, W. Zhang, Y.Z. Zuo, Z.L. Yu and Y. Wang 684

**Research of Soundless Crack with Different Number of Drillholes**
L.X. Tang, D. Zhang, Z.T. An and J.Y. Zhang 689

**Research on Negative Skin Friction on Pile by a Simple Model Experiment**
T. Huang, J.H. Zheng and W.M. Gong 693

**Research on Stability of Foundation Pit Construction**
H.S. Dai and T. Yang 697

**Research on the Effect of One Debris Flow along Bailong River**
Y.Q. He, Y. Wu and S.L. Li 701

**Research on the Retention Capacity of Ruins Soil under Drying Condition**
P. Liu, H.Y. Zhang, Y. Chen, X.X. Shao and X.Y. Fu 705

**Stability Analysis on Anti-Slide Pile to Reinforce Slope Based on ABAQUS**
X.J. Gu, T.Q. Zhou and S.L. Lu 711

**Study on Optimization of Design Parameters for Composite Foundation with Cement-Fly Ash-Gravel Piles**
P.F. Luo, J.X. Tong, X.H. Sun, X.H. Yang, J. Zhang and M.L. Yan 715

**Study on the Design Method of Different Thickness-Diameter Ratios for Composite Foundation with Rigid Long and Short Piles**
J.X. Tong, X.H. Sun, P.F. Luo, N. Jia, X.H. Yang and M.L. Yan 723

**Study on the Effects of the Rainwater Seepage on Slope Stability**
J.S. Xun, X.T. Xu and R.Q. Bai 729

**Study on the Lateral Displacement of Super-Long Pile under a Asymmetrical Surcharge Load in Soft Clay**
Q. Li and X.L. Lu 733

**Temperature Field Numerical Analysis of Different Freeze Pipe Spacing of Vertical Frozen Soil Wall Reinforcement at Shield Shaft**
J. Hu, B.S. Jiang, H. Zeng, Y.N. Chen and Y.Y. Zhu 738

**The Applied Research of Underwater Vacuum Preloading Method in Soft Soil Foundation**
Y.Q. Feng and L. Zhang 742

**The Bearing Characteristics and its Influencing Factors of Reinforced Soil Foundation**
Y. Jiang, X.M. Wang, W.B. Sun and Y. Dong 746

**The Instability Mechanism of Soil-like Slope under the Action of Acid Corrosion in Open-Pit Copper Mine**
H.Y. Ju, G.Q. Gao, S.L. Liu, C.T. Luo and J.H. Li 750

**The Optimum Design of Slope Angle Based on Critical Sliding Field**
S.G. Sun, Y.N. Yi, Q.H. Cui and L. Jin 755

**Theoretical Analysis on Underwater Vibrating Compaction Technology of Scattering-Filling Rubble Stone Layer**
J.B. Fu, S.W. Yan and Z.J. Chen 760

**Three-Dimensional DEM Numerical Simulation of Rock Failure Progress with Different Microscopic Heterogeneities**
H. Chen, R. Fang, Y.J. Li and F.C. Zhang 767

**Analysis of Structural Soil's Shear Strength under Arbitrary Degree of Consolidation**
Y. Liu, C. Sun and S. Li 774

**Stability Monitoring Analysis on Side Slope Engineering Management of Longmenhao Primary School**
L.M. Wu, Z.J. Wang and S.Y. Liu 778

**The Stability of 3D-Geomat in Different Slope Gradient**
G.Y. Wang, J.P. Zhang and Y.S. Sun 782

**Monitoring and Analysis on the Supporting Structure for Deep Foundation Pit**
H.X. Sun, K. Zhang and S.L. Chen 787

**Numerical Analysis of Floatation Response of Buried Pipeline in Liquefied Soil**
S.N. Deng, W.T. Peng and J.Q. Lin 791

**Research on the Construction Monitoring for Enclosure Structure of Working well**
Y. Liao, J.H. Zhan and C. Li 797

**Experimental Study on Bearing Mechanism of Jacked Pipe Pile in Sand**
J.T. Wang 801

**On Stability and Deformation of Slurry-Trench Affected by Formation Equipment**
M.Y. Shi and F.G. Song 805

**Two-Dimensional Problem of Moisture Elasticity of Inhomogeneous Spherical Array with Cavity**
V.I. Andreev and A.S. Avershyev 812

## Chapter 1: Geotechnical Engineering

**Development of the Monitoring Guidance System for Slope Engineering**
D.H. Kong, Y.K. Ruan, Z.G. Zhang, W.F. Mao and M. Li 819

**The Application of BP Artificial Neural Network in Geotechnical Engineering**
N. Zhao 823

**Numerical Simulation of Slope Excavation in Highway Renovation and Expansion Project**
G.C. Luo, Z.M. He, X. Luo and Q.G. Hu 827

**On Fire Severity of Flammable Gas**
W.Z. Wu 831

**Study on Cover Backfilling of Open Pit to Underground Basing on Natural Classification**
C. Chen, D.Q. Gan, C.Q. Yu, A.D. Song, S. Wang, H.J. Lu and W.H. Zhang 835

## Chapter 2: Geological Engineering

**A New Geometrical Model of Fluid Flow in Rock Fractures for Valid Application of the Cubic Law**
H.G. Zhu, Y.D. Jiang, C. Yi and H.P. Xie 841

**Control Function of Corrosion of Calcareous Sandstone over Rock Mass Quality in One Hydroelectric Station on the Jinsha River**
S.Q. Lu and P. Zhu 847

**Dynamic Mechanism Research on the Tectonic Activation of Anninghe Rift**
J.Q. Liu and Y.S. Li 851

**Searching for the Shortest Seepage Path of 3D Network in Fractured Rock Masses**
B. Pan and Y.S. Zhang 857

**Development Features and Fractal Research of Fault Structure of No.5 Coal Seam in Chenghe-Second Coal Mine**
X.C. Xue and J. Wang 862

**The Application of Reservoir Geo-Modeling Technology in Section07, Ticleni Oilfield**
L.Y. Pang 866

**The Classification and Quality Evaluation of Rock-Mass Based on Limited Geological Information**
X.G. Wu, Z.Q. Yang, Q. Gao and D.H. Ba 870

**The Genesis Mechanism Analysis of Qinglong Landslide in the Central Region of Yunnan Province Water Source Diversion Reservoir Area of the Jinsha River**
T.J. Song, J.P. Chen, X.J. Li and J.Y. Yan 875

**Experimental Investigation on the Physical and Mechanical Features of Clay Shale in Bayingobi Basin of Inner Mongolia**
H.A. Liang, Q.R. Lu, S.J. Chen and H.Y. Hu 879

**Growth and Mechanics of Brittle Fault Systems in Rock Mass: An Example of Baihetan Hydropower Dam Area**
W.Q. Cheng, S.J. Di, X.Y. Xu and G. Song 883

**Sleeve Valve Pipe and Steel Pipe Micropile Fractured Tensile Reinforcement in Combination with the Application of a Mined-Out Area**
S.L. Tang, L. Yang, L.H. Sun and X.W. Li 887

**Evolution Characteristics of Permeability and Porosity of Mudding Weak Permeability Media with Nonlinear Flow**
Y.E. Deng, J. Yu and X. Peng 893

**Stability Analysis of Gypsum Mine Goaf Surface Based on Discrete Element Method**
X.M. Liu, C.X. Chen, K.Z. Xia and P.L. Huang 897

**Automated Analyzer, LOI and other Methods for Determination of Soil Organic Carbon**
Y.Y. Zhang and W.H. Zhang 903

**Determination of Volumetric Joint Count Based on 3D Fracture Network and its Application in Engineering**
J.L. Wu and J. He 907

**Relations between Paleoclimatological Conditions and Mineralogical Characteristics of Clays in Miocene Sediments at Linxia Basin, China**
N. Yu, H.L. Hong, Z.H. Li, K.X. Zhang and R.B. Li 912

**Research about Control Factors and Early Warning System of Early Warning System in Song Fangtun Oilfield**
N. Lv, Y.M. Wang and H.Y. Liu 919

**Stability Analysis of Puzi Landslide in Chongqing**
K. He and C.L. Chen 923

**The Landslides Developed with the Evolution of the River Terraces in the Loess Plateau, China**
X.L. Xing, X.K. Hou, T.L. Li and P. Li 927

**Application of Self-Drilling Anchor on Coal Gangue Slope Treatment**
T.L. Chen, J. Zhou, A.M. Wang and H. Li 935

**Researches on Slope Treatment Technologies under Complicated Geological Conditions in High Temperature and Rainy Regions**
R.X. Shan and H.P. Li 940

**Research on Two-Dimensional Landslide Model Control System Based on Support Vector Machine Modeling**
Z.T. Liu and Z.H. Feng 947

**Uncertainty Analysis and Monitoring of Earth Dam**
L.Q. Yang, R. Gao and Y. Wang 954

**Study on Rock Strength Characteristic by Point Load Test**
R.H. Wang, Y.Z. Jiang, J.L. Guo and T.C. Tang 958

**Research on the Mechanical and Thermophysical Properties of Frozen Soil in Cretaceous Formation**
H.D. Dai, M.L. Yin, T.Y. He, K. Liu, T. Li and T.Q. Zheng 962

**Coordinate Transformation and the Volume Covering Fractal Algorithm of Rock Surface Morphology**
K. Man, Y. Zhao and H.F. Li 966

**Study on Control Technology of Slope in Mountainous Areas of Southwest China under Complex Geological Conditions**
W. Yang and H.P. Li 971

**Anisotropic Bounding Surface Model in ABAQUS Software**
Y.Z. Qin and Q. Chen 977

## Chapter 3: Tunnel, Subway and Underground Facilities

**Construction Methods for Long-Span and Bifurcation Tunnel Structure**
C.L. Xin and B. Gao 983

**Effect of Time-Varying on Shield Tunnel Lining Structure**
F.J. Liu and J.F. Chen 987

**Analytical Hierarchy Process Based Post-Earthquake Health Diagnosis Method for Tunnel in South of China**
H. Huang, W. Zhang, L.F. Yang and Z. Chen 991

**Numerical Analysis of Construction Method in Shallow-Buried Large-Section Loess Tunnel**
Z.J. Sun 997

**Numerical Simulation of Effect of Foundation Pit Excavation on Underlain Shield Tunnel**
G. Wei, L.W. Hu and K.L. Chen 1001

**On Karst Water Inrush (Gushing) Geological Environment in Pingyang Tunnel**
Q.Q. Zhu, Q.Q. Miao and S.P. Jiang 1008

**Preliminary Ideas of the Metro Station Constructed by Shield Tunneling Method Combined with Prefabricated Method**
H.F. Su, W.N. Liu and F.C. Liu 1013

**Pre-Stressed Reinforcement and Security Analysis of Tunnel Lining with Dislocation and Cracks**
J.W. Zhang 1019

**Research on Layout of Measurement Points in Tunnel Lighting Experiment**
Q. Yang, B. Liang, G.B. Pan, S.Y. He, W. Chen, X.Y. Dang and Z.W. Wu 1024

**Study of Life Safety on the Fire Accidents in the Subway Station**
H. Xie, Y.Y. Xu, X. Zhang and J. Chen 1029

**Study on Emergency Evacuation in the Subway Fire Accidents**
H. Xie, Y.Y. Xu, X. Zhang and J. Chen 1033

**Study on Fire Smoke Movement of Urban Traffic Link Tunnel**
X.L. Yao and Z.G. Zhang 1037

**Research on the Regional Stress Field of Underground Powerhouse at the Right Bank of Baihetan Hydropower Station**
Q. Zhao, X.L. Leng and X. He 1042

**Study on the Blasting Excavation Method of Urban Shallow Tunnel**
Z.Q. Li and Z. Li 1051

**The Monitoring and Numerical Simulation Analysis on the Construction of a Shallow Underpass**
L.S. Liu and J. Zhao 1056

**Metro Station Deformation Caused by Deep Foundation Pit Construction**
C.L. Xin and B. Gao 1061

**New Developments and Applications in Rail Transit Construction Technology**
R.J. Li, R.L. Shan, Q.L. Liao and F.M. Wu 1065

**Numbering Analysis of Ground Settlement by Shield Method Based on the Model of Corrected 'Equivalent Circle Zone'**
Z.L. Zhou and S.G. Chen 1072

**Numerical Analysis on Interaction Induced by Crosswise Tunneling**
P.L. Gan, X.W. Tang, W.M. Shen and H.Y. Wang 1076

**Research on Key Technology of Shield Machine Main Drive Sealing**
R.J. Li, R.L. Shan, Y.X. Gui, J.Z. Yang and J. Liu 1081

**Review of Testing and Analysis on Metro-Induced Vibration**
J.W. Li 1088

**Stability Analysis of Wall Structure which its Depth is over Thousand m**
Y.H. Wang, X.C. Fu and X.H. Jing 1092

**Design of High Speed Railway Tunnel and its Construction Method in Abrupt Slope with Loose Rockmass**
X.J. Zhou, B. Jiang, R. Yang and C. Ning 1096

**Numerical Simulation for Construction Process Large-Span Flat Tunnel under the Condition of Shallow Buried**
J.J. Li, L. Tuo and G.J. Zhang 1100

**Study on FEM Numerical Simulation and Strain Monitoring of Tunnel Secondary Lining**
Y.N. Li, M. Liu, S. Wu, H. Liu, J.K. Su, Z.L. Zhang and C. Li 1105

**Study on Simulation Analysis of Excavation Deep Foundation Pit in Qingnian Road Station of Tianjin Subway Line 2**
Y. Bai, P.B. Cui, J.B. Wu and L. Wu 1112

**The Application of Getting $R_c$ Value from Point Load Test and Rebound Test by Tunnel Surrounding Rock Classification System**
R.X. Wang and Z.C. Yuan 1116

**The Dynamic Response of Shallow Buried Structure under the Action of Explosion Load**
Q. Zhang, H.B. Wei and J.H. Zhao 1122

**Discussion on Highway Tunnel Monthitoring Measurement Control Standards**
L.J. Tan, H.Q. Zhou and K.S. Chen 1127

**Research on early Concrete Crack Control of Shijiazhuang Subway Construction in Winter**
X.M. Yu, L.J. Cao and D.Y. Geng 1134

**Response of the Spiral Conveyor Spewing in Water-Rich Sand**
Y.R. Song, J. He, G.F. Chen, M. Hong and P.B. Li 1138

**Study on Deformation Prediction of the Tunnel Surrounding Rocks Based on Non-Equal Time-Interval Grey Model**
P.F. Geng, C.M. Yang, W.D. Guo and P. Wang 1143

**Mechanical Calculation for Collapse Mechanism of Surrounding Rock on Shallow Tunnel**
Y. Peng, J.S. Yang, Y.H. Shen and J.H. Liu 1148

**The Research on Environment Vibration due to Subway with Rail Pads of Frequency-Dependent Stiffness**
F. Yang, K. Wei and Y.C. Song 1153

**Tunnel Collapse Treatment Technique Research in Xinjiang Tianshan High-Altitude, Low-Temperature Mountain**
C.S. Zhu and X.H. Yang 1161

**Tunnel Lining Microstructure and Mechanical Properties of Evolutionary Analysis**
Y.D. Ma and S. Liang 1168

**BIM Technology Used in Underground Subway Station Planning Simulation**
H.K. Pu and Q.C. Wei 1174

**Comfortable Quality Analysis of Subway Station Vibration Induced by Multiple Trains**
B.Q. Zhang 1178

**Optimization of Tunnel Support Type through Fault Zone**
K. Li and H. Guo 1184

**Force Analysis of the Middle Wall in Multi-Arch Tunnel under Central Hole + CRD Method**
J. Li and Z.L. Wang 1188

**Force State of Country Rock and Supporting Structure in Multi-Arch Tunnel under Central Hole + CRD Method**
J. Li, Z.L. Wang and J.F. Zhong 1192

**Key Construction Technology of Shield Machine Passing through the Airport Apron in Shallow Soft Soil**
R.J. Li, R.L. Shan, R.S. Li, J.Y. Lv and Y.W. Song 1197

**Optimization of Construction Method for Shijiazhuang Xinbai Subway Station**
C.Y. Gao, J.G. Niu and D.Y. Geng 1203

**Study on Classification and Regulation for Defects on Railway Tunnel**
J.W. Zhang, S. Wang and H.X. Huang 1207

**The Dynamic Response of Zhengyangmen Gate Tower Induced by Beijing Metro Line 2**
Q. Song, J.Q. Guo, W.H. Chen and P. Guo 1212

**Study on Investigation and Analysis of Existing Railway Tunnel Diseases**
D.P. Zhao, X.R. Tan and L.L. Jia 1218

**Development States and Existing Problems Research of Nondestructive Testing of Bolt**
X.K. Bao, H.H. Liu and L.J. Liang 1223

**Identification of Surrounding Rock Parameters Based on MSVR**
X.L. Li, J.J. Zhang, F.M. Wang and B. Zhang 1227

**Kinematics Analysis of Working Edge Point for Gauge Disc Cutter in Cutterhead of Tunneling Machine**
Q.X. Wu, G.F. Tian, L. Chen and H.W. Ma 1232

**Mechanism Analysis and Prevention Method for Tunnel Fire**
J. Wu, F.M. Shen and P. Jiang 1238

**Metro Construction Safety Risk Assessment Based on the Fuzzy AHP and the Comprehensive Evaluation Method**
X. Zheng and F.H. Ma 1243

**Monitoring and Analysis for the Deformation of SMW Retaining Structures in Subway Station**
J.T. Xia, S.F. Zhang, H.R. Shen, Z.J. Liu and S.Q. Huang 1249

**Approach on Pollution Gases Diffusion Path of Small Spacing Tunnel Entrance Based on CFD**
Y.Y. Xing 1254

**Influence of Foundation Pit Excavation on Existing Shield Tunnel and its Protection Range**
X. Wen and C.R. Pang 1258

**LS-SVM-Markov Model for Tunnel Deformation Prediction**
G.T. Cai and S.J. Hu 1264

**Optimization of Stope Structural Parameters in Phosphorite Mine and its Stability Analysis**
X.X. Li and K.G. Li 1268

**Research of the Key Control Parameters Standard for Shield Tunnel Under-Crossing High Speed Railway**
Z. Liu and P. He 1273

**Research on Defects of Tunnel Portals during the Operation**
K.Z. Zhu and J.H. Luo 1279

**Study on Risk Trend Assessment of Metro Tunnel Crossing Underground Pipeline Based on Partial Connection Number**
H.T. Xie, B. Li and Y.S. Zhao 1283

**Water Inrush Risk Evaluation into the Tanjiaba Tunnel**
Y.B. Sun and M.Y. Feng 1288

**Numerical Analysis of Two Structural Schemes of the HK-Zhuhai-Macau Immersed Tunnel**
Y.J. Dai, M.J. Zhou, Y.F. Kong, X.D. Liu and Z.G. Zhang 1293

**The Deformation Characteristics Analysis of Metro Tunnel in Complicated Geological Conditions**
D.H. Qiu, S.C. Li, Y.G. Xue and F.D. Xie 1297

**Auger Bored Piles Application Works in the Subway**
Y. Wu 1301

**Impact of Urban Rail Transit on Residential Property Values in Hangzhou**
L.F. Ruan and J.P. Yin 1306

**Dynamic Accumulation Damage Characteristics of Initial Cracks for the Lining of High-Speed Railway's Tunnel**
X.Q. Wang and B. Cai 1311

**A Numerical Investigation on Time-Dependent Failure of Tunnels Based on the Long-Term Strength Characteristics of Rocks**
L.C. Li and M. Xing 1315

**Measurement and Research on Broken Zone of Surrounding Rock in Cha Zhen Tunnel**
R. Wang, Y. Liang and W. Qin 1321

**Numerical Simulation Study on Three-Step Method Construction for Neighborhood Tunnel**
L.L. Cai, X.Y. Yang and N. Guo 1327

**Study on Pressure Observation of Fully Mechanized Caving Faces in Coal Seams with Rock Burst Danger in Xiagou Coal Mine**
Z.C. Tian, Y.J. Liu, W.C. Wang and Y.H. Ren 1331

**Research on Geostatic Stress and Optimization of Bolt Support for Tilted Strata Roadway**
R.L. Shan, L. Tian, W.F. Zhao, J.Y. Lv, Y.H. Xiao, L.F. Wei and X.Y. Hao 1335

**Construction Monitoring Technology Analysis for Railway Tunnel**
J.F. Hou, J. Chen and R.L. Wang 1342

**Application of Grouting Reinforcement Technology in Pingshan Shaft Station**
L. Tian, J.Y. Xi, J. Liu, X.D. Liu, F. Shang and X. Dong 1347

**Research Status and Development Trends of Roadway Surrounding Rock Stability Classification**
R.L. Shan, X.S. Kong, J. Liu, J.F. Li, Y. Bai and Y.W. Song 1352

**Analysis on Changes of Mechanical Properties of Lining of Tunnels in Huangtu Regions Taking Account of Loess Cavity by Using ADINA**
H.P. Zhou, E.Y. Wang, Y.X. Hu, Z.Q. Liu and J.B. Cui 1358

**Research of Fractured Surrounding Rock Physical and Mechanical Characteristics in Shuguang Mine No.2 Mining Area**
H.J. Xue, J.L. Xue, M.L. Yin, J. Kong and Z.M. Gao 1364

**Finite Element Analysis on Causes of Crack in Large Underground Garage**
B. Shu and J.H. Peng 1369

**The Application of Fracture Mechanics in Highway Tunnel Lining Cracking**
S.Z. Chen 1377

**Studies on Damage Distinguishing of Underground Tunnel Structure Based on BP Neural Network**
X. Zuo, G.X. Chen and W.Q. Li 1382

**Non-Linear Free Vibration of Submerged Floating Tunnel Tether**
Z.B. Su and S.N. Sun 1388

**Numerical Simulation Method Utilization in Water Gushing Yield Forecasting of Paoziling Tunnel in Hunan Province, China**
Y.N. Yang, Q. Zhang and M. Xu 1392

**Reliable Design and Study on Highway Tunnel Lining Structure**
Z.L. Niu, Y.B. Qi, J.S. Huang, C. Wang and J.L. Li 1398

**The Example Analysis of the Transfer Stations of Subway**
L.J. Yu, Y.L. Li and K.M. Chen 1402

**Subway Station Group Decision and Evaluation of Fire Emergency**
L.J. Cao, X.M. Yu and D.Y. Geng 1408

**Based on Effect Coefficient Method of Metro Tunnel Collapse Risk Evaluation Model and its Application**
P.L. Cai, J. Wang and S.W. Tian 1412

## Chapter 4: Seismic Engineering

**Application of FEM Strength Reduction Dynamic Analysis in the Seismic Design of Reinforced Earth-Retaining Wall with Geo-Grid**
X.S. Tang, Y.R. Zheng and L. Jie 1419

**Damage Mechanism of Yiliang Earthquake on September 7, 2012**
Z. Lin, M. Tian, D.B. Chen and C.F. Li 1426

**Deformation and Energy-Based Seismic Damage Evaluation of Steel Reinforced Concrete and Reinforced Concrete Piers**
J.J. Lin, A.R. Liu, Q.C. Yu and J.D. Deng 1430

**Experimental Study on Dynamic Mechanical Properties of Galvanized Iron Wire under Seismic Strain Rate**
H. Zhang, J.H. Zhang, D.B. Wang and X. Li 1435

**Peak Story Drift of a Building Structure Subjected to Earthquakes**
J.H. Lin 1439

**Research Advances in Seismic Behaviors of Shear Wall with Opening**
L.Y. Gong, J.W. Chen and Y.P. Su 1443

**Response Modification Factor for Y-Eccentric-Braced Steel Frame Structures Designed Based on Chinese Code**
W.X. Yang, Q. Gu, P.Z. Cao and R.J. Shi 1449

**Seismic Performance of the Reinforced Concrete Frame Structures with Infilled Walls of Different Configuration**
M.S. Guan, H.B. Du, W. Chen and Y.H. Wu 1458

**Shaking Table Test Analysis of Bottom-Business Multi-Story Masonry Structure in Small and Middle Towns in the Southward**
Y.D. Liang, X. Guo, H.W. Yi, Y.Z. Li and J.Z. Jiang 1463

**Shaking Table Test of Reinforced Concrete Frame-Wall Model**
H. Zhang, B. Li, X. Li and D.B. Wang 1467

**Analysis on Self-Centering Capacity of Prefabricated Frame Joints**
Y. Zou, H. Lin and W.Q. Ma 1471

**The Effect of Damping on Seismic Performance of Steel Frame**
X.W. Wang and C.J. Hu 1477

**The Influence Analysis of Mechanical Behavior between Pile and Soil on End Bearing Pile Foundation's Dynamic Characteristic**
W. Hu, Y.H. Zhang and Y. Zhang 1481

**The Present Situation of Rural Housing and the Seismic Performance Analysis**
H. Li 1486

**Geotechnical Seismic Isolation System - Further Experimental Study**
W. Xiong, M.R. Yan and Y.Z. Li 1490

**Seismic Response Analysis of Deep Water Bridges with Pile Group Foundations**
D.X. Zhao, J.J. Wang and J.S. Su 1494

**Analysis of Strong Ground Motion Characterization in the 2013 Lushan Earthquake**
T. Yu, M. Lu and X.J. Li 1499

**Development and Prospect of China's Bridge Seismic Bearing**
L. Zhang, C.H. Zhao, L. Li and B.B. Fan 1506

**Feasibility Analysis of Applying Biomechanical Properties of Human Body to Seismic Design of Building Structure**
S.S. Wu, G.C. Kang, S. Wang and J.Y. Lian 1511

**A Method for Checking Eccentricity of Solid Concrete Piers with Low Longitudinal Reinforcement Ratio under a Minor Earthquake**
X.C. Chen, Z.W. Liu, Y.L. Zhang and L. Pei 1515

**Application of the Jerk Feedback on the Shaking Table**
F.F. Li, J.B. Ji, X.J. Li and N. Li 1521

**Data Processing and Preliminary Analysis of Strong Motion Records from the Ms7.0 Lushan, China Earthquake**
H.Y. Yu, B.F. Zhou, W.X. Jiang, C. Yang, Q.C. Xie, P.Y. Tan, S.M. Xu and X.F. Zhao 1528

**Permanent Displacement Identification Analysis in 2011 Mw9.0 Tohoku Earthquake, Japan**
B.F. Zhou, T.S. Song, R.Z. Wen and L.L. Xie 1533

**Research on Shaking Table Control Parameter Tuning Technology Based on System Identification**
J.B. Ji, L.J. Sun, P.Y. Zhan, J.K. Wang and L.L. Song 1538

**Research Summary of Vibration Reducing Performance for Infilled Wall**
M.S. Sun, S.Y. Qu, F.B. Meng and C.L. Li 1545

**Analysis on Seismic Performance of Beam and Plate Converter Floor**
G.T. Zhao and X.T. Kou 1551

**Ultimate State of Bridges with Rocking Isolation under Extreme Earthquakes**
T.Y. Lee, M.Y. Huang and K.J. Chung 1555

**Verification of LSSRLI-1 Applicability on Soft Sites Using Exact Solution**
R.S. Li and X.M. Yuan 1559

**Controls on Material and Mesh for Structural Nonlinear Time-History Analysis**
X.M. Chen, J. Duan, H. Qi and Y.G. Li 1564

**Influence of Saturation Degree on Deamplification of $P_1$ Wave through Multilayered Porous Media**
M.Y. Mehiaoui Hadjebar, M. Hadid and M. Berrah 1570

**Precise Integration Method of Pseudo-Dynamic Testing of Structures**
H.B. Wang and R. Liu 1574

**Reliability Analysis in Performance-Based Earthquake Engineering**
A. El Ghoulbzouri, Z. El Alami and S. El Hannoudi 1581

**An Energy Dissipation Device Based on Shape Memory Alloys for Frame Structures**
Y. Chen, N.L. Zhu and S. Gao 1591

**Analysis of the Influence of Mortise-Tenon Joint Damage on Seismic Performance of Ancient Timber Structure**
X.L. Wang and L. Jin 1595

**Demand Diagrams Based on Inelastic Spectra: A Proposal for the Implementation of the Capacity Spectrum Method in the Romanian Seismic Design Code**
I.G. Craifaleanu 1600

**Research of Soil Layers Amplification Effect Based on Strong Seismic Records and Calculations**
L. Wang and Y. Su 1604

**Research on Performance-Based Seismic Levels of Nonstructural Components**
H.H. Zhu and G. Zhao 1609

**Research on Seismic Damage of Buildings in the Beichuan Earthquake**
F. Wang and C. Ning 1613

**Seismic Analysis of 5-Span High-Speed Railway Continuous Girder Bridge**
J.H. Guo and M.Q. Lu 1618

**Seismic Performance Analysis of Steel Frame with Wedge Devices Based on the Energy Dissipation**
J.S. Lei, W.X. Luo, J.L. Jiang and W. Zhang 1624

**Seismic Performance Analysis on Single-Storey Masonry House with Sliding Damping Technology**
K. Yuan, Y.M. Li and B. Kang 1629

**Seismic Reduction and Control Analysis of Hybrid Structure with Viscous Dampers under Strong Earthquake**
S. Qiu, S.C. Deng and Z.Q. Zhu 1633

## Chapter 4: Seismic Engineering

**Simplified Dispersion Curves of Earthquake Love Wave for Rotational Seismic Motion Estimation**
Y.W. Liu and H.N. Li 1639

**Study on Seismic Behavior of Self-Centering Precast Frame**
H. Lin, T.Q. Li and Q. Wang 1645

**Study on Seismic Detection Applied in Mine Advance and Side**
Y.B. Hu, Y. Wang, Y.Q. Wu and Z.X. Liu 1649

**Study on the Anti-Seismic Performance of New Swing Structure System Based on PUSHOVER**
D. Liu 1653

**Study on the Seismic Safety of the Qinghai Traditional Dwellings**
M.J. Zhang, L.X. Liu and Y.N. Shi 1658

**A Suggestion on Uncertainty Correction of Ground Motion Attenuation in Probabilistic Seismic Hazard Assessment**
C.F. Wang, X.X. Tao, A. Z, K. Zhao and W. Jiang 1662

**Average Damage Ratio and Earthquake Damage Matrix of Non-Engineered Building in Seismogenic Provincial Regions in China**
J.H. Xing, M. Lu, Y.M. Zhao and Y. Yu 1667

**Collapse-Resistance Measure for the Bottom Frame Structure under Earthquake**
D.Z. Wang, J.W. Dai and R.C. Shan 1676

**Dynamic Analysis of Artificial Boundaries in Gravity Dam-Foundation Rock Interaction System**
W. Qiao and G.M. Liu 1680

**Dynamic Analyses of a Self-Anchored Suspension Bridge under Seismic Excitations**
C. Wang and Y.X. Wang 1687

**Inertial Coefficient Adopted in Pile-Pier Structure under Deep Water**
G.S. Sun, C. Liu, J. Xie and F.J. Ma 1692

**Numerical Analysis of Seismic Behavior of a Concealed Bracing Connection for Precast Concrete Shear Walls**
Q. Jin, W.N. Guo, W.J. Zhao, B. Zhang and D.P. Zhang 1696

**Seismic Performance of Base-Isolation Building Subjected to Near-Fault Ground Motion with Velocity Pulse**
Q.M. He, Y.Q. Li, Y.M. Zhao and Y. Yang 1700

**Seismic Response Analysis of Free Long-Span Submarine Flexible Pipelines under Earthquakes**
Y.L. Deng, Y. Bian and F. Lei 1704

**SRC Frame-RC Core Wall Hybrid Structures Collapse-Resistant Design**
Y.Y. Wu, Z.K. Cui, Q.Q. Gong and L. Zeng 1708

**Study on Seismic Performance of Irregular RC Frame with Specially Shaped Columns**
J. Tang and L. Wu 1712

**Study on Seismic Response Characteristics of Step-Terrace Frame Structure on the Slope**
L.P. Liu, J.J. Liu, A.L. Li and M.Z. Tan 1718

**Study on Simplification Conditions of Curved Regular Bridges under Seismic Effect**
T.Y. Song, Y. Shen and G.P. Li 1723

**Study on the Characters of Seismic Response Spectra Based on China Financial Information Mansion**
M. Li, Y.Q. Wang, W. Tao, B. Wang, Q.X. Yu, L.L. Wu and R.L. Shan 1729

**Time-Frequency Analysis of Non-Stationary Ground Motions via Multivariate Empirical Mode Decomposition**
Y.W. Su, G.Q. Huang and L.L. Peng 1734

**Study of Intake Tower under an Earthquake Using the Power Spectral Method Based on ANSYS**
X. Hua, C.Q. Yu, W.H. Zhu, K. Zhao and C.L. Huang 1742

**Studies on Seismic Measures to Improve Masonry Infilled Wall**
Y.J. Zhang, X.S. Duan, X.Y. Wang, C.L. Zhou and Y. Sun 1746

**A Suggestion to the Vertical Earthquake Action Stipulated in Seismic Design Specification**
H.M. Liu, X.X. Tao and J.Y. Wang 1750

**Seismic Response Analysis for Assembled Precast Concrete Residence**
Z.B. Meng, Y. Cao, G.D. Qiao and Y.S. Zhao 1755

**Study of Ultimate Displacement of Timber Structures in Chinese Ancient Buildings**
M.G. Xu and Z.W. Ding 1759

**Expected Annual Earthquake Loss Analysis Based on CMR of Structures**
L.N. Xian and X.Y. Ou 1763

**Earthquake Mitigation Effect Analysis of Hysteretie DamPers in Steel Frame**
C. Xu, Y.F. Niu and Y.X. Zhao 1767

**Analysis of Earthquake Damages and Seismic Reinforcement of Bridges**
B.B. Fan, C.H. Zhao, L. Zhang and L. Li 1771

**Research on Shaking Table Test of Base and Story Isolation Structures**
G.C. Zheng and H.L. Xu 1776

**Vulnerability Analysis of Existing Buildings under Seismos**
X.H. Meng and G.Z. Yang 1782

**Finite Element Analysis of Seismic Responses of a Large-Cantilever Stadium Structure**
Z.Y. Sun, Q. Jin, L.G. Jia, Q. Wang, Y. Ma and C. Xu 1786

## Chapter 5: Hydraulic Engineering, Water Resources and Hydrology

**A Two-Dimensional Numerical Model for Shallow Water Flows over Variable Topographies**
B. Lv and S.X. Li 1793

**An Inversion Method of the Material Parameters for Gravity Dams**
D.D. Zhang, X. Feng and J. Zhou 1799

**An New Approximate Formula for Contracted Depth in Quadratic Parabola Shaped Channels**
F.L. Li 1803

**Analysis of the Influence of Bottomland Change on Waterway Conditions in Liyushang in Middle Reaches of the Yangtze River**
Y.D. Zhu and J. He 1807

**Analysis on Hydrodynamic Load that Induces High Dam Body Vibration**
C.T. Wang, H.X. Ding and H. Lv 1812

**Analysis on Seepage Effects of Plastic Concrete Cut-Off Wall in Construction and Operation Period of Hydropower Station Tail Channel**
G.X. Yan and W. Wu 1816

**Application of MIKESHE Model in Water Environmental Management for Guishui River Basin**
Z. Zheng, J. Zhang, H.L. Gong and J.W. Huang 1823

**Design of a Pressurized Trapezoidal Shaped Conduit Using the Rough Model Method (Part 2)**
B. Achour and A. Bedjaoui 1828

**Evaluation of the Effects of Channel Regulation Engineering Works in Typical Braided Reach**
J.Q. Han and L.Q. Li 1842

**Experimental Study on Engineering Properties of Cemented Sand and Gravel**
H. Fu, J.G. Feng, H.Q. Han and H. Ling 1846

**Finite Element Analysis of Stress Deformation of Earth-Rock Dam on Narrow Valley**
F.Y. Chu 1852

**Philosophical Reflections on Chinese Water Resource Management**
Y.F. Liu, B.Q. Ruan and C.C. Xie 1856

**Research and Discussion of Impervious Wall Construction Based on Continuous Vertical Slotting Technology**
L.X. Zhang, Y. Li, Z. Zhang, J.T. Niu and H.Y. Yu 1860

**Research of Eco-Compensation among Basin Cascade Hydropower Station Development and Management**
X.M. Zhou and M. Zhao 1864

**Research on Channel Regulation Parameters of Daijiazhou Reach in Middle Yangtze River**
W.L. Liu 1870

**Research on the Feasibility of Water Diversion Project**
L.H. Zhang, G.H. Wang and X.H. Hao 1874

**Simulation Method of Particle Size Scale for Fine Sand Model**
W.L. Liu, X.F. Liu and P.J. Yue 1878

**Study on Navigation Technology of Waterway at Hub Downstream and Bridge Area Overlapping**
X. Liu 1883

**Study on Sandy Pebble Reach Riverbed Erosion and Deposition Basic Law after the Three Gorges Reservoir**
X.F. Liu, M.L. Zhang and Z.W. Ye 1888

**Study on the Horizontal Velocity Distribution in Natural Rivers**
H. Ge, L.L. Zhu and X.B. Zhang 1893

**Study on the Uplift Force of Plunge Pool Slab**
C.T. Wang, B.H. Xie and W.H. Zeng 1897

**The Direct Solution on Normal Depth of an Egg-Shaped Section Tunnel**
H. Wen 1901

**The Study of Available Water Resources in Northern Shaanxi**
X.J. Wu 1906

**Mechanical Characteristics Analysis on Flexible Mattress in Downstream Sinking Based on Lumped Mass Method**
Z.H. Sun and M.L. Cheng 1910

**Research on Navigable Ship Model Test in Curved Waterway**
C.H. Wang and X.B. Cheng 1918

**Data Assimilation of River Networks Using Extended Kalman Filter**
Y.F. Chen and J.L. Qian 1923

**Numerical Analysis of the Influences of Water Level on Seepage Stability of Tailing Dam**
F.D. He, X.F. Cao, X. Yang and Z.D. Zhou 1928

**Experimental Study on the Air-Cooling of Concrete Aggregate**
M. Zeng, C.H. Guo, Z.M. Kang, W. Guan, F. Lu, G. Wang and D.W. Tang 1932

**Sensitivity Analysis of Concrete Face Rock-Fill Dam Parametric Based on the Intelligent Algorithm**
Q. Yan, Z.H. Gao and Z.C. Song 1940

**Study on the Present Situation and Development of Groundwater Monitoring Technology**
Q.H. Guan, F.L. Li, X.Q. Chen, Y.F. Zhang and C.J. Tian 1946

**Impact of the Cascaded Reservoirs and the Tributaries Confluence on the Eco-Hydrology of the Reserve in the Upper Reaches of Yangtze River**
L. Zhao, Q.D. Peng, Q.C. Chen, C. Li and Z.J. Yin 1953

**Shape Optimization for Arch Dam with Sequential Quadratic Programming Method**
Y. Duan, W. Yuan and H.B. Liu 1961

**Unsteady Flow Impact on Downstream Waterways and Control Measures Research of Pingban Hub in Nanpanjiangjiang River of Guizhou**
X. Liu 1966

**3D Dynamic Numerical Simulation of Water Flow in Stilling Basin with Flaring Gate Pier**
C. Qiu and C.L. Liu 1971

**Finite Element Analysis of Seismic Response of Exposed Steel Penstock in Hydropower Station**
Y. Liu, C.Z. Shi and H.G. Wu 1975

**Joint Regulation and Storage of Surface Water and Groundwater in Rushan River Basin**
M.H. Niu, Z.H. Xu and X. Wang 1981

**Comprehensive Evaluation for Utilization Efficiency of Rain-Flood Resources in Rushan River**
S.F. Zhou, Z.H. Xu, S.S. Yang, K. Kong and Y. Xiu 1985

**Study on Tidal Current and Sediment for Dredging Project in Yamen Channel**
J. He, L.P. Shi and Y.J. Sun 1989

**Analysis of Monitoring and Settlement Prediction of Wenzhou Shoal Seawall**
H.Y. Wei, G.Q. Liang and C.J. Zhang 1993

**Comparative Study on Design of Exposed Penstock Laid on Ground Using Chinese and American Specifications**
L. Hu, H.G. Wu, C.Z. Shi and Y.H. Xie 2000

**Current Situation and Development of SHPF Project in China**
C.M. Guan 2007

**Geo-Stress Direction Evaluation Method Based on Numerical Simulation**
S.C. Xu and C.Y. Jin 2011

**Influence of the Bridge on the Flood Controlling in the River**
X.Z. Zhang, X.P. Dou, Z.X. Jiao and Y.Y. Song 2015

**Monthly Rainfall Analysis in West Part of Chongqing**
L. Qin, J.Y. Jin, Q. Zhang and D.K. Wang 2019

**Optimization Study on Drainage System for Canal of Middle Route Project of SNWT in Expansive Soil Area with High Groundwater Level**
H.d. Cui, J.F. zhang, G.S. zhu, D.X. Wu, W. Zhang and J.L. Wang 2023

**Precipitation Characteristics and Trend in the Hsiao-Ching River Basin of Jinan City during the Past 50 Years**
L. Lin, J. Liu, J.W. Huang, X.Q. Chen, Q.H. Guan and Y. Tang 2029

**Research on Structure Design of U Type Canal of Seepage-Proofing**
J.L. Sun, B. Zhang and S.J. Zhang 2033

**Simulation Study on Deposition Downstream Floodgates in Estuarine**
X.Z. Zhang, Y.Y. Song and S.M. Chen 2037

**Study on Time Effect of Rock Fill Dam Seepage Line**
X.Y. Tao, D. Xiang, W. Sun and Y. Li 2041

**Temperature Rebound Influenced by Environment Temperature Analysis of the Irrigated Area of a High Arch Concrete Dam under Constrcution**
X.H. Chen, Y.Y. Huang, B.L. Xu, D.D. Liu and X.B. Wei 2045

**The Numerical Simulation of the Flow Field in the Micro-Pressure Inner Loop Reactor**
J.C. Liu, Z.G. Yin and W. Ji 2050

**Vibration Analysis and Human Comfort Evaluation of Underground Hydropower House**
D. Fu and H.G. Wu 2055

**Working Performance of Anti-Arch Segments on the Left Bank Slope of Xiangjiaba Gravity Dam**
Q.J. Zhou, P. Gao, Z.G. Gong and H.F. Li 2063

**Main Engineering Geological Problems and Evaluation on the Reservoir Engineering of Yellow River Water Diversion and Irrigation Area**
Z.Q. Huang, T.L. Chen and A.M. Wang 2071

**Research on the Calculation Method of Earth Pressure on the Back Side of Large Cylinders**
J.L. He 2074

**Utilizing GIS in the Development of Water Quality River Modeling for Penchala River, Malaysia**
F. Othman, A.E. Mohamed Elamin, S.A. Hezza Azahar and S.A. Muhammad 2078

**Data Mining Model in Regional Target Decomposition of Water Resources Utilization Efficiency**
H.W. Chen, J.W. Huang, B. Li, S.D. Fu and X. Zhang 2082

**The RCC Arch Dam Analysis during Overload**
Y. Xia, Y.Y. Yu, X.L. Zhao and Z.Q. Zhang 2088

**Study on Damage of Concrete Dam Subjected to Combined Action of Earthquake and Slide Surge**
J. Li, Q. Xu, J.Y. Chen and G.S. Lu 2092

**Research on the Dam Foundation Stability and Reinforcement Measures of the 12th Sluice Section of Xiangjiaba Hydropower Station**
X.J. Wang and X.X. Zhao 2096

**Experimental Investigation on the Segregation of Landslide Dam Materials**
M. Zhang, F. Wang, G.J. Mouse, W.T. Luo, H.W. Zhang and Y.R. Liu 2103

**Relaxation Analysis of the Arch Dam Foundation Rock Masses of Jinping I Hydropower Project**
B. Xiao, D.N. Zhou and Z.H. Min 2108

## Chapter 6: Coastal Engineering

**Research on the Influence of Diking in Shallow Sea of Tangdao Bay on Marine Environment**
Y.H. Xu, X.H. Hao and X.M. Dong 2115

**System Analysis of Construction Quality Control Measures of Coastal Levee**
X.Q. Wang, H. Li and S.Y. Han 2120

**Experimental Study on Mooring Manner and Safety Operation for 450,000DWT Supertanker**
B. Jiang, X.J. Huang, Y.X. Lv and X.B. Zhang 2124

**Experimental Study on the Offshore Positioning and Installing of Large Caisson**
X.J. Huang, W.Z. Zhang, B. Jiang and Y.X. Lv 2129

**Two-Dimensional Finite Element Analysis of Laboratory Seawall Model**
J. Zhang, J.F. Zhai, X.M. Wang and J. Chen 2134

**Accuracy Comparison for the Ocean Tide Models in Estuarine Tidal Prediction, the Pearl River Estuary**
L. Zhu, X.L. Yin and L. Jiang 2141

**Numerical Model on Hydrodynamic Impact from HZM Bridge**
J. He, Y.J. Sun and X.S. Zhao 2146

**The Research of Flow Resistance Property in the Tugging and Mooring of Tube Segment**
Z.Z. Qiu and M. Dong 2150

**Tieshan Port Development Plan: Evaluation of the Long Wave Induced Resonance Using a Numerical Mild-Slope Model**
H.J. Zhao, J. Yang and G.P. Chen 2154

**Wave Kinematics and Pressure Field of Third-Order Theory for Bichromatic Bi-Directional Waves in Water of Finite Depth**
H. Huang and G.L. Li 2166

**A Kind of Floating Breakwater Sheltering Deep Water Aquaculture**
X.F. Cheng 2170

**Analysis of Gravity Foundation for Offshore Structure under Cyclic Loads**
R. Gao, L.Q. Yang and Y. Wang 2177

**Application Status and Development Trend Research of Ecological Revetment in Jiangsu Inland Waterway**
J. Zhang, J.F. Zhai, X.M. Wang and J. Chen 2181

**Computation and Analysis of Buttressed Quay's Floor**
Q.C. Ning, X. Yang, Y. Shi and L. Li 2185

**Research of Sediment Transport Trend and Erosion-Deposition Characteristic of Yangma Island Sea Area**
Y. Wang, W. Ye and M.C. Li 2189

**Study on the Evolution of Artificial Beach in Xiamen**
G.L. Wang 2194

**Three Dimensional Physical Model Study on Penang Fishing Port Project**
C.H. Zhang and B.L. Geng 2198

**Study on the Panel of the High-Pile Wharf Near Estuary Based on the Finite Element Method**
X. Yang, Q.C. Ning, Y. Shi and G.X. Xia 2202

**Appropriate Jackup Selection in Disturbed Wellsite by Pile Inserting and Pulling in Offshore Oilfield**
Y.N. An, Q.F. Song and J. Li 2206

## Chapter 7: Construction Technology

**Complementary Use of Inductive Test and Bending Test for the Characterization of SFRC**
L. Liao, S. Cavalaro, A. de la Fuente and A. Aguado 2213

**Research on New Type Quantitative Nondestructive Pre-Stress FRP Sheet Tension Fixture**
G.S. Zhu, L.S. Bao and C. Guo 2220

**Analysis on Impact of the Node Connection Pattern for Fastener-Style Steel Pipe Formwork Support**
L. Liu, B. Wang, J.C. Wang and Y.N. Liu 2224

**Analysis on Lateral Deformation of High-Formwork in Different Column's Spacing of Bridging**
L. Liu, B. Wang, Y.N. Liu and J.C. Wang 2228

**Influence of Bridging Arrangement Location on the Mechanical Characteristics of the High-Formwork Support System**
L. Liu, Y.N. Liu, B. Wang and J.C. Wang 2232

**Research on Influence of Concrete Pouring Sequence on Stability of High-Formwork Support System**
L. Liu, J.C. Wang, B. Wang and Y.N. Liu 2235

**The Integration of New Technology Research on Composite Inorganic Fiber Acoustic Insulation Spray in Engineering Construction**
J.Y. Shao and D. Wang 2239

**The Technology Innovation of Green Soft Ground Handling Based on Squeezing and Consolidation Composited**
J.Y. Shao and X. Zhang 2244

**Causes and Solutions for the Common Problems in Rotary Drilling Cast-in-Place Pile Construction**
Z.Y. Zhou and C.Y. Zhang 2249

**Determining the Degree of Mobility of Building Systems**
P.P. Oleinik, L.S. Grigoryeva and V.I. Brodsky 2253

**Engineering Application of Precast Assembly Integral Shear Wall Structure on Housing Industrialization**
Y. Wang, Y.N. Zhang, F. Yang and X.X. Xia 2257

**Features and Construction of Prefabricated Buildings**
Y.H. Zhao 2262

**Connecting Passage Construction for the Foundation Pit under Existing Optical Fiber Cable**
H.Q. Cao, N. Lou and W.J. Cui 2266

**Experimental Study of Effects of Operation Parameters on Efficiency of Vibratory Pile Driving**
H.P. Zheng, L. Chen, W. Wang, L.Q. Peng and J.Y. Zhang 2272

**The Study about Anti-Seismic Structures Stirrup Construction Blanking Length Theory Calculation**
H.L. Li, X.X. Cui and Y.H. Zhao 2277

**Components and Guidance for Constructional Rearrangement of Buildings and Structures within Reorganization Cycles**
A. Volkov, V. Chulkov, R. Kazaryan, M. Fachratov, O. Kyzina and R. Gazaryan 2281

**Mold-Unloading-Lifting and Lifting-Transportation's Construction Checking of Composite Wallboard in Industrial Production**
C.Y. Xu, L. Yan, C.L. Xu and S.K. Jiang 2285

**Discussions on Foundation Pit Construction Scheme of Large Building in Mountain Area**
M.J. Lin 2289

**Outstripping Engineering Preparation of Construction Sites**
P.P. Oleinik, L.S. Grigoryeva and V.I. Brodsky 2294

**Research on the Problems and Countermeasures for Steam Curing of Assembled Composite Wallboard**
C.Y. Xu, L. Yan, C. Li and Z.W. Cao 2299

**Temperature Cracks of Concrete Engineering Analysis and Treatment Measures**
G. Zhang 2303

**The Double-Layer Nonstationary Heat Conduction Measures to Prevent the Formation Ice-Dams on the Roof**
M. Petrichenko, D.V. Nemova, D.S. Tarasova and A.A. Staritcyna 2308

**Construction Technology of High-Rise Building Structure**
P. Cheng, X.F. Chen and L. Wu 2316

**Research on the Characteristics and Status of Recycled Concrete Filled Steel Tube**
B. Wang, X. Liu and X. Yu 2320

**The Countermeasures on Temperature and Shrinkage Crack of Mass Concrete**
X.C. Zheng, P.F. Li and S.Z. Sun 2324

**Reinforcement Method Choice of Deep Soft Soil Foundation**
C.M. Zhang, L.J. Liang and C. Huang 2328

**Bending Resistance of a Slender Plate Girder with Longitudinal Stiffener**
S.I. Gutiu and C. Moga 2332

**Processing Status and Utilization of Construction Waste in China and the West**
F.J. Liu and F.F. Suo 2336

## Chapter 8: Water Supply and Drainage Engineering

**Effects of Different Irrigation Amount on Yield and Quality of Greenhouse Tomatoes**
Z. Chen and M.A.M. Abdalhi 2343

**Emergency Supply of Drinking Water**
M. Teichmann, F. Kuda and Z. Proske 2346

**Integrated Fuzzy Evaluation of Raw Water Eutrophication Based on GIS**
J.P. Liu, J.W. Shao, F.L. Dong and X.Y. Ma 2350

**Research of Hydrodynamics of Biofilter with Surface Feed**
E.S. Gogina, O.V. Yantsen and O.A. Ruzhitskaya 2354

**Research on UV/$TiO_2$ Photocatalytic Oxidation of Organic Matter in Drinking Water and its Influencing Factors**
J.H. Zhao 2358

**The Development of Prestressed Concrete Cylinder Pipe in China**
H.Y. Zhang, H. Peng and X. Chen 2363

**The Single-Sludge Denitri-Nitrification System in Reconstruction of Wastewater Treatment Plants in the Russian Federation**
E. Gogina and I. Gulshin 2367

**Study on the Treatment of Compound Micro-Polluted Groundwater by Contact Oxidation Process under Different Filtration Rates**
Y.H. Zhao, J. Cheng, X. Yan and D. Wang 2370

**Ultra-High-Rise-Building Water Supply and Drainage System Design**
Y.N. Si, M. Zhou, Y.H. Liu and L. Deng 2374

**Treatment of Raw Water in Yangtze Chenhang Reservoir by Diatomaceous Earth Precoat Filtration**
W.Q. Zhou, D. Zhang, H. Ye, Z. Wang, Z. Yang and C.L. Zhang 2380

**Choosing an Optimal Trenchless Renovation Method for Pressure and Non-Pressure Pipes**
V. Orlov and I. Averkeev 2384

**Design and Development of the Urban Water Supply Pipe Network Information System Based on GIS**
X.H. Wang, Y.J. Liu, Z. Wang and W. Zhang 2389

**Model Precision Assessment of Water Distribution System Based on Uncertainty Analysis**
S.H. Shu, X.M. Zheng and J.L. Ruan 2394

**The Selection of Priority Pipe Sections for Sewer Network Renovation**
V. Orlov and A. Andrianov 2398

**Hydraulics of Looping**
J. Zolotova 2403

**The Water Usage Method and Spatial Structure Type of Spring Village in Northern China**
Y.W. Kong 2408

## Chapter 9: Heating, Gas Supply, Ventilation, Air Conditioning Works and Daylighting Design

**Simulation and Analysis of Thermal Performance of Internal Recycle Double Skin Facades**
C. Hui, Y.Q. Wang, B. Wang, W. Tao and S.L. Zheng 2415

**Analysis and Evaluation for the Economic Performance of Ground Source Heat Pump System with Waste Heat Recover**
Z.C. Zhao, W.X. Feng, H.J. Mi and Y. Xue 2421

**Experimental Investigations on Effect of Particles Removal in Cleanroom with Non-Unidirectional Airflow**
Y. Wang 2428

**Calculation and Analysis of Gravity Head Coefficient in Hot Water Heating System**
W.W. Xie and Y.Z. Fu 2432

## Chapter 9: Heating, Gas Supply, Ventilation, Air Conditioning Works and Daylighting Design

**Study on the Current Situation of Economic Analysis of Ice Storage Air-Conditioning System**
Y.N. Li, S.F. Wang, T.Z. Lv and S.F. Lang 2441

**A CFD Simulation of Indoor Natural Ventilation of a Residential District in Zhuzhou**
Z.Y. Wang, S.F. Yang, C.R. Liu, T.Y. Zhang and N. Cui 2447

**Analysis of Influence Factors on the Internal-Melt Ice-on-Tube while Melting**
Y. Liu 2452

**Effect of the Circulation Flow Velocity in Ground Heat Exchangers on System Operation**
Z.S. Qi, Q. Gao, Y. Liu, Z.H. Gao and L. Bai 2457

**Energy Saving Design of a Training Center in Dongguan**
X.J. Lai, Z.H. Du and Z.Q. Zhang 2461

**Calculation of the Maximum Length of the Directly Buried Cooling Pipes Applied in the District Cooling System (DCS)**
C.Y. Tan, H.H. Hu, M.M. Wang, Z.Z. Pan and H.Q. Wang 2466

**Discussion on Ventilation Requirement for Meeting Indoor Air Quality**
M.J. Lin, Q.Q. Liu and Z.M. Peng 2471

**Simulation Study on Characteristics of Ultra-Low Temperature Heat Pump Air Conditioning System for Pure Electric Vehicles**
H.J. Li, G.H. Zhou, A.G. Li, X.G. Li, J. Chen and T. Chen 2475

**The Effectiveness of Implementing Automated Ventilation System in Premises Intended for Public Using**
S. Shilkina and A. Trusov 2480

**"Breathing House" – New Air System for Healthy Residential Buildings**
T.X. Dong and Z.Y. Yan 2484

**Research on the Construction Technology of Radial Underground Heat Exchanger and its Heat Exchange Performance**
R.H. Wang, Q.H. Wang and Y. Feng 2488

## Chapter 10: Oil, Gas and Mineral Exploration

**Optimization of Acid Fracturing Design in Yubei Fractured Reservoir**
L.Y. Song, X.R. He and J.C. Zhang 2495

**Optimization of Black Oil Model-CO2 Flooding in Low Permeability Reservoir**
L.Y. Song, J.C. Wei, X.M. Xu and T. Gao 2502

**Experimental Study of Self-Suction Spraying with Pressure Gas and Water**
Z.F. Ma, G.R. Lin, Z. Zhang and H.L. Xie 2508

**Study on Surface Deformation Law of Western Chengchao Iron Induced by Underground Mining**
Y.C. Zhou, C.X. Chen, X.M. Liu and K.Z. Xia 2513

**Adsorption Research of Polymer on Oil Sands in Qidongyi Block of Xinjiang Conglomerate Reservoir**
X.B. Nie, Y. Guo, Q.X. Lou, W.D. Liu, L.H. Sun and J.Y. Li 2518

**Analysis on Permeability of High Permeability Layer-Penetration Oil Influencing Factors**
Y. Fang 2524

**Industry Clusters Innovation Action Model Based on the CAS Theory – Shanxi Magnesium Industry**
F.Z. Luo and S.L. Liu 2528

**Research on Construction Technology of the High Permeability Type Layer-Penetration Oil Production**
G. Hu 2533

**Research on High Permeability Layer-Penetration Oil Production**
Q. Guan 2539

**The Influences and the Mechanism of Action of Grinding Aid Agent during Micro Fine Particle of Lean Hematite Ore of Grinding Operation**
B. Liang, J.R. Zhang, M.M. Han and L.B. Zhao 2545

**Rapid Excavation Technical Research of Blasting Mining Face in Liangzhuang Mine**
Z.B. Yan, X. Xu, T.T. Li, S. Wu and S.Y. Ma 2550

**Numerical Simulation Study on Setting Stopping Line of Working Face in Shuguang Mine**
H.J. Xue, J. Chen, B. Liu, J. Kong and Z.J. Hao 2554

**The Research of Gas Drainage Technology in Daning Coal Mine**
Z.M. Zhao and G. Wang 2558

## Chapter 11: Disaster Prevention and Mitigation

**Analysis on Wind-Induced Vibration of Tall Buildings in Hilly Terrain**
Y. Sun, N. Deng and Z.L. Li 2567

**Energy Absorption Numerical Analysis of Mine Impingement Thin-Walled Components with Different Configurations**
Z. Tang, Y.S. Pan and X.J. Zhu 2572

**Freezing Damage Analysis of Jintaizi Fishing Floor Engineering in Fuyu**
L.J. Dou, W. Wang and M.Y. Xu 2579

**Mechanical Properties and Calculation Method for Monolayer Cable Net Glass Curtain Wall under Fire Conditions**
L.F. Gong, Y. Bai and S.Q. Li 2583

**Pregnant Mechanism and Mechanical Model of Rock Landslides in Chair-Shaped Cataclinal Bank Slopes**
X.C. Ma, X.C. Chen and Y.J. Feng 2589

**Research on Method for the Weight Definition of Evaluation Indicator in Dump Landslides Based on Rough Set**
T.T. Luan, Z.H. Xie and S.S. Liang 2600

**Study on Ignition Time of Radiation Cargo in Irradiation Room under Stuck Radioactive Sources**
X.L. Yao 2607

**The Coupling Interaction in the Rankine Method for Concrete Filled Steel Tube Columns under High Temperatures**
Y. Yao and X.X. Hu 2612

**The Design of Unascertained Fire Risk Evaluation System for High-Rise Civil Building Based on VB**
L.N. Zhang, J. An and Q. Zhang 2616

**A Study of Storm Surge Risk Index System**
Q. Liu and Z.Z. Yuan 2622

**Review of Different Methodologies and Risk Assessment Models Instorm Surge Disaster Management**
Q. Liu and S. Yang 2628

**A Forecast and Risk Assessment Model for Storm Surge Impacts**
L. Zhang, Q. Liu and S. Yang 2635

**Survey of Fire Load in Building Furniture Store**
J.P. Wang 2642

**The Research on Structure Fire Resistance Test of Fire Retardant Rigid Polyurethane**
J.P. Wang 2646

**Tornado Hazard Loss of Nuclear Power Plant Building during Design Service Period**
T. Song and L.Y. Lu 2649

**Comparative Analysis of Wind Load for Transmission Tower between Chinese and American Codes**
Z. Xu, Y.J. Zeng, D.J. Cao, X.J. Lang and L. Tian 2654

**Landslide Susceptibility Zonation Based on the Analytic Hierarchy Process and Information Method**
D.D. Qiu, R.Q. Niu and Y.N. Zhao 2658

**Modelling of the Human Behavior in Evacuation**
L. Wei, C.Y. Zhao and W.F. Yuan 2663

**Numerical Simulation on Ghosting Fire in the Confined Underground Space**
P.H. Zhang, X.W. Lu and X.M. Zhang 2667

**Research on Concrete Columns Seismic Performance of Super Early-Strength Composite Fibers after High Temperature**
C.Z. Sun, R.X. Wu and H.N. Zhao 2671

**The Analysis of Hysteretic Behavior of Concrete Filled Double Skin Steel Tubular after Exposure to Fire**
X. Liu, J.T. Bao and B. Wang 2675

**The Construction of Emergency Logistics System Framework and Information Platform System**
W.K. Chen and C. Hua 2679

**Vulnerability Assessment of Truss Structure Based on Strain Energy and Damage Scenarios**
Y. Xu, X.C. Yu and W.B. Li 2686

**Deformation Monitoring and Prediction of a Reservoir Landslide in Sichuan Province, China**
B. Han, S.S. Hou, B. Zhu, L.C. Wang, A. Li and H.J. Ye 2694

**Mechanical Performance Calculation of Single-Layer Cable Mesh Point-Supported Glass Curtain Wall under Fire Conditions**
L.F. Gong, Y. Bai and S.Q. Li 2702

**Design and Realization of 3S Technology-Based Geological Disaster Database System in Liaoning Province**
H. Ding, L.S. Sun, J.L. Wang and X. Wang 2708

**Monitoring of Flooding Water under Coal Mine Based on Improved Fuzzy Clustering**
M.Y. Nie, M.R. Zhou and X.Q. Fu 2713

**Review on Study of Fire Behavior of Bridges in China**
Y.J. Liu, Y. Yao, X.X. Li and X.D. Chen 2717

**Risk Assessment of Debris Flow Based on Multi-Objective Fuzzy Pattern Recognition Method in Mountain Highway Construction**
Y. Wang 2722

**Case Study of Fire Risk Management of Tourist Hotels**
R.J. Shiu, S.T. Cheng and I.T. Liu 2727

**Multivariate Geometric Factors Contributing to Crashes and Injuries in Mountainous Freeways: A Case Study from Jiangxi, China**
M. Li, Y.G. Wang and X. He 2731

**The Analysis of Safety Investment Behavior of the Long-Term Incentive Mechanism in Construction Enterprise**
Y.B. Shui, Q. Li and H. Li 2735

**Research on Functional Adaptation of Sport Venues as a Disaster Prevention Refuge**
L.D. Huang and T.Y. Zhang 2740

## Chapter 12: Cartography and Geographic Information System

**A Research on Digital City Three-Dimensional Visualization System Based on Skyline**
H.B. Dai, X.J. Yue and J.Y. Xu 2745

**A Study on Informatization Construction of Sharing "One Map" between Land and Planning Departments**
G. Yang and T.T. Zhou 2749

**The Visualization of Health Monitoring System for Bridge Using CORS and GIS**
Q.L. Kong, Y.H. Li, L.T. Han and J.Y. Guo 2756

**Research on the 3-D Scene Quick Build Method of Virtual City and Implementation Method of Basic GIS Function**
C. Yang, H. Li, P. Gao and R.C. Zhang 2760

**Application of Three-Dimensional Visualization Technology in Real Estate Management**
J. Cui, J.J. Ma, D.L. Ma and N.N. Yang 2765

**Calculation of Land Consolidation Potential Based on GIS**
Y.H. Liu and W.Q. Chen 2769

**Information Management of Maritime Work Based on GIS**
J.P. Liu, F.L. Dong and J.W. Shao 2774

**Design and Fabrication of Dynamic Thematic Maps Based on Flash**
Y.X. Xu and J.W. Yang 2778

**Development of Topographic Maps Symbols Library**
C.M. Sun and Y.X. Xu 2782

## Chapter 13: Surveying Engineering

**Application of Total Station in the Measurement of Transmission Line**
F.R. Gui 2789

**Chinese Geodetic Coordinate System 2000 and its Comparison with WGS84**
H.P. Li, S.F. Bian and Z.M. Li 2793

**Discussion on the Measurements in Cantilever Construction with Guyed Hanging Basket**
F.R. Gui 2797

**Error Analysis of the Settlement Observation**
L. Wang, L. Fang, B. Zhang and C.C. Huang 2801

**Application of Stereo Vision Measurement Technology in the Detection of Round Hole**
Q. Wang, X.M. Cui, C. Li, J.J. Cui and L.J. Li 2805

**Application of Model GM (1,1) to Settlement Forecast of High-Fill Airport**
Y.P. Wu, J.B. Wang and C.T. Wang 2810

**Research and Extended of Semi-Parametric Model Additional System Parameter**
Y.P. Wu, C.T. Wang and J.B. Wang 2815

**Research on Control Methods of Measuring Super High-Rise Buildings**
X.Y. Xie 2820

**Correction of Atmospheric Effect in EnviSAT ASAR Repeat-Pass Interferometry with MODIS Water Vapor**
G.T. Sun, P. Song and X.Y. Liu 2824

**Analysis of Underground Space Azimuth Measuring and Data Processing in a Tunnel**
T. Wang, H.R. Duan, L.T. Jiang and S. Liu 2828

**Study on Application of Terrestrial 3D Laser Scanning Technology in the Calculation of the Fine Earthwork**
X.G. Feng, M. Li and J.X. Liu 2833

**Application and Research of 3D Laser Scanning Technology in Steel Structure Installation and Deformation Monitoring**
D.L. Ma, J. Cui and S.Y. Wang 2838

**Discussion on the Application of GPS Technology in Bridge Construction Plane Control Net and in Survey of Bridge Axis Lofting**
S.Y. Jiang 2842

**Improved BP Neural Network Model Applied in Settlement Analysis**
L.B. Gao 2848

**Multi-Scale Classification Based on Remote Sensing**
P.L. Li, W.P. Ti and J.C. Li 2853

**Research on GPS Height Partition Fitting Method**
C. Wang 2860

**GPS RTK Techniques for Construction Monitoring of Super Deep-Water Open-Caisson**
Y.G. Hao, X.L. Liu and J.B. Liu 2865

**Triangle Interpolation on Discrete Point Set**
H.F. Jiang 2872

## Chapter 14: Applied and Computational Mechanics

**Effect of Ring Support Position and Geometrical Dimension on the Free Vibration of Ring-Stiffened Cylindrical Shells**
X.W. Liu and B. Liang 2879

**Increment-Dimensional Precise Integration Method of Oil-Water Coupling Flows in a Low Permeability Reservoir with Capillary Pressure**
F.L. Mei and G.L. Li 2883

**Influence of Vertical Vibration on Surface Velocity of a Liquid Bridge**
R.Q. Liang, Z.H. Zhang, T.Y. Gao and F.S. Yan 2890

**Linear Analysis of the Constitutive Relation of Concrete Elastoplastic Disturbance**
J.M. Liu, W.N. Wang and S. Liu 2894

**Method of Extended Domain and General Principles of Mesh Approximation for Boundary Problems of Structural Analysis**
P.A. Akimov and M.L. Mozgaleva 2898

**Numerical Simulations of the Internal Fluid Field for Porous Scaffold Used in Tissue Engineering**
Q.G. Liu, J.Z. Jiang, H.T. Cui, X.Q. Yu and P.Y. Peng 2903

**Preliminary Application of Software Package GPPS to Spare Linear Systems from Meso Scale Simulation of Concrete Specimen**
J.P. Wu, H.F. Ma, J. Zhao and S.C. Wang 2907

**Mechanical Behavior Analysis of Concrete Short Columns Pushed out from Over-Thick Steel Tube**
J.M. Liu, J.L. Yang and S. Liu 2912

**Study on Numerical Simulation of Explosion in Soil Based on Fluid-Solid Coupling Arithmetic**
J. Song and S.C. Li 2916

**Study on Stability of Functionally Graded Cylindrical Shells Subjected to Hydrostatic Pressure**
X.W. Liu, B. Liang and R. Li 2920

**Theoretical Foundations of Correct Wavelet-Based Approach to Local Static Analysis of Bernoulli Beam**
P.A. Akimov and M. Aslami 2924

**Theory Analysis of Functionally Graded Materials Cylindrical Shell Buckling under Pure Bending**
W. Cheng, Z.G. Wang and S.C. Long 2928

**Numerical Decision of Problems of Structural Mechanics with Nonideal Unilateral Constraints**
A. Lukashevich and L. Rozin 2932

**Some Recent Developments in Coupling of Finite Element and Boundary Element Methods - Part I: An Overview**
W. Elleithy and L.T. Leong 2936

**Some Recent Developments in Coupling of Finite Element and Boundary Element Methods - Part II: Dynamic Procedures for Determining the Relaxation Parameters for the Mixed Dirichlet-Neumann Domain Decomposition FEM-BEM Coupling Method**
W. Elleithy and L.T. Leong 2943

**State Space Solution of Response for Piles Subjected to Lateral Loads**
F.L. Mei and G.L. Li 2948

**Study on Downburst Wind Field Characteristics under Mountainous Terrain**
H.T. Shi, Y.Z. Wu, S. Yi and B.F. Ji 2954

**Study on Downburst Wind Load under Characteristic Topography**
Y.Z. Wu, Y. Sun, H.T. Shi and B.F. Ji 2958

**The Study on Differential Equations Method for Solving Column-Pile Structural System Internal Forces**
D.C. Fu, Y.H. Wen and L. Wang 2962

**Theory of Duality Disturbance of Elastoplasticity**
J.M. Liu, S. Liu, J.L. Yang and Y.Z. Sun 2966

**Thermocapillary Convection of Low Prandtl Number Fluids under Uniform Magnetic Fields**
R.Q. Liang, D. Bei, F.S. Yan and D.Q. Geng 2970

**Two-Dimensional Problem Moisture Elasticity for Inhomogeneous Flat Annular Area**
A.S. Avershyev and V.I. Andreev 2974

**Application of Energy Method for Determining Loss Factor in Dynamic Systems with Hysteretic Damping**
V. Smirnov and V. Mondrus 2978

**Hexahedron-Dominant Mesh Generation for Blocks with Constrained Triangulated Boundary Surfaces**
X.B. Pei and N.X. Xu 2983

**High-Precision Structured Finite Volume Model for Numerical Simulation of Dam-and Dyke-Breach Flow**
Y.T. Ye, L.L. Liang, S.H. Zhang and Y.Z. Jiang 2990

**Novel Partitioned Integration Method Based on Newmark's Scheme for Structural Dynamic Problems**
C.G. Jia, Y.M. Li, H.L. Xia and L.P. Liu 2996

**Subgrade Limit Bearing Capacity Calculation Using Slip Line Method**
Q.Q. Sun, T.Q. Zhou and X.J. Gu 3003

**3-D Numerical Simulation of Flow Structures in a Sharp Bend of the Lower Yangtze River**
D.D. Jia, Y.J. Lu, X.N. Zhang and X.B. Zhang 3007

**About Verification of Correct Wavelet-Based Approach to Local Static Analysis of Bernoulli Beam**
P.A. Akimov and M. Aslami 3013

**Determining the Frequency of Free Oscillations Geometrically Nonlinear Shell Using the Mixed Finite Element Method**
L.U. Stupishin and K.E. Nikitin 3017

**Dynamical Analysis on Underground Powerhouse of Yixing Pumped-Storage Power Station**
F. Han, D.W. Zhong, J.Y. Mo and G.J. Chen 3021

**Experimental and Finite Element Study on the Fatigue Growth of a Semi-Elliptical Surface Crack in a X80 Pipeline Steel Specimen**
Q. Jin, Z.Y. Sun and W.N. Guo 3026

**Finite Element Analysis on Negative Wind Pressure Stress of External Wall Insulation Layer**
Y.H. Zhang, L.P. He, Y.J. Zhang and C. Li 3030

**Mechanics Analysis of Tower Crane**
Z.J. Yang, Z.D. Ai and H.W. An 3034

**Mixed Time Integration Parallel Algorithm for Nonlinear Dynamic Analysis**
C.J. Fu 3038

**A Comparison between the Matrix Displacement Method and the Finite Element Method in Solving Frame Structure with SM Solver Software**
L.J. Cheng and X.C. Yan 3042

**Crack Extension Calculation under Tensile and Shear Load by XFEM**
M. Yu, Z.H. Dai and G.J. Hu 3046

**Finite Element Solution in Fluid Mechanics Using Exponential Function Based Interpolation**
S.W. Fang, X.F. Yuan, R.J. Qian and S.H. Jiang 3051

**Numerical Simulation of Flow around High-Rise Buildings Based on Reynolds Stress Model**
Z.P. Zhang, W. Zhang and G.P. Chen 3057

**Reconstruction of Shallow Shells for Increase Bearing Capacities and Operating Characteristics**
L.U. Stupishin and A.G. Kolesnikov 3062

**Study on Reduced Order Model in Large-Span Roof Vibration under Wind Actions**
F.J. Sun and D.M. Zhang 3066

**The Coupling of Pseudo-Spectral Method and Domain Decomposition Method for the Elastostatic Problem**
R. Ding, F.J. Chen, Q. Shen and L. Liu 3071

**The Foundation of Nonlinear Finite Element Model**
B. Wang, X. Liu and B.D. Zhao 3075

**Properties and Moving Time Average for Lévy Walks with Power-Law Waiting-Time Distributions**
K.Y. Deng and J.W. Deng 3079

**The Scattering of Circular Cylindrical Cavity with Time-Harmonic SH Waves in Infinite Strip Region**
L.M. Cai, H. Qi and X.N. Pan 3083

**Numerical Simulation of the Wind Load on the Mast at Different Wind Angles**
R.S. Cao, Y.Y. Fang and L. Wang 3089

**MIDAS-Based Finite Element Analysis of the Short Line Method of the Precast Segmental Bridge Construction**
L.K. Guan, X.D. Zhang and H. Lei 3093

**Simulation of Acoustic Cavitation Bubble Motion by Lattice Boltzmann Method**
X. Zhou, M.L. Shan, C.P. Zhu, B.Y. Chen, C. Yin, Q.G. Ren, Q.B. Han and Y.B. Tang 3098

**Research and Development on Similarity Principle of Model Pile**
X.Q. Wang, S.M. Zhang, J. Liao and Y.S. Huang 3106

**Study on the Downburst Field Characteristics under the Influence of Two-Dimensional Continuous Mountains at Different Distance**
Y. Sun, Y.Z. Wu, H.T. Shi and B.F. Ji 3111

**Investigation on the Wind Pressure Asymmetric Coefficient of Transmission Line**
W. Hao, B. Li, J.B. Yang and F.L. Yang 3115

**Three-Parameter Damage Evolution for Quasi-Brittle Solids**
J. Zhang 3119

## Chapter 15: CAD/CAE/Computer Technology

**An Integrated Simulation System for Building Structures**
J. Duan, X.M. Chen, H. Qi and Y.G. Li 3127

**Simulation Analysis of Built Environment Based on Design Builder Software**
L. Zhang 3134

**Simulation on SHTB Apparatus Design Based on ANSYS/LS-DYNA**
G.F. Xiao, X.Q. Jiang, Y.C. Zhou and J. Yan 3138

**Numerical Simulation of SHPB Test for Concrete under Confining Pressure**
H. Zhang, A.Y. Xie and Y.W. Gao 3144

**Engineering Practice of Elasto-Plastic Time-History Analysis on Super High-Rise Using ABAQUS**
Y. Zhou, S.R. Hong and Y. Chen 3149

**Calculation on Internal Force Effect of a High-Speed Highway Prestressed Concrete Extra-Dosed Cable-Stayed Bridge**
X.Z. Chen 3154

**Establishing the Digital Model of Hydraulic System in Simulation Vibration Table**
R. Li, X.S. Li and H. Xu 3158

**Research on SketchUp Application in Graphing of Civil Engineering**
Q. Dong and Y.S. Yang 3163

**Analysis of the Flow Characteristics of Multiphase Flow Fields in the Mixing Agitator**
X.B. Wang 3167

**Building Information Modeling (BIM) and Analysis of more Traditional CAD**
J. Li 3171

**From CAD to the Rapid Development of BIM**
J. Li 3175

**Model Reuse Technology in Building Electrical Parameters Design**
H.K. Pu and Q.C. Wei 3179

**Normally Consolidated Subgrade Limit Bearing Capacity Calculation Using Slip Line Method**
M. Chen and T.Q. Zhou 3183

**Numerical Simulation and Testing of 45 Architecture Steel Welded Based on Gaussian Heat Source**
J.B. Ji, J.Z. Zhang and L. Zhang 3187

**Research on Tunnel Construction Quality Based on Visualization Management**
Q. Li 3192

**Analysis on Application Prospect of BIM Technology in Granary Designing**
G.X. Chen, B.H. Hao and Y.Q. Zhao 3196

**Intelligent and Complex Monitoring in Intelligent Buildings**
A. Volkov and K. Latyshev 3204

**Numerical Analysis of Bridge Expansion-Induced Rail Deformation of Ballast Truck**
Z.W. Xiong, X.L. Liang, X.X. Dai and P. Wang 3208

**Real-Time Dynamic Simulation System for Tunnel Construction Based on OpenGL**
Q. Li 3215

**Study on Multiple Points Matching in Different Images of Intelligent Building**
Z.L. Lin, E.Z. Dong and P. Ju 3219

**The Soft Soil Foundation Consolidation Numerical Simulation Based on the Model of Modified Cam-Clay**
X.J. Gu, T.Q. Zhou and S. Cheng 3223

**3D Models as Vista Information Management Governance in the Field of Development of Underground Space in Cities**
V. Belyaev 3227

**Using CAD for Selecting Different ACS Engineering Systems of Buildings and Structures in the Presence of Interference and Restrictions**
A. Volkov, A. Sedov, P. Chelyshkov and A. Doroshenko 3231

**The Integration of BIM and the Reinforcement Information Expressions**
C. Shen and D.H. Li 3234

# CHAPTER 1:

# Geotechnical Engineering

*Applied Mechanics and Materials Vols. 580-583 (2014) pp 3-8*
*© (2014) Trans Tech Publications, Switzerland*
*doi:10.4028/www.scientific.net/AMM.580-583.3*

# 3D Finite Element Analysison Behaviour of Piled Raft Foundations

Anhtuan Vu[1,2,a], Ducphong Pham[1,3,b], Tuonglai Nguyen[1,c], Yu He[3,d]

[1]Instituteof Techniques for Special Engineering, Le Quy Don Technical University, Hanoi, Vietnam

[2]Graduate School of Natural Science and Technology, Kanazawa University, Kanazawa, Japan

[3] School of Civil Engineering, Southwest Jiaotong University, Chengdu, China

[a]vuanhtuan@mta.edu.vn, [b]ducphong357@gmail.com, [c]lainthn@gmail.com, [d]352866785@qq.com

**Keywords:**Piled raft, Settlement, Plaxis 3D Foundation

**Abstract.**This paper highlights settlement behaviour of piled raft foundation by 3D finite element analysis through Plaxis 3D Foundation program. The effects of pile number, pile length, pile layout and pile spacing on the behaviour of piled raft foundation were studied.The numerical results show that:Piled raft foundation has much more efficency to reduce settlement than that of traditional raft foundation. The value of vertical defomation decreases as the result of the increase of pile number, pile length, pile spacing and vice versa. Pile layout has significant effect on both value and location of maximum settlement of piled raft foundation.

## Introduction

In the recent years, piled raft foundation (PRF) has been more and more popularly applied to increase load capacity and reduce settlement in a very economic way comparing with traditional foundation concepts. Many researchs on piled raft foundation engineering have been published, such asBaziar et al. [1], Poulos et al. [2], Poulos[7], Randolph[8], Poulos and Davis [9]. Analysis methods related to PRFwere presented in[3-6].

This study concentrates on the effect of engineering factors related to pile in raft foundation such as number of pile, pile length, pile layout and pile spacing on the behaviour of the piled raft foundation; analysis is carried out by 3D finite element method via Plaxis 3D Foundation software.

## Finite Element Modelling

Among different numerical modeling approaches, finite element technique is popular in recent years in the field of foundation engineering. To date, a variety of finite element computer programs have been developed with a number of useful facilities and to suit different requirements. The analysis method in this study refers to three dimensional finite element methods (FEM)[10] via Plaxis 3D Foundation software. In the analysis, raft and piles are in elastic state. The nonlinear behavior of soil has been modeled with elastic idealplastic constitutive model with a Mohr Coulomb yield criterion.

The finite element mesh can be generated automatically after the full geometry model has been defined and all the components have their initial properties. The elements used for meshing of subsoil are 15-node wedge elements.

## Numerical examples and parametric studies

A 8x8x1m piled raft with massive circular piles which have diameter of 0.4m and length of 10m is used as numerical example for parametric studies. Foundation is subjected to a 100KN/m$^2$ uniformly distributed load. The displacement due to effect of selfweight was ignored.The model was extended in both horizontal directions to a width of 16m to advoid any influence of the outer boundary. Number of pileswas varied to investigate the effect on the settlement of foundation with different layout such as: raft foundation without piles, raft foundation with various pile layouts from one to nine piles.This raft was also used to consider the influence of the pile length and the pile layout.Horizonal dimensions of the raft were changed according to the change of pile spacing

butthe dimension between the border pile row and the raft edge of 2D (D is pile's diameter) was kept remain.

The surveyed ground includes 2 layers with the thickness of layers are 5m and 18m respectively. Soil properties and material model are shown in the

Table 1. Pile and raft are concrete with the behaviour of linear elastic and Young modulus of $2.9*10^7 kN/m^2$.

Table 1. Soil properties

| Properties | Layer 1 | Layer 2 |
|---|---|---|
| Depth (m) | 0-5 | 5-23 |
| Unit weight ($kN/m^3$) | 16 | 17 |
| Material model | Mohr Coulomb | Mohr Coulomb |
| Cohesivec ($kN/m^2$) | 10 | 5 |
| Internal friction angle (degree) | 15 | 25 |
| Deformation modulus ($kN/m^2$) | 4500 | $2*10^4$ |
| Poisson's ratio | 0.3 | 0.2 |

### *3.1. Effect of number of piles*

Apiled raft foundation 8x8x1m, which has variablenumber of piles was loaded with a uniformly distributed force of $100kN/m^2$. The results of settlement of the foundation in cases of raft only, raft with single pile, raft with 3 piles, raft with 5 piles and raft with 9 piles were illustrated in Fig. 1(a-e) respectively.

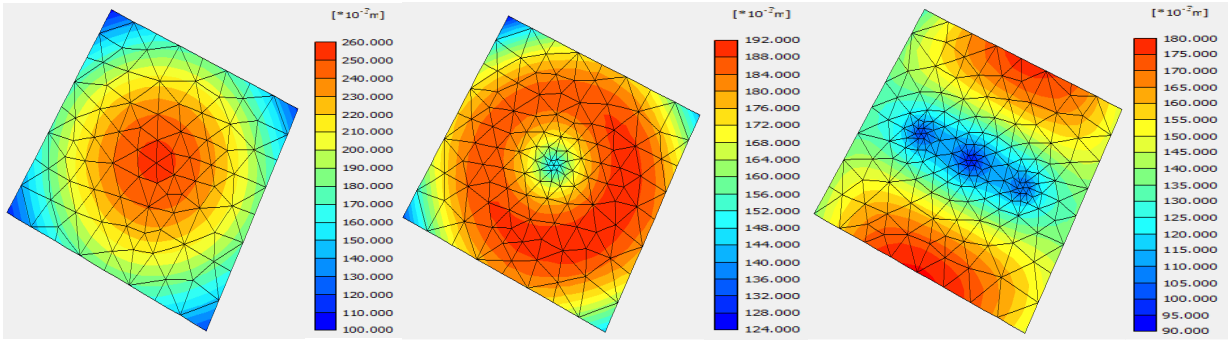


a) Raft without piles $U_{max}= 252.55*10^{-3}m$

b) Raft with 1 pile $U_{max}= 190.78*10^{-3}m$

c) Raft with3 pile $U_{max}= 176,41*10^{-3}m$

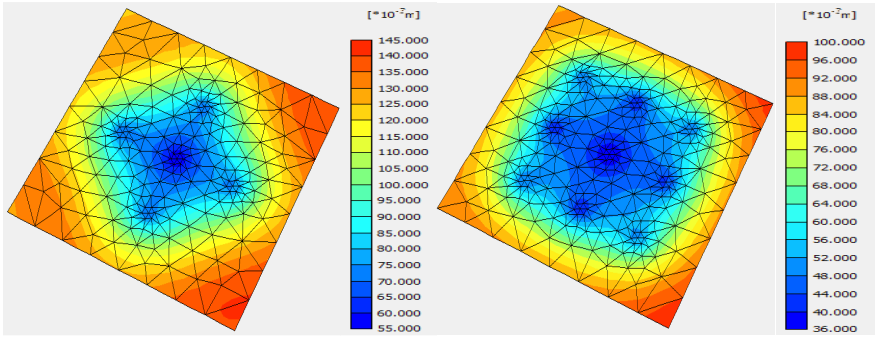


d) Raft with 5 piles $U_{max}= 140.44*10^{-3}m$

e) Raft with 9 piles $U_{max}= 98.15*10^{-3}m$

Fig. 1Settlement of the raft with different number of piles

Fig. 2 and Fig. 3show the load-settlement curves at center of the raft and at midle point of the raft edge.

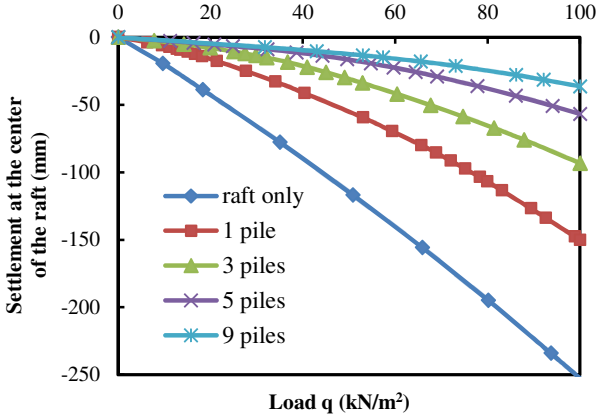


Fig. 2 Load-settlement curve at the centre of the raft

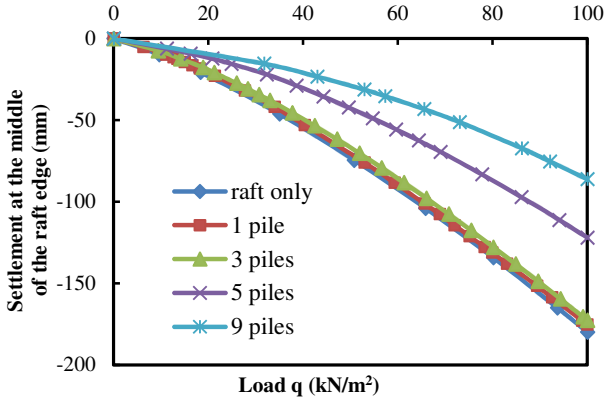


Fig. 3 Load-settlement curve at the middle of the raft edge

The numerical results show that: piled raft foundation is more efficient than traditional raft foundation in reducing settlement. The increase of pile number results in the decrease of global and diffirential settlement and vice versa.

### *3.2. Effect of pile length*

A piled raft foundation 6x6x1m, which was reinforced by 9 piles with diameter of 0.4m,was loaded with a uniformly distributed force of 100kN/m$^2$. The pile spacing was S=5D=2m. The distance from border pile row to the raft edge was 2.5D=1m. The Fig. 4(a-d) show the results of the foundation settlement in cases thatthe length of piles were 6m, 8m, 10m and 12m respectively.

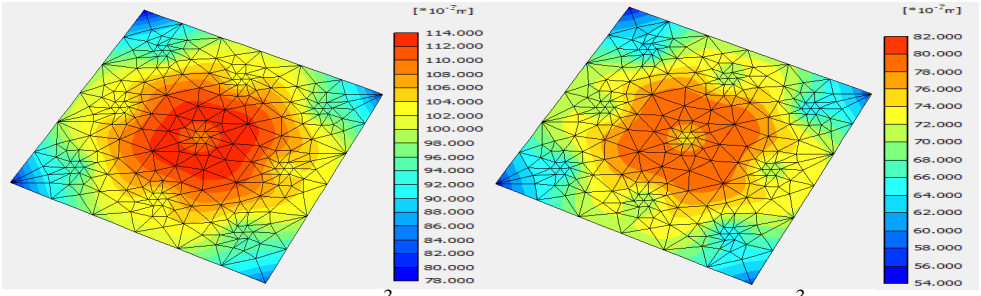

a) $L_p$ = 6m, $U_{max}$ = 113.2*10$^{-3}$mb) $L_p$ = 8m, $U_{max}$ = 80.03*10$^{-3}$m

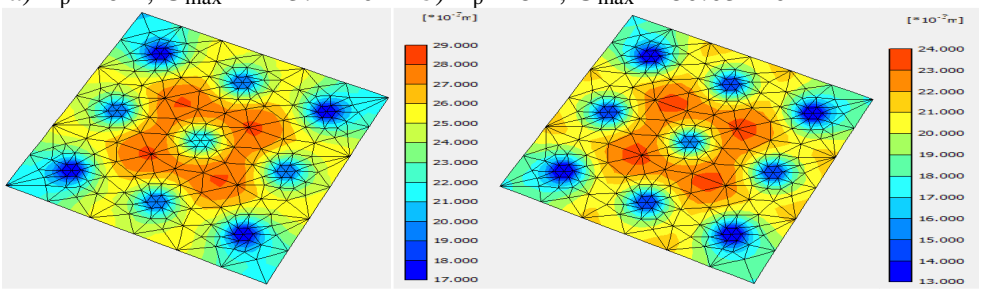

c) $L_p$ = 10m, $U_{max}$ = 28.26*10$^{-3}$md) $L_p$ = 12m, $U_{max}$ = 23.38*10$^{-3}$m

Fig. 4Settlement of the raft with different piles length, number of piles are 9

Numerical results show that the vertical displacement declined due to the growth of pile length. However, the efficency in the settlement decrease is not the same in cases of different pile length increases. The maximum settlement was reduced by 33.17*10$^{-3}$m from 113.2*10$^{-3}$m to 80.03*10$^{-3}$m, approximate 29.3% when the pile length varied from 6m to 8m. The maximum settlement was reduced significantly by 51.77*10$^{-3}$m from 80.03*10$^{-3}$m to 28.26*10$^{-3}$m, approximate 64.7% when the pile length varied from 8m to 10m. Meanwhile, the maximum settlement unnoticealely

decreased only by 4.88*10$^{-3}$m from 28.26*10$^{-3}$m to 23.38*10$^{-3}$m, approximate 17.3% when the pile length increase from 10m to 12m.

### *3.3. Effect of pile layout*

Both the location and the value of the maximum settlement was highly infuenced by the pile layout.Fig. 5(a-c)express the different results on the settlement when the raft was embeded with the same 9 piles but different layout.Fig. 5a and b (pile spacing was 5D and 8D respectively) illustrate the similar value around 98*10$^{-3}$mbut different location of maximum settlement to each other. Meanwhile, the maximum settlement in Fig. 5c (pile spacing S=2D and piles concentrated to the center of the raft) was 154.30*10$^{-3}$m which was much bigger than those in the previous cases. TheFig. 5d shows the settlement of the raft which was embeded with 5 piles. As can be seen that this value was smaller than the value in Fig. 5c although there were more piles in Fig. 5c (9 piles) comparing toFig. 5d (only 5 piles).

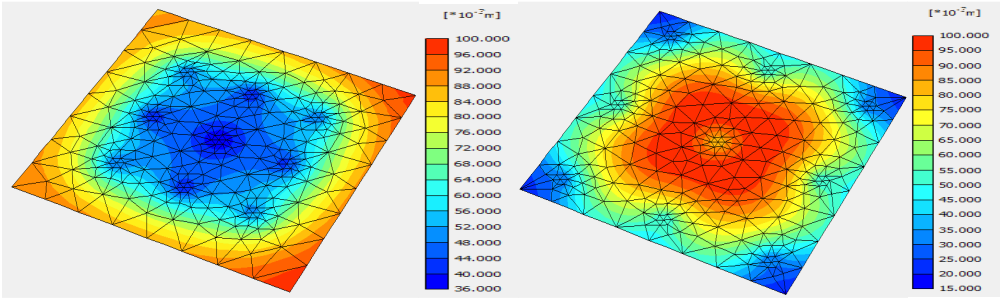


a) Raft with 9 piles, S=5D, $D_b$=2mb) Raft with 9 piles, S=8D, $D_b$=0.8m

$U_{max}$ = 98.15*10$^{-3}$m $U_{max}$ = 98.83*10$^{-3}$m.

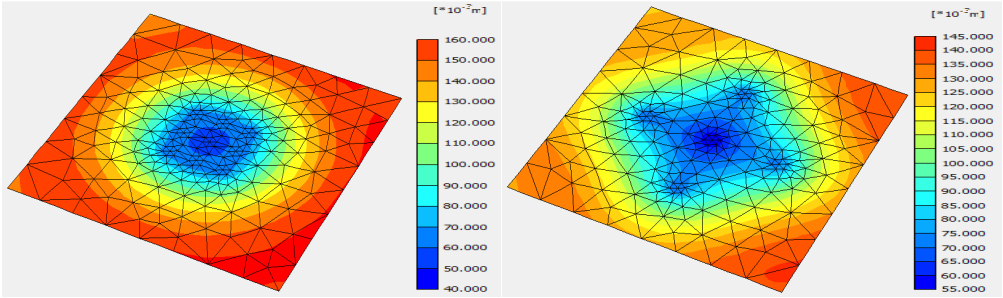


c) Raft with 9 piles, S=2D, $D_b$=3.2md) Raft with 5 piles, S=5D, $D_b$=2m

$U_{max}$ = 154.30*10$^{-3}$m $U_{max}$ = 140.34*10$^{-3}$m.

Fig. 5 Effect of pile'slayout on the maximum settlement of the foundation

### *3.4. Effect of pile spacing*

Effect of pile spacing was studied by using 9-pile-rafts, which had varied pile spacing as 2D, 4D, 6D and 8D and unchanged dimention from border pile row to the raft edge of 2D.The results shown in Fig. 6illustrate that the settlement will increase due to the growth of pile spacing and vice versa. However the effect of increase of pile spacing on the settlement was not unchanged. The maximum vertical displacement grew up only by 5.64*10$^{-3}$m (about 53%) when the spacing increased from 2D to 4D. Meanwhile, when the spacing increased from 4D to 6D and from 6D to 8D, the maximum settlements experienced the growths from 16.26*10$^{-3}$m to 42.37*10$^{-3}$m (increase about 160%) and from 42.37*10$^{-3}$m to 98.83*10$^{-3}$m (increase about 133%).

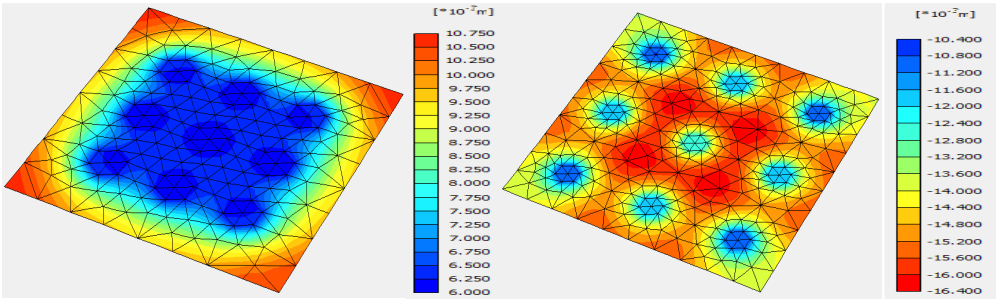


a) Pile spacing S=2D
$U_{max} = 10.62*10^{-3}$m

b) Pile spacing S=4D
$U_{max} = 16.26*10^{-3}$m

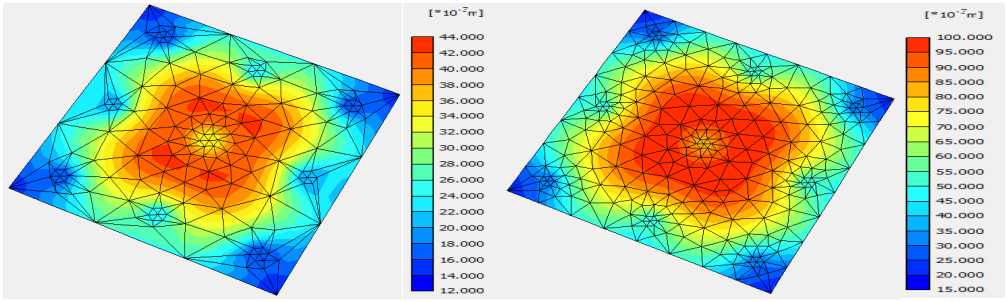


c) Pile spacing S=6D
$U_{max} = 42.37*10^{-3}$m

d) Pile spacing S=8D
$U_{max} = 98.83*10^{-3}$m

Fig. 6 Effect pile spacing on the settlement of the foundation

## Conclusion

The numerical results reveal the following conclusions:

(1) The settlement behaviour of piled raft foundation was depended on several factors such as number of piles, pile length, pile layout and pile spacing.

(2) The increase of pile number will lead to the decrease of both global and differential settlement.

(3) The settlement of the foundation will be reduced due to the growth of pile length and vice versa.

(4) The layout of piles have significant effect on not only the value but also the location of maximum settlement.

(5) The settlement behaviour of pile raft foundation is also affected by pile spacing, an increase of pile spacing will lead to an increase of settlement and vice versa.

## References

[1] M.H. Baziar, A. Ghorbani, R. Katzenbach: Small-scale model test and three-dimensional analysis of pileraft foundation on medium-dense sand, International Journal of Civil Engineering, 2009,Vol. 7(3), pp. 170-175.

[2] H.G. Poulos, J.C.Small and H.Chow: Piled raft foundation for tall buildings, Geotechnical Engineering Journal of the SEAGS & AGSSEA, 2011, Vol. 42(2), pp.78-84.

[3] C.J. Lee, M.D. Bolton, A.Al-Tabbaa:Numerical modelling of group effects on the distribution of dragloads in pile foundations, Geotechniques, 2002, Vol. 52(5), pp. 325- 335

[4] Pastsakorn Kitiyodom, Tatsunori Matsumoto and Ryuuichi Sonoda: Approximate numerical analysis ofa large piled raft foundation, Soils and Foundations, Japan, 2011, Vol.51(1), pp.1-10.

[5] G. Beer, J.R. Booker, J.P. Carter, eds: Computer Methods and Advances in Geomechanics, A.A. Balkema, Rotterdam, The Netherlands, 1991, Vol. 2, pp. 183-191.

[6] H.G. Poulos: An approximate numerical analysis of pile-raft interaction, International Journal of Numerical and Analytical Methods in Geomechanics, 1994, Vol. 18(2), pp. 73-92.

[7] H.G.Poulos: Piled raft foundations - Design and applications, Geotechnique, 2001, Vol. 51(2), pp. 95-113.

[8] M.F. Randolph (1983). Design of piled raft foundations. CUED/D, CambridgeUniversity, U.K, 1983, Vol. 143, pp. 1-22.
[9] H.G.Poulos and E.H. Davis: The settlement behaviour of single axially-loaded incompressible piles and piers, Geotechnique, 1968, Vol. 18(3), pp. 351–371.
[10] L.J. Novak, L.C. Reese, S.T. Wang: Analysis of piled-raft foundations with 3D finite-element method, Proceedings of the 2005 Structures Congress, New York, Structural Engineering Institute of ASCE, (2005), pp. 1-12.

*Applied Mechanics and Materials Vols. 580-583 (2014) pp 9-16*
*© (2014) Trans Tech Publications, Switzerland*
*doi:10.4028/www.scientific.net/AMM.580-583.9*

# A modified method to fit probability distributions of geotechnical parameters using stochastic weighted entropy principle

ZHANG Shu-jun[1,2,a], XU Zhi-jun[3,b], ZHONG Luo[1,c], Xiao Zhaoran[3,d]

[1]Wuhan University of Technology, School of Civil Engineering and Architecture, Wuhan 430070, China

[2]Nanyang University of Technology, School of Civil Engineering, Nanyang 473004,China

[3]School of Civil Engineering and Architecture, Henan University of Technology, Zhengzhou 450001, China

[a]s-j-z668@163.com, [b]zj.xu_hust@qq.com, [c]zl@whut.edu.cn, [d]cexzr@163.com

**Key words:** geotechnical parameter; entropy principle; small samples; stochastic weighted; probability distribution

**Abstract.** Due to various uncertainties, most of geotechnical parameters are small samples, which causes much trouble when the probability distribution of geotechnical parameter is fitted using traditional distributions. This paper uses stochastic weighted method to improve the small samples of Geotechnical parameters into big samples, thus solving the problems caused by the small samples. Meanwhile, the probability density function of geotechnical parameter is derived based on maximum entropy principle, the advantage of presented method is verified through Kolmogorov-Smirnov Test. Case study shows that the proposed method not only overcomes the dependence of conventional fitting methods on classical probability distributions, but also the fitting more close to the fact because the data come from the big sample improved by geotechnical parameters, which has important engineering significance.

## Introduction

It is well accepted that uncertainties in geotechnical engineering design are unavoidable and numerous practical advantages are realizable if uncertainties and associated risks can be quantified[1]. The values of soil properties used in geotechnical engineering and geomechanics involve a significant level of uncertainty arising from several sources such as: inherent stochastic heterogeneity (also referred to as spatial variability), measurement errors, statistical errors (due to small sample sizes), and uncertainty in transforming the index soil properties obtained from soil tests into desired geomechanical properties[2].

The reliance on the observational method is an implicit recognition of this critical aspect. There is a growing awareness that explicit recognition and treatment of uncertainties can serve to supplement traditional risk reduction methods such as the observational method. Deng presented a distribution-free algorithm by combing maximum entropy with sample moments for estimating probability curves directly from experimental or field sample data of rock stochastic variables. Zheng[3] study Each stochastic variable influencing on the reliability of the vertical bearing capacity for pile in the dimensionless limit state equation, and use the maximum entropy principle to transform iterative calculation of reliability index into a maximum entropy density function calculation.

Based on the principle of information spread, Gong[4] proposed normal information spread estimation method(NISEM) to generate probability density functions ogeotechnical parameters with small samples. Zhou[5] employed the polynomial approximation based on stochastic weighted method to generate probability density functions of geotechnical parameters with small samples, and used stochastic weighted method to resample from the present samples so as to get the origin moment of the total. Zhang[6], Kwak[7], Li[8] and Dithinde[9] used normal distribution and log-normal distribution to fit the bias factor of axial capacity for piles aiming to analysis reliability influenced by various uncertainties.

Currently, Maximum entropy(Maxent) principle has been increasingly used to calculate the probability distribution. Jaynes[9] presented the maximum entropy(Maxent) principle as a rational approach for choosing the most unbiased probability distribution, amongst all possible distributions. When only moment constraints are considered, Phillips[10] introduced the use of the maximum entropy(Maxent) method for modeling species geographic distributions with presence-only data. Hyon[11] employed the maximum entropy principle for finite extensible nonlinear elasticity(FENE) model to obtain the solution which maximizes the entropy of FENE model in stationary situations. Zhao[12] proposed the fuzziness of the damage process to be given full consideration when to analyze the reliability of vertical capacity of pile under the condition of the model subjected to vertical load of pile using the principle of maximum entropy(MaxEnt). Banavar[13] presented an application of the principle of maximum entropy(MaxEnt) to understanding species diversity in ecology and introduce a new statistical ensemble corresponding to the distribution of a variable population of individuals into a set of species not defined a priori. The deficiency of above studies is dependent on classical probability distributions.

This paper uses the stochastic weighted method to improve the small samples of geotechnical parameters into big samples. Meanwhile, the probability density function of geotechnical parameter is derived based on maximum entropy principle. Finally, the validity of presented method is illustrated through case study.

## Stochastic weighted method

Stochastic weighted method proposed by Zheng[14] overcome the deficiencies of Bootstrap method used to deal with confidence interval and estimating error. Currently, stochastic weighted method has been employed to solve the problems caused by small sample of engineering.

Assuming the geotechnical parameters $X=(x_1,x_2,\cdots,x_n)$ as independent and identical distribution, the mean and variance of independent and identical distribution are $\bar{x}$ and $S_X^2$. The mean and variance of total sample for geotechnical parameters are $\mu$ and $\sigma^2$. Therefore, there is a deviation between fact value and statistic characteristics of geotechnical according to statistic principle, which is

$$R_n^{(1)}=\bar{x}-\mu_x, R_n^{(2)}=\frac{n}{n-1}S_x^2-\sigma_x^2 \tag{1}$$

Based on stochastic weighted method, establishing the weighted statistic of deviation $R_n^{(1)}$ and $R_n^{(2)}$ as

$$\left.\begin{aligned} D_n^{(1)} &= \sum_{i=1}^{n} V_i x_i - \bar{x} \\ D_n^{(2)} &= \frac{n}{n-1}\sum_{i=1}^{n} V_i (x_i - \bar{x})^2 - \frac{n}{n-1} S_x^2 \end{aligned}\right\} \tag{2}$$

where $(v_1, v_2, \cdots, v_n)$ is Dirichlt variables obeying $\mathrm{D}(1,1,\cdots,1)$.

According to Eq.(1) and Eq.(2), the following equation can be obtained

$$E[D_n^{(1)}] = E[R_n^{(1)}], \quad E[D_n^{(2)}] = E[R_n^{(2)}] \tag{3}$$

Based on Eq.(3), the statistic characteristics of $\mathrm{D}_n^{(1)}$ and $\mathrm{D}_n^{(2)}$ can approximately replace statistic characteristics of $R_n^{(1)}$ and $R_n^{(2)}$, respectively. Consequently, according to Eq.(1), Eq.(4) can be written as

$$\mu_x = \bar{x} - R_n^{(1)}, \quad \sigma^2 = \frac{n}{n-1} S_x^2 - R_n^{(2)} \tag{4}$$

Substitution of Eq.(2) into Eq.(4) and subsequent equation leads to the following solution:

$$\left.\begin{aligned} \hat{\mu}_x &= 2\bar{x} - \sum_{i=1}^{n} V_i x_i \\ \hat{\sigma}_x^2 &= 2\frac{n}{n-1} S_x^2 - \sum_{i=1}^{n} V_i (x_i - \bar{x})^2 \end{aligned}\right\} \tag{5}$$

where $\hat{\mu}_x$ and $\hat{\sigma}_x$ are the estimated values of the mean $\mu$ and the variance $\sigma^2$.

**Maximum entropy principle and computational process**

How to ensure which result occurs is the main characteristic of a stochastic test, it is an important problem because the uncertainties caused by a stochastic test can be quantitatively analyzed if the results are available. Zheng[3] defined a measure of uncertainty, referred to as entropy, similar to that used in thermodynamics and statistical mechanics to solve above problem. For a continuous stochastic variance *x*, the entropy can be expressed as

$$H[f(x)] = -\int_R f(x) \ln f(x) dx \tag{6}$$

where $f(x)$ is the probability density function of $x$; $R$ is the domain of $x$; $H[f(x)]$ is the information entropy of $x$.

Based on probability statistics theory, the main probabilistic characteristics of stochastic variables can be described using first four moments. Accordingly, the probability density function should satisfy the following conditions

$$\left.\begin{aligned} & f(x) \geq 0 \\ & \int_R x^i f(x) dx = \mu_i \quad i = 0,1,2,3,4 \end{aligned}\right\} \tag{7}$$

Information entropy is a parameter to measure system information, and the less degree of system uncertainty is, the less entropy is, but system can offer more information; In contrast, larger entropy can be obtained when the degree of system uncertainty becomes larger, and then less information from system is available. Therefore, if the entropy of a distribution subjected to a set of constraints reaches the maximum value, then the information of this distribution is most objective, and the model of this distribution can be formulized as[3]

$$\text{Max.} \quad H = -\int_R f(x)\ln f(x)dx \tag{8}$$

Eq.(8) is a optimization model containing constraint conditions, which can be solved using variation method. Dividing the domain $R$ into $2n$ equal segments described in Fig.(1), and the step length is $h$, hence $x_i = ih$. Therefore, Eq.(7) and Eq.(8) can be transform as

$$\int_{-n}^{n} a_i f(ih)dx = \mu_i \quad i = 0,1,2,3,4 \tag{9}$$

$$H = -\sum_{i=-n}^{n} hf(ih)\ln f(ih) \tag{10}$$

where

$$\begin{cases} a_0 = h;\ a_1 = ih^2;\ a_2 = (i^2 + 0.083)h^3; \\ a_3 = (i^3 + 0.25i)h^4; a_3 = (i^4 + 0.125i^2 + 0.0125)h^5 \end{cases} \tag{11}$$

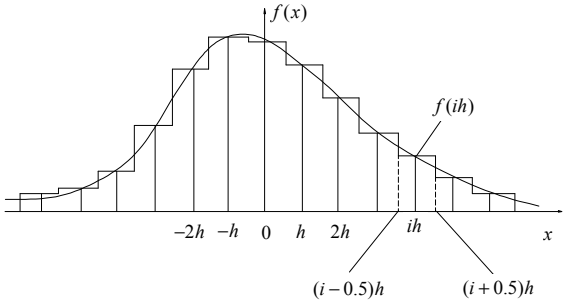


**Fig 1. The diagrammatic sketch of the defining field of stochastic variable** $x$

Based on lagrange multiplier $\lambda_0, \lambda_1, \lambda_2, \lambda_3, \lambda_4$, Establishing Lagrangian function as

$$L = \sum_{i=-n}^{n} [f(ih)(-\ln f(ih) + \sum_{j=0}^{4} a_j \lambda_j) \tag{12}$$

According to Fermat's theorem and $\frac{\partial L}{\partial f(ih)} = 0$, Eq.(13) can be obtained

$$f(ih) = \exp(-1 + \sum_{j=1}^{5} a_j \lambda_j) \tag{13}$$

$f(ih)$ is a function including five variables according to Eq.(11) and Eq.(13). Substitution of Eq.(13) into Eq.(9) and subsequent equation leads to a nonlinear equations including five variables $\boldsymbol{\lambda} = \lambda_0, \lambda_1, \lambda_2, \lambda_3, \lambda_4$ as

$$F(\boldsymbol{\lambda}) = 0 \tag{14}$$

Newton iteration method is a good method to solve the nonlinear equations, which is employed the nonlinear equation as Eq.(14), and the computation is come true using MANLAB programming language.

**Computation step of stochastic weighted entropy**

In engineering practice, geotechnical parameter samples are mostly small samples due to various uncertainties arising from the variability exhibited by properties of geotechnical materials from one location to the other, even within nominally homogeneous profiles. The geotechnical parameters $x_0, x_1, \cdots, x_n$ is from total distribution. Based stochastic weighed entropy, the probability density function of geotechnical parameters can be obtained using following steps.

Firstly, the data from engineering are arranged as the observed sample $X = (x_0, x_1, \cdots, x_n)$, thus the observed sample is a small sample.

Secondly, the small sample $X = (x_0, x_1, \cdots, x_n)$ of geotechnical parameters is improved into big samples, thus solving the problems caused by the small samples $\widehat{X_i} = \sum_{i=1}^{N} v_i x_i$. To improve the computational accuracy, weighted times should be as many as possible.

Thirdly, The subsample of geotechnical parameter is given through *N*-times simulations using Monte Carlo simulation method.

Fourthly, the first four moments of probability density function for geotechnical parameters is computed using subsample.

Fifthly, the entropy density function of geotechnical parameters is calculated using maximum entropy principle.

**Case study**

Dithinde[9] presents four load test databases from South Africa for driven piles in noncohesive soils (29 tests), bored piles in noncohesive soils (33 tests), driven piles in cohesive soils (59 tests), and bored piles in cohesive soils (53 tests). Xu[15] used a method for data processing and optimization in geotechnical engineering to optimize above data, and good data are obtained in table 1 and table 2. In table 1 and table 2, $\lambda_R$ is the ratio of measured value and calculated value of capacity for piles.

Based on classical probability distributions, the statistical parameters and types of distributions optimal probability distribution are shown in table 3.

**Tab.1 Good data of $\lambda_R$ for driven piles**

| Case number | $\lambda_R$ | Case number | $\lambda_R$ |
|---|---|---|---|
| 1 | 0.93 | 6 | 0.96 |
| 2 | 0.95 | 7 | 1.21 |
| 3 | 0.85 | 8 | 1.10 |
| 4 | 1.13 | 9 | 1.00 |
| 5 | 1.33 | 10 | 1.05 |

**Tab.2 Good data of $\lambda_R$ for bored piles**

| Case number | $\lambda_R$ | Case number | $\lambda_R$ |
|---|---|---|---|
| 1 | 1.04 | 11 | 1.03 |
| 2 | 1.22 | 12 | 0.80 |
| 3 | 1.11 | 13 | 1.02 |
| 4 | 0.97 | 14 | 0.79 |
| 5 | 1.13 | 15 | 0.97 |
| 6 | 1.15 | 16 | 1.27 |
| 7 | 0.93 | 17 | 0.99 |
| 8 | 1.02 | 18 | 0.78 |
| 9 | 0.83 | 19 | 0.86 |
| 10 | 0.97 | 20 | 0.90 |

**Table 3 Statistical parameters and probabilistic distributions of parameters**

| Types of piles | Statistical parameters | Types of distribution |
|---|---|---|
| driven piles | $\mu = 1.275, \sigma = 0.198$ | Normal distribution |
| bored piles | $\alpha = 1.81, \beta = 2.15$ | $\beta$ distribution |

Testing sample is weighted by 100-times using the proposed method, then employing maximum entropy principle to fit the probability distribution of weighted sample, the entropy density function $f(x)$ of $\lambda_R$ can be obtained. Fig.2 and Fig.3 shown the comparisons of distribution curves of experimental data for driven piles and bored piles.

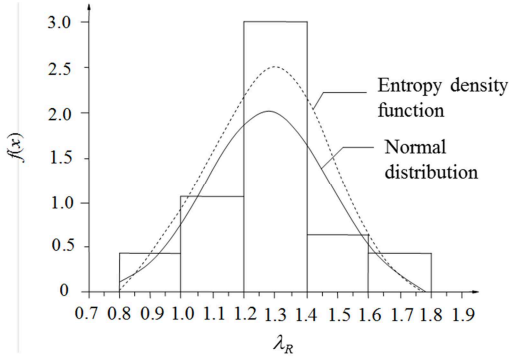


**Fig.2 Comparison of distribution curves of experimental data (driven piles)**

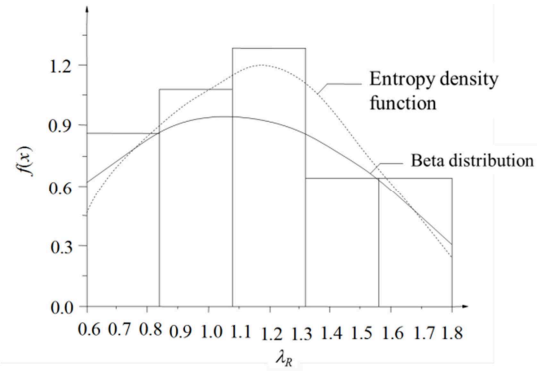


**Fig.3 Comparison of distribution curves of experimental data (bored piles)**

From Fig.(2) and Fig.(3), the proposed method has an advantage that its fitting is more accuracy than classical probability distribution.

In order to further test the valid of the proposed method, K-S(Kolmogorov-Smirnov) testing method is used to compare with the two methods. Assuming the empirical distribution and total distribution are $F_n(x)$ and $F(x)$, respectively. The maximum difference between $F_n(x)$ and $F(x)$ is $D_n$ which can be written as

$$D_n = \max |F_n(x_i) - F(x_i)| \quad i = 1, 2, \cdots, n \tag{15}$$

Assuming the testing level and critical value are $\alpha = 0.05$ and $D_{n,\alpha}$, respectively. According to K-S(Kolmogorov-Smirnov) testing method, the probability distribution of geotechnical parameters accept the distribution of $F(x)$ if the statistic value $D_n$ is not less than critical value $D_{n,\alpha}$.

On the condition that the testing level is $\alpha = 0.05$, the probability distribution of geotechnical parameters may accept several types of probability distributions. Accordingly, to improve the fitting accuracy, a goodness-of-fit test is employed, and the fitting degree is [16]

$$\varphi = 1 - \frac{D_n}{D_{n,\alpha}} \tag{16}$$

Based on Eq.(16) and K-S(Kolmogorov-Smirnov) testing method, the testing results are shown in table 4. From table 4, the fitting accuracy of proposed method is better than traditional method.

**Table. 4 Results of Kolmogorov-Smirnov testing**

| Types of piles | Significance level $\alpha$ | Critical value $D_{n,\alpha}$ | Traditional method $D_n$ | Proposed method $D_n$ |
|---|---|---|---|---|
| driven piles | 0.05 | 0.25907 | 0.07992 | 0.06965 |
| bored piles | 0.05 | 0.28724 | 0.14131 | 0.06098 |

## Conclusion

Due to soil parameter uncertainty arises from the variability exhibited by properties of geotechnical materials from one location to the other, even within nominally homogeneous profiles, geotechnical parameters samples are mostly small samples. This paper put forward a modified method to fit probability distribution of geotechnical parameters according to stochastic weighted entropy, and the following results can be obtained:

(1) This paper uses the stochastic weighted method to improve the small samples of geotechnical parameters into big samples, thus solving the problems caused by the small samples;

(2) Based on maximum entropy principle and stochastic weighted method, the entropy density function of geotechnical parameters is calculated, which not only assures the convergence, but also successfully eliminates the dependence on classical probabilistic distribution. The calculation results are closer to the fact since the data directly comes from samples;

(3) Whether From the comparisons of histogram and curve fitting, or from the results of K-S(Kolmogorov-Smirnov) testing method, the fitting accuracy of proposed method is better than traditional method.

## Reference

[1] K. K. Phoon. Reliability-based Design in Geotechnical Engineering: Computations and Applications(New York and London: Taylor & Francis, 2008).

[2] M. Dithide, K. K. Phoon, D. M. WET, et al(2010). Characterization of model uncertainty in the static pile design formula. J. Geotech. Geoenviron Eng, 137(1): 70-85.

[3] J. J. Zheng, Z. J. Xu, Y Liu, et al(2010). Reliability analysis for vertical bearing capacity of pile based on the maximum entropy principle. Chinese J. Geotech Eng, 32(11): 1643-1647.

[4] F. Q. Gong, X. B. Li, J. Deng.(2006). Probability Distribution of small of Geotechnical Parameters Using Normal Information Spread Method. Chinese J. Rock Mech. Eng, 25(12): 2559-2564.

[5] J. L. Zhou, C. F. Zhao, T. Qian(2009). Probability distribution of small samples of geotechnical parameters using stochastic weighted method. Low Temperature Architecture Technology, 31(10): 59-61.

[6] L. M. Zhang, D. Q. Li, W. H. Tang(2005). Impact of routine quality assurance on reliability of bored piles. J. Geotech. Geoenviron Eng, 132(5): 622-630.

[7] K. Kwak, K. J. Kim, J. Hub, et al(2010). Reliability-based calibration of resistance factors for static bearing capacity of driven steel pipe piles. Cana. Geotech. J, 47(4): 528-538.

[8] D. Q. Li, L. M. Zhang, W. H. Tang(2005). Reliability evaluation of cross-hole sonic logging for bored pile integrity. J. Geotech. Geoenviron Eng, 131(9):1130-1138.

[9] E. T. Jaynes(1957). Information theory and statistical mechanics. Physic Review, 106(4):620-30.

[10] S. J. Phillip, R. P. Anderson, R. E(2006). Schapire. Maximum entropy modeling of species geographic distributions. Eco Mode, 190(3-4): 231-259.

[11] Y. Hyon, J. A. Carrillo, Q. Du, et al(2008). A maximum entropy principle based closure method for macro-micro models of polymeric meterals. Kinetic. Related Models, 1(2): 1-14.

[12] W. Y. Zhao, Z. J. Xu, J. J. Zheng(2010). Reliability Analysis of vertical bearing capacity of pile using stochastic-fuzzy entropy principle. Sixth International Conference on Natural Computation (ICNC 2010), Yantai, 4198-4193.

[13] J. R. Banayar, A. Maritan, I. Volkov(2010). Applications of the principle of maximum entropy: from physics to ecology. Journal of Physics: Condensed Mater, 22(6):1-13.

[14] Z. G. Zheng(1987). Stochastic weighted method. Journal of Applied Mathematics,10(2): 247-253.

[15] Z. J. Xu(2012). Reliability analysis of bearing capacity and reliability-design optimization of piles. Wuhan: Huazhong University of Science & Technology.

[16] A. H. S Ang, W. H. Tang. Probability Concepts in Engineering: Emphasis on Applications to Civil and Environmental Engineering, 2nd edition(New York: John Wiley & Sons, 2006).

*Applied Mechanics and Materials Vols. 580-583 (2014) pp 17-23*
*© (2014) Trans Tech Publications, Switzerland*
*doi:10.4028/www.scientific.net/AMM.580-583.17*

# A Research on Elastoplastic Theory Based on Full State Function

Zhenhai Wei [1, a], Mengshu Wang [2] and Dingli Zhang [2]

[1]Logistics Academy Beijing 100858, China

[2] Beijing Jiaotong University, Beijing,100044, China

[a]email: wzhai@vip.sina.com

**Keywords:** complex materials; structural materials; full state function; strength theory; constitutive relation.

**Abstract.** The analysis of structural materials, especially the theoretical research, is always a challenge. Starting from the structural characteristics of the material, the theory of full state function about the strength - stiffness - strain that reflects the properties of structural material is established on the basis of the structural state of the material. The full state function is an important method to solve this problem. In order to further analyze the characteristics of the full state function, the full state function, strength theory of the material and the constitutive relation found are first studied. It is found that the full state function can more comprehensively reflect the properties of the structural material. The full state function accommodates the strength theory in the classical elastic-plastic theory. The full constitutive relation of the materials can be derived from the full state function. That is to say, the full state function can unify the strength theory and constitutive relation in the classical theory and can be used for the analysis of the structural materials. The full state function is more than a mere form, because it has explicit physical and mechanical meanings.

## Introduction

In order to describe and solve the structural problems of the materials on the macroscopic scale, literature [1-5] put forward the full state function to describe the properties of the structural materials. The elastic properties of the materials mainly refer to the properties and characteristics of the materials when the morphology of the material remains unchanged. However, the plastic properties of material in the macroscopic sense are the manifestation of the properties of material in the process from one structural state to another. Under a specific structural state, the stress intensity, stiffness and geometric pattern of the material constitute the basic features of the material. In the macroscopic sense, the statistically continuous variations of the material described by the critical strength, stiffness and geometry in all structural states constitute the full state function that reflects the material properties. In the classical elastic-plastic theory, the methods describing the plastic properties are mainly divided into strength theory and constitutive relation. But the classical elastic-plastic theory is only suitable for simple materials without structurality. For materials with strong structurality, the full state function theory works better. This article mainly discusses the mutual influence between the full state function, strength criterion and constitutive relation of the material.

## Conditions for deriving the full state function and its meaning

The full state function theory is based on the basic assumption that the material has structure, which is the cornerstone of this theory. This is essentially different from the classical elastic-plastic theory and falls into the category of mechanical theory for complex materials.

The basic assumptions for the existence of full state function:

(1) Any material has structurality that exists on different scales of the material. The structurality of the material varies with the scale.

(2) The structurality of the material can be described by the model of granular material.

(3) The structural state of the material can be described by the connections between granules and the resulting geometry and constitutive relation in the model of granular material.

(4) Any structural state of the material can be homogenized over a certain area (statistical domain) to obtain the changing values of structural strength, stiffness and geometric pattern under this particular state.

(5) The shift from one structural state to another of the material complies with certain rules [4-5].

The structure of the material will change when influenced by environmental factors, that is, it will shift from one structural state into another. In the granular material model, the structural state is closely related to the granule morphology, granule size distribution, spatial scale and density of granules in space. Of all possible structural state, one structural state cannot shift into another state unless under appropriate conditions. Some structural states can be mutually transformed, but others cannot. The structural states that can be reached are called the attainable structural state. All the attainable structural states form the network of attainable structural states. The values of critical strength, stiffness and geometric variation of structure in all structural states can be fitted into hypersurface equation in the σ-D-ε phase space according to the network of attainable structural states.

$$\Phi\ (\sigma_{ij}^{s}, D_{ijkl}^{e}, \varepsilon_{ij}^{s}) = 0 \tag{1}$$

$\sigma_{ij}^{s}, D_{ijkl}^{e}, \varepsilon_{ij}^{s}$ are corresponding to the critical strength, structural stiffness and the strains of geometric variation between adjacent structures under a specific structural state. This function describes the relation between the critical strength, stiffness and geometric strain under different structural states of the material macroscopically. Thus, it is called the full state function of materials.

For the classical elastic-plastic material which is isotropically continuous, $D^e$ is a constant. Thus equation (1) can be written in the following form:

$$\Phi\ (\sigma_{ij}^{s}, \varepsilon_{ij}^{s}) = 0$$

This, in fact, is the strength criterion of the homogeneous materials, or known as yield function.

**Elastoplastic Theory Based on Full State Function**

According to the definition, full state function reflects the basic performance of materials under a unification framework, so the performance characteristics of materials described by the classical elastoplastic theory can be fully reflected by full state function. Starting with the theory of full state function in this article, the loading condition, flow rule, strength theory and constitutive relation in the classical elastoplastic theory are discussed in the following contents.

**Increments and energy equations in the form of full state function of materials**

According to the form of full state function, its full state potential function is the surface equation in phase space that is determined by modulus of elasticity, critical structural strength and strain tensor.

$$\Phi\ (D_{ijkl}^{e}, \sigma_{ij}^{s}, \varepsilon_{ij}^{p}) = 0$$

It is a hypersurface in phase space σ-D-ε. Its tangent plane equation is solved:

$$\frac{\partial \Phi}{\partial D_{ijkl}^{e}}(D_{ijkl}^{e} - D_{ijkl}^{e0}) + \frac{\partial \Phi}{\partial \sigma_{ij}^{s}}(\sigma_{ij}^{s} - \sigma_{ij}^{s0}) + \frac{\partial \Phi}{\partial \varepsilon_{ij}^{s}}(\varepsilon_{ij}^{p} - \varepsilon_{ij}^{p0}) = 0 \tag{3}$$

Where $D_{ijkl}^{e0}$, $\sigma_{ij}^{s0}$ and $\varepsilon_{ij}^{p0}$ are coordinate values on the surface of the selected point.

Suppose $dD_{ijkl}^{e} = D_{ijkl}^{e} - D_{ijkl}^{e0}$, $d\sigma_{ij}^{s} = \sigma_{ij}^{s} - \sigma_{ij}^{s0}$, $d\varepsilon_{ij}^{p} = \varepsilon_{ij}^{p} - \varepsilon_{ij}^{p0}$ that, an equation in the incremental form can be obtained:

$$\frac{\partial \Phi}{\partial D_{ijkl}^{e}} dD_{ijkl}^{e} + \frac{\partial \Phi}{\partial \sigma_{ij}^{s}} d\sigma_{ij}^{s} + \frac{\partial \Phi}{\partial \varepsilon_{ij}^{s}} d\varepsilon_{ij}^{p} = 0 \tag{4}$$

where *i, j* and *k* are summation subscripts. Where the material structure is considered, the incremental form is used to represent a full constitutive relation of the material.

This full constitutive relation contains the constitutive relation of simple and homogeneous materials in the classical theory in form.

For elastic-perfectly plastic materials, it can be considered that

When $D_{ijkl}^{e} = \text{constant}$, $dD_{ijkl}^{e} = 0$, so equation (4) is converted into

$$\frac{\partial \Phi}{\partial \sigma_{ij}^s} d\sigma_{ij}^s + \frac{\partial \Phi}{\partial \varepsilon_{ij}^s} d\varepsilon_{ij}^p = 0 \tag{5}$$

Given that the total strain of the material is, $d\varepsilon_{ij} = d\varepsilon_{ij}^e + d\varepsilon_{ij}^p = \frac{d\sigma_{kl}^s}{D_{ijkl}^e} + d\varepsilon_{ij}^p$ ,It is substituted into the above equation to obtain $d\varepsilon_{ij}^p = d\varepsilon_{ij} - \frac{d\sigma_{kl}^s}{D_{ijkl}^e}$,

$$\frac{\partial \Phi}{\partial \sigma_{ij}^s} d\sigma_{ij}^s + \frac{\partial \Phi}{\partial \varepsilon_{ij}^s} (d\varepsilon_{ij} - \frac{d\sigma_{kl}^s}{D_{ijkl}^e}) = 0 \tag{6}$$

After sorting,

$$(\frac{\partial \Phi}{\partial \sigma_{ij}^s} D_{ijkl}^e - \frac{\partial \Phi}{\partial \varepsilon_{ij}^p}) d\sigma_{ij}^s = -\frac{\partial \Phi}{\partial \varepsilon_{ij}^p} D_{ijkl}^e d\varepsilon_{kl} \tag{7}$$

In addition, under the incremental form, the increasing amount of energy can be shown by the following equation:

$$\Pi = \sigma_{ij}^s d\varepsilon_{ij}^s + \frac{1}{2} d\varepsilon_{ij}^s d\sigma_{ij}^s \tag{8}$$

Considering plastic deformation, i.e. the structural change of material, must be located on a surface of full state function, so the surface is equivalent to a constraint condition of energy variation. In other words, when stress and strain increments are variables, the range of variation must be constrained by the surface (equation 5). Thus, according to Lagrangian method, there is

$$\Pi = \sigma_{ij}^s d\varepsilon_{ij}^s + \frac{1}{2} d\varepsilon_{ij}^s d\sigma_{ij}^s + \lambda (\frac{\partial \Phi}{\partial \sigma_{ij}^s} d\sigma_{ij}^s + \frac{\partial \Phi}{\partial \varepsilon_{ij}^s} d\varepsilon_{ij}^p) \tag{9}$$

Where $\boldsymbol{\lambda}$ is the constraint constant. This is the energy variation equation when stress and strain increments are variables.

Based on the principle of minimum energy, the stationary point of energy variation can be solved. The following equation is obtained:

$$\frac{\partial \Pi}{\partial (d\varepsilon_{ij}^s)} = \sigma_{ij}^s + \frac{1}{2} d\sigma_{ij}^s + \lambda \frac{\partial \Phi}{\partial \varepsilon_{ij}^s} = 0 \tag{10}$$

$$\frac{\partial \Pi}{\partial (d\sigma_{ij}^s)} = \frac{1}{2} d\varepsilon_{ij}^s + \lambda \frac{\partial \Phi}{\partial \sigma_{ij}^s} = 0 \tag{11}$$

If simultaneous equation is established with equation (5), the expressions of the stress and strain increments of the stationary point can be solved.

**Loading condition under full state function of materials**

When the stress increment is an independent variable, according to the definition of full state function of materials, all components of stress increment will change on the surface of the full state function. This condition can be solved according to equation (10):

$$\lambda = -\frac{\sigma_{ij}^s + \frac{1}{2} d\sigma_{ij}^s}{\frac{\partial \Phi}{\partial \varepsilon_{ij}^s}} = -\frac{\sigma_{kl}^s + \frac{1}{2} d\sigma_{kl}^s}{\frac{\partial \Phi}{\partial \varepsilon_{kl}^s}} \tag{12}$$

This is the loading condition under full state function. From equation (12) it can be seen that the variation of stress increment should meet a certain condition. This condition is related not only to the stress increment, but also to the strength of structural status and derivative of component in the strain direction of the full state function. Moreover, this condition has the stronger constraint than the loading condition in the classical elastoplastic theory. That is because once any component of stress increment is determined, other components are also determined.

**Flow rule under full state function of materials**

Equation (11) is converted into

$$d\varepsilon_{ij}^{s} = -2\lambda \frac{\partial \Phi}{\partial \sigma_{ij}^{s}} \tag{13}$$

If $k = -2\lambda$ , there is $d\varepsilon_{ij}^{s} = k \frac{\partial \Phi}{\partial \sigma_{ij}^{s}}$. This is similar to the flow rule in the classical elastoplastic theory.

Thus, it can be seen that the flow rule is the relationship between strain increment and full state function obtained based on the energy principle, in the concept of full state function, and under the condition that components of the stress increment are variables. Besides, the equation of the stationary point of surface constraint of the full state function is also considered.

**Constitutive relation under full state function of the materials**

According to equation (10),

$$\frac{\partial \Phi}{\partial \varepsilon_{ij}^{s}} = -\frac{\sigma_{ij}^{s} + \frac{1}{2} d\sigma_{ij}^{s}}{\lambda} \tag{14}$$

It is substituted into equation (3) to obtain

$$\frac{\partial \Phi}{\partial \sigma_{ij}^{s}} d\sigma_{ij}^{s} - \frac{1}{\lambda}(\sigma_{ij}^{s} + \frac{1}{2} d\sigma_{ij}^{s}) d\varepsilon_{ij}^{s} = 0 \tag{15}$$

Let $H = (\sigma_{ij}^{s} + \frac{1}{2} d\sigma_{ij}^{s})\, d\varepsilon_{ij}^{s}$ , this is the expression of energy increment. That is

$$\frac{\partial \Phi}{\partial \sigma_{ij}^{s}} d\sigma_{ij}^{s} - \frac{1}{\lambda} H = 0 \tag{16}$$

Moreover, equations (10) and (11) are converted into

$$\begin{cases} \sigma_{ij}^{s} + \frac{1}{2} d\sigma_{ij}^{s} = -\lambda \frac{\partial \Phi}{\partial \varepsilon_{ij}^{s}} \\ d\varepsilon_{ij}^{s} = -2\lambda \frac{\partial \Phi}{\partial \sigma_{ij}^{s}} \end{cases} \tag{17}$$

These equations are multiplied with each other and summation is performed to obtain

$$(\sigma_{ij}^{s} + \frac{1}{2} d\sigma_{ij}^{s}) d\varepsilon_{ij}^{s} = 2\lambda^{2} \frac{\partial \Phi}{\partial \sigma_{ij}^{s}} \frac{\partial \Phi}{\partial \varepsilon_{ij}^{s}} \tag{18}$$

Thus, $H = 2\lambda^{2} \frac{\partial \Phi}{\partial \sigma_{ij}^{s}} \frac{\partial \Phi}{\partial \varepsilon_{ij}^{s}}$ , which is substituted into equation (16) to obtain

$$\frac{\partial \Phi}{\partial \sigma_{ij}^{s}} d\sigma_{ij}^{s} - 2\lambda \frac{\partial \Phi}{\partial \sigma_{ij}^{s}} \frac{\partial \Phi}{\partial \varepsilon_{ij}^{s}} = 0 \tag{19}$$

According to the rule of work hardening in the classical elastoplastic theory, [6] is obtained.

$$A = (-1) \frac{\partial F}{\partial H_{a}} \frac{\partial H_{a}}{\partial \varepsilon_{ij}^{s}} \frac{\partial g}{\partial \sigma_{ij}^{s}} \tag{20}$$

Where $A$ is the parameter of work hardening, and $\boldsymbol{F}$, $\boldsymbol{H_a}$ and $\boldsymbol{g}$ are the plastic potential function, the strain hardening function and the yield function, respectively.

If it is considered that the full state function consists of plastic potential function and yield function, there is

$$A = (-1) \frac{\partial \Phi}{\partial \sigma_{ij}^{s}} \frac{\partial \Phi}{\partial \varepsilon_{ij}^{s}} \tag{21}$$

Thus,

$$\frac{\partial \Phi}{\partial \sigma_{ij}^s} d\sigma_{ij}^s + 2\lambda A = 0 \tag{22}$$

If equation (13) and $d\varepsilon_{ij}^p = d\varepsilon_{ij} - \frac{d\sigma_{kl}^s}{D_{ijkl}^e}$ are considered,

$$d\sigma_{ij}^s = (D_{ijkl}^e - \frac{\frac{\partial \Phi}{\partial \sigma_{ij}^s} D_{ijpq}^e D_{qpkl}^e \frac{\partial \Phi}{\partial \sigma_{kl}^s}}{A + \frac{\partial \Phi}{\partial \sigma_{mn}^s} D_{mnuv}^e \frac{\partial \Phi}{\partial \sigma_{uv}^s}}) d\varepsilon_{ij} \tag{23}$$

In this way, the expression of constitutive relation of a material is obtained. It is similar to that in the classical elastoplastic theory. However, the function reflecting the material performance in this article is the full state function of the materials.

**Stress-strain path with the minimum energy under full state function of materials**

According to the principle of the minimum energy, equations (10) and (11) can be obtained, and simultaneous equations are established with (5):

$$\sigma_{ij}^s + \frac{1}{2} d\sigma_{ij}^s + \lambda \frac{\partial \Phi}{\partial \varepsilon_{ij}^s} = 0, \quad \frac{1}{2} d\varepsilon_{ij}^s + \lambda \frac{\partial \Phi}{\partial \sigma_{ij}^s} = 0, \quad \frac{\partial \Phi}{\partial \sigma_{ij}^s} d\sigma_{ij}^s + \frac{\partial \Phi}{\partial \varepsilon_{ij}^s} d\varepsilon_{ij}^p = 0 \tag{24}$$

By solving,

$$\lambda = -\frac{1}{2} \frac{\frac{\partial \Phi}{\partial \sigma_{ij}^s} \sigma_{ij}^s}{\frac{\partial \Phi}{\partial \sigma_{ij}^s} \frac{\partial \Phi}{\partial \varepsilon_{ij}^s}}, \quad d\sigma_{ij}^s = \frac{\frac{\partial \Phi}{\partial \sigma_{kl}^s} \sigma_{kl}^s}{\frac{\partial \Phi}{\partial \sigma_{mn}^s} \frac{\partial \Phi}{\partial \varepsilon_{mn}^s}} \frac{\partial \Phi}{\partial \varepsilon_{ij}^s} - 2\sigma_{ij}^s, \quad d\varepsilon_{ij}^s = \frac{\frac{\partial \Phi}{\partial \sigma_{kl}^s} \sigma_{kl}^s}{\frac{\partial \Phi}{\partial \sigma_{mn}^s} \frac{\partial \Phi}{\partial \varepsilon_{mn}^s}} \frac{\partial \Phi}{\partial \sigma_{ij}^s} \tag{25}$$

This is the change path of stress-strain in the incremental form under the condition of minimum energy. Starting with the initial point of stress state, which may be under the minimum energy state, the stress-strain changes along the surface of full state function of the material, i.e. the path of changes, form the minimum energy path. The meaning of the minimum energy path is that the material structural change, which is the plastic change macroscopically, has the condition of deformation optimization, and this provides a new solution for some problems (such as plastic working and material creep).

## Discussions on Full State Function and Relevant Issues

The presentation of full state function of materials is to suggest a concrete idea and analytical method for solving the problems of structural materials. Through the above discussion, with full state function as the constraint condition, the principle of minimum energy is adopted to derive nearly all theoretical points and conclusions involved in the classical elastoplastic theory. These mainly include loading condition, flow rule, strength theory and constitutive relation. According to the principle of minimum energy, when the strain increment is a variable, the loading criterion can be obtained based on the equation of stationary point, when the stress increment is a variable, the flow rule will be obtained based on the equation of stationary point; when strain and stress increments are both variables, the constitutive relation is obtained. Therefore, the theoretical method of full state function cannot only help build a new theoretical system for solving the problems of structural materials, but also completely covers the main theoretical points and conclusions in the classical elastoplastic theory.

Loading condition, flow rule, strength theory and constitutive relation in the classical elastoplastic theory are all based on a series of assumptions. The reason is that these assumptions generally consider the homogeneous materials, but neglect the material structures. In other words, the important natures of structural materials are simplified, which make the features of the materials to lose their important inner connections. As a result, the connections between these features have to be rebuilt by relying on certain assumptions. The theory of full state function of materials takes structural materials as the research basis and restores the nature of material plasticity into variation of material structures, which fundamentally reflects the material performance. In this way, the theories of loading condition, flow rule, strength theory and constitutive relation are unified with their methods.

For stress-strain paths of materials, the theory of full state function of materials can provide good explanation and analysis. The surface of full state function of the materials is affected not only by stress state, but also by strain and structural stiffness of the material. Therefore, the stress state does not comprehensively reflect the actual state of the materials, and different stress paths or stress-strain paths are reflected on different points on the surface of full state function. In addition, the stress-strain path with the minimum energy reflects an important feature of materials, i.e. stress and deformation of the materials will occur along this path or around the path to the greatest degree. This provides important guidance for the optimization of material processing and analysis of creep property.

## Conclusion

According to the previous discussion, it can be found that the full state function, strength criterion and constitutive relation of the materials are the function reflecting the properties of the material with structurality. The full state function unifies the strength criterion and constitutive relation in then sense of both form and concept. According to the relationship between they, the following conclusions can be explicitly obtained:

(1) The full state function based on the variation of the structural state of the material is the envelope surface of the strength surface under all structural states.

(2) From the equation of a tangent plane in full state function, the full constitutive relation of the material in the increment form can be derived.

(3) According to the principle of minimum energy, full state function of the materials can be used to derive the main theoretical conclusions in the classical elastoplastic theory, including loading condition, flow rule, strength theory and constitutive relation.

(4) Form the above three conclusions, it can be deduced that the full state function of the materials is the ideal approach to fully describe the performance of the structural materials. Theoretically, it is a method that can unify strength theory, flow rule and constitutive relation, and has beauty in coordination and consistency.

(5) The full state function accommodates the strength theory and constitutive relation with clear physical and mechanical meanings. It represents a complete system.

The derivation of the specific form of the full state function for the material needs to combine with the structure model of the material. At present, this article only preliminarily explores the characteristics, meaning and usage of the full state function of the materials. Many other related problems remain to be studied.

**References**

[1] Wei ZhenHai, Wang MengShu, Zhang DingLi, Study of constitutive relationship model of material structure based on full state function, The 2nd International Conference on Civil Engineering, Architecture and Building Materials (CEABM 2012),2012.5

[2] Wei ZhenHai, Wang MengShu, Zhang DingLi,THE CONSTITUTIVE RELATIONSHIP MODEL OF BASED ON THE FULL STATE FUNCTION, PROCEEDINGS OF THE TWENTY-FIRST NATIONAL CONFERENCE ON STRUCTURAL ENGINEERINGTHE,2012.10

[3] Wei ZhenHai, Wang MengShu, Zhang DingLi, A research on the full state function constitutive relation model, The Second International Symposium on Constitutive Modeling of Geomaterials: Advances and New Applications 2012.10

[4] Wei ZhenHai Research on the Geomaterials Structure[D] Beijing Jiaotong University 2012. In Chinese.

[5] Wei ZhenHai, Wang MengShu, Zhang DingLi, Structure Analysis of Rock and Soil[M]. China WaterPower Press, 2012.12, In Chinese.

[6] Gong XiaoNan, Soil Plasticity[M] ZheJiang University Press 1997.7 P139.

*Applied Mechanics and Materials Vols. 580-583 (2014) pp 24-27*
*© (2014) Trans Tech Publications, Switzerland*
*doi:10.4028/www.scientific.net/AMM.580-583.24*

# Affect of Large Deep Foundation pit dewatering on the Neighboring Buildings

Kewei Ding[1, a],Fan Zhao[2, b],Xiaozhi Zhang[3, c]

[1]School of Civil Engineering, Anhui Jianzhu University, Hefei 230601, PR China

[2]School of Civil Engineering, Anhui Jianzhu University, Hefei 230601, PR China

[3]School of Civil Engineering, Anhui Jianzhu University, Hefei 230601, PR China

[a]dingkw@aiai.edu.cn, [b]634907130@qq.com, [c]847911955@qq.com

**Keywords**:foundation pitdewatering;environmental impact appraisal model ;FLAC$^{3D}$; surface subsidence;

**Abstract:**Take the *ground-water lowering of foundation pit project* in DA Dongmen subway station in Hefei as an example, introduce a kind of environmental impact appraisal model,using softwareFLAC$^{3D}$ to imitate the key index--surface subsidence, offers relevant safe bases to construct security monitoring department.

## Introduction

With the constant development of the urban construction in china, more and more cities start the construction of the subway. Subway Foundation Pit always construct in dense buildings,so we must calculate and control the surface subsidence owing to pit dewatering for the purpose of reduce the influence of groundwater decline before pit construct on neighboring buildings. Especially to the large deep pit with complex hydrogelogical conditions , whose dewatering is a large area project , which influence more, forming precipitation funnel curve to produce additional deformation on structure around and do great damage to surrounding environment.

## 2.Engineering Situation

### 2.1Subject of the station

The station is the transfer of subway line one and line two, total construction area is 34837m$^2$. Station one is four floor three-span undergorund box-type frame structure,station standard is 145.44m long,23.5m wide and 31.7m deep; station two is three floor three-span undergorund box-type frame structure,station standard is 220.5m long,23.5m wide and 24.4m deep; The abnormal joints of the two station is threefloor many-span box-type structure. The most kind of soil thickness of the station is about 4m,the minimum is 1m and the maximum is 5.3m. The enclosure structure adopts the diaphragm wall, cross plate joint,which is 1.2m thickness in station one and 2.0m thickness in station two. All usingcover and excavation top-down method to construct.

### 2.2 Hydrology geological condition in this field

The subway station includes two layers of groundwater---perched water and confined water.Perched water: buried 1.35 ~ 5.50m deep; 10.17m ~ 13.98m elevation. Aquifer include powder quality clay and miscellaneous fill lay.Confined water: buried 1.2 ~ 4.9m deep; 10.77m ~ 14.77m elevation. Aquifer include Powder soil fine sand lay.( Permeability coefficient are 5.8*10$^{-4}$cm/s and 2.3*10$^{-3}$cm/s).

Geological parameter of the station as the following table shows:

**Table.1 Geological parameter**

| Soil layer | Thickness (m) | Density (kg/m3) | Shear modulus (Mpa) | Volume modulus (Mpa) | Permeability coefficient m2/Pa.sec | Poisson ratio |
|---|---|---|---|---|---|---|
| Powder soil | 2 | 1.7 | 4.32 | 7.45 | $2.7*10^{-13}$ | 0.4 |
| Flour sand | 10 | 1.87 | 9.92 | 17.1 | 1.3*10-$^{12}$ | 0.35 |
| Powder quality clay | 14 | 1.77 | 10.83 | 18.6 | $1.0*10^{-15}$ | 0.35 |
| Sandstone | 4 | 1.9 | 11.36 | 19.6 | $1.3*10^{-15}$ | 0.32 |
| Rock | 10 | 2.1 | 20.6 | 35.6 | $2.8*10^{-19}$ | 0.3 |

## 3. Appraise system in environmental impact of precipitation

The dewatering of the large deep pit causes the surface subsidence around, leading to the fact the building around and underground pipeline slope, crack. So, it is a very important job to carry on the analysis of environmental impact as to the precipitation project of the area where the geological condition of hydrology is complicated. There have foundation of counting based gray theory, BP nerve networkmethod, GIS environmental impact method,etc. At present we introduce a environmental evaluation method.

This kind of method is based on a simple, scientific appraisal method of fuzzy mathematics, it considers the inherent environment (Hydrology geological condition of the project) and two pieces of influence of response of the surrounding environment,constructs 8 kinds of evaluation indexes,dispel dimensional difference, carry on standardized treatment, correspond to four think result (excellent, good, medium, and poor) . The evaluation indexes include precipitation patterns,compressibility,hydrological effects ,the water volume of foundation pit lateral wall, boundary load distribution,subsequent life of buildings,foundation form of buildings and the uneven settlement .The Correspondingweight matrix is[0.2376 0.0594 0.0179 0.0950 0.0505 0.1239 0.0659 0.3498]

## 4. The settlement imitate calculating

### 4.1Set up models and net subdivision

For simplified calculation, a longitudinal section which fetches the foundation pit imitates and analyzes, the length of foundationpit is 6m, width 24m, excavate deep 32m, adopts the underground continuous wall as enclosing and protecting structure and concurrently stagnant water curtain when excavated of foundation pit, it is here from the foundation pit to dredge the dry well and fix up. The final size of the model is confirmed as 6m * 180m * 60m cuboid as shown in Fig. 1.

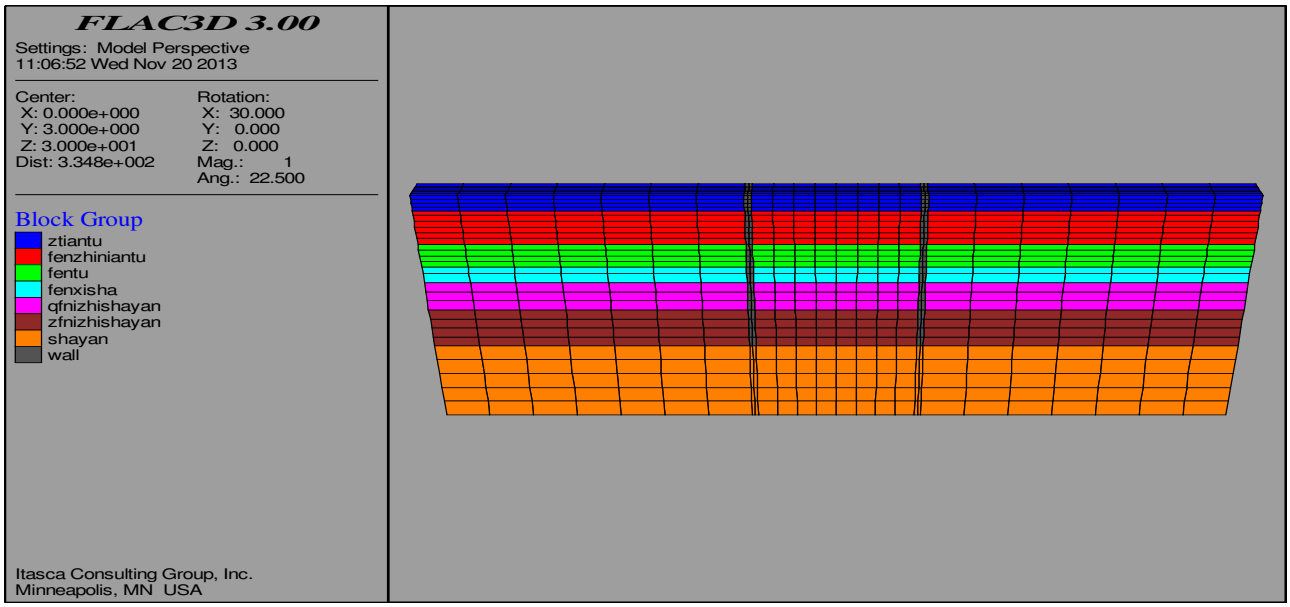


**Fig .1 Calculate models**

### 4.2 Establish the border and initial condition

Set up the horizontal direction to restrain on both sides of the model, exercise restraint in moving horizontally; Above surface freedom border, bottom set up competence and verticality restrain, restrain competence from, move vertically, the bottom of the model is the waterproof border, it is the border of influent to lower the well.

### 4.3 Model calculating andResult of calculation of simulation

We can realize precipitation by establishment of the hole water pressure strength. Divided into two steps specifically: First of all, change hole water pressure model behind the strength, carry on fluid flow calculation of the steady state; Then close the influent mode subsequently, only carry on quiet strength analysis.Then choose the earth's surface, and several point of 60m order as the characteristic of studying from foundation pit 0 - 20 - 40 edge, click these and join to transform into the straight line of the characteristic, characteristic deformation situation of straight line that choose at observing the earth's surface come, describe different water level ground verticality displacement situation lower dark, curve out of shape of straight line of characteristic (subside groove) Paint it in Fig2.

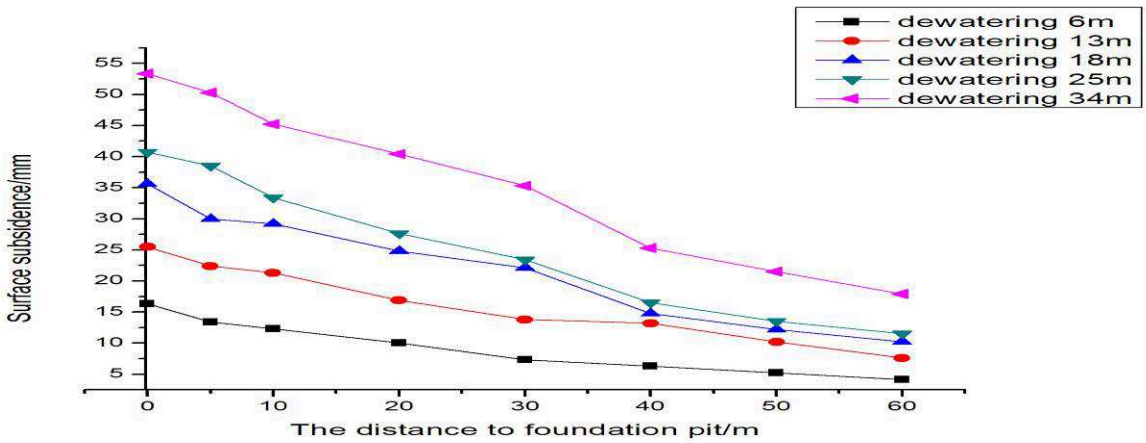


**Fig .2The curve of finite element**

## Conclusion

From the appraisal system of the environmental impact of precipitation,we can know in order to reduce the influence on the environment of precipitation of large area in the large deep foundation pit, we must control the ground and subside and the building does not subside evenly in the coverage of precipitation radius in a situation that geological condition of hydrology and precipitation are designed and has been already made. Take DA Dongmen subway station in Hefei as an example,we must set up the monitoring point in sphere of influence buildings, such as four corners in the building corner, the connects place with new of old building, expansion joint and both sides deep foundation that bury different. Each building assign subside measuring point and tilt measurement points. The address select of cracks observed situation monitoring points combined buildings are arranged on the side of a building near the wall surrounding the crack spacing of 20 ~ 30m uniform layout level observation wells. Site monitoring using the method offollow-up observations timed observation combining. Monitoring frequency can be adjusted according to changes in the size of the monitoring data, monitoring data when there are mutations, monitoring frequency encryption to 2 to 3 times / d.

Through the observation of the water level observation wells in precipitation process,we must ensure that the groundwater level changes between successive walls and buildings within the specified range, kept lowering the water table depth within 1m. By monitoring the building ,we found there is no cracks in the building , meetting regulatory requirements of the maximum settlement building and the maximum tilt , to protect the safety of the building.

## Acknowledgements

This project is supported by Anhui Provincial Laboratory Project Funding through grant No. 1106c0805024.

## References:

[1]Qu Junbiao Li Tao: FLAC$^{3D}$ calculates application in the pit precipitation of the deep foundation[A] Building of Shanxi(2006)

[2]Du Mingyu Ruan Qinsong:Construct and appraise analyzing to the environmental impact around in the deep foundation pit of subway station[A] Railway building(2013)

[3]Wang Jianxiu Wu Lingao:The deep foundation pit precipitation of subway station brings out and subsides the mechanism and computing technology[A]Rock mechanics and project journal(2009)

[4]Zhao Ming Yu Kailin:Appraise system to study in pit precipitation environmental impact of the foundation[A] Construction technology (2011)

[5]Linin LuJianyong: Foundation pit precipitation analyze to peripheral building and qualification on influence of surface subsidence [A] Architecture science(2010)

[6]LouRongxiang ZhouNianqing:The pit precipitation numerical simulation of deep foundation stands in Subway Line No. 11 Xujiahui of Shanghai [A] Underground space and project journal (2011)

[7]Zhang Zhengshuan :The pite precipitation of the foundation causes the crack of building around analysis [A] Project quality (2012)

[8]Wang Wenfeng:To the predict building subside caused by the pit precipitation of thefoundation and give prevention measure[A] Reconnoitre in the railway(2013)

*Applied Mechanics and Materials Vols. 580-583 (2014) pp 28-33*
*© (2014) Trans Tech Publications, Switzerland*
*doi:10.4028/www.scientific.net/AMM.580-583.28*

# Analysis of Monitoring Results of a Deep Foundation Pit with Pile-Anchor Retaining Structure

Xiaohua Yang[a], Fangwu Wu[b], Teng Chen[c], Xing Liu[d]

Schools of Civil Engineering, Hunan University of Technology, Zhuzhou 412007, China

[a]yangsheep@126.com, [b]285206736@qq.com, [c]chengteng1987@126.com, [d]416107079@qq.com

**Keywords:** deep foundation pit; structure monitoring; settlement

**Abstract.** According to characteristics and surrounding environments of a deep foundation pit with pile-anchor retaining structure, a monitoring program was developed. The monitoring focused on horizontal displacements of retaining piles, subsidence of soil surrounding foundation pit and settlements of buildings near foundation pit. The results show that the maximum displacements are in middle position of sides and at corners of foundation pit. The horizontal displacements and settlements of pits are efficiently rejected by anchors. The displacements of buildings near foundation pit are affected by many factors, such as the excavation speed and anchor. The displacement exists characteristics of time and spatial effects. The monitoring results provide a reliable basis for the safety construction and rational organization of construction.

## Introduction

With the rapid developments of city, the spaces are limited more and more. If construction project is in a limited space, had to development to underground. To build a large-scale underground building first needs to carry on excavations and supports of deep foundation pit. In construction process, pressure states of soil inside and outside foundation pit have being changed from static earth pressure to passive or active earth pressure, which lead deformations of soil[1]. In order to ensure safety and quality of foundation pit, it need to timely evaluate the effectiveness of support structure. It is important that real-time monitoring has been built for support structures, surrounding soils and adjacent buildings. Monitoring data can be referred to as "thermometer" for buildings[2]. By analyzing the monitoring data have become one of the main methods to study deep foundation pit[3].

Pile anchor retaining structure consists of pile and prestressed anchor, which widely applied in deep excavation projects. In construction of pile anchor structure, the first work is to do retaining piles and stratified to move soil, and then do prestressed anchors hierarchically from top to bottom in retaining piles. Because retaining piles and prestressed anchors into working states are different and supporting structures to withstand pressures of soil are increasing, the stresses states of retaining piles and anchors have been changed. In this paper, based on the monitoring data, it will be analyzed horizontal displacements at top of supporting piles, ground surface settlements and changes of building displacements near pit to study deformation rules of pile anchor retaining structure and influence rules for surrounding environment.

## Engineering situations

The project is a public service building with 16 floors and a large underground parking which site was hillside with high to southwest and low to northeast. The excavation depth of pit for underground parking is changed with site topography, depth ranges are from 8m to 13m and the maximum depth is in southwest corner. Foundation plane sizes are about 85m in length and 30.9m in width. A 3m high stone masonry bulkhead built by adjacent department is about 4m far from west side of pit, there are two buildings with single storey near southwest corner and a six storey building far from 11m on south side and a road with width of 5m adjacent to east side. The city main road locates in north side which is far away from pit that can not consider the influences of foundation pit. According to

environmental conditions, pile anchor retaining structures are set in west, south and east side. 1 to 4 prestressed anchors are set up respectively in dado piles with the different height of soil retaining. The total length of pile anchor retaining wall is about 145m.

**Engineering geological conditions**

According to geological survey report, the site stratums from top to bottom were plain fill layer, silty clay layer and gravel with clay layer. The natural foundation bearing capacities of each soil layer and representative values of main properties in physical and mechanical are shown in table 1.

Table 1 Physico-mechanical parameters

| Geotechnical layer | State | Characteristic value of foundation bearing capacity [$f_{ak}$/kPa] | Modulus of elasticity [$E_s$/MPa] | Internal friction Angle [$\Phi$/°] | Cohesion [$C$/kPa] |
|---|---|---|---|---|---|
| Plain fill | Losse-slightly dense | 80 | 4.3 | 6.5 | 10.0 |
| Silty clay | Hard plastic | 220 | 7.0 | 17.0 | 22.0 |
| Silty clay | Hard plastic | 230 | 7.1 | 17.0 | 22.5 |
| Silty clay | Waxiness-soft plastic | 120 | 4.8 | 10.0 | 16.0 |
| Gravel with clay | Moderate density | 420 | 20.0 | 30.0 | / |
| Limestone | Slightly weathered | 5000 | | | |

The hydrogeological conditions of site are in moderate. Perched water from domestic water and atmospheric precipitation is filled with in plain fill layer and excreted to low-lying place. The moisture content in silty clay layer is poor which is relatively impermeable layer. The layer of gravel with clay is aquifer and strong permeable layer in which has rich phreatic water. A small amount of bedrock fissure water contains in limestone fissures. The depth of static water level at each hole is between 2.00m to 7.20m.

Plain fill, silty clay and gravel with clay soil represented as special soil. The distribution of plain fill layer is uneven and bearing capacities are low, this layer is not foundation bearing stratum. During foundation pit excavation, slope gradient should be increased in plain fill layer. Silty clay represented as state of hard plastic and soft plastic, buried depth is deeper and partial thickness is larger which brings adverse effects to pile foundations. It should be considered carefully influences in easy deformations if select pile foundation. Layer of gravel sand with clayey soil contain rich water and is a strong permeable layer, pile foundation construction in this layer is difficult. The geological distributions in influence depth of dado pile are shown in Fig.1.

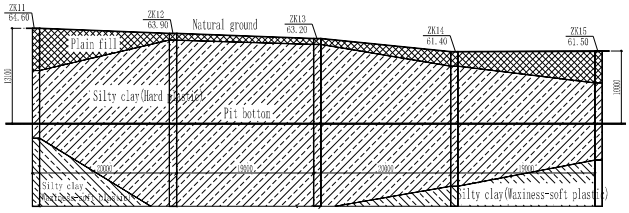


Fig. 1 Geological distribution of retaining pile excavation depth range

**Monitoring schemes of foundation pit**

The stabilities of retaining structure is not only related to safety of projects, but also to protect buildings, roads and pipeline facilities near foundation pit. Therefore, it must be taken the information

management methods to control constructions and effective monitoring for foundation pits. The arrangements of monitoring points for retaining structure should be able to reflect the actual states and change trends and meet the requirements of monitoring. Safety level of this foundation pit is in second stage determined by national standrads[4]. With the requirements[5], monitoring points are arranged at the key feature points of internal forces and deformation in supporting structure. The layout of monitoring points is shown in Fig.2.

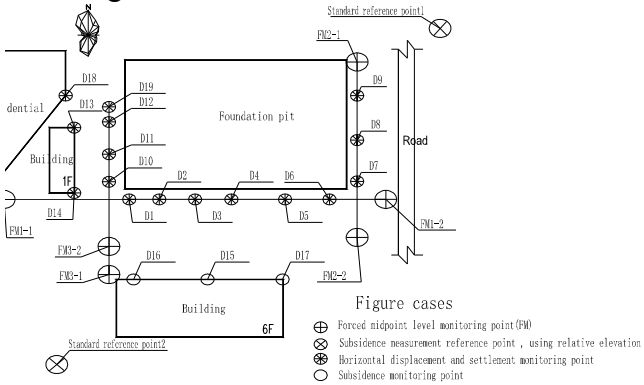


Fig. 2 Schematic drawing of monitoring points arrangement

## Monitoring method

The monitoring instruments and measurement methods are chosen by current national codes[5]. Differential settlements are measured by DSZ2 water levels and DS1 level micrometers and by using micrometer method. Horizontal displacements are observed by DJ2 level optical theodolites and by using collimation line method and small angle measurement method.

The monitoring datum points buried for horizontal displacements are met up with current national codes[6]. The observation piers for forced to center are set up and using precision optical devices for centering detections, the error of centering measure is less than 0.5mm.

## Analysis of monitoring results

There are two purposes for monitoring deep foundation pit which are foundation pit monitoring and environmental monitoring. Foundation pit monitoring includes monitoring for retaining pile wall, supports, anchors, stresses and deformations of soil as well as underground water level changes. Environmental monitoring includes monitoring for displacements and deformations of stratum surrounding deep foundation pit, underground pipelines, buildings and roads nearby deep foundation pit. With actual characteristics of this project, the monitoring works are for horizontal displacements and settlements of pile anchor retaining structure and buildings near foundation pit.

## The horizontal displacements at top of retaining wall piles

The monitoring results at piles top on south side of deep foundation pit are shown in Fig.3.

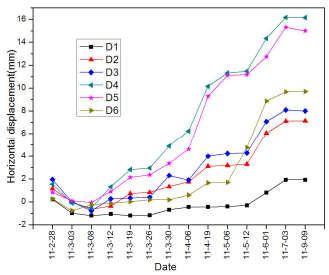


Fig.3 Curves of horizontal displacement with times at pile top on south side

It can be seen from Fig.3 that horizontal displacements with excavation are presented as a step by step process which are increased at first, then partial reduced and tended to stable. Horizontal displacements tend to increased with excavation, the growths were become slowly after last row of anchors completed, and then finally tended to stable. Horizontal displacements in middle place of side were decreased after building basement floors have been done. The reasons for this phenomenon are that there are earth pressures on retaining piles which lead retaining pile slip to foundation pit and bending deformations. With increase of depth, earth pressures increase which caused horizontal displacements to increase continuously. When excavation to a certain depth, the first row of prestressed anchor on retaining piles has been constructed, the bending deformations of retaining piles are in control soon and this made retaining piles produce large anti-pressure to soil. When excavation to another depth, horizontal displacements will increase again. With second rows of prestressed anchor completed, the bending deformations of retaining piles are under control and make back pressure to soil. After basement floor completion, horizontal displacements appear rebound phenomenon because the actions of prestressed made by anchors and earth pressures decreased with retaining soil thickness changed by basement floor. The basement floor stiffness is larger and has obviously embedded effects to retaining piles. Prestressed anchors can effectively restrain horizontal displacements of retaining pile and improve whole supporting structure stiffness. Further studies showed that horizontal displacements can be reduced by the second rows of prestressed anchor.

The maximum horizontal displacement is in middle of south side and value is 16.16mm which illustrated this supporting structure are meet with requirements of national standards and the structure has been in safe state. The monitoring results are consistent with research conclusions that the larger deformations are in middle of sides and corners of foundation pit.

## The settlements of pile

The settlement results of pile on south, west and east side of foundation pit are given in Fig.4 to Fig.6.

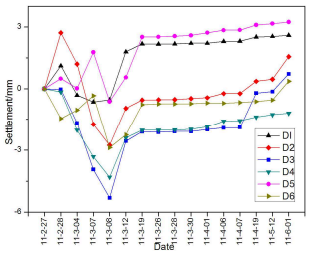


Fig.4 Settlements on south side

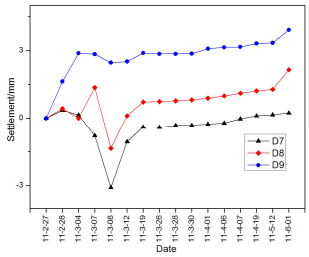


Fig.5 Settlements on west side

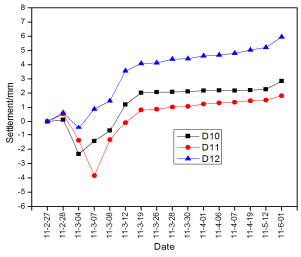


Fig.6 Settlements on east side

It is shown from Fig.4 to Fig.6 that the settlements of pile at beginning of excavation were increased. After the first row of anchor completed, the growths of settlements were become slowly and even trend to rebound. With excavation depth increase, settlements of piles began to increase again, then rebounded slightly after the second rows of anchor completed and trended to stable. The reasons for this are due to inhibitions of prestressed anchor on retaining pile settlements. The maximum settlement points are located in corners and in middle place of long sides. In process of construction, the monitoring in these areas should be strengthened. If an exception occurs, must alarm immediately to prevent accidents.

## Spatial and Time effects

With engineering practices, it can be found that distances from pit edges, arrangements of supporting structure, time effects and applied effective prestress of anchors have obvious influences on settlements of building near foundation pit. According to monitoring data, the settlement curves of buildings near south and west side of pit are shown in Fig.7 and Fig.8.

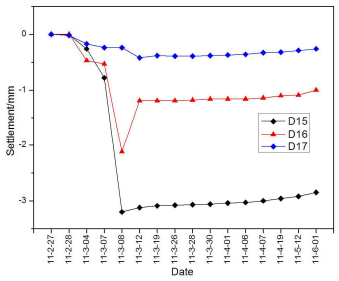


Fig.7 Settlements of building on south side

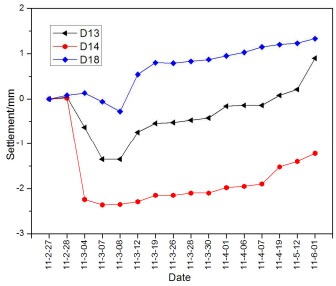


Fig.8 Settlements of building on west side

The maximum settlements are in southwest corner and central of south side, the values are 2.36mm and 3.20mm. Theoretical analysis show that deformations are most sensitive at corners and center of sides. Ground settlement near these places is also larger. After excavation, states of soil surrounding pit are changed to free and make soil slip slowly to free surfaces which causes soil shear failure and leads soil near pit sides to become soft and compressibility, then leads nearby buildings to produce new settlements. The influences for building settlements are greatly by distances far from pit. The changes of settlement have obvious spatial effects.

Building settlements near pit are changed slowly in initial period and the amount of settlements is small. After a row of prestressed anchors completed, building settlements are changed obviously, then tends to stable. Settlements have obvious hysteresis characteristics with depth of pit, thus settlements of buildings have been manifested after a depth completed for periods of time. The main reasons are that slip creep and shear failure occurred to soil near foundation pit has a lag phase which caused process of settlements has significant time effects.

## Conclusion

Settlements and horizontal displacements of supporting structure and ground surfaces, vertical displacements of buildings nearby foundation pit are all within bounds of current national standards, supporting structures are in safety and stability. The environment monitoring results are particular and true. With analysis, the conclusions can be obtained as following:

1) Displacements and settlements of pile anchor retaining structure were influenced greatly by prestressed anchor. It can effectively reduced horizontal displacements and settlements of supporting structure. By observing horizontal displacements and settlements, it can effectively monitor the states of supporting structures and find abnormal phenomena in time.

2) During excavation, the maximum deformations appeared in middle part of sides and at corners of foundation pit.

3) There are many factors influenced settlements of buildings, such as distances from pit boundaries, arrangements of supporting piles, time effects and so on. The greatest impact is distances between buildings from pit boundaries. Process of settlements of buildings nearby pit has significant spatial and time effects.

## References

[1] An Guanfeng, Gao Junyue. Comprehensive Analysis of Deep Foundation Pits for Underground Space in Guangzhou, Chinese Journal of Geotechnical Engineering, 29(2007), pp.872-879. (in Chinese).

[2] Liu Guobin, Wang Weidong. Excavation Engineering Handbook, China Architecture and Building Press, 2009.

[3] Li Shu, Zhang Dingli, Fang Qian. Research on Characteristics of Ground Surface Deformation During Deep Excavation in Beijing Subway, Chinese Journal of Rock Mechanics and Engineering, 31(2012), pp.189-198. (in Chinese).

[4] Technical Specification for Retaining and Protection of Building Foundation Excavations (JGJ120-2012), China Architecture and Building Press, 2012.

[5] Technical Code for Monitoring of Building Foundation Pit Engineering (GB50497-2009), China Architecture and Building Press, 2012.

[6] Code for Deformation Measurement of Building and Structure (JGJ8-2007), China Architecture and Building Press, 2007.

*Applied Mechanics and Materials Vols. 580-583 (2014) pp 34-37*
*© (2014) Trans Tech Publications, Switzerland*
*doi:10.4028/www.scientific.net/AMM.580-583.34*

# Analysis on Strengthening of Plant to slope soil under orthogonal states

Junbin Gu

Architecture and Civil Engineering School, Inner Mongolia University of Science and technology, Baotou, 014010, China

gu613@163.com

**Keyword:** the orthogonal states, plant, soil, strengthening

**Abstract.** In the traditional slope engineering, the slope processing mainly emphasizes the strength effect, and ignore the damage to the environment. Along with people are to landscape and strengthening of environmental protection consciousness, the slope protection method of tradition can not satisfy the requirement of people.Use Interaction of plant roots and rock-soil body to reinforcement and anchorage on the slope surface protection and reinforcement, which can meet the design requirement for stability of slope surface and restore the damaged natural ecological environment. This paper set up the relations between the tensile strength of plant root and the root diameter, establish the theoretical calculation model of the interaction between plant roots and soil, and study the strengthening of plant roots to soil.

## Introduction

In recent years, the slope plant protection research has been carried out both at home and abroad and has a lot of literature.But the research of plant protection mainly explore the construction technology and protective effect of slope plants for further study the slope plant protection. And in order to prevent blindness in design and construction must intensive study the mechanism action of the slope plant protection.Through the data access and analysis, the plant roots have the anchoring effect of deep roots and the reinforcement effect of shallow root, and both can reinforce the slope from the mechanics aspects. The deep vertical root through the potential shear surface to resist the shallow landslide; the small diameter and high dense fibrous improve soil shear strength [1]. So this paper mainly study the strengthening of plant root to soil in the plant slope protection.

## The mechanical effect and mechanical model of plant protection

**The mechanical effect of plant protection.** The vertical root of plants through the shallow slope to loose the weather belt, and anchorage on the depth and stability rock layer to have the effect of prestressed anchor: The plant lateral roots form the reticular structure in the surface soil, lash the soil around and make into soil form the reinforcement whole, so form the three-dimensional structure of solid protective with vertical root have net and pile effect in soil structure, increased the tensile strength and shear strength in the soil, so as to improve the safety factor of slope as shown in Fig.1. Root reinforcement effect of slope soil related to the root distribution form,the root content in the soil and the root strength[2], the herbs as the example for research in this paper.

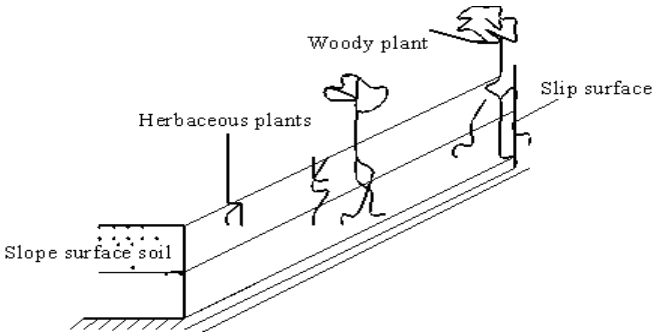


Fig.1 The map of plant roots and slope effect

**The mechanics model of interaction between Plant roots and soil.**The herbs roots distribution characteristics shown that root distribution density gradually decreases and thin down from the surface in soil, the slope soil can be regarded as soil and root composite material in the scope of the root intertwining,and the herb roots as the fiber function so according to the reinforced soil principle analyze on the stress state of the upper slope, the roots distribution in the soil as the the reinforced fiber distribution and the three-dimensional reinforcement. Below to establish the mechanics model of interaction between Plant roots and soil[3] as shown in Fig.2, which shown the extension direction of the root and soil shear zone orthogonal conditions[4].

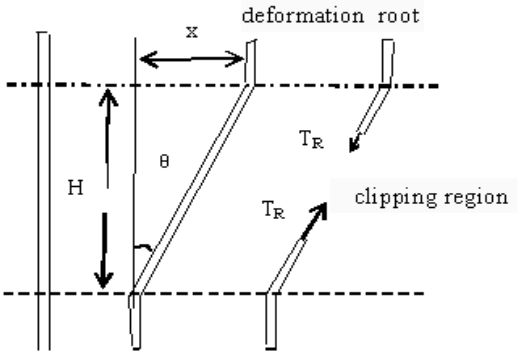


Fig.2 The mechanism analysis diagram of balance model for single root force under orthogonal status

Orthogonal:

$$\tau_R = \frac{T}{a}\sin\theta + \frac{T}{a}\cos\theta\tan\varphi \tag{1}$$

In the formulas, $\tau_R$ for due to the effect of root reinforcement to increase the shear strength of soil; T for the single tensile resistance; $a$ for the soil area of single function; $\theta$ for shear angle; $\varphi$ for the internal friction angle of soil.

## Research strengthening of plant roots to soil

**The relationship between tensile strength and root diameter of the plant root.**In the experiment, selected the bermudagrass, White clover and amorpha fruticosa as test object, select several root form each plant roots type and make its diameter distribution change is larger and continuous. The root tensile strength may refer to applied for the calculation method of steel reinforced concrete structures:

$$P = 4F / \pi D^2 \tag{2}$$

In the formulas,P for the root tensile strength; F for the root tensile resistance (the root is pulled when the weight of the sandbags); D for the section diameter when root tensile (assume the root end face is round).Test results of statistics as shown in Tab.1and the relation curve of the root tensile strength and the root diameter as shown in Fig.3, Fig.4, Fig.5.

Tab.1 The relationship statistics data between the root tensile strength and the root diameter

| | | the root diameter for D(mm)and the root tensile strength for P(MPa) | | | | | | |
|---|---|---|---|---|---|---|---|---|
| Bermud | The root section diameter | 0.240 | 0.283 | 0.383 | 0.480 | 0.700 | 0.720 | 0.780 |
| agrass | The root tensile strength | 58.83 | 65.05 | 65.06 | 48.58 | 26.50 | 24.82 | 23.34 |
| White | The root section diameter | 0.887 | 0.927 | 0.986 | 1.265 | 1.724 | 2.020 | 2.053 |
| clover | The root tensile strength | 9.74 | 11.54 | 11.75 | 11.50 | 9.10 | 8.88 | 8.56 |
| amorpha | The root section diameter | 0.67 | 1.28 | 1.70 | 1.78 | 1.81 | 1.85 | 2.20 |
| fruticosa | The root tensile strength | 10.32 | 10.54 | 10.25 | 10.16 | 10.10 | 10.02 | 9.86 |

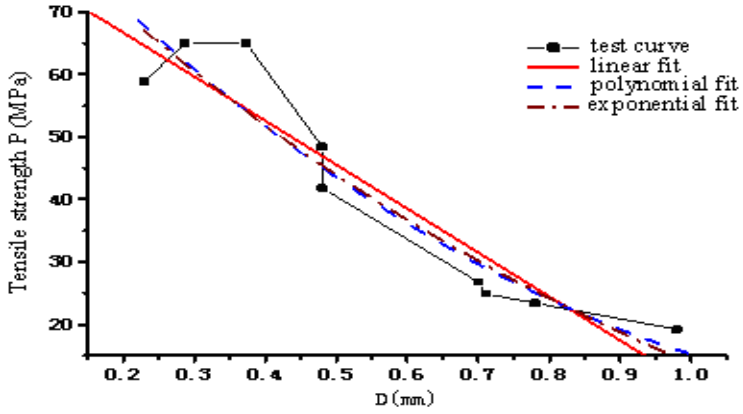


Fig.3 The relationship between the root tensile strength and the root diameter for Bermuda grass

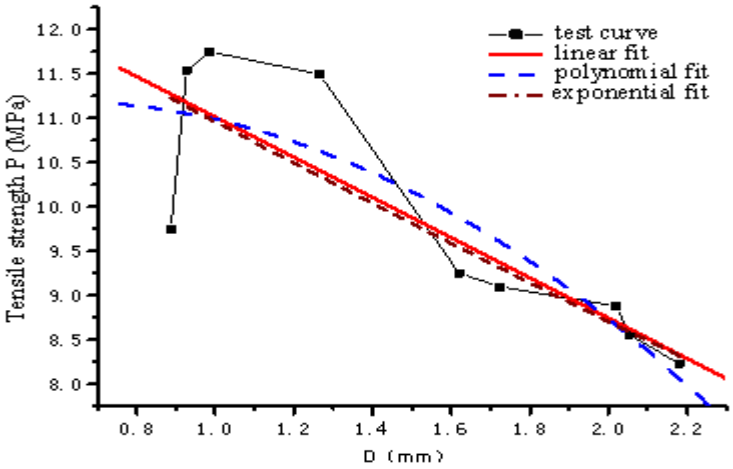


Fig.4 The relationship between the root tensile strength and the root diameter for White clover

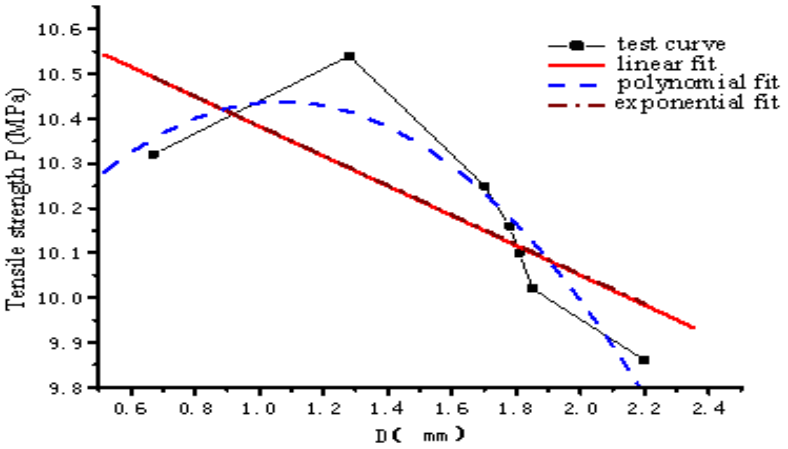


Fig.5 The relationship between the root tensile strength and the root diameter for Amorpha fruticosa

The fitting effect found that polynomial fitting is better for Bermuda grass and Amorpha fruticosa, and exponential fit is better for White clover.Analyzed on the relationship between the root deformation angle and the soil shear strength under orthogonal state for three roots meet above conditions, and the relationship between the root tensile strength and the root of the roots diameter (d = 0.1 ~ 0.3 mm) are as follows:

Bermuda grass : $y = 44.4314x^2 - 123.4059x + 93.1668$

White clover: $T(N) = -21.3117 + 34.6929e^{-0.0724d}$ (3)

Amorpha fruticosa: $T(N) = -0.5137d^2 + 1.0992d + 9.8501$

**Research results**.Using the formula (1) and (3) calculate the reinforcement effect of three plants to soil ,and the results are shown in Tab.2. Further analyze the change law of the soil shear strength with the deformation Angle change by MATLAB is shown in Fig.6.

Tab.2 The strengthening effect of different plants to soil

| Plant Type | Bermuda grass | White clover | Amorpha fruticosa |
|---|---|---|---|
| $\tau_R$ (KPa) | 1424.36 | 250.275 | 193.519 |

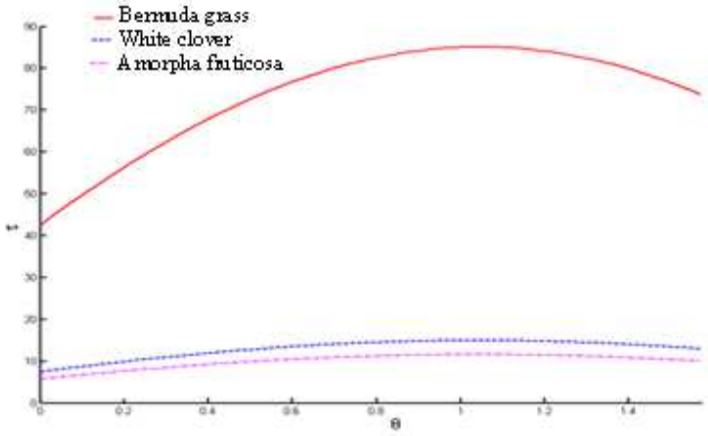


Fig.6 The relationship between the soil shear strength and the root deformation angle under orthogonal state

Angle increased in a certain Angle, when the deformation Angle reaches to1 radian, the soil shear strength reach to the maximum, and the soil shear strength has the decrease tendency along with the deformation Angle continues to increase. This phenomenon is due to the reinforcement effect of root to soil by the synthesis function of two component of the root tensile strength. When the deformation Angle increases, the root tensile strength in the horizontal component increases and the vertical component decreases. Due to the root reinforcement effect is the synthesis of the two parts, Fig.6 is obtained when the extent of the increase is greater than the extent of decrease.

## Conclusion

Plant roots have a strengthening effect on slope soil, on the other hand, the plant also cannot leave the soil environment,which need to achieve the desired mineral nutrients and moisture from the soil. so the effect of plants and slope soil is mutual, plant roots affect the stability of the slope geotechnical by mechanics effect .The slope plants have similar function as anchor or pile, but should not simply analogy of the mechanical strengthening effect of the slope plants and the effect of anchor or pile, should put the favorable and unfavorable factors taken together to study the strengthening effect of plant roots to soil slope.

## References

[1]Dengpei ZHOU, Junyun ZHSANG.Plant slope protection engineering technology[M].China Communications Press,2003.7

[2]VAN BEEK L P H, WINT J, CAMMERAAT L H, etc.Observation and simulation of root reinforcement on abandoned Mediterranean slopes[J]. Plant and soil,2005.278(1/2):55-57.

[3]Qinqin YU, Na QIAO, Haijing LU, XiaSong HU, etc.Research reinforcement effect of plant root on soil[J].Chinese Journal of Rock Mechanic and Engineering.2012.5,31(S1):3216-3222.

[4]Chunhui CHEN, Echuan YAN.Research on the effects of plant roots on soil shear strength[J]. Geological Science and Technology Information.2012.07,31(4):123-126.

*Applied Mechanics and Materials Vols. 580-583 (2014) pp 38-47*
*© (2014) Trans Tech Publications, Switzerland*
*doi:10.4028/www.scientific.net/AMM.580-583.38*

# Centrifuge Model Study of High Strength Piles Composite Foundation Settlement & Instability under Embankment in Different Kind Soils by Different Pile Spacing

Qingjian Wang[1,a] , Shujie Zhang [2,b], [*]Chao Guo [3,c] and Zhengran Lu [3,d]

[1]China Railway Sixth Group Shijiazhuang Railway Construction Co. Ltd, Shijiazhuang 050010, China

[2]CCCC First Harbor Consultants Co. Ltd, Tianjin 300222, China

[3]Shenyang Jianzhu University, Shenyang 110168, China

[a]wangqingjian70@163.com, [b]zhangshujie2014@163.com,

[c]guochaoglovel@126.com , [d]luzhengranglovel@126.com

**Keywords:** Centrifuge Model; Composite Foundation; High Strength Piles; Embankment; Instability.

**Abstract:** A series of centrifuge model tests has been conduced to examine the behavior of high strength piles composite foundation stability under railway embankment in silt or clay or sand different kind of soils. The high strength composite foundation has a symmetrical plan layout consisting of 3×4, 4×6, and 5×8 piles with a center-to-center spacing of 6 or 4 or 3 times pile width. The piles are under the same height of railway embankment, with the same length, and on the same lying soil layer. The high strength composite foundation stability test results are expressed in terms of soils kinds-pile displacement response of the composite foundation, embankment load experienced by soil between piles and piles in the composite foundation, and bending moment profile along individual pile. It is established that the high strength composite foundation stability efficiency reduces significantly with decreasing of the strength of soil between piles in composite foundation. The tests reveal the shadowing effect phenomenon in which the marginal piles experienced larger laterally and bending moment than that of the central piles. The shadowing effect is most significant for the lead row piles and considerably less significant for subsequent rows of middle piles. The approach adopted by many researchers of taking the average performance of piles in the same row is found to be inappropriate for the middle rows, of piles for composite foundation as the outer piles in the row carrying significantly more laterally load and experience considerably higher bending moment than those of the inner piles.

## Introduction

The performance of high strength composite foundations subject to embankment load is of considerable importance in Chinese super railway practice, for mostly Chinese super railway embankment foundations are reinforced by high strength piles during the past ten years (for example, Beijing-Shanghai High Speed Railway et al. 2011). In the field, piles are often arranged in gropes, and the behavior of piles of composite foundation may differ substantially from that of a single pile. The composite modulus (JGJ 79-2002 Technical Code for Ground Treatment of Buildings of China) is commonly employed to evaluate the stability of high strength composite foundation. Several full-scale field tests on composite subject to embankment loads have been reported. These include studies on composite foundation (for example, Cui 2009). Some degree of understanding on the performance of high strength composite foundation has been gained from these field studies.

Laboratory studies such as centrifuge model tests could provide further insight on the behavior of composite foundations. At present, much of the centrifuge model studies on composite foundation were carried out (for example, Wang et al. 2010; BUI et al. 2009). Relatively few centrifuge model studies were conducted to investigate the stability of composite foundation and majority of these studies concentrated on the study of settlement (for example, Wang et al. 2010). A series of centrifuge

model tests was, therefore, initiated to examine the behavior of high strength composite foundation in silt or clay or sand to research the soil between piles character effect on the composite foundation stability. In addition, the test observations are compared with those obtained from field studies.

## Experimental Setup

All the tests were conducted at 50 g on the Southwest Jiaotong University (SJU) of China, which has a radius of 3 m and comprises a balanced arm with dual swing platforms. The centrifuge has a capacity of 100 g tones and a maximum acceleration of 200 g. Details of the SJU Centrifuge are given in BUI et al. (2009). Fig.1 shows a sketch of the model setup. The rectangular stainless steel model container has an internal diameter of 600×600×800mm.

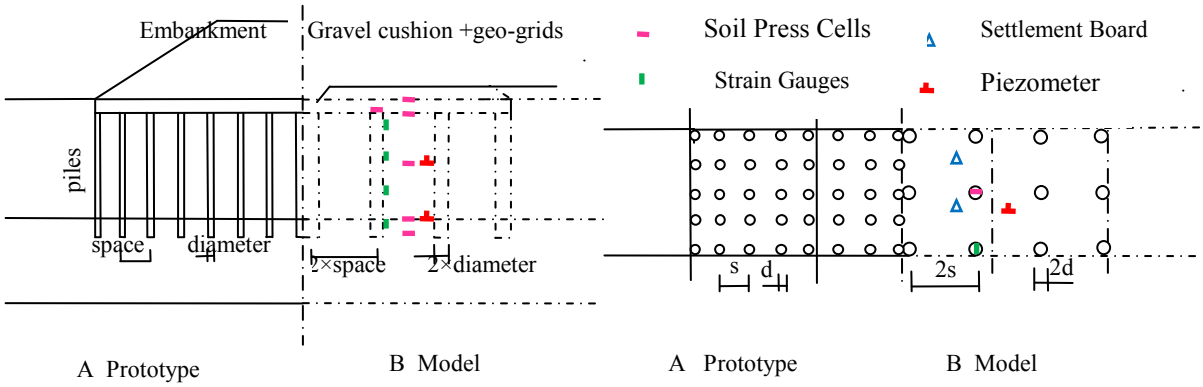


Fig.1. Centrifuge model setup

Tab.1 Physical and mechanical parameters of model

| | Parameter | Com Mod | Ten Str | Ela Mod | Un-Com Str | Max Dry Den | Max Dia |
|---|---|---|---|---|---|---|---|
| Materials type | | $E_{1-2}$ | $\sigma_t$ | E | $\sigma_c$ | $\rho_{dry}$ | D |
| | | (MPa) | (kN/m) | (MPa) | (MPa) | (kN/m$^3$) | (mm) |
| Soils | Silt | 2.28 | | | | | |
| | Clay | 4.30 | | | | | |
| | Sand | 6.25 | | | | | |
| Geo-grille | Gauge | | 1.60 | | | | |
| Pile | Concrete | | | 1417 | 8.4 | | |
| Emb | Granite | | | | | 19 | |
| Cushion | Sand | | | | | | 1.5 |

The model pile is 20 cm long with the lower 2 cm pile length to be inserted into the sand lying layer. At 50 g, the simulated prototype embedment pile length is 10 m. The geo-grille is made of gauge, that tensile strength is 1.6 kN/m (80 kN/m prototype scales). The gravel cushion is made of 10 mm (0.5m prototype scale) thick sand, which maximum diameter is 0.4 mm (2 cm prototype scales). It is very difficult to layered setup embankment, so the whole embankment is made of 120 mm (6 m prototype scale) thick weathered granite once. Train and rail load is replaced by 65mm×14mm (3.25m×53.8kPa prototype scale) steel plate.

The model pile is made of the real material as cement gravel (gravel size 1:50 scale reduction) instrumented with 14 coordinate points to enable bending moment measurements along the pile profiles, 4 strain gauges (from pile top 1, 7, 13, 19 cm) to enable pile stain along the piles. At each

level, two active strain gauges were glued onto the opposite faces of the model pile and connected to two dummy gauges on a strain meter mounted on board the centrifuge to form a Wheatstone full bridge circuit. The instrumented pile surface was glued by a thin layer of sand to enhance the interaction with the soils having a final pile width of 2cm.

Three soil press cells (from pile top 0,9,18 cm) were installed in the soils between piles to enable soil press along the pile depth, two soil press cells in cushion and lying soil layer, and one soil press cells on the pile top, respectively. Two settlement boards were instrumented on the surface of cushion at the center and toe of embankment, respectively. Two pore water pressure gauges (from pile top 9, 18 cm) were instrumented.

The material parameter of the model embankment fill, piles, and soils between piles equals to the prototype, for select the real material in the model. Tab.1 shows the details of the materials parameter of the test. For the soil lying layer, a 30-mm-thick sand layer was first placed at the bottom of the model container before placement of soils between piles.

The soils between piles were prepared in the following manner. First, the soil was then placed in the model container to a height of about 200 mm and then consolidated under its self-weight in the centrifuge at 50 g to allow the express pore water pressure in the soil to dissipate through the soil surface and the openings located close to the bottom of the container via the bottom sand layer. Ground settlements and pore water pressures in the soil were measured to monitor the progress of soil consolidation.

## Test Procedure and Configurations

After completion of consolidation for soils between piles, the centrifuge was stopped to facilitate pile and embankment installation. The test pile was precast, for facilitating strain gauges; the other piles were cast-in-place. The pile installation had to be done at 1 g, as it was very difficult to control the pile penetration depth in soil under high-g condition. Fig.2 shows test loading progress. As the embankment was whole precast, that changed the acceleration of the test by trisection to simulate the embankment filling progress. After that, if the model didn't destructed, put on the steel plate, and went on accelerating for 3.5 h to simulate the foundation consolidation 1 year under train and rail load.

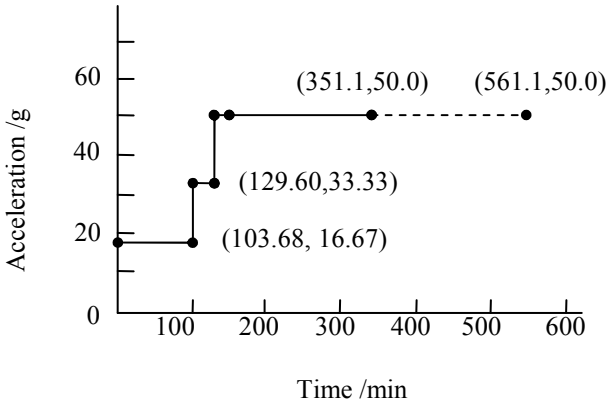


Fig.2. Test loading progress

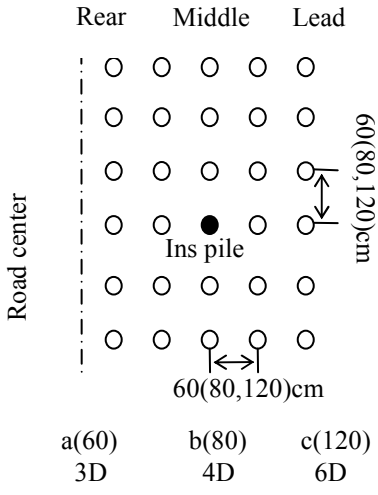


Fig.3. Plan view of pile configuration

Composite foundation of up to 40 piles was investigated in the present study. Figs.3 provide a plan view of the composite foundation configuration for tests involving piles with center-to-center pile spacing 3(4, 6) D (D=pile width). In all cases, tests were carried out in all silt, clay, and sand. The definition of lead row piles (piles in the row furthest away from the center of the embankment), middle row piles (middle second and third rows in the case of 5×8 pile group) and rear row piles as well as center piles for individual pile row is also given in Fig.3. Owing to limited number of recoding

channels in the strain meters, only one pile can be instrumented in one test. The location of the instrumented pile for each test is also shown in Fig.3.

## Load-settlement Responses of Composite Foundation

From this point onwards, all the test results are presented in prototype scale unless otherwise stated. The strain-length of piles in silt, clay, and sand are represented by the curve in Figs. 4 (a-c), respectively. As expected, the piles strains are not fixed values but variables along the pile length, which are corresponding to the following theoretical calculations. In the calculations, the piles stresses are a group of curves, from stress-strain compatible theory, the piles strains are also a group of curves. There are the maximums of the piles stresses in the piles up middle, and minimums in the pile two tops. These deformation and stress phenomena are coinciding with the composite foundation settlement theory reported by Guo. (2012). on it, there is an equal settlement surface in the composite foundation, where the settlements of soils and piles are equal. The axial forces of the piles are a group of exponential curves, and the maximums on the upper third of the piles.

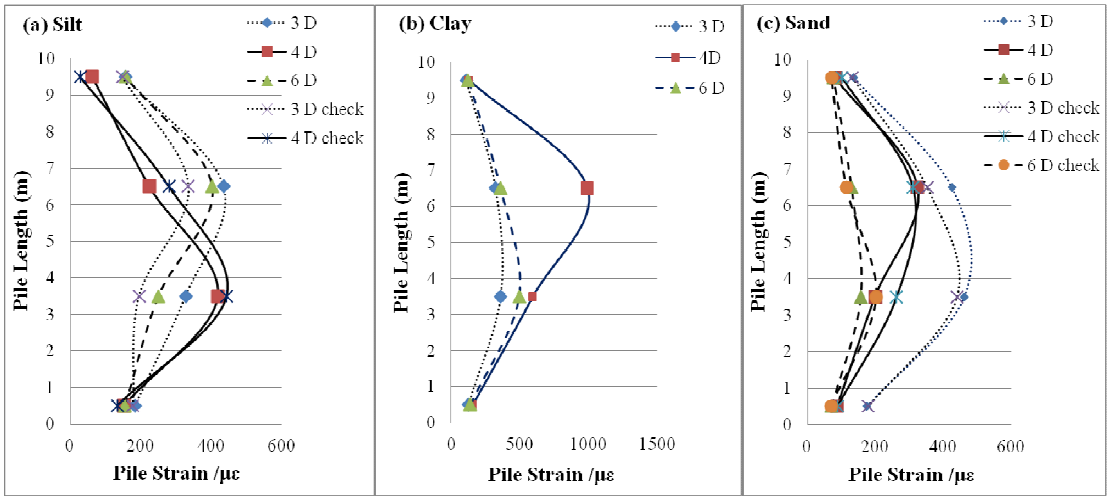


Fig.4. Pile length-strain of different soils

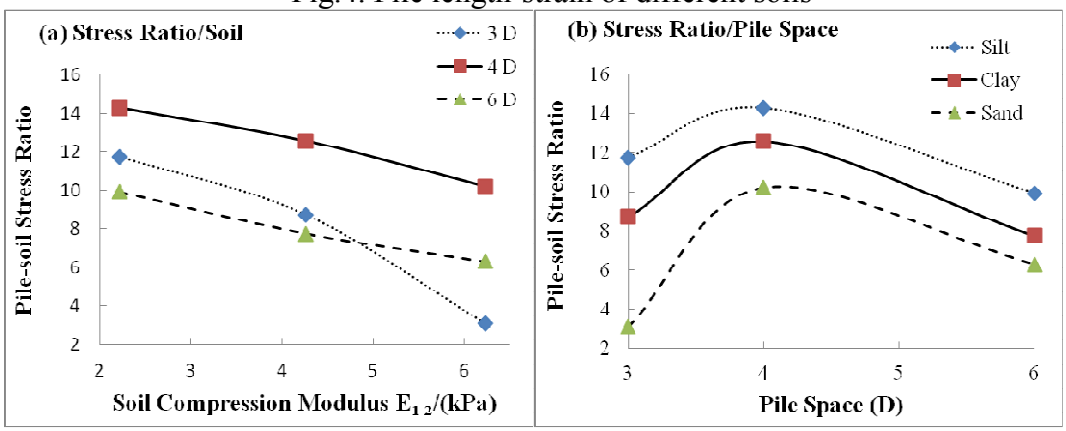


Fig.5. Pile-soil stress ratio at top

In silt, the pile strains along the length are complicated. There is not a clear rule to reflect the piles strains along the length with different piles spaces. It is similar that the 3D and 4D are larger than 6D in the middle of piles. It because that the geo-grids on the top of 6D piles were impaled, which leaded the 6D piles couldn't be fully used as the 3D and 4D piles to bear the embankment load.

In clay, the 4D are larger than 3D and 6D obviously, which illustrated the 4D piles is fully used. It because that the geo-grids on the top of 6D piles were impaled, which leaded the 6D piles couldn't be fully used as the 3D and 4D piles to bear the embankment load. The single pile in 3D piles group bead fewer loads than 4D, for the 3D's replacement ratio larger than 4D's. We can conclude the 4D piles space is optimal space in clay.

In sand, the 3D are larger than 4D, and 4D larger than 6D recursive, which illustrated the single pile in 3D piles group bead fewer loads than 4D, and 4D fewer than 6D, for the 3D's replacement ratio larger than 4D's, and 4D's larger than 6D's.

The pile-soil stress ratios at top changing with different kind soils and pile spaces are represented by the curve in Figs. 5 (a-b), respectively. As expected, the pile-soil stress ratio decreases with the soil compression modulus E1-2 increasing, but the 4D's ratio is always larger than the others, by different soils' modulus. The pile-soil stress ratio first increases then decreases with the soil pile spaces increasing, and at the 4D has the maximum; that ratio in silt is larger than clay, and in clay larger than sand, by different pile spaces.

As the sand is stiffer than clay, and clay is stiffer than silt, the load-displacement response of a pile in sand is stiffer than that of clay, and in clay is stiffer than that of silt. However in silt of 6D space, the geo-grids may be impaled by piles, which may lead to the stress between piles and soils renew distribution. By the Figs. 4 to 5, we can conclude that the 4D pile space is the most economic and reasonable to control the composite foundation settlement, in different kind soils.

**Load-instable Responses of Composite Foundation**

The load-instable responses of composite foundation in silt, clay, and sand with 3D, 4D, and 6D spaces are researched in these tests. The failure models of high strength composite foundation are affected by multi-factors, as embankment stiffness, piles and soils strength, and pile spaces etc. By preliminary analysis, the failure models can be itemized as pile impale geo-grids and cushions, slope shear failure, and piles flexural failure are represented by the pictures in Figs. 6 to 8, and failure types schematic diagram Fig.9, respectively. These failure types are similar to that that reported on piles in clay by A.T.C.Goh. (1997).

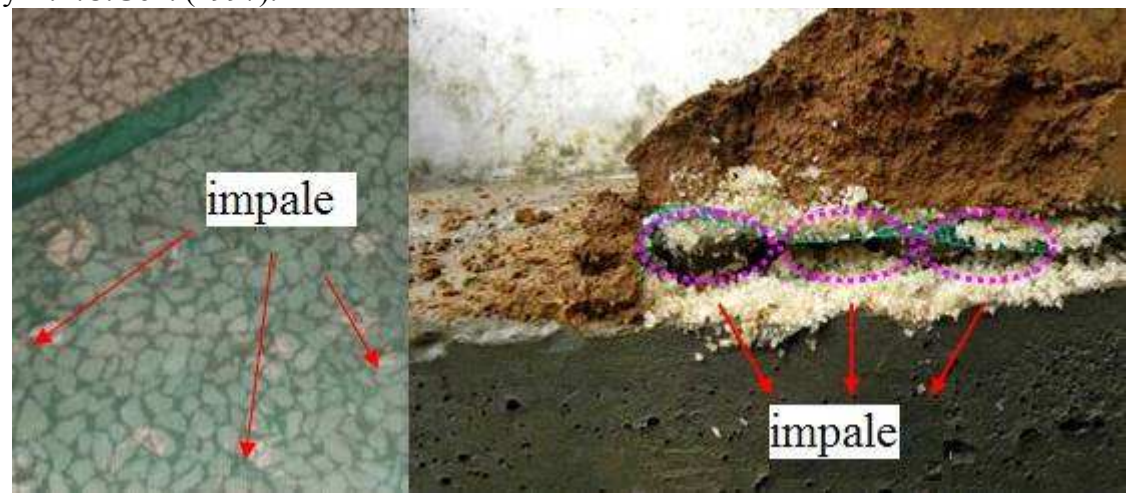


Fig.6. Piles impale geo-grids and embankment

Piles impaled geo-grids and cushions in all cases. There are many holes in the geo-grids impaled by piles, obviously cracks on the pile top embankment slope. Because the piles strength is much larger than soils, that make differential stress between piles and soils, and lead to the stress concentration in the pile top gravel cushion and geo-grids. There are radial cracks in embankment toe on piles top, which even leads to the embankment hang in the air. If the impaling too large, the piles and soils cooperative work will be destroyed, and then the composite foundation will be make part failure. It is unavoidable of pile impaling in the geo-grids and cushion, which is the precondition of the soils between piles playing a role in composite foundation (for example, Guo et al. 2010). That can be reduced by put reinforced concrete caps on the piles top (for example, BUI et al. 2009), in practice engineering.

Slope shear failures took place in clay and silt of 6D spacing in these series tests. Soils masses of lateral toe of slope are out-shifting significantly, there are a series cracks near the slope toe, obviously impaling on the most lateral piles top geo-grids and cushion. The most outsides row piles near the

slope toe outward inclined significantly, some of them even break, the next decreased, and the center hardly inclined. Shear failure plane cut off the outsides piles and breakthrough the slope toe. This observation on piles and embankments slope shear failures is similar to that reported on piles in clay by Zheng. (2012).

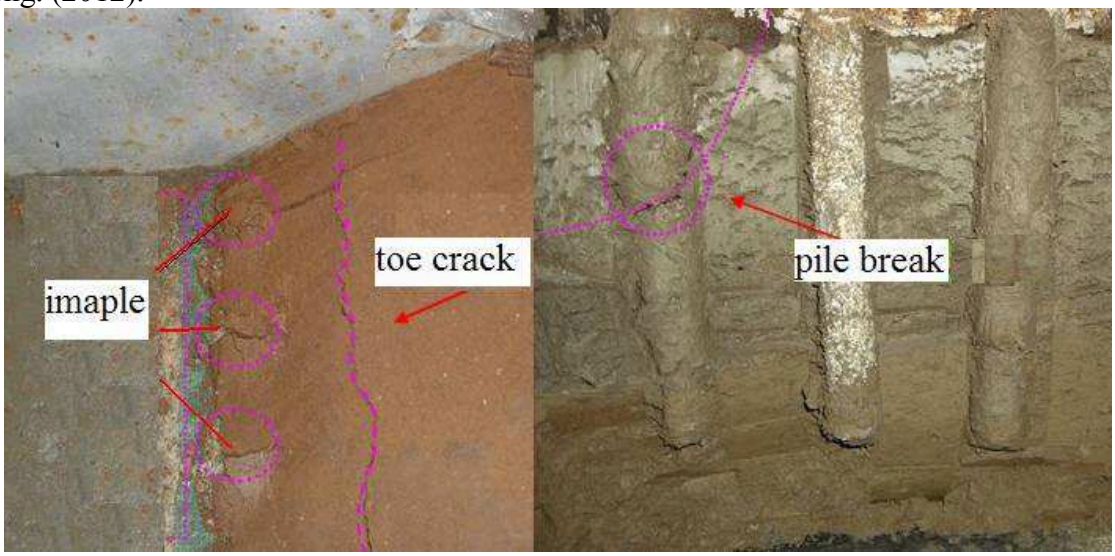


Fig.7. Slope shear failure

Because of the shape of embankment slope and mechanical characters of railroad, there are larger shear stresses in the embankment, especially at the slope toe. The shear stresses are mostly supported by the outside piles and soils, however the insides piles and soils little, for the symmetry of embankment structure and the barrier effect of piles group. From the deformation of different parts of composite foundation, the lateral displacement is decreasing from slope toe to center, the inside piles are just major vertical settlement. From the stress distribution of the foundation, in the center piles and soils lateral deformations are confined by the interactions of piles. However, the outside piles and soils lack lateral constrained and bearing the larger shear stresses, which make them easy fracture. When the outside piles and soils cannot support the shear stress, the foundation will take place shear failure. The theory on composite foundation failures are demonstrated by Guo. (2012).

Piles flexural failure took place in silt of 6D spacing in these series tests. The most outsides piles have significantly incline and flexural deformation; the piles top are excluded the slope toe; there are a lot of radio cracks on the piles top slope toes. From the composite foundation outside to inside, the piles inclination decreased, the most inside piles just have only micro scale inclination. The most outside row piles and the next break at middle section or on the soil interface. There are obviously out-up-shifts of the soils between the outside and next row piles, at the same time, the embankment having a larger settlement. This observation on piles and flexural failures is similar to that reported on piles in clay by Zheng. (2012). However, the model piles are replaced by aluminium alloy pipe, which could not reflect the true failure character of piles, especially the brittle fracture of the concrete type material piles.

Fig.8. Piles flexural failure

The main reasons of piles flexural failure are the larger piles spacing and lower strength of soils between piles. From outside to inside of the composite foundation, the main load directions supported by piles are changing from incline to vertical. There are settlement and lateral sway of the soils between piles under the embankment load. If the pile spacing is too large (6D in these tests), the strength of soils too low (silt in these tests), and the embankment too high, the lateral sway of inside soils will make the pile subject to bending load, which lead to piles flexural failure. As the outside row piles failure, the next row piles will continue failure, that make the lateral support of piles further weakened. At the same time, the soils between piles will support increased load, if the soils strength is too low, the composite foundation will be overall instable. While soil strength difference between the upper and lower soil interface (silt and sand interface in these tests) is too large, the piles is more like cantilever beam, that make the piles flexural failure at interface.

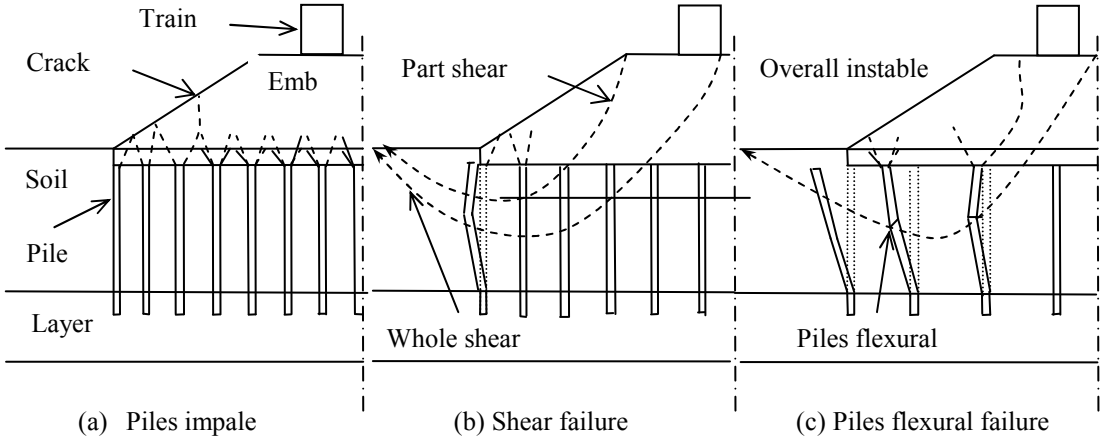


Fig.9. Composite foundation failure types

Considering the variation in soil properties in various piles spacing studies, the experimental failure types observed in the present study are reasonably consistent with those obtained from the early studies.

## Conclusions

Centrifuge model tests have been performed to investigate the behavior of high strength piles composite foundation in silt, clay, and sand under railway embankment and train load. The tests involved the high strength piles number ranging from 12 to 40, with center-to-center pile spacing of 3, 4, or 6D. The following conclusions can be obtained from the present study:

1. The embankment load of per pile supported is complicated in different kinds of soils with various piles spacing in the composite foundation. If the soils strength between piles is too low (silt in these tests) the load of per pile supported have not obvious regular with the pile spacing changing. The writer think that, as the soils strength is too low and the piles too high, the piles and soils cannot coordinate work together. It means that cannot make up the true composite foundation, for the soils between piles cannot give piles enough lateral constraint. That makes the piles like alterable system in structure engineering; there are no constraints on piles. It is no use to increase the piles number in composite foundation to decrease the pile spacing, consequently decrease per pile supported load. That has been proved by engineering practice in Xia-Shen railway of china, where the piles spacing is 3D, the soils between piles is silt. However, the embankment also took place overall instability when filling to 6m. It can conclude that the high strength piles composite foundation is not suitable using in soft soils as silt and mud areas.

2. With the soils strength increasing (clay in these tests), the soils and piles can constitute a coordinate work group as composite foundation, where the soils and piles can transfer load interaction effectively. There is an optimal piles spacing (4D in these tests), at this piles spacing, the piles strains

have a maximum at the up third of piles, the piles-soils stress ratio also has a maximum. By the optimal piles spacing, the piles and soils strengths can get a full used to realize the safety and economic of composite foundation. It can give a good reference to designer to determine the piles spacing in composite foundation, which has been used in Shi-Ji passenger special line of china. In sand, as its strength is high, the piles-soils stress ratio is less than in clay at the same pile spacing, which means the piles cannot be full used as in clay. It is diseconomy to constitute high strength piles composite foundation in sand.

3. In line with the findings of Guo et al. (2012) and Dong et al. (2010), the equal settlement surface of composite foundation is observed in the up third of piles, where the soils and piles have an equal settlement. The piles stress along length is an exponential function curves, and at the equal settlement surface, it has the maximum. On the up conclusions, Guo et al. (2012) deduced a series group stress-strain coordinate function of soils and piles in composite foundation under embankment load. By which, the strain and stress of the piles, soils between piles and cushion are separated calculated, it is good supplement to composite modulus calculating method of composite foundation settlement (JGJ 79-2002 Technical Code for Ground Treatment of Buildings of China).

4. the composite foundations failure types under a higher embankment load in 3,4,6D piles spacing, including piles impale geo-grids in every test, part shear failure in clay (4D) and whole shear failure in silt (6D), overall instable of piles flexural failures in silt (6D) are observed, respectively. The piles up stick gravel cushion, and under stick layers soils are necessary to constitute the composite foundation, in Guo et al. (2010). However, the pile impale geo-grids is need avoid, which can be resolved by giving a reinforced concrete cap on the pile top in engineering practices. The shear failures are a more general phenomena than others failure types, especially in homogeneous ground. However, in composite foundation the high strength piles can lead to more complicated failures types. The shadowing effect is most significant for the lead row piles and less significant on subsequent rows of trailing piles. Hence, if uniform pile type and size have been adopted for a composite foundation, appropriate checks should be conducted to evaluate whether the lateral load carrying and bending moment capacity of the lead row piles, in particular the outer lead piles, would be exceeded. In many previous research studies, the average performance of piles in the same row rather than the performance of individual piles is employed in the analysis. This simplification is found to be acceptable for the lead and rear row piles where the behavior of the outer and center piles do not differ much (Zheng et al. (2010)). However, for the middle pile rows (middle row in the case of the 4D, middle second and third rows in the case of the 3D), the present study reveals that the center piles often carries much less load and bending moment than those of the outer piles in the same row. Thus, appropriate caution should be taken when designing piles in the middle rows of a large composite foundation in view of the large difference in the load and bending moment between the outer and center piles.

**Acknowledgments**

The present study is part of the research collaboration between the Southwest Jiaotong University of China and The Third Railway Survey and Design Institute Group Corporation of China. The writers would like to express their gratitude to the technical staff of the Geotechnical Centrifuge Laboratory at Southwest Jiaotong University of China for their assistance and contributions in conducting the centrifuge model tests. The professor of Qian-Su in reviewing some of the testing schedule is gratefully appreciated. The authors sincerely thank the National Natural Science Foundation of China for the financial support provided to this research project (Grant No. 51308255).

**References**

[1] JGJ 79—2002 Technical code for ground treatment of buildings[S]. 2002. (in Chinese)

[2] JTG D30—2004 Specifications for design of highway subgrades[S].2004. (in Chinese)

[3] JTS 147—1—2010 Code for ground of port engineering[S]. 2010. (in Chinese)

[4] TB 10001—2005 Code for design on subgrade of railway[S]. 2005. (in Chinese)

[5] ZHENG Gang, LIU Li, HAN Jie. Stability of embankment on soft subgrade reinforced by rigid piles(I)—Background and single pile analysis[J]. Chinese Journal of Geotechnical Engineering, 2010, 32(11): 1648–1657. (in Chinese)

[6] ZHENG Gang, LIU Li, HAN Jie. Stability of embankment on soft subgrade reinforced by rigid inclusions(II)—group piles analysis[J]. Chinese Journal of Geotechnical Engineering, 2010, 32(12): 1811–1820. (in Chinese)

[7] HAN J, HUANG J, PORBAHA A. 2D Numerical modeling of a constructed geosynthetic-reinforced embankment over deep mixed columns[C]// ASCE GSP 131, Contemporary Issues in Foundation Engineering, 2005.

[8] HUANG J, HAN J, PORBAHA A. Two and three-dimensional modeling of DM columns under embankments[C]// ASCE GeoCongress, 2006.

[9] NAVIN M P, FILZ G M. Numerical stability analyses of embankments supported on deep mixed columns[C]// ASCE GSP 152, Ground Modification and Seismic Mitigation,2006.

[10] TERASHI M, TANAKA H, KITAZUME M. Extrusion failure of the ground improved by the deep mixing method[C]// Proceedings of the 7th Asian Regional Conference on Soil Mechanics and Foundation Engineering: Haifa, Israel, 1983:313–318.

[11] MIYAKE M, AKAMOTO H, WADA M. Deformation characteristics of ground improved by a group of treated soil[C]// Centrifuge 91. Rotterdam: Balkema, 1991: 295–302.

[12] HASHIZUME H, OKOCHI Y, DONG J, et al. Study on the behavior of soft ground improved using deep mixing method[C]// Proc of the International Conference on Centrifuge 98, 1998: 851–856.

[13] KITAZUME M, OKANO K, MIYAJIMA S. Centrifuge model tests on failure envelope of column type deep mixing method improved ground[J]. Soils and Foundations, 2000,40(4): 43–55.

[14] KITAZUME M, MARUYAMA K. Collapse failure of group column type deep mixing improved ground under embankment[C]// Proc. of the International Conference on Deep Mixing, ASCE, 2005: 245–254.

[15] KITAZUME M, MARUYAMA K. External stability of group column type deep mixing improved ground under embankment loading [J]. Soils and Foundations, 2006, 46(3):323–340.

[16] KITAZUME M, MARUYAMA K. Internal stability of group column type deep mixing improved ground under embankment loading [J]. Soils and Foundations, 2007, 47(3):437–455.

[17] BROMS B B. Can lime/cement columns be used in Singapore and Southeast Asia[R] 3rd GRC Lecture, Nanyang Technological University and NTU-PWD Geotechnical research Centre, 1999: 214.

[18] ZHENG G, LIU L. Numerical analysis of the pile lateral behavior and anti-slip mechanism of rigid pile supported embankments[C]// Advances in Ground Improvement: Research to practice in the United States and China-Proceedings of the 2009 US-China Workshop on Ground Improvement Technologies, 2009: 63–72.

[19] SHI Dan-da. Micromechanical simulations of sand behavior under monotonic and cyclic loading[D]. Shanghai: Tongji University, 2007. (in Chinese)

[20] BUI Phu Doanh, LUO Qiang, ZHANG Liang,et al. Analysis on pile spacing effect of composite foundation with high strength piles by centrifugal model test[J]. Journal of the China Railway Society, 2009, 31(6): 69–75. (inChinese)

[21] HUANG Jing. Experimental analysis of CFG pile composite foundation under embankment load [D]. Chengdu: Southwest Jiaotong University, 2008. (in Chinese)

[22] T. Ilyas, C. F. Leung, Y. K. Chow, and S. S. Budi. Centrifuge Model Study of Laterally Loaded Pile Groups in Clay [J]. Journal of Geotechnical and Geoenvironmental Engineering, 2004, 130(3):274-283.

*Applied Mechanics and Materials Vols. 580-583 (2014) pp 48-51*
*© (2014) Trans Tech Publications, Switzerland*
*doi:10.4028/www.scientific.net/AMM.580-583.48*

# Comparative Experimental Research of Soil Freezing with Pressure and Non-pressure

Zhang shiyin

School of Civil Engineering and Architecture, Anhui University of Science and Technology, Huainan Anhui 232001

**Keywords:** Freeze under pressure; Freeze without pressure; Contrast test

**Abstract:** Use two kinds of soil, processes the uniaxial compressive strength test under the condition of pressure and zero pressure freeze, concludes different test results. That is the uniaxial compressive strength of frozen soil under pressure is higher than that without pressure, and laboratory test data as the basis for the design of the temporary support is relatively safe.

## Introduction

Freezing method uses the technique of artificial refrigeration, ices the water in the formation. So the natural soil turns into frozen soil. It can increases strength and stability of soil, and can isolate the connection of groundwater and underground engineering, in order to excavation and ling construct the underground engineering in the protection of frozen wall. The essence is using artificial refrigeration changes soil properties temporarily to consolidate layer. At present, freezing construction method applied in coal mine construction, currently frozen construction method is widely used in engineering, it is not only used in mine construction, foundation, but used in urban underground railway, river tunnels and other projects. But when the natural soil turn into frozen soil, its strength has relationship with its composition, moisture content, density, liquid limit, pressure and salinity. Now, in the design of frozen soil wall, strength index of frozen soil is usually settled in the laboratory, but the soil in the depths is under pressure in all directions, when the soil is taken into lab, crustal stress has been released, that is to say the strength index is measured after the crustal stress has been released. So whether the measured the frozen strength under stress and it at no stress is equal is a deep research of us.

## The contents and methods of test

Strict implementation of《Standard for Soil Test Method》GB/T 50123-1999 standard and《Physical and Mechanical Properties Experiment of Artificial Frozen Soil》MT/T 593-2011. Test content includes homemade container that the volume won't expansion when freeze, conventional physical property test of soil, Including moisture content, density, liquid limit and plastic limit, unconfined compressive strength test of soil, uniaxial compressive freezing strength test of soil samples without restrictions around, uniaxial compressive freezing strength test of soil samples in the condition of restrictions around.

## Soil sample and instrument

Soil sample is from a mine shaft of Huaibei, depth of 130 to 140 meters, taking into account the soil deep in the ground pressure and soil samples frozen frost force basically the same, tests using different clay and sand, test instrument is the self-developed WDT-100KN electro hydraulic soil pressure testing machine. (See Fig 1)

The test uses remolded soil, in order to compare the sample uniform, contrast, all of the soil sample after drying and pulverizing together with an amount of water, making certain the soil moisture content. Then wet 48 hours and sufficiently stirred to a uniform moisture content of the soil samples. The soil properties shown in table1.

Fig1 Testing machine

Table1 Soil properties

| Level number | Name of soil sample | Depth | Moisture content W% | Wet density ρ g/cm3 | Dry density ρ d g/cm3 | Liquid limit $W_l$% | Plastic limit Wp% | Plastic limit index Ip | Liquid limit Index Il |
|---|---|---|---|---|---|---|---|---|---|
| 1 | clay | 132.9 | 20.92 | 2.05 | 1.70 | 43 | 23 | 20 | -0.104 |
| 2 | Fine sand | 140.6 | 17.83 | 2.09 | 1.77 | | | | |

## Test results and analysis

### Test results

The test results shown in table2.

Table2 Test results

| Level number | Name of soil sample | The experimental condition | Test temperature (℃) | Test force (kN) | Stress (kN) | Axial deformation (mm) | Axial strain (%) |
|---|---|---|---|---|---|---|---|
| 1 | clay | No pressure, room temperature | 15 | 1.19 | 0.61 | 19.65 | 19.56 |
| 1 | clay | No pressure, room temperature | 15 | 1.29 | 0.66 | 18.20 | 19.00 |
| 2 | Fine sand | No pressure, room temperature | 15 | 1.46 | 0.74 | 16.31 | 19.14 |
| 2 | Fine sand | No pressure, room temperature | 15 | 1.58 | 0.80 | 16.71 | 19.64 |
| 1 | clay | No pressure, frozen soil | -5 | 4.61 | 2.39 | 14.36 | 19.20 |
| 2 | Fine sand | No pressure, frozen soil | -5 | 4.55 | 2.38 | 13.41 | 16.77 |
| 1 | clay | Pressure, frozen soil | -5 | 4.95 | 2.52 | 13.16 | 16.45 |
| 2 | Fine sand | Pressure, frozen soil | -5 | 5.11 | 2.62 | 13.35 | 16.69 |
| 1 | clay | No pressure, frozen soil | -10 | 7.53 | 3.88 | 11.35 | 13.57 |
| 2 | Fine sand | No pressure, frozen soil | -10 | 7.95 | 4.15 | 10.63 | 13.48 |
| 1 | clay | Pressure, frozen soil | -10 | 8.77 | 4.41 | 10.35 | 12.87 |
| 2 | Fine sand | Pressure, frozen soil | -10 | 8.87 | 4.62 | 10.43 | 12.68 |
| 1 | clay | No pressure, frozen soil | -15 | 10.94 | 5.55 | 9.65 | 12.07 |
| 2 | Fine sand | No pressure, frozen soil | -15 | 11.44 | 5.81 | 9.81 | 12.27 |
| 1 | clay | Pressure, frozen soil | -15 | 11.82 | 6.12 | 5.95 | 5.97 |
| 2 | Fine sand | Pressure, frozen soil | -15 | 11.89 | 6.09 | 7.79 | 9.74 |

**The uniaxial compressive strength of frozen soil is larger than the one of normal soil**
According to the test results, the uniaxial compressive strength of frozen is larger than that of no-frozen, and generally 2-4 times, what's more, the lower the temperature, the greater its compressive strength, but to a certain low temperature, with the decrease of temperature, the compressive strength increase is not obvious. For some formation, lower freezing temperature is good for enhance the strength of soil, but to a certain temperature, increase its strength by reducing the temperature is limited.

**The compressive strength of frozen soil under pressure is higher than that without pressure**
As we all know, deep soil layer is affected by the overlying strata pressure, it has some stress, tests have proved that, the compressive strength of frozen soil under stress is larger than that after release the stress, this has a certain relationship with the condition of freezing.

## Analysis

According to analysis of test results, there are several points that the axial compressive strength of samples under pressure is larger than without pressure.
1, The specimens have frost heave, from the freezing test have found that samples is limited in the lateral, but after the soil specimen whose ends have no restrictions(under no pressure) freeze, two ends of the sample have bulging phenomenon, it is obviously that the sample has frost heave in the freezing. So it is indicating that when the specimen is freezing, the volume increases, the density becomes small.
2, Usually, sample freezing in sealed container will produce frost heave, but there are constrains on sample from container in all directions, specimen size can not be increases, but with the same quality, the density will larger than it in no constraint.
3, For the sample is restrained by the fix container device, and the specimen produces frost heave force in freezing, but the frozen sample volume is still the same with before freezing, samples must digest the volume that was produced when freezing, so the sample particle must be rearranged, it will into an more reasonable and close state, therefore, the density under pressure frozen is larger than that without pressure frozen, this is the reason why the uniaxial compressive strength under pressure is larger than it without pressure.

## The conclusion

According to the above analysis, the compressive strength of frozen soil under pressure is larger than it without pressure, the frozen test data that usually completed in the laboratory, its strength is lower than it in the original deep frozen soil, so using laboratory test data as the basis of engineering design for the temporary support is relatively safe.

## References:

[1] 《Standard for Soil Test Method》GB/T 50123-1999,China Planning Press.

[2] 《Test Method for the Triaxial Shear Strength of Artificial Frozen Soil》MT/T593.5-1996.

[3] Qian chunchun, Tian yahu, Improvement on Experimental Method of Frost Heaving[J].Low Temperature Construction Technology.2007.（5）102-103.

[4] Wang renhe, Li dongwei, Model Test of Multiple Circle Pipes Freezing and Mathematical Model Study of Water Heat Coupling [J] .Journal of Hefeiu University.2007.(11)1481-1485.

[5] Wang renhe, zhuang rui, Li dongwei, Frost Heaving Force Measurement Study in Formation and Melting of Multi Ring Pipe Frozen Wall [J].Journal of Glaciology and Geocryology. 2010, 32(3): 538-542.

[6] Tang yiqun, Hong jun, Experimental Study on Frost Heaving Characteristics of Mucky Clay under Artificial Freezing [J].Chinese Journal of Geotechnical Engineering. 2009, 36(6): 359-365.

[7] Peng liyun, Liu Jiankun, Tian yahu, Research on Frost Heaving Characteristics of Silty Clay [J].Hydrogeology and Engineering Geology. 2009, 36(6): 359-365.

[8] Wang yansen, Li binsheng, Numerical Simulation Method of Temperature Field of Freezing Shaft Out- wall[J].Mining and Engineering Safety Journal. 2007.(9)316-320.

*Applied Mechanics and Materials Vols. 580-583 (2014) pp 52-55*
*© (2014) Trans Tech Publications, Switzerland*
*doi:10.4028/www.scientific.net/AMM.580-583.52*

# Discussion on Treatment Technology of Reinforcement Pile in Karst Area

Zheng ChengBo [1, a], Xu Jie[1, a]

[1] School of Architecture, Linyi University, Linyi, Shandong, China

[2]The 7th Institute of Geology & Mineral Exploration of Shangdong Province, Linyi, Shandong, China

[a]15653971769@163.com, [b]zhengchengbo@lyu.edu.cn

**Keywords:** Limestone cave;Reinforcement;Pressure grouting;High pressure grouting; Supplementary pile

**Abstract.** With the example of pile foundation engineering in the limestone karst fissure reinforcement, discusses the principle of reinforcement of pile foundation in karst area, introduces some construction technology of pile foundation reinforcement, the reinforcement design principles and the reinforcement scheme is briefly discussed, and combined with the engineering practice and put forward a set of safety, economy and reasonable treatment plan, to reinforcement technology promote the karst pile foundation bottom cave, fracture.

## Introduction

With the rapid development of Chinese economy, more and more high-rise building project, the bearing capacity of foundation design requirement is more and more big, need to design of bored pile foundation in karst area, and is often accompanied by cave, resulting in pile foundation bearing capacity decreased significantly, and the adverse effects of great uncertainty, impact structure safety engineering; these problems according to the own experience analysis.

## Introduction to engineering

### 1.1 Engineering survey

A university library, the library is something 150m, north-south width of 157m, 7 layers, high41.7m, frame structure, the foundation for bored pile foundation pile, single column, pile diameter is 600mm, φ800mm, φ1000mm and φ1200mm, a total of 362 trees. The pile foundation construction ends with drilled core testing, test results showed the presence of karst cave, fissure part of pile end below 5 meters, the cave filling of clay in different degree, rock crushing, does not meet the specification requirements; safety, economy and reasonable based on the principle, must exist at the ends of piles or fissure cave on the shallow part of the reinforcement, ensure the safety of the building.

### 1.2 Engineering geological conditions

According to the "report" the geotechnical engineering investigation, site soil layer from top to bottom are as follows:

The miscellaneous fill: the average thickness of 1.46m; ②The average thickness 2.77 m; ③Clay: the silty clay: the average thickness of 1.02 m; ④The average thickness of sand: 3.52 m; ⑤The average thickness of clay: 3.12 m; ⑥The whole weathered diorite Bin Yan: exposing the maximum thickness of 31.20m (nonexposed); ⑦The strong weathered diorite Bin Yan: exposing the layer 1.80 ~ 12.30m; ⑧The weathered diorite Bin Yan: to expose the thickness of 1.2 ~ 6.10m, ⑨Limestone weathering: the main form in karst caves fracture, exposing the maximum thickness is 18.90m.

## Reinforcement scheme design

### 2.1 Design principles

According to the characteristic of bearing capacity of single pile foundation of different values, respectively, for each problem pile according to current calculation of the bearing capacity of pile bearing capacity, compared with the lack of data [1], consider using pressure grouting, grouting pressure, grouting and grouting strengthening side, adding the bored pile, processing method based on fourth, lack of size selection of bearing capacity of the different processing methods, selection of reinforcement method is mainly based on the following principles:

(1) When the bearing capacity of single pile pressure grouting is greater than the bearing capacity of single pile and pile end value, no cave development, the core drilling hole sealing treatment using pressure grouting method (I).

(2) When the pile end existent cave, pile bearing stratum of rock fragmentation, pile bearing stratum argillaceous limestone or porphyrite, pile end rock cracks developed, if after grouting reinforcement of bearing capacity of single pile is larger than the single pile stress value, through core drilling hole using high pressure grouting the reinforcement treatment on the method (II).

(3) When after grouting reinforcement of bearing capacity of single pile bearing capacity of single pile is less than the value, if the difference between the two is smaller, the pile end of karst strata on the top of thick, strengthened by grouting and the side grouting reinforcement (III).

(4) When after grouting reinforcement of bearing capacity of single pile bearing capacity of single pile is less than the value, if the pile end of karst strata on the top of the thinner or single pile bearing capacity than the bearing capacity of single pile is small is big, the addition of bored pile reinforcement (IV).

### 2.2 Reinforcement schemes

According to the design drawings [2] all kinds of pile bearing capacity of single pile, survey report and core drilling test results on the problems of the pile one one was used to analyze the bearing capacity calculation, the final classified on the need to deal with the pile; do not meet the design requirements of a total of 197 tall pile, classified processing in accordance with the above four kinds of processing methods, so this part of the bearing capacity of pile foundation can meet the design requirements, which uses two times of high pressure grouting bolt (in bored pile construction of pile side is φ220) was used to reinforce the 10 trees, using pressure grouting plugging of drilling core hole 66 trees, high-pressure grouting (only φ48 steel tube as the high pressure grouting pipe), the 89 trees strengthen the pile pressure grouting, supplement 10, and 22the diameter of 600mm or 800mm. Pressure grouting, grouting by drilling core drilling test of the implementation of the original.

## Reinforcement construction scheme

### 3.1 Pressure grouting construction

3.1.1 Pressure grouting construction method

Pressure grouting construction method is as follows: decentralization of grouting pipe, hole cleaning, grouting, repeated grouting, the next cycle of operation.

(1) To the grouting pipe: according to the design drawings in the pile hole grouting plastic tube (or pipe down). The grouting pipe length should be greater than the grouting depth 30cm ~ 50cm for grouting and ground pipe connected.

(2) The hole cleaning: after running the grouting pipe, the grouting pipe connection to the mud pump through grouting hose ground detection hole, wash with water, back out until the hole in the water not containing impurities.

(3) Slip casting : the special mixing barrel grouting and grouting pump, injection pump working pressure should meet the requirements of construction (less than 0.5MPa). According to the design, preparation of slurry, slurry mixing evenly, with the mix with the use of grouting slurry pump to be reinforced with Kong Zhong, grouting with the grouting pipe up, but ensure the nozzle always buried in the slurry below 1 ~ 1.5 meters.

(4) Repeated grouting: by perfusion of the water cement ratio, along with the solidification cement grout, grouting holes will have certain decline in [3], in order to ensure grouting and the existing pile surface as high, at the first end 45min grouting to a grouting, grouting, grouting pipe end to enter into the liquid level of not less than 50cm, grouting slurry returning to the pile surface. Liquid filling slurry to repeatedly until after the final set of pile top elevation consistent before the slurry coagulation.

3.1.2 Quality assurance measures

(1) Water cement ratio is 0.6 ~ 0.7, to ensure that the use of cement and water to be weighing.

(2)The water to be neutral water does not contain impurities.

(3) The grouting pipe to ensure smooth and at any time to check the dimensions on the grouting pipe.

(4) Grouting pressure is 0.2 ~ 0.5Mpa.

**3.2 High pressure grouting and high-pressure grouting strengthening**

3.2.1 The process

The process is as follows: embedded grouting pipe and an exhaust pipe→ sealing hole→hole cleaning→ water pressure→high pressure grouting→the next cycle of two high-pressure grouting→ plugging grouting pipe→ the next cycle.

(1) Embedded grouting pipe and the exhaust pipe: according to the design drawings in the pile hole to pre process of high pressure grouting good pipe, and the sealing position with steel welded tripod 6.5, the exhaust pipe is tied to the high pressure grouting pipe, the exhaust pipe mouth over the tripod position 5 ~ 10cm high; pressure grouting pipe length should be greater than the grouting depth 30cm ~ grouting hose to the ground and connected with the 50cm tube

(2) Sealing: dry cement mortar rigid according to the sealing length of hole sealing, dry harden cement mortar shall be compacted layer by layer.

(3) The hole cleaning: sealing 24 ~ 48 hours after injection to be empty, strengthened by high pressure grouting hole, until the exhaust hole in the water does not contain impurities square hole cleaning.

(4) Water pressure: empty after water pressure with wedge, exhaust hole is blocked, carry out the high water pressure, the pile bottom sediment and soft soil is split, the pressure is not less than 0.2MPa.

(5) High pressure grouting: high pressure grouting pressure after the water, open the exhaust pipe, high pressure grouting, when the slurry from the exhaust pipe to return does not contain impurities, the exhaust pipe is welded, then the high pressure grouting in high pressure grouting pipe. Grouting slurry to a special stirring barrel and grouting pump, injection pump working pressure should meet the requirements of construction (less than 5MPa). According to the design, preparation of slurry, slurry mixing evenly, with the mix with the mud pump to be reinforced hole grouting, grouting pressure not less than the design pressure, and loading time of not less than 5min.

(6) Plugging grouting pipe: high pressure grouting sealing grouting pipe after the high pressure grouting pipe welded to prevent slurry returning to surface.

3.2.2 Quality assurance measures

(1) Water cement ratio is 0.6 ~ 0.7, the cement and water to weighing.

(2) The water to be neutral water does not contain impurities.

(3) Grouting pipe to ensure the smooth and have good weldability.

(4) High pressure grouting pressure is 2 ~ 3Mpa, grouting pressure with shockproof pressure meter, loading time must use the meter

(5)The high pressure grouting pipe machining welded to ensure weld height, the electrodes shall comply with the relevant standards of the state.

**Comparison of the test, test and economic effect**

Do not meet the requirements of the specification of the pile after treatment, entrust the local detection unit for the treatment of pile load test, the core drilling test and dynamic test and other

methods of detection, the pile can meet the design requirements, to achieve the desired results, treatment scheme of the project than the conventional filling pile or pile again drilling, a comprehensive analysis on the basis of pile bottom karst fissure size and distance from the bottom of pile is different, different processing methods for the project to save millions of dollars, but also saves time, achieved very good results.

## Conclusion

Treatment technology of grouting pile foundation construction in karst area is currently the most effective method of treatment, reliable reinforcement, it is a settlement of single pile construction in the reconstruction of the investigation report and the actual construction geology is inconsistent, and provides a new idea of pile end rock integrity can not meet the specification requirements of processing. Individually for each does not meet the requirements of the standard calculation of pile separately, comparing several schemes, different requirements by different processing plan.

## References

[1] Cheng ye, Zhao Minghua, Cao Wengui. Strength reduction method of [C] / / ninth soil mechanics and geotechnical engineering academic conference papers stability evaluation of karst cave roof under pile foundation.2003

[2] Zhao Minghua, Yuan Tengfang, Li Li, Jiang Desong. The karst pile capacity calculation of safety thickness of strata layer on [J]. highway, 2003, (1):124-128

[3] Li Zhirong, Wang Zhenyu. Bored pile in karst area design and construction of [J]. engineering construction and design, 2000, (1):56-57

*Applied Mechanics and Materials Vols. 580-583 (2014) pp 56-60*
*© (2014) Trans Tech Publications, Switzerland*
*doi:10.4028/www.scientific.net/AMM.580-583.56*

# Effect of Variable Permeability Coefficient on Consolidation of Ultra-soft Ground under Vacuum Preloading

Binbin Xu[1, a], Aihua Liang[2, b] and Mingying Li[3, c]

[1]Key Lab. of Geotechnical Engineering of Tianjin, Tianjin, China; Key Lab. of Geotechnical Engineering, Ministry of Communication, Tianjin, China; Tianjin Port Engineering Institution, Ltd. of CCCC., Tianjin, China

[2]Key Lab. of Geotechnical Engineering of Tianjin, Tianjin, China; Key Lab. of Geotechnical Engineering, Ministry of Communication, Tianjin, China; Tianjin Port Engineering Institution, Ltd. of CCCC., Tianjin, China

[3]Key Lab. of Geotechnical Engineering, Ministry of Communication, Tianjin, China; Tianjin Port Engineering Institution, Ltd. of CCCC., Tianjin, China

[a]xubinbin@tpei.com.cn, [b]Liangah75@sina.com, [c]limingying@tpei.com.cn

**Keywords:** Ultra-soft ground; Vacuum preloading; Finite element; Variable permeability coefficient

**Abstract.** In this paper, a soil-water coupled finite element analysis incorporated the macro-element method is carried out to investigate the effect of variable permeability coefficient on the consolidation of the ultra-soft ground using vacuum preloading. Sys cam-clay model is employed as the constitutive model of the ultra-soft soils. When the drain space becomes from 60cm to 40cm, there is significant acceleration in the numerical settlement of the ground using the constant permeability coefficient, which is quite different from the observational results. When the variable permeability coefficient where a liner relationship between the void $e$ and the logarithmic value of permeability coefficient $\ln k$ is adopted is employed, there is a good accordance between the numerical and observational settlements. According to the distribution of variation in the void, the largest variation in the void occurs at the top several layers and therefore the predominant settlement can be attributed to the volumetric compression of the top several layers.

## Research Background

Land reclamation has been the main treatment to relieve the land shortage in Binhai New Area of Tianjin. The reclaimed ground consists of ultra-soft dredged soils from Bohai sea, which is of very high water content, low bearing capacity and small permeability. The vacuum preloading has been extensively used in the land reclamation in the coastal region. Large-scale field tests about the vacuum preloading of the ultra-soft ground have been carried out by Liang et al. [1] and they found that when the space of the plastic vertical drain varies from 60cm to 40cm, the degree of vacuum pressure increases correspondingly but there is no obvious acceleration in the settlement, which may attribute to the decreasing void during the vacuum preloading. In order to explain the above phenomena, many scholars have investigated the influence of the variable permeability caused by the decreasing void on the vacuum preloading theoretically and numerically [2,3,4]. However, there is no systematical finite element analysis about the influence of variable permeability coefficient on the consolidation of the ultra-soft ground. In this paper, a soil-water coupled finite element analysis incorporated the macro-element method is carried out to demonstrate the effect of the variable permeability coefficient on the vacuum preloading.

## Introduction of the Macro-element Method

One of the difficulties in the numerical calculation of the vacuum preloading is the mesh partition. It is well known that there is much difference between the size of the ground and the size of the plastic vertical drain. If specific meshes are assigned to the vertical drain, the mesh will become too fine to

finish the calculation in a rational period. In addition, when a three-dimensional vacuum preloading problem is simplified as a two-dimensional plane strain problem the numerical drain space ratio and discharge capacity should be adjusted artificially according to the practical ones [5,6]. Based on the soil-water continuity equation proposed by Akai and Tamura [7], Seikiguchi et al. [8] introduced the concept of the macro-element method for two-dimensional consolidation problems. As shown in Fig. 1, the plastic vertical drain is simplified as the pore water pressure $u_D$ inside the element, which is not necessary to designate specific meshes for the vertical drains. Through changing $u_D$, the pore water can flow into/out of the element and the volume of element is variable as if there were plastic vertical drains.

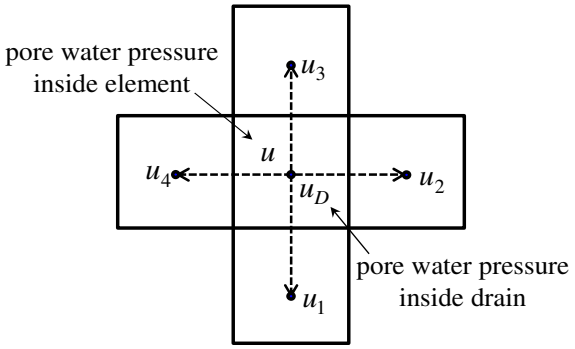


Fig. 1. Sketch of pore water flow among element, vertical drain and adjacent elements

## Calculation Conditions

**Mesh Partition.** The reclaimed ground is with the width of 96m, length of 150m and depth of 4m with ultra-soft dredged soils. The plastic vertical drain is placed with the width of 14m and the depth of 3.5m, where the improved area is marked as the macro-element area in Fig. 2. Based on the practical field tests, the equivalent well space $d_e$, the well diameter $d_w$ and the discharge capacity $k_w$ are 0.6 or 0.4m, 6.75cm and 4.0cm/s respectively, that is the drain spacing ratio $n = d_e / d_w$ is around 9 or 6. The hydraulic boundary is also shown in Fig. 2, where the vacuum pressure -80kPa is applied at the top of the plastic vertical drain. The undrained boundary is applied at the bottom of the drain to represent the sealing of the drain at the bottom. At the right side of the macro-element area, the undrained condition is applied from the top surface until 1.5m underground to act as the clay sealing wall. In the left side of the ground, the undrained condition is used considering the symmetry

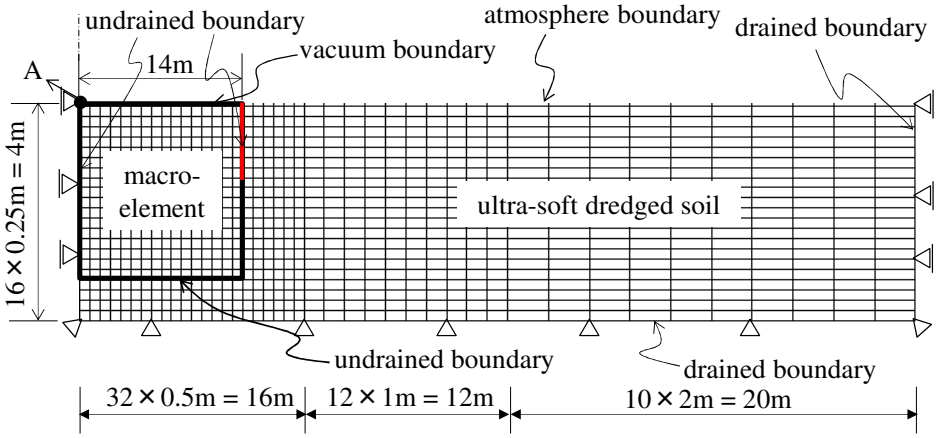


Fig. 2. Mesh partition and boundary conditions

**Soil Parameters.** The sys cam-clay model [9], which is able to describe the different extent of disturbance of soils by introducing the concept of structure, overconsolidation and anisotropy, is employed as the constitutive model of the ultra-soft soils. Through the curve fitting of the experimental and numerical results of the one-dimensional compression test as shown in Fig. 3, the

soil parameters can be determined in Table 1. In Fig. 3, there is a sudden decrease in the specific volume around 10kPa. Through assigning appropriate degree of structure and overconsolidation, such decrease can be reproduced accordingly.

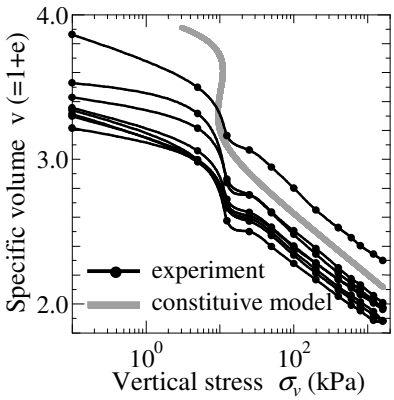


Fig. 3. Curve fitting of experimental and numerical results for one-dimensional compression test

Table 1 Soil parameters and initial values of ultra-soft soil

| *Elasto-plastic parameters* | | *Initial values* | |
|---|---|---|---|
| compression index $\tilde{\lambda}$ | 0.29 | specific volume $v_0$ | 4.0 |
| swelling index $\tilde{\kappa}$ | 0.015 | stress ratio $\eta_0$ | 0.75 |
| critical state constant M | 1.4 | degree of structure $1/R_0^*$ | 950 |
| intercept of NCL*) N | 0.8 | degree of OC $1/R_0$ | 3.5 |
| poisson's ratio $\nu$ | 0.4 | degree of anisotropy $\varsigma_0$ | 0.0 |
| *Evolutional parameters* | | soil particle density $\rho_s$ [g/cm$^3$] | 2.76 |
| degradation index of structure $a$ | 0.88 | permeability coefficient $k$ [cm/s] | $5\times10^{-8}$ |
| degradation index of OC $m$ | 0.8 | | |

*) specific volume on NCL of fully remolded soil when $p'$=98.1kPa, $q$=0

## Calculation Results

**Settlement.** The observational and numerical settlements at node *A* in Fig. 2 when the drain spacing ratio is 9 are shown in Fig. 4. As can be seen, there is a good accordance between two settlements, which proves that the soil parameters employed in Table 1 is reliable. The slight differences may attribute to the instable vacuum pressure at the initial stage.

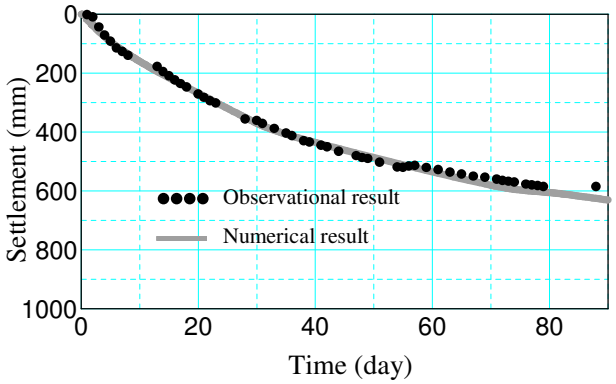


Fig. 4. Observational and numerical settlements at node *A* ($n$=9)

As explained by Xu et al. [10], one of the merits of the macro-element method is that it is unnecessary to re-divide the mesh when different drain spacing ratios are employed. Therefore, using the same mesh partition the numerical settlement can be presented in Fig. 5. Initially, the numerical result corresponds to the observational one very well until around 20d after the application of the vacuum pressure. However, the difference becomes more and more remarkable as the time of the vacuum preloading elapses when the constant permeability coefficient $k$ is adopted, which can attribute to the decreasing permeability caused by the decreasing void as the progress of the vacuum preloading.

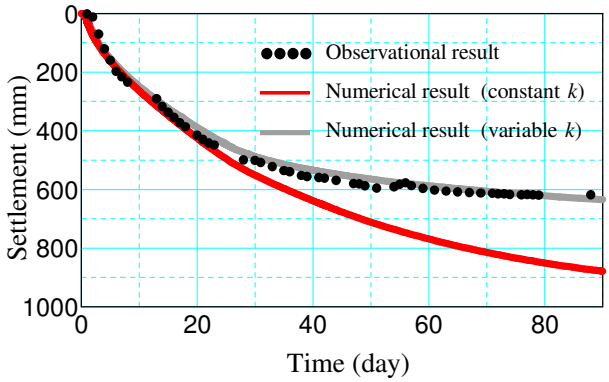


Fig. 5. Observational and numerical settlements at node $A$ ($n$=6)

In order to investigate the effect of the variable permeability coefficient $k$ on the vacuum preloading, a linear relationship between the void of the ultra-soft soil and the permeability coefficient is used as shown in Eq. (1). Here, $e_0$ is the initial void and $k_0$ is the initial permeability coefficient. $c_k$ can be determined by the try-and-error method. Limited to the space of this paper, the determination of $c_k$ is neglected and we directly assign 0.8 to it. Fig. 5 also presents the settlement of node $A$ when the variable permeability coefficient is employed, in which Eq. (1) is used. As can be seen, there is a very good correspondence between the observational and numerical settlements. Compared with the case where the constant $k$ is used, the permeability coefficient gradually decreases as the void becomes smaller in the variable-$k$ case. Moreover, the smaller the drain space is, the larger the variation of the permeability is. Therefore, it is very necessary to consider the variation of permeability coefficient for the consolidation of the ultra-soft ground, especially when there is a considerable change in the void of the ground.

$$e - e_0 = c_k \left( \ln k - \ln k_0 \right). \tag{1}$$

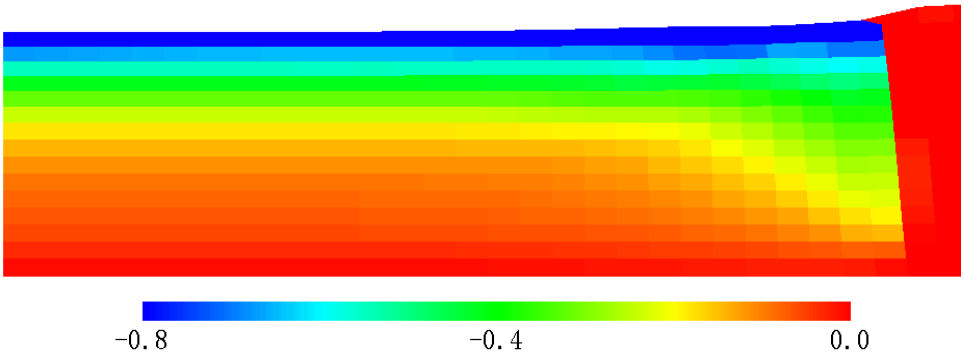


Fig. 6. Distribution of variation in the void in the ground of the improved area when 70d vacuum consolidation ($n$=6)

**Distribution of Variation of the Void.** The distribution of variation in the void of the improved ground after the vacuum pressure has been applied for 70d is shown in Fig. 6. In the color legend, the red end (0.0) represents that there is no void change and the blue end (-0.8) means that there is void decreasing, namely volumetric compression. As can be seen, the decrease of the void becomes smaller and smaller from top to bottom. Therefore, the decrease of the permeability coefficient also becomes smaller and smaller downward. In addition, the predominant volumetric compression concentrates at the top several layers. It can be known that the volumetric compression in the top several layers contributes to the main settlement at the ground surface, even though the length of the plastic vertical drain is very large. At the boundary of the improved area and unimproved area, due to the undrained condition of the clay sealing wall, there is no variation of void in the unimproved area.

## Conclusions

In this paper, a soil-water coupled finite element analysis incorporated the macro-element method is carried out to investigate the effect of variable permeability coefficient on the consolidation of the ultra-soft dredge ground during the vacuum preloading. The conclusions are as follows:

(1) In the vacuum preloading of the ultra-soft ground, it is necessary to consider the decrease of the permeability coefficient when the void becomes smaller accompanying the volumetric compression.

(2) As the drain space changes from 60cm to 40cm, there is no obvious acceleration in the settlement of the surface due to the significant decrease of the permeability. The smaller the drain space is, the larger the variations of the void and the permeability coefficient are.

(3) The variation of the void gradually decreases from top to bottom, namely the variation of permeability coefficient deceases downward and the settlement of at the ground surface can be mainly attributed to the volumetric compression of the top several layers.

**Acknowledgements**
The authors would like to thank *Assoc. Prof. Yamada* and *Dr. Son* in *Nagoya University* for their valuable suggestions in the calculation.

**References**

[1] A.H. Liang, J.J. Liu, M.Y. Li and W. Li: Chinese Journey of Geotechnical Engineering Vol. 35 Supp. 2 (2013), p. 712-716. (In Chinese)

[2] H.Y. Lei, W.Z. Zhang, P. Han, M.S. Huang, X.C. Wang and L. Chen: Chinese Journey of Geotechnical Engineering Vol. 35 No. 12 (2013), p. 2328-2333. (In Chinese)

[3] C.L. Qiu, S.W. Yan, L.Q. Sun and Y.C Ji: Rock and Soil Mechanics Vol. 34 No. 3 (2013), p. 631-638. (In Chinese)

[4] L.Q. Sun, A.W. Yang, R. Liu and C.L. Qiu: Journal of Engineering Geology Vol. 21 No. 3, p.476-480. (In Chinese)

[5] B. Indraratna, I. Sathananthan, C. Rujikiatkamjorn and A. Balasubramaniam: International Journal of Geomechanics, Vol. 5, No. 2 (2005), p. 114-124.

[6] J. C. Chai, J. Carter and S. Hayashi: Journal of Geotechnical and Geoenvironmental Engineering, Vol. 131, No. 12 (2005), p. 1552–1561.

[7] Akai, K.; Tamura, T.: Proceeding of JSCE, (1978) , p. 98–104. (In Japanese)

[8] H. Sekiguchi, T. Shibata, A. Fujimoto and H. Yamaguchi: Proceeding of the 31st Symposium on JGS, (1986), p. 111–116. (In Japanese)

[9] A. Asaoka, T. Noda, E. Yamada, K. Kaneda, and M. Nakano: Soils and Foundations, Vol. 42, No. 5 (2002), p. 47–57.

[10] B. Xu, A.H. Liang, J.B. Fu, J.F. Hou and J.S. Li: submitted to Hydro-science and Engineering (2013). (In Chinese)

*Applied Mechanics and Materials Vols. 580-583 (2014) pp 61-67*
*© (2014) Trans Tech Publications, Switzerland*
*doi:10.4028/www.scientific.net/AMM.580-583.61*

# Experimental application of fractal theory into selection of subgrade filling materials

Xigang Wang[1, a]

[1]College of resources and civil engineering , Liaoning institute of science and technology,176 xianghuai Road, shiqiaoziDistrict, Benxi city, Liaoning province, China 117004

[a]fx_wxg@163.com

**Keywords:**fractional dimension; dopant amount; settlement and deformation; prediction model

**Abstract.**To investigate the settlement deformation of subgrades, we used fractal theory and soil section technology to study the original foundation soil, and soils filled with 4%, 8%, 12%, 16%, 20% and 24% of A material. The results show that under consolidation pressure of 500 KPa and after one dry-wet circulation, the fractal dimension was 1.7 in the original soil, 1.78 in the soil filled with 4% A material, and 1.93 in the soil filled with 24% A material. Along with the increased dopant amount of A material, the fractal dimension of soil mass gradually increased, but after the dopant amount reached 24%, the increasing rate was very slow. With the increased addition of A material, the compression deformation gradually weakened, but after the dopant amount reached 24%, the changing rate was very small. We derived a prediction model between the dopant amount at a certain particle size and the fractional dimension. This model can be used to predict the dopant amount at a certain size. The reasonableness of this model when using single size was validated via engineering practice.

## Introduction

Because of the formation history and stress history, rock-soil porous materials will lead to heterogeneity in rock-soil engineering materials. Unsaturated rock-soil mass is largely affected by porosity and suction. The key in studying the macromechanic properties of rock-soil materials is how to accurately describe their microstructral composition. It is hard to study the internal microstructure of soil mass via traditional geometrical methods.

Based on fractal geometry theory and related experimental data, we analyzed the pore microstructure of rock-soil porous media and found the obvious fractal properties of rock-soil materials. Studying the macromechanic properties of rock-soil materials via analysis of internal microstructure will help to better serve engineering practice [1,2].

The subgrades of high-speed rails require strict settlement control, thus raising demand for the properties of filling materials to be used in subgrades. Generally, the quality of the original foundation soil does not meet engineering demands, and in most cases, we have to dope additional materials to improve the soil mass. However, a low addition will not yield the expected effect, while a high addition is not economic. In this paper, thus, based on engineering practice, we use fractal theory to analyze the soil mass materials, to determine fractal dimensions, and determine the dopant amount of materials on basis of relationship between fractional dimension and soil-mass compressed deformation. We expect to provide better services for engineering.

## Experimental analysis

Images were recorded by electron microscopy and processed on Image-Pro Plus (IPP). The original foundation soil, and the soils filled with 4%, 8%, 12%, 16%, 20% and 24% of A material were marked as groups 1 to 7.

### 1.1 Sample collection

Three types of soil were collected with a thin-walled steel cylinder (height 30 cm, radius 12 cm). Each type of soil was set with 4 samples, which underwent 0, 1, 3, and 5 dry-wet circulations respectively. The samples were consolidated under 500 KPa.

### 1.2 Preparation of soil sections

The soils were compressed under the consolidation pressure to a height < 30 cm. Considering the boundary effect, we cut off the uppermost 4 cm soil from each sample. Then a soil section was collected at each 3 cm. Seven sections were cut from each sample.

## Soil-mass fractional dimension

### 2.1 Fractal dimension of original area distributing of particles

The rock soil mass is composed of a pore structure and a particle structure. Via soil sections and IPP [3,4,5,6], we obtained pore distribution rules, pore number and size, relationship between pore area and size. Based on these data, the fractal dimension of particle original area distribution was used via box counting method as follows:

$$A(\geq R) = A_T\left[1\text{-}(\frac{R}{R_{max}})^{2\text{-}D_0}\right] \quad (1)$$

where R——reference particle size

$R_{max}$——maximum particle size

$A(\geq R)$——total area of particles≥R

$A_T$——total area of the reference range

$D_0$——fractal dimension of pore original area distribution

Logarithm of two sides of Eq. (1) yields:

$$\ln[1 - A(\geq R)/A_T] = (2 - D)\ln(R/R_{max}) \quad (2)$$

With $\ln[1 - A(\geq R)/A_T]$ as Y-axis and $\ln(R/R_{max})$ X-axis, the experimental data were fitted to obtain a linear slope k. The fractal dimension of original area of foundation soil was calculated as follows:

$$D_0 = 2\text{-}k \quad (3)$$

### 2.2 Distributing fractal dimension of tested soils

Based on soil section technology and image processing technology, with particle sizes 4, 3.5, 2, 3, 2.5, 2.5, 1, 0.5 cm as dividing sizes, the experimental data were used to analyze the relationships between fractal dimension of original area of foundation soil and particle size (Fig. 1).

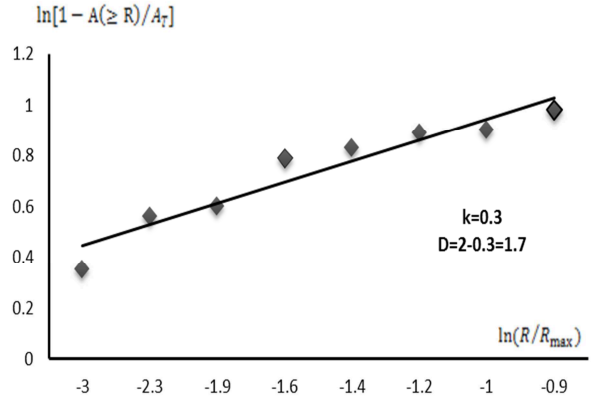


Fig.1 Fractal dimension of original area of foundation soil

Figure 1 shows that the logarithms of particle size and particle area are in linear relationship, with slope of 0.3. Based on Eq. (3), the fractal dimension of original particle is 1.7.

Similarly, the soil masses of groups 2 -7 were analyzed, and the relationships between the fractal dimension of original area and particle size are showed in Fig. 2.

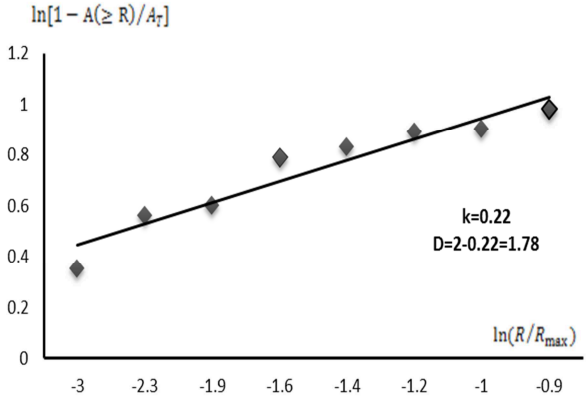


a:dopant amount of material A = 4%

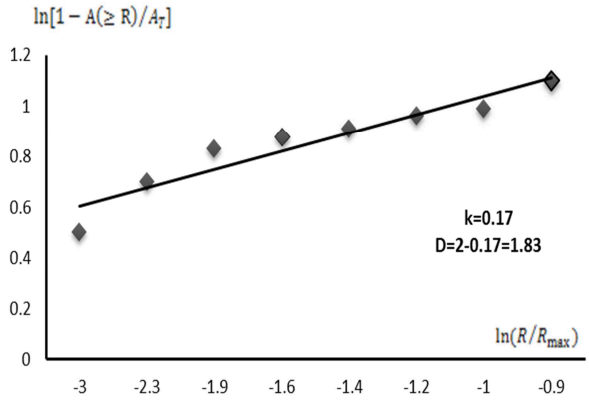


b:dopant amount of material A = 8%

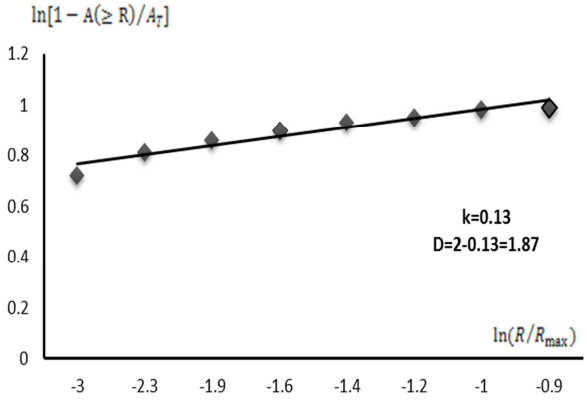


c: dopant amount of material A =12%

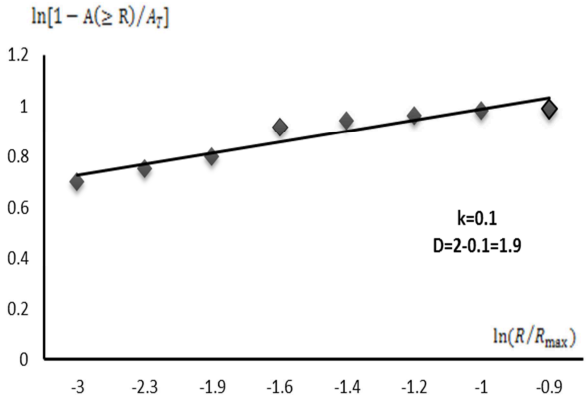


d:dopant amount of material A =16%

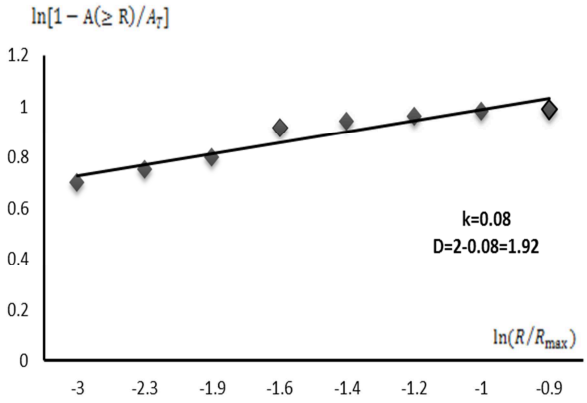


e:dopant amount of material A = 20%

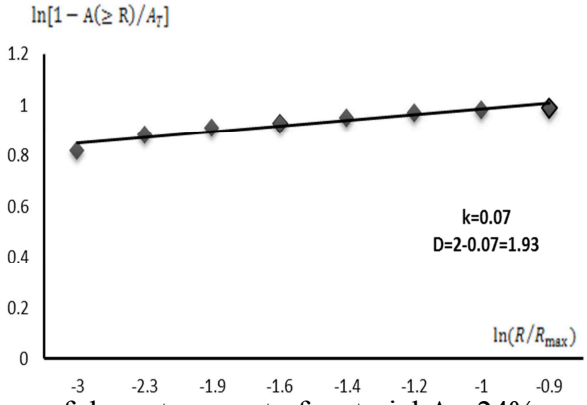


f:dopant amount of material A =24%

Fig. 2 Relationship between fractal dimension and dopant amount of A material

Figure 2 shows that the fractal dimensions of groups 2 to 7 are 1.78, 1.83, 1.87, 1.9, 1.92, and 1.93, respectively.

The relationship between dopant amount of A material and fractal dimension is showed in Fig. 3.

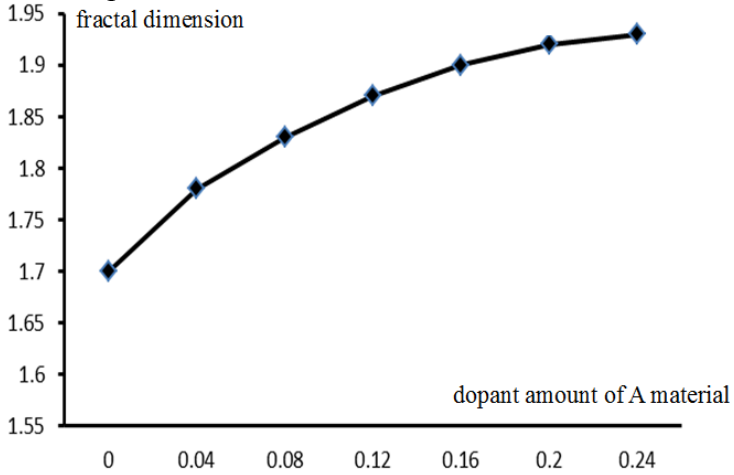


Fig.3 Relationship between fractal dimension and dopant amount of A material

Clearly, along with the increased dopant amount of A material, the fractal dimension of soil-mass original area distribution gradually increases; at dopant amount of 20% or 24%, the increasing rate of fractal dimension slows down, indicating that A material effectively fills the pores of large particles.

Each soil sample was cut into 7 sections which were not of the same the depth. Experiments show that the soil-mass fractal dimensions from each section are inconsistent, and the relationships between fractal dimension and depth are showed in Fig. 4.

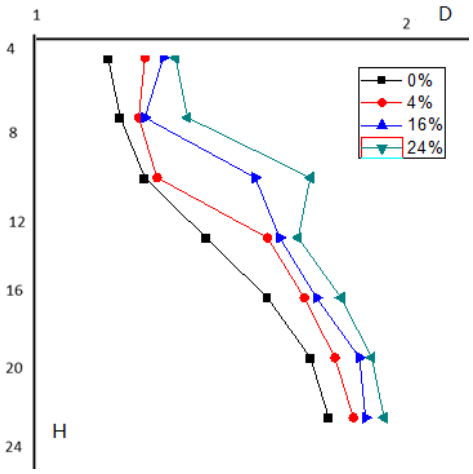


Fig. 4 Relationship between fractal dimension after 1 dry-wet circulation and depth

Clearly, for the same soil sample, under the consolidation pressure, the soil-mass fractal dimension gradually increased along with the increased depth; at the same depth, the fractal dimension also rose along with the increased dopant amount of A material.

### 2.3 Deformation and distributing fractal dimension

By measuring the deformation of each type of soil, we built the relationships between fractal dimension and deformation (Fig. 6).

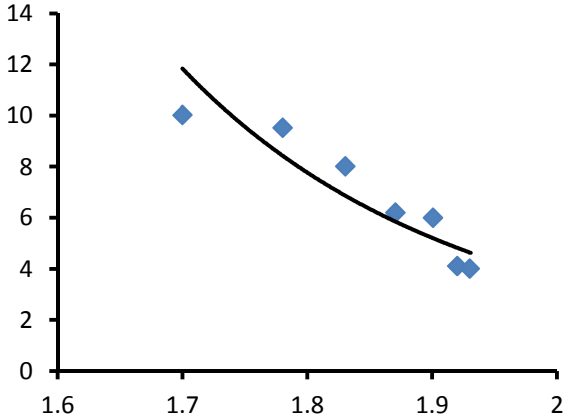


Fig. 5 Relationship between fractal dimension and deformation

Clearly, the deformation was maximized in the original foundation soil; along with the increased dopant amount of A material, soil-mass deformation was enhanced; when the dopant amount was 20%, the soil mass deformation changed very slightly; the deformations were not very different between dopant amounts of 24% and 20%. These results indicate that the dopant amount of 24% A material could well inhibit the soil mass deformation. In this project, addition of 24% A material into the original foundation soil can improve the deformation resistance of soil mass.

### Relationship between fractal dimension and dopant amount

We suppose the volume of original foundation soil is V, the addition of the modifying soil is a*V; when the addition of the modifying soil is equal to the volume of particles with size > R in the original soil, then most pores in the original soil will be filled in, resulting in small consolidation deformation in the mixed foundation soil.

The modified soil was further divided to obtain the relationship between particle size and pore volume. Then we can know the volume of pores between particle sizes R1→R2 (R1<R2). This interval of pores will be filled in with a modifying material with single particle size of R1. In this way, in each interval, we can obtain the particle size of the doped modifying material. Based on the pore

volume, we can determine the dopant amount. A more detailed division will result in less sedimentation in the original foundation soil.

Based on fractal theory and by studying Menger sponges, we obtain the pore volume of particle size ≥ R1 in the modified soil is:

$$V(R_1) = V * （R_1/R_{max}）^{3-D} \quad (4)$$

The pore volume of particle size ≥ R2 in the modified soil is

$$V(R_2) = V * （R_2/R_{max}）^{3-D} \quad (5)$$

where $V(R_1)$ and $V(R_2)$ are the pore volumes of particle size ≥ R1 and ≥ R2 respectively;$R_{max}$ is the maximum particle size. Then the pore volume in the interval R1→R2 (the added volume of the modifying material) is:

$$V(R_1 \to R_2) = V(R_1) - V(R_2) = V * (\frac{R_1 - R_2}{R_{max}})^{3-D} \quad (6)$$

Then the ratio of the modifying material to the modified soil is:

$$a = V(R_1 \to R_2)/V = (\frac{R_1 - R_2}{R_{max}})^{3-D} \quad (7)$$

Then we will study one and two modifying materials.

When the project only utilizes modifying material A with a single particle size, then the dopant amount of A material is:

$$a_1 = \frac{\int_R^{R_{max}} V*(\frac{R-R_{max}}{R_{max}})^{3-D} dR}{V} = \frac{-（R-R_{max}）^{4-D}}{{R_{max}}^{3-D}} \quad (8)$$

If the particle size of material B is R1, the particle size of material C is R2, then the dopant amounts of B and C are:

$$b_1 = \frac{\int_{R_1}^{R_2} V*(\frac{R_1-R_2}{R_{max}})^{3-D} dR}{V} = \frac{-（R_1-R_2）^{4-D}}{{R_{max}}^{3-D}} \quad (9)$$

$$c_1 = \frac{\int_{R_2}^{R_{max}} V*(\frac{R_2-R_{max}}{R_{max}})^{3-D} dR}{V} = \frac{-（R_2-R_{max}）^{4-D}}{{R_{max}}^{3-D}} \quad (10)$$

Then the equation will be validated using the material A with single particle size. Based on the relations between fractal dimension and deformation (Fig. 5), we obtain a suitable fractal dimension, which is in 2D plane, but the fractal dimensions obtained from Eqs. (7-10) are in 3D space. Thus, the fractal dimension in 2D is transformed to the fractal dimension in 3D as follows:

$$D = D_0 + 1 \quad (11)$$

In Fig. 5, D0=1.93, D=2.93, the particle size of material A is 0.16 cm, and the maximum particle size of original foundation soil is 0.4 cm. With Eq. (8), we know when the dopant amount of material A is 23%, the result was close to the dopant amount of 24% in the experiment, thus validating the reasonableness of the equation.

## Conclusions

(1) Along with the increased amount of material A, the fractal dimension of filling material distribution gradually increases, and the fractal dimension of soil mass gradually increases. At dopant amount of 24%, the changing rate of fractal dimension slows down. Along with the increased amount of material A, the compressed deformation was weakened, and after 24%, the deformation was reduced.

(2) Based on fractal theory, we built a prediction model between the dopant amount of modifying material and the distributing fractal dimension. The applicability of this model was validated via engineering practice.

**References**

[1] Zhu Hua. fractal theory and its application [M]. Science press (Beijing), 2011. (in Chinese)

[2] Xie Heping. Introduction into fractal-rock mechanics [M]. Science press (Beijing), 1995. (in Chinese)

[3] Wang Guoliang, Zhou Shenglu, Zhao Qiguo. Volume fractal dimension of soil particles and its application in land use [J]. ActaPedologicaSinica, 2005,42(4):545-550. (in Chinese)

[4] Li Xiangquan, Hu Ruilin, Zhang Li. Microstructure effect of clay soil during consolidation [J]. Geotechnical Engineering Technique, 1999,3(3)52-56. (in Chinese)

[5] XuYongfu, Fu Deming. Structural strength of unsaturated soil [J]. Engineering Mechanics, 1999,35(1):32-36.(in Chinese)

[6] XuYongfu, Dong Ping. Fractal models for soil-water characteristics of unsaturated soils [J]. Rock-Soil Mechanics, 2002,23(4):400-406. (in Chinese)

[7] Tao Gaoliang. Fractal approach on pore structure of rock and soil porous media and its applications [D]. Wuhan University of Technology, 2010.(in Chinese)

*Applied Mechanics and Materials Vols. 580-583 (2014) pp 68-72*
*© (2014) Trans Tech Publications, Switzerland*
*doi:10.4028/www.scientific.net/AMM.580-583.68*

# Experimental study of static disintegration on unsaturated soil

Nianqin Wang[1,a] , Qingtao Wang[1,b] , Qian Xue[2,c]and Xiaoling Liu[1,d]

[1]College of Geology and Environment, Xi'an university of Science and Technology, Xi'an, Shanxi, 710054, China

[2]School of Telecommunication and Information Engineering,XI'an University of Posts & Telecommunications,Xi'an, Shanxi, 710061, China

[1a]nianqinwang@163.com, [1b]wangnish@163.com, [2c]562594509@qq.com,[1d]dizhigcliu@163.com

**Keywords:** Unsaturated Loess; Disintegrating test; Moisture content; Degree of compaction

**Abstract.** In order to explore the disintegration characteristics of compacted loess, through the unsaturated soil disintegration instrument by independently developed,conduct the soaking disintegration experimental study on remolded soil unsaturated samples,obtained a series of experimental results:①The curves can be divided into the slow disintegration, rapid disintegration and stabilization of disintegration in three stages，the degree of compaction and water rate impact on rapidly disintegrating stage;②When the degree of compaction is certain,the disintegration rate decreased with the water contented increasing,the decreased amplitude is increasing with the moisture content increased to18%,the disintegration characteristics disappeared with the moisture content increased to 22%;③When the initial moisture content is certain, the disintegration rate decreased with the degree of compaction increasing, The time significantly prolonged when the disintegration completed. the decreased amplitude is increasing with the degree of compaction increased to 95%,the disintegration characteristics basically disappeared. Based on the relationship of degree of compaction and the moisture content to void ratio, the thesis establishes the model between the disintegration rate and the effective porosity ratio,the formula can be used to calculate the disintegration rate of compacted loess.The specific conclusions are:①When the critical moisture content increased to 22%,the disintegration characteristics disappeared;②When the critical degree of compaction increased to95%， the disintegration characteristics also disappeared.

## Introduction

Because of the special properties of water-sensitive of Loess,The slope(manmade slope ) destruction caused by the disintegration (wet)plagued the construction in Loess areas.Studies have shown that:the disintegration not only beneficial to the slope remodeled,which can emptied slope with the intensified corroding, also can changed the slope shape and slope[1].For this reason,exploring the process and the mode of action of disintegration on unsaturated soil has practical value.A lot of research has been carried out about disintegration on unsaturated soil, [2~3]Carried out soaking disintegration experiments on compacted loess,analyzed the disintegration law influenced by the degree of compaction and moisture content,establishment the correlation between the rate of disintegration and the void ratio,illustrates the nature impact on disintegration by the degree of compaction and moisture content;[4]Analyzed the relationship between the disintegration amount with different depths and the roots;[5]Carried the disintegration experiment with the samples of different initial matric suction by self-made instrument;[6]Conducted disintegration test and triaxial permeability under different initial states on compacted loess；

[7]partitioned the Chinese loess region based on the differences of disintegration characteristic;[8~9]analyzed the disintegration mechanism in the embankment slope in situ test.Due to the hysteresis of its research methods and means,so far there is no general applicability of the disintegration experimental apparatus on unsaturated soil. In this paper,we try to developed the experimental apparatus,to explore the disintegration mechanism on unsaturated soil .

## Experimental Equipment and Scheme

**Experimental Equipment.** Based on the knowledge of soil-water action process, the thesis designed disintegration tester for unsaturated soil as (Fig.1) shows.The experimental instruments constitute of disintegrating device, water control device and the iron sets.The advantages show as follows: ① The water control device can automatically recharge the disintegrating device by the F1 type float valve,the Water supply device can achieve high automation and accurate level;②the test instrument has the advantages of simple structure,reasonable design and manufacture easily,and the error is small, the results are accurate.

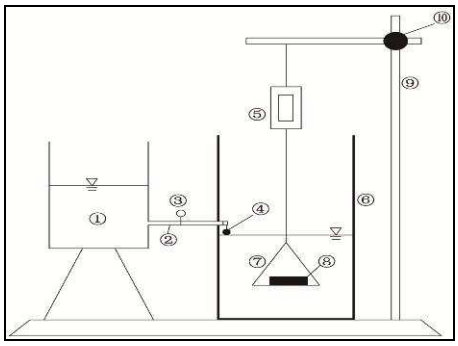


Remarks:①water control device②glass catheter③The switch④the F1 type float valve⑤E-Rally⑥Plexiglas cylinder (diameter 15cm)⑦Barbed plate (size 10cm × 10cm, mesh0.5cm × 0.5cm )⑧Soil samples⑨the iron sets⑩The lifting switch

Fig.1 The disintegration device for unsaturated soil

**Experimental Scheme**. Sample preparation: Take an undisturbed Lishi loess as studying object, prepare 20 cylindrical samples groups which volume is 200cm$^3$,the degree of compaction are 85%, 90%, 95%, 100%; 10%, water content are12%,14%, 16%, 18%, 22%.

In order to eliminate the dimension of the test, represented by the cumulative disintegration disintegration of modulus, calculated by the following equation:

$$B_t = \frac{M_0 - M_t}{M_0} \tag{1}$$

Formula: Bt cumulative disintegration modulus (dimensionless), M0 is Rally initial reading, Mt tension meter readings at time t;

Disintegration rate calculated by the following equation:

$$V = \frac{B_b - B_a}{T_a - T_b} \tag{2}$$

Formula: V is the rate of disintegration (min-1), Bb, Ba, respectively corresponding to the point b and a cumulative disintegration modulus, Tb, Ta b, respectively, and a point corresponding to the point of disintegration time (min) .

The test process:① determination of soil natural moisture content, liquid limit, plastic limit and other basic physical parameters;②determination of unsaturated soil under different degree of compaction conditions, disintegrating relationship between the amount of time;③determination of unsaturated soil under different moisture conditions, disintegrating relationship between the amount of time. During the experiment, the water temperature controlled at 20 ~ 22 °, the disintegration of

the dissolution of the body characteristics observed specimen to specimen disintegration is complete, collation and analysis of data.

**Analysis of Experimental Results**

**The effect of initial moisture content to the disintegration.**Figure 2 is the disintegration curve between the modulus (Bt) and time(T) under different moisture conditions when the degree of compaction is 95%.Analyzed of experimental data shows that:(1)the disintegration curve can be divided into three sections: the samples did not change significantly in the stages 0 ~ 5min , only a small sample of soil particle caving out the surface,this stage reflects the process of the water enters the sample porosity when the specimen immersion in water,5 ~ 20min is the rapidly disintegration stage,with the gradual increase of the moisture content in the sample, the soil particles disintegrant off from outside to inside like the flocculent or Chunky.However,the disintegration rate is stable,the disintegrating basically completed used 20min,the disintegrant modulus at around 0.8;However, the sample still ongoing disintegrant at steady rate with the water content was 22%.（2）When the degree of compaction at a certain level,the total sample disintegration rate decreases with increasing water content.（3）When the initial moisture content of the sample is not the same,the completion time is also showing slight difference,the completion time take 11min, 14min, 16min, 18min, 20min under the initial moisture content are 10%, 12%, 14%, 18%, 16%.This shows that,the initial water content is not only reduced the water absorption capacity of specimen, also has a certain effect to Slow down the disintegration rate.Figure 3 is the disintegration curve between the modulus (Bt) and time(T) under different moisture conditions when the degree of compaction is 85%.Which has the same disintegration law to Figure2, the total sample disintegration rate decreases with increasing water content.We can get the law from Figure2 and Figure3 that the decreased amplitude is increasing with the moisture content increased to18%,the disintegration characteristics disappeared with the moisture content increased to 22%.The disintegration rate calculated by formula (2) as the results in table1.The relationship between disintegrating rate and moisture content as shown in Figure6.

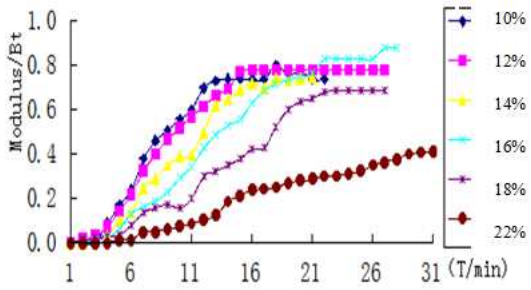


Fig.2 The disintegration curve on different moisture content of the degree of compaction is 95%

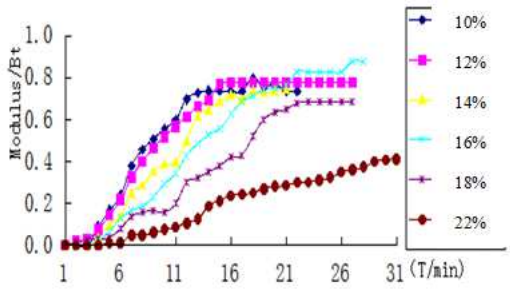


Fig.3 The disintegration curve on different moisture content of the degree of compaction is 85%

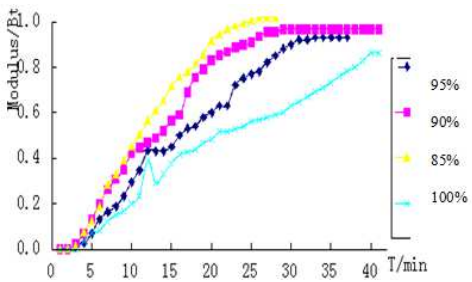


Fig.4The disintegration curve on different degree of compaction of the initial moisture content is 12%

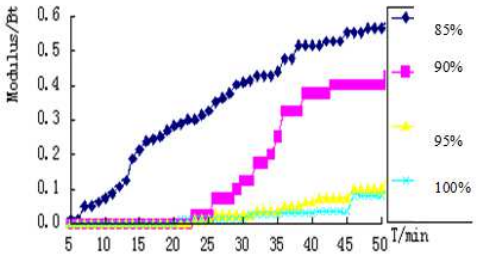


Fig.5The disintegration curve on different degree of compaction of the initial moisture content is 20%

**The effect of the degree of compaction to the disintegration.**When the unsaturated soil compacted,the structure changed, the soil porosity and water absorption capacity decreased,the disintegration rate also slowed down significantly.Figure4 and Figure5 are the disintegration curve between the modulus (Bt) and time(T) under different degree of compaction when the initial moisture conditions are 12% and 20%.Analyzed of experimental data shows that:The disintegration curve are similar with Figure2 and Figure3,also with obvious stages;the total sample disintegration rate decreases with increasing degree of compaction.the disintegration characteristics disappeared with the degree of compaction increased to 95%.Figure 5 indicates that the regularity of the disintegration characteristics performance significantly influenced by the degree of compaction.

**prediction of disintegration rate based on the effective porosity ratio**

the effective porosity ratio refers to ratio of the volume of air in soil to the volume of soil particles.It has the correlation between moisture content and degree of compaction as follows:

$$e_i = \rho_s\left(\frac{100}{K\rho_{\max}} - \frac{\omega}{100}\right) - 1 \qquad (3)$$

Formula:$e_i$ is effective porosity ratio; $\rho_s$ as particle density (g/cm$^3$); ω is the moisture content (%); $\rho_{max}$ is the maximum dry density of soil (g/cm$^3$); K is the degree of compaction (%). In this experiment: $\rho_s$ is 2.7g/cm$^3$, $\rho_{max}$ is 1.97g/cm$^3$.

After the regression analysis,get the relationship between the rate of disintegration and effective porosity ratio,as table 2 and Figure 7.The regression results as follows:

$$V_i = 0.0134 + 4.3019e_i - 13.98e_i^2 \qquad (4)$$

The correlation coefficient is $R^2$=0.856,achieved a high correlation level.

Table1 The relationship between the rate of disintegration and the initial moisture content

| | K=85% | K=90% | K=95% | K=100% |
|---|---|---|---|---|
| ω=10% | 0.14 | 0.13 | 0.076 | 0.051 |
| ω=12% | 0.125 | 0.12 | 0.11 | 0.05 |
| ω=14% | 0.074 | 0.07 | 0.063 | 0.031 |
| ω=16% | 0.049 | 0.044 | 0.032 | 0.021 |
| ω=18% | 0.04 | 0.03 | 0.027 | 0.011 |
| ω=20% | 0.036 | 0.028 | 0.017 | 0.006 |
| ω=22% | 0.012 | 0.01 | 0 | 0 |

Table2 The relationship between the rate of disintegration and the the effective porosity ratio

| $V_i$ | $e_i$ | $V_i$ | $e_i$ | $V_i$ | $e_i$ |
|---|---|---|---|---|---|
| 0.006 | \ | 0.032 | 0.123 | 0.12 | 0.283 |
| 0.011 | 0.011 | 0.063 | 0.163 | 0.13 | 0.323 |
| 0.021 | 0.051 | 0.11 | 0.203 | 0.012 | 0.172 |
| 0.031 | 0.091 | 0.076 | 0.243 | 0.036 | 0.212 |
| 0.05 | 0.131 | 0.01 | 0.083 | 0.04 | 0.252 |
| 0.051 | 0.171 | 0.028 | 0.123 | 0.049 | 0.292 |
| 0 | 0.003 | 0.03 | 0.163 | 0.074 | 0.332 |
| 0.017 | 0.043 | 0.044 | 0.203 | 0.125 | 0.372 |
| 0.027 | 0.083 | 0.07 | 0.243 | 0.14 | 0.412 |

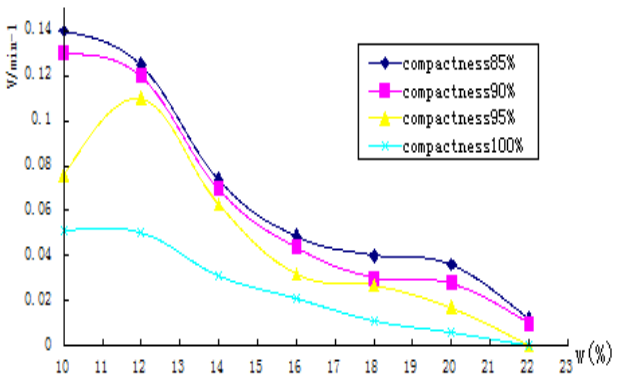


Fig.6 The relationship between the rate of disintegration and the initial moisture content

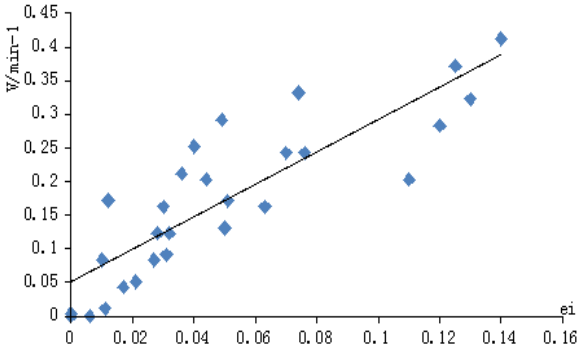


Fig.7 The relationship between the rate of disintegration and the the effective porosity ratio

## Conclusion

(1)The disintegration of unsaturated soils developed instrument can achieve the disintegration experiment of unsaturated soil in hydrostatic water.The water control device can realized automatic replenishment, and the precision could meet the test requirements.

(2) The degree of compaction and moisture content are the main factors affecting disintegration of unsaturated soil.The disintegration rate presents decrease trend with the increasing of The initial moisture content and the degree of compaction.

(3) Based on the relationship of degree of compaction and the moisture content to void ratio, the thesis establishes the model between the disintegration rate and the effective porosity ratio,the formula can be used to calculate the disintegration rate of compacted loess.

**Acknowledgment**

This research work was supported by the key Project of China （41130753）and the National Natural Science Foundation of China （40972174, 40972215）

## References

[1]Li Xi'an,Huang Runqiu,Peng Jianbing.Experimental research on disintegration of loess.Chinese Journal of Rock Mechanics and Engineering,2009,28(S1):3207-3213.

[2]Li Jiachun,Tian Weiping.Experiment of compacted loess disintegration.Journal of ChongQing Jiaotong University,2005,24(5):74-77.

[3]Li Jiachun,Cui Shifu,Tian Weiping.Erosion characteristic of road slope and test of soil disintegration.Journal of Chang'an University(Natural Science Edition),2007,27(1):23-26+49.

[4]Ma Xiao,Zhu Shoujun.Soil disintegration characteristics of terrace hedgerows in Loess hilly-gully areas.Journal of Northwest Forestry University,2013,28(4):21-25.

[5]Wang Jing'e,Xiang Wei,Bi Renneng.Experimental study of influence of matric suction on disintegration of unsaturated remolded loess.Rock and Soil Mechanics,2011,32(11):3258-3262.

[6]Yuan Kekuo,Dang Jinqian,Wang Zikui,Zhuo Li.Study on water character of compacted loess.Yangtze River,2009,40(20):34-37.

[7]FULLER M L. Some unusual erosion feature in the loess of China[J].Geographical Review,1922,12(4):570-584.

[8]WILSON G V ， PERIKETI R，FOX G A，et al. Seepage erosion properties contributing to streambank failure[J]. Earth Surface Processes and Landforms,2007,32(3):447-459.

[9]BRIVOIS O ，BONELLI S，BORGHI R. Soil erosion in the boundary layer flow along a slope:a theoretical study[J]. European Journal of Mechanics(B/Fluids),2007,26(6):707-719.

*Applied Mechanics and Materials Vols. 580-583 (2014) pp 73-77*
*© (2014) Trans Tech Publications, Switzerland*
*doi:10.4028/www.scientific.net/AMM.580-583.73*

# Experimental Study on Bubble Curtain Technology Applied in Underwater Blasting Damping

HU Hai-ying[1 a] ZHANG Yu-cheng[2,3,4 b] HUANG Zhong-ming[5 c]
PENG Chang-xue[6 d]

[1.] College of Hydraulic and Civil Engineering,South China Agricultural University,Guangzhou 510642

[2.] GuangDong Research Institute Resources and Hydropower,GuangZhou, 510610,China

[3.] The Geotechnical Engineering Technology Center of Guangdong Province, Guangzhou 510610, China

[4.]The Emergency Technology Research Cente of Guangdong Province for Public Events Guang-Zhou,510610

[5.] School of Civil Engineering and Transportation, South China University of Technology, Guangzhou 510641

Architectural Design and Research Institute, South China University of Technology, Guangzhou 510641,China

[a] 282392530@qq.com [b] 125340752@qq.com [c] 352452082@qq.com [d] 45547572@qq.com

**Keywords:** bubble curtain, shield, underwater blasting, wave absorbing, damping

**Abstract:** With the further development of urban construction, engineering blasting has had a wide range of applications. However, its application environment has become more and more complex relatively. Underwater blasting, one of the applications of engineering blasting, has been increasingly used in construction of subsea tunnel and immersed tube in recent years though it has a complex influence on surroundings in operation. For the study of shock wave absorption technology of underwater blasting, this paper analyses the effectiveness of bubble curtain shielding technology used in the underwater explosion by field experiment. The test result shows that intensity of underwater shock wave approximately reduced by 80% after passing through the bubble curtain, which indicates that the bubble curtain can effectively reduce the shock wave pressure in water; vibration caused by shock wave in water approximately reduced by 20% after passing through the bubble curtain, which reflects propagation law of shock wave has changed due to the effect of the curtain.

## Introduction

With the development of urban large-scale underground construction, the range of applications of blasting has become wider and wider, transferred from sparsely populated wilderness to densely populated city, extended from land to water. Blasting greatly accelerates construction speed and saves construction cost, which has a remarkable technical and economic effect. However, because of the increased complexity of blasting situation, people are increasingly concerned about its harm to the surrounding environment. Blasting seismic effects have varying degrees of influence or damage on the buildings and facilities in surrounding area. In this regard, to reduce or eliminate the effects of blasting on the surrounding environment through blasting vibration reduction technology is very urgent and important in engineering practice.

There are both similarity and difference between underwater blasting and land blasting. The former not only generates seismic wave, but also produce water shock wave. The hazard of water shock wave cannot be ignored, which has characteristics of big impulse and slow damping and threatens security of aquatic life, water construction, ships and underwater operation personnel. To the land bursting, because of its current extensive applications, there are many more mature shock absorption technologies now, such as millisecond blasting shock absorption technology, pre-split blasting shock

absorption technology, isolation holes (slots) damping technology, etc. Because of the different construction environment between the underwater blasting and the land blasting, the shock absorption technology of underwater blasting still needs more research and development and to be tested by applying it to engineering practice.

This paper analyses the effectiveness of bubble curtain shielding technology used in the underwater explosion by field experiment, so as to provide more experience for its applying to the engineering practices.

## Bubble Curtain Shielding Technology

The concept of the bubble curtain was first proposed by engineer Adolph in Canadian Industrial Co. Ltd. and applied to underwater blasting in construction of Canada Ortario hydropower station [1,2]. Subsequently, the bubble curtain technology had been widely used and studied in countries due to the significant effect on attenuation of underwater shock wave and seismic effect in underwater blasting. Our predecessors had explained the bubble curtain attenuation law from the viewpoint of acoustic and thermodynamic or from the point of view of energy, and made a theoretically reasonable exposition by introducing Bp value which is parameter to describe the reduction degree of underwater shock wave [3]. The bubble curtain can well weaken underwater shock wave pressure so that constructions around the blasting area can be protected effectively [4].

Bubble curtain shielding technology means: One or more bubble curtains are laid between explosive and object of protection. When underwater shock wave reaches the bubble curtain, diffuse reflection is generated on surface of rising bubbles. Meanwhile, underwater shock wave compresses the bubbles, which makes most energy of the shock wave expended during the bubble compression process, so that the pressure caused by underwater shock wave is greatly reduced and thus the object is protected.

## Bubble Curtain Decompression Experiment

To test shock wave absorption effect of bubble curtain, an experiment was designed, and its plane layout is shown in Figure 1，field test results is shown in Figure 2 and Figure 3.

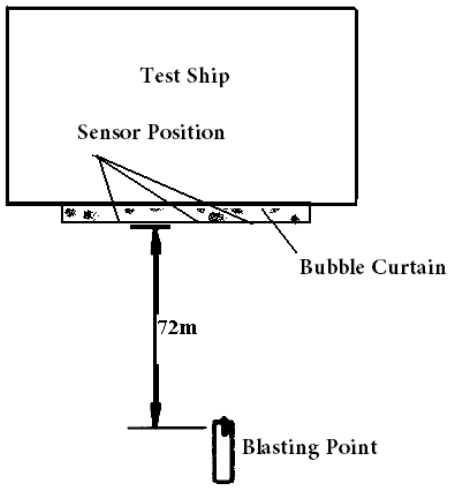


Fig. 1 Bubble Curtain Installation Diagram

Fig.2 Field Test photo (Sensor placement site)

Fig. 3 Field Test photo (Bubble curtain generator site)

Monitoring equipment selected in the experiment is a high-resolution seismograph of Strata View TM type developed by EG & G which is an American company and it has a total of 24channels, referred to as R-24. This instrument has high-performance with the characteristics of automatic gain and accurate 18-bit analog conversion. Measured dynamic range is up to 113db; tuning distortion is less than 0.01%; sensitivity is 57.6mv/cm after enlargement process.

Curtain parameters are shown in Table 1, and blasting parameters in test are shown in Table 2.

Tab. 1 Bubble Curtain Parameters

| Air Jet Pipe | | | | Air Jet Hole | | | | Air Demand | Pressure |
|---|---|---|---|---|---|---|---|---|---|
| Diameter (mm) | Length (m) | Space (m) | Row | Hole Space (mm) | Hole Number | Aperture (mm) | Reflex Angle (degree) | ($m^3$/min) | (MPa) |
| 80 | 24 | 0.5 | 2 | 20 | 236 | 3 | 90 | 25.5 | 1.03 |

Tab. 2 Blasting Parameters

| Test Number | Total Quantity (kg) | Largest Quantities of Once Blasting (kg) | Hole Number | Aperture (mm) | Hole Space (m) | Hole Depth (m) | Row Space (m) | Distance (explosive source to measuring point) (m) |
|---|---|---|---|---|---|---|---|---|
| 1 | 210 | 25 | 74 | 105 | 2.2 | 1.93 | 1.6 | 72 |
| 2 | 267.5 | 35 | 72 | 105 | 2.2 | 1.90 | 1.6 | 72 |
| 3 | 252.5 | 30 | 60 | 105 | 2.2 | 2.17 | 1.6 | 72 |
| 4 | 155 | 17.5 | 46 | 105 | 2.2 | 1.92 | 1.6 | 72 |

## Experiment Results

Field test results are shown in Table 3. It can be seen from the table, the underwater shock wave pressure behind the bubble curtain is far less than that in front of the curtain and the strength of the shock wave is reduced by 80%, which indicates that the bubble curtain can effectively reduce the underwater shock wave pressure. Unlike the changes of pressure, underwater shock wave vibration is not reduced significantly, by about 20%, which reflects the propagation law of the "new" shock wave changes after it passes through the bubble curtain.

Tab. 3 Site Monitoring Results

| Test Number | Total Quantity (kg) | Largest Quantities of Once Blasting (kg) | Distance (explosive source to measuring point) (m) | Underwater Shock Wave Pressure(MPa) | | Underwater Shock Wave Vibration Velocity (cm/s) | |
|---|---|---|---|---|---|---|---|
| | | | | in front of the Curtain | behind the Curtain | in front of the Curtain | behind the Curtain |
| 1 | 210 | 25 | 72 | 0.0277 | 0.0046 | 1.06 | 0.75 |
| 2 | 267.5 | 35 | 72 | 0.0340 | 0.0075 | 1.21 | 0.96 |
| 3 | 252.5 | 30 | 72 | 0.0317 | 0.0053 | 1.15 | 0.89 |
| 4 | 155 | 17.5 | 72 | 0.0236 | 0.0051 | 0.97 | 0.78 |

## Conclusion

Field test of bubble curtain shows that the bubble curtain shielding technology has significant influence on reducing shock wave pressure generated by underwater blasting. However, its effect on vibration reduction is not very obvious relatively. In this regard, consider a way that combines the bubble curtain technology with the damping technology in land blasting and apply it to the underwater blasting, which can achieve the great effect on pressure and vibration reduction at the same time, but this requires a further study.

## Acknowledgements

This paper is supported by three funds--The National Natural Science Foundation of China (Project Grant No.: 51378131). The Water Science and Technology Innovation Foundation of Guangdong(Item Number： 2009-25) and The Foundation of Guangdong Provincial Highway Administration(Item Number：2012-09). Thanks for this three foundations.

**References**

[1] Feng Shu-yu, Ma Nai-yao. Blasting [M] Beijing: Railway Press, 1980(in Chinese)

[2] Yang Guang- xu. Underwater Blasting [M] Beijing: Ocean Press, 1992(in Chinese)

[3] Garr BB (USSR), etc. Underwater Blasting [M] Wang Zhong-qian, Lu Yi, etc. translate, Bei-Jing: People's Publishing House, 1992(in Chinese)

[4] Wang Zhong-qian. Underwater Blasting Shock Wave [A] Underwater Demolition Anthology [C] Beijing: People's Communications Press, 1980. (in Chinese)

[5] ZHANG Yu-cheng,YANG Guang-hua,JIANG Yan. Numerical simulation analysis of influence of blasting construction of foundation trench of immersed tunnel on stability of embankment Rock and Soil Mechanics, 2010, 31(Supp.1). (in Chinese)

[6] ZHANG Yu-cheng. Stability research of soil slopes based on deformation field and Stress Field [D].WUHAN,wuhan university,2007(in Chinese)

[7] YANG Guang-hua, ZHANG Yu-cheng, ZHANG You-xiang. Variable modulus elastoplastic strength reduction method and its application to slope stability analysis, Chinese Journal of Rock Mechanics and Engineering, 2009, 28(7): 1506-1512. (in Chinese)

*Applied Mechanics and Materials Vols. 580-583 (2014) pp 78-82*
*© (2014) Trans Tech Publications, Switzerland*
*doi:10.4028/www.scientific.net/AMM.580-583.78*

# Experimental Study on the Position of Balanced Point of Large-tonnage Pile with Self-balanced Load Method in the Northwest Region

Ying Xin [1,a], Feng Yue [1,b], Ping Li [1,c] and Gongsheng Wang [2]

[1] School of Civil Engineering, Lanzhou University of Technology, No.287 Langongping Street, Lanzhou and 730050, China

[2] Gansu Building Research Institute, Lanzhou and 730050, China

[a] xyinglut@163.com, [b] YueFeng_666@163.com, [c] liping@lut.cn

**Keywords:** Loess region, Large-tonnage pile, Self-balanced load test, Balanced point position

**Abstract.** The self-balanced test technology has been widely applied in the eastern soft soil region for many years due to its economy and convenience. However, few engineering practices could be found in the northwest loess region. In this paper, self-balanced load tests were conducted in the large-tonnage piles of a bridge project in Gansu Province. The methods determining the position of pile balanced point were studied. The positions of balanced points of test piles were also simulated using Finite Element Method (FEM). The test results show that the self-balanced method has good applicability for loess in the northwest region. The pile side friction is fully exerted and the test data could be reasonable and reliable. Besides, the shortages of traditional empirical method could be made up for if FEM is adopted, which makes the accuracy of the balanced point position improve effectively and provide a reference for field trials.

## Introduction

In recent years, with the increase of engineering construction, the tonnage and diameter of pile has been larger and larger and higher bearing capacity is designed. Traditional static load test is costly and time-consuming, as well as the test results could not meet the design requirements frequently especially for large-tonnage piles [1,2]. The self-balanced test technology could solve these problems well, so it has been widely applied in the eastern region [3]. However, few engineering practices could be found in the loess of the northwest region. Effective local experience is scant especially for piles with large tonnage and high bearing capacity.

In this paper, a bridge project in Gansu Province was taken as an example to study the method of determining the position of balanced point of pile. The self-balanced load tests were conducted in the large-tonnage piles and the balanced point positions of test piles were simulated by FEM, which could provide practical experience for further application in the northwest region.

## Project Profile

The bridge project was located in the intersecting site of the two main roads near the Yellow River. The bridge spanned 240m and was between stations 0+240 and 0+480. Continuous box girders with variable cross-section were used on the main bridge and small precast box girders were adopted for 1~30m in the west and 2~30m in the east on the approach bridge. The pile foundation was taken. The technical indexes of the soil were shown in Table 1.

Three piles were selected to be tested respectively. All the test piles were designed as friction piles with the pile diameter of 1.5m and the standard value of concrete compressive strength of 30MPa. The designed ultimate bearing capacity of a single pile ranged from 3400kN to 10000kN. The whole test was conducted according to the specifications to verify whether the bearing capacity of pile meet the design requirements.

Table 1 Technical indexes of the soil

| Number | Stratum | Thickness (m) | Allowable values of foundation bearing capacity (kPa) |
|---|---|---|---|
| 1 | miscellaneous fill | 0.7～2.4 | 110 |
| 2 | silt | 3.2～7.0 | 130 |
| 3 | round gravel | 0.3～1.5 | 400 |
| 4 | egg stone | 5.4～6.6 | 500 |
| 5 | sandstone of strong weathering | 3.0～3.5 | 300 |
| 6 | sandstone of middle weathering | 25～27 | 400 |

**Estimated Results of Load Cell Position**

The upper and lower sections of pile would reach the ultimate bearing capacity at the same time and be in a state of equilibrium if the load cell is located in the actual position of pile balanced point. Combined with the geotechnical parameters of the test pile area, the position of load cell could be estimated by:

$$Q_{au}^{R}+G_{u}=Q_{ad}^{R}+Q_{d} \tag{1}$$

$$Q_{au}^{R}=UL_{a}\tau_{-}^{R} \tag{2}$$

$$G_{u}=\frac{\pi D^{2}}{4}L_{a}\gamma \tag{3}$$

$$Q_{ad}^{R}=U(L-L_{a})\tau_{+}^{R} \tag{4}$$

$$Q_{d}=\frac{\pi D^{2}}{4}q_{pk} \tag{5}$$

Where $L$, $L_a$ and $D$ were the parameters representing the whole pile length, the length of the upper pile and the diameter of pile respectively. $Q_{au}^{R}$ and $Q_{ad}^{R}$ were the parameters which showed the side frictions of the upper and the lower pile. $G_u$ and $Q_d$ were equal to the dead weight of the upper pile and the bearing capacity of pile tip. $\gamma$ was a parameter that represented the density of pile. $\tau_{-}^{R}$, $\tau_{+}^{R}$ and $q_{pk}$ were the parameters showing the standard values of both side friction of the two sections and resistance of pile tip. According to the technical indexes of the soil, the load cell positions of test piles could be estimated and listed in Table 2.

**Simulation of Balanced Point Position**

**Numerical Models.** The traditional empirical method could not reflect the influence of pile-soil interaction on large-tonnage piles and large errors could be found in the test results [4]. Therefore, the finite element software MIDAS was used to simulate the load cell position. The position estimated by the traditional formulas was adopted. According to the results of the soil tests and design documents, the technical indexes of the simulated models were listed in Table 3.

Table 2 Technical indexes of test piles

| Test pile number | 1# | 2# | 3# |
|---|---|---|---|
| Effective length(m) | 42.0 | 30.0 | 30.0 |
| Load cell position (over the pile tip) | 13.5m | 10.0m | 10.0m |
| Designed ultimate bearing capacity (kN) | 10000 | 7200 | 5000 |
| Two-way loading maximum (kN) | 6000 | 4320 | 3000 |

Table 3 Technical indexes of the simulated models

| Item | Elastic modulus (GPa) | Poisson ratio | Cohesion (kPa) | Friction angle (°) |
|---|---|---|---|---|
| Loess | 0.025 | 0.38 | 25 | 30 |
| Breccia | 0.04 | 0.2 | 50 | 40 |
| Silt | 0.017 | 0.4 | 23 | 26 |
| Reinforced concrete pile | 23 | 0.2 | —— | —— |

The pile 1# was chosen to be simulated in this paper. The load cell position was estimated 13.5m over the pile tip, which divided the pile into the upper and the lower sections. The thickness of the load cell was not considered in comparison with pile length. Linear elastic model was for pile and D-P model was for soil in the process of simulation. Both the pile and the soil were set as the solid elements. The finite element models were shown in Fig. 1.

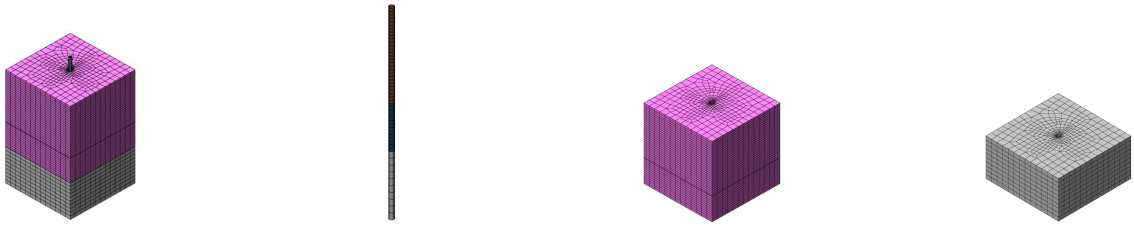

(a) (b) (c) (d)

(a)Model for the whole pile-soil element (b) Model for the pile
(c)Model for the loess (d) Model for the silt

Fig. 1 The finite element models

**Results of Numerical Simulation.** The load was added to the model of 600kN each grade of 10 grades. Part of the simulated displacement figures of the upper and the lower piles were listed in Fig.2. The corresponding displacements were listed in Table 4.

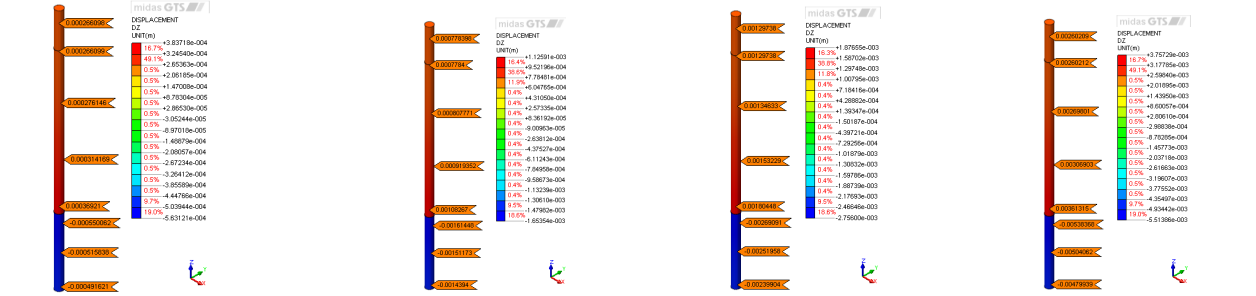

(a)Loading 600kN (b)Loading 1800kN (c)Loading 3000kN (d)Loading 6000kN

Fig. 2 Simulated displacements of the upper and the lower piles

Table 4 Simulated displacement values of pile 1#

| Item | Load (kN) | Displacements of upper pile (mm) | Displacements of lower pile (mm) |
|---|---|---|---|
| 1 | 600 | 0.36 | -0.56 |
| 2 | 1200 | 0.75 | -1.1 |
| 3 | 1800 | 1.13 | -1.65 |
| 4 | 2400 | 1.51 | -2.2 |
| 5 | 3000 | 1.89 | -2.76 |
| 6 | 3600 | 2.26 | -3.31 |
| 7 | 4200 | 2.64 | -3.86 |
| 8 | 4800 | 3.02 | -4.41 |
| 9 | 5400 | 3.4 | -4.96 |
| 10 | 6000 | 3.78 | -5.51 |

As shown in Table 4, the displacement values of the lower pile were larger than that of the upper pile in the same grade when the load cell was 13.5m over the pile tip. The lower pile would reach the ultimate bearing capacity and be destroyed first, which indicated that the position of balanced point

estimated by the traditional empirical method was not fully accurate and was lower than the actual balanced position of pile [5,6].

**Self-balanced Test**

Considering the results of numerical simulation, the patented load cell with 70cm in height and 15cm in range was put 16m over the pile tip in the self-balanced test. The displacements were measured by the displacement sensor of the accuracy of 0.01mm.The slow load method was adopted in accordance with the specifications. The test results of pile 1# were shown in Table 5.

Table 5 Test results of pile 1#

| Number | Load (kN) | Accumulative upward displacements (mm) | Accumulative downward displacements (mm) |
|---|---|---|---|
| 0 | 0 | 0 | 0 |
| 1 | 600 | 0.06 | 0.29 |
| 2 | 1200 | 0.17 | 0.66 |
| 3 | 1800 | 0.29 | 1.14 |
| 4 | 2400 | 0.48 | 1.75 |
| 5 | 3000 | 0.7 | 2.29 |
| 6 | 3600 | 1.01 | 2.76 |
| 7 | 4200 | 1.39 | 3.26 |
| 8 | 4800 | 1.91 | 3.79 |
| 9 | 5400 | 2.51 | 4.31 |
| 10 | 6000 | 3.27 | 5.12 |

The pile-soil correction factor $\gamma$ of the upper pile was 1.0. The ultimate bearing capacity of pile 1# could be determined by formula (6).

$$Q_u=\gamma(Q_{us}-W)+Q_{ud}=(6000-\pi\times0.752\times28.5\times25)\times1.0+6000=10742\text{kN} \quad (6)$$

**Results Comparison**

From Table 4 and Table 5, the simulated values and measured values of longitudinal displacement for pile 1# at each grade could be compared and analyzed in Table 6. The corresponding load-settlement curves were shown in Fig. 3. A conclusion could be found that measured values of downward and upward displacement approximated the simulated values at the same load. Meanwhile, measured pile bearing capacity could meet the design requirements when the load cell was put over the pile tip for 16m. It indicated that this position approached the actual balanced point position and the self-balanced test results were reasonable and reliable.

Table 6 Contrastive results of simulated and measured displacements

| Load (kN) | Displacements of upper pile (mm) | | Displacements of lower pile (mm) | |
|---|---|---|---|---|
| | Simulated values | Measured values | Simulated values | Measured values |
| 600 | 0.36 | 0.06 | -0.56 | -0.29 |
| 1200 | 0.75 | 0.17 | -1.10 | -0.66 |
| 1800 | 1.13 | 0.29 | -1.65 | -1.14 |
| 2400 | 1.51 | 0.48 | -2.20 | -1.75 |
| 3000 | 1.89 | 0.70 | -2.76 | -2.29 |
| 3600 | 2.26 | 1.01 | -3.31 | -2.76 |
| 4200 | 2.64 | 1.39 | -3.86 | -3.26 |
| 4800 | 3.02 | 1.91 | -4.41 | -3.79 |
| 5400 | 3.40 | 2.51 | -4.96 | -4.31 |
| 6000 | 3.78 | 3.27 | -5.51 | -5.12 |

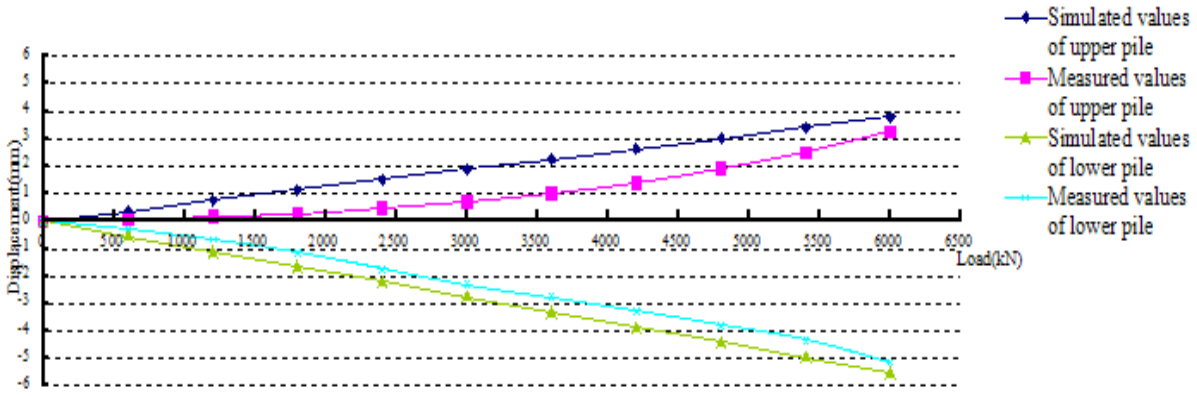


Fig. 3 Load-settlement curves of the simulated and measured values

## Conclusions

Based on the results obtained from the self-balanced tests and numerical simulation of large-tonnage piles, the following conclusions could be drawn:

(1) According to the traditional empirical formulas from (1) to (5), the load cell position of pile 1#could be estimated to be 13.5m over the pile tip.

(2) Numerical simulation of pile 1# was done, which indicated that the displacement values of the lower pile were larger than that of the upper pile at the same grade when the load cell was 13.5m over the pile tip. The lower pile would reach the ultimate bearing capacity and be destroyed first, showing that the position of balanced point estimated by the traditional empirical method was lower than the actual balanced position of pile.

(3) The self-balanced test was conducted after the load cell position of pile 1# was adjusted to be 16m over the pile tip. The test results approximated the simulated results, showing that this position was closer to the actual balanced point position of pile and the self-balanced test results were reasonable and reliable.

## Acknowledgements

This research is supported by the 2012 Technology Project Plan of Urban and Rural Housing Construction in Gansu Province (Project account: JK2012-32).

## References

[1] D. A. Bruce: *Ground Engineering*. Vol. 19 (1986), p. 9-15

[2] Jori O.Osterberg: *Piling and Deep Foundations*. A.A.Balkema Rotterdalll, Netherlallds (1989), p. 421-427

[3] Weiming Gong. *Journal of Building Structures*.Vol. 23 (2002), p. 82-88 (In Chinese).

[4] H.G. Poulos: *Proceedings of the Instititon of Geotechnical Engineering* (2008), p. 17-27

[5] K.S. Wong: *J.Geoteeh. Engng.* Vol. 121 (1995), p. 457-465

[6] Fellenius: *Geotechnical News-Vancouver* .Vol. 24 (2006), p. 43

*Applied Mechanics and Materials Vols. 580-583 (2014) pp 83-88*
*© (2014) Trans Tech Publications, Switzerland*
*doi:10.4028/www.scientific.net/AMM.580-583.83*

# Finite Element Simulation and Stability Analysis of Composite Soil Nailing

Jie Zhao [1, a], Lingli Wang [1,b]

[1] The R&D Center of the Civil Engineering Technology, Dalian University, Dalian 116622, China

[a]zhaojie_gd@163.com, [b]1184396960@qq.com

**Keywords:** composite soil nailing; finite element analysis; deformation; incidence-angle of soil-nails; safety factor.

**Abstract.** Under the condition of plane strain, a 2D elastoplastic FEM is used to analyze the behavior of composite soil nailing bracing of deep excavation, then finite element method of stability analysis is applied to evaluate the stability of the soil-nail wall. The authors analyzed the difference between composite soil nailing and normal soil nailing. Through analyzing the effect of bracing parameters on the deformation behavior and stability of the excavation, some useful conclusions are obtained to provide certain references for the design and construction of composite soil nailing.

## Introduction

Composite soil nailing technique is a geotechnical comprehensive bracing technology composite with other soil-reinforcement technologies in the soil nailing structure. It maintains the advantages of traditional soil nailing, brings about small deformation and has extensive application. Composite soil nailing is a joint application of active bracing and passive bracing and a combination of flexible bracing and rigid bracing. Its mechanism can be summarized as load sharing, impermeability and sealing, passing loads, partial stabilization and advanced reinforcement. There are three basic forms of common composite soil nailing, such as soil-nail with cement - soil piles (waterproof curtain), soil-nail with advanced micro-piles and soil-nail with pre-stressed anchor (rope).

Many Chinese scholars did some researches on the new form of composite soil nailing. Yang Linde et al [1] conducted elastoplastic analysis on the composite soil nailing of Cement - soil Piles by means of FEM based on mucky-excavation engineering practice of Shanghai and explored its law of deformation and mechanism. Song Erxiang et al [2] focused on the soil deformation and the selection of mechanical parameters under the excavation condition for composite soil nailing FEM. Song conducted more thorough researches on the composite soil nailing in the joint form of cement-mixing piles and soil-nails. It is believed that there are significant differences on the mechanism of the composite soil nailing and the normal soil nailing. Xu Changjie et al [3] discussed the effect of different bracing methods and bracing parameters on the deformation in the way of plane elastic-plastic FEM on the basis of engineering practice. Yang Qian et al [4] studied the action principle of composite soil nailing through model testing. Li Xiangfan et al [5] observed on the scene that the composite soil nailing deformation could be divided into three stages according to location, size and priorities of cracks and analyzed the production mechanism of cracks in each stage. Although many researchers yielded fruitful results, engineering practice is still ahead of the theoretical study in the current status.

Taking composite soil nailing bracing combined of the soil-nails and the soil-cement mixing piles for example, the partial excavation and bracing process of composite soil-nail wall with the cement mixing piles is simulated through elastic-plastic finite element analysis of the composite soil nailing plane with Z_Soil (a geotechnical engineering FEM software).Its action principle is also analyzed and compared with pure soil nailing excavation. Then the excavation stability is been evaluated by finite element stability analysis, which provide certain references for the design and construction.

## Finite Element Simulation of Composite Soil Nailing

**Constitutive Model of Soil**. Drucker-Prager model and Mohr-Coulomb model are two common elastoplastic constitutive model in geotechnical engineering. They both consider the influence of hydrostatic pressure on the yield strength. However, D-P model has many advantages over M-C. model. D-P model has smooth yield surface and it's easy to determine parameters and calculate etc. Therefore, the D - P model is adopted in the elastic-plastic model calculation during the excavation in this paper. Its yield function is expressed as:

$$F = \alpha I_1 + \sqrt{J_2} = k \,. \tag{1}$$

Equation (1) is a general expression of geotechnical materials. $I_1$ is the first invariant tensor, $J_2$ is the second invariant of stress deviator, $\alpha$ and $k$ are the strength parameters of geotechnical materials. Different yield criterion can be achieved in the FEM by changing the expression of $\alpha$ and $k$. When equation (1) is compared with the Mohr-Coulomb formula on the condition of plane strain, non-associated flow rule ( $\varphi = 0$ ) is adopted to obtain the following formula

$$\alpha = \frac{\sin\phi}{3}, k = c\cos\phi \,. \tag{2}$$

The criterion precisely matches M-C criterion and it still belongs to the generalized Mises criterion.

**Build Computation Model**. The bracing system is simplified as a two-dimensional plane-strain problem. Quadrilateral parametric element is used to discrete soil. Soil-nails are simplified as a elastic rod unit only in tension. Drucker-Prager ideal-elastoplastic model is applied to the soil and mixing piles. According to engineering experience and measured results, force on the sprayed concret surface in composite soil nailing is small, so the effect of surface-layer is omitted in calculation. The concept of interface units is introduced to simulate the interaction between soil and soil-nails and an elastoplastic model is used to describe the characteristic of the interface.

When the interface unit is elastic, shear stress:

$$|\tau| < \sigma_n \tan\phi_i + c_i \,. \tag{3}$$

When the interface unit is plastic, shear stress:

$$|\tau| = \sigma_n \tan\phi_i + c_i \,. \tag{4}$$

In the formulas, $\phi_i$ and $c_i$ are the friction angle and cohesion of interface unit, $\sigma_n$ is the normal stress on the interface unit, $\tau$ is the shear stress. Parameters of Soil contact-surface is discounted from soil-strength parameters. Cohesion and friction angle of contact-surface is 70% of the soil cohesion and friction angle.

## Finite Element Analysis of the Excavation Stability

The traditional method of excavation stability analysis uses limit equilibrium method [6,7] .These analysis methods usually assume the sliding-surface shape to be fold line, single arc, double arc and logarithmic spiral line etc. without considering the stress-strain relationship of soil when seeking safety factor. Neither the joint action nor the deformation coordination of the soil and retaining structures (soil-nails and cement mixing piles) is considered.

As a powerful numerical method, FEM considers the stress-strain relationship of soil. It can not only calculate the internal force of nail and simulate excavation process etc., but also consider the

non-uniformity and the anisotropic character of the soil. In this paper, FEM is applied to evaluate the stability of excavation slope. As to the plane strain, shear strength of soil obeys Mohr-Coulomb strength criterion. So the soil shear strength of any point on the potential sliding surface is [8]

$$\tau_f = \sigma_n \tan\phi + c \,. \tag{5}$$

In the formula, $\sigma_n$ is normal stress, $\phi$ and $c$ are internal friction-angle and cohesion of the soil. Stability safety-coefficient along the sliding surface is defined as

$$F_s = \frac{\int_l (\sigma_n \tan\phi + c) dl}{\int_l \tau dl} \,. \tag{6}$$

FEM is adopted to analyze composite soil nailing to get the stress distribution of excavation- soil. Then pattern searching method of the generalized mathematical programming is adopted to analyze potential sliding surface. The stability safety-coefficient is regarded as the objective function and the minimum value of the objective function among the assumed sliding surface is searched out as the most dangerous sliding surface.

## Analysis of an Engineering Example

**Project Overview.** As shown in Fig.1, half of the calculation model is analyzed according to the Symmetry of the excavation structure. The overall height of the model is 18m, width is 30m. The depth of the excavation is 8m, which is divided into 6 steps, 1.5m for the former five steps and 0.5m for the last step. Five rows of soil-nails are established, whose level interval is 1.0m, vertical distance is 1.5m,length is 8m.Drilling diameter of soil-nails is 0.1m. Diameter of cement-soil mixing piles is 1.0m, length is 12m. The excavation is vertical. Calculation parameters are listed in table 1.

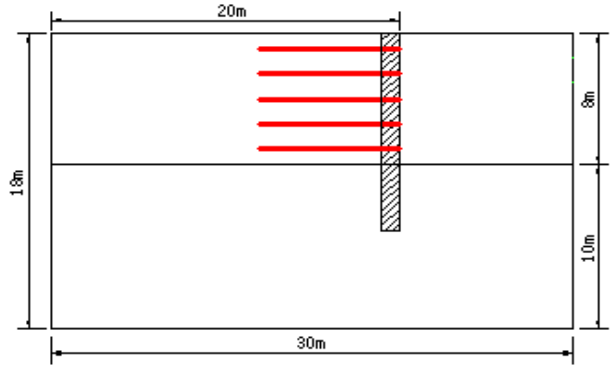


**Fig. 1** Finite element model

**Table 1** Calculation parameters of Composite soil nailing

| | $\gamma$ kN·m$^{-3}$] | $c$ kPa | $\varphi$ ° | $k$ | $n$ | $E$ Gpa | $\upsilon$ | $f_y$ Mpa |
|---|---|---|---|---|---|---|---|---|
| Soil | 20 | 10 | 30 | 200 | 0.5 | | 0.3 | |
| Soil-nail | 25 | | | | | 30 | 0.2 | 310 |
| Mixing Pile | 20 | 120 | 30 | | | 0.1 | 0.25 | |

**Note:** soil-nails use the equivalent elastic modulus. The elastic modulus of the soil is determined by the equation $E = kp_a\left(\frac{\sigma_{3\max}}{p_a}\right)^n$ .

**Computational Results. (1) Horizontal displacement of excavation sidewall.** Figure 2 shows the comparison of the horizontal displacement of the excavation sidewall between pure soil nailing and composite soil nailing. Compared with the pure soil nailing, the excavation-sidewall deformation of composite soil nailing is in bulging shape. The maximum horizontal displacement location is not on the top of the excavation, but in the middle to the lower part; Due to mixing piles, the horizontal displacement is greatly reduced. Mixing piles belong to the pre-reinforcement, the composite soil nailing deformation depends on the joint influence of the mixing pile stiffness and strengthened soil stiffness. Since the mixing pile stiffness is larger, its effect on the deformation is dominant. As a result, composite soil nailing deformation is greatly reduced.

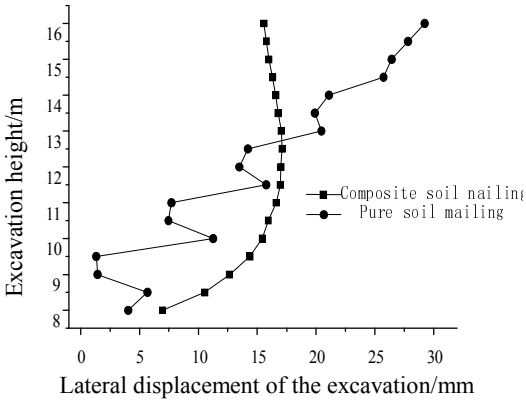


**Fig. 2**Horizontaldisplacement of excavation sidewall

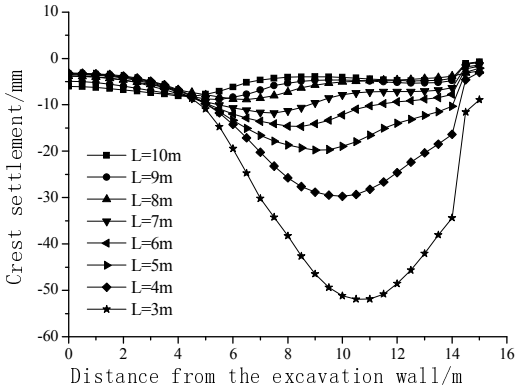


**Fig. 3**Influence of soil-nail length on the subsidence of excavation ground

**(2) Settlement of the excavation surface.** The largest settlement of composite soil nailing is located near 0.9H after mixing piles, which is different from that of pure soil nailing. The maximum settlement location of the pure soil nailing excavation-surface is near the top of the slope. Because of mixing piles, the composite soil nailing surface settlement is greatly reduced than that of pure soil nailing. It is suggested that mixing piles play an important role in restricting on the surface settlement.

**(3) Stability of the excavation.** Safety factor of pure soil nailing excavation is 1.37 in the FEM. While the one of composite soil nailing excavation is1.71. So cement mixing piles greatly improve the stability of the excavation.

**Analysis of Composite Soil Nailing Influence Factors. (1) Influence of soil-nail length.** Considering the influence of soil-nail length, soil nails were horizontally arranged. And the length varied from 3m to 10m. Figures3and4 show the influence of soil-nail length on the excavation deformation. Figure 5 shows the influence of soil-nail length on the excavation stability. As can be seen, with the increase of soil-nail length, firstly not only the ground settlement and lateral deformation of the excavation are greatly reduced but also the stability of the excavation is improved; secondly, the maximum settlement location of the excavation surface moves away from the excavation wall and the maximum lateral displacement location of the excavation moves down; Thirdly, surface-settlement and horizontal displacement of the excavation walls of soil-nail cement-mixing pile composite bracing decrease and the reducing speed also decreases slowly; Moreover, safety factor of the excavation increases, but the reducing speed decreases slowly. In conclusion, it is effective on controlling displacement and improving the stability to increase the soil-nail length. But it seems not very economical to increase the soil-nail length in engineering when it is a little longer.

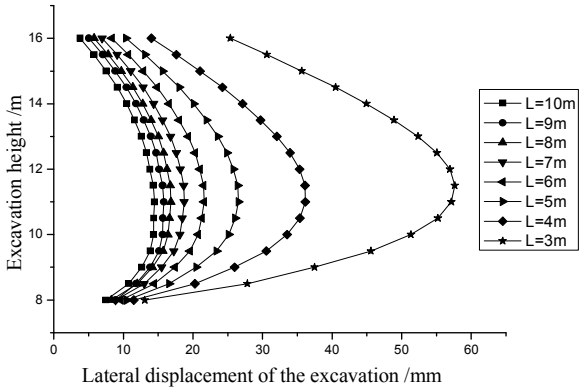


**Fig. 4** Influence of soil-nail length on the excavation lateral displacement

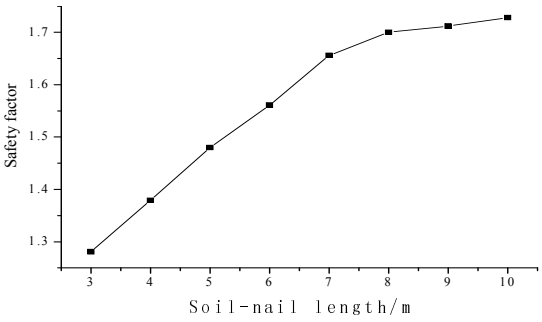


**Fig. 5**Influence of soil-nail length on the excavation stability

**(2) Influence of soil-nail inclination on stability.** Many scholars analyzed the best angle of setting soil-nails. However, most of them took the limit equilibrium method and only conducted research on pure soil nailing. In this paper, FEM was adopted to analyze the stability of the excavation and study the variation by setting the soil-nails into different angles. The results show that when soil-nails are long enough (L>H), the safety factor decreases as soil-nail inclination increases and the optimal incidence-angle of the soil-nails is horizontal. When soil-nails are a little shorter (L<H), the safety factor firstly increases and then decreases as soil-nail inclination increases. The optimal incidence-angle of the soil-nail tilts downward about 10 °.

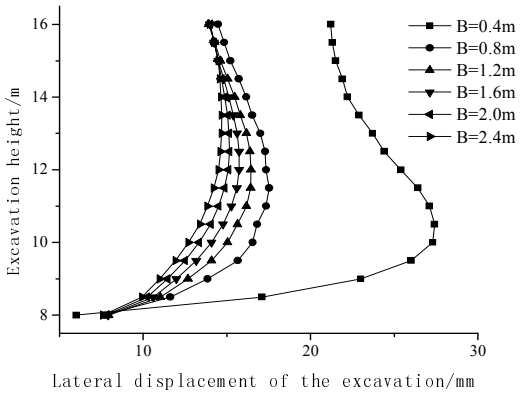


**Fig. 6** Excavation lateral displacement of different mixing-pile thicknesses

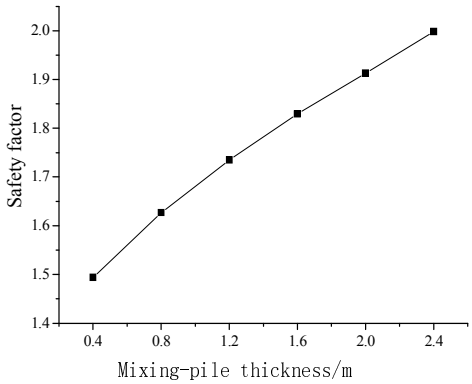


**Fig. 7** The excavation safety-factor of different mixing-pile thicknesses

**(3) Influence of mixing pile thickness.** The thicknesses of the cement mixing piles (B) were set into 0.4m, 0.8m, 1.2 m, 1.6m, 2.0m and 2.4m. As shown in figure 6, the horizontal displacement form of the excavation wall remains the same under different mixing pile thicknesses. The maximum displacement occurs in the lower part of the excavation. The maximum lateral displacement location moves up as the mixing pile thickness increases. When the mixing pile thickness reaches a certain value, the decrease of displacement is smaller as the mixing pile thickness increases. Obviously it is not economical in the project. As can be seen in the figure7, within a reasonable range of mixing pile thicknesses, safety factor almost increases linearly as the mixing-pile thickness increases. If the mixing pile thickness continues to increase, it will result in waste in the project.

## Conclusions

Through the finite element analysis for simulation and stability of composite soil nailing structure and the comparison with the normal-pure soil nailing, there is obvious difference between the two mechanisms. Deformation of composite soil nailing is greatly reduced and the maximum horizontal displacement location is in the middle to the lower part which improves the stability of the excavation bracing system.

Through the analysis of different bracing parameters and the research of excavation deformation and stability, we can get the following conclusions, which provide certain references for the design and construction.

(1) The increase of soil-nail length reduces the deformation of the excavation. However, it seems not very economical to increase the length of the soil-nail in engineering when it reaches a certain length.

(2) When the soil-nail is long enough, the safety factor decreases as soil-nail inclination increases. The optimal incidence-angle of the soil-nail is horizontal. When the soil-nail is a little shorter, the safety factor first increases and then decreases as soil-nail inclination increases. The optimal incidence-angle of the soil-nail tilts downward, about 10 °.

(3) As the mixing pile thickness increases, safety factor of the excavation almost increases linearly. But when the mixing pile thickness increases to a certain extent, it is not obvious to control the deformation of the excavation.

## References

[1] Linde Yang, Xiangfan Li, Zhengxiong Zhong, Nonlinear finite element analysis of composite soil-nail wall [J] .Journal of Geotechnical Engineering,2001,23(3): 149-152. (In Chinese)

[2] Erxiang Song, Yue Qiu. Finite element analysis of composite soil nailing excavation bracing [J].Rock and Soil Mechanics, 2001, 22 (3): 241-245. (In Chinese)

[3] Changjie Xu, Qinjin Li, Influence of bracing parameters on the composite excavation deformation [J].Rock and Soil Mechanics,2005,26(2):295-298. (In Chinese)

[4] Qian Yang, Mingju Zhang, Tiecheng Sun, Experiment on soft soil of composite soil nailing [J]. Rock and Soil Mechanics,2004,25(9):1401-1408. (In Chinese)

[5] Xiangfan Li, Ji Yin, Fei,Guan, Composite soil nailing excavation in the soft strata [J].Chinese Journal of rock mechanics and Engineering,2005,24(21):3876-3881. (In Chinese)

[6] Ji Yin, Fei Guan, Junfeng Xu, Discussion on the relationship between the composite soil nailing stability-calculation method and slope crack [J].Geotechnical Engineering World, 2004,7(4):50-54. (In Chinese)

[7] Tiecheng Sun, Mingju Zhang,Qian Yang,Stability analysis method of composite soil nailing deep-excavation and its application [J] .Engineering Mechanics,2005,22(3)126-133.(In Chinese)

[8] Longtan Shao, Hongxiang Tang , Guocheng Han, Finite element analysis for slope stability and its application [J].Chinese Journal of Computational Mechanics,2001,18(1):81-87. (In Chinese)

*Applied Mechanics and Materials Vols. 580-583 (2014) pp 89-92*
*© (2014) Trans Tech Publications, Switzerland*
*doi:10.4028/www.scientific.net/AMM.580-583.89*

# Fuzzy Mathematical Method of Slope Reliability Analysis in Surface Mine under Seepage Conditions

Kun Yang [1, a], Hua-xue Li [1,b], Hao Han [1,c]

[1]Key Laboratory of Mining Disaster Prevention and Control, Ministry of Education, Shandong University of Science and Technology, Qingdao, Shandong 266590, China

[a]Kunyang11@163.com, [b]302675605@qq.com, [c]hanhao1013@qq.com

**Keywords:** Surface mine; Reliability analysis; Fuzziness;Fuzzy point evaluation

**Abstract.** With the development of the economy, the increasing height of slopes in surface mine will seriously threaten the security in Coal Mine Area. Therefore, how to accurately evaluate slope stability has become one important problem. Based on reliability theory and fuzzy theory, a new reliability analysis method-fuzzy point evaluation method is presented in this paper. It is more practical and efficient for slope reliability assessment because traditional evaluation method doesn't consider the fuzziness of parameters. As a typical example, we applied the technique to a surface mine case under seepage conditions, and made comparison with the traditional reliability analysis approach. The results indicate that the conclusions from both methods are essentially consistent. However, because considers the fuzziness of parameters, fuzzy point evaluation method has more actual instructive significance comparing with the traditional mothod.

## Introduction

China is a large country of coal consumption. Large-scale coal mining will produce a large number slopes in surface mine. With the development of the economy, the increasing height of slopes will seriously threaten security in Coal Mine Area Therefore, how to accurately evaluate the stability of slopes in open-pit mine has become one important problem which has to be solved as soon as possible.

The variability of physical and mechanical parameters exists objectively. When the variability is considered, reliability method is more consistente with the actual project situation. However, traditional reliability analysis only take into account the randomness of parameters but ignore the fuzziness. For the uncertain parameters influenceing the stability of slopes, their fuzziness is impersonally existent and it comes from people's awareness. Therefore, There are some limitations by classical random reliability analysis. in this case, using a fuzzy number to reflect the uncertainty is warranted. In this paper, a fuzzy point estimate method are put forward for the reliability analysis of coal gangue hills based on reliability theory and fuzzy theory. This mehtod fuzzily processes every uncertain parameter and each of the fuzzy variables is to be discretized into appropriate $\alpha$-cut. Through taking finite $\alpha$ values on the interval [0,1], reliability index and failure probability are obtained. Therefore, this method is more practical and efficient and also consistent with people's experience.[1,2]

## Fuzzy point evaluation method

**Trapezoid Membership Function.** The membership function of a trapezoid fuzzy number is as shown in fig 1.

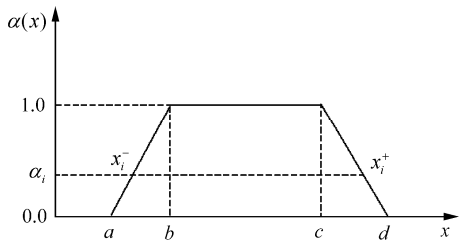


Fig.1 Trapezoidal fuzzy number

a，b，c and d can be calculated according to formulae (1) :

$$\left.\begin{aligned} a &= E(x_i) - m_1\sigma(x_i) \\ b &= E(x_i) - m_2\sigma(x_i) \\ c &= E(x_i) + m_2\sigma(x_i) \\ d &= E(x_i) + m_1\sigma(x_i) \end{aligned}\right\} \tag{1}$$

Where: $m_1$， $m_2$ can take values on the interval [0.5,3]. So, the membership function could be written:

$$\alpha(x) = \begin{cases} \dfrac{x-a}{b-a} & (a < x \le b) \\ 1 & (b < x \le c) \\ \dfrac{d-x}{d-c} & (c < x \le d) \end{cases} \tag{2}$$

**Fuzzy Point Evaluation Method.** In classical reliability theory, structure state was decided by function $z = g(x_1, x_2, \cdots, x_n)$. When take a $\alpha$-level, the rth origin moments of the function can be denoted as below[3~5]:

$$z_{\alpha_i}^r = p_+ g^r(x_{\alpha_i}^+) + p_- g^r(x_{\alpha_i}^-) \tag{3}$$

Where: $i = 1, 2, \cdots, N$； $r = 1, 2$； $p_+$ and $p_-$ are obtained by the following formula:

$$p_\pm = 1 \pm \sum_{i=1}^{M-1} \left( \sum_{j=i+1}^{M} \frac{\rho_{ij}}{\sqrt{\prod_{i=1}^{M}\left[1 + \left(\frac{\beta(1)_i}{2}\right)^2\right]}} \right) \tag{4}$$

Where: $\rho_{ij}$ is correlation coefficient between $x_i$. $\beta(1)_i$ is skewness coefficient of $x_i$. When don't consider the correlation between mechanical parameters, there are $p_+ = p_- = 1$.

The rth origin moments of the function can be calculated according to:

$$E[z^r] = \frac{\sum_{i=1}^{N} \alpha_i z_{\alpha_i}^r}{N} \tag{5}$$

So, the reliability index can be calculated:

$$\beta = \frac{E(z)}{E(z)} \tag{6}$$

## Engineering project

In order to study the feasibility of the reliability analysis method mentioned above, we carried out validation through an engineering project as below. As shown in figure 2, the mining was conducted in the area on three levels of 320m, 300m and 280m of the north-east of Xue-feng sandstone open pit.[6]. The statistical results of cohesion and friction coefficient as shown in table 1.

Table 1 Statistical results of mechanical parameters

| statistic characters | | means | standard deviations | coefficients of variation |
|---|---|---|---|---|
| Ⅰ interlayer | Frictioncoefficient | 0.725 | 0.092 | 0.127 |
| | cohesion（Mpa） | 0.055 | 0.002 | 0.042 |
| Ⅱ interlayer | friction coefficient | 0.692 | 0.092 | 0.133 |
| | cohesion（Mpa） | 0.057 | 0.003 | 0.053 |
| Ⅲ interlayer | friction coefficient | 0.714 | 0.085 | 0.119 |
| | cohesion（Mpa） | 0.058 | 0.002 | 0.041 |
| Rock density (g/cm3) | | 2.70 | 0.299 | 0.111 |

In this paper, steady seepage conditions were considered. The adopted water levels are 60m on the upper reaches acnd 40m in the downstream. The calculated equipotential lines are shown in fig 3.

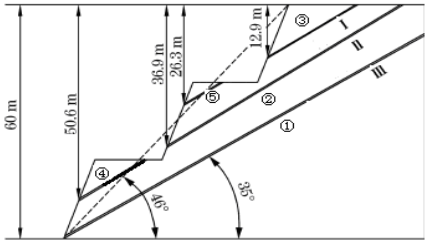


Fig.2 Section of a slope with several slide surfaces

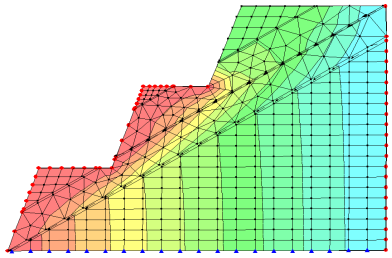

Fig.3 Equipotential lines of steady seepage

$g(x) = FS - 1$ was adopted in calculating reliability index of five sliding surfaces. Where: $FS$ is safety factor and it is obtained by Janbu method in this paper.

First, the reliability index $\beta$ under seepage conditions was calculated by traditional method which doesn't consider the fuzziness of parameters . The results are listed in table 2.

Table 2 Reliability index calculated by traditional method for different sliding surface

| Number of sliding surface | ① | ② | ③ | ④ | ⑤ |
|---|---|---|---|---|---|
| Reliability index $\beta$ | 2.41 | 3.02 | 3.64 | 4.27 | 4.67 |

Then, we adopt fuzzy point evaluation method to calculate $\beta$ for different sliding surface on eight $\alpha$-cuts. When $m_1$=1, $m_2$=0.5, the 1st and 2nd order moment of $FS$ are shown in table 3.

Table3 The 1st and 2nd order moment of function for different α –levels for every slip surface

| Slip surface | ① | | ② | | ③ | | ④ | | ⑤ | |
|---|---|---|---|---|---|---|---|---|---|---|
| $\alpha$ | FS+ | FS- | FS+ | FS- | FS+ | FS- | FS+ | FS- | FS+ | FS- |
| 0.1 | 1.762 | 1.410 | 1.986 | 1.584 | 2.415 | 1.820 | 2.786 | 2.011 | 3.024 | 2.432 |
| 0.2 | 1.758 | 1.419 | 1.975 | 1.592 | 2.407 | 1.828 | 2.780 | 2.018 | 3.018 | 2.439 |
| 0.3 | 1.749 | 1.427 | 1.967 | 1.607 | 2.398 | 1.840 | 2.771 | 2.031 | 3.011 | 2.447 |
| 0.4 | 1.740 | 1.436 | 1.952 | 1.614 | 2.391 | 1.851 | 2.764 | 2.047 | 3.004 | 2.459 |
| 0.5 | 1.732 | 1.448 | 1.944 | 1.628 | 2.383 | 1.859 | 2.759 | 2.054 | 2.994 | 2.470 |
| 0.6 | 1.726 | 1.450 | 1.929 | 1.635 | 2.371 | 1.866 | 2.750 | 2.063 | 2.989 | 2.582 |
| 0.7 | 1.721 | 1.467 | 1.920 | 1.650 | 2.364 | 1.874 | 2.742 | 2.075 | 2.981 | 2.596 |
| 0.8 | 1.628 | 1.479 | 1.912 | 1.662 | 2.354 | 1.901 | 2.735 | 2.082 | 2.976 | 2.701 |

According to formula(6), the reliability index can be calculated and the rusults are shown in table 8.

Table 8 Reliability index calculated by fuzzy point evaluation method for different sliding surface

| Number of sliding surface | ① | ② | ③ | ④ | ⑤ |
|---|---|---|---|---|---|
| Reliability index $\beta$ | 2.53 | 3.26 | 3.92 | 4.57 | 5.02 |

Compare the results of the two methods, reliability indexes are shown in figure 4.

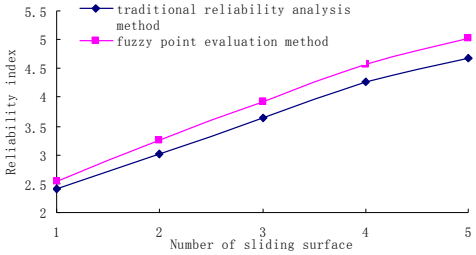


Fig 4. Comparison of reliability indexes by two methods

From the above figure, we can see that the reliability indexes of slide surfaces calculated by fuzzy point evaluation method are essentially consistent with the results by traditional method, which shows this method is feasible. Furthermore, because considers the fuzziness of parameters, fuzzy point evaluation method has more actual instructive significance comparing with the traditional method.

## Conclusions

In this paper, a fuzzy point estimate method for slopes in surface mine under seepage conditions is presented based on reliability theory and fuzzy theory. Because considers the fuzziness of parameters, it is a more practical and efficient stability assessment method comparing with the traditional reliability analysis method. However, further study should be done in the following aspects:

In this paper, the parameters are assumed independent. So, considering the influence of correlation is the next thing to do.

The selection of membership function lacks of enough practice. It should be perfected by engineering experience.

## Acknowledgements

This work was financially supported by the Chinese National Natural Science Foundation (51379119,51109124, 51274135) and SDUST Research Fund (2010kytd106)

## References

[1]YANG Kun, ZHOU Chuang-bing, ZHANG Xin. FUZZY-RANDOM RELIABILITY ANALYSIS OF BLOCKY ROCK MASS IN SLOPES[J]. Chinese Journal of Rock Mechanics and Engineering, 2006,25(2)：407-413

[2] YANG Kun , WANG Tongxu, MA Zhitao. Application of cusp catastrophe theory to reliability analysis of slopes in open-pit mines. [J]. Mining Science and Technology，2010，20（1）：71-75

[3] Klir G. Fuzzy Sets：an Overview of Fundamentals，Applications and Personal Views[M]. Beijing：Beijing Normal University Press，2000.

[4]Wang Guangyuan，Liu Yubin. Practical calculation method for fuzzy random reliability of structures[J]. Earthquake Engineering and Engineering Vibration，1995，15(3)：38–46.

[5] Giasi C I，Masi P，Cherubini C. Probabilistic and fuzzy reliability analysis of a sample slope near Aliano[J]. Engineering Geology，2003，(67)：391–402.

[6] Huang Wei, Yang Shijiao. Fuzzy Reliability Analysis of the Slope with Several Slide Surfaces in Xuefeng Open Sandstone Pit[J] Mining Research and Development. 2007，27(3):22-24

*Applied Mechanics and Materials Vols. 580-583 (2014) pp 93-97*
*© (2014) Trans Tech Publications, Switzerland*
*doi:10.4028/www.scientific.net/AMM.580-583.93*

# Influence of Density on Mechanical Properties for Coarse-grained soil Based on Percolation Theory

Yidan HUANG[1, a], Lingkan YAO[1,b], Jian Wang[1,c]

[1]School of Civil Engineering, Southwest Jiaotong University, Chengdu, Sichuan 610031, China

[a]huangyidan@home.swjtu.edu.cn, [b]yaolk@home.swjtu.edu.cn, [c]crest01@qq.com

**Keywords:** percolation; coarse-grained soil; renormalization group; density

**Abstract.** Coarse-grained soil is the main material of embankment dams, it is one of the major study objectives of soil mechanics. This paper introduces a method that utilizes percolation theory to explore the influence of soil density on mechanical property from the micro perspective. First it proposes the concept of stress network among particles; then it introduces the method of applying renormalization group theory for deducing; finally it derives the conclusion that in a uniform coarse-grained soil, the porosity and the mechanical property present a relationship of linear.

## Introduction

Soil is generally composed by solid particles, liquid phase and gas phase, while the liquid and gas phases can also be called as pore phase so as to form non-uniform aggregation with random structure. Hence, the properties of the three components as well as their proportion and interaction determine the physical and mechanical property of the soil. Currently, the study on soil mechanical property is mainly under the assumption condition of continuity, utilizes the overall medium as calculation model for the actual granule, and the model nature is represented by the constant determined by the experiments. Theories considering the actual soil particle composition structure, and studying the granular medium model of single particle and overall performance still need further development. This paper introduces a method that utilizes percolation theory to explore the influence of soil density on mechanical property from the micro perspective.

## Definition of stress network among particles

The first task is to make the soil structure abstract as the model required in percolation theory[1]. The natural structure of coarse-grained soil is featured with the point-to-point single-grained structure among particles. If the dry interspace is considered only, which means the interspace pressure is atmospheric pressure, the force in the granular system will be spread by contact points under load effect. The stress transmitted through contact system is called intergranular stress. As for the particles than can be simplified into balls, it is believed that the stress transmission path between the two contacted particles is a straight-line segment connecting the two sphere centers, and this line segment obviously passes the contact points. Such line segment is defined as “key” in the stress network among particles, and the corresponding segment endpoints or the particle center is defined as “base” (or grid point), and the integration of all bases and keys forms the so-called stress network among particles. Therefore, when the soil particle structure determines, the stress network among particles is also uniquely determined. It is also thought that the granular interaction obeys the probability principle, which is reflected that key or base is connected through a certain probability rate of $p$. However, the size of $p$ depends on the physical property and contact status of the particle itself such as the influence of irregular particle surfaces on the contact degree, but has nothing to do with the particle structure. It can be regarded that the mechanical phenomenon represented by stress network among particles is to make the soil structure abstract as 3D structure. When $p=1$, the constructional elements in the same structure is with the largest mechanical strength. On the other hand, when $p<1$, for network with different structures, there will be a critical connection probability $p_c$ for each. When

$p<p_c$, the network structure is broken into limited-sized fragments like the rickety components that can not bear strength. When $p \geq p_c$ , it can be expanded into limitless connected network, and $p_c$ is called percolation threshold value. However, $p \geq p_c$ is regarded as the necessary condition for soil to become the stress body; meanwhile, the mechanical strength will be higher when the value of $\Delta p = p - p_c$ is larger. In this sense, $p_c$ also becomes an indicator for reflecting the soil mechanical property. Its feature is that $p_c$ has nothing to do with the physical property of particles but it is only determined by the topological structure of stress network among particles. As for the soil with the same physical property but different granule structure, $p$ is a fixed value, while the changes of $\Delta p$ depends on the changes of $p_c$. Based on this, quantitative analysis for the influence of soil structure on mechanical property can be conducted and the concept of stress network among particles makes percolation model theory become possible.

**Deducting percolation threshold value with renormalization group theory**

Taking the theoretically densely-ranged balls of the same particle diameter as the example, this paper introduces the method of applying renormalization group theory[2] for deducing $p_c$. As shown in figure1a, when investigating under the 2D situation, the stress network among the densely-ranged balls is the two-dimensional lattice of triangles.

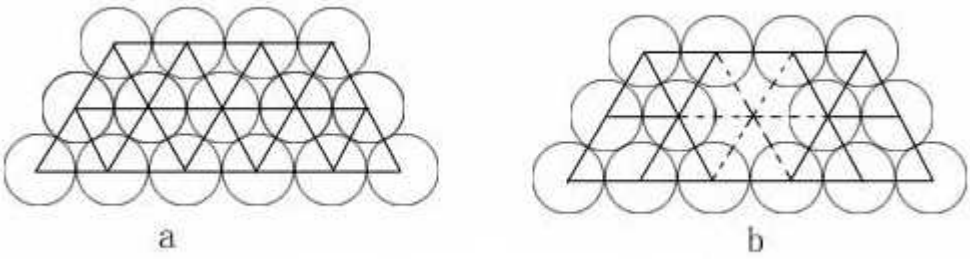


**Fig. 1. Diagram of stress network among particles**

If some place lacks one particle, which means there is a hole, the stress network will show the state of solid lines in Figure 1.b. However, it can still be regarded that the stress network is still a complete triangle lattice, but the corresponding base and key at the hole (as shown by the dotted lines in Figure 1.b) are always at non-conducting state. The purpose of such processing is to apply the renormalization group theory in the positional space to deduct percolation threshold value when hole occurs. Take the base percolation model as the example, and the operation process of renormalization group theory is as follows:

1. As a kadanoff's transformation[3], the lattice constant will be expanded into three times so as to transform the original lattice into new triangle lattice. Here it is unnecessary to worry about the problem of prominent "surface effect" caused by the small value of cell, for what matters is the interrelation of hole probability $h$ and $p_c$ not the absolute value of $p_c$.

2. Formulate the conducting direction of cells. It is believed stress can be transmitted in any direction; hence the conducting cells will be in conducting state as long as there are two lattice points in the cells. For instance, the Figure 2.a is a cell in the conducting state. If the lattice point at the right bottom corner becomes a hole in such cell, this cell is still in a conducting state as in Figure 2.b. However, if the lattice point at left bottom corner also becomes a hole, this cell is no longer conducting as in Figure 2.c. According to this, the conducting state of cells can be determined by the conducting state of lattice points and the distribution state of holes.

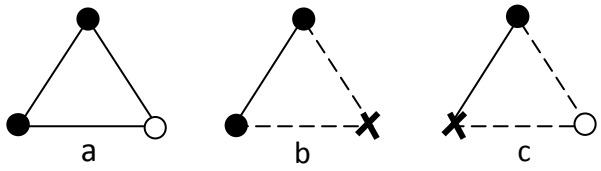


**Fig. 2. Configuration example for lattice points and holes**

●--- Lattice points in conducting state

○--- Lattice points in non-conducting state

×---Holes

3. Calculate the conducting probability of cells. According to the above provisions, 10 kinds of conducting configurations from 64 kinds of configurations can be found so as to draw out $p'$, the conducting probability of cell.

$$p' = p^3[(1-h)^3 + 3h(1-h)^2] + 3p^2(1-p)[(1-h)^3 + h(1-h)^2] \quad (1)$$

In this formula, $p'$refers to the conducting probability of cells， $p$ refers to the conducting probability of lattice points, while $h$ means hole ratio.

4. Determine the fixed points under renormalization group transformation. $p'$ is the function of $p$ and $h$, that is, $p' = R_b(p,h)$. From the definition of fixed points in renormalization group, it can be obtained that

$$R_b(p^*,h) = p^*(1-h) \quad (2)$$

When various numbers of $h$（$0 \le h \le 0.5$）are substituted into Formula(2), the corresponding points can be obtained. If $h$=0.06, the equation will be

$$p^* = 1.0528p^{*3} + 2.82p^{*2}(1-p^*) \quad (3)$$

For $p^* > 1$ is of no meaning, in the range of $0 \le p^* \le 1$, it can be obtained

$$p_1^* = 0; p_2^* = 0.531915$$

As the critical points can be corresponded only in unstable fixed points, it can be obtained that $p_c = p_2^* = 0.531915$, which is the percolation threshold value of stress network among soil particles when $h$=0.06. In this way, the relation curve of $p_c$ and $h$ is shown in Figure 3.a.

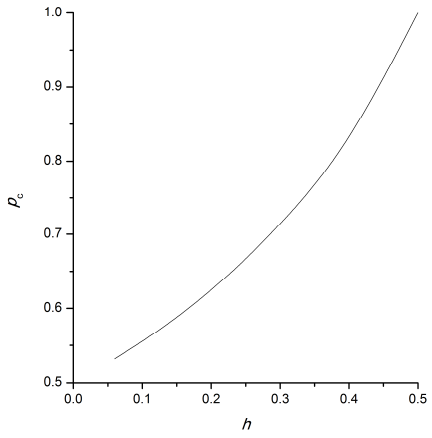


**a**

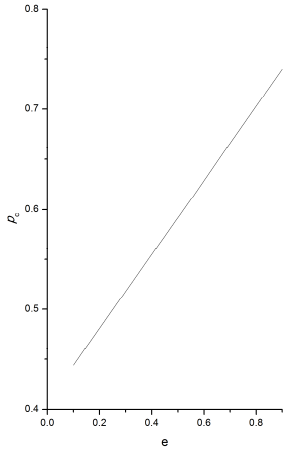


**b**

**Fig. 3. The relationship of $p_c$ and h, $p_c$ and $e$**

## Summary

If the proportion of particle volume to the total soil volume is $V_0$ when there is no hole, the void ratio will be $e=\frac{1-V_0}{V_0}$. When the soil hole ratio is $h$, it can be obtained that

$$e=\frac{(1-V_0)+V_0h}{V_0(1-h)} \tag{4}$$

In this way, the derivation method of composite function can be applied to solve the derivative of $p_c$ to $e$. Moreover, the densely-ranged balls of the same particle diameter $V_0$ =0.74 is substituted to solve

$$\frac{dp_c}{de}=\frac{dp_c}{dh}\cdot\frac{dh}{de}=\frac{4p_c^2h-4^2p_c+3p_c}{4p_ch^2+8p_ch-4p_c+3h+3}\cdot\frac{1}{V_0(1+e)}=0.37 \tag{5}$$

That $\frac{dp_c}{de}$ is equal to a constant proves the linear relationship between $p_c$ and $e$. In this way, after using e for coordinate conversion of $h$, the relation curve of $p_c$ and $h$ shown in Figure 3.a will become a straight line as in Figure 3.b. Such linear relationship is determined by the renormalization group Formula (2), while the renormalization group formula depends on the topological structure of stress network among particles and kadanoff's transformation method. As the topological structure of stress network of unchanged holes is adopted and the processing method of reflecting its influences only in transformation law is applied, strictly educing the functional relation between $p_c$ and $e$ in mathematics becomes possible, which further realizes the goal of quantitative analysis for the influences of soil density on mechanical property from micro perspective. According to the indoor experimental results, when the sandy soil is of different void ratio, its corresponding mechanical property index is as shown in Table 1[4]. From Table 1, it can be found that the relation between $e$ and $\varphi$ in silt is completely non-linear; the relation between $e$ and $E_0$ in fine sand is non-linear; while the relationship between $\varphi$ or $E_0$ and $e$ for either coarse sand or medium sand is definitely linear.

**Table 1. The average mechanical property index of sandy soil**

| Type | Void ratio e | Internal friction degree φ (degree) | Modulus of deformation E0 (MPa) |
|---|---|---|---|
| Coarse sand | 0.4~0.5 | 42 | 46 |
| | 0.5~0.6 | 40 | 40 |
| | 0.6~0.7 | 38 | 33 |
| Medium sand | 0.4~0.5 | 40 | 46 |
| | 0.5~0.6 | 38 | 40 |
| | 0.6~0.7 | 35 | 33 |
| Fine sand | 0.4~0.5 | 38 | 37 |

| | | | |
|---|---|---|---|
| | 0.5~0.6 | 36 | 28 |
| | 0.6~0.7 | 32 | 24 |
| | 0.5~0.6 | 36 | 14 |
| Silt | 0.6~0.7 | 34 | 12 |
| | 0.7~0.8 | 28 | 10 |

There are many other factors affecting the soil mechanical property. As for cohesiveless soil, the influence of density on mechanical property is large. The bigger the density is; the more soil contact points are, the stronger the connection is, the weaker the soil compression is, and the larger the internal friction angle is. That is, the higher the soil strength is. This is a well-known rule. On the other hand, for the sandy soil with bigger particle diameter, it is general with the property of uniform-sized particles and obvious single grain structure, which is similar to the established model with the balls of the same diameter as the background. Therefore, the conclusion that the influence of void ratio on mechanical property is linear can be applicable to it, and can be reflected from the indoor experimental data. This conclusion also has guiding significance for analyzing the influence of homogeneous gravel soil density on mechanical property.

## Acknowledgements

This work was financially supported by a grant from the National Natural Science Foundation of China (No.41172321, No.41030742, No.51308474). The corresponding author: Lingkan Yao

## References

[1] Yici Zhang: Percolation Theory. Chinese Journal of Applied Probability and Statistics ,1986.

[2] Kenneth G. Wilson: The Renormalization Group and Critical Phenomena.Reviews of Modern Physics, Vol. 55, No. 3, July 1983, p. 583~600.

[3] Houqiang Li, Guangyue Cheng: Fractals and Fractal Dimension. Chengdu: Sichuan Education Press,1990, p. 86~107.

[4] Engineering Geology Manual, China architecture & Building Press,1992, p. 195.

*Applied Mechanics and Materials Vols. 580-583 (2014) pp 98-104*
*© (2014) Trans Tech Publications, Switzerland*
*doi:10.4028/www.scientific.net/AMM.580-583.98*

# Justification for determination of the depth of an active zone based on the II group of limiting states

Nurumbayeva Lunara Maksotovna[1,a], Badanin Andrey Nikolaevich[2,b]

[1]Saint-Petersburg State Polytechnical University, Polytechnicheskaya, 29. St.Petersburg, 195251 , Russian Federation

[2]Saint-Petersburg State Polytechnical University, Polytechnicheskaya, 29. St.Petersburg, 195251 , Russian Federation

[a]telman_lunara@mail.ru, [b]chinnab@mail.ru

**Key words:** depth of the active zone, thickness, geomechanics, soil mechanics, calculation of (soil) settlement.

**Abstract.** The problems of the amendments in the updated edition of SNIP 2.02.01-83 * "Foundations of buildings and structures" SP 22.13330.2011 "Foundations of buildings and structures" are discussed in the article". Theoretically, the depth of the core is not justified anywhere and the restrictions are made only on the basis of experimental data. The importance of the amendments should be displayed theoretically.

In according to the newly adopted regulatory framework the results of the foundation settlement calculations for the limited states of the second (II) group by the layer-stack summation method with the justification of the amendments in the updated edition of SNIP 2.02.01-83 * "Foundations of buildings and structures" SP 22.13330.2011 "Foundations of buildings and structures" are shown in this article.

In the second part of the article the optimum width selection calculation results of projected foundation and identification of the economic benefits of decisions made are shown.

## Introduction

The main and obligatory calculation is designing based on the II group of limiting states [2-5]. For a foundation [8] this is mainly a definition of its settlement. Definition of the foundation settlement [9] is an integral part of designing since bases and foundations are the most important bearing elements of buildings and constructions [13-17]. Reliability of a construction [12], by which we understand the ability of a construction to carry out demanded functions within the calculated period of exploitation, as a whole depends on the correct calculation of the designed foundation and the base beneath the foundation.

The cost of a foundation [20, 21] if a building or a construction is erected is estimated as 12% of the entire cost, if we talk about working hours they reach up to 15% and more of the whole number of working hours, and as to the duration of works to construct a foundation it takes up to 20% of the construction period. If there are immersed parts of buildings or hard soil conditions the above mentioned figures may significantly increase [6]. Therefore improvements in designing and technological solutions in the area of foundation construction lead to saving of budget and working resources as well as to shortening of construction period [6].

Updated edition of SNIP 2.02.01-83 * "Foundations of buildings and constructions" SP 22.13330.2011 was released on 28.12.2010 in which there were changes related to conditions of the definition of the depth of the active zone as well as to foundation settlement [1, 10].

Analysis of the amendments to the regulatory document revealed the absence of the theoretical justification of the decrease of the depth of the active zone, limitations for the depth of the active zone were accepted on the basis of experimental data or test data also a question related to methodology or to the absence of methodology of calculation of foundation settlement based on SP 22.13330.2011 "Foundations of buildings and constructions" emerged [7].

**Design conditions**

It was possible to theoretically justify [23] the amendments made with the help of calculation of settlement by the means of layer by layer summation of mat footing of the following parameters: width b=1,2 m., depth of base of the foot of foundation allocated above the natural relief d=1,8 m., average pressure beneath the foot of foundation P=285 kPa. The base is arranged in the following layers:

1. Fine sand of the specific weight $\gamma_1$=18,7 kN/m$^3$ , deformation module $E_1$=14,4 MPa;
2. Sand of average size of the specific weight $\gamma_2$=19,2 kN/m$^3$, deformation module $E_2$=18,6 MPa;
3. Sand of average size of the specific weight $\gamma_2$=19,8 kN/m$^3$, deformation module $E_2$=18,8 MPa

Received results are displayed in the Table 1.

**Results and discussion**

Settlement of such foundation [18,19] calculated in accordance with SNIP 2.02.01-83 * "Foundations of buildings and constructions" where the depth of the active zone should meet the condition,

$$\max\sigma \leq 0{,}2\gamma H \quad (1)$$

and according to SP 22.13330.2011 "Foundations of buildings and constructions" with the condition,

$$\max\sigma \leq 0{,}5\gamma H \quad (2)$$

does not exceed the permissible therefore the depth of the active zone with the changes made is mathematically justified [7].

Results of the comparison of the active regulatory documents (a SP 22.13330.2011 Updated version of 2.02.01-83 * "Foundations of buildings and constructions" at the moment functions only like a recommendation designer has a right to use the definition of the depth of the active zone in accordance with the both documents) demonstrate that there is no significant loss of the reliability of foundations (picture 1). Moreover the limitation of the depth of the active zone according to SNIP 2.02.05-.85* “Bases of hydro technical constructions” is $\max\sigma \leq 0{,}2\gamma H$ [11].

The investigations [22] of calculation under which settlement does not exceed the acceptable with a huge bias, sets a new goal. Namely working hours needed to construct a foundation should be optimized. It is possible by the means of a calculation of the settlement of foundation based on the method layer by layer summation decreasing the width of foundation.

Results of the calculation of foundation settlement for a foundation with the following parameters width b=1 m. are given in the Table 2, and width b=0.8 m are given in the Table 3.

Table 1

| № | Type of soil layer | Absolute depth z [m] | Relative depth ξ=2z/b [m] | Coeffi-cient of tension change acc. to depth α | Additional pressure σzp [kPa] | Everyday pressure σzg [kPa] | 0,2 σzg | 0,5 σzg | Module of defor-mation E [MPa] |
|---|---|---|---|---|---|---|---|---|---|
| 1 | Fine sand | 0 | 0 | 1,000 | 251,340 | 33,660 | 6,73 | 16,83 | 14,4 |
| | | 0,24 | 0,40 | 0,977 | 245,559 | 42,640 | 8,53 | 21,32 | |
| | | 0,72 | 1,20 | 0,755 | 189,762 | 51,620 | 10,32 | 25,81 | |
| 2 | Sand of average size | 1,20 | 2,00 | 0,550 | 138,237 | 60,836 | 12,17 | 30,42 | 18,6 |
| | | 1,68 | 2,80 | 0,420 | 105,563 | 70,052 | 14,01 | 35,026 | |
| | | 2,16 | 3,60 | 0,337 | 84,702 | 79,268 | 15,85 | 39,634 | |
| | | 2,64 | 4,40 | 0,280 | 70,375 | 88,484 | 17,70 | 44,242 | |
| | | 3,12 | 5,20 | 0,239 | 60,070 | 97,700 | 19,54 | 48,85 | |
| | | 3,60 | 6,00 | 0,208 | 52,279 | 106,916 | 21,38 | 53,458 | |
| | | 4,08 | 6,80 | 0,185 | 46,498 | 116,132 | 23,23 | 58,066 | |
| | | 4,56 | 7,60 | 0,166 | 41,722 | 125,348 | 25,07 | 62,674 | |
| | | 5,04 | 8,40 | 0,150 | 37,701 | 134,564 | 26,91 | 67,282 | |
| 3 | Sand of average size | 5,52 | 9,20 | 0,137 | 34,434 | 144,068 | 28,81 | 72,034 | 18,8 |
| | | 6,00 | 10,00 | 0,126 | 31,669 | 153,572 | 30,71 | 76,79 | |
| | | 6,48 | 10,80 | 0,117 | 29,407 | 163,076 | 32,62 | 81,54 | |

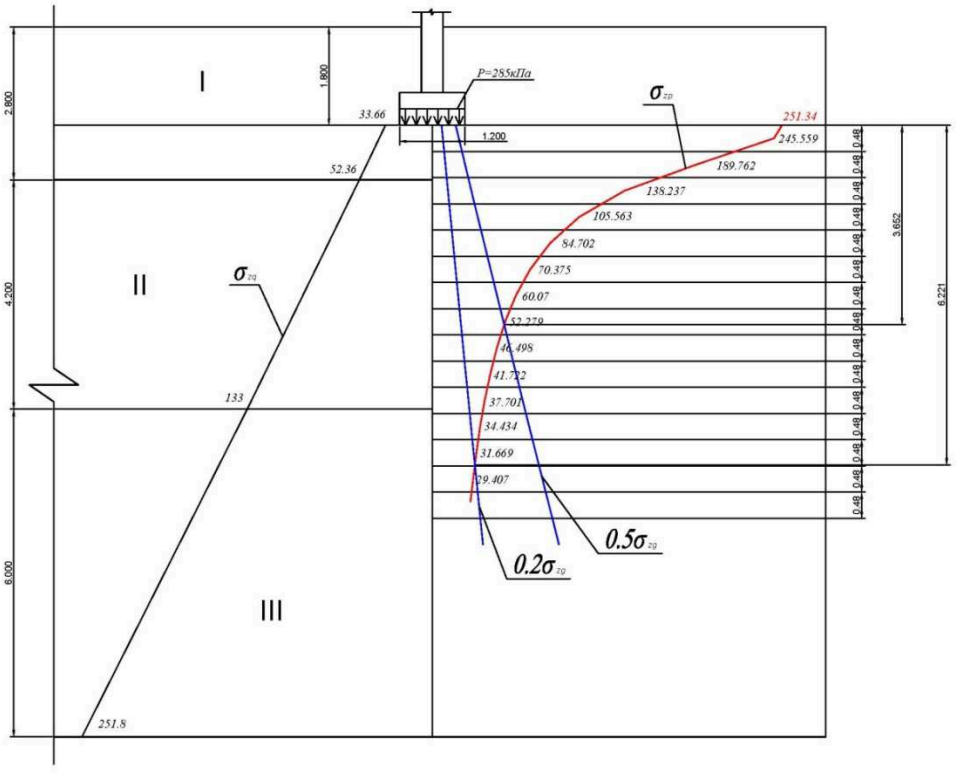


Figure 1. Calculation scheme of compressive stress by the means of layer by layer summation acc. to old and new regulations.

Table 2

| № | Type of soil layer | Absolute depth z [m] | Relative depth ξ=2z/b [m] | Coeffi-cient of tension change acc. to depth α | Additional pressure σzp [kPa] | Everyday pressure σzg [kPa] | 0,2 σzg | 0,5 σzg | Module of defor-for-mation E [MPa] |
|---|---|---|---|---|---|---|---|---|---|
| 1 | Fine sand | 0 | 0 | 1,000 | 308,340 | 33,660 | 6,73 | 16,83 | 14,4 |
| | | 0,24 | 0,48 | 0,958 | 295,328 | 42,640 | 8,53 | 21,32 | |
| | | 0,72 | 1,44 | 0,687 | 211,891 | 51,620 | 10,32 | 25,81 | |
| 2 | Sand of average size | 1,20 | 2,40 | 0,477 | 147,078 | 60,836 | 12,17 | 30,42 | 18,6 |
| | | 1,68 | 3,36 | 0,359 | 110,756 | 70,052 | 14,01 | 35,026 | |
| | | 2,16 | 4,32 | 0,285 | 87,939 | 79,268 | 15,85 | 39,634 | |
| | | 2,64 | 5,28 | 0,236 | 72,707 | 88,484 | 17,70 | 44,242 | |
| | | 3,12 | 6,24 | 0,201 | 61,915 | 97,700 | 19,54 | 48,85 | |
| | | 3,60 | 7,20 | 0,175 | 53,960 | 106,916 | 21,38 | 53,458 | |
| | | 4,08 | 8,16 | 0,155 | 47,731 | 116,132 | 23,23 | 58,066 | |
| | | 4,56 | 9,12 | 0,138 | 42,613 | 125,348 | 25,07 | 62,674 | |
| | | 5,04 | 10,08 | 0,125 | 38,604 | 134,564 | 26,91 | 67,282 | |
| 3 | Sand of average size | 5,52 | 11,04 | 0,115 | 35,336 | 144,068 | 28,81 | 72,034 | 18,8 |
| | | 6,00 | 12,00 | 0,106 | 32,684 | 153,572 | 30,71 | 76,79 | |
| | | 6,48 | 12,96 | - | - | 163,076 | 32,62 | 81,54 | |

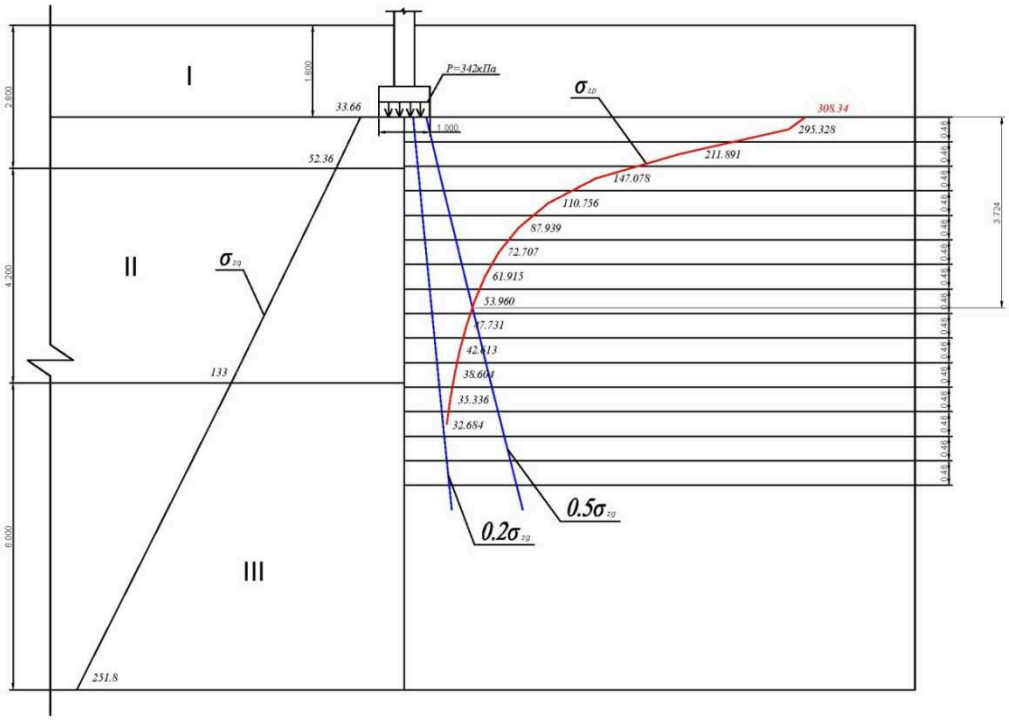


Figure 2. Calculation scheme of compressive stress by the means of layer by layer summation acc. to new regulations where b = 1 m.

Results of the calculation of foundation settlement for a foundation with the width b=0.8 m are given in the Table 3:

Table 3

| № | Type of soil layer | Absolute depth z [m] | Relative depth ξ=2z/b [m] | Coeffi-cient of tension change acc. to depth α | Additional pressure σzp [kPa] | Everyday pressure σzg [kPa] | 0,2 σzg | 0,5 σzg | Module of defor-mation E [MPa] |
|---|---|---|---|---|---|---|---|---|---|
| 1 | Fine sand | 0 | 0 | 1,000 | 393,840 | 33,660 | 6,73 | 16,83 | 14,4 |
| | | 0,24 | 0,60 | 0,929 | 365,877 | 42,640 | 8,53 | 21,32 | |
| | | 0,72 | 1,80 | 0,596 | 234,729 | 51,620 | 10,32 | 25,81 | |
| 2 | Sand of average size | 1,20 | 3,00 | 0,397 | 156,354 | 60,836 | 12,17 | 30,42 | 18,6 |
| | | 1,68 | 4,20 | 0,293 | 115,395 | 70,052 | 14,01 | 35,026 | |
| | | 2,16 | 5,40 | 0,231 | 90,977 | 79,268 | 15,85 | 39,634 | |
| | | 2,64 | 6,60 | 0,191 | 75,027 | 88,484 | 17,70 | 44,242 | |
| | | 3,12 | 7,80 | 0,162 | 63,802 | 97,700 | 19,54 | 48,85 | |
| | | 3,60 | 9,00 | 0,140 | 55,138 | 106,916 | 21,38 | 53,458 | |
| | | 4,08 | 10,20 | 0,124 | 48,738 | 116,132 | 23,23 | 58,066 | |
| | | 4,56 | 11,40 | 0,111 | 43,716 | 125,348 | 25,07 | 62,674 | |
| | | 5,04 | 12,60 | - | - | 134,564 | 26,91 | 67,282 | |
| 3 | Sand of average size | 5,52 | 13,80 | - | - | 144,068 | 28,81 | 72,034 | 18,8 |
| | | 6,00 | 15,00 | - | - | 153,572 | 30,71 | 76,79 | |
| | | 6,48 | 16,20 | - | - | 163,076 | 32,62 | 81,54 | |

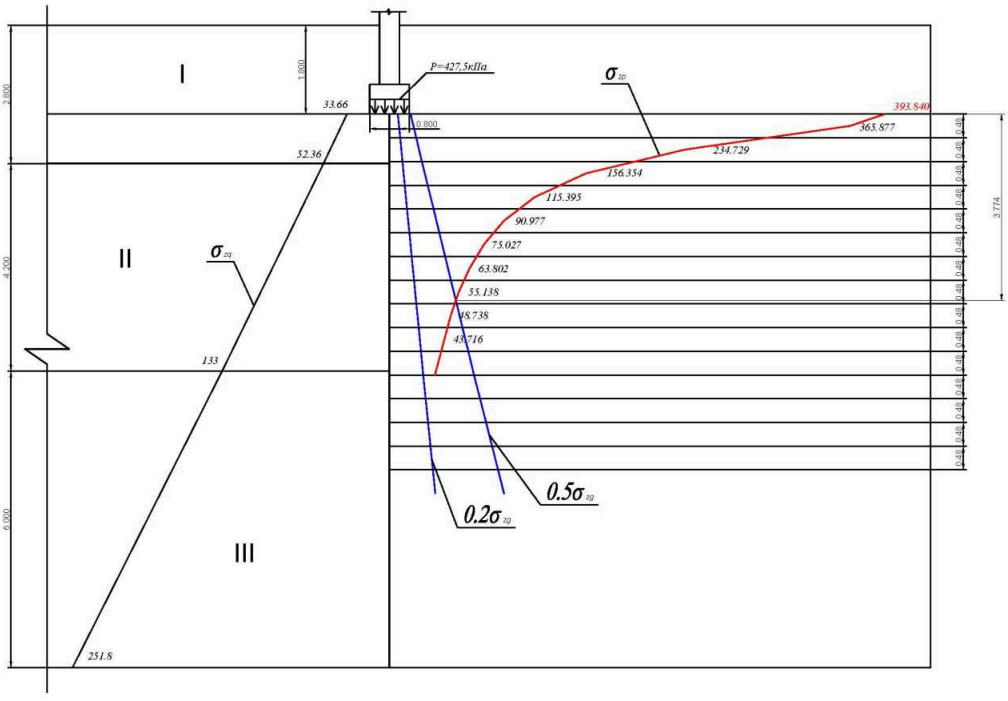


Figure 3. Calculation scheme of compressive stress by the means of layer by layer summation acc. to new regulations where b = 0,8 m.

Results of working hours spent and materials used are displayed in Table 4.

Table 4.

| Foundation width [m] | Working hours for ground works [%] | Used materials [%] | | |
|---|---|---|---|---|
| | | concrete | broken stone | sand |
| 1,2 | 100 | 100 | 100 | 100 |
| 1 | 92,74 | 83,33 | 90,91 | 90,91 |
| 0,8 | 85,58 | 66,67 | 81,82 | 81,82 |

According to the calculations settlement of foundation despite the decrease in width stays within acceptable limits therefore working hours may be optimized and reduced by 7,26 – 14,42 % as well as materials used by 34,69 – 69,69 %.

## Summary

1. Foundation settlement calculated according to new regulations in all studied cases stays within acceptable limits which allows to decrease working hours and amount of materials used.
2. Production approach for the choice of optimal width of designed foundation may be used as a recommendation and may function as a starting point for a research of shallow foundations of other types and sizes.

## References

[1] Actualized edition SNIP 2.02.01-83* "Foundations of buildings and structures": SP 22.13330.2011 "Foundations of buildings and structures".

[2] Zytovych N. A. Soil Mechanics (brief course). 6th edition. M.: Vyshaya shkola, 2011, 272 p.

[3] Bugrov A. K. Soil mechanics. SPb. Publishing of SPbSPU, 2007, 170-175 pp.

[4] Reznik Y.M. Determination of active zones below footings. Art of Foundation Engineering Pratice Congress, 2010, 554-564 pp.

[5] Dalmatov B. I. Soil mechanics, bases and foundations (including engineering geology course). 2rd edition. Lan' publishing. 2012, 415 p.

[6] Arhipov D.N. Interaction of the soil basis and the combined tape bases with geometrically changeable form of a sole. Avtoref. Novocherkassk, 2006, 153 p.

[7] Badanin A.N., Nurumbaeva L.M. Modern calculation of foundations for the group II limit states and its features. Construction of unique buildings and structures, 2013, №4 (9), 6 p.

[8] Utkin V.S. The reliability calculation of foundations under eccentric load in the operation phase. Magazine of Civil Engineering. 2013, №5, 69 p.

[9] Melnikov V. A., Zarubin P. E. The comparative analysis of methodologies for calculating settlement of pile foundations. Construction of unique buildings and structures, 2013, №8 (13), 43-45 p.

[10] SNiP 2.02.01-83* "Foundations of buildings and structures".

[11] SNiP 2.02.01-85* "Foundation of hydraulic structures".

[12] Utkin V.S., Shepelina E.A. Calculation of reliability of foundation bed in the deformations at the operational stage. Magazine of Civil Engineering, 2013, №4, 13 p.

[13] Uhov S. B., Semenov V. V., Znamenskiy V. V. Soil mechanics, bases and foundations. 4th edition. 2007, 566 p.

[14] Nelson J., Overton D., Durkee D. Depth of Wetting and the Active Zone. Expansive Clay Soils and Vegetative Influence on Shallow Foundations. 2001, 95-109 pp.

[15] Zytovych N. A. Permafrost engineering: General and Applied. “Stereotip” publishing. 2013, 448 p.

[16] Braja M. Das. Advanced soil mechanics. New York: Taylor & Francis Group, 2008, 567 p.

[17] Punmia B. C., Ashok Kumar Jain, Arun Kr. Jain. Soil mechanics and foundations. Firewall Media, 2005, 940 p.

[18] Harr M. E. Foundations of theoretical soil mechanics. NY McGrow Hill, 1966.

[19] Harr M. E. Mechanics ob particulate media: a probiemisting approach. New York: 1977. 543 p.

[20] Venkatramaiah C. Geotechnical engineering. New Age International, 2007. 926 p.

[21] Whitlow R. Basic soil mechanics. Prentice Hall, 2001. 592 p.

[22] Bocheninskii, V.P., Vatin, N.I., Shmarov, V.S. Rezul'taty issledovaniya perekhodnykh protsessov v zhidkometallicheskikh konturakh s mgd-nasosami, 1981, 20 p.

[23] Badanin A.N., Bugrov A.K., Krotov A.V. The determination of the first critical load on particulate medium of sandy loam foundation. Magazine of Civil Engineering, 2012, №9, 31 p.

*Applied Mechanics and Materials Vols. 580-583 (2014) pp 105-108*
*© (2014) Trans Tech Publications, Switzerland*
*doi:10.4028/www.scientific.net/AMM.580-583.105*

# Mechanics Analysis of semi-rigid subgrade pavement structure

Liya Su

Architecture and Civil Engineering School, Inner Mongolia University of Science and technology, Baotou, 014010, China

suliya1@.imust.cn

**Keyword:** Asphalt Pavement, Semi-rigid foundation, modulus of elasticity, reasonable thickness

**Abstract.** The semi-rigid base asphalt pavement structure was choose often used to the highway in our country, but the semi-rigid base asphalt pavement early damage almost has become a common phenomenon.In this paper, the rule and trend of mechanics response about pavement structure (the vertical displacement and tensile stress) were analyzed under the semi-rigid base choose different elasticity modulus and thickness by ANSYS for muti-layer foundation of semi-rigid base pavement design to provide reference.

## Introduction

The semi-rigid base asphalt pavement is the main road structure form in China[1], the many advantages of the semi-rigid base material for thinning, and reduced the construction cost to provide the reliable guarantee for asphalt layer, but with the increase of traffic volume and vehicle load, the semi-rigid base itself defects and overloading problems caused the early damage,which reduce the service life and service quality of Pavement in a large extent. Among the reason is complex, pavement structure is the key factor. Therefore, it is necessary to analyze mechanical state of pavement structure select different structure parameters combination under the load ,so as more clear understand stress distribution of the semi-rigid base asphalt pavement under different structure combination state and determine the reasonable structure and horizon of pavement structure, which makes the good performance of pavement structure has meet the traffic demand.

## Establish the finite element model of semi-rigid pavement

The pavement structure is actually a three-dimensional engineering structures, it can support any form load,so describing the road system performance of the best model is 3D model.The three-dimensional finite element model is realized in three-dimensional space within the scope of discure pavement structure and consider any distribution load form.The size of the model will not be taken to infinity in Finite element analysis, the model size will get as larger as possible, but the size is too large will greatly increase the computational effort. So we should rationally determine the size of the calculation model and don't increase too much computation work guarantee the calculation accuracy[2].

In ANSYS analysis,Different element meshing have a great influence on computed result,and the precision of calculation results improve with the rapid growth of grid from the basic theory of finite element.But the grid too small to need improve the performance of the computer, and element increase will increase the rounding error of computation. So this paper the element meshing adopt mapped mesh method, In the load was divided secretly, and element division gradually increased away from the traffic load, soil base divided relatively sparse as shown in Fig.1.

In the calculation process, the the boundary conditions of model are as follows: a certain depth of soil base bottom is fixed and the constraint around.The two face parallel to the z axis no displacement along x direction, before and after plane perpendicular to the z axis no the displacement along y direction, each structural layer of pavement adopt completely continuous contact and Bond together by glue of Booleans to simulate the completely continuous calculation. The maximum deflection,the peak value of maximum stress and its location of pavement structure were analyzed when conditions.

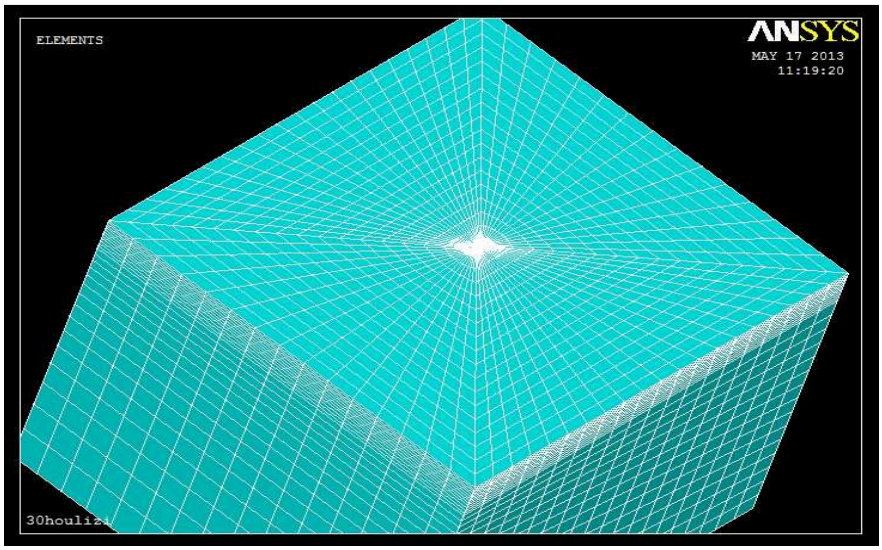


Fig.1 Grid Meshing by ANSYS

Pavement as a kind of multilayer elastic system, each structure layer on its stress state will be different degrees impact under the load. For pavement model under wheel load , the displacement and stress values were calculated to comparison. A single axle beer load two-wheel group 100kN as standard axle load by BZZ-100 said in the calculations,a single wheel surface equivalent diameter from 21.3cm and the center distance of two rounds for1.5 times the equivalent diameter [3].

Maximum stress of each layer reduced with the center distance of two rounds increased , so the center of two rounds was selected as the calculation basis by changing the elastic modulus or thickness of semi-rigid base to analyze its reasonable value range.

**Mechanics effect of elastic modulus on pavement structure**

Analyzed on the deflection value and stress to get the reasonable value range of elastic modulus about semi-rigid base under the condition of the semi-rigid base thickness unchanged and change the elastic modulus as shown in Tab.1.

Tab.1 The structural parameters I of semi-rigid base asphalt pavement

| | elastic modulus(MPa) | thickness (cm) |
|---|---|---|
| asphalt concrete pavement | 1400 | 20 |
| semi-rigid base | undetermined | 30 |
| semi-rigid bottom base | 600 | 20 |
| soil matrix | 60 | 600 |

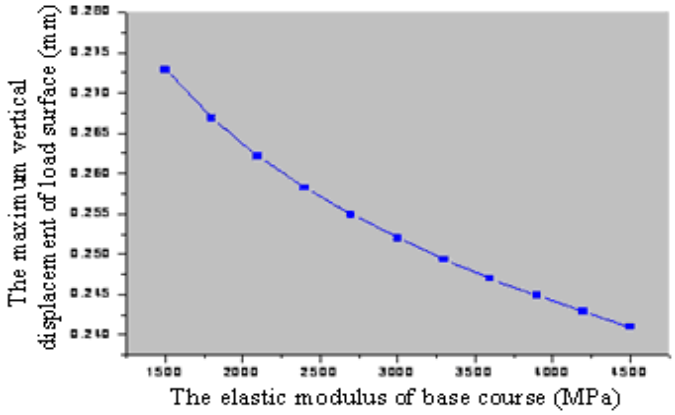


Fig.2 The relation of base elastic modulus and maximum load surface vertical displacement

Road surface deflection value and the elastic modulus of semi-rigid base meet linear relationship. With the elastic modulus of semi-rigid base materials increased, road deflection value decreases as shown in Fig.2. when elastic modulus of base layer reaches a certain value, the road deflection may not decrease.

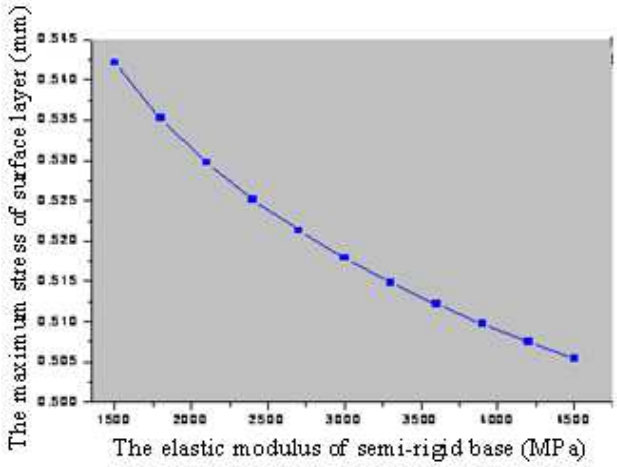


Fig.3 The relation of base elastic modulus and maximum surface layer stress

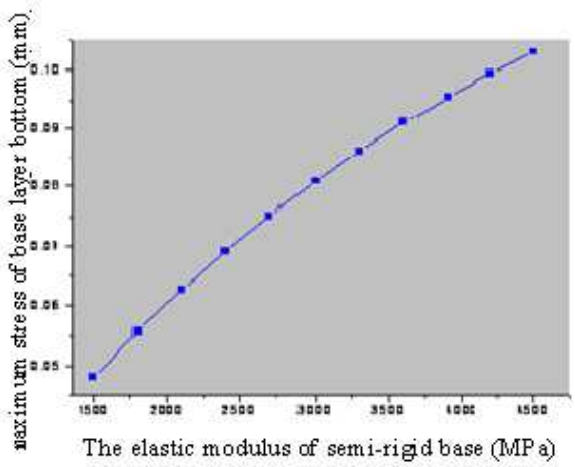


Fig.4 The relation of base elastic modulus and maximum base layer bottom stress

Fig.3 and Fig4 shown that the relationship between elastic modulus of base layer and the various structural layers of the tension and compression stress, for the surface layer, the influence of elastic modulus on resilient deflection reduced with the increase of material elastic modulus, and the curve slope gradually reduce, the sensitivity get smaller and smaller.Tensile stress of base layer bottom increased with the elastic modulus of base layer increased, but when the elastic modulus of base layer reach 4500MPa, the tensile stress of base layer bottom still in the range of allowable stress. Accordingly, elastic modulus of base layer have a reasonable value range.

**Mechanical effect of the basic thickness on pavement structure**

keeping the constant elastic modulus of the semi-rigid base and changing the thickness of the semi-rigid base, through analyzed on the deflection value and stress value to conclude that the reasonable value range of thickness about semi-rigid base and the relationship with the condition of pavement structure,as shown in Tab.2.

Tab.2 The structural parameters II of semi-rigid base asphalt pavement

| | elastic modulus(MPa) | thickness (cm) |
|---|---|---|
| asphalt concrete pavement | 1400 | 20 |
| semi-rigid base | 1500 | undetermined |
| semi-rigid bottom base | 600 | 20 |
| soil matrix | 60 | 600 |

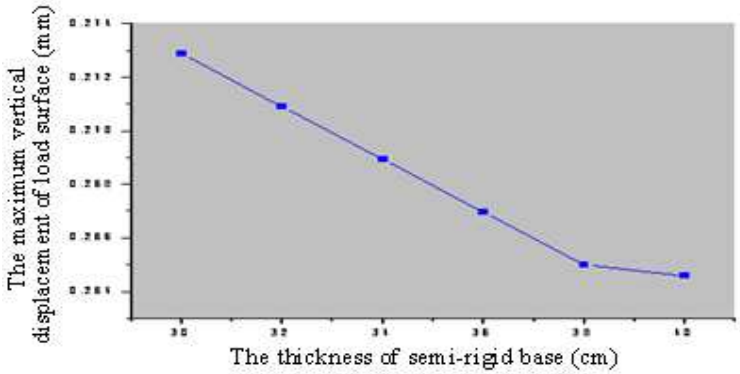


Fig.5 The relation of base thickness and maximum load surface vertical displacement

Fig.5 shown that the influence of the thickness of semi-rigid base on deflection and the influence of elastic modulus is the same.

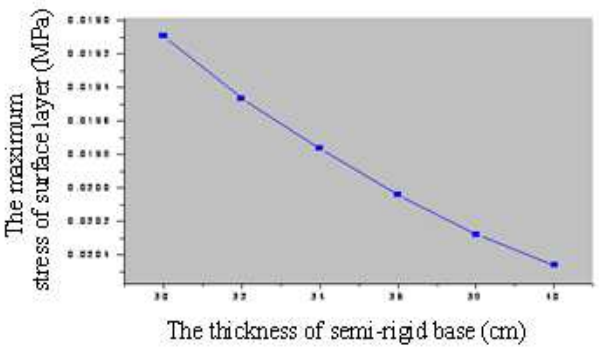


Fig.6 The relation of base thickness and maximum surface layer stress

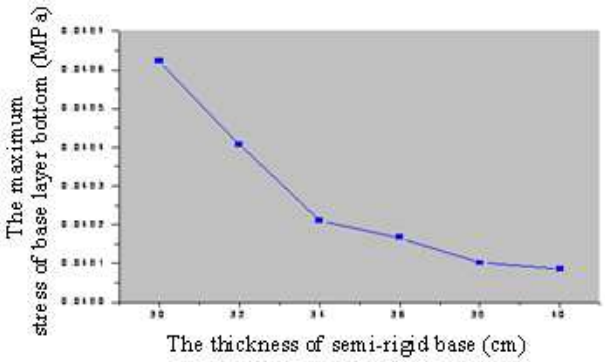


Fig.7 The relation of base thickness and maximum base layer bottom stress

Fig.6 and Fig.7 shown that the changing rule of the normal stress of each layer or base bottom with the thickness of semi-rigid base is similar as with the elastic modulus change. Both of the influence law of tensile stress about various structural layers in the bottom is the same.

## Conclusion

Mechanics analysis of the semi rigid base asphalt pavement structural by the ANSYS. When select different elastic modulus and thickness of semi-rigid material, analysis and checking calculation of the mechanical response of various design parameters on pavement under the traffic load (stress and displacement component).Through calculation and analysis get the following conclusions:

Elastic modulus of semi-rigid base materials between1500MPa and 3000MPa, and thickness control under 35cm is more reasonable. Many units construction in this area in the process, thickness generally is 32cm, thickness of the semi-rigid base about Prominent sections could reach 40cm in the overload and heavy load problem.

Sensitivity index of general mechanical on the semi rigid base change decreased with the elastic modulus and thickness of semi-rigid base increase. With elastic modulus and thickness of the semi-rigid base increased, the change value of each index is more and more small, so the blind increased elastic modulus and thickness of semi-rigid base no practical significance.

At present, many units are studying a new pavement structure form [4], such as in the laying thickness is less than 30cm of flexible base asphalt and aggregate on semi-rigid base, or directly adopt asphalt stabilized macadam base and grading macadam road base combination for whole flexible asphalt pavement structure. Research results shown that the new type pavement structure has better mechanical properties and the thinner thickness, the overall performance,anti-rutting ability and the resist fatigue cracking ability are superior to the traditional semi-rigid base structure. This new structure will be the future trend and direction of the road structure design.

## References

[1] Peng LIN.Analysis on reasonable thickness and horizon of semi-rigid base[D],Tianjin:Hebei University of Technology, 2010.

[2] Xiaonian CHEN.Analysis on the mechanical response of asphalt pavement by three-dimensional finite element [D],Lanzhou:Lanzhou university of technology,2006.

[3] Haiyan ZHU, Xuanchang WANG, Baogui CAO. Stress analysis on the composite pavement of elastic foundation[J],Journal of chang ’an university,2008,28,25-29.

[4] Jingli ZHANG.Analysis on the limitations and new development direction of the classical pavement structure[J],Technology of Highway and Transport ,2004,1,16-18.

*Applied Mechanics and Materials Vols. 580-583 (2014) pp 109-112*
*© (2014) Trans Tech Publications, Switzerland*
*doi:10.4028/www.scientific.net/AMM.580-583.109*

# Model Test Study of Squeezed Branch Pile under Horizontal Vibration Load

Bing LV[1, a] ,Xiaojuan GAO[1, b]

[1] School of Civil Engineering, Henan University of Science and Technology, China, Luoyang, 471023

[a]lvbing1987.happy@163.com, [b]gaoxjly@163.com

**Keywords**: squeezed branch pile, horizontal vibration, model test, pile-soil dynamic interaction

**Abstract.**Based on the self-design model experimental system of dynamic soil-pile dynamic interaction, strong horizontal dynamic load was exerted to two models of squeezed branch pile, and the bearing plate location of the two squeezed branch piles is different. The model experiment adopt digital frequency converter to control the loading frequency, and use spring of different stiffness coefficient to achieve different load level. In order to analyze the action of bending moment and the status of lateral earth pressure changes, different sizes of excitation frequency and excitation load were setted during the test.

## Introduction

As the squeezed branch pile is widely used in civil engineering structures, relevant technical regulations are designed, especially construction machinery equipment and technology are becoming ripe gradually. The superior economic and technical performance of squeezed branch pile are gradually recognized. Due to its special section properties, the plates or branches of pile increase the inertia moment of pile body and the ability of resistancing loads, so its bearing capacity is greatly improved [1]. There are many engineering examples and theoretical analysis about squeezed branch pile under horizontal static load and vertical static load, while related research of the squeezed branch pile under horizontal dynamic load is rare and there is no theoretical analysis. But in practical engineering, pile foundation is often under the horizontal vibration load, such as: wave load, continuous running vehicle load, mechanical vibration load and earthquake load, wind load, etc. Under the effect of strong horizontal vibration force, the pile foundation is a complex system of pile-soil dynamic interaction. As time went on, stiffness of pile and the energy of the system lost due to damping [2]. Roger and Harry found the most significant factor of pile foundation dynamic is the yield displacement of soil and soil spring [3]. Novak has carried on the large size model pile dynamic test research, and the experimental results showed that dynamic response have some typical nonlinear characteristics. Under the circular vibration loads, a separation gradually created between pile and soil, which lead to a decline of stiffness and damping of the pile [4]. In general, experimental study on horizontal dynamic load of pile foundation is relatively few, and the level of dynamic load test of squeezed branch pile is more rarely.

## Summary of the test

**Study of model test facility.** To study the bearing capacity of squeezed branch pile under lateral vibration load, the model test of squeezed branch pile was conducted in cohesive soil. The soil taken from the construction site was divided three layers and put into box and tamped. After the soil was tamped, the physical and mechanical properties were measured again to made the tamped soil be same as the natural soil .The soil box used for model test is 1.2m length, 0.8m width and 1.0m height. One side of the box are made in glass, another threes sides are made in steel. The model pile made with steel of 0.8mm depth, the pile is 900mm length, 800mm length of pile was embedded in soil and 100mm length was exposed in air to convenience to application load (Fig.1). The diameter of the pile is 60mm, and eight strain gauges were attached symmetrically to each pile to measure the strain of measurement points during loading. Strain gauges were coated with structural plastic to prevent

moisture. Three pressure cells were buried in front of the pile 30mm in different depths along the pile for measure the earth pressure. The experiment facility is shown in Fig.2.

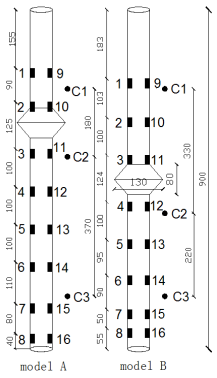


Fig.1 Sketch of model piles, strain gauges and pressure cells(unit: mm)

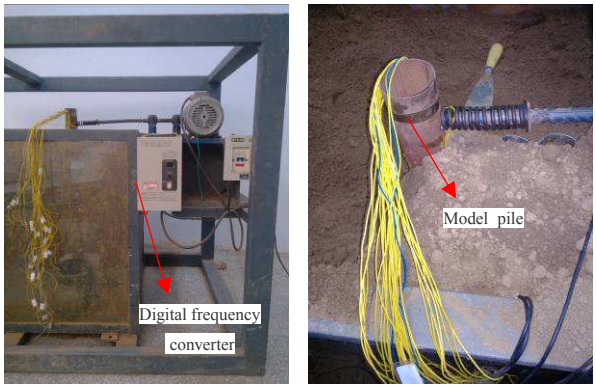


Fig.2 Sketch of test set

**Load control.** To achieve circular horizontal vibration loads, a motor was used to drive the eccentric wheel to rotate, and the eccentric wheel was contacted with a dowel bar. A spring is sheathed on the dowel bar and in contact with the pile. When the motor is started to work, the rotating speed of motor is excitation frequency of the load. Eccentricity of the eccentric wheel is 5mm. Loading position at a distance of pile top is 60mm. The magnitude of the load depends on the spring's stiffness coefficient and expansion. Expansion of spring is determined by the position and the size of eccentric wheel. Four springs with different stiffness coefficients are applied to the test. The determination of four loads' amplitude are respectively 45.1N, 78.4N, 141.1N, 220.5N. In order to measure the effect of vibration frequency, set the vibration frequency in the range of 1~30 Hz. Due to the pile-soil system is nonlinear, the size of dynamic loads and the loading process all have influence on its dynamic characteristics, so set the excitation load and excitation frequency from small to large during the test

## Results analysis

**Effects of excitation frequency.** The load bearing behaviors of the squeezed branch pile under horizontal dynamic load are shown in Fig.3 and Fig.4. As shown in Fig.3, with the increase of excitation frequency, the dynamic bending moment decreases in the upper part and the lower portion is gradually increased. On the whole, the maximum bending moment is occurs in about 1/3 the depth

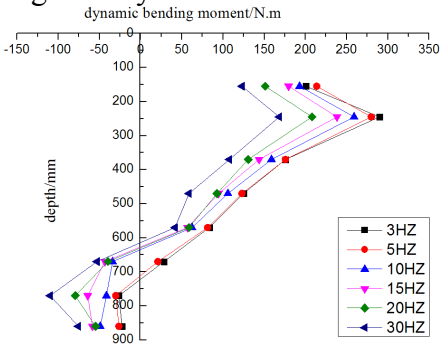


Fig.3 Relationship of dynamic bending moment and excitation frequency of model A(220.5N)

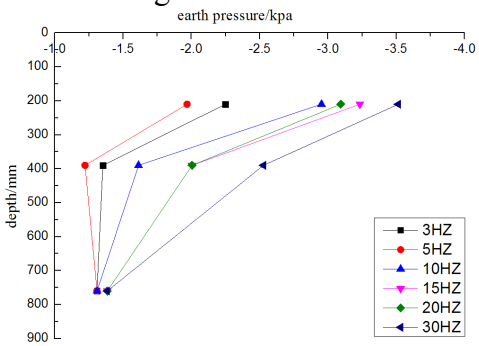


Fig.4 Relationship of earth pressure and excitation frequency of model A (45.08N)

of the pile top. The inflection points appeared in 724mm, 710mm, 634mm, 630mm, 632mm, 610mm depth, respectively, which have a upward trend. In practical engineering, this means the anti-lateral displacement ability of super-structures is improved. Fig.4 shows that under certain load, with the increase of excitation frequency, lateral earth pressure showed an increasing trend on the whole, and the main influence depth is in a 2/3 length from the top of the pile. Select the load level is 78.4N and measuring point is 2 of model A, and the time-strain curve of measuring point under the action of

different frequency is plotted in Figure 5. It can be seen strain in the excitation frequency of 3 Hz and 7 Hz mainly concentrated in 10μ~50μ;when the excitation frequency is 20 Hz, strain mainly concentrated in 10μ~40μ;when the excitation frequency is 30 Hz, strain mainly concentrated in 15μ~30μ. Other measuring points have the similar statistical variation. This shows that with increase excitation frequency, stress conditions of pile is changed, meanwhile the deformation of the cross-section is reduced. As can be seen from Fig 3 to Fig 5, with the increase of the excitation frequency, bearing capacity of pile-soil system is increased. This indicates that increase the excitation frequency has a better influence on the dynamic bearing capacity of squeezed branch pile. It has increased the level of dynamic bearing capacity.

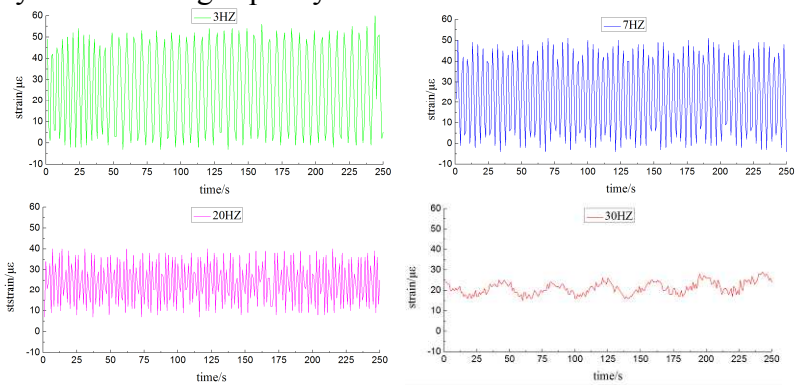


Fig.5 Time-strain curve of measuring points under the action of different frequency

**Effects of excitation load.** Set the excitation frequency of 3 Hz, and the load bearing behaviors of the squeezed and branch pile under different horizontal dynamic loads is shown in Fig.6.It can be seen from Figure 6, increase dynamic excitation load level has a significant impact to the bearing capacity of the pile. With increase the excitation load, dynamic response of squeezed branch pile gradually decreased with depth. Set the excitation frequency of 15 Hz, and the behaviors of lateral earth pressure is shown in Fig.7. It can be seen that the increase of excitation load will cause a significant increase in lateral earth pressure.

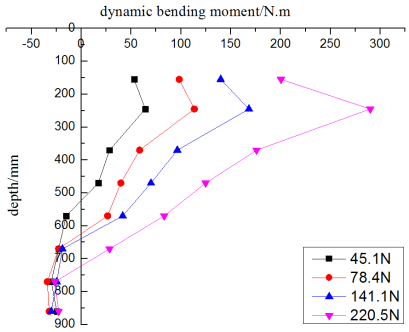


Fig.6 Relationship of dynamic bending moment and horizontal dynamic load of model A (3Hz)

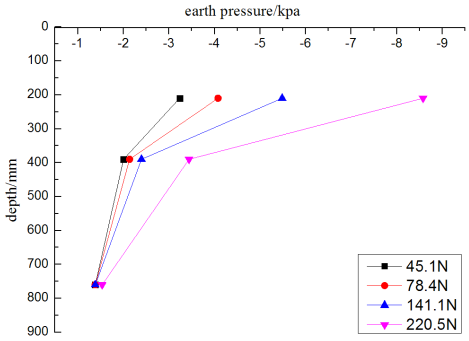


Fig.7 Relationship of earth pressure and horizontal dynamic load of model A (15Hz)

With the increase of depth, the variation amplitude decreased gradually. Figure 6 and Figure 7 shows that, with the increase of excitation load, bending moment and soil pressure showed a phenomenon of nonlinear increase. One reason is that the material of pile and soil is nonlinear, and the other reason is because the soil is elastic-plastic material. Soil resistance not only depends on the excitation load size and the deformation velocity of pile, but also depends on residual deformations of the soil. The gap between pile and soil has not been filled with new soil and creates separation, then generate a dynamic amplification phenomenon. Obviously, this situation is not conducive to the absorption of vibration energy.

**The influence of bearing plate's position.** It is worth mentioning that bearing plate's position changed the stress of squeezed branch pile obviously. Compare Figures 6 and 8, set the excitation frequency of 3 Hz. when the excitation load is 141.1N , the maximum dynamic bending moment of

model A is 70.2N.m, which occurred in the measuring point 2 ; the maximum dynamic bending moment of model B is 176.1N.m, which occurred in the measuring point 2 .When the excitation load is 220.5N, the maximum dynamic bending moment of model A is 290.2N.m, which occurred in the measuring point 2 ;the maximum dynamic bending moment of model B is 297.7N.m, which occurred in the measuring point 3.

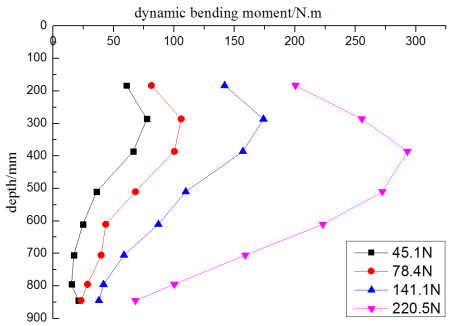


Fig.8 Relationship of dynamic bendingmomentand horizontal dynamic load of model B (3Hz)

The maximum bending moment of two piles both occurred in about 1/3 the depth of pile top, but under the same excitation frequency and excitation load, envelope of bending moment size of model A is significantly smaller than model B. That is to say the setting of bearing plate changed the deformation and stress state of squeezed branch pile, and the ability of pile body balance bending moment is improved. Setting bearing plate in the upper position of the pile body is beneficial to the improvement of the horizontal dynamicbearing capacity. In Fig.6, the rotation centers are respectively appeared in 526mm,627mm, 645mm, 726mm depth, which have a downward trend, while the rotation center of model B is close to the bottom of pile. Obviously, the model A's ability of constraint upper building to resist horizontal dynamic load is weaker than model A

## Conclusions

This paper designed the device of squeezed branch pile under horizontal vibration load. Two different bearing plate position of squeezed branch pile model tests were carried out. The main conclusions are shown as follows:

1. The test results revealed that with the increase of vibration frequency, the dynamic response of squeezed branch pile has a tendency to decrease on the whole. With the increase of excitation load, dynamic bending moment and lateral earth pressure gradually increased. The dynamic response of squeezed branch pile decreases with depth, and the influence is mainly distributed in 2/3 of the depth from the top of the pile.
2. The setting of bearing plate changed the deformation and stress state of squeezed branch pile. The ability of pile body balance bending moment is improved, which is a structure optimization design of pile foundation. Setting bearing plate in the upper position of the pile body is beneficial to the improvement of the horizontal dynamic bearing capacity.
3. Circular vibrating load will make the soil residual deformation gradually increased, and the soil's capacity to absorb vibration energy descend. The effects of the dynamic magnification phenomenon caused by excitation load will reduce the bearing capacity level of squeezed branch pile.

## References

[1] GAO Xiaojuan,LIU Fengjun,LI Yuehui etc. *Engineering mechanics* Vol.26(7)(2009),p.97 (InChinese)
[2] HU Anfeng. Studies on theory and behavior of lateral vibration of pile foundation, *Zhejiang university*, 2002(In Chinese).
[3] Roger A, Harry M. *OTC1695* (1972) ,p.687
[4] HAN Yingcai, NOVAK M. *Earthquake Engineering and Engineering Vibration*, Vol.9(2)(1989),p.97 (In Chinese).

*Applied Mechanics and Materials Vols. 580-583 (2014) pp 113-117*
*© (2014) Trans Tech Publications, Switzerland*
*doi:10.4028/www.scientific.net/AMM.580-583.113*

# Model Tests of Foundation Bearing Capacity of Sandy Soil and Pile Foundation Bearing Capacity

Shijie Lu[1, a], Huadong Chen[1, b], Wei Chen[1, c],Tong Xiang[1, d] and Xiefeng Hong[1, e]

[1]Department of Civil Engineering, Zhejiang University of Technology, Hangzhou, 310014, China

[a]dickyou88@126.com, [b]18868812697@163.com, [c]m18868812700@163.com, [d]xiangtong1993@163.com, [e]hxf201104160407@163.com

**Keywords:** Foundation Settlement, Bearing Capacity, Pile Foundation, Sandy Soil, Model Test

**Abstract.** Using self-made model device, researchers studied the characteristics of foundation settlement of sandy soil and pile foundation load-bearing in sandy soil. Through weight loading, researchers analyzed the phenomenon of foundation settlement. Then, researchers embedded friction piles in sand, so as to analyzed pile foundation bearing capacity. The methods and results of the research can provide guidance for teaching of Soil mechanics and foundation engineering.

## Introduction

The settlement in foundation engineering has always been one of the main topics of soil mechanics. Because of the growing scarcity of land resources，high buildings are rising and a large number of high buildings and municipal engineering have to be built over soft foundation due to urban development. Under this background, the problems in the foundation engineering must be focused on. There are a lot of methods for foundation treatment. During the construction, we commonly used foundation or pile foundation to bear load. So, it is a priority of foundation engineering to correctly recognize the load-bearing characteristics of foundation and pile foundation.

In the past, most of the research for the two bearing problems adopted theoretical analysis, while less involved model tests. Therefore, in view of the characteristics of foundation settlement of sandy soil and pile foundation load-bearing in sandy soil, researchers designed two model tests to study the settlement and bearing capacity of foundation engineering. The result can provide some theoretical guidance for foundation treatment in practical engineering.

## Test Methodology

In this experiment, dry sand was chosen to simulate the foundation soil. Before the test, it is necessary to determine some relevant physical indicators of sandy soil. First of all, 300 grams of sand soil was taken to determine particle proportion, water content and grain size distribution respectively. These experimental results show that the soil particle proportion is 6.8%,and the water content of soil is $2.66g/cm^3$.In addition，the grain size analysis test results are showed in table1 and figure1.

Table 1 Soil sieving results

| Sieve pore diameter d / mm | Quality of soil on sieve m / g | The proportion of soil on sieve ω / % | The proportion of soil which smaller than Sieve pore diameter Σ ω / % |
|---|---|---|---|
| 1 | 13.329 | 4.46 | 95.54 |
| 0.5 | 45.697 | 15.30 | 80.24 |
| 0.25 | 157.213 | 52.62 | 27.62 |
| 0.125 | 79.335 | 26.56 | 1.06 |
| 0.075 | 2.471 | 0.83 | 0.23 |
| <0.075 | 0.696 | 0.23 | |

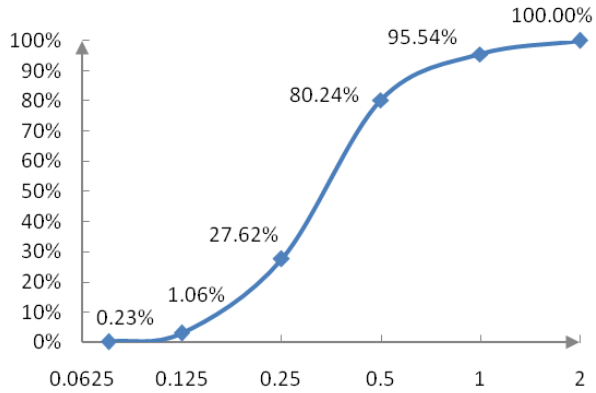


Fig. 1 Particle grading curve

From figure 1，it is possible to work out some physical indicators of soil. The results are as follows.

Non-uniformity coefficient: $C_u = \frac{d_{60}}{d_{10}} = 1.542$

Curvature coefficient: $C_c = \frac{d_{30}^2}{d_{60} \times d_{10}} = 1.104$

Fineness modulus: $M_x = \frac{(A_{0.15} + A_{0.3} + A_{0.6} + A_{1.18} + A_{2.36}) - 5A_{4.75}}{100 - A_{4.75}} = 1.64$

According to the result of fineness modulus, the sandy soil must be classified as fine sand. Also, on the basis of non-uniformity coefficient, the soil sample is uniform. So, the soil has poor compactness, which be recognized as badly graded soil.

**The Model Test of Foundation Bearing Capacity.** The figure 2 shows the device schematic drawing.

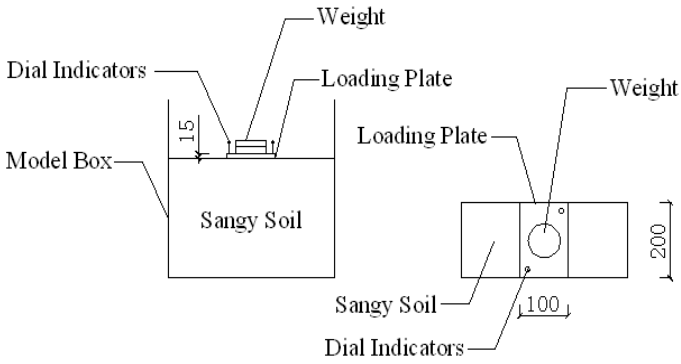


Fig. 2 Device schematic drawing

In this test, the sandy soil which had been determined particle proportion, water content and grain size distribution was used to simulate the foundation soil. And a steel plate which was 20cm long, 10cm wide and 1.5cm thick was used to simulate the foundation. Also, it was able to simulate the phenomenon of foundation settlement through loading on steel plate.

Two dial indicators installed diagonally on the bearing plate were used for the test. Before the test, initial reading should be record. In data processing, average reading of dial indicators was taken as the actual settlement under load. The method of loading step by step was used for this test. To be specific, the weight of 10.2 kg per level should be load on, so as to generate same load size to facilitate comparison of the test results. After each loading, the researchers recorded readings 3 minute intervals until the difference of the latter and the former is less than 0.01 mm. Notice that the weight must be handled with care each time to avoid disturbing steel plate. Also, it is vital to make sure that weights remain upright to prevent the non-uniform stress.

Stop loading the moment that following situation appears:
(1) The soil around bearing plate presents lateral extrusion obviously.
(2) The foundation settlement increases sharply.
(3) Due to leaning of bearing plate, weight cannot be load on.

**The Model Test of Pile Foundation Bearing Capacity.** This test, only a few different from the former, mainly researched the character of load-bearing of friction pile group foundation. In this test, researchers used a steel plate which was 20cm long, 20cm wide and 1.5cm thick to simulate the foundation.and embedded four aluminum half-round tubes of which radius was 1.5cm and length was 20cm to simulate friction piles. The device schematic drawing is as figure 3 shows. The four tubes were pre-buried in soil under the corners of the steel plate to guarantee consistency for the position of each one relative to the center of pile cap which aimed to eliminate the influence of pile group effect caused by pile cap stiffness.

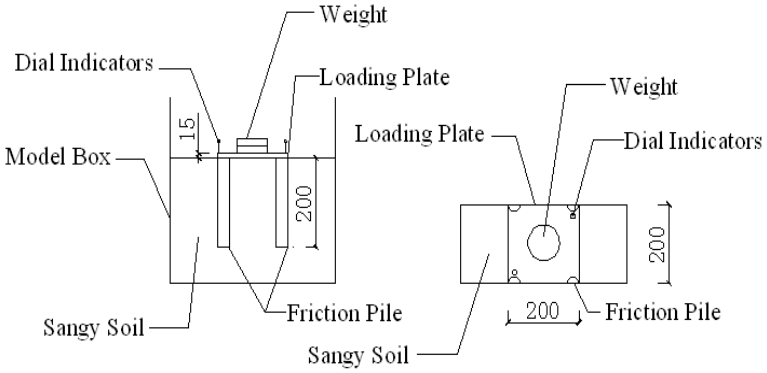


Fig. 3 Device schematic drawing

In the process of embedment, each tube must be straight and at the same height, while flat surface of aluminum half-round tubes were ensured to be pressed hardly to glass wall of model box. When placing bearing plate, researchers made it direct connected with tip of pile to guarantee effective simulation of pile bearing. The steps of loading weight and the termination conditions were same as the model test of foundation bearing capacity of sandy soil.

## Results and Analysis

**The Model Test of Foundation Bearing Capacity.** The figure 4 and 5 respectively show the **foundation settlement of the second and the ninth weight grades.**

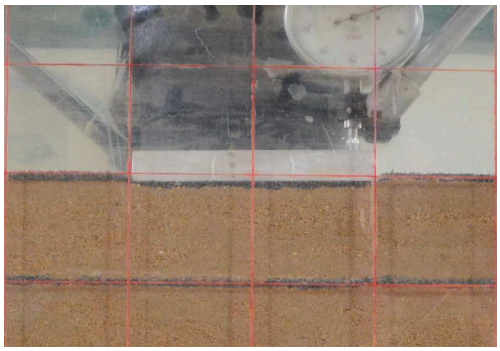

Fig. 4 Foundation settlement of the second weight grades

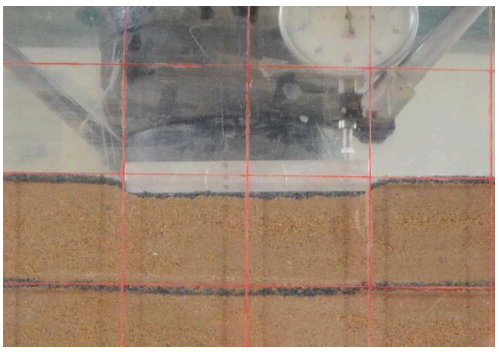

Fig. 5 Foundation settlement of the ninth weight grades

According to the results of model test of sandy soil foundation bearing capacity，researchers plotted a p-s curve as figure 6 shows.

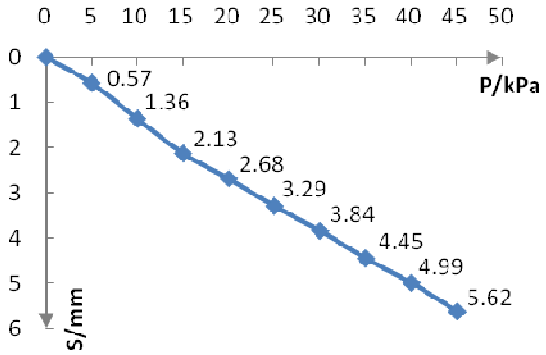


Fig. 6 P-s curve

Researchers calculated absolute value of the slope of straight lines connecting adjacent two points. The results are as follows: 0.114, 0.158, 0.154, 0.110, 0.122, 0.110, 0.122, 0.108 and 0.126. From the slope change, it can be analyzed that, except a few points, most of them can be connected as a straight line. It shows that the soil were in compaction stage, a linear change phase, in the process of loading. In this stage, the soil kept elastic equilibrium, and shear stress of any point in the soil was less than the shear strength of soil. As weight loading step by step, elastic deformation was undergoing in the foundation soil, while foundation settlement was increasing gradually. However, the load caused by upper structure had not reached critical edge pressure of foundation soil and it had not appeared plastic deformation in the foundation.

When reached the tenth weight grades, bearing plate tilted and weight cannot be load on any more, so the test was terminated. In order to guarantee the accuracy of test data, researchers taken the first nine sets of results of the dial indicator reading for analysis.

The cause of bearing plate tilting was the eccentricity pressure. In the process of loading, researchers could not strictly guarantee weight vertical loading which led to uneven settlement of foundation. When differential settlement of both sides accumulated to a certain extent, the upper structure collapsed marking the termination of the test before reaching critical edge pressure.

**The Model Test of Pile Foundation Bearing Capacity.** Figure 7 shows pile foundation settlement of ultimate bearing capacity. According to the results, researchers plotted a p-s curve as figure 8 shows.

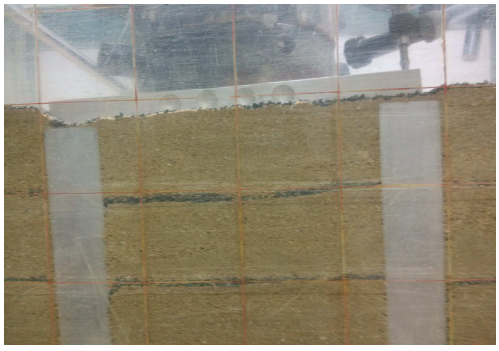

Fig. 7 Ultimate bearing capacity

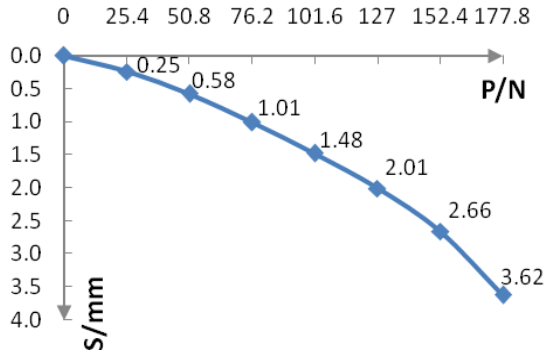


Fig. 8 P-s curve

When reached the eighth weight grades (each pile was under the load of 203.2 N theoretically), pile foundation settlement was increasing so sharply that led to weight collapsed, then, the test terminated. The moment of collapsing, bearing plate tilted greatly. Therefore, the pile foundation settlement under the eighth weight grades could not be read accurately by dial indicators. In order to guarantee the precision of the test results, researchers took the first seven sets of data to plot a p - s curve.

The pile foundation bearing capacity of the test depends on three aspects:

(1) The strength of pile body material
(2) The bearing capacity of foundation soil
(3) The influence of the pile group effect

In the test, aluminum half-round tubes were chosen to simulate friction piles due to high strength. Thus, in this test, the material strength of pile body was not the main influence on pile foundation bearing capacity. This conclusion can be proved from the result that the pile had not been destroyed. At the same time, on the premise of pile body material strength was enough high, and the pile group effect under vertical load was not the main role in pile foundation bearing capacity. Therefore, in this test, the bearing capacity of foundation soil had most impact on pile foundation bearing capacity. In other words, the process of loading step by step was also the process of foundation destruction.

From figure 8, with the method of slope analysis similar to the model test of foundation bearing capacity, it is possible to plot a p-s curve formed by the first five results, which is nearly a straight line. It suggests that before the sixth time loading, the soil should be in compaction stage keeping elastic equilibrium. After the sixth time loading (each pile loaded 152.4 N), the p -s curve slope increased obviously, and after that it is still increasing. It indicates that foundation soil were into shear stage. Thus, the time for foundation reaching plastic load was between the fifth time loading and the sixth time loading. In the shear stage, the p - s curve no longer keep linear, and it developed plastic deformation area in foundation soil. As the load increasing, the plastic deformation area is expanding, and the elastic deformation area is narrowing down with it, until a continuous slip plane is formed in the soil when the external load comes to the ultimate load of foundation. (Researchers did not draw the point of ultimate load in figure 7)

## Conclusion

This paper reflects the process of sandy soil foundation settlement and pile foundation settlement through two model test. Also, it reasonably explains the mechanism of two kinds of settlement and summarizes its characteristics through the analysis of test results. However, the test equipment this paper introduced has certain limitation to simulate the whole process of sandy soil foundation settlement.

## Acknowledgment

National College Students' Innovative Training Program (NO. 201310337017)

## References

[1] H.Y. Xu, M.Q. Zhou and X.M. Lou: Chinese Journal of Geotechnical Engineering, Vol. 33 (2011) Supp. 2, p.139. (In Chinese)

[2] Y.D. Chen, X.D. Wang and J.M. Zai: Journal of Sichuan University, Vol. 43 (2011) No.5, p.45. (In Chinese)

[3] Z.Y. Lin, Z.H. Dai and M.X. Su: Journal of Fuzhou University, Vol. 37 (2009) No.5, p.737. (In Chinese)

[4] R.W. Liang and E.B. Pei: Sci-tech Information Development & Economy, Vol. 20 (2010) No.2, p.171. (In Chinese)

[5] C.G. Zhao and B. Bai: *Fundamentals of Soil Mechanics* (Tsinghua University Press, China 2009), p.305. (In Chinese)

[6] G. Zheng, Y.J. Pei and S.J. Liu: Rock and Soil Mechanics, Vol. 29 (2008) No.11, p.2912. (In Chinese)

*Applied Mechanics and Materials Vols. 580-583 (2014) pp 118-122*
*© (2014) Trans Tech Publications, Switzerland*
*doi:10.4028/www.scientific.net/AMM.580-583.118*

# Numerical simulation of load transfer mechanism of T-shaped soil-cement deep mixing column

Peisheng Xi[1,a], Xiaotao Zhang[1,b*], Bo Liu[1,c]

[1]Department of civil engineering, Anhui jianzhu university, Hefei, Anhui, 230601, China

[a]xipeisheng@163.com, [b]zhangxt21@163.com, [c]aualiubo@163.com

**Keywords:** T-shaped soil-cement deep mixing column; Load transfer; Numerical simulation; Design parameter.

**Abstract:** T-shaped soil-cement deep mixing column load transfer mechanism is different from the general section column. Basing on the fast Lagrangian finite difference method, we study the load transfer mechanism of T-shaped soil-cement deep mixing column at different load levels, expanding head height and the ratio of upper and lower pile diameter. By the numerical simulation we obtained that the axial force plummeted value of expanding head flange increases with the load and the ratio of upper and lower pile diameter increasing, it will decreases when the height of expanding head increasing.This paper can provide a reference for the design of T-shaped soil-cement deep mixing column.

## Introduction

T-shaped soil-cement deep mixing column is a kind of new technology which combain bidirectional soil-cement deep mixing column with the section-varied soil-cement deep mixed column. It was designed after analysis the shortcomings of the existing soil-cement deep mixing column and the load transfer mechanism of soil-cement deep mixing column foundation and the soil arching effect[1-3]. In process of generate column, the power system driven two groups mixing blades that install drill pipe and the blades forward and reverse rotationon mixing soil-cement, by the mixing blades automatic retractable, it will make the upper section of the pile expanding and form a shape similar nails soil-cement deep mixing pile [1,4], shown in Figure 1.

## Material parameters and calculation models

As a new kind of soft soil foundation treatment method, if we want to accurately grasp the design and construction methods, we need to study its axial force transfer mechanism. In this paper, basing on the field and laboratory tests obtain the parameters of pile and soil, using the fast Lagrangian finite difference method calculate load transfer mechanism, analysis the parameters at difference load level, expanding head height and the ratio of upper and lower pile diameter impact on the load transfer mechanism.

The model uses the finite difference numerical simulation software FLAC3D, while the calculation range meet certain conditions, then the model constraint type of lower and side boundary has little effect on the results[1], considering the meshing influence computing speed, set the model bottom boundary two times the pile length from the surface and horizontal boundary has a distance of 20m to the center of the pile, fixed the model lower boundary, the side boundary only constraint corresponding horizontal displacement. Due to FLAC3D internal no thickness of contact element, this can solve the existing problem of shear between the pile and soil. Contact surface calculation parameters take normal stiffness was 0.53MPa, shear stiffness was 0.26Mpa, cohesion was 30kPa, friction was 15 degree.The pile calculation parameters shown in Table 1, calculate soil parameters shown in Table 2.

Mohr-Coulomb model is most widely used soil constitutive model in geotechnical engineering, general soil test can determine the soil parameters, not need do Senior experiments, so select this

model to calculate and checking this model can better control accuracy 5% .Build calculation model shown in Figure 2.

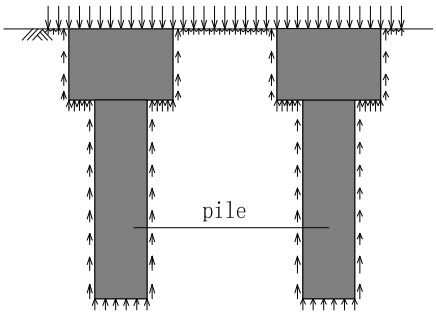


Fig. 1 T-shaped soil-cement deep mixing column schematic

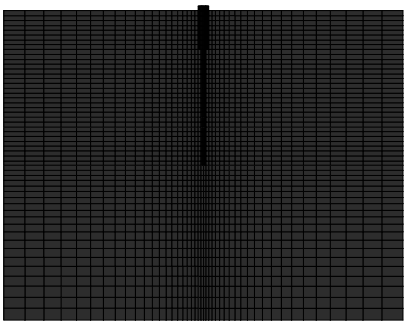

Fig. 2 Computing model meshing

Table1 T-shaped soil-cement deep mixing column calculation parameters

| parameter | elasticity (MPa) | poisson ratio | density ($kg \cdot m^{-3}$) | cohesion (kPa) | friction (°) |
|---|---|---|---|---|---|
| expanding head | 150 | 0.24 | 2100 | 230 | 35 |
| lower column | 120 | 0.25 | 2050 | 190 | 32 |

Table2 Physical and mechanical parameters

| layer | layer thickness (m) | elasticity (MPa) | poisson ratio | density ($kg \cdot m^{-3}$) | cohesion (kPa) | friction (°) | permeability coefficient ($cm \cdot s^{-1}$) |
|---|---|---|---|---|---|---|---|
| topsoil | 2 | 7.90 | 0.33 | 1938 | 25.2 | 15 | $1.05\times10^{-5}$ |
| muddy loam | 12 | 1.35 | 0.40 | 1755 | 11.6 | 10 | $1.52\times10^{-6}$ |
| loam | 2 | 9.66 | 0.32 | 1955 | 21.0 | 15 | $1.62\times10^{-5}$ |
| earing stratum | 18 | 16 | 0.28 | 2000 | 28.0 | 20 | $2.55\times10^{-5}$ |

## Research column load transfer mechanism

To study the influence of load level, expanding head height, ratio of upper and lower pile diameter to T-shaped soil-cement deep mixing column load transfer mechanism and characteristic parameters(the variable cross-section of the axial force plummeted value), table 3 for the numerical simulation (column length were taken 16.5m, rigid pile load).

Table3 List of numerical simulation conditions

| parameter | conditions one | conditions two | conditions three |
|---|---|---|---|
| load | change | ultimate bearing capacity | |
| expanding head height | 4m | change | 4m |
| upper and lower pile diameter ratio | 2 | 2 | change |
| lower pile diameter | 500mm | 500mm | 500mm |

## Comparison of numerical simulation and measured data.

To verify the numerical simulation results whether accurately reflect the T-shaped soil-cement deep mixing column load transfer mechanism, test highway T-shaped soil-cement deep mixing column section A, K30+100~140 in Shanghai, Jiangsu and set stress gage on column (column length was 16.5m, upper and lower pile diameter was 1000mm and 500mm, expanding head height was 4m), At the end of pile construction set stress gage within two hours. Ensure the stress gage location accurate include level and depth direction in the process. Upper four stress gage range is 1MPa, the lower two range is 0.6MPa, stress gage depth in Figure 3.

Figure4 was numerical simulation and measured data contrast, the curve was the relationship on axial force and depth under 250kN and 550kN in top of the pile. From Figure 4, the axial force have a big chance in depth 4m and this place was expanding head height, we can conclusion that expanding head height have an influence on axial force transfer. It was obvious that in depth range of stress gage

the numerical simulation results was very consistent with field data, so the numerical simulation results can reflect the true work condition of T-shaped soil-cement deep mixing column.

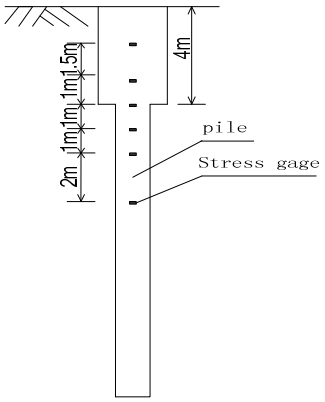


Fig. 3 Stress gage depth

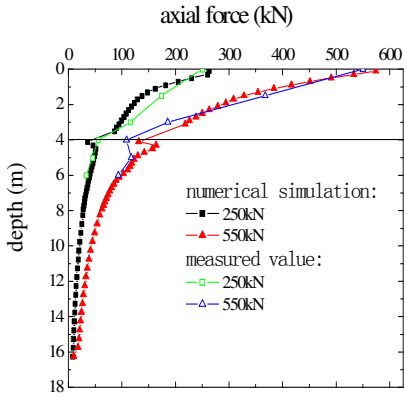


Fig. 4 Comparison numerical simulation and measured data

**Load grade impact on load transfer mechanism.**

Working condition one: load transfer mechanism numerical simulation under different load level results in Figure 5, Figure 6

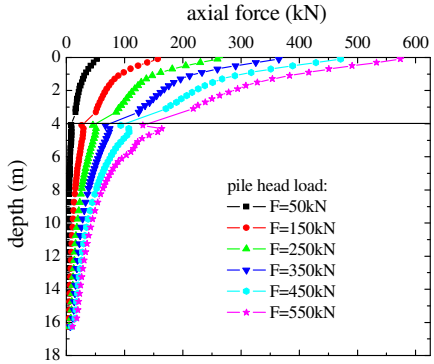


Fig. 5 Axial force change at different load levels

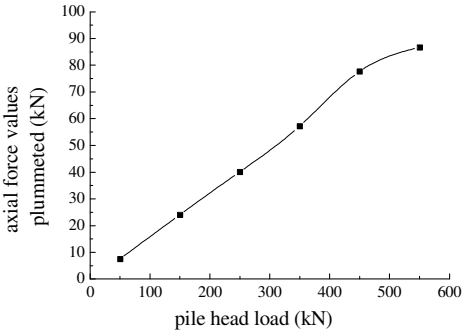


Fig. 6 Variable cross-section of the axial force plummeted values and the load curve

Figure 5, Figure6 show: axial force gradually decay with depth increasing, axial force range in expanding depth decay faster than the lower axial force, variable cross-section axial force appears plummeted phenomenon, plummeted value( the minus on upper and lower axial force in variable cross-section)increases linearly with the pile head load growth, but when the pile head load close to the ultimate load, plummeted value rate of increase was significantly smaller. This is mainly due to the expanding head flange of pile action and the pile load transfer to the soil under flange, so that axial force appears plummeted.

T-shaped soil-cement deep mixing column bearing capacity offered by the soil around the pile, the pile tip resistance and soil supporting force under expanding head flange composed, collaborative work, when pile bearing capacity close to the limit load, the soil bearing capacity under expanding head flange close to the limit[8], a small load increments, may have a relatively large soil subsidence, therefore can provide support force for the pile is relatively small increments. Due to the expansion head flange effect, part of the pile axial force is transmitted to the soil around the pile, produce a negative relative displacement between pile and soil in the lower part of the expanding head flange 30cm, pile-soil contact surface appearance of negative skin friction[9,10], leading to the maximum axial force lower expanding head occurs in 0.1 ~ 0.3m.

**Expanding head height impact load transfer mechanism.**

Working condition two: when expanding head height was 1m, 2m, 3m, 4m, 5m, 6m 16.5m, the ultimate bearing capacity have the simulation results shown in Figure 7, Figure 8.

Figure 7, Figure8 show: in ultimate load, axial force gradually decay with increasing depth and expanding head height greater the axial force increases, but the axial force attenuation trend consistent; the axial force range of expanding head depth decay faster than the lower decay rate; in variable cross-section the axial force appears plummeted phenomenon and plummeted value decreases with expanding head height increases, plummeted value come to stable when the expanding head height increased to 3m later. It is worth noticing that different expanding head height of deep mixing column, the lower section of the pile maximum axial force basically the same under ultimate load.

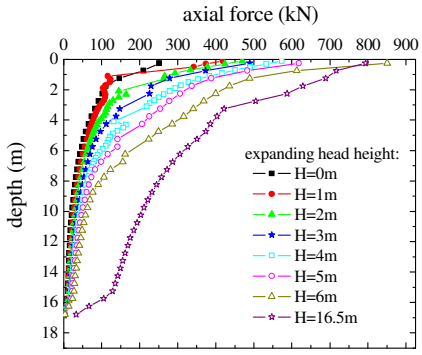


Fig. 7 Axial force curve in different expanding head height under ultimate load

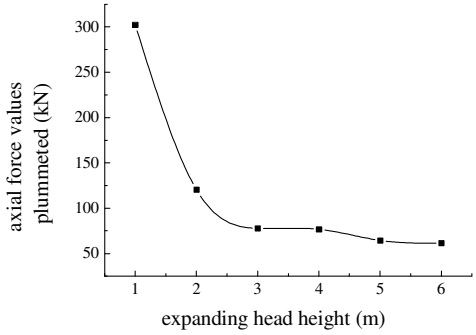


Fig. 8 Variable cross-section of the axial force values plummeted and expanding head height curve

Diameter 1000mm conventional bidirectional soil-cement deep mixing column (H=16.5m), the axial force was significantly higher than other shaped deep mixing column under ultimate load; while diameter 500mm conventional bidirectional soil-cement deep mixing column (H=0m), in the range of expanding head depth axial force was significantly lower than other shaped deep mixing column under ultimate load, but the depth below 1m and expanding head height 1m they axial force curve are basically the same; the ultimate bearing capacity of expanding head height 6m deep mixing column slightly lower than the diameter 1000mm conventional bidirectional soil-cement deep mixing column.

**The ratio of upper and lower pile diameter impact load transfer mechanism.**

Working condition three: the ratio of upper and lower diameter is 1.2, 1.6, 2.0, 2.4, 2.8 and 3.2, the numerical simulation results under ultimate bearing capacity shown in Figure 9, Figure 10.

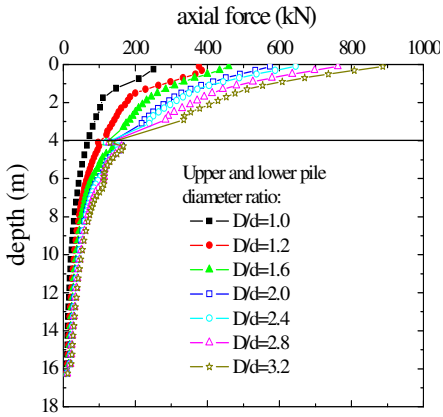


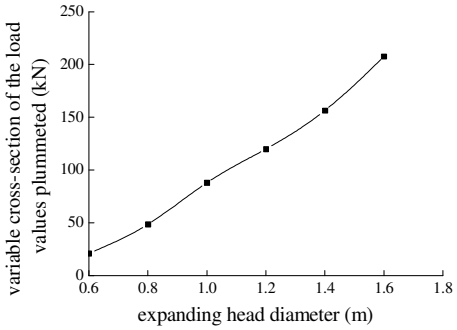


Figure 9, Figure10 show: under ultimate load, the axial force gradually decay with increasing depth; in variable cross-section axial force appears plummeted phenomenon, plummeted value increase with

the ratio of upper and lower pile diameter geater and the relationship obedience quadratic relationships. This mainly due to axial load consistent in ultimate load, but the flange area and expanding diameter into a quadratic relationship. In addition, for different expanding head diameters deep mixing column, the maximum axial force is very close below variable cross-section. In the role of ultimate load for expanding head height 4m deep mixing column, the ratio of upper and lower pile diameter should be controlled within 2.0.

## Conclusions

Through the numerical simulation on load transfer mechanism of T-shaped soil-cement deep mixing column, finally we obtain the following conclusions:

(a) The axial force increases with the load levels increasing.
(b) The axial force decay velocity of expanding head is much faster than the lower part.
(c) Axial force plummeted value under expanding head flange increases with the load and the ratio of upper and lower diameter increasing, but it will decreases when the expanding head height increasing. The changes amplitude relative decreases when expanding head height is greater than 3m.
(d) Within 30cm below the expanding head flange occurs negative friction zones; The influence sphere has connection to load and the ratio of upper and lower pile diameter, it will increase when the ratio of upper and lower pile diameter increasing.

## References

[1] Peisheng Xi. Bidirectional deep mixing column with a variable cross-section method and its bearing capacity behavior [D]. Doctor thesis, Southeast University, 2007. (in Chinese)
[2] Peisheng Xi, Songyu Liu. Construction Technology, 2006, 35(1): 2-5. (in Chinese)
[3] Peisheng Xi, Nenghe Gong, Haiyan Chu, et al. Construction Technology, 2007, 36(1): 5-8. (in Chinese)
[4] Songyu Liu, Zhiduo Zhu, Peisheng Xi, et al. Chinese Journal of Geotechnical Engineering, 2009, 31(7): 1059-1068. (in Chinese)
[5] FLAC-3D Fast Lagrangian Analysis of Continua in 3 Dimensions, Version 2.0, User's Manual, Itasca Consulting Group, Inc. USA.
[6] Randolph M F, Worth C P. Application of the failure state in undrained simple shear to the shaft capacity of driven piles[J]. Geotechnique, 1981, 31(1):143-157.
[7] Randolph M F. Science and empiricism in pile foundation design[J]. Geotechnique, 2003, 53(10): 847-875.
[8] O'Neill, M.W., Hawkins, R.A., Mahar, L.J. Load-transfer mechanisms in piles and pile groups[J]. Journal of the Geotechnical Engineering Division, ASCE, 1982, 108(12): 1605-1623.
[9] Songlin XU, Yushan Wu. Rock and Soil Mechanics, 1996, 17(2): 42－52. (in Chinese)

*Applied Mechanics and Materials Vols. 580-583 (2014) pp 123-128*
*© (2014) Trans Tech Publications, Switzerland*
*doi:10.4028/www.scientific.net/AMM.580-583.123*

# One-dimensional consolidation modelling for unlayered soil

Issam Hanafi [1,a], Fouad Dimane [1,b], Francisco Mata Cabrera[2,c], José Tejero Manzanares[2,d]

[1]Group of Material Science, Energy and Environnement, Ecole Nationale des Sciences Appliquées d'Al Hoceima (ENSAH), BP 03 Ajdir, 32000 Al Hoceima, Morocco.

[2]University Polytechnic School Of Mining and Industrial Engineering of Almaden, 1 Plaza Manuel Meca, 13400 Almaden, Spain.

[a]hanafi.issam@yahoo.fr, [b]dimane.fouad@gmail.com, [c]francisco.mcabrera@uclm.es, [d]jose.tejero@uclm.es

**Keywords:** consolidation, modeling, one dimension, unlayerd soil.

**Abstract.** In this work, one-dimensional problem has a well-known linear solution and, thus, provides a simple verification of the consolidation capability using numerical solution. The coupling is approximated by the effective stress principle, which treats the saturated soil as a continuum, assuming that the total stress at each point is the sum of an effective stress carried by the soil skeleton and a pore pressure in the fluid permeating the soil. This fluid pore pressure can change with, and the gradient of the pressure through the soil that is not balanced by the weight of fluid between the points in question will cause the fluid to flow: the flow velocity is proportional to the pressure gradient in the fluid according to Darcy's law. A typical case is a consolidation problem. Here the addition of a load to a body of soil causes pore pressure to raise initially; then, as the soil skeleton takes up the extra stress, the pore pressures decay as the soil consolidates. The Terzaghi problem is the simplest example of such a process. For illustration purposes, the problem is treated with and without finite-strain effects. The numerical solution agrees reasonably well with the analytical solution, with some loss of accuracy at later times.

## Introduction

The one-dimensional consolidation theory by Terzaghi & Fröhlich constitutes the basis of Soil Mechanics [1]. Evaluation of expected settlements depends on the determination of consolidation parameters, which could be evaluated by laboratory tests, field tests, and empirical correlations. Consolidation parameters interpreted from laboratory tests could be subject to inaccuracies resulting from factors such as sample disturbance, sample size, and strain rate. For field tests, existing correlations are typically used to interpret consolidation parameters.

A numerical solution of one-dimensional consolidation of layered soils with such defined boundaries is derived by using the method of Laplace transform and its numerical inverse. The solution is explicitly expressed and conveniently coded into a computer program for ease and efficiency of practical use. Analytical solutions of one-dimensional consolidation of single-layered soil are also derived by using the method of analytical inverse Laplace transform and the method of separation of variables as well. By comparing these two analytical solutions and comparing with an available analytical solution for two-layered soil with pervious boundaries, the proposed numerical solution for layered soils is validated. Good agreement is obtained, and the accuracy of the numerical solution is verified. Moreover, the dissipation of excess pore water pressure and the increase of degree of consolidation with time for a four-layered soil are investigated to assess the effects of the adopted drainage boundary conditions on consolidation [2]. Other authors presented an analytical solution to the problem of 1-D consolidation of single-layered soil, wherein $k_v$ is constant and Es varies with depth, with this problem considered as a special case of the problem of consolidation of non-homogeneous soil above. The semi-analytical solution for the consolidation problem of

single-layered or multi-layered soil with $k_v$ and $m_v$ varying with depth, but this solution may only be applicable to NC clay. Based on this solution, the consolidation behavior can be discussed [3].

some studies were conducted on the 1-D nonlinear consolidation problem, in which the coefficient of permeability $k_v$ and that of volume compressibility $m_v$ both directly relate to $c_v$ and vary with the effective stress and void ratio [4]. For single-layered foundation, this paper takes into consideration single-drainage situation and time-dependent loading.

**One dimensional modelling**

The problem is shown in a body of soil 2.54 m high is confined by impermeable, smooth, rigid walls on all but the top surface. On that surface perfect drainage is possible, and a load is applied suddenly. Gravity is neglected. Because of the boundary conditions, the problem is one-dimensional, the only gradient being in the vertical direction.

The soil is assumed to be linear elastic, with a Young's modulus of 689.5 GPa and Poisson's ratio of 0.3. The specific weight of the pore fluid is assumed to be 276.8 $10^3$ N/m$^3$. The permeability is assumed to vary linearly with the void ratio, with a value of 8.47 $10^{-8}$ m/sec at a void ratio of 1.5 and a value of 8.47 $10^{-9}$ m/sec at a void ratio of 1.0. The void ratio is assumed to be 1.5 initially throughout the sample. Abaqus uses effective permeability, which is permeability divided by the specific weight of the pore fluid. Therefore, the fluid in this problem is assigned the value 276.8 $10^3$ N/m$^3$ for the specific weight and the permeability is scaled accordingly.

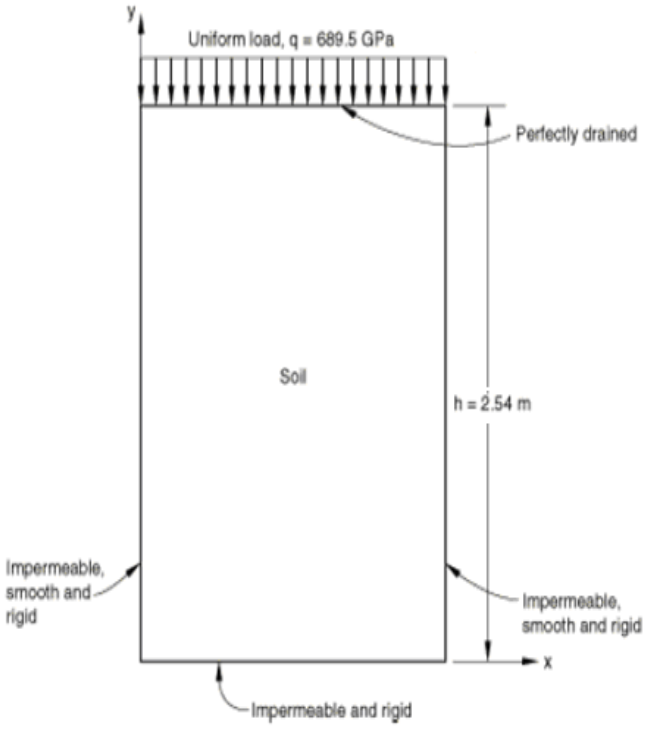


Figure 1. Consolidation problem geometry

The boundary conditions are as follows: On the bottom and two vertical sides, the normal component of displacement is fixed, and no flow of pore fluid through the walls is permitted. This latter is the natural boundary condition in the fluid mass conservation equation, so no explicit specifications need to be made. On the top surface a uniform downward load is applied suddenly. The magnitude of this load is taken to be 689.5 GPa. This large load will cause considerable deformation, thus illustrating the difference between the small- and large-strain solutions. This surface allows perfect drainage so that the excess pore pressure is always zero on this surface.

The problem is run in two steps. The first step is a single increment of a soil consolidation analysis with an arbitrary time step, with no drainage allowed across the top surface. This establishes the initial

solution: uniform pore pressure equal to the load throughout the body, with no stress carried by the soil skeleton. The actual consolidation is then done with a second soils consolidation step, using automatic time stepping.

An important issue in such consolidation problems is the choice of initial time step. As the governing equations are parabolic, the initial solution (immediately after the sudden change in load) is a local, "skin effect," solution. In this one-dimensional case the form of the initial solution is sketched in figure 2 for illustration purposes. With a finite element mesh of reasonable size for modelling the solution at a later time (when the changes in pore pressure have diffused into the bulk of the body soil), this initial solution will be modelled poorly. With smaller initial time steps the difficulty becomes more pronounced, as sketched in figure 2.

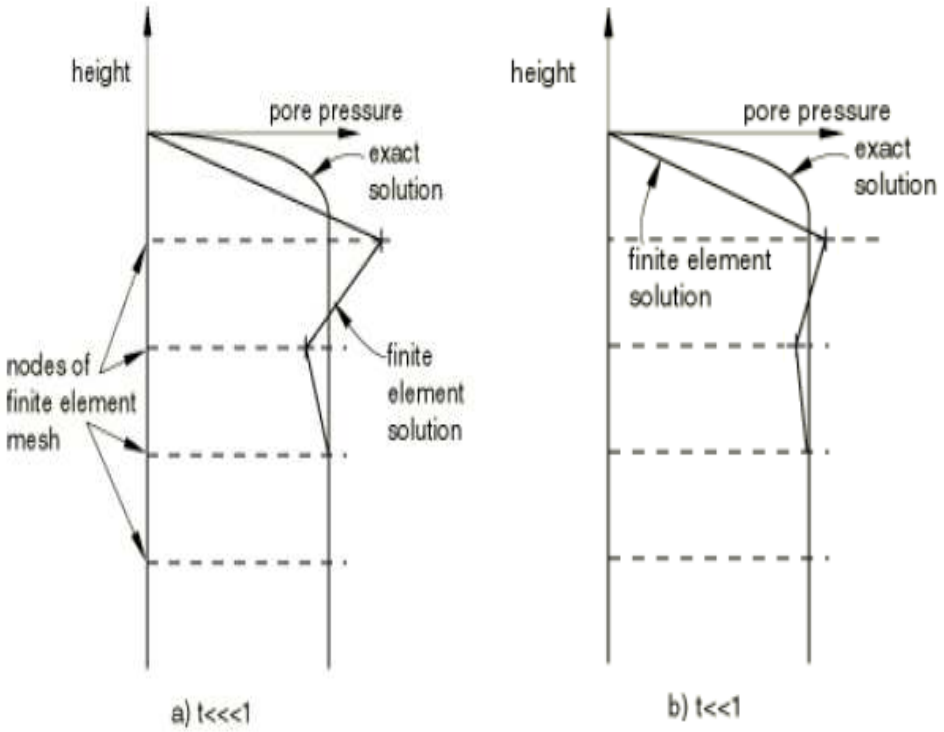


Figure 2. Solutions at t <<1

As in any transient problem, the spatial element size and the time step are related to the extent that time steps smaller than a certain size give no useful information. This coupling of the spatial and temporal approximations is always most obvious at the start of diffusion problems, immediately after prescribed changes in the boundary values. For this particular case the issue has been discussed in detail by Vermeer and Verruijt [5], who suggest the simple criterion:

$$\Delta t \geq \frac{\gamma_w}{6Ek}(\Delta h)^2 \tag{1}$$

where $\Delta h$ is a characteristic element size near the disturbance (that is, near the draining surface in our case), E is the elastic modulus of the soil skeleton, k is the soil permeability, and $\gamma_w$ is the specific weight of the permeating fluid. For our model we choose $\Delta h = 254$ mm (10 in); and we have $E = 689.5$ GPa, $k = 8.47\ 10^{-8}$ m/s, $\gamma_w = 2.768\ 10^5$ N/m3, which gives $\Delta t \geq 0.05$ s. Based on this calculation, an initial time step of .06 sec is used. This gives an initial solution with no "overshoot" at all, as expected. In this case we wish to continue the analysis to steady-state conditions. This is defined by asking Abaqus to stop when all pore pressure change rates fall below 11.5 KN/m$^2$/s.

**Results and conclusion**

In the small-strain analysis the steady-state condition (rate of change of pore pressure with time below the prescribed value) is reached after 20 increments, the last time increment taken being 491 seconds — about 8000 times the initial time increment. This very large change in time increment size is typical of such diffusion systems and points out the value of using automatic time stepping with an unconditionally stable integration operator for such problems.

The results of the small-strain analysis are summarized in figures 3-4. Figure 3 shows pore pressure profiles (pore pressure as a function of elevation) at various times in the solution.

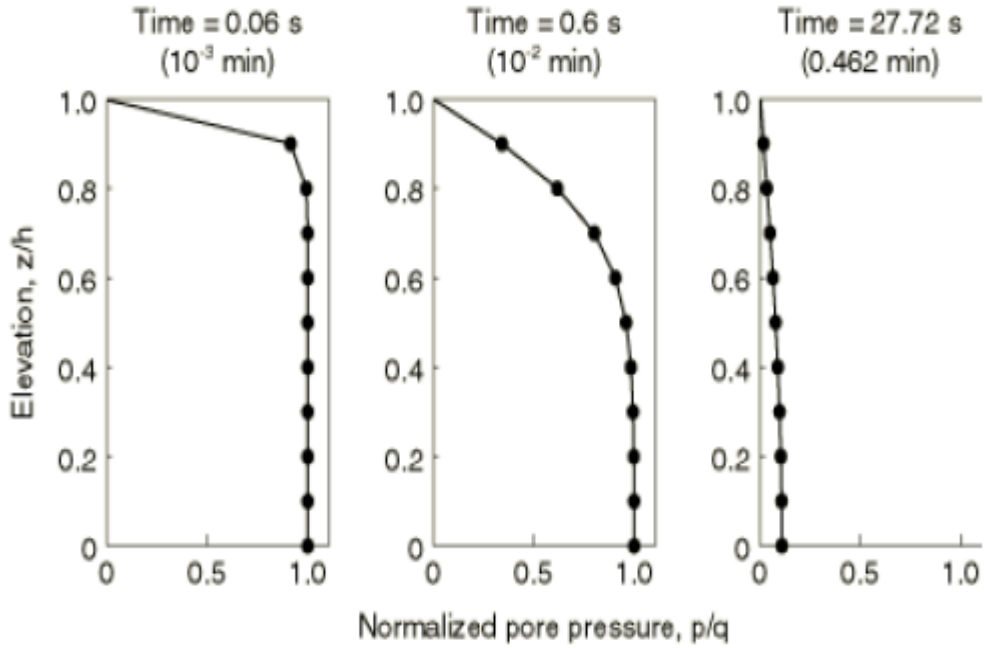


Figure 3. Pore pressure at various times

As we would expect, the solution begins by rapid drainage at the top of the sample and loss of pore pressure in that region. This effect propagates down the sample until the entire sample is steadily losing pore pressure throughout its length. At steady state the solution has zero pore pressure everywhere, with the load being carried as a uniform effective vertical stress. Figure 4 shows this transfer of load from the fluid to the skeleton at the 1.905 m elevation as a function of time.

Figure 5 compares these numerical results with the solution quoted in Terzaghi and Peck [1]. Here the downward displacement of the top surface of the soil, as a fraction of its steady-state value (the degree of consolidation), is plotted as a function of normalized time, defined as:

$$time\ factor = \frac{kE}{H^2 \gamma_w} t \tag{2}$$

Where k is the permeability of the soil, E is the Young's modulus of the soil, $\gamma_w$ is the specific weight of the pore fluid, H is the height of the soil sample, and t is time.

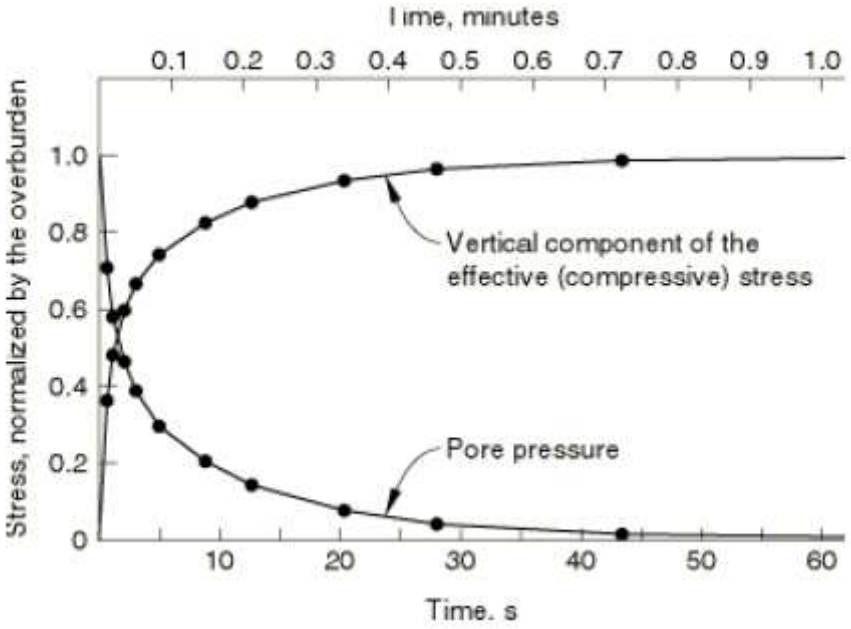


Figure 4. Pore pressure and effective stress

Figure 5 shows that the numerical solution agrees reasonably well with the analytical solution, with some loss of accuracy at later times. This latter effect is attributable to the coarse time stepping tolerance chosen. Higher accuracy could be obtained with a tighter tolerance on the allowable pore pressure stress change parameter. However, the solution is clearly adequate for design use.

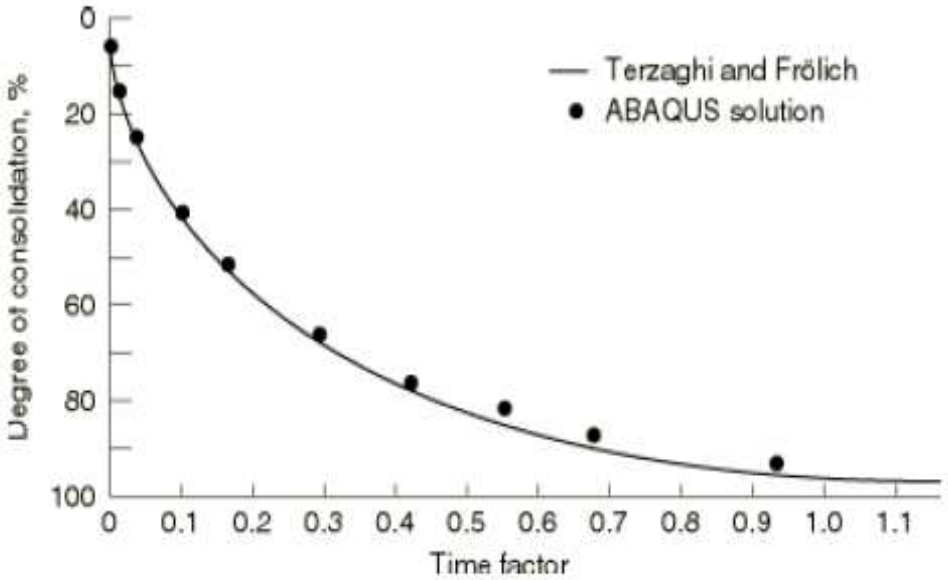


Figure 5. Degree of consolidation Vs time factor

In the finite-strain analysis of soils, changes in the void ratio can lead to large changes in permeability, therefore affecting the transient response in a consolidation analysis. Typical soils show a strong dependence of permeability on the void ratio (as soil compacts, it becomes increasingly harder for fluid to pass through it), with the consequence that “plugging” may result. This means that a soil that was relatively permeable in its original state becomes less permeable as it consolidates.

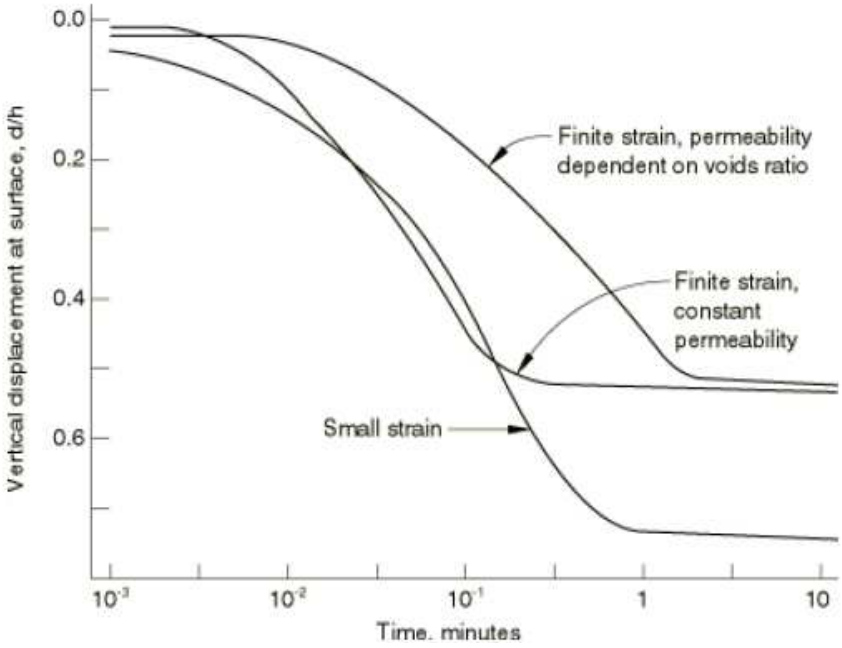


Figure 6. Comparisons of finite- and small-strain solutions to the Terzaghi consolidation problems

In this work the permeability of the soil is assumed to decrease by an order of magnitude as the void ratio decreases from its initial value of 1.5 to a value of 1.0. Such logarithmic dependence of permeability on the void ratio is not uncommon in fully saturated clays. Two finite-strain analyses are run, one with permeability treated as a constant and a second with this variation in permeability. The results are shown in figure 6, together with the results of the small-strain analysis under similar load. The "plugging" effect of void ratio dependence of permeability is clearly seen in this figure. Since the permeability decreases with the consolidation of the soil, the time required for all excess pore pressure to dissipate increases. The final value of displacement under the applied load is not a function of permeability and is correctly predicted by both large-strain analyses. It is interesting to observe that, if the permeability is not dependent on the void ratio, the finite-strain results show more rapid initial consolidation than the corresponding small-strain analysis.

**References**

[1] K., Terzaghi and R. B. Peck: John Wiley and Sons, New York, 2nd, 1948.

[2] J.C., Liu and G.H., Lei: Computers and Geotechnics Vol. 54 (2013) p. 202.

[3] K. Xie, J. Wen, J. Xia: Journal of Zhejiang University Science Vol. 6 (2005) p. 29.

[4] K.H., Xie, X.Y., Xie, W., Jiang: Computers and Geotechnics Vol. 29 (2002) p. 151.

[5] P. A.,Vermeer and A., Verruijt: International Journal for Numerical and Analytical Methods in Geomechanics Vol. 5 (1981) p 1.

*Applied Mechanics and Materials Vols. 580-583 (2014) pp 129-134*
*© (2014) Trans Tech Publications, Switzerland*
*doi:10.4028/www.scientific.net/AMM.580-583.129*

# Practical and Experimental Study of Grouting Anchor in Slope Reinforcement Engineering

Lu Guo-ren[1, a*], Zhang Le-wen[2], Wang Hong-bo[2]

[1]Shandong Jianzhu University, Jinan, Shangdong, China 250101

[2]Shandong University, Jinan, Shangdong. China 250061

[a]luguoren65@163.com

**Keywords:** Grouting anchor; Slope strengthening; Experimental study; Effective anchorage length

**Abstract.** Anchoring technique has been widely used in slope engineering because of its reinforcing function to rock and soil mass. Yet the full understanding of the anchoring mechanism still lags behind the engineering practice. This paper introduces the design process and construction technology of the grouting anchor in slope reinforcement engineering. Based on bolt grouting test, it is found that the effective anchorage length of the grouting anchor depends on the size of the anchor solid and relative physical and mechanical properties of surrounding rock and soil. Research shows that the distribution of shear stress is uneven along the anchoring length. It mainly amasses within the front 1/3 part of the anchoring and increases with the development of outside load. The conclusion is helpful to describe the anchoring mechanism and instructive for engineering practice.

## Introduction

Engineering practice shows that the rock anchorage technique can fully call their own strength in rock and soil mass and has the fewer disturbances to the rock mass itself; in addition, it is an efficient economy reinforcement technique. So rock anchorage technique attracts the favor of the engineers and has been widely used in geotechnical engineering[1-3]. Although certain progress of rock anchorage technique has been made in experimental study and in application, the full understanding of the anchoring mechanism obviously lags behind the engineering practice. The anchorage parameters mostly depend on practical experience and engineering analogy method, which cannot fully reflect the anchoring performance of slope rock mass mechanical behavior. Design method, mechanical effect and reinforcement mechanism of rock anchorage technique need to be further studied. In this paper, the experimental study of rock anchorage technique was performed based on an engineering practice of highway slope reinforcement and the findings were helpful for reveal the anchoring mechanism and engineering practice.

## Application of grouting anchor in slope reinforcement of Dongguan to Shenzhen expressway

**Project profile.** This project is located in K15 section of Dongguan to Shenzhen expressway. And the pile number is K15 + 720 to K15 + 904, and the vertical height of slope is 53.94 m.

Due to the poor cohesive force of upper debris slope, the well-developed fractures of lower strongly weathered argillaceous siltstone, and the enough region rainwater, the whole slope can't be natural stability. Considering the physical and mechanical properties of rock mass slope and other influencing factors on slope stability, spray anchor reinforcement measures were adopted in this project.

**Outline of grouting anchor design.** The design process of the anchor rod was shown in figure 1.

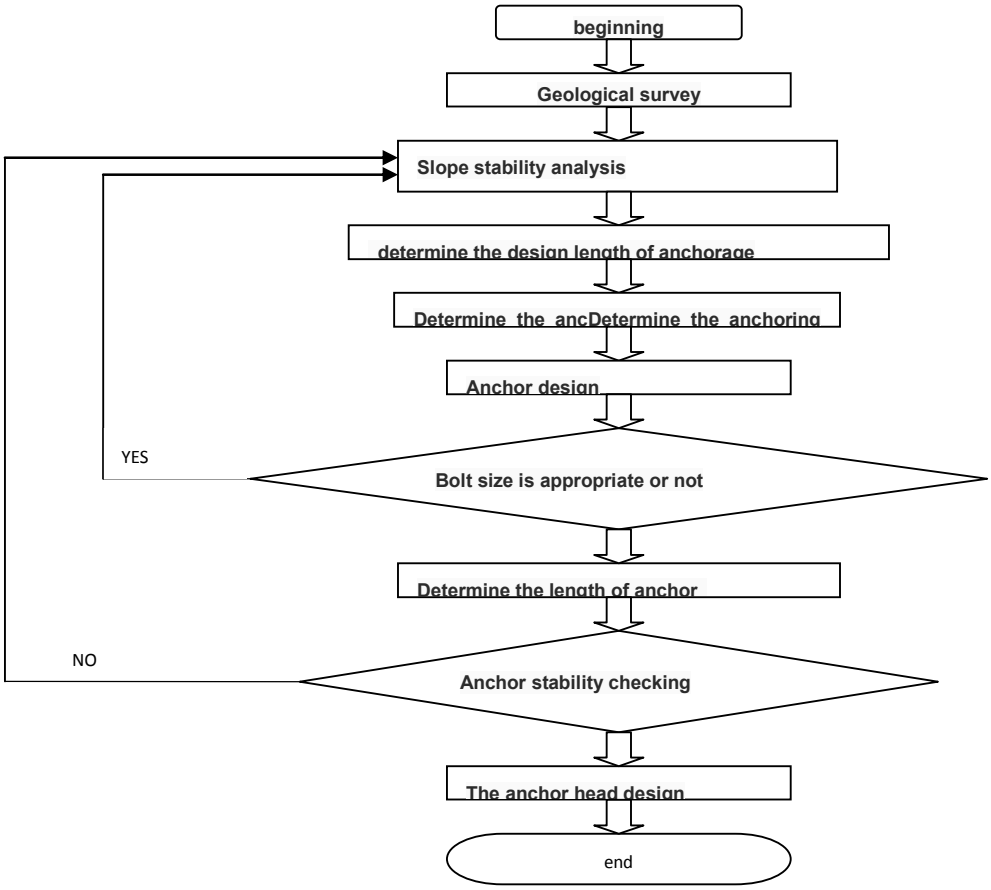


Fig.1 Design process of bolt

The slope stability analysis and the calculation method of anchoring force are as follows: Circular arc failure mode was chosen considering that the slope was mainly composed of diluvial gravel soil and broken rock mass. Based on Swedish article point's method, the slope safety factor calculation formula was obtained as

$$Fs = \frac{\text{Anti-sliding moment}}{\text{Slipping torque}} = \frac{CL + tg\phi \sum (W_{\mathrm{i}} \cos \alpha_{\mathrm{i}} - U_{\mathrm{i}})}{\sum W_{\mathrm{i}} \sin \alpha_{\mathrm{i}}} \tag{1}$$

where $C$ is cohesive force of rock and soil mass, $L$ is the length of the sliding surface, $\varphi$ is the frictional angle of rock and soil mass $W_i$ is the $i$th market its own weight, $\alpha_i$ is the $i$th strips sliding surface inclination and $U_i$ is the $i$th strips surface water pressure.

When the anchoring force $T$ was applied to the slope, the formation of safety coefficient can be described as

$$F_s = \frac{CL + \left[\sum (W_i \cos\alpha - U_i) + T\cos\theta\right] tg\varphi}{\sum W_i \sin\alpha_i - T\sin\theta} \tag{2}$$

in which, θ is the vertical angle between the anchor axis and the sliding surface.

And Equitation (3) can be easily gotten with Equitations (1) and (2)

$$T = \frac{[F_S] \cdot \sum W_i \sin\alpha_i - tg\varphi \sum (W_i \cos\alpha_i - U_i) - CL}{[F_S]\sin\theta + \cos\theta\, tg\varphi} \tag{3}$$

in which, [ $F_s$ ] is the allowable slope safety factor.

Specially, in the grouting bolt[4], the anchoring force can be described as

$$T = \pi L d q_s \tag{4}$$

where $L$ the length of the anchoring body, $d$ is the diameter of anchor solid and $q_s$ is the bond strength between anchor solid surface and the surrounding rock mass.

According to the calculating results, design length of anchor was 10 meters to 14 meters, the lip angle between anchor and horizontal plane was 15 degree, and the spacing of anchors was 2 meters to 4 meters. Rebar with diameter of 25 mm was chosen as the material type of anchor, poured with cement paste around the total length of the anchor.

## Construction technology.

### Anchor hole forming

A diameter of 110mm was set as the aperture of anchor hole, and QZ100K portable pneumatic DTH drilling rig was used for the anchor hole forming. During the forming process of anchor hole, residue was timely cleaned and a bracket with lip angle of 15 degree was used to control the forming angle of drilling rig.

### Manufacture and installation of anchor

Anchors were made with rebar of 25mm in diameter, and before that rust cleaning was performed on rebar materials. Position brackets were installed every two meters to ensure the center position of anchor with enough thickness of the protective layer. Precise process control during installation process of anchors was carried out to prevent anchor hole collapse.

### Cement slurry preparation and its grouting process

Cement slurry was made of No. 425 Portland cement with a water cement ratio of 0.45 to 0.5, the mixing time was set as no less than 3 minutes. And when the anchor grouting pipe was extended to about 10 cm to 15 cm distance from the bottom of anchor hole, the cement slurry then was started pouring into the anchor hole. During the pouring course of cement slurry, the anchor grouting pipe was gradually pulled out but should guarantee that the nozzle was always buried in the slurry till cement slurry overflowing from orifice. Then sealing belt was filled in the orifice under a pressure of 0.2 MPa to 0.5MPa.

## Field experiment

To study the anchorage mechanism of anchor and evaluate the rationality of the design, anchor test in the construction site was carried out.

**Overview.** The field test of anchor includes two parts, drawing test and strain monitoring test. For the former one, the purpose is to estimate the average surface friction stress $q_s$ between anchors and the anchor hole wall as well as the impact of anchorage length on anchors. For the latter one, the purpose was to investigate the distribution of axial stress and cohesive stress, which was implemented by setting strain sensor on the surface of anchor body.

Two sets of drawing tests were performed, one was located in the soil and the other was located in the rock mass. In each group, three anchor bolts with different anchorage length, which was 3.5 m, 5.5 m and 11.5 m, respectively, were tested independently. Fig. 3 shows the results of the drawing test.

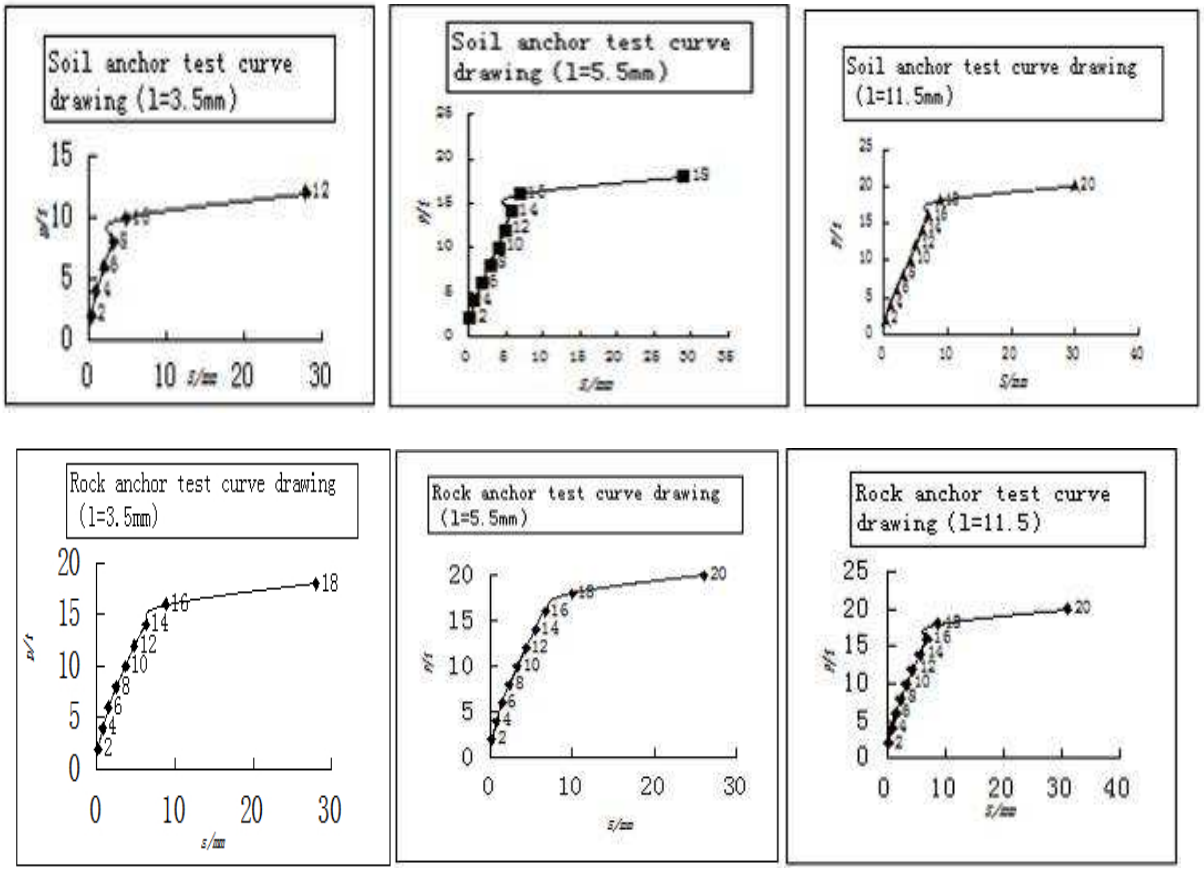


Fig.2 Drawing test results

For the strain monitoring test, two anchor bolts, with a bolt length of 14 m, there into, non anchorage length of 1.5 m and anchorage length of 12.5 m, were pasted with strain sensors. One anchor was located in the soil and the other was in rock mass.

As paste technology of strain sensors is one of the most important factors that influencing the test results, the below process was carried out in this research: the gauge location of the anchor bolt was polished well and carefully cleaned with acetone, then strain sensors were pasted. Yet only the anchor bolt located in soil and its sensors was well preserved in this research, and the cable of sensors placed on anchor in rock mass was destructed because of the curiosity of field workers. Table 1 shows the measured data of strain during drawing test.

Table 1 Measured strain on anchor bolt during drawing test

| Length along anchor bolt/m | Strain data under different drawing load (kN) /microstrain | | | | | | | | |
|---|---|---|---|---|---|---|---|---|---|
| | 40 | 60 | 80 | 100 | 120 | 140 | 160 | 180 | 200 |
| 1 | 412 | 628 | 834 | 1038 | 1293 | 1458 | 1673 | 1986 | 2288 |
| 2 | 118 | 295 | 442 | 683 | 898 | 1201 | 1412 | 1785 | 2011 |
| 4 | 8 | 16 | 20 | 138 | 326 | 528 | 735 | 892 | 1025 |
| 6 | 0 | 5 | 1 | 0 | 38 | 66 | 152 | 223 | 358 |
| 8 | 4 | 4 | 5 | 3 | 16 | 25 | 38 | 71 | 112 |
| 12 | 2 | 4 | 3 | 0 | 5 | 10 | 12 | 33 | 48 |

**Analysis of experimental results.**

**Analysis of drawing test results**

Observing the loading curves in Fig. 2, it can be seen that the anchorage force increase with the anchoring length, but there is a effective anchorage length, over that the further augment of

anchoring length cannot significantly increase the anchorage force of anchor bolt. Fig. 3 gives the comparison of anchorage force and anchoring length located in the soil and in the rock mass, and it can be concluded that the value of effective length relates to the characteristics of hole wall. It's about 6.0m in the soil and about 4.0m in the rock mass.

The average surface friction resistance $q_s$ can be calculated using equation (4) and the relationship curve between $q_s$ and anchoring length can be obtained, shown in Fig. 4. It can be concluded that the average surface friction resistance decreases with the increase of the anchorage length.

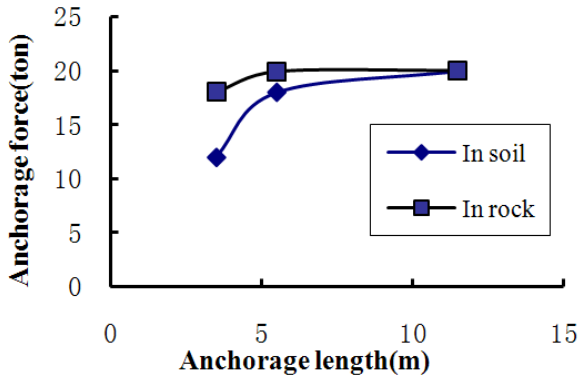


Fig.3 Relation curve between anchorage force and length

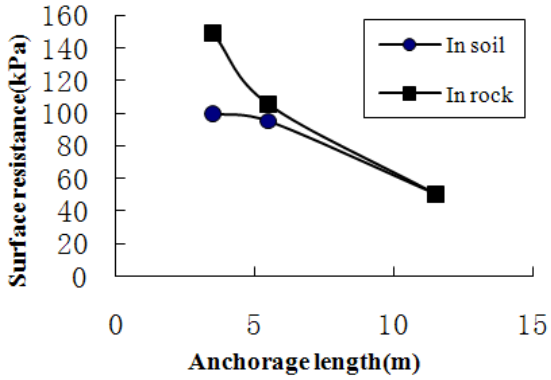


Fig.4 Relationship between average surface friction resistance and anchoring length

**Axial force and shear stress distribution along anchorage section**

According to the measured data in Table 1, anchor axial force $P$ is calculated by

$$P = K_0 EA\varepsilon \tag{5}$$

where $K_0$ is coefficient related to sensitivity of sensor resistors and cable length, $E$ is the elastic modulus of anchor bolt, which was $2\times10^5$ MPa, $A$ is the cross-sectional area of anchor bolt and $\varepsilon$ is the strain.

The calculation results of axial force $P$ is shown in Fig. 5. It can be seen that the axial force mainly concentrated in the front of anchor bolt while subjected to external load, and in the root of anchoring segment there was almost no axial force emerged. With the increase of external load, the distribution range of axial force gradually developed, that is to say, the spread of the axial force exhibits be progressive.

Shear stress between the anchor and cement paste (that is the cohesive force on the anchor bolt) can be calculated by the difference of axial stress in different cross sections of anchor bolt, and Fig. 6 shows the distribution of shear stress.

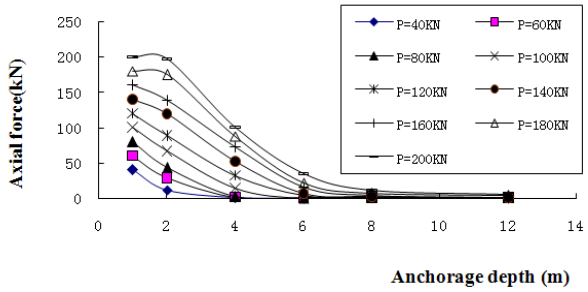


Fig. 5 Axial force curve of every measured point on bolt

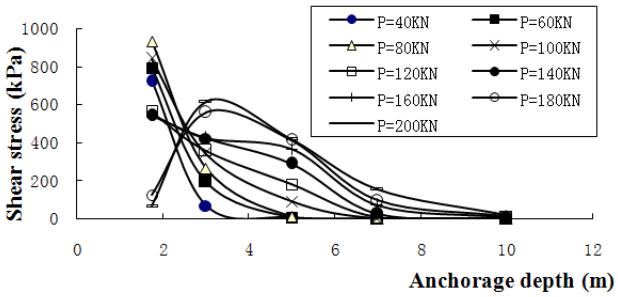


Fig.6 Distribution of shear stress between bolt and grouting

It is known from Fig. 6 that shear stress between slurry and anchor was unevenly distributed along the depth of grouting anchor, and mainly concentrated in the first third segment. Yet the peak value of shear stress moves to the bottom with the increase of the external load. But drawing test, which was traditionally adopted as the standard of grouting effect and capacity of anchor solid, can only examine the front part of grouting body. For grouting anchor bolt, drawing test can't well access the solidity of cement past and it's not comprehensive taking drawing test as the exclusive criteria, especially for grouting anchor with long length in rock mass.

## Conclusions

Based on the above test and analysis results, following conclusion can be concluded:

(1) There is an effective anchoring length in anchor grouting, which depends on the physical and mechanical properties of anchor solid and surrounding media.

(2) Shear stress in anchor solid unevenly distributes along the length of anchoring section, and mainly concentrated in the former 1/3 segment of anchor bolt. With the increase of external load, peak value of shear stress moves to the bottom of grouting anchor.

(3) It's not comprehensive taking drawing test as the exclusive criteria for grouting anchor with long length.

## Acknowledgements

The work presented in this paper was sponsored by Scientific Research Foundation of Shandong Jianzhu University (No. 010171105), for which the authors are grateful.

## References

[1] Cheng Liangkui. Present situation and the development of Chinese geotechnical anchoring technology. See: editor in chief of the Chinese rock and earth anchoring construction association. Anchorage technology in geotechnical engineering, Beijing: earthquake publishing house, 1992,125

[2] Sun Jun. Application and development of geotechnical anchoring technology in China. Xiong Houjin editor. New progress of international geotechnical anchoring and grouting . Beijing: China building industry press, 1996, 27 ~ 32.

[3] Peng Zhenbin editor. The anchoring engineering design and construction. Wuhan: China university of geosciences press, 1997, 30 ~ 31.

[4] Cheng Liangkui, Zhang Zuomei, Yang Zhiyin compiled. Rock and soil reinforcement and practical technology. Beijing: the earthquake publishing house, 1994.

*Applied Mechanics and Materials Vols. 580-583 (2014) pp 135-142*
*© (2014) Trans Tech Publications, Switzerland*
*doi:10.4028/www.scientific.net/AMM.580-583.135*

# Reliability Analysis on the Foundation Bearing Capacity in Ningbo Rail Transit Engineering

ZHU Jian-feng[1,a], LIU Gan-bin[1,b], YE Jun-neng[2,c]

[1] Faculty of Architectural Civil Engineering and Environment, Ningbo University; Ningbo, Zhejiang 315211 China

[2] Ningbo Urban Rail Transit Project Construction Headquarters, Ningbo, Zhejiang 315012, China

[a]zhujianfeng0811@163.com, [b]liuganbin@nbu.edu.cn, [c]yjn75@139.com

**Keywords:** foundation bearing capacity; reliability; checking point; natural density; vane strength

**Abstract:**According to the first-stage geologic investigation reports of the line 1 and line 2 in Ningbo rail transit, the natural density ($\rho$) and the vane strength ($C_u$) probability distribution of the typical layers in Ningbo area were studied in this paper. Besides, the reliabilities of the typical layers foundation bearing capacity in Ningbo area were evaluated by the checking point method. It is found that (1) the natural densities of the typical layers in Ningbo area show good normal distribution as their corresponding variation coefficients ($\delta$) are small. Unfortunately, the vane strengths of the typical soils in Ningbo area show poor normal distribution as their corresponding variation coefficients ($\delta$) are large. (2) The soil parameters variation has significant influence on the reliability index $\beta$. Moreover, $\beta$ is more sensitive to the variation of $\rho$ than to the variation of $C_u$. (3) As the safety coefficient methods can not consider the influence of the soil parameters variation on the foundation stability, it is suggested that the foundation stability in Ningbo area should be evaluated by the reliability analysis method.

## Introduction

Soil is a natural and historical product. As the different physical and chemical reactions and different historical conditions and different transportations and migrations, soil has significant variation. Therefore, the soil at different points has different physical and mechanical properties even if they look like uniform ostensibly[1]. The constant variation of soil varies with the mineral composition and buried depth and stress history and water content and density during the formation of soil and it does not decrease with the increase of the tests and the improvement of test technology. Therefore, how to consider the uncertainty of soil has become one of the important problems for most engineers.

Foundation bearing capacity is an important research subject in soil mechanics. Unfortunately, the randomness of geological conditions and the discreteness of the sampling sites in investigation always are not considered in dealing with the problem of the foundation bearing capacity. Then, the safety factor method in which all the soil parameters are considered to be constant is used in practical engineering. However, it is not coincided with the fact and results in a large number of engineering accidents[2].

Reliability analysis methods can consider the uncertainties of soil and should be widely used in the geotechnical design theoretically. However, the probability distribution of soil parameters cannot be determined accurately due to the limited investigation data. Then, the application of reliability theory into geotechnical engineering is restricted[3-6].

In this study, the physical parameter including the natural density ($\rho$) and the vane strength ($C_u$) probability distributions of the typical soils were studied in Ningbo area based on the first-stage geologic investigation reports of the line 1 and line 2 in Ningbo rail transit. Then, the reliability of the foundation bearing capacity in Ningbo rail transit engineering was analyzed by the checking point method. The reliability analysis method can be widely used in the geotechnical design in Ningbo rail transit engineering.

**Physical parameters probability distribution of typical layers in Ningbo area**

The Ningbo city is on the east of the Ningbo-Shaoxing plain of Zhejiang in China, and some typical layers such as mucky clay, slush, clay-silt sand, clay, sandy silt, silt and so on had been spontaneously developed during the long and complex geologic evolution. As there is little work on the statistic analysis of the physical parameters in Ningbo area, the application of the reliability theory into the geological design had been seriously limited.

The line 1 in Ningbo rail transit is the main trunk in the east-west direction of the Ningbo rail transit network planning. Meanwhile, the line 1 with a total of 45.99 km long runs through the Haishu Old City, Sanjiankou, Jiangdo New City. Moreover, it is surrounded by the central region of Beilun to its east, Gaoqiao town to its west. The line 2 with a total of 50 km long in Ningbo rail transit is the main trunk in the southwest-northeast direction of the Ningbo rail transit network planning, and it begins at Gulin in Yingzhou and ends in Beilun. According to the first-stage geologic investigation reports of the line 1 and line 2 in Ningbo rail transit with a total of 4 bid sections and 2343 effective borehole and 58984 effective data, The statistic analysis on the physical parameter of every layer such as the natural density ($\rho$) and the vane strength ($C_u$) in Ningbo area were studied. Due to space limitation, only 4 typical layers shown in Table 1 are selected to study the bearing capacity reliability of foundation soil in Ningbo area.

**Table1 Category and depth of typical layers in Ningbo area**

| Soil Numbers | Soil categories | Average depth $h$(m) | Average buried depth $H$(m) |
|---|---|---|---|
| ①$_{3\text{-}0}$ | mucky clay | 2.0 | -2.0 |
| ②$_{2\text{-}1}$ | slush | 2.5 | -4.5 |
| ③$_{2\text{-}0}$ | silty clay | 9.5 | -14.0 |
| ④$_{2\text{-}0}$ | clay | 8.0 | -22.0 |

**1.1 Distribution of natural density**

The frequency histogram of the natural density associated with every typical layers are shown in Fig 1. Moreover, the statistical indexes of the natural density associated with every typical layers including the average value ($\mu$) and standard deviation ($\sigma$) and the variation coefficient ($\delta$) are shown in Table 2.

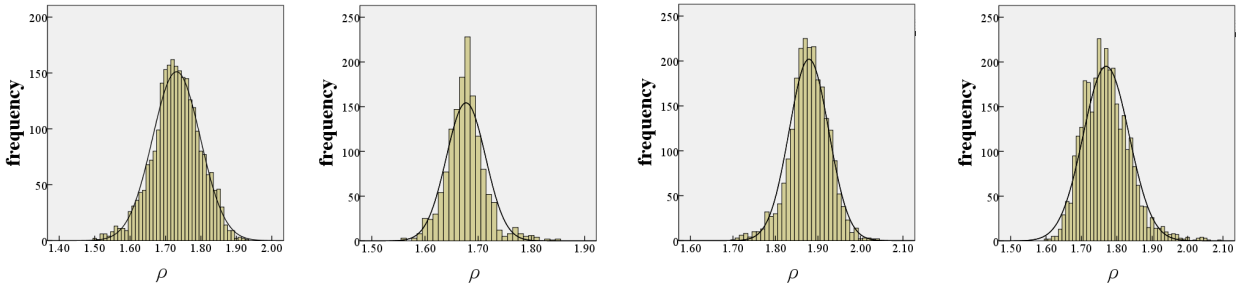


**(a) Layer ①$_{3\text{-}0}$ (b) Layer ②$_{2\text{-}1}$ (c) Layer ③$_{2\text{-}0}$ (d) Layer ④$_{2\text{-}0}$**

**Fig.1 Natural density histograms of typical layers**

**Table2 Natural density probability statistical table of typical layers**

| Layers | $N$ | $\mu$ (g/cm$^3$) | $\sigma$ (g/cm$^3$) | $\delta$ |
|---|---|---|---|---|
| ①$_{3\text{-}0}$ | 2557 | 1.731 | 0.068 | 0.039 |
| ②$_{2\text{-}1}$ | 2078 | 1.675 | 0.039 | 0.023 |
| ③$_{2\text{-}0}$ | 2361 | 1.879 | 0.047 | 0.025 |
| ④$_{2\text{-}0}$ | 3119 | 1.770 | 0.062 | 0.035 |

From Fig.1 and Table 2, it can be seen that: the variation degrees of the natural density ($\rho$) are low, where the maximum variation coefficient is 0.039 and minimum variation coefficient is only 0.023. Furthermore, the natural density probabilities of all typical layers in Ningbo area show good normal distribution.

### 1.2 Distribution of vane strength parameters

The Vane test has proven to be a simple but effective method in measuring the shear strength of soft soil since they have a flow on smooth surfaces and are common in devices used in different types of rheometers (parallel disc rheometers or coaxial cylinders). Therefore, the vane strength ($C_u$) of four typical layers in Ningbo area is tested and the frequency histogram of the vane strength associated with every typical layers are shown in Fig 2. Moreover, the statistical indexes of the vane strength associated with every typical layers including the average value ($\mu$) and standard deviation ($\sigma$) and the variation coefficient ($\delta$) are shown in Table 3.

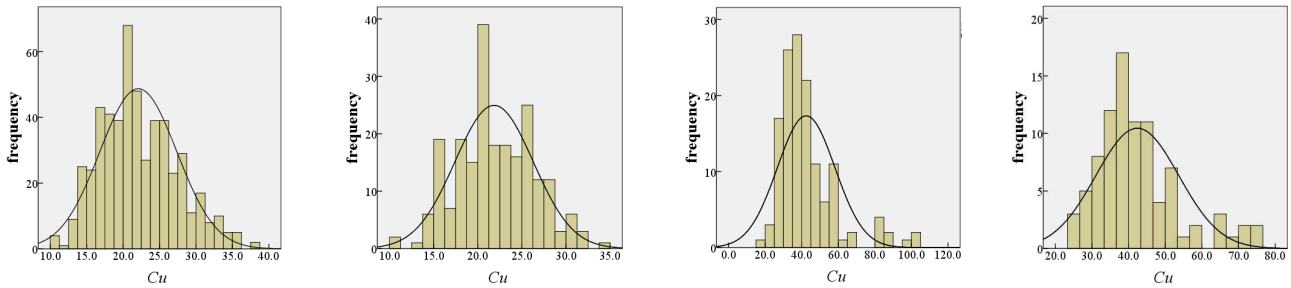


**(a) Layer ①$_{3\text{-}0}$** **(b) Layer ②$_{2\text{-}1}$** **(c) Layer ③$_{2\text{-}0}$** **(d) Layer ④$_{2\text{-}0}$**

**Fig.2 Vane strength $C_u$ histograms of typical layers**

**Table3 Vane strength probability statistical table of typical layers**

| Layers | $N$ | $\mu$ (g/cm$^3$) | $\sigma$ (g/cm$^3$) | $\delta$ |
|---|---|---|---|---|
| ①$_{3\text{-}0}$ | 517 | 22.086 | 5.290 | 0.240 |
| ②$_{2\text{-}1}$ | 222 | 21.847 | 4.436 | 0.203 |
| ③$_{2\text{-}0}$ | 137 | 42.392 | 15.765 | 0.372 |
| ④$_{2\text{-}0}$ | 89 | 42.366 | 11.326 | 0.267 |

From Fig.2 and Table 3, it can be seen that: the variation degrees of the natural density ($\rho$) are low, where the maximum variation coefficient is 0.372 and minimum variation coefficient is only 0.203. Furthermore, the natural density probabilities of all typical layers in Ningbo area show normal distribution.

### Checking point method

In the standardized normal space, the reliability index is defined as the minimum distance between the origin of coordinates and the limit state curve by Hasofer and Lind (1974). Then, the vertical line is drawn through the origin of coordinates to the limit state curve and the intersection is called checking point.

In the checking point method, all the random variables are considered to be in normal distribution. Its procedure is as follows:

(1) Supposed that the random variables including $X_1$, $X_2$,…, $X_n$ are in normal distribution. Then, the performance function of the structure is $Z$=g($X_1$, $X_2$,…, $X_n$). Given that the checking point $\boldsymbol{X}^*$ is $(x_1^*, x_2^*, \cdots, x_n^*)$ and by taking the first-order terms of a Taylor series expansion the performance function is derived as:

$$Z \approx g(x_1^*, x_2^*, \cdots, x_n^*) + \sum_{i=1}^{n} \frac{\partial g(x^*)}{\partial X_i}\left(X_i - x_i^*\right) \tag{1}$$

The associated average value ($\mu$) and standard deviation ($\sigma$) are

$$\mu_Z = E(Z) = g(x_1^*, x_2^*, \cdots, x_n^*) + \sum_{i=1}^{n} \frac{\partial g(x^*)}{\partial X_i}\left(E(X_i) - x_i^*\right) = g(x_1^*, x_2^*, \cdots, x_n^*) + \sum_{i=1}^{n} \frac{\partial g(x^*)}{\partial X_i}\left(\mu_{X_i} - x_i^*\right) \tag{2}$$

$$\sigma_Z^2 = E(Z - E(Z))^2 = \sum_{i=1}^{n}\sum_{j=1}^{n} \frac{\partial g(x^*)}{\partial X_i}\frac{\partial g(x^*)}{\partial X_j} E[(X_i - \mu_{X_i})(X_j - \mu_{X_j})] = \sum_{i=1}^{n}\left[\frac{\partial g(x^*)}{\partial X_i}\sigma_{X_i}\right]^2 \tag{3}$$

The associated reliability index is

$$\beta = \frac{\mu_Z}{\sigma_Z} = \frac{g(x_1^*, x_2^*, \cdots, x_n^*) + \sum_{i=1}^{n} \frac{\partial g(x^*)}{\partial X_i}\left(\mu_{X_i} - x_i^*\right)}{\sqrt{\sum_{i=1}^{n}\left[\frac{\partial g(x^*)}{\partial X_i}\sigma_{X_i}\right]^2}} \tag{4}$$

As the checking point $\boldsymbol{X}^* = (x_1^*, x_2^*, \cdots, x_n^*)$ is unkown, the reliability index cannot be computed by equations.

Moreover, the relationship between the checking point and the reliability index can be[2]:

$$x_i^* = \mu_{X_i} + \beta\sigma_{X_i}\cos\theta_{X_i} \tag{5}$$

In the standardized normal space, the sensitivity coefficient $\alpha_{Xi}$ can be :

$$\alpha_{X_i} = \cos\theta_{X_i} = \frac{-\frac{\partial g(x^*)}{\partial X_i}\sigma_{X_i}}{\left(\sum_{i=1}^{n}\left[\frac{\partial g(x^*)}{\partial X_i}\sigma_{X_i}\right]^2\right)^{1/2}} \tag{6}$$

where, $\alpha_{Xi}$ is the sensitivity coefficient which denotes the relative influence of the $i^{th}$ random variation on the standard deviation.

The failure probability can be:

$$P_f = 1 - \Phi(\beta) \tag{7}$$

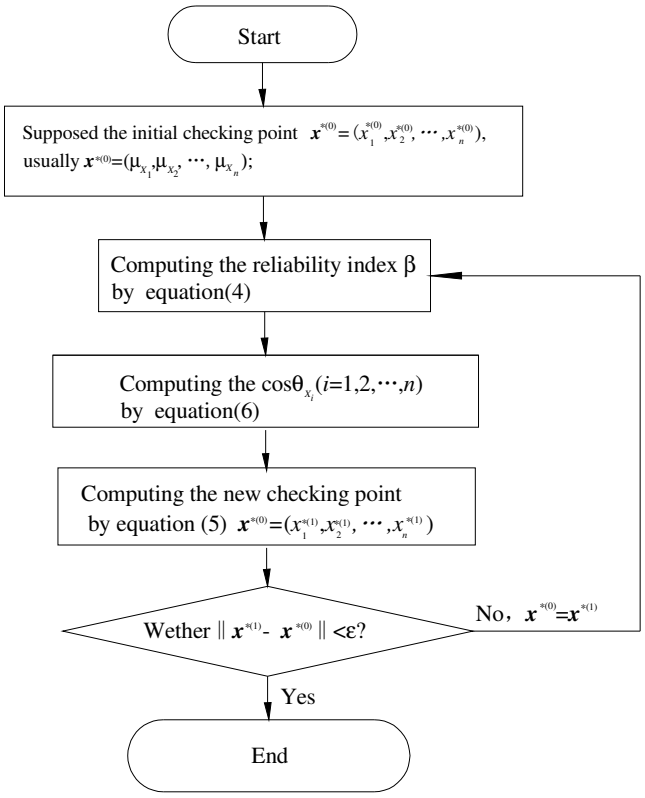


**Fig.3 Flow chart of the checking pint method**

where, $\Phi(\beta)$ denotes the cumulative probability function on normal distribution.

Based on the above formulae, the reliability index can be performed and the incremental procedure can be implemented as shown in Fig. 3. Furthermore, the correspondent failure probability can be computed by the equation (7).

## Reliability analysis on the foundation bearing capacity in Ningbo rail transit engineering

### 3.1 Stability analysis on the soil foundation

The vane shear test can be used to predict the foundation bearing capacity of soft clay such as mucky clay and slush and collapsible loess and so on. The empirical formula is:

$$f_a = 2C_u + \gamma H \tag{8}$$

where

$C_u$ is the modified vane shear strength of soil (kPa);

$\gamma$ is the unit weight of foundation soil (kN/m$^3$);

$H$ is the foundation buried depth (m).

The correspondent safety factor $F_s$ is:

$$F_s = \frac{2C_{um} + \gamma_m H}{p_m} = \frac{2C_{um} + \rho_m g H}{p_m} \tag{9}$$

where

$p_m$ is the mean value of the foundation pressure (kPa);

$C_{um}$ is the mean value of the shear strength of foundation soil (kPa);

$\gamma_m$ is the mean value of unit weight of foundation soil (kN/m$^3$);

$\rho_m$ is the mean value of natural density of foundation soil (g/cm$^3$);

$g$ is the acceleration of gravity (m/s$^2$)。

### 3.2 Limit state equation

The correspondent limit state equation is :

$$p - 2C_u - \gamma H = p - 2C_u - \rho g H \tag{10}$$

where

$p$ is the foundation pressure (kPa);

$\rho$ is the natural density of the foundation soil (g/cm$^3$).

### 3.3 Determination of the random variation

Based on the above engineering condition, the foundation buried depth $H$ and the acceleration of gravity $g$ can be considered as constant in the practical reliability design. However, the variation of other parameters such as the shear strength $C_u$ and the natural density of foundation soil and the foundation pressure are large and they should be considered as random variation.

### 3.4 Computation of the reliability index

The mean value of the foundation pressure $p_m$ is 200 kPa and its correspondent variation coefficient $\delta_p$ is 0.25. Moreover, in each layer the vane shear strength $C_u$ and the natural density $\rho$ are independent on each other and both of them are in good normal distribution. The statistic results are shown in Table 4.

**Table4 Calculation parameters of each typical layer**

| Layers | $H$(m) | $C_u$ | | $\rho$ | |
|---|---|---|---|---|---|
| | | $\mu$ (kPa) | $\delta$ | $\mu$ (g/cm$^3$) | $\delta$ |
| ①$_{3-0}$ | 2.0 | 22.086 | 0.240 | 1.731 | 0.039 |
| ②$_{2-1}$ | 4.5 | 21.847 | 0.203 | 1.675 | 0.023 |
| ③$_{2-0}$ | 14.0 | 42.392 | 0.372 | 1.879 | 0.025 |
| ④$_{2-0}$ | 22.0 | 42.366 | 0.267 | 1.770 | 0.035 |

As shown in Table 5, the reliability index $\beta$ and the failure probability $P_f$ of each layer can be computed by equations (4)-(7).

**Table5 Foundation bearing capacity calculated results of each typical layer**

| Layers | $F_s$ | $\beta$ | $P_f$(%) |
|---|---|---|---|
| ①$_{3-0}$ | 0.390 | -2.33 | 99.01 |
| ②$_{2-1}$ | 0.588 | -1.50 | 93.32 |
| ③$_{2-0}$ | 1.289 | 2.54 | 0.55 |
| ④$_{2-0}$ | 2.332 | 4.72 | 0.00 |

From Table5, it can be shown that:

(1) As the safety factors are less than 1 and the failure probabilities are more than 93%, both the layer ①$_{3-0}$ and ②$_{2-1}$ cannot be used as the foundation bearing layer.

(2) The safety factor and the failure probability of layer ③$_{2-0}$ are 1.289 and 0.55%, respectively. Moreover, the safety factor of layer ④$_{2-0}$ is 2.332 and its correspondent failure probability is 0.

Although it is theoretically valid to take the layer ④$_{2-0}$ as the foundation bearing layer, the construction cost is greatly raised as the buried depth of layer ④$_{2-0}$ is large than layer ③$_{2-0}$. Therefore, it is more reliable to choose the layer ③$_{2-0}$ as the foundation bearing layer.

### 3.5 Sensibility analysis on the variation

Supposed that the The mean value of the foundation pressure $p_m$ is 200 kPa and its correspondent variation coefficient $\delta_p$ is 0.25. The layer ③$_{2\text{-}0}$ and layer ④$_{2\text{-}0}$ are taken as the foundation bearing layer, respectively. Their correspondent mean values of the vane shear strength and the natural density are kept invariant and their variation coefficients change from 0.1 to 0.7. Then, the correspondent reliability indexes are shown in Fig.4 and Fig.5.

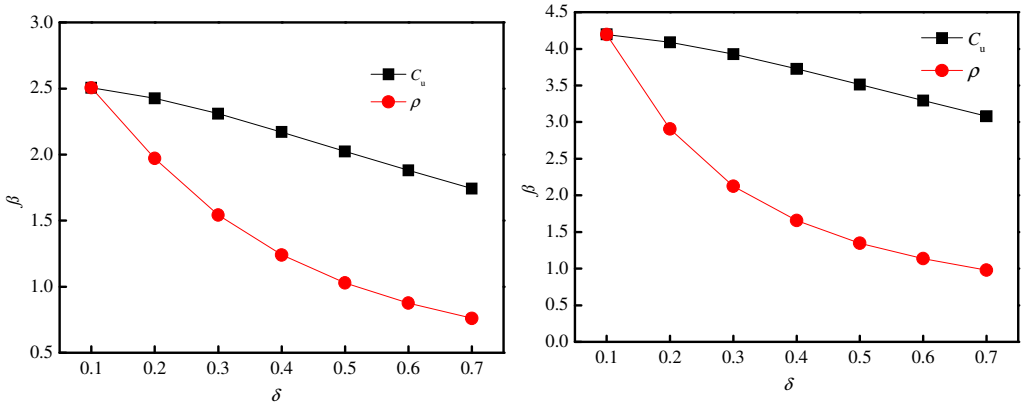


**Fig.4 Relationship between the variation coefficient and reliability in layer ③$_{2\text{-}0}$ and ④$_{2\text{-}0}$**

From Fig.4 and Fig.5, it can be seen that:

(1) The variation of soil parameter has a significant influence on the reliability index. Furthermore, the reliability index is more sensitive to the natural density than to the vane shear strength.

(2) As the mean value of the vane shear strength and the natural density and the foundation pressure are instant, the safety factor of layer ③$_{2\text{-}0}$ and layer ④$_{2\text{-}0}$ computed by equation (9) are 2.07 and 2.332, respectively. Furthermore, the stability of each layer is safe.

(3) However, the reliability index has a significant change due to the different variation coefficients. With the increase of variation coefficient, the reliability index of layer ③$_{2\text{-}0}$ decreases from 2.51 to 0.76 and the correspondent failure probability increase from 0.60% to 22.36%. Moreover, the reliability index of layer ④$_{2\text{-}0}$ decreases from 4.20 to 0.98 and the correspondent failure probability increase from 0 to 16.35%.

(4) From analysis it above can be seen that, safety factor method cannot consider the influence of the variation coefficient and may provide the wrong conclusion. However, the reliability analysis method can reflect the influence of the variation coefficient on the failure probability of foundation soil. Therefore, it is suggested that the safety of the foundation soil should be assessed by the reliability analysis method in practical engineering.

## Conclusions

(1) The natural density of every typical layer in Ningbo area has little variation and shows good normal distribution. In addition, the variation degree of the vane shear strength of every typical layer in Ningbo area is high and shows normal distribution.

(2) The variation of soil parameter has a significant influence on the reliability index and the reliability index is more sensitive to the natural density than to the vane shear strength.

(3) Safety factor method cannot consider the influence of the variation coefficient and may provide the wrong conclusion. It is suggested that the safety of the foundation soil should be assessed by the reliability analysis method in practical engineering.

**Acknowledgements**

The National Nature Fund of China (Grant No. 51278256) and the Public Welfare Technology Application Research of Zhejiang Province of China (Grant No. 2012C21058) and the Natural Science Fund in Ningbo University of China (Grant No. 2012A610160, XKL11D2076) are acknowledged for their financial support. This paper was also sponsored by K. C. Wong Magna Fund in Ningbo University of China.

**References**

[1] Morgenstern N. R. Performance in geotechnical practice. The Inaugural Lumb Lecture. The Hong Kong Institution of Engineers (2000).

[2] Baecher G. B., Christian J. T. *Reliability and statistics in geotechnical engineering*[M]. West Sussex: John Wiley & Sons Ltd, (2003).

[3] Chen C. F., Zhu J. F. Calculation method of earth slope reliability based on response surface method and Morgenstern-Price procedure[J]. Engineering Mech- anics, Vol.25(2008), p.166-172. (in Chinese)

[4] El-Ramly H., Morgenstern N. R., Cruden D. M. Probabilistic stability analysis of a tailings dyke on pre-sheared clay shale[J]. Canadian Geotechnical Journal, Vol.40(2003), p.192-208.

[5] Zhu J. F., Chen C. F., Xu R. Q. An optimization method of reliability analysis of foundation pit reinforced with soil nailing [J]. Rock and Soil Mechanics, Vol.31(2010), p.2336-2341. (in Chinese)

[6] Low B. K. Reliability analysis of rock slopes involving correlated nonnormals[J]. International Journal of Rock Mechanics and Mining Science, Vol.44(2007), p.922-935.

*Applied Mechanics and Materials Vols. 580-583 (2014) pp 143-147*
*© (2014) Trans Tech Publications, Switzerland*
*doi:10.4028/www.scientific.net/AMM.580-583.143*

# Research on the Anchorage Technology of Steep Slope in Sanitary Landfill

Ping Li [1,a], Heng Wang [1,b] and Ying Xin [1,c]

[1] School of Civil Engineering, Lanzhou University of Technology, No.287 Langongping Street, Lanzhou and 730050, China

[a] liping@lut.cn, [b] wangheng217@126.com, [c] xyinglut@163.com

**Keywords:** Sanitary landfill, HDPE membrane, Anchoring trench, Limit equilibrium theory

**Abstract.** The process of urbanization has brought prosperity of economy and improvement of people's living standard, but larger and larger life garbage in the city could be found due to excessive concentration of population. Sanitary landfill method has been widely applied in many cities for convenience and economy. Anti-seepage treatment and anchorage technology are two key issues to reduce the pollution of leachate on surrounding environment and underground water sources with construction of modern sanitary landfill area. In this paper, the anchorage technology of high-density polyethylene (HDPE) membrane was researched on the steep slope in the valley-type sanitary landfill. The test and theory of anchorage were also studied in the northwest region. The results show that anchorage force reaches the maximum when the anchoring platform is horizontal. It keeps the geomembrane more stable if the slope angle is within 45° when the slope height is over 6m.

## Introduction

Many landfill sites in the northwest region locate in the steep valley, with the slope more than 45° and the slope height more than 8m, which makes it difficult to lay and anchor the HDPE membrane[1]. Therefore, how to prevent seepage in northwest is a difficult problem in sanitary landfill design and construction. The fixation of HDPE geomembrane on the side slope of landfill site depends on anchorage facilities at the foot of each slope. Anchoring trench is adopted in the rock and soil foundation, while the anchor bolt, nail, or a special HDPE geomembrane embedded lock bar in the concrete, masonry and reliably batholith. At present, anchoring trench is the main form, the direction of the anchoring platform is horizontal and the form of cross section of the anchoring trench is rectangle. However, the earthwork excavation volume with this method is large and the cost is high. In order to reduce the cost, a proposed anchoring trench form along the direction of the slope is adopted, but the anchoring force by this method is lesser and geomembrane may take off the anchor. In order to guarantee the integrity and avoid the damage of the geomembrane, it should prevent geomembrane from excessive tensile stress [2,3]. Generally, tensile strength of the geomembrane is calculated by limit equilibrium method of slope stability analysis and researched through experiment combined with limit equilibrium theory [4].

## Limit Equilibrium Analysis Method of Geomembrane Anchorage

**Analysis of the Vertical Pressure of Dump Body.** The structure diagram of dump body in landfill was shown in Fig. 1.The dump body was assumed to be uniform distribution, whose initial unit weight before compaction was $\gamma_0$ and unit weight after compaction was $\gamma_1$. $\theta$ standed for the slope angle of the sanitary landfill area and h was for the height of the slope. The angle of repose of dump body on the anchoring platform was $\beta$ as well as the foot of the slope was set to be the coordinate origin for 0.

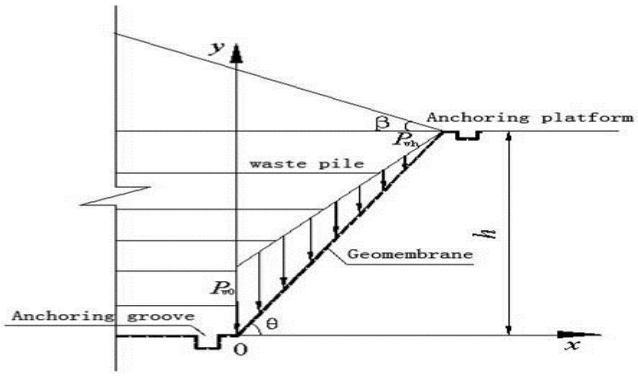


Fig. 1 Structure diagram of dump body

On the top of the anchoring platform, namely the position of y=h, the vertical earth pressure $P_{vh}$ of overlying soil adding to the geomembrane was zero. While for y=0, the vertical earth pressure $P_{vh}$ of the foot of the slope could be calculated by formula (1-1):

$$P_{v0} = \gamma_1 h(1+\cot\theta\cdot\tan\beta) \tag{1-1}$$

Then the vertical earth pressure $P_{vy}$ of overlying soil at $y=y_0$ could be given by:

$$P_{vy} = \gamma_1\left[h+(h-y_0)\cot\theta\tan\beta\right] \tag{1-2}$$

The vertical pressure that geomembrane received was non-uniform distribution and the maximum would occur at the foot of the slope, which was shown in Fig. 1. The total vertical pressure of HDPE for unit width was calculated by formula (1-3):

$$P_{v,total} = \frac{1}{2}\gamma_1 h^2(1+\cot\theta\tan\beta) \tag{1-3}$$

The additional stress at the foot of the slope was caused by the compaction of garbage layer and given by:

$$P_r = (\gamma_1-\gamma_0)\cdot h\cdot(1+\cot\theta\tan\beta) \tag{1-4}$$

The total average additional tension along the slope surface that geomembrane received was calculated by:

$$P_T = \frac{1}{2}(\gamma_1-\gamma_0)h^2(\sin\theta+\cos\theta\tan\beta) \tag{1-5}$$

**Calculation of the Residual Downward Tension of Geomembrane.** Here was a assumption that the geotextile was fully contacted with the geomembrane without relative sliding. The friction $P_\tau$ of both the upper and the lower surfaces of geomembrane was obtained as follows:

$$P_\tau = P_{\tau au} - P_{\tau ad} = (C_{au}-C_{ad})\cdot\frac{h}{\sin\theta}+\frac{1}{2}\gamma_1 h^2(1+\cot\theta\tan\beta)\cos\theta(\tan\delta_u-\tan\delta_d) \tag{1-6}$$

Where $C_{au}$ was a parameter showing the cohesion of geomembrane and the upper geotextile while $C_{ad}$ represented the cohesion of geomembrane and the lower compacted soil respectively. $\delta_u$ and $\delta_d$ were the corresponding friction angels.

The unbalanced tension and anchorage force were needed to make the geomembrane stable if $P_T > P_\tau$. When the landfill body tension $P_T=P_\tau$, The geomembrane could be in limit equilibrium state and remain the tensile stability if $P_T = P_\tau$ .The geomembrane would not slide along the slope and anchorage treatment was not required if $P_T < P_\tau$.

The average residual downward tension of geomembrane along the slope was calculated by:

$$P_r = P_T - P_\tau = \frac{1}{2}h^2\cdot(1+\cot\theta\tan\beta)\left[(\gamma_1-\gamma_0)\sin\theta-\gamma_1\cos\theta(\tan\delta_u-\tan\delta_d)\right]-\frac{(C_{au}-C_{ad})\cdot h}{\sin\theta} \tag{1-7}$$

**Calculation of Geomembrane Tension and Anchorage Force.** The geomembrane tension and the anchorage force of anchoring platform must be used to balance the residual downward tension of geomembrane. Based on this theory, the following assumptions could be made:

(1) There was no relative sliding between the geomembrane and the geotextile.

(2) The geomembrane tension that was close to the anchoring platform was regarded as non-uniform distribution.

(3) The stress-strain relations of geomembrane conformed to the characteristics of elastic material when the tensile rate was less than the yielding tensile rate of geomembrane.

According to the above assumptions, the tension of geomembrane could be given by:

$$P_t = E\Delta l \tag{1-8}$$

Where $E$ was a parameter that represented the elastic modulus of geomembrane and $\Delta l$ was the parameter showing the elongation of geomembrane along with the slope surface.

According to the design and stability requirements of sanitary landfill area, the tensile strength of HDPE should be less than or equal to the tensile yield strength of geomembrane, namely $[P_t] \le T_f$ .The direction of anchoring platform was horizontal and rectangular cross section was adopted for anchoring trench as shown in Fig. 2.

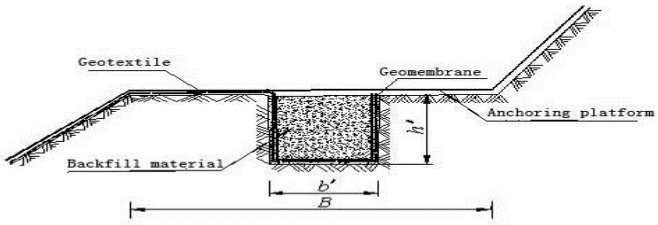


Fig. 2 Sectional view of anchoring trench on anchoring platform

According to the principle of unbalanced friction, the anchorage force Pa provided by the anchoring trench was obtained by:

$$P_a = 2\left[\left(C'_{\mathrm{au}} - C'_{\mathrm{ad}}\right)\cdot h' + \frac{1}{2}\gamma_2 h'^2 k_0\left(\tan\delta'_{\mathrm{u}} - \tan\delta'_{\mathrm{d}}\right)\right] + \left[\left(C'_{\mathrm{au}} - C'_{\mathrm{ad}}\right)\cdot b' + \frac{1}{2}\gamma_2 h'^2(\tan\delta'_{\mathrm{u}} - \tan\delta'_{\mathrm{d}})\right]$$
$$+\left[\left(C'_{\mathrm{au}} - C'_{\mathrm{ad}}\right)\cdot b' + \frac{1}{2}\gamma_2 h'^2(\tan\delta'_{\mathrm{u}} - \tan\delta'_{\mathrm{d}})\right] \tag{1-9a}$$

Where $C'_{\mathrm{au}}$ was a parameter showing the cohesion of geomembrane and the upper geotextile while $C'_{\mathrm{ad}}$ represented the cohesion of geomembrane and the lower compacted soil respectively. $k_0$ was a coefficient representing the static pressure of lateral and equaled to 0.5. $\gamma_2$ was on behalf of the unit weight of packing in the anchoring trench. $\delta'_{\mathrm{u}}$ and $\delta'_{\mathrm{d}}$ were the corresponding friction angels. The formula (1-9a) could be simplified as follows:

$$P_a = (C'_{\mathrm{au}} - C'_{\mathrm{ad}})(2h' + b') + \gamma_2 h'^2(\tan\delta'_{\mathrm{u}} - \tan\delta'_{\mathrm{d}}) \tag{1-9b}$$

The rectangular anchoring trench was adopted for the steep slope in order to decrease excavated volume and construction cost, which was shown in Fig. 3. If the friction and cohesion between the materials and geomembrane were ignored at the top of anchoring trench, the anchorage force of anchoring trench could be given by:

$$P_a = (C'_{\mathrm{au}} - C'_{\mathrm{ad}})(h' + b') + \frac{3}{4}\gamma_2 b'^2(\tan\delta'_{\mathrm{u}} - \tan\delta'_{\mathrm{d}}) \tag{1-9c}$$

(1) The geomembrane would slide or fracture along the slope surface if $P_r > P_t + P_a$ .The above phenomenon could be distinguished by the following three conditions:

- The phenomenon of anchor falling would happen in geomembrane if $[P_t] > P_a$ .
- The phenomenon of anchor falling or fracture would happen with the same probability in geomembrane if $[P_t] = P_a$ .
- The phenomenon of fracture would happen in geomembrane if $[P_t] < P_a$ .

(2)The geomembrane stayed in the limit equilibrium state if $P_r = P_t + P_a$ .

(3)The geomembrane was in stable state if $P_r < P_t + P_a$ , which was expressed in two ways:

- The slope geomembrane could remain stability relying on the anchoring platform only without tensile deformation if $P_r \le P_a$ , which indicated $P_t = 0$ .

Tensile deformation could be found in the geomembrane if $P_r > P_a$ , namely $P_t > P_r - P_a$ .

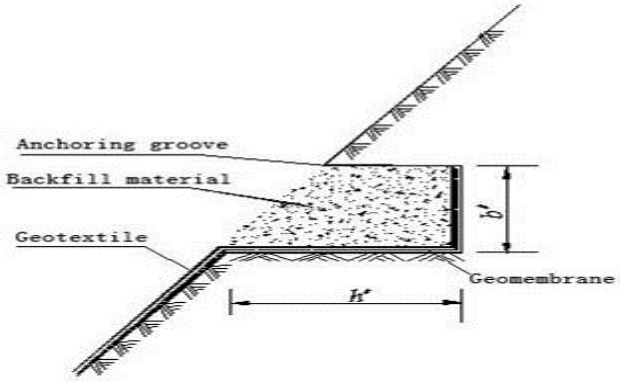


Fig. 3 Sectional view of anchoring trench along the slope surface

## Engineering Examples

**Parameter Selection.** The calculated parameters of anchorage force of geomembrane on the steep slope were showed in Table 1. If the influences of the construction process on the compactness of dump body and the slope geomembrane were ignored, the initial weight $\gamma_0$ and final unit weight $\gamma_1$of dump body were set 11kN/m$^3$ and 15kN/m$^3$.The three kinds of anchoring trenchs with the rectangular cross-section of 0.5m, 0.8m, 1.0m in depth and 0.5m, 0.8m, 1.2m in width were adopted respectively. The unit weight $\gamma_2$ of cohesive soil after compaction was 19kN/m$^3$. In this study, the anchoring technology of HDPE for steep slope was researched ,which indicated the angel of slope was ranging from 40 ° to 60 ° and the height of slope was 6 m, 8 m, 10 m and 12 m respectively. Considering the whole stability of dump body with the increase of height, the value of tan$\beta$ was equal to 0.33 according to the engineering experience.

Table 1 Calculated parameters of anchorage force of geomembrane on the steep slope

| Item | Example 1 | Example 2 | Example 3 (Test) |
|---|---|---|---|
| $C_{au}$(kPa) | 2 | 1 | 0.27 |
| $C_{ad}$(kPa) | 0.5 | 0.5 | 0.15 |
| $\delta_u$(°) | 15 | 10 | 17 |
| $\delta_d$(°) | 5 | 3 | 5 |
| $C'_{au}$(kPa) | 3 | 2 | 0.27 |
| $C'_{ad}$(kPa) | 1 | 0.4 | 0.15 |
| $\delta'_u$ (°) | 20 | 15 | 17 |
| $\delta'_d$(°) | 5 | 5 | 5 |

**The Anchoring Force Calculation.** The cross section with $b' \times h'$ of 0.5×0.5m, 0.8×0.8m and 1.2×1.0m referred to as section 1, section 2 and section 3 respectively, the anchoring force of the level and the vertical anchoring trench were represented by $P_1$ and $P_2$ respectively. Anchoring force in different examples was shown in Table 2.

Table 2 The anchoring force

| Section Type | Section Size ($b' \times h'$) (m) | Example 1 (kN·m$^{-1}$) | | Example 2 (kN·m$^{-1}$) | | Example 3 (kN·m$^{-1}$) | |
|---|---|---|---|---|---|---|---|
| | | $Pa_1$ | $Pa_2$ | $Pa_1$ | $Pa_2$ | $Pa_1$ | $Pa_2$ |
| section 1 | 0.5×0.5 | 4.3 | 3.0 | 3.3 | 2.2 | 1.2 | 0.9 |
| section 2 | 0.8×0.8 | 8.2 | 5.7 | 6.0 | 4.2 | 2.9 | 2.2 |
| section 3 | 1.2×1.0 | 11.7 | 10.1 | 8.6 | 7.2 | 6.4 | 3.4 |

**Geomembrane Residual Tension Under P*r* in Calculation.** According to the formula (1-9), residual tension Pr was calculated with different geomembrane anchoring height and different slope angle, the results were shown in Table 3.

Table 3 Residual tension $P_R$ (Unit: kN·m$^{-1}$)

| Height(m) | Angle(°) | | | | | | | | |
|---|---|---|---|---|---|---|---|---|---|
| | 40º | | | 45º | | | 50º | | |
| Example | 1 | 2 | 3 | 1 | 2 | 3 | 1 | 2 | 3 |
| 6 | -1.4 | 24.2 | 0.5 | 9.3 | 32.1 | 11.3 | 18.8 | 39.1 | 21.2 |
| 8 | 3.5 | 45.1 | 1.3 | 22 | 58.9 | 20.5 | 38.6 | 71.3 | 38 |
| 10 | 11.4 | 72.3 | 2.5 | 40 | 93.8 | 32.7 | 65.3 | 114 | 60 |
| 12 | 22 | 106 | 4.1 | 62.7 | 136.7 | 47.5 | 98.8 | 163.6 | 86.7 |

| Height (m) | Angle(°) | | | | | |
|---|---|---|---|---|---|---|
| | 55º | | | 60º | | |
| Example | 1 | 2 | 3 | 1 | 2 | 3 |
| 6 | 27.4 | 45.4 | 30.2 | 35 | 50.9 | 38.4 |
| 8 | 53.4 | 82.4 | 54 | 66.7 | 92.1 | 68.6 |
| 10 | 88.2 | 130.1 | 84.9 | 108.7 | 145.3 | 107.6 |
| 12 | 131.4 | 188.8 | 122.6 | 160.6 | 210.5 | 155.3 |

## Geomembrane Tensile Slope Stability Analysis

In this study, geomembrane was assumed to meet the stress-strain relationship of elastic material before reaching the tensile strength. Taking geomembrane allowing tension as the maximum tension, then the maximum tensile force $P_{max}$ of geomembrane on the slope of reservoir could be expressed by formula (2-1). In order to prevent a larger tensile deformation of geomembrane which could cause damage to the landfill anti-seepage engineering, the allowing tension of 30kN/m is adopted in this study (i.e., the tensile strength of HDPE membrane was 20MPa).

$$P_{t\max} = [P_t] + P_a \tag{2-1}$$

## Conclusions

(1) In the three kinds of working conditions, the anchoring force increased with the increasing section size of anchoring trench.

(2) In the same condition, anchorage force reached the maximum when the direction of the anchoring platform was horizontal.

(3) The friction angle had larger influence on the anchoring force than the cohesive force.

(4) Residual tension increased with the increase of the slope angle or the slope height. In the three kinds of working conditions, example 2 had the largest residual tension. When the slope height was over 6m, it should keep the slope angle within 45° to make the geomembrane stable.

## References

[1]Gabr MA, Valero S.N. *Geotechnical Testing Journal*. ASTM Vol. 18 (1995), p. 241-251

[2]Koerner R.M.: *Geotextiles and Geomembranes.* Vol. 10 (1991), p. 335-355

[3] David E.D: *Journal of Geotechnical and Geoenvironment Engineering*.Vol.124(1998),p.628–637

[4]Gilbert R.B, LONG J.H, DALY J.J.: Structural Integrity of Composite Geosynthetic Lining and Cover Systems. Geosynthetics'93 Conference Proceedings, Canada(1993), p.1389–1401

*Applied Mechanics and Materials Vols. 580-583 (2014) pp 148-151*
*© (2014) Trans Tech Publications, Switzerland*
*doi:10.4028/www.scientific.net/AMM.580-583.148*

# Study on Graphic Method for the Stability of High Loess Slopes Based on MATLAB

HU JIAN-Chun[1,a], GAO JIAN-Yong[2,b] and CHEN YAN-Xia[3,c]

[1]Engineering & Technology Department of Xichang College,Sichuan,China

[2]China Institute of Water Resources & Hydropower Research,Beijing,China

[3]China Institute of Water Resources & Hydropower Research,Beijing,China

[a]7346868@qq.com, [b] 21659747@qq.com, [c] 21087539@qq.com

**Keywords:** Water contents, Stability analysis, Graphic method, MATLAB,GUI.

**Abstract.** High loess slopes are easily unstable because of the water sensitivity of loess, therefore, the study on stability of high loess slopes is a very important task for water and soil conservation on loess plateau. Forcus on the inefficiency of current graphic method, after considering main influencing factors of stability of high loess slopes, such as lithology, topography, groundwater conditions, slope water content and seismic intensity, etc., on the basis of graphic method, an automatic table lookup program was developed, moreover, the interfaces of graphic method were compiled based on MATLAB platform, which could automatically generate plenty of obvious characteristics of slope data for further modeling.

## Introduction

Because loess has water sensitivity, high loess slopes tends to lose stability when they encounter water. Therefore, it is quite necessary to study stability of high loess slopes to reduce losses caused by landslide hazard. Generally, methods for stability analysis of loess slopes can be divided into qualitative analysis method, quantitative analysis method, uncertainty analysis method and intelligent analysis method [1]. In detail, because analysis charts about stability of slopes are easy to use and their results are visual, they are advocated by people being engaged in slope design and monitoring. In 1937, Taylor [2] put forward a stability chart for the first time. Later, Bishop and Morgenstern (1960) [3,4], Morgenstern(1963)[5] and Spencer(1967) [6] et al. designed various kinds of nomograph. In 1998, Jing Li and Xinhua Zhou et al.[7] improved Bishop method, considered main factors that affected high loess slopes simultaneously and designed an analysis chart related to stability of loess slopes. The chart solution is simple and direct, while its chart lookup efficiency is low. Thus, we need to improve the analysis chart about stability and develop an automatic chart lookup program to generate a number of slope data with obvious features. This seems to be quite necessary and is of practical significance. This thesis takes high slopes at tablelands on the left bank of Weihe River water transfer channel of Baiji Valley as an example and develops an automatic table lookup program on the basis of graphical method. Based on MATLAB platform, it generates a number of slope data with obvious features automatically, which provides data support for follow-up modeling.

## Research thought

The research thought is shown as follows. First of all, according to the feature that loess has water sensitivity, this thesis mainly considers the factor water content and obtains the relationship between cohesive force and internal friction angle as well as that between cohesive force and water content (i.e., $w \sim c$ and $w \sim \phi$) by experimental data fitting. Besides, it achieves the relationship between weight and water content according to empirical formula. Then, it takes high slopes at tablelands on the left bank of Weihe River water transfer channel of Baiji Valley as an example to determine data range of each impact factor (IF) and generate calculating parameters about slopes by random

assortment. Finally, it improves the graphical method, develops an automatic table lookup program according to calculating parameters about slopes, obtains safety factors via table lookup and gets safe states in accordance with specifications. In doing so, it obtains slope data for use of BP neural network modeling.

**Data acquisition**

**3.1 Impacts of water content on physical and mechanical parameters.**Impacts of water content on cohesive force are very obvious. According to researches implemented by Li Wang, Jinqian Dang[8] and Sen'an Zhang[9] et al., quantitative relational expression about cohesive force $c$ and water content $w$ is obtained.

$$\lg\left(\frac{c}{100}\right) = A - Bw \tag{1}$$

Where $c$ stands for cohesive force of soil body (kPa);

$w$ represents water content of soil body (%);

$A, B$ are parameters, whose values vary with changes in regions. According to average values of measured data about the three places including Qianyang, Binxian County and Baoji, their average is A=0.709 and B=0.044 [8], respectively.

Jinqian Dang et al. [10] carried out profound researches on water content and intensity parameters of Malan loess in Guanzhong area, Shaanxi Province. In accordance with experimental data fitting, they obtained the relational expression about the internal friction angle $\phi$ and the water content $w$, as shown in the following:

$$\phi = 24.3 - 0.1096w \tag{2}$$

The research shows that wet unit weight grows with increase in water content under the condition that dry unit weight is constant [8]. Average dry unit weight of loess is 15kN/m3 [11]. According to empirical formula, the relational expression about weight of soil body $\gamma$ and water content $w$ is shown as follows:

$$\gamma = 15(1 + w) \tag{3}$$

Where $\gamma$ and $w$ represent weight (kN/m$^3$) and water content (unit: 1) of loess.

**3.2 Value range of Ifs.** Analyses and selection of soil indicators are keys to analyses related to stability of high loess slopes. Researches indicate that stability of high loess slopes are mainly affected by seven factors including weight of soil body, cohesive force, internal friction angle, slope ratio, slope height, pore pressure and seismic intensity [12]. This thesis takes high slopes at tablelands on the left bank of Weihe River water transfer channel of Baiji Valley as an example and determines reasonable value range of each IF.

**3.2.1 Water content of high slopes' soil body.** In accordance with results of actual measurement on water content of high slopes' geological sections at Bapji Valley, water content of parts whose distance to the surface of slopes is 20-30m is 20%-26% generally. Rainfall and changes in surface water have significant impacts on water content of soil body. Specifically, if there is heavy rainfall a wet year appears, water content of soil body will be improved, the state that water content is saturate or partially saturate will appear and high slopes may be damaged. The value range of water content, which this thesis selects, is [15%, 28%], including the whole range of variation from unsaturation to saturation of soil body.

**3.2.2 Intensity index.** Thus, based on Formula (1) and Formula (3), we can confirm that range of cohesive force is [30 kPa,110 kPa] and weight is [17.28 kN/m3,19.20 kN/m3]. In addition, a relatively large range is set for internal friction angle, i.e., [22°, 30], in order that most values of internal friction angle about loess can be contained.

**3.2.3 Slope height.** The research finds that height of the high slope with the most serious destroy is 40- 73m [13]. Therefore, value range of high slopes, which is set in this thesis, is [30 m, 105 m].

**3.2.4 Slope ratio.** In consideration of abrupt slopes and steep slopes, gradient in this thesis is 15° $\varphi_f$ ≤m≤70°. Then, slope ratio is 0.4≤m≤3.7, where the slope ratio m=1/tan($\varphi_f$).

**3.2.5 Pore water pressure coefficient.** The research points out that underground water depth at edge of tablelands is between 30m and 60m [8]. It is assumed that underground water depth is 45m and pore water pressure in soil body is calculated according to hydrostatic pressure ($\gamma_u = -1$) and three situations about pore water pressure coefficient, i.e., $\gamma_u = 0$, $\gamma_u = 0.25$ and $\gamma_u = 0.5$. In this way, range of pore water pressure coefficient is confirmed to be {-1,0,0.25,0.5}.

**3.2.6 Seismic intensity.** This thesis confirms that value of seismic intensity is {0,7,8,9}, which equals earthquake magnitudes 0, 5.5, 6.0 and 6.5.

**3.2.7 Generate samples.** According to value range of each IF, $c$, $\phi$, m and slope height H are generated randomly. Meanwhile, $\gamma_u$, seismic intensity q and weight $\gamma$ are combined randomly. As a result, calculating parameters of slopes are obtained, and safety factors of slopes are got by table lookup.

**3.2.8 Conformation of safe state.** By consulting original Technical Summary about Weihe River Water Transfer Project of Baoji Valley, slopes are considered to be destroyed and stable when Fs<1.1 and Fs>1.1, respectively [14]. According to this, s safe state of slopes is confirmed (when they are stable, s=1; when they are destroyed; s=0). Accordingly, data about high loess slopes when changes in water content are considered are generated. Besides, it considers that generated data have consistency and satisfy requirements of follow-up BP neural network modeling.

## Analytical system by the graphical method

In accordance with the literature [8], the graphical method is remolded and the analytical system by the graphical method is developed. Fig. 1 shows the interface that appears after entering the system from menus in the main interface.

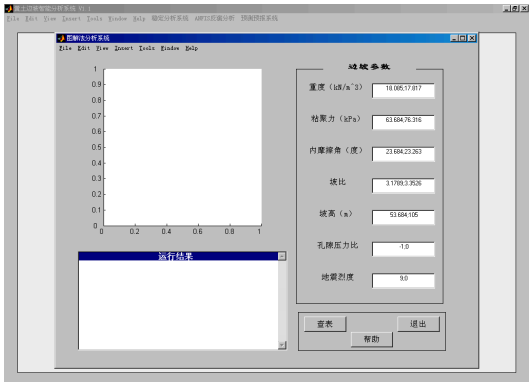

Fig. 1 Design about interface of the analytical system

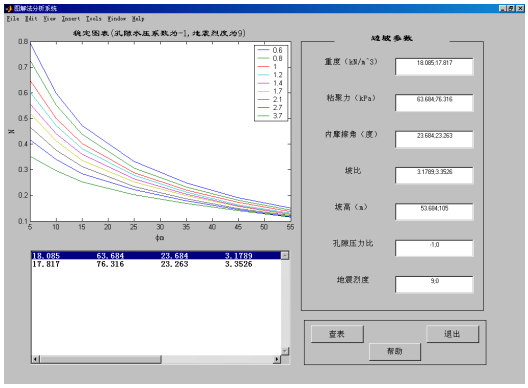

Fig. 2 Functional design of the analytical system

**4.1 Calculate safety factors by table lookup.** In the column of slope parameters, semicolons are used for partition. After each group of parameters has been input, values of each group of safe factors can be obtained by chart lookup function. Besides, each group of slope parameters and safety factors are shown in listbox at left bottom of the interface.

**4.2 Display functions of searched charts.** If we click any group of data in the listbox, the searched chart will appear in the plotting area. Besides, chart title will show corresponding values of the two parameters pore pressure ratio and seismic intensity. Additionally, abscissa $\phi_m = arctg(c/\gamma Htg\phi)$ and ordinate $N = \tan\phi / F$, as shown in Fig. 2, where the legend refers to slope ratio.

## Conclusion

This thesis takes high slopes at tablelands on the left bank of Weihe River water transfer channel of Baiji Valley as an example, regards water content as a main factor, extends functions of the graphical method based on MATLAB, improves the graphical method, develops an automatic table lookup program and generates data about high loess slope under the situation that changes in water content is considered. Such data have consistency and satisfy data requirements of BP neural network modeling.

## References

[1]Gao Jianyong. Intelligent analysis and prediction on high loess slope[D].Northwest A&F University: Northwest A&F University,2007

[2]Taylor, D.W. Stability of Earth Slopes[J]. Journal of Boston Society of Civil Engineers,1937,(24): 197-246.

[3]Bishop AW,Morgenstern NR. Stability coefficients for earth slopes[J]. Geotechnique,1960,10(4): 129-150.

[4]Bishop AW. The use of the slip circle in the stability analysis of slopes[J]. Geotechnique,1955,5(1):7-17.

[5]Morgenstern N. Stability charts for earth slopes during rapid rundown[J]. Geotechnique,1963,13(2): 121-131.

[6]Spencer EA. Method of analysis of the stability of embankments assuming parallel inter-slice force[J].Geotechnique, 1967,17(1):11-26.

[7]Li Jing,Zhou Xinhua,Dang Jinqian. Graphic method for the stability of loess slopes[J].Chinese Journal of Geotechnical Engineering,1998,20(4):40-43.

[8]Zhou Xinghua. Analysis of loess slope stability graphical method[D].Yanglin: Northwest A&F University: Northwest A&F University,1997

[9]Zhang Senan. Section of old loess (Q1) determination of engineering properties and nonlinear parameters of Jiuzhoutai Section[J].1994,(5):22-25.

[10]Dang Jinqian,Hao Yueqing. Effect of water content on the structure strength of loess[J]. Journal of Water Resources and Water Engineering,1998,9(2):15-19.

[11]Liu zudian.Loess Mechanics and Engineering[M].Xi'an: Shanxi science and technology Press,1997

[12]Gao Jianyong,Chen Yanxia,Dang Jinqian. Analysis of influencing the stability of loess slope norm based on Grey Relational Analysis[J].Yangtze River,2008,39(8): 81-83.

[13]Wang weisheng,Lei Xiangyi. Stability analysis of loess slope bases on neural network[J].Journal of Northwest University(Natural Science Edition) ,2001,31(3): 267-270.

[14]Chen Li. Analysis of distortion demolish occurred at high slope section of Baojixia canal al ong the plateau edge and design for slope cutting[J]. Journal of Shanxi Water Power,2001,17(1): 23-26.

*Applied Mechanics and Materials Vols. 580-583 (2014) pp 152-155*
*© (2014) Trans Tech Publications, Switzerland*
*doi:10.4028/www.scientific.net/AMM.580-583.152*

# Analysis about Stability of a Slope

Yajun Yin[1,a], Guanghan Xu[1,b], Yongmei Qian[1,c]

[1]Jilin Jianzhu University, Changchun, China

[a]1638715111@qq.com, [b]513917884@qq.com, [c]654675316@qq.com

**Keywords:** Slope; Stability; Analysis

**Abstract.** Based on the engineering geological conditions of an artificial slope is analyzed using a combination of numerical simulation, the slope ratio method and other methods, the slope stability was evaluated, It has a certain reference to artificial slope stability evaluation that similar to a combination of soil and rock.

## Introduction

The rear side of the new factory building form an L-shaped artificial slope after excavation, maximum slope height of nearly 22m, the length of nearly 300m, As the impact of the recent rain, the local section appears landslide phenomenon.

Original topography of slope area belongs to the hilly and alluvial plain border zone, currently, the plant has undergone significant changes in topography situation affected by pre-construction.

The study focused on the eastern side of the north-south direction of slope, slope length of about 145m, high maximum slope about 22m.To facilitate the study of the problem, according to the slope morphology of the slope, slope height, slope and material composition ,lithology characteristics, etc, the current slope is divided into three sections. Ⅰ area locates by the eastern side of north zone of slope along the SN trending, Ⅱ area for its southerly zone; southern slope of the EW trending is divided Ⅲ area.

District Ⅰ mainly soil slope, slope shape irregular, slope height and slope changes greater, lush vegetation on the slope; Ⅱ area covers with a thin layer of Quaternary on the slope, the highly weathered granite is exposed, the moderately weathered granite appears at the slope toe. Slope shape more complete, high slope greater maximum 22m, slope about 51 °;Ⅲ district slope is the recent formed by the artificial slope cutting, the highly weathered granite is exposed in the slope, smaller slope height, max 8.5m, an average slope is 38 °.

According to the classification principles of building slope engineering technical specification, Ⅰ area, Ⅱ district slope is secondary slope;Ⅲ district slope is three-level slope.

## the Stability Study of Slope

**Formation Lithology.** The main substance of slope is: (1) containing gravel silty clay, Quaternary eluvial, slope wash, plastic - hard plastic state; (2) strongly weathered granite; (3) moderately weathered granite.

**the Mode Research of Slope Instability.** Complexity, diversity, and environmental differences in the occurrence of rock structure, determine its modes are varied. The rock slope instability modes are summarized by the former as flat, circular, wedge, dumping, outburst and other forms. Therefore, study the stability of a slope, you first need to determine likely instability modes under certain geological conditions, on this basis, then for the unstable modes have been identified

through analysis of mathematical mechanics and test methods to determine the security situation of slope.

1. Ⅱ zone structure characteristics of slope rock mass

a. The rock mass weathering characteristics

Weathered rock is mainly affected by topography, lithology, structure, groundwater and other factors,Grading of the weathering degree of rock mass in the slope can be simply divided into strongly ~ moderately weathered, weathering forms are mainly dominated by area. As the top of the slope at the excavation of relatively shallow, thick Quaternary cover, under which is strongly weathered granite, rocks are weathered becoming gravel block whose color is dark brown,the trock mineral composition is difficult to distinguish, softer rock.

Excavation at the slope toe is the deepest, and appears massive rock, mineral composition is difficult to distinguish, relatively hard rock is characterized by medium weathered state, but the number of exposed scale is not big.

b. Structural characteristics of rock mass

Within the range of rock slope there is a series of internal discontinuities, the structural surface rock, mainly for construction joint surface and weathered surface fissures. Geological survey of surveying and mapping and the revelation through exploratory trench at slope toe, reflect the region densely jointed rock slope, poor integrity of the rock mass.

Strongly weathered granite is showed as crushing, structural surface is given priority to with weathering fracture, soft rock, rock is scattered structure, which belongs to the structure of the overall fragmentation.

Moderately weathered granite is hard rock, surface structure based mainly on construction joints, there are larger differences in the joints intensity, in the fractured parts of the joints, the rock is broken, showing cracked mosaic structure. Local joint fissure that was not developed assumes fractured block structure. Comprehensive evaluation, it generally belongs to cracked mosaic structure.

2. Ⅱdistrict jointed rock mass slope fracture development features

Site slope outcrop in poor condition, so dig the trench where the toe of the slope and the slope are, through artificial way to expose, and conduct a statistical work of joints.From the statistical results of joint fissures of slope rock mass, cracks in the direction of the N-W gives priority to, a few for east-west, inclination concentrated between 50°~ 70, is steeply dipping fractures.

3. Ⅱdistrict slope hydrogeological conditions

Nearby slope range groundwater is main types of bedrock fissure water (shallow weathered fissure water), aquifer for weathered granite, average water depth is 3.60m-8.50m, the water level elevation generally is 99.22m-111.79m. Groundwater recharge mainly depends on rainfall, drainage through underground runoff. There is relationship between groundwater flow and topography, flow direction from the terrain height to low-lying. Trench excavation of the site accumulated a certain amount of water, can consider to seep from the slope groundwater as part of the sources, which can be inferred from the bedrock groundwater water level line.

4. Ⅱarea slope instability mode

A large number of studies show that, similar to District II slope characteristics, the main consideration should be given to the slope in rock slope as the basic characteristics of the unstable mode.

As mentioned earlier, area II slope surface covered with residual thin sediment layer, the slope angle is 51 °, no deformation. But the slope toe outcropped granite, under the condition of slope toe was excavated two groups, affected by the failure phenomenon, the wedge sliding. affected by the

surface structure of the two groups, there has been sliding wedge failure phenomena. From the analysis of development characteristics of slope rock mass joint fissure, most joints fissure in NW-NNW direction, tendency of SW, it is the main control structure of causing planar sliding surface,meanwhile, this group fissure combines with joint fissure of another group nearly EW can cause sliding wedge.

**Stability Analysis of Slope.** 1. Slope stability analysis based on strength subtraction. Slope stability has been a hot research topic in the field of geotechnical engineering, people usually adopt safety coefficient method to evaluate the stability of the state. Its principle is simple, clear physical meaning, is still the most important indicators and concepts for the slope stability analysis. Strictly speaking, the safety factor is an evaluation index based on limit equilibrium analysis methods, numerical simulation is parallel with the limit equilibrium analysis methods, focusing on rock mass stress - strain that the analysis of failure mechanism. In the early days of slope stability analysis, which does not exist intersection points between the two. Strength reduction method based on numerical simulation technology changes this situation.

In the strength reduction method, safety factor of slope stability is defined as: While the slope just reaches the critical failure state, the degree reduce on rock soil shear strength, that safety factor is defined as ratio of the actual shear strength of rock soil and the shear strength after reduction when happens critical failure.Points of strength reduction method is using type 1, type 2 to adjust the strength indicators $c$ and $\phi$ of rock and soil ( in the type, $c_F$ is cohesive force after the reduction, $\phi_F$ is friction angle after the reduction, $F_{trial}$ is reduction factor), then make numerical analysis for the slope stability, continuously increase the reduction factor, calculate repeatedly, until it reaches the critical damage, the reduction factor is the factor of safety. The calculation formula is as follows:

$$c_F = c / F_{trial} \tag{1}$$

$$\phi_F = \tan^{-1}((\tan\phi) / F_{trial}) \tag{2}$$

In this slope, strongly weathered granite is considered as structure characteristics of cataclastic rock mass, moderately weathered granite is considered as the structure character of inlaid cataclastic rock mass. Integrating structural characteristics of rock mass, referring to successful cases at home and abroad other slope engineering, mechanics parameters of the slope granite are recommended as shown in table 1.

Table 1 Mechanical properties of granite indicators recommended values

| Project | The recommended value of strongly weathered granite | The recommended value of weathered granite |
|---|---|---|
| Natural density (KN/m3) | 23.3 | 25.5 |
| Shear wave velocity (m/s) | 587 | 1230 |
| The internal friction angle (degrees) | 32 | 40 |
| Cohesion (kPa) | 30 | 45 |
| Poisson's ratio | 0.36 | 0.25 |
| The softening coefficient | 0.56 | 0.87 |

This paper adopts the fast Lagrange difference algorithm, uses Mohr Kulun constitutive model, puts convergence in numerical calculation as a criterion of instability, to make calculation of fast Lagrange finite difference. The data as shown in table 2.

Table 2 Numerical calculation parameters of slope

| Strata \ Parameters | Density ρ(kg/m3) | Cohesion c（kPa） | The angle of internal friction Φ（°） |
|---|---|---|---|
| Residual gravel containing silty clay | 1960 | 22.3 | 14.5 |
| Strong weathered granite | 2300 | 30 | 32 |
| Moderately weathered granite | 2500 | 45 | 40 |

According to the calculation knows that the safety factor of slope is 2.25, the overall security is assured, however, in view of the analysis of eluvial soil at top of slope shows that there is a trend that soil displacement occurs. Calculations indicate that the plastic deformation occurs only in a shallow portion of soil distribution.

2. The slope ratio method. According to "technical code for building slope engineering" (GB 50330-2002)Chapter 12, when engineering conditions permit, should give priority to the slope ratio method for stability analysis.

The site survey results shows that, Ⅱ area upon slope is covered by a thin layer of clay, the rock in the slope is moderate weathering granite, the slope rock mass can be divided into class ii, put the slope covered with soil as loading into account, rock slope is height of about20m, according to Table 12.2.2, which allows the value of the slope ratio (aspect ratio) is 1:0.35 to 1:0.5, which allows a maximum slope angle should be 60 °, the actual average slope slope angle is 51, within the allowable range of the slope ratio. Even taking into account the unfavorable loading factors on the slope, the slope stability is also no problem.

## Conclusions

For the slope be given priority to with the soil and cataclastic rock slope, the rain wash out is not only the various influence on slope stability, but is very active. It turns out that most of the damage and the sliding of slope are concerned with the role of water. Waterproof slope is very important, the use of spray anchor bracing approach to security closure slope to prevent water entering, excluding the impact of water, is a good way to maintain slope stability.

The project involves the slope according to the morphological characteristics, lithology, rock mass structural features, such as rock engineering geological conditions and the distribution of positions, is divided into three different sections, respectively, according to the specific circumstances of different sections of the slope, using the corresponding appropriate analytical methods, its stability was evaluated.

## Reference

[1] Liu Tong, etc. Analysis and Prediction of Stability on Ancient Landslide Number Ⅷ Underground Reservoir at Xiaban, Xinjiang. [J], Journal of Engineering Geology, 2005.13.

[2] Yin Hongfeng, etc. Meigu Luo Cha Landslide Stability Analysis [J], Journal of Natural Disasters, 2007.12.

*Applied Mechanics and Materials Vols. 580-583 (2014) pp 156-159*
*© (2014) Trans Tech Publications, Switzerland*
*doi:10.4028/www.scientific.net/AMM.580-583.156*

# Analysis of Micro-seismic Monitoring Vibration on the Adjacent Buried Pipeline Affected by Impacting of Punching Pile Construction

Yanhua She

College of Urban Construction, Yangtze University, Jingzhou 434023 China

syh916@126.com

**Keywords:** punching pile construction; buried pipeline; micro-seismic monitoring; vibration control

**Abstract.** Impact loads caused by punching pile construction of highway bridges are bound to disturb stratum surrounding the buried pipeline adjacent to, which would adversely affect the normal use and safe operation of buried pipelines. Through developing field micro-seismic trial, the characteristics of vibration attenuation and sphere of influence were analyzed, in order to assess its impact on buried pipeline nearby. It drew conclusions that the amplitude of vibration energy had been enlarged with the presence of the pipeline; It should conduct the surface peak velocity above the pipeline as the main control index in routine vibration monitoring of pile foundation construction adjacent to buried pipeline; by positioning analysis of impacting vibration source, the rupture area of rock and soil around the pipeline caused by the vibration was determined, and security measures for pipeline protection was proposed. It provides a new method of control technology for pile foundation construction.

## Introduction

Pile foundation construction of highway bridge adjacent to pipeline once caused the leakage of natural gas pipeline, it would bring about serious social damage. Therefore, the influence of vibration caused by impact drilling construction of bridge pile foundation on buried pipeline must be carried on the safety monitoring and control effectively. The vibration produced by construction impact loads is extremely complex on the role and influence of pipe soil coupling. Both theoretical analysis and numerical calculation are considerable limitations. To explore other research methods, especially the field measurement method has been the goal of many researchers pursuing. This paper attempts to use HZ-MS48 microseismic signal data acquisition system to carry on the test, recording the transmitted signal of vibration wave propagation in rock and soil medium and analyzing attenuation characteristics and influence scope of vibration waves, in order to assess its impact on the adjacent buried pipeline. The research also is further exploration for the study on microseismic monitoring technology application in geotechnical engineering about pile construction vibration.

## Microseismic Monitoring Study

The researchers has been made a lot of achievements on the application of microseismic technique to different extent such as the oil and gas[1], mining[2-3], underground engineering [4], civil engineering[5] and so on. But many problems in theory research and application remain to be resolved.

To understand the effect of construction vibration on buried pipeline clearly, microseismic monitoring test was carried on the field. The test site located in Juma River No.8 bridge of Zhang jiakou to Shi jiazhuang expressway from Laiyuan to Laishui. Shaanxi-Beijing natural gas pipeline crossed the bridge between the fourth and fifth hole, with the nearest distance of 6.3m from pipe. Bridge pile foundation mainly adopted the impact drilling to construct.

**The Testing Arrangement.** The distance between the pipeline and impact pile hole center was 8.12m. Pipe buried 1m depth. Three measuring points were arranged along the pipe axis (x axis) and four measuring points were arranged along the pipe radial direction (y axis), where except 3# and 5# measuring points arranged on the pipeline, others assigned on the ground. The layout of three

component geophones were shown in Fig.1. Measuring point coordinates were shown in Tab.1. Microseismic monitoring on test was shown in Fig.2.

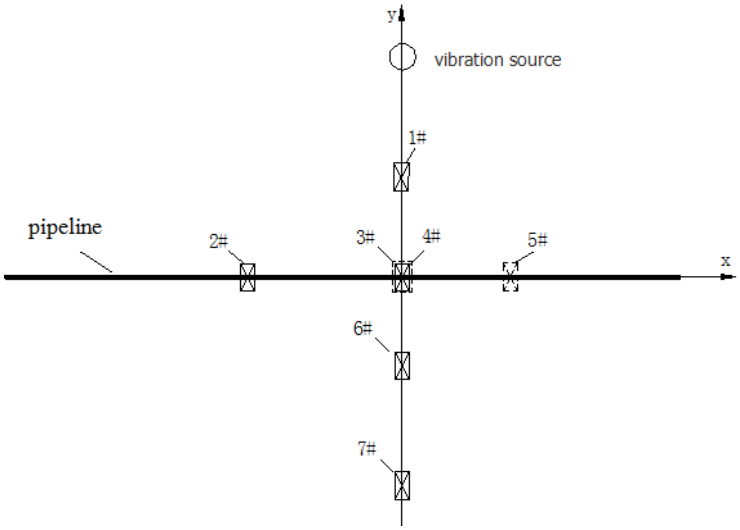


Fig.1 Layout of three component geophone

Tab.1 Coordinate of testing points

| measuring points | | 1# | 2# | 3# | 4# | 5# | 6# | 7# |
|---|---|---|---|---|---|---|---|---|
| coordinate (m) | x(East) | 0.00 | -4.18 | 0.00 | 0.00 | 2.09 | 0.00 | 0.00 |
| | y(North) | 2.00 | 0.00 | 0.00 | 0.00 | 0.00 | -2.00 | -6.05 |
| | z(Elevation) | 0.00 | 0.00 | 0.90 | 0.00 | 0.90 | 0.00 | 0.00 |
| remarks | | Test points 1,4,6,7 were used to analyze the vibration attenuation with distance; Test points 3,4 used to analyze the vibration velocity relationship between pipeline and ground; Test points 1,2,3,5 were used to analyze the impact vibration energy and vibration properties. | | | | | | |

(a) monitoring device (b) geophone embedding (c) data acquisition

Fig.2 Real-time monitoring by micro-seismic system

**Signal Acquisition.** The parameters of punching hammer were: weight m=5t ,bottom radius R=0.9m, punching depth from 0m to h=10m. When punching depth was 1.3m, the vibration source basically was at the same level of the pipeline, with vibration source coordinates (0,8.12,1.30). Microseismic events were collected at s=0.5m~2.5m for the stroke. By the field test and measurement, the typical microseismic events of points 1, 3, 4, 6 were shown in Fig.3 and Fig.4(n-horizontal radial, e-Horizontal tangential, v-vertical direction).

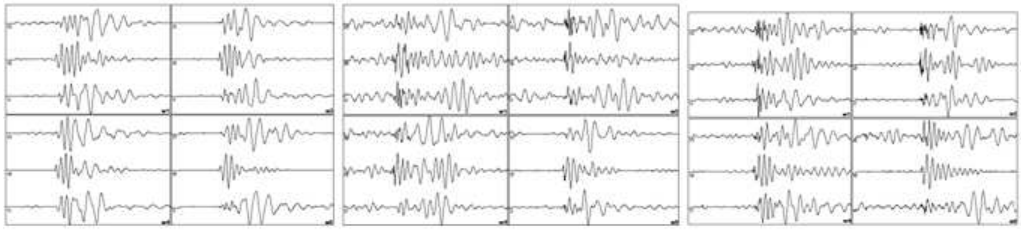


Fig.3 Three component velocity waveforms of microseismic events of different stroke

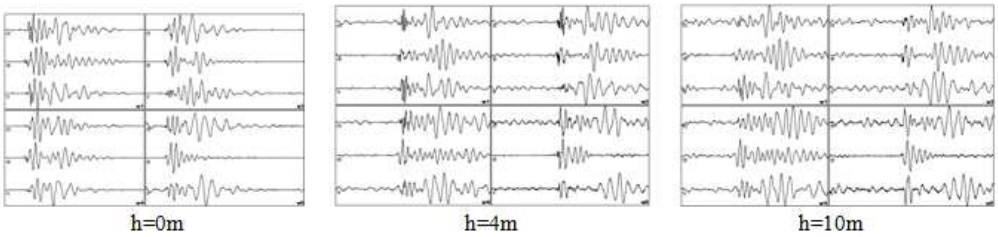


Fig.4 Typical velocity waveforms of microseismic events on different vibration source

## The Test Data Processing and Analysis

**Analysis of The Vibration Characteristics and Effect on Buried Pipeline.** The power spectral characteristics of typical microseismic signal were shown in Fig.5. From the figure, the energy of vibration wave focused on low frequency range of 10~50Hz. It had high signal-to-noise ratio and the vibration energy in other frequency bands was very small.

As shown in Fig.6, vibration velocity of testing points before and after buried pipeline decreased first and then increased, that was vibration energy had been enlarged because of the pipeline.

Considering the different impact source location, vibration velocity in three direction of measuring points was shown in Tab.2.

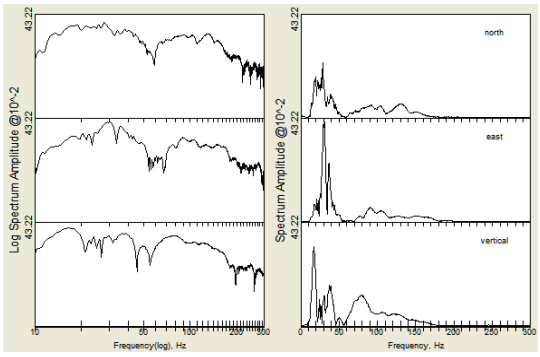


Fig.5 Spectrum analysis of typical microseismic signal

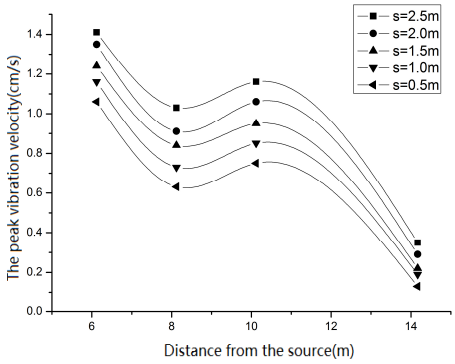


Fig.6 Curves of vibration velocity attenuation along horizontal distance

Tab.2 The peak vibration velocity of testing points on diffent vibrating source

| source position (m) | velocity of measuring point (cm/s) | | | | | |
|---|---|---|---|---|---|---|
| | 3#(on the pipe) | | | 4#( ground above the pipe) | | |
| | n | e | v | n | e | v |
| H=0.0 | 1.28 | 0.56 | 1.43 | 1.33 | 0.62 | 1.52 |
| H=1.3 | 1.56 | 0.73 | 1.41 | 1.24 | 0.58 | 1.48 |
| H=4.0 | 1.30 | 0.42 | 1.11 | 1.06 | 0.39 | 1.21 |
| H=8.0 | 0.92 | 0.25 | 0.74 | 0.63 | 0.18 | 0.85 |
| H=10.0 | 0.77 | 0.16 | 0.48 | 0.42 | 0.10 | 0.65 |

As shown in Tab.2, vertical vibration velocity on ground above the pipe was primary monitoring target, in the conventional vibration monitoring of pile foundation construction adjacent to buried pipeline. When the peak vibration velocity on ground being controlled, it can guarantee vibration velocity of the pipeline in the safe range. It also concluded that when the pile hole was close to buried pipeline, adopting manual excavation pile hole to the depth below the pipeline level can be adopted , in order to effectively reduce the pipeline vibration velocity and ensure the safe operation of the pipeline.

**Determine the Impact Rupture Zone.** Selecting microseismic events at 1, 2, 3, 5 measuring points, source localization analysis was be carried on. P wave arrival time picking of one microseismic event was as shown in Fig.7. The positioning results were as shown in Fig.8, with vibration position(0,8,1.5),which was in comparison with the actual.

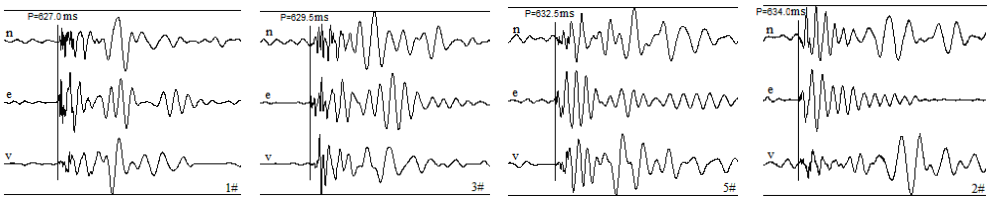


Fig.7 Picking out arriving time of P-wave

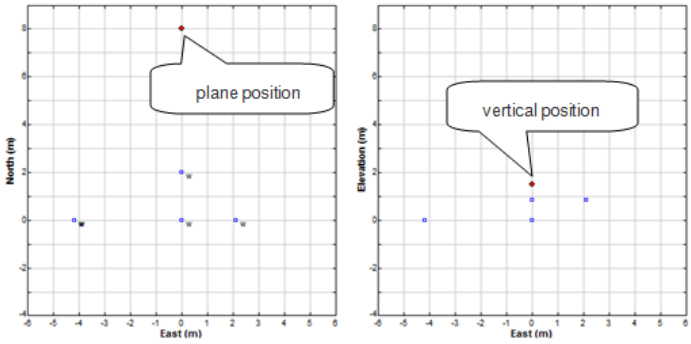


Fig.8 Location result of microseismic events

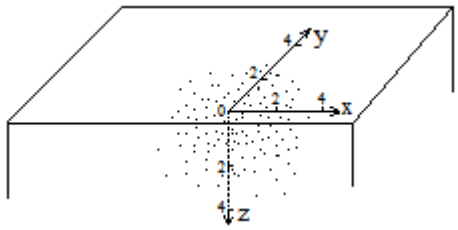


Fig.9 Failure region caused by vibration(unit：m)

Location analysis for all microseismic events can obtain the rupture area of rock and soil caused by vibration, approximately three times of hammer radius, as shown in Fig.9. Therefore, if the pipeline was located out of three times hammer radius (3R), it can guarantee the vibration caused by impacting construction producing no damage for rock soil around the pipe, so as to avoid the threat of pipeline safety.

## Conclusions

Vibration velocity of testing points before and after buried pipeline decreased first and then increased, that was vibration energy had been enlarged because of the pipeline. Vertical vibration velocity on ground above the pipe was primary monitoring target. When the peak vibration velocity on ground being controlled, it can guarantee vibration velocity of the pipeline in the safe range. Failure region of rock and soil caused by vibration was about 3 times of the hammer radius. Therefore, if the pipeline was located outside 3 times of the hammer radius, rock soil around pipe can be guaranteed no damage .It put forward a new method for researching the vibration caused by bridge pile foundation construction.

## Acknowledgements

This work is financially supported by Key Lab. for the Exploitation of Southwestern Resources & the Environmental Disaster Control Engineering, Ministry of Education Visiting Scholar Foundation of China (20091230).

## References

[1] Dong Shitai,Gao Hongxia: Petroleum Instruments.Vol.18(2004),P.5(in Chinese)

[2] Milev A M, Spottisswoode S M: Pure Appl. Geophys. Vol.159(2002),P165

[3] M.Cai, P.K.Kaiser:Tunneling and Underground Space Technology Vol.20(2005),P301

[4] Jiang Fuxing, Yang Shuhua, ChengYunhai, et al. Cinese Journal of Geophysics. Vol. 49(2006), P1511(in Chinese)

[5] She Yanhua, Su Huayou,Xiao Zhengxue:China Journal of Highway and Transport. Vol. 22(2009), P40(in Chinese)

*Applied Mechanics and Materials Vols. 580-583 (2014) pp 160-164*
*© (2014) Trans Tech Publications, Switzerland*
*doi:10.4028/www.scientific.net/AMM.580-583.160*

# Consolidation of Unsaturated Soils Due to Dissipation of Pore-air Pressure

XU Hao-feng[a], WANG Wen-jun[b], ZHA Zhi-xiang[c]

Ningbo Institute of Technology, Zhejiang University, Ningbo 315100, China

[a]xuhaofeng@nit.zju.edu.cn, [b]wwjcumt@nit.zju.edu.cn, [c]zhazx71@126.com

**Keywords:** unsaturated soils; consolidation; pore-air.

**Abstract.** One-dimensional consolidation equation of unsaturated soils was derived in order to solve this special case of consolidation. The presented equation, not similar to Terzaghi's equation, is a type of absolute nonlinear partial differential equation, and it was solved by finite difference method. An example was analyzed and the case of incompressible fluid consolidation was compared. Finally the experimental results from laboratory tests reported in the literature, was fitted by the presented equation, and the agreement was good. The results show that (1) the process of pore-air pressure dissipation is similar to that of pore-water pressure of saturated soils; (2) the compressibility of pore fluid is not an advantageous factor to quicken the consolidation; (3) the presented equation is effective to analyze the process of consolidation of unsaturated soils which consolidate mainly due to the dissipation of pore-air pressure.

## Introduction

According to existence style of air phase (or water phase), there are three types of unsaturated soils[1]. The first type of unsaturated soils is soils of which the degree of saturation is very high ($S_r$>85%) and the pore water contains air bubbles. The second type of unsaturated soils is soils where both air phase and water phase are continuous. The third one is soils that the air phase is continuous while the water phase is discontinuous and the degree of saturation is very low ($S_r$<40%). Because of the complexity of air phase, the consolidation of unsaturated soils is more difficult than saturated soils.

Studies on consolidation of unsaturated soils are often on the first and the second types[2-10]. And there are few researches about the third type of unsaturated soils. Only in Fredlund's monograph[11], the one dimensional consolidation equation of dry soils has been mentioned. It is necessary to research the consolidation of the third type of unsaturated soils. If the consolation rule of the third one could be understood, it would advantage the research on consolidation of the second type of unsaturated soils. It has been discovered that the consolidation process of the second type of unsaturated soils could be divided to two parts: the pressure of pore air has been dissipated firstly, and secondly it is followed by the dissipation of pore water pressure [12].

The consolidation caused by pore air would be different to the dissipation of pore water pressure of equation of saturated soils- Terzaghi's equation.

In this paper, the one dimensional consolidation equation of unsaturated soils due to dissipation of pore-air pressure is derived. Subsequently it is solved by finite difference method. And the characteristic of consolidation has been discussed. In addition, the experimental results from laboratory tests reported in the literature [13], is fitted by the presented equation.

## Organization of the Text One-dimensional consolidation equation due to dissipation of pore air pressure

Hypotheses are following: (1) only air can flow through the pore and the infiltration of pore water can be neglected; (2) pore air is perfect gas, and it is isothermal process; (3) both pore water and pore air would not transform to each other; (4) the deformation is small and the soil skeleton is linear elastic; (5) both soil grain and pore water are uncompressible; (6) soil is homogeneous, and the coefficient of

compressibility and the coefficient of infiltration of pore air are constant. Then the equations can be provided as following.

**Continuity equation of pore air.** According to the conservation of mass, the continuity equation of pore air can be expressed as

$$\frac{\partial(\rho_a n_a)}{\partial t} = \nabla \cdot (\rho_a v_a) + q \tag{1}$$

Where, $\rho_a$ is density of pore air (kg/m$^3$); $n_a$ is pore air porosity of soil $n_a=V_a/V$, ($V_a$, V are volume of pore air and soil respectively); $v_a$ is flow velocity of pore air (average velocity relative to the whole section)( m/s); q is the unit injection into the collection or the unit outflow from the source (kg/(m$^3$•s), if there is no collection or source, then q=0.

**Expression of pore air's density.** According to ideal gas equation, we can get

$$\rho_a = \frac{u_a \omega}{RT} \tag{2}$$

Where, $u_a$ is absolute pressure of gas (kPa); R is gas factor (J/(mol•K)); ω is molecular weight of gas (g/mol); T is absolute temperature (K).

**Equation of motion of pore air (Darcy's law).** Supposing gas seepage accords with Darcy's law, we can get

$$v_a = \frac{k}{\mu} grad(u_a) \tag{3}$$

Where, k is valid permeability of pore air in soil (m$^2$); μ is coefficient of viscous of gas (Pa•s).

**Formula of effective stress of pore air.** The formula of effective stress about pore air can be expressed as

$$\sigma = \sigma' + u'_a \tag{4}$$

Where, σ is the total stress on soils (kPa); σ′ is effective stress; u′$_a$ is excess pore air pressure.

**Relationship of stress and strain.** Supposing the volume of pore water is constant during the process of consolidation, we can get

$$\frac{\partial n_a}{\partial t} = \frac{\partial n}{\partial t} = -m_v \frac{\partial \sigma'}{\partial t} \tag{5}$$

Where, $m_v$ is the coefficient of volume compressibility of soil (kPa$^{-1}$); n is porosity of soil.

**One-dimensional equation of consolidation due to dissipation of pore air pressure.** Substituting these above expressions into the equation of continuity and supposing the total stress σ is constant, we can get

$$(n_a + m_v u_a)\frac{\partial u_a}{\partial t} = \frac{k}{\mu}[(\frac{\partial u_a}{\partial z})^2 + u_a \frac{\partial^2 u_a}{\partial z^2}] \tag{6}$$

The above expression is just the one-dimensional consolidation equation of unsaturated soils due to dissipation of pore air pressure.

## Solution for consolidation equation

**Analytic model of consolidation.** The thickness of soil stratum loaded by p is 2H, two sides are air permeable. The boundary condition is: if z=0 or z=2H, then $u_a=p_{atm}$ (t>0); if t=0, then $u_{a0}=p_{atm}+p_0$

(where is initial increment of pore air pressure). Because of the compressibility of pore air, $p_0$ is not equal to the load p. Supposing the instantaneous deformation is $\Delta h_{is}$ and the final deformation is $\Delta h$, $p_0$ can be defined as

$$p_0 = (1 - \frac{\Delta h_{is}}{\Delta h}) p \tag{7}$$

**Solution by finite difference method.** The style of consolidation equation is elegant, but it is not easy to be solved. In order to solve this whole nonlinear partial differential equation, the finite difference method is adopted in the paper. Supposing the space step length is $\Delta z$, the time step length is $\Delta t$, the number of time node is i (i=0,1,2,…), the number of space node is j (j=0,1,2,…,n), the equation can be transferred as

$$u_{ai+1,j} = \frac{k\Delta t}{\mu(n_a + m_v u_{ai,j})(\Delta z)^2}[(u_{ai,j+1} - u_{ai,j})^2 + u_{ai,j}(u_{ai,j+1} - 2u_{ai,j} + u_{ai,j-1})] + u_{ai,j} \tag{8}$$

Where, $\Delta z=2H/n$. And by analysis the increment of time $\Delta t$ can be gotten as

$$\Delta t = \frac{\mu(n_a + m_v u_{a0})(\Delta z)^2}{\chi k u_{a0}} \tag{9}$$

Where, coefficient $\chi$ is used to adjust the time step length in order to control the speed of convergent. The smaller the coefficient $\chi$ is, the fast the convergent is. However if the convergent is too fast, the analysis would not be stable. So the appropriate value of coefficient $\chi$ should be selected according to the fact.

The condition of certain solution can be transferred and expressed as: initial condition is $u_{a0,j}= p_{atm}+p_0$ (j=0,1,2,…,n); boundary condition is $u_{ai,0}= u_{ai,n}=p_{atm}$ (i=0,1,2,…), where $p_{atm}$ is atmosphere pressure (kPa).

## Example and discussion

**Example analysis.** Supposing the parameters for analysis in the soil stratum as following: $\mu=1.3\times10^{-8}$ kPa•s, $k=1.6\times10^{-12}m^2$, $n_a=0.5$, $m_v=2.0\times10^{-4}kPa^{-1}$, $p_{atm}=100kPa$, $u_{a0}=400kPa$, 2H=20m, $\Delta z=1m$, $\chi=2.8$, we can get $\Delta t=4.21s$. So the distribution of pore air pressure along depth with time can be analyzed, as shown in Fig.1.

It is obvious that the process of consolidation due to dissipation of pore air pressure can be simulated successfully by finite differential method.

**Comparison with consolidation of incompressible fluid.** If the pore fluid is incompressible, then the equation of consolidation can be derived as Eq.10.

$$\frac{\partial u_a}{\partial t} = \frac{k}{\mu m_a}\frac{\partial^2 u_a}{\partial z^2} \tag{10}$$

If the boundary condition and the initial condition are same, we can get the analytic solution of Eq.10 as Eq.11.

$$u_a(z,t) = p_0 \sum_{m=1}^{\infty} \frac{2}{M} \sin\frac{Mz}{H} e^{-M^2 T_v} + p_{atm} \tag{11}$$

Where,

$$M=(2m-1)\pi/2,\ T_v=\frac{kt}{\mu m_a H^2} \tag{12}$$

Then the process of consolidation due to compressible fluid can be compared with incompressible fluid. The results have been shown in Fig.2.

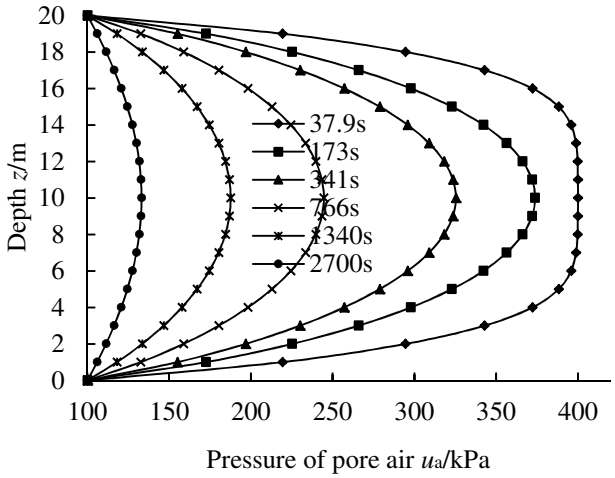


Fig. 1 Distribution of pore-air pressure along depth in different time

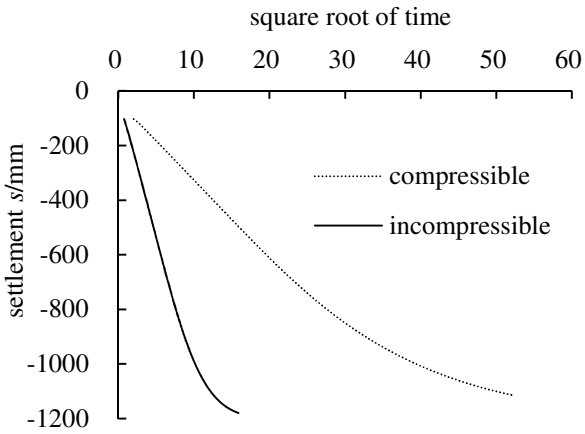


Fig. 2 Comparison of compressible and incompressible fluid's consolidation- Settlement versus time

From Fig.2, it can be concluded that the compressibility is not an advantageous factor to quicken the consolidation. As we all know, the instantaneous deformation would occur because of the compressibility of pore fluid. But the residual settlement would be finished slowly.

## Comparison with experimentation

There are trial datum of confined compression test in Shao et.al [13]'s research on remolding unsaturated loess. The parameters' values of soil are: $d_s$=2.7, $w_l$=30.6%, $w_p$=18.7%, w=14%, $\rho_d$=1.60g/cm$^3$, $S_r$=55%. Analyzing the typical deformation curve in that paper, the process of consolidation can be divided into two stages as shown in Fig.3. This viewpoint is also indicated by Ausilio, et.al.[12]

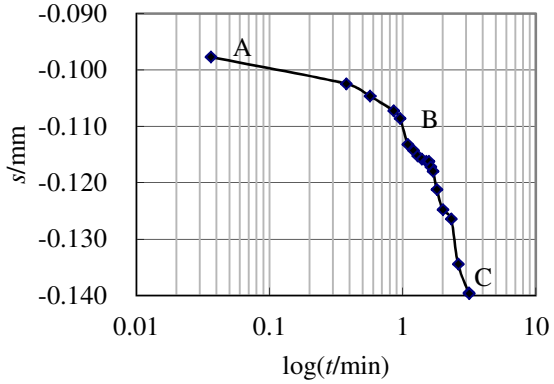


Fig. 3 The s-logt's curve in consolidation process of unsaturated soil

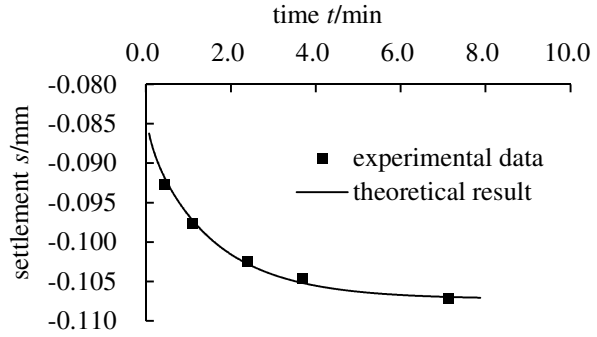


Fig.4 Comparison between experimental results and the numerical results of consolidation analysis by this study

The stage of AB in Fig.3 can be regarded as the stage of consolidation due to dissipation of pore air pressure. And according to the equation provided in the paper, comparison between the result of analysis and trial datum can be drawn as shown in Fig.4. The values of parameters for analysis are following: $\mu=1.3\times10^{-8}$kPa•s, $k=6.67\times10^{-18}$m$^2$, $n_a$=0.18, $m_v=3.5\times10^{-5}$kPa$^{-1}$, the initial settlement $s_0$=0.082mm, $\Delta z$=1mm, $\chi$=2.8, $\Delta t$=0.72s and the initial pore air pressure $u_{a1}$=182.6kPa, the pore air pressure in the end of stage AB $u_{a2}$=146.5kPa. And the height of soil is 2cm.

It can be seen from Fig.4 that the simulation is very perfect. And it indicates that the equation of consolidation for dissipation of pore air pressure can be used to analyze the first stage of consolidation of unsaturated soils.

## Conclusions

The consolidation of unsaturated soils can be divided into two stages. The equation which can describe the first stage of consolidation has been derived and founded in this paper. The conclusions are following:

(1) The equation is very different to Terzaghi' equation. It is a whole nonlinear partial differential equation.

(2) The characteristic of dissipation of pore air pressure in consolidation of unsaturated soils is similar to that of pore water pressure in saturated soils.

(3) The compressibility of pore fluid would slow down the consolidation.

The equation founded in the paper has been validated by the experimental results. And it is able to simulate the consolidation due to dissipation of pore air pressure.

## Acknowledgements

This work was financially supported by Ningbo Natural Science Foundation (2013A610202), the Zhejiang Natural Science Foundation (Y1111240) and the National Natural Science Foundation of China (51378469).

## References

[1] L. Barden: Geotechnique Vol. 3 (1965), p. 257
[2] M. A. Biot: Journal of Appolied PhysicsVol. 12 (1941), p. 155
[3] R. F. Scott: *Principles of soil mechanics* (Mass: Addison-Wesly Pub Company, Inc, 1963)
[4] C. S. Chang: International Journal for Numerical and Analytical Methods in Geomechanics Vol. 7 (1983), p. 39
[5] Daiquan Yang, Zhujiang Shen: Chinese Journal of Geotechnical Engineering Vol. 13 (1991), p. 70
[6] Zhenghan Chen，Dingyi Xie，Zudian Liu: Applied Mathematics and Mechanics Vol. 14 (1993), p. 127
[7] Haiyun Wei, Liangtong Zhan, Yunmin Chen: Chinese Journal of Geotechnical Engineering Vol. 28(2006), p. 264
[8] Zongze Yin, Hua Ling: Chinese Journal of Geotechnical Engineering Vol. 29 (2007), p. 633
[9] Z. Y. Ai, C. Wu, J. Han: International Journal of Engineering Science Vol. 46 (2008), p. 1111
[10] Z. Lou, C. H. Juang: Journal of GeoEngineering Vol. 7 (2012), p. 59
[11] D. G. Fredlund: *Soil mechanics for unsaturated soils* (Translator: Zhong-yi CHEN, et al: China Architecture & Building Press, Beijing 1997)
[12] E. Ausilio, E. Conte: *Remarks on consolidation in unsaturated soils from experimental results* (Springer-Verlag Berlin, Berlin 2005)
[13] Shengjun Shao, Ting Wang, Qinggao Yu: Chinese Journal of Geotechnical Engineering Vol. 31 (2009), p. 1037

*Applied Mechanics and Materials Vols. 580-583 (2014) pp 165-168*
*© (2014) Trans Tech Publications, Switzerland*
*doi:10.4028/www.scientific.net/AMM.580-583.165*

# Determine the Shear Strength of Aeolian Sand and Bearing Capacity

Yingzi Yin [1, a] , Yalei Wang [1,b]

[1]Architecture and civil engineering school , Inner Mongolia University Of Science & Technology, Baoyou 014010, China

[a]yinyingzi2005@126.com

[b]414287459@qq.com

**Key Words** : shear strength; cohesion; internal friction angle; bearing capacity

**Abstract**: In this article, through aeolian sand sample study in Inner Mongolia Baotou area, to determine the aeolian sand maximum dry density and optimum moisture content. On this basis, the aeolian sand cohesion and internal friction angle were measured by the quick direct shear test when aeolian sand was at the optimum moisture content and near the most largest compactness. And the bearing capacity of retaining wall model which regarded aeolian sand as fillers was determined. Then bearing capacity change of aeolian sand wrapped before and after was compared. Experimental results showed that: when the aeolian sand was in the wet and compacted state, its cohesion was 3.31 kPa and internal friction angle was 36.8°. The aeolian sand bearing capacity was 153.8kPa by the plate loading test. The aeolian sand wrapped with a geotextile bearing capacity was 194.1kPa. Through the aeolian sand research of Baotou area, it provides a useful reference for the construction of highway and railway and application of wrap-reinforced retaining wall which is a new retaining structure in the region, and the aeolian sand is treated as a special filling material in these structures.

## Introduction

In the vast desert areas in China, especially in the western arid regions, the natural environment is very harsh and the economy is backward. But there are abundant natural gas, oil, coal and other resources. In order to speed up the economic development of these areas，the research for construction of roads and railways in desert regions is an urgent demand. These areas lack of building materials, only aeolian sand can be provided. The bearing capacity of aeolian sand is small, and it is not easy to compact. In this paper, the shear strength and bearing capacity of aeolian sand in Baotou area were studied through experiment. The results show that the aeolian sand package can effectively improve the bearing capacity. This provides a reference for the railway and highway construction in desert areas and the application of wrap-reinforced retaining wall in this area.

## Shear strength of aeolian sand

2.1 *Experimental Procedure*

(1) Compacted the aeolian sand with standard heavy compaction test method, and we could obtain that the maximum dry density and optimum water content were respectively 1.576g/cm$^3$ and 17%.

(2) Added a certain amount of water into the Aeolian sand to adjust to the optimum water content and compact the sand. Taked the aeolian sand Sample with foil sample, the volume of foil sample was 60.351cm$^3$, the height was 2cm, A=30.16 cm$^2$, C=1.549kPa/0.01mm, and quick direct shear test was made.

(3) The experimental results are shown in table 1 below.

**Table 1 Test results of experimental**

| Vertical pressure (kPa) | 50 | 100 | 200 | 300 | 400 |
|---|---|---|---|---|---|
| Shears trength | 37.176 | 66.607 | 168.841 | 243.193 | 286.565 |

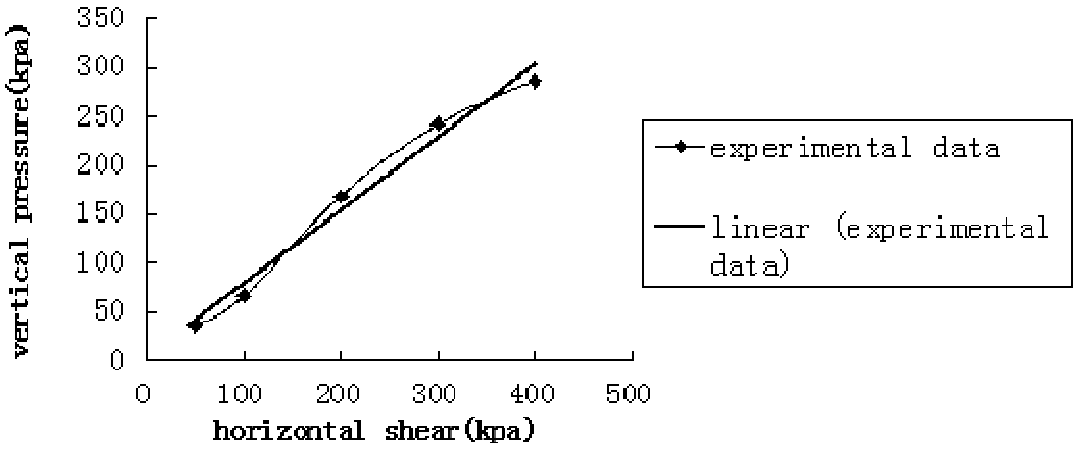


**Figure 1 The shear strength and vertical pressure relation curve of aeolian sand under wet condition**

2.2 *Analysis of experimental results*

It can be concluded from the test results that in the wet state, the cohesion c=3.31kPa, Internal friction angle is36.8° . In general, aeolian sand in natural condition has a very low moisture content, the cohesions is almost 0. The aeolian sand in optimum moisture content and compaction condition shows a false cohesive force phenomenon because of water.

## Bearing capacity of aeolian sand

3.1 *Model of package reinforced retaining wall*

As shown in Figure 2, the model is 150cm in height, 180cm in width, 200cm in length. According to the data of previous test about lay-down thickness on wet aeolian sand, Each layer of lay-down thickness is 40cm. Put the next layer after compaction, and each layer of eolian sand is usually set.

**Figure 2 Model of package reinforced retaining wall**

3.2 Measure the bearing capacity of the aeolian sand with plate load test

3.2.1 Experimental Procedure

(1) Spread the geotextile(5m in length, 1.8m in width) on the test ground, then mixed a certain amount of aeolian sand in accordance with the optimum water content(about 17%). Then put the sand on the geotextile. The range was 2m long, 1.8m wide. The lay-down thickness was 40cm.

(2) Compacted the aeolian sand uniformly with small ramming machine, made sure the compacting factor was greater than 0.96, then pack with the geotextile.
(3) According to the above method, and then put two layer and compact.
(4) Fixed a 500mm*500mm*20mm steel plate on the bottom of test case, and placed it in the middle of the aeolian sand, and fixed the four corners of the top surface of the wooden case with four pins. Recorded the height with level before loading.
(5) Each level was loaded in accordance with 25kPa. Observed a sedimentation of bearing plate with level. Took the load when l/b=0.01, namely, sedimentation was 5mm. The results were shown in Table 2. From the experimental data in the Table 3-1, it can be obtained that the bearing capacity of aeolian sand after packaging was 194.1kPa.

**Table 2 Aeolian sand packaged by geotextile at optimum moisture content and compaction degree was 0.96**

| load(kPa) | 25 | 50 | 75 | 100 | 125 | 150 | 175 | 200 | 225 |
|---|---|---|---|---|---|---|---|---|---|
| sedimentation (mm) | 0.07 | 0.17 | 0.29 | 0.47 | 0.97 | 2.22 | 3.87 | 5.35 | 6.7 |

The bearing capacity of aeolian sand before packaging could be measured by the above similar experimental procedure. The results were shown in Table 3. Took the load when l/b=0.01, namely, sedimentation was 5mm, and from the experimental data in the Table, it could be obtained that the bearing capacity of aeolian sand before packaging was 153.8kPa.

**Table 3 Aeolian sand with optimum moisture content and compaction degree was 0.96**

| Load(kPa) | 25 | 50 | 75 | 100 | 125 | 150 | 175 | 200 | 225 |
|---|---|---|---|---|---|---|---|---|---|
| Sedimentation (mm) | 0.25 | 0.5 | 0.55 | 1.38 | 3.7 | 4.58 | 5.80 | 6.73 | 7.7 |

3.3 *Comparison of aeolian sand's bearing capacity before and after packaging*
From the Table 3, it can be obtained that the bearing capacity of compact aeolian sand before packaging is 153.8kPa. From the Table2, it can be obtained that the bearing capacity of compact aeolian sand after packaging with geotextile is 194.1kPa. Obviously, the bearing capacity of aeolian sand after packaging is effectively improved. From the experimental data we can learn that the bearing capacity of aeolian sand after packaging increases by 26.2%. As the aeolian sand is packaged with geotextile, the aeolian sand is provided a lateral restraint force with the geotextile. Thus it obviously improves the bearing capacity of aeolian sand.

## Conclusion

This paper studies the aeolian sand by experiment in west area, Inner Mongolia. The results show that：
(1) It can be concluded from the test results that in the wet state the cohesion c=3.31kPa, and internal friction angle is $36.8^{\circ}$ for aeolian sand. The aeolian sand at optimum moisture content and compaction condition shows a false cohesive force phenomenon because of water.
(2)Measured the bearing capacity of the aeolian sand before and after packaging with plate load test. The result shows the bearing capacity of aeolian sand before packaging is 153.8kPa, the bearing capacity of aeolian sand after packaging is 194.1kPa. Obviously the bearing capacity of aeolian sand after packaging is effectively improved. The bearing capacity of aeolian sand after packaging increases by 26.2% compared with before.

**Reference**

[1] Zhang,Zhanzhi, Gong,Haike, Xie,Yongli, & Yang,Xiaohua.The engineering property of aeolian sand in Inner Mongolia[J]. Journal of Hebei University of Technology. 2006.35(3):112-117.

[2] Yuan, Yuqing, & Wang,Xuancang. Experimental research on compaction characteristics of aeolian sand [J]. Chinese Journal of Geotechnical Engineering [J].2007,29(3):360-365.

[3] Wu,Jinghai, Wang,Dequn, & Chen,Huan. Study on geosynthetic reinforced sand by triaxial compression test [J]. Chinese Journal of Geotechnical Engineering,2000,22(2):199-204.

[4] Sheng,Anlian. Highway design in desert region[M].Beijing: China Communications Press,1996.

[5] Huo,Yongcheng, & Xin,Shuzhen. Experimental research on compaction characteristics and bearing capacityof aeolian sand [J]. Railway Engineering,2007(9).

[6] You,Fuxiang. Determination of subgrade bearing capacity of aeolian sand[J].Coal Engineering,2008(8),

*Applied Mechanics and Materials Vols. 580-583 (2014) pp 169-174*
*© (2014) Trans Tech Publications, Switzerland*
*doi:10.4028/www.scientific.net/AMM.580-583.169*

# Dynamic Response of Two-dimensional Fluid-saturated Porous Beam

Fengxi Zhou [1,a], Qiang Ma [2,b]

[1] Western Engineering Research Center of Disaster Mitigation in Civil Engineering of Ministry of Education, Lanzhou University of Technology, Lanzhou, Gansu 730050, China

[2] School of Civil Engineering, Lanzhou University of Technology, Lanzhou, Gansu 730050, China

[a] zfx620@163.com, [b] maqiang0104@163.com

**Keywords:** Theory of saturated porous media, Two-dimensional beam, Dynamic response, Dynamic characteristics

**Abstract.** The dynamic response of the two dimensional fluid-saturated porous beam has been studied based on the linear elastic theory and the Biot's model for saturated porous media, in which the compressibility of solid particles and fluid and the viscosity of pore fluid are taken into account. By adopting Fourier series expansion and solving ordinary differential equations, the calculation formula for dynamic response of a two dimensional simply-supported fluid-saturated porous beam is established. The dynamic response characteristics of the forced vibration under uniformly distributed harmonic load are analyzed as a numerical example. Moreover, the solid displacement and pore fluid pressure of the two-dimensional fluid-saturated porous beam would be affected by the surface in filtration conditions, pore fluid permeability coefficient and loading frequency parameters etc.

## Introduction

Since Biot (1956) put forward the basic equations describing the dynamic characteristics of saturated porous media, many scholars have studied the problem of saturated porous medium dynamic from different aspects, including analytical studies of dynamic response of saturated porous media problems [1,2], numerical solution analysis [3,4] and wave propagation characteristics of saturated porous media analysis [5,6] and so on. The current research on the saturated porous media wave problems mainly focus on the geometric characteristics of geotechnical materials infinite half space domain or a layer of finite thickness, and on the research of all kinds of fluid saturated porous material fluid solid coupling dynamic static response is far behind the development of single-phase continuum elastic mechanics.

In terms of fluid saturated porous medium beam and rod structure, Li [7] application of Biot wave model has studied the vibration and quasi-static response of saturated porous elastic beam and rod in the case of liquid along the axial diffusion, pointed out that the phenomenon of Mandel-Cryer also exists in the porous elastic deformation response of beams and rods, and on this basis has studied the dynamic buckling of the porous elastic beam. Based on the three-dimensional equations of incompressible saturated porous media theory, Yang Xiao established the mathematical model of micro- incompressible saturated porous beam and rod linear deformation, using Laplace transform studied the quasi-static and dynamic bending at both ends of the permeable cantilever, and analytical studies the linear dynamic response of simply supported saturated porous elastic, for the analysis of the saturated porous elastic beam nonlinear bending problem. In addition, the saturated porous elastic beam non-linear bending problems were analyzed.

All above, simplified theoretical modeling analysis was adopted in the current research on fluid-saturated porous material of structure. However, studies showed that the mechanical quantity could not be polynomial along the thickness of coordinate variables. Given various simplified theories, only the partial fundamental equations could meet the required conditions and this error would increase with the increase of girder thick. Based on the Biot theory of porous media, the dynamic response governing equation of two dimensional fluid-saturated porous beam was established in this paper. The transient vibration response of simply supported fluid saturated porous beam was researched. Moreover, the influence on the solid displacement and pore fluid pressure of

the two-dimensional fluid-saturated porous beam was studied as different surface infiltration conditions, pore fluid permeability coefficients and loading frequency values.

## The Governing Equation of Fluid-saturated Porous Beam and Transient Response

**Basic Equation.** Based on the Biot theory of porous media, the basic equation of homogeneous saturated porous media was

$$\sigma_{ij} = \lambda\varepsilon_{kk}\delta_{ij} + 2\mu\varepsilon_{ij} - \alpha p\delta_{ij} b = 1/K_f \tag{1}$$

$$p = M\zeta - \alpha \mathrm{M}\varepsilon_{kk}\zeta = -w_{i,i} \tag{2}$$

$$\varepsilon_{ij} = \frac{1}{2}(u_{i,j} + u_{j,i}) \tag{3}$$

$$\sigma_{ij,j} = \rho\ddot{u}_i + \rho_f\ddot{w}_i \rho = (1-n)\rho_s + n\rho_f \tag{4}$$

$$-p_{,i} = \rho_f\ddot{u}_i + m\ddot{w}_i + b\dot{w}_i \tag{5}$$

The governing equation could be obtained from (1) to (5):

$$\mu\nabla^2 \mathrm{u} + (\lambda + \mu + \alpha^2 M)\mathrm{grad}e - \alpha M\mathrm{grad}\zeta = \rho\ddot{\mathrm{u}} + \rho_f\ddot{\mathrm{w}} \tag{6}$$

$$\mathrm{grad}(\alpha Me - M\zeta) = (\rho_f\ddot{\mathrm{u}} + m\ddot{\mathrm{w}}) + b\dot{\mathrm{w}} \tag{7}$$

In the above equations, $u$ and $w$ were the displacement vectors of the solid skeleton and pore fluid. $\zeta = -w_{i,i}$; $\varepsilon_{ij}$ was the strain vectors of the solid skeleton. $m = \rho_f / n$ ,where $n$ was the porosity of soil. $\rho_f$ was pore fluid pressure. $\mu$ and $\lambda$ were Lame constants of solid skeleton; $\rho$ was total density of the saturated soil and could be derived by $\rho = (1-n)\rho_s + n\rho_f$ ,where $\rho_s$ and $\rho_f$ were density of solid grains and pore fluid respectively. $b = 1/k_f$ , $k_f$ was the dynamic permeability. $\alpha$ and $M$ were the Biot parameters of the two-phase material compressibility. Moreover, $\alpha = 1 - K/K_s$ , $1/M = (\alpha - n)/K_s + n/K_f$ . $K$ , $K_s$ $K_f$ were the Bulk modulus of the solid skeleton, solid particles and pore fluid.

**Dynamic Models of Two Dimensional Simply Supported Beam.** The beam length and depth were denoted by *L* and *h* as shown in Fig. 1.

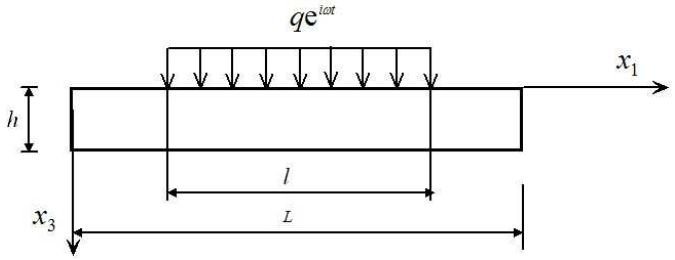


Fig. 1 Simply-supported two dimensional fluid-saturated porous beam

Eages of the beam were assumed to be simply supported as shown in formula (8)

$$\sigma_{11} = 0\ ,\quad u_3 = 0\ ,\quad w_3 = 0 \quad \text{at } x_1 = 0, L \tag{8}$$

This set of edge conditions was identically satisfied by setting

$$u_1 = \sum_{m=0}^{\infty} U_1(x_3)\cos\frac{m\pi x_1}{l}\mathrm{e}^{iwt}\ ,\quad w_1 = \sum_{m=0}^{\infty} W_1(x_3)\cos\frac{m\pi x_1}{l}\mathrm{e}^{iwt} \tag{9a}$$

$$u_3 = \sum_{m=0}^{\infty} U_3(x_3)\sin\frac{m\pi x_1}{l}\mathrm{e}^{iwt}\ ,\quad w_3 = \sum_{m=0}^{\infty} W_3(x_3)\sin\frac{m\pi x_1}{l}\mathrm{e}^{iwt} \tag{9b}$$

Substitute Eq.(9) into Eq.(6) and Eq.(7) and the matrix equation could be obtained:

$$\begin{bmatrix} \rho w^2-\mu\xi_1^2-(\lambda+\mu+\alpha^2M)\xi_1^2+\mu F^2 & \rho_f w^2-\alpha M\xi_1^2 & (\lambda+\mu+\alpha^2M)\xi_1 F & \alpha M\xi_1 F \\ \rho_f w^2-\alpha M\xi_1^2 & mw^2-ibw-M\xi_1^2 & \alpha M\xi_1 F & M\xi_1 F \\ -(\lambda+\mu+\alpha^2M)\xi_1 F & -\alpha M\xi_1 F & \rho w^2-\mu\xi_1^2+(\lambda+\mu+\alpha^2M)F^2+\mu F^2 & \rho_f w^2+\alpha MF^2 \\ -\alpha M\xi_1 F & -M\xi_1 F & \rho_f w^2+\alpha MF^2 & mw^2-ibw+MF^2 \end{bmatrix} \begin{bmatrix} P_1 \\ P_2 \\ P_3 \\ P_4 \end{bmatrix} = \begin{bmatrix} 0 \\ 0 \\ 0 \\ 0 \end{bmatrix} \tag{10}$$

Where $F = \mathrm{d}/\mathrm{d}x_3$ . The non-trivial solution of equation (10) yielded (11)

$$\begin{bmatrix} U_1 \\ W_1 \\ U_3 \\ W_3 \end{bmatrix} = \begin{bmatrix} h_i & h_1 & h_3h_4 & -h_3h_4 & h_5 & -h_5 \\ 1 & 1 & h_3 & -h_3 & h_6 & -h_6 \\ h_1h_2 & -h_1h_2 & h_4 & h_4 & h_7 & h_7 \\ h_2 & -h_2 & 1 & 1 & 1 & 1 \end{bmatrix} \begin{bmatrix} A\mathrm{e}^{r_1x_3} \\ K\mathrm{e}^{-r_1x_3} \\ B\mathrm{e}^{r_3x_3} \\ R\mathrm{e}^{-r_3x_3} \\ C\mathrm{e}^{r_5x_3} \\ S\mathrm{e}^{-r_5x_3} \end{bmatrix} \tag{11}$$

Where $A, K, B, R, C, S$ were six arbitrary constants. Using stress-displacement relationships the following expressions for stresses were obtained:

$$\begin{bmatrix} \sigma_{11} \\ \sigma_{33} \\ \sigma_{13} \\ p \end{bmatrix} = \begin{bmatrix} \sigma_{11}' \sin\xi_1 x_1 e^{iwt} \\ \sigma_{33}' \sin\xi_1 x_1 e^{iwt} \\ \sigma_{13}' \cos\xi_1 x_1 e^{iwt} \\ p' \sin\xi_1 x_1 e^{iwt} \end{bmatrix} \tag{12}$$

Where

$$\begin{bmatrix} \sigma_{11}' \\ \sigma_{33}' \\ \sigma_{13}' \\ p' \end{bmatrix} = \begin{bmatrix} g_1 & g_1 & g_2 & -g_2 & g_3 & -g_3 \\ g_4 & g_4 & g_5 & -g_5 & g_6 & -g_6 \\ g_7 & -g_7 & g_8 & g_8 & g_9 & g_9 \\ g_{10} & g_{10} & g_{11} & -g_{11} & g_{12} & -g_{12} \end{bmatrix} \begin{bmatrix} A\mathrm{e}^{r_1x_3} \\ K\mathrm{e}^{-r_1x_3} \\ B\mathrm{e}^{r_3x_3} \\ R\mathrm{e}^{-r_3x_3} \\ C\mathrm{e}^{r_5x_3} \\ S\mathrm{e}^{-r_5x_3} \end{bmatrix} \tag{13}$$

Take the local load by Fourier series expansion into the following form:

$$q_n = \begin{cases} \dfrac{l}{L}q & n=0 \\ \dfrac{2q}{n\pi}\sin(\dfrac{n\pi l}{L}) & n>0 \end{cases} \tag{14}$$

Therefore, according to the boundary conditions of upper and lower beam surfaces, Eq.(11) and Eq. (13) could determine the undetermined constants *A, K, B, R, C* and *S*, combined (9) and (11) - (14) could get dynamic response of displacement and stress under local load.

**Numerical Examples and Analysis**

In order to analyze the fluid saturated porous two-dimensional beam under dynamic load response, the physical and mechanical parameters of saturated porous materials were selected including $n$=0.19 $E = 1.44\times10^7\,\mathrm{pa}$ , $\nu = 0.2\,pu_3 f = 50Hz$ , $\rho_s = 2.458\mathrm{kg/m}^3$ , $\rho_f = 1.000\mathrm{kg/m}^3$ , $K_s = 3.6\times10^7\,\mathrm{pa}$ , $K_f = 3.3\times10^6\,\mathrm{pa}$ and $k_f = 1.9\times10^{-7}\,\mathrm{m}^4/\mathrm{kNs}$ .When dynamic load amplitude $q = 1000\mathrm{pa}$ , the changing curves of the beam middle pore fluid pressure $p$ and vertical displacement $u_3$ along the

beam height were analyzed at different load frequencies, permeability coefficients and harmonic load frequency of 5Hz，50Hz，100Hz，150Hz respectively. As can be seen from Fig. 2 and Fig.3, whether the upper and lower surfaces were permeable freely or completely not, the cross-section of the pore fluid pressure in the magnitude and vertical displacement would increase with load frequency rising, but the flooding conditions of the upper and lower surfaces had little effect on the vertical displacement of the solid skeleton in this paper.

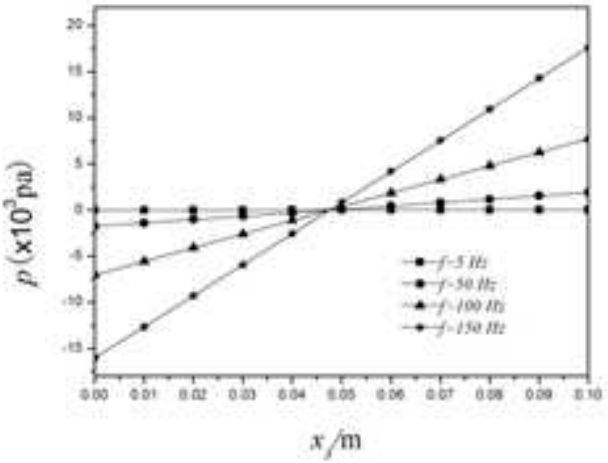


Fig. 2 The fluid pressure along the beam thickness varying with $f$ under free permeable condition

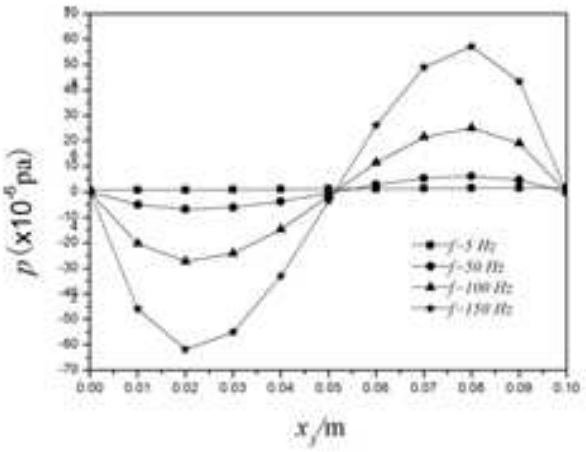


Fig. 3 The fluid pressure along the beam thickness varying with $f$ under impermeable condition

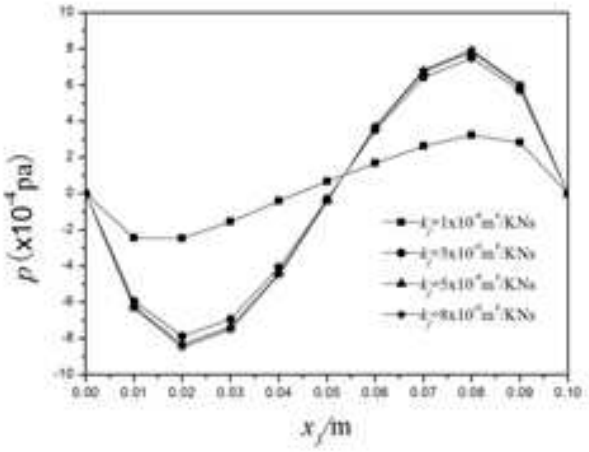


Fig. 4 The fluid pressure along the beam thickness varying with $k_f$ under free permeable condition

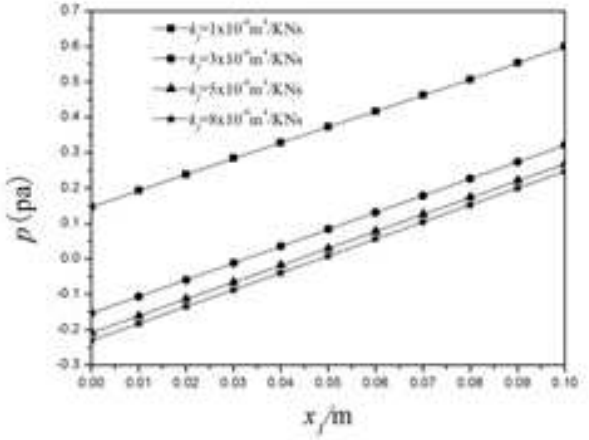


Fig. 5 The fluid pressure along the beam thickness varying with $k_f$ under free impermeable condition

In order to analyze the influence of dynamic response that permeability coefficient to fluid-saturated porous beam, Fig. 4 and Fig. 5 were plotted in the upper and lower surface of freedom permeable or completely impermeable the cross-section of the pore fluid pressure $p$ and vertical displacement $u_3$ along the curve beam height when load frequency was f=50Hz. As can be seen from the diagrams, the influence of fluid permeability coefficient and the permeable conditions of upper and lower surfaces on the fluid pressure was large, but little effect could be found on the vertical displacement of the solid skeleton.

## Conclusions

Based on the results obtained from the numerical example, the following conclusions could be drawn:

(1) In the role of local harmonic load, the cross-section of the pore fluid pressure in the magnitude and vertical displacement increases with load frequency increasing, but the flooding conditions of the upper and lower surfaces has little effect on the vertical displacement of the solid skeleton.

(2) Large influence of fluid permeability coefficient and the permeable conditions of the upper and lower surfaces could be found on the fluid pressure, but little on the vertical displacement of the solid skeleton. Moreover, the changes of both permeability coefficient and load frequency has little effect on the total stress components of the beam cross-section.

**Acknowledgements**

This work was supported by the Chinese Natural Science Foundation (Grant No.51368038), the Fund of Education Department of Gansu Province of China for Master's Tutor (1103-07) and the Fundamental Research Funds for the Gansu Universities (Grant No. 1104ZTC140).

**References**

[1] Gajo A, Mongiovi L.: *International Journal of Rock Mechanics and Mining Sciences and Geomechanics Abstracts*, Vol. 3 (1996), p. 399-413

[2] Yang X , Pan Y. : *Applied Mathematics and Mechanics*, Vol. 2 (2010), p. 193-204

[3] Zienkiewicz O C, Shiomi T. :*Int. J. Numer. Analyt. Methods Geomech*. Vol. 8 (1984), p. 71-96

[4] Fengxi Zhou, Yuanming Lai: *Chinese Journal of Theoretical and Applied Mechanics.* Vol. 44 (2012), p. 943-947 (In Chinese).

[5] De Boer R, Liu Z F.: *International Journal of Rock Mechanics and Mining Sciences and Geomechanics Abstracts*. Vol. 32 (1995), p. 378-378

[6] Polenov V S, Chigarev A V.: *Journal of Applied Mathematics and Mechanics*. Vol. 74 (2010), p. 198-203

[7] Li L P, Cederbaum G, Schulgasser K.: *International Journal of Solids and Structures*. Vol. 35 (1998), p. 4931-4943

*Applied Mechanics and Materials Vols. 580-583 (2014) pp 175-179*
*© (2014) Trans Tech Publications, Switzerland*
*doi:10.4028/www.scientific.net/AMM.580-583.175*

# Process Simulation and Formation Mechanism of Shear Band in Soil

SHIWEI HOU[1, a], JINHONG QU[2,b], YIFANG ZHANG[1,c] and XIULI DU[3,d]

[1] School of Civil Engineering, Shenyang Jianzhu University, Shenyang 110168, China

[2] Liaoning Electric Power Exploration and Design Institute, Shenyang 110179, China

[3] Key Laboratory of Urban Security and Disaster Engineering of Ministry of Education, Beijing University of Technology, Beijing 100124, China

[a]hsw1375@126.com, [b]qujinhong@lepdi.com.cn, [c]786898732@qq.com, [d]duxiuli@bjut.edu.cn

**Keywords:** shear band; strain energy; deformation process; formation mechanism

**Abstract.** Shape multiformity and formation mechanism of shear band in normal consolidated soil were analyzed based on Modified Cam-Clay model under plane strain condition. The results proved that shear band forms because of impact action caused by strain energy releasing. End restraint and initial defect can induce and control the formation process and shape of shear band. The interaction of different boundary and initial defect settings was analyzed in order to obtain the mechanism and deformation process of shear band.

## Introduction

Progressive development of shear band is a hot spot and a difficult point on geotechnical research. The formation mechanism of shear band is the research base on both soil body stability and progressive failure. The remarkable understanding to process of shear band would have great helpful to the civil engineering design and construction.

Numerical simulation can be used as methods of finite difference, finite element, discrete element method and so on. Zienkiewicz [1] first proposed the adptive mesh technique to refresh the finite mesh in order to satisfy the failure question. Belytschko et al [2] raised extended finite element thought and meshless method. Wang et al [3] used discrete element to research particle breakage under high pressure and plane strain conditions. Powrie et al [4] researched end friction of triaxial test by using particle flow method. Castelli et al [5] simulated the propagation law of shear band in defect material using boundary element method. Lu [6] came forward principal stress conditions of shear band process and failure under plane strain conditions.

Formation mechanism and development process of shear band under plane strain condition using modify cam model was analyzed in this paper. The results show that strain energy is the formation mechanism of shear band. The development process of shear band has the relationship with interaction of boundary and initial defect, local strains of different parts also have progressive order.

## Formation Mechanism of Shear Band

The soil parameters used in constitutive model was the same as parameters of Sam [7], in which $\alpha$=50kPa, $\beta$=1.0, M=1, $\lambda$=0.174, $\kappa$=0.026, $e_0$=0.889, $\mu$=0.28, k=25mm/s. Pore pressure element CPE8RP was used. Sample size was 50mm$\times$100mm, and was divided into 20$\times$40=800 elements. The simulation process was two steps, the cell pressure 100kPa was put in first step, strain controlled loading under unconstrained condition was put in second step. Top and bottom of sample were displacement boundary conditions, left and right boundaries were stress conditions. Fig.1 is the vertical log strain results of one defect element which location at top left corner of sample. The initial yield strength of defect element was 15kPa, while other elements were 50kPa [8].

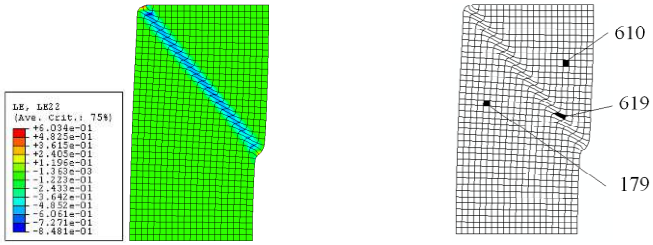


**Fig.1 Log strain result and location of representative elements**

The formation mechanism of shear band is analyzed using strain paths and deformation characters of elements in shear band and non shear band area. As fig.1 shows that the elements named 179, 610, 619 were selected to do comparative analysis. The effective stress paths of the three elements are showed in fig.2. The three stress paths are same before peak stress value, while the shear stresses are all decreasing after peak shear stress value. The average stress laws are different. The element 610 is above the shear band, the average effective stress is decreasing lightly after peak value. While the element 619 is in the shear band, the average effective stress is decreasing greatly after peak value. And the element 179 is below the shear band, the average effective stress is increasing after peak value. The analysis results of effective stress path show that the element porosity in shear band area is increasing, the bearing capacity decreased rapidly, the weak element that can endure deformation is formed. A series of continuous weak elements are formed in sample after peak shear stress, which offered conditions for formation of macro shear band.

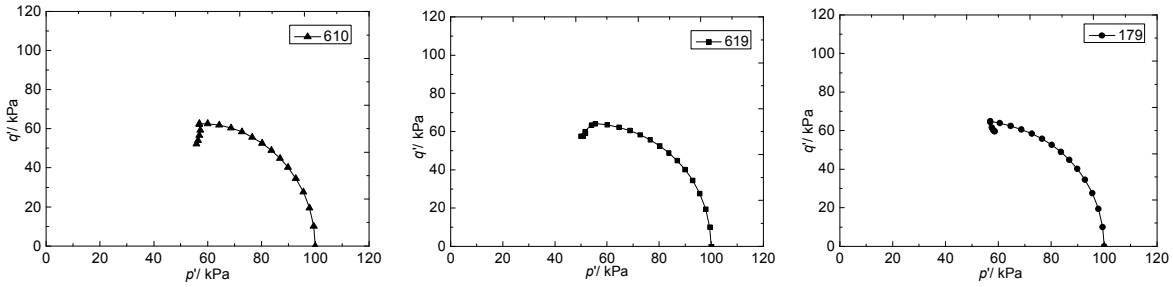


**Fig.2 Effective stress path of the representative elements**

The vertical stress-strain curves of the three representative elements are contrasted in fig.3. Element 610 and 619 are in the same vertical line. Element 179 and 619 are in the same horizontal line. Element 610 and 179 in non shear band area are in a state of unloading, while deformation of element 619 in shear band is increasing rapidly.

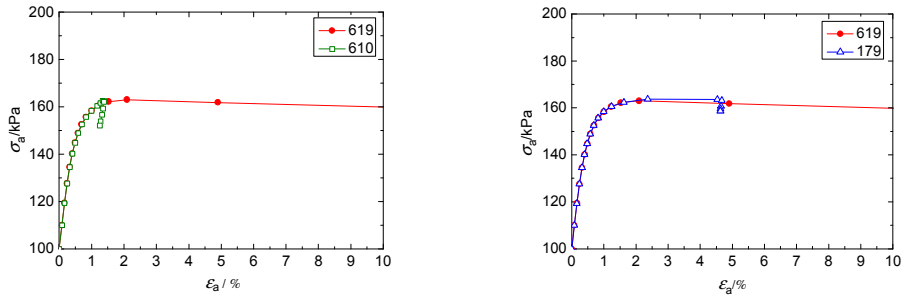


**Fig.3 Vertical stress and strain relationship of the representative elements**

The reason can be explained with strain energy mechanism. The internal strain energy of element is increasing to the maximum value during loading until the peak stress. Element 619 can not bear the strain energy because of porosity increasing and stiffness decreasing after peak stress. The released energy of 610 is put on 619 rapidly, which cause the deformation of 619 increasing rapidly. Then the macro shear band is formed. The element 610 is in a state of unloading because of energy releasing.

Table 1 shows strain change of the two representative elements in non shear band area. The relative response is the ratio between difference of peak strain and final strain and peak strain value.

The non shear band area has response phenomenon which means the area in a unloading state during the shear band development process. For this kind of single shear band as the element 179 and 610 results shows, the upper shear zone is given priority to vertical response, lower shear zone is given priority to level response. Just like the fault in geology, predominantly vertical response of the upper plate and predominantly level response of the lower plate interacts together, then releasing strain energy, the shear band of sample is formed followed the maximum shear stress surface.

**Table 1 Element strain in non shear band area**

| Element number | Strain type | Peak value time | Peak value strain | Final strain | Relative response |
|---|---|---|---|---|---|
| 179 | $\varepsilon_a$ | 500 | -0.04637 | -0.04558 | 1.7% |
| | $\varepsilon_r$ | 500 | 0.04674 | 0.04632 | 0.9% |
| 610 | $\varepsilon_a$ | 460 | -0.01591 | -0.01475 | 7.3% |
| | $\varepsilon_r$ | 460 | 0.01387 | 0.01248 | 10.0% |

In conclusion, the fundamental cause of formation of shear band is the releasing of elastic strain energy. Based on the MCC model, shear process is controlled by strain. The physical process of shear band formation is presented as follows. Defect element induces the inhomogeneous deformation, the element on some shear surface first reaches the shear strength and is unable to bear the loading, while elements in other area that do not reach the shear strength still can resist. To break this balance by keep loading, the results are strain response of element which does not reach the strength. The releasing elastic strain energy make the weak element which reaches the strength happen deformation. The response impact action is the reason that loading decreasing and deformation increasing at the same time, then continuous and macro shear band is formed.

## Formation Process of Shear Band

The formation process of shear band is complicate and effected by boundary conditions. For the same initial defect and different boundary displacement condition, the formation processes of shear band are completely different.

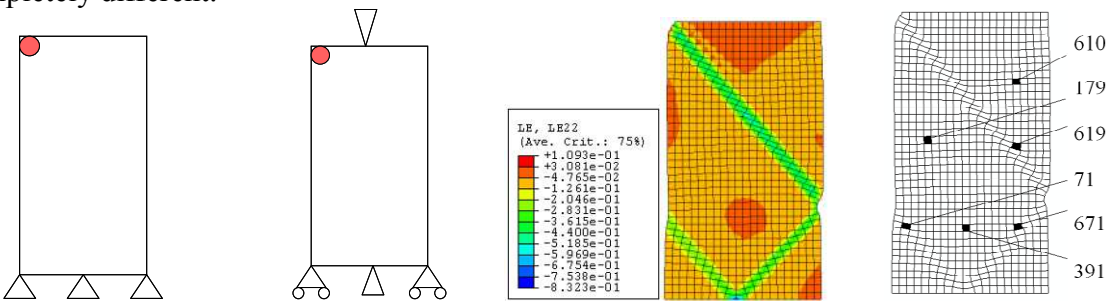


**(a) Boundary condition 1 (b) Boundary condition 2 (c) Strain nephogram (d) Responsible element location**

**Fig.4 Boundary conditions and results**

Take the conditions in fig.4 (a) (b) as an example, the formation process of shear band is researched. They have the same final type of shear band as fig.4 (c) shows. The location of representative elements is showed in fig.4 (d).

Fig.5 is the stress relationship under interaction of boundary condition 1 and 2. Six representative time points for each condition are selected to explain the deformation process of shear band, the corresponding vertical strain nephograms are presented in fig. 6. Shear stresses are both have softening phenomenon for the two conditions. For the condition 1, the interaction of fully end friction and initial defect is clearly effect the strain localization as the strain nephograms of point 1 and 2 shows. The strain localization area is cross, but initial defect win the competition in the end. For the condition 2, top displacement boundary is not strong enough to compete with initial defect, so the shear band is single section mainly controlled by defect. After the stress peak value, the types of shear band are same as strain nephogram of point 5 and 6 shows.

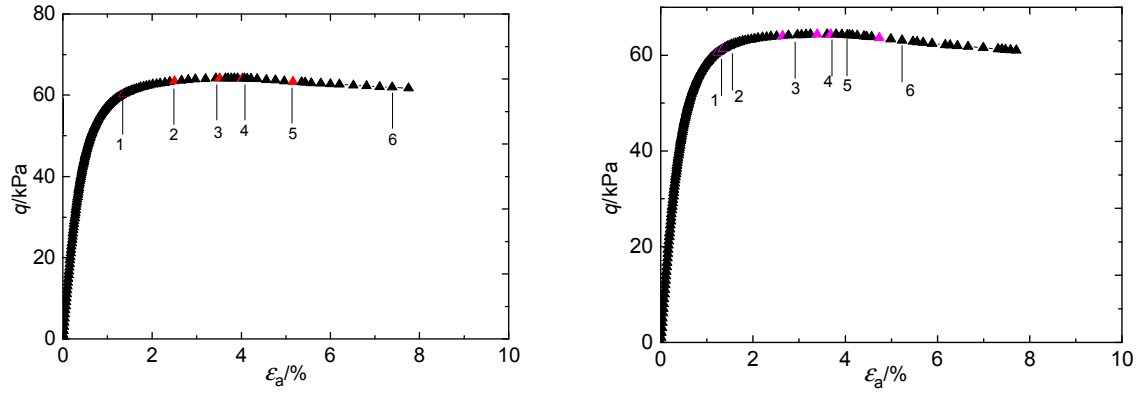


(a) Boundary condition 1 (b) Boundary condition 2

**Fig.5 Stress relationship under interaction of boundary condition 1 and 2**

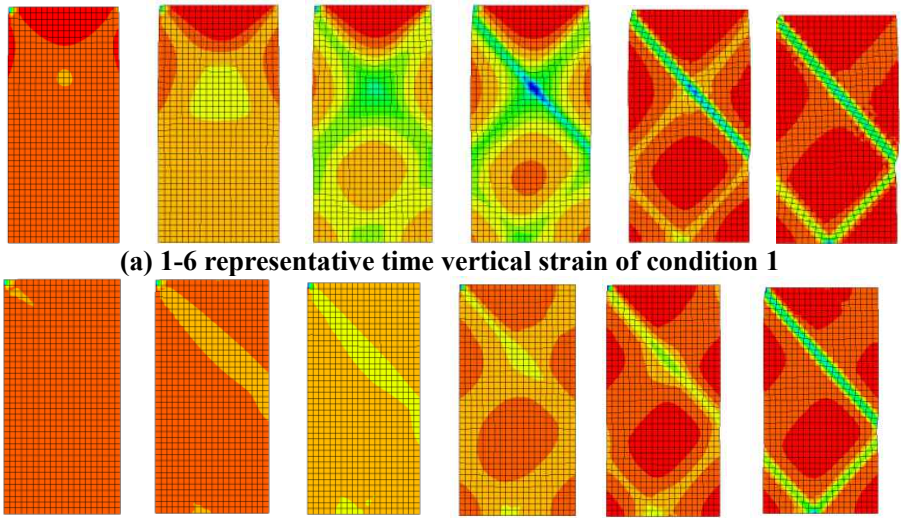

(a) 1-6 representative time vertical strain of condition 1

(b) 1-6 representative time vertical strain of condition 2

**Fig.6 Formation progress under interaction of boundary condition 1 and 2**

Representative elements 179,391,610,619,671,716 in fig. 4 (d) are used to analyze the process of shear band. The elements 619,671,71 are in the three section shear band respectively. Fig.7 is the strain curve with time of the representative elements. It can be seen that strains of 619, 671 and 71 are increasing at different time which means that the different section of shear band has order to develop. The conclusion is match with the strain results and also shows the formation process of shear band.

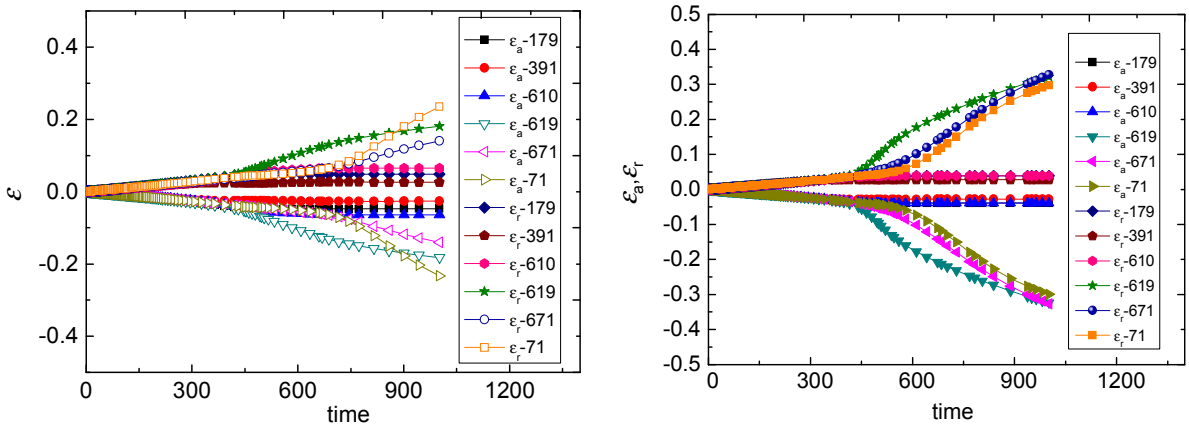


(a) Boundary condition 1 (b) Boundary condition 2

**Fig.7 Strain and stress of the representative elements**

## Conclusions

Formation mechanism and development process of shear band under plane strain condition were researched using numerical simulation method.

The fundamental cause of formation mechanism of shear band is the releasing of elastic strain energy. The response impact action is the reason that loading decreasing and deformation increasing at the same time, then continuous and macro shear band is formed.

The formation process of shear band is complicate and effect by boundary conditions. For the same initial defect and different boundary displacement condition, the formation process of shear band are completely different and effect by competition and interaction of boundary and initial defect, local strains of different parts also have different progressive orders.

## Acknowledgements

This work was financially supported by the National Natural Science Foundation of China (51308355) and opening project of the Key Laboratory of Urban Security and Disaster Engineering of Ministry of Education, Beijing University of Technology.

## References

[1] O C Zienkiewicz, M S Huang, M Pastor. Int. J. Numer. Anal. Meth Geomech, Vol. 19(1995), p.127

[2] T Belytschko, T Black. Int. J. Numer. Meth Engng, Vol. 45(1999), p.601

[3] J F Wang, H B Yan. Procedia Engineering, Vol. 14(2011), p.1713

[4] W Powrie, Q Ni, R M Harkness, et al. Geotechnique, Vol. 55(2005), p. 297

[5] M Castelli, A Allodi, C Scavia. Int. J. Numer. Anal. Meth Geomech, Vol. 33(2009), p.1561

[6] D C Lu, Y P Yao, A N Zhou. Chinese Journal of Rock Mechanics and Engineering, Vol. 25(2006), p.2320, in Chinese

[7] H Sam. *Applied soil mechanics with ABAQUS applications*. (John Wiley & Sons, Inc, USA 2007)

[8] X L Du, S W Hou, D C Lu, et al. Rock and Soil Mechanics, Vol. 33(2012), p.1281, in Chinese

*Applied Mechanics and Materials Vols. 580-583 (2014) pp 180-184*
*© (2014) Trans Tech Publications, Switzerland*
*doi:10.4028/www.scientific.net/AMM.580-583.180*

# Research of the Shear Strength Test of the Soil on the Surface of Lop Nor Gobi

Liang Yin[1, a*], Shi Qiu[1,b], Wenjie Li [2,c], Hao Hu[1,d] and ZHongkai CHen[1]

[1]Northwest Institute of Nuclear Technology, Xi'An, Shanxi, 710024, China

[2]Academy of Equipment Command & Technology, Beijing, 102249, China

[a]yinliang12@nudt.edu.cn, [b]qiushiln@sohu.com, [c]cfanlwj@sohu.com, [d]hhlyx@sohu.com, [e]chzhk@mail.ustc.edu.cn

**Keywords:** Lop Nor, gravelly gobi, surface soil, shear strength, in-situ shear test

**Abstract.** By applying the self-made field in-situ direct shear equipment, it makes a series of in-situ direct shear test researches on the soil （＜10cm）on the surface of the gravelly gobi in Lop Nor, Xinjiang, achieving its shear strength parameter. The conclusion that this paper gets not only provides the key parameters needed for the design of the gobi surface soil collection machine and the relevant assessment experiments, but also offers the reference for evaluating the similar soil shear strength of the gobi engineering construction.

## Introduction

According to the regional development plan, it intends to apply the milling collection machine to collect a certain thick surface soil from the region of Lop Nor gobi. In this field, the design and calculation of the milling collection machine are of great importance. Firstly, it must know the material indexes of the research object such as the shear strength parameter of the surface soil to be collected.

Based on the current literature[1] released, there is few research about the characteristics of Lop Nor gobi. Also, the cognition on the characteristic of the physical parameter of the soil is limited. Most of soil parameters are not well determined. Even, some parameters are unknown. The soil in the region of Lop Nor gobi is generally the gravelly soil with quite poor viscosity. So, it is very hard to obtain the undisturbed sample of the soil for the laboratory test according to the demand. The test result also has quite great limitation. The regular height of the strain-controlled direct shear apparatus is only 20mm, which cannot be taken for the test on the gravelly soil sample[2]. Thus, considering the current situation of the shortage of the research on the characteristics of the surface gravelly soil in the gobi region, this paper, on the basis of Mohr-Coulomb principle, measures the shear strength parameters of the surface soil with a certain thickness with the self-made field in-situ direct shear apparatus, to provide the reference for the design of the milling collection machine and calculation.

## Introduction of Components of Gobi Soil in the Research Area

Due to the long synthetic effects of the wind transport, freeze-thaw cycle, hydration-dehydration cycle and the crystallization & dissolution of the salt, the surface gobi soil in the research zone is mostly covered by the gravel, which is called gravel screen. Its particle is quite even. The material source is the broken objects of the mountain through the weathering. The substance components are basically same. With regard to the lithology, most are quartzite, granite and sandstone. According to the atomic absorption spectrometry analysis, its chemical components are listed in the table 1.

Table 1 Main chemical components of the gobi soil in Lop Nor region

| SiO2 | Al2O3 | Fe2O3 | CaO | MgO |
|---|---|---|---|---|
| 59.59% | 10.64% | 2.48% | 13.71% | 1.76% |

Through the analysis on the screen experiment of the particles sampled from the soil, the particle grading of the soil is measured and tested. From it, it can be seen that the surface soil is generally composed of lots of gravels and sands. The grading is not good (Cu=20~25). Also, it contains a small quantity of argillaceous interstitial matrix, of which the content of the gravel（＞2.0mm）is about 30%~50% and the content of the sand with the coarse sand (1~0.25mm) is about 47%~68%. The content of the silt and the argillaceous matrix is less than 5% of the overall contents, evenly spreading between the sand and gravel. The gobi particle grading of the research zone is shown in fig.1.

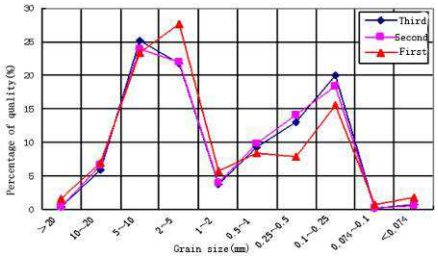


Fig.1 Particle grading curve of the gobi sol in Lop Nor region

## Content and Method of the Test

### Design of Field In-situ Direct Shear Apparatus[3]

The in-situ shear test is a kind of test method to measure the gobi gravel soil shear strength (cohesion C and internal friction angle Φ) value. This method takes into account the influence of the structural plane of the sand. The test result is quite consistent with the actual situation.

The in-situ direct shear test belongs to the on-site quick shear test. Because the regular field direct shear apparatus cannot meet the demand of the test on the shear strength characteristics of the gobi gravelly surface soil, the author makes a set of field in-situ direct apparatus by himself to conduct a series of tests on the gobi surface soil in the Lop Nor region, as shown in Fig.2.

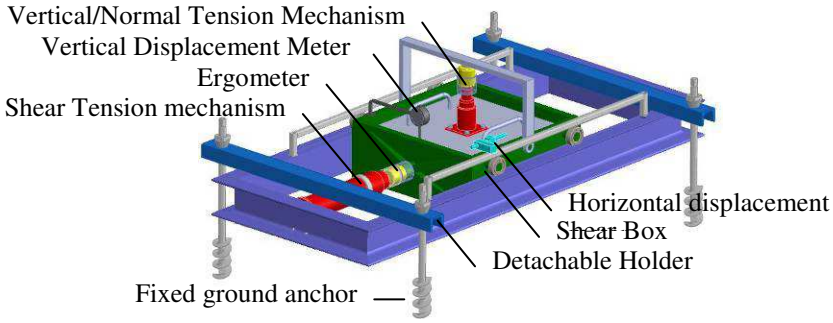


Fig.2 Field In-situ Direct Shear Apparatus Design Model

The field in-situ direct shear apparatus is designed based on the principle of the stain-controlled direct shear apparatus. This apparatus has the structure in split mounting type, chiefly consisting of the detachable outside frame, shear transmission mechanism, vertical tension mechanism and shear box as well as measurement system. Through adding a certain vertical load and horizontal shear force on the gobi sand soil, the shear plane of the sample determined is broken and then the shear stress of the sample is recorded. The sand sample is obtained in the way of pressing the shear box into the soil. According to the regulation of GB/T 50123-1999 Soil Test Method Standard, to measure the strength index of the coarse-grained soil, the specification of the shear box can be generally computed in accordance with the formula (1).

$$\frac{D}{d_{\max}} \geq 8 \sim 12, \quad \frac{H}{d_{\max}} \geq 4 \sim 8 \tag{1}$$

In the formula, d max refers to the largest size of the sand particle(mm); D is the diameter of the sample(mm) and H is the sample height(mm).

According to the sampling analysis of gobi gravelly soil in the Lop Nor region, the largest particle size of the soil collected should be Φ2.5cm. Through the calculation, the size range of the shear box is

D≥20～30cm and H≥10～20cm. The design of the shear box is square. The square shear box has the high stiffness and highly accurate measurement with the convenient installation of the measurement instruments while it stands the shear stress. Hence, while the round shear box is equivalent to the square one, the size of its section ranges from L≥17.7～26.6cm.

The performance indexes of the field in-situ direct shear apparatus design are that the clearance area of the shear box is 1000cm$^2$(preparation) and the vertical pressure is 30kN as well as the horizontal thrust is 40kN. It all takes the jack for loading. Four~six helical vane fixed steel chisels fix the outside frame. Compared with the regular direct shear apparatus, it is more suitable for measuring the shear strength of the coarse particle material such as the sand and gravelly soil.

**Test Method**

Based on the principle that the test point must be representative and easy to guarantee, it selects three sample zones to carry out the test of the gobi surface soil shear strength parameter measurement. The depths of three soils tested are respectively 2cm, 5cm and 10cm. For each depth, 4 samples are prepared. It is actually an unconsolidated and undrained quick shear test.

Fig.3 Field In-situ Direct Shear Test Site

After the test zone is selected on site, the contour with the area of 1000m2 is marked on the earth’s surface. Meanwhile, the rock and earth mass outside the line is dug to the deep layer needed for the test and then the shear box covers on the prepared sample. The fine sand is used to fill the gap between the shear box and the soil sheared. Next, the equipments (fig.3) including the force transferring rectangular tube columns, jack, ergometer, compression frame and the fixed steel chisel are installed in proper order. When the test holder is installed, it applies the flat-pushing way to implement the shear test. The normal stress gradually increases by using 30kN jack according to the preset values of 25kPa, 50kPa, 100kPa and 200kPa. In the pressure increase course, the normal stress doesn’t change. Besides, the action point of the normal stress and the shear stress goes through the center of the sample. The horizontal shear stress is added by using 40kN jack from 8th to 10th grade. The shear stress loading rate takes the time as the control factor. The rate should be controlled within 3mm/min. Each 1min, it is read. And then, it carries out shearing till the sample is broken or cut. While the shear deformation reaches the sample length of 0.05~0.10 or while the shear displacement greatly changes during a period and the shear and normal stress tend to be unstable, it is judged that the sample shear is broken. After the accomplishment of the shear test, the largest shear stress and the corresponding normal stress(the normal stress value may grow in the implementation of the shear engineering) values are recorded, to describe the geology of the sample. Besides, the up and down difference of the shear plane is measured. The actual shear area is checked. The relationship curve between the shear stress and normal stress is drawn. The simple linear regression equation is achieved. Finally, according to the graphical method, the eigenvalue of the gobi surface soil shear strength is acquired.

**Analysis of the Test Results[4]**

**The Deformation Characteristics of Gobi Surface Soil**

As a whole, the characteristic curve of the relationship between the gobi surface soil shear stress and the horizontal displacement(please see fig.4) is inclined to the downward concave. The expression of the soil sheared is reflected by the existing peak strength. In terms of the relationship between the

stress and strain, it is usually reflected through the obvious resultant stress-strain curve. While we observe the broken plane after the soil shearing, the bottom slip surface of the broken plane of the sample appears downward cambered shape. It is due to the up and down change while it is in the place with quite large particles. In other words, the situation that the broken plane bypasses the stones for the upward bend occurs while other broken planes are quite flat. It is because the broken plane can directly go through the place with quite small particles by cutting stones. It is a significant feature of the gravelly surface soil used to tell from other materials.

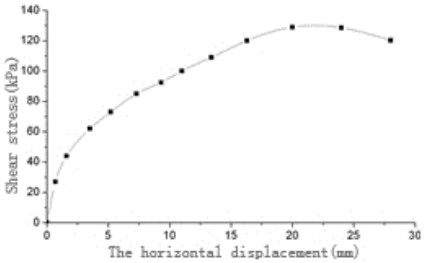


Fig.4 Shear stress-displacement characteristic curve

**Calculation of the Shear Strength Parameters of the Gobi Surface Soil**

According to the soil shear strength formula proposed by the Mohr-Coulomb principle[3], it can be known that there is the linear relationship between the shear strength r and the normal stress σ for cutting the broken plane. As long as the cohesion c and internal friction angle ϕ, the shear strength of the gobi surface soil can be solved.

In accordance with the test plan, it makes three groups of tests aiming to the layer of different depths. After the test result is organized, the curves of the relationship between the normal load of different-layer failure planes and the shear strength are drawn, as presented in fig.5.

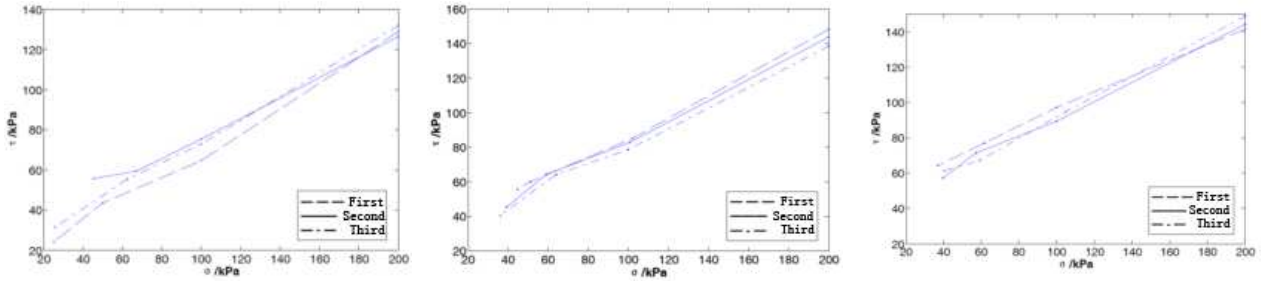


1) 2cm 2) 5cm 3) 10cm

Fig.5 The curve of the relationship between the normal load of different layer and the shear strength

Through the curve of the relationship between the normal loading of the failure plane and the shear strength, the simple linear regression equation is obtained. The shear strength parameters of the gobi surface soil in the test place are solved, as table 2 shows.

Table 2 Result of Lop Nor gobi soil in-situ shear test

| Depth | 2cm | 5cm | 10cm |
|---|---|---|---|
| Internal Friction Angle ϕ (°) | 20.4～25.3 | 25.2～25.7 | 20.7～24.2 |
| CohensionC (kPa) | 15.3～23.5 | 27.2～33.1 | 41.5～51.6 |

Through analyzing the rule of the shear strength, the following conclusion can be gotten.

From Fig.5, we can see that there is nearly the linear relationship between the shear strength τ and the normal stress of the sheared failure plane σ. We get that the relevant coefficient[5] of the simple linear regression equation is 0.98. It proves that the Mohr-Coulomb principle is applicable for the gobi surface soil. Also, it indicates that the way of using the self-made field in-situ direct shear apparatus to measure the gobi surface soil shear strength parameter is feasible.

The cohesion of the gobi surface soil significantly changes with the change of the depth. c=15.3kPa ～ 51.6kPa. The soil structure refers to the shape, size, arrangement and mutual relationship of the soil particles or soil aggregation. The soil structure can be classified into three

basic types that are the single grain structure, honeycomb structure and flocculent structure[6]. According to the formation of the gobi soil, it can be classified as the single grain soil. However, the gobi soil has the great cohesion. It is not the pure single grain soil. Its cohesion has been beyond the range of the single grain soil. It is because a small quantity of clays in the gobi soil form a colloidal shape between the gravel and heap sand to make them be a whole under the long-time pressure of its self-weight. Meanwhile, the sizes of the gobi soil particles are different. They occlude and embed each other, greatly enhance the cohesion of the gobi soil. What's more. The deeper the soil is, the larger the cohesion will be. It is a soil that is never mentioned in the regular classification. Therefore, for some aspects in the engineering work, it only takes the relevant regulations in the standard for reference.

The change of the internal friction angle of the gobi surface soil is relatively small. $\varphi$=20.4°～25.7°. It is obviously affected by the water content of the soil and the density. The water content of the surface soil is basically same as the size of the void content. They are respectively 0.9% and 35%.

From the curve relationship between the shear stress and the vertical stress shown in Fig.5, Fig.6 and Fig.7, the shear strength of the sand increases with the growth of the vertical pressure. The shear deformation regularity of three-layer depth is quite good, with the low dispersion. It indicates that the data achieved under such experimental conditions is reliable.

## Conclusions

Through proving that Mohr-Coulomb standard is applicable for the gobi surface soil with the test, it verifies that the method of using the self-made field in-situ direct shear apparatus to measure the shear strength parameter of the gobi surface soil is feasible. Compared with the common direct shear apparatus, it is practical and time-saving, with the simple structure.

- The cohesion of the gobi surface soil strengthens with the increase of the depth. c=15.3kPa～51.6kPa. The change of the internal friction angle is relatively small. $\varphi$=20.4°～25.7°.
- The shear strength of the gobi surface soil increases with the rise of the vertical pressure. The shear deformation regularity of the soil of different depths is quite good, with the low dispersion. Thus it can be seen that the data obtained under such experimental conditions is reliable.
- The gobi surface soil can be interpreted by the resultant stress-strain relationship curve. Yet, it has the features significantly different from other materials. That is, the failure plane can either cut the small neighboring stone or bypass the big stone depending on the difference of the shear strength.
- The field in-situ test makes up some defects of the laboratory soil test. The indexes gotten are the real and natural reflection of the soil. So, it is more scientific and reasonable to use it for the engineering design.

## References

[1] HU Yin-qiao,GAO You-xi,WANG Jie-min. Some new under-standing of land-surface processes in arid area from the HEIFE[J]. ACTA Meteorologica Sinica , 1996, 10(2) :232～246

[2] MEI Ying-bao, YAN Jia-ping. Direct shear test of gravel and viscosity soil[J]，Subgrade Engineering, 2000(5)，36-37,In Chinese

[3] MENG Gao-tou. Physical geography in the arid areas of china[M]. Beijing: Geologic Press, 1991,In Chinese

[4] GUAN Jian-min, LI Jing-hui. A discuss on construc -tion performance of gobi soil in JiaYuGuan[J]. Gansu Science and Technology, 2009, 25(22), 136-138,In Chinese

[5] CHEN Jiu-yu, LIN Jian. Physical geography in the arid areas of china[M]. Shanghai: Science Press, 1985,In Chinese

[6] XIA Xun-cheng. Physical geography in the arid areas of china[M]. Beijing: Science Press, 1989,In Chinese

*Applied Mechanics and Materials Vols. 580-583 (2014) pp 185-190*
*© (2014) Trans Tech Publications, Switzerland*
*doi:10.4028/www.scientific.net/AMM.580-583.185*

# Study of Soil Structural Parameters Based on the Gunary Model

Xuefeng HUANG[1, 2 a], Yang KONG[1, b], Baoshan YANG[3, c], Pingfu ZHEN[3, d]

[1]School of Civil Engineering, Lanzhou University of Technology, Lanzhou, Gansu 730050, China;

[2]Chongqing Key Laboratory of Geomechanics & Geoenvironmental Protection, LEU, Chongqing 401311, China;

[3]Electronic Comprehensive Investigation and Surveying Institute of Ministry of Information Industry, Xi′ an, Shanxi, 710054, China

[a]hxfen60@163.com, [b]gongzuo99033@163.com, [c]13909186522@163.com, [d]872915023@qq.com

**Keywords:** confined compression; compacted loess; the stress-strain relationship; structural parameter; the Gunary Model; the two-parameter liner reciprocal function

**Abstract.** Structural study of the soil is an important research content of soil mechanics. Based on the previous research results of soil structure, this paper puts forward the Gunary Model as a completely new form to describe the stress-strain relationship of soil, to discuss the method to determine soil strain considering structural parameter under the new model, to give the relevant function of the stress controlling structural parameter with stress. The results show that the Gunary Model is applicable to characterize the stress-strain relationship of soil, the parameter $c$ controls the fitting accuracy and decides the curve shape; by using the stress-strain expression of the Gunary Model, this paper finds the calculated value of stress controlling structural parameter and stress meets the two-parameter linear reciprocal function form.

## Introduction

SHEN Z J refers structural study of the soil as "the core of soil mechanics of the 21st century" [1]. XIE D Y summarizes the study results, and believes that the research method of micro-structure morphology, solid mechanics and soil mechanics are three basic ways of research on structural study of the soil, and he proposes a method to determine the soil strain considering structural parameter [2]. LUO Y S believes that the method to determine the soil strain considering parameter has many flaws under complex stress state, through the research of loess under dynamic, static stress state, proposes the method to determine the soil stress considering structural parameter [3].CHEN X analyzes two typical methods about how to determine the soil structural parameter, and puts forward an expression with an unified form and simple style [4].The value of soil structural parameter is determined by test data of undisturbed, remolded and saturated undisturbed soil samples. At present, there is more and more research on the soil structural parameter, there has been confined compression consolidation test, conventional triaxial compression test, and unsaturated soil triaxial compression test. The research involves in soil damage, complex stress and other fields, research results are increasingly rich.

The method to determine the soil strain considering structural parameter is the first canonical method that being proposed. The purpose of this study is to use a new description of the soil stress-strain relationship, combining with the relevant experimental results, to discuss the method about how to determine soil strain considering structural parameter under the new model, to give the relevant function of the stress controlling structural parameter with stress, and to validate the rationality of the new model.

## The proposal and application of a new model

**Propose a new model.** Under the confined compression state, $\sigma$ represents the vertical compression stress, $\varepsilon$ represents the vertical compression strain, then the soil stress-strain curve is shown in Fig.1.

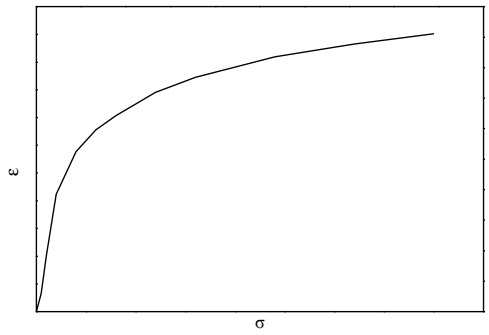


Fig.1 The curve of soil stress-strain relationship under confined compression

Fig.1 shows the soil stress-strain relationship under confined compression. As can be seen from Fig.1, the soil stress-strain curve under confined compression can be simply considered as a monotonically increasing convex function, with the increase of stress, the strain is increasing more and more slowly. In 1963, Konder proposed the Hyperbolic Model to characterize the dynamic skeleton curve of soil stress and strain [5], so, the soil stress-strain relationship can be expressed as formula (1).

$$\varepsilon = \frac{\sigma}{a + b\sigma} \tag{1}$$

Where $\varepsilon$ = the vertical compression strain of soil; $\sigma$ = the vertical compression stress of soil; $a$, $b$ =the test parameters.

It is clear that the Hyperbolic Model curve form and the soil stress-strain relationship curve form are very close with each other, so the Hyperbolic Model is widely recognized and used.

With the development of the urban road traffic, housing and other livelihood infrastructures in the northwest loess area, studies of compacted loess are increasing, and its main research content is the study of deformation characteristics. A lot of experiments prove that the soil secant modulus-stress linear relationship can not reflect the actual situation of loess in a higher compactness because in this case the soil secant modulus-stress relationship is appearing as a non-linear form. Base on the study of highway, airport construction and other projects in loess region, CHEN K Y and HU C M believe that the stress-strain relationship of compacted loess conform the power function form [6, 7]. The author finds by experimental studies that the power function has a higher fitting precision in high compactness conditions, but with the decrease of compactness the fitting accuracy and stability are decreasing too, at the same time, the soil secant modulus-stress relationship appears as a linear form, therefore, the form of power function cannot be applied. Thus, to construct a new model which has an extensive applicability, fitting accuracy and high stability is very important. The author extents the Hyperbolic Model, and introduces a new parameter to get the new model which is named as the Gunary Model, the specific form as shown in formula (2).

$$\varepsilon = f(\sigma) = \frac{\sigma}{a + b\sigma + c\sqrt{\sigma}} \tag{2}$$

Where $\varepsilon$ = the vertical compression strain of soil; $\sigma$ = the vertical compression stress of soil; $a$, $b$, $c$ =the test parameters.

As can be seen from formula (1) and formula (2), when the value of parameter $c$ is small, the Gunary Model approaches to the Hyperbolic Model, when the value of parameter $c$ is zero, the Hyperbolic Model can be considered as a special case of the Gunary Model. In order to visualize fitting curve shape of the Gunary Model, the numerical curves are shown in Fig.2.

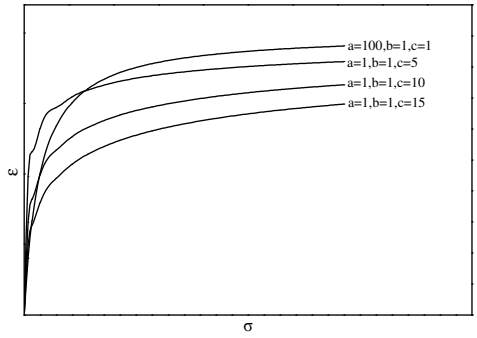


Fig.2 Fitting curves using the Gunary Model

Fig.2 shows the fitting curves using the Gunary Model. As can be seen from Fig.2, the Gunary Model fitting curve form meets the stress-strain relationship curve form under confined compression. Under the same stress if the formula has equal $a$ and $b$ value, the smaller $c$ value the lager strain value, similar to the lower compactness of compacted loess. Under the same lower stress if the formula has equal $b$ and $c$ value, the larger $a$ value the smaller strain value, when the stress exceeds a certain value, the stress-strain curve tends to approach gentle by requiring a higher stress.

**The application of a new model.** This article will list Yan' an compacted $Q_2$ loess research achievements and quote partial reference [4] original date, the Gunary Model will be extended to the general soil stress-strain relationship description, and the details as shown in Fig.3.

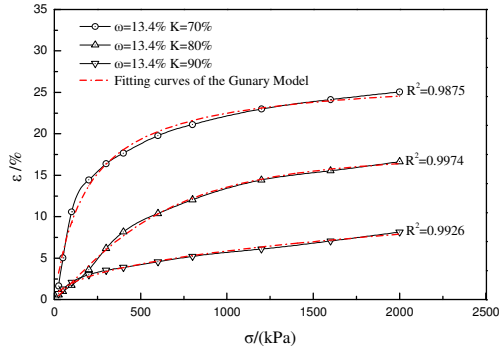


(a) Compacted $Q_2$ loess in Yan' an region

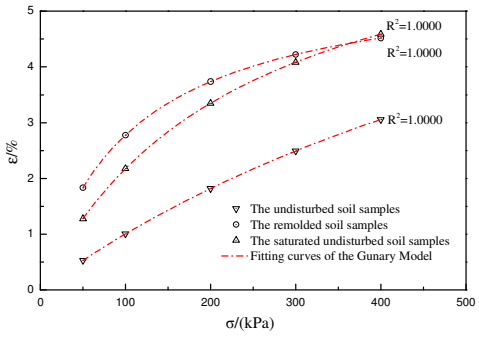


(b) Loess in Yang' ling region

Fig. 3 The curves of stress-strain relationship of different kinds of loess

Where $K$ = compactness; $\omega$ = moisture content; $R^2$ = the correlation coefficient.

Fig. 3 shows the curves of the stress-strain relationship of different kinds of loess. It can be seen from Fig.3 that the Gunary Model can describe different types of loess and various forms of stress - strain curves, the fitting curves meet the development of actual form, meanwhile, it has a higher accuracy. Fig.3-(b) shows the correlation coefficient of the undisturbed, the remolded, the undisturbed saturated soil samples are all 1.0, indicating that Gunary model is suitable to describe the general soil stress-strain relationship, structural parameters study below will use the Gunary Model soil stress-strain relationship.

## Formula derivation and test methods

**Structural parameters.** By using unconfined compression test to make compression curves about the undisturbed soil samples, the remodeled soil samples, the undisturbed saturated soil samples of the same kind of soil, that is, three-line method. By using three-line method the author discusses the method to calculate strain considering structural parameter, it can also be called the stress controlling method, and the specific form as shown in formula (3).

$$m_\sigma = \frac{m_1}{m_2} = \frac{\varepsilon_s / \varepsilon_o}{\varepsilon_o / \varepsilon_r} = \frac{\varepsilon_s \varepsilon_r}{\varepsilon_s^{\,2}} \tag{3}$$

Where $m_\sigma$ = stress controlling structural parameter; $m_1$ =variability; $m_2$ = stability; $\varepsilon_o$, $\varepsilon_r$, $\varepsilon_s$ = strain of undisturbed, remolded, undisturbed saturated samples.

$E_{\sigma i} = \sigma / \varepsilon$ is defined as the stress controlling secant modulus under the confined compression, by introducing the secant modulus method, formula (3) is converted to formula (4).

$$m_\sigma = \frac{\varepsilon_s \varepsilon_r}{\varepsilon_s^{\,2}} = \frac{(\sigma_s / E_{\sigma s})(\sigma_r / E_{\sigma r})}{\sigma_o / E_{\sigma o}} = \frac{E_{\sigma o}^{\,2}}{E_{\sigma s} E_{\sigma r}} \tag{4}$$

Where $\varepsilon_o$, $\varepsilon_r$, $\varepsilon_s$ =strain of undisturbed, remolded, undisturbed saturated samples; $\sigma_o$, $\sigma_r$, $\sigma_s$ = stress of undisturbed, remolded, undisturbed saturated samples; $E_{\sigma o}$, $E_{\sigma r}$, $E_{\sigma s}$ = secant modulus of undisturbed, remolded, undisturbed saturated samples.

As mentioned above, the soil stress-strain relationship under confined compression meets the Gunary Model, here, the author controls the same value $\sigma$ as the stress of undisturbed, remolded, undisturbed saturated samples, so the strain considering structural $m_\sigma$ can be got by

$$E_{\sigma i} = h(\sigma) = a + b\sigma + c\sqrt{\sigma} \tag{5}$$

$$m_\sigma = \frac{E_{\sigma o}^{\,2}}{E_{\sigma s} E_{\sigma r}} = \frac{h(\sigma_o)^2}{h(\sigma_s) h(\sigma_r)} \tag{6}$$

Where $E_{\sigma i}$ = stress controlling secant modulus under confined compression; $a$, $b$, $c$ = the test parameters.

**Test methods.** Test soil samples are taken from Yang' ling, Shan' xi province, confined compression consolidation stress test will be controlled at 50kPa, 100kPa, 200kPa, 300kPa, 400kPa, including the same moisture content, dry density natural undisturbed soil samples, remodeled soil samples and natural saturated undisturbed samples[4].

## Results and analysis

**Structural parameter based on the Gunary Model.** Results of soil stress-strain relationship based on the Gunary Model are shown in Table 1 and Fig.3-(d).

Table 1 The stress-strain relationship fitting parameters based the Gunary Model

| Samples | $a$ | $b$ | $c$ | $R^2$ |
|---|---|---|---|---|
| The undisturbed samples | 89.1058 | 0.1043 | -2.3484E-13 | 1.0000 |
| The remolded samples | 18.4887 | 0.1752 | 4.8771E-14 | 1.0000 |
| The saturated samples | 32.2181 | 0.1375 | -1.08867E-14 | 1.0000 |

Note: The original test data from the reference [4]; E(n) means 10 ^ (-n)

Where $R^2$ = the correlation coefficient; $a$, $b$, $c$ = the test parameters.

As can be seen from Table 1 and Fig.3-(d) that the Gunary Model can characterize soil stress - strain relationship, the correlation coefficients are all 1.0, the fitting precision is of high value, $c$ value, although it is a very small number, but here, it cannot be ignored because that $c$ value plays a controlling role for fitting accuracy, if the value is taken as 0, the fitting expression turns into a form

of the Hyperbolic model equation, although the correlation coefficient is approximately 1.0, but the three-parameter fitting accuracy is better than two-parameter fitting. Meanwhile, the study of the deformation properties of compacted loess in Yan' an find the $c$ value determines the shape of the secant modulus-stress curve, the smaller the $c$ value, the closer the curve tends to linear relationship.

Using formula (2) - (6) to calculate the stress controlling structural parameters, and finishing the test results are shown in Table 2, Fig.4.

Table 2 The measured and calculated values of stress controlling structural parameters

| $\sigma$/kPa | $m$ | $m_\sigma$ | $\delta$/% |
|---|---|---|---|
| 50 | 6.77 | 8.352 | 23.36 |
| 100 | 6.49 | 5.985 | -7.77 |
| 200 | 3.66 | 3.783 | 3.36 |
| 300 | 2.80 | 2.777 | -0.82 |
| 400 | 2.21 | 2.216 | 0.26 |

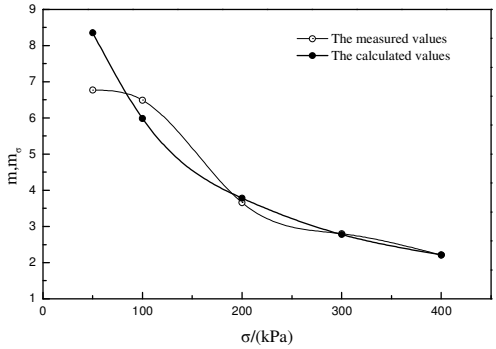


Fig.4 The curve of the measured and calculated values of stress controlling structural parameters

Where $\sigma$=stress; $m$=the measured stress controlling structural parameter; $m_\sigma$ = the calculated stress controlling structural parameter; $\delta$ = relative tolerance.

Fig.4 shows the curve of the measured and calculated values of stress controlling structural parameters. As can be seen from Table 2 and Fig.4 the measured and calculated stress controlling structural parameter values relative tolerance is lager at lower stress, when the stress is 50kPa, the relative tolerance is the biggest one. With the increase of stress, the relative tolerance gradually decreases and tends to 0. The measured results and the calculated results have a higher agreement, and explain the applicability of the Gunary Model. The measured and calculated stress controlling structural parameter value all decrease with the increase of stress, the measured values present in a form of anti-S-curve diminishing, the calculated values present in the form of a concave curve diminishing with a gradually decreasing rate.

With the increase of stress, the calculated parameter is decreasing regularly, the author finds that the calculated stress controlling structural parameters can be described by the two-parameter liner reciprocal function, and the specific form as shown in formula(7).

$$m_\sigma = \frac{a}{1+b\sigma} \tag{7}$$

Where $a$, $b$ = the test parameters.

Using formula (7) represents the relationship between the calculated stress controlling structural parameter and stress, and finishing the test data as shown in Fig.5.

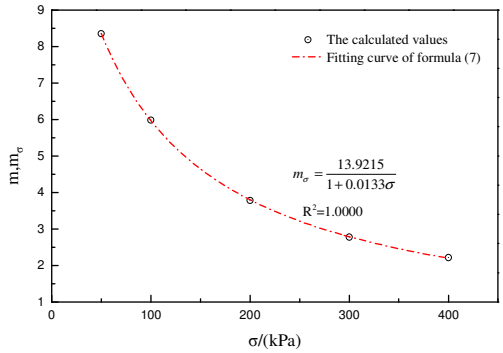


Fig.5 The fitting curve of the relationship between the calculated stress controlling structural parameter and stress

Fig.5 shows the fitting curve of the relationship between the calculated stress controlling structural parameter and stress. As can be seen from Fig.5, the fitting correlation coefficient is 1.0, the fitting accuracy is very high, and nearly perfectly correlate, indicating that the relationship between the calculated stress controlling structural parameter and stress can be described by the two-parameter liner reciprocal function.

## Summary

The Gunary Model from is applicable to characterize the soil stress-strain relationship, the parameter $c$ controls the fitting accuracy and decides the curve shape. By using the stress-strain expression of the Gunary Model, this paper finds the calculated stress controlling structural parameter and stress meets the two-parameter linear reciprocal function form.

## Acknowledgements

This work was financially supported by the 2013 National Science and Technology Support Program (2013BAJ06B00), Shanxi Provincial Science and Technology Co-ordination Innovation Project (2012KTDZD03-04). Thanks to the partial original data provided by reference [4].

## References

[1] SHEN Zhu-jiang: Chinese Journal of Geotechnical Engineering Vol. 18-1 (1996), p. 95-97(in Chinese).

[2] XIE Ding-yi, QI Ji-lin: Chinese Journal of Geotechnical Engineering Vol. 21-6 (1999), p. 651-656(in Chinese).

[3] LUO Ya-sheng, XIE Ding-yi, SHAO Sheng-jun, et al: Chinese Journal of Rock Mechanics and Engineering Vol. 23-24 (2004), p. 4248-4251(in Chinese).

[4] CHEN-Xi, LUO Ya-sheng, CHENG Da-wei, et al: Rock and Soil Mechanics Vol. 34-5 (2013), p. 1253-1258(in Chinese).

[5] Kondner R L: Journal of the soil mechanics and foundations division, ASCE Vol. 89-1 (1963), p. 115-143.

[6] CHEN Kai-sheng, SHA Ai-min: Rock and Soil Mechanics Vol. 31-4 (2010), p. 1023-1029(in Chinese).

[7] HU Chang-ming, MEI Yuan, WANG Xue-yan: Engineering Mechanics Vol. 30-10 (2013), p. 108-114(in Chinese).

*Applied Mechanics and Materials Vols. 580-583 (2014) pp 191-194*
*© (2014) Trans Tech Publications, Switzerland*
*doi:10.4028/www.scientific.net/AMM.580-583.191*

# Study on static strength of Aeolian sand before and after cyclic loading

Dapeng Liu[1,a*], Xiaohua Yang [1,b], Jing Wang [2,c] and Zhengjun Mao[3,d]

[1]School of Highway, Chang'an University, Xi'an 710064, China

[2]Gansu Construction Vocational Technical College, Lanzhou 730050,China

[3]Xi'an University of Science and Technology, Xi'an 710054, China

[a]839289786@qq.com, [b]xiaohuay@126.com, [c]136089261@qq.com, [d]136895123@qq.com

**Keywords:** Aeolian sand; static strength; confining pressure; cyclic loading; consolidation ratio; initial static deviator stress

**Abstract.** Aeolian sand is one commonly used subgrade filling in Xinjiang Oasis-desert region, engineering practices also proved its applicability as subgrade filling. In order to find the law of Aeolian sand subgrade static strength after cyclic loading, the paper studied the static strength of Aeolian sand before and after cyclic loading through the dynamic and static triaxial tests. It is concluded that the greater cyclic loading is, the more Aeolian sand static strength peak decreases. When cyclic loading is small, the bigger confining pressure and consolidation ratio are, the static strength peak increases more after cyclic loading. The bigger initial static deviator stress is, the more Aeolian sand static strength peak reduces. The frequency of cyclic loading has little effect on static strength. In order to keep the stability of low embankment, we should restrict overload , ensure subgrade and foundation consolidation adequately, use gravel or geosynthetic materials to package edge of roadbed, so as to increase confining pressure. The research results can provide reference for the design and construction of Aeolian sand low subgrade in Xinjiang Oasis-desert region.

## Introduction

Highway will appear large settlement under long time traffic cyclic loading, this will lead to a lot of diseases of pavement, especially for the low embankment expressway. To this kind of expressway, dynamic stress which is transmitted to subgrade and foundation from vehicle is larger. Strength and stiffness of subgrade and foundation will reduce, the same situation to bearing capacity of foundation. These will lead to more larger settlement and early damage of pavement structure. The research of low embankment expressway is carried out in Xinjiang Oasis-desert region now. The static strength of Aeolian sand before and after cyclic loading is one of the important works to the highway whose subgrade is filled with Aeolian. We can take effective measures to prevent the road early damage after we know the strength change of Aeolian. For the strength change of geotechnical materials after the cyclic loading, many scholars have carried on the related research work. Saturated soft clay shear strength changes after cyclic loading was studied by Wang[1]. The degradation of undrained shear strength of undisturbed and remolded marine clay after cyclic loading was studied by Wang[2]. The degradation of static shear strength of undisturbed silt soft clay in the Yangtze estuary after complex cyclic loading was studied by Luan[3]. As to the degradation static strength of Aeolian sand before and after cyclic loading, there is almost no research focusing on it. The paper studied it through dynamic and static triaxial tests and got some laws which can be reference to the Aeolian embankment road design and construction in Xinjiang Oasis-desert.

## Laboratory test

The Aeolian sand used in the tests comes from Xinjiang Oasis-desert region. The parameters of the Aeolian sand is shown in table 1.

Table 1 Parameters of Aeolian sand

| sample | Dry density/g/cm$^3$ | optimum water content/% | the quality percentage of different size | | | | Cu | Cc |
|---|---|---|---|---|---|---|---|---|
| | | | 0.3-0.6 | 0.15-0.3 | 0.15-0.074 | <0.074 | | |
| Aeolian sand | 1.811 | 12 | 15.4 | 70.9 | 10.8 | 2.9 | 1.7 | 0.75 |

The test equipment is the hollow cylinder torsional shear apparatus(HCA) that was produced by GDS company. HCA is mainly composed of confining pressure controller, back pressure controller, inner pressure controller, pressure chamber, the axial load drive, measurement equipment, data acquisition instrument, computer etc. , the equipment can be used to the static and dynamic real triaxial shear test. HCA can applicate radial and ring load, the maximum load frequency is 2hz and the maximum axial load is 10kn. Loading waveform can be generated by the servo system, which can be sine wave, triangle wave, square wave, half sine wave and user-defined waveforms. In this paper, dynamic loading waveform is half sine wave. The stress and the strain control method can be used in static triaxial test, The paper used the strain control method.

The experiment is divided into two parts, the first part is direct to carry on the static load test. The second is carrying on a certain cycles of dynamic load tests and then carrying on the static load test[4-5]. Specific testing schemes are shown in table 2.

Table 2 Triaxial test schemes

| sample number | Confining pressure | Cyclic dynamic stress | Consolidation ratio | Load frequency | initial static deviator stress | Loading way |
|---|---|---|---|---|---|---|
| S1 | 20 | | 1 | | 0 | Carrying on static load under strain control |
| S2 | 30 | | 1 | | 0 | |
| S3 | 40 | | 1 | | 0 | |
| S4 | 20 | 20 | 1 | 1 | 0 | Carrying on static load after 5000 times cyclic loading |
| S5 | 20 | 30 | 1 | 1 | 0 | |
| S6 | 20 | 40 | 1 | 1 | 0 | |
| S7 | 20 | 20 | 1.5 | 1 | 0 | |
| S8 | 20 | 20 | 2 | 1 | 0 | |
| S9 | 20 | 20 | 1 | 1.2 | 0 | |
| S10 | 20 | 20 | 1 | 1.5 | 0 | |
| S11 | 20 | 20 | 1 | 1 | 10 | |
| S12 | 20 | 20 | 1 | 1 | 20 | |
| S13 | 30 | 20 | 1 | 1 | 0 | |
| S14 | 40 | 20 | 1 | 1 | 0 | |

Test procedure can be divided into three steps. The first step is making samples based on the maximum dry density that was gotten from the Aeolian sand compaction test, then the sample is placed on the base of the pressure chamber, in the process of placing to prevent disturbance of the sample. The second step is injecting water to pressure chamber and the sample is saturated. Then samples consolidate under different confining pressure and consolidation completion standard is back pressure volume remaining constant. The third step is applying on static load and different cyclic dynamic loading on sample. For dynamic loading samples, static load is applied on after 5000 times cyclic dynamic loading.

## Test results

Samples S1, S2 and S3 respectively consolidated under effective confining pressure 20Kpa, 30Kpa, 40Kpa, then were applied on static load directly. Static strength and strain relationships are shown in fig.1, we can see from fig.1 that static strength of S1, S2 and S3 is increasing when strain is increasing in the early stage of the load. When the strain is 2% or so, the three samples static strength reach the peak. The peak respectively are 147Kpa, 169Kpa and 186Kpa. After reaching peak, the sample structure damaged. When strain further increasing, the static strength slowly began to decrease.

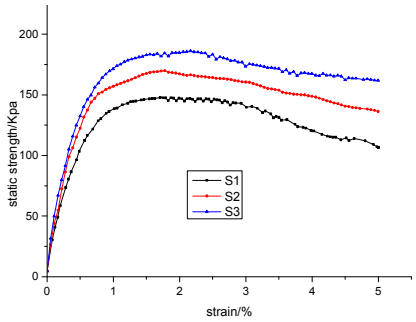


Fig.1 Relationships of static strength and strain under different size static loading

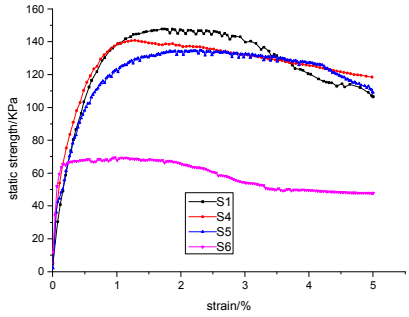


Fig.2 Relationships of static strength and strain under different size cyclic loading

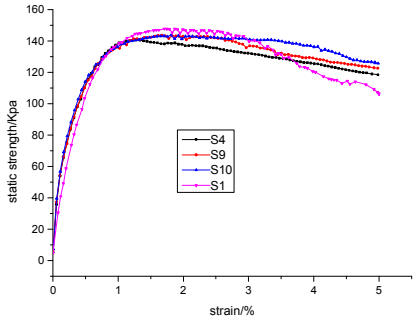


Fig.3 Relationships of static strength and strain under different cyclic loading frequency

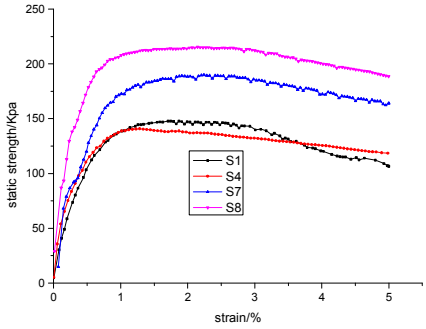


Fig.4 Relationships of static strength and strain under different consolidation ratio

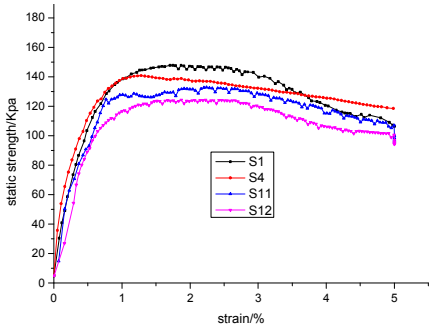


Fig.5 Relationships of static strength and strain under different initial static deviator stress

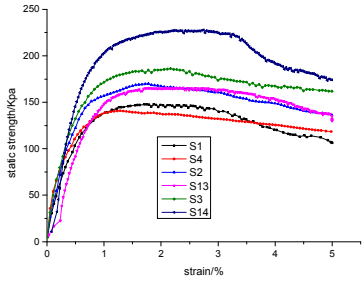


Fig.6 Relationships of static strength s and strain under different confining pressure before and after cyclic loading

Sample S4, S5 and S6 consolidated under 20kpa effective confining pressure ,then were applied on 20kpa, 30kpa and 40kpa cyclic loading for 5000 times, after that the samples were applied on static load. The results are shown in fig.2, meanwhile we compared the result with the result of S1. From fig.2, we can see that the static strength peak of S4 has little change comparing with S1, this shows that 5000 times cyclic loading of 20kpa has little influence on static strength. when cyclic loading is 30kpa, the static strength peak decreases from 147kpa to 134kpa, This shows that 5000 times cyclic loading of 30kpa has certain influence on static strength. when cyclic loading is 40kpa, the static strength peak is 70kpa, this is consistent with that S6 has a larger cumulative plastic deformation after 5000 times cyclic loading, and at the same time the sample structure is damaged. Because the dynamic stress passed from overload vehicles to Aeolian sand subgrade is bigger and it is easy to cause subgrade destruction, in order to prolong the service life of road, we should restrict overload, especially serious overload in practice.

The relationships between static strength of S1, S4, S9 and S10 and strain are shown in fig. 3. From fig. 3, we can see that when cycle loading is 20kpa and cycle loading frequency are respectively 1hz, 1.2hz and 1.5hz, the static strength after 5000 times cycle loading has little change with S1 that has no cycle loading. The static strength peak of S1, S4, S9 and S10 is about 140kpa, so it shows that cycle loading frequency has little effect on static strength as long as the size of the dynamic load is in a low level.

The relationships between static strength of S1, S4, S7 and S8 and the strain are shown in fig.4. From fig. 4, we can see that the greater consolidation ratio, the greater the static strength. When consolidation ratio is 1,1.5 and 2, the static strength peak are respectively 140kpa, 180kpa and 215kpa after 5000 times 20kpa cyclic loading. This shows that the greater consolidation ratio is, the more compact the Aeolian sand structure is, the greater the static strength peak is regardless of having cyclic loading or no. So for Aeolian sand subgrade, foundation and roadbed having fully consolidation and keeping enough compaction has vital significance to ensure the roadbed strength.

The relationships between static strength of S1, S4, S7 and S8 and the strain are shown in fig. 5. It shows in fig. 5 that the larger the initial static deviator stress is, the smaller the static strength peak is after cyclic loading. When static deviator stress are 0kpa, 10kpa and 20kpa, the static strength peak are 140kpa,132kpa and 123kpa respectively. It shows that the degradation of static strength is larger after cyclic loading when the initial static deviator stress is larger.

The relationships between static strength of S1, S2, S3,S4,S13 and S14 and the strain are shown in fig. 6. We can see from fig. 6 that the greater confining pressure is, the bigger static strength peak is when other conditions are equal. When confining pressure is 20kpa, static strength peak of S4 is slightly less than that of S1 .When confining pressure is 30kpa, static strength peak of S13 is basically equal to that of S2 .When confining pressure is 40kpa, static strength peak of S14 is greater than that of S3. It shows that Aeolian sand became more compact when confining pressure is 40kpa after 5000 times cyclic loading, so static strength peak becomes bigger.

In practice, gravel or geosynthetics is used to package edge of Aeolian sand subgrade, this increases Aeolian sand subgrade confining pressure, so Aeolian sand strength after cyclic loading will increase and the stability of subgrade is ensured.

## Conclusions

Static strength peak decreases with the increase of cyclic loading at a certain confining pressure. Aeolian sand sample structure has been damaged after 5000 times cyclic loading When cyclic loading is 40kpa and static strength peak is only 70kpa decreasing by about 50% comparing with sample applied on static load directly. So in practice, we should restrict overload to ensure subgrade stability. Cycle loading frequency has little effect on static strength as long as the size of the dynamic load is in a low level. The greater consolidation ratio is, the more compact the Aeolian sand structure is, the greater the static strength peak is regardless of having cyclic loading or no. So for Aeolian sand subgrade, foundation and roadbed having fully consolidation and keeping enough compaction have the vital significance to ensure the roadbed strength. The degradation of static strength is larger after cyclic loading when the initial static deviator stress is larger. The greater confining pressure is, the bigger static strength peak is.

## References

[1] X.P.Wang, H.P.Liu, H.Zhou, J.Wang. Study on saturated soft clay shear strength changes after cyclic loading[J]. Railway Engineering, 2006,4:56-58. (in Chinese)

[2] S.Y.Wang, Z.G.Lou. The degradation of undrained shear strength of undisturbed and remolded marine clay after cyclic loading[J]. Rock and Soil Mechanics, 2000, 21(1):20-27. (in Chinese)

[3] M.T.Luan, G.X.Liu, Y.Guo，Z.T.Wang. Study on the degradation of static shear strength of undisturbed silt soft clay in the Yangtze estuary after complex cyclic loadings[J]. Journal of Hydraulic Engineering，2010,41（12）:1407-1415. (in Chinese)

[4] B.Huang, H.Ding, Y.M.Chen. Simulation of high-speed train load by dynamic triaxial tests[J]. Chinese Journal of Geotechnical Engineering ,2011,33(2):195-202. (in Chinese)

[5] C.J.Wang，Y.M.Chen. Study on effect of traffic loading induced static deviator stress on undrained cyclic properties of saturated soft clay[J]. Chinese Journal of Geotechnical Engineering , 2007,29(11):1742-1747. (in Chinese)

*Applied Mechanics and Materials Vols. 580-583 (2014) pp 195-200*
*© (2014) Trans Tech Publications, Switzerland*
*doi:10.4028/www.scientific.net/AMM.580-583.195*

# Study on the development of plastic zone based on strain expressed Mohr- Coulomb yield condition

Cai Yang [1,2,a], Tu-gen Feng [1,2,b]

[1]Key Laboratory for Geotechnical Engineering of Ministry of Water Resource, Nanjing 210098, China

[2]Research Institute of Geotechnical Engineering, Hohai University, Nanjing 210098,China

[a]yang668411@126.com, [b]tgfeng75@163.com

**Keywords:**slope stability; Mohr- Coulomb yield condition;plastic zone; strength reduction FEM

**Abstract:** At present, there is a lot of research for slope stability, the inherent reason of slope instability is geotechnical material will get plastic deformation under load. In this paper, Mohr-Coulomb yield condition is transformed strain expressed to stress expressed.Based on this, analysis the effects that geotechnical material parameters internal friction angle φ,cohesion c and Poisson's ratiovto Mohr- Coulomb yield condition and the development of soil plastic zone.In addition, using the strength reduction FEM simulating the change of plastic zone distribution caused by change of the geotechnical materials parameters .The results show that the internal friction angle φ, cohesion c are reducted, the plastic zone expand;Increasing the Poisson's ratio ν, narrowing the slope's plastic zone;Plastic zone's different distribution is caused by different material parameters affect the yield surface.

## Introduction

In the analysis of slope stability, finite element method can overcome the disadvantage that soil hypothesis as a rigid by limit equilibrium method, considering the nonlinear constitutive relation and can be applied to any complex boundary conditions[1]. Strength reduction FEM was first proposed by Zienkiewicz[2] in 1975 is becoming a new trend. Ugai (1989) [3], Matsui and San (1992) [4], Dawson and Roth (1999) [5] all have done further research, The results show that strength reduction FEM and limit equilibrium can be made almost close to the safety factor and the critical slip surface.

The soil produces plastic deformation is the intrinsic reasons of slope's failure. So it is necessary to start from the classical elastic-plastic theory, analysis of rock and soil mechanical parameters for the development of plastic zones. In this paper ,writer deduced strain expressed Mohr- Coulomb yield condition to analysis of the effect of parameters on the yield condition .The results are verified with the strength reduction FEM.

## The strain expressed Mohr- Coulomb yield condition

**Deduction.** When the objects within a point to produce plastic deformation, strain components need to meet the conditions is called the strain expressed yield condition. The material is assumed isotropic,yield function's strain space in six-dimensional can be discussed in the three-dimensional[6]. The strain yield function can be expressed as:

$$\left.\begin{aligned} f(\varepsilon 1, \varepsilon 2, \varepsilon 3)=0 \\ f(I_1', J_2', J_3')=0 \\ f(I_1', J_2', \theta\varepsilon')=0 \end{aligned}\right\} \quad (1)$$

By the generalized Hooke's law: $\sigma_{ij}=\frac{E}{1+\nu}(\varepsilon_{ij}+\frac{\nu}{1-2\nu}\varepsilon_{ij}\delta_{ij})$ （2）

The stress tensor and the deviatoric stress tensor invariants for（3）:

The strain tensor and the deviatoric strain tensor invariants for（4）:

$$\left.\begin{aligned} I_1&=\sigma_1+\sigma_2+\sigma_3\\ I_2&=-(\sigma_1\sigma_2+\sigma_2\sigma_3+\sigma_3\sigma_1)\\ I_3&=\sigma_1\sigma_2\sigma_3\\ J_1&=0\\ J_2&=\frac{1}{2}s_{ij}s_{ij}\\ J_3&=S_1S_2S_3 \end{aligned}\right\} \quad (3) \qquad \left.\begin{aligned} I_1'&=\varepsilon_1+\varepsilon_2+\varepsilon_3\\ I_2'&=-(\varepsilon_1\varepsilon_2+\varepsilon_2\varepsilon_3+\varepsilon_3\varepsilon_1)\\ I_3'&=\varepsilon_1\varepsilon_2\varepsilon_3\\ J_1'&=0\\ J_2'&=\frac{1}{2}e_{ij}e_{ij}\\ J_3'&=e_1e_2e_3 \end{aligned}\right\} \quad (4)$$

According to the formula (3), (4) and (2), the invariants' transformation formulas between stress space and strain space is (5):

$$\left.\begin{aligned} I_1&=\frac{E}{1-2\nu}I_1'=3K\,I_1'\\ J_2&=(\frac{E}{1+\nu})^2J_2'=4G^2J_2'\\ J_3&=(\frac{E}{1+\nu})^3J_3'=8G^3J_3'\\ I_3&=(\frac{E}{1+\nu})^3J_3'-\frac{1}{3}\frac{E}{1-2\nu}(\frac{E}{1-2\nu})I_1'J_2'+\frac{1}{27}(\frac{E}{1+\nu})^3(I_2')^3 \end{aligned}\right\} \quad (5)$$

and $\theta_\sigma=\theta_\varepsilon$ ； $\mu_\sigma=\mu\varepsilon$ （6）

The stress expressed Mohr- Coulomb yield condition:

$$F=\frac{1}{3}I_1\sin\varphi+(\cos\theta_\sigma-\frac{1}{\sqrt{3}}\sin\theta_\sigma\sin\varphi)\sqrt{J_2}-c\cos\varphi=0 \quad (7)$$

The conversion formula (5) into (7) can get the strain expressed Mohr- Coulomb yield condition:

$$f=2\sin\varphi\frac{1+\nu}{1-2\nu}\varepsilon_m+2(\cos\theta_\varepsilon-\frac{1}{\sqrt{3}}\sin\theta_\varepsilon\sin\varphi)\sqrt{J_2'}-\frac{1+\nu}{E}c\cos\varphi=0 \quad (8)$$

convert the formula (8) into the general form of generalized Mises yield condition:

$$\alpha' I_1'+\sqrt{J_2'}-k'=0 \quad (9)$$

which $\alpha'=\frac{1}{3}\sin\varphi\frac{1+\nu}{1-2\nu}/(\cos\theta_\varepsilon-\frac{1}{\sqrt{3}}\sin\theta_\varepsilon\sin\varphi)$ $k'=\frac{1+\nu}{E}c\cos\varphi/[2(\cos\theta_\varepsilon-\frac{1}{\sqrt{3}}\sin\theta_\varepsilon\sin\varphi)]$

**Analysis of generalized Mises yield condition (α', k').**In stress space, When the yield condition should be invariant of stress tensor function, can be written as follows:$F=F_1(I_1)+F_2(J_2,\theta_\sigma)$.Similarly, can also use the strain tensor invariant to describe: $f=f_1(I_1')+f_2(J_2',\theta_\varepsilon)$

Which $f_1(I_1')$ only affect hexagonal size in π plane; $f_2(J_2',\theta_\varepsilon)$ determin the shape of the yield locus in π plane.

The yield surface of Mohr- Coulomb yield condition is a cone surface of an irregular hexagon section,because the geotechnical materials in the compressed states and extended state have different strain Rhodes angle θε.

We assume that the shape of the yield surface has been determined, the impact functions on the yield surface are mainly a 'and k', the derivative of material parameters as follows:

The partial derivative of the Poisson's ratio ν：

$\partial \alpha'/\partial \nu = \sin\varphi/[(1-2\nu)^2.(\cos\theta_\varepsilon - \frac{1}{\sqrt{3}}\sin\theta_\varepsilon\sin\varphi)]$

$\partial k'/\partial \nu = c\cos\varphi/[2E.(\cos\theta_\varepsilon - \frac{1}{\sqrt{3}}\sin\theta_\varepsilon\sin\varphi)]$

the range of strain Rhodes angle: $-\frac{\pi}{6} \le \theta\varepsilon \le \frac{\pi}{6}$, then $\cos\theta\varepsilon - \frac{1}{\sqrt{3}}\sin\theta\varepsilon\sin\varphi > 0$,so $\partial \alpha'/\partial \nu \ge 0$，$\partial k'/\partial \nu \ge 0$.To Mohr- Coulomb yield surface ,when the Poisson's ratio ν is greater，pyramid surface of hexagonal cross-section will expand in the longitudinal and transverse in the strain space.Strain space is divided into two parts，f（εij）<0，as elastic state；f（εij）=0，the material in yield surface has begun to yield. With yield surface expand, the degree of difficulty of geotechnical materials reach yield condition increases,then the plastic zone's development will decrease.

Similarly ,the partial derivative of the rock soil cohesion c ：

$\partial k'/\partial c = (1+\nu)\cos\varphi/2E(\cos\theta_\varepsilon - \frac{1}{\sqrt{3}}\sin\theta_\varepsilon\sin\varphi) > 0$

The cohesion c is larger, the larger k' constant.Pyramid surface of hexagonal cross-section is longitudinal extending in the strain space,the yield surface expand,then the plastic zone's development will decrease.

The partial derivative of internal friction angle φ ：

$\partial\alpha'/\partial\varphi = (1+\nu)\cos\theta_\varepsilon\cos\varphi/[3(1-2\nu)(\cos\theta_\varepsilon - \frac{1}{\sqrt{3}}\sin\theta_\varepsilon\sin\varphi)^2] > 0$

The internal friction angle increases, the yield surface will be expanded.The plastic zone's development will decrease.

$\partial k'/\partial\varphi = (1+\nu)\cos\theta\varepsilon(\frac{1}{\sqrt{3}}\tan\theta_\varepsilon\sin\varphi)/2E(\cos\theta_\varepsilon - \frac{1}{\sqrt{3}}\sin\theta_\varepsilon\sin\varphi)^2$, when $\frac{1}{\sqrt{3}}\tan\theta_\varepsilon\sin\varphi > 0$, $\varphi < 19.47°$, the φ is larger, the larger k constant,pyramid surface of hexagonal cross-section is longitudinal extending in the strain space,the yield surface expand.Then the plastic zone's development will decrease. Contrarily ,when$\varphi > 19.47°$,the plastic zone's development will increase.

**The basic idea.** Based on strain expressed Mohr- Coulomb yield condition, this paper has theoretically analyzed the effect the Poisson's ratio ν, internal friction angle φ, cohesion c to yield surfaces and plastic zone's development[7].Combine a classic example of slope stability analysis ,using the strength reduction FEM to validate the analysis[8,9].

## Example and numerical simulation

**Parameters of the model .** A homogeneous slope is shown in figure 1, height of slope H=10.0m,soil bulk density γ=20kN/m3,cohesion c=12.38kPa, elastic modulus E=100Mpa,take a different value of internal friction angle $\varphi$ as 10°,15°,20°,25°,30°. Reduct the shear strength parameters c and φ[10].

$$\tau_r = \frac{\tau_f}{F_r} = \frac{\sigma\tan\varphi + c}{F_r} = \sigma\frac{\tan\varphi}{F_r} + \frac{c}{F_r},\ \varphi_r = \arctan(\frac{\tan\varphi}{F_r}),\ c_r = \frac{c}{F_r} \quad (10)$$

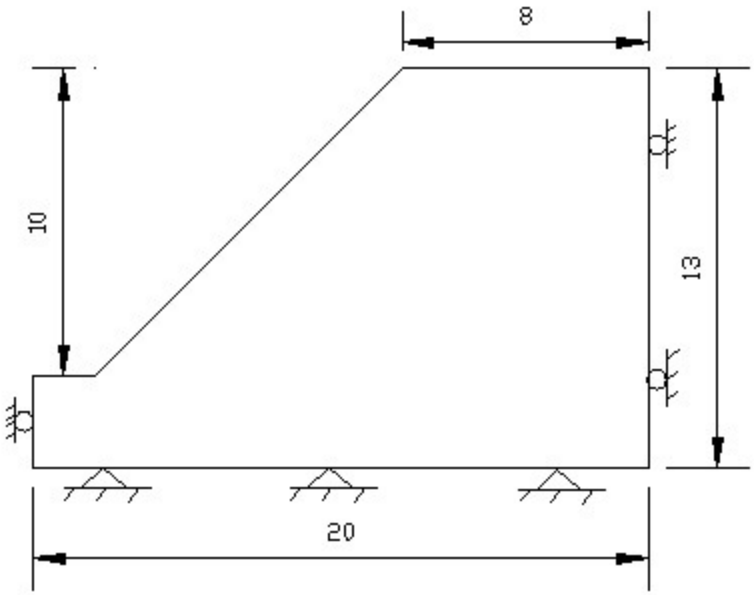


Fig.1 Computational geometry model

**Effect of friction angle and cohesion changes on the plastic zone development**. Strength reduction principle is gradually reducting the soil shear strength c and $\varphi$ according to formula (10) in a certain ratio.With increasing the reduction factor Fr， the plastic zone development increased significantly.When the friction angle is 20 °， The plastic zone of slope distribution shown in Figure 2.when $\varphi$ gets other values, development of plastic zones are in the same law.

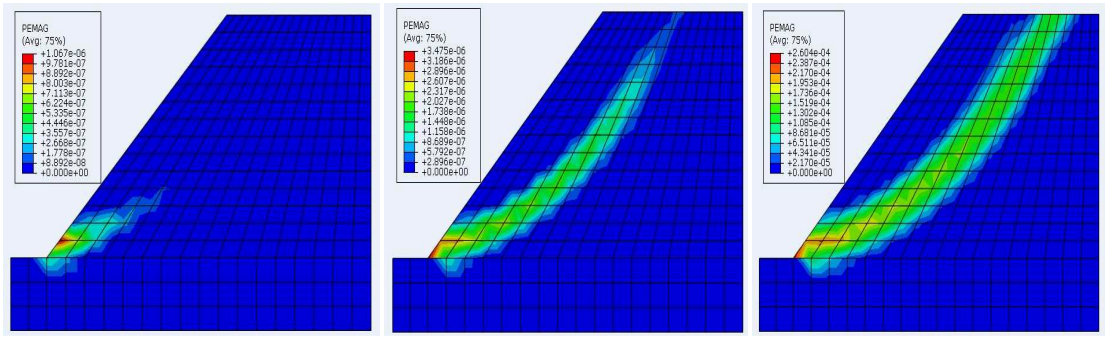

$F_r$=0.94 $F_r$=0.98 $F_r$=1.00

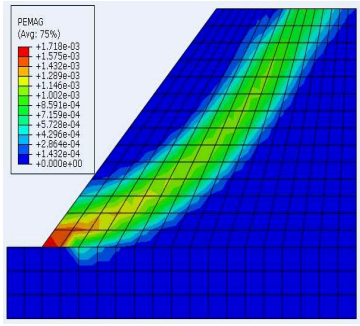

$F_r$=1.05

Fig.2 The plastic zone distribution

**Effect of Poisson's ratio ν on the plastic zone development.** The plastic zone distribution with Poisson's ratio ν variation in internal friction angle 25 °,shown in figure 3.From the plastic zone distribution， the influence of Poisson's ratio ν for the development of the plastic zone is very

obvious，With the increase of Poisson's ratio ν, plastic zone decreases. when φ gets other values, development of plastic zones are in the same law.

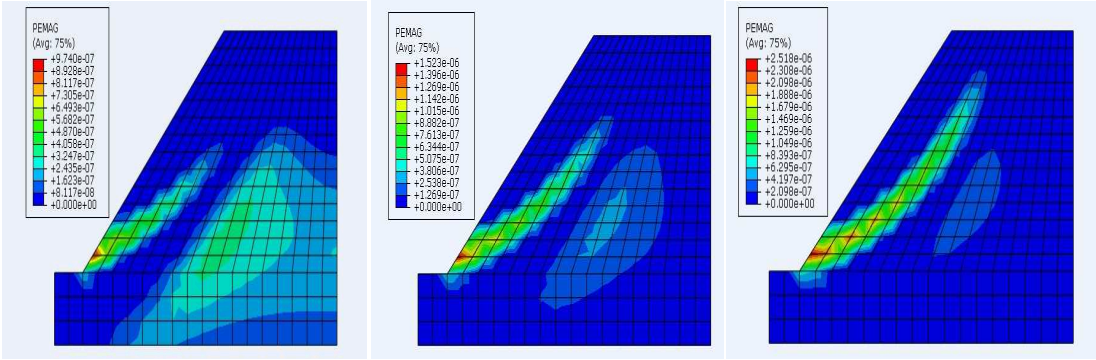


v=0.25 v=0.29 v=0.33

Fig.3The plastic zone distribution of different v values when φ=25°

## Conclusion

In this paper, using the classical elastic-plastic mechanics theory, convert stress expressed Mohr- Coulomb yield condition to strain expressed Mohr- Coulomb yield condition, then get the effects that the parameters of geotechnical materials Poisson's ratio ν, cohesion c and internal friction angleφ to Mohr- Coulomb yield surface. With increasing the reduction factor Fr (so the cohesion c and internal friction angle φ decrese),the plastic zone development increased significantly. With the increase of Poisson's ratio ν, plastic zone decreases. Results of numerical simulation are consistent with the theoretic analysis. Therefore, the plastic zone distribution of slope is internal caused of geotechnical material parameters' effect on the yield surface . For the slope with different characters of soil , the distribution of plastic zone development must be different.This research has guiding significance for practical engineering applications

## Acknowledgements

This work was financially supported by Natural Science Foundation (51009054), The Ministry ofEducation, Science and Technology Research Projects（109077） and The Natural Science Foundationof Jiangsu Province (BE2010513)

## Reference：

[1]LIAN Zhenying,HAN Guocheng,KONG Xianjing.Stability analysis of excavation slope by Strength reduction FEM[J]. Chinese.Journal of Geotechnical Engineering, 2001,23(4):407-411(in Chinese)

[2] Zienkiewicz O C, Humpheson C, Lewis R W. Associated and non-associated visco-plasticity and plasticity in soil mechanics[J]. Géotechnique, 1975, 25(4): 671-689.

[3]UgaiK. A method of calculation of total factor of safety of slopes by elasoplastic FEM[J].Soils and Foundations,1989,29(2):190-195

[4]Matsui T,San K C.Finite element slope stability analysis by shear strength reduction technique[J].Soils and Foundations,1992,32(1):59-70

[5]Dawson E M,Roth W H,Drescher A.Slope stability analysis by strength reduction [J].Geotechnique,1999,49(3):387-403

[6]ZHENG Yingren,GONG Xiaonan. Plactic Theroy of Geotechnics[M].Beijing: China Building Industry Press,1989

[7]LUAN Maotian,WU Yajun,NIAN Tingkai.A Criterion for evaluating slope stability based on development of plastic zone by shear strength reduction FEM[J].Journal of Disaster Prevention and Mitigation Engineering,2003,23(3):1-8
[8]YIN Zongzhe,et. Geotechnical principles[M].Beijing: China Water Conservancy and Hydropower Press,2007
[9]ZHAO Shangyi,ZHENG Yingren,ZHANG Yufang.Study on slope failure criterion in strength reduction finite element method[J].Rock and Soil Mechanics,2005,26,(2):332-336
[10]FEI Kang,ZHANG Jianwei. Application of ABAQUS in geotechnical engineering[M].Beijing: China Water Conservancy and Hydropower Press,2010

*Applied Mechanics and Materials Vols. 580-583 (2014) pp 201-204*
*© (2014) Trans Tech Publications, Switzerland*
*doi:10.4028/www.scientific.net/AMM.580-583.201*

# Testing study on the effects of water content on permeability for coal

C.H. Zhang[1,a] , X.P. Xu[1,b]

[1,2]School of Civil Engineering, Hebei University of Science and Technology, Shijiazhuang，Hebei 050018,China

[a]zhangchunhui789@163.com, [b]xuxiaopan@sohu.com

**Keywords:** water content, coal, permeability, slippage effects

**Abstract.** To obtain the effects of water content on the permeability of coal, briquette specimen were obtained from Wulong Mine, Liaoning Province. The permeability of the air drying, bounding water and saturating specimens were tested with self-made equipment respectively, and the effects of water content on permeability for coal were studied. The results showed that: (1)The permeability of specimens decreases with confining pressure increasing, and the air drying and bounding water specimens take on obvious slippage effect. However the saturated specimens never take on slippage effects. It is because the channels of saturated coal sample are occupied by water. When the gas goes through specimens, gas never is absorbed. Collision between gas and the channel wall decreases, and the slippage effect disappears. (2) With water content increasing, the permeability of specimens decreases. (3)The permeability of specimens increases when pore pressure increases.

## Introduction

Scientific prediction of gas flow and aggregation in coal seams is the key issue to prevent the disaster of methane [1-3]. Permeability of coal, affected by stress, temperature and many other factors, is a pivotal parameter to predict gas flow in coal seams.

C.H. Zhang[4] carried out experiments of gas flow on coal and the effects of pore pressure on coal permeability and slippage was analyzed. Y.J. Yu[5] studied the effects of temperature and failure on permeability. Z.P. Meng[6] explored coal's permeability under whole stress-strain curves. J. Xu[7] researched permeability of coal containing gas under varying temperatures and stress. Coal samples containing gas were tested by Z.H. Zhu[8], and the permeability was studied by varied stress path. The effects of coal matrix shrinkage on permeability were studied by S.J. Peng[9]. The effects of temperature and the average effective stress on coal permeability was analyzed by Z. Wang[10]. The effects of ultrasonic functions for coal with low permeability on desorption was tested by X.C Xiao [11].

Coal always suffers from groundwater. It is of great significance to study the effects of groundwater on permeability of coal for prediction of the gas flow and accumulating laws. However, the present researches rarely are reported.

In this paper, the briquette specimens were obtained from Fuxin Mine in Liaoning Province. The self-made tri-axial experiment setup of coupled deformation and gas flow was employed to test the permeability of the drying, bounding water and saturating samples under varying confining pressure and pore pressure. The effects of water content on permeability for coal were studied, and the results are provided to help the prediction of gas flow.

## Experiment

**Preparation** The raw coal was obtained from Fuxin Mine in Liaoning Province. Due to the heterogeneity of raw coal, the briquette specimens were used in the experiment. The raw coal was powdered less than the size of 0.15 mm. The coal powder was mixed with proper water. Then the coal powder with water was put in the forming mould, and 25 ton pressure was kept 20 min by testing machine. As a result 6 standard samples with the size of Φ 50 mm x 100 mm were made. The porosity of the samples was about 14%. The samples were kept 48 hours in a drying baker at the temperature of 100. After that 2 drying samples, 2 samples with bounding water and 2 saturating samples were

made respectively. The average water content for every group was 0.01%, 3.6% and 9.9%, respectively.

**Experimental Equipment and Experimental Procedures** In this paper the self-made tri-axial stress-seepage equipment was used. The equipments includes true triaxial permeameter, test hydraulic pump, digital pressure gauge, regulating pressure valves, six-port valve, pipes, nitrogen and energy storage tank, et al. And it can be seen in Figure 1.

The basic steps can be followed as: First, the prepared standard coal sample was put into the tri-axial stress gripper, and was sealed with heating shrinkable tube. Second, confining pressure was constantly applied, and then pore pressure was applied (nitrogen). When that was stable he gas flow was measured and the permeability was calculated according to the following formula:

$$k = \frac{2p_0 Q\mu L}{A(P_1^2 - P_2^2)} \quad . \tag{1}$$

Where, $k$ is permeability, $\mu m^2$; $P_0$ is standard atmospheric pressure，MPa; $P_1$ is gripper inlet pore pressure，MPa; $P_2$ is gripper outlet pore pressure ;$L$ is the length of the coal samples, in mm; $Q$ is standard atmospheric pressure(20°) air flow, in ml/min; $\mu$ is the gas dynamic viscosity coefficient, in Pa·S; $A$ is section area of coal samples，$mm^2$.

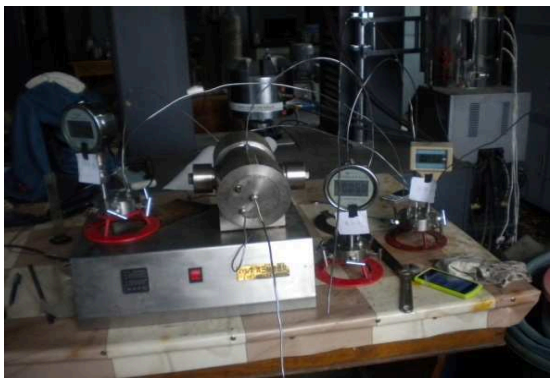

**Fig.1** Permeability test equipment
(Real Photo of Permeability Apparatus：Gas permeability equipment )

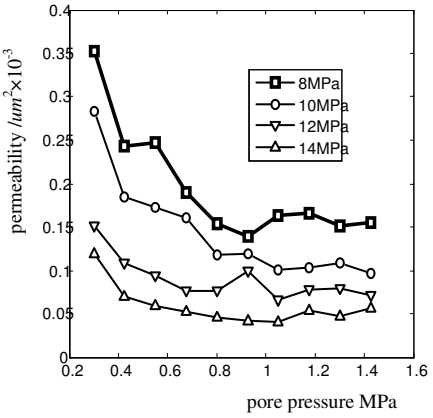


**Fig.2** Permeability of dried coal

**Experimental Results and Analysis** The average permeability of the three different groups under varying confining pressure and pore pressure is obtained through the experiment. The results are shown from Fig.2 to Fig.4.

Fig.2 is the permeability of the dry coal sample under varying confining pressure and pore pressure. It can be seen from Fig.2 with the confining pressure increasing the permeability decreases. While with pore pressure increasing, the permeability initially decreases then increases slowly. That approximately takes on a "V" curve, and it is so called *slippage effects* (or *Klinbenberg effects*). In Fig.3 the permeability of bounding water specimen is seen under varying confining pressure and pore pressure. It can be seen from Fig.3 that the relationship between pore pressure and permeability is similar with that of drying coal samples. Namely that also takes on slippage effects.

Comparing Fig.2 with Fig.3, it can be seen that the permeability of bounding water specimen is significantly lower than that of drying specimen. It is mainly because that the existence of bounding water occupies partial space of pores or fracture in specimen, and the flow channel becomes narrow. The slippage effects can be described by Klinbenberg equation as:

$$k = k_0(1 + \frac{b}{p}) \quad . \tag{2}$$

Where, $k_0$, $b$ are fitting coefficient, determined by fitting the experimental data, $p$ is pore pressure.

Eq.2 is employed to fit the experimental data in Fig.2and Fig.3, and the fitting results are listed in Table 1.It can be seen from Table.1 that the relationship between pore pressure and permeability for drying and bounding water specimens can be well fitted by.Eq.2.

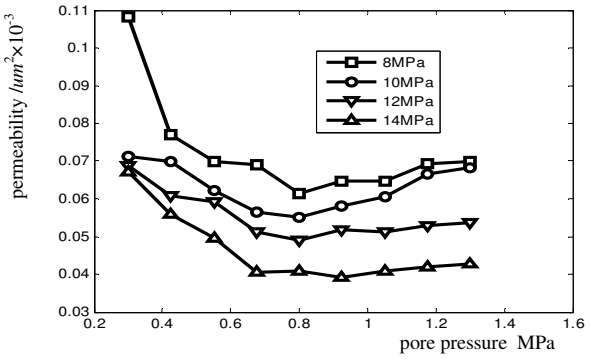


**Fig.3** Permeability of bounding water specimen

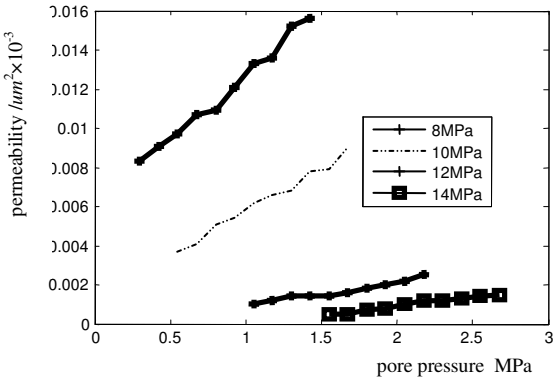


**Fig.4** Permeability of saturating coal sample 1

The relationship between pore pressure and permeability of saturated specimens under varying confining pressure can be seen in Fig.4. It can be seen from Fig.4 that the permeability gradually increases when port pressure increases, and the slippage effects disappear. The main reason is the channel in saturated specimens is occupied by water, when the gas goes through, the gas can't be adsorbed by the channel wall. As a result, the slippage effects disappear. The permeability of saturated water specimens increases when pore pressure increases.

**Table.1** Fitting results for drying, bounding water and saturating specimens

| groups | confining pressure/MPa | $k_0$ | $k_1$ | $b$ | correlation coefficient |
|---|---|---|---|---|---|
| drying | 8 | 0.085 | / | 0.897 | 0.957 |
| | 10 | 0.046 | / | 1.496 | 0.980 |
| | 12 | 0.050 | / | 0.548 | 0.906 |
| | 14 | 0.023 | / | 1.040 | 0.891 |
| bounding water | 8 | 0.050 | / | 0.290 | 0.874 |
| | 10 | 0.058 | / | 0.062 | 0. 849 |
| | 12 | 0.045 | / | 0.152 | 0.910 |
| | 14 | 0.030 | / | 0.354 | 0.951 |
| saturating | 8 | / | 0.637 | 0.561 | 0.994 |
| | 10 | / | 0.612 | 0.518 | 0.988 |
| | 12 | / | 1.341 | 0.653 | 0.986 |
| | 14 | / | 0.974 | 0.576 | 0.975 |

It also can be seen from Fig.4 that the permeability of saturated specimens decreases significantly. That is mainly because that free water occupies partial space of pores and fractures and the gas flow is blocked. With confining pressure increasing, the permeability of saturated specimens decreases. When pore pressure increases the permeability increases as well. Obviously the permeability of saturated specimens is decided by confining pressure. It is because under the effective confining pressure the coal has a tendency of being pressed, which makes pores space smaller, and the permeability decreases. The relationship between effective confining pressure and permeability can be written by:

$$k = k_1 \exp(-a\sigma') . \quad (3)$$

*Where,* $k_1$, $a$ are fitting coefficient, respectively, $\sigma'$ is effective confining pressure.

Eq.3 is employed to fit the experimental data in Fig.4, and the fitting results are listed in Table 1.

It can be seen from Table.1 that the relationship between permeability and effective confining pressure can be well fitted by Eq.3. In other words, the permeability of saturated specimens takes on negative exponent form with effective confining pressure.

## Conclusions

In this paper effects of water content and confining pressure on the permeability are studied by tri-axial seepage experiments, and our main conclusions include:

(1)The permeability of specimens decreases with confining pressure increasing, and air drying and bounding water specimens take on obvious slippage effect. However the saturated specimens never take on slippage effect. It is because the channels of saturated coal sample are occupied by water. When the gas goes through specimens, gas never is absorbed. Collision between gas and the channel wall decreases, and the slippage effect disappears.

(2) With water content increasing, the permeability of specimens decreases.

(3)The permeability of specimens increases when pore pressure increases.

(4) The permeability of saturated specimens takes on negative exponent form with effective confining pressure.

## Acknowledgements

The authors would like to show great gratitude to the Key National Natural Science Foundation of P. R. China for its financial support. (Grant No. 51274079, 51308182).

## References

[1] C.H. Zhang. Seepage-stress coupled model of heterogeneous and random fractured rock mass [J].Journal of China Coal Society, 2009, 34(11): 1460－1464.

[2] C.H. Zhang, Y.J. Yu, Q.S. Zhao. Seepage-stress elastoplastic coupling model of heterogeneous coal and numerical simulation [J]. Rock and Soil Mechanics. 2009, 30(9):2837-2842.

[3] J.P. Tang, Y.S. Pan, S.L. Yang. Experimental study of coal and gas outburst under tridimensional stresses [J]. Chinese Journal of Rock Mechanics and Engineering. 2013, 32 (5):960-965.

[4] C.H. Zhang, Y.J. Yu, H.L Yue, et al. Seepage-stress coupled model of coal with Klinbenberg effect [J].Rock and Soil Mechanics. 2010, 31(10):3217-3222.

[5] Y.J. Yu, H. Zhang, C.H. Zhang, et al. Experiments of effects of temperature and stress on permeability of standard coal briquette specimen [J]. Journal of China Coal Society.2013, 38(6):936-941.

[6] Z.P Meng, B.Y. Wang, X.T. Xie, et al. Mechanical properties of coal deformation and its influence on permeability [J].Journal of China Coal Society. 2012, 37(8):1342-1347.

[7] J. Xu, S.J. Peng, Y.Q. Tao, et al. Experimental analysis of influence of creep on permeability of gas-bearing coal [J]. Chinese Journal of Rock Mechanics and Engineering. 2009, 28(11):2273-2279.

[8] Z.H. Zhu, T. Feng, D.H. Xie, et al. Seepage property of coal containing gas under different paths in laboratory [J].Journal of Mining & Safety Engineering. 2012, 29(4):570-574.

[9] S.J. Peng, J. Xu, G.Z. Yin, et al. Experimental analysis of matrix shrinkage's influence on mechanical permeability of gas filled coal [J]. Journal of Chongqing University. 2012, 35(5):109~114.

[10] Z .Wang, M. Yuan, M.H. He,et al. Experiment study on influence of stress field and temperature on permeability of coal samples [J]. Coal Technology .2013, 32(2):103-104.

[11] X.C. Xiao, J. Xu, Y.S. Pan. Experiment study of promoting methane desorption law in coal considering power ultrasound effect [J]. Chinese Journal of Rock Mechanics and Engineering. 2013, 32(1):65-71.

*Applied Mechanics and Materials Vols. 580-583 (2014) pp 205-208*
*© (2014) Trans Tech Publications, Switzerland*
*doi:10.4028/www.scientific.net/AMM.580-583.205*

# The application of cubic spline interpolation function in determining rock rheological long-term strength

Moli Zhao[a] , Qiangyong Zhang[b]

Geotechnical and Structural Engineering Research Center，Shandong University，Jinan，Shandong 250061，China

[a]hello-zml@163.com, [b]qiangyongz@sdu.edu.cn

**Keywords:** Rock rheological mechanics; Rheological long-term strength; Isochronous curve method; Cubic spline interpolation; Maximum deviation point

**Abstract.** The rheological long-term strength is determined according to the triaxial rheological test data of diabase at the dam area of Dagangshan Hydropower Station. Firstly, based on the stress-strain isochronous curve method and connected the test points with cubic spline interpolation function, the maximum deviation point in the long-term interval is determined as the turning point and established the long-term strength by nonlinear least square method. The results show that this method is consistent with the other methods. Finally, the advantage and disadvantage of this method is analyzed. This method can overcome the randomness of artificial selecting the turning points. Therefore, maximum deviation point method is relatively a reasonable and effective method to determine the rheological long-term strength of rock.

## Introduction

Long-term strength as a time effect parameter is one of the important parameters in the long term stability analyses. When the stability of geotechnical engineering is calculated, the long-term strength will always be considered as an important index[1,2]. In geotechnical engineering with long term loading, the actual stress must less than the long-term strength in order to limit the rock creep. The long-term strength of rock is the maximum stress of rock with long time loading and no destruction.

Generally, the long-term strength is calculated by the triaxial rheological tests[3]. Direct method and indirect method are two mainly methods to determine the value of long-term strength[4]. Chen[5] proposed the third yield value theory, which is a popular method to determine the value of long-term strength using stress-strain isochronous curves. Li[6] obtained the long-term value used three method they are isochronous stress strain cluster method, the relationship between steady state creep rate and stress, crash time with damage stress in fractures and creep loading pressure.

However, it is artificial that use the method of isochronous stress strain cluster to obtain the long-term strength through selecting the turning points. The artificially selecting the turning point are daunted in some papers[7,8]. Then, in this paper, the cubic spline interpolation function and calculating the maximum deviation points method are used to obtain the turning points. This method can overcome the randomness of artificial selecting the turning points.

## Fundamental principles

In order to obtain the long-term strength of diabase with triaxial loading, Dagangshan hydropower bedrock diabase triaxial rheology test data are used. The cylinder diabase specimens have diameter of 50mm and high 100mm. The creep tests were carried out by using rock servo-controlled triaxial rheology equipment RLW-1000KN with 20±1°C room temperature. For diabase specimens, the triaxial creep tests were performed under the condition of confining pressures of 10MPa and 20Mpa. During the creep tests, pre-determined multi-step loading stress levels were applied in steps. Fig.1-2 show the two kinds of tests axial creep curves with specific confining pressure. Fig.3-4 are the isochronous spline cluster of diabase under multi-stage axial loading at confining pressure 10MPa and20MPa.

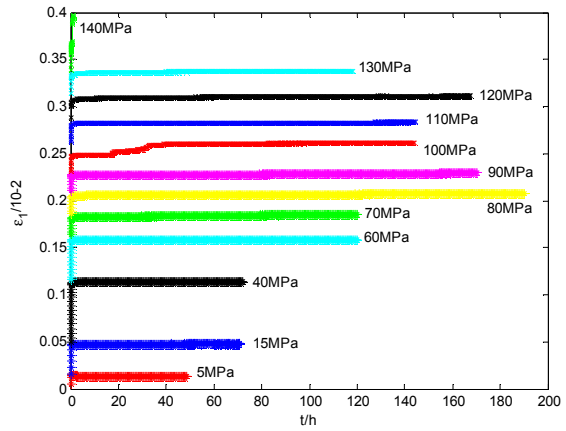


Fig.1 Axial creep curves of jointed diabase under multi-stage axial loading at confining pressure of 10MPa

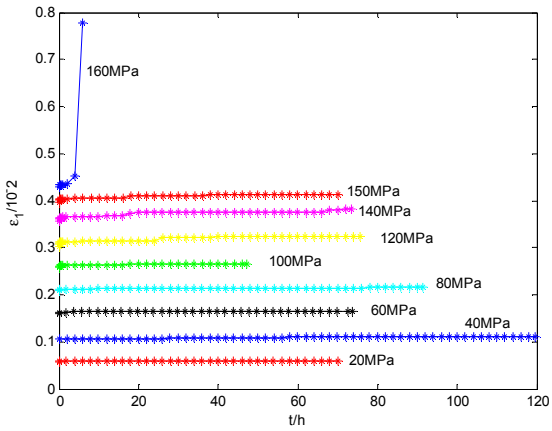


Fig.2 Axial creep curves of diabase under multi-stage axial loading at confining pressure of 20MPa

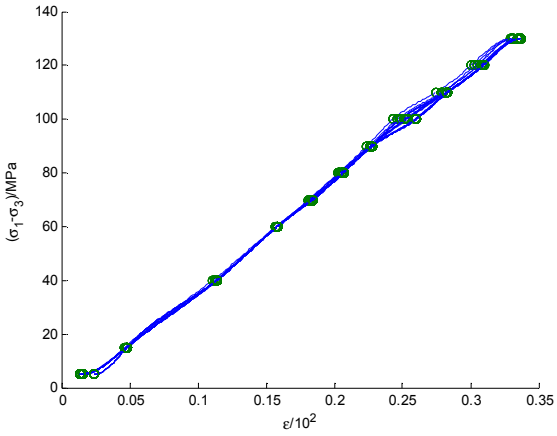


Fig.3 Isochronous spline cluster of jointed diabase under multi-stage axial loading at confining pressure of 10MPa

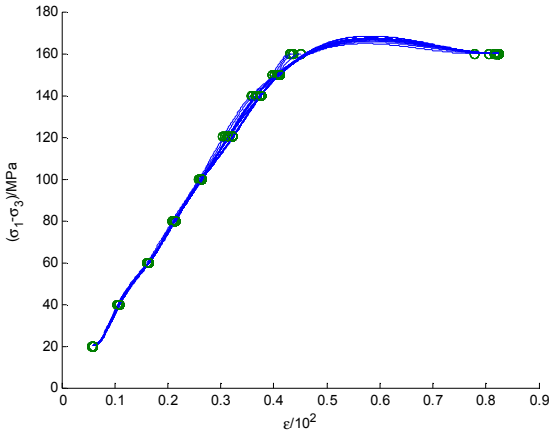


Fig.4 Isochronous spline cluster of diabase under multi-stage axial loading at confining pressure of 20MPa

**The range of Long-term strength**

From Fig.3 with the differential stress increasing at confining pressure of 10MPa, it is obtained that the increase rate of strain with differential stress more than 90MPa is bigger than the differential stress in 0-80MPa. Hence, under the confining pressure of 10MPa the value of long-term strength added the confining pressure must be in the range [100, 110] MPa. At the confining pressure of 20MPa the value of long-term strength added the confining pressure must be in the range [120,140] MPa. Because the creep property of the rock are strongly linked with the stress value, the stable creep or acceleration creep will be appear when the axial loading increased to a limited value of stress. The range of long-term strength using this method is coincidence with the method unstable creep criterion. So, the range will be used to get the third yield point.

**Calculating the Long-term strength value**

Using the data of the tests at the confining pressure of 10MPa and 20MPa, the cubic polynomials are obtained using the cubic spline interpolation method. Then, the maximum deviation point in the range of long-term strength will be found as the turning point. Supposing the function of the cubic polynomial is $y=f(x)$ and $a$, $b$ are the x-axis coordinate of the internal endpoint. So the maximum deviation point is the point on the curve of the cubic polynomial in the range, which has the maximum distance from the points on the line to the line AB. Fig.5 shows the geometric relationship of the maximum deviation point. The x-axial coordinate of the maximum point can be obtained using

$$f'(c)=\frac{f(b)-f(a)}{b-a}. \tag{1}$$

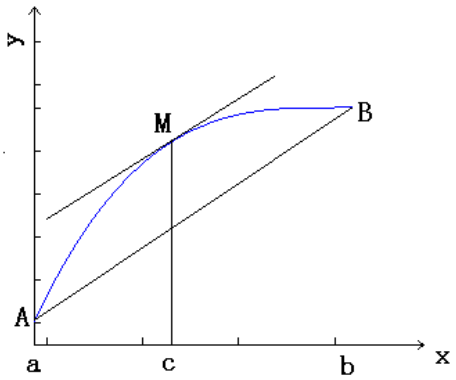


Fig.5 Maximum deviation point M

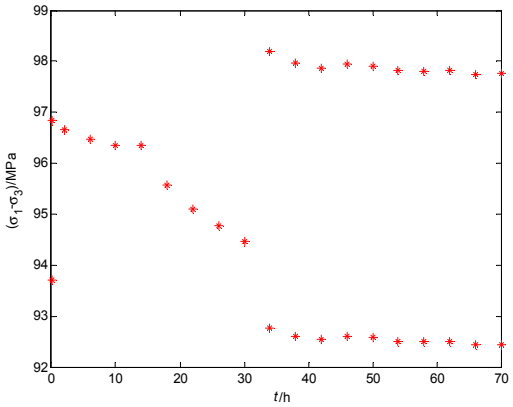


Fig.6 Maximum deviation points of diabase under multi-stage axial loading with confining pressure of 10MPa in ($\sigma_1$-$\sigma_3$)-t figure

From the results of calculation, not all ranges have only one maximum deviation point. Some ranges have two maximum deviation points. Because the function is cubic polynomial, in the case of $x\in[a, b]$ with $f''(x)=0$ , the range will has two deviation points as in Fig.6. If the range has two deviation, we will choose the lower stress value as the established maximum deviation point. The exponential equation (2) is used to determine the long-term strength value

$$\sigma = A + B\exp(-at) \tag{2}$$

Where A, B are the undetermined coefficient. So, the stress $\sigma$ reaches $\sigma_\infty$ with the time $t$ tending to positive infinity. Then the equation (2) can be expressed as

$$\sigma = \sigma_\infty + (\sigma_0 - \sigma_\infty)\exp(-at) \tag{3}$$

Where $\sigma$ is the differential stress of the maximum and minimum principle stress. Fitting the maximum deviation points with nonlinear least square method, the undetermined coefficient and $\sigma_\infty$ can be found. The value of $\sigma_\infty$ is the long-term strength of the rock with respect to the corresponding confining pressure. At confining pressure 10MPa, the long-term strength $\sigma_\infty$ is 103.5088MPa, the creep fracture strength $\sigma_f$ is 150MPa and $\sigma_\infty/\sigma_f$ =0.69. At confining pressure 20MPa, the long-term strength $\sigma_\infty$ is 124.94MPa, the creep fracture strength $\sigma_f$ is 180MPa and $\sigma_\infty/\sigma_f$=0.693.

## Comparison analyses with different method

Table 1 gives the data comparison of various methods to determine the long-term strength. It is demonstrated the long-term strength obtained with unstable creep criterion is lower than the value with other methods. The reason of this phenomenon is the value of the long-term strength with unstable creep criterion equaling to the stress of the first point in the range. While the value of the long-term strength with the isochronous stress strain method and the maximum deviation point method in this paper equaling to the stress of the turning point in the range. Considering the limitation of the test, it is impossible to divide the stress stage very closely. Therefore, the unstable creep criterion is more conservative and the value is more lower than other methods. We also find that the value of long-term strength with deviation point method is approximately with the value used by isochronous stress strain method. Deviation point method making use of the cubic spline interpolation function to fit the test data which can keep the smooth and continuity of the whole system. This method can overcome the randomness of artificial selecting the turning points. Even though, sometimes we will get two deviation points in the range. In order to the safety of engineering, it is reasonable to choose the lower value as the deviation point. So the deviation point method is a reliable method to acquire the value of long-term strength.

Table 1 Comparison of various methods to determine the long-term strength

| Methods | | Confining pressure/MPa | |
|---|---|---|---|
| | | 20MPa | 10MPa |
| Isochronous stress strain method | $\sigma_\infty$/MPa | 124.4 | 104.2 |
| | $\sigma_\infty/\sigma_f$ | 0.691 | 0.695 |
| Unstable creep method | $\sigma_\infty$/MPa | 120 | 70 |
| | $\sigma_\infty/\sigma_f$ | 0.667 | 0.467 |
| Volume method | $\sigma_\infty$/MPa | 124 | 50 |
| | $\sigma_\infty/\sigma_f$ | 0.689 | 0.333 |
| Maximum deviation point method | $\sigma_\infty$/MPa | 124.9 | 103.5 |
| | $\sigma_\infty/\sigma_f$ | 0.693 | 0.69 |

## Conclusions

A method for determining the long-stem strength value is presented in order to overcome the randomness of artificial selecting the turning points. This maximum deviation point method can be obtained the long-term strength value using the triaxial creep test data at different confining pressure. This method is easily programming and standardizing. From the results of calculation, the value of long-term strength with deviation point method is approximately with the data obtained by isochronous stress strain method. The long-term strength value with unstable creep criterion is lower than the value with other methods. From the results we can see the deviation point method is a reliable method to determine the value of long-term strength.

## References

[1] V. I. Pushkarev, B. G. Afanas'ev: J. Min. Sci., vol. 9(1973), No.5, p.558

[2] C. M. Sangha, R. K. Dhir. Int. J. Rock Mech. and Mining Sci., vol. 9(1972), No.3, p.343

[3] Z. Szczepanik, D. Milne, K. Kostakis and E. Eberhardt, in Handley, M., and Stacey, D., eds., Technology roadmap for rock mechanics: Pretoria, South African Institute of Mining and Metallurgy, Tenth Congress of the International Society for Rock Mechanics, Johannesburg, (2003) , p. 1179

[4] J. Sun: Chinese J. Rock Mech. Eng., vol.26(2007),No. 6, p.1081(In Chinese)

[5] Z. Chen: Chinese J. Rock Mech. Eng., vol.1(1982), No. 1, p.1(In Chinese)

[6] L. Li, W. Xu, W. Wang, et al.: Eng. Mech., vol.27(2010), No. 11, p.127(In Chinese)

[7] X. CUI, C.She: J. Rock Mech. Eng., vol. 30(2011), Supp.2, p. 3899(In Chinese)

[8] Q. Zhang, W.Yang, F. Cheng, et al: Chinese J. Geotechinical Eng., vol. 33(2011), No.12, p.1910(In Chinese)

*Applied Mechanics and Materials Vols. 580-583 (2014) pp 209-212*
*© (2014) Trans Tech Publications, Switzerland*
*doi:10.4028/www.scientific.net/AMM.580-583.209*

# The Application of Vacuum Preloading Method in Soft Soil Foundation Underwater

Yuqin Feng[1,a], Lu Zhang [2,b]

[1]The school of Architecture and Civil Engineering , Inner Mongolia University of Science & Technology, Baotou 014010, China

[2]The Nuclear Industry 208 Battalion, Baotou 014010, China

[a]btfyq@126.com, [b]zllxy_love@126.com

**Keywords:** Soft foundation, Shear strength, Vacuum preloading, Construction technology

**Abstract.** On the basis of engineering project in coastland, this article analyzes the construction technology and reinforcement mechanism of vacuum preloading reinforces soft soil foundation. By indoor soil test of Reinforcement of soil before and after processing, comparing the change of the physical and shear strength index, verify vacuum preloading method underwater is effective means in handing soft ground and provide some experience for regional development and promotion of underwater application of vacuum preloading technology.

## Introduction

With the development of high heavy buildings in coastal cities, Traditional foundation treatment methods cannot satisfy the requirement of engineering practice, Some composite foundation treatment methods and new foundation treatment technology have been applied in engineering practice. Composite foundation treatment method is not permutation and combination of simple foundation treatment method. It needs reasonable combination to achieving the goal of 1+1>2. The soft soil foundation vacuum preloading underwater is one of composite foundation treatment technology. It could quicken the progress of soil consolidation and strength, reducing project duration, saving material and cost of investment. In order to develop and disseminate vacuum preloading underwater technology, this article combining an engineering example in the coastal area, analyze the application problems of vacuum preloading underwater technology handing soft ground to provide some experience for construction technology and design of vacuum preloading underwater in the coastal areas.

## Project Overview

One construction sites being high-rise and super-tall residential groups, locate one provinces and cities area, belonging to coast accumulation landforms. Proposed projects main building is 12~33 layers, above the ground height being 48~100m, setting 2 layers basement. This project ±0.00 height is 4.9m, the basement floor bottom elevation being -5.6m, cushion layer thickness being 0.2m, the upper structure with frame-shear wall or frame shear wall structure. The primordial terrain belong coast accumulation landforms and now formed by man-made. The land form is flat and the site leveling elevation is 5.9m. The field southwest, southeast and northeast still exist surface water for a long time, surface water depth being about 1.00m. In view of silt soft soil layer which appeared saturated flow state is thick of 0.00m~20.10m has widespread distribution in this area and the overlying filling being owe consolidation soil, for reducing the adverse effects of consolidation settlement which occurred in the soft soil layer in the stage of the project being completed. So this silt soft soil layer site will use vacuum preloading underwater method to reinforce foundation.

From top to bottom soil name and lithology abased on drilling results are shown in table 1.

**Table 1. The name, Thickness and Status of Soil Layer**

| Number | Code | Soil Name | Thickness (m) | Geotechnical Condition |
|---|---|---|---|---|
| ① | $Q_1^{ml}$ | Artificial Filled Soil | 0.50~8.60 | Loose State |
| ② | $Q_2^{ml}$ | Artificial Reclaimed Soil | 0.50~14.00 | Saturation and Loose State |
| ③ | $Q_2^{mc}$ | Sludge | 1.40~18.80 | Saturation and Flowing Plastic |
| ④ | $Q^{el}$-1 | Clay | 0.70~4.80 | Saturation and Plasticity |
| ⑤ | $Q^{el}$-2 | Gravelly Sand | 0.80~5.95 | Saturation and Slightly Less Dense |
| ⑥ | $Q^{el}$-3 | Gravelly Cohesive Soil | 1.00~5.70 | Saturation and Hard Plasticity |
| ⑦ | $\gamma_4$ | Completely Weathered Granite | 0.70~12.70 | Earthy |
| ⑧ | $\gamma_3$ | Intensely Weathered Granite | 0.15~15.50 | Soil Clip Pieces |
| ⑨ | $\gamma_2$ | Moderately Weathered Granite | 0.50~5.60 | Core Into Earthy |

## The Construction Process

Place the sand blanket after site clearing , make the curtain of construction clay and drive plastic drainage plate (Type B plastic drainage plate of the SPB100 series, section size 4’100mm),layout vacuum lines (PVC outer membrane type filter tubes, pipe diameter>50mm), inbuilt vacuum probe, inbuilt monitoring devices, excavation pressure membrane channel, pave earthwork cloth, vacuum membrane, fill the cofferdam and impoundment while evacuating (pour the water being pumped into the cofferdam, forming constant water load), after prepressing the load 90 days, go on evacuating if the degree of consolidation can not meet the requirements, otherwise, unloading, completion and acceptance can be performed.

## Reinforcement Mechanism of Vacuum Preloading Underwater

Reinforcement mechanism of vacuum preloading have three point. The first point is that the load coming into thin film above is equal to the load coming into inside and outside differential pressure; The second point is that the underground water level lower, additional stress increasing, couple with additional pressure of foundation soil increasing. The third point is that closed bubbles discharge, the permeability of soil increasing. Under positive pressure, saturated soil has a small number of closed bubbles which have plugged gap to reduce the permeability of soil, speeding up the consolidation process. In this project, vacuum conditions need to extract a large number of groundwater, together with auxiliary seal measures of membrane, like membrane ditch stored water together, enclosed sheet pile wall stored and so on. Membrane water storage can play a role of sealing membrane to ensure the membrane under vacuum degree; it also could have the effect of preloading load. The actual load is equal to the membrane under vacuum preloading load and the sum of membrane water pressure load. In vacuum load and membrane water pressure load, pore water was ruled out slowly and the volume decrease slowly, foundation consolidation deformation, and the same time, with the super hydrostatic pressure disappearing gradually, effective stress increase gradually, the strength of the foundation soil increasing gradually. Like this using water as extraction by the preloading load, could avoid using large material stack, reducing the construction cost greatly, getting on economic and practical effect.

**Analysis of Indoor Soil Test Results Before and After Processing**

The project had indoor geotechnical experiment for mud soil before processing and made an evaluation of the physical and mechanical properties of soil. According to the national standard «Standard for soil test method» (GB/T50123-1999), this test takes with 21 pieces of undisturbed soil sample. Test results are shown in Table 2.

**Table 2. Mud Soil Before Processing Physical and Mechanical Properties Statistical Table**

| Items | Min | Max | Average Value | Standard Deviation | Coefficien of Variation | Correction Factors | Standard Values |
|---|---|---|---|---|---|---|---|
| Water Content $w$ (%) | 52.40 | 71.30 | 60.90 | 6.140 | 0.10 | 1.039 | 63.200 |
| Density $\rho$ (g/cm$^3$) | 1.550 | 1.670 | 1.620 | 0.034 | 0.021 | 1.008 | 1.63 |
| Proportion $G$s | 2.660 | 2.690 | 2.670 | 0.009 | 0.003 | 0.999 | 2.670 |
| Void Ratio $e$ | 1.406 | 1.938 | 1.660 | 0.150 | 0.090 | 1.035 | 1.718 |
| Liquid Limit $w_L$ (%) | 42.70 | 54.00 | 47.50 | 3.960 | 0.083 | 1.030 | 48.90 |
| Plastic Limit $w_P$ (%) | 25.10 | 31.30 | 27.60 | 2.098 | 0.076 | 0.973 | 26.90 |
| Plasticity Index $I_P$ | 17.60 | 24.20 | 19.90 | 1.979 | 0.100 | 1.038 | 20.60 |
| Liquidity Index $I_L$ | 1.530 | 1.790 | 1.670 | 0.080 | 0.048 | 1.018 | 1.700 |
| Coefficient of Compressibility $a_{1\text{-}2}$ ( $MP_a^{-1}$ ) | 1.060 | 1.950 | 1.320 | 0.306 | 0.232 | 1.099 | 1.450 |
| Compression Modulus $E_{1\text{-}2}$ ($MP_a$ ) | 1.500 | 2.500 | 2.100 | 0.318 | 0.154 | 0.934 | 1.900 |
| Internal Friction Angle $\varphi$ ($^0$) | 2.000 | 4.200 | 3.100 | | | | |
| Cohesive Force $c$ ($kP_a$ ) | 2.000 | 5.000 | 3.500 | | | | |

In this field, mud soil adopt vacuum joint impoundment preloading to reinforce, According to the national standard «Standard for soil test method» (GB/T50123-1999), this test takes with 21 pieces of undisturbed soil sample. Test results are shown in table 3.

From table 2 and table 3 above it can be seen that the natural water content of processed mud soil detected in the field has decreased 3.8% in the measuring depth, void ratio decreased 2.56% liquidity index decreased 3.6%, coefficient of compressibility decreased 10.34%, modulus of compression increased 5.2%, cohesion increased 47.7%, illustrating that this field's mucky soil layer which take the method of vacuum combined with water storage stack preloading to reinforce do has certain effects.

**Table 3. Mud Soil After Processing Physical and Mechanical Properties Statistical Table**

| Items | Min | Max | Average Value | Standard Deviation | Coefficien of Variation | Correction Factors | Standard Values |
|---|---|---|---|---|---|---|---|
| Water Content $w$ (%) | 50.60 | 68.30 | 59.00 | 5.125 | 0.087 | 1.032 | 60.80 |
| Density $\rho$ (g/cm$^3$) | 1.580 | 1.700 | 1.630 | 0.034 | 0.021 | 1.002 | 1.65 |
| Proportion $G$s | 2.660 | 2.730 | 2.680 | 0.016 | 0.006 | 0.998 | 2.680 |
| Void Ratio $e$ | 1.421 | 1.874 | 1.619 | 0.141 | 0.087 | 1.032 | 1.670 |
| Liquid Limit $w_L$ (%) | 44.10 | 52.40 | 47.30 | 2.160 | 0.046 | 1.016 | 48.00 |
| Plastic Limit $w_P$ (%) | 25.90 | 30.70 | 28.00 | 1.481 | 0.053 | 0.982 | 27.50 |
| Plasticity Index $I_P$ | 18.20 | 22.00 | 19.70 | 0.972 | 0.049 | 1.018 | 20.00 |
| Liquidity Index $I_L$ | 1.400 | 1.800 | 1.600 | 0.134 | 0.084 | 1.031 | 1.640 |
| Coefficient of Compressibility $a_{1\text{-}2}$ ( MP$_a^{-1}$ ) | 0.940 | 1.470 | 1.190 | 0.179 | 0.150 | 1.088 | 1.300 |
| Compression Modulus $E_{1\text{-}2}$ (MP$_a$ ) | 1.800 | 2.600 | 2.200 | 0.281 | 0.130 | 0.924 | 2.000 |
| Internal Friction Angle $\varphi$ ($^0$) | 2.000 | 2.600 | 2.400 | 0.154 | 0.065 | 0.964 | 2.300 |
| Cohesive Force $c$ (kP$_a$ ) | 2.000 | 9.000 | 5.100 | 1.868 | 0.367 | 0.797 | 4.000 |

## Conclusions

- Vacuum preloading underwater has a certain reinforcement effect for mud soil in coastal region.
- Vacuum preloading underwater can improve the physical and mechanical properties index of mud soil.
- Vacuum preloading underwater can improve the shear strength of mud soil.

## References

[1] Technical Code for Ground Treatment of Buildings, (JGJ 79-2012), (in Chinese).

[2] Code for Design of Building Foundation, (GB 50007-2011), (in Chinese).

[3] Guanbao Ye,etc: *Foundation Treatment* (*the third edition*).( China Building Industry Press, 2009),(in Chinese).

*Applied Mechanics and Materials Vols. 580-583 (2014) pp 213-218*
*© (2014) Trans Tech Publications, Switzerland*
*doi:10.4028/www.scientific.net/AMM.580-583.213*

# The Microstructure Formation Process Research in Loading Condition of Dredger Fill

Jia WANG , Penglin CAI

College of Construction Engineering Jilin university, Changchun 130062,China

**Keyword:** reclaimed soil; microstructure; Consolidation settlement

**Abstract.** This paper takes some sections of Tianjin coast for example, explore the microstructure morphology and index-load combination in the condition of different settling time with load combination about reclaimed soil on the basis of sampling and testing of original state reclaimed soil. Including apparent form, size, directionality gap , formation of the skeleton and bulk density changes of the flocculation body aggregate. It found the characteristics and regularities of microstructure of reclaimed soil in the initial settlement. The research claims the structure of reclaimed soil is enhanced and the change of soil microstructure has positive significance to the engineering geological properties. in the process of consolidation

## The introduction

In coastal areas, it is relatively prominent problem about shortage of land resources in the process of urbanization. The geographical expansion of cities is strictly limited by the land use of construction land, Reclaimed soil[1] is using dredge and mud to pump mud and port formed by hydraulic fill by sedimentary soil at the bottom of the rivers. It has the high water content, high compressibility, high clay content, organic matter, flow, etc. This article mainly research self-organizing microstructure of reclaimed soil[2]

## Test method and instruments

Test instrument has adopted by the vacuum freeze-drying (dexa), scanning electron microscopy fracture method is used to carry on the processing in the microstructure of soil samples in the sample preparation, soil sample is cutted into appropriate size of the soil sample in the beginning. Then sublimating freeze-dried in freeze-dried instrument, after the sample is freeze-dried thoroughly, breaking out the fracture surface at one end of the article in the soil sample as the microstructure of soil test ,last, getting the microstructure image information after coating the ESM scanning electron microscopy (esm) analysis.

## 3 Results and discussion

3.1. The flocculation body and aggregate

This paper studies aggregate collection in the apparent morphology, flocculation body size of aggregate, flocculation body aggregate stereospecificity, flocculation body internal mineral aggregate stereospecificity, reunion body porosity and degree of osteoporosis on the free settling 0 days, five days, ten days, 20 days of reclaimed slurry flocculation body in the process of self-organization and observes its change with time and load regulation.

By the above-mentioned, as the free settling time increased, reclaimed slurry aggregate is smaller from 0 to 10 days in compaction process beginning to form mineral composition with smaller clay

mineral aggregate from high moisture content and solid mineral composition of low flocculation body[3] .Since 10 ~ 40 days, these small molding clay mineral aggregate is forming larger aggregates the new self organization core under the action of self organization in reclaimed mud system.

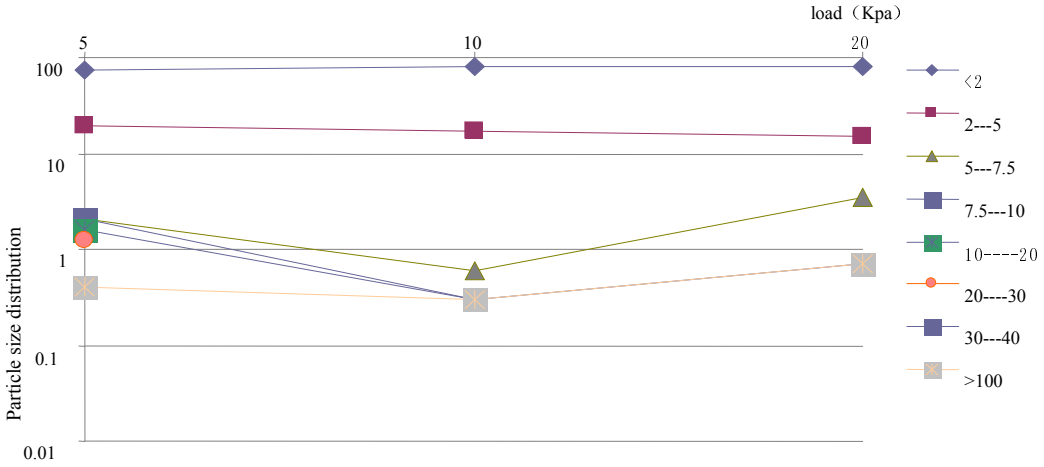


Fig.1 Particle size composition （10d）

3.2 The change of particle diameter

Particle size composition has also changed in the whole process of subsidence. <2 μ m particle concentration is stable and 2～5 μ m particles showed a trend of decrease in the initial settlement, And 7.5 to 10 microns particles, > 100 microns particles increased obviously, it is Show that 2 ~ 7.5 microns particles are widely involved in 7.5 ~ 10 microns particle, > 100 microns particle group formation. the effect of the < 2 microns particle was not significant as shown in figureTo the middle and later periods of the settlement , < 2 microns particles is reducing in a certain degree , The 2 ~ 5 microns particles increased, it shows that < 2 microns particles are widely involved in the formation of 2 ~ 7.5 microns particles. The general trend is: Growth over time, Smaller particles gradually is consumed in the process of large particles formed, But the vast majority of < 2 microns mineral particles is independent individual form in the aggregate ,as show in fig.1.

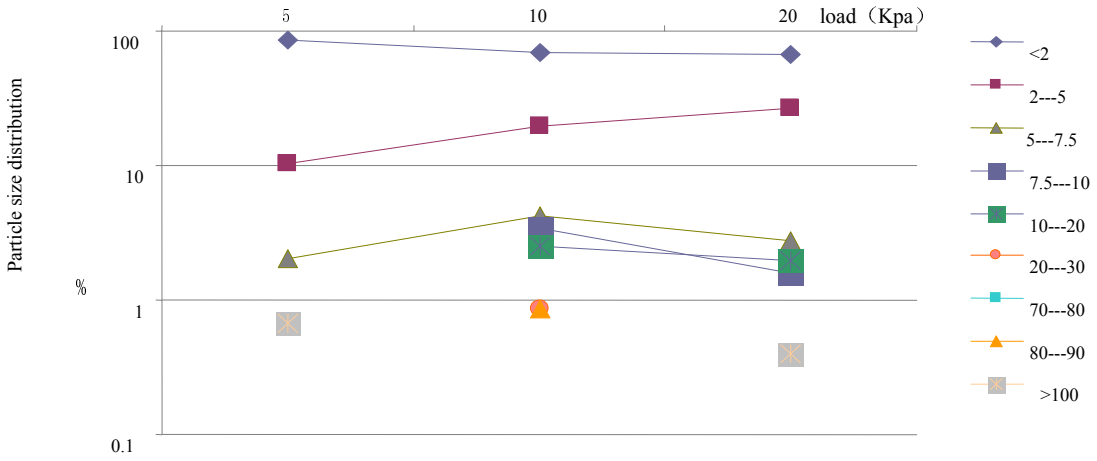


Fig.2 Particle size composition （40d）

3.3 Mineral grain orientation in the aggregate

The directionality of internal mineral of clay mineral aggregate is divided into two stages in the condition of different settling time and load.

The first stage is the initial settlement. Internal mineral aggregate of directional property mainly depends on its initial core directional property of minerals. Some layer or flaky mineral around the core minerals in a smaller angle, However, filamentous with layered clay minerals contact in the form of the point – surface for the most part of The columnar filamentous clay mineral. porosity is larger and aggregate density is low. As show in the fig(3 ,4).

The second stage is the combination of self-organization between aggregate[4]. Especially under the load, The arrangement of collection is in order 。And internal mineral aggregate tend towards the direction of perpendicular to the load, parallel to the horizontal direction. Aggregate in the process may be the whole rotation in the process.

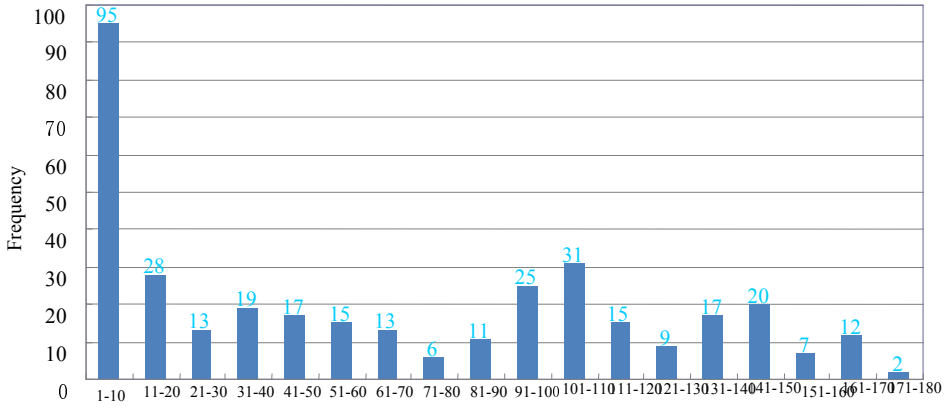


Fig.3 Distribution of long axis and the X axis Angle distribution internal mineral aggregate (10 days 10kPa-4000times)

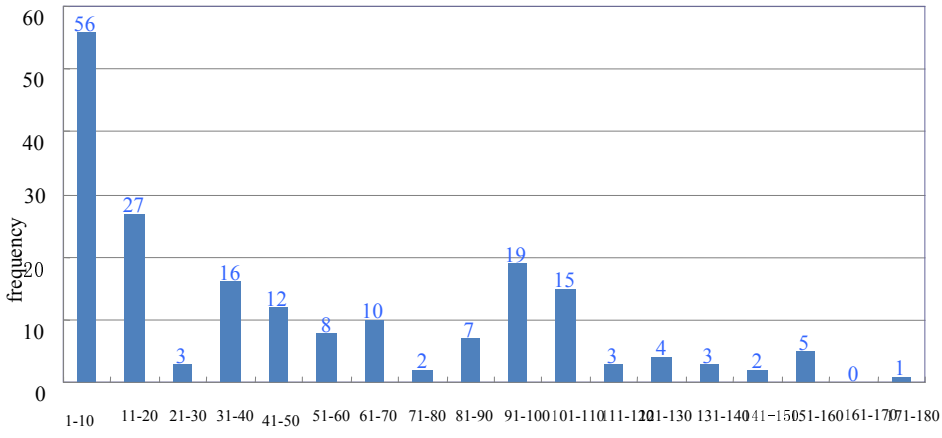


Fig.4 Distribution of long axis and the X axis Angle distribution internal mineral aggregate (10 days 20kPa-4000times)

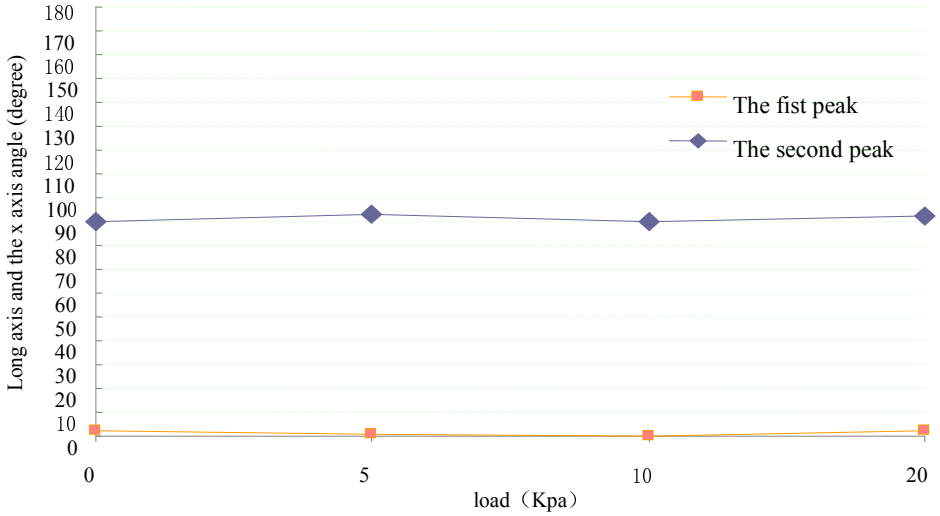


Fig.5 Distribution of long axis and the X axis Angle distribution internal mineral aggregate (40 days 0kPa-4000times)

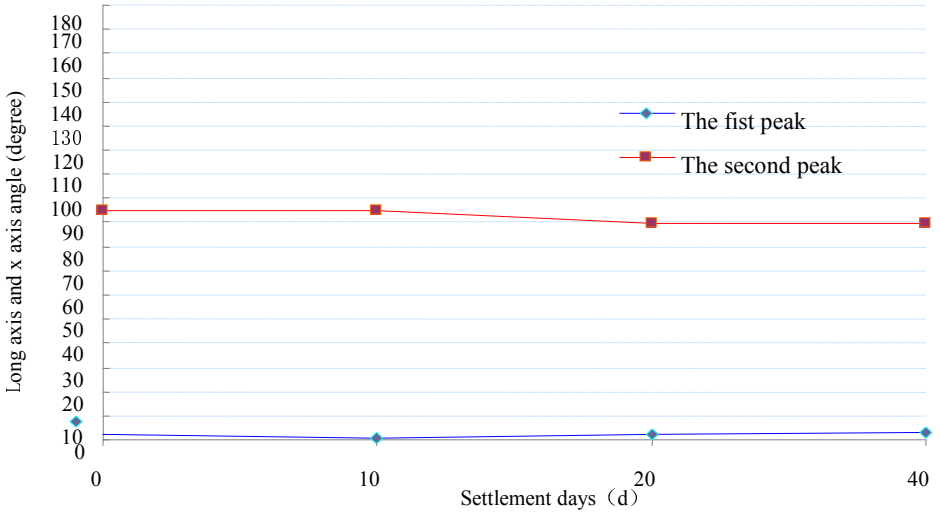


Fig.6 Distribution of long axis and the X axis Angle distribution internal mineral aggregate (40 days 0kPa-4000times)

3.4 Aggregate surface morphology

The aggregate surface morphology has experienced from complex to simple.

The aggregate surface is irregular and there are seemingly villous flake and filamentous clay minerals attached on the surface of the flocculation body aggregate disorderly in the beginning. Flake clay mineral attached to the surface of the flocculation body aggregate irregularly in the condition of no load in ten days of settlement. After loading, The surface morphology is changed .For example mineral particles disappear, clay minerals present layer accumulation, flaky mineral almost parallel to surface, the surface is relatively dense. From 20 days to 40 days, self organization restructuring of aggregate has been completed ,the surface of the aggregate is formed by a collection of complex curved surface, The two clay mineral is closely adsorbed on the surface collection. The direction of mineral plane approach aggregation .The surface of aggregate is smooth and dense. There will be no loose mineral On the surface and cascading mineral edge is visible. It shows that aggregate has a great influence on the surface morphology of form in drainage consolidation of compaction .Surface morphology of the aggregate can also be seen as a factor in reclaimed soil density index[5]. as show in the fig.5

3.5 Gap and bulk density changes of the flocculation body and aggregate

The aggregate pore become close in the body in the process of self-organization of the flocculation body and aggregate，As shown in fig.6.，Suspension of flocculating substance turns into solid flocculation body[6] and Loose flocculating body forms and encrypts fast in the initial flocculation body formation from 0 to 10 days. Flocculation body shapes preliminary through the formation of self-organization of original clay mineral flocculating substance. Micrograph shows that loose mineral stack and small clay mineral particles adsorbed on the surface of the flocculation body astatic. But not dense, irregular surface morphology, villous, sheet, flocculation body has a bigger hole, higher osteoporosis. Self- organization of flocculation structures again under the synergy from 10 to 20 days.

During this period small flocculation body gradually become adsorbed or united by bulky flocculation or aggregation then become honeycomb or grid frame structure and appear larger pores. Composite flocculation body or collection experience drainage consolidation process which the pore water gradually eliminate and the pore become smaller again under the load from 20 to 40 days . As shown in fig.7 its bulk density also increases dramatically in the whole settlement and loading process.

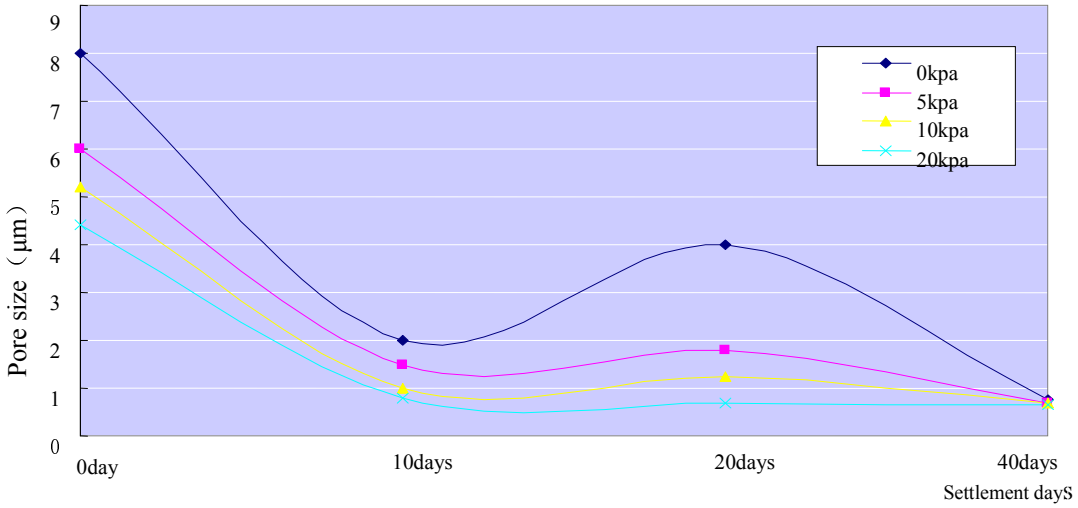


Fig.7. The change of Bulk density and void ratio in the process of initial settlement about filling slurry

3.6 The formation of the skeleton

Test shows that mineral grains and aggregate reclaimed soil skeleton basic form, as well as different forms of changes have taken place in the connection form under the condition of different load or different settlement time. The basic form of skeleton is loose mesh sheet cellular structure and the main connection form is edge surface and mineral grains of linear flake the flocculation body aggregate. The basic form of skeleton is from loose mesh flake honeycomb to the density of honeycomb irregular crumb and crumb honeycomb assembly as the settling time increase. The strength of the reclaimed soil continuously strengthen because skeleton experienced from a single mineral to aggregate skeleton, the structure strength of monomer fossil skeleton is low but structure strength of the aggregate skeleton is higher in the whole[7].

## Conclusions

1. Reclaimed aggregate generated in mud from big to small of the formation of compact process to form small clay mineral aggregate as the free settling time increased. The directional property of internal mineral of aggregate occur two stages of differentiation in the condition of different settlement time and load combination. The first stage is directional property of internal mineral aggregate mainly depends on its initial core directional property of minerals. The second stage is the tendency of internal mineral of the organization is perpendicular to the load.

2. The pores become compacted in aggregate. The pore surface form of reclaimed soil is related to settling time and soil skeleton connection form has changed. for example, skeleton structure is from a single mineral transform into aggregates. The trend of particle size composition is the smaller particles gradually is consumed in the process of large particles formed but the vast majority of < 2 microns mineral particles in the aggregate keep the independent individual form of minerals with growth time in the whole process of settling

## References

[1] Niu C c. 2012,Fractal feature Of Microstructure In The Process of The Seepage Consolidation About Reclaimed Soil [J]. Journal of Southwest Jiaotong University,

[2] SHEN Z w e,WANG J ,2006 . Some discussion of issues about self organizing principle[J].JOURNAL OF SYST EMS SCIENCE , ( 01) :14-18

[3] Yang A w, Du D j.2010 ,Reclaimed soil sedimentary features and the micro structure of the research in Tianjin[J] .Hydrogeology engineering geology,37（5）83-87

[4] Shi b. 1997, Quantitative research of microstructure orientation about cohesive soil [J]. Journal of geological, Vol.71(1)

[5] CHENG Y X ,2008.The Structural Strength Formation Mechanism of Sea shore Dredger Fill and Key Technique of Vacunm Preload Method[D]

[6] Yang J ,2009.Simulation study on structural strength of dredger fill with high clay content during consolidation progress[D].

[7] Cheng Y x, Du D j.2010, Strength growth mechanism of reclaimed soil structural in Tianjin binhai [J]. The coal geological exploration，38（1）：45-49

*Applied Mechanics and Materials Vols. 580-583 (2014) pp 219-223*
*© (2014) Trans Tech Publications, Switzerland*
*doi:10.4028/www.scientific.net/AMM.580-583.219*

# The research on mean spacing of rock fracture

Lu Jiang[1,a], Yangsong Zhang[2,b]

Department of Civil Engineering, Nanjing University of Science and Technology, Nanjing, China

[a]jianglu070903@163.com, [b]zysnj318@126.com

*Corresponding author. E-mail address: zysnj318@126.com (Yangshong Zhang)

**Keywords:** Rock Fracture; Mean Spacing; Linear Density; Linear Density Correction

**Abstract.** The mean spacing of rock fracture is a very important parameter base to evaluate rock mass，a number of rock studies base on it. Object of this paper is Beishan preselected area in Gansu Province, China. A uthor use GPS-RTK to measure the fracture's endpoints and inflection, then process the resulting coordinate, building a three-dimensional model of rock fracture by using three-dimensional software and meshing the three-dimensional model, Through the analysis of fractures in each grid to calculate the linear density of rock fracture, after the orientation and inclination correction on linear density, it can be converted to an mean spacing of rock fractures. The mean spacing of rock fracture can be directly used for rock mass classification in GSI rock systems, and has a great significance in rock engineering studies.

## Introduction

In the study of stability in geotechnical engineering, the study of engineering rock mechanics parameters is one of the key issues[1]， the rock mass engineering support, stability evaluation and numerical simulation all need a selection of mechanical parameters on rock mass strength, and the choice of parameters plays a vital role which result the accuracy of the calculated[2]. Situ testing of rock mechanics parameters has a long cycle, high cost and testing difficulty, Moreover the test results are often presented certain discrete[3]. In the current surrounding rock grading system, only GSI surrounding rock grading system is directly related to rock parameters (such as the Hoek-brown strength criterion and Mohr-Coulumb strength criteria parameters and rock modulus). Through the quantitative surrounding rock grading system, it can reduce the reliance on engineering experience and very convenient[4]. In the process of calculation GSI, the selection of the mean spacing of rock fracture is particularly important, it is difficult to measure directly, so in this paper study the rock fracture's mean spacing through the the endpoints and the inflection point coordinates of rock fracture and other basic information.

## Mean Spacing

The mean distance between Structural plane can be estimated by studying its linear density, Its reciprocal is the mean spacing. Order to area C's third group of field(Area C' fracture is characterized by occurrence can be divided into three groups) in Bei Shan as the research object, first simple treatment the endpoints and inflection point coordinates of fracture which measured by GPS, then establish fracture geometry by using three-dimensional modeling software, finally derived each fissure lines' information.

First read the endpoint and inflection point coordinates of fracture which measured by GPS, as shown in figure 1. Then read the fissure line information which obtained by three-dimensional modeling software, on this basis, according to the point and line information to create fracture line, as shown in figure 2.

According to the read point and create line fitted to free-form surfaces, can reflect the surface fluctuation of the actual area to a certain extent, as shown in figure 3. Subsequently, from the x, y, z three directions will be cut off from the surface every 5m, forming the 5 m intervals grids, as shown in figure 4.

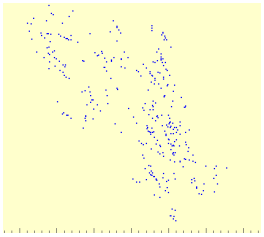

Fig.1 The endpoint and inflection point of fracture's figure

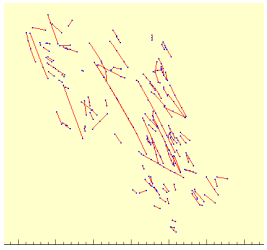

Fig.2 Points and lines created by fractures

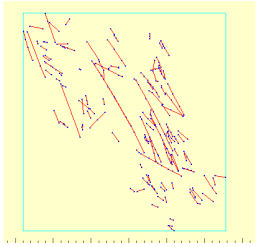

Fig.3 Point and line created by fracture fitted to free-form surfaces

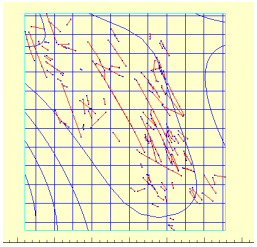

Fig.4 Fracture fitting surface mesh

Figure 3 is the top view of mesh surface of fractures in area C third group, and it can be understood as the grid projected on the horizontal plane. In Figure, Y direction refers to the North, X direction refers to the East. The statistical linear density in both directions that is north-south direction and east-west direction, denoted $n_{SN}$ and $n_{EW}$. The value approach to a grid that is 5m as a unit, optional 5m, 10m, 15m ..... to calculate the length L, count the number of fractures m in the calculation of the length L. The ratio of the number of fissures m to the calculation of the length L is linear density. To reduce the linear density error, number of fractures m in each length L must be greater than or equal 3, selected five groups of maximum linear density in each direction for conservative considering, denoted $n_{SNi}$ and $n_{EWi}$. Then average linear density in each direction, we can obtained the linear density of fractures $n_{SN}$ and $n_{EW}$ in both directions. The judgment is beginning with minimum length that L is 5m, and then expand the length if the data is not enough.

$$n_{SNi} = \frac{m_{SNi}}{L_{SNi}}, \quad n_{EWi} = \frac{m_{EWi}}{L_{EWi}} \tag{1}$$

$$n_{SN} = \frac{\sum_{1}^{5} n_{SNi}}{5}, n_{EW} = \frac{\sum_{1}^{5} n_{EWi}}{5} \tag{2}$$

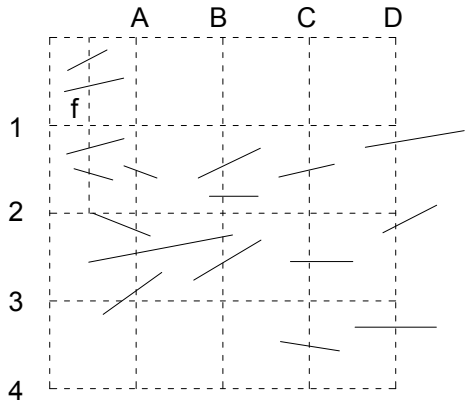


Fig.5 Example of extracting the value of linear density

Considering the diversity of the selected object , here is a small example that counting linear density $n_{SN}$ of north-south direction in order to facilitate understanding and easy to get linear density of fractures (Figure 5). First, consider the case that only a single grid and gauge length is 5m,

only A2 ~ A3 segment has three fissures in Fig, record 1 data; Object that is extended to two grids and gauge length is extended to 10m, B1~B3 segment has four fissures, which also consider the case that fractures does not on the grid line, for example, there are four fissures on the line f, record two copies of the data; Then object that is extended to three grids and gauge length is extended to 15m, C1~C4 and D1~D4 segment both has three fissures, record two copies of the data. Linear density is 0.6,0.4,0.4,0.2,0.2 respectively obtained from five data, and average linear density $n_{SN}$ is 0.36.

Table 1 is data of linear density for the third group of area C, including five linear density statistics of north-south and east-west direction. The intensity of this group can be found better, fissures are more than three in a grid, and the resulting of each linear density rather average.

Table 1 Value of linear density (Unit: bar / m)

| set | North-south direction | | | | East-west direction | | | |
|---|---|---|---|---|---|---|---|---|
| | Number of fissures $m_{SN}$ | Gauge length $L_{SN}$ | Linear density $n_{SNi}$ | Average linear density $n_{SN}$ | Number of fissure $m_{EW}$ | Gauge length $L_{EW}$ | Linear density $n_{EWi}$ | Average linear density $n_{EW}$ |
| 1 | 4 | 5 | 0.8 | | 5 | 5 | 1.0 | |
| 2 | 4 | 5 | 0.8 | | 5 | 5 | 1.0 | |
| 3 | 4 | 5 | 0.8 | 0.76 | 6 | 5 | 1.2 | 1.0 |
| 4 | 3 | 5 | 0.6 | | 4 | 5 | 0.8 | |
| 5 | 4 | 5 | 0.8 | | 5 | 5 | 1.0 | |

**Tendency correction of linear density**

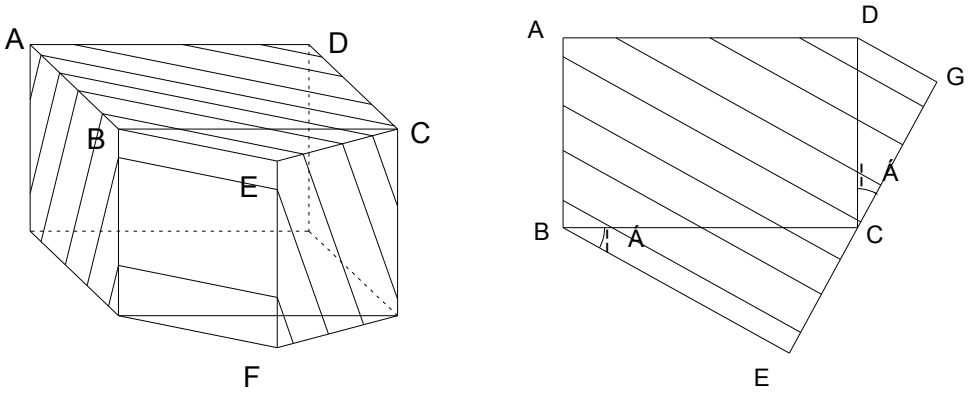


a）Perspective view b）Top view

Fig.6 Tendency correction of linear density

According to the above method to find a linear density inaccurate. In Figure 1.6, ABCD surface is horizontal, BA refers to the North, BC refers to the east, the value of linear density in east-west direction is equal to the number of fractures on BC segment divided by the length of BC segment, the value of linear density in north-south direction is equal to the number of fractures on CD segment divided by the length of CD segment. But in the top view, fissures is not perpendicular to BC or CD segment, when considering only factors of the horizontal plane, the actual value of linear density in east-west direction should be equal to the number of fractures on BC segment divided by the length of CE segment, empathy the actual value of linear density in north-south direction should be equal to the number of fractures on CD segment divided by the length of CG segment. So it needs to be tendency correction for the linear density, as follows:

When the tendency that $\alpha = 0$: no tendency correction, $n_{EW}$ is the linear density .

When the tendency that $0 < \alpha < 90$：

$$n_{SN}' = \frac{n_{SN}}{\sin\alpha}, n_{EW}' = \frac{n_{EW}}{\cos\alpha} \tag{3}$$

When the tendency that $\alpha = 90$： no tendency correction, $n_{SN}$ is the linear density.

When the tendency that $90 < \alpha < 180$：

$$n_{SN}' = \frac{n_{SN}}{\sin\alpha}, n_{EW}' = -\frac{n_{EW}}{\cos\alpha} \tag{4}$$

When the tendency that $\alpha = 180$： no tendency correction, $n_{EW}$ is the linear density .

When the tendency that $180 < \alpha < 270$：

$$n_{SN}' = -\frac{n_{SN}}{\sin\alpha}, n_{EW}' = -\frac{n_{EW}}{\cos\alpha} \tag{5}$$

When the tendency that $\alpha = 270$： no tendency correction, $n_{SN}$ is the linear density .

When the tendency that $270 < \alpha < 360$：

$$n_{SN}' = -\frac{n_{SN}}{\sin\alpha}, n_{EW}' = \frac{n_{EW}}{\cos\alpha} \tag{6}$$

When the tendency that $\alpha = 360$： no tendency correction, $n_{EW}$ is the linear density .

The consolidated available:

$$n_{SN}' = \begin{cases} \dfrac{n_{SN}}{|\sin\alpha|}, & \text{if } \alpha \neq 0、90、180、270 \text{ or } 360 \\ n_{SN}, & \text{if } \alpha = 90 \text{ or } 270 \\ \text{Not exist}, & \text{if } \alpha = 0 \text{ or } 180 \text{ or } 360 \end{cases} \tag{7}$$

$$n_{EW}' = \begin{cases} \dfrac{n_{EW}}{|\cos\alpha|}, & \text{if } \alpha \neq 0、90、180、270 \text{ or } 360 \\ \text{Not exist}, & \text{if } \alpha = 90 \text{ or } 270 \\ n_{EW}, & \text{if } \alpha = 0 \text{ or } 180 \text{ or } 360 \end{cases} \tag{8}$$

**Inclination correction of linear density**

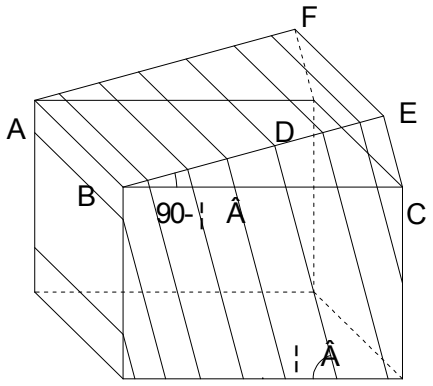


Fig.7 Inclination correction of linear density

Linear density represents linear density that in the horizontal after tendency correction, is not the linear density that in the vertical plane. In Figure 7,the value of linear density is equal to the number of fractures on BC segment divided by the length of BE segment after tendency correction, Therefore, there is a need for further inclination correction of linear density, as follows:

$$n_{SN}''=\frac{n_{SN}'}{\sin\beta},\quad n_{EW}''=\frac{n_{EW}'}{\sin\beta} \tag{9}$$

Where $\beta$ is the Inclination of the fracture, $n_{SN}'$ and $n_{EW}'$, respectively, are line density for the north-south and east-west direction after tendency correction.

**The corrected average distance**

Model and mesh three sets of data of area C respectively, then statistics linear density of north-south and east-west direction, after tendency and inclination correction of the linear density can get the average density of three groups of fractures respectively, and finally get the average fracture spacing of the three groups, as shown in Table 2.

Table 2 The mean spacing of rock fractures case

| set | Propensity (deg) | Dip (deg) | $n_{SN}$ (/m) | $n_{EW}$ (/m) | $n_{SN}'$ (/m) | $n_{EW}'$ (/m) | $n_{SN}''$ (/m) | $n_{EW}''$ (/m) | Mean spacing(m) |
|---|---|---|---|---|---|---|---|---|---|
| 1 | 99.23 | 22.25 | 0.54 | 0.80 | 0.55 | 4.99 | 1.44 | 13.17 | 0.14 |
| 2 | 302.34 | 86.39 | 1.44 | 1.56 | 1.70 | 2.92 | 1.71 | 2.92 | 0.43 |
| 3 | 47.00 | 83.86 | 0.76 | 1.00 | 1.04 | 1.47 | 1.05 | 1.47 | 0.79 |

**Conclusion**

Three-dimensional model of the joints created based on three-dimensional software effectively utilizes the existing GPS-RTK coordinates of rock fractures, there is no need to repeat the measurement data, and mean spacing of rock fractures can be calculated according to the three-dimensional model. Work does not need to operate in the field, this approach allows more convenient for field measurements. However, data processing and modeling process is somewhat complicated, it will take some time to complete, therefore hope that future research can raise more convenient method to calculate the mean spacing of rock fissures.

**Acknowledgements**

This research presented in this paper has been supported jointly by National Natural Science Foundation(NNSF) of China(40872172) and State Administration of National Defense Science and Technology industry (Department Two-2012-491).

**References**

[1] WANG Shu-ren, ZHOU Hong-bin, WU Chong-fu, et al.Research on rock mechanics parameters by using comprehensive evaluation method of rock quality grade-oriented[J]. Rock and Soil Mechanics, 2007, 28(Supp.): 202－206.

[2] ZHANG Zhi-gang, QIAO Chun-sheng. Improved empirical determination of strength parameter for jointed rock masses and its application in engineering[J]. Journal of Beijing Jiaotong University, 2006, 30(4): 46－49.

[3] HOEK E, DIEDERICHS M S. Empirical estimation of rock mass modulus[J]. International Journal of Rock Mechanics & Mining Sciences, 2006, 43: 203－215.

[4] CAI M, KAISERA P K, UNOB H, et al. Estimation of rock mass deformation modulus and strength of jointed hard rock masses using the GSI system[J]. International Journal of Rock Mechanics & Mining Sciences, 2004, 41: 3－19.

*Applied Mechanics and Materials Vols. 580-583 (2014) pp 224-230*
*© (2014) Trans Tech Publications, Switzerland*
*doi:10.4028/www.scientific.net/AMM.580-583.224*

# The Research Review of Underground Continuous Wall on Deformation Characteristic

Shimin Zhang[1,a], Tengkun Yuan*[2, b], Yangkai Zhou[3,c], Denghui Li[4,d], Kaihang Zhuo[5,e]

[1] Zhejiang University City College, Hangzhou, China

[a]zhangsm@zucc.edu.cn,

[b]923586244@qq.com,[c]714833229@qq.com,[d]510341785@qq.com,[e]zkh657@qq.com

**Keywords:** Underground Continuous Wall, Deformation Characteristic, Calculation Method

**Abstract.** Underground continuous wall has received more and more attention in the construction field as the important part in the foundation engineering. Pointing at the deformation characteristic of continuous wall, the factors which influent the deformation of continuous including the intrinsic mechanical characteristic and time effect in the construction area. The main calculation methods and various of calculation models are concluded as well as the construction technology, which concludes the research production in the continuous wall field and pointing the direction for the following research.

## Introduction

The underground continuous wall technology was first applied in impermeable wall in Santa Malia Dam in Italy. The appearance of numerous construction machines applied in continuous wall in Japan in the 1960s offer a condition which promotes this technology progress in the global scope. The first case applying the continuous wall technology in high-rise buildings in China is a bank building in Taiwan in 1971.Since then, the continuous wall technology has drawn great attention and obtained a widespread application in the deep foundation construction.

At the same time, the calculation methods and construction technology is updating rapidly which adding the fresh blood to the underground continuous wall construction. For example, Jun Sun`[1] put forward the predict method of continuous wall based on immune RBF neural network in 2003, and the efficient construction method named "Three Walls in One Wall" proposed by Fen Yuan[2]. All these late-model technology together promote the development of underground continuous wall technology.

## Deformation factors

There are two main aspects that influence the deformation of underground continuous wall,one is a series of internal factors like the depth ratio and reinforcement ratio of the underground continuous wall, the other is the construction conditions and time effect. For the internal factors,the depth ratio and reinforcement are regarded as elements forming the fuzzy relationship matrix to conclude the fuzzy principle of the deformation which is almost the same comparing the result in traditional calculation method[3]. The result of the above method indicate that when the depth ratio is constant, the value of deformation is decrease with the increase of the reinforcement ratio,but it is nor a linear relationship. At the same time,the principle concluding from the practical projects is the same with the result calculating through the above theory method[4].

Compared with the internal factors, the influence of construction condition to the underground continuous wall is more unpredictable and diversification. For example,the main reason of the tremendously increasing of the pit deformation is the not timely supporting and dewatering. While the loading around the pit is also an important reason to explain the deformation of the pit.Mingtao Lu[5] emphasize the influence of the surcharge behind the underground continuous wall and proposes a series of guiding suggestions of the continuous wall construction combining the monitoring data of a deep pit in Wuhan. At the same time, Zhongjun Wang[6] also put forward similar views and undertake the research in the area of how the confined water and loading affect the stability of continuous wall through finite element analysis.

In addition, Wei Fan[7] raise the opinion that contact surface of soil also have a certain effect on the deformation of underground continuous wall. The result that put the contact surface of soil into consideration is more consistent than the result not, which is lower in the pit deformation and ground subsidence outside the pit.

The principle of the underground continuous wall deformation is confirmed in the No.1 subway construction projects in Hangzhou last year.Lishen Hu[8] combine the monitoring data in deep pit of Train Station and the finite element analysis,bring the view that the supporting and dewatering problem are the main reasons for the continuous wall deformation.Cong Lei[9] also draws a similar conclusion through the design and monitoring data of continuous wall in the construction process in Pengbu Station.

## Calculation method

The main part of the underground continuous wall design is to calculate and design the exterior-protected construction. Hence, choosing a appropriate approach is the key to design the continuous. These methods can roughly divided into three groups: the conventional design method(the static equilibrium method),the elastic resistance method,the finite element method.

**Confirm the value of m** The value of m(proportional coefficient of horizontal resistance coefficient) is a discrete quantity in the design of underground continuous wall. There are two approaches to confirm this value in standard:horizontal loading test of single pile method and empirical formula calculation method. However, both of them exist defects and have a large deviation to the actual value.

Qiang Wang[10] proposes the method that back calculate the value of m through the real deformation of underground continuous wall. First of all, analyze the elastic foundation beam to establish the calculation function to get the value of m,and then optimize the result to confirm the value of m to forecast the next stage of the deformation. This method takes full advantage of the actual working conditions,which makes the result relatively accurate. At the same time, Xiliang Gao[11] holds the opinion that the deviation of the value of m have a large effect on the calculation of continuous deformation,and verify the accuracy of the method that use displacement to back calculate m.

**Incremental iteration method** Incremental iteration method is been applied widely in the practical projects process as a design method which takes the relationship of underground continuous wall construction into consideration.Shijin Feng[12] puts forward apply the incremental iteration method considering the influence of wall displacement to analyze the situation of undergrounder continuous wall's displacement. The influence that incremental displacement affect the incremental loading is linear.

$$\Delta p_{i+1}^{n} = \Delta p_{i}^{n} \pm \Delta \delta_{i}^{n} k_{s}^{n} \quad (1)$$

In the function, i means computation times in the incremental iteration method,i=1,2,3$\cdots$. $\Delta \delta_{i}^{n}$ means the displacement in the i time. $k_{s}^{n}$ means the rigidity of soil spring in the No.n construction condition. $\Delta p_{i}^{n}$ means the increasing load in the i time.

The overall stiffness matrix $[K_{n}^{p}]$ is used to calculate the final incremental displacement and loading as this stage of displacement and loading adding up to the last stage to get the total displacement and internal force.

**Fuzzy reliability analysis** Yongjin Tang[13] expand the the fuzzy relation matrix adding the thickness of the continuous wall, the depth of the pit,the depth ratio and the reinforcement ratio based on the previous matrix to forecast the horizonal displacement of continuous wall. Comparing the theory result with the displacement data of practical projects, the success rate (means the error is less than 2‰)reach 75% which can definitely illustrate that this method is reasonable and pertinence in the forecast of the deformation of the underground continuous wall.

It seems that the notion of fuzzy reality has been introduced into the analysis of construction reality,but there are also some problems to be solved,among which the standard of function choice is the most difficult to choose. Because the function is the precondition of the analysis,which has a direct effect on the calculation result. Different function has different result.Jie Sun[14] chooses three typical function: the falling trapezoid distribution,second-degree parabola distribution and the ridge shaped distribution to infer the influence of different function choice. The general principles are concluded by analyzing and comparing：second-degree parabola distribution is the most successful function in these three ones which is consistent with theoretical results;the falling trapezoid distribution gets a conservative results compared with the ridge shaped distribution.

**Conclude the principle of deformation in statistical method** Hu Feng[15] collects a great deal of practical project data on underground continuous wall, concludes the principle of continuous wall deformation. In this research, Hu Feng collects 58 monitoring data in Shanghai arear and apply the statistical theory to analyze the relationship among the displacement of maintenance system, soil properties and the system stiffness. Some laws can been concluded,displacement of the continuous wall appears over the excavation face and the relationship between the the thickness of soil and the deformation of continuous is close.

At the same time, Zhonghua Xu[16] also collect the monitoring data in Shanghai arear to confirm the above research,which promotes the development of the statistical theory in the civil engineering research.

## Model establishment

**Soil coupled creep model** According to the accumulation of practical experience, Haizhu Guo[17] finds that model combined time hardening exponential function law and failure criterion of Druker-Prager can reflect the time effect in the pit construction. The data from the model is coincide with that from the real construction process utilizing the data in the triaxial rheology experiment as the model's parameters.

If the Soil coupled creep model is extended and applied in the 3D simulation of deep pit supporting system, which will better reflect the effect of time and space. Compared with the elastic model and elastoplastic model, this model is more consistent with the actual projects.

Zhao baoyun[18] combined the creep model with $FLAC^{3D}$ software to explore the application in the design of slope stability whose working mechanism is similar withe continuous wall.

**Mohr Coulomb elastoplastic model** Dongxu Shang[19] applies the simulation software,simulating an underground continuous wall project of a building to analyze the deformation of the pit and the soil subsidence around the pit. In the process of the model construction, the soil model is Mohr Coulomb model,the steel support model is beam unit model,and the continuous wall model is shell unit model. According to the data from the simulation soft, the result shows a obvious tendency toward the monitoring data.

**Mechanical model of tubular pile (closed wall)** Based on the principle of elastic mechanics, Hua Wen[20] puts forward mechanical model of tubular pile (closed wall),which use semi-inverse method and principle of superposition to get side friction on both side of the pile. In this way, the analytical solution of axial strain on the surface of the pile and the unit side friction.

This method points at the rectangular closed continuous wall which can not calculate in the traditional method for the foundation subsidence and inner friction existence. The application of analytical solution is introduced by the model test of the rectangular closed continuous wall which offer the theory evidence for the data analysis of the rectangular closed continuous wall.

**Parabolic cylinder model** Based on the underground continuous wall in the station pit in Lingbo, Shilong Ding[21] apply the parabolic cylinder model in the analysis of cell wall stability in the situation of overloading. The purpose of this research is to explore how the model parameters affect the sensitivity and safety factor of cell wall stability. The result is verified by the monitoring data of the position, depth an verticality of cell wall which offer the theoretical and practical basis for the similar projects in Lingbo arear.

## The deformation law of continuous wall in the vertical force

**The research of closed continuous wall** The rectangular closed continuous wall is new type of bridge foundation, which is connected by rigid joint to form the closed rectangular frame.Hua Wen [22]applies the simulating method to explore how the distance of closed wall affect the group effect in the vertical load. Two model wall in different section size are used in the test,where the length of the model wall in group A is shorter than that in group B while the thickness and heigh is the same. According to the figure analysis after the test, several conclusion can be got,the character of closed wall is to form a group of walls rather than a single wall, the work principle of which is also totally different from the single wall. Enlarging the distance between the walls can promote the effect of internal resistance force and the soil stress. In the situation of keeping the thickness and heigh are uncharge, enlarging the wall in a certain value can improve the group effect and carrying capacity effectively to gain better economic benefit.

At the same time, Bo Zhang[23] and Zhang Song [24]simulate analyze the closed continuous wall in the FLAC-3D to explore the influence of the angle of internal friction on the closed wall in the vertical force,concluding that the most of the load is born by the side friction of the continuous wall foundation. The principle of the bearing mechanism is similar with the end bearing friction pile foundation, the vertical bearing capacity increase significantly with the increase of soil modulus.

**Continuous wall is born the vertical force in the soft soil** To improve the continuous pressed capacity in the soft soil is a unsolved problem.Yin Jiao[25] put forward to apply wall grouting to improve the compressive strength of underground continuous wall, which has been proved by the simulation method in the construction scene. According the analysis data, several conclusion can been shown, firstly, wall grouting can significantly improve the limit vertical compressive capacity and vertical stiffness,specially the resistance force in the end of the continuous wall. After the wall grouting, the main settlement of the continuous wall is result from the elastic deformation of wall subsoil.

Yu Weijian[26] used numerical analysis model and calculation to find out the stability situation of the surrounding rock in the vertical which is helpful to the research of continuous wall. Combined with safety monitoring, Liang Gui-lan[27] also discuss the stability Analysis of surrounding rock, getting the likely research result with Yu Weijian

## New technology of construction

**"Three Walls in One Wall"** Combining the reforming project in Shanghai the Bund, Fen Yuan proposes the new conception of "Three Walls in One Wall",which utilizes the continuous wall and inner wall as the flood control wall, developing the function of enclosure wall,load bearing wall and flood control wall for continuous wall.

There are two key technologies in this project,one is rotary drilling to clean the riprap layer near the river,which minimizes the adverse effects on the flood control wall foundation. The other is cell wall reinforcement to connect the continuous curtain cutting off the connection with the water. The depth of the curtain reach the impermeable layer,which enhance the stability of the cell wall.

**Construction method of barrette** Barrette is a single rectangular continuous wall to bear the load from the upper part of the structure. The surface area and flexural rigidity is bigger than the circular pile which can fully utilize the side resistance force and improve the bearing capacity. In the last several years, this pile have been widely applied in the high-rise buildings, elevated road and other foundational constructions[28].

Guohui Lei[29] make 3D discrete of the pile body along the depth and cross section in 3D analysis, applying the Mindlin function and the static equilibrium law to construct the displacement function of pile and the soil around the pile, which infer the equation describing the relationship between the load on the barrette and the displacement of pile.

## Construction materials and components

**GFRP bar** Glass Fiber Reinforced polymer(called GFRP foe short)is a new type of fibrous composite.GFRP replaces traditional bar in shield driving part for which is lighter than others. The GFRP bar is usually used in the continuous wall because it will not influent the mechanical performance of the continuous wall and can directly drill the continuous wall when the shield In and out of the tunnel[30].

**The I-shaped steel joints** Aiming to solve the difficulties in the locking pipe and joint box connecting in underground continuous wall, Jian Shen[31] combines the project in the Shanghai World Expo to introduce the I-shape steel joints application in the continuous wall. This type of joint can be a permanent part of the continuous wall which solve the pipe laying problem in the continuous

wall construction. According to three dimensional finite element analysis, the joint proved to be safe and reliable.

**Combine continuous wall and steel support** Based on the metro station pit project in Shengzheng, Qinxi Zhang[32] explore the supporting system combining the continuous wall and steel support in the soft simulation and field measurement. The result show that the restriction of the steel supporting is a vain effect in controlling the pit deformation. Hence, minimizing the stress loss and supporting the frame in time should be promised during the progress of the pit digging.

At the same time, Meng Qingshan[33] also utilize the steel pile to enhance the strength of retaining wall whose mechanical principle is likely with the continuous wall. This construction method has been widely used in the practical projects.

## Summary

The development of continuous wall at the present stage, the latest construction technology and conception have been introduced in this article. For making the design of the continuous wall trend to be more reasonable and normative, the next study can be turned to the below arear.

The time and space effect is unpredictable when it influent the continuous wall deformation. In the deformation prediction progress, more factors should be taken into consideration to make it more comprehensive and reasonable. At the same time, the management in the construction field should trend to standardization, avoiding the bias loading phenomenon.

The vertical load is not frequent like the lateral load ,but the vertical also has a certain effect on the continuous wall. For this reason, the deformation forecast of continuous in the vertical force should also be taken into consideration to make the forecast more reasonable.

The design of underground continuous wall combining with new materials and various of functional joints have been arisen in the construction technology. This technologies not only enhance the stability of the continuous wall, but also realize various of continuous wall for different functions, which improve construction efficiency.

## Acknowledgements

The work is fully supported by Science Technology Department of Zhejiang Province(2013C31041)

## References

[1] Sun J. and Zhao Q.H. and Xiong X.B.,Rock and Soil Mechanics,3(2003),p.24-27.
[2] Yuan F.,Chinese Journal of Underground Space and Engineering ,5(2)(2009),p.1736-1740.
[3] Tang Y.J.,Chinese Journal of Underground Space and Engineering ,1(1)(2005),p.102-107.
[4] Li G.,Chinese Journal of Building Construction,6(2008),p.100-103.
[5] Lu M.T.,Xing X.K. and Song Z.P.,Journal of Water Resources and Architectural al Engineering,9(4)(2011),p.109-123.
[6] Wang Z.J.,JOURNAL OF SHUIAZHUANG RAILWAY INSTITUTE(NATURAL SCIENCE)23(1)(2010),p.59-61.
[7] Fan W.,Wang J.H. and Chen J.J.,JOURNAL OF SHANGHAI JIAOTONG UNIVERSITY,40(12)(2006),p.2119-2121.
[8] Hu L.S.,Subgrade Engineering,3(2011),p.90-93.

[9] Lei C.,Chinese Journal of underground engineering,5(2011),p.79-83.
[10] Wang Q.,Liu S.Y. and Tong L.Y. JOURNAL OF SOUTHEAST UNIVERSITY (Natural Science Edition,41(2)(2011),p.352-358.
[11] Gao X.L.,JOURNAL OF RAILW_AY ENGINEERING SOCIETY,2(2008),p.1-5.
[12] Feng S.J.,Chen X.X. and Gao G.Y.,Rock and Soil Mechanics,30(1)(2009),p.226-230.
[13] Chen Y.X.,JOURNAL OF NINGBO UNIVERSITY(NSEE),24(3)(2011),p.76-79.
[14] Tang Y.J.,Chen Z.F.and Huang C.F.,Chinese Journal of Geotechnical Engineering, 27(3)(2005) ,p.288-293.
[15] Sun J.,Zhang X.and Mou Z.G.,Rock and Soil Mechanic,29(3)(2008),p.838-840.
[16] Feng H.,Liu G.B.and Zhang W.L.,Chinese Journal of Underground Space and Engineering, 6(1)(2010),p.151-156.
[17] Guo H.Z,Zhang Q.H.and Zhu J.W.,Rock and Soil Mechanics,30(3)(2009),p.688-698.
[18] Zhao B.Y.,Liu D.Y.and Zheng Y.R.,,Disaster Advances,5(4)(2012),p.1231-1236 .
[19] Shang D.X.,Yi M.,Journal of North China Institute of Water Conservancy and Hydroelectric Power,2(2008),p.26-28.
[20] Wen H.,Cheng Q.G.and Song Z.,Rock and Soil Mechanics,29(12)(2008),p.3342-3348.
[21] Ding S.L.,Dong J.Z.and Liu G.B.,JOURNAL OF NINGBO UNIVERSITY (NSEE), 29(4)(2010),p.107-111.
[22] Wen H.,Cheng Q.G.and Chen X.D.,Rock and Soil Mechanics,30(1)(2009),p.152-156.
[23] Zhang B.,Chen X.D.,Journal of Earth Sciences and Environment,32(3)(2010),p.311-315.
[24] Song Z.,Chen Q.G.and Meng F.C.,29(3)(2008),p.2183-2208.
[25] Jiao Y.,CHINA CIVIL ENGINEERING JOURNAL,41(3)(2008),p.84-90.
[26] Yu W.J.,Zhai S.H.and Gao Q.,Disaster Advances, 5(4)(2012),p.120-126 .
[27] Liang G.L.,Disaster Advances, 5(4)(2012),p.312-330 .
[28] Lei G.H.,Hong X.and Shi J.Y.,CHINA CIVIL ENG EERING JOURNAL,38(4)(2005),p.103-109.
[29] Lei G.H.,Hong X.and Shi J.Y.,Rock and Soil Mechanics,25(4)(2004),p.590-600.
[30] Li H.X.,Lu Q.and Yuan J.B.,Journal of Hebei University of Engineering (Natural Science Edition),28(1)(2011),p.22-24.
[31] Shen J.,NORTHESTERNSEISMOLOGICALJOURNAL,33(2011),p.316-320.
[32] Zhang Q.X,Ma Q.X.and Zhang M.J.,Geotechnical engineering technique,25(2)(2011),p.95-100.
[33] Meng Q.S.,Kong L.W.and Tan F.Y.,isaster Advances, 5(4)(2012),p.417-421.

*Applied Mechanics and Materials Vols. 580-583 (2014) pp 231-237*
*© (2014) Trans Tech Publications, Switzerland*
*doi:10.4028/www.scientific.net/AMM.580-583.231*

# The rheological properties and yield stress model of high-density slurry added with coarse sands

ZHANG Xiu-xiang[1, a], QIAO Deng-pan[1, b]

[1.] Faculty of land and resources engineering, Kunming University of Science and Technology , Kunming 650093, China

[a:]15887221514@163.com，[b:]1215550723@qq.com

**Key words：** Coarse sands; Rheological properties; High-density slurry; Yield stress model;

**Abstract：** In order to determine the concentration range of high-density slurry with coarse sands for suiting pipeline transportation in Jinchuan mine, at the same time find a suitable model to predict yield stress. In this paper, based on the coarse sand of Jinchuan mine as material to prepare high-density slurry, studied on the rheological properties. Through two-factor variance analysis, qualitative and ration analysis of the effect was conducted on the cement content and mass concentration to rheological parameters. The results show that the rheological model of the coarse sand is similar to that of Bingham plastic fluid, the mass concentration has a significant effect on viscosity and yield stress, and the viscosity is significantly affected by the cement content. The mass concentration of 82%-84% is suitable gravity transportation in pipeline. Meanwhile the relation model is established between yield stress and water-cement ratio, aggregate volume concentration, the model has high precision. These provide technical basis for designing filling system and ensuring the stability of slurry transportation, and a new idea for the research of rheological properties.

## Introduction

For filling mining method, whether the slurry can realize steady transmission in tube is the key, the liquidity must content with the requirements of pipeline. On the premise of confirming stowing gradient, it is the prerequisite that ensure smoothly transport the slurry to the mined empty area in the form of gravity or pumping [1, 2]. Solving some technical problems which including preparation craft of slurry, the resistance calculation, pipeline design, and parameter optimization of pipeline transportation has a direct relationship with rheological properties and influencing factors of slurry.

In this paper, on the basis of the experiment carried out rheology test for high-density slurry of coarse sand, provided qualitative and quantitative analysis to the influence of cement content on the rheological parameters, revealed its influences and identified optimal concentration for pipeline. Yield stress model was put forward.

## 1 Test

### 1.1 Experimental material

(1)The coarse sands come from Jinchuan mine. The density of coarse sand is 2409 $Kg \cdot m^{-3}$, packing density is 0.595 by experimental determination.

(2) The result of grading is in Tab 1 through experimental determination.

**Tab 1** Grading of coarse sands

| Sieve mesh/（mm) | Cumulative distribution of screen underflow/（%） |
|---|---|
| 16 | 97 |
| 10 | 83 |
| 5 | 61 |
| 0.3 | 25 |
| 0.08 | 3 |

This engineering practice has showed that if the value of fine aggregate is too low, it will cause clogging in pipeline.

Tab 1 show that the particle which less than 0.3 mm is 25%, accords with the regulations of < construction code of pumped concrete> in AIJ, as well as china's regulations specify that the sand content of passing 0.315 mm mesh is no less than 15%[3]. So it is suitable for pipeline transportation.

1.2 Testing instrument

The test used Brookfield（DV-Ⅱ+Pro) , chose the HA (# 2) rotor, the computer program was set as 50 speed point that the rotor speed increase from 20 RPM to 200 RPM, each speed point wait 5s,1s gather a numeric, five data of each speed point take the average.

1.3 The design and method of experiment

The slurry for rheological test need to the conditions of high concentration and high flow， it still disagree about that the definition of high concentration and high flow [4,5]， Through a lot of experiments, this paper thinks the standard of high concentrations and high flow is that the slurry keep no separation and non-hierarchical after standing five minute and has the characteristics of slow slump-loss and non-bleeding, furthermore, slump is greater than or equal to 220mm, divergence is greater than 450mm, collapsed slump is less than 1s. Configuring slurry which concentration is from76% to 85% for observing in the lab, results show that 76%-79% have serious segregation, 80% is mild segregation, when comes to 81% has been basically no segregation. Slump, divergence and collapsed slump have reached the above requirement. So this test configures19 groups slurry which added quantity concrete separately are310 $kg \cdot m^{-3}$,280 $kg \cdot m^{-3}$,250 $kg \cdot m^{-3}$ and 220 $kg \cdot m^{-3}$ , mass concentration is from81% to 85%, (as when added quantity concrete of the slurry is 220 $kg \cdot m^{-3}$ , mass concentration is 81% ,the slurry had mild segregation, so didn't do rheological) , put the slurry into 1000 ml beaker with stirring for rheological test. The experimental scheme is shown in Table 2.

**Tab 2** The pilot scheme of rheology

| Slurry with coarse sands | Added quantity concrete/($kg \cdot m^{-3}$) | mass concentration/（%） |
|---|---|---|
| Rheological experiments | 310, 280, 250, 220 | 81%, 82%, 83%, 84%, 85% |

## 2. Experimental results and analysis

Drafted curves according to the shear stress and shear rate which get from different added quantity concrete and mass concentration:

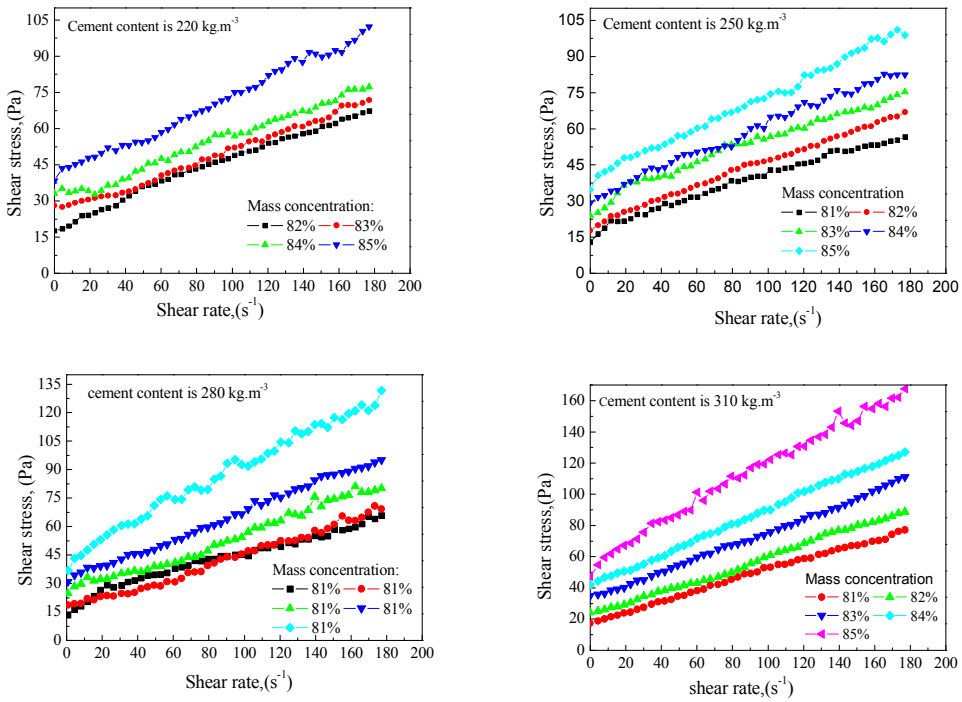


**Fig 1** Relation curve between shear rate and shear stress when cement content is separately 310 kg·m$^{-3}$, 280 kg·m$^{-3}$, 250 kg·m$^{-3}$, 220 kg·m$^{-3}$

Fig. 1 show that the rheological curve is a straight line of not through the origin. Straight line has an intercept on shear stress axis, the rheological process shows the characteristics of viscoplastic body , slope of the line is the plastic viscosity, the rheological index is one, belongs to Bingham plastic model(see Eq.(1))：

$$\tau = \tau_0 + \eta\gamma \qquad (1)$$

Where τ is the shear force (Pa), $\tau_0$ is the yield stress (Pa), η denotes the consistency coefficient (Pa·s), γ represents the shear rate(s$^{-1}$).

Used regression analysis software applying Bingham plastic model to fit the curves for obtaining the value of yield stress and viscosity, the results put in Tab3.

**Tab 3** Rheological parameters of regression analysis about the experiment of coarse sand

| Cement content (kg·m$^{-3}$) | Mass concentration (%) | Water-cement ratio | Volume concentration of aggregate | Yield stress （Pa) | Viscosity （Pa·s) | Correlation index |
|---|---|---|---|---|---|---|
| 310 | 81 | 1.262 | 0.5087 | 13.01 | 0.334 | 0.997 |
| | 82 | 1.211 | 0.5245 | 17.14 | 0.380 | 0.996 |
| | 83 | 1.159 | 0.5408 | 22.97 | 0.430 | 0.998 |
| | 84 | 1.105 | 0.5574 | 31.69 | 0.488 | 0.999 |
| | 85 | 1.050 | 0.5746 | 46.16 | 0.633 | 0.991 |
| 280 | 81 | 1.395 | 0.5190 | 18.25 | 0.261 | 0.983 |
| | 82 | 1.339 | 0.5348 | 19.68 | 0.299 | 0.993 |
| | 83 | 1.281 | 0.5510 | 24.18 | 0.324 | 0.983 |
| | 84 | 1.221 | 0.5676 | 31.53 | 0.366 | 0.996 |
| | 85 | 1.161 | 0.5847 | 44.01 | 0.484 | 0.989 |

| | | | | | | |
|---|---|---|---|---|---|---|
| 250 | 81 | 1.560 | 0.5292 | 19.11 | 0.227 | 0.988 |
| | 82 | 1.497 | 0.5450 | 20.25 | 0.264 | 0.997 |
| | 83 | 1.433 | 0.5612 | 25.47 | 0.283 | 0.989 |
| | 84 | 1.366 | 0.5779 | 31.37 | 0.305 | 0.995 |
| | 85 | 1.298 | 0.5949 | 39.06 | 0.350 | 0.995 |
| 220 | 82 | 1.699 | 0.5553 | 20.03 | 0.258 | 0.993 |
| | 83 | 1.625 | 0.5714 | 24.81 | 0.263 | 0.994 |
| | 84 | 1.550 | 0.5881 | 30.34 | 0.267 | 0.988 |
| | 85 | 1.472 | 0.6051 | 39.69 | 0.346 | 0.992 |

## 3 Analysis the influencing factor of rheological parameters

### 3.1 The impact analysis for viscosity

Used analysis of variance to judge whether every factor has a significant influence on viscosity, the results are shown in Tab.4：

**Tab. 4** Two-factor variance analysis of viscosity

| Soruce of variation | SS | Df | MS | F Value | P-value |
|---|---|---|---|---|---|
| FactorA | 0.1002 | 3 | 0.0334 | 27.2643 | 7.54E-05 |
| FactorB | 0.0555 | 3 | 0.0185 | 15.1097 | 0.0007 |
| Error | 0.0110 | 9 | 0.0012 | | |
| Sum | 0.1667 | 15 | | | |

Note：Factor A represents cement content, factor B represents mass concentration

Significance test:：

Tab.4 shows that FA=27.2643>$F_{0.99}(3,9)$=6.99，FB=15.1097> $F_{0.99}(3,9)$=6.99, so factor A and factor B are highly significant. But cement content has more influence on viscosity.

According to the result of two-factor variance analysis, drew curves about factors which are highly significant and yield stress, as shown in Figure 2, 3.

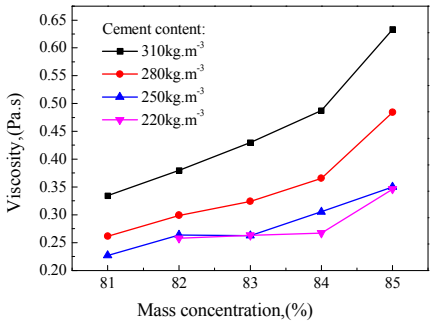


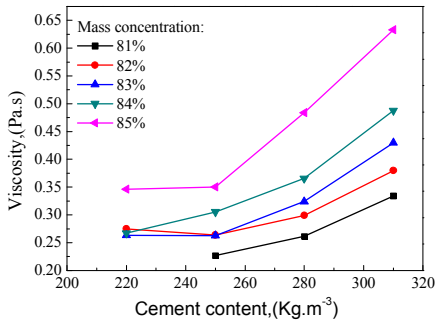


**Fig 2** Effect of mass concentration on viscosity **Fig 3** Effect of cement content on viscosity

Fig2 shows that under certain cement content, viscosity presents a growing trend with increasing concentration. The increase of concentration means the decrease of water-cement ratio, free water of slurry becomes less, unit of skeleton structure becomes more, the internal friction of slurry grows, and the final viscosity becomes larger. The viscosity increases relatively moderate from 81% to 84%, but increases greatly from 84% to 85%. When choose the concentration for pipeline should be less than 84%.

Fig3 shows under a certain mass concentration, the more the cement content increases, the bigger the viscosity is, the increase in the amount of cement makes W/C become smaller, makes the

slurry thickening, and the volume of coarse sand, friction becomes bigger, ultimately viscosity becomes larger. The viscosity changes little from 220 kg·m$^{-3}$ to 250 kg·m$^{-3}$, then rises quickly between 250 kg·m$^{-3}$ and 310 kg·m$^{-3}$.

### 3.2 The impact analysis for yield stress

In order to examine the influence of cement content and mass concentration on the yield stress, the double factors variance analysis is presented in Tab 5.

**Tab 5** Two-factor variance analysis of yield stress

| Soruce of variation | SS | Df | MS | F-Value | P-value |
|---|---|---|---|---|---|
| FactorA | 1.1635 | 3 | 0.3878 | 0.0425 | 0.9873 |
| FactorB | 1089.2872 | 3 | 363.0958 | 40.2566 | 1.53E-05 |
| Error | 81.1758 | 9 | 9.0195 | | |
| Sum | 1195.2681 | 15 | | | |

Significance test:

Tab.5 shows that FA = 0.0425<$F_{0.99}$(3,9)=6.99, FB=40.2566>$F_{0.99}$(3,9)=6.99, factor B are highly significant, that is, mass concentration has more influence on viscosity.

In order to clearly observe the influence of concentration on yield stress plotted curves as follow Fig4:

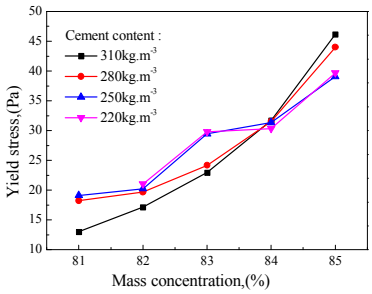


**Fig.4** Effect of mass concentration on yield value of stress

Four curves from Fig.4 show under the same cement content, with the increase of concentration, yield stress shows a clear upward trend. when the concentration is less than 84%, the more the amount of cement added, the smaller the yield stress is, can be explained that the increase of cement means the decrease of coarse sand and the contact points between particles, the opportunity to form a skeleton structure becomes small, the resistance of the slurry becomes small; When the slurry concentration reaches 85%, yield stress becomes larger obviously. So the concentration should be less than or equal to 84% for pipeline.

### 3.3 The model of yield stress

It is apparent from the description, the value of yield stress has close relationship with water, cement and aggregate, so the three factors should be considered. In order to explore the quantitative relationship between them, put the values of three factors inTab3. The relation curves between yield stress and aggregate volume concentration ($C_V$) as well as water-cement ratio (W/C) see Fig 5, 6; get the regression equations using curves in Fig5, 6 are shown in Tab 6.

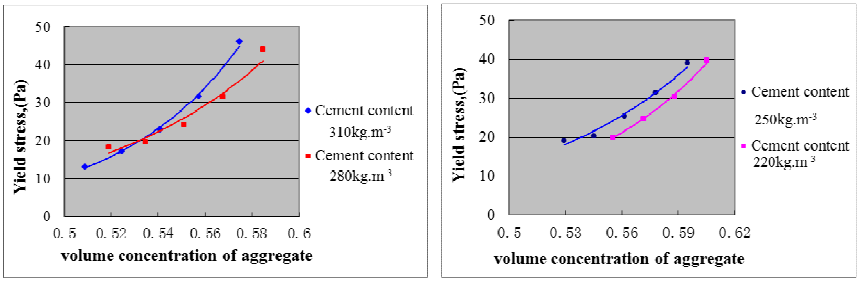


**Fig. 5** The relation curves between aggregate volume concentration and yield stress

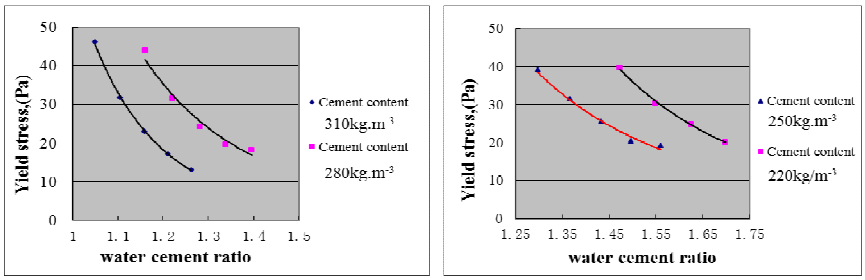


**Fig .6** The relation curves between water-cement ratio and yield stress

**Tab. 6** The equation of the relation between yield stress and $C_V$ as well as W/C

| Cement content ($kg \cdot m^{-3}$) | The relation equation between $C_V$ and yield stress | $R^2$ | The relation equation between W/C and yield stress | $R^2$ |
|---|---|---|---|---|
| 310 | $Y=0.0008e^{19.127x}$ | 0.998 | $Y=63.52x^{-6.813}$ | 0.970 |
| 280 | $Y=0.0143e^{13.617x}$ | 0.964 | $Y=85.97x^{-4.883}$ | 0.999 |
| 250 | $Y=0.0433e^{11.398x}$ | 0.977 | $Y=111.20x^{-4.072}$ | 0.982 |
| 220 | $Y=0.0106e^{13.573x}$ | 0.997 | $Y=245.11x^{-4.729}$ | 0.998 |

Tab.6 shows that the volume concentration of aggregate has exponent relation on yield stress, there lies in an negative exponential function between W/C and yield stress. Put forward the yield stress model：

$$\tau_0 = \alpha * \exp(C_V) * \left(\frac{W}{C}\right)^b \quad (2)$$

Where $\tau_0$ is the yield stress (Pa), W/C denotes water cement ratio, α and b are constant, $C_V$ represents aggregate volume concentration.

Moreover，W/C, volume concentration and packing density in expression are dimensionless quantity; the dimension of yield stress is only related to α, so set the dimension of α as Pa.

According to the data in Tab 3, used Eq. 2 to regression, the value are shown in Tab 7：

**Tab. 7** The regression model at each dosage of cement

| Cement content ($kg \cdot m^{-3}$) | Regression model | Correlation $R^2$ | F value | Significance |
|---|---|---|---|---|
| 310 | $\tau_0 = 35.596 * \exp(C_V) * \left(\frac{W}{C}\right)^{-6.606}$ | 0.9992 | 14591.101 | highly significant |
| 280 ` | $\tau_0 = 50.109 * \exp(C_V) * \left(\frac{W}{C}\right)^{-4.964}$ | 0.9734 | 712.012 | highly significant |
| 250 | $\tau_0 = 69.726 * \exp(C_V) * \left(\frac{W}{C}\right)^{-4.401}$ | 0.9741 | 2206.195 | highly significant |
| 220 | $\tau_0 = 99.638 * \exp(C_V) * \left(\frac{W}{C}\right)^{-4.013}$ | 0.9906 | 5253.134 | highly significant |

Tab.7 shows that as the cement content decreasing, coefficient α and b take on an increasing tendency, accords with the physical laws. The correlations are greater than 0.97, shows the accuracy and reliability of the model. The coefficient α still needs further research.

## Conclusion

1. Under a certain mass concentration the more the cement content increases, the bigger the viscosity is. When the slurry concentration reaches 85%, yield value of stress becomes larger obviously，under a certain cement content, viscosity with increasing concentration presents a growing trend, increases greatly from 84% to85%. From 81% to 84% is suitable for pipeline, considering the dehydration of underground, suggest that the range of concentrations is 82%-84%.

2. A large number of rheological experiments show that under the same cement content, with the water-cement ratio reducing, the yield stress is significantly increased; W/C is a negative exponential function with yield stress. With the increase of aggregates and concentration，yield stress becomes larger. The volume concentration of aggregate has exponent relation on yield stress. After synthetically consider the influence of water, cement and the property of aggregate on yield stress, the prediction model of yield stress is proposed, this equation has some advantages such as simple formula, definite physical meaning and high accuracy etc.

Equation is as follows:

$$\tau_0 = \alpha * \exp(C_v) * \left(\frac{W}{C}\right)^b$$

This equation can reduce a large number of complex experiments in mine for obtaining yield stress, and has a significance to be promoted.

## Acknowledgements

This work was financially supported by National Natural Science Foundation of China (51164016) and the key science and technology projects of Gansu Province (1203GKDC003).

## References

[1]. Deng-pan Qiao, Wei-hua Chen, Lei Zhang, Wei-xin Yao, Xian-lai Wang, Hu Wang. The modern concept of mining and filling mining. *Non-ferrous Metal Science*, 2011.2(2):7-14.(in Chinese)

[2]. Long-sheng Zhao, Heng-hu Sun, Wen-biao Sun, Jian-zhuang Liu. Study on the rheological characteristic and effect of paste-like slurry. *China Mining*, 2005, 14(10):45-48. (in Chinese)

[3]. Wasp.E.J, Kenny.J.P, Gandhi.B.L, *Solid-Liquid flow slurry pipeline transportation*. Clausthal: *Trans Tech Publications*, 1977:102-184.

[4]. Yu-hai Xu, Xin-qi Xu, Jian-xiong Li. Rheological behavior of high-density backfill and reasonable determination of the parameters for its gravity-flow transport//*Eighth International Filling Mining Conference Proceedings of China Nonferrous Metals Society*. Beijing, 2004:234-236. (in Chinese)

[5]. Yuan-hong Zeng. Research the rheological properties of cement mortar and predict the rheological parameters [Dissertation]. Chongqing: Chongqing University, 2009:1-35. (in Chinese)

*Applied Mechanics and Materials Vols. 580-583 (2014) pp 238-242*
*© (2014) Trans Tech Publications, Switzerland*
*doi:10.4028/www.scientific.net/AMM.580-583.238*

# 3-D Numerical Study of Mechanical Behaviors of Pile-anchor System

Richeng Liu[1,2,a], Bangshu Xu2[2,b], Bo Li[1,c], Yujing Jiang[1,d]

[1] Graduate School of Engineering, Nagasaki University, Nagasaki 8528521, Japan

[2] School of Civil and Hydraulic Engineering, Shandong University, Jinan 250061, China

[a] email:my1122002006@126.com, [b] email:xubangshu@sdu.edu.cn

[c] email:libo@nagasaki-u.ac.jp, [d] email: jiang@nagasaki-u.ac.jp

**Keywords:** pile-anchor system; sensitivity analysis; numerical simulation; FLAC$^{3D}$

**Abstract:** Mechanical behaviors of pile-soil effect and anchor-soil effect are significantly important in supporting engineering activities of foundation pit. In this paper, finite difference method (FDM) was utilized to perform the numerical simulation of pile-anchor system, composed of supporting piles and pre-stressed anchor cables. Numerical simulations were on the basis of the foundation pit of Jinan's West Railway Station, and 3D simulation analysis of foundation pit has been prepared during the whole processes of excavation, supporting and construction. The paper also analyzed the changes of bending moments of piles and axial forces of cables, and discussed mechanical behaviors of pile-anchor system, through comparisons with field monitoring. The results show that the parameters concluding vertical gridding's number, cohesion of pile and soil, and pile stiffness have robust influences on supporting elements' behaviors. Mechanical behaviors of supporting pile and axial forces of anchor cable changed dramatically, indicating that the potential failure form was converted from toppling failure to sliding failure.

## Introduction

Pile-anchor supporting system is consisted of supporting pile and anchor cable. The system can robustly control the displacement of soil, by utilizing the passive stress mechanism of pile and active stress mechanism of anchor cable, and finally maintain the safety of the foundation pit. This system can strictly dominate the displacement of foundation pit, having the merits of strong supporting effects, low-cost and easy-construction [1].

Shen and Bang [2] studied the influents of supporting parameters during the process of excavation, using the finite element method (FEM). Jiang and Lin [3] exhibited an expression to calculate the maximum displacement of pile-anchor supporting system, based on the abundant monitoring data. Their expresses theoretically depicted the relations of maximum displacement and various engineering aspects. However, the thorough understanding of mechanical behaviors of pile-anchor supporting system is still a difficult task, due to the complexities and uncertain of geo-technical conditions.

In this paper, finite difference method (FDM) was utilized to perform the numerical simulation of pile-anchor system, composed of supporting piles and pre-stressed anchor cables. Numerical simulations were on the basis of the foundation pit of Jinan's West Railway Station, and 3D simulation analysis of foundation pit has been performed during the whole processes of excavation, supporting and construction.

## Project overview

The foundation pit of station square located in Jinan city of Shandong province, China, with a length of 470m and a width of 346m. The depth of the foundation pit is approximately 15m, and the underground water level is in the range of -14m ~ -19m. The foundation is mainly composed of clay soil, as well as a portion of land pebble.

According to the engineering geology, hydrogeology, the surrounding environment and the correlated technical specifications, the foundation pit of station square is designed with pile-anchor supporting system. The depth of the foundation pit is 14m. The pile-anchor supporting system is composed by a row of pile and four rows of pre-stressed anchor cables, as shown in Fig. 1.

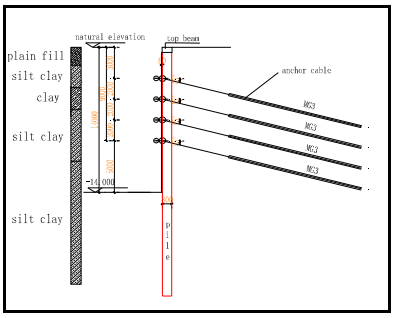


Fig.1 Supporting scheme

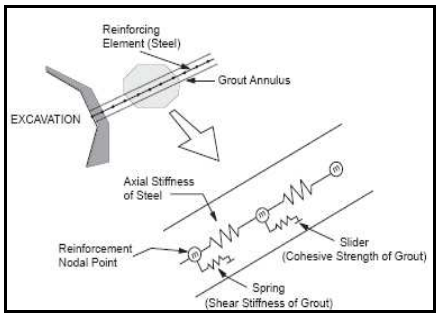


Fig.2 Mechanical representation of fully bonded reinforcement

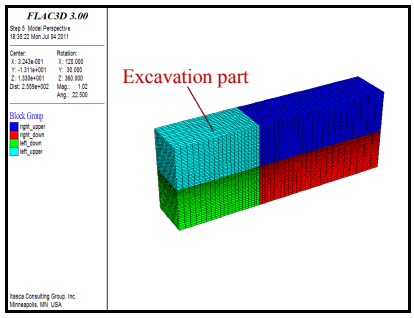


Fig.3 Calculating model

## Basic theories

The interaction effects of cable, grout and rock/soil are investigated by using spring-slider model system. This model can reflect the shear properties of interaction between cable and rock. The maximum shear force robustly depends on the shear stiffness of grout. The shear stiffness $K_g$ of grout for unit thickness can be expressed by:

$$k_g = \frac{2\pi G}{\ln(1 + 2t / D)} \tag{1}$$

where, $G$ is the shear modulus of grout, $t$ is the thickness of grout annular and $D$ is the diameter of anchor cable. The shear force $\tau_g$ of grout intersection can be calculated by:

$$\tau_g = \frac{G}{(D/2 + t)} \frac{\Delta u}{\ln(1 + 2t / D)} \tag{2}$$

where, $\Delta u$ is the relative displacement of grout and rock/soil.

In evaluating the axial forces that develop in the reinforcement displacements are computed at nodal points along the reinforcement axis, as show in Fig. 2. Out-of-balance forces at each node are computed from axial force in the reinforcement, as well as shear forces contributed through shear intersection along the grout annulus. Axial displacements are computed by integrating the nodal accelerations using the out-of-balance axial force and a mass lumped at each node.

**Modelling and parameters**

The height of the model is about 2.1 times of the depth of excavation, while the length of the model is about 3.3 times of the length of excavation. The length of the model is 130m, with the depth of 30m. The length of excavation is 39m, with the depth of 14m, as shown in Fig. 3. Physical and mechanical properties of soils, cables and piles are shown in Tables 1 ~ 3.

Table1 Physical and mechanical properties of soils

| Number | Soil type | Thickness of soil (m) | Modulus of deformation (MPa) | Poisson's ratio | Saturated unit weight ($kN/m^3$) | Cohesion (KPa) | Internal friction angle (º) |
|---|---|---|---|---|---|---|---|
| 1 | plain fill | 1.5 | 13.17 | 0.27 | 19.0 | 10.0 | 10.0 |
| 2 | silt clay | 2 | 20.70 | 0.30 | 19.3 | 26.3 | 19.4 |
| 3 | silt | 2 | 27.33 | 0.28 | 19.1 | 25.7 | 23.4 |
| 4 | silt clay | 5 | 17.31 | 0.32 | 19.6 | 25.0 | 21.9 |
| 5 | silt clay | 11 | 20.49 | 0.30 | 19.4 | 24.8 | 21.0 |
| 6 | clay | 10 | 26.40 | 0.30 | 19.6 | 34.2 | 24.9 |
| 7 | silt clay | 25 | 30.33 | 0.30 | 19.4 | 45.7 | 22.9 |

Table2 Physical and Mechanical Properties of Anchor Cable

| Num-ber | Type | Density $\rho$ ($kg/m^3$) | Elasticity modulus E(GPa) | Cross-section area A($mm^2$) | Grout cohesion $C_g$(N/m) | Grout stiffness $k_g$(N/m/m) | Grout perimeter $P_g$(mm) | Tensile strength $F_t$ (KN) |
|---|---|---|---|---|---|---|---|---|
| 1 | Freedom segment | 7800 | 195 | 181.37 | 1 | 1 | 471 | 337.35 |
| 2 | Anchorage segment | 7800 | 195 | 181.37 | $2\times10^5$ | $1.75\times10^7$ | 471 | 337.35 |

Table3 Physical and Mechanical Properties of Pile

| Num-ber | Type | Density $\rho$ (kg/m3) | Elasticity modulus E(GPa) | Poisson's ratio ν | Cross-section area A($mm^2$) | Cohesion of pile and soil Pg (N/m) | Interface stiffness $k_g$ (N/m/m) | Friction angle $\phi_g$ | Pile perimeter $P_g$ (mm) |
|---|---|---|---|---|---|---|---|---|---|
| 1 | pile | 2500 | 31.5 | 0.3 | 5024 | 0.96e7 | 1.3e7 | 9.6 | 252 |

## Results and analysis

Figs. 4(a) and 4(b) show the results of bending moment of pile and axial force of anchor cable with varying grid layers in the vertical direction in numerical model. With the increment of grid layer, the bending moment of pile and the axial force of anchor cable increase too. When the number of grid layer exceeds 50, the increment of bending moment and axial force is not remarkable, however, the computing time is increasing significantly. Figs. 4(c) and 4(d) depict the changes of bending moment of pile and axial force of anchor cable under different cohesions of pile and soil. As the cohesion increases, the bending moment of pile and the axial force of anchor cable increase, too. This is because the increasing cohesion results in a better bonding effect of pile and soil, leading to more stress applying on pile. Figs. 4(e) and 4(f) illustrates the variations of bending moment of pile and axial force of anchor cable with increasing stiffness of pile. The increasing stiffness causes the increase of bending moment of pile and decrease of axial force of anchor cable. The reasons may be that with the increase of pile stiffness, the supporting pile would suffer more stress of soil, making the soil suffering less stress and resulting in the increase of bending moment of pile and decrease of axial force of anchor cable.

Fig. 5 and Table 4 present the comparison results of monitoring data and calculated results. The monitoring data shows that the maximum interior bending moment is 158.7kN•m located in $z$ = -10m, while the numerical results are 159.79kN•m located in $z$ = -9.15m. The maximum exterior bending moment of monitoring data is -152.3kN•m in the depth of $z$ = -14m, while the maximum exterior bending moment of calculated results is -139.68kN•m in the depth of z = -14.64m. The monitoring data agree well with the measured data, showing the accuracy and reliability of the numerical simulation.

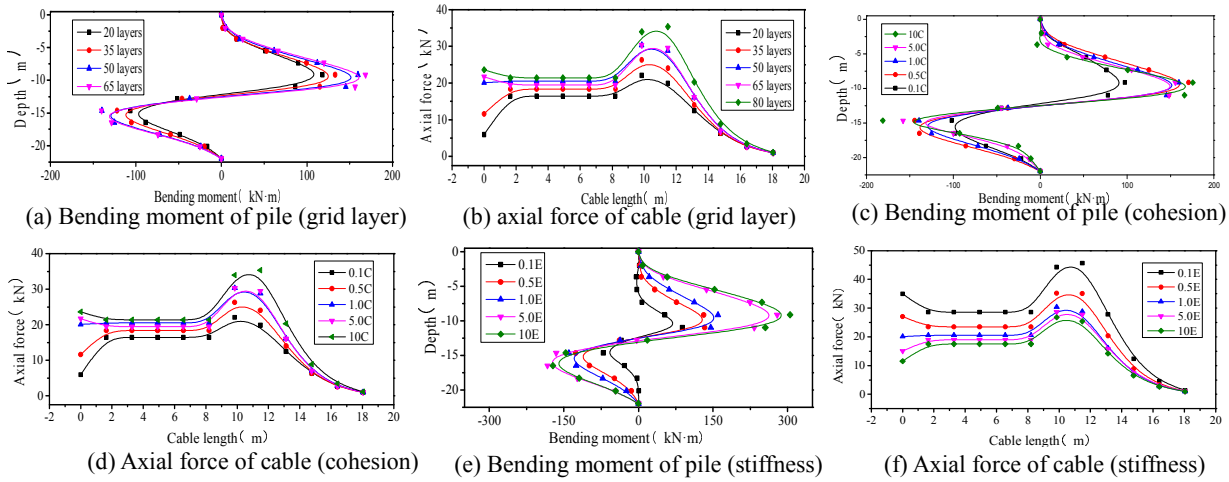


(a) Bending moment of pile (grid layer) (b) axial force of cable (grid layer) (c) Bending moment of pile (cohesion)

(d) Axial force of cable (cohesion) (e) Bending moment of pile (stiffness) (f) Axial force of cable (stiffness)

Fig. 4 Bending moments of pile and axial forces of cable with varying grid

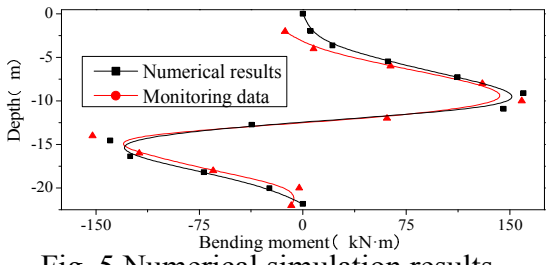


Fig. 5 Numerical simulation results and measured data

Table 4 Measured data and numerical simulation data

| Data source | Max interior bending moment | | Max exterior bending moment | |
|---|---|---|---|---|
| | value（kN•m） | depth（m） | value（kN•m） | depth（m） |
| Monitoring | 158.7 | -10 | -152.3 | -14 |
| Calculating | 159.79 | -9.15 | -139.68 | -14.64 |
| Errors(%) | 0.7 | 8.5 | 8.286 | 4.571 |

## Conclusions

The comparisons of monitoring data and numerical simulations show that when obtaining the reasonable parameters and considering the interaction effects of soil, cable and pile, the numerical simulation is accurate and reliable. The vertical grid layer, the cohesion of pile and soil, the pile stiffness and other parameters can significantly influence on the mechanical behaviors of pile and anchor cable. When excavation is finished, the results show the maximum axial force of anchor cable located in the former part while its value is constant for freedom segment, which agrees well with other researchers' results.

## References:

[1] JB Cao. Study on mechanics and application of pile-anchor in deep foundation pit [D]. Wuhan: China University of Geosciences, 2010. (in Chinese)

[2] CK Shen, S Bang and LR Herrman. Ground movement analysis of earth support system [J]. J. Geotech. Engrg.Div, ASCE, 1981,107(12):1609-1624.

[3] CG Jiang, XX Lin, JX Huang, GD Lv and SF Yu. Deformation monitoring and primary analysis of supporting structure of pile-anchor system in foundation pit [J]. Geotechnical engineering, 2002,5(8):55-56. (in Chinese)

*Applied Mechanics and Materials Vols. 580-583 (2014) pp 243-249*
*© (2014) Trans Tech Publications, Switzerland*
*doi:10.4028/www.scientific.net/AMM.580-583.243*

# A General Criterion for Complex Rocks and Soils and Its Application

Huaining Ruan[1, a], Manlu Luo[2], Di Wang[1] and J. W. Ju[3]

[1] School of Civil and Transportation Engineering, Hohai University,

Nanjing 210098, China

[2] School of Internet of Things Engineering, Hohai University

[3] Department of Civil and Environmental Engineering, University of California,

Los Angeles, CA 90095, USA

[a]hnruan@hhu.edu.cn

**Keywords:** Failure Condition, Complex Rocks and Soils, Anisotropic, Nonlinear, Engineering Application

**Abstract.** A failure criterion is proposed for complex rocks and soils. Their anisotropic and nonlinear behavior is analyzed theoretically and experimentally. The influence of the intermediate principal stress is taken into account. The nonhomogeneous strength and the effect of geological temperature are also discussed. Many classical failure criteria are special cases of the proposed condition. The criterion is applied in the analysis of the bedrock of Ankang Dam in China. The case study illustrates the potential of the proposed general model in engineering application.

## Introduction

When engineering works are constructed in a soil or rock, two issues need to be addressed. One is whether shear stresses exceed the shear strength of soil so that the soil failure will cause catastrophic collapse of structures. The other is whether consolidation deformations are so large that total or differential settlement will result in damage to structures. In practice, both strength and consolidation should be considered. At this point, soil strength is examined in detail. Soil failure is an essential topic for engineering purposes. It is concerned with bearing capacity of foundations, stability of slopes, earth pressure, etc.

In studying soil strength, a useful method is to establish a failure criterion, which links limiting combinations of stresses and describes behavior of soil strength effectively. In plasticity theory, the Tresca and the Mises criteria are commonly used. However, Tresca's yield condition indicates that the normal stress on slip planes does not affect shear strength. Mises' model states that the hydrostatic stress has no influence on failure. Therefore both the criteria take no account of internal friction of rocks and soils. In soil and rock mechanics, the Mohr-Coulomb criterion is widely used. Nevertheless, this model ignores the intermediate principal stress. This is not true in many cases. Drucker and Prager suggested an extended Mises criterion, in which the octahedral shear stress is a function of the octahedral normal stress. This model is generally employed in the FEM analysis. Basically, all the criteria mentioned above are applicable to homogeneous and isotropic rocks and soils only, and all of them are linear functions in stress space.

In fact, soil and rock behavior is extremely complicated (Xu, 1993; Qian and Yin, 1994) [1, 2]. The authors have conducted constitutive modeling for non-ideal materials involving their evolutionary elastoplastic damage (Ju and Ruan, 2002; Ju, Ruan and Ko, 2004) [3, 4]. Specifically for complex soils, Shen (2000) [5] cited Ruan and Xu's extended strength theory as an analysis basis. Due to vertical consolidation in field, different geological environments, and many other reasons, rocks and soils sometimes behave anisotropic, heterogeneous, and nonlinear. In order to deal with all these characteristics, a comprehensive failure criterion is proposed. This model embraces many advantages of available theories and agrees with experimental data very well.

**General Criterion**

Anisotropic behavior is common for many soils and rocks due to preferred orientation of mineral grains or bedding planes. Strengths parallel and perpendicular to weakness planes are quite different. Donath (1964) [6] performed strength and deformability tests on slate. Here the three principal stresses are denoted by $\sigma_1$, $\sigma_2$, and $\sigma_3$, and it is assumed that $\sigma_1 \geq \sigma_2 \geq \sigma_3$.

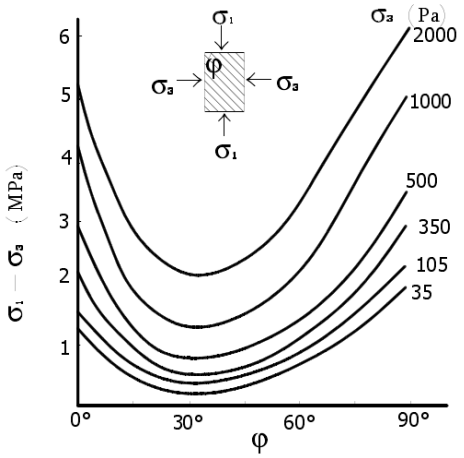


Fig. 1 Triaxial compression test on slate

Figure 1 shows that the limiting stress difference $\sigma_1$-$\sigma_2$ is related to loading direction. When the major principal stress $\sigma_1$ is inclined with bedding planes at an angle of some 30°, the strength reaches its minimum. Jaeger (1960) [7] extended the Mohr-Coulomb criterion for anisotropic rocks. He suggested that the shear strength parameters are expressed as continuous functions of direction. In many cases, the intermediate principal stress $\sigma_2$ cannot be ignored. Hill (1950) [8] developed a model for anisotropic metal as follows

$$F(\sigma_y - \sigma_z)^2 + G(\sigma_z - \sigma_x)^2 + H(\sigma_x - \sigma_y)^2 + 2L\tau_{yz}^2 + 2M\tau_{zx}^2 + 2N\tau_{xy}^2 = 1 \tag{1}$$

where $\sigma_x$, $\sigma_y$, and $\sigma_z$ are the normal stresses in three co-ordinate directions, $\tau_{xy}$, $\tau_{yz}$, and $\tau_{zx}$ are the shear stresses, and $F$, $G$, …, and $N$ are material parameters characterizing anisotropy. In fact, this is a model obtained by generalizing the Mises criterion for anisotropic materials. For anisotropic soils and rocks, a better model is Pariseau's criterion (1972) [9]

$$\left[F(\sigma_y - \sigma_z)^2 + G(\sigma_z - \sigma_x)^2 + H(\sigma_x - \sigma_y)^2 + 2L\tau_{yz}^2 + 2M\tau_{zx}^2 + 2N\tau_{xy}^2\right]^{\frac{n}{2}} = 1 + (U\sigma_x + V\sigma_y + W\sigma_z) \tag{2}$$

in which $U$, $V$, and $W$ are additional parameters describing anisotropy, and $n$ is a nonlinear constant. Considering layered soils, Saada (1973) [10] introduced the Gol'denblat-Kopnov criterion which is written

$$\frac{1}{2}\left[U(\sigma_x + \sigma_y) + W\sigma_z\right] + \left[F(\sigma_x^2 + \sigma_y^2) + H\sigma_z^2 + I(\sigma_y\sigma_z + \sigma_z\sigma_x) + K\sigma_x\sigma_y + 2L(\tau_{yz}^2 + \tau_{zx}^2) + 2N\tau_{xy}^2\right]^{\frac{1}{2}} = 1 \tag{3}$$

In this equation the anisotropy parameters are reduced to eight, namely, $U$, $W$ …, and $N$. The model implies that soils behave transversely isotropic, and their strengths parallel to the $x$ and $y$ axes are the same but that perpendicular to the $z$ axis is different. Both Eqs. (2) and (3) are generalized forms of the Drucker-Prager criterion. They are experimentally confirmed to a sufficient degree of accuracy for some soils. These two failure conditions involve the hydrostatic stress, and state that the compressive strength differs from the tensile strength. Therefore, the models account for internal friction of soil. Including the advantages of the above models, a universal failure criterion is suggested as follows

$$i_1 = U\sigma_x + V\sigma_y + W\sigma_z \tag{4}$$

$$j_2 = F\sigma_x^2 + G\sigma_y^2 + H\sigma_z^2 + I\sigma_y\sigma_z + J\sigma_z\sigma_x + K\sigma_x\sigma_y + L\tau_{yz}^2 + M\tau_{zx}^2 + N\tau_{xy}^2 \tag{5}$$

$$j_2^{\frac{n}{2}} = 1 + i_1 \tag{6}$$

In reality, $i_1$ comes from the expansion of the first stress invariant $I_1$ to anisotropy, and $j_2$ is reached by generalizing the second deviator stress invariant $J_2$. The nonlinear relationship between $i_1$ and $j_2$ is established in the form of power function. This model is used to describe anisotropic and nonlinear behavior of soil. In Eq. (6), $j_2$ is of the anisotropy type of the Gol'denblat-Kopnov (G-K) criterion, and thus it is capable of describing a higher degree of anisotropy than Pariseau's criterion of Eq. (2). The nonlinear relationship between $i_1$ and $j_2$ is in the form of the Pariseau criterion, and therefore this power law illustrates much more potential than the linear G-K model of Eq. (3).

Laboratory and *in situ* tests show that failure lines are nonlinear for certain soils and rocks. Temporarily $\sigma_2$ is ignored. The stress difference $q$ is defined as $q=(\sigma_1-\sigma_3)/2$, and the mean stress as $p=(\sigma_1+\sigma_3)/2$. Based on theoretical and experimental analysis, the power law is presented to depict nonlinear relationship between $q$ and $p$. This model takes the form

$$q^n = A_1 p + B_1 \tag{7}$$

where $A_1$ and $B_1$ are strength parameters.

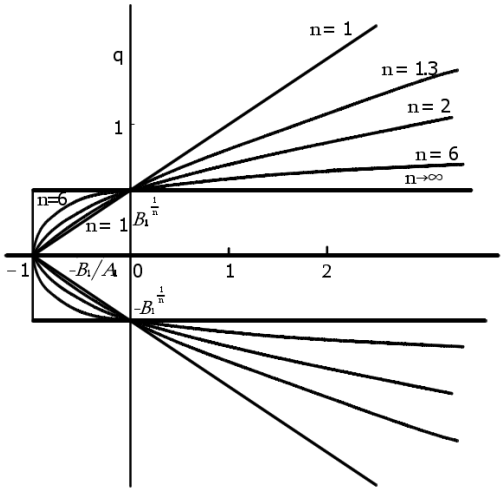


Fig. 2 Failure lines of power law

In Figure 2, nonlinear strength lines are demonstrated in several types of power law. Actually both linear and nonlinear failure criteria are expressed in terms of power function. When $n=1$, Eq. (7) gives a linear criterion. Under the linear condition, Eq. (7) is the Mohr-Coulomb criterion when $A_1 \neq 0$, and it reduces to the Tresca criterion if $A_1=0$. When $n=2$, the failure locus is a parabola. This kind of criterion is sometimes used for soft rocks and soils.

Now the intermediate principal stress $\sigma_2$ is taken into consideration. For isotropic solids, the power function between $p$ and $q$ is extended to the relationship between the first stress invariant $I_1$ and the second deviator stress invariant $J_2$. This model is expressed as

$$J_2^{\frac{n}{2}} = A_2 I_1 + B_2 \tag{8}$$

In Eq. (8), there are also two parameters besides the power $n$. When anisotropic soils are dealt with, Eq. (8) is expanded as

$$j_2^{\frac{n}{2}} = i_1 + 1 \tag{9}$$

This is Eq. (6). $i_1$ and $j_2$ are denoted by Eqs. (4) and (5). Therefore, Eq. (6) is a failure criterion characterizing both anisotropic and nonlinear behavior of soils.

It is common that several types of rock or soil are encountered in a single engineering site. Their mechanical properties are different from position to position. For heterogeneous soils and rocks, strength parameters may be expressed as functions of location. Thus Eqs (4) ~ (6) can be rewritten in terms of co-ordinates

$$i_1 = U(x,y,z)\sigma_x + V(x,y,z)\sigma_y + W(x,y,z)\sigma_z \tag{10}$$

$$j_2 = F(x,y,z)\sigma_x^2 + G(x,y,z)\sigma_y^2 + H(x,y,z)\sigma_z^2 + \cdots \tag{11}$$

$$[j_2(x,y,z)]^{\frac{n}{2}} = 1 + i_1(x,y,z) \tag{12}$$

In practice, the material parameter functions of *U(x,y,z)*, *V(x,y,z)*, … will be determined from tests or observations for various locations. In geological problems, high temperature and high pressure deep in the earth's crust will affect strength and deformability of rocks. Moreover, it is known that geothermal fields are not uniform. A regular variation is that temperature rises with depth. Set

$$t = t(x,y,z) \tag{13}$$

Strength parameters become functions of temperature *t*. Eqs. (10) ~ (12) are rewritten

$$i_1 = U(x,y,z,t)\sigma_x + V(x,y,z,t)\sigma_y + W(x,y,z,t)\sigma_z \tag{14}$$

$$j_2 = F(x,y,z,t)\sigma_x^2 + G(x,y,z,t)\sigma_y^2 + H(x,y,z,t)\sigma_z^2 + \cdots \tag{15}$$

$$[j_2(x,y,z,t)]^{\frac{n}{2}} = 1 + i_1(x,y,z,t) \tag{16}$$

In effect, the influence of non-uniform temperature is the same as that of material heterogeneity. Meanwhile, some other thermal properties of soils and rocks, such as thermal expansion, will also cause stress alteration. This topic will be covered in other relevant research.

**Special Cases of the Proposed Criterion**

The failure criterion of Eqs. (14) ~ (16) is a comprehensive model dealing with heterogeneous, nonlinear, and anisotropic materials. Many classical criteria are its special cases. When the material parameters do not change with position and temperature, Eq. (16) reduces to Eq. (6). It is a nonlinear and anisotropic criterion for homogeneous medium. In Eq. (6), let

$$n = 1 \tag{17}$$

It is simplified into

$$j_2^{\frac{1}{2}} = 1 + i_1 \tag{18}$$

This is the three-dimensional Gol'denblat-Kopnov criterion. In Eqs. (4) ~ (6), assume

$$\begin{cases} I = F - G - H = -2F' \\ J = G - H - F = -2G'' \\ K = H - F - G = -2H \end{cases} \tag{19}$$

Substituting Eq. (19) to Eqs. (4) ~ (6) yields

$$\left[F'(\sigma_y - \sigma_z)^2 + G'(\sigma_z - \sigma_x)^2 + H'(\sigma_x - \sigma_y)^2 + L\tau_{yz}^2 + M\tau_{zx}^2 + N\tau_{xy}^2\right]^{\frac{n}{2}} = 1 + (U\sigma_x + V\sigma_y + W\sigma_z) \tag{20}$$

which is the Pariseau criterion. Now the hydrostatic stress is neglected. That is

$$U = V = W = 0 \tag{21}$$

Eq. (20) becomes the Hill criterion

$$\left[F'(\sigma_y - \sigma_z)^2 + G'(\sigma_z - \sigma_x)^2 + H'(\sigma_x - \sigma_y)^2 + L\tau_{yz}^2 + M\tau_{zx}^2 + N\tau_{xy}^2\right]^{\frac{n}{2}} = 1 \tag{22}$$

When isotropic soil is under consideration, there are relationships in Eq. (20)

$$\begin{cases} F'=G'=H' \\ L=M=N=6F' \\ U=V=W \\ n=1 \end{cases} \tag{23}$$

Substituting Eq. (23) in Eq. (20) gives

$$\left\{\frac{1}{6}\left[(\sigma_y-\sigma_z)^2+(\sigma_z-\sigma_x)^2+(\sigma_x-\sigma_y)^2+6(\tau_{yz}^2+\tau_{zx}^2+\tau_{xy}^2)\right]\right\}^{\frac{1}{2}} = (6F')^{-\frac{1}{2}}+U(6F')^{-\frac{1}{2}}(\sigma_x+\sigma_y+\sigma_z) \tag{24}$$

This is the celebrated Drucker-Prager criterion. Further, the mean stress is ignored, and then

$$U=0 \tag{25}$$

Eq. (24) reduces to

$$\frac{1}{6}\left[(\sigma_y-\sigma_z)^2+(\sigma_z-\sigma_x)^2+(\sigma_x-\sigma_y)^2+6(\tau_{yz}^2+\tau_{zx}^2+\tau_{xy}^2)\right]=(6F')^{-1} \tag{26}$$

It is the famous Mises criterion.

Eq. (26) is applicable to isotropic metal. Eq. (24) is suitable for isotropic soil and rock. Eq. (22) can be used for anisotropic metal. Eqs. (20) and (18) may be employed for anisotropic soil and rock with nonlinear and linear behavior respectively. The criterion of Eq. (16) presented in this paper can be applied for heterogeneous, nonlinear, and anisotropic geomaterials.

## Case Study of the Proposed Model

The Ankang Dam is taken as an example. It is shown how to apply the proposed criterion for actual engineering projects. Rock foundations of the Ankang dam consist of metamorphic rock formed in the Sinian Period. Phyllite and schist are widely distributed. Experimental data show that these rocks exhibit strong anisotropy. Rock specimens are prepared from drill cores. Specimens are made dry, wet, and saturated separately. Unconfined compression tests are carried out. Loads is applied perpendicular, parallel, and inclined to weakness planes of rock respectively. When weaknesses are inclined, the load orientation varies from 10° to 60°. For a transversely isotropic medium, the proposed criterion of Eqs. (4) ~ (6) may be expressed as

$$\left[F(\sigma_x^2+\sigma_y^2)+H\sigma_z^2+I(\sigma_y\sigma_z+\sigma_z\sigma_x)+K\sigma_x\sigma_y+L(\tau_{yz}^2+\tau_{zx}^2)+N\tau_{xy}^2\right]^{\frac{n}{2}} = 1+U(\sigma_x+\sigma_y)+W\sigma_z \tag{27}$$

Here the *z* axis is normal to geological planes. The loading direction changes within the *zx* plane. In this example, $\sigma_y=0$. Substituting into Eq. (27) yields

$$\left(F\sigma_x^2+H\sigma_z^2+I\sigma_z\sigma_x+L\tau_{zx}^2\right)^{\frac{n}{2}}=1+U\sigma_x+W\sigma_z \tag{28}$$

where there are seven parameters totally. The Mohr circle of stress for unconfined compression can be applied in the stress analysis. The stress components with reference to co-ordinates can be calculated using the following

$$\begin{cases} \sigma_x=\sigma\sin^2\theta \\ \sigma_y=\sigma\cos^2\theta \\ \tau_{zx}=\sigma\sin\theta\cos\theta \end{cases} \tag{29}$$

where $\theta$ is the angle between the *z* axis, i. e. the normal to weaknesses, and the load is $\sigma$. Substituting Eq. (29) in Eq. (28) gives

$$\left(F\sigma^2 \sin^4\theta + H\sigma^2 \cos^4\theta + I\sigma^2 \sin^2\theta\cos^2\theta + L\sigma^2 \sin^2\theta\cos^2\theta\right)^{\frac{n}{2}} = 1 + U\sigma \sin^2\theta + W\sigma \cos^2 \tag{30}$$

It has been verified that a parabolic failure curve is applicable to some soft rocks. This is the case for the Anking dam according to investigation. Let $n=2$. Substituting to Eq. (30) and rearranging it yields

$$F\sigma^2 \sin^4\theta + H\sigma^2 \cos^4\theta + I\sigma^2 \sin^2\theta\cos^2\theta + L\sigma^2 \sin^2\theta\cos^2\theta - U\sigma \sin^2\theta - W\sigma \cos^2\theta = 1 \tag{31}$$

In order to determine the six parameters in the above equation, six sets of $\theta$ versus $\sigma$ data are obtained from tests. Saturated phyllite specimens are prepared and tested. The experimental data are shown in Table 1.

Table 1 Unconfined compression test results for Ankang phyllite

| θ(°) | 0 | 45 | 50 | 60 | 70 | 90 |
|---|---|---|---|---|---|---|
| σ(MPa) | 69.167 | 36.250 | 45.700 | 26.500 | 64.150 | 55.025 |

In Eq. (31), the parameters $I$ and $L$ are identical. Therefore, only five sets of experimental data are necessary. Select five groups in Table 1. Substitute to Eq. (31) and solve the system of equations for the parameters. Finally the following results are obtained

$$\begin{cases} F = -8.47450094\times10^{-4} \\ H = -3.30567059\times10^{-4} \\ I + L = -1.41260893\times10^{-3} \\ U = -6.480586986\times10^{-2} \\ W = -3.73229342\times10^{-2} \end{cases} \tag{32}$$

This is the failure criterion for the Ankang rock foundation. The model is applied for stability analysis of the rock masses. The bearing capacity of the foundations, the safety factor of the slopes, and many other solutions for the Ankang project are determined. The elastoplastic analysis using the finite element method containing the present criterion is performed. All the study indicates the proposed criterion displays good potential in application.

## Conclusions

A failure criterion for heterogeneous, nonlinear, and anisotropic geomaterials is proposed. It accounts for the influence of the intermediate principal stress. Anisotropy arising from weakness planes is considered. Nonlinear envelopes to Mohr's circles are involved. Heterogeneous media and non-uniform thermal fields are discussed.

This model is highly comprehensive. It may reduce to the Mises criterion, the Drucher-Prager criterion, the Hill criterion, the Pariseau criterion, and the Gol'denblat-Kopnov criterion. There are totally thirteen parameters in this criterion. They can be determined from conventional tests of unconfined compression, uniaxial tension, biaxial compression, and direct shear.

A case study of the Ankang dam illustrates that the proposed criterion is applicable to actual engineering. It demonstrates good potential in stability analysis of complex soils and rocks.

## Acknowledgements

This work was financially supported by the National Natural Science Foundation of China (Grant No. 51379065 and 50539090) and sponsored in part by the National Science Foundation (USA), Mechanics and Materials Program, under the PYI Grant MSS-9157238. These supports are gratefully acknowledged.

**References**

[1] Zhiying Xu, Rock Mechanics, Third Edition, Water Publisher, Beijing, 1993. (in Chinese)

[2] Jiahuan Qian and Zongze Yin, Principles and Computational Methods in Soil Engineering, Second Edition, Water Publisher, Beijing, 1994. (in Chinese)

[3] J. W. Ju and H. N. Ruan, Effective elastoplastic damage model for fiber reinforced metal matrix composites with evolutionary complete fiber debonding, Proc. of 15th ASCE Engineering Mechanics Conference, ASCE Press, Reston, 2002.

[4] J. W. Ju, H. N. Ruan and Y. F. Ko, Micromechanical evolutionary elastoplastic damage model for FRMMC with complete fiber debonding, ASME, Applied Mechanics Division, 255 (2004) 9-14.

[5] Zhujiang Shen, Theoretical Soil Mechanics, Water Publisher, Beijing, 2000. (in Chinese)

[6] F. A. Donath, Strength variation and deformational behavior in anisotropic rock, in: W. R. Judd (Ed), State of Stress in the Earth's Crust, Elsevier, New York, 1964, pp. 281-297.

[7] J. C. Jeager, Shear failure of anisotropic rocks, Geological Magazine, 97 (1960) 65-72.

[8] R. Hill, The Mathematical Theory of Plasticity, Oxford University Press, London, 1950.

[9] W. G. Pariseau, Plasticity theory for anisotropic rocks and soils, Proc. of 10th Symposium on Rock Mechanics, AIME, 1972, pp. 267-295.

[10] A. S. Saada, Strain-stress relations and failure of anisotropic clays, J. Soil Mech. Found. Div., ASCE, 99 (1973) 1091-1111.

*Applied Mechanics and Materials Vols. 580-583 (2014) pp 250-255*
*© (2014) Trans Tech Publications, Switzerland*
*doi:10.4028/www.scientific.net/AMM.580-583.250*

# A method to determine GSI value by using P-velocity and its application in engineering

Zhao Yuan[1,a], Wang Liangqing[2,b*], Zhou Peng[3,c], Han Yue[4,d], Chen Guorong[5,e]

[1] Engineering Faculty, China University of Geosciences, Wuhan 430074, China

[2] Engineering Faculty, China University of Geosciences, Wuhan 430074, China

[3] Engineering Faculty, China University of Geosciences, Wuhan 430074, China

[4] Wuhan Municipal Engineering Design and Research Institute Co.Ltd, China

[5] Engineering Faculty, China University of Geosciences, Wuhan 430074, China

[a] 283068458@qq.com, [b] wlq027@126.com

**Key words**: GSI; P-velocity; Hoek-Brown; Mechanical parameters;

**Abstract.** Rock mass mechanical parameters play a significant role in geotechnical engineering design, slope stability evaluation and numerical simulation, which is commonly determined by GSI method. The simplified method using P-velocity to determine GSI (Geological Strength Index) values is proposed in this study, avoiding the limitations of Hoek-Brown method. The relationship between GSI and P-velocity is established through data collected from several projects in China. Then the dam site of Rumei hydropower station, Tibet, China has been taken as a case study to validate this relationship. This method can be utilized directly in engineering projects since it can meet with the engineering accuracy requirement and reduce the cost.

## Introduction

With the progressive proceeding of hydropower engineering, the determination of rock mass deformation modulus has become more and more important in geotechnical engineering design, rock mass deformation analysis, slope stability evaluation and numerical simulation et al..

The common processes for determining rock mass deformation modulus consist of in situ test method (Rocka and Dasilv, 1970), numerical method (Kawamoto and Ichikawa, 1988) and rock mass classification method (Bieniawski, 1978; Hoek and Brown, 1997). However, some of these methods have large limitations in the following ways. Firstly, it is time consuming and expensive for in situ test; secondly, for numerical method, it is difficult for general engineers to establish the complex constitutive models; thirdly, the selection of training samples is subjective for artificial neural network method. Nevertheless, the rock mass classification method with the properties of simplicity, accuracy and money-saving, has being widely used in engineering practice.

For this reason, many researchers proposed some empirical relations based on the rock mass classification method (Q, RMR, GSI and RQD method) to predict rock mass deformation modulus. Amongst those empirical formulas, the most commonly utilized and effective method is GSI method proposed by Hoek and Brown, since the estimated values can be employed in the practical engineering directly, especially for the closely jointed and heterogeneous rock mass.

Sonmez and Ulusay (1999) proposed an empirical approach for the prediction of rock mass deformation modulus based on the quantitative GSI system and suggested to consider disturbance factors, and then Sonmez and Ulusay (2002) slightly modified the quantitative GSI chart. Marinos and Hoek (2000) suggested adding intact or massive rock into the top row of the GSI system. Hoek (2006) studied to take into account the properties of the intact rock as well as the effects of disturbance due to blast damage or stress relaxation in GSI system. Cai (2007) presented a method to extend the GSI system for the estimation of rock mass residual strength, which is proposed to adjust the peak GSI to the residual GSI value based on the two major controlling factors—the residual block volume and the residual joint condition factor. Russo (2009) put forward a new approach for a quantitative assessment of the GSI values based on the relationship between GSI and

joint parameter used in RMi system. Okay Aksoy (2012) made comparisons of different empirical equations of rock mass deformation modulus including GSI method with numerical model results.

Unfortunately, although the GSI (Hoek-Brown) method has been used widely in recent decades, the disadvantages of this method cannot be ignored especially for those who are short of geological experience, because the GSI values obtained from the chart can only be a range due to the lack of the accurate measurable parameters to describe the characteristics of rock mass structure and the conditions of discontinuities. Meanwhile, the quantitative assessment of the GSI values proposed by some researchers is sometimes complicated and inconvenient for engineering practice. Therefore, it is crucial to find a simplified method to estimate GSI values to meet the need of practical engineering.

The purpose of this study is to propose a new method to determine the GSI values more simply by establishing the relationship between GSI and P-velocity (Vp) using the data collected from several large-scale projects in China. Then the comparisons of the GSI prediction performance between the P-velocity method and Hoek-Brown method were made to validate the accuracy of this relationship through Rumei hydropower station engineering, Tibet, China, which provides the scientific basis for engineering practice.

**Structure of the database**

The data for this study were collected from 14 dam sites in China, namely the Yinpan dam in Wujiang river, the Three Gorges Dam, the Jinshuitan dam, the Gezhou dam, the Longyangxia dam, the Longtan dam, the Tongjiezi dam, the Pubugou dam, the Baozhusi dam, the Manwan dam, the Goupi dam, the Enshi dam, the Maerdang dam and the dam in Lancang river.

Table 1 The statistical evaluations of some parameters provided from the studied locations

| properties | locations | Min | Max | Mean | Count |
|---|---|---|---|---|---|
| GSI | the Yinpan dam | 26.71 | 68.25 | 52.48 | 9 |
| | the Three Gorges dam | 55.86 | 80.87 | 71.08 | 7 |
| | the Jinshuitan dam | 51.76 | 78.76 | 66.56 | 3 |
| | the Gezhou dam | 30.59 | 65.91 | 44.96 | 6 |
| | the Longyangxia dam | 60.1 | 66.42 | 63.22 | 2 |
| | the Longtan dam | 58.17 | 68.36 | 63.81 | 3 |
| | the Tongjiezi dam | 42.98 | 60.02 | 54.19 | 4 |
| | the Pubugou dam | 58.42 | 60.78 | 59.6 | 2 |
| | the Baozhusi dam | 43.31 | 64.09 | 54.02 | 4 |
| | the Manwan dam | 47.58 | 71.83 | 61.51 | 3 |
| | the Goupi dam | 42.90 | 71.52 | 61.05 | 13 |
| | the Enshi dam | 7.53 | 82.22 | 54.91 | 79 |
| | the Maerdang dam | 61.73 | 74.02 | 70.32 | 10 |
| | the dam in Lancang river | 53.09 | 67.04 | 61.93 | 5 |
| Vp (m/s) | the Yinpan dam | 2680 | 5450 | 4004.4 | 9 |
| | the Three Gorges dam | 5250 | 5890 | 5552.9 | 7 |
| | the Jinshuitan dam | 3000 | 5028 | 4342.7 | 3 |
| | the Gezhou dam | 2780 | 4000 | 3146.7 | 6 |
| | the Longyangxia dam | 4760 | 5400 | 5080 | 2 |
| | the Longtan dam | 4600 | 5520 | 5146.7 | 3 |
| | the Tongjiezi dam | 2350 | 4230 | 3390 | 4 |
| | the Pubugou dam | 4360 | 5600 | 4980 | 2 |
| | the Baozhusi dam | 3000 | 4200 | 3550 | 4 |
| | the Manwan dam | 4300 | 5286 | 4795.3 | 3 |
| | the Goupi dam | 2800 | 5146 | 4220.2 | 13 |
| | the Enshi dam | 1806 | 6414 | 3923.1 | 79 |
| | the Maerdang dam | 3930 | 5515 | 5002.5 | 10 |
| | the dam in Lancang river | 3096.8 | 4549.5 | 3983.3 | 5 |

## The determination of GSI values by utilizing P-velocity

### The qualitative method to determine GSI by Hoek and Brown

The geological strength index (GSI) method was put forward and developed by Hoek and Brown, which can be used to estimate rock mass deformation modulus of different geological conditions, especially for the closely jointed and heterogeneous rock mass, hence, it overcomes the deficiency of RMR method and becomes the widely used method in the world. The GSI values are estimated from the rock mass structure and the discontinuities surface condition, and the deformation modulus can be deduced from formula (1) (Hoek,1997).

$$E_m = \sqrt{\sigma_c / 100} * 10^{((GSI-10)/40)} (GPa) \quad (1)$$

Where $\sigma_c$ is the uniaxial compressive strength of intact rock, $GSI$ is the geological strength index, and $E_m$ is the deformation modulus of rock mass.

### The quantitative method to determine GSI by using P-velocity

Although the GSI method has been utilized widely in recent decades, the drawbacks of this method cannot be neglected. Without the accurate measurable parameters to describe the characteristics of rock mass structure and the conditions of discontinuities, the GSI values can merely be range values from the chart above, which leads to large errors especially for the engineers who are lack of experience. Meanwhile, the quantitative assessment of the GSI values put forward by some researchers is sometimes complex and difficult for engineers to grasp. Therefore, under the condition to meet the need of engineering projects, it is crucial to find a simplified method to estimate GSI values.

In general, the larger the sound wave velocity is, the better the rock mass integrity is, the higher the rock mass quality is, and the larger the corresponding GSI value is. Therefore, both the GSI and P-velocity have the tendency to increase with the increasing of rock mass integrity.

To find the specific relationship between the GSI and P-velocity, the data collected from above were imported into the Statistica software, resulting in the logarithmic relationship presented in Figure 1. The results shows that the fitting relationship is very good.

$$GSI = 76.61 \lg V_p - 216.56 \qquad r^2 = 0.8475 \quad (2)$$

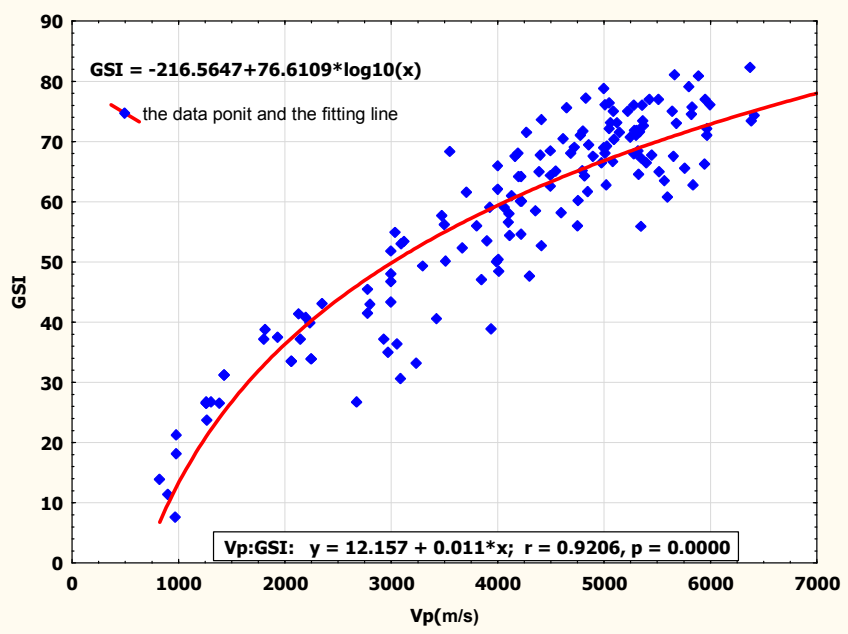


**Figure 1.**The fitting relationship between P-velocity and GSI

## The validation of using P-velocity to determine GSI value

### The research background for engineering project

Rumei hydropower station is located in the Mangkang County, Changdu district, Tibet, China, along Lantsang River. The Rumei hydropower station dam is about 315 m high, the drainage area of Lantsang River is $7.94\times104$ km$^2$, and the average river discharge is 653m$^3$/s.

The dam site encompasses three different formations, namely, the Triassic Series of Zhuka Formation ($T_2z$) for which the predominant lithology is dacite; the Jurassic Series Huakai formation ($J_2h$) for which the lithology includes sandstone and mudstone with the same amount; the Quaternary (Q). The large scale of geological structure observed at the dam site is Zhuka Fault (F), which is located about 0.8 kilometers away from left dam abutment. Gentle dipping advantage discontinuities are developed on both sides of the valley, and secondary discontinuities, small faults and cracks are developed randomly in this area.

In situ tests were carried out on dacite rock mass of Rumei dam site through scientists and engineers from Guiyang Investigation and Design Institute, State Power Corporation, China. The Schmidt hammer test, P-velocity tests and plate-loading tests were conducted to obtain the uniaxial compressive strength of intact rock, P-velocity and deformation modulus of rock mass. The GSI values can be deduced backwards from formula (1).

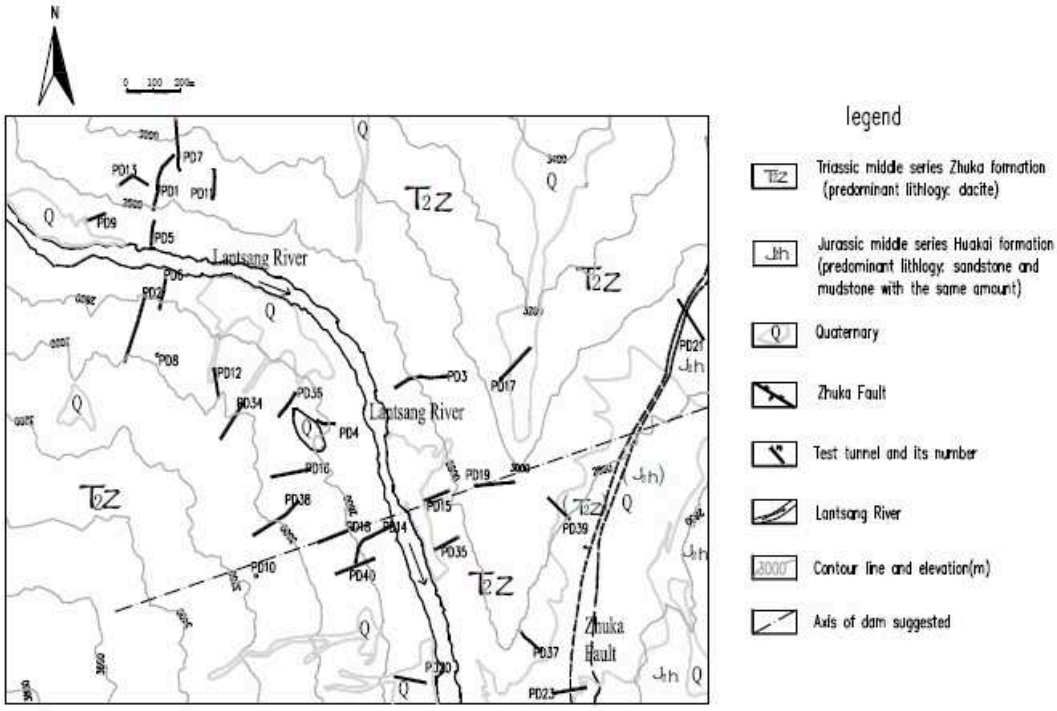


**Figure 2.** The engineering geological figure of this dam site

**Table 2** Rock mass deformation modulus, uniaxial compressive strength and P-velocity results from in situ tests

| | Tunnel number and location of test point (from the tunnel entrance) | Deformation modulus (Em, GPa) | Uniaxial compressive strength (UCS, MPa)* | P-velocity (Vp, m/s) | GSI （Hoek-Brown method） |
|---|---|---|---|---|---|
| 1 | PD17 (22m) | 4.36 | 16.3 | 2506.5 | 51.34 |
| 2 | PD19 (11m) | 9.06 | 40.85 | 2566 | 56.06 |
| 3 | PD5 (31m) | 13.68 | 61.45 | 3675 | 59.67 |
| 4 | PD19 (30m) | 14.67 | 50 | 3229 | 62.68 |
| 5 | PD1 (68m) | 15.81 | 59.5 | 4905 | 62.47 |
| 6 | PD19 (134m) | 16.45 | 58.6 | 4356 | 66.41 |
| 7 | PD3 (72m) | 17.07 | 45.4 | 4155 | 66.15 |
| 8 | PD15 (12m) | 17.11 | 48.6 | 4075 | 65.60 |

| | | | | | |
|---|---|---|---|---|---|
| 9 | PD1 (85m) | 17.28 | 60.75 | 5235 | 63.83 |
| 10 | PD3 (63m) | 17.63 | 53.65 | 3940 | 65.26 |
| 11 | PD3 (115m) | 18.31 | 55.2 | 4540 | 65.67 |
| 12 | PD5 (63m) | 18.57 | 64.45 | 4425 | 64.57 |
| 13 | PD19 (52m) | 19.37 | 56.7 | 4356 | 66.41 |
| 14 | PD5 (77m) | 20.2 | 61.65 | 4675 | 66.42 |
| 15 | PD15 (33m) | 21.21 | 45.1 | 5255 | 65.98 |
| 16 | PD15 (70m) | 22.87 | 42.9 | 5050 | 71.72 |
| 17 | PD15 (98m) | 25.32 | 59.3 | 5415 | 70.68 |

*Note: Uniaxial compressive strength is obtained by rebound apparatus

**The comparisons of GSI values between P-velocity method and Hoek-Brown method**

The GSI values of this dam site based on P-velocity method can be obtained by formula (2), therefore, the results presented in table 3 show that the prediction performance of using P-velocity method to determine GSI values is good when compared with the Hoek-Brown method, meanwhile, the relationship between GSI and P-velocity based on 14 dam site in China is accurate which can be used to determine GSI values for other engineering projects.

**Table 3** The comparisons of GSI values between two methods

| | GSI（Hoek-Brown method） | GSI（P-velocity method） | error |
|---|---|---|---|
| 1 | 51.34 | 43.85 | 0.146 |
| 2 | 56.06 | 44.63 | 0.204 |
| 3 | 59.67 | 56.58 | 0.052 |
| 4 | 62.68 | 52.27 | 0.166 |
| 5 | 62.47 | 66.18 | 0.059 |
| 6 | 66.41 | 62.23 | 0.017 |
| 7 | 66.15 | 60.66 | 0.083 |
| 8 | 65.60 | 60.02 | 0.085 |
| 9 | 63.83 | 68.35 | 0.071 |
| 10 | 65.26 | 58.89 | 0.098 |
| 11 | 65.67 | 63.61 | 0.031 |
| 12 | 64.57 | 62.76 | 0.028 |
| 13 | 66.41 | 62.23 | 0.063 |
| 14 | 66.42 | 64.59 | 0.028 |
| 15 | 65.98 | 68.48 | 0.021 |
| 16 | 71.72 | 67.15 | 0.064 |
| 17 | 70.68 | 69.47 | 0.017 |

**Conclusions**

The simplified method using P-velocity to determine GSI values is proposed and validated in this study.

The relationship between GSI and P-velocity is established through 150 data collected from 15 large-scale projects in China, and the fitting relationship is obtained as GSI=76.61lgVp-216.56 ($r^2$=0.8475). Then the dam site of Rumei hydropower station, Tibet, China has been taken as a case study to validate this relationship. The results show that the error of using P-velocity method and Hoek-Brown method to determine GSI values is small, resulting in the conclusion that the method to determine GSI values by using P-velocity is reasonable.

The P-velocity method overcomes the limitations that the GSI values based on Hoek-Brwon method cannot be obtained accurately in the non- isotropic rock mass of multilayers with different lithology and strength, which provides a new way for this type of rock mass to determine GSI values.

In conclusion, using P-velocity method to determine GSI values provides a feasible, rapid and economical method for the estimation of rock mass mechanical parameters. This method can be utilized directly in engineering projects if the in-situ shear tests are not carried out, since it can meet with the engineering accuracy requirement and reduce the cost.

**Acknowledgements**

The work was funded by National Basic Research Program of China (973 Program) (No.2011CB710604), the National Natural Science Foundation of China (No. 41372310), the Special Fund for Basic Scientific Research of Central Colleges, China University of Geosciences (Wuhan) (CUG090104).

**References**

[1] Barton, N., Choubey, V.. The shear strength of rock joints in theory and practice. Rock Mech 10, 1-54(1977).

[2] Bieniawski, Z.T.. The geomechanics classification in rock engineering applications. International Society for Rock Mechanics(1979).

[3] Cai, M., Kaiser, P.K.. Determination of residual strength parameters of jointed rock masses using the GSI system. International Journal of Rock Mechanics and Mining Sciences 44(2), 247–265(2007).

[4] Gokceoglu, C., Sonmez, H., Kayabasi, A.. Predicting the deformation moduli of rock masses. Int J Rock Mech Min 40(5), 703–12(2003).

[5] Hoek, E., Brown, E.T.. Practical estimates of rock mass strength. Rock Mechanics and Mining Sciences 34(8), 1165-1186(1997).

[6] Hoek, E., Diederichs, M.S.. Empirical estimation of rock mass modulus. International Journal of Rock Mechanics and Mining Sciences 43(2), 203–215(2006).

[7] Kawamoto, T., Ichikawa, Y.. Deformation and fracturing behaviour of discontinuous rock mass and damage mechanics theory. International Journal for Numerical and Analytical Methods in Geomechanics 12, 1-30(1998).

[8] Marinos, P., Hoek, E.. A geologically friendly tool for rock mass strength estimation. In: Proceedings of the international conference on geotechnical and geological engineering (GeoEng2000), Melbourne, Australia, 1422–1440(2000).

[9] Okay Aksoy, C., et al.. A comparative study of the determination of rock mass deformation modulus by using different empirical approaches. Engineering Geology 131-132, 19–28(2012).

[10] Palmstrom, A., Singh, R... The deformation modulus of rock masses—comparisons between in-situ tests and indirect estimates. Tunneling Underground Space Technol 16, 115–31(2001).

[11] Rocka, M., Dasilv, J.N.. A new method for the determination of deformability in rock masses. International Society of Rock Mechanics, Proceedings 2-21, 423-437(1970).

[12] Russo, G.. A new rational method for calculating the GSI. Tunnelling and Underground Space Technology 24(1), 103-111(2009).

[13] Serafim, J.L., Pereira, J.P.. Considerations on the geomechanical classification of Bieniawski. Proceedings of the symposium on engineering geology and underground openings, 1133–1144(1983).

[14] Sonmez, H., Ulusay, R.. Modifications to the geological strength index (GSI) and their applicability to stability of slopes. Int J Rock Mech Min 36, 743–60(1999).

*Applied Mechanics and Materials Vols. 580-583 (2014) pp 256-259*
*© (2014) Trans Tech Publications, Switzerland*
*doi:10.4028/www.scientific.net/AMM.580-583.256*

# Analysis of Engineering Characteristics of Cement Soil with Low Mix Additions

Ai Min Liu

CCCC-Tianjin Port Engineering Institute, Ltd., Key Laboratory of Geotechnical Engineering, Ministry of Communications; Key Laboratory of Geotechnical Engineering of Tianjin, West District, Tianjin, China, 300222

liuaimin1987@163.com

**Keywords:** Low mix additions; cement soil; engineering characteristics

**Abstract.** The mold bag cement soil was used to be as the material of dike core while building cofferdam. So the engineering characteristics of cement soil with low mix additions were analyzed in this paper. It was pointed out the unconfined compressive strength of cement soil is mainly related to the property of soil, water content, cement mixing content and degree of mixing uniformity, but has little to do with curing condition, cement adding way and the property of mixing water.

## Introduction

When building cofferdam and bank revetment in region with soft clay in our country, the riprap mound breakwater and backfilling sand dike are the common structural style. In the region with lacking sand and stone resources, large amount of fund needs to be invested for the procurement and transportation of sand stone materials, which makes the costs for building riprap mound breakwater and backfilling sand dike are very high[1,2]. Therefore, the new cofferdam type has been tried to develop. The successful applications of cement soil cofferdams with low mix additions in Tianjin and Lianyungang have great significance for building cofferdam in region lacking sand and stone materials.

By adopting cement soil with low mix additions as dike core of cofferdam, its engineering characteristics shall be analyzed so as to guide and optimize the design and reduce engineering cost.

## Research Approach

There are many factors to affect the strength of cement soil. The mainly factors are as follows: (1) Cement: the type, mix proportion and mixing content of cement; (2) Soil property: the property of soil in different area is difference, and even for the soil of different type in the same area, there is also relatively large difference; (3) Degree of mixing uniformity: It is the degree of mixing uniformity of cement. These factors will affect the strength of cement soil. Therefore, the tests were done regarding several main influential factors.

## Research Results

Main test materials are soil sample, water and curing agent. The soil sample used in test is from the seabed of Port of Tianjin. They were mainly mucky clay and ultra-soft clay. Table 1 is the main physical mechanical properties of the soil samples. The water used in test is sea water at the place with soil borrowing. And the fresh water for comparative test is from the running water of residents. Cement used in test is P.O.32.5 Portland cement.

**Table 1 Statistical table of main physical mechanical properties of soil sample**

| Description of soil | Water content % | Unit weight kN/m$^3$ | Porosity ration | Plasticity index | Liquidity index | UU strength index | | Coefficient of compressibility MPa$^{-1}$ | Modulus of Compressions MPa |
|---|---|---|---|---|---|---|---|---|---|
| | | | | | | c(kPa) | φ(°) | | |
| Ultra-soft clay | 63.7 | 16.2 | 1.747 | 25.9 | 1.55 | 5.23 | 0.1 | 1.52 | 1.86 |
| Mucky clay | 41.0 | 18.1 | 1.149 | 17.1 | 1.25 | 10.91 | 4.36 | 0.83 | 2.99 |

**Relation between Mixing Amount of Cement and Strength.** As cement is the major material in this test, its consumption has great influence on the cost of project. Thus, it is very important to select a proper mixing proportion which could meet the strength requirement while reducing construction cost to a maximum extent.

In the cement soil cofferdam, the strength of cement soil does not need to be as high as that of ordinary cement mixing soil. Therefore, cement mixing content needn't too high for unnecessary waste, but its strength shall neither be too low, as it will have influence on the stability of mold bag and construction progress. For this purpose, the cement mixing content is 6～10% (mass ratio between cement mixing content and the soil to be mixed). It is resulted that the strength of cement soil is greatly improved comparing with that of previous soft clay, but the strength of cement soil is still very low in case cement mixing content is 6%. When cement mixing content exceeds 7%, the shaping state of cement soil is greatly improved. Thus, the cement mixing content of project site is intended to be 8%. It is because that the operation condition in laboratory test is better than that of project site. The construction effect at site shows about 8% cement mixing content could better ensure the stability of cement soil mold bag and the interval with the filling construction of mold bag of the next layer.

Figure 1 is the relation between unconfined compressive strength and curing period. The laboratory test condition was P.O.32.5 Portland cement, standard curing condition (20±3 ℃, immersed).

It can be seen from the Figure 1 that the larger the cement mixing content is, the higher the strength of cement soil is. The unconfined compressive strength of cement soil with 8% cement mixing content and 11 days curing period is to 0.69MPa.

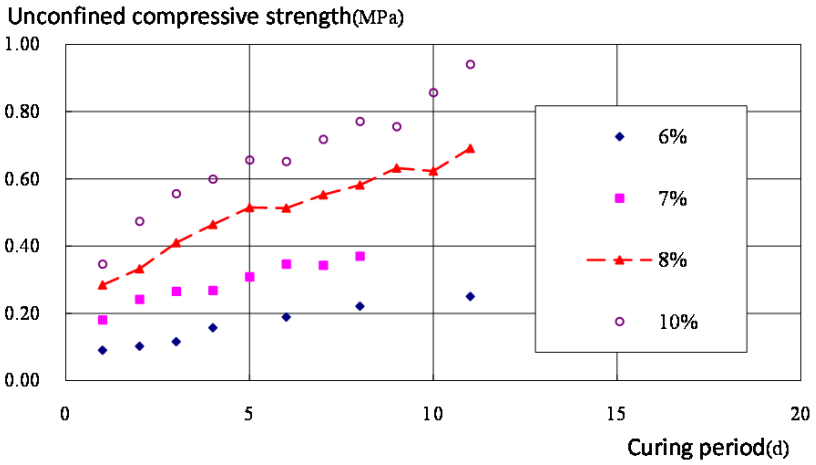


**Fig.1 Strength of cement soil with different mixing contents**
(P.O.32.5 Portland cement , water content is 58%)

**Relation between Water Content of Soil and Strength.** Figure 2 is the correlation curve of strength of cement soil with the same cement mixing content and different water contents. Under the same

curing condition, it is shown that the lower the water content of soil is, the higher the unconfined compressive strength of cement soil with the same cement mixing contents.

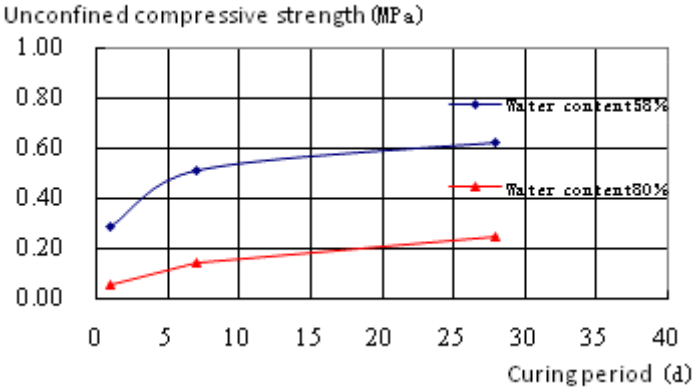


**Fig.2 Correlation curve of strength of cement soil with different water contents**
(8% cement mixing content)

**Relation between Soil Property and Strength.** The comparative tests for cement soil strength of ultra-soft clay, mucky clay, mucky silty clay and silt of Port of Tianjin were done. The results are shown on Figure 3.

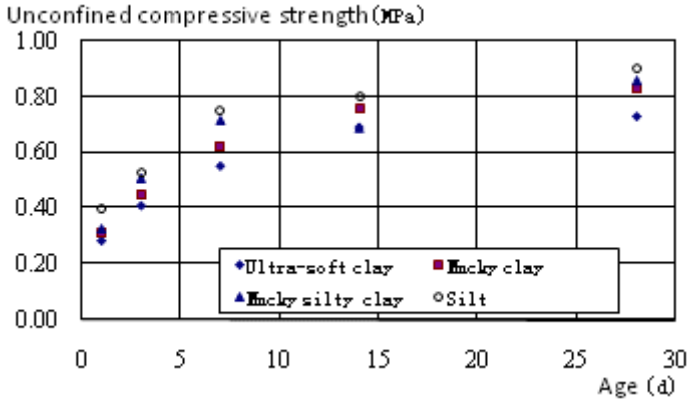


**Fig.3 Strengths of four kinds of soil under the same test condition**
(8% cement mixing content and P.O.32.5 Portland cement)

Test result shows the strengths of cement soil made with mucky silty clay and silt are higher than the strengths of cement soil made with ultra-soft clay and mucky clay under the same cement mixing content. This result is convenient to borrow soil at project site. The soft clay of seabed could be used as wanted.

**Relation between Degree of Mixing Uniformity and Strength.** Generally, the degree of mixing uniformity has a large influence on the strength of cement soil. The better the mixing uniformity is, the higher the strength of cement soil is, while the worse the mixing uniformity is, the lower the strength of cement soil is. Two kinds of cement soil with the same cement mixing content were made, one was uniformly mixed in laboratory and the other was incompletely mixed at project site, and the comparative tests of cement soil strength were done under the different ages and the same curing condition. The result shows the unconfined compressive strength of cement soil (P.O.32.5 Portland cement mixing content is 8%) prepared in laboratory with seabed soft clay could reach 0.69MPa after 11 days, and test condition is standard curing condition (20±3℃, immersed, water content of cement soil is about 58%), see Figure 1. Under the same standard curing condition, the strength of cement soil mixed at site is only 0.243MPa after 14 days (See Figure 4), which is obviously lower than the unconfined compressive strength of cement soil mixed in laboratory. The main reason is the degree of

mixing uniformity at site is relatively low. As there are few test samples of cement soil at site, the formula of relation between site strength and indoor strength cannot be found out for the moment.

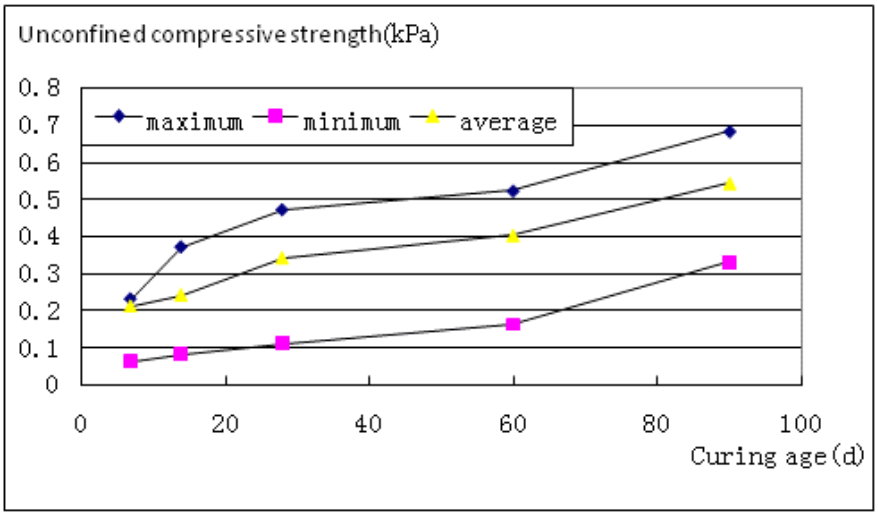


**Figure 4 Strength of on-site shaped cement soil with 8% mixing content under indoor curing condition**

In addition, the laboratory tests were also done for the influence of mixing form of cement, curing condition and test water on strength of low mix addition cement soil. The results show there is no obvious influence on unconfined compressive strength of cement soil whether mixing dry or wet cement, or whether sea water or fresh water. And the influence of the change of curing temperature (10℃～30℃) on strength is also very small.

## Conclusions

(1)The unconfined compressive strength of cement soil is mainly related to the property of soil, water content, cement mixing content and degree of mixing uniformity, while has little to do with curing condition, the mixing form of cement and mixing water.
(2)The unconfined compressive strength of cement soil uniformly mixed in laboratory is far higher than that mixed at site under the same curing condition.

## References

[1] Zhang Jing, Miao Zhonghai, Liu Aimin, etc. *General Report on Technical Research of Cofferdams for Marine Works of Mold Bagged Cement Soil* [R]CCCC Tianjin Port Engineering Institute, Ltd., 2005. (in Chinese)

[2]Guo Shujun and Zhu Yaoting. *Research Report on Engineering Characteristics of Cement Soil*[R]CCCC Tianjin Port Engineering Institute, Ltd.,2005. (in Chinese)

*Applied Mechanics and Materials Vols. 580-583 (2014) pp 260-263*
*© (2014) Trans Tech Publications, Switzerland*
*doi:10.4028/www.scientific.net/AMM.580-583.260*

# Energy characteristics of brittle rock in failure process

Tang Aijun[a], Shi Chenggong[b], Wang Ying[c], Wang Jianhua[d]

Jinan sijian construction group co.,ltd, China

[a]Jnsjjtjyb@126.com, [b]3884640@qq.com, [c]252945337@qq.com, [d]294721610@qq.com

**Keywords:** Brittle rock; failure; energy; high geostress

**Abstract.** Energy transformation in rock failure process is a complicate process, especially in the high geostress conditions. First from the point of energy, analysis and study on the rock deformation and failure process under uniaxial compression and triaxial compression condition. Based on the test results, the deformation failure characteristics and its energy in triaxial compression are analyzed. Reveal the energy dissipation and energy release characteristics in the process, and found the internal causes is stored elastic in rock mass unit can release suddenly and cause rock damaged. Especially in the high geo-stress condition, the compressed engineering rock mass are often faced with the risk of unloading damage. After add anchor, the mechanics performance of specimen after peak period is significantly improved, and can absorb more of the release of strain energy, which is helpful for maintaining the overall stability of surrounding rock.

## Introduction

With the human activity spread to the underground space, more and more underground engineering are constructed in high geostress area. For example, the biggest geostress of lashiwa hydropower station underground workshop is 29.6 MPa, the maximum principal stress value of jinping I hydropower station underground workshop is 37.5 MPa, and the measured the maximum principal stress value of Jinping II long tunnel of hydropower station is as high as 42 MPa. The part west-line project of south-to-north water transfer project in planning will meet 50MPa squeezing stress when excavated. The above projects belong to high geostress underground engineering in reference [1].

In the high geostress condition, unloading rock mass action can cause internal the agglomeration of elastic strain energy release suddenly for excavation, and in the long-term of the geological tectonic movement rock as a kind of inhomogeneous multiphase composite structure material, internal formed a wide variety of scale joints and fissures, and had a random state distribution. When get the outside effect, the internal defects of micro occurring regularly evolution, crack gradually expand, in local form breakthrough area. Along with the increase of external function, these tiny crack development into cracks. Bearing force over the limit, crack extension forward quickly, resulting in rock instability and failure, causing the surrounding rock and pineapple rock burst occurred brittle failure phenomenon, to the stability of surrounding rock and personnel equipment safety brought serious threat, so study under high geostress underground rock destruction of energy to ensure the safety of the engineering characteristics and the stability of the major research value.

## Relationship between failure and energy

Figure 1 is the uniaxial compression stress strain curve, generally, the whole process of the rock deformation can be divided into five stages in reference [2], the five stages corresponding to different energy into form.

1) Compress dense phase (OA) : When rock in compression, the internal defects gradually closed, input in the conversion of energy for rock elastic energy stored in internal; If unload the part of the energy and can be released.

2) Elastic stage (AB) :Rock will produce linear elastic deformation, the outside world can input into the rock elastic energy. If in the range and unloading, energy and can be released, and will not cause damage to the destruction of the rock.

3) Stable cracking stage of development (BC) : After the elastic limit, rock come into the plastic deformation stage,the micro crack began to appear as stress rupture and poor and the increase of development, when the stress remain unchanged, the rupture also stop development. The tester input energy into elastic energy.

4) Unstable cracking stage of development (CD): In this stage micro broken development came a qualitative change, elastic energy storage is abate, due to the rupture process caused by stress concentration effect significantly, and even work stress unchanged, broken still keep progressive development, make the weak link in damage. At this time, body strain to inflation, axial strain rate and lateral strain rate increase accelerated.

5) Strain softening stage (DE): The microcrack join into and produce the macro rock ,which lead to the overall destruction. The storage of elastic energy released, transformation, such as kinetic energy to surface, all kinds of radiant energy increase a lot.

From the above it can be seen in the whole process of rock deformation, the different stage have different ways of energy conversion, the general can think, in the peak intensity D point before the performance for the slow the energy dissipation process, and the peak value point is energy change is sharply after the release of the process.

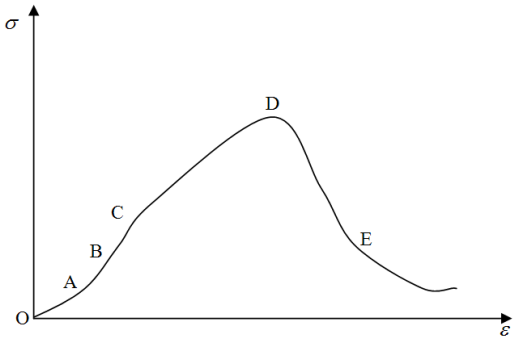


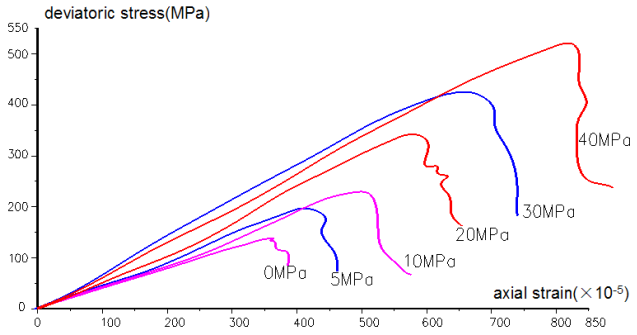


**Fig. 1 Curve of rock stress-strain Fig.2Curve of stress-strain under pseudo triaxial compression**

## Test research on energy characteristic in failure process

This test is developed by rigid pressure in the testing machine. In the experiment, the axial displacement and transverse displacement rate joint control, axial displacement load rate is 0.002 mm/s, and transverse displacement load rate is 0.0005 mm/s (in confining pressure). Processing molding the specimens for cylindrical, a diameter of 50 mm and 100 mm high. The rock specimen is loaded by the axial displacement control loading mode. In the process, the axial displacement of the 5 mm D1117 sensor measuring axial displacement, 100 kN load sensor measuring of the rock axial load, and the testing machine to be automatic conversion into the corresponding strain and stress the output to data collection system. The 5 mm diametral strain of chain sensor record was adopted.

Conventional triaxial compression test confining pressure are chosen 5, 10, 20, 30, 40 MPa. Test the axial displacement control early loading mode; When curve deviates from the straight start segment, the switch as horizontal displacement control loading mode. Begin by hydrostatic pressure conditions on the reservation gradually to the confining pressure value (confining pressure loading using manual control mode, the loading process in two to three minutes to complete), and then keep the confining pressure constant and continuous sinusoidal axial pressure test until the end.

Conventional rock uniaxial compression and triaxial compression test have been mechanical parameters are given in table 1, including confining pressure for rock damage instantaneous confining pressure value, strength in the rock for confining pressure under the condition of the axial load-bearing capacity, and elastic modulus for rock is axial compression curves straight segment of the slope.

**Tab. 1 Rock mechanics parameters**

| NO. | Loading mode | Confining/MPa | Strength/MPa | Elastic modulus/Gpa | Passion ration |
|---|---|---|---|---|---|
| ETD-1 | Unaxial compression | 0.0 | 142.27 | 32.28 | 0.246 |
| ETD-2 | | 0.0 | 143.84 | 33.08 | 0.248 |
| ETD-3 | | 0.0 | 141.39 | 32.08 | 0.244 |
| ETD-4 | | 0.0 | 145.38 | 33.65 | 0.252 |
| ETD-5 | | 0.0 | 138.98 | 31.58 | 0.241 |
| ETD-6 | | 0.0 | 139.24 | 31.89 | 0.245 |
| ETD-7 | | 0.0 | 128.18 | 22.11 | 0.237 |
| ET-1 | Triaxial compression | 5.0 | 198.50 | 32.26 | 0.249 |
| GT-2 | | 10.0 | 229.08 | 33.10 | 0.261 |
| GT-4 | | 20.0 | 343.57 | 35.79 | 0.264 |
| GT-5 | | 30.0 | 418.34 | 36.19 | 0.253 |
| GT-6 | | 40.0 | 519.78 | 37.21 | 0.247 |

## Energy characteristic

The generation of new fracture rock material need energy dissipation, fracture surface of the sliding between to energy dissipation, rock material of the yield of destruction and damage fracture is essentially an energy dissipation process. Axial compression, the initial testing machine is the work done by the energy dissipation of the rock material. But in confining pressure under the action of core distortion, confining pressure also the initial work is done. And derived from [3] in confining pressure the energy dissipation for actual rock is

$$U = \int \sigma_1 d\varepsilon_1 + 2\int \sigma_3 d\varepsilon_3 \tag{1}$$

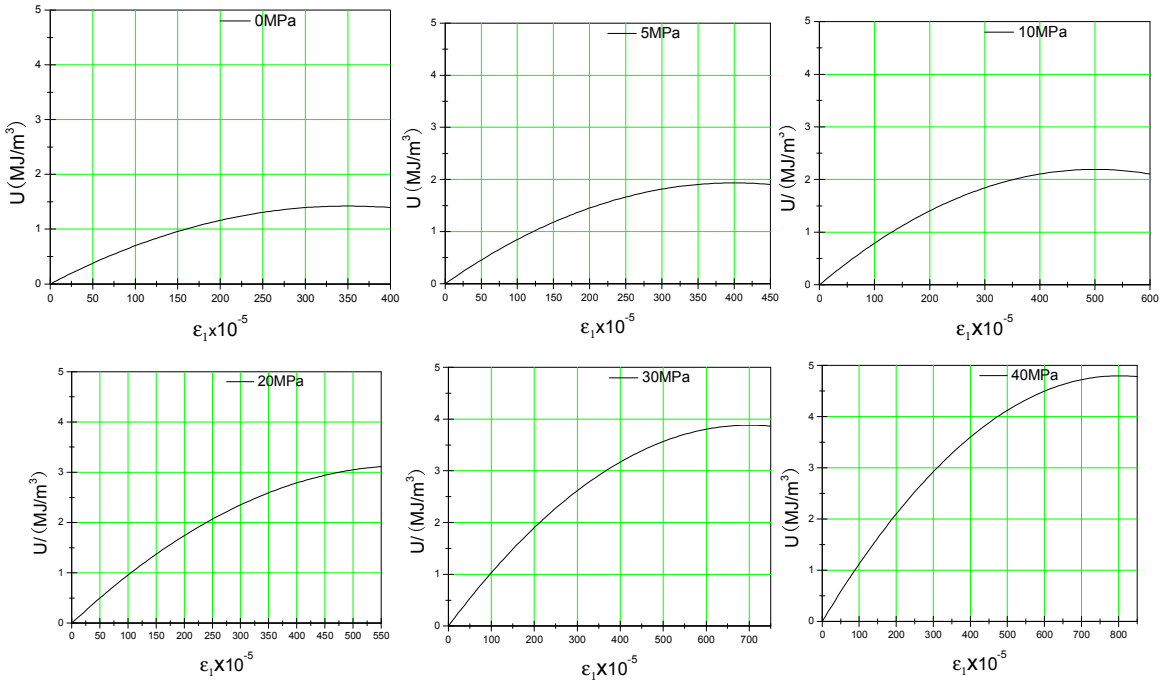


**Fig.3 Energy dissipation properties under different confining pressures**

Figure 5 gives different confining pressure under the effect of axial compression damage of rock energy analysis. The chart shows, online elastic stage, the rock of the actual absorption energy roughly into parabolic increase. Rock began to yield, as the axial stress increase slowly and ring to deformation increase quickly, rock sample of actual absorption energy increase speed slow. After the peak intensity, of the rock deformation change, the absorption of energy with the axial deformation also changes the speed increase further reduced. It is worth noting that, when rock has broken down completely, produce the macro fracture surface, change is shear failure surface friction between the work done. From this may know, is in peak strength of rock after absorbing energy is mainly used to internal material plastic sliding between doing work. And with the increase of confining pressure, absorb energy of rock gradually increase. Low confining pressure when the energy of the actual absorption of rock specimens is very little, and relatively slow increase; But high confining pressure when the energy of the actual absorption of rock specimens is very big, and increase more quickly.

## Summary

The destruction of the rock material and energy is closely related to the changes, especially in the high ground stress conditions. Under the condition of high ground stress in surrounding rock of the damage characteristics of energy, respectively, the deformation and energy surrounding rock the relationship of change, anchor on the influence of the fracture energy and excavation process release of energy and transfer, get the following conclusion:

(1) In the whole process of rock deformation, the different stage have different ways of energy conversion, the general can think, is in peak strength point before the performance for the slow the energy dissipation process, and the peak value point is energy change is sharply after the release of the process. Dissipation to a certain extent inevitable to release the transition, the energy dissipation of strength of rock of that reduce, energy release is a rock reckoning the real cause of the damage.

(2) Rock mass unit stored elastic energy released is a unit of rock mass destruction suddenly internal causes. Especially in the high ground stress condition, for excavation unloading rock mass action can cause internal agglomeration elastic strain can suddenly released, can cause rock destruction, to the stability of surrounding rock and personnel equipment safety brought serious threat;

(3) In three axis of stress state of engineering, and if some of the direction of stress suddenly drops, cause rock in lower stress state damage, so the rock of actual absorption energy is reduced, the original rock stored elastic strain energy release will be foreign, converted to rupture the kinetic energy of rock, rock, rock burst fracture may occur and pineapple brittle failure phenomenon.

## References

[1] Hawkes I and Mellor M. Uniaxial testing in rock mechanics laboratories. Engineering Geology. No.4 (1970), p.177-285.

[2] Peng S D and Johnson A M. Crack growth and faulting in cylindrical specimens of granite . International Journal of Rock Mechanics & Mining Sciences, No.9 (1972), p.37-86.

[3] Li C. And Stillborg B. Analytical models for rock bolts. Int. J. of Rock Mech. Min. Sci., Vol.36 No.8 (1999), p.1013-1029.

*Applied Mechanics and Materials Vols. 580-583 (2014) pp 264-267*
*© (2014) Trans Tech Publications, Switzerland*
*doi:10.4028/www.scientific.net/AMM.580-583.264*

# Estimation Study on Shear Wave Velocity of Seabed Using GRNN

Di Shengjie[1, 2 a], Shan Zhigang[1,b], Xu Xueyong[1,c]

[1] HydroChina Huadong Engineering Corporation, Hangzhou, Zhejiang 310014, China.

[2] Research Center of Coastal and Urban Geotechnical Engineering, Zhejiang University, Hangzhou, Zhejiang 310058, China.

[a]di_sj@ecidi.com; [b]shan_zg@ecidi.com; [c]xu_xy@ecidi.com

**Keywords:** prediction method; shear wave velocity; in-situ test; offshore engineering; GRNN.

**Abstract.** Characterization of the shear wave velocity of soils is an integral component of various seismic analysis, including site classification, hazard analysis, site response analysis, and soil-structure interaction. Shear wave velocity at offshore sites of the coastal regions can be measured by the suspension logging method according to the economic applicability. The study presents some methods for estimating the shear wave velocity profiles in the absence of site-specific shear wave velocity data. By applying generalized regression neural network (GRNN) for the estimation of in-situ shear wave velocity, it shows good performances. Therefore, this estimation method is worthy of being recommended in the later engineering practice.

## Introduction

Values and vertical gradients of shear wave velocity ($V_s$) are important physical and mechanical properties of soils. They are used in both basic and applied engineering geology and civil engineering. They are important in determining the soil dynamic behavior and liquefaction susceptibility, as well as in static loading situations, including site classification, hazard analysis, site response analysis, and soil-structure interaction [1-3]. Many building and geotechnical engineering investigation codes now require consideration of site response when estimating the seismic demand on a structure and rely on a time averaged shear wave velocity $V_s$ to a depth of 20m or 30m for this evaluation. In addition, several geological investigations have recently used correlations between geological parameters and $V_s$ in predicting the foundation properties [4].

The $V_s$ can be measured using different in-situ tests such as seismic cone penetration test, seismic dilatometer test, down-hole test, cross-hole test, suspension logging and spectral analysis of surface wave. Also different empirical correlations have been developed between $V_s$ and cone penetration test data. Baldi et al. correlated $V_s$ in Italian sands with cone tip resistance of cone penetration test (CPT) and the effective overburden stress [5]. Mayne and Rix found that $V_s$ in clays is statistically correlated with cone tip resistance and void ratio [6]. In-situ measurement of $V_s$ has become the preferred method for estimating the small-strain shear properties and has been incorporated into site classifications systems and ground motion prediction equations. The paper presents a new method for estimating the shear wave velocity profiles in the absence of site-specific shear wave velocity data.

The generalized regression neural network (GRNN) is a kind of intelligent algorithms. It has some advantages such as simple design, perfect convergence and high accuracy etc, so it has been widely used for complex nonlinear forecasting model [7]. A model based on GRNN is established to estimate the $V_s$ at the offshore site using the physical and mechanical parameters of samples.

## In-situ test and prediction study

The feasibility of the in-situ test for $V_s$ is studied in both technologically and economically at the offshore wind farm construction site. We used the XG-I suspension logging instrument for testing the shear wave velocity because of low-cost and high-precision. At the same time, the instrument is put

into the drilling hole and it detects $V_s$ point to point from bottom to top. The test site of offshore wind farm and the test instrument are show in Fig. 1.

**Fig.1.** Offshore wind farm construction site and test instrument of shear wave velocity

The conventional estimation methods for shear wave velocity are often using the empirical equations such as regression formulas based on the test data and test depth. However, the different regression formulas present different results even though they are showing the good correlation. We take the part test points for example, the estimation depths for $V_s$=500m/s between power function and polynomial function show that the estimation error is very big (see Fig.2).

In addition, Mayne's equations for estimating the value of $V_s$ based on CPT data are shown as equations (1) and (2). The estimation and comparison results of construction site based on the equations and test data are also shown in Fig.2. As can be seen from the Fig.2, the equation (2) has good applicability. But it is a problem to estimate the values of $V_s$ without the in-situ test results such as the CPT data. We can establish an applicable non-linear mapping relation using the soil parameters and $V_s$ data already known to estimate the new $V_s$ data at other construction site.

$$V_s = 118.8\log_{10}(f_s) + 18.5 \quad (1)$$

$$V_s = [(10.1\log_{10}(q_c) - 11.4]^{1.67}(100 f_s / q_c)^{0.3} \quad (2)$$

where $f_s$ is the side friction of CPT (kPa), and $q_c$ is cone tip resistance of CPT (kPa).

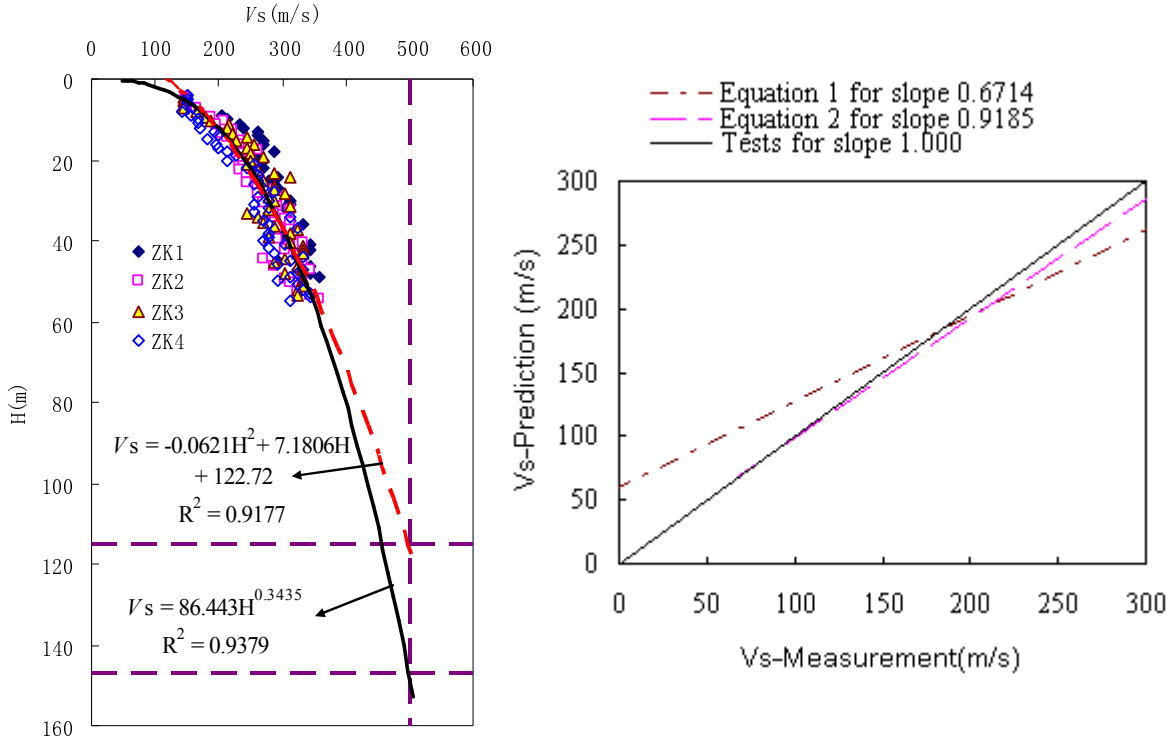


**Fig.2.** Regression method and experienced method for predicting shear wave velocity

**GRNN method and conclusions**

The factors of shear wave velocity of soils in seabed have been studied by statistical analysis. The affecting factors mainly include the physical and mechanical properties of foundation soils, such as standard penetration test (SPT) number $N$, side friction $f_s$ of CPT, cone tip resistance $q_c$ of CPT, depth $z$, void ratio $e$, compression modulus $E_s$, water content $w$, density $\rho$, specific gravity of soil grain $G_s$ and type of soils $T$. Then we use GRNN model to estimate $V_s$. The affecting factors are defined as the input samples and the corresponding $V_s$ as output samples. The minimum error corresponding to spread of GRNN is the final network selected value, which is shown as follows:

$$E(spread) = \frac{1}{n}\sum_{i=1}^{n}(e_i)^2 = \frac{1}{n}\sum_{i=1}^{n}[Y_i(X_i) - Y_i]^2 \quad (3)$$

where spread is the undetermined parameter of the GRNN, $n$ is number of samples, $e$ is corresponding error, $X_i$ is input sample and $Y_i$ is the corresponding output sample of each input sample. With the training samples gathered from the test results before, the optimal value of spread is obtained. Some training samples of input and output data are shown in Table 1.

**Table.1.** Some training samples of GRNN

| $V_s$ | $N$ | $f_s$ | $q_c$ | $z$ | $e$ | $E_s$ | w | $\rho$ | $G_s$ | $T$ |
|---|---|---|---|---|---|---|---|---|---|---|
| *m/s* | — | *KPa* | *MPa* | *m* | — | *MPa* | % | $Kg/m^3$ | — | — |
| 121.6 | 8.27 | 33.86 | 3.31 | 1.70 | 0.883 | 12.84 | 31.30 | 1.85 | 2.70 | 1 |
| 132.1 | 10.19 | 41.04 | 3.50 | 3.65 | 0.845 | 12.79 | 30.00 | 1.86 | 2.70 | 1 |
| 155.5 | 13.67 | 69.00 | 6.62 | 8.15 | 0.820 | 11.10 | 29.10 | 1.88 | 2.70 | 1 |
| 181.9 | 21.50 | 99.60 | 9.04 | 12.90 | 0.781 | 15.91 | 27.60 | 1.89 | 2.69 | 1 |
| 227.0 | 30.30 | 130.68 | 11.77 | 17.20 | 0.769 | 20.31 | 27.20 | 1.90 | 2.69 | 1 |
| 204.8 | 15.40 | 76.31 | 5.91 | 21.95 | 0.828 | 10.94 | 29.40 | 1.87 | 2.70 | 1 |
| 235.0 | 5.00 | 85.45 | 2.99 | 25.65 | 0.930 | 5.71 | 33.10 | 1.83 | 2.70 | 2 |
| 237.7 | 21.00 | 81.21 | 6.55 | 33.85 | 0.864 | 11.43 | 30.80 | 1.86 | 2.70 | 1 |
| 274.9 | 28.60 | 110.38 | 9.36 | 35.35 | 0.815 | 16.26 | 28.90 | 1.88 | 2.69 | 1 |
| 283.0 | 34.60 | 140.10 | 12.91 | 37.75 | 0.795 | 18.26 | 28.20 | 1.88 | 2.68 | 1 |
| 288.4 | 14.45 | 98.22 | 5.59 | 39.35 | 0.988 | 6.35 | 35.60 | 1.81 | 2.70 | 1 |
| 297.7 | 23.20 | 104.18 | 3.23 | 41.35 | 0.767 | 6.78 | 27.50 | 1.92 | 2.72 | 2 |
| 310.1 | 22.90 | 137.31 | 7.48 | 46.55 | 0.762 | 9.26 | 27.10 | 1.91 | 2.70 | 2 |
| 294.5 | 35.10 | 177.50 | 15.18 | 48.55 | 0.803 | 8.76 | 28.70 | 1.89 | 2.71 | 1 |
| 169.0 | 5.00 | 17.60 | 0.66 | 8.00 | 1.232 | 4.03 | 43.60 | 1.76 | 2.72 | 2 |
| 251.4 | 17.60 | 72.60 | 6.72 | 13.20 | 0.726 | 10.67 | 24.09 | 1.97 | 2.69 | 1 |
| 218.6 | 5.00 | 33.50 | 0.98 | 17.95 | 1.067 | 3.32 | 37.44 | 1.82 | 2.73 | 2 |
| 217.0 | 13.90 | 96.571 | 5.22 | 28.80 | 0.721 | 10.78 | 24.00 | 1.94 | 2.69 | 1 |
| 229.0 | 17.80 | 85.61 | 2.32 | 32.30 | 0.747 | 6.05 | 26.90 | 1.99 | 2.74 | 2 |
| 243.0 | 8.80 | 55.50 | 2.60 | 36.50 | 0.800 | 6.20 | 29.70 | 1.90 | 2.70 | 2 |
| 294.5 | 38.00 | 127.44 | 9.15 | 45.45 | 0.778 | 12.13 | 25.80 | 1.90 | 2.69 | 1 |
| 132 | 12.40 | 45.71 | 3.48 | 7.10 | 0.730 | 9.67 | 25.40 | 1.96 | 2.70 | 1 |
| 165 | 17.00 | 67.26 | 6.37 | 13.20 | 0.692 | 11.25 | 24.90 | 1.99 | 2.70 | 1 |
| 231 | 26.60 | 102.19 | 10.67 | 21.80 | 0.681 | 13.02 | 23.50 | 1.98 | 2.69 | 1 |
| 195 | 6.40 | 51.11 | 2.61 | 23.00 | 0.724 | 9.44 | 25.20 | 1.96 | 2.69 | 2 |
| 205 | 12.70 | 66.31 | 5.25 | 24.00 | 0.736 | 9.69 | 25.10 | 1.94 | 2.70 | 1 |
| 250 | 17.70 | 83.72 | 8.11 | 26.40 | 0.666 | 11.95 | 23.80 | 2.00 | 2.69 | 1 |
| 235 | 17.60 | 88.54 | 2.45 | 29.40 | 0.720 | 5.62 | 25.70 | 2.00 | 2.73 | 2 |
| 238 | 8.60 | 56.90 | 2.70 | 30.70 | 0.823 | 5.52 | 29.00 | 1.92 | 2.71 | 2 |
| 248 | 12.20 | 95.76 | 5.58 | 32.60 | 0.764 | 9.26 | 26.00 | 1.93 | 2.70 | 1 |
| 258 | 31.80 | 109.20 | 9.77 | 38.50 | 0.791 | 12.52 | 27.10 | 1.91 | 2.69 | 1 |

Considering the excellent classification property of GRNN, the types of soils are introduced to the training samples. The cohesive soils are represented by the number 1, and non-cohesive soils by the number 0. The trained network will automatically make the soils classifications, which as one of the input samples affect the shear wave velocity. For example, when the input number of soil type is 0, the trained GRNN can identify automatically the characteristics of non-cohesive soils and seek the corresponding shear wave velocity. The mechanical and physical parameters of the seabed soils of in-situ test and indoor test from the offshore construction site as the predicting samples, the predicted values of $V_s$ can be obtained based on the trained GRNN. Some predicting samples of GRNN can be shown in Table 2.

Because the GRNN estimation model considering the comprehensive factors, the predicted results show good agreement with the actual values. The example analysis shows that the method has the good forecast precision and useful value. In addition, the estimation of GRNN can offer reference to other engineers and researchers.

**Table.2.** Some predicting samples of GRNN

| Predicting samples | | | | | | | | | | Predicted values | Actual values |
|---|---|---|---|---|---|---|---|---|---|---|---|
| $N$ | $f_s$ | $q_c$ | $z$ | $e$ | $E_s$ | w | $\rho$ | $G_s$ | $T$ | $V_s$ | $V_s$ |
| — | *KPa* | *MPa* | *m* | — | *MPa* | % | $Kg/m^3$ | — | — | *m/s* | *m/s* |
| 12.20 | 61.23 | 4.92 | 2.10 | 0.774 | 9.56 | 26.10 | 1.92 | 2.70 | 0 | 110.0 | 119.5 |
| 12.90 | 62.70 | 4.84 | 7.10 | 0.731 | 9.57 | 25.40 | 1.96 | 2.70 | 0 | 142.6 | 139.0 |
| 19.60 | 42.42 | 8.99 | 16.50 | 0.847 | 6.84 | 29.40 | 1.90 | 2.70 | 1 | 165.5 | 152.0 |
| 6.90 | 68.861 | 1.96 | 21.60 | 0.752 | 8.69 | 26.40 | 1.95 | 2.70 | 0 | 197.9 | 181.5 |
| 13.90 | 96.571 | 5.22 | 28.80 | 0.721 | 10.78 | 24.00 | 1.94 | 2.69 | 0 | 224.8 | 217.0 |
| 17.80 | 85.61 | 2.32 | 32.30 | 0.747 | 6.05 | 26.90 | 1.99 | 2.74 | 1 | 235.9 | 229.0 |
| 8.80 | 55.50 | 2.60 | 36.50 | 0.800 | 6.20 | 29.70 | 1.90 | 2.70 | 1 | 251.4 | 243.0 |
| 38.00 | 127.44 | 9.15 | 45.45 | 0.778 | 12.13 | 25.80 | 1.90 | 2.69 | 0 | 302.6 | 294.5 |

**Acknowledgements**

This work was financially supported by the National Natural Science Foundation of China (41101519), Major Science and Technology Project of China Hydropower Engineering Corporation (GW-KJ-2011-18) and the Postdoctoral Advanced Research Programs Class II of Zhejiang Province (No. BSH1302013), China.

**References**

[1] E. L. Hamilton: A review, Geophysics, Vol. 41 (1976), p. 985-996.

[2] T.L. Youd and I.M. Idriss: J. Geotech. Geoenviron. ASCE. Vol. 127 (2001), p. 297-313.

[3] B. O. Hardin and F. E. Richart: J. Soil Mech. Found. Div. Vol. 98 (1972), p. 603-624.

[4] R. D. Borcherdt: Earthquake Spectra. Vol. 18 (2002), p. 189-217.

[5] G. Baldi, R. Bellotti, V. N. Ghionna, M. Jamiolkowski and D. C. F. Lo Presti: Proceedings, 12th International Conf. on Soil Mech. and Found. Eng. Vol. 1 (1989), p. 165-170.

[6] P. W. Mayne and G. J. Rix: Soils and Foundation. Vol. 35 (1995), p. 193-194.

[7] D. F. Specht: IEEE Transaction on Neural Network. Vol. 2 (1991) p. 568-576.

*Applied Mechanics and Materials Vols. 580-583 (2014) pp 268-272*
*© (2014) Trans Tech Publications, Switzerland*
*doi:10.4028/www.scientific.net/AMM.580-583.268*

# P-wave attenuation mechanism of calcareous sand under explosion

XU Xue-yong[1,a], Di Sheng-jie[1,b], Cheng Wan-qiang[1,c], LI Wei[1,d], DU Wen-bo[1,e]

[1]HydroChina Huadong Engineering Corporation, Hangzhou, Zhejiang 310014, China.

[a] xu_xy@ecidi.com; [b]di_sj@ecidi.com; [c]cheng_wq@ecidi.com;

[d]li_w@ecidi.com;[e]du_wb@ecidi.com

**Keywords:** marine geotechnical medium; calcareous sand; P-wave attenuation; particle breakage; explosion energy

**Abstract.** Calcareous sand is a special marine geotechnical medium that exhibits interesting physical and mechanical properties resulting from its composition and structure. In the current paper, the blasting compression wave (P-wave) attenuation mechanism of calcareous sand under explosion was studied through explosion experiments. The decay law of the P-wave was obtained based on the earth pressure at different distances from the blast center. The results show that, the broken, compress, and damage zones were formed under the effect of blasting load, many particles were broken near the blasting zone. Calcareous sand exhibits strong absorption and attenuation effects on the P-wave because of its particle breakage characteristics.

## Introduction

Calcareous sand is a special marine geotechnical medium composed primarily of calcium carbonate. The special sedimentary environment of calcareous sand, particularly its deposition process which does not involve long-distance transport, resulted in the preservation of the small pores in the original skeleton[1-2]. Studies have shown that the irregular shape and particle breakage characteristics of calcareous sand account for its engineering properties, which are significantly different from those of other terrestrial sand[3-5].

At present, docks, airport runways, collecting tanks, and other kinds of civil and military infrastructures are constructed on coral reefs because of necessity, as well as for protection and the development of marine resources. These infrastructures potentially cause accidental and man-made explosions. Thus, studies on explosion safety and protection for these buildings are becoming increasingly significant.

Calcareous sand is the most common material medium on coral reefs, and its mechanical properties significantly affect the propagation and attenuation of the explosion wave. In recent decades, extensive studies on the dynamic characteristics of terrestrial sand or soil have been conducted. For example, VAN IMPE W F *et al.* (1989) [6], Gohl W B *et al.* (2000) [7], Dontsov V E *et al.* (2001) [8],WANG Ming-yang *et al.* (2002) [9], Qu Jun-tong *et al.* (2006) [10], MU Chao-min *et al.* (2010) [11]. These studies can be classified into two categories, namely, the experimental method and numerical simulations. The experimental method obtains the relationship between the material medium parameter and the explosion load. For example, different densities, grain compositions, and sand saturation exhibit different characteristics in response to explosions. On the other hand, numerical simulations are mostly performed by establishing physical models based on experimental test results and then using the ANSYS/LS-DYNA software to imitate the explosive process[12]. Studies on the dynamic response characteristics of calcareous sand under explosion are rare. Hence, the

conduct of research on this field is necessary. Understanding the explosion compression wave propagation and attenuation can provide basic information for engineering constructions. In the current paper, the explosion compression wave propagation and attenuation of calcareous sand would be examined through indoor explosion experiments.

## Experiment material

The calcareous sand used in this experiment was sampled from China Nansha Islands. The physical parameters were determined and a granulometric analysis experiment was conducted prior to the indoor explosion experiment. The results show that 50% of the particles have sizes larger than 0.5 mm, and the non-uniform coefficient is 7.83, indicating that the samples could be classified as coarse sand. Table 1 and Fig. 1 show the detailed physical properties of the calcareous sand and the results of the granulometric analysis experiment, respectively:

**Table 1** Physical properties of calcareous sand

| $D_{60}$ (mm) | $D_{30}$ (mm) | $D_{10}$ (mm) | $e_{max}$ | $e_{min}$ | $d_s$ |
|---|---|---|---|---|---|
| 0.876 | 0.579 | 0.112 | 1.405 | 0.766 | 2.76 |

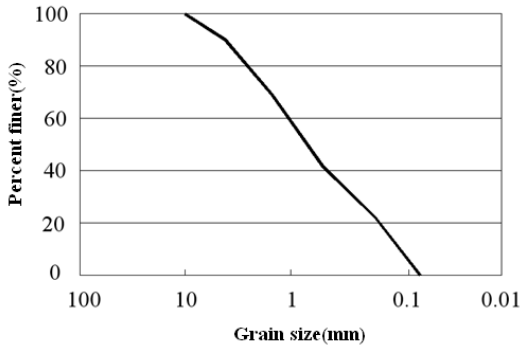


**Fig. 1** Granulometric analysis of calcareous sand

## P-wave attenuation test

High-temperature and high-pressure gas are produced after an explosion and rapidly expands, resulting in a huge energy explosion. This energy acts on the surrounding medium and then spreads in the form of an explosion wave.

Shi Jiao-wang et al. (1992) [13] tested the earth pressure of terrestrial sand after it was subjected to an explosion experiment. The shock wave rapidly attenuated in the impact zone, and the measured waveform basically turned into a compression wave outside the impact zone. The earth pressure increased because of the P-wave compression action. The propagation and attenuation of the explosion compression wave was then obtained based on a complete analysis of the test results.

A 100 cm × 100 cm × 100 cm steel box was used for the mini-explosion experiment. Given that the boundary constraint and stress wave reflection significantly affects the precision of the experiment, a 2 cm thick foam mat was placed around the inside wall of the experiment box for the multiple comparison of experimental data. The results indicate an efficient improvement.

Three earth pressure strain gauge-type sensors were disposed along the horizontal direction of the experiment box at a depth of 40 cm. The distances from the explosion were 30, 50, and 70 cm. Fig. 2 shows the size of the experiment box and the position of the sensors, with TY01 to TY03 representing the three earth pressure strain gauge-type sensors.

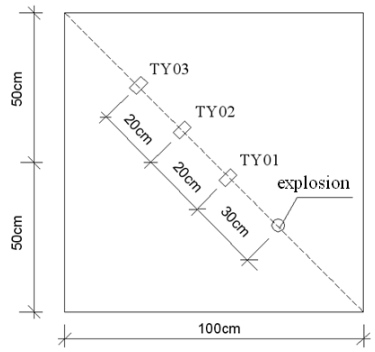


**Fig. 2** Size of the experiment box and the position of the sensors

## Test results

Fig. 3 shows the earth pressure–time history curve of the calcareous sand, in which the overpressure from the explosion reaches a peak value within 1 ms to 6 ms followed quickly by an attenuation and then by a negative pressure.

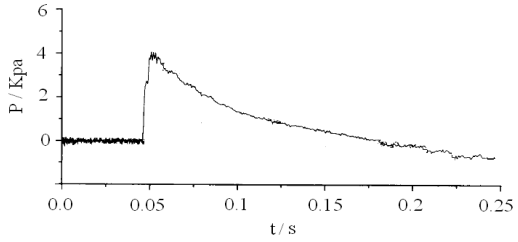


**Fig. 3** Typical earth pressure time–history curve of the calcareous sand

Fig. 3 shows that the maximum earth pressure is 4.13 kPa. However, when the mechanics of the explosion [Eqs. (1) and (2)] are used to calculate the overpressure from the explosion in the water, the water pressure on the same explosive distance is 16.18MPa, which is far greater than the maximum earth pressure of the calcareous sand. These differences indicate that the calcareous sand has greater absorption and attenuation effect. Calcareous sand is a non-continuous medium mainly consisting of loose particles and pore water. Thus, the deformation of loose particles and the effect of the explosive stress wave between the particles can lead to a greater loss on the explosive wave energy.

$$\Delta P_m = 53.3\left[\frac{\sqrt[3]{Q}}{R}\right]^{1.13} \tag{1}$$

$$\Delta P_m = \frac{35.5}{R^0} + \frac{15.5}{(R^0)^2} - \frac{0.024}{(R^0)^3} \tag{2}$$

$$R^0 = \frac{\sqrt[3]{Q}}{R} \tag{3}$$

where $\Delta P_m$ is the overpressure from the explosion, $R$ is the distance from the explosion, and $Q$ is the number of explosives.

**Regression analysis of the P-wave attenuation mechanism**

According to the blast similarity law, when two explosives with the same properties but different quantities explode in the same medium, their stress or deformation field is broadly similar. Thus, the geometry terms can be expressed as the relative distance, as shown in Eq. (4):

$$R_1 / \sqrt[3]{Q_1} = R_2 / \sqrt[3]{Q_2} \tag{4}$$

The explosive pressure can be expressed as a function of the relative distance, as follows:

$$\sigma = f(\sqrt[3]{Q} / R) = \sum_{i=1}^{n} K_i (\sqrt[3]{Q} / R)^{\alpha_i} \tag{5}$$

where $K$ and $\alpha$ are the attenuation parameters associated with the explosive conditions and the wave dissemination media. The first-series solution can be used to establish the experimental formulas, as shown in Eq. (6):

$$\Delta P_m = K \ (\sqrt[3]{Q} / R)^{\alpha} \tag{6}$$

By defining $\rho = \dfrac{\sqrt[3]{Q}}{R}$, and through the logarithmic transformation of Eq. (6), a linear equation is derived, as follows:

$$\lg \Delta P_m = \alpha \lg \rho + \lg K \tag{7}$$

By defining $y = \lg \Delta P_m$, $a = \lg K$, $b = \alpha$, $x = \lg \rho$,

$$y = a + bx \tag{8}$$

$a$ and $b$ can be obtained through a linear regression analysis, and the attenuation parameters ($K$ and $\alpha$) can be obtained. The decay law of the P-wave with the distance can then be calculated using Eq. (9).

$$\Delta P_m = 24.36 \left( \frac{\sqrt[3]{Q}}{R} \right)^{1.76} \tag{9}$$

Fig. 4 shows the fitted curve of the experimental results.

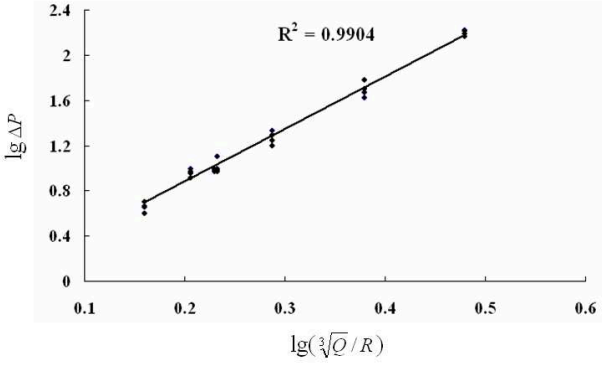


Fig. 4 Decay law of the P-wave through a linear regression analysis

**Conclusions and Discussions**

The attenuation mechanism of the P-wave was examined through blasting test, main conclusions are summarized as follows:

(1) The effects of absorption and attenuation of the compression wave were very strong for saturated calcareous sands. In the current study, the attenuation law was expressed as $\Delta P_m = 24.36\left(\frac{\sqrt[3]{Q}}{R}\right)^{1.76}$.

(2) Under the effect of blasting load, many particles were broken near the blasting zone. The broken, compress, and damage zones are formed, which consume most of the energy and result in an increase in the attenuation effect. The energy for the formation of the broken, compress, and damage zones will be calculated through theoretical method in the later study.

**Acknowledgements**

This work was financially supported by the Natural Science Foundation of China (41101519) and Key Technologies Program of HydroChina Huadong Engineering Corporation(KY2011-02-17-01).

**References**

[1]Liu Chongquan, Yang Zhiqiang, Wang Ren. The present condition and development in studies of mechanical properties of calcareous soils[J], *Rock and Soil Mechanics*, 1995, 16(4):75–83.

[2]Wang Ren, Song Chaojing, Zhao Huanting. Engineering Geological Properties of Coral Reefs on Nansha Islands[M]. *Beijing: Science Press*, 1997.

[3]ZHANG Jiaming, ZHANG Lin, JIANG Guosheng, et al. Research on particle crushing of calcareous sands under triaxial shear[J]. *Rock and Soil Mechanics*, 2008, 29(10):2789–2793.

[4]WANG Xinzhi, WANG Ren, MENG Qinshan, et al. Study of plate load test of calcareous sand[J]. *Rock and Soil Mechanics*, 2009, 30(1): 147–156.

[5]CHEN Qingyun, SUN Jizhu, WANG Ren. Triaxial experiment study of acoustic emission laws of calcareous sand. *Rock and Soil Mechanics*, 2009, 30(7):2027–2036.

[6]VAN IMPE W F, MEYUS I. Soil Compaction by Blasting in the Zeebrugge Area[C]. 1st Iranian Int. Sem. On SMFE, Tehran, Iran. 1989.

[7]GOHL W B, JEFERIES M G, HOWIE J A. Explosive Compaction: Design, Implementation and Effective- ness[J]. *Geotechnique*,2000,50 (6):657－665.

[8]DONTSOV V E, NAKORYAKOV V E. Enhancement of shock waves in a porous medium saturated with a liquid containing gas bubbles[J]. *International Journal of Multiphase Flow*, 2001, (27): 2033－2041.

[9]WANG Ming-yang, ZHAO Yue-tang, QIAN Qi-hu. Study on dynamic behaviour and numerical method for saturated sand[J]. *Chinese Journal of Geotechnical Engineering,* 2002, 24(6): 723－729.

[10]Qu Jun-tong, Zhou Jian, Wu Xiao-feng. Explosive Compaction of Sand Ground Foundation[J]. *Engineering Blasting,* 2006,12(3):14-17.

[11]MU Chao-min, REN Huiqi, LI Yongchi, et al. Propagation laws of blast wave in saturated soils with high saturation degree[J]. *Rock and Soil Mechanics*, 2010，31(3)：875-880.

[12]GUO Sheng-bing, GAO Peizheng, PAN Yuefeng, et al. Explosive wave propagation in quasi-saturated sandy soil[J]. *Rock and Soil Mechanics*, 2004, 25(12):1897–1899.

[13]Shi Jiaowang, Tong Jinyue, Xiong Changhan, et al. An Experimental Research on Compaction of Saturated Sand Soil by Explosion[J]. *Journal of Yangtze River Scientific Research Institute*, 1992, 9(4):25–32.

*Applied Mechanics and Materials Vols. 580-583 (2014) pp 273-277*
*© (2014) Trans Tech Publications, Switzerland*
*doi:10.4028/www.scientific.net/AMM.580-583.273*

# Response of Non-homogeneous Saturated Soils and Free-field to Incident Plane SH Wave

Fengxi Zhou[1,2,a], Ruixia Song[1,b]

[1]School of Civil Engineering, Lanzhou University of Technology, Lanzhou, Gansu in China,730050;

[2]Western Engineering Research Center of Disaster Mitigation in Civil Engineering of Ministry of Education, Lanzhou University of Technology, Lanzhou, Gansu in China, 730050.

[a]geolut@163.com, [b]songrx365@163.com

**Key words:** Non-homogeneous Saturated Soil, SH Wave, Dynamic Response, Reflection and Transmission

**Abstract.** Based on the Biot's Theory, the dynamic response of non-homogeneous saturated soil has been studied using Helmholtz vector decomposition principle and Exact Dynamic Stiffness Method (EDSM). Reflection and transmission of SH wave in non-homogeneous saturated soil have also been analyzed in considering the continuous variation of physical and mechanical properties of saturated foundation along the thickness. The general calculation formula about the reflection and transmission coefficients of bedrock and free field on both surfaces was achieved. Assuming that the material properties have an exponential law distribution and gradient variation along the thickness-coordinate, the dynamic response of non-homogeneous saturated soils under incident plane SH wave was discussed by numerical examples. The results show that the incident angle, the thickness and heterogeneity index of saturated soil have significant influences on the ratio of the ground displacement and bedrock displacement.

## Introduction

Dynamical response of soil subjected to earthquake is one of the major considerations in the field of geotechnical engineering and earthquake engineering. Biot's theory has been widely applied in geomechanics to study the wave propagation in fluid-saturated poroelastic medium subjected to seismic wave action [1,2]. Knopoff [3], Gilbert and Backus [4] assumed that the covering soil layers upon bedrock as ideal elastic, homogeneous, isotropic media and then derived the exact dynamic-stiffness matrices for the soil layer and half-space, with that a complete theory for wave propagation in layered soils was derived, and widely been used in civil engineering. Curtis and Redwood [5], proposed a solution for the dispersion characteristics of SH wave in a piezoelectric material and the conditions for the existence of various modes. Buchen[6,7] studied the reflection, transmission, and diffraction of SH waves excited by a line source in layered half space. However, very few studies have considered the influence of non-homogeneous saturated soils. In this paper, SH wave in a layered structure of non-homogeneous saturated soils is investigated under the varying with incident angle, the thickness and heterogeneity index of saturated soil, the numerical results are presented and discussed.

## Theoretical Formulations

The saturated soil foundation model is shown in Fig.1; the thickness of saturated soil above bedrock is $H$, and SH wave is incident from bedrock.

**In Bedrock**. The potential function of bedrock can be introduced here [8] :

$$\Phi = 2B_e \mathrm{e}^{i(k_{1R}x_1 + k_{3R}x_3 - \omega t)} \tag{1}$$

Where $B_e$ , $B_r$ are the amplitude coefficient of incident and reflected SH wave in bedrock, respectively, and $B_e$=$B_r$ ; $k_{3R}=(\omega\cos\theta)/v$ , $k_{1R}=(\omega\sin\theta)/v$ ; $v$ is the velocity of incident SH wave, and $v=\sqrt{\mu/\rho}$ ;

The calculation formula of displacement component is:

$$u_{R2}(x_1,x_3,\mathrm{t})=\frac{\partial^2\Phi}{\partial x_1^2}+\frac{\partial^2\Phi}{\partial x_3^2} \tag{2}$$

Using the stress-strain relations and wave equation, we can get the following forms of function relation between the stress and the potential function,

$$\tau_{R23}=\mu\frac{\partial}{\partial x_3}\left(\nabla^2\Phi\right) \tag{3}$$

Physical quantities of bedrock are:

$$u_{R2}(x_1,x_3)=-2\left(k_{1R}^2+k_{3R}^2\right)B_e\mathrm{e}^{i(k_{1R}x_1+k_{3R}x_3-\omega t)} \tag{4a}$$

$$\tau_{R23}=-2i\mu k_{3R}\left(k_{1R}^2+k_{3R}^2\right)B_e\mathrm{e}^{i(k_{1R}x_1+k_{3R}x_3-\omega t)} \tag{4b}$$

**In Saturated Porous Media.** Assuming that the soil skeleton is uncompressible and the fluid viscosity is incorporated into the dynamic permeability, the control equations for saturated soil [9] are:

$$\mu\nabla^2\mathbf{u}+\mathrm{grad}\left[\left(\mu+\lambda+\alpha^2M\right)e\right]-\mathrm{grad}\left(\alpha M\zeta\right)=\rho\ddot{\mathbf{u}}+\rho_f\ddot{\mathbf{w}} \tag{5a}$$

$$\mathrm{grad}\left(\alpha Me-M\zeta\right)=\left(\rho_f\ddot{\mathbf{u}}+m\ddot{\mathbf{w}}\right)+b\dot{\mathbf{w}} \tag{5b}$$

In the above equations, $u_i$ and $w_i$ are the displacement vectors of the solid skeleton and pore fluid, respectively; $e=u_{i,i}$ , $\zeta=-w_{i,i}$ ; $\lambda$ and $\mu$ are Lame constants of solid skeleton; $\alpha$ and $M$ are the compressibility parameters of the two-phase medium.; $\alpha=1-K/K_s$ , $1/M=(\alpha-n)/K_s+n/K_f$ , $K_f$ is bulk modulus of pore fluid; $\rho$ is total density of the saturated soil, and can be derived by $\rho=(1-n)\rho_s+n\rho_f$ , where $n$ is porosity, $\rho_s$ and $\rho_f$ are density of solid grains and pore fluid, respectively; $b=\eta/k_f$ ; $\eta$ is the fluid viscosity, $k_f$ is the intrinsic permeability; $\nabla$ denotes the Laplace operator.

According to Helmholtz vector decomposition principle, it's convenient to introduce potentials $\varphi_u$ , $\psi_u$ , $\varphi_w$ and $\psi_w$ , then the solid skeleton and pore fluid displacements $u_i$ and $w_i$ can be expressed as:

$$\boldsymbol{u}=\nabla\varphi_u+\nabla\times\boldsymbol{\psi}_u,\quad \nabla\cdot\boldsymbol{\psi}_u=0 \tag{6a}$$

$$\boldsymbol{w}=\nabla\varphi_w+\nabla\times\boldsymbol{\psi}_w,\quad \nabla\cdot\boldsymbol{\psi}_w=0 \tag{6b}$$

Substituting Eq.(6) into Eq.(5), differential equation of S wave can be given as:

$$\mu\nabla^2\boldsymbol{\psi}_u-\rho\ddot{\boldsymbol{\psi}}_u-\rho_f\ddot{\boldsymbol{\psi}}_w=0 \tag{7a}$$

$$\rho_f\ddot{\boldsymbol{\psi}}_u+m\ddot{\boldsymbol{\psi}}_w+b\dot{\boldsymbol{\psi}}_w=0 \tag{7b}$$

Introduced displacement potential function of saturated soil skeleton:

$$\Psi=\left(Ae^{-iv_tx_3}+De^{iv_tx_3}\right)\mathrm{e}^{i(k_1x_1-\omega t)} \tag{8}$$

We can get the following physical quantities of saturated soil:

$$u_2(x_1,x_3)=-\gamma_t^2\left(Ae^{-iv_tx_3}+De^{iv_tx_3}\right)\mathrm{e}^{i(k_1x_1-\omega t)} \tag{9a}$$

$$\tau_{23}=i\mu v_t\gamma_t^2\left(Ae^{-iv_tx_3}-De^{iv_tx_3}\right)\mathrm{e}^{i(k_1x_1-\omega t)} \tag{9b}$$

Where $A$ , $D$ are the amplitude coefficient of transmission and reflection for SH wave in saturated soil, respectively; $k_1=k_{1R}=(\omega\sin\theta)/v$ ; $v_t^2=\gamma_t^2-k_1^2$ ; $\gamma_t^2=-\beta_3/\mu\left(m\omega^2-i\omega b\right)$ ; $\beta_3=\omega^2\rho\left(m\omega^2-i\omega b\right)-\omega^4\rho_f^2$ .

**Propagation of SH Wave in Non-homogeneous Saturated Soil Layer**

According to the different environment, geography and climate conditions, the soil physico-mechanical properties have great difference along the depth. The control equation of non-homogeneous saturated soils is partial differential equations with variable coefficients, and it is difficult to get analytical solutions. To solve this problem, the non-homogeneous saturated soil layer along the thickness is simplified as many homogeneous thin layer of saturated soil, as is shown in Fig.2. The layer number *N* is decided by precision. The wave transmission and reflection of SH wave in the *jth* layer is also shown in Fig. 2.

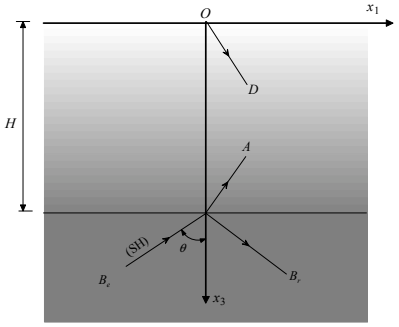


Fig.1 Diagram of non-homogeneous saturated soil foundation

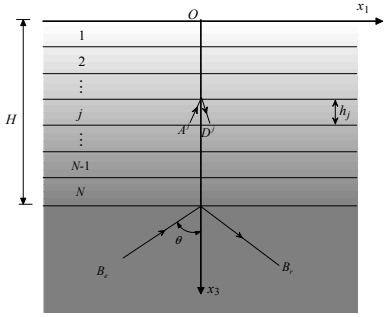


Fig.2 The laminate model of non-homogeneous saturated soil

**Transfer Matrix.** SH wave is incident from bedrock, reflected and transmitted in non-homogeneous saturated soil, from formula (9), and using Exact Dynamic Stiffness Method (EDSM), we get:

$$\mathbf{U}^j = \mathbf{F}^{(j)} \cdot \mathbf{A}^j \cdot \mathrm{e}^{i(k_1 x_1 - \omega t)} \tag{10}$$

Where superscript *j* represents the *jth* layer of non-homogeneous saturated soil; $\mathbf{U}^j = \left(u_2^{(j)} \quad \tau_{23}^{(j)}\right)^T$, $\mathbf{A}^j = \left(A^j \quad D^j\right)^T$, $\mathbf{F^{(j)}} = \begin{bmatrix} -\gamma_t^2 e^{-iv_t x_3} & -\gamma_t^2 e^{iv_t x_3} \\ i\mu v_t \gamma_t^2 e^{-iv_t x_3} & -i\mu v_t \gamma_t^2 e^{iv_t x_3} \end{bmatrix}$.

The formula (10) is applicable to any depth from 0 to *h*. When $x_3 = 0$, we can get the value of displacement and stress component on the top surface of the *jth* layer, and $\mathbf{F}_0^{(j)}$. According to the continuity conditions of boundary surface, The displacement and stress component on the top surface of the *jth* layer are equal with the corresponding values of the (*j-1*)*th* layer on the bottom. In the follow formula, subscript B represents the bottom surface, and subscript T represents the top surface:

$$\mathbf{U}_{\mathrm{B}}^{j\text{-}1} = \mathbf{F}_0^{(j)} \cdot \mathbf{A}^j \cdot \mathrm{e}^{i(k_1 x_1 - \omega t)} \tag{11}$$

From formula (10) and (11), the relation expression of displacement and stress between the *jth* and the *(j-1)th* both on the bottom layer can be obtained:

$$\mathbf{U}_B^j = \mathbf{G}_{h_j}^{(j)} \cdot \mathbf{U}_{\mathrm{B}}^{j\text{-}1} \tag{12}$$

Where, $\mathbf{G}_{h_j}^{(j)} = \mathbf{F}_{h_j}^{(j)} \mathbf{f}_{\mathbf{0}}^{(j)}$; $\mathbf{f}_0^{(j)}$ is the inverse matrix of $\mathbf{F}_0^{(j)}$.

According to the formula (12), we can get recursive relation expression of displacement and stress on the bottom of the *jth* and the *(j-1)th* layer. The displacement and stress of the *(N-1)th* bottom layer are equal with the corresponding values of the *Nth* layer on the top, therefore, the displacement and stress relations on the top of the *Nth* layer and the first layer can be expressed as follows:

$$\mathbf{U}_{\mathrm{T}}^{N}=\mathbf{M}\cdot\mathbf{U}_{\mathrm{B}}^{\mathbf{1}} \tag{13}$$

Where: $\mathbf{M}=\prod_{m=N-1}^{2}\mathbf{G}_{h_m}^{(m)}=\mathbf{G}_{h_{N-1}}^{(N\text{-}1)}\cdot\mathbf{G}_{h_{N-2}}^{(N-2)}\cdot\cdots\cdot\mathbf{G}_{h_2}^{(2)}\cdot$

Consider the displacement and stress of the top and the bottom of the first layer and the *Nth* layer both on the top, we can obtained:

$$\mathbf{F}_{\mathbf{0}}^{(N)}\cdot\mathbf{A}^{N}=\mathbf{M}\cdot\mathbf{F}_{h_1}^{(1)}\cdot\mathbf{A}^{\mathbf{1}} \tag{14}$$

**Boundary Conditions.** At the interface of the saturated soil and bedrock, $u_{R2}=u_2^N$, $\tau_{R23}=\tau_{23}^N$, we get:

$$2\left(k_{1R}^2+k_{3R}^2\right)B_e=\gamma_t^2\left(A^N e^{-iv_t h}+D^N e^{iv_t h}\right) \tag{15a}$$

$$-2i\mu k_{3R}\left(k_{1R}^2+k_{3R}^2\right)B_e=i\mu^N v_t^N\gamma_t^2\left(A^N e^{-iv_t h}-D^N e^{iv_t h}\right) \tag{15b}$$

According to formula (14) and (15), we can establish a system of linear equations:

$$\mathbf{A}\bullet\mathbf{X}=\mathbf{B} \tag{16}$$

Where, $\mathbf{X}$ is the unknown amplitude vector of the first and the *Nth* of saturated soil layer, $\mathbf{X}=\left[A^1\ \ D^1\ \ A^N\ \ D^N\right]^T$; $\mathbf{A}=\left[a_{ij}\right]_{4\times4}$; $\mathbf{B}=\left[0\ \ 0\ \ 2\left(k_{1R}^2+k_{3R}^2\right)B_e\ \ -2i\mu k_{3R}\left(k_{1R}^2+k_{3R}^2\right)B_e\right]$.

Solving the formula (16) when $B_e$=1, we can get unknown amplitude coefficient of the first, the *Nth* of saturated soil layer. Bringing the amplitude coefficient into equation (4) and (9), and $x_3=0$, we can get the displacement ratio of saturated soil and bedrock both on the top surface.

## Numerical Results and Discussion

Considering a saturated soil with a thickness of *H*, assuming the porosity of the saturated soil is varying along the thickness as an analytic function of power law [10] as follows:

$$n(x_3)=\left[n(0)-n(H)\right]\left(\frac{H-x_3}{H}\right)^{\gamma}+n(H) \tag{17}$$

$$k_f=k_{f0}\left(\frac{n}{n_0}\right)^{\kappa},\quad G(n)=G_0\left(\frac{1-n}{1-n_0}\right)^{\kappa} \tag{18}$$

Where $\gamma$ is a non-homogeneous parameter, and different values of $\gamma$ dictate that the material properties have different non-homogeneous distributions along the thickness; $\kappa$ denotes the change in the index of the physical and mechanical properties of the soil with porosity; $G$ represents the parameters of the saturated soil, such as $\mu$, $\rho$ and $\rho_f$; $n_0$, $k_{f0}$ and $G_0$ are the porosity, permeability and the corresponding physical and mechanical parameters at initial state, respectively.

The porosity of the upper surface ( $x_3=0$ ) is $n(0)=0.45$, and other physico-mechanical parameters in saturated soil are chosen as follows: $n(H)=0.25$, $\mu_0=2.70\times10^9\ \mathrm{N/m^2}$, $\rho_0=2100\ \mathrm{kg/m^3}$, $\rho_{f0}=1000\ \mathrm{kg/m^3}$, $k_{f0}=6\times10^{-4}\ \mathrm{cm/s}$. And physico-mechanical parameters of bedrock are presented as: $\mu_R=1.70\times10^9\ \mathrm{N/m^2}$, $\rho_R=2640\ \mathrm{kg/m^3}$. In the example the calculation frequency for the seismic simulation is 5Hz, and the soil is divided into 100 layers.

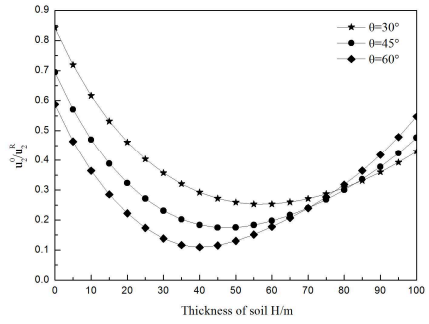


Fig.3 Curves of displacement ratio varying with soil thickness at different incident angles

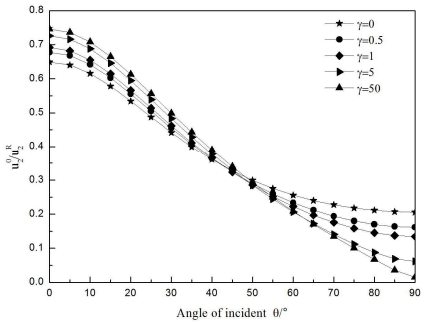


Fig.4 Curves of displacement ratio varying with incident angles at different heterogeneity indexes

Considering the influence of incident angle and soil thickness on the response, the displacement ratio varying with soil thickness under three different inclined angles ($30^\circ$, $45^\circ$, $60^\circ$) is presented in Fig.3 when $\gamma$=1 .The curve ranges parabola, and the displacement ratio gets its minimum varying with soil thickness near 40m. Displacement ratio decreases varying with the incident angle while the thickness is less than 80m; and it increases while more than 80m.

For study the influence of non-homogeneous on the response under the inclined SH seismic wave, displacement ratio with incident angle changing in different heterogeneity index is shown in Fig.4 when the soil thickness is 20m. Displacement ratio decreases varying with the incident angle. Displacement ratio increases varying with the heterogeneity index while the incident angle is less than $45^\circ$; and it decreases while more than $45^\circ$.

## Conclusions

(1) EDSM is applicable to analyzing SH wave propagation in non-homogeneously saturated soil. It has clear formulations and can solve the complex wave equations.

(2) Considering the material properties vary along $x_3$, the incident angle, the thickness and heterogeneity index of saturated soil play an important role on the dynamic response of non-homogeneously saturated soil.

## Acknowledgements

This work was supported by the National Natural Science Foundation of China (Grant No. 11162008), the Fund of Education Department of Gansu Province of China for Master's Tutor (1103-07) and the Fundamental Research Funds for the Gansu Universities (Grant No. 1104ZTC140).

## References

[1] Deresiewicz H, R Skalak.: *Bull Seism Soc Amer*. Vol. 53 (1963), p.783–789

[2] Hajra S, Mukhopadhyay A: *Bull Seism Soc Amer*. Vol. 72 (1982), p.1509–1533

[3] Knopoff L: *Bull seism soc Amer*. Vol. 54 (1964), p.431–438

[4] Gilbert F, Backus G E: *Geophysics*. Vol. 31 (1966), p.326–332

[5] R. G. Curtis and M. Redwood: *Journal of Applied Physics*. Vol. 44 (1973), p. 2002-2007

[6] Buchen PW. *Geophys J R astr Soc*. Vol. 25 (1971a), p.97-113

[7] Buchen PW: *Geophys J R aser Soc*. Vol. 23 (1971b), p.531-542

[8] Guitong Yang, shanyuan Zhang. Elastodynamics[M]. Beijing: *China Railway Publishing House*. 1988 (In Chinese)

[9] Shiming Wu. Soil Dynamics[M]. Beijing: *China Building Industry Press*. 2000 (In Chinese)

[10] Fengxi Zhou, Yuanming Lai, Ruixia Song: *Science China: Technological Sciences*. Vol. 02 (2013), p.131-140

*Applied Mechanics and Materials Vols. 580-583 (2014) pp 278-282*
*© (2014) Trans Tech Publications, Switzerland*
*doi:10.4028/www.scientific.net/AMM.580-583.278*

# Study of Key Parameters in the Process of Aeolian Sand Compactibility

Yingzi Yin [1, a] , Yalei Wang [1,b]

[1]Architecture and civil engineering school , Inner Mongolia University Of Science & Technology, Baoyou 014010, China

[a]yinyingzi2005@126.com

[b]414287459@qq.com

**Key Words:** aeolian sand; compatibility; optimum moisture content; maximum dry density; compactness; compatibility times; lay-down thickness

**Abstract:** The main factors affecting soil compatibility include moisture content, compaction work, soil type, grading and coarse material content etc.. The effects of compaction work are as follows: the stronger compaction work is, the more larger soil dry density is. The optimum moisture content decreases with the compaction work increasing. This paper mainly studies the effect of compaction work to aeolian sand compatibility. Its lay-down thickness is about 30-50cm when we use vibratory roller to compact aeolian sand in practical engineering. This paper analysis's and studies the maximum dry density and the optimum moisture content of aeolian sand in the middle region of Inner Mongolia, and achieves its lay-down thicknesses are 30cm,40cm,and 50cm respectively at the optimum moisture content. We use 85kg vibration-impact rammer instead of YZ 18 vibratory roller to simulate the aeolian sand compaction effect at the optimum moisture content. The specification does not specify the number of compatibility times, but it is generally 3 to 5 times in the actual project .We choose the most suitable compatibility times and lay-down thickness through anglicizing the Aeolian sand compactness for vibration-impact rammer rolling on eloign sand 3 times,4 times, and 5 times respectively at 3 different kinds of lay-down thicknesses. Through the study of the Inner Mongolia area Aeolian sand, it provides a useful reference for highway and railway construction in the desert area as well as the encapsulated layer thickness of reinforced retaining wall, a new type support structure.

## Introduction

Previous technical specification for construction of highway sugared provisions: the highway and a highway should be tested according to lay-down thickness 30cm, to ensure the uniformity of the compacted layer. Now the technical specification for construction of highway sugared rules: each packing lay-down thickness should be determined by test. But for the lay-down thickness in the process of aeolian sand compatibility, specification is not clearly defined. In practical engineering, its lay-down thickness is about 30-50cm. The main factors affecting soil compatibility include moisture content, compaction work, soil type, grading and coarse material content etc. The effects of compaction work are as follows: the more stronger compaction work is, the more larger soil dry density is. The optimum moisture content decreases with the compaction work increasing. This paper studies aeolian sand compatibility in Inner Mongolia area when its lay-down thicknesses are 30cm, 40cm, and 50cm respectively at the optimum moisture content. Due to the limitation of experimental conditions, vibration-impact rammer can not be directly used for aeolian sand compatibility study. In this experiment. We use 85kg vibration-impact rammer instead of YZ 18

vibratory roller to simulate the aeolian sand compaction effect at the optimum moisture content. The number of compatibility times is generally 3 to 5 times in actual project . Vibration-impact rammer is used to roll on aeolian sand 3 times4 times, and 5 times respectively at 3 different lay-down thicknesses in this test. The cutting ring method detects the aeolian sand compactness. Based on experimental results, the most suitable compatibility times and lay-down thickness are selected, which provides a useful reference for highway and railway construction in the desert area as well as the encapsulated layer thickness of reinforced retaining wall, aeolian sand as fillers.

## Experiment with small tamping machine and YZ 18 vibratory roller

2.1 The determination of various parameters of experiment with small tamping machine and YZ 18 vibratory roller

Small tamping machine is used for the test of HCD85-A type vibration shock ramming, the motor power is 30 kW, the quality of 85kg, and the jump height is 40 to 60mm, the impact frequency is 480 to 650 times / min, forward speed is 10 to 14m/min. In order to facilitate the calculation, the average values is selected. The jump height is 50mm, the impact frequency is 565 times / min, forward speed is 12m/min. The lower section size of small ramming machine is 25mm * 27mm. Vibratory roller is a more efficient compatibility machinery, it is widely used in all kinds of highway construction. For earth-rock foundation, technical specifications for construction of highway sugared rule: compatibility machinery should be choused based on the weight of no less than 18 tons of vibration road roller.

2.2 Calculation of key parameters of using small ramming machine to simulate compatibility effect of road roller

In 1 to 2 times of compatibility, the total power consumption of YZ 18 vibratory roller is 87.2 kW. In 3 to 8 times, the total power consumption of YZ 18 vibratory roller is 124.1 kW. And the roller in the process of compatibility, its maximum speed of calculation is the first gear, v=6km/h=1.67m/s. The basic parameters are shown in Reference 1**.** We can control the experiment used small ramming machine's working time to simulate approximately the wet aeolian sand compaction effect of YZ 18 vibratory roller. Rolling section is 25cm * 54cm. The calculation results are shown in Table 1.

**Table 1. Small ramming machine simulated the calculation results of YZ 18 vibratory roller**

| Compactibility times | 3 times | 4 times | 5 times |
|---|---|---|---|
| Rolling area（$cm^2$） | 1350 | 1350 | 1350 |
| Power（kW） | 298.5 | 422.6 | 546.7 |
| Working time（s） | 28.4 | 40.1 | 51.9 |

## Use small ramming machine to simulate the experimental process and result of YZ 18 vibratory roller

3.1 The steps of the experiment

(1) Weighed a sufficient amount of aeolian sand, and added appropriate amount of water to the optimum moisture content and mixed well. In this experiment, the aeolian sand is from the central area of Inner Mongolia, the maximum dry density and optimum moisture content is 1.576g/$cm^3$ and 17% respectively.

(2) Found a flat area as a test site, and poured enough mix of aeolian sand down at the test site, measured and controlled aeolian sand lay-down thickness, its lay-down thicknesses were respectively 30cm, 40cm and 50cm. To flatten the aeolian sand surface, as shown in Figure 1.

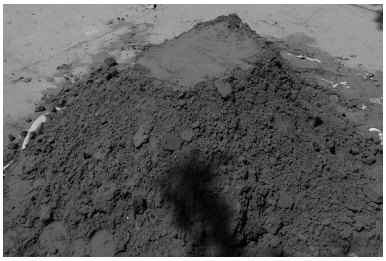

**Figure 1. Aeolian sand-pine lay on the ground**

(3) Small tamping machine rolled uniformly on three kinds of lay-down thicknesses respectively, and stopwatch controlled each small tamping machine's working time. Small tamping machine was used to simulate approximately the YZ 18 vibratory roller 3 times, 4 times and 5 times compaction effect.

(4) Every compatibility was completed, and the cutting ring method was used to measure the compactness. Used the cutting ring to take samples in accordance with the top, middle and bottom order respectively after compacting the aeolian sand. Then flattened the aeolian sand surface and weighed the weight. Recorded the data and calculated the compactness.

(5) Calculation of the compactness. In this experiment, the cutting ring with inner diameter of 61.9mm and height of 20mm, and its weight was 46.6g. The calculation formula of the compactness:

$$\text{Compactness}=\frac{m-46.5}{\pi\times(\frac{6.19}{2})^2\times 2\times\rho_{\max}}$$

Of which: $\rho_{\max}$ refers to the wet density corresponding to the optimum moisture content, take 1.84g/cm$^3$.

3.2 *The compatibility effect for lay-down thickness of 30cm*

Speeded enough wet aeolian sand on the experiment site, and divided the sand into three mounds evenly. The lay-down thickness was 30cm,flattened the aeolian sand surface, Small tamping machine rolled uniformly on three mounds in accordance with 3 times, 4 times and 5 times respectively to simulate approximately the YZ 18 vibratory roller compaction effect Then the cutting ring method was used to measure the compactness of three mounds. As seen from Table 2, when the aeolian sand lay-down thickness is 30cm, its compactness has a downward trend from the top to down, and the bottom compactness is comparatively small. The bottom compactness increases with compatibility times increasing. The number of compatibility times is 5 times, the compactness meets and exceeds the compactness requirements of highway and road to highway sugared. Soil sugared compactness standards are shown in Reference 1.

3.3 *The compatibility effect for lay-down thickness of 40cm*

According to the same experimental steps, spreaded enough wet aeolian sand on the experiment site, divided the sand into three mounds evenly. The lay-down thickness was 40cm.The measured compactness results are shown in Table2. It can be seen from Table 2, the aeolian sand compactness of the top and middle is higher in general than the bottom. And the bottom compactness increases with compactibility times increasing. When the number of compatibility times was 5 times, the bottom compactness reached a relatively large value. At this time, the bottom aeolian sand compactness had reached 96%. This accorded with the compactness requirements of highway and a highway.

**Table 2. The compaction results for lay-down thickness of 30 cm /40cm/50cm**

| Compatibility times | Top compactness （%） | Middle compactness （%） | Bottom compactness （%） |
|---|---|---|---|
| 3 times | 95.8/94.8/92.8 | 92.1/91.1/90.1 | 88.9/85.9/82.9 |
| 4 times | 98.1/97.1/94.1 | 96.2/95.2/91.2 | 95.1/93.6/85.6 |
| 5 times | 99.2/99.5/96.2 | 98.6/97.8/92.4 | 97.2/96.2/86.5 |

3.4 The compactibility effect for lay-down thickness of 50cm

According to the same experimental methods and steps, spreaded enough wet aeolian sand on the experiment site, divided the sand into three mounds evenly. The lay-down thickness was50cm.Small tamping machine rolled uniformly on three mounds in accordance with 3 times, 4 times and 5 times respectively to simulate approximately the YZ 18 vibratory roller compaction effect. Then the cutting ring method was used to measure the compactness's of three mounds. The measured results are shown in Table 2. It can be seen from the experimental data in Table 2, when the aeolian sand lay-down thickness is 50cm at optimum moisture content, its compactness has a downward trend from the top to down, and the bottom compactness is comparatively small than the compactness of the top and middle. According to whether the bottom compactness meets the specification requirements or not, to determine whether the compacted sugared achieves the levels of compactness requirements or not. Table2 shows the aeolian sand bottom compactness and the number of compatibility times curve for lay-down thickness of 50cm. As can be seen from the graph, along with the increase of the number of compatibility times, the compactness is increased. When times is 5 times, the compactness is the largest. But even so, the compactness is only 86.5%, and it can not meet the requirements of the highway sugared compactness.

3.5 Three kinds of lay-down thicknesses comparison

Comparison of Table2 experimental data shows: when the aeolian sand has the same lay-down thickness and compatibility times, the compactness from top to bottom gradually decreased. Regard the number of compatibility times for the 5 times as an example, as shown in Figure 2. And with the decrease of lay-down thickness, the compactness difference between the top and bottom becomes smaller. In this experiment, When the compatibility times is 5 times and lay-down thickness is 50cm, the compactness difference between the top and bottom is 9.7%. When the lay-down thickness is 40cm, the compactness difference between the top and bottom is 3.3%. When the lay-down thickness is 30cm, the compactness difference between the top and bottom is 2%.

The test for three kinds of different thicknesses was studied. We can see from Figure 3: when the lay-down thicknesses are 30cm, 40cm and 50cm, along with the increase of compatibility times, the bottom aeolian sand compactness increases. From the experimental data, when compatibility times is 3 times, three kinds of lay-down thicknesses can not meet the compactness requirements of highway and a highway. When compatibility times is 4 times and the lay-down thickness is 30cm,the wet aeolian sand compactness meets the requirements of two grade highway and approach the requirements of first grade highway.

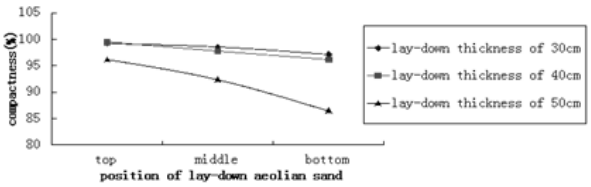


**Figure 2. It is the relationship curve of aeolian sand compactness and position at different lay-down thicknesses when compatibility times is five times**

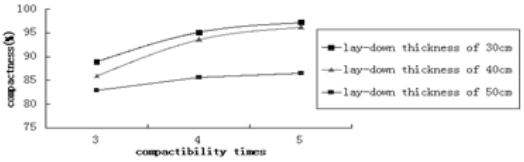


**Figure 3. It is the relationship curve of bottom aeolian sand compactness and compatibility times**

## Conclusion

According to Inner Mongolia region aeolian sand experimental research, The results show that:

(1) The compactness from top to bottom gradually decreased, and with the decrease of lay-down thickness, the compactness difference between the top and bottom becomes smaller. Generally the bottom compactness is the most minimum， which can be used as a reference standard to determine the aeolian sand compactness requirements.

(2) From the experimental data, in three different kinds of lay-down thicknesses, with the increase of the number of the compatibility times, the compaction has varying degrees of increase, namely, the compaction work is stronger, the generated soil compactness is large. And the lay-down thickness is small, and compaction work improves the aeolian sand compactness smelly.

(3) From the experimental data, when compatibility times is three times, three kinds of lay-down thicknesses can not meet the requirements of the compactness. When compatibility times is 4 times and the lay-down thickness is 30cm, the wet aeolian sand compactness meets the requirements of two grade highway and approaches the requirements of highway and a highway. When the compatibility times is 5 times, in lay-down thicknesses of 40cm and 30cm, the wet aeolian sand compactness meets highway and a highway requirements.

(4) From the experimental data and the compaction effect, this paper suggests that wet aeolian sand can be used when its compatibility times is 5 times and lay-down thickness is 40cm.

## Reference

[1] The Ministry of communications of the people's Republic of China. The technical specification for construction of highway subgrade (JTJF10-2006)[M]. Beijing: China Communications Press

[2] Zhou, Tiequn. Development of YZ 18 type vibratory roller.: [Master degree from Hunan University, Changsha: Thesis]. Hunan University Institute of Mechanical Engineering., 2008,37-38

[3] Cao, Yuanwen., Li, Zhiyong., & Liang, Naixing. Aeolian sand roadbed compactibility technology and method of analysis. [J]. Chongqing Jiaotong Institute Proceedings. 2004,23 (4): 64-67

*Applied Mechanics and Materials Vols. 580-583 (2014) pp 283-286*
*© (2014) Trans Tech Publications, Switzerland*
*doi:10.4028/www.scientific.net/AMM.580-583.283*

# Construction Techniques and Mechanism of Pre-Anchoring Fissured Stope Hangingwall by Fully-Grouted Cable Bolts

Fenglin Zhan[1, a *], Ping Ye[2, b]

[1]School of Architectural and Surveying Engineering, Jiangxi University of Science and Technology, Ganzhou, Jiangxi, China, 341000

[2] School of Continuing Education, Jiangxi University of Science and Technology, Ganzhou, Jiangxi, China, 341000

[a]zhanfenglin7278@sina.com, [b]yeping2938@sina.com

**Keywords:** Mechanism, Pre-Anchoring, Fissured Stope Hangingwall, Fully-Grouted Cable Bolts.

**Abstract.** The construction techniques and anchoring mechanism of pre-anchoring fissured stope hangingwall of some copper mine in China by fully-grouted cable bolts are explored. The construction stages such as drilling anchor holes, making anchorage cables and cement mortar, grouting, and curing are expounded. A combined action mechanism of pre-anchoring fissured stope hangingwall by fully-grouted cable bolts is presented. The achievements are helpful and beneficial to the design and construction of rock engineering projects which need anchoring reinforcement, such as slopes, tunnels, deep foundation pit, caverns, and underground mining.

## Introduction

The anchoring techniques of fully-grouted cable bolts [1, 2] find a wide application in the reinforcement of slopes, tunnels, deep foundation pit, caverns and underground mine stopes. The construction techniques and anchoring mechanism of pre-anchoring fissured stope hangingwall of some copper mine in China by fully-grouted cable bolts are explored. The embedded depth, horizontal section width along inclined direction, strike length, vertical height, and pitch angle of the studied mine stope are 89.75m, 12.5m, 7m, 32.5m, and 30° respectively. The surrounding rock of the stope hangingwall is fissured granite porphyry [3].

## Pre-Anchoring Construction

Anchor holes in the unstable fissured hangingwall are drilled by YGZ-90 type drilling equipment. The diameter and depth of an anchor hole are 55 mm and 10.5 m respectively. Upward anchor holes in a row form a vertical fan shape. The corresponding anchor holes in two adjacent rows use staggered arrangement. The row spacing is 3 m. Fan-shaped layouts of anchor holes in two adjacent rows are as shown in Fig. 1. Every anchor hole is cleaned with high-pressure water or compressed air.

An anchor cable uses 20 mm diameter steel wire rope with the length of 11 m. 6 ~ 8 strands of steel wires are taken out from one end of steel wire rope and are bent into 5 ~ 10 cm long agnail around the outer wire rope as anchor cable head. Finally the steel bar hook (see Fig. 2) is strapped on anchor cable head with iron wire and the anchor cable is pushed into the bottom of the hole by using pushing rods.

Ordinary Portland cement is used and the largest particle size of sand is not more than 5 mm. Cement mortar is made underground and the mixing weight ratio of cement : sand : water = 1 : 1 : 0.3. For each anchor hole 25 kg cement and 25 kg sand are approximately used. Injection pump is employed for injecting cement mortar into anchor holes.

After grouting, anchor hole orifices are plugged with cork, cotton, or cement bag paper lest mortar outflow from anchor holes. Mortar strength has relation to curing time. To assure quality mortar should be cured for at least half a month and the best curing time is a month or more. The deformation of the unstable fissured hangingwall can be inhibited by the hardened fully-grouted cable bolts combined with fissured hangingwall.

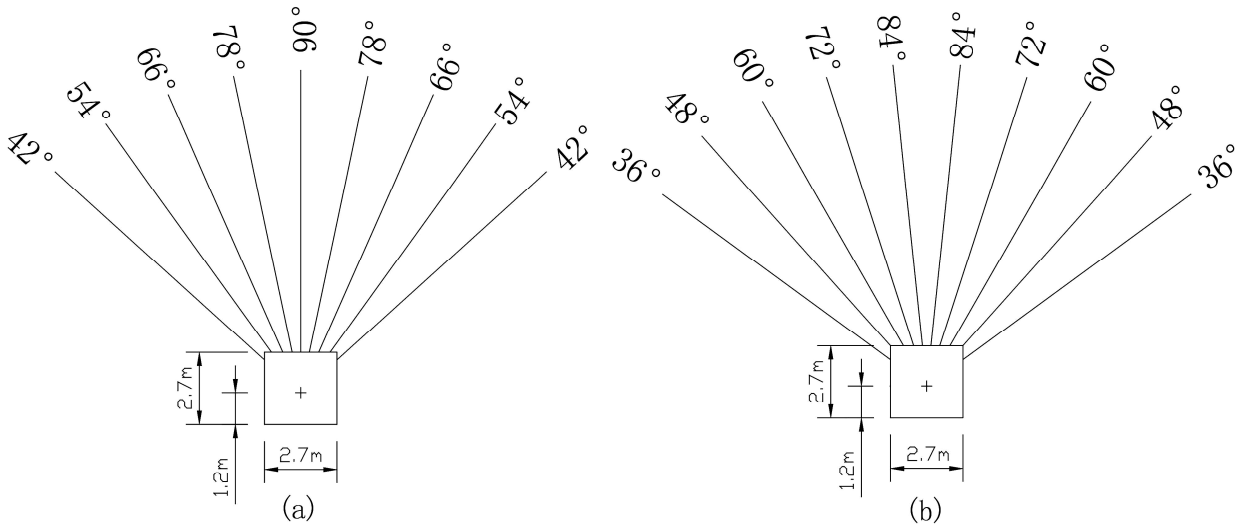


Fig. 1 Fan-shaped layouts of anchor holes in two adjacent rows

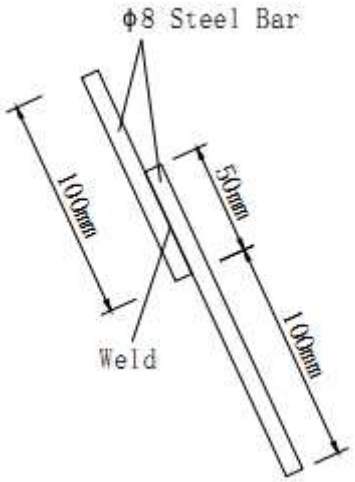


Fig. 2 Steel bar hook

Fig. 3 shows the schematic vertical section of the test mine stope and fissured stope hangingwall pre-anchored by fully-grouted cable bolts along inclined direction.

## Mechanism

The mechanism of pre-anchoring fissured stope hangingwall by fully-grouted cable bolts is a combined action. It includes the following five main effects.

**Hanging Effect.** Cable bolts are different from bolts. The flexibility of cable bolts is something like that of ropes. Action of faults can make a cable bolt become curved or appear a broken line, but its anchoring force still exists. In-situ we have occasionally observed that fully grouted cable bolts hang some unstable rock blocks on the stope hangingwall surface and the rock blocks can not drop.

**Effect of a Laminated Beam.** Fully-grouted cable bolts, which are something like linen thread in the sole of cloth shoes, sew up the rock layers of stope hangingwall together to form a laminated component as a whole. Resisting force between rock layers increases greatly, and the bending strength, shear strength, and rigidity of hangingwall also grow.

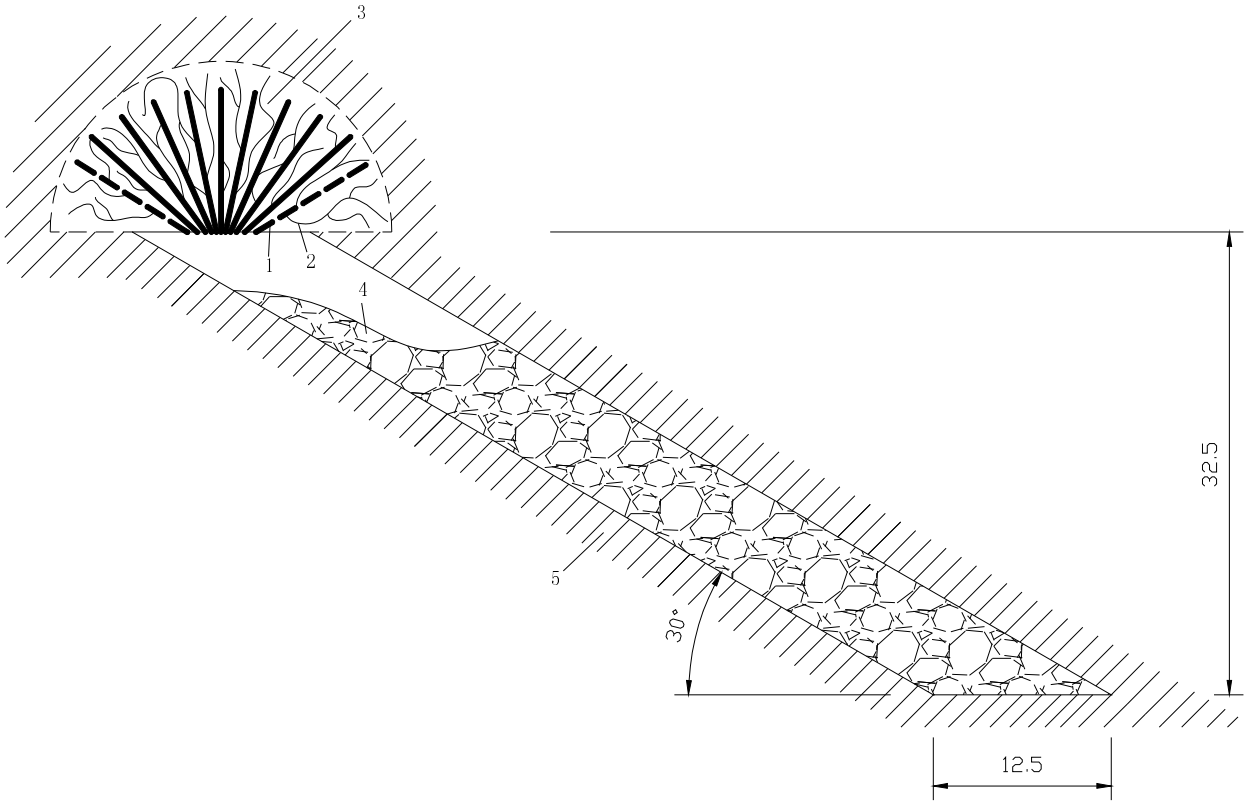


Fig. 3 Schematic vertical section of the test mine stope and fissured stope hangingwall pre-anchored by fully-grouted cable bolts along inclined direction 1) Fully-grouted cable bolts 2) Faults and fissures 3) Fissured mine stope hangingwall pre-anchored by fully-grouted cable bolts 4) Ore 5) Surrounding rock

**Effect of Injection Anchorage.** That cement mortar injects and fills faults, fissures, and cleavages makes rock being in a 1D or 2D stress state become in a more stable 3D one. Injection can also increase the strength and deformation modulus of soft constructional surfaces in surrounding rock. Strip-shaped and pulse-shaped grouting, which is something like the root hair of a tree, wraps fissured hangingwall into a wedge-shaped thing. This wedge wedges the top part of the stope. The space system of forces of the whole stope is balanced, and therefore no hangingwall collapse occurs.

**Waterproof and Impervious Effect.** Injection fills faults, fissures, and cleavages in surrounding rock to form an artificial impervious hangingwall with certain thickness. Influence of water on surrounding rock is alleviated or effectively protected. This waterproof and impervious effect is the same as principles of water-protection, sand-fixation, and water and soil conservation of tree roots.

**Effect of Anchoring in Advance.** Fully grouted cable bolts reinforce stope hangingwall in advance before in-situ rock is disturbed. The strength of surrounding rock itself is maintained and acquires further improvement and enhancement owning to the fact that fully-grouted cable bolts restrain deformation of surrounding rock. It is protected that a 3D stress state of surrounding rock is transformed into a plane stress state in the process of mine extraction. The stability of mine stopes is guaranteed.

## Conclusions

Active support can be formed by pre-anchoring. The mine stope hangingwall pre-anchored by fully-grouted cable bolts can immediately and actively support surrounding rock and bear loads to prevent the further development of rock strata movement when the mined-out space is formed.

During test and production process, persistent safety production of the mine stope pre-anchored by fully-grouted cable bolts is ensured due to the reliable anchorage performance and stable work space. The ore recovery rate and profits of the mine are increased.

A combined action mechanism of pre-anchoring fissured stope hangingwall by fully-grouted cable bolts is presented. The combined action includes hanging effect, effect of a laminated beam, effect of injection anchorage, waterproof and impervious effect, and effect of anchoring in advance. The achievements are helpful and beneficial to underground deep mining, and the design and construction of rock engineering projects which need anchoring reinforcement, such as slopes, tunnels, caverns, and mine stopes.

**Acknowledgements**

This work was financially supported by the scientific and technological fund of Education Department of Jiangxi Province (GJJ08292).

**References**

[1] Fenglin Zhan, Meifeng Cai, Influence of high temperature on anchoring system of cable bolts at stope hangingwall, Journal of Liaoning Technical University 4 (2007) 524-526. (In Chinese)

[2] Fenglin Zhan, Ping Ye, ANSYS simulating analysis of 3D single-cable temperature model of fully-grouted cable bolts, Proceedings of 2012 International Conference on Electric Technology and Civil Engineering (ICETCE 2012), Institute of Electrical and Eletronics Engineers, Inc., USA, 3(2012) pp. 1391-1394.

[3] Fenglin Zhan, Ping Ye, ANSYS simulating analysis of a 3D high-temperature stope reinforced in advance with fully grouted cable bolts, in: Mingjin Chu, Xiangran Li, Jingzhou Lu, Xingmin Hou, and Xiaogang Wang (Eds.), Progress in Civil Engineering (Part 1), Trans Tech Publications Ltd, Switzerland, 2012, pp. 525-528.

*Applied Mechanics and Materials Vols. 580-583 (2014) pp 287-290*
*© (2014) Trans Tech Publications, Switzerland*
*doi:10.4028/www.scientific.net/AMM.580-583.287*

# Numerical Analysis of the Bearing Behavior of Single Pile under Horizontal Load

Defu Ma[1,a,*], Guangjun Guo[2,b], Xia Yang[1] and Zhidong Zhou[3,c]

[1]Hydraulic Research Institute of Shandong Province, Jinan,250014,China

[2] Department of Water Resources of Shandong Province ,Jinan,250014,China

[3]School of Civil Engineering, Shandong University,Jinan,250061,China

[a]6974554@126.com, [b]6974470@126.com, [c]zhouzhidongdzd@163.com

[*]corresponding author

**Keywords:** foundation engineering; single pile; horizontal load; p-y curve; numerical analysis.

**Abstract.** Understanding the pile behavior and predicting the capacity of piles under horizontal load are important topics in foundation design. In this paper, the mechanical characteristics of single pile under horizontal load is analyzed based on FLAC3D finite difference software, and the load-displacement curve, the bending moment, shear force, soil resistance under all levels of load and the distribution law of p-y curve along the pile shaft are obtained. accordingly the following conclusions can be made: the bending moment of the upper part of pile body is big, the maximum bending moment is at the height of 2~3 meters and it is almost zero below the depth of 9 meters. The bending moment increases with the increase of load, the point of maximum bending moment moves down along the pile body with the increasing of horizontal load. and the location of the point of maximum bending moment moves from 2 meters below the ground to 3 meters below it. The distribution of soil resistance along the pile shaft is a reverse "S", the maximum of pile lateral soil resistance is at the height of about 2~3 meters below the ground.

## Introduction

Pile foundation is widely used as one kind of important foundation forms in civil engineering. With the constant improvement of the level of bridge construction and the development of economic in China, across the strait channel will be built at the Bohai bay, the Taiwan strait and the Qiongzhou strait and sea-crossing bridge is the most competitive solution to the problem of crossing the straits. The application of deep water foundation will be more and more common, the horizontal loadings, such as the wave loading, static dynamic water pressure and wind loading, the ship collision loading, etc. the deep water foundation sustained are much bigger than that of the land building, which makes it have equal importance with the vertical loads[1-4]. In this paper, combined with the engineering geological data, the finite difference method is adopted to study the horizontal bearing performance of single pile and its bearing capacity, which is aimed at providing basis and references for the design of the horizontal bearing pile.

## The numerical calculation model

### Calculation parameters

In this paper, finite difference program FLAC3D based on the fast Lagrangian method is used to calculate and analyze the working traits of single pile under horizontal load. In the calculation, Mohr-Coulomb model is used for the soil , the Elastic model is used for Pile, Pile size (diameter 600 mm, wall thickness 130mm, buried depth 15 m). It is sandy loam and silt of the main aquifers. In the depth of exploration, Quaternary overburden is completely developed with: foundation for artificial accumulation, sandy loam, loam, the foundation strata belongs to Quaternary Holocene alluvial deposits($Q4_{a1}$), and from top to bottom are as follows:①sandy loam;②silt;③clay;④sandy loam;⑤ clay. The physical and mechanical properties of field test area's foundation soil is illustrated in Tab.1.

According to Equation (1) and (2), the bulk modulus and shear modulus can be converted from elasticity modulus.

Bulk Modulus: $$K = \frac{E}{3(1-2\upsilon)} \quad (1)$$

Shear Modulus: $$G = \frac{E}{2(1+\upsilon)} \quad (2)$$

Tab.1 The physical and mechanical properties of field test area's foundation soil

| Soil class | Thickness (m) | ω (%) | $e$ | $\rho$ (kg/m$^3$) | $E_s$ (MPa) | $c$ (kPa) | $\varphi$ (°) |
|---|---|---|---|---|---|---|---|
| sandy loam | 7 | 25.8 | 0.883 | 1960 | 4.93 | 21.0 | 11 |
| silt | 7 | 20.9 | 0.660 | 1970 | 10.65 | 25.0 | 10 |
| clay | 3 | 35.4 | 1. 171 | 1880 | 3.92 | 18.2 | 19 |
| sandy loam | 2 | 24.2 | 0.736 | 1990 | 4.83 | 19.4 | 18 |
| clay | 3 | 21.7 | 0.743 | 2040 | 4.62 | 18.1 | 16.6 |

**Numerical computational model**

Interface command is used in the pile - soil interface, sliding and separation are allowed in it and the normal stiffness and shear stiffness of the interface are 10 times of the equivalent stiffness of the pile[5].Grading one-way maintain load time step control is adopted in the calculation and the top pf the pile is free. Computational geometry model is shown in Fig. 1.

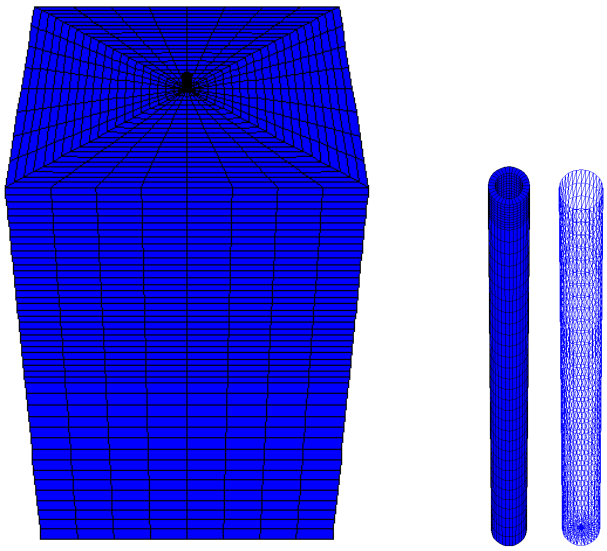

Fig.1 Numerical computational model

**The analysis of numerical calculation results**

The largest single pile load can be forecast according to the regulations. The load increment of per load level is about 1/10 ~ 1/15 of the estimated maximum horizontal load. Therefore, the design load per level is 15kN and there are 10 levels at all. One-way maintain load method is used to applied the load and the loading ends when there is a mutation of the displacement of the pile top.

The curve of horizontal displacement of the pile top under the action of all levels of load is drawn and the result is shown in Fig. 2.

According to the [6], for precast reinforced concrete pipe pile, the horizontal bearing capacity characteristic value of single pile can take 75% of that of the load that causes the horizontal displacement at the earth's surface to be 10 mm, while 6mm for buildings that are sensitive to horizontal displacement according to the results of static load test. It can be known from the horizontal load displacement curve shown in Fig. 2 that the horizontal displacement of 6 mm is corresponding to the load of 98kN while the horizontal displacement of 10 mm is corresponding to the load of 126kN.

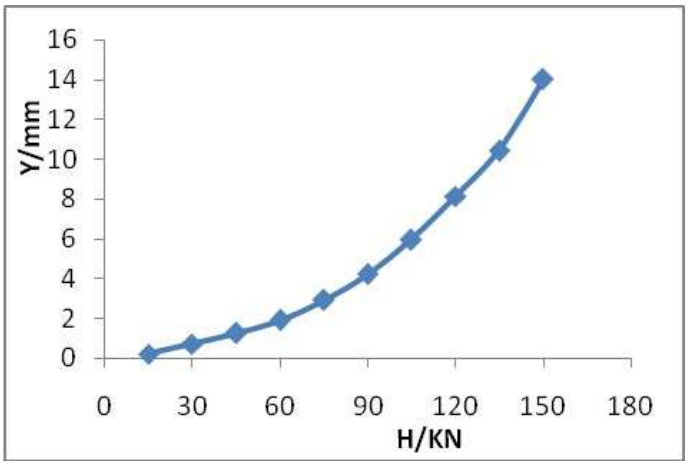


Fig.2 The p-y curve

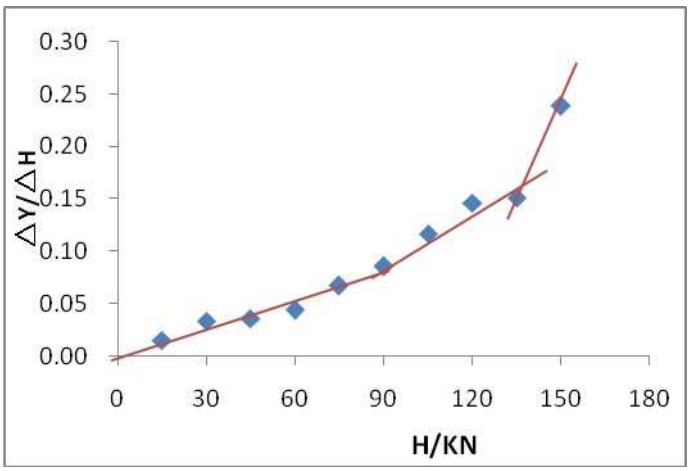


Fig.3 The p-y gradient curve

The determine for the critical load usually based on the result shown in Fig. 3. As the result of numerical calculation shows, the load of the first turning point on the gradient curve which is 90kN is chosen as the horizontal critical load of the single pile, while that of the second turning point as the horizontal ultimate load which is 135kN.

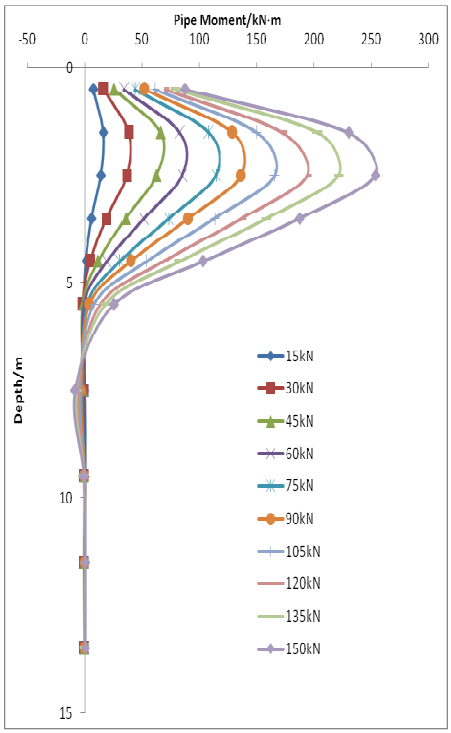


Fig.4 The bending moment of pile

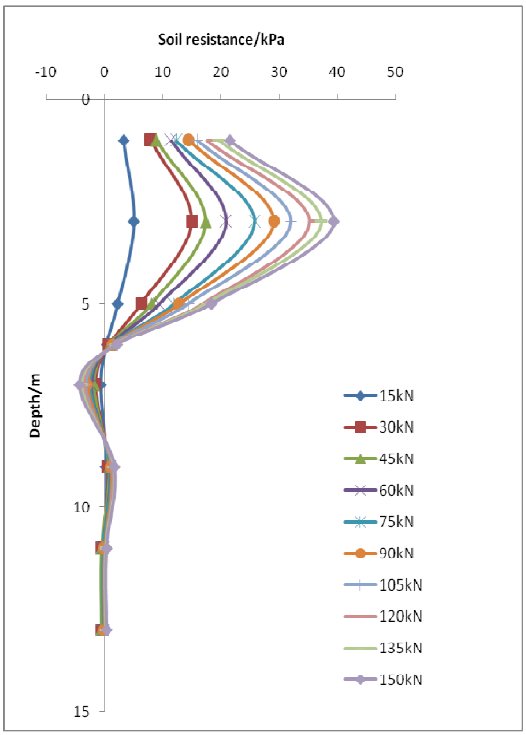


Fig.5 Distribution of soil resistance along the pile shaft

As Fig.4 shows, the bending moment of the upper part of pile body is big, the maximum bending moment is at the height of 2~3 meters, while the bending moment of the lower part of pile body is small and it is almost zero below the depth of 9 meters.

The bending moment increases with the increase of load, the point of maximum bending moment moves down along the pile body with the increasing of horizontal load. As the horizontal load increases from 15kN to 150kN gradually, the maximum bending moment of pile shaft increases from 16.0kN·m to 254.1kN·m, and the location of the point of maximum bending moment moves from 2 meters below the ground to 3 meters below it.

The zero moment point moves down along the pile body as the load increasing, it moves from 5.2 meters below the ground to 7.5 meters with the increasing of load, which indicates that the soil is in the elastic state during the initial state of horizontal loading. With the increasing of load, the soil changes from elastomer to plastomer, the influence depth increases as well, the deeper soil participate in the effect to resist horizontal load.

As Fig.5 shows, the distribution of soil resistance along the pile shaft is a reverse "S", the maximum of pile lateral soil resistance is at the height of about 2~3 meters below the ground, while the negative peak of it is in the middle of the pile shaft, and the absolute value of the negative peak is less than the positive peak of the soil resistance, the pile lateral soil resistance is almost zero below the depth of 9 meters. As the horizontal load increases, pile lateral soil resistance gradually come into operation and point of maximum soil resistance moves down along the pile shaft.

## Conclusions

The paper mainly conducts the horizontal bearing performance of single pile and its bearing capacity, accordingly the following conclusions can be made: the bending moment of the upper part of pile body is big, the maximum bending moment is at the height of 2~3 meters and it is almost zero below the depth of 9 meters. The bending moment increases with the increase of load, the point of maximum bending moment moves down along the pile body with the increasing of horizontal load. and the location of the point of maximum bending moment moves from 2 meters below the ground to 3 meters below it. The distribution of soil resistance along the pile shaft is a reverse "S", the maximum of pile lateral soil resistance is at the height of about 2~3 meters below the ground.

## Acknowledgements

This work was financially supported by Binhai comprehensive utilization of water resources and the most strict water resources management and demonstration (201201116).

## References

[1]S. Karthigeyan, V.V.G.S.T. Ramakrishna, K. Rajagopal. Influence of Vertical Load on the Lateral Response of Piles in Sand[J]. Computers and Geotechnics, 2006, 33(2):121-131.

[2]HSIUNG Y M, CHEN S S, CHOU Y C. Analytical Solution for Piles Supporting Combined Lateral Loads [J]. Journal of Geotechnical and Geoenvironmental Engineering, ASCE, 2006, 132(10): 1315-1324.

[3]GUO W D. Nonlinear Response of Laterally Loaded Piles and Pile Groups[J]. International Journal for Numerical and Analytical Methods in Geomechanics, 2009, 33(7): 879-914.

[4]SEO H, YILDIRIM I Z, PREZZI M. Assessment of the Axial Load Response of an H Pile Driven in Multilayered Soil [J]. Journal of Geotechnical and Geoenvironmental Engineering, ASCE, 2009, 135(12): 1789-1804.

[5]ZHUANG P Z, QI L, ZHOU Z D. Influencing Factors Analysis of Horizontal Bearing Capacity of Single Pipe Pile[J]. Highway, 2013, (8): 12-18.

[6]JGJ 94-2008. Technical Code for Building Pile Foundations[S]. Beijing: China Architecture & Building Press, 2008.

*Applied Mechanics and Materials Vols. 580-583 (2014) pp 291-295*
*© (2014) Trans Tech Publications, Switzerland*
*doi:10.4028/www.scientific.net/AMM.580-583.291*

# Simplified Bishop method homogeneous soil slope stability analysis based on the C# language

Haibing Wei[1, a *], Qian Zhang[1,b], Junhai Zhao[1,c]

[1] Chang'an Road No.161, Chang'an University, Xi'an 710064, China

[a]1583576542@QQ.com, [b]563178082@QQ.com, [c]zhaojh@chd.edu.cn

**Keywords:** C# language; simplified Bishop method; slope stability; the factor of safety; the critical slip surface

**Abstract.** A computer program was compiled based on the C# language of Microsoft Visual Studio 2008 and the principle of simplified Bishop method. The program will calculate the minimum factor of safety, and automatically draw the two-dimensional(2-D) critical slip surface after user input the basic parameters. Through testing a lot of examples, the program has good stability, high precision, fast speed and good visibility.

## Introduction

The slope stability problem is an ancient and young subject. During 240 years evolution, slope stability analysis went through a long and hard journey, In general, slope stability analysis methods are divided into three categories: qualitative analysis, quantitative analysis and uncertainty analysis.

Qualitative analysis methods mainly include: historical causes analysis, expert system method and graphical method[1]. These methods have distinct empirical in common, so qualitative analysis can only be used for preliminary and rough assessment.

Quantitative analysis methods are divided into two categories: one is the article points method based on the theory of the rigid body limit equilibrium theory, the other is the numerical analysis method based on the theory of elastic-plastic theory. The origin of the former was very early and withstood the test of practice, and a large number practice have proved that the simplified Bishop method often could get enough precision for homogeneous soil slope. However, the latter's accuracy and reliability is to be measured based on the former.

Uncertainty analysis methods mainly include: the dissipative structure theory, catastrophe theory, etc[2]. These methods consider the uncertainty of the factors, but there are a lot of shortcomings: (1) the theoretical is strong, it's difficult to master them; (2) starting late, the computer program is less;(3) lack of mechanics analysis, focus on the accidental factors.

For the reasons above, the computer program is compiled based on the simplified Bishop method.

## The overview of slope stability analysis software status

At present, the commercial software in geotechnical engineering field are foreign products, such as ANSYS, FLAC, MARC, ABAQUS, MIDAS/GTS, etc. We can obtain the safety factor and the most disadvantageous slide surface nephogram by using them, the criterions include: (1)the characteristics of main parts of displacement mutation. (2) the numerical convergence. (3) the plastic zone through[3].

The advantages of the slope stability analysis by finite element method are: (1) they can give the size and distribution of stress and strain in soil. (2) they don't need to assume the shape and position of sliding surface. But the controversy of this method are: (1) the effectiveness of the slope instability criterion is controversial. (2) factors influence the accuracy are various. (3) the location of the sliding surface could not be determined accurately. (4) they require high quality of science and technology for the user. (5) they generally more expensive.

In contrast, there are more weaknesses and shortcomings for the development of the domestic software: (1) foreign software outshine others, there is no place for domestic software. (2) domestic software in early time more use the process oriented language, the visualization is low and human-computer interaction is relatively poor. (3) few people dare to try programming.

For the reasons above, the purpose of this paper is to use Visual C # language of the Microsoft Visual Studio 2008 to develop a simple, friendly, fast and accurate visualization software, the software can read basic parameters well, obtained the minimum safety factor, and automatically draw the two-dimensional(2-D) critical slip surface.

## The program design

### C # language features

C # is a kind of development language designed specifically for the .Net framework, the characteristics are: (1) fully Object Oriented Programming, and visualization degree is high; (2) programming based on component, and be more likely to achieve modular; (3) the grammar is free and be easy to understand; (4) does not support pointer by default, program safety is high; (5) automatic memory management, save space.

### Program module analysis

Program development uses modular design, according to the calculation principle and personal analysis, the program is divided into five modules: Center of the circle search module, angle calculation module, weight calculation module, safety factor module and the minimum safety factor choose and the most disadvantageous slide surface determines module. Due to the limited space, only the center of the circle search module is analyzed.

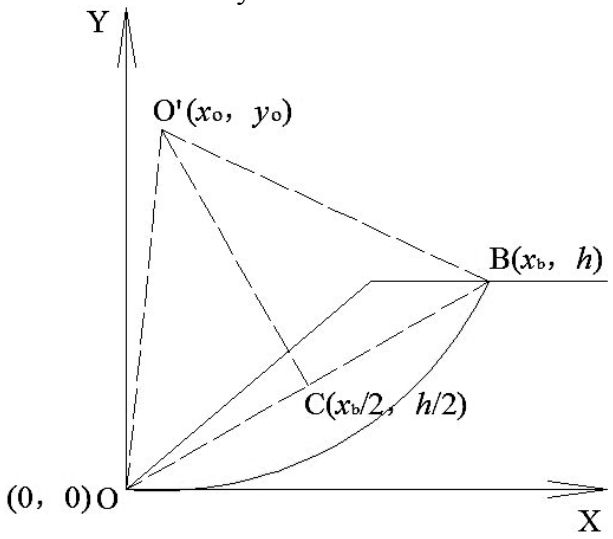


Fig.1. Slope calculation diagram

The XOY rectangular coordinate system is shown in Fig.1. O(0, 0) is the sliding out point, B ($x_b$, $h$) is the falling point, $h$ is the height of slope. O′($x_o$, $y_o$) is the center of arc OB, it must be on the perpendicular bisector of OB. The perpendicular bisector of OB and OB intersect at point C($x_b$/2，$h$/2). The slope of line OB is:

$$K_{AB} = \frac{y_B - y_A}{x_B - x_A} = \frac{h}{x_b}. \tag{1}$$

$$\because OB \perp O'C$$

$$\therefore K_{OB} \cdot K_{O'C} = -1$$

$$K_{OC} = -\frac{x_b}{h}. \tag{2}$$

The equation of O′C is:

$$y - \frac{h}{2} = -\frac{x_b}{h}(x - \frac{x_b}{2}). \tag{3}$$

When determining the scope of $x_o$, we take $h \leq y \leq 3\ h$[4].

When $y_0=h$:

$$x_0 = \frac{x_b}{2} - \frac{h^2}{2x_b}. \tag{4}$$

When $y_0=3h$:

$$x_0 = \frac{x_b}{2} - \frac{5h^2}{2x_b}. \tag{5}$$

And $h>0$，$x_b>0$:

$$\frac{x_b}{2} - \frac{5h^2}{2x_b} \le x_o \le \frac{x_b}{2} - \frac{h^2}{2x_b}. \tag{6}$$

By the Fig.2:

$$x_b \ge h \cdot \cot\alpha. \tag{7}$$

After many trial:

$$x_b \le h \cdot (1 + \cot\alpha). \tag{8}$$

α is the slope angle, so the scope of $x_b$ is:

$$h \cdot \cot\alpha \le x_b \le h \cdot (1 + \cot\alpha). \tag{9}$$

The scope of $x_b$ is determined, then the scope of $x_o$ is determined, and then the scope of the $O(x_o,y_o)$ is also determined, the analysis of the module is over.

After the program running, first, through the "New" command under the "Project" menu, create a new project shown in Fig.2. then click "OK" to enter the engineering interface shown in Fig.3, engineering interface is consist of three parts, the top of the left side is the parameter input window, the bottom of the left side is the data output window, and the right side is graphics output window. After entering the parameters, click the "Calculate" button to calculate, the result will be shown in Fig.3. Click "Save" button, the program will automatically save the results, Through the "History" command under the "Project" menu, you can also view the history.

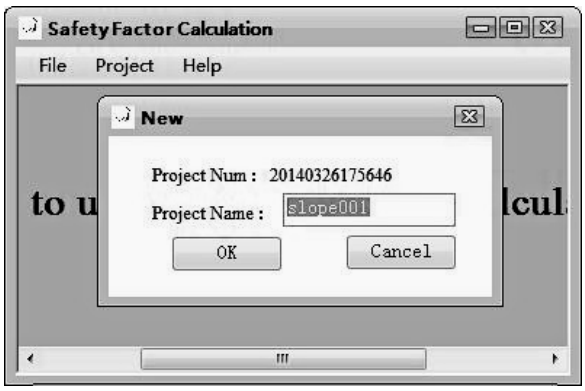


Fig.2. Start Interface

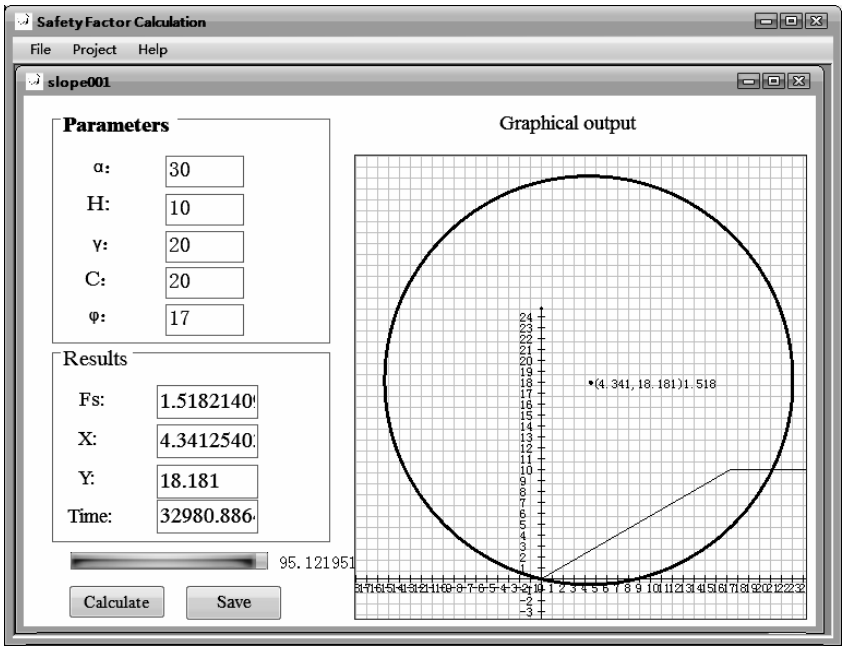


Fig.3. Engineering Interface

**To verify**

In order to test the stability and reliability of the program, a large number of examples are tested, due to the limited space, just list some results shown in table 1, and the most dangerous sliding surface of Num2, Num4 and Num5 are shown in Fig.4, Fig.5 and Fig.6.

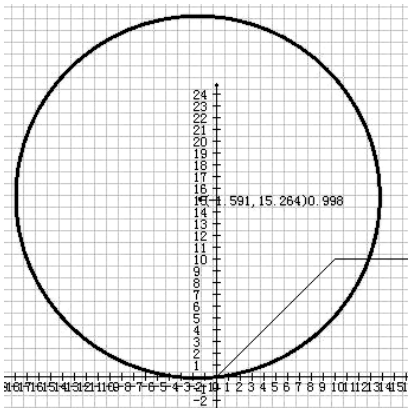


Fig.4. Num2 sliding surface

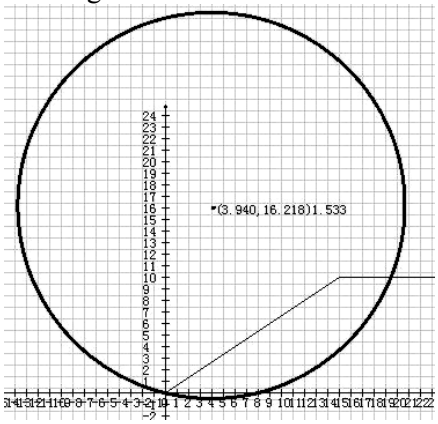


Fig.5. Num4 sliding surface

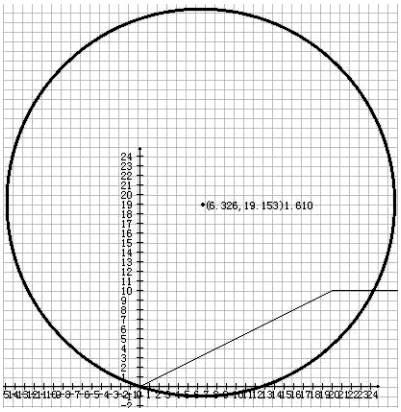


Fig.6. Num5 sliding surface

Table1. Test results

| Num | α (°) | H (m) | γ (KN/m$^3$) | C (Kpa) | φ (°) | Fs (Liter-ature) | Fs (Prog-ram) | Error (%) | Time (s) | example source |
|---|---|---|---|---|---|---|---|---|---|---|
| 1 | 30.00 | 10.00 | 18.00 | 10.00 | 25.00 | 1.522 | 1.522 | 0.000 | 26.9 | Lizheng |
| 2 | 45.00 | 10.00 | 20.00 | 12.38 | 20.00 | 1.000 | 0.997 | -0.30 | 16.2 | [5] |
| 3 | 50.00 | 20.00 | 20.00 | 42.00 | 17.00 | 1.118 | 1.118 | 0.000 | 43.1 | [6] |
| 4 | 33.69 | 10.00 | 19.00 | 24.50 | 15.00 | 1.534 | 1.533 | -0.06 | 29.4 | [7] |
| 5 | 26.57 | 10.00 | 19.00 | 21.00 | 15.00 | 1.612 | 1.610 | -0.12 | 34.1 | [7] |
| 6 | 45.00 | 20.00 | 19.62 | 28.60 | 20.00 | 1.080 | 1.078 | -0.15 | 46.3 | [8] |
| 7 | 35.54 | 20.00 | 18.82 | 41.65 | 15.00 | 1.362 | 1.360 | -0.15 | 60.5 | [9] |
| 8 | 35.00 | 21.00 | 19.06 | 11.71 | 20.00 | 0.922 | 0.924 | 0.217 | 55.0 | [10] |
| 9 | 55.00 | 15.00 | 15.00 | 10.00 | 20.00 | 0.720 | 0.723 | 0.417 | 24.2 | [11] |
| 10 | 40.00 | 15.00 | 25.00 | 20.00 | 25.00 | 1.190 | 1.192 | 0.168 | 33.7 | [12] |

## Conclusions

Through the examples above, the programm has the following features:

(1) The calculation accuracy is high, it firstly ensures the practicability and reliability of the program.

(2) The calculation speed is fast, it meets the time requirements for the user.

(3) The operation interface is simple, input parameters quickly, and the output results are abundant and easy to understand.

## Acknowledgements

This work was financially supported by Natural Science Foundation of China (41202191), China Postdoctoral Science Foundation (2012M520079, 2013T60868), Doctoral Fund of Ministry of Education of China (20110205130001, 20120205120001) and Natural Science Foundation of Shannxi Province of China (2011JM7002).

## References

[1] Yuefeng Li. Analysis on Stability of High Filled Slope[D]. Changsha Hunan: Central South University of Forestry and Technology,2012.In Chinese.

[2] Shayi Wang. Study on Disaster System and Theoretical Basis of Dynamics of Disaster[D]. Zhejiang: Zhejiang University,2008.In Chinese.

[3] Yuanchuan Chen. Research on Calculation of Soil-slope safety Factor by Strength Reduction Finite Element Method[D]. Chongqing: Chongqing Jiaotong University, April, 2009. In Chinese.

[4] Ming Li, Dexin Ding. The most dangerous sliding slope arc center position of the search and application program[J]. Journal of south China university, 2004, 18(4): 63-66. In Chinese.

[5] Qing Lu. Study on Prevention and Treatment Technology of Slope Engineering Disasters[D]. Zhejiang: Zhejiang University, April, 2006. In Chinese.

[6] Jie Zhao. The Research of Some Application Problems in Finite Element Method for Slope Stability Analysis[D]. Dalian :Dalian University of Technology, July, 2006. In Chinese.

[7] Zhihe Wang. Loess Landslide, High Slope Stability Analysis and Engineering Application[D]. Xi'an :Xi'an University of Architecture and Technology, April, 2012. In Chinese.

[8] Zibin Zhou. Study of Slope Stability Based on Limit Equilibrium Method and Finite Element Method[D]. Nanjing: College of Civil Engineering Hohai University, Mar, 2004. In Chinese.

[9] Lijun Su. Study of Earth Slope Stability Based on Limit Equilibrium Method and Finite Element Method[D]. Sichuan: Xihua University, May, 2012. In Chinese.

[10] Xinke Wang. The Stability Analysis and Research of Soil Slopes[D]. Anhui: Hefei University of Technology, May, 2007. In Chinese.

[11] Lipeng Liu, Hongjie Yu, Qi Chen. Mechanical and geometrical parameters on the sensitivity analysis of soil slope stability[J]. Geotechnical Engineering Technique, 2008, 22(3): 123-126. In Chinese.

[12] Liu Han, Senshu Ji, ect. Circular sliding stability analysis and the software realization of mining research and development[J]. Mining Research and Development, 2011, 31(4): 40. In Chinese.

*Applied Mechanics and Materials Vols. 580-583 (2014) pp 296-301*
*© (2014) Trans Tech Publications, Switzerland*
*doi:10.4028/www.scientific.net/AMM.580-583.296*

# Study on Engineering Behavior of Non-Embedded Pile-Board Structure Crossing Over-Shallow-Embedded Metro

Chuan-bin ZHOU[1, a], Qian SU[1, b *], Hao BAI[2, c], Yu HE[1, d], Wen-hui ZHAO[1, e]

[1]MOE Key Laboratory of High-speed Railway Engineering, Chengdu 610031, China

[2]Engineering Construction Department, Sichuan Expressway Construction and Development Co., Chengdu 610041, China

[a]chbweek@126.com, [b]suqian@126.com, [c]secdcbh@126.com, [d]352866785@qq.com, [e]841858571@qq.com

**Keywords:** Deep soft ground; Non-embedded pile-board structure (NEPBS); Engineering behavior; In-situ test; Over-shallow-embedded metro

**Abstract:** It's the first application of NEPBS crossing over-shallow-embedded metro in deep soft ground on new *Shanghai-Hangzhou passenger dedicated railway* (SHPDR) in China. It's necessary to study the engineering behavior of NEPBS in complex geology field. Long-term observation systems were installed at the typical test sections of SHPDR; Combined with theoretical analysis model, the mechanical properties and deformation laws were analyzed and tested. Measurement results show that the test reinforcement stresses of loading plates and supporting beams are small; the test bending moments agree well with the theoretical bending moments, which are far less than the resistance bending moments; the piles improved the mechanical properties of deep soft ground, so the plate-soil contact stresses are small, the maximum value is 132 kPa; 45 days after the train operation, the post-construction settlement is 1.86 mm; the settlements of individual test points are not yet stable, but they tend toward stability, which can meet the requirements of settlement control of SHPDR.

## Introduction

The new SHPDR is a high standard passenger railway, which intersects Shanghai metro 9 at 87° in zone DK5+344.8~DK5+374.8 in deep soft ground[1]. The embedded depth of metro tunnel is less than 8m, abutment excavation could make the tunnel rise and a lot of existing structures in the subgrade clearances in common subgrade scheme. Therefore, the design department put forward the NEPBS subgrade with strong adaptability in crossing underground pipelines and structures.

NEPBS is a new subgrade form of Ballastless track railway, which has high bearing capacity and good dynamic properties, and it is very economical too. In recent years, NEPBS has been successfully applied in Zhengzhou-Xi'an dedicated passenger railway and many other high-speed railways [2-4]. It's the first application of NEPBS crossing over-shallow-embedded, and the engineering behaviors of NEPBS in complex geology field are not known exactly, thus, it's necessary to study the engineering behavior of NEPBS in SHPDR. Combined with the SHPDR project, the engineering behavior of NEPBS and the tunnel-NEPBS interaction were tested, so as to verify that the NEPBS can meet the construction requirements of high-speed railway, and to provide scientific basis of the application of NEPBS in deep soft ground and other complex geology fields.

## In-situ Test Condition

**Engineering Overview.** The new SHPDR stands on the coastal plain with open flat terrain. The Shanghai metro-9 consists of three parallel over-shallow-embedded shield tunnels, and the surrounding rock is muddy clay. The interval between two tunnels is 10 m. The NEPBS is composed of reinforced concrete loading plates, supporting beams and cast-in-situ bored piles. One

continuous unit of NEBPS is composed of three spans. There are 4 piles on one lateral section, the diameter is 0.8m and the length is 46 m. The supporting beam is on the top of 4 piles with the size of 9.64×1.50×1.60 m. And we set two loading plates on 4 supporting beams with the size of 30.0×4.4×1.0 m (see Fig. 1~3).

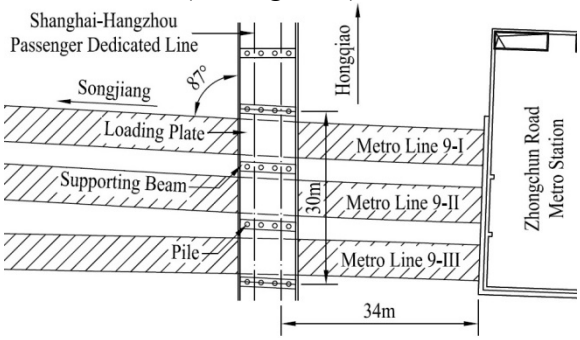


Fig. 1 Layout chart of NEPBS and metro

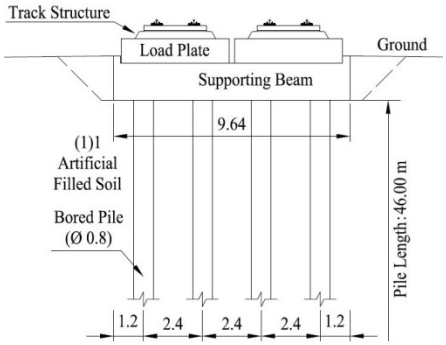


Fig. 2 Layout chart of NEPBS cross section (Unit: m)

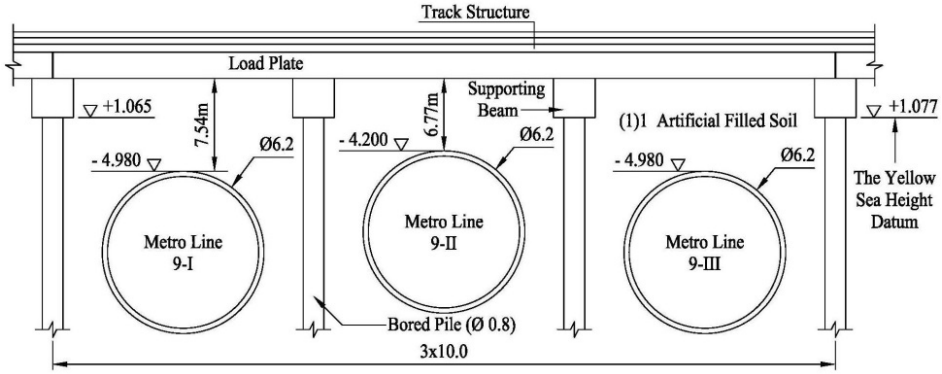


Fig. 3 Layout chart of NEPBS profile (Unit: m)

**Physical Mechanical Indexes of Soil.** The main foundation soil is soft clay or silt. According to geological prospecting materials, in the range of 60 m below the ground, the bearing capacity of soil is very low. The physical mechanical indexes of soil are listed in Tab 1.

Tab 1 Physical mechanical indexes (natural soil)

| Soil layer | Name | Thickness (m) | Density (g/cm$^3$) | Void ratio | Bearing capacity (kPa) | Cohesion (kPa) | Internal friction angle (°) |
|---|---|---|---|---|---|---|---|
| 3(1) | Muddy clay | 2.0 | 1.79 | 1.16 | 60 | 9.11 | 6.66 |
| 4 | Muddy clay | 6.6 | 1.80 | 1.13 | 80 | 9.70 | 7.13 |
| 6(1) | Silty clay | 8.4 | 1.99 | 0.72 | 180 | 18.04 | 14.06 |
| 7(1) | Silt | 5.5 | 1.95 | 0.75 | 150 | 12.59 | 17.04 |
| 7(2) | Fine sand | 7.6 | 2.05 | 0.64 | 160 | 19.00 | 22.40 |
| 8(2) | Silty clay | 12.5 | 1.87 | 0.93 | 150 | 15.88 | 12.64 |

**In-situ Testing Scheme.** In order to study and predict the engineering behavior of NEPBS, the in-situ observation systems were established. The test content included the internal force of loading plate and supporting beam, the plate-soil contact stress, and the settlement of plate. The arrangement of test components is shown in Fig. 4.

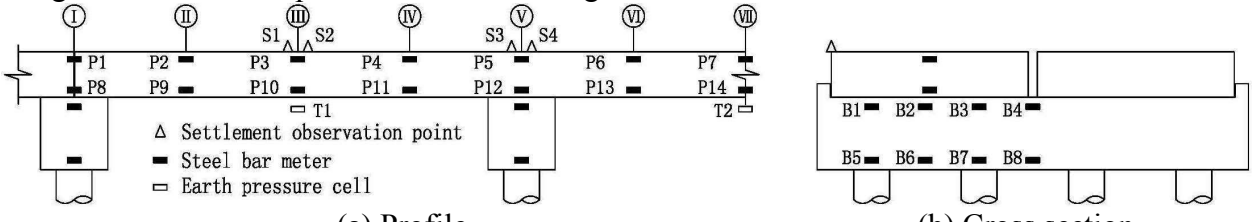


(a) Profile (b) Cross section

Fig. 4 Arrangement of test components

## Design and Calculation Method

**Design and Calculation Thoughts.** The design methods of NEPBS include allowable stress method (ASD) and limit state method (LSD) at present. LSD is more reasonable than ASD. LSD is better than ASD in theoretically, however, the dynamic properties of NEPBS under the train load are not known enough, therefore, ASD is still being used. NEPBS is a statically indeterminate structure, which can be analyzed by analytical method after being simplified.

**Calculation Models.** Based on equal rigidity, NEPBS can be simplified as lateral and longitudinal plane models because the load is strip load, and the loading plate is a textural one-way slab. The soil has strong transverse effect on piles; therefore, comprehensive rotation rigidity $G$ is introduced in the simplified plane models to describe the ability to resist rotation deformation of piles under the soil-pile interaction [5,6]. The comprehensive rotation rigidity is represented by the following equation:

$$G = \frac{1}{\varphi_0} = \frac{\alpha E_1 I (A_3 B_4 - B_3 A_4)(B_3 D_4 - D_3 B_4)}{(C_3 A_4 - A_3 C_4)(B_3 D_4 - D_3 B_4) + (C_4 B_3 - C_3 B_4)(D_3 A_4 - A_3 D_4)} \tag{1}$$

where $\varphi_0$ represent rotation, $\alpha$ represent pile deformation coefficient, $E_1$ is elastic module, $I$ is pile moment of inertia, and $A_3$, $A_4$, $B_3$, $B_4$, $C_3$, $C_4$, $D_3$, $D_4$ are undetermined constants. In order to further simplify the calculation, conversion pile length $h_{\text{con}}$ independent of pile-soil interaction is introduced instead of real pile length. The conversion pile length is represented by the following equation:

$$h_{con} = 3E_1 I / G \tag{2}$$

**Design load.** Construction load and other load in service life should be considered into the design of NEPBS. The design loads include structure weight, train live load, temperature load, centrifugal force, swaying force and so on. In this static test, only the structure weight of NEPBS and the load from track structure were considered to calculate the theoretical internal forces and bending moments when test results were compared with theoretical calculation results.

## Results and Analysis

**Reinforcement Stress.** The load from track structures was transferred to loading plates, then, transferred to supporting beams and soil under plate; the load on the supporting beams was transferred to the pile, then, transferred to the bearing soil stratum. Supporting beam was rigidly connected to pile, and loading plate and supporting beam formed hinged or rigid structure. The measurement results of reinforcement internal force of loading plate and supporting beam are shown in Fig. 5~6.

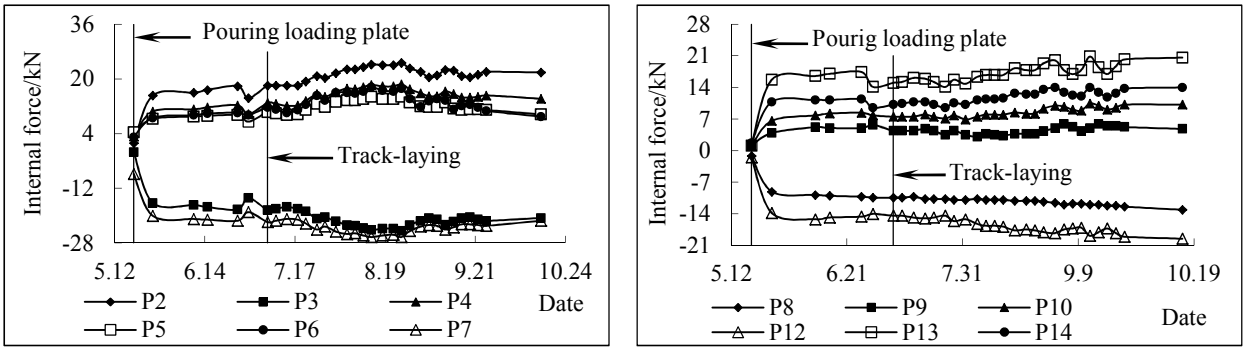


(a)Top (b) Bottom

Fig. 5 Time-history curves of reinforcement internal force of loading plate

After the completion of loading plate pouring, the hydration heat of concrete could make the test values of steel bar meter fluctuate acutely so that the test would not have high precision. The data after temperature stabilized were analyzed, in Fig. 5~6, the positive represent tension, and the negative represent pressure. The loading plates and supporting beams are in the working state of beam with compression steel. The maximum reinforcement tensile stresses of loading plates are

24.0 MPa at the bearing and 22.7 MPa at the span center, and the maximum reinforcement compressive stresses are 31.7 MPa at the bearing and 42.7 MPa at the span center. The maximum reinforcement tensile stresses of supporting beams are 11.9 MPa at the bearing and 17.0 MPa at the span center, and the maximum reinforcement compressive stresses are 12.7 MPa at the bearing and 20.0 MPa at the span center. After the completion of subgrade and track engineering, the test values were tend toward stability because the supporting effect of soil increased with the increase of settlement. The average values of reinforcement stresses at all sections were conversed to the bending moment of loading plate (see Fig. 7).

In Fig. 7, the test bending moment values agreed well with theoretical values of NEPBS which is subjected to the structure weight and the load from track structure. In theoretically, the bending moment at the bearing of side span should be zero, however, the test bending moment values were not zero because the real bearing was not a point but a plane. Therefore, the ends of loading plate need to be designed especially. What's more, the test bending moment values were far less than the design resistance moment values, which showed that the design resistance is safe and reliable.

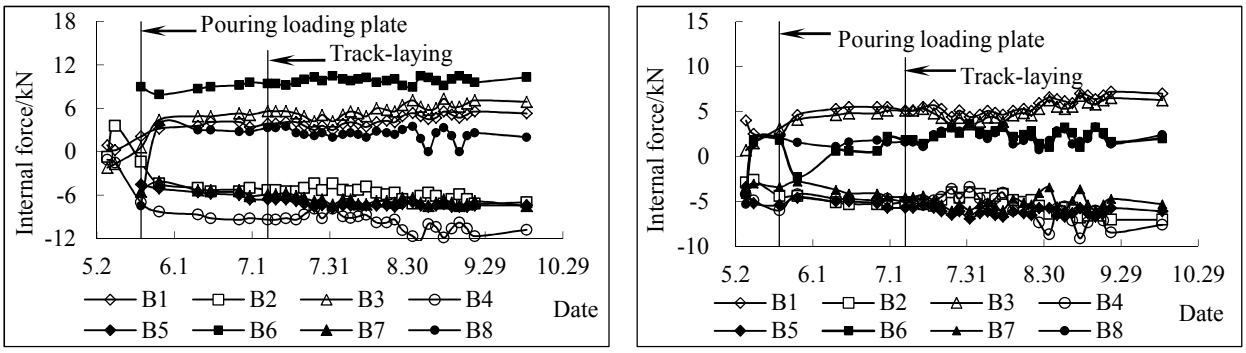


(a)Section I (b)Section V

Fig. 6 Time-history curves of reinforcement stress of supporting beam

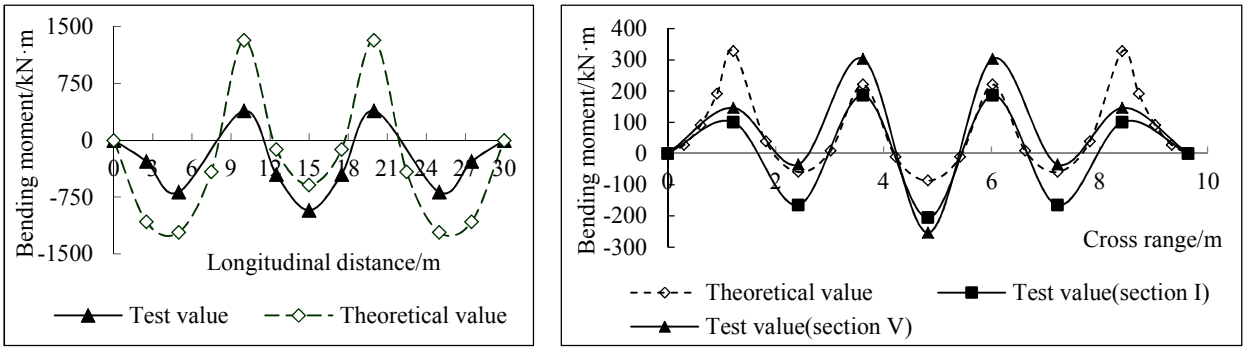


(a)Loading plate (b) Supporting beam

Fig.7 Comparison between test and theoretical bending moment

**Analysis of Plate Soil Contact Stress.** In theoretical design, the supporting effect of soil is often ignored, which is treated as safety margin. The stronger supporting effect of soil becomes, the bigger foundation coefficient is, and the smaller settlement of loading plate is. Foundation coefficient can be back calculated by the plate-soil contact stress. In order to get the plate-soil contact stress, earth pressure cells were set below the loading plate at the center line of the track (represented by *zx*) and one rail (represented by *zz*). The measurement results are shown in Fig. 8.

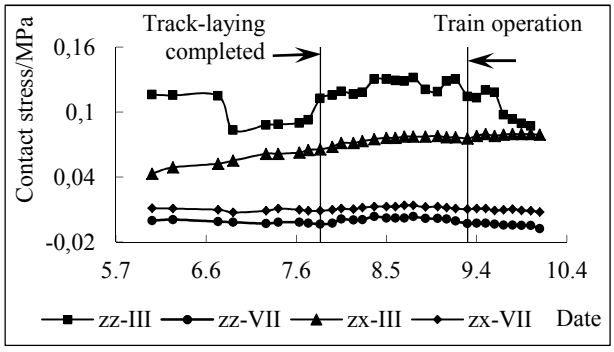


Fig.8 Time-history curves of plate-soil contact stress

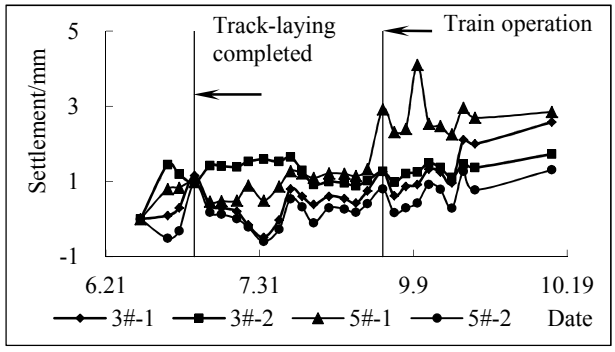


Fig.9 Time-history curves of settlement

The test contact stresses are small, the maximum value is 132 kPa. There is a great rigidity difference between pile and soil, and the supporting effect weakened gradually with the soil-pile interaction so that the upper load was transferred to the top of piles. Moreover, with the settlement increase and long-term interaction of NEPBS and soil, the contact stresses changed a little which can indirectly reflect that the metro tunnels didn't rise basically.

**Settlement Analysis of Pile-Board.** The deformation stability of NEPBS can be verified by the settlement test. The measurement results are shown in Fig. 9. Measured data shows that the initial settlement rate was fast, and then decreased with the lapse of time. After the train operation, settlement increased obviously again. 45 days later, the total settlements of section III and VII were 1.73mm and 2.85mm; and the post-construction settlements were 0.76mm and 1.86mm. The settlement of individual observation points were not yet stable, however, the settlements tended toward stability according to the prediction, and the settlements could be less than 15mm which is the requirement of design code.

## Conclusions

**Mechanical Properties.** NEPBS has the features of stressing definite, reasonable structure, clear path of force transfer and strong anti-disturbance capability, which can improve the bearing capacity of soft soil efficiently.

**Influence on metro.** With the settlement increase, the metro tunnels didn't rise. NEPBS has little influence on metro on SHPDR project, which can guarantee the stability of metro tunnels.

**Safe and reliable design.** The test bending moments agree well with theoretical moments, and they are far less than the resistant bending moment. Some internal forces of loading plates increased first and then decreased because of the supporting effect of foundation soil.

**Contact stress.** Foundation soil has certain supporting effect. The plate soil interaction can make most of load be transferred to the top of piles so that the load on soil would be reduced.

**Settlement.** The total settlements of NEPBS are small, and which has a slow trend of increase. According to the prediction, the settlement can meet the construction requirements of SHPDR using the NEPBS.

## Acknowledgements

This work was financially supported by the national key technology R&D program of China (Grant No.2011BAK12B03), and the fundamental research funds for the central universities (Grant No.SWJTU11ZT03). These supports are greatly appreciated.

**References**

[1] Qian Su, Hao Bai, Long-biao Liang et al.: Applied Mechanics and Materials Vol. 71-78(2011), p.388-392, in Chinese.

[2] SU Qian, BAI Hao, HUANG Junjie et al.: Journal of Southwest Jiaotong University Vol. 47(2012), p.181-186, in Chinese.

[3] BAI Hao, SU Qian, HUANG Jun-jie, et al.: Rock and Soil Mechanics Vol. 33(2012), p.3753-3759, in Chinese.

[4] BAI Hao, SU Qian, LIANG Long-biao, et al.: China Safety Science Journal Vol. 21(2011), p.144-150, in Chinese.

[5] SU Qian, WANG Wu-bin, BAI Hao, et al.: Journal of Traffic and Transportation Engineering Vol. 12(2012), p.19-24, in Chinese.

[6] SU Qian, LUO Zhao-xin, WANG Xun: Theory and Practice of Non-Embedded Pile-Plank Structure of High-Speed Railway Subgrade (China Railway Publishing House, China 2011).

*Applied Mechanics and Materials Vols. 580-583 (2014) pp 302-307*
*© (2014) Trans Tech Publications, Switzerland*
*doi:10.4028/www.scientific.net/AMM.580-583.302*

# The Analysis on Bearing Characteristic of Residue Pile Composite Foundation Formed by DDC

Zengrong Liu [1, a], Qingjuan Sun[1, b] and Zhifang Yan [1, c]

[1]School of Civil Engineering, Xi'an University of Architecture and Technology, Xi'an, Shaanxi, 710055, China

[a]1305636339 @qq.com, [b] sunqingjuan@yeah.net, [c]yanzhifang594@163.com

**Keyword:** Residue pile, Composite foundation, Bearing characteristic, ANSYS finite element analysis

**Abstract.** The bearing capacity of residue pile composite foundation formed by deep dynamic compaction, shorted for DDC, is calculated and analyzed by ANSYS finite element software. The analysis results show that pile body and soil between piles have a good coordination, residue pile composite foundation is semi-flexible and semi-rigid and the effect of consolidating foundation is obvious. The purpose of foundation treatment should be taken into consideration primarily to provide reference for future similar projects.

## Introduction

The residue pile composite foundation is filled with soil, sand, rock, broken bricks, concrete blocks, industrial wastes and mixtures of inorganic waste solids and formed by deep dynamic compaction method. At present, it is common to study the residue pile composite foundation applied in engineering, while the numerical simulation analysis is rare. This paper calculates and analyzes the bearing characteristic changes of residue pile in different factors, such as bearing characteristic analysis of residue pile, bearing characteristic analysis of soil between piles, elasticity modulus of pile body and soil between piles, pile-soil stress ratio, and pile length. The general bearing characteristic regulation of residue pile composite foundation is analyzed in detail.

## Build the finite element model of residue pile composite foundation

Based on the actual project, the holes diameter of residue pile composite foundation is 1.2m. After deep dynamic compaction, the holes diameter is 1.8m and pile length is 12m. The pile bodies are filled with residue and the properties of soil between piles has been strengthened. Model parameters mainly are come from laboratory soil test and construction experience. Poisson ratio of residue pile and soil between piles is taken from the references [1], and the specific parameters are shown in table 1.

Table 1 Model parameters of residue pile composite foundation

| Materials | modulus of compressibility $E_s$ (Pa) | Poisson ratio $\mu$ | Cohesive strength $c$ (Pa) | Internal friction angle $\varphi$ (°) |
|---|---|---|---|---|
| Pile body | $2.4e^8$ | 0.27 | | |
| Load board | $2e^{10}$ | 0.15 | | |
| mattress | $5.0e^7$ | 0.25 | 0 | 38 |
| soil between piles | $4e^7$ | 0.35 | $3.2e^4$ | 23.2 |

Under vertical load of residue pile composite foundation, it can be regarded as axially symmetric load. Therefore, the space problem of residue pile composite foundation under vertical load can be simplified plane problem in finite element calculation process. The model is symmetric, so take half of single pile composite foundation to carry out numerical simulations. Element type applies for Plane42. In fact, because pile and soil between piles sustain larger top loads within a certain range, refine them on grids. That is to say, divide X axis positive direction by 2.5 percent to achieve the exact solution.

According to contact elements provided by ANSYS finite element software, use surface contact element target169 and contact170 between pile and soil to simulate relative sliding efficiently. Friction coefficient should be determined to make contact analysis. There exists occlusion effect between piles and soil based on the reinforcement mechanism of DDC, the divide is not clear, so friction coefficient is large. The friction coefficient is 0.5 in this paper. Assuming that no relative slip between the piles and mattress when calculating, it applies for coupling connection. Set contact element between piles and soil to simulate the relative sliding effectively.

Before the numerical simulation, there are some assumptions including soil is isotropy; residue piles are elastic material; soil between piles is elastic-plastic material; the effect of history stress, soil displacement and initial stress of soil in pile-forming process are left out.

According to the reference[2] and trial calculation, dimensions of calculation model take 1 time pile length horizontally and twice times vertically. Boundary conditions are side of the model has no horizontal displacement, the bottom is completely fixed and surfaces are free. The finite element model of residue pile composite foundation and mesh are shown in Fig.1.

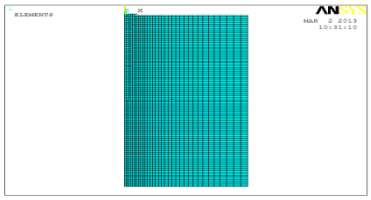

Fig.1 Element partition of residue pile composite foundation

## The analysis on bearing characteristic of residue pile composite foundation

Bearing characteristic of composite foundation lies in coactions of piles and soil between piles, and sustaining top load. By studying the mechanism of reinforcement and load bearing, this paper analyzes the bearing characteristic of composite foundation in the aspects of composite foundation, single residue pile and soil between piles respectively.

**The analysis on bearing characteristic of composite foundation** .From the (a) of Fig.2 below, it can be seen that the effect of vertical pressure stress of residue pile is obvious under the action of superstructure, and the stress is very large leading to stress concentration at the top and tip of piles. Pile stress is 172.7kPa, taking 35.4 percentage of top loads. It is shown from data analysis that pile side resistant of residue pile composite foundation plays a major role which taking 64.6 percentage of top loads.

From the (b) of Fig.2 below, it is found that there is different degrees of sedimentation of piles and soil around piles. Vertical displacement of soil is 18.6mm under load board, and the average displacement of soil around load board is 9.3mm. The compressive deformation of soil is obvious under load board. The sedimentation of composite foundation decreases gradually from top to bottom presenting layer status. It can be seen clearly that piles and soil between piles of composite foundation under load board move down together basically, which means piles and soil between piles play a very good teamwork.

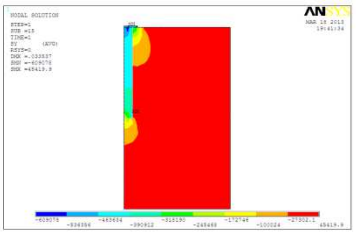

（a）vertical stress nephogram

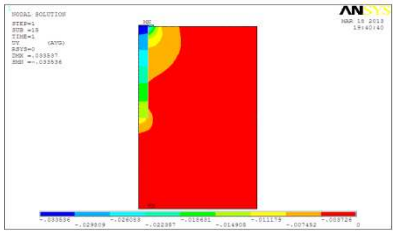

（b）vertical deformation nephogram

Fig.2 Numerical simulation result of composite foundation at 500kPa

Fig.3 is a curve about load and settlement of composite foundation by numerical simulation. From the curve, it can be seen that residue pile composite foundation changes evenly under the range of 800kPa, and the p-s curve is gentle and smooth. Known from reference[3], for composite foundation filled with soil, sand, rock, residue pile, industrial waste and so on, the load is characteristic value of bearing capacity of single pile corresponded by s/d=0.015. Therefore, the bearing capacity of composite foundation is 380kPa in such conditions.

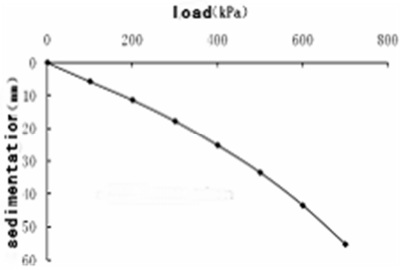


Fig.3 Loading-settlement curve of residue pile composite foundation

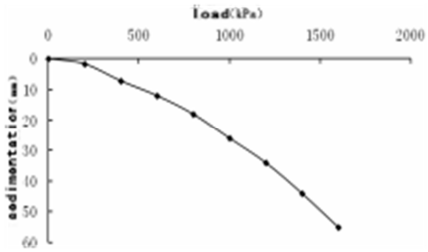


Fig.4 Loading-settlement curve of residue pile

**The analysis on bearing characteristic of residue pile body** .It is controversy to calculate bearing capacity of residue pile composite foundation. In some references, it is calculated by treating as dispersive pile or bonding materials pile in the other references. In the model, length of residue pile is 12m and diameter is 1.8m. Treated as Brauns dispersive piles, ultimate bearing capacity of single pile is 695kPa. While it is 1380kPa treated as bonding materials pile. Fig.4 is p-s curve of residue pile by numerical simulation. From the curve, it can be seen that ultimate bearing capacity of single residue pile is 1400kPa, which is higher than ultimate bearing capacity of dispersive pile. Difference between numerical simulation results and the ultimate bearing capacity by treating as bonding materials pile is small. It indicates that residue piles belong to bonding materials pile, and they are also frictional piles whose lateral friction is larger.

As shown in Fig.5, the difference of stress between top and tip of residue piles is large. With increasing the pile length continually, the stress of pile body decreases gradually due to the existence of the friction along the pile side and resistance of pile body material. And the stress of pile body increases with raising the load. However, load increment of pile top is 200kPa, and load increment of tip of piles is 28kPa. So, load increment of pile top is bigger than load increment of tip of piles. The reason is that the friction along the pile side is larger than tip resistance which is a stable value with increasing of the load.

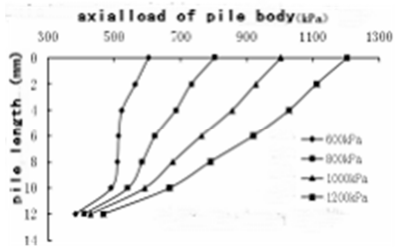


Fig.5 Axial Load distribution curve of pile body

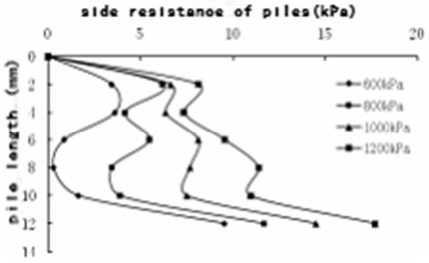


Fig.6 The distribution curve of side resistance of piles

From Fig.6, it can be found that the side resistance of piles has certain regulations along pile body length with increasing top load. From the distribution curve of side resistance along pile body, the changes of side resistance is divided into three a stage roughly. In stage1, the side resistance of top of the piles increases linearly. With increasing load of top piles, the side resistance increases gradually. But the side resistance decreases when top load increases to a certain extent. In stage2, if pile length is 2 to 8 meters, the side resistance decreases gradually after the peak. In stage3, the side resistance has a tendency to sudden increase at the tip piles, which is caused by strengthening effect of the side resistance. Due to diversity of residue pile materials, distribution laws of residue piles are different. However the overall trend is that the side resistance increases gradually as the load increases.

Above all, by theory calculation, comparing numerical simulation and load transmission laws of pile body, the residue pile composite foundation meets bond bearing capacity of friction pile and the reinforcement mechanism. Therefore, the residue piles are adhesive friction piles.

**The analysis on bearing characteristic of soil between piles .**Fig.7 is a relationship curve about stress of soil between piles and load in different depth of burial. It shows that stress of soil between piles enlarges with the increase of load in the same depth of burial, and there is a great difference in different depth of burial that stress of soil between piles decreases with the increase of depth of burial. Stress of soil between piles is lower around tip of piles, which is only about 50kPa.

Fig.8 is a relationship curve about deformation of soil between piles and load in different depth of burial. It show that sedimentation of soil between piles increases as the load enlarges. The deformation curve and stress curve are both gentle, which means soil between piles has better work performance sustaining top loads. From loading-settlement curve of soil between piles, the bearing capacity of soil between piles can reach 250kPa through DDC, which indicates that DDC has a significant effect on reinforcement for soil between piles.

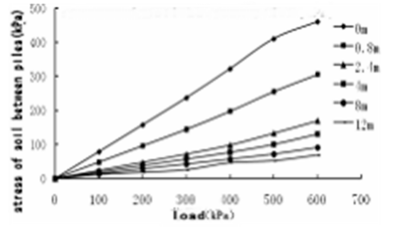


Fig.7 Relationship curve about stress of soil piles and load

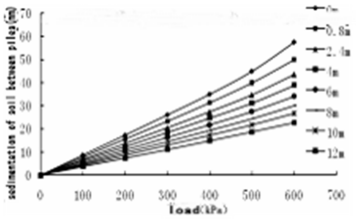


Fig.8 Relationship curve about deformation of between soil between piles and load

**The analysis on pile-soil stress ratio .**From Fig.9, pile-soil stress ratio of residue pile composite foundation changes slightly with the changing of load. Known from the figure above, when pile-soil stress ratio changes between 2.3 to 3, the load fluctuates within a narrow range, which agrees with the properties of dispersive pile composite foundation[4]. In terms of residue pile composite

foundation, the main reason is that the rigidity of residue pile is not very large, belonging to semi-flexible and semi-rigid piles in among bonding materials piles.

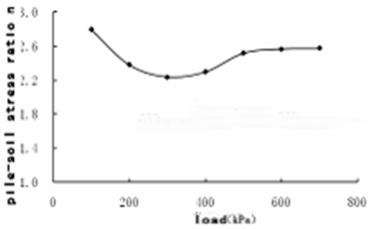


Fig.9 Relationship curve about pile-soil stress ratio and load

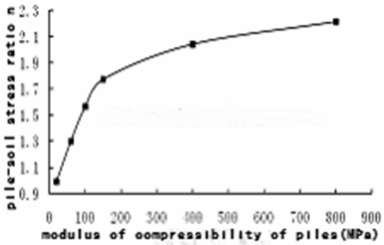


Fig.10 Relationship curve about $E_p$ and n

**The analysis on influencing factors of residue pile composite foundation**

**The effect of modulus of compressibility on bearing characteristic of composite foundation .**From Fig.10, modulus of compressibility of piles has a greater impact on sedimentation of composite foundation. It can be seen from modulus of compressibility of piles and pile-soil stress ratio that pile-soil stress ratio starts from1 when modulus of compressibility of piles and soil between piles is equal, which means that pile-soil stress ratio is about 2.5 with increasing modulus of compressibility of piles when they sustain equal loads.

From Fig.11, sedimentation of composite foundation decreases as modulus of compressibility of piles increases. At the beginning, the sedimentation decreasing is fast. And it is stable when modulus of compressibility of piles reaches to 800MPa. It indicates that increasing the modulus of compressibility of residue pile may enhance bearing properties of composite foundation and reinforcement effect.

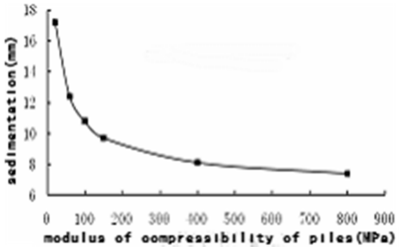


Fig.11 Relationship curve about $E_p$ and sedimentation

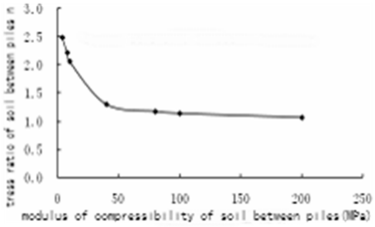


Fig.12 Relationship curve about $E_p$ and n

**Conclusions**

The finite element model about bearing characteristic of residue pile composite foundation is established by applying for ANSYS. By comparing the model and theories, this paper analyzes bearing capacity and mechanism of residue pile composite foundation formed by DDC, and studies the impact of modulus of compressibility of piles and soil between piles on bearing properties of residue pile composite foundation. Using the concept of composite foundation and theories, the article regards residue piles as semi-flexible and semi-rigid piles, which have large differences with dispersive piles. The main contents are given as follows:

The curve about load and sedimentation of single residue pile composite foundation is achieved by numerical simulation, and it is gentle, which means piles and soil have a better cooperation. The bearing capacity of composite foundation is 380kPa, which shows that soft foundation can achieve better reinforcement by choosing residue pile composite foundation.

Calculate the bearing capacity of single residue pile by using the formula of dispersive pile and bonding materials pile, then establish numerical model. It shows that the bearing capacity of single

residue pile is appropriate to bonding materials pile's, and has big differences with dispersive pile. And it can be found that residue pile composite foundation belongs to bonding materials pile. By analyzing the pile-soil stress ratio of residue pile composite foundation, residue piles are semi-flexible and semi-rigid.

The piles and soil between piles of residue pile composite foundation sustain top load together and have good compatibility. Soil between piles works well though DDC, which has reached around 250kPa. It indicates that compactness of soil between piles overcomes natural foundation.

**References**

[1] X.N.Gong: Theory and Engineering Application of Composite Foundation (China Architecture and Building Press, China, 2007).

[2] JGJ79: Technical Regulation of Foundation Treatment for Buildings (China Architecture and Building Press, China, 2002).

[3] Z.J.Xu, B.W Si: New Technique of Foundation Treatment–DDC (China Architecture and Building Press, China, 2011).

[4] CECS197: Technical Regulations of DDC (Beijing Planning Press, China, 2006).

[5] F.Y. Tan: Rock and soil mechanics, Vol. 32（1）（2011）, p.288

[6] Z.Z.Zhang, and Z.L.Wang: New Development of Rammed Soil-cement Pile Composite Foundation Technology(China Planning Press, China, 2007).

[7] The standards of China Association for engineering construction Standardization: Technical regulations of DDC (Beijing Planning Press, China, 2006).

[8] P.J.Jiang and Z.Y.Guo: GEO Foundation, Vol. 14(2)(2000）, p.24

*Applied Mechanics and Materials Vols. 580-583 (2014) pp 308-311*
*© (2014) Trans Tech Publications, Switzerland*
*doi:10.4028/www.scientific.net/AMM.580-583.308*

# The Explanation of Yield Surface Rotation of Sands by Principle of Thermodynamics with Internal Variables

Jingyu Chen[1, a], Ying Hai[2,b]

[1]School of Civil Engineering and Architecture, Jiaxing University, Jiaxing 314001, P.R. China

[2]School of Mechanical and Electrical Engineering, Jiaxing University, Jiaxing 314001, P.R. China

[a]jxxy_chen@126.com, [b]haiying@mail.zjxu.edu.cn

**Keywords:** Dissipation function. Yield function. Yield surface rotation. Saturated sands. Thermodynamics with internal variables.

**Abastract**：Using constitutive modelling principle of thermodynamics with internal variables, the yield surfaces rotation of saturated sands subjected triaxial compression stress state are justified and explained. The explanation for the yield surfaces rotation of saturated sands prove the correctness and feasibility for the principle of thermodynamics with internal variables to construct elastoplastic constitutive relation of saturated soils.

## Introduction

With the thermal-mechanical coupling phenomena research, theory of thermodynamics of continuua has developed a lot since the 80's of the last century. Results of thermodynamics of continuua enriched the constitutive theory of continuum mechanics, and provided new ideas and methods for soil constitutive modelling. Collins and Houlsby *et al.* applied principles of thermodynamics of continuua to geomaterial constitutive modelling, and used two scalar founctions: free energy founction and dissipation founction (or yield founction), in theory of thermodynamics with internal variables, to establish constitutive model. Once the form of the free energy and dissipation potential functions have been specified, the corresponding yield loci, flow rules, isotropic and kinematic hardening rules as well as the elasticity law can be deduced in a systematic manner[1,2].

It is now well understood that whilst volumetric hardening models are normally sufficient to describe the behaviour of clays. It is necessary to additionally introduce shear hardening to model the observed behaviour of sands. It is shown in this paper that in order to keep the thermomechanical models internally consistent, the introduction of shear hardening implies that the yield surfaces must necessarily rotate in stress space and the material response immediately becomes anisotropic. This is, of course, already well recognized observationally and is a feature of a number of recent sand models. This paper provides justification and explanation for the yield surfaces rotation of saturated sands subjected triaxial compression stress state, by constitutive modelling principle of thermodynamics with internal variables(T.I.V). The explanation for the yield surfaces rotation of saturated sands prove the correctness and feasibility for the principle of thermodynamics with internal variables to construct elastoplastic constitutive relation of saturated soils. [3,4].

## The Dissipation Function and Yield Surface of Clay′s Isotropic Models

To specify $\boldsymbol{\alpha} = \boldsymbol{\varepsilon}^p = (\varepsilon_v^p, \varepsilon_d^p)$ an internal variable, $\varepsilon_v^p$ is the volume strain and $\varepsilon_d^p$ is the shear strain of a saturated soil element，the element is in a two-dimensional stress state in triaxial compression test. Use $p$, $q$ to represent the effective mean stress and the effective shear stress, respectively, the stess tensor is then specified by $\boldsymbol{\sigma} = (p, q)$. The dissipation function of isotropic models has the form

$$D(\boldsymbol{\sigma}, \boldsymbol{\alpha}, \dot{\boldsymbol{\alpha}}) = \sqrt{A^2 \left(\dot{\varepsilon}_v^p\right)^2 + B^2 \left(\dot{\varepsilon}_d^p\right)^2} \qquad (1)$$

where $A=a_1p'+a_2q+a_3p_c'$ , $B=b_1p'+b_2q+b_3p_c'$ ; $a_1,a_2,a_3,b_1,b_2,b_3$ are dimensionless coefficients. When $a_1=a_2=b_1=b_2=0,$ the dissipation function is

$$D(\boldsymbol{\sigma},\boldsymbol{\alpha},\dot{\boldsymbol{\alpha}})=p_c'\sqrt{(a_3\dot{\varepsilon}_v^{\mathrm{p}})^2+(b_3\dot{\varepsilon}_d^{\mathrm{p}})^2}$$

According to thermodynamics with internal variables the dissipative stresses are

$$\chi_p=\frac{\partial D}{\partial\dot{\varepsilon}_v^{\mathrm{p}}}=p_c'\frac{a_3{}^2\dot{\varepsilon}_v^{\mathrm{p}}}{\sqrt{(a_3\dot{\varepsilon}_v^{\mathrm{p}})^2+(b_3\dot{\varepsilon}_d^{\mathrm{p}})^2}},\quad \chi_q=\frac{\partial D}{\partial\dot{\varepsilon}_d^{\mathrm{p}}}=p_c'\frac{b_3{}^2\dot{\varepsilon}_{\mathrm{s}}^{\mathrm{p}}}{\sqrt{(a_3\dot{\varepsilon}_{\mathrm{v}}^{\mathrm{p}})^2+(b_3\dot{\varepsilon}_{\mathrm{s}}^{\mathrm{p}})^2}} \tag{2}$$

From Eq.(19) we obtain the yield surface equation in dissipative stress space

$$\left(\frac{\chi_p}{a_3p_c'}\right)^2+\left(\frac{\chi_q}{b_3p_c'}\right)^2=1 \tag{3}$$

this yield surface is shown in Fig. 1. The shift stress is $\boldsymbol{\rho}=(\rho_p,\rho_q)=(\gamma p_c',0),$ so $\chi_p=p-\gamma p_c'$, $\chi_q=q$ , the yield surface equation in true stress space is

$$\left(\frac{p-\gamma p_c'}{a_3}\right)^2+\left(\frac{q}{b_3}\right)^2=p_c'^2 \tag{4}$$

As $a_3=1/2,b_3=M/2,\gamma=1/2$ , where the $M$ is the slope of the critical-state line in the $(p,q)$ plane, Eq.(4) becomes

$$\left(p-\frac{p_c'}{2}\right)^2+\left(\frac{q}{M}\right)^2=(\frac{p_c'}{2})^2 \tag{5}$$

This is the yield surface equation the modified Cam-Clay model given by Burland（1965）in the Cambrige University, the yield surface is shown in Fig. 2.

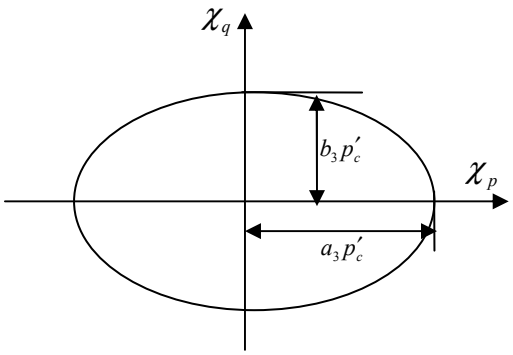


**Fig.1 Yield surface in dissipative stress space**

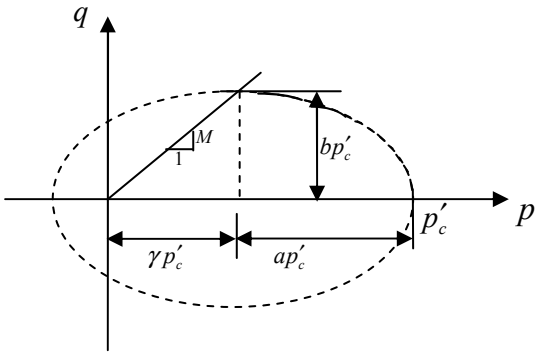


**Fig.2 Yield surface in true stress space**

**The Dissipation Function and Rotational Yield Surface of Sands**

As the dissipation function involves the product of the plastic volumetric and shear strain increment components, the dissipation function becomes

$$D(\boldsymbol{\sigma},\boldsymbol{\alpha},\dot{\boldsymbol{\alpha}})=\sqrt{A^2\left(\dot{\varepsilon}_v^p+\tan\theta_n\dot{\varepsilon}_d^p\right)^2+B^2\left(\dot{\varepsilon}_d^p\right)^2} \tag{6}$$

where, as will be shown, the new parameter $\theta_n$ is the slope of the NCL in the current state of anisotropy. A similar form for the dissipation function was considered, in a micro-mechanical context, by Muhunthan *et al.* [ 5 ]. The dissipative stress components are hence given by

$$\begin{aligned}\chi_p&=\partial D/\partial\varepsilon_v^p=A^2\left(\dot{\varepsilon}_v^p+\tan\theta_n\dot{\varepsilon}_d^p\right)/D\\ \chi_q&=\partial D/\partial\varepsilon_d^p=(A^2\left(\dot{\varepsilon}_v^p+\tan\theta_n\dot{\varepsilon}_d^p\right)\tan\theta_n+B^2\dot{\varepsilon}_d^p)/D\end{aligned} \tag{7}$$

from which it follows that

$$\chi_q-\chi_p\tan\theta_n=B^2\dot{\varepsilon}_d^p/D \tag{8}$$

By eliminating the plastic strain increments between (7)–(8), the equation of the inclined, elliptical yield locus (Figure 3) is obtained as

$$\frac{\chi_p^{\,2}}{A^2}+\frac{(\chi_q-\chi_p\tan\theta_n)^2}{B^2}=1 \tag{9}$$

Inverting (7), the normal flow rule for the plastic strain increments is obtained

$$\dot{\varepsilon}_v^p = D\left[\frac{\chi_p^{\,2}}{A^2}-\frac{(\chi_q-\chi_p\tan\theta_n)\tan\theta_n}{B^2}\right] \quad \text{and} \quad \dot{\varepsilon}_d^p = D\frac{(\chi_q-\chi_p\tan\theta_n)}{B^2} \tag{10}$$

Since the shear strain increment is zero on the current NCL, it follows from Equations (7), (8) and (10) that on this line

$$\chi_p=\pm A \quad \text{and} \quad \chi_p/\chi_q=\tan\theta_n \tag{11}$$

so that $\tan\theta_n$ is the slope of the **NCL** in dissipative stress space, and $(\pm A,\ \pm A\tan\theta_n)$ are the associated dissipative pressures and shear stresses at yield. The **NCL** in dissipative stress space is the chord of the ellipse joining the two points where the normals are in the $\chi_p$ direction, as shown in Figure 3. Similarly the **CSL** is the chord joining the points where the normals are in the $\chi_q$ direction, so that the volumetric strain increment is zero. If the origin in true stress space is to be on all the yield loci, the shift stress components must be related by

$$\rho_q=\rho_p\tan\theta_n \tag{12}$$

It follows that the slope of the NCL in true stress space, is identical to $\theta_n$. If we represent A by the linear function of the basic stress parameters as in the previous section, the pressures at the two ends of the **NCL** are

$$p'=\rho_p\pm A=\rho_p\pm(a_1p'+a_2q+a_3p_c') \tag{13}$$

The positive sign corresponds to $p'=p_c'$, so

$$p'=\rho_p+[a_1p_c'+a_2(\rho_q+(p_c'-\rho_p)\tan\theta_n)+a_3p_c'] \tag{14}$$

whilst, the negative sign gives yield at zero pressure $p'=0$, so that

$$0=\rho_p-[a_2(\rho_q+(p_c'-\rho_p)\tan\theta_n)]+a_3p_c' \tag{15}$$

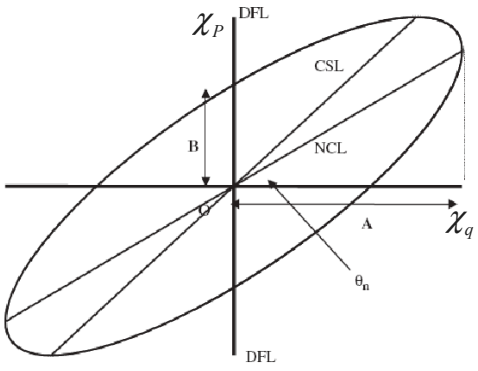


**Fig. 3 Rotated elliptical yield locus in dissipative stress space**

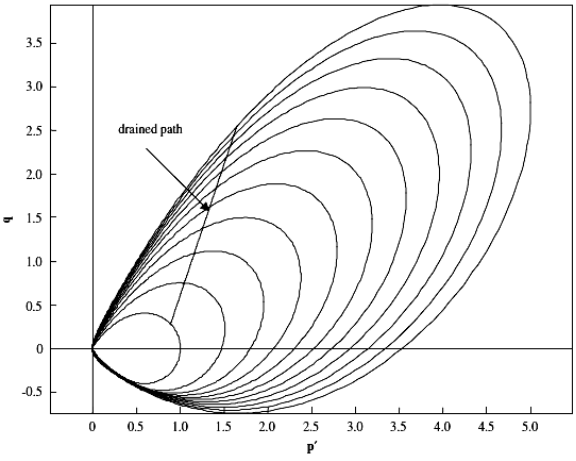


**Fig. 4 Rotational yield loci of a loos sand under triaxial compression**

The shift stress components, and the coefficients of $A$ hence satisfy:

$$\rho_p=\frac{1}{2}\gamma p_c' \quad \text{and} \quad \rho_q=\frac{1}{2}\gamma p_c'\tan\theta_n \tag{16}$$

where $a_1=1-\gamma,\ a_2=0,$ and $a_3=\frac{1}{2}\gamma$.

Since the two components of the shift stress have been found in (16), the equation or the yield locus in true stress space can be written as

$$\frac{(p-\gamma p_c'/2)^2}{A^2}+\frac{(q-p'\tan\theta_n)^2}{B^2}=1 \tag{17}$$

Dimensionless coefficients $b_1$、$b_2$、$b_3$ in $B=b_1p'+b_2q+b_3p_c'$ can be deduced from the slopes of the critical state lines in compression and extension.

Since we are trying to model the effect of shear strain hardening, it is perhaps natural to assume that the rotation angle depends on the plastic shear strain, so that we can write

$$\tan\theta_n=\tan\theta_f\left[1-\exp\left(-\beta\varepsilon_d^p\right)\right] \tag{18}$$

where $\theta_f$ is the ultimate value of $\theta_n$, $\beta$ is a model parameter of the rotational harding law (18).

According to the harding law $(\lambda-\kappa)dp_c'/p_c'=d\varepsilon_v^p+\tan\theta_n d\varepsilon_d^p$, the rotational harding law (18) and Eq.(17), giving a loose sand model parameters $\lambda=0.15,\kappa=0.01,M_c=1.2,M_e=0.86,\gamma=0.4,\alpha=03,\theta_f=30^0$ and $\beta=10$, the rotational yield loci are drawn in Fig.4 with the computer software Matlab.

## Summary

To take $\boldsymbol{\varepsilon}^p=(\varepsilon_v^p,\varepsilon_d^p)$ as an internal variable, when the dissipation function does not include the product of the plastic volumetric and shear strain increment components, the yield surface just shifts from dissipative stress space to true stress space without change of shape. But when the dissipation function includes the product of the plastic volumetric and shear strain increment components, the yield surfaces rotate in dissipative stress space and true stress space, and the material response immediately becomes anisotropic. Principles of thermodynamics of continuua with internal variables present good explanations of yield surface rotation of saturated sands.

## Acknowledgements

This work was financially supported by the ZHEJIANG PROVINCIAL NATURAL SCIENCE FOUNDATION (LY13A020005，Y14E070022).

## References

[1] Collins, I. F., Houlsby, G. T. Application of thermomechanical principles to the modelling of geotechnical materials[J]. Proceedings of Royal Society of London, 1997, Ser. A 453: 1975－2001.

[2] Houlsby, G. T. & Puzrin, A. M. A thermomechanica framework for constitutive models for rate-independent dissipative materials[J]. International Journal of Plasticity, 2000, 16: 1017－1047.

[3] Puzrin, A. M. & Houlsby, G. T. (2001c). A thermomechanical framework for rate-independent dissipative materials with internal functions[J]. Int. J. Plasticity 17, 1147–1165.

[4] Chen, Jingyu&Ying, Hai. The Modified Cam-Clay Model and The Constitutive Relation Principle of Thermodynamics with Internal Variables[J]. Applied Mechanics and materials,Vols. 353-356(2013).

[5] Muhunthan，B., Chameau，J. L., Masad E. Fabric effects on the yield behaviour of soils. Soils and Foundations, 1996, 36: 85–97.

*Applied Mechanics and Materials Vols. 580-583 (2014) pp 312-315*
*© (2014) Trans Tech Publications, Switzerland*
*doi:10.4028/www.scientific.net/AMM.580-583.312*

# The studies of rock damage softening Statistical constitutive model under true triaxial stress state

Huimei Zhang [1,a], Xiangmiao Xie[1,b] and Gengshe Yang[2,c]

[1]Department of Mechanics, Xi′an University of Science and Technology, Xi′an, Shaanxi 710054, China; [2]College of Architecture and Civil Engineering, Xi′an University of Science and Technology, Xi′an, Shaanxi 710054, China

[a]zhanghuimei68@163.com, [b]1050486898@qq.com, [c]yanggs@xust.edu.cn

**Key Words:** True triaxial stress state; Poisson random distribution; D-P criterion; Constitutive relation

**Abstract**: From the feature of rock micro-unit failure obeys Poisson random distribution, the damage softening statistical constitutive of was established under true triaxial confinement based on D-P criterion, so the impact of the intermediate principal stress on rock deformation and failure was considered in theory, and the actual engineering rock complex stress path evolution was reflected more realistically. Furthermore, according to the geometrical conditions of stress-strain relationship, the theoretical relationship between constitutive model parameters and the stress-strain curve characteristic parameters during the process of rock softening and deforming, which enhance the adaptability of the model. Finally, the rationality of the model verified by the measured data.

## Introduction

The concept of damage was first used by the Soviet Union plastic mechanics Kachanov home in 1958 when the creep rupture studied. In 1976, Dougill first proposed the study of rock material damage mechanics, which introduced the concept of damage to the study of rock [1]. Rock is a porous medium, and its constitutive equation has obvious nonlinear characteristics, thereby, how to create the stress-strain relationship can reflect rock in the process to the damage is one of the hot and difficult rock mechanics studies [2]. To this, the researchers conducted a great deal of research, and made some encouraging research achievements, especially after the introduction of statistical methods, the research of rock damage softening statistical constitutive relations have made great progress[3-5]. In [6] the strain equivalence hypothesis was proposed, and the damage variable D is introduced into the constitutive model of rock, which opened the study of rock damage softening constitutive model. In [4] based on D-P criterion,the three-dimensional rock damage evolution equation and rock damage softening constitutive equations were established , which describes the rock mechanism of damage. In [7] the parameters can reasonably describe rock micro-element strength were introduced based on the assumption that the strength of the rock micro element obeys normal distribution.

However, the above triaxial constitutive theory model mainly focus in the conventional triaxial model without considering the impact of the intermediate principal stress. In fact, a lot of rocks true triaxial compression test results indicate that [8-10], the strength and failure of rock were not only affected by the maximum principal stress and minimum principal stress, but also affected by the intermediate principal stress, namely the so-called intermediate principal stress effect. And the evolution of complex stress path resulted from underground rock excavation can only reflected by true triaxial constitutive model.

In this paper, on the basis of predecessors' research, the true triaxial stress state of rock damage softening constitutive model was established, and the theoretical expression of model parameters was deduced based on the Poisson, and the correctness of established formula finally verified through the test data.

**The established of rock damage statistical constitutive model**

Using the J. Lemaitre strain equivalence hypothesis [6], the basic formula of rock damage constitutive model is

$$\{\sigma\}=[C]\{\varepsilon\}(1-D) \tag{1}$$

where, $\{\sigma\}$ is the nominal stress vector, $[c]$ is elastic matrix, $\{\varepsilon\}$ is strain vector, $D$ is damage variable.

Based on the heterogeneity of rock meso structure [4], the physical property of material internal micro elements are of probabilistic, assuming they obey Poisson statistical distribution. Under the action of load, the gradual destruction of material caused by the micro cracks and micro pore aggregation can represented by the damage of available $D$,its expression is [11]

$$D=1-\left(\left(\frac{\varepsilon}{\varepsilon_0}\right)^m+1\right)\exp\left(-\left(\frac{\varepsilon}{\varepsilon_0}\right)^m\right) \tag{2}$$

where, $\varepsilon$ is the strength of micro element, $m,\varepsilon_0$ are model parameters.

According to D-P failure criterion, $\varepsilon$ is

$$\varepsilon=\left[\frac{\sin\varphi}{\sqrt{9+\sin^2\varphi}}\frac{E(\sigma_1+\sigma_2+\sigma_3)}{\sigma_1-\mu\sigma_2-\mu\sigma_3}+\frac{E\sqrt{(\sigma_1-\sigma_2)^2+(\sigma_2-\sigma_3)^2+(\sigma_3-\sigma_1)^2}}{\sqrt{6}(\sigma_1-\mu\sigma_2-\mu\sigma_3)}\right]\varepsilon_1 \tag{3}$$

where, $E$ is elastic modulus, $\mu$ is poisson ratio, $\varphi$ is internal friction angle, $\varepsilon_1$ is the max principal stress.

Therefore, by Eq. 1and Eq. 2 the statistical constitutive model of rock damage was established

$$\begin{cases}\sigma_1=E\varepsilon_1\left(\left(\frac{\varepsilon}{\varepsilon_0}\right)^m+1\right)\exp\left(-\left(\frac{\varepsilon}{\varepsilon_0}\right)^m\right)+\mu(\sigma_2+\sigma_3)\\ \sigma_2=E\varepsilon_2\left(\left(\frac{\varepsilon}{\varepsilon_0}\right)^m+1\right)\exp\left(-\left(\frac{\varepsilon}{\varepsilon_0}\right)^m\right)+\mu(\sigma_3+\sigma_1)\\ \sigma_3=E\varepsilon_3\left(\left(\frac{\varepsilon}{\varepsilon_0}\right)^m+1\right)\exp\left(-\left(\frac{\varepsilon}{\varepsilon_0}\right)^m\right)+\mu(\sigma_1+\sigma_2)\end{cases} \tag{4}$$

Since the Eq. 4 contains the intermediate principal stress, so the Poisson distribution variables may reflect the impact of the intermediate principal stress on rock strength.

The above derivation based on Poisson distribution function, the damage model of rock was described from a statistical point of view, however, the parameters of the model have not been determined. In previous studies, the majority of the constitutive model parameters were determined by using the test curve fitting method, which has obvious limitations. In order to enhance the adaptability of the model, the theoretical relationship between model parameters and rock deformation and the stress-strain curves characteristic parameters in failure process must be studied, based on it , the expression the model parameters under complex stress state of were established.

**Determine of model parameters**

In this section, we took the Total differential method to deduce the model parameters. Typical triaxial test curve satisfies the following conditions at the extreme points of the geometry

$$\begin{aligned}&(1)\,\varepsilon_1=\varepsilon_c,\sigma_1=\sigma_c;\\ &(2)\,\varepsilon_1=\varepsilon_c,\frac{\partial\sigma_1}{\partial\sigma_2}=0.\end{aligned} \tag{5}$$

The model parameters are (the solution is ignored)

$$\begin{cases}\left(\left(\dfrac{\varepsilon_c}{\varepsilon_0}\right)^m+1\right)\exp\left(-\left(\dfrac{\varepsilon_c}{\varepsilon_0}\right)^m\right)=\dfrac{\sigma_c-\mu\sigma_2-\mu\sigma_3}{E\varepsilon_c}\\ \left(\dfrac{\varepsilon_c}{\varepsilon_0}\right)^m+1=m\left(\dfrac{\varepsilon_c}{\varepsilon_0}\right)^{2m}\end{cases} \tag{6}$$

Let $x=\left(\dfrac{\varepsilon_c}{\varepsilon_0}\right)^m$, then Eq .6, simplified to

$$\begin{cases}(x+1)\exp(-x)=\dfrac{\sigma_c-\mu\sigma_2-\mu\sigma_3}{E\varepsilon_c}\ \text{(a)}\\ x+1=mx^2\qquad\qquad\qquad\text{(b)}\end{cases} \tag{7}$$

The parameter $x$ can be solved from Eq .7(a), then the parameter $m$ can be calculated from Eq .7(b), finally get the value of $\varepsilon_0$, so far the rock damage softening Statistical constitutive model under true triaxial stress state are finally determined.

**Verification of model**

The maximum principal stress and maximum principal strain theory curve about different intermediate principal strain under complex stress state can be obtained from Eq .3, Eq .4 and Eq .6, and contrasted it with the test data provided from [9],as shown in Fig.1 The rock elastic modulus $E$=4.866GPa, poisson ratio $\mu$=0.25, internal friction angle$\varphi$=44.70.And Peak point parameters under different intermediate principal stress are shown in Table 1.

Table 1 Sandstone parameters under different intermediate principal stress

| $\sigma_2$/MPa | $\sigma_c$/MPa | $\varepsilon_c$/‰ |
|---|---|---|
| 1.2483 | 10.6359 | 19.7582 |
| 2.2622 | 11.4578 | 14.1821 |

To highlight reflect the impact of the intermediate principal stress on rock failure, especially selected two different intermediate principal strain cases when the minimum principal strain were the same in literature [9]. In Fig.1 (a), $\sigma_3=0.78$MPa, and the ratio of the intermediate principal stress and the minimum principal strain is $\sigma_2/\sigma_3=1.6$; In figure 1 (b), $\sigma_3$= 0.78MPa, and the ratio of the intermediate principal stress and the minimum principal strain is $\sigma_2/\sigma_3=2.9$.

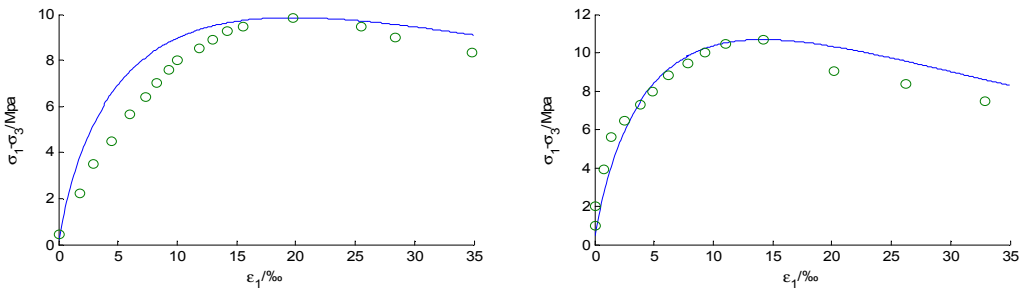


（a）（$\sigma_3$=0.78MPa,$\sigma_2/\sigma_3$=1.6）　（b）（$\sigma_3$=0.78MPa,$\sigma_2/\sigma_3$=2.9）

Fig.1 The verification curves of true triaxial rock theoretical model under different confining pressure

As can be seen from Fig.1, the stress-strain relationship theoretical curve of rock damage constitutive model established in this paper matched with test data, so the rationality of constitutive model were verified.

## Conclusions

1. In this paper, assuming that rock micro element obey Poisson statistical distribution, the rock damage statistical constitutive model was established based on the D – P criterion, which considering the effect of intermediate principal stress on rock failure strength in theory;
2. The theoretical relationship between model parameters and rock deformation and the stress-strain curves characteristic parameters in failure process were established, the Parameter $m, F_0$ can only be determined by using peak point stress and strain information of test curve and rock elastic modulus, poisson ratio, and these parameters can be easy to get in the conventional mechanical properties test;
3. Through the model verification show that the rock damage statistical constitutive model under true triaxial stress state established in this paper matched with test data.

## Acknowledgments

Supported by the National Natural Science Foundation of China (11172232, 41272340), Natural Science Foundation of Shaanxi (2011JM1003), New Century Talent Support Program of Ministry of Education(ACET-12-1044) and the Special Foundation of Education Department of Shaanxi (11JK0525, 11JK0542).

## References

[1] Xingchun Su, Lianjin Tao, Wengui Cao. Rock mechanics [M]. Beijing: Higher Education Press, 2005(In Chinese)

[2] Heping Xie. Rock and damage mechanics [M]. Beijing: China University of Mining and Technology Press, 1990(In Chinese)

[3] Weiya Xu, Lide Wei. Study on statistical damage constitutive model of rock [J]. Chinese Journal of Rock Mechanics and Engineering, 2002, 21(6): 787-791(In Chinese)

[4] Wengui Cao, Zulie Fang, Xuejun Tang. A study on statistical of constitutive model for soft and damage rocks [J]. Chinese Journal of Rock Mechanics and Engineering, 1998, 17(6): 628-633(In Chinese)

[5] Wengui Cao, MInghua Zhao, Xuecheng Liu. Study on the model and its modifying method for rock softening and damage based on Weibull random distribution [J]. Chinese Journal of Rock Mechanics and Engineering, 2004, 23(19): 3226-3231(In Chinese)

[6] Lemaitre J. How to use damage mechanics [J]. Engineering and Design, 1984, 80: 233-245

[7] Wengui Cao, Peng Li, Minghua Zhao, Xuecheng Liu. On statistical damage constitutive model and its parameters for rock based on normal distribution [J]. Hydrogeology & Engineering Geology, 2005, 32(3):11-14(In Chinese)

[8] Jihua Yang, Handong Liu. True triaxial experimental study on rock strength and deformation [J]. Journal of North China Institute of Water Conservancy and Hydroelectric Power, 2007, 28(3):66-68(In Chinese)

[9] Rajendra P, Tiwari, K. Seshagiri Rao. Post failure behavior of a rock mass under the influence of triaxial and true triaxial confinement [J]. Engineering Geology, 2006,84:112-119

[10] Jingtao Chen, Xiating Feng. True triaxial experimental study on rock with high geostress [J]. Chinese Journal of Rock Mechanics and Engineering, 2006, 25(8): 1537-1543(In Chinese)

[11]Chunan Tang. Catastrophe in rock unstable failure [M]. Beijing: China Coal Industry Publishing House, 1993(In Chinese)

*Applied Mechanics and Materials Vols. 580-583 (2014) pp 316-319*
*© (2014) Trans Tech Publications, Switzerland*
*doi:10.4028/www.scientific.net/AMM.580-583.316*

# A New Algorithm For Computing Threshold Value Used To Image Segmentation

Guoyan Chen[1,a], Dequn Liang[2,a] , Ying Zhang[1,a],Haiyan Xie[1,b]

[1]Department of Mathematics, Dalian Maritime University , Dalian,Liaoning,116026

[2]School of Information Science and Technology, Dalian Maritime University , Dalian,Liaoning 116026,China

[a]guoyanch@sina.com, [b]winteriscoming@sina.com

**Keywords:** Threshold, Image segmentation, Degree of membership

**Abstract.** With the development of computer technology, digital image technology is also to grow rapidly. At present, the image processing has become a popular research field. Segmentation is a very important critical step in image processing tasks, which directly affects the subsequent analysis results. Cluster analysis belongs to the category of unsupervised classification and it is not depended on any prior knowledge of the category, so it usually serves as a basic tool to be used for the initial stage of image segmentation. In this paper, we propose a weighted fuzzy threshold algorithm based on fuzzy relations. This algorithm determines the fuzzy membership function according to the similar relationship between pixels, and emphasizes influence of sharpening features of Gaussian function. The new method overcome the drawbacks of clustering algorithms such as, sensitive to the initial value, need to pre-set number of categories. The numerical results show the effectiveness of the new method.

## Introduction

Image segmentation is to divide the input image into a disjoint set of physically meaningful, quasi-homogeneous regions. The partition is made according to some perceptual attributes like color, boundary information, or a certain application-dependent region uniformity criterion. Since it provides the basis and precondition for the further analysis of the image, it is useful for feature extraction and pattern recognition. It has been well studied in the past decades. For example, Ben et al. [1] do the image segmentation by employing the color clustering method. Bu et al. [2] do the image segmentation by employing the Fuzzy cluster method (FCM). However, the image segmentation is till a hot research area as there exists no a common method.

Image segmentation technology is a multi-factor, multi-index classification problem. Lots of the threshold algorithms for image processing ignore some similarities between pixels and are affected by some extent abnormal pixel values. Cluster analysis is an effective tool for dealing with data classification. As it does not depend on any prior knowledge of the category, cluster analysis is an unsupervised classification method. Until now, researchers have proposed lots of clustering algorithms, which can be divided into two categories based on the nature of the general classification algorithm. One is hard clustering method with the representation K-means clustering method and another one is the fuzzy clustering algorithm with representation FCM. However, both categories of cluster algorithms depend on the cluster number which needs to be given first, and they are sensitive to initial conditions. Moreover, the running time depends on the size of the data. In the recent years, many of researchers have focused on improving the cluster methods mentioned above. For example, [3] improved the FCM by introducing the entropy constraint into FCM. On the other hand, the new proposed method still has some drawback of limitations. The methods proposed in [4-5] only perform well when there is a small gap between the actual image and the ideal result. Moreover, the algorithms are very complex. The membership-based threshold segmentation algorithm provided by [6] has ignored the similarity of the image.

In the field of data processing, the received data may be uncertainty. Since the following operation will be affected by the uncertainty, it is very important in the process of analysis. Fuzzy theory is good at dealing with uncertainty and has been widely applied to the field of image processing such as image enhancement, image segmentation. Then we may get stable results if we employ the fuzzy theory in process of data clustering.

In this paper, we propose a weighted fuzzy threshold algorithm based on fuzzy relations, the new method overcome the drawbacks of clustering algorithms such as, sensitive to the initial value, need to pre-set number of categories. The numerical results show the effectiveness of the new method.

## Definition of image segmentation

Image segmentation is proposed in 1992 and its aim is to divide the image into small regions. The mathematical formulations of image segmentation are as what follows. Let R denote the entire area of the image. The image segmentation is to divide R into some sub-areas which satisfy:

1) $\bigcup_{i=1}^{n} R_i = R$ ;

2) $R_i$ is a connection region, for $i = 1,2,\cdots,n$ ;

3) $R_i \cap R_j = \varnothing$ , $i, j = 1,\cdots,n, i \neq j$ ;

4) $P(R_i) = TRUE$ , $i = 1,2,\cdots,n$ ;

5) $P(R_i \cup R_j) = FALSE$ , for any adjacent areas $R_i$ and $R_j$ .

Here $P(R_i) = TRUE$ means that all points in $R_i$ satisfy some given properties and $P(R_i \cup R_j) = FALSE$ means that the adjacent areas $R_i$ and $R_j$ satisfy the different properties.

## The threshold clustering method based on fuzzy theory

Segmentation is a critical step in the image processing as it affects the following steps of segmentation analysis directly. In fact, the image segmentation algorithm can be taken as the clustering method. Due to the intuitive nature and simplicity, the threshold plays a key role in the image segmentation. By taking advantage of the fuzzy membership function, we sharp the impact of singular value to the threshold of the image and strengthen the impact of the similarity to the threshold of the image. The algorithm for calculating the threshold of clustering algorithm based on membership is as follows.

Suppose that there are *m* sample vectors and *n* variables, where $X_i = (x_{i1}, x_{i2}, \cdots, x_{in})$ denotes the *i*-th sample. When estimating the threshold value, we use the Euclidean distance to calculate the similarity between *i*-th and *j*-th sample, that is, $d_{ij} = \sqrt{(x_{i1} - x_{j1})^2 + (x_{i2} - x_{j2})^2 + \cdots + (x_{in} - x_{jn})^2}$ , $i, j = 1,2,\cdots,m$ .

Step 1.Calculate the similarity of the samples and denote $D_i = \{d_{i1}, d_{i2}, \cdots, d_{im}\}, i = 1,2,\cdots,m$ .

Step 2.Rearrange the elements of $D_i$ , and write by $S_i$ ,

$$S_i = \{d_{ip}, d_{ik}, \cdots, d_{it}\} = \{s_{i1}, s_{i2}, \cdots, s_{in}\}, i = 1,2,\cdots,m, \text{ where } d_{ip} > d_{ik} > \cdots > d_{it}.$$

Step 3.Rearrange the samples based on the order of $S_i$ , write by $S_{X_i}$ ,

$$S_{X_i} = \{X_p, X_k, \cdots, X_t\} = \{X_1^i, X_2^i, \cdots, X_m^i\}, i = 1,2,\cdots,m.$$

Step 4.Construct membership functions $g_{ij} = \exp\{-\frac{(d_{ij} - \overline{d}_i)^2}{\sigma_i^2}\}$, where

$$\sigma_i^2 = \frac{1}{n-1}\sum_{j=1}^{m}(d_{ij} - \overline{d}_i)^2 \text{ and } \overline{d}_i = \min\{S_i\}.$$

Step 5.Calculate the fuzzy center with respect to $i$-th sample and denote them by $C_i = \{c_{i1}, c_{i2}, \cdots, c_{in}\}$, where $c_{ij} = \dfrac{\sum_{k=1}^{m} g_k x_{kj}^i}{\sum_{k=1}^{m} g_k}$, $i = 1,2,\cdots,m,\ j = 1,2,\cdots,n$.

Step 6.Calculate the value of the threshold

$$\theta = \frac{\sum_{i=1}^{m}\sum_{j=1}^{m}\sqrt{(c_{i1}-c_{j1})^2 + (c_{i2}-c_{j2})^2 + \cdots + (c_{in}-c_{jn})^2}}{m^2 - m},$$

specially, $\theta = \dfrac{\sum_{i=1}^{m}\sum_{j=1}^{m} | c_i - c_j |}{m^2 - m}$, if $n = 1$.

Step 7. Split or merge regional clusters.

In our algorithm, Step 1 depicts the similarity to the threshold of the image by a similar distance. This make our algorithm need not provide the cluster number with the lack of the priori knowledge and avoid the influence of the initial value. Step 4 can escape from the affected of the singular values by defining the membership function as $\exp(-\dfrac{(x-\mu)^2}{\sigma^2})$. Step 7 can make the algorithm insensitive to the order of input samples by merging clustering algorithm.

## Two numerical experiments

### A numerical experiment of FCM

We choose ten 2-dimensional samples as in Table 1 and cluster the data by FCM.

Table1 Ten 2-dimensional samples

| Sample | $X_1$ | $X_2$ | $X_3$ | $X_4$ | $X_5$ | $X_6$ | $X_7$ | $X_8$ | $X_9$ | $X_{10}$ |
|---|---|---|---|---|---|---|---|---|---|---|
| $x_1$ | 0 | 0.5 | 0 | 0.5 | 1.5 | 1.5 | 2.5 | 2.5 | 3 | 3 |
| $x_2$ | 0 | 0 | 1 | 1 | 0 | 1 | 0 | 1 | 0 | 1 |

As FCM need the number of clusters, we test FCM by setting the number of clusters as 2. The result is shown as in Figure 1.

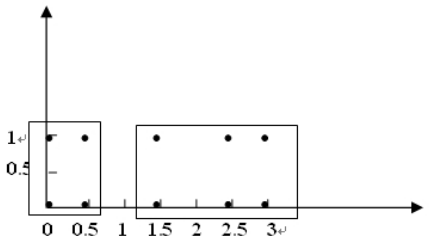


Fig 1 FCM (with 2 clusters)

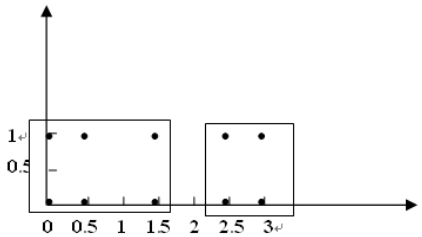


Fig 2 Change in the inputting order

The above numerical experiment shows that we can use FCM to cluster according to the given cluster numbers. If we change the inputting order of the data (see Figure 2), we get the different results, which means that the FCM depends on the order of the inputting of the data.

### A numerical experiment of the new algorithm

FCM depends on the given cluster number. But in general, we can not always know in advance except that we can have a thorough understanding of the data. The proposed method does not need to provide

the cluster number. It can cluster the dada by setting the threshold. Moreover, it does not depend on the inputting order. Next we show the improvement by an actual image example.

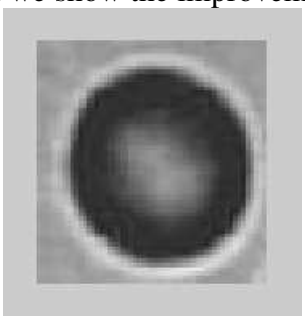

Fig 3 Original image

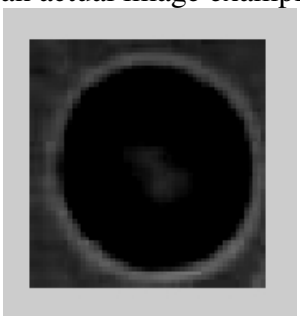

Fig 4 Fuzzy center

The images after segmentation：

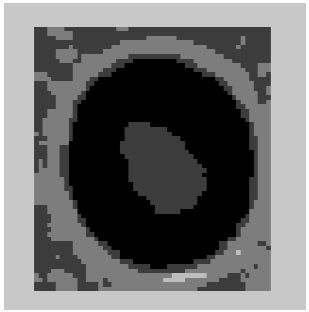

Fig 5 FCM (with 4 clusters)

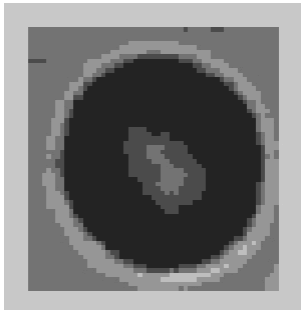

Fig 6 Results of the our method

## Conclusions

In this paper, we propose a weighted fuzzy threshold algorithm based on fuzzy relations. Compared with the existing clustering algorithms dealing with image segmentation, our algorithm can sharp the impact of singular value to the threshold of the image and strengthen the impact of the similarity to the threshold of the image. But with different forms of the membership function, we may get different results. In the future, the algorithm may be improved in this aspect.

## Acknowledgment

This work was financially supported by the Liaoning Provincial Natural Science Foundation of China Under contract No.201102015, the College Scientific Research Projects, Department of Education in Liaoning Province under contract No. L2013209, and the Fundamental Research Funds for the Central Universities Under contract No. 3132013332. The work was also financially supported by the Fundamental Research Funds for the Central Universities.

## References

[1] Zhiwei Ben, Yunjie Zhao, in: Computer Applications and Software, Vol.27 (2010), p.11. (In Chinese).

[2] Juan Bu, Xiangyang Wang, Yifeng Sun, in: Journal of Image and Graphics, Vol.13 (2008), p.1837. (In Chinese).

[3] Jun Tian, Yongxuan Huang, Yalin Yu, in: Pattern Recognition and Artificial Intelligence, Vol.21 (2008), p.221. (In Chinese).

[4] Chaira T, Ray A K, in: Pattern Recognition Letters, Vol.24 (2003), p.1837-1844.

[5] Chaira T, Ray A K, in: Appl, Soft Comput, Vol.8 (2008), p.919-927.

[6] Guo X.J., Zhang H.H., Chang Z., in: ICIC Express Letters, Vol.3 (2010), p.1059.

*Applied Mechanics and Materials Vols. 580-583 (2014) pp 320-323*
*© (2014) Trans Tech Publications, Switzerland*
*doi:10.4028/www.scientific.net/AMM.580-583.320*

# COMPARISON ANALYSIS OF BUILDINGS SETTLEMENT, CALCULATED IN ACCORDANCE WITH RHEOLOGICAL PROPERTIES OF SOILS

## (basedon the geotechnicalconditions of St. Petersburg)

Astafyeva Ekaterina

Russia, Saint-Petersburg State Polytechnical University (Institute of Civil Engineering)

astafyeva.ekaterina@gmail.com

**Keywords:**foundation settlement, soft soils, soil models, Plaxis, Fem-models, rheological model, hardening soil model, field observations, monitoring

Soft soils are well represented as the foundation of buildings all over the world. Settlements of buildings that are built on soft soils are developing over decades and often uneven. This can cause structural damages to constructions and as consequence unplanned repairs or even collapses of buildings in general.

Tojustify the useof different modelsof soil mechanicsit is necessary to carry outtheir verification. Verification of the modelconsists of complianceto the simple laboratoryexperimentsand of theadequacy ofthe field tests description. And the most important thing is that theresults of calculations should be based oncomparison between series of field observations.The principaldifficulty ofcomparingcalculation resultswithfield observationsisthat the actualsoil deformationisdeveloping over a longtime, andmost of thecalculation methods are aimed to obtainfinite values ofdeformations. Comparison between dataof finite deformations and data of field observationsis not quite correct, because, asa rule, in-situ (field)observationsrecordedincompletedevelopment process of deformations but not only the final resultof settlement. Therefore, to comparethese calculationsand observations we should selectcalculation modelsthat canexamine the development ofdeformationsin time.

Based on the above, it is interesting to analyzethe applicability ofthe most commonengineeringmethodsandcalculation models ofthe soils that underlie different calculation programsused in practice.

### Geotechnical engineering software

For calculating settlement geotechnics usually use engineering methods described in the regulatory literature: SNiP[1] and SP [2](Russian norms), Eurocode[3] (EU norms) and standards of other countries.Calculations of buildings settlement are alsocan be done with use ofnumerical methods (software).Manysoftware products, such as«Plaxis», «Ansys», «Abaqus», «Fem-Models», are developed to studythe stress-strain state of grounds. Basically, theseprograms use thefinite element method.

Numericalmethods for determining in-timesettlement are basedon two types oftasks:

1) based onsolvingthe filtrationcomponents (the first type)[4];
2) based onthe rheological modelofsubgrade (the second type)[5].

For solving the first type tasksRussiangeotechnicalengineers usually use calculation software «Plaxis» and for solving tasks of the second type – software package «Fem-models».Mostoftento calculatebuildings settlement Russian engineersuseHardening Soil model(«Plaxis»),as well asElastoviscoplastic (rheological)model («Fem-models»). The Hardening Soil modelallows to estimateonly the finalsettlement,the rheological model – a development of the settlementintensityover time.

**Comparison analysis of settlement calculations: numerical orengineering methods?**

Several historicbuildings were selected in St. Petersburg (Russia): House of Soviets, Krylov State Research Centre. The data offield observationsover about pastseventyyears was collected [6]. For them were made calculations usingnumerical and engineeringmethods for determining in-timesettlement. Finally was made comparison analysis with field observations results.In this paper the House of Sovietsis considered.

Figures 1 and 2 present the main resultsof the calculation in software «Plaxis»for the House of Soviets.The figure 2 showsthat prolongedsettlement ofwesternwing is about 403 mm.

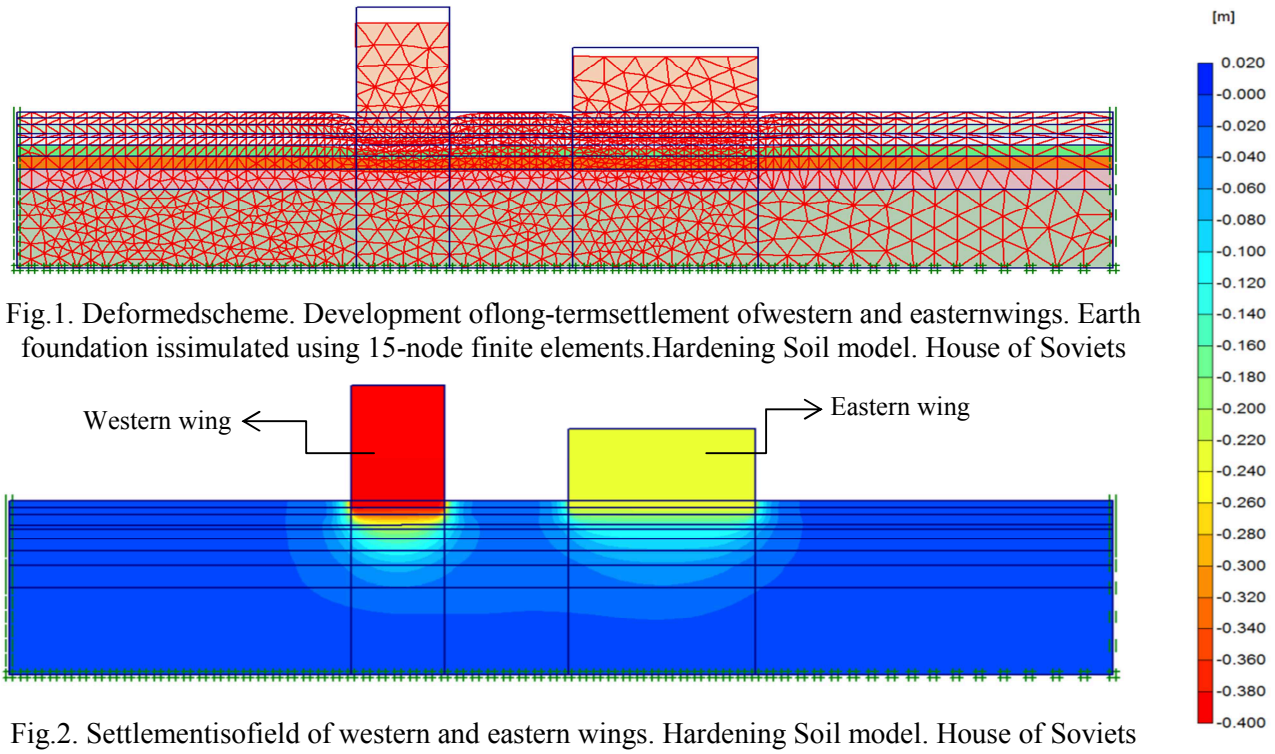


Fig.1. Deformedscheme. Development oflong-termsettlement ofwestern and easternwings. Earth foundation issimulated using 15-node finite elements.Hardening Soil model. House of Soviets




Fig.2. Settlementisofield of western and eastern wings. Hardening Soil model. House of Soviets

A figure 3 showsthe resultsof numerical method using software «Fem-models»[5] for the House of Soviets.Averagesettlement of the most loaded western wing is 398mm.

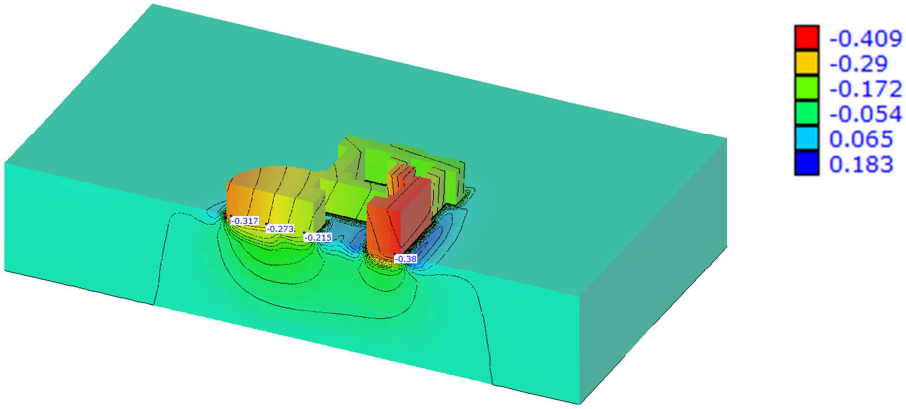


Fig.3. Settlementisofield (m) of the western andeastern wings. rheologicalmodel. House of Soviets

Figure 4 shows theoverlaygraphs of developmentin timesettlementof the western wingfor 70 years, which reached 398 mm in 1967 year,according tofield observationsandthe results ofa numerical calculationsbased onthe simulationofthe «Fem models»rheologicalmodel.

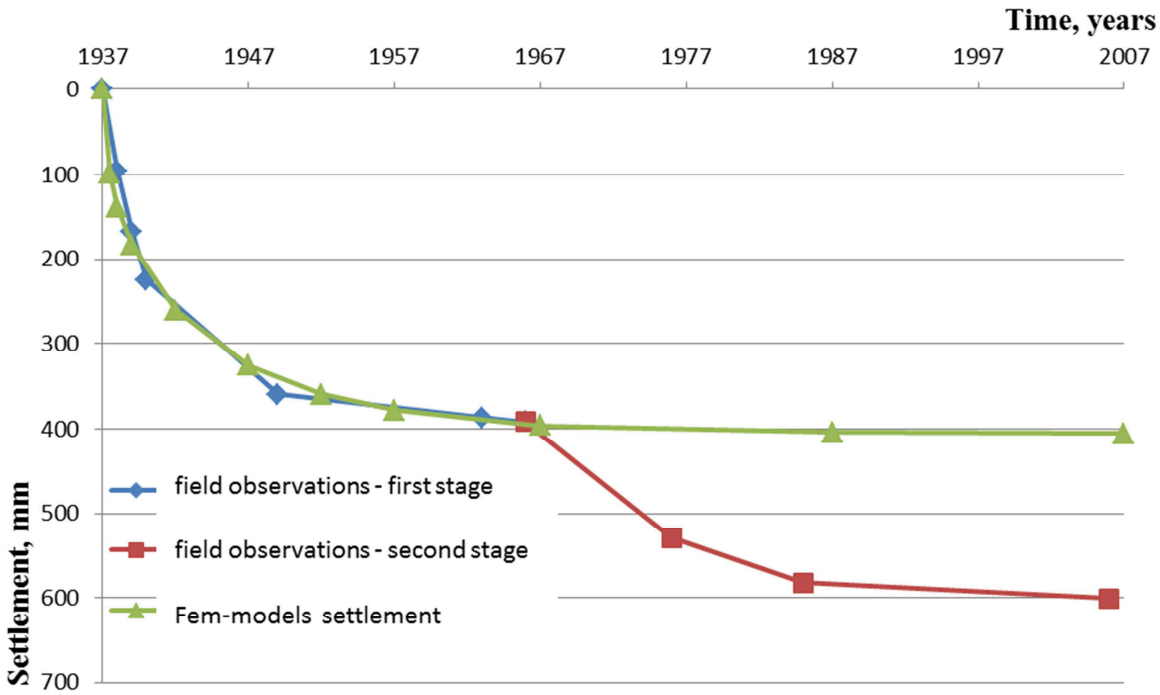


Fig. 4. Graphscomparingthe calculatedsettlement (mm) of the western wing with the results oflong-term observations. Calculationsare based on therheological model. House of Soviets

According to the figure 2and figure 4 following conclusions can be done:

1)The numerical forecast in «Fem-models» fairly accurately correlated with the datum of field observations thatwas 395 mm in 1967 (until possible anthropogenic impact due to which after 1967 the western wing precipitate was further developed).

2) Final settlementof 403 mm, calculated in «Plaxis», is sufficiently close to the observed long-term settlement.

3) Also it may be notedresults match of long-term settlement calculation using Hardening Soil model («Plaxis») and nonlinear Elastoviscoplasticmodel («Fem models»).In Hardening Soil model the developmentof the building settlementwas modeledwithdrainedconditions,in Elastoviscoplastic model–with undrainedconditions.In both cases,identicalresultsare due to the ratherlowshearmoduliof weakclay soils.

Engineering calculations results of final settlement of the western wingwere made using different methods:

1) 360 mmbySNIP 2.02.01-83* [1];
2) 301 mm bySP 22.13330.2011[2];
3) 358 mm by method Egorova [1];
4) 371mm by Eurocode 7 [3].

Results of engineering calculations show thatcurrent standards of engineering calculation methods underestimate the final settlement on more than 10%.

## Conclusions

Usinglong-situ observations in researchis essential, as it allows to evaluate the accuracyof geotechnicalpredictionsusing differentmodelsof soil mechanics:

1) In the case of use «Plaxis» with Hardening soil model (drained working conditions) Russian geotechnics should consider a number offactors and constraints [7].Be aware that themodel was developedfor denseclay andsand soils. Use of Hardening soil modelwithoutcostlystabilometrictestsinvolves administeringactuallyequal tothe shear modulus$E_{50}$odometer$E_{oed}$,thatis not the sameforsoft soils. In addition, deformation modules given in geotechnical investigations reports by Russian geologists are artificially led to the results of stamp tests using coefficient Agishev. Using"table" deformation modulescan belogical forengineering calculationsof settlement, but the use of suchmodulesinnumerical methodsis incorrectbecause it unreasonablyoverstatesthe shearmodulusand, consequently,reduces thesheardeformationdeviatorpart, which in turnreduces the overalldeformationof the soilarray. Accountingof thesefeaturesHardening soil modelprovides a goodconsistency withlong-situ observations.

2)Viscoelastoplasticmodel («Fem-models»), giventhe actual valuesof shear deformationunderundrainedsoilconditions,can achieve results which arecloseto collected innatural conditionsdeformation of buildingsconstructedon soft soils.

3) Engineering calculating methods are not accurate. They need to be deeply researched and developed.

It is necessary to develop existing rheological models which taking into accountlong-termsheardeformationandrelaxation coefficientson the basis of verification between field observations data.

## References

[1] SNiP 2.02.01-83* Foundations of buildingsand structures. Moscow.: Stroyizdat, 1986 – 45 s. (rus)

[2] SP 22.13330.2011 Foundations of buildingsand structures. – Moscow.:2011 – 161 s. (rus)

[3] EN 1997-1: Eurocode 7: Geotechnical design –Annex F

[4] R.B.J. Brinkgreve, editor. Plaxis, 2D Version 8. AA. Balkema, 2002

[5] Shashkin A.G. Vyazko-uprugo-plasticheskaya model povedeniya glinistogo grunta. Magazine of Reconstruction of historical cities and geotechnical engineering. St-Petersburg. 2011. No13. pp.174-205 (rus)

[6] TsytovichN.A., PolyakovA.P., YevgenyevN.S. Report about soils and foundationssettlements researchesofVolodarskogoHouseof Sovietsin Leningrad– Leningrad.:1939 – 44 p. (rus)

[7] T. Schanz, P.A. Vermeer, and P.G. Bonnier. Beyond 2000 in Computational Geotechnics, chapter Fotmulation and verification of the Hardening- Soil Model, pages 281-290. Balkema, Rotterdam, 1999

*Applied Mechanics and Materials Vols. 580-583 (2014) pp 324-328*
*© (2014) Trans Tech Publications, Switzerland*
*doi:10.4028/www.scientific.net/AMM.580-583.324*

# Stability Analysis of Jinghua Gypsum Mine golf in Jingmen city

Congxin Chen, Kaizong Xia, Yuanbin Dong,
Xiumin Liu, Pinglu Huang

（State Key Laboratory of Geomechanics and Geotechnical Engineering, Institute of Rock and Soil Mechanics, Chinese Academy of Sciences, Wuhan 430071, China）

Xiakaizong1988@sina.com

**Keywords:** Mining engineering, underground mining, Gypsum mine, golf, Stability

**Abstract.** According to golf's distribution and occurrence situation of Jinghua Gypsum Mine circumstances in Jingmen city, The golf is divided into general golf, filling golf, then the stability of column and covering layer of the two kinds of golf are analysed. It is shown that: For the general golf, A large range of column is stable within a relatively short period of time in the process of underground mining. it will be unstable for local small column because of it was bore weight of overlying strata. After the column was soaked, its strength will be greatly reduced, and the long term stability of column will not be guarantee. Complementary, the covering layer is basically critical stable state; For the filling golf, A large range of column is stable, and the covering layer is also basically critical stable state. It can promote the control of mining disaster and the protection of ecological environment and similar engineering with a high theoretical and practical value.

## Introduction

The formation of the geological strata structure is changed caused by underground Mining, including drainage and the stress state, which exceeds he natural resilience of the environment, and its impact was far beyond the scope of time and space mines exist. The goaf caused by underground mining is the potential geological disasters [1-4].

Jinghua gypsum mine is located in Hua Zhu Cun of the former Dongbao area Bai Miao Jie, designed annual production capacity is 150000 t in 1982, and the mine design life is 28.64 years, and the mining is due at September 2011.While the relevant departments is no extension. Jinghua Gypsum Mine Gob approximately 0.6 square kilometers, the vertical depth is 70-150 meters from the ground. The golf area caused by mining is large, so it is extremely difficult to deal the golf and restore the geological environment.

## The classification of golf

According to golf's distribution and occurrence situation of Jinghua Gypsum Mine Gob circumstances in Jingmen, The golf is divided into general golf, filling golf

### 2.1 the general golf

When the ore is exploited from the underground mining, no filling or caving process, also did not appear obvious roof fall accident in goaf. According to the relevant data and field survey, the general golf is about 126800 $m^2$ in Jinghua gypsum mine.

After the research of main column and rooms in filling golf of Jinghua gypsum mine,the survey result is described in the following: the general golf of Jinghua gypsum mine(X group), the maximum column is 8.8×5.9m and the minimum is 4.4m×2.2m, so 5.9m×4.3m is regarded as the average size. The maximum space between column is 8.2m×7.9m and the minimum space is 6.0m×3.2m ,so 7.5m×6.0m is regarded as the average space. The maximum height is 9.1m and the minimum height is 6.9m, so 8.0m is regarded as the average height. In consideration of the irregular column size, 5.0m×4.0m is regarded as effective size of column, 8.0m×7.0m is regarded as average space and 8.0m is regarded as average height.

The irregular column or small column in general golf of Jinghua gypsum mine is shown in Figure 1.

Fig.1 The irregular column or small column in ordinary golf of Jinghua gypsum mine

**2.2 the Filling golf**

If the golf is filled by waste rock after mining, calling the filling golf. Relevant information and field surveys show the filling golf total area is about 37,000 $m^2$ in Jinghua gypsum mine, which are mainly distributed in 310,311,312 mining area

After the research of main column and rooms in filling golf of Jinghua gypsum mine, the survey result is described in the following: the filling golf of Jinghua gypsum mine(X group), the maximum column is 6.5m×5.0m and the minimum column is 6.3m×3.0m ,so 6.6m×3.8m is regarded as the average size. The maximum space between columns is 8.2m×7.9m and the minimum space is 6.1m×5.5m, so 7.3m×6.6m is regarded as the average space. The maximum height is 5.0m and the minimum height is 4.0m, so 4.7m is regarded as the average height. In consideration of the protective effect to column by waste rock, 6.0m×4.0m is regarded as effective size of column, 7.0m×6.5m is regarded as average space and 4.5m is regarded as average height.

**Stability analysis of golf**

Surface stability of golf at gypsum mine depends on the stability of column and overlying. Based on the results of the stability study have been made in column, stability is determined by several key parameters in the following:

**3.1 Stability analysis of general golf**

Golf surface stability in gypsum mine depends on the stability of column and overburden [5-8]. Therefore, based on the stability results of the study have been made in golf, stability is determined by two key parameters in the following.

**3.1.1 Stability analysis of column**

When using the room and column method of mining, column strength on the stability of golf plays a big role. Slightly inclined ore and column calculation method is used to estimate the stability of golf. column's relative area of the mine should satisfy the following formula:

$$S_0 / S \geq \gamma hnk / \sigma_0 k_f \tag{1}$$

where $S$ —area of column support($m^2$); $S_0$—column cross-sectional area ($m^2$); $k$—load factor, and relate to the rock property, according to the characteristics of gypsum mine, reference information, take = 1; $\sigma_0 k_f$—uniaxial compressive strength of ore cube specimen(MPa); $n$—safety factor when the column without long-term retention, take 2 to 3, the surface does not allow collapse or require column long-term retention, take 3-5; $k_f$ — column shape factor; $\gamma$—Overburden density; $h$—depth from golfto surface (m).

Safety factor can be obtained when given the size of column and room.

$$n=\frac{S_0}{S}\times\frac{\sigma_0 k_f}{\gamma hk}=\frac{S_0}{S}\times\frac{R_C}{\gamma hk} \tag{2}$$

In consideration of the exist of argillaceous siltstone in the mine roof and its strength is lower than ore, so the compressive strength of the mine roof written as $R_c$ is selected to replace $\sigma_0 k_f$. According to survey data, take $\gamma$=24 $KN/m^3$; $k$=1; $R_c$=27.6Mpa; $h$=40～119m.

Research result shows that in golf of Jinghua gypsum mine(X group), the maximum column is 8.8×5.9m and the minimum column is 4.4m×2.2m ,so 5.9m×4.3m is regarded as the average size. The maximum space between columns is 8.2m×7.9m and the minimum space is 6.0m×3.2m ,so 7.5m×6.0m is regarded as the average space. The maximum height is 9.1m and the minimum height is 6.9m ,so 8.0m is regarded as the average height. In consideration of the irregular column size ,5.0m×4.0m is regarded as effective size of column, 8.0m×7.0m is regarded as average space and 8.0m is regarded as average height.

Thus can calculated the minimum cross-sectional area accounted for 8.5 percent of the column supporting area,and with an average of 14.0 percentage in golf at Jinghua gypsum mine. According to the above formula, the average safety factor range is from 1.4 to 4.0 , and the minimum safety factor is 0.8.

Relevant research results show that the strength of saturated gypsum mine will be greatly reduced, softening coefficient is about 0.8, strength reduction factor due to the rheological is 0.66, thus the average long-term safety factor range is from 0.7 to 2.1, the minimum safety factor is 0.4.

This shows that in the majority golf column in the underground mining process is stable within such a relatively short period of time, some small column can not bear the weight of overlying rock will be unstable. After the underground golf of a certain time, especially after the column saturated, its strength will be greatly reduced, long-term stability of the column will not be protected.

### 3.1.2 Stability analysis of covering layer

Shown in Figure 2, the overlying rock abdc will sink due to gravity after mining, and both sides of the wedge abm and cdn also impose its horizontal pressure force written as P, so friction resistance effect produced by P is happened in planes written as ab and cd, now unit length in mining area (gateway) is taken as the calculational unit body, so the pressure written as Q which is acted on the unit length of the roadway roof is:

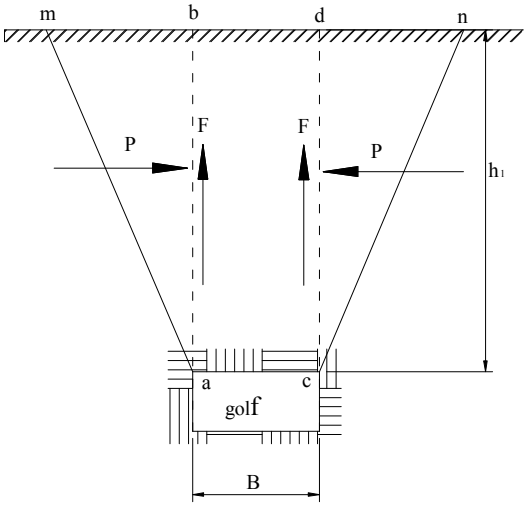


Fig.2 Schematic of depth calculated from golfroof to the surface

$$Q=G-2F \tag{3}$$

Where $G=B\gamma h_1$; $B$-tunnel width(m); $h_f$—depth from roof to the surface(m); $\gamma$-unit weight of overburden,KN/$m^3$.

$$F=p\cdot\tan\Phi \tag{4}$$

Where $p$ - compressive stress in the ab plane or cd produced by wedge abm and cdn; $\Phi$ -Angle of internal friction of rock.

When $p$ is taken as its maximum:

$$P = \frac{\gamma \cdot h_1^2}{2} tg^2(45^\circ - \frac{\Phi}{2}) \tag{5}$$

So $Q = B\gamma h_1 - \gamma h_1^2 tg(45^\circ - \Phi/2)tg\Phi$

From the above equation, when h1 large to a certain depth, the rock layer above the roof can maintain balance and not collapse, at this time $Q$ is zero and $h_1$ is named critical depth written as $h_0$:

$$h_0 = \frac{B}{tg^2(45^\circ - \Phi/2)tg\Phi} \tag{6}$$

The stability of roof can be evaluated by critical depth $h_0$ .When $h_0 < h_1 < 1.5\,h_0$ , the stability of roof is worst; when $h_1 > 1.5\,h_0$ ,the roof is in stable condition.

At Jinghua gypsum mine, the overlying strata of golf are mainly composition by silty mudstonepelitic pelitic siltstone and surface dust producted in Quaternary, as the largest thickness come from siltstone and its friction resistance and weight takes the largest proportion, so siltstone's friction angle written as $\Phi$ is selected. According to related date , $\Phi$ =48.5° ; This formula applies to the stability calculation of the roadway and the roof of golf which is supported bu strip column , due to Jinghua gypsum mine is supported by the point column, so mining width B is selected as 8m which is larger than ordinary ,and $h_0$ = 50m can be obtained when the parameters taken into the above formula. This means when the depth from golfroof to the surface , $h_1$ >75, the roof is stable.

On Jinghua gypsum mine overburden's thickness is 40 ~ 119m, the overburden in golf is in the critical stability condition.

### 3.2 Stability analysis of covering layer of filling golf

#### 3.2.1 Stability analysis of column

After the research of main column and rooms in filling golf of Jinghua gypsum mine, the survey result is described in the following: in filling golf of Jinghua gypsum mine(X group), 6m×4.0m is regarded as the average size; 7.0m×6.5m is regarded as the average space; 4.5m is regarded as the average height and 82~96m is regarded as the depth between golf to the suffice.

Thus can calculated the minimum cross-sectional area accounted for 14.9 percent of the column supporting area,and with an average of 17.3 percentage in the golfat Jinghua gypsum mine. According to the above formula, the average safety factor range is from 2.1 to 2.4 , and the minimum safety factor is 1.8.

Relevant research results show that the strength of saturated gypsum mine will be greatly reduced, softening coefficient is about 0.8, strength reduction factor due to the rheological is 0.66, thus the average long-term safety factor range is from 1.1 to 1.3, the minimum safety factor is 1.0.

So we can make the conclusion that mainly columns in filling golf is safety.

#### 3.2.2 Stability analysis of rocky covering of filling golf

The depth written as $h_0$ between roof and the surface of earth is called critical depth, when the rocky overburden can maintain its balance and not collapse, in addition, Q is just equal to zero.

$$h_0 = \frac{B}{tg^2(45^\circ - \Phi/2)tg\Phi} \tag{7}$$

The roof's stability can be evaluated by critical depth. When $h_0 < h_1 < 1.5\,h_0$ ,the stability of roof is worst ; when $h_1 > 1.5\,h_0$ ,the roof is in stable condition.

At Jinghua gypsum mine, the overlying strata of golfare mainly composition by silty mudstonepelitic pelitic siltstone and surface dust producted in Quaternary, as the largest thickness

come from siltstone and its friction resistance and weight takes the largest proportion, so siltstone's friction angle written as $\Phi$ is selected. According to related date , $\Phi$=48.5° ; This formula applies to the stability calculation of the roadway and the roof of golf which is supported bu strip column , due to Jinghua gypsum mine is supported by the point column, so mining width B is selected as 7m which is larger than ordinary ,and $h_0$ = 43m can be obtained when the parameters taken into the above formula. This means when the depth from golfroof to the surface , $h_0$>65, the roof is stable.

On Jinghua gypsum mine overburden's thickness is 82 ~ 96m, the overburden in golf is in the critical stability condition.

## Conclusions

After studying this article, the following conclusions can be drawn:

(1) According to golf's distribution and occurrence situation of Jinghua Gypsum Mine Gob circumstances in Jingmen, The golf is divided into general golf, filling golf

(2) For the general golf, A large range of column is stable within a relatively short period of time in the process of underground mining . it will be unstable for Local small column because of it was bore weight of overlying strata. After the column was soaked, its strength will be greatly reduced, and the long term stability of column will not be guarantee. Complementary, the covering layer is basically critical stable state.

(3)For the filling golf, A large range of column is stable, and the covering layer is also basically critical stable state

## Acknowledgements

This work was financially supported by the National Natural Science Foundation of china (No. 51274188)

## References

[1] Guoqing He, Lun Yang, Tigeng Ling, et al. Mining subsidence school [M]. Xuzhou: China University of Mining Press, 1991.( In Chinese)

[2] Zhipan He. stability analysis and control technology research Mined areas under the new highway [Master thesis][D]. Chasha: Central South University, 2004.( In Chinese)

[3] Lizhen Shi. study on stability of placer gold goaf in Ludila hydro power station after Storing the Water [Master thesis][D]. Chendu: Chengdu University of Technology, 2008.( In Chinese)

[4] Liyuan Tong, Yu Song, YuQiu, et al. Current research state of problems associated with mined-out region under expressway and future development. Chinese Journal of Rock Mechanics and Engineering, 2004, 23(7): 1198-1202.( In Chinese)

[5] Jiangteng Li. Study on instability and time dependence of pillar in hard rock mass [Master thesis][D]. Chasha: Central South University, 2006.( In Chinese)

[6] Peipei Chen, Hongquan Liu. Determination of water proof rock pillar height with the top coal caving under sea [J].Journal of China Coal Society, 2009, 34(7): 875-880.( In Chinese)

[7] Chun'an Tang, He Qiao, Xiaohe Xu, et al. Numerical simulation on pillar failure and associated acoustic emissions[J]. Journal of ChinaCoal Society, 1999, 24(3): 266-269.( In Chinese)

[8] Changyou Xu. Mining from Open Pit to Underground [M]. Wuhan: Wuhan University of Technology Press, 189.( In Chinese)

*Applied Mechanics and Materials Vols. 580-583 (2014) pp 329-333*
*© (2014) Trans Tech Publications, Switzerland*
*doi:10.4028/www.scientific.net/AMM.580-583.329*

# Study on deformation property of coarse particles (sulfate) saline soil with field test

Peng Yang[1, a], Yafeng Liu[2,b], Haizhen Mi[3,c], Yanpeng Zhu[4,d]

[1]Lanzhou University of Technology, Lanzhou, china, 730050

[2]Electric Power Design Institute of Gansu Province, Lanzhou, china, 730050.

[3]Lanzhou University of Technology, Lanzhou, china, 730050

[4]Lanzhou University of Technology, Lanzhou, china, 730050

[a]y491016333@163.com, [b]zhoushur@yahoo.com.cn, [c]Mihz@lut.com, [d]Zhuyp@lut.com

**Keywords:** Coarse particles saline soil, Field test, Salt content, Salt expansion rate.

**Abstract.** Salt expansion was the main diseases of the salty foundation. In order to study the deformation regularity and quantitative description of coarse particles saline soil ground in natural condition, a field test was conducted in Dunhuang area. The exploratory well with 7.5 m depth (deeper then annual temperature change layer) was excavated on site, and the data of salt content \water content \ground temperature \salt expansion rate were collected. From the test it was found that : salt expansion mainly decided by salt content, salt content and salt expansion rate have approximately a quadratic function relationship; the minimum salt content could cause soil expansion is 1.5‰; The salt expansion force was strong, and the gravitational stress could not suppress the deformation.

## Introduction

A lot of construction projects in the Hexi corridor region face the salt expansion deformation problem. In earlier years, the investigation of the engineering properties of this kind ground was not very deep. But now with higher safety standard, the issues of salt expansion became more and more important. We had known that the salt expansion amount of coarse saline soil after repeated freeze-thaw cycles was less than fine-grained soil in an open system[1], and the salt expansion amount was not only associated with the dry density and water content of soil, but also with the pressure and the content of fine particles[2.3], and the sensitive temperature of salt cementation layer between 3~7 $^{o}$C and 12~15 $^{o}$C, but for the loose soil, the sensitive temperature between 0~-7 $^{o}$C [4], and the sand layer exist was very important to form the salt cementation layer[5], and so on. These studies used indoor simulation experiments mostly, and lack field measurement for verification. In order to study the engineering properties of coarse saline soil and quantitative evaluate its characteristics, it was necessary to take in-site experiments. The authors took an in-site experiment in Dunhuang area in winter (from October 19, 2011 to March 7, 2012) and measured the salt expansion amount of ground. It was found that some regularity and quantitative description of salt expansion deformation.

## The condition of experiment

### Purpose and test methods

This experiment aimed to study the salt expansion regularity of coarse particles saline soil. During the test, water content, salt content, ground temperature and salt expansion rate were measured to study the relationship among them.

First of all, a 1.2 m diameter, 7.5 m depth exploratory well was excavated in ground. The schematic of exploratory well was shown in Fig.3, and the stratigraphic column was shown in Fig.4**.** A settlement observation stick placed in the center of well which did not move in vertical. Meanwhile, the horizontal observations sticks were set at different depths to measure the salt

expansion amount of each soil layer. The moisture meter and ground temperature gauge were set next to horizontal observations sticks.

The observation stick used in experiment was $12\times10^{-3}$ m diameter galvanized pipe, and the ground temperature gauge wasYH5000 temperature gauge, and the moisture meter was ST-TW moisture meter.

In order to ensure the compactness and humidity of the soil filled in well was similar with undisturbed soil, we took some watering when fill back.

**Salt and water conditions of the test site**

The ground was divided into eight layers in depth corresponding to the location of observation stick. The soil parameter of each layers was shown in Table 1.This kind of foundation (gravel) had a high permeability, so the content of water was low (most of samples less than 8%), the curve of water content and salt content along depth direction is shown in Fig.1 and Fig.2. From the literature we knew that it could not have frost heaving under this water content. All expansion deformation was caused by salt expansion.

**Tabel.1 The average salt content and water content of the original ground**

| sequence | interval [m] | Anion content [mg·kg$^{-1}$] | | | | Action content [mg·kg$^{-1}$] | | | | salt content [‰] | Water Content [%] |
|---|---|---|---|---|---|---|---|---|---|---|---|
| | | $CO_3^{2-}$ | $HCO_3^-$ | $SO_4^{2-}$ | $Cl^-$ | $Ca^{2+}$ | $Mg^{2+}$ | $Na^+K^+$ | $NH_4^+$ | | |
| 1 | 0.1~0.5 | 0 | 178 | 2706 | 569 | 914 | 68 | 554 | undetected | 4.95 | 7.62 |
| 2 | 0.5~1.0 | 0 | 176 | 2434 | 176 | 710 | 61 | 414 | undetected | 3.94 | 4.02 |
| 3 | 1.0~1.5 | 0 | 172 | 2031 | 124 | 569 | 63 | 345 | undetected | 3.33 | 3.88 |
| 4 | 1.5~2.0 | 0 | 160 | 1625 | 18 | 446 | 67 | 211 | undetected | 2.55 | 4.7 |
| 5 | 2.0~3.0 | 32 | 205 | 821 | 87 | 70 | 18 | 436 | undetected | 1.60 | 3.76 |
| 6 | 3.0~4.5 | 18 | 168 | 1047 | 124 | 236 | 34 | 324 | undetected | 1.97 | 5.63 |
| 7 | 4.5~6.0 | 16 | 183 | 1542 | 267 | 370 | 30 | 512 | undetected | 2.91 | 3.47 |
| 8 | 6.0~7.5 | 16 | 189 | 1369 | 302 | 423 | 36 | 381 | undetected | 2.70 | 3.32 |

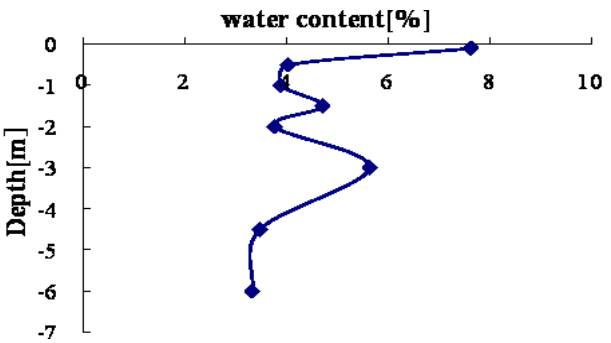


Fig.1 Natural water content curve with the depth

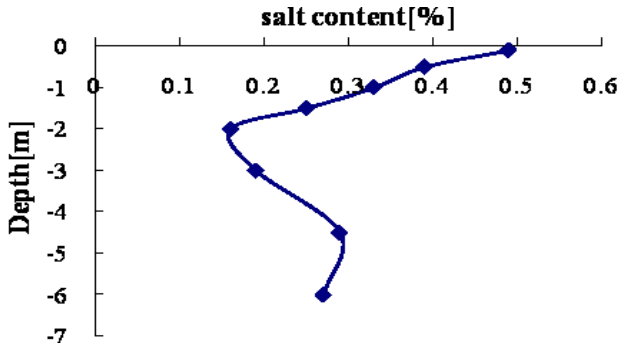


Fig.2 Natural salt content curve with the depth

## Experimental procedure and data

### The condition of ground temperature

The ground temperature curves of each depth were shown in Fig.5. We could know that, 6.0 m depth strata temperature change less than 0.6 $^{o}$C in whole winter, and the depth of zero annual amplitude was about 7.5 m. The minimum temperature of 0.1 m depth was -6.1 $^{o}$C and frozen depth in this region about 1.0 m. The Surface of foundation was frozen about 82 days in winter.

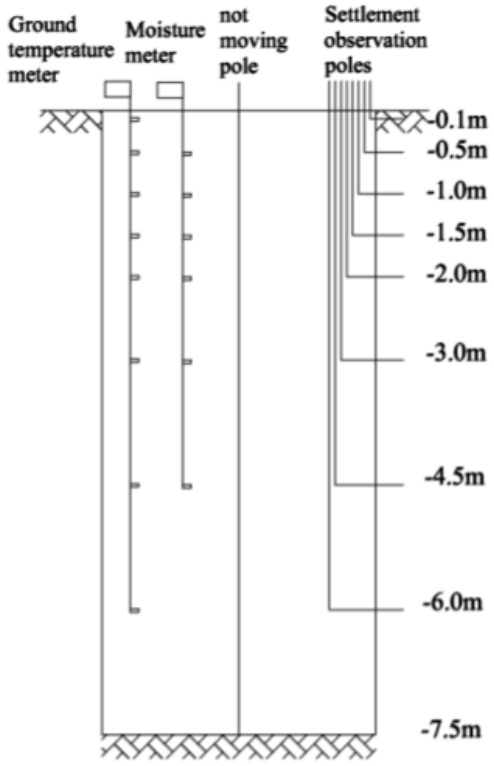


Fig.3 Schematic diagram of exploratory well

| Sequence | Thickness /m | Interval /m | Stratigraphic column | Stratigraphic description | Note |
|---|---|---|---|---|---|
| 1 | 0.4 | -0.1~-0.5 | | Gravel: grey , rounded, particle size 5~20mm, | there are six salt cementation layers in the exploratory well and located at -0.1m -0.3m、-0.6m -1.4m、-1.6m -1.8m。the thickness of salt cementation layer between 30~100 mm. |
| 2 | 0.5 | -0.5~-1.0 | | Sand : dry, dense. | |
| 3 | 0.5 | -1.0~-1.5 | | Gravel: gray, Secondary rounded. | |
| 4 | 0.5 | -1.5~-2.0 | | Sand : dry,dense . | |
| 5 | 1.0 | -2.0~-3.0 | | Gravel: gray, Secondary rounded. Sand : dry,dense . | |
| 6 | 1.5 | -3.0~-4.5 | | Gravel: gray, Secondary rounded. Sand : dry,dense . Gravel: grey ,Secondary rounded, Mixed with some stone. | |
| 7 | 1.5 | -4.5~-6.0 | | Sand : dry,dense . Gravel: grey Secondary rounded, Mixed with some stone. | |
| 8 | 1.5 | -6.0~-7.5 | | Sand : dry,dense Gravel: grey ,Secondary rounded, Mixed with some stone. | |

Fig.4 Stratigraphic column

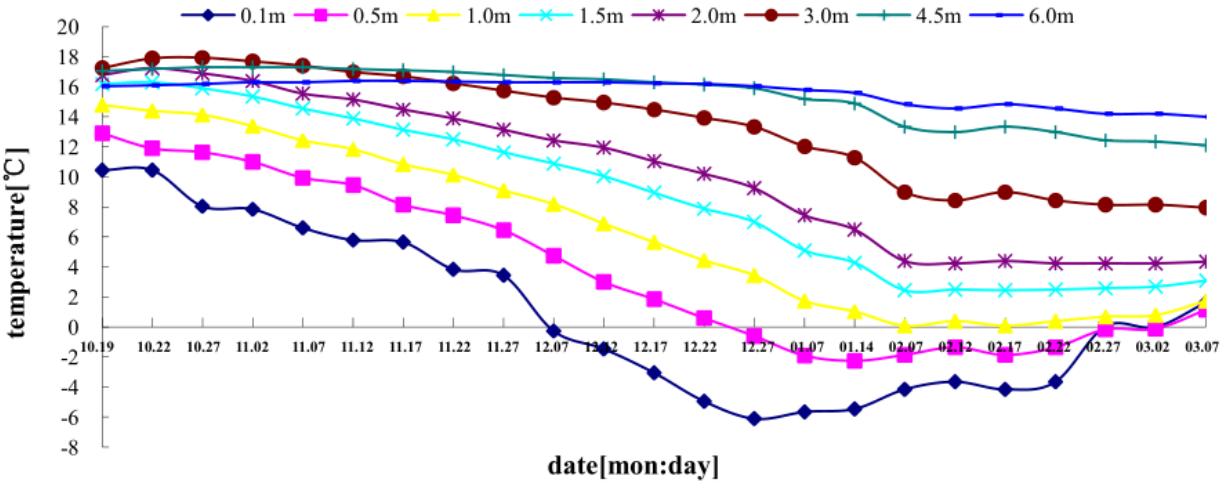


Fig.5 Ground temperature curve

**The effect of salt content on salt expansion rate**

22 group data of strata expansion amount were recorded during the whole experiment period, and the results was shown in Fig.6. Based on above data, we got the average salt expansion amount and salt expansion rate of each stratum which shown in Fig.7 and Fig.8. The amount of salt expansion deformation of every stratum increased in winter. Especially, the expansion amount of 0.5 m and 4.5 m depth were the most prominent. So the curve of salt expansion looks like a bow. This phenomenon was related to the salt content. It proved that salt content, which directly decided the amount of expansion, was the most important affecting factor of expansion deformation. And the temperature, which was the secondary affecting factor, became lower could induce crystallization and expansion among soil particles.

The salt content of 4.5 m depth was more than 2.0 m depth, so it caused the amount of salt expansion was more than 2.0 m depth. But in the later days, the surface ground temperature became lower and lower, so more and more salt migrated from deep to shallow of ground, which was why the expansion amount of 2.0 m depth continued to grow subsequently.

The relationship between salt content and salt expansion rate was shown as formula1 and Fig.9. According to formula **1** we could calculate the minimum salt content of coarse particles saline soil. The minimum salt content of coarse particles saline soil is about 1.5‰, and it was lower than fine-grained soil.

$$\eta=0.4889(\omega)-0.1466 . \quad (1)$$

note：η——salt expansion rate[%].

ω——salt content [‰].

$R^2$——The correlation coefficient of polynomial，$R^2$=0.8043.

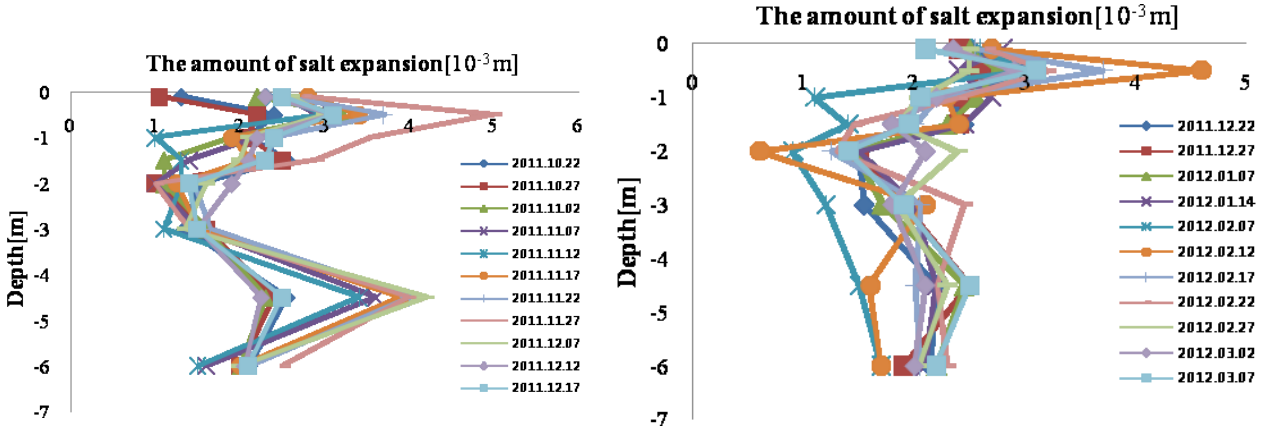


**Fig.6 The salt expansion curves of each stratum**

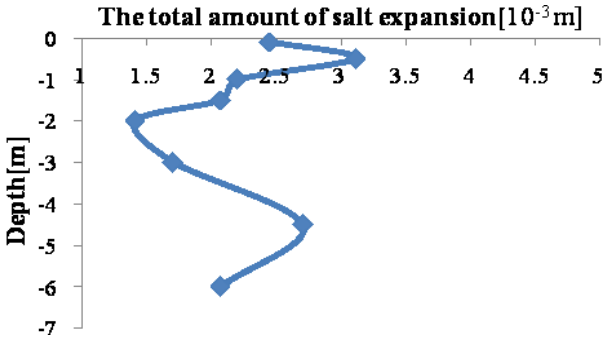


**Fig.7 Measured average salt content curve**

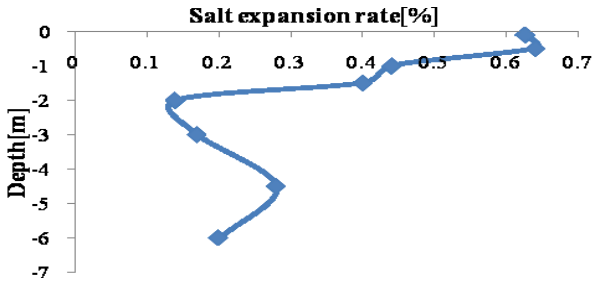


**Fig.8 Measured average salt expansion rate curve**

**The effect between water content and salt expansion rate**

Experiment simulated rainfall, and the amount of watering equivalent to the annual maximum rainfall in this region. According to the experiment recording we found that the rainfall could cause salt expansion indeed. The amount of salt expansion of each stratum increased after rainfall and the average expansion amount reached $2.04\times10^{-3}$ m. Especially, the salt expansion developed very fast in a short time after rainfall. After the water penetrates to deeper location, water content of foundation became lower, the speed of salt expansion slows down. It indicated that when water content was low, it just participated in the process of crystallization, but had almost no effect on the migration of salt. Under this condition, water barely causes salt migrated from deep to shallow. Therefore, water was a necessary condition of salt expansion, but it contribution depended on its amount.

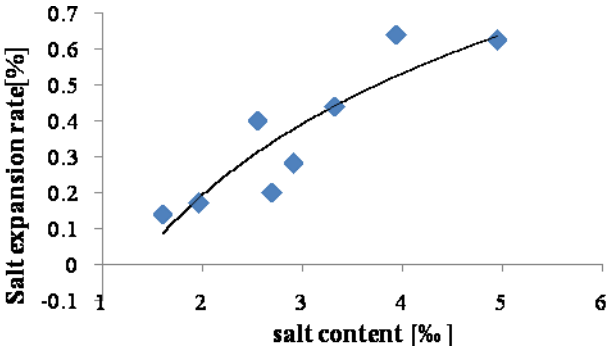


**Fig.9 The salt content and salt expansion rate curves**

## Conclusion

From this experimental observation and data analysis, we could know that:

1. Salt expansion problem does exist in coarse particles saline soil, but the expansion amount was very limited. This experiment discovered that the total expansion amount was about $6.9\times10^{-3}$ m within range of 7.5 m depth in ground. Though this expansion amount was limited, it would happen every year. So this kind of harm to projects will last forever. Meanwhile, this experiment discovered several salt-rich layers within range of 0.1 m~2.0 m depth in ground , it could be considered as direct evidence of salt migrated from deep to surface in ground. The salt migration would last in the future; it was shown that this problem was extremely complex.

2. From data analysis we could know that 1.5‰ salt content was the minimum salt content for coarse particles saline soil, which was lower than Fine- grained soil (almost 3‰~5‰).

3. For coarse particles saline soil, salt content was the most important factor affect salt expansion deformation. There was an approximately quadratic relationship between salt content and salt expansion rate. Water content was hardly affect salt expansion deformation when it was low, while water content increased immediately, the destruction showed a sudden increase in the amount of salt expansion.

4. Since the test conditions was limited, we could not measured the salt expansion force directly. But we measured the salt expansion deformation in 6.0 m depth in ground; it proved that the salt expansion force was very significant.

## References

[1] Hui Bing, Ping He. Experimental study of water and salt redistributions of saline soil with different freezing modes [J]. Rock and Soil Mechanics, 2011(8): 2307-2312.

[2] Shasha Zhang, Xiaohua Yang, Zhiren Dai. Freezing-thawing Cycles and Salt Expansion Test of Crude Coarse Grain Clay Salty Soil [J].China Journal of Highway and Transport, 2009(4): 28-32.

[3] Weixing Bao, Xiaohua Yang, Yongli Xie. Research on salt expansion of representative crude saline soil under freezing and thawing cycles [J]. Rock and Soil Mechanics, 2006(11): 1991-1995.

[4] Qingbai Wu, Tao Sun, Zhaoxiang Tao, Qiang Li. Experimental Studies on the Salt Expansion of Coarse Grain Saline Soils Under Constant Temperature[J]. Journal of Glaciology and Geocryology, 2001(3): 238-243.

[5] Xiangrong Yang, Yafeng Liu, Peng Yang, HaizhenMig. In-site test study on causes of cemented layer in hexi sandy saline (sulfate) land base [J], Journal of Engineering Geology, 2013(8): 535-539.

*Applied Mechanics and Materials Vols. 580-583 (2014) pp 334-337*
*© (2014) Trans Tech Publications, Switzerland*
*doi:10.4028/www.scientific.net/AMM.580-583.334*

# Study on the value range of horizontal ground stress in initial geostress field based on the Generalized Hoek - Brown criterion

Zhe Ou[1, a*], Congxin Chen[1,b], Hua Fu[1,c], Yichao Zhou[1,d]

State Key Laboratory of Geomechanics and Geotechnical Engineering, Institute of Rock and Soil Mechanics, Chinese Academy of Sciences, Wuhan, Hubei 430071, China,
[a]quqianzhekou@163.com, [b]cxchen@whrsm.ac.cn, [c]510125890@qq.com, [d]28926531@qq.com,

**Keywords:** Generalized Hoek-Brown criterion; initial geostress field; horizontal ground stress; calculation model of value range

**Abstract.** On the conditions that assuming vertical ground stress and horizontal ground stress are both principal stress, a calculation model of horizontal ground stress value range with depth change in initial geostress field is built by formula derivation, according to the Generalized Hoek-Brown failure criterion, and the reasonability of the calculation model is verified by the geostress measured value. The results show that, there is a good consistency at the distribution range of horizontal ground stress calculated value and horizontal ground stress measured value, it is proved that the the calculation model is reasonable. The calculation model gives new methods and thinking for evaluation of the initial geostress field.

## Introduction

Ground stress is the fundamental forces inducing geological disasters such as landslide, collapse, ground subsidence, rock burst and so on, especially when the balance of initial geostress field has been destroyed by rock mass excavation makes ground stress releasing. So, it has a important implications to prevention and control of geological disasters by a effective evaluation of initial ground stress field. Ground stress can be decomposed into vertical ground stress and horizonta ground stress, vertical ground stress can be estimated by the average unit weight of rock mass times the depth of rock mass [1], however, it is hard to estimate horizontal ground stress by such parallelapproach [2] . So, how to stimate horizontal ground stress is a key point in initial geostress field evaluation.

In this paper, a calculation model of horizontal ground stress value range with depth change in initial geostress field is built by formula derivation, according to the Generalized Hoek Brown failure criterion [3], and the reasonability of the calculation model is verified by the geostress measured value. The results show that, there is a good consistency at the distribution range of horizontal ground stress calculated value and horizontal ground stress measured value, it is proved that the the calculation model is reasonable. The calculation model gives new methods and thinking for evaluation of the initial geostress field.

## The Generalized Hoek-Brown criterion

Hoek and Brown bringed up the Hoek-Brown criterion at 1980[4], and it is widely used in giving joint rock mass strength parameters. The Generalized Hoek-Brown criterion bringed up by E. Hoek and so on, is a correction on the problems founded when the initial criterion has been using, and its specific expression is shown in Eq. 1:

$$\sigma_1 = \sigma_3 + \sigma_c \left( m_b \frac{\sigma_3}{\sigma_c} + s \right)^a \tag{1}$$

$\sigma_1$ and $\sigma_3$ are the maximum and minimum principal stress when rock mass damage; $\sigma_c$ is The rock uniaxial compressive strength; $m_b$ and $s$ are the material parameter related to the characteristics of rock mass; $a$ is the constant of joint rock mass. The computational formulas estimating $m_b$, $s$ and $a$ are respectively shown in Eq. 2:

$$\left.\begin{aligned} m_b &= m_i \exp\left(\frac{GSI-100}{28-14D}\right) \\ s &= \exp\left(\frac{GSI-100}{9-3D}\right) \\ a &= \frac{1}{2} + \frac{1}{6}\left(e^{\frac{-GSI}{15}} - e^{-\frac{20}{3}}\right) \end{aligned}\right\} \tag{2}$$

$m_i$ is intact rock empirical constant; $GSI$ is geological strength index; $D$ is rock mass disturbance parameters, $D$ equals to 0 in initial geostress field.

**Calculation model of horizontal ground stress value range**

Rock mass are most in limit equilibrium state or steady state in initial geostress field. According to Generalized Hoek-Brown failure criterion, if rock mass wants to keep steady, its internal stress field shall meet the conditions are shown in Eq. 3:

$$\sigma_1 \le \sigma_3 + \sigma_c \left( m_b \frac{\sigma_3}{\sigma_c} + s \right)^a \tag{3}$$

Although, $a$ is determined by $GSI$ as shown in Eq. 1, $a$ can be equaled to 0.5 according to the Hoek-Brown criterion for concisely. So Eq. 3 can be changed to Eq. 4:

$$\sigma_1 \le \sigma_3 + \sqrt{m_b \sigma_c \sigma_3 + s\sigma_c^{\,2}} \tag{4}$$

In addition to the near the big fault, vertical ground stress ($\sigma_V$) and horizontal ground stress ($\sigma_H$) are both principal stress as a general rule in the crustal rock mass [1]. There are two stress condition ($\sigma_H < \sigma_V$ and $\sigma_H > \sigma_V$) shall be consider.

1st condition: if $\sigma_H < \sigma_V$, then $\sigma_H = \sigma_3$ and $\sigma_V = \sigma_1$. So, Eq. 4 can be changed to Eq. 5:

$$\sigma_V \le \sigma_H + \sqrt{m_b \sigma_c \sigma_H + s\sigma_c^{\,2}} \tag{5}$$

Solve the inequation Eq. 5 about $\sigma_H$, then Eq. 5 can be changed to Eq. 6:

$$(\sigma_V + \frac{1}{2} m_b \sigma_c) - \sqrt{m_b \sigma_c \sigma_V + \frac{1}{4} m_b^{\,2} \sigma_c^{\,2} + s\sigma_c^{\,2}} \le \sigma_H \le (\sigma_V + \frac{1}{2} m_b \sigma_c) + \sqrt{m_b \sigma_c \sigma_V + \frac{1}{4} m_b^{\,2} \sigma_c^{\,2} + s\sigma_c^{\,2}} \tag{6}$$

2nd condition: if $\sigma_H > \sigma_V$, then $\sigma_H = \sigma_1$ and $\sigma_V = \sigma_3$. So, Eq. 4 can be changed to Eq. 7:

$$\sigma_H \le \sigma_V + \sqrt{m_b \sigma_c \sigma_V + s\sigma_c^{\,2}} \tag{7}$$

If rock mass want to keep steady in the two conditions above, $\sigma_H$ must meet Eq. 6 and Eq. 7 at the same time, so $\sigma_H$ must meet the intersection between Eq. 6 and Eq. 7. Because the right side of Eq. 6 is bigger than the right side of Eq. 7, so the intersection between Eq. 2 and Eq. 7 can be wrtten as Eq. 8:

$$(\sigma_V+\frac{1}{2}m_b\sigma_c)-\sqrt{m_b\sigma_c\sigma_V+\frac{1}{4}m_b{}^2\sigma_c{}^2+s\sigma_c{}^2}\le\sigma_H\le\sigma_V+\sqrt{m_b\sigma_c\sigma_V+s\sigma_c{}^2} \quad (8)$$

Inequation Eq. 7 is the calculation model of horizontal ground stress value range in initial geostress field. According to research content above, $\sigma_V$ can be wrtten as Eq. 9:

$$\sigma_V=\gamma h \quad (9)$$

$\gamma$ is average unit weight of rock mass; $h$ is depth of rock mass. So Eq. 8 can be wrtten as Eq. 10 :

$$(\gamma h+\frac{1}{2}m_b\sigma_c)-\sqrt{m_b\sigma_c\gamma h+\frac{1}{4}m_b{}^2\sigma_c{}^2+s\sigma_c{}^2}\le\sigma_H\le\gamma h+\sqrt{m_b\sigma_c\gamma h+s\sigma_c{}^2} \quad (10)$$

**Calculated values of horizontal ground stress**

The right and left side of inequality sign of Eq. 10 are the lower upper limit values of horizontal ground stress, they are can be written as $\sigma_{H\min}$ and $\sigma_{Hmax}$. So, Eq. 10 can be changed to Eq. 11:

$$\sigma_{H\min}\le\sigma_H\le\sigma_{H\max} \quad (11)$$

In order to verify the calculation model, give $m_i$ a value range of 5~15, give $GSI$ a value range of 52.5~67.5, give $\sigma_c$ a value range of 20MPa~100MPa, give $\gamma$ a value range of 0.02MN/m³ ~0.03MN/m³ .Divide the value ranges of $m_i$, $GSI$, $\sigma_c$ and $\gamma$ into 5 sections, so there are 6 groups values of $m_i$, $GSI$, $\sigma_c$ and $\gamma$, they are shown at table 1.

Table 1. Values of calculation model parameters

| group | GSI | $m_i$ | $\sigma_c$(MPa) | $\gamma$(MN/m$^3$) |
|---|---|---|---|---|
| 1 | 67.5 | 15 | 100 | 0.030 |
| 2 | 64.5 | 13 | 84 | 0.028 |
| 3 | 61.5 | 11 | 68 | 0.026 |
| 4 | 58.5 | 9 | 52 | 0.024 |
| 5 | 55.5 | 7 | 36 | 0.022 |
| 6 | 52.5 | 5 | 20 | 0.020 |

Give $h$ a value range of 0~3000m, substitute the values at table 1 in Eq. 10 to calculate the values of $\sigma_{H\min}$ and $\sigma_{Hmax}$ in every 200m, there are 6 groups of $\sigma_{H\min}$ and $\sigma_{Hmax}$. According to the results above, the calculated values of $\sigma_H$ with $h$ change can be shown in Fig. 1.

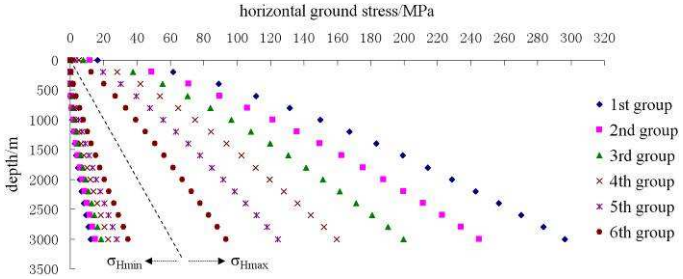


Fig. 1. Calculated values of $\sigma_{Hmin}$ and $\sigma_{Hmax}$ change with depth

Analyzing the calculated values of $\sigma_H$ in picture 1 can get the conclusion as follows: The value range of $\sigma_H$ is growing bigger from the earth's surface to earth's deep. As the values at table 1 are growing bigger , the growing speed of the value range of $\sigma_H$ is more and more faster.

## Verification of the calculation model

Compare to the measured values of $\sigma_H$ can verify the reasonability of the calculated values. G. Ranalli[4] collected more than 150 measured values of $\sigma_H$ from all of the world, and divided these measured values of $\sigma_H$ into 3 types (shield region, folt belt, sedimentary cover) according to the geological tectonic environment, the research results have been shown in Fig. 2 (a).

In order to compare conveniently, clip the section of picture 1 make the value range of $\sigma_H$ from 0 to 100MPa, shown in Fig. 2 (b). Find two minimum values of $\sigma_H$, and link them to a line as the lower boundary of $\sigma_H$, and then get the upper boundary of $\sigma_H$ using the same method. Link the 6th group of $\sigma_{H\min}$ and $\sigma_{Hmax}$ to lines respectively in the Fig. 2 (b), the line on the left and right are the lower and upper boundary of $\sigma_H$ respectively.

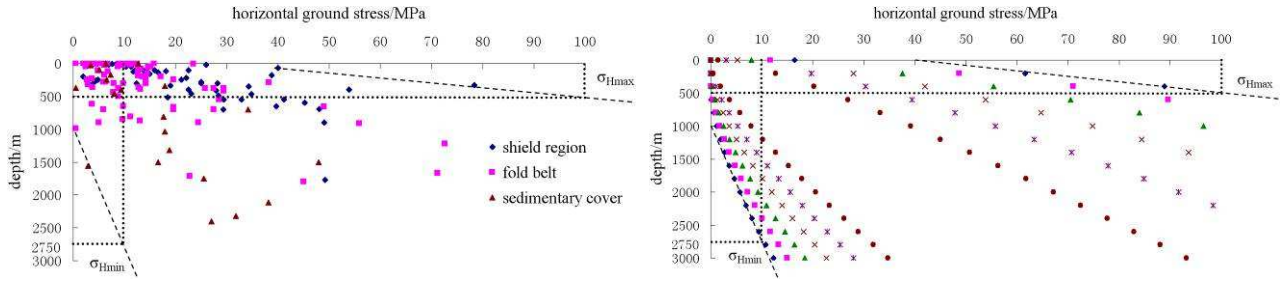


(a) measured values of $\sigma_H$ (b) calculated values of $\sigma_H$

Fig. 2. Comparison between measured values and calculated values of $\sigma_H$

The upper boundary values of $\sigma_H$ are both about 100MPa when $h$ is 500m in Fig. 2 (a) and Fig. 2 (b). The upper boundary values of $\sigma_H$ are both about 10MPa when $h$ is 2750m in Fig. 2 (a) and Fig. 2 (b). Near the surface, the value ranges of $\sigma_H$ are both 0~20MPa in Fig. 2 (a) and Fig. 2 (b). According to the above analysis, there is a good consistency on distribution ranges between measured values and calculated values of $\sigma_H$, and it is proved that the calculation model of horizontal ground stress value range is reasonable.

## Conclusions

The calculation model of horizontal ground stress value range is induced based on the Generalized Hoek-Brown failure criterion, and the reasonability of the calculation model is verified by the geostress measured value.

The results show that, there is a good consistency on distribution ranges between measured values and calculated values of $\sigma_H$, and it is proved that the calculation model of horizontal ground stress value range is reasonable.

The calculation model gives new methods and thinking for evaluation of the initial geostress field.

## References

[1] HOEK E, BROWN E T. Underground Excavations in Rock [M]. London, UK: The Institution of Mining and Metallurgy, 1980: 93－101.

[2] ROMAN D C, MORAN S C, POWER J A, et al. Temporal and spatial variation of local stress fields before and after the 1992 eruptions of Crater Peak vent，Mount Spurr volcano, Alaska [J]. Bulletin of the Seismological Society of American, 2004, 94: 2366－2379.

[3] HOEK E, CARRANZA-TORRES C, CORKUM B. Hoek-Brown failure criterion [C] // Proceedings of NARMS-TAC Conference. Toronto: [s.n.], 2002: 267－273.

[4] Ranall G., Geotectonic relevance of rock-stress determinations, Tectonophysics, Vol.29, No.1－4, 1975.

*Applied Mechanics and Materials Vols. 580-583 (2014) pp 338-343*
*© (2014) Trans Tech Publications, Switzerland*
*doi:10.4028/www.scientific.net/AMM.580-583.338*

# Analysis of Long-term Deformation of Reinforced Retaining Wall using Optical Fiber Sensor Geotextile

Liang Lu[1, 2,a], Zongjian Wang[3,b], Huan Feng[1, 2,c] and Katsuhiko Arai[4,d]

[1]School of Civil Engineering, Chongqing University, Chongqing 400045, China

[2]Key Laboratory of New Technology for Construction of Cities in Mountain Area (Chongqing University), Ministry of Education, Chongqing 400045, China

[3]Institute of Geotechnical Engineering, Chongqing Jiaotong University, Chongqing 400074, China

[4]NPO Research Institute of Ground Disaster Prevention of Fukui Region, Fukui 910-0004, Japan

[a]luliangsky@163.com, [b]wangzongjiansky@163.com, [c]shimuyan1227@126.com, [d]geotech@u-fukui.ac.jp

**Keywords:** deformation, geotextile, optical fiber sensor, reinforced retaining wall

**Abstract.** Geotextiles have been widely used in the reinforced retaining wall, but it is not easy to measure the deformation of the wall during and after construction. To assess the deformation stability of the reinforced retaining wall, an optical fiber sensor was used in geotextile. Based on the measurement accuracy of strain for the sensor geotextile, an actual geotextile-reinforced retaining wall was studied using the fiber sensor geotextile. The experimental results were compared with the results from a numerical procedure, which employs the Mohr-Coulomb yield criterion and an initial stress method and determines the plastic displacement at collapse represented by the distribution of yield elements. The comparison shows that the numerical results have a good agreement with the corresponding measurement values. The result shows the possibility that the procedure gives the realistic evaluation of long-term deformation of reinforced retaining wall.

## Introduction

Due to cost-saving, ease of construction and ability to improve the visual appearance, the geosynthetics has been widely applied in the embankment construction. With the development of reinforced soil, a number of recent papers have examined different aspects of their design and behavior [1,2]. A lot of literatures proved that the reinforced have the merit of high bearing capacity [3,4]. However, geotextile play the role of reinforcement when reinforced soil occurs a certain amount of deformation. To analyze the deformation behaviors of geosynthetics applied to a reinforced soil structure, the load-elongation properties of the geosynthetics and local deformation measurement data are required.

Field observation for the geotextile is carried out to assess the stability of the reinforced retaining wall during and after construction. The deformation of the geosynthetics installed in soil was usually evaluated through strain gauge. Leshchinsky and Fowler have suggested using silicon to attach strain gauges to the woven geotextile [5]. Strain gauges can be attached directly to woven geotextiles and geogrids, however, the local deformation of nonwoven geotextile is difficult to measure with strain gauges. Huang used a method of attaching strain gauges to the surface of non-woven geotextile composed of a core layer of knitted textile and needle-punched double layer of non-woven geotextile, by using gauge cement [6]. Won et al. proposed a strain-gauge attachment method [7] to attach strain gauges to geogrid, woven geotextile or nonwoven geotextile using an adhesive, results in less resistance against tension stress, due to its ductile and elastic properties, and it also prevents the water rising from below. But no matter what, the strain gauge is difficult to install and provides only local measuring points because of it lacking durability.

To measure the strain of geosynthetics for long term periods, an optical fiber sensor is used to geotextile reinforcement [8,9].The accuracy of the sensor geotextile on strain measurement had been confirmed through a laboratory tensile test by Tsuji et al [10]. Application of the sensor geotextile to

actual reinforced retaining wall showed that the deformation of the reinforced soil wall can be evaluated continuously during and after construction, and for long term maintenance operations. It proves that the assessment system using the sensor geotextile is useful to evaluate the stability of the wall.

Based on Mohr-Coulomb yield criterion and an initial stress method, a numerical procedureis proposed to evaluate the stability of retaining wall. Compared with the case study, it showed the possibility that the procedure gives the realistic evaluation of stability assessment of reinforced retaining wall.

## Optical Fiber Sensor Geotextile and Measure Method

**Optical Fiber Sensor Geotextile.** To measure the strain of reinforced soil wall in one direction for long term periods, an optical fiber sensor geotextile was applied. The optical fiber sensor geotextile is manufactured by inserting a single-mode optical fiber sensor with a diameter of 0.9 mm longitudinal into the geogrid. As shown in Fig. 1, the geogrid includes a core of optical fiber sensor surrounded by light-weight and high-strength synthetic fiber which is covered by high-density polyethylene resin.

**Strain Measure Method.** Employing the Brillouin Optical Time Domain Reflectometry (BOTDR) system through the optical fiber sensor inserted in geogrid, the strain distribution of geogrid and deformation of reinforced earth wall was measured.

When strain occurs in the optical fiber sensor, the peak frequency of the Brillouin scattered light changes in proportion to the magnitude of the strain of optical fiber sensor. According to the linear relationship between the frequency distribution of Brillouin scattered light with the strain of optical fiber, the strain distribution along the entire length of the geogrid was monitored by the BOTDR system. Moreover, the position of the strain can also be identified by measuring the return time with the BOTDR system.

In the actual field, the initial value of strain can be measured after the optical fiber sensor geotextile is installed in the way as normal geotextile.

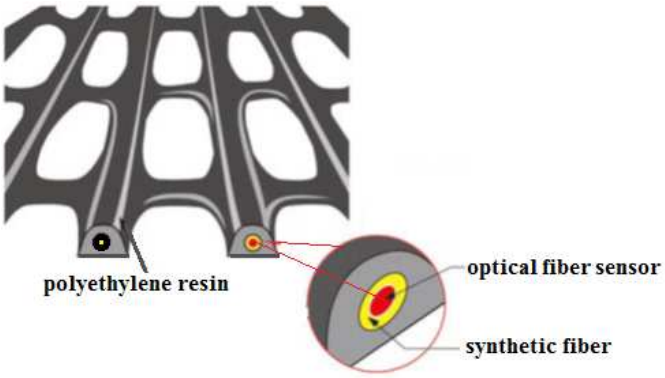


**Fig. 1** Diagrammatic sketch of optical fiber sensor geotextile

## Numerical Procedure

The stability of reinforced retaining wall is also estimated by a numerical procedure to compare with the measurment results. Wang et al. concluded that the slope failure occurs when the cumulative plastic displacement exceeds a certain critical value at collapse [11]. To estimate the critical value at collapse, a numerical procedure which considers the stiffness and strength of materials is proposed to evaluate the stability of reinforced retaining wall.

Employing Mohr-Coulomb (Eq. 1) and Coulomb (Eq. 2) yield criteria to vertical fill and friction interface respectively.

$$F_M = \{(\sigma_x - \sigma_y)^2 + 4\tau_{xy}^2\}^{1/2} - \{(\sigma_x + \sigma_y)\sin\phi + 2c\cos\phi\} = 0 \quad (1)$$

$$F_C = /\tau_{xy}/ - c - \sigma_t \tan\phi \quad (2)$$

where, $\sigma_x$, $\sigma_y$ and $\tau_{xy}$: stress components, and $\sigma_t$ and $\tau_{st}$: normal and shear stresses in friction interface, c: cohesion and $\phi$: internal friction angle.

In actual ground, when applying further $\sigma_3$ or $\sigma_n$ after yield point A, the stress state will move along the yield surface as seen in Fig. 2. At the elasto-plastic state from point A to B shown in Fig. 2, we employ a simple non-associated flow rule, where $F_c$: yield function; $Q_c$: plastic potential; $\{\delta\varepsilon_p\}$: increment of plastic strain. Here, we employ the simple plastic potential $Q_M$ and $Q_c$ as defined by Eqs. (3) and (4) respectively for Mohr-Coulomb and Coulomb material.

$$Q_M = \{(\sigma_x - \sigma_y)^2 + 4\tau_{xy}^2\}^{1/2} - 2g = 0 \quad (3)$$

$$F_C = /\tau_{xy}/ - g = 0 \quad (4)$$

where g: a hypothetical parameter which is not cited actually because plastic potential Qc and $Q_M$ are used only by the differential form. By applying the initial stress method described later, all elements of fill are assumed to bear no tensile stress, and reinforcement material is assumed to sustain no compression stress.

To evaluate the stability analysis of vertical fill mainly by its final state as treated in the limit equilibrium analysis. The distribution of yield elements calculated by the initial stress method presented by Zienkiewicz et al. [12] is relatively accordance with the final collapse pattern of slope. Two types of nonlinearity (nonlinear stress-strain relationship and no tension) are well treated by the initial stress method. To apply the initial stress method at only one loading stage as shown in Fig. 3, the fundamental flow diagram of calculation is shown in Fig. 4.

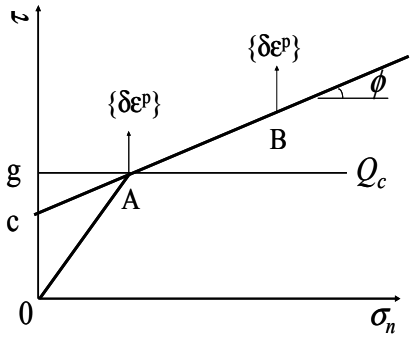


**Fig. 2** Flow rule along yield line

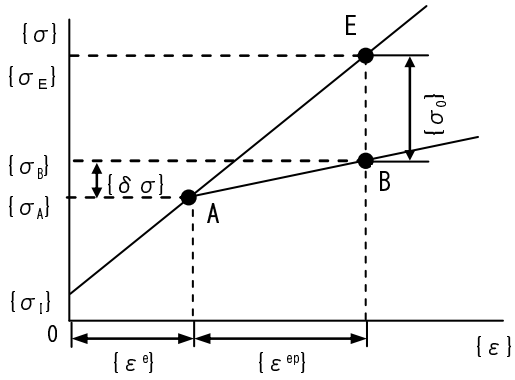


**Fig.3** Initial stress method

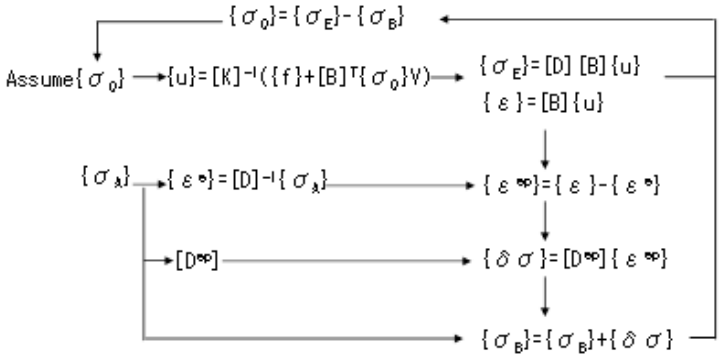


**Fig. 4** Flow diagram of iteration

### Case study of Application Geotextile of Sensor Gegeotextile

A cross-section of the geotextile- reinforced retaining wall is shown in Fig. 5, in which configuration of geotextile and measuring sensors is also shown. The wall was 9.5m high and the overburden backfill was constructed to a height of 30m with gravelly sandy with fines as shown in Table 1. Particle size distribution of backfill: 37.7% Gravel, 53.0% sand and 9.3%. In the actual field, the installation and type of geotextile changes along the height of fill according to limit equilibrium method. The properties of geotextile are also shown in Table 1.

From the laboratory tensile tests, the relationships between strain and tensile strength for the two types of geotextile used in the reinforced wall are given in Fig. 6. The horizontal displacements of wall surface after completing the construction are compared with numerical results respectively in Fig. 7. Both the measuring and numerical results show a shape of horizontal displacement that curves outward. Fig. 8 compares the strain distributions measured using optical fiber sensors with numerical results in different time point of construction. It is obvious that the optical fiber sensor can measure a continuous strain distribution in a geotextile. The strain is largest near the wall in Geotextile A, which is located close to the bottom of the wall, and in the middle the strain close to the rear on geotextile B.

**Table 1** Properties of Case study

| Density [g/cm$^3$] | Dry Density [g/cm$^3$] | Maximum Dry Density [g/cm$^3$] | Optimum Water Content [%] | C [kN/m$^2$] | φ [ °] |
|---|---|---|---|---|---|
| 2.67 | 1.75 | 1.83 | 13.0 | 10.5 | 38.4 |

| Particle Size Distribution | | | Geotextile A | | Geotextile B | |
|---|---|---|---|---|---|---|
| Gravel [% ] | Sand [%] | Silt [%] | Design Strength [kN/m] | EI [kN/m] | Design Strength [kN/m] | EI [kN/m] |
| 37.7 | 53.0 | 9.3 | 120 | 3290 | 80 | 2030 |

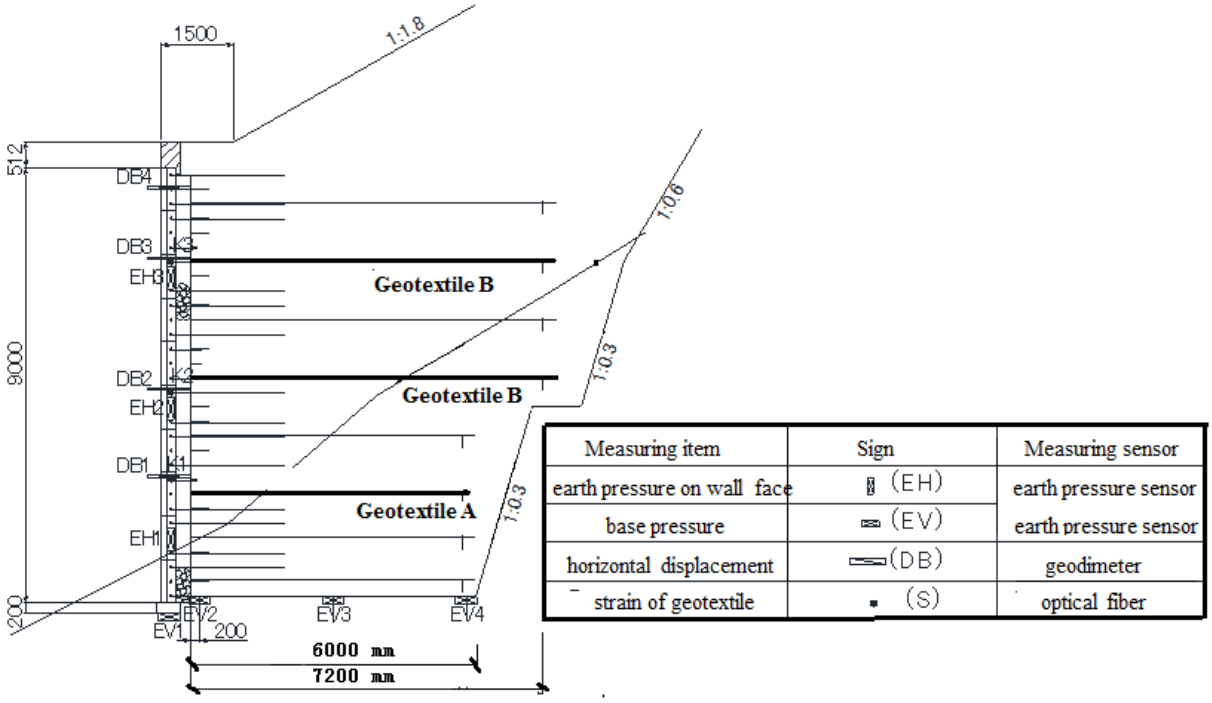


**Fig. 5** Cross section of geotextile-reinforced retaining wall

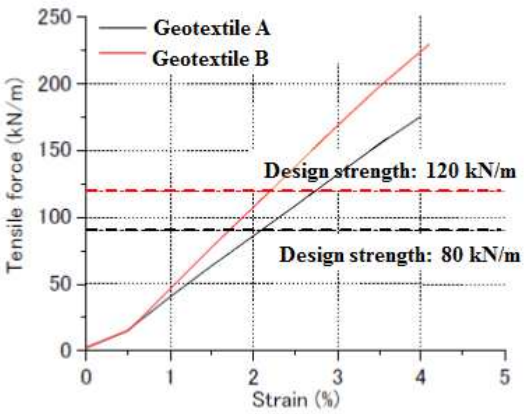


**Fig. 6** Relationship between strain and tensile strength

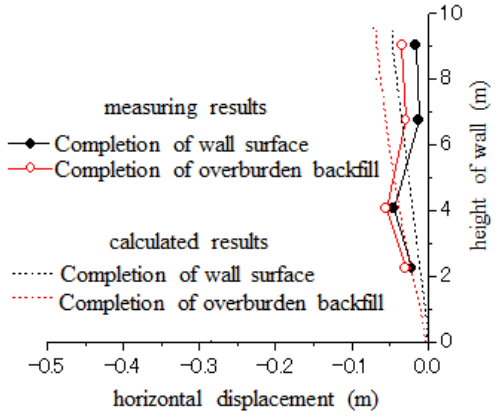


**Fig. 7** Horizontal displacement of wall

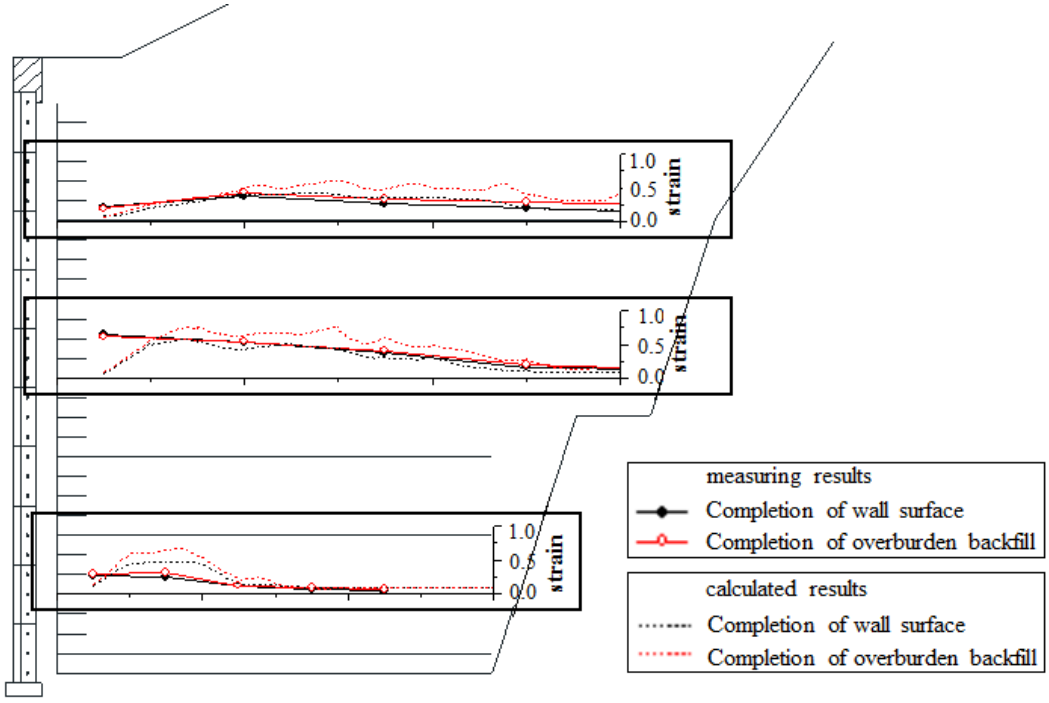


**Fig. 8** Strain distributions

## Discussions

Fig. 6 shows the tensile characteristics and the design tensile strength of the two types of geotextile respectively. The design tensile strength is based on maximum tensile strength considering the reduction of creep, durability and installation damage factors. The strain corresponding to the design tensile strength of geotextile is about 2.0 % to 2.5 %, as shown in Fig. 6. Based on the limit value of strain, the stability of reinforced retaining wall can be evaluated by the measured strain. The reinforced retaining wall is considered to be stable when the measured strain is less than 2.0 %, which represents the tensile force acting in the geotextile less than the design tensile strength. When the measured strain is greater than 2.5 %, the corresponding tensile force of the geotextile is greater than the design tensile strength, the reinforced retaining wall is considered unstable.

For the actual reinforced retaining wall using sensor geotextile, as shown in Figs. 7 and 8, the calculated result agree fairly well with the measured one. The maximum value of strain during and after construction of reinforced retaining wall, either in measurement or numerical procedure, is below 1 % for Geotextile B and C and about 0.6 % for Geotextile A, which shows that the tensile strength induced in the geotextile is less than the design tensile strength. Correspondingly, the wall is considered stable.

## Conclusions

To evaluate the stability of reinforced retaining wall during and after construction, an optical fiber sensor geotextile was used to measure the strain of geotextile embedded in the soil and a numerical procedure was applied to calculate the strain of geotextile. The following conclusions can ne drived from the experimental and numerical results in this paper:

1) The application of optical fiber sensor geotextile to an actual case showed that the optical sensor can measure a continuous strain distribution in the geotextile and enable to provide the strain distribution close with the numerical result.
2) The proposed procedure used a simple model which only requires a small number of soil parameters and provided reasonable results in the critical state, in which the collapse mode is represented by the distribution of yield elements.
3) According to the critical value of strain, the case study proved that the stability of the geotextile reinforced retaining wall can be evaluated by the maximum strain.
4) Case study showed the possibility that the proposed procedure gives the realistic evaluation of stability of reinforced retaining wall and provides a useful engineering tool for the design of reinforced retainig wall.

## Acknowledgements

This work was financially supported by the Chongqing Natural Science Foundation (cstc2012jjA0510, cstc2013jcyjA30014), Fundamental Research Funds for the Central Universities (CDJZR12200011) and Scientific Research Foundation for the Returned Overseas Chinese Scholars, State Education Ministry.

## References

[1] H. Liu: Geotextiles and Geomembranes Vol.32 (2012), p. 18

[2] D.T. Bergado and C. Teerawattanasuk: Geotextiles and Geomembranes Vol. 26 (2008), p. 39

[3] L. Lu, K. Arai and Z.J. Wang: Journal of Applied Mechanism, JSCE Vol. 10 (2007), p. 351

[4] S. Alamshah and N. Hataf: Geotextiles and Geomembranes Vol. 27 (2009), p. 217

[5] D. Leshchinsky and J. Fowler: Geotextiles and Geomembranes Vol. 9-2 (1990), p. 145

[6] C.C. Huang: Geotextiles and Geo- membranes Vol. 16 (1998), p. 175

[7] M.S. Won and Y.S. Kim: Geotextiles and Geomembranes Vol. 25 (2007), p. 10

[8] A.Yashima, S. Tsuji, K. Yoshida and Y. Yokota: Geosynthetics International 16 (2009), p. 238

[9] K. Yoshida, N. Tatta, Y. Yokota, S. Tsuji and H. Ohta, in: Application of Reinforced Soil Wall having Self Monitoring System to Actual Embankment Construction Project, edited by EM. Palmeira, Geosynthetics for a Challenging World, 9Icg Brazil 2010 Conference Secretariat Publishers (2011).

[10] S. Tsuji, N. Tatta and Z. J. Wang, in: Stability Assessment of Geotextile-reinforced Soil Wall using Optical Fiber Sensor, edited by Y. Miyata, T. Okayasu, H. Furuya, T. Uchimura and J. Otani/ Research Publishing, Proc. of the International Workshop on ICT in Geo-Engineering, Kyoto Japan(2012).

[11] Z.J. Wang, K. Arai, N. Tatta, A. Yamaguchi and S. Furukawa: Journal of Applied Mechanism, JSCE Vol. 10 (2007), p. 363 (in Japanese)

[12] O.C. Zienkiewicz, S. Valliappan and I. P. King: Internal Journal of Numerical Methods Engineering Vol. 1 (1969), p. 75

*Applied Mechanics and Materials Vols. 580-583 (2014) pp 344-348*
*© (2014) Trans Tech Publications, Switzerland*
*doi:10.4028/www.scientific.net/AMM.580-583.344*

# Analysis of Platform on Piles Application on Deformation Control of Underground Pipe in Reclamation Areas

Dongni Zhou[1, a], Qin Shang[2,b] and Bi Xiao[3,c]

[1]Changjian Institute of Survey, Planning, Design and Research, Wuhan, 430010, China

[a]bonyblue1111@163.com, [b]shangqin@cjwsjy.com.cn, [c]xiaobi@cjwsjy.com.cn

**Keywords:** reclamation, soft soil, existing pipeline, settlement of foundation, platform on piles

**Abstract.** At coastal beach soft soil area, reclamation projects may have great effect on the deformation of the existing underground pipeline. In this paper, the engineering specification method and the finite element method are used respectively for the pipe deformation calculation of the application of platform on piles to handle such underground pipeline deformation control. The results show that the application of platform on piles can effectively diminish the settlement deformation of the existing underground pipe. Co mparing the two calculation results and the monitoring results, the finite element calculation results are more in line with the actual. By appropriately increasing the width of the platform and the pile spacing, the initial design program can achieve a more optimal solution.

## Introduction

At coastal beach soft soil area, it is widely distributed underground pipeline which have strict deformation control requirements. Reclamation project may have effect on the deformation of the existing underground pipeline. Pile foundation is a very commonly used in industrial and civil engineering infrastructure. But it pours rare that platform on piles of the engineering project is built above the protection target and shares the upper-loading. The problem is how to calculate the deformation of the pipe for the platform on piles treatment, whether this treatment is effective and how to fix the specific dimensions for the platform and the piles.

## Project overview

The length of the cofferdam is 12.2 km; the area of the reclamation is 6395 mu. There 6 existing underground pipelines are distributed through the body of the cofferdam. The pipe tube center elevation is -6.5m, all of which were laid underground with pipe jacking method. The main material of the cofferdam is sandbag. The crest elevation is 7.3m and the original ground elevation is about -0.43m. Levee foundation widely distribute compression larger heavy silt loam and silty clay silt . The main foundation soil physical and mechanical parameters are showed in Table1.

Table 1 The main foundation soil physical and mechanical parameters table

| Layer No. | Soil Classification | Basic Physical Indicators | | | | Consolidation Fast Shear | Consolidation Test |
|---|---|---|---|---|---|---|---|
| | | Water Ratio | Wet Density | Dry Density | Cohesion | Internal Friction Angle | Modulus of Compression |
| | | $\omega$ (%) | $\rho$ ( g/cm$^3$) | $\rho_d$ ( g/cm$^3$) | $c_{cq}$ (KPa) | $\varphi_{cq}$ | $E_s$ (MPa) |
| 1 | Heavy silt loam | 36.2 | 1.84 | 1.35 | 13.1 | 11.1 | 4.36 |

| | | | | | | | |
|---|---|---|---|---|---|---|---|
| 2 | Heavy silty loam | 27.4 | 1.93 | 1.51 | 4.9 | 20.4 | 10.42 |
| 3 | Rock Flour With a Little Gravel | 28.7 | 1.9 | 1.48 | 4.2 | 22.1 | 9.13 |
| 4 | Heavy Silt Loam | 34.4 | 1.86 | 1.38 | 16.9 | 14.1 | 4.66 |

**Pipe Deformation Control Analysis of platform on Piles Program**

As the existing water pipeline with steel material, its strength, stability has a larger surplus. But related specifications have strict requirements on the longitudinal strain of the pipelines. According to the relevant regulatory requirements, the largest settlement of the pipeline project should be controlled in less than 18cm. Thus, this requirement proposed pipe cap reinforcement program are as follows:

Drive caisson pile φ800 on both sides of the pipeline. According to the upper load and sedimentation control requirements pile length segments using 38m, 28m and 18m in three sizes. On top of the pile design longitudinal pile capping beam, with width of 1m, height of 0.8m. Cast unidirectional platform plate on the pile beam in situs, with board thickness of 1m and board top elevation of 0.00. The cofferdam was constructed on the area of the platform board. Consider subsidence space reserved between platform and the ground, and the sand leak holes were also reserved in the platform board. After the foundation settlement stable, fill sand in the space between platform and the ground through the sand leak holes reserved before. The platform on piles reinforcement program layout is showed in Fig.2.1.

There are many methods to calculate the foundation settlement, most of them can be categorized into theoretical formulation method based on Terzaghi' s consolidation theory, simulating three dimensional consolidation theory and Biots consolidation theory, and numerical computing method based on finite element theory. Therefore, these two methods will be used to do analysis as follows.

**3.1 Engineering Specification method**

3.1.1 Assuming Boundary Conditions

(1) Take the cofferdam as load

As the analysis concerns the settlement of foundation not the deformation of the cofferdam, to simplify the calculation model, take the cofferdam as an external load.

(2) Soil uniaxial compression

The calculation model (one-dimensional model) only considers a vertical compression without considering lateral deformation.

(3) Pipes have the same nature with the soil layer where it placed

To simplify the calculation model, not consider the differences between the water pipes and the soil where it placed and take the pipe and the foundation soil the same nature to calculate.

(4)Take the settlements of the soil below pipes as the settlements of pipes

Assume the pipes together with the settlement of the pile, without considering the longitudinal stiffness of pipes, nor consider the relationship between the pipes, soil and rigid pile.

3.1.2 Calculation method

Settlement deformation is calculated by using relevant formula from "Building Pile Technical Specifications". As the pile spacing of this project is about 6 times the pile diameter, for the sake of caution, the calculation methods of clustered pile foundation (pile spacing less than 6 times pile

diameter )and sparse pile foundation (pile spacing more than 6 times pile diameter) are taken respectively and adopt the greater result.

For the pile spacing of not more than 6 times the pile diameter pile , the final settlement adopt using Boussinesq's solution, according to the sum of physical stratification method of deep foundation. For the pile spacing of more than 6 times the pile diameter pile, the bottom soil of the platform not share the load and the subsidiary stress caused by piles is determined by the Mindlin's solution. Adopt one-way compression method to calculate the sum of stratified soil subsidence, by the superposition calculation of the subsidiary stresses caused by all the piles in the horizontal range of the calculation point, taking into account the pile compression.

#### 3.1.3 Calculation Result

According to calculations, the maximum settlement of the platform is 0.05m; the maximum settlement of the pipe is 0.05m. Considering the reserved settlement differences between the platform and the ground, the settlement of pipes will be very small, almost zero.

### 3.2 Finite Element method

#### 3.2.1 Assuming Boundary Conditions

(1) Take cofferdam as area load.

(2) Take the influence depth calculated by regulation formulation as the lower boundary and the 2 times influence depth as the horizontal boundary. The bottom boundary apply 3-dimention displacement constrains, and the border boundary apply normal displacement constrains.

(3) Use shell elements to simulate pipe body.

(4) Use solid elements to simulate ground foundation. Apply DP model comes with ANSYS to do the calculation. The DP model is an ideal elastic-plastic model, which compliance with Drucker-Prager criterion based on M-C criterion presented by D.C Drucker and W.Prager. It is needed to input 3 parameters, cohesion force c, internal friction angle φ, and expansion angle φf which is to control the expansion. As the main soil type of this project is sandy clay, normally consolidated or unconsolidated soil, which would occur only shear compression, expansion angle φf is zero.

(5) Use solid elements to simulate pile, applying concrete material model.

(6) Add contacting elements (no separation type) between ground soil and pipes, allowing sliding without friction occur in a small area.

(7) Add contacting elements (Frictional type) between ground soil and pipes, allowing the two contacting surfaces transfer a certain shear stress before relative sliding occurs. As long as the shear stress come over this value, the relative sliding will occur between the two contacting surfaces.

Fig.1 shows the finite element model.

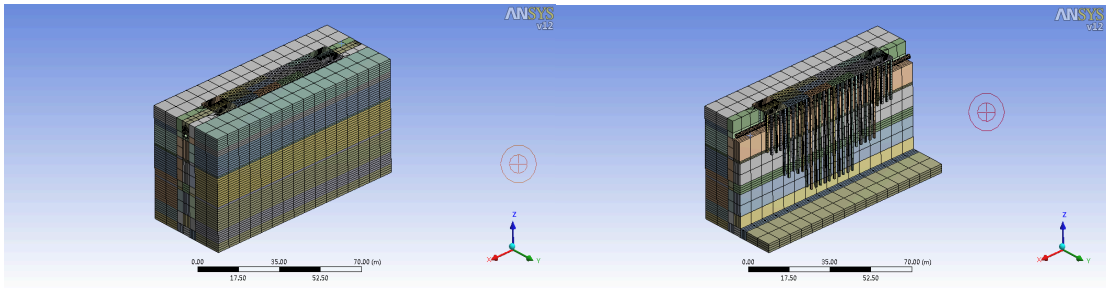

Fig.1 Finite element model

3.2.2 Calculation Result

The settlement of pipe foundation is 0.16m; the maximum vertical deformation of pipe is 0.15m, as the maximum radial deformation is 0.001m. The vertical deformation of pipe is controlled under the values specification allows, but is far more than the result calculated by specification method.

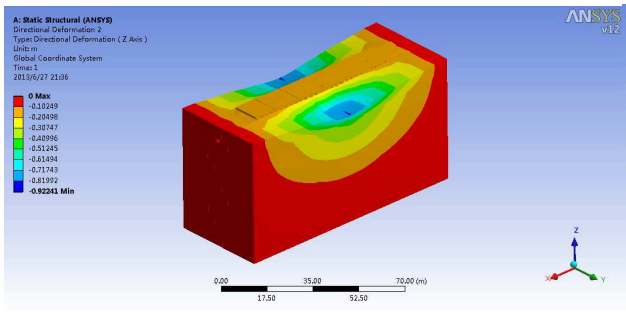


Fig.2 Foundation deformation diagram

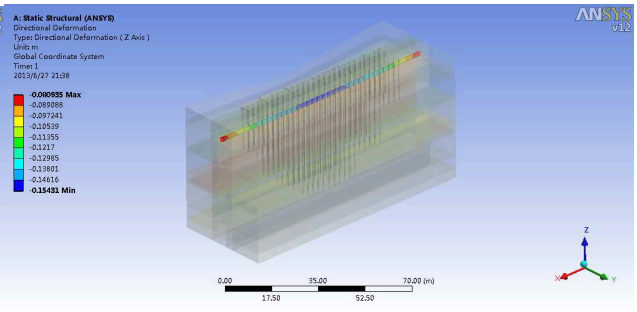


Fig.3 Water pipe deformation diagram

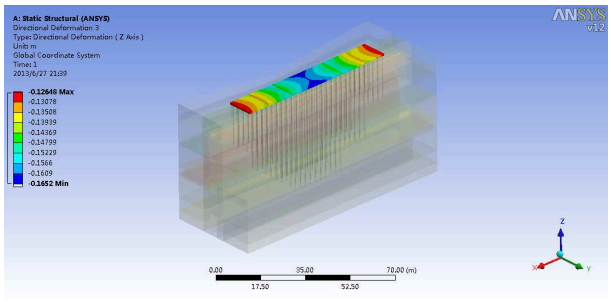


Fig.4 Platform deformation diagram

Fig.2 and Fig.3 show that the foundation treatment of platform on piles has significant effect on settlement control. Fig.4 shows that, the reserved settlement differences between platform and ground is surplus. As the differences of settlement between piles and the soil around are great, the leakage channel is more likely to be formed.

### 3.3 Results Analysis

The calculation result of finite element method is larger than the specification method. Analyzing the reasons, there may be several factors as below:

Factor 1: The specification method assumes the pipe, pile and the soil between piles subside together. The settlement deformation is comprised of the settlement deformation of soil under the piles and the pile compression which is very small because of the large pile stiffness.

Factor 2: The specification method not takes effect from the lateral loads into consideration.

Factor 3: The specification method cannot calculate the negative friction force caused by the differences of settlement between pile and the soil around it.

The main factors are factor 1 and factor 2. Comparing to the general calculation, it is very different cases that the protected object is located under the platform. Due to the limited width, the platform can only share the load directly to the upper part of the cofferdam, and the edge loads would have a greater impact to the soil among piles.

Factor 3 is also very important. Because of the less settlement of the piles and the more settlement of the soil around piles, it would generate large negative friction force. The more densely arranged in piles, the greater its negative friction force.

The pile platform and pipes of this project are arranged monitoring facilities, according to the monitoring results at completion of this project, the maximum settlement of the pipe is 47 mm, the maximum settlement of the steel concrete caisson pile is 49 mm. According to the experience of

similar projects in the past, it can be expected that, within 50 years of engineering use fixed number of year, the final settlement of the water pipe will be about 100 mm. The results are greater than the results calculated by engineering specification method and slightly smaller than the finite element method. The monitoring results show that the settling amount of the pipe is approximately the same as that of the caisson pile at completion of the project, which is very different from the engineering specification method calculation results. So the finite element method calculation results are more in line with the actual.

According analysis of the calculation and the monitoring results, the initial design of the platform on piles can also be optimized from the following several aspects:

(1) Appropriate increase cap width

It can be seen from the calculation results, the edge loads are the most important factors to generate vertical deformation of the pipe. The platform can only reduce the shallow foundation stress, where is under the platform and above the pipe. With increasing depth, the foundation stress increases rapidly until almost the same with the same depth of soil, at the meantime the protection effect of the platform is weakened and exhausted. But as the increase width of the platform the investment increase, the platform can be of different design programs for the width election to achieve the optimal design.

(2) Appropriate increase pile spacing

According to the results, the pile strength is still surplus. By increasing pile spacing, especially to increase the distance between the pile and the pipes can save investment, while also reducing the effects of pile lateral friction to the pipes. At the same time, as the loads of single pile increasing, settlement of the pile would increase. But it can be solved by increase the reserved gap between the platform and the ground.

## Conclusions

In the coastal reclamation projects, applying platform on piles design can effectively solve the settlement problem of existing pipeline caused by the upper large area loading. By appropriately increasing the platform width and the pile spacing, it can achieve a more optimal solution. In accordance with regulatory requirements, while increasing the pile spacing, it must guarantee the pile bearing capacity not exceed its ultimate bearing capacity. When the pile bearing capacity exceeds its ultimate bearing capacity, the result is the soil at the bottom of the pile would occur plastic damage and the pile would continue to subside, but it is impossible to subside unlimitedly. To some deep, the stresses would achieve a re-balance. It is necessary to do further analysis for the stress-strain state of the foundation soil while increasing the pile spacing, which can create a greater space for the design optimization.

## References

[1] Chang Shibiao, Zhang Sumin. Engineering Geology Manual (In Chinese) [M]. China Building Industry Press, 2011

[2] Karl Terzaghi. Theoretical Soil Mechanics [M].Chapman and Hall, Limited John Wiley And Sons, Inc. 1944

[3] Zhu Bofang. Finite element method theory and applications [M] (In Chinese). 3nd ed. Beijing：China Water Power Press，2009.

[4] Drucker D.C and Prager W. Soil Mechanics and Plastic Analysis for Limit Design [J]. Q, April, Math, 1952,（10）: 157～165

[5] Gong Xiaonan. Foundation Treatment Manual [M] (In Chinese). Beijing: China Building Industry Press, 2008

[6] GB50007-2002. Code for Design of Building Foundation [S] (In Chinese). Beijing: China Building Industry Press, 2002

*Applied Mechanics and Materials Vols. 580-583 (2014) pp 349-354*
*© (2014) Trans Tech Publications, Switzerland*
*doi:10.4028/www.scientific.net/AMM.580-583.349*

# Research on Water Temperature Change of Hot Dry Rock Fracture Storage Layer in Shenyang

Jianbin Zhao[1,a], Haidong Song[2,b], Di Li[3,c], Zheng Zhang[4,d]

[1,2,3,4]Department of Civil Engineering, Shenyang Jianzhu University, Shenyang 110168,China

[a]cejbzhao@163.com,[b]174445300@qq.com,[c]1061825140@qq.com,[d]294471341@qq.com

**Keywords**: Hot Dry Rock, Heating,Fracture storage layer, Water temperature change

**Abstract**. Hot dry rock(HDR) provides heat through fracture storage layer. The purpose of research on water temperature change of hot dry rock fracture is to study that whether heat energy can satisfy five months winter heating or not. Research method is establishing model of hot dry rock fractured storage layer by means of numerical simulation software FLUENT according to the rock physical properties in Shenyang region. The depth of drilling is 4000m and the water flow rate is 1cm/s. Research principle is high temperature underground rock transfer heat to medium water in the fracture by coupling. Conclude water temperature change equation every two weeks. The results of the study is that fracture water temperature distribution can be approximated taken as linear distribution. According to the slope K, we can conclude water temperature change formula(3.10), and we can use it to infer fracture water temperature.

## Introduction

In the Shenyang area, winter heating consumes a lot of mineral fossil fuel for five months. The burning products critically affect air quality and undermine the sustainable development. Hot dry rock has obtained more and more people's attention.Because the enormous pre-development costs, the research work is still in the theoretical stage[1]. In this paper, we study water temperature change of fracture storage layer. It is critical step in the development of hot dry rock heating system.It directly affects the prime cost of hot dry rock research.It is also the basis of studying the fracture storage layer rock temperature distribution.

## Working mechanism of hot dry rock heating system

Hot dry rock heating system consists of injection wells, extraction wells and artificial fracture storage layer. Fractured storage layer is located between the injection wells and the extraction wells. Fracture storage layer is built by massive hydraulic fracturing technology. Its working mechanism is injecting high-pressure water through the injection wells to the high-temperature rock. The high-pressure water is heated in a boiling state through the fractured storage layer. Then the high-temperature water is transmitted through the extraction wells.The low-temperature water is injected into injection wells for recycling.Fracture storage layer is the place where medium water and high-temperature rock exchange heat energy and thermal conductivity [3,4].Environmental conditions of artificial fracture storage layer play an important role to analysis energy absorption. Working Mechanism diagram is shown in Figure 1.1.

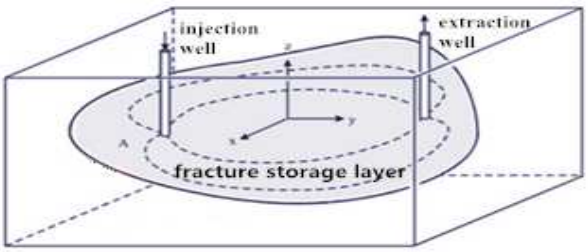


Fig1.1 Working mechanism diagram of HDR

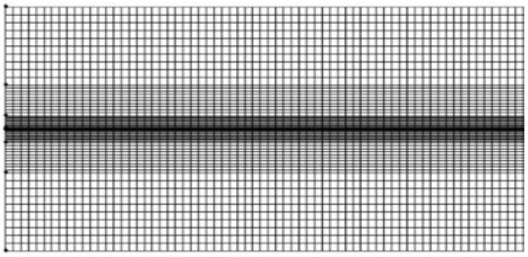

Fig 2.1 HDR retention layer crack model

**Assumptions.** Rock blocks are intended to simplify homogeneous and isotropic continuum models. Fracture is simplified fractured media model. Water storage and water permeability of rock are negligible. Because of the high-pressure, water vaporization does not occur. The model can be considered saturated with water. The density of water is 1.0g/cm$^3$ all the time. Rock transfer heat by conduction, convection, radiation. And the radiation component of hot dry rock model is negligible. Water flow rate only relate to the pressure difference between the injection wells and production wells. To simplify the mathematical modeling, model can be seen a rotating body as the axis of fracture, according to the assumptions. Thereby simplifying the model into a two-dimensional calculation model [2,3]. The model is shown in Figure 2.1.

**Fracture water temperature control equation.** In the HDR system, the movement of water is mainly controlled by the pressure difference between the injection wells and the production wells, and the free convection caused by the temperature change is generally negligible. Thus the heat transfer equations and fluid motion equations can be independently solved. Therefore, forced convection is the only factor to consider in the heat transfer equation [5].According to the norm of conservation of energy, quantity of heat of per unit area along the axis direction is $Q_1$

$$Q_1 = -\lambda_w \nabla T \tag{2.1}$$

The effect of fluid movement, control body of per unit area along the axis direction is $Q_2$

$$Q_2 = c_{vw} \bullet \rho_w \bullet v_i \bullet T \tag{2.2}$$

The heat conduction from the rock to fracture water is $Q_3$

$$Q_3 = -\frac{\lambda_r}{\delta}(T_{rb} - T_w) \tag{2.3}$$

Therefore, according to the norm of conservation of energy infer the heat transfer equation

$$c_{vw}\rho_w \frac{\partial T_w}{\partial t} + Q_1 + Q_2 + Q_3 = 0 \tag{2.4}$$

Putting(2.1 ~ 2.3) into (2.4) can infer

$$c_{vw}\rho_w \frac{\partial T_w}{\partial t} = \lambda_w \nabla^2 T - c_{pw} \bullet \rho_w \bullet \nabla(v_i \bullet T_w) + \frac{\lambda_r}{\delta}(T_{rb} - T_w) \tag{2.5}$$

The seepage of water obeys Darcy's law, can infer

$$v_i = q_i = k_f \nabla p \quad i = x, y, z \tag{2.6}$$

Therefore, putting the formula (2.6) into (2.5) can get complete fracture water temperature field equations

$$c_{vw} \frac{\partial(\rho_w T_w)}{\partial_t} = \lambda_w \nabla^2 T - c_{pw} \bullet \nabla(\rho_w \bullet k_f \bullet \nabla p \bullet T_w) + \frac{\lambda_r}{\delta}(T_{rb} - T_w) \tag{2.7}$$

In the equation: $\lambda_w$ is the thermal conductivity of water, $c_{vw}$ is constant volume specific heat of water, $c_{pw}$ is constant pressure specific heat of water, $\rho_w$ is density of water, $\lambda_r$ is thermal conductivity of rocks, $\delta$ is 1/2 slit width, $T_{rb}$ is crack rock edge temperature, $T_w$ is water temperature, $v_i$ is water flow rate, $q_i$ i290s ratio of flow rate, $k_n$ is seepage coefficient.

**Water temperature change in fracture storage layer**

In order to research the water temperature change in entire fractures. Research on the fracture water temperature distribution during different time periods. Calculate and analysis the data of system every two weeks. Concrete analysis of the situation is as follows:

From Figure 3.1, we can summarize temperature distribution of water in the fracture after the 2 weeks' running of system. The line of cracks in the first 200m range extent straightly. Temperature of water in fracture distributes linearly. Within the range from 200m to 500m, the image is curve state. After the system runs two weeks, the temperature distribution of the fissure water can not be accurately expressed the relationship linear distribution.

From Figure 3.2, we can summarize temperature distribution of water in the fracture after the 4 weeks' running of system. The image of fracture linearly extend in the front 300m range, fissure water temperature changes linearly distributed. Within the range of 300m to 500m, the image is bent. Four weeks after the system runs, the fissure water temperature distribution can be summarized as the range of linear increase than two weeks ago,but the overall linear relationship is still not accurately expressed.

From the Figure 3.3 can summarize fracture water temperature distribution after system runs six weeks.Fracture water temperature change trend is close to linear. The linear equation can be approximately defined as:

$$T = T_0 + 0.09L \tag{3.1}$$

In the equation: $T_0$ is the injection water temperature. $T$ is the temperature of random point in the crack. $L$ is the distance from fractured to the injection wells.

The hot dry rock system fracture water temperature distributions of eight weeks and ten weeks can be summarized from the Figure 3.4 and Figure 3.5. Compared to the water temperature distribution of six weeks, change trend of fracture water temperature is closer to linear. The linear equation can be approximately defined as:

$$T = T_{_0} + 0.08L \tag{3.2}$$

$$T = T_0 + 0.076L \tag{3.3}$$

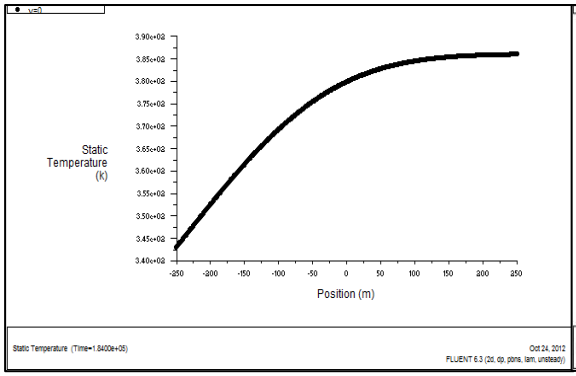


Fig 3.1 Cracked after two weeks the water temperature distribution 4000m 1cm/s

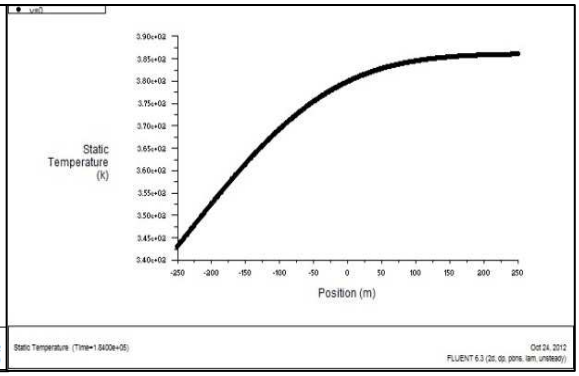


Fig 3.2 Cracked after four weeks the water temperature distribution 4000m 1cm/s

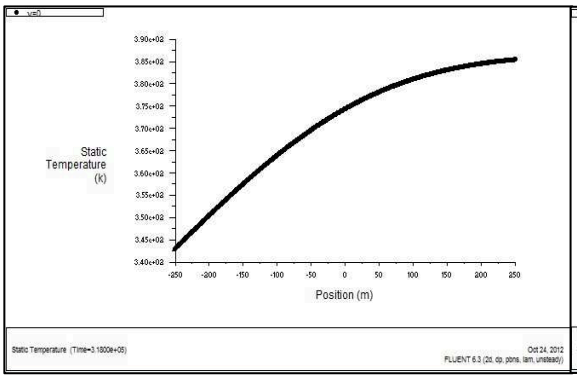


Fig 3.3 Cracked after six weeks the water temperature distribution 4000m 1cm/s

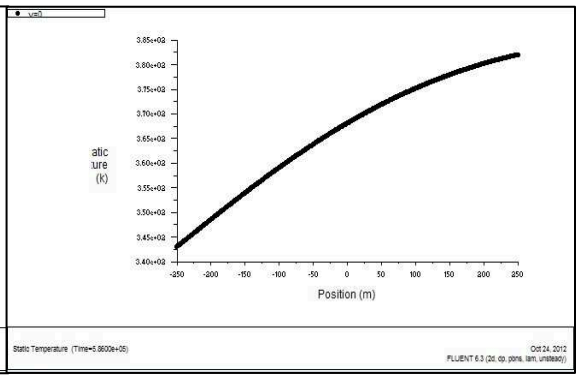


Fig 3.4 Cracked after eight weeks the water temperature distribution 4000m 1cm/s

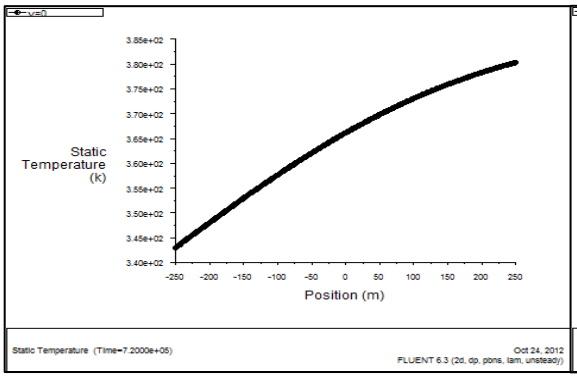


Fig 3.5 Cracked after ten weeks the water temperature distribution 4000m 1cm/s

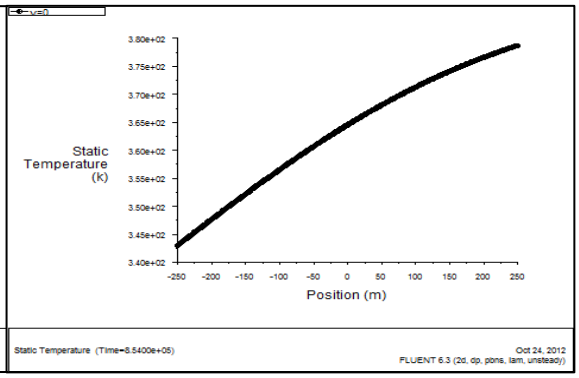


Fig 3.6 Cracked after 12 weeks the water temperature distribution 4000m 1cm/s

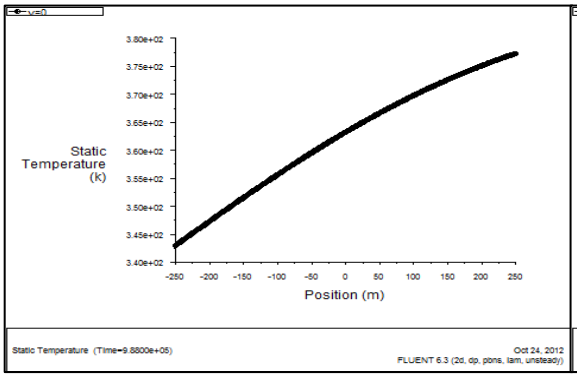


Fig 3.7 Cracked after 14 weeks the water temperature distribution 4000m 1cm/s

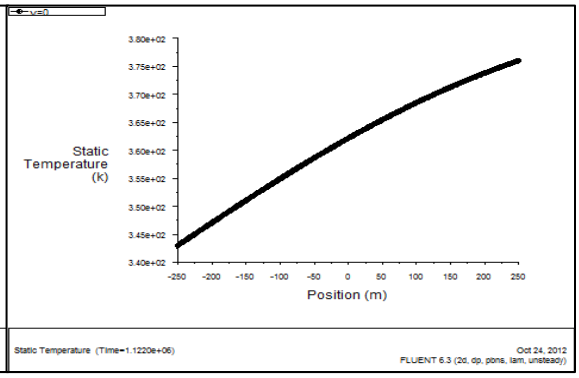


Fig 3.8 Cracked after 16 weeks the water temperature distribution 4000m 1cm/s

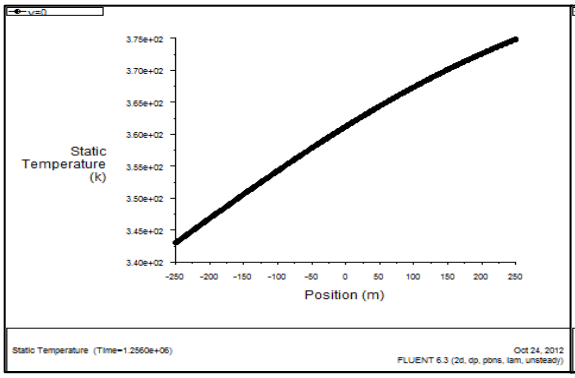


Fig 3.9 Cracked after 18 weeks the water temperature distribution 4000m 1cm/s

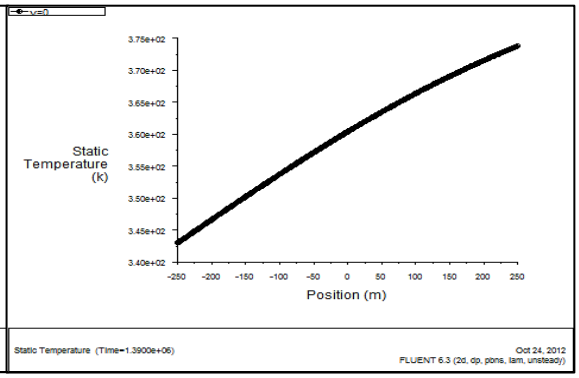


Fig 3.10 Cracked after 20 weeks the water temperature distribution 4000m 1cm/s

The hot dry rock system fracture water temperature distribution of twelve weeks, fourteen weeks, sixteen weeks, eighteen weeks, twenty weeks can be summarized from the Figure 3.6~Figure 3.10,The linear equation can be respectively defined as equation(3.4) ~ (3.8) :

$$T = T_0 + 0.072L \tag{3.4}$$

$$T = T_0 + 0.07L \tag{3.5}$$

$$T = T_0 + 0.068L \tag{3.6}$$

$$T = T_0 + 0.064L \tag{3.7}$$

$$T = T_0 + 0.062L \tag{3.8}$$

Table 3.1 Slopes calculated from Fig 3.3 to Fig 3.10

| Time | 6 | 8 | 10 | 12 | 14 | 16 | 18 | 20 |
|---|---|---|---|---|---|---|---|---|
| Slope | 0.09 | 0.08 | 0.076 | 0.072 | 0.07 | 0.068 | 0.064 | 0.062 |

Fig 3.11 shows the tendency of change of slope with time goes by

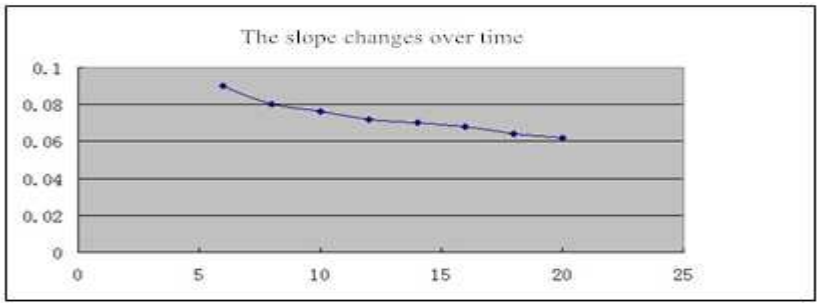


Fig 3.11 The slope changes over time

We can infer the equation 3.9 which the change of slope K with time goes by. The equation can be approximately defined as:

$$k = 0.092 - 0.0015t \tag{3.9}$$

In the equation: $k$ is water temperature slope of the curve variation with time. $t$ is the running time of the hot dry rock system. The unit is weeks.

Thus, the equation of water temperature variation with the time is equation 3.10.

$$T = T_0 + (0.092 - 0.0015t) \bullet L \tag{3.10}$$

In the equation:$T$ is the water temperature in different fracture locations. $T_0$ is injection water temperature. $t$ is the time of the hot dry rock system runs. $L$ is the distance from the injection wells.

**Conclusions**

(1) With the system running, the rate of change of water temperature distribution gradually tends to change linear.
(2) When the system runs five months, fracture water temperature distribution can be approximated as linear distribution.
(3) With the system running, the rate of change of temperature distribution of water in the fracture decrease following the increase of the length of crack.
(4) The depth of drilling is 4000m and the water flow rate is 1cm/s. We can use the equation (3.10) to study and predict fracture water temperature

$$T = T_0 + (0.092 - 0.0015t) \bullet L \tag{3.10}$$

In the equation: $T$ is the water temperature in different fracture locations. $T_0$ is injection water temperature. $t$ is the running time. $L$ is the distance from the injection wells.

**References：**

[1]Jianbin Zhao, Xiaoyan Feng, Keqi Yan:The key technical analysis on the hot dry rock in northeast cold in china, Applied and Materials (ISSN: 1660-9336).2011.8
[2]Jianbin Zhao, Kun Zhao: Research of Hot Dry Rock Mechanics on Fracture Temperature Distribution of Storage Layer in Shenyang, Progress in Civil Engineering.2012.5
[3]Hayashi K, Willis-RichardsJ, HopkirkRJ, NiiboriY: Numerical models of HDR geothermal reservoirs: a view of current thinking and progress[J]. Geothermic 1999; 28:507-518.
[4] DUCHANE D V. Geothermal energy production from hot dry rock: operational testing at the Fenton Hill, New Mexico HDR test facility[J]. American Society of Mechanical Engineers, Petroleum Division(Publication)PD, Emerging Energy Technology,1994,57：169-174.
[5]Jianbin Zhao, Xiaoyan Feng,Keqi Yan: Hot dry rock in LiaoShen winter heating technical analysis [J]. The 13th annual meeting of China association for science and technology the 14th at the venue- The exploitation and utilization of geothermal energy and low carbon economy international symposium,2011.(In Chinese)

*Applied Mechanics and Materials Vols. 580-583 (2014) pp 355-358*
*© (2014) Trans Tech Publications, Switzerland*
*doi:10.4028/www.scientific.net/AMM.580-583.355*

# Studies about creep characteristic of silty clay on triaxial drained creep test

WANG YanFang[1, a],Zhou ZhiGang[2,b]and CaiZhengYin[3,c]

[1]Jin Ling Academy, Nanjing University Jiangsu, Nanjing 210093, China

[2]Jiangsu Province Water Engineering Sci-tech Consulting Co. LTD, Jiangsu, Nanjing 210029, China

[3] Nanjing Hydraulic Research Institute, Jiangsu, Nanjing 210014, China

[a]wyf_02@163.com, [b]hbzzkong@sina.com, [c]zycai@nhri.cn

**Keywords:** silty clay; $k_0$ consolidation; triaxial drained creep test; creep coefficient;

**Abstract：** The creep characteristic of saturated silty clay was studied by triaxial drained creep test through two stress paths of axial loading and lateral lightening. According to test data, some conclusions were submitted. First, the axial creep laws between the two stress paths were consistent on the drainage conditions. Volume strains were much smaller than axial strains. Volume strains presented shear dilatancy along with lightening confining pressure. The silty clay creep coefficient was put forward and its variation law was summarized. The silt soil creep coefficient was closely related to the deviatoric stress level. The two had a linear relationship. The silt soil creep coefficientincreased with deviatoric stress level and had no matter with the confining pressureand loading path.

## Introduction

The deformation of soil is not just a transient, but also increases with a certain speed, and it has some creep characteristics.The experimental studies on creep characteristics of soil most based on conventional undrained consolidation triaxial test, without considering drained conditions effects on the soil creep characteristic. There were many researches about silty clay's creep properties [1-2]. But the drainage creep characteristics of silty clay were seldom studied on the condition of preconsolidation state. The purpose of this paper is to study the creep characteristic of saturated silty clay with triaxial test by $k_0$ consolidation and drainage conditions, and to explore differences of the soil creep properties through two stress paths of axial loading and lateral lightening.

## Triaxial Drained Creep Test

The triaxial drainage creep tests of saturated remoulded soil with axial loading or lateral unloading were carried on by takinga certain amount of silt soil. The previous $k_0$ consolidation was completed according to the sampling depth before the creep tests. In this paper, the $k_0$ value was 0.45. Test apparatuseswere the modified stress controlling triaxial apparatuses. The creep tests scheme was shown in table 1.

Table 1 The loading scheme of silt soil creep test

| Loading paths | Consolidation pressure （kPa） | | Creep paths |
|---|---|---|---|
| Axial loading | Confiningpressure | 50 | Confining |
| | Axial pressure | 111 | pressure is |

| | | | |
|---|---|---|---|
| | Confiningpressure | 100 | constant, and |
| | Axial pressure | 222 | Axial pressure is |
| | Confiningpressure | 250 | increasing step by |
| | Axial pressure | 555 | step |
| Lateral lightening | Confiningpressure | 50 | Axial pressure is constant, and Confining pressure is decreasing step by step |
| | Axial pressure | 111 | |
| | Confiningpressure | 100 | |
| | Axial pressure | 222 | |
| | Confiningpressure | 250 | |
| | Axial pressure | 555 | |

**Analysis of Test Results**

It was shown from fig.1 that axial strain and volume strain were consistent between axial loading and lateral unloading conditions. It was shown that from the trend of the curve the creep strain increment increased with stress levels, and the accelerated creep did not appear for the two strains. Regardless of high or low stress levels, both were degenerative patterns. There were no uniform creep and accelerated creep. The volume strain showed much difference between axial loading and lateral unloading conditions. When $\sigma_3 = 250\text{kPa}$ with lateral unloading, it showed shearing shrinkage tendency and was the same as the axial loading conditions. But with increasing of shear stress levels, this increment in volume deformation gradually decreased. From fig.1 (f) showed that volume deformation increments of the two lateral levels were fewer than the first two levels. When $\sigma_3 = 100\text{kPa}$ with lateral unloading, it showed tendency of shear shrinkage after shear dilatancy. But When $\sigma_3 = 50\text{kPa}$ with lateral unloading, it showed shear dilatancy tendency beginning at the first level. This showed that under the condition of lateral load shedding, silty clay creep has a certain volume dilatancy characteristics, and with the decrease of consolidation confining pressure, the dilatancy properties were more obvious.

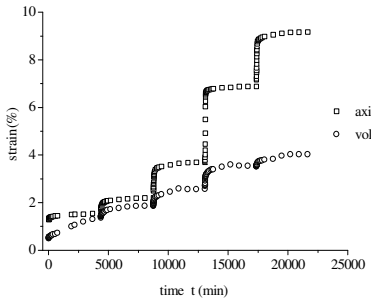


(a) $\sigma_3 = 50\text{kPa}$ withaxial loading

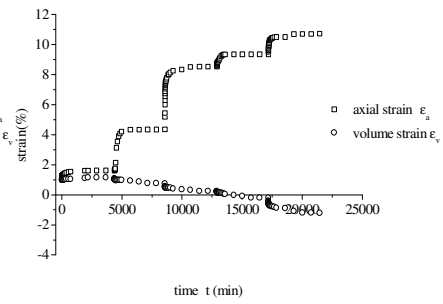


(b) $\sigma_3 = 50\text{kPa}$ with lateral lightening

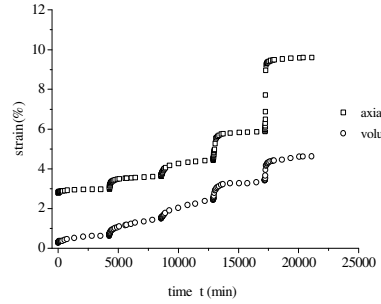


(c) $\sigma_3 = 100\text{kPa}$ withaxial loading

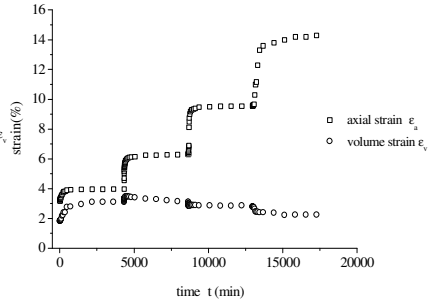


(d) $\sigma_3 = 100\text{kPa}$ with lateral lightening

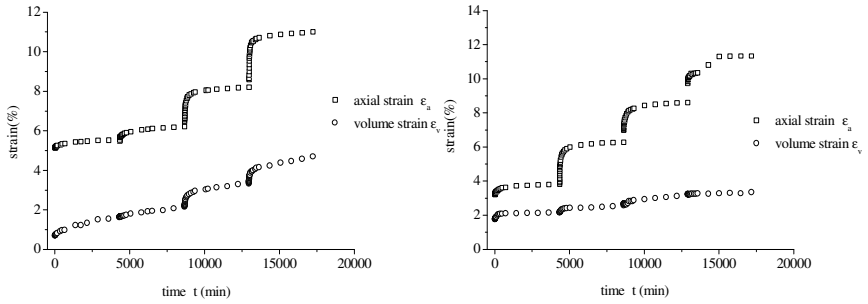


(e) $\sigma_3$ = 250kPa with axial loading (f) $\sigma_3$ = 250kPa with lateral lightening

Fig.1 Creep strain curves of silt soil with triaxial drained creep test

## Creep Coefficient

For one-way consolidation compression test, coefficient of secondary compression was used to describe the creep properties of soil. After pore pressure dissipate, the characteristic quantities used void ratio changes to represent creep deformations under effection of effective stress. Similarly, concept of creep coefficient for triaxial drained creep test was defined as the gradient between creep strain and logarithmic time. The expression is shown as Eq.(1):

$$C_\varepsilon = \frac{\varepsilon - \varepsilon_0}{\log(t / t_0)} \qquad (1)$$

For Eq.(1): $t_0$ is creep starting time of soils, $\varepsilon_0$ is creep value for creep starting time. The value was 80 min here.

The relationship curves between axial strain and logarithmic time under different deviatoric stress was shown in Fig.2. The slope factor of fitting line represented the creep coefficient, which increased with stress levels from Fig.3. All creep coefficients of six soil samples under different stress levels were plotted out in Fig.3. According to Fig.3, it showed that regardless of confining pressure and loading path, creep coefficients increased up with stress level, and basically the relationship line was a straight line. Under the same loading path and the same deviatoric stress level, the creep coefficient changed unobviously with consolidation confining pressure. The relationship curves of the two creep path with axial loading and lateral unloading was similar. The conclusion was that creep coefficients of soil sample was closely related to deviatoric stress levels, but had little relationship with consolidation confining pressure and creep loading path.

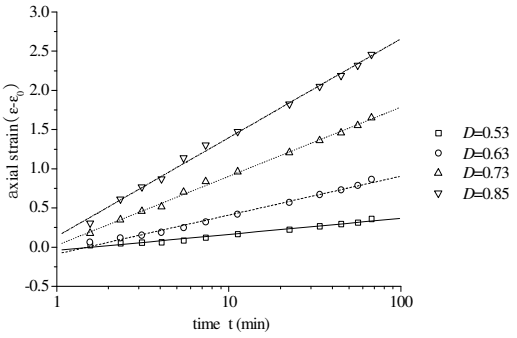


Fig.2 Relationship between axial creeps and logarithmic times at $\sigma_3$ =250kPa with axial loading

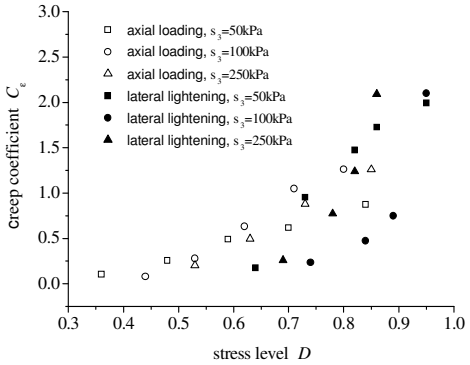


Fig.3 Relationship between stress levels and creep coefficients of six soil samples

## Conclusions

There were many researches about silty clay's creep properties. The drainage creep characteristics of silty clay were studied by the paper on condition of preconsolidation state. The conclusions from experimental results and related analysis were as follows:

(1) Volume strains were significantly less than axial strains. For the two stress path of axial loading and lateral unloading, the creep laws were fundamentally consistent in triaxial drained creep test.

(2) Volume strains showed much difference between axial loading and lateral unloading conditions. Volume strains presented shearing dilatancy characteristic. The lower consolidation confining pressure was, the more clearly shearing dilatancy characteristic was.

(3) Concept of creep coefficient was drew up. According to test data, creep coefficients of soil sample were closely related to deviatoric stress levels, but had little relationship with consolidation confining pressure and creep loading path.

## References

[1] Yuan J Y, Zhao X H, Yang X Zh, et al. Experimental study of the strength and deformationeffect of $k_0$-consolidation condition to Shanghai soft soils[J]. Site Investigation Science and Technology,1995,(6):22-25. (in Chinese).

[2] ZHU H H，CHEN X P，CHENG XJ, et al.Study on creep characteristics and model of soft soil considering drainage condition［J］.Rock and Soil Mechanics, 2006, 27(5):694－698.(in Chinese).

*Applied Mechanics and Materials Vols. 580-583 (2014) pp 359-363*
*© (2014) Trans Tech Publications, Switzerland*
*doi:10.4028/www.scientific.net/AMM.580-583.359*

# Test study on effects of temperature, sand mix ratios and dry density on soil water characteristic curves of bentonite-sand mixtures

Xiang-wei FANG[1, a], Chun-ni SHEN[2, b], Chun-hai LI[1], Long WANG[1]

[1]Chongqing Key Laboratory of Geomechanics & Geoenvironmental Protection, Department of Civil Engineering, Logistical Engineering University, Chongqing 401311, China

[2]Chongqing University of Science and Technology, Chongqing 401331, P.R. China

[a]fangxiangwei1975@163.com, [b]scn1999@163.com(Corresponding author)

**Keywords:** bentonite-sand mixtures; soil-water characteristic curve; moisture balance method; suction

**Abstract:** A series of tests on the soil water characteristic curve through moisture balance method were conducted to study the effects of temperature, sand mix ratios and dry density on the soil water characteristic curve of bentonite-sand mixture. The test results show that with the increase of temperature, the water retention capacity of the mixture significantly decreased. Within the test control suction range, sand mix ratios at the low suction had obvious effects on the soil water characteristic curve and at high suction the effects gradually decreased. Dry density had no effects on the soil water characteristic curve of bentonite-sand mixture. In accordance with the test data, an experience model of soil water characteristic curve of bentonite-sand mixtures considering temperature and sand mix ratios is established.

## Introduction

With the development of the use of nuclear energy and nuclear engineering, safe disposal of the (high-level radioactive waste) is raising the concern of the world as well as the use of nuclear energy. At present, deep geological disposal is universally recognized as a viable solution placing the high-level radioactive waste solidification down to 500-1000 meters in the underground repository, to achieve the purpose of isolation from living environment of mankind. Buffer/backfill material used in the construction of an underground repository is one of the important aspects, and the bentonite sand mixed buffer/backfill materials have become popular around the world. As Canada mixed Avonseal bentonite and sand at a proportion of 5:5; Japan add 30% quartz sand into Kunigel V1 as the preferred buffer/backfill material[1]. China, after a comprehensive studying, has preliminarily identified the Inner Mongolia GMZ bentonite as our preferred buffer/backfill material.

Soil water characteristic curve shows the relationship between the unsaturated soil suction, water content and saturation. scholars have done a lot of work on the soil water characteristic curve of bentonite and mixtures. For example, G.X.Tang et al.[1] studied the soil water characteristic curve, through the filter paper method, of the mixture with sand mix ratios of 50% at different temperatures. A.C.Jacinto et al.[2] studied water retention curves of MX-80 bentonite of different temperatures and dry density and then used them in the analysis of the thermal-hydraulic-mechanical coupling. E.E.Alonso et al.[3] using the vapor balance method, studied the soil water characteristic curve of compacted FEBEX bentonite with different temperatures and dry density. G.F.N.Gitiranar et al.[4] studied impact factors of the equation of soil water characteristic curve of the bentonite. Ye et al.[5] studied the impact of temperatures and free expansion in unconfined condition on highly compacted pure GMZ bentonite SWRC under high suction. Zhang et al.[6] using the pressure plate and the vapor balance method studied the GMZ bentonite under different initial saturation conditions at room temperature, the significant influence of saturation, sand mix ratios and the dry density of bentonite-sand mixture on the water retention capacity. Studies above on soil water characteristic curve of bentonite and the mixture of bentonite and sand are carried out under normal temperature, therefore studies on buffer/backfill material under different temperature, sand mix ratios and dry

density and its water retention capacity under the influence of residual radiant heat by geological disposal of high level radioactive waste have practical importance both in theoretical analysis and engineering.

This paper studies soil water characteristic curve of the mixed buffer/backfill material of bentonite with sand through the vapor balance method, analyzed the influence of temperature, sand mix ratios and dry density on soil water characteristic curve of the compacted mixture and establishes empirical model that can predict reference to the soil water characteristics curves of mixture of different sand mix ratios and temperature.

## Preparation of test specimens and the test methods

### 1.1 Test materials and preparation of sample

Bentonite used in the test is produced from Gaomiaozi area in Inner Mongolia, and quartz sand aggregate is the manually processed local quartz sand. The basic performance of the bentonite is presents a liquid limit of 318%, a plastic limit of 38%, a grain weight of 2.66[7], and the sand is presents grain size of 49.72% within 0.6~0.3mm and 45.64% within 0.3~0.15mm. Sand mix ratios is defined as the ratio of dry sand to dry bentonite. Fully stir and mix the bentonite with the initial water content of 12.59% and dry quartz sand with sand mix ratios at 0, 10, 20, 30, 40, 50 and 60% and leave them alone for one week. Samples of the mixture are made by statically compacted to a cylinder with diameter of 20mm and height of 10mm through specialized sample preparation apparatus, with dry density, respectively 1.7, 1.8, 1.9 and 2.0g/cm$^3$. After that, put samples in small aluminum boxes, and measured their weight.

### 1.2 Test procedures and determination of soil water characteristic curve

The samples placed in the aluminum capsule are placed in the moisturizing vessel with saturated salt solution at the same time, the samples are on the humidor aperture ceramic board, and the prepared saturated salt solution is placed at the bottom. Saturated salt solution is used to control soil suction and the relative humidity (RH) relationship can be determined according to the thermal dynamics, the following relationship exists between the suction and relative humidity[8]:

$$\psi = -\frac{RT\rho_w}{\omega_v}\ln(RH) \quad (1)$$

Temperature is controlled according to test requirements, and samples are weighted by high-precision electronic balance (with accuracy of 0.0001g) every one to two weeks. When two consecutive weight remains unchanged (two measurements within the range of 0.001g), the exchange of water vapor between the soil samples and steam is considered to reach a equilibrium, at this time the weight of test sample can be recorded and final moisture can be calculated. Elevated temperatures can significantly shorten the time to reach the final balance during the test. Tests are conducted at the temperature of 20, 40, 60 and 80℃ respectively in a incubator with an accuracy of ± 0.5℃. The whole process lasts for three months. Saturated salt solution, and their corresponding suction values under different temperatures are shown in Table 2. Relative humidity translation are cited from DEAN J. A. et al.[9]. Suction balance of tests in this paper mainly relies on free diffusion of water vapor.

## Analysis of test results

### 2.1 Influence of temperature on the soil water characteristic curve of the mixture

Figure 2 gives Influence of temperature on the soil water characteristic curves of bentonite-sand mixture. It can be seen from figure 2 that under the same sand mix ratios(30%) and dry density(1.80g/cm$^3$), when the temperature increases, water retention capacity of the mixture decreases. To observe and analyze better, fitted soil water characteristic curves of mixture of various temperatures are given, in the semi log coordinate, soil water characteristic curves of various temperatures are roughly parallel. When the temperature was raised from 20℃ to 80℃, the controlled suction of the saturated salt solution increased from 4MPa to 367MPa, while the water content of the

mixture decreased from 33.2% to 1.0%. Due to space limitations, Figure 2 lists the soil water characteristic curve of a sand mix ratio (30%) at different temperatures, under other sand mix ratios, as the temperature increases, the behavior of the mixture of soil water characteristic curve is consistent. The finding above is consistent with literature[3-5]. This is because, soil suction is controlled in the suction vapor equilibrium method, and the total suction is equivalent to the free energy of the water in the soil; for higher suction, the dominate factor of adsorption of soil transited from capillary action into the water retention. With increasing temperatures, free energy of water molecules increases freely, with more adsorbed water molecules escaped, the moisture content is decreased.

**2.2 Influence of dry density on soil water characteristic curves of the mixture**

Impact of dry density on soil water characteristic curves of bentonite mixed with sand of are shown in Figure 3. As can be seen from Figure 3 test, the suction controlled with the same sand mix ratios (40%) and under the conditions of temperature (60℃), soil water characteristic curves of the mixture at the different dry density coincidence. It can be seen that the dry density had no effect on the moisture content of the mixture. Scholars who studied FEBEX bentonite[3,4], GMZ bentonite[5,6] observed a similar phenomenon in the test, that the dry density of the soil water characteristic curves of the mixture had no effect. This is because the water in the soil is mainly adsorbed on the mineral surface, while compaction is difficult to change the impact of mineral water adsorption capacity. Suction controlled in the test is within high suction condition, and the dry density has no effect on the soil water characteristic curves of the mixture.

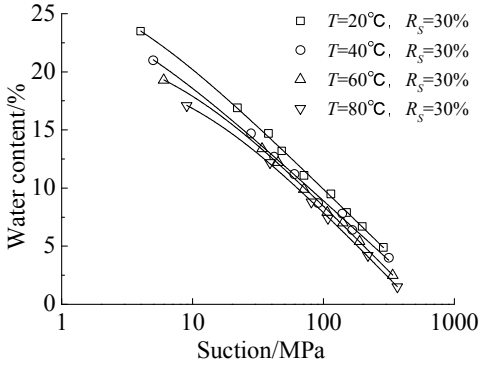


Fig.1 Influence of SWCCs on bentonite-sand mixtures at different temperature

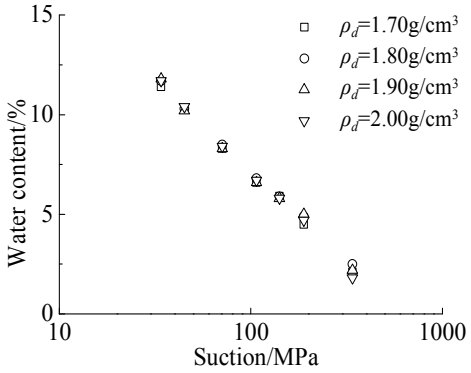


Fig.2 Influence of SWCCs on bentonite-sand mixtures under different dry densities

**2.3Influence of sand mix ratios on the soil water characteristic curves of the mixture**

Soil water characteristic curves of bentonite-sand mixture of sand mix ratios at different temperatures (20℃, 40℃, 60℃and 80℃) and under the conditions of the same dry density (1.80g/cm$^3$) are shown in Figure 4 (soil water characteristic curves of mixture at 20℃ and 60℃ are listed). At the same temperature (see Figure 4 (a) and Figure 4 (b)), as sand mix ratios increases water retention capacity of a mixture significantly reduces, within the suction range of the test control, and a low power segment, water content of sand mix ratios of a mixture are significantly affected; When the suction increase under different sand mix ratios, water content of the mixture decreases. It is the same in the performance of soil water characteristic curves of the mixture at other temperatures. This is mainly because the contact manner between the bentonite particles is changed, in the compacted sample, at this test of lower suction; soil suction is caused by capillary action. the void between the structure in the soil particles affect the soil water characteristic curves; For higher suction, the free energy of soil water can be increased, thus reducing soil adsorption of water, a mixture of different sand mix ratios would lose a large amount of water, then the suction is the main factor of water retention curves. The law, found by Zhang et al.[6], of soil water characteristic curves of GMZ mixture of different mixing sand ratios is consistent with what is found by vapor balance method under normal temperature conditions.

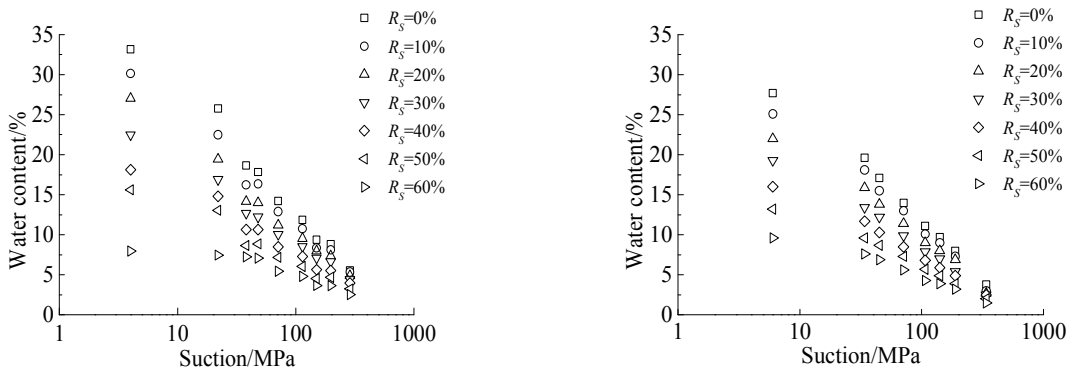


（a）SWCCs on bentonite-sand mixtures at 20℃ （b）SWCCs on bentonite-sand mixtures at 60℃

Fig.3 Influence of SWCCs on bentonite-sand mixtures under different sand mix ratios

## The construction of empirical model of soil water characteristic curve

### 3.1 Empirical model

According to the test data to be analyzed in the semi log coordinate system within a range of test controlled suction, when the suction increases, the moisture content of the mixture shows a decreasing trend. Different temperatures and mixing sand ratios under the conditions of moisture and suction followed the relationship:

$$\omega_T = a - b\ln(\psi + c) \quad (2)$$

Where, $\omega_T$ is the water content of the mixture at different temperatures; $\psi$ is the suction corresponding to different temperatures; *a, b, c* are equation coefficients.

To fit the experimental data under different temperatures, get the series fitting equation by analyzing under different conditions of temperature and sand mix ratios. With the increase of sand mix ratios, the average of parameters shows a decreasing trend, the test parameter c shows an increasing trend with the temperature. A relationship can be found between equation coefficients a, b and mixing sand ratio, presented in (3) and (4).A relationship also exists between the equation coefficient c and temperature，presented in (5).

$$a = k_1 R_s + \lambda_1 \quad (3)$$

$$b = k_2 R_s + \lambda_2 \quad (4)$$

$$c = k_3 e^{\alpha T} \quad (5)$$

Where， $k_1, k_2, k_3$ are 0.49, -0.08, and 1.49; $\lambda_1, \lambda_2$ are respectively 44.58, 6.95; and $\alpha$ is 0.01. Incorporate (3), (4) and (5) into (2), we obtain the equation of soil water characteristic curve of mixture in any temperature and sand mix ratios:

$$\omega_T = k_1 R_s + \lambda_1 - (k_2 R_s + \lambda_2)\ln(\psi + k_3 e^{\alpha T}) \quad (6)$$

### 3.2 Validation of empirical model

Validation of soil water characteristic curve model of mixture under any temperature and sand mix ratios is considered below. Temperatures are taken at 20℃, 40℃, 60℃ and 80℃, sand mix ratios are 0, 20, 40 and 60%, respectively; validation of the established empirical model of soil water characteristic curves of a mixture is carried out. The predicted curve is shown in Figure 5: the forecast curve with the experimental data fits better.

## Conclusion

(1) Within the scope of this article, the dry density has no effect on the soil water characteristic curves of the mixture; impact of temperature, sand mix ratios on oil water characteristic curves of the mixture is obvious; as the temperature increases, water retention capacity of the mixture decreases. For lower suction, when mixing sand ratio increases, the water retention capacity decreases

significantly. For higher suction the impact of the increasing sand mix ratios on the water retention capacity of the mixture is not obvious.

(2) In the semi log coordinates, different temperatures, sand mix ratios are considered, and empirical model of soil water characteristic curve, of a mixture is obtained. The empirical model is used to predict soil water characteristic curves of the mixture of different temperatures and sand mix ratios. Predicted results and experimental data agree with each other well.

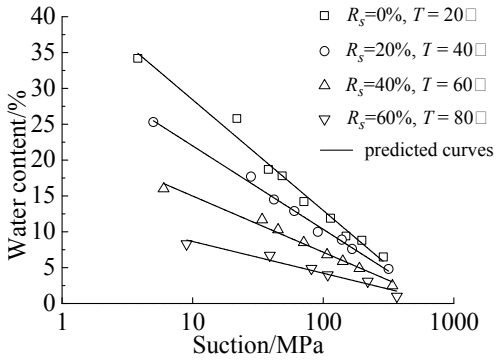


Fig.4 Comparison between measured and predicted results

**Acknowledgements**

This work was financially supported by General Logistics Department Science Research Project (No.BY211C014) and the National Natural Science Foundation of China (No.11272354 ) and Academic Innovation Foundation Project of Logistical Engineering University(No.YZ11-42201).

**References**

[1] Gary X.Tang，James Graha，James Blatz，et al. Suctions, stresses and strengths in unsaturated sand-bentonite[J]. Engineering Geology，2002, (64)：147-156.

[2] Abel Carlos Jacintoa，María Victoria Villar，Roberto Gómez-Espina，et al. Adaptation of the van Genuchten expression to the effects of temperature and density for compacted bentonites[J]. Applied Clay Science，2009, (42)：575-582.

[3] E.E. Alonso，E. Romero，C. Hoffmann，et al. Expansive bentonite-sand mixtures in cyclic controlled-suction drying and wetting[J]. Engineering Geology，2005, (81)：213-226.

[4] Gilson de F. N. Gitirana Jr.,Delwyn G. Fredlund, M.ASCE. Soil-Water Characteristic Curve Equation with Independent Properties[J]. Journal of ggeotechnicail and geoenvironmental engineering，2004, 30(2)： 205-209.

[5] YE Wei-min, WAN Min, CHEN Bao，et al. Effect of temperature on soil-water characteristics and hysteresis of compacted Gaomiaozi bentonite[J]. J.Cent. South Univ. Technol. 2009, 16：821-826.

[6] ZHANG Hu-yuan，ZHANG Ming，CUI Su-li，et al. Determination and modification of soil-water characteristic curves of bentonite-sand mixtures as high-level waste backfill/ buffer material[J]. Chinese Journal of Rock Mechanics and Engineering，2011, 30(2)：382-390.

[7] LIU Yue-miao，WEN Zhi-jian. Study on clay-based materials for the repository[J]. Jmineral petrol，2003, 23 (4)：42-45.

[8] FREDLUND D G, RAHARAJO H. Soil mechanics for unsaturated soil[M]. New York：John Wiley & Sons，Inc.，1993：78-79.

[9] DEAN J A. Lange's handbook of chemistry[M]. 15th ed. New York: McGraw-Hill, 1999：4-5.

*Applied Mechanics and Materials Vols. 580-583 (2014) pp 364-370*
*© (2014) Trans Tech Publications, Switzerland*
*doi:10.4028/www.scientific.net/AMM.580-583.364*

# The prediction of northern slope deformation and failure caused by the transformation of open-pit to underground mining in the Yanqianshan iron mine

Anlin Shao[1, a], Hailong Feng[2,b]

[1]Mining Company, Anshan Iron and Steel Group Corporation, Anshan, Liaoning, China

[2]School of Engineering & Technology, China University of Geosciences, Beijing, China

[a]agkyjs@163.com, [b]fenghailongvip@126.com

**Keywords:** Transformation of open-pit to underground mining; Deformation and failure of slope; Method of limit equilibrium.

**Abstract.** The Yanqianshan iron mine is preparing to transform from an open-pit mine to an underground mine. We adopt the non-pillar sublevel caving approach to exploit the particularly thick steep ore bodies within the range from -183 m to -500 m from top to bottom. According to the features of ore body distribution and the approaches of exploitation, we expect that underground mining will result in the loss of stability on the northern slope of the open pit, causing traction-type landslides. Moreover, along with increasing the depth of the mining operation, the range of slope failure will continue to expand and further affect the safety of drainage features and roads distributed on the north side of the open pit. For this purpose, we select four sections along the trending direction of ore bodies and apply the limit equilibrium method to predict the failure process and characteristics on the northern slope according to the stratified mining process.

## Introduction

The Yanqianshan iron mine was founded in 1960 under open-pit mining practices, which were halted in September 2012. The resulting open pit is 1,410 m long in the east-west direction and ranges from 570 m - 710 m wide in the north-south direction. The elevation of the closed loop is 93 m, and the eventual elevation of the bottom of the open pit is -183 m (Figure 1). The ore bodies of the iron mine are located in the middle of the open-pit, and the trending direction is approximately east-west, tipping in the northeast or southwest directions at a dip angle of 70°-88°, and partially upright. According to the distribution features of ore bodies and the mining methods, we predict that underground mining will result in the loss of stability on the northern slope of the open pit, causing traction-type landslides as a result.

To solve the problem of pit slope deformation and failure caused by the transformation from open-pit to underground mining of metal mines, scholars mainly adopt numerical simulation, model experiment, and on-site monitoring methods. Liu et al. used 2D-Block to study the impact of the transformation of open-pit to underground mining on the slope in the Shizishan mining area of the Daye iron mine [1]. Zhao et al. combined the GPS monitoring data of surface rock movement and FLAC3D numerical simulation to study the impact of the transformation of open-pit to underground mining in the Longshou mine on the stability of rock on the slope, investigating the movement and deformation of wall rocks, the distribution of stress fields, and the failure mechanism [2]. Yang et al. applied FLAC to analyze the displacement field and stress field of the slope during the transformation of open-pit to underground mining in the Nanfen iron mine, in addition to the possible regions of instability [3]. Wang et al. combined PFC and a similar material experiment to study the failure regularity and disaster mechanism of slopes due to the transformation of open-pit to underground mines [4]. Some scholars used similar material model tests to study the failure mechanism of rock layers during the transformation of open-pit to underground mining and the regularity of slope deformation and failure. Sun et al. combined the results obtained for a model test and measurements of mine exploration to investigate the mechanisms of deformation and failure of rock bodies during

the transformation of open-pit to underground mining [5]. Zhang et al. studied the Longshou mine in Jinchuan and analyzed the mechanism of deformation caused by the transformation of open-pit to underground mining in the high-stress area dominated by horizontal tectonic stress, according to the GPS measurement data [6].

To predict the process and regularity of pit slope failure caused by the transformation of open-pit to underground mining and to avoid the loss of personnel and property caused by sudden failure, we apply the limit equilibrium approach and investigate the process and characteristics of failure on the northern slope of an open-pit caused by underground mining according to the actual underground mining process underway in this location. We carry out our study by following the procedure of cyclic analysis as a "simulation of the underground mining-computation of the slope stability-simulation of landslide." Hence, we are able to determine the range of failure on the ground and provide a basis for the layout of drainage and road systems.

## Geology of the mining area and an overview of mining

The Yanqianshan iron mine is located 5 km northeast of the Qianshan scenic area in Anshan City, Liaoning Province, and is 22 km to the west of the center of Anshan City. The southern slope of the iron mine is mainly distributed with mixed rock formations, including gneissic mixed rocks, and granite-like mixed rocks. The basic structural pattern in the mining area is a steep monoclinic structure trending in the direction of 270°-300°, with a dip direction in the northeast or southwest and a dip angle of 70°-88°; that is, the structure is partially upright. The faults in the mining area can be divided into strike faults, oblique faults, and transverse faults, which destroy the integrity of the ore bodies; the main faults are F13, F20, F19, and Fm-1 (Fig.1). The overall trending direction of the ore bodies is 270°-300°., which includes three ore bodies, i.e., Fe1, Fe2, and Fe3; the composition is dominated by ore body Fe1, which is 1,600 m long in the east-west direction and ranges from 55-194 m wide in the north-south direction (Fig.1).

In May 2012, the Yanqianshan iron mine began mining the ore bodies on the eastern and western slopes. The range of mining on the western slope includes the ore bodies to the west of exploration line XIV with an elevation in the range of 21 m to -183 m, and the range of mining on the eastern slope includes the ore bodies to the east of exploration line VII-50 with an elevation in the range of -47 m to -183 m. After mining the eastern and western slopes, the underground ore bodies will be mined, and the range of underground mining includes the ore bodies between exploration lines XVI-IX+100 with elevation in the range of -183 m to -500 m (Fig. 1). The mining activity on the eastern and western slopes and the underground exploration have adopted the non-pillar sublevel caving method, proceeding from the top to the bottom in a horizontal layer approach with an inter-lay thickness of 18 m.

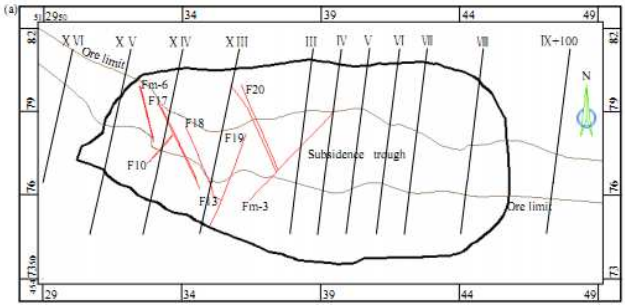


Fig. 1 The geological plan of Yanqianshan iron mine.

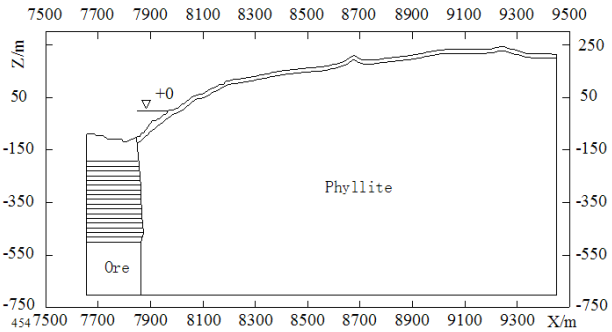


Fig. 2 Computational model of section IV.

## Prediction of the failure process on the northern slope caused by underground mining

**Methods of analysis.** Based on the distribution features and mining methods of ore bodies, we predict the rock movement and failure process caused by the underground mining as follows: (1) After commencing the underground mining practices on the eastern and western slopes, a collapse groove

will appear in the open pit along the trending direction of the ore veins, and the collapse groove will grow increasingly deeper with mining progress on the eastern and western slopes and underground. (2) Along with the deepening of the collapse groove, the rock bodies adjacent to both sides of the collapse groove will displace and begin to slide toward the collapse groove. (3) The collapse of rock bodies adjacent to the two sides of the collapse groove will then cause the loss of the stability of the northern and southern slopes of the open pit, resulting in traction-type landslides. (4) The aforementioned movement and failure of the rock layers will happen repeatedly as the increase of the mine depth, and the range of rock movement and failure caused by underground mining will continue to expand.

In contrast to the conventional analysis of slope stability, during the mining process, the slope of the open-pit discussed in this paper is subject to continuous landslides and collapse that continuously develop into the deeper layers of rock, causing the range of surface failure to undergo continued expansion. Therefore, we select profiles III-VI (Fig. 1) as the typical profile of the northern slope, and we apply the limit equilibrium method to investigate the process and characteristics of failure on the northern slope of the open-pit caused by underground mining. We carry out our analysis in accordance with the actual process of underground mining by following the procedures of cyclic analysis as a "simulation of the underground mining-computation of the slope stability-simulation of landslides." The detailed analytical processes performed for each profile are as follows.

Step 1: According to the stratified process of underground mining, modify the calculation model and simulate the horizontal mining from the current layer downward to the next layer, with a stratified thickness of 18m.

Step 2: Apply the limit equilibrium method to calculate the slope stability after the exploration of one layer, and search and draw the potential sliding surface that corresponds to different safety coefficients.

Step 3: If a sliding surface exists with a safety coefficient smaller than 1.0, cut off the sliding bodies along the minimum sliding surface, and carry out the simulation of landslides and collapse during the mining process.

Step 4: Continue the previous step until there is no remaining sliding surface with a safety coefficient smaller than 1.0.

Step 5: Repeat the procedures of Step 1-Step 4 until the exploration reaches the level of -500 m.

**Determination of the physical mechanical parameters of rock bodies.** In this paper, all of the computation profiles are located in the same partition, and a given type of rock body can use the same physical mechanical parameters. According to the survey report, we determined the physical mechanical parameters for different types of rock bodies, as shown in Table 1.

Table 1 The physical mechanical parameters of rock bodies.

| Rock | Density [g/cm$^3$] | Cohension [Mpa] | Fraction angle [°] |
|---|---|---|---|
| Phyllite | 26.8 | 500 | 40 |
| Ore | 32.7 | 1300 | 41 |

**Model of calculation.** Fig. 2 is the calculation model for profile IV. In the model, the direction of the X-axis points from south to north, and the direction of the Z-axis points from low elevation to high elevation. The range of the computation model is specified as follows: the coordinates of the northern boundary are X = 4, 549, 450 m, and the south side extends to the southern boundary of the ore veins. The Z coordinate for the bottom of the model is -700 m, and the upper part reaches the ground surface. The mining activity in the first step reaches the elevation of -194 m; then, mining proceeds layer-by-layer in 18-m increments, before eventually reaching the elevation of -500 m. The calculation model used for the other profiles is similar to that of profile IV and, hence, is not reiterated here.

**The process of slope failure and an analysis of the characteristics.** With the method of analysis described in section 3.1, we analyze the process and characteristics of failure on the northern slope (profiles III-VI) of the open-pit. The procedures for the analysis of underground mining, the computation of slope stability, and the simulation of landslides are the same for different computation profiles. However, due to the difference in the geometric morphology of the slopes, there is also a difference in the relationship between the slope failure process and mining depth and the position of the most dangerous sliding surface. Fig. 3(a)-(d) give the relationship between the minimum safety coefficient and mining depth for the slopes with profiles III-VI, and Fig. 4(a)-(d) give the relationship between the position of the most dangerous sliding surface and the mining depth for profiles III-VI. In the following, we use profile IV as an example, and we present details about the slope failure process while carrying out the underground mining practice.

Before the underground mining practice is initiated, the minimum safety coefficient of the slope with profile IV is 1.891, and the slope is in a stable state. According to the relevant designs, mining advances to the elevation of -194 m at the first step and then continues for 17 steps, with a mined layer measuring 18 m at each step. To facilitate the narration, we use $\lambda$ to represent the horizontal distance from the intersection between the most dangerous sliding surface and the ground surface to the northern margin of the model. The process and characteristics of failure for the slope with profile IV are as follows.

(1) When the mining activity reaches the elevation from -194 m to -212 m, the slope is in a stable state without landslides, but the minimum safety coefficient of the slope decreases to 1.004. Additionally, the most dangerous sliding surface of the slope moves northward, and the $\lambda$ value is 1, 540 m.

(2) When the mining activity reaches the elevation from -212 m to -230 m, the minimum safety coefficient of the slope is 0.909, and $\lambda$ is 1, 540 m. We cut off the landslide along the sliding surface of the slope that corresponds to the minimum safety coefficient, and then, we calculate the stability of the slope, where the safety coefficient of the slope reaches 1.056. The stability of the slope after a landslide increases, and the most dangerous sliding surface moves northward by 52 m.

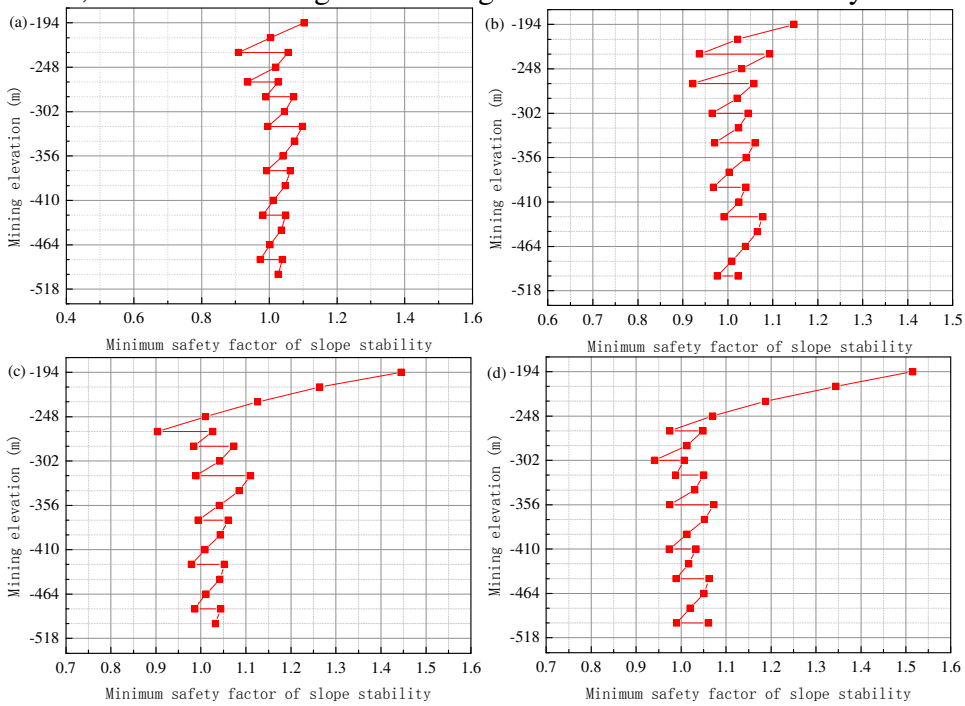


Fig. 3 Relationships between slope failure and mining depth at different sections: (a) Sec. IV, (b) Sec. III, (c) Sec. V, (d) Sec. VI.

(3) When the mining activity reaches the elevation from -230 m to -248 m, the minimum safety coefficient of the slope is 1.017, and $\lambda$ increases from 1, 488 m to 1, 505 m. This indicates that after the first simulation of slope cutting, the stability of the slope increases, and the most dangerous sliding surface moves slightly southward.

(4) When the mining activity reaches the elevation of -266 m, the minimum safety coefficient of the slope is 0.936, and $\lambda$ is 1, 425m. After performing slope cutting on the corresponding sliding surface according to the minimum safety coefficient, we again calculate the stability of the slope, finding that the minimum safety coefficient increases to 1.026 and that the $\lambda$ value becomes 1, 492 m. This indicates that after the second slope-cutting event, the stability of the slope increases again, and the most dangerous sliding surface continues to move northward by 67 m.

(5) When the mining activity reaches the elevation of -284 m, the minimum safety coefficient of the slope is 0.990, and $\lambda$ is 1, 342 m. After performing slope cutting on the corresponding slide surface according to the minimum safety coefficient, we calculate the stability of the slope. The minimum safety coefficient increases to 1.072, with a $\lambda$ value of 1, 434 m. This indicates that after the third landslide simulation, the slope again reaches a stable state, and the most dangerous sliding surface moves significantly northward by 92 m. When the mining activity reaches from -284 m to -302 m, the minimum safety coefficient of the slope is 1.050, and the variation of $\lambda$ is very small. At this time, the slope is in a stable state.

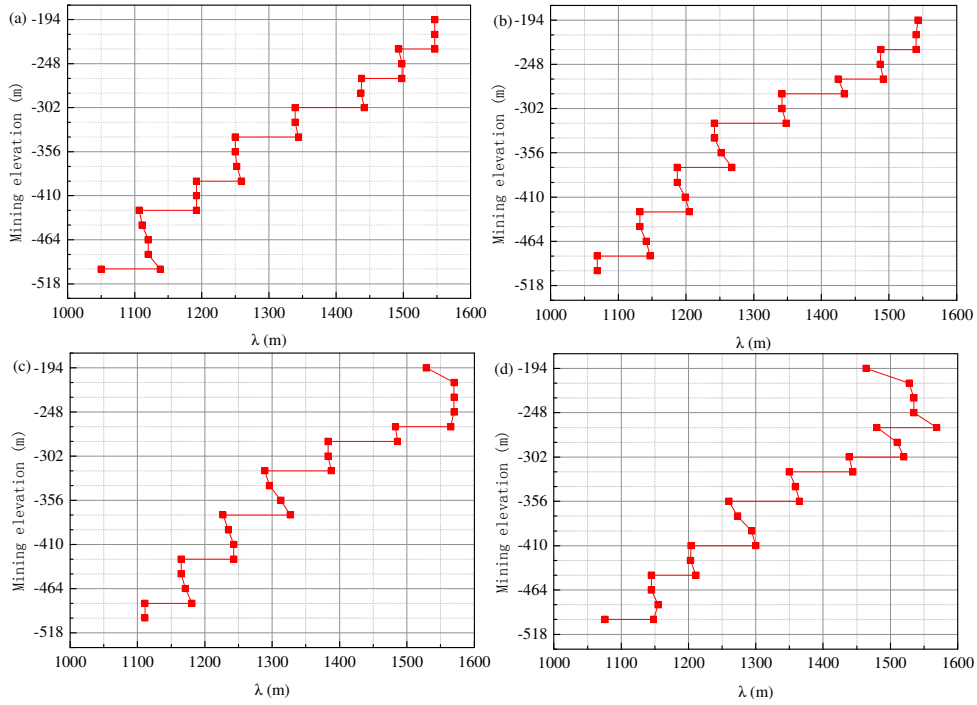


Fig. 4 Relationship between most dangerous sliding surface and mining depth at different sections: (a) Sec. III, (b) Sec. IV, (c) Sec. V, (d) Sec. VI.

(6) When the mining activity continues, reaching the elevation of -320 m, the minimum safety coefficient of the slope is 0.996, and $\lambda$ is 1, 242 m. After the landslide simulations, the minimum safety coefficient is 1.098, and $\lambda$ changes to 1, 348 m. This indicates that when the mining activity reaches the elevation of -320 m, the implementation of a fourth simulated landslide causes the slope to reach a stable state, and the most dangerous sliding surface again moves significantly northward by 106 m. When the mining continues to -338 m, the minimum safety coefficient of the slope is 1.075, without significant change in the most dangerous sliding surface, and the slope is still in a stable state. When the mining activity reaches from -338 m to -356 m, the minimum safety coefficient of the slope is 1.040, and the most dangerous sliding surface again moves slightly southward, with the slope in a stable state.

(7) When the mining activity reaches the elevation of -374 m, the minimum safety coefficient of the slope is 0.992, and $\lambda$ is 1, 187 m. Again, we perform the slope cutting along the sliding surface that

corresponds to the minimum safety coefficient, and we derive the minimum safety coefficient to be 1.062. This indicates that after the fifth simulated landslide, the minimum safety coefficient increases, and the stability of the slope also increases. As a result, the most dangerous sliding surface moves northward by 81 m, and $\lambda$ is 1, 268 m. When the mining activity continues to -392 m, the minimum safety coefficient of the slope is 1.047, without significant change in the most dangerous sliding surface, and the slope is still in a stable state. When the mining reaches from -392 m to -410 m, the minimum safety coefficient of the slope is 1.010, and the most dangerous sliding surface again moves slightly southward, with the slope in a stable state.

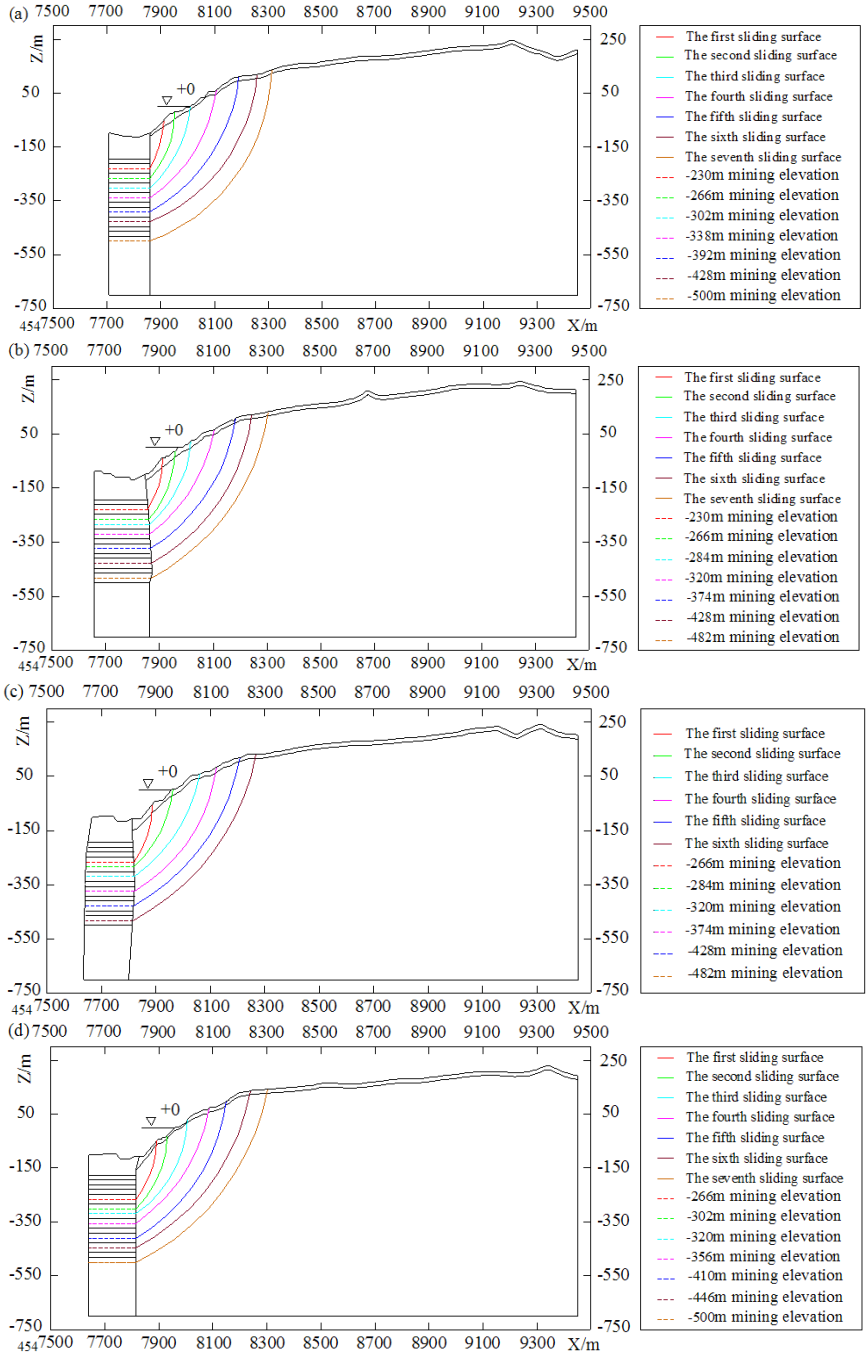


Fig. 5 Relationship between most dangerous sliding surface and mining depth: (a) Sec. III, (b) Sec. IV, (c) Sec. V, (d) Sec. VI.

(8) When the mining activity reaches the elevation of -428 m, the minimum safety coefficient of the slope is 0.981, and $\lambda$ is 1, 132 m. After slope cutting, the calculated minimum safety coefficient is 1.048, and $\lambda$ becomes 1, 205m. It can be seen that when the mining reaches the elevation of -428 m, after the sixth simulated landslide, the minimum safety coefficient increases, and the stability of the slope also increases, and the most dangerous sliding surface moves northward by 73 m. When the

mining activity continues to the elevation of -446 m, the minimum safety coefficient of the slope is 1.036, without a change in the value of $\lambda$; hence, the slope is still in a stable state. When the mining reaches from -446 m to -464 m, the minimum safety coefficient of the slope is 1.020, and the most dangerous sliding surface again moves slightly southward.

(9) When the mining activity reaches the elevation of -482 m, the minimum safety coefficient of the slope is 0.974, and $\lambda$ is 1, 069 m. The minimum safety coefficient with the simulation of slope cutting is 1.039. That is, after the seventh landslide simulation, the minimum safety coefficient increases, as does the slope stability; furthermore, the most dangerous sliding surface again moves northward by 78 m, and $\lambda$ is 1,147 m. When the mining reaches -500 m, the position of the most dangerous sliding surface experiences an insignificant change.

Fig. 5 (a)-(d) give the position of the most dangerous sliding surface with a safety coefficient smaller than 1.0 for profiles III-VI during the mining process. From these figures, it can be seen that during the underground mining activity, seven landslides occur for profile III. After the final landslide, the minimum safety coefficient of the slope is 1.023; a total of seven landslides occur for profile IV, and the minimum safety coefficient of the slope is 1.039; a total of six landslides occur for profile V, and the minimum safety coefficient of the slope is 1.044; a total of seven landslides occur for profile VI, and the minimum safety coefficient of the slope is 1.061.

## Conclusions

(1) The Yanqianshan iron mine is preparing to transform from open-pit exploration to underground mining practices. According to the distribution features of ore bodies and the method of exploration, underground mining will cause the loss of stability on the southern and northern slopes of the open-pit, resulting in traction-type landslides. Moreover, in addition to increasing the depth of the mine, the landslide will continuously occur on the northern and southern slopes of the open-pit, and the range of failure will continuously expand, endangering the nearby buildings and facilities on the surface.

(2) In this paper, we select profiles III, IV, V, and VI for the northern slope of the open-pit as the typical profiles, and we apply the limit equilibrium method to investigate the process and characteristics of failure on the southern slope of the open-pit caused by underground mining. We carry out our investigation according to the actual process of underground mining by following the procedures of cyclic analysis as a “simulation of the underground mining-computation of the slope stability-simulation of landsides.”

(3) We establish the minimum safety coefficient and relationship between the location of the most dangerous sliding surface on the slope and mining depth for the slope of each typical profile. Additionally, we predict the process of slope failure, and we analyze the impact of the range of slope failure on the buildings and facilities on the ground surface.

## References

[1] H. Liu, W.S. Chen, X.T. Feng and Q.R. Chen: Rock and Soil Mechanics Vol. 25 (2004), p. 1413-1417

[2] H.J. Zhao, F.S. Ma, and Y.C. Li: Journal of China Coal Society Vol. 36 (2011), p. 1635-1641

[3] W. Yang, S.J. Cai, and Y.C. Li: Nonferrous Metals Vol. 64 (2012), p.75-78

[4] Y.F. Wang, and F.P. Zhong: Journal of China Coal Society Vol. 38 (2013), p. 64-69

[5] S.G. Sun, M.F. Cai and S.J. Wang: Chinese Journal of Rock Mechanics and Engineering Vol. 19 (2000), p. 126-129

[6] Y.M, Zhang, F.S. Ma, J.M. Xu, H.J. Zhao and Y.L. Gao: Rock and Soil Mechanics Vol. 32 (2011), p.590-595

*Applied Mechanics and Materials Vols. 580-583 (2014) pp 371-375*
*© (2014) Trans Tech Publications, Switzerland*
*doi:10.4028/www.scientific.net/AMM.580-583.371*

# The study on the engineering properties of squeezed branch piles under combined load

Weifeng Han Binbin Feng Jing Zhou Chenyuan Lu

(College of Architecture & Civil engineering, Zhejiang University of Technology, Hangzhou 310014, China)

(College of Architecture & Civil engineering, Zhejiang University of Technology, Hangzhou 310014, China)

(Hangzhou urban construction development group co., LTD, Hangzhou 310014, China)

(College of Architecture & Civil engineering, Zhejiang University of Technology, Hangzhou 310014, China)

532218982@qq.com, 490275262@qq.com,179303444@qq.com, 393767655@qq.com

**Key words:** squeezed branch pile; combined load; bearing properties; model test

**Abstract.** In this article, we design an experiment about model piles to study their bearing capacity and deformation properties under uplifting load of different angles, model piles include the equivalent-diameter pile, the squeezed branch pile with single plate and the squeezed branch pile with two plates. The test shows, the bearing capacity of squeezed branch pile is higher than the equivalent-diameter pile, and its plates can resist the horizontal load on the top of pile better.

In the actual project, pile foundation often bears various loads, such as vertical load, horizontal load and bending moment, etc. The bearing properties of squeezed branch pile under one-way load have been studied many times, but the study of bearing properties under combined load has not been reported almost. In this article, we carry out a model experiment of the squeezed branch pile under vertical load and horizontal load together to increase access to its bearing properties.

## The brief test introduction

There are 3 model piles in this experiment, no.1 is the equivalent-diameter pile, no.2 is the squeezed branch pile with single plate and no.3 is the squeezed branch pile with two plates, as shown in Figure 1. The pile shaft is a steel pipe with 50mm in diameter and 60mm in length, and the plate is a steel plate with 120mm in diameter and 20mm in thickness. In order to increase the model pile's surface roughness, we brush a layer of cement slurry on the steel pipe. We carry out this experiment in the soil tank of Geotechnical Laboratory of our college, its plane dimension is 0.6*1.5m and its depth is 0.85m, the test soil sample is generic homogeneity silt from Xiasha Hangzhou. We bury the three model pile into the soil tank in place and tamp the test soil sample in layers before the experiment, the place as shown in Figure 1.

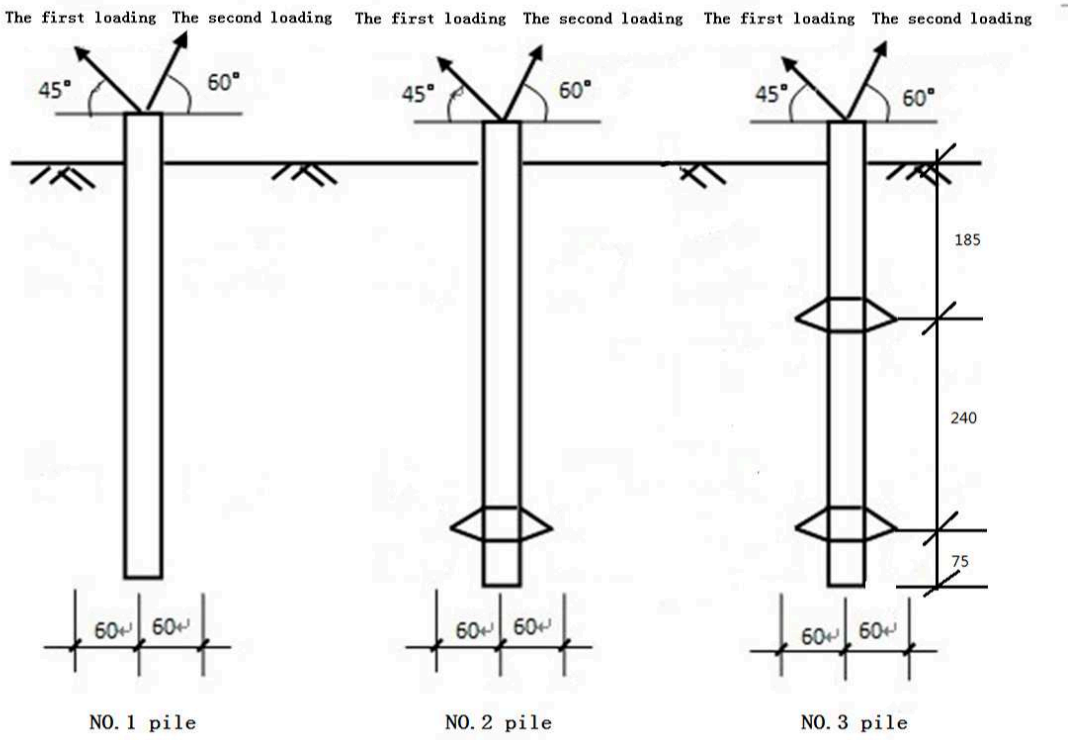


Fig.1 The model piles and loading schematic diagram

For comparison, two groups of loading are be designed in this experiment, in the first group, three piles are studied under uplifting horizontal load of 45 degree angle, in the second group, three piles are studied under uplifting horizontal load of 45 degree angle.

## Q-S curve analysis

According to the load and horizontal displacement measured by experiment, we can get the Q-Sv curve as shown in the figure below:

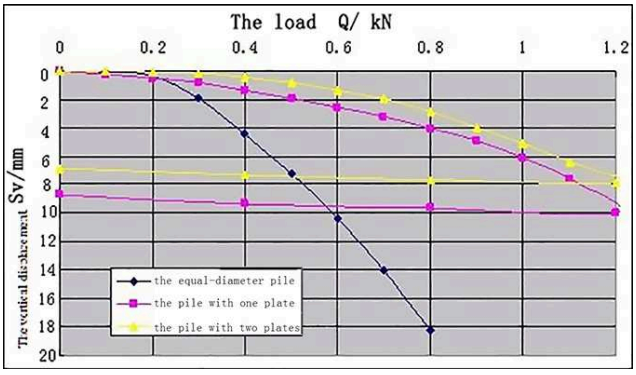


Fig.2-1 The Q-$S_v$ curve when the load inclination is 45 degree

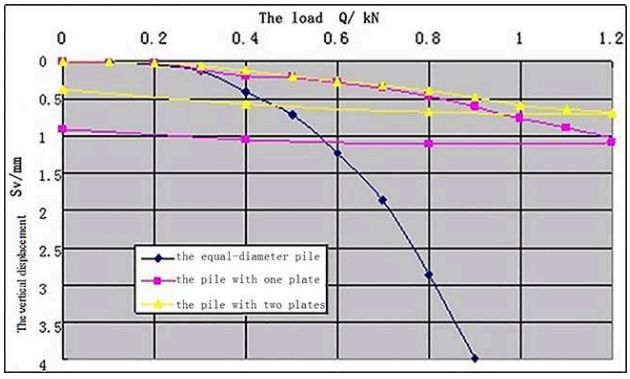


Fig.2-2 The Q-$S_v$ curve when the load inclination is 60 degree

According to the load and horizontal displacement measured by experiment, we can get the Q-Sh curve as shown in the figure below:

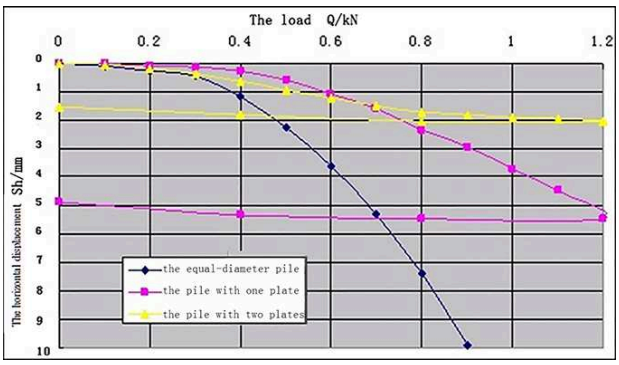


Fig.2-3 The Q-$S_h$ curve when the load inclination is 45 degree

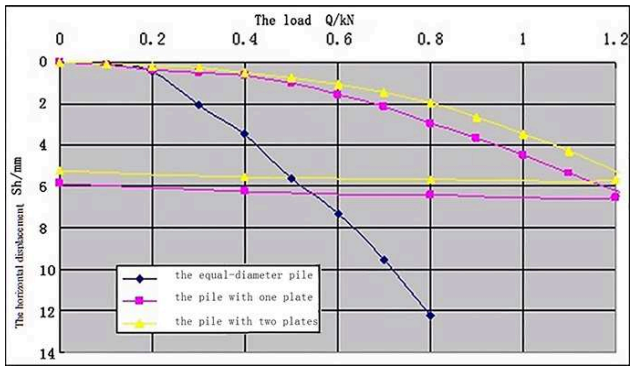


Fig.2-4 The Q-$S_h$ curve when the load inclination is 60 degree

To analyze the curve features above-mentioned, we can get the following results:

1) According to the analysis of figure 2-1~2-4, we find the Q-Sv curve and Q-Sh curve of the squeezed branch pile is more flat without steep drop, compared with general equivalent-diameter piles, under inclined load. If determine the bearing capacity with the equal displacement, we can find the bearing capacity of squeezed branch pile is higher than the general pile's, which fully embody the advantage of the squeezed branch pile's bearing capacity.

If take horizontal deformation of 4 mm as a control condition of bearing capacity, we find the bearing capacity of the equivalent-diameter pile is about0.62kN and of the squeezed branch pile with single plate is about 1.03kN when 45 degree load inclination. The bearing capacity of the squeezed branch pile with single plate increase by 66%, compared with the equivalent-diameter pile, and the bearing capacity of the squeezed branch pile with single plate is much higher(because the displacement of two plates pile do not load to 4mm, it is not strictly comparable).

When 60 degree load inclination, the bearing capacity of the equivalent-diameter pile is about 0.43kN and of the squeezed branch pile with single plate is about 0.94kN, compared with the equivalent-diameter pile, the bearing capacity of the squeezed branch pile with single plate increase by 119%

2) To displacement, when the load inclination is 45 degree and the load is 0.8kN, the vertical displacements of three piles are 2.86mm, 0.47mm, 0.39mm, we can find the displacements of the single plate pile and two plates pile are 16 and 14 percent of the equivalent-diameter pile's. Meanwhile, the horizontal displacements of three piles are 7.39mm, 2.37mm, 1.72mm, and the displacements of the single plate pile and two plates pile are 32 and 23 percent of the equivalent-diameter pile's displacements. So the squeezed branch pile has the better capability to resist deformation caused by horizontal load and uplifting load, and the more plates, the more favorable.

3) Different load angles, that is to say, the proportion of horizontal load and vertical load is different, have an effect on the load-bearing performance of piles. For the equivalent-diameter pile, when 45 degree load inclination, its Q-Sv curve is no obvious steep fall, but when 60 degree load inclination,

the steep fall point is obvious. According to the phenomenon, we can assume that when the load horizontal component is larger, the friction increases as the increase of pressure on pile-soil interface, thus the uplift bearing capacity increases.
For squeezed branch piles, the phenomenon of high uplift bearing capacity caused by large horizontal load is obvious, especially the pile with two plates, there appear a inflection point in its Q-Sv curve, when the load increase to a value, the deformation of piles with two plates is insensitive to load, it is called “uplifting stamina”.

4) According to the test data when the load inclination is 45 and 60 degree, we can get the ratio $S_v/S_h$ between the vertical and horizontal displacement as shown in the table below:

Table.1 The ratio $S_v/S_h$ when the load inclination is 45 degree

| The pile mark | NO.1 pile | NO.2 pile | NO.3 pile |
|---|---|---|---|
| $S_v/S_h$ | 0.39 | 0.2 | 0.23 |

Table.2 The ratio $S_v/S_h$ when the load inclination is 60 degree

| The pile mark | NO.1 pile | NO.2 pile | NO.3 pile |
|---|---|---|---|
| $S_v/S_h$ | 1.5 | 1.37 | 1.44 |

From the above tables, we can assume that the load inclination is sensitive to the deformation in both directions when the pile foundation bears the uplifting and horizontal load. When the load inclination is 45 degree (the load ratio is 1:1 in vertical and horizontal directions), the horizontal displacement of three piles is larger than the uplifting. But when the inclination increase 15 degree to 60 degree (the load ration is 1.73:1 in vertical and horizontal directions), the horizontal displacement of three piles is less than the uplifting displacement.

So in the actual project, we should consider that the combined load composed of uplifting and horizontal load is sensitive to the displacement variation. For example, when it requires high level for deformation control in one direction, we should emphasize to strengthen the anti-deformation design of pile foundation in the direction.

**Conclusions**

1) Compared to the equivalent-diameter pile with the same length and diameter, the load bearing behavior of squeezed branch piles under uplifting inclined loads is similar with the behavior loaded in one way(horizontal or vertical direction), and There is a significant increase in the bearing capacity of squeezed branch piles, especially the piles with two plates.

2) The squeezed branch pile has a better capability to resist deformation caused by horizontal and uplifting loads, and the more plates, the more favorable.

3) When the proportion of horizontal load and vertical load is different (the load inclination is different), there is an effect on the load-carrying properties of piles. The appropriate horizontal load can increase the pressure on pile-soil interface, and increase the friction force, and enhance the uplifting bearing capacity.

4) The experiment shows that the combined uplifting inclination is very sensitive to the deformation in two directions.

**Acknowledgements**

This work was financially supported by Science and Technology Innovation Activities Plan of Zhejiang college students.

**Reference**

[1] Chen Lun, Jiang Li, Wang Haiyan.et al. Field full- scale test study on tension bearing mechanism of DX piles cast in-situ. Industrial Construction, 2004,34(10):33.

[2] DENG You-sheng, GONG Wei-ming, DAI Guo-liang. Comparative test study on extraction characteristics of both compactions-under reamed. Building Science, Vol. 22, No. l Feb. 2006.

[3] LU Cheng-yuan, MENG fan-li, WANG long. Test study of model piles with branches and plates [J]. Rock and Soil Mechanics. 2004，25（11）：1809-1813.

[4] LU Cheng-yuan, MENG fan-li, WANG Zhang-jie. Test of model piles with branches and plates in unsaturated silty clay [J]. Chinese Journal of Geotechnical Engineering, 2004，26（4）：522-525.

[5] QIAN De-ling. A study of compression and extraction resistance behavior of squeezed supporting disk pile [I]. Rock and Son Mechanics, 2003, 24(supp.): 517 — 520.

[6] QIAN De-ling. Study on loading transfer law and FEM simulation of squeezed branch piles [J]. Chinese Journal of Geotechnical Engineering, 2002, 24(3): 3 7 I —375.

[7] DENG You-sheng, GONG Wei-ming, DA I Guo-liang, HAN Jin-sheng. Field Comparative Experimental Study on Bearing Capacity of Both Bored Pile with Branches and Plates and Column Bored Pile at the Same Site. Journal of Chongqing Jianzhu University, Vo1. 27 No. 5 Oct 2005.

*Applied Mechanics and Materials Vols. 580-583 (2014) pp 376-379*
*© (2014) Trans Tech Publications, Switzerland*
*doi:10.4028/www.scientific.net/AMM.580-583.376*

# Triaxial test study on Marine Sediments Sample with Simulated Combustible Ice

Xiaoliang Wang[1,a], Guangfan Li[1,b,*] and Juan Du[1,c]

[1]College of Civil Engineering & Architecture, Hainan University, Haikou 570228, PR China

[a]wayne0509@163.com, [b]lgf1728@163.com ([*]corresponding author) , [c]sharondj1978@sohu.com

**Keywords:** Combustible ice, Marine sediments, Triaxial test, Mechanical property

**Abstract.** Combustible ice is a kind of efficient and clean energy that has the potential to be exploited in the future, exploiting combustible ice needs to understand its mechanical properties. Combustible ice is another important feature of soil which is different from soil, in order to correctly understand the distinction, this paper using soil mechanics triaxial test method, to study the mechanical properties of combustible ice. Different from previous study, this article put forward the concept of simulated combustible ice, namely through baking powder, sodium chloride, and Marine sedimentary soil to simulate flammable ice, explore a new method for sample preparation to study the mechanical property of combustible ice.

## Introduction

Combustible ice is a kind of cage ice crystals generated by gas and water in a range of high pressure and low temperature conditions, so is also called gas hydrate. It widely distributed in the mainland, deep sea and some inland lake. It is a new energy with huge reserves [1-2]. According to statistics, the total energy of gas hydrate in the world is about 2~3 times more than coal, oil and gas, 27% of the mainland and 90% of the sea containing gas hydrate [3]. As the world's energy dried up, Combustible ice has got more and more attention as a kind of clean energy. In recent 10 years, combustible ice is known as the crown of 21st century new energy [4].

Before exploiting gas, we must carry on the experiments of gas hydrate research. Research on simulation test, Hyodo [5] and Clayton [6] created the integration of triaxial test apparatus. Experimental study on the mechanical properties of hydrate sediments at home and abroad work started relatively late, so the literature of hydrate sediments mechanical properties research reports is limited to the laboratory test results of Winters, Hyodo, Masui and Clayton et al. The study of hydrate sediments stress-strain relationship and strength characteristics need to be further [7].

It is tedious and expensive to improve equipment and prepare simulated sample in the study of combustible ice. That goes against the fundamental research of combustible ice. Relative to the complex equipment modification and sample preparation, this paper proposes a new idea, simulated combustible ice which means using conventional materials to simulate the structure form of combustible ice, get the mechanics performance through triaxial test and analysis the geological problems may encounter in the process of exploit combustible ice.

## Test introduction

Domestic experts agreed in three basic aspects about the study on combustible ice [8-10]: ①Macroscopic mechanical properties of combustible ice difference is mainly caused by the different methods of its formation; ②Combustible ice strength characteristics associated with test conditions, such as confining pressure, initial porosity and so on; ③The strength of combustible ice is associated with the particle properties of sediments. At home and abroad for the simulation of combustible ice is used more high voltage equipment simulated conditions of combustible ice generated at low temperature, at the same time, take advantage of highly visual equipment to observe the formation and decomposition of combustible ice. But for the mechanics characteristic test, these test conditions are not important. Therefore, the author thought that as the key models of combustible ice is mainly

focused on three aspects: ①The choice of skeleton particles; ②The cellular structure of sediment; ③The simulation of combustible ice crystal particles.

**Skeleton Particle.** Skeleton particles of test sample preparation using Marine sedimentary soil. Marine deposit refers to the Marine environment by Marine dynamic process to produce a series of deposits, including debris from land and Marine biological bone and debris, ash and cosmic dust, etc, with a series of lithologic features and biological characteristics of Marine environment. Marine sediments is the breeding of oil and gas, selected areas of Hainan island coastal deposition by dry sieving to make combustible ice soil sample can suit the requirements of triaxial test.

**Cellular Structure.** Cellular structure is due to leave the sediment space after the release of crystals gas. The cellular structure is accomplished by baking powder. The acid salt in baking powder can react with carbonate and control the speed of gas velocity. Carbonates are hydrolyzed in water balance:

$$HCO_3^- + H_2O \Leftrightarrow H_2CO_3 + OH^- \quad (1)$$

$$H_2CO_3 \Leftrightarrow H_2O + CO_2 \uparrow \quad (2)$$

Reaction to the right to produce large amounts of gas when the system of ph or temperature changes. Acidic salt by hydrolysis or ionization effect change system of ph in the reaction process, thus affecting the carbonate gas.

**Crystal Particle.** The most common type of combustible ice crystal structure form is six sides cube. In order to achieve the simulation test under atmospheric pressure, select properties of stable and crystal particles with six sides of the cube sodium chloride is most appropriate.

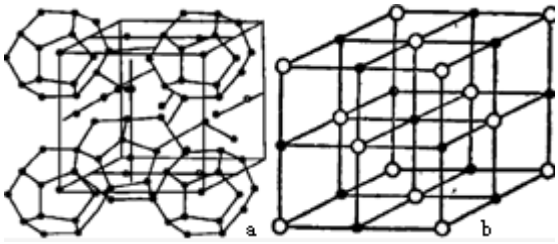


Fig. 1 Comparison of Gas hydrate and Sodium chloride

(a-Gas hydrate the diamond cubic structure diagram; b-Sodium chloride cubic structure diagram). As can be seen from the figure 1 both gas hydrate and sodium chloride are six sides cube. Experiment chose the sun sea water to prevent crystallization of large granular sodium chloride crystals test of sodium chloride in the process of early into the soil.

**Test Set.** Combustible ice is another important characteristic of soil and different from the soil. Triaxial test can correctly understand the difference. Triaxial test set to three kinds: consolidation test; consolidation undrained test; not consolidated undrained test. Simulations of combustible ice exploit process in different project environment.

## Combustible Ice Sample Triaxial Test

**Consolidation-Drainage Triaxial Test (CD).** Consolidation drained shear test set $\sigma_3 = \sigma_c$, five consolidation pressures $\sigma_c$ rank: 0kPa; 50kPa; 75kPa; 100kPa; 150kPa. Reverse pressure saturated samples first, then consolidated under $\sigma_c$, drainage shear keep $\sigma_3 = \sigma_c$ at last. Each level cell pressure 1 set of tests are carried out, sample size: $\phi 50 \times 100$.

The stress strain curve is shown in figure 2. From figure 2 we can see sample of combustible ice present plastic damage, the higher confining pressure, the greater intensity.

**Consolidated-Undrained Triaxial Test (CU).** The strength index of consolidated undrained can be used for seabed combustible ice under the water level change suddenly during exploit. Test set five cell pressures: 0kPa, 50kPa, 75kPa, 100kPa, 150kPa. Each level cell pressure 1 set of tests are carried out, sample size: $\phi 50 \times 100$.

The stress strain curve is shown in figure 3. From figure 3 we can see sample of combustible ice present plastic damage, the higher confining pressure, the greater intensity.

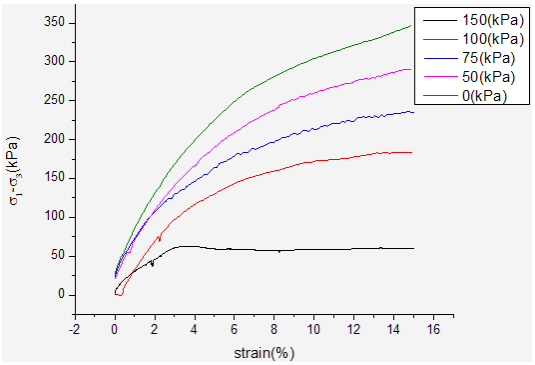


Fig. 2 The stress-strain diagram of CD

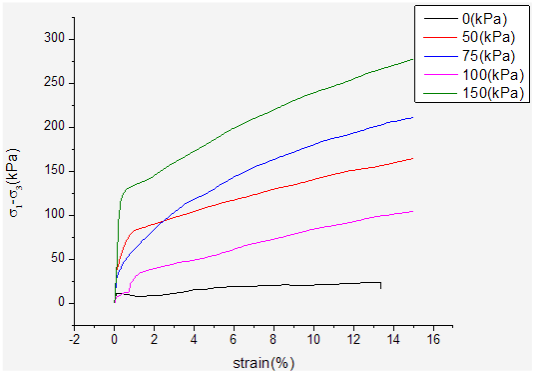


Fig. 3 The stress-strain diagram of CU

**Unconsolidated-Undrained Triaxial Test (UU).** Undrained strength is used to the pore water pressure dissipation caused by load increase and density not remains the same. If the viscosity of combustible ice carrier soil is big and permeability is little, we should use this strength when drainage condition is poor. This test is divided into two groups, a set of crystal content 5%, and another group of crystal content 10%. The group of 5% has five cell pressure levels: 50kPa; 100kPa; 150kPa; 200kPa; 300kPa. The group of 10% has four cell pressure levels: 50kPa; 100kPa; 150kPa; 200kPa.

Crystal content 10% obtained a set of test stress strain curve as shown in figure 4 and crystal content 5% obtained a set of test stress strain curve as shown in figure 5.

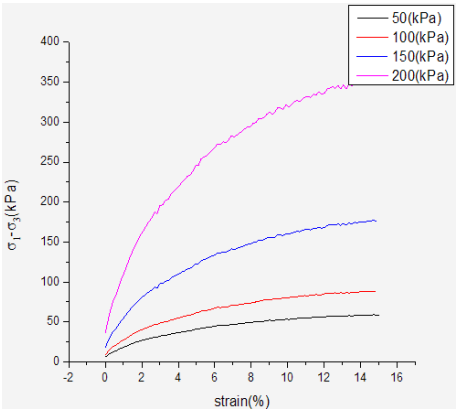


Fig. 4 The stress-strain diagram of UU (10%)

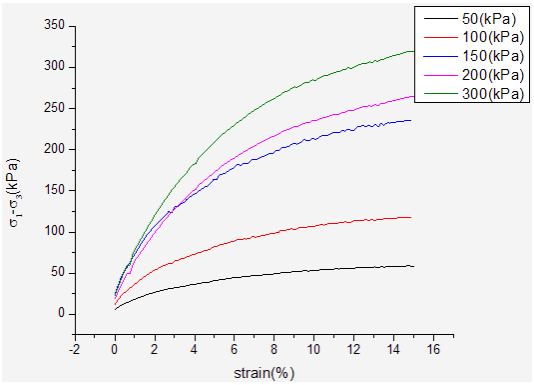


Fig. 5 The stress-strain diagram of UU (5%)

By comparing the figure 4 and figure 5 can be learned, the peak compressive strength difference of combustible ice sample with different crystal content under same cell pressure is very big, to compare the same cell pressure with different contents of crystal to analyze the crystal content on the compressive peak as combustible ice peak compressive strength of Marine sediment sample, draw the table 1:

Table 1 The same cell pressure the comparison of different crystal content compressive peak

| Cell pressure | Peak strength（5%） | Peak strength（10%） | Strength added(kPa) |
|---|---|---|---|
| 50kPa | 58.68 | 63.72 | 5.04 |
| 100kPa | 88.02 | 117.36 | 29.34 |
| 150kPa | 176.04 | 234.72 | 58.68 |
| 200kPa | 264.25 | 352.08 | 87.83 |

Table 1 illustrates that peak strength of combustible ice sample increased along with the increase in crystal content under the same cell pressure. At the same time, the peak strength of combustible ice sample increased along with the increase of cell pressure. This is because the crystals in combustible ice sample played the cementation in traxial shear compression process and the greater the cell pressure cementation, the more obvious.

## Conclusion and Outlook

Using baking powder, sodium chloride and Marine sedimentary soil to simulate combustible ice sample is feasible. Compared the CD and CU test, crystal affect little to the internal friction angle of

combustible ice sample, mainly because of the cementation of pore water pressure and crystal of combustible ice sample's cohesive force. The cellular structure produced by baking powder generated gas to combustible ice sample peak compressive strength effect remains to be further research. Different skeleton materials combustible ice samples should be studied by means of triaxial test in response to the kinds of geological environment during exploiting combustible ice.

**Acknowledgements**

This work was financially supported by the the Natural Science Foundation of Hainan province [No. 513139], the Midwest Key Areas Construction Project Plan of Hainan University.

**References**

[1] KVENVOLDEN K A, LORENSON T D. The global occurrence of natural gas hydrate[J]. Geophysical Monograph, 2001, 124: 3-18.

[2] KLAUDA J B, SANDLER S I. Global distribution of methane hydrate in ocean sediment[J]. Energy and Fuels, 2005,19:459-470.

[3] Zhang Wenliang, He Yanmei, Sun Yuhong. The course of study and the trend of development of natural gas hydrate[J]. Fault-Block Oil & Gas Field, 2005, 12(2): 8-10. (in Chinese)

[4] Ye Yuguang, Zhang Jian, Diao Shaobo, Liu Changling, Ren Sihong, Sui Weidong. Experimental Technique for Marine Gas Hydrates[J]. MARINE GEOLOGY & QUATERNARY GEOLOGY, 2003, 23(1): 119-123. (in Chinese)

[5] HYODO M, NAKATA Y, YOSHIMOTO N, ORENSE R. Shear behaviour of methane hydrate-bearing sand[C]// Proceedings of 17th International Offshore and Polar Engineering Conference. [S.1.]: The International Society of Offshore and Polar Engineers. 2007: l326—l333.

[6] CLAYTONC R I, PRIEST J A, BEST A I, The effects of disseminated methane hydrate on the dynamic stiffness and damping of a sand[J]. Geotechnique, 2005, 55(6): 423--434.

[7] WANG Shuyun, LU Xiaobing. Advances of research Oil mechanical properties of gas hydrate deposits[J]. Advances in Mechanics, 2009, 39(2): l76—l88. (in Chinese)

[8] WAITE W F, WINTERS W J, MASON D H. Methane hydrate formation in partially water-saturated Ottawa sand[J]. American Mineralogist, 2004, 89: 1202–1207.

[9] MIYAZAKI K, MASUI A, YAMAGUCHI T, et al. Investigation of deformation mechanism for methane hydrate sediment based upon mechanical properties in unloading and reloading process under triaxial compression[C]// The Proceedings of the 8th ISOPE-OMS. Chennai, 2009: 102–106.

[10] YUN T S, SANTAMARINA J C, RUPPEL C. Mechanical properties of sand, silt and clay containing tetrahydrofuran hydrate[J]. Journal of Geophysical Research-Solid Earth, 2007, 112(B4): 1-13.

[11] LI Yanghui, Song Yongchen, Liu Weiguo. TRIAXIAL COM PRESS ION TEST OF NATURAL GAS HYDRATE[J]. NATURAL GAS EXPLORATION & DEVELOPMENT, 2010, 33(2): 51-55. (in Chinese)

[12] Bai Yuhu, Li Qingping, Zhao Ying. The effects of parameter model on the simulation of gas hydrate dissociation in porous media by depressurization[J]. Petroleum Drilling Techniques, 2009, 37(6): 11—17. (in Chinese)

*Applied Mechanics and Materials Vols. 580-583 (2014) pp 380-385*
*© (2014) Trans Tech Publications, Switzerland*
*doi:10.4028/www.scientific.net/AMM.580-583.380*

# Weak Form Quadrature Element Analysis of Diaphragm Walls

Ye Li[1,a], Hongzhi Zhong[1,b]

[1] Department of Civil Engineering, Tsinghua University, Beijing 100084, China

[a]superl_y@sina.com, [b]hzz@mail.tsinghua.edu.cn

**Keywords:** weak form quadrature element; diaphragm wall; Rankine's earth pressure theory

**Abstract.** In combination with Rankine's earth pressure theory, a weak form quadrature element formulation is established for analysis of diaphragm walls. Results are compared with those of Paroi2, a finite element software package for diaphragm walls, to demonstrate the effectiveness and the advantages of the present formulation. Accurate results are obtained with only a few weak form quadrature beam elements, contrasting with dense finite element division that is needed for complex load distributions over the diaphragm wall.

## Introduction

For large-scale suspension bridges, the entire loads on the girder are transmitted to the tower through cables. As a result, the main cable usually bears large force. In order to provide a strong constraint at the end of the main cable, an anchorage is designed effectively to transmit the cable force to the basis.

Depending on the attachment of cables, there are two-types of suspension bridges: self anchored and earth anchored; while the earth anchored suspension bridges are further classified into rock anchor bridges and gravity-type anchor bridges. A gravity-type anchor balances the main cable tension with the anchorage gravity, and bears most action of gravity during construction. The anchorage with diaphragm wall is an important type of gravity-type anchor. Yangluo Yangtze River Bridge [1] and Humen No.2 Bridge both use diaphragm wall anchorage foundation.

Diaphragm walls, buried deeply in the ground, usually form a circular or rectangular cross section envelope of anchor. It ensures the stability of the structure during layerwise excavation inside the diaphragm wall and adding support on the inner side of the diaphragm wall at the same time. After the formation of foundation trench, cylindrical or cubic shape of mass concrete anchorage foundation would be built by placing concrete inside and capping.

It is important to ensure the serviceability of diaphragm walls all the time. Not only during normal operation phase but also during the construction is the analysis of diaphragm wall integral to its reliability. With the continual excavation of one side soil and adding support, the stress of the diaphragm wall varies from time to time. Therefore, engineers need to calculate the bending moment envelope curve of diaphragm walls and design parameters accordingly.

## Diaphragm wall and soil pressure

As shown in Fig.1, each section of diaphragm wall is simplified into a strut [2]. For cylindrical anchorage foundation, the diaphragm walls form a circular ring. Normally a section of diaphragm wall deforms in the radial direction and lateral sides of the section are constrained. In calculation, the lateral constraint is simplified as additional distributional stiffness acting on the diaphragm wall.

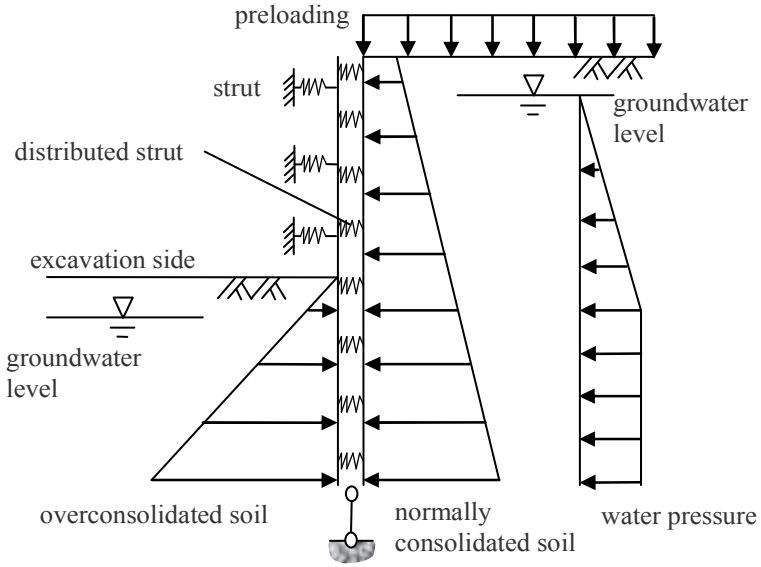


Fig 1. Strut model of diaphragm wall

Before excavation, there is a certain preloading on the ground. With progress of excavation, the groundwater level of the excavation side declines at the same time. Water and soil are treated separately to gain the force exerted on the wall. Static pressure is taken as water pressure, disregarding the impact of seepage. Soil stress is calculated based on Rankine's earth pressure theory [3] for which the stress-strain relationship is shown in Fig 2. On the excavation side, over consolidated soil model is used while normally consolidated soil model is used on the other side.

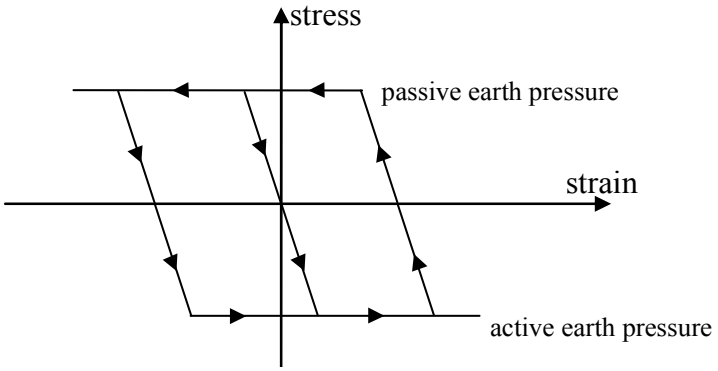


Fig. 2 Stress-strain relationship of soil based on Rankine's earth pressure theory

Paroi2 is a specific finite element software package for analysis of diaphragm walls which is currently used in some bridge design institutes. Usually, the finite element beam element is only suitable for uniform additional stiffness and load. Consequently, large result errors may arise if coarse finite element mesh is used in the case of nonlinearly distributed soil pressure.

In contrast, weak form quadrature beam element has shown its advantages in dealing with complex load distribution in previous studies [4-8]. In addition, weak form quadrature element analysis can achieve accurate simulation with sparse element division.

**A quadrature element for diaphragm wall**

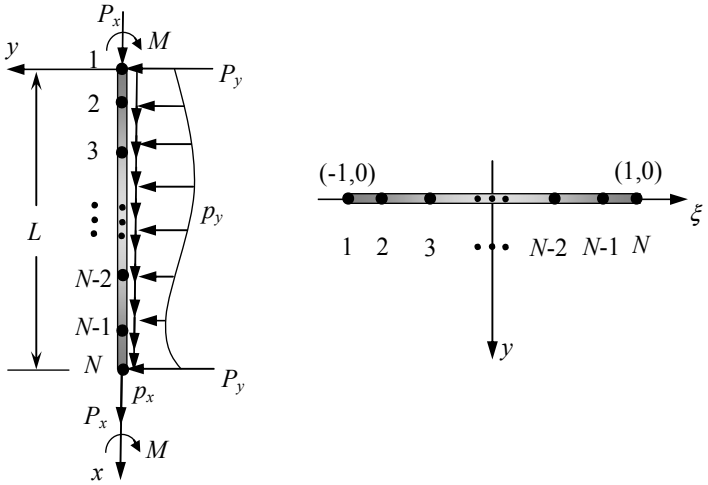


Fig 3. Quadarture element and integration points

As shown in Fig 3, a quadrature element, an abbreviation for weak form quadrature element, is mapped onto the normalized coordinate before analysis. Coordinate transformation formula is chosen as [8]

$$\xi = x/S - 1, S = L/2 . \tag{1}$$

The black dots in Fig 3 are integration points. There are two translational degrees of freedom at every integration point, while each end point is endowed with a rotational degree of freedom additionally.

The element displacement vector can be expressed as

$$\mathbf{d}^{(\mathrm{e})} = \left[\mathbf{d}_1^{\mathrm{T}} \quad \mathbf{d}_N^{\mathrm{T}} \quad \mathbf{d}_2^{\mathrm{T}} \quad \cdots \quad \mathbf{d}_{N-1}^{\mathrm{T}}\right]^{\mathrm{T}} \tag{2}$$

$$\mathbf{d}_i^{\mathrm{T}} = \begin{cases} \left[u_i \quad v_i \quad \left(\dfrac{\mathrm{d}v}{\mathrm{d}\xi}\right)_i\right], & i = 1, N; \\ \left[u_i \quad v_i\right], & i = 2, ..., N\text{-}1. \end{cases} \tag{3}$$

The strain vector is given as

$$\overline{\boldsymbol{\varepsilon}}(x) = \begin{Bmatrix} \varepsilon \\ \kappa \end{Bmatrix} = \begin{Bmatrix} \dfrac{\mathrm{d}u}{\mathrm{d}x} \\ \dfrac{\mathrm{d}^2 v}{\mathrm{d}x^2} \end{Bmatrix} \tag{4}$$

which is related to the strain vector in the normalized coordinate through

$$\overline{\boldsymbol{\varepsilon}}(x) = \mathbf{D}\boldsymbol{\varepsilon}_0(\xi) \tag{5}$$

where

$$\mathbf{D} = \begin{bmatrix} \dfrac{1}{S} & 0 \\ 0 & \dfrac{1}{S^2} \end{bmatrix}, \ \boldsymbol{\varepsilon}_0(\xi) = \begin{Bmatrix} \dfrac{\mathrm{d}u}{\mathrm{d}\xi} \\ \dfrac{\mathrm{d}^2 v}{\mathrm{d}\xi^2} \end{Bmatrix}. \tag{6}$$

The quadrature element formulation is established based on the virtual work principle. The expressions of external and internal virtual work can be given as

$$\delta U_{\text{ext}}^{(\text{e})} = -S\int_{-1}^{1}(p_x\delta u + p_y\delta v)\mathrm{d}\xi - (P_x\delta u + P_y\delta v + \frac{M}{S}\frac{\mathrm{d}v}{\mathrm{d}\xi})\Big|_{\xi=\pm1} \tag{7}$$

$$\delta U_{\text{int}}^{(\text{e})} = S\int_{-1}^{1}\delta\overline{\boldsymbol{\varepsilon}}^{\mathrm{T}}\mathbf{R}\mathrm{d}\xi + S\int_{-1}^{1}k_y v\delta v\mathrm{d}\xi + K_y v\delta v\Big|_{\xi=\pm1} \tag{8}$$

The soil pressure is taken into account in external virtual work, and the effect caused by soil pressure is included in internal virtual work. In Eq. (8), $\mathbf{R}^T=[N(\xi)\quad M(\xi)]$ is section internal force vector; $k_y$ is distributional additional stiffness resulting from variation of soil pressure and lining support; $K_y$ is elastic support stiffness at ends. It is noteworthy that repeated calculation of elastic support at ends should be avoided.

Lobatto quadrature with $N$ sampling points is used to evaluate the integrals in Eqs. (7) and (8) which are rewritten as

$$\delta U_{\text{ext}}^{(\text{e})} = -\delta\mathbf{d}^{(\text{e})\mathrm{T}}\mathbf{F}^{(\text{e})} \tag{9}$$

$$\delta U_{\text{int}}^{(\text{e})} = S\sum_{i=1}^{N}W_i\delta\overline{\boldsymbol{\varepsilon}}_i^{\mathrm{T}}\mathbf{R}_i + S\sum_{i=1}^{N}W_i k_{yi}v_i\delta v_i + K_{yi}v\delta v\Big|_{\xi=\pm1} \tag{10}$$

where $W_i$ are the weighting coefficients for Lobatto quadrature.

The virtual work principle states

$$\delta U_{\text{ext}}^{(\text{e})} + \delta U_{\text{int}}^{(\text{e})} = 0 \tag{11}$$

which gives the equilibrium equations. To find the solution of the equilibrium equations, an incremental form of the equilibrium eqautions is needed, which can be written in matrix form as

$$\delta\mathbf{F}^{(\text{e})} = \mathbf{K}^{(\text{e})}\delta\mathbf{d}^{(e)} \tag{12}$$

where $\mathbf{K}^{(\text{e})}$ is the tangent stiffness matrix given by

$$\mathbf{K}^{(\text{e})} = S\sum_{i=1}^{N}W_i\mathbf{B}_{0i}^{\mathrm{T}}\mathbf{D}\mathbf{k}_i\mathbf{D}\mathbf{B}_{0i} + \overline{\mathbf{K}}_a \tag{13}$$

where $\overline{\mathbf{K}}_a$ is a diagonal matrix representing the additional stiffness matrix, i.e.

$$\overline{\mathbf{K}}_a = diag\left(\mathbf{K}_{a1}\quad 0\quad \mathbf{K}_{aN}\quad 0\quad \mathbf{K}_{a2}\quad \mathbf{K}_{a3}\quad \cdots\quad \mathbf{K}_{a(N-1)}\right) \tag{14}$$

$$\mathbf{K}_{ai} = \begin{cases}\left[0\quad SW_i k_{yi} + K_{yi}\right], & i=1,N;\\ \left[0\quad SW_i k_{yi}\right], & i=2,...,N-1;\end{cases} \tag{15}$$

and

$$\begin{aligned}&\mathbf{B}_{0i} = \left[\mathbf{B}_{0i,2}\quad \tilde{\mathbf{B}}_{0i,1}\quad \mathbf{B}_{0i,N+1}\quad \tilde{\mathbf{B}}_{0i,N+2}\quad \mathbf{B}_{0i,3}\quad \cdots\quad \mathbf{B}_{0i,N}\right]\\ &\mathbf{B}_{0i,j} = \begin{bmatrix}C_{i(j-1)}^{(1)} & 0\\ 0 & G_{ij}^{(2)}\end{bmatrix}, \tilde{\mathbf{B}}_{0i,j} = \begin{bmatrix}0\\ G_{ij}^{(2)}\end{bmatrix}\end{aligned} \tag{16}$$

where $C_{ij}^{(1)}$ and $G_{ij}^{(2)}$ are the weighting coefficients for the differential quadrature analog and the generalized differential analog [8], respectively. The section stiffness matrix of the element is given by

$$\mathbf{k}(x)=\begin{bmatrix} EA & 0 \\ 0 & EI \end{bmatrix}. \tag{17}$$

**An example**

The anchor of Humen No.2 Bridge is examined here to verify the quadrature element formulation. The anchor is in the shape of a circular cylinder with 90m in diameter and 27m in depth. It is a reinforced concrete structure.

The diaphragm wall under consideration consists of 4 soil layers: mucky soil, gravelly sand, strong weathered shaly sandstone and weathered sandstone. The parameters of the soil are taken from the geological exploration report. It is 36m from the ground plane to the bottom of the diaphragm wall. During construction, the foundation trench is excavated for 9 times with 3m excavating depth each time.

Paroi2 and the quadrature beam element are used to calculate the internal forces respectively and results are compared. In analysis with Paroi2, the diaphragm wall is divided into 27 segments and 5 elements per segment. In quadrature element analysis, the diaphragm wall is modelled with 13 beam elements, each with three integration points.

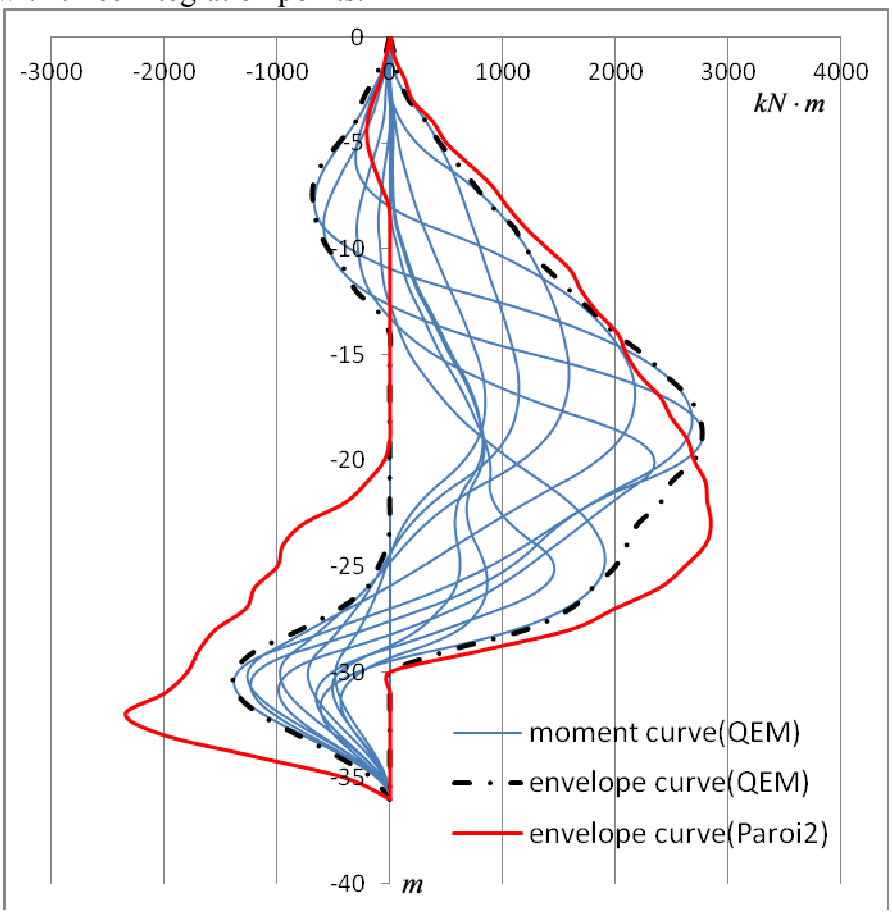


Fig 4. Envelope of bending moment

The envelop curve of the bending moments at all excavation stages is obtained as shown in Fig 4. It is seen that the quadrature element result conforms to that of Paroi2, indicating that it is effective to calculate the diaphragm wall with the quadrature beam element. Paroi2 uses 135 beam elements to acquire convergent results, contrasting to 13 elements in quadrature element analysis.

The maximum bending moment is found to be $2819\,\mathrm{kN\cdot m}$ from Paroi2 runs, while $2769\,\mathrm{kN\cdot m}$ is obtained for the quadrature element analysis, there being a 1.8% difference. However, the deviation of the negative moment of the diaphragm wall of Paroi2 from that of quadrature element analysis is relatively larger.

The difference between the results is believed to come from the modeling difference. Loads and additional stiffness are treated differently in Paroi2 and the quadrature element formulation. As less simplification is introduced in the present quadrature element formulation, the results of quadrature element analysis are believed to be more reliable.

## Conclusions

It has been shown that quadatrture element is effective in analysis of diaphragm walls in combination with Rankine's earth pressure theory. Compared with finite element analysis, quadature element analysis can offer accurate results with fewer elements.

## Acknowledgements

This work was financially supported by the National Science Foundation (51178247).

## References

[1] G Xu, M Liu, Diaphragm wall design of southern anchorage of Yangluo Yangtze River Bridge (in Chinese). Highway, 2004, 10:11-14

[2] Highway bridge foundation and foundation design specifications (China)(JTG D63-2007)

[3] W J M Rankine, On the stability of loose earth, Philosophical Transactions of the Royal Society of London, 1857, 147: 9-27.

[4] H Zhong, T Yu, Flexural vibration analysis of an eccentric annular Mindlin plate, Archive of Applied Mechanics, 2007, 77(4): 185-195

[5] H Zhong, M Gao, Quadrature element analysis of planar frameworks, Archive of Applied Mechanics, 2010, 80(12), 1391-1405

[6] H Zhong, R Zhang And H Yu, Buckling analysis of planar frameworks using the quadrature element method, International Journal of Structural Stability and Dynamics, 11(2):363-378, 2011

[7] N Xiao, H Zhong, Nonlinear quadrature element analysis of planar frames based on geometrically exact beam theory, International Journal of Non-Linear Mechanics, 47(5): 481–488, 2012

[8] R He, H Zhong. Large deflection elasto-plastic analysis of frames using the weak-form quadrature element method, Finite Elements in Analysis and Design, 2012, 50: 125-133

*Applied Mechanics and Materials Vols. 580-583 (2014) pp 386-390*
*© (2014) Trans Tech Publications, Switzerland*
*doi:10.4028/www.scientific.net/AMM.580-583.386*

# A CHEMO-ELASTO-PLASTIC COUPLING MODEL FOR SANDSTONE CONSIDERING pH EFFECT

Xuehao Li [1,2, a], Wei Wang[1,2,b] , Zhenyuan Tian [1,2,c] and Weiya Xu[1,2,d]

[1] Key Laboratory of Ministry of Education for Geomechanics and Embankment Engineering, Hohai University, Nanjing, China

[2]Geotechnical Research Institute, Hohai University, Nanjing, China

[a]Lixuehao12345@163.com, [b]wwang@hhu.edu.cn, [c]tianzhy163@126.com, [d]wyxu@hhu.edu.cn

**Keywords:** Sandstone, chemo-mechanical coupling, constitutive model,pH

**Abstract.** In this paper, we present a numerical modeling of chemo-mechanical behaviour of sandstone. An internal variable is introduced in this model for the purpose of describing pH effect on elasto-plastic properties. A new chemo-elasto-plastic model is proposed for sandstone. The proposed model is applied to predict material responses in triaxial compression tests of sandstone after soaking in different pH acidic solutions. We concluded with good agreement between numerical simulations and experimental data.

## Introduction

In recent years, research interest in the chemo-mechanical behavior of soils and rocks has been enhanced, as a result of the increasing geomechanical problems evolved due to the chemical effects. Many applications based on the study of chemo-mechanical behaviour can be found in the practice, especially for corrosion due to industrial waste water and acid rain, petroleum drilling,etc. A large number of experimental investigations involving in-situ tests and laboratory tests have been performed[1-5]. Based on these experimental results, similar conclusions have been drawn. Chemical degradation induces an increase in material porosity, which ultimately causes the deterioration of mechanical properties, especially the acidic environment has an influence on the elastic properties as well as the plastic properties and induces the yield limit to shrink with increase in concentration of acid.

A good understanding and prediction of these mechanisms, therefore, is necessary for the performance of fully coupled chemo-mechanical numerical analysis. Different numerical models taking into account chemical effects have been proposed [6,7]. These models deal with the chemo-mechanical coupling problem by damage statistics model or mathematical models. However, these models lack of mechanical meaning.

In this study, a new chemo-elasto-plastic model is presented in order to describe the chemo-mechanical behaviour of sandstone. An internal variable is introduced in this model to describe the pH effect to sandstone in acidic solution; the numerical results are given in the paper.

## Modeling of chemo-mechanical behavior of Sandstone

In this part, the variable $\theta$ denotes the change in pH of acidic environment with respect to a reference value:

$$\theta = \frac{pH}{7} \tag{1}$$

In order to take into account the chemical effect of plastic deformation, an internal state variable called chemical hardening variable, noted by $\gamma_\theta$ is proposed; this variable physically represents the

concentration of $H^+$ in acidic solution induced by change of microstructure of material. In consideration of chemo-mechanical coupled behavior, we assume that $\gamma_\theta$ can be defined by:

$$\gamma_\theta = \frac{pH}{7} \cdot \left( \frac{\sigma_c}{p_0} \right)^3 \quad (2)$$

Where pH represents the concentration of $H^+$ in acidic solution, $\sigma_c$ is the confining pressure. The fixed reference pressure $p_0$ =1MPa is used to make the parameter $\gamma_\theta$ dimensionless.

In this work, a quadratic function is used to describe plastic yielding and failure surface [8], the yield function is expressed as below:

$$f = q^2 + A\alpha_p (p - C_0) = 0 \quad (3)$$

Where $p$ is the mean stress, $q$ is deviatoric stress .The parameter $C_0$ represents the material tensile property and $A$ represents the frictional angle. The fixed reference pressure $p_0$ =1MPa is used to keep the parameter $A$ dimensionless. The plastic hardening is described by the increasing function $\alpha_p$ of the generalized plastic shear strain $\gamma_p$ and chemical internal state variable $\gamma_\theta$ . Based on the experimental data obtained from the tests on sandstone [9,10], we use the following form:

$$\alpha_p(\gamma_p, \gamma_\theta) = \alpha(\gamma_\theta) \left[ \alpha_p^0 + (1 - \alpha_p^0) \frac{\gamma_p}{B + \gamma_p} \right] \quad (4)$$

$$\gamma_p = \int \sqrt{\frac{2}{3} de_{ij}^p de_{ij}^p} \quad (5)$$

The parameter $B$ determines the plastic hardening rate.

The function $\alpha(\gamma_\theta)$ is introduced here for the description of chemical effect on the evolution of material mechanical property. In the absence of relevant data and for the sake of simplicity, a quadratic functions is used:

$$\alpha(\gamma_\theta) = a\gamma_\theta^{\,2} + b\gamma_\theta + c \quad (6)$$

$a$ , $b$, $c$ are the parameters related to the chemical hardening of material, and can be obtained from fitting the experimental data.

Here we use a non-associative plastic flow rule. Taking into account the chemical effect on the material friction coefficient, the following plastic potential is used:

$$g = q + A\eta\alpha(\gamma_\theta)(p - C_0) \ln\left( \frac{p - C_0}{I_0} \right) \quad (7)$$

By using this potential, the stress space is divided into two zones, which are plastic compressibility and dilation. The boundary between these two zones is defined by the condition $\partial g_\sigma / \partial p = 0$ and this boundary can be approximated by a linear function[8]:

$$f_d = q - A\eta(p - C_0) \quad (8)$$

The parameter $\eta$ is the slope of the boundary line between compressibility-dilation zones.

**Numerical simulations of triaxial compression tests on Sandstone with chemical corrosion**

In this section, the proposed model is used to simulate the triaxial compression tests of sandstone under different confining pressures(4MPa and 6MPa) after soaking in three solution with different pH values (pH =3 and 7) [2]. Totally, the proposed model contains 10 parameters to describe the chemo-elasto-plastic behavior of sandstone, which can be entirely determined from interpretation of tri-axial compression tests. The initial elastic constants ($E_0$ and $\mu_0$) can be obtained from the linear part of stress–strain curves in a tri-axial compression test. We use the average values obtained from

various tests. The parameters $A$ and $C_0$ can be deduced by drawing the locus of peak stresses in $p$–$q$ plane, while the parameter for the initial yield surface $\alpha_p^0$ is captured from the locus of stresses at onset of inelastic strains. We can obtain the value of parameter $\eta$ by identifying stress points corresponding to $\partial g_\sigma / \partial p = 0$ on stress–strain curves. The plastic hardening parameter $B$ can be obtained by drawing the function $\alpha_p$ versus plastic deviatoric strain $\gamma_p$, the parameters $a$, $b$ and c for the description of chemical effect in $\alpha(\gamma_\theta)$ can obtained by drawing the function $\alpha(\gamma_\theta)$ versus plastic deviatoric strain $\gamma_\theta$.

In order to evaluate the performance of the proposed model, the parameter sensibility of pH to the mechanical response is carried out. Different values of pH (pH=7,5,4,1) are used in the simulation while the confining pressure is fixed at 6 MPa. The comparison of simulation results are shown in Fig.3. It is noticed that the strength increase with the increasing value of pH.

By fitting the experimental data by above methods, we have obtained the following values of parameters shown in Table 1:

**Table 1**. Representative values of parameters for sandstone

| Elastic parameters: | Plastic parameters: | |
|---|---|---|
| $E_0$=3.65MPa | $A$=52 | $a$= -2.10e-5 |
| $\mu_0$=0.45 | $C_0$=8 | $b$=0.00788 |
| | $\alpha_p^0$=0.19 | $c$= 0.339 |
| | $B$=0.00075 | |
| | $\eta$=-0.022 | |

By using these parameters, numerical simulations of tri-axial compression tests of sandstone soaked in the solutions bearing different pH values (pH=3 and 7) were performed. The relation between deviatoric axial stress and axial strain is simulated.

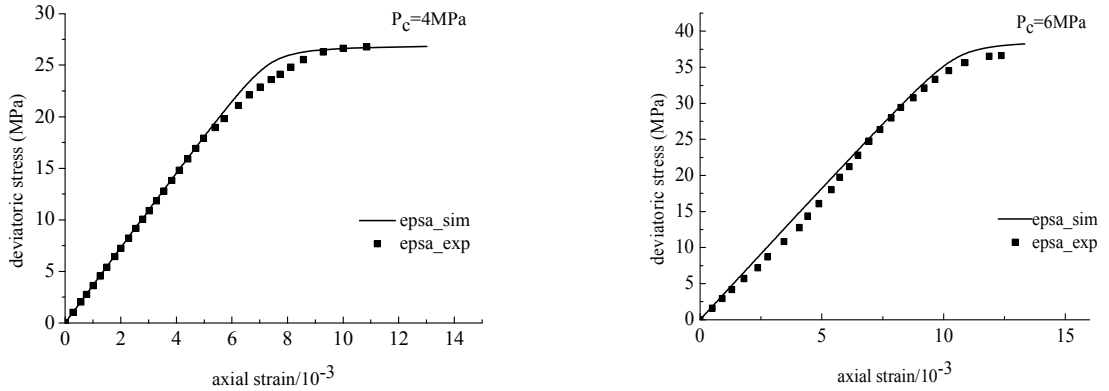


**Fig.1**. Simulations of triaxial compression tests on sandstone under different confining pressures at pH=7.

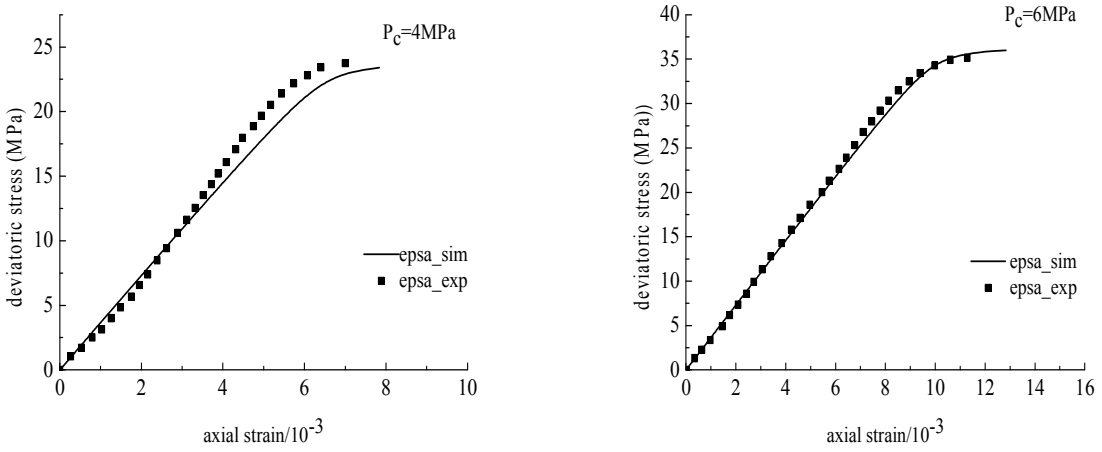


**Fig. 2**. Simulations of triaxial compression tests on sandstone under different confining pressures at pH=3.

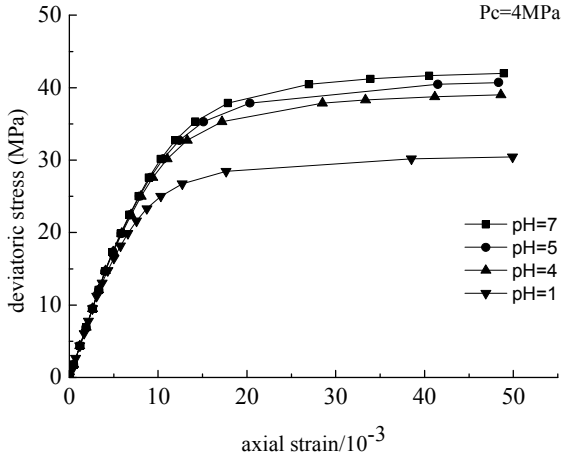


**Fig. 3**. Simulations of triaxial compression tests on sandstone under different pH at confining pressures fixed at 6 MPa.

Fig.1,2 and 3 show the comparisons between test data and numerical simulations. From the figures, with the increase in confining pressure and pH value, the strength increase. It seems that the model can well describe the feature. Moreover, in spite of simplifications and assumptions used, a general good agreement is obtained between the experimental data and simulation results for the stress-strain relationships. Qualitatively, the proposed model can correctly describe the general trend observed in the test data.

## Conclusions

In this study**,** numerical modeling of the chemo-mechanical behavior of sandstone is presented. The evolution of microstructure due to chemical effect is quantified through an internal variable, taking into account the effect of pH of acidic solution on the mechanical properties of sandstone. A quadratic function is used to describe the plastic yielding and failure surface. The triaxial compression tests on sandstone soaked in different pH (pH=3, 7) solutions are simulated. In spite of limited data available, the proposed model seems to describe well the main features observed in experiments. However, the proposed model should be verified by other experimental data and this will be done in the further study.

**Acknowledgements**

The work was financially supported by the National Science Foundation of China (Grant no. 51109069, 11272114, 11172090) and National Program on Key Basic Research Project (973 Program) (Grant no. 2011CB013504).

**References**

[1]. S.Y. Xie, J.F. Shao, W.Y. Xu: International Journal of Rock Mechanics & Mining Sciences. Vol. 48(2011), p.741-747
[2]. W.Wang, T.G.Liu, J.Lv, R.B.Wang, W.Y. Xv, B.Jian: Chinese Journal of Rock Mechanics and Engineering. Vol.31(2012),p.3608
[3]. J.Xv,H.Wu,L.C.Cheng,et al: Chinese Journal of Rock Mechanics and Engineering ,In Chinese.2012,Vol31(2),p.3898-3903
[4]. L.S.Tang,Z.P.Cheng,S.J.Wang: ChineseJournal of Rock Mechanics and Engineering ,In Chinese. 2002,Vol.21(4),p.526-531
[5]. X.T.Feng, W.X.Ding: International Journal of Rock Mechanics & Mining Sciences.Vol.44 (2007) , p.437–448
[6]. R.K. Huo, N.Li, H.D.Liu: Chinese Journal of Rock Mechanics and Engineering. Vol.24 (2005),p.1853
[7]. L.C.Jiang, Y.Wen: Chinese Journal of Rock Mechanics and Engineering. Vol.42(2011),p.3503
[8]. J.F. Shao, Q.Z,Zhu,K.Su: Computers and Geotechnics Vol.30 (2003) ,p.549–555
[9]. F.Bourgeois,J.F.Shao,O.Ozanam: Mechanics Research Communications Vol.29(2002), p.383-390.
[10]. Z.Yan, Z.M.ZHANG, J.F.SHAO: ENGINEERING MECHANICS ,In Chinese Vol.23(2006).p.153-156

*Applied Mechanics and Materials Vols. 580-583 (2014) pp 391-394*
*© (2014) Trans Tech Publications, Switzerland*
*doi:10.4028/www.scientific.net/AMM.580-583.391*

# A critical-line-based predictive model for landslides

Gordon Tung-Chin Kung [1,a], and Yu-Geng Tang [2,b]

[1] Sustainable Environment Research Laboratories, National Cheng Kung University, No. 500, Sec. 3, Anmin Rd., Annan District, Tainan City, TAIWAN

[2] Department of Architecture, Haw-Hsia Institute of Technology, No.111, Gongzhuan Rd., Zhonghe District, New Taipei City, TAIWAN

[a] tckung@mail.ncku.edu.tw, [b] tang@cc.hwh.edu.tw

**Keywords:** Landslide, rainfall, critical line, rainfall intensity, accumulated rainfall.

**Abstract.** This paper developed a critical-line-based method for predicting the occurrence of landslides using two rainfall indices, the rainfall intensity and the accumulated rainfall, based on four landslide case histories recorded in a county. Specifically, the rainfall records of the four cases were used to compute the 60-minute rainfall intensity and accumulated rainfall prior to the occurrence of landslides. Although the meteorological and geological conditions as well as other crucial factors are not considered in the development of the intended model, the analysis results indicated that the developed critical-line-based predictive model can reasonably identify the boundary between occurred and non-occurred zones. The developed model has the potential to be a useful tool for predicting the occurrence of landslides according to the rainfall conditions.

## Introduction

Taiwan is a mountainous country and located in the routes of typhoons in southeastern Asia. Landslides are occasionally triggered by the heavy rainfall during typhoon or Mai-yu seasons and caused tremendous damage and lost in Taiwan. According to the records by the SWCB [1], the number of landslides recorded every year increases after the 1999 Chi-Chi earthquake. This means that slopes may be disturbed and the factor of safety of stability may be reduced. Over the past decades, many methods have been developed for predicting the landslide occurrences using meteorological factors all over the world [2-6]. It is desirable to develop a local predictive model for landslides in Taiwan.

Landslides may be caused by a large number of various factors such as meteorological factors, geological factors, vegetation, construction of roads, earthquakes, and so on. However, the rainfall factors are generally recognized to be ones of most crucial factors causing landslides. According to the past studies, the intense rainfall has been recognized as the primary factor to trigger landslides. In addition, accumulated rainfall is commonly recognized as a secondary landslide-triggering meteorological factor [7]. Therefore, the objective of this study is to develop a simplified model for predicting the occurrence of landslides with use of two rainfall indices, the rainfall intensity and the accumulated rainfall.

## Collection of landslide cases

The SWCB [1] delivered the reports annually to record and analyze the slope failure events in Taiwan, including landslides and debris flows. Based on the annual reports by the SWCB, the present study collected four landslide case histories occurred in Renai Township, Nantou County, Taiwan in various years. Specifically, two of them occurred in Datong Village in 2006 and 2007, while the other two occurred in Cueihua Village in 2006 and 2008. All the four landslide cases were triggered by the heavy rainfall. Detailed information such as location, rainfall history (as shown in Fig. 1), rainfall station name, time of landslide occurrence, hydrogeology conditions, vegetation condition, description and in-situ photos of failure, and so on, were collected for each of the four landslide cases.

Overall, the four landslide cases are located in a relatively small region and the use of them to develop the simple model for predicting the occurrence of landslides intends to reduce the effect of other influence factors on the landslides as much as possible.

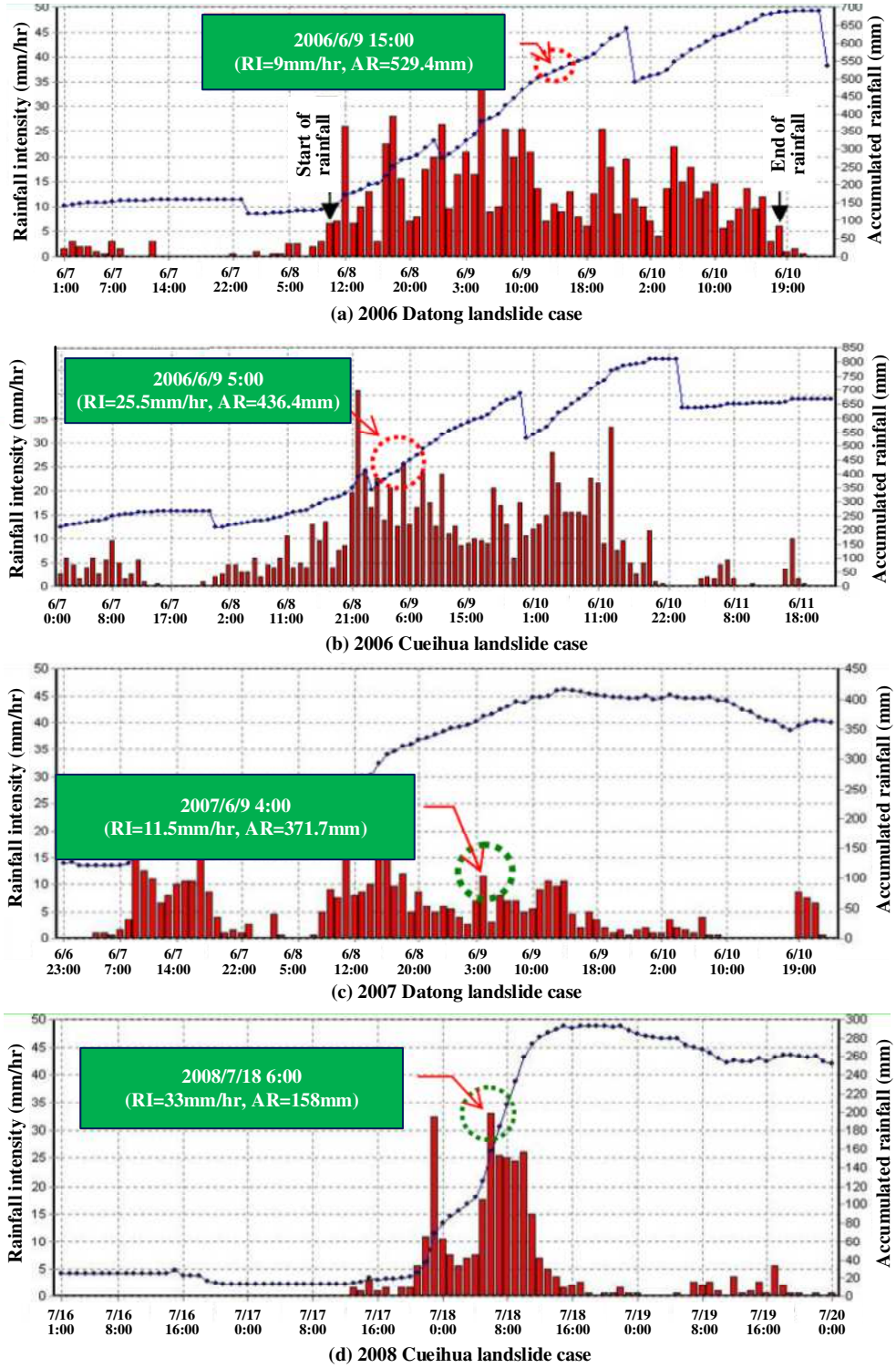


Fig. 1 Rainfall records for the four landslide cases collected.

## Calculation of rainfall indices

For the calculation of the rainfall intensity and the accumulated rainfall, the following definitions are employed: (1) the sum of rainfall within 60 minutes is called the rainfall intensity, and (2) the rainfall accumulated from the start of the rainfall event to a certain time is named as the accumulated rainfall.

With these definitions, the rainfall intensity and the accumulated rainfall at every hour can be obtained prior to the occurrence time of landslides for each of landslide cases. It should be noted that the rainfall records after the occurrence of landslides were not employed in this present study. Then, all the data points (the combination of the rainfall intensity and the accumulated rainfall) calculated are employed together to develop the critical line for predicting the occurrence of landslides.

**Analysis results**

Figure 2 reveals the analysis results of four landslide case histories. The solid points represent the values of the rainfall intensity and the accumulated rainfall when the landslide occurred, while other hollow points are hourly data calculated prior to the occurrence of landslide with respect to various time. It should be noted that the data after the occurrence time of landslides are not incorporated into the figure. Based on those data points, a critical line for predicting the occurrence of landslides in Renai Township, Nantou County was established. As mentioned previously, the critical line is the boundary for identifying the occurrence of landslide. The scenario that hollow points are located inside the critical line and solid points are located outside the critical line represents the capacity of the critical line for estimating the occurrence of landslides is good. On the contrary, the critical line established is not satisfactory provided the hollow points are located outside the critical line and solid points are located inside the critical line.

As shown in Fig. 2, only five hollow points are outside the critical line as well as only one solid point is inside the critical line. This means the developed critical line may be capable of identifying the boundary for predicting the occurrence of landslide by using two indices, the rainfall intensity and the accumulated rainfall. However, it is desirable to incorporate more landslide data to validate the capacity of the developed critical line. In addition, the critical line developed in Fig. 2 is only valid to Renai Township, Nantou. The simple methodology exhibits a high potential to be employed in other vulnerable area to develop the critical line for predicting the occurrence of landslides.

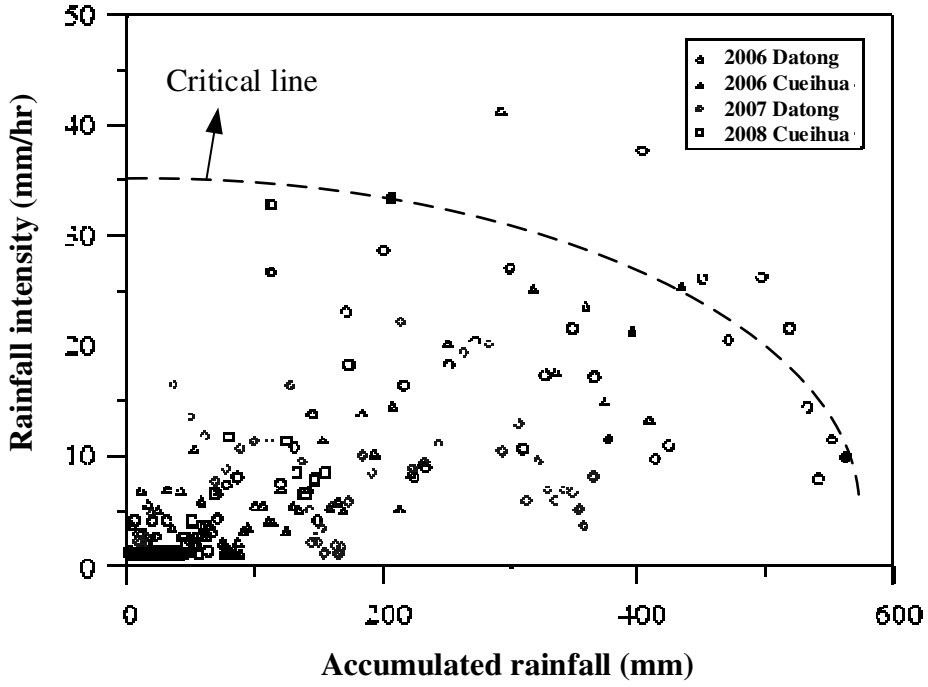


Fig. 2 The developed critical line using two rainfall indices for prediction of landslides in Renai Township, Nantou County

**Summary**

This study collected four landslide case histories occurring in Renai Township, Nantou County in various years to develop a critical-line-based model for predicting the occurrence of landslides. The analysis results displayed that the developed critical line is capable of identifying the boundary for predicting the occurrence of landslide based on two rainfall indices, the rainfall intensity and the accumulated rainfall. The results of the present study indicated that the critical-line-based model established based on the data of landslide case histories located within a small area, e.g., 5km×5km or 10km×10km, could be applicable to predict the occurrence of landslides. Although additional studies are required to validate the developed predictive model, it has the potential to be a useful tool to predict the occurrence of landslides.

**Acknowledgements**

This work was financially supported by the National Science Council, Taiwan through Grants NSC 100-2628-E-006 -012 and NSC 101-2628-E-006 -007.

**References**

[1] The Soil and Water Conservation Bureau, Council of Agriculture, Executive Yuan, Taiwan: Information on http://www.swcb.gov.tw

[2] M.C. Ke, S.C. Lin, Y.J. Chen, L.K. Chen, Y.T. Wang, H.T. Chou, The Research on Integrated Landslide Disaster Early Warning System, 2009 Resource and Environment Research Conference, Hualien, Taiwan (2009).

[3] C.H. Tan, C.Y. Ku, S.Y. Chi, Y.H. Chen, L.Y. Fei, C.F. Lee, T.W. Su, Assessment of Regional Rainfall-Infiltration Landslide Susceptibility using the 3S-Based Hydrogeological Model, The 10th International Symposium on Landslides and Engineered Slopes, June 30~July 4 2008, Xi'an, China (2008).

[4] C.T. Lee, C.C. Huang, J.F. Lee, K.L. Pan, M.L. Lin, J.J. Dong, Statistical approach to storm event-induced landslide susceptibility, Natural Hazard and Earth System Sciences, 8 (2008) 941-960.

[5] R.M. Iverson, Landslide triggering by rain infiltration, Water Resource Research, 36(7) (2000) 1897-1910.

[6] A. Carrara, Multivariate models for landslide hazard evaluation, Mathematical Geology, 15(3) (1983) 403-427.

[7] G.F. Wieczorek, T. Glade, Climatic factors influencing occurrence of debris flows. In: Jakob M, Hunger O (eds) Debris-flow Hazards and Related Phenomena, Praxis, Springer Berlin Heidelberg, 2005, pp. 325-362. Information on http://www.weld.labs.gov.cn

*Applied Mechanics and Materials Vols. 580-583 (2014) pp 395-400*
*© (2014) Trans Tech Publications, Switzerland*
*doi:10.4028/www.scientific.net/AMM.580-583.395*

# Analysis and Process Control of the Deformation for Deep Excavation in Soft Clay

Hui Liu[1, a], Weibin Li[2,b] and Hongtao Liu[3,c]

[1]School of Civil Engineering, Southeast University, Nanjing, Jiangsu, 210018, China

[2]School of Civil Engineering, Southeast University, Nanjing, Jiangsu, 210018, China

[3]The Fifth Research and Design Institute of Nuclear Industry, Zhengzhou, Henan, 450000, China

[a]894718743@qq.com, [b]liwbliwb@163.com, [c]6268655@qq.com

**Keywords:** soft clay, deep excavation, finite element, back-analysis from measured displacement, dynamic prediction, process control.

**Abstract.** Mechanisms of the distortion of deep excavation in soft clay are recommended on the beginning. Plane FEA method is combined with back-analysis from displacement on this paper to establish a dynamic prediction system of the distortion of deep excavation, which is proved to be viable by practice. Combining with the idea of process control, a process control model of the distortion of deep excavation is established on this paper. It is divided into three parts: advance control, observation and dynamic prediction, process control in the construction.

## Introduction

With the rapid development of urban construction, more and more underground space is applied, after what lots of deep excavation produced. With the increase in scale and depth of excavation, a series of challenges are put forward to the design and construction of the pit currently.

The excessive deformation of excavation will cause uneven settlement or cracking of the surrounding buildings, roads, pipelines and other important facilities [1], furthermore it will affect the normal use function. Therefore, the deformation control has become an important link of design and construction of deep foundation pit engineering, especially in the construction of deep foundation pit in soft soil area, the environmental effects caused by excavation is more obvious, the deformation control of deep excavation in soft soil is particularly important.

## Deformation Mechanism of Deep Excavation in Soft Clay and Finite Element Analysis

**Deformation Mechanism.** Excavation deformation consists of three parts, which are the wall deformation, the bottom uplift and the surface settlement around foundation pit. Pit excavation process is unloaded process of the excavation of soil. The process not only leads to mainly upward displacement produced by the bottom of the soil, but also causes horizontal deformation of the enclosure wall, which results in plastic uplift of the bottom soil. The two parts are also main causes of the surrounding ground movement.

**The Time-Space Effect of deep Excavation in Soft Soil.** Earth pressure on the supporting structure is changing, the deformation of foundation pit also changes with time. In addition to soil properties and supporting structure parameters, the deformation of foundation pit is also related to

excavation method, time, excavation sequence, space, and so on. This is the rule of space-time effect of deep the deformation of foundation pit.

**The Finite Element Analysis Model of foundation pit.** It is divided into plane model and 3-D model. For the long strip pit, we usually use the first model. Due to the existence of large space effect obviously, we use the other one to the foundation pit which has complex shapes.

The plane finite element model is as follows. In consideration of symmetry between the shape and excavation of the foundation pit, one side of the symmetry axis is usually taken as the computational domain during the plane finite element analysis in deep foundation pit. The influencing width is three to four times longer than the depth, and the influencing depth is two or four times longer than the depth or as long as the depth between the surface and the hard soil of the bottom of the foundation pit, as shown in Fig.1.

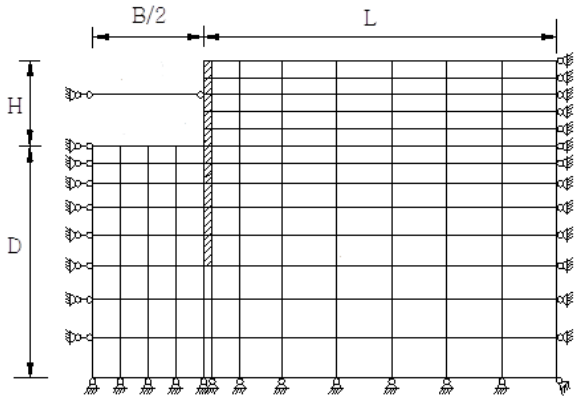


H—The depth of excavation B—The width of excavation
L—Width range D—Depth range

Fig.1 The plane finite element model

3-D finite element model is as follows. In the establishment of 3-D finite element model, when layout of the supporting structure and excavation method are satisfied with the condition of symmetry, we can choose a half or a quarter of the side of symmetry axis as the computational domain. The determination of the overall size is same as the model of plane finite element.

**Simulation of the Interaction between Retaining Structure and Soil.** The contact can be divided into two types in ANSYS, which are the rigid-flexible contact and the flexible-flexible contact. There are three ways to simulate contact, which are the point to point, the point to surface and the surface to surface.

The contact between pile and soil contact is the rigid-flexible contact. The pile is defined as the target body, while soil is defined as the contact body. These two surfaces together are regarded as a contact pair. By defining a lot of contact pairs, the simulation of the pile-soil contact can be come true. Each contact pairs is recognized by a set of constants alone, as shown in Fig.2.

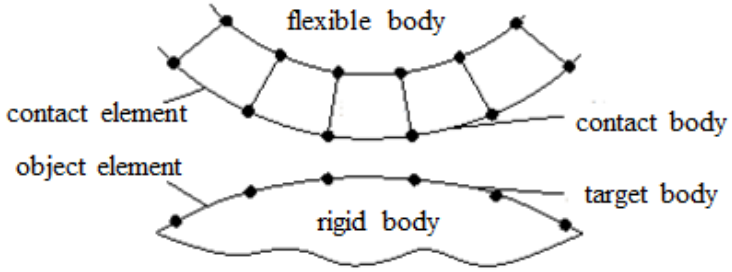


Fig.2 Simulation of surface-surface contact in ANSYS

**Consideration of the Initial Stress.** There are two ways to consider self-weight stress in ANSYS [2]. The first one is to regard the weight as the load and impose it on the ground. The ground emerge displacement under its own weight. While continuing to analyze the subsequent construction, the results of displacement is the accumulation of the initial displacement, while in reality the initial displacement is long over. Therefore behind each construction stage analysis of the displacement field, we need to subtract the initial displacement field. The second one is to apply weight first and obtain the initial stress field. The results will be saved as a file. During analysis of excavation, the initial stress will be read directly into the soil element, so that the displacement field is zero under self-weight stress. Then the result is the actual displacement field.

**The Simulation of Excavation and Support Processes.** These processes can be effectively simulated by using the "life and death" technique of unit in ANSYS [2]. During the excavation of deep foundation pit, we can directly select the soil element that is removed and "kill" it, in order to simulate the excavation. When erecting support, we can “active” the corresponding part that is killed in the excavation. The unit should become zero when it is activated. It is important to note that these units that input initial strain in form of real constant are not affected by birth and death element options.

## Dynamic Prediction for the Deformation of Foundation Pit based on Anti-Analysis

In geotechnical engineering, the certain physical quantities which are obtained by field measurement to reflect the system mechanical behavior can be used to calculate various parameters or some initial parameters of the system. We usually call this method anti-analysis.

**Target Parameters Selection of Anti-Analysis.** The target parameters are unknown parameters that to be solved in the process of anti-analysis. Different constitutive model of soil can be used in finite element analysis，which resulted in different target parameters of anti-analysis. The details are shown in Table1.

[Table 1 Selection of target parameters in anti-analysis]

| Constitutive model of soil | Target parameters of anti-analysis |
|---|---|
| Elastic model | Elastic modulus and Poisson's ratio |
| Elastic-plastic model | Elastic modulus, Poisson's ratio μ, Cohesion and Internal friction angle |
| Viscoelastic model | Elastic constants and Viscous constants |

**Objective function based on the relative displacement.** Before establishing the objective function, displacements calculating by the finite element analysis should be conducted. the calculated displacements of each points should subtract the calculated displacements from the bottom of points, then a relative displacement could be obtained, after that we can establish the objective function through the relative displacement which measured by taking the bottom of the tube as a fixed point. The equation is shown in Eq.1.

$$J=\sum_{i=1}^{m}(U_i-\triangle U_i^*)^2 \tag{1}$$

In the formula: $m$ —The total number of measurement points;

$U_i$ —The measured displacements of the point i;

$\triangle U_i^*=U_i^*-U_m^*$ —Relative displacement by calculation.

**Optimization and solution of the objective function.** Selected the appropriate way to optimize and solve function optimization can greatly improve the convergence speed of the objective function, so as to improve the efficiency of back analysis. Here mainly introduce two common methods.

Firstly, the golden section method in single-parameter solution is as follows. The interval (a, b) should be divided and supposing breakpoints are c and d. The equation is shown in Eq.2.

$$\begin{cases} c = (1-\alpha)a + \alpha b \\ d = \alpha a + (1-\alpha)b \end{cases} \quad (2)$$

In the formula, $\alpha$ =0.618. After calculating the values of this function in c and d, we should do the following comparison.

（1）If f(c)< f(d), then the interval (a, d) is used as the new interval ($a_1$,$b_1$).

（2）If f(c)>f(d), then the interval (c, b) is used as the new interval ($a_1$,$b_1$).

We should continue to compare the values of the function at all points by using segmentation method, namely it is not until the minimum meet the accuracy requirements that the interval can be stopped shortening, by doing what we can calculate the similar minimum.

Secondly, Modified simplex algorithm [3] is as follows. The basic idea is as follows. Establishing an n-dimensional space, in which we can compare the values of the function in these n+1 points and remove the point which makes the objective function get the maximum and is replaced by a new point. The new simplex replaces the old one constantly by iterated operation and is designed to close to the minimum of J(x). In the process, the power continues to shrink automatically, and get the minimum point finally.

**Deformation Dynamic Forecast based on the Anti-Analysis Method.** Taking comprehensive parameters obtained from anti-analysis into normal analysis and predicting internal force and deformation in the excavation process can not only help to test anti-analysis, but also improve the accuracy of it. The flow chart is shown in Fig.3.

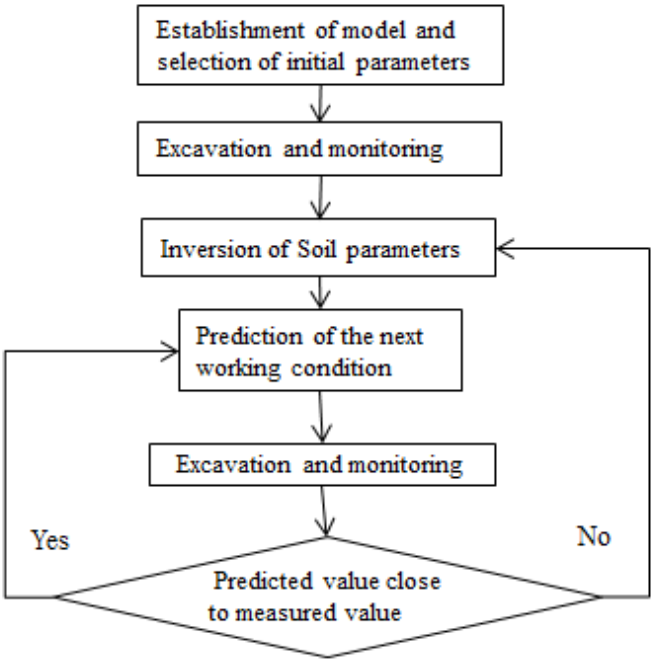


Fig.3 Flowchart of dynamic prediction for pit deformation

**Process Control for Deformation of Deep Excavation in Soft Soil**

Process control for deformation of deep excavation in soft soil can be divided into three parts, which are prior pre-control, construction monitor and dynamic forecast and construction control.

**Identify of Deformation Control Objectives.** Before deciding the objective of deep excavation deformation control, we should make a careful investigation of the engineering geological conditions and the surrounding environmental conditions, then study and calculate the allowable deformation of surrounding buildings, structures and pipelines, on this basis, determine the allowable value of deformation for the supporting structure caused by excavation and settlement of surrounding ground, finally we regard it as the deformation control objective of deep excavation.

**Construction Supervision.** The content of excavation monitoring can broadly divide into three parts that are displacement monitoring, stress monitoring and auxiliary monitoring. In early excavation, information acquisition cycle can be longer. With the depth increasing, the deformation scale of exterior-protected construction increases, then the acquisition cycle should be shortened. After collecting all kinds of information, we should input the computer for data processing promptly and draw the curves. At the same time, we should analyze bad data to find out causes and make improvements timely. After processing the information, it should be feedback to the designer, builder, superior and developer and submitted monitoring report timely.

**Measures of Process Control during Construction.** The first one is Construction measures considering time-space effect. The main construction parameters are lift height, intermediate dimension, excavation time and exposure time without the support. The determination of lift height and intermediate dimension should consider the location of strut and soil conditions. During excavation, we should make full use of their own strength and let excavation alternates with strut. If the excavation time or the exposure time is too long, the deformation will also be increased. Therefore, it is necessary to reduce the excavation time. After excavation, we should set up the strut timely and inflict the pre-stress to avoid long exposure time without the support.

The second one is add axial force of strut and adjust the position of strut.

The third one is tracking the grouting reinforcement.

The last one is emergency measures in construction Cantilever excavation depth caused by excessive horizontal displacement of pile top is too large. The details are shown in Table2.

[Table2 Common problems of deep foundation pit in soft soil and emergency measures]

| Types and causes of danger | Measures |
|---|---|
| Long depth of Cantilever excavation leads to long horizontal displacement of pile top | Unloading outside the pit and setting support immediately |
| Leakage of waterproof curtain leads to large settlement of ground | Grouting plug and setting recharge wells |
| Shallow embedment depth results in pile introversion or skirting instability | Unloading, heaping pile foot and reinforcing soil of passive zone |
| Excessive excavation leads to large deformation of the supporting structure | Stopping digging and setting strut immediately |
| Long exposure time causes deformation increasing | Setting strut immediately or refilling pre-stress |

## Conclusions

Deformation problems of deep excavation in soft soil have been attracted much attention for a long time, which is a focus and difficulty in excavation engineering. This paper combines the anti-analysis technology of displacement and method of finite element analysis and analyzes the deformation of supporting structure caused by excavation, which is also an important trend in the deformation analysis of foundation pit. From the finite element, selection of constitutive model and related parameters is still a problem, which needs a further study in the future. The anti-analysis model used in this paper is based on the elastic plane finite element model, but it cannot consider local deformation caused by soft soil rheology.

Deformation control of deep excavation is a complex process, this paper analyzes its control method and basic process from the technical aspects only, it needs a further study in the application and promotion in practical engineering.

## Acknowledgements

This paper is completed under the careful guidance of teacher Li, so I want to say thank you to him firstly. At the same time, I want to thank you the author of all references and teachers and friends providing help for thesis writing.

## References

[1] Jianhang Liu, Xueyuan Hou: China Building Industry Press, 1997.4.
[2] Wenhua Hao: Beijing: China Water Power Press, 2005.1.
[3] Mingguo Xu: Seismological Press, 2003.6.

*Applied Mechanics and Materials Vols. 580-583 (2014) pp 401-404*
*© (2014) Trans Tech Publications, Switzerland*
*doi:10.4028/www.scientific.net/AMM.580-583.401*

# Analysis of the Interaction of Foundation Pit Supporting Structure and Soil

Yuqin Feng[1,a], Chenxi Liu[2,b]

[1]The school of Architecture and Civil Engineering , Inner Mongolia University of Science & Technology, Baotou 014010, China

[2]Zhuhai Institute of Architectural Design, Zhuhai 519000, China

[a]btfyq@126.com, [b]lcx_1209@126.com

**Keywords:** Foundation Pit, Supporting Structure, Soil Anchor, Soil Pressure

**Abstract.** This paper analyzes an engineering in an area of China which was processed by vacuum preloading technology in the silt soft soil. This engineering was used rigid supporting structure technology of piles in row and bolts for large area of deep foundation pit supporting. It compared the realistic measure soil pressure and theoretical concluded soil pressure, and got the soil pressure distribution mode which is suitable for silt soft soil processed in this way. The conclusion can provide a reference for similar supporting structure system to calculate earth pressure.

## Introduction

Foundation pit engineering is a very complex system engineering, with a strong regional, comprehensive, practical and risk. Excavation structure is a complex structure with the interaction of structure and surrounding soil. The ways of supporting include using structural obstructing soil, using materials reinforced soil and retaining structures obstructing soil, using retaining structures and anchored rock reinforcing soil. Supporting structure, no matter what methods, it's forces are all complex and it's analytical methods all involve the problem of retaining structures and geotechnical cooperative work. This paper analyzes an engineering in an area of China which is processed by vacuum preloading technology in the silt soft soil. This engineering is used rigid supporting structure technology of piles in row and bolts for large area of deep foundation pit supporting. Combined with the monitoring results of axial tension and earth pressure, this paper analyzes the interaction of of soil and the pile anchor supporting system and the deformation of foundation pit for soil pressure. It provides some reference for complex conditions of large area deep foundation pit supporting engineering's design and construction.

## Project Overview

A building site into various high-rise housing complex, located in an province. Its original coastal geomorphic units are stacked landscape. The main building of the proposed project from 11 to 32 floors, above ground level 41~100m, with 2 floors basement. ±0.00 elevation equivalent to an absolute elevation 4.90m. Bottom elevation of the basement floor is -5.60m. Cushion thickness is 0.20m. Actuality ground elevation is 2.00~2.50m. Considering cap excavation depth is 0.50m. The foundation pit's perimeter of this project is about 1054 meters. The foundation pit's design depth is 8.30~8.80m. The security level is level 1. The importance factor of excavation sidewalls is 1.1. The groundwater level of proposed site has great differences Buried underground water depth ranged from 0.10 to 1.20 meters , equivalent to 0.89 to 2.60 meters above sea level. The site has been processed by vacuum preloading technology.

According to the results of the survey report, the name, thickness, physical properties indicators of soil which are related to excavation of foundation pit are in Table 1 from top to bottom.

**Table 1. Physical Properties of Soil Indicators**

| Number | Soil Name | Strata Thickness (m) | Severe ($kN/m^3$) | Floating Severe ($kN/m^3$) | Cohesion (kPa) | Internal Friction Angle ($^0$) |
|---|---|---|---|---|---|---|
| ① | Plain Fill | 8.50 | 18.5 | - | 14.0 | 14.0 |
| ② | Plain Fill | 1.20 | 18.4 | 8.5 | 14.0 | 14.0 |
| ③ | Silt | 3.80 | 16.5 | 6.5 | 6.7 | 3.1 |
| ④ | Silt | 5.80 | 16.1 | 6.1 | 5.3 | 2.9 |
| ⑤ | Silt | 9.95 | 16.1 | 6.1 | 5.2 | 2.7 |
| ⑥ | Gravelly Sand | 1.50 | 19.0 | 9.0 | - | - |
| ⑦ | Strong Weathered Rock | 0.72 | 19.5 | 9.5 | - | - |
| ⑧ | Strong Weathered Rock | 3 .50 | 20.0 | 10.0 | - | - |
| ⑨ | Middle Weathered Rock | 15.60 | 21.0 | 22.0 | - | - |

## Foundation Pit Supporting Program

This project's foundation pit designed according to the principles of economic, safety, easy of construction, using rigid supporting structure form of piles in row and bolts. Piles in row are constructed by rotary digging pile machine or auger drill (red). Pile's diameter is 1.20m and spacing is 1.50m. Clear distance between piles is 0.30m, using 0.60m diameter high pressure jet grouting pile to check water between piles between piles. Top elevation of crown beam is 1.30m. Concrete strength grade of pile is C35 and reinforcement is HRB400; stirrups is HRB300. Rock bolts are compose of high strength steel wire mesh, using a dedicated machine bolt into the hole , and the use of the casing wall holing. Bore diameter is 150mm, steel strand is $\Phi^s$ 15.2mm. The tensile strength of the standard value is 1860 N/mm. Grouting materials used 42.5R ordinary portland cement paste, adding the amount of cement 0.3% FDN superplasticizer.

## Analysis of Retaining Structure and Soil Interaction

### *Computed Result of Retaining Structure's Soil Pressure*

There are five sectional supporting on the south side pit. The perimeter of foundation pit is 150 m. Each level of excavation is divided into one, two , three , etc. drill excavation. Excavation must be balanced stratified open digging, digging depth should not exceed bolt on each storey 20cm. After the excavation, each layer of anchor bolt should be constructed and prestressing force should be brought to bear, of and prestressed anchor. Earth pressure is the side thrust that applied to the soil structure, and also the main load bared by retaining structures. The construction of soil pressure value of the working condition of each role in supporting anchor structure is calculated by Leading deep foundation pit construction design software. The model of soil pressure calculating used elastic soil pressure model and classical soil pressure model. The results are shown in Figure 1.

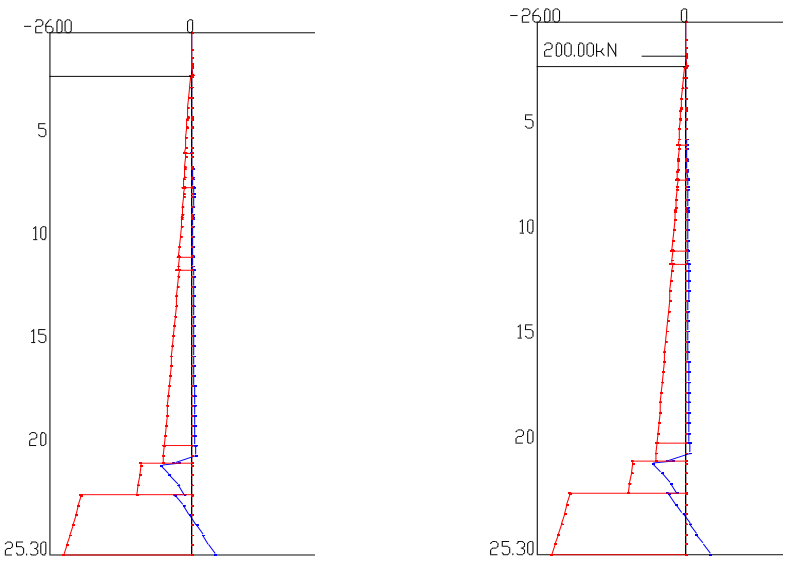


**Condition 1 ( excavation 4.6m)** **Condition 2 ( excavation 6.6m)**

**Fig. 1. Distribution of calculation soil pressure (kN/m)**

As can be seen from the figure the value of earth pressure distribution over the use of theoretical calculations are always on the small great.

### *Analysis of Calculation Soil Pressure Retaining Structure and Measured Results*

The pit sets 28 observation points in total, using resistance strain gauges to test the pit active soil pressure. Measured anchored piles' soil pressure distribution is shown in Figure 2. In the figure, The measured soil pressure distribution approximation a triangle that up and down small and middle large. For the pile anchor supporting structure, because that rock bolts are all prestressed bolts, bolts' prestress have changed soil pressure distribution, made the soil pressure that near bolts increasing, at the bottom of pit decreasing.

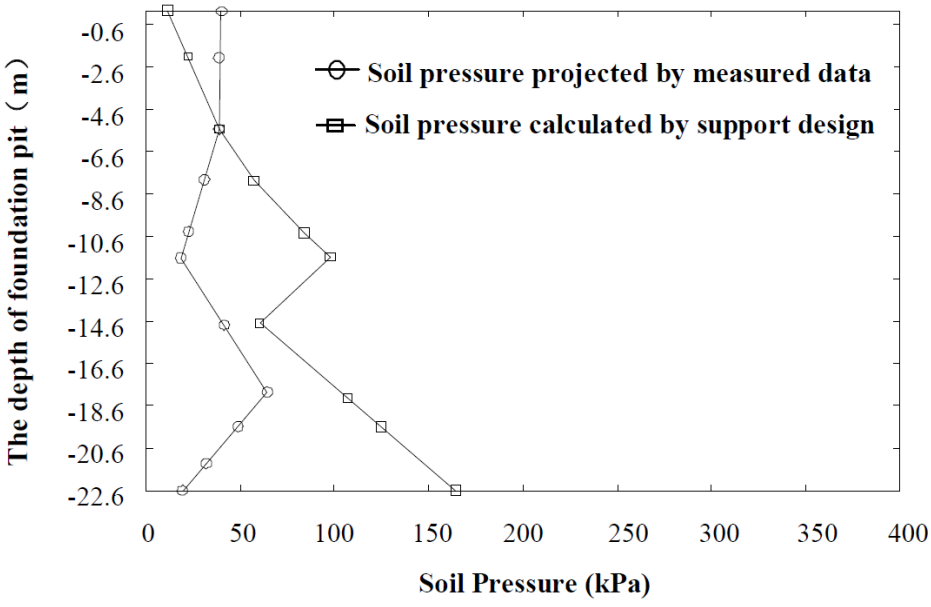


**Fig. 2. Realistic measure soil pressure and theoretical concluded soil pressure compare**

## Conclusions

- Via this engineering example, it proves that in the silt soft soil foundation using vacuum preloading for large area of deep excavation , piles in row and bolts pit supporting structure technology is feasible.
- In the supporting system, soil piles and anchors are complementary and mutually reinforcing.
- The measured soil pressure distribution approximation a triangle that up and down small and middle large. It can be corrected by theoretical formula when design calculating.

## References

[1] Technical Code for Building Pile Foundations, (JGJ94-2008), (in Chinese).

[2] Technical Specification for Retaining and Protection of Building Foundation Pit, (JGJ120-2012), (in Chinese).

[3] Technical Specification for Ground Anchors, (CECS22: 2005), (in Chinese).

*Applied Mechanics and Materials Vols. 580-583 (2014) pp 405-408*
*© (2014) Trans Tech Publications, Switzerland*
*doi:10.4028/www.scientific.net/AMM.580-583.405*

# Calculation for Earth Pressure of Cavity Expansion Considering Displacement

WUMEI ZHANG[1, a], XIN HUANG[2,b]

[1,2]School of Transportation Science and Engineering BUAA, Beihang University, 37 Haidian Street ,Beijing, 100191, P. R. China

[a]may3718@163.com, [b]hx2000@buaa.edu.cn

**Keywords:** finite element method; passive earth pressure; cavity expansion.

**Abstract.** Most of the studies on cavity expansion are about the analytical solutions of the stress distribution, and not related to the effect of soil properties on earth pressure. Aiming at the problem, the change law of passive earth pressure is analyzed by using the Mohr-Coulomb model, and the formula of earth pressure is summarized. The error value of calculation and simulation is small that the formulas can be directly used in practical engineering.

## Introduction

Cavity expansion has been widely used in many geotechnical engineering such as underground excavation and pile foundation. The classical earth pressure theories are used in calculation of the limit state of soil, without considering the change of earth pressure with the displacement. The process of the displacement magnitude of the retaining structure under the condition of plane displacement has been researched [1-4]. The earth pressure is related to the displacement mode of the retaining structure. It is static earth pressure when the displacement is zero. With the increasing of displacement, the earth pressure becomes the passive earth pressure until it reaches a maximum passive earth pressure. The analytical solutions of the stress distribution due to the cavity expansion have also been studied, without the formula of passive earth pressure [5-7].

In this paper, the variation trend of passive earth pressure of soft soil with initial aperture will be simulated by using the finite element software of ABAQUS. The change law of passive earth pressure is analyzed by calculation qualitatively and quantitatively in the process of displacement loading on the soil, and the formula of passive earth pressure in the expansion process is summarized.

## Calculation method and numerical model

The existing studies have indicated that the passive earth pressure will increase when the displacement increases gradually until it reaches the passive state of limit equilibrium. At present, the constitutive model of rock and soil are mainly divided into the theory of elasticity, viscoelastic and viscoelastic plasticity theory and elastic-plastic theory. And elastic-plastic model is the most consistent with the characteristics of soft soil which is the main research object of this paper. The commonly used yield criteria of ideal elastic-plastic model are the D-P model, the Mohr-Coulomb model and the Cam-Clay model. The Mohr-Coulomb model is widely used, and it has fewer parameters which are easy to identify. The analysis of soil is using the Mohr-Coulomb model and the parameters of soft soil can be searched in engineering geology manual. Take different parameter

value in the range into numerical simulation model, extract and process the data from the models, and summarize the change trend between the earth pressure and the parameters.

Building finite element model includes building apart, input parameters, input load, establish grid. The displacement load is applied to enlarge the aperture of the soil, so axial symmetric model is chosen, and the depth and width of model should not affect the calculation results of different depth and aperture of the hole, and the depth of 20m, width of 40m can meet the conditions. 36 models were established, the depth of hole $H$ are 5, 6, 7, 8, 9, 10m and the initial radius of hole $r$ are 0.06, 0.07, 0.08, 0.09, 0.1m respectively. Without considering the friction effect between the soil units and retaining structure, the input material parameters includes: gravity of soil $\gamma$ (KN/m$^3$), elastic modulus $E$ (KPa), soil cohesion $c$ (KPa), Poisson ratio $\mu$, frictional angle $\varphi$(º), void ratio $e$, Saturation $\omega$, osmotic coefficient $k$ (cm/s), and each parameter selects 4 or 5 different number, assuming the distance between a point on the wall of the hole and the ground is $h$ (m), initial radius of the hole is $r$ (m), the expansion displacement of the wall is $x$ (m). The establishment of the grid has great influence on the results of finite element analysis, aiming at the problem, the grid properties of various models are same, and decrease the grid density until effect of grid on the earth pressure can be neglected, and the grid density is 0.25m.

The earth pressure formula summarized principles: 1. The various parameters are derivative to approximate a function. 2. To reduce the complexity of the formula, parameters with negligible effect on the final data will be ignored. 3. Each parameter's dimension will be regardless, KPa is the unit of earth pressure $\sigma$.

**Numerical analysis and earth pressure formula summary**

The main purpose is to calculate the passive earth pressure of the cavity expansion. Therefore, data extracted from the models are the node force $F$, which is horizontal direction on the wall. $F$ is the horizontal resultant of the scope of the nodes of the elements.

$$F=\sigma\times 0.25\times 2\,\pi(r+x) \tag{1}$$

The formula of $F$ must be summarized before the formula of the earth pressure is summed up. Passive earth pressure is a function associated with the parameters.

$$F = f(\gamma, E, c, \varphi, e, \omega, k, h, r, H, x) \tag{2}$$

In order to simplify the model, linear Function is used to fit the curve, all the terms in the formula of $F$ are of the first degree. When calculating the passive earth pressure, the Equation. 2 should be derivation and decomposition.

$$F = f_x' x + f_1(\gamma, E, c, \varphi, e, \omega, k, h, H, r)$$

$$F = f_{xE}'' xE + f_2\ (\gamma, c, \varphi, e, \omega, k, h, H, r)x + f_{1e}'(\gamma, c, \varphi, e, \omega, k, h, H, r)E + f_3\ (\gamma, c, \varphi, e, \omega, k, h, H, r)$$

…… (3)

And so on, the various parameters derivation of the formula of the passive earth pressure is achieved, and put the solution into the formula, and some parameters have less influence on calculation, those will be ignored for simplification.

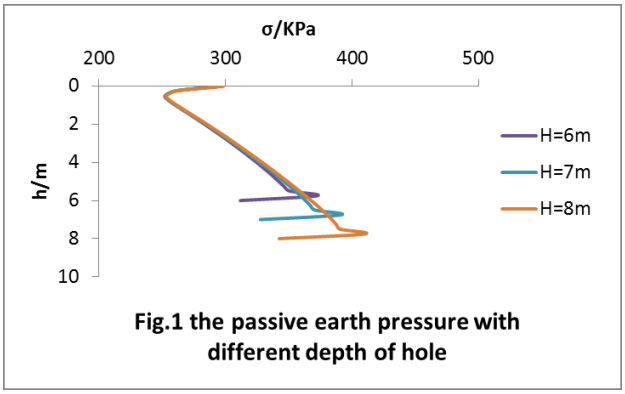


Fig.1 the passive earth pressure with different depth of hole

In Figure 1, the passive earth pressure in same conditions is almost the same except the soil near the top and bottom of the hole, the earth pressure of the soil near the top and bottom is irregular unlike the middle, because the constraints are different. Therefore, the formula of the passive earth pressure is only suitable for the middle part of the soil and the pressure is unrelated to the depth of hole.

By changing the parameter values, it can be learned that void ratio $e$, Saturation $\omega$, osmotic coefficient $k$ and Poisson ratio $\mu$ do not affect the formula. When $h$ and $r$ is unchanged, with the increase of $x$, $E$, $c$, $\gamma$ and $\varphi$ have large effect to the passive earth pressure.

Figure 2-5 are the curves of relationship between earth pressure and displacement with different single parameter under the same other conditions respectively. The earth pressure can be considered as two stages, the elastic stage that the pressure raises rapidly and the elastic-plastic stage that the pressure increases slowly. In the elastic stage, elastic modulus $E$ is the main effect and the other parameters are quite opposite. Therefore, the passive earth pressure is only related to $E$, $x$, $h$, $r$, that it increase when those parameter increase.

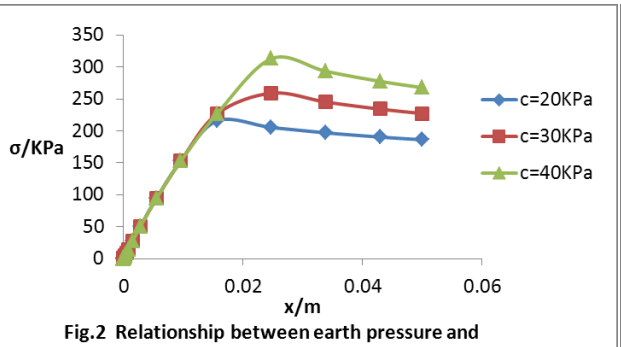


Fig.2 Relationship between earth pressure and displacement with different c

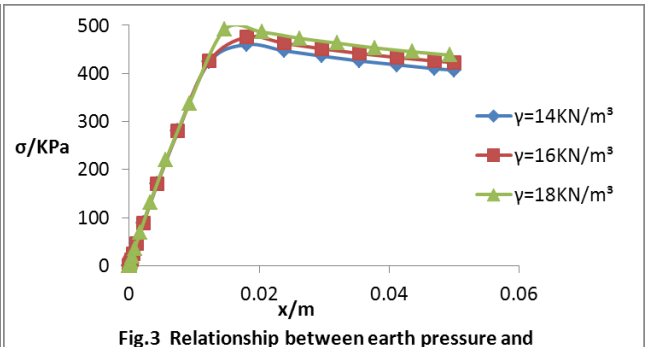


Fig.3 Relationship between earth pressure and displacement with different γ

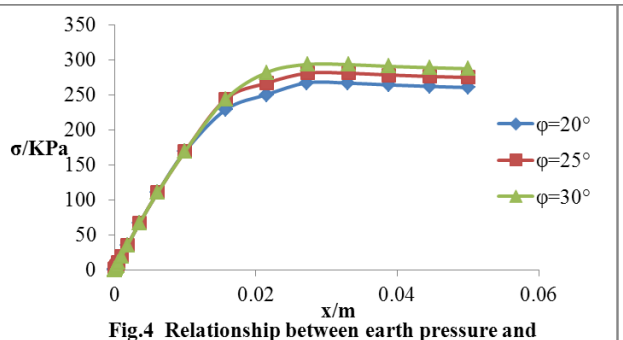


Fig.4 Relationship between earth pressure and displacement with different φ

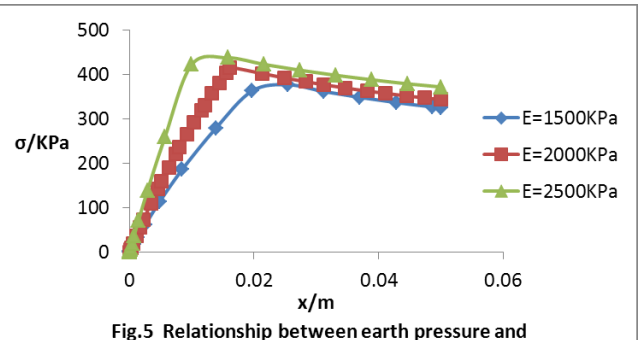


Fig.5 Relationship between earth pressure and displacement with different E

After calculation and summarizing, passive earth pressure in elastic stage should be in calculated in accordance with Equation 4.

$$\sigma=[(1.3081E+249hr+12.h-15r+1)x+3\times10^{-5}]/0.5\pi(r+x) \quad KPa \tag{4}$$

In the elastic-plastic stage, the passive earth pressure changes slowly, and each parameter has impact on it, passive earth pressure in elastic-plastic stage should be in calculated in accordance with Equation 5.

$$\sigma=[(0.0044rhE+22.015rh+0.0007Eh+0.1201rE-21.3713r+1.3973h+0.00266E)x-0.00011\gamma\varphi ch+0.008\gamma\varphi h+0.0013\gamma ch+0.07657\gamma\varphi c-0.1101\gamma+0.00206,.c\varphi h-0.059\varphi h-0.03953ch+0.00264\varphi c+0.67c-0.088\varphi-0.24h+1.9802]/0.5\pi(r+x) \quad (KPa) \tag{5}$$

Random selections of parameters are putted into Equation 4-5, and the results are compared with finite element simulation results in Table 1, there are a few differences between the results. Therefore, the passive earth pressure can be directly calculated according to the formula.

Table.1 Comparison between calculation and simulation with different parameters

| parameters | $\gamma$=18, r=0.08, h=2, e=1500, c=50, $\varphi$=30°, x=0.466, H=6 | $\gamma$=18, r=0.08, h=2.75, e=1500, c=50, $\varphi$=30°, x=0.466, H=8 | $\gamma$=18, r=0.08, h=2, e=2000, c=40, $\varphi$=25°, x=0.0138, H=8 |
|---|---|---|---|
| calculation(KPa) | 269.22 | 283.3 | 316.28 |
| simulation(KPa) | 274.34 | 290.37 | 318.36 |
| error amount | 1.86% | 2.43% | 0.65% |

## Conclusions

(1) The earth pressure can be considered as two stages, the elastic stage that the pressure raises rapidly and the elastic-plastic stage that the pressure increases slowly. In the elastic stage, the passive earth pressure is only related to *E*, *x*, *h*, *r*, and in the elastic-plastic stage, each parameter has impact on the value of pressure.

(2) By simulation, the formulas of the two stages are summarized, and the error value is small, formulas can be directly used to calculate the earth pressure except the soil near the bottom and the top. The earth pressure is not compared with the actual ones due to the lack of real data, but considering the numerical simulation and the formula derivation method is reasonable, the formulas of earth pressure can be applied to practical engineering.

## References

[1] Guosheng Lu: Rock and Soil Mechanics, Vol. 25 No. 4 (2004), p. 586-589.
[2] Kunlin Lu and Yang Yang: Rock and Soil Mechanics, Vol. 30 No. 2(2009), p. 553-557.
[3] Yekai Chen, Yimin Wang, Riqing Xu and Xiaonan Gong: Chinese Journal of Rock Mechanics and Engineering, Vol.23 No.6 (2004), p. 980-988.
[4] Mei Guoxiong and Jinmin Zai: Rock and Soil Mechanics, Vol.22 No.1 (2001), p. 83-85.
[5] Zhaoran Xiao，Zhao Zhang and Mingfang Du: Rock and Soil Mechanics, Vol.25 No. 9(2004), p.1373-1378.
[6] He Tao, Mingwen He, Junguo Xiao: Acta Mech. Sin. (2011) 27(6):1001–1012.
[7] Dongxue Hao, Rong Chen, Chengshun Xu and Chuncheng Liu: Rock and Soil Mechanics. Vol. 34 No. 10 (2013), p.2781-2789.

*Applied Mechanics and Materials Vols. 580-583 (2014) pp 409-414*
*© (2014) Trans Tech Publications, Switzerland*
*doi:10.4028/www.scientific.net/AMM.580-583.409*

# Experimental Study on Shear Strength of Different Types of Soil

CHEN Hui-man[1,a] GUO Fei-hu[1,b] ZHOU Xian-qi[1*,c]

[1]Department of construction engineering,Xiamen University of Technology,Xiamen 361024,China
[a]hmchen@xmut.edu.cn,[b]474270226@qq.com,[c]xqzhou@xmut.edu.cn

**Keywords:** Red clay;Triaxial test;Engineering property;moisture content;shear strength

**Abstract:** Red clay belongs to region special soil.It has engineering geological properties that are different from general soils.The natural red clay has high ratio void ratio,high moisturecontent,low density and so on.But red clay has non-corresponding high strength,bearing capacity of foundation and low compressibility. With the high speed development of China economy,the main soil named red clay in South is used as bearing stratum of many building foundations.However,when red clay is used as foundation,it is regarded as gerenal clay to consider its bearing capacity of foundation.So this will cause two disadvantages.First,potential is not given full play,resulting in considerable waste.Second,red clay has some special properties,such as high woid ratio,softening in water.These properties will bring hidden troubles,causing some bad accidents.These are caused by lacking of knowledge to engineering properties.Xiamen locates in southeast of China,and red clay is widely distributed.It is formed by accumulation through laterization of granites and basalts.So it is essential to study red clay.In this article,literatures of red clay in Xiamen are collected.Indoor conventional geotechnical tests are done,some engineering property parameters are obtained.

## Introduction

Red clay belongs to region special soil,formed in tropical and sub tropical zones.It experiences different degree of laterization.It is rich in iron,aluminum oxide and much clay content,not containing base composition[1-3]. Engineering properties of red clay are different from that of general soil.Red clay under native state generally has high void ratio,high moisture content,low density and so on. But red clay has non-corresponding high strength,bearing capacity of foundation and low compressibility[4-7].

In our country,distribution of red clay is very extensive.According to preliminary statistics,there are more than 2 million square kilometers that are converd by red clay in our 9.6 million square kilometers.Its range is roughly from Changjiang River to Hainan,from Taiwan and the Penghu Islands to Yunnan-Guizhou Plateau and Hengduan Mountains.It refers to 14 provinces and regions.It is one of the most extensively distributing soils[8].It is observed from distributing regions that almost the South region is covered by red clay.I t is a parlance in China that is north of the loess,south red soil.

Xiamen locates in southeast in China.And it is extensive distribution of red clay in Xiamen.The land area of Xiamen is 1565 square kilometers,belonging to subtropical climate.

With the high speed development of China economy, the main soil named red clay in South is used as bearing stratum of many building foundations. However,when red clay is used as foundation,it is regarded as gerenal clay to consider its bearing capacity of foundation.So this will cause two disadvantages.First,potential is not given full play,resulting in considerable waste.Second,red clay has some special properties,such as high woid ratio,softening in water.These properties will bring hidden troubles,causing some bad accidents.These are caused by lacking of knowledge to engineering properties.So it is essential to study the red clay.

On the basis of collecting literatures,reading literatures and analysizing literatures in this article,study on shear strength of red clay in Xiamen is done.The main works are following.

(1) Reading literatue of red clay.

literatures about red clay are collected,read and analysed.

(2) Laboratory experiments of engineering characteristics of red clay.

It is regarded red clay in each region of Xiamen as the object of study.Samples of red clay are taken,the physico-mechanical indexes,such as moisture contents,are obtained by common physical experiments.

(3) doing Triaxial experiments of red clay.

Through triaxial experiments(triaxial consolidation draining shear test(CD), triaxial consolidation undraining shear test(CU), triaxial unconsolidation undraining shear test(UU)).Shear parameters of $c$ and $\varphi$ in Xiamen are determined.

**Routine laboratory experiments of red clay in Xiamen**

In order to know shear parameters of red clay in Xiamen,disturbed soils are sampled in some regions of Xiamen and moisture content experiments are done.

Table 1 Moisture content experiment

| Name | Testing samples | Teams |
|---|---|---|
| Sample1 | 1-9 | 3 |
| Sample2 | 1-9 | 3 |
| Sample3 | 1-9 | 3 |

In order to measure moisture content of disturbed samples exactly,sampling should obey priniples which is far from ground surface,keeps soils wet,and decreases evaporation of water as far as possible.

**Experimental methods and equipments**

Experimental methods of moisture content mainly have oven drying method,alcohol burning method,frying dry method,specific gravity method and so on.In this testing, oven drying method is used.9 specimens are sampled in each site,and are dryed for 8hours under 105-110°C,and the average value of 9 moisture contents are taken for moisture content of specimens

testing equipments:oven box which is heated by electricity and can keep 105-110°C;balance that its accuracy is 0.01g; small aluminum box and so on.

**Experimental datum**

moisture contents of specimens are obtained through meticulously experiments.The main datum are in the following table.

Table 2 Moisture content of specimens

| Name | Team | Quality of aluminum box(g) | Quality of soil and aluminum box(g) | Quality of dry soil and aluminum box (g) | moisture content (%) | The average value of moisture contents of each team(%) | The average value of moisture contents of each sample(%) |
|---|---|---|---|---|---|---|---|
| Sample 1 | 1 | 9.596 | 23.797 | 21.405 | 16.844 | 16.432 | 16.599 |
| | | 9.560 | 24.989 | 22.508 | 16.080 | | |
| | | 9.501 | 23.909 | 21.550 | 16.373 | | |

| | | | | | | | |
|---|---|---|---|---|---|---|---|
| | 2 | 9.561 | 24.243 | 21.718 | 17.198 | 16.565 | |
| | | 9.557 | 24.181 | 21.821 | 16.138 | | |
| | | 9.297 | 21.962 | 19.890 | 16.360 | | |
| | 3 | 9.549 | 21.304 | 19.384 | 16.334 | 16.800 | |
| | | 9.543 | 23.373 | 21.019 | 17.021 | | |
| | | 9.556 | 23.542 | 21.158 | 17.046 | | |
| Sample 2 | 1 | 9.596 | 20.870 | 17.912 | 26.237 | 26.235 | 26.131 |
| | | 9.560 | 22.048 | 18.767 | 26.273 | | |
| | | 9.501 | 21.183 | 18.123 | 26.194 | | |
| | 2 | 9.561 | 21.822 | 18.592 | 26.344 | 26.139 | |
| | | 9.557 | 21.867 | 18.604 | 26.507 | | |
| | | 9.297 | 22.850 | 19.385 | 25.566 | | |
| | 3 | 9.549 | 22.383 | 19.053 | 25.947 | 26.020 | |
| | | 9.543 | 22.177 | 18.889 | 26.025 | | |
| | | 9.556 | 21.638 | 18.486 | 26.088 | | |
| Sample 3 | 1 | 9.595 | 23.733 | 20.842 | 20.448 | 20.319 | 20.202 |
| | | 9.552 | 23.102 | 20.365 | 20.199 | | |
| | | 9.501 | 21.181 | 18.809 | 20.308 | | |
| | 2 | 9.545 | 20.436 | 18.248 | 20.090 | 20.166 | |
| | | 9.557 | 22.845 | 20.114 | 20.552 | | |
| | | 9.287 | 23.359 | 20.565 | 19.855 | | |
| | 3 | 9.570 | 19.043 | 17.118 | 20.321 | 20.121 | |
| | | 9.559 | 20.911 | 18.681 | 20.206 | | |
| | | 9.573 | 22.862 | 20.226 | 19.836 | | |

**Analysis of testing datum**

From above table,it is concluded that the difference of moisture contents of specimens is bigger.The moisture contents of three samples are 16.599%, 26.131%, 20.202% respectivlely.

**Triaxial shear experiments of red clay in Xiamen**

Triaxial shear experiment is a method of testing shear strength.Generally 3-4 cylinder specimens are used in this experiment.Ttrixial compression(difference of principal stress $\sigma_1$-$\sigma_3$) is loaded under constant confining compression(minor principal stress $\sigma_3$) to shear until break.Then according to Mohr-coulomb theory, parameters of shear strength are obtained.

Triaxial experiments are divided into triaxial consolidation draining shear test(CD), triaxial consolidation undraining shear test(CU), triaxial unconsolidation undraining shear test(UU).In this experiment,these three experiments are done successively.

**Introduction of triaxial apparatus**

TSZ micro-control triaxial testing apparatus uses newest technology,gathering machine,electronic technique,automatic control technology,sensor automatic measurement technology and computer technology.Basic equipment could do routine stress-strain unconfined test,UU,CU,CD and so on.Different equipments of test vessels and control modules could do Ko consolidation test,static lateral pressure coefficient,triaxial test of multiple stress path,tensile test,elasticity modulus test,bearing ratio test and so on.If consolidation modules are equiped,step loading test and continuous loading testing are done.If vibration modules are equiped, micro-control vibration triaxial testing could done.

Fig. 1 TSZ micro-control triaxial testing apparatus

**Testing method**

Triaxial testing is composed of specimen preparation,specimen installation,consolidation stage,shear stage.

**Specimen consolidation**

(1) Confining compression is applied through control cabinet,and when it approachs to setting value,it is started.

(2) open drain valve.

(3) Pore water is drained through confining pression until pore water pressure decreases more than 95%.

(4) consolidation finishs and drain valve is closed.

**Analysis of testing datum**

Three testings are done to specimens: triaxial consolidation draining shear test(CD), triaxial consolidation undraining shear test(CU), triaxial unconsolidation undraining shear test(UU).The datum are following.

Testing results of triaxial unconsolidation undraining shear test(UU)

Table 3 UU testing datum

| Name | Team | value of C | average value of C | Value of $\varphi$ | average value of $\varphi$ |
|---|---|---|---|---|---|
| Sample 1 | 1 | 59.20 | 61.07 | 15.00 | 14.6 |
| | 2 | 61.10 | | 15.10 | |
| | 3 | 62.90 | | 13.70 | |
| Sample 2 | 1 | 12.70 | 15.80 | 19.90 | 19.73 |
| | 2 | 15.70 | | 19.90 | |
| | 3 | 19.30 | | 19.40 | |
| Sample 3 | 1 | 40.70 | 38.90 | 4.00 | 3.97 |
| | 2 | 32.80 | | 5.30 | |
| | 3 | 43.50 | | 2.60 | |

Testing results of triaxial consolidation undraining shear test(CU)

Table 4 CU testing datum

| Name | Team | value of C | average value of C | Value of $\varphi$ | average value of $\varphi$ |
|---|---|---|---|---|---|
| Sample 1 | 1 | 53.20 | 53.50 | 18.50 | 19.57 |
| | 2 | 56.30 | | 19.60 | |
| | 3 | 51.00 | | 20.60 | |
| Sample 2 | 1 | 12.70 | 16.10 | 19.90 | 19.73 |
| | 2 | 19.90 | | 19.40 | |
| | 3 | 15.70 | | 19.90 | |
| Sample 3 | 1 | 41.00 | 51.50 | 8.70 | 7.30 |
| | 2 | 57.00 | | 6.30 | |
| | 3 | 56.50 | | 6.90 | |

Testing results of triaxial consolidation draining shear test(CD)

Table 5 CD testing datum

| Name | Team | value of C | average value of C | Value of $\varphi$ | average value of $\varphi$ |
|---|---|---|---|---|---|
| Sample 3 | 1 | 19.40 | 42.43 | 23.50 | 21.73 |
| | 2 | 61.90 | | 20.10 | |
| | 3 | 46.00 | | 21.60 | |

Analysis of testing datum

It is concluded from table 6 and table 7 that parameters of shear strength will change with the change of testing method.Draining mode and consolidation mode have unconspicuous influence law to cohesions,but have conspicuous influence law to frictional angles.With improvement of consolidation and draining conditions, friction of soil increases showing the increasement of effective indexes of soil.This coincides with practical engineerings.

Table 6 Changes of cohesion C（KPa）under three testing conditions

| | UU | CU | CD |
|---|---|---|---|
| Sample 1 | 61.07 | 53.50 | |
| Sample 2 | 15.80 | 16.10 | |
| Sample 3 | 38.90 | 51.50 | 42.43 |

Table 7 Changes of frictional angle $\varphi$(°)under three testing conditions

| | UU | CU | CD |
|---|---|---|---|
| Sample 1 | 14.60 | 19.57 | |
| Sample 2 | 19.73 | 19.73 | |
| Sample 3 | 3.97 | 7.30 | 21.73 |

**Conclusions**

On the basis of collecting literatures,reading literatures and analysizing literatures in this article,study on routine experiments and shear strength experiments of red clay in Xiamen is done.The main conclusions are following

(1) moisture content relates to distributing sites of soil.

Difference of moisture content of samples is bigger.The moisture contents of samples are 16.599%, 26.131%, 20.202% respectively.

(2) Laboratory experiments of engineering properties of red clay.

It is regarded red clay in each region of Xiamen as the object of study.Samples of red clay are taken,the physico-mechanical indexes,such as moisture contents,are obtained by common physical experiments.

(3) doing Triaxial experiments of red clay.

Through triaxial experiments(triaxial consolidation draining shear test(CD), triaxial consolidation undraining shear test(CU), triaxial unconsolidation undraining shear test(UU)).Shear parameters of $c$ and $\varphi$ in Xiamen are determined. Parameters of shear strength will change with the change of testing method.Draining mode and consolidation mode have unconspicuous influence law to cohesions,but have conspicuous influence law to frictional angles.With improvement of consolidation and draining conditions, friction of soil increases showing the increasement of effective indexes of soil.This coincides with practical engineerings.

**Acknowledgements**

This work was financially supported by the University Students' Innovative Training Program (2012).

**References：**

[1] WANG qing,CHEN jianping,MA liying.Study on Chinese Red Clay and Evaluation of Bearing Capacity of Foundation.Exploration Engineering,4(1995),P.15-17.

[2] HUANG zhihong,ZHU lijun,LIAO yiling et al.Mechanical properties of Red Clay under Different Stress Paths. Journal of Rock Mechanics and Engineering, Vol.23-15(2004),P. 2599-2603.

[3] GAO guoduan.Micro Structure and Engineering Properties of China Red Soil [J]. Journal of Geotechnical Engineering, Vol.7-5(1985),P.10-21.

[4] MA lin. A Study on Constitutive Model and Tests on Influence of Free Ferric Oxide on Increasing of Strengh of Granite Residual Red Soil.PHD,Jilin University,2007.

[5] LI ping.Discussion about the Geotechnical Character of Granite Residual Soil in Fujian Province [J].URBAN GEOTECHNICAL INVESTIGATION & SURVEYING, Vol.6(2006),P. 78-79.

[6] LIU yanghua.Red Clay's Geotechnical Engineering Property at Dongan in Hunan. Journal of Gulin Institute of Technology, Vol.22-4(2002),P.476-480.

[7] HE guangxiang,PEI yongwei,YANG chengfu et al. The Influence of Groundwater Line Lowing to the Building Cracking in the Red Clay Region.Guizhou Geology, Vol.25-2(2008),P. 139-141.

[8] WANG yuhua. Distribution Characteristics of Red Soil and Red Clay in China[A].Conference Prceeding of New Progress of Engineering Geology of China.Edited by Press of Chengdu University of Science and Technology,1989,in Press.

*Applied Mechanics and Materials Vols. 580-583 (2014) pp 415-419*
*© (2014) Trans Tech Publications, Switzerland*
*doi:10.4028/www.scientific.net/AMM.580-583.415*

# Failure mechanism of strip footing on geotextile- reinforced soil

Zongjian Wang[1,a], Liang Lu[2,3,b] and Bin Zheng[2,3,c]

[1]Institute of Geotechnical Engineering, Chongqing Jiaotong University, Chongqing 400074, China

[2]School of Civil Engineering, Chongqing University, Chongqing 400045, China

[3]Key Laboratory of New Technology for Construction of Cities in Mountain Area (Chongqing University), Ministry of Education, Chongqing 400045, China

[a]wangzongjiansky@163.com, [b]luliangsky@163.com, [c]20131602077@cqu.edu.cn

**Keywords:** failure mechanism, geotextile-reinforced soil, deformation, bearing capacity

**Abstract.** Several laboratory model tests were carried out on the bearing capacity of strip footings on reinforced soil foundation and reinforced slope. Compared with unreinforced cases, the deformation and failure of reinforced earth in different foundation conditions were monitored and analyzed. In order to visualize a failure mechanism when the ground reaches the state of limit equilibrium, a new numerical procedure was proposed. Assuming an elastic-perfectly plastic model, a smeared shear band approach and a modified initial stress method enable the proposed procedure to create an explicit collapse mode by the stress yield condition. On the basis of the development of failure mode and deformation of foundation, the bearing capacity of strip footings can be significantly increased by the inclusion of geotextile. And because the procedure considers the stiffness and deformation of the material, it may be applied to complex stability problems.

## Introduction

The technology of geosynthetics reinforced soils is applied more and more in recent geotechnical engineering practice. Among the possible applications, the beneficial use of foundation reinforcement to improve the bearing capacity has attracted a great deal of attention, and there have been numerous studies on this subject [1, 2]. These investigations have demonstrated that both the ultimate bearing capacity and settlement performance of shallow foundation can be improved by the inclusion of geosynthetics in the ground, and have proven the reinforced soil foundation to be a cost-effective foundation system.

When a footing is rested on sloping ground, the bearing capacity of footings may be significantly reduced. Yoo presented a possible measure of reinforcing the sloping ground with layers of geogrid to improve the bearing capacity [3]. To design a footing on a reinforced slope requires a thorough understanding of the mechanical behavior in addition to the bearing capacity behavior of the reinforced slope.

Most of previous studies concerning the design methods for the reinforced soil foundation and reinforced slope are based on the limit equilibrium which represents kinematical conditions only by using the mechanically reasonable shape of failure [4, 5]. However, the limit equilibrium-based stability analysis often tends to become uncertain and unreliable for a soil stratum which consists of multiple layers, or which includes materials having quite different stiffness like earth reinforcement material. This is because this method evaluates the material properties only by its final strength, and does not explicitly allow considering the stiffness and deformation of materials which may play an important role for evaluating earth reinforcement, and which may affect the globe failure mechanism. Although numerical analyses such as the finite element or finite difference analysis have become popular in design practice, no rational evaluation for the failure and deformation stability for determination of ultimate bearing capacity on reinforced foundation. Many researches show that the classical FEM does not necessarily provide a reasonable failure mechanism [6].

This study aims at establishing a rational method to examine the effect of geosynthetics on improvement of bearing capacity behavior based on the formation of failure collapse and deformation stability and to estimate the stability of rigid strip footing on reinforced soil ground and reinforced

slope. Firstly, several laboratory model tests were carried out to investigate the failure and deformation behavior of rigid strip placed on level ground and on top of slope with and without layers of geotextile. Then, combined a smeared shear band approach with a modified initial stress, a numerical procedure based on FEM was proposed to create a failure mechanism by stress yield condition. In addition, the proposed numerical procedure employs requires a small number of soil parameters to reduce the numerical efforts and to be applied directly to practical design works. Finally, the mechanical behavior of reinforced soil is discussed and analyzed by comparing the location and collapse of failure and deformation of reinforced earth with the unreinforced cases.

## Laboratory model tests

**Test configuration.** A series of laboratory model tests were executed in a test box made of a steel frame, having inside dimension of 70×10mm in plane and 55mm in height. The two sidewalls of the test box were constructed using transparent glasses marked in grids with side length of 5cm size for ease of monitoring the deformation and failure mechanism during testing. In addition, a rough base condition of a 0.15m model footing made of steel prepared at the bottom of the footing. Since the walls of the test box were firmly held in position by steel melting and the wall friction was kept to the minimum by using a thin rubber membrane smeared with a thin layer of silicon grease on the surface of sidewalls, plane strain conditions were considered for all model tests. In order to observe the experimental behavior, a hardened glass is fixed on one side of the soil stratum. Fig. 1 shows different parts and locations of testing apparatus for the case of slope, while the model footing and Bellofram cylinder used for applying the loading pressure to the footing should be rested on the middle of surface of ground.

All tests of slope were conducted with an artificially made slope of 1(V): 1.73(H). The model strip footing was located on the edge of slope, with the length of the footing equal to the full width of the soil tank in order to maintain the plane strain conditions. The two ends of the rigid model footing were polished smooth to minimize the end friction effects. A rough base condition was provided by rough sand paper on the bottom of model footing. The model tests considering the effect of reinforcement material were also performed. For the case of level ground, only one layer of geotextile is placed 130 mm deep in the ground according to the calculated position of active wedge below the model footing. For the case of sloped ground, the effect of reinforced soil was discussed through the two cases setting up one layer and two layers of reinforced material respectively, as shown in Fig. 2, besides Case 1 for natural unreinforced one.

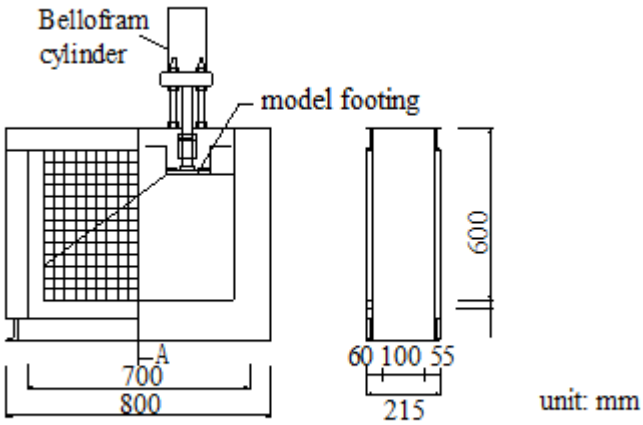


**Fig. 1** Schematic view of experimental apparatus

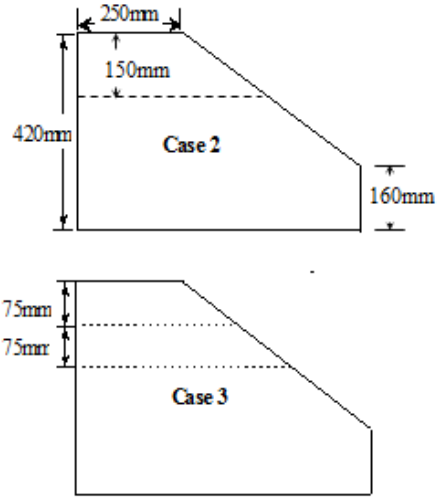


**Fig. 2** Arrangement of reinforced slope

**Materials used for the testing.** The sand used in the model ground was mountain sand taken from Mikuni region of Fukui in Japan. The soil parameters are shown in Table 1, in which c, φ: Mohr-Coulomb strength parameters, E: Young's modulus of the soil stratum, γ: unit weight of soil,

and μ: Poisson's ratio. In the experiments, c and φ were obtained by a direct shear test. E is back calculated by the footing settlement observed. Note that because of different locations of soil sample in two tests for level ground and slope, the parameters taken from soil test were different. Considering the effect of reinforcement material, one type of woven geotextile is used to the reinforced subsoil. Table 2 shows the properties of the woven geotextile.

**Test results.** Test relationship between load pressure and settlement of footing on natural level ground is compared with the reinforced case in Fig.3. The test results show that the bearing capacity and settlement is considerably improved by use of geotextile. The test results for three cases of sloping ground are shown in Fig. 4. Compared with Case 1 of natural subsoil without reinforced material, Case 2 with one layer of geotextile or Case 3 with two layers of geotextile has a higher failure load and a lower settlement respectively.

**Table 1** Soil Parameters

| Case | c (kpa) | φ (°) | E(kPa) | γ (kN/m$^3$) | μ |
|---|---|---|---|---|---|
| Level ground | 12.25 | 30.96 | 3924 | 15.66 | 0.33 |
| Slope ground | 7.85 | 15.9 | 5886 | 14.03 | 0.33 |

**Table 2** Properties of Geotextile

| length (mm) | width (mm) | thickness (mm) | E (MN/ m$^2$) | strain at tensile failure | tensile strength (kN/m) | mass (g/ m$^2$) |
|---|---|---|---|---|---|---|
| 900 | 200 | 0.21 | 4900 | 19% | 950 | 130 |

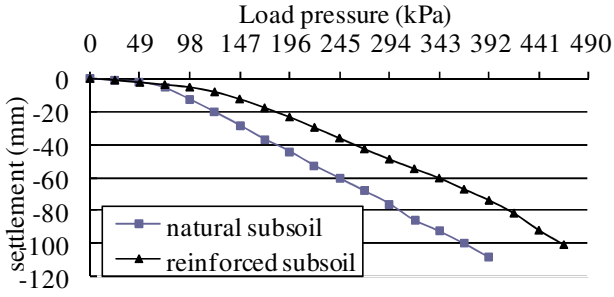


**Fig. 3** Load pressure-settlement relationship (Level ground)

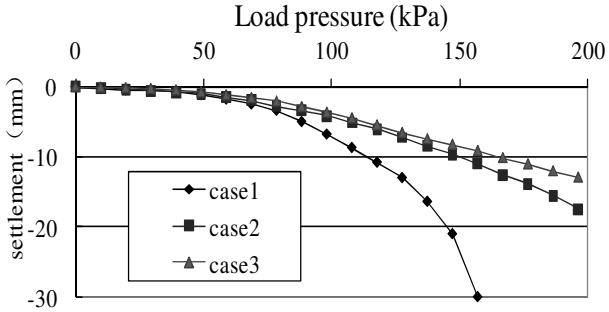


**Fig. 4** Load pressure-settlement relationship (Sloping ground)

## Numerical modeling

To relate the proposed procedure to conventional stability analysis, Mohr-Coulomb and Coulomb yield criteria were employed respectively to soil mass in plane strain condition and to the interface between the footing and the ground surface. To explain the effect of geosynthetics on improvement of bearing capacity and deformation behavior, a numerical procedure enables to get a definite failure mechanism was proposed. To obtain a rational failure mechanism analogous to that assumed in limit equilibrium method, three assumptions are followed [7]: 1) Assume an active wedge below footing; 2) Assume the yield element as a stratified material based on the smeared shear band approach; 3) Perform a nonlinear FEM based on the modified initial stress method [10].

**Numerical analysis.** Applying the numerical procedure to the laboratory model tests, the footing is modeled by beam elements and represented by its elastic modulus $E=2.1\times10^7$kPa, cross area $A=0.012m^2$ and moment of inertia $I=1.44\times10^{-7}m^4$. The shear modulus G of interface elements is given as $E/2(1+\mu)$ by using E and μ of subsoil. Many experimental researches have observed actually the active wedge developing below footing. However, when a footing rested on the slope the active wedge may be changed based on the relationship between major principle and direction of shear band rather than the most fundamental expression.

**Numerical results.** Due to the assumption of the smeared shear band for yield element, it may create an estimated slip surface by the distribution of yield element. Figs. 5 and 6 shows the yield regions given by the proposed procedure, in which a solid line in some finite element represents the correspongding element has yielded and shows the direction of shear band. In this study, the failure mechanism can be defined when the yield elements are connected to form a continous slip surface, accordingly the corresponding load $q$ determined as ultimate bearing capacity. Figs. 7 and 8 shows the numerical relationships between load and settlement for all cases in comparison with the test results, in which solutions of bearing capacity are shown supported by the formation of failure mechanism.

## Discussions

For the case of level ground, Fig. 7 illustrates the earth reinforcement effect on the bearing capacity in comparison with natural subsoil. FE meshing and material parameters are the same as those on unreinforced cases except the geotextile is practiced by truss material. The results show that the geotextile improves the bearing capacity because the geotextile restrict the extension of yield regions for reinforced subsoil in Fig. 5 which also contains a conventional slip surface presented by Prandtl .

For the case of slope, Fig. 6 compares the distribution of yield elements when the foundation reaches the ultimate bearing capacity $q$ for three cases. Because the position of geotextile in Case 2 is much deeper than the region of failure mode in Case 1 as shown in Fig. 6 (a), the geotextile little improves bearing capacity. While the geotextile of upper layer in Case 3 largely improves bearing capacity, for its position rather restricts the expansion of failure surface. Because the yield elements are mainly concentrated on the region upper the geotextile, the bearing capacity and deformation of reinforced soil foundation is improved, as shown in Fig. 8. In addition, it can be found that the bearing capacity of slope is less than the level ground because the failure surface cut through the side of slope prior to the surface of ground.

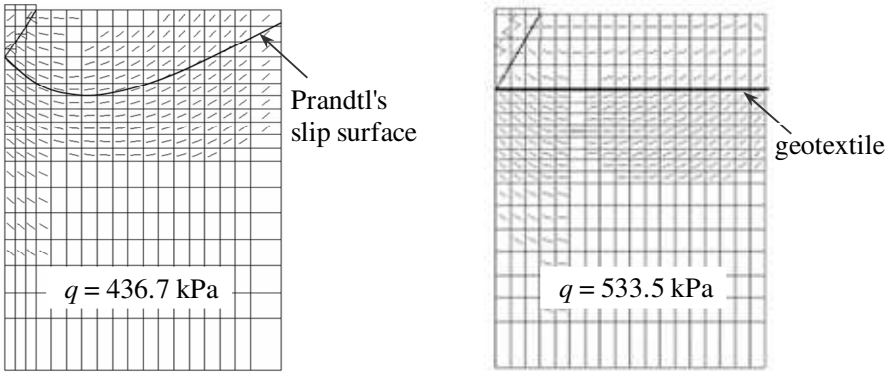


**Fig. 5** Failure collapse and yield regions for right half partof level ground: (a) unreinforced case (b) rienforced case

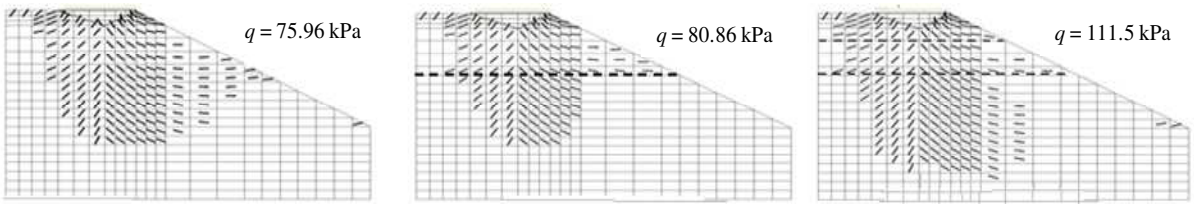


**Fig. 6** Filure collapse and yield regions of sloping ground: (a) Case 1 for natural slope (b) Case 2 for slope with one layer of geotextile (c) Case 3 for slope with two layers of geotextile

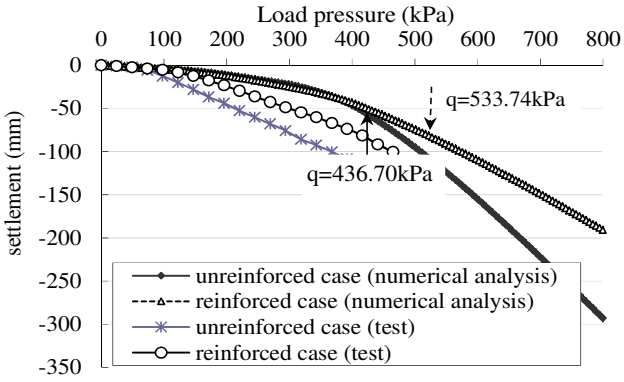


**Fig. 7** Load pressure - settlement relationship (Level ground)

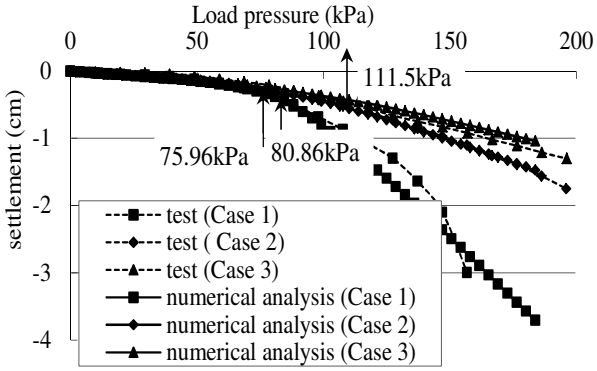


**Fig. 8** Load pressure-settlement relationship (Sloping ground)

## Conclusions

On the basis of the development of failure mode of foundation, the bearing capacity behavior of strip footings on reinforced soil was discussed. The following conclusions can be derived :

1) In order to fill a gap existing between limit equilibrium method and classical FEM, a numerical procedure was proposed to provide a reasonable failure mechanism in the course of design. Because the procedure considers the stiffness and deformation of the material, it may be applied to deal with the reinforced soil problems.
2) The bearing capacity can be determined by the failure collapse represented by yield elements; in any case the earth reinforcement gives much larger bearing capacity and restricts the settlement of foundation because the collapse mode is observed to be restricted to a narrow limit and to restrain the unconstrained plastic flow by geotextile especially by the upper geotextile.
3) In all cases the bearing capacity and failure collapse provided by the proposed procedure agrees fairly well with the test results. The results show that the geotextile placed different positions improve the bearing capacity behavior in different degrees, which agrees well with the experiment.

## Acknowledgements

This work was financially supported by the Chongqing Natural Science Foundation (cstc2012jjA0510), Fundamental Research Funds for the Central Universities (CDJZR12200011), Project (KJTD201305) supported by the Innovation Team Building Programs of Chongqing Colleges and Universities, Scientific Research Foundation for the Returned Overseas Chinese Scholars, State Education Ministry.

## Literature References

[1] P.K. Basudhar, S. Saha, and K. Dab: Geotextiles and Geomemnranes Vol. 25(6) (2007), p. 377

[2] M. Ghazavi, and A.A. Lavasan: Geotextiles and Geomemnranes Vol. 26(5) (2008), p. 404

[3] C. Yoo: Geotextiles and Geomembrans Vol 19 (2001), p. 279

[4] J.G. Zornberg, N. Sitar, and J.K. Mitchell: Journal of Geotechnical and Geoenvironmental Engineering Vol. 124(8) (1998), p. 684

[5] J.N. Mandal, and L. Labhane: Geotehnical and Goelogical Engineering, Vol. 10(4) (1992), p. 291

[6] Y. Hu, and M.F. Randolph: Soils and Foundations, 38(1) (1998), p. 241

[7] L. Lu, K. Arai, and Z.J. Wang: Journal of Applied Mechanics Vol. 10 (2007), p. 351

*Applied Mechanics and Materials Vols. 580-583 (2014) pp 420-423*
*© (2014) Trans Tech Publications, Switzerland*
*doi:10.4028/www.scientific.net/AMM.580-583.420*

# Horizontal Displacement of GFRP bars and PC Strand Combination of Technology Supporting Piles

Xiuhua Li[1,a] , Yanyan Gao[1,b] , Chenxi Yue[1,c] and Chunqing Hu[2,d]

[1]Department of Architectural Engineering, HuaiYin Institute of Technology,

[2]Huaian Guangsha Building Design Co., Ltd.

Huaian, Jiangsu, 223001, China

[a]lixiuhuayou@163.com, [b]gaogua@163.com, [c]ycxmail@163.com, [d]hcqme@163.com

**Keywords:** GFRP bars; PC Strand; Supporting Piles; Engineering Field Test; Horizontal displacement; Energy principle.

**Abstract.** GFRP bars and PC strand composite pile is a new supporting piles, according to the engineering field test and analysis of experimental data prove that there is a significant effect on the control aspects of the horizontal displacement of supporting piles. Principle energy method can calculate the horizontal displacement of pile foundation pit in theory, by comparing the size of the horizontal displacement of the supporting piles of ordinary reinforcement, to demonstrate the feasibility of using GFRP bars and PC strand combination of techniques to reduce the horizontal displacement of excavation, provide reference for future engineering practice.

## Introduction

In recent years, with the accelerated progress of urbanization, urban population continues to gather, as land resources are very limited, the city would like the building height and depth inevitable. Along with high-rise buildings, large-scale development and construction of municipal facilities and underground space, the project site appears a lot of deep excavation, in order to ensure safety during construction excavation site and the surrounding environment, the horizontal displacement of foundation pit structure is not can be too much, so how to limit lateral excavation engineering practice structure is an urgent problem to be solved.

## GFRP bars and PC strand combination technique

**GFRP bars characteristics compared to ordinary steel.** Glass fiber reinforced (GFRP bars) as a new wire, used in China has just started. GFRP bars by using multi-strand continuous glass fibers as the polyethylene resin, epoxy glue, through a special pultrusion die. GFRP bars compared with ordinary steel, the main features are: (1) GFRP bars tensile strength than ordinary steel; low (2) shear modulus, ease of removal after the end of engineering support piles; (3) bulk density of small , is about 25% of the ordinary steel; (4) good corrosion resistance. Between these characteristics, GFRP bars replace bar in the supporting structure is entirely feasible, but it is reasonable.

**Combination technique of GFRP bars and PC strand in the supporting piles.** The use of low shear strength of GFRP bars, brittleness easy removal and post-tensioned steel noose recyclable characteristics, reduce excavations abandoned after the difficulty and cost of demolition, environmental protection, green construction has significance.

GFRP bars and PC strand combination pile that is configuration GFRP bars in the compression zone of the general pile, in the tension zone configuration PC strand. Pile construction is completed and before the excavation, applied partially prestressed for the tension zone of PC strand, so that GFRP bars in tension, with the excavation pit, GFRP bars tendons pulling force gradually reduced; When the excavation to a certain depth, the second prestressed steel strand so until the excavation is completed. In summary, the technology features is GFRP bars, concrete piles, PC strand all in tension. This makes full use of the concrete compression performance, GFRP bars and PC strand tensile good performance characteristics.The GFRP bars arranged on the pressure side of the row of piles, PC

strand disposed in pit row piles in tension side, shown in Figure 1, Figure 2. The use of pre-stressed technology, making the total cross section of the concrete is always compressed state (no tension zone), while the GFRP bars and the strand is always in tension, and through hierarchical prestressed GFRP bars tensile stress remains under control status, you can give full play to the advantage of material, making the material properties into full play, for material savings, lower costs of practical significance.

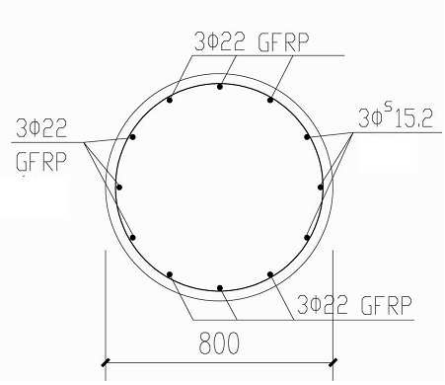

**Figure 1 Portfolio section pile reinforcement** **Figure 2 Combination trailer coupling**

## Energy Method Principle

**Energy Act introduced**. In static structural analysis, can be applied directly equilibrium conditions, geometric deformation conditions and physical conditions for solving the structure of the internal forces and displacements, which is generally static method, according to the most general case, its calculation of a total 15 unknown amount, there is the corresponding 15 equations, even for a simplified plane problem is, there are still six unknowns, ie there are six equations to be solved, the difficulty of solving these equations are equations without saying and Yu. If the equilibrium conditions or conditions with the corresponding geometric deformation energy principle instead solution as the basis for the establishment of the energy method is called. There are two basic methods in the static method, namely displacement method (to shift the basic structure of an unknown quantity) and power law (in some internal forces as the basic unknowns). Correspondingly, the energy principle also has two basic principles: the displacement method corresponds to the principle of minimum potential energy (potential energy in value theorem), and the corresponding force method is the minimum complementary energy principle. Algorithm on the horizontal displacement of the supporting piles mentioned below uses a minimum potential energy theorem, namely the potential in value theorem.

**Principle of stationary energy.** The total potential energy of the system by the criteria used to determine whether the structure of the stable equilibrium state. Energy criterion contains two common energy principle for the principle of stationary potential energy and minimum potential energy principle. Principle of stationary potential energy is when the system is in equilibrium, the total potential energy of a first-order change into zero, that is the total potential energy of this system is a stationary value:

$$\delta \prod = 0$$

Where in the total potential energy of the system has indicated that it is the strain energy and force potential U and W.

## Engineering Field Test

**Project Overview.** Golden Plaza project is located in Huaian City at the southwest corner of the word dam. The project set a floor basement. This is a basement excavation works. Engineering ± 0.00 equivalent absolute elevation 10.00m, excavation area 42000m$^2$ about pit perimeter around 1000m.

Natural ground level within the site about 8.50m, ± 0.00 equivalent absolute elevation 10.00m, Bottom elevation -7.00m, so the actual excavation of the pit depth 5.50m. The excavation depth of 5.50m, the environment in general, support the design level of safety to take two, namely the importance of the coefficient γ= 1.0.

**Engineering Hydrogeological Conditions.** ① Miscellaneous fill: taupe, gray-yellow, mainly clay, more than 30 years backfill time, the layer of soil audience distribution, thickness 4.00 ~ 8.10m. ② Silty clay: gray, soft plastic, widely distributed field area, thickness 3.70 ~ 8.00m. ③ Clay: brown, plastic, widely distributed field area, thickness 0.60 ~ 4.50m.

Each soil calculation parameters are shown in Table 1.

**Table 1 Calculation parameters for each soil**

| Layer No. | Strata Title | Severe | Solid fast direct shear | | Permeability coefficient recommended value |
|---|---|---|---|---|---|
| | | | Cohesion | Angle of internal friction | |
| | | γ | C | ϕ | K |
| | | KN/m$^3$ | KPa | Degree | (cm/s) |
| ① | Miscellaneous fill | 17.3* | 6.0* | 17* | 3e-4 |
| ② | Silty clay | 17.5 | 26.0 | 12.0 | 6.2e-5 |
| ③ | Clay | 19.2 | 49.0 | 18.3 | 3e-6 |
| Remark | In the table ,C, φ is the standard value, the rest is the average and marked with * are empirical values. | | | | |

**Test data processing.** According to the experimental data obtained pit displacement drawn through the measured data shown in Figure 3. After analysis, the true and reliable experimental data, through PC strand tensioning graded approach is applied to the control pit displacement effect is obvious, GFRP bars and PC strand combination supporting piles experiment was successful basically successful, can be used for further study.

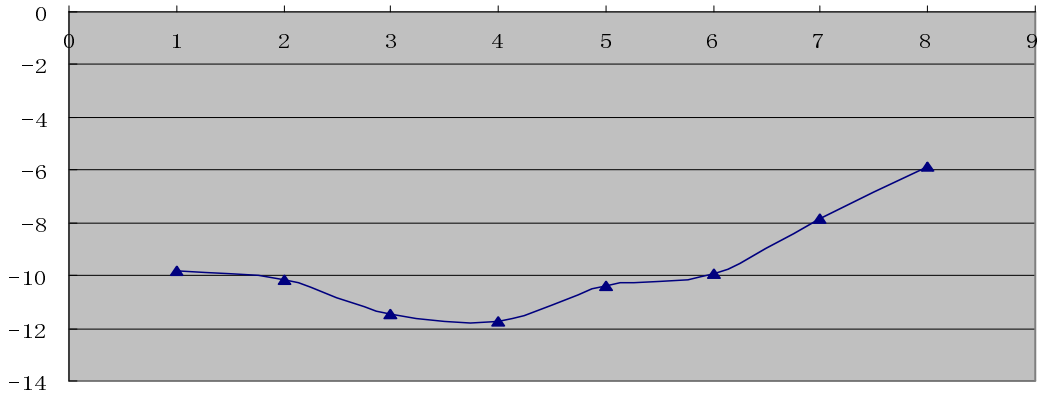


**Figure 3 The map of pit displacement**

## Using the energy method to calculate the lateral supporting piles

In order to reduce the horizontal displacement of the pile excavation, pile on the Strand in the tension zone of prestressing. After the excavation, in the role of supporting piles of earth pressure and prestressed re-equilibrium. Here in value theorem using the potential energy method to recalculate the amount of horizontal displacement after prestressing supporting piles.

By substituting the data and calculated: lateral reinforcement piles under normal circumstances occurred to 17cm, the maximum rear sway prestressed piles happen to 12cm, can be seen through the GFRP bars and prestressing strand combination of technology, the amount of horizontal displacement pile excavation reduction compared to ordinary reinforcement in the case of about 30%, and with the increasing depth of the excavation carried out repeatedly applied prestressing, the lateral row of piles will decrease to some extent.

## Conclusion

GFRP bars and PC strand combination of technology in the excavation of the theory is still in the research stage, by using the principle of energy method for the actual maximum lateral displacement of the pile calculation of the amount, and excavation pile comparison proved the feasibility of reducing the horizontal displacement of the pile excavation GFRP bars and PC strand combination technique. GFRP bars and because of low shear modulus characteristics, structure excavation as a temporary structure after the demolition of the construction problems have been resolved, not only reduced the waste, to achieve green building, but also for the future of the surrounding buildings construction brought convenience.

## References

[1] Xueyi Yu: submitted to Journal of Construction Technology. 2011, 40(S1): 218-220.

[2] Shaoqing Shi,Yingfang Liu and Ping Yin: submitted to Journal of Engineering Plastics Application. 2004, 32(6): 43-45.

[3] Weichen Xue, Qiaowen Zhen and Yu Yang: submitted to Journal of Civil Engineering. 2007, 40(12): 59-68.

[4] Weichen Xue: submitted to Journal of Glass Reinforced Plastics / Composites. 2003, 5: 10-13.

[5] Hui Peng: submitted to Journal of China Municipal Engineering. 2008, 4:60-62.

[6] Yiheng Ge, Kejiong Ye and Lisheng Chen: submitted to Journal of Shanghai Construction Science & Technology. 2010, 2: 50-52.

[7] Xiuhua Li, Weimin Cong, Chenxi Yue and Chunqing Hu: Construction Techniques and Measures of GFRP Bars Pile in the Excavation. ICCET 2013

[8] Xiuhua Li, Weimin Cong, Chenxi Yue and Jianxiong Liu: Research on the technology of GFRP bars and PC strand combined supporting piles by experiment. GCCSEE 2013

[9] Guoshu Shen: submitted to Journal of Zhuzhou Institute of Technology.2006,6:90-93

[10] Chonghu Jiang: submitted to Journal of Highway and Automotive.2008, 2:133-135

*Applied Mechanics and Materials Vols. 580-583 (2014) pp 424-431*
*© (2014) Trans Tech Publications, Switzerland*
*doi:10.4028/www.scientific.net/AMM.580-583.424*

# Numerical Analysis of Stabilization of Slopes Overlying Bedrock Using Piles and Effect of Socketed Length of Pile on Stability

Mudthir Bakri[1, a], Yuanyou Xia [1,a], Huabin Wang [2,b]

[1,] Wuhan University of Technology, Wuhan, 430070,China

[2]Huazhong University of Science and Technology, Wuhan 430074, China

[a]mbbakri@hotmail.com, [b]xiayy1965@126.com, [c]huabin@mail.hust.edu.cn

**Keywords:** slope stability; factor of safety; socketed pile length; strength reduction method.

**Abstract.**Piles are used widely for stabilization of landslides. To stabilize a slope settled on bedrock with piles the required factor of safety must be checked, and pile should be designed properly. Piles should be socketed into firm rock to prevent uprooting or overturning .In this research it is aimed to look into the socketed length of pile in bedrock. Therefore the parameters that affect the factor of safety of slope/pile system such as location, length, spacing and diameter of piles are analyzed. The effect of socketed length of pile in rock on pile behavior is investigated by plotting the shear force and bending moment diagrams along pile. The optimal pile position is found to be located slightly upper of the middle of the slope. The minimum socketed length after which the factor of safety will be remained constant is found to be 0.12L where L is pile length.FLAC3D computer code based on finite difference method is used to simulate the slope/pile system.

## Introduction

Anti-slide piles are utilized for the stabilizing of unstable slopes, and have been established as efficient stabilizing technique. The piles employed in stabilization of slopes and landslides are regarded as passive piles since they are generally subjected to lateral force developing from the horizontal movements of the surrounding soil. The Problem in the case of passive piles is complicated because the lateral forces acting on the piles are dependent on the soil movements, which are in turn affected by the presence of the piles. A pile will serve by its shear strength, which is different from an anchor or soil nail. [1]

For slopes with great depth between ground surface and stiff stratum or stable layer (bedrocks), the solution is impractical to embed piles into bedrock or a stable layer (infinite pile length assumption). Thus, the embedded length of piles is an issue and attracts great attention. Many studies have analyzed the embedded length of piles due to lateral soil movements. Ito et al. investigated the design method for a row of piles in a slope with a fixed slip surface, and analyzed the effect of pile length above the slip surface on the factor of safety of pile-slope system[2][2]. Poulos[3] introduced a design method of piles to reinforce slopes by a computer program ERCAP, and examined the impression of embedded length on resistance of piles. Chen and Poulos et al. [4] described a series of laboratory tests on single-instrumented model piles embedded in calcareous sand undergoing lateral soil movements, and analyzed the effect of the ratio of embedded pile length in the upper "unstable" sand layer to that in the lower "stable" sand layer on the maximum bending moment. Griffiths et al. [5] uses two-dimensional plane strain to examine the influence of pile reinforcement on stability of slopes by numerical analysis, and presented the effects of pile length on stability and factor of safety of slope; the uses of two dimensional plane strain would not reflect the actual pile-slope interaction.

Guo and Qin [6] developed an experimental setup to look into the behavior of vertically loaded free-head piles in sand subjected lateral soil movements.

The embedded length of piles subjected to lateral soil movements or in unstable slopes has been referred to either by model tests or by numerical simulations. However, only two parameters, the embedded pile length above the slip surface and the ratio of embedded pile length in the upper "unstable" layer to that in the lower "stable" layer, have been analyzed. More systematic studies are needed to better understand the pile-slope interaction. In the present study, the socketed length of pile in stable rock layer is analyzed, and the influence on safety factor and pile behavior is analyzed with three-dimensional elastoplastic shear strength reduction method.

**Analysis method**

The stability of slopes reinforced with one row of piles is commonly estimated using pressure or displacement based methods, applying an assumed or measured pressure or displacement distribution on piles according to experiences or in-situ measured values caused by lateral soil movements. But it cannot describe the actual coupled pile-soil interaction, and may cause some inaccuracies. Alternatively, the shear strength reduction finite element/finite difference methods can be a good choice, because it cannot only simulate the coupled pile-slope interaction but also calculate the global factor of safety conveniently. The definition of global factor of safety of slopes reinforced with one row of piles in shear strength reduction method is identical to the one in limit equilibrium method. The reduced shear strength parameters, $c_{rd}$ and $\phi_{rd}$, are defined as

$$C_{rd} = \frac{C}{FOS} \tag{1}$$

$$\phi_{rd} = \tan^{-1}(\tan\phi / FOS) \tag{2}$$

Where $C$ and $\phi$ are the actual shear strength parameters of the sliding soil layer; and FOS is the SSRM reduction coefficient; it is considered as the global safety factor of the pile stabilized slope.

**Slope reinforcement system**

**3.1 Model Geometry and Meshing**

The construction of three-dimensional finite difference models is processed using ANSYS 14.5 because it is accurately creating a refine meshed models. The generated meshed model is transferred to FLAC3D using special code written using C++ language. The FEM mesh in ANSYS is well fine-tuned at the pile zone and the near region to enable a closer examination of the state of stresses and displacements of the pile. The selected size of the pile element is 0.40 m and 0.50 m at the adjacent zones of sliding soil and rock layer. The maximum element size in the model does not exceed 2.0 m .In order to minimize the effect of boundaries; the least distant left at both sides back and front the anti sliding pile is 10 times pile diameter . The basic model was reinforced with a row of piles socketed into rock with different socketed length.

**3.2 Constitutive model and parameters:-**

The constitutive behavior of soil continuum is modeled using Mohr-Coulomb model. The Mohr-Coulomb strength criterion has been widely used for geotechnical materials. The position of a stress point on this envelope is controlled by a non-associated flow rule for shear failure, and an associated rule for tension failure. Constitutive behavior of anti slide pile and stable rock layer is considered as isotropic elastic model. The principal parameters of the base model are selected to let

the slope model at verge of failure (FS=1.0). The main parameters required in model calculation are shown in table1.Slope angle was selected to 35° while S/D is selected to be 3 in the base model and the anti slide pile diameter is 2.0 m.

Table 1. Material Properties required in the model computations

| Material Properties | Antislide Pile | Sliding soil | Rock |
|---|---|---|---|
| Density (Kg/m$^3$) | 2500 | 2000 | 2200 |
| Elastic Properties | | | |
| Young's Modulus (Mpa) | 1.04E+06 | 2.00E+02 | 2.39E+04 |
| Poissison's Ratio | 0.2 | 0.3 | 0.2 |
| Strength Properties | | | |
| Cohesion (Kpa) | | 20 | |
| Friction Angle(°) | | 10 | |

For slope-pile analysis, the use of interface elements is essential; the use of them allows relative movements between the soil and the pile, and between sliding and stable soil layers. The apparent stiffness of an element in the normal direction ( kn ) is

$$kn = ks = 10 \times \max\left[ (K + \frac{4}{3}G) \Big/ \Delta Z_{\min} \right] \tag{3}$$

Where : $K$ = bulk modulus of the stiffest neighbouring element

G =shear modulus of the stiffest neighbouring element

$\Delta Z_{\min}$ = smallest dimension of an adjoining element in the normal direction

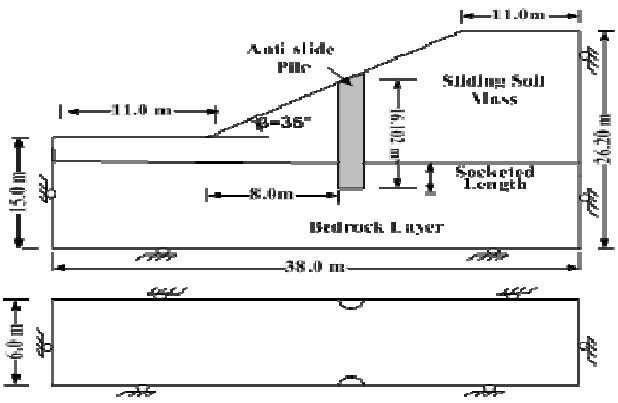


Fig. 2 Model Layout

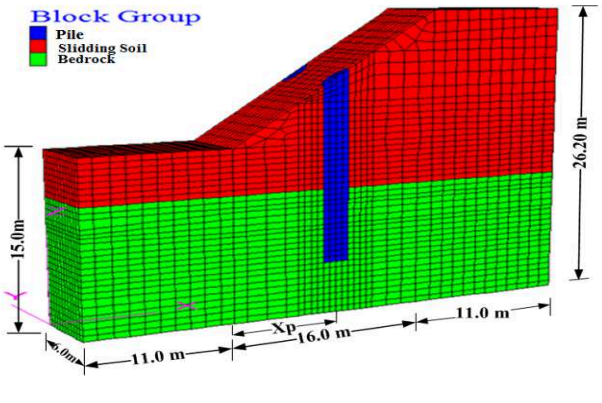


Fig. 1 Slope Model and Finite Difference mesh

## Results and discussions

### 4.1 Effect of pile location

In slopes and landslides stabilized with the piles, the location of the pile has an important role in the stability of slopes reinforced with piles. Many authors studied and investigated the effect of the pile location; they apply using different analysis techniques. As presented in Fig. 2, the pile location in the slope is determined by utilizing a dimensionless ratio ( $x_P/X$ ) where ( $x_P$ ) is the distance from the slope toe, and ( X ) the horizontal length of the slope.

Previous studies on one layer slopes have shown that the optimal pile location is not dependent on the distance between the piles[1]. Consequently, the location of a pile (S=3D) will be employed to find of the optimal location of the piles in a three-dimensional analysis.

The variations of the pile location with the factor of safety of reinforced slope for different slope angles are shown in Fig. 3. The embedment length in rock is considered large enough so that the maximum factor of safety can be obtained at each location. The results show that the maximum value of factor of safety is obtained when the stabilizing piles are installed in the upper middle part of the slope and this result is the same as results of other studies that have been carried out using shear strength reduction method. For the purpose of determination of the exact optimal location of pile, more models with different slope angles with different pile location are analyzed.

From the results shown in Fig. 3 the location of optimal position the pile tended to be within the upper middle of the slope for the different slopes. The optimum location of the pile tends to be towards the upper middle with the increase of slope angle (SA). All Slopes presented in Fig. 3 has factor of safety of 1.0 before installation of pile, consequently after pile installation the maximum factor of safety ranged from 1.49 to 1.53 and $X_P/X$ ranged from 0.53 to 0.59.

Xinpo et.al [7] used FLAC two-dimensional plane strain model found that the exact optimal location of the pile for slopes when the $X_P/X$ is 0.53. Won et al.[8] employing FLAC3D found the optimum pile location for slope when $X_P/X$ is 0.51, however, Hassiotis et al.[9] used the friction circle method to conduct the couple effect found the optimum $X_P/X$ to be 0.72. Hence, the results obtained in the present study are close to the findings from the authors who used FLAC3D to conduct such as a problem.

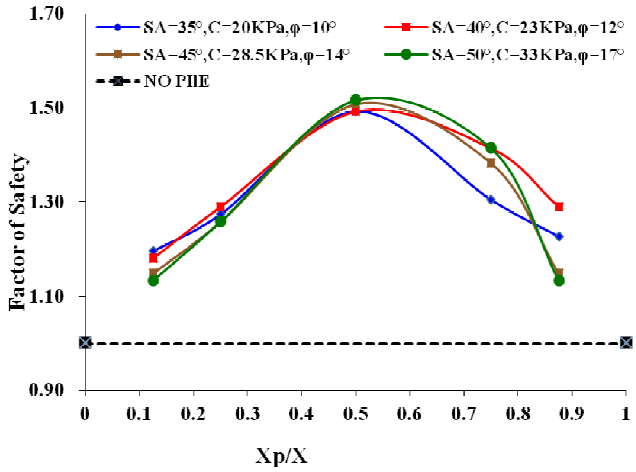


Fig. 3 Effect of Pile location on Safety Factor

**4.2 Effect of socketed pile length in stable layer (Sliding soil Thickness):-**

The impression of the coupled effect of The Stabilizing pile and soil can alter the depth of sliding surface. In effect, the thickness of sliding layer varying for slope to and another and at the same time, there is no determined pile length to be used in all slopes since it is dependent on the proportions of the slope and the depth of the critical slip surface. Therefore, in order to evaluate the effect of socketed length of the pile in stable layer the ratio $L_R/L$ ( $L_R$ , Length of Socketed length of the pile portion in stable layer, $L$ , length of piles) is used for the piles located at the middle of the slope.Fig. 4 shows the effect of the socketed ratio on the factor of safety of the reinforced slope. As expected, the results show that the factor of safety of the reinforced slope will increase with increasing of the socketed ratio. However, after a specified socketed ratio which is termed as the critical socketed ratio, the factor of safety will be remained constant. These results are similar to the results obtained by Griffith and Yang for the slope of one soil layer reinforced with one row of pile [5] . Thus, assumption of unlimited pile length in analysis is excessive and will make the designers to conduct an uneconomic design.

The results of analyzed models for different pile socketed lengths at the spacing of 2D are shown in Fig. 5 as the pile socketed length decreases; the pile deflection at the failure mode of slope will be increased, and comes to fully failure when the socketed length decreases as shown in displacement. The displacement of the pile along its length is relatively increased as shown when SR=0.0 and 6.0% consequently. It should be noted that when the pile socketed ratio is less than the critical socketed length; the deflection increases almost linearly with the depth. It emanated from less anti-slide force provided by the bottom of the piles and increase of sliding soil area in the top parts above the socketed portion.

It is observed that the bending moment of the piles as presented in Fig. 5 is increased in the socketed portion with the reduction of the socketed ratio. The position of the maximum bending moment is always slightly above the contact surface between sliding and stable soil layers, and whenever this surface move up or down the position of the maximum moment moves correspondingly. The distribution of the pile shear force as shown in Fig. 5c has two peak points. In the sling soil layer where the negative portion of the pile shear forces distribution, it is observed that the pile shear force increases with decreasing pile socketed ratio, and the point of the maximum shear force moves correspondingly with the move of the surface between sliding and stable layer until the pile socketed ratio less than the critical value. When the socketed ratio below the critical socketed length the shear force and bending moment in the pile are showing big reduction, in other words, the pile seems malfunction compared to the status where the socket ratio is greater than the critical value.

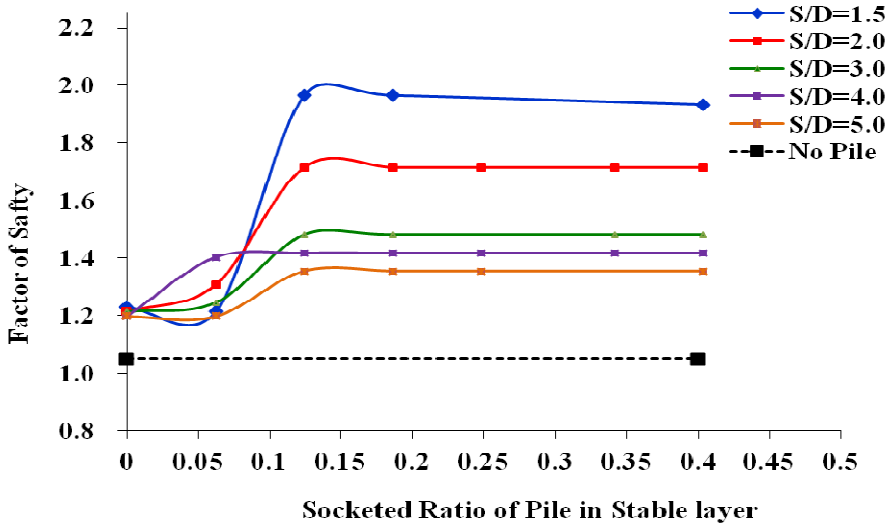


Fig. 4 Effect of Socketed length on factor of safety

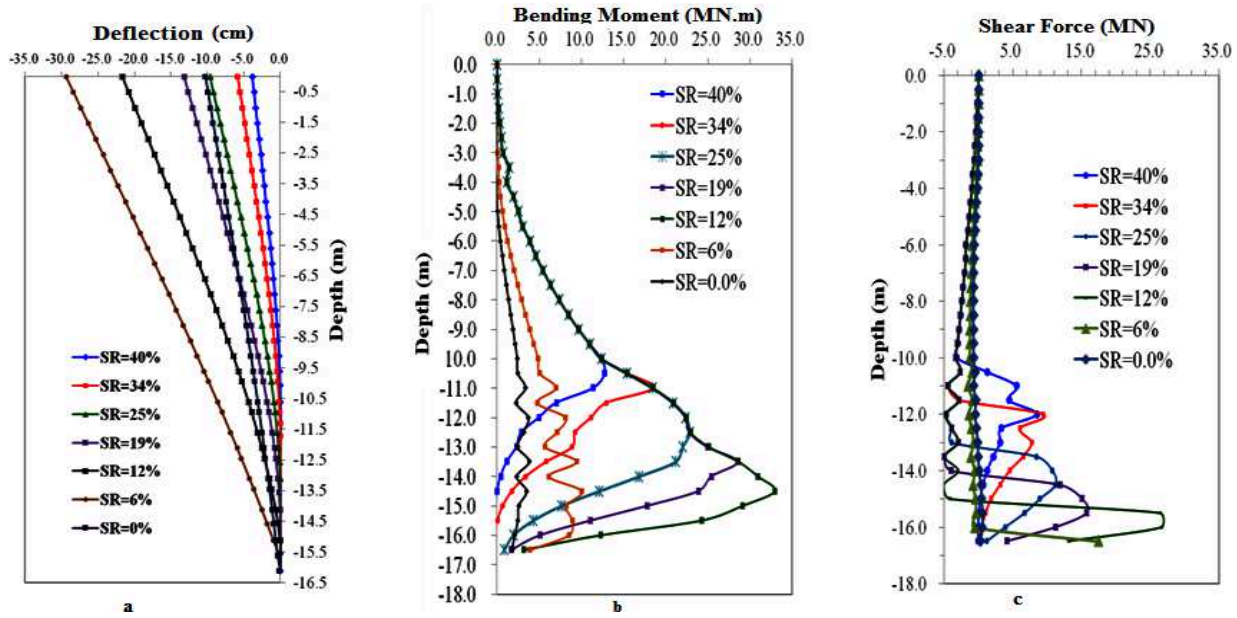


Fig. 5 Effect of socketed ratio on pile behavior

### 4.3 Effect of pile spacing

The influence of pile spacing on factor of safety with socketed ratio is present in Figure , it is noticed for smaller socketed ratio less than the critical $SR$ the effect of $S/D$ is small whereas the factor of safety for variant pile spacing was close together while the effect is considerable after the socketed length become greater than the critical SR and factor of safety show no increase after the critical socketed ratio. The effect of pile spacing on the factor of safety of reinforced slope for the piles installed where $x_P/x$ is equal to 0.5 is shown in Fig. 6. As anticipated, the factor of safety is reduced with increasing pile spacing. Similar curves have also been obtained by Cai and Ugai [10] and Jeong et al. [8] using coupled and uncoupled analyses, respectively. As shown in Fig. 6 ,at the beginning, as the pile interval increased the factor of safety decreases rapidly but the increase of the pile spacing contributes to a gradual decrease in the factor of safety. When the spacing of piles is $5.0D$ the factor of safety is 1.3, which is slightly greater than the recommend value by the Chinese code. Since, in practice, the pile spacing usually is not taken a very large value, regarding a small range for the pile spacing is enough in the analysis.

Fig. 7shows the effect of the socketed pile spacing on the pile behavior for the reinforced slope. With the reduction of pile spacing, the behavior of piles are more like to a continuous materials and the consequence of soil arching and load sharing of the pile turns to be more apparent so that the soil with a big displacement is arrived into the limit state. The behavior of the pile can be manifested by the deflection of piles at the failure mode of the slope for different pile spacings Fig. 7.a. The bending moment Fig. 7.b and the shear force of the piles for different pile spacings are shown in Fig. 7.The results show that with increasing pile spacing, the bending moment of the piles' increases and the position of the maximum bending moment is slightly above the surface between the sliding and stable soil layer. In other words, with increasing pile spacing, the value of the maximum bending moment increases. The same tendency also occurs within the shear force distribution of the piles. This can be explicated by the fact that the loading zone of each pile, impressed by lateral movements of soil (Sliding), is consequently increased with the increase of spacing between piles. It is also detected that the rate of change in the behavior of piles with small spacings is faster than piles with large spacings. This is in a well agreement with the results formerly obtained about the factor of safety of the reinforced slope for various pile spacings and also the results obtained by Yang et al.[5].

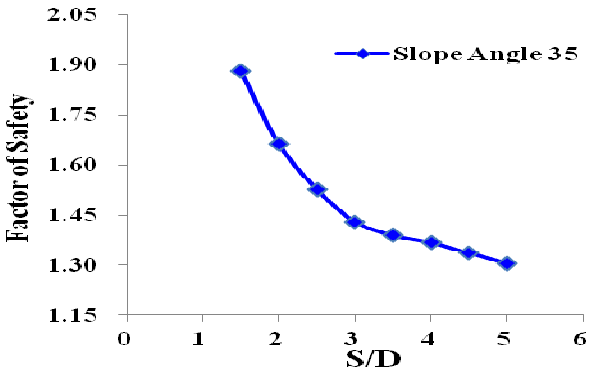


Fig. 6 Effect of S/D on Factor of safety

## Conclusions

The Socketed length of anti-slide pile used in slopes overlaying bedrock is analyzed employing three dimensional shear reduction method .From the result of the numerical model following conclusions can be drawn.(1) Pile position significantly affects the factor of safety of reinforced slope; the optimum position was found to be within the upper middle of the slope; when the slope angle increased the optimum pile location is prompting slightly up.(2) The socketed length is affecting safety factor of the slope; the minimum socketed length to gain the maximum safety factor was found to be 12% of the pile length.(3) Pile behavior is affect by socketed length with the increase of socketed length the maximum bending moment and shear force are increased, the position of peak value always located slightly above the bedrock layer.(4) Bending moment and shear force is increased with the increase of pile spacing due to the extension of loading zone of each pile.

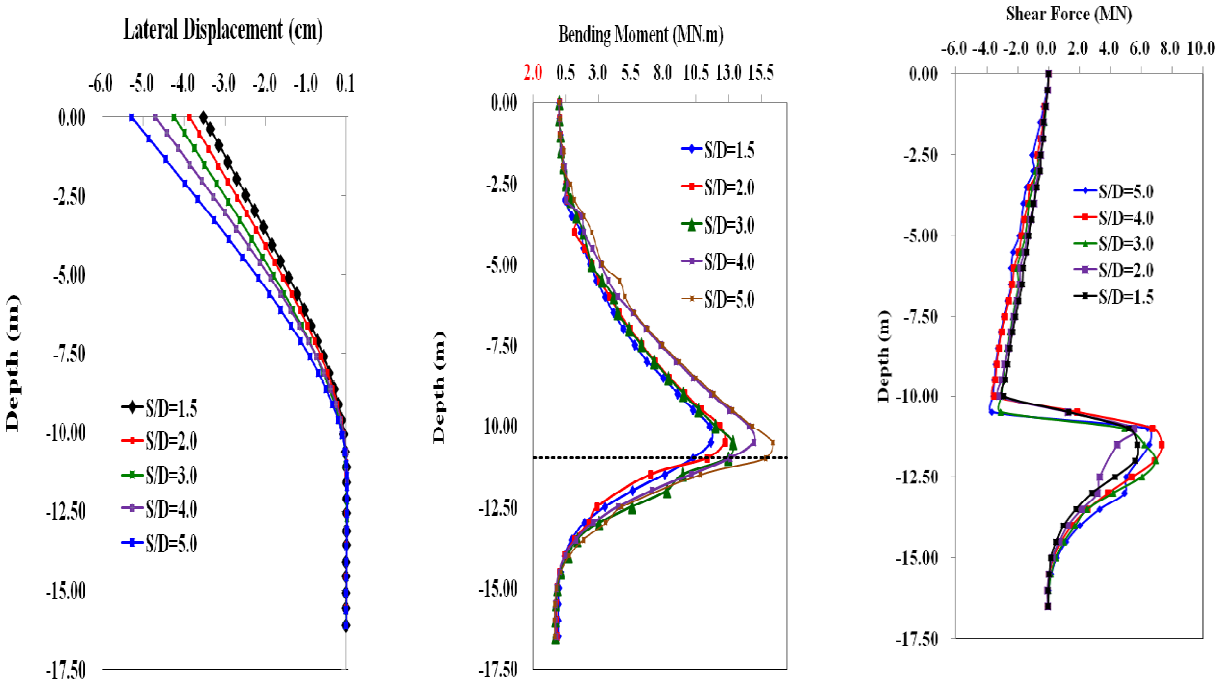


(a) (b) (c)

Fig. 7 Effect of Pile spacing on pile behavior

**References**

[1] W. Wei and Y. Cheng, submitted to journal of computers and Geotechnics , (2009)
[2] T. Ito and T. Matsui, submitted to journal of Soils and foundations,(1975)
[3] H. G. Poulos, submitted to journal of the soil mechanics and foundations division(1973)
[4] L. Chen, H. G. Poulos, and T. S. Hull, submitted to journal of soils and foundations,(1997)
[5] S. Yang, X. Ren, and J. Zhang, submitted to journal Journal of Rock Mechanics and Geotechnical Engineering,(2011)
[6] M. Ashour and H. Ardalan, submitted to journal Computers and Geotechnics, (2012).
[7] X. Li, S. He, Y. Luo, and Y. Wu, submitted to journal of Geomechanics and Geoengineering,(2011)
[8] J. Won, K. You, S. Jeong, and S. Kim, submitted to journal of Computers and Geotechnics,(2005)
[9] S. Hassiotis, J. Chameau, and M. Gunaratne, submitted to journal of Geotechnical and Geoenvironmental, 1997.
[10] F. Cai and K. Ugai, submitted to journal of Soils and foundations, (2000)

*Applied Mechanics and Materials Vols. 580-583 (2014) pp 432-435*
*© (2014) Trans Tech Publications, Switzerland*
*doi:10.4028/www.scientific.net/AMM.580-583.432*

# Numerical Simulation Analysis of Bearing Characteristics on Super-large Diameter Rock Socketed Pile

Chengzhong Gong[1,2,a], Chunlin He[1,b], Mingxing Zhu[2,c]

[1]Huaiyin Institute of Technology 223001 China

[2] Southeast University, 210096 China

[a]gcz2008@sina.com, [b]c.l.he@163.com, [c] 413464031@qq.com

**Keywords:** Bridge Engineering, Bearing Characteristics, Numerical Simulation, Rock-socket pile, Side Friction

**Abstract.** Wujiang Bridge is located on the Wujiang River in Chongqing Province in China. Based on test method of numerical simulation, the bearing characteristics of this large-diameter rock-socket pile with super-thick pile caps have been analyzed, including pile foundation load-bearing characteristics, pile-soil load sharing, and stress flow analysis of thick pile caps. The results indicated that Q-s curve of this kind of pile is approximate to linear. Under the action of ultimate load, the main load was supported by pile end résistance. And according to main stress distribution of pile cap, there is an obvious spatial truss effect phenomenon in it.

## Introduction

With the development of large span bridge structure, the large diameter rock-socket pile has been widely used in bridge engineering [1, 2]. The mechanism research on stress and deformation is more and more at present, but the research about the mechanism of super-large diameter rock-socket pile is comparatively rare, and lack of the necessary reference data. The main research methods are field test and laboratory tests [3, 4]. Based on the Wujiang bridge pile foundation project, the finite element analysis method is used to study the load bearing characteristics in this article.

## Project Overview

Wujiang Bridge, which is 630m length, is located over the Wujiang River at the Fuling of Chongqing Province in China. The structural style is twin towers and double cable plane cable-stayed bridge as shown in figure 1. The main beam is 26.9m width, and 2.73m high. The high span ratio is 1/117.2. On the west side of river the tower is 206.3m height, east tower is 198.3m height. The concrete strength of the pylon is $C_{50}$, The large diameter group pile foundation, using $C_{40}$ concrete poured, is used in this project. The cap size is 20m×16.4m×7.5m. The four piles under the cap is cast-in-place pile, which is 4.0m diameter, 38.5m length. The bearing layer at the tip of pile is weathered limestone.

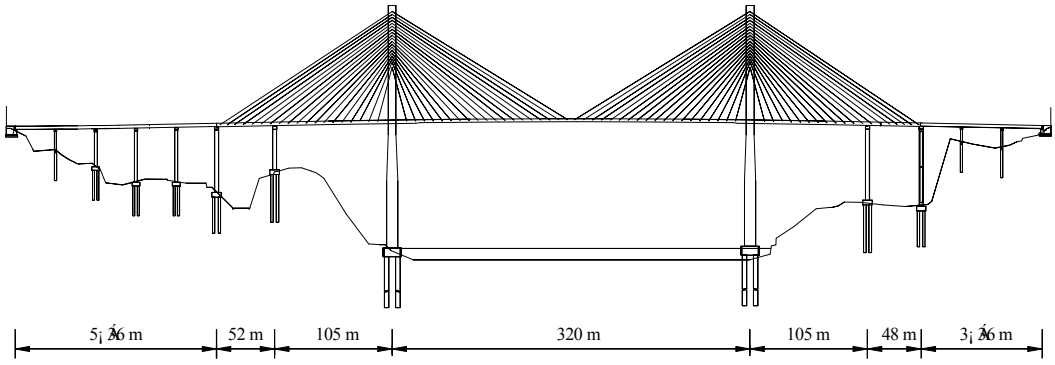


Fig.1 Schematic diagram of Wujiang Bridge

## Established the finite element model

**Model unit.** Numerical simulations of soil, pile cap, pile are used in 3D modeling in this paper. Considering the restrictions of computing speed and accuracy of the results, the C3D8R unit is selected in the modeling. Soil are divided into about 100000 grid units, the four piles are divided into 15000 grid units and pile cap is divided into 9000 grid units. The number of the grid can ensure the accuracy of numerical analysis enough.

**Material parameters of the model.** The material of pile and pile cap is reinforced concrete, the isotropic elastic model, its parameters as shown in chart 1. The soil around the piles is used in Mohr - Coulomb model. Due to the more soil can bring more inconvenience to contact calculation, soil is simplified into three layers according to the geological exploration report, and its parameters are shown in chart 2.

Chart1 Elastic Parameters of Pile Model

| name | elasticity modulus (MPa) | Poisson's ratio | density (kg/m$^3$) |
|---|---|---|---|
| concrete | 30000 | 0.22 | 2500 |

Chart2 Physical and Mechanical Parameters of Soil

| layer | elasticity modulus (MPa) | Poisson's ratio | Cohesion (kPa) | internal friction angle | Density (kg/m$^3$) |
|---|---|---|---|---|---|
| soil-1 | 7 | 0.30 | 22 | 35 | 1950 |
| soil-2 | 10.9 | 0.30 | 0.025 | 35 | 1950 |
| rock | 455 | 0.25 | 690 | 51 | 2200 |

**Model size and boundary conditions.** According to the modeling of the relevant engineering experience, the soil model is 77 m length, 60 m width, and 80 m depth, as shown in figure 2.

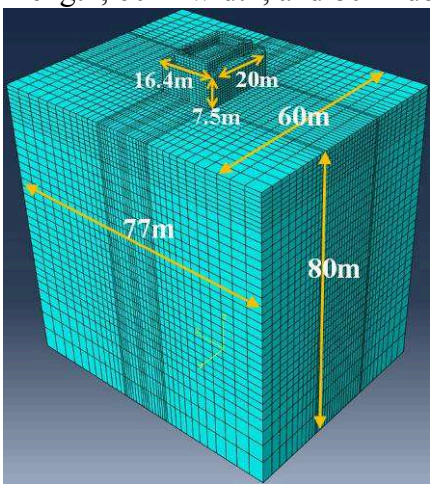


Fig.2 Model for the numerical simulation

## Numeric Simulation Results and Analysis

**Pile foundation load-bearing characteristics.** In order to learn the transfer mechanism of pile-pile caps- soil system, the vertical ultimate load for 67800 T, which is provided by designing institute, is selected to impose on the model. Under the vertical load the stress and displacement cloud charts as shown in figure 3 and 4.

From the perspective of the stress cloud charts of z axis, under the action of ultimate load, it can be seen that the soil at the bottom of the pile and soil-pile friction beard the upper load, side friction was more noticeable.

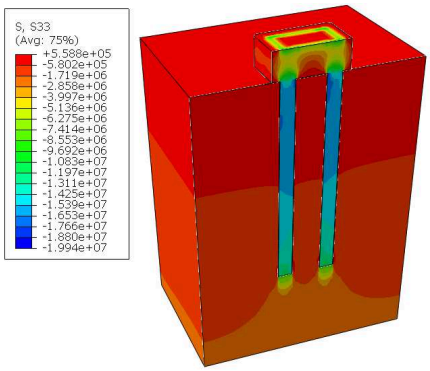


Fig.3 Stress cloud maps of z axis

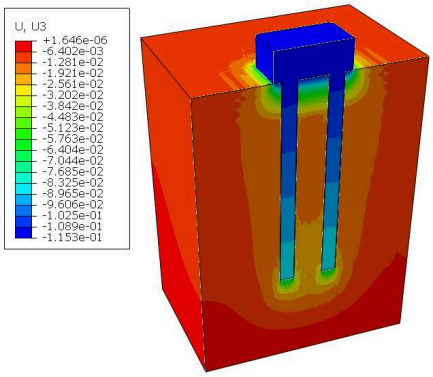


Fig.4 Displacement cloud maps of z axis

The load-settlement relationship of pile is shown in figure 5. As shown in the picture, load-settlement curve is gentle, which is approximate to linear. The reason is that the pile foundation of Wujiang Bridge is rock-socketed pile, its diameter and length is deeper. So its bearing capacity is high and the settlement is less. Besides, its bearing layer is weakly weathered limestone, which can effectively reduce the settlement. The relative stiffness of pile caps is bigger than pile. It has good coordination ability to differential settlement of pile.

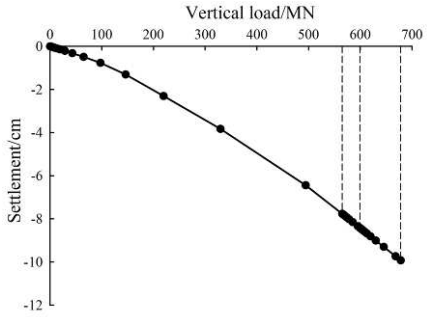


Fig.5 Load - settlement curve of group Piles

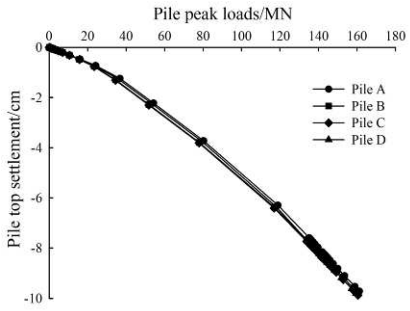


Fig.6 Load - settlement curve of each pile

From figure 5, the curve has not been a turning point. This is because with the load increasing, the elastic slip between pile and rock wall get increasing, the upper load shall be done by the pile end. Under the pile end is full of high strength of rock, so the curve does not appear obvious turning point.

**Load-settlement curve of each pile.** Q-s curve of single pile in group pile as shown in figure 6. With the increase of load on pile caps, the settlement of pile top has been increased too. The curve presented a linear relationship. When load added to limit state, there are still no obvious turning points. This shows that the bearing capacity of pile foundation has a high security reserves. From the settlement of each pile, it can explain the ultra thick pile cap has very good coordination ability to differential settlement. It is also a very important control parameter in the process of bridge construction.

**Analysis of Pile-soil load sharing.** With the load at the top of the cap increase, the pile tip resistance and pile side resistance and soil at the bottom of the pile caps has changed as shown in figure 7.

From the diagram it can be seen that, at the beginning of loading, side friction sustained majority of the load, while the rest of load was supported by the rock of pile end. The load, shared by the soil at the bottom of the pile caps, is small. With the increase of load, pile side friction began to increase slowly, and reached limit value, the load, which the soil at the bottom of the pile caps sustained, would increase slowly, however, the quantity is very limited. By contrast, the bearing capacity of pile end was increased dramatically.

The load sharing ratio is shown in figure 8. It can be seen clearly the proportion relationship among the pile tip resistance and pile side resistance and soil at the bottom of the pile caps in the process of loading. We can draw a conclusion that the load is mainly composed of pile side friction and pile end resistance, the load which soil at the bottom of the pile caps bear is small, it can be neglected in large diameter super thick pile caps in pile foundation system.

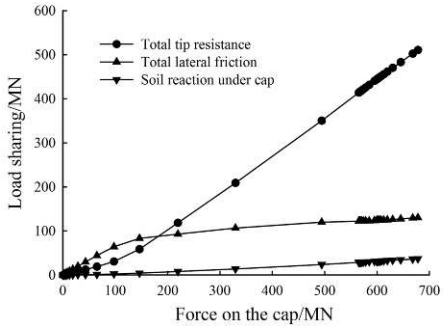


Fig.7 Load sharing

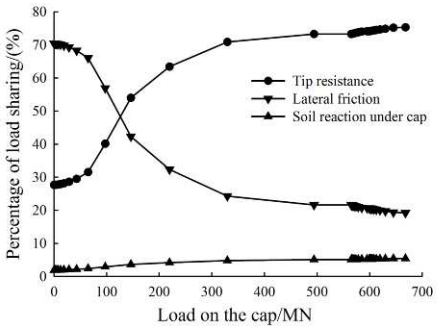


Fig.8 Percentage of load sharing

**Load transfer stress flow analysis of thick pile caps.** In the process of load transfer of pile foundation, thick pile caps can appear the obvious effect of thick pile caps. In order to be more intuitive understanding of its mechanical characteristics, the finite element data was processed, and entity graph of internal compressive stress flow on pile caps is shown in figure 9.

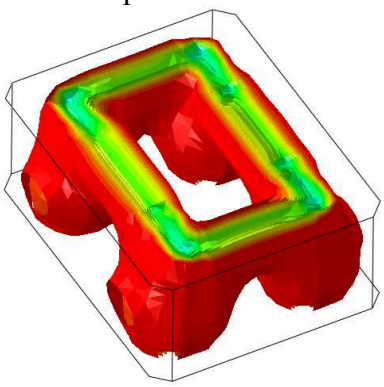

Fig.9 Entity graph of ompressive stress flow

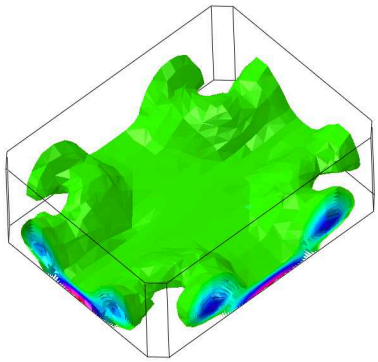

Fig.10 Entity graph of tensile stress flow

It can be seen from the figure 9. a compressive stress arch will be formed between two adjacent piles. Upper load pass directly to the pile top through stress arch foot. The entity stress flow graph is shown in Figure 10. Through the picture it can be clearly seen the area where the tensile stress distributed in the process of force transmission. The main distribution was at the bottom of the thick pile caps. According to main stress distribution of pile cap, we can know where reinforced should be set up in pile cap design. This not only ensures the safety of the structure, but also save material, avoids waste in the whole cross section of encryption.

## Summary

In pile foundation system of large diameter super thick pile caps, the load is mainly supported by side friction and pile end resistance, the load which soil at the bottom of the pile caps bear is small. According to main stress distribution of pile cap, there is an obvious spatial truss effect phenomenon in it. This is completely different to the general pile caps.

## References

[1] HE Chunlin, G.Chengzhong: *Civil Structure and Environmental Engineering*, edited by Xiangdong Zhang,Bin Zhang. Trans tech publications Ltd. (2013).

[2] G.Chengzhong, HE Chunlin and G.Weiming: submitted to Journal of Civic Architectural and Environmental Engineering (2013)

[3] HE Chunlin, G.Chengzhong: submitted to Journal of China and Foreign Highway (2013)

[4] HE Chunlin, G.Chengzhong: submitted to Journal of Highway (2012)

*Applied Mechanics and Materials Vols. 580-583 (2014) pp 436-439*
*© (2014) Trans Tech Publications, Switzerland*
*doi:10.4028/www.scientific.net/AMM.580-583.436*

# Prediction of Displacement Time Series based on Support Vector Machines-Markov Chain

Fei Xu[1, a] *,Wenxiong Xu[2, b] and Ke Wang[1, c]

[1]Hainan Highway Survey and Design Institute, Haikou, Hainan, 570206, China

[2]School of traffic and transportation engineering, CSUST, Changsha, 410114, China

[a]xfawy@hhu.edu.cn, [b]21141940@qq.com, [c]496258148@qq.com

**Keywords:** Support Vector Machines, Markov Chain, Displacement Time Series, Particle Swarm Optimization.

**Abstract.** A new displacement time series predicting model was proposed by combining the Support Vector Machines and the Markov Chain, which was named as Support Vector Machines and Markov Chain (SVM-MC) model. Through studying the measured displacement, SVM optimized by particle swarm optimization (PSO) was used to forecast the trend of macro development in roll. Markov chain was applied to compute State Transition Probability Matrix. By classifying system state and calculating absolute error and relative error between measured value and SVM fitting value, the predicting results are improved. The model was used on predicting displacement time series of a high slope of a permanent lock. The engineering case studies indicated that the model was scientific and reliable, and there was engineering practical value for displacement time series forecasting.

## Introduction

The rock mass displacements show some characteristics of random fluctuations for both the internal factors (geological structure, the nature of the rock, rock structures, etc.) and external factors (excavation, blasting, rainfall, etc.). The prediction of the displacement timing of geotechnical engineering could be used to accurately predict the deformation of rock and soil with the monitoring data collected. Thus the feedback is helpful in adjusting the construction program and taking urgent measures. Currently the major modeling methods used to predict the timing of displacement are time series analysis methods and intelligent rock mechanics methods. However, there are defects in all of these methods[1-2].

SVM (support vector machines, SVM) is a kind of machine learning techniques based on structural risk minimization principle, which can solve the practical problems of small samples, nonlinearity, high dimension and local minima. Applicable to volatile random time series forecasting, the Markov Chain (markov chain, MC) system can better reveal the performance randomly generated influenced by a variety of complex factors. In order to improve the prediction result, obtaining a more accurate timing of displacement, the two algorithms is proposed to be integrated and the support vector machine - Markov chain model (SVM-MC) is proposed.

## SVM-MC Model Building

**Support Vector Machines.** Given the training sample set $(x_i, y_i)_{i=1}^{l} \in R^n \times R$, $x_i$, $y_i$ is the input and output variables respectively, $l$ is the sample number. SVM [3] uses the linear regression function to fit the sample set as follows:

$$y(x) = w\phi(x) + b\,. \tag{1}$$

Where, $w$ is the weight vector, $b$ is the bias, $\phi(x)$ is the non-linear mapping. Assume that all training samples within the precision $\varepsilon$ is error-free fitting using linear function. Considering the existence of the fitting error, the non-negative slack variables $\xi_i$ and $\xi_i^*$ are introduced. Using duality theory, turned the optimization problem into the following optimization problem:

$$\max\{-\frac{1}{2}\sum_{i=1}^{l}\sum_{j=1}^{l}(\alpha_i-\alpha_i^*)(\alpha_j-\alpha_j^*)K(x_i,x_j)-\varepsilon\sum_{i=1}^{l}(\alpha_i-\alpha_i^*)+\sum_{i=1}^{l}y_i(\alpha_i-\alpha_i^*)\}$$
$$St\sum_{i=1}^{l}(\alpha_i-\alpha_i^*)=0(\alpha_i,\alpha_i^*\in[0,c]) \quad . \tag{2}$$

Here, $K(x_i,x_j)$ is the kernel function. According to KKT theorem, $\alpha_i,\alpha_i^*,b$ can be obtained for the SVM:

$$f(x)=\sum_{i=1}^{l}(\alpha_i-\alpha_i^*)K(x_i,x)+b\,. \tag{3}$$

Here, the kernel function $K(x_i\cdot x_j)=\phi(x_i)\phi(x_j)$. The Gaussian radial basis function is used in this paper.

**Particle Swarm Optimization.** PSO uses the velocity - position search model. Each particle represents a candidate solution of the solution space. A fitness function is defined to evaluate each particle solution. The velocity $v_i=\{v_{i1},v_{i2,}\cdots,v_{in}\}$ determines the $i$ th particle's distance of each iteration in the solution space. A group of random particles is initialized, among which the location of $i$ th particle in the $n$ -dimension solution space could be represented by $x_i=\{x_{i1},x_{i2},\cdots,x_{in}\}$. Particles update their velocity and position through tracking the individual extreme values $f_i=\{f_{i1},f_{i2},\cdots,f_{in}\}$ and the global ones $g=\{g_1,g_2,\cdots,g_n\}$ dynamically. The formula is as follows:

$$\begin{aligned} v_{id}^{k+1}&=wv_{id}^k+c_1r_1(f_{id}^k-x_{id}^k)+c_2r_2(g_d^k-x_{id}^k)\\ x_{id}^{k+1}&=x_{id}^k+v_{id}^{k+1}\end{aligned} \quad . \tag{4}$$

Where, $w$ is the inertia weight factor; $r_1,r_2$ present the random number uniformly distributed in the interval $(0,1)$ ; $c_1,c_2$ are the learning factors; $i=1,2,\cdots,N$ , $N$ is the number of particles; $v_{id}^k,x_{id}^k$ are the $i$ th particle's $d$ -dimensional component vector of the velocity vector and the position one respectively; $f_{id}^k,g_d^k$ are the $i$ th particle's $d$ -dimensional component vector of the optimal individual location and the global optimization one, $d=1,2,\cdots,n$ ; $n$ is the dimension number.

**Dynamic Trend Forecast.** The first step of dynamic trend forecast is to prediction the $p$ time series $\{x_m,x_{m+1},\cdots,x_{m+P-1}\}$ after $m$ using $m$ time series $\{x_i,x_{i+1},\cdots,x_{i+s}\}$ $(i=0,1,\cdots,\ m-s-1)$ , $m-s$ group time series. With the $p$ time series obtained, $\{x_0,x_1,\cdots,x_{P-1}\}$ is replaced by the $p$ time series. The new $m$ time series is used in the $p$ time series prediction next time, and so on[4].

When using SVM modeling, the selection of penalty factor $C$ and kernel function parameter $\sigma^2$ directly affect the prediction accuracy. PSO is induced to optimize its parameters.

**Improvement of Prediction by Markov Chain.** The displacement time series is divided into several states with the different upper and lower thresholds of the relative error $\Delta$ between the displacement measured value and support vector machine fitting results chosen as the criteria for classification denoted $S1,S2,\cdots,Sn$ . $n$ is the number of states. Assuming the probability of the sequence number $Si$ in the displacement state is $m_i$ . The probability of state $Si$ transferred to state $Sj$ after $k$ steps is $m_{ij}(k)$ . The probability of the state $Si$ transferred to state $Sj$ of displacement sequences after $k$ steps is:

$$P_{ij}^{(k)}=\frac{m_{ij}(k)}{m_i}(i,j=1,2,\cdots,n) \quad . \tag{5}$$

Since the last state of displacement timing shift is uncertain, so the last $k$ timing data is to be removed.With the transition probabilities calculated, the displacement time state transition matrix is created.Giving state transition matrix established, the trend of the system can be predicted by examining the state transfer matrix $P(k)$. Preparation table is enquired before forecast.

Determining the future steering of the displacement time series, the variation range of SVM prediction value is determined. The most likely predicted value may be the midpoint of the interval:

$$F(x) = (1+\overline{\Delta}) f(x) = (1+\overline{\Delta})(\sum_{i=1}^{n} (\alpha_i - \alpha_i^*) K(x_i \cdot x) + b) \ . \tag{6}$$

Where, $\overline{\Delta} = (\Delta_{up} + \Delta_{down})/2$ is the average relative error, $\Delta_{up}, \Delta_{down}$ respectively presents the upper and lower limits of the interval; $F(x)$ is the improved predicted value by Markov chain; $f(x)$ is the predicted value of support vector machine. The variation range of the predicted value is $(1+\Delta_{up}) f(x) \sim (1+\Delta_{down}) f(x)$. Equation (6) is the SVM-MC model .

## Project Applications

The permanent ship lock in a project is huge, technically complex. And it comprehensive benefits significantly. A lot of monitoring instruments is settled in the south, the northern slope and central pier for real-time monitoring of the deformation of the slope. The monitor displacement of observation points outside the lock TP/BM27GP02 from 14 January 1998 to 14 May 2001 were analyzed using the proposed method. Monitoring interval is one month, with totally 41 steps.

**Displacement timing fitting by SVM.** After SVM trial, select $C = 62.43$, $\sigma^2 = 7.98$, $s = 10$, $p = 1$, take the first 37 time steps to construct 27 learning samples, while the last four steps as the test samples. Table 1 lists the measured displacement value of 27 learning samples, fitted values of support vector machines , absolute error, and relative error.

Table 1 Measured value and fitting value of SVM

| Time Step | Measured Value / mm | SVM Fitted Value / mm | Absolute Error / mm | Relative Error (%) | State | Time Step | Measured Value / mm | SVM Fitted Value / mm | Absolute Error / mm | Relative Error (%) | State |
|---|---|---|---|---|---|---|---|---|---|---|---|
| 11 | 15.39 | 15.64 | -0.25 | -1.62 | *S*2 | 25 | 29.97 | 29.14 | 0.83 | 2.77 | *S*4 |
| 12 | 19.19 | 18.65 | 0.54 | 2.81 | *S*4 | 26 | 31.08 | 30.99 | 0.09 | 0.29 | *S*3 |
| 13 | 18.69 | 18.78 | -0.09 | -0.48 | *S*2 | 27 | 31.48 | 31.54 | -0.06 | -0.19 | *S*2 |
| 14 | 21.69 | 22.71 | -1.02 | -4.70 | *S*1 | 28 | 33.25 | 33.05 | 0.20 | 0.60 | *S*3 |
| 15 | 23.69 | 24.32 | -0.63 | -2.66 | *S*1 | 29 | 32.50 | 32.98 | -0.48 | -1.48 | *S*2 |
| 16 | 25.76 | 26.42 | -0.66 | -2.56 | *S*1 | 30 | 32.63 | 32.74 | -0.11 | -0.34 | *S*2 |
| 17 | 28.39 | 27.68 | 0.71 | 2.50 | *S*4 | 31 | 32.46 | 32.25 | 0.21 | 0.65 | *S*3 |
| 18 | 28.69 | 28.52 | 0.17 | 0.59 | *S*3 | 32 | 34.09 | 34.92 | 1.17 | 3.43 | *S*4 |
| 19 | 29.92 | 29.45 | 0.47 | 1.57 | *S*3 | 33 | 33.33 | 33.65 | -0.32 | -0.96 | *S*2 |
| 20 | 30.33 | 29.42 | 0.91 | 3.00 | *S*4 | 34 | 33.97 | 34.02 | -0.05 | -0.15 | *S*2 |
| 21 | 30.51 | 30.15 | 0.36 | 1.18 | *S*3 | 35 | 34.76 | 34.25 | 0.51 | 1.47 | *S*3 |
| 22 | 31.70 | 31.03 | 0.67 | 2.11 | *S*4 | 36 | 34.76 | 34.99 | -0.23 | -0.66 | *S*2 |
| 23 | 32.21 | 31.52 | 0.69 | 2.14 | *S*4 | 37 | 32.90 | 35.02 | -2.12 | -6.44 | *S*1 |
| 24 | 31.28 | 31.12 | 0.16 | 0.51 | *S*3 | | | | | | |

**Improvement of Displacement Timing by Markov Chain.** Divided state based on the relative error $\Delta$ of the measured value and the displacement values support vector machines fitted. Taking into account the convenience of calculation the timing displacement is divided into four states (Table 2). According to Table 2, in which the state of learning samples is divided( Table 1).

Table2 The state division standard

| Status codeS | *S*1 | *S*2 | *S*3 | *S*4 |
|---|---|---|---|---|
| State numeric limits (%) | [-8,2) | [-2,0) | [0,2) | [2,8] |

After a number of steps to the state according to Table 1, may be determined for each state, but also can determine the number of state occurs.

According to the distance from the forecast step, numbers of shift steps are set 1,2,3,4. In the transition matrix corresponding to the shift steps, the row vectors of the initial state is selected to form a new probability matrix. Sum the new column vector. The state corresponding to the shift steps with the largest sum is the steering state of the system. Table 3 shows the results of the states the 38'th step is in. Seen from Table 3, in the total column, the possibility state $S1$ and $S2$ appear is the largest and nearly equal, which means that the error of the measured and predicted values of the 38'th step is most likely in the range constituted by $S1$ and $S2$. Therefore, the error of the midpoint of the range is taken as the possible errors of predicted values. According to formula (6) it is obtained

$$F(x) = (1+\bar{\Delta}) f(x) = (1+{}^{(-8)}\!/_{2}\,\%) \times 35.95 = 34.512$$

In this case, the measured value is 34.60mm. The predictive value using support vector machine model is 35.95mm. SVM-MC effectively improve the prediction accuracy.

Table 3 The table of state forecasting of the 38th time step

| Time step | Initial Status | Shift Steps | *S*1 | *S*2 | *S*3 | *S*4 |
|---|---|---|---|---|---|---|
| 37 | *S*1 | 1 | 0.667 | 0 | 0 | 0.333 |
| 36 | *S*2 | 2 | 0.143 | 0.428 | 0.286 | 0.143 |
| 35 | *S*3 | 3 | 0 | 0.428 | 0.428 | 0.144 |
| 34 | *S*4 | 4 | 0.333 | 0.333 | 0.167 | 0.167 |
| | Total | | 1.143 | 1.189 | 0.881 | 0.787 |

When the measured value of the 38'th step ia obtained, deleting the data of the first time step, add the data of the 38'th time steps, and form learning sample of fixed length, ensuring the latest observational data is used in each prediction. Seen from Table 4, SVM-MC predicted values and the measured ones are in good agreement, the error is small, and the prediction accuracy has been greatly improved compared with SVM.

Table4 Comparison of the measured value and predicted value of displacements

| No. | Measured Value /mm | SVM Predicted Value/mm | SVM Relative Error （%） | SVM-MC Predicted Value /mm | SVM-MC Relative Error (%) |
|---|---|---|---|---|---|
| 38 | 34.60 | 35.95 | -3.902 | 34.52 | 0.254 |
| 39 | 35.78 | 36.98 | -3.354 | 35.50 | 0.783 |
| 40 | 34.53 | 36.86 | -6.748 | 34.87 | -0.985 |
| 41 | 33.99 | 37.04 | -8.973 | 35.02 | -3.030 |

## Conclusions

Combining SVM and MC, SVM-MC for displacement timing prediction is proposed. SVM-MC boasts both advantage of SVM and MC. SVM is adopted to predict the macroscopic development law of the timing displacement. The state transition probability of MC is applied to characterize the microscopic fluctuations feature of the timing displacement, thereby improving the accuracy of prediction. Project application shows that the model is feasible, enhancing the single prediction accuracy of SVM model. Thus the mode could be promoted in displacement timing analysis.

## References

[1] J.G.Chen, L.D.Zhu: Computer Engineering and Application, Vol (2006), p.225-226.(In Chinese)

[2] K.Y.Liu, C.S.Qiao, W.Y.Teng: Chinese Journal of Geotechnical Engineering, Vol.26(2004), p. 57-61. (In Chinese)

[3] N.V. Vladimirapnik: The Nature of Statistical Learning Theory, edit by NY: Springer-Verlag(1995).

[4] A.N.Jiang: Rock and Soil Mechanics, Vol.6(2007), p.1176-1180. (In Chinese)

*Applied Mechanics and Materials Vols. 580-583 (2014) pp 440-444*
*© (2014) Trans Tech Publications, Switzerland*
*doi:10.4028/www.scientific.net/AMM.580-583.440*

# Project Design of Dewatering for Deep Foundation Pit in Dalian

Bailiang Guo[1, b],Hongbin Liu[1,a]

[1] School of Civil Engineering, University of Science and Technology Liaoning, Liaoning, China

[a]binbinliu999@126.com, [b]908663979@qq.com

**Keywords:** Deep Foundation Pit, Dewatering Design, Well-Points Dewatering

**Abstract.** Tube well dewatering is widely applied in deep foundation pit for its large water discharge, good dewatering effect, simple equipment and easy maintenance. In this paper, rube well dewatering is designed for the temporary project of foundation pit according to the engineering characteristics and stratum and underground water distribution with the deep foundation pit engineering as the background. The required parameters and design process of well tube dewatering are illustrated, and experience of applying tube well dewatering in evacuation of deep foundation pit is accumulated, which will be of certain referential significance for similar projects.

## Introduction

With the continuous rapid development of economy, the construction of underground urban space develops at an unprecedented speed. As a result, substantial foundation pit engineering occurs, and its depth increases constantly. The security of foundation pit turns to be extremely significant, while the construction of foundation pit is usually below the underground water, For avoiding the quick sand, piping and sudden surge at the bottom of pit, and preventing the earth from collapsing. As a result, it is quite necessary to conduct dewatering design for the foundation pit. In this paper, combining certain foundation engineering in Dalian, the tube well dewatering technology of foundation pit is introduced.

## Project overview and geological site condition

### Project overview

Locating in the northeast side of Gangwan Square of Zhongshan District in Dalian, this project is consisted of a high tower and low skit building. The tower is about 244 meters in height, with 4 underground floors and 51 above-ground floors. Its structural system is steel reinforced concrete frame-tube formed by concrete shear wall, inner shear wall, concrete filled steel tubular column, and overlapped incline support. It is tube-in-tube structure, with 18 meters of depth.

### Geological site condition

The main stratum structure of this site is that the overlaying soil is miscellaneous fill and sludge, while the underlying bedrock is strong and intermediary weathered sandstone. There is no active fault structure around the site. The lithology, depth and thickness parameters of each soil layer are shown in table 1.

Table 1 Lithology, depth and thickness of each soil layer

| number | Soil layer name | Layer top elevation [m] | Average thickness [m] |
|---|---|---|---|
| 1 | Miscellaneous fill | 3.25~6.57 | 5.8~11.4 |
| 2 | Muck | -2.17~7.27 | 0.40~1.20 |
| 3 | Completely weathered rock slate | -2.47~-7.77 | -5.68~16.60 |
| 4 | Strongly weathered slate | -1.37~16.60 | 1.0~11.20 |
| 5 | Weathered slate | -3.67~19.6 | 26.6 |
| 6 | Weathered gray-green rock | -34.8 | |

The underground water type of this site is the quaternary system pore water and bedrock fissure water. The buried depth of groundwater is about 2.8 m. The basal water is the fill stratum, sludge and complete weathering slate and intense weathering slate. The underground water is mainly filled by the atmospheric precipitation and ditch permeation. The thickness of the water-bearing stratum is about 26m.

**Dewatering project design**

The total precipitation area of this site is $9873.5m^3$, with the osmotic coefficient $1.4 m/d$. In the deep foundation pit, two approaches are adopted for dewatering. One is surface dewatering, and the other is the tube well dewatering [1]. According to the groundwater buried depth and excavation depth of this site, the tube well dewatering is adopted. Considering the economic factors, the tube well dewatering method with relatively low cost is employed. Tube wells with certain water are arranged around the foundation pit, and the underground water shall be extracted. The underground water around the foundation pit will flow into the foundation pit, so that the underground water level decreases by 0.5m below the excavation face, as shown in Fig. 1.

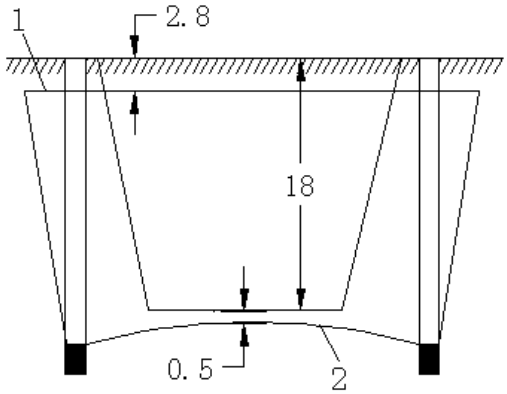


Fig.1. Water level schematic diagram

**Precipitation influence radius**

When the cone of depression is basically stable, the precipitation influence radius is related to the designed drawdown, permeability coefficient, and thickness of water-bearing stratum. The calculation Eq. 1[2] is:

$$R = 2S\sqrt{KH} = 2\times 15.7\times\sqrt{1.4\times 26} = 189.4m \tag{1}$$

In which, R is the precipitation influence radius, S is the designed drawdown, K is the permeability coefficient, and H is the thickness of water-bearing stratum.

**Equivalent radius of foundation pit**

$r_0$ is the illusion radius, and it is related to the excavation area and form of the foundation pit. The calculation Eq. 2[4] is:

$$r_0 = \sqrt{A/\pi} = \sqrt{9873.5/3.14} = 56m \tag{2}$$

In the equation, $r_0$ is the equivalent radius of the foundation pit, and A is the excavation area.

**Water inflow of the foundation pit**

It employs fully penetrating well, and the water inflow can be calculated with large well method, and the calculation Eq. 3[4] is:

$$Q = 1.366K\frac{(2H-S)S}{\lg R - \lg r_0} = 2060.3\, m^3/d \tag{3}$$

In which, $Q$ is the water inflow of the foundation pit, $K$ is the permeability coefficient, $H$ is the thickness of water-bearing stratum, $S$ is the designed drawdown, $R$ is the precipitation influence radius, and $r_0$ is the equivalent radius of foundation pit.

**Single-well water yield**

The single-well water yield is determined by the well with maximum interference in group well dewatering, and the calculation Eq. 4[2] is:

$$q = 120\pi r_s l\sqrt[3]{K} = 120\pi \times 0.3 \times 2.5 \times \sqrt[3]{1.4} = 87\, m^3/d \tag{4}$$

In which, $q$ is the maximum water yield of single-well well casing, $r_s$ is the radius of the filter, $l$ is the length of the filter, and $K$ is the permeability coefficient

**Number of well point required**

Elements such as blocking shall be considered when calculating the well points, and as a result, it should multiply by 1.1, and the calculation Eq. 5[3] is:

$$n = 1.1\frac{Q}{q} = 1.1\frac{2060.3}{87} = 26.04 \tag{5}$$

Therefore, 27 wells will be arranged.

In which, $n$ is the number of well points, $Q$ is the water inflow of the foundation pit, $q$ is the maximum permitted water yield of single well tube.

**Well point pipe spacing**

The well points are arranged in equal-gap method, and the calculation Eq. 6 is:

$$a = \frac{(L_1 + L_2 + B_1 + B_2)}{n} = 14.8m \tag{6}$$

In which, $a$ is the inter-well gap, $L_1$ is the upper base of the trapezoid foundation pit, $L_2$ is the lower base of the trapezoid foundation pit, $B_1$ and $B_2$ are the two sides of the trapezoid foundation pit.

**Design of precipitation well**

The Eq. 7[5] for calculating the depth of the precipitation well is:

$$\begin{aligned} H_W &= H_{W1} + H_{W2} + H_{W3} + H_{W4} + H_{W5} + H_{W6} \\ &= 18 + 0.5 + 6 + 1 + 2.5 + 1.5 \approx 30m \end{aligned} \tag{7}$$

In the equation, $H_W$ is the depth of the precipitation well, $H_{W1}$ is the depth of the foundation pit, $H_{W2}$ is the distance of the precipitation water level from the required depth, $H_{W3}$ is $ir_0$, $i$ shall be within the precipitation distribution range of the water conservancy, $1/15 \sim 1/10$, $r_0$ is the equivalent radius of the rainfall distribution or $1/2$ of the inter-well gap, $H_{W4}$ is the range of stage during dewatering period, $H_{W5}$ is the working length of the filter of the precipitation well, and $H_{W6}$ is the length of sand setting tube.

The diameter of the tube well is 0.3m, the diameter of the filter tube is 0.168m, 1.5 m sand setting tube is set, and it is filled by the natural gravel, while the mater convolvulus is sealed by clay. The structure is shown in fig. 2.

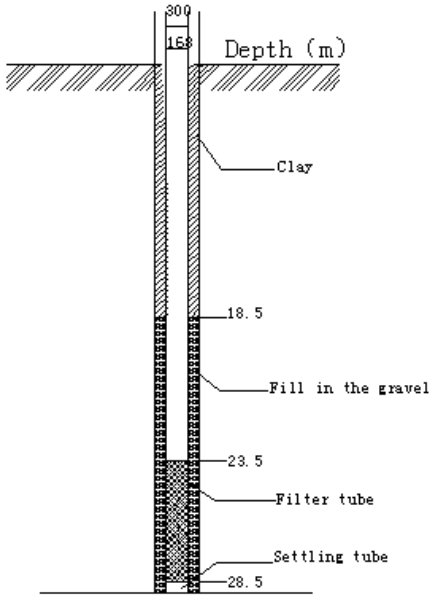


Fig.2. Precipitation well structure diagram

**Arrangement of precipitation well**

The precipitation well is arranged in circle about 1m distant from the side boundary of the foundation pit, and 27 wells are set. Meanwhile, two observational wells shall be set in the center of the foundation pit. The arrangement plan is shown in Fig. 3.

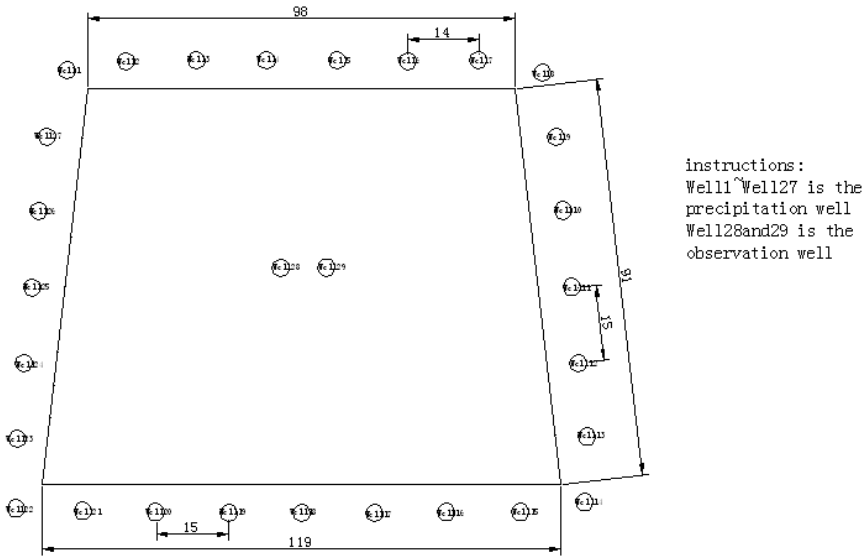


Fig.3. Precipitation well layout

**Verification of drawdown**

After the number of tube well, gap and arrangement method are determined, the fully penetrating well of the foundation pit can be taken advantage of for predicting the depth of foundation pit with Eq. 8[6].

$$S = H - \sqrt{H^2 - \frac{Q}{1.366K}\left[\lg R - \frac{1}{n}\lg(r_1 \cdot r_2 \cdot r_3 \cdots r_n)\right]} \tag{8}$$

In which, $S$ is the water level drawdown, $H$ is the thickness of the water-bearing stratum, $R$ is the precipitation influence radius, $Q$ is the water inflow of the foundation pit, $K$ is the permeability coefficient, $r_1 \cdot r_2 \cdot r_3 \cdots r_n$ is the distance from the foundation pit center to each well point.

Substitute it into the above equation, and it is concluded that $S = 18.6 > 15.7$, satisfying the requirements of drawdown.

**Control over the land subsidence caused by the precipitation**

During the dewatering process, with the decrease of underground water, it may give rise to the deformation of ground or land subsidence. In this project, filling method is employed for preventing the ground settlement, as shown in Fig. 4.

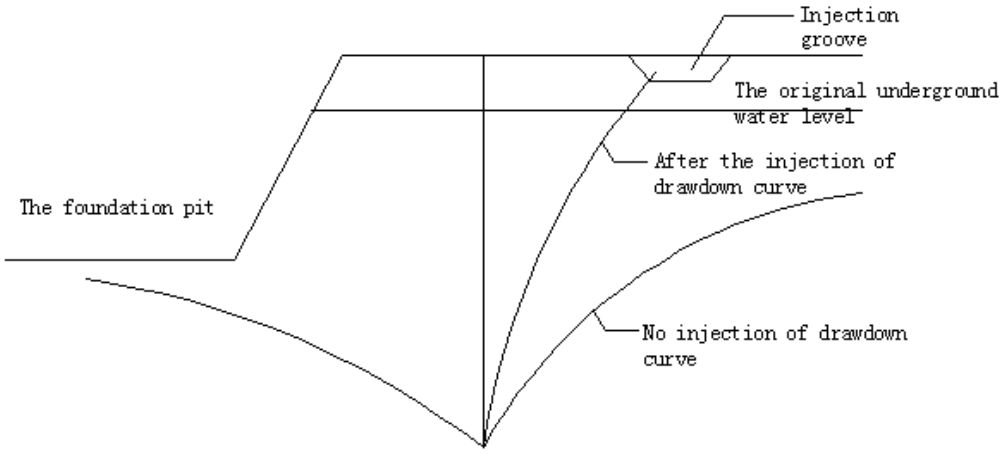


Fig.4. Injection method of schematic diagram

**Conclusion**

After calculation, there are 27 precipitation wells arranged around the foundation pit, about $30m$ in depth, and $300mm$ in diameter. The water outflow of single well is $87 m^3/d$, and two observational wells are set. According to the calculation result, it satisfies the requirements of the foundation pit.

The preliminary precipitation design plan is workable. In order to guarantee the construction security of the foundation pit, the precipitation effect shall be monitored. If it cannot satisfy the requirements, future optimization design shall be conducted.

**References**

[1] Qin Lu and Jun Xiong : Low temperature Architecture Technology Vol. (2)(2005), p. 71

[2] Shengshen zhang: Shanxi Architecture Vol. 36(2010), p. 103

[3] Peng Deng, Xiaola Feng, Yan Tang and Jun Feng: Safety and Environmental Engineering Vol. 19(2012), p. 119

[4] Tianqiang Yao and Zhenhua Shi: Handbook of foundation pit precipitation(China Building Industry Press, Beijing2006)

[5] Chen Yang,Shilan Wang and Caijun Li: Water Conservancy Science and Technology and Economy Vol. 15(2009), p. 273

[6] Liqing Wu: Electric Power Construction Vol. 24(2003), p. 26

*Applied Mechanics and Materials Vols. 580-583 (2014) pp 445-449*
*© (2014) Trans Tech Publications, Switzerland*
*doi:10.4028/www.scientific.net/AMM.580-583.445*

# Reinforcement and Characteristic Analysis of Bolt Technology Applied in Bedding Rock Slope

Enhua Wang [1,a], Zhide Wang [2,b], Limin Jiang [3,c], Luo Hao[4,d],An ran[1,e]

[1]Guizhou Highway Engineering Group Co., LTD, China

[2]Civil Engineering and Architecture School, Wuhan University of Technology, China

[3]Wuhan Building Material Industry Design and Research Institute Co., LTD, China

[4]Shenzhen Engineering Design Co., Ltd of China Aerospace Construction Group, China

[a]Lanxin778@163.com,[b]wangzhide-wuhan@163.com, [c]jianglimin0714@126,

[d]comrohaun@163.com, [e]707482213@qq.com

**Keywords:** Bolt technology; Bedding Rock Slope; Stability of Slope; Reinforcement

**Abstract.** Discrete element software is used to simulate the excavation of a rock slope in Puli-Xuanwei Expressway in Yunnan Province. Through monitoring displacement development characteristics in different positions of slope, the result shows that the minimum horizontal displacement under excavation exists in the top of the slope, meanwhile the maximum horizontal displacement occurs in the foot and waist of the slope, and the maximum vertical displacement occurs in the top of the slope. Comparing rock slope in such conditions as different stratum angles, directions, rock characteristics and thickness, it concludes possible failure modes of slope and the variation law of safety coefficient under different conditions. This paper is instructive and offers reference for the practical engineering.

## Introduction

The slope locates on the right of K3+580, it is 26.6m high, there is tectonic denudation canyon and karst landform in line area. Terrain slope ranges from 15° to 24°, the earth's surface is Quaternary holocene diluvial clay and consist of clay limestone gravels and rubbles, rubbles present angular shape and the diameter ranges from 3 to 86 mm; underlying bedrock is limestone, and its colors present gray and dark gray, the core of the rock disintegrates, which is the main characteristic in line area. The type of groundwater in line area is mainly pore phreatic water in loose rock mass and the water forms in rainy days and disappears in sunny days, so there is no uniform water level in line area.Slope has its structural surface,and the angle of dip is 36°, importance should be attached to the slope with structural surface, and appropriate support shold be taken. At home and abroad the most common way for slope reinforcement is mainly bolt technology, pre-stressed anchor cable and slide-resistant pile. These method play a role and are widely used in practical engineering.

## Selection of Calculation Parameters

According to the engineering geological survey data, Rock and soil parameters of slope are as follows: density of limestone rock is 24KN/m, angle of internal friction $\varphi$=22°, cohesion equals to

55KPa, concrete C30 is used for slope reinforcement, design value of the bond strength between mortar and reinforced bar $f_{bi}$=2400kPa, bond strength between bolt and rock $f_{rb}$=180kPa.

**Calculation of bolt design**

Limit equilibrium method is used for checking the safety factor of slope $k$, when $k$ is greater than or equal to 1, the slope is thought to be safe but according to design requirements from highway embankment design specifications, safety factor $k$ should be greater than or equal to 1.3. The following formula is used to calculate $k$ in limit equilibrium method:

$$k = \frac{R}{T} \quad , \quad R = N \cdot \tan\varphi + c \cdot L \tag{1}$$

In the equation, $R$ and $T$ represent sliding resistance force and slide force (KN) in the direction parallel to the surface structure; $N$ represents positive pressure on structure surface(KN); $c$ represents cohesion on structure surface(KN/m$^2$); $\varphi$ represents friction angle of structure surface; $L$ represents the length of structure surface(m).

In calculation, the gravity of slope is considered but earthquake and groundwater impact is out of consideration. After calculating by limit equilibrium method, total slide force is 2975.6 KN, total sliding resistance force is 3430.4 KN, security coefficient is 1.153. Calculation model is shown in figure 1, the slope is basically stable but the coefficient does not meet the requirements of design specifications, so reinforcement measures are needed to be taken on the slope and bolt technology is used in the engineering.

Firstly the state of slope under gravity is discussed and then the supporting force of bolt on slope is analyzed.

$$T = T_1 + T_i \, , \qquad N = N_1 + N_i \tag{2}$$

**A. calculation of slope gravity**

$$T_1 = W \cdot \sin\alpha \, , \quad N_1 = W \cdot \cos\alpha \, , \quad W = \sum A_i \cdot \gamma_i \tag{3}$$

In the equation, $N_1$ and $T_1$ represent two component forces of gravity (KN) in the directions of vertical and parallel to the structure surface; $W$ represents gravity of sliding body; $\alpha$ represents dip angle of structural plane; $A_i$ represents the total area (m$^2$) of rock stratum $i$; $\gamma_i$ represents the density (kN/m$^3$)of rock stratum $i$.

**B. calculation of bolt anchoring force**

The two component forces of bolt vertical and parallel to the structure surface $N_t$ and $T_t$ are calculated according to Equation 4.

$$T_t = \sum T_{ti} \quad , \qquad N_t = \sum N_{ti} \tag{4}$$

The two component forces of each installed bolt vertical and parallel to the structure surface $N_{ti}$ and $T_{ti}$ are calculated according to Equation 5.

$$N_{ti} = R_{mi}\sin(\alpha+\theta_i) \quad , \quad T_{ti} = -R_{mi}\cos(\alpha+\theta_i) \tag{5}$$

In the equation, $\theta_i$ represents incidence angle of installed bolt $i$; $R_{mi}$ represents anchorage (KN) of installed bolt $i$, its value equals to the minimum among uplift bearing capacity $R_{mi1}$, tensile resistance of steel bar $R_{mi2}$, pullout resistance of steel bar and mortar $R_{mi3}$. $R_{mi} = \min\{R_{mi1}, R_{mi2}, R_{mi3}\}$

$$\begin{cases} R_{mi1} = \xi_1 \dfrac{\pi D_i \sum q_{sik} L_{ia}}{s_{ix}} \\ R_{mi2} = \dfrac{\xi_2}{\gamma_0} \cdot \dfrac{n_i \cdot \pi \cdot d_i^{\,2} \cdot f_{yi}}{\gamma_s \cdot 4 s_{ix}} \\ R_{mi3} = \dfrac{\xi_3}{\gamma_0} \cdot \dfrac{n_i \cdot \pi \cdot d_i \cdot f_{bi} \cdot L_{ia}}{\gamma_s \cdot s_{ix}} \end{cases} \tag{6}$$

In the equation, $D_i$ represents the diameter (mm) of anchoring segment $i$; $n_i$ represents steel $i$; $q_{sik}$ represents friction resistance (KPa) of rock and bolt $i$; $L_{ia}$ represents length of effective anchorage section $i$; $\gamma_s$ represents coefficient of load component; $s_{ix}$ represents horizontal spacing of bolt $i$; $d_i$ represents the diameter of the steel bar in bolt $i$; $\gamma_0$ represents importance coefficient of slope; $\xi_1$, $\xi_2$, $\xi_3$ separately represents applying condition coefficient in bond of anchor body and formation, tensile of steel bar in bolt and bond of steel bar and mortar; $f_{bi}$ represents the bond strength (KPa) of steel bar and mortar; $f_{yi}$ represents tensile strength of steel bar ($N/mm^2$).

The excavation body was broken like before support of slope, there is a slip down trend along the surface structure, bolt support belongs to an active support technology. Not only can this support technology control anchored slope sliding along structure surface, but it can also conduct the overall control on broken crack-like slope, so it maintains the integrity of the slope.

Based on dates from geological survey information and considering dip angle of the structure surface, a space layout as up-wide and down-narrow forms in the slope. The length of bolt in the upper part is 12 meters, in the middle and lower part is 10 meters, so as to make bolt pass through the structure of the surface. Deformed steel bar HRB335 is used in the bolt and the diameter of the steel bar is 28 mm, the diameter of anchoring segment is 91 mm, bolts are layer in 3.0×3.0 square shape in spatial distribution of slope, the angle of bolt with the horizontal plane is 20°.

After calculating by limit equilibrium method, total slide force of slope under bolt supporting is 2779.5 KN, total sliding resistance force is 36391KN, security coefficient is 1.309.The resistance

each bolt bearing is 49 KN, bolt supporting structure and calculation model is shown in Fig.1, the result shows that the slope is in a stable state, and this proves that bolt plays an important role in supporting slope.

**Analysis on the effect of bolt**

Assume the other things keep constant, then change the incidence angle of bolt ranges from 0~40°, it can be found that when the incidence angle increase from 0~10°, FOS of slope has an increasing trend and it reaches the maximum at 10°; when the incidence angle increase from 10~40°, the coefficient has an decreasing trend, the relation between the incidence angle and FOS is shown in Fig.2, it proves that the incidence angle has a great impact on the effect of slope reinforcement.

Assume the other things keep constant, then change the diameter of drilling anchor from 30~120mm. It can be found that when the diameter is less than 70 mm, safety coefficient of slope increases with the increasing of the diameter; when the diameter is greater than 70 mm, safety coefficient keeps constant. It proves that there is an extreme value to bolt diameter, the relation between slope safety factor and drilling anchor diameter is shown in Figure 3. It plays a key role in determining drilling anchor diameter meanwhile ensure slope stability and it takes a good effect on controlling the project cost.

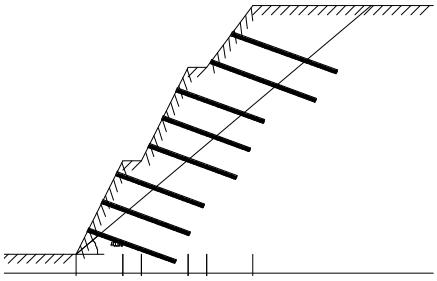

Fig.1 Cross-sectional of slope under bolt support

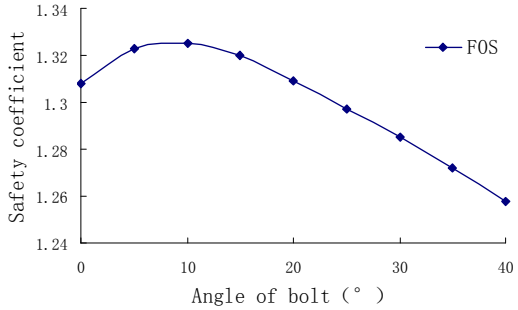


Fig.2 Relation of slope FOS and angle of bolt

Assume the other things keep constant, then change the diameter of bolt from 16~32 mm. Safety coefficient of slope increases in a second-order parabola with the increasing of the diameter, the relation is shown in Fig.4. In the control of slope stability, the diameter of bolt can be chosen according to practical engineering so as to improve the stability of slope.

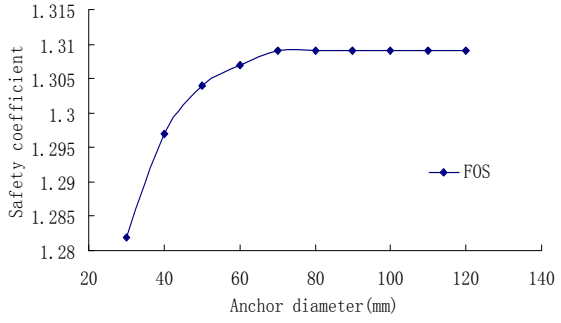


Fig.3 Relation of FOS and drilling anchor diameter

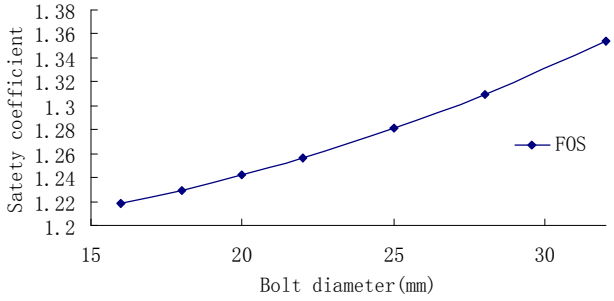


Fig.4 Relation of slope FOS and bolt diameter

**Summary**

By calculating stability of slope on the right of K3+580 locating in Puli-Xuanwei Expressway in Yunnan, the result shows that the safety coefficient does not meet the requirements of design specifications when there is not any support for slope. Such measure as bolt supporting is proposed

to improve the stability of slope, and the effect of bolt on slope reinforcement is proven. After changing the parameter of bolt , following conclusion can be reached:

（1）Different incidence angle has impact on the effect of slope reinforcement, and the optimal incidence angle should be taken into consideration in order to take the optimal supporting effect.

（2）In bolt construction diameter of the drilling anchor significantly affected the stability of slope, and when the diameter reaches a certain value, safety coefficient keeps constant. The critical value should be applied in the engineering so as to take optimum efficiency on slope reinforcement.

（3）The diameter of bolt plays an important role in slope stability, so the diameter can be limited in a certain range to ensure the stability of slope in practical engineering

By calculating and contrast above, bolt reinforcement takes some effect on slope stability. After analyzing the change rule among different parameters, the relation between safety coefficient and parameters can be determined and it has significance in guiding slope reinforcement.

**Acknowledgements**

This work was financially supported by the Science and technology research projects from Department of Transportation of Yunnan Province [Yun Jiao Ke 2010（A）07-a].

**References**

[1] Yang Feng, Wang Lian-guo, He An-min. Failure Mechanism and Bolting Support Technique of Complex Roof[J].Journal of mining and safety engineering, (2008) 03,286~289.

[2] Kang Hong-pu, JIANG Tie-ming, Gao Fu-qiang. Design for pretension rock bolting parameters[J].Journal of china coal society,(2008) 07.721~726.

[3] Chen Guo-zhou, Zhang Jian-xun, Jia Jin-qing. Three-dimensional stability analysis of anchored rock slope and its application to practical engineering[J].Journal of shandong uniersity of technology(science and technology) ,(2010) 02.12~15.

[4] Dong Hanxiong. Application of Pretested Anchored Cable in Reinforcement of Side Slope[J].Railway investigation and surveying,(2009)02.32~34.

[5] LUAN Chuanbao, XIE Song- fang, WANG Zhiwen. Application of prestressed anchor cablestechnology in hign cutting slop construction [J].Journal of Inner Mongolia Agricultural University,(2008)01.152~154.

*Applied Mechanics and Materials Vols. 580-583 (2014) pp 450-454*
*© (2014) Trans Tech Publications, Switzerland*
*doi:10.4028/www.scientific.net/AMM.580-583.450*

# Analysis on influencing factors of cement stabilized macadam base of compressive strength in Shenyang area

Yan Xu[1, a], Chunzhen Bai[1,b], Yifang Zhang[1,c], Xiao Liu[1,d]andDi Li[1,e]

[1] Shenyang Jianzhu University, Shenyang, Liaoning province, 110168, China

[a]xy_zsl@163.com, [b]1039471842@qq.com, [c]786898732@qq.com, [d]10732420@qq.com, [e]1061825140@qq.com

**Keywords:** grain size distribution, forming method, curing age, strength influencing factors

**Abstract.** The compressive strength of cement stabilized macadam base is an important index to evaluate the quality of road construction. In this paper, investigation and field sampling were conducted on roads in Shenyang city, and, indoor experiment study was then adopted to analyze effects of particle grade, cement dosage, molding method, compaction and curing age on compressive strength. The results show that rational particle grade greatly enhances the strength. Strength of vibration molding sample is closer to the field sample strength and is 0.6 times bigger than that of static pressure molding sample. 1% increment of construction compaction degree will induce 10% increment of compressive strength. Increment of cement dosage and curing age will induce increment of compressive strength, but the effect is limited. Studied in paper can provide a theoretical basis for site construction in Shenyang area.

## Introduction

The cement stabilized macadam base with its high strength, good board, good erosion resistance, and economy becomes the main structure of our country highway semi-rigid base, standard requirements for 7 days on the base of the cement stable class unconfined compressive strength to achieve 2.5 ~ 4.5 MPa in China[1]. However, there are many and complex factors which can affect the strength of cement stabilized macadam roadbase.

## Raw material properties

Table 1 Raw material sampling

| Number | Mixing station | Construction route | Particle size composition(cm) | Stone origin |
|---|---|---|---|---|
| 1 | Shenbeicui gongbao | Pingwang route,Nongwang engineering | 1~3,1~2,0.5~1;attle | Tieling |
| 2 | Shenyan | Shenyan route | 1~3,1~2,0.5~1;attle | Fushun |
| 3 | Xinmin | Jiangzhang route | 1~3,0.5~1;attle | Tieling |
| 4 | Hunnansifang | Xinlibao route | | |
| 5 | Hunnanlixiang | Shenli route, Yonghong route | mixture, attle | Liaoyang |
| 6 | Liaozhong | Gaonen route | | |

## Analysis of the formation mechanism of the strength of cement stabilized gravel

Table 1 shows. Under the pressure of mechanical compaction, the gap between coarse aggregate in the mixture is filled with a mixture of cement and fine aggregate, the air in the pore is discharge; Cement and gravel particles close to each other, so as to achieve solid state[2].Subsequently, the formation of its strength mainly depends on the cement hydration and hardening. The cement hydration generating have cementation ability of hydration products of hexagonal $Ca(OH)_2$, C-S-H, square plate hydrated calcium aluminate. The hydration products of cement hydration, intertwined overlap, the aggregate particles wrapped together to form the skeleton structure[3].

**The influence of particle gradation for strength**

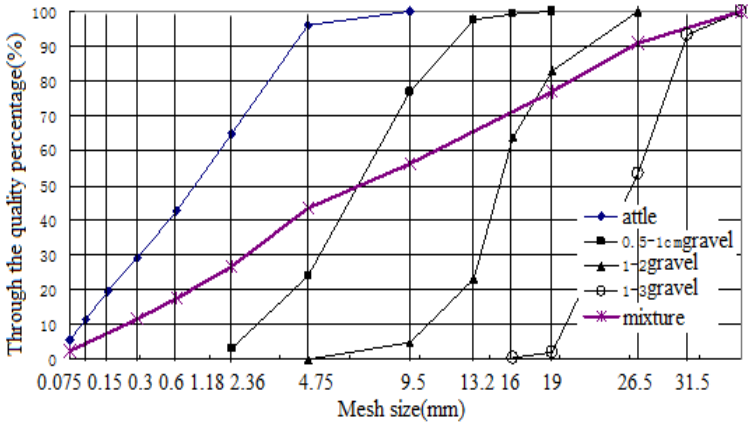


Fig.1 Nongwang engineering of the particle size sieving curve

Figure 1 shows. Construction mixture gradation curve reflects in less than 2cm of coarse particles, 1-2cm grain accounts for larger proportion, through the quality percentage is low, particle partial thick; Greater than 2cm of the gradation curve is located in the middle of the upper and lower curves. So the above mix proportion mixing mixture has not been a skeleton structure, the content of fine particles on the pore filling is less. Although the gravel composed of 3-4 grade according to the standard[4], but the average value is 2.9MPa, mixture gradation needs to be optimized.

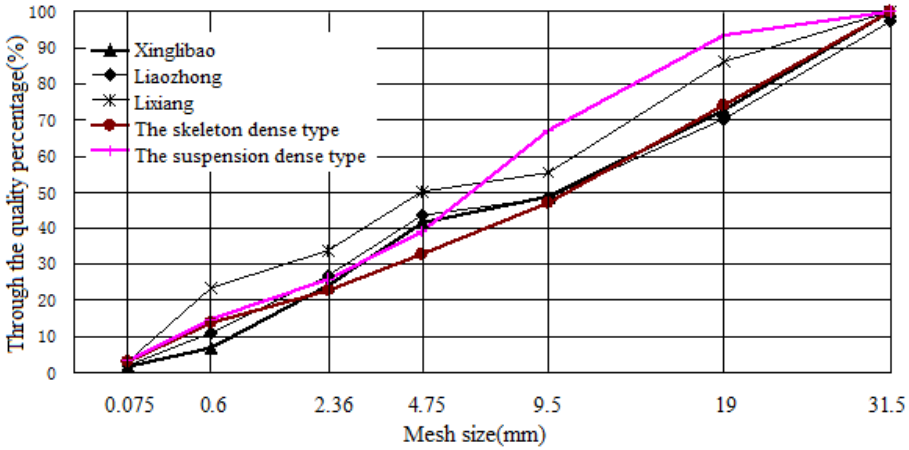


Fig.2 Mixture gradation curve distribution characteristics of Liaozhong, Xinlibao, Lixiang

As shown in figure 2, Liaozhong and Xinlibao mixture gradation curve at greater than 9.5mm larger particles part close to the skeleton dense type curve, the mixture of the coarse particle content is larger, more than 9.5mm particles above 50%; Mixture in 4.75mm~9.5mm particle quality is less than 10% of the total. Because of the pore filling between the skeleton is not real, so improve the strength of the effect is not obvious, and the specimen prone to segregation and cellular phenomenon. In Lixiang, mixture content of fine particles less than 4.75mm, reached 50% of the total, the larger particles content of more than 20mm smaller than other mixing station mixing scheme, less than 15%, gradation curve closer to suspended dense type grading curve.

**The influence of cement dosage for strength**

To investigate the cement dosage effect on the strength of the cement stable macadam mixture, adopting Lixiang mixing station mixing ratio, cement dosage by 4%, 4.5% and 5%, and indoor experiments, the results are shown in table 2.

Table 2 Different cement dosage on the influence on the strength of cement stabilized gravel base

| Number | Mixture ratio | Cement dosage（%） | Molding method | Unconfined compressive strength of the average value（MPa） | | |
|---|---|---|---|---|---|---|
| | | | | 7d | 28d | 90d |
| 1 | gravel：attle =1:1 | 4.0 | static pressure | 3.41 | 3.88 | 5.86 |
| 2 | gravel：attle =1:1 | 4.5 | static pressure | 3.68 | 3.95 | 6.03 |
| 3 | gravel：attle =1:1 | 5.0 | static pressure | 3.86 | 4.04 | 6.24 |

From table 2 shows, the degree of compaction and distribution under the same conditions, the cement dosage had no significant effect on the compressive strength, When the cement dosage increased by 1%, the compressive strength of the 7 d growth is 0.45 MPa, the growth rate is 13%, the 28 d compressive strength growth is 0.16MPa, the growth rate is 4%, the 90 d compressive strength growth is 0.38 MPa, growth rate of 6.4%.Visible cement dosage effect on the strength is not obvious, and with the increase of age, strength increase value and ratio is to reduced compared with early strength. Therefore, considering the shrinkage cracks and other factors, suggestions appropriate to reduce the dosage of cement in engineering.

**The influence of molding methods impacting for strength**

Take the gravel materials from Lixiang mixing stations , according to the construction mix stirring the mixture, the dose of cement is 4.5%, use static pressing and vibration molding specimens respectively, standard of the compacted degree is of 97%. Among which vibration molding uses two molding time which are 75s and 100s , obtaining the results of 7d unconfined compressive are shown in Table 3.

Table 3 Comparison of 7d compressive strength of different molding methods (MPa)

| Isostatic pressing $R_{cj}$ | Vibration molding (75s) $R_{cz1}$ | Vibration molding (100s) $R_{cz2}$ | Core sample at site $R_{cx}$ | $R_{cj}/ R_{cx}$ | $R_{cz1}/ R_{cx}$ | $R_{cz2}/ R_{cx}$ |
|---|---|---|---|---|---|---|
| 3.68 | 5.87 | 8.06 | 6.14 | 0.60 | 0.97 | 1.31 |

Table 3 shows that the average intensity value of isostatic pressing is 3.68MPa, the average of vibrating 75s is 5.87MPa, increasing 60% compared to isostatic pressing; The average of vibrating 100s is 8.06MPa, increasing 119% compared to isostatic pressing; The intensity of 7 d of vibration time which is 75s is closest to core samples strength, the value of the site is 0.97 times the field strength of the core sample, showing vibration molding is greatest similarity for construction process of the rolling process.

**Analysis of effects of the degree of compaction on the strength**

Based on previous research, on the conditions of meeting the standard of compact degree, for static pressing specimens, the degree of compaction is increased by 1%, the corresponding 7d unconfined compressive strength is increased by 0.2 ~ 0.3MPa and is about 10% of the measured values[5]. If you do not meet the requirements of the degree of compaction,when degree of compaction is reduced by 1% for each , the decreased value of intensity will be greater than 0.3MPa. With increasing age, the strength of cement stabilized gravel affected by the degree of compaction shows a decreasing trend.

**Analysis of effects of age on the strength**

For the analysis of the relationship between cement stabilized macadam mixture curing age and compressive strength, and in the testing process, respectively parts, conserve 7d, 28d and 90d, test unconfined compressive strength.

Table 4 Compressive strength test value in different age

| Num | Route | Mixture ratio | Cement dosage | Compressive strength R(Mpa) 7d | 28d | 90d | R7/R28 (%) | R7/R90 (%) |
|---|---|---|---|---|---|---|---|---|
| 1 | Jiangzhang route | 1-3cm:0.5-1cm: attle=25:25:50 | 5% | 3.4 | 4.4 | 4.7 | 77.3 | 72.3 |
| 2 | Xinlibao | Attle:gravel (mixture)=45:55 | 5% | 2.7 | 3.5 | 3.8 | 77.1 | 71.1 |
| 3 | Shenyan route | 1-3cm:1-2cm: 0.5-1cm:attle=10:25:20:45 | 5% | 2.3 | 3 | 3.4 | 76.7 | 67.6 |
| 4 | Nongwang engineering | 1-3cm:1-2cm: 0.5-1cm:attle=20:20:20:40 | 5% | 2.9 | 3.7 | 4.4 | 78.4 | 65.9 |
| 5 | Shenli route | Gravel:attle=50:50 | 5% | 3.5 | 4.4 | 5 | 79.5 | 70.0 |
| average value | | | | 2.96 | 3.8 | 4.26 | 77.8 | 69.4 |

Table 4 shows, with the increase of age, the compressive strength of cement stabilized gravel increases, the slope of the intensity distribution curve decreases, indicating that the growth rate of the compressive strength decreases. The average of 7d compressive strength is 77.8% of 28d compressive strength , is 69.4% of 90d compressive strength. Mix in tests of five groups, the average of 7d compressive strength is greater than 65% of 90d compressive strength values. Because cement stabilized gravel is relatively quick in the cement hydration process, so the early strength is higher. Therefore, in the construction process roadbed should focus on early conservation in order to the cement hydration and then promotes the formation of early strength of cement stabilized macadam. Meanwhile, the problem of shrinkage cracks should be considered fully, early strength should not be too high and should be controlled in a reasonable range.

## Conclusions

In plurality of cement stabilized macadam mixing plant of Shenyang region (involving more than one route), project team samples for laboratory tests to analyze the development of the rule and impact factors of compressive strength in Shenyang, the following conclusions:

(1)The mix of laboratory test used is construction mix and cement dose is 4% -5%. The average of the laboratory tests of 7d unconfined compressive strength is more than 2.0MPa, meeting the indicator of secondary and the following secondary road base which are provided by(highway subgrade technical specifications).

(2)Mixture gradation is an important factor of 7d compressive strength, in the construction the gradation which is used is close to a lower limit of gradation range which is in the specifications, but part of the particle content of the mix is less and not yet form a gradation of a skeleton dense. So the integrity of the specimen decreases and the intensity values reduces.

(3)The impact of doses of cement on strength is small, in laboratory tests 4.0% of dose of the cement mix of 7d unconfined compressive could meet strength values of regulatory requirements, so in the project considering the shrinkage cracks，project cost and other factors may appropriately reduce the dose of cement.

(4)Forming method has a greater impact on the strength of cement stabilized crushed stone, 75s vibration compaction intensity used in the experiment is closest to the measured values. The intensity value of 75s indoor vibration is about 170% of isostatic pressing and this shows vibration molding methods make the strength greatly improved.

(5)The degree of compaction is a key indicators which ensure the strength of cement stabilized macadam base, when the degree of compaction is reduced by 1%, the strength is reduced by about 10%, so the standards of compact degree should be strictly controlled in the construction.

(6)With the age increasing, the strength of cement stabilized macadam base increases, the rate of early strength increases rapidly, the rate of late strength decline. 7d compressive strength is above 65% of 90d compressive strength, early conserve should be paid great attention to ensure the growth of early strength in the construction.

**References**

[1] Road base construction technical specification (Beijing: China Communications Press 2009). In Chinese.

[2] Zhendong Qian,Leilei Chen,Changjiang He,Dongliang Fu. (2008). Highway, 6, 180-182. In Chinese.

[3] Qingying Meng,Weifeng Zhou, Ke Zhao. (2007). Highway traffic science and technology, 1(24), 21-23. In Chinese.

[4] Highway asphalt pavement design specification(Beijing: China Communications Press 2006). In Chinese.

[5] Huimin Hu. (2005). Asphalt pavement construction quality variability study. PhD dissertation, university of changan. In Chinese.

*Applied Mechanics and Materials Vols. 580-583 (2014) pp 455-459*
*© (2014) Trans Tech Publications, Switzerland*
*doi:10.4028/www.scientific.net/AMM.580-583.455*

# Experimental study on dynamic characteristics of tailings

Jianbin Zhao[a], Yingchun Ji[b], Xiao Liu[c] and Di Li[d]

Shenyang jianzhu university, Shenyang, Liaoning 110168, China

[a]cejbzhao@163.com, [b]ycstudyji@163.com, [c]liuxiao_sy@163.com, [d]1061825140@qq.com

**Keywords:** cyclic triaxial test; dynamic modulus; damping ratio; tailings.

**Abstract:** In this paper, the dynamic characteristics for three different kinds of copper tailings are studied through a series of cyclic triaxial tests. It is found that under confining pressure 200 and 300 kPa, elastic modulus raises with the increasement of coarse grain content to a certain degree and then declines, and the maximum elastic modulus corresponds to good gradation. While, as for confining pressure 100 kPa, elastic modulus raises with the increasement of fine grain content. It is also found that elastic modulus raises with the increasement of confning pressure. And, damping ratio raises with the increasement of shear strain and finally to a stable value. Finally, the fitting $G_d/G_{dmax} \sim \gamma$ curve for three kinds of tailings shows the reasonableness of test results.

## Introduction

Mine mining ore through beneficiation process to select the valuable ore. Tailings, the remaining waste is discharged through the water head processed to form slurries and stored in the storehouse lastly. There're are over 2,700 tailings existing in China, most of which are constructed in upstream method and because of inadequate drainage system the invasion line of the dams is very high [1]. These tailings in the dams usually in saturated and loose state. Tailings deposition from coarser below to finer is regular, the upper mostly fine sand, silty sand and sub-sand mostly in central and bottom is mud tailings which are quite different from ordinary clay and mechanical properties are very complex, especially in the earthquake they are easily liquefaction and destructive deformation [2-3].

Current researches related to the dynamic characteristics of tailings dam are still relatively small, the results of researches are very limited. It is mainly because of the experiment of dynamic characteristics has high requirements on equipment and it needs a long experimental time. In this paper, basing on a copper in Shenyang, we focus on dynamic characteristics of different particle size of tailings. The past experiment mainly studies the affect of density, consolidation ratio, confining pressure on the dynamic characteristics of tailings, while, different tailings on the particle size distribution are very different, which also affects the dynamic characteristics. Basing on the law of tailings deposition, we configure three kinds of tailings namely tail fine sand, tail silty sand and tail floury soil to study their dynamic characteristics under cyclic loading.

## Laboratory instruments and solutions

This experiment uses VJT5010 bidirectional dynamic triaxial test system which produced by Vjtech company, the sample size is $\phi 39.1 \times 80mm$. Exicitation frequency of cyclic loading is 1Hz, the wave of vibration is sin wave.

Tailings material used in the experiment taken from a copper mine in Shenyang and considering representative samples, physical experiment and particle size analysis experiment carried out on the samples. The maximum diameter of copper mine tailings is no more than 2mm, nonuniformity coefficient Cu = 4.1 ~ 11.0, coefficient of curvature Cc = 2.0 ~ 5.2, which are poorly graded tailings. According to the data in this experiment, we configure three kinds of tailings material, namely 1 # tail fine sand, 2 # tail silty sand and 3 # tail floury soil. Physical properties of three kinds of tailings are shown in table 1.

The experiment uses dry packing method and hierarchical compaction according to the dry density measured in the site. After preparation, placing the specimen to the vacuum device, pumping and then passing into the degassed water from the bottom to make the specimens saturated, so that the pore water pressure coefficient B reaches 0.95. After saturation, samples drainage consolidates under confining pressure 100, 200 and 300 KPa. Consolidation ratio Kc = 1. Then the dynamic stress is applied under undrained conditions. According to the relevant specification when generally elastic strain and plastic strain of the sample reaches to 5%, the sample is damage [4].

Table 1 Physical properties of three kinds of tailings

| Number | Soil type | Composition | $d_s$ | e | w | $\rho_d$ | $c_u$ | $c_c$ |
|---|---|---|---|---|---|---|---|---|
| 1# | Tail fine sand | >0.075mm 85%<br><0.075mm 15% | 2.98 | 0.861 | 28.4% | 1.68 | 4.2 | 2.18 |
| 2# | Tail silty sand | >0.075mm 64%<br><0.075mm 36% | 2.96 | 0.858 | 27.8% | 1.64 | 3.8 | 5.0 |
| 3# | Tail floury soil | >0.075mm 19%<br><0.075mm 81% | 2.92 | 0.856 | 28.1% | 1.63 | 3.9 | 2.3 |

## Experimental results and analysis

### Curve analysis dynamic elastic modulus and dynamic strain

At confining pressure 100, 200 and 300kPa, relationship between dynamic modulus and strain curves of the three Tailing's dynamic triaxial tests are shown in Fig.1.

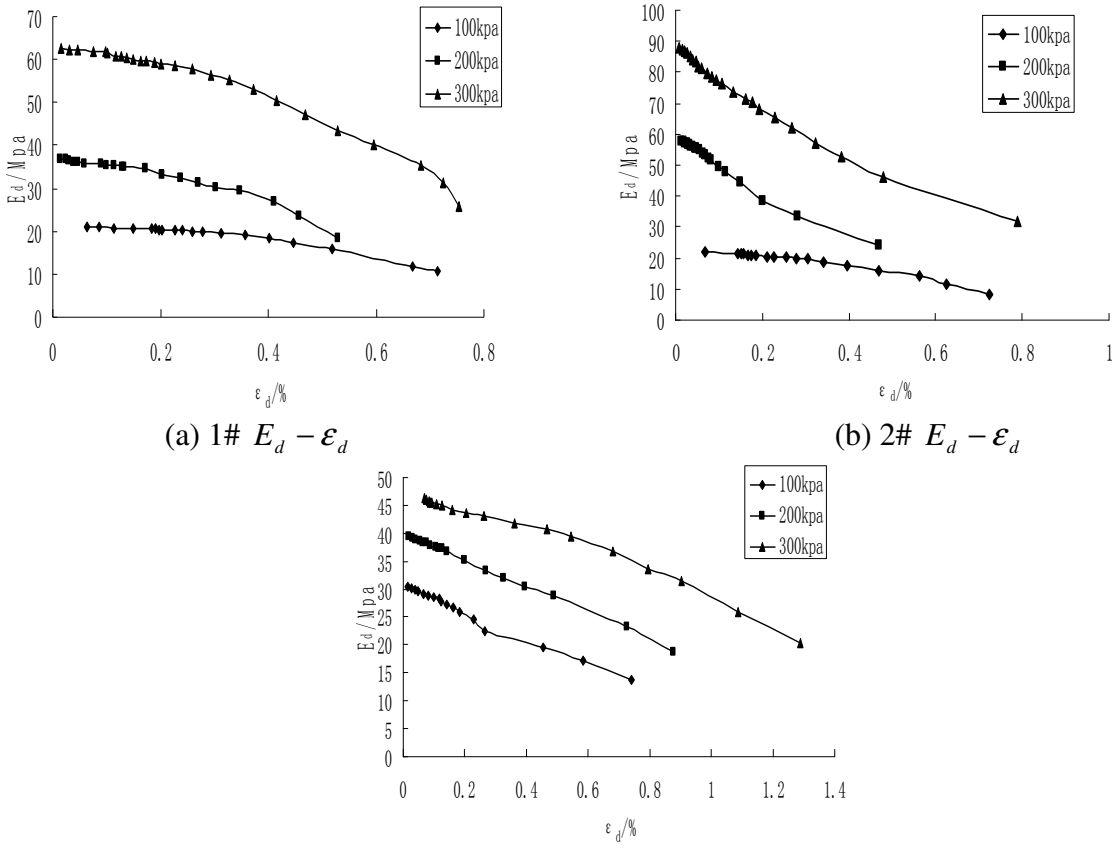


(a) 1# $E_d - \varepsilon_d$ (b) 2# $E_d - \varepsilon_d$

(c) 3# $E_d - \varepsilon_d$

Fig.1 Dynamic elastic modulus - dynamic strain relation curves

By the curve, we can see that:

（1）With the increasing of strain, dynamic modulus decreases. In the same consolidation ratio, when the confining pressure is200 or 300KPa, dynamic modulus of Silty sand is bigger than fine sand; dynamic modulus of fine sand is bigger than Floury soil. This is because silty sand not only contains coarse particles but also contains a certain amount of fine particles, the two particles working with each other, forming a good gradation, which is better to resist the elastic deformation. While the particle content of fine sand and floury soil is relatively simple, so the ability to resist deformation is weak. At the same time because of the sbility of the coarse particles to resist deformation is larger than fine particles, so elastic modulus of fine sand whose main composition is coarse particle is greater than floury soil. By contrary, when the surrounding pressure is 100KPa, dynamic modulus of floury soil is bigger than the others, the reason is the floury soil has a certain amount of fine particles. So when the surrounding pressure is little this will make it even more easier to squeeze particles.

（2）Dynamic modulus has a certain relationship with confining pressure. In the same strain, the elastic modulus of soils under surrounding pressure of 300KPa is bigger than the soils under surrounding pressure of 100 and 200KPa. This is because the surrounding pressure will apply bond stress on the tailings material, making it more dense, and consequently the ability to resist deformation improves.

**$G_d/G_{dmax}\sim\gamma$ line fitting and comparative analysis**

We experimentally measured dynamic triaxial dynamic elastic modulus axial and axial dynamic strain, according to the translation of the relationship, we can obtain dynamic shear strain and dynamic shear modulus.

$$\gamma_d = \varepsilon_d(1+\mu) \tag{1}$$

$$G_{\mathrm{d}} = E_d / 2(1+\mu) \tag{2}$$

The experiment was carried out in 100,200 and 300kpa confining pressure on tailings and then three kinds of data integration together confining pressure curve fitting. $G_d/G_{dmax}\sim\gamma$ relation curves are shown in Fig.2.

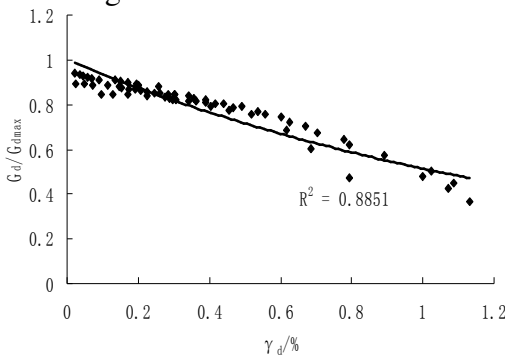


(a) 1# $G_{\mathrm{d}} / G_{d\max} - \gamma_d$

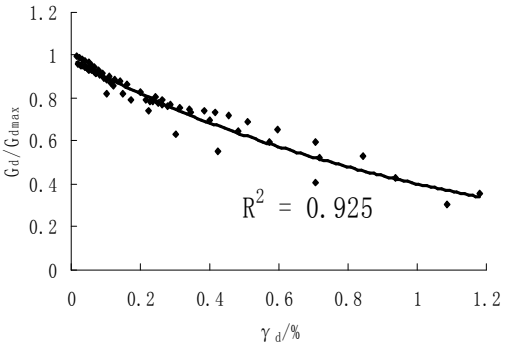


(b) 2# $G_{\mathrm{d}} / G_{d\max} - \gamma_d$

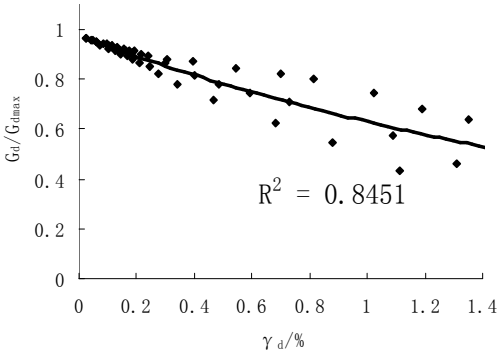


(c) 3# $G_{\mathrm{d}} / G_{d\max} - \gamma_d$

Fig.2 Dynamic shear modulus ratio – dynamic shear strain relation curves

For fine sand,

$$G/G_{d\max} = 0.9983e^{-0.6645\gamma} \tag{3}$$

For silty sand,

$$G/G_{d\max} = 0.9825e^{-0.8964\gamma} \tag{4}$$

For silt,

$$G/G_{d\max} = 0.9732e^{-0.4337\gamma} \tag{5}$$

From the curves we can see that:

（1）For fine sand, data distribution is relatively concentrated, while, it is discrete when the shear strain is larger.

（2）For silty sand and floury soil, data distribution is concertrated when the shear strain is less than 0.4%, while, data distribution is discrete when the shear starin is more than 0.4%.

（3）Shear modulus increases with decreasing shear strain and, because with increasing shear strain, the ability to resist deformation of the specimen decreases.

（4）Exponential fitting may well reflects the relationship between the shear modulus and shear strain. From the viewpoint of the limit, when the shear strain tends to infinity the shear modulus ratio tends to zero. From this point of view, realistic exponential is fitting.

**Analysis of damping ratio and dynamic shear strain curve**

Due to the presence of the damping ratio, In the process of vibration, the change of the stress strain is slower than the change of the stress state , we also called it hysteresis. The relationship between damping ratio and dynamic shear strain is shown in Fig.3.

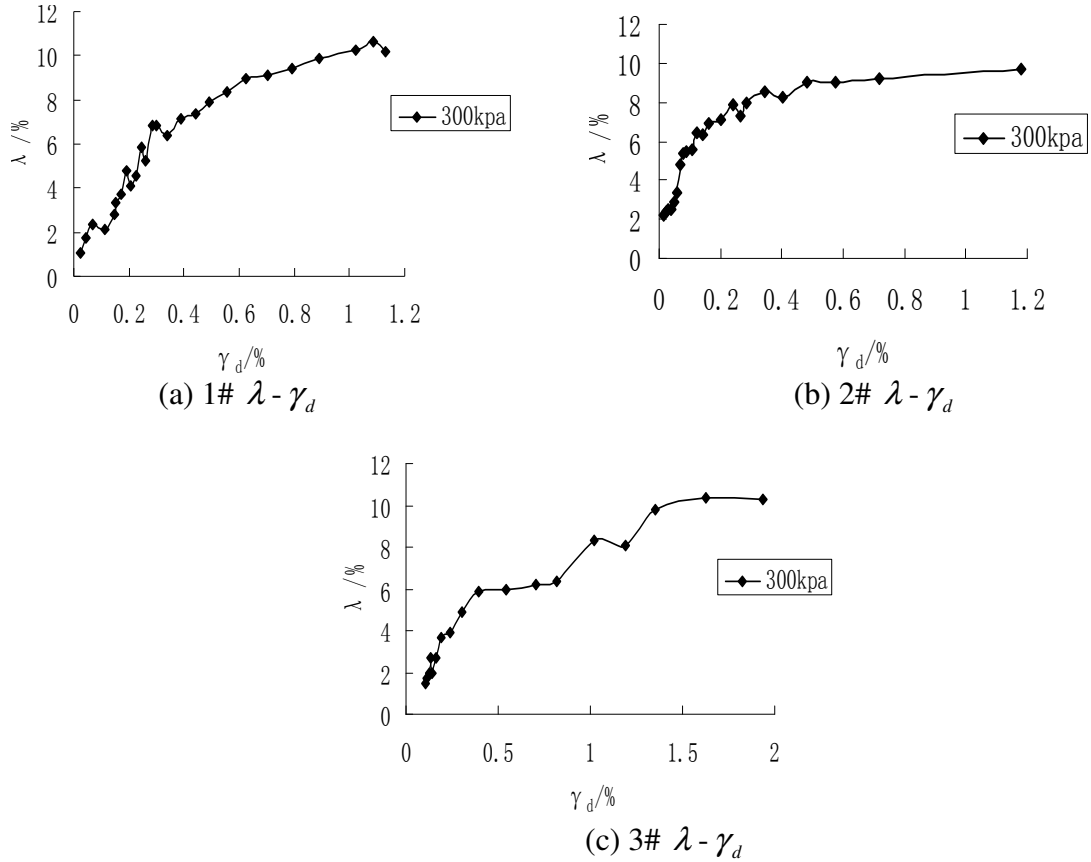


(a) 1# $\lambda$ - $\gamma_d$ (b) 2# $\lambda$ - $\gamma_d$

(c) 3# $\lambda$ - $\gamma_d$

Fig.3 Damping ratio - dynamic shear strain relation curves

From the chart we can see that:

（1）With the increasing of the shear strain, the damping ratio increase, which is worth noting that when the strain is small, the damping ratio increases rapidly with the increasing of strain, after that the rate of increasing slows down.

（2）There is no significant increase in the damping ratio when the shear strain increases to a certain value, in fact, it is gradually approaching a certain fixed value. That is to say the lag of stress relative to strain has a limit value.

## Conclusions

In this paper, by applying cyclic loading on three kinds of tailings which include fine sand, silty sand and floury soil, analyzing the dynamic parameters of elastic modulus and damping ratio, we obtained the following conclusions:

（1）With the increasing of the strain, the dynamic modulus decreases. In the same consolidation ratio, when the confining pressure is 200 or 300KPa, dynamic modulus of Silty sand is bigger than fine sand; dynamic modulus of fine sand is bigger than Floury soil, when confining pressure is 100Kpa, the dynamic modulus of Floury soil is greater than the other two.

（2）Dynamic modulus have a certain relationship with confining pressure. With the same shear strain, the higher the confining pressure, the greater dynamic modulus.

（3）According to the experimental data, fitting out three Tailings $G_d/G_{dmax}\sim\gamma$ curve. When the shear strain tends to infinity the shear modulus ratio is zero, this fits fact.

（4）Damping ratio increases with increasing shear strain, there is no significant increase in the damping ratio when the shear strain increases to a certain value, in fact, it is gradually approaching a certain fixed value.

## References

[1] Chunli Chen, Junfang He,Zaiqiang Hu.Study on dynamic deformation and dynamic strength properties of tailings sand[J]. Journal of Hydraulic Engineering,2007,(3):365-370.(in chinese)

[2] Yuancheng Ruan,Xin Guo.Experimental study of saturated tailings material static,dynamic strength properties [J]. Journal of Hydraulic Engineering,2004,(1):67-73.(in Chinese)

[3] Jinan Yan,Wulin Wang.Study on dynamic properties of tailings sand [J].Rock and Soil Mechanics,1990,(4):69-74.(inchinese)

[4] Ministry of Water Resources of the People's Republic of China.SL237-1999 Specification of soil test[S].beijing: China water conservancy and Hydropower Press.

[5] Seed H B, Lee K L, Idriss I M, et al. The slides in the San Fernando Dams during the earthquake of February 9, 1971[J]. Journal of Geothechnical Engineering, 1975,101(GT7):637-652.

[6] Changrong He. Dynamic modulus and damping ratio of dynamic triaxial experimental study[J]. Chinese Journal of geotechnical engineering,1997,19(2):39-48.(in chinese)

[7] Vick S G.Risk based approach to seismic stability and Inundation Hazard for upstream tailings dams.[A].Proceedings of international symposium on safety and Rehabilitation of tailings dams[c].Sydney:[s.n.],1990.

*Applied Mechanics and Materials Vols. 580-583 (2014) pp 460-463*
*© (2014) Trans Tech Publications, Switzerland*
*doi:10.4028/www.scientific.net/AMM.580-583.460*

# Experimental Study on Engineering Characteristics of Basalt Residual Soil on High Slope

Kai Cui[1, a], Ye Yang[2, b]

Department of Civil Engineering, Southwest Jiaotong University, Chengdu, Sichuan, 610031, China

[a]acuikai@swjtu.cn, [b]86352218@qq.com

**Keywords:** BiWei Highway, Basalt Residual Soil, Engineering Characteristics.

**Abstract.** The basalt residual soil of high slope of BiWei highway in Guizhou province belongs to regional special soil. Comprehensive and systematic evaluation for engineering geologic characteristics of residual soil on basalt is necessary to the construction in this area and geological engineering investigation. Kaolinite is dominant in clay mineral of this soil, which has a higher clay particle content. The special material composition and structural morphology make it have the physical properties of high porosity, low density and high water content. But it has mechanical properties of higher strength. The soil has a low expansibility and weak water-resistance. Moreover, the soil is sensitive to environmental factors such as temperature and humidity. The mechanical properties become weak after soaking, leading to a larger collapse deformation and a heavy disintegration. Therefore, it is important to focus on the engineering disasters caused by rain water for example.

## Introduction

The basalt residual soil has characteristics such as low density, high water content, high saturation, high void ratio, high compressibility, low capacity, maldistribution, and unstable properties. The Permian basalt is widely distributed in Guizhou province and rock joints and fractures develop in the indexing lot where it exists. The rock broke into pieces after weathering and then become residual soil. It is widely overlying strata and it has greater thickness [1,2]. It will lead to the collapse of slope, heavy slumping, large-scale landside [3] and other geological hazards [5,6], which is a serious threat to the country's economic construction and people's lives and property safety. In-depth study on the engineering mechanical properties of the highway building in basalt residual area is important to elevate the highway construction technology in basalt residual area. Scholars have researched on physical and mechanical index [7-10], permeability [11,12], strength [13], disintegrative [7,14], mineral composition [15] and microstructure [16]. The previous studies indicate that different basalt residual soils of varioius regions show the similar engineering mechanical properties and also their respective regional characteristics. In view of the above situation, in this paper, the basalt residual soil in high slope in BiWei highway K86+700-+960 was studied. The engineering mechanical properties of the basalt residual soil in this area was studied through a lot of experiments, consolidation test, direct shear test, permeability test, and disintegration test. And then the strength and deformation characteristics of the basalt residual soil is analyzed, which can provide some theoretical support for the guidance of highway construction and the prevention of geological disasters in the region.

**Physical properties of basalt residual soil**

The basalt residual soil in this area has high water content (33%), low natural density (1.6g/cm$^3$), and big pore. It is between hard plastic and waxiness in the natural state. The basalt residual soil particle size distribution curve showed that the soil clay has large content, non-uniform coefficient $c_u$ is 31, the curvature coefficient $c_c$ is 2.33, belonging to good gradation. Mineral composition analyzed by X ray showed that kaolinite minerals is a main component with the basalt residual soil clay minerals.

**Mechanical properties of basalt residual soil**

The WG-4 portable consolidation apparatus is used to determine the compressibility. The test method is uniaxial consolidation compression test. The results showed that BiWei basalt residual soil compression coefficient $a_{1\text{-}2}$=0.3MPa$^{-1}$, belongs to medium compressible soil.

The remolded soil is used to conduct the direct shear test. Remolded soil is compounded according to bulk density of undisturbed soil, divided in six water content grades including 20% (dry state), 33% (natural water content), 45% (saturated state) and three middle values. Each water is graded with three samples, each sample of the void ratio is controlled in natural void ratio (1.2), and peak strength $c$, $\varphi$ and residual strength $c_r$, $\varphi_r$ of M-C model are determined by repeated shear test. The test results showed that the high cohesion of the residual soil is similar to cohesive soil and the high internal friction angle is similar to silty soil. It showed that in the natural state, although the structure of soil is lost, the coupling force between soil particles is still strong. The soil has better mechanical characteristics. At the same time, like other types of basalt residual soil, the soil becomes wet when it encounters water, which leads to soil degradation. Before and after the basalt residual soil is saturated, by comparing the changed strength, we can find that the variation amplitude of cohesion is significantly greater than the internal friction angle, the soil deterioration is caused by the decrease of particle cohesion. In addition, the residual strength significantly reduced compared with the peak strength, the $c$ decreased by 50%-70% with the $\varphi$ value of decline 2°-8°. Fig. 1 and Fig. 2 show that the relationship curves of cohesion and residual cohesion change with the water content. Fig. 3 and Fig. 4 show that the relationship curves of internal friction angle and residual internal friction change with the water content. The figures show that cohesion is influenced obviously by the change of water content. The general tendency is that it reduces obviously with the increase of water content. Also, residual cohesion also decreases with the increase of water content, but the trend is relatively slow. The internal friction angle and residual friction angle have a downward trend with the increase of water content, but the change is slow.

Basalt residual soil has poor water resistance, so it is easy to be disintegrative in a certain state. After immersion in water, the original basalt residual soil is not to be disintegrative in 24 hours. After soaking in water 24h and 3 to 4 cycles of wetting and drying, the original basalt residual soil begin to be the small block disintegration, and the disintegration is in a matter of chunky, with weak disintegration under natural state. The test also shows that the degree of disintegration and rate of disintegration is higher than undisturbed soil. While the temperature and humidity cycle will also accelerate the disintegration, the disintegration of basalt residual soil is influenced importantly by the changes of water content. In general, the disintegration of clayey soil and clay rock is caused by the structure of destruction, which is composed of soil surface water hydration expansion. But kaolinite mineral is the main components of the BiWei basalt residual soil mineral, which has poor hydrophilicity and expansion. Mineral composition should not be the main reason of this kind of soil disintegration. We believe that the main factors of different state of disintegration of basalt

residual soil is not the same. The disintegration under natural soil is the fracture expansion, and the disintegration phenomenon is caused by the original structure defect expansion, because the majority of fine pores in soil are bigger than surface area. The adsorption effect, the air of soil fissure and structural flaws is pressed by the water, to produce super tension. Residual soil is sensitive to cycles of wetting and drying process. Dehydration in a dry environment, cementing material bonding of particles occur dehydration hardening. Although it may become quasi crystalline or crystalline iron oxide in certain circumstances, to form aggregates coated surface coverage, enhance the agglomeration degree, but the whole structure is loose structure, the connection of the structure strength turns weak. At the same time, the electrostatic repulsion between the surface of clay particles turns weak by the concentration of colloidal iron oxide, when it turns wet again, the harden condensation water can not be restored to the original state, it causes the cement performance of particles turns weak, structure strength turns weak. When the water immerses, the micro structure of soil is disturbed and damaged, strong disintegration phenomenon is happened, therefore, the disintegration of remolded soil and dry-wet cycling soil are dispersed disintegration.

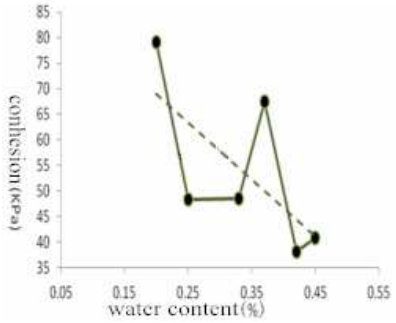


Fig. 1 Cohesion-water content relationship curve

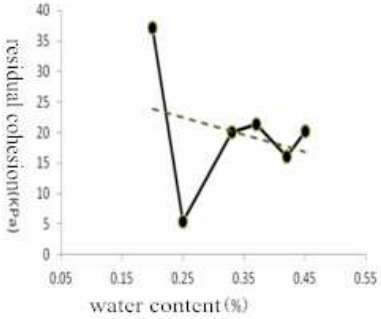


Fig. 2 Residual cohesion-water content relationship curve

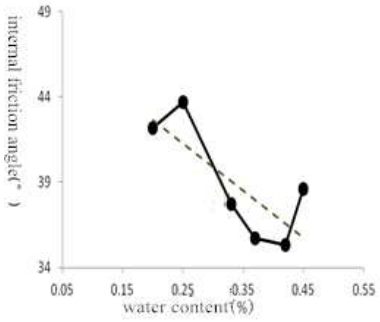


Fig. 3 Internal friction angle-water content relationship curve

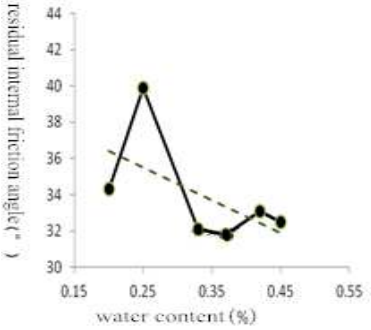


Fig. 4 Residual internal friction angle-water content relationship curve

The permeability coefficient of soil samples at 20℃ is determined by TST-55 varying-head permeameter. The average of permeability coefficient $K_{20}$ of the basalt residual soil is $2.49\times10^{-4}$cm/s, belonging to the high permeability. This is mainly because kaolinite mineral is the main component of basalt residual soil clay minerals, hydrophilic is weak, water molecules are easy to pass through the soil, and permeability is strong. In addition, in the process of penetration test, obvious swelling phenomenon is not found.

## Conclusions

The high slope of BiWei highway basalt residual soil was a kind of special regional soil with poor physical characteristics (high porosity, low density, high water content)and better mechanical properties(high intensity).

BiWei highway basalt residual soil was sensitive to water, and the characteristics of water resistance were poor. After soaked and saturated the mechanical properties deteriorated significantly, which also led to disintegration, especially when the structure suffers disturbance and dry-wet cycle, the phenomenon is enhanced. Construction should focus on the engineering disaster caused by rain.

**Acknowledgements**

This paper was supported by the Fundamental Research Funds for the Central Universities and the open research fund Key Laboratory of Seismic Technology of Sichuan Province, Southwest Jiaotong University.

**References**

[1] Q. Shen, C.X. Chen and R. Wang: Rock and Soil Mechanics, Vol. 27(12) (2006), p.2309 (In Chinese)

[2] B. Yu, H.Y. Sun, Y.Q. Shang et al: The Chinese Journal of Geological Hazard and Control, Vol. 18(2) (2007), p.17 (In Chinese)

[3] X.J. Li, H.M. Ma and H.G. Wu: Journal of Engineering Geology, Vol. 18(1) (2010), p.60 (In Chinese)

[4] Z.H. Li, X.H. Yang, F.P. Lai, et al: Journal of Engineering Geology, Vol. 16(6) (2008), p.806 (In Chinese)

[5] Y.H. Liu, C. Tang, T.F. Li, et al: Journal of Engineering Geology, Vol. 17(5) (2009), p.656 (In Chinese)

[6] J.X. Wang, L.Z. Yang and J. He: Journal of Geological Hazards and Environment Preservation, Vol. 13(2) (2002), p.17

[7] X.W. Zhang, L.W. Kong and M. Zang: Chinese Journal of Geotechnical Engineering, (2013), in press (In Chinese)

[8] H. Rahardjoa, K.K. Aung, E.C. Leong et al: Engineering Geology, Vol. 73(1) (2004), p.157

[9] P.R. Vauhgan, M. Maccarini, S.M. Mokhtar: Quarterly Journal of Engineering Geology, Vol. 21 (1988), p.69

[10] G.H. Wang, H.M. Chen: Journal of North China Institute of Water Conservancy and Hydroelectric Power, Vol. 32(3) (2011), p.67 (In Chinese)

[11] S.A. Ola: Quarterly Journal of Engineering Geology, Vol. 13(2) (1980), p.87

[12] X.B. Tian, X. Liu: Soil Engineering and Foundation, Vol. 26(4) (2012), p.123

[13] N. Loganathan, D.S. Suraj and A. Thurairajah: Journal of Geotechnical Engineering, Vol. 118(4) (1992), p.593

[14] S.M. Rao, K. Revanasiddappa: Geotechnical and Geological Engineering, Vol. 24(3) (2006), p.725

[15] M.T.G.D. Oliveira, M.L.L. Formoso, et al: Journal of South American Earth Sciences, Vol. 11(4) (1998), p.365

[16] L.D. Wesley: Journal of Geotechnical Engineering, Vol. 116(4) (1990), p.589

*Applied Mechanics and Materials Vols. 580-583 (2014) pp 464-468*
*© (2014) Trans Tech Publications, Switzerland*
*doi:10.4028/www.scientific.net/AMM.580-583.464*

# Influences of Cross Section Parameters on Bending Resistance of TSC Pile

Xinquan WANG[1, a *], Shimin ZHANG[1, b], Juan LIAO[1, c] Yingsheng HUANG[1, d]

[1]Department of Civil Engineering, Zhejiang University City College, Hangzhou 310015, China

[a]awangxq@zucc.edu.cn, [b]zhangsm@zucc.edu.cn, [c]liaoj@zucc.edu.cn and [d]huangys@zucc.edu.cn

**Keywords:** TSC pile, ultimate flexural capability, cross section parameter, mid-span deflection

**Abstract.** Precast thin-wall steel and spun concrete composite pile (TSC pile) is a kind of new type of steel-concrete composite pile whose bearing performance is between steel pile and concrete pile. This article adopted FEM software to set up 3D TSC pile model to analyze its performance. Through the comparison with actual pure bending bearing experiment results, the model's reliability was verified and the results showed that the model was reliable. Then lots of bending bearing capacity contrast calculations were conducted by using different cross section parameters (outside diameter, concrete pipe's wall thickness and steel pipe's wall thickness), and the influences of these parameters on bending resistance of TSC pile were discussed. The results showed that: with the increase of outside diameter, concrete pipe's wall thickness and steel pipe's wall thickness, TSC pile's ultimate flexural bearing capacity increased. The influences of different parameters were not the same, outside diameter was the most important parameter, then concrete pipe's wall thickness, and the last one was steel pipe's wall thickness.

## Introduction

Precast Thin-wall Steel and spun Concrete composite Pile (the abbreviation is TSC pile[1]) is a kind of new type of foundation pile which is made by pouring concrete into the curl formed steel pipe, made by Q235B or Q345B steel plate (steel belt), and then centrifuging in centrifuge to form the shape. Concrete compression strength is not lower than 80MPa, which can bear large vertical load and horizontal load. TSC pile is a new type of steel-concrete composite structure whose bearing performance is between steel pile and concrete pile, and it owes the advantages of steel pile and concrete pile, and can avoid the defects of these two kinds of piles when they are used alone: outside steel pipe's stability will be increased by inside concrete pipe; Inside concrete pipe's compression capacity will be greatly increased by the "lock ring effect" of outside steel pipe, which turn the stress state of concrete pipe from one-way to three-dimensional stress state[2]. TSC pile owes lots of advantages: high anti-hammering capacity, high penetrating power, fast driving speed, good endurance quality, good forming equality, low material cost and so on[3].

TSC pile has already successfully been used in practical engineering projects in industry, electricity power, transportation and some other field [4]. Harbor engineering projects usually use piles with large diameter, and commonly, the pile obviously bears the effect of wind, wave and some other horizontal loads effect, which need high flexural capacity. Now, there were already many scholars studied the flexural performance of TSC pile through laboratory tests method[5], the results showed that TSC pile's flexural capability is good, and also indicated that cross section properties of pile had a greater impact on its bending performance, but the specify influence degree of each parameter was not clear. Model test and numerical computation are the most effective methods to study the pile loading behavior[6-8]. For the fully play of performance of steel pipe and concrete material in TSC pile, optimizing cross section parameters, and then improve its bending resistance capacity, this article simulated TSC pile with varied cross section parameters (outside diameter, wall thickness and steel pipe's wall thickness) to discuss the influence of different parameters on the bending performance of TSC pile, the results were valued for TSC pile's designing and producing.

## Analysis methods

Large-scale FEM software Abaqus was used in the analysis. Abaqus is one of the most efficient and reliable nonlinearity software in the world now, and owes obvious advantages in solving varied nonlinearity problems in civil engineering projects, and provides many material constitutive models.

Based on the pure bending test date, the analysis model's rationality was verified. The laboratory test loading diagram is shown in Fig.1.In laboratory test, TSC pile's diameter is 1000mm, pile length is 13m, total wall thickness is 130mm, the outside steel pipe uses Q235 steel and its wall thickness is 10mm, inside concrete is C80 concrete. The loading sketch map of prototype is showed in the figure 1. L is pile's length (value in test is 13m), *a* is 1/2 loading span (value in test is 0.5m). In the numerical simulation, concrete damage plasticity model was used to display the characters after pile material entering into the plasticity status, and the steel adopted elastic-plastic model.

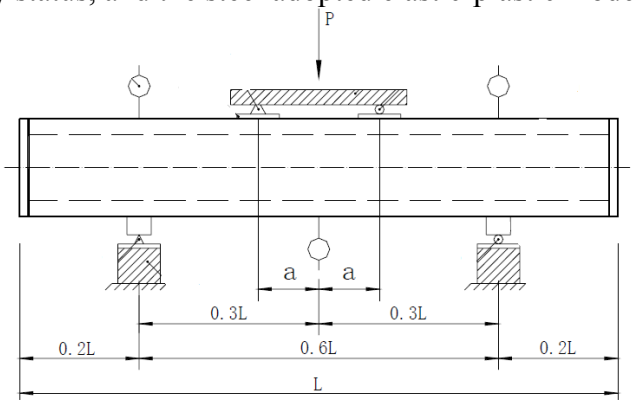


**Fig. 1 Laboratory test loading diagram**

Fig. 2 shows load-mid-span deflection curves which measured in test and calculated in FEM method. The figure indicates that the numerical modeling results are close to the test measured results. This numerical modeling can better show the elastic status, elastic-plastic status and plastic status of the pile under the effect of bending moment, which shows that the FEM used in this study is reliable. The ultimate flexural bearing capacity calculated by this numerical modeling is 5687 $kN \bullet m$.

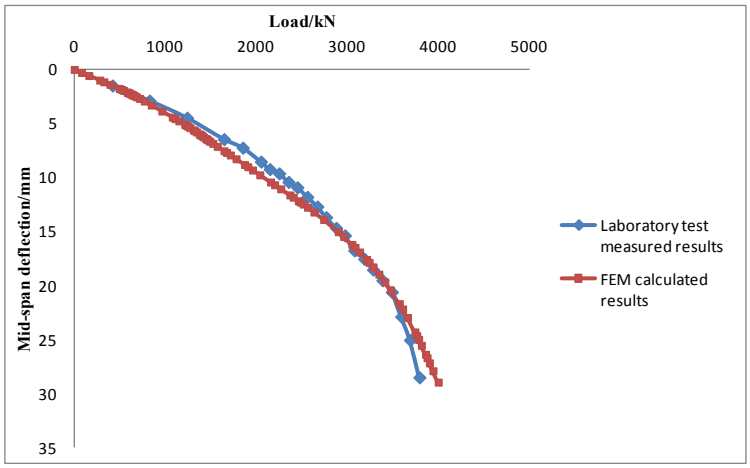


**Fig. 2 Load-mid-span deflection curve of TSC piles**

The below are TSC pile's numerical analysis with varied cross section parameters, different cross section properties are discussed to analyze their influences on the bending resistance performance of pile. The pile uses C80 concrete and Q235 steel. Through numerical modeling method, different cross section parameters (outside diameter, concrete pipe's wall thickness and steel pipe's wall thickness) are used respectively in comparison calculations, the calculation length of pile is 15m, and specific parameters can be seen in table 2.

**Table 1Calculation parameters for numerical modeling comparison**

| sorts | Parameters/(mm) |
|---|---|
| Pile outside diameter | 600,800,1000,1200 |
| Concrete pipe's wall thickness | 110,120,130,150 |
| Steel pipe's wall thickness | 8,10,16,20 |

## Analysis of calculation results

**Influence of pile's outside diameter on the bending resistance performance.** Fig. 3 shows the influence of varied pile outside diameters on the load-mid-span deflection. In the comparison calculations, the same cross section total wall thickness, same steel pipe's wall thickness, same pile length (t=100mm, ts=10mm, L=15m) are used and pile material is also the same. The figure indicates that load-mid-span deflection curves of piles with different outside diameters are similar to each other, deflection changes linearly under small load, and the pile begins to enter into the plastic status with the increase of load, finally, regional pile material enter into plastic yield status, the pile reaches its ultimate flexural bearing capacity, mid-span deflection begin to increase greatly. With the increase of outside diameter, under the same load, the mid-span deflection decrease obviously. Even when the load is small, diameter variation will cause bigger variation of mid-span deflection, this is because that, with the increase of load, the pile gradually enters into the plastic status, which indicates that diameter has a great impact on bending resistance capacity of TSC pile.

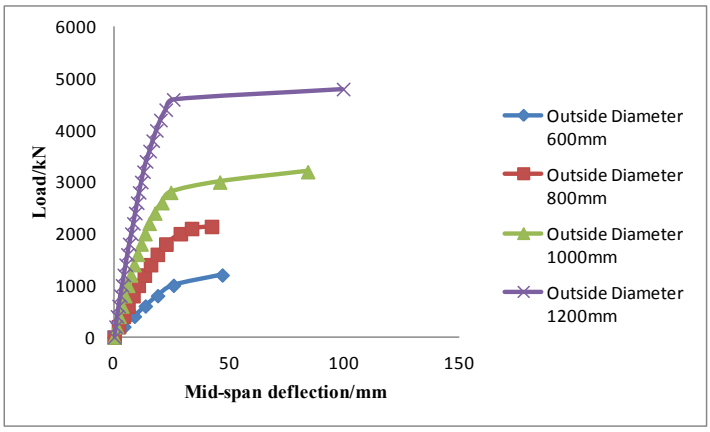


**Fig. 3 Load-mid-span deflection curves of piles with different outside diameters**

**Influence of concrete pipe's wall thickness on the bending resistance.** Fig. 4 shows that influence of different concrete pipe's wall thickness on the load-mid-span deflection of pile. In the comparison calculations, the pile's outside diameters, steel pipe's wall thickness, pile's length are the same (D=1000mm, ts=10mm, L=15m) and also the material. The actual changed parameter is the wall thickness of concrete pipe. Figure 6 shows that the variation trends of piles, when concrete pipe's wall thickness changes, are closed to each other, and the variation trend is basically linear when the load is small; With the increase of load, the pile gradually enters into plastic status, the curve doesn't change in linear; With the increase of load, material's plastic zone continuously extend, the deflection begins to increase greatly. With the increase of concrete pipe's wall thickness, under the same load, the mid-span deflection is decreased. When the load is small, the influence of concrete pipe's wall thickness is small, with the increase of load, the mid-span deflection of pile with small concrete pipe's wall thickness will increase dramatically, this is because that, with the increase of load, the pile begin to enter into plastic deformation status.

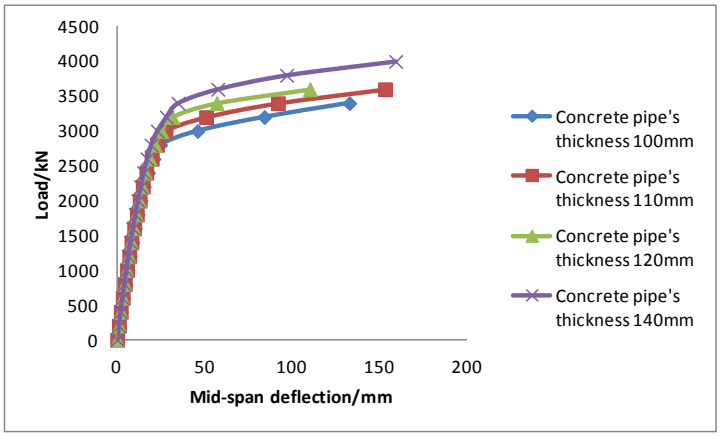


**Fig. 4 Load-mid-span deflection curves of piles with different concrete pipe's wall thickness**

**Influences of steel pipe's wall thickness on the bending resistance.** Fig. 5 shows the influences of steel pipe's wall thickness on load-mid-span deflection. In the comparison calculations, the total wall thickness, outside diameter, the length of pile are all the same (D=1000mm, t=130mm, L=15m), and also the pile material, steel pipe's wall thickness is the only changed parameter. The figure indicates that load-mid-span deflection curves' tracing pattern do not change when steel pipe's wall thickness change, and the pile also experiences three main status, linear status, plastic status and plastic yield status. When pile material enters into plastic yield status, the mid-span deflection changes dramatically. With the increase of steel pipe's wall thickness, under the same load, mid-span deflection decreases obviously. When the load is small, the influence of steel pipe's wall thickness on the deflection is small, with the increase of load, the mid-span deflection of pile with thin steel pipe will increase dramatically, this is mainly because that, with the increase of load, pile with thin steel pipe will first enter into the plastic deformation status till plastic yield status.

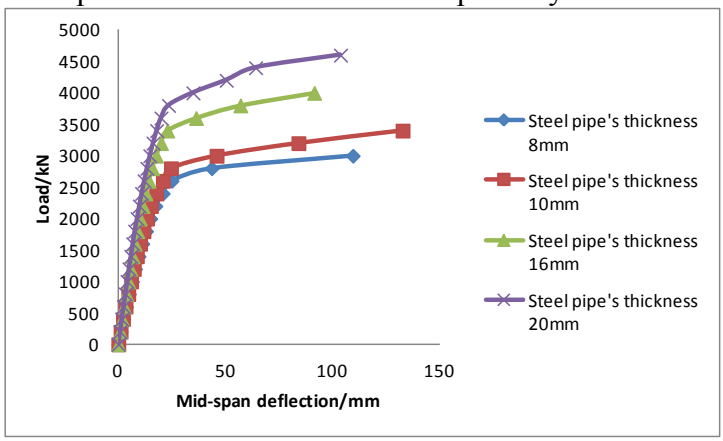


**Fig. 5 Load-mid-span deflection curves of pile with different steel pipe's wall thickness**

## Conclusions

Through numerical modeling, the bearing characteristics of TSC pile under the effect of bending moment are discussed, different cross section parameters (outside diameter, total wall thickness and steel pipe's wall thickness) are chosen in the comparison calculations, and the influences of different parameters on the bending resistance performance are analyzed, the main conclusions are as follows:

(1) Through the comparison with the laboratory test date, the feasibility of finite element model for analyzing the ultimate flexural capability of pile is verified.

(2) With the increase of outside diameters, mid-span deflection decreases obviously, the ultimate flexural capability of pile increases dramatically. But the varying patterns of piles' mid-span deflection with different outside diameters were similar. Each pile experiences three status, elastic deformation status, plastic deformation status and plastic yield status.

(3) With the increase of concrete pipe's wall thickness, under the same load, the mid-span deflection is decreased, and the pile's ultimate flexural capability is increased. When the load is small, the influence of concrete pipe's wall thickness on the mid-span deflection is small, with the increase of load, the influence becomes obviously gradually. With the increase of concrete pipe's wall thickness, the increase trend of ultimate flexural capability of pile becomes gently gradually.

(4) With the increase of steel pipe's wall thickness, under the same load, the mid-span deflection is decreased, and the ultimate flexural capability is increased. With the increase of steel pipe's wall thickness, the ultimate flexural capability of pile increase in linear trend.

**Acknowledgements**

This material is based upon work funded by Zhejiang Provincial Natural Science Foundation of China under Grant No. LQ12E09002; Project(51308497) supported by National Natural Science Foundation of China.

**References**

[1] JG/T272-2010, Precast thin-wall steel and spun concrete composite pile [s]. Beijing: China Standards Press, 2010 (in Chinese).

[2] ZHUO Yang, CAO JIN-JIE, QIU Song, Flexural capacity of large-diameter thin-wall steel and spun concrete composite piles [J]. 2011.10: 135-138 (in Chinese).

[3] LIN Zhiqing, Brief talk of applications of precast thin-wall steel and spun concrete composite pile (TSC pile) in engineering projects [J]. 2013.11: 54-56 (in Chinese).

[4] WANG Hua-zhong, WANG Fa. Application and Advancement of Steel Tubular Pile in Baosteel Project [J]. Chinese Journal of Underground Space and Engineering, 2009, 5: 1696-1703(in Chinese).

[5] Song Hongzhao, Lu Liang. Experimental study on behavior of TSC pile subjected to pure bending [J]. Chinese Journal of Structural Engineers, 2011, 1:146-150 (in Chinese).

[6] Liu Hanlong, Tan Huiming, Peng jie, Zhang Jianwei. Development of large scale pile foundation model test system [J]. Chinese Journal of Geotechnical Engineering, 2009, 31(3): 452-457. (in Chinese)

[7] Tan, H.M.; Liu, H.L.; Deng, A. Numerical analyses on geogrid-reinforced cushion in pile-supported composite foundation . Geotechnical Engineering, 2009, 40(1), 25-30. (in Chinese)

[8] Tan, Huiming, Gao, Zhibing, Huang, Yonglin. Calculation method of pile-supported geogrid-reinforced embankment based on elastic large deflection theory. 2011 International Conference on Electric Technology and Civil Engineering, ICETCE 2011-Proceedings, 2011, 2974-2978. (in Chinese)

*Applied Mechanics and Materials Vols. 580-583 (2014) pp 469-473*
*© (2014) Trans Tech Publications, Switzerland*
*doi:10.4028/www.scientific.net/AMM.580-583.469*

# Roadbed Treatment Research in Expansive Soil Area

FENG ZHen[1, a], LI Cong-Jie[2,b] , GAO Xue-Li[3,c]

[1]College of Civil Engineering, Hebei University, Baoding, 071002, China

[2]College of Civil Engineering, Hebei University, Baoding, 071002, China

[3]College of Civil Engineering, Hebei University, Baoding, 071002, China

[a]Robertvon@163.com, [b]Licj@163.coml, [c]Gaoxl@163.com

**Keywords:** expansive soil; roadbed; swell shrink mechanism; treatment

**Abstract.** This paper elaborate the bad geological characteristic and the huge disaster caused by expansive soil. When constructing the road or railway in expansive soil area, the roadbed disease such as slope stability failure, roadbed settlement, mud pumping, ballast bag and so on is elaborated. The expansion and shrinkage mechanism of expansive soil has been studied from such aspects as physical-chemistry-mechanics effect, material composition, external influencing factors and so on. In expansive soil area, such expansive soil treatment and reinforcement methods as physical improvement, chemistry improvement, biological improvement are summarized and proposed.

## Introduction

There are more than 35 countries where exists the expansive soil which spreads six continents. In China, the expansive soils create the extremely huge harm, the loss that the expansive soil creates is double more than the loss sum created by such disasters as flood, hurricane, earthquake and so on in American, the economic loss for the expansive soil question approximately amounts to $20 billion every year. In China railway engineering the expense used for treatment the expansive soil foundation reach ten million Yuan each kilometer. Therefore, treatment research of expansive soil geological disasters has the significant economic significance and project practice value [1,2].

## Engineering Characteristic and Swell Shrink Mechanism

*1). Engineering Characteristic.* Expansive soil distribute broadly, is one kind of more crevasses and having remarkable swell-shrink characteristics geologic body, its distribution are very widespread. The expansive soil's clay ingredient is mainly composed by the strongly hydrophilic mineral and other clay mineral, as one kind of high plastic clay which is sensitive to the environment moist-heat change, its chief feature is that the expansive soil is rich water affinity clay , richly big the liquid limit, big swell-shrink characteristics, absorbing water swell and softening, dehydration shrink and hard crack, more crevice, distortion repeatedly and so on, in the soil body the crevasse disorderly distribute, and do the special harm to all kinds of shallow light engineering construction[2,3].

*2). Swell Shrink Mechanism of Expansive Soil.* The swell-shrink of expansive soil, in fact, are the soil body mechanics characteristic change caused by the soil water “gain and loss”. It is the quite complex physical-chemistry-mechanics effect action process, it is not only decided by its material composition and microstructure characteristic, but also having close relation with the environmental condition in which it locates. The expansive soil swell-shrink mechanism's explanation theory mainly includes the crystal lattice expansion theory, the double-electrode layer theory, the microstructure theory and so on.

The physical mechanics theory about expansive soil includes mainly effective stress theory, capillary vessel theory, elastic theory and so on. These theories thought that the swell of the expansive soil is caused by the physical mechanics effect which produced by the water-soil interaction under certain external process. After fractional saturation expansive soil absorbing water, the soil pore water pressure and the effective stress will change, the capillary vessel potential energy and the surface tension change accordingly, and caused the pellet elasticity effect, thus caused the volume of the expansive soil to increase.

**The Roadbed Failures in Expansive Soil Area**

In road or railway engineering, because of surface layer weathering effect, swell with wet and shrinkage with dry effect, as well as the insufficient compaction or protection and so on, many roadbed is distressing [4].

Under the wet cyclical effect in the dry season and the rainy season, in addition the vehicles travel load's action, the expansive soil roadbed which is not be replaced or sealed treatment will be caused superficial relaxation. Thus causes the roadbed to produce mud pumping phenomenon. The roadbed mud pumping phenomenon often is followed by the roadbed bigger settlement and the pavement wave distortion, therefore, it seriously influence traffic safety and even cause the traffic interruption.

After roadbed soil sliming, base course's crushed stone and so on is easy to fall into or is pushed in foundation bedding soil and forms the saccate structure. The ballast pouches will cause the pavement structure to destroy, at the same time, become the water seepage channel and water carrier in the roadbed, further cause deep soil body wet and sliming, thus intensify the ballast pouch's development, finally result in the vicious circle.

Usually, because of the mechanical roller compaction not arriving the road border section, the later settlement of road border become bigger, and also because of its free face, it is specially sensitive to the atmospheric physics action, therefore after water loss the shrinkage strain of road border is far bigger than that of dike body under the alternation of wetting and dry action. Road border longitudinal crack phenomenon occurs more in the dry season. After the road border has the longitudinal crack, although it does not immediately influence road's security of service, but if it is not repaired promptly, the longitudinal crack forms the seep channel of roadbed, causes the surface water very easily permeate roadbed, thus easy to cause the road border collapse.

**Roadbed Treatment Methods of Expansive Soil**

According to the improvement mechanism, the methods of expansive soil improvement may divide into three types, one is physical property improvement methods, for example to add coarse sand filling materials and so on, the other is chemistry improvement methods, for example to add lime, cement, gypsum, sodium silicate and so on, the next other is biological improvement methods, in order to reduce or permanently control disease.

*1). Physical property improvement methods*

The physical improvement methods include such many methods as soil replacement method, humidity control method, compaction control method, totally closed method, mixing sand method, Geo-cell or Geo-grid reinforcement method, Geo-textile reinforcement method, soil nail wall reinforcement method, the pile foundation reinforcement method and so on[4~5].

a) Humidity control method includes two methods, pre-wetting method and maintaining stable water content method. In order to control the change of expansive soil water content, to maintains water content little evaporation and prevent rain water to permeate in the roadbed slope or the foundation soil during construction, some necessary measures should be adopted, for example, in the construction process reserving covering layer, before lining soaking the expansive soil and

controlling critical humidity and so on, sometimes using the plastic membrane or the asphalt to cover on expansive soil slope face.

b) Soil replacement method is to dig out the part expansive soil and enclosed with the un-expansive cohesive soil or coarse-grained soil. The replacement roadbed soil thickness should consider the soil water content rapid change zone's depth which is caused by rain. The road slope protection effect of soil replacement is closely related with such construction factors as the soil water content, dry unit weight, soil type, soil block size, laying soil thickness, rolling quality and so on. If the quality of replacement soil meets each technical specification requirement and some supporting measures are taken, this method is really effective to the roadbed stability of slope.

c) Totally closed method is also named cover method, is to fill in the expansive soil in the core of bank and encircle the dike body with the non-swelling earth. The thickness of cover soil layer should not be smaller than 1m, and the cover soil layer should be built tightly and totally close the expansive soil in order to restrict the temperature' change in the dike, namely waterproof and preservation moisture, but the side slope spot is often the construction roller compaction weak spot. If the closed soil layer and the embankment soil are constructed in layered filling and roller compaction together to reach the similar compactness, then the treatment effect will be better.

d) Compaction control method is to make the expansive soil's compaction to the request density. The method can reduce effectively the swell of expansive soil when it is in low dry density and high moisture content, but the high water content's expansive soil is very difficult to gain compaction, when soil body roller compaction is under the volume weight, the strength of it is smaller. Similarly, it cannot meet the engineering need. The compaction control method has low expense, but has certain sphere of application, generally it is suitable for the weak expansive soil ground. After expansive soil compaction its dry density will increase, moreover the cohesion and the angle of internal friction will also increase, ground bearing capacity will enhance.

e) Mixing sand method is to do the expansive soil improvement through adding non-expansive coarse sand filling materials and so on, the main role is to change the constitutive property, particle combination of the natural or disturbed expansive soil, and make the expansive soil to become the non-swelling earth or to reduce its swell-shrink characteristics. If mixed the sandy gravel in the lime to synthetically treat expansive soil embankment, the swell shrink characteristics of expansive soil is eliminated in chemistry, the grain composition is optimized in physics and its compaction character and bearing capacity is improved. Before applying mixing sand method, the reasonable mixture ratio of mixed material must be determined, and the construction technology feasibility must be demonstrated.

f) Geo-cell or Geo-grid reinforcement method is that through laying the level Geo-cell or Geo-grid in the expansive soil embankment of construction, to make the best of the friction force and the snap-in force between Geo-net and filling soil, to increase the shearing strength of the soil body, to restrict expansive soil' swell distortion, and finally to achieve the stable roadbed the goal. Because expansive soil embankment's weathering depth is generally in 2m, adding Get-net length in the soil is within limits slope surface certain scope, and the construction is convenient. It is a kind of method which is worth using and promoting.

*2). Chemistry improvement methods*

Using chemical methods to improve expansive soil, it includes the following methods[6].

a) Lime stabilization method is the most commonly-used improvement methods in engineering practice. The lime solidification appears as a result of the base exchanges, the cementation, interaction of clay particle and lime. The reinforcement mechanism of lime stabilization foundation soil is mainly because expansive soil contains major content dissociation aluminum silicon ions,

after mixed with lime, the expansive soil carry on the cation exchange action, aggregation, solidification like the cement effect, after the curing the plastic limit of the soil may be enhanced greatly and its plasticity index may be reduced great degree, finally the swell-shrink behavior of expansive soil is eliminated. The lime action on earth level relates to the lime dose, degree of grinding of soil and lime, mixing uniformity, age and so on.

b) Chemical improvement fluid method, through the microscopic analysis and the physical mechanics experiment to the soil mass improved by modifier, we know that Certain organic positive ion compound can change the charge distribution of the montmorillonite mineral crystal structure, weaken the negative electricity repulsion, and stop hydrone to enter the crystal layer and the granule, increase adsorption and the cementation between the loose particle, keep down the swell-shrink distortion of the expansive soil. After improvement the expansive soil's shearing strength parameter also has comparatively large degree enhancement. Simultaneously, the organic chemistry grouting material is one kind of non-toxic, tasteless, odourless liquid. After chemistry solution is firmly adsorbed by earth, it will not drained and not create the environment pollution.

c) Fly ash, cement, lime mixed modification method. The fly ash, cement, lime mixed modification method is one kind of quite ideal improvement method, the proportion of additives should be decided according to the improvement earth’s request. In this kind of mixed chemical additive, the lime obviously reduces the earth expansion rate and the cement increases the earth the strength characteristic. After fly ash and the quicklime mixed, under certain moisture content condition they has a series of hydration reaction, and produce such compounds which is water-fast stable crystallization resultant as hydrated Calcium silicate, hydrated Calcium aluminate, as well as hydrated Calcium ferrite and so on, these compounds may harden gradually in the air and water, and play the reinforcement role to expansive soil so as to limit its expansibility.

d) Mixing cement improvement method, The cement chemical composition is mainly Tricalcium silicate, Dicalcium silicate, Tricalcium aluminate and so on, after these mineral of clinker in the cement meeting the water, they have the chemical reaction, hydrated reaction, and produce such main hydrated products as Calcium silicate hydrate, Calcium hydroxide, hydrated Calcium aluminate, hydrated Calcium ferrite, hydrated Calcium sulphoaluminate and so on.. When the cement content increases, the improvement earth's expansion ratio reduces, the reducing reason is similar to the lime, but the cement will have the bigger condensation which transforms the clay into the even more granular earth, thus cause the expansion rate to decrease, but lime is more effective than cement with aspect to reducing the expansion rate.

e) Mixing slag composites improvement method. Such composites as expansive soil, slag, cement, lime, sand and so on is called “the slag composites earth” which is put into mortar as slope protection material. The expansive soil improved by slag composite may basically lose the expansibility. The slag composites earth’s strength changes with the age, the strength of age one year is 3-8 times of age 28d, moreover the slag composites earth have good property to resist swelling with wet and shrinkage with dry[6].

f) The pressure injection grouting improvement method is to apply the lime white or the cement mortar injection scheme to reinforce expansive soil slope, under the high pressure the lime white enters the earth from lateral and longitudinal direction of grouting hole, along the soil body crevasse or the new fracture face caused by grouting precipitate and form many lime arteries or the lime thin layer. Using jet grouting, directional jet grouting or sprinkler irrigation, the grout under high pressure form not only the pulpous state structure, but also may form the lime or soil cement coagulation bodies which have certain structure and shape, or forms the boards and piles composite anti-slide body which can adapt to the bigger distortion.

*3).* Biological *improvement methods*

Physics-chemistry improvement reinforcement method is applying both physical and chemical effect to improve the expansive soil. It is refers to according to the certain proportion mixing expansive soil with lime, cement, fly ash, slag as well as the mixture of them, and adding ration active catalyst to promote modifier and earth to react each other, and finally achieving the goal to stabilize expansive soil.

The biological improvement method is to make use of the biology surface active agent to attach on the clay mineral surface, so it can reduce the liquid level tension, cause the clay mineral surface hydrophobization, break down mineral surface hydration shell or cause it to become thin, thereby cause the intergranular cohesive force to increase, enhance the earth shearing strength, and finally reduce the swell-shrink characteristic of expansive soil.

## Summary

In expansive soil area, the roadbed disease such as slope stability failure, roadbed settlement, mud pumping, ballast bag and so on is elaborated emphatically. Expansive soil treatment and reinforcement methods as physical improvement, chemistry improvement, biological improvement are summarized and proposed. But on the part of the expansive soil treatment technology, many further deep researches need to be done, aiming at the key question of expansive soil embankment fill, based on preserving moisture and anti-seepage, carry on the expansive soil embankment filling technology deep study. In order to determined the best mixed dosing and effective construction technology of expansive soil distribution area. The expansion and shrinkage mechanism of expansive soil has been studied from such aspects as physical-chemistry-mechanics effect, material composition and external influencing factors and so on.

## Acknowledgements

The research work of this paper is supported by Natural Science Fund Project of Hebei University (No.2009-151), and The Office of Housing and Urban-Rural Construction Fund Project of Hebei Province (No. 2009-279 ,No.2010-245), and the Hebei Education Department Fund Project (No. 2010111)

## References

[1] Shiwen Liao, The expansive soil and railway engineering. Beijing: Chinese Railroad Publishing House, 1984.

[2] *FENG Zhen* ,On the Road Construction and Environmental Protection. WECT2010, 2010.6,1748~1751

[3] Guolin Yang, The test study on engineering characteristics of Tan-Shao freeway expansive soils. Journal of Railway Science and Engineering, Vol 2, pp.62-67, 2005(1).

[4] Jianpu Zhou, Research into compaction expansive clay distortion curve characteristic. Highway, pp.25-29, 2003(1).

[5] Xianmin Li, Study on Treatment Theory and Technique for Expansive Soil Geological Disasters, RSETE, 2011.6, 802~806.

[6] Tuode Li, Improvement engineering properties of expansive soil with slag composite materials. Chinese Journal of Geotechnical Engineering, Vol 15, pp.11-13, 1993(5). 806

*Applied Mechanics and Materials Vols. 580-583 (2014) pp 474-480*
*© (2014) Trans Tech Publications, Switzerland*
*doi:10.4028/www.scientific.net/AMM.580-583.474*

# Simplified Method for Estimating the Inner Support and Internal Force through Stand Column Uplift of Foundation Pit in Soft Soil

Yan Liu [1, a], Junyan Liu [1,b], Tao Liu[2,c]

[1]School of Civil Engineering and Architecture, University of Jinan, Jinan ,Shandong

[2] College of Enviromental Science and Engineering,Ocean University of China,Qingdao,Shandong
[a]liuyan322@163.com, [b]liujunyan@vip.sina.com, [c] ltmilan@163.com

**Keywords:** Foundation pit in Soft Soil, Stand column bulge, Additional bending moment.

**Abstract.** In the excavation process of Foundation Pit in Soft Soil area, it will cause the large uplift of stand column, and may cause the instability and failure of foundation pit in case of being serious; but the additional internal force of support system caused by the uplift and sinking of stand column currently has no practical calculation model in the foundation pit design. This article discusses the reason and mechanism for uplift of stand column in the foundation pit, proposes the simplified calculation method of estimating the additional bending moment of inner support through uplift of stand column in allusion to two main influence factors of bottom heave and vertical load caused by the excavation of foundation pit, inversely calculates the permissible additional bending moment of inner support based on this, verifies by combining the monitoring data for uplift of stand column in the actual project, and finally, further proposes the project measures corresponding to the uplift of stand column, hoping to provide beneficial reference for the similar project.

## Introduction

In recent years, our rail transit construction has been rapidly developed, the safety and stability problem of foundation pit of metro station is also increasingly concerned by people, and the deformation size and change rule of foundation pit is not only related to the safety of foundation pit, but also to the safety of surrounding building and underground pipeline. The foundation pit of many metro stations in the soft soil is used inner structural support system; and in the foundation pit project design and construction, the overall stability of foundation pit project, horizontal deformation of retaining structure and internal force are calculated and studied. But there are few studies on the vertical displacement of stand column pile in the foundation pit [1]; and if the vertical displacement amplitude of stand column is too big, it may enlarge the lateral displacement of retaining structure of foundation pit, intensify the uplift of bottom soil of foundation pit, and increase the vertical displacement of stand column, thus causing the vicious cycle, causing the adverse effect to the environmental protection around, and then causing the project accident. This article discusses the reason and mechanism for uplift of stand column in the foundation pit, analyzes the additional bending moment produced by vertical displacement and influence for overall stability of foundation pit, proposes the method and standard of calculating the permissible vertical displacement of stand column, and finally verifies by combining the some project cases.

## Reason and Mechanism for Vertical Displacement of Stand Column

In all factors impacting on the vertical displacement of stand column, the bottom heave and vertical load of foundation pit are main two aspects [2]. The direct action of earth excavation in the foundation pit causes the uplift and deformation of soil layer below the excavation face, and the bottom heave will cause the floating of stand column pile; and the vertical load mainly causes the sinking of stand column pile. Sometimes, the design considers the effect of vertical load, but the stand column pile still has displacement upward, the reason is that the condition of foundation pit during the construction is relatively complicated and the actual variability of used vertical load value and condition of

geological soil layer is relatively big. When the foundation pit is excavated, the stress of bottom is released, the soil in the pit is rebounded, the upper part of pile body is born the positive frictional resistance upward, and the stand column pile is lifted; and the deep soil of foundation pit prevented the lifting of pile, and produces the frictional resistance downward to the pile to prevent the lifting of pile. The lifting of pile will prompt the stress release of soil of pile tip, the soil of pile tip will also produce the uplift, the pile will also be lifted, but the continuous loading of upper structure and construction load with big variability will cause the sinking of stand column, therefore, it can be seen that the mechanism for vertical displacement of stand column is relatively complicated. Therefore, it is relatively difficult to calculate and forecast whether the stand column pile is lifted or sunk finally through data, and it is more difficult to calculate the final displacement quantitatively, which can be controlled and adjusted through monitoring in real time only.

## Harm for Vertical Displacement of Stand Column

If the vertical displacement amplitude of stand column is too big, it may enlarge the lateral displacement of retaining structure of foundation pit, intensify the uplift of bottom soil of foundation pit, and increase the vertical displacement of stand column, thus causing the vicious cycle, causing the adverse effect to the environmental protection around (which is shown in the Figure 1). The nonuniformity of vertical displacement of stand column will cause the differential displacement of all points of support system on the vertical plane and plane, and finally cause the support to produce bigger secondary stress (this part of stress is not considered generally in the support structure design), and if there is bigger differential settlement among the stand columns or between the stand column and underground diaphragm wall, it will cause the eccentric compression of support system and even instability, and then cause the project accident [3].

The change for shaft force value obtained before and after the stand column has vertical displacement is not big, the shaft force in most of the bars is increasing trend, but the absolute amount increased is not big. But because the additional bending moment of support caused by the vertical displacement of stand column is relatively big, the bending moment is even several times before the stand column has displacement. For the bending component, it should check and calculate its stable condition in the plane of bending moment effect and outside the same respectively according to the code for design of steel structures; for the component like 609 steel pipe of which the second moment of area of two directions is same, this problem is very serious; but for the I-steel and other components, it should pay special attention, to prevent the occurrence of local instability; for the inclined strut close to the retaining wall, it should pay special attention; and for the component of which the change of bending moment is relatively big, it should check and calculate separately, to prevent its instability, and impacting on the normal work of whole support system.

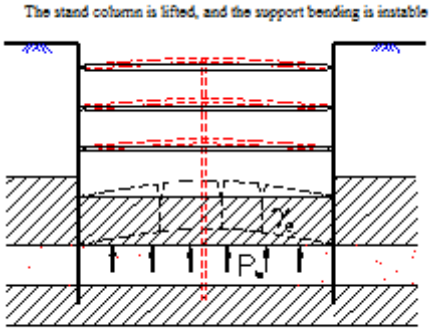


Fig.1 Sketch for retaining instability caused by uplift of stand column

## Discussion for Additional Bending Moment and Permissible Displacement

**Calculation method of additional bending moment.** Due to the reason of analysis above and effect of confined water head pressure of bottom, it is easy to produce the floating phenomenon of stand column pile, and then drive the support to float, in this way, it will produce the additional bending moment to support. The difference deflection of support will change the stress state of support, which is very easy to cause the instability and failure of support. For the reinforced concrete support, the floated and deformed additional bending moment can use the calculation model shown in Fig.2, the differential deformation of support and underground diaphragm wall is equivalent to the beam fixed at two ends, and the support base will produce the vertical deflection. It can obtain the bending moment produced by deflection according to the method of structural mechanics, shown in Fig.2.

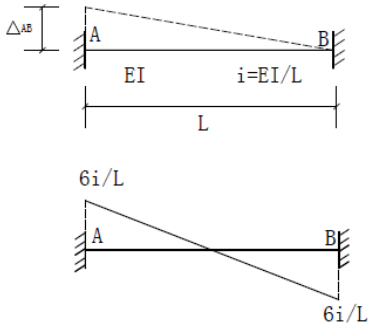


Fig.2 Calculation model for additional bending moment of support with differential settlement

Maximum bending moment of supported after deflection

$$M_{\max} = 6EI\Delta_{AB} / L^2 \quad (1)$$

Except the additional bending moment produced by floating the stand column, the foundation pit support is compression member, and the additional bending moment will also be produced due to the pressure effect, which can be obtained by the following formula

$$M_N = N \cdot \Delta_{AB} \quad (2)$$

In the formula, N——Support shaft force;

$\Delta_{AB}$——Support deflection value

The maximum additional bending moment produced by uplift of stand column is in the middle part of support and at endpoints of two ends, of which the value is

$$M_{总} = M_{\max} + M_N = \frac{6EI\Delta_{AB}}{L^2} + N \cdot \Delta_{AB} \quad (3)$$

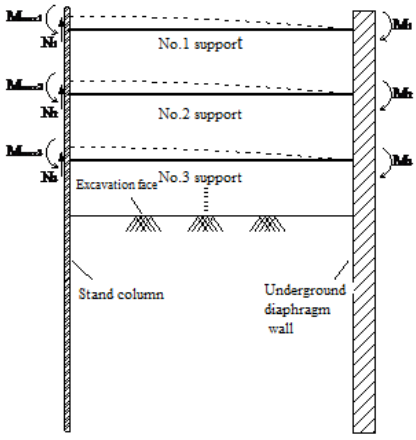


Fig.3 Calculation chart for floating force of stand column

The floating force acted on the stand column can be calculated through $M_{\max}$

The force acted on the stand column according to the principle of theoretical mechanics is

$$N_{总}=\sum_{i=1}^{n} N_i = \sum_{i=1}^{n} \frac{M_{\max i}}{L} \quad (4)$$

In the formula, n——floating support number.

**Ultimate bending moment of support and permissible differential settlement.** The calculation formula of ultimate bending moment of concrete support is as follows

$$M_u = f_y b h_0^2 \rho (1-0.5\rho \frac{f_y}{f_{cm}}) \quad (5)$$

In the formula: $f_y$—— Bending compressive strength of steel bar;

b—— Width of section;

$h_o$—— Effective height of section;

ρ ——Reinforcement ratio of longitudinal tensile reinforcement;

$f_{cm}$ ——Bending compressive strength of concrete.

Since the bending moment caused by eccentricity is smaller than the bending moment caused by lifting stand column, it can ignore the bending moment caused by eccentricity conservatively, and the maximum permissible differential settlement shall be inversely calculate with ultimate bending moment.

$$\Delta_{AB} = \frac{M_u \times L^2}{6EI} \quad (6)$$

**Estimation for vertical displacement of stand column.** Assuming that the underground diaphragm wall is not sunk and controlled through the differential settlement of each support, thus, the permissible lifting amount of stand column of each support is equal to $\Delta_{AB}$ + lifting amount of stand column and underground wall settlement when the support is completed. The minimum in the permissible lifting amount of each support is taken as the limit value of uplift of stand column.

## Project Case

Some foundation pit has length of 174.08m at the east side and 62.53m at the west side, and has width of 22.30m; and the excavation depth H of standard section is 38m (wherein the end well is 41.2m), and the retaining wall is underground diaphragm wall of which the thickness is 1200mm, of which the depth is 65m.

Since the depth of foundation pit is deep and the risk is big, all foundation pits use 9 concrete supports during the construction, and the middle part of foundation pit is equipped with bearing support of stand column pile. The stand column pile uses the cast-in-place pile of which the pile diameter is 1200mm, of which the depth is 75m. Since the depth of foundation pit is deep and the risk is big, the construction process is monitored in all directions; and in addition, the upper part has much unloading and the substratum has confined water, so the uplift of strand column becomes a main monitoring content, which should pay close attention. Up to September 15, 2006, the lifting amount and differential settlement of each support is shown in Table 1 according to the monitoring data.

Table 1 Lifting amount and differential settlement of each support

| Support No. | Lifting Amount of Support/mm | Differential Settlement/mm | |
|---|---|---|---|
| | | Left Wall | Right Wall |
| No.3 | 24.92 | 20.06 | 16.76 |
| No.4 | 23.39 | 18.44 | 15.22 |
| No.5 | 19.85 | 14.88 | 11.07 |
| No.6 | 17.92 | 12.93 | 9.74 |
| No.7 | 8.4 | 4.3 | 2.1 |
| No.8 | 1.5 | -4.03 | -7.25 |
| No.9 | -2.7 | -7.55 | -10.80 |

For this project, the support uses the reinforced concrete support,E= $3.25\times10^{10} N/m^2$, $I=\frac{bh^3}{12}$, L=22.3/2=11.15m, $\Delta_{AB}$ is shown in the Table 1; and the additional bending moment produce by floating the stand column of foundation pit is calculated according to formula (1), shown in the Table 2. The ultimate bending moment of concrete support calculated by formula (4) and reinforcement of reinforced concrete support are shown in the Table 3: the interface size of each support and permissible differential settlement value calculate by formula (5) are shown in the Table 4. The limit value of uplift of stand column calculated according to the permissible lifting amount of stand column is equal to $\Delta_{AB}$ + lifting amount of stand column and underground wall settlement when the support is completed. Thus, it can obtain that the limit value of uplift of stand column is the minimum of each permissible lifting amount, 42.251mm; and the limit value of differential settlement is: 42.251-5.41 =36.841mm. According to the principle above and calculation process, the bending moment and floating forced of each support can be obtained when the lifting amount of stand column is 30mm, shown in the Table 6. The measured duration curve of stand column lifting is shown in Fig.4 and Fig.5.

It can be known through the calculation that, in this case, the uplift of stand column does not exceed the maximum permissible uplift amount, but has been relatively close, which should be concerned and taken the corresponding project measures.

Table 2 Additional bending moment of support for floating stand column

| Support No. | Lifting Amount/mm | Differential Settlement/mm | | $M_{max}$ /kN.m | $M_N$ /kN.m | $M_T$ /kN.m |
|---|---|---|---|---|---|---|
| | | Left Wall | Right Wall | | | |
| No.3 | 24.92 | 20.06 | 16.76 | 1 340 | 46.311 | 1 380 |
| No.4 | 23.39 | 18.44 | 15.22 | 1 230 | 62.483 | 1 290 |
| No.5 | 19.85 | 14.88 | 11.07 | 2 300 | 52.171 | 2 350 |
| No.6 | 17.92 | 12.93 | 9.74 | 2 600 | 83.164 | 2 680 |
| No.7 | 8.4 | 4.3 | 2.1 | 890 | 51.390 | 940 |
| No.8 | 1.5 | -4.03 | -7.25 | 1 500 | 90.370 | 1 590 |
| No.9 | -2.7 | -7.55 | -10.80 | 1 690 | 60.237 | 1 750 |

Table 3 Ultimate bending moment of each concrete support

| Support No. | Section Size/m | Ultimate Bending Moment /kN•m |
|---|---|---|
| No.4 | 1.0×0.8 | 4 348.840 1 |
| No.5 | 1.2×1.0 | 5 760.072 0 |
| No.6 | 1.2×1.1 | 6 632.848 9 |
| No.7 | 1.2×1.1 | 7 373.298 5 |
| No.8 | 1.2×1.1 | 8 143.536 9 |
| No.9 | 1.2×1.0 | 2 104.577 2 |

Table 4 Permissible differential settlement of each support

| Support No. | Ultimate Bending Moment/kNm | E/kN/m2 | Width/m | Height/m | I/m4 | Permissible Differential Settlement ΔAB(mm) |
|---|---|---|---|---|---|---|
| No.4 | 2 485.052 | 3.25E+07 | 1.0 | 0.8 | 0.042 67 | 64.982 |
| No.5 | 3 200.040 | 3.25E+07 | 1.2 | 1.0 | 0.100 0 | 36.723 |
| No.6 | 3 834.017 | 3.25E+07 | 1.2 | 1.1 | 0.133 1 | 31.771 |
| No.7 | 4 119.161 | 3.25E+07 | 1.2 | 1.1 | 0.133 1 | 35.318 |
| No.8 | 4 402.909 | 3.25E+07 | 1.2 | 1.0 | 0.100 0 | 51.931 |
| No.9 | 1 223.59 | 3.25E+07 | 1.2 | 1.0 | 0.100 0 | 13.417 |

Table 5 Permissible lifting amount of each stand column

| Support No. | Permissible differential settlement/ΔABmm | Minimum Land Settlement/mm | Lifting Amount of Stand Column when the Support is Completed/mm | Permissible Lifting Amount/mm |
|---|---|---|---|---|
| No.4 | 64.982 | 5.41 | 1.53 | 71.922 |
| No.5 | 36.723 | 5.41 | 5.07 | 47.203 |
| No.6 | 31.771 | 5.41 | 7.00 | 42.251 |
| No.7 | 35.318 | 5.41 | 16.52 | 47.728 |
| No.8 | 51.931 | 5.41 | 23.42 | 80.761 |
| No.9 | 13.417 | 5.41 | 27.62 | 46.447 |

Table 6 Bending moment of each support when the lifting amount of stand column is 30mm

| Support No. | Lifting Amount of Support/mm | Maximum Differential Settlement/mm | $N_i$ | $N_T$ | $M_T$ | Ultimate Bending Moment/kN•m | Play Ratio/% |
|---|---|---|---|---|---|---|---|
| No.4 | 28.47 | 23.06 | 144.430 | 1 001.87 | 1 610.399 | 4 348.840 1 | 37.03 |
| No.5 | 24.93 | 19.52 | 279.148 | 1 001.87 | 3 126.459 | 5 760.072 0 | 54.27 |
| No.6 | 23.00 | 17.59 | 335.737 | 1 001.87 | 3 760.263 | 6 632.848 9 | 56.69 |
| No.7 | 13.48 | 8.37 | 162.079 | 1 001.87 | 1 815.294 | 7 373.298 5 | 24.63 |
| No.8 | 6.58 | 1.17 | 131.859 | 1 001.87 | 344.090 | 8 143.536 9 | 4.22 |
| No.9 | 2.38 | -3.03 | 48.619 | 1 001.87 | 544.532 | 2 104.577 2 | 25.86 |

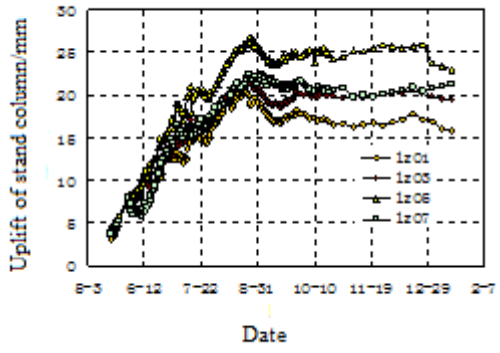


Fig.4 Changing curve for measured value

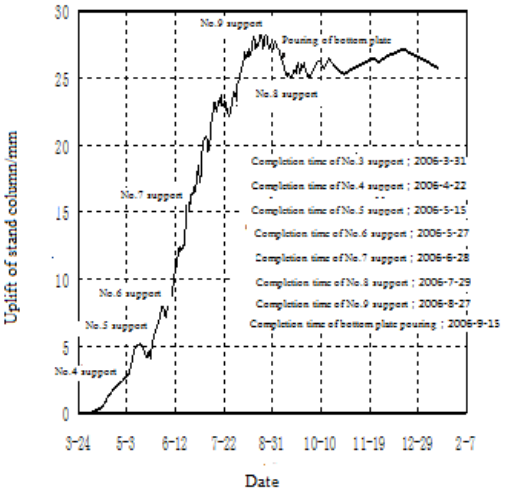


Fig.5 Curve for uplift of stand column Z04 with time

**Construction measurement of reducing deformation of stand column**

In the normal state, the vertical deformation of stand column can be effectively controlled by taking measures from the following aspects according to the reason and mechanism that the stand column produces the vertical displacement:

- For the bottom heave has big influence to the stand column lifting, the reduction of bottom heave can reduce such influence.
- The stand column and retaining structure of underground diaphragm wall shall be subjected to the settlement estimation according to the construction state, on this basis, coordinating the excavation of foundation pit or applying the load on the stand column, so that the differential settlement among the stand column, underground diaphragm wall and other retaining walls meets the requirement of structural design.
- Form the entity with big rigidity between the stand column and support and among the support, underground diaphragm wall and other retaining structure, and coordinate the non-uniform deformation jointly.

- Consider reducing the settlement through enlarging the bearing capacity of stand column pile.
- The frictional resistance of pile soil interface will have direct influence to the stand column pile lifting, therefore, it can reduce the influence of the excavation of foundation pit to the stand column pile lifting through reducing the frictional resistance above the stand column pile.
- Strengthen the settlement observation of stand column, support, underground diaphragm wall and others, and feed back to guide the information construction.
- Displacement control of stand column caused by temperature change and other factors.

## Conclusion

With deeper and deeper depth of foundation pit, the uplift of stand column in the foundation pit becomes a problem which is not ignored. It occasionally happens the accident of foundation pit brought that the retaining structure of foundation pit is damaged due to the uplift of stand column. This article obtains the following conclusion through analyzing the harm of uplift of stand column to the foundation pit project:

- The mechanism for uplift of stand column is relatively complicate. The main influence factors have bottom rebound, confined water and upper load. The soil rebound and confined water cause the stand column to uplift upward, and the continuous load of upper structure and construction load with big variability will cause the settlement of stand column, therefore, at current, it is very difficult to calculate the final displacement of stand column quantitatively, and the best method is still depended on the field monitoring and real-time feedback to guide the construction.
- Analyze the additional bending moment of support caused by the uplift of stand column, and propose the calculation formula of calculating the permissible deflection of stand column according to the ultimate bending moment of support.
- Strengthen the statistical analysis of monitoring data of uplift of stand column, and summarize the change rule and calculation method appropriate for the vertical displacement of stand column of Foundation Pit in Soft Soil from mass data.

## Acknowledgements

The author would like to thank for the support from the Jinan science and technology plan projects(NO: 201201142) and the national natural science fund projects(NO: 51208228) of China.

## References

[1] Liu Jianhang, Hou Xueyuan. Foundation pit project manual [M]. Beijing: China Architecture Press, 1997. (In Chinese)

[2] Mao Jinping, Xu Wei, Lv Peng. Analysis for vertical displacement of stand column of deep foundation pit [J]. Building technology, Volume 35, No.5 2004, P342-343. (In Chinese)

[3] Liu Guobin, Hou Xueyuan. Residual stress method for bulge and deformation of Foundation Pit in Soft Soil [J]. Underground Engineering and Tunnels, No.2 1996, P1-7. (In Chinese)

*Applied Mechanics and Materials Vols. 580-583 (2014) pp 481-485*
*© (2014) Trans Tech Publications, Switzerland*
*doi:10.4028/www.scientific.net/AMM.580-583.481*

# Slope Early Warning System Design and Preliminary Practice

Fei Xu[1, a], Wenxiong Xu[2,b] and Ke Wang[1,c]

[1]Hainan Highway Survey and Design Institute, Haikou, Hainan, 570206, China

[2]School of traffic and transportation engineering, CSUST, Changsha, 410114, China

[a]xfawy@hhu.edu.cn, [b]21141940@qq.com, [b]496258148@qq.com

**Keywords:** Slope Stability, Slope Early Warning System, Early Warning Criterion, Warning Thresholds.

**Abstract.** Early warning thresholds for slope instability were discussed in this study by means of rheological tests and field measurements due to availability and effectiveness of the data. Five warning levels were specified to take proper measures in different emergent cases. The left bank slope of Jinping I hydropower station was studied as an instance to implement the strategies introduced in the study. The surface displacement thresholds were obtained by analyzing long-term observed displacements (the former three warning levels) and the rheological tests on the rock mass (the last two levels). The results gave out that the thresholds of surface displacement rate for different warning levels were 0.30mm/d, 1.15mm/d, 3.00mm/d and 5.00mm/d. These results could be potential references for other projects.

## Introduction

The slope warning system was put forward to manage the safety of these slopes. The slope early warning system was consisted of several parts in this study: the data acquiring modulus, the data processing modulus, the forecasting modulus, the early warning modulus. The first three parts were not included hereby despite the need for further research.

Research on slope forecast and monitoring alarm for landslide disaster had been a worldwide challenge. The US Geological Survey and US Weather Bureau had collaborated to establish the real-time regional landslide warning system by means of long-term statistics of relationship between landslide occurrence and the precipitation[1]. In China, research on geologic hazard system survey and monitoring warning system for slopes had been entirely started round the Three Gorges Reservoir Area since the late 1990s, and had obtained some valuable achievements[2]. The top key issue on forecast and warning of slopes to prevent instability hazards was the analysis and identification of critical warning criterion[3]. In the slope warning stage, the warning thresholds for the warning criteria were often the top key issues accounting for the accuracy and reliability of the slope warning system. So far, researchers had been doing intensively on surface features and the inducing factors of slope failures from different aspects, like the deformation capacity, crack of slopes, precipitation, seism, underground water and so on[4] although research on this issue was under exploratory stage.

The work hereby was closely related to the left bank slope of Jinping I hydropower station. It was aimed to develop a reliable approach to specify the thresholds of the slope early warning criteria with multiple warning levels. It first presented the guide lines for selection of the slope warning criteria. And then gave the framework of five level warning for the safety of high-steep slopes. The surface displacement and the precipitation of the area were specified as the two key warning indicators for the slope safety warning. Afterwards, the threshold values of the warning criteria were discussed. The work could provide references for slopes with similar conditions.

## Slope Early Warning System Design

The purpose of slope early warning was to warn people before the potential slope hazards and so as to keep them and the properties from suffering. It can be implemented through the slope early warning system. As described above, slope early warning system was consisted of four stages: data collection, data processing, forecasting and early warning, which was shown in Fig.1.

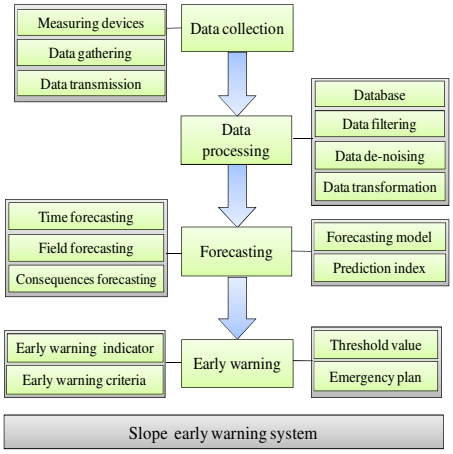


Fig1. The composition of slope early warning system

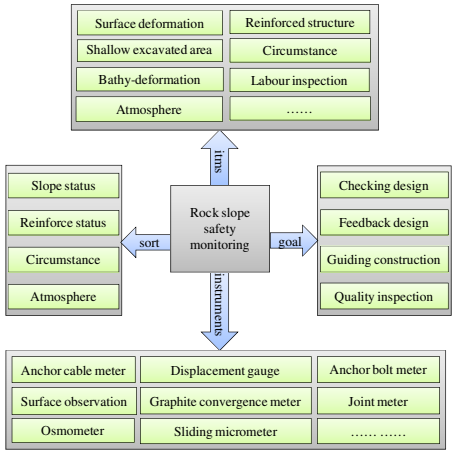


Fig.2 Monitoring design of the rock slope

Data collection was the beginning of slope early warning. It involved data acquiring instruments and measuring technologies. Also, some data gathering devices may be needed in this stage to obtain sufficient data. Then data transmission technologies need be applied to transmit data gathered by measure devices to the data collection devices which could be recognized by working staffs. The stage of data processing was the construction of data base and execution of data pre-processing for the slope safety analysis downwards. Data base was firstly needed to manage the huge amount of data collected in the stage of data collection. Afterwards, some pre-processing technologies were needed to reduce the influences of the random errors or the potential measuring faults. The data collected by the apparatus could be affected by many factors, such as the temperature, human activities and other kinds of uncertain causes, thus data filtering should be executed to remove the "fake" data component collected during the process of data collection. Also, there may be noise in the initial data collected and in this way "data de-noising" was needed to remove the affection of noise. Meanwhile, the process of data transformation was often needed to translate data into other forms. Sometimes, the accumulative displacement was needed, and in other cases the deformation rate may be the focus.

As to the "forecasting" stage, it had plenty of usage since it can tell people in advance the event of slope instabilities about the occurring time, location and potential consequences to human beings and their properties. Time forecasting was to tell the time of slope movement before its occurrence with some forecasting techniques like the forecasting model and the prediction index. Field forecasting was to broadcast the location where slope instabilities would happen or the region that would be affected by the slope instabilities. In this way, human activities within the region would be avoided. Massive of works had been done on the movement of landslide for forecasting the occurring time. Mainly, the forecasting model and prediction index were the two key issues for the forecasting of landslide events. With the proper forecasting model, the monitoring data collected can be organized in a rational way in order to obtain the expected results to pre-tell the occurrence of slope hazard, like the landslide and rock fall.

Early warning stage was designed for proper management of slope instability events. It aimed to not only tell people the occurrence of slope instabilities, but also to provide or propose pre-designed policies and measures for disaster prevention and mitigation when these disasters happened. Also, it can design different warning levels and thus can give different suggestions in variant emergent situations.

## Warning Criteria and the Thresholds

The first step in the early warning stage was to identify the early warning criteria that could be used as the standard to label the stability status of the slope. The process of identifying the warning criteria may be involved many aspects of the slope conditions. The research aim on slope warning criteria is to identify the threshold values for early warning indexes on different warning levels. It was difficult

and complex for identification of slope warning criteria and the thresholds since that the potential evolutionary process of rock slope was unforeseen and difficult to reveal desperately so far. That's to say, the principles for slope evolution were uncovered implicitly at present. Many works[5] had contributed differently on the warning criteria of landslide performance for forecasting landslide event. The works showed that it would be unpractical at present to completely discover the rules of slope evolution especially for those high-steep slopes with complex conditions. These effects were the external feedback of the potential evolutionary process of high-steep slopes. Slope displacement was the most common one among the entire monitoring index and thus it was used mostly often for analysis of slope stability. In this way, slope displacement was adopted as the main indicator to execute early warning of high-steep slopes.

**The Five-level Early Warning Method.** In the five-level early warning method, slope early warning was designed with five warning levels. Each level was represented as a basic status of slope stability. The relationship of the five-level warning design with the stage of slope stability evaluation and the warning signals were shown paralleled in Table 1. To this end, the five-level early warning design could be accord with the results of slope stability evaluation and can be represented easily with a suitable warning signal which could be recognized by people without academic background. It should be stated that the five-level warning design concerned nothing with the form of the warning criteria. It was proposed for each warning criterion with five ranges of values and thus there were four thresholds to be specified as shown in Table 1. The thresholds $a_i (i = 1, \cdots 4)$ denoted the critical value of a criterion which indicated that the slope stability status would involve to the $i$ th warning level.

Table1 The five-level early warning design for early warning

| Stability Status | Highly Stable | Stable | Average Stable | Unstable | Extremely Unstable |
|---|---|---|---|---|---|
| Warning Level | V | IV | III | II | I |
| Warning Signal | Green | Blue | Yellow | Orange | Red |
| Thresholds | $[0,a_4]$ | $[a_4,a_3]$ | $[a_3,a_2]$ | $[a_2,a_1]$ | $[a_1,\infty]$ |

The process of slope early warning could be carried out with the method introduced in this study in the following ways. Let denote the present value of the warning criterion and $s_i^*$ be the threshold value corresponding to the $i$ th warning level. If satisfied

$$s_{i-1}^* (s_{i+1}^* < s_i^*, i = 4,3,2) or \quad s > s_i^* \quad (i = 1) \quad or \quad 0 \le s < s_{i-1}^* \quad (i = 5). \tag{1}$$

Then, it indicated that the slope system would execute the ith warning level. The output of Equation (1) indicated that the larger value of the criterion, the more unstable of the slope. These were suitable for most criteria, for example the accumulative displacement, the strain rate level of the slope material and the precipitation of the region. While, there may be the criteria with the opposite effect of their value, like the reinforced strength and the strength of the rock mass. It could be transferred easily to the other kind with the normalization method for these kinds of criteria (the larger of the value the safer of the system).

**Slope Introduction.** Jinping I hydropower station located in Yalong River and situated in Yanyuan and Mulu of Liangshan District, Sichuan Province, southwest of China. The concrete dam was an arch dam with double curvature and was the top highest arch dam worldwide so far with the height 305m. In the dam site, the mountain was tremendous with high steep valleys and bareness basement. It was a typical V-like deep valley with relative height difference more than 1000m. The tendency of rock formation was general in accord with the direction of the river. The left bank slope was escarpment slope with none large profound gully. The main rock formations exposed were marble and green schist. The thickness of marble was about 600m and lay into valley slope under the height of 1820m and the river bed. Many weak geological structure surfaces were exposed in the rock slope, such as the faults, the dike X and deep seated crack. Several kinds of structural planes crossed mutually and there were several potential slipping blocks and sliding patterns [6].

**Slope Monitoring Design.** The safety monitoring system of the rock slope was installed to check the design and guide the construction activities. The monitoring of the excavated slope of the left abutment was aimed to firstly check the slope designs and provide data for feedback analysis, and

secondly guide the construction and confine its quality. Constructing supports would be strengthened according to the monitoring results to safeguard the project. Meanwhile, the data obtained by the monitoring system can reveal the comprehensive information related to the deformation and stability of the slope which was affected assembly by the external triggering factors and the geological factors. The composition of the monitoring system was shown in Fig.2.

**Thresholds of Surface Displacement**. The evolution process of rock slope from initial steady status to its failure divided into five stages from the view of creep theory[7]. The goal hereto was to identify the threshold values for each of the five warning levels shown in table 1. Firstly, the statistical analysis on the monitoring information of the slope was carried out to obtain the threshold values for the warning level IV in the term of an interval. Secondly, the rheological experiments were taken to reveal the thresholds for warning level III, II and I, i.e. the thresholds. The procedure was given as follows.

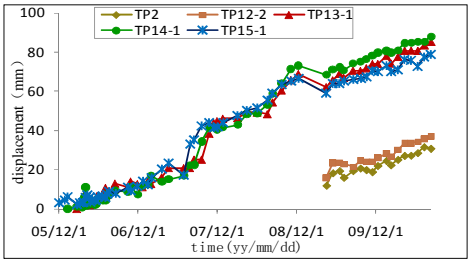


Fig.3 Monitoring results of slope surface displacement

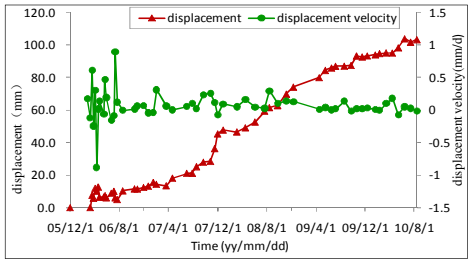


Fig.4 Deformation curves of monitoring point TP14-1

The displacements obtained from five monitoring points were shown in Fig.3. It can be noticed that the rules and trends were mainly the same for the five different monitoring results. Thus statistical analysis could be taken to analyze the monitoring information for each typical monitoring point. Here we chose, TP14-1, the one with the largest accumulative displacement. The deformation features of monitored point TP14-1 were shown in Fig.4 with the accumulative displacement and the displacement rate. As to obtain the thresholds, we firstly rejected the noisy data by "3σ-rule" in the deformation series which were shown at the beginning of the curves, and then selected the displacement rate as the warning criterion. In this way, the problem was settled to identify the threshold values of different warning levels.

It can be found from the figures that the maximum displacement rate of TP14-1 was 0.30mm/d. And the mean and the variance of the displacement rate were 0.07 and 0.22 respectively. Two different formulas were set to calculate the thresholds of warning level IV.

$$a_3 = \max\left\{V_1, V_2\right\}(V_1 = V_{\max} + 2\sigma, V_2 = \overline{V} + 5\sigma)\,. \tag{2}$$

Where, $V_{\max}$ denoted the maximum displacement rate; $\overline{V}$ and $\sigma$ represented the mean and variance of the displacement rate, respectively. The threshold was specified as the maximum value of historical data of the monitoring displacement rate. To this end, the interval $[a_4, a_3]$ was obtained as $[0.30, 1.15]$.

As for the interval thresholds $[a_2, a_1]$, other method must be applied to identify the values as we could not foresee the instability process of the slope. In this study, the rheological experiment was tried to reveal the whole deformation features of the rock mass of the slope. We carried out the whole rheological test in the rock automatic tri-axial rheological servo apparatus to obtain the features during the whole process of the rock mass from loading until its failure. The lateral strain and strain rate were recorded during the whole test. In this way, the deformation rate could be obtained as the reference for determination of threshold values.

The results of lateral accelerating rheological and rheological rate of marble and greenschist were shown in Fig.5 and Fig.6. It can be drawn from the figures that the lateral strain of the rock mass had evolved the stage of initial rheology, steady rheology and boosting rheology before its failure. Also it could be noted that the rheological rate of deformation at the beginning of boosting stage was about

1.0mm/d. In the primary period of boosting rheology it was between 1.0mm/d to 2.5mm/d, while in the later period it reached about 2.5mm/d to 5.0mm/d, and over 5.0mm/d in the failure period. Encouraged by the results and by reference to the creep theory, the threshold values of the warning level II were specified as 2.5mm/d and 5.0mm/d. Thus we obtained $a_2$ = 2.5mm/d , $a_1$ = 5.00mm/d . Therefore the thresholds $a_4, a_3, a_2, a_1$ have all been obtained.

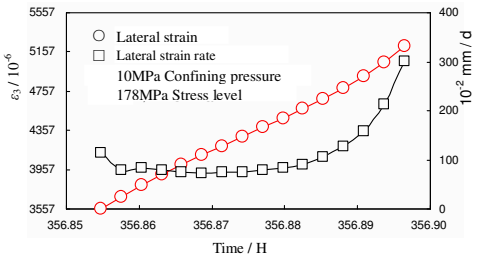


Fig.5 Results of the rheological test for marble

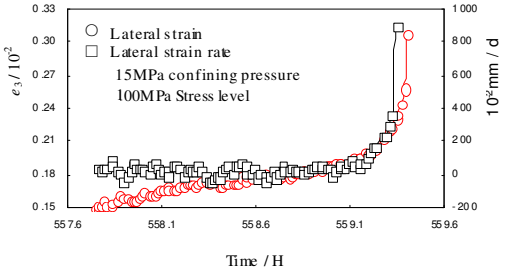


Fig.6 Results of the rheological test

## Conclusions

Slope safety early warning can be analyzed in different warning levels to take different measures in variant emergent situations. Slope early warning system was an efficient method to safeguard slope stability with multiple source data like the field monitoring and laboratory test.

Slope early warning could be executed with the five-level warning method on condition that the warning criteria were efficient to label the safety status of the slope and the data could be obtained properly. Surface displacement rate was studied as the major warning indicator in this study and was specified as a criterion for execution of slope early warning. Threshold values of slope surface displacement rate for different warning levels were determined as 0.30mm/d, 1.15mm/d, 3.00mm/d and 5.00mm/d for left bank slope of Jinping I hydropower station, respectively.

## References

[1] D.K.Keefer, R.C.Wilson, R.K.Mark: Science, Vol.238(1987), p. 921-925.

[2] S.R.Wu, Y.M.Jin: Journal of Jilin University, Vol.34(2004), p.596-600. (In Chinese)

[3] Z.Liu, W.Xu, K.Zhang: Journal of Hohai University(Natural Sciences), Vol.37(2009), p. 313-316. (In Chinese)

[4] D.N.Petley, F.Mantovani, M.H.Bulmer: Geomorphology, Vol.(2005), p.133-147.

[5] Q.Xu, Y.P.Zeng: Chinese Journal of Rock Mechanics and Engineering, Vol.28( 2009), p.1099-1099. (In Chinese)

[6] S.W.Qi, F.Q.Wu, H.X.Lan: Chinese Journal of Geotechnical Engineering, Vol.24(2002), p.596-599.

[7] R.R.Cornelius, P.A.Scott: Rock Mechanics and Rock Engineering, Vol.26(1993), p.233-252.

*Applied Mechanics and Materials Vols. 580-583 (2014) pp 486-489*
*© (2014) Trans Tech Publications, Switzerland*
*doi:10.4028/www.scientific.net/AMM.580-583.486*

# Slope Stability Evaluation based on PSO-PP

Ke Wang[1, a], Fei Xu[1, b *]

[1]Hainan Highway Survey and Design Institute, Haikou, Hainan, 570206, China

[a]xfawy@hhu.edu.cn, [b]496258148@qq.com

**Keywords:** Slope, Stability, Projection Pursuit, Particle Swarm Optimization, Logistic Curve Function.

**Abstract.** Evaluation of slope stability is a complex system problem with uncertainties. Based on the Projection Pursuit (PP), the Particle Swarm Optimization (PSO) and the Logistic Curve Function (LCF), a new model for evaluation of slope stability is developed, which is referred as Projection Pursuit based on Particle Swarm Optimization (PSO-PP). The model, on the one hand, uses PSO to optimize the projection index function and the parameters of LCF. Thus it would ensure the accuracy of the parameters used in the model. On the other hand, the nonlinear relationship between projection values and empirical grades is established according to LCF. The test results of the model show that the model has a very good precision. In this study, the evaluation results obtained by applying the model developed here into Jinping I site hydropower plant are well consistent with the practice situation. It indicates that the model here is feasible and effective in the evaluation of slope stability.

## Introduction

The stability of the slope is affected by many factors internal and external that is fuzziness, randomness and variability. Thus the slope stability evaluation is a complex system of uncertain. This paper attempts to combine projection pursuit algorithm (Projection Pursuit, PP), particle swarm optimization (Particles Swarm Optimization, PSO) and a logistic curve function (Logistic Curve Function, LCF) in one model, that is, Projection Pursuit based on Particle Swarm Optimization, PSO-PP, to conduct the slope stability evaluation. The principles, algorithms and steps of the mode is put in detail. Then the new model is applied to a project.

## Projection Pursuit Model PSO (PSO-PP)

**Projection Pursuit.** The basic idea of Projection Pursuit [1] (PP) is to projected high-dimensional data onto low-dimensional subspace ones through computer technology. The projection index function is used to evaluate the possibility of a projection structure for projection configuration. The minimization of projection index function helps in seeking the optimal projection value, based on which the structure and characteristics of the original high-dimensional data is analyzed. Besides the prediction value and the scatter diagrams could also be used to establish regression model to predict the system.

**Particle Swarm Optimization.** PSO uses the velocity - position search model. Each particle represents a candidate solution of the solution space. A fitness function is defined to evaluate each particle solution. The velocity $v_i = \{v_{i1}, v_{i2,} \cdots, v_{in}\}$ determines the $i$ th particle's distance of each iteration in the solution space. A group of random particles is initialized, among which the location of $i$ th particle in the $n$ -dimension solution space could be represented by $x_i = \{x_{i1}, x_{i2}, \cdots, x_{in}\}$. Particles update their velocity and position through tracking the individual extreme values $f_i = \{f_{i1}, f_{i2}, \cdots, f_{in}\}$ and the global ones $g = \{g_1, g_2, \cdots, g_n\}$ dynamically. The formula is as follows:

$$v_{id}^{k+1} = wv_{id}^{k} + c_1 r_1 (f_{id}^{k} - x_{id}^{k}) + c_2 r_2 (g_d^{k} - x_{id}^{k}); \quad x_{id}^{k+1} = x_{id}^{k} + v_{id}^{k+1}. \tag{1}$$

Where, $w$ is the inertia weight factor; $r_1, r_2$ present the random number uniformly distributed in the interval $(0,1)$ ; $c_1, c_2$ are the learning factors; $i = 1, 2, \cdots, N$ , $N$ is the number of particles; $v_{id}^{k}, x_{id}^{k}$ are

the $i$ th particle's $d$ -dimensional component vector of the velocity vector and the position one respectively; $f_{id}^k, g_d^k$ are the $i$ th particle's $d$ -dimensional component vector of the optimal individual location and the global optimization one, $d = 1, 2, \cdots, n$; $n$ is the dimension number of the solution dimension.

**Logistic Curve.** Mathematical equation of logistic curve is:

$$x(t) = K / (1 + e^{a-rt}) . \tag{2}$$

Where, $x(t)$ is the predicted value of the time $t$; $K$ is the saturation limit for the predicted value; $r$ is the growth rate; $a$ is integration constant..

**The PSO-PP Model of Slope Stability Evaluation.** The process of PSO-PP modeling is as follows:

Step 1, generate the projection data. Establish sample sets $(x_{ij}^*, y_i)$ $(i = 1, 2, \cdots, n; j = 1, 2, \cdots, m)$ based on the index of slope stability evaluation. $x_{ij}^*$ is the evaluation index and $y_i$ presents the level of experience evaluation. $n$ is the number of samples. $m$ is the evaluation value of indicators.

Set the strength of slope stability criteria are: the number of slope level increases with the stability of slope, level one is the most stable, level $N$ stage the most unstable. Establish PSO-PP mode of the slope stability evaluation is to establish the nonlinear relationship between $x_{ij}^*$ and $y_i$. To realize dimensionless $x_{ij}^*$ is normalized to $x_{ij}$ by the following formula:

$$x_{ij} = (x_{ij}^* - Ex_j) / Sx_j \, (i = 1, 2, \cdots, n; j = 1, 2, \cdots, m) . \tag{3}$$

Where, $Ex_j$ is the expectation value of the $j$ th evaluation index and $Sx_j$ is the standard deviation.

Step 2, calculate of the projection values. Set the vector $\vec{a} = (a_1, a_2, \cdots, a_m)$ as the projection direction. Then PSO-PP project $m$ dimensional evaluation index $x_{ij}$ onto $\vec{a}$ to obtain projected $z_i$.

$$z_i = \sum_{j=1}^{m} a_j \cdot x_{ij} , (i = 1, 2, \cdots, n; j = 1, 2, \cdots, m) . \tag{4}$$

Step 3, establish the projection index function. During integrated projection, it is required that the projection value $z_i$ is set as close as possible to the variability information of the evaluation index, that is, the standard deviation $S_z$ of $z_i$ should be as large as possible and the local density $D_z$ of $z_i$ reaches a maximum at the same time [2]. Thus, the projection index function $Q(a)$ is:

$$Q(a) = S_z \cdot D_z ; S_z = [\sum_{i=1}^{n} (z_i - E_z)^2 / n]^{1/2} ; D_z = \sum_{i=1}^{n} \sum_{j=1}^{n} (R - r_{ij}) f(R - r_{ij}) . \tag{5}$$

Where, $E_z$ is the mathematical expectation of $\vec{a}$ 's projected value; $r_{ij} = \left| z_i - z_j \right|$ is the sample distance; $R$ is the density window breadth, $(\max(r_{ij}) + m / 2) \le R \le 2m$; unit step function is:

$$f(R - r_{ij}) = \begin{cases} 1 & , \quad R > r_{ij} \\ 0 & , \quad R \le r_{ij} \end{cases} . \tag{6}$$

Step 4, optimize the projection index function. As projection index function $Q(a)$ change with $\vec{a}$, reflect the structure of the data type. The most optimum projection direction $\vec{a}$ is the most possible to reveal a structure's projection direction of high-dimensional data of. The optimal projection direction could be determined by solving the optimization formula (7):

$$\max Q(a) = S_z \cdot D_z \quad S.t. \sum_{j=1}^{m} a_j^2 = 1 . \tag{7}$$

It is difficult to solve the problem by conventional methods unless using PSO.

Step 5, establish PSO-PP regression model. Set the best projection direction $\vec{a}^*$ obtained from step 4. The optimum projected value $z_i^*$ is generated by substituting $\vec{a}^*$ into equation(5) . The corresponding mathematical model is established based on the scatter $z_i^*$ and $y_i$. Research shows it is suitable to apply the logistic curve to describe the relationship between $z_i^*$ and $y_i$, that is,

$$y_i^* = N / (1 + e^{a - r \cdot z_i^*}) . \tag{8}$$

Where, $y_i^*$ is the calculation of the sample $i$ th slope grade value; $N$ is the number of slope stability classification, which is the upper limit of the curve as well; $a$ is the integration constant of the logistic curve function and $r$ is the increase rate parameters. $a$ and $r$ is determined by the following minimization problem:

$$\min F(a, r) = \sum_{i=1}^{n} (y_i^* - y_i)^2 . \tag{9}$$

PSO is used for the optimization whose process refers to step 4.

## Project Applications

**Select Evaluation Index and Determine Slope Grade.** The Factors affecting slope stability is very complex among which the most important one is the rock and soil type and its nature, geological structure, hydro geological conditions. From the aspects like terrain features, rock features and monitoring status, eight factors are selected as evaluation index of slope stability. They are the slope height ( $H$ ), slope angle ( $\phi$ ), cohesion ( $C$ ), internal friction angle ( $\varphi$ ), rock quality index ( $RQD$ ), rock integrity coefficient ( $K_V$ ), slope deformation rate ( $V$ ), anchoring force growth anchor proportional ( $P$ ):

By referring to the relevant literature [3-4], and with reference to five slope stability system, stable (I), relatively stable (II), basically stable (III), unstable (IV) extremely unstable (V). Each index's classification criteria are listed in Table 1. Taking into account that calculated value of PSO-PP is continuous real number, that there might be certain errors near the endpoint value of the level classification zone, and that the output value of PSO-PP is in a threshold range, the "rounding" rule is applied and the threshold averaged if a slope level is between two categories. Set the level threshold of slope stability as follows in Table 2.

Table 1 Classification standard for the discrimination indices of slope stability

| Evaluation index | Stable （I） | Relatively stable （II） | Basically stable （III） | Unstable （IV） | Extremely unstable （V） |
|---|---|---|---|---|---|
| $H$/m | 0~30 | 30~45 | 45~60 | 60~80 | >80 |
| $\phi$/° | 0~20 | 20~35 | 35~45 | 45~60 | >60 |
| $C$/MPa | >0.22 | 0.22~0.12 | 0.12~0.08 | 0.08~0.05 | 0.05~0 |
| $\varphi$/° | >37 | 37~29 | 29~21 | 21~13 | 13~0 |
| $RQD$ | >90 | 90~75 | 75~50 | 50~25 | 25~0 |
| $K_v$ | 1~0.75 | 0.75~0.55 | 0.55~0.35 | 0.35~0.15 | 0.15~0 |
| $V$/mm/m | 0~2 | 2~3 | 3~5 | 5~8 | >8 |
| $P$/% | 0~8 | 8~15 | 15~20 | 20~25 | >25 |

Table 2 Classification threshold value of PSO-PP

| Slope level | I | II | III | IV | V |
|---|---|---|---|---|---|
| PSO-PP Result | <1.50 | 1.50~2.50 | 2.50~3.50 | 3.50~4.50 | >4.50 |

**Engineer Applications.** Zone I Slope of Left Bank Slope, the Hydropower Station I, Jinping, Yalong river is 90 meters high. The slope angle is 63.5 ° deduced from excavation breaking rate 1:0.5. Seen from the deformation and stability analysis of the left bank slope and the safety monitoring analysis of left bank slope[5], the relevant parameters of slope zone I is: slope height is 90m, slope angle is 63.43°, cohesion is 0.07*MPa*, internal friction angle is 22.8°, *RQD* is 89, rock integrity index is 0.78, deep deformation rate is 0.32mm / m, the proportion of anchor that anchoring force increases is 7%. The projection value obtained by PSO-PP is -0.265. So the calculation result of slope level is 1.97. Seen from Table 2, the stability of the slope is between stable (I) and relatively stable (II), and is finally determined level II. Similarly, the stabilization level discrimination of other slopes are in Table 3. Discrimination results are consistent with the three-dimensional limit equilibrium calculations. In the pre-set guideline "the better slope stability, the lower the levels", the district of the slope is sorted from high to low as follows: zone II, zone I, zone I.

Table 3 Grade discrimination of left bank slope of Jinping I site hydropower station

| Slope No. | Projection value | PSO-PP result | Level |
|---|---|---|---|
| Zone I | -0.265 | 1.97 | II |
| Zone II | -0.311 | 1.86 | II |
| Zone III | -0.235 | 2.04 | II |

## Summary

Combining PP, PSO and logistic curve, the mode Projection Pursuit based on Particle Swarm Optimization (PSO-PP) is established. PSO is used to realize the global optimization of the logistic function parameters. The logistic function described the relationship between scatters of projection value and experience one.

Taking advantage of the superior capacity of PSO optimization, the accuracy of the projection direction and logistic curve parameters is guaranteed, ensuring the reliability and objectivity of the PSO-PP evaluation.

Based on PSO-PP result and slope stability criteria set in advance, the stability of slope from the same level could be compared, enhancing the accuracy of the analysis.

## References

[1] J.H.Friedman, J.W.Tukey: IEEE Trans Comput, Vol.23(1974), p.881-890.

[2] R.E. Ren, H.W.Wang. Multivariate statistical data analysis-Theory, Methods and Examples, edit by Beijing: National defense Industry Press(1998).(In Chinese)

[3] B.Y.Yuan, Z.F.Yang, D.A.Liu: Chinese Journal of Rock Mechanics and Engineering, Vol.2(1999),p.166-169. (In Chinese)

[4] X.L.Tan, W.Y.Xu, G.L.Liang: Chinese Journal of Rock Mechanics and Engineering, Vol.28(2009), p.2503-2509. (In Chinese)

[5] W.Y.Xu: The report of safety monitoring analysis of left bank slope of Yalong river Jingping I site hydropower plant, edit by Nanjing: Hohai university Press(2009). (In Chinese)

*Applied Mechanics and Materials Vols. 580-583 (2014) pp 490-493*
*© (2014) Trans Tech Publications, Switzerland*
*doi:10.4028/www.scientific.net/AMM.580-583.490*

# Stability Analysis of Tower Foundation for Transmission Line

Zhen Chen

School of Electromechanical and Architectural Engineering, Jianghan University, Wuhan, Hubei, 430056, China

184139321@qq.com

**Keywords:** Transmission Line, Tower Foundation, Stability Analysis.

**Abstract.** On basis of geological hazard survey for dangerous tower foundations of transmission line in the sphere of influence of some goaf, stability analysis is conducted for dangerous towers by use of statistical approach in accordance with relevant regulations, to propose recommended treatment measures. The method suggested in this paper can provide references for stability analysis on dangerous towers of transmission lines. The recommended measures can be served as a reference for actual projects.

## Introduction

Due to mineral resources development and other human activities, part of transmission line tower position may suffer impacts of geological disasters such as landslides, mudslides, collapse, ground subsidence, ground fissures and so on to cause tower base collapse, power failure and other accidents so that power supply for surrounding areas will be affected. In this paper, impacts of mining subsidence in tower position stability are evaluated by use of statistical approach in accordance with relevant regulations on basis of geological hazard survey for dangerous tower section of some transmission line. Dangers of geological disasters such as ground subsidence and ground fissures caused or intensified by coal mining on towers are analyzed to propose recommended treatment measures for protection of line sections and tower bases subject to impacts and damage.

## Overview of Evaluation Area

**Meteorological and Hydrological Conditions.** Survey area is located in the Pearl River Basin. Designed line tower positions are higher than maximum flood level of surface rivers in the area, the towers are less affected by surface rivers. There is no large surface water body but some seasonal creeks in the area which is recharged mainly by atmospheric precipitation and largely affected by climates. In accordance with observational data from local weather bureau, annual rainfall is not even in the area where rainy season accounts for 77% of annual rainfall while dry season only 10% of annual rainfall, with maximum temperature of 30℃ and minimum temperature of -5℃.

**Geomorphic Feature and Structure.** Lines in the area need to run through mountains. Tower site is mainly subject to denudation landform of lower-medium and medium-high mountains and has a terrain of valleys between mountains. Vegetation mainly consists of miscellaneous trees and bushes and some of cultivated lands are distributed in gentle slopes and low-lying areas.

Exposed strata include Permian Longtan Formation (P3l), Lower Triassic Feixianguan (T1f) and Quaternary (Q). Rock strata near towers are of monocline structure with attitude of 190∠66°. There are reverse faults about 250m west of 009 tower for I circuit in the strike of S37~40°W, tendency of

SE, dip angle of 54 ~ 46 °, horizontal fault displacement of 20 to 90m and vertical fault displacement of 20 to 60m.

In accordance with the Zoning Plan of Chinese Seismic Response Spectrum eigenperiod and Zoning Plan of Chinese Ground Motion Peak Acceleration Area, the area reaches the seismic response spectrum eigenperiod of 0.35 to 0.40s, ground motion peak acceleration of 0.05g and seismic basic intensity of below VI.

**Engineering Geological Conditions.** Based on mechanical properties of rocks, lithology and composition relationships, rock strata in the survey area can be classified into soft and loose engineering geology rocks.

Main human activities in the area mainly include coal mining and road construction. Coal mining has a long history in the area where small coal mines and old caves ate distributed complexly to largely affect tower base of ground lines.

The coal mine at dangerous towers which seam dip is 43~50° adopts inclined shaft development and retreat mining along strike long wall. Its mining elevation is 1600~1400m and it applies full falling roof management mode. For coal seam outcrops and shallow coal seam zone, small coal mines have a long history with a general mining depth of 30 to 60m to cause fragmented goafs. 1 coal seam is mainly mined and it has been mined to the elevation of 1445m between F54 and F57.

## Stability Analysis of Dangerous Tower Section

**Safe Mining Depth of Coal Mines.** In accordance with Literature [1] and people-oriented geological disaster prevention principle, 220kV and 500kV transmission lines have ground facilities at protection class of Ⅱ and security coefficient of K=150. Safe mining depth is calculated based on the formula (1):

$$H_{\delta} = M_n \cdot K \tag{1}$$

Where, Hδ is the safe mining depth, Mn is the coal seam mining height or combined action thickness, and K is the safety coefficient(K=150).

**Surface Movement and Deformation Expectation**. Surface movement and deformation in the tower position can be predicted by use of probability integration method and empirical formula[2].

$$W_{(x)} = \frac{W_0}{2}[1 + \mathrm{erf}(\sqrt{\pi}\frac{x}{r})] \tag{2}$$

$$U_x = W_{(x)} \cdot \left(b + \eta \cdot \mathrm{tg}\alpha - \frac{h}{H}\right) \tag{3}$$

$$\varepsilon_x = \frac{dU_x}{dx} \tag{4}$$

$$T_x = \frac{dW_{(x)}}{dx} \tag{5}$$

Where, $W_{(x)}$ is the subsidence of any point, $U_x$ is the horizontal displacement of any point, $\varepsilon_x$ is the horizontal deformation of any point, $T_x$ is the inclination of any point, r is the major radius of influence, h is the average thickness of soil layer, H is the average mining depth, b is the horizontal movement factor and $b = 0.3 \times (1 + 0.0086\alpha)$, α is the seam dip, and η is the subsidence factor(taking 0.7).

**Building Damage Level.** Building damage in the goaf is classified into four levels[2], shown in Table1.

Table 1. Building damage level

| Level | Possible Maximum Settlement (mm/m) | Horizontal Deformation (mm) | Inclination (mm/m) | Damage Level |
|---|---|---|---|---|
| Ⅰ | - | ≤2.0 | ≤3.0 | Slight |
| Ⅱ | - | ≤4.0 | ≤6.0 | Minor |
| Ⅲ | - | ≤6.0 | ≤10.0 | Moderate |
| Ⅳ | 200 | >6.0 | >10.0 | Serious |

**Coal Mine Overview.** The coal mine is located above Triassic Feixianguan formation as an immediate roof of coal-bearing stratum. There are more than 10 faults, most of which are reverse

faults. The area is of anticline structure with a stratigraphic dip of 30° to 50 °. The coal seal is inclined with a thickness of 1.4 to 3.0m and mining elevation of 1600 to 1400m and mined by use of inclined shaft development and retreat mining along long wall, of which roofs are managed by full falling method. Existing production scale of the coal mine is 210,000 t / year. For coal seam outcrops and shallow coal seam zone, small coal mines have a long history with a general mining depth of 30 to 60m to cause fragmented goafs. 1 coal seam is mainly mined and it has been mined to the elevation of 1445m between F54 and F57 faults.

**Geological Disasters Near Towers.** No geological disasters such as collapse, landslides and ground subsidence are found along the transmission line. Small coal mines have a long history to cause small goafs. There are surface cracks of 1 to 2m long and 5 to 15cm wide near the towers, but they are covered with agricultures. Tower base has two cracks of 4 to 5cm wide.

**Safe Mining Depth of Coal Mines.** Combined action thickness of coal seam mining is calculated as shown in Table 2. As shown from formula (1), the coal mine has an existing average mining depth of 212m and future average mining depth of 234m, much smaller than the safe mining depth of 2505m, and overlying rocks of the goaf are poor in the stability.

Table 2. Combined action thickness of coal seam mining

| No. | Workable seam | Seam thickness M1(m) | Seam mining height M(m) | Seam spacing H(m) | H/M | C | Combined action thickness $M_n$(m) |
|---|---|---|---|---|---|---|---|
| 1 | 1 | 2.42 | 2.42 | 0.0 | 0.00 | 1.00 | 2.2 |
| 2 | 5 | 1.98 | 2.20 | 20.0 | 9.09 | 1.00 | 4.4 |
| 3 | 6 | 1.51 | 2.20 | 11.6 | 5.27 | 1.00 | 6.6 |
| 4 | 10 | 3.00 | 3.00 | 34.0 | 11.33 | 1.00 | 9.6 |
| 5 | 12 | 3.10 | 3.10 | 16.1 | 5.19 | 0.75 | 11.9 |
| 6 | 17 | 2.90 | 2.90 | 33.0 | 11.38 | 1.00 | 14.8 |
| 7 | 19 | 1.40 | 2.20 | 35.0 | 15.91 | 0.85 | 16.7 |

**Determination of Coal Mining Range of Influence.** Lithological rocks in the area mainly comprise the upper Permian Longtan coal measures ($P_3l$), Triassic Feixianguan ($T_1f$) argillaceous siltstones, fine sandstones and silty mudstones, belonging to medium hard overlying rocks. The coal seam has a dip angle of 43° to 50 °, 47 ° on average, so it is an inclined coal seam. Unconsolidated formation bears water with a thickness of 0 to 20m, 10m on average. Considering importance of transmission lines, weak foundation and other conditions, surface influence range shall be delineated to the maximum extent. Downhill boundary angle of $\beta_0$= 44° is taken by graphical method based on Literature [2] and mining influence radius.

**Tower Stability Evaluation.** The coal mine has an existing average mining depth of 212m and future average mining depth of 234m respectively with a mining depth-thickness ratio of 86 and 14, much lower than safety coefficient K=150 of surface facilities at protection class of II.

By using probability integral method[2], possible maximum settlement, horizontal deformation, horizontal deformation, inclination and damage in the position of dangerous towers under existing goaf conditions can be calculated, as shown in Table 3.

Table 3. Stability of dangerous tower positions

| Tower | Profile | Position | Maximum Subsidence (mm) | Horizontal Deformation (mm/m) | Inclination (mm/m) | Damage Level |
|---|---|---|---|---|---|---|
| I009 | Fig.1 (a) | Inside Goaf | 1042 | 0.3 | 0.2 | Serious Damage |
| I010 | Fig.1 (b) | Outside Goaf 42m | 1066 | 1.6 | 1.4 | Serious Damage |
| Ⅱ 008 | Fig.1 (a) | Outside Goaf 8m | 1050 | 1.3 | 1.1 | Serious Damage |
| Ⅱ 009 | Fig.1 (b) | Inside Goaf | 1048 | 0.4 | 0.3 | Serious Damage |

All the above tower sections are located within the influence range of future mining surface subsidence. With further mining of coal mines, goaf influence range will be expanded to possibly cause geological disasters such as surface cracking, subsidence of ground and so on. Under existing conditions, tower position stability is poor where towers may suffer geological disasters with large possibility, risk and hazard. It is suggested to change transmission lines and ensure a distanced of 200m from future goaf influence range [3,4].

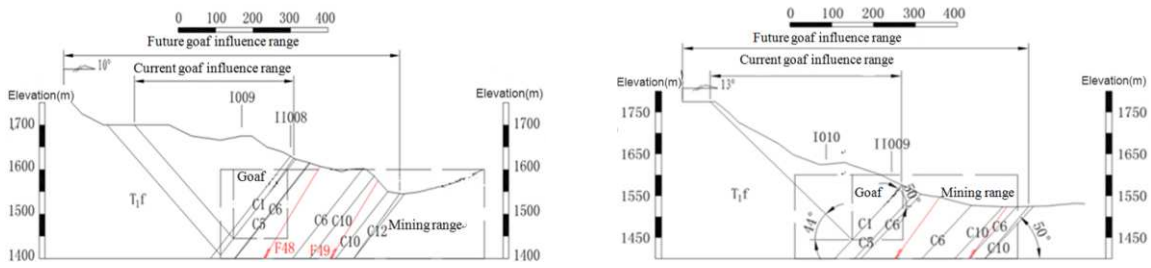


(a) (b)

Figure 1. Tower section

**Suggested Prevention Measures For Dangerous Tower Sections**

To prevent geological disasters, including surface cracking, ground subsidence as well as resulting landslide and collapse, from causing tower base collapse, line power failure and even power supply problem affecting surrounding areas, the following prevention measures are suggested based on stability of dangerous tower sections (Table 3):

(1) All tower sections are within the influence range of future mining ground subsidence, they may suffer geological disasters at a higher level of influence, risk and hazard. Tower base is poorly stable and suffer serious safety hazards. It is suggested to change route of the above tower sections and ensure a distanced of 200m from future goaf influence range[5].

(2) Associated with future mining of coal mines around towers, coal mining is highly possible to cause and intensify surface cracking, ground subsidence and other geological disasters. Towers and foundation have no significant deformation. It is suggested to strengthen monitoring and change routes if tower and foundation deformation exceeds the allowable value[6].

(3) Old goafs affect towers outside the goaf influence range. It is suggested to strengthen monitoring.

(4) During coal mining, security coal pillars must be reserved near the tower base according to relevant requirements of Literature [2] to ensure existing tower base is protected from geological disasters.

(5) Appropriate measures shall be taken to ensure adjacent tower base is not affected when a tower base is collapsed to cause power failure in extreme cases and even the collapsed tower base can be recovered as soon as possible.

(6) Future line construction shall avoid coal mining influence areas to the greatest extent.

**References**

[1] Xu-min Tian and Li Tian. *The local coal mine practical handbook*. (China Mining Press, Xuzhou 2006).

[2] State Coal Industry Bureau. *Buildings, water, railway and main tunnel coal pillar setting and Coal mining regulations*. (China Coal Industry Publishing House, Beijing 2000).

[3] Yong Zhang, Wen-long Gao and Yun-yun Zhao: Influence research of coal seam mining and pole foundation stability of 1000 kV UHV transmission line. Rock and Soil Mechanics.Vol.30 (2009), p. 1065

[4] Zhen-hua Li, Xiao-jun Cui, Jin-sheng Que and Hai-lin Lai: Stability Analysis of Tower Foundation Along 1000kV Ultra High-voltage Transmission Line in Mine Goaf. Electric Power Survey & design. Vol.12(2010), p. 18

[5] Jian-hua Yang, Xi-bin Tang, Jian Zhao, Hai-zhou Luo and Jian-ping Ding: Safety evaluation on tower foundation of transmission lines within coal mine goaf and its emergency treatment[J]. Journal of Liaoning Technical University(Natural Science).Vol.8(2012),p. 458

[6] Y. Zhang, M.F. Cai, Y.Y. Zhao and P. Luo: Mining of coal seam under mined out space and foundation stability of transmission tower. Proceedings of the International Young Scholars' Symposium on Rock Mechanics - Boundaries of Rock Mechanics Recent Advances and Challenges for the 21st Century( 2008),p.766

*Applied Mechanics and Materials Vols. 580-583 (2014) pp 494-498*
*© (2014) Trans Tech Publications, Switzerland*
*doi:10.4028/www.scientific.net/AMM.580-583.494*

# Study on Sheltering Effect of Underground Building to Horizontal Displacement of Retaining Wall of Foundation Pit

Yan Liu[1a], Junyan Liu[1,b] Shanbing Cai[1,c]

[1]School of Civil Engineering and Architecture, University of Jinan, Shandong Jinan 250022

[a]liuyan322@163.com, [b]liujunyan@vip.sina.com,[c]treasure168@126.com

**Keywords:** Foundation pit, Displacement field, Underground building.

**Abstract.** Due to the existence of underground building, the distribution of displacement field of adjacent foundation pit is obviously different from that of general foundation pit, and it is of great significance to correctly understand the sheltering effect of underground building to displacement field for determining the protection class of foundation pit while supporting design of foundation pit, and protecting the safety of metro station built near and surrounding buildings during the construction. Relying on the foundation pit project of metro station and combining the sensitivity theory through mechanism analysis, this article discovers that the sheltering effect is most obvious when the spacing between the underground building and retaining wall of foundation pit is 0.5H, and the sheltering effect can be ignored when the distance is more than 2H.

## Introduction

With the extension and development of rail transit network, more and more foundation pits near the underground building had (such as metro station, basement and the like) are excavated. There have been many studies on the influence of excavation of foundation pit to adjacent underground building currently, and many advanced construction technologies of foundation pit to adjacent construction are also developed. During the construction, the horizontal displacement for retaining wall of foundation pit will also be strictly controlled in general, to reduce the influence to the station, but it does not say that the nearer the distance from the underground building to foundation pit is, the stricter the control displacement is, instead, there is a sensitive area, however, the study on this is not perfect [1].

## Mechanism for sheltering action of underground building to displacement field of foundation pit

The foundation pit is excavated to unload the retaining wall body to displace towards the pit, and when the insertion ratio is not big enough, the soil behind the wall will also have the plastic flow towards the pit, both of which will cause the ground loss behind the wall; and the upper soil will compensate the loss behind the wall in the effect of self weight, thus causing that the soil behind the wall is displaced horizontally and vertically. Due to the large horizontal integral rigidity, the old station behind the wall will produce reversed sheltering action to the soil displacement, thus reacting on retaining wall of foundation pit and uplift in the pit [2-4].

This sheltering action will make the horizontal displacement of retaining wall body of foundation pit is much less than the displacement value of those without underground building.

**Project background.** The new station is located at the south side of station operated in parallel, the parallel spacing of the second floor underground of two stations is about 5m, and the foundation pit is excavated with one underground diaphragm wall in the first floor underground totally. The station has length of 241.2m, the main structure has width of 20.6m, the maximum burial depth of bottom plate of end well is 16.59m, and the buried depth of bottom plate of standard section is 14m, which are in the double column three-span underground two-tier architecture. The retaining structure of station is underground diaphragm wall of which the thickness is 800mm and the depth is 26m. The

finite element model shall be built to analyze the sheltering action of underground building, shown in the Figure 1.

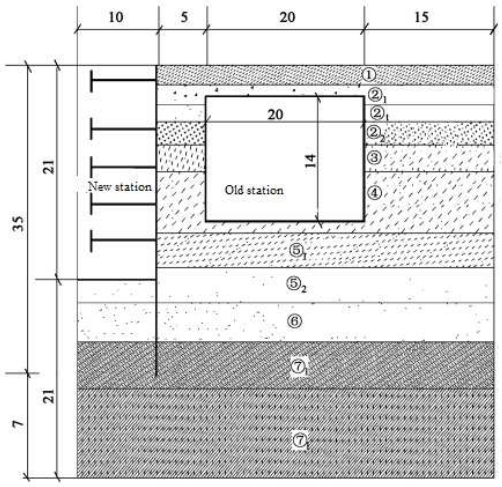


Fig.1 Calculation Model

**Analysis for sheltering effect of different spacings.** Fig.2 (a)-(e) is the deformation diagram of retaining structure in the different working conditions and soil widths.

6m and 9m of curve in Fig.2 (a)-(e) respectively indicate that the distance from the underground structure to foundation pit is 6m and 9m, we indicates that others are similar in case of no

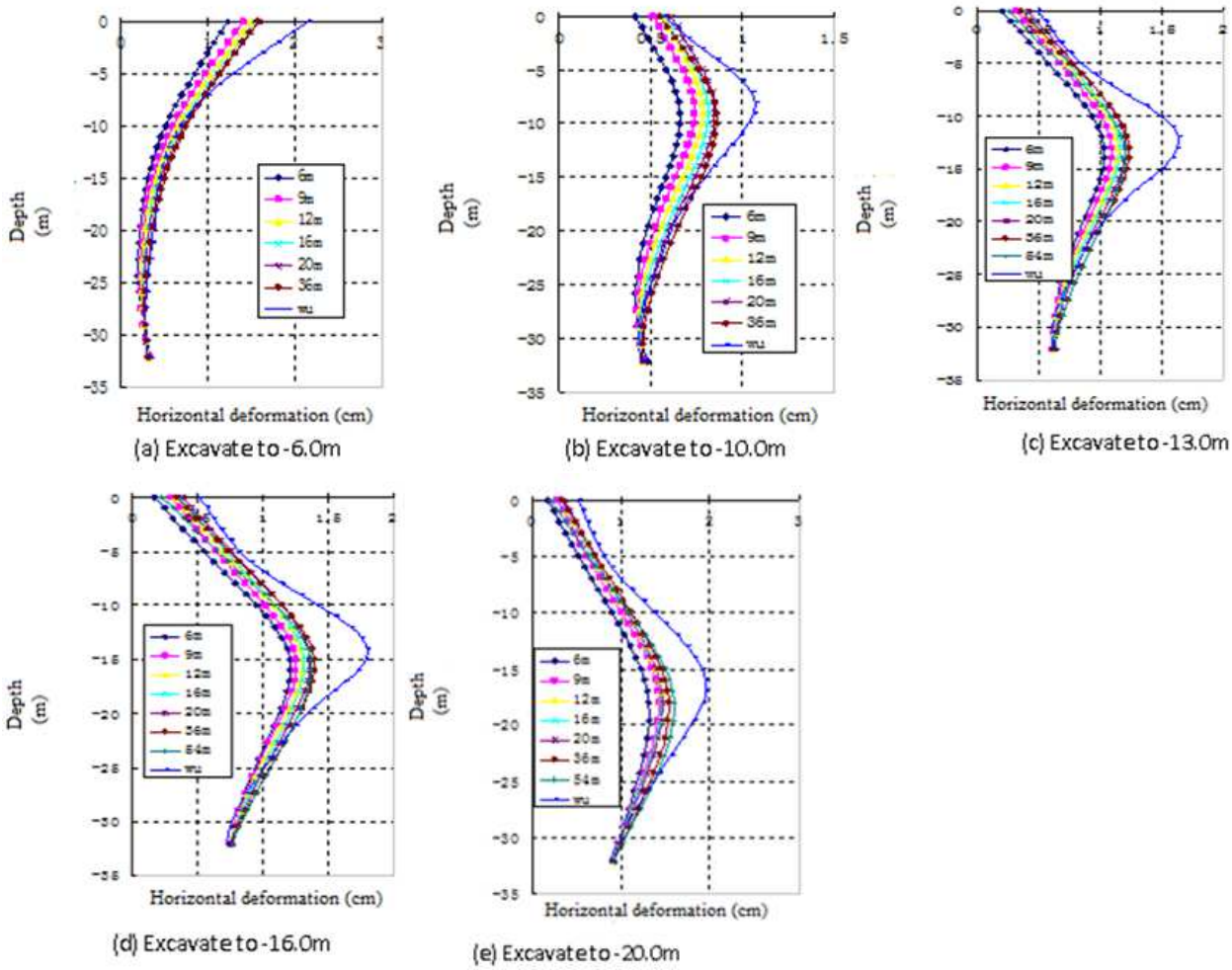


Fig.2 Deformation diagram of retaining

It can be seen from the figure that the existence of underground building has certain influence to the horizontal deformation of retaining structure of foundation pit, and especially, the influence for maximum deformation value of supporting structure is relatively big. The distance from the

underground building to the supporting structure of foundation pit is inversely proportional to the sheltering effect of underground building and proportional to the horizontal displacement produced by the retaining structure.

Respectively taking the spacing from the old station to wall of foundation pint is 0m, 5m, 10m, 15m, 20m, 30m, 40m and 50m, the relation between its spacing and maximum horizontal deformation of wall of foundation pit while excavating to the bottom (20m) is shown in the Figure 3.

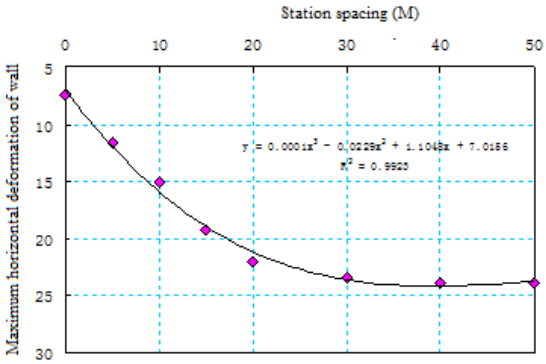


Fig.3 Relation diagram for maximum horizontal deformation and spacing of wall of foundation pit

**Sensitivity Analysis of Spacing to Horizontal Deformation of Retaining Wall**

In virtue of sensitivity analysis method in the system analysis, seek the sheltering effect of old station with changed spacing to the wall deformation of foundation pit.

Set a system, of which the system characteristic P is mainly decided by the n factors, i.e.

$$P = f(a_1, a_2, ...a_n) \qquad (1)$$

In some a reference state , the system characteristic is P*. Respectively order that each factor is changed within its possible range respectively, and analyze the trend and degree of system characteristic P while deviating the reference state P* due to the change of these factors, such analysis method is called as sensitivity analysis [5,6]. The sensitivity function [5] can be defined after each physical quantity is subjected to the dimensionless method:

$$S(k) = \frac{\left(\frac{|\Delta P|}{P^*}\right)}{\left(\frac{|\Delta a|}{a_k^*}\right)} \qquad (2)$$

$$P^* = f(a_1^*, a_2^*, ..., a_n^*) \qquad (k = 1, 2, ..., n) \qquad (3)$$

It can be seen from the formula above that the calculation of sensitivity function is closely related to the reference value. By taking the reference value $l^*$ of spacing from the wall of old station to that of new foundation pit is 5m, 10m,15m, 20m ,30m, 40m and 50m, it can obtain the relation of $d_{\max} / d_{\max}^*, l / l^*$ , shown in the figure 4 respectively.

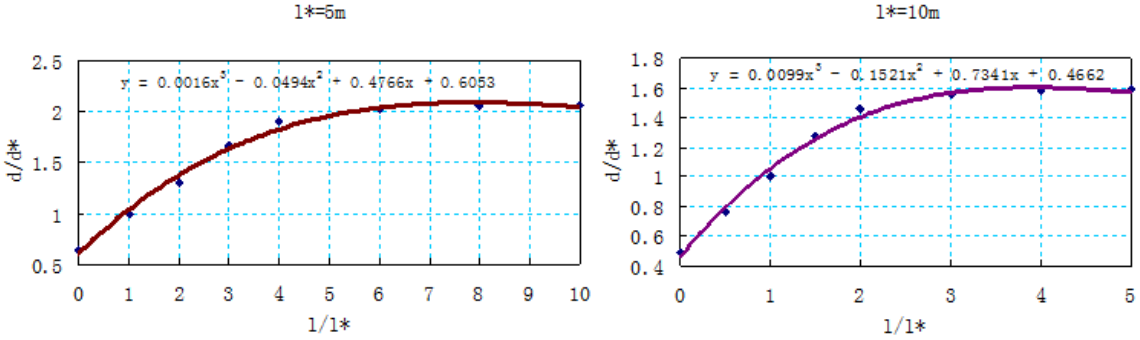

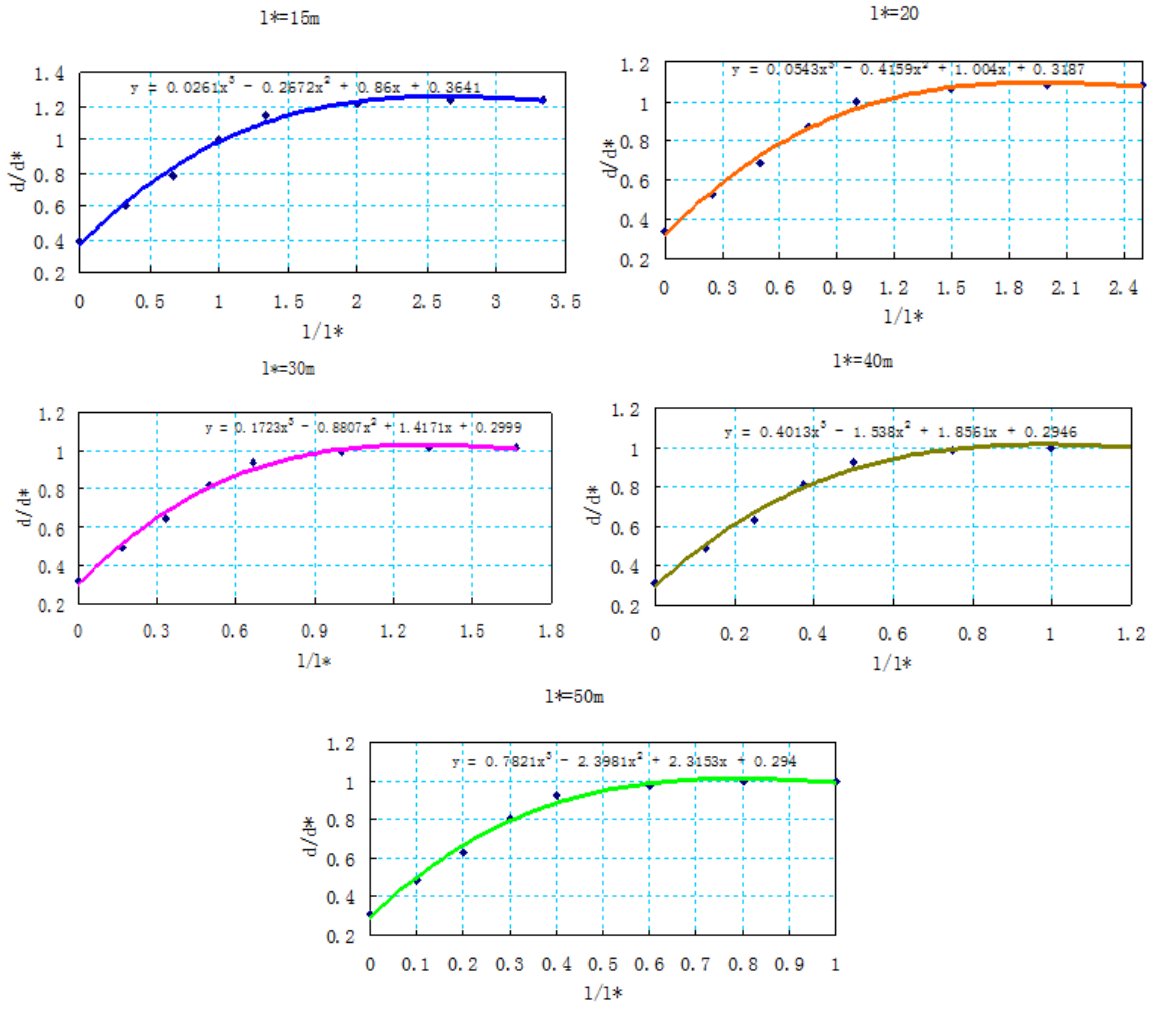


Fig.4 Relation of $d_{\max}/d^*_{\max}, l/l^*$

In the figure, when is 5m, it can obtain from the curve fitting:

$$y = 0.0016x^3 - 0.0494x^2 + 0.4766x + 0.6053 \quad (4)$$

Thus, it can obtain that the sensitivity function of is

$$S(l) = \left|y'\right| = \lim_{\Delta\to 0}\left|\frac{\Delta y}{\Delta x}\right| = \lim_{\Delta\to 0}\left|\left(\frac{\Delta d_{\max}}{d^*_{\max}}\right) \Big/ \left(\frac{\Delta l}{l^*}\right)\right| = \left|0.0048x^2 - 0.0988x + 0.4766\right| \quad (5)$$

It can be know from the formula above that the sensitivity factor of is S ($l^*$) = 0.3826 when $l^*$ is 5m, meaning that the relative error d of parameter will cause that the relative error of maximum horizontal displacement of station is 0.3826d. Similarly, it can be obtained that the sensitivity factors of are 0.4593, 0.4039, 0.3351, 0.1726, 0.0819 and 0.1346 when $l^*$ takes 10, 15, 20, 30, 40 and 50m.

Table 1 Sensitivity Factor of Different Reference Values

| | l*=5m | l*=10m | l*=15m | l*=20m | l*=30m | l*=40m | l*=50m |
|---|---|---|---|---|---|---|---|
| Influence coefficient of horizontal displacement | 0.3826 | 0.4593 | 0.4039 | 0.3351 | 0.1726 | 0.0819 | 0.1346 |
| Influence coefficient of wall settlement | 0.5033 | 1.6507 | 0.9020 | 0.2620 | 0.5856 | 0.0762 | 0.1794 |

When $l^*$ is 40m, the sensitivity factor of parameter is the smallest, so it can think that when the spacing from the wall of old station to that of new foundation pit is more than 40m, the influence of underground structure to the foundation pit can be ignored, thus, it can take 2H (which is excavation depth of foundation pit) as boundary recommended value for the existence of underground structure

to vertical displacement of foundation pit. And when the distance is 0.5H, the sheltering effect of underground station to the horizontal deformation of retaining wall of foundation pit should be the most obvious.

## Conclusion and Prospect

It is not hard to see though the analysis above that when then spacing from the underground building to the retaining wall of foundation pit is 0.5H in the soft soil area, the sheltering action is the most obvious, therefore, at this time, in the excavation process of foundation pit, it should strictly control the deformation of retaining wall body, reasonably determine the construction alarm value, and reasonably determine the design grade of foundation pit.

When the distanced is more than 2H, the sheltering effect of underground building to the retaining wall body of foundation pit can be ignored.

It shall need the further study for considering the design mode of foundation pit of such sheltering action.

## Acknowledgements

The author would like to thank for the support from the Jinan science and technology plan projects(NO: 201201142) and the national natural science fund projects(NO: 51208228) of China.

## References

[1] Liu Yan. Study on construction influence of station built behind the metro transfer hub. Tongji University. Doctor' s thesis.2007.9. (In Chinese)

[2] Wang Hongxin. Influence for the construction of foundation pit to adjacent metro station being operated and study of its corresponding deformation control technology. Tongji University. Master' s thesis. 2003.3.8. (In Chinese)

[3] Wang Yibin. Deformation control study of parallel transfer node station. Tongji University. Master' s thesis. 2005.3.1. (In Chinese)

[4] Dong Haibin. Study of interaction in the construction of parallel metro station. Tongji University. Master' s thesis.2004.8.1(In Chinese)

[5] Zhang Guang, Zhu Weishen. Parameter sensitivity analysis and test scheme optimization [J]. Rock and Soil Mechanics, 1993, 14(1): 51-58. (In Chinese)

[6] Zhu Weishen, Zhang Guang. Sensitivity analysis of jointed rock parameter to influence of surrounding rock damaged area [J]. Underground space.1994, 14(1):11-12 . (In Chinese)

*Applied Mechanics and Materials Vols. 580-583 (2014) pp 499-502*
*© (2014) Trans Tech Publications, Switzerland*
*doi:10.4028/www.scientific.net/AMM.580-583.499*

# Study on the stress and strain of EPS silt light-weight soil by laboratory test

Yong Feng [a] , Yubin Pei [b]

School of Civil Engineering,Henan University of Technology,Zhengzhou ,Henan,China

[a]51433719@qq.com, [b]874769620@qq.com

**Keywords:** EPS silt mixed lightweight soil; Stress and strain; Laboratory test

**Abstract.** EPS is silt mixing light-weight soil by expanded polystyrene, curing agent, mixture mixing and has a certain strength, lightweight synthetic packing. This article is based on laboratory test, using the uniaxial and triaxial compression test on the relationship between stress and strain, research has shown that the strain values are greatly influenced by the EPS content ratio, strength is mainly composed of cement mixing ratio control. Triaxial test results show that only when the cement mixing is larger, mixed soil shear strength characteristics with general soil has a great deal of similarity.

## Introduction

EPS technology silt mixing light-weight soil from a new point of view that the sludge as a resource, by adding the waste foamed polystyrene, curing agent, mixture mixing and has a certain strength, lightweight synthetic packing. due to its stable physical properties, won't produce the soil pollution problem, at the same time, the technology can be abandoned foamed material and silt into high quality filling construction materials, To waste recycling is the environmental geotechnical engineering is on the rise and development of one of the main research direction.

This article mainly USES the indoor experiment study of the stress-strain relationship, is the purpose of the study for EPS silt mixed lightweight soil engineering application provides reasonable geotechnical parameters, for the selection, preparation has a clear service engineering properties of EPS silt mixing light-weight soil, can be widely applied to facilitate the green technology.

## Under the conditions of uniaxial compression of light-weight soil stress-strain relationship

### Different EPS content of light-weight soil stress-strain relationship analysis

Fig.1 is the changing rule of the stress of the lightweight soil with strain. In the figure 5 curve we can see that every curve has obvious peak stress strain curve for processing softening type curve, it shows that the formation of lightweight soil is of obvious structural.

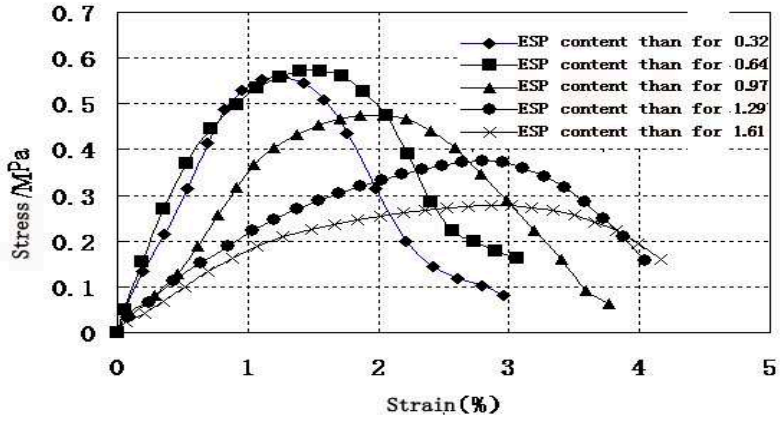


Fig.1 Different EPS content of light-weight soil stress-strain relationship

The whole stress-strain relationship curve is divided into three stages. Line segment, the first stage is the initial load time, increases with the strain, stress increasing, before reach the yield stress, stress-strain relationship is close to linear relationship, but the short line segment. Linear

relationship suggests that samples in the elastic state, samples, there is no obvious cracks deformation basically can be restored. The second phase of material plastic yielding phase, with the increase of load, a new crack sample, the original cracks is also improved, soil by contraction to inflation, the growth of strain growth speed is greater than stress, stress-strain relationship clearly into curve, stress increases to the peak. Sharp decline in the third stage is the failure stage, stress, and that the slope of the curve to become negative.

Although different EPS content than the case of light-weight soil stress-strain relationship characteristics are consistent, but there is a big difference strain values. Can be seen from the diagram, the strain value increases with the increase of the ratio of the mixed quantity of EPS, and the plastic zone range is obviously increased, but lower strength.

**Different cement mixing ratio of light-weight soil stress-strain relationship analysis**

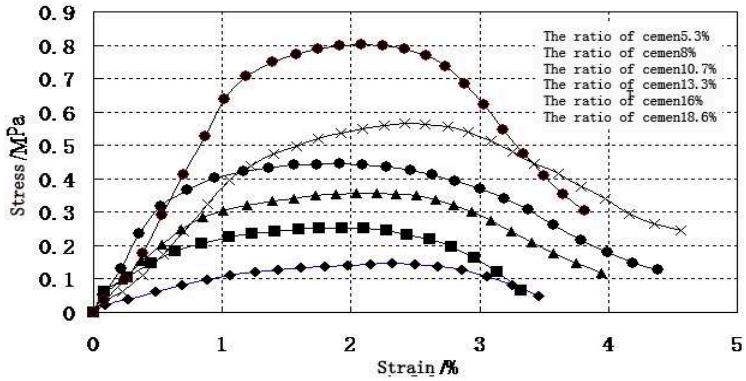


Fig.2 Different cement dosage of light-weight soil stress-strain relationship

Fig.2 for cement ratio 5.33 to 18.6% of light-weight soil stress-strain curve, we can conclude that the changing rule of the stress and strain are the same as shown in Fig.2, presents the processing softening type curve. Different cement ratio stress-strain relationship characteristics of lightweight soil is relatively consistent, but at different curve. Cement ratio is high, the stress strain curve is steep, high stress strength, failure strain is small, about 2%, mainly brittle failure; Than low dosage of cement, the stress strain curve and stress intensity is low, failure strain, about 3%, plastic damage is given priority to. Both strain values were similar, therefore, can not consider the effect of cement content on strain value.

**Triaxial compression under the condition of the light-weight soil stress-strain relationship**

**Triaxial compression test comparative study on the stress and strain**

Uniaxial compression test is still not fully reflect the characteristics of lightweight TuShiYang stress and strain, so the triaxial tests are needed to further study and discussion.

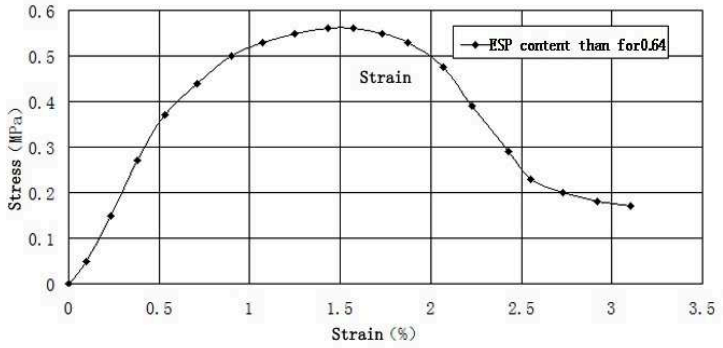


Fig.3 Typical mixing light-weight soil stress-strain relationship curve

EPS of silt mixing light-weight soil triaxial stress strain curve as shown in Fig.3, under the condition of confining pressure is 200 kPa, for mixing water, 20% of cement is 13%, the density of 0.823 g/cm3, age 28 days sample separately not consolidated undrained stress-strain test and consolidated undrained stress-strain test, to conduct comparative analysis.

Fig.4 and Fig.5 shows the mixed lightweight soil triaxial stress strain curve has the same rule, namely the characteristic of nonlinear and hardening characteristics of obvious. At the initial stage, the main differential stress and axial strain relationship curve of the initial phase of approximate to linear, show that hybrid lightweight soil in the elastic state, when the stress reaches a critical value, the stress-strain relationship is nonlinear, and proved that there are lightweight soil mixed plastic deformation. At the same time, in the process of loading, material after entered the stage of elastic-plastic deformation, stress and constantly improve, with the increase of strain curve, no obvious peak hardening characteristics of stress - strain relationship is obvious.

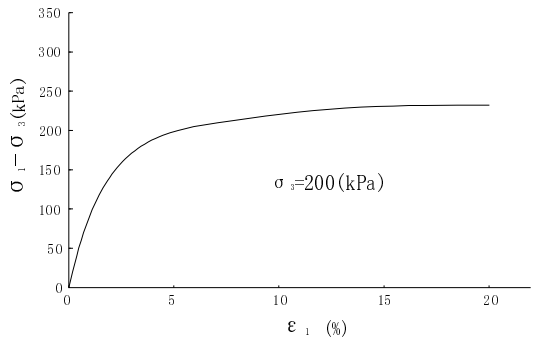


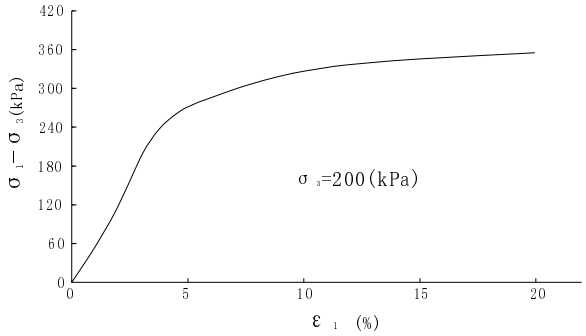


Fig.4 No consolidation undrained stress-strain curve Fig.5 Consolidated undrained stress-strain curve

At the same time, the comparative Fig.4 and Fig.5, you can see that consolidation undrained stress strain test of maximum principal stress difference is greater than consolidation undrained stress-strain test, and also compared with high yield stress.

Respectively under the consolidated undrained triaxial compression test and consolidated undrained triaxial compression test respectively to investigate and analysis the characteristics of stress and strain.

**No consolidated undrained triaxial compression test stress and strain characteristics**

EPS particles in silt mixing lightweight soil soil cohesive action mainly depends on the cement bonding between the degree of shear process can be considered as a lightweight structure failure process of soil itself. When the cement dosage is small, weak bonding effect, the higher the confining pressure, the extent of damage, the greater the light-weight soil and the lower the strength. When the cement dosage is bigger, bonding effect is strong, its high strength, lightweight soil with a relatively low confining pressure effect on lightweight soil, the characteristics of lightweight soil is close to the general characteristics of soil.

Cement mixing ratio of 16% and 22%, the same confining pressure conditions, the principal stress difference along with the confining pressure increases. Accordingly, when the cement mixing ratio of 10% and 13%, under the same confining pressure, the principal stress difference is small, the main differential stress decreases with increasing confining pressure.

Experiment also found that when the cement mixed with more hours, no obvious effect on the size of the principal stress difference, when the cement mixing is larger, influence on the size of the principal stress difference is obvious. Principal stress difference and gradually increase with the increase of cement mixing ratio, the high stress approximate linear increase

**Consolidated undrained triaxial compression test stress and strain characteristics**

In the consolidated undrained triaxial compression test, the extraction of sample saturated, sample density in the range of 0.823 to 0.987 g/cm3, 10-22% cement mixing ratio, mineral water, 20% (28 days, respectively in confining pressure 50 kPa, 100 kPa, 200 kPa and 300 kPa under the action of the stress strain curve of sample.

Obviously found in the process of test, with the continuous development of axial strain, principal stress difference increasing, confining pressure is greater than 50 kPa, the stress strain curve for strain hardening; Principal stress difference increases with the increase of confining pressure on, this of conventional triaxial compression test results of soil with general similar.

Found in the experiment: cement mixing ratio within a certain range, confining pressure, respectively, in the 50 kPa, 100 kPa, 200 kPa and 300 kPa, under the action of EPS silt mixed lightweight soil stress - strain curve has obvious nonlinear features and hardening. With confining pressure increasing, the stress strain curve in the initial period of linear degree and the tangent slope gradually decreases, and when the strain hours, confining pressure is higher, the initial elastic modulus and principal stress difference is small; When large strain, high confining pressure, the principal stress difference increasing, hardening characteristics more obvious.

Experiment also found at the same time, the cement mixing ratio of beads has greater effect on the size of the principal stress difference, the main differential stress increases with the increase of cement mixing ratio, the high stress approximation of linear increase relation, but compared with not consolidated undrained triaxial compression test, the smaller of absolute value of the slope.

## Conclusion

Strain values increase with the increase of the ratio of the mixed quantity of EPS, and the plastic zone range is obviously increased, but lower strength. Situation of different cement lightweight soil stress-strain relationship characteristics are consistent, and the small strain values, the maximum stress when the strain value is about 2%.

Through the consolidated undrained triaxial compression test results of analysis, the EPS of silt mixing light-weight soil shear strength properties. Shear strength index of the internal friction Angle and cohesive force of the cement mixing ratio, density, and varies according to age, only when the cement mixing is larger, mixed soil shear strength characteristics of great similarity with general soil. Experiment also found that the cement mixing ratio has a certain influence on the size of the principal stress difference, the difference of principal stress that increases with the increase of cement mixing ratio, the high stress approximate linear increase.

## Acknowledgements

This work was financially supported by the 2013 ZhengZhou city science and technology plan projects "EPS silt renewable hybrid lightweight soil technology and application" (20130820) and ZhengZhou city science and technology plan projects (academician workstation construction plan) (project number: 131 pysgz205) funding.

## References

[1] Kamaluddin, M., Balasubramanium.A.S., Overconsolidated behavior of cement treated soft clay, Proceedings of Tenth Asian Regional Conference on Soil Mechanics and Foundation Engineering, DunodDunod ,2006,44:407-412.

[2] Helene Tremblay, Serge Leroueil, Jacques Locat.Mechanical improvement and vertical yield stress prediction of clayed soils from eastern Canada treated with lime or cement, Canadian Geotechnical Journal, Canada, 2010, 92:1753-1761.

[3] Tianshun Hou, Guangli Xu.Foam particle mixing lightweight soil triaxial stress - strain - pore pressure characteristics test [J]. China journal of highway, In Chinese, ,2009,22(6):10-17.

[4] Tianshun Hou, Guangli Xu.Foam particle mixing lightweight soil shear strength characteristics of experimentalstudy[J].Journal of China university of mining, In Chinese, 2010,39(4):534-540.

[5] Jian Jiang, Zhanyou Luo, Tang Jie. Building sand mixing lightweight soil preparation technology and the orthogonal experiment research [J]. The Chinese and foreign road, In Chinese, 2010,30(2):200-204.

*Applied Mechanics and Materials Vols. 580-583 (2014) pp 503-508*
*© (2014) Trans Tech Publications, Switzerland*
*doi:10.4028/www.scientific.net/AMM.580-583.503*

# The Analys of Stability of Composite Soil Nail

Yong Zeng[1,a]

[1]Jiangxi Transport Consultation Company,Nanchang,330008,China

[a]14263330@qq.com

**Keywords**：Composite soil nailing technology; New technology; Main form of structure; Main principle

**Abstract.** Composite soil nailing technology is a new technology which developed on the basis of the soil nailing supporting technology. This new technology has a very important practical significance to the construction, for which the scale is larger and larger, the condition is more and more complex and the excavation of foundation is more and more deep. Composite soil nailing technique is mainly introduced in this paper by its main form of structure and the main principle, which draw a conclusion that different forms of the combination of support types have different effects on the stability of structure, by analyzing the support stability. This thesis shows that we should adjust measures to local conditions, choose the right organic combination. At the same time it also provides the basis for the practical application of engineering support.

## Introduction

Along with the construction of high-rise buildings, municipal engineering of underground space development unceasingly, in order to meet the requirements of building's using function, meet the requirements of excavation depth and area of growing demand, support technology must be improved to a certain height. Composite soil nailing supporting construction gets more and more favor of engineering application, due to its economical, safe and reliable features. There is no formal definition about the composite soil nail. According the reference experience and theory[1,2] we can get that: the composite soil nailing technology is a support technology which takes the soil nail as a solidified body, allying with the other ground treatment technology to support the soil pressure. Because composite soil nailing technology can be applied to the complicated geological conditions[3,4], it can save project investment, and has a good application prospect. So far the composite soil nailing technology is widely used. However, there are still few research reports about the theory and experimental research of composite soil nailing support, working mechanism and design calculation .the design and analysis method of composite soil nailing technology is still very lack. Although there have been some research, and have provided a certain theoretical basis, there is no analysis method that has been agreed about the composite soil nailing technology. And we also have not enough acknowledge about the working performance of the composite soil nailing support technology, we needs further research. Recently , with the support of natural science , the civil engineering department of Tsinghua university are doing some research about the working mechanism and design theory of the composite soil nailing support technology, and will hopefully get a series of achievements in the past two or three years.

## Main types of composite soil nail

In the existing engineering examples, there are mainly the following categories about the composite soil nail.

1) Soil nailing and waterproof curtain composite support

When the water table is high or the foundation pit is in anti-seepage requirement. (to prevent ground subsidence caused by the large decline of the water table) , in the weak soil stratum, we can use the

technology of soil nailing and waterproof curtain composite support. This support technology solves the issues of water seepage after the excavation of soil and the soil instability, basement high, piping problem caused by the decrease of strength of soil. Meanwhile, as a result of the foundation pit supporting in a timely manner, the slope is vertical flat and dry, when the support completes.

2) The soil nailing with micro pile composite supporting

When the water table is deep or there is no requirement about water seepage, we can adopt the technology of soil nailing with micro pile composite supporting. This supporting technology is available to prevent the basement from uplifting and from the local lane in the process of the excavation. Generally use the root pile or micro column steel tube, sometimes using a stake.

3) The soil nailing and the pre-stressed anchor composite supporting

Pre-stressed anchor is a useful and effective form in the composite soil nail supporting, especially when the foundation pit is deep ,the geological conditions, the surrounding environment is complex, and we have a strict requirement for the deformation of the foundation pit, it will show its advantage. Its main characteristic is governing the deformation displacement of side wall by applying pre-stressed. There are two kinds of the supporting, one is implanted in a row or two rows of pre-stressed anchor; the other is that A pit bottom with pre-stressed anchor, the anchor rod arranged on the bottom.

4) Soil nailing and waterproof curtain, steel pipe pile composite supporting

Cement mixing pile can stop water seepage, and the advanced micro pile has large stiffness. In order to give full play to the advantages of both, we can combine the two, together with the soil nailing to form a kind of new composite soil nailing support type ------ a soil nailing and waterproof curtain, steel pipe pile composite support. If we have a strict requirement in displacement of excavation in the practical engineering, we can join the pre-stressed anchor; If required the displacement and settlement of excavation, we can exert a certain pre-stress on soil nailing.

**The mechanism of action of composite soil nail**

1)The mechanism of the waterproof curtain

The water curtain often consists of cement mixing pile. In the application of cement-soil mixing pile, the width of the single pile is 0.5 m, width of double row piles is 1.0m. According to the soil conditions and the depth of excavation, we will decide to adopt the single row pile or double row pile. There are two aspects about the mechanism of the water curtain: (a) Get the problems of self-stability and seepage of pit side solved. When the water content of side wall is large, the net shotcrete layer is not easy to bond together with the soil, if spray layer spray directly on soil-cement mixed pile, it's easy to bond together.(b) because of the better work performance of the cement soil than the undisturbed soil, when the cement-soil pile set in the basement below a certain depth(the grave ratio between 0.7~1.0), play an important role to resist the uplift of the basement and piping.

2)mechanism of the advanced micro pile

Advanced micro pile is grouted by steel pipesφ48-φ108 or drill pipe, and spacing of 0.5-1m, This kind of micro pile can not form waterproof curtain, but can increase the self-stability of each layer soil in case of uplifting the basement. Meanwhile, it also plays a very important role for the stability of the supporting system.

3)The mechanism of the pre-stressed soil nails and pre-stressed anchor

There is a difference in structure between the pre-stressed soil nail and common soil nail. The body of pre-stressed soil nail is twisted steel atφ20-φ32 and total length of grouting. At the free period, add a sleeve on the steel body. We need take some measures of grouting seal before adding a sleeve. Covering a panel on the head of nail and tighten with nuts. The pre-stress was applied to implement by locking the nut. This kind of pre-stress was often small, less than 50KN. The place of

soil nail has a role of group nail and the construction technology is common with soil nail. This type of pre-stressed soil nail can be placed according to the actual conditions, like setting few rows above or the overall layout or interval setting. While the pre-stress applied is lesser, the density is bigger, and avail the deformation of side wall. This kind of soil nail will show its superiority for the soil of low bond strength. If we use the pre-stressed anchor to reinforce the soil, the pre-stress is bigger and the anchor is easy to pull out to failure.

**Analysis on stability of soil nail**

3.1 The calculation principle of stability of composite soil nail

Based on engineering application situation and the research methods of analysis on stability of composite soil nailing, we get the conclusion that the main consideration should be given to determine the stability safety factor of slope, the determination of the most dangerous slip surface, the calculation on stability of the supporting, the stability in construction process, the influence of the water in the soil, the effect of pre-stressed anchor, the role of soil-cement mixing pile retaining wall and nano-pile, etc.

3.2 The calculation of slope stability safety coefficient

At present, there are two types of calculations about the slope stability safety coefficient. One is calculated by the torque, the other is calculated by the strength. The former is Peterson ke. Petteson calculation method and phelan Newcastle (W.F ellenius) calculation method I[5], the latter is phelan Newcastle (W.F ellenius) calculation method II[6]. Although the two methods both get the same expression about the safety coefficient, the meaning is different. The method of according to the strength to calculate slope stability safety coefficient explains the safety of the anti-sliding force reserves, which is obtained by the moment balance, implying static unbalance; the method of according to the torque to calculate slope stability safety coefficient is static balance, implying moment unbalance, and explains the safety reserve of the anti-sliding moment reserves.

3.3 The determination of the most dangerous slip surface

In order to study the most dangerous sliding surface of the soil, we usually assume that the most dangerous sliding surface is a circular arc. When we use the circular arc method to determine the slid surface, the key is how to determine the center of the circular arc in the circle. Now there are two kinds of methods to determine the center of the circular arc: the traditional method and the geometrical parameters control method[7-9].

The most important method in the traditional method is exhaustion and search method. As shown in fig.3-1, the specific search method is: first to determine the slope toe point O, then slip arc destruction endpoints P can be extended from the top point A extends outward along the direction of A to B in the step length of 0.05H. Finally determine the center F of the slip circle arc fracture surface, the center when the safety factor is Minimum is the most dangerous slip surface circle center. Geometric parameter control method, as shown in fig. 3-2, the specific method is: set a sliding surface after A and B, A is in the foundation pit slope toe (the toe that dig each layer of slope or the time of completion of the excavation slope toe), B is the point of intersection with the top surface. Connect line AB, Over A,B as a circular arc and tangent to the vertical line after B. The relative height between A and B is H, draw a line parallel X axis in the point where is H/2 and intersect AB at D, intersecting the circular arc at F. The most dangerous sliding surface can only exist between the AB line and AFB arc. If the soil is plain soil, the most dangerous sliding surface can be determined by the formula (1)

$$F_s = \frac{M_R}{M_s} = \frac{\sum (C_i L_i + W_i \cos\theta_i tg\phi_i)}{\sum W_i \sin\theta_i} \quad . \tag{1}$$

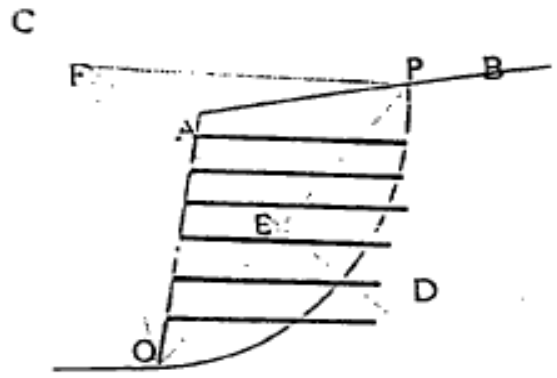


Fig.3-1.The most dangerous sliding surface determined by exhaustion and search method

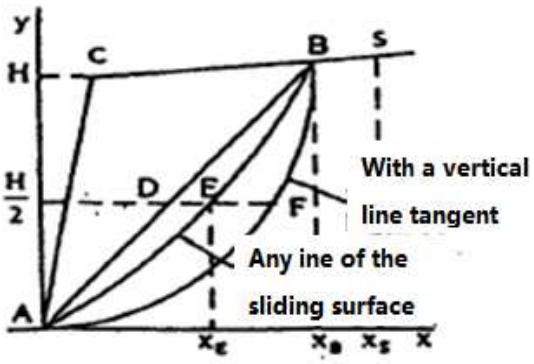


Fig.3-2. The most dangerous sliding surface determined by geometrical parameters control method

**The influence factor of stability of composite soil nailing support**

4.1 The influence of water

At present, there are many forms of composite soil nailing but the literature is rare. The stability ultimately depends on the organic combination of the composite form. In addition, water is also an important factor in the complex geological conditions, also has an important influence on the stability of foundation pit. The influence of water on soil is expressed by the effective stress principle that studying the difference between the stress between grains and pore water pressure in saturated soil and the relationship between the both and total pressure; total stress method and the effective stress method is that the proper strength index C and $\phi$ got from the different trials and the influence on strength that the pore water pressure has in the specific circumstance; select the fair use of shear strength parameters and bond strength indicators reasonably, and use tri-axial test and direct shear test to analyze the effect of water on the slope stability. No matter which method to choose, the key of stability analysis is to select appropriate shear strength index.

4.2 The effect of pre-stressed anchor rod (rope)

The palisade structure of the pre-stressed anchor rod and the traditional plate, pile, wall support, which mainly bear the soil pressure and water pressure exerting on envelope, anchoring force of stable soil is used to maintain the stability of the supporting structure and soil. The stability analysis also included the overall stability of soil. Due to instability of slope or the action of load, the foundation bottom of the wall will slide and push out, the whole system will slide down along the surface, and the soil will uplift from the outside corner of the wall, the whole soil anchor is within the deep slip surface of soil, causing overall instability. The article stability analysis can be used in Sweden point method, and stability safety coefficient is not less than 1.5. Internal stability refers to the stability calculation on deep slip surface of soil anchor and the wall foundation between the imaginary fulcrum, the usually calculation method is Kranz stability analysis.

4.3 The effect of Cement soil mixing pile retaining wall and the advanced micro pile

Cement-soil mixing pile retaining wall usually used in soft soil, high water table of foundation pit supporting, and play an important role in seepage prevention, resistance to uplift and resistance to

horizontal slip and to overthrow, allying the soil nailing, also plays an important role in the internal stability of foundation pit. Meanwhile, it also solved the problem that the nit-suspended spray on the surface is not easy to bond. If the internal stability checking of combined support system can meet the requirements of resistance, the bottom of slide and resistive overturning safety factor is enough. The combination of the advanced micro piles with soil nailing plays an important role for the internal stability of soil.

## Conclusions

The composite soil nailing developed at the base of soil nailing has mainly several types. Such as advanced micro pile composite soil nailing support, soil nailing + pre-stressed anchor rod composite soil nailing support, soil nailing + advanced micro piles + pre-stressed anchor rod composite support, soil nailing + soil-cement mixing pile waterproof curtain composite support, Soil nailing + cement soil mixing pile water stop curtain (including single pile and double pile) + pre-stressed anchor (cable) composite support, Mechanism of action on the composite soil nailing is mainly about the soil nailing, according to different soil conditions, engineering environment, with the help of cement soil mixing pile water stop curtain, advanced micro pile and pre-stressed anchor and other components of the joint action to stabilize the soil and slope. Stability of composite soil nailing analysis show that the slope stability safety coefficient, the most dangerous slip surface and waters in the soil, setting up advanced micro pile, adding pre-stressed anchor has significant effect on the stability of slip plane. At present, the composite soil nailing technology building its application in many areas of foundation pit supporting in China, but in the mountain slope reinforcement and under complicated geological conditions, such as supporting engineering in soft soil area, it is not very wide. However, it has a very long term application of significance. In the future research, we can try to perfect the supporting theory, improve the construction technology, and make it develops in a direction of gradually replacing the traditional supporting technology.

## Reference

[1] Hongqi Shao. Study on Interacting Mechanism and the Load Transfer Regularity of Rock Anchonage [D] Xi'an University of Architecture and Technology .(2009).

[2] Yuelian Li .Working Mechanism Analysis of Pre-stressed Anchors [D] Jinlin University. (2008).

[3] Huazong Xia. Jianguo Lv. Research Status of the Compound Earth nail wall supported by micro steel pipes in Advance.[J] Journal of North China Institute of Science and Technology: (2007),4(2) :41-43

[4] Xiangfan Li Shuigen Xu .Study of the Compound Nailed Retaining Wall. Shanghai Geology

[5] Clifton B. Farnsworth, Blaine Leonard, Darin Sjoblom, Quality Assurance of Soil Nail Grout for Provo Canyon Reconstruction Project [J].(2010) Earth Retention Conference, 278-285.

[6] V. Elias，I. Juran Soil Nailing for Stabilization of Highway Slopes and Excavation，FHWA/RD-89-198，June.，(1991)

[7] Yutian Huang Reinforcing Technique for Excavation Slop With Bars in High Underground Water Level Zone WanGuo Press.

[8] Xinde Deng Xincheng Deng. The Application of Soil Nailing Anchor Combined Support Structure in the Treatment of Foundation Pit Accident. [J] Science and Technology Innovation Herald: (2008). 81-83

[9] Qie Yang, Mingju Zhang. Jianguo Zhang. Study on the Composite Soil Nailing Working Mechanism [J] Chinese Journal of Underground Space and Engineering. (2005)，1(3) : 409-412.

*Applied Mechanics and Materials Vols. 580-583 (2014) pp 509-513*
*© (2014) Trans Tech Publications, Switzerland*
*doi:10.4028/www.scientific.net/AMM.580-583.509*

# The Application of Origin Software in the Data Processing of Rock Creep Experiment

Chunyan Gao[1, ,2,a], Jianguang Niu[2,b] and Quanchen GAO[1,c]

[1]School of Mechanics & Civil Engineering,China University of Mining & Technology(Beijing),China

[2]School of management science and Engineering,Shijiazhuang University of Economics,China

[a]gaochunyan2010@163.com, [b]niujianguang10@163.com, [c]gqc@cumtb.edu.cn

**Keywords:**data processing, rheological experiment, Origin software, curve fitting.

**Abstract.** The rheological experiment is one of main methods in studying rock's long-term mechanical properties, with the characteristic of mass data and numerous relevant parameters. In this paper, the data of surrounding rock's rheological experiment in Zhuji Coal Mine roadway is processed by Origin software, including drawing the creep experiment curves, taking derivatives of curves and then drawing the curves of creep rate and acceleration, curve fitting and parameter estimation, etc. The results show that the data it does not need to programme when using the software to process and it is convenient and time-saving with high precision and is worthy of popularization and application.

## Introduction

The rheological experiment is one of main methods in studying rock's rheological features. Compared with other general experiments, it has the characteristic of mass data and numerous relevant parameters, and has to face the issues of drawing the creep experimental curves, taking derivatives of curves and nonlinear constitutive equation model fitting and parameters estimation, etc. In order to solve those problems, MATLAB software requires users to have the ability of calculation and programme to deal with the data in the process, and the adjustment of software needs some necessary time and energy. However, users of Origin do not need to programme and they could process data directly and draw curves conveniently.

Origin is the data analysis and draw software exploited by American company OriginLab, and also the advanced data analysis and drawing tool often used by researchers and engineers. The data analysis of Origin includes various perfect mathematical analysis functions such as curve fitting, sorting, adjustment and computing, statistics, spectrum transform, and it could draw dozens of two-dimensional and three-dimensional graphs based on the template. People get rid of the process of operating directly on the computer hardware resources by using Fortran and C programming language, professional software such as MATLAB provide rich resources of function, which frees the programmer from tedious program code, and Origin does not need users to write any code but brings users the most direct and simple data analysis and drawing environment.

This paper takes the surrounding rock's rheological experiment in Zhuji Coal Mine roadway as an example to introduce the specific application of Origin8.0 in the data processing of rheological experiment, mainly including data imputing, graph exporting, drawing curves, the derivation of curves, and function fitting, etc.

## Main functions of Origin

The window of Work Sheet and input of data

When users start Origin or create a new file, the default setting is to open a worksheet window, in which there are two columns named A(x), B(y), representing independent variable and dependent variable respectively. Clicking on the Column's Pull-down Menu or Add New Columns of the right mouse button, users can add the required number of columns. Double clicking on the top of columns,

users could change names and set types of columns, and then they could import the data in the Excel files or directly input data or copy and paste the data from Excel files into worksheet.

Drawing and modifying graph

Origin offers the drawing templates including alignment chart, scatter diagram, point plot and pole coordinates, etc. When users draw graph, they could pick the drawing area directly in the worksheet, then click on the orders such as line, symbol to draw alignment chart and scatter diagram, or click on the drawing order first, picking coordinate axis, drawing area in the pop-up message, and then click OK to finish graph.

Users also could click on the generated graph to pop-up dialog box, and then click the "independent" in the message box to modify each line gradually or follow the default "dependent" to finish all curves linear and color changes.

Curve fitting

Origin software provides the orders such as linear fitting, nonlinear curve fitting, and a custom function fitting. Firstly, users should activate drawing window Graph where the data curve to be fitted is, then choose the menu Analysis→Fit…to get the corresponding fitting. After fitting finished, the fitting curve will appear in the graph window and give the fitting model function and parameters.

The output of graphics

Origin has two ways to put Graph graphs into the word file: one of them is saving Graph graphs as images and then inserting them into various files. Choosing File→Export page, and then selecting parameters of type of files and others according to needs, users could save the graphs in the specified path, then open the word file and insert picture to finish the whole process. The other way is taking graph as the Origin file to paste it in the Word page. In the Origin page, users choose File→Export page, and copy the graph in the Graph window to the clipboard, then click right mouse button to choose "Paste" or "Paste Special" to finish the whole process. When using the "Paste Special", if users want to choose graph in the importing of Origin graph object, all they need to do is to double click the graph and then enter Origin Page to reedit the graph. After modifying, users could directly save the changed graph into the source file through closing Origin.

## Main tasks in the data processing of surrounding rock's rheological experiment in Zhuji Coal Mine road way

Zhuji Coal Mine is located in the junction of Panji and Huaiyuan districts in Huainan city, Anhui Province, which is around the area of Wuqian and Qilong villages. Its coal-bearing stratus are Carboniferous system and Permian system, in which the Shanxi Formation in the Permian system and the upper and lower Shihezi Formation are main coal-bearing layers. The main mineable layers immediate roof and seam floor both consist of mud rock. RQD of mud rock is between 0.74 and 1.27, and the average number is 0.95. The rock mass quality is generally medium, and minority is good, which belongs to the range of instability to moderation. Especially the roof and floor are carbonaceous mudstone and mudstone containing carbon, with small thickness and low compressive strength, most of which belong to soft rock with low to medium stability. In the process of engineering, unstable situation such as floor heave happens a lot, so it is necessary to study the rheological features of mudstone.

The purpose of rock creep experiment is to study rock's character of deformation under the long-term load. Through the study of damage condition of rock sample and measured creep curves, researchers could confirm the rheological model, using regression analysis to identify the rock creep experimental curves, and then get the corresponding rheological mechanical parameters. The main tasks of creep test data processing are: To draw strain-time curve under the condition of a certain load and observe the change rule of strain; To take derivatives of curves, drawing curve of strain rate changing over time, and study strain's rate of convergence and mechanical property of rock sample to confirm mechanical components and the corresponding model in constitutive model; To do the curve fitting, then confirm the mechanical parameters and establish the creep equation.

## The Application of Origin in the Data Processing of Rock Rheological Experiment

This paper takes the sample single-shaft axial rheological experiment of mudstone roof of the Zhuji coal mine roadway named "roof 2/6-7" as an example to do data processing. The load continuously loads in classification and computer collects data automatically in the process of experience. For the limitation of this paper, the forth grade load is taken as an example to do the data analysis, and its stress is 44.9MPa, the sample interval is 0.5h, ignoring the instantaneous deformation when it is loading, the data of axial direction strain are shown in the table 1.

Tab. 1 Axial direction strain when the stress is 44.9MPa

| | | | | | | | |
|---|---|---|---|---|---|---|---|
| Time (h) | 0.123177 | 0.624305 | 1.125694 | 1.626909 | 2.211632 | 3.214236 | 4.216666 |
| Strain1 (%) | 0.657360 | 0.660019 | 0.661371 | 0.663309 | 0.664466 | 0.666156 | 0.667320 |
| Time (h) | 5.219097 | 6.221527 | 7.223958 | 8.224926 | 9.224946 | 10.224966 | 11.224986 |
| Strain1 (%) | 0.668387 | 0.669303 | 0.670122 | 0.670600 | 0.670900 | 0.671100 | 0.671400 |
| Time (h) | 12.225006 | 13.225026 | 14.225046 | 15.225066 | 16.225086 | 17.225106 | 18.225126 |
| Strain1 (%) | 0.671600 | 0.672000 | 0.672400 | 0.672600 | 0.672900 | 0.673200 | 0.673400 |
| Time (h) | 19.225146 | 20.225166 | 21.225186 | 22.225206 | 23.225226 | 24.225246 | |
| Strain1 (%) | 0.673600 | 0.673900 | 0.673900 | 0.674200 | 0.674400 | 0.674600 | |

Drawing curves of axial direction creep

Importing the data form Excel files, saving accumulated measurement time in column A and measured value of axial strain in column B, setting the time column's name is time and the unit is h, naming strain column "strain", the unit is %, and the annotation is "stress 44.9MPa", after selecting time column and strain column, users only need to click on "scatter" to draw scatter diagram, as shown in Figure 1.

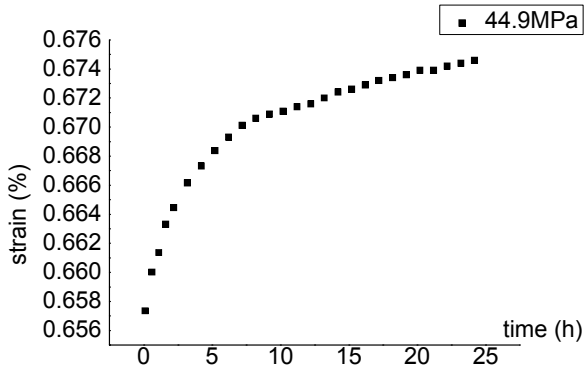


Fig. 1 Scatter diagram of axial strain creep experiment

Drawing curves of creep rate and creep acceleration

When study of rock's rheological properties, researchers need to confirm the mechanical properties and the form of constitutive model through creep rule reflected by the change of creep rate and creep acceleration. The curves of rock creep rate and creep acceleration are first derivative and second derivative curves of creep to time. There are two conditions of creep rate: $\varepsilon'=0$, which means the deformation is stable; $\varepsilon'>0$, which means the deformation is increasing. And there are three conditions of creep acceleration: $\varepsilon''<0$, the creep rate is decreasing, and the rock is in the period of creep attenuation; $\varepsilon''=0$, creep rate is a constant value, and the rock is in the period of creep stability; $\varepsilon''>0$, the creep rate is increasing, and the rock is in the period of creep acceleration, and it will be damaged soon.

After drawing the creep curve, click the graph window, select differentiate in mathematics of the analysis menu, and then open differential window to set the proper parameters. If users want the number of creep rate, input "1" in derivative order; if want that of creep acceleration, input "2", and then click OK to return to book window, users could see there is a new-added data column of differential results, and use this column data to draw graph, as shown in Figure 2 and 3.

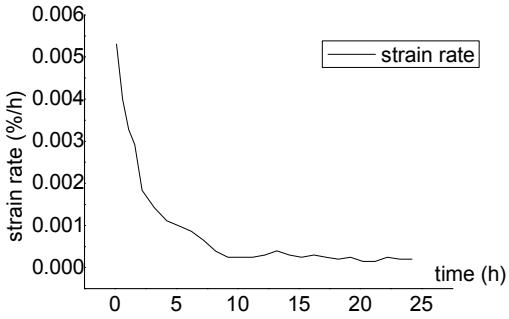


Fig. 2 Curve of axial creep rate

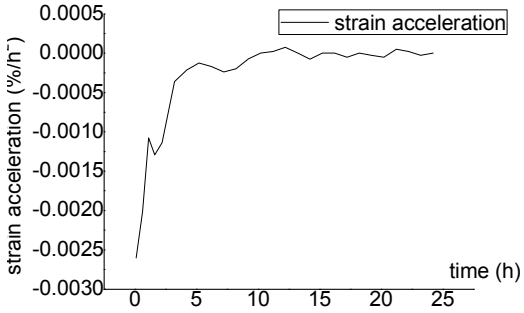


Fig. 3 Curve of axial creep acceleration

From Figure 2 and Figure 3, when axial direction stress is 44.9MPa, in the first 1 hour of load, the creep rate ε' changes a lot, when ε"<0, the creep rate decreases rapidly, and the rock is in the period of creep attenuation; then the change speed of ε" become stable, within 2 hours, the creep rate decreases to a non-zero value. When ε"=0, creep rate is a constant value and the rock is in the period of creep stability. Therefore, the constitutive equation could choose model burgers. Model burgers are made up by Maxwell and Kelvin in series, which could describe two periods of rock creep, namely, rock creep attenuation and rock creep stability.

If ε">0, and the creep rate ε' is increasing gradually and the rock is in the period of creep acceleration, researchers should choose nonlinear viscous component model.

Axial direction creep curve fitting

There are various rheological models and different rock materials should take diverse models with various forms and parameters. In order to get the proper parameters, users should use optimization algorithm such as simple algorithm, genetic algorithm to do programming calculation. And Origin software could solve the problem of programming calculation and use the custom function of nonlinear curve to do the fitting.

The creep equation of Burgers model is:

$$\varepsilon = \frac{\sigma_c}{E_1} + \frac{t}{\eta_1}\sigma_c + \frac{\sigma_c}{E_2}\left(1 - e^{-\frac{E_2}{\eta_2}t}\right). \tag{1}$$

In order to input parameters easily, order $A=\sigma_c/E_1$, $B=\sigma_c/\eta_1$, $C=\sigma_c/E_2$, $D=-E_2/\eta_2$, $x=t$,$y=\varepsilon$, then the creep equation becomes:

$$y = A + Bx + C(1 - e^{Dx}). \tag{2}$$

After drawing the creep curve, click the analysis→fitting→nonlinear curve fit in the menu and open the NLFit message box. In the settings, select new in drop-down menu of "Function", it will pop up Fitting Function Organizer, which is the Fitting function editor. Input parameters in the editor: the name of function is Burgers, the names of coordinate are X and Y, the Function parameters are A, B, C, D, the form the function is origin c, the inputting function expression is y=A+B×x+C-C×exp(D×x) according to the C programming language rule. Then click on the upper right red arrows in the function edit box to enter the compiling page, and check whether the edition is successful or not by clicking "Compile".

After successful editing, click right "save" and "ok" in order to exit function editor until get to the NLfit message box. Then click on "Parameters" to set the initial values, inputting the initial values in the value column in turn, choosing "Fitting to the convergence", then the software begin to do the fitting, to calculate the parameters and draw the fitting curve.

Please notice that the biggest difficulty in using custom function to do the fitting in the nonlinear fitting box is the confirmation of parameters' initial values. If the setting values are not proper, it would be hard to get the satisfied fitting results. For instance, the initial values of A, B, C, D are all the

same: 0, the similarity of fitting is just 0.81627, and the fitting results is too large, which means the fitting curve is not matching the experimental curve. If users set the initial values in this way: A=0.2,B=0.000,C=0.02,D=-0.2, the similarity of fitting is 0.99874, the standard errors are all small, which matches the fitting results, and the fitting curve is close to the experimental curve. Therefore, researchers should do the preliminary estimation of parameters first when they begin the fitting.

After fitting, users could see that on the base of scatter diagram in the drawing window, the fitting curve is added, and the window also provide the fitting similarity and the main parameters and standard errors of them, as shown in the Figure 4. the fitting results are: A=0.65706, B=0.000236172, C=0.01195,D=-0.38153, therefore $E_1$=68.33470MPa, $\eta_1$=190115.67840MPa.h, $E_2$=3757.32218MPa, $\eta_2$=9848.03862MPa.h.

The equation after fitting is:

$$\varepsilon = \frac{\sigma_c}{68.33470} + \frac{t}{190115.67840}\sigma_c + \frac{\sigma_c}{3757.32218}\left(1 - e^{-\frac{3757.32218}{9848.03862}t}\right) \tag{3}$$

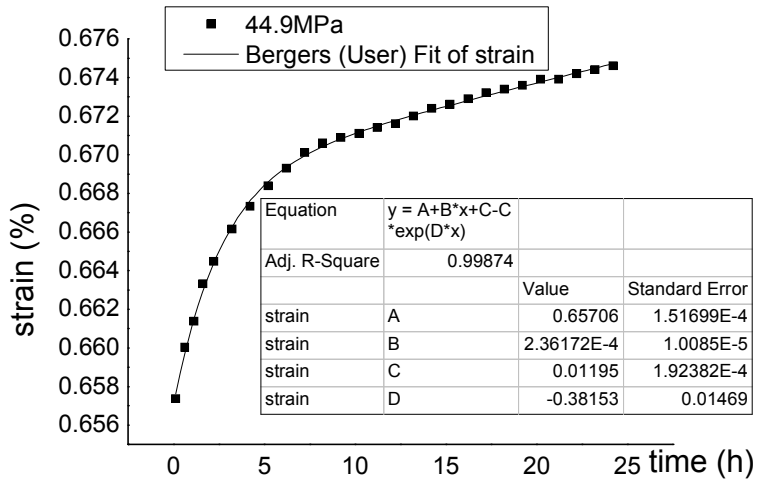


Fig. 4 Fitting Curve and Main Parameters

## Conclusion

Origin software has powerful function of data analysis, calculation and drawing. Through the data processing of creep experiment of rock sample in the Zhuji Coal Mine roadway when the stress is 44.9MPa, the results show that this software could drew creep curve, take derivatives of curves and do the curve fitting and parameters estimation without programme, which is easy to operation, has quick speed and high efficiency, and is worthy of popularization and application.

## Acknowledgments

This work was financially supported by The Doctoral program of Higher Education Research Foundation (20120023110007), Technical Economics and Management of Academic Discipline Project of Hebei .

## References:

[1] Jun Sun： *Rheology and engineering application of geotechnical materia*l. Beijing: China Architecture and Building Press,(1999).In Chinese

[2].K. S.Chan ,D. E. Munson, et al. in： *Int J of Damage Mechanics*, 1996: 293－314.

[3].Qingzhong Fan, Yanfa Gao. in： *Chinese Journal of Rock Mechanics and Engineering*, 2005(11):1273.In Chinese

*Applied Mechanics and Materials Vols. 580-583 (2014) pp 514-517*
*© (2014) Trans Tech Publications, Switzerland*
*doi:10.4028/www.scientific.net/AMM.580-583.514*

# The experimental study of the influence of the matric suction on the unsaturated soil strength

CuiRan Liu

Luoyang Institute of Science and Technology,China

liucuiran@163.com

**Keywords:** unsaturated soil, matric suction, triaxial apparatus, shear strength

**Abstract.** With modified unsaturated soil triaxial apparatus, unsaturated soil shear strength of the tests under the condition of different water contents are done. Experimental results show that the matric suction exist in unsaturated soil and increases with the decrease of moisture content. And the shear strength of unsaturated soil is higher than that of saturated soil. Shear strength of unsaturated soil varies as the matric suction and water content. The shear strength increases when the matric suction increases. when soil tend to be saturated, the matric suction will tend to be zero. And the shear strength of unsaturated soil values gradually close to the strength of the saturated soil.

## Introduction

The strength of the soil is one of the important mechanical properties of soil. The strength of the unsaturated soil is more complex [1] than that of saturated soil largely due to the presence of matric suction. The matric suction is capillary part of the free energy of water in soil. It is determined by the equivalent suction through the measure of vapor pressure which balances water in soil. It can be thought for the difference values of the pore air pressure and pore water pressure. It is the essential feature of unsaturated soil which differs from the saturated soil. There exists a close relationship between saturated soil and unsaturated soil at the same time and they can be reciprocally transformed with the changes of water content in the soil pore.

## Unsaturated soil strength theory

So far, the shear strength research of unsaturated soil has a history of more than forty years. Generally, the strength parameters are selected on the basis of the Mohr-coulomb strength theory of saturated soil. Several different shear strength formulas were put forward from different perspectives and point of view combined by studying the properties of soil. At present, the following two shear strength formulas have been widely accepted by people.

(1) Bishop (1960) shear strength the theoretical formula

$$\tau_f = c' + (\sigma - u_a)_f tg\phi' + \chi(u_a - u_w)_f tg\phi' \tag{1}$$

Bishop proposed his unsaturated soil shear strength formula combining his effective stress principle [2] of unsaturated soil with Mohr - Coulomb failure criteria. The $\chi$ is a parameter which is related to saturation, soil category, dry-wet circulation and loading paths. It is difficult to determine, the formula is not widely applied.

(2) DG. Fredlund (1978) effective shear strength formula

$$\tau_f = c' + (\sigma_f - u_a)_f tg\phi' + (u_a - u_w)_f tg\phi^b \tag{2}$$

Fredlund formula was put forward with presence of double stress principle [3]. When $(\sigma - u_a)$ is fixed and $(u_a - u_w)$ can be changed, different $\tau$ can be obtained. So the $\varphi^b$ can be obtained from the $\tau \sim (u_a - u_w)$ figure. Ten different test results compiled by Fredlund show that the $\varphi^b$ is smaller than $\phi'$.

**Triaxial shear test of unsaturated soil**

(1) The experimental principle and method

Triaxial test is one of the most commonly used method indoor measuring soil shear strength. According to the drainage, triaxial strength test of unsaturated soil can be divided into: consolidation drainage experiment, constant moisture content test, consolidated undrained tests, undrained tests and the unconfined compression test. According to the practical drainage situation of unsaturated soil, the drainage consolidation test method is adopted in this paper. It can respectively control and measure pore air pressure and water pressure and can accurately measured volume change of samples in the test. In order to avoid vaporization of measurement of pore water pressure system, axis-translation technology is adopted in test process [4-5]. In test, dry density of the specimens is controlled as 1.51 kg/cm$^3$ and water content was respectively controlled as 5%, 10%, 15% and 20%. The specimens are cylindrical and the diameter is 6.18 cm with 12.5 cm height. Under confining pressure is respectively controlled as 100KP$_a$, 200KP$_a$, 300KP$_a$ and 400KP$_a$ during test. The matric suction is controlled and measured.

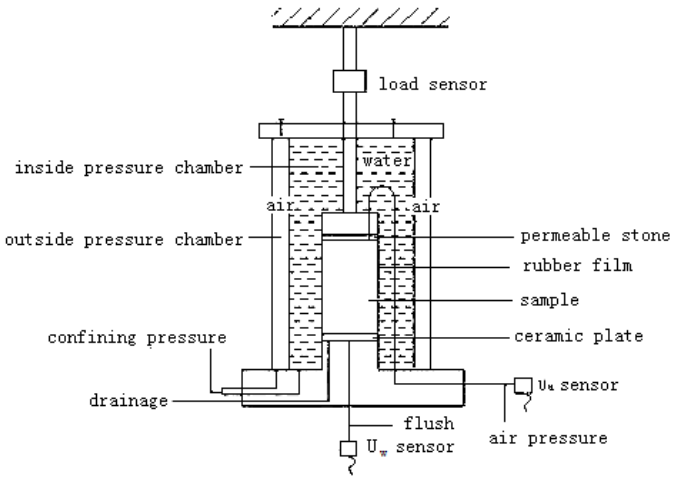


Fig.1 Triaxial Pressure Chamber of unsaturated soil

(2) Test results

According to the test results, stress-strain curves and strength envelopes of unsaturated soil with water content of 5%, 8%, 10%, 15% and 20% are obtained. Due to the limited space, only stress-strain curves and strength envelopes of water content 5%, 10%, 20% are listed in this article as figure2～4.

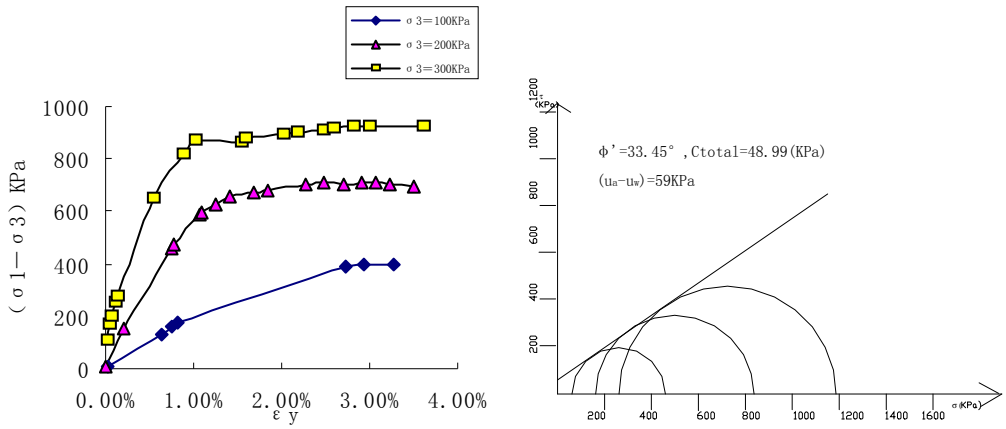


Fig. 2 The stress-strain and Mohr-Coulomb curves of unsaturated soil with 5% water content.

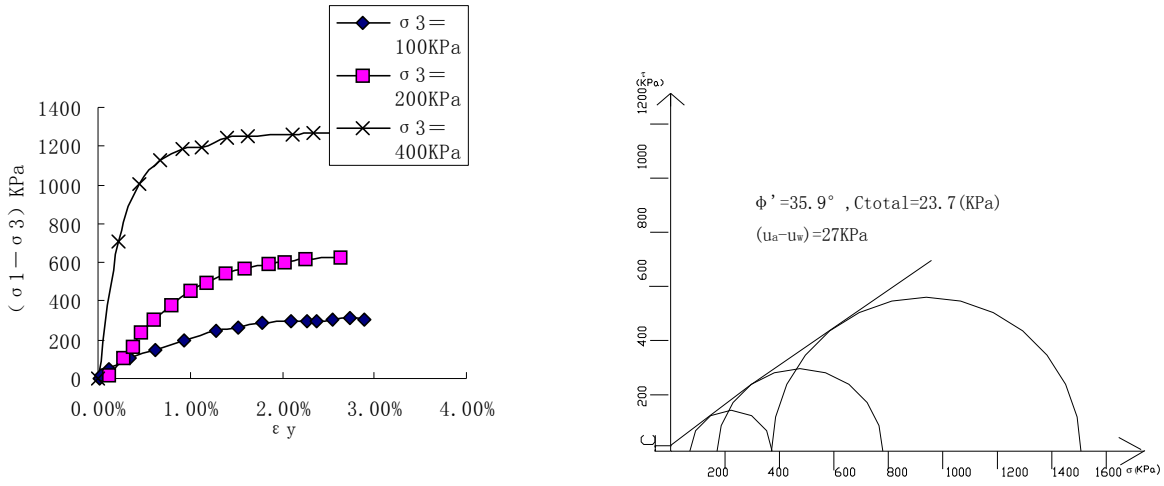


Fig.3 The stress-strain and Mohr-Coulomb curves of unsaturated soil with 10% water content.

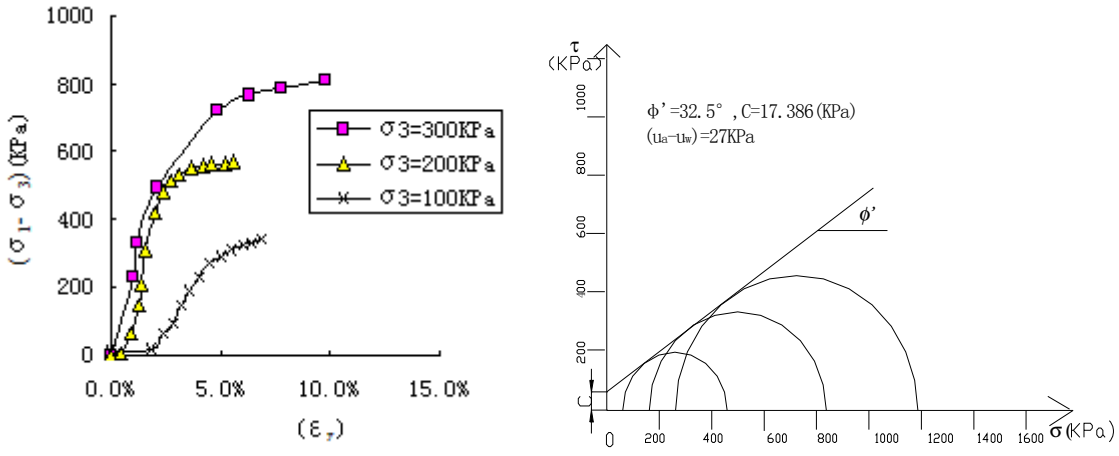


Fig.4 The stress-strain and Mohr-Coulomb curves of unsaturated soil with 20% water content.

(3)Strength formula of unsaturated soil

According to shear test, the Parameters of shear strength of unsaturated soil are obtained as in table 1.

Tab.1 Parameters of shear strength of unsaturated soil

| Moisture content | Matric suction | Internal friction Angle | Total cohesion | Saturation |
|---|---|---|---|---|
| w | Us（KPa） | φ（°） | $C^{'}$（KPa） | Sr |
| 5% | 59 | 33.44848 | 48.990201 | 16.39% |
| 10% | 27 | 35.89876 | 19.744096 | 32.78% |
| 15% | 25 | 32.67281 | 17.366 | 49.20% |
| 20% | 11 | 33.2952 | 17.052282 | 65.59% |

The unsaturated soil shear strength formula is fitted as (formula3) according to the test data using the least squares method.

$$\tau_f = (\sigma_f - u_a)_f tg\phi + \exp(a + b/(u_a - u_w) + c\ln((u_a - u_w))) \quad (3)$$

A, b, c are fitting coefficients and respectively is 3.86, 23.90 and 23.90 in the formula.

(4) The relationship between the matric suction and shear strength Unsaturated soil

From table 1, effective friction angle value calculated by the unsaturated soil test results is slightly affected by water content. Therefore, the author thinks that the effective friction angle of some specific unsaturated soil can be thought of as a fixed value. But because of the matric suction, the total cohesion is strongly influenced by water content. When the matric suction is larger, the greater the

total cohesion becomes and the shear strength of unsaturated soil increase accordingly. But the relationship between the shear strength and matric suction is not linear and is unstable. Using the data in the table 1, the scatter diagram between total cohesion and matric suction is drawn as figure 5.

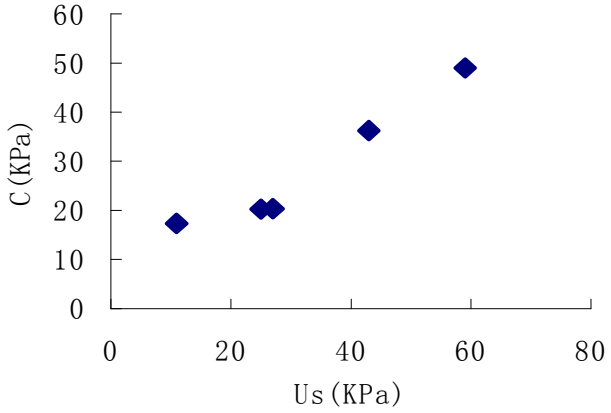


Fig. 5 The curve of relationship between matric suction and total cohesion

## Conclusion

(1) Due to the existence of adsorption frictional force of unsaturated cohesive soil skeleton, the strength of the unsaturated cohesive soil is generally greater than that of the saturated cohesive soil. Its value is not affected by the influence of applied stress, but is greatly influenced by water. When the water content reaches a certain value, the adsorption frictional force decreases rapidly. So contribution of the matric suction to unsaturated soil shear strength is a limit value and unstable.

(2) Effective internal friction Angle of unsaturated cohesive soil saturated cohesive soil is not affected by external forces and suction, its value depends on the mineral composition of soil and stress history.

## References

[1] Bao Chenggang,Gong Biwei,Zhan Liangtong,Properties of unsaturated soils and slope stability of expensive soils, proceedings of the Second International Conference on Unsaturated Soils,Beijing,1998,Vol.2.

[2] Bishop A W. Blight G E. Some aspects of effective stress in saturated and partly saturated soils. Geotechnique, 1963,13(3):177-179.

[3] Fredlund D G, Mongerstem N R, Widger R S. The shear strength of unsaturated soils. Can.Geotech,J,1978,15(3):313-321.

[4] Lu Zhao Jun．Shear strength and Inflation pressure of unsaturated soil, Journal of geotechnical, 1992，14(13)：1－8.engineering .

[5] Miu Lin Chang,Yin Zong Ze,Liu Song Yu. The conventional triaxial soil strength test of unsaturated soil soil. Journal of Southeast University, 2000，30（1）：121-125.

*Applied Mechanics and Materials Vols. 580-583 (2014) pp 518-523*
*© (2014) Trans Tech Publications, Switzerland*
*doi:10.4028/www.scientific.net/AMM.580-583.518*

# The settlement analysis of the cement fly-ash gravel pile composite foundation of Baotou

Juan Li[1, a], Yao Xu[2, b] and Jun Yin[3, c]

[1] School of architectural and civil engineering, Inner Mongolia University of Science and Technology, Baotou 014010, China

[2]BaoGang Real estate development company, Baotou 014010, China

[3]Baogang Group Design & Research Institute, Baotou 014010, China

[a]teleiweili@163.com, [b]xuyao225b@tom.com, [c]yinjun8277@tom.com

**Keywords:** Cement fly-ash gravel pile composite foundation, Resilience-recompression, Consolidation settlement, Settlement analysis.

**Abstract.** This paper analyzes the causes of larger differences of final settlement calculated value of cement fly-ash gravel pile (CFG pile) composite foundation of Baotou with actual observed result of it. On the basis of analysis on a number of practical engineering data of Baotou, we modify the settlement formula of the CFG pile composite foundation and gain the modified coefficient applied to the settlement calculation of the CFG pile composite foundation of Baotou. The modified formula and coefficient proposed in this paper have a positive effect on the accurate settlement calculation of puting forward a more accurate correction formula and coefficient of the calculation of the CFG pile composite foundation of Baotou.

## Introduction

In recent years, high-rise buildings in Baotou area are increased year by year, and the the CFG pile composite foundation has been widely used. However, a large number of engineering practices of Baotou show that there are large differences between the calculated value of the final settlement of the CFG pile pile composite foundation of Baotou and actual observed result of the settlement according to the formula recommended by the standards. The research of the CFG pile composite foundation conducted by many scholars is mainly concentrated in the pile side resistance, load transfer of piles and soil [1~ 6], the common stress of soil and pile and the performance of material in pile body, there are only a few researches on the settlement deformation of the CFG pile composite foundation. While the researches on the settlement deformation of the CFG pile composite foundation of Baotou are still a blank.

The causes of larger differences between the calculated value of the final settlement of the CFG pile composite foundation of Baotou and actual observed result of the settlement mainly consist two aspects: First, the final settlement of the CFG pile composite foundation should include settlement deformation of the springback recompression when the foundation embedded deeper, while the specification does not consider this; Second, the correction coefficient of the settlement calculation of the CFG pile composite foundation directly comes from the specification, while the compression modulus value of the settlement calculation of the CFG pile composite foundation of Baotou by the depth range beyonds the scope of coefficient values given by specification, resulting in the bias of correction coefficient of the settlement calculation of the CFG pile composite foundation of Baotou.

In regarding to the two points presented in this paper, according to the settlement mechanism of the CFG pile composite foundation and the basis of analysis and research on a number of practical engineering data of Baotou, we modify the formula of the final settlement of the CFG pile composite foundation of Baotou and gain the modified coefficient applied to the settlement calculation of the CFG pile composite foundation of Baotou.

**The problems in the application of the of the settlement deformation formula of the CFG pile composite foundation recommended by the norm**

The geological conditions in Baotou area are good, when building foundations are buried shallowly, it can be used as supporting layer of the natural foundation, and it does not need to do ground treatment. So the technology the CFG pile composite foundation of Baotou can be used when the building foundations buried deeply. However, the final settlement formula of the CFG pile composite foundation is applied to the conditions that the building foundation is embedded shallowly. The formula which recommended by the specification takes the consolidation settlement deformation into consideration which is produced by the average additional stress $p_0$ [7,8], but does not consider the settlement deformation of the springback recompression. However , when the building foundation is embedded deeply, from the excavation of the foundation ditch to the use of buildings, the final settlement of the foundation consists of the settlement deformation produced by the springback recompression and the consolidation settlement in the foundation. Some high-rise buildings in the basement have 3 ~ 4 layers (or even more layers), the total load $p$ may be equal to or less than the weight $p_c$ of the overlying soil, the settlement deformation of the high-rise building foundation will be only decided by the deformation of the compression deformation. Therefore, when calculating the final settlement deformation of high-rise building foundation, the deformation of the compression deformation is more important in the total settlement and should attached importance to it and considered.

**Correcting and deducing the computational formula of final settlement of the CFG pile composite foundation**

When the building foundation in Baotou area is buried deeply, the excavation of the foundation ditch will unload the foundation and cause the springback deformation of foundation soil (Fig. 1 (a)). With the external load $p$ in the upper structure gradually increasing , when the external load $p$ is less than or equal to the gravity $p_c$ of the foundation pit soil , the settlement deformation $s_1$ of the springback recompression in the CFG pile composite foundation will occur (Fig. 1 (b)). When the external load $p$ is increasing and will be greater than the weight of foundation pit soil $p_c$, the consolidation settlement deformation $s_2$ in the the CFG pile composite foundation also will happen (Fig. 1 (c)). So the final settlement of the CFG pile composite foundation $s = s_1 + s_2$ ($p > p_c$).

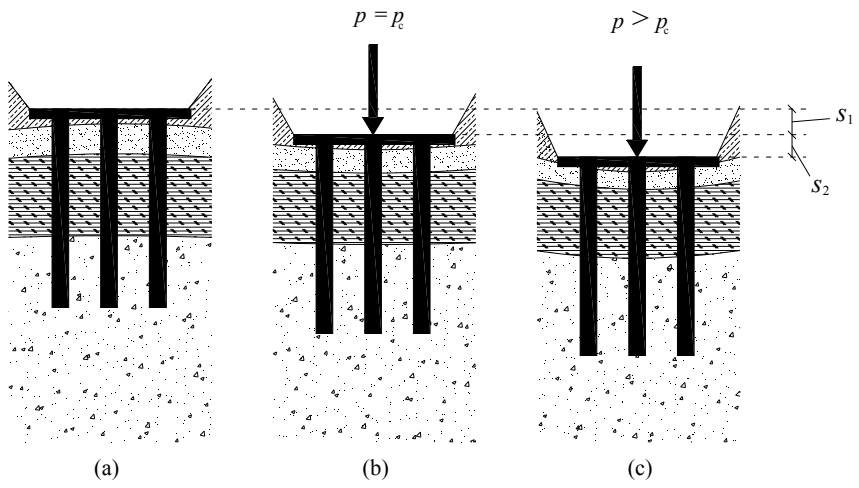


Fig.1 The settlement calculation of the CFG pile composite foundation

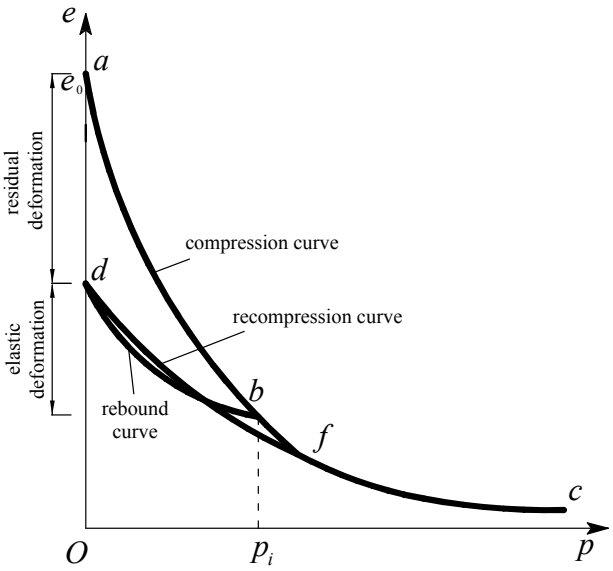


Fig.2 The springback recompression in the soil body and compression curve

The springback recompression in the soil body and compression curve in Fig.2 shows that the rebound curve of the soil body can not coincide with the original compression curve. The slope of recompression curve is much smaller than the original compression curve. After the deformation of the soil unloading $p_i$ becoming stability, then exert external load $p_i$ again, at this point the void ratio of recompression curve of soil is less than the void ratio of the compression which exerted the same loading pi, thus the settlement deformation of springback recompression $s_1 > 0$.

This article uses the layer-wise summation method, and takes the continuous process of settlement deformation of the springback recompression and consolidation settlement deformation in the CFG pile composite foundation into consideration, and introduces a new correction coefficient $\psi'_{sp}$ of the final settlement calculation in the CFG pile composite foundation, then modifies the standard formula, finally deduces the modified formula of the final settlement calculation in the CFG pile composite foundation when considering the situation that the foundation is buried shallowly.

$$s = \psi'_{sp}\{[\sum_{i=1}^{n}\frac{p_c}{E'_{spi}}(\overline{\alpha}_i z_i - \overline{\alpha}_{i-1}z_{i-1}) + \sum_{i=n+1}^{m}\frac{p_c}{E'_{si}}(\overline{\alpha}_i z_i - \overline{\alpha}_{i-1}z_{i-1})] + [\sum_{i=1}^{n}\frac{p_0}{E_{spi}}(\overline{\alpha}_i z_i - \overline{\alpha}_{i-1}z_{i-1}) + \sum_{i=n+1}^{m}\frac{p_0}{E_{si}}(\overline{\alpha}_i z_i - \overline{\alpha}_{i-1}z_{i-1})]\} \quad (1)$$

Where:

$n$ —— the soil layers within the scope of the CFG pile composite foundation

$m$ —— the total soil layer within the depth range of the settlement calculation in the CFG pile composite foundation

$p_c$ —— be equivalent to the base pressure of gravity in the soil of the upper pit depth (kPa)

$E'_{spi}$ —— the modulus in the i-th layer of the composite soil in the CFG pile composite foundation affected by the external load (the gravity in the soil of the upper pit depth) (MPa), $E'_{spi}=\xi E'_{si}$

$E'_{si}$ —— the modulus in the i-th layer below the composite soil in the CFG pile composite foundation affected by the external load (the gravity in the soil of the upper pit depth(MPa)

$z_i$, $z_{i-1}$ —— the distance from the bottom of foundation to the first layer and to the i-1 layer of soil background (m)

$\overline{\alpha}_i$ , $\overline{\alpha}_{i-1}$ —— the average coefficient of additional stress within the bottom of foundation to the first layer and to the i-1 layer of soil background

$\xi$ —— the increased coefficient of the compression modulus in the composite soil which located in the CFG pile composite foundation $\xi = f_{spk} / f_{ak}$

$\psi'_{sp}$ —— the modified coefficient of the final settlement in the CFG pile composite foundation

**The value analysis on the modified coefficient of the final settlement calculation in the CFG pile composite foundation when the foundation is buried deeply**

With the modified formula (not including the modified coefficient)of the final settlement in the CFG pile composite foundation mentioned above, we calculate five typical engineering examples in different areas of the Baotou area, and obtain the five engineering total settlement value before the five engineering settlement values are amended. With the value and the analysis of the observed settlement results, we get the modified coefficient value of the final settlement in the CFG pile composite foundation when considering the influences of settlement deformation of the springback recompression . The correction coefficient of the values are shown in Table 1.

Table 1. The modified coefficient table of the final settlement of the CFG pile composite foundation in the engineering examples

| Serial number | The equivalent value of the compression modulus $\overline{E'}_s$ | The final settlement before the method of calculation is modified S(mm) | The actual final settlement S′ (mm) | $\psi_{sp}' = S'/S$ |
|---|---|---|---|---|
| Case 1 | 55.312 | 52.0 | 9.9 | 0.178 |
| Case 2 | 41.151 | 115.0 | 19.3 | 0.168 |
| Case 3 | 37.446 | 190.9 | 36.5 | 0.191 |
| Case 4 | 51.078 | 195.8 | 35.4 | 0.176 |
| Case 5 | 87.133 | 71.8 | 12.4 | 0.173 |

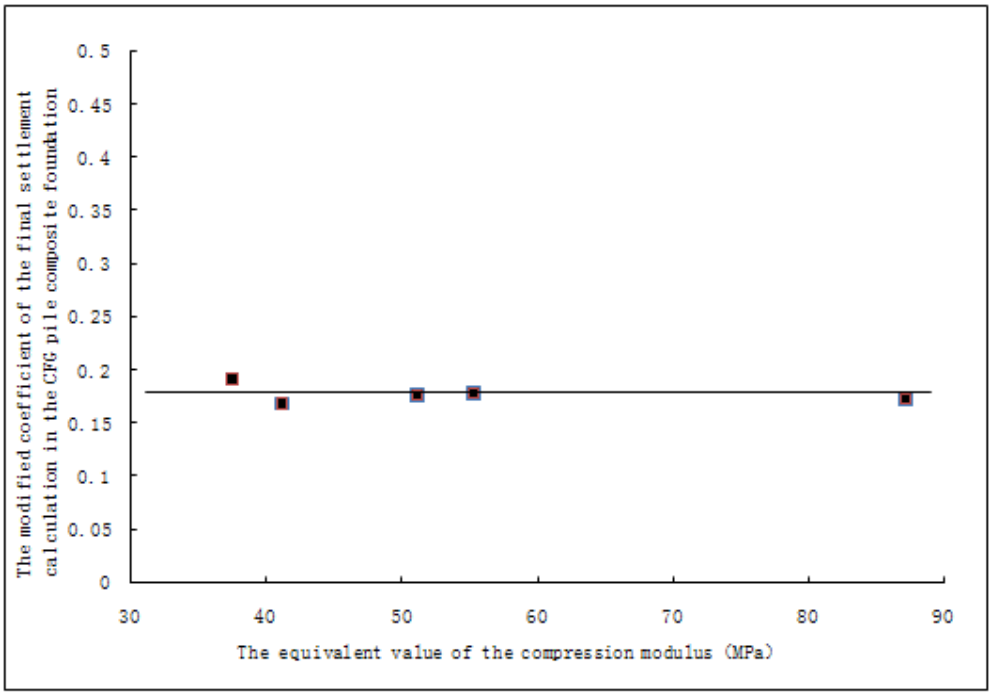


Fig.3 The distribution diagram of modified coefficient of the settlement calculation

The relation of the modified coefficient of final settlement calculation in the CFG pile composite foundation in the engineering examples of Baotou is shown in Fig.3.

Fig.3 shows that the approximate distribution of the modified coefficient of the final settlement calculation in the CFG pile composite foundation is on both sides of $\psi'_{sp} = 0.178$ when the equivalent value of the compression modulus in five engineering examples $\overline{E'_s}$ >35Mpa. We can get $\psi'_{sp} = 0.178$ when $\overline{E'_s}$ >35Mpa in Baotou area.

**The tests on the modified calculation formula and the correction and applicability of modified coefficient proposed in this paper**

By separately using the calculation proposed in this paper and the formula recommended by the norm, we calculate the settlement in another practical engineering examples chosen in Baotou area (example 6), and compare with the observed data in an engineering practice. In an engineering example, the soil physical and mechanical indexes in various soil layer and the parameters of the settlement calculation in foundation are shown in Table 2. The calculation results of the final settlement are summarized in table 3.

Table 2. The soil physical and mechanical indexes and the parameter table of the settlement calculation in foundation

| Soil layer | Thickness $h_i$(m) | Severe $\gamma$(kN/m$^3$) | compression modulus $E_s$ (MPa) | Limit shaft resistance $q_{si}$ | Ultimate tip resistance $q_p$ | Comprehensive vale of bearing capacity $f_{ak}$ (kPa) |
|---|---|---|---|---|---|---|
| ①miscellaneous fill | 0.45 | 17 | 3 | | | |
| ② collapsible silt | 1.43 | 17.3 | 6 | | | 160 |
| ③gravel sand | 3.81 | 20 | 30 | 60 | | 280 |
| ④silty clay | 6.73 | 19.7 | 7 | 60 | | 180 |
| ⑤silty clay | unrevealed | 19.7 | 8 | 70 | 1200 | 190 |

Table 3. The summary sheet of final settlement in the CFG pile composite foundation

| Characteristic value of loading capacity of single pile (kN) | Characteristic value of loading capacity of Composite foundation (kPa) | The equivalent value of the compression modulus (Mpa) | The final settlement calculated by normative formula (mm) | The final settlement calculated by modified formula (mm) | The actual observed final settlement (mm) |
|---|---|---|---|---|---|
| 2931.5 | 512.3 | 38.3 | 25.7 | 34.3 | 36.0 |

The Table 3 shows that the final settlement calculated by the modified formula proposed in this paper is very close to final settlement in the engineering practice, the error is within 5%,. However, there is a large difference between the final settlement calculated by the formula which is recommended by the norm and final settlement in the engineering practice. Thus, the modified formula of the final settlement calculation in the the CFG pile composite foundation proposed in this paper and it is correct. The modified formula and coefficient proposed in this paper will have a positive effect on the refined calculation of the final settlement in the CFG pile composite foundation of Baotou.

**References**

[1] Mylonakis G, Gazetas G. Settlement and additional internal forces of grouped piles in layered soil [J]. Geotechnique, 1948, 48(1) :55-72.

[2] Colye, H B, Reese, L C. Load Transfer for Axially Loaded Piles in Clay [J]. J.S.M.F.D. ASCE,1966, (92) :1-26.

[3] Randolph M F, Worth C P. Analysis of deformation of vertically load piles [J]. Geotechnical engineering division. Proceedings of the American Society of Civil Engineers. 1978,(104) : 1465-1488.

[4] Randolph M F, Worth C P. An analysis of vertical deformation of pile groups [J].Geotechnique. 1979, 29(4) :423-439.

[5] Paolo Carrubba. Skin friction of large-diameter piles socketed into rock [J].Can.Geotech. 1997, (34):230-240.

[6] Seed H B, Reese L C. The action of soft clay along friction piles [J]. Trans. ASCE, 1957, 122:731-754.

[7] JGJ6-2011,Technical Code for Tall Building Box Foundations and Raft Foundations [S].BeiJing: China Building Industry Press,2011:21-34(In Chinese).

[8] Jianguo Dong,Xihong Zhao. The theoretical and practical of soil-foundation interaction for tall building[M].ShangHai: Tongji University press,1997:41-54(In Chinese).

*Applied Mechanics and Materials Vols. 580-583 (2014) pp 524-531*
*© (2014) Trans Tech Publications, Switzerland*
*doi:10.4028/www.scientific.net/AMM.580-583.524*

# Three-Dimensional Numerical Analyses of Pile Response due to Braceded Excavation-Induced Lateral Soil Movement

Lin Li[1,a], Xiaoxin Hu[2,b], Guanghui Dong[3,c] and Ju Liu[4,d]

[1,2,4] School of Civil Engineering, Tianjin Key Laboratory of Soft Soil Characteristics and Engineering Environment, Chengjian University, Tianjin 300384, People's Republic of China

[3]The Metro Corporation of Tianjin, Tianjin 300051, People's Republic of China

[a]lilintjuci @126.com,[b]hu_xiaoxin @126.com, [c]dgh_8888@163.com, [d] l_b_t_x@126.com

**Keywords:** Braced excavation, Lateral displacement , Distance, Pile stiffness, Axial load.

**Abstract.** Using the explicit finite difference code FLAC3D, the behavior of pile adjacent to braced excavation is investigated. The Modified-cam clay constitutive model was employed to model the non-linear stress-strain soil behavior, and the pile was assumed to have linear elastic behavior. The interface model incorporated in FLAC3D code was used to simulate the soil/pile contact, The built-in 'fish' language was used to calculate the data demanded. The pile response such as pile deflection, bending moment and lateral soil pressure were studied, and it is shown that the pile response is different from that caused by the excavations which are unstructted. In "standard" problem, the effect of different pile head constraints on the pile response was investigated, the effect of lateral displacement of the wall, distance from the excavation face, pile stiffness, pile length and axial load on the pile response are also investigated when the pile head is constrained from deflection. The research finding was compared with other published case history and reasonably good agreement was found between them.

## Introduction

In dense urban environments where land is scarce and buildings are closely spaced, deep excavation for basement construction and other underground facilities is unavoidable. Deep excavation work for a new building would result in soil movement behind the retaining structure. The soil movement might induce considerable bending moment and deflection on the pile foundations supporting existing structures nearby. As pointed out by Poulos, the lateral soil movement is considered to be more critical for adjacent piles, especially concrete pile, as piles are often not designed to sustain significant lateral loading.

This problem has been investigated extensively by many authors. For example, Yang and Zhou(2005)[1] employed the three-dimensional elastic-plastic finite element method to study the pile response due to unstructted excavation-induced soil movements. Zheng and Yan(2007) [2]performed a field measurement and the influences of various parameters on pile response due to adjacent excavation were studied with three-dimensional finite element mode. Chen and Wang(2008) [3]used the geotechnical finite element numerical analysis software Plaxis 8.2 to simulate the effect of many factors on the behaviors of adjacent piles. Poulos and Chen(1996, 1997) [4,5]used two-stage analysis involving the finite-element method and the boundary-element method to study the pile response due to excavation-induced lateral soil movement and design chart for estimating the pile moments and deflections were presented. A. T. C. Goh and K.S. Wong(2003) [6] carried an actual full-scale instrumented study to examine the behavior of an existing pile due to nearby excavation activities resulting from the construction of a 16m deep cut-and -cover tunnel. C. F. Leung, Y. K. Chow and R. F. (2000) [7], D. E. L. Ong, C. E. Leung and Y. K. Chow (2006) [8]carried out centrifuge model studies to investigate the effect of the excavation-induced soil movement on adjacent single pile in sand and clay.

Although lots of numerical studies were carried out, some disadvantage still existed, such as the ideal elastic-plastic model was employed for the excavation simulating and the pile was modeled

using beam element. In this paper, using the commercially available three-dimensional code FLAC3D, the behavior of the pile adjacent to excavation is investigated, this code used an explicit finite difference program to study numerically the mechanical behavior of a continuous 3D medium as it reaches equilibrium or steady plastic flow, the explicit Lagrangian calculation scheme and the mixed-discretization zoning technique used in FLAC3D ensure that plastic failure and flow are modelled very accurately.

## Details of Numerical Model

For simplifying the numerical analysis, the model was cut out from a rectangular foundation pit. The length of the model is only 20m, only 1/2 model was conducted for symmetry, as is shown in Fig. 1. The thickness of the diaphragm wall is 0.8m and the height is 26m. The width of the foundation pit is 10m(1/2 model) . The boundary conditions for the soil are as follows: the nodes at the top face are free to move, the nodes at the bottom face of the soil are fixed vertically, and the nodes at other faces are fixed horizontally. A total of 37200 elements and 43582 nodes were used for this analysis.

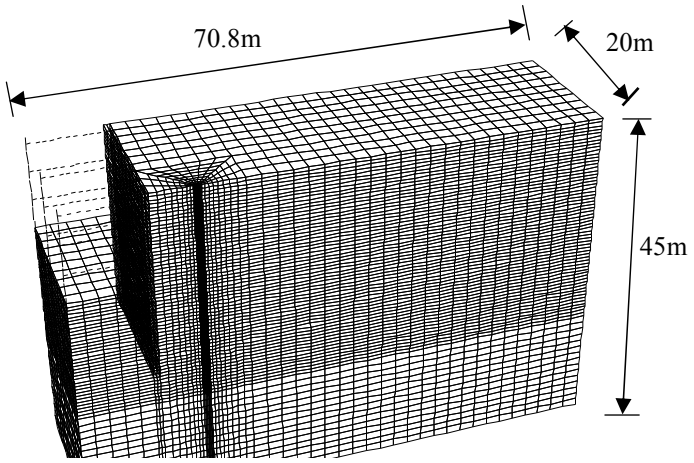


Fig.1. Three dimensional finite difference model

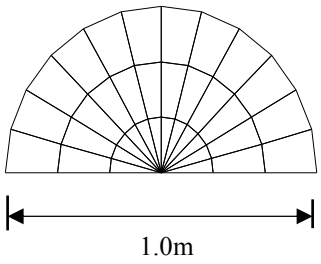


Fig. 2. Cross section of pile

The modified-cam clay constitutive mode was employed to model the non-linear stress-strain soil behavior. Total stress analysis with undrained conditions was assumed with the following soil parameters: the unit weight of the soil $\gamma$=1.9kN/m$^3$, the void ratio e=0.62, the coefficient of earth pressure at rest $K_0$=0.5, $\lambda$=0.09, $\kappa$=0.0093, M=0.90, poisson's ratio $\mu$=0.35, and over consolidation ratio OCR=1. The parameters of the soil is equal to the 5th layer soil of Tianjin , which is modified by considering the structural property of the soil(Meng, 2009) [9].

The solid elements used for modeling the pile were assumed to have linear elastic behavior. Poisson's ratio of $\mu$=0.3 was used. The diameter of the pile is 1.0 m, the adopted mesh of the pile section is shown in Fig. 2.

The calculation steps of the numerical model are presented in Table 1.

Table 1. Calculation Steps of Excavation

| Step | Construction Conditions |
|---|---|
| 0 | Compute the initial ground stress |
| 1 | Excavate to -1.5m and install the first level struts |
| 2 | Excavate to -5.5m and install the second level struts |
| 3 | Excavate to -9.5m and install the third level struts |
| 4 | Excavate to -13.0m |

## Results and Discussions

In general, the response of the pile adjacent to excavation is relevant to the lateral wall displacement, which was related to the relative stiffness parameter EI/h$^4$(EI is the bending rigidity of the wall, h is

the vertical space of the structs)and other factors . In "standard" problem, the maximum lateral displacement of diaphragm wall was 0.30%H(H is the maximum excavation depth ).

In the following analyses, a "standard" problem with constant "standard" parameters is analyzed first, and then some key parameters are varied to investigate their influence on pile response. The parameters defining the "standard" problem are as follows: X=6m, distance from the excavation face; Lp=30m, pile length; Ep=30GPa, modulus of elasticity of the pile; $\delta_{hmax}$=0.3%H, the maximum lateral displacement of the diaphragm wall.

Because three pile head restraints condition are used, the pile response for "standard" problem are shown in Fig. 3, Fig. 4 and Fig. 5. A negative value of deflection indicates that the deflection is moving towards the excavation face, A positive value of bending moment indicates that the side of the pile which is far away from the excavation is in tension, and a positive value of lateral soil pressure indicate the lateral soil pressure acted on the side of pile which are far away from the excavation. Pile deflection is monitored at the centre of the pile elements. The forces per unit length acting on the pile node are calculated by summation the component of the normal forces acting on the interface nodes and the shear drag forces around the pile shaft in the direction of soil displacement at the same level of pile length.

**Result for "standard " problem.** The pile response under different head constraints for 4 stages of the excavation are shown in Fig. 3, Fig. 4 and Fig. 5. It can be seen that the pile response increase with increasing excavation depth.

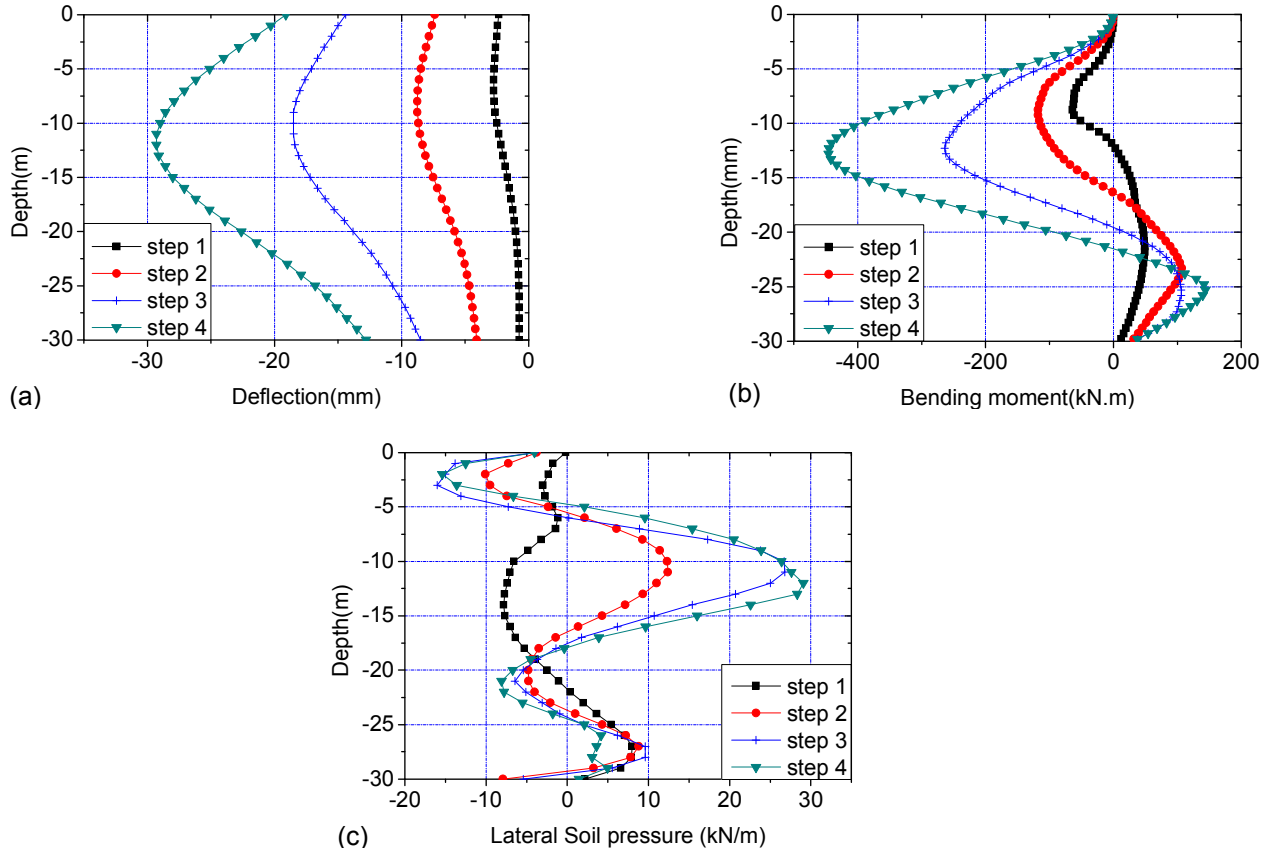


Fig. 3. Pile response for "standard" problem (free-headed)

Fig. 3 shows the pile response under free head condition(free-headed). For braced excavation, the movement of the top of pile was slightly larger than the surface lateral soil movement, so a 'negative' soil pressure is introduced on the upper part of the pile shaft, i.e. soil pressures acting on the opposite side of the pile on the top of the pile. With the depth increasing, the 'negative' soil pressure on the upper part of the pile shaft turned to 'positive' soil pressure in the middle part of the pile.

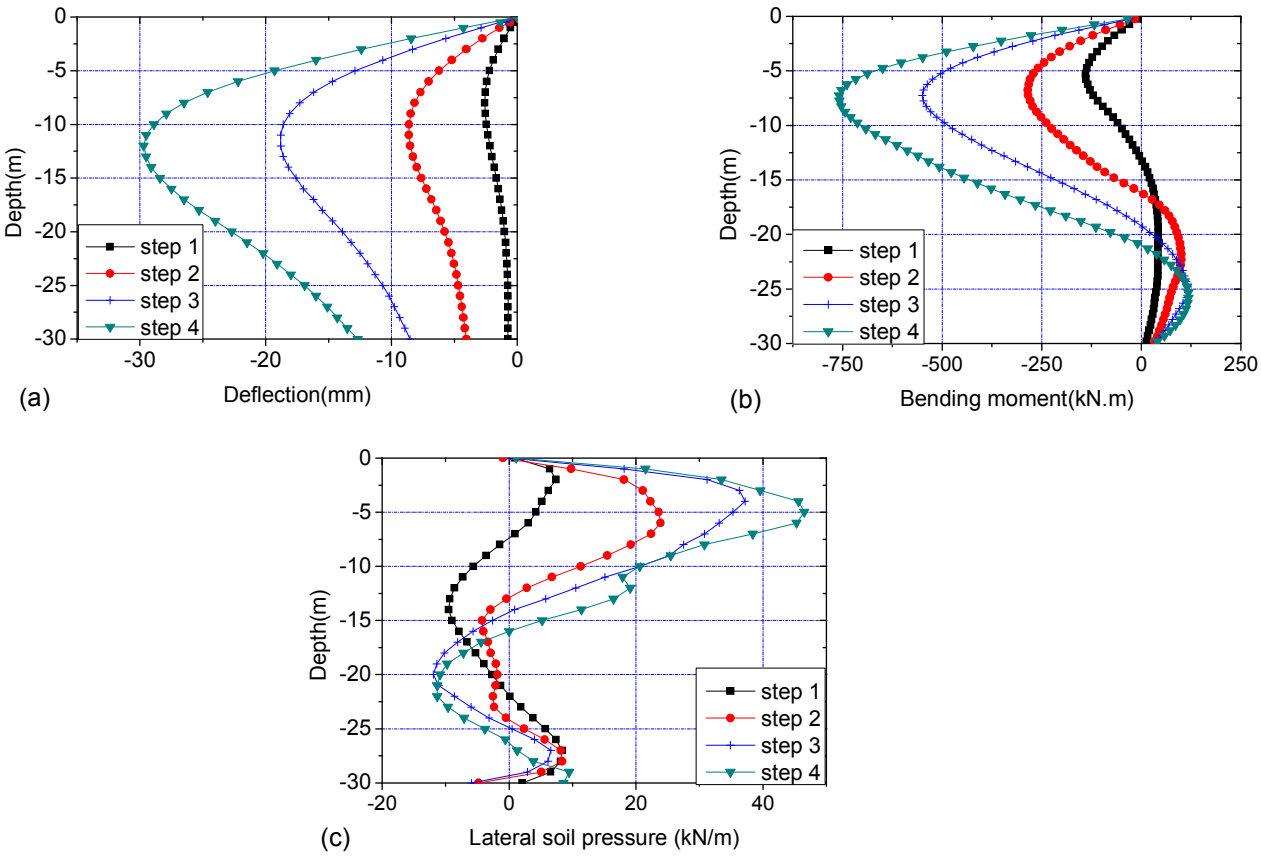


Fig 4. Pile response for "standard" problem(fixed deflection-free rotation)

Fig. 4 shows the pile response when the pile head is constrained from deflection. But the rotate is allowed(fixed deflection-free rotation). This corresponds to the situation that the single pile supporting superstructure columns connected by tie beam to enhance the overall foundation stability, The tie beam are usually long and slender with the main function of providing lateral support to the individual piles without much restriction on the pile-head rotation, thus connection between the tie beam and the piles maybe approximately assumed as a hinge connection. The pile head deflection is effectively eliminated, no bending moment developed at the pile head, but the negative moment and the lateral soil pressure along the upper pile shaft have a remarkably increase, the depth of the maximum negative moment is -7m, that is higher than -12m which is the depth under free head condition.

Fig.5 shows the pile response when the pile head is fixed against both deflection and rotation(fixed-fixed condition), which is likely to correspond to the situation where a massive pile cap is restrained by ground beams, or when the pile is part of pile raft foundation for a large structure, A signification positive bending moment developed at the pile head due to the constraint in rotation besides the pile head deflection is effectively eliminated. The lateral soil pressure on the pile shaft is the largest among the three constraints cases.

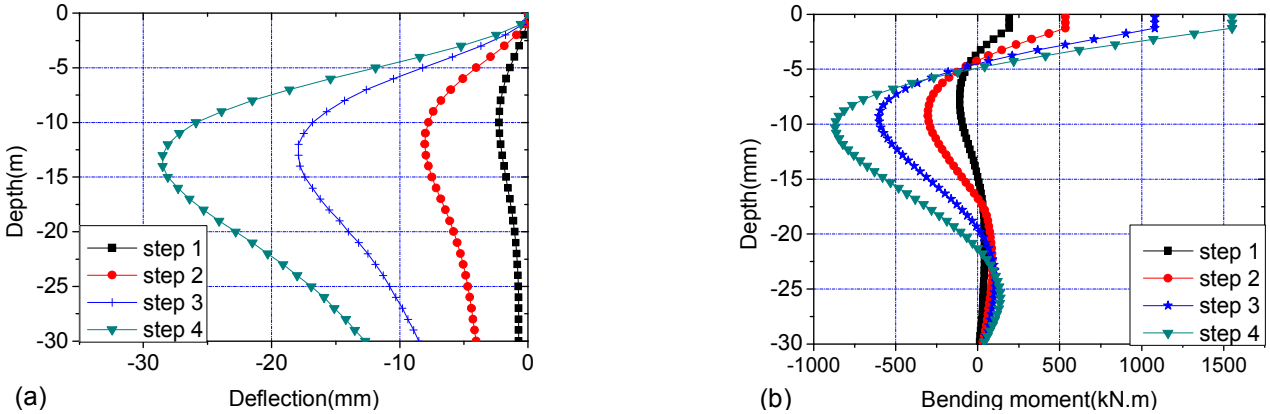

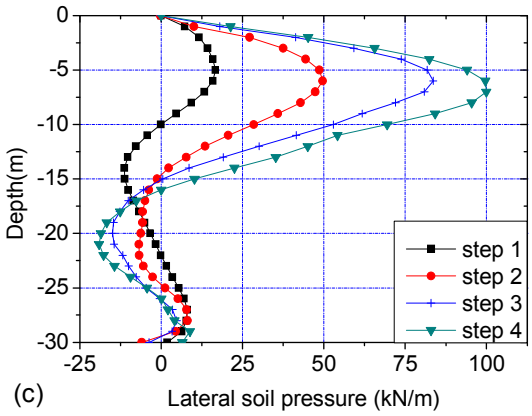


Fig. 5. Pile response for "standard" problem(fixed-fixed )

**Influence of the lateral displacement of the wall.** In engineering practice, the lateral displace--ment of the wall may vary in large scope. The influence of lateral displacement of the wall on the pile response for maximum excavation depth is shown in Fig. 6， the maximum lateral displacement of the wall is respectively be 0.28%H, 0.3%H, 0.35%H and 0.45%H(H is the maximum excavation depth ).

The pile head condition is constrained from deflection and the distance from excavation face is 6m in this case. It can be seen that the deflection, the bending moment and the lateral soil pressure all significantly increase with the increasing lateral displacement of the wall.

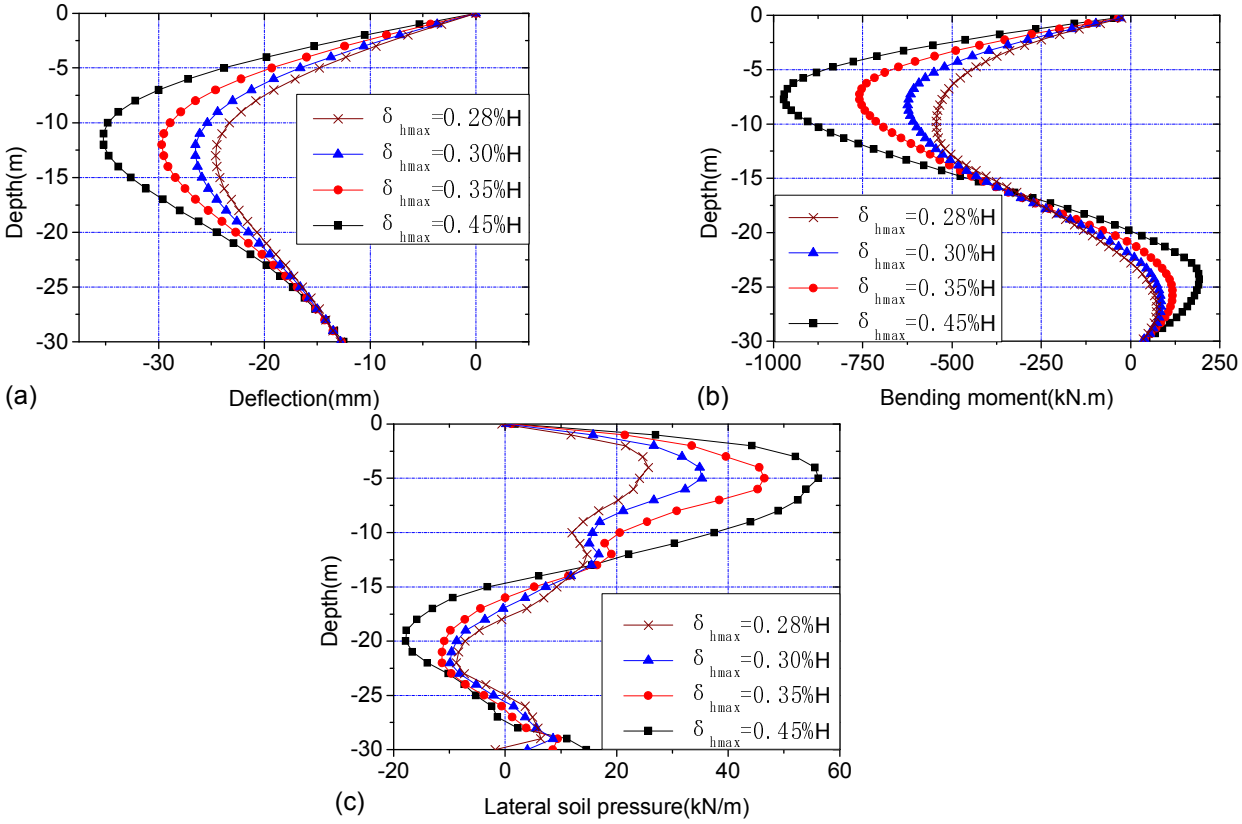


Fig. 6. Effect of retaining wall stiffness on the response of pile

**Influence of the distance from the excavation face.** When the pile head only constrained from deflection(fixed deflection-free rotation), the influence of distance on the pile response for maximum excavation depth is shown in Fig. 7. The distribution of the deflection, bending moment and lateral soil pressure are quite similar in shape at various distance, but the maximum value decreases with the distance increasing.

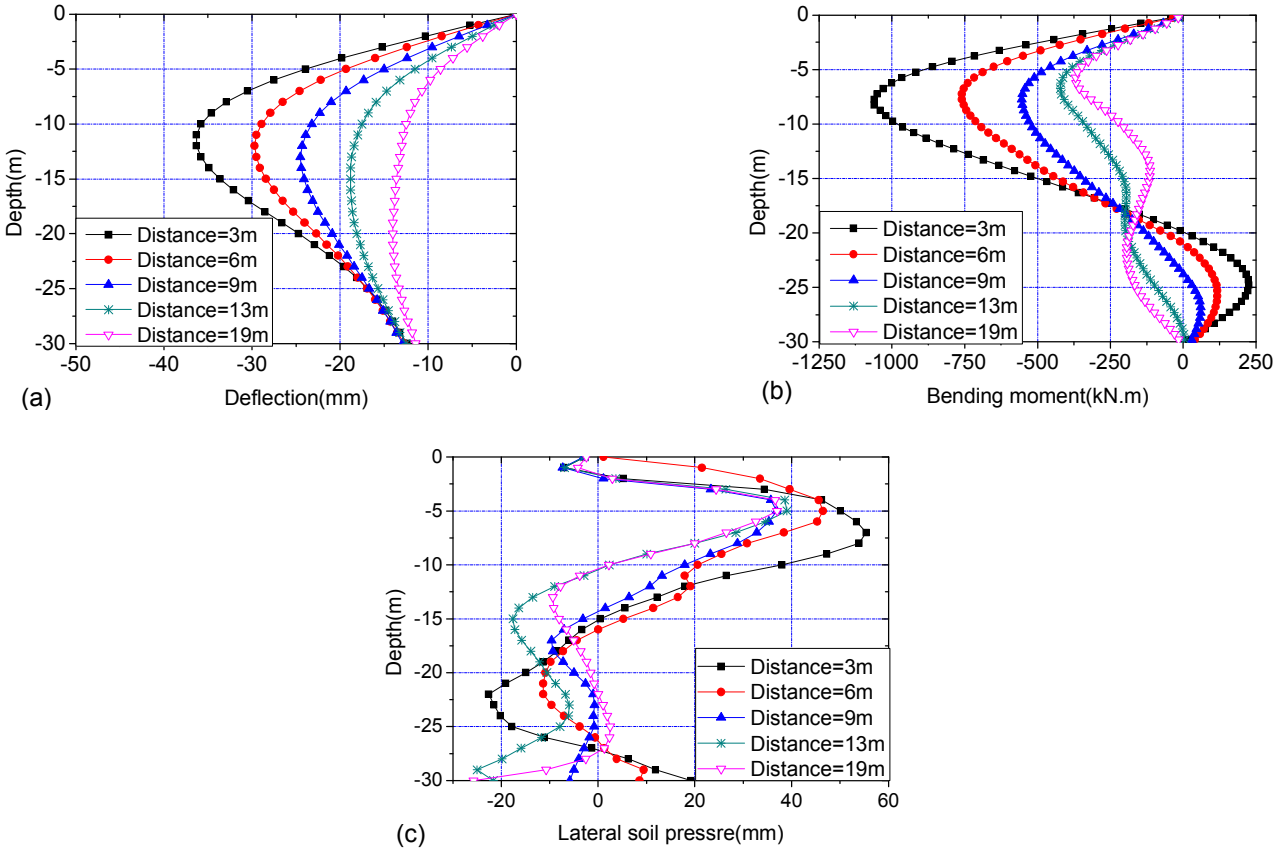


Fig. 7. Effect of distance from excavation face on the response of pile

**Influence of the pile stiffness.** When the pile head only constrained from deflection(fixed deflection-free rotation), the influence of pile stiffness on the pile response for maximum excavation depth is shown in Fig. 8. Only the young's modulus of pile stiffness is varied. It can be seen that the pile deflection decreases with the pile stiffness increases, and the pile bending moment and lateral soil pressure increase greatly with the pile stiffness increases.

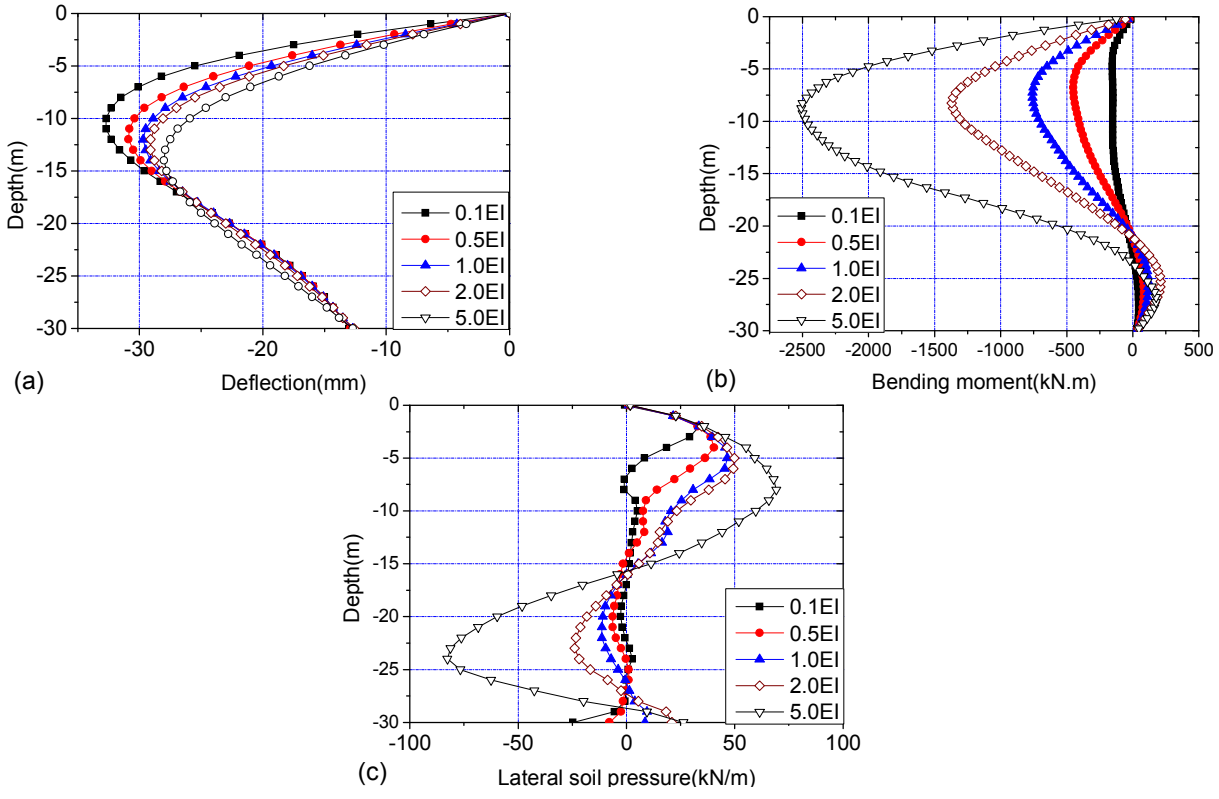


Fig. 8. Effect of pile stiffness on the response of pile

**Influence of pile length.** A cases of pile(pile head only fixed deflection) have been studied. The pile behavior is quite similar when the pile length is more than 22 m. When the pile length is less than 10 m, the deflection of the pile is near to a straight line, and the bending moment of the whole pile is negative.

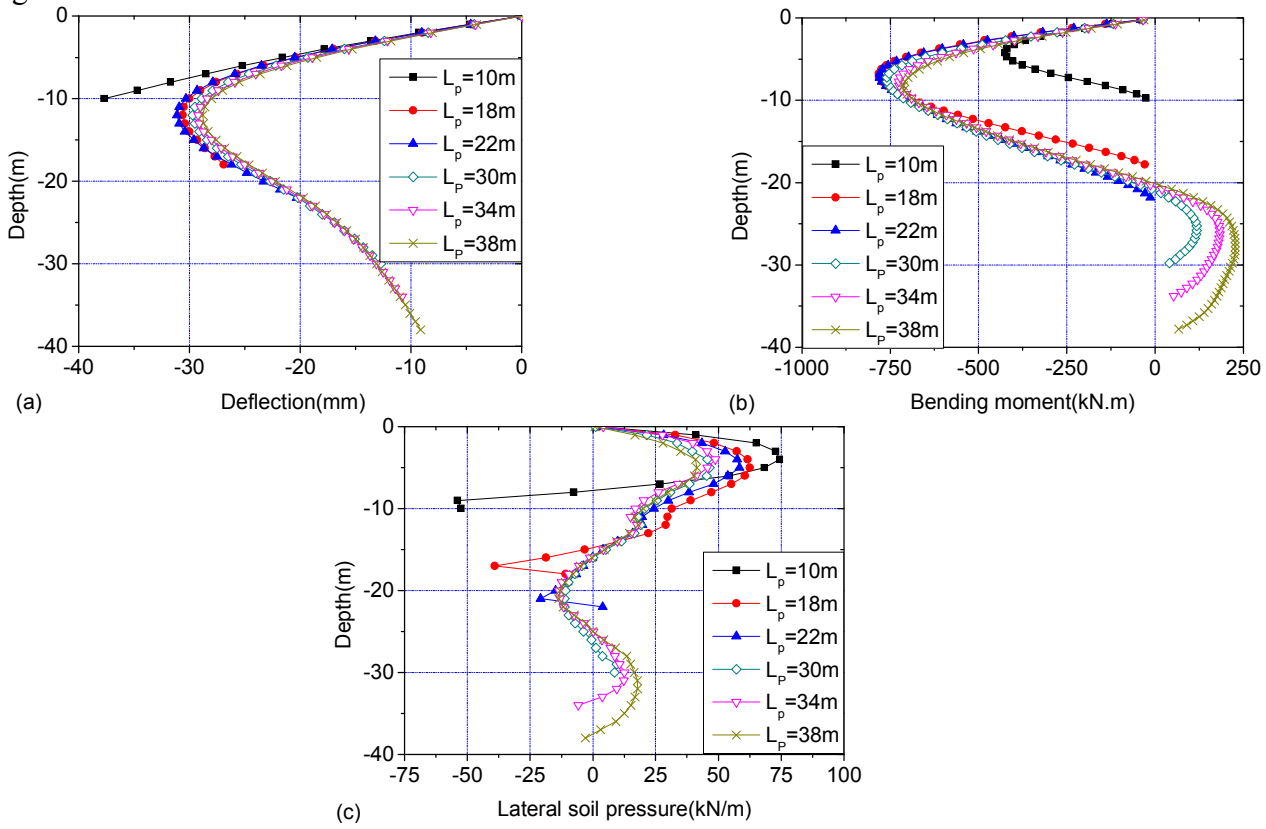


Fig. 8. Effect of pile length on the response of pile

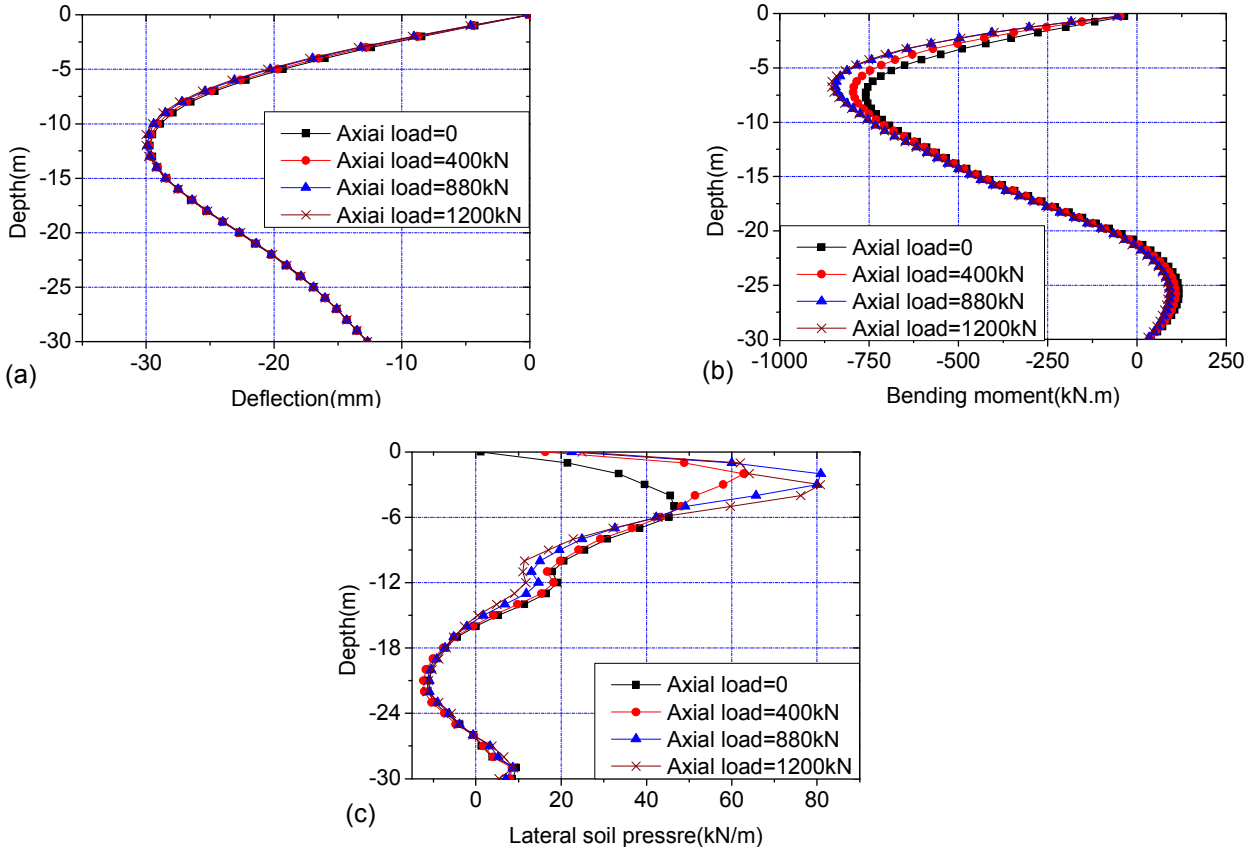


Fig. 9. Effect of axial load on the response of pile

**Influence of axial load.** The effect of axial load on pile response for maximum excavation depth is shown in Fig. 9, Only the pile head in the fixed deflection-free rotation case is introduced. It can be seen that the pile deflection, bending moment, and lateral soil pressure increase with the axial load increases, but the increase is very small due to the constraint of the surrounding soil. This shows little difference with Guo and Ghee (2006)[10], but the effect of the axial load is less than that of Guo and Ghee (2006).

## Conclusions

The influence of braced excavation on adjacent pile was studied by numerical analysis, the distribution of deflection, bending moment and lateral soil pressure along the pile is significantly different from that caused by unstructted excavation[11], but the laws of the influence of some parameter on pile response are similiar. The results given by the numerical analysis indicate that the pile response increase with the increasing excavation depth and the increasing lateral displacement of the wall. With the increasing distance from the excavation face, the pile response decrease. With the pile stiffness increasing, the pile deflection decrease, the pile bending moment and lateral soil pressure increase. The pile response increase with the axial load increasing, but the increase is very small.

## Acknowledgements

The authors would like to acknowledge the National Nature Science Foundation of China(Found No:41172233)for financial support.

## References

[1] Min Yang, Hongbo Zhou. China Civil Engineering Journal, Vol. 38(2005), p. 91(in chinese).

[2] Gang Zheng, Zhixiong Yan, Huayang Lei and Yang Lei. Chinese Journal of Geotechnical Engineering, Vol. 29(2007), p. 638(in chinese).

[3] Chen, F. Q. and Wang, J. W：Chinese Journal of Rock and Soil Mechanics, Vol. 29(2008), p. 1971 (in chinese).

[4] H. G. Poulos and L. T. Chen. Canadian Geotech. J. Vol. 33(1996). p. 670

[5] H. G. Poulos and L. T. Chen. J. Geotechnical and Geoenvironmental Engineering, Vol. 123(1997) p. 94.

[6] A. T. C. Goh, K. S. Wong, C.I. Teh and D. Wen. Journal of Geotechnical and Geoenvironmental Engrg. Vol. 129(2003), p. 383.

[7] C. F. Leung, Y. K. Chow, and R. F. Journal of Geotechnical and Geoenvironmental Engrg, Vol. 126(2000), p. 947.

[8] D. E. L. Ong, C. E. Leung, and Y. K. Chow. Journal of Geotechnical and Geoenvironmental Engrg, Vol. 132(2006), p. 36.

[9] Meng, L."Study on structural property and constitutive model for tianjin soft clay." Master's thesis(2009), Tianjin University, Tianjin, China(in chinese).

[10] W. D. Guo and Ghee E.H. *Behavior of axial loaded pile Groups subjected to lateral soil movement.* Proceedings of Sessions of GeoShanghai., GSP2006, 153. p.174

[11] Lin Li, Guanghui Dong, Fenghui Zhang and Min Yang. T*hree-Dimensional Numerical Analyses of Pile Response due to Unstructted Excavation-Induced Lateral Soil Movement.* Submitted to the 3rd GeoShanghai International Conference, accepted.

*Applied Mechanics and Materials Vols. 580-583 (2014) pp 532-538*
*© (2014) Trans Tech Publications, Switzerland*
*doi:10.4028/www.scientific.net/AMM.580-583.532*

# 3D finite element numerical analysis for stability calculation of high steep rock slope

Xiaofeng Xie[1,a] Yuanliang Liu[1,b] Jiayong Han[1,c] Liang Xing[1,d]

[1] Guangdong Provincial Academy of Building Research, No.121, Xianliedong Road, Guangzhou City, Guangdong Province, China.

[a]email:xiexf2000@263.net, [b]email:liang801014@126.com, [c]email:garvens@126.com, [d]email:304717049@qq.com

**Key words:** High steep rock slope; 3D finite element numerical analysis; Stability analysis.

**Abstract.** Due to the high steep rock slope stability analysis its complex geological conditions and other factors, its stability calculation has been a technical problems the field of slope engineering, in this paper, 3D finite element calculation software Midas GTS for side slope surface topography and slope internal faults, weak structural plane of complex three-dimensional geological modeling, it overcomes the complex slope geological modeling problem and simulates rainfall, earthquakes and other factors affecting the stability on the slope, calculated results more in line with reality, and the software calculates is in accordance with fact, it provides a useful reference for slope engineering.

## Introduction

Stability analysis of high steep rock slope has been a technical problem in the fields of engineering, if the slope stability can be calculated accurately, that is not only can predict slope failures or not, and the calculated results provides a scientific basis for later design and monitoring. However, due to the complex geological conditions, accurate analysis for its stability is not easy, this paper is on the basis of actual slope stability assessment project, Midas GTS finite element numerical simulation software is used for three-dimensional modeling of complex slope geological structure and analyzes the stability of the slope.

## Overview of high steep rock slope engineering

There was a rock slope engineering in Guangdong Province, the height is about 130m and length is about 302m, according to engineering survey data show that the overburden of bedrock is artificial fill soil and slope residual soil, its thickness is 2.30 ~ 8.45m, the lithology of bedrock are: shale, sandstone, geological conditions is complex, rock boundaries, fractures, weak structural plane are staggered, and there are another two through fractures $F_1$ and $F_2$, $F_1$is major fracture, trending toward is NE9°, the tendency is NW279°, the average angle is 78°; $F_2$ fault: trending toward is NW316°, the tendency is SW226°, dip 78°.

## 3D modeling of high steep rock slope

Midas GTS is an excellent finite element method (FEM) 3D numerical simulation software in engineering field which has fast and intuitive three dimensional modeling, rapid and very powerful ability in mesh generation, professional geotechnical analysis capabilities and intuitive analysis results, etc., it has been applied to the field of geotechnical engineering widely.

As the geological conditions of this rock slope is very complicated, rock boundaries , faults, weak structural plane are staggered , so three dimensional modeling is difficult, but Midas GTS is used to geometric modeling and mesh generation of slope geological and structural, focused divided slope complex surface, geography, stratified structure of rock, faults , weak structural plane , crush belt and son on, making it be closer to the actual three dimensional simulation geometry and spatial

distribution of slope ,it can more realistically simulate a three dimensional stress state and reflect rock and soil slope of actual slope, the calculated results are more in line with reality, and then using the finite element method to calculate the slope stability, specific process of three dimensional modeling is as follows:

**Three dimensional surface and geography generation of slope generated**. Using Midas GTS software terrain generator modules (TGM), import 3D DXF CAD in line (with real elevation contour lines, shown in Figure 1), the points is sampled as much as possible, because the more sampling points, the higher precision, and then it generates complex slope terrain and surface. (Shown in Figure 2)

**Using generated surface to segmentation entity to get slope model**. It is to ensure the boundaries of a solid model are level. On the basis of the solid model, according to the rock slope three dimensional coordinates of points, spatial distribution, fault strike, dip, spatial location of weak structural plane to generate a three dimensional curved surface and divided solid model, carved out of rock units, faults, weak structural plane, (Shown in Figure 3).

**Solid mesh is divided.** Generally it is divided tetrahedral mesh, the meshing size is smaller, the accuracy is higher, but the spent time calculating is longer, for some important key parts, such as faults, weak structural plane, bottom of slope and so on should be divided a little fine mesh to ensure its accuracy (Shown in Figure 4).

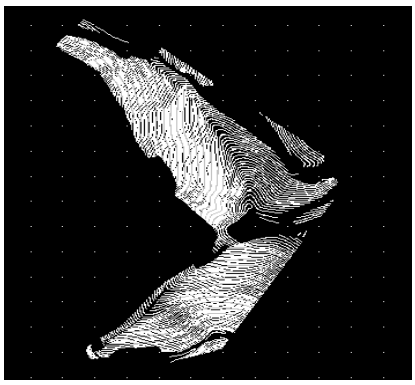

**Figure 1. Slope contour map**

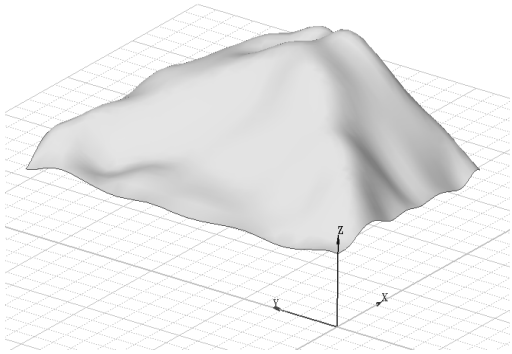


**Figure 2. Generated slope surface and geography**

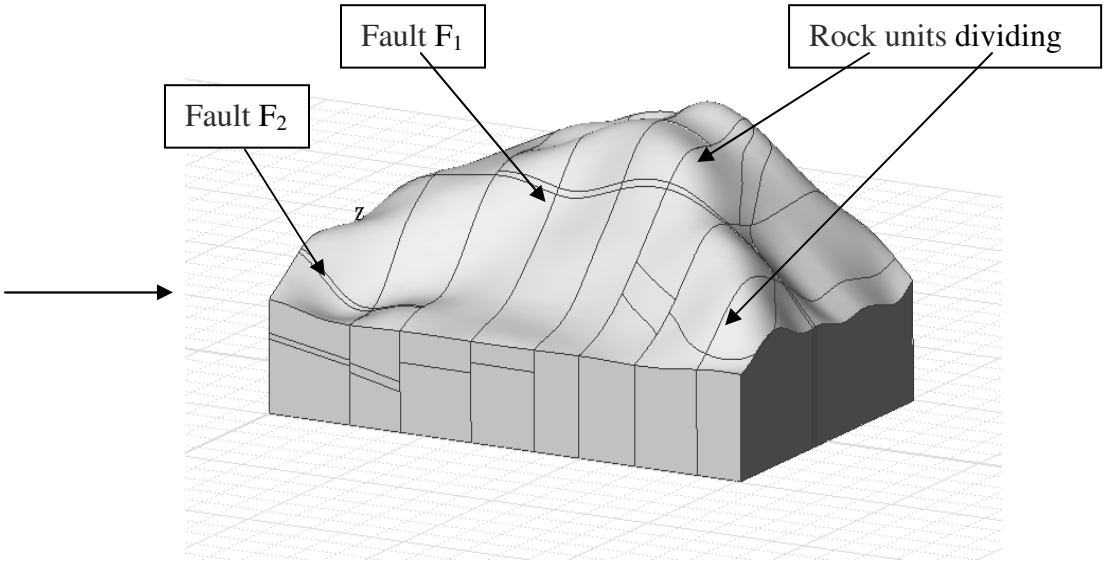


**Figure 3. Solid mesh of rock units, faults is divided**

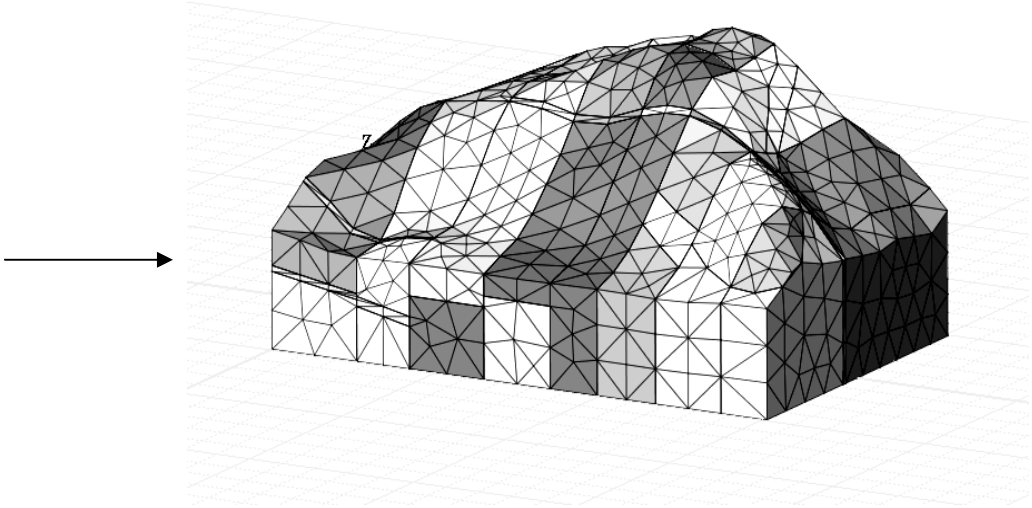

**Figure 4. Solid mesh is divided**

**Slope stability calculation**

**The rock unit calculation parameters.** Mechanical parameters of rock units are shown in Table 1.

**Table 1. Rock unit calculation parameters**

| Rock level | Rock unit classes and code | | Gravity Density (kN/m$^3$) | Shear Strength | |
|---|---|---|---|---|---|
| | | | | Angle of internal friction (°) | Cohesion (MPa) |
| Ⅳe | Good combined N5 | | 26.00 | 31.15 | 0.147 |
| Ⅴd | General combined N4 | | 25.50 | 29.00 | 0.120 |
| Ⅴc | Bad combined N3 | N3-3 | 25.00 | 19.00 | 0.080 |
| | | N3-2 | 25.00 | 18.50 | 0.070 |
| | | N3-1 | 25.00 | 18.00 | 0.060 |
| Ⅴb | very bad combined N2 | | | 13.00 | 0.035 |
| | | | | 18.00 | 0.030 |
| | | N2-2 | 24.50 | 12.50 | 0.045 |
| | | N2-1 | 24.50 | 12.00 | 0.040 |
| Ⅴa | extreme bad combined N1 | N1-5 | 22.00 | 8.55 | 0.033 |
| | | N1-4 | 23.00 | 8.55 | 0.030 |
| | | N1-3 | 24.00 | 8.50 | 0.030 |
| | | N1-2 | 20.50 | 13 | 0.030 |
| | | N1-1 | 23.50 | 8.45 | 0.030 |

## Engineering conditions analysis

**Groundwater level and rainfall.** According to the water table for each drill hole sectional view of survey data, a cross section water line is drawn, while the groundwater pressure is as external load, directly on the slope structure, it is in order to achieve a common effect of rainfall and the water table. According to the national weather station records of local rainfall condition, it is shown that local maximum 24 hours rainfall is 213.1 mm, there time is August 2, 1997 (statistical life :1956-2013 year). In finite element model, this is achieved by node flow of 2.5e-6m3 / s in slope model.

**The seismic fortification intensity.** According to《Seismic Design Code》（GB50011-2010）, local seismic intensity is 6 degrees, the design peak of acceleration is 0.05g. The project site conditions is rock, hence the earthquake seismic waves using class Ⅰ site seismic waves of GTS software, adjust amplitude reaches 0.05g, while duration is 24.96s,acquisition time interval is 0.01s, the seismic process is shown in Figure 5.(Ordinate is acceleration values (g), abscissa is time (s))

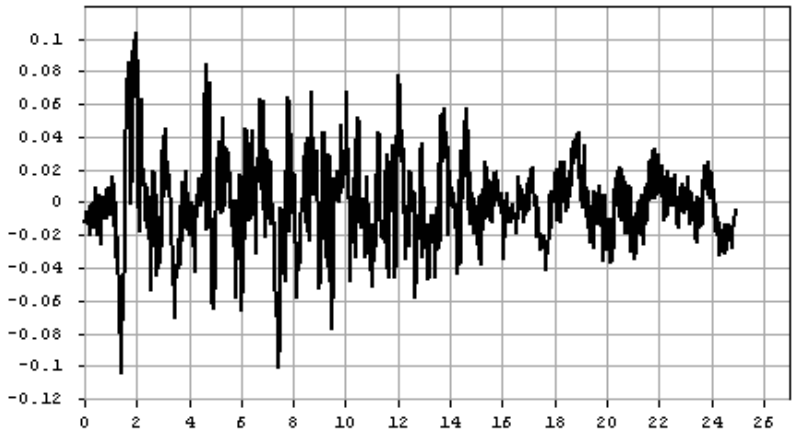


**Figure 5. Earthquake time curve**

Using the strength reduction method, rock slope is three dimensional analyzed under its own weight, heavy rainfall, earthquake three conditions effect, obtained the safety factor, the maximum shear strain (potential slip surface) of slope, shown in Figure 6～10.

## Numerical calculation results

### Under the action of gravity

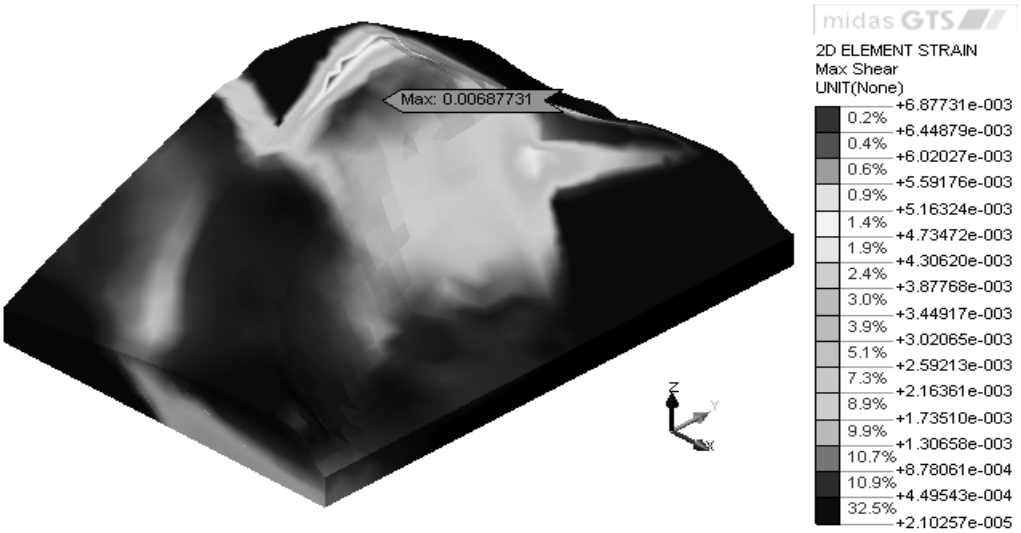


**Figure 6. The maximum shear strain**

**Under rainfall infiltration**

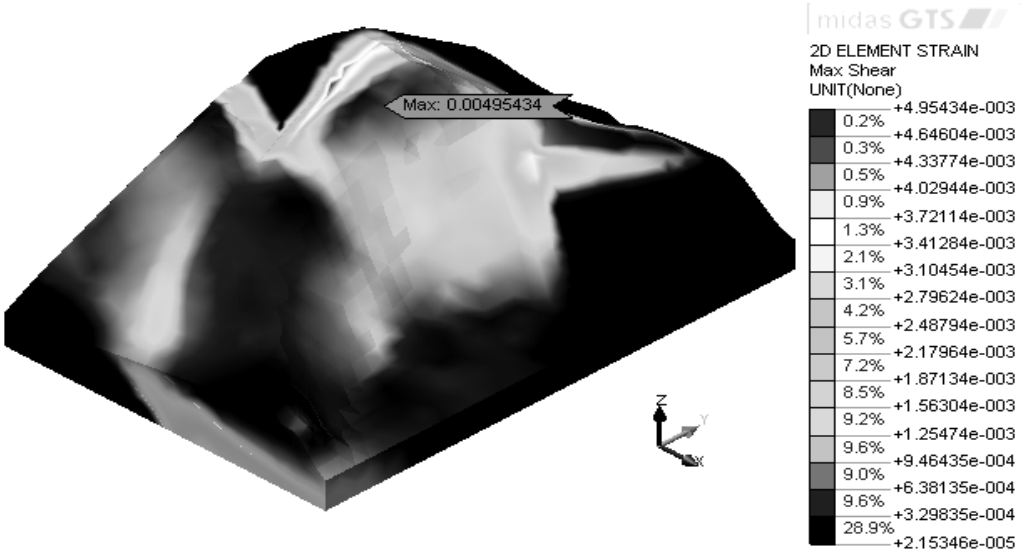


**Figure 7. The maximum shear strain**

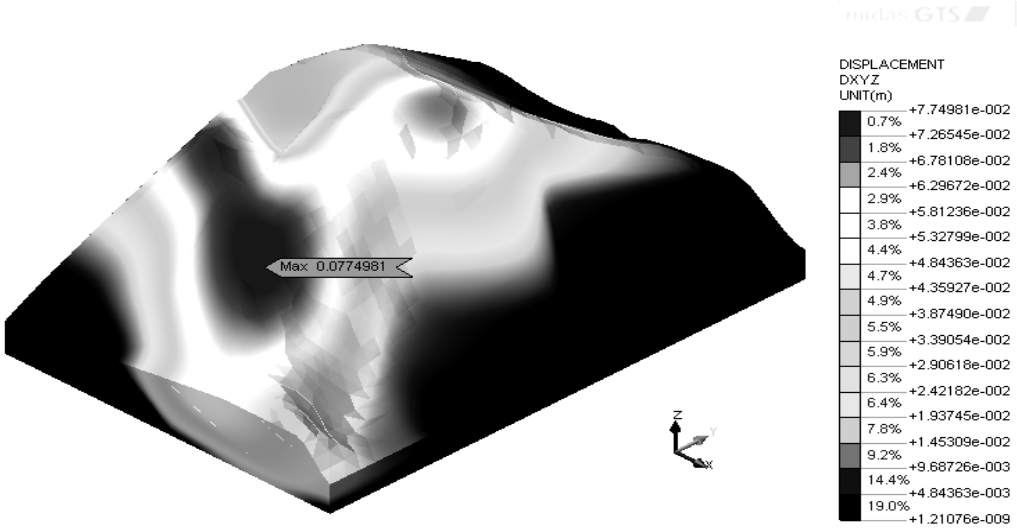


**Figure 8. Displacement**

**Under the action of earthquake**

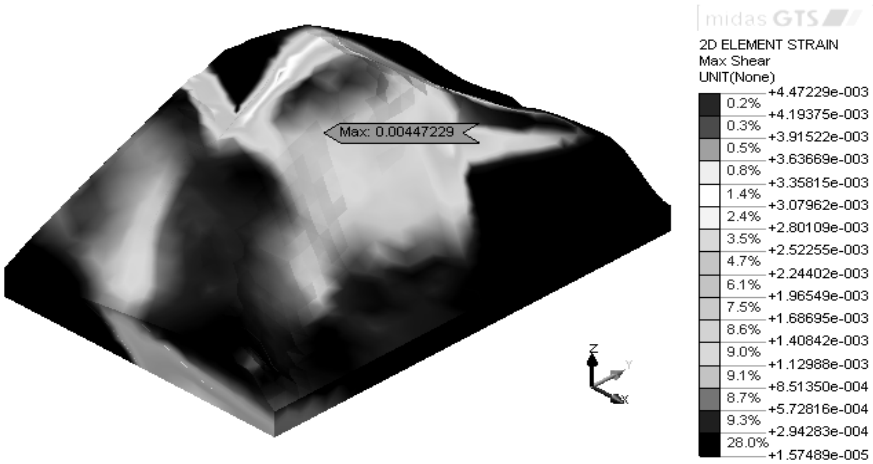


**Figure 9. The maximum shear strain**

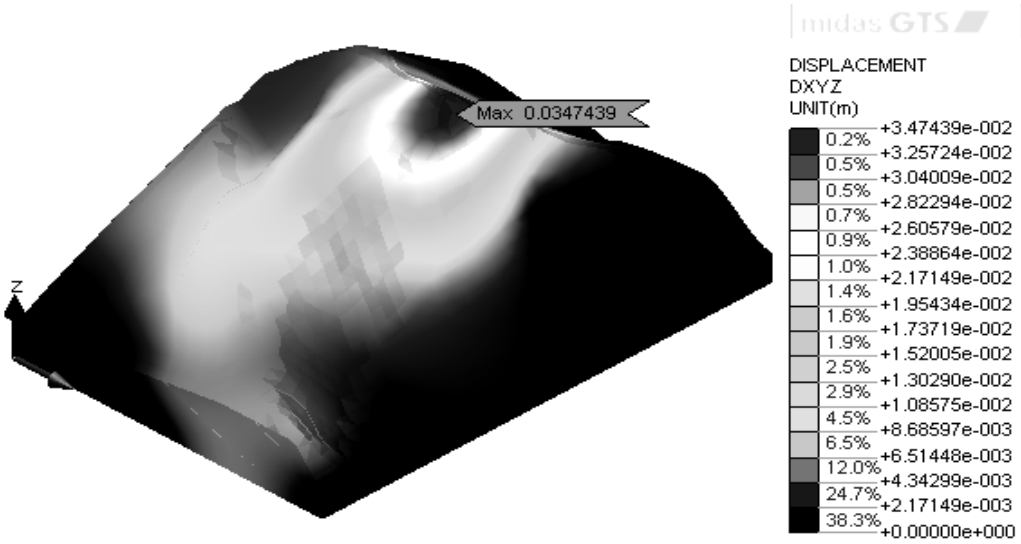


**Figure 10. Displacement**

**Stability calculation results**

**Table 2 Stability calculation results**

| Conditions effect, | Safety Coefficient | The maximum displacement (m) | The maximum limit yield stress （KPa） | The maximum Shear strain |
|---|---|---|---|---|
| Under the action of gravity | 1.2125 | —— | 1179.07 | 0.0033 |
| Under rainfall infiltration | 1.0875 | —— | 1114.39 | 0.0013 |
| Under the action of earthquake | 1.1625 | —— | 1126.71 | 0.00257 |
| Displacement under the action of gravity | —— | 0.158 | 1042.04 | 0.0035 |
| Displacement of Seismic time history analysis | —— | 0.0677 | 180.57 | —— |

**Based on the above calculated results:**

The slope is generally stable under action of gravity, but stability is bad in local section.

Three-dimensional analysis for large displacement and shear deformation of slope residual soil are main factor affecting slope safety.

Safety coefficient is reduced about 20%, the maximum displacement reaches 158mm under heavy rain seepage, under seismic safety factor is reduced about 15%, the maximum displacement reached 67.7mm, so in heavy rain and earthquakes, the slope is instable. The maximum stress occurs in the vicinity of the rupture zone, the security is determining the distribution of stress field across the slope here.

Verified by actual monitoring data show that the calculated results are accordance with reality.

## Conclusion

In this paper, Midas GTS finite element calculation software is used for complex geological bodies 3D modeling such as geological terrain and surface, internal faults, weak structural plane, it overcomes the difficult problem of slope complex geological modeling, and slope stability is calculated under simulating rainfall, earthquakes and other factors affecting, the results are accordance with reality, it provides a useful reference for slope engineering.

## References

[1] Chen Z,Wang X,Haberfield C,Yin J,Wang Y. A three-dimensional slope stability analysis method using the upper bound theorem,part 1: Theory and method[J]. International Journal of Rock mechanics and Mining Sciences, 38: 369-378, (2001).

[2] ChenZ,MiH,ZhangF,WangX. A simplified method for 3D slope stability analysis [J]. Canadian Geotechnical Journal, 40: 675-683, (2003).

[3] Huang C C,Tsai C C,Chen Y H. Generalized method for three-dimensional slope stability analysis[J]. Journal of Geotechnical and Geo-environmental Engineering, ASCE. 128(10): 836-848, (2002).

[4] Chen Mi H,Wang X. A three-dimensional limit equilibrium method for slope stability analysis[J] Chinese Journal of Geotechnical Engineering, 23(5)：525-529, (2001).

[5] Xie M,Esaki T,Zhou G,Mitani Y. GIS-based 3D critical slope stability analysis and landslide hazard assessment [J] Journal of Geotechnical and Geo-environmental Engineering, ASCE, 129(12): 1109～1118, (2003).

*Applied Mechanics and Materials Vols. 580-583 (2014) pp 539-543*
*© (2014) Trans Tech Publications, Switzerland*
*doi:10.4028/www.scientific.net/AMM.580-583.539*

# A Certain Foundation Pit Support Design and Construction in Baotou

Xiankai Bao[1, a],Menghui Que[2,b]

[1,2]College of Architecture and Civil Engineering, Inner Mongolia University of Science andTechnology, Baotou, Inner Mongolia China 014010

[a] E-mail:bxkzlm@163.com, [b]157336347@qq.com

**Key words:** Foundation pit support, soil nailing wall, supporting, construction.

**Abstract.**We adopt the supporting scheme of soil nailing wall by comparison and selection combining engineering geological conditions and surrounding buildings load situations. And introduce focally its supporting principles and major parameters and main construction points. The scheme meets the engineering requirements proved by the construction acceptance inspection with its safe and rational design and construction convenience.

## Introduction

The soil nailing wall is a supporting technique strengthening slope and excavation soil stability developing in resent two or three decades [1].It is a self stabilization and retaining-soil behind the wall supporting structure. By a combined action of top-bottom slender and dense soil nailing in situ soil, steel mesh reinforced shotcrete and reinforced soil mass. And the wide applications of the structure in slope enhancing and foundation pit supporting at home and abroad benefited from its characters of non pollution, low noise, stability and reliability, obvious social effect and economic effect comparing with other structures. The technology applies in parts above groundwater level or artificial fill, cohesive soil and weakly consolidated sand after artificial precipitation [2] [3].

## Project profile

### Brief Introduction

It is a geotechnical engineering reconnaissance task in detail survey delegated by China IPPR International Engineering Corporation for proposed Baotou Steel Xinxingshuian garden engineering. It is located in east of Kunriver road, north of Qingnian road, and south of Baiyan road. It is a flat terrain, Lower from north to south, of ground level from 1066.38～1068.59m, alluvial fan front edge of Kun river, and rich in quaternary sediment in thickness. The site with 65m length and 5.5m height in 2m north of D business district was sloped 1: 0.3 due to the location limits. But it partial collapsed in rain flood season because of simple laying of Φ8@200 steel mesh and thinner C20 concrete than <50mm.So we proposed soil nailing wall for re-supporting considering the engineering conditions and technical and economical factors.

### Engineering Geology and Hydrological Conditions

Besides artificial miscellaneous fill(thickness of 0.2～0.4m)in surface in the engineering investigation, It is Holocene rushed diluvia all above 35.0m depth range and stated according lithology and engineering properties:

The First layer is a little wet and dense collapsible silt, with mica and white stripe and macroporous structure, and soaking collapsibility. Its thickness is between 1.7～5.3m, layer level is between 1061.05～1064.98m.

The second layer is tawny fine sand of feldspathic and quartziferous, a little wet and dense to middle dense in natural state. Its thickness is between 0.3～4.2m, layer level is between 1059.02～1063.74m.The third level is variegated gravelly sand of feldspathic and quartziferous, with good grain composition and a little grait. Its thickness is between 14.9～19.7m, layer level is between 1040.55～1046.58m.The third[1] level is tawny silty clay of mica and iron oxide, plastic state in natural state, Its thickness is between 0.3～4.4m, layer level is between 1049.58～1053.57m.

The forth level is silt and part silty clay of feldspathic and quartziferous, tawny to taupe, with feldspathic and quartziferous granular mineral, middle dense in natural state. Its thickness is between 0.3～4.7m, layer level is between1040.23～1046.55m.The fifth layer is taupe grit and partial fine sand and silt clay interlayer or lenticle of feldspathic and quartziferous, saturation and middle dense in natural state. And we don't expose the layer in the reconnaissance. he initial underground water level is 25m in the location reconnaissance, and didn't measure the stable underground water level because of the mud counterfort in exploitation.The stable underground water is hidden 20m under the earth surface and is phreatic water according existing data of nearby regions. We can ignore the influence of underground water due to its depth and take 10kPa for surrounding load.

The table below of definite soil layers and mechanical characteristics for slope supporting and construction range according to the location reconnaissance:

Table 1 Soil layers and parameters in construction range

| Layer | Average depth (m) | gravity density $\gamma(kN/m^3)$ | cohesion c(kPa) | internal friction angle $\varphi(^\circ)$ | cohesive τ(kPa) |
|---|---|---|---|---|---|
| artificial miscellaneous fill ① | 1.2 | 19.0 | 5 | 10 | 16 |
| collapsible silt ② | 3.7 | 16.5 | 13 | 30.3 | 80 |
| gravelly sand ③ | 0.6 | 19.0 | 0 | 18 | 130 |

## Pit Supporting Method Selection and Design

### Selection

The slope protection range is on the east of the 10th building, 65m longitude 2m north of D business district, and 12.5m in the northeast corner with average 5.5m height of "┘"shape.The top and bottom slope lines are all certain in the excavation. We proposed initially soil nailing wall or anchoring for supporting comparing with location limitations, security and economic problems of gravity retaining wall and the sheet pile supporting. We decided the soil nailing wall for its low cost, fast construction speed, simple equipment, convenient operation, less noise and the owners' requirements of quick supporting engineering finish for the end of construction of the 10th building and D business district.

### design of soil sailing wall

For location limitation, the soil nailing wall lever pitch is $\beta = 73.3^\circ$ （1: 0.3slope）,soil nailing and horizontal plane angle is $\alpha = 15^\circ$,soil nailing horizontal spacing is $s_x = 1.2m$,vertical spacing is $s_y = 1.4m$, the artificial borehole aperture is 110mm.

(1) the soil nailing lateral pressure: $\sigma_{ai} = (q + \gamma_i h_i)K_{ai} - 2c_i\sqrt{K_{ai}}$ .

in the equation: $q$ —The ground overload from simple work shed

So: $\gamma_i$ —the soil weight of the layer I row soil nailing in

$h_i$ —the distance between the I row soil nailing and slope top

$K_{ai}$ —The coefficient of active earth pressure in the layer the I row in, $K_{ai} = \tan(45^\circ - \frac{\varphi_i}{2})$ ,

$\varphi_i$ is the internal friction angle of the I row soil

$c_i$ —the soil nailing cohesion of the layer the I row in

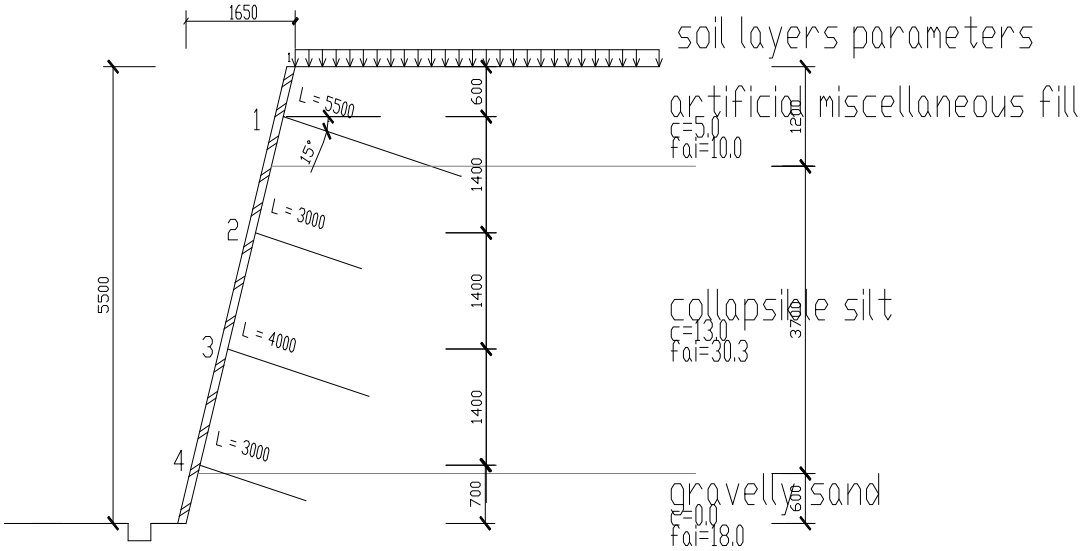


Fig1 Calculation diagram

(2) The reduction coefficient of active earth pressure

$$\xi_1 = \tan\frac{\beta - \varphi_1}{2}[\frac{1}{\tan\frac{\beta + \varphi_1}{2}} - \frac{1}{\tan\beta}] / \tan^2(45° - \frac{\varphi_1}{2}) = 0.722$$

$$\xi_2 = \tan\frac{\beta - \varphi_2}{2}[\frac{1}{\tan\frac{\beta + \varphi_2}{2}} - \frac{1}{\tan\beta}] / \tan^2(45° - \frac{\varphi_2}{2}) = 0.583$$

$$\xi_2 = \xi_3 = \xi_4 = 0.583$$

(3) the standard tensile load values $T_i = \xi_i \sigma_{ai} s_x s_y / \cos\alpha$

(4) tensile load design value,the important factor of the foundation pit side wall $\gamma_0 = 1.0$

(5) soil nailing length design

①effect length of anchoring end

$l_j = \frac{T_{uj}\gamma_s}{\pi d_j \tau_i}$ pulling safety coefficient $\gamma_s$=1.3,drilling diameter of the j row soil nailing $d_j$=110mm

$\tau_i$ —soil cohesive strength of the I layer

② free segment length

$L_{fi} = \frac{H - Z_i}{\sin\beta}\sin(\beta - \frac{\beta+\alpha}{2}) / \cos(90° - \alpha - \frac{\beta-\alpha}{2})$,

slope height H=5.5m, $Z_i$ —height of slope top and soil nailing in I row

③ $L_i = l_i + L_{fi}$ the whole soil nailing length

(6) bolt diameter calculation

$As = \frac{kTmax}{fy_k} = \frac{1.3\times 54430}{335} = 211.2mm^2$, secondary steel of 20mm diameter

$As = 314mm^2$, secondary steel of 20mm diameter for vertical stress, surface concrete thickness of 80mm and Φ8@200×200mm steel shed.

Table 2 Values according layer coefficients

| Row No. | Lateral pressure （kPa) | reduction coefficient | standard tensile load values (kPa) | tensile load design value (kPa) | whole soil nailing length (m) | Practical soil nailing length(m) |
|---|---|---|---|---|---|---|
| 1 | 6.68 | 0.722 | 8.39 | 10.49 | 5.37 | 5.5 |
| 2 | 0.21 | 0.583 | 0.21 | 0.26 | 2.07 | 3 |
| 3 | 33.72 | 0.583 | 34.19 | 42.74 | 3.25 | 4 |
| 4 | 42.95 | 0.583 | 43.54 | 54.43 | 2.97 | 3 |

(7) interior pulling check calculation

$L_{fi} + \frac{F_{sd}T_{ui}}{\pi d\tau_i} < L_i$ and the value is ,partial stability safety coefficient of soil nailing $F_{sd}$=1.3

(8) check calculation of stability against sliding

$E_{\alpha x} = s_x s_y \sum[(q + \gamma_i h_i)k_{ai} - 2c_i\sqrt{k_{ai}} = 130.76kN$

$F_t = (w + qB)s_y \tan 18° = 191.5kN$; so: $Kn = \frac{F_t}{E_{ax}} = \frac{191.5}{130.76} = 1.46 > 1.3$, meets the requirements of stability against sliding.

(9) check calculation of stability against overturning, moment against overturning $M_w = (w + qB)s_y \frac{B}{2} = 1178.8kN \cdot m$ ,overturning moment $M_0 = \sum[(q + \gamma_i h_i)k_{ai} - 2c_i\sqrt{k_{ai}}]s_x s_y \frac{H}{3} = 239.75kN \cdot m$

so: $K_q = \frac{M_w}{M_0} = 4.92 > 1.3$ , meets the requirements of stability against overturning.

So: $K_q = \frac{M_w}{M_0} = 4.92 > 1.3$

**Conclusions**

(1) And we got the geological coefficients based on detailed geological survey report in the design of soil nailing wall. But we took the conservative coefficient of artificial miscellaneous fill according to local experience because of its complex and various properties and influences of environment, human and seasons

(2) We adopted 2m width of Reinforced concrete flanging and Φ6@200×200mm steel shed to ensure slope stability due to the 1m thick artificial miscellaneous fill in the slope top.

(3) The whole supporting system is rational and reliable according to the monitoring results of horizontal displacement less than 14mm,vertical less than 16mm and no obvious crack.

(4) We should give priority to the soil nailing wall for a narrow location and tense construction period by comparison other supporting systems.

**References:**

[1]Liu Xiangyi, Wei Huanwei, ZhangXin, The Technique of Foundation Pit Excavation for Deformation Control and Neighboring Building Protection [J]. Industrial Architecture 2007, 37(1):69-72

[2] JGJ 94-2008, Pile Foundation Technology Standard［S］.

[3] Gao Wensheng, Liu Jinli. Pile Foundation Design and Construction and Testing［M］. Beijing: China Building Materials Press,2001:31-42.

*Applied Mechanics and Materials Vols. 580-583 (2014) pp 544-551*
*© (2014) Trans Tech Publications, Switzerland*
*doi:10.4028/www.scientific.net/AMM.580-583.544*

# A Study on Micro Pile Reinforcement Technology for the Accumulative landslide of Expansive Soil

Hui He[1,a], Yue Xu[2,b], Zhaozhao Huang[2,c], Zhi Li[2,d]

[1]College of Civil Engineering,Xi'an technological university,Xi'an,shaanxi 710036 China

[2]College of Civil Engineering,Xi'an technological university,Xi'an,shaanxi 710036 China

[a]Hehui710032@163.com,[b] xuyuexa@163.com ,[c]hzzxab@163.com ,[d] lizhi1d@163.com

**Keywords**: accumulative, landslide,expansivesoil,micro pile,failure mode,design technique

**Abstract.**This paper studies the micro pile technology for the accumulative landslide reinforcement of expansive soil, putting forward the three failure modes of the micro pile strengthening accumulative landslides of expansive soil and design principles of the micro pile, and then illustrating its calculation methods. Those finding have been applied into 22 landslide disasters for the micro pile design, landslide treatment engineering in south mountainous area of Shaanxi Province in China, which attaches theoretical and practical importance to the design and treatment of micro piles reinforcing the same type of landslide.

## Introduction

Accumulative landslides are widely distributed in China, and there were 6535 landslides in the south mountainous area of Shaanxi Province according to the geological survey, in which the accumulation landslides accounted for about 92.3% in total, and shallow landslides with thickness less than 6m were made up for 51%, therefore those landslides has provided a broad space for the use of miniature piles[1-4].In China, the formula for micro pile can be roughly divided into three categories--- General theoretical method to calculate anti-slide pile, Cantilever pile calculation method and Equivalent calculation method.

Technically from the aspect of General theoretical method to calculate anti-slide pile, slope load is borne by the body of micro pile, and its effect is equivalent to the ordinary anti-slide pile without taking into account of the anti-sliding function for the soil between piles, which could turn into a conservative calculating result. The cantilever pile calculation suggests that the micro diagram of the micro pile is equivalent to cantilever structure anchoring below the sliding surface, and technology personnel is more likely to use this method due to its simple calculation, but the hypothesized landslide thrust and distribution condition of anti-sliding resistance before piles are not accurately assumed, so there exists a huge difference between the calculating results and the actual monitoring results of the spots. Based on Equivalent calculation method, the pile spacing is small, and micro pile and its surrounded soil form an integrated structure to share load, which could serve as a composite structure equivalent to the soil retaining structure in traditional way, then deducing the results according to the calculating method of the soil retaining structure. The last method is the combination of theory and experience, but the thickness of the retaining soil is often difficult to estimate, therefore it is difficult to avoid the errors in design and calculation. So far, our country has not yet developed a set of sound and systematic calculation theory and design method of miniature piles, impacting the wide application and development of micro piles.

The design techniques for the micro pile reinforcement of accumulative expansive soil landslide are studied based on laboratory research, field monitoring and miniature pile reinforcement practical operations for 22 landslides in the southern region of Shaanxi Province.

## Micro pile reinforcement of slope failure mode

Studies have shown that the failure mode of micro pile reinforcement accumulative landslide consists of three types—the overall failure of the micro pile, the single pile failure of the micro pile and the local failure of the micro pile[1,5,6].

**The overall failure of the micro pile.**In the landslide reinforcement engineering, the composite structure of micro pile is often formed by the single piles in rows according to certain combination. The test research indicates that the overall failure mode are basically same as that of a single tiny single pile, showing that in the surrounded sliding surface, there exist the cutting deformation of failure, and bending of pile body within the destructive areas, many oblique cracks, basically being vertical of pile's anchoring section, loaded pile tilting towards front edges of slides, different bearing force in rows of piles , the destruction decreasing in line with the sliding orientation, as the result, the shear calculation is used to calculate for the design of micro pile.

**The single pile failure of the micro pile**.In the process of using micro pile to reinforce expansive soil landslide, the maximum bending moment and shear force is close to the sliding surface, and the single pile failure is often characterized by shear fracture caused by inadequate shear carrying capacity of single piles, and the destruction area of the piles roughly ranges 60 cm or so in the slip surface.

**The local failure of the micro pile.**Due to uneven distribution for the soil nature, there is loose soil between piles in certain area of micro pile reinforcement engineering, with relative large spacing between piles, under the effect of sliding force, the soil body between piles slip away; in the destructive area, the bearing shear force for a number of micro piles close to the sliding surface exceeds the shear strength, and results in shear failure, or excessive deformation of pile body. The occurrence makes the micro pile composite structure seriously damaged in certain area or loses bearing ability of anti-slope slide, leading to the destruction of the local structure, or the failure as a whole eventually .

## Design principles[1,7,8,9,10]

(1)Miniature pile supporting system belongs to the interaction of piles and soil, and the design must take the pile-soil interaction problem into consideration.

(2)In the reasonable arrangement of piles, even if only a tiny relative displacement of piles and soil takes place, the shapes of arching soil look similar under irregularly distributed load, with different pile-soil load sharing ratio, pile bearing 80%, while soil accounting for 20% .

(3)With reasonable pile spacing for micro pile composite structure , anti-resistance to slide force of pile in rows is of difference, and the design should be took consideration about different resistance of pile in rows, with load sharing ratios of 1:0.7:0.6 respectively for the first row, the second one and the third row of piles

(4)In the process of arrangement, it is advisable to leave pile spacing to (8 ~ 10) d, pile row distance to (5 ~ 10) d, pile of anchoring depth to (1/3 ~ 2/5) L.

(5)Micro pile group is often designed for multiple pile body, and the top of pile shall be designed for coupling beam, which pile efficacy can be adjusted to a certain extent to control and avoid the displacement of pile top.

(6)In the working process, the maximum bending moment and shear force of micro pile are near the sliding surface, and their moment and shear force values are taken as the design basis for micro pile to guarantee the bending and shear strength of pile body as a whole.
(7)It is crucial to design a perfect drainage system on the micro pile reinforcement of accumulation of expansive soil landslide. Intercepting drains, torrent gutter, side ditches, drainage and build-in slope pipes in the slope, etc should be jointly considered and developed with project situations.
(8)The cracking or fracture disturbed in the slope surface should be filled solidly, reducing water infiltration into the slope, to control cracking and fracture, to adjust the soil stress state, to improve the soil strength, and to avoid generation of secondary sliding surface.
(9) Micro steel pile should be set up by open-off cut to have pressure grouting in certain depth of sliding surface, in order to reinforce the sliding zone of pile and soil strength. Experience about engineering and project has shown that the ratio of grouting is around between 1.6 ~ 3.5.

**The design calculation method of micro pile reinforcement**

**Design concept.**Micro pile reinforcement system is the interaction of piles and soil body, landslide load is shared by piles and soil on pro rata basis, and bearing capacity of piles in rows is not identical in group. In the micro pile design, the resistance of soil between piles should be fully considered according to the different pile-soil load share ratio and different bearing capacity of piles in rows. With reasonable spacing pile design, down force of the landslide is allocated to the group micro piles and the soil between piles in the proportion 8:2, and the total assigned load on bearing should be distributed in the proportion 1: 0.7:0.6to the piles in rows. The pile body is under the uniform distributed load, acting on the piles above the sliding surface. Given to the pile anchoring end as the fixed bearing, we may simplify micro pile and beam connection by rigid connections to generate the calculation of the internal force of each item based on structure internal force calculation method, to check reinforcement system in the terms of the overall damage, the destruction of the local structure and single pile failure modes.

**Arrangement patterns and drainage design:**

(1) The layout

Expansive soil landslide failure forms of performance failure for shallow slip, in order to prevent the shallow slip of Expansive soil form landslide failure and to guarantee the effect of micro pile the reinforcement. We often use laterally linear connection to reinforce the single slope, or equip the single piles in vertical and horizontal (longitudinal and cross)frame structure, as shown in Figure 1. & 2.

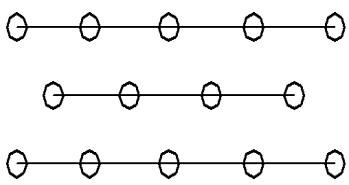

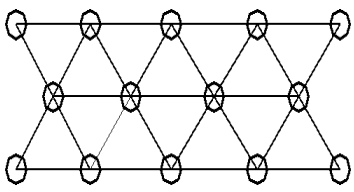

**Fig.1 Single pile lateral connection form Fig.2 Single pile lateral and longitudinal connection form**

(2)Drainage design

Accumulative landslide of expansive soil induced by rainfall erosion and water infiltration in southern Shaanxi will seriously affect the stability of the slope, so measures must be adopted to

protect the sliding surface, such as, intercepting drains, torrent gutter, side ditches, drainage and build-in pipes in the slope to be set up in the certain depth of the slope body to drain off the water in time.

**Design calculation method:**

(1)Calculation assumption

1)Assuming landslide thrust of micro pile composite structure above sliding surface is a uniformly distributed load;

2)Stating the micro pile below the surface as the fixed end set in the bedrock;

3)Calculating the length of each micro pile approximately from the top of the pile to the sliding surface at L/3 below;

4)The stress of the each single pile of the same row being same ;

5) Assuming the connection between each micro pile and connecting beam for the fixed one, while compared with the pile ,the beam structure member being regarded as a rigid one;

6)Letting the connecting beam be only horizontal displacement and horizontal displacement of the pile tops being equal in the connecting beam.

(2)A sketch of calculation

According to the above calculation assumption, the calculating model of expansive soil micro pile as shown in figure 3:

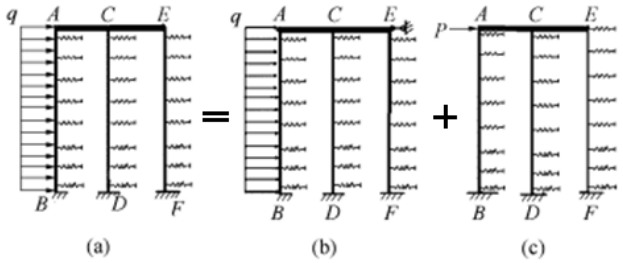


**Fig.3 The calculation model for landslide reinforcement with micro pile**

(3)The landslide thrust calculation

There are multi-formula to compute the landslide thrust to compute. The transfer coefficient method is simple, and we assume that the direction of the force between the bars parallels to the ground, not taking the specific form of landslides destruction into account, and could derive the force in accordance with the transfer coefficients. Landslide thrust by the transfer coefficient calculation method is shown in Figure 4.The calculation is assumed as the follow: 1) we assert the landslide body to slide down as the whole but incompressible based on the assumption of no extruding deformation between the bars or plates; 2) there is no cracking or fracture between the bars or plates, so no pulling force is transmitted only for the thrust; 3) the thrust between the bars is inferred to function at the midpoint of the interface; 4) we may take the sliding body as the calculation item with formulating 1.0 m of length unit on a central axis at the sliding surface without considering shaft or side resistance.

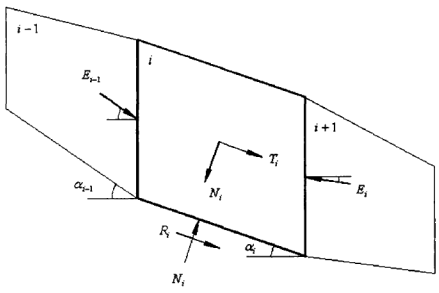


**Fig.4 Transfer coefficient method to calculate the landslide thrust**

From the above pictured, we may take the Separated Slider i for example, and the inclined forces are resolved into different components on the sliding surface:

$N_i=W_i\sin\alpha_i$

$T_i=W_i\cos\alpha_i$(1)

Based on the equilibrium conditions, the left force of the Separated Slider i will be inferred as follows:

$E_i= W_i\sin\alpha_i- W_i\cos\alpha_i\tan\varphi_i-c_il_i+\psi_iE_{i-1}$(2)

In the Formula: $\varphi_i$ for the angel of internal friction ($^O$) ; $C_i$ for the cohesive force of Separated Slider i on the surface of the sliding body (kN/m) ; $L_i$ for the length of the sliding surface of the landslide mass (m); $\psi_i$ for the Transfer coefficient;

$$\psi_i=\cos(\alpha_{i-1}-\alpha_i)-\sin(\alpha_{i-1}-\alpha_i)\tan\varphi_i \quad (3)$$

We may calculate the landslide thrust to ensure landslide stability. If the thrust of the last slider is positive, the landslide is unstable; If the thrust value of some piece is less than or equal to zero, then the landslide turn into more stability in geotechnical engineering. Due to full consideration about the stability of landslide in an actual engineering project, so we are supposed to assume the safety coefficient of slope stability to calculate the landslide thrust, so the safety coefficient could be defined as the ratio of overall anti-sliding resistance of the Slider i to the sliding-down force or the thrust through the effect of gravity.

$$F_s=\frac{E_i+W_i\cos\alpha_i\tan\varphi_i+ c_il_i-\psi_iE_{i-1}}{W_i\sin\alpha_i} \quad (4)$$

In the Formula: $F_s$ for safety coefficient, usually ranging 1.05 ~ 1.25.

So the landslide thrust could be concluded as follows:

$$E_i=F_sW_i\sin\alpha_i-W_i\cos\alpha_i\tan\varphi_i-c_il_i+\psi_iE_{i-1} \quad (5)$$

In addition, if the calculated interface containing reverse slopes, the value of $W_i\sin\alpha_i$ is negative, thus $W_i\sin\alpha_i$ being a resistance, and then we will not multiply safety coefficient at this time.

(4) Determined landslide thrust of row piles

We conduct the uneven distribution coefficient of thrust force being as 1:0.7:0.6 based on the numerical analysis, physical model tests, field monitoring tests and the previous findings, which derives from a comprehensive analysis.

(5) Single pile reinforcement calculation

Steel piles are widely used into micro pile reinforcement engineering, and the reinforcement calculation would be determined and generated as the followings:

Firstly, the landslide thrust and sliding resistance are calculated. Setting the horizontal component for the landslide thrust of the first row pile to be $E_n$, the sliding resistance for the last row pile being $P_n$,of horizontal component in the calculation unit, the lateral force of the micro pile group should be $T_n$ , as shown below:

$$T_n = E_n - P_n \tag{6}$$

Then based on the assumption of landslide thrust distributed evenly on the pile, the cross section As of each row steel pile reinforced area for per calculated width is indicated as follows.

$$A_s = \frac{T_n}{n \cdot f_v} \tag{7}$$

In the Formula: fv for reinforcement value of shear strength; Tn for lateral force of micro pile; n for row number of micro pile arrangement.

As heterogeneity reflected in the design of pile stress, uneven distribution coefficient of a landslide thrust should be introduced , and the resulting revised reinforcement area of row pile for per calculated width goes below:

$$A_{si} = \eta \cdot A_s \tag{8}$$

In the Formula: Asi for the actual reinforcement area of row pile ranking i; As for the average of micro pile reinforcement area;ηfor 1:0.7:0.6(inferred on the basis of the numerical analysis, physical model experiment, field monitoring and previous research findings after a comprehensive analysis ), that is to say, the ratio of the row pile landslide thrust for the No. 1 row, No.2 row and the No. 3 row respectively .

(6)The determination of pile length and pile spacing

Miniature pile length can be obtained by the following formula (determined the total length for the length of each micro pile above the sliding surface plus with the pile anchorage length at L / 3 below the sliding surface):.

$$L = L_1 + L_2 \tag{9}$$

$$L_2 = \frac{A_c \sigma_R}{\pi d \tau_2 10^2} \tag{10}$$

In the above Formula: $L_1$ stands for pile length from sliding line to slope surface (m); $L_2$ is for pile length of anchored section (m);$\tau_2$ is for the weighted average of cohesive force ($N/cm^2$) between the pile and the soil mass under the calculated sliding line; d means a micro pile diameter (cm); $A_c$ is for cross section area of micro pile ($cm^2$); $\sigma_R$ refers to compressive stress acted on the cement mortar ($N/m^2$).

In the engineering, the expansive soil micro piles are arranged in different rows and groups toensure the effectiveness of spacing effect . In order to guarantee the soil mass not flow around single piles, this kind of composite structure can play a normal role effectively. Some scholars assume that the estimated value of friction resistance acted upon between soil mass and side pile is greater than the landslide thrust to commonly determine the anti-slide pile spacing, and other scholars calculates the pile spacing through the strength of the soil arch conditions. But these two methods have advantages and disadvantages. The former failed to give full consideration to the strength of the soil arching conductive to be conservative in calculation, while the latter ignored the static equilibrium conditions produced by the interaction between the pile shaft resistance and landslide thrust, though soil arching strength was considered. The estimation of pile spacing for the micro pile composite structure is practically expected to be as (8 ~ 10) d in the reasonable way.

(7)Micro pile composite structure calculation

Miniature single pile calculation. In the landslide reinforcement project, , three conditions should be met with to maintain the stability of the composite structure simultaneously: no sliding failure in the whole body, no general shear failure on the sliding surface of soil, no general shear for the single rank of piles

1) The safety coefficient to calculate the anti-sliding stability of pile composite structure is not less than 1.25

2) Shear capacity for the micro pile composite structure is no less than the landslide thrust to satisfy the general shear on the sliding surface:

$$R=n[\tau]A>E_i \tag{11}$$

In the Formula:[τ] stands for shear strength of steel pipe (125Mpa); n means the number of miniature pile per meter arranged; A is for cross-sectional area of steel tube.

3) When local failure of micro pile composite structure occurs, the main reason is to blame for low mechanic parameters of soil mass between piles not enough to form effective soil arching or too large pile spacing, whereas spacing of micro pile in expansive soil is generally accepted as (8 ~ 10) d , not feasible for the larger one .

(8)Engineering applications

The anti-slide technology for micro piles are applied into the design of 22 small-scale landslides control engineering in southern mountains of Shaanxi Province for 5 years since 2009, which have gained lots of social and economic benefits. The practical application shows that micro pile reinforcement technology is an effective control method of expansive soil landslide.The practice of landslides monitoring, such as Mu-Shang Village landslide, Kimcheon Temple landslide, a landslide took place at Lao-dao-si , and landslides at the Town of New Street yangjiawan village, reaching a conclusion, we can appropriately enlargement of the pile spacing and row distance to get better technical advancement and economic benefits in other similar engineering design.

## Conclusions

(1) The micro pile composite structure of accumulative landslide is under reinforcement system with space force, so spatial structure can be transferred to a flat or level steel structure embedded in the rock and soil mass under the certain calculation assumptions. We may simplify anchored pile as the fixed support, micro pile and beam connection by rigid connections to draw the calculation.

(2) The three failure modes of micro pile are determined , respectively, for the overall destruction, destruction of single pile and local damage, to carry on the corresponding calculation.

(3) Micro single pile layout should be arranged in the Quincunx shape (conventionally in three rows), pile spacing composed as the (8 ~ 10) d rows to lay out, the pile row distance used in accordance with (5 ~ 10) d to arrange , and anchoring depth of pile being (1/3 ~ 2/5) L of the length of the pile

(4) Anti-slide pile- soil interaction should be taken into account in the reasonable pile design and arrangement. When calculating the internal force for each row pile, downslide thrust force should be acted upon by the external force on the whole structure in the rectangular distribution.

(5)Reinforcement technology of micro pile anti-sliding composite structure , its design thoughts, approaches and procedures are given.

Author brief introduction: Hui He(1962-),male, Xi'an Technological University professor ,The main research area for geotechnical engineering design and construction technology. E-mail: hehui710032@163.com.

**References**

[1] Xi'an Institute of Survey and Design of Chinese Nonferrous Metal industry ,Xi'an Technological University and so on. Research on the Key Technology of the Control of Landslide Disaster in the Mountainous Area in Southern Shaanxi [R].Xian: Science and Technology Department of Shaanxi Province,2013.(In Chinese)

[2] Gongxian Wang. Current Situation of Engineering Measures for Preventing Landslide at Home and Abroad[J].The Chinese Journal of Geological Hazard and Control,1998,9(1):1-9. (In Chinese)

[3] YuZheng.The Development of Micro Pile in Foreign Countries[J].Port Engineering,1990,(5):43-49. (In Chinese)

[4] Xiaoming Li. Engineering Practice of Expressway Landslide Control in South of Jiangsu area[J].Journal of Huaihai Institute of Technology ,2005,24(21):3954-3958. (In Chinese)

[5] Shufeng Wang, Yu-ming Men. Study on Failure Mode of Micro Pile on Loess Landslide[J]. Engineering Survey,2010,（1）:19-22. (In Chinese)

[6] Jinkai Yan, Yue-ping Yin, Yu-ming Men. A Study on the Distribution Law of Micro Pile Stress and Failure Model Experimental[J].The South to North Water Diversion and Water Science & Technology,2010,8（1）: 44-88. (In Chinese)

[7] Yanbing Liu. The mechanism of Micopiles Reinforce Shallow Expansive Soil Landsides [D]. Xian:Journal of Xi'an Institute of Technology ,2012. (In Chinese)

[8] Hui He, Gengshe Yang, Kou-xin Fan.The Accumulation Layer Expansion Arch Test Study on the Effect of Soil between Piles Soil Landslide Mini Pile[J].Journal of Xi'an Institute of Technology,2013. (In Chinese)

[9] Hui He, Yanbing Liu.An Analysis of Numerical Simulation of Micropiles Reinforcing Shallow Landslide[J].Advanced Materials Research Vols, 2012,446-449:2663-2666.

[10]HuiHe, Zhiyu Li.Analysis on Mining the Potential Landslide Stability Based on FLAC3D[J].Journal of Gansu Sciences,2013,2（3）:32-35.(In Chinese)

*Applied Mechanics and Materials Vols. 580-583 (2014) pp 552-555*
*© (2014) Trans Tech Publications, Switzerland*
*doi:10.4028/www.scientific.net/AMM.580-583.552*

# Analyses of Anti-Seepage Measure for Expansive Soil Subgrade in Hefei

Yuan Wei[1,a] and Weizhong Xing[2,b] Yan Shao[3, c],

[1,2]Anhui University of Architecture, Hefei, Anhui, 230601, China

[a] weiyuan155@163.com, [b] xwz19901012@163.com, [c] shaoyan@aiai.edu.cn

**Keywords:** Expansive Soil, Anti-seepage measure, Subgrade engineering, Water content, Numerical analysis

**Abstract.** Deformation of expansive soil subgrade depends on moisture content. Anti-seepage measure of unsaturated expansive soil was carried out using ABAQUS as for the influence of atmosphere. The results show that there is large change in water content using anti-seepage measure measure. After using anti-seepage measure, range of water content decreases. At the same time, range of water content value obviously decreases with the increase of the depth of seepage control. Therefore, damage of pavement caused the deformation can decrease by seepage control measure. The results could be used for engineering design and numerical calculation.

## Introduction

Moisture content changes of expansive soil casue expansion, contraction, intensity changes and also influence slope stability. With the growth of moisture content of expansive soil, the expansive force grows gradually. When the expansive force exceeds the upper loads, the subgrade will appear serious disintegration partial collapse, uplift and crack. When the moisture content of the expansive soil subgrade reduces, the road will crack. In case of rain or snow, water seeping into the soil, the soil will lose bearing capacity. [1-3]

Hefei is one of typical expansive soil coverage region in our country. Moisture content changes casued by rainy season, monsoon and temperature. Facts proved that, the moisture content of the expansive soil shifted and transformed with climate, geological environment and construction activities. The effective cohesion of the soil was declined by cycle dry shrinking and wet expanding, and lead to reduce the strength of soil. [4]

In this paper, we adopt the finite element software ABAQUS to simulate the effect of rainfall. Through application of the software, we can analysis the difference between using anti-seepage measure and no anti-seepage about moisture content changing in Hefei. We can use ABAQUS to analysis the effect of speeage and the influence of seepage depth to moisture content. The results could be used as reference for engineering designing and numerical calculation.[5-6]

## Unsteady seepage finite element analysis

(1)Anti-seepage scheme and geometric model

Figure 1 is the geometric model of numerical calculation. There are two kinds of anti-seepage scheme. The seepage depth are 500mm and 1000mm.

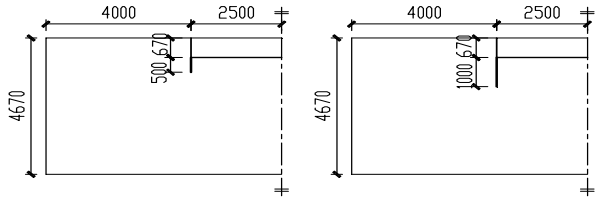


Fig. 1 The geometric model of anti-seepage measure

Divide the unit after the finite element model, as shown in figure2.

(2) Material parameters and boundary conditions

(a) physical property Initial water content 25%;initial void ratio 0.75;density 1.92g/cm3;permeability coefficient 3.06×10-8m/s.Expansive soil subgrade soil water characteristic curve are shown in figure 3 below.

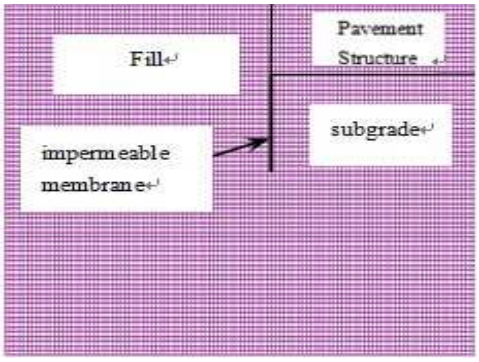


Fig.2 Diagram of finite element

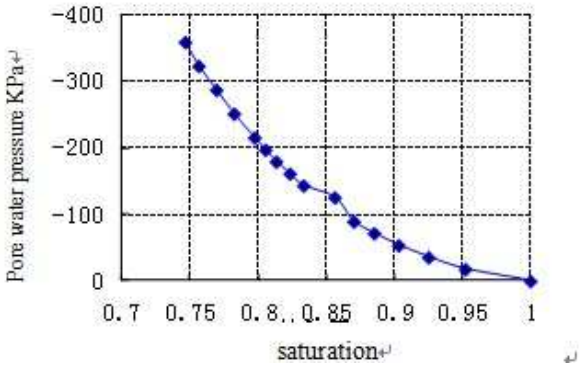


Fig.3 Soil water characteristic curve

(b) boundary of flow

Reference to the expansive soil area construction technical specification, July is the largest rainfall in Hefei area, the rainfall is 181.5 mm. Considering the largest rainfall month, we can take the precipitation of heavy rain in July. Assuming that there are 5 days of precipitation, then the precipitation is 181.5÷5 = 36.5 mm/d. Because of the low soil permeability, we can use two kinds of boundary condition; The first is that we can use flow boundary condition before surface pore pressure approach 0. The precipitation is: 0.0365÷24 =0.00152m/h. The second is using head boundary condition after the surface pore pressure approach 0 : the surface matrix suction is 0.

2 Anti-seepage calculation results and analysis

In this paper, the ABAQUS software is used to conduct 3 kinds of caculation about moisture content changes. These three kinds of situations are no seepage measure, anti-seepage measure 0.5 m and anti-seepage measure 1.0. Figure 4 is different location node marker in subgrade. The saturation distribution map of three schemes are showed in figure 5 to 7.

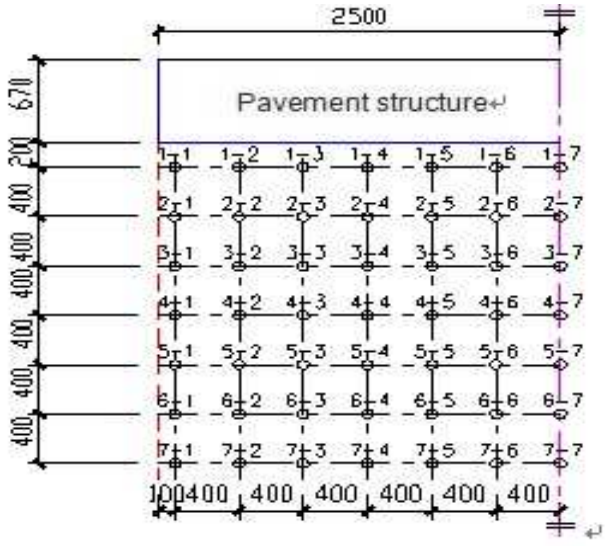


Fig.4 Different location node diagram in subgrade

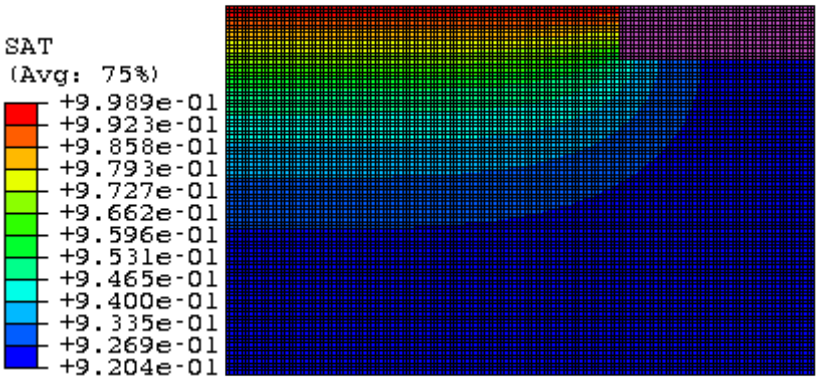


Fig. 5 Water content after no anti-seepage measure

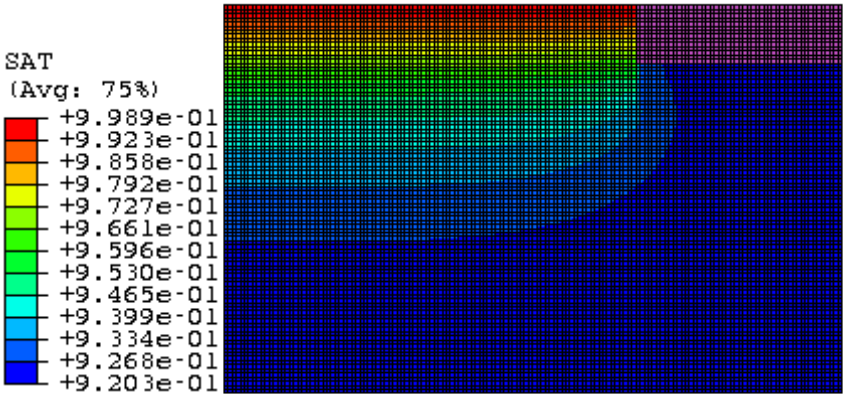


Fig. 6 Water content at 0.5 m after anti-seepage measure

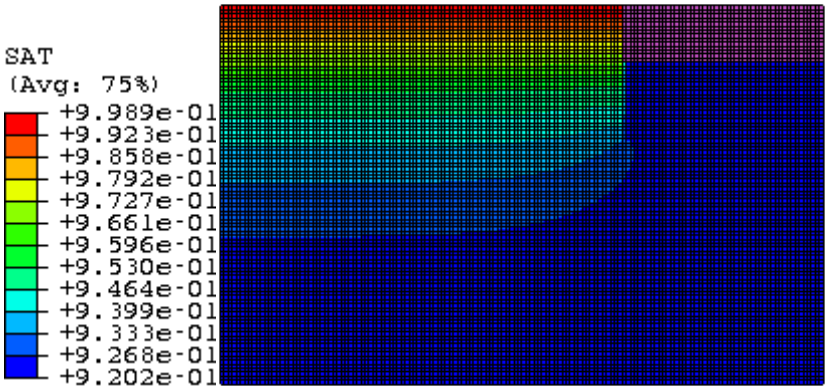


Fig. 7 Water content at 1.0 m after anti-seepage measure

Figure 5 is no anti-seepage measure. Changes of water content caused by rainfall have directly effect on roadbed, which will lead to remarkable expansion deformation. Figure 6 ~ 7 are anti-seepage measure. The moisture content changes occur under the seepage film. With the increasing of seepage depth, the infiuence of roadbed will be reduced.

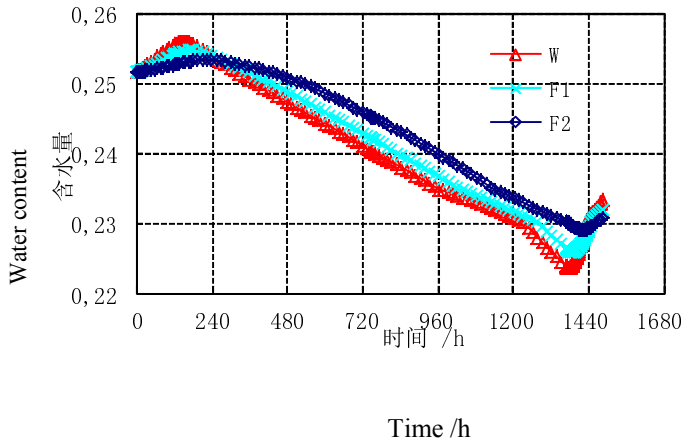


Fig. 8 Curve of water content at 2-2 section in subgrade

Figure 8 is subgrade of node 2-2 ( in figure 4) moisture content curve. The W means no seepage control scheme, F1, F2 refer seepage control scheme 1, 2 respectively. As it showed in figure 8, after take anti-seepage measure, the curve is more smooth.Seepage scheme can reduce the deformation of expansive soil.

## Conclusions

Through the above analysis, we can draw the following conclusions:
(1) Expansion and deformation of subgrade soil depends on the distribution and changes of moisture content, anti-seepage measures can reduce the extent and inhomogeneity of water content in subgrade soil.
(2) Anti-seepage measures can reduce the non-uniform deformation of subgrade soil. Therefore, the non-uniform deformation of pavement structure will be reduced after take anti-seepage measures.
(3) Moisture content in subgrade soil are significantly declined after using anti-seepage measure under rainfall. Because of water seepage channel was obstructed by anti-seepage measures, and the effect of anti-seepage measures are more obvious with the improvement of seepage depth.

## References

[1] GBJ112-87,*Expansive Soil Region Construction Technical Specification*.(In Chinese)

[2] Fabao Wu, Wenhua Yang:*Guangdong Building Materials*, 2011,(07) :129～130. (In Chinese)

[3] Quanhui Liang: *Public Science & Technology*, 2010,(09):98～107. (In chinese)

[4] Jun Zhou,Jiang Zhu,Jun Cai: *Journal of Soil and Water Conservation*,2000,14(3):92-95. (In Chinese)

[5] Dinghua Yang,Lvhua Gong,Fan Ji: *Modern knowledge publishing house*,2000. 314-317. (In Chinese)

[6] Binmin Du: *Communications Science and Technology Heilongjiang*,2009,(06):19-20. (In Chinese)

*Applied Mechanics and Materials Vols. 580-583 (2014) pp 556-559*
*© (2014) Trans Tech Publications, Switzerland*
*doi:10.4028/www.scientific.net/AMM.580-583.556*

# Analysis on Deformation and Support Technology of Deep Soft Rock roadway

Yongsheng Liu* Wang Liu Xingyu Dong

School of Civil Engineering and Architecture, East China Jiaotong University, Nanchang China

Yshliu07@126.com, 136890023@qq.com, 894684981@qq.com

* corresponding author. Tel:+85-971-87046707, E-mail: yshliu07@126.com

**Keyword**: soft rock roadway; deformation; mechanical mechanism; support technology

**Abstract:** The deformation and support technology of soft roadway is a very important problem in mine. Based on the roadway's deformation of Jian Xin Mine of Jiangxi Fengcheng Mining Bureau, the mechanics mechanism and reasons of the soft rock roadway deformation are analyzed. And the three kinds of support technologies which are suitable for soft rock roadway are put forward. The support technologies have been used in the soft rock roadway of coal mine and have achieved good results. The research has important reference value for soft rock roadway supporting technology and its stability maintenance.

## Introduction

In recent years, the pressure control and supporting problem of soft rock mine roadway is more and more brought to the attention of the experts with the increasing of mining depth [1-3]. In our country, many mines have great difficulty in soft rock roadway supporting and become the main factors that influence the mine development and the economic benefit [4]. The buckling deformation of soft rock roadway excavation happens easily, and it shows as floor heave and two roadsides crowded and folded, roof causes layer off the top or roof fall, etc by fracture and abscission. When using the traditional supporting of soft rock roadways, it results in roadway maintenance difficulties, disrepair seriously, high maintenance costs for many times, low mine production efficiency [5-6]. The depth of Jiangxi Jian Xin Mine is -700m at present, thereby the pressure is high, the litho logy is poor and the roadway had several large deformations. Combined with the actual situation of Jian Xin Mine, this paper describes support technology of deep soft rock roadway briefly, provides support and references for mining for deep coal rock roadway excavation safety.

## Project overview

Jian Xin Mine is located in the north of Qujing syncline in Xianguling Mine. The overall structure of the mine is monoclinic, the strata is the North-East and East-West, dip direction is South and Southeast and the inclination angle is 8° to 10°.The mine develops a structural anticline—Xiufangshan anticline, it is located in the secondary level West Wing mining area, axial is between N40°-60°E, the inclination angle is 0° to 8°,the local rises, south west inclines, exposes in the western mountain and Xiufangshan line, east wing rock strata dips and the dip angle is small, the west wing steepens and dip is 12°- 25°。

## Deformation and mechanics mechanism

### 3.1 Deformation

Due to deep mining and poor geological conditions, many roadways deform in Jian Xin Mine. The typical is the 7 # in the central panel of the wind roadway, the deformation of the roadway is shown in Fig. 1. Field test demonstrates that the original arch turns to concave, arch point sink

generally and the maximum arch deformation of the most serious transverse section is about 60 cm, as shown in Fig.2.

Fig.1 Deformation of the roadway

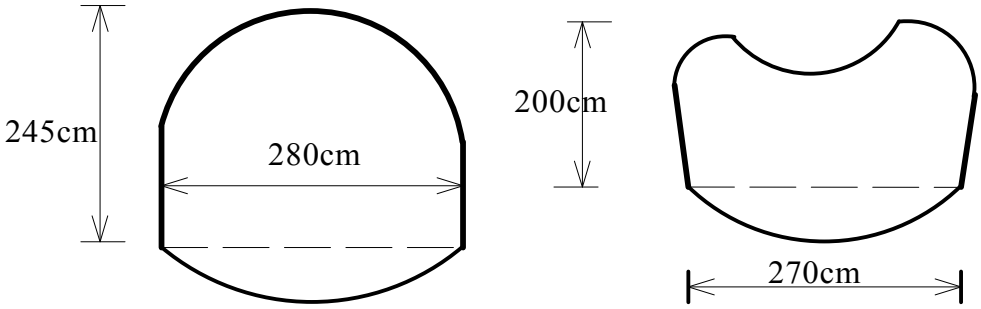


（a）design pattern （b） deformation pattern

Fig.2 Design chart of the roadway

**3.2 Gravity stress of Rock mass**

With the roadway depth increasing, the internal elastic energy stored in rock mass increases. When roadways be excavated, rock mass stress state disturbances, the original stable three dimensional stress field to unstable two-dimensional stress field and release huge strain energy which can lead to deformation and failure of roadways. Especially for deep soft rock roadways, this situation is more obvious. Buried depth on the surrounding rock affects deformation of roadway strongly; it may cause damage because of large deformation fast and instability if not take effective support timely.

**3.3 Geological condition**

The stability of the roadway not only depends on the strength of the rock itself, more important is on the geological conditions of roadway. This includes the development situation of rock mass, groundwater, etc. Generally, the more the geological structure of surrounding rock develops, the worse the integrity of the surrounding rock is and the more serious the deformation and failure of roadways are under the same pressure load. In addition, the groundwater is the important factors influencing the deformation of soft rock roadway excavation. Because the soft rock mostly contains minerals such as kaolinite, montmorillonite and others, it not only produces expansion strain and stress, causes uneven internal stress of rock mass, reduces the strength of the rock and leads to deformation serious when water molecules in rock mass.

**3.4 Environment disturbance**

The deep soft rock roadway excavation deformation is highly affected by the external disturbance. construction in adjacent roadways, mine moving on working face and so on change the size of soft rock’s stress, cause the non-uniform deformation of roadway and even instability.

**Support technology**

**4.1 Anchor combined support technology**

Anchor bolting is regarded surrounding rock as active supporting body and roadways anchor before the large deformation of roadway surrounding rock. By making full use of the bearing capacity of surrounding rock itself, taking variable load as the supporting body and making the whole of the surrounding rock formation to be a larger rigidity, abscission layer extension is prevented and reduced[7-8]. For further improving the stability of soft rock roadway excavation, bolt is often applied to bolt-mesh-spurting technology and bolt-grouting technology. In bolt mesh spurt technology, bolts anchor on no damage of rock mass to prevent surrounding rock loose deformation and failure, shotcrete is used closing surface of surrounding rock and the supporting bolt of surrounding rock in lays to prevent surface rock caving and the steel mesh laid in the spray layer increases the strength and flexible of the shotcrete layers and improves the integrity of the support. Anchor combined anchor, concrete spray layer and steel fabric closely with the surrounding rock bear the weight together, it gives full play to the bearing capacity of surrounding rock, provides timely resistance in the process of deformation with the surrounding rock together and limit excessive deformation of surrounding rock to maintain the stability of roadway.

Bolt-grouting support is closing the surrounding rock of roadway with shotcrete to prevent further weathering of surrounding rock after the roadway excavation, and then putting bolt-grouting anchors into the surrounding rock grouting for reinforcement. Bolt-grouting anchor has both the characteristics of bolt support and grouts through this bolt grouting to surrounding rock. Through grouting, grout filling and pressure dense fissure space, the unconstrained loose state of the surrounding rock before grouted into joint support system adapted to the complex state of stress and strain (compression, shear, tensile)with the combined action of the rock, slurry and the surrounding rock.

Jian Xin Mine's roadways are buried deeply, complicated geological conditions, long service life and the serious deformation. In roadways repair reinforcement, it effectively control the deformation of surrounding rock by using the above technology, ensure the stability of roadway, achieve good socioeconomic benefits.

**4.2 U-shape compressible support and wall backfilling technology**

Its greatest advantage is that when the surrounding rock pressure reaches a certain value, the u-shaped bracket occurs to yield reduction and a result of yield is decreasing surrounding rock pressure acting on the support, avoiding the support destruction caused by the surrounding rock pressure is greater than the bearing capacity of the stent and ensuring the normal use of roadway. But new roadway surroundings are uneven and cause stress concentration because it contacts the smooth u-shape support unevenly. In order to reduce the uneven contact, between u-shape flexible support and roadway wall, it often packs some adhesive materials to make the force uniform. After filling in the back of the wall, the interactive system of roadway surrounding rock and support changes from the "support - surrounding rock" system without wall backfilling into the trinity function system of "support –filling layer-surrounding rock". Support and filling layer makes up the composite support structure and it makes the change from the effect alone of support on filling layer without wall after filling into the interaction of the support and filling layer together on surrounding rock. Through the wall pack will support and surrounding rock couplet one, form the joint bearing, more advantageous to play since the bearing capacity of surrounding rock. After wall filling with concrete jet u-shape set direct injection filling, filling is close-grained, not only effect is good, and construction craft simple, the technical main point easy to grasp, greatly reduces the labor intensity of workers, to speed up the advance. U-shape Steel support wall backfilling with concrete spraying machine grouting directly and filling is filling density and good effect, and the construction process is simple, the technical essentials is easy to master, greatly reduces the labor intensity of works and accelerates the driving speed.

### 4.3 Secondary coupling support technology

In general, with soft roadway having the features of deforming speedily, large deformation and long creep duration, etc, therefore roadway is quick to pressure, pressure big, low success rate of one supporting after roadway excavation. According to the principle of the combination of supports and surrounding rock, control technology of soft rock roadway's surrounding rock is used with a certain deformation of the flexible supports and carries on the secondary support. One flexible supporting depressurization leads to the rock stress reaching the mechanical equilibrium under lower deformation rate, and it gives full play to the bearing capacity of surrounding rock. The stiffness of secondary support reduces the deviatory stress of rock mass of roadway, decreases the tangential stress of surrounding rock of roadway relatively, increases the radial stress relatively and promotes the stress stability of surrounding rock. Flexible support is anchor support, bolt-grouting support or the combined support of anchor and metal net, the stiffness of support is used stone arch or u-shaped bracket supporting method, etc.

## Conclusions

The supporting technology of soft rock roadway excavation is a complicated work, especially in the poor condition called "three high and one disturbance" after the deep mines transfer. And the stability of surrounding rock of roadway is the important premise of the mine economic benefits and the security situation. Therefore, it is necessary to study the deformation mechanism of deep soft rock roadway excavation and determine the reasonable way of supporting technology are the. Under the condition of deformation mechanism of soft rock roadway excavation in the specific analysis, Jian Xin Mine gets the ideal supporting effect with the supporting technology combined a variety of techniques.

## Acknowledgements

This work was financially supported by the Chinese Natural Science Foundation (51274101, 51074076) and JiangXi Science and technology support program (20121BBG70064).

## References

[1] He Manchao, Jing Haihe, Sun Xiaoming. Soft rock engineering mechanics[M].Beijing: Science Press, May 2002 （in Chinese）

[2] Zhou Xiangzhi. Mechanism of soft rock roadways deformation analysis and the main countermeasures[J]. Coal Mining Technology, 2011, (3):41-44 (in Chinese)

[3] Wang Haidong, Zhang Yongji. The support mechanism and application of soft rock roadway excavation[J]. Journal of Liaoning Technical University, 2005, (supplement):26-28 (in Chinese)

[4] Li Guofeng, Cai Jian, Guo Zhibiao. The researches and applications of anchor support technology in deep soft rock roadway excavation [J]. Coal Science and Technology, 2007, (4):44-47 (in Chinese)

[5] Zhang Jianhua, Zhai Jin, Lv Zhaohai. Study on Mechanism analysis and control technology of deformation occurred in mine watery soft rock roadway [J]. coal engineering,2014,46(1):53-55 (in Chinese)

[6] Fang Tengjiao, Liao Xuedong, He Lubin. Failure mechanism and control of soft rock roadway under mining disturbance [J]. COAL GEOLOGY & EXPLORATION , 2014,42(2):67-70 (in Chinese)

[7] Sun Xiao-ming , He Man-chao. Numerical simulation research on coupling support theory of roadway with in soft rock at depth[J]. Journal o f China University of Mining & Technology, 2005, 34(2):166-169 (in Chinese)

[8] Gao Zhengyong, Fan Zhengxing. Secondary roof bloting with anchor and wire mesh support technology of soft rock roadway in deep mine [J]. Coal science and technology, 2014, 42(2):11-15 (in Chinese)

*Applied Mechanics and Materials Vols. 580-583 (2014) pp 560-565*
*© (2014) Trans Tech Publications, Switzerland*
*doi:10.4028/www.scientific.net/AMM.580-583.560*

# Analytical Solution for Contaminant Extraction Using Well Injection Depth Extraction Technology Considering the Effect of Smear Zone

Hengyu Wang[1,a], Xiaowu Tang[1,b] and Penglu Gan[1,c]

[1]Research Center of Coastal and Urban Geotechnical Engineering, Zhejiang University, China

[a]email: why303433506@gmail.com, [b]email: tangxiaowu@zju.edu.cn,

[c]email: dennis19900828@gmail.com

**Keywords:** Contaminant Extraction; Smear Effect; Analytical Solution; Well Injection Depth Extraction (WIDE)

**Abstract.** The smear zones are usually caused by the installation of vertical drains in fine-grained soil. An analytical solution for contaminant extraction using well injection depth extraction (WIDE) system considering the smear effect was developed. The injection rate was assumed to be equal to the retrieval rate to maintain full saturation and steady-state seepage flow. The results obtained by the proposed analytical solution agree well with those obtained from the finite element method. An illustrative example was presented to show the influence of the smear zones and results reveal that the smear zone can have a great influence on the contaminant extraction from soils. The 500-hour base concentration of acetone in the middle of the contaminated soil increases by a factor of approximately 1.9 when the effect of the smear zone is considered in the model.

## Introduction

Well injection depth extraction (WIDE) is an improved pump-and-tread system in which prefabricated vertical wells (PVW) installed in a relatively close spacing shorts the flow path. It is demonstrated to be effective for depth-specific removal of contaminants in fine-grained soils [1-3]. Welker et al. [1] developed MODFLOW with MT3D method to numerically model the bench-scale PVD remediation system. Sharmin et al. [2] analyzed the impact of the extraction process of WIDE technology on the groundwater head distribution and contaminant transport using the finite element model. Although many sophisticated problems must be solved numerically, simplified analytical solutions are still an economical and efficient alternative to the numerical models. Gabr et al. [3] presented the analytical solution for contaminant extraction through an axisymmetric model.

The installation of vertical drains by means of a mandrel causes significant remolding of the subsoil, especially in the immediate vicinity of the mandrel [4-6]. The characteristics of the smear zone investigated using a large-scale consolidometer are found with reduced permeability, decreased water content and increased compressibility [4, 5]. Therefore, it is of great importance to research the smear effect on contaminant extraction in contaminated soils.

In this paper, an analytical solution of 1D contaminant extraction using WIDE system considering the smearing effect is obtained under conditions of steady-state flow. In order to simplify the sophisticated problem and emphasize the smear effect on contaminant extraction, the PVWs are substituted by sand-wall (Fig. 1). The presented model is described as an idealized three-zone model, where the smear zone is the disturbed region in the immediate vicinity of the sand-wall, and the middle zone is the intact region. The results obtained by the proposed method are compared with those obtained by the finite element method (FEM). An illustrative example is performed to investigate the smear effect based on the proposed analytical solution.

**Mathematical model**

As shown in Fig. 1, the flushing solutions are injected through a row of sand-wall, and retrieved through another row of sand-wall that runs parallel to the injection sand-wall, and the rate of the injection which remains constant is equal to the rate of the extraction. The model mainly includes the sand-walls, the smear zones, and the undisturbed contaminated soil which are considered to be homogeneous and fully saturated. The co-ordinate x has its origin at the border of the injection sand-wall, and its direction is parallel to the ground surface. It is assumed that the piezometric heads in the injection sand-wall and extraction sand-wall are steady. Based on Darcy's law, the flow of the flushing solution can be occurred only in the x direction and if the piezometric heads in the injection sand-wall and extraction sand-wall are fixed, the seepage velocity must be invariable.

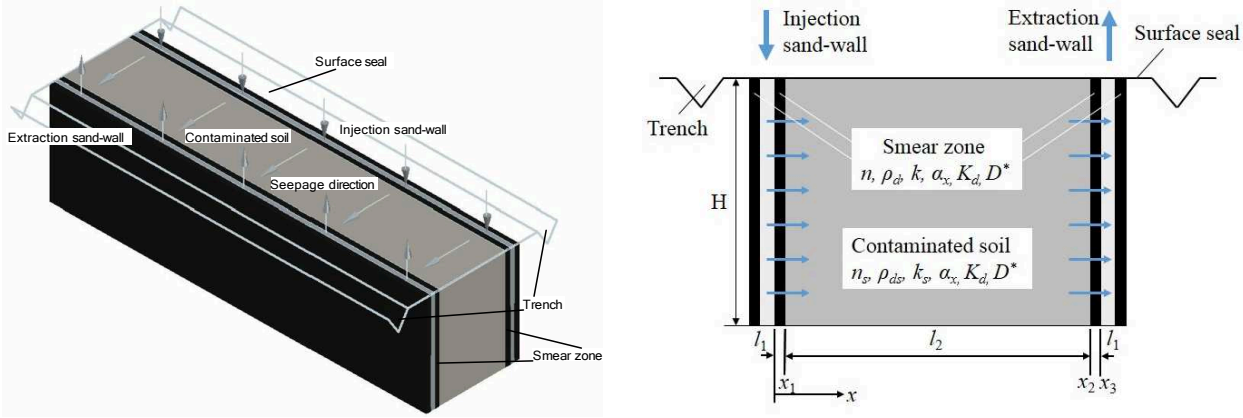


(a) Spatial pattern (b) Analysis scheme

**Fig. 1** Schematic diagram of contaminant extraction considering smear zones.

The governing equation for solute transport through the smear zones and the undisturbed contaminated soil at a particular distance $x$ and time $t$ is:

$$R_{di}\frac{\partial C_i(x,t)}{\partial t}=D_i\frac{\partial^2 C_i(x,t)}{\partial x^2}-\frac{1}{n_i}\frac{q_x\partial C_i(x,t)}{\partial x}\quad (i=1,2,3). \tag{1}$$

where $R_{d1}$, $R_{d3}$ are the retardation factors of the smear zone; $R_{d2}$ is the retardation factor of the undisturbed soil; $C_1$ is the contaminant concentration in the smear zone near the injection sand-wall; $C_2$ is the contaminant concentration in the undisturbed soil; $C_3$ is the contaminant concentration in the smear zone near the extraction sand-wall; $D_1$, $D_3$ are the coefficients of the hydrodynamic dispersion of the smear zone; $D_2$ is the coefficient of the hydrodynamic dispersion of the undisturbed soil; $n_1$, $n_3$ are the porosity of the smear zone, i.e. $n_s$; $n_2$ is the porosity of the undisturbed soil, i.e. $n$; and $q_x$ is the seepage velocity in the contaminated soil. Based on the Darcy's law, $q_x$ is determined as

$$q_x=k_H\frac{\Delta h}{L}=\frac{l_1+l_2+l_3}{l_1/k_s+l_2/k+l_3/k_s}\frac{\Delta h}{L}. \tag{2}$$

where $k_H$ is the horizontal equivalent permeability coefficient; $k_s$, $k$ are the permeability coefficients of the smear zone and the undisturbed soil, respectively; $\Delta h$ is the water head difference between the injection sand-wall and extraction sand-wall; $l_1$, $l_3$ are the width of the smear zone; $l_2$ is the width of the undisturbed soil; and $L$ is the span between the injection sand-wall and the extraction sand-wall.

Using the Henry's law, $R_{di}$ can be represented as follows:

$$R_{di} = 1 + \rho_{di} K_d / n_i \quad (i = 1, 2, 3) . \tag{3}$$

where $\rho_{d1}$, $\rho_{d3}$ are dry bulk density of the smear zone, i.e. $\rho_{ds}$; $\rho_{d2}$ is dry bulk density of the undisturbed soil, i.e. $\rho_d$; and $K_d$ is the equilibrium distribution coefficient. For the soil type of the smear zone and undisturbed zone are same, $K_d$ in both smear zone and undisturbed soil are assumed to be the same.

Based on Eq. (2), $D_i$ can be determined by

$$D_i = D^* + \alpha_x k_H \frac{\Delta h}{n_i L} . \tag{4}$$

where $D^*$ is the effective diffusion coefficient; and $\alpha_x$ is the dispersivity of the x direction, likewise, $D^*$ and $\alpha_x$ in both regions are assumed to be the same.

The initial condition is

$$C_i(x, 0) = C_0 \quad (i = 1, 2, 3) . \tag{5}$$

where $C_0$ is the initial contaminant concentration in the contaminant zone.

For the left boundary, the contaminant concentration of the flushing solution is zero:

$$C_1(0, t) = 0 . \tag{6}$$

The Neumann boundary condition is considered at the right boundary:

$$\frac{\partial C_2(x, t)}{\partial x}\Big|_{x=L} = 0 \tag{7}$$

The contaminant concentration at the interface of the smear zone and the undisturbed zone are the same, and the continuity of the contaminant flux must be obeyed as well:

$$-n_i D_i \frac{\partial C_i(x_i, t)}{\partial x} + q_x C_i(x_i, t) = -n_{i+1} D_{i+1} \frac{\partial C_{i+1}(x_i, t)}{\partial x} + q_x C_{i+1}(x_i, t) \quad (i = 1, 2) . \tag{8}$$

$$C_i(x_i, t) = C_{i+1}(x_i, t) \quad (i = 1, 2) . \tag{9}$$

**Analytical solution**

Similarly to the problem of one-dimensional consolidation of layered systems, the method of separation of variables is applied. The solution to the governing Eq. (1) satisfying the boundary conditions given by Eqs. (6), (7) and the continuity conditions given by Eqs. (8), (9) can be expressed as follows:

$$C_i(x,t) = C_0 e^{\frac{q_x x}{2n_i D_i} - \frac{q_x^2 t}{4n_i^2 R_i D_i}} \sum_{m=1}^{\infty} \xi_m g_{im}(x) e^{-\beta_{im} t} \quad (i = 1,2,3) \tag{10}$$

where

$$g_{im}(x) = A_{im} \sin\left(\mu_i \lambda_{im} \frac{x}{l_1}\right) + B_{im} \cos\left(\mu_i \lambda_{im} \frac{x}{l_1}\right), \qquad \lambda_{im} = l_1 \sqrt{\frac{R_{d1}\beta_{im}}{D_1}}, \qquad \mu_i = \sqrt{\frac{R_{di} D_1}{R_{d1} D_i}},$$

$$\xi_m = \frac{e^{\frac{q_x x_1}{n_1 D_1} + \frac{q_x x_2}{n_2 D_2}} \int_0^{x_1} g_{1m}(x) e^{-\frac{q_x x}{2n_1 D_1}} dx + \frac{R_{d2} n_2}{R_{d1} n_1} e^{\frac{q_x x_1}{n_2 D_2} + \frac{q_x x_2}{n_2 D_2}} \int_{x_1}^{x_2} g_{2m}(x) e^{-\frac{q_x x}{2n_2 D_2}} dx + e^{\frac{q_x x_2}{n_3 D_3} + \frac{q_x x_1}{n_2 D_2}} \int_{x_2}^{L} g_{3m}(x) e^{-\frac{q_x x}{2n_3 D_3}} dx}{e^{\frac{q_x x_1}{n_1 D_1} + \frac{q_x x_2}{n_2 D_2}} \int_0^{x_1} g_{1m}^2(x) dx + \frac{R_{d2} n_2}{R_{d1} n_1} e^{\frac{q_x x_1}{n_2 D_2} + \frac{q_x x_2}{n_2 D_2}} \int_{x_1}^{x_2} g_{2m}^2(x) dx + e^{\frac{q_x x_2}{n_3 D_3} + \frac{q_x x_1}{n_2 D_2}} \int_{x_2}^{L} g_{3m}^2(x) dx}$$

The coefficients $A_{im}$ and $B_{im}$ can be determined by the following recurrence equation:

$$\left.\begin{aligned} &\left[A_{1m} \quad B_{1m}\right]^T = \left[1 \quad 0\right]^T \\ &\left[A_{(i+1)m} \quad B_{(i+1)m}\right]^T = S_{im} \left[A_{im} \quad B_{im}\right]^T \quad (i = 1,2) \end{aligned}\right\}. \tag{11}$$

in which:

$$S_{im} = \zeta_i \begin{bmatrix} E_{im}F_{im} + \eta_i G_{im}H_{im} & E_{im}H_{im} - \eta_i G_{im}F_{im} \\ G_{im}F_{im} - \eta_i H_{im}E_{im} & G_{im}H_{im} + \eta_i E_{im}F_{im} \end{bmatrix}, \quad E_{im} = \sin\left(\mu_{i+1}\lambda_{(i+1)m} \frac{x_i}{l_1}\right), \quad F_{im} = \sin\left(\mu_i \lambda_{im} \frac{x_i}{l_1}\right),$$

$$G_{im} = \cos\left(\mu_{i+1}\lambda_{(i+1)m} \frac{x_i}{l_1}\right), \quad H_{im} = \cos\left(\mu_i \lambda_{im} \frac{x_i}{l_1}\right), \quad \zeta_i = e^{-(\frac{q_x}{2n_{i+1}D_{i+1}} - \frac{q_x}{2n_i D_i})x_i}, \quad \eta_i = \frac{n_i \lambda_i}{n_{i+1}\lambda_{i+1}} \sqrt{\frac{D_i R_{di}}{D_{i+1} R_{d(i+1)}}}$$

The determinant of the following which is equal to zero yields the values of $\lambda_{im}$:

$$\left| S_3 \cdot S_2 \cdot S_1 \cdot \left[1 \quad 0\right]^T \right| = 0 \tag{12}$$

in which

$$S_3 = \begin{bmatrix} \frac{\lambda_{3m}}{l_1} \sqrt{\frac{R_{di} D_1}{R_{d1} D_i}} H_{3j} + \frac{q_x}{2n_3 D_3} F_{3j} \\ -\frac{\lambda_{3m}}{l_1} \sqrt{\frac{R_{di} D_1}{R_{d1} D_i}} F_{3j} + \frac{q_x}{2n_3 D_3} H_{3j} \end{bmatrix}^T, \quad \lambda_{1m}^2 = \lambda_{3m}^2 = \lambda_{2m}^2 + (\frac{q_x^2}{4n_2^2 R_{d2} D_2} - \frac{q_x^2}{4n_1^2 R_{d1} D_1}) \frac{l_1^2 R_{d1}}{D_1}$$

**Comparisons with the finite element method**

To demonstrate the method is reasonable and verify the analytical solution gives the correct results, the proposed analytical solutions are compared with the finite element method (FEM) provided by

GeoStudio 2007. The width of the sand-wall is assumed to be 4cm and smear zone is taken to be 0.1m, which is 2.5 times the width of the mandrel based on large-scale consolidation studies, as described by Sathananthan et al. [4]. The porosity and permeability in the undisturbed contaminated soil and the smear zone are extracted from Indraratna et al. [5, 6]. Toluene is chosen to represent the contaminant in the soil, and the initial constant concentration of toluene is assumed to be 1mg/L. The material and chemical properties of the soil are taken directly from Foose et al. [7] for the similar property of the compacted clay liner from Foose et al. [7] and the clay used in Indraratna et al. [5]. The properties of the undisturbed zone and smear zone are shown in Table 1.

The comparisons of contaminant concentration profiles in contaminated soil consisting of two smear zones and an undisturbed zone obtained by the presented analytical solution and GeoStudio 2007 are shown in Fig.2. The presented analytical solutions are agreed with the results obtained by the finite element method excellently. This result further validates the proposed analytical solutions.

**Table 1** Parameters of the model for comparison with GeoStudio 2007

| **Soil type** | $n_s$ | $n$ | $\rho_d$[g/cm$^3$] | $\rho_{ds}$[g/cm$^3$] | $k$[cm/s] | $k_s$[cm/s] |
|---|---|---|---|---|---|---|
| Clay | 0.52 | 0.55 | 1.25 | 1.30 | $3.36\times10^{-7}$ | $2.7\times10^{-8}$ |
| **Contaminant** | $K_d$[ml/g] | $D^*$ [cm$^2$/h] | $\alpha_x$[m] | $\Delta h$[m] | $l_1$, $l_3$[cm] | $l_2$[cm] |
| Toluene | 1.0 | $7.34\times10^{-3}$ | 2.0 | 12 | 10 | 80 |

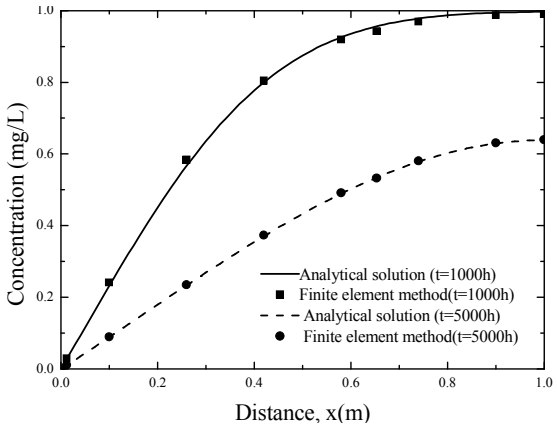


**Fig. 2** Comparisons of the analytical solution with the finite element method

## Results and discussion

An illustrative example is presented to show the influence of the smear zones. Acetone is selected to represent the contaminant in the soil. The initial constant concentration of acetone is assumed to be 1mg/L. The diffusion and distribution coefficients of the clay are from Kalbe et al. [8]. The properties of the smear zone and the undisturbed zone are extracted from Indraratna et al. [5, 6]. The material and the chemical properties of the undisturbed zone and smear zone are summarized in Table 2.

**Table 2** Parameters of the model for analysis

| **Soil type** | $n_s$ | $n$ | $\rho_d$[g/cm$^3$] | $\rho_{ds}$[g/cm$^3$] | $k$[cm/s] | $k_s$[cm/s] |
|---|---|---|---|---|---|---|
| Clay | 0.52 | 0.55 | 1.25 | 1.30 | $3.9\times10^{-8}$ | $3.4\times10^{-9}$ |
| **Contaminant** | $K_d$[ml/g] | $D^*$ [cm$^2$/h] | $\alpha_x$[m] | $\Delta h$[m] | $l_1$, $l_3$[cm] | $l_2$[cm] |
| Acetone | 0 | $1.22\times10^{-2}$ | 2.0 | 12 | 10 | 30 |

Two conditions are considered for this discussion. The comparison of the concentration profile for the case considering the effect of the smear zone and that assuming no smear zone is shown in Fig. 3.

Both concentration profiles of the two cases are obtained on the basis that the water head difference is maintained at 12m, and correspondingly the seepage velocities of the two cases are $6.49\times10^{-6}$m/h and $3.37\times10^{-5}$m/h respectively. The 500-hour base contaminant concentration at the distance of 0.25m decreases from 0.88 for the case considering the smear zone to 0.46 for that assuming no smear zone. Meanwhile, the contaminant concentration at the distance of 0.5m decreases from 0.996 to 0.66 when the smear zone is not considered in the model. The results suggest that the smear zone has a great effect on the contaminant extraction from contaminated soils.

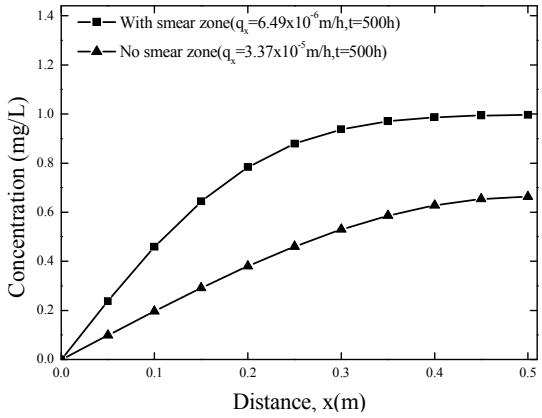


**Fig. 3** Effect of smear zone on contaminant concentration profiles.

## Conclusions

An analytical solution for one-dimensional contaminant extraction considering the effect of the smear zone is presented in this paper. The results obtained by the proposed analytical solution agree well with those obtained by the finite element method. The results suggested that the smear zone can have a great influence on the contaminant extraction from contaminated soils. The 500-hour base concentration of acetone at the distance of 0.25m increases by a factor of approximately 1.9 when the effect of the smear zone is considered in the model.

## Acknowledgements

The authors would like to express their sincere gratitude to National Natural Science Foundation of China (Grant No. 51179168) for the financial support to this study.

## References

[1] Welker AL and Gilbert RB: J. Geotech. Geoenviron. Eng., Vol. 129 (2003), p. 81
[2] Sharmin N, Kunberger T, Gabr MA, Quaranta JD and Bowders JJ: Geosynthetics International, Vol. 15 (2008), p. 205
[3] Gabr MA, Wang J and Bowders JJ: J. Geotech. Eng., Vol. 122 (1996), p. 914
[4] Sathananthan I and Indraratna B: J. Geotech. Geoenviron. Eng., Vol. 132 (2006), p. 942
[5] Indraratna B and Redana IW: J. Geotech. Geoenviron. Eng., Vol. 124 (1998), p. 180
[6] Indraratna B and Redana IW: Canadian Geotechnical Journal, Vol. 37 (2000), p. 132
[7] Foose G, Benson C and Edil T: J. Geotech. Geoenviron. Eng., Vol. 128 (2002), p. 391
[8] Kalbe U, Müller WW, Berger W and Eckardt J: Appl. Clay Sci., Vol. 21 (2002), p. 67

*Applied Mechanics and Materials Vols. 580-583 (2014) pp 566-571*
*© (2014) Trans Tech Publications, Switzerland*
*doi:10.4028/www.scientific.net/AMM.580-583.566*

# Application of Fuzzy Set Theory to Evaluate the Stability of Slopes

Tarig Mohamed[1, a] and Anuar Kasa[2, b]

[1]Department of Civil & Structural Engineering, UKM, Malaysia

[2]Department of Civil & Structural Engineering, UKM, Malaysia

[a]tarigmohalam@gmail.com, [b]anuar@eng.ukm.my

**Keywords:** Fuzzy logic, ANFIS, Slope stability prediction.

**Abstract.** An artificial intelligence tools, Adaptive Neuro Fuzzy Inference System (ANFIS), was used in this study to predict the stability of slopes. Data used in this study were 300 various designs of slope. Those designs were created by using Slope/W which calculated factors of safety using various limit equilibrium methods (LEM) such as Bishop, Spencer and Morgenstern-Price. The input parameters consisted of height of slope, H (1–10 m), unit weight of slope material, $\gamma$ (15-22 kN/m$^3$), angle of slope, $\theta$ (11.31°-78.69°), coefficient of cohesion, c (0-50 kN/m$^2$) and internal angle of friction, $\phi$ (20°- 40°) and the output parameter is the factor of safety. To build the fuzzy inference system, 243 rules were used at 60 epochs. The number of membership function for the any input was three and the type of membership function for output was linear. ANFIS obtained regression square ($R^2$) of one for Bishop, one for Janbu, one for Morgenstern-Price and one for Ordinary. The result proved that ANFIS may possibly predict the safety factor with good precision and nearly to the target data.

## Introduction

An exposed ground surface that stands at an angle with the horizontal is called slope. Slope stability problem has been an important issue in geotechnical engineering. Slope failure is a common natural disaster which takes place around the world. The evolution of slope stability analyses in geotechnical engineering has followed closely the developments in soil. Geotechnical engineers have to pay particular attention to geology, ground water and shear strength of soils in assessing slope stability. Therefore, slope investigation and classification are important for the community [1,2,3,4,5].

Geotechnical engineers frequently use limit equilibrium methods (LEM) of analysis when studying slope stability problems. The methods of slices have become the most common methods due to their ability to accommodate complex geometrics and variable soil and water pressure conditions. During the past three decades approximately one dozen methods of slices have been developed. They differ in (i) the statics employed in deriving the factor of safety equation and (ii) the assumption used to render the problem determinate [6,7,8,9].

System modeling based on conventional mathematical tool is not well suited for dealing with ill-defined and uncertain systems. By contrast, a fuzzy inference system (FIS) employing fuzzy if-then rules can model the qualitative aspects of human knowledge and reasoning processes without employing precise quantitative analyses. This fuzzy modeling or fuzzy identification, first explored systematically by Takagi and Sugeno, has found numerous practical applications in control, prediction and inference. However, there are some basic aspects of this approach which are need of better understanding. More specifically (i) no standard methods exist for transforming human knowledge or experience into the rule base and database of a fuzzy inference system, (ii) there is a need for effective methods for tuning the membership functions (MFs) so as to minimize the output error measure or maximize performance index [10,11,12,13,14].

Fuzzy if-then rules or fuzzy conditional statements are expressions of the form *IF A then B*, where *A* and *B* are labels of fuzzy sets characterized by appropriate MFs. Due to their concise form, fuzzy if-then rules are often employed to capture the imprecise modes of reasoning that play an

essential role in the human ability to make decisions in an environment of uncertainty and imprecision. Another form of fuzzy if-then rules, proposed by Takagi and Sugeno, has fuzzy sets involved only in the premise part. Both types of fuzzy if-then rules have been used extensively in both modelling and control. Through the use of linguistic labels and MF, a fuzzy if-then rule can easily capture the spirit of "rule of thumb" used by humans. From another angle, due to the qualifiers on the premise parts, each fuzzy if-then rule can be viewed as local description of the system under consideration [10,15,16,17].

Fuzzy inference systems (FIS) are also known as fuzzy-rule-based systems, fuzzy models, fuzzy associative memories (FAM), or fuzzy controllers when used as controllers. Basically a fuzzy inference system is composed of five functional blocks: (1) a rule base containing a number of fuzzy if-then rules, (2) a database which defies the membership function of the fuzzy sets used in the fuzzy rules, (3) a decision-making unit which performs the inference operations on the rules, (4) a fuzzification interface which transforms the crisp inputs into degrees of match with linguistic value, (5) a defuzzification interface which transform the fuzzy results of the inference into crisp output. Usually, the rule base and the database are jointly referred to as the knowledge base [10].

Depending on the types of fuzzy reasoning and fuzzy if-then rules employed, most fuzzy inference systems can be classified into three types: (1) the overall output is the weighted average of each rule's crisp output induced by the rule's firing strength and output MF, (2) the overall fuzzy output is derived by applying "max" operation to the qualified fuzzy outputs, (3) Takagi and Sugeno's fuzzy if-then rules [10,15,18,19,20].

The power of Artificial Intelligent (AI) becomes more authoritative when the system is programmed to cater the need of complex applications. Adaptive Neuro-fuzzy Inference System (ANFIS) Model using neuro adaptive learning techniques which are similar to those of neural networks was originally presented by Jang. Given an input/output data sets, ANFIS constructs FIS whose MF parameters are adjusted using back propagation algorithm or other similar optimization techniques. Hence, the advantages of a fuzzy system can be combined with a learning algorithm [21,22,23,24].

## Methodology

The methodology for this study could be divided into three steps; (i) Designing slopes. Height of slope (H), unit weight of soil (γ), angle of slope (θ), coefficient of cohesion (c) and internal angle of friction ($\phi$) were used as input parameters. To design the slopes, many possibilities were considered for the input parameters by fixing some of them and changing the others. The angles of slope were calculated by considering horizontal and vertical length of the slope, (ii) Calculation of safety factors. Slope/W which applied limit equilibrium methods i.e. Bishop, Janbu, Morgenstern-Price and Ordinary, was used to compute factors of safety for 300 different designs. The comprehensive formulation of the software made it possible to easily analyze both simple and complex slope stability problems using a variety of methods, (iii) Adaptive Neuro-Fuzzy Inference Systems (ANFIS) prediction. After carrying out the stability analyses, ANFIS was used to formulate the mapping from a given input to an output. For this research, linear output and 243 rules were used for generating fuzzy inference system (FIS). For training the FIS, 60 epochs, hybrid method and zero errors tolerance were used. The mapping then provided a basis from which decisions could be made.

## Results and Discussion

The result of this research can be divided into three parts; (i) Designed slopes. In this research, 300 different designs of slopes were established. Different variables including height of slope (H), unit weight of soil (γ), angle of slope (θ), coefficient of cohesion (c), and internal angle of friction ($\phi$) were used as the input parameters for designing, (ii) Factors of safety. The results of the calculated

safety factors can be classified as (1) less than one, (2) greater than one, and (3) greater than 1.5, (iii) Prediction by Adaptive Neuro Fuzzy Inference Systems (ANFIS). By using 300 training data, ANFIS model was used as a function of different parameters. Prediction using ANFIS produced average percentage error of 0.0915 for Bishop, 0.0928 for Janbu, 0.0917 for Morgenstern-Price and 0.0935 for Ordinary. Figure 1 until 4 show the comparison of calculated factors of safety using LEM and predicted factors of safety using ANFIS. In addition, ANFIS obtained regression square ($R^2$) of one for Bishop, one for Janbu, one for Morgenstern-Price and one for Ordinary.

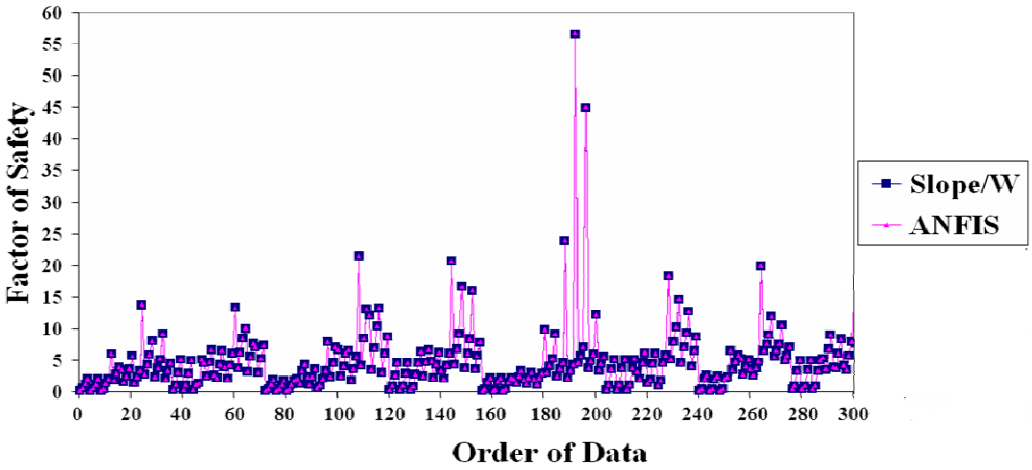


Fig.1 Comparison of calculated factor of safety using Bishop and predicted using ANFIS

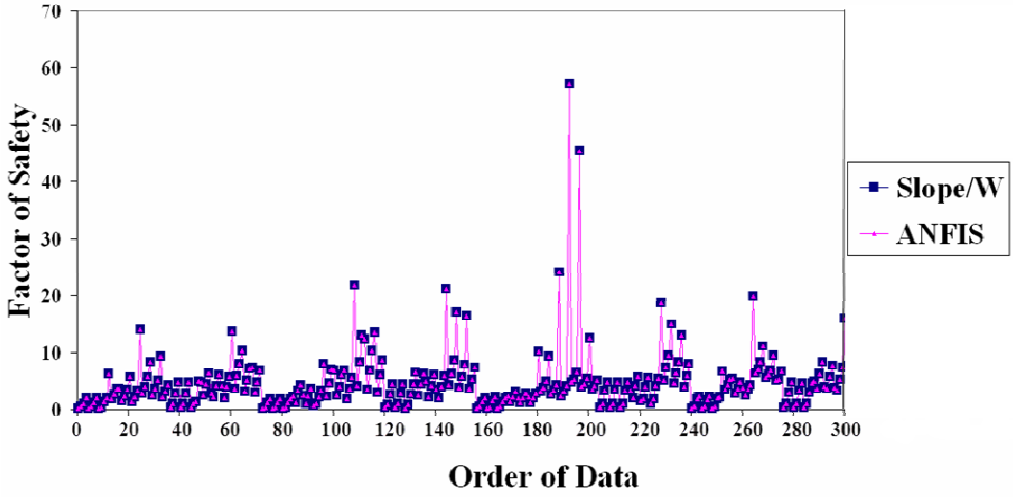


Fig.2 Comparison of calculated factor of safety using Janbu and predicted using ANFIS

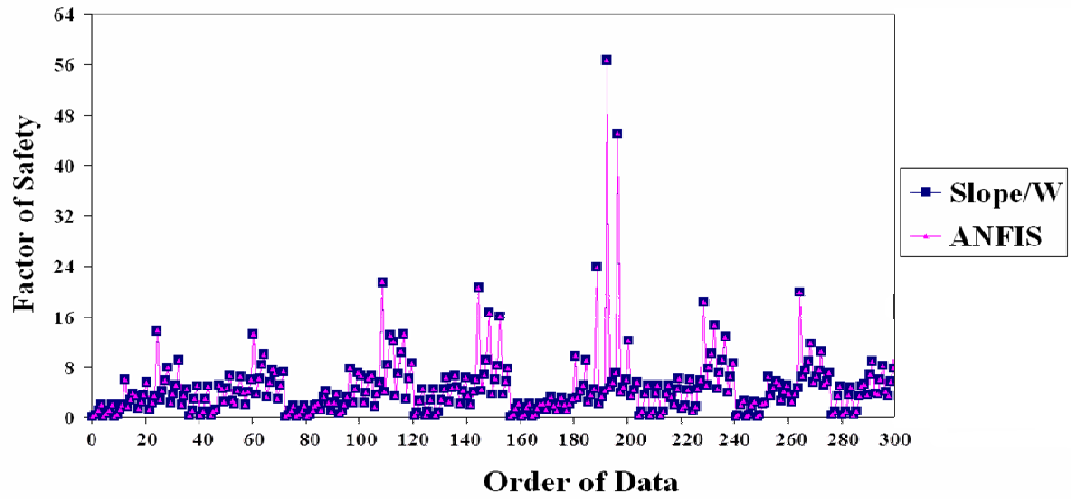


Fig.3 Comparison of calculated factor of safety using Morgenstern-Price and predicted using ANFIS

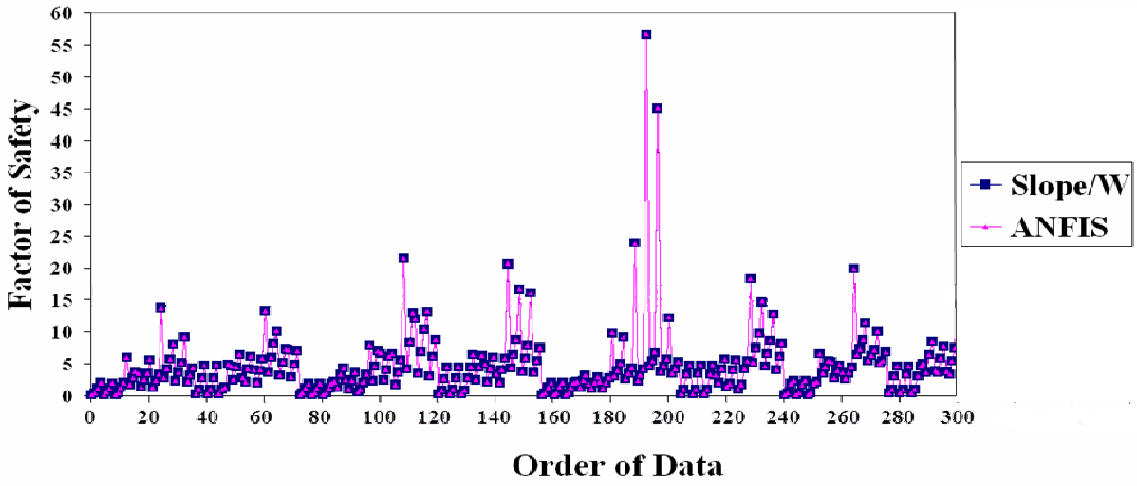


Fig.4 Comparison of calculated factor of safety using Ordinary and predicted using ANFIS

## Conclusion

As a conclusion, this research has achieved all the desired objectives. The results of this study can be considered as a major contribution to the field of knowledge since the use of Adaptive Neuro Fuzzy Inference Systems (ANFIS) for prediction of slope stability as carried out in this research has not been conducted before. The results show that ANFIS could really predict the factor of safety very well since the values of $R^2$ for all cases are very close to one and could predict the safety factors with high accuracy compared with other methods. Thus, ANFIS could be a suitable tool for predicting the stability of slope in future research.

## Acknowledgment

Authors would like to thank the National University of Malaysia for funding this project through the University Research Grant.

**References**

[1] Lee, W.A., Thomas, S.L., Sunil, S. & Glenn, M. Slope stability and stabilization methods. Ed. th-2. New York: John Wiley & Sons (2002)..

[2] Choobbasti, A.J., Farrokhzad, F. & Barari, A. Prediction of slope stability using artificial neural network. Arabian Journal of Geosciences 2(4): 311-319 (2009).

[3] Ping, K.Z. & Zhi, Q.C. Stability prediction of tailing dam slope based on neural network recognition. Proceeding of the International Conference on pattern Environmental and Computer Science 380-383 (2009).

[4] Vector, Y. Application of soil nailing for slope stability purpose. Thesis B.Sc. University of Technology (2008).

[5] Braja, M.D. Principles of geotechnical engineering. Ontario: Nelson (2007).

[6] Fredlund, D.G. & Krahn, J. Comparison of slope stability methods of analysis. Canadian Geotechnical Journal 14: 429-439 (1977).

[7] Terzaghi, K. & Peck, R.B. Soil mechanics in engineering practice. Ed. the-2. New York: John Wiley & Sons (1967).

[8] Wright, S. A study of slope stability and the undrained shear strength of clay shales. Thesis Ph.D. University of California (1969).

[9] Fredlund. A comprehensive and flexible slope stability program. The Roads and Transportation Association of Canada Meeting (1975).

[10] Jang, J.S.R. ANFIS: adaptive-network-based fuzzy inference system. IEEE Transactions on System Man and Cybernetics 23(3): 665-685 (1993).

[11] Pedrycz, W. Fuzzy Control and Fuzzy Systems. New York: John Wiley & Sons (1989).

[12] Sugeno, M. Industrial applications of fuzzy control. North Holland: Elsevier Science (1985).

[13] Kandel, A. Fuzzy expert systems. Boston: Addison Wesley (1988).

[14] Kandel, A. Fuzzy expert systems. Boca Raton: CRC (1992).

[15] Takagi, T. & Sugeno, M. Derivation of fuzzy control rules from human operator's control actions. Proceeding of the IFAC Fuzzy Information Knowledge Representation and Decision Analysis 55-60 (1983).

[16] Zadeh, L.A. Fuzzy sets. Information and Control 8: 338-353 (1965).

[17] Zadeh, L.A. Outline of a new approach to the analysis of complex systems and decision processes. IEEE Transactions on System Man and Cybernetics 3: 28-44 (1973).

[18] Lee, C.C. Fuzzy logic in control systems: fuzzy logic controller-part 1. IEEE transactions on Systems, Man, and Cybernetics 20(2): 404-418 (1990a).

[19] Lee, C.C. Fuzzy logic in control systems: fuzzy logic controller-part 2. IEEE transactions on Systems, Man, and Cybernetics 20(2): 419-435 (1990b).

[20] Tsukamoto, Y. An approach to fuzzy reasoning method. Advances in Fuzzy Set Theory and Applications 137-149 (1979).

[21] Sivarao, Peter, B. & El-Tayeb, N.S.M. A new approach of adaptive network-based fuzzy inference system modeling in laser processing-a graphical user interface (GUI) based. Journal of Computer Science 5(10): 704-710 (2009).

[22] Merikoski, S., Laurikkala, M. & Koivisto, H. An adaptive neuro-fuzzy inference system as a soft sensor for viscosity in rubber mixing process. Automation and Control Institute: Tampere (2001).

[23] Jang, R. Neuro-Fuzzy and Soft Computing: A Computational Approach to Learning and Machine Intelligence. New Jersey: Prentice Hall (1996).

[24] Sakellariou, M.G. & Ferentinou, M.D. A study of slope stability prediction using neural networks. Geotechnical and Geological Engineering 23: 419–445 (2005).

*Applied Mechanics and Materials Vols. 580-583 (2014) pp 572-578*
*© (2014) Trans Tech Publications, Switzerland*
*doi:10.4028/www.scientific.net/AMM.580-583.572*

# Application Research on Distributed Optical Fiber Monitoring Technology in Static Load Test of Large Diameter and Post-grouting Filling Pile

Jiaxing Chen[1, a], Tonghe Zhou[2, b] and Yuancheng Guo[3, c]

[1]Zhengzhou city engineering quality surveillance Zhengzhou Economic and Technological Development Zone Substation, China

[2]Design and research institute of Zhengzhou University, China

[3]Zhengzhou University, China

[a]13603868660@126.com, [b]zth1964@126.com, [c]guoyuancheng@163.com

**Keywords:** distributed optical fiber, post-grouting filling pile, bearing character

**Abstract.** The Static load test of the post-grouting filling pile in Zhengzhou city's third ring road rapidness project, uses strain gauge and distributed optical fiber to track and monitor the evolution rule of load-settlement, pile body stress, pile side resistance, etc., interprets bearing properties of large diameter post-grouting filling pile, contrasts and analyzes the monitoring data obtained by optical fiber and strain gauge at the same time. The result shows that, the monitoring effect of the pile body stress obtained by distributed optical fiber technology is superior to the strain gauge, but the data of them still needs to verify each other.

## Introduction

In recent years, with the development of optical fiber technology, the distributed optical fiber technology is widely used in geotechnical engineering and underground engineering [1-8]. Compared with the strain gauge, the measuring point of the distributed optical fiber is simple to embed, a higher monitoring precision and automatically collecting data, the ability to monitor continuously in a complex environment. So far the monitoring technology is mainly used to monitor the internal force of tunnel structure in geotechnical and underground engineering, rarely used in ground treatment. Thus, Through Zhengzhou city's third ring road rapidness project, the distributed optical fiber technology is applied to the large diameter post-grouting filling pile load test, analyzing the bearing character of the large diameter post-grouting pile and comparing with the monitoring data obtained by the strain gauge to discuss the applicability of the technology.

## Overview of Test

This test depends on the Zhengzhou city's third ring road rapidness project. Test area is located at crossing of Hanghai road and Jingguang road. The district is mainly the quaternary alluvium and the soil geotechnical properties are shown in Table 1.

Table 1 Soil physical and mechanical index

| Soil layer number | Soil | Depth (m) | Bearing capacity basic allowable value [$f_{a0}$] (kPa) | Pile flank friction force standard value $q_{ik}$ (kPa) | Soil layer introduction |
|---|---|---|---|---|---|
| ② | Floury soil | 15.30～18.20 | 200 | 50 | The most shallow buried, structural is poorer, engineering properties of groundwater is sensitive, not as foundation bearing layer of the project |

| | | | | | |
|---|---|---|---|---|---|
| ③$_1$ | Floury soil | 8.40～16.80 | 240 | 70 | No significant difference engineering properties, structural, not easily affected by groundwater are bearing layer can be used as a basis |
| ③$_2$ | Silty clay | 3.30～11.70 | 390 | 80 | |
| ③$_3$ | Floury soil | 7.60～21.20 | 220 | 70 | |
| ③$_4$ | Silty clay | | 410 | 80 | |

The single pile static load test was divided into six groups, one group of the piles was conducted without post-grouting, two groups were conducted post-grouting at the bottom of the pile, three groups were conducted composite grouting between the bottom of the pile and the side of the pile. Loading method is anchor-pile method. Maximum loading of test pile is 22000kN, the diameter of test piles is 1.2m, anchor-piles (using composite post-grouting) diameter is 1.5 m, the strength grade of the concrete is underwater C30, the length of the piles is 38m, and the depth inserted into the soil is 40 m. Before grouting, ultimate bearing capacity of the single pile is 9900kN. The plane position of the test pile and scene photos is shown in Fig. 1 and Fig. 2.

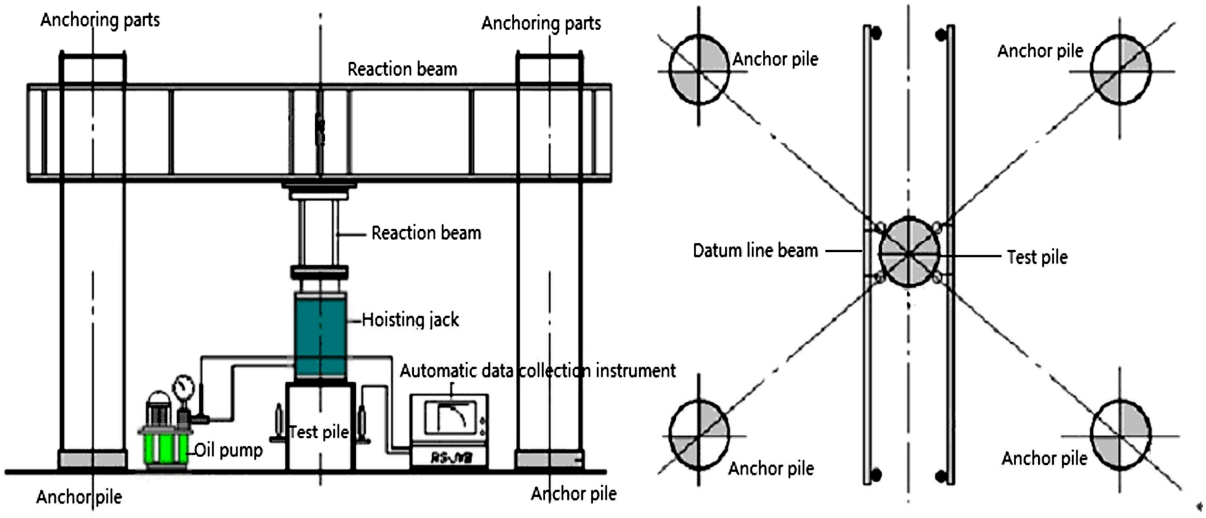


Fig. 1 The piles arrangement

Fig. 2 The scene photos of the static load test of single pile

**Monitoring of Distributed Optical Fiber**

**Basic Principle** Brillouin scattering is affected by strain and temperature at the same time. When the temperature along optical fiber changes or axial strain exists, the light frequency of the optical fiber in the back of the Brillouin scattering will drift, the degree of the frequency drift and the change of optical fiber strain and temperature had a good linear relationship, so by measuring the degree of the frequency drift of the back on to the natural optical fiber Brillouin scattering light can retained the information of the optical fiber temperature and strain distribution.

**Method of Embedding Optical Fiber Sensor** In the test, before lifting the first section of reinforcing cage, two relatively main reinforcements of steel cage were selected as distributed optical fiber's attachment objects, along the main reinforcements inside of the steel cage from bottom to up began tie the optical fiber, and maintain fiber straight when tying, close to the main reinforcement inside of the reinforcing cage, used nylon cable to tie every 100 mm to 150 mm to fix the optical fiber to ensure the uniform deformation of fiber and concrete. In order to avoid the adverse effect on the distributed optical fiber like break points in the pouring and construction process in the later stage at the same time. The optical fiber was protected with metal corrugate pipe when laying, then cling the bellows to reinforcing rib at the bottom of reinforcement cage to form "U" glyph circuits. Nylon cable ties were used to assemble in every 100mm and waterproof tape was adopted to waterproof. At the junctions of the main reinforcements and the reinforcing ribs of reinforcement cages, namely the transitions of the optical fiber from the main reinforcements to the reinforcing ribs and from the reinforcing ribs to the main reinforcements, where the hollow area was formed and optical fibers were easily damaged when pouring concrete, triangle plastic foam is adopted to fill in these areas and the foam is tied with waterproof tape in order to avoid water and cement paste flowing into the area when pouring concrete or post grouting and negative effect on the optic fiber, The photos of optic fibers banging are shown in Fig. 3 and Fig.4.

Lay the optical fiber at the head of pile. The protection tube of the pile is made of steel plate welded whose thickness is 5mm, the inner diameter 1200mm, the length 1.2 m. In order to avoid the damage when making the head of pile in later stage, the optical fiber shall be protected by metal corrugate pipe in a distance of 3.0m to the top of the pile, sealed with waterproof tape and loaded in PVC plastic pipe whose length is about 2.0m, fixing the PVC plastic pipe on steel cage's main bars with iron wires. The optical fibers above PVC plastic tube head were treated with waterproof tape and put them all in nylon bag and marked beside pile and buried them in the soil for protection.

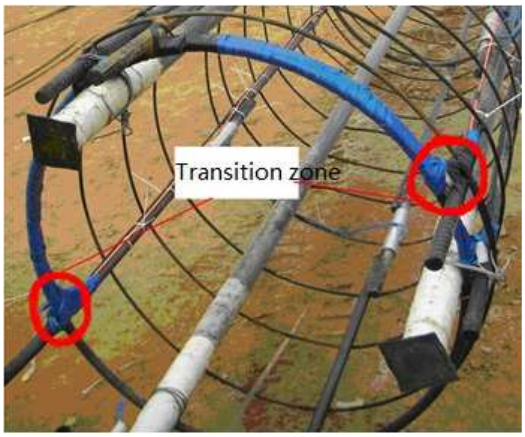


Fig. 3 Optic fibers laying at the bottom of the steel cage

Fig. 4 Optical fibers banging in the steel cage

After finishing the pile body concrete pouring, curing was asked for 28 days. Before the static load test of pile foundation, the optical fibers buried in the soil in the earlier stage were found out according to the mark to be butted joint to the optical fibers whose functions were just sensing with PCF fusing machine. Then circuit testing was conducted with BOTDR optical fiber strain analyzer to determine the effect of optical fiber welding quality.

**Data Collection** BOTDR instrument tracked and monitored the loading and unloading process of the test piles. The test of each stage of loading starts before the time when the displacement observation is stable 10 minutes. Next stage of loading was loaded (unloaded) after the data was collected. The initial strain value of the pile foundation load can be forecasted and obtained before the experiment and the strain can be considered to be the initial strain in free state. The difference between the strain produced by each stage of loading and the initial strain could be taken as the strain value in this stage of loading.

## Results Analysis of the Experiment

This experiment data is selected every 0.4 m. Pile 4 # (composite grouting in the side and bottom of pile) was taken as the analysis object. The data of composite grouting pile settlement, pile body parameters such as strain, stress and axial force were analyzed respectively, comparing the strain and the optical fiber strain data at the same time.

**P-s Curve** As is shown in Fig. 5, with the load increasing, the settlement of pile top increases gradually. The ultimate bearing capacity of single pile is 20000 kN.

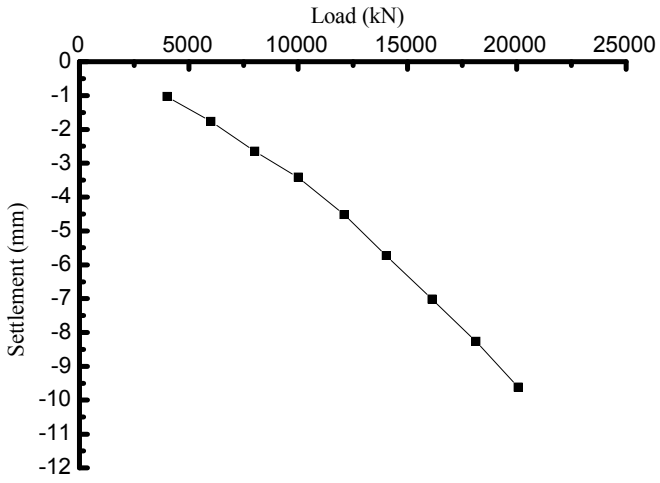


Fig. 5 The p - s curve of test pile 4#

**Pile Body Stress** Fig. 6 shows that, with the increasing of upper load, pile body stress increases gradually. The principle of stress variation is consistent with the strain of the pile. The reduction of pile stress fluctuates from the top of the pile to the bottom of the pile.

The main factors to induce the monitoring data fluctuation include the change of the pile diameter, monitoring accuracy, embedment method, construction technology and so on. Increasing the diameter of the pile made the pile stress reduce under the same axial force. Material changes in temperature affected the monitoring accuracy of the optical fiber sensor and data transmission error occurred. When pouring concrete, temperature changes of different depths of concrete hydration heat affected the monitoring results. Since the fiber was flexible material, there would be local bend in laying and it would also affect the accuracy of the monitoring to some extent. After grouting, side friction resistance of the pile increased in the test and pile stress reduced relatively with the same axial force.

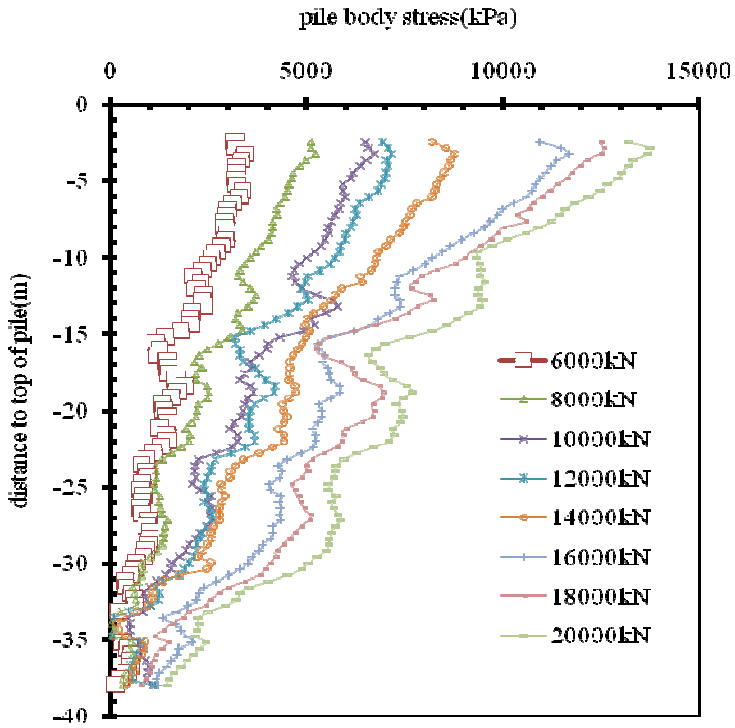


Fig. 6 The pile body stress curve of test pile 4#

**Comparison Analysis of the Strain Measured with two Methods** In the test, the strain gauges and optical fibers were embedded at the same time, the data obtained from two methods was in contrast and analyzed. The results are shown in Fig. 7.

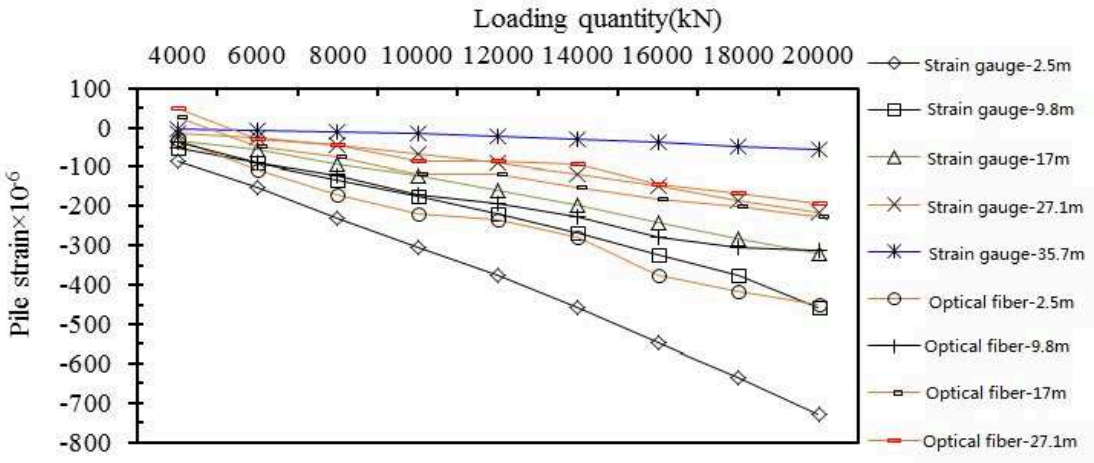


(a)

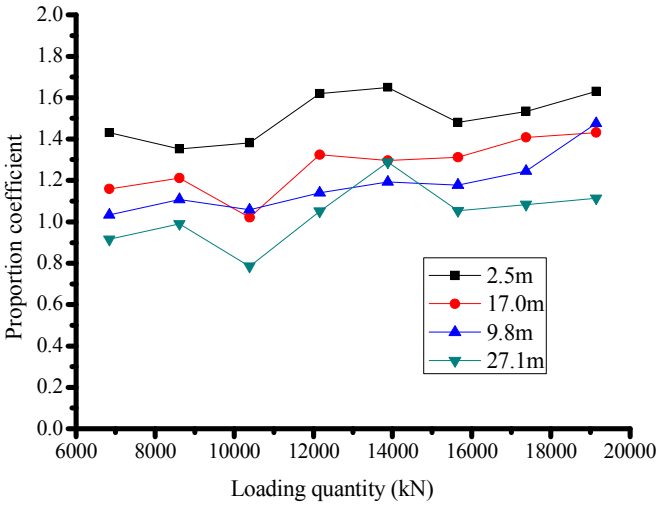


(b)

Fig.7 Strain data contrast curves of test pile 4# of the strain gauge and optic fiber

As is shown, at the same location, two kinds of data have the same evolution law: with the load increasing, the strain increases gradually and it presents a linear growth, the ratio of strain measured by two methods between 0.9~1.6.

## Conclusions

The experiment of post-grouting filling pile in Zhengzhou city's third ring road rapidness project, study the evolution of large diameter and post-grouting filling pile about the settlement of pile top and pile body stress. Contrast and analyzing the data of strain gauge and optic fiber, the main conclusions are as following: With the upper load increasing, pile strain, pile stress and pile axial force increases gradually. The test data accuracy will be affected by the change of pile diameter, monitoring accuracy, embedment method, construction technology, temperature change of material, etc. Strain ratio measured with optical fiber and strain gauge at the same position is 0.9~1.6. With the load increasing, difference of the strain data measured with the two methods increases gradually. Distributed optical fiber measurement can be applied to monitor the pile body stress continuously and has obvious advantage in monitoring pile axial force, pile stress, pile strain, pile side resistance and so on over strain gauge. But the data needs to be modified with the strain gauge data.

## References

[1] Guangqing Wei, Bin Shi and Xiaokui Yu, etc: BOTDR distributed detection technology in complex formation drilling filling pile test [J]. Journal of engineering geology, 2008, 16(6): 826~832. In Chinese

[2] Huawei Guo and Chuanhui Cheng: BOTDR fiber optical strain test pile body measurement [J]. Journal of pingdingshan institute of technology, 2007, 16(3): 55~58. In Chinese

[3] Yong Ding: Tunnel structure health monitoring research based on BOTDR [D]. Nanjing: Nanjing University, 2005. In Chinese

[4] Design and research institute of Zhengzhou University: The report of grouting shaft piles compressive static load test of distributed optical fiber inspection in East district of Zhengzhou [R]. Zhengzhou: Design and research institute of Zhengzhou University. 2007. In Chinese

[5] Yaxing Pei, Xiankang Tan and Aixun Wang: Application of the optical fiber sensing technology in prestressed anchor rod stress test [J]. The people of the Yangtze river, 2004, 35(1): 25-27. In Chinese

[6] Bin Shi, Xuejun Xu and Di Wang, etc: Research on tunnel health diagnosis of BOTDR distributed fiber optic strain monitoring technology [J]. Journal of Rock Mechanics and Geotechnical Engineering2005, 24(15): 2622-2628. In Chinese

[7] Dan Zhang : Research on distributed optical fiber sensing technology based on BODTR and its application in tunnel deformation monitoring [D]. Nanjing: Nanjing University, 2004. In Chinese
[8] Suozhu Ma: The application of optical fiber sensing technology in underground engineering [J]. Journal of Railway Engineering Society, 2006, 2: 67-70. In Chinese
[9] Shenghe Sun, Tingyun Wang and Ying Xu: Optical fiber measurement and sensing technology (Edition 2) [M]. Haerbin: Harbin industrial university press, 2002. In Chinese

*Applied Mechanics and Materials Vols. 580-583 (2014) pp 579-584*
*© (2014) Trans Tech Publications, Switzerland*
*doi:10.4028/www.scientific.net/AMM.580-583.579*

# Coaction analysis on pile-net-cushion-soil

Ruifang Wang[1, a],Keyu Wang[2,b]

[1]Department of Civil Engineering of Urban Construction College,Wuhan University of Science and Technology,China, 430065

[2] Institute for Building Science of Hubei, China,430071

[a] 865140840@qq.com [b]272575226@qq.com

**Keywords**：analytic calculation;flexibility matrix;field experiment;finite element numerical calculation

**ABSTRACT**： In accordance of the principles of stress continuousness and displacement coordination, the interactions model of pile and pile, pile and soil are set up； Accoring to the symmetry of the models,1/4 of the models are extracted to set up three-dimension multipile composite foundation models.The flexibility matrix of the three reinforcements are modified to build a global flexibility matrix with the consideration of cushion's compression； Interaction coefficients of the analytic calculation are lower than those of the finite element when pile lengthen is diversity.The comparison between the on-site measured data from the literature review and results of the analytic calculation shows the settlements in the analytic calculation are smaller than those in the measured data, and the model measurements are very close to the curves from the analytic calculation. All these prove that the analytic methods proposed by this research are accurate and may function as a reference to engineering.

## Introduction

Pile-net composite foundation is made of reinforced sand-pile-soil,they coundertake embankment loads and traffic loads.The methods about the joint actions of pile and soil include:load transfer-method[1][2],shearing displacement method[3],elasticity theory,numerical calculation.The paper adopt shearing displacement method to analy the coactions of group piles-nets-soil-cushion under the embankment loads.

## Basic assumption

Due to the coactions mechanism of the piles-soil-cushion is complex,the minor factors are neglected in analytic calculation,material properties are assumpted,the assumptions are ut infra:

(1) Pile-net-cushion-soil are homogeneous,isotropic,ideal elastic mass;
(2) The bearing of net is neglected;
(3) Relative displacement of frictional resistance of pile side are ideal elastoplasticity ;
(4) The actions of soil around piles are neglected when the coactions among piles are analyzed.

## Flexibility matrix of the bearing system

The matrix of displacements and loads about group piles is:

$$\{w\}=[\delta]\{P\} \quad (1)$$

In formula (1), $[\delta]$ is the flexibility matrix of the bearing system,partitioned matrix is represented

$$[\delta]=\begin{bmatrix}\delta_{mm} & \delta_{mn} & \delta_{ms}\\ \delta_{nm} & \delta_{nn} & \delta_{ns}\\ \delta_{sm} & \delta_{sn} & \delta_{ss}\end{bmatrix} \tag{2}$$

3.1 Softness factor of coactions about piles

Material,physical dimension of piles are ipentity,according to the action model of piles were deduced by Mylonakis and gazetas[4] ,as shown in Fig.1:

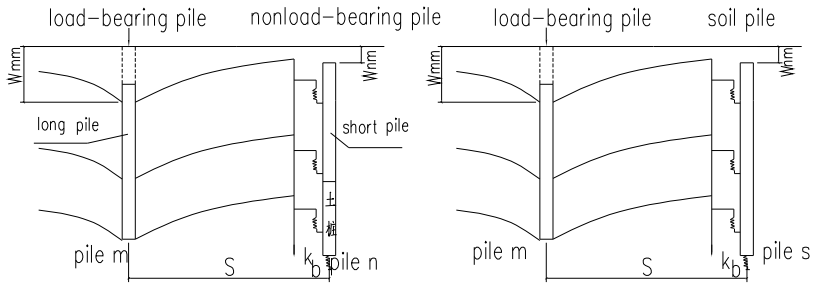


(a) Interact model of piles (b) Interact model of pile and soil

Fig.1 Interact model of load-bearing pile and nonload-bearing pile

Pile body shear stress of load-bearing pile m is created by applied load $\sigma_p$, Shear stress is transferred along radial,arrive the soil around piles,settlement of the soil is

$$w_s=\psi(s)_{mn}w_{mm} \tag{3}$$

$$\psi(s)=\frac{w_s(s,z)}{w_s(r_p,z)}=\begin{cases}\dfrac{\ln r_m-\ln s}{\ln r_m-\ln r_p} & r_p\le s\le r_m\\ 0 & s>r_m\end{cases} \tag{4}$$

Directed pile n,relative displacement of pile depth z is $w_{mn}-w_s$, According to Winkler model,the pile side resistance of pile n is $k_{zn}(w_{nm}-w_s)$, Vertical unit differential of pile n is

$$A_{pn}E_{pn}\frac{d^2w_{nm}(z)}{dz^2}-k_z[w_{nm}(z)-w_s(z)]=0 \tag{5}$$

Assumpt $\lambda_m=\sqrt{\dfrac{k_{zm}}{A_{pm}E_{pm}}}$, subscript m of $\lambda_m,k_{zm}$ represent pile m load transfer coefficient and pile side Winkler coefficient, $w_{mm}(z)$ is displacement of pile body due to the own load of pile cap,according to the displacement formula of the single pile $w_p(z)=C_1e^{\lambda z}+C_2e^{-\lambda z}$ ,the solution of formula (5) is:

$$\frac{d^2 w_{nm}(z)}{dz^2} - \lambda_n^2 w_{nm} + \lambda_n^2 \psi(s)(c_1 e^{\lambda_m z} + c_2 e^{-\lambda_m z}) = 0 \quad (6)$$

According to formula (6),obtain pile body displacement $w_{nm}(z)$ ,substitute into $P(z) = -E_P A_P \frac{dw(z)}{dz}$ The axis force of pile body $p_{nm}(z)$ is ,

$$w_{nm}(z) = \frac{\lambda\psi(s) z(-D_1 e^{\lambda z} + D_2 e^{-\lambda z})}{2} + D_3 \cdot z \cdot e^{\lambda z} + D_4 \cdot z \cdot e^{-\lambda z} \quad (7)$$

$$P_{nm}(z) = \frac{\lambda\psi(s)}{2} A_P E_P [D_1(1+\lambda z)e^{\lambda z} - D_2(1-\lambda z)e^{-\lambda z}] + A_P E_P \cdot \lambda(D_3 e^{\lambda z} + D_4 e^{-\lambda z}) \quad (8)$$

Integration constant $D_1, D_2$ are drawn from the terminal condition of pile m:

$$D_1 = \frac{P_{bm} - A_{pm} E_{pm} \lambda_m P_{bm} / k_{bm}}{-2A_{pm} E_{pm} \lambda_m e^{\lambda_m l_m}}, \quad D_2 = \frac{P_{bm} + A_{pm} E_{pm} \lambda_m P_{bm} / k_{bm}}{2A_{pm} E_{pm} \lambda_m e^{-\lambda_m l_m}} \quad (9)$$

When the pile depth $z = l_n$ , $w_{bnm}(z) = w_{bnm}(l_n)$ , $P_{bnm}(z) = P_{bnm}(l_n)$ ; When $z = 0$, $P_{nm}(0) = 0$ , The relation of the end resistance $P_{bnm}(l_n)$ and the end displacement $w_{bnm}(l_n)$ is

$$P_{bnm}(l_n) = k_{bn} w_{bnm}(l_n) \quad (10)$$

$$D_3 = -\frac{\psi(s)}{2} \frac{-P_{mm} l_n + l_n k_m w_{mm} l_m - \frac{l_n k_{bn}}{A_p E_P} P_{mm} l_n - \frac{P_{mm}(0) e^{-\lambda l_n}}{A_p E_p \lambda}(k_{bn} - A_P E_P \lambda)}{e^{\lambda l_n}(k_{bn} + A_P E_p \lambda) + e^{-\lambda l_n}(k_{bn} - A_P E_P \lambda)} \quad (11)$$

$$D_4 = \frac{\psi(s)}{2} \frac{-P_{mm} l_n + l_n k_m w_{mm} l_m - \frac{l_n k_{bn}}{A_p E_P} P_{mm} l_n + \frac{P_{mm}(0) e^{-\lambda l_n}}{A_p E_p \lambda}(k_{bn} + A_P E_P \lambda)}{e^{\lambda l_n}(k_{bn} + A_P E_p \lambda) + e^{-\lambda l_n}(k_{bn} - A_P E_P \lambda)} \quad (12)$$

are deduced[5].

When the load $P_{mm}(0) = 1$ ,affect the pile cap m,numerical displacement of nonload bearing pile n is the softness factor $\delta_{nm}$ is: $\delta_{nm} = \frac{w_{nm}(0)}{P_{mm}(0)} = \frac{D_3 + D_4}{-A_p E_p \lambda(D_1 - D_2)}$ (13)

3.2 The interaction of pile and soil

The interaction of pile and soil can change to the action of pile and soil pile,The interaction model of pile and soil as shown in Fig.1(b),that is

$$A_{Ps} E_{Ps} \frac{d^2 w_s(z)}{dz^2} - k_z w_s(z) = 0 \quad (14)$$

The displacement equation of soil pile is obtained according to formula(6),in formula(15), $w_s(z)$ is the answer to the formula(3).When we solve formula(14),the flexibility coefficient of adjacent soil pile $\delta_{sm} = \psi(s) \cdot \delta_{mm}$ (15)

According to the reciprocal displacement law,when the load bearing pile is soil pile,the relation about flexibility coefficient of the affected pile is $\delta_{nm} = \delta_{mn}$ (16)

3.3 Flexibility coefficient $\delta_{ss}^{`}$ of soil pile

When exert load to the soil surface, $\delta_{ss}^{`}$ is the self-displacement under the unit load.Suppose it is Winkler foundation model to analy the interrelation of soil piles:

$$\delta_{ss}^{`}=\begin{cases}\frac{1}{c} & i=j\\ 0 & i\neq j\end{cases} \tag{17}$$

When it is the soil around pile,c is Winkler bedding coefficient ; When it is pile end soil,according to $P_b=k_b w_b$ ,c is $c=k_b=\frac{P_b}{w_b}$.

3.4 The simulation of cushion action

Due to the depth of cushion is thin,we regard it is distributed spring,rigidity of spring is $k_c=\frac{EA}{h_c}$, revised flexibility matrix is

$$\delta=[\delta]=\begin{bmatrix}\delta_{mm} & \delta_{mn} & \delta_{ms}\\ \delta_{nm} & \delta_{nn} & \delta_{ns}\\ \delta_{sm} & \delta_{sn} & \delta_{ss}\end{bmatrix}+\begin{bmatrix}\frac{h_c}{EA} & 0 & 0\\ 0 & \frac{h_c}{EA} & 0\\ 0 & 0 & \frac{h_c}{EA}\end{bmatrix}=\begin{bmatrix}\delta_{mm}+\frac{h_c}{EA} & \delta_{mn} & \delta_{ms}\\ \delta_{nm} & \delta_{nn}+\frac{h_c}{EA} & \delta_{ns}\\ \delta_{sm} & \delta_{sn} & \delta_{ss}+\frac{h_c}{EA}\end{bmatrix} \tag{18}$$

## 4. Contrast verification

We contrast such analytic formula and finite element numerical calculation and field test data,to verify the rationality of these analytic solution.

4.1 Contrast with finite element numerical calculation

Consider symmetry ,we give 1/4 part model to numerical calculation,symmetry restrain is applied to 1/4 boundary, normal restrain to the cross-section are applied to the other two side,fixed end restrain are applied to the end.1/4 part pile is pile m,the other pile is pile n.Diagrammatic sketch and finite mesh are shown in Fig.2 and Fig.3.

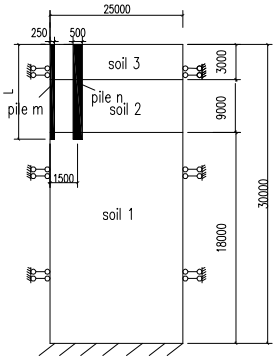


Fig.2 Calculation model diagrammatic sketch

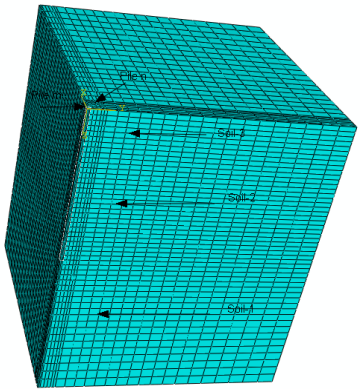


Fig.3 Finite mesh of 1/4 double piles

Unit load is respectively applied to pile m and pile n.We count the settlements of pile cap and soil among pile,the interaction coefficients are shown in table1.

Table 1 Pile length affect to the interaction coefficients

| pile length /m | finite element numerical calculation | | | | | | Analysis of the thesis | | | | | |
|---|---|---|---|---|---|---|---|---|---|---|---|---|
| | $\delta_{mm}$ | $\delta_{mn}$ | $\delta_{ms}$ | $\delta_{nm}$ | $\delta_{nn}$ | $\delta_{ns}$ | $\delta_{mm}$ | $\delta_{mn}$ | $\delta_{ms}$ | $\delta_{nm}$ | $\delta_{nn}$ | $\delta_{ns}$ |
| 8 | 0.95 | 0.95 | 1.02 | 0.95 | 0.95 | 1.02 | 0.87 | 0.865 | 0.99 | 0.865 | 0.87 | 0.99 |
| 15 | 0.696 | 0.777 | 1.01 | 0.695 | 0.779 | 1.01 | 0.68 | 0.679 | 0.96 | 0.679 | 0.68 | 0.96 |
| 20 | 0.598 | 0.597 | 1.00 | 0.6 | 0.6 | 1.00 | 0.56 | 0.554 | 0.95 | 0.554 | 0.56 | 0.95 |

4.2 Contrast with field experiment

In order to study the interact coefficient of piles under work load,Cooke[6] took a series of experiments to obtain measured value about interact coefficient.The test respectively drive three steel tubular piles,their lengthen are 4.5m,outside diameter is 168mm,wall thickness is 6.4mm,pile space is three times as much as pile diameter.The paper assume the elastic modular ratio of steel tubular pile is $2.1\times10^5$MPa,the Poisson ratio of soil is 0.5.When the load is 20KN,the settlement of pile A is 0.153mm.Literature 6 gave the measured value of interact coefficient when the pile space is 3d and 6d(d is pile diameter),individual is: $\delta_3$ =0.22 and $\delta_6$=0.1.In order to test the accuracy of the interact coefficient in the paper,the paper determine the revise coefficient by the foundation shear modulus from the literature[6],when l/d is 25, the interact coefficients of different pile space are obtained,as shown in Fig.4.

From Fig.4,the results of numerical calculation is close to the analysis which is put forward by the text.When s/d is identical,the coefficient of the numerical calculation and the analysis of the paper are somewhat greater than the site measured values.That is when the pile was driven in soil,the soil was compacted,intensity of the soil was intensifying.But we ignore the intersity,so the measured value of interact coefficient is less than the other two.

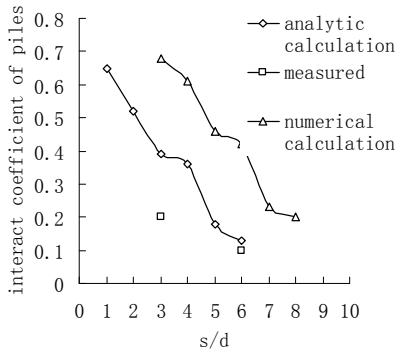


Fig.4 Comparison of interact coefficient

## Conclusions

Generally,the analytic solution is less than the finite element results.Contrast the results of site test and analytic solution,the settlement of analytic calculation is lower than the measured settlement,these maybe ascribe to analytic calculation ignore the group piles effect.

**References**

[1] Seed H B,Reese L C.The action of soft clay along friction piles.Transactions,ASCE, 122：731-754(1957)

[2] Colyle H M,Reese L C.Load transfer for axially piles in clay.Journal of the Soil Mechanics and Foundation Division,ASCE,92(2)：1-26(1996)

[3] Cooke R W.The settlement of friction pile foundation .Proc.Conference on Tall Buildings,Kuala Lumpur(1974)

[4] Mylonakis G, Gazetas G. Settlement and additional forces of grouped piles in layered soil[J].Geotechnique,48(1):55-72(1998)

[5] LU Xu-Wen .Experiment and Study of Composite Foundation with Long-short Piles to ImDrove Deep Soft under Embankment Load[D]. Nanjing HydrauIic Researeh Institute in Fullfillment of the Requirement (2007)

[6] COOKE R W, PRICE G & TARR K.Jacked Piles in London Clay： Interaction and Group Behaviour under Working Conditions [J].Geotechnique, 30 (2)：449-471(1980)

*Applied Mechanics and Materials Vols. 580-583 (2014) pp 585-588*
*© (2014) Trans Tech Publications, Switzerland*
*doi:10.4028/www.scientific.net/AMM.580-583.585*

# Cone penetration test study of ultra soft soil after vacuum preloading

Jiongqi Yu[1, a], Hongwen Li[1,b] and Wen shuang Wang[1, c]

[1] Zhejiang Institute of Hydraulics and Estuary, Hangzhou 310020, China

[a]yujiongqi@163.com, [b]496962410@qq.com, [c]1614921526@qq.com

**Keywords:** No sand cushion; Ultra soft soil; Vacuum preloading; Surface-layer improvement; Cone tip resistance.

**Abstract.** No sand cushion vacuum preloading method is one of the construction technology for treating the ultra soft soil formed with hydraulic fill at present. The practice is ahead of the scientific research work, as the effect detection technology of the surface-layer improvement is still in the stage of exploration. In this paper, the cone penetration test (CPT) is used to detect the effect of the surface-layer improvement of the ultra soft soil based on one case in Zhejiang province in China. The result shows that the cone tip resistance is at the range of 0.08 ～ 0.40MPa and the thickness varies about 1.5 to 2.2 m of the treated ultra soft soil. The cone tip resistance along the depth has two kinds of curve shape and four zones.

## Introduction

Tianjin, Zhejiang, Fujian and other coastal areas in China have formed a large number of land space by reclamation, whereas the ground elevation cannot satisfy subsequent development requirements for factories, industrial, road and other constructions. One preferred solution is to fill the ground up to the required elevation with the ultra soft soil transporting from the near sea. At the same time, the traditional vacuum preloading method with sand cushion is difficult to excute in the ultra soft soil, so no sand cushion technology is developed to meet the requirements of the reality [1]. As a new construction technology, no sand cushion vacuum preloading method is still in the stage of exploration, so the treatment effect need to detect and analyze at present. This paper tries to analyze the treated effect of the ultra soft soil by the cone penetration test (CPT), and to provide reference of technology applicability and guidance of process improvement and detection technique development.

The CPT has been widely used as an important field test in geotechnical engineering where penetration is possible[2, 3, 4]. The CPT provides near-continuous penetration test datu to draw test curve and determine soil type and soil mechanical properties and analyze space changing law.

**Table 1 Particle size, moisture content and depth of the initial ultra soft soil**

| Soil layer number | moisture content | Particle size | | | | | Depth |
|---|---|---|---|---|---|---|---|
| | ω(%) | | $d_{60}$(mm) | $d_{50}$(mm) | $d_{30}$(mm) | $d_{10}$(mm) | H(m) |
| 0-1 | 126.9 | Max | 0.011 | 0.007 | 0.003 | 0.002 | ≤2m |
| | | Min | 0.005 | 0.003 | 0.002 | 0.002 | |
| | | Average | 0.007 | 0.005 | 0.002 | 0.002 | |
| 0-2 | 92.1 | Max | 0.012 | 0.008 | 0.004 | 0.002 | 2～2.5m |
| | | Min | 0.005 | 0.004 | 0.002 | 0.002 | |
| | | Average | 0.009 | 0.006 | 0.003 | 0.002 | |
| 0-3 | 73.9 | Max | 0.012 | 0.010 | 0.004 | 0.002 | ＞2.5m |
| | | Min | 0.008 | 0.005 | 0.002 | 0.002 | |
| | | Average | 0.010 | 0.007 | 0.003 | 0.002 | |

## Description of the case

The case is located on one coastal areas of east Zhejiang in China. The reclamation ground has a certain slope and covers an area of 125000 $m^2$. First, fill the reclaimed area with the sedimentary soil from the near sea. Then no sand cushion vacuum preloading method was applied to improve the ultra soft soil. The soil characteristic parameters of the ultra soft soil before improvement as shown in table 1.

The CPT was applied to detect the improvement effect of the ultra soft soil after vacuum preloading treatment, and the test points were arranged in square layout with 50 m x 50 m, and the total test point number was 50.

## Curve shapes of the cone tip resistance

Due to the difference of the vacuum pump position and the transferring effect of the vacuum pressure in horizontal direction and depth direction and the phenomenon of soil column surrounding the vacuum drainage channel, etc., the improvement effect may be different in each test point and lead to form the different curve shapes of the cone tip resistance. The test curve of the cone tip resistance to depth can be divided into two kinds of shape, namely uniform shape and peak shape, and the peak shape can be divided into unimodal shape and bimodal shape.

The uniform shape curves as shown in fig. 1, the cone tip resistance changes within a small range along the top and middle of the vertical direction. The unimodal shape curves as shown in fig. 2, the cone tip resistance has a bulge in the middle of the vertical direction. The location of the bulge has a wide range in the depth direction, and the peak value also changes in some degree. The bimodal shape curves as shown in fig. 3, the cone tip resistance has two bulges in the middle of the vertical direction. The bimodal shape is a variant of the unimodal one.

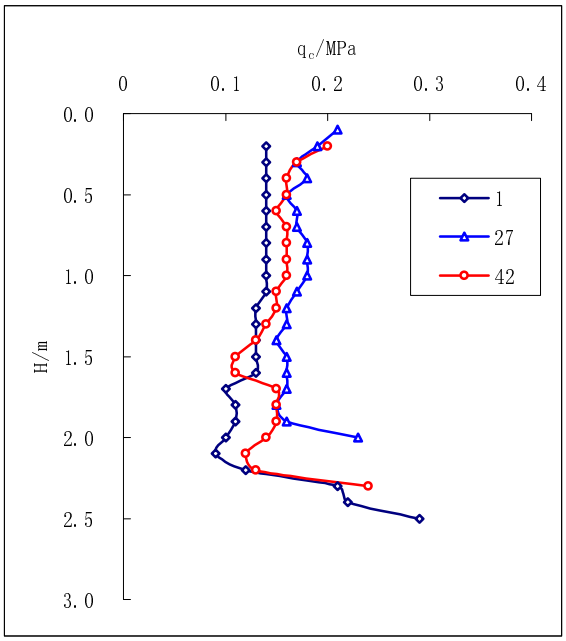


Fig. 1 The uniform shape curves

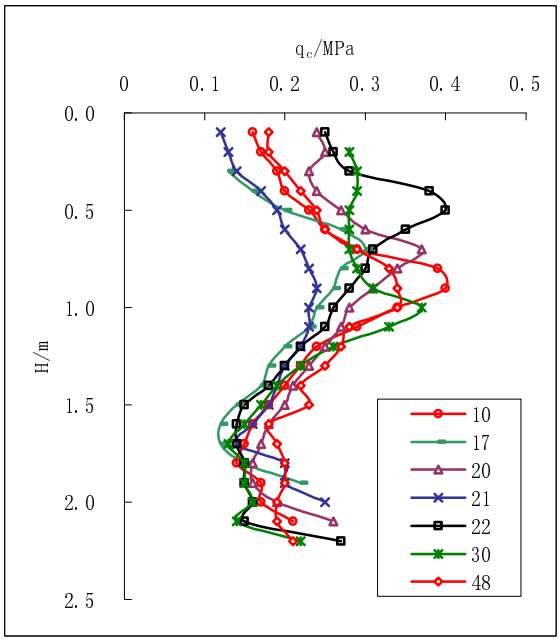


Fig. 2 The unimodal shape curves

## The thickness of the improved ultra soft soil

The junction between the bottom of the ultra soft soil and the natural soil is a weak zone with vacuum preloading treatment, where the cone tip resistance of the ultra soft soil is smaller and the cone tip resistance of the natural soil is bigger. So the changing trends of the cone tip resistance with depth can reflect the thickness of the improved ultra soft soil. The cone tip resistance to depth curves related to the maximum thickness and the minimum thickness of the test points as shown in fig. 4, the minimum

thickness is about 1.5m in test point No.3 and the maximum thickness is about 2.2m in test point No.5, namely the range of the thickness of the improved ultra soft soil is about 1.5 ~ 2.2 m. The result is corresponding with the initial ground slope.

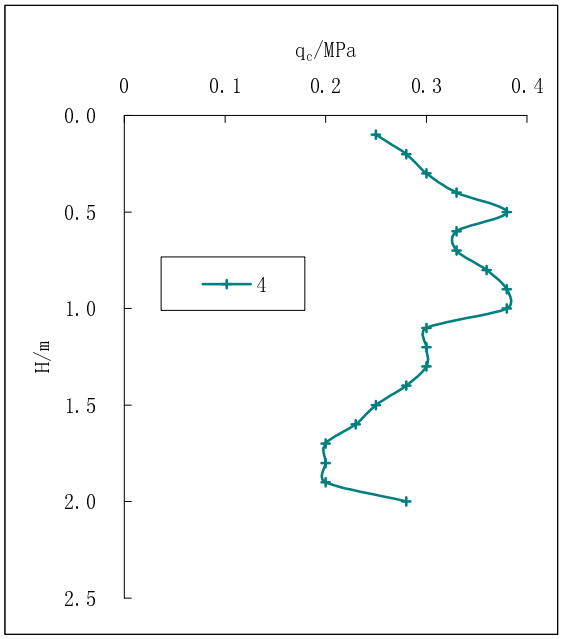


Fig. 3 The bimodal shape curves

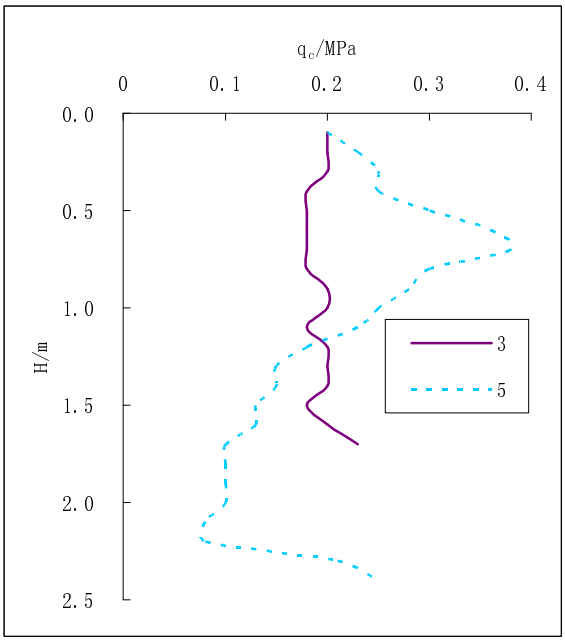


Fig. 4 The $q_c$ – H curves related to the maximum and the minimum thickness of improved soil

**The change laws of the cone tip resistance**

The scatterplot of the cone tip resistance to depth as shown in fig. 5. There are four bandwidth zones of the cone tip resistance down the depth.

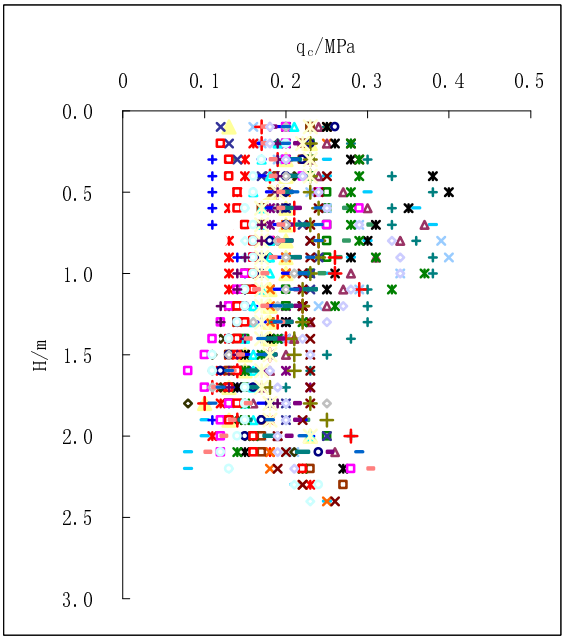


Fig. 5 The scatterplot of the cone tip resistances

At the surface, there is a monotonic increase bandwidth zone of the cone tip resistance down the depth within 0～0.4 m, where the minimum value varies between 0.11 and 0.12 MPa and the maximum value varies between 0.26 to 0.40 MPa. In the upper middle, there is a uniform bandwidth zone of the cone tip resistance down the depth within 0.4～1.0 m, where the minimum value varies

between 0.11 and 0.13 MPa and the maximum value varies between 0.38 to 0.40 MPa. In the lower middle, there is a monotonic decline bandwidth zone of the cone tip resistance down the depth within 1.0～1.5 m, where the minimum value varies between 0.10 and 0.13 MPa and the maximum value varies between 0.25 to 0.38 MPa. At the bottom, there is a uniform bandwidth zone of the cone tip resistance down the depth within 1.5～2.2 m, where the minimum value varies between 0.08 and 0.10 MPa and the maximum value varies between 0.19 to 0.25 MPa.

## Conclusions

Following the analysis, there are some interesting things:

According to the detection result of the CPT, it can be obtained that the thickness of the ultra soft soil after vacuum preloading varies about 1.5 to 2.2 m in the case of east Zhejiang in China.

The cone tip resistance curves along the depth can be divided into two kinds of shape, namely uniform shape and peak shape as the later mainly belongs to the unimodal shape.

Due to the difference of the vacuum pump position and the transferring effect of the vacuum pressure in horizontal direction and depth direction and the phenomenon of soil column surrounding the vacuum drainage channel, etc., the improvement effect may be different in each point.

According to the test scatterplot, the cone tip resistance can be divided into four zones, namely monotonic increase bandwidth zone down the depth at the range of 0 ~ 0.4 m and uniform bandwidth zone at the range of 0.4 ~ 1.0 m and monotonic decline bandwidth zone at the range of 1.0 ~ 1.5 m and uniform bandwidth zone at the range of 1.5 ~ 2.2 m.

## Acknowledgements

This work was financially supported by the Zhejiang Science and Technology Innovation Team on Water Conservancy Project Safety Study (2010R50035) and Public Welfare Industry Scientific Research Special Funds of the Ministry of Water Resources (201201043) and the Central Subsidies to Local Science and Technology Basic Condition Construction Special Funds of the Ministry of Finance (Zhejiang Finance Education [2011] No. 179).

## References

[1] Cao Yonghua, Li Wei, Liu Tianyun (2011). Surface-layer improvement technology for ultra soft soil by vacuum preloading[J]. *Chinese journal of geotechnical Engineering* **33,** No. S1, 234 – 238. (in Chinese)

[2] Meng Gaotou. Theory, method and its engineering application of soil test in situ[M]. Beijing: Geological Publishing House, 1997. (in Chinese)

[3] Zhu Longgen, Liu Limin, Geng Naixing. New testing technology for foundation[M]. Beijing: China Machine Press, 1999. (in Chinese)

[4] Shuttle, D.A. & Cunning, J. (2007). Liquefaction potential of silts from CPTU. *Can. Geotech. J.* **44**, No. 1, 1 – 19.

*Applied Mechanics and Materials Vols. 580-583 (2014) pp 589-595*
*© (2014) Trans Tech Publications, Switzerland*
*doi:10.4028/www.scientific.net/AMM.580-583.589*

# Defects Discrimination and Error Analysis of Wharf Bored Piles Detected by Low Strain Reflection Wave Method

Tao Li [1, a], Qingchang Qiu [2,b] and Jing Wang [3,c *]

[1] CCCC Fourth Harbor Engineering Institute Co.,Ltd. , Guangzhou 510230, China;

CCCC Key Lab of Environmental Protection & Safety in Foundation Engineering of Transportation, Guangzhou 510230, China;

[2] CCCC Fourth Harbor Engineering Institute Co.,Ltd. , Guangzhou 510230, China;

[3] CCCC Fourth Harbor Engineering Institute Co.,Ltd. , Guangzhou 510230, China;

Civil and transportation institute, South China University of Technology, Guangzhou 510641, China;

CCCC Key Lab of Environmental Protection & Safety in Foundation Engineering of Transportation, Guangzhou 510230, China

[a]litao_geo@163.com, [b]qiuqch@tom.com, [c]phdwangjing@126.com

**Keywords:** low strain method, bored pile, error analysis

**Abstract:** Based on the field test of bored piles at wharf detected by low strain reflection wave method, time-history curve features and defect position of intact piles and defective piles contrastively analyzed, with verification of on-site drilled core testing. The reason for discrimination error between specific defect position and actual data when processing low strain reflection wave method are derived, based on the analysis of effect of defective piles strengthened by pressure grouting method retested by low strain testing, practical measures of on-site low strain reflection wave testing are purposed to improve detection accuracy.

## Introduction

The bored pile is refers to pile that first forms borehole with drilling machine, steel tube or artificial excavation, then proceed with reinforcing cage placing and concrete casting. With the development of construction technology, due to advantages of low noise, small vibration, high load capacity and broad applicable scope, bored pile is used widely in infrastructure engineering such as pavement, railway, bridge and wharf, etc. [1-4]. However, as a kind of concealed work, 5% - 20% of the bored piles appear different levels of quality problems. Therefore, it could effectively avoid quality accidents if the testing to foundation pile is enhanced in construction stage, also contemporaneous remedy could be adopted to reduce economic loss [5-10].The low strain dynamic testing is regarded as an effective testing method, with advantages of convenience, expeditiousness, low cost and wide coverage [11-13].

Based on engineering example of defect detection to bored piles at wharf tested by low strain reflection wave method, testing waveform of intact piles and defective piles are analyzed and discriminated, to compare the results of core samples drilled from defective piles, the reason for to occur error on the defective interface during actual defect position discrimination is proposed. Based on large number of practical experience, the method to strengthen quality of signal acquisition is also proposed, which aims to improve discrimination accuracy of low strain reflection wave testing. However, during the low strain reflection wave testing to foundation pile, discrimination to testing data often meets error problems. Hence, testing technology should be enhanced, the ability of data analysis should be upgraded, and consequently the accuracy of testing data discrimination is improved.

## Engineering background

The project is bored piles in a port engineering, low strain reflection wave method is used for discriminating pile structure integrity.

The project is located in ground surface with stratum in Beihai Fm, middle Pleistocene and Eopleistocene largely outcropped, whereby Beihai Fm stratum is a set of littoral facies deposit, which is the main stratum constituting low terrace on both sides of harbor banks. The Eopleistocene stratum is a set of river delta facies deposit that sand interbeds with caly, with mottled caly layer, laterite layer and ferruginous cementation layer on top. As the erosion surface showing, the Eopleistocene stratum has a unconformable contact with Beihai Fm stratum, also it often outcrops near the high tidal mark and on the bottom of gulf bank. On the top of borehole drilled in waters, mottled clay and silty clay are exposed as Beihai Fm stratum. On the lower part of borehole, grey clay, grey clay interbedded with sand, grey sand layers(silty fine sand, medium coarse sand, gravelly sand) are exposed as Eopleistocene stratum, while the soft soil layers or loose sand layers exposed on the upper part of borehole, what refers to silt, silty soil, silt mixed with sand, sand mixed with silt, silty fine sand, medium coarse sand with grey or grayish yellow belong to stratum in Holocene of Quaternary.

The drilling soil layers distribution is shown as：①Plain fill, grey to grayish yellow, abandoned dredged fill, mainly consists of flowing mud, silt, cohensive soil and medium coarse sand, 1.03m average layer thickness. ②Medium coarse sand, grey to grayish yellow, saturated and loose, minor shellgrit contained. Lens in distribution, 3.24m average layer thickness. ③Sand with cohensive soil mixed (interbedded), grayish yellow, grayish white to purplish pink, saturated, loose to slightly dense, mainly medium coarse sand, partially interbedded with cohensive soil, 2.88m average layer thickness. ④Clay, rey, wet, plastic to hard plastic, partially interbedded with multi-thin-layer silty sand, minor rotten wood fragment contained, 11.42m average layer thickness. ⑤ Medium coarse sand, grey to light grey, saturated, medium dense to dense, poor sorting features, partially interbedded with cohensive soil, 1.86m average layer thickness. ⑥Clay, grey, slightly dense and wet, hard plastic, partially hard, partially interbedded with multi-thin-layer silty sand, minor rotten wood fragment contained, 6.04m average layer thickness. ⑦Medium coarse sand, grey, light grey to grayish white, saturated, medium dense to dense, partial extreme dense, poor sorting features, partially minor cohensive soil and rotten wood fragment contained, 6.34m average layer thickness. ⑧ Clay, grey, wet, hard plastic to hard, partially plastic, partially minor silty sand contained, or interbedded with multi-thin-layer silty sand, 9.03m average layer thickness.

The wharf uses 3-storey frame structure that gross area is approximately 800m$^2$, bored piles are selected for the foundation design, the design strength grade of concrete is C35, design pile bearing capacity is 3400kN, the diameter and length of pile is respectively 1.0m and 43m, the bearing stratum is clay. The piles pertain to ultra long pile engineering in soft soil area.

## Principles and apparatus of testing

Generally, foundation pile low strain dynamic testing is applied to pile integrity and concrete quality testing, preliminary inspection of pile bearing capacity, later the foundation pile quality is evaluated. The Principles of foundation pile low strain dynamic testing is principles of reflection and refraction that strain wave propagates in elastomer. As the pile bolck subjecting to temporary mechanical vibration, particle on pile will be extruded and vibrates along pile shaft to propagate strain wave downward. When the strain wave encounters abrupt interface, such as pile end, mud layer, fracture or serious expanding, refraction wave will appear immediately. The quality data including reflection signals will be recorded by high sensitive sensor placed on pile block, then converted to digital signals by high speed A/D converter. Based on the features of waveform, the change of wave impedance can be determined that pile integrity will be discriminated too. The testing standard or testing basis is applied according to Specification for Dynamic Testing of Piles in Port Engineering, JTJ249-2001.

The testing apparatus adopts PIT-Collector foundation pile integrity tester produced by Pile Dynamics, Inc.

Assuming the pile is one-dimensional linear elastic bar, whose pile length is *L*, cross sectional area is *A*, elastic modulus is *E,* mass density is $\rho$ and generalized impedance is $Z = A\rho C$ ; The one-dimensional wave equation can be obtained as

$$\frac{\partial^2 u}{\partial t^2} = c^2 \frac{\partial^2 u}{\partial x^2} - \frac{R}{\rho \cdot A} \tag{1}$$

where *R=R(x,t)* is soil resistance activated by hammer percussion per unit length along pile axis, $C = \sqrt{E/\rho}$ is elastic wave velocity of pile.

$$x = \frac{1}{2} \bullet \frac{c}{\Delta f_i} \tag{2}$$

Assuming impedance somewhere in the pile has changed, when strain wave moves from mediator I（$Z_1 = \rho_1 \bullet C_1 \bullet A_1$） to mediator II（$Z_2 = \rho_2 \bullet C_2 \bullet A_2$）, it will produce velocity reflection wave $V_r$ and velocity transmission wave $V_t$.

To let pile integrity coefficient $\beta = Z_2 / Z_1$ , then

$$V_r = V_i \cdot \frac{1-\beta}{1+\beta} \tag{3}$$

$$V_t = V_i \cdot \frac{2}{1+\beta} \tag{4}$$

where incident wave $V_i$， transmission wave $V_t$ and reflection wave $V_r$ are values in the interface between mediator I and mediator II. Influenced by damping of pile material and pile shaft soil resistance, both the amplitude of incident waves and reflection waves received from pile bolck and interface are different, while the corresponding phases are the same. Pile shaft defects position is calculated by equations below

$$x = \frac{1}{2000} \bullet \Delta t_i \bullet c \tag{5}$$

$$x = \frac{1}{2} \bullet \frac{c}{\Delta f_i} \tag{6}$$

In low strain testing, pile integrity types should be synthetically discriminated with consideration of defect depth, test signal attenuation, pile type, stake technology, geological condition, construction condition and test signal features in time domain or frequency domain. According to *Specification for Dynamic Testing of Piles in Port Engineering,* the pile integrity are classified to 4 types. According to response signals from sensor, wave train figure is plotted. Considering the phase of incident wave and reflection wave in wave train figure, vibration frequency and relevant wave arrival time, pile integrity type can be discriminated. When performing testing analysis, reflection signal at pile end should be found first, if the signal is weak, processing signal can be zoomed in appropriately until clear signal emerges, then to discriminate waveform through contrastive analysis. If the waveform is regular, no defect reflection occurs in pile, the reflection at pile end is clear, the pile should be classified as type I. If the waveform is basically regular, small defect reflection occurs in pile, the reflection at pile end is basically clear, the pile should be classified as type II. If the waveform occurs serious defect reflection wave or periodic reflection wave and no reflection occurs at pile end, or due to serious defect at upper part of pile, low frequency vibration of waveform decays sharply, no reflection occurs at pile end, the pile should be classified as type IV. If there is obvious defect reflection wave in time domain signal, other features intervene type II and type IV, the pile could be classified as type III.

## Testing results

In the pile integrity testing, bore piles at wharf in the project are tested by low strain reflection wave method, the reflection wave time-history curves of testing results are shown in Fig. 1and Fig. 2.

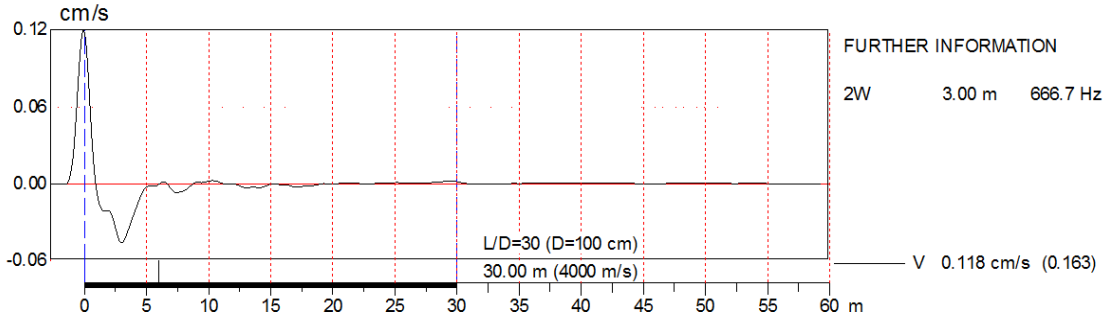


**Figure 1 Reflection wave time-history curve of intact pile**

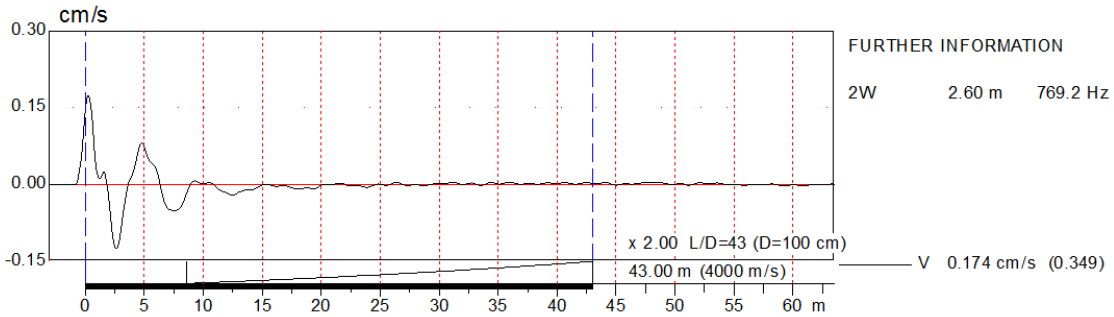


**Figure 2 Reflection wave time-history curve of defect pile**

According to the reflection waveform time-history curve shown in Fig. 1, reference wave velocity is 4000m/s. The peak of incident wave occurs in the position of 0m, pile length is 30m. It has clear wave train and regular waveform, no abnormal reflection occurs, that means wave velocity is normal and no defect occurs in pile. Hence, the pile should be classified as type I. The piles belong to super-long piles in soft soil area, strain wave in piles generally occur sharp attenuation, what leads to detection difficulty of reflection wave signal at pile end. Therefore, not only reflection signal at pile end, but also the testing results of drilled core method and high strain method, construction records should be taken into account to discriminate pile integrity.

According to the reflection waveform time-history curve shown in Fig. 2, there are obvious anomalies revealed through the curve, that means clear synclastic reflection wave peak occurs in the position of 5m, manifesting as necked-in defect. Furthermore, the signals at pile end is weak, so the defective pile should be classified as type III.

For the defective pile tested by reflection wave method in Fig. 2, drilled core method is applied for detection. The drilled core method is a concrete strength testing method that to drill core sample from foundation pile by dedicated drill, the thickness of sinking slag at pile end and bedrock strength also can be tested with application of the method. Drilled core method has the advantages of intuition, reliability, high precision, but the cost is relatively high. The pictures of core samples drilled from bored piles are shown in Fig. 3.

As shown in Fig. 3, the core samples appear as fragmentized in the position of 8m, with length of about 3m, it has poor cementation near the fragmentary part, voids and pits occurs on the side face of core samples, fracture on piles are in good agreement and appear as prismatic, part of the samples are trenched and compact, thus, the piles can be discriminated as defective piles. The results tested by drilled core method is basically in accordance with those tested by low strain method, however, there are some error in the discrimination of exact position of the defect, the result of drilled core appears to be about 8m, while the result of waveform time-history curve is 5m, which is 3m shallower than actual depth.

**Figure 3 Core samples drilled from defect bored piles**

According to the engineering example mentioned above, there are certain limitations for low strain reflection wave method. When testing pile integrity with the method, the initial exciting wave received by station varies from different distance that the station away from exciting point, that leads to various degree of lag occurs when compared with the exciting point. However, he time that reflection wave at pile end from each point reaches pile bolck is identical，that causes smaller time difference between incident wave and reflection wave on interface, so the predicted pile length or position of defect interface is shallower than actual situation. Hence, the error analysis of defect discrimination should be noticed in actual application of low strain method.

According to the results of low strain testing data and on-site core drilling, serious defect occurs in the pile, certain remedy needs to be adopted. After full discussion among quality supervision department, supervision unit and construction unit, pressure grouting method is adopted to strengthen the defect part in pile. Based on high pressure, cement slurry is forced to diffuse to poor cementing part of concrete and seepage discretion occurs, after the cement becomes solid, process to grout under the pressure, and then retest the strengthened pile. In order to verify the strengthening effect of pile treated by pressure grouting method, low strain reflection wave testing are adopted for detection, as shown in Fig. 4.

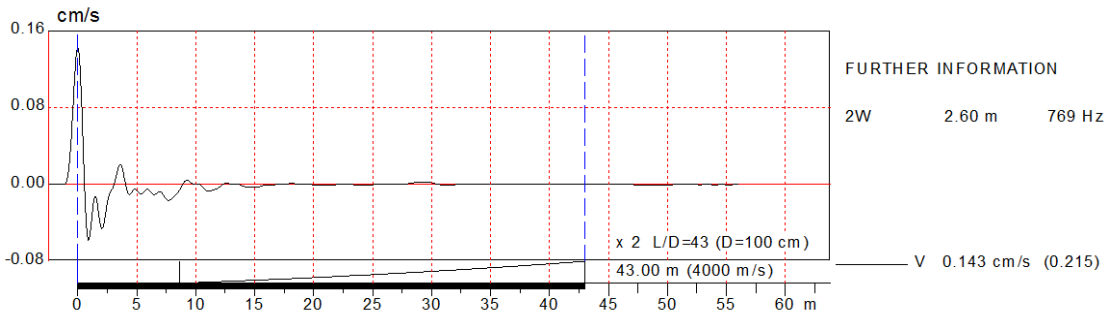


**Figure 4 Reflection wave time-history curve of intact pile after pressure grouting**

It can be discerned from the waveform time-history curve of strengthened piles shown in Fig. 4, that the waveform degenerates in a regular way with normal wave velocity, slightly defect of incident wave occurs in the position of 4m, that means slightly defect occurs in pile, the piles can be classified as type II and used as engineering piles.

The results of low strain reflection wave testing show that pressure grouting is a effective way to dispose of quality defect such as breaking piles, serious segregation and loosening of concrete, and bottom sediment. With the advantages of simple construction process, low cost, short construction period, convenience in execution and quality control, the application of pressure grouting technology is more widely than other reinforcement methods. Therefore, it can be regarded as a reference to similar projects.

## Testing measures

In foundation pile testing, low strain reflection wave is a semi-direct testing method (nondestructive testing method) that is able to detect foundation pile integrity thoroughly and effectively, it has an important effect on detecting quality of piles. However, the use of low strain dynamic testing of foundation pile is unilateral, the analysis results of testing curve are influenced by plenty factors such as pile concrete uniformity, compactness, accuracy of parameters of pile length, size effect, frequency response and excitation energy, etc.

As for the discrimination of abnormal piles, not only defect in pile causes irregularity of curve，but also test results are affected by external test condition, it still confined to qualitative analysis at present. Hence, on the premise that accuracy of data is ensured, pile integrity types should be analyzed and discriminated with consideration of the depth of defect position, attenuation characteristics of test signal, pile type design, stake technology, geological condition, construction situation, measured time domain or amplitude frequency signals， etc. In order to avoid safety and quality accidents in construction caused by misjudgment, to improve the accuracy of testing, alternative testing method should be adopted for contrast verification, if necessary, which favors adopting targeted remedy promptly and reducing unnecessary economic loss caused by misjudgment.

Based on the experience of massive low strain testing, actual operation process of low strain reflection wave method is concluded empirically to improve the accuracy of foundation pile low strain dynamic testing.

For site sampling, the selection of sampling parameters are different under varied field and weather conditions, this is because electric apparatus leakage happened in rainy humid weather and excessive vibration in piling field interfere with sampling accuracy, that leads to misjudgment of defects in piles. Hence, weather factor is ineligible on site sampling.

Usually, it will produce the inferior laitance part on the top of engineering pile during construction, so station must be positioned on dense part of concrete and preferably in the middle of reinforcing cage.

To avoid quality problems on the top of testing piles, laitance should be cleaned up and pile head should be leveled off in case of porosity. The connection between sensor and concrete generally is bonded with plaster powder or grease, there is a huge strength difference between plaster powder and concrete, so the dosage of plaster powder needs to be considered carefully. During site test, the concrete mark of engineering piles all around the field should be discriminated accurately, because the speed wave in concrete is determined by concrete strength grade, which will affect the results of pile length testing and defects position discrimination.

During the foundation pile testing, try to make the force acts perpendicular to pile head when doing the percussion, it is conducive to suppress particle lateral vibration and avoid secondary pulse ，thereby preventing from the subsequent wave interference. It is a good choice to percuss with short-handled impact hammer or impact bar. Short-handled impact hammer is easy to make the force acts perpendicular to pile head, while the magnitude of every percussion is hard to control that causes poor waveform repeatability；With impact bar free falling at a certain height, the force exerted on pile head reveals verticality and uniformity, also fine signal repeatability is obtained, whereas secondary pulse is easy to appear.

## Conclusions and suggestions

With applying low strain reflection wave method to test the bored piles，conclusions below are obtained through defects discrimination and error analysis.

(1) The view that geological condition of soft soil and excessive pile length can lead to low reflection effect at the bottom of pile is raised, after analyzing the time-history curve of reflection wave in bored piles low strain test and comparing characteristics curve and defect positions between intact piles and defective piles.

(2) In low strain reflection wave testing, various degree of lag occur at initial exciting wave and exciting point received from measuring point at varied distance, which leads to error in actual location and experimental data of the defective piles.

(3) According to the low strain retest result of defective piles strengthen by pressure grouting, fine strengthening effect is verified.

(4) The actual operation of low strain reflection wave method on bored pile at construction site is proposed, that both accuracy and quality of testing are enhanced.

**References**

[1] XU Zhi-ping. *Application of PIT in Testing of Cast-in-Situ Concrete Piles for Bridges* [J]. China Harbour Engineering. 2004(5): 47-48.

[2] GUO De-Ling. *Case Study of Low Strain Integrity Testing of Shallow Defects of Bored Pile* [J]. Science & Technology Information 2012(11): 380, 393, 394.

[3] JING Wei-zhuang, LIU Dong-jia, SHUAI Chang-e. *The Data Processing of Low Strain Test Pile on Cast-in-situ Bored Pile and the Matching Analysis*[J]. Chinese Journal of Engineering Geophysics. 2009, 6(1): 105-110.

[4] WANG Kai-jun, GUO Jia-kai. Cheng Shi Jian she Li Lun Yan Jiu. *Application of low strain reflected wave method in the quality testing of concrete grouting pile* [J].ChengShi Jianshe LiLun Yan Jiu 2011(14).

[5] KE Zhai-bang, LIU Dong-Jia. *Numerical computation of axisymmetric problems in low strain integrity tests on piles* [J].Chinese Journal of Geotechnical Engineering. 2006, 28(12): 2111-2115.

[6] LIU Dong-Jia, LIU Yu-zhou, WANG Jie-ying. *Theoretical study on torsional wave applied in low strain dynamic testing of piles* [J]. Chinese Journal of Geotechnical Engineering. 2003, 25(3): 283-287.

[7]WANG Jian-hua, ZHI Sheng-ying. *Daming Coefficients of Pile-soil Interation with Low Strain* [J]. Chinese Journal of Rock Mechnics and Engineering. 2007, 26(9): 1800-1808.

[8] HU Xin-fa，LIU Jian-xin. *Study of Inaccuracy of P-wave Velocity in Piles by Low Strain Integrity Testing* [J]. Chinese Journal of Rock Mechanics and Engineering2013(z2): 4183-4189.

[9] ZHANG Liang-jun, WANG Jing-tao, LI Guo-cheng. *Application of Wavelet Transforming Integrity Testing of Piles* [J]. Chinese Journal of Rock Mechnics and Engineering. 2002, 21(11): 1735-1738.

[10] ZHANG Xian-min, LI Shao-bo. *Determination of Pile's Defect Degree with Low-strain Energy Analysis* [J]. Chinese Journal of Rock Mechnics and Engineering. 2006, 25(z1): 3198-3205.

[11] DING Xuan-ming, CHEN Yu-min, KONG Gang-qiang. *Formation mechanism of velocity waves in low strain integrity testing of PCC pile*[J]. Rock and Soil Mechanics. 2012, 33(1): 154-161.

[12] FEI Kang，LIU Han-Long，ZHANG Ting. *Three-dimensional effects in low strain integrity test of PCC pile* [J]. Rock and soil mechanics. 2007, 28(6): 1095-1102.

[13] LU Zhi-tang，WANG Zhi-liang，LIU Dong-jia. *Analysis of 3-D Effects in Low Strain Testing of Pipe Pile* [J]. Journal of Tongji University (Natural Science) 2012, 40(11): 1603-1607, 1653.

*Applied Mechanics and Materials Vols. 580-583 (2014) pp 596-600*
*© (2014) Trans Tech Publications, Switzerland*
*doi:10.4028/www.scientific.net/AMM.580-583.596*

# Double-row composite anchor bolt design and construction monitoring analysis of green building

Hongxia Li[1, a],Yongwei Wang [2,b],Fang Gaokui[3,c]

[1.2]Huanghe Science and Technology College Institute of Technology, Zhengzhou 450000, China;
[3]Zhengzhou University, Zhengzhou 450000, China

[a]737801521@qq.com, [b] 65839177@qq.com, [c] 637801526@qq.com

**Keywords:** composite supporting, double-row piles, anchor, soil nailing, numerical simulation

**Abstract:** Zhengzhou East Green high-speed rail block D6 site supporting of deep foundation pit engineering, double row pile composite retaining structure design and data analysis. Through specific examples of projects, based on the measured data shows that support form of the rationality and practicality.

## 0Introduction

As the city construction land increasingly nervous, more and more high-level, high-rise building, the excavation of foundation pit depth increases gradually, technology requirements for design and construction of supporting structure growing, is composed of a single form of multiple compound supporting system of foundation pit supporting in China gradually become the main development direction and research hot spot.

Double row pile composite anchor as a new type of composite retaining structure, double row pile and anchor by the reasonable design consists of a whole, the formation of double row pile composite bolt support system, give full play to the double row pile and anchor their technical advantages, technical and economic benefit is remarkable.

All manuscripts must be in English, also the table and figure texts; otherwise we cannot publish your paper.

## Project summary, geological hydrology conditions

### 1.1Project summary

High-tech development zone green high iron D6 block including two 36 class an office building and attached three layers such as commercial podium. The main building foundation pit depth of 17 m, podium, underground garage foundation pit depth is 16 m. D6 plot on the east side, the south 5 m for land red line, land outside the red line, respectively for the two urban trunk road; Red line on the west side, north of 5 m for land, land outside the red line is 20 m wide green belts.

### 1.2Geological and hydrological conditions

According to the geotechnical engineering investigation report, the green high iron D6 plot field of geotechnical engineering information is as follows:

1) Geological conditions

(1) Topography site for cultivated land, basic flat terrain, ground geomorphic units for the Yellow River flood plains, and the whole field within the scope of the investigation found no bad geological phenomenon.

(2) According to the litho logy and mechanics characteristics of foundation soil layer from top to bottom is divided into 12. Design USES the soil parameter is as follows:

2) Hydrological conditions

Groundwater types is diving, stable water depth of 10.2 ~ 11.0 m.

**Double row pile supporting scheme and the calculation model for software of FLAC3D**

**Table 1 Soil design parameters**

| soil | geotechnical category | soil thickness/m | severe/kg/m$^3$ | angle of internal friction / ° | cohesion/KPa | anchor side resistance/KPa | compression modulus/MPa |
|---|---|---|---|---|---|---|---|
| 1 | silty soil | 3.01 | 18.0 | 23 | 12 | 57 | 7.1 |
| 2 | silty soil | 1.98 | 17.8 | 25 | 13 | 66 | 9.7 |
| 3 | silty soil | 1.66 | 18.2 | 24 | 18 | 60 | 6.6 |
| 4 | silty clay | 1.46 | 18.2 | 16 | 18 | 72 | 6.2 |
| 5 | silty soil | 1.04 | 18.0 | 26 | 18 | 75 | 10.2 |
| 6 | silty clay silt | 1.30 | 18.0 | 11 | 15 | 66 | 6.8 |
| 7 | silty soil | 1.34 | 19.0 | 26 | 14 | 78 | 11.2 |
| 8 | silty clay | 3.7 | 18.2 | 10 | 15 | 60 | 7.2 |
| 9 | silt | 1.22 | 18.5 | 28 | 4 | 87 | 23.0 |
| 10 | fine sand | 6.76 | 18.8 | 30 | 2 | 114 | 34.0 |
| 11 | silty clay | 2.70 | 19.5 | 19 | 24 | 102 | 12.7 |
| 12 | fine sand | 3.96 | 19.0 | 32 | 2 | 120 | 35.0 |

## 2.1 Double row pile supporting scheme

The foundation pit adopts the upper slope, lower double row pile composite bolt support scheme. Support plan section diagram is shown in figure 1. Pile diameter 800 mm, 1500 mm longitudinal spacing, double row pile row distance 2700 mm. Anchor adopted three rows, from top to bottom length of 26 m respectively, 22 m, 22 m, is apart from the pile top is 1 m, 4 m, 6.5 m respectively. Upper part put slope using soil nail and soil nail length is 12 m, soil nail spacing is 1.0 m, the longitudinal spacing is 1.3 m.

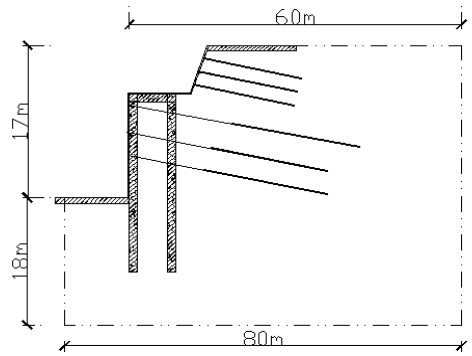


**Figure 1 Double row pile composite bolt support structure profile sketch**

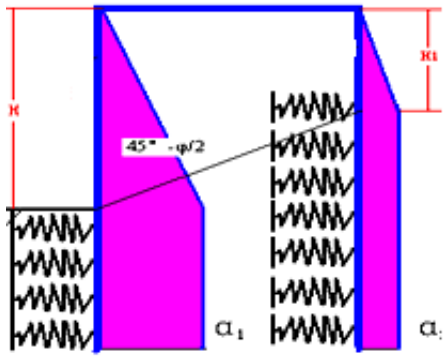


**Figure 2 Is double row pile design calculation software model**

## 2.2 Richard software for double row pile design calculation model

This project adopts the principle is the foundation pit design software to calculate, before the calculation according to certain earth pressure model is given. Calculation model diagram as shown in figure 2, The H1 for equivalent excavation depth, Has the excavation depth。

## 2.3 FLAC3D software double row pile design calculation model

Selected by FLAC3D and the boundary the conditions, the definition of foundation pit excavation presents point as the origin of coordinates, excavation length direction along the Y axis is outspread, width along the X axis is outspread, excavation the depth along the Z axis negative stretch. The Analysis calculation, the model around four symmetry constraint, which is restricted to the X and Y respectively to the below of foundation pit at the bottom of the fixed constraint.

FLAC3D finite difference software analysis of foundation pit excavation calculation model diagram as shown in figure 3 to figure 5:

**Richard software and FLAC3D numerical results contrast analysis**

Calculation process because of the two kinds of software, using two kinds of software of double row pile composite anchor and lateral bending moment calculation results contrast analysis to better understand the performance of double row pile composite anchor.

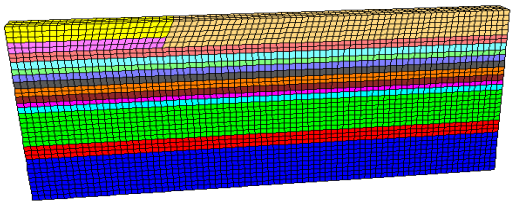

**Figure 3 Not when excavation of double row pile composite bolt support structure model diagram**

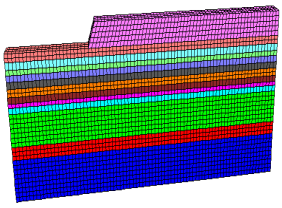

**Figure 4 Slope excavation supporting model diagram**

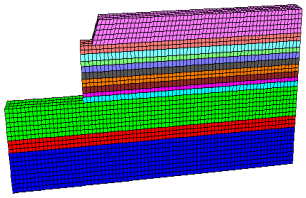

**Figure 5 Excavation on the supporting model diagram**

Reason is the calculation results show that before and after double row pile lateral and bending moment diagram in the form of expression is significantly different. In front of the deformation of the pile for curved scissors, back row pile characterized by pure bending shape, only the last step when Before and after row pile lateral trend to show the consistent, illustrate a few steps before the deformation of the excavation Before and after double row pile, only to the last step before and after double row pile show good work mechanism.

Before and after double row pile bending moment diagram of the first three steps in applying bolt and the last step is obvious different, mutation happened when excavation bottom, especially the back pile bending moment diagram. Whether in theory or the measured before and after double pile bending moment should show the gradient, as to why in excavation on deformation and bending moment are why, unlike before a few steps, worth exploring.

In view of the above two problems, we should start with double row pile soil pressure calculation model considering. Reason is the earth pressure calculation model is shown in figure 6.

Double row piles is only active earth pressure calculation, consideration of the soil on earth pressure between piles of transference, normally in front of the pile and the back pressure of piles and soil is different. In the front row piles on the soil pressure according to the actual excavation surface, and the rear pile as defined by the equivalent excavation surface soil pressure.

1. Equivalent depth excavation face

$$L_O = H\tan(45° - \varphi/2) = 5.78 \tag{1}$$

Because $L_0 > L$

$$H_1 = H - \frac{L}{\tan(45° - \varphi/2)} = 6.39 \tag{2}$$

so

$$\varphi = \frac{\sum_{i=1}^{n} h_i \varphi_i}{\sum_{i=1}^{n} h_i} \tag{3}$$

Type:

$H_1$ - The back pile equivalent excavation depth (m);

$H$ - The foundation pit excavation depth (m);

$L$ - Front of the pile row distance (m);

$L_0$ - Sliding surface extends to the surface to the edge of the foundation pit horizontal distance (m);

$\varphi$ - Internal friction Angle of soil, a weighted average of the values for the excavation surface above the soil.

Front and back row pile soil pressure

Double row piles is calculated according to their equivalent Front and back row pile excavation surface when the value of earth pressure calculation their Ea, then share multiplied by the coefficient of Front and back row pile respectively, have effect on Front and back row pile soil pressure, when decorate a form for rectangular double row piles is calculated as follows:

$$\alpha = \frac{L_0}{L} < 1 \tag{4}$$

$$\alpha = \frac{2L}{L_0} - \left(\frac{L}{L_0}\right)^2 = 0.716 \tag{5}$$

Front of the pile $P_A = \alpha e_a 0.716 \mathrm{E}_a$ (6)

Back row pile $P_B = (1-\alpha)E_a = 0.284E_a$ (7)

Reason is that the calculated results of the distribution of earth pressure and calculation. And adopt some assumption, which is associated with the project, double row piles without considering any slope, slope line up from behind the double-row piles; In front of the resistance of pile elastic range from excavation face downwards, back row pile resistance elastic range from H1 face downwards; Back row pile equivalent above the excavation surface soil before the passive earth pressure.

Can be seen from the used FLAC3D calculation results from the front of the excavation to the beginning of the excavation before and after double row pile deformation are identical. The change of various working conditions in the process of excavation is gradient, no obvious mutation, the third and fourth largest lateral at the top of the pile, compared to a few steps behind the main reason is that the excavation depth is small, but by carefully observe the deformation of the overall trend and a few steps behind the fact is the same.

Constantly, is a dynamic soil pressure, So any form of distribution is appropriate in advance, only the measured is reliable, but the actual is to get after excavation, only feedback adjustment, and can be measured to the true earth pressure is also very difficult. And when is obtained by using the FLAC3D is modeled according to the actual situation, not in front of the excavation to the size of the earth pressure, but let it automatically generated in the process of excavation to the role of supporting structure, the actual situation and is consistent, the precision of calculation is higher also.

**Monitoring result analysis**

Foundation pit safety level to level. Groundwater types for diving, stable water level is 10.2 ~ 11.0 m. Foundation pit supporting the main way is: the top 5 m by soil nail wall, bottom and even beam with double column piles and anchor rope combined support.

Building foundation pit engineering monitoring technical specification requirement level of foundation pit does not exceed the maximum lateral value of 50 mm, when the excavation is one of the biggest lateral value of 25.7 mm specification requirements is far less than 50 mm and satisfies the requirement of monitoring. Show that composite bolt support structure with double-row piles meet the requirements of the foundation pit engineering.

From the monitoring result analysis, before and after double row pile deformation trend is consistent, roughly from start construction to the excavation to the end, no mutation and achieve value. The same condition, the back pile the maximum lateral value is greater than the front pile, but

before and after double row pile basically equal on the top of the pile lateral values, give full play to the role of coupling beam, make Front and back row pile forced deformation of the pile is coordinated. Different condition, the back pile of pile top lateral value is the same, maximum lateral gradually increases with the increase of excavation depth, but the maximum point remains unchanged. Again, in front of the pile displacement of pile top is basically remain unchanged, from pile head to 5 m strength of pile lateral value is nearly equal, the reason is that the bolt through the waist beam direct effect on the front row piles, equivalent to three rows of supporting pile in the front row, this and FLAC3D calculations in front of the pile deformation curves are very similar.

From the measured values shows that Front and back row pile deformation trend is roughly similar, show that double row pile composite the wholeness of the anchor supporting form is very good, always maintain coordination double row pile deformation, and work together. Overall Front and back row pile deformation monitoring data and calculation result of finite difference software, verify the accuracy of FLAC3D numerical model.

Monitoring results show that the deformation of the measured values is less than the calculated value, fully achieve the desired goal. In a word, the principle is, though cannot be accurately according to the actual earth pressure for the design of supporting schemes, but this kind of calculation method of design guide the construction is safe and reliable. Practice proved that is feasible.

## Summary

1) Double row pile composite supporting structure for anchor supporting of foundation pit lateral, can satisfy the requirements of specification, and in construction process found no crack is not conducive to the construction of more obvious.

2) The principle is the software, though cannot be accurately according to the actual earth pressure for the design of supporting schemes, but this kind of calculation method of design is used to guide the construction is safe and reliable;

3) The use of double row pile composite bolt supporting of foundation pit lateral capacity, under the same conditions is less than the pure double row pile and pile anchor support.

## References

[1] Wu Gang, Bai Bing, Nie Qingke. The double-row piles retaining structure for deep excavation design calculation method [J]. Rock and soil mechanics, 2008, 29(10): 2753~ 2758.

[2] Nie Qingke, Hu Jianmin, Wu Gang. The double-row piles retaining structure for deep excavation deformation and earth pressure [J]. Rock and soil mechanics, 2008, 29(11): 3089~ 3094. (In Chinese)

[3] Edited by Huang Qiang. Building foundation pit supporting technology for Application Manual [M]. Beijing: China Building Industry Press, 1999.

[4] Gong Xiaonan, editor-in-chief of high tide. Design and construction of deep foundation pit [M]. Beijing: China Building Industry Press, 1998.

[5] GB50497-2009monitoring of building excavation engineering technical specification [S]. Beijing: China Building Industry Press, 1992.

*Applied Mechanics and Materials Vols. 580-583 (2014) pp 601-605*
*© (2014) Trans Tech Publications, Switzerland*
*doi:10.4028/www.scientific.net/AMM.580-583.601*

# Experiment research of rock anchor foundation on sandstone ground in transmission line

Yan Zhang[1, a*], Weifeng Zheng[1,b]

[1]China Electric Power Research Institute 100192, China

[a]zhangyan2009@gmail.com, [b]zhengweifeng1977@126.com

**Keywords:** transmission line; rock anchor foundation; sandstone ground; ultimate uplift bearing capacity; failure mode

**Abstract.** Rock anchor foundation can be widely used for the practical transmission line engineering in mountain areas. On strong-weathered sandstone ground, ten sets of uplift static load test of single rock anchor foundation were carried out. Based on the testing results, the typical failure modes and the ultimate uplift bearing capacity of foundations were obtained. Internal force distribution and effective anchorage depth were investigated through stain measurements. Design parameters of rock anchor foundation on sandstone ground were proposed, which can provide a reference for transmission line engineering design.

## Introduction

Rock anchor foundation is a new type of transmission tower foundation which consists of anchor rod and pile caps [1]. Because of taking full advantage of the mechanics performance of original rock mass, rock anchor foundation has excellent pull-out bearing performance. Compared with regular foundation, rock anchor foundation can reduce excavated volume, concrete dosage and project cost significantly which make it an environmental protection foundation type.

Under uplift load condition, the load transfer mechanism of rock anchor foundation is very complicated and ambiguous. In order to investigate the failure characteristics and load-bearing mechanism of rock anchor foundation systematically, this paper will analyze the load-displacement relation and the law of internal force distribution of rock anchor foundation based on uplift field load test on sandstone ground.

## General situation of test

**Engineering geological conditions.** This field test site is located in Lingwu City of Ningxia Hui Autonomous Region. The surface of ground is silty sand layer which is about 0.5m~1.5m thick. The bottom of ground is strong-weathered sandstone layer with more than 10m thickness. According to the result of point load test, the hardness degree of sandstone can be defined as relatively hard rock. The physical and mechanical properties of sand and rock mass are shown in Table1.

Table1. Physical and mechanical properties of sand and rock mass

| Lithology | Thickness [m] | Natural unit weight [kN/m$^3$] | Cohesion [kPa] | Internal friction angle [°] | Shear strength [kPa] | Eigenvalue of bearing capacity [kPa] |
|---|---|---|---|---|---|---|
| Silty sand | 0.5~1.5 | 15.0 | 0 | 15 | / | / |
| Sandstone | >10 | 21.0 | 0 | 55 | 20 | 400 |

**Experimental foundation design scheme.** Ten sets of single rock anchor foundation are designed for field static load test. The diameter of anchor bar is 36mm. The material of anchor bar is HRB400. The diameter of anchor hole is 100mm. The strength grade of fine stone concrete is C30. The depth and quantity of single rock anchor foundation are shown in Table2.

Table2. Depth and quantity of single rock anchor foundation

| Serial number | D0.5 | D1.0 | D1.5 | D3.0 | D4.5 |
|---|---|---|---|---|---|
| Depth [m] | 0.5 | 1.0 | 1.5 | 3.0 | 4.5 |
| Quantity | 2 | 2 | 2 | 2 | 2 |

**Loading device and testing system**. The loading device consists of reaction force steel beams and hollow tension jack. The counterforce device consists of wood block and natural ground. The test devices are RS-JYC static load meter and DH3816 strain gauge. The uplift loading system is shown in Fig1.

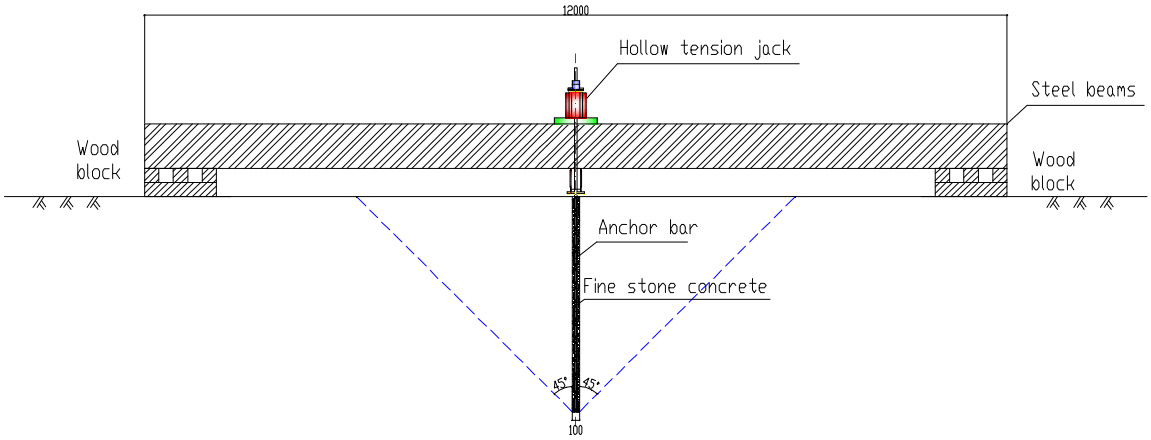


Fig1. Sketch of uplift loading system of single rock anchor foundation

**Loading method.** According to relevant technical standard [2], static load test adopts slow maintenance loading method. Uplift load is applied on foundation step by step. The step number of load cannot be less than 8. The maximum uplift load must be greater than 2 times of design load. The displacement of rock anchor foundation should be recorded right after each loading step immediately. The test data should be recorded every 5 minutes till the deformation is less than 0.01 mm 4 times in a row.

## Analysis of test results

**Typical failure mode.** The failure mode of foundation is the macro performance of the reaction between anchor and rock ground. The failure mode which can reflect the load-bearing characteristics directly is also one of important basis of design parameters. Under uplift load, single rock anchor foundation has four kinds of potential failure modes which are anchor bar tensile failure, anchor pile pull-out failure, anchor bar pull-out failure and rock mass shear failure depending on the depth of anchor, anchor bar features, properties of rock mass and construction quality. Anchor bar tensile failure and anchor pile pull-out failure are the main failure modes of this field test. The failure photos of this field test are shown in Fig2.

**Analysis of uplift bearing capacity of single rock anchor foundation.** The load-displacement relations of single rock anchor foundation of different anchorage depth are shown in Fig3.

The displacement of single rock anchor foundation refers to the displacement of top of anchor bar. Learn from Fig3, the ultimate uplift bearing capacity of foundations of different anchorage depth are 240kN, 450kN, 450kN, 465kN and 475kN respectively. The ultimate uplift bearing capacity of 0.5m deep foundations is less than the foundations of other anchorage depths obviously. This is because the failure mode of 0.5m deep foundations is anchor bar tensile failure while the failure mode of foundations of other anchorage depth is anchor pile pull-out failure.

(a) Anchor bar tensile failure (b) Anchor pile pull-out failure

Fig2. Two kinds of failure photos

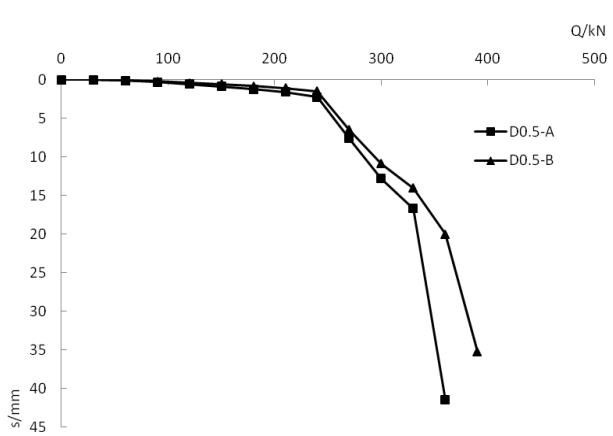


(a) Anchorage depth=0.5m

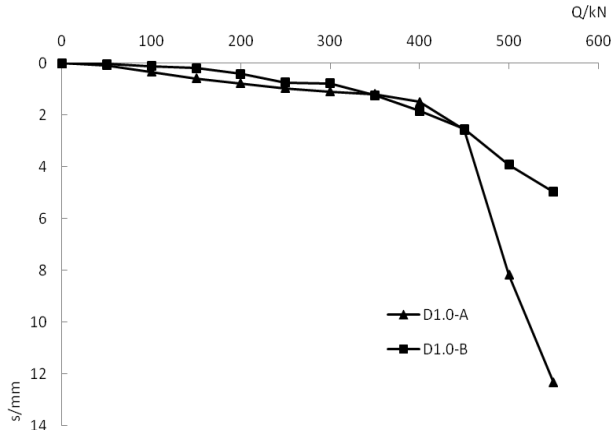


(b) Anchorage depth=1.0m

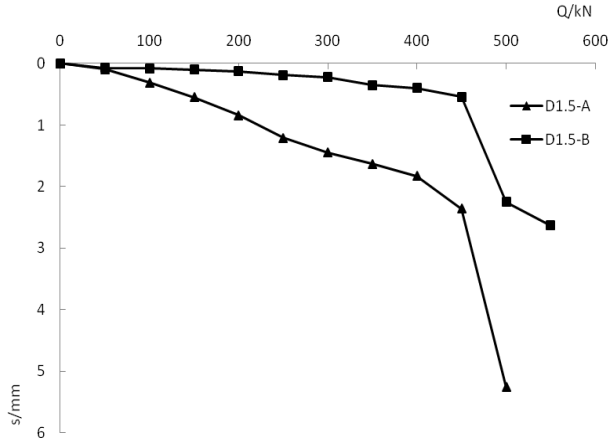


(c) Anchorage depth=1.5m

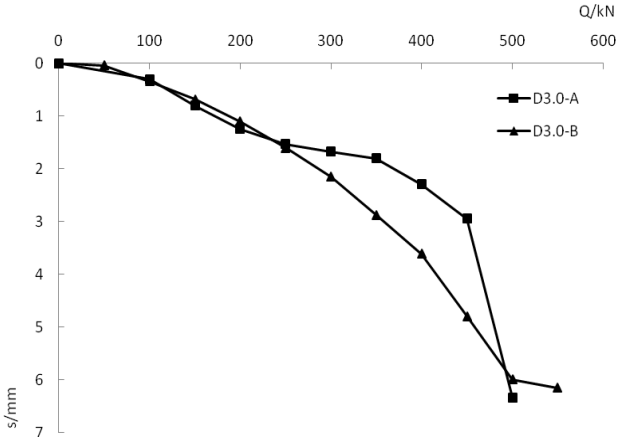


(d) Anchorage depth=3.0m

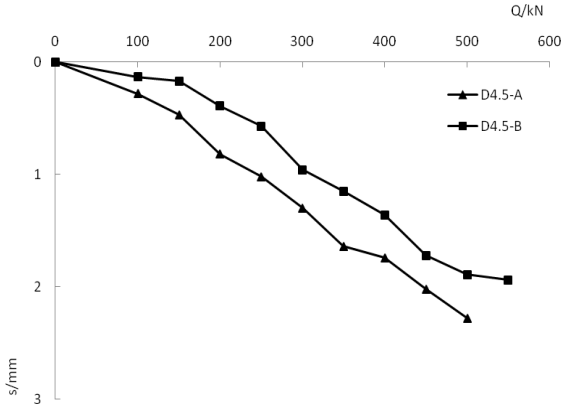


(e) Anchorage depth=4.5m

Fig3. The load-displacement relations of single rock anchor foundation

**Analysis of internal force distribution of anchor bar.** Based on stain measurement results of anchor bar in loading process, the internal force distribution along the depth of anchor bar is shown in Fig4.

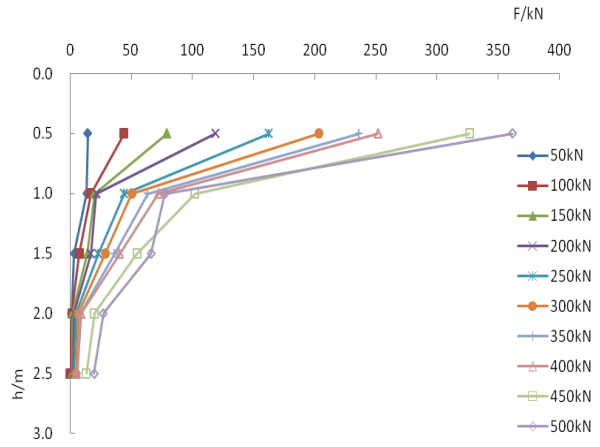


(a) Anchorage depth=3.0m

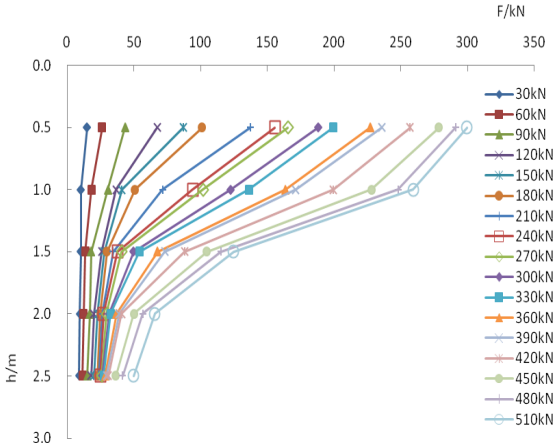


(b) Anchorage depth=3.0m

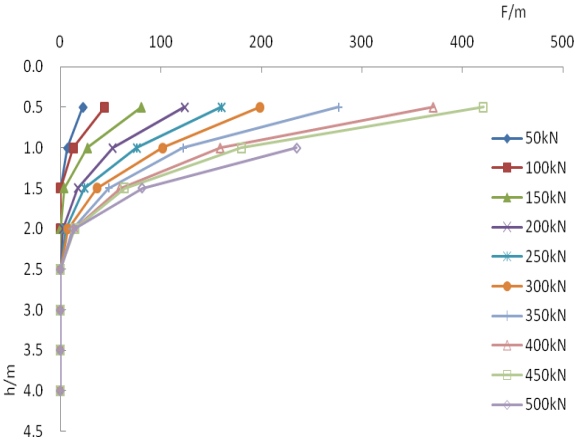


(c) Anchorage depth=4.5m

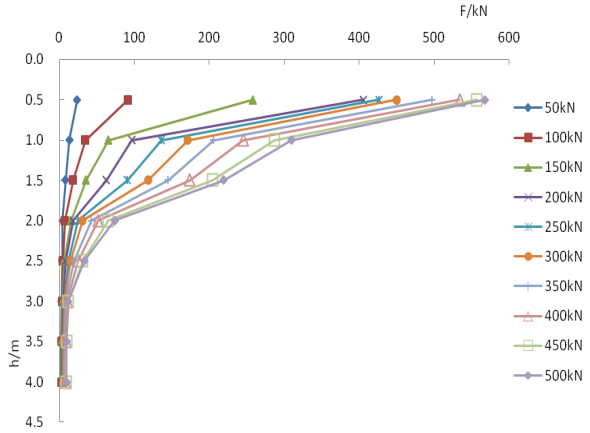


(d) Anchorage depth=4.5m

Fig4. The internal force distribution of anchor bar

Learn from Fig4, the internal force distribution of anchor bar increase with load and decrease with increasing depth. When the depth is larger than 2.5m, the internal force of anchor bar is less than 10% of current load. Therefore, the effective anchorage depth can be considered as 2.5m.

**Analysis of design parameters of rock anchor foundation.** According to the test result of single rock anchor foundation of 0.5m depth, the bond strength between anchor pile and rock mass can be calculated by Eq. 1 directly. Where $T_u$ is the ultimate uplift bearing capacity; $D$ is the diameter of anchor pile; $h_0$ is effective anchorage depth. Internal force distribution and effective anchorage depth are obtained.

$$\tau_b = \frac{T_u}{\pi D h_0} = \frac{240}{3.14 \times 0.1 \times 0.5} = 1528 \quad \text{kPa} \tag{1}$$

## Conclusions

On basis of the uplift static load test of single rock anchor foundations on strong-weathered sandstone ground, this paper analyzes the typical failure modes and the ultimate uplift bearing capacity of foundations. The bond strength between anchor pile and sandstone rock mass is proposed

**References**

[1] Cheng Yongfeng，Shao Xiaoyan，Zhu Quanjun: Current situation of foundation works and existing problems for transmission lines in China. Electric power construction Vol. 23, No.3 (2002), p. 32~34.

[2] Code for design of building foundation. GB 50007-2011.

[3] Zheng Weifeng, Deng Haiji, He Jinye: Experimental research on rock anchor foundation in transmission line. Building Science Vol. 28, No. 9 (2012), p. 57~59.

[4] Ding Shijun, Lu Xianlong: Loading test of rock anchor foundation for transmission lines. Electric power construction Vol. 31, No. 11 (2010), p. 1~5.

[5] Sun Yizhen, Zheng Weifeng, Fan Zhiqiang: Tension model test research on grouted bolts foundation in jointed rock masses for transmission lines. Rock and Soll Mechanics Vol. 33, No. 1 (2012), p. 78~82.

[6] Zheng Weifeng, Lu Xianlong, Cheng Yongfeng, Feng Zixia: Experimental study on rock anchor foundation in transmission lines. Geotechnical investigation & Surveying Vol. 1 (2010), p. 5~8.

[7] He Hongbo: Antilift tests of transmission line embedded rock foundation. Electric power construction Vol. 28, No.9 (2007), p. 18~20.

[8] Fei Xiangze, Cheng Yongfeng, Su Xiucheng: Experiment study on anchor-shaft rock foundation in

North China transmission line construction. Electric power construction Vol. 28, No.1 (2007), p. 26~28.

[9] Technical regulation for designing foundation of overhead transmission line. DL/T 5219-2005.

*Applied Mechanics and Materials Vols. 580-583 (2014) pp 606-609*
*© (2014) Trans Tech Publications, Switzerland*
*doi:10.4028/www.scientific.net/AMM.580-583.606*

# Experimental Studies on Acoustic Emission of Different Damaged Concrete

Hongguang Ji [1,a], Xurong Li[1,b], andChenglin Song[1,c]

[1]School of Civil and Enviromental Engineering,University of Science and Technology Beijing, Beijing,China

[a]jihongguang306@ces.ustb.edu.cn, [b]lixr0911@163.com,[c]lianyi6789@163.com

**Key words:** Concrete; Damage; Acoustic emission signal.

**Abstract.** Through to conduct uniaxial compression test on concrete of suffering sulfate attack, the frequency characteristics of acoustic emission signal are analyzed in the corrosion concrete failure process. The results show that: the acoustic emission ringing counts show phases developmental rule with the relative stress increased.When the relative stress is low, acoustic emission signal of the damaged concrete $S_1$ is intensive and large amplitude, while the acoustic emission signal of the no damage concrete $S_0$ is active - relative quiet - active - relative quiet and the acoustic emission signal of the damaged concrete $S_2$ is active - quiet - active.

## Introduction

For the corrosion concrete materials, the failure process of concrete and the internal micro crack evolution process are consistent. Concrete cracking is mainly the initial expansion of the internal micro crack. It produces the acoustic emission phenomenon because generation and propagation of micro cracks cause the stress relaxation and the part energy stored suddenly released in the form of stress wave [1,2]. Frequency characteristic of acoustic emission signal is an important aspect of acoustic emission signal analysis [3,4].The relationship of the frequency characteristics of concrete material acoustic emission and the mechanical parameters of concrete material is an important basis of sensor selection, effective characteristic selecting and signal analysis in the testing of the concrete material acoustic emission [5,6,7,8].Developing research of characteristics of acoustic emission signal in the corrosion concrete failure process and revealing the relations between the failure process of concrete and acoustic emission characteristic parameters are helpful for understanding the failure mechanism of the corrosion concrete. In order to study the relationship between the mechanical parameters of corrosion concrete material and the frequency characteristics of the AE signal, uniaxial compression tests are conducted on the no damage concrete and the damage concrete immersed in sulfate solution in 9% after seven months.

## Experimental Design

In order to study the relationship between the mechanical parameters of the corrosion concrete and the frequency characteristic of the acoustic emission, the C30 concrete specimens were made. The specimen size is 100mm*100mm*100mm. Specific parameters of the mixture ratio of the concrete material can be seen in table 1. Sulfate solution of sodium sulfate and magnesium sulfate mixed of the 9% sulfate ion concentration was compounded. Concrete was stirred in forced action mixer and was vibrated compacting in shaking table. The forms of the concrete specimens were removed after twenty-four hours then they were standard cured in standard curing room. Three concrete specimens were directly put into the sulfate solution after curing 28 days, labeled as $S_0$.Three concrete specimens were pressurized to 50% of the ultimate load then unloading, then put they into sulfate solution, labeled as $S_1$.Three concrete specimens were pressurized to 70% of the ultimate load then unloading, then put they into sulfate solution, labeled as $S_2$.Uniaxial compression test and acoustic emission testing are conducted on all the specimens of soaking in sulfate solution after seven months.

Table 1 Mix proportion of concrete

| Concrete mark | Water-cement ratio W/C | Water [kg/m$^3$] | Cement [kg/m$^3$] | Sand [kg/m$^3$] | Stone [kg/m$^3$] | Water Reducer [kg/m$^3$] | Nacl [kg] | $NaNO_2$ [kg] | Trolamine [kg] |
|---|---|---|---|---|---|---|---|---|---|
| C30 | 0.49 | 196 | 400 | 620 | 1224 | 34.20 | 4 | 4 | 0.2 |

**Appearance Features**

The surface of the concrete appears variation of different degree with increasing corrosion time after the concrete was corroded by sulfate solution. These specimens have no obvious changes in the first one month then the color of the concrete is slightly pale over the next few months. The concrete's surface appears slightly sand phenomenon and some parts of the specimen which were exposed to the air began to produce crystal in the sixth month. The concrete specimens have slight spalling in the seventh month. The surface of the concrete specimens after being taken out from the solution gradually appears a lot of white crystals of salt in the dry process. Because of the crystalline absorption effect of concrete in the air, the drying time of the specimen is relatively long, and there are a large number of salt on the surface of the concrete and some have entered the concrete surface area( see figure 1).

S0 S1 S2

Fig.1 Concrete of different damage in sulfate solution after soaking seven months photograph comparing

**Concrete Acoustic Emission Parameters and Corresponding Relation between Stress and Strain**

Through uniaxial compression test on corrosion concrete, using acoustic emission detection system, conducting the acoustic emission signal waveform acquisition and stress-strain observation in a whole process, the acoustic emission ring counts that corresponding to each time period are obtained in uniaxial compression process of the corrosion concrete. Combined with the process of the stress of corrosion concrete, by using data from the press, stress,strain and time corresponding relationship of the corrosion concrete can be obtained. When the stress value is converted into the corresponding relative stress value, after finishing, the corresponding relationship can be obtained on the relative stress and AE counts and the strain and acoustic emission counts.

Acoustic emission ring refers to the time-domain graphics of the acoustic emission wave, transducer each shocking one time, the output of a pulse called "ring". Acoustic emission ring count is number that acoustic emission signal exceeds a certain threshold. The relative stress is defined as the ratio that the stress value of a certain point of time in the compressive process and the maximum stress value that concrete bears, expressed as a percentage. The reference of corresponding stress level, which have a more clear understanding of the concrete in the loading process stage.

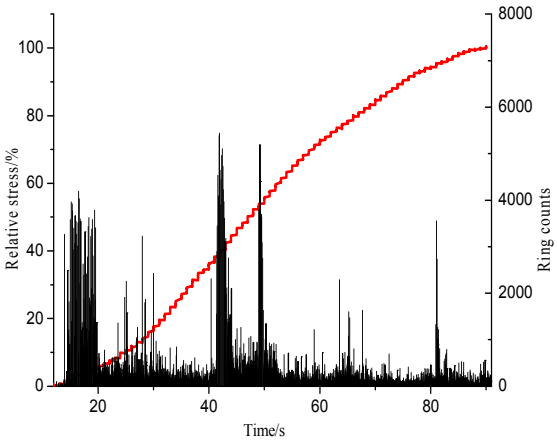


Fig.2 9%-$S_0$ Concrete relative stress -time-ring count diagram

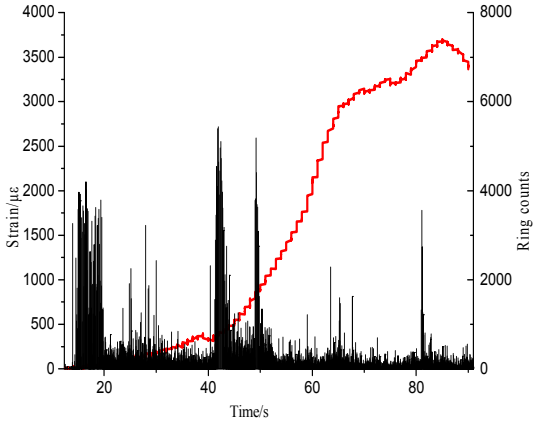


Fig.3 9%-$S_0$ Concrete strain-time-ring count diagram

From figure 2 and figure 3 can be seen, no damage concrete specimens were corroded in sulfate solution after seven months, which acoustic emission mainly occurs in 10% of the relative stress and 40% of the relative stress in the process of uniaxial compression. The acoustic emission counts decrease during the late stage of the specimen deformation.

Analysis reasons: because no damage concrete specimens were corroded by sulfate solution, the main reaction products are gypsum and ettringite, which the micro internal structure changes. The deformation of the concrete is not obvious in the initial loading stage, but acoustic emission counts are relatively high because of the effect of ettringite.

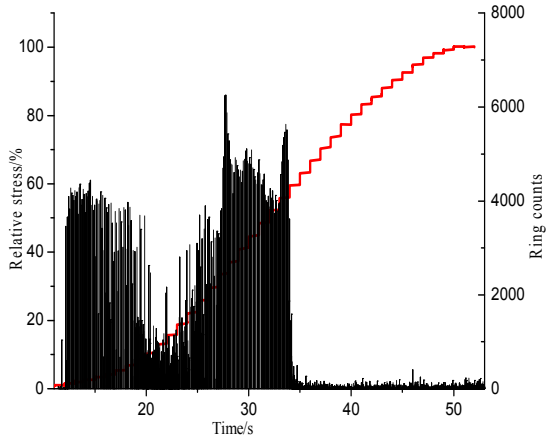


Fig.4 9%-$S_1$ Concrete relative stress -time-ring count diagram

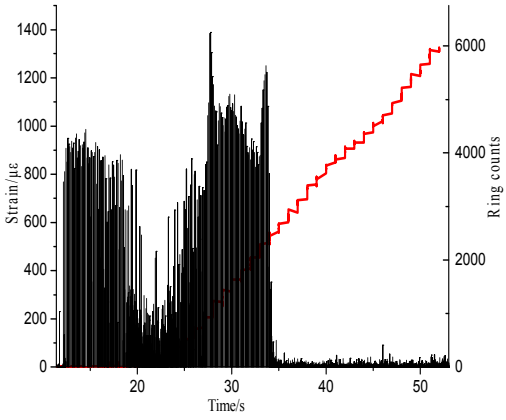


Fig.5 9%-$S_1$ Concrete strain-time-ring count diagram

From figure 4 and figure 5 can be seen, damage concrete specimens $S_1$ were corroded in sulfate solution after seven months, which acoustic emission mainly occurs in 5%-10% of the relative stress and 20%-50% of the relative stress in the process of uniaxial compression. The acoustic emission counts also show a downward trend and calm in the late stage of the specimen deformation.

Analysis reasons: the gypsum and ettringite of reactive formation are more because the number that sulfate ions get into the concrete is more after the concrete suffered damage and sulfate erosion. Furthermore, the early acoustic emission counts are relatively high and relatively dense because the gypsum and ettringite are belong to the brittleness material.

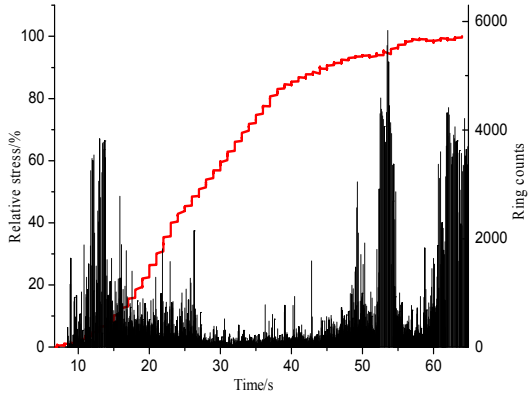


Fig.6 9%-$S_2$ Concrete relative stress -time-ring count diagram

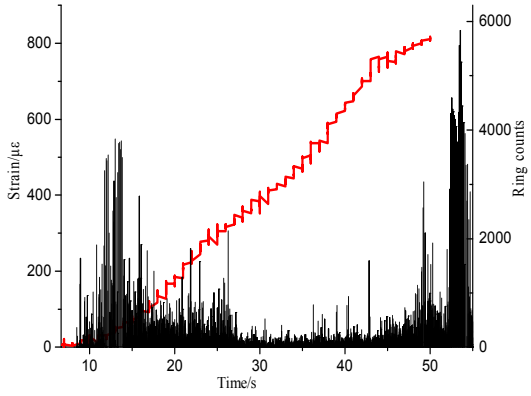


Fig.7 9%-$S_2$ Concrete strain-time-ring count diagram

From figure 6 and figure 7 can be seen, damage concrete specimens $S_2$ were corroded in sulfate solution after seven months, which the acoustic emission process is divided into three stages, namely initial stage, quiet period and active period in the process of uniaxial compression.

Analysis reasons: the internal concrete is density because the concrete specimens have been loaded 70% of the ultimate load in the initial stage. The sulfate ion is not easy to enter the concrete and produce the gypsum and ettringite so that the initial deformation of the corrosion concrete is not too large. The acoustic emission counts of the concrete specimen $S_2$ decreased relative to the acoustic emission counts of the concrete specimen $S_1$. Acoustic emission signal seems relatively calm in the middle of loading. The corrosion concrete performance is more brittle and acoustic emission activity is enhanced sharply when it reached the ultimate load.

## Conclusions

(1). Frequency characteristics of the acoustic emission signal is not very dense for no damage concrete specimen $S_0$ in the whole uniaxial compression process. Initial AE activity is stronger than the late AE activity.

(2). Initial acoustic emission signal of damage concrete specimen $S_1$ are stronger than that of the concrete specimen $S_2$, and performance is obviously very dense. The acoustic emission process of the damage concrete specimen $S_2$ is divided into three stages, namely the initial stage, calm stage and active stage.

## References

[1] H.G Ji. *Research and Application on Acoustic Emission Performance of Concrete Material.* (China Coal Industry Publishing House, China 2004),p13. (In Chinese)

[2] E.Y.Wang, X.Q.He and Z.T.Liu, et al: Journal of China Coal Society,Vol. 29 (2003) No.3, p.289. (In Chinese)

[3] Y.H.Chen,S.F.Liu and R.S.Geng, et al: Nondestructive Testing ,Vol. 24 (2002) No.9, p.394. (In Chinese)

[4] H.G.Ji and M.F.Cai:Chinese Journal of Rock Mechanics and Engineering, Vol. 22 (2003) No.2, p.227. (In Chinese)

[5] H.G.Ji and M.F.Cai:Chinese Journal of Rock Mechanics and Engineering,Vol. 18 (1999) No.9, p.157. (In Chinese)

[6] X.S.Zhang, J.W.Sun and X.M.Zhao:Journal of Astronautic Metrology and Measurement, Vol. 15 (1995) No.5, p.34. (In Chinese)

[7] H.G.Ji,L.H.Jia andZ.D.Li: Acta Acustica, Vol.21 (1996) No.4, p.601. (In Chinese)

[8] H.G.Ji,T.S.Zhang and Z.Y.Zhang, et al: Nondestructive Testing,Vol. 23 (2001) No.7, p.289. (In Chinese)

*Applied Mechanics and Materials Vols. 580-583 (2014) pp 610-613*
*© (2014) Trans Tech Publications, Switzerland*
*doi:10.4028/www.scientific.net/AMM.580-583.610*

# Experimental study on post-peak failure behavior of rock masses with persistent joint

Lei Wang[1, a], Jiang Yu [1, b], Xue Hua[1, c],

[1]PLA Institute of Engineering Corps, Xuzhou, Jiangsu 221004, China

[a]wljdd@foxmail.com, [b]yj20051202@163.com, [c]huaxue@163.com

**Keywords:** transfixion joint; post-peak; joint inclination angle; uniaxial compression

**Abstract.** The uniaxial compression test on pre-existing persistent jointed rock cylindrical standard specimen made by high stiffness servo control testing machine, systematic researched the relationship between jointed rock post-peak stress-strain curve, the destroy form of rock masses with dip angles of persistent joints. And the results reveal that: (1) The post-peak stress - strain curves of specimens with joint inclination angle of 15°and complete specimens are basically the same, but the difference of post-peak stress - strain curves of specimens with the joint inclination angle from 30°to 60°and complete specimens is vary greatly; (2) The post-peak failure modes of specimen change with different joint inclination. The research result can reflect mechanics and deformation and damage characteristics under uniaxial compressive loading in the phase of post-peak of rock masses with different dip angle pre-existing persistent joints.

## Introduction

Rock mass are mostly containing multiple irregular joints. In underground engineering surrounding rock is despite the destruction, many joints and even rupture state is more serious, but the failure of surrounding rock after mostly remained relatively stable, especially in Anchorage under the action of the stress field around the change, can form a stable structure and rupture the suitable, so studying the jointed rock after peak strength and deformation characteristics, is practical for the current project. Currently there are studied by means of mathematical calculations [1] [2], numerical analysis [3] [4], field testing and laboratory model tests.

Model test carried out in the laboratory is the better method. Because the rock is a complex containing much messy joint body, research ideas we can make to the process with a plurality of joints of rock from the intact rock into single jointed rock gradually carried out research on [5].

Domestic and foreign scholars regarding the mechanics of jointed rock compression through many experiments[6]-[9], but the study for post peak characteristics of jointed rock is few, for this paper, several groups through the joints of precast standard specimens containing different angle uniaxial compression tests carried out, through a systematic study of the uniaxial compression joints under different inclination failure mode peak after peak after the apparent relationship between the Poisson's ratio-strain curves - and post-peak stress.

## Experimental methodology

**Preparation of specimens.** Specimens for high 100mm diameter 50mm standard specimens, see Figure 1. Values were 15 °, 30 °, 40 °, 45 °, 50 °, and 60 °.

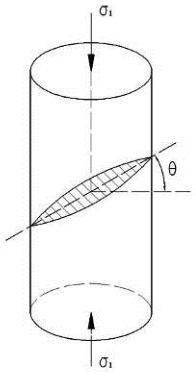


Fig.1 Schemes of jointed specimen

The cement mortar samples were produced by mixing of 425R OPC, sand and water at the ratio 1: 2.6: 0.35, respectively, by quality. To ensure the maximum possible homogeneity and isotropy of the overall compound, the OPC and silica sand were initially mixed together prior to the addition of water. Subsequently, water at room temperature was added to the dry mix of the constituents and thoroughly remixed. Grooves were cut on the two longer sides of the mold to insert thin galvanized sheets (0.1mm thick) in between them to create persistent (through-going) joints inclined angle which is 15°, 30°, 40°, 50°and 60° before initial setting, in order to simulate prefabricated through the fractured joints.

After the initial setting and final setting, the block will automatically make the fracture aperture closed to ensure that prefabricated fractured joints have certain cohesion. Each sample was kept under room temperature for 24 hours after being taken out of the mold, and then placed for 28 days, before cylindrical specimens with diameter 50 mm were cored from them. Individual cores were cut with a diamond saw to produce a set of cylindrical cement-mortar specimens 100 mm in height.

**Testing procedure.** Uniaxial Compressive Strength tests were carried out for the testing programme described below. All experiments were performed at TAW-2000 microcomputer control high stiffness servo testing machine. Methodologies utilized for the experimental work followed the ASTM specified standards for UCS testing.

## Results

**The post peak stress - strain curve.** The joint angle, the axial stress - strain curve shown in figure 2. The graph shows the difference of stress strain curve of the 15 ° joint angle specimen and complete specimen is very small. Great influence and joint angle from 30 °, 40 °, 50 °, 60 °, stress strain curve. As can be seen, the specimen in comparison with integrity, including joint angle at 30 ° to 60 ° between the specimen, the stress-strain curve from a single peak curve into a multi peak curve.

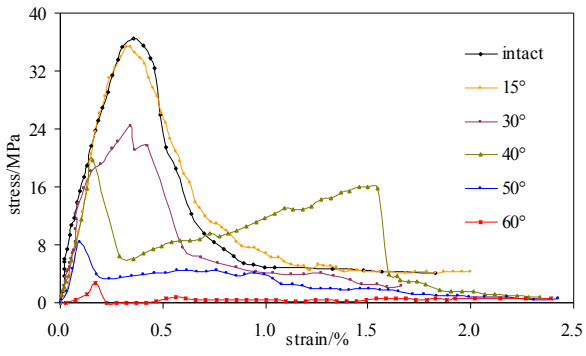


Fig.2 Axial stress-strain curves for specimens with different joint inclination angles

**Post peak failure mode.** Through the joint angle $\theta$ =15°, damaging effects of joints on the specimen is very weak, the specimen is still in accordance with the splitting failure. Through the joint angle $\theta$=30°to $\theta$=50°until failure forms of joint angle, the size of the specimen has great influence $\theta$=30°, the joint surface sliding failure and specimen overall splitting failure is almost the same time; =40°, first along the joint plane sliding failure, then produce overall splitting failure; $\theta$=45°, is still the first along the joint plane sliding failure, then produce overall splitting failure; $\theta$ =50° destruction, just along the joint surface sliding, does not produce splitting failure. Through the joint angle $\theta$=60°, along the joint plane sliding failure phenomenon is more obvious, there is no splitting failure.

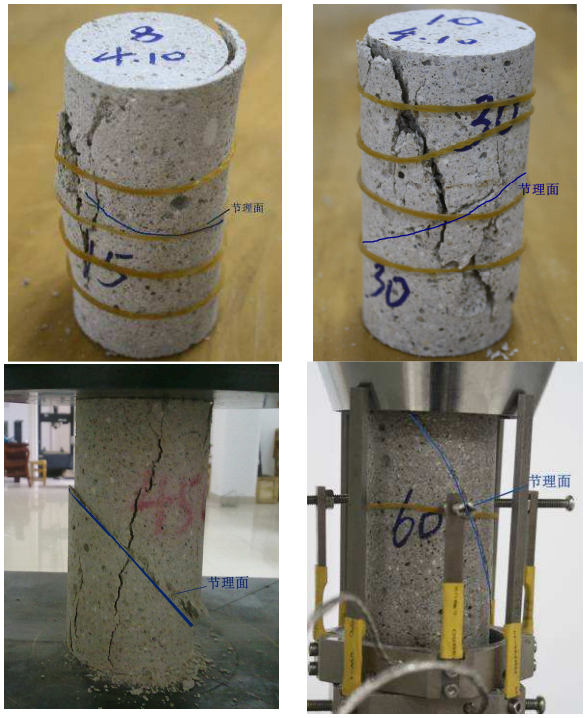


Fig.8 Post peak damage morphology of jointed rocks in turn with the joint inclination from 15°, 30°, 45°to 60°

## Discussion

When $\theta$=30°, 40°, 45°, stress-strain curve appeared multi peak phenomenon =30° time curve remains and complete curve similar, just after the strength peak curve has a small fluctuation of second small peak; but after $\theta$=40°, 45° stress-strain curve is greatly change the first peak, then there will be second, third or even more of the peak, the peak strength of will and the back is greater than the first peak intensity value. The first peak is the specimen damage in the joints, and the peak is due to the specimen had a splitting shear failure and produced, $\theta$=40°, 45° specimen easily along the joint surface damage, as the pressure increases further the two part separated off specimen is further compression (main factors at joints has not influence), which reached second peak, and this season will have a sliding surface, so the stress began to decline, but with the specimen is further compressed, pressure drop to the bottom and the gradually increased, it will repeat the last action, this is the reason why $\theta$=40°, 45°when there are multiple peak. 60°$\geq\theta\geq$50°, direct shear failure along the joint plane. To achieve greater angle this paper does not research.

Through jointed rock specimen failure with the different point of view, we can see the damage in the form of joint angle of peak after the main factors. The joint angle at $\theta$=15° when damage is splitting, the joint surface almost no effect, its failure forms and complete specimens were similar; $\theta$=60° failure is mainly shear failure, the failure is the main failure along the joint surface; $\theta$=30° and $\theta$=45° is splitting and shear failure mode, first damage along the joint surface, with the pressure increase joint friction is relatively stable, and began to produce specimens of splitting failure.

## Discussion

In this paper, a different angle of prefabricated jointed rocks through uniaxial compression test specimens were studied through joints inclination on the stress - strain curves and forms of destruction. From the experimental results obtained:

(1) With the change of joint angles, the post peak stress - strain curve significantly, jointed inclination $\theta$= 15° stress - strain curves and complete specimen similar, jointed inclination from 30°, 40°, 45°, 50°, 60° , the stress - strain curves and complete specimen obvious differences, stress - strain curves produce multiple peak after peak phenomenon, particularly evident at 40°.

(2) Different angle joints, different specimens after the peak phase of the failure mode. After the dip $\theta$= 15° when the specimen failure mode for the peak splitting, inclination $\theta$= 50°, 60° when the specimen after the destruction of the peak shear, angle of $\theta$= 30°, 40°, compared with 45°, splitting and shear cut the hybrid model.

## References

[1] Jaeger J.C.，N.J.W. Fundamentals of Rock Mechanics [M]. Fourth Edition Chapmen and Hall, London，2007.

[2] Yan Shilin, Huang Yuying, Chen Chuanyao. An equivalent model for jointed rock mass with persistent joint and its elastic parameters [J]. Journal of Huazhong University of Science and Technology，2001，29 (6)：60–63. (in Chinese)

[3] Wong, R. H. C., C. A. Tang, K.T Chau, P Lin. Splitting failure in brittle rocks containing pre-existing flaws under uniaxial compression[J]. Engineering Fracture Mechanics, 2002, 69(17): 1853-1871.

[4] LI Shuchen, FENG Xianda, LI Shucai, et al. Numerical simulation of zonal disintegration for deep rock mass [J]. Chinese Journal of Rock Mechanics and Engineering, 2011, (7):1338-1344. (in Chinese).

[5] B.H.G.Brady, E.T.Brown. Rock Mechanics for underground mining [M].New York, Boston, Dordrecht, London, Moscow: Kluwer Academic Publishers, 2005.

[6] XIA Caichu, LI Hongzhe, LIU Sheng. Study of deformation properties of jointed specimens under unloading conditions [J]. Chinese Journal of Rock Mechanics and Engineering, 2010, (4):697-704.(in Chinese).

[7] LI Hongzhe, XIA Caichu, WANG Xiaodong, et al. Experimental study on deformation and strength properties of jointed marble specimens [J]. Chinese Journal of Rock Mechanics and Engineering, 2008, (10):2118-2123. (in Chinese).

[8] P.H.S.W. Kulatilake, W. He, J. Um, H. Wang. A physical model study of jointed rock mass strength under uniaxial compressive loading [J].International Journal of Rock Mechanics and Mining Sciences, Volume 34, Issues 3–4, April–June 1997, Pages 165.e1-165.e15.

[9] S.Q. Yang, Y.H. Dai, L.J. Han, et al. Experimental study on mechanical behavior of brittle marble samples containing different flaws under uniaxial compression[J].Engineering Fracture Mechanics, Volume 76, Issue 12, August 2009, Pages 1833–1845.

*Applied Mechanics and Materials Vols. 580-583 (2014) pp 614-618*
*© (2014) Trans Tech Publications, Switzerland*
*doi:10.4028/www.scientific.net/AMM.580-583.614*

# Explanation of Phenomenological Characteristics in Seepage Force Concept system

Yang Shen [1, a], Wenhan Du [1, b]

[1]Key Laboratory of Ministry of Education for Geomechanics and Embankment Engineering, Hohai University, Nanjing, 210098, China

[a]shenyang1998@163.com, [b]gsyygsyy@163.com

**Keywords:** The seepage force; Phenomenological characteristics; Soil clod analysis; Soil particle analysis

**Abstract:** Soil mechanics has been developed for a long time and its concept system is basically complete. But there are still some concepts not being defined clearly. The unclear concepts of seepage force are stated from three phenomenological characteristics aspects in this paper. The difference between loaded object and calculated range is cleared. The contact rule of solid phase and liquid phase is illustrated. The mathematical meaning of seepage force is clarified. Though judging the critical hydraulic gradient of soil flow on surface of cohesionless soil, the difference and correlation of the soil particle and clod analysis based on the phenomenological characteristics will be illustrated.

## Introduction

Soil mechanics has developed for nearly 90 years since Terzaghi put forward the effective stress principle and one dimensional consolidation theory as the foundation of this subject. Water is important in the status of soil mechanics. Its influences on consolidation, strength, permeability, and many other theories have been caused wide attention and discussion in science and engineering. As the intersection of hydraulics and soil mechanics, the researchers in different disciplines have different understanding in the concepts and application of seepage. The concept of seepage force, for instance, has not been used in the hydraulic field because the main research object of which is a fluid. However, there are still some unclear and inoperable explanations in soil mechanics, which is especially disadvantage for beginners understanding and application of the knowledge. At present, the concept of seepage force which is defined by Chinese current soil mechanics teaching material[1]-[11] can be generally divided into the following two categories: (1) Seepage of water in the void of soil cold will drag on it. The stress and strain of soil can be changed by this force. The drag force on soil particles in the unit volume of soil is called seepage force; (2) While groundwater flow in the soil, head pressure will change due to the resistance of soil particles. From the point of the principle of action and reaction, the flow will surely exert a force on soil particles. For convenience, this force on unit volume in soil particles is named as seepage force.

Physically, the forces under seepage should be consisted of the normal water pressure on the surface of soil particles and the tangential force caused by viscosity of water. This kind of description also has been referred in hydraulics[12]. But in soil mechanics, viscous tangential force does not appear in the description of seepage force. And it is classified as the drag of water on soil particles or the soil particles' resistance to flow. Literally, the description of seepage comes from the angle of the water movement but not according to the objective existence of force itself, which will puzzle beginners. For example, whether the seepage force can be equated to the flow viscous tangential force which is mentioned in hydraulics? If it does, how can it be calculated?

In order to clarify the concept of seepage force and apply it to engineering, some phenomenological characteristics in the concept of seepage force will be explained first. The concept of loaded object and calculated range, solid-liquid contact rules, and the mathematical meaning of the drag force will be made clear. The domestic soil mechanics teaching material is draw to descript abstract concept of seepage force, which is the drag force of seepage flow applied to soil particles in unit soil.

**Explanation of the phenomenological characteristics in the seepage force concept**

So-called phenomenological characteristic is concluded from the study of surface phenomenon, which can explain the phenomenon but is not the accurate intrinsic reason of these phenomena. It is particularly prominent for the phenomenological characteristics in the concept of seepage force. The following will focus on the triple phenomenological characteristics in the concept of seepage force.

**(1)Disunity of loaded object and calculated range**

In order to understand the concept of seepage force, the loaded object and calculated range of research must be understood first. By definition, the loaded object is the soil particles in soil while the calculated volume range is the unit of the whole soil in the case of seepage. On the surface, it is unreasonable to establish such mathematical model for seepage force. When the seepage force was analyzed from a macroscopic perspective, the object analyzed is the general soil rather than the soil particle. It will not create a big impact on the final result in actual application based on the model and is convenient to apply theory to practice.

Similar ways of expression might be found in many concepts of soil mechanics. For example, the permeability coefficient is defined as the flow water cross the unit in the section of the soil. Actually, the section includes the cut surface of the soil particle and the pore. The seepage can only happen in the pore among the soil particle but not the whole section. In another word, seepage can only happen in the pore while the calculated object is the whole section. From this point of view, the definition of the permeability coefficient also reflects the disunity between actual analysis object and calculated one.

**(2) Contact rules of solid phase and liquid phase**

When setting up the mathematical model of the seepage, the mutual contact soil particles and water also should be taken into consideration besides considering applying object and forced object. The contact rules means: In the case of regarding the saturated soil clod unit (including soil particles and water in the pores of the soil particles) as the modeling object, it must be sure that the internal soil particles contact external soil particles and internal water contacts external water. That is to say the internal soil particles will not contact the external water or internal water will not contact the external soil particles at the contacting surface between clod units. To put it simply, there is no contact between different phases (as shown in Fig. 1).

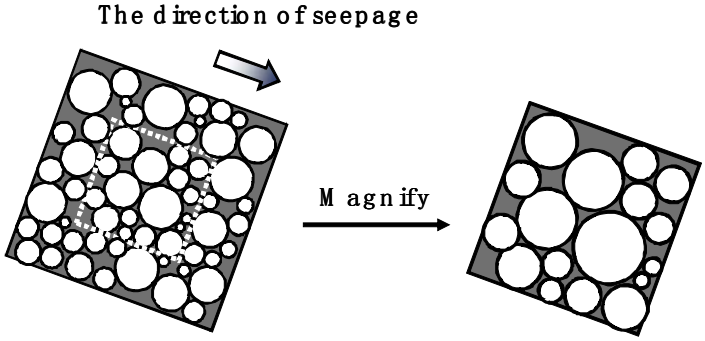


**Fig. 1 Solid-liquid phase contact in soil clod**

Physically, the contact between different phases certainly exists. The rule only caters to the modeling characteristics of a special classification method. There are several purposes as follows:

First, the resistance which soil particles put on the flow water can be solved under the condition of the model when regarding water as the analyzed object, thus the seepage force which is the reaction of resistance can be obtained;

Second, as the object of study, pore pressure is only generate between the water-water touching surface for soil cold. And this rule is in agreement with the calculating premise that pore pressure cannot cause the deformation of soil skeleton. It stays the same with the modeling of the effective stress principle.

Third, the viscous shear stress which is vertical to the pore pressure (that means the direction is tangent to soil particle surface) will not appear. The shear stress will only arise when solid is in contact with solid, and the water pressure will only arise when water contact with water.

**(3) The mathematical clarity of seepage force**

The drag in the definition of seepage force emphasizes the force which water applies on the soil particles under the condition of flowing. Due to the loaded object in the seepage force mathematical model is soil particle, the soil particle under the condition of static water is only loaded by buoyancy force. And the soil particle is also loaded by the reacting force of water resistance under the condition of seepage in addition to the buoyancy of water. Thus, the so-called drag force is the part of acting force of water flow on the soil particles except buoyancy. In addition to the seepage force and buoyancy, there is no more force imposing on the soil particles.

Saying from the physics, the force stressed by flow on the soil particle is the result of superposition of pore pressure and viscous force, or also can be seen as the result of superposition of seepage force and buoyancy(as shown in Fig. 2). The "force" in the two groups can not appear at the same time. Because the researchers are very clear to the method of the seepage force calculating, this kind of system is more inclined to adopt in the actual calculation. Although buoyancy and seepage force are not of real objective existence.

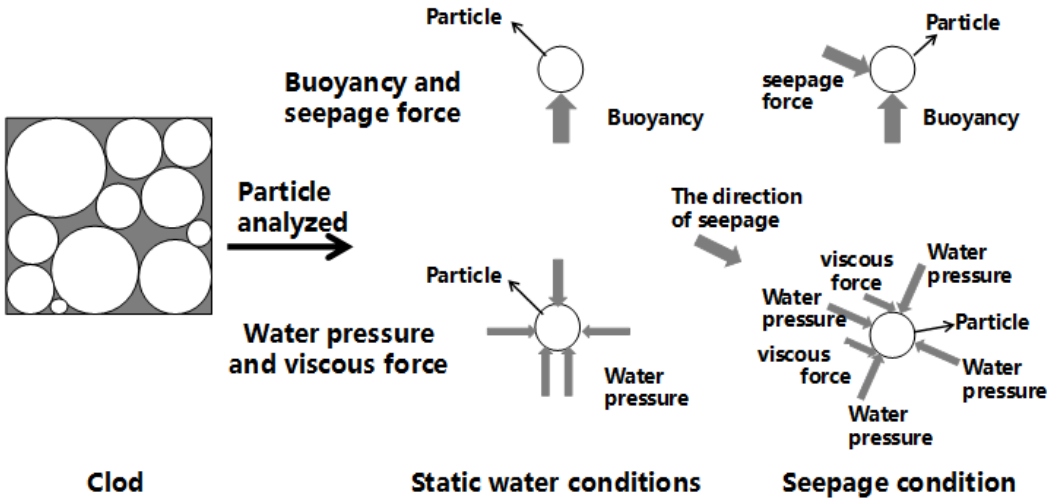


**Fig. 2 Two kind of force stressed on the soil particle**

To sum up, the definition of seepage force is put forward based on the above stating: Under seepage condition (or flowing condition) the water would load on the soil particles. Such load in the unit volume of soil cold consists of two parts. The buoyancy is the one part, and the seepage force is the rest part.

## Soil particle and soil clod analysis based on the phenomenological characteristics

Based on three layers of phenomenological characteristics mentioned above, water in soil mechanics shows two ways of the effect on the different mechanical objects while stress analysis was carried out on the soil particles or the clods. The third layer of phenomenological characteristics can help analysis the force of water putting on the soil particle in the system consist of buoyancy and seepage force when regarding soil particle as the research object. And the second phenomenological characteristics according to the above can help study the force condition of soil clod with pore pressure and effective stress analysis. The difference and correlation of the two methods will be illustrated with a simple example. It is the judgment of critical hydraulic gradient of soil flow on surface of cohesionless soil.

**(1) Seepage force analysis method with soil particles as the study object**

Seepage force analysis is used for studying soil particle under the soil flowing condition. As shown in Fig. 3, when the vertical upward seepage happens in soil, the soil particle in the soil clod is forced by the vertical gravity and vertical upward buoyancy put on. At the same time, due to the effect of

seepage water, soil particle will inevitably suffer the vertical seepage force. The two components together with the effective stress of soil particles are balanced. According to the mathematical model of seepage force in the volume of soil cold, the soil particle stress vertical balance can be set up:

$$\sigma' A = W_s - F_b - J = G_s V_s \gamma_w - V_s \gamma_w - i\gamma_w V = \gamma_w V[(G_s - 1)(1-n) - i] \quad (1)$$

Where: $\sigma'$—— Effective stress loading on the particles;

$A$——Area of the end of the infinitesimal clod;

$W_s$——Gravity of particles in the infinitesimal soil clod;

$F_b$——Buoyancy of particles in the infinitesimal clod;

$J$——Seepage force of particles in the infinitesimal clods;

$G_s$——Proportion of soil particles;

$V_s$——Volume of soil particle;

$\gamma_w$——Specific gravity of water;

$i$——Hydraulic gradient of infinitesimal clod;

$V$——Volume of infinitesimal clod;

$n$——Porosity of infinitesimal clod.

When the soil flowing occurs, the effective stress is zero. The critical hydraulic gradient can be easily got through the relevant formula translation:

$$i_{cr} = (G_s - 1)(1-n) \quad (2)$$

Where: $i_{cr}$——Critical hydraulic gradient of soil.

The third layer of phenomenological characteristic help deriving the balance. Through the analysis, the soil is the calculated range while the soil particle is the real loaded object.

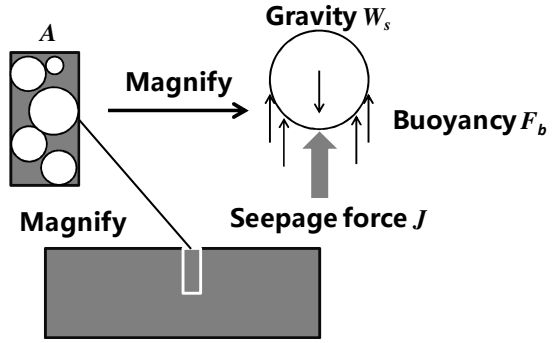


**Fig. 3 Effective stress analysis method based on the soil particle**

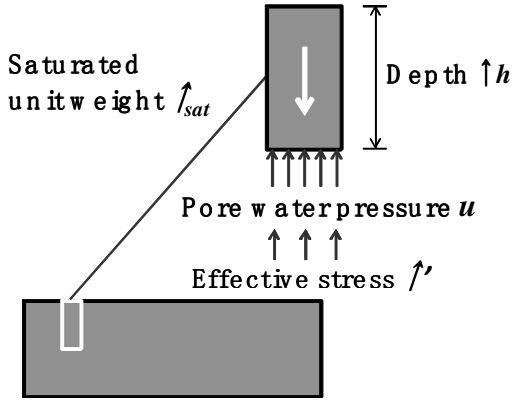


**Fig. 4 Effective stress analysis method based on the soil clod**

**(2) Effective stress and pore pressure analysis method with soil clods as the study object**

Similarly, the critical hydraulic gradient also can be analyzed with effective stress on soil clod.

There is a soil clod in the soil surface as shown in Fig. 4 being regarded as the analysis object. Its depth is $\Delta h$, which is very close to zero in the numerical value. The clod can be seen as an infinitesimal volume. The total stress $\sigma$ at the bottom is $\gamma_{sat}\Delta h$, the pore pressure $u$ is $\gamma_w \Delta h + i\gamma_w \Delta h$. When vertical seepage occurred, at the condition of soil damage critical state, the effective stress is zero, which means that the pore water pressure is equated with the total stress at the bottom. That is:

$$\gamma_{sat}\Delta h = \gamma_w \Delta h + i\gamma_w \Delta h \quad (3)$$

Through some formula translations, the critical hydraulic gradient can be expressed as the ratio of effective weight of soil to specific weight of water:

$$i_{cr} = \frac{\gamma'}{\gamma_w} \quad (4)$$

Where: $\gamma_{sat}$——Saturated specific gravity of Infinitesimal clod;

$\Delta h$——Height of infinitesimal clod;

$u$——Pore water pressure of the infinitesimal clod of by at the bottom of it;

$\gamma'$—— Effective specific gravity of infinitesimal clod.

Although (4) and (2) type is different in form, but the same result can be got by comparing the nature indicators of soil:

$$i_{cr} = \frac{\gamma'}{\gamma_w} = \frac{\frac{(G_s - 1)\gamma_w}{1+e}}{\gamma_w} = \frac{(G_s - 1)}{1+e} = (G_s - 1)(1-n) \tag{5}$$

Where: $e$——Void ratio.

From stating above, the hydraulic gradient can be got with the different ways with effective stress analyzing. Although the form is different, the result is unified. Also, the effective stress and pore pressure analysis method with soil particle or clod as the study object is feasible can be approve

## Conclusion

The three layers of phenomenological characteristics in the concept of seepage force system are stated above. In this paper, the acting force of water flow is clearly distinguished in the modeling of soil mechanics. And the assumption of single-phase contact is emphasized, when the soil clod is the analyzed object. The assumption guarantees that the effect of water flow only performance on the pore pressure, thus the modeling system of pore pressure and effective stress can be established. Based on the perspective of soil particle, the effect of water flow can be divided into two components including buoyancy and seepage force. And then the mathematical significance of seepage force from soil mechanics is explained. The correlating analysis not only strengthens the understanding of soil mechanics concepts but also promote the maneuverability of calculation in seepage.

## References

[1] Zhongyi Chen, Jingxing Zhou, Hongjin Wang: *Soil mechanics* (Tinghua University Press, China 1994).

[2] Minghua Zhao: *Soil mechanics and foundation engineering* (Wuhan University of Technology Press, China 2009).

[3] Tinghao Lu: *Soil mechanics* (Hohai University Press, China 2005).

[4] Baolong Zhu, Jinjun Guo: *Soil mechanics* (Water Resources and Hydropower Reasearch of China Press, China 2011).

[5] Huaijing Zhang: *Soil mechanics* (China Machine Press, China 2011).

[6] Peiyi Lu: *Soil mechanics* (China Building Materials Press, China 2000).

[7] Chenghua Wang: *Principle of Soil mechanics* (Tianjin University Press, China 2002).

[8] Xiangdong Zhang: *Soil mechanics* (China Communication Press, China 2011).

[9] Ping Yang: *Soil mechanics* (China Machine Press, China 2005).

[10]Jinkun Li, Shimin Yu, Hongjin Wang: *Soil mechanics and foundation engineering* (Earthquake Press, China 1992).

[11]Chenghua Wang: *Soil mechanics* (Huazhong University of Science and Technology Press, China 2010).

[12]Zhenxing Zhao, Jianjing He: *Hydraulics(the second edition)* (Tinghua University Press, China 2010).

*Applied Mechanics and Materials Vols. 580-583 (2014) pp 619-622*
*© (2014) Trans Tech Publications, Switzerland*
*doi:10.4028/www.scientific.net/AMM.580-583.619*

# Finite element analysis of rock bolt foundation in metallurgical industrial plant

Mengxi Tan[1b] Hongbin Liu [2a]

[1] China University of Geosciences, beijing,China

[2] School of Civil Engineering, University of Science and Technology Liaoning, Liaoning, China

[a]binbinliu999@126.com, [b]441670016@qq.com,

**Keywords:** Rock bolt foundation; Foundation design; Static load test; finite element simulation

**Abstract.** Based on the application of Rock Bolt Foundation in metallurgical industrial plant foundation design, this paper utilized bolt deformation formulas that derived by Gu Shuancheng and others to calculate deformation of rock blot. The result is consistent with the experimental value, the authors can further verify the experimental and theoretical calculation value eventually by finite element analysis software ANSYS, which provides a reference for practical application of rock bolt foundation in metallurgical industrial plant.

## Introduction

Industrial plant is located in the seaside of Bayuquan Development Zone, which is a steelmaking continuous casting plant, rocks of this region possess a layer structure of shale. Large in density and slight slope, the bearing capacity of the bedrock is relative high. These plants adopt whole steel structure, its building area is approximately 150000 square meters, the height of plants can reach 65 meters, the converter charging span of crane beam is defined as heavy duty, which lifting load is 450 tons. According to practical condition of site, suppose that the foundations of plant employ the technique of traditional design into column foundations, however, it will inevitably lead to a waste of bearing capacity for rock subgrade. A large quantity of experimental date and analysis show that it is available to employ rock bolt foundation. In this case, rocks are taken as load bearing stratum, anchor erected in foundation base. Moreover, bedrock and foundation are connected into entirety to bear the moment so as to reduce the size of base and buried depth, which can save project cost.

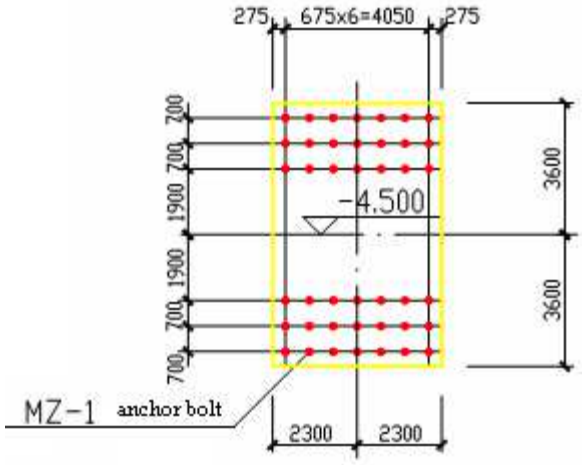


Fig. 1 Arrangement diagram of anchor bolt.

**Rock bolt foundation treatment**

Due to the plant structure is influenced by moment. Compared with others plans, the bolt can exert a better function when it is settled at the edge of foundation (Figure.1). Although calculation of bolt tension in the "Code for design of building foundation GB50007-2011" and "Code for design of high-rising structures GB50135-2006" accord the same set of formulas to obtain uplift capacity, calculations proceed without considering the force interaction between foundation and bedrock calculation, while actual bedrock owns a higher bearing capacity, one can ignore the compressive capacity of bolt. Therefore, the formula is applicable for the foundation with anchor bolt. Assignment of bolt for this project is relative unreasonable so that the author takes reaction of bedrock into account, which is reliable for the model.

**Single anchor uplift static load testing and theoretical analysis**

**Program of bolt detector and arrangement.** This static load testing commences with a ZY-50 type radial bogie, its operations are as follows: 1.Connecting the radial bogie with anchor bolts that to be measured, in addition, work-table of the hydraulic cylinder and bolts should be adjusted appropriately to make sure that bolts tolerate vertical load.2.Placing the value in the middle and it should be connected with pipe, then unscrewing the cover of hand pump.3. Pressing digital pressure gauge switch and adjusting to following state.4.Ensuring that all instruments are feasible, then the valve switch is placed in the "load" and "unload" position, which conducts pre-loading and unloading experiments.5.Since there is no issue, one can commence with the test of anchor bolt.6.It is desirable to turnoff gauge switch so that service life of battery can be prolonged after the test.7.Overloading is forbidden, digital pressure gauge can not exceed the maximum range.

In this construction the bedrock is mainly composed of moderate weathering rock, to reach its design elevation, bedrock is filled with 100~2000 mm concrete C15 as cushion. Bolt adopt two-stage Φ 32 hot rolled ribbed bar (HRB335), which diameter is 100mm and design depth of anchor rock is 4.0 m, afterward, pouring micro hole perfusion GJ type of secondary grouting material to guarantee the eigenvalues of a single anchor uplift loading is 130KN.

According to extract 5% of the total number for bolt, specify its position and check the site elevation for design of the foundation, bolts to be inspected in three days after perfusion.

**Bolt detector and theoretical calculation.**It is difficult to confirm uplift capacity and deformation of the bolt in engineering, furthermore, body material, rocks around the bolt, geometry characteristics of interface and physical properties of the bolt also effect its mechanics. At present, anchor design is still in state of experience and semi-empirical, for the acknowledge of mechanism in rock bolt is vague, it is especially complicated to estimate of the deformation and rigidity.

In this paper, the author employs the formula deduced by Gu Shuancheng, the total displacement of anchor S is divided into free section elastic displacement S1 and interface of relative shear displacement S2, expressed in a formula, the relationship can be written as $S= S_1+S_2$. Based on local deformation of theory, one can conclude ideal elastic-plastic load transfer model as the instruction, when drawing force is increased to a certain extent, surface of anchored rock and soil will gradually appear to current plastic condition. Before the capacity of anchor reach its ultimate capacity, the anchor rod section remains elastic. After a series of the deduction, the deformation of anchor bolt can be denoted by

$$S=[\frac{4L_1}{\pi E_s d^2}+\frac{4}{\pi D^2 E_a \beta}(\frac{1}{\beta L_b}+\frac{\beta L_b}{3})]p \qquad (1)$$

In which, P is the tension of the bolt, the freedom length of the bolt $L_1$ is 1.6m, the anchored segment of bolt $L_b$ is 4m, the diameter of anchorage D is 100mm, the interface tension of anchor in elastic limit is $p_e$, $E_s=2.06\times10^5 MP_a$, $E_r=3.25\times10^4 MP_a$.

$$\beta=\sqrt{\frac{4K_s}{DE_a}};E_a=\frac{E_r(D^2-d^2)+E_Sd^2}{D^2};K_s=\frac{3DE_a}{3\pi D^2E_a[S/P_e-4L_1/(\pi E_Sd^2)]L_b-4L_b^2}$$

On the basis of calculation, deformation of bolt can be figured out when the load applied to 52 kN, 78 kN ,104 kN, 130 kN ,156 kN, 182 kN ,208 kN, 234 kN and 260 kN. By extracting ten pillars of 34 bolts, one can make a comparison of its theoretical and experimental value.

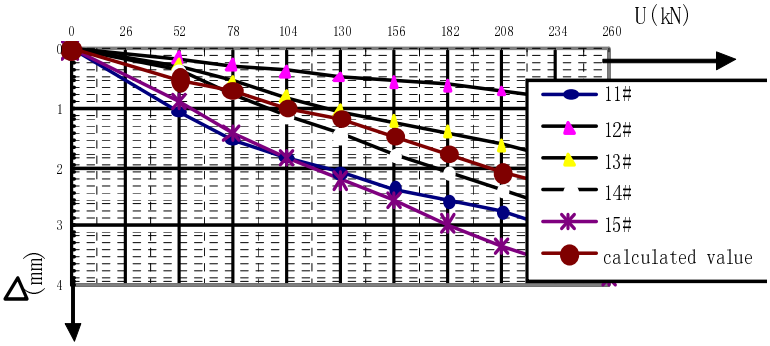


Fig.2 11-15# the curve of theoretical and experimental value U~Δ

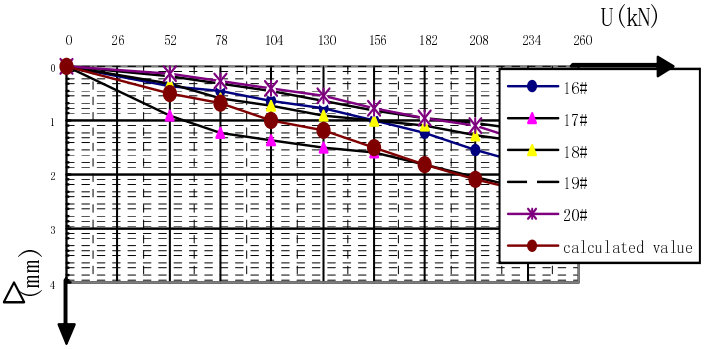


Fig.3 16-20# the curve of theoretical and experimental value U~Δ

By contrast the result obtained is in agreement with the experimental value, due to the distribution of shear stress along the anchor rod is uneven, anchor solid and rock interface between the limit of the shear strength and stiffness of bolt will generate a direct influence for stress distribution law, based on the factors as has been noted, it is difficult to determine bolt deformation directly by theory, bolt deformation formula inquires to be further improved. Meanwhile, specifics are to specific analysis, only by combination of theory with practice can ensure the safety of project.

**ANSYS finite element analysis**

The anchor bolt employs the element of LINK, Micro-swelling agent utilizes the element of PLANE42. Geometric parameters as follows: Freedom length of the bolt is 1600mm, anchored segment of bolt is 4000mm, diameter of anchorage is 100mm and its aperture is 32mm, diameter of the rock is 300mm. Mechanical parameters: Elastic modulus of rebar is $3.25\times10^4$MPa, the Poisson's ratio is 0.3, the strength of GJ Micro-swelling agent is equivalent with concrete C40, which elastic modulus is $2.06\times10^5$MPa, the Poisson's ratio is 0.27, elastic modulus of rock is $15\times10^9$MPa, the Poisson's ratio is 0.25. Graphs below plot the deformation of anchor after calculation:

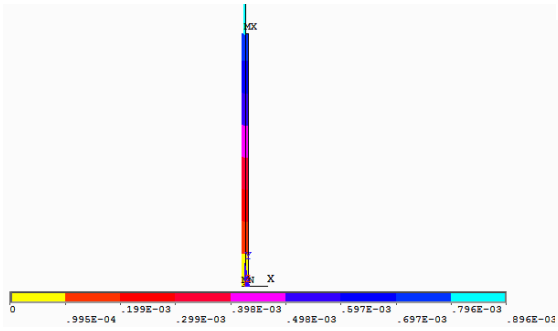


Fig.4 Y-Component of displacement ,Y=104KN

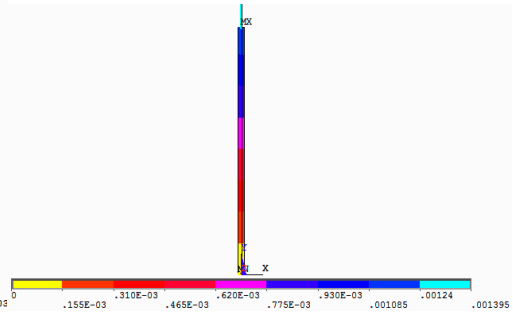


Fig.5 Y-Component of displacement,Y=156KN

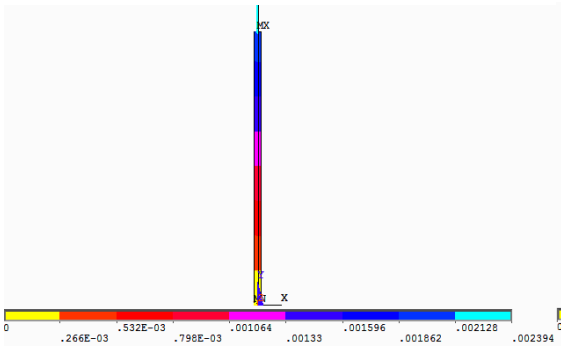


Fig.6 Y-Component of displacement ,Y=208KN

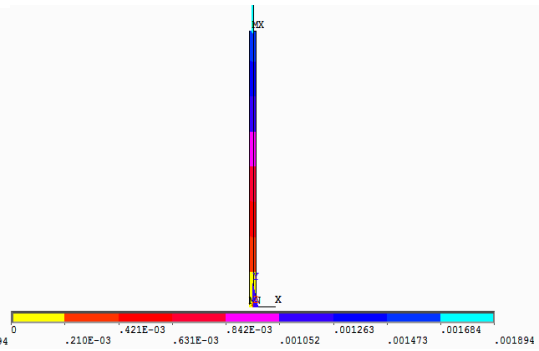


Fig.7 Y-Component of displacement ,Y=260KN

Through contrast one can conclude that the consequence fits into the computer simulation because of discreteness, reading error and initial eccentricity. Finite element analysis employs a simplified model, it is impossible to accurately simulate the stress of anchor rod, the main reason is that bonding effect between bolt and micro expansion agent is difficult to measure.

## Conclusion

The displacement of anchor bolt is a complex problem, there are many factors that can influence its deformation. These uncertain factors cause difficulties of simulation, to accurate calculation of the bolt deformation, either from theory or from practice are not possible. In this paper, result of the theoretical calculation is in line with the deformation value performed by ANSYS, moreover, the safety of anchor bolt is verified that provides a valuable reference for practical engineering. While bonding effect between bolt and micro -swelling agent are difficult to calculate and simulate, which deserves further research.

## References

[1] GB50007-2011,Code for design of building foundation[S] .In Chinese

[2] GB50135-2006, Code for design of high-rising structures[S] .In Chinese

[3] Shuancheng Gu, Genfei Ye and Xian Chen: Experiment on Limit Shearing Strength Parameters of Bolt Anchored Section， Coal Science and Technology Vol. 38(2010), p. 37

[4] Daocheng Wang: The Experiment Study of Anchor Inspection on Optical Fiber Sensor[D] .Xi'an University of Science and Technology, Xi'an ,2011

*Applied Mechanics and Materials Vols. 580-583 (2014) pp 623-627*
*© (2014) Trans Tech Publications, Switzerland*
*doi:10.4028/www.scientific.net/AMM.580-583.623*

# Laboratory Studies on Acoustic Emission Characteristics to Coal Dynamic Response under Variable Accelerative Load

Xinghui Liu[1,a *], [T]Chuanxiao Liu[1,b], Shuai Zhuang[1,c], Long Wang[1,d] and Shusen Lin[1,e]

[1]College of Water Conservancy and Civil Engineering, Shandong Agricultural University, Tai'an 271018, China

[a]wennuan2003@126.com, [b]lchuanx@163.com, [c]zhuangshuai6688@163.com, [d]wlo1988@aliyun.com, [e]sender2008@163.com

**Keywords:** Impact Load, Coal Failure, Acoustic Emission, Monitoring and Prediction

**Abstract.** To simulate the fracture of the coal under impact load, uniaxial pressure test of coal which retrieved from KongZhuang coal mine-DaTun coal and electricity Company of China coal group was done in the manner of strain control which rest with a function of uniform variable acceleration. Through researches on the stress-strain relationships and acoustic emission characteristics, the relationship between ring count rate and time series was founded, and the process before failure of coal was divided into four stages: low-level ringing count rate, higher level, highest level and peaceful period. Through the comparison and analysis, it is founded that acoustic emission characteristics in the stage of higher level of ringing count rate can be regarded as a basis for the prediction of coal fracture. According to three obvious rise stages of acoustic emission signal in the process before failure of coal, growth factor of climbing speed $\mu$ is introduced and the values are calculated between 2 to 4, and it is conferred that the value of $\mu$ is proportional to compressive strength of coal and loading rate. It is of great significance for the prediction of coal fracture by acoustic emission characteristics in the stage of new cracks.

## Introduction

The rock acoustic emission is a phenomenon that rocks release strain energy in pulse wave forms when its creek is extended. Since American scholar Obert discovered this phenomenon in the 1930s, study on acoustic emission is gradually developed and it is also applied in the structure engineering and mine monitoring in foreign countries. Chinese scholars conducted many studies on the technology of rock acoustic emission since 1980s. Because of its low technique requirement, simple and intuitive analysis mode, fast analysis, good real-time performance, easy master and operation, the technology of rock acoustic emission has been widely used in the mine ground pressure research and it has become one of the main means in the modern engineering monitor.

The signals of rock acoustic emission are always obtained through conventional uniaxial or triaxial pressure test, which contain abundant information includes rock damage and rupture. In engineering practice, the coal seams at the working face of deep mine usually bursts due to the impact which is caused by high stress disturbance on the top of the face. Study on the coal acoustic emission is widely developed in recent years and varieties of research thinking and analysis methods are adopted. So, plenteous research achievements are achieved. However, not so many scholars study on the effect of impact to coal, and existing prediction of coal burst caused by surge pressure in engineering are more depends on the experience. The failure of coal at working face caused by surge pressure is simulated approximatively through the coal specimen uniaxial pressure test under variable accelerative control. It has vital significance in the coal seam failure monitor and prediction to analyze the acoustic emission signals and to resolve the failure process and characteristics of signals.

**The coal specimen acoustic emission test under uniaxial pressure**

The diameter of the cylindrical coal specimen is 48mm and more details can be seen in Table.1.

Table.1 Numbers and heights of specimens

| Number | Height（mm） |
|---|---|
| Coal 01 | 100 |
| Coal 02 | 90 |
| Coal 03 | 76 |

In the test, the coal specimen is loaded through SAW-2000 Electro-hydraulic Servo- controlled Rock Mechanics Testing System and the acoustic emission signals are received by AE21C Acoustic Emission Instrument.

In the uniaxial pressure test, the specimen is under a dead load at first and then, to simulate the actual coal seam failure under surge pressure in the engineering by the strain-controlled method of ramped acceleration function. First, the coal specimen is applied a constant load in 2kN to simulate the dead load state of coal seam in stable period. From the first 30 seconds, the strain is changed based on the variety of the $\varepsilon = \frac{1}{6}\alpha t^3$ function. That is to say, the designed strain is changed in a ramped acceleration way at the acceleration $a = \alpha t$.

The controlling coefficient $\alpha$ of the coal sample01, 02, 03, is 0.003, 0.002 and 0.002 separately and all of them are under variable accelerative strain control to simulate the impact approximatively.

**The result and analysis of the coal dynamic response test**

At the beginning of the 30 seconds before the set function works, the constant load value is 2kN, the strain value is 0 and acoustic emission signal is not produced. During the period, time from the beginning of the strain controlled load to the damage of the specimen is very short. The dynamic load value gets the highest at almost 12s, 13s and 14s, and the specimen is damaged.

**The strain-stress relationship.** As is shown in Fig.1, the strain-stress relationship of the specimen follows the typical rock strain-stress relationship law.

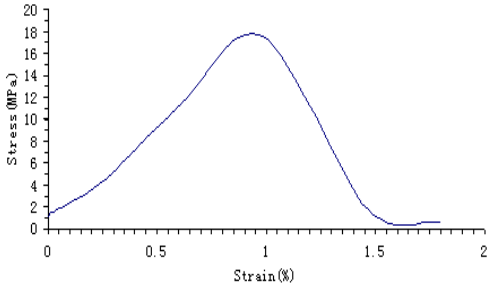


(a) coal01

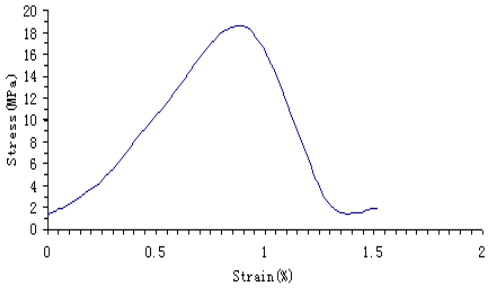


(b) coal02

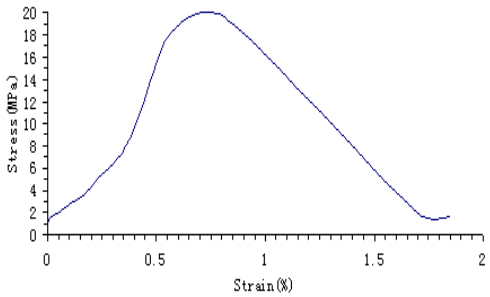


(c) coal01

Fig.1 Relations of strain-stress for coal

According to the conversion formula provided from *Concise Handbook of Engineering Geology*, the uniaxial compressive strength value of non-standard specimen is corrected and the translated values can be seen in Table.2.

Table.2 Compressive strength of standard specimens

| Number | Coal 01 | Coal 02 | Coal 03 |
|---|---|---|---|
| Compressive strength (MPa) | 18.1 | 18.3 | 19.3 |

It can be inferred from the relationship of the compressive strength value and the strain value at the peak point of the stress that, the quantity of the internal cracks of coal 03 is the smallest and the degree of the joint is the lowest and it is the hardest. The crack development degree of coal 01 and coal 02 is close.

**The relationship of the ring count rate and the time series.** In the application of the acoustic emission techniques, the ring count is considered to be a parameter that can best reflect the variation of the material property in a variety of parameters. In the forecast of rock break, the monitor and prediction are achieved through parameter changes with time series. So, it is analyzed mainly through the relationship of ring count and time series. The results are as follows:

When the load maintains in 2kN, there is little acoustic emission or not and it can be considered that there is no acoustic emission produced. The ring count- time series curves before the specimen damaged are depicted in Fig.2.

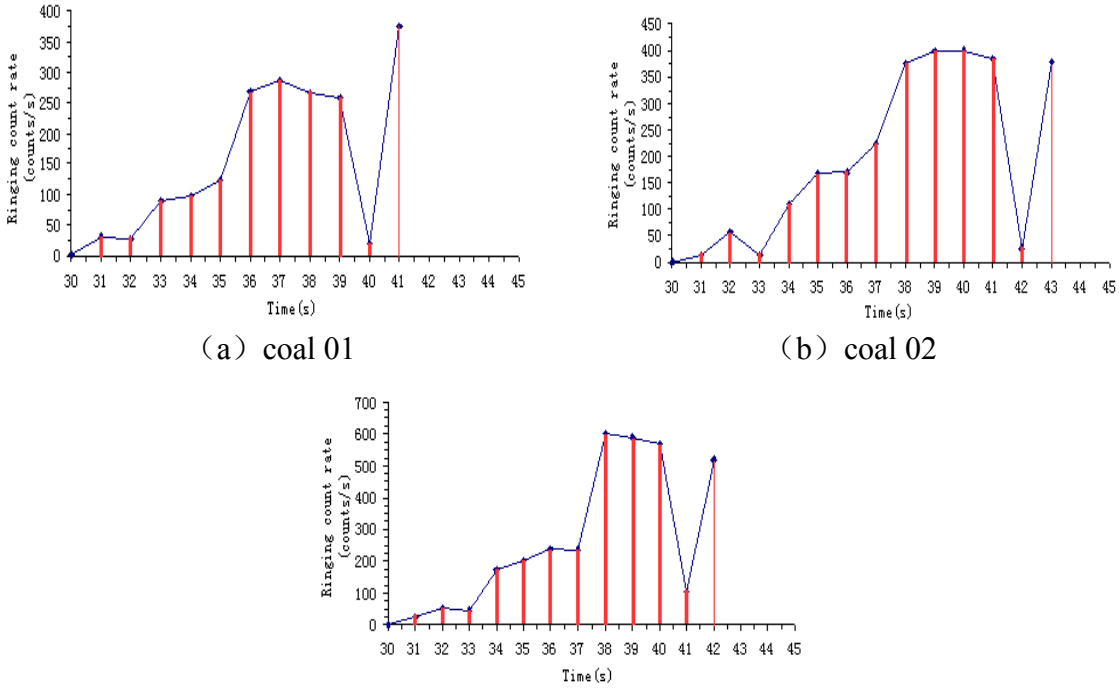


（a）coal 01 （b）coal 02

（c）coal 03

Fig.2 Changes of ring-down accumulation counts over time for coal prior failure

The ringing count rate-time series curves of three specimens are quiet similar and four obvious stages are founded: ring count low level stage, higher level stage, highest level stage and peaceful stage. Thus, the typical ring count- time series cure can be described in Fig.3.

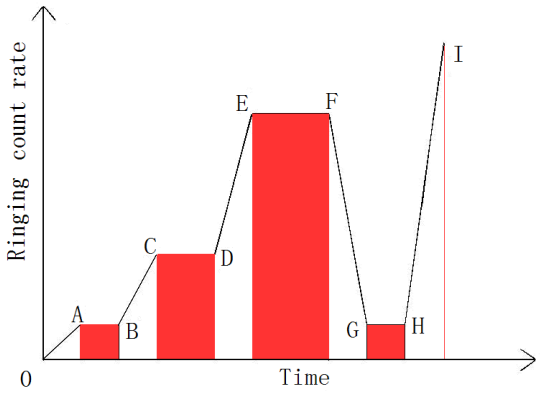


Fig.3 Diagram of typical changes of ringing count rate over time for coal under impact load

In the application of engineering prediction, the signals at peaceful stage are not suitable to regard as a characteristic signal to predict the coal damaged because coal is destroyed very soon after peaceful stage. If regard the signals at low level stage as monitoring signals, it may lead to false alarm. This is because the signal level is low and duration is very short, and the signals can be disturbed by the messy and irrelevant ones easily. According to the comprehensive analysis of the signal characteristics and time series, it is reasonable to regard signals at higher level as basis of coal failure prediction. During this period, the ringing count rate begins to appear continuous signal, maintains a lower level after rise, and rises up to a higher level after a short time. This time could be regarded as forecast period.

**The analysis of growth rate of acoustic emission signal.** The coal is damaged very soon after the peaceful stage and before this stage, the curve of ring count rate and time series has three obvious upward phrases. The mean upward rate of each phrase is defined as $k_1$, $k_2$, $k_3$ by the time order. The $k$ value calculated by test data can be seen in Table.3.

Table.3 Rates of mean in different rise stages

| | $k_1$ (counts·s-2) | $k_2$ ( counts·s-2) | $k_3$ ( counts·s-2) |
|---|---|---|---|
| Coal 01 | 29 | 61 | 145 |
| Coal 02 | 28 | 64.5 | 104 |
| Coal 03 | 26.5 | 127 | 365 |

It can be known from Table.3 that the $k$ value double increases with time, i.e., the ring count rate double increases at each stage. Average growths $\mu$ of each specimen can be seen as follows: $\mu_{01} = 2.239$, $\mu_{02} = 1.958$, $\mu_{03} = 3.832$. The interval of the $\mu$ value is (2, 4) and this means each stage ring count rate is 2 to 4 times to its previous one.

Combined with compressive strength of each specimen and the analysis of loading rate, conclusion can be inferred as follows: for the coals have the same compressive strength, the higher loading rate, the bigger $\mu$ value; for the coals under the same loading rate, the bigger compressive strength, the bigger $\mu$ value. That is to say, the compressive strength and loading rate have direct ratio relation with $\mu$ value separately.

Due to the limitation of the numbers of specimen and the loading rate, deep relationships of the growth multiple $\mu$, coal compressive strength and the loading rate need to be studied further.

## Conclusions

(1) The simulant impact test of coal is achieved through variable accelerative strain controlled method and it is more consistent with practical engineering situation.

(2) The characteristics of acoustic emission signals are analyzed and four obvious stages before coal damaged are founded: Ringing count rate's low level stage, higher level stage, highest level stage and peaceful stage. And the relationship of coal ringing count rate and time under variable acceleration load is gained.

(3) The ringing count rate at higher level stage can be regard as forecast basis of coal failure. The ringing count rate begins to appear continuous signal, maintains a lower level after rise, and rises up to a higher level after a short time and maintains stable. This time could be regarded as forecast period.

(4) The growth multiple $\mu$ of acoustic emission signal rate is introduced and the interval of the $\mu$ value is (2, 4). It can be inferred that the $\mu$ value has direct ratio relation with the compressive strength and loading rate separately. This is of great significance to predict the coal failure through ring count rate at higher level stage.

**References**

[1] Jan Vilhelm , Vladimír Rudajev , Tomáš Lokajíček , Roman Živor: Application of autocorrelation analysis for interpreting acoustic emission in rock. International Journal of Rock Mechanics and Mining Sciences, 2007,45(7):1068-1081.

[2] V. Rudajev , J. Vilhelm , T. Lokajíček: Laboratory studies of acoustic emission prior to uniaxial Compressive rock failure. International Journal of Rock Mechanics and Mining Sciences, 2000,37(4):699-704.

[3] Xinming Peng, Youhong SUN, Anning LI: Application present of the rock acoustic emission technique. World Geology, 2000,19(3):303-306.

[4] Yong Chen: Application of acoustic emission techniques to rock mechanics research. Acta Geophysica Sinica, 1997,20(4):312-322.

[5] Chun-an Tang: Numerical simulation of AE in rock failure. Chinese Journal of Rock Mechanics and Engineering, 1997,16(4):368-374.

[6] Ru Zhang, Heping Xie, Jianfeng Liu, et al: Experimental study on acoustic emission characteristics of rock failure under uniaxial multilevel loadings. Chinese Journal of Rock Mechanics and Engineering, 2006,25(12):2584-2588.

[7] Hu Qin, Gun Huang, Weizhong Wang: Laboratory studies on Acoustic Emission characteristics to whole process of compressed coal petrography deformation and failure in different moisture content. Chinese Journal of Rock Mechanics and Engineering, 2012,31(6):1116- 1121.

*Applied Mechanics and Materials Vols. 580-583 (2014) pp 628-631*
*© (2014) Trans Tech Publications, Switzerland*
*doi:10.4028/www.scientific.net/AMM.580-583.628*

# Mechanical model of pile-soil work together

Sujuan Zhang

Civil Engineering School, Shandong Jiao Tong University, Jinan, Shandong, 250023, China

Zhangsujuan2007@sina.com

**Keywords:** pile-soil-foundation, mechanical model, the analytic method

**Abstract.** Come up with of pile-soil-(foundation) pile cap interaction grounded upon penetration deformation of pile ends and compression of soil between piles. Hyperbolic model is adopted to simulate the development of tip resistance and side resistance in accordance with deformation to reflect the nonlinearity of pile-soil work, Boussinesq solution is utilized to calculate the stresses generated in soil by foundation (pile cap)plate, Mindlin stress solution is used to calculate the stress produced in the soil between piles by side resistance and end resistance, and the stress of soil is the superposition of the two solutions.

## Introduction

## The play function of tip resistance and side friction with the change of penetration deformation

In view of previous scholars' research results, this paper use hyperbolic function to simulate the development of side resistance, compared with the relative displacement of pile-soil, and the development of pile tip resistance with normalized penetration deformation.

(1)Normalized settlement curve of pile tip resistance:

$$q_{cal} = \frac{K_p\left(\frac{s}{d}\right)}{n + m\left(\frac{s}{d}\right)} \tag{1}$$

In this formula: $K_p$ is correction coefficient, $s$ is amount of pile tip penetration, $d$ is diameter of pile, $m$ is the reciprocal of ultimate pile tip resistance $m = 1/q_{pcal}$ , $n = (s/d)_{ref}/q_{pcal}$ ,in most cases, median is more acceptable, namely, $(s/d)_{ref} = 0.235$, it can also be determined by fitting formula through experiment measuring. Without measured data, it may also be determined by making the following formula as a reference in standard value of pile end tip resistance.

$$q_{cal} = K_p\left\{\frac{\left(\frac{s}{d}\right)}{0.30+\left(\frac{s}{d}\right)}\right\}^{\frac{0.44}{0.33}} q_{s\tan dard} \qquad \frac{s}{d} \le 0.2 \tag{2}$$

(2) Similar to pile tip resistance, hyperbolic function is adopted to simulate the play of side resistance with pile-soil relative displacement:

$$f = \frac{K_S z}{a_f + b_f z} \tag{3}$$

In this formula: $K_s$ is correction coefficient, $f$ is frictional resistance, $z$ is pile-soil relative displacement, $a_f, b_f$ is constant. $b_f$ is reciprocal of ultimate frictional resistance of pile side $b_f = 1/f_{uit}$ , parameter $a_f$ is reciprocal of stiffness of initial tangent, the value is usually dependent upon measured data, on Hirayama's advice, the value can be $a_f = z_{reff} / f_{uit}$ ,and $z_{reff}$ can be 0.004Ds(Ds is diameter of pile); it can also be determined by fitting formula through test results.

**The determination of stress in soil**

2.1 The distribution assumption of foundation (pile cap) in sharing the stress

Assume that soil stress distribution of calculation unit in calculated foundation (pile cap) is rectangular footing with uniform distributed loading.

2.2 Layered property of soil and distribution assumption of side friction

Similar to load transfer method, the pile is divided into several segments, each of which is a calculation unit. Considering different soil properties, adopting different calculation parameters, the soil layers in calculated areas are set as calculated areas accordingly. when calculating, in accordance with the different soil properties in each calculated layer, we choose calculation properties of different soil properties. For the sake of analysis, two soil layers are considered, soil layers between piles and bearing course at pile end. As for the soil layers under the surface of pile end, they also receive stratified treatment when calculated.

2.3 The determination of additional stress in soil

Soil stress consists of three parts, namely, additional stress generated in soil by the load-sharing of foundation (pile cap), additional stress produced in soil by side friction and that brought out by pile tip resistance in soil. Elastic solution is still used to analyse the stress in soil layers in the situation of pile-soil interaction.

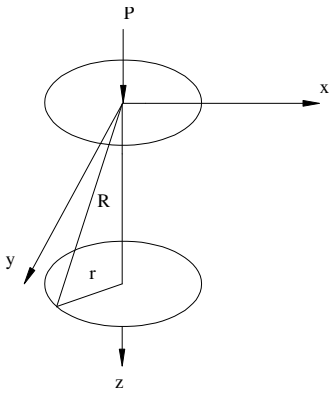


Fig. 1, Schematic analysi diagram for the surface stress of semi-infinite body

2.3.1 The solution of additional stress produced by bearing sheet in soil

Calculate the additional stress generated by foundation (pile cap) in soil, (Bossinesqsolution[1]) is used, which can calculate the vertical concentrated forces imposed on the elastic surface of semi-infinite body. See Fig. 1, under the action of vertical force, the stress components of additional stress in vertical direction is:

$$\sigma_z = \frac{3P}{2\pi} \frac{Z^3}{\left(r^2 + Z^3\right)^{\frac{5}{2}}} \tag{4}$$

The stresses of each point under foundation(pile cap) can go through integral solution with above formula, then additional stress in soil produced by foundation(pile cap) is defined.

2.3.2 The solution of additional stress generated by side friction and pile tip resistance in soil

(1) Geddes stress solution

To calculate the stress and settlement under soil layers of a single pile and piles, Geddes stress solution, integral expression of Mindlin stress solution, is employed. Geddes stress solution assumes that soil is a semi-infinite body which is isotropic, uniform and elastic, Geddes holds that the load on pile top of a single pile p consists of three parts, see See Fig. 2,

$$P = P_b + P_\gamma + P_t = P_b + P_\tau \tag{5}$$

$$P_b = \alpha P \tag{6}$$

$$P_\tau = \beta P \tag{7}$$

$$P_t = (1-\alpha-\beta)P \tag{8}$$

In this formula:

$P_\tau$ is aggregate side friction, $P_\gamma$ is side friction of rectangular distribution（kN）, $P_t$ is resultant force of triangular distribution side friction(KN); $\alpha, \beta$ is load distribution coefficient of pile tip resistance and rectangular distribution side friction respectively.

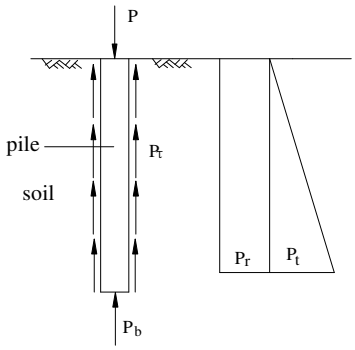

Fig. 2, Schematic analysis diagram of a single pile stress

Under action of the above internal forces, vertical additional stress of any point M(r,z)in soil can be solved according to the following formula, see Fig. 3,

$$\sigma_z = \sigma_{zb} + \sigma_{zr} + \sigma_{zt} = \frac{P_b}{L^2} I_b + \frac{P_r}{L^2} I_r + \frac{P_t}{L^2} I_t \tag{9}$$

In this formula:

$L$ is embedded depth of pile, $I_b, I_\gamma, I_t$ is additional stress coefficient of any point in soil under action of pile tip resistance, frictional resistance of rectangular distribution and frictional resistance of triangular distribution respectively. Geddes also gives the vertical additional stress coefficient in soil.

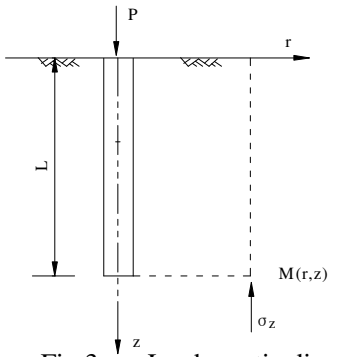

Fig.3, r,z,L schematic diagram

(2)additional stress produced by side friction in soil

The intensity of side friction can be fixed with the formula (3). Suppose side friction is evenly distributed in the calculated pile, pile-soil relative displacement is determined by the middle point of calculation unit of pile and that of the corresponding calculated soil layer.

Adopting integral expression of Geddes on Mindlin stress solution to solve the additional stress produced by pile in the soil, because the given side friction is the average side friction of each pile,

when using the formula, superposition is imperative, see Fig. 4, pile is divided into n units, top depth of the unit k is ht, k, bottom depth is h, k, then additional stress produced by the frictional resistance of unit k in points of the soil is $M(h_t,k)$-$M(h_b,k)$.

Function M (h) indicates the pile with the length, the pile side resistance of which is the additional stress generated by the average frictional resistance of unit in points of the soil, and additional stress generated by side friction of the whole pile in points of the soil is

$$\sum_{i=1}^{n} M\left(h_{t,i}\right) - M\left(h_{b,i}\right) \tag{10}$$

In this formula:

M (h) can be solved by Geddes based upon side friction influence coefficient formula of Mindlin solution.

(3)additional stress set off by pile tip resistance in the soil

Formula (1) is used to determine the intensity of pile tip resistance. As for the additional stress set off by pile tip resistance in the soil, integral expression of Geddeson Mindlin stress solution is used.

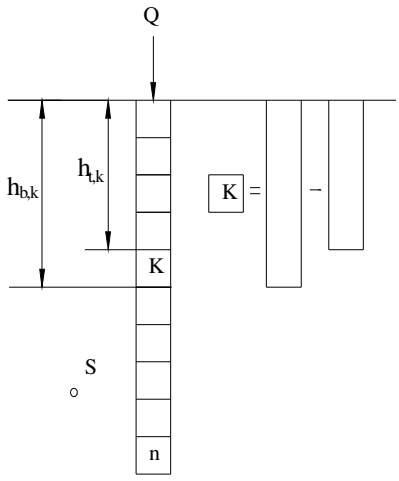


Fig. 4, K additional stress calculation produced by side friction of a single pile in points in soil

**Determination of soil deformation**

After additional stress of soil is fixed, additional stress layer-wise summation method is used to determine soil deformation. Compression modulus, which is defined according to e～p curve, is helpful in reflecting the nonlinearity of soil.

**Summary**

This paper puts forward stress model based upon micro pile-soil-foundation (pile cap) interaction, analyzes different stress stages and calculation method of foundation sedimentation value in each stage. Based upon penetration deformation theory, related calculation program is developed in accordance with pile-soil interaction.

**References**

[1] Shu Xiang, Yuan Li-min. Unified approach to the Calculation of Single Pile Settlement Based Upon Geddes Formula[J]. Industrial Architecture, 1998

[2]China Academy of Building Research. JGJ94-2008 Technical Code For Building Pile Foundations[S]. Bei Jing: China Architecture and Building press, 2008

[3] Hu Peng-fei, Zhang Zai-ming. Integral of Mindlin's Stress Formula by Mathematics Software and Its Application in Geotechnical Engineering [J]. Geotechnical Engineering Technique, 2008

*Applied Mechanics and Materials Vols. 580-583 (2014) pp 632-635*
*© (2014) Trans Tech Publications, Switzerland*
*doi:10.4028/www.scientific.net/AMM.580-583.632*

# Mechanics analysis of flexible base Pavement Structure

Liya Su

Architecture and Civil Engineering School, Inner Mongolia University of Science and technology, Baotou, 014010, China

suliya1@.imust.cn

**Keyword:** Asphalt pavement; Flexible base; Elastic modulus; Reasonable thickness

**Abstract.**With the rapid development of traffic cause in our country, the operating requirement of driving load factors to pavement structure become higher and higher. The Semi-rigid base asphalt pavement structure exposed some defects and shortcomings, so the study of flexible base asphalt pavement structure is put on the agenda under the circumstances.Based on the research achievements at home and abroad of the existing asphalt pavement structure , choosing different elastic modulus and thickness to calculate and analyze the flexible base by ANSYS, gaining the law and trend of mechanics response (the vertical displacement and tensile stress) about pavement structure for the flexible base pavement of each layer foundation to provide the design reference.

## Introduction

The semi-rigid base asphalt pavement structure of domestic traditional appear constantly early damage problems such as local network crack, pavement crack and push, which affect seriously the our country development of transportation and economy, so flexible base have good development and application prospect [1], and the basic types pavement structure has been used widely. According to foreign experience, it has the some advantages but the semi-rigid base is not ,and overcome some shortcomings of the semi-rigid base, but domestic research has just started in this field. For that reason, further systematic research the flexible base asphalt pavement structure for our country development of road pavement structure has the profound significance [2].

## Establishment the finite element model of flexible pavement

Pavement structure is actually a three-dimensional engineering structures can bear any form load, so the best model describing the road system work is the 3D model [3] as shown in Fig.1. The concrete form of flexible base pavement have many kinds, which can be roughly divided into surface course, base course, subbase and soil matrix.

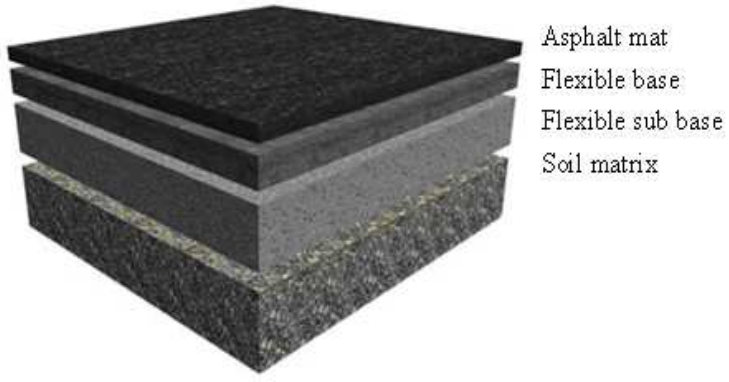


Fig.1 A typical flexible base asphalt pavement structure

In order to apply the above calculation model and finite element method to analyze the force mechanism of flexible base asphalt roadbed by ANSYS, the material properties and the structure characteristics of the model for the following assumptions: the layers are continuous, completely

elastic, homogeneous and isotropic; the next layer is infinite in the horizontal direction and vertical direction; layers contact condition for completely continuous; and the weight of each layer was Ignored[4].

Model geometry size and the actual size is similar, the road width for 6m, the base thickness for 6 m and the length along road direction for 7m. According to the design specifications of highway asphalt pavement (JTGD50-2006) [5] known that standard axle load for BZZ -100, the tire ground pressure for 0.7MPa, when the radius of circle for 10.65cm, two rounds of center distance for1.5cm*10.65cm. In order to calculate conveniently, the wheel load is simplified to square uniformly distributed load for19 cm*19 cm, contact area for 361 square centimeters and double center distance for 32 cm. The entity model after the mesh as shown in Fig.2.

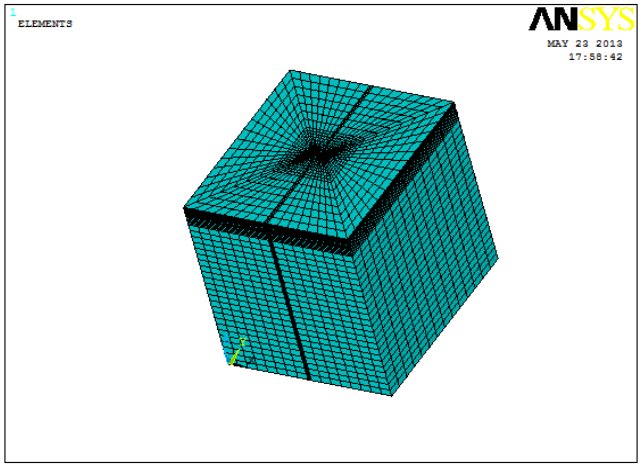


Fig.2 Grid Meshing by ANSYS

**Mechanics effect of Elastic modulus for pavement structure**

Changing the elastic modulus to study the change rules of deflection value and stress under the condition of the flexible base thickness unchanged,the rustle as shown in Tab.1, Fig.3 and Fig.4.

Tab.1 The structural parameters of the flexible base for asphalt pavement

| | elastic modulus(MPa) | thickness (cm) |
|---|---|---|
| asphalt concrete pavement | 1400 | 17 |
| flexible base | undetermined | 23 |
| flexible subbase | 800 | 30 |
| soil matrix | 60 | 600 |

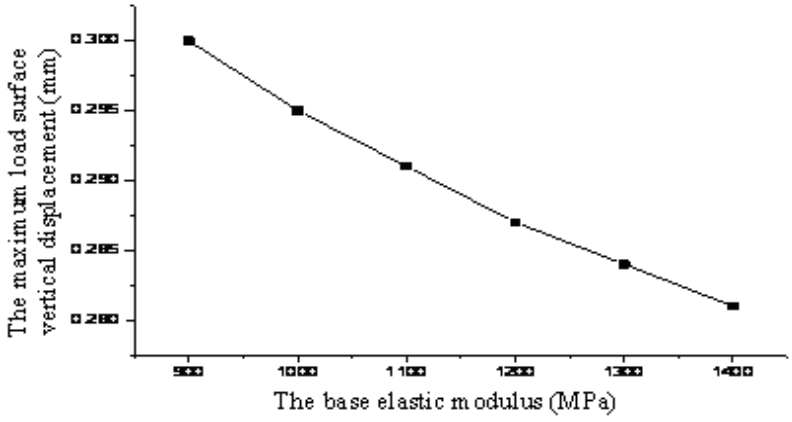


Fig.3 The relation of base elastic modulus and maximum load surface vertical displacement

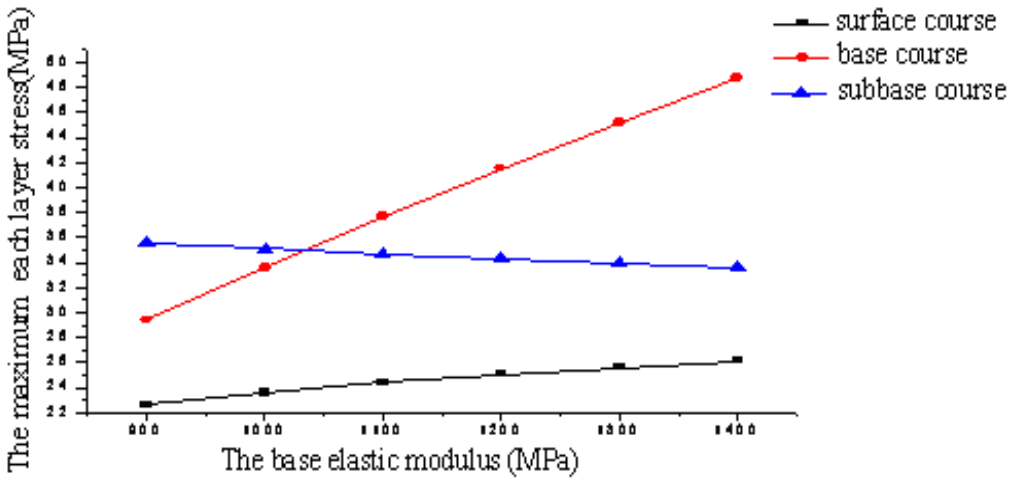


Fig.4 The relation of base elastic modulus and maximum each layer stress

The deflection value of road surface and the elastic modulus of flexible base meet to linear relationship. With the increase of elastic modulus about flexible base materials, the deflection value of road surface decreases gradually as shown in Fig.3. The tensile stress increased by 15.4% at the bottom of the surface layer, tensile stress increases 0.93 times at the bottom of base layer, and tensile stress decreases by 6.8% at the bottom of the subbase as shown in Fig. 4.

**Mechanical effect of the basic thickness for pavement structure**

Changing the flexible base thickness to study the value of deflection and stress under the condition of the elastic modulus unchanged, the result as shown in Tab.2,Fig.5 and Fig.6.

Tab.2 The structural parameters of the flexible base for asphalt pavement

| | elastic modulus(MPa) | thickness (cm) |
|---|---|---|
| asphalt concrete pavement | 1400 | 17 |
| flexible base | 1200 | undetermined |
| flexible subbase | 800 | 30 |
| soil matrix | 60 | 600 |

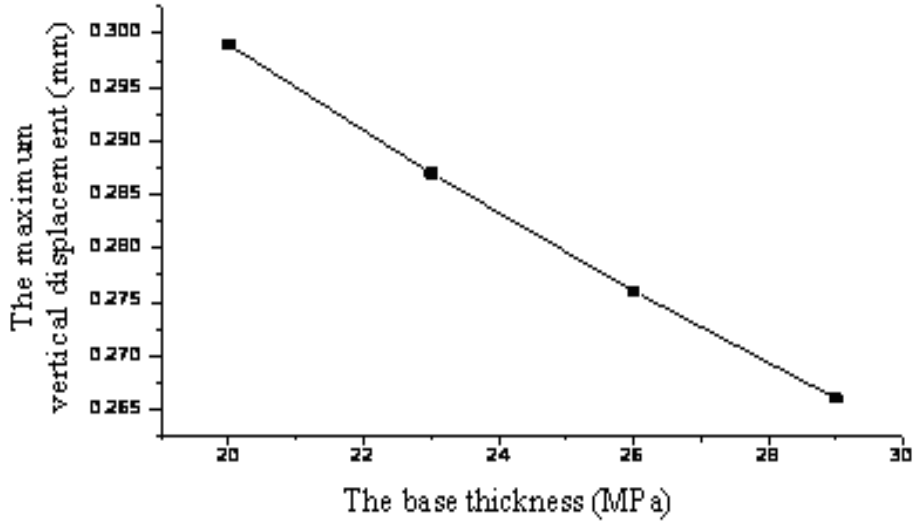


Fig.5 The relation of base thickness and maximum vertical displacement

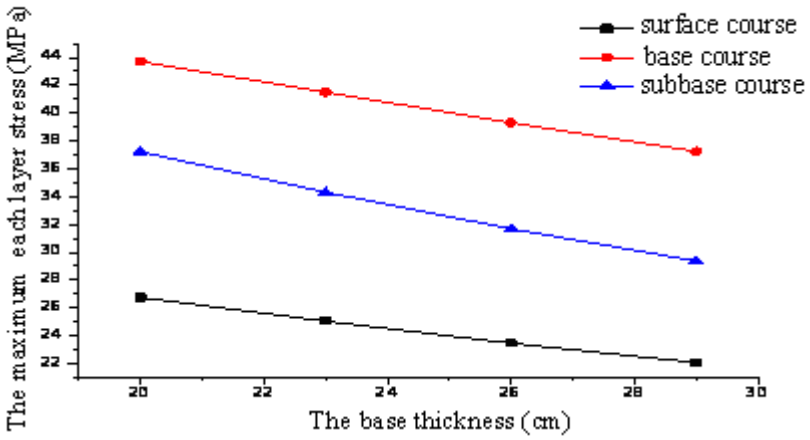


Fig.6 The relation of base thickness and maximum each layer stress

Fig.5 shown that the influence of flexible base thickness and the influence of elastic modulus to road surface deflection is the same, and Fig.6 shown that the increase of base layer thickness will make the tensile stress decrease in different degree at the bottom of each layer.

## Conclusion

Mechanics analysis of flexible base asphalt pavement structure by the ANSYS. When select different elastic modulus and thickness of flexible material, analysis and checking calculation the mechanical response of various design parameters on pavement under the traffic load (stress and displacement component).Through calculation and analysis get the following conclusions:

The influence of structural base elastic modulus for the mechanics index is obvious, The increases of base elastic modulus lead to the maximum vertical displacement reduced,which indicate the bigger the material modulus, the smaller the deflection value. In order to make the large deformation of pavement structure was not produced , the use of materials need have enough modulus.Because the changes of base modulus can affect the tensile stress at the bottom of each layer, the increased of base modulus will make tensile stress at the bottom of base layer increase.

The increase of the base thickness lead to the value of pavement structure deflection depress, and the base thickness increase also can make the tensile stress have the different reduction at the bottom of each layer.

## References

[1] Huan WANG.Analysis on structure mechanical characteristics of the flexible base asphalt pavement [D].Wuhan University of Technology,2010.06.

[2] Yiru LIU.Research of flexible base asphalt pavement structure design[D].Hebei University of technology, 2007.06.

[3] Peng LIN.Analysis on reasonable thickness and horizon of semi-rigid base[D],Tianjin:Hebei University of Technology, 2010. 06.

[4] Bo YANG,etc.Finite element analysis on three dimensional viscoelastic of the flexible base asphalt pavement [J].Highway Engineering ,2009,34(3):58-63.

[5] Specifications for Design of Highway Asphalt Pavement (JTGD50-2006)[M].Industry standard of the People's Republic of China,2006.

*Applied Mechanics and Materials Vols. 580-583 (2014) pp 636-640*
*© (2014) Trans Tech Publications, Switzerland*
*doi:10.4028/www.scientific.net/AMM.580-583.636*

# Monitoring analysis and safety evaluation of deep foundation pit under complex conditions

Xutao Zhang[1,2,a], Qiangyong Zhang[1,b], Chao Wang[1,c] , and Youfa Wang[1,d]

[1]Geotechnical and Structural Engineering Research Center of Shandong University, Jinan, Shandong 250061, China

[2]School of Architecture and Engineering, Liaocheng University, Liaocheng, Shandong 252059, China

[a]zhangxutao@lcu.edu.cn, [b]qiangyong@sdu.edu.cn, [c]122256121@qq.com, [d]631427813@qq.com

**Keywords:** deep foundation pit; deep horizontal displacement; deformation control; monitoring analysis

**Abstract.** The horizontal displacement of pit top and horizontal displacement in deep soil of underground garage deep foundation pit in Radio and TV centre of Shandong province was analyzed. Combing the deformation control value of foundation pit, we thought that the supporting structure was safe and reliable. The supporting structure could not only meet the strength requirements but also meet the deformation control requirements. This deep foundation pit was a successful case under complex conditions. Analyzing the variation rules between monitoring data and construction time, the instructive conclusions were obtained. The deformation of foundation pit external corner was largest. The external corner should be avoided in foundation pit. The dynamic loads around foundation pit had a great influence on the safety and stability of pit. The rainfall was disadvantage factors, so the construction of foundation pit should keep away from the rainy season. The foundation pit floor could limit soil deformation and improve the safety of pit. The pit floor should be constructed as early as possible.

## Introduction

In the recent twenty years, the foundation pit engineering has become a hot issue and difficult problem in the field of geotechnical engineering [1]. The foundation pit engineering is a comprehensive system engineering. It is related to not only the soil strength and stability but also the collaborative work of soil and supporting structure. The design and construction of foundation pit is to ensure the safety and stability of supporting structure, but also to ensure the safety of the surrounding buildings and facilities [2-4]. At present, a lot of dangerous accidents have happened in the foundation pit engineering. In many accidents, the collapse of foundation pit has brought destructive impact on the surrounding buildings and facilities and caused incalculable losses [5, 6]. The accidents have a lot to do with the complex and imperfect design theory of foundation pit engineering. Based on the present situation, the monitoring analysis of foundation pit engineering and typical engineering experiences have become very important. The underground garage deep foundation pit in Radio and TV centre of Shandong province is a deep, large, complex engineering. Combing with the monitoring data of this engineering, the deformation of pit soil and surrounding buildings with foundation pit construction has been analyzed, and the safety and stability of the pit engineering has been evaluated. Some instructive conclusions are obtained, and these conclusions can provide references for similar engineering.

## Project Overview and Reinforcement Scheme

The underground garage deep foundation pit in Radio and TV centre of Shandong province is located in north-west corner of intersection of Youth East Road and Jingshi Road in Jinan. The surroundings around foundation pit are complex. There are buildings and underground pipelines near the foundation pit. The foundation pit excavation depth is 17.9m, the width is about 30m, and the length

is about104m. Because of the deep excavation depth, the complex surrounding environment and the restriction of excavation site, the supporting structure of foundation pit is required. According to the engineering geological and hydro-geological conditions, combing with the surrounding environment, the safety grade of the foundation pit shall be class A. The lateral wall of foundation pit is vertical, the steel pipe piles and pre-stressed anchors are used to support foundation pit. The diameter of steel pipe pile is 200mm, the effective length of pile is 20.5m, and the spacing of pile is 600mm. The rod body material of anchor is 2φ28 steel bars. The anchored length of pre-stressed anchors is 13m, and the free length is 7m. The horizontal spacing of anchors is 1.5m, and the vertical distance is 2.5m. Reinforced shotcrete is used for surface protection.

## Monitoring Scheme of Foundation Pit

The safety grade of the foundation pit is class A. The working time of foundation pit is 18 months. According to the regulations of Technical Code for Monitoring of Building Foundation Pit Engineering, monitoring items of the foundation pit engineering should include: the horizontal and vertical displacement of pit top, the horizontal displacement in deep soil, the settlement of surrounding buildings, the internal force of supporting pile structure, etc. Because of the limited space of this article, only the horizontal displacement of pit top and the horizontal displacement in deep soil were analyzed in this paper. Fig.1 is the monitoring plane layout of foundation pit.

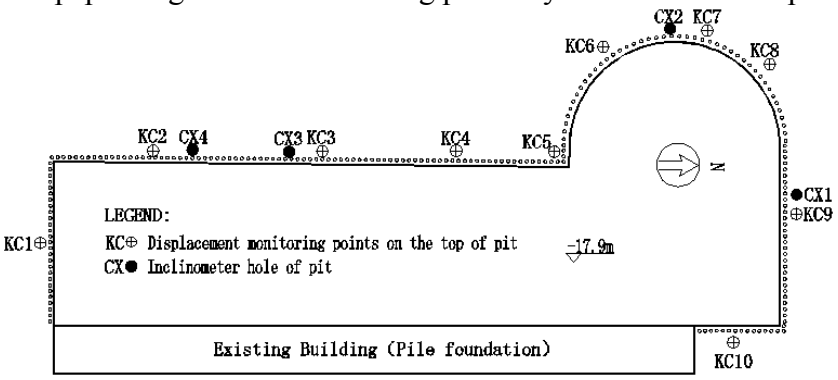


Fig.1 Monitoring plane layout of foundation pit

## Monitoring Results and Analysis

**Corresponding Relations between Key Time and Construction Content.** From the pit excavation to the construction of underground garage structure is a longer period of time, and a large number of monitoring data is gained. Analysis of all of the monitoring data is very difficult and not easy to find out the rules. Therefore, the monitoring data of several key time was analyzed. In order to obtain the instructive monitoring conclusions, the corresponding relations between the key time and the foundation pit construction content should be clear firstly. Table 1 is the corresponding relations between key time and foundation pit construction content.

Table 1 Corresponding relations between key time and construction content

| Key time | Construction content and related events | Cumulative time / d |
|---|---|---|
| April 13, 2011 | Set monitoring point, Install inclinometer tube, excavate earthwork | 0 |
| July 10, 2011 | Excavate to -5.5m, install the first and second rows of pre-stressed anchor | 88 |
| September 15, 2011 | Excavate to -11m, install the third and fourth rows of pre-stressed anchor | 155 |
| November 15, 2011 | Excavate to -16m, install the fifth and sixth rows of pre-stressed anchor; continuous and heavy rain | 216 |
| December 20, | Excavate to the final depth -17.9m | 251 |

| | | |
|---|---|---|
| 2011 | | |
| March 25, 2012 | Complete the construction of the cushion and floor of underground garage | 346 |
| September 15, 2012 | Complete the construction of underground garage; ready to backfill | 460 |

**Horizontal Displacement of Pit Top.** Fig.2 is the correlation between horizontal displacement of pit top and cumulative time. The positions of monitoring point KC1, KC3, KC5, KC7 and KC9 are marked in Fig.1. The horizontal displacement of pit wall is negative, which indicates the deformation of foundation pit is towards inside. In order to analyze the monitoring datas, the details of some monitoring points are as follows: KC5 is located in west external corner position of the foundation pit; KC7 is located in west internal corner position of the foundation pit; KC9 is located in the north central position of the foundation pit, there are dynamic loads in the vicinity.

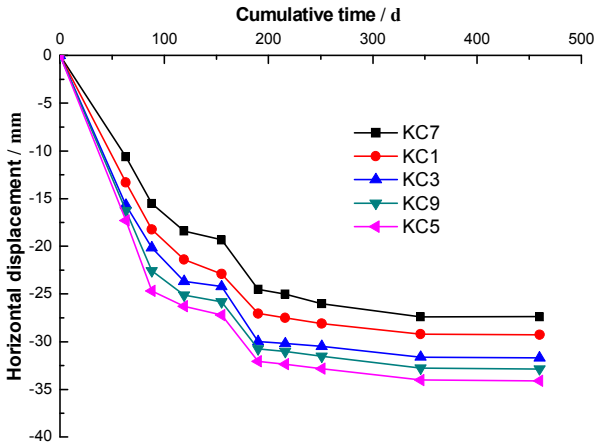


Fig.2 Correlation between horizontal displacement and cumulative time

The horizontal displacement of monitoring point KC7 is the smallest, and the ultimate displacement value is -27.39mm. The horizontal displacement of monitoring point KC5 is the biggest, and the ultimate displacement value is -34.13mm. The horizontal displacement of foundation pit external corner position is far greater than the internal corner position. Therefore, external corner should be avoided in the design of foundation pit. The horizontal displacement of monitoring point KC9 is relatively large and close to the control value, and the ultimate displacement value is -32.85mm. This shows that the dynamic load on the north side of foundation pit has great influence on the safety of the foundation pit. In the cumulative time from 155 days to 216 days, there has been a bigger increase in the horizontal displacements of all five monitoring points. Considering the rainfall in this period, rainfall has a great influence on the safety of foundation pit. In the cumulative time from 251 days to 346 days, the horizontal displacement increases continuously, while the horizontal displacement remains unchanged in the cumulative time from 346 days to 460 days. This shows that foundation pit floor is very important to the safety of foundation pit.

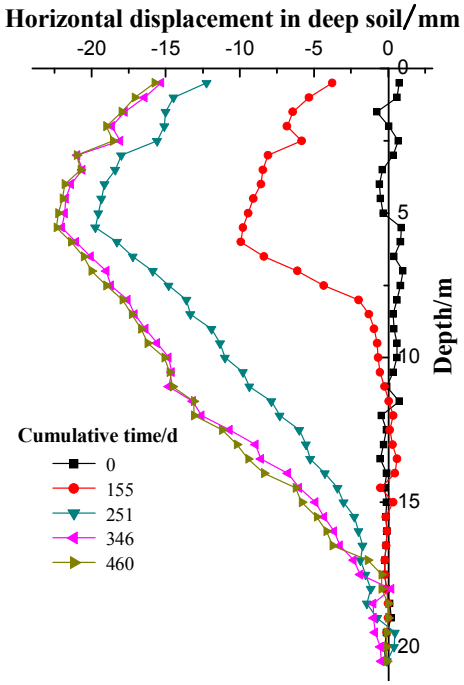


Fig.3 Correlation between CX1 horizontal displacement and depth

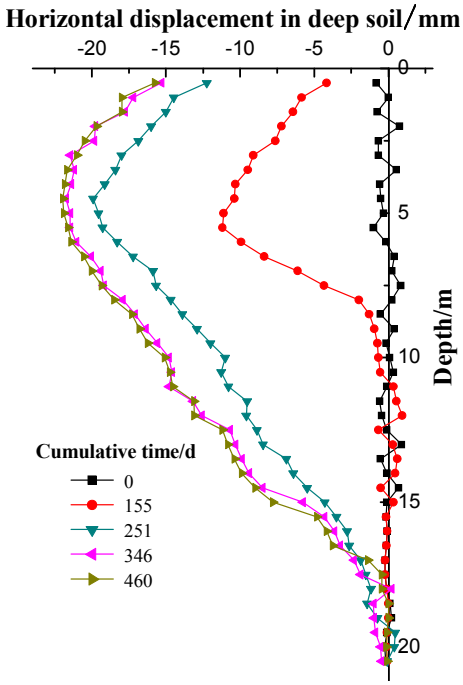


Fig.4 Correlation between CX1 horizontal displacement and depth

**Horizontal Displacement in Deep Soil.** The inclinometer is a device used for monitoring the horizontal displacement in deep soil. It can monitor the magnitude and direction of horizontal displacement. The project provided four inclinometer holes, their position are shown in Fig.1. Fig.3 and Fig.4 is the relationship curve between deep horizontal displacement and depth of CX1 and CX3. The variation rule of the deep horizontal displacement is consistent basically in Fig.3 and Fig.4, but it is worth noting that: (1) in the cumulative time from 155 days to 251 days, the horizontal displacement has more than doubled. Considering the rainfall in this period, rainfall has a great influence on the deep horizontal displacement of foundation pit. (2) Comparing the three curves of cumulative time 251 days, 346 days and 460 days, we find that the horizontal displacement of deep soil has not change after the completion of foundation pit floor, while the soil displacement is still increasing before the completion of foundation pit floor. This indicates that foundation pit floor is favorable factors for the safety of foundation pit.

## Summary

After finishing the analysis of the foundation pit monitoring data, we find that foundation pit supporting structure is safe and reliable. The supporting structure can control soil deformation effectively. It is a successful deep foundation pit case under complex conditions. Further analysis of monitoring data variation, we get the following instructive conclusions: (1) the deformation of foundation pit external corner is the largest; and the external angle should be avoided in the foundation pit. If the external corner can not be avoided, the supporting structure should be strengthened and the monitoring frequency should be increased. (2) Dynamic load around foundation pit has a great influence on the pit safety. If the dynamic load can not be avoided, enough safe distance should be provided. (3) The rainfall is disadvantage factors for the safety and stability of foundation pit engineering. The construction of foundation pit engineering should avoid the rainy season; otherwise the monitoring frequency should be increased. (4) The pit floor can limit soil deformation and improve the safety of pit. Therefore, the pit floor should be as soon as possible constructed.

**Acknowledgements**

This work was financially supported by Ji'nan Institute of Surveying and Mapping Reseach Project (2011JK057).

**References**

[1] Xiaonan Gong: China Civil Engineering Journal Vol. 38 (2005), p. 99-102. (In Chinese)

[2] Guanghua Yang: Chinese Journal of Geotechnical Engineering Vol. 20 (1998), p. 113-115. (In Chinese)

[3] Juncai Li, Zhuoyuan Zhang and Guoyu Luo: Rock and Soil Mechanics Vol. 24 (2003), p. 812-816. (In Chinese)

[4] Guanfeng An and Junyue Gao: Rock and Soil Mechanics Vol. 26 (2005) p. 1837-1840. (In Chinese)

[5] Jianhang Liu and Xueyuan Hou: *Excavation engineering handbook* (China Architecture and Building Press, Beijing 1997) (In Chinese)

[6] Yeqing Tang, Qimin Li and Jiangyu Cui: *Excavation engineering accident analysis and processing*. (China Architecture and Building Press, Beijing 1999) (In Chinese)

*Applied Mechanics and Materials Vols. 580-583 (2014) pp 641-650*
*© (2014) Trans Tech Publications, Switzerland*
*doi:10.4028/www.scientific.net/AMM.580-583.641*

# Analysis of Coral Reef Rock Mass Integrity Based on RMDI Method

Jinchao Wang[1, a *], Chuanying Wang[2,b] and Zengqiang Han[3,c]

[1,2,3]Institute of Rock and Soil Mechanics, Chinese Academy of Sciences, Wuhan 430071, China

[a]wangjinchao_88@163.com, [b]chywang@whrsm.ac.cn, [c]hanzengqiang01@163.com

**Keywords:** borehole camera, geological survey, coral reef, rock mass integrity.

**Abstract.** At present, relatively few drilling surveys have been conducted on coral reefs, and comprehensive geological info on coral reefs is difficult to obtain. However, research of coral reef is of great importance to our development and exploitation of maritime resources. The survey of Chenhang Island in Paracel (Xisha) Islands saw China's first usage of digital borehole camera technology, which resulted in a large amount of first-hand geological data. We have utilized the rock mass integrity index (RMDI) method in our analysis of coral reef integrity, and with reference to the rock mass classification standard, formulated the correlation between RMDI values and coral reef intactness, enabling the engineering evaluation of coral reef integrity. Through statistical analysis of camera data gathered along the CK2 borehole's approx. 1km length, we performed an integrity evaluation of the entire borehole length using the RMDI classification, and created a coral reef stratum development diagram which is consistent with the actual cores. The results indicate: (1) the classification system based on RMDI is feasible in the integrity evaluation of coral reefs; (2) the coral reef integrity values obtained using the RMDI method are accurate; (3) borehole camera survey and statistical analysis are of great utility in the study of coral reefs.

## Introduction

Coral reefs are rock and soil structures formed by the remains of scleractinian corals (refer with: Fig. 1) after long-term geological effects[1]. They can be found widely and prominently around islands and certain coastlines in South China Sea. They may function as symbols of China's sovereignty over its territory, and valuable sites for exploitation of maritime resources and construction of airborne and seaborne transportation facilities in South China Sea. As the history of corals spans from the Paleozoic Era to the present, they can also be used as important indicators for stratum designation and analysis of past climate and geography. Coral reefs are affected by crust movements. They are generally formed in shallow areas 50m below low tide line, with reefs above sea level indicating an upward movement of crust or lowering of sea level, and lower reefs indicating a downward crust movement. Coral reefs are also often found near abundant oil and natural gas resources. Coal, bauxite, manganese ore and phosphate rock have been found in the sediments of coral reefs and their lagoons, and strata-bound mineral deposits with multiple metals including copper, lead and zinc have been found through the rudaceous rocks of reef bodies. The coral limestone can be used as a raw material for lime and cement, the corals can be used as decorations, and many coral reef regions have been developed for tourism. In summary, the study of coral reefs is of great significance.

The main component of coral reef rock mass is calcium carbonate (CaCO3). As shown in Fig.2, it is porous and brittle, low in both hardness and strength. Drilling is an indispensable method in the background survey of coral reefs, but due to characteristics of their structure and limitations of technology, such as mechanical disturbances which may result in low or even zero coring rates, the geological info obtained is often incomplete, rendering traditional analytical methods inaccurate. As coral reef rocks tend to shatter under high pressure, it is easy for the drilling process to damage the intactness of coral rocks, which is impossible to determine through rock cores. Therefore, a singular reliance on drilling would affect the accuracy of coral reef research and even cause erroneous results. A better evaluation of their rock mass would require a combination of drilling and other complementary techniques. The digital borehole camera[2,3,4] system has integrated digital video

and computer control by using optical sensors for close observation of rock mass inside the borehole. The acquired information is processed with computer to generate digital column-shaped image of the borehole walls (refer with: Fig. 3), solving the integrity and accuracy problem of geological info acquisition in coral reef boreholes.

Fig. 1—Remains of scleractinian corals.

Fig. 2—Rock cores obtained from coral reefs.

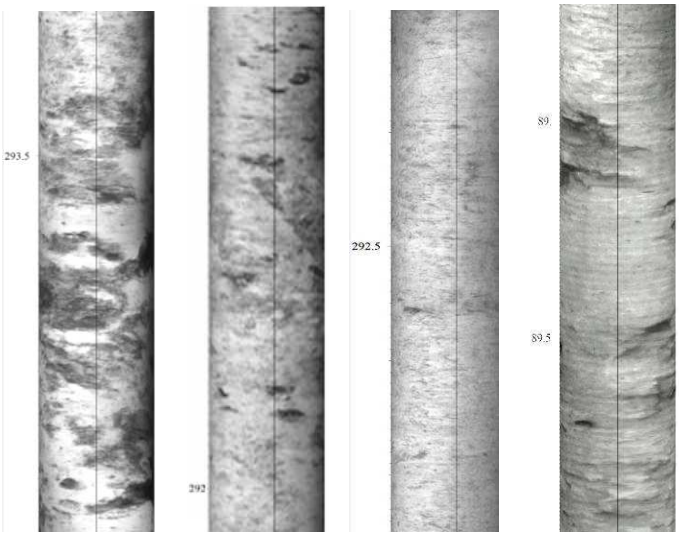


Fig. 3—Borehole camera images.

The basic quality of a rock mass is an inherent fundamental property that affects its stability in engineering projects. It depends on internal factors of the rock structure, of which rock mass integrity is a controlling factor. The borehole camera system has enabled us to evaluate the geometric (macroscopic) intactness of a rock mass. RMDI method is used in evaluation of coral reef integrity, but there is not a detailed standard of evaluation. Hence, this paper provides an in-depth comparison between results of RMDI method and actual engineering, by comparing the RMDI values acquired from borehole CK2 at Chenhang Island, Xisha (Paracel) Islands with geological info obtained using other methods. The rock mass classification standard is then used to help determine the corresponding degrees of rock mass intactness for the RMDI values.

**Borehole Camera**

The key to the digital panoramic borehole camera system lies in breakthroughs of panoramic (reflector on the conical surface) and digital (digital video and imaging) technologies. The panoramic technologies enable a 2-dimensional representation of the 360° borehole wall, which is overlayed with directional info, creating a panoramic image; digital technologies allow the digitization of videos, which are processed with inverse transformation algorithms to construct a model of the borehole wall and generate a digital vertical image. The borehole camera image is an intuitive representation of the cavities and other geological info from the borehole wall. By processing this info, a complete database can be generated, which can be used to statistically determine the number and sizes of visible cavities in the image. Fig.4 is a schematic diagram of borehole camera imaging.

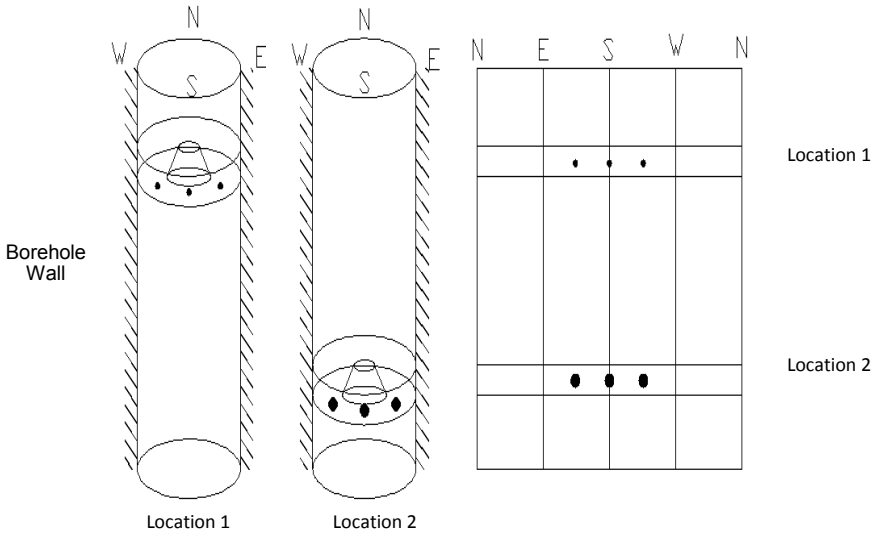


Fig. 4—Schematic diagram of borehole camera imaging.

**RMDI Method Overview**

**The Lumpiness Function**. The formation of coral reef rock mass is affected by multiple factors. Its special characteristics caused the rock mass to have multiple sections of intact rocks in addition to multiple hollow and broken sections. For the purpose of evaluating the maximum value of intact rock height within a unit depth, we establish the lumpiness function $\ell(z)$, expressed as

$$\ell(z) = L/H. \quad (1)$$

Where H is the depth to be measured; L is the maximum height of intact rock within the depth to be measured; generally $0 \le L \le H$. If the value of the lumpiness function $\ell(z)$ is zero, it indicates the given section of rock mass is hollow.

**The DIDF Function**. Since the coral reef rock mass is a complex entity formed from geological structures of the coral reef, the integrity shown in borehole images or lack thereof depends directly on its geological structures. For instance, a very small number of tiny cavities have little effect on the rock mass integrity, and its image shows even distribution of colours, which is an indication of high integrity; a relatively high number of large cavities break up the rock mass, causing its image to show great variation in colours and signs of fragmentation. We establish a single-variable function that varies along the borehole axial direction, the rock mass integrity index density function (DIDF)[5], represented as f(z) where z is depth, expressed as

$$\alpha = \ell(z). \quad (2)$$

Where 0≤α≤1. If the value of f(z) is 1 or approximating 1, it indicates the rock mass at the given depth has high integrity; the smaller the f(z) value is, the lower the integrity is, and the more fragmented the rock mass appears.

**The Coefficient α.** The coral reef rock mass integrity is affected by the size effect of lumpiness. The coefficient α in the DIDF represents the effect, with their relations expressed as

$$\alpha = \ell(\mathrm{z}). \tag{3}$$

**The RMDI Value.** The coral reef rock mass integrity index density function DIDF is a reflection of rock mass intactness along borehole axial direction. The rock mass integrity index (RMDI)[5] refers to the proportion of intact rock bodies within a given range, expressed as a percentage, where the given range can be a part of the borehole or the entire depth. If the given depth range is [h1, h2], the RMDI can be expressed as a definite integral of DIDF within the range, expressed as

$$\mathrm{RMDI} = \frac{\int_{h_1}^{h_2} f(\mathrm{z})\mathrm{dz}}{\int_{h_1}^{h_2} 1\mathrm{dz}}. \tag{4}$$

## Correlation Between RMDI and Rock Mass Intactness

**Classification of Rock Mass Intactness.** Rock mass intactness refers to the extent of development of various geological interfaces, mainly the fissures and faults. It is a generalized representation of the rock mass structures, and is determined by many factors including the shearing of structural planes, the sizes of structural bodies, and the cementation between bodies. A high-intactness rock mass has fewer faults, and a low-intactness rock mass contains more faults. It is one of the most important signifiers of rock mass quality, used in rock engineering as an overall indicator. Thus it is significant for rock engineering to find methods that allow simple and scientific evaluation of rock mass intactness.

The various classification schemes for rock mass, whether focusing on qualitative classification or quantitative assessment, all must take integrity into account, as it is an important signifier for rock mass strength and transformative properties. China's engineering geologists have always used properties of joints and fissures (which directly affect rock mass integrity) to describe the engineering characteristics of rock mass, especially the distances between joints and fissures. Table 1 shows the classification standards based on joint spacing by China's "Code for investigation of geotechnical engineering", "Technical code of railroad engineering geology", "Code of engineering geological survey" and "Code for hydropower engineering geological investigations", and the joint spacing standard recommended by International Society for Rock Mechanism[6,7,8,9]. Table 2 shows the qualitative classification from "Standard for engineering classification of rock masses" (GB50218-94)[10].

Table 1—Classification based on rock mass joint spacing.

| Standard | Structure Type | | | | |
|---|---|---|---|---|---|
| | Intact | Lumpy | Bedded | Fragmented | Granular |
| Code for investigation of geotechnical engineering GB50021-2001 | >1.0m | >1.0m<br>>0.4~1.0m | 0.4~1.0m<br>0.2~0.4m | 0.2~0.4m<br>≤0.2m | |
| Technical code of railroad engineering geology TBJ12-85 | >1.0m | >0.4m | <0.4m | <0.2m | |
| Code of engineering geological survey ZBJ14003-89 | >1.0m | 0.5~1.0m | 0.3~0.5m | <0.3m | |
| Code for hydropower engineering geological investigations GB50287-2006 | >1.0m | 0.5~1.0m | 0.3~0.5m | 0.1~0.3m | <0.1m |
| ISO/TC182/SC/WGI0 | >0.6m | | 0.2~0.6m | <0.2m | |

Table 2—Qualitative classification of rock mass intactness.

| Name | Development of Structural Planes | | Cementation of Main Structural Planes | Types of Main Structural Planes | Corresponding Structural Types |
|---|---|---|---|---|---|
| | No. of Groups | Mean Spacing | | | |
| Intact | 1~2 | >1.0m | Strong or average | Joints, fissures, beddings | Intact or very thick bedded structure |
| Moderately intact | 1~2 | >1.0m | Weak | Joints, fissures, beddings | Lumpy or thick bedded structure |
| | 2~3 | 1.0~0.4m | Strong or average | | Lumpy structure |
| Moderately fragmented | 2~3 | 1.0~0.4m | Weak | Joints, fissures, beddings, minor faults | Fissured lumpy or medium thick bedded structure |
| | ≥3 | 0.4~0.2m | Strong | | Mosaic fractured structure |
| | | | Average or weak | | Medium & thin bedded structure |
| Fragmented | ≥3 | 0.4~0.2m | Weak | Various types | Fissured lumpy structure |
| | | ≤0.2m | Average or weak | | Fractured structure |
| Highly fragmented | Disordered | | Very weak | | Granular structure |

As the standards differ with regards to classification of rock mass intactness, and no prior examples exist for coral reef rocks, grading their intactness can be difficult. With the comprehensive geological info acquired by borehole camera system, we attempted to conduct the rock mass integrity evaluation of coral reefs using the RMDI method, and explored the correspondence between the RMDI values and rock mass intactness.

**Correlation between RMDI and Rock Mass Intactness.** During the geological survey on coral reef islands in the central northern parts of South China Sea, a panoramic digital camera survey was completed along the full length of the CK2 borehole in Chenhang Island, with the depth of the survey ranging from 22 to 924m. An info database was created through acquisition of info from borehole walls, which was processed by computer to generate the borehole image. The sizes and numbers of visible cavities in the image were statistically analysed, and the DIDF value of the rock mass was calculated using Equations 1, 2and 3, as shown in Fig.5:

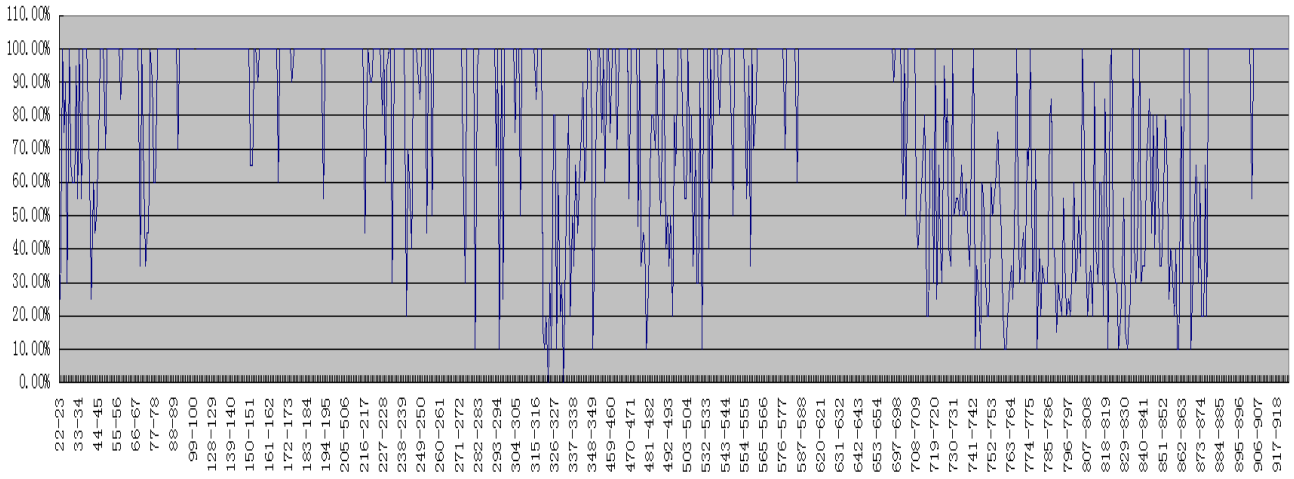


depth (m)

Fig. 5—Coral reefs integrity index density function (DIDF).

As the CK2 is a relatively deep borehole approximating 1km in length, we choose 10m as the basic unit to simplify the calculation and assessment of RMDI (refer with: Fig. 6).

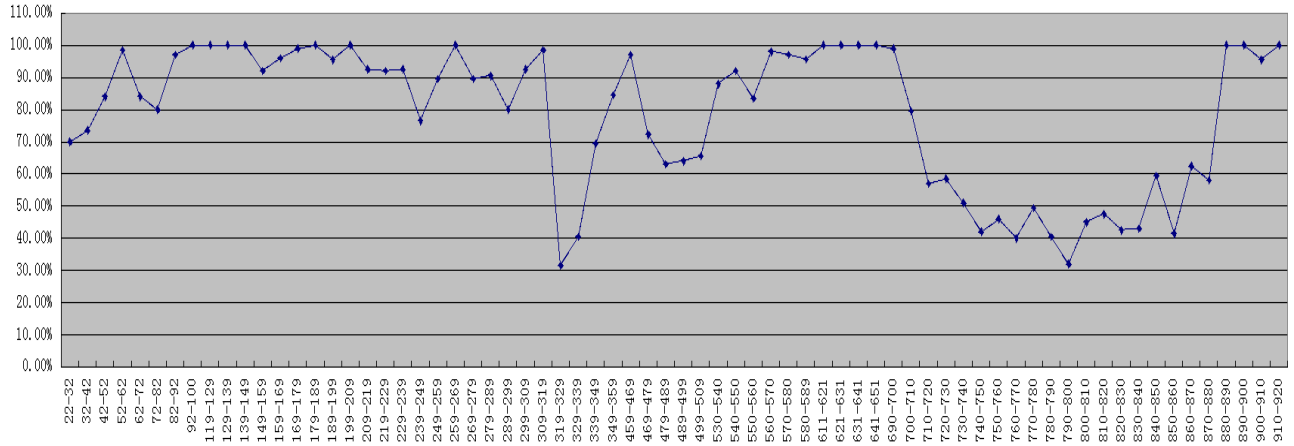


depth (m)

Fig. 6—Coral reef rock mass integrity index (RMDI).

As shown in Fig.6, the RMDI stays relatively high in the segment from CK2 depth 82 to 229m, at values above 0.85. Based on drilling log and rock core photos (refer with: Fig. 7), the rock cores of the segment are intact. Moreover, the intact cores from this segment are all longer than 1m (the cores shown in the figure have been broken up for the purpose of storage). We treat the length of intact cores to be the spacing between joints or structural planes, therefore this segment corresponds to the "intact" type in the qualitative classification of rock mass intactness from Table 2. Thus we consider the segment of coral reef rock mass to have high intactness.

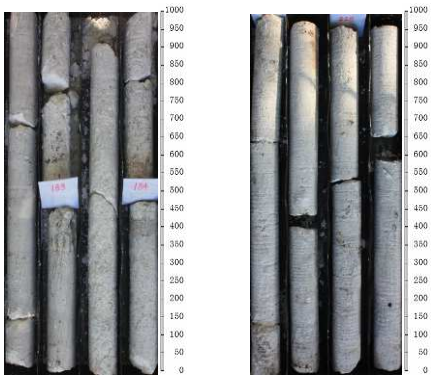

129~133m 169~173m

Fig.7—Some cores from coral reef rock mass.

At the segment from depth 319 to 339m, the RMDI is below 0.4. Based on drilling log and rock core photos (refer with: Fig. 8), the cores obtained from this segment are more fragmented, the heights of intact cores are less than 0.2m, and the structures display weak cementation. These cores correspond to the "highly fragmented" type in the qualitative classification, thus we consider the segment to have low intactness.

324~329m 333~338m

Fig.8—Some cores from coral reef rock mass.

At the segment from depth 469 to 509m, the RMDI is between 0.55 and 0.75. Based on drilling log and rock core photos (refer with: Fig. 9), the intact cores from this segment have an average length around 0.5m. The cores display medium thick bedded structures, with average cementation, which corresponds to the "moderately fragmented" type in the qualitative classification. Thus we consider the segment to have average intactness.

475~479m 505~509m

Fig.9—Some cores from coral reef rock mass.

The feasibility and accuracy of the RMDI method has already been established in prior studies on coral reef rock mass integrity evaluation. Through the comparison between RMDI and other data shown above, with reference to the classifications based on joint spacing (refer with: Table 1) and qualitative classification of intactness, the correlation between coral reef RMDI and rock mass intactness can be formulated (refer with: Table 3).

**Evaluation of the CK2 Borehole.** Based on the correlation between RMDI and intactness from Table 3, an evaluation of intactness throughout CK2 can be made. The intactness of coral reef rock mass can be deemed to be the degree of cementation in the coral reef. A comprehensive coral reef stratum development diagram can be constructed using RMDI, as shown in Fig.10(b).

TABLE 3—Correlation between RMDI and coral reef rock mass intactness.

| Intactness | High | Moderately high | Average | Moderately low | Low |
|---|---|---|---|---|---|
| Homogeneity | 1.00~0.85 | 0.85~0.70 | 0.70~0.55 | 0.55~0.40 | <0.40 |

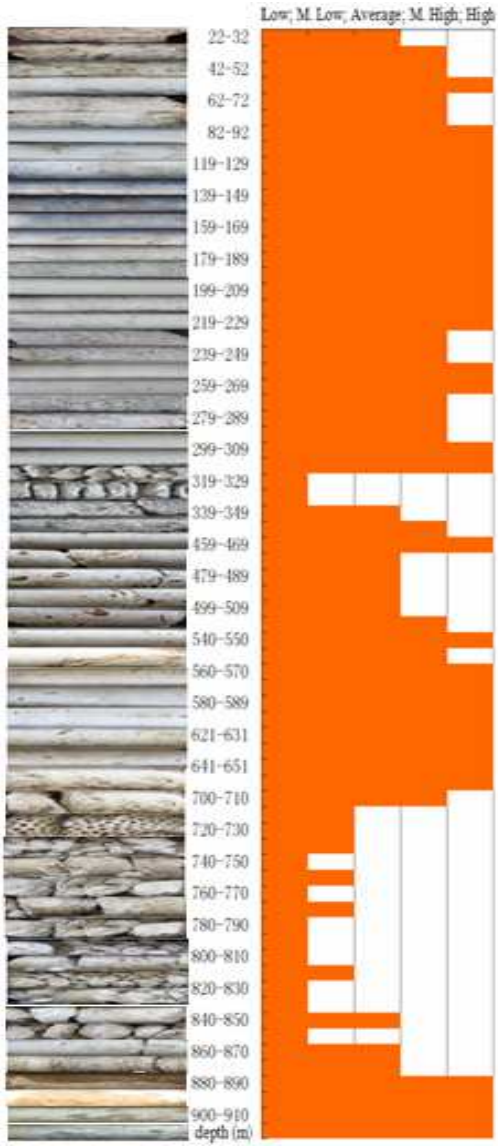


(a) (b)

(a) Selected photos of rock cores

(b) Diagram of coral reef stratum development

Fig. 10—Comparison of rock cores and RMDI evaluation results.

A comparison of actual rock cores and results of RMDI-based assessment (refer with: Fig. 10) shows that the RMDI results are generally consistent with actual cores. Through the evaluation of rock intactness throughout the CK2 borehole, we discovered that the intactness in coral reef is alternately interleaved along the depth. The 82 to 229m, 560 to 700m and 880 to 924m segments have high intactness, with strong cementation in the corresponding cores, high coring rates, and more intact cores; the 319 to 349m and 740 to 860m segments have low intactness, with weak cementation, low coring rates, and fragmented cores. The construction of coral reef development stratum structures will be of great significance to the identification of geological stratums and investigation of past climates and geography.

## Conclusion

Through detailed comparative analysis of RMDI values and info from the entire approx. 1km length of the CK2 borehole, and with reference to the rock mass classification standards, we formulated the correlation between RMDI values and coral reef rock mass intactness, conducted an integrity evaluation of the CK2 borehole, and constructed a coral reef development stratum structure diagram. The results of RMDI evaluation also prove generally consistent with other evaluation methods. It can be concluded that: (1) the classification system based on RMDI is feasible in the integrity evaluation of coral reefs; (2) the coral reef integrity values obtained using the RMDI method are accurate; (3) borehole camera survey and statistical analysis are of great utility in the study of coral reefs.

## References

[1] Wei, X., Jia, C., and Meng, W., Dolomitization Characteristics of Carbonate Rock in Xisha Islands and Its Formation:A Case Study of Well Xichen-1, Journal of Jilin University (Earth Science Edition), 2008, 38(2), pp. 217–224.

[2] Prensky, S. E., Advances in borehole imaging technology and application, Borehole Imaging: Applications and Case Histories, London, Geological Society, 1999, pp. 1–43.

[3] John，H., and Carole, D., Acoustic and optical borehole-wall imaging for fractured-rock aquifer studies, Journal of Applied Geophysics, 2004, 55:151-159.

[4] Wang, C., Ge, X., and Bai, S., The digital panoramic borehole camera system and its application, Rock and Soil Mechanics, 2001, 22(4), pp. 522–525.

[5] Wang, C., Hu, P., and Sun, W., Method for evaluating rock mass integrity based on borehole camera technology, Rock and Soil Mechanics, 2010, 31(4), pp. 1326–1330.

[6] Ministry of Construction of the People's Republic of China, GB50021-2001, Code for investigation of geotechnical engineering, Beijing, China Architecture & Building Press.

[7] Ministry of Railways of the People's Republic of China, 1996, TBJ12-85, Technical code of railroad engineering geology, Beijing, China Railway Press.

[8] Ministry of Water Resources of the People's Republic of China, GB50287-2006, Code of engineering geological survey, Beijing, China Planning Press.

[9] Ministry of Geology & Mineral Resources of the People's Republic of China, ZBD14003-89, Code of engineering geological survey, Beijing, Ministry of Geology & Mineral Resources of the People's Republic of China.

[10] Ministry of Water Resources of the People's Republic of China, GB50218-94, Standard for engineering classification of rock masses, Beijing, Ministry of Water Resources of the People's Republic of China.

*Applied Mechanics and Materials Vols. 580-583 (2014) pp 651-654*
*© (2014) Trans Tech Publications, Switzerland*
*doi:10.4028/www.scientific.net/AMM.580-583.651*

# Application of Curve Model Fitting Methods to Settlement Prediction

WU Ming[1, a] , NIU Jialun[2, b]

[1] Hangzhou Bureau of Quality and Safety supervision of Traffic Engineering, Hangzhou, China 310014

[2] Chang'an University, Xi'an, China 710064

[a] windtg1009@126.com [b] 13484523466@qq.com

**Keywords:** soft sub-grade; settlement prediction; Hyperbolic model; Logistic curve model

**Abstract.** Both Hyperbolic model and Logistic curve model have certain applicability to settlement prediction of soft sub-grade. Based on the observational settlement data of soft sub-grade in an industrial zone, the features of Hyperbolic model and Logistic curve model are studied. By using curve fitting methods with Origin software to predict the sub-grade settlement value and analyze the simulation results, compare these two models to determine which one is more reasonable. The results show that the Logistic curve model is more accurate and reasonable, it has the value of popularization and application in engineering.

## Introduction

Soft soil is characterized by features of high compressibility, high water content, low strength and poor permeability. It's deformation is quite complex in the soft sub-grade treatment works. The deformation is related to its own characteristics, in addition, it's influenced by filling traits, filling speed and soft foundation treatment methods. So, the study of soft sub-grade settlement issues has important significance.

Engineering practice situations indicate that accurate calculation of soft sub-grade settlement, especially prediction of settlement after construction is the key issue in engineering construction. While the measured data of settlement is the standard of testing calculation results, it's important to analyze the measured data of settlement. It's of great value in project to use the settlement data observed during pre-construction sufficiently and rationally to find out settlement regularity, thus we can predict the settlement during post-construction and after completion according to settlement regularity.

The commonly used method to predict soft soil sub-grade settlement according to measured data is to assume that sub-grade settlement regularity obeys some kind of mathematical model form. Determining the undetermined coefficient of model dynamically by using measured data samples, thus after construction settlement and final settlement can be predicted. Such mathematical model are mainly two types, one which regards Logarithmic model and Hyperbolic model(He et al., 2009). as representative to predict after construction settlement, the other which contains the growth curve model(GOMPERTZ B., 1825) and Weibull model to predict the whole process. The growth curve generally contains Logistic curve equation and Gompertz(Zai et al., 2000) curve equation.

This paper relies on a filling project of soft soil area road at an industrial zone. By using its settlement observation data, we can predict the settlement value of this road with origin software(Xiao et al., 2009) which based on analysis of Hyperbolic model and Logistic curve model, in order to verify the scientificalness and rationality of models and determine the optimal prediction method of settlement value in projects.

## Building and Analysis of Settlement Prediction Model

**Hyperbolic Model.** Hyperbolic model is an empirically derived method which assumes the average speed of sinking resumes in the form of hyperbolic. Expression is expressed as,

$$s_t = s_a + \frac{t - t_a}{\alpha + \theta(t - t_a)} \qquad \text{(a)}$$

Formula (a) can be rewritten as formula (b),

$$\frac{t-t_a}{s_t-s_a}=\alpha+\theta(t-t_a) \qquad \text{(b)}$$

In formula(a) and formula(b), $t_a$ and $s_a$ are respectively the time and settlement value of fitting calculation starting reference point, t and $s_t$ are the time and settlement value of any point on the fitting curve, α and θ are the coefficients obtained from the measured value which respectively represent intercept and slope of lines.

When $t\rightarrow\infty$ ,we can get the final settlement value formula(c),

$$s_\infty=s_a+\frac{1}{\theta} \qquad \text{(c)}$$

**Logistic Curve Model.** Logistic curve belongs to growth model curve, it's S-curve shape and found by a German mathematician, biologist P.F.Verhus in 1837 when he studied population.

Jinmin Zai etc (Zai et al., 2000) consider that the process of things reflected by growth model curve happen, develop, mature, then reach a certain limit is similar to the process of sub-grade loading progressively infliction with corresponding settlement gradually occurrence. Settlement increases linearly in the initial stages when immediate settlement mainly occurs. After the first turning point occurs, settlement rate increases along with the increase of land filling height, at this time main consolidation settlement mainly occurs. Another turning point appears after that, the settlement rate slows down gradually to a steady value which is named the final settlement, during this stage, secondary consolidation settlement mainly occurs. The whole process of settlement curve is an anti-S shape. So, we can use this curve to fitting the whole process soft soil sub-grade settlement and predict final settlement.

The Logistic curve equation is,

$$S_t=\frac{A_1-A_2}{1+(t/t_0)^p}+A_2 \qquad \text{(d)}$$

In this equation, $s_t$ represents the cumulative settlement value at time t, $A_1$, $A_2$, p and $t_0$ are fitting parameters.

According to this equation, when the Logistic curve function is fitted by measured S-t data, if $t\rightarrow\infty$, $S_\infty\rightarrow A_2$,it means that parameter is the predicted final settlement value.

A typical Logistic curve is shown (in Figure. 1)

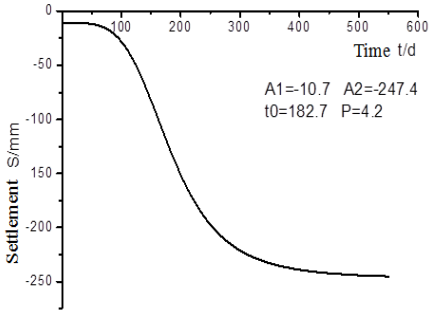


Figure1 Typical Logistic Curve Model

**Engineering Case Analysis.**

Soft soil sub-grade distributes widely in an industrial zone. In the construction of municipal roads, to control the settlement value of sub-grade, the sub-grade is reinforced by equal load preload, DJM, and geogrid. Among them, the observed values of some observation points in this industrial area are showed in (Table. 1), sub-grade is dealt by preload. The settlement is observed between May 17 to September 30, totally 136 days, the embankment is divided to 9 grades, the cumulative land filling height is 4.3m.

Table1 Settlement Observation Data

| Observation time | Time interval *t*/d | Cumulative time *t*/d | Cumulative settlement *S*/cm | Land filling height *H*/m |
|---|---|---|---|---|
| May 17 | 0 | 0 | 0.0 | 0.0 |
| May 24 | 7 | 7 | 5.7 | 0.3 |
| May 30 | 6 | 13 | 10.0 | 0.9 |
| June 7 | 8 | 21 | 13.3 | 1.5 |
| June 14 | 7 | 28 | 16.1 | 2.0 |
| June 21 | 7 | 35 | 17.9 | 2.6 |
| June 27 | 6 | 41 | 19.1 | 3.0 |
| July 3 | 6 | 47 | 20.0 | 3.4 |
| July 13 | 10 | 57 | 20.6 | 4.0 |
| July 20 | 7 | 64 | 21.1 | 4.3 |
| July 27 | 7 | 71 | 21.8 | 4.3 |
| August 5 | 9 | 80 | 22.2 | 4.3 |
| August 19 | 14 | 94 | 22.3 | 4.3 |
| September 1 | 13 | 107 | 22.5 | 4.3 |
| September 16 | 15 | 122 | 22.6 | 4.3 |
| September 30 | 14 | 136 | 22.6 | 4.3 |

**Rationality of Comparative Model.**Hyperbolic curve and Logistic curve are used to predict the settlement of this road, results are shown in (Figure. 2),

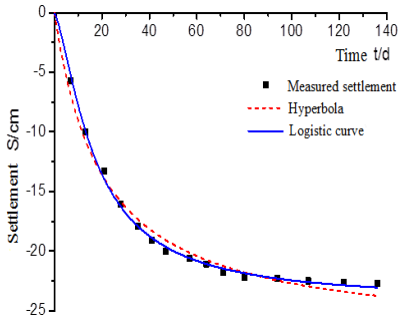


Figure2 Prediction of Settlement by Hyperbolic and Logistic Curve

It's can be seen from (Figure. 2) that both of Hyperbolic model and Logistic curve model can reflect the development regular pattern of sub-grade settlement. However , comparing with measured settlement value, the predicted value of Hyperbolic model appears a phenomenon of large early value, small medium value and large late value. The "S" development mode of Logistic curve model fits with measured settlement curve at any stages, this indicates that Logistic curve model can reflects the sub-grade settlement accurately than Hyperbolic model.

The predicted values of two methods in (Figure. 2)are summarized and compared as Table2 shows. According to the predicted results of settlement in (Table. 2), the predicted settlement values of both Hyperbolic model and Logistic curve model are larger than measured settlement value. According to the error of settlement value, the error of predicted settlement value of Logistic curve model is less than Hyperbolic model for about 13.6%. According to the standard error which is used to evaluate model prediction accuracy indicators, Logistic curve model is smaller than Hyperbolic model, means that the predicted accuracy is more exact. To sum up, the predicted settlement value of Logistic curve model is more accurate.

Table2 The predicted results of Hyperbolic and Logistic curve model

| Simulation Model | Curve Equation | Standard Error | Predicted Settlement $S_t$/cm | Measured Settlement S/cm | Settlement Error /% |
|---|---|---|---|---|---|
| Hyperbolic Model | y=P1*x/(P2+x) | 0.62986 | 27.24 | 22.6 | 20.5 |
| Logistic Curve Model | y=A2+(A1-A2)/(1+(x/x0)^p) | 0.32519 | 24.17 | 22.6 | 6.9 |

**The Effectiveness Analysis of Curve Model.**There are 16 actual numbers of observation among the given data in (Table. 1). Taking three types of prediction of 1-8times, 1-12times and 1-16times, namely using Hyperbolic model and Logistic curve model respectively to predict the observational data within 47d, 80d and 136d. Comparing predicted results, the results are shown in (Table. 3),.

Table3 The Effectiveness Analysis of Settlement Prediction

| Categories | Categories | Cumulative Time | Predicted Settlement $S_t$/cm | Measured Settlement S/cm | Settlement Error/% |
|---|---|---|---|---|---|
| Hyperbolic Model | Point8 | 47d | 34.14 | 22.6 | 51 |
| | Point12 | 80d | 29.74 | 22.6 | 31.6 |
| | Point16 | 136d | 27.24 | 22.6 | 20.5 |
| Logistic Curve Model | Point8 | 47d | 29.16 | 22.6 | 29 |
| | Point12 | 80d | 25.58 | 22.6 | 13 |
| | Point16 | 136d | 24.17 | 22.6 | 6.9 |

It's can be seen from the effectiveness analysis of settlement prediction(Table3):

(a).The settlement error of Logistic curve model is always smaller than the settlement error of Hyperbolic model by comparing settlement error at any same monitoring time and monitoring data of two types of curve model, namely it's more accurate. The accuracy of Hyperbolic model needs more monitoring time and monitoring data.

(b).From the predicted results analysis of Logistic curve model, it's can be seen that the predicted value has a large difference with measured settlement value at point8, the predicted values are close to measured results at point12 and point16. It showed that it's insufficient to meet the characteristic of curve model and the prediction accuracy is not enough when measured data are not enough. Only taking enough measured data(at point12 or point16), can we achieve good prediction effectiveness. (Xu et al., 2007)

## Conclusion

(a).Establish Hyperbolic model and Logistic curve model, analyze the application in predicting settlement value of two models.

(b).Compared with Hyperbolic model, Logistic curve model can reflect the laws of sub-grade settlement change accurately, have more accurate prediction results and higher prediction accuracy.

(c).To achieve a certain prediction accuracy, Hyperbolic model needs more monitoring time and monitoring data than Logistic curve model. The more measured data to fitting, the more accurate predicted results are.

## References

[1] He, L, Jiang, Y., 2009, The application of Hyperbolic model in Predicting sub-grade settlement: *Journal of Hehai University (Nature Science)*, 200937(2): 200-205

[2] GOMPERTZ B. On the function expressive of the law of human mortality and on a new method of determining the value of life contingencies [M]// Philosophical Transactions of the Royal Society of London. Series A. Mathematical and Physical Sciences, 1825: 513-585.

[3] Xiao, X., 2009, Origin8.0 practical tutorial-Technology mapping and data analysis: *China Electric Power Press*. 2009:160-163.

[4] Zai, J, and Mei, T, 2000, The application of growth curve in predicting sub-grade settlement: *Journal of Nanjing architectural engineering school*. 2000, 53(2): 9-12.

[5] Zai, J, and Mei, T., 2000, The study of whole process of settlement's prediction methods: *Rock and Soil Mechanics*, 2000, 21(2):322-325.

*Applied Mechanics and Materials Vols. 580-583 (2014) pp 655-658*
*© (2014) Trans Tech Publications, Switzerland*
*doi:10.4028/www.scientific.net/AMM.580-583.655*

# Effect of overload on bearing capacity of FRP reinforced ground

Chongxi Bai [1,a], Xinyan Shao [1,b], Qiuping Wang [1,c]

[1] (School of Water Conservancy and Building, Northeast Agricultural University, Harbin 150030，Heilongjiang, P. R. China)

[a]bcxzcx@163.com, [b]shaoxinyan2005@126.com, [c]81018881@qq.com

**Keywords:** Overload; Reinforced ground; Bearing capacity; Settlement; Model test

**Abstract.** Concrete blocks were arranged on both sides of the strip foundation to simulate overload. Model tests with overload or not were conducted, for four test programs including pure sand ground, single plate reinforced ground, double plates reinforced ground and single plate with two anchorage ends reinforced ground. The influence of overload on bearing capacity and settlement of ground, earth pressure and strain of FRP was analyzed. The test results showed that overload can enhance the bearing capacity, and reduce the ground settlement in a certain extent, with the beneficial effects of overload on reinforcement effect being decreased while the amount of reinforcement was increased.

## Introduction

Fiber reinforced polymer (FRP) material has good performance such as corrosive resistance, water resistance, high temperature resistance, high strength, high modulus of elasticity, light weight, and so on, so it's application is more and more widely in civil engineering and hydraulic engineering. FRP material can be used to improve reinforcement effects significantly and improve durability of traditional reinforcements.

In recent years, the reinforcement mechanism has been in–depth studied by domestic and foreign scholars. Wei has discussed the size and distribution of internal force of reinforcement [1]. Huang believed that the reinforcement mechanism being diffusion mechanism and deep foundation mechanism [2, 3]. Yamanouchi has analyzed lateral pressure effect and tension membrane effect of geogrid [4]. Patra has researched the effect of embedment depth of strip foundation on the bearing capacity [5]. Li proposed the bearing mechanism of reinforced aeolian sand [6]. Huang considered stress diffusion effect from friction of reinforcement and earth as reinforcement mechanism [7]. Du has researched settlement and slope stability of embankment reinforced with CFRP [8].

Tests on a pure sand ground program and three reinforced ground programs were completed, with overload or not. Influence law of overload on reinforcement effect was analyzed.

## Experiment overview

Loading tests were completed in the model box which was made of the steel box embedded by 1.5cm thick transparent organic glass plate along walls. The length, height and underside width of strip foundation were 46 cm, 14 cm and 10 cm respectively. Stress-strain curve of FRP was a straight line approximately. The fine sand screened from dry sand was made as ground.

There were four test programs, including pure sand ground (program *a*), single plate reinforced ground (program *b*), double plates reinforced ground (program *c*) and single plate with two anchorage ends reinforced ground (program *d*), with overload or not for each program. "N" was used to mark no overload program.

The size of plate and arrangement of strain gauge were shown in Fig. 1, with shaded area being anchoring ends. There were no anchoring ends for program *a*, *b*, *c*. Width and height of each anchoring end were 2cm and 1.2cm respectively. Placement of reinforcement and earth pressure gauge was shown in Fig. 2. There was no reinforcement for program *a*.

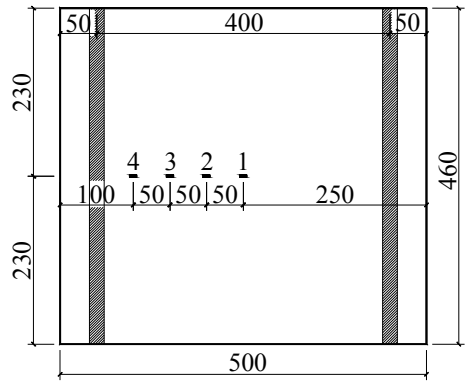


Fig. 1 Arrangement of strain gauge

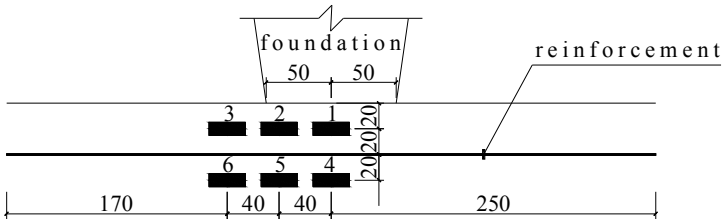


Fig. 2 Reinforcement and earth pressure gauge

## Test results and analysis

**Contrast for Curves of load and settlement.** Contrast for curves of foundation pressure and ground settlement was shown in Fig. 3. The results showed that overload can increase the bearing capacity and reduce ground settlement for program *a*, *b*, *d*. Overload can both increase bearing capacity and ground settlement for program *c*. There was earth shear failure for unreinforced ground, and there were reinforcement extrusion and earth shear failure for reinforced ground.

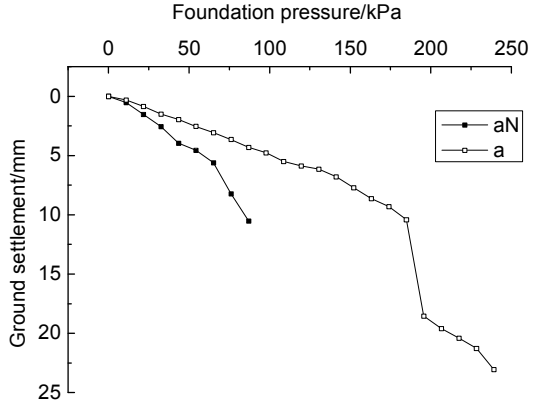


(a) program *a*

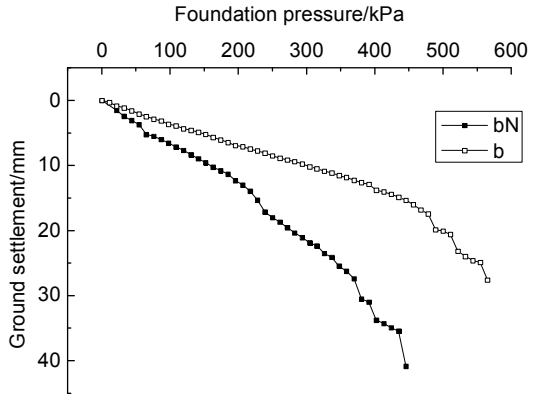


(b) program *b*

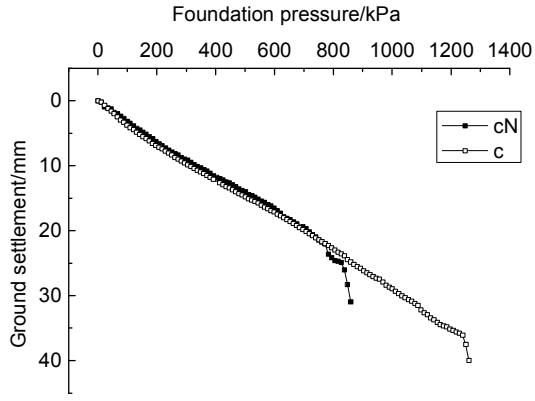


(c) program *c*

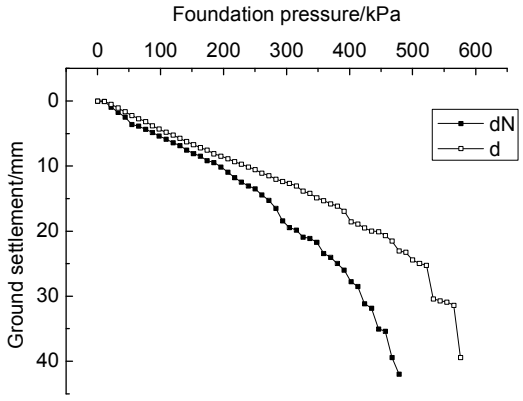


(d) program *d*

Fig. 3 Contrast of pressure-settlement curves

**Contrast for Curves of load and strain of reinforcement.** Contrast for curves of foundation pressure and strain of reinforcement was shown in Fig. 4 for reinforced programs. We can saw that overload can reduce strain value of 1 and 2 measuring points for program *b* and *d*, and the influence of overload on strain value for program *c* was small.

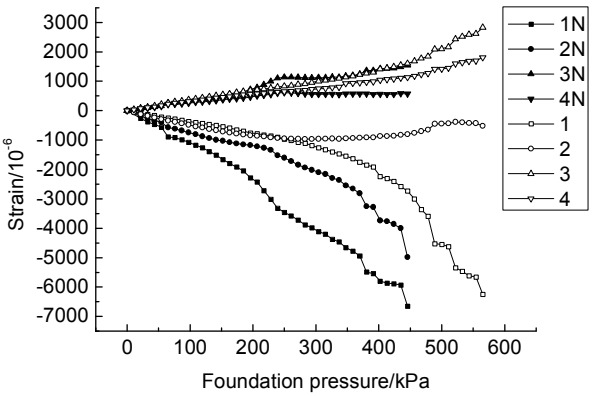


(a) program *b*

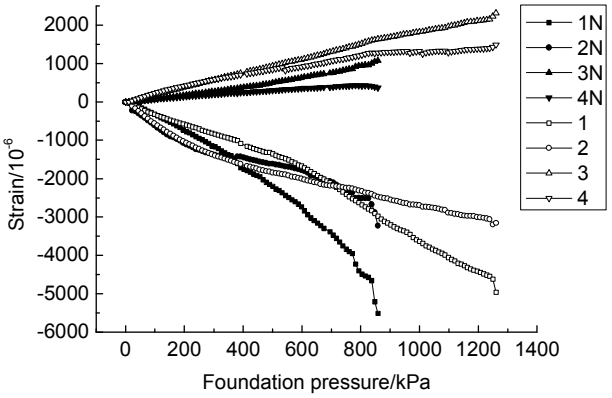


(b) upper layer reinforcement of program *c*

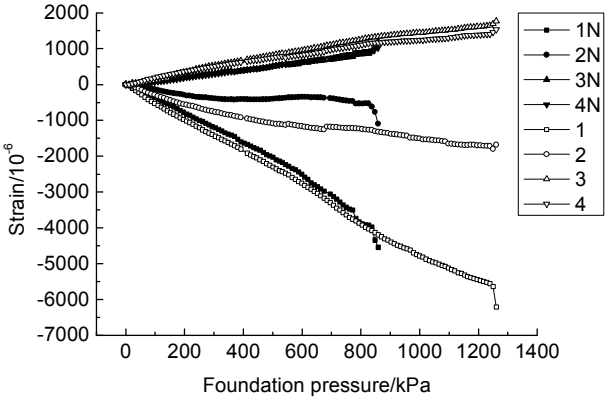


(c) under layer reinforcement of program *c*

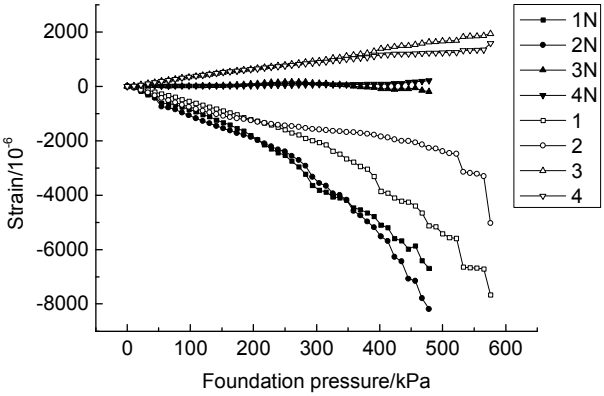


(d) program *d*

Fig. 4 Contrast for curves of foundation pressure and strain

**Contrast for Curves of load and earth pressure.** Contrast for curves of foundation pressure and earth pressure was shown in Fig. 5. Earth pressure value of 3 and 6 measuring points was small, so the remaining four points were shown in Fig. 5. The comparison result showed that there was no influence of overload on distribution of earth pressure nearly.

## Conclusions

Earth shear failure emerged for unreinforced ground, and reinforcement extrusion and earth shear failure emerged for reinforced ground. Overload can enhance the bearing capacity of ground, and can reduce the settlement of ground and the deformation of reinforcement in a certain extent, but the overload had little effect on the distribution of earth pressure. The beneficial effects of overload on reinforcement effect were decreased while the amount of reinforcement was increased.

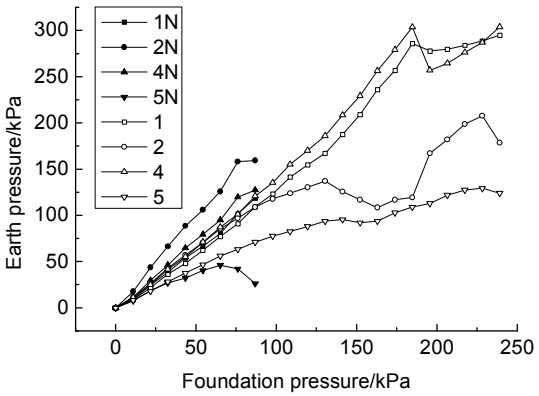


(a) program *a*

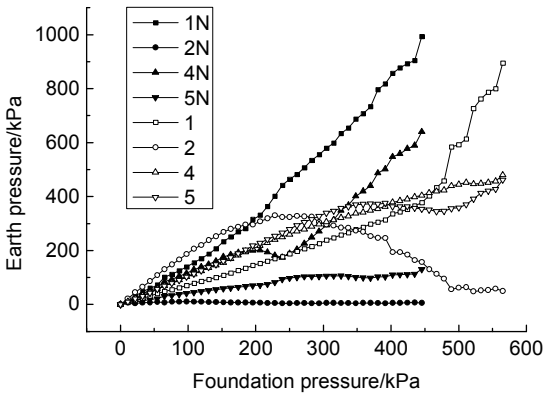


(b) program *b*

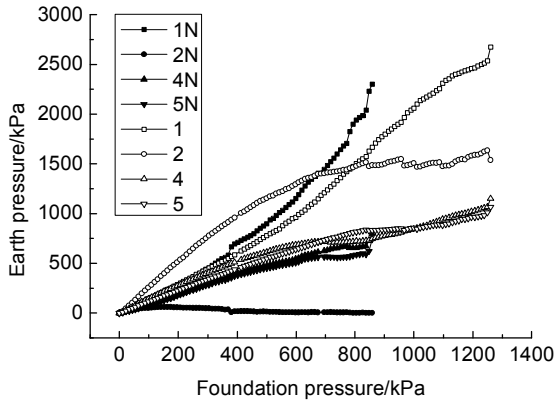


(c) program *c*

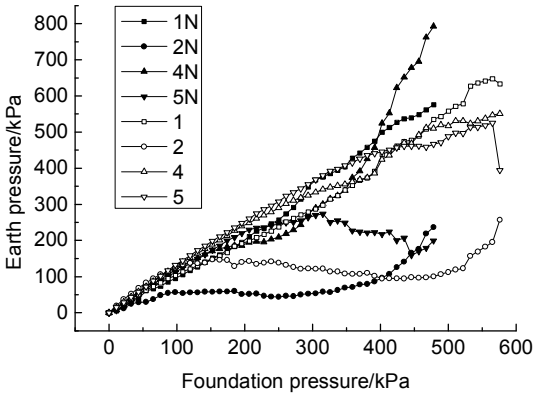


(d) program *d*

Fig. 5 Contrast for curves of earth pressure and foundation pressure

**Acknowledgements**

The research reported in this paper is supported by the Heilongjiang Province of China Postdoctoral Financial Assistance (Grant No.LBH-Z12043), the Doctoral Starting up Foundation of Northeast Agricultural University of China (Grant No.2012RCB33). The financial support is highly appreciated.

**References**

[1] Wei L L, Hua Z K. Measurement and analysis of reinforcement tension for earth foundation[J]. Chinese Journal of Geotechnical Engineering, 1997(1):15-21.( In Chinese)

[2] Huang C.C., Tatsuoka F.. Bearing capacity of reinforced horizontal sandy ground[J]. Geotextiles and Geomembranes,1990,9(1):51-82.

[3] Huang,C.C., Menq,F.Y.. Deep-footing and wide-slab effects in reinforced sandy ground[J]. Journal of Geotechnical and Geoenvironmental Engineering,ASCE,1997,123(1):30-36.

[4] Yamanouchi,T., Gotoh,K.A.. A proposed practical formula of bearing capacity for earthwork method on soft clay ground using a resinous mesh[R]. Technology Report of Kyushu University,1970,52(3):201-207.

[5] Patra,C.R., et al. Bearing capacity of embedded strip foundation on geogrid-reinforced sand[J]. Geotextiles and Geomembranes,2005,23(5):454-462.

[6] Li C, Liu L. Study of indoor model test of spread foundation on the reinforced aeolian sand subgrade[J]. Chinese Journal of Geotechnical Engineering, 2003, 25(4):441-444. ( In Chinese)

[7] Huang X Z. Measurement of soil pressure in geobelt-reinforced foundation and analysis of reinforcement mechanism [J]. Chinese Journal of Geotechnical Engineering, 2012, 34(9):1691-1694. ( In Chinese)

[8] Du Y X. Application and research of CFRP prestressed reinforced earth technology[D]. Changsha: Hunan University, 2003. ( In Chinese)

*Applied Mechanics and Materials Vols. 580-583 (2014) pp 659-664*
*© (2014) Trans Tech Publications, Switzerland*
*doi:10.4028/www.scientific.net/AMM.580-583.659*

# Influence of Density on the Hydraulic and Mechanical Properties of Sands

Osvaldo de Freitas Neto[1,a], Olavo Santos[2,b] and Ricardo Severo[3,c]

[1]Federal University of Sergipe, Aracaju-SE, Brazil

[2]Federal University of Rio Grande do Norte, Natal-RN, Brazil

[3]Federal Institute of Education, Science and Technology of Rio Grande do Norte

[a]osvaldocivil@yahoo.com.br, [b]olavo@ct.ufrn.br, [c]ricardosevero2003@yahoo.com.br

**Keywords:** Relative density, Shear strength, Permeability.

**Abstract.** This article aims at assessing the influence of relative density on the hydraulic conductivity and shear strength of two sands, denominated S01 and S02, derived from different regions and formation processes. S01 is wind-blown and S2 alluvial. The results of characterization and hydraulic conductivity in constant head tests were presented for both samples. The results of direct shear tests with sand S01 prepared with 5 different void ratios were also presented, for a vertical stress of 100kPa. The S02 sample was prepared with 4 different void ratios and these underwent direct shear testing with vertical stresses of 25kPa and 150kPa. This sample was prepared with the maximum and minimum void ratio and submitted to strength tests at CD triaxial compression with confining stresses of 50kPa, 100kPa and 200kPa. Results showed that even with different grain sizes, and under different density conditions, there were no significant variations in the permeability of the materials. With respect to shear strength, sand S01 obtained higher angle of friction values than sand S02, even though the latter had a higher percent coarse fraction. Sand S02 was relatively similar in terms of friction angle values obtained in direct shear and triaxial compression strength tests.

## Introduction

Relative density is a function of the void ratio of the soil that interfere in the strength of a granular soil. It provides an indication of the state of compactness of a mass of natural or compacted soil. A number of properties used in engineering can vary with the state of soil compactness, These include shear strength, compressibility and permeability of a soil. However, different soils in the same state of compactness can exhibit differences in these properties. Thus, it is important to accurately relate engineering properties to this ratio. [1] and [2], among others, conducted strength tests on compact and loose sands. [3] show that the lower the shear strength of a sand the greater the tendency to dilatancy (expansion) in the shear phase. [4] underscores that the lower the confining stress applied to compact sand, the greater the expansion during shear.

This study aims at assessing the influence of relative density on the hydraulic conductivity, compressibility and shear strength of two sands, one wind-blown from the city of Natal, Brazil, denominated S01, and the other alluvial from the city of São Carlos, Brazil, denominated S02. Moreover, we intend to compare compressibility behavior and angle of friction values of sample S02 obtained in direct shear and CD triaxial compression tests.

## Materials and Methods

Granulometric analysis [5], maximum [6] and minimum [7] void ratios and the specific gravity of solids [8] were conducted to characterize these sands. To determine the hydraulic conductivity of the 2 samples, permeability tests [9] were carried out at constant head in the maximum and minimum state of compactness. Sand S01 underwent direct shear testing with a normal stress of approximately 100kPa, for samples with void ratios (e) of 0.45, 0.55, 0.64, 0.75 and 0.88 respectively.

Sand S02 was submitted to direct shear testing with normal stresses of 25kPa and 150kPa, when void ratios (e) were 0.53, 0.55, 0.60 and 0.63 respectively. In this sample, for the direct shear tests, these

parameters were grouped according to the following nomenclature: Group A (e = 0:53 and normal stress of 25kPa and 150kPa), Group B (e = 0:55 and normal stress of 25kPa and 150kPa ), group C (e = 0.60 and normal stress of 25kPa and 150kPa) and group D (e = 0.63 and normal stress of 25kPa and 150kPa). Furthermore, this sample was subjected to two stages of CD triaxial compression strength tests, with 3 tests in each stage. In the first series of assays the test specimens were molded under maximum relative density, that is, with a minimum void ratio. The second series of tests was performed in test specimens molded under minimum relative density. A strain rate of 0.5mm/minute was used in all the tests.

## Results

### Characterization

Figure 1 shows the particle size distribution curves of the 4 samples, and Table 1 summarize the characterization test results of the samples as well as their classification according to Unified Soil Classification (USC). Table 2 presents the permeability test results of the 4 samples.

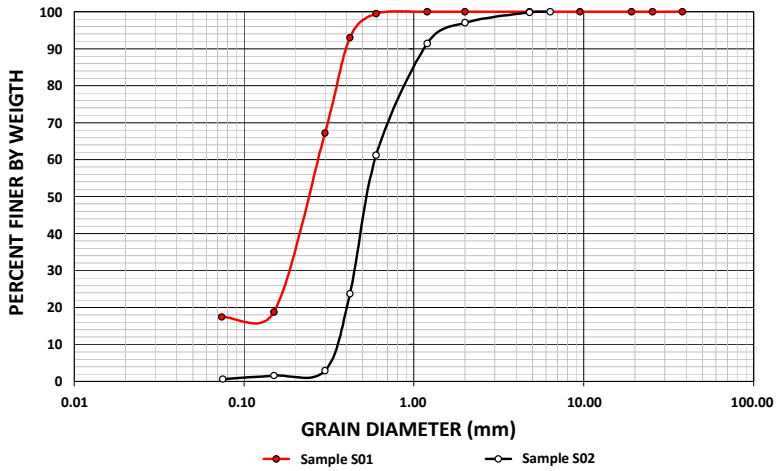


Figure 1: Particle size distribution curves of the 2 samples.

Table 1: Particle size characteristics of the 2 sands.

| Samples | Gravel (%) | Coarse Sand (%) | Medium Sand (%) | Fine Sand (%) | $C_u$ | $C_c$ | $\rho_s$ (g/cm³) | $e_{max}$ | $e_{min}$ | Classification - USC |
|---|---|---|---|---|---|---|---|---|---|---|
| **S01** | 0.0 | 1.1 | 68.9 | 30.0 | 1.53 | 0.90 | 2.65 | 1.10 | 0.35 | Medium to fine sand - **SP** |
| **S02** | 3.0 | 36.0 | 59.0 | 2.0 | 1.71 | 0.96 | 2.67 | 0.75 | 0.50 | Medium to coarse sand - **SP** |

Table 2: Permeability test results of the 2 samples

| Samples | S01 | S02 |
|---|---|---|
| **k (cm/s) - $e_{max}$** | $8.9 \times 10^{-2}$ | $1.2 \times 10^{-1}$ |
| **k (cm/s) - $e_{min}$** | $1.2 \times 10^{-2}$ | $5.4 \times 10^{-1}$ |

Direct Shear Tests: S01

As mentioned above this series of tests was conducted under normal stress of 100kPa. Figures 2 and 3 show the results obtained by [2]. With these results the angle of friction was determined for each sample. Figure 4 exhibits the angles of friction as a function of the variation in void ratio in the samples [2].

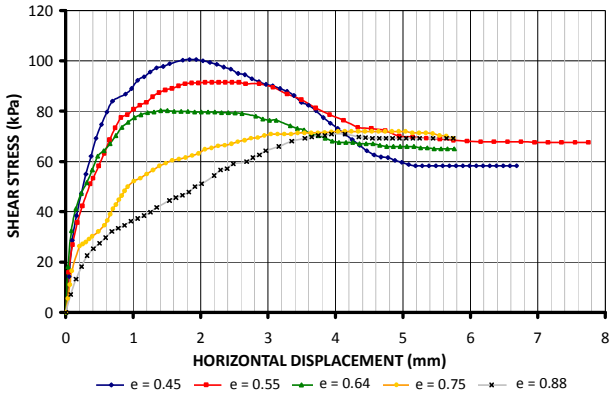


Figure 2: Shear stress x horizontal displacement – Sand 1. [2]

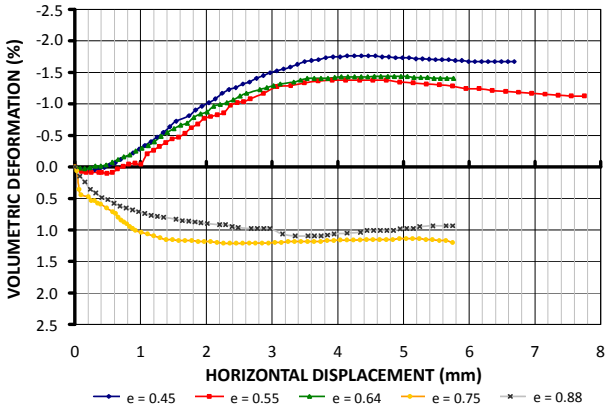


Figure 3: Volumetric deformation x horizontal displacement – Sand 1. [2]

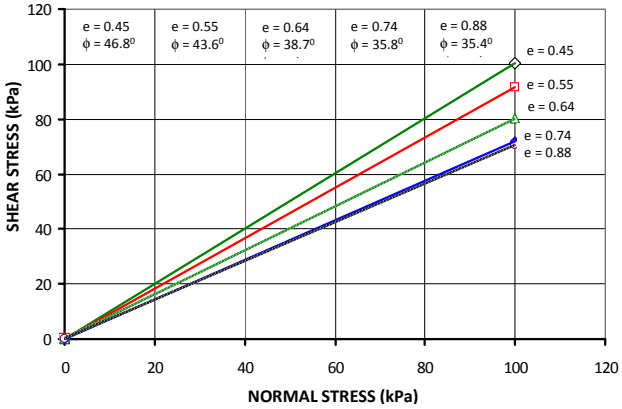


Figure 4: Angle of friction of sand S01 for the 5 compactness conditions and vertical stress of 100kPa. [2]

Direct Shear Tests: S02

Test results of these samples are presented in Figures 5, 6 and 7. Figure 8 shows strength envelopes obtained for this material, where the angles of friction range from 36.6º to 40.5º.

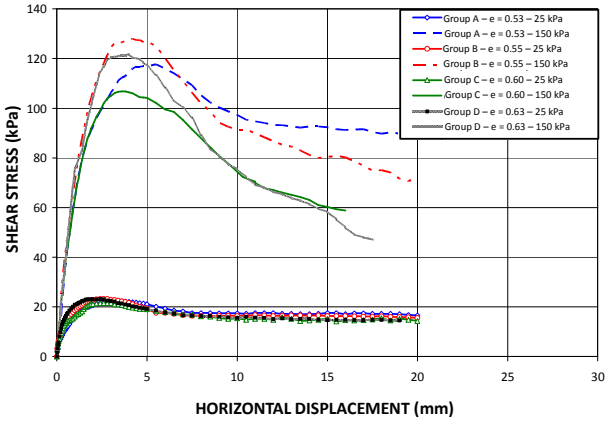


Figure 5: Shear stress x horizontal displacement for the 4 molding conditions of sand S02.

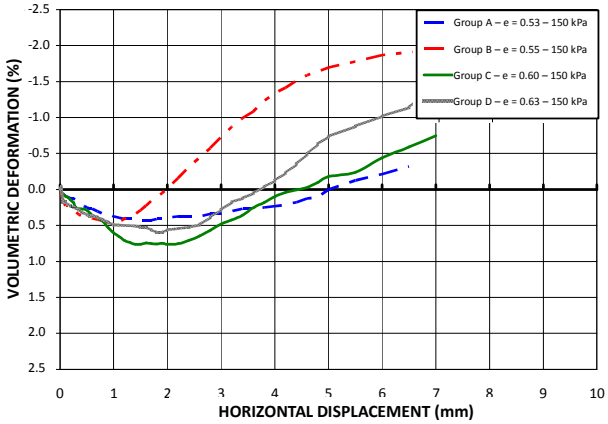


Figure 6: Volumetric deformation x horizontal displacement for the 4 molding conditions of sand S02 under vertical stress of 150kPa.

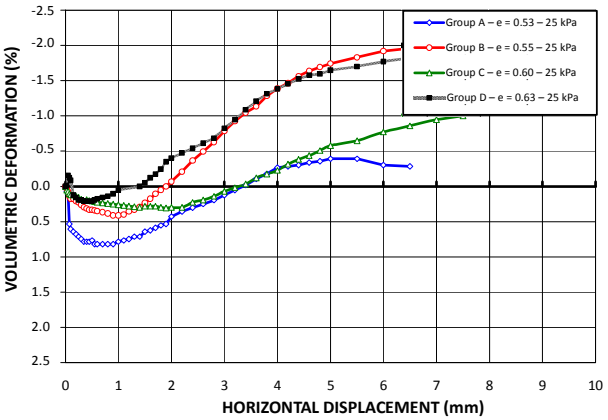


Figure 7: Volumetric deformation x horizontal displacement for the 4 molding conditions of sand S02 under vertical stress of 25kPa.

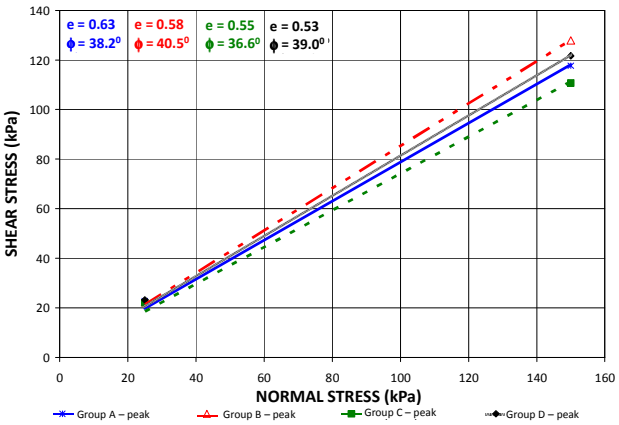


Figure 8: Shear stress x normal stress for the 4 molding conditions of sand S02.

Triaxial Compression Strength Tests – CD Test: S02

Figures 9, 10, 11 and 12 show the results of these tests. Figure 13 exhibits the envelopes in terms of the s x t diagram of this series of tests, as well as angles of friction of the soil, with respect to the Mohr-Coulomb envelope.

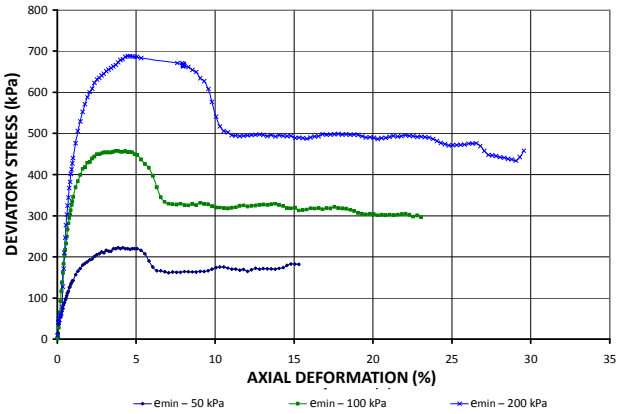


Figure 9: Deviatory stress x axial deformation of sand S02 in the dense state.

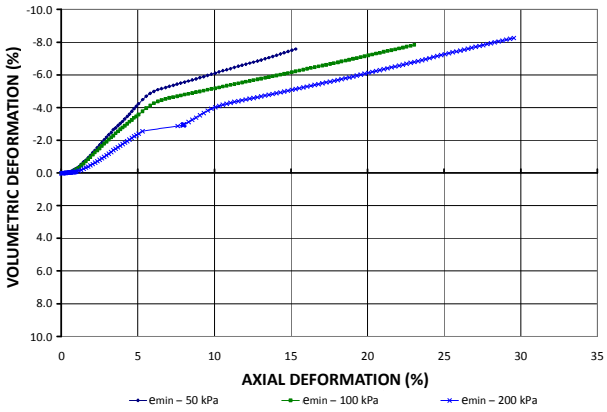


Figure 10: Volumetric deformation x axial deformation of sand S02 in the dense state.

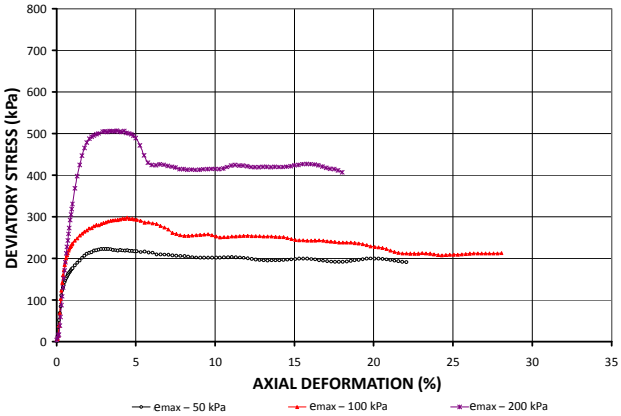


Figure 11: Deviatory stress x axial deformation of sand S02 in the loose state.

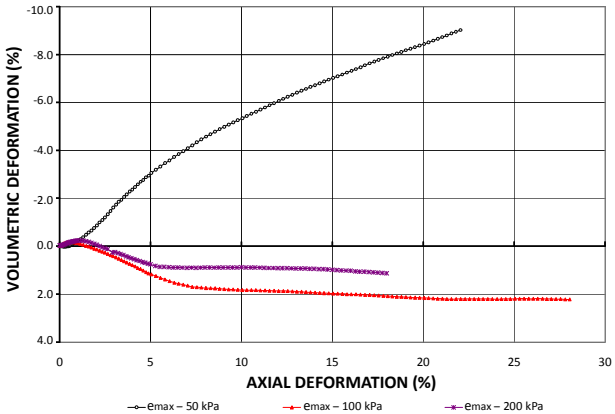


Figure 12: Volumetric deformation x axial deformation of sand S02 in the loose state.

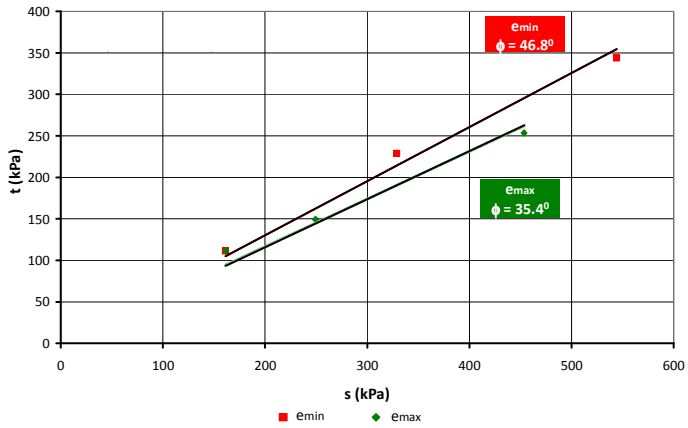


Figure 13: *s x t* diagram of sample S02.

## Analysis of Results

Sands S01 and S02 were classified according to USC as medium to fine and coarse to medium sand, respectively, both poorly graduated. The coefficient of permeability obtained for S01 sand was around 10 times smaller than that obtained for S02 sand. Relative density did not significantly influence the permeability of the samples.

With respect to shear Strength of sand S01, a well-defined peak can be observed in tests with void ratios between 0.45 and 0.64. In these tests there was a slight tendency to compression, followed by volumetric expansion (dilatancy) during the test (Figures 2 and 3). It is hypothesized that the critical void ratio for this material under these conditions is between 0.64 and 0.75. In this series of trials the angle of friction ranged from 35.5º, in a less compact state, to 46.8º, in the denser state (Figure 4). These values corroborate the limits established by [10] and [11].

Sand S02, for the series of direct shear tests, with vertical stress of 150kPa, showed no tendency to an increase in shear strength with a rise in relative density. This is evidenced, for example, when the shear strength of Group B, which, as previously mentioned, has 65% relative compactness, is compared with that obtained by Groups C and D.

The results of tests with 25kPa of normal stress showed no discrepancies. The initial condition of the samples, for this level of vertical stress, seemingly did not influence their shear strength (Figures 5). The angles of friction for this sample ranged from 36.6º to 40.5º (Figure 8). It is hypothesized that the divergent results are related to the lack of uniform testing. A tendency to compression was observed in all the tests of this sand (S02), followed by dilatancy, from 2 millimeters of horizontal displacement onwards (Figures 6 and 7).

The triaxial tests conducted with sand S02 showed greater deviatory stress with both an increase in confining stress and a rise in relative density (Figures 9 and 11).

As depicted in Figure 10 regarding the behavior of the material in terms of volumetric variation with an increase in axial deformation, test specimens molded with a minimum void ratio show a tendency to compression followed by dilatancy of test specimens. This dilatancy increased with a decline in confinement level. In tests where test specimens were molded with relative density in terms of maximum void ratio, confining stresses of 100kPa and 200kPa showed expansion followed by compression, whereas in the test with confining stress of 50kPa expansion only occurred in the shear phase (Figure 12).

The effective angles of friction for the sample in states of minimum and maximum compactness obtained from triaxial tests were 35.4º and 40.7º respectively. These values are similar to those obtained from the direct shear test in this sample. [12] reported the similarity of angles of friction obtained from direct shear and drained triaxial tests. He states that for practical purposes the direct shear test can be used to determine the angle of friction of sands.

If the angles of friction for the two samples are compared in their maximum and minimum states, it can be observed that in the loose state, the angle of friction of the samples is similar, while in the compact state, the angle of friction at peak strength of sand S01 is around 7 times higher than in

sand S02. In regard to critical values, this difference is less than in samples with lower relative density, as illustrated in Figures 2, 5 and 11, where after resistance peak, the residual strength was somewhat similar.

## Conclusion

According to the results of this study, it is concluded that an increase in relative density in the sands did not significantly influence their permeability.

A rise in relative density generally results in greater interaction between grains of sand, which has a direct effect on the shear strength of a material and, in turn, on the angle of friction of the samples. Irrespective of the tendency to increased strength as a function of relative compactness, if the highest and lowest angle of friction values found for sand S01 and S02 are compared, it can be observed that the values obtained for sand S01 are significantly higher than those of sand S02, which contrasts the notion that grain size determines the strength of a granular material.

The results of triaxial compression tests show a tendency towards increased strength, with both a rise in confining stress and an increase in relative density. Under conditions of maximum compactness, as expected, it was found that the lower the confining stress, the higher the tendency of the material to expand during the shear phase. Under conditions of minimum compactness, the behavior of dense sand was observed in the test with 50kPa of confining stress and loose sand in confined samples with 100kPa and 200kPa.

## References

[1] Lee, K. L. and Seed, H. B. Drained strength characteristics of sands. J. Soil Mech. Fdns Div. Am. Sot. Ciu. Engrs 93, SM6, 117-141, (1967).

[2] Freitas Neto, O., Costa, F. A. A., Lima, V. A, Pereira, J. R. C. and Santos Jr. O. F. Determination of the geotechnical properties of eolian sediments of Natal-RN. II Geojovem. (In Portuguese), (2006).

[3] Lambe, T. W and Withman, R. V. Soils Mechanics, John Wiley & Sons, New York, (1970).

[4] Vilar, O. M. Soil Mechanics - Shear Strength. (Class notes). (In Portuguese), (2006).

[5] Associação Brasileira de Normas Técnicas – ABNT – NBR 7181 – Soil – Granulometric analysis. (In Portuguese), (1984).

[6] Associação Brasileira de Normas Técnicas – ABNT – MB – 3324 – Soil – Determination of the maximum void non-cohesive soil. (In Portuguese), (1990).

[7] Associação Brasileira de Normas Técnicas – ABNT – MB – 3388 – Soil – Determination of the minimum void of non-cohesive soil. (In Portuguese), (1991).

[8] Associação Brasileira de Normas Técnicas – ABNT – NBR – 6508 – Soil – Determination of specific gravity of solid. (In Portuguese), (1994).

[9] Associação Brasileira de Normas Técnicas – ABNT – NBR 13292 – Soil – Coefficient of permeability of granular soils with constant load. (In Portuguese), (1995).

[10] Terzaghi, K. and Peck, R.B. Soil Mechanics in engineering practice. 2ed. New York: Jonh Wiley and Sons Co. 729p, (1967).

[11] Sousa Pinto, C. Basic class in soil mechanics. In 16 lessons. Oficina de Textos. Sao Paulo. (In Portuguese), (2002).

[12] Mello, V. F. B. Contribution to the study of shear strength of soils. Tese. (In Portuguese), (1956).

*Applied Mechanics and Materials Vols. 580-583 (2014) pp 665-668*
*© (2014) Trans Tech Publications, Switzerland*
*doi:10.4028/www.scientific.net/AMM.580-583.665*

# Numerical Simulation of Failure Process on Soil Slope with Different Support Measures

Yu-wei Zhang[1,a] , Lie-xian Tang[1,b*], Da-chuan Bai[1,c], Peng Zhou[1,d]

[1] University of Science and Technology Liaoning, Anshan, China, 114051

[a] zhangweitian5425@163.com, [b] t7766@sina.com, [c]1129105052@qq.com, [d]396282411@qq.com

**Key words：** Numerical Simulation; RFPA-Centrifuge; Soil Slope; Support Measure

**Abstract：** In conventional analysis methods of soil slope, we must presume potential sliding surface at first and then gain the safety factors, judge the stability of slope by the safety factors. In fact, if we know a slope is unstability but don't know where will be slide or failure, we can't adopt effective measures to support and prevent the sliding accidents appearing. This paper use RFPA-Centrifuge to numerical simulate the failure of soil slope with different support measures without presume any potential sliding surface, success to gain the failure process and the corresponding safety factors. From the calculate results of RFPA-Centrifuge, we can find where is the first failure point and all the slide mass. So if we can use good analysis software to simulate the failure process of slope and adopt corresponding support measures before the engineering beginning, the stability of slope will be better and the accidents will be disappeared or reduced.

## Introduction

In conventional analysis methods of soil slope, we must presume potential sliding surface at first and then gain the safety factors, judge the stability of slope by the safety factors[1-3]. In fact, if we know a slope is unstability but don't know where will be slide or failure, we can't adopt effective measures to support and prevent the sliding accidents appearing. The authors of this paper hope to resolve above problems through a numerical analysis method.

## Essential Principle

RFPA (Realistical Failure Process Analysis) is a professional series software to failure process analysis in geotechnical engineering. RFPA-Centrifuge is based on the principle of geotechnical centrifuge model tests, the weights of all cells are increased step by step in a certain coefficient, without change other parameters. At first to calculate stress for given increment of weight in every step, and then check every cell based on a certain criteria, increase next increment and calculate next step if every cell has not change, calculate stress again in current step if some cells be changed until no new changed cell is checked. Repeat continually above process, the relatively weak cell will failure when the load stress over its carrying capacity. The macroscopical failure surface will be transfixed with the amount of fail cells increase continually [4].

## Unstable Criterion

There are two primary unstable criterions in slope analysis software, the first criterion is regarding convergence as the unstable indication of slope which adopting stress and displacement to getting answers in calculate process of finite element methods, the second criterion is regarding connectedness of strain from slop toe to crest as the unstable indication of slope. The finite element calculate adopt whole loading in RFPA-Centrifuge, there are converge results every step, so this method regard the max failure elements as the unstable indication of slope. RFPA-Centrifuge will record automatically the number of failure elements in every loading steps, so this method judge the stability of slope is simple and effective.

The safety factor of RFPA-Centrifuge is defined with the specific gravity of element which failure surface connected divide the initial specific gravity of element, equation is following:

$$\gamma=\gamma_0[1+(n-1)\times\Delta]$$

remark：γ —— the specific gravity of elements when failure surface connected;
$\gamma_0$ —— the initial specific gravity of element;
n —— loading steps when failure surface connected;
Δ —— centrifuge loading coefficient.

$$K=\frac{\gamma}{\gamma_0}=1+\frac{b}{b_0}\cdot(n-1)\cdot\Delta$$

remark：$K$ ——safety factor，$b_0$——size of prototype，b——size of model.

## Engineering Instance of Soil Slope

There is a typical engineering instance in reference [5], the road between Chongqing to Zhanjiang occured slope slippage in Guizhou province. Undercut slip mass 5-6m cause the slope active and continue development, at last being many slide surfaces in soil and airslake layer. It will cause slip mass slide if dig continue with design parameters. So adopted support measures with anti-slide pile adding pre-stressed anchor cable. Typical cross-section and sketch of finite element strength reduce mesh for landslide are showed in Fig.1 and the mechanical parameters are showed in table 1. The sketch of RFPA-Centrifuge is showed in Fig.2, including only anti-slide pile model and anti-slide pile adding pre-stressed anchor cable model.

Table.1 Mechanical parameters of the slope

| Material name | Weight /KN.m$^{-3}$ | Elasticity modulus /MPa | Poisson's ratio | Cohesive strength /kPa | Internal frictional angle /(º) |
|---|---|---|---|---|---|
| Slip mass | 21 | 30 | 0.30 | 25.5 | 24.5 |
| Sliding bed | 24 | $10^5$ | 0.25 | 200 | 30.0 |
| pile(C25concrete) | 24 | $2.9\times10^4$ | 0.20 | Regarding elastic material | |

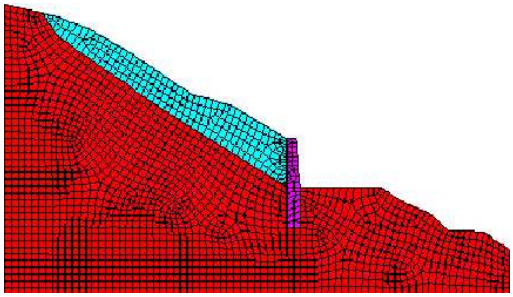

Fig.1 Typical cross-section and sketch of finite element strength reduce mesh for landslide

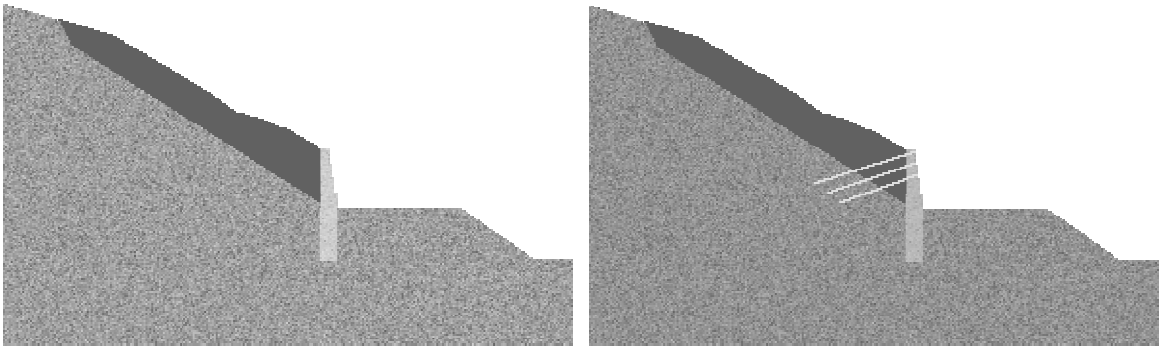

(a) only anti-slide pile (b) anti-slide pile adding pre-stressed anchor cable

Fig.2 Sketch of RFPA-Centrifuge model for landslide

**Numerical Calculation Results**

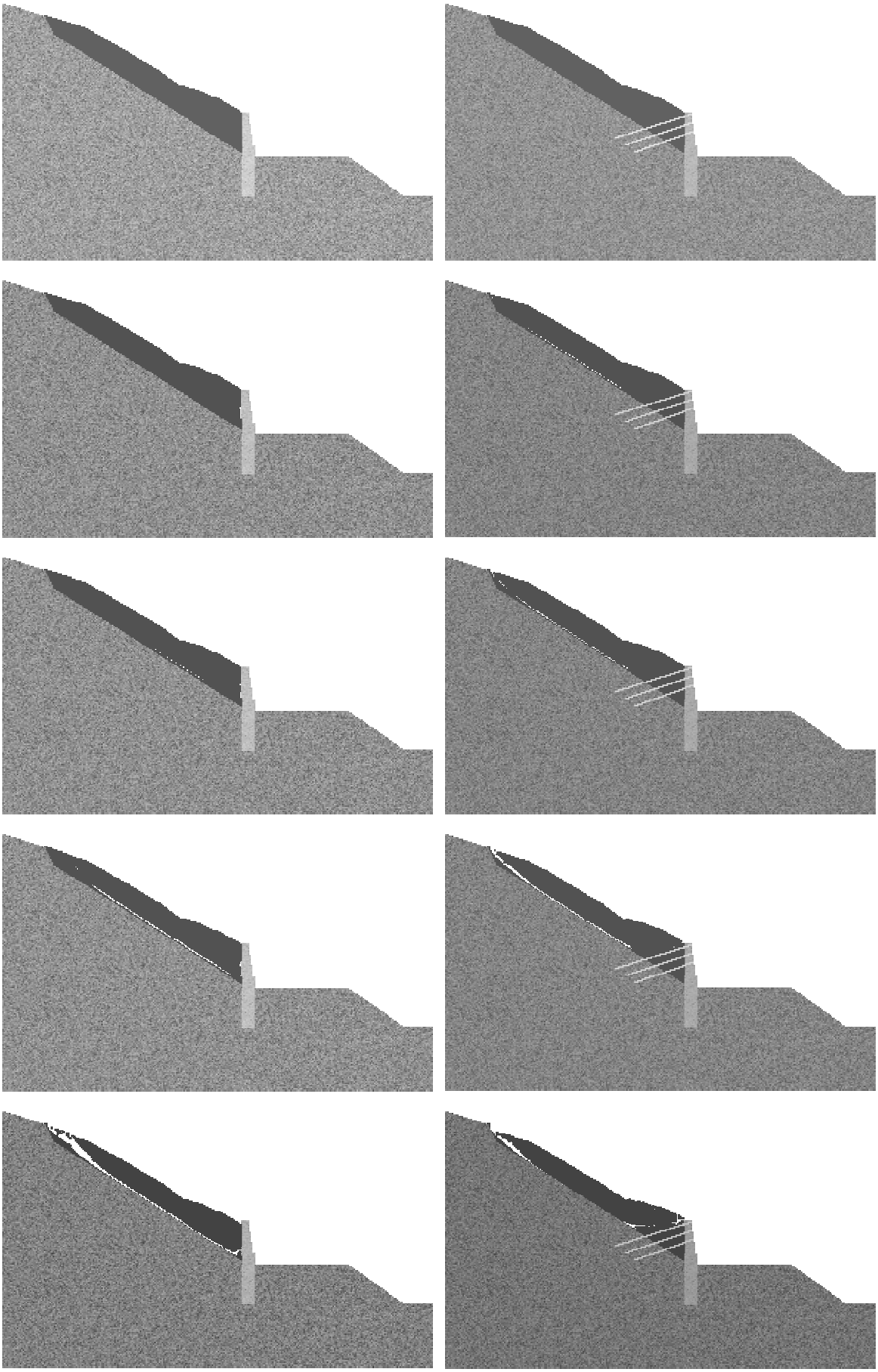

(a) only anti-slide pile (b) anti-slide pile adding pre-stressed anchor cable

Fig.3 Failure process showed by RFPA-Centrifuge

Fig.3 shows the failure process of landslide with different support measures by RFPA-Centrifuge. From this picture, we can see that the results which anti-slide pile adding pre-stressed anchor cable are same to the result of finite element strength reduce method(showed in Fig.4), the slide surface occurred at the top of anti-slide pile, however the slide surface didn't occurred at the top of the anti-slide pile which adopted only anti-slide pile to support the landslide.

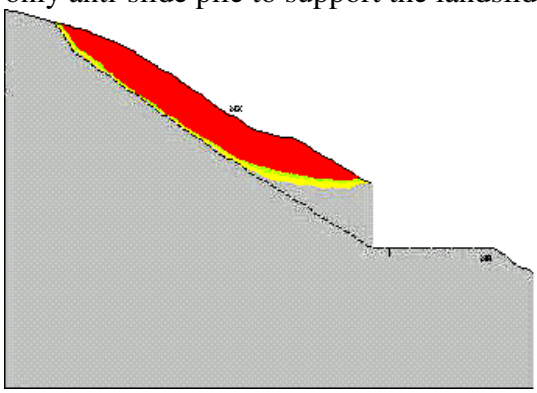

Fig.4 Result of strength reduce method

In calculation results of RFPA-Centrifuge, the safety factor which adopted only anti-slide pile is 1.14, and the safety factor which adopted anti-slide pile adding pre-stressed anchor cable is 1.36. Therefore, we can find that adopted anti-slide pile adding pre-stressed anchor cable, the stability of slope is improved greatly.

## Conclusions

From the calculate results of soil slope with different support measures by RFPA-Centrifuge, we can find that this software can simulate the failure process of slope without presume any potential sliding surface, at the same time we can gain the corresponding safety factors.

Before the engineering beginning, if we can use good analysis software to simulate the failure process of slope and adopt corresponding support measures, the stability of slope will be better and the accidents will be disappeared or reduced.

## Acknowledge

(1) Excellent Young Scholars Growth Plans of Liao'ning Educational Committee (LJQ2013033)
(2) Youth Foundation of University of Science and Technology Liaoning (2012QN07)

## References

[1] Chen Zu-yu. Principles for soil slope stability analysis. methodology. program [M]，Beijing: China Water & Power Press,2005,1-2. in Chinese

[2] Griffiths D V，Lane P A. Slope stability analysis by finite elements[J]. Geotechnique，1999, 49(3):387-403.

[3] Dawson E M，Roth W H，Drescher A. Slope stability analysis by strength reduction[J]. Geotechnique,1999,49(6):835-840.

[4] Tang Chun-an, Tang Lie-xian, Li Lian-chong, Li Chang-wen. Centrifugal loading method of RFPA for the failure process analysis of rock and soil structure[J]. Chinese Journal of Geotechnical Engineering, 2007, 29(1): 71-76. in Chinese

[5] Zheng Ying-ren, Zhao Shang-yi. Calculation of inner force of support structure for landslide/slope by using strength reduction FEM[J]，Chinese Journal of Rock Mechanics and Engineering,2004, 23(20):3552-3558. in Chinese

*Applied Mechanics and Materials Vols. 580-583 (2014) pp 669-673*
*© (2014) Trans Tech Publications, Switzerland*
*doi:10.4028/www.scientific.net/AMM.580-583.669*

# Prediction of Composite Foundation Settlement Based on Multi-Variable Gray Model

Yue Wang[1,a] Guang Yang[2,b]

[1]Inner Mongolia KaiTong Construction Co., Ltd

Erdos Street, Huhehaote, 010010，China

[2]School of Engineering and Technology, China University of Geosciences

29 Xueyuan Road, Beijing, 100083, China

[a]ktwy6789@sina.com, [b]gyang@126.com

**Keywords:** MGM (1, n) model, composite foundation settlement, prediction

**Abstract.** In this paper, based on the principle of gray theory, MGM(1,n) multi-variable settlement prediction model was established. Combined with specific examples of projects, settlement of rigid pile composite foundation was predicted, and the prediction results are compared with both prediction results of GM(1,1) gray model which is currently comparatively mature and the settlement observation results. The study shows that it is effective to use MGM(1,n) multivariate gray model to predict composite foundation settlement.

## Introduction

Settlement is an important indicator to measure whether the buildings are security and stability. The purposes of monitoring the composite foundation settlement lie not only in monitoring every moment of settlement in the project, but also in predicting possible settlement at a future time by establishing settlement model which is based on the settlement monitoring data, and then analyzing its security, take measures in advance to minimize or inhibit the harm caused by ground subsidence. Currently, there are a lot of composite foundation settlement prediction methods, such as curve fitting method, regression cut method, determine function method, the gray model method and so on[1]. Composite foundation settlement which is fuzzy and uncertain is affected by many factors. Therefore, to predict foundation settlement using the gray model method which is based on the gray theory is favored by people. Gray theory is to make a scientific prediction of the future state of the system through processing original data, establishing the grey model and calculating the related-parameters of the model. In composite foundation settlement predictions, the gray GM(1,1) model is widely used. Actually, foundation settlement deformations in each monitoring point are not independent, associated with settlement of other monitoring points around and influenced by them. Multi-variable grey model can consider the impact of relevant variables and reflect the settlement law better, thus predict the settlement more accurately [2, 3].

## Establish Multi-Variable Gray Settlement Model

**MGM(1,n) Gray Settlement Model.** MGM(1,n) gray settlement model is a first order ordinary differential equations with n variables. It is promoted from GM(1,1) settlement prediction model in the case of n variables. Let $x_i^{(0)}(k)(i=1,2,\cdots,n)$ be a sequence of n original settlement monitoring, $x_i^{(1)}(k),(i=1,2,\cdots,n)$ is the liner accumulated generating sequence correspondingly, which means

$$x_i^{(i)}(k)=\sum_{j=1}^{k}x_i^{(0)}(j)$$

The first order ordinary differential equations with n variables of MGM(1,n) settlement model is:

$$\left.\begin{aligned}
&\frac{dx_1^{(1)}}{dt} = a_{11}x_1^{(1)} + a_{12}x_2^{(1)} + \cdots + a_{1n}x_n^{(1)} + b_1 \\
&\frac{dx_1^{(1)}}{dt} = a_{11}x_1^{(1)} + a_{12}x_2^{(1)} + \cdots + a_{1n}x_n^{(1)} + b_2 \\
&\vdots \\
&\frac{dx_1^{(1)}}{dt} = a_{11}x_1^{(1)} + a_{12}x_2^{(1)} + \cdots + a_{1n}x_n^{(1)} + b_n
\end{aligned}\right\} \tag{1}$$

Written in matrix form as:

$$\frac{dX^{(1)}}{dt} = AX^{(1)} + B \tag{2}$$

Where:

$$A = \begin{pmatrix} a_{11} & a_{12} & \cdots & a_{1n} \\ a_{21} & a_{22} & \cdots & a_{2n} \\ \vdots & \vdots & & \vdots \\ a_{n1} & a_{n2} & \cdots & a_{nn} \end{pmatrix} \quad ; \quad B = \begin{pmatrix} b_1 \\ b_2 \\ \vdots \\ b_n \end{pmatrix} \quad ; \quad X^{(1)}(t) = (x_1^{(1)}(t), x_2^1(t), \cdots, x_n^1(t))^t$$

Based on integral transformation principle, pre-multiply both side of the equation (2) by $e^{-At}$ can get formula (3).

$$e^{-At}\left(\frac{dX^{(1)}}{dt} - AX^{(1)}\right) = e^{-At}B \tag{3}$$

After the integration in the interval [0, $t$], time-varying settlement model can be got, whose expression is formula (4).

$$X^{(1)}(t) = e^{-At}(X^{(1)}(1) + A^{-1}B) - A^{-1}B \tag{4}$$

**Solve the Model Parameters A and B.** The equation (1) is discretized, and least square method is used to estimate, which can get formula (5).

$$H = (S^T S)^{-1} S^T Y \tag{5}$$

Where:

$$S = \begin{pmatrix} z_1(2) & z_2(2) & \cdots & z_n(2) & 1 \\ z_1(3) & z_2(3) & \cdots & z_n(3) & 1 \\ \vdots & \vdots & & \vdots & \vdots \\ z_1(m) & z_2(m) & \cdots & z_n(m) & 1 \end{pmatrix}; \quad Y = \begin{pmatrix} x_1^{(0)}(2) & x_2^{(0)}(2) & \cdots & x_n^{(0)}(2) \\ x_1^{(0)}(3) & x_2^{(0)}(3) & \cdots & x_n^{(0)}(3) \\ \vdots & \vdots & & \vdots \\ x_1^{(0)}(m) & x_2^{(0)}(m) & \cdots & x_n^{(0)}(m) \end{pmatrix}; \quad H = \begin{pmatrix} a_{11} & a_{21} & \cdots & a_{n1} \\ a_{12} & a_{22} & \cdots & a_{n2} \\ \vdots & \vdots & & \vdots \\ a_{1n} & a_{2n} & \cdots & a_{nn} \\ b_1 & b_2 & \cdots & b_n \end{pmatrix}$$

$$z_i(k)=\frac{1}{2}(x_i^{(1)}(k)+x_i^{(1)}(k-1)),\quad (i=1,2,\cdots,n;k=2,3,\cdots,m)\,.$$

$\hat{A}$ and $\hat{B}$ which are identification values of $A$ and $B$ can be obtained from the matrix H:

$$\hat{A}=\begin{pmatrix}\hat{a}_{11} & \hat{a}_{12} & \cdots & \hat{a}_{1n}\\ \hat{a}_{21} & \hat{a}_{22} & \cdots & \hat{a}_{2n}\\ \vdots & \vdots & & \vdots\\ \hat{a}_{n1} & \hat{a}_{n2} & \cdots & \hat{a}_{nn}\end{pmatrix};\qquad \hat{B}=\begin{pmatrix}\hat{b}_1\\ \hat{b}_2\\ \vdots\\ \hat{b}_n\end{pmatrix}$$

The formula (3) can be written in the form of a discrete model in formula (6).

$$\hat{X}^{(1)}(k)=e^{-\hat{A}(k-1)}(\hat{X}^{(1)}(1)+\hat{A}^{-1}\hat{B})-\hat{A}^{-1}\hat{B} \tag{6}$$

Where: $e^{-\hat{A}(k-1)}=I+\sum_{i=1}^{\infty}\frac{\hat{A}^i}{i!}(k-1)$

The formula (6) is inverse accumulation restored, which can get formula (7).

$$\hat{X}^{(0)}(k)=\hat{X}^{(1)}(k)-\hat{X}^{(1)}(k-1),\quad (k=1,2,3\cdots) \tag{7}$$

When k≤m, $\hat{X}^{(0)}(k)$ is the analog value of the settlement; when k＞m, $\hat{X}^{(0)}(k)$ is the predicted value of the settlement.

**Modeling Precision.** $\delta^2$ which is the average fitting precision of the settlement model is calculated as formula (8).

$$\delta^2=\frac{\sum_{i=1}^{n}V_i^TV_i}{nm} \tag{8}$$

Where: residuals $v_i(k)=x_i^{(0)}(k)-\hat{x}_i^{(0)}(k)$,

$$V_i=(v_i(1),v_i(2),\cdots,v_i(m))^T\quad (i=1,2,\cdots,n;k=1,2,\cdots,m)$$

In projects, the smaller average fitting precision is, the higher the precision of the MGM(1,n) settlement model is.

For ease of calculation, the MGM(1,n) multi-variables gray settlement prediction program is compiled by the author using MATLAB software. In this program, the settlement analog values, the settlement predictive value as well as errors and precision can be quickly calculated after input composite foundation settlement observations.

## Application Examples

A 24 layers high-rise building is 85 meters high, whose main structure is frame structure, using CFG pile composite foundation. Since the beginning of the building construction, four settlement monitoring points (P1, P2, P3, P4) are laid around the building. Setting the settlement observation interval of one month, 16 times of settlement monitoring data is listed in Table 1. Now the previous

12 times of data is used to establish the model, and the last 4 times of data is used to compare with the predicted settlement values.

Table 1. Settlement Observation Data

| Observation points | Settlement /mm | | | | | | | | | | | | | | | |
|---|---|---|---|---|---|---|---|---|---|---|---|---|---|---|---|---|
| | 1 | 2 | 3 | 4 | 5 | 6 | 7 | 8 | 9 | 10 | 11 | 12 | 13 | 14 | 15 | 16 |
| P1 | 4.9 | 10.8 | 11.4 | 12.0 | 13.2 | 14.5 | 17.9 | 21.2 | 22.8 | 24.6 | 25.2 | 26.9 | 28.3 | 29.4 | 30.7 | 31.4 |
| P2 | 6.2 | 7.1 | 7.3 | 7.8 | 8.1 | 9.6 | 11.8 | 13.7 | 14.3 | 14.9 | 16.0 | 17.0 | 17.8 | 18.5 | 19.2 | 19.8 |
| P3 | 5.2 | 5.4 | 5.6 | 6.7 | 7.7 | 8.8 | 10.3 | 11.9 | 13.6 | 14.2 | 14.9 | 15.8 | 16.7 | 17.5 | 18.3 | 19.0 |
| P4 | 4.1 | 4.2 | 4.3 | 4.7 | 6.0 | 6.5 | 8.1 | 9.4 | 10.9 | 11.5 | 12.0 | 12.8 | 13.5 | 14.3 | 14.8 | 15.6 |

**Establish the Settlement Prediction Model.** In this example, n=4. According to formula (1) to (7), MGM(1,4) settlement model established on points P1, P2, P3 and P4 is formula (9).

$$\hat{x}_{1i}(1+k) = e^{\overline{A}k}\begin{pmatrix} -194.8559 \\ -115.2984 \\ -116.9452 \\ -99.5635 \end{pmatrix} - \begin{pmatrix} -199.7559 \\ -121.4984 \\ -122.1452 \\ -103.6635 \end{pmatrix} \tag{9}$$

Where:

$$\overline{A} = \begin{pmatrix} -3.0419 & -3.9042 & 1.1453 & -0.0159 \\ -1.9200 & 2.1720 & 1.4568 & -0.5392 \\ -1.0547 & 1.3859 & 1.0733 & -0.8577 \\ -1.1606 & 1.3727 & 1.0567 & -0.5982 \end{pmatrix}; \quad \overline{B} = \begin{pmatrix} -4.9562 \\ -2.4057 \\ -0.6217 \\ -1.9942 \end{pmatrix}$$

The analog values calculated from settlement model which is established using previous 12 times of data are listed in Table 2. It can be seen from Table 2 that all the relative errors of analog values and observation values are less than 0.5%. The average goodness of fit is 0.0773, and the value is relatively small, indicating that the settlement model established by using MGM(1,4) gray model has higher precision and can be used to predict the composite foundation settlement.

Table 2. Settlement Analog Results of MGM(1,4) Model

| Observation sequences | Analog values /mm | | | | Measured values /mm | | | | Residuals /mm | | | |
|---|---|---|---|---|---|---|---|---|---|---|---|---|
| | $x_1$ | $x_2$ | $x_3$ | $x_4$ | $y_1$ | $y_2$ | $y_3$ | $y_4$ | $v_1$ | $v_2$ | $v_3$ | $v_4$ |
| 1 | 4.9 | 6.2 | 5.2 | 4.1 | 4.9 | 6.2 | 5.2 | 4.1 | 0 | 0 | 0 | 0 |
| 2 | 10.86 | 7.19 | 5.27 | 4.09 | 10.8 | 7.1 | 5.4 | 4.2 | 0.06 | 0.09 | -0.13 | -0.11 |
| 3 | 11.40 | 7.26 | 5.87 | 4.39 | 11.4 | 7.3 | 5.6 | 4.3 | 0 | -0.04 | 0.27 | 0.09 |
| 4 | 11.86 | 7.52 | 6.58 | 4.83 | 12.0 | 7.8 | 6.7 | 4.7 | -0.14 | -0.28 | -0.12 | 0.13 |
| 5 | 13.07 | 8.40 | 7.63 | 5.67 | 13.2 | 8.1 | 7.7 | 6.0 | 0.17 | 0.30 | -0.07 | -0.33 |
| 6 | 15.20 | 9.87 | 8.99 | 6.86 | 14.5 | 9.6 | 8.8 | 6.5 | 0.70 | 0.27 | 0.19 | 0.36 |
| 7 | 17.87 | 11.59 | 10.49 | 8.20 | 17.9 | 11.8 | 10.3 | 8.1 | -0.03 | -0.21 | 0.19 | 0.10 |
| 8 | 20.54 | 13.19 | 11.92 | 9.48 | 21.2 | 13.7 | 11.9 | 9.4 | -0.66 | -0.51 | 0.02 | 0.08 |
| 9 | 22.82 | 14.48 | 13.16 | 10.56 | 22.8 | 14.3 | 13.6 | 10.9 | 0.02 | 0.18 | -0.44 | -0.34 |
| 10 | 24.61 | 15.46 | 14.22 | 11.46 | 24.6 | 14.9 | 14.2 | 11.5 | 0.01 | 0.56 | 0.02 | -0.04 |
| 11 | 26.03 | 16.23 | 15.14 | 12.23 | 25.2 | 16.0 | 14.9 | 12.0 | 0.83 | 0.23 | 0.24 | 0.23 |
| 12 | 27.27 | 16.92 | 15.98 | 12.95 | 26.9 | 17.0 | 15.8 | 12.8 | 0.37 | -0.08 | 0.18 | 0.15 |

**Subsidence Prediction.** Settlement prediction results (13-16 times) of MGM(1,4) model are listed in Table 3, and the prediction precision is showed in Table 4. It can be seen from Table 4 that the prediction errors of the MGM(1,4) model are in 0.06~0.3 mm, whose fitting precision is 0.0045, compared with GM(1,1) settlement model, it has higher precision, whose prediction values are closer to the measured values.

Table 3. Contrast of Forecasted Settlement Using Three Different Methods

| Observation | MGM(1,4) model /mm | | | | GM(1,1) model /mm | | | | Measured values/mm | | | |
|---|---|---|---|---|---|---|---|---|---|---|---|---|
| sequences | $x_1$ | $x_2$ | $x_3$ | $x_4$ | $x_1$ | $x_2$ | $x_3$ | $x_4$ | $y_1$ | $y_2$ | $y_3$ | $y_4$ |
| 13 | 28.47 | 17.61 | 16.79 | 13.66 | 27.82 | 18.30 | 17.11 | 14.06 | 28.3 | 17.8 | 16.7 | 13.5 |
| 14 | 29.62 | 18.28 | 17.53 | 14.35 | 28.93 | 19.59 | 18.38 | 15.22 | 29.4 | 18.5 | 17.5 | 14.3 |
| 15 | 30.67 | 18.87 | 18.19 | 14.97 | 29.96 | 20.93 | 19.71 | 16.45 | 30.7 | 19.2 | 18.3 | 14.8 |
| 16 | 31.50 | 19.30 | 18.70 | 15.47 | 30.92 | 22.33 | 21.09 | 17.75 | 31.4 | 19.8 | 19.0 | 15.6 |

Table 4. Prediction Precision Using Two Different Methods*

| Observation | MGM(1,4) model | | GM(1,1) model | |
|---|---|---|---|---|
| points | $\delta^2$ | $v$ | $\delta^2$ | $v$ |
| P1 | 0.0448 | 0.115 | 0.333 | 0.567 |
| P2 | | 0.310 | 2.430 | 1.405 |
| P3 | | 0.073 | 1.825 | 1.198 |
| P4 | | 0.063 | 2.156 | 1.320 |

* $\delta^2$ is the prediction precision; $v$ is mean residual.

## Conclusion

In this paper, multi-variable gray settlement prediction model is established. Using MATLAB software gray settlement model program is developed. With specific project example, the composite foundation settlement is simulated and predicted. The results show, MGM(1,n) gray prediction model has better fitting precision and prediction precision. Based on the settlement monitoring, this model can be used to predict composite foundation settlement. Once the predicted value exception occurs, remedial measures can be taken early enough to ensure the safety of the building.

MGM(1,n) gray prediction model is a nonlinear predictive model, which is a single-point extension model in the multi-points condition considering the related information among the monitoring points. Compared with GM(1,1) model, it has higher analog precision and prediction precision. And MGM(1,n) gray model can get n points prediction values, which need to establish one model, but GM(1,1) model need to establish n models, which need more work. So the MGM(1,n) gray model is more convenient.

To ensure the precision of the settlement prediction, along with the constantly updated monitoring data, old data can be removed, and the latest data can be used to correct prediction model to improve the sensitivity of the model, which can make more accurate composite foundation settlement prediction.

## References

[1] Julong Deng. Grey Control System, Huazhong University press, Wuhan (1993)

[2] Bing Chen, Xiaodong Chen, Application of multivariate gray model in prediction of deep-mixing pile compound roadbed settlement, Journal of Liaoning Technical University, Vol.26 No.3(2007), p.378-380

[3] Feng Ren, Xianwei Zhao, Forecasting of Daping Landslide Based on the Grey Model, Chinese Journal of Engineering Geophysics, Vol.8, No.5 (2011), p.627-630

*Applied Mechanics and Materials Vols. 580-583 (2014) pp 674-678*
*© (2014) Trans Tech Publications, Switzerland*
*doi:10.4028/www.scientific.net/AMM.580-583.674*

# Preparation of a new type of joint filler and study on adhesion performance

Xiaowei Li[1, a], Chuan Sha[2,b]

[1]Xijing University,xian,shanxi Province, China

[2]zhongjiaoluqiao,jishucorporation,Beijing, China

[a]lixiaowei_2005@163.com, [b]sxwhsc@163.com

**Keywords:** Adhesion performance. Joint filler. Tensile strength. Humidity.

**Abstract.** Aiming at a new joint filler for pitch concrete pavement, processing it in different condition of water, determining the tensile strength through tensile experiment, analyzes the effect of adhesion performance from joint filler in water surrounding; does analysis to the adhesion performance of the recurrent tensile test in identical water surroundings.It evidenced that the new joint filler is much less affected in water surronuding than rubber modified bitumen,which is made by CARFCO inUSA,what meas that the new joint filler is much better than rubber modified bitumen on adhesion performance.

## Introduction

With the extension of highway asphalt pavement total milestone in chine, because the effect of the presence of water and repeat traffic load, there is a serious disease asphalt pavement[1, 2], and surface cracking is one of the major diseases of the road. Cracks not only undermine the structural integrity of the road, but also reducing the comfort and safety of the road[3, 4], so the research of cracks problems is urgent.

Filling cracks can prevent and stop water infiltration road deep, and delay the further develop of diseases of the road. Filling cracks is an important means of asphalt pavement maintenance department of Early Crack. Caulking material is a common way of repairing cracks. Zhen Wu [5] , who have had a single -component polyurethane caulk synthetic material; Dongchang Zhang [6] , who have developed a new type of long-life sealing material , the main component is silicone; Songqi Shou [7], who had been working on material for polyurethane caulk, and developed a silicone-modified polyurethane prepolymer and two-component polyurethane caulks , and then prepared composite caulking material combined with the advantages of polyurethane caulks and silicone caulks. However, these caulks have their shortcomings, especially sensitive to humidity, furthermore can't play the ideal adhesion effect because of the impact of water. So it's need to develop a new type caulks which is less sensitivity to water. Based on rubber modified asphalt (hereinafter referred to as American products), which is produced by the company of CARFCO in the United States, this paper studies the effect of water on a new sealing material adhesion by tensile test method. It's hope to play a guiding role in preparing caulks, improving the crafts, extending pavement performance, improving the level of road maintenance, saving the cost of long service asphalt pavement.

## Materials and methods

### 1.1 Preparation of materials

A new joint compound ( compatible agent+tackifier+SBS +crumb rubber +stabilizer) was studied. The preparation flowchart is shown in Figure.1.

To ensure the best performance of the asphalt under the same conditions the optimum technic index of modified asphalt was determined: test temperature is 180 ℃, shear rate is 3000r/min, shearing time was 40min, development time was 30min. After the above process and a method of making a new type of joint compound performance index is shown in Table.1.

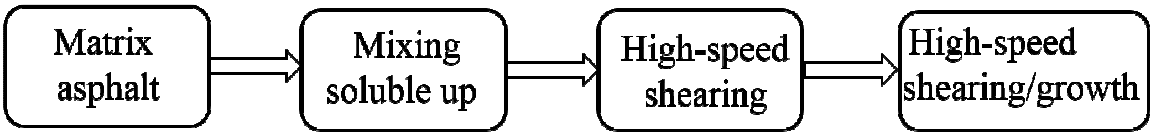


Fig.1. Preparation flow chart of the modified asphalt

Table.1.Performance metrics of a new joint sealant

| Property | New joint sealant | Experimental method |
|---|---|---|
| softening point（℃） | 90.6 | T0605 |
| Ductility（5℃，cm） | 21.6 | T0606 |
| Thixotropic Index（25℃，mm） | 52 | T0604 |
| Elastic recovery（25℃，%） | 94.0 | T0603 |
| TFOT | | |
| Ductility（5℃，cm） | 13.1 | T0606 |
| Thixotropic Index（25℃，mm） | 45 | T0604 |
| Elastic recovery（25℃，%） | 88.2 | T0603 |

**1.2 Tensile tests**

Tensile tests was finished by GF multifunctional road interlayer force tester using mixture cylinder (d=100mm) as specimen. Test tensile rate was first set as 1.2mm/min, and both ends of the specimen were fixed by clamps and stretched till the stretch distance was 2 cm, and then the tensile load and displacement of the specimen were output by the computer. Tensile testing process and real die pictures is shown in Figure.2.

Test pieces were prepared as follows. the mixture cylinder of which diameter was100mm and height was 63.5mm first went through surface treatment. A certain amount of filler material was then heated to 140 ℃ and painted evenly on the surface of the cylinder. The two cylinders butt was jointed by adhesive tape to prevent material spillage. Secondly,test material was placed at room temperature for more than 4h, and three specimens were shaped in each group. Finally, every specimen was placed onto GF multifunctional road interlayer force tester and stretched with failure load recorded, and then tensile strength was calculated according to formul is shown in Eq.1.

$$P=F/A \quad (1)$$

Remark:P – Adhesion strength, Mpa;F-The maximum load,N;A - Drawing area, mm2.

The test results to three decimal places to the arithmetic average of the three test specimens as a result.

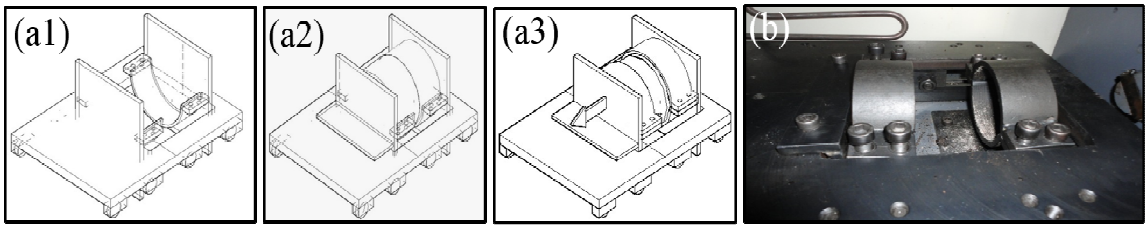


Fig.2. (a) diagram of Tensile test loading process (b) mould real figure

After drawing the specimen, the sealing material has a strong elastic recovery, some time later the test piece is placed spontaneously revert to the state before stretching, Specific specimen state diagram as in Fig.3. Tensile specimens were repeated for 5 cycles, Researching Caulks adhesion variation.The results is shown in Figure.5.

Under different water environments specimen preparation : ( 1 ) on the cylinder surface dust, dried , heated to 140 ℃ of caulking material to the cylinder surface evenly , butt shape. The group measured

the adhesion strength of the dry cleaner environment caulking material . ( 2 ) to clean the surface of the cylinder , into the water ( tap water ) in 40min ~ 60min, wipe the surface and more water will be heated to a caulking material evenly cylindrical surface 140 ℃, the docking molding.The group measured the adhesion strength under wet conditions caulking material . ( 3 ) to clean the surface of the cylinder,into the water ( tap water ) to soak 40min ~ 60min, excess water on the surface without any processing, the material is heated to 140 ℃ of caulk evenly to the cylinder surface,docking molding. The group measured the adhesion strength under water environment caulking material . ( 4 ) for the cylinder surface clean after the heat evenly to caulks 140 ℃,the docking molding into the water ( tap water ) to soak more than 4h . The group measured the specimen under the influence of caulking material to soak adhesion strength .

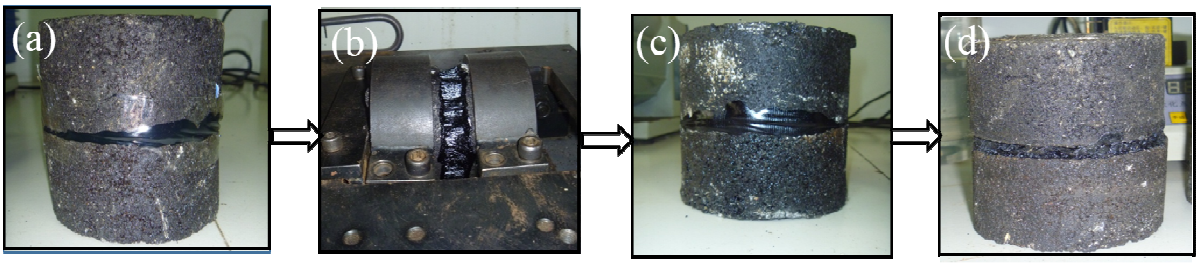


Fig.3. Process state diagram of Specimen tensile (a) original specimen.(b) tensile specimen during process (c) specimen before stretching (d) specimen after stretching

Production scheme will be different between the test piece good road GF multi layer testing tensile strength tester , the peak force recorded test results is shown in Table 2 . Making a set of three test specimens , the result of a test specimen , if more than 10 % of the average , be removed. If two test results of more than 10 % of the average , the group results void.

Table.2. Effect of humidity on adhesion property between United States product and new joint sealant

| Interface environment | New joint sealant（MPa） | | | | | United States product（MPa） | | | | |
|---|---|---|---|---|---|---|---|---|---|---|
| | One | Two | Three | Four | Five | One | Two | Three | Four | Five |
| Planning A | 0.593 | 0.427 | 0.344 | 0.330 | 0.311 | 0.400 | 0.325 | 0.284 | 0.230 | 0.146 |
| Planning B | 0.549 | 0.387 | 0.271 | 0.268 | 0.249 | 0.235 | 0.207 | 0.205 | 0.203 | 0.134 |
| Planning C | 0.540 | 0.362 | 0.277 | 0.245 | 0.217 | 0.221 | 0.192 | 0.183 | 0.170 | 0.112 |
| Planning D | 0.580 | 0.413 | 0.311 | 0.308 | 0.301 | 0.343 | 0.286 | 0.264 | 0.222 | 0.145 |

## Results and analysis

### 2.1 The effect of joint filler on adhesion performance about Humidity

Compared with humidity on the new caulking material impact on the adhesion properties of U.S. products, and its comparative test results is shown in Figure 4.To ensure the accuracy of the test data results , select the first tensile test results as a ratio . The results can be obtained from Figure 4 , the interface environment from the dry - wet - water environment changes , the new joint filler adhesion strength decreased 7.4% and 8.9 %, respectively , specimens less impact on water soaking conditions caulking material adhesion properties , filling sewing material adhesion strength decreased ratio of 2.2%.American products decreased rates were 41.2% and 44.7%,the proportion of the adhesion strength decreased 14.2% under the conditions of the test piece flooding .

The results showed that: the presence of water weakens the adhesion of the joint compound . Analyze the reasons : ① water in the adhesive film formed on the interface of the tiny cracks and

holes to fill on the interface , resulting in the formation of joint compound inaccessible physical anchor , leading to loss of adhesion properties of caulking material [8]; ② caulk first, the adhesive material in the course of the water film instead of contacting the mixture, can not form an effective adhesion; ③ water is much greater than the polarity of the polarity of caulking material, the molecular orientation according to the theory of joint compound has water peeling , leading to loss of adhesive properties of joint compound.

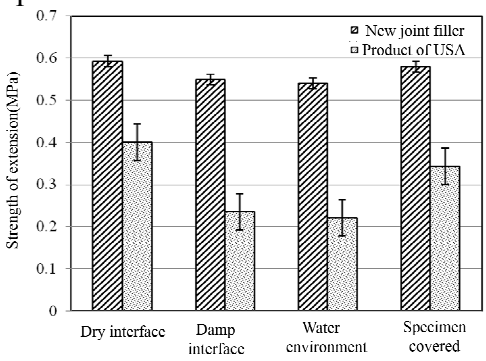


Fig.4. Effect of humidity on adhesion property between United States product and new joint sealant

Contrast adhesion properties of new materials and caulk U.S. products , the impact of the new water sealing material adhesion by less than U.S. products.The new joint compound mixed with thickeners , adhesion thickener provided to ensure that the new caulking material can firmly adhere to the interface , reducing the water may be stripped . In addition , according to the rotational viscosity test results , the United States is greater than the product 's viscosity and consistency of the new joint compound [9,10] , the water film will fill small cracks and holes on the interface , resulting in the loss of material adhesion properties , the impact on U.S. products to far greater than the new caulking material .

### 2.2 Repeated tensile test under the same humidity

(1) The changes of joint filler on adhesion performance on repeated tensile test.

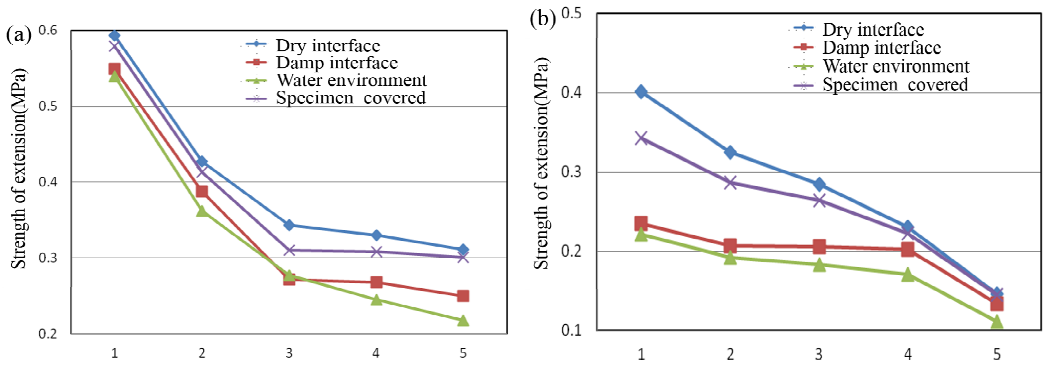


Fig.5. Adhesion property between United States product and new joint sealant（a）new joint sealant（b）United States product

Under different circumstances , the new adhesive caulk material changes have the same pattern: the first three , the new joint filler adhesion strength greater magnitude of change , the next three new caulking material adhesion basically stable. American products in repeated tensile test results with the new caulking material vary, the first four stretching, changing its adherence to a lesser extent , the results of the fifth stretch material adhesion began to have a greater attenuation.

(2) Observation during tensile test

Figure.6 (a) (b) (c) (d) and (a1) (b1) (c1) (d1) can be seen, a good adhesion of the new sealing material, such that it exists in the water film able to firmly adhere to the interface, keeping water

tightness. Greater impact on the adhesion of American products by water, has been cracking during stretching.

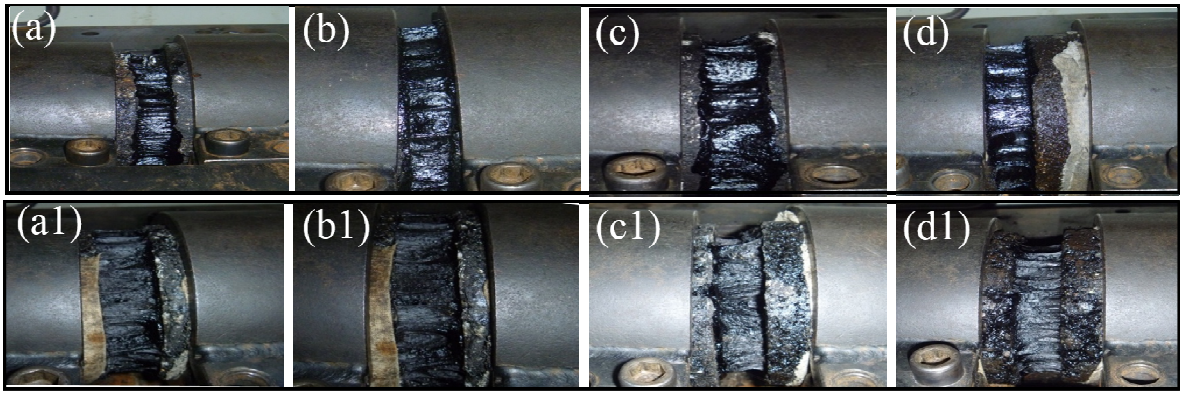


Fig.6. The repeated tensile test results between new joint sealant and United States product with under the same water environment. (a)(b)(c)(d) are results of United States product. (a1)(b1)(c1)(d1) are results of new joint sealant. (a, a1) dry interface, (b, b1) damp interface , (c, c1) water environment,(d, d1) specimen covered

In summary, there is a water film on the one hand the interface hindered caulks anchor role in the formation of interfacial adhesion; hand water caulks cause spalling, resulting in loss of joint compound adhesion properties. For new caulking material, its good adhesion properties to its adhesion properties of the water has little effect on U.S. products, due to the greater consistency and viscosity of the material, its greater impact on the presence of water, resulting in material tensile process appears.

## Conclusions

(1) The presence of a water film interface hinders the formation of joint compound anchor role in the adhesion interface, resulting in loss of joint filler adhesion performance.

(2) Compare U.S. products, new joint filler excellent adhesion performance reduces the sensitivity to water.

(3) Fracture under high humidity conditions, decrease in adhesiveness of the specimen is more serious, the tensile strength greatly decreased..

## Acknowledgements

This work was finally supported by the school funds of Xijing university (xj130229)

## References

[1] Jun Pei.Liaoning transportation science and technology,2004,(1):27-29 (In Chinese)

[2] Ruilong Xu, Wenhua Hu. East China Highway,2003,(4):20-21(In Chinese)

[3] Wenjuun Liu. Modern highway,2010.(23):217-219 (In Chinese)

[4] Hetie Tang. Highways & Automotive Applications.2003,(4);29-31(In Chinese)

[5] Zhen Wu, Qing Guo. Chemical materials for construction,2001(3):27-29(In Chinese)

[6] Dongchang Zhang, Liqin Long.Technology of highway and transport. 2009(6):52-53

[7] Chongqi Shuo, Shang Lou. Jouranl of china foreign highway.2009.29(6):224-227

[8] Odum-ewuakyeb, Attoh-Oking N. Construction and building materials,2006,20,78-82

[9] Wei Wu, Guanghua Cui. Foreign Sciences Section on Pharmacy, 2000, 27 ( 5):292 － 297

[10] Abu-izzaka, Garciacontrerasl. Journal of Pharmaceutical Sciences, 1996, 85 ( 2 ):144-149

*Applied Mechanics and Materials Vols. 580-583 (2014) pp 679-683*
*© (2014) Trans Tech Publications, Switzerland*
*doi:10.4028/www.scientific.net/AMM.580-583.679*

# Probability Statistical Model and Network Simulation Technology of Random Fractured Rock Mass

Chunxiu Han[1,2,a], Donghua Zhou[2,b], Wenyuan Liao[2,c], Xu Chen[2,d], Longqi Li[2,e], Kaicheng Yao[2,f]

[1]Architectural Engineering Faculty, Kunming Metallurgy College, Kunming 650033, Yunnan, China;
[2]Faculty of Civil Engineering, Kunming University of Science and Technology, Kunming 650504, Yunnan, China
[3]Yunnan TST Engineering Examination Co., Ltd., Kunming, Yunnan, 650000, China
[a]593416010@qq.com, [b]stahlverbundbau@yahoo.com.cn, [c]373537671@qq.com, [d]xuchen_22@163.com, [e]lilongqiqingdao@sina.com, [f]765304571@qq.com

**Keywords:** fractured rock mass, statistical analysis, probabilistic model, network simulation

**Abstract.** Based on field investigation of random fractured rock mass, the sample parameters are put to statistical analysis, and 2-D fracture network model is established with probability-statistics theory and Monte-Carlo simulation technique. Finally, 2-D fracture network model is formed, which gain fracture distributed regularity in statistical sense, and is of important meaning to describe the fracture geometrical characteristics.

## Introduction

International Society for Rock Mechanics defines discontinuity as a fracture surface of faults, weak surface, most of rock joint, weak schistosity and weak belt caused by various mechanical factors[1]. One of them, rock joint is a crack of rocks, which is no obvious displacement, and is also one of the weak structural plane most extensive developing in upper crustal rocks[1]. These rock joints change the damage and instability way of rock mass. Hence researching distribution features of fractured rock mass is of great engineering significance, is also rock force frontier and hot topic.

Randomness of the distribution of rock mass and the diverse and complex space combination make it a difficult task to describe fractured rock mass accurately. In fact, the fractured rock mass distribution with stochastic uncertain, is also certainly. The distribution parameter values can be statistics, and then a probability model is established. With the rapid development of computer technology, structural plane network technology based on statistics and probability theory is able to widely use in engineering. Monte-Carlo method is adopted in this paper to be used in fracture network model, which can show its geometric characteristics of rock distribution in the study area.

## Theory of fractured rock mass statistical analysis

In the perspective of mathematical statistics, a large amount of sample data is from rock mass structure and reflects the characteristics of them. The sample may be defined as a individual one extracted from rock mass of the structure, and the rock mass structure itself as a collection of all individuals, namely totality[3]. Based on limited data obtained from field investigation of rock mass structure, the general characteristics of rock mass structure are derivated, namely the overall distribution calculated by the sample distribution.

### 1.1 Fitting sample parameter distribution

Some parameters are defined as follows: $x_1, x_2, \ldots, x_n$ as a sample of Populations $X$, statistic for $T = T$（$x_1, x_2, \ldots, x_n$）, probability density function as $f(x)$, with mean $\bar{x}$ and variance $s^2$, a maximum as $b$ and a minimum as $a$. According to statistics of sample characteristics $a$ and $b$, $k-1$ points with $t_1, t_2, \ldots, t_{k-1}$ are selected from sample values in the interval $[a, b]$ to divide into $k$ intervals of $[a, t_1], (t_1, t_2], \ldots, t_{k-1}, b]$, as shown in fig. 1.

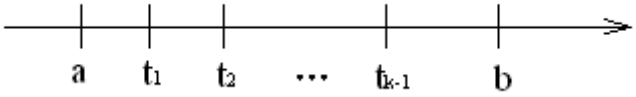


Fig.1 Segmentation interval of random variable

Setting $n_i$ As the number of the interval of $i$ (known as frequency) of sample $x_1, x_2, \ldots, x_n$, and the values of $f(x)$ in interval $[a, b]$ are represented by a histogram of measured data, then a probability density curve is described roughly.

**1.2 Non-parametric hypothesis test**

Hypothesis testing is a process of inference, which judge hypothesis according to the samples: inspection the same of guess distribution $F(x)$ and distribution. Hypothesis test is divided into parameter test and non-parametric test[3]. The former is testing some parameters according to known population distribution, and the latter is to examine some parameters for unknown population distribution.

In the statistical analysis of rock mass structure, population distribution type indicated rock mass structure is unknown normally, at this time its inspection method is non-parameter method[3]. Commonly used methods are fitting inspection of *Pearson* $\chi^2$, $k-s$ test, etc.

**Probability analysis and simulation principle of fractured rock mass**

Owing to limitations of rock outcrops, Some of structural plane trace length measured in the field site are full trace length, while some others are half trace length, some even are abridged part of the trace length with unseen both ends of the trace.

Probability density function of trace length is set as $f(l)$, and probability density of joint trace length is $g(l)$, average of population trace length is $\mu_L$:

$$g(l) = \frac{lf(l)}{\mu_L} \tag{1}$$

Probability density function of half-trace length is set as $h(l)$,and population trace length is $m$, $F(l)$ is cumulative probability of $f(m)$:

$$F(l) = \int_0^l f(m)dm \tag{2}$$

$$g(l) = \frac{1-F(l)}{\mu_L} \tag{3}$$

According to analysis by Priest and Hudson(1998)**,** under the condition of negative exponential distribution, the mean trace length intersect with survey line is$2\mu_L$, while uniform distribution which is $\frac{4}{3}\mu_L$,normal distribution.

Monte-Carlo simulation is based on the measured data of field fracture geometry characteristic parameters, fitting out probability density function of the occurrence, trace length and spacing parameters, and then mapping fissure network with computer[3]. Statistical analysis is carried out on the fracture azimuth firstly, and advantage direction of rock fracture group is determined, then parameters distribution law is fitted to generate random numbers separately for each fracture, which produces random variables of geometric parameters, and calculates halfway point of the crack position, dip angle and train long respectively. This group of crack is generated when the sampling area, generating a second group of fracture group, until all finished growing in a crack in the group are generated. Read the store in a crack in the data, graphic display fracture network, finally output graphics.

## Examples of application

YanJin Bridge Reservoir in RenHua, Guizhou province, is a comprehensive water conservancy for purpose of irrigation, power generation, water supply and travel. Elevation of dam riverbed is 569 m, and normal water level is 650 m. Downstream of right dam abutment is compound brae, whose terrain is steep cliffs with terrain slope Angle of 70 ~ 80°, relative level difference of about 124 m. There is empty face between 597 ~ 660 m elevation of 20 ~ 50 m from dam side downstream. The outdoor layer is fine-crystalline dolomite, dolomite and thin layer of argillaceous dolomite, and weak intercalated layer. For the bedding rock slope, combined with fracture, the dam abutment stability is seriously affected. Therefore, recognizing and describing fracture distribution accurately is particularly important.

### 3.1 Sample parameter distribution fitting

In the right abutment downstream, the dominant orientation is shown by survey data, and three groups of cracks, its occurrence, respectively, are 1)N72°E/80°NW, 2)N23°E/40°SE and 3)N33°W/20°NE. Then fit fissure angle distribution on three groups, as described in Fig.2, Fig.3 and Fig.4.The results show that sample fracture trace length is logarithmic normal distribution.

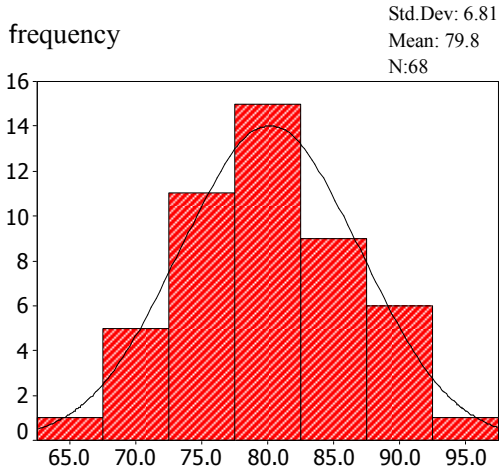


Fig.2 Fracture dip angle in 1)group(°)

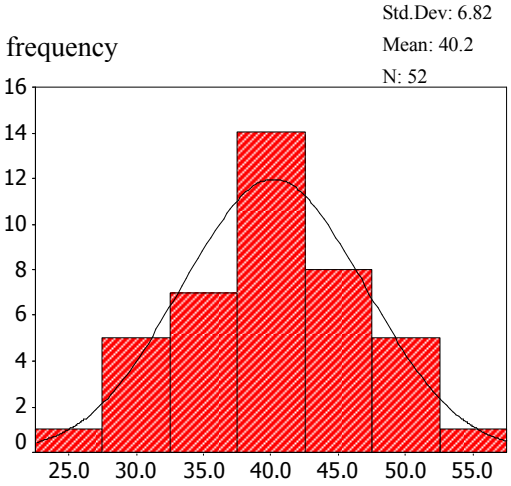


Fig.3 Fracture dip angle in 2)group(°)

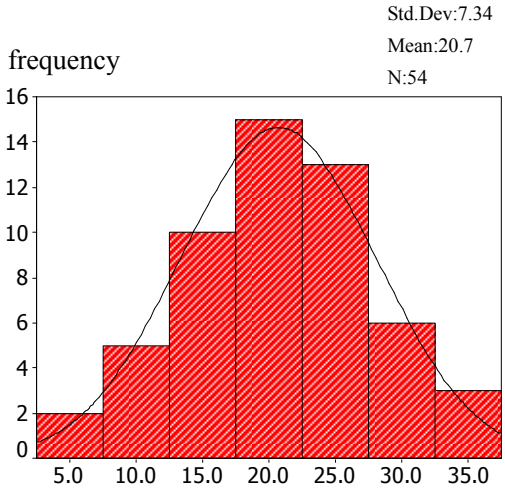


Fig.4 Fracture dip angle in 3)group(°)

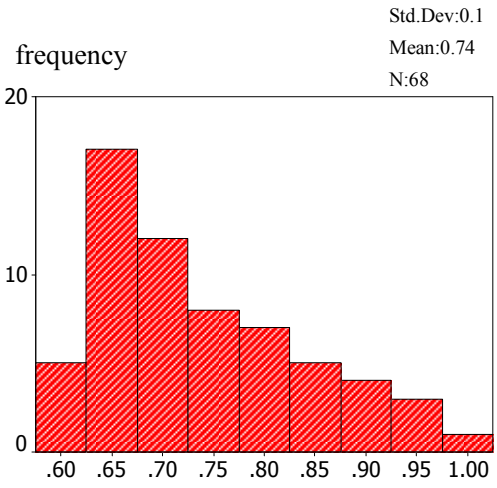


Fig.5 Fracture train length(m)

### 3.2 *pearson* $\chi^2$ fitting testing

Set a sample cumulative probability distribution as $F(x)$, with null hypothesis $H_0$: global cumulative probability distribution function as $F(x)$,and with alternative hypothesis $H_1$: global cumulative probability distribution function not as $F(x)$.

Set $n_i$ As the number of interval $i$ (known as frequency) of sample $x_1, x_2, \ldots, x_n$, and the total samples number as $N$, then the value $\frac{n_i}{N} - p_i$ should be small, otherwise, reject the hypothesis $H_0$ and accept $H_1$ [4]. Under conditions of $H_0$, the Statistic is,

$$\chi^2 = \sum_{i=1}^{k} \frac{(n_i - e_i)^2}{e_i} \tag{4}$$

Take equation(4) to distribution as $\chi^2(k-1-r)$ ,there $r$ is the number of unknown parameters in the overall. On the calculation of, $p_i$ can be replaced by $\hat{p}_i$ [4]. Giving significance level $\alpha$ and distribution tables of $\chi^2(k-1-r)$, $\chi^2_\alpha$ can be obtained. If $\chi^2 \le \chi^2_\alpha$,it means numerator of $\chi^2$ small, then the value $\frac{n_i}{N} - p_i$ is small, which reject the hypothesis $H_0$ ,otherwise, accept $H_1$. The hypothesis test results of angle, trace length of crack are shown in table 1.

Table1 Distribution form of Rock fracture angle and train in the study area( $\alpha = 0.05$)

| statistics | occurrence | sample number | mean | standard deviation | $\chi^2$ | $\chi^2_\alpha$ | distribution form |
|---|---|---|---|---|---|---|---|
| Dip angel | N23°E/40°SE | 68 | 79.8° | 6.81° | 1.334 | 11.143 | normal distribution |
| | N33°W/20°NE | 52 | 40.2° | 6.82° | 1.259 | 11.143 | normal distribution |
| | N72°E/80°NW | 54 | 20.5° | 7.34° | 0.896 | 11.143 | normal distribution |
| train | — | 68 | 0.74m | 0.1m | 5.286 | 22.362 | lognormal distribution |

### 3.3 Generation of two-dimensional fracture network

Two-dimensional fracture network is made up of different length and Angle fracture trace length according to the statistical parameters and generate statistical model. The steps are as follows:

(1)Determine generating area: considering some cracks center in the outside of study area but closing to the border, the train length may be extended to the field, so the fracture area extends outward half an average train length ( $\mu_L/2$) from study area boundary[5].

(2)Determine number of trace center in generated field: frequency per unit area is obtained by $i$ group fracture with statistical data, and the midpoint number of the group fracture in generated field.

(3)Generation of trace crack position, Angle, and train length: picks a random number in (0,1) with congruence method, and generate random variables coordinates $x_i$ and $y_i$ based on normal distribution; generate angle random value based on normal distribution; then generate train length random value based on lognormal distribution. After that, determine position 0f fracture in study area. Finally, two-dimensional fracture network is obtained[5].

It is simulated with VBA, which is second development technology of AutoCAD. The simulation results as shown in figure 6. Combined with actual situation and exploration data, this method was used to simulate two-dimensional fracture network model and in accordance with the actual situation, which find fracture regularity in statistical sense. As can be seen from fig. 5,

fracture for bedding, fracture connectivity rate of Angle 40°is high, which affect the stability of slope seriously. With fracture network diagram, fracture network hydraulic calculation can be got,

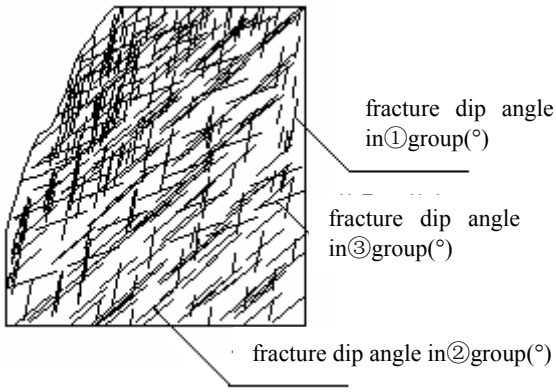


Fig.6 2-D fracture network

and then the connectivity rate and slope stability analysis can further calculated on the basis of network model. Therefore, fracture network diagram is the basic work for the security of engineering.

## Conclusion

(1) The existence of rock fracture damage rock mass integrity, influence on rock mass deformation and failure mode, and control seepage and stability characteristics of rock mass. Therefore, understanding and the way of depicting the existence of fractures accurately is very important.

(2) Because of the complexity of rock fracture, it is hard to describe fracture characteristics with completeness and certainty. Research shows that: fracture characteristics can be described statistically with application method of probability and mathematical statistics, combined with Monte-Carlo simulation technology, rock fracture two-dimensional network is carried out and receive good results.

(3) The secondary development technique programming of VBA is a good way to stimulate fracture, for it is contained in shared memory space with CAD, which has faster application execution speed than C language and VB language. The method can be used for the simulation of rock fracture.

## References:

[1] Xu Kaili, Zhuzhicheng. Structural Geology[M]. Beijing: Geological Publishing House, 2005. (in Chinese)

[2] Zhu Zhende. Rheological model research and application of fractured rock mass damage[D]. Postdoctoral degree thesis, 1999. (in Chinese)

[3] Huang Runqiu, etc. The complex rock mass structure fine description and its engineering applications[M]. Beijing: science press, 2004. (in Chinese)

[4] Ma Qingguo. Management, data acquisition, statistical principle and SPSS tools and application[M]. Beijing: Science press, 2004. (in Chinese)

[5] Zhang Youtian. Rock hydraulics and engineering[M]. Beijing: China WaterPower Press, 2005. (in Chinese)

*Applied Mechanics and Materials Vols. 580-583 (2014) pp 684-688*
*© (2014) Trans Tech Publications, Switzerland*
*doi:10.4028/www.scientific.net/AMM.580-583.684*

# Pullout Test Research on Interfacial Interaction of Reinforced Band and Gravelly Soil

WANG Yanli[1, a], CHENG Zhanlin[1, b], ZHANG Wei[1, c], ZUO Yongzhen[1, d], YU Zhenlin[2, e] and WANG Yong[3, f]

[1]Key Laboratory of Geotechnical Mechanics and Engineering of the Ministry of Water Resources, Yangtze River Scientific Research Institute, Wuhan 430010, China

[2]State Key Laboratory of Geomechanics and Geotechnical Engineering, Institute of Rock and Soil Mechanics, Chinese Academy of Sciences, Wuhan 430071, China

[3]Changjiang Institute of Survey, Planning, Design and Research, Wuhan 430010, China

[a]wyldhh@126.com, [b]chengzl@mail.crsri.cn, [c]zhangwei@mail.crsri.cn, [d]284128990@qq.com, [e]895772705@qq.com, [f]wang831yong@163.com

**Keywords:** Pullout test, Interfacial interaction, reinforced band, water content

**Abstract.** Taking steel-plastic composite reinforced band (CAT) and gravelly soil as the test materials, the pullout tests of reinforced band in gravelly soil with different water contents have been carried out by the laminated shear test instrument. The interface friction characteristics between reinforced band and gravelly soil are studied, and the influences of water content on the interaction characteristics are also discussed. Results show that (1) the extraction of reinforced band is a gradual process. The anchor end began to move firstly because of the extensibility of reinforced belt itself. As interface friction gradually transfer backward by, the free end start to move onward, then displacement schedule curves of the anchor end and the free end are gradually parallel, the whole movement of reinforced belt happens immediately. (2) Pulling force and displacement curve of the pullout friction test displays obviously nonlinear characteristics. Pulling force of the reinforced band increases greatly with increasing displacement at the beginning of the test, then decrease with the increasing displacement after the peak value is reached, the force-displacement curves generally exhibit strain soften characteristics. But it present strain hardening trend under greater normal stress, and pullout frictional strength increases with the increasing normal stress. (3) The pullout friction coefficient of the interface is sensitive to water content. It decreases linearly with the increasing water content.

## Introduction

Reinforced soil retaining wall is a kind of retaining structure with certain flexibility and deformation ability, which could improve the soil deformation and its engineering property by shear friction between reinforced band and filling to achieve soil reinforcement stability. As a new flexible structure, reinforced retaining wall has been widely used in various fields such as the highway and railway epaulement, abutment, vertical quay, revetment, and so on. The interfacial characteristic of reinforced material and filling directly determine the safety and stability of reinforced retaining wall. The pullout test and direct shear test are typically used for reinforced soil interfacial interaction for indoor test research (Shi et al. 2009)[1]. Scholars at broad [2-6] obtained a great deal of achievements through pullout test and direct shear test to study interface characteristic of synthetic material and filling. While domestic scholars in China developed related research on the interface characteristic of synthetic material and packing as well. Scholars [7-9] successively carried out the geo-grid and filling pullout test to study the influence of loading mode, packing thickness, compaction degree, reinforcement rigidity, reinforced structure form, buried length, vertical effective stress on the pulling characteristics of reinforced soil. The reinforced materials in the above research are mostly geo-grid or soil fabric and the filling materials are sand or clay, in which little research was made on reinforced

band, and the water content was seldom considered as the factor on the pulling characteristics of reinforced soil. In southwest of China, reinforced band is widely used in embankment and revetment engineering as the reinforcement material. At the same time, the reservoir water level fluctuation will lead to water content change of packing material, which will then affect the stability of the reinforced structure. Therefore, the research on the influence of different water content on the interfacial friction characteristic of reinforced band and characteristics is of great significance.

Based on the reinforced soil retaining wall in a project in Chongqing of China, in which the CAT steel-plastic composite reinforced band and sand gravel are as the test materials, pullout test of reinforced band and gravelly soil with different water content were conducted by using large shear test instrument to study the interface friction characteristic of them. Then the interface friction coefficient was obtained, and the water content's influence on interface friction characteristic was analyzed in the paper to provide reference for reinforced soil engineering.

## Pullout Test

**Test Equipment.** Pullout test was conducted on DHJ60 large scale simple shear apparatus jointly developed by Yangtze River Scientific Research Institute and Huaxi Geotechnical Instrument Research Institute of Sichuan University, This equipment is mainly consisted of vertical and horizontal loading equipments, shear box, stress and displacement data collection system. The equipment adopts the plate frame structure with hydraulic loading method, which horizontal load uses strain type control mode and could achieve step-less speed regulation at 0.03~20mm/min. The upper shear box is composed of 10 overlaying rings, which is 30mm high and numbered from top to bottom. The rolling shafts are equipped between and beside the overlaying rings to minimize the shear resistance. The vertical and horizontal loads are measured by using load sensor, and 100mm resistance type displacement meter is used to measure the overlaying ring displacement, which is exported through eight-channel digital inspection instrument.

**Test material.**The test material is gravelly soil selected from retaining wall site in Chongqing of China, because the largest grain size in the field is greater than 60 mm, in situ grain size distribution need be modified to fit in the test apparatus, which is 60 mm in diameter. The simulation curve of grain size distribution using the Equivalent Weight Replacement method is shown in Figure 1. The reinforcement material used CAT steel-plastic composite reinforced band produced by Chongqing Yonggu Engineering Reinforced Band Co., LTD, which is geo-synthetics composed of carbon spring steel wire wrapped with polyethylene composite band. The product specification is CAT30020B and the width is 30 mm and thickness is 2.0mm.

**Test method.**The soil sample was compacted by layers according to the density and water content requirement. After the soil was filled in lower shear box, the reinforced band assembled with displacement measurement wire was laid on soil sample with equal spacing to ensure the horizontal pulling force and the geotechnical band are in the same horizontal plane. Then the soil sample of upper rings were filled by layer and compacted before rigid bearing plate was covered with vertical stress force exerted to make soil consolidation. After stable consolidation, horizontal load was applied in strain control mode with 0.3 mm/min pullout rate for pullout test, and the horizontal tension and pulling displacement were recorded. When the pulling force reached peak value and eventually stably dropped or displacement occurred at free end of reinforced band with stable movement rate, it was then regarded that the reinforced soil interface had been completely destroyed, and the test could be stopped. During the test process, the water content's influence on reinforced soil interface friction was the key point to consider. In order to increase the test accuracy, 3~5 geo-band equally spaced were laid on the interface (see figure 2).

**Test scheme.**The significant factors that affect the soil interfacial interaction property of reinforced band in the pullout test include normal stress, pulling speed, reinforced material strength, size, and different water content of soil sample, dry density state, and etc. For the actual engineering conditions, the increase of reservoir water level would greatly influence the water content of gravelly

soil, and the change of water content would affect the interfacial interaction characteristic of geotechnical band and sand gravel. Therefore, this paper intends to carry out the pullout test for gravelly soil in three different water contents and reinforced band, and the test scheme is as shown in the table 2.

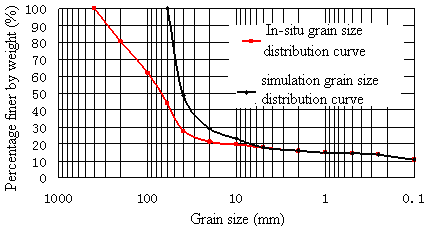


Fig 1. Grain size distribution curves of in situ and reconstituted specimen

Fig. 2. The geo-band laying view

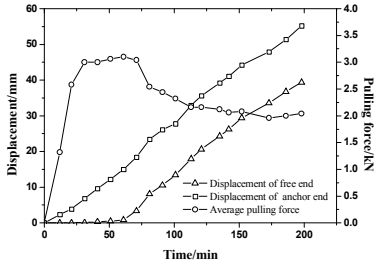


Fig. 3. Time-history curve of pulling force and displacement for reinforced band

Table 2. Pullout test scheme

| Test No. | Vertical load kPa | Pulling rate mm/min | Number of geo-band | Gravelly soil | |
|---|---|---|---|---|---|
| | | | | Water content w (%) | Dry density ($g/m^3$) |
| 1 | 300 | 0.3 | 5 | 3.7 | 2.24 |
| 2 | 400 | 0.3 | 5 | 3.7 | 2.24 |
| 3 | 500 | 0.3 | 3 | 3.7 | 2.24 |
| 4 | 300 | 0.3 | 3 | 4.7 | 2.24 |
| 5 | 400 | 0.3 | 3 | 4.7 | 2.24 |
| 6 | 500 | 0.3 | 3 | 4.7 | 2.24 |
| 7 | 300 | 0.3 | 3 | 5.7 | 2.24 |
| 8 | 400 | 0.3 | 3 | 5.7 | 2.24 |
| 9 | 500 | 0.3 | 3 | 5.7 | 2.24 |

## Test Result Analysis

**Calculation formula.**The interface pulling friction strength is calculated as the formula below:

$$\tau_f = \frac{T_p}{2BL} \tag{1}$$

Where $\tau_f$ is the pulling friction strength; $T_p$ is the total horizontal tension at peak value; B, L is the buried width and length in the soil.

The earth is calculated as below--pulling friction factor of geosynthetics materials:

$$f = \frac{\tau_f}{p} \tag{2}$$

Where p is the normal pressure; $\tau_f$ is the pulling friction strength corresponding to p.

**Pulling force and pulling displacement.** Figure 3 is the time-history curve of pulling force and displacement for reinforced band in test No.1. It can be seen from the graph that when the reinforced band that buried in the sand gravel is subject to a horizontal pull, the stress and deformation are to be generated in the pulling direction. At the beginning of the test, when the pulling force was small, the anchored end was pulled out first with displacement expanded as the pulling force increased, and free end displacement remained unchanged. When the pulling force gradually increased to a certain value, the interface friction was gradually delivered to back end and relative displacement in the reinforced soil increased in slow pace. When the pulling force reached to maximum value, the pulling end and

free end had displacement, the time-interval graph gradually paralleled, and the reinforced band immediately had integral displacement.

**Pullout test graph.** Figure 4 is the relationship between pulling force and displacement of the reinforced band in gravelly soil with three different water contents and in different normal stress. It can be seen from the figure that, the overall trends of the relationship between pulling force and pulling displacement under different water content are basically same, but which showed obvious nonlinear characteristic in the pullout test with the same water content. When the reinforced band was pulled at beginning, the pulling force increased with increased displacement, and the pulling decreased as the pulling displacement increased after the pullout force reached peak value. The pulling graph was featured by strain softening characteristic, but tended to be strain-hardening under greater normal stress. The greater the normal stress was, the higher peak pulling force would reach, which was due to that the contact between reinforced band and gravelly soil particles were more compact. The pulling force mainly comes from friction between the reinforced band and gravelly soil, and the friction resistance is larger required by same displacement produced by reinforced band, thus the peak value of pulling force is higher. The water content of packing material has great influence on interface friction coefficient. Under same normal stress, the higher the water content is, the lower the pulling friction strength will be.

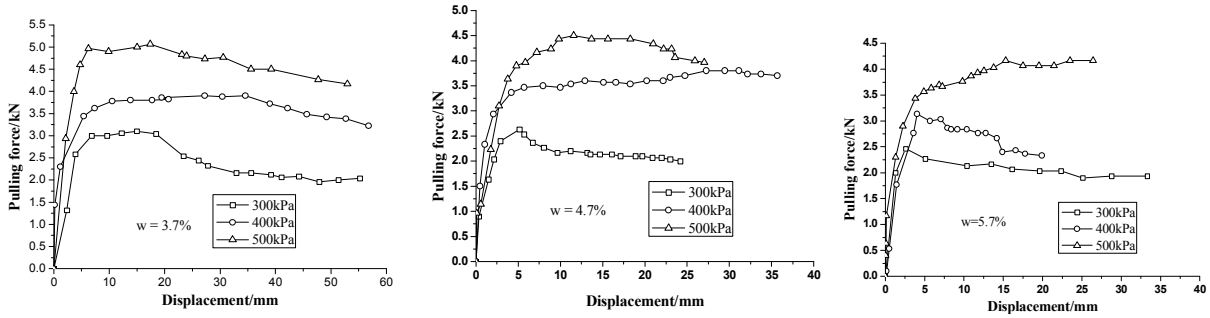


Fig. 4. Graph for pulling force and pulling displacement

Table 3. Results of pullout test

| Test No. | Vertical load p (kPa) | Water content of sand gravel w (%) | Total horizontal tension at peak value $T_P$(kN) | Pulling friction strength $\tau_f$ (kPa) | Pulling friction coefficient $f$ | Average pulling friction coefficient $\bar{f}$ |
|---|---|---|---|---|---|---|
| 1 | 300 | 3.7 | 3.10 | 86.111 | 0.287 | |
| 2 | 400 | 3.7 | 3.90 | 108.333 | 0.271 | 0.280 |
| 3 | 500 | 3.7 | 5.07 | 140.741 | 0.281 | |
| 4 | 300 | 4.7 | 2.63 | 73.148 | 0.244 | |
| 5 | 400 | 4.7 | 3.80 | 105.556 | 0.264 | 0.253 |
| 6 | 500 | 4.7 | 4.50 | 125.000 | 0.250 | |
| 7 | 300 | 5.7 | 2.47 | 68.519 | 0.228 | |
| 8 | 400 | 5.7 | 3.13 | 87.037 | 0.218 | 0.226 |
| 9 | 500 | 5.7 | 4.17 | 115.740 | 0.231 | |

## Conclusions

(1) The pull out of reinforced band is processed gradually. Due to the flexibility characteristic of reinforced band, at the beginning of the test, the anchored end was pulled out first with displacement expanded. When the pulling force gradually increases to a certain value, the interface friction is gradually delivered to back end and relative displacement in the reinforced soil increased in slow pace. When the pulling force reaches to maximum value, the pulling end and free end begin to take

place displacement, the time-history curve gradually paralleled, and the reinforced band immediately had integral displacement.

(2) The relationship between pulling force and pulling displacement in the test shows obvious nonlinear characteristic. When the reinforced band is pulled at beginning, the pulling force increases with increased displacement, and the pulling decreases as the pulling displacement increases after the pullout force reaches peak value. The pulling curve is featured by strain softening characteristic, but tends to be strain-hardening under big normal stress. The pulling friction strength increases as the vertical load increases.

(3) The water content of filling material has great influence on soil interface friction coefficient. Under the same normal stress, the higher the water content is, the lower the pulling friction strength will be. When the water content increases from 3.7% to 5.7%, the linear of average pulling friction coefficient decreases from 0.28 to 0.226, which is decreased around 19%.

**Acknowledgements**

This work was financially aided by the National Natural Science Foundations of China (51309027 & 51102229), the Postdoctoral Science Foundation of China (2013M531688), the Open Research Fund of State Key Laboratory of Geomechanics and Geotechnical Engineering (Institute of Rock and Soil Mechanics, Chinese Academy of Sciences) (Z012009) and the Foundation of State Key Laboratory for Geomechanics and Deep Underground Engineering (SKLGDUEK1110).

**References**

[1] Shi, D.D., Liu W.B., Shui, W.H., et al. "Comparative experimental studies of interface characteristics between uniaxial/biaxial plastic geogrids and different soils." Rock and Soi1 Mechanics, Vol. 30 (2009), p.2237-2244.

[2] Ochiai, H., Otani, J. and Hayashic, S. E. A.. "The pull-out resistance of geogrids in reinforced soil." Geotextiles and Geomenbranes, Vol. 14 (1996), p.19-42.

[3] Marc, J., Good, H., Tuncer, B., et a1. "Interaction of Foundry Sands with Geosynthetics." J. Geotechnical & Geoenv. Engrg., ASCE, Vol. 127 (2001), p. 353-362.

[4] Sugimoto, M. and Alagiyawanna, A. "Pullout behavior of geogrid by test and numerical analysis." Journal of Geotechnical and Geoenvironmental Engineering, Vol. 129 (2003), p 361-371.

[5] Fleming, I. R., Sharma, J. S. and Jogi, M. B. "Shear strength of geomembrane-soil interface under unsaturated conditions." Geotextiles and Geomenbranes, Vol. 24 (2006), p. 274-284.

[6] Mocraci, N. and Recalcati, P. "Factors afecting the pullout behaviour of extruded geogrids embedded in a compacted granular soil." Geotextiles and Geomenbranes, Vol. 24 (2006), p. 220-242.

[7] Zhang, W.H., Wang, B.T., Zhang, F.H., et al. "Test study on interaction characteristics between two-way geogrids and clay." Rock and Soil Mechanics, Vol. 28(2007, p. 1031-1033.

[8] Yang, G.Q. and Sui, C.Y. "Experimental Research on Interface Friction Characteristics of Geogrids and Soil." Journal of Shijiazhuang Tidao Nniversity (Natural Science), Vol. 23 (2010), p.46-52.

[9] Wang, M.Y., Bao, C.G., Ding, J.H., et al.. "Effect of some test conditions on pull-out behaviors of interface between geogrids and compacted expansive soils." Rock and Soil *Mechanic*s, Vol. 29 (2008), p.442-448.

*Applied Mechanics and Materials Vols. 580-583 (2014) pp 689-692*
*© (2014) Trans Tech Publications, Switzerland*
*doi:10.4028/www.scientific.net/AMM.580-583.689*

# Research of Soundless Crack with Different Number of Drillholes

Lie-xian Tang[1,a*], Dong Zhang[2,b], Zhen-tong An[1,c], Jun-yan Zhang[1,d]

[1] University of Science and Technology Liaoning, Anshan, China, 114051

[2]Ansteel Group Corporation, Anshan, China, 114000

[a] t7766@sina.com, [b] zhangdong8821@126.com, [c]771917861@qq.com, [d]1205175890@qq.com

**Key words:** Numerical Simulation; Soundless Crack; Failure Process; RFPA

**Abstract:** The special advantages of Soundless Crack method are safety and environmental protection. Soundless Crack is widely used in stone exploitation, partly crack of brittleness materials such as rock and concrete, and backout of building in city. In these engineering, we must drill many holes for loading Soundless Cracking Agents, but the drilling cost is expensive including human cost and materials cost, at the same time need much time to drill these holes. So we hope to gain the best crack results at the minimum drillhole numbers. This paper used RFPA software to set up some models with different drillhole numbers, gained different failure process of models. Adopted different drilling plan will occur different results. We should drill more holes if we need partly crack smoothly. We can plan the number of drillholes based on our need if we can use RFPA to simulate the failure process before beginning.

## Instruction

Soundless Cracking Agent(SCA) is a farinose material with high distensibility, mixed with water and then fill into drillholes of rock or concrete, dilation and induration happened at the same time, became a new dilated material which volume increase thrice and produce dilated power above 2.94 million Pa. Producing great dilated power in a period of times and loading to wall of drillholes, beginning appear crackle when tensility inside is bigger than the strength of cracking body, the crackles develop along with the continue action of dilate power, at last the cracking body is broken. Comparing with conventional explosive blast method, the Soundless Crack method low blasting velocity and slow loading, can gain blasting results without shake, noise, fly rock, bad gas, pollution. It is an important complementarity and development for blast technology, and easy to transportation, storage and operation, so it is widely use to building backout, especially in backout engineering which can't use blast method, and stone exploitation and cutting[1-4].

In all Soundless Crack engineering, should drill many holes for filling the Soundless Cracking Agent, but drill holes need cost, so we must gain the requisite results at minimum drillholes number. This paper used RFPA (Realistic Failure Process Analysis[5-7]) to numerical simulation of failure process on soundless crack with different drillholes, hoped to show the primary crackle developing process and provide reference evidence for actual engineering.

## Numerical Models and Results

Primary mechanics parameters of numerical models reference paper[7], the material is concrete, compressive strength is 38.6 MPa and tensile strength is 1.9 MPa, the elasticity modulus is 36977MPa, poisson's ratio is 0.2. Built four type of models, 300*300 mm with one hole in the middle of the model(Fig.1 (a)), 600*300mm with two holes which distance was 300mm(Fig.1 (b)), 600*300mm with three holes(Fig.1 (c)) and five holes (Fig.1 (d)), the calculation results are showed in Fig.1.

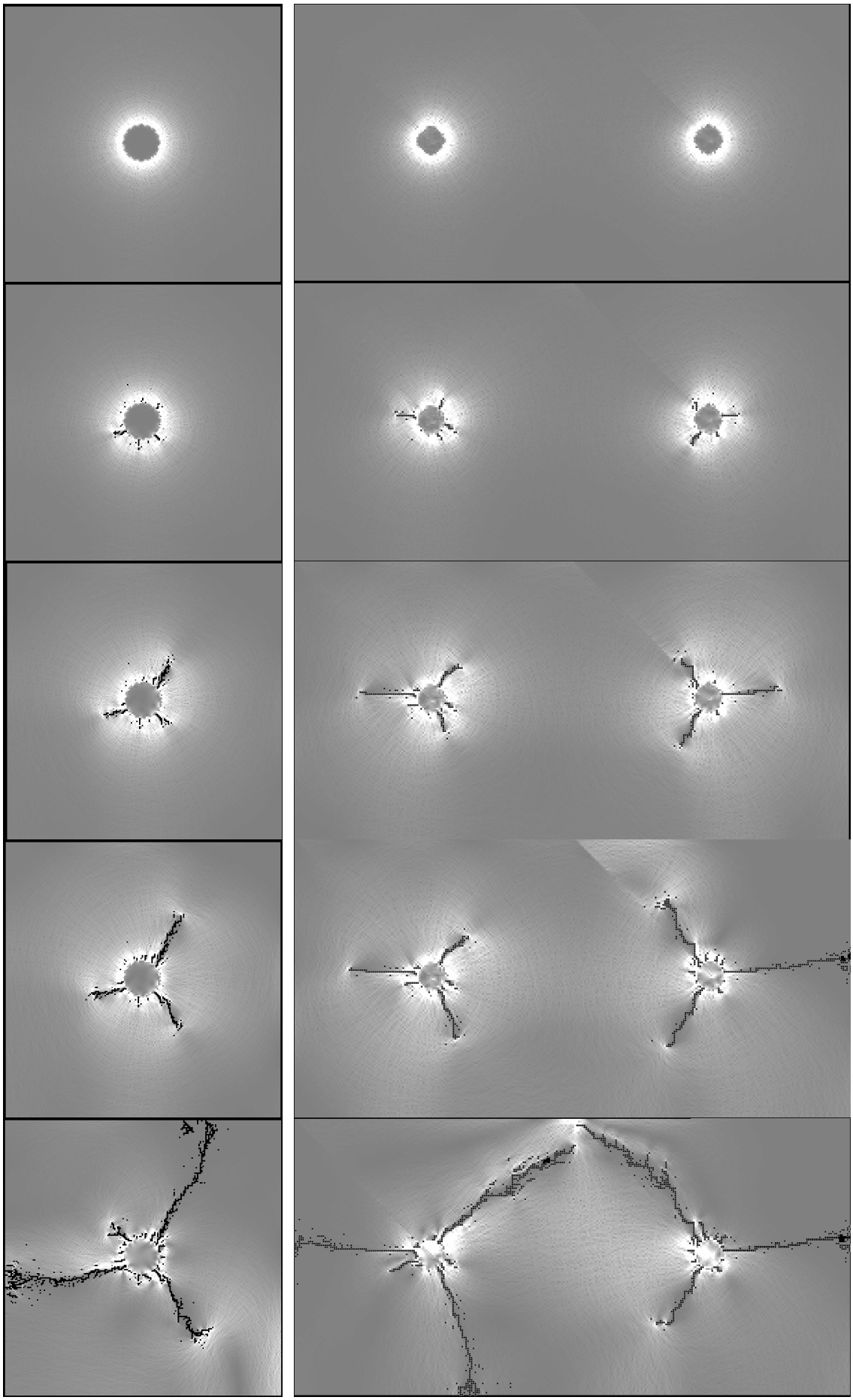

（a）300*300mm model （b）600*300mm model with 2 drillholes

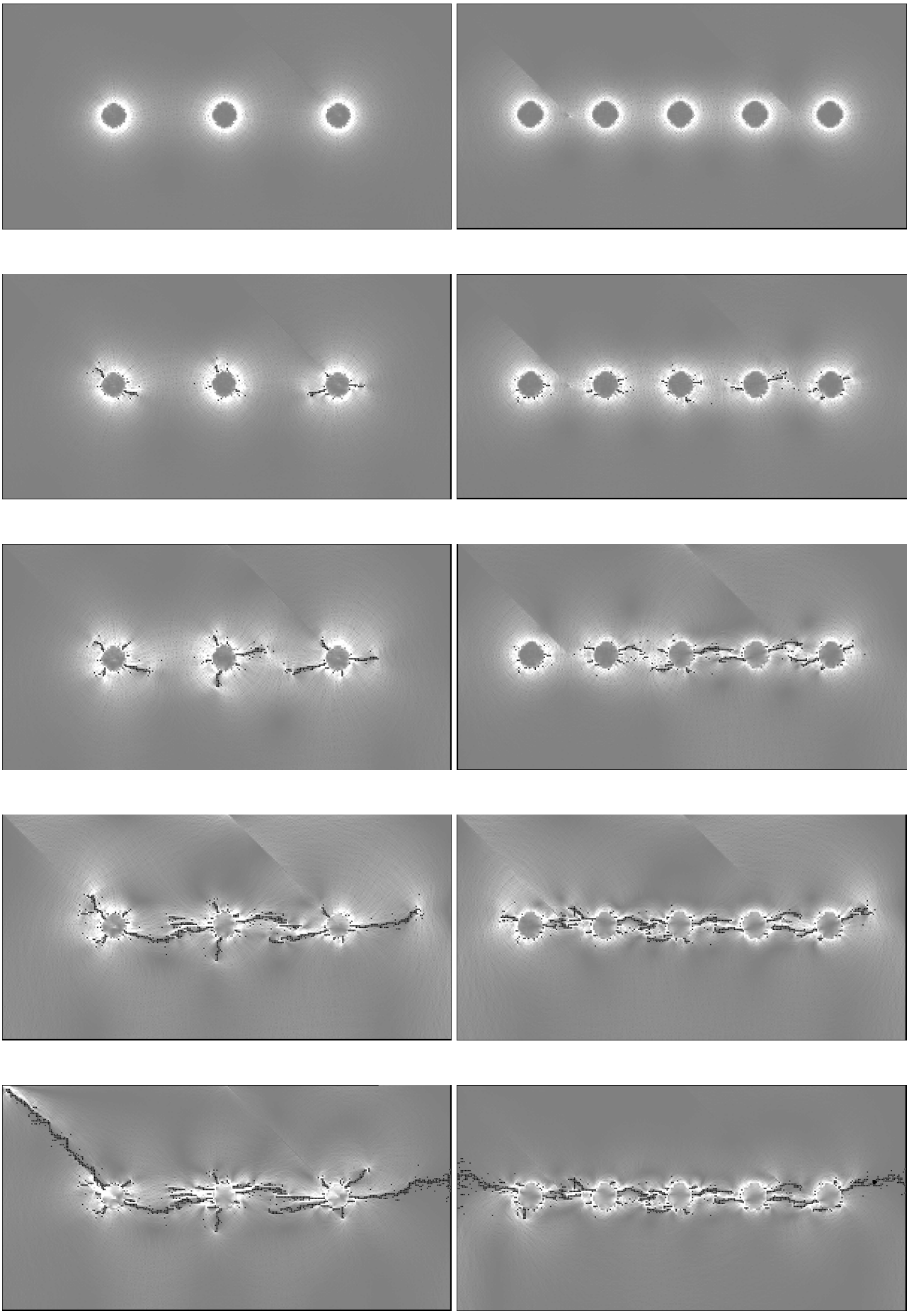

（c）600*300mm model with 3 drillholes （d）600*300mm model with 5 drillholes

Fig.3. Failure process of different number of drillholes

## Results Analysis

For the 300*300(mm) model with one drillhole in the middle of the model, there are three stochastic crackles. For the 600*300(mm) model with two drillholes which distance is 300mm, every drillhole has three stochastic crackles too. For the 600*300(mm) model with three drillholes which distance is 150mm, primary crackle connected but some crackle are stochastic. For the 600*300(mm) model with five drillholes which distance is 50mm, primary crackle connected as a beeline.

## Conclusions

From the calculation results by RFPA about soundless crack with different number of drillholes, we can find that the failure process of soundless crack are different because of the drillholes number, we have to drill different holes based on our need, we may drill much less holes if we need to break all of the objective, contrarily, we should drill more holes if we need to crack partly of the objective. If we can know the mechanics parameters of the materials, we can numerical calculation the failure process before drilling, rectify the planning distance between holes to gain the best cracking results. If the parameters are enough nicety, we can calculate the maximum distance between holes while be satisfied with break requirement.

## Acknowledge

(1) Youth Foundation of University of Science and Technology Liaoning (2012QN07)
(2) Excellent Young Scholars Growth Plans of Liao'ning Educational Committee (LJQ2013033)

## References

[1] Yin Guo-wei, Wen Xiang-yong. Application of soundless broken preparation in concrete and steel reinforced concrete demolishment[J]. Journal of Heilongjiang Hydraulic Engineering College. Vol.28 No.1 2001.3: 78~80

[2] Zhu Hui.The application of soundless breaking agent in stone demolition construction[J]. Shanxi Architechture. Vol.28 No.6 2002.6:55~56

[3] Tang Lie-xian, Tang Chun-an, Tang Shi-bin. Pysical experiment and numerical tests of soundless cracking on concrete [J]. Concrete, 2005, (8) :3-5 (in Chinese)

[4] Tang Lie-xian, Tang Chun-an, Tang Shi-bin. Pysical experiment and numerical tests of soundless cracking[J]. Journal of Geotechnical Engineering, 2005, 27(4):437-441 (in Chinese)

[5] Tang Chun-an, Tang Lie-xian, Li Lian-chong, Li Chang-wen. Centrifugal loading method of RFPA for the failure process analysis of rock and soil structure[J]. Chinese Journal of Geotechnical Engineering, 2007, 29(1): 71-76

[6] Tang Chun-an, Li Lian-chong. RFPA centrifugal mode-theory and application[J]. Failure Mechanics Letters, 2005, 3:41-42

[7] Zhu Wan-cheng, Tang Chun-an, Yang Tian-hong, Liang Zheng-zhao. Constitutive relationship of mesoscopic elements used in RFPA2D and its validations[J]. Chinese Journal of Rock Mechanics and Engineering, 2003, 22(1): 24-29.

*Applied Mechanics and Materials Vols. 580-583 (2014) pp 693-696*
*© (2014) Trans Tech Publications, Switzerland*
*doi:10.4028/www.scientific.net/AMM.580-583.693*

# Research on Negative Skin Friction on Pile by a Simple Model Experiment

Ting Huang[1, 2, a], Jinhai Zheng[1], Weiming Gong[2]

[1]College of Harbour, Coastal and Offshore Engineering, Hohai University, Nanjing, P.R.China

[2]Key Laboratory of Hydraulic and Waterway Engineering of the Ministry of Education, Chongqing Jiaotong University, Chongqing, P.R.China

[3]School of Civil Engineering, Southeast University, Nanjing, P.R.China

[a]huangting@hhu.edu.cn

**Keywords:** pile; negative skin friction; model experiment; sand; settlement.

**Abstract.** Accompanied by the substantive construction of domestic ports, the negative skin friction on pile becomes a common problem. In order to provide references for the related experiment research in the future, the designs of model experiments reported in the literatures were emphatically analyzed and compared. Compared to conventional pile model test, the model test on negative skin friction on pile needs to apply load on soil surface and it is difficult to simulate large surcharge by conventional test methods. An experimental scheme which could produce large surcharge load by conventional test conditions is given in this paper. Pile stress, displacement of pile top and layered settlement of soil was tested under different surcharge level. The depth of neutral point and the group effect of NSF are discussed.

## Introduction

Pile foundation is used widely because of good applicability for foundation soil. However, there are still some problems in the appliance of pile foundation, such as negative skin friction (NSF). If the pile foundation passes through the high compressibility of soil, the axial force of pile and the pile settlement will increase when the soil settlement increases and exceeds pile settlement. The strength failure of pile, the failure of pile bearing stratum and the failure of superstructure due to differential settlement may occur in severe case. Therefore it is important to pay attention to the problem of NSF on pile.

The concept of NSF was first presented in the 1930's when Terzaghi and Peck researched on the problem of differential settlement for the building adopted pile foundation. A lot of research on NSF of pile foundation has been conducted. This paper mainly discusses the experiment research on NSF.

## The Experiment Research on NSF

**Field Experiment.** A lot of field experiments of NSF were conducted through the nineteen-sixties and nineteen-seventies [1]. The NSF induced by the settlement of clay under surcharge load was studied mainly which was focused on the dragload and neutral point. The common law of neutral point of pile with different pile bearing stratum was obtained. Furthermore, the adhesion factor $\alpha$ and effective stress friction factor $\beta$ which were back calculated by field experiments provided important references for calculation and design. The measured dragload and neutral point also showed obvious time effect due to the slowness of clay consolidation. After the late 1970's, bitumen coated piles were proposed and some contrast experiments were conducted. The experiment results indicated that the NSF could be reduced effectively by setting up the coating on pile surface. Consequently, this method was used widely as the way to solve NSF.

Accompanied by the substantive construction of domestic ports, the negative skin friction on pile becomes a common problem because bitumen coated steel pipe pile is not widely used. However, the

research in this aspect is relatively lagging in domestic, and many researchers are attracted in field experiment.

**Model Experiment.** Field experiments on NSF, which research contents were relatively homogeneous, were mostly aimed at single pile and were time consuming and labor intensive processes owing to the time for clay consolidation. Unlike field experiments, the number of model experiments was less. In order to study group effect and validate the law from field experiments, there have been some scholars which researched NSF by model experiment and obtained valuable results since 1980's. Some research surveys are shown in Table 1.

Table 1. General Situation of Model Experiments on NSF

| Literature | Material of Pile | Loading Method of Soil (Max. Load) | Main Research Contents |
|---|---|---|---|
| Shibata et al [2] | Thin-Wall Steel Pipe | Rubber Pneumatic Bag (60 kPa) | Group Effect of Vertical and Inclined Pile Groups |
| Toma [3] | Brass Pipe | Rubber Pneumatic Bag (90 kPa) | Relationship Between NSF and Surcharge or Soil Shear Strength |
| Leung et al [4] | Aluminum Pipe | Heaped Load In Centrifuge (70 kPa) | Influence of Load On Pile Top on NSF |
| Charles et al [5] | Aluminum Pipe | Heaped Load In Centrifuge (45 kPa) | Influence of End Condition and Group Effect on NSF |

Model experiments on NSF are also carried out in recent years in China. The methods of the simulation of the surcharge load at soil surface can be divided into heap soil and load by loading plate and jack. Lu [6] studied the NSF on single pile and pile groups by model experiments respectively, and he adopted the method of heaping soil on the surface of clay and the max. value of surcharge load was 11.5 kPa. It can be found that the max. value of surcharge load was small by heaping soil, and that may lead to the soil settlement and the dragload too small. Larger surcharge load can be produce by setting the loading plate on soil surface and loading it. Yang [7] conducted the model experiment on NSF on single pile by using the loading plate, and the max. value of surcharge load was 100 kPa. Yang researched the law of neutral point and the dragload when the rate of water content of silt changed.

In conclusion, different experiment devices were designed to simulate surcharge load and studied NSF on pile. The method of heaping soil on soil surface does not need high requirement of experiment condition, but the data measured may be small and deviation may be large. The method of setting rubber pneumatic bag on soil surface can produce large surcharge loading (such as, Shibata [2] and Toma [3]), but the requirement of experiment condition is much higher. The method of setting loading plate on soil surface also can produce large surcharge load, but it just applied to single pile experiment. By contrast, centrifuge experiment shows great advantages.

## A Simple Model Experiment for NSF

**Test Description.** This paper suggests an experimental scheme which could realize large surcharge load by simple experiment conditions. The model experiment apparatus of pile groups are shown in Fig. 1. Reinforcing bands is welded on tank side to reduce the tank deformation caused by applying surcharge load on soil surface. The settlement plates are set on several soil layers inside and outside the pile groups in order to measure layered settlement. The down loading plate, which is prepared from 20 mm thickness steel plate and opened holes for model piles and settlement plates, is put on the sand surface. The up loading plate, which is prepared from 30 mm thickness steel plate and welded with four legs, is put on the down loading plate. The surcharge load on soil surface is simulated by the jack which uses down and up loading plate to ensure the surface load uniform. Two balance beams and small counterforce frame are fixed at tank wall. The model pile can be step-loaded by using

weight or jack. Pile stress, displacement of pile top and layered settlement of soil can be tested under different surcharge level.

According to the above method, a single pile test was conducted firstly. Model pile, which was embedded in 1 m thick homogeneous saturated sand bed, was prepared from thin-wall steel pipes of 1.4 m length, 40 mm outer diameter and 1.18 mm thickness with strain gauges at the inner wall of pipe pile. The load on pile top was step-loaded to 250 N, and the surcharge load was step-loaded to 120 kPa.

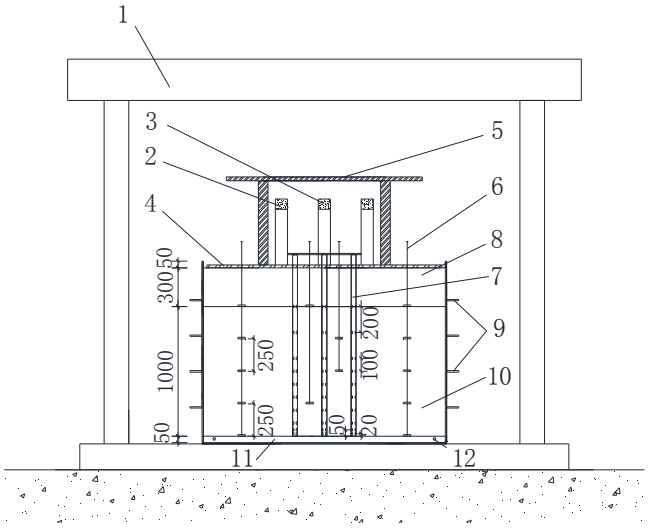


Fig. 1. Layout of model test (mm): 1-big counterforce frame; 2-balance beam; 3-small counterforce; 4-down loading plate; 5-up loading plate; 6-settlement plate; 7-model pile; 8-sand surcharge; 9-reinforcing band; 10-sand; 11-gravel sand; 12-drain valve.

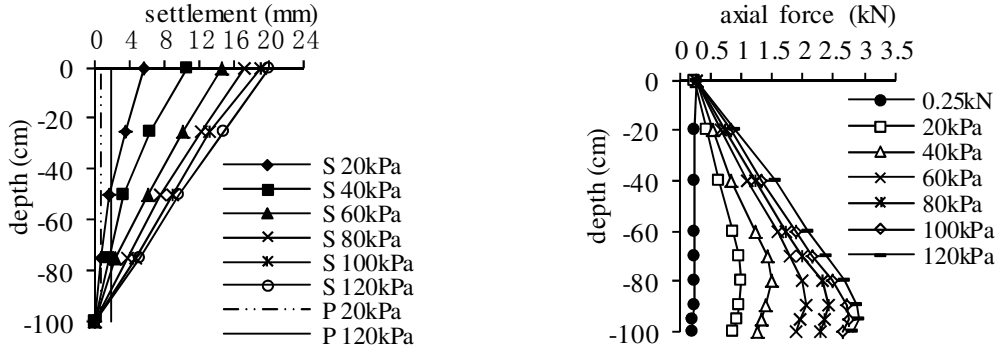


(a) (b)

Fig. 2. The test result of single pile: (a) The layered settlement of soil and the single pile settlement; (b) The relationship between axial force of pile and surcharge load on soil surface.

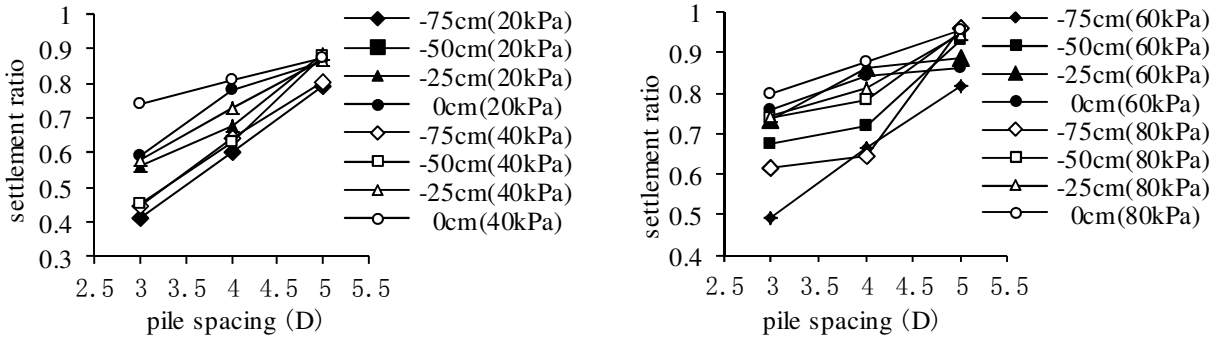


(a) (b)

Fig. 3. The soil settlement ratio inside and outside pile groups: (a) surcharge load 20 kPa - 40 kPa; (b) surcharge load 60 kPa - 80 kPa

**Results and Discussion.** The test result is shown in Fig. 2. Fig. 2(a) shows that the layered settlement of soil increases with the increase of surcharge load, but the increment decreases. The axial force of pile indicates that the depth of neutral point varies from 0.8 L (the length of pile in soil) to 0.95 L and the dragload varies from 0.77 kN to 2.64 kN as shown in Fig. 2(b). The effect of NFS is obvious in the test.

In order to study the NSF of pile groups, four different tests, such as 3×3 pile group test with pile spacing of 3 D (pile diameter), 4 D and 5 D under different surcharge load were designed. The group effect coefficient of NFS can be characterized by relative settlement of the soil inside and outside the groups. The soil settlement ratio inside and outside pile groups is shown in Fig. 3. The test result indicates that the ratios of inner to outer settlements increase with the increase of pile spacing or surcharge load, and decrease with the increase of soil depth. When pile spacing reaches 5 D, the soil settlement ratio is close to 1 and the difference between the inside and outside settlement is little.

## Conclusions

Accompanied by the substantive construction of ports in China, the problem of NSF on pile is needed to pay more attention. Some useful conclusions can be obtained by the model experiment.

(1) The model tests of NSF on pile and pile groups in sand, which surcharge load was simulated by sand and the jack with down and up loading plate, were designed and conducted. The axial force of pile, the settlement of pile top and the layered settlement of soil were obtained under different surcharge load.

(2) When the surcharge load was step-loaded from 0 kPa to 120 kPa, the axial force of pile indicates that the depth of neutral point varies from 0.8 L to 0.95 L in the tests. According to the test result of soil settlement ratio inside and outside pile groups, it indicates that the group effect can be ignored when pile spacing reaches 5 D.

## Acknowledgements

This work was financially supported by the Fundamental Research Funds for the Central Universities (No. 2013B03214), the Natural Science Foundation of Jiangsu province (No. BK20130843), the Jiangsu Planned Projects for Postdoctoral Research Funds (No. 1302048B) and the Key Laboratory of Hydraulic and Waterway Engineering of the Ministry of Education (No. SLK2013B01).

## References

[1] M. Endo, K. Minou and T. Shibata: *Negative Skin Friction Acting on Steel Pipe Piles in Clay*, Proceedings of the 7th International Conference on Soil Mechanics and Foundation Engineering, Mexico City, Vol. 2 (1969), p. 85-92.

[2] T. Shibata, H. Sekiguchi and H. Yukitomo: Soils and Foundation, Vol. 22 (1982), p. 29-39.

[3] T M. Toma: A model study of negative skin friction on a fixed base pile in soft clay (edinburgh: Heriot-Watt University, department of civil engineering. 1989)

[4] C. F. Leung, B. K. Liao and Y. K. Chow et al.: Soils and Foundations, Vol.44 (2004), p.17-26.

[5] W. W. Charles, G. P. Harry and S. H. Vincent, et.al: Journal of Geotechnical and Geoenvironmental Engineering, Vol.134 (2008), p.1245-1260.

[6] Mingsheng Lu: Port and Water Engineering, Vol. 5 (1997), p. 54-58. (In Chinese)

[7] Qing Yang, Gangqiang Kong, Pengyi Zheng and Maotian Luan: Rock and Soil Mechanics, Vol. 29(2008), p. 2805-2810. (In Chinese)

*Applied Mechanics and Materials Vols. 580-583 (2014) pp 697-700*
*© (2014) Trans Tech Publications, Switzerland*
*doi:10.4028/www.scientific.net/AMM.580-583.697*

# Research on Stability of Foundation Pit Construction

Hengsan Dai[1, a] Tao YANG[2, b]

[1]Faculty of Construction Management & Real Estate, Chongqing University, Chongqing 400015

[2]Central and Southern China Municipal Design and Research Institute Co.,Ltd, Wuhan,430010

[a]E-mail: 47846552@qq.com

[b]E-mail:02765666@sohu.com

**Keywords:** Strength Deduction Method; Foundation Pit; Support of Foundation Pit; Continuous Wall; Finite Element; Estimation on Stability

**Abstract:** In geotechnical engineering, the support pattern regularly applied is continuous wall, whose high security, strong adaptability, good stability and other characteristics have been widely appraised in engineering circles. This paper use Midas to build the three-dimensional research model on varied construction stages of foundation pit, in which the foundation pit applies the scheme of combing continous wall and inner support. Further more, this paper makes estimation on the machenical stability in varied construction stages of foundation pit and use strength deduction method to analyze the stress and strain conditions of foundation pit in different working states, the results acquired from which researches have certain reference to the engineers.

## Introduction of the Model

### 1.1 The Characteristics & Applicable Scope of Continuous Wall

The underground continuous wall is applicable to soft soil, sand soil or other places with high requirements. The main benefits is good waterproof performance, high structural security[1], capability of combing construction with jamb wall of basement and good integration. However, it is also featured by hard construction technology, slow construction speed, high requirement for machinery and large occupation of site[2].

### 1.2 Building of Model

This three-dimentional support system of foundation pit chooses the scheme of combining underground continuous wall and inner support. The foundation pit is rectangular shape with excavated depth of 18m, length of 22m and width of 12m. Within the foundation pit, angle braces and cross braces are seperately applied in four corners and horizontal direction with a section of supporting beam: BxH=900x700mm. The soil mass is divided into claypan and decomposed rock; regarding to claypan, we set elastic modulus E to be 6e4kpa, cohesive strength c to be 45kpa, angle of internal friction φ to be 12° , gravity of soil mass γ=18KN/m3, saturation gravity γsat=22KN/m3, and poisson ratio v to be 0.35; in the second interface of decomposed rock, we set elastic modulus E to be 3.4e45kpa, cohesive strength c to be 65kpa, angle of internal friction φ to be 40° , gravity of soil rock mass γ=22KN/m3, saturation gravity γsat=21KN/m3, and poisson ratio v to be 0.3. The reinforcing cage and concrete placement shall be applied in the underground continuous wall, which will conform to the the construction technology and process of underground continuous wall during construction; while the wall thickness shall be 700mm. See Fig. 1 & 2 below for the three-dimensional model of foundation pit.

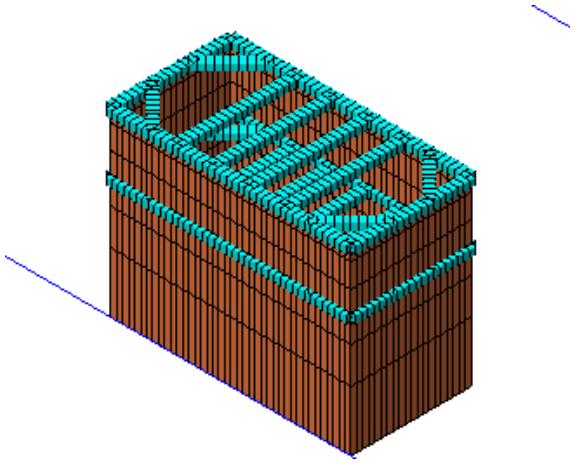

Fig. 1 Combined System of Underground Continuous Wall and Internal Support for Foundation Pit

## Examination of Results of Varied Construction Stages

### 2.1 The Displacement Change in Varied Construction Conditions

The deformation monitoring and control in foundation pit construction are focal contents of informatization construction, therefore, it is essential of an immediate monitoring to the displacement change after completion of varied construction conditions in the construction. See Fig. 3～11 below for the displacement change of foundation pit in varied construction stages.

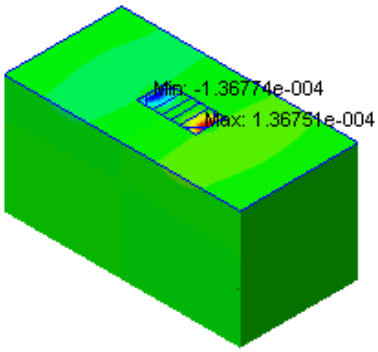


Fig. 2 Displacement along X Direction of Foudation Pit after Excavation 1

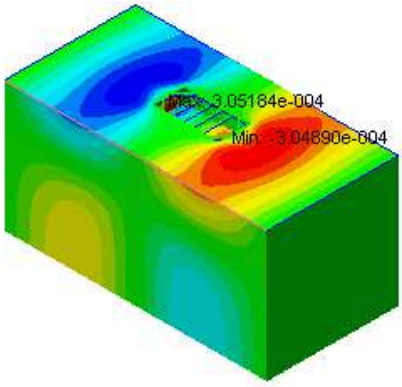


Fig. 3 Displacement along X Direction of Foudation Pit after Brace 1 and Excavation 1

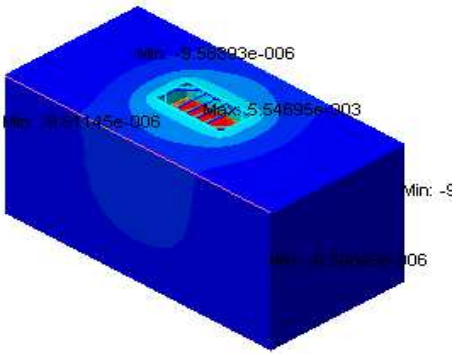


Fig. 4 Displacement along Z Direction of Foudation Pit after Excavation 1

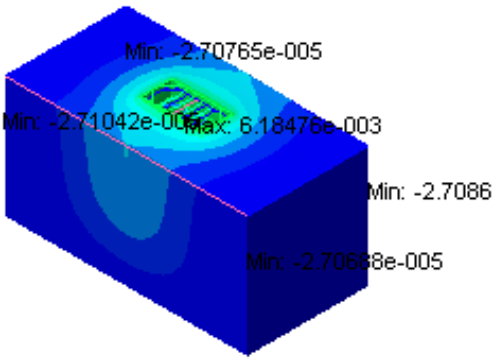


Fig. 5 Displacement along Z Direction of Foudation Pit after Brace 1 and Excavation 2

### 2.2 Comparison of Bracing Internal Force

As it includes many result options of internal forces within the varied construction conditions such as axial force, shear force and bending movement, so this paper chooses the change conditions of representative Fy and My. The result indicates that the internal force Fy changes in the horizontal direction along two left/right ends of cross brace with a large value; and the large section of My distributes in brace ends and midspan positions, of which the ends bear large compressive stress and the midspan produces upper blending and deformation. See Fig. 12～13 below.

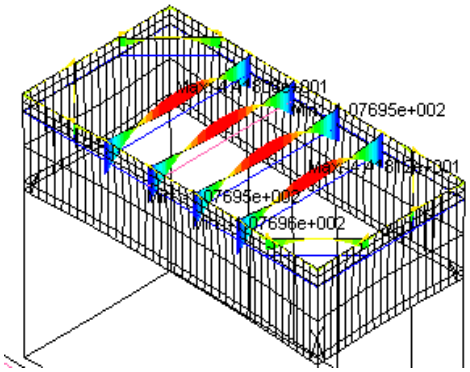


Fig.6Distributuon of $M_y$ during Brace 1 and Excavation 2

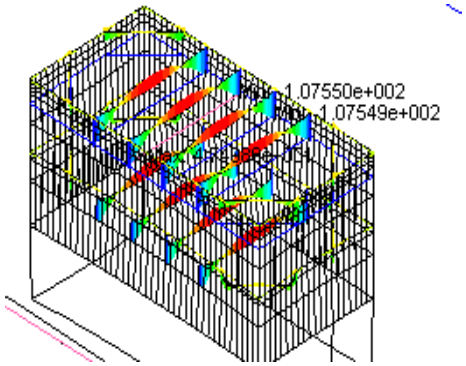


Fig.7 Distributuon of $M_y$ during Brace 2 and Excavation 3

### 2.2 Internal Forces of Continuous Wall

Under various conditions, there are also many forcing conditions of continuous wall, therefore, this paper chooses the internal force along X direction as reference. See Fig. 16 & 17 below for the the internal force along X direction of continuous wall.

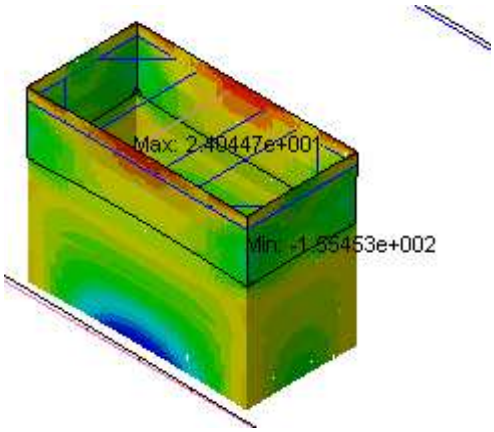


Fig. 8 Internal Force along X Direction of Continuous Wall after Brace 1 and Excavation 2

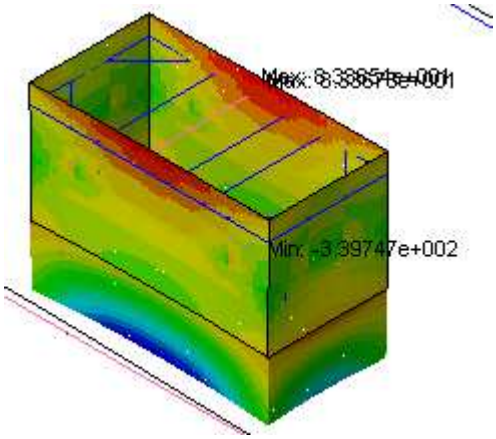


Fig. 9 Internal Force along X Direction of Continuous Wall after Brace 2 and Excavation 3

### Conclusions

This paper use Midas-GTS to build a three-dimensional calculation and analysis model for varied construction stages of foundation pit, in which the foundation pit applies a bracing system of combining underground continuous wall with inner braces and the construction procedure is divided into three stages: excavation1, brace 1 followed by excavation 2, and brace 2 followed by excavation 3. After operation and analysis, the displacement changes, internal force and stress of

inner bracing, internal force and stress changes of underground continuous wall are examined in directions of X, Y and Z of foundation pit during varied construction stages. Due to so many datas of varied costruction conditions in analysis, only several datas such as displacement changes in varied costruction conditions, Fy and My changes of inner bracing and the distribution condition of internal force along X direction of underground continuous wall are selected to get conclusions as follows:

The model built seems too conservative; in varied construction stages, the displacement changes along X and Y directions of foundation pit are all very small as to be less than 1mm, so does it along Z direction; the maximum displacement in final construction stage is about 6.31mm.

**Reference**

[1] Yang Guanghua, The Practical Calculation Method of Bracing Structure in Deep Foundation Pit and Its Application [M], published by Beijing: Geological Press, 2004.
[2] Huang Shixiang, Pan Jiang, Liu Hong, etc., A Discussion on Design of Bracing Structure of Foundation Pit in Wushan Station of Guangzhou Subway [C], selected from Proceedings of Cross-Strait Soil and Rock Engineering in 2004.
[3] Xiao Shaoran, Soil Mechanics [M], published by Zhengzhou: Zhengzhou University Press, in 2007.

*Applied Mechanics and Materials Vols. 580-583 (2014) pp 701-704*
*© (2014) Trans Tech Publications, Switzerland*
*doi:10.4028/www.scientific.net/AMM.580-583.701*

# Research on the Effect of One Debris Flow Along Bailong River

He Yongqiang[1,a], Wu Yun[1,a] ， Li Suling[2,a]

[1] School of Civil Engineering, Northwest University for Nationalities, Lanzhou 730030, P.R. China
[2] School of Highway, Chang'an University, Xi'an 710064, P.R. China

[a]mdtmhyq@163.com

**Key words:** Bailong River; debris flow; character; hazards assessment

**Abstract:** Earthquake can cause heavy casualties and property losses immediately, and induced a mass of secondary mountainous disasters such as collapse, landslide and debris flow. Collapse and landslide provide abundant incompact solid matter for movement of debris flow directly, which makes the debris flow ravines be active in a long period in the future. Taking one debris flows on Bailong River as an example. Based on the analysis of the valley features and the forming condition scientific prediction for the trend of the debris flow activities and estimates the hazards situations have been achieved.

## Introduction

southern of Gansu is the severe earthquake disaster area, and is one of the landslide, debris flow distribution area, its geological hazard development degree, frequency , scope and damage is in the first place in China[1] .

it has an important significance for people's life, property and hydropower Project construct to research the formation condition and motion feature of debris flow, predict its develop tendency and hazard.

## Formation Condition of Debris Flow

### 2.1 Terrain Condition

The gully lies in middle-mountain of Bailong River right bank, Its area is 2.6 km$^2$ with the shape of "willow-leaf-alike', the highest elevation is 2430m, lowest elevation is 900m, relative height difference is 1530m. the length of the main gully is 10.15km, and the shape is "U" in downstream, there are many waterfall scarps along main gully. As a whole, the terrain condition of the gully is beneficial to water collecting in short time, surface and brunch gully water gain energy in main gully quickly, then the scale and peak of debris flow in main gully will upgrade quickly. It provides a beneficial condition for debris flow.

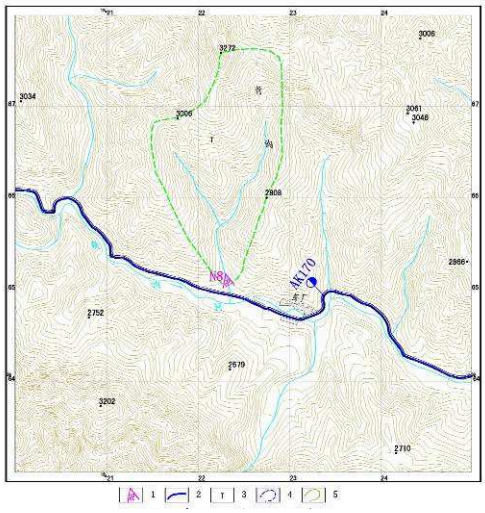

### 2.2 Recharge Condition of Solid Mass

There are precipitous topography, loose rock, developed Weathering, Influence of geological structure and earthquake in the gully, disasters such as collapse, landslide are very developed. These will supply rich solid loose mass for debris flow. ① Landslide: According to Investigation, there are 18 landslides in the gully. Including 220 loess-bedrock landslides, 2 loess landslides, 2 bedrock landslide. ② Collapse and slump: earthquake induced many collapses and slumps; it becomes the resource for soiled material for debris flow. Collapse masses are bedrock and loess-bedrock collapses in the gully. most of them are loess collapse. ③ Gully bed debris: debris distributed in channel and entrance of debris flow, the shape is cone at entrance. ④ Slope loose debris: Include slope coprolite and wash, loose loess and weathered clastic stones and etc.

A lot of researches show that the critical rainfall of debris flow in southern of Gansu is 15-20mm per hour, 8-10mm per ten minutes; it is the lowest district in Gansu province. In this area, the maximum rainfall is 90.5mm per 24 hours, 40mm per hour, 16.2mm per 10 minutes. Since 1939, the rainfall of 25~50mm/ day is 2-3 times per year, 50~75mm/day and more than 75mm/day is about 2-3 times per 10 years. There is a concentrate rainfall, with a character of intensity rainstorm, and local heavy rainfall, all of these supply a hydrodynamic condition for debris flow.

## Influence Evaluation for hydropower project

### 3.1 Prediction of Risk Range

The risk range of debris flow is the region where may be damaged by debris flow. in this paper, once and maximum debris flow accumulation range model was used, which mentioned by paper [7], a model of debris flow was appropriately readjusted combined with field survey of the gully debris flow and related parameters from indoor and field tests. The accumulation pattern after debris flow of the gully was speculated when reservior is full and empty.

Prediction model of debris flow accumulation range:

$$a = 0.49312 \tag{1}$$

$$l = 2.5748\left(V \times G \times r_c / \ln r_c\right)/3 \tag{2}$$

$$d = 0.254/\left[V \times r_c /\left(G_2 \times \ln r_c\right)\right] \cdot 1/3 \tag{3}$$

Where, a is the area of once debris flow accumulation（$m^2$）; $l$ is the length of maximum accumulation（m）; D is the depth of once debris flow accumulation（m）.V is once solid loose mass maximum recharge capacity（$m^3$）; G is the accumulation area slope (°); rc is the gravity of debris flow($g/cm^3$);

Applicable condition, when $r_c$=1and G=0, the model is unfit, prediction accuracy is average relative error of a is 11.83%； prediction accuracy is average relative error of 1 is 9. 5%； Prediction accuracy is average relative error of d is 7.8%.

When the area of once debris flow accumulation is predicted with this model, once solid loose mass maximum recharge capacity can use the calculation result of once debris flow solid loose mass, G is the accumulation area average slope, longitudinal gradient is 3° ~5° , the average value is 4° , gravity is designed frequency unit weight of debris flow. Let designed parameters to the above mentioned formula, the area of once debris flow accumulation parameters with designed frequency can be calculated. Calculation parameters and accumulation range of the gully is showed in table 1.

**Table 1 Calculation parameters of designed frequency and accumulation range**

| designed frequency P（%） | 5 | 3.333 | 2 | 1 |
|---|---|---|---|---|
| V($10^4m^3$) | 9.2 | 12.2 | 14.8 | 18.5 |
| G（° ） | 4 | 4 | 4 | 4 |
| $r_c$ ($g/cm^3$) | 1.75 | 1.75 | 1.75 | 1.75 |
| $a$($m^2$) | 35940 | 43194 | 52073 | 56991 |
| $l$(m) | 269.8 | 296.4 | 325.1 | 340.5 |
| $d$(m) | 4.53 | 4.7 | 4.9 | 5.2 |

From the calculation results of accumulation forecasting model for every frequency of the gully debris flow, debris flow of 50—year frequency and 100—year frequency can reach upper damsite and open diversion canal, this will lead to the Direct threaten of sludge buried, impaction and scouring. Debris flow of 50—year frequency and 100—year frequency also can reach the other bank of Bailong river, and it is possible to block the river and form dammed lakes, it will threat to the safety and operation of downstream hydropower station. It will not be sludge buried by debris flow to Wuguan expressway and , Chengyu railway. From the calculation results of every frequency flow accumulation model, the debris flow has a little effect for middle dam-site.

### 3.2 Prediction of River Blocking

Debris flow always takes a lot of solid loose mass into Main River. If there are too much solid mass, Main River may be blocked, and there will come to a provisional dam, after some time, the impoundment will cause dam-break. In addition, sediment clogged also will cause a part of riverbed deposit and River course change, then a large number of sediments are inputted in Main River, sediment content of Bailong river will increased, and power generation benefit and coastal flood control will also be affected. Take conversion coefficient of false or true volume ratio to 0.8, then the scale of once debris flow blocking at the entrance is:

$$W_t = \frac{0.8W}{C_V - P_S C_V} = \frac{(\frac{1}{2\tan 14^\circ} + \frac{1}{2\tan\varphi}) \times 0.8B \times H^2}{C_V - P_S C_V} \tag{4}$$

Where, $W_t$ is the total amount of solid mass($m^3$)； B is the width of Main River (m); H is the depth of Main River (m), take 5; $\varphi$ is internal friction angle of debris flow (°)， take 25; $C_v$ is the volume concentration of soil in debris flow, take 1.45; Ps is the weight percentage between sand and soil in flow, take 0.21.

The amount of once debris flow enter hydropower station can be calculated by the flowing formula

$$V_{s0} = \alpha_p \times V_s \tag{5}$$

Where, $V_{s0}$ is the volume of debris flow entering into hydropower station under some designed frequency（$m^3$）; $V_s$ is total quantity of debris flow solid mass under some designed frequency（$m^3$ ）; $\alpha_P$ is storage factor of debris flow solid mass under some designed frequency.

$\alpha_P$ of 100—year frequency can be gotten by from near entrance accumulation character investigation and analysis inverse computation during blocking the river, other frequency can be get by analyzed combing with experience, then storage amount of once debris flow can be gotten. The lifetime of station is set to 100 years, assume there are 10 times debris flow of 10—year frequency, 5 times of 20—year frequency, twice of 50—year frequency, once of 100—year frequency. Then the possible maximum storage amount is show in table 2.

**Table 2 The possible maximum storage amount（$10^4m^3$）**

| items | Designed frequency P（%） | | | |
|---|---|---|---|---|
| | 10 | 5 | 2 | 1 |
| Once storage amount under every frequency | 1.82 | 2.14 | 3.95 | 5.55 |
| Possible times | 10 | 5 | 2 | 1 |
| storage amount | 18.2 | 10.7 | 7.9 | 11.1 |
| storage amount of 100—year frequency | 56.42 | | | |

Calculation results show that, the maximum possible storage amount of debris flow solid mass is $56.42\times10^4m^3$ during life tome of the station, if adopting upper dam site, total storage capacity is $220\times10^4m^3$， so it is significantly compared that debris flow affect storage capacity of upper dam site. It is relatively smaller for middle damsite.

## Conclusions

Wudu region of southern of Gansu province is one of the most serious hazards of debris flow. the basin area of the debris flow gully has abundant of loose mass, The main hazards are landslides, collapses and appearance erosion, it belong to viscous debris flows, the flow rate of 100—year frequency is 351m3/s, these will have a threaten of buried and impact washing, and blocking the river.

## Acknowledgements

This work was financially supported by the fundamental research founds for universities (31920130019).

## References

[1] Chen Zuyu. The Stability Analysis of Soil Slope (China Water Conservancy and Hydropower Press, Beijing, 2003)

[2] Chi Shulan, Kong Shuxiang: embankment engineering．(Chinese Railway Press, Beijin 2002)

[3] ZHUANG Jian-qi1 ,CUI Peng, Ge Yong-gang, etc. Hazard Assessment of Debris Flow Valleys Along Dujiangyan -Wenchuan H ighway After “5·12”W enchuan Devastating Earthquake [J], Journal of Sichuan University （Engineering Science Edition）, 2009, 41, (3): 131-139.

[4] Chen Xiaoqing, Cui Peng, Zhao Wanyu. Optimal timing for the control of debris flow in wenchuan earthquake area [J]. Journal of Sichuan University （Engineering Science Edition）, 2009. 42, (3):125-130

[5] Huang zhongshu, Yu Yingzhong. Debris Flow Distribution and Development Character in Southern of Gansu Province Upper Yangtze River [J], Yangtze River, 1998，29(7)：44.

*Applied Mechanics and Materials Vols. 580-583 (2014) pp 705-710*
*© (2014) Trans Tech Publications, Switzerland*
*doi:10.4028/www.scientific.net/AMM.580-583.705*

# Research on the retention capacity of ruins soil under drying condition

Ping Liu[1,2,a], Huyuan Zhang[1,2,b] , Yi Chen [1,2,c], Xianxian Shao [1,2,d] and Xinyuan Fu [1,2,e]

[1]Key Laboratory of Mechanics on Disaster and Environment in Western China (Lanzhou University), Ministry of Education, Lanzhou, China 730000

[2]School of Civil Engineering Mechanics, Lanzhou University, Lanzhou, China 730000

[a]liuping@lzu.edu.cn, [b]Zhanghuyuan@lzu.edu.cn, [c] sxjzyscy@163.com, [d] shaoxx11@lzu.edu.cn, [e] fuxy11@lzu.edu.cn

**Keywords:** retention capacity, ruins, matric suction, shrinkage

**Abstract.** The soil water characteristic curve (SWCC) has been tested during the drying process. In order to define the relationship between suction, degree of saturation and void ratio, fitting models of SWCC was established. Studies have shown that the shape of SWCC of three kinds of samples (taken from Jiaohe, Gaochang and Jiuzhoutai) was similar to the inverted "S", the relationship between water content and matric suction was inversely proportional. Under the condition of the same moisture, the matric suction of the Jiaohe and Gaochang samples were greater than the Jiuzhoutai samples, and the changes of pore water pressures showed the same trend. The degree of saturation began to decrease when the water content reduced to the air entry value. When the degree of saturation was greater than 90%, the volume of soil samples contracted significantly, and when saturation is below 80%, volume shrinkage stopped.

## Introduction

A large number of ancient earthen architecture ruins were left along the Silk Road in arid and semi-arid areas of northwest region, and these earthen ruins were constructed by clay or sand, or by directly digging raw soil, or by utilizing sun-dried mud bricks [1]. Compared with rocks, the soil is characterized by low strength and weak water resistance, which determines that it is extremely difficult to protect the earthen cultural ruins, especially the immovable earthen architecture ruins preserved in the open air. Benefiting from the unique climatic conditions of being arid and rainless, some open-air earthen ruins in the northwestern region have been preserved well until now. However, due to the physical and chemical weathering, the function of building materials (mainly the soils) continually degraded. These earthen ruins were suffering from devastating damages [2-4]. So it was a priority to carry out the work of conservation in earthen ruins.

## Experimental Materials and Methods

**Experimental Materials.** Test soil samples are taken from Jiaohe ruins and Gaochang ruins located in Turpan city, Xinjiang province. The region surrounding Turpan belongs to continental warm temperate zone arid desert climate, and the annual precipitation is 16.2mm. However, there were several times of heavy storms with precipitation reaching 40~50mm in the history. In addition, the recorded maximum daily temperature difference was 21.9°C (July 1994), the maximum ground temperature reached 44.5°C [5]. Engineering drilling ascertained that the ruins were located on the alluvial or lake stratum which is mainly composed of silt, clay, and fine sand inter-bedded layer.

Under rainfall conditions, soils on the ruins' surface a first saturated, mud are formed. After the rain, as the moisture content reducing, mud turns to crust. At the same time, shrinkage cracks on the surface of crust generate and expand during the drying process [4]. Therefore, remolded soils which are initially saturated are chosen to test for the study. In order to contrast the test data, loess samples retrieved from Jiuzhoutai in Lanzhou are selected as the comparative samples. To avoid the impact of

large particles in the soils, soil samples are sieved. The diameter of the mesh is 1mm. In tests, automatic laser particle size analyzer (Mastersizer 2000) is used in particle test, and Powder X-ray diffractometer (X'Pert Pro MPD) is used in mineral composition test. Other parameters of physical properties are tested according to the Standard for Soil Test Method (GB/T50123-1999). The test results are listed in Table 1, Table 2 and Figure 1.

Table 1 Physical properties of the soil samples

| sample | specific gravity | Liquid limit /% | Plastic limit /% | Plasticity index | Clay /% | silt /% | sand /% | specific urface area/$m^2 \cdot g^{-1}$ |
|---|---|---|---|---|---|---|---|---|
| Jiaohe | 2.719 | 34.0 | 22.4 | 11.6 | 25.1 | 67.4 | 7.5 | 1.19 |
| Gaochang | 2.714 | 30.7 | 18.5 | 12.2 | 25.0 | 60.3 | 14.7 | 1.07 |
| Jiuzhoutai | 2.722 | 28.1 | 17.6 | 10.5 | 11.2 | 70.5 | 18.3 | 0.64 |

Table 2 Results of analysis by X-ray diffraction of test soil samples

| sample | Montmorillonite | Illite | Plaster | Kaolinite | Chlorite | Quartz | potash feldspar | anorthose | Calcite | Dolomite |
|---|---|---|---|---|---|---|---|---|---|---|
| Jiaohe | 2.3 | 2.1 | 0.1 | 2 | 0 | 39.2 | 18.3 | 34.9 | 0 | 0.3 |
| Gaochang | 2.1 | 4.7 | 0 | 2.1 | 1.6 | 37.2 | 13.6 | 22.3 | 14.6 | 0.4 |
| Jiuzhoutai | 1.4 | 6.9 | 0.1 | 3 | 1.7 | 48.4 | 11.2 | 15.9 | 8.9 | 1.9 |

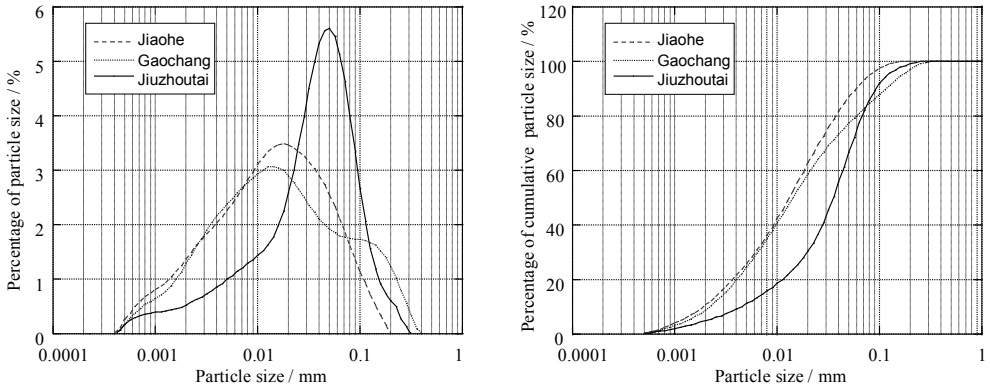


Particle size frequency curve Cumulative grain size curves

Fig.1 Grain size distribution curve of soil samples

**Test principle.** With the decreasing of water content, the matrix suction is increasing during the shrinkage of the saturated soils. The relationship between the matrix suction and water content during the drying process is defined by the soil water characteristic curve (SWCC). In this paper, the pressure plate extractor (Figure 2) is used to test the SWCC of ruins' soil samples.

Fig.2 Photograph of the 15bar pressure plate extractor

Test principle of pressure plate extractors: A wetted porous ceramic plate is backed by a fine mesh screen which also provides a passage way for the extracted solution, and is further sealed by a rubber membrane backing. The soil samples are placed directly onto the ceramic plate and are saturated on the plate. After bolting the extractor lid onto the Extractor, air pressure may be increased to the value of the test. (0.1 to 1500kPa). As soon as air pressure inside the chamber is raised above atmospheric pressure, the higher pressure inside the chamber forces excess water through the microscopic pores in the ceramic plate. The high pressure air , however, will not flow through the pores since they are filled with water and the surface tension of the water at the gas-liquid interface at each of the pores supports the pressure much the same as a flexible rubber diaphragm. At any given air pressure in the chamber, soil moisture will flow from around each of the soil particles and out through the ceramic plate until such time as the effective curvature of the water films throughout the soil are the same as at the pores in the membrane. When the air pressure in the Extractor is increased, flow of soil moisture from the samples starts again and continues until a new equilibrium is reached. At equilibrium, there is an exact but opposite relationship between the air pressure (positive force) in the extractor and the soil suction (negative force). Water content by weight or by volume can be determined for the sample that was at equilibrium with the pressure in the extractor.

**Test procedure.** The process of sample preparation is the same with the one mentioned in reference [8]. The saturated mud is still chosen as the initial sample. Prior to testing, the 15bar pressure plate is first put under the water until it is fully saturated. Then, remove the pressure plate onto the table, put the cutting rings on the pressure plate, putting a piece of round filter paper underneath each ring, then squeeze the mud out of the V-type plastic bag into the rings, smooth the top of mud samples in the rings, and then place them together into the extractor. Exert different pressures on the extractor. In each pressure level, when it is in equilibrium, open the extractor, take out a set of samples to test the water content, and then recover the extractor exert the next pressure. Repeat the above steps until it reaches the set pressure value. The test process is shown in Fig.3.

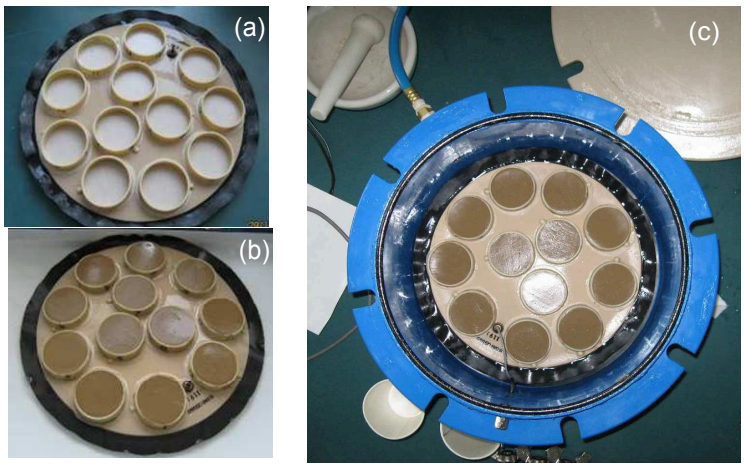


a. saturate the pressure plate b. pour the mud into cutting rings
c. placed the samples into pressure plate extractors

Fig.3 Testing process of the SWCC

## Analysis and Discussion of Test Results

The obtained values of water content versus imposed suction are plotted in Fig. 4. Fitting formulas and associated parameter values of corresponding curves are given in Table 3.

The results showed that the shape of SWCC is substantially similar for the 3 kinds of samples, water content and suction showed an inverse relationship. From the slope variation of the curve, when the suction at the range of 90-500kPa, with gradually decreasing of water content, suction increased slowly. When the suction is less than 90kPa or greater than 500kPa, with gradually decreasing of water content, the suction increased rapidly.

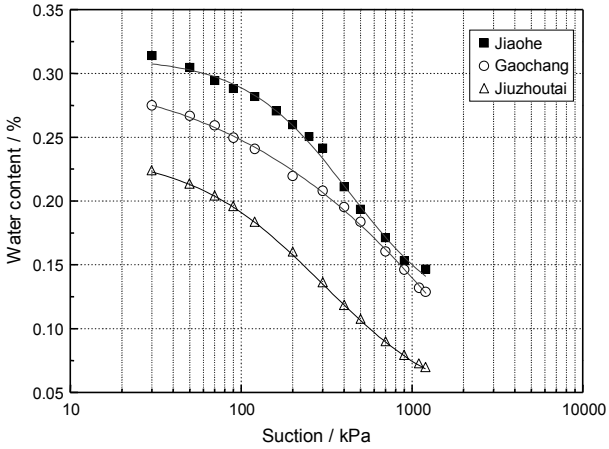


Fig.4 Soil shrinkage characteristic curves of three kinds of samples

Table 3 Fitting formulas and parameters

| Sample | Fitting formula | Parameters | Correlation coefficient |
|---|---|---|---|
| Jiaohe | $y=\beta+\frac{\alpha-\beta}{1+(x/\gamma)^{\lambda}}$ | $\alpha=0.3132$<br>$\beta=0.10289$<br>$\gamma=428.322$<br>$\lambda=1.42626$ | $R^2=0.99557$ |
| Gaochang | | $\alpha=0.30788$<br>$\beta=-0.24682$<br>$\gamma=4510.09$<br>$\lambda=0.55311$ | $R^2=0.99855$ |
| Jiuzhoutai | | $\alpha=0.23677$<br>$\beta=0.03352$<br>$\gamma=299.72$<br>$\lambda=1.1317$ | $R^2=0.99983$ |

Seen from the figure, at the same water content, suction values of Jiaohe and Gaochang samples are greater than that of Jiuzhoutai samples. And when the suction values are the same, the water content of Jiuzhoutai samples is lower than that of the others. It can be concluded that under the condition of the same water content, the pore water pressure of Jiaohe and Gaochang samples are lower than that of Jiuzhoutai samples. According to Kelvin capillary model equations, under the condition of same pore pressure, the pore water pressure (negative) decreases as the curvature radius of the gas-liquid interface decreases. In other words it is that the pore pressure decreases as the pore radius decreases [6-7].

The SEM photographs of three kinds of samples are presented in Fig. 5. As can be seen from the photographs, the pores of Jiaohe and Gaochang samples are significantly smaller than that of Jiuzhoutai samples. The corollary above is proved to be correct.

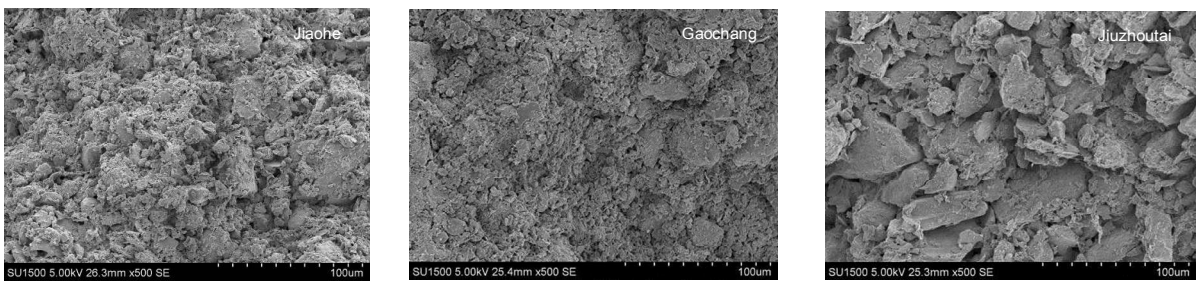


Fig.5 SEM photographs of three kinds of samples

Based on the data of SWCC and the results gained from reference [8], the corresponding s-e (suction-void ratio) and s-$S_r$ (suction-degree of saturation) curves are given in Fig. 6-7. The figures show that with the evaporation of water, the suction increases, and the degree of saturation decreases, along with reducing of the void ratio and the shrinking of samples volume.

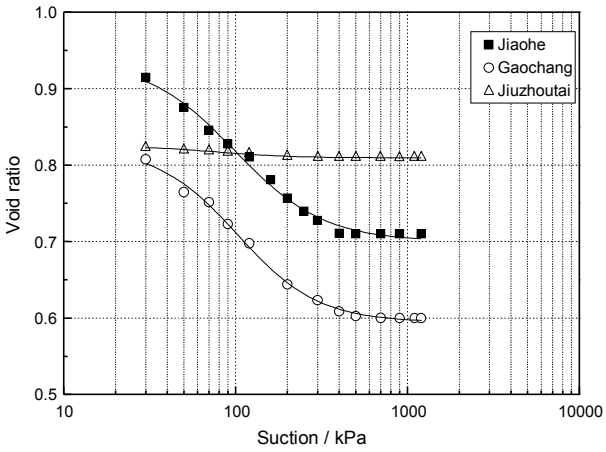


Fig.6 Relationship between suction and void ratio

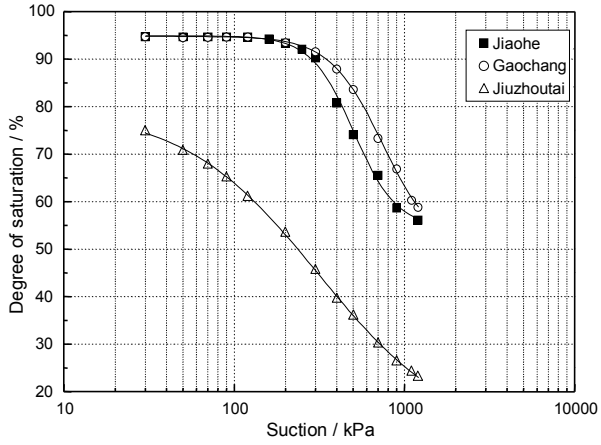


Fig.7 Relationship between suction and degree of saturation

Fig.6 shows that when the suction increases to a certain extent, the void ratio of samples remain unchanged, the corresponding point is defined as the shrinkage limit suction (SLS). The SLS should be consistent with the suction which is gained at the shrinkage limit water content. Fig.7 shows that in the early dryness for the Jiaohe and Gaochang samples, the decrease in water volume results in an equal decrease in bulk soil volume, with the internal pores still being fully saturated, so the degree of saturation remains unchanged. With the decrease of water content, air enters the internal pores, since then, the degree of saturation begins to decrease, until the water content reach to the humidity of the ambient air outside, the decrease can stop and reaches a certain value. For the Jiuzhoutai samples, the situation is different. Due to the presence of large particles, in the early dryness of the Jiuzhoutai samples, the decrease in water volume results in an smaller decrease in bulk soil volume, so air quickly enters the internal pores, resulting in the decrease of degree of saturation in the early period[9].

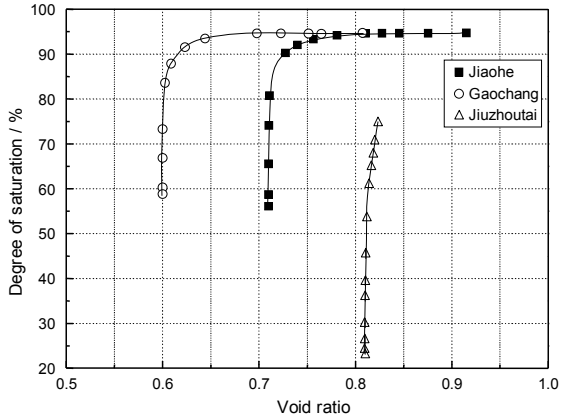


Fig.8 Relationship between degree of saturation and void ratio

During the drying process of samples, the relationship between degree of saturation and void ratio is given in Fig.8. It shows that when the degree of saturation is higher than 90%, the void ratio of Jiaohe and Gaochang samples changes very obviously. As the degree of saturation continues to decrease (in the range of 80-90%), the reduced amplitude of void ratio becomes smaller. When the degree of saturation is lower than 80%, decrease of the void ratio stops. For the Jiuzhoutai samples, because of the large particles skeleton, the volume of the soil samples change a little, so the amplitude of the void ratio shows a similar trend, i.e., little change.

**Conclusions**

(1) The results show that the shape of SWCC of three kinds of samples taken from jiaohe, gaochang and jiuzhoutai is similar to the inverted letter S, the relationship between water content and matric suction is inversely proportional.

(2) Under the condition of the same water content, suction values of Jiaohe and Gaochang samples are greater than that of Jiuzhoutai samples. And when the suction values are the same, the water content of Jiuzhoutai samples is lower than that of the others. It can be concluded that under the condition of the same water content, the pore water pressure of Jiaohe and Gaochang samples are lower than that of Jiuzhoutai samples.

(3) When the water content reaches the air entry value, the degree of saturation begins to decrease, when the degree of saturation is below 80%, decrease of the void ratio stops, the main shrinkage process of samples volume usually occurs before the degree of saturation reduces to 90%.

**Acknowledgements**

This work was financially supported by the Foundation of Key Laboratory of Mechanics on Disaster and Environment in Western China (Lanzhou University), Ministry of Education (201204), the Natural Science Foundation for Young Scientists of Gansu Province, China (1208RJYA040), the Specialized Research Fund for the Doctoral Program of Higher Education of China(20120211120008), the Special Research Foundation of Gansu Electric Power Design Institute of China Energy Engineering Group (Y490891001).

**References**

[1] Z.X. Li, X.D. Wang, M.L. Sun: *Research on consolidation techniques for conserving the ancient city of Jiaohe* (Science Press, Beijing 2008). (In Chinese)

[2] Z.X. Li: *Conservation of ancient sites on the Silk Road* (Science Press, Beijing 2003). (In Chinese)

[3] Z.X. Li, L.X. Zhao, M.L. Sun: Chinese Journal of Rock Mechanics and Engineering. Vol. 28(2009), p. 1047. (In Chinese)

[4] H.Y. Zhang, P. Liu, J.W. Wang, et al.: Rock and Soil Mechanics. Vol. 30(2009): p. 1883. (In Chinese)

[5] Y.H. Xie: *Preservation and research of the ancient ruins of Jiaohe* (Xinjiang People's Publishing House, China 1999). (In Chinese)

[6] I.G.B. Indrawan, H. Rahardjo, E.C. Leong: Engineering Geology, Vol. 82(2006): p.154.

[7] W.M. Cornelis, J. Corluy, H. Medina, et al.: European Journal of Soil Science, Vol. 57(2006): p. 258.

[8] P. Liu, H.Y. Zhang, G.S. Yan, et al.: Chinese Journal of Rock Mechanics and Engineering, Vol. 29(2010): p. 842. (In Chinese)

[9] D.L. Wang, M.T. Luan, Q. Yang: Chinese Journal of Rock Mechanics and Engineering, Vol. 26(2007): p. 1862. (In Chinese)

*Applied Mechanics and Materials Vols. 580-583 (2014) pp 711-714*
*© (2014) Trans Tech Publications, Switzerland*
*doi:10.4028/www.scientific.net/AMM.580-583.711*

# Stability analysis on anti-slide pile to reinforce slope based on ABAQUS

Xiaojie Gu[1, a], Taiquan Zhou[1, b], Shilong Lu[1,c]

[1] School of Environment and Civil Engineering, Jiangnan University, Wuxi, China, 214122

[a]416704023@qq.com, [b] 846158321@qq.com, [c] 916303231@qq.com

**Keywords:** ABAQUS finite element method, anti-slide pile, soil slope, stability

**Abstract**

The research uses the method of three-dimensional finite element analysis combined with the actual project application to study the slope reinforced by anti-slide pile. The research analyses the influence of reinforcement that the anti-slide exert on the soil and shows the changes of the sliding surface properties by establishing the finite element numerical model. The conclusion can be made that the ABAQUS finite element method is visual and practical. The study is of great benefit to the actual engineering.

## Introductions

Landslide is one of the most common accidents in the project. Many factors cause the landslide that will seriously affect the safety of traffic and people's lives once it happens. In the study of prevention and control of landslide, a variety of engineering measures are put forward. The methods of anti-slide pile which are widely used occupy the important position. Materials making anti-slide piles include the earliest application of piles, the steel pile and the most widely used reinforced concrete pile. Different from common pile foundation, anti-slide pile mainly bears lateral loads, which is similar with the stress characteristics of the beam. However, the sliding surface and the effect of soil resistance make it a kind of statically indeterminate structure which is different from that of the simple beam. According to the plenty of research on slide problems and the anti-slide pile by theoretical studies ,numerical model and field monitor conducted by scholars at the country and abroad.This article utilizes ABAQUS finite element and Shear Strength Reduction Factor method to demonstrate the effect of anti-slide pile, on the basis of previous studies and combined with the actual project.

## SSRF (Shear Strength Reduction Factor)

**1.1 Introduction of Shear Strength Reduction Factor.** Shear Strength Reduction Factor is presented by Zienkiewicz and his colleagues, which widely adopted by many scholars now. They proposed a shear strength reduction factor ($F_r$). Under the condition of invariable loads, $F_r$ means maximum shear strength in the soil dividing by the actual shear stress produced by external load.
In a limit condition, actual shear stress produced by external load is equal to minimum shear strength that is same as shear stress identified after reduction. Shear strength parameters can be expressed as Eq.1

$$C_m = \frac{c}{F_r}$$

$$\varphi_m = \tan^{-1}\left(\frac{\tan\varphi}{F_r}\right)$$

**Eq.1 Shear strength parameters**

In the equation $C$ and $\varphi$ are shear strength in the soil, $C_m$ and $\varphi_m$ are the actual shear stress produced by external load. $F_r$ is shear strength reduction factor. The initial value of $F_r$ is little enough to ensure stability of soil. The value of it does not increase until soil slope becomes instability

**1.2 The advantage of SSRF compared with other method.** (1) Complex landform and geology slope can be easily calculated. (2) Take soil constitutive relation and effect of deformation on stress

into consideration. (3) Simulate the shape of slip plane; the shape of slip plane is usually determined by the shear strain or displacement increment (4) Consider combined action between soil and supporting structure (fore poling, soil nailing, surface, etc.) (5) No necessary to premise the shape of slip surface and no need to slice.

**1.3 SSRF in ABAQUS.** From the basic principle, the essence of SSRF is that $C$ and $\varphi$ gradually reduce by time which results in a unit of the internal force beyond the yield surface. The stress cannot be bear will be gradually transferred to the soil around the unit. After the sliding surface appears, soil becomes instability. The parameters of the material in ABAQUS can change with temperature and field variables; can be easy to implement process of the decreased strength parameters. The followings are the procedure:

Step1. We should define a field variable; usually reduction factor is equal to the field variable.

Step2. Material parameters that are changed with field variables are realized in this step.

Step3.When analysis starting, we specify the magnitude of field variables .At the same time, gravity is working. To avoid destruction, $F_r$ is quite little even less than 1.

Step4. In the subsequent analysis steps, Fr increases linearly. When the calculation aborted (Numerical convergence), we analyze results. By evaluation criterion of instability, we work out the safety factor.

## Establishment of the numerical model

**2.1Model overview.** There is a soil slope reinforced by an infinite long friction pile . The height of soil is 10.0 m with a 2 in 3 slope; Diameter of the anti-slide pile is 0.8 m; pile length is 15.5 m; pile spacing is 4 times the pile diameter; the position of the pile is 10.5 m away from slope foot.

**2.2 The establishment of the initial state**

(1) Definite the model size according to the general situation . We should reserve zone of pile on the soil when establishing the parts of soil and pile, like **Fig.1.**

(2) Set up the material and sectional property. The soil obeys Mohr - Coulomb model (an ideal linear elastic), at the same time the pile is suppose to be elastic material. Soil and pile parameters list as **Table 1**.

(3) Analysis step is used to apply gravity load as the initial stress state to realize strength reduction

**Table.1 Parameters of the numerical model**

| Materials | Density /kg·m$^{-3}$ | Poisson's ratio | Young's modulus/ MPa | Cohesion /Kpa | friction angle/° |
|---|---|---|---|---|---|
| Soil | 1900 | 0.3 | 60 | 35 | 35 |
| Pile | 2400 | 0.25 | 30 000 | | |

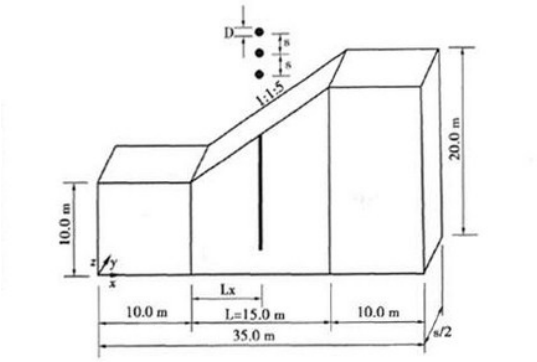


**Fig.1 Establishment of the model**

**2.3 Realization of interaction.** Contect between pile and soil has a great influence on the calculation results. The numerical model set up interaction property at the beginning and use the algorithm of master-slave surface. The master one is surface of pile, to the contrary soil is the slave surface. Normal contact obeys hard contact. We use penalty function as frictional characteristic with 0.51 as its friction coeff

**2.4 Boundry conditons.** Given full consideration to the actual working condition, the numerical calculation model of boundary conditions are as follows:

(1) Restrain x displacement both side of model.(2) Restrain y displacement front and back(3) Fixed bottom of model ,that is to say, restrain three orientations displacements.(4) Restrain y displacement of the symmetry plane on the pile

**2.5 Realization of strength reduction.**Import data from the initial stress state, then modify the material properties and add *Reduce* analysis step to realize linearly increasing of field variable.After that , creat job and submit it.

## Calculation results analysis

**3.1 The analysis of the initial state.** It is initial but the most importment when ground stress is balanced at the beginning. As shown in **Fig.2**, displacements are calculated respectively before and after the reinforcement. Existence of anti-slide pile makes the settlement of roadbed overall reduced, but the effect is not obvious.

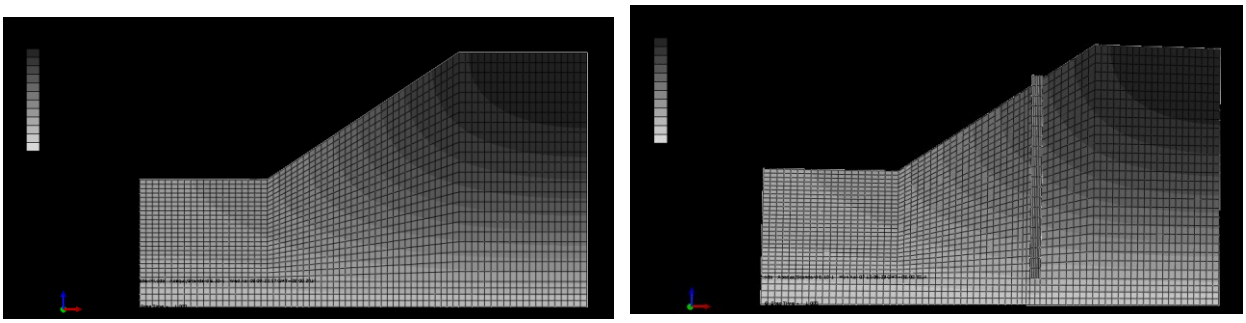

**A.non-pile** **B. with pile reinforcement**

**Fig.2 Displacements before and after the reinforcement**

**3.2 After considering strength reduction.** Continuous sliding zone of slope has been formed before reinforcement, nonetheless, the existence of the anti-slide pile make great difference on cloud picture of displacement increment. The anti-slide pile effectively prevented the sliding of upper soil, and as a result, the overall circular slip surface does not appear. But the preceding soil still could be pulled away from the anti-slide pile, the thrust of soil is borne by pile.

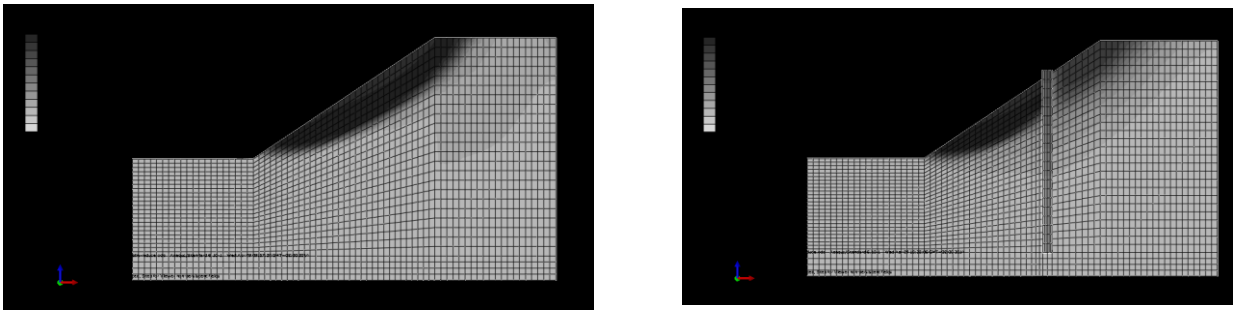

**A.non-pile** **B. with pile reinforcement**

**Fig.3 Displacement increment before and after the reinforcement**

**3.3 Deformation of the pile and the soil pressure of the pile body**

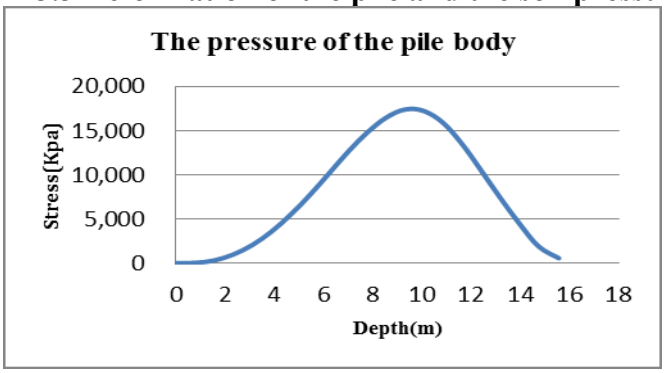


**Fig.4** Soil pressure of the pile body

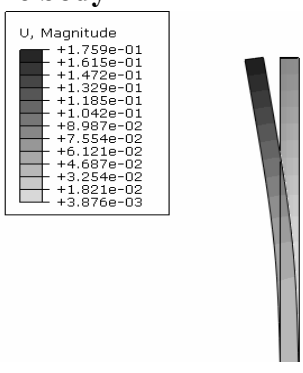


**Fig.5 Deformation of the pile**

**Fig.4** pile pressure value maximum at a depth of 10 m that is easy to destory.
Buckling deformation of pile is given in **Fig.5**, and shows the top of the pile produced bending deformation, while the lower present a good anchor that is a typical long pile deformation model.

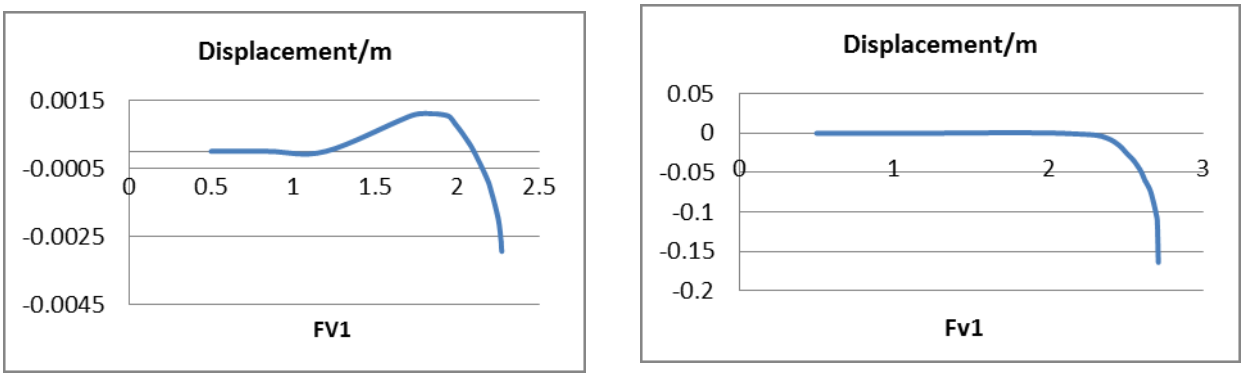


**A.non-pile** **B. anti-slide pile**

**Fig.6 The relationship between FV1 (Fr) and U1**

By **Fig.6**, the displacement of the inflection point is taken as the evaluation standard. the safety coefficient of reinforced soil is 2.20, while before reinforced is 2.50. The strengthening effect of anti-slide pile is obvious.

## Conclusions

(1) Accuratly prediced instability of slip crack surface form and potential destory location before and after reinforcement, at the same time proved the correctness of the numerical simulation.
(2) In the initial stress state, the impact of the anti-slide pile is not so big for the displacement of soil, but for the vertical stress distribution has great influence.
(3) It sets the anti-slide pile in the soil of the reinforced soil mass in front of the safety coefficient increases sharply when considering strength reduction. The thrust of soil is borne by pile which effectively reduce the deformation of the pile and inhibit the formation of sliding zone when soil pulled away from the pile.

## References

[1] FeiKang.: *ABAQUS application in the geotechnical engineering*. (Beijing: China water conservancy and hydropower press, 2009) (in Chinese)

[2] Dawson E M, Roth W H and Drescher A. Slope stability analysis by strength reduction [J].Geotechnique,1999,49(6):835-840

*Applied Mechanics and Materials Vols. 580-583 (2014) pp 715-722*
*© (2014) Trans Tech Publications, Switzerland*
*doi:10.4028/www.scientific.net/AMM.580-583.715*

# Study on Optimization of Design Parameters for Composite Foundation with Cement-fly Ash-gravel Piles

Pengfei Luo[1,2,a], Jianxing Tong[1,2], Xunhai Sun[1,2], Xinhui Yang[1,2], Jie Zhang[3] and Mingli Yan[1,2]

[1] China Academy of Building Research, Beijing, 100013, China

[2] State Key Laboratory of Building Safety and Built Environment, Beijing, 100013, China

[3] North China Electric Power University Science & Technology College, Hebei, 071051, China

[a] lpfcabr@sina.com

**Keywords:** Composite foundation with cement-fly ash-gravel piles; design optimization analysis; pile-soil interaction; thickness-diameter ratio.

**Abstract.** Based on theoretical analysis and experimental result, the principle as well as the interaction between pile and soil, the design parameters of composite foundation with cement-fly ash-gravel piles (CFG piles for short) are optimized, which are pile length, pile diameter, pile spacing, pile strength and thickness of cushion layer, in order to put forward the reasonable design parameters for reaching economic and reasonable target. Through the optimized analysis, it is put forward that bearing stratum of pile tip should select a relatively better soil layer, the diameter of CFG pile is usually appropriately to select between 350mm and 500mm, it is usually appropriately to select larger pile spacing under the permissible range between 3*d* and 5*d* being ruled by standard, it is appropriately to enlarge the pile diameter to reduce the requirement of pile strength in high rise and super high rise building which requiring bearing capacity of single pile is high, and the thickness of cushion layer is appropriately to select between 0.4 and 0.6 times of the pile diameter.

## Introduction

The technology of composite foundation with cement-fly ash-gravel piles (CFG piles for short) was invented by Institute of Foundation Engineering of China Academy of Building Research around 1990 [1, 2]. This kind of composite foundation, because of the existence of cushion layer, achieved interaction between pile and soil. It was applied in multistoried building at first, and extended into high-rise and super high-rise building widely through more than twenty years of scientific research and engineering practice. Remarkable economic and social benefit is obtained. There are five design parameters in design of composite foundation with CFG piles, which are pile length, pile diameter, pile spacing, pile strength and thickness of cushion layer. How to optimize the design parameters of composite foundation with CFG piles, in order to reach the purpose of the economic and reasonable, is discussed in this study.

## Pile Length Optimized

**Distribution of Vertical Stress Field in Soil.** The distribution of additional stress of the soil along the depth in natural foundation and composite foundation with CFG piles are shown in Fig. 1.

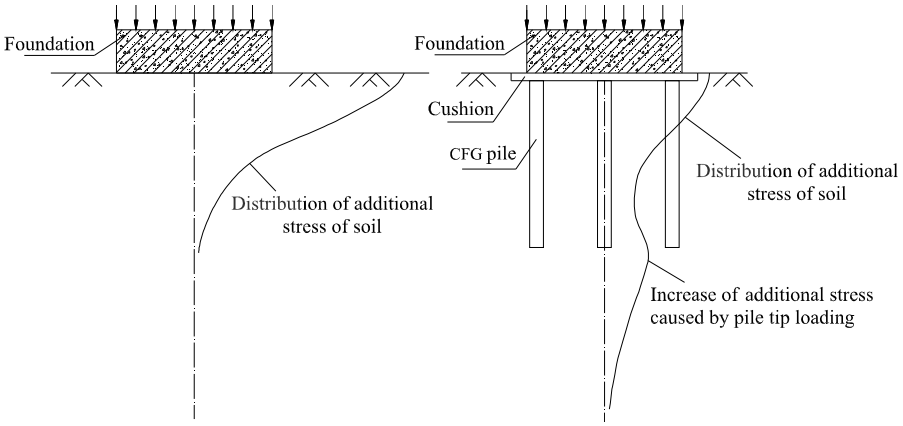


(a) Natural foundation (b) Composite foundation with CFG piles

**Fig. 1 Distribution of additional stress of the soil along the depth**

It can be drawn from Fig. 1 that there is a world of difference between the distribution of additional stress of the soil along the depth in natural foundation and composite foundation with CFG piles. The additional stress of the soil among piles is increased in the tip of piles, as the action of piles tip load.

**Present Problems and Measurement.** During composite foundation design with CFG piles, it usually selects the bearing stratum at pile tip according to investigation report at first, then preliminary determining the pile length.

The bearing stratum of pile tip is usually appropriate to select the soil layer, whose bearing capacity and compression modulus are relatively higher (such as gravel layer), as the additional stress of the soil among piles is added for piles tip loading around the tip of piles. However, it caused a lot of problems for the relatively low of bearing capacity and compression modulus soil layer (such as silty clay layer) is selected as the bearing stratum of pile tip by a lot of designers in many projects. The dotted line above is silty clay layer in Fig. 2, and below is gravel layer which has a relatively higher of bearing capacity and compression modulus. Two kinds of piles are designed in Fig. 2, which are short pile (shown in Fig. 2a) and long pile (shown in Fig. 2b), and the bearing stratums of pile tip are silty clay layer and gravel layer.

Under the same loading effect, two kinds of composite foundation with CFG piles can be analyzed as following:

First, above the dotted line in Fig. 2, assuming A1 is the area of additional stress of composite foundation with short CFG piles in Fig. 2a, and it is bigger than A2 in Fig. 2b. Therefore, the settlement of composite foundation with short CFG piles above dotted line is much more than the composite foundation with long CFG piles. Second, below the dotted line in Fig. 2, assuming B1 is the area of additional stress of composite foundation with short CFG piles in Fig. 2a, and it is smaller than B2 in Fig. 2b. Thus, the settlement of composite foundation with short CFG piles bellow dotted line is less than the composite foundation with long CFG piles. But overall, the settlement of composite foundation with short CFG piles is bigger than the composite foundation with long CFG piles. Furthermore, the bearing capacity of single short pile is smaller than the long pile, for both pile length and the bearing stratum of pile tip, as the long pile has a relatively better bearing layer because the bearing capacity and compression modulus are relatively higher.

Therefore, considering both bearing capacity and deformation, it leads problem to increase the numbers of piles because of adopting the short piles scheme. Assuming it only needs three hundred long piles, and it may need five hundred short piles. It causes the increasing of wasted mixtures, reducing the construction efficiency and bringing adverse effects about constructed piles as the numbers of piles increased.

Thus, during foundation design with CFG piles composite, the relatively better bearing layer should be selected as the bearing stratum of pile tip, whose bearing capacity and compression modulus are relatively higher. So it can control the overall deformation better, play the end resistance of pile tip well, and also avoid the uneven settlement building which may cause by the large changing of the ground lithology. The higher the bearing capacity and compression modulus of the pile tip bearing stratum are, the faster the building settlement stability is [1].

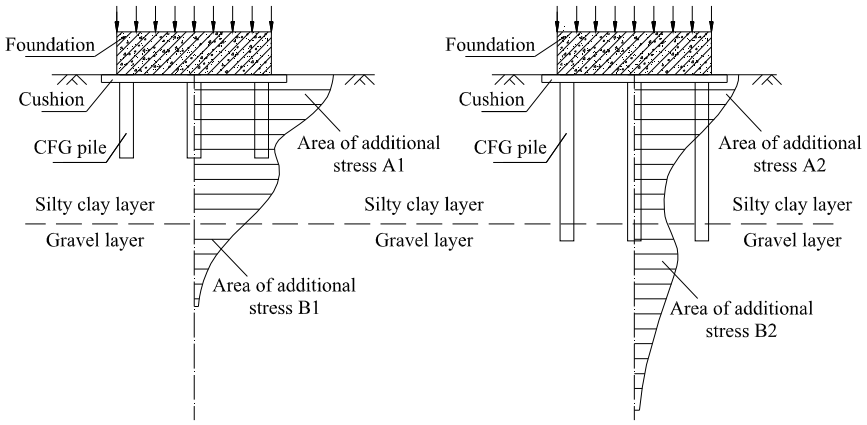


(a) Composite foundation with short CFG piles, (b) Composite foundation with long CFG piles

**Fig. 2 Distribution of additional stress of the soil among piles along the depth**

**Pile Diameter Optimized**

Characteristic value of single CFG pile bearing capacity can be assumed by following [4]:

$$R_a = u_p \sum_{i=1}^{n} q_{si} l_{pi} + \alpha_p q_p A_p \quad (1)$$

Where, $u_p$ is circumference of pile, $q_{si}$ is the side resistance characteristic value of the *i* soil layer around pile, $l_{pi}$ is the thickness of the *i* soil layer of pile length within the range, $q_p$ is the characteristic value of pile tip resistance, $A_p$ is sectional area of the pile, and $\alpha_p$ is play coefficient of pile tip resistance, which can be taken as 1.0 for CFG pile.

Supposing bearing capacity provided by unilateral concrete is $f_{Ra}$, and it can be written as follow,

$$f_{Ra} = R_a / V \quad (2)$$

Supposing pile length is $l_p$ ($l_p = \sum_{i=1}^{n} l_{pi}$), then needed mixtures of one single pile can be calculated as following,

$$V = \pi d^2 l_p / 4 \quad (3)$$

$f_{Ra}$ can be calculated from Eq. 1, Eq. 2 and Eq. 3,

$$f_{Ra} = 4 \sum_{i=1}^{n} q_{si} l_{pi} \Big/ (d l_p) + q_p / l_p \quad (4)$$

Based on Eq. 4, when the side resistance characteristic value $q_{si}$, characteristic value of pile tip resistance $q_p$, and pile length $l_p$ are determined, the larger the pile diameter $d$ is, the smaller the bearing capacity $f_{Ra}$ provided by unilateral mixture is.

The changing of bearing capacity value $f_{Ra}$ provided by unilateral concrete with the pile diameter under the same condition is shown in Table 1 and Fig. 3.

**Table 1 $f_{Ra}$ changing with the pile diameter under the same condition**

| Pile diameter (m) | Pile length (m) | $R_a$* (kN) | Needed mixture of one single pile ($m^3$) | $f_{Ra}$ ($kN/m^3$) |
|---|---|---|---|---|
| 0.3 | 10 | 324.99 | 0.71 | 460.00 |
| 0.6 | 10 | 734.76 | 2.83 | 260.00 |
| 0.9 | 10 | 1229.31 | 6.36 | 193.33 |
| 1.2 | 10 | 1808.64 | 11.30 | 160.00 |
| 1.5 | 10 | 2472.75 | 17.66 | 140.00 |
| 1.8 | 10 | 3221.64 | 25.43 | 126.67 |

*Side resistance characteristic value $q_{si}$ is 30kPa and pile tip resistance characteristic value $q_p$ is 600kPa.

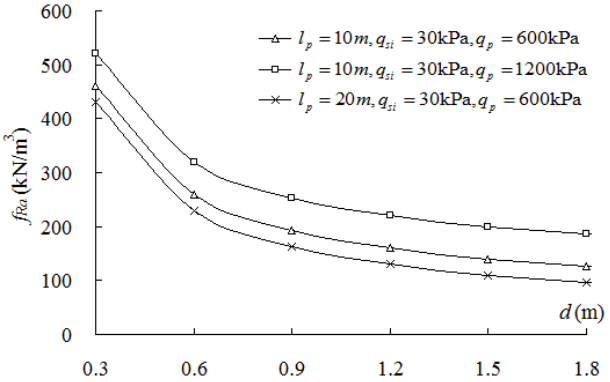


**Fig. 3 $f_{Ra}$ changing with the pile diameter under the same condition**

It can obtain from Table 1 and Fig. 3 that the larger the pile diameter is, the lower the bearing capacity value $f_{Ra}$ is, which is provided by unilateral concrete under the same condition. So the thick pile is not economic. The smaller the pile diameter is, the larger the pile specific surface area is, and the bearing capacity value provided by unilateral mixture is the higher. However, the construction quality can not be controlled easily if the pile diameter is too small. Therefore, the diameter of CFG pile is usually appropriate to select between 350mm and 500mm, when the requirement of bearing capacity of single pile is not high.

## Pile Spacing Optimized

A project has adopted the construction technology of composite foundation with CFG piles to reinforce in northeast China. The pile diameter is 500mm, pile length is 15m, and pile spacing is 1.5m. The bearing stratum of pile tip is silty clay ⑤ layer (shown in Fig. 4). It is happened fleeing bore while piling, and it is still fleeing bore while jumping the pile spacing (pile spacing is 3.0m). Through analyzing, it is caused by the pile spacing, which is too small as it is only 3*d* (*d* is the pile diameter). It is easy happening fleeing bore at the silty clay ② layer and saturated silt ④ layer. After redesigning, the pile diameter is 400mm, pile length is 24m, bearing stratum of pile tip is coarse sand ⑥ layer, and pile spacing is 5*d* (*d* is the pile diameter). Few fleeing bore is happened while piling. The pile spacing should be determined to meet the design requirement of bearing capacity of composite foundation, control the settlement of building, soil characteristics, and construction technology. The pile spacing is not the smaller the better. Considering from the angle

of construction, it should enlarge the pile spacing as possible, in order to prevent adverse effect on piled pile from new piling pile.

Pile spacing can be adjusted by changing pile length, under the condition of bearing capacity and deformation requirements, and it should select a relatively better bearing layer used as the bearing stratum of pile tip, whose bearing capacity and compression modulus are relatively higher. It is usually appropriate to select larger pile spacing, under the permissible range between 3*d* and 5*d* being ruled by standard [4] (*d* is the pile diameter).

**Pile Strength Optimized**

According to "Technical code for ground treatment of buildings" (JGJ 79-2012) [4], when does not need making depth correction of bearing capacity of composite foundation carrying on embedded depth of foundation, it should meet the following requirement,

$$f_{cu} \geqslant 4\lambda R_a / A_P \tag{5}$$

Where, $f_{cu}$ is the cube compressive strength average value of pile body cubic (the side length of the cube is 150mm) of 28 days under the standard curing condition (kPa); $R_a$ is characteristic value of single pile bearing capacity (kN); $A_p$ is section area of pile ($m^2$); $\lambda$ is exerting coefficient of single pile bearing capacity.

Determining single pile bearing capacity of $R_a$, assuming pile diameter is $d$ , the pile strength is $f'_{cu}$ , and it can be written as the following,

$$f'_{cu} = 4\lambda R_a / A_P = 16\lambda R_a / (\pi d^2) \tag{6}$$

Base on Eq. 6, when single pile bearing capacity of $R_a$ is determined, the smaller the pile diameter is, the higher the pile strength is. The pile strength and corresponding strength grade of concrete under different conditions are shown in Table 2 and Fig. 5.

**Table 2 Pile strength and corresponding strength grade of concrete under different conditions**

| Pile Diameter (m) | $R_a = 500$kN | | $R_a = 1000$kN | |
|---|---|---|---|---|
| | Pile strength (MPa) | Concrete strength | Pile strength (MPa) | Concrete strength |
| 0.3 | 25.48 | C30 | 50.96 | C65 |
| 0.6 | 6.37 | C15 | 12.74 | C15 |
| 0.9 | 2.83 | C15 | 5.66 | C15 |
| 1.2 | 1.59 | C15 | 3.18 | C15 |
| 1.5 | 1.02 | C15 | 2.04 | C15 |
| 1.8 | 0.71 | C15 | 1.42 | C15 |

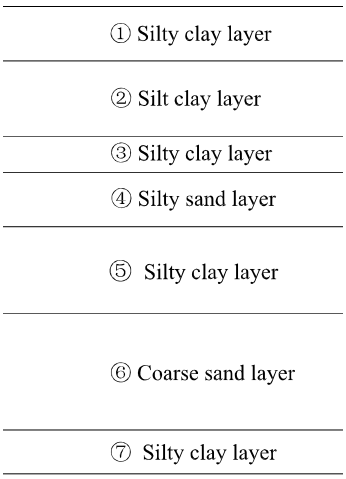


**Fig. 4 Schematic diagram of typical geological profile of ground**

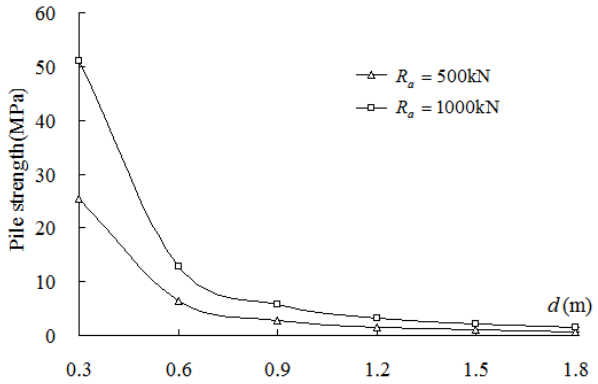


**Fig. 5 Pile strength and corresponding concrete strength under different conditions**

It can be obtained form Table 2 and Fig. 5 that the smaller pile diameter is, the higher pile strength is. Under the same condition of pile diameter, the larger bearing capacity of single pile is, the higher pile strength is. Thus, pile diameter is usually appropriate to select between 350mm and 500mm, while the strength grade of concrete is between C15 and C40. It is appropriate to enlarge the pile diameter to reduce the requirement of pile strength in high rise and super high rise building, which requiring higher bearing capacity of single pile.

### Thickness of Cushion Layer Optimized

The technology of cushion layer is the key technology of composite foundation with CFG piles. The existing of cushion layer guarantees the soil among piles to work throughout under normal condition, achieve interaction between pile and soil, and take important part in improving the distribution loading of pile and soil in foundation.

Therefore, the thickness of cushion layer is one of the main factors of exerting coefficient of pile and soil bearing capacity, which is usually expressed as thickness-diameter ratio (the ratio of the thickness of cushion layer to pile diameter is defined as thickness-diameter ratio). When the rigidity foundation and pile diameter is given, the thicker cushion layer is, the smaller the exerting coefficient of pile bearing capacity is, and the thinner cushion layer is, the smaller the exerting coefficient of soil bearing capacity is. It can define the ratio of pile top stress to characteristic value of single pile bearing capacity is $\lambda_1$, and the ratio of soil stress to characteristic value of foundation bearing capacity is $\lambda_2$, when the loading reaches the characteristic value of composite foundation bearing capacity.

The tests indicate that the smaller thickness-diameter ratio is, the larger exerting coefficient of single pile bearing capacity is, and exerting coefficient of bearing capacity of soil among piles is the smaller. The tests also indicate that larger thickness-diameter ratio is, the smaller exerting coefficient of single pile bearing capacity is, and exerting coefficient of bearing capacity of soil among piles is the larger. The exerting coefficient of single pile and soil bearing capacity is more fully, when the thickness-diameter ratio is in the range of 0.4 to 0.6 (shown in Fig. 6).

Thus, the thickness of cushion layer is appropriately to select between 0.4 and 0.6 times of the pile diameter. The appropriate material of cushion layer includes medium sand, medium sand, graded sand-gravel and gravel, etc.

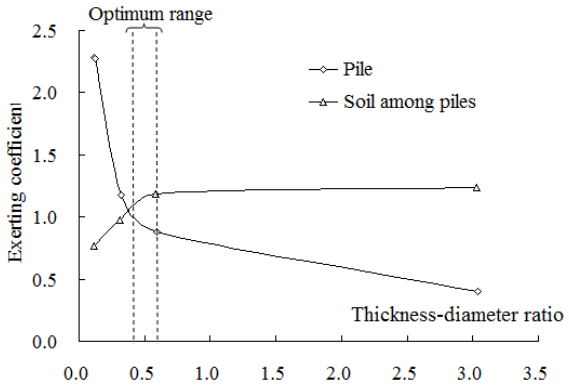


**Fig. 6 Relationship curve for exerting coefficient of single-type-pile and soil bearing capacity of composite foundation with CFG piles and thickness-diameter ratio [5]**

(When the loading reaches the characteristic value of composite foundation bearing capacity)

## Conclusions

The following conclusions can be drawn from this study.

(1) Bearing stratum of pile tip should select the soil layer, whose bearing capacity and compression modulus are relatively high.

(2) Diameter of CFG pile is usually appropriately to select between 350mm and 500mm, when the requirement of bearing capacity of single pile is not high.

(3) Pile spacing should be determined to meet the design requirement of bearing capacity of composite foundation, control the settlement of building, soil characteristics, and construction technology. The pile spacing is not the smaller the better. Considering from the angle of construction, it should enlarge the pile spacing as possible in order to prevent adverse effect on piled pile from new piling pile. Pile spacing can be adjusted by changing pile length, under the condition of bearing capacity and deformation requirements, and it should select the relatively better bearing layer for the bearing stratum of pile tip, whose which bearing capacity and compression modulus are relatively higher. It is usually appropriately to select larger pile spacing, under the permissible range between 3*d* and 5*d* being ruled by standard (*d* is the pile diameter).

(4) Pile diameter is usually appropriately to select between 350mm and 500mm, while the strength grade of concrete is between C15 and C40, in multistoried building, which requiring bearing capacity of single pile is not high. It is appropriately to enlarge the pile diameter to reduce the requirement of pile strength in high rise and super high rise building, which requiring bearing capacity of single pile is high.

(5) Thickness of cushion layer is appropriately to select between 0.4 and 0.6 times of the pile diameter. The appropriate material of cushion layer includes medium sand, medium sand, graded sand-gravel and gravel, etc.

**References**

[1] M.L. Yan, J. Yang, C.L. Wu, et al. Experimental study on composite foundation with CFG piles [R]. Beiing: China Academy of Building Research, 1992 (in Chinese).

[2] X.L. Huang. Deformation of lime-fly-ash columns and cement-flyash-stone columns reinforced composite foundation [C]. Nanjing: Ground Treatment and Pile Foundation International Symposium, China, 1992.

[3] M.L. Yan, D.G. Zhang. Technology and engineering practice of composite foundation with CFG piles [M]. 2nd ed. Beijing: China Water Power Press, 2006 (in Chinese).

[4] Technical code for ground treatment of buildings (JGJ 79-2012) [S]. Beiing: China Architecture and Building Press, 2012 (in Chinese).

[5] J.X. Tong. Experimental study on lateral pressure under local rectangle surcharge and relation between thickness-diameter ratio and pile-soil exertion of composite foundation with CFG piles [D]. Beiing: China Academy of Building Research, 2007 (in Chinese).

*Applied Mechanics and Materials Vols. 580-583 (2014) pp 723-728*
*© (2014) Trans Tech Publications, Switzerland*
*doi:10.4028/www.scientific.net/AMM.580-583.723*

# Study on the Design Method of Different Thickness-diameter Ratios for Composite Foundation with Rigid Long and Short Piles

Jianxing Tong [1, a], Xunhai Sun [1], Pengfei Luo [1], Ning Jia [1], Xinhui Yang, and Mingli Yan [1]

[1] Institute of Foundation Engineering, China Academy of Building Research, 30#, Bei San Huan Dong Lu, 100013, Beijing, China.

[a] tjxcabr@sina.com

**Keywords:** Composite foundation with rigid long and short piles; Thickness-diameter ratio; Exertion of bearing capacity; Thickness of cushion

**Abstract**. Composite foundation can be designed as long and short piles that lie on different bearing strata with high bearing capacities. Researches have shown that for foundation with sufficient stiffness, the ratio of the thickness of cushion to pile diameter (thickness-diameter ratio) plays an important role on the exertion of bearing capacities of pile and soil between piles. Traditional method just applies equal thickness-diameter ratio to design composite foundation with long and short piles, which hinders the exertion of bearing capacity of composite foundation. To overcome this defect, this paper studies the relations between thickness-diameter ratio and the exertions of bearing capacities of pile and soil between piles. The design method of thickness-diameter ratio for composite foundation with long and short piles is also proposed in this study.

## Introduction

When there are two bearing strata with high bearing capacity in the different buried depths of foundation soil, within the reasonable ranges of pile length and spacing of composite foundation with rigid pile, if short piles are used, bearing capacity can satisfy requirement, but the deformation of foundation is likely to be too large. If long piles are applied, both bearing capacity and deformation can satisfy requirement, but bearing capacity may be too high, which induces conservation and waste of the project. In this condition, composite foundation can be designed as long and short piles that lie on different bearing strata [1 - 3].

If composite foundation with long and short piles is applied, it is optimal that long pile, short pile and soil between piles reach their bearing capacities simultaneously, which means that the exertion coefficients of bearing capacities of long pile ($\gamma_1$), short pile ($\gamma_2$) and soil between piles ($\beta$) all equal 1.0. To achieve this goal, the current existing problems are: (1) Determining how to adjust parameters of composite foundation to fully exert the bearing capacity of pile. (2) Under what conditions that the bearing capacities of pile and soil between piles reach their characteristic values simultaneously?

Researches [4 - 6] have shown that for foundation with sufficient stiffness, the ratio of the thickness of cushion to pile diameter (thickness-diameter ratio) plays an important role on the exertion of bearing capacities of pile and soil between piles. Traditional method just applies equal thickness of cushion and pile diameter to design Composite foundation with long and short piles,

which hinders the exertion of bearing capacity of composite foundation. To overcome this defect, this paper studies the relations between thickness-diameter ratio and the exertions of bearing capacities of pile and soil between piles. The design method of thickness-diameter ratio for composite foundation with long and short piles is also proposed in this study.

## Exertion of bearing capacities of pile and soil between piles using equal thickness-diameter ratio

**Exertion of bearing capacities of pile and soil between piles for composite foundation with single pile type.** Fig. 1 shows the relations between $\alpha$ and exertion coefficients of bearing capacity of pile ($\gamma$) and $\beta$ when the bearing capacity of composite foundation with single pile type reaches its characteristic value.

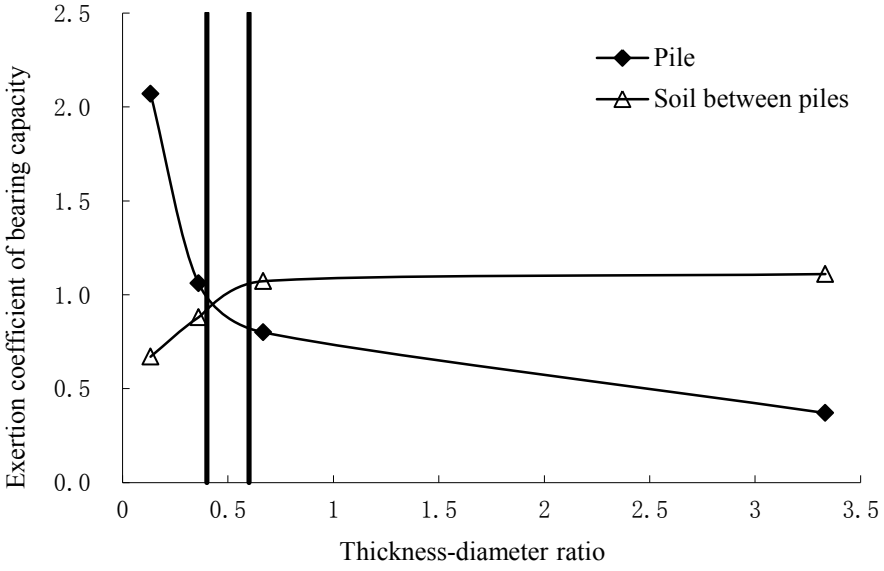


**Fig. 1 Relations between thickness-diameter ratio and exertion coefficients of bearing capacities of pile and soil between piles for composite foundation with single pile type (when the loading equals the characteristic value of bearing capacity for composite foundation)**

From Fig. 1, it can be seen that $\gamma$ decreases with the increase of $\alpha$. when $\alpha \leq 0.361$, the bearing capacity of pile can be fully exerted while the bearing capacity of soil between piles cannot be fully exerted. If $\alpha = 0.133$, $\gamma$ could reach as high as 2.07 which means that ultimate bearing capacity of pile is reached. But $\beta$ is just 0.67 in this condition. When $\alpha \geq 0.667$, the opposite trend is observed. The bearing capacity of soil between piles can be fully exerted while $\gamma$ is all along lower than 1.0. When $\alpha = 3.333$, $\gamma$ is only as low as 0.37.

The optimal range of $\alpha$ for composite foundation with single pile type is 0.4-0.6. Within this extent, the ranges of $\gamma$ and $\beta$ are 0.82-0.98 and 0.93-1.06.

**Exertion of bearing capacities of pile and soil between piles for composite foundation with long and short piles.** Fig. 2 shows the relations between $\beta$ and $\gamma_1$ *and* $\gamma_2$ when the bearing capacity of composite foundation with long and short piles reaches its characteristic value using equal $\alpha$.

From the figure, it can be seen that the bearing capacities of long pile, short pile and soil between piles cannot be fully exerted simultaneously (close or a little bit higher than the characteristic value of bearing capacity) if the same $\alpha$ is used. when $\alpha = 0.333$, the bearing capacities of long pile and short pile are over exerted, which are close to their ultimate bearing capacities, while $\beta$ is just 0.61. When $\alpha = 0.667$, $\gamma_1$, $\gamma_2$ and $\beta$ are 0.65, 0.96 and 1.17 respectively, which means that except long

pile, the bearing capacities of short pile and soil between piles can be exerted. When $\alpha \geq 1.333$, exertion Coefficients of bearing capacities of long and short piles are relatively low and the bearing capacities of piles cannot be fully exerted.

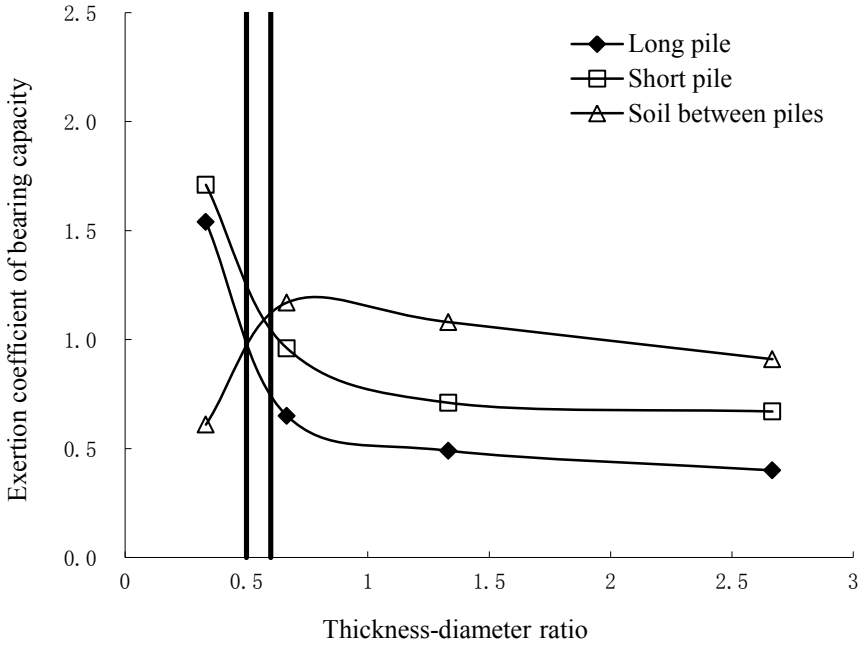


**Fig. 2 Relations between thickness-diameter ratio and exertion coefficients of bearing capacities of long pile, short pile and soil between piles for composite foundation with long and short piles (when the loading equals the characteristic value of bearing capacity for composite foundation)**

The optimal range of $\alpha$ for composite foundation with long and short piles is 0.5-0.6 using the equal $\alpha$. Within this extent, the ranges of $\gamma_1$, $\gamma_2$ and $\beta$ are 0.75-0.98, 1.04-1.25 and 0.98-1.12, respectively.

**Exertion of bearing capacities of pile and soil between piles for composite foundation using different thickness-diameter ratios**

Under the condition that equal $\alpha$ is used, it is difficult that the bearing capacities of long pile, short pile and soil between piles are fully exerted just by the means of adjusting the value of $\alpha$.

Table 1 shows the values of $\gamma_1$, $\gamma_2$ and $\beta$ when the bearing capacity of composite foundation with long and short piles reaches its characteristic value using equal thickness-diameter ratio.

From the table, it can be concluded that:

- If the fixed pile diameters are used and the thickness of cushion is increased for short pile and decreased for long pile, when the bearing capacity of composite foundation reaches its characteristic value, $\gamma_1$ is higher than the condition that the same thickness of cushion is used. Although $\gamma_2$ decreases slightly, the bearing capacity of soil between piles can be fully exerted. The bearing capacity of composite foundation with different thicknesses of cushion is larger than the condition that equal thickness of cushion is used.
- If the fixed thicknesses of cushion are used and the diameter of long pile are increased, when the bearing capacity of composite foundation reaches its characteristic value, $\gamma_1$ is higher than the condition that the equal pile diameter is used. Although $\gamma_2$ decreases slightly, the bearing capacity of soil between soils can be fully exerted.

- For long pile, if the thickness of cushion is decreased and the pile diameter is increased at the same time, $\gamma_1$ can be increased more rapidly.

**Table 1 Exertion Coefficients of pile and soil between piles for composite foundation with long and short piles using different thick-diameter ratios**

| Test No. | Design method | $\alpha$ of long pile | $\alpha$ of short pile | $\gamma_1$ | $\gamma_2$ | $\beta$ |
|---|---|---|---|---|---|---|
| 1# | Equal pile diameter and different thicknesses of cushion | 0.333 | 0.667 | 1.02 | 0.89 | 1.14 |
| 2# | Equal thickness of cushion and different pile diameters | 0.341 | 0.5 | 0.95 | 0.88 | 1.10 |
| 3# | Different thicknesses of cushion and pile diameters | 0.333 | 0.5 | 0.90 | 0.97 | 1.12 |

**Design method of different thickness-diameter ratios for composite foundation with long and short piles**

On the premise that the bearing capacity of soil between piles are fully exerted, the bearing capacities of long pile, short pile and soil between piles can be exerted in an ideal combination by applying different $\alpha$ for long and short piles. The suitable ranges of $\alpha$ for long and short piles are 0.35-0.5 and 0.5-0.65. If there is no big difference between the bearing capacities of long pile and short piles, it is suggested to adopt lower value for long pile and higher value for short pile, or vice versa.

There are two design methods of $\alpha$ for composite foundation with long and short piles: (1) fixing pile diameter, $\alpha$ can be changed by using different thicknesses of cushions for long pile, short pile and soil between piles (Fig. 3); (2) Fixing the thickness of cushion, $\alpha$ can be changed by using different pile diameters for long and short piles (Fig. 4).

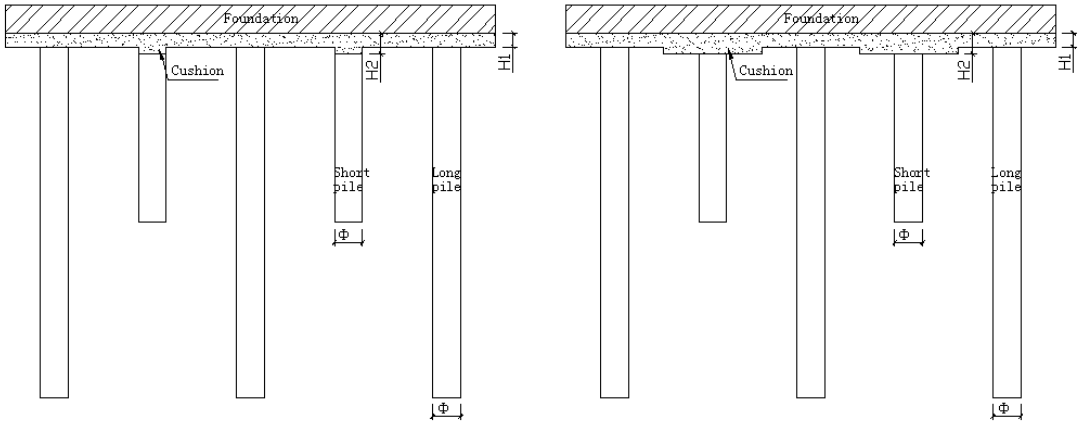


(a)Thickness of cushion is changed based on the areas of long and short piles

(b) Thickness of cushion is changed only within the range of short piles

**Fig. 3 Illustration of different thicknesses of cushion for composite foundation with long and short piles**

Fig. 4 (b) is another kind of method that changes the pile diameter. Smaller $\alpha$ can be achieved by applying pile cap and increasing cross section of pile top.

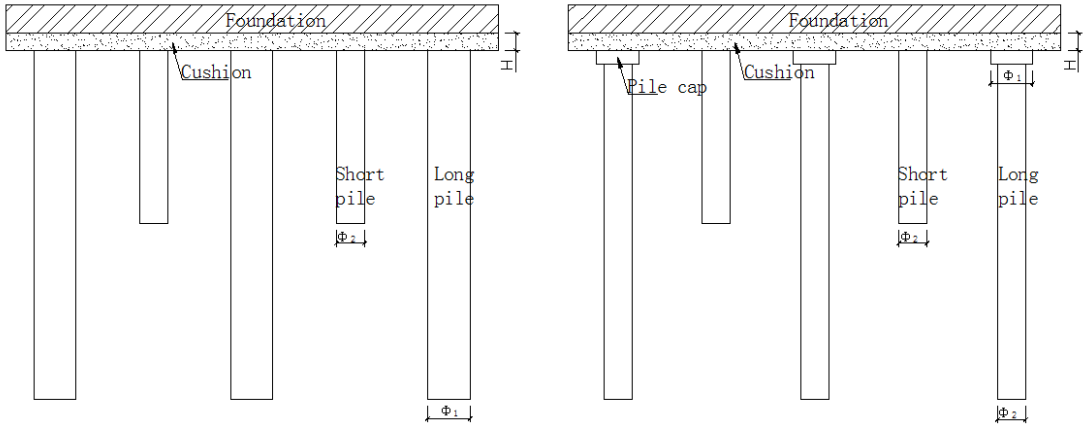


(a) The diameters of long and short piles are different

(b) The diameters of long and short piles are the same and pile cap are used for long pile

**Fig. 4 Illustration of different pile diameters for composite foundation with long and short piles**

It should be noted that when applying different $\alpha$ to design composite foundation with long and short piles, although decreasing the thickness of cushion can increase the bearing capacity of long pile, if the cushion is too thin, stress concentration will appear on the pile top, which is adverse to the punch resistant capability of foundation slab. Moreover, when the foundation bears horizontal loads, horizontal loads will also concentrated on the pile top, which violates the basic principal of composite foundation that mainly vertical loads are born. Therefore, the aim of adjusting the thickness of cushion is not to make the bearing capacities of long and short piles fully exerted. In other words, to ensure that pile doesn't punch the foundation and there is no excessive stress concentration on the pile top, it is not practical to make $\gamma$ equals 1.0. The usefulness of cushion for composite foundation with rigid pile is that it can ensure the exertion of bearing capacity of soil between piles and make the bearing capacities of long and short piles exerted in a relatively high level, which maximizes the total bearing capacity of composite foundation.

## Conclusions

This paper studies the relations between thickness-diameter ratio and the exertion of bearing capacities of pile and soil between piles of composite foundation with long and short piles. The following conclusions can be drawn from this study:

(1) The ratio of thickness to diameter for composite foundation with rigid reinforcement has a great influence on the exertion of bearing capacity of pile and soil between piles. The optimal range of $\alpha$ of composite foundation is 0.4-0.6.

(2) if $\alpha$ remains constant and is in the range of 0.5 and 0.6, the exertion coefficients of bearing capacity of long pile is less than that of short pile which is further less than that of soil between piles. It is difficult that the bearing capacities of long pile, short pile and soil between piles are fully exerted just by the means of adjusting the value of $\alpha$.

(3) The method of applying different $\alpha$ should be used in the design of composite foundation with long and short rigid piles. The suitable values of $\alpha$ for long and short piles are 0.35-0.5 and 0.5-0.65. If there is no big difference between the bearing capacities of long pile and short pile, it is suggested to adopt lower value for long pile and higher value for short pile, or vice versa.

(4) There are two design methods of $\alpha$ for composite foundation with long and short piles: (i) fixing pile diameter, $\alpha$ can be changed by using different thicknesses of cushions for long pile, short pile and soil between piles. (ii) Fixing the thickness of cushion, $\alpha$ can be changed by using different pile diameters for long and short piles.

**References**

[1] JGJ 79-2002 Technical code for ground treatment of buildings[S]. Beiing: China Architecture and Building Press 2012. (in Chinese)
[2] M.L. Yan, J. Yang, C.L. Wu, et al. Experimental study on CFG pile composite foundation[R]. Beiing: China Academy of Building Research, 1992. (in Chinese)
[3] M.L. Yan, D.G. Zhang. CFG pile composite foundation technology and engineering practice [M]. 2nd ed. Beijing: China Water Power Press, 2006. (in Chinese)
[4] M.S. Wang. Study on the effect of piles and soil in composite foundation[D]. Beiing: China Academy Of Building Research, 2005. (in Chinese)
[5] J.X. Tong. Experimental study on lateral pressure under local rectangle surcharge and relation between thickness-diameter ratio and pile-soil exertion of CFG pile composite foundation[D]. Beiing: China Academy of Building Research, 2007. (in Chinese)
[6] X.H. Sun. Effect of foundation rigidity and cushion thickness on rigid pile composite foundation bearing capacity [D]. Beiing: China Academy of Building Research, 2010. (in Chinese)

*Applied Mechanics and Materials Vols. 580-583 (2014) pp 729-732*
*© (2014) Trans Tech Publications, Switzerland*
*doi:10.4028/www.scientific.net/AMM.580-583.729*

# Study on the effects of the rainwater seepage on slope stability

Jusheng Xun[1,a], Xiangtian Xu[1,b*], Ruiqiang Bai[1,c]

[1]Department of Transportation, Inner Mongolia University, Hohhot 010070, China.

[a]2584157731@qq.com, [b]49940655@qq.com(*Corresponding Author), [c]brq1269977095@qq.com

**Keywords:** Highway slope, rain infiltration, seepage, safety factor

**Abstract.** The work condition of the highway, which is usually built in mountainous regions, is complex relative to the ordinary road. Slope instability accident caused by the seepage of rainwater usually occurred in the rainy season. The mechanism for seepage failure of slope was investigated by used the Mohr-Coulomb criterion and the principle of effective stress. The effect of rain intensity on slope stability was equivalently instead by the effect of moisture content on slope stability. The influence of moisture content on the safety factor of slope stability was further calculated according to the Bishop's method. The degeneration of safety factor follow to the moisture content was presented in the percentage.

## Introduction

With the development of transportation construction, there is a steady increase of road constructions in mountain area, but it is inevitable to build higher and dig deeper in the process of such constructions. Moreover, the roads were destroyed by continuous heavy rainfall, such as erosion of gaps that cause landslides. If not treated in a timely, it will cause more serious consequences (Wang, 1994). By the analysis of geomorphic and geologic characteristics of Chongqing, Lin (2001) concludes that when the rainfall intensity is greater than or equal to 100mm /d, the stability is poor and the slopes which are on the fringe of steady state may possibly transformed, partially damaged; When the rainfall intensity is greater than or equal to 150 mm/d, the fragile slopes will be transformed, damaged, collapse, and even cause the disasters of landslides and mud avalanche. Shimada (Shimada, et al., 1995) used finite element method to analyze the value of the slope stability. The influenced factors, such as the rainfall intensity, rock and soil strength were also investigated. The result shows that safety factor value of slope model observably reduces as the rainfall intensity increase; in term of rock-soil water retention curve closed to the saturated, a little change of matrix suction can result in significant reductions for slope safety factor. A key step of analysis the slope stability under the rain seepage is to determine the unsaturated soil's stability coefficient which is associated with water content. If the calculating capacity of the limiting equilibrium method can describe the changing process of safety factor, the reliable parameters for the slope safety protection will be provided to further guide the preventive works. According to the unsaturated earth drained shear strength theory, the influence of water content on unsaturated shear strength was analyzed in this paper. The calculation of slope stability under the rain seepage condition was carried out by applying simplified Bishop's method.

## Influence factors

**Geographical and geological influences.** Complex geological environment of the mountain is an important factor for the slope stability, especially fault unconformity mountain, creating the conditions for the surface runoff, which decline strength of soil and rock, seriously affecting highway slope stability.

**Rainfall infiltration and surface runoff influences.** A large number of construction cases show that more than ninety percent slope instability accident was occurred under condition of rainfall (Sun, et al., 1998). The main reason for this phenomenon is that pore water pressure and soil pressure rise with the increase of rainfall intensity and emerges seepage force to reduce cohesive force and friction

angle, which leads to the decrease of soil strength and slope stability. So this can be looked as a transformation process from unsaturated soil to saturated soil.

**Water influences.** Mohr-Coulomb raised the theory of unsaturated soil from the experiment of sand.

$$\tau_f = c + \sigma \tan \varphi \tag{1}$$

Where $\tau_f$ is the shear strength, $\sigma$ is stress on the sliding surface, $c$ is soil cohesion, $\varphi$ is Angle of internal friction of soil. As Fig.1 shown, where O is the center of the circle of the sliding surface, R is radius, $AD$ is the sliding surface, W is soil self weight. According to the limiting equilibrium method, we have

$$K = \frac{\tau_f \hat{L} R}{Wa} \tag{2}$$

Where, $K$ is the safety factor of slope stability, $\hat{L}$ is the length of the sliding surface, $a$ is the horizontal distance between O and the landslide body center of gravity. Equation (2) shows that the safety factor degenerated with the increase of the moisture content.

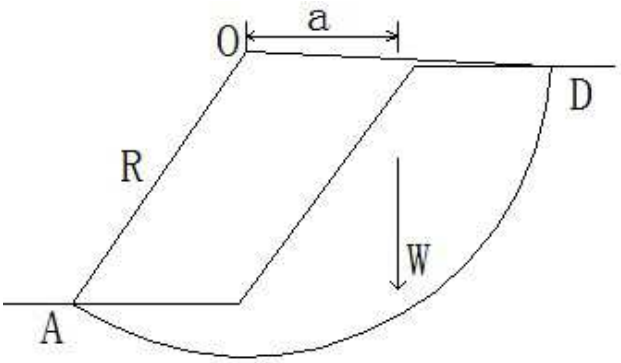


**Fig.1 Overall slope stability analysis**

## Analysis

With the rapid development of applied mathematics, many analysis methods for slope stability has presented, which can be generally classified as certain analysis method and uncertain analysis method. Limiting equilibrium method needs to split the unsaturated soil, according to the inter-slice force of soil that can be classified as Fellenius' method(Bishop, 1995), Bishop's method( Bishop,1995) and Janbu's method(Janbu,1954). Bishop's method proposed by Bishop in 1950, compared with other methods, it is easier to acquire and has more accuracy, which applies to soil slope and rock slope with broken and loose structure, it is considered as the most common method to calculate the safety factor of the sliding surface. This paper uses simplified Bishop's method.

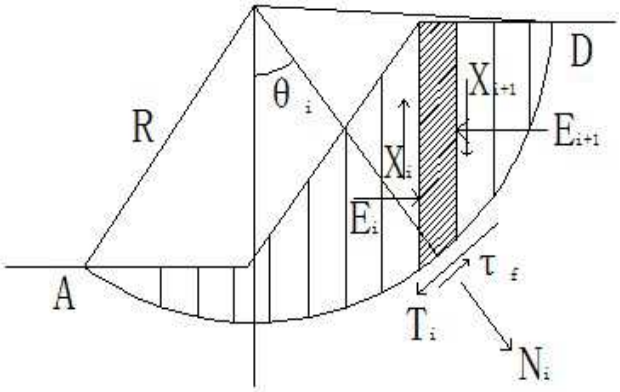


**Fig. 2 Schematic stress analysis of soil**

As Fig.2 shown, the limit equilibrium equation is

$$T_i = \frac{N_i \tan\varphi + c_i l_i}{K},$$

Where $T_i$ is tangential force, $N_i$ is normal force, $c_i l_i$ is cohesion.

According to force balance, we have:

$$W_i + X_{i+1} - X_i - T_i \sin\theta_i = N_i \cos\theta_i \quad (3)$$

$$N_i \cos\theta_i + T_i \sin\theta_i = W_i + \Delta X_i \quad (4)$$

Where $W_i$ is the soil self weight of *i*-th section, $X_i$ is the inter-force of adjacent soil body, $\theta_i$ is radius angle, where $\Delta X_i = X_{i+1} - X_i$ .By Eqs.2, 3 and 4,we have :

$$T_i = \tau_{f_i} l_i = \frac{c_i l_i + N_i \tan\varphi}{K}$$

$$N_i = \frac{W_i + \Delta X_i - \frac{c_i l_i}{K}\sin\theta_i}{\cos\theta_i + \frac{\sin\theta_i \tan\varphi}{K}}$$

Where $\Delta H_i = H_{i+1} - H_i$, it is negligible, so

$$K = \frac{\sum_{i=1}^{n} \frac{1}{m\theta_i}(W_i \tan\varphi_i + c_i l_i \cos\theta_i)}{\sum_{i=1}^{n} W_i \sin\theta_i}$$

Written in the form of effective stress:

$$K = \frac{\sum_{i=1}^{n} \frac{1}{m\theta_i}(W_i - u_i l_i \cos\theta_i)\tan\varphi_i' + c_i' l_i \cos\theta_i}{\sum_{i=1}^{n} W_i \sin\theta_i} \quad (5)$$

It does not meet the conditions of moment equilibrium apparently with respect to that the normal force between soils tripe makes no difference to the slope safety factor, but this method proves the theoretical of closed theory, moment equilibrium of the landslide and the limit equilibrium theory. The slope safety factor calculated by Bishop's method reduces with the increase of moisture content in the soil as can be seen from the Eq.5,which is very detrimental to slope stability.

The research material was taken form bare soil of Northeast Forestry University, Harbin (Jiang, et al., 2009).The direct shear test under the condition of 100kpa, and the results were as follows:

**Table 1. Test results**

| Moisture content $\omega$ （%） | Cohesion $c(kpa)$ | Angle of internal friction $\varphi$ (°) |
|---|---|---|
| 10 | 17.225 | 25.2 |
| 12 | 14.902 | 24 |
| 14 | 13.648 | 22.5 |
| 16 | 12.477 | 20 |
| 18 | 11.389 | 19 |
| 20 | 10.385 | 17 |

According Eq.1, we can calculate the shear strength of soil body under difference moisture content as follow:

**Table 2. $\omega$ and $\tau_f$**

| Moisture content $\omega$ | 10% | 12% | 14% | 16% | 18% | 20% |
|---|---|---|---|---|---|---|
| $\tau_f$ （kpa） | 64.28 | 59.42 | 55.06 | 48.87 | 45.82 | 42.88 |

Table 2 shows that the shear strength declines with the increase of moisture content in the soil. According Eq.2, we can calculate the safety factor reduced percentage with the moisture content ranged from 10% to 20% as shown below:

**Table 3. Computational results**

| Moisture content $\omega$ | 12% | 14% | 16% | 18% | 20% |
|---|---|---|---|---|---|
| relative reduction ratio of stability coefficient | 7.56% | 14.34% | 23.97% | 28.72% | 33.29% |

## Conclusion

The main conclusions can be drawn as follows:
(1)The slope safety factor will be lower under the condition of rainfall seepage.
(2) As increase of rainfall intensity, the moisture content will be increased and the factor of slope stability will be reduced, which will lead to decrease of the slope safety factor.
(3)More attention be should taken in the engineering where the soil has high moisture content.

## Acknowledgments

This research was supported by the program of Innovation and Entrepreneurship for Undergraduates of the Inner Mongolia University (201318275), Natural Science Foundation of Inner Mongolia (No. 2013MS0702, No. 2010MS0708) and the Program of Higher-level talents of Inner Mongolia University (30105-125146).

## References

[1] Wang,G.T., Geotechnical Engineering :Stability analysis of high fill embankment road.(1994(1))
[2] Lin, X.S.,Geological Hazards and Environment: landslide and rainfall study,12( 3),1-7. (2001)
[3] Shimada, K., Fujii, H.,et al.,Unsaturated Soils: Stability of unsaturated slopes considering Changes of matric suction,1.(1995)
[4] Sun,G.Z..Science:typical landslide ,4-5,Beijing,China.(1998)
[5] Bishop, A.W.,Geotechiqne.X: The Use of the Slip Circle in the Stability Analysis of slopes. No,1.(1995)
[6] Janbu, N.,Stability of Earth Slope: Application of Composite Slip Surface for Stability Analysis,Proc, European Conf, Sweden.(1954)
[7] Jiang, H.H., Dong, X.B., et al.,.Forest Engineering: Affect soil moisture for different soil shear strength Slope Vegetation, 25(3):78-80.(2009)

*Applied Mechanics and Materials Vols. 580-583 (2014) pp 733-737*
*© (2014) Trans Tech Publications, Switzerland*
*doi:10.4028/www.scientific.net/AMM.580-583.733*

# Study on the Lateral Displacement of Super-long Pile under a Asymmetrical Surcharge Load in Soft Clay

Qi Li[1, a], Xiaoli Lu[2,b]

[1]College of Machinery and Engineering, Taishan University, Taian, Shandong 271000, China

[2]Department of Architectural Engineering, Taishan Polytechnic, Taian, Shandong 271000, China

[a]eqnoi@163.com, [b]115530@163.com

**Keywords:** soft clay; super-long pile; pile side displacement; surcharge load; ABAQUS

**Abstract.** The pile will have a large lateral displacement in soft soil under the role of heaped load. Based on Biot consolidation theory, combined with a certain highway project, a three-dimensional FEM model is established, the process that the soil lateral deformation under heaped load lead to the pile side displacement was simulated. On the ground of the former result, the influence factors for the displacement of pile top and the pile displacement field distribution are analysed. The results show that, the building load area, load grade and the distance from loading area to pile have a major influence on the pile side displacement. On the other hand, the load on pile top have a very small contribution for stability of anti side displacement. The buildings nearby the area of pile foundation should be given attention in practical engineering.

## Introduction

At present the research on passive pile in deep soft foundation is much less than that on active pile. Chinese freeways are mainly distributed in the southeast area. The coastal freeways take quite a large proportion in these ways. In coastal area, the foundations are mostly soft soil. The characteristics of soft soil is weak, low strength, high compressibility, low permeability, prone to plastic flow and so on[1] and it has caused great difficulties to the foundation treatment of road engineering. Therefore, using pile foundation to meet the requirements of settlement and stability in coast section with deep soft soil. However, if there is surcharge load on deep soft foundation where is the construction sector of expressway pile, the load will be transferred to the pile by the soil around. The pile will be caused great accessional vertical settlement and lateral displacement[2]. This will lead to cracking or destroying of pavement.

In this paper, based on the Biot consolidation theory[3], combined with the case that a super-long pile have undergone the effect of the role of heaped load in coastal tideland reclamation area, a 3D elastic-plastic finite element model is established. On the ground of the former result, the influences on the deformation and displacement of pile which come from different load area or different distance are analysed.

## Description of the Finite Element Model

**Project Background.** A coastal highway project which goes by the coastal tidal flat partly, intend to use Pile supported viaduct to go through. Similar geological conditions for the bridge, located in the coastal reclamation zone. The upper layer is soft soil, whose thickness is about 30m. It is mainly silt and silt clay. And its property is poor. The middle layer is mainly thick layer of mild clay and clay, where hard plastic and soft plastic appear alternately. The lower layer is hard plastic clay , gravel and cobble layer.

**Mode**l. By using the finite element software ABAQUS[4], the 3-D model was established according to the geological data of bridge pile foundation and the size of the pile foundation which were provided in construction design stage. The center of pile cross-section is the origin of coordinates. The horizontal soil boundary is X= ± 100m, Y= ± 100m.The gravity direction is used as

Z axis direction. We use a circular pile whose diameter is 2m, length 90m, buried depth 77m, to drive into the bearing layer (gravel and silt) 2m.The 3-D model is shown in fig. 1.

**Working conditions**.According to the distance from loading area to the pile (L=10m, 20m, 30m) and the area of heaped load(S=100m$^2$, 200m$^2$), the working conditions are divided into 6 conditions(as shown in fig. 2). We considered the pile top load which is 0 or 4700kN in each condition.The load with 4700kN is design load in traffic conditions. The surcharge loading method is asymmetrical.

## Calculation Parameters

The soil is seen as an elasto-plastic body, the constitutive model based on Mohr Kulun model and the simulation of pile is elastic[5]. The pile is loaded from 0 to 100kPa step by step. There is 10kPa in each load level for 15 days. The whole loading cycle is 150 days. The bottom boundary of model with all displacement constraint is undrained boundary. The boundary around with horizontal displacement constraint is undrained boundary also. In addition to the surcharge load area, the surface of soil is drainage boundary. The parameters of pile and soil are shown in table 1.

Table 1. Soil/Pile Calculation Parameters[6,7]

| Layer/Pile | Depth (m) | $E$ (MPa) | $v$ | $\gamma$(kN/m$^3$) | $C$(kP$_a$) | $\varphi$(°) | Permeability Coefficient（m/s） | |
|---|---|---|---|---|---|---|---|---|
| | | | | | | | Horizontal | Vertical |
| Silt Clay | 30 | 2 | 0.35 | 17.9 | 12.0 | 2.5 | $3\times10^{-8}$ | $3\times10^{-8}$ |
| Silty Clay | 75 | 25 | 0.25 | 20.0 | 65.0 | 20.0 | $10\times10^{-8}$ | $10\times10^{-8}$ |
| Gravel and Silty Sand | 80 | 6,500 | 0.20 | 25.3 | 10.0 | 35.0 | $2\times10^{-4}$ | $2\times10^{-4}$ |
| Clay | 100 | 25 | 0.25 | 22.1 | 65.0 | 20.0 | $8\times10^{-8}$ | $8\times10^{-8}$ |
| Pile | 77 | 30,000 | 0.17 | 24.0 | / | / | / | / |

## Results and Analysis in the condition of L=10m

As shown in fig. 3, we selected the point M in pile-top as calculation point.The displacement changes of pile foundation in X direction which is caused by surcharge load in action period are calculated. We also analyzed the linear OP's displacements on the pile in fig. 3 at the end of loading.

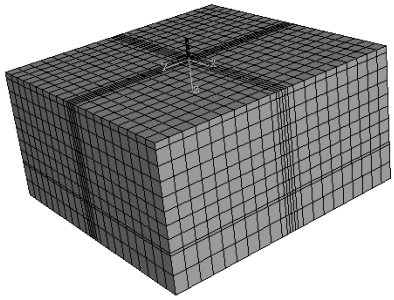

Fig. 1. Finite Element Model

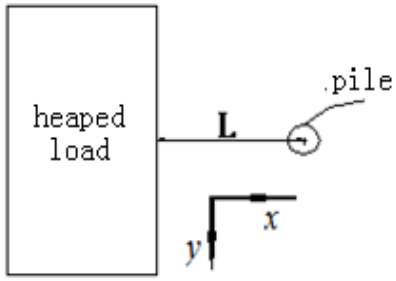


Fig. 2. Relative Position of Heaped Load and Pile

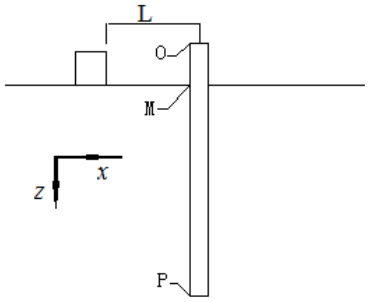


Fig. 3. Relative Position of Calculation point

The displacements of point M in X direction when L=10m and S＝100m2 or S＝200m2 are respectively shown in fig. 4 and fig. 5.

From fig. 4, we can see that the horizontal displacement of M is having an increasing rise with the increase of load level. The maximum is 21.2mm when the surcharge load is 100kPa. The analysis shows that the horizontal displacements of pile are affected obviously by the load level. We must emphatically consider this influence in practical engineering. As shown in fig. 4, the two curves are the lateral displacements of pile which have pile-top load of 0 and 4700kN, respectively. The shift of point M with pile-top load is less than that without pile-top load. Its fig shows the pile-top load has a stabilizing effect on pile foundation.

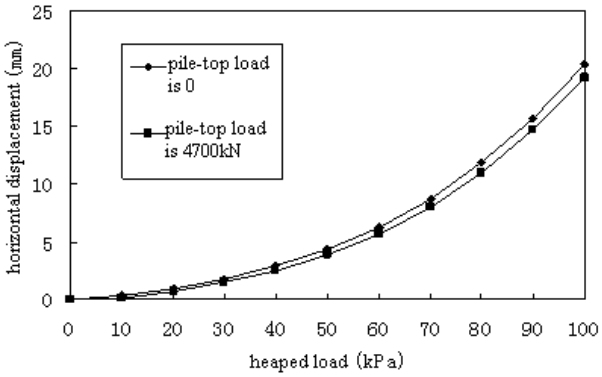


Fig. 4. Horizontal Displacement of M in L=10m, S＝100m$^2$ Condition

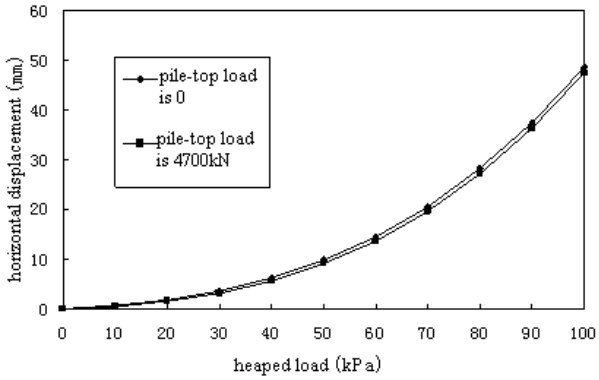


Fig. 5. Horizontal Displacement of M in L=10m, S＝200m$^2$ Condition

From fig. 5, we can see that, when S＝200m$^2$, the low of horizontal displacement of M is similar as the S＝100m$^2$, but the overall value is about 2.4 times larger than the case of S＝100m$^2$. The maximum displacement of S＝200m$^2$ is 48.5mm when the load is 100kPa. The analysis shows that the horizontal displacements of pile are affected obviously by the surcharge load area. So, in practical engineering, large area loading should be tightly restricted nearby the pile in soft clay.

After the end of loading, the linear OP's displacements on the pile when L=10m and S＝100m$^2$ or S＝200m$^2$ are respectively shown in fig. 6 and fig. 7.

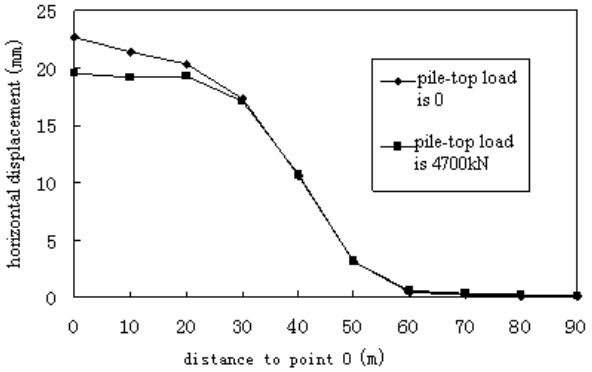


Fig. 6. Horizontal Displacements of Linear OP in L=10m, S＝100m$^2$ Condition

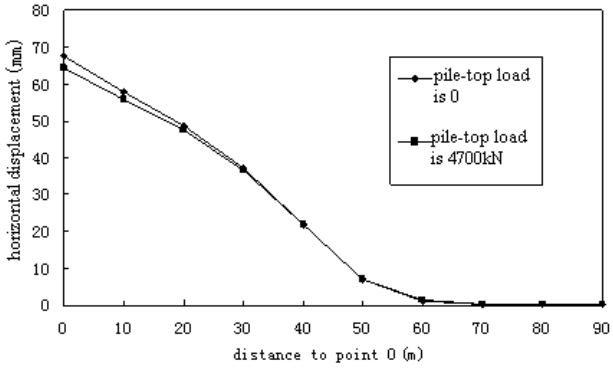


Fig. 7. Horizontal Displacements of Linear OP in L=10m, S＝200m$^2$ Condition

As shown in fig. 6, that's more than other points the horizontal displacements of point O with pile-top load and without pile-top load, which have amounts of 19.5mm and 22.6mm, respectively.Because the pile hadn't tilted absolutely, the lateral displacements of linear OP decreased slowly from pile-top to the ground. In the silt soil, the displacements started to decrease rapidly, it is only 3mm in the 50m depth. At length farther than 60m, the shift is close to 0, it shows that in this depth the effects of heaped load on soil deformation have almost disappeared.

Fig. 7 shows that the horizontal displacements of point O with pile-top load and without pile-top load are 64.4mm and 67.1mm respectively, they are larger than the amounts of S＝100m$^2$ condition. The pile body was in a state of incline

## Comprehensive and Comparative Analysis in Different Conditions

From the L=10m conditions,we can see that the influence of pile-top load for pile's lateral displacements is very small, and it is smaller in L=20m and L=30m conditions. So here we selected all conditions with 4700kN pile-top load to analyze comprehensively. The extreme displacements of pile were shown in table 2.

As we can see from fig. 8, the horizontal displacement of M is having an increasing rise with the increase of load level in all conditions. With the same area and the same load, the horizontal

displacement of M which caused by less distance from loading area to the pile is large then others. With the same distance and the same load, the displacement caused by larger load area is larger then others. The maximum displacement is 47.4mm when the heaped load reach 100kPa in the condition of S＝200m$^2$, L＝10m. In general, in the condition of a more heaped load, it's influence in the horizontal displacement of M will be significantly diminished with the increase of distance to pile foundation and the decrease of load area.

As we can see from fig 9, the maximum displacements of points on linear OP are in the condition of S＝200m$^2$, L＝10m, and their maximum value is 64.4mm. The horizontal displacements of the pile vary with the depth. The point which has maximum horizontal displacement is not fixed, If the heaped load is far from the pile, the maximum displacement point will be stability in the lower of silt soil. If the heaped load could make the pile in a state of incline, the maximum horizontal displacement appear at the top of pile. Now the influence for practical engineering which caused by the pile's displacements will not be ignored. Moreover, at 47m depth below the ground, 60m far from the pile top, the shift is close to 0 in all conditions, it shows that in this depth the deformation of soil caused by heaped load is very small. In the soil above the depth of 47m to the clay layer on top, the shift increases rapidly. In the silty clay, the increase is slowing down, the displacement even appear to decrease if the heaped load area is far from the pile enough.

Table 2. Extreme Displacements of Pile

| Conditions | Maximum Displacement of M (mm) | Maximum Displacement of Points on Linear OP (mm) |
|---|---|---|
| S=200m$^2$, L=10m | 47.41 | 64.36 |
| S=100m$^2$, L=10m | 19.27 | 19.49 |
| S=200m$^2$, L=20m | 21.51 | 23.79 |
| S=100m$^2$, L=20m | 9.56 | 11.58 |
| S=200m$^2$, L=30m | 15.73 | 16.95 |
| S=100m$^2$, L=30m | 7.40 | 8.39 |

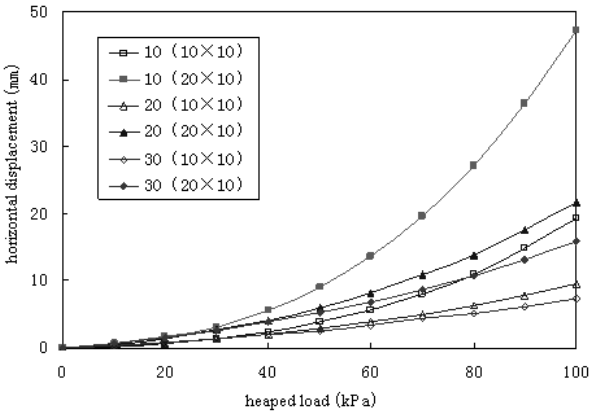


Fig. 8. Horizontal Displacement of M in Different Conditions

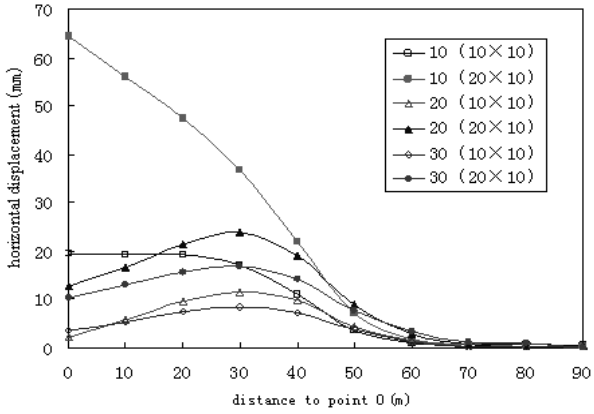


Fig. 9. Horizontal Displacements of Linear OP in Different Conditions

## Conclusions

The pile-top load has certain contribution to the stability of the pile for standing up to the lateral displacement of soil. But the contribution is too small to be ignored in practical design.

The heaped load area and load level have a great influence on the lateral displacements of pile foundation, the lateral shifts unlinearly increases with the increase of the load area or the load level in the same distance from heaped load to pile. So the buildings with super-large area or high-rise should be avoid nearby the pile in soft clay. At the same time, the surcharge load should be loaded synchronously and symmetrically as far as possible.

The horizontal displacements of pile decrease with the rais of distance from heaped load to the pile. If heaped load area is too close to the pile foundation, it will cause large lateral shift. For the project analyzed in this paper, the distance proposed from heaped load area to pile foundation should be more than 15m.

## References

[1] J. Han, K. Akins. Use of geogrid-reinforced and pile-supported earth structures. Proceedings of International Deep Foundation Congress, ASC:E, Orlando (2002), 668-679.

[2] E.A Ellis, S.M Springman. Full-height piled bridge abutments constructed on soft clay. Geotechnique, (2001), Vol. 51 No. 1: 3-14.

[3] B. Indraratna,, A. S. Balasubramaniam, P. Phamvan. Development of negative skin friction on driven piles in soft Bangkok clay. Can. Geotech. J., (1992) Vol. 29 No. 3): 393-404.

[4] Z. X. Yu, H. Gao, Y. D. Hu. Study on Applieation of ABAQUS in Analysis during Consolidation of Soft Soil Foundation. Journal of China & Foreign Highway, Dec. (2007), Vo1. 27 No. 6: 11-14. (In Chinese)

[5] T. Shibata, H. Sekiguchi, H. Yukitomo. Model test and analysis of negative friction acting on piles. Soils and Foundations, (1982), Vo1. 22 No. 2: 29-.39.

[6] Z. Q. Ye, A. Q. Li, G. H. Yang. Study of Permeability for Cohesive Soil. Journal of Southeast University(Natural Science Edition), Sept. (1999), Vo1. 29 No. 5: 121-125. (In Chinese)

[7] J. M. Wu, J. H. Wei, J. X. Du. Generation mechanism of negative skin friction for cast-in-place piles in offshore tidal environment. Journal of Hohai University(Natural Sciences), May (2009), Vol. 37 No. 3: 299-303. (In Chinese)

*Applied Mechanics and Materials Vols. 580-583 (2014) pp 738-741*
*© (2014) Trans Tech Publications, Switzerland*
*doi:10.4028/www.scientific.net/AMM.580-583.738*

# Temperature Field Numerical Analysis of Different Freeze Pipe Spacing of Vertical Frozen Soil Wall Reinforcement at Shield Shaft

Jun Hu[1,a], Baoshi Jiang[1,b], Hui Zeng[2,c], Yanan Chen[1,d], Yunyun Zhu[1,a]

[1]College of Civil Engineering and Architecture, Hainan University, Haikou, Hainan, 570228, China

[2]School of Civil Engineering and Architecture, Wuyi University, Guangdong, 529020, China

[a]hj7140477@hainu.edu.cn, [b]lanbaoshi-hit@qq.com, [c]wyunjfu@126.com, [d]576167462@qq.com

**Keywords:** Shield Launching, Vertical Frozen Soil Wall, Freeze Pipe Spacing, Temperature Field

**Abstract.** Determining the freezing pipe spacing, the freezing reinforcement required range and method, acquiring the development and distribution patterns of frozen soil wall temperature field are the key issues needed to be addressed when using vertical freezing method for the soil reinforcement at shield shaft. Based on the shield launching project of the cross-river shield tunnel of Nanjing subway line 10 and the finite element numerical analysis software, the development and distribution patterns of different distance between freezing pipes of the vertical frozen wall are studied. The numerical simulation shows that, it is feasible to use the numerical model to simulate the temperature field of vertical frozen wall. Decreasing the distance between freezing pipes causes a greater impact on the temperature field. When freezing pipe spacing increases to 0.1m, frozen wall cross-lap time increases of about 1 day. With the freezing pipe spacing increasing, the cross-lap time increases linearly. The temperature of frozen wall decreases with the distance between freezing pipes decreasing, and the strength of frozen wall is more uniform. Results and conclusions form this research may play a useful role to aid designs of similar projects in future.

## Introduction

The methods of reinforcement for Shield shaft end typically include deep mixing method, high-pressure rotary-spray method, SMW working method, artificial freeze method, grouting method, plain concrete pile method, and dewatering method. Soil reinforcement can be performed with single or multiple methods. These reinforcement methods can be categorized into two types: (1) chemical reinforcement methods (e.g., high-pressure rotary-spray method, deep mixing method, grouting method, plain concrete pile method); (2) physical reinforcement methods (e.g., artificial freeze method, dewatering method) [1]. For soft soil region, the reinforcement can be carried out through vertical frozen working method, as mixing pile and rotary-spray pile methods could not be made due to the limitation of ground conditions. The vertical frozen method can also be used when severe water or soil leaking were found at hand-hole after chemical reinforcement. Vertical frozen working method is designed based on tabular frozen reinforcement theory. In this method, a certain number of vertical frozen holes are placed at the end of shield shaft. The frozen soil curtains at the holes resist soil and water pressure of broken shield, preventing the collapse of soil and mud from falling into the working well [2]. Based on the shield launching project of the cross-river shield tunnel of Nanjing subway line 10 and the finite element numerical analysis software, this paper studies the development and distribution patterns of different distance between freezing pipes (0.6m, 0.8m, 1.0m, 1.2m and 1.4m) of the vertical frozen soil wall.

## Engineering Background

The total length of Nanjing subway route-10 is 41.4 km, with 20 stations. The river tunnel (double-lane single tunnel) is constructed with large diameter shield tunneling. According to exploration data, the east side shield launching well is located at high water pressure sandy strata, and the characteristics in this strata behave high porosity, high ground water pressure, and low strata load capacity. Under unfavorable geology conditions and high water pressure, it is under high risk to have shield-launching works. Therefore, the soil body at the end of shield shaft should be reinforced.

According to the conditions discussed above, this launching project applies the method with tri-axial deep stirring pile + vertical frozen. The detail of this method is summarized here: the primary reinforcement type usesΦ1000@750 tri-axial stirring pile. The reinforcement region covers 5 m at both sides of shield shaft. Ground dielectric constant elevation is reinforced to 6m away from arch bottom, and longitudinal reinforcement is 17 m along the working direction of shield. To improve the cementation strength of enclosure structure between stirring pile and middle airshaft, two vertical freezing pipes are placed along the working direction outside of enclosure structure at the east shield well with both array spacing at pipe spacing of 800 mm.

Vertical frozen are arranged with two-row frozen holes in a flower arrangement way. The distance between row A and diaphragm retaining wall is 0.4 m, and the distance between row A and B is 0.8 m. Hole-spacing is 0.8 m. Total number of frozen hole is 57, with 29 placed at row A and 28 at row B. The length of each hole is 31.152m, and depth of hole is 1775.7m. Frozen pipes used here are Φ127×4.5mm seamless steel pipes. Φ48×3.5mm seamless steel pipes are used as fluid supply pipes. During formable period of freezing, brine temperature is in the range of -28℃～-30℃, and brine temperature is in the range of -25℃～-28℃ during freezing maintain period. It is noted that the duration of formable period of freezing is 30 days.

## Construction of Three-dimensional Model

The computational model for temperature field used here is transient heat conduction model with phase transition. According to the suggested frozen-hole arrangement plan, this study applies the simulation of half region to obtain the best computation efficiency due to symmetry of the problem. The origin of coordinate is selected on the ground right above the tunnel face, and longitudinal length (x axis)×transverse width (y axis)×vertical height (z axis) =3m×12m×32m. Two-row frozen is applied as the vertical frozen method in a flower arrangement way. The distance between row A and diaphragm retaining wall is 0.4 m, and the distance between A and B is 0.8 m. Hole-spacing is 0.8 m (this sentence is duplicated). The number is 14.5 for row A and 14 for row B. The frozen pipe diameter is 127 mm, with each frozen-hole length of 31.152m. This simulation applies four-node mesh format, and finer meshes are placed close to the frozen pipes. Total element in the model is 815788, with 149000 nodal points.

Table. 1 Physical thermal parameters after cement improvement

| Soil type | Density /(Kg·m$^{-3}$) | Water content/% | Hear conductivity / ( KJ·m$^{-1}$·d$^{-1}$·℃$^{-1}$ ) | | Specific heat /(KJ·Kg$^{-1}$·℃$^{-1}$) | | Latent heat /(×10$^{8}$J/m$^{3}$) | Temperature of freezing/ (℃) |
|---|---|---|---|---|---|---|---|---|
| | | | Unfrozen soil | Frozen soil | Unfrozen soil | Frozen soil | | |
| Cement soil | 2040 | 11.6 | 180 | 205 | 1.60 | 1.66 | 0.81 | [-2,0] |

Table.2 The cooling plan of brine temperature

| Time/d | 0 | 1 | 5 | 10 | 15 | 20 | 30 | 40 |
|---|---|---|---|---|---|---|---|---|
| Temperature/℃ | 30 | 0 | -12 | -20 | -25 | -28 | -30 | -28 |

The soil frozen experiment is carried out with the soil samples taken from the project site. Physical thermal parameters after cement improvement by tri-axial deep stirring pile are listed in Table 1. Due to the reinforcement of the end with tri-axial deep stirring pile, the ground temperature under effect of cement hydration heat would increase by approximately 10℃. Typically constant temperature at 10 m under ground is 19-20℃. Therefore, the initial temperature of ground under cement reinforcement is set as 30℃ before freezing. The temperature at the boundary of the model is kept constant. The outside boundary of the computational area is treated as adiabatic boundary, and the frozen pipes surface is treated as thermal loading boundary. The brine temperature is used as the boundary loading, and the cooling plan of brine temperature during formable period of freezing is listed in Table 2. According to this plan, the freezing time is set to be 40 days, with each step of 24 hours.

**Computation Results and Analysis of Temperature Field**

Figure 1 shows the different freezing tube spacing z = 0 cross-section at different times 0 ˚C isotherm.

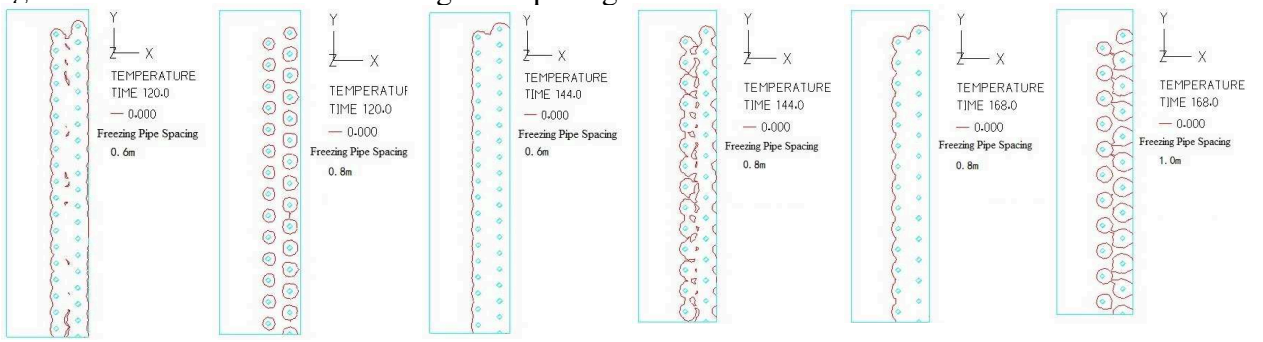


a) 5 days after frozen b) 6 days after frozen c) 7 days after frozen

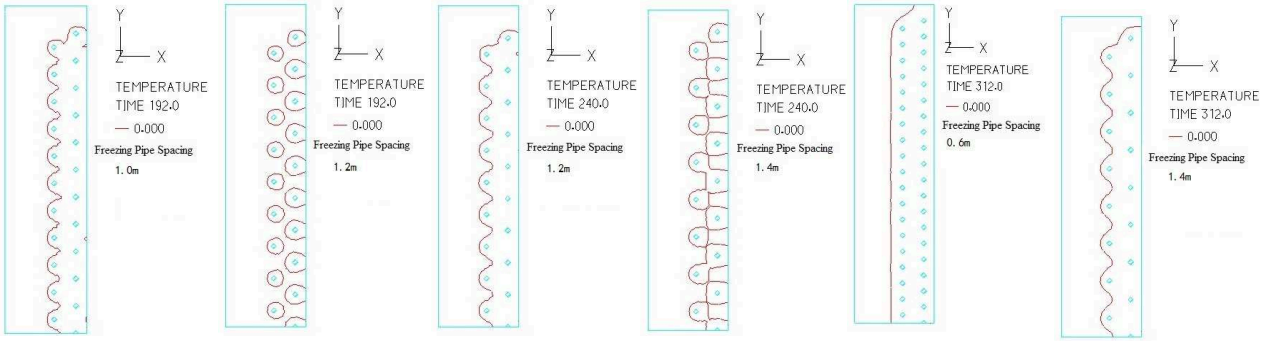


d) 8 days after frozen e) 10 days after frozen f) 13 days after frozen

Fig.1 0˚C isotherm for z=0 profile at different times of varied freezing pipe spacing

It can be seen: in the frozen pipe unpaid ring 0 ˚C isotherm to freeze a circle concentric pipe distribution, A row cylindrical frozen permafrost development speed tube formation is greater than B row cylindrical tube formed frozen permafrost, which mainly because the B row around the tube is not frozen permafrost a large range of heat exchange and thermal convection more, so the development of permafrost cylindrical slower. Frozen pipes freeze single-row spacing of 0.6m tube 4 days began to freeze pay in circles, frozen 5 days between rows and rows of circles began to pay freeze 6 days to form a continuous vertical wall of permafrost. Freezing tube spacing 0.8m single and double row frozen pipes from freezing circle began to pay 6 days, 7 days form the overall frozen permafrost wall. Freezing tube spacing 1.0m in freezing day 7 A row of freezing pipes and tubes not yet pay freeze row B ring, but the row between the row and start mutual exchange rings. The reason is the distance between each row of freezing pipes 1.0m, while the distance between the rows and rows of 0.8m, due to the heat from the exhaust and the exhaust heat is less than the distance between each row of freezing pipes between the rows and rows of it first began to pay between laps. Freeze 8 days, A row of freezing, there are still unfrozen area between the tube and the building envelope. Permafrost frozen nine days to form a vertical wall. Freezing tube spacing 1.4m slowest lap time of delivery, frozen for 10 days between the first row and the rows start mutual exchange rings, when frozen soil wall forming a continuous 13 days. With the freeze time increases, the vertical distance between the different freezing pipes freeze wall continues to develop, deliver laps zero isotherm curvature gradually slows tending to straight line, increasing the wall thickness of the permafrost.

Time seen, different spacing freezing pipes freeze wall post to form a closed loop time that vertical wall were frozen: frozen pipes spaced 0.6m for the six days, freezing pipes spaced 0.8m to 7 days, freeze tube spacing of 1.0m 9 days, freezing tube spacing 1.2m for the 11 days, freezing tube spacing 1.4m for the 13 days. Post spacing of 0.6m lap time than 1.4m when the seven days ahead of time, reducing the visible effects of freezing tube spacing on the temperature field is more significant. The freezing tube spacing increases every 0.1m, freeze wall post lap time increased by about one day. With the freezing tube spacing increases, frozen wall post lap time increases linearly.

Frozen pipes by different spacing z = 0 cross-section 30 days of freezing temperatures contours can be seen in Figure 2: 30-day freeze, freezing tube spacing between 0.6m and 0.8m of B row frozen pipe and envelope (blue area) are concentrated in the temperature of -26.67 ˚C, continuous and uniform thickness 1.2m. Freezing tube spacing 1.0m of -26.67 ˚C isotherm at reducing the scope of the package, freezing tube spacing 1.2m when the blue area is divided into two parts, exhaust temperature between B and A row of frozen pipes concentrated in -20 ˚C ~ -26.67 ˚C, A row between the tube and the envelope freezing temperatures are concentrated in -26.67 ˚C. When the temperature of the freezing tube spacing 1.4m blue area is mainly focused on the following -20 ˚C, -26.67 ˚C isotherm only appear in each row A frozen pipe around.

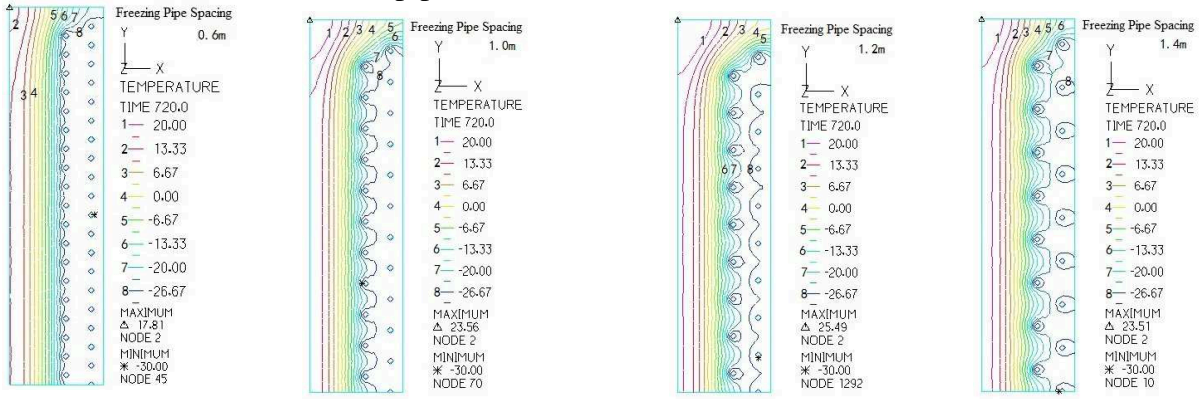


a) Freezing pipe spacing 0.6 b) Freezing pipe spacing 1.0 c) Freezing pipe spacing 1.2 d) Freezing pipe spacing 1.4

Fig.2 Temperature contour of z = 0 section frozen for 30 days for different freeze pipe spacing

## Summary

(1) Different tube spacing freeze pay freeze wall to form a closed loop of time that the walls were vertical permafrost: Spacing 0.6m for the six days, seven days spaced 0.8m, 1.0m spacing is 9 days, spaced 1.2m 11 days, 13 days 1.4m spacing. Exchange lap time than when the spacing distance between 0.6m 1.4m seven days ahead of time, reducing the visible effects of tube spacing freezing temperature field is more significant.

(2) Each frozen tube spacing increases 0.1m, freeze wall post lap time increased by about one day. With the freezing tube spacing increases, frozen wall post lap time increases linearly.

(3) Freeze tube spacing, the lower the curtain vertical permafrost temperature, the more uniform vertical wall strength permafrost formation.

## Acknowledgment

This research was sponsored by the scientific research start-up fund program of Hainan University ( Program No. kyqd1241), the Midwest Key Areas Construction Project Plan of Hainan University and 2014 Hainan national science foundation.

## References

[1] Hu Jun, Zeng Hui, Wang Xiaobin. Numerical Analysis of Temperature Field of Cup-shaped Frozen Soil Wall Reinforcement at Shield Shaft[J]. Applied Mechanics and Materials,2013,341-342(5): 1467-1471.

[2] Hu Jun,Zeng Hui,Wang Xiaobin. Experimental Research on the Physi-mechanical Performances of Geosynthetics[J]. Applied Mechanics and Materials,2013,341-342(5): 33-37.

*Applied Mechanics and Materials Vols. 580-583 (2014) pp 742-745*
*© (2014) Trans Tech Publications, Switzerland*
*doi:10.4028/www.scientific.net/AMM.580-583.742*

# The Applied Research of Underwater Vacuum Preloading Method in Soft Soil Foundation

Yuqin Feng[1,a], Lu Zhang [2,b]

[1]The school of Architecture and Civil Engineering , Inner Mongolia University of Science & Technology, Baotou 014010, China

[2]The Nuclear Industry 208 Battalion, Baotou 014010, China

[a]btfyq@126.com, [b]zllxy_love@126.com

**Keywords:** Foundation treatment, Vacuum preloading, Site test, Shear strength

**Abstract.** On the basis of engineering project using underwater vacuum preloading method to strengthening the soft foundation, under the specific geological conditionsthis article analyzes the construction technology and reinforcement mechanism of underwater vacuum preloading of the soft soil foundation. By indoor soil test of Reinforcement of soil before and after processing, compared the change and improve of soil shear strength indexes before and after the reinforcement, it is verified that the underwater vacuum preloading method is a effective mean in handing soft ground, and can be further promoted as a means of handling soft ground along the coastal area of China.

## Introduction

With the development of high heavy buildings in coastal cities, Traditional foundation treatment methods cannot satisfy the requirement of engineering practice, Some composite foundation treatment methods and new foundation treatment technology have been applied in engineering practice. The soft soil foundation underwater vacuum preloading is one of composite foundation treatment technology.The water pulled out when vacuum is as a heap of cargo stack preloading, using the vacuum produced by negative hydrostatic pressure and the membrane water load, to speeding up the progress of consolidation and the strength of the soft soil.In order to develop and disseminate underwater vacuum preloading technology, combining an engineering example in the coastal area, this article analyzes the application problems reinforcement mechanism of underwater vacuum preloading technology handing soft ground and evaluates of reinforcement effect

## Project Overview

The project is a more multi-storey, small high-level, high-rise and high-rise residential buildings in China, in which the main residential area is 11~32 layer, 41~100 m above the ground, has 1~2 layers basement embedded in the depth of 7.20 m. The frame and shear wall or frame shear wall structure are used in this project. The original landform types of the venue is the coastal tidal flats, by the artificial reclaimed, the terrain is relatively flat, the surface elevation is about 2.0~3.0 m, the venue leveling elevation is 5.9 m. But the surface water in the southwest, southeast and northeast of the field is long-standing existed, whose depth is about 1.00 m. By surveying, each hole orifice elevations are measured between 1.60~3.82 meters. In view of silt soft soil layer which appeared saturated flow state is thick of 0.00~18.40 m has widespread distribution in this area and the overlying filling being owe consolidation soil, with an average of about 7.2 m, has a high water content, high thixotropic , low intensity, for reducing the adverse effects of consolidation settlement which occurred in the soft soil layer in the stage of the project being completed. So this silt soft soil layer venue will use underwater vacuum preloading method to reinforce foundation.

From top to bottom soil name and lithology abased on drilling results are shown in table 1.

**Table 1. The name, Thickness and Status of Soil Layer**

| Number | Soil Name | Thickness (m) | Geotechnical Condition |
|---|---|---|---|
| ① | Artificial Filled Soil | 1.00~2.70 | Loose State |
| ② | Artificial Filled Soil | 0.80~7.70 | Loose State |
| ③ | Sludge | 2.60~8.70 | Saturation and Flowing Plastic |
| ④ | Sludge | 2.00~10.00 | Saturation and Flowing Plastic |
| ⑤ | Gravelly Cohesive Soil | 3.40~8.90 | Saturation and Flowing Plastic |
| ⑥ | Completely Weathered Granite | 2.50~8.60 | Earthy |
| ⑦ | Intensely Weathered Granite | 3.70~8.60 | Soil Clip Pieces |
| ⑧ | Moderately Weathered Granite | 4.80~10.10 | Core Into Earthy |

## The Construction Process

Place the sand blanket after site clearing , make the curtain of construction clay and drive plastic drainage plate (Type B plastic drainage plate of the SPB100 series, section size 4×100mm),layout vacuum lines (PVC outer membrane type filter tubes, pipe diameter>50mm), inbuilt vacuum probe, inbuilt monitoring devices, excavation pressure membrane channel, pave earthwork cloth, vacuum membrane, fill the cofferdam and impoundment while evacuating (pour the water being pumped into the cofferdam, forming constant water load), after prepressing the load 90 days, go on evacuating if the degree of consolidation can not meet the requirements, otherwise, unloading, completion and acceptance can be performed.

## The Reinforcement Mechanism of Underwater Vacuum Preloading

Underwater vacuum preloading method is a vacuum stack preloading method that combines surcharge preloading with vacuum preloading; it is more effective to treat soft foundation. Vacuum negative pressure and positive pressure to heap load could add to form vacuum stack preloading method. Vacuum preloading method technology is that in first lay sand cushion layer in soft foundation, burying vertical drainage well, and then cutting off from the atmosphere using closing membrane buried in the grave, through embedding shaft vacuum suction. Passing air exhaust forms negative pressure in sand cushion layer and drainage well. Pore water continuously discharge from drainage well in back pressure to strengthen soil. In engineering construction of Underwater vacuum preloading method, vacuum conditions need to extract a large number of groundwater, together with auxiliary seal measures of membrane. Membrane water storage can play a role of sealing membrane to ensure the membrane under vacuum degree; it also could have the effect of preloading load. The actual load is equal to the membrane under vacuum preloading load and the sum of membrane water pressure load. In vacuum load and membrane water pressure load, pore water was ruled out slowly and the volume decrease slowly, foundation consolidation deformation, and the same time, with the super hydrostatic pressure disappearing gradually, effective stress increase gradually, the strength of the foundation soil increasing gradually.

## Vane Shear Strength Test

This project adopts vane shear strength test to evaluate treatment soft ground test data. So it could get the objective and scientific evaluation of soft foundation treatment effect.

The vane shear strength test gets undrained shear strength Cu that mainly reflects the vertical plane strength of the soil. This experiment adopts resistance strain type cross slab, using static sounding instrument injection device to press the cross slab into different test depth. With the help of a rotary vane head gear torque device, using LMC - D310 static microcomputer of soil resistance torque, so as to calculate the shear strength unearthed. Vane shear strength test structure shown in table 2.

**Table 2. Vane Shear Strength Test Statistics**

| Items | Intensity Index (kPa ) | Statistical Depth (m) | Range Value (m) | Average Value (kPa ) | Standard Deviation | Coefficien of Variation | Standard Values (kPa ) |
|---|---|---|---|---|---|---|---|
| Before the vacuum preloading | Cu | 0~5.0 | 16.92~26.59 | 20.12 | 3.335 | 0.166 | 17.86 |
| | Cu' | 0~5.0 | 4.05~7.87 | 5.90 | 1.441 | 0.244 | 4.92 |
| | *S*t | 0~5.0 | 3.03~4.18 | 3.49 | 0.396 | 0.144 | 3.22 |
| After the vacuum preloading | Cu | 0~5.0 | 19.39~31.82 | 25.05 | 3.000 | 0.120 | 23.84 |
| | Cu' | 0~5.0 | 5.92~10.15 | 7.92 | 1.030 | 0.130 | 7.50 |
| | *S*t | 0~5.0 | 3..05~3.29 | 3.17 | 0.075 | 0.024 | 3.14 |
| Before the vacuum preloading | Cu | 5~10.0 | 18.93~29.74 | 25.41 | | | |
| | Cu' | 5~10.0 | 5.39~8.78 | 7.10 | | | |
| | *S*t | 5~10.0 | 3..33~4.02 | 3.60 | | | |
| After the vacuum preloading | Cu | 5~10.0 | 19.44~39.00 | 25.68 | 5.110 | 0.200 | 23.33 |
| | Cu' | 5~10.0 | 6.27~11.22 | 8.05 | 1.500 | 0.190 | 7.36 |
| | *S*t | 5~10.0 | 2..99~3.48 | 3.19 | 0.150 | 0.050 | 3.12 |
| After the vacuum preloading | Cu | >10.0 | | 30.19 | | | |
| | Cu' | >10.0 | | 9.82 | | | |
| | *S*t | >10.0 | | 3.07 | | | |

Indicated: Cu: Undrained shear strength of undisturbed soil;
Cu': Undrained shear strength of remoulded soil;
*S*t: Sensitivity of clayey soil.

From the table 2 it can be see clearly that after treatment the average value of shear strength for the undisturbed soil is 25.40, in which within 0~5 meters deep the average shear strength of undisturbed soil is increased by 24.50%,the average shear strength of remoulded soil is increased by 34.24%; within 5~10 meters deep the average value of shear strength is increased by 1.06%, the average shear strength of remoulded soil is increased by 13.42%, under 10 meters the shear strength of the silt soft soil is 30.19 kPa, in other depth within the scope of the test results, the average shear strength of undisturbed soil and remoulded soil are also increased. The vane shear strength changes before and after the foundation treatment are shown in table 3.

**Table 3. Vane Shear Strength Average Value Comparison Table Before and After The Foundation Treatment**

| Stage | | Depth (m) | | |
|---|---|---|---|---|
| | | **0~5.0** | **5.0~10.0** | **>10.0** |
| **Before Soft Ground Treatment** | **Cu** | 20.12 | 25.41 | 30.19 |
| | ***St*** | 3.49 | 3.60 | |
| **After Soft Ground Treatment** | **Cu** | 25.05 | 25.68 | 30.19 |
| | ***St*** | 3.17 | 3.19 | |
| **Decrease Ratio** | **Cu** | 24.50% | 1.06% | |
| | ***St*** | 9.17% | 11.39% | |

From table 3 it can be clearly see that the vane shear strength were increased of the silt soft soil layer depth within the scope, in which the vane shear strength within the scope of 5 meters of the top silt layer is significantly increased, below 5 meters the vane shear strength is increased slightly, sensitivity of soil in detecting depth range are reduced to a certain extent, in a word, the underwater vacuum preloading method has a certain effect in the consolidation processing of soft soil.

## Conclusions

- Underwater vacuum preloading has a certain reinforcement effect for mud soil in coastal region.
- Underwater vacuum preloading can improve the shear strength of mud soil.
- Underwater vacuum preloading can lower the sensitivity of mud soil.

## References

[1] Technical Code for Ground Treatment of Buildings, (JGJ 79-2012), (in Chinese).

[2] Code for Design of Building Foundation, (GB 50007-2011), (in Chinese).

[3] Standard for Soil Test Method, (GB 50123-1999), (in Chinese).

[4] Electrical Measuring Vane Shear Test Procedures, (YS 5220-2000), (in Chinese).

[5] Guanbao Ye,etc: *Foundation Treatment* (*the third edition*).( China Building Industry Press, 2009),(in Chinese).

*Applied Mechanics and Materials Vols. 580-583 (2014) pp 746-749*
*© (2014) Trans Tech Publications, Switzerland*
*doi:10.4028/www.scientific.net/AMM.580-583.746*

# The Bearing Characteristics and its Influencing Factors of Reinforced Soil Foundation

Yang Jiang[1,2,a], Xiaomou Wang[2] , Wenbin Sun[1,b], Yun Dong[1,c]

[1]Faculty of Architecture and Civil Engineering, Huaiyin Institute of Technology, Huaian, China

[2]School of Highway, Chang'an University, Xi'an, China

[a]jy_12345678@163.com, [b]sunwb1969@163.com, [c]dyunhyit@163.com

**Keywords:** Reinforced soil foundation, Bearing capacity, Influencing factors, Finite element method

**Abstract.** The reinforced soil foundations have been widely used in various geotechnical engineering applications, such as bridge approach slab, bridge abutment and so on. However, many problems of reinforced foundation still need to be solved and the behavior of the reinforced foundation requires further study. Therefore, finite element analyses were conducted on unreinforced and reinforced clay subgrade soil to evaluate the influence of various factors affecting the performance of strip footing on studied soils. Conclusions are drawn: the effective reinforcement depth is about 1.5B for the reinforced soil and it is independent of the geogrid type; At a given settlement, the bearing capacity of the footing decreases with the increase in reinforcement spacing, with larger decrease rates at small spacings; A geogrid with a tensile modulus ranging from 5MPa to 25MPa will maximize the benefits of the reinforced soil footing, etc.

## Introduction

The concept of reinforced soil as construction material is based on the existence of soil-reinforcement interaction due to tensile strength, frictional and the adhesion properties of the reinforcement and was first introduced by the French architect and engineer Henri Vidal in the 1960s. In the past three decades, reinforced soil foundations (RSF) have been widely used in various geotechnical engineering applications, such as bridge approach slab, bridge abutment, building footings, and embankment.

Researchers have shown that the inclusion of reinforcement in soil foundations is a cost-effective solution to increase the ultimate bearing capacity or reduce the settlement of shallow footings compared to the conventional methods. The most common type of reinforcement used in soil foundation applications are geogrids.

Meanwhile, the improve performance of reinforced soil foundation can be attributed to three fundamental reinforcement mechanisms as described below: (a) Rigid boundary; (b) Membrane effect; (c) Lateral restraint effect [1].

In order to get more behavior of the RSF, the influence of various factors on the performance of footings on reinforced soil foundation was investigated by finite element analyses. The factors are as follows: spacing between reinforcement layers, tensile modulus of reinforcement, soil-reinforcement interaction coefficient, optimum top spacing for the single-layer and multi-layer reinforced soil, footing width, etc. The influence of these factors will be discussed in the following sections [2].

For each case, the load-deformation curve, obtained from the finite element simulation, was used to determine the ultimate bearing capacity and settlement of the footing. The benefits of RSF were assessed in terms of the bearing capacity ratio (BCR) and settlement reduction factor (SRF).

## The fundamental behavior of the reinforced soil foundation

The influence of the location of first reinforcement layer (H) on the BCR is discussed in this section, based on the FEM analyses for the footing (B=1.2m) placed on single-layer, two-layer and three-layer geogrid-reinforced soil systems with varying depth.

In the single-layer reinforcement case, the BCR increases first with the increase of the depth ratio (H/B) and then decrease after a threshold value of H/B. This threshold depth ratio (H/B) is around 0.5, where the BCR gets the highest value. The variation of the BCR with depth ratios (H/B) is similar in the two-layer and three-layer reinforcement cases. However, the threshold depth ratio slightly decreases with the number of reinforcement layers around 0.4 in two-layer reinforcement case and around 0.3 in three-layer reinforcement case [3].

The design of reinforced soil foundations requires the determination of the effective depth of the reinforced zone, below which reinforcement will not have appreciable benefit on footing performance. To identify the effective depth, finite element analyses were conducted on a footing (B=1.2m) using three types of geogrid reinforcements placed uniformly either at 30cm interval or 60cm interval.

Three types of geogrid (I, II, and III) were included to investigate the dependence of effective depth on geogrid's properties. Type I geogrid has a relatively low tensile modulus, Type II has a medium tensile modulus, and type III represents a stiff geogrid.

For each type of geogrid, a series of finite element analyses were conducted with the number of reinforced layers increasing till the reinforced depth reaches 2.5B. The bearing capacity ratio was calculated from load-deformation curves for each case.

What can be seen from Fig. 1(a) (for the 30cm reinforcement spacing, the number of reinforcement layers increases from one to ten) and Fig. 1(b) (for the 60cm reinforcement spacing, the number of reinforcement layers increases from one to five), the BCR of the reinforced footing increased as the number of reinforcement layers increased, but at a decreasing rate. For the 30cm spacing cases, there is no significant improvement in the BCR when the number of reinforcement layers exceeds 6, which corresponds to a depth of 1.5B=1.8 m. Similarly, no further significant improvement in BCR was achieved for the 0.6 m spacing as the number of layers exceeds 3, which is also corresponds to 1.5B depth. Accordingly, the effective reinforcement depth expressed as the strip footing's width will be equal to 1.5B for the soil in question.

As seen in Fig. 1(a) and Fig. 1(b), the improvement trend in BCR is the same for all the three types of geogrid that been investigated, which also indicated that the effective reinforcement depth is independent of the geogrid type.

## Influence of various factors on the bearing capacity ratio

### Reinforcement Spacing

The effect of reinforcement spacing on the footing's bearing capacity and settlement was investigated by changing the spacing of reinforcement layers within the effective reinforcement depth of 1.5B. A series of finite element analyses were conducted on the footing- reinforced soil model using three geogrid types placed at five different spacing. The following reinforcement layers configurations were considered: three layers with 60cm spacing, four layers with 45cm spacing, six layers with 30cm spacing, nine layer with 20cm spacing, and twelve layers with 15cm spacing. For each case, the BCR and the settlement reduction factor (SRF) at the ultimate load capacity of a 3-layer Type II reinforced soil were calculated. The results show that at a given settlement the

bearing capacity of the footing decreases with the increase in reinforcement spacing, with larger decrease rates at small spacing. Besides, the footing settlement at the ultimate load capacity of a 3-layer Type II reinforced soil is smaller for closer reinforcement spacing. The reduction effect of footing settlement is more remarkable when the spacing ratio reduced.

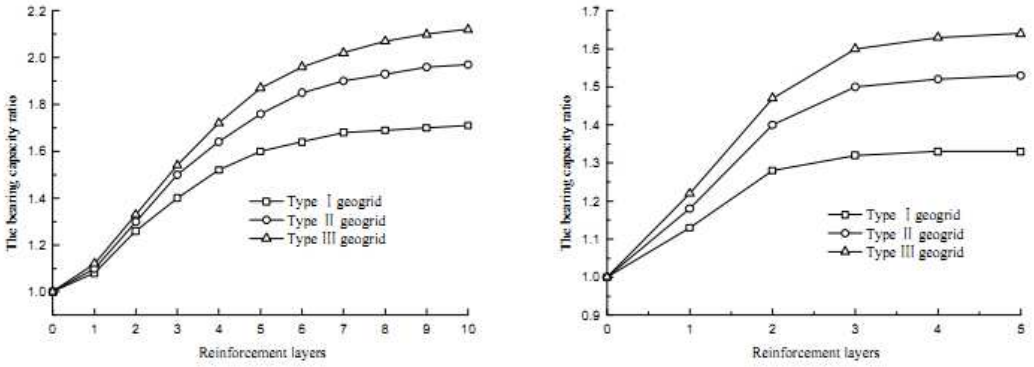


(a) 30cm spacing (b) 60cm spacing

Fig. 1 Variation of BCR with reinforcement layers

**Reinforcement Tensile Modulus**

A series of finite element analysis were conducted for each tensile modulus using 3, 6 and 9 layers of reinforcement placed within the effective depth of 1.5 B at a uniform spacing. Regardless of the number of reinforcement layers, the footing with geogrids of higher tensile modulus has a larger bearing capacity. Moreover, this modulus-related increase in the BCR is more remarkable at lower geogrid stiffness and gradually weakens as the tensile modulus of geogrid exceeds 35MPa. At the same time, the SRF decreases with the increase in reinforcement tensile modulus at a gradually reducing rate. In general, the study indicates that a better reinforcement effect in terms of higher ultimate bearing capacity and smaller settlement can be achieved from higher tensile modulus of the geogrid. In addition, a geogrid with a tensile modulus ranging from 5MPa to 25MPa will maximize the benefits of the reinforced soil footing [4]. No more significant improvement is achieved when the tensile modulus of geogrid exceeds 35MPa.

**Geogrid-Soil Interaction**

The influence of the geogrid-soil interaction coefficient on the BCR and SRF is examined when the coefficients range from 0.4 to 0.8 with equal interval of 0.1. The results show that, as the interaction coefficient increases, the BCR increases and SRF decreases for all studied geogrid reinforced soil footings, which means that better interaction between soil and geogrids always provide better performance of RSF. On the other hand, the increase rate in the BCR or the decrease rate in the SRF is relatively independent of the type of geogrids.

**Footing Embedment Depth**

The variation of the BCR and the variation of SRF with footing embedment depth were analyzed using the FEM model. With the increase of the embedment depth for the footing, both the BCR and the SRF slightly decrease at an approximately linear manner. There is a slight reduction trend of the BCR with the increase of the embedment depth, which can be explained by the fact that the increase

of the embedment depth increases the bearing capacity of the unreinforced footing more than that of the reinforced footing [5].

### Footing Width

In this section, the effect of footing width on the BCR and SRF of reinforced soil footings was studied by changing the width of strip footing from 0.9 m to 1.8m. The results show that with the increase of footing width, both the BCR and the SRF decrease at a linear manner. It is due to larger increase in the bearing capacity of the unreinforced footing compared to the reinforced footing brought up by the increase of the footing width, which consequently causes a decrease trend in the BCR. And thus it can be concluded that increase in footing width cannot bring more benefit in increasing BCR, however, it can reduce more footing settlement. The benefit in reducing the settlement can be explained by the fact that wider footing can distribute overlying load in a wider range and thus the corresponding settlement reduces.

### The Friction Angle and Cohesion of Soil

The effect of soil friction angle on the BCR and SRF of reinforced soil footings was studied by varying it from 25°to 45°while all the other parameters of the soil remained unchanged. The effect of cohesion was also analyzed else.

The results show that with the increase in friction angle or cohesion, both the BCR and SRF decreased, which means that the increase in friction angle and cohesion of soil cannot bring benefit in increasing its bearing capacity. This can be explained that the increase in friction angle or cohesion results more increase in the bearing capacity of the unreinforced soil compared to the reinforced soil, which consequently causes a decrease in the BCR.

## Conclusions

The effective reinforcement depth is about 1.5B for the reinforced soil and it is independent of the geogrid type; At a given settlement, the bearing capacity of the footing decreases with the increase in reinforcement spacing, with larger decrease rates at small spacing; A geogrid with a tensile modulus ranging from 5MPa to 25MPa will maximize the benefits of the reinforced soil footing; Better interaction between soil and geogrids always provide better performance of RSF; With the increase in the embedment depth of the footing, both the BCR and the SRF slightly decrease at an approximately linear manner; Increase in footing width cannot bring more benefit in increasing BCR, however, it can reduce more footing settlement; With the increase in friction angle or cohesion, both the BCR and SRF decreased.

## References

[1] C. Yoo: Geotextiles and Geomembranes Vol.19 (2001), p. 279

[2] J. G. Collin, T.C. Kinney and X. Fu: Geosynthetics International Vol.3 (1996), p. 537

[3] D.K. Maharaj: The Electronic Journal of Geotechnical Engineering Vol.8 (2003)

[4] M.T. Adams and J.G. Collin: Journal of Geotechnical and Geoenvironmental Engineering Vol.123 (1997), p. 66

[5] E.C. Shin, B.M. Das, E.S. Lee and C. Atalar: Geotechnical and Geological Engineering (2002), p. 169

*Applied Mechanics and Materials Vols. 580-583 (2014) pp 750-754*
*© (2014) Trans Tech Publications, Switzerland*
*doi:10.4028/www.scientific.net/AMM.580-583.750*

# The instability mechanism of soil-like slope under the action of acid corrosion in open-pit copper mine

Haiyan Ju [1, a], Guiqing Gao [1,b], Shaolin Liu [1,c], Changtai Luo [1,d], Jianhua Li [1,e]

[1] Nanchang Institute of Technology, Nanchang 330099, Jiangxi, China

[a]jhyhgw@qq.com,[b]guiqingg@qq.com,[c]1196827270@qq.com,[d]40340035@qq.com, [e]gdwjljh@163.com

**Keywords:** open-pit copper mine; soil-like slope; the acid wastewater; instability mechanism

**Abstract.** Combined with the engineering geological conditions and geological characteristics of soil-like slope in a certain open-pit copper mine, based on the experiments and theoretical analysis, the instability mechanism of soil-like slope under the action of acid mine wastewater is researched. Because the acid wastewater goes into the weak structural plane, reacting with the constitutional materials and fillings in slopes, the react change the microstructure of the rock and soil, and replace, dissolve the components, causing the cohesion and internal friction angle of slope reducing eventually and slope failure.

## Introduction

With the rapid development of social and economic, human's demand for mineral resources is growing, environmental problems arise from the growing mine drainage, and the pollution will become a global problem which will gradually attract people's attention [1,2]. The widest pollution and the greatest harm of mine drainage is acid mine drainage AMD (Acid Mine Drainage). Reported in the literature, 70% acid in the water is from the mine drainage [3]. According to incomplete statistics [4], in all accidents of open-pit copper mine, about 70% are due to the instability mechanism of slope, and most of the instability of slope are soil-like slope, and acid mine drainage leading to the destroying of metal mine slope is a special way. The soil-like slope in open-pit mine occur all types of slope instability or landslide events constantly, which caused a huge threat and loss to the production and life of mine enterprises.

At present, the experimental research about the mechanical properties and corrosion mechanism of soil-like slope in the role of acid mine drainage domestic and foreign has been reported rarely in domestic and foreign, and mostly related research is about the erosion or corrosion mechanism of reinforced concrete under acidic water conditions or cement soil, or research on acidic soils. This thesis based on laboratory experiments and theoretical analysis reveals the instability mechanism of soil-like slope in open-pit copper mine, which provides a theoretical basis for the maintenance and reinforcement of the mine's slope.

## Project Overview

The copper mine lies in Jiangxi Province. Its length from north to south is 1700 m, width from east to west is 600-900 m, and its open-pit mining highest elevation is 475 m, the lowest elevation design is -26.0 m, and the maximum height of the slope of 501 m, which is a large open pit mines. The mine belongs to the subtropical monsoon climate, and the climate is warm and humid, annual average rainfall is 1908.9 mm. In this region the stratum mainly include Cambrian, Triassic, Jurassic, Quaternary and early of Yanshan magmatic intrusions and dikes class. Its geological structure is relatively simple, and it doesn't found that there is major fault fracture zone passing.

Following an inspection, the shallow surface soil of the mine's slope behaves the whole strongly weathered, reddish brown, brown, gray, gray brown, and other blended color. the mine's slope is original rock structure, and the structure is not easy to identify, feldspar has kaolinised, is gray, quartz is granular, whose size is generally 0.3-3mm, part is 5-10mm, and the slope's fissures are developed,

where there is a large of Fe, Mn and filling. Lower part of the rock is mixed rock which is slightly weathered, and was reddish brown, brown, gray, gray brown and other blended color. It is granular and massive structure, less fissures in which there is a small Fe, Mn. The core show short column-shaped and pieces blocks, and the lithology is better. The open-pit mine's slope belongs to soil-like slope (Fig. 1).

Fig.1 Copper mine's soil-like slope

**The instability mechanism of soil-like slope**

Soil-like slope is between the rock slope and soil slope .It is composed of soil material substance or crushed rock which is formed by the weathering of original rock and they retain and some inherited the structure surface of the original rock.Soil-like slope of mine have the characteristics of the soil-like slope, apart from this it also contains large amounts of sulfide minerals [5], which produces highly acidic water after reaction with water and air, and the acidic water can take place chemical reaction with the contacted slope body very easily. The chemical reaction will change the composition of slope body's skeleton and internal molecular structure, reducing the cohesion and internal friction angle of slope body and making slope easier instability.

**The formation mechanism of acidic water.** The major waste rock of metal mine are minerals mica, quartz and pyrite. The acid mine drainage is mainly produced by the weathering of pyrite, and the water quality changes depending on the oxidation of pyrite caused by [6,7]. During the reaction, the sulfide, water, oxygen is involved, bacteria (mainly iron and sulfur Bacillus subtilis), redox potential, temperature and so on are the reaction conditions. Part of the chemical reaction equation is as follows:

$$2FeS_2 + 7O_2 + 2H_2O \rightarrow 2Fe^{2+} + 4SO_4^{2-} + 4H^+ \quad (1)$$

$$4Fe^{2+} + 10H_2O + O_2 \rightarrow 4Fe(OH)_3 + 8H^+ \quad (2)$$

$$4Fe^{2+} + O_2 + 4H^+ \rightarrow 4Fe^{3+} + 2H_2O \quad (3)$$

$$FeS_2 + 14Fe^{3+} + 8H_2O \rightarrow 15Fe^{2+} + 2SO_4^{2-} + 16H^+ \quad (4)$$

Taking the water around the area of projects, founding that the components of environmental water's quality are complex, and its pH value is about 3.23, which belongs to the strong acidic water, moreover the water contains strong erosion and contains a lot of heavy metal ions, which in addition to Pb ions, other content of Cu, Zn, Cd plasma seriously overweight.

**Study on mechanical characters of soil-like slopes by acid mine drainage.** Combined with the engineering geological, some samples are taken. The surface of rock and soil slope and the deep of rock and soil are taken and both are three groups. Three tests are respectively conducted for compression test, direct shear test and the longitudinal wave velocity tests.

**Compression test results analysis.** Based on the results analyzed for drainage in project area, $H_2SO_4$ is formulated as solution of pH 3.23, and put the six groups of samples into the solution, observe the changes in compressive strength for 0d, 5d, 10d, 15d, 20d. The results are shown in table 1 and Fig. 2. The test results show that with the increasing of immersion time, the compressive strength of rock and soil in surface and deep show a decreasing trend, and the compressive strength of the surface is less than the deep.

**Direct shear test results analysis.** Each sample is carried out shear test, and take the results of the sample into regression analysis, then gain the parameter of shear strength of the corresponding state of the soil .The parameter are cohesion(c)and internal friction angle (Φ), the results are in table 2, Fig. 3

and Fig. 4. According to the test results, the shear strength of the surface is less than the deep. With the growth of time of the effect in the acidic solution, the shear strength of rock and soil in surface and deep shows a decreasing trend.

Table 1 Compression test results

| The sample | | Compressive strength/MPa | | | | |
|---|---|---|---|---|---|---|
| | | 0d | 5d | 10d | 15d | 20d |
| The surface of rock and soil | 1 | 83.36 | 80.14 | 76.64 | 64.32 | 52.08 |
| | 2 | 81.65 | 78.31 | 75.52 | 63.34 | 50.34 |
| | 3 | 82.32 | 79.01 | 77.19 | 63.96 | 51.27 |
| The deep of rock and soil | 1 | 92.61 | 88.06 | 83.56 | 72.56 | 60.35 |
| | 2 | 94.24 | 90.12 | 86.05 | 73.24 | 61.25 |
| | 3 | 93.15 | 89.45 | 82.98 | 72.35 | 61.05 |

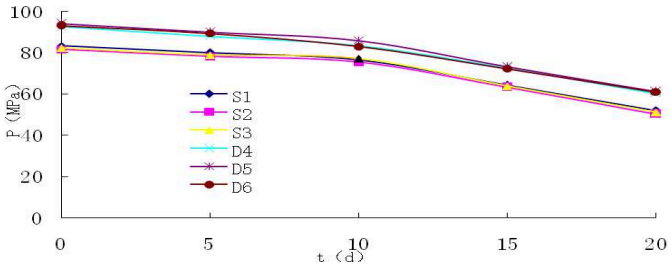


Fig. 2 The relationship between the compressive strength of surface soil and deep soil with the immersion time

Table 2 Direct shear test results

| The sample | | | The immersion time/d | | |
|---|---|---|---|---|---|
| | | | 0 | 10 | 20 |
| The surface of rock and soil | 1 | Cohesion /MPa | 10.829 | 10.712 | 10.606 |
| | | Internal friction angle / $^0$ | 42.06 | 41.35 | 39.98 |
| | 2 | Cohesion/MPa | 10.632 | 10.596 | 10.487 |
| | | Internal friction angle / $^0$ | 43.16 | 42.04 | 40.21 |
| | 3 | Cohesion /MPa | 10.735 | 10.621 | 10.514 |
| | | Internal friction angle / $^0$ | 42.28 | 41.67 | 40.12 |
| The deep of rock and soil | 1 | Cohesion /MPa | 12.031 | 11.957 | 11.842 |
| | | Internal friction angle / $^0$ | 45.96 | 44.85 | 43.21 |
| | 2 | Cohesion /MPa | 12.697 | 12.524 | 12.379 |
| | | Internal friction angle / $^0$ | 45.41 | 43.98 | 42.13 |
| | 3 | Cohesion /MPa | 12.785 | 12.713 | 12.605 |
| | | Internal friction angle / $^0$ | 46.26 | 45.19 | 44.31 |

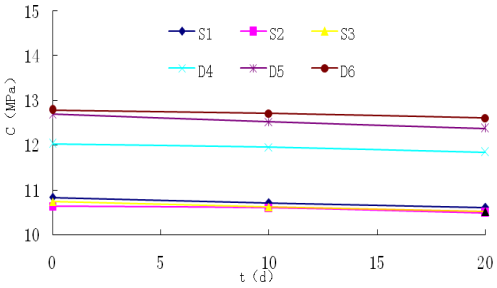


Fig.3 The relationship between the cohesion of surface soil and deep soil with the immersion time

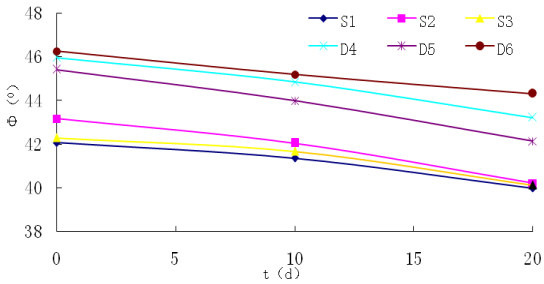


Fig.4 The relationship between the internal friction angle of surface soil and deep soil with the immersion time

**Analysis on the relationship between porosity with longitudinal wave velocity.** Survey and evaluate the initial porosity, the initial longitudinal wave velocity, porosity after soaking 20d and longitudinal wave velocity after soaking 20d. The changes are shown in table 3, the porosity of the surface is more than the deep, and with the growth of immersion time, the porosity of the rock and soil show a growing trend, and longitudinal wave velocity show a decreasing trend.

Table 3 The comparison sheet of soil's porosity and longitudinal wave velocity

| The sample | | The initial porosity /% | After soaking porosity/% | The initial longitudinal wave velocity/(m/s) | After soaking longitudinal wave velocity/(m/s) |
|---|---|---|---|---|---|
| The surface of rock and soil | 1 | 11.956 | 12.032 | 3579 | 3289 |
| | 2 | 11.845 | 11.958 | 3555 | 3275 |
| | 3 | 11.765 | 11.924 | 3550 | 3267 |
| The deep of rock and soil | 1 | 10.689 | 10.795 | 3842 | 3547 |
| | 2 | 10.364 | 10.468 | 3836 | 3529 |
| | 3 | 10.562 | 10.627 | 3839 | 3531 |

## Conclusion

Because soil-like slopes have weak structural plane, so their failure forms are very different to general rock slopes and soil slopes. And in the weak structural plane produce a large number of capillary pores due to weathering, these fissures or pores will become the center of acidic mine water absorption , while soil-like slopes' joints and cracks filled with a lot of rocks, clay minerals siliceous and carbonate rocks, which are highly corrosive under acidic conditions. Therefore, the instability mechanism of soil-like slopes along the weak structural plane mainly lies in the acid mine drainage go into the weak structural plane, react with the constitutional materials and fillings in slopes, the react change the microstructure of the rock and soil , and replace, dissolve the components. As a result the cohesion and internal friction angle of slope reduce eventually, so that causing slope failure. Meanwhile, acid mine drainage will increase the size of weak structural plane and bring new fracture which increase the probability of slope failure.

In summary, when analyze the stability of soil-like slope in open-pit copper mine and reinforcement it, not only should pay attention to the structural characteristic of soil-like slope, but also particularly attention to the comfortable drainage design, reduce the slope runoff and reduce erosion damage due to the effect caused by acid mine drainage, improve the cohesion and angle of internal friction of rock and soil, and effectively improve the physical and mechanical properties of rock and soil.

**Acknowledgement**

Supported by the Jiangxi provincial education department of science and technology project (GJJ13755, KJLD12048, GJJ13753, GJJ13741 and GJJ13756), Jiangxi province science and technology support program(20122BBG70174), Nanchang Institute of Technology Young Fund Project (2012KJ007a and 2012SK008) and Nanchang Institute of Technology students research training program in 2013.

**References**

[1] Di Pingkuan, Shan Zhongjian. Environmental pollution and its control method on mine wastewater [J]. Environmental Engineering, 1989,7(1):14-17.
[2]Liu Zhiyong, Chen Jianzhong .Study on treatment of acid mine drainage [J] Yunnan Environmental Science,2004,23(Supplement,1):152-156
[3] Zhou Zhihua. Strengthen the sustainable development of minie and promote environmental protection in mine.[M].Chinese mining industry.1994. (2):9-13.
[4] Xiong Ziying. Study on the characteristics of soil-like slope[J].Sichuan Building,2004(3):43-44.
[5] Zhao Xiaoyan, Hu Houtian, Shi Yanbing. Preliminary study on soil-like slope[J].Journal of Engineering Geology,2005,13(1):81-84.
[6] Cai Meifang, Dang Zhi.Progress pyrrhotite oxidation mechanism and prevention of acid mine drainage. [J]Environmental Pollution and Control,2006.28 (1):58-61.

*Applied Mechanics and Materials Vols. 580-583 (2014) pp 755-759*
*© (2014) Trans Tech Publications, Switzerland*
*doi:10.4028/www.scientific.net/AMM.580-583.755*

# The Optimum Design of Slope Angle Based on Critical Sliding Field

Shiguo SUN [1,a], Yanan YI [1,b], Qinhuan CUI [1,c] and Lu JIN [1,d]

[1] North China University of Technology Beijing 100041

[a] ssg59@tom.com, [b] 562482528@qq.com, [c] lumia1988@foxmail.com, [d] 781559582@qq.com

**Key wards:** slope stability, critical sliding field, geometric form, optimum design

**Abstract.** The optimum design of final highwall is a multivariable and complex technical problem that every change in any factor will influence the stable state. Based on the history-case, this paper applied the critical sliding field to search the critical slip and evaluate the stability of slope with different geometric forms. Comprehensively compared the global and local slope stability and its economic benefits, finally achieved the optimum design of final highwall.

## Introduction

In the design of open-pit mining projects, the slope angle concerns both enterprise's revenue and resource's utilization. The angle of slope has a significant impact on the stability of the slope, the economic benefits of open-pit mining and the safety of the life and equipment. Therefore, the slope stability is a key factor of normal production in open-pit mine. It is significant to design the maximum slopes angle under the condition of the established safe reserve.

Jinchuan quartz mine mining will enter final highwall mining stage. Many parts of the slope have different degree of deformation and failure. The production states can affect the company's economic benefit. Therefore, how to determine the optimum slope angle becomes a problem to be solved. This paper do some research on the subsequent deep level mining and the optimum design of final highwall, aiming at ensure the slope stability, reducing the loss rate of mineral resources, so as to achieve maximum economic benefits.

## Engineering geological conditions and mining profile

Mining area which is high in northwest while low in southwest belongs to hilly terrain. After years of exploration, the area formed an open pit which is low in the middle while relatively high on the other three sides including the south side, the west side, and the north side, all of which have become slopes with multistep shape. The middle area which has some simple roads connecting to working platform is relatively flat. The top of north slope is almost covered with waste mining rock while some local area is bedrock exposed. There are many cracks on the earth's surface which is near to slope boundary. The mining area has experienced many faulting activities and the fracture has fully developed.

The mining basin distributed in a stripe shape extending towards northeast and southwest. The stratum consists of lower Paleozoic erathem, Devonian system, Permo-carboniferous system, Tertiary strata and quaternary strata. The exposed layer below natural ground consistbreccia, sandstone, slate and so on. There are some pieces of fault fracture zone and coal between local layers.

The stope is a deep sunken open pit with 1000 meters long, 390 meters wide and 160 meters high. The elevation of the lowest platform is 1756 meters. The height of the slope is about 90 meters except for the lower unfinished part which is about 50 meters. So it's the key point that how to

make the best of ore resources while the slope is kept stable. This paper talked about how to design this slope using Critical slip field method.

## The fundamentals of optimum design

**The residual thrust method.** The residual thrust method assumes that the force between two slices is parallel to the bottom plane of the previous block, when the sliding force is greater than the anti-sliding force, it will have a trend of downward sliding [1-3]. The formula is as follows:

$$P_i = F_s w_i \sin\theta_i - \left(w_i \cos\theta_i - P_{i-1}\sin\Delta\theta_i\right)\tan\phi_i - c_i l_i + P_{i-1}\cos\Delta\theta_i , \quad (1)$$

or $$P_i = F_s w_i \sin\theta_i - w_i \cos\theta_i \tan\phi_i - c_i l_i - P_{i-1}\psi_i , \quad (2)$$

where $P_i$ and $P_{i-1}$ are the remaining force of blocks, $F_s$ is safety factor, $w_i$ is the block weight, $c_i$ is cohesion, $\phi_i$ is angle of friction, $\theta_{i-1}$ is the upper block bottom angel, $\theta_i$ is the nether block bottom angel, $\Delta\theta_i = \theta_i - \theta_{i-1}$, $\psi_i = \cos\Delta\theta_i + \sin\Delta\theta_i \tan\phi_i$ is thrust coefficient. Safety factor $F_s$ is calculated by iterating, $F_s$ is the solution when $P_{n+1} = 0$.

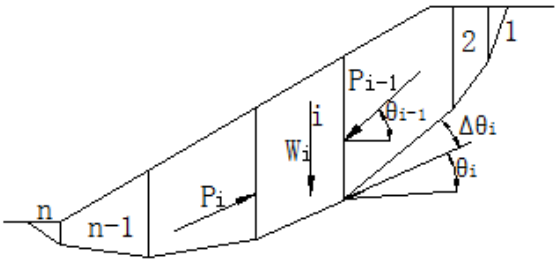


Fig 1 Residual thrust method calculation icon

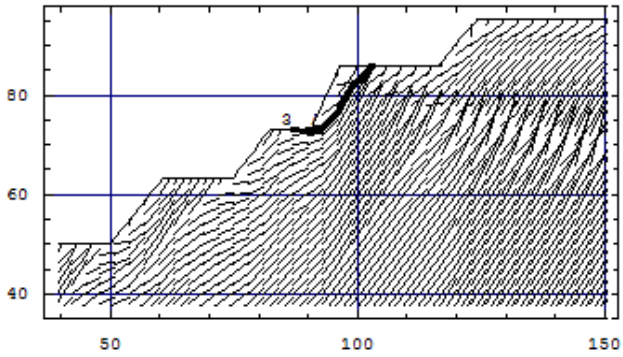


Fig2 The critical sliding surface of present slope in 3-3 profile

**Fundamental of critical sliding field method.** Critical sliding field method is on basis of residual thrust method, probing the critical sliding surface under the condition that exit and entry is specified. The slope is divided into a number of dangerous blocks, and the contact surface is divided into several points for the search. When given a safety factor, the slope body's strength expressed by a uniform proportion, the arbitrary point has a sliding direction and the maximum remaining thrust P. When researching, the direction of nether bulk' maximum residual thrust is the most dangerous sliding direction, and so on to get the maximum residual thrust slip surface [4-6]. Adjusting the safety coefficient of $F_S$ when the maximum residual thrust is zero to get the critical sliding field, and which is the most dangerous slip surface.

## The optimum design and analysis of slope angle

**Design standards.** In the process of open-pit mining, the maximum allowable slope angle should be calculated under the premise that the FOS (factor of safety) is greater than 1.05. In this study the method of Ordinary, Bishop, Janbu, and Morgenstern-Price are used to analysis slope stability. The search for dangerous sliding surface and the analysis for stability of slope are based on

the limit FOS that the minimum value of the four methods is greater than 1.05. If the residual thrust of the sliding surface is zero or near zero, then the angle of this slope is the maximum allowable value under the condition of the established safe reserve, which can meet the requirements of optimization slope angle.

Table 1 Parameters of faults and physical properties of rocks

| | C (Kpa) | Φ(°) | γ(KN/m³) | E(Mpa) | μ |
|---|---|---|---|---|---|
| rubble | 26 | 26 | 16.5 | 1038 | 0.15 |
| sandstone | 109.44 | 29.75 | 26.2 | 1520 | 0.14 |
| killas | 147.06 | 28.05 | 27.8 | 1192 | 0.21 |
| shattered fault zones | 20 | 23.8 | 22 | 88 | 0.26 |
| quartzite | 148.2 | 29.3 | 27 | 1798 | 0.24 |

**The sliding surface search of critical state for present slope.** This paper takes jingchuang open-pit mine north wall as a case to search and analysis the final highwall's critical sliding surface. The engineering geological condition is shown in the figure 3, and the parameters of stratum are shown in the table 1. The dangerous sliding surface of present slope is searched on the premise of the allowable minimum FOS at 1.05. Based on this residual thrust, the minimum of FOS is found out while the residual thrust is zero. And then, figure out the maximum slope angel by optimum design. After systematic search, the maximum residual thrust is closed to zero when the slope angle is 32°. This angle is in accordance with the current slope angle， it illustrates that the present situation of the slope basically meets the safety requirements in engineering. The global slope is stable, but local failure occurs at the steps as shown in figure 2. So the deep level mining chose to mine directly along this angle.

**Optimum design for deep mining.** 3-3 profile's engineering geological distribution as shown in figure 3. Including quaternary diluvial layer adopting the mechanical parameters of sandstone, carbonaceous mudstone and extrusion belt adopting mechanical parameters of fault fracture zone, mixed zone cladding on the slate using the mechanical parameters of gravel. Exploit the deep resources extending mining at the angle 32° downwards, considering the comprehensive economic rationality, it only allows its depth down to 1706 levels. Under this condition, make an optimum design, and through the sliding surface search and evaluating slope stability, the maximum residual thrust near to zero when $F_S$ = 0.982. The minimum stability coefficient in the four calculation methods is only 0.94, with a mean of 0.99.Therefore, the slope stability does not meet the safety requirements.

Against the formation distribution characteristics and the analysis of engineering geological conditions, it can be found that the main cause of instability in the profile is mass strength of fracture zone rock range from 1756 to 1732 levels is low. Carrying capacity of the slope waist insufficient, thus inducing the instability and failure of slope as a whole after deep mining. Reducing the overall slope angle makes stripping amount too large causes poor economic benefit. Through a series of scheme comparison and analysis, reduce local slope angle appropriately in order to ensure the safety of the fracture zone. Then considering the strength characteristics of slate below 1732 levels, increase its deep slope angle to form a convex type slope can reduce the stripping amount and increase production [7,8], so as to guarantee the whole slope angle of the same or slightly changed.

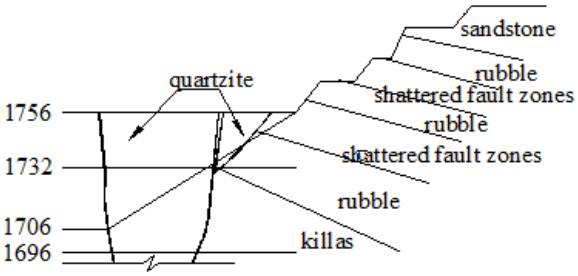


Fig3. 3-3 profile by extending deep mining at 32° plan and stratigraphic distribution

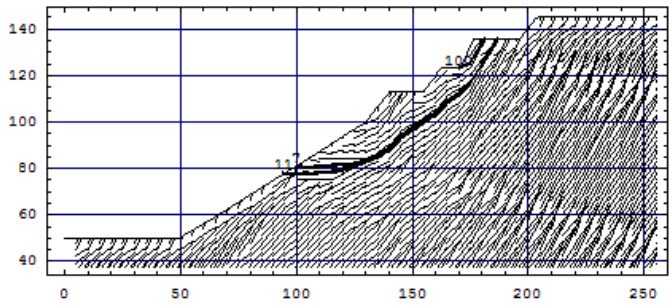


Fig4. Slope sliding surface of 3-3 profile by extending deep mining at 32 °

Firstly, optimize the design of the upper fracture zone of slope, through a series of calculation and analysis, when mining the fault fracture zone at 23°, the bearing capacity of the bottom of the fracture zone can meet the safety requirements, namely first by extending the deep to 1732 levels at 23°, to ensure the local stability of slope. Then taking the $F_S$ = 1.05, search the slope lower slope , get the lower slope Angle was 40°, the integral sliding surface maximum residual thrust is close to zero ( figure 5). The whole slope Angle is 32°, which allows extending down to 1708 levels. The convex type slope's minimum stability coefficient through the four calculation methods is above 1.05, with a mean of 1.14 (table 2), the overall stability meets the engineering requirements. finally, by setting a series of safety coefficient for the slope sliding surface analysis, get when FS = 1.02, the local slope's maximum residual thrust is close to zero (figure 6), the slope's minimum stability coefficient through the four calculation methods is above 1.05, with a mean of 1.10, the local slope stability either meets the engineering requirements.

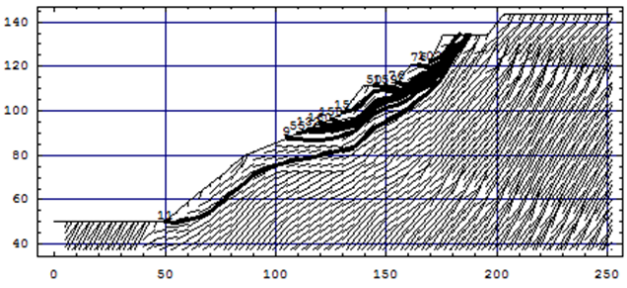


Fig5. Overall slope sliding surface of 3-3 section by extending deep mining at 32 ° +40 °

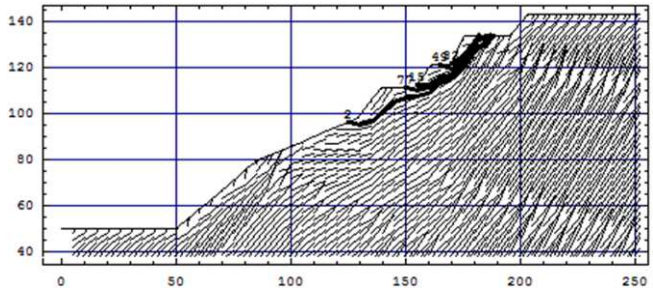


Fig6. Local slope sliding surface of 3-3 section by extending deep mining at 32 ° +40 °

Finally, design exploitation angle is 32°+23°+40°, the whole slope angle for 32, with a raised top and a concave bottom, which is just like convex type slope of combination. The plan is to ensure the overall stability of the slope and promoted the local stability of the slope, so as to achieve to meet the overall stability under the premise of exploiting resource at maximum level. The optimum design of final highwall provides a new train of thoughts, can reduce the magnitude of t scheme design, simplify the design process.

Table 2 Slope stability evaluation results of 3-3 profile

| evaluation content | Current slope angle（°） | Extending slope angle（°） | Overall slope angle（°） | Ordinary | Bishop | Janbu | M-P | Mean value |
|---|---|---|---|---|---|---|---|---|
| overall | 32 | 23+40 | 32 | 1.10 | 1.22 | 1.10 | 1.13 | 1.14 |
| local | 32 | 23+40 | 32 | 1.07 | 1.16 | 1.05 | 1.13 | 1.10 |

## Conclusions

Based on the residual thrust method, critical slip field theory determines accurately sliding surface of slope has important theoretical significance and practical application value. Its main advantages are that it can eliminate the influence of artificial factors, ensure the actual reliability of the evaluation, and avoid the same project with different evaluation conclusion by different technical personnel.

According to jinchuan quartz open-pit mine resources occurrence characteristics and engineering geological conditions, critical slip field theory is applied to the optimization design to the final highwall's research. In consideration of the special engineering geological conditions and mining method based on economy, convex type slope mining scheme is presented in this paper, its main characteristic is to use such control measures local fracture zone slope angle gently, hard segment steep, to ensure that the overall slope stability, so as to ensure the effective resource development and safety production.

## Acknowledgements

This work was financially supported by National Natural Science Foundation in China (41172250), Scientific Support Project of National Twelfth Five-year (2012BAK09B06), Beijing innovation team upgrade project (IDHT20140501), Construction of Beijing Scientific Research Base-Scientific Research Innovation Platform, and Beijing Science and Technology Achievement Transformation Project.

## References:

[1] DaYong ZHU, Qihu QIAN, Zaosheng ZHOU et al. Slope critical sliding field Based on the residual thrust method[J]. Chinese Journal of Rock Mechanics and Engineering.1999,18(6):0667～0670.

[2] Shiguo SUN, Qifa RAN, Guozu LI. Method of optimum design using technology of critical sliding field[J]. China Mining Magazine,2006,15(8):0072～0074.

[3] DaYong ZHU, Hongdao JIANG. Method and application of Slope critical sliding field(Ⅰ)—theoretical basis[J]. 2000,20(3):0063～0066.

[4] Deyi JIANG, Hehua ZHU, Yungui DU. Slope stability analysis and landslide prevention[M]. Chongqing University Press:ZHANG Ge-sheng,,in 2007 2nd Edition.

[5] DaYong ZHU, Zaosheng ZHOU. Slope globally critical slip field (GCSF) theory and engineering application[J]. China Civil Engineering Journal. 1999,32(3):0066～0072.

[6] Shiguo SUN, Yinghui CUI. The application of critical slip field method in Buzhaoba open-pit slope[J]. Morden Mining,,2010(5):0067～0069.

[7] Jiachen WANG, Jingzhong DU. Level convex type slope failure analysis[J]. Journal of China University of Mining and Technology. 1992,21(2):0102～0107.

[8] Lielie LI. The study on the analytical method and numerical simulation of three-dimensional convex curve slopes[D]. Master thesis, Central South University,2011.

*Applied Mechanics and Materials Vols. 580-583 (2014) pp 760-766*
*© (2014) Trans Tech Publications, Switzerland*
*doi:10.4028/www.scientific.net/AMM.580-583.760*

# Theoretical Analysis on Underwater Vibrating Compaction Technology of Scattering-filling Rubble Stone Layer

Jianbao Fu [1,a], Shuwang Yan [2,b] and Zhijun Chen[3,c]

[1] School of Civil Engineering, Tianjin University, Tianjin 300072, China
CCCC Tianjin Port Engineering Institute Co., Ltd. , Key laboratory of Port Geotechnical Engineering of the Ministry of Communication, Key laboratory of Port Geotechnical Engineering of Tianjin, Tianjin, 300222, China
[2] School of Civil Engineering, Tianjin University, Tianjin 300072, China
[3] CCCC Tianjin Port Engineering Institute Co., Ltd. , Key laboratory of Port Geotechnical Engineering of the Ministry of Communication, Key laboratory of Port Geotechnical Engineering of Tianjin, Tianjin, 300222, China
[a]fujianbao@tpei.com.cn, [b]slq0532@126.com, [c]chenzhijun@tpei.com.cn

**Keywords:** Underwater vibrating compaction; Scattering-filling rubble stone layer; Effect analysis of parameters; Theoretical analysis.

**Abstract.** This paper studied on the underwater vibrating compaction technology of scattering-filling rubble stone layer. At HongKong-Zhuhai-Macao bridge project, in order to satisfy the project time limit, underwater vibrating compaction technology with hydraulic hammer instead of conventional dynamic compaction technology was used to tamp scattering-filling rubble stone layer with no dead angle in a short time. Owing to the shortage of engineering example, the theoretical analysis was needed before field application. In this paper, the rubble stone layer and the vibration system were simplified to a mechanical model. Vibration system's work on rubble stone was obtained by mathematical derivation, and effects of parameters were analyzed. The result shows that work on scattering-filling rubble stone layer increases with the increase of system quality, equivalent damping, exciting force and angular velocity and decreases with the increase of equivalent stiffness, water stiffness and buoyancy.

## Introduction

To promote economic development, Chinese government invested about 700 billion yuan to build the HongKong-Zhuhai-Macao bridge[1]. In the project, the foundation treatment in immersed tube section of tunnel and islands project used stone bed compaction technology. The total length of stone bed is about 4.8 kilometers. The width is about 42 meters. The thickness is about 1.9 meters. On the stone bed, there is scattering-filling rubble stone layer with 0.6 meters thick. The maximum water depth of the scattering-filling rubble stone layer is 44 meters. The scattering-filling rubble stone layer should be tamped to make it more compact and smooth.

Figure 1 The vibrating compaction system

Conventional dynamic compaction technology could not tamp the scattering-filling rubble stone layer with no dead angle in a short time due to the project construction period. Therefore, a new underwater damping method was needed. The construction unit of the bridge was to be used

underwater vibrating compaction method with hydraulic hammer. The vibrating compaction system is shown in Fig. 1. Owing to the shortage of engineering example, the theoretical analysis was needed before field application.

In this paper, the scattering-filling rubble stone layer and the vibrating compaction system were simplified as a mechanical model. The work equation was obtained through mathematical derivation. And effects of system parameters were analyzed. The work of this paper provided theoretical support for underwater vibrating compaction technology.

## Establishment and Solution of the Vibration Equation

Supported by available literature [2-4], the vibrating compaction system and the rubble stone layer were equivalent to a simplified model which was composed of quality, spring and damping.

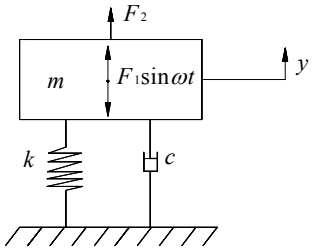


Figure 2 Simplified mechanical model

Fig. 2 shows the simplified mechanical model. In the model, the positive direction of vertical displacement is upward. In Fig. 2, parameter $m$ is compaction system quality. Parameter $k$ is equivalent stiffness of rubble stone layer. Parameter $c$ is system equivalent damping. Parameter $c$ contains two parts: equivalent damping of $c_1$ rubble stone layer and water damping $c_2$. Parameter $F_1$ is exciting force amplitude. Parameter $F_2$ is buoyant force of compaction system. Parameter is angular velocity.

According to the vibration model, the vibration equation was established.

$$my'' + \left(c_1 + c_2\right) y' + ky = F_2 - W + F_1 \sin \omega t \,. \tag{1}$$

The characteristic equation of Eq. 1 is shown in the following equation.

$$r^2 + \frac{c_1 + c_2}{m} r + \frac{k}{m} = 0 \,. \tag{2}$$

According to the practical engineer, the following equation can be obtained.

$$\left(\frac{c_1 + c_2}{m}\right)^2 - 4\frac{k}{m} = \frac{\left(c_1 + c_2\right)^2 - 4mk}{m^2} < 0 \,. \tag{3}$$

Then Eq. 2 has two conjugate complex roots as following equation.

$$r_{1,2} = \frac{-\left(c_1 + c_2\right) \pm i\sqrt{4mk - \left(c_1 + c_2\right)^2}}{2m} \,. \tag{4}$$

General solution of the homogeneous equation corresponding to Eq. 1 is shown in Eq. 5.

$$Y = e^{\alpha t}\left(C_1 \cos \beta t + C_2 \sin \beta t\right) \,. \tag{5}$$

In Eq. 5, $C_1$ and $C_2$ are arbitrary constants. $\alpha = -\frac{(c_1 + c_2)}{2m}$, $\beta = \frac{\sqrt{4mk - (c_1 + c_2)^2}}{2m}$.

Because $\pm i\omega$ are not the roots of the characteristic equation, Eq. 1 has the following special solution.

$$y = Q + R_1 \cos \omega t + R_2 \sin \omega t . \tag{6}$$

$$y' = -\omega R_1 \sin \omega t + \omega R_2 \cos \omega t . \tag{7}$$

$$y'' = -\omega^2 R_1 \cos \omega t - \omega^2 R_2 \sin \omega t . \tag{8}$$

Substitute above three equations into Eq. 1. Then the following equation will be obtained.

$$\left(kR_1 - m\omega^2 R_1 + (c_1 + c_2)\omega R_2\right)\cos \omega t + \left(kR_2 - (c_1 + c_2)\omega R_1 - m\omega^2 R_2\right)\sin \omega t + kQ = F_2 - W + F_1 \sin \omega t \tag{9}$$

Comparing Eq. 9 on both sides, in order to make sure the equation correct at any moment *t*, the following three conditions are needed.

$$R_1 = \frac{(c_1 + c_2)\omega}{2mk\omega^2 - k^2 - m^2\omega^4 - (c_1 + c_2)^2 \omega^2} F_1 . \tag{10}$$

$$R_2 = \frac{m\omega^2 - k}{2mk\omega^2 - k^2 - m^2\omega^4 - (c_1 + c_2)^2 \omega^2} F_1 . \tag{11}$$

$$Q = \frac{F_2 - W}{k} . \tag{12}$$

Then the general solution of Eq. 1 is shown in following equation.

$$Y = e^{\alpha t}\left(C_1 \cos \beta t + C_2 \sin \beta t\right) + \frac{F_2 - W}{k} + R_1 \cos \omega t + R_2 \sin \omega t . \tag{13}$$

Initial conditions of Eq. 1 are shown in Eq. 14.

$$\begin{cases} Y\big|_{t=0} = 0 \\ Y'\big|_{t=0} = 0 \end{cases} . \tag{14}$$

According to Eq. 13 and Eq. 14, Eq. 15 and Eq. 16 will be obtained.

$$C_1 = \frac{W - F_2}{k} - R_1 . \tag{15}$$

$$C_2 = \frac{1}{\beta}\left(R_1 \alpha - \frac{W - F_2}{k}\alpha - \omega R_2\right). \tag{16}$$

Now parameters in Eq. 13 all have a clear expression. Eq. 13 is the vibration displacement.

In order to observe the variation of the displacement y, give a set of parameters: $m$=35×10$^3$ kg, $k$=4.2×10$^7$ N/m, $c_1$=1.5×10$^5$ N•s/m, $c_2$=1×10$^4$ N•s/m, $F_1$=1456 kN, $F_2$=70 kN, $\omega$ =1846π rad/min. Taken these parameters into Eq. 6, the time displacement curve will be obtained. The curve is shown in Fig. 3.

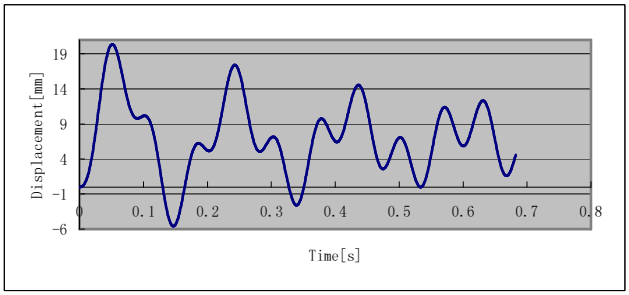


Figure 3 Displacement-time curve

In Fig. 3, the regularity of displacement-time curve is poor. It is very difficult to calculate system work according to the displacement shown in Fig. 3.

With further analysis, the displacement $Y$ can be split into two parts: $y_1$ and $y_2$.

$$\begin{cases} y_1 = e^{\alpha t}\left(C_1 \cos \beta t + C_2 \sin \beta t\right) \\ y_2 = \dfrac{F_2 - W}{k} + R_1 \cos \omega t + R_2 \sin \omega t \end{cases}. \tag{17}$$

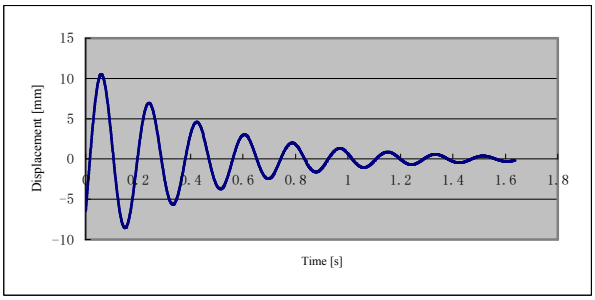


Figure 4 $y_1$ displacement-time curve

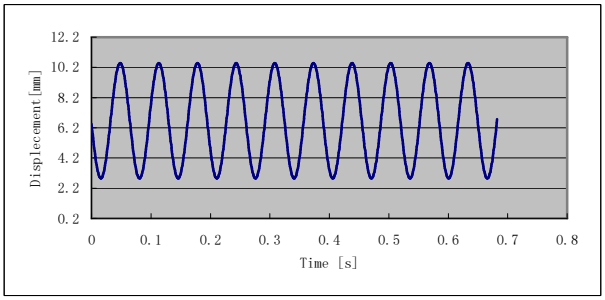


Figure 5 $y_2$ displacement-time curve

In Fig.4, the displacement $y_1$ attenuates along with time periods. Through the attenuation trend, displacement $y_1$ will attenuate to zero in a few seconds. A vibrating compaction period is at least a few minutes in practical project. So the contribution of displacement $y_1$ to the vibrating compaction process is very small. Displacement $y_1$ can be neglected in the whole compaction period.

In Fig.5, displacement $y_2$ is a harmonic function of time. It is stable in the whole compaction process. It is the steady-state response of the system. Therefore, the contribution of displacement $y_1$ is neglected, and only the contribution of displacement $y_2$ is considered in the vibrating compaction progress in this paper.

Displacement $y_2$ can be changed to Eq. 18.

$$y_2 = \frac{F_2 - W}{k} + R\sin\left(\omega t + \varphi\right). \tag{18}$$

In Eq. 18, $R = \sqrt{R_1^2 + R_2^2}$, $\varphi = \arctan\dfrac{R_1}{R_2}$.

The vibrating velocity is shown in Eq. 19.

$$v = y_2{}' = R\omega\cos\left(\omega t + \varphi\right). \tag{19}$$

In actual project, the compaction system works on the rubble stone layer when the system moves downward. When the compaction system moves upward, it doesn't work on rubble stone layer. And one part of system's work is used to overcome buoyancy and resistance of water. So the work on

rubble stone layer is equal to the difference between the work when compaction system moves upward and the work done by buoyancy and water resistance.

According to Eq. 19, in time 0~T, the time span when compaction system moves downward is $\left[\frac{\pi-2\varphi}{2\omega},\frac{3\pi-2\varphi}{2\omega}\right]$. Then the system work on rubble stone layer is shown in Eq. 20.

$$P=\int_{\frac{\pi-2\varphi}{2\omega}}^{\frac{3\pi-2\varphi}{2\omega}}\left(F_2-W+F_1\sin\omega t\right)dy_2-\int_{\frac{\pi-2\varphi}{2\omega}}^{\frac{3\pi-2\varphi}{2\omega}}c_2 v dy_2=2\left(W-F_2\right)R-\frac{1}{2}\pi F_1 R\sin\varphi-\frac{1}{2}c_2R^2\omega\pi\,. \tag{20}$$

**Determining Method of Equation Parameters**

Supported by available literatures [5], determination of equivalent stiffness is shown in Eq. (21).

$$k=\frac{1.1E}{1-\nu^2}\sqrt{BL}\,. \tag{21}$$

In Eq. 21, $k$ is equivalent stiffness and its unit is N/m. $E$ is elastic modulus and its unit is Pa. $\nu$ is Poisson's ratio. $B$ is the width of vibration plate and its unit is m. $L$ is the length of vibration plate and its unit is m.

Table 1 Interpolation table of damping ratio

| Mass ratio $b$ | Poisson's ratio | | | | | | |
|---|---|---|---|---|---|---|---|
| | 0 | 0.25 | 0.30 | 0.35 | 0.40 | 0.45 | 0.50 |
| 20 | 0.196 | 0.207 | 0.215 | 0.224 | 0.234 | 0.245 | 0.257 |
| 40 | 0.139 | 0.147 | 0.153 | 0.160 | 0.167 | 0.176 | 0.185 |
| 60 | 0.114 | 0.121 | 0.126 | 0.131 | 0.137 | 0.144 | 0.152 |
| 80 | 0.099 | 0.105 | 0.109 | 0.114 | 0.119 | 0.125 | 0.132 |

Equivalent damping can be determined by Eq. 22 [5,6].

$$\mathrm{c}=2\mathrm{D}\sqrt{mk}\,. \tag{22}$$

In Eq. 22, $D$ is damping ratio. $D$ can be determined through Table 1 with certain mass ratio and Poisson's ratio. Mass ratio $b$ can be calculated by following equation.

$$b=\frac{m}{\rho r_0^3}. \tag{23}$$

In Eq. 23, $\rho$ is the density of rubble stone layer. $r_0$ is the equivalent radius of vibration plate. $r_0=0.56\sqrt{BL}$.

Water damping is related with properties of water and the shape of vibration compaction system. The effect of system shape is even larger than water properties. The determination of water damping needs field test.

## Effects Analysis of Parameters

In order to analyze effects of parameters on system work, give a set of parameters: $m$=30×10$^3$ kg, $k$=4×10$^8$ N/m, $c_1$=1×10$^6$ N•s/m, $c_2$=1×10$^5$ N•s/m, $F_1$=1400 kN, $F_2$=60 kN, $\omega$ =1800π rad/min. Change a parameter with 10% amplitude 4 times when other parameters remain unchanged, and collect the changed parameter and corresponding system work in a vibration cycle as shown in Fig. 6~12, then effects of parameters are obtained.

Fig. 6 is the influence curve of system quality on the system work, which shows that the system work on rubble stone layer increases with the increase of system quality. But the relationship between quality and the work is not linear. The curve is downward convex. With the increasing of system quality, the influence on system work is more and more heavy.

Fig. 7 is the influence curve of equivalent stiffness on the system work, which shows that the system work on rubble stone layer decreases with the increase of equivalent stiffness. The relationship between equivalent stiffness and the system work is not linear. The curve is downward convex.

Fig. 8 is the influence curve of equivalent damping on the system work, which illustrates that the system work on rubble stone layer increases with the increase of equivalent damping. The relationship between equivalent damping and the system work is not linear. The growth of system work is smaller and smaller with the increase of equivalent damping.

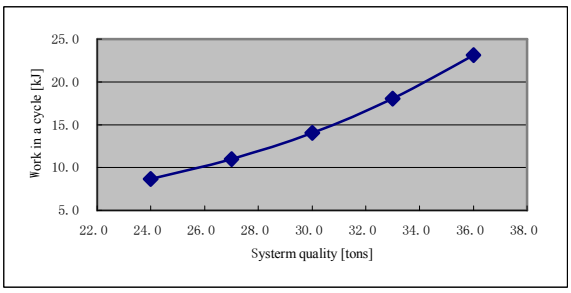


Figure 6 Effect of system quality on system work

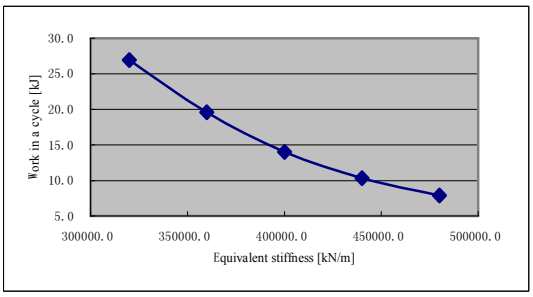


Figure 7 Effect of equivalent stiffness

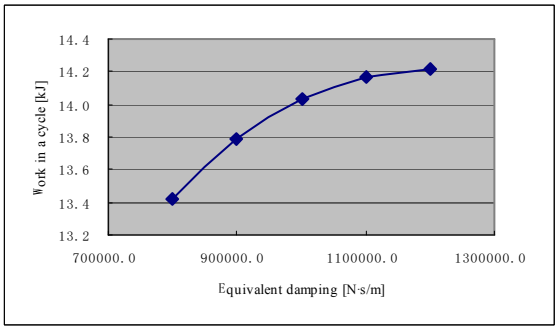


Figure 8 Effect of equivalent damping on system work

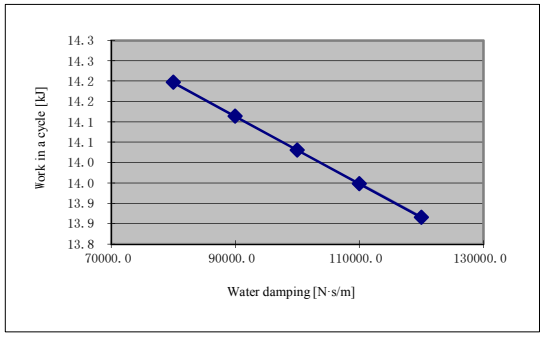


Figure 9 Effect of water damping

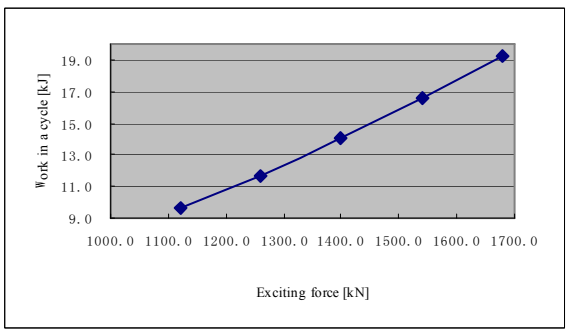


Figure 10 Effect of exciting force on system work

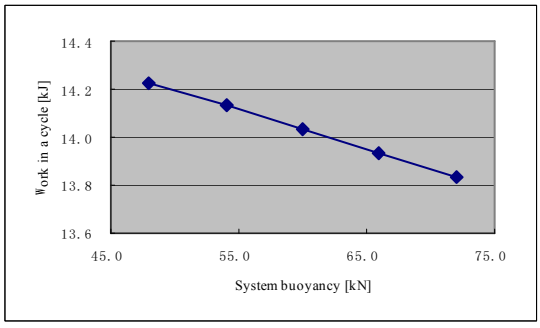


Figure 11 Effect of buoyancy on system work

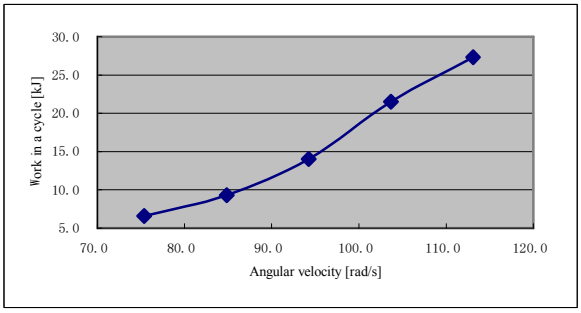


Figure 12 Effect of angular velocity on system work

Fig. 9 is the influence curve of water damping on the system work, which shows that the system work on rubble stone layer almost linear decreases with the increase of water damping.

Fig. 10 is the influence curve of exciting force on the system work, which demonstrates that the system work on rubble stone layer almost linear increases with the increase of exciting force.

Fig. 11 is the influence curve of buoyancy on the system work, which gives that the system work on rubble stone layer decreases with the increase of buoyancy. The relationship between buoyancy and the system work is almost linear.

Fig. 12 is the influence curve of angular velocity on the system work, which presents that system work on rubble stone layer increases with the increase of angular velocity. The relationship between angular velocity and the system work is not linear.

The above analysis shows that the work on scattering-filling rubble stone layer increases with the increase of system quality, equivalent damping, exciting force and angular velocity and decreases with the increase of equivalent stiffness, water stiffness and buoyancy.

## Conclusions

This paper investigated on the underwater vibrating compaction technology of scattering-filling rubble stone layer. Vibration compaction system and rubble stone layer were simplified to a mechanical model and the vibration equation was established. Through rigorous mathematical derivation, this paper gave equations of the vibration displacement, the vibration velocity and the system work on rubble stone layer. Lastly the influence of parameters on the system work was analyzed. The results show that the work on scattering-filling rubble stone layer increases with the increase of system quality, equivalent damping, exciting force and angular velocity and decreases with the increase of equivalent stiffness, water stiffness and buoyancy. This study can provide theoretical support for underwater vibrating compaction technology of scattering-filling rubble stone layer. It has important theoretical and engineering significance.

## References

[1] Information on http://www.cccchzmb.com

[2] Z.Q. Wang: *Study and practice of plate vibratory compactor*. Tianjin: Hebei University of Technology (2002). (in Chinese)

[3] Z.H. Ni: *Vibration mechanics*. Xi'an: Xi'an Jiao Tong University Press (2002). (in Chinese)

[4] Z.G. Ou: Hubei Water Power, Vol. 1 (1991), p. 10-14. (in Chinese)

[5] Y. Ouyang: *Optimization design and simulation analysis of high power vibratory plate compactor*. Xi'an: Chang'an University (2006). (in Chinese)

[6] S.Y. Zhang: Construction Machinery and Equipment, Vol. 1 (1998), p. 5–8. (in Chinese)

*Applied Mechanics and Materials Vols. 580-583 (2014) pp 767-773*
*© (2014) Trans Tech Publications, Switzerland*
*doi:10.4028/www.scientific.net/AMM.580-583.767*

# Three-Dimensional DEM Numerical Simulation of Rock Failure Progress with Different Microscopic Heterogeneities

He Chen[1,2,a *], Rui Fang[1,2,b], Ya Jun Li[1,2,c] and Fa Chun Zhang[1,2,d]

[1] National engineering laboratory for surface transportation weather impacts, Kunming, Yunnan, 650041, China;

[2] Yunnan planning, design and research institute of transportation, Kunming, Yunnan, 650041, China;

[a]2012_chenhe@tongji.edu.cn, [b]1134524638@qq.com, [c]5754419@qq.com, [d]735705125@qq.com

**Key words**: heterogeneity; crack propagation; macroscopic property; failure characteristic

**Abstract**: A three-dimensional DEM numerical model for analyzing rock failure process was developed by taking heterogeneities on microscopic scale into account with statistical mechanic. Failure processes of a series of rock samples with different heterogeneities were numerical simulated by uniaxial compressive tests. The influences of microscopic heterogeneity on macroscopic mechanical properties and failure behaviors were investigated. The results demonstrate that the numerical tests are able to illustrate the crack propagation occurring in different stages, and to predict the characteristic stresses and strains. With the increasing of heterogeneity index, except for Poisson's ratios and crack damage strains that almost maintain constant, deformation parameters as well as characteristic stresses and strains increase following exponent functions. As heterogeneity increases, elasticity deformation of rock samples becomes longer, volume compression reduces, brittle failure characteristic presents more significant, failure mode changes from "X" pattern to coalescence surface pattern forming through the whole rock samples.

## Introduction

Rock can be represented as an assembly of cemented mineral grains which can be described by its internal microstructures. The intact crystalline rock consists of a variety of mineral grains of different sizes, and of close contacts between mineral grains and microscopic defects in the form of cracks and holes [1]. Such microscopic structure causes rock to be a heterogeneous material. Heterogeneity is one of most important factors determining mechanical behaviors of rocks. Hence, taking heterogeneity into account for an investigation on rock failure process is a fundamental research for rock engineering.

However, heterogeneity is difficult to be described in laboratory even with the most advanced techniques. Therefore, some researches have been carried out concerning methods to mimic heterogeneity. Tang et al. [2] studied the failure processes of rock specimens with different heterogeneities under uniaxial compressive loading using a rock failure process analysis code (RFPA2D) by assuming mechanical properties subordinate to a statistical distribution. Ke et al. [3] studied the effects of mesoscopic heterogeneous material parameters on macroscopic mechanical behavior by employing a virtual internal bond model. Luo et al. [4] carried out an investigation into relationship between macroscopic and mesoscopic mechanical properties of heterogeneous rock materials based on types and contents of minerals. Lan et al. [1] developed a grain-based universal distinct element model and studied crack propagation in brittle rock samples with different heterogeneities. Xu et al. [5] studied mesoscopic structures of heterogeneous materials based on digital image processing technique. The macroscopic heterogeneity performed by rock samples under uniaxial or biaxial compressive loading is primarily caused by microscopic heterogeneity. Hence, numerical simulation method which is able to take microscopic heterogeneity into account is regarded as an effective tool for investigating rock mechanical behaviors. However, most researches were carried out using two-dimensional numerical model, which is not able to reflect the spatial distribution of heterogeneity.

Continuum medium models based on the assumption of homogeneity are not be able to describe local failure caused by heterogeneity of rock itself [3]. In comparison, Distinct element method (DEM), developing for analyzing rock mechanical behaviors originally, is a suitable method for studying the failure behavior of rock and describing crack propagation and rock fracture both from the macroscopic and microscopic point of views. In addition, DEM is able to deal with material failure from micro crack to macro failure and does not require the formulation of complex constitutive models. This method is therefore often used to investigate mechanical behavior and failure mechanism of rocks recently. The bonded particle model (BPM) proposed by Potyondy and Cundall [6] has drawn attention for its ability to reproduce the main mechanical behavior of Lac du Bonnet granite using DEM uniaxial and triaxial compression tests. Wang and Tonon [7]developed a distinct element code and applied it to model the mechanical behavior of a crystalline rock such as Lac du Bonnet granite. Christian et al. [8] proposed a progressive failure model and reproduced many features observed during rock failure experiment.

The approach and benefits of DEM are compelling, but the literature using this method to study the effects of heterogeneity on rock mechanical behaviors is rarely reported.

Thus, based on statistics characteristic of microscopic mechanical properties in rock material [9], a statistical distribution function was used to describe heterogeneity of rock sample and implemented into three-dimensional bond contact model. A series of uniaxial compressive tests on rock samples with different heterogeneities were simulated. The effects of microscopic heterogeneity on macroscopic mechanical properties and failure processes were investigated. Some significant conclusions were obtained finally.

## DEM Numerical Method

**Mechanical Response.** The mechanical response of bond contact model was established firstly through reasonable theoretical derivation, and then it was verified by a series of laboratory tests on the cemented samples [10]. Fig. 1(a) presents the normal mechanical response which is composed of tension and compression directions. In tension, the normal contact force $F_n$ between two particles is a product of normal stiffness coefficient $\bar{k}_n$ and tension displacement $u_n$ before its value reaches the normal bond strength. When the force arrives at the normal bond strength, the bond is broken and the normal force abruptly reduces to zero. In compression, the contact force is always a product of $\bar{k}_n$ and compression displacement, $u_n$. Fig. 1(b) presents the tangential force-displacement relationship. The shear force increases linearly with the increasing of tangential displacement $u_s$ up to shear strength. After the peak value is reached, the bond breaks and tangential force drops to the residual frictional shear strength. In Fig 1(c), the mechanical response on rolling contact direction is similar to that on tangential direction, the moment, $M$, is a product of rolling stiffness, $\bar{k}_r$, and relative rolling rotation $\theta$, and then it drops to zero.

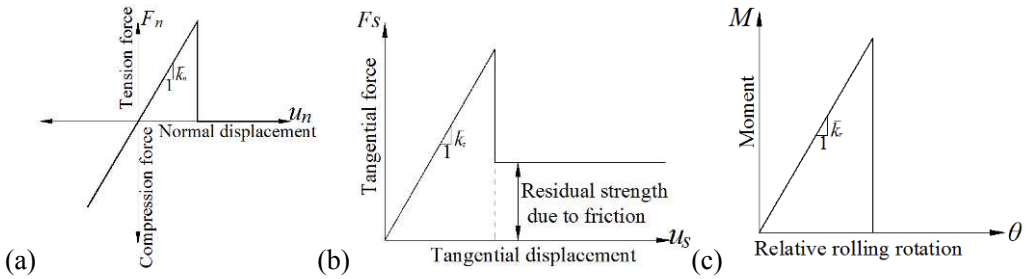


Fig. 1 Mechanical response of bond contact model: (a) normal mechanical response; (b) tangential mechanical response; (c) rolling mechanical response.

**Strength Envelope.** The normal stress and shear stress are derived by the beam theory, simplifying the microscopic bonded particles as a macroscopic beam, as shown in Fig. 2. The strength envelope bond contact model obtained by a simple transformation of the originally proposed equation is expressed by:

$$\sigma_c = -\frac{F_n}{A} + \frac{|M^s|\overline{R}}{I} \tag{1}$$

$$\tau_c = -\frac{|F^s|}{A} + \frac{|M^n|\overline{R}}{J} \tag{2}$$

where $\sigma_c$ and $\tau_c$ are the maximum tensile stress and the maximum shear stress, respectively; $A$, $I$ and $\overline{R}$ are the area, moment of inertia and radius of parallel bond, respectively.

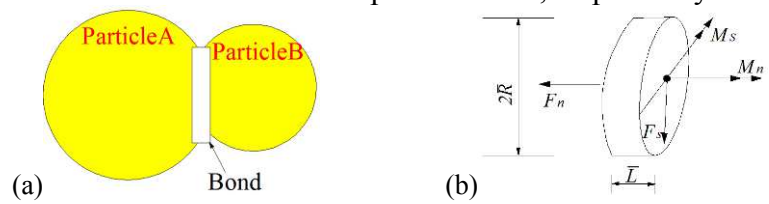


Fig. 2 Bond and its applied forces in bond contact model: (a) bond; (b) applied forces.

## Generation of DEM Rock Samples with Different Heterogeneities

DEM procedures for generating rock samples with different heterogeneities were compiled. Radius expansion method was employed to generate DEM rock samples. The samples were composed of 14923 particles with a maximum diameter of 1.05 mm, a minimum of 0.6 mm, and an average ($d_{50}$) diameter of 0.825 mm. The numerical samples are 30 mm wide, 30 mm long and 60 mm high. The initial void porosity is 0.35, which is representative of a dense sample, as shown in Fig. 3(a). After the generation, the sample was consolidated in 1D under the specific vertical pressure by lowering the top rigid wall and uprising the upper rigid wall with fixed side walls until the equilibrium state. Force distribution presenting in Fig. 3(b) shows that the force is distributed uniformly. In order to obtain densely packed and well-connected assembly, floating particles that have less than the specified contact number were deleted and simultaneously the radii were expanded aiming at increasing contact number. After these processes, the final average contact number arrived at 4.18, which satisfies the requirement of rock sample.

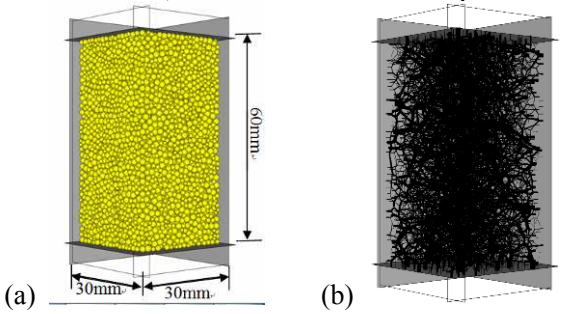


Fig. 3 DEM rock sample and force distribution

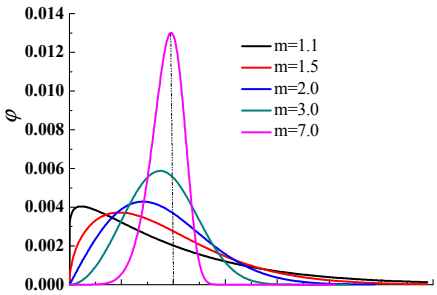


Fig. 4 Weibull distributions

Table 1 Microscopic parameters used in DEM simulation

| particles | | | |
|---|---|---|---|
| Density $\rho_s$ | Mean elastic modulus $E_0$ | Ratio between normal stiffness and tangential stiffness $k_n/k_s$ | Friction $\mu$ |
| 2360 $kg/m^3$ | $2.0\times10^{10}$ P$a$ | 2.5 | 0.5 |
| Interparticle bonds | | | |
| Mean elastic modulus $E_0$ | Ratio between normal stiffness and tangential stiffness $k_n/k_s$ | Mean tensile strength of bonds $\sigma_0$ | Mean tangential strength of bonds $\tau_0$ |
| $2.0\times10^{10}$ P$a$ | 2.5 | $2.0\times10^{7}$ P$a$ | $6.0\times10^{7}$ P$a$ |

For heterogeneity, the material properties for particles and interparticle bonds are randomly distributed throughout the samples by following a Weibull distribution:

$$\varphi = \frac{m}{\sigma_0}\left(\frac{\sigma}{\sigma_0}\right)^{m-1} e^{\left[-\left(\frac{\sigma}{\sigma_0}\right)^m\right]} \tag{3}$$

where $\sigma$ is the bond strength and $\sigma_0$ is the mean strength of interparticle bonds. For an elastic modulus $E$ of particles and interparticle bonds, the same distribution is used. $m$ is homogeneity index implies a more heterogeneous material and vice versa, as shown in Fig. 4.

Tab. 1 presents the microscopic parameters for particles and interparticle bonds used in DEM simulation. According to Ref. [6], the ratios between normal stiffness and tangential stiffness for particles and interparticle bonds were chosen to be 2.5. The friction coefficient 0.5 was used for particles. The elastic and strength parameters illustrating in Tab. 1 were finally selected by adjusting microscopic parameters until the mechanical properties obtained were consistent with experimental data. Eight samples with different heterogeneity indexes, m = 1.1, 1.5, 3.0, 7.0, 15.0, 30.0, 80.0, 300.0, representing materials for relative heterogeneity to relative homogeneity (Fig. 4)

## Numerical Simulation Results

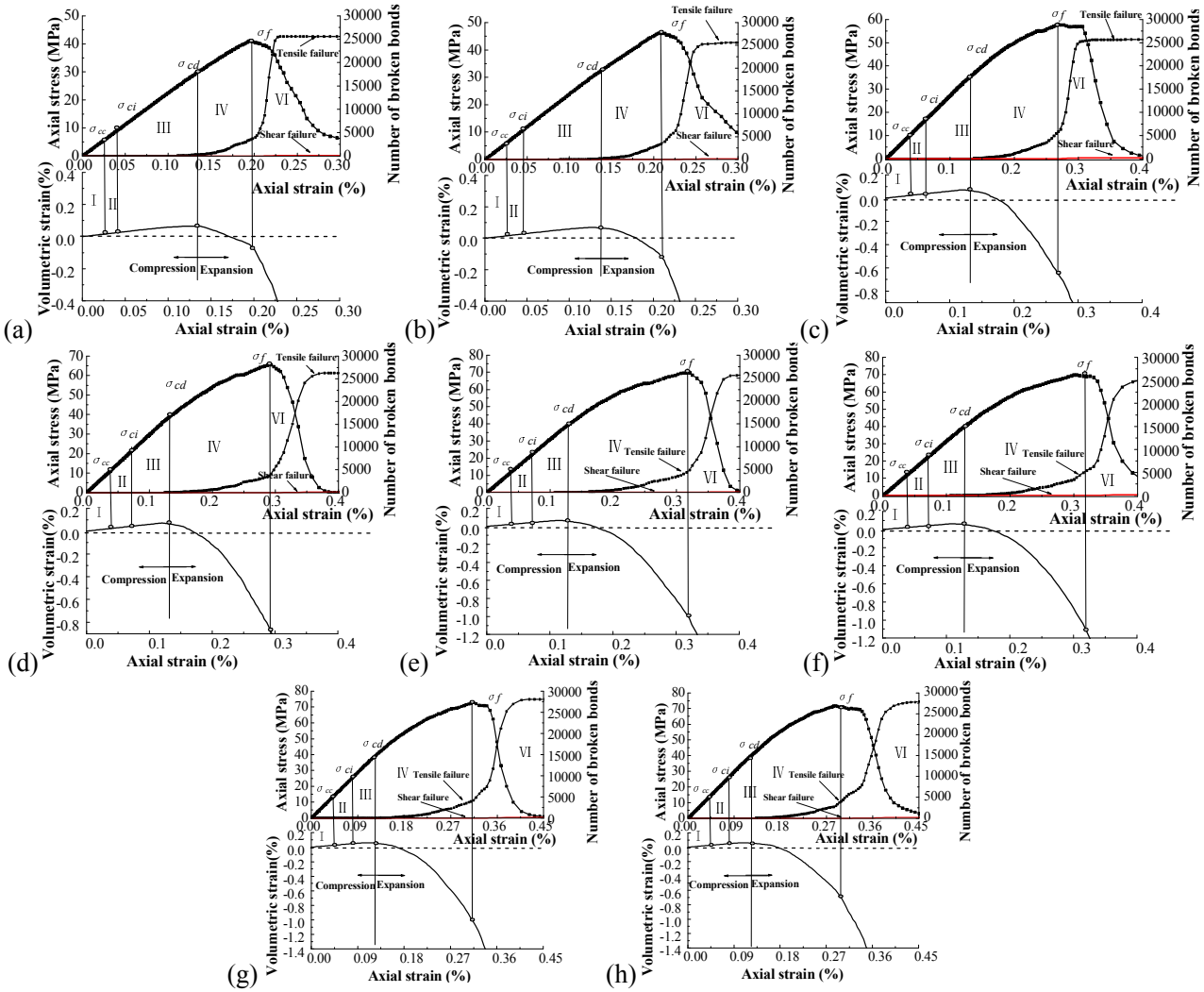


Fig. 5 Relationships between stress, the number of broken bonds, volumetric strain and axial strain obtained from DEM uniaxial compressive tests: (a) m=1.1; (b) m=1.5; (c) m=3.0; (d) m=7.0; (e) m=15.0; (f) m=30.0; (g) m=80.0; (h) m=300.0.

**Effects of Heterogeneity on Macroscopic Mechanical Behaviors.** Fig. 5 presents the stress-strain relationship and the number of broken bonds with axial strain obtained from numerical uniaxial compressive tests. The macroscopic failure of the rock samples is caused by the initiation and propagation of micro cracks which can be identified by looking at the history of the number of broken bonds in the DEM simulation (Fig. 5). In addition, all strains were computed by monitoring the motion of pairs of gauge particles that lie along the global coordinate axes at the centers of the sample faces in order to remove the influence of overlap between wall and boundary particle. The failure process of the DEM rock sample can be classified into five distinct stages as follows:

*Stage I*. Crack closure region. No crack occurs and the compression deformation is mainly from closure of original material defects. This region may or may not be present depending on the initial crack density and crack geometry. However, stress-strain relationship is almost linear which is different from experimental observation. Such discrepancy may arise from the fact that the DEM sample is consolidated before loading which leads to partial closure of initial pores.

*Stage II*. Elastic deformation region. No new cracks generate since number of broken bonds remains zero at this stage. Likewise, elastic deformability plays a dominant role because the relationships between stress, volumetric strain and axial strain are all linear.

*Stage III*. Crack initiation and stable growth region. The onset of failure indicates the start of third region and the corresponding stress is referred to as crack initiation stress, $\sigma_{ci}$, in DEM simulations. As a result of crack generation, stress and lateral strain against axial strain depart from linearity. Moreover, the volumetric strain reaches its peak value at the end of this phase due to the increasing rate of lateral strain exceeding that of axial strain.

*Stage IV*. Crack damage and unstable growth region. The axial stress level at the volumetric strain reversal marks the beginning of this stage, and it is referred to as crack damage stress, $\sigma_{cd}$. Besides, it can be observed by the slope of the number of broken bonds-axial strain curve that cracks generate rapidly, which is in good agreement with the main characteristic of the unstable crack region in real rocks.

*Stage V*. Post peak region. Appearance of the peak stress $\sigma_f$ marks the beginning of the post-peak behavior. After the peak, both lateral strain and volumetric strain responses display a continuing dilation, while a residual strength determined by friction is reached. Similarly to axial stress, the relationship between broken-bond number and axial strain tends to stabilize.

Moreover, Fig. 5 shows that crack number and type is almost unrelated with heterogeneities. As heterogeneity index increases, elastic deformation region increases, volumetric strain reduces before crack damage stress, the failure characteristic in post peak region become more significant. These conclusions drawn from Fig. 5 are in agreement with other numerical simulations [2].

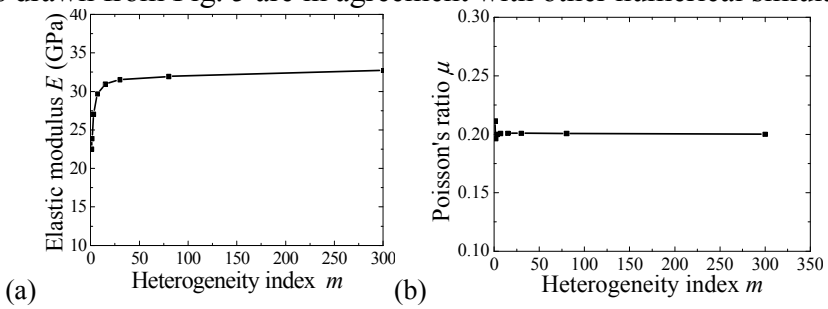


Fig. 6 Relationships between deformation parameters and homogeneity indexes: (a) elasticity modulus; (b) Poisson's ratio

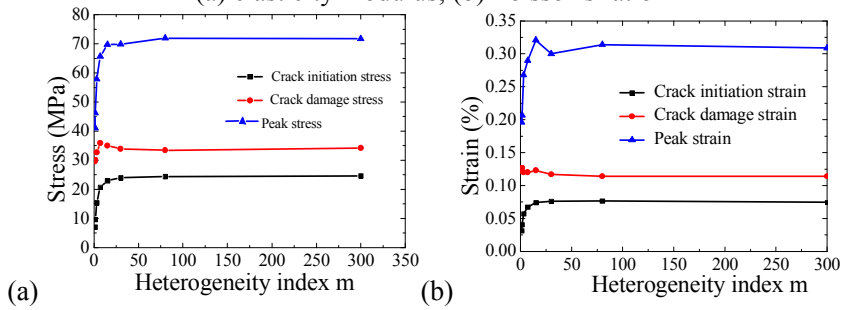


Fig. 7 Relationships between characteristic stresses, characteristic strains and homogeneity indexes: (a) characteristic stresses; (b) characteristic strains

Fig. 6 presents the relationships between deformation parameters and heterogeneity indexes. It is shown that with the increasing of heterogeneity index, elastic modulus increases rapidly first, and then reach stabilizing, but Poisson's ratio almost keeps a constant value. Fig. 7(a) shows that crack initiation stress, crack damage stress and peak stress increase with the heterogeneity index up until a constant value. In Fig. 7(b), the variation on crack initiation strain and peak strain are similar with that on stress. However, crack damage strain almost unchanged.

As mentioned above, when the heterogeneity index is higher, much more deformation and strength parameters of bonds approach mean values shown in Tab. 1. These bonds may reach limit state and break simultaneously. However, for samples with lower heterogeneity indexes, the microscopic parameters are so distinct that cracks initiate and failure surfaces develop much more easily, which causes mechanical properties lower.

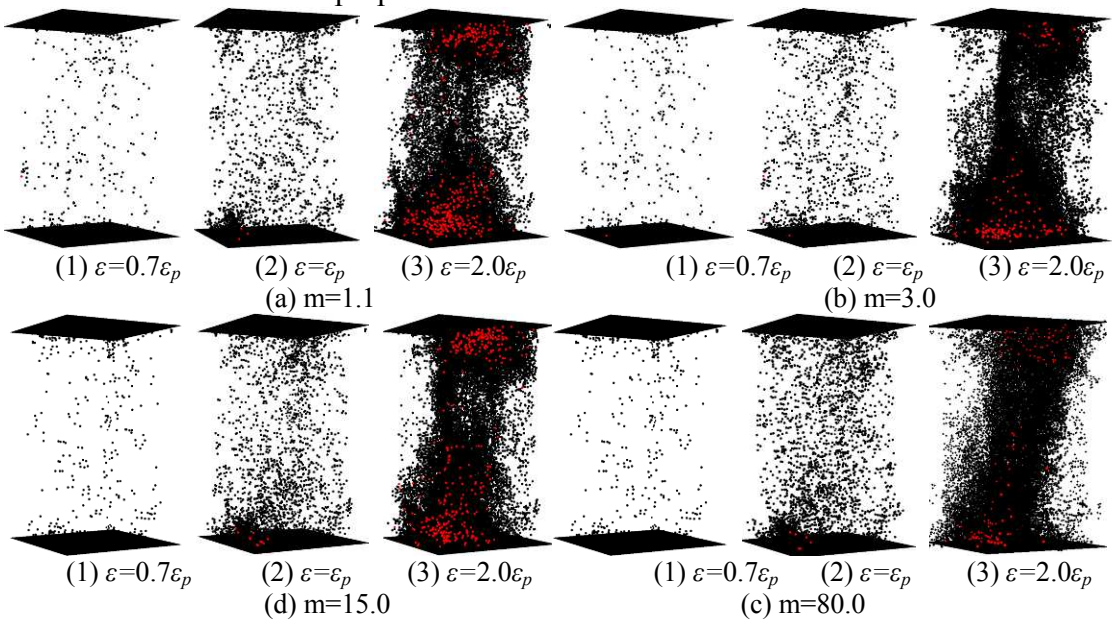


Fig. 8 Broken bond distributions of heterogeneous DEM rock samples under different axial strains

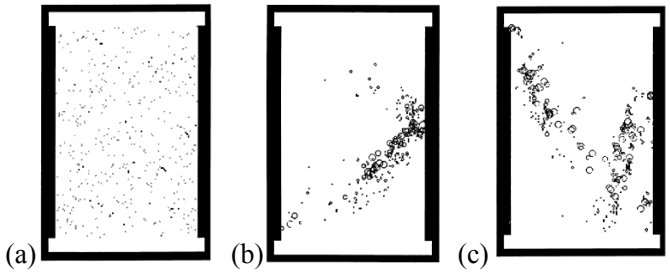


Fig. 9 Plots of simulated AE locations obtained from RFPA$^{2D}$ simulation:
(a) 56% peak stress; (b) 100% peak stress; (c) 92% peak stress [2].

**Effects of Heterogeneity on Failure Progresses.** Fig. 8 presents broken bond distributions of four heterogeneous DEM rock samples under different axial strains. $\varepsilon_p$ represents peak strain when stress reaches peak value. For broken bonds shown in Fig. 8, red indicates shear-induced bond failure for which bond shear strength has been exceeded and black implies tension-induced bond failure for which tensile strength has been exceeded.

It can be seen that the onset of failure in the samples subjected to uniaxial compressive loading is first indicated by the formation of isolated fractures caused mainly by tensile broken bonds. Such local fracturing is almost not affected by heterogeneity indexes, only results from tension stress concentration. When the strain reaches axial strain $\varepsilon_p$, broken bonds began to localize. This characteristic becomes more significant with the increasing of heterogeneity index. The broken bond distributions at the strain 2.0$\varepsilon_p$ are influenced by heterogeneity remarkably. For samples with a lower heterogeneity index, most of fractures distribute along the loading surfaces, "X" failure pattern appears. As heterogeneity index increases, fractures diffuse from ends to center, samples express coalescence surface failure mainly caused by tension-induced broken bond. The failure progress is in good agreement with other simulation as shown in Fig. 9. In rock mechanics, shale often presents local failure, while homogeneous basalt and granite presents coalescence surface failure.

## Conclusions

Three-dimensional DEM numerical model incorporated with random assignment code for taking heterogeneities on microscopic scale into account was used to analyze rock failure process. A series of rock samples with different heterogeneities were numerical simulated by uniaxial compressive tests. The influences of microscopic heterogeneity on macroscopic mechanical properties and failure behaviors were investigated. The following conclusions can be made from this study:

(1) The proposed three-dimensional DEM numerical model was successfully calibrated to match the five-stage stress-strain and volumetric strain-axial strain relationships. In addition, the recorded evolution of the number and type of bond failures not only can be used to identify crack propagation stages but also can predict the characteristic stresses and strains.

(2) Fracture number and its type developed in DEM samples are almost unrelated with heterogeneity. However, with the increasing of heterogeneity, elastic deformation region become longer, volumetric strain reduce, brittle failure characteristic after peak stress presents more significant. These results are in good agreement with other simulations.

(3) Except for Poisson's ratios and crack damage strain that almost maintain constant, deformation parameters as well as characteristic stresses and strains increase following exponent function.

(4) As heterogeneity increases, failure modes change from "X" pattern to coalescence surface pattern forming through the whole rock sample, but tension-induced cracks initiate first and the proportion of these cracks is higher.

Note that one of our main aims was to establish an effective method to describe rock heterogeneity, and apply the advantages of DEM simulation means to analyze mechanical behaviors of rock. One of our future works is to use this method to simulate boundary-value problems and compare with experiment data, such as the instability of rock slopes.

## Acknowledgements

The work reported in this paper was funded by National High Technology Research and Development Program of China (863 Program), with grant NO. 2012AA112502. The support of the Itasca Consulting Group is also gratefully acknowledged. All the supports are greatly appreciated.

## References：

[1] H.X. Lan, C.D. Martin and B. Hu: Journal of Geophysical Research, Vol. 115(2010), p. 1-14.
[2] C.A. Tang, H. Liu, P.K.K. Lee, Y. Tsui and L.G. Tham: International Journal of Rock Mechanics and Mining Sciences, Vol. 37(2000), No.4, p. 555-569.
[3] K. R. Ke, J.L. Jiang, X.R. X.R. Ge and M.L. Xiao: Chinese Journal of Rock Mechanics and Engineering, Vol. 30(2011), No. 2, p. 4093-4098. (in Chinese)
[4] R. Luo, Y.W. Zeng and X. Du: Chinese Journal of Geotechnical Engineering, Vol. 34(2012), No. 12, p. 2331-2336. (in Chinese)
[5] W.J. Xu, R.L. Hu and Y.P. Wang: Journal of China Coal Society, Vol. 32(2007), No. 4, p. 358-362. (in Chinese)
[6] D.O. Potyondy, P.A. Cundall: International Journal of Rock Mechanics & Mining Science, Vol. 41(2004), No. 8, p. 1329-1364.
[7] Y. Wang, F. Tonon: International Journal for Numerical and Analytical Methods in Geomecnanics. Vol. 34(2010), No. 5, p. 447-469.
[8] E. Christian, S. Robert and E. Peter: Granular Matter, Vol. 13(2011), No. 4, p. 341-364.
[9] J.G.M Van，V.M.R.A. Van and T.K. Wang: Mechanics of Materials, Vol. 34(2002), No. 11, p. 705-724.
[10] M.J. Jiang, Y.G. Sun, L.Q. Li and H.H. Zhu: Mechanics and Materials, Vol. 55(2012), p. 1-15.

*Applied Mechanics and Materials Vols. 580-583 (2014) pp 774-777*
*© (2014) Trans Tech Publications, Switzerland*
*doi:10.4028/www.scientific.net/AMM.580-583.774*

# Analysis of structural soil's shear strength under arbitrary degree of consolidation

Yang Liu[1, a], Chao Sun[1,b] and Shuang Li[1,c]

[1]Department of Civil Engineering, University of Science and Technology Beijing, 100083, China

[a]oceanly@gmail.com, [b]429417359@qq.com, [c]1060673242@qq.com

**Keywords:** soft clay; shear strength; structure of soft soil; degree of consolidation.

**Abstract.** Mohr-Coulomb strength theory is the most widely used in practical engineering, however, it is difficult to predict the cohesion and internal friction angle precisely. In fact, soft clay's shear strength varies with the change of stress path and consolidation history, so it is vital to predict the shear strength in different construction phases, and the influence of soil structure is necessary to be taken into consideration to predict the shear strength under under arbitrary degree of consolidation. This study proposed a simple shear strength fomula under arbitrary degree of consolidation considering the enfluce of soil structure. The derived formula is much more convenient to plug the changing strength index into program.

## Introduction

One of the most important researches of soil mechanics is the shear strength, which is used in the research of the stability of slope, the bearing strength of foundation soil and the calculation of retaining wall pressure. How to predict the shear strength's changing is vital to the practical engineering. At present, effective stress method proposed by Zen Guoxi(1975)[1] and effective consolidation stress method proposed by Zhao Lingwei and Shen Zhujiang(1962)[2], He qun(2005)[3] studied the shear strength's changing rule with the changing degree of consolidation via many soil tests. Yang Rongchang(2001)[4] studiedthe relationship between shear strength and arbitrary degree of consolidation on the base of stress path.

## Derivation of the undrained shear strength

Zen Guoxi[1] proposed a method which can predict the change of shear strength with the changing of degree of consolidation. He suggests that the shear strength of foundation soil grows continuously as the increasing degree of consolidation. The shear strength of foundation is shown as follows,

$$\tau_f = \eta(\tau_{f0} + \Delta\tau_f). \tag{1}$$

Where $\tau_{f0}$ is the natural shear strength before loading, $\Delta\tau_f$ is the increase of shear strength because of consolidation, $\eta$ is the reduction coefficient considering the shear slid

Yang Rongchang(2001)[4] get the cohesion and internal friction angle of arbitrary degree of consolidation as follows,

$$\begin{cases} \sin\phi_i = \dfrac{U_i \sin\phi_{cu}}{1-(1-U_i)\sin\phi_{cu}} \\ c_i = \dfrac{(1-U_i)(1-\sin\phi_{cu})}{1-(1-U_i)\sin\phi_{cu}} \dfrac{c_u}{\cos\phi_i} \end{cases}. \tag{2}$$

where $U_i$, $c_i$ and $\varphi_i$ is the soft clay's intensity index under the arbitrary degree of consolidation. $c_{cu}$ and $\phi_{cu}$ is the intensity index under consolidated undraind case. $c_u$ is the intensity index under unconsolidated undrained case.

The index $c_{cu}$ and $\phi_{cu}$ is obtained from consolidated undrained test. In order to find the relationship between strength under arbitrary degree of consolidation and unconsolidated undraind test index ($c_{cu}$ and $\phi_{cu}$), the relationship must be established between the index under arbitrary degree of consolidation ($U_i$, $c_i$ and $\varphi_i$) and unconsolidated undraind test index ($c_{cu}$ and $\phi_{cu}$), which has been derived by Yang Rongchang, then this paper establish the relationship between the intensity index ($c_i$ , $\phi_i$) and shear strength of soft clay under arbitrary degree of consolidation.

The angle between failure surface and the surface major principle stress surface is 45°. In Fig.1, the strength at point c is the consolidated undraind strength $\tau_c$ .

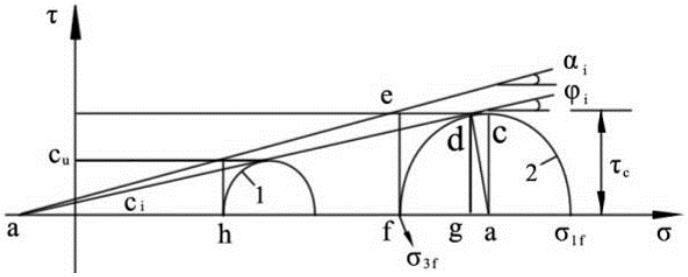


**Fig.1 The increase of shear strength under arbitrary degree of consolidation**

As shown in Fig.1, stress circle 1 is the initial state circle which correspond to the strength of natural soft clay, stress circle 2 is obtained from undraind test under the arbitrary degree of consolidation($U_i$) when the confining pressure increases by $\Delta\sigma_3$. One can obtain the follos from Fig.1,

$$fb = cb = bd = ef = \tau_c \tag{3}$$

$$af = ab - fb = \frac{bd}{\sin\phi_i} - fb = \frac{\tau_c}{\sin\phi_i} - \tau_c \tag{4}$$

$$\tan\alpha_i = \frac{ef}{af} = \frac{\tau_c}{\frac{\tau_c}{\sin\phi_i} - \tau_c} = \frac{\sin\phi_i}{1-\sin\phi_i} \tag{5}$$

$$\tau_c = af\tan\alpha_i = (c_i\cot\phi_i + \sigma_{3f})\tan\alpha_i = (c_i\cot\phi_i + \sigma_{3f})\frac{\sin\phi_i}{1-\sin\phi_i} \tag{6}$$

Formula (6) can be transferred to formula (7) ,

$$\Delta\tau_c = \frac{\sin\phi_i}{1-\sin\phi_i}\Delta\sigma_{3f} \tag{7}$$

Where $\Delta\tau_c$ is the increase of shear strength.

The soft clay always been a K0 consolidation state in field, the above formula (6) and formula (7) is limited. The general method to solve this trouble is establishing a relationship as follows,

$$\begin{cases} \sigma_{3f} = \frac{1}{2}(1+K_0)\sigma_z & (a) \\ \sigma_{3f} = \frac{1}{3}(1+2K_0)\sigma_z & (b) \end{cases} \tag{8}$$

Where $\sigma_z$ is the vertical consolidation stress. Then formula (6) can be changed to formula (9),

$$\begin{cases} \tau_c = [c_i\cot\phi_i + \frac{1}{2}(1+K_0)\sigma_z]\frac{\sin\phi_i}{1-\sin\phi_i} & (a) \\ \tau_c = [c_i\cot\phi_i + \frac{1}{3}(1+2K_0)\sigma_z]\frac{\sin\phi_i}{1-\sin\phi_i} & (b) \end{cases} \tag{9}$$

where $\sin\phi_i$ and $c_i$ is the same with formula (2). The increase of strength is obtained from formula (7),

$$\begin{cases} \Delta\tau_c = \dfrac{1}{2}(1+K_0)\dfrac{\sin\phi_i}{1-\sin\phi_i}\Delta\sigma_z & (a) \\ \Delta\tau_c = \dfrac{1}{3}(1+2K_0)\dfrac{\sin\phi_i}{1-\sin\phi_i}\Delta\sigma_z & (b) \end{cases} \tag{10}$$

**The influence of soft clay's structure on strength**

According to the influence of structure on the clay's strength, the envelope line can be assumed that the line can be divided into two parts, as shown in Fig.2. Critical stress $\sigma_{pc}$ correspond to the intersection of those two part of lines, the natural strength $c_u$ can be obtained from effective consolidation stress method, those two lines indicate three strength index ( $c_{cu1}$, $\phi_{cu1}$ and $\phi_{cu2}$ ), the first part of the line's strength index are $c_{cu1}$ and $\phi_{cu1}$, that of the second part of the line are $c_{cu2} = 0$ and $\phi_{cu2}$, then the natural structural soft soil's undrained strength can be divided into two part to be normalize.

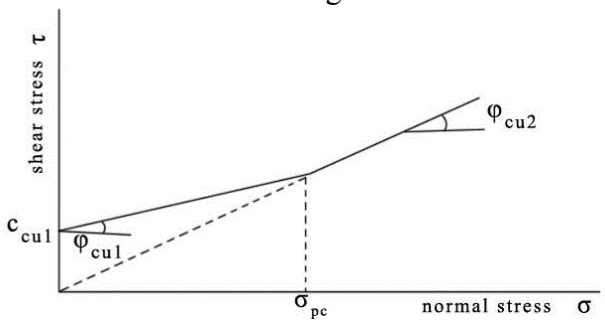


**Fig.2 The strength of structural soft clay(Shen Zhujiang, 1998)**

The strength of structural soft clay under arbitrary degree of consolidation can be wriiten as follows,

$$\tau_c = [c_i \cot\phi_i + \frac{1}{2}(1+K_0)\sigma_z]\frac{\sin\phi_i}{1-\sin\phi_i} \tag{15}$$

Where $\sigma_z$ is the vertical consolidation stress at field.

Then if $\sigma \le \sigma_{pc}$ ( $\sigma$ is effective stress, $\sigma_{pc}$ is the critical stress)

$$\begin{cases} \sin\phi_i = \dfrac{U_i \sin\phi_{cu1}}{1-(1-U_i)\sin\phi_{cu1}} \\ c_i = \dfrac{(1-U_i)(1-\sin\phi_{cu1})}{1-(1-U_i)\sin\phi_{cu1}}\dfrac{c_u}{\cos\phi_i} \\ c_u = \dfrac{\cos\phi_{cu1}}{1-\sin\phi_{cu1}}c_{cu1} + \dfrac{1}{2}(1+K_0)\dfrac{\sin\phi_{cu1}}{1-\sin\phi_{cu1}}\gamma h \end{cases} \tag{16}$$

If $\sigma > \sigma_{pc}$

$$\begin{cases} \sin\phi_i = \dfrac{U_i \sin\phi_{cu2}}{1-(1-U_i)\sin\phi_{cu2}} \\ c_i = \dfrac{(1-U_i)(1-\sin\phi_{cu2})}{1-(1-U_i)\sin\phi_{cu2}}\dfrac{c_u}{\cos\phi_i} \\ c_u = \dfrac{1}{2}(1+K_0)\dfrac{\sin\phi_{cu2}}{1-\sin\phi_{cu2}}\gamma h \end{cases} \tag{17}$$

Or

$$\tau_c = [c_i \cot \phi_i + \frac{1}{3}(1 + 2K_0)\sigma_z]\frac{\sin \phi_i}{1 - \sin \phi_i} \tag{18}$$

If $\sigma \le \sigma_{pc}$

$$\begin{cases} \sin \phi_i = \dfrac{U_i \sin \phi_{cu1}}{1 - (1 - U_i)\sin \phi_{cu1}} \\ c_i = \dfrac{(1 - U_i)(1 - \sin \phi_{cu1})}{1 - (1 - U_i)\sin \phi_{cu1}} \dfrac{c_u}{\cos \phi_i} \\ c_u = \dfrac{\cos \phi_{cu1}}{1 - \sin \phi_{cu1}} c_{cu1} + \dfrac{1}{2}(1 + K_0)\dfrac{\sin \phi_{cu1}}{1 - \sin \phi_{cu1}} \gamma h \end{cases} \tag{19}$$

If $\sigma > \sigma_{pc}$

$$\begin{cases} \sin \phi_i = \dfrac{U_i \sin \phi_{cu2}}{1 - (1 - U_i)\sin \phi_{cu2}} \\ c_i = \dfrac{(1 - U_i)(1 - \sin \phi_{cu2})}{1 - (1 - U_i)\sin \phi_{cu2}} \dfrac{c_u}{\cos \phi_i} \\ c_u = \dfrac{1}{2}(1 + K_0)\dfrac{\sin \phi_{cu2}}{1 - \sin \phi_{cu2}} \gamma h \end{cases} \tag{20}$$

The line of strength turns at the critical point, which suggests that the structure of the soft clay can't be ignored. Formulas of (16), (17), (19) and (20) are the derived expression of undrained strength under arbitrary degree of consolidation considering the soil's structure.

## Summary

This study proposed a simple shear strength fomula under arbitrary degree of consolidation considering the enfluce of soil structure.Tthe increase of the undrained strength under arbitrary degree consolidation is the same with that of effect consolidation stress method, while the derived formula in this paper is much more convenient to plug the changing strength index ($c_i$, $\phi_i$) into program combing with the formula proposed by Yang Rongchang. Soil's structure has a great influence on the strength, the strength considering this influence is obtained.

## Acknowledgements

This work was financially supported by the Youth Talent Plan of University in Beijing and Training Talents Funded by Organization Department of CPC Beijing Committee.

## References

[1] Guoxi Zeng: Foundation treatment manual: China building industry press (1988). (In Chinese)

[2] Linwei Zhao, Zhujiang Shen: nanjing hydraulic research institute (1962). (In Chinese).

[3] Qun He, Wuming Len, Limin Wei: Railway science and engineering journal, Vol.2, No.2 (2005), p.51. (In Chinese)

[4] Rongchang Yang: Journal of nanjing institute of civil engineering and architecture.Vol.4 (2001), p.20.(In Chinese)

*Applied Mechanics and Materials Vols. 580-583 (2014) pp 778-781*
*© (2014) Trans Tech Publications, Switzerland*
*doi:10.4028/www.scientific.net/AMM.580-583.778*

# Stability Monitoring Analysis on Side Slope Engineering Management of Longmenhao Primary School

Liming Wu[1,2, a], Zijian Wang[3,b],Shiyang Liu[1,c]

[1]Chongqing Jiaotong University,Chongqing 400074,China

[2]Chongqing University of Science&Technology,Chongqing 401331,China

[3]Chongqing Technology and Business Institute,Chongqing 400052,China

[a]58432053@qq.com, [b]121687678@qq.com, [c]758481739@qq.com

**Keywords:** Slope treatment, Stability monitoring, Displacement rate, Warning.

**Abstract.** Through doing spot monitoring on stability of slope engineering management of Longmenhao Primary School, this paper does analysis on monitoring data for one month. Analysis results show that all of accumulation maximum displacement, change rate of horizontal displacement and accumulation maximum settlement of slope of Longmenhao Primary School do not surpass warning value thus knowing that slope of this section is basically stable which also provides references for stability detection analysis of engineering management.

## Introduction

Cracking and settlement appeared on the ground of slope crest when 52m long and 7.5-8.0m high of cut slope were dug on the foundation trench of 1# rib-plank anchored bolt retaining wall on Tushan Road on September 21, 2013. Through actual measurement, width of the crack was 1 to 12cm and settlement was 1 to 34cm. The crack, running parallel to side slope direction, lied along the ground beam on the west side of teaching building of Longmenhao Primary School which tended to be closed from south to north. Maximum values of horizontal displacement and settlement of side slope existed between south side of it which was the original Longmenhao Kindergarten and teaching building. Pile foundation at south-west corner of teaching building was exposed. Bulge crack appeared on the rock mass of retaining wall foundation trench side slope where slope toe squeezed cut and hillslope locally collapsed. Width of deformation body range was 13 to 20m and length of it was about 60m whose horizontal displacement direction was basically perpendicular to side slope trend. This very deformation body endangered the safety of teaching building and teachers and students (including 979 students and about 80 teachers).

Fig.1 Side Slope Engineering Management of Longmenhao Primary School

**Monitoring Significance.** Rail transit Line 6 of Chongqing City starts in tea garden city sub-center of Nan'an District and ends in Beibei District whose route crosses Yangtze River and Chialing River, runs through five administrative districts of Nan'an District, Yuzhong District, Jiangbei District, Yubei District and Beibei District, connects three CBD of Danzishi, Jiefangbei and Jiangbeicheng also prospective administration center and Dazhulin, Lijia and Cai Jia Zu Tuan.

As foundation trench of track loop at the bottom of Tushan road in this project is deep, side slope height above the road is high and the section upside is teaching building of Longmenhao Primary School, disturbance during construction process would influence the teaching building thus influencing teaching security. Also because this project would plan to construct Ramp B. The minimum distance between Ramp B and house plane of Longmenhao Kindergarten in which the digging of ramp may present influences on the structure safety of kindergarten house (as shown in Fig.1). Therefore it seems particularly important to monitor the side slope of Longmenhao Primary School and Kindergarten.

**Monitoring Purposes.**Through monitoring measurement data accumulation and displacement-time curves, influencing degree of deep foundation trench of Line 6 and construction of Ramp B on side slope of Longmenhao Primary School and Kindergarten should be decided to adopt relevant protective measures in time to guarantee the safety of teaching buildings of Longmenhao Primary School and Kindergarten.

**Monitoring Work Content.**Contents of monitoring measurement on foundation trench and side slope engineering of Longmenhao Primary School in Nan'an District, Chongqing City include settlement of side slope outside teaching building, horizontal displacement of side slope outside teaching building and deep displacement of side slope outside teaching building whose time interval is September 29 - Octorber 29 during which details of the finished workload are presented in Tab.1.

Tab.1 Monitoring Measurement on Workload List of this Stage

| Sequence Number | Monitoring Items | Unit | number of the first stage |
|---|---|---|---|
| 1 | settlement of side slope outside teaching building | dot.times | 648 |
| 2 | horizontal displacement of side slope outside teaching building | dot.times | 276 |
| 3 | deep displacement of side slope outside teaching building | dot.times | 493 |

## Monitoring Program and Data Analysis on Engineering Management of Side Slope

**Settlement of Side Slope Outside Teaching Building.** Setting work of monitoring point CJ1+~CJ8 on settlement of side slope outside teaching building of Longmenhao Primary School was finished on September 28, 2013. Changing rate and accumulative variation of each observing point in the first stage are seen in Tab.1 and their relevant tendency charts are in Fig.2.

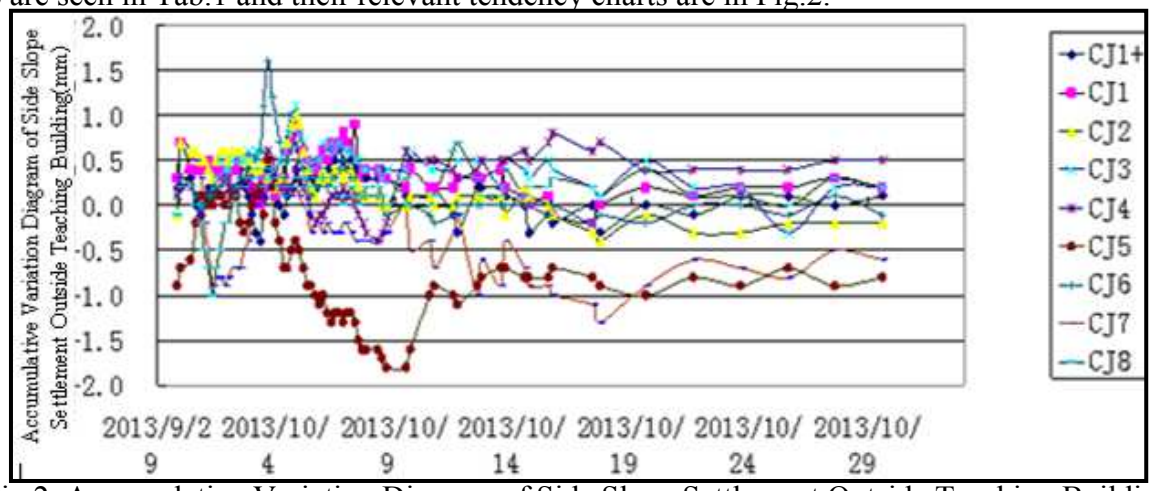


Fig.2 Accumulative Variation Diagram of Side Slope Settlement Outside Teaching Building

**Horizontal Displacement of Side Slope Outside Teaching Building.** Setting work of monitoring point W1~W4 on horizontal displacement of side slope outside teaching building of

Longmenhao Primary School was finished on September 28,2013.Changing rate in X, Y directions and accumulative variation of each observing point in this stage are seen in Tab.2 and their tendency charts are in Fig.3-Fig.4.

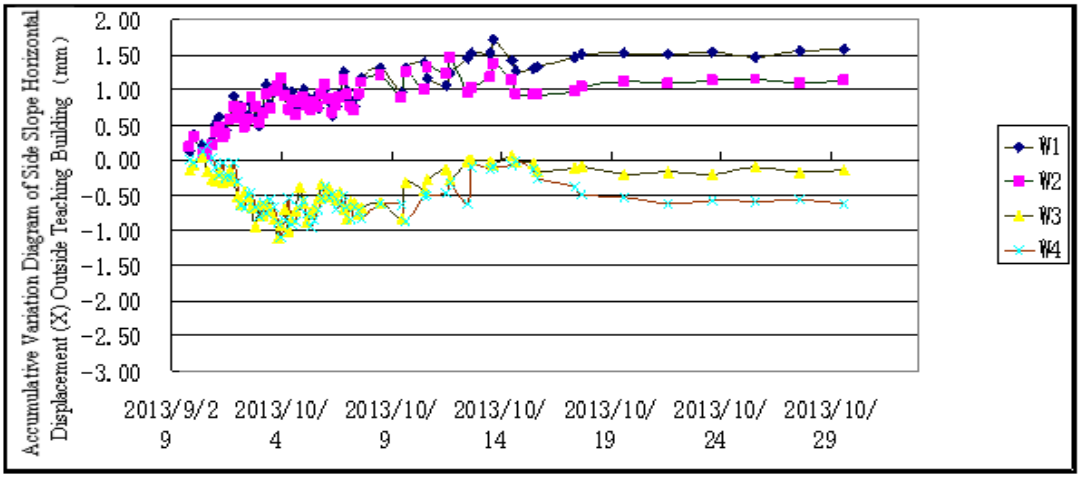


Fig.3 Accumulative Variation Diagram of Side Slope Horizontal Displacement (X) Outside Teaching Building

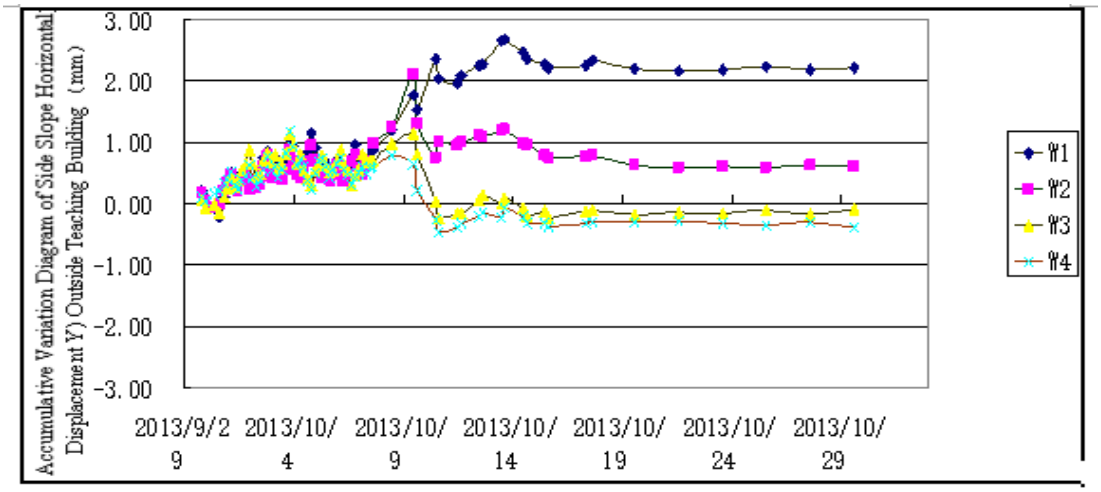


Fig.4 Accumulative Variation Diagram of Side Slope Horizontal Displacement(Y)Outside Teaching Building

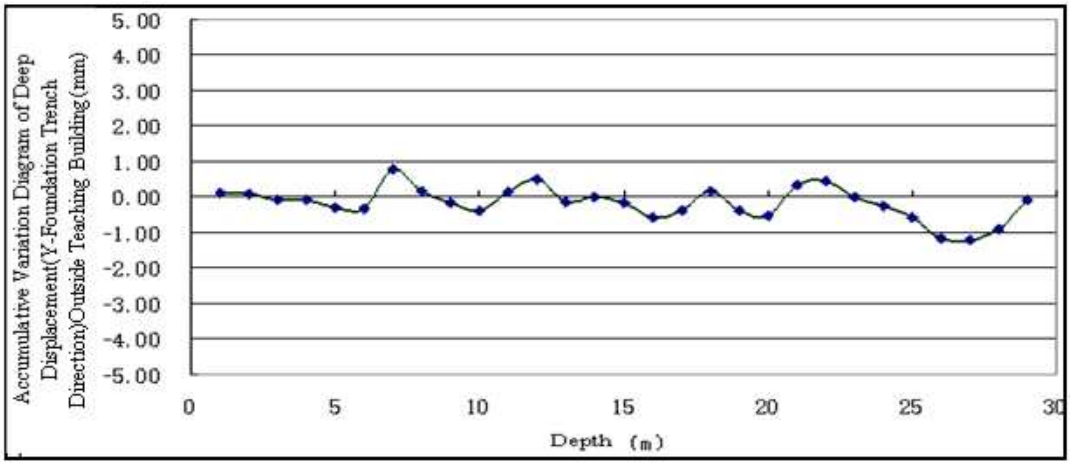


Fig.5 Accumulative Variation Diagram of Deep Displacement (Y-Foundation Trench Direction)Outside Teaching Building

**Deep Displacement of Side Slope Outside Teaching Building**. Setting work of monitoring section on deep displacement of side slope outside teaching building of Longmenhao Primary School

was finished on September 28, 2013. Changing rate in Y, X directions and accumulative variation of observing points in each depth in this stage are seen in Fig.5-Fig.6 .

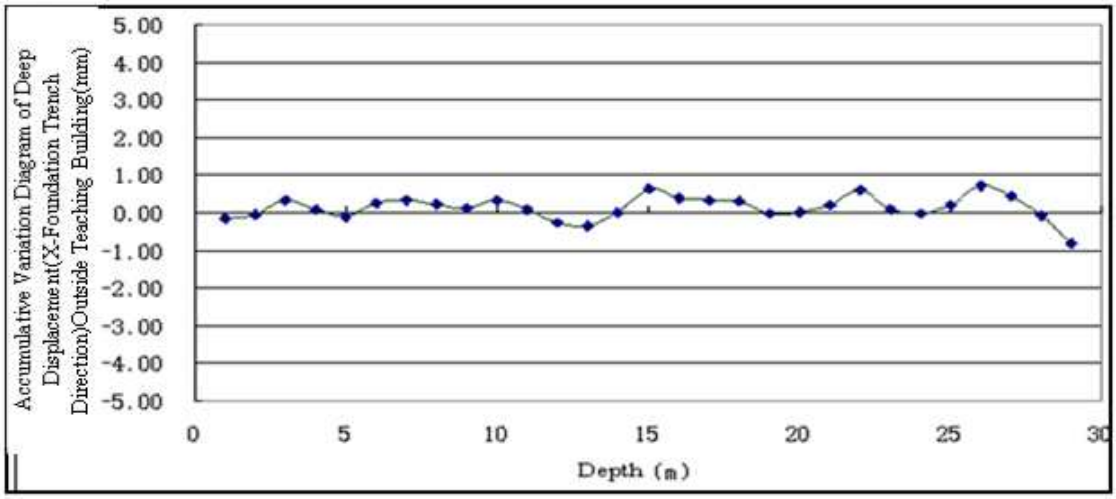


Fig.6 Accumulative Variation Diagram of Deep Displacement
（X-South Side）Outside Teaching Building

**Prewarning Value and Controlling Value of Side Slope**

According to 9.2.12 Rule in GB50843-2013 and combining with monitoring condition of site operation, it is protocoled that prewarning value of side slope displacement towards inside of foundation trench is 4mm/d whose opposite direction is 3mm/d and cumulative maximum horizontal displacement is 20mm or horizontal displacement rate keeps to be more than 2mm for three consecutive days. Meanwhile controlling value is 8mm/d whose opposite direction is 5mm/d. Prewarning value of settlement of side slope is 4mm/d whose opposite direction is 3mm/d and controlling value is 8mm/d whose opposite direction is 5mm/d.

**Summary**

Analyzing through the data above, it is seen that accumulative maximum horizontal displacement of side slope of Longmenhao Primary School does not surpass prewarning value, changing rate of horizontal displacement during consecutive days does not exceed prewarning value, settlement and horizontal displacement of side slope outside teaching building tend to be stable, changing amplitude of deep displacement of side slope is small and side slope is basically stable. Therefore it is suggested that monitoring should be continued.

**References**

[1] JGJ/T8-2007 Code for deformation measurement [S].BeiJing: China architecture&Building press,2007,9
[2] GB50330-2002 Technical code for building slope engineering[S]； BeiJing: China architecture& Building press,2002,5
[3] YS5229－1996 Code for monitoring of geotechnical engineering[S]. BeiJing:China planning press,1996,11
[4] GB50308-2008 Code for urban rail transit engineering survey[S]. BeiJing: China architecture&Building press,2008,3
[5] GB50497-2009 Technical code for monitoring of building excavation engineering[S]. BeiJing:China planning press,1996,11.2009,3
[6] JGJ120-99 Technical specification for retaining and protection of building foundation excavations[S]. BeiJing: China architecture&Building press,2012,10

*Applied Mechanics and Materials Vols. 580-583 (2014) pp 782-786*
*© (2014) Trans Tech Publications, Switzerland*
*doi:10.4028/www.scientific.net/AMM.580-583.782*

# The stability of 3D-geomat in different slope gradient

Guangyue Wang, Jianpeng Zhang and Yuanshuai Sun

School of Civil Engineering, Shandong University, Jinan, Shandong, 250061, China

wgyue@sdu.edu.cn, 569031356@qq.com,570582410@qq.com

**Keywords:** 3D-geomat; safety factor; finite element; stability

**Abstract.**3D-geomat protective slope is a new type of protective slope form which combines the 3D-geocell with the planting grass. Because the complex and dense spatial structure can tie the slope soil and has a reinforced effect on the slope surface, it has the advantage in soil and water conservation and ecological protection, and it gets more and more widely used in the present engineering construction. By using the finite element model, we compare the whole stability in the 3D-geomat slope and unprotective slope under the condition of different slope gradient. And then we get the relative results.

## Introduction

In recent years, with the development of the economic and construction in our country, the projects of highway, railway and road are increasing, a lot of artificial slope appear, but the scour erosion, soil erosion and local landslide also exist on these slopes [1].As a new type of technology in ecological slope protection, the 3D-geomat has the effect on soil and water conservation and ecological protection, and it has been developing rapidly in recent years. Liansheng Li and Yuzhong Huang get the result that the comprehensive cost of the 3D-geomat can reduce investment by 47% than other slope protection by using the method of field test [2]. Hengin Xiao, Zhao Wang and Jinfeng Zhang systematically analyzed the designed mechanics index of the 3D-geomat, and solved the corresponding problem in some extent [3]. Xiaolu Liu and Henglin Xiao detail the establishment of protection system in 3D-geoamt slope through selecting material in different slope and the grass in different areas [4]. In this paper, by using the finite element software ABAQUS, based on practical engineering, we apply the method of numerical simulation, and analyze the integrity of the slope for the presence or absence of the 3D-geomat in different slope gradient.

## The solid model in finite element

**Modeling.** The first contract section K18+132~K18+250 between Wei Jie and Ma Duan in Qing-Hong expressway uses the technology of 3D-geomat grassed slope.

The engineering parameters: the soil of slope is homogeneous; the total height is 15m; the slope angle is 40° and the type of the 3D-geomat grassed slope is EM4.

Based on the practical engineering, we use three-dimensional model, the vertical depth is 10m, the length of the slope is 15m and the height of the slope is 9m.

The geometry size is shown in figure 1(unit/m) and the three-dimensional view of the slope is shown in figure 2:

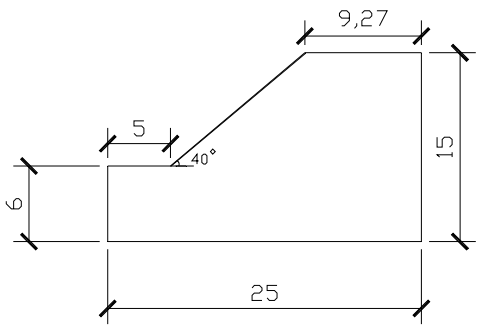


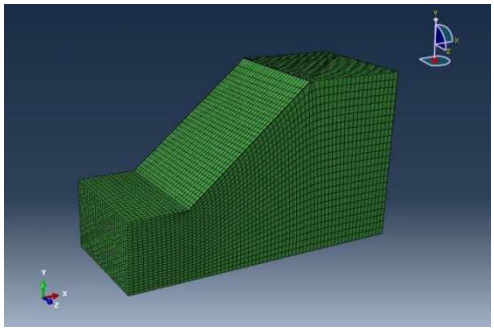

Fig.1 The geometry size of the model Fig.2 The three-dimensional view of the slope

**Mesh dividing.** The structure of 3D-geomat is a net in space. For the slope soil section, because it involves the rainfall infiltration, we use the hexahedral element--C3D8P, which possesses pore pressure degree of freedom. This kind of element has eight degrees of freedom (including pore pressure degree of freedom), the soil slope is divided into 42000 units. In order to make the calculation of the model easy to converge when simulating the numerical calculation, the continuous medium model in which the slope soil and the reinforced soil of 3D-geomat has the same nodes but varies in nature of the material is adopted. The whole model has a total of 46098 nodes. The mesh dividing of the model is shown in figure 3:

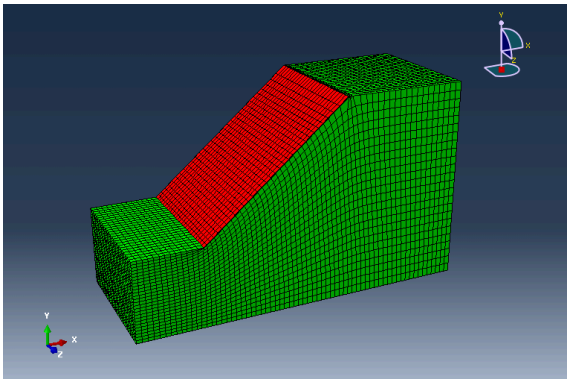

Fig.3 The mesh dividing of 3D-geomat protective slope

**Boundary conditions.** Because the slope is continuous as a whole, the model is taken as part of the overall slope to analyze, the boundary is defined as (As shown in figure 4):

(1)Limit the degree of freedom of the normal direction of the four facades.

(2)Limit the degree of freedom of three directions for x, y, z at the bottom of the model.

(3)We set the boundary conditions of the static water pore pressure that have a linear increase with depth below the water level in front facade and behind facade of the slope. The bottom, the front facade and behind facade sets the undrained boundary condition.

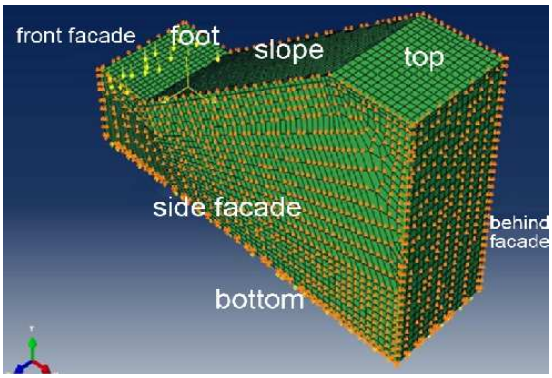


Fig.4 Boundary sketch

## The analysis of computing results

**Calculating parameter.** The calculating parameters of the model are shown in table 1

Table 1 Calculating parameters of slope model

| Material | Elasticity modulus | Poisson's ratio | Cohesive force | Internal friction angle | Dry density | Permeability coefficient |
|---|---|---|---|---|---|---|
| Soil | 20 | 0.3 | 24 | 20 | 1.81 | 1.2E-6 |
| 3D-geomat | 60 | 0.25 | -- | -- | -- | 1.2E-6 |

**The analysis of computing results in the different slope gradient.** The figure 5 gives us the changing rule of the safety factor in the different slope gradient. From the picture, we can see that along with the increase of the slope angle, the safety factor decreases accordingly, and the decrease trend of the safety factor becomes gradually slow. The variation of the safety factor is very small when the slope angle increases to 50 °.The two curves also shows that the difference of the safety factor is greater when the slope angle becomes larger. That is to say, the protecting effect of the 3D-geomat is more and more obvious with the increase of slope angle.

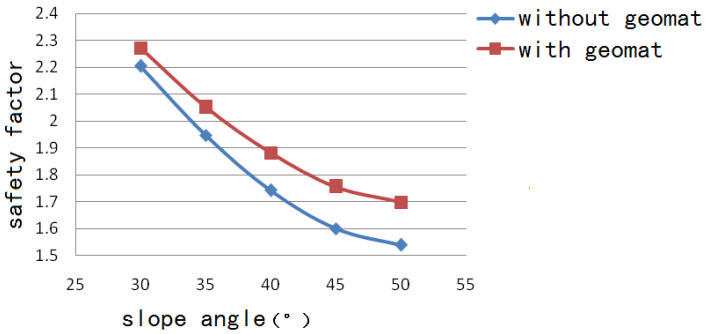


Fig.5 The changing curve of the safety factor in the different slope angle

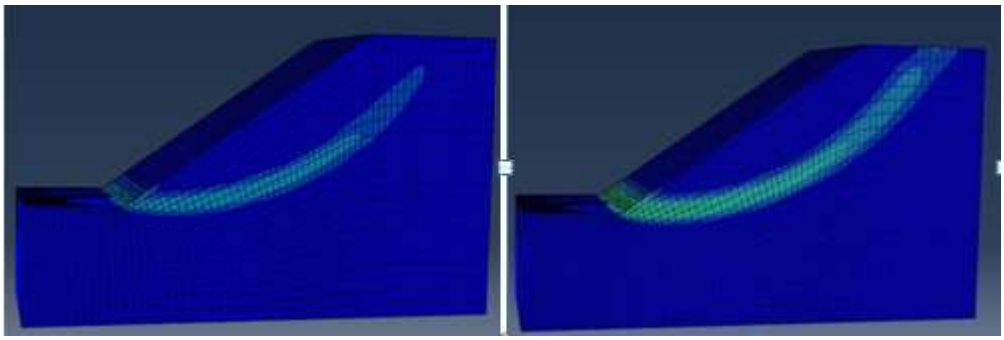

Without protection Protection with geomat

Fig.6 The comparing cloud picture in the same slope angle (35°)

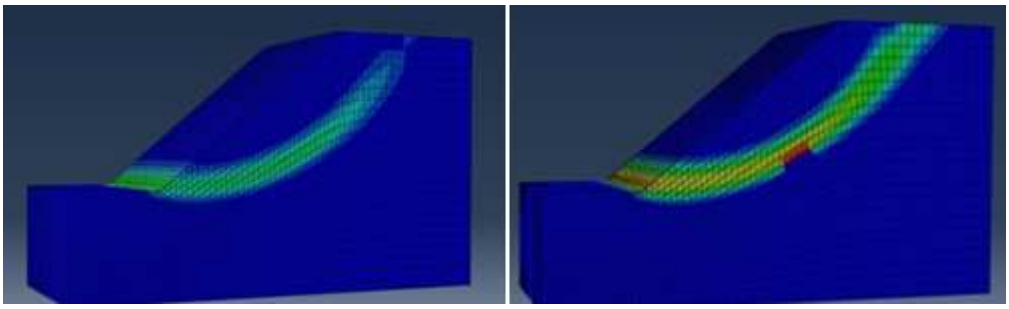

Without protection Protection with geomat

Fig.7 The comparing cloud picture in the same slope angle (40°)

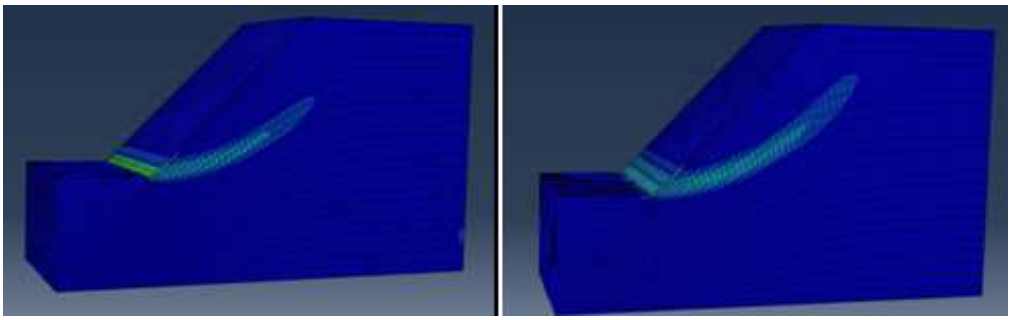

Without protection Protection with geomat

Fig.8 The comparing cloud picture in the same slope angle (45°)

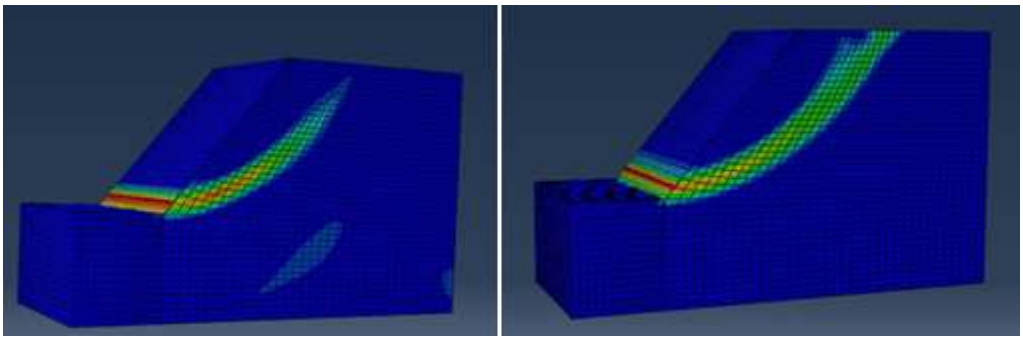

Without protection Protection with geomat

Fig.9 The comparing cloud picture in the same slope angle (50°)

According to figure 6 to 9, we know that the plastic strain range with 3D-geomat is larger than the slope without 3D-geomat under the same condition of rainfall infiltration, and the protective effect

increases with the increase of slope gradient within a certain scope of slope gradient. So the 3D-geomat has an enhanced effect on the stability of the slope.

## Conclusions

(1)The 3D-geomat has an enhanced effect on the stability of the slope.
(2)It has a significantly protective effect in the range of 30° to 50° of the slope angle.
(3) The protective effect increases with the increase of slope angle.

## Acknowledgments

This project was supported by the National Natural Science Foundation of China (Grant No.11072133).

## References

[1] Guangyue Wang, Xinghua Wang, Jinxiang Wei. the Erosion Characteristics of the Slope Surface with the Geocell[J]. Basic Science and Engineering, 2013, 21(2):249-256.
[2] Liansheng Li, Yuzhong Huang. the Application Analysis of Grassed Protective Slope with the 3D-geomat[J]. Soil and Water Conservation in China. SWCC, 2004, 8:39-40.
[3] Henglin Xiao, Zhao Wang, Jinfeng Zhang. the Research of Design Indicators about 3D-geomat[J]. Rock Mechanics and Engineering, 2004, 25(11), 1800-1804.
[4] Xiaolu Liu, Henglin Xiao. the Brief Talk about the Establishment of Protection System for 3D-geomat Slope[J]. Subgrade Engineering, 2006, 6:114-116.

*Applied Mechanics and Materials Vols. 580-583 (2014) pp 787-790*
*© (2014) Trans Tech Publications, Switzerland*
*doi:10.4028/www.scientific.net/AMM.580-583.787*

# Monitoring and Analysis on the Supporting Structure for Deep Foundation Pit

Haixia Sun [1, a], Ke Zhang [1,b], Sili Chen [1,c]

[1]Shenyang University of Technology, Shenyang 110870, Liaoning, China

[a]sunhx99@126.com, [b]805850569@qq.com, [c]chen1458@sina.com

**Keywords:** deep foundation pit, fender pile, deformation, monitoring

**Abstract.** This article mainly expounds the importance of in-situ monitoring on the construction process of deep foundation pit. Taking the deep foundation pit of some Shenyang metro station for example, the deformation features of the supporting structure and the internal and external of foundation pit is analyzed, according to the monitoring data of the fender pile displacement during the excavation of deep foundation pit. The conclusion is obtained that the timely and accurate in-situ monitoring information is necessary to guaranteeing construction safety. We should pay more attention to the excavation speed and exert the interior support timely during the excavation of foundation pit to avoid large deformation and danger. The analytical results of monitoring data shows that the whole stage of foundation pit excavation is stable and the fender pile with internal supports can guarantee the stability of foundation pit.

## Introduction

Lots of foundation pit engineering is focused on the poor geological conditions, narrow construction site, complicated construction conditions and built-up area. In this condition of the foundation pit supporting system can not only ensure the safety of the excavation and supporting structure , but also the safety and normal use of the surrounding building and municipal facilities. That is to say that environmental effects problem exists in the foundation pit engineering. Strengthen the in-situ monitoring of deep foundation pit, it is more important to guide the construction of deep foundation pit. In deep foundation pit engineering, the deformation of fender structure and foundation pit plays an important role in guiding the design and construction. Give deformation forecast for each construction stage to monitoring has more practical significance in deformation analysis, so as to make timely construction decisions, optimize the construction process, and ensure the construction safety.

## Project profile

This station adopted open construction. Hun River high floodplain, Hun River new fan, and Hun River old fan stratum consists of a set of sedimentary layer which gradually turn fine grain into coarse grain. They generally consist of clay, silt, medium sand, coarse sand, gravel, sand, gravel soil, silt and little fine sand. Local area part of the stratum is missing. The southwest of station is 5 to 7 storey residential building, the northeast is a standard factory and sanitation, and the northwest side is a hotel. The south of Road construction has 66 kv high voltage towers in the green belt. The station underground pipeline: there are 12 plastic communication cable with a diameter of 0.1 meters and gas pipe (iron) with a diameter of 0.3 meters; The sewage pipe under the middle of the north of Road Construction about 3.3 meters to the edge of the structure, there is a east-west sewer with cross-section 2.4 m×1.8 m in the south of the station about 23 meters.

The principal building envelope adopted 1000 @1200 bored piles, the pile structure diagram was shown in the fig.1.

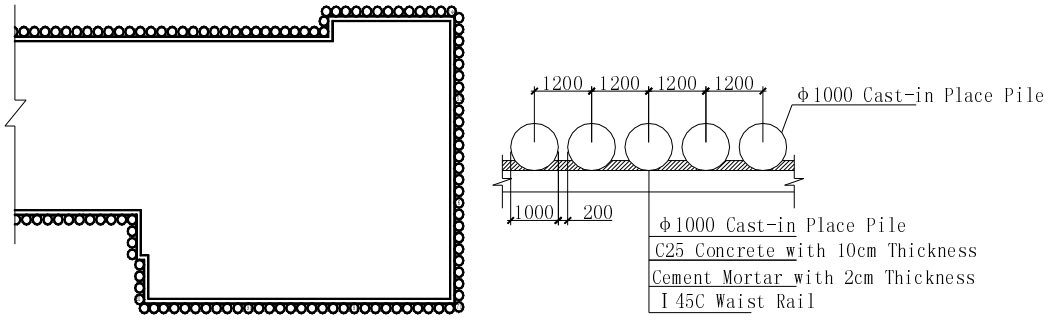


**Fig.1**. Building envelope of foundation pit

**Monitoring program of construction**

Monitor the displacement of fender piles during the metro construction, provide timely and reliable information for proprietor to assessing the environment effects of metro construction, and make a timely and accurately forecast to the possible risks of environment safety.

**Monitoring items and monitoring instrument.** Monitoring items is including horizontal displacement on the pile top and pile inclinometer. Monitoring instrument includes: Leica TCRA1201R300 total station, deformation observation for indium ruler, inclinometer ROCTEST RT-20, and dip tube;

**Measuring point layout standard.** Lay one monitoring point every 15 meters, combining with foundation pit characteristics. Monitor 3-4 times after constructing the fender pile and top beam. Monitor once during the process of foundation pit excavation every 1-2 days. Monitor once during the construction of the principal part 3-7 days.

**Monitor and control standard.** Adopt class Ⅲ monitoring and management for Code for shot crete-bolt construction method of railway tunnel(TBJ108-92) and cooperate with displacement rate as monitoring and control datum, that is to say, take three-quarters of allowed values as warning value, one third of allowed values as a reference. The values between the warning value and allowable values is called warning range, it should give warnings when the measured value is in this area, and the construction countermeasures should be discussed and adopted to prevent the end displacement more larger. In the table, $U_0$ as measured value; $U_n$ as allowable value. The foundation pit is stable if the measured value below the reference value.

**Monitoring allowable value.** Due to the foundation pit excavation depth is more than 14 meters and has pipeline and other municipal facilities in the three times of excavation depth, so the foundation pit belongs to the first level protection level in the deformation control of Shenyang metro foundation pit. In accordance with the relevant rules, regulations, similar engineering experience and relevant requirements of first level foundation pit, the engineering monitoring allowed values are shown in the following table 2.

**Table 2** Monitoring measurement value $U_n$

| Monitoring program | Monitoring Value (mm) | Design Value (mm) | The displacement rate control (mm/d) |
|---|---|---|---|
| Displacement of pile top | 30≤0.2%H | 40 | 2mm/day |

Note: H is the depth of foundation pit

The set and application of the displacement control index must be used with the displacement rate control index at the same time. Compared with the displacement, displacement rate control index has a clear physical meaning. It reflects the development trends along with the time of deformation.

**Monitoring time.** The monitoring of program conducted from April 2006 to August 2007, that is, since the construction of foundation pit building envelope until the end of the main work engineering. In implementation, each monitoring program and relevant construction process are synchronous, and

do some corresponding adjustment according to the adjustment of construction schedule to ensure the monitoring timely and accurately.

**Monitoring results and analyze**

Taking monitoring data of four stakes from No.1 to No.4 as an example in the south for example, shown in fig.2, analyze the process of foundation pit excavation and offset condition of inclinometer.

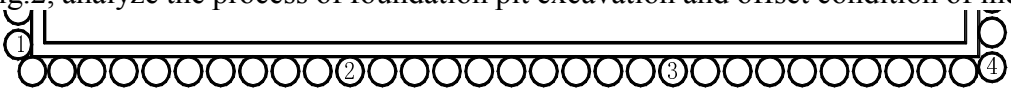


**Fig.2**. Pile position of foundation pit monitoring in the South

The offset curve obtained from monitoring of survey is shown in Fig3. The positive value indicated the displacement fronts on the inside of foundation pit, and the negative value indicated the displacement fronts on the outside of foundation pit.

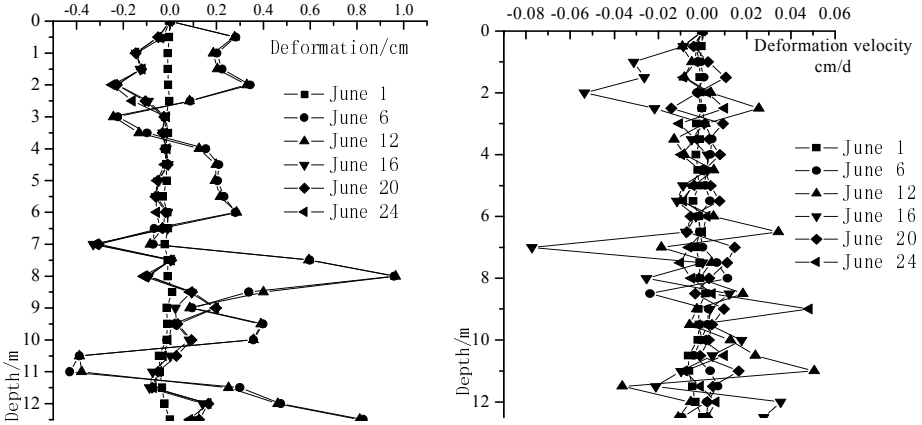


a) Deformation b)Deformation velocity

**Fig.3**. Displacement curve of 1 pile

Seen from the fig.3, in 6th of June and 12th of June appeared relatively large displacement at the depth of 8.0 meters and 12.5 meters, then the displacement tends to stability. Because the excavation depth of foundation pit is more than 10 meters, and the second corner brace steel support is not applied, resulting in larger pile displacement. Deformation is reduced and stabilized after applied corner brace 16 days later. In the June16th, the displacement velocity is fairly large at the depth near 7 meters, and the direction is to the periphery of foundation pit. This is because that the applying of the second steel supports. The accumulative displacement and displacement velocity do not exceed the limit value, and indicates the excavation of foundation pit and supports are reasonable.

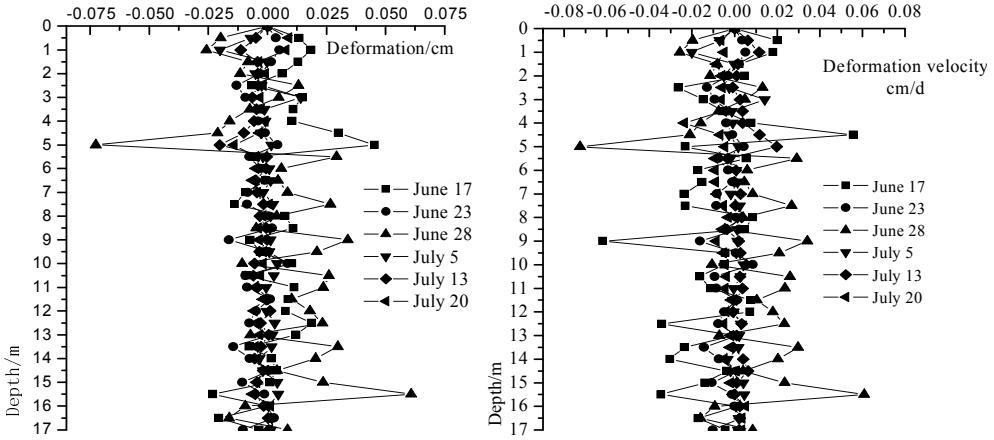


a) Deformation b)Deformation velocity

**Fig.4**. Displacement curve of 3 pile

Seen from the fig.4, at the depth of 5 meters in the foundation pit on June 17th, accumulative displacement increases suddenly, the pile deformed to the inside of foundation pit. By June 28th, the

pile caused larger deformation to the outside of foundation pit. This is because the second steel support is applied in June 28th. Meantime, at the end of pile the deformation is to the inside of foundation pit. The measurement of the displacement rate change is basically the same as the accumulative displacement trend. The accumulative displacement and displacement variation speed do not exceed the limit value.

It can be seen from the fig.5, the accumulative displacement measured on June 10th and on June 14th is larger. The largest accumulative displacement is close to 1 cm, which appeared at the depth of 8 meters. The displacement mutation also can be seen at the depth of 4 meters. After applied the second steel support on June 20th, the displacement tends to stabilize, the value is much small. The variation of displacement velocity value is very small. The accumulative displacement and displacement velocity do not exceed the limit value.

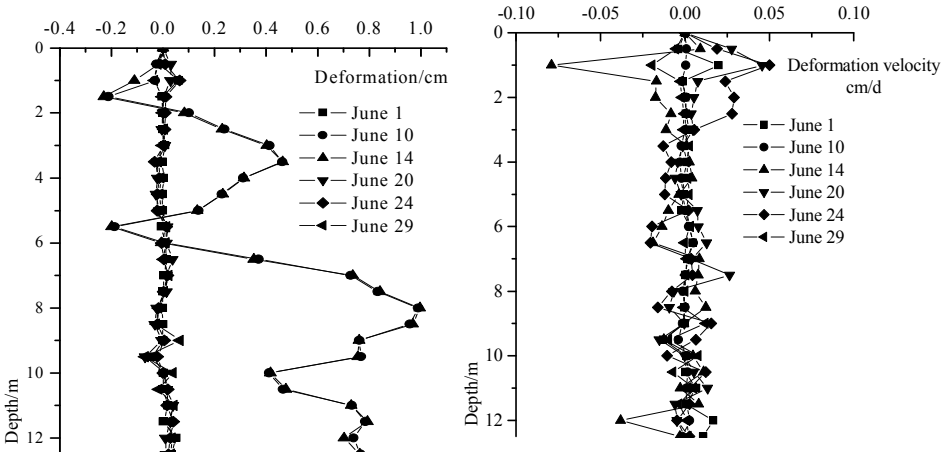


a) Deformation b)Deformation velocity

**Fig.5**. Displacement curve of 6 pile

## Conclusions

Timely and accurate in-situ monitoring information is the prerequisite to ensure the safety of construction. Excavation rate should be paid more attention during the excavation of foundation pit, and applied internal support timely in order to avoid excessive deformation and danger.

The analytical results of monitoring data shows that the whole stage of foundation pit excavation stability is good and the fender pile with internal supports can guarantee the stability of foundation pit.

## Acknowledgements

This work was financially supported by the Liaoning Provincial Education Department Scientific Research General Foundation (201164119) and the National Natural Science Foundation (51279109).

## References

[1] Cunbao He. The application of survey monitoring in construction of the deep foundation pit. Science Technology and Engineering, 2008:8 (23), 6406-6417.

[2] The ministry of railways of the People's Republic of China. Railway tunnel spray anchor construction technique rules TB10108-2002. Beijing: China railway publishing company, 2002.

[3] The ministry of construction of the People's Republic of China. Code for investigation of geotechnical engineering GB50021-2001. Beijing: China building industry press, 2001.

*Applied Mechanics and Materials Vols. 580-583 (2014) pp 791-796*
*© (2014) Trans Tech Publications, Switzerland*
*doi:10.4028/www.scientific.net/AMM.580-583.791*

# Numerical Analysis of Floatation Response of Buried Pipeline in Liquefied Soil

Deng Sunan [1,], Peng Wentao [2,a] and Lin Junqi [3,]

[1] School of Energy and Power Engineering, Wuhan University of Technology,Wuhan,430070, China

[2] School of Civil Engineering and Architecture, Wuhan University of Technology,Wuhan,430070, China

[3] Institute of Engineering Mechanics, CEA, Harbin, China

[a] pwtao2006@163.com

**Keywords:** soil liquefaction, buried pipeline, floatation response

**Abstract.** In this paper, the formulae are deduced for the floatation response of pipeline buried in liquefied soil. The beam model based on the theory of beam on elastic foundation is used for the pipeline buried in non-liquefied and liquefied soil. The soil property is nonlinear, the floating force induced by the soil liquefaction is related to the position of pipeline, is nonlinear also. For the convenience and simplification of analysis, the nonlinear increment element method was used and lots of numerical analysis was conducted, including: the floatation response of pipeline buried in homogeneous soil, the floatation response of pipeline buried in non-homogeneous soil, and the floatation response of pipeline buried in discontinuous liquefied area. The influential factors on the floatation response of buried pipeline buried in liquefied soil including spring stiff of liquefied soil, the initial deformation, the length of liquefied area, the axial force acting on the pipeline, the material of pipeline, and the diameter of pipeline. The calculation results of discontinuous liquefied area draw a significant conclusion that for a long liquefied area, to make the soil non-liquefied in the middle of liquefied area may decrease the length of liquefied area and reduce the flotation displacement of pipeline greatly.

## Introduction

Buried pipeline is the important part of city's lifeline. During an earthquake, not only the buried pipeline itself get damaged and the economical loss is large, but also the damage of buried pipeline will induce the functional loss of the lifeline system and severe secondary hazard. The earthquake field observations show that there are three major causes of damage to buried pipeline during earthquakes: soil liquefaction, fault movement and seismic ground shaking. Soil liquefaction is one of the major causes to the damage of buried pipeline. The damage investigations revealed that the damage ratio of pipeline (number of breaks/per km) has much larger values in liquefied soil compared with that in shaking ground without liquefaction. The difference of earthquake response of buried pipeline in liquefied soil and that without liquefaction lay in that, the buried pipeline in liquefied soil not only suffer the earthquake shaking acting on the pipeline along or transverse to pipeline axis, but also the pipeline suffers the floating force due to soil liquefaction. The floating force make pipeline deformed in the vertical plane along the pipeline axis, and will make the pipeline get out the ground surface, which is called pipeline floatation. The floatation response of pipeline will make pipeline seriously damaged. All the theoretical and experimental study on the floatation response have got lots of beneficial results, but some conclusion are not the same such as: the effect of the length of liquefied region on the floatation response; the effect of axis force on the floatation response; the effect of pipeline depth on the floatation response, and so on. It shows that the study on floatation response of buried pipeline in liquefied soil is complicated so that need further study and the results need to be verified in the future earthquake.

**Analysis Method**

During an earthquake, the liquefaction of soil will make the soil shear strength much smaller than that without liquefaction, and also add a floating load on the pipeline buried in, those two reasons make the buried pipeline to float upward, and the pipeline will deform upward in the vertical plane through the pipeline axis. In some situations the pipeline may partly get out of the surface of ground and get damaged seriously. So the occurrence of floatation response of buried pipeline needs two conditions: a) is that the constraint force of soil acting on the pipeline is small enough. Experimental study shows that the constraint force of liquefied soil on the pipeline is 1/3000 to 1/1000 of the value without liquefaction; and b) is that the floating force that the liquefied soil acting on the pipeline is larger than the sum of the weight of pipeline and the weight of material transported in the pipeline.

Basing on the principals of virtual work, the beam model based on the theory of beam on elastic foundation is used for the pipeline buried in non-liquefied and liquefied area (figure 1), the equilibrium equations can be write as follow:

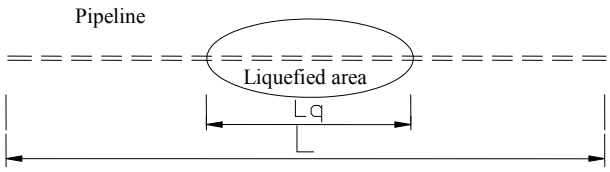


Figure 1 Pipeline buried in non-liquefied and liquefied soil

$$\int M\delta w''dx - \int \bar{N}\,\delta\varepsilon_a dx + \int P_s \delta w dx - \int P_f \delta w dx + \int P_g \delta w dx = 0 \tag{1}$$

Where,

M is the bending moment, and express as $M=EI\,w''$;
EI is the bending stiffness of pipeline section;
w is floatation response of pipeline;
$\bar{N}$ is the axial force acting on the pipeline;
Pg is the weight of pipeline and the material in the pipeline;
Pf is the floating force on the pipeline and induced by the soil liquefaction. The floating force is varied with the position of pipeline in the liquefied soil shown in figure 2. There are three occasion: a) when the pipeline is totally in the liquefied soil (w≤H-R), the floating force is $F_f = \gamma_s \pi R^2$; b) when the pipeline is partly out the surface of ground (H-R≤w≤H+R), the floating force is $F_f = A_s\gamma_s = \pi\gamma_s R^2(\pi - \varphi + \frac{1}{2}\sin 2\varphi)$; and c) when the pipeline is totally out the surface of ground (H+R≤w), the floating force is zero;

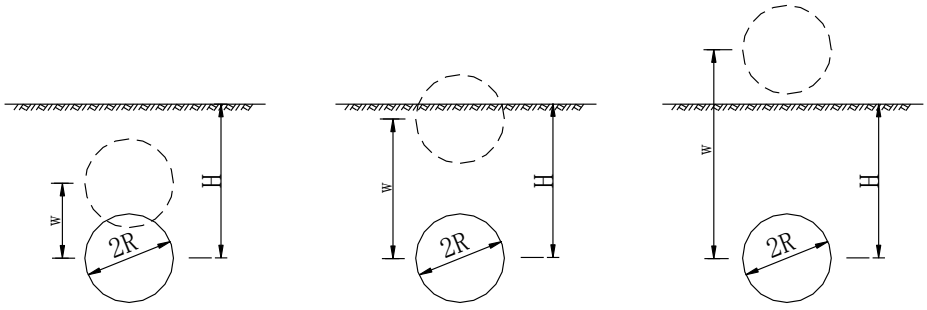


Figure 2 The positions of pipeline in liquefied soil

$\gamma_s$ is the density of liquefied soil;
H is the buried depth of pipeline;
R is the diameter of pipeline;

. $A_s$ is the sectional area of pipeline under the ground surface; and $\varphi = \frac{1}{2}\cos^{-1}(\frac{H-w}{R})$;

$\varepsilon_a = \frac{1}{2}(w'')^2$ is the axis deformation induced by the lateral deformation of pipeline;

Ps is the soil lateral constraint force on pipeline, and is nonlinear force, shown in figure 2. In the non-liquefied region, the soil lateral constraint force is express as:

$$P_s = \begin{cases} K_d w & \mathbf{w} \le \mathbf{0} \\ K_u w & \mathbf{0} < \mathbf{w} \le \bar{\mathbf{w}} \\ \bar{P}_s & \bar{\mathbf{w}} \le \mathbf{w} \end{cases}$$

where， $K_d$ , $K_u$ are the spring constants when pipeline moves down or move up respectively, $\bar{P}_s$ is the largest constraint force when pipeline moves upward, and $\bar{\mathbf{w}}$ is the displacement related with $\bar{P}_s$ . In the liquefied region, $P_s$ =0 or a very small value.

By the finite element method (see reference 1, 2, 3 for detail deduction), equation (1) change to:

$$[K_p + K_s - K_N - K_f]\{w\} + \{P_g\} - [K_p - K_N]\{w_g\} = 0 \quad (2)$$

Equation (2) can be express in increment as below:

$$[K_p - K_N]\{w_g\} - [K_p - K_N]\{w_0\} - \{P_g\} - \{P_{s0}\} + \{P_{f0}\} \ [K_p + K_s - K_N - K_f]\{\Delta w\} = \quad (3)$$

Where,

$K_p$ is the bending stiffness matrix of pipeline;

$K_s$ is the constraint stiffness matrix of soil on pipeline;

$K_N$ is the axial force stiffness matrix of pipeline or geometric stiffness matrix;

$K_f$ is the floating force stiffness matrix;

$\{\Delta w\}$ is the floatation response increment vector;

$\{w_0\}$ is the calculating floatation displacement result vector of last step, and is the input of next step;

$\{w_g\}$ is the initial deformation vector of pipeline;

$\{P_g\}$ is the weight vector of pipeline and material transported in pipeline;

$\{P_{s0}\}$ and $\{P_{f0}\}$ are the initial soil constraint vector and the initial floating force vector in the calculation step respectively, and the their values are calculated from $\{w_0\}$.

The floatation response vector $\{w\}$ is obtained by using iterative method to equation (3).

**Numerical Calculation Results**

During the calculation of the floatation of buried pipeline, the initial deformation of pipeline is assumed to be: $w_0 = A_0 \sin\frac{\pi}{L}x$ and $\theta_0 = A_0 \frac{\pi}{L}\cos\frac{\pi}{L}x$, here, L is the length of liquefied region. The convergent criterion is $|\Delta w_i| \le 0.001$. The thickness of the pipeline is 0.01m, the outer diameter of the pipeline is 0.4m, the length of the pipeline is 200m, the bending stiffness of pipeline (EI) is 2.64×108Nm2, the density of liquefied soil (γs) is 2.0×104N/m3, and the average density of pipeline (γg) is 7.65 × 103N/m3.Some calculation results of pipeline floatation response in homogenous liquefied soil are shown in figure 3 to figure 6.

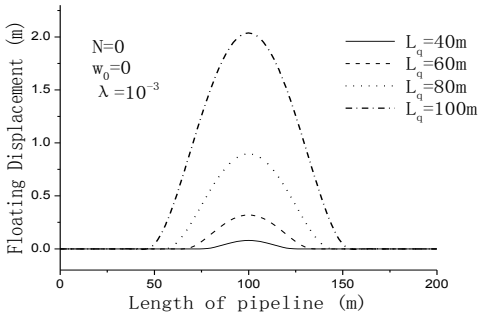


Figure 3 The effect of length of liquefied region

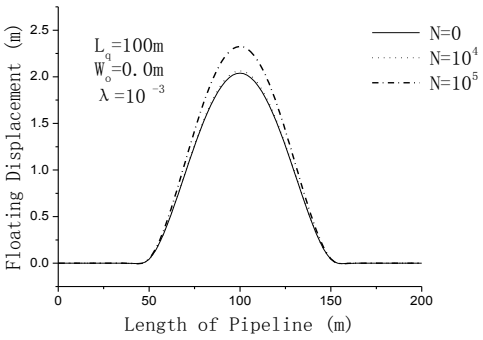


Figure 4 The effect of axial force

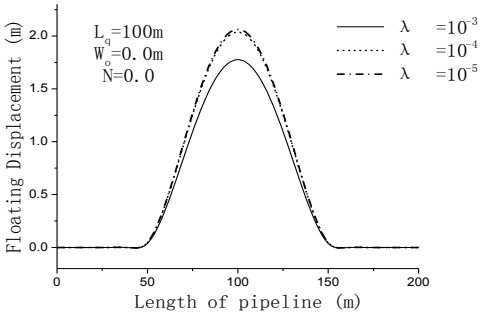


Figure 5 The effects of spring constant

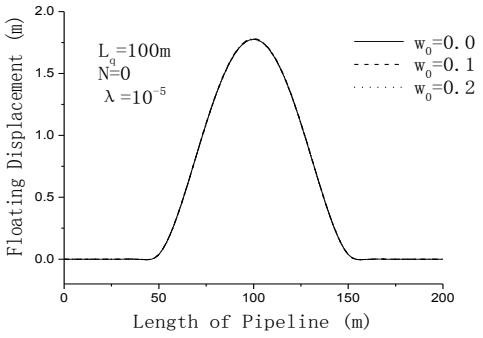


Figure 6 The effect of initial deformation

Figure 3 gives the effect of the length of liquefied region on the floatation of the buried pipeline. It shows that the floatation response varies with the length of liquefied region greatly, a smaller length of liquefied region gets a smaller floatation, and this is in agreement with the experimental results [4], but as the length of liquefied region gets larger, the floatation becomes larger rapidly, and this can not be simulated in the laboratory test. Figure 4 gives the results of the effect of axial force on the floatation response. It can be seen form figure 4 that the floatation response of buried pipeline gets lager when the axial force gets larger, and when the axial is too large, the pipeline would be unstable, and the iteration procedure is not convergent. Figure 5 gives the effect of the spring constant of liquefied soil on the floatation of pipeline, and it shows that a lower spring constant makes the floatation lager. Figure 6 gives the effect of initial deformation on the floatation, and shows that the initial deformation of the pipeline has little effect on the floatation of buried pipeline. From the calculation, it can be seen that the bending strain is larger when the length of liquefied region and the axial force get lager.

Figure 7 to figure 11 give the calculation results of pipeline floatation buried in two different liquefied soils. Figure 7 gives the effects of two kinds of soil constraint on the floatation response. It can be seen that the maximum flotation displacement occurs in the area with smaller soil spring stiffness. The effects of nonlinear soil constraint and the initial deformation, the length of liquefied area, and the axial force acting on the pipeline is the same as in homogenous soil.

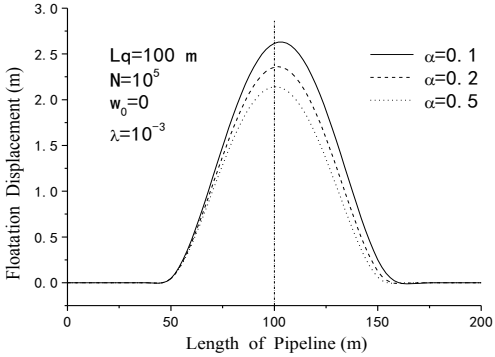


Figure 7 The effect of soil property

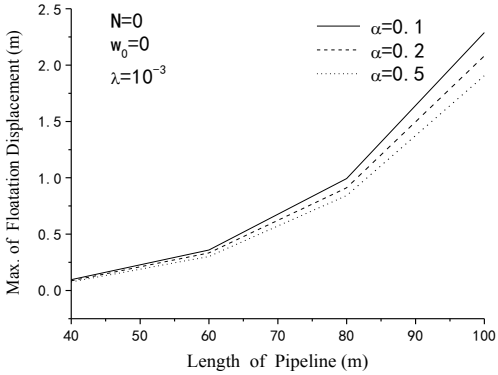


Figure 8 Effect of length of liquefied region

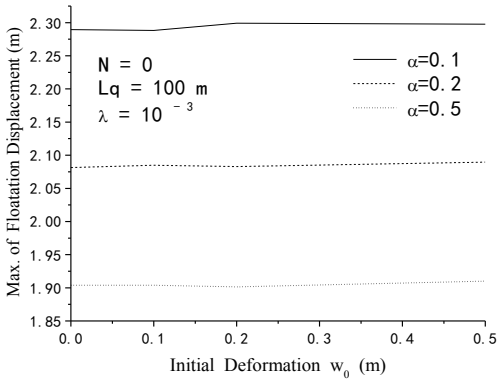


Figure 9 The effect of initial deformation

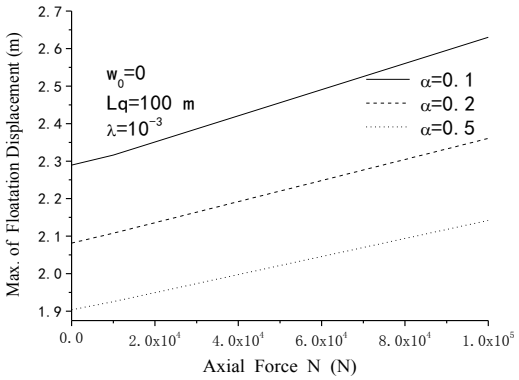


Figure 10 The effect of axial force

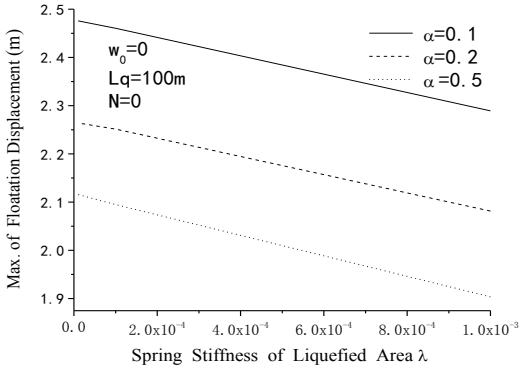


Figure 11 The effects of spring constant

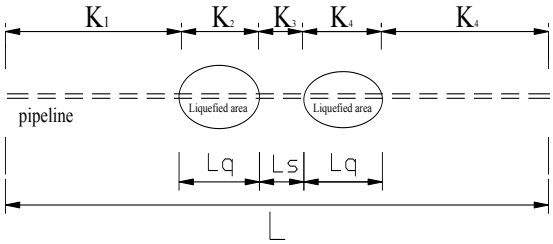


Figure 12 Discontinuous liquefied region

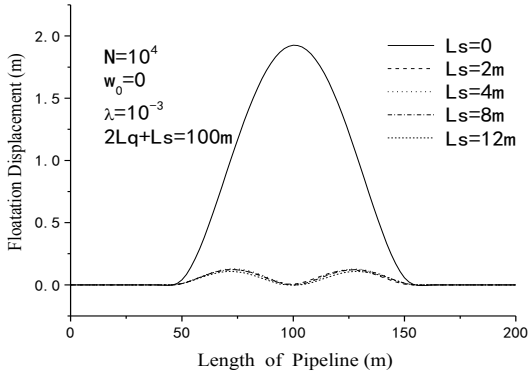


Figure 13 Effect of length of Ls

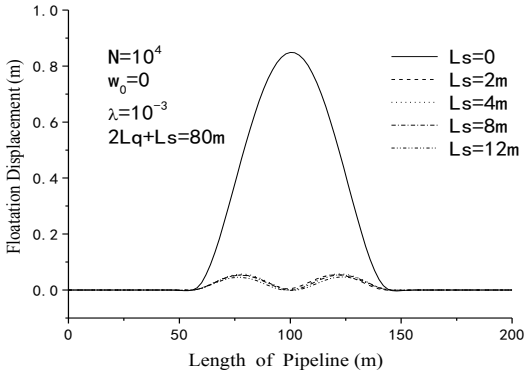


Figure 14 Effect of length of Ls

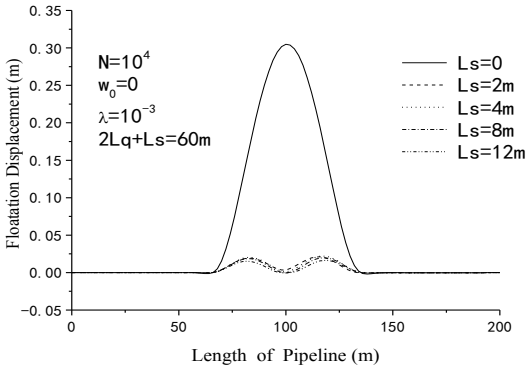


Figure 15 Effect of length of Ls

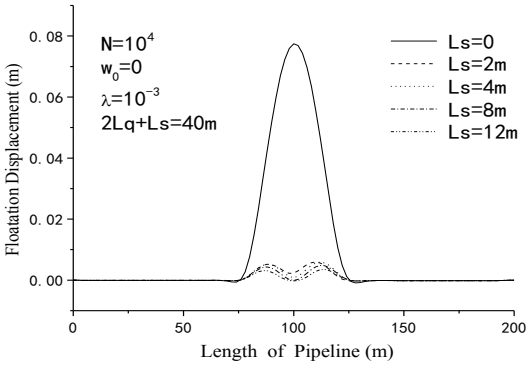


Figure 16 Effect of length of Ls

Figure 13 to figure 16 give the calculation results of pipeline floatation response in discontinuous liquefied region as shown in figure 12. The figures give respectively the floatation response of buried pipeline, when the whole length of liquefied area and the length of intermediate non-liquefied area are different. It can be seen from the figures that the intermediate part of liquefied area, that is no-liquefied soil part, will decrease the floatation response obviously. In all the calculations, the peak

value of floatation response is nearly the same value and varied little with the length of intermediate non-liquefied area.

## Conclusion

1) In homogeneous soil, the length of liquefied region has very large effect on the floatation of buried pipeline, and the floatation displacement gets larger as the length of liquefied region gets longer.
2) In homogeneous soil, the axial force has some effect on the floatation response, and larger axial force makes lager floatation displacement.
3) In homogeneous soil, the spring constant of liquefied soil has a great effect on the floatation response, and a lower spring constant of liquefied soil makes the floatation displacement lager.
4) In homogeneous soil, the initial deformation of the pipeline has little effect on the floatation of buried pipeline.
5) The effects of the axial force on the pipeline, the initial deformation, and the equivalent spring stiffness of liquefied soil on the floatation response in no-homogeneous soil are the same with the results of homogeneous soil.
6) The maximum floatation displacement of pipeline occurs in the area with smaller soil spring stiffness in two kinds of soils. The soil is much more no-homogeneous, the floatation response is much bigger
7) The calculation results of two liquefied soil with non-liquefied intermediate part draw a significant conclusion that for a long liquefied area, to make the soil non-liquefied in the middle of liquefied area may decrease the length of liquefied area and reduce the flotation displacement of pipeline greatly.
8) Based on the calculation results, to dispose the liquefied soil, the length of disposed area is 2m can achieve a good effect of reducing the floatation. In addition, when the length of liquefied area less than 40m, the floatation response of pipeline is very small. These conclusions can be referenced in actual engineering.

## References

[1] Lin Junqi, Xiong Jianguo, Analysis of Floating Response of Buried Pipeline in Liquefied Soil, Earthquake Engineering and Engineering Vibration, Vol.20 No.2 2000 (in Chinese)
[2] Gan Wenshui, Hou Zhongliang, Floatation Response of Buried Pipeline in Liquefied Soil, Special Structures, Vol.6 No.3 1989 (in Chinese)
[3] Xiong Jianguo et al, Study on Seismic Problems of Oil Supply Pipeline in Liquefied Soil, Technical Report of Seismological Institute of Laoning Earthquake Adiministration, 1993 (in Chinese)
[4] K. Shimamura et al，Experimental and Analytical Study of the floatation of Buried Gas Steel Pipe Due to Liquefaction, 12WCEE, 2000, Paper No.1385
[5] Zou Degao et al, Experimental Study on the Floatation Behavior of Pipeline in Saturated Sand Foundation and Earthquake Resistant Measures during an Earthquake, Chinese Journal of Geotechnical Engineering, Vol.24 No.3 2002 (in Chinese)
[6] Hou Zhongliang et al，Anti-seismic of Buried Pipeline, Academic Books and Periodicals Press, 1990 (in Chinese)
[7] Hu Yunxian, Earthquake Engineering, Seismological Press, 1990 (in Chinese)
[8] Lin Junqi, Li Zuohua, Hu Mingyi, Study on Floatation Response of Buried Pipeline Induced by Soil Liquefaction, Earthquake Engineering and Engineering Vibration, Vol.24 No.3 2004(in Chinese)
[9] Lin Junqi, Li Zuohua, Hu Mingyi, Study on Floatation Response of Buried Pipeline due to Non-homogenous Soil Liquefaction, Earthquake Engineering and Engineering Vibration, Vol.24 No.4 2004(in Chinese)

*Applied Mechanics and Materials Vols. 580-583 (2014) pp 797-800*
*© (2014) Trans Tech Publications, Switzerland*
*doi:10.4028/www.scientific.net/AMM.580-583.797*

# Research on the Construction Monitoring for Enclosure Structure of Working Well

Yuan Liao[1,2,a], Jianhui Zhan[1], Chen Li[2]

[1]Hubei Provincial Communication Planning and Design Institute, Wuhan 430051, China

[2]Wuhan University of Technology, Wuhan 430063, China

[a]737030309@qq.com

**Keywords:** the Diaphragm Wall; Construction Monitoring; Data analysis.

**Abstract:** Working well of nanjing city latitude three pass by river channel project is taken for example. Underground continuous wall was adopted in this project. Detailed monitoring scheme was formulated and lots of date was obtained by foundation pit. The monitoring data changed sharply analysis shows that the maximum horizontal displacement and the maximum strut axial forces is located near the excavation surface and along with the soil excavating. After structure construction, the change of deformation and internal force of enclosure structure gradually became stable. The theoretical analysis and test results are tend to be consistent. But this two have certain differences due to the influence of various factors.

## Introduction

Foundation pit engineering is a kind of high risk project. Once the accident happened, the projects not only suffer from delays and cost overruns but also endanger surrounding buildings, people's life and property safety. In this paper, base on the monitoring date of working well of latitude three pass by river channel project, the law of displacement and internal force were studied.

## Engineering situation

The shortest distance of work well and Yangtze river levee is about 53 m. The safety grade of Work well palisade structure is grade I. Table 1 shows the soil physical properties of the work well.

Table 1 Physico-mechanical properties of soils and rocks

| The number of Layer | The name of Geotechnical | Bulk Density/ γ | Poisson Ratio/ν | Coefficient of Lateral Earth Pressure/ξ | Coefficient of quick shear tests/ | | Coefficient of Subgrade Reaction | |
|---|---|---|---|---|---|---|---|---|
| | | | | | | | Late-ral | Horizon-tal |
| | | [kN/m3] | - | - | [kPa] | [°] | [m/d] | |
| ①0 | Miscellaneous Fill | 18.4 | 0.35 | 0.53 | / | / | 5 | / |
| ②1 | Clay | 18.3 | 0.39 | 0.65 | 30 | 4.9 | 15 | 18 |
| ②2 | Mucky Silty Clay | 18.1 | 0.42 | 0.72 | 16 | 2.6 | 8 | 8 |
| ③1 | Silt Clay | 18.5 | 0.40 | 0.68 | 25 | 4.6 | 10 | 15 |
| ⑥1 | Round Gravel Clamp Pebble | 20.6 | 0.20 | 0.25 | 0 | 40.0 | 60 | 80 |
| ⑥2 | Silt | 17.7 | 0.28 | 0.38 | 7 | 29.1 | 30 | 40 |

The thickness of the diaphragm wall is 1.2 m, the excavation depth is 25.783 m, the deep of diaphragm wall is 44 m and the size of diaphragm wall is 20 m × 20 m. The build-in depth of the diaphragm wall is 18.217 m and the toe of wall insert in the ③1 layer silty clay. By the way, two - row reinforced concrete support structure and four - Row steel support structure (Φ 609 x 16 steel pipes) composes support structure system. Fig.1 shows the elevation drawing of work well.

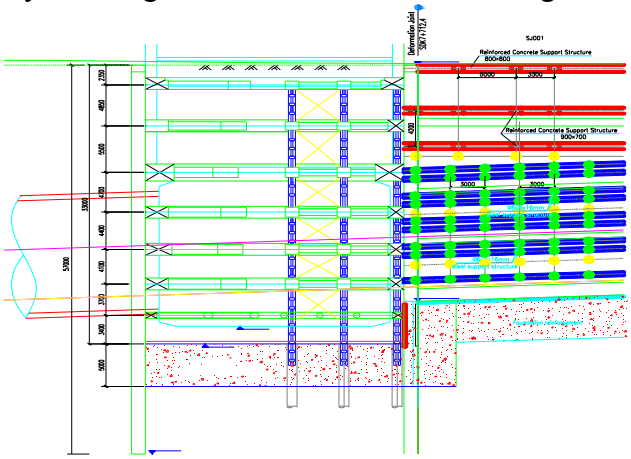

Fig.1 Elevation drawing of monitoring sites in deep excavation pit

## The monitoring items and test point arrangement of Foundation pit

After a comprehensive consideration, the monitoring items (see table 2) and test point arrangement (see fig.2) are determined.

Table 2 Comparison between initial stresses and stresses got in the back analysis

| Test Item | Ground settlement | Horizontal and Vertical displacement for pile, wall and soil | Strut axial forces | Lattice column settlement | Ground water | Deflection of diaphragm wall |
|---|---|---|---|---|---|---|
| Test instrument | Electronic Level | Electronic Level, Inclinometer | Axial Force and Strain Testing Sensor | Electronic Level | Water Level Gauge | Electronic Level, Electronic Theodolite |

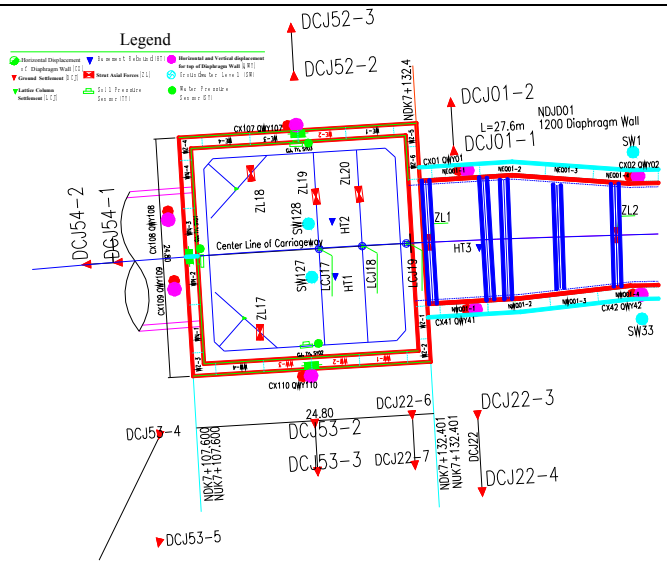


Fig.2 Plane layout of monitoring sites in deep excavation pit

## Monitoring data analysis

### Displacement data analysis for top of diaphragm wall

There are totally four displacement monitoring points for diaphragm wall, including horizontal and vertical displacement, which are QWY107, QWY108, QWY109 and QWY110. Fig.3 shows the displacement–time curves.

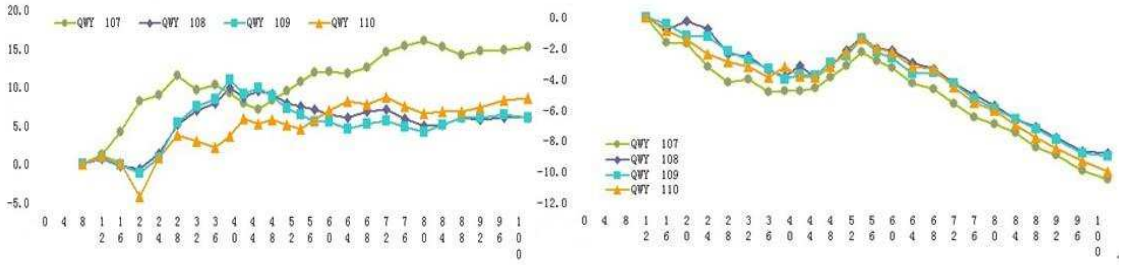


Fig.3 Horizontal and Vertical displacement(mm)-time(Day) curves of diaphragm wall

The fig.3 illustrates that, with the excavation, the horizontal direction of diaphragm wall start to Migrate to pit inside and the Vertical direction of is settlement. The maximum vertical displacement point is located in test point QWY107 and the cumulate depth change is 10.5 mm. At the same time, the maximum horizontal displacement point is also located in test point QWY107 and the cumulate change is 15.2 mm. The reason why the maximum displacement change test point is QWY107 is that it is just seated near road. At present, all measuring points are in safe.

**Displacement data analysis for Lattice column**

There are totally three displacement monitoring points for lattice column, which are LCJ17, LCJ18 and LCJ19. Fig.4 shows the settlement–time curves of lattice column.

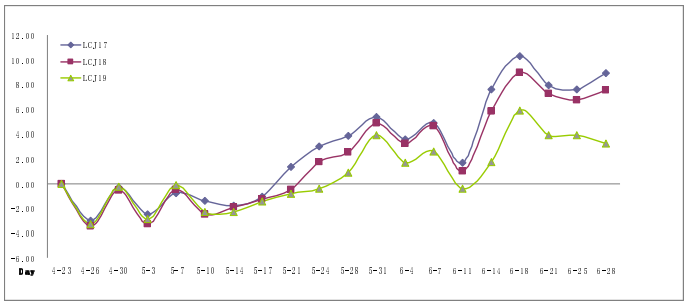


Fig.4 Lattice column settlement(mm)-time(Day) curves

With the excavation, difference rebound of lattice column increase furtherly and the biggest difference value is 5.7 mm. The maximum cumulate change test point is located in LCJ17 and the value is 9.1 mm; The change rate is the highest with test point LCJ17 and LCJ18, the value of which is -0.7mm/d which are all in safe.

**Horizontal displacement data analysis for diaphragm wall**

There are totally four displacement monitoring points for horizontal displacement of diaphragm wall, which are CX107, CX108, CX109 and CX110. Fig.5 shows the curves of horizontal displacement vs depth .

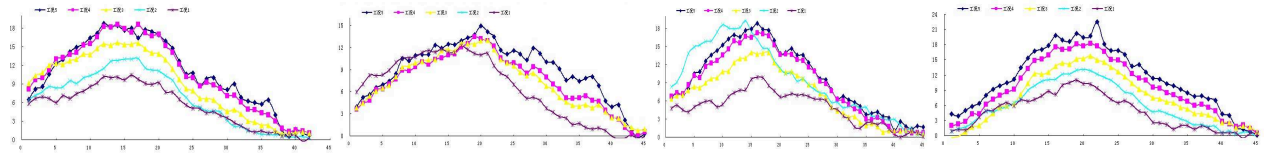

Fig.5 Horizontal displacement(mm) vs. Depth(m) for CX107, CX108, CX109 andCX110

With the excavation, the horizontal displacement increase and the position of maximum horizontal displacement gradually move down. The characteristics of each curves in fig.5 is that deformation of both side is small and the middle is larger. The range of each maximum horizontal displacement of test points , changing from 15 mm to 25 mm, is even.

**Strut axial forces data analysis**

There are totally twenty-eight axial force testing sensors. Fig.6 shows the curves of horizontal measuring inner axial force-time

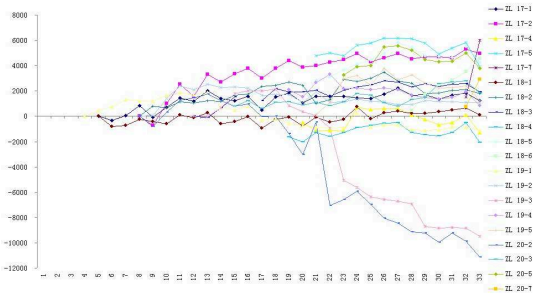

Fig.6 Horizontal Measuring inner axial force(KN)-time(Day) curves

With the excavation, the strut axial forces of each support structure increase. And the support stucture which increasing fast is near the bottom of foundation pit. After construction of baseplate, each strut axial forces tend to be stable. The maximum strut axial force test point is ZL17-7, which is up to 17515.5 KN; The change rate is the highest also with test point ZL17-7, the value of which is 15393.5KN/d.

## Water and soil pressure data analysis

There are totally three soil pressure sensors and three water pressure sensors, which are SY01, SY02, SY03 and TY01, TY02, TY03.. Fig.7 shows the curves of soil and water pressure-time.

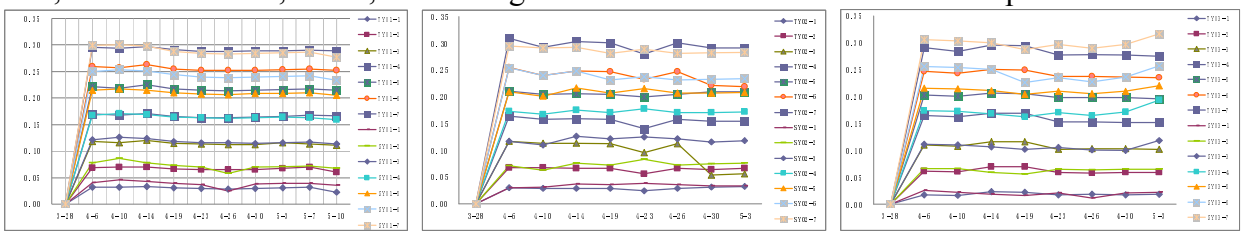

Fig.7 Soil and water pressure(Mpa)-time(Day) curves for TY01\SY01, TY02\SY02 and TY03\SY03

The maximum water pressure test point is SY3-7, which is up to 0.30 Mpa and the maximum water pressure test point is TY1-7, which is up to 0.27 Mpa, which are all in contorl.

## Conclusions

In order to ensure the safety of life and property for people, it is necessary to monitor the construction of foundation pint. Through monitoring and analyzing the working well of latitude three pass by river channel project, the law of displacement and internal force were studied, which can guide the construction and design of other similar engineering structure.

## References

[1] Zeng Guo-xi, Pan Qiu-yuan, Hu Yi-feng. The behavior of excavation in soft clay group[J]. Chinese Jounal of Geotechnical Engineering, 1988, 10(3): 13-22. (in Chinese)

[2] Bai Yong-xue. Effect factor and control method on deformation of deep foundation pit of the subway station in soft soil[D]. Chengdu:Southwest Jiaotong University, 2006. (in Chinese)

[3] Liu Jian-hang, Hou Xue-yuan. Handbook of deep excavation engineering[M]. Beijing: China Architecture and Building Press, 1997. (in Chinese)

[4] Jiang Hong-sheng, Liu Guo-bing. Time-space effect on strut force in deep excavation of soft soil[J]. Chinese Journal of Geotechnical Engineering, 1998, 20(6):105－107. (in Chinese)

[5] JGJl20—99 Technical specification for retaining and protection of building foundation excavation[S]. 1999. (in Chinese)

[6] Ou C Y. Deep Excavation: Theory and practice[M]. New York: Taylor & Francis, 2006.

*Applied Mechanics and Materials Vols. 580-583 (2014) pp 801-804*
*© (2014) Trans Tech Publications, Switzerland*
*doi:10.4028/www.scientific.net/AMM.580-583.801*

# Experimental Study on Bearing Mechanism of Jacked Pipe Pile in Sand

Jiatao Wang[1, a *]

[1]Department of Civil Engineering, Shandong Water Polytechnic, Rizhao, Shandong, China

[a]wy_wjt@126.com

**Key words:** Jacked pipe pile; side resistance; tip resistance

**Abstract:** Study on bearing mechanism of jacked pipe pile in sand is useful of optimizing the pile foundation design, and the research of the regularity of side resistance and tip resistance of pile has a very important theoretical significance. In this paper, a new effective method is used to test the tip resistance of the jacked pipe pile during the press-in process, and then the side resistance can be deduced [1]. Based on the field tests, the inherent laws of interaction between pile and soil in sand is explored, which provides some theoretical basis for the pile foundation design and engineering application.

## Introduction

In recent years, jacked pipe pile has been widely used in industrial and civil buildings, railways, highways, bridges, ports and other projects in China. Study on bearing mechanism of jacked pipe pile in sand soil will have a very important theoretical significance and application value. Therefore, the correct understanding of the bearing capacity of piles is of great significance in the design of the project [2].

Based on the field tests, the inherent laws of interaction between pile and soil in sand is discussed, which provides some theoretical basis for the pile foundation design and engineering application.

## The pile foundation test

**Preparations for the tests.** A steel pipe pile is used in this test, with the thickness of 6mm, the length of 2.8m, and the diameter of 500mm.

In order to measure the value of the pile tip resistance of the pile, a special testing device is used in this test, as shown in Figure 1.

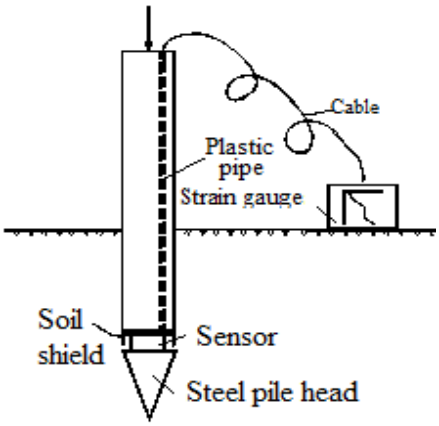


Fig.1 Testing device of pile tip resistance

Different from the traditional test of jacking force measurement, in this test a self-made pile pressure sensor is placed near the end of pile [3], [4]. After the sensor is done, curve of the

relationship between stress and strain is calibrated in laboratory. Then transported to the site, install the pile, forming a whole pile. Lead by the pile tip force sensor embedded in a thin plastic tube inside the pile piercing, connected to the intelligent resistance strain gauges.

At the construction site, static pile driver is used to press pile into the soil. After the stability of soil, the static load test is carried on. During the static load test, the strain of the pile can be measured by the testing device. Then tip resistance is got, which can be based on to get the pile side resistance. The test is divided into two parts: one is the measurement of the steel pipe piles indentation process; another is the measurement process of the static load test after the consolidation of the soil.

**Steel pipe pile press-in process.** Test site soil is fine sand. Groundwater level is 5.5m. Shear strength of sand ($C$) is of 5 kPa, and $\phi$ is of 36 degrees.

The strain is recorded during pipe pile press-in process, and then pile the tip resistance is obtained. Since the total pile resistance is known, the pile side resistance can be got. It can be seen from the data of the test, pile side resistance increases with the buried depth increase, but reaches a certain depth basically unchanged; also can be seen that at the same depth, the lateral friction decreases with the increase of the length of the pile buried in soil. Pile resistance is not like some of the information referred tip resistance accounted for the major part of the total, the proportion of both pile resistance is a variable value. The ratio of pile side resistance and tip resistance to total jacking force is shown in Figure 2, in which R1 is the ratio of pile tip resistance to total jacking force, R2 is the ratio of pile side resistance to total jacking force.

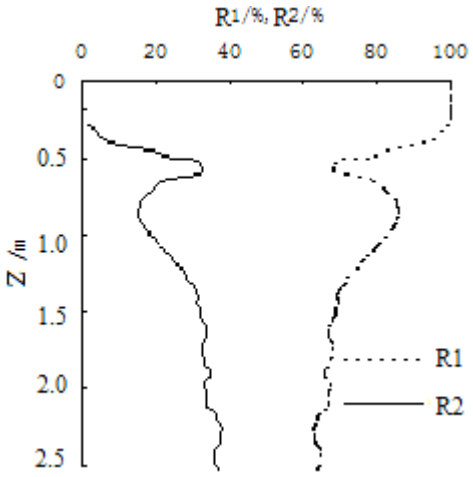


Fig.2 The ratio of pile side resistance and tip resistance to total jacking force

It can be seen from Figure 2, under the experimental conditions of the sand soil, when the pile end through non-hard soil, the pile side resistance is larger than the tip resistance, not like some of the information referred tip resistance is always accounted for the major part. In fact, only when pile tip reaches a hard layer, the pile tip resistance will dramatically increase, as a major part of the total resistance of the pressure pile.

**The static load test**

The static load test is carried on after ten days of the construction of the jacked pipe pile [5], [6]. During the process of the test, the pile strain is measured to get the pile tip resistance and side resistance, which can be seen in Figure3 and Figure 4.

It can be seen that the tendency of pile p-s curve in pile static load test is different from the pile press-in test. Comparison of two curved shape, analyze its variation, the P-S curve is divided into three stages [7]: the elastic stage, the yield stage, and the failure stage, shown in Figure 3. In the

elastic stage, the load is increased from 0KN to 200KN. The P-S curve of the pile top is basically linear, the pile top settlement changes from 0mm to 10.5mm, while pile end settlement is small, essentially unchanged. In the yield stage, the load is increased from 200KN to 300KN, P-S curve of the pile top and end both appear as curved segments, the pile top settlement increased to 34mm, and the pile end settlement also increased to 16mm. In the failure stage loads of 300KN to 350KN, both pile top and pile end P-S curves occur a sharp decline, and the pile top settlement reaches 73mm, pile end settlement to 53mm.

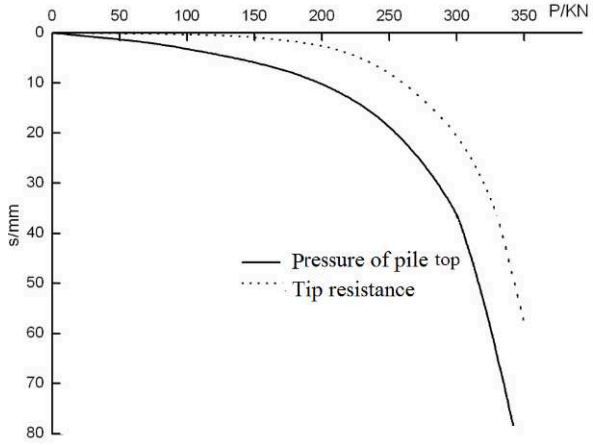


Fig.3 Curves of pressure -settlement

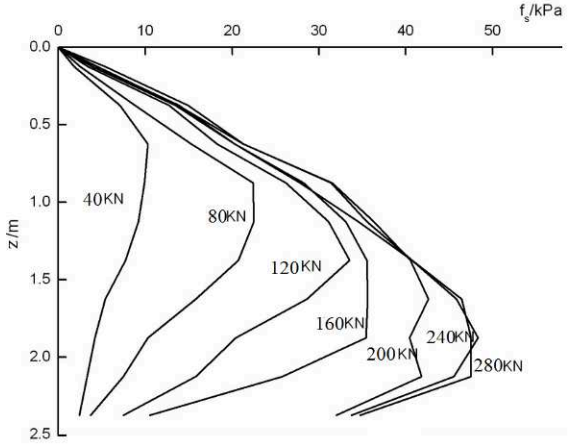


Fig.4 Curves of pile side friction under different levels load

Distribution curves of pile side friction under different levels load in the site load test are shown in Figure 4. It can be seen from figure that the value of side friction along the pile increases at the first, but decreases at last. In the same location, pile-soil friction resistance increases rapidly at first, but with the increasing of the load, growth slows or even decreases. That's to say, with the increasing of the load, the upper load along the pile height gradually pass on to the end of the pile, and the soil at the end of pile occurs the plastic deformation.

As can be seen from the above analysis of single pile settlement laws in sandy soils: the elastic stage, suffered a smaller load, pile load is mainly undertaken by the pile skin friction, tip resistance basically do not play. But when the load reaches 200KN, the yield stage beginning, the pile tip resistance began to play, and now the pile frictional resistance has largely played to the limit. The load continues to increase, the pile tip resistance gradually plays a main role to bear the increased load, and pile end began piercing distortion. When the load increases to 300KN, tip resistance plays a critical point, to yield, which lead to piercing damage. Large settlements occur both in pile top and pile end, and then the failure of the whole pile occurs.

## Summary

(1) The basic principle of this test method is obtained by measuring the pile strain to get pile tip resistance, and then calculates the pile side resistance. It's a good solution to the shortcomings of traditional test methods.

(2)It can be seen from the pile site indentation test that pile side resistance increases with the buried depth, but reaches a certain depth basically unchanged; also can be seen that at the same depth, the lateral friction decreases with the increase of the length of the pile buried in soil. During the press-in process, when buried shallow depth of the pile, because the pile lateral friction is not fully played, the pile tip resistance accounts for a larger proportion of pile resistance; with the increasing of the piles buried depth, the cumulative value of the pile side friction also increases, the proportion of pile side resistance will increase.

(3) The tendency of pile p-s curve in pile static load test is different from the pile press-in test [8]: the elastic stage, suffers a smaller load, pile load bears mainly by the pile skin friction, tip resistance basically do not play; but he pile tip resistance begins to play when the yield load reaches, and the pile side resistance has largely played to the limit at this time. If the load continues to increase, the pile tip resistance gradually plays a main role to bear the increasing load and pile end begins piercing distortion. When the load achieve to a critical point, the tip resistance comes to yield.

(4) According to the current pile foundation design specifications, the load used in the pile design is generally in the elastic stage and the tip resistance has not been effectively play [9]. It is necessary to consider the bearing capacity of larger settlement of pile top, give full play to the role of pile tip resistance, so as to reduce the project cost, and to optimize the design of pile foundation.

**Acknowledgements**

This work was supported by the Shandong Province college science and technology plan project (J12LG56).

**References**

[1] Brucy F, Meunier K, Nauroy J F. Behavior of pile plug in sandy soils during and after driving [J]. 23rd Offshore Technology Conference, Houston, 1991: 145-154.

[2] Hu Zhong-xiong. The increasing bearing capacity of the single pile with time in saturated soft soil [J]. Chinese Journal of Rock Mechanics and Engineering, 1985, 7(3): 58-61.

[3] FEI Qin-fa, MA Hai-long. Study on time effect of skin friction of soil displacement pile in saturated soft soil [J]. Journal of Science and Technology of Suzhou University. 1995, 8(4): 35-40.

[4] Li Xiong, Liu Jin-li. Time effect of bearing capacity of precast pile in saturated soft soil [J]. Chinese Journal of Rock Mechanics and Engineering, 1992, 14(4): 9-19.

[5] Zhang Mingyi, Shi We. Time effect on the ultimate bearing capacity of static pressed pile [J]. Chinese Journal of Rock Mechanics and Engineering, 2002, 12(2): 2601－2604.

[6] Kenneth G. Gavin and Brendan C. O'Kelly. Effect of friction fatigue on pile capacity in Densen sand[J]. Jour. of Geo. Geoenvir. Engng. ASCE, 2007, 133(1): 63–71.

[7] Heerema E.P. Predicting pile driveability: Heather as an illustration of the "friction fatigue" theory[J]. Ground Engng, 13(3), 1980: 15–20.

[8] Seed, Reese. The action of soft clay along friction pile [J]. Civil Engineers, 1995, 81: 840－842.

[9] Wang Jiatao, Zhou Jian, Zhang Mingyi. Computation of bearing capacity of jacked piles based on spherical cavity expansion theory and time effect [J]. Chinese Journal of Underground Space and Engineering, 2010, 6(5): 964-968.

*Applied Mechanics and Materials Vols. 580-583 (2014) pp 805-811*
*© (2014) Trans Tech Publications, Switzerland*
*doi:10.4028/www.scientific.net/AMM.580-583.805*

# On Stability and Deformation of Slurry-trench Affected by Formation Equipment

Maoyin Shi[1, a], Fugui Song[1,b]

[1]The Key Laboratory of Road and Traffic Engineering, Ministry of Education, Tongji University, Shanghai 200092, China

[a]1234462@tongji.edu.cn, [b]623031143@qq.com

**Keywords:** slurry-trench; formation equipment; instability mechanism; deformation

**Abstract**. A synthesized investigation is conducted of trench formation machine's effect on trench wall in soft soil area. The failure pattern of the slurry-trench is analyzed by means of 3D FEM based on strength reduction method. The investigation shows that the global instibility occurs in the superficial layers and speads along the trench segment. The grab movement in slurry has an instant impact on the trench wall and may cause local instability. The overload and construction technique of trench formation equipment are both important concerns during trench construction to ensure safetry.

## Introduction

With the advantages of high stiffness, high security and small deformation of support structure, diaphragm wall is widely used in excavation especially in complicated environment with high protection demands. During the diaphragm wall construction, because of lateral unloading, trench excavation may cause lateral deformation and vertical settlement. In soft soil area, trench wall may collapse. It's accepted that trench excavation is the most important stage of diaphragm wall construction and it is key to improving construction efficiency and project quality[1].

The stability of trench wall mainly depends on bentonite slurry in the trench. There has been some research on the instability mechanism of trench wall and factors that influence trench stability. Scholars researched the influence of the slurry property, soil condition, underground water, additional ground load, trench shape and size et al[2-5]. However, the effect of trench equipment and its excavation techniques on trench wall stability and deformation is rare. The paper makes an investigation of the trench formation equipment and its effect on the trench wall.

## Techniques of the trench equipment by hydraulic power

The trench machine by hydraulic power is widely applied in trench excavation. The grab cut soil with gear and the soil is took out with the bucket. When raised up onto the ground, the grab opens its bucket and dumps the soil.The process continues until the trench is completed.The grab activity is shown in Fig.1a).

Common trench segments are 3.8~7.2m wide generally. The trench is excavated by one grab or several grabs. The excavation order of several grabs is shown inFig.1b).

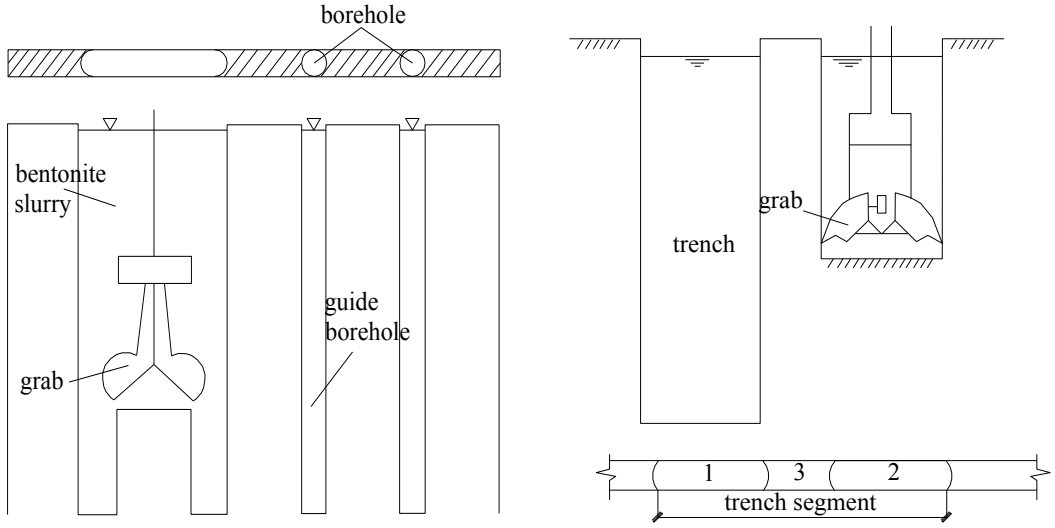


a) Drill and grab workmanship b) Excavation order of wide trench

Fig.1 Working patterns of hydraulic grab

Except big float rock and bedrock, trench equipment with hydraulic grab adapts in kinds of soils, such as clay, sand and gravel soil. It makes little noise and little vibration with high efficiency and accuracy. Most is equipped with bore-hole surveying and correcting device to correct the verticality of trench wall when necessary.

In the paper, equipment effect is investigated in two aspects: the machine itself and construction technique. The machine itself is divided into two parts: the weight itself and its vibration. To be precise, the technique factor means the impact of slurry flow on the trench wall caused by the grab's moving up and down in slurry.

**Project background**

The soft clay in a station pit of Ningbo Rail transit is investigated. The main soil layers are shown in Table 1. There is mainly clay and silty clay, sandwiched with clayey silt ③$_1$, 1.7m thick. The soil is of high rheology. The trench is 6m wide, 1m thick and 46m deep. The guide wall is 0.25m thick and 1.8m deep and 1m wide along the ground.

Table 1 Soil properties

| Soil layer | Thickness[m] | $\gamma$[kN/m$^3$] | $E_{s0.1\text{-}0.2}$[MPa] | $\Phi$[°] | $c$[kPa] | $K_0$ | $qu$[kPa] |
|---|---|---|---|---|---|---|---|
| ①$_{3T}$ | 0.5~2.9 | 18.2 | 3.17 | 11.0 | 21.0 | 0.52 | 40.3 |
| ①$_3$ | 0.9~3.4 | 17.4 | 2.49 | 8.5 | 13.8 | 0.66 | 20.4 |
| ②$_1$ | 0.5~2.3 | 18.6 | 3.74 | 11.7 | 19.9 | 0.58 | 39.8 |
| ②$_{2\text{-}2}$ | 3.3~7.5 | 17.5 | 2.48 | 9.4 | 15.5 | 0.65 | 22.9 |
| ②$_3$ | 1.8~6.1 | 18.2 | 2.90 | 9.8 | 16.7 | 0.63 | 33.3 |
| ③$_1$ | 1.7~4.7 | 19.3 | 5.54 | 24.6 | 6.5 | 0.45 | 43.7 |
| ④$_{1\text{-}1}$ | 1.7~5.3 | 18.1 | 3.13 | 10.5 | 17.4 | 0.60 | 32.8 |
| ④$_2$ | 1.0~11.8 | 17.8 | 3.10 | 11.2 | 21.6 | 0.58 | 46.0 |
| ⑤$_1$ | 1.3~6.8 | 19.7 | 6.39 | 16.5 | 42.6 | 0.42 | 95.0 |
| ⑤$_2$ | 0.5~10.4 | 19.4 | 5.22 | 16.0 | 35.2 | 0.45 | 87.0 |
| ⑥$_2$ | 8.6~17.5 | 18.7 | 4.20 | 13.0 | 25.7 | 0.50 | 83.1 |
| ⑦$_1$ | 2.1~10.3 | 20.0 | 6.68 | 18.2 | 46.0 | 0.48 | 164.0 |

**Effect of the trench machine itself**

The analysis is conducted from two perspectives: additional static load and dynamic load caused by vibration. In this part, 3D numerical modeling is used to investigate the instability mechanism of trench wall and the effect of the equipment.

**Static load of the machine weight.** The static load of the machine weight shall be considered as ground overload. Because of the existence of the trench, the overload effect cannot be calculated with Boussinesq method. To analyze the instability pattern of the trench with ground overload，a 3D FEM based on strength reduction method is set up. As shown in Fig.2a), the trench size is 6m(wide) ×1m(thick)×46m(deep), and the model size is 24m(wide) ×16m(thick)×60m(deep).

The specification of the trench machine is shown in Table 2. The machine load is simplified as uniformly distributed load 165.4kPa, 0.8m×6m and located 0.5m away from the trench wall.

Table 2 Specification of the trench cutter machine

| Type | Unit | Jintai SG40A |
|---|---|---|
| Weight of main machine | t | 63 |
| Grab weight | t | 18.344 |
| Track length | mm | 5680 |
| Track width | mm | 800 |

By means of the finite element model based on strength reduction method, aimed at the typical soft soil layer ② in Ningbo, the 3D instability mechanism and its failure mode under overload is investigated. The soil is simulated with 15-node triangular element of high order and Mohr-Couloumb elastoplastic constitutive model. Reduction coefficient $R_i$ is used to reflect the stiffness relationship between contact surface and the soil. $R_i$ =0.65. The criterion of instability is to form a complete plastic zone. The model grid is shown in Fig.2b).

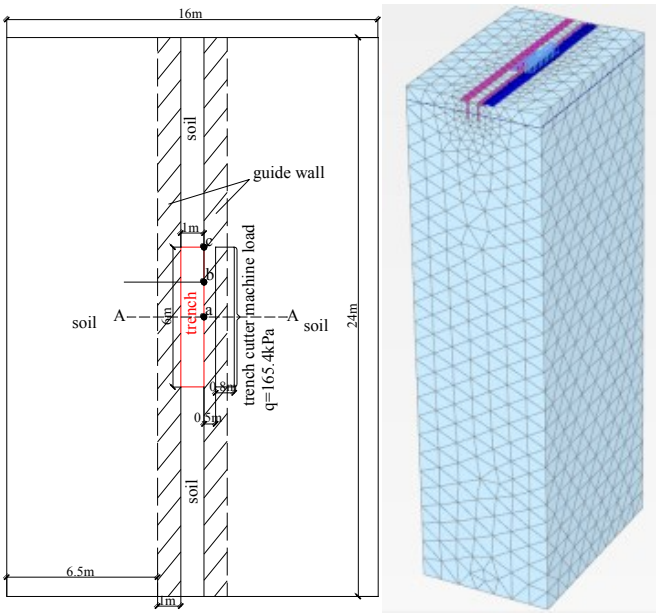


a) top view b)3D finite element model grid

Fig.2 FEM model of trench with machine load

The slide face is shown in Fig.3. Changes occur within the superficial layer, approximately 6m from the ground surface (see Fig.3a)). The upside of the guide wall is cut off by the tension of the deformed soil below. The soil below the guide wall bulges towards the trench, namely ‘necking down’ in clay soil (see Fig.3b)). The plastic zone spread along the trench width(see Fig.3c)).

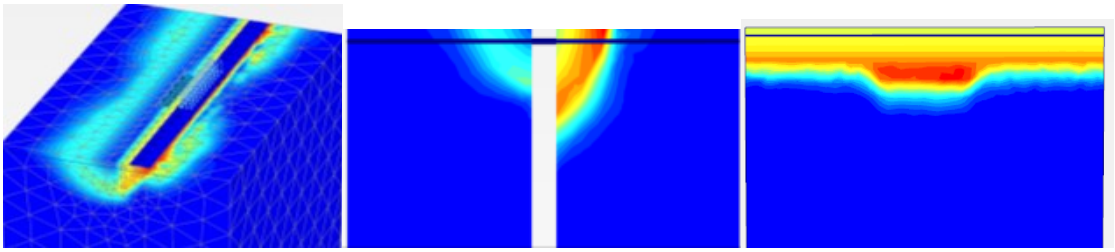

a) 3D instability pattern b) slide face on cross-section A-A c) incremental deformation of trench wall on load side

Fig.3 The instability pattern of trench under machine load condition

The lateral deformation of the trench wall is investigated with 3D FEM. The intersecting line of cross-section A-A(see Fig.2a)) and the trench wall on load side is picked out. With different overload values, the horizontal deformation follows the same rule but variable values (see Fig.4). The soil right below the load is firstly compressed. Due to the elastic guide wall, the topside of the wall tends to deform towards the load side. The deformation decreases along the trench depth. In the soft clay ② 2-2, the deformation rebounds a little then goes on attenuation.

The maximum horizontal deformation towards the trench under the machine weight 165.4kPa is 20mm. The deformation increments with the incremental load value tends to be larger and approaches to shear failure. For safe sake, the trench cutter equipment should be chosen reasonably according to the soil condition and it's necessary to reinforce the superficial layers and to lay thick steel panel under the machine to decrease the uniformly distributed load.

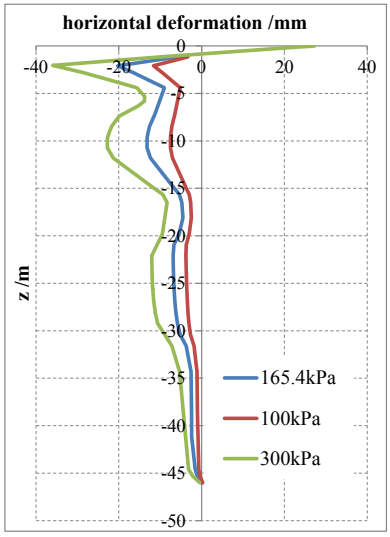


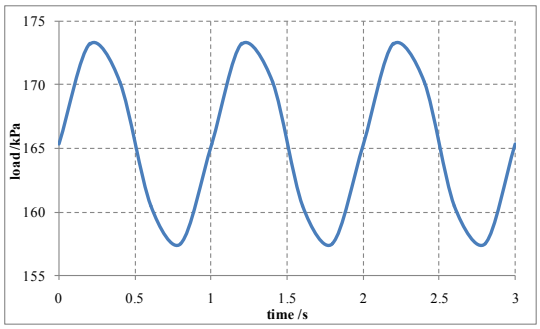


Fig.4 Horizontal deformation of trench centerline Fig.5 Dynamic load curve over time

**The machine vibration.** Addition to the overload, the mechanical vibration is inevitable. It may change the soil properties and lead to large deformation and further endanger the stability of the slurry-trench.

To investigate the instant elastic deformation of the trench wall and then to evaluate the instantaneous safety during the trench exposure period, 3D numerical modeling is conducted. The soil is modeled with 3D-Solid material. The slurry-trench size is above-mentioned. The model size is 12m×9m×48m. The dynamic load is simplified as sinusoidal load as shown in Fig.5 whose cycle is 1s and the value is G±5%G. Viscoelastic artificial boundary is set at the fourvertival sides and the bottom of the model to simulate the radiation damping of continuum. With the damping, the scattered wave made by the structure and load goes through the boundry without rebounding And the model domain can be smaller thereby to reduce the computing time. The model is shown in Fig.6.

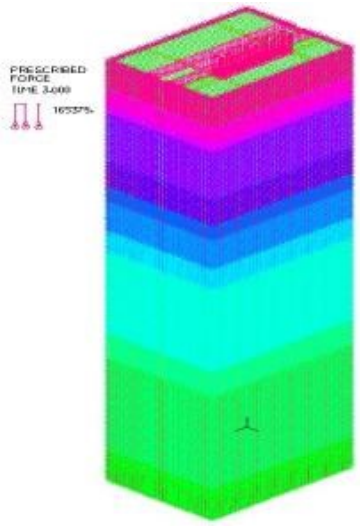


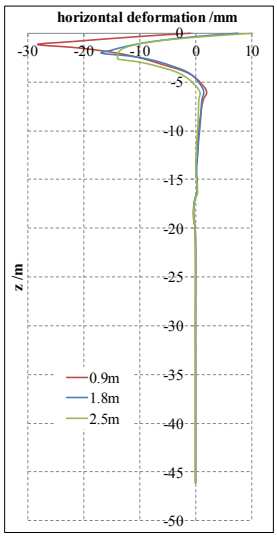


Fig.6 FEM model Fig. 7 Horizontal deformation of trench centerline with different guide wall depth

Pick the centerline of the trench wall (the intersecting line of cross-section A-A and the trench wall on load side.) as the object. With the dynamic load, the trench wall tilts towards the trench(see Fig.7). The influence range is from the ground surface to 6m below, which is similar to the static load situation. As shown in Fig.7, with the deepening of the guide wall, there shows a reduction of the horizontal deformation. When the depth changes from 0.9m~1.8m and 1.8m~2.5m, the deformation reduces 35.7% and 16.7% respectively. We can assume that there is an optimal guide wall depth *h*. When the guide wall is deeper than *h*, the deformation of trench wall would decrease but with a small amplitude. In practice, the guide wall shall be reasonably determined based on soil condition and surrounding environment to fulfill the balance between the effect and cost.

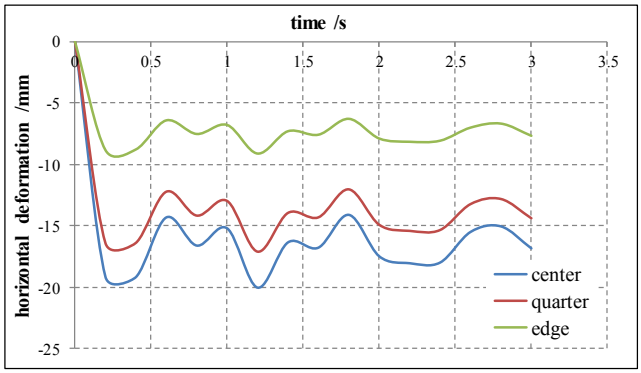


Fig.8 Horizontal deformation of typical points on trench wall

To investigate the response characteristics of trench wall deformation with time, three typical points are picked out. They are of the same elevation and respectively locate at the center of the trench wall(a), 1/4 trench width away from the centerpoint(b) and at the edge of the trench(c). Their deformations along with the loading time are shown in Fig.8. The deformation curves follow the same rule but of different values. At the beginning of the loading, the deformation develops linearly towards the trench and then fluctuates at a magnitude level.

The nearer to the centerline of the trench, the larger deformation occurs, which ss easily found in Fig.9. The instant deformation of the horizontal lines 0.9m and 1.8m below the ground is shown in Fig.9. At the edge of the trench segment at -0.9m, there is a border of the guide wall and the surrounding soil. So there is a sudden change. The deformation along the trench width makes a tank towards the trench similar to the Peck subsidence tank. The characteristic of horizontal deformation of trench wall under dynamic loads shall be described with Peck subsidence formula if necessary.

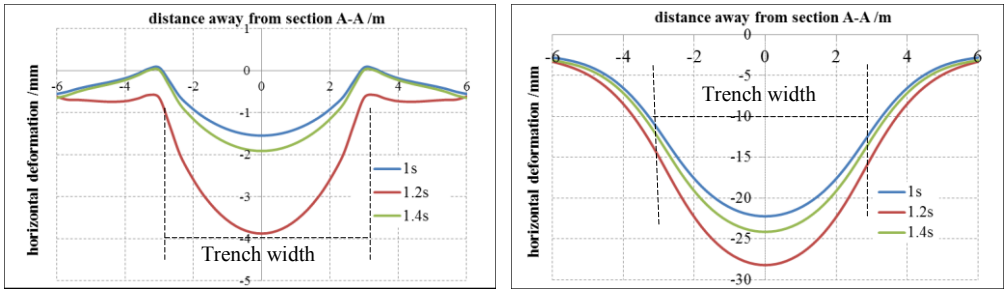


a) -0.9m b) -1.8m

Fig. 9 Horizontal deformation of trench wall cross-section in different depth

The numerical analysis of trench wall by simplifying the machine weight as static and dynamic load shows that the change caused by the machine mainly occurs in the superficial layers. The influence recesses rapidly along the soil down. The result follow the law obsevered in the centrifuge test by W. Powrie and C.Kantartzi[6] and the elasoplastic FEM analysis by P. Oblozinsky[7]. Instability in upper layers is the main pattern of instability especially under three-dimension conditions.

**Movement of the grab**

Trenches become deeper and several crawls are necessary to make a trench segment. The grab has to move up and down frequently. The moving velocity will cause the flow of the slurry. Moving up arouses negative pressure on the trench wall and moving down causes positive pressure. Repeated movements may greatly impact the slurry wrap on the surface of the trench wall and make adverse effects on local stability of the trench.

The paper deals with the effect of working technique as a hydromechanics problem. If slurry flow changes from laminar flow to turbulent flow, the risk of slurry wrap being damaged and local instability will increase sharply. Ref.8 and 9 analyzed the effect of velocity of grab movement $v_w$ on the stability of trench wall. The velocity of slurry flow is calculated with Eq.1.

$$v_s = \frac{A_w v_w}{A_k - A_w} \tag{1}$$

The equivalent hydraulic diameter of slurry flow is as Eq.2

$$D = \frac{4(A_k - A_w)}{p_{kw}} \tag{2}$$

Where $A_k$-$A_w$ is the cross-section area of slurry flow; $P_{kw}$ is the wetted perimeter of slurry flow. The Hedstrom number can be calculated with Eq.3.

$$H_e = \frac{\tau_s D^2 \rho_s}{\mu_s^2} \tag{3}$$

The corresponding Reynolds number is as Eq.4.

$$Re = \frac{v_s D \rho_s}{\mu_s^2} \tag{4}$$

Where $\rho_s$ means the fluid density， t/m$^3$; $v_s$ means the average flow velocity, m/s; $\mu_s$ means the fluid dynamics viscosity, kPa·s.

By the relationship between friction coefficient and Hedstrom number together with Reynolds number of Bingham fluid, we can figure out whether the slurry flow is laminar flow or turbulent and then determine the moving speed of the grab.

The excavation orifice diameter of a 1m-diameter grab can generally reach 1.2m. Assume that the grab moves down the trench at 1m/s, the flow speed of slurry will be 2.27m/s according to Formula 1 and 2. The equivalent hydraulic diameter is 0.2m. As for the slurry, assume $\tau_s$=6.7×10$^{-3}$kPa, $\mu_s$ =8×10$^{-6}$ kPa·s, $\rho_s$ =1.03t/m$^3$ with Eq.3 and 4, the Hedstrom number and the Reynolds number are 4.32×106 and 5.8×104 respectively. The critical corresponding Reynolds number from laminar to turbulent is 5.0×104. If the moving velocity of the grab is over 1m/s, the slurry flow may turn into turbulent flow[9]. Thus, the operation velocity of the trench cutter machine shall be restricted into a reasonable level to ensure safety.

## Conclusions

Trench formation equipment plays a remarkable role in trench excavation. In this paper, a thorough investigation is carried out of how the formation machine works and its effect on the trench wall stibility and deformation.The overload and workmanship of the formation machine are both negative.

The 3D failure mechanism is derived from the 3D FEM based on strength reduction method. It shows that the additional load on ground surface mainly influence the range of 6m below ground surface, namely superficial layer instability. Static and dynamic analysis reach to the same conclusion. In the background project in Ningbo, the maximum deformation caused by formation equipment is 20mm. The horizontal deformation curve across the trench segment is similar to the Peck subsidence tank. The analysis method and results shall be a reference for similar projects.

The grab's moving up and down in slurry may lead the slurry flow into turbulence. The turbulent flow may greatly impact the trench wall and take the slurry wrap away from the trench sidewall. It makes a risk of local instibility. For safe sake, assume the laminar flow is necessary. According to the Bingham fluid theory, the reasonable velocity of the grab movement is 1m/s.

## References

[1] Guobin Liu, Weidong Wang: Manual of Excavation Engineering[M]. China Building Industry Press. 2009, 2rd Edition.(in Chinese)

[2] TSAI J S: *Canadian Geotechnical Journal*,3,189,1997.

[3] Pengming Jiang et al: *Chinese Journal of Geotechnical Engineering*,21,338, 1999. (In Chinese)

[4] Shiyong Shi, Wei Zhang: *Journal of Geotechnical Engineering*. S1,1418, 2006.(in Chinese)

[5] Yonggang Xu et al: *Journal of Rock Mechanics and Engineering*,S2,3464, 2011.(in Chinese)

[6] Powrie W，Kantartzi C: *Geotechnique*. 46(4),725,1996.

[7] Oblozinsky P, Ugai K, Kataguri M, et al:*Computers and Geotechnics*.28(2):145, 2001

[8] Guogang Lei etal:*Advances in Science and Technology of Water Resources*.01,82,2006.(in Chinese)

[9] Washbourne J: *Ground Engineering the Magazine of the British Geotechnical Association*, 18(05),18,1985.

*Applied Mechanics and Materials Vols. 580-583 (2014) pp 812-815*
*© (2014) Trans Tech Publications, Switzerland*
*doi:10.4028/www.scientific.net/AMM.580-583.812*

# Two-dimensional Problem of Moisture Elasticity of Inhomogeneous Spherical Array with Cavity

Vladimir I. Andreev[1, a], Anatoliy S. Avershyev[2, b]

[1,2] Moscow State University of Civil Engineering, Jaroslavskoje sh., 26 Moscow, Russia

[a]asv@mgsu.ru, [b] fullbass-@mail.ru

**Keywords:** moisture-elasticity, inhomogeneity, induced deformations, thick-walled shells, moisture transfer, soil, clay

**Abstract**: The numerical-analytical solution of the axisymmetric problem of moisture-elasticity for hollow spherical soil massive is provided. We consider the steady-state water transfer. Inhomogeneity of the array due to the dependence of the deformation modulus on the soil moisture. Stress state of the array caused by forced deformations and uneven pressure rebuff of the soil. The method for solving non-axisymmetric problems with radial inhomogeneity in polar coordinates is described. Diagrams on the stress fields in homogeneous and inhomogeneous formulations of the problem are provided. It describes a method of calculating radial inhomogeneous axisymmetric problem of theory of elasticity for thick-walled spherical shell.

## Introduction

Typical problem of moisture-elasticity is the problem of pipeline rupture. In the present study we considered this problem for an inhomogeneous spherical soil array. At relatively low depth of cavity the pressure of the ground on the outer surface of array is uneven. The paper investigates the effect of external pressure and mass forces on the stress state of a spherical array with cavity. We consider the problem of pipeline rupture at a depth *H*. Assuming that the water extends from the hole along the spherical surface we consider an array of spherical radius *b at condition a<<b<H,* where *a* – radius of water source. Thus pressure on the outer surface of the array is a variable and the unevenness of pressure is balanced by the mass forces $\gamma$ (Fig. 1).

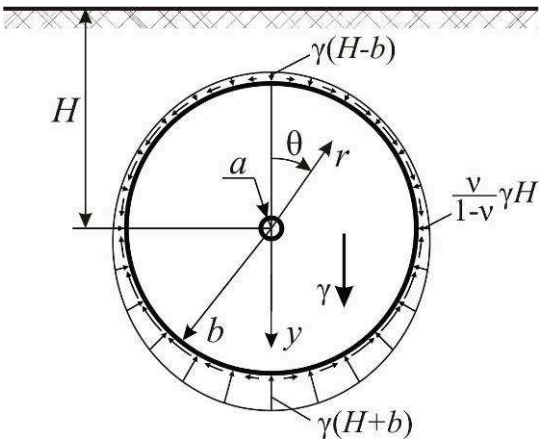


Fig. 1 The settlement scheme

## Moisture transfer

Problem of the distribution of moisture in solids is described by Fick's second law [1, 2] and corresponds to the diffusion process. We have considered a stationary process of moisture conductivity with Dirichlet boundary conditions:

$$\frac{\partial^2 w}{\partial r^2}+\frac{2}{r}\cdot\frac{\partial w}{\partial r}=0;\quad r=a:\quad w=w_s;\quad r=b:\quad w=w_0. \tag{1}$$

Here $w_s$ – moisture of saturated soil, $w_0$ – natural moisture of soil. The solving of problem (1) has a form:

$$w(r)=\frac{a\cdot b\cdot(w_s-w_0)}{b-a}\cdot\frac{1}{r}-\frac{a\cdot w_s-b\cdot w_0}{b-a}. \tag{2}$$

It is known that in many soils (clay, loess, peat) at moistening the Deformation modulus is reduced [3]. For example for clay this dependence can be approximated by the function:

$$E(w) = E_0 \cdot (w/w_s)^{-\alpha}, \tag{3}$$

where $E_0$ – deformations modulus for de-moisturized clay. Below we use next values: $E_0 = 19.88$ MPa; $w_s = 0.363$; $\alpha = 2.4$.

**Calculation of stress state**

The problem is solved in spherical coordinates $r, \theta, \varphi$. In view of the axial symmetry with respect to the axis $y$ (Fig. 1), we assume $w = 0$, $\frac{\partial}{\partial \varphi} = 0$. From the Duhamel-Neumann relations we obtain expressions for the stresses:

$$\begin{aligned}
\sigma_r &= \lambda \cdot \left( \frac{\partial u}{\partial r} + \frac{2u}{r} + \frac{1}{r} \cdot \frac{\partial v}{\partial \theta} + \frac{v}{r} \cdot \operatorname{ctg}\theta \right) + 2\mu \cdot \frac{\partial u}{\partial r} - 3K \cdot \varepsilon_f; \\
\sigma_\theta &= \lambda \cdot \left( \frac{\partial u}{\partial r} + \frac{2u}{r} + \frac{1}{r} \cdot \frac{\partial v}{\partial \theta} + \frac{v}{r} \cdot \operatorname{ctg}\theta \right) + 2\mu \cdot \left( \frac{1}{r} \cdot \frac{\partial v}{\partial \theta} + \frac{u}{r} \right) - 3K \cdot \varepsilon_f; \\
\sigma_\varphi &= \lambda \cdot \left( \frac{\partial u}{\partial r} + \frac{2u}{r} + \frac{1}{r} \cdot \frac{\partial v}{\partial \theta} + \frac{v}{r} \cdot \operatorname{ctg}\theta \right) + 2\mu \cdot \left( \frac{u}{r} + \frac{v}{r} \cdot \operatorname{ctg}\theta \right) - 3K \cdot \varepsilon_f; \\
\tau_{r\theta} &= \mu \cdot \left[ r \cdot \frac{\partial}{\partial r}\left( \frac{v}{r} \right) + \frac{1}{r} \frac{\partial u}{\partial \theta} \right]; \quad \tau_{r\varphi} = 0; \quad \tau_{\theta\varphi} = 0.
\end{aligned} \tag{4}$$

Here $\lambda, \mu$ – Lame parameters, $K$ – the bulk modulus, $\varepsilon_f$ – forced (humidity) strains. The latter are determined by the formula

$$\varepsilon_f = \int_{w_0}^{w} \beta(w) dw, \tag{5}$$

where $\beta$ – swelling coefficient. If $\beta$=const [3] $\varepsilon_f = \beta(w - w_0)$.

Substituting (4) into the equations of equilibrium we obtain an analogue Lame equations but unlike them having dependence of mechanical characteristics on the coordinates. If we consider only the radial inhomogeneity of the material, these equations take the form:

$$\begin{aligned}
&\mu \cdot \nabla^2 u + 3(\lambda + \mu) \cdot \frac{\partial \varepsilon_{av}}{\partial r} - \frac{2\mu}{r^2} \cdot \left( u + \frac{\partial v}{\partial \theta} + v \cdot \operatorname{ctg}\theta \right) + 3\frac{\partial \lambda}{\partial r} \cdot \varepsilon_{av} + 2\frac{\partial \mu}{\partial r} \cdot \frac{\partial u}{\partial r} - 3\frac{\partial}{\partial r}(K \cdot \varepsilon_f) + R = 0; \\
&\mu \cdot \nabla^2 v + \frac{3(\lambda + \mu)}{r} \cdot \frac{\partial \varepsilon_{av}}{\partial \theta} + \frac{\mu}{r^2} \cdot \left( 2\frac{\partial u}{\partial \theta} - \frac{v}{\sin^2 \theta} \right) + \frac{\partial \mu}{\partial r} \cdot \left( \frac{1}{r} \cdot \frac{\partial u}{\partial \theta} + \frac{\partial v}{\partial r} - \frac{v}{r} \right) - \frac{3}{r}\frac{\partial}{\partial \theta}(K \cdot \varepsilon_f) + \Theta = 0.
\end{aligned} \tag{6}$$

We seek a solution of (6) as expansions of functions $u$ and $v$ in series of Legendre polynomials [4]:

$$u(r,\theta) = \sum_{n=0}^{\infty} u_n(r) \cdot P_n(\cos\theta); \quad v(r,\theta) = \sum_{n=1}^{\infty} v_n(r) \cdot \frac{\partial P_n(\cos\theta)}{\partial \theta}. \tag{7}$$

Volume loads and forced deformations included in the system of equations (6)can also be expanded in Fourier series in Legendre polynomials:

$$R(\theta) = \sum_{n=0}^{\infty} R_n \cdot P_n(t); \quad \Theta(\theta) = \sum_{n=1}^{\infty} \Theta_n \cdot \frac{\partial P_n(t)}{\partial \theta}; \quad \varepsilon_в(r,\theta) = \sum_{n=0}^{\infty} g_n(r) \cdot P_n(t), \tag{8}$$

where the expansion coefficients $R_n$, $T_n$ and $g_n$ are defined by:

$$R_n = \frac{2n+1}{2}\int_{-1}^{1} R(t)P_n(t)dt; \quad \Theta_n = \frac{1}{\int_{-1}^{1}\left(\frac{\partial P_n(t)}{\partial\theta}\right)^2 dt}\int_{-1}^{1}\Theta(t)\frac{\partial P_n(t)}{\partial\theta}dt; \quad g_n(r) = \frac{2n+1}{2}\int_{-1}^{1}\varepsilon_{\text{в}}(r,t)P_n(t)dt. \tag{9}$$

After the series expansions of all components of the system (6) we can obtain a number of systems of two ordinary differential equations for the functions $u_n(r)$ and $v_n(r)$ for each $n$:

$$(\lambda+2\mu)\cdot u_n'' + \left[\frac{2(\lambda+2\mu)}{r} + (\lambda+2\mu)'\right]\cdot u_n' - \left[\frac{n\cdot(n+1)\cdot\mu + 2(\lambda+2\mu)}{r^2} - \frac{2\lambda'}{r}\right]\cdot u_n +$$

$$+ n\cdot(n+1)\cdot\left[-\frac{\lambda+\mu}{r}\cdot v_n' + \left(\frac{\lambda+3\mu}{r^2} - \frac{\lambda'}{r}\right)\cdot v_n\right] - 3(K\cdot g_n)' + R_n = 0; \tag{9}$$

$$\mu\cdot v_n'' + \left(\frac{2\mu}{r} + \mu'\right)\cdot v_n' - \left[n\cdot(n+1)\cdot\frac{\lambda+2\mu}{r^2} + \frac{\mu'}{r}\right]\cdot v_n + \frac{\lambda+\mu}{r}\cdot u' + \left[\frac{2(\lambda+2\mu)}{r^2} + \frac{\mu'}{r}\right]\cdot u_n + \Theta_n = 0.$$

Given that $\varepsilon_{\text{f}} = \varepsilon_{\text{f}}(r)$; $R = -\gamma\cdot\cos\theta$; $\Theta = \gamma\cdot\sin\theta$ in (9) we will have:

$$g_0(r) = \varepsilon_{\text{f}}\cdot P_0(t) = \varepsilon_{\text{f}}(r); \quad R_1 = -\gamma; \quad \Theta_1 = \gamma, \tag{10}$$

Others $g_i = R_i = \Theta_i = 0$.

The boundary conditions in stresses can be written as:

$$r = a: \quad \sigma_r = 0; \quad \tau_{r\theta} = 0;$$

$$r = b: \begin{cases} \sigma_r = -\gamma\cdot(H - b\cdot\cos\theta)\left(\dfrac{\nu}{1-\nu} + \dfrac{1-2\nu}{1-\nu}\cdot\cos^2\theta\right); \\ \tau_{r\theta} = \dfrac{\gamma}{2}\cdot(H - b\cdot\cos\theta)\dfrac{1-2\nu}{1-\nu}\cdot\sin 2\theta. \end{cases} \tag{11}$$

Presenting stress (4) in the form of series (7) (11), we obtain

at the boundary $r = a$: $\sigma_{r,n}^a = 0$; $\tau_{r\theta,n}^a = 0$, $n = 0, 1, 2, 3$;

at the boundary $r = b$:

$$\sigma_{r,0}^b = -\frac{1+\nu}{1-\nu}\cdot\frac{\gamma\cdot H}{3}; \quad \sigma_{r,1}^b = \frac{3-\nu}{1-\nu}\cdot\frac{\gamma\cdot b}{5}; \quad \sigma_{r,2}^b = -\frac{1-2\nu}{1-\nu}\cdot\frac{2\gamma\cdot H}{3}; \quad \sigma_{r,3}^b = \frac{1-2\nu}{1-\nu}\cdot\frac{2\gamma\cdot b}{5};$$

$$\tau_{r\theta,1}^b = \frac{1-2\nu}{1-\nu}\cdot\frac{\gamma\cdot b}{5}; \quad \tau_{r\theta,2}^b = -\frac{1-2\nu}{1-\nu}\cdot\frac{\gamma\cdot H}{3}; \quad \tau_{r\theta,3}^b = \frac{1-2\nu}{1-\nu}\cdot\frac{2\gamma\cdot b}{15}.$$

Thus the final solution has the form $u = \sum_{n=0}^{3} u_n(r)\cdot P_n(t)$; $v = \sum_{n=1}^{3} v_n(r)\cdot\frac{dP_n(t)}{d\theta}$.

**Results and discussion**

Numerical solution of the system (9) with boundary conditions (11) was implemented in the software package Matlab. In calculations other than the initial data specified after equation (3) we used the following values: $a$ = 0.25 m; $b$ = 2.5 m; $H$ = 5 m; $\gamma_s$ = 26.95 kN/m$^3$; $\beta$ = 0.6; $\nu$ = 0.4. Fig. 2 shows the distribution of stresses $\sigma_r$ and $\sigma_\theta$ for the characteristic values of the angle $\theta$. The curves $\sigma_\varphi$ is almost completely coincide with the stresses $\sigma_\theta$ that usually happens for spherical bodies in problems with central symmetry. In turn, the shear stresses are much smaller

than normal stresses. Computations have shown that the highest values $\tau_{r\theta}$ do not exceed 0.03 MPa, which is two orders of magnitude less than the mean values of normal stresses. The dotted lines in Fig.2 show the curves corresponding to the homogeneous array for the average value of the deformation modulus $E_{\text{cp}} = \int_a^b E(w(r))dr/(b-a) = 64.68$ MPa at $\theta = 45^\circ$.

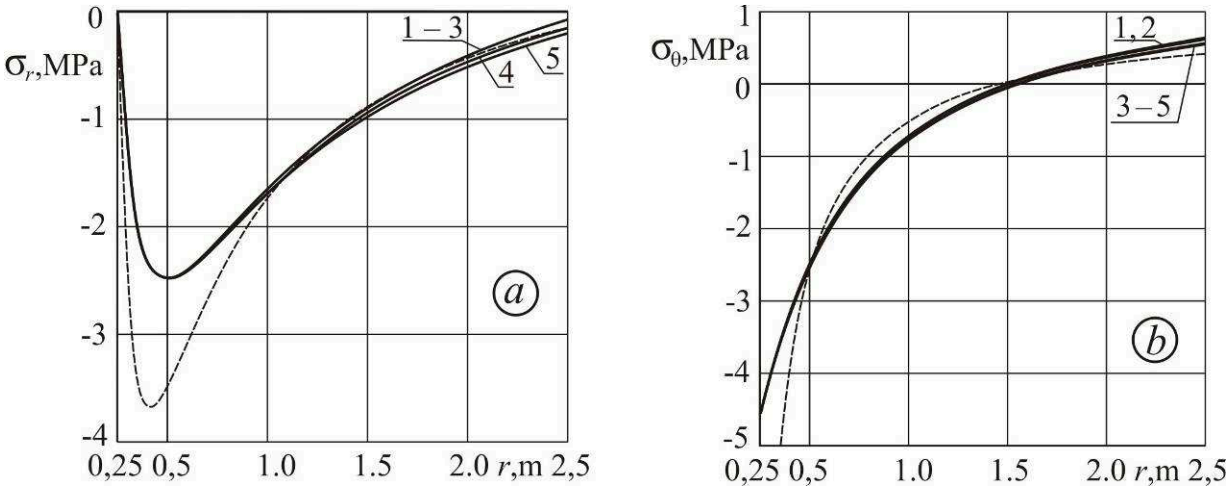


Fig. 2. Distribution of the stresses $\sigma_r$ (*a*) and $\sigma_\theta$ (*b*) along the radius for different values θ:
$1 - \theta = 0$; $2 - \theta = \pi/4$; $3 - \theta = \pi/2$; $4 - \theta = 3\pi/4$; $5 - \theta = \pi$.
—— considering inhomogeneity; - - - - excluding inhomogeneity.

**Conclusions**

Comparing values of the stresses $\sigma_r$ and $\sigma_\theta$ for the inhomogeneous ground (solid lines) at different directions (different $\theta$) we can note that they are almost identical. Small differences are near $r = b$. These differences are due to different soil pressure on the outer surface of the array. In general, the contribution the account of influence of pressure on the stress state near the cavity is negligible compared to the stresses caused by the swelling soil. Hence we can conclude that the problem can be solved in a simpler - centrally symmetric formulation excluding the variability of soil pressure.
Particular attention should be paid to Influence of Inhomogeneity on the stresses. Tear the outer contour of array there are tensile stresses that can be dangerous for soil.

**References**

[1] Lykov A.V. *The theory of heat conduction*. Moscow, "Vysshaya shkola" (1967) 599 p.
[2] Ter-Martirosyan Z.G. Soil mechanics. Moscow , Publ. house “ASV” (2005) 488 p.
[3] Golly O.R. Using laws of swelling clay soils in construction: Reconstruction cities and Geotechnical Engineering #8 (2004) pp. 131-141
[4] Andreev V.I. *Some problems and methods of mechanics of inhomogeneous bodies*. Moscow, Publ. house “ASV” (2002) 286 p.
[5] Kamke E. *Differetialgleichungen*. Leipzig (1969) 576 p.
[6] Andreev V.I., Avershyev A.S. Stationary Problem of Moisture-elasticity for Inhomogeneous thick-walled Shells. Advanced Materials Research, Vols. 671-674 (2013) pp. 571-575. Trans Tech Publications, Switzerland,

# CHAPTER 1:

# Geotechnical Engineering

*Applied Mechanics and Materials Vols. 580-583 (2014) pp 819-822*
*© (2014) Trans Tech Publications, Switzerland*
*doi:10.4028/www.scientific.net/AMM.580-583.819*

# Development of the monitoring guidance system for slope engineering

Deheng Kong[1, a], Yunkai Ruan[1, b], Zhigang Zhang[2, c], Wenfei Mao[1, d], Ming Li[1, e]

[1] College of Construction Engineering, Jilin University, 938 Xinminzhu Street, Chaoyang District, Changchun, China,130026

[2]School of Civil Engineering, Tongji University, 1239 SiPing road, Yangpu District, Shanghai City, China, 200092

[a]kongdeheng@163.com, [b]ruanyunkai@163.com, [c]jiath0815@qq.com, [d]mao361560@163.com, [e]1101173473@qq.com

**Keywords:** Landslides, Slope Monitoring, Software Design, Visual Basic.

**Abstract.** The slope monitoring is an important part of the slope engineering. Through the reasonable monitoring, the engineers can get all kinds of information and the state of slope stability; provide scientific basis for the forecast about instability. Facing various methods and diverse information, the engineers can not consult books and make project efficiently. Based on the objective of safe construction, a database system including a comprehensive range of information about monitoring design, construction technology and equipment is built by achieving the design ideas of rapid and concise. By utilizing the development tools of Visual Basic and database platform of Access, the monitoring guidance system is developed with the consultation, editing, and analysis functions. The system provides a complete slope monitoring information platform to guide the engineering staff to quickly and accurately develop the design of slope monitoring.

## Introduction

Slope is formed in the natural gravity or the human action of soil or rocks, and is one of the most basic geological environments of human engineering activities, as well as the most common form of engineering construction [1]. As one of the three global major geological disasters (earthquakes, floods, landslides and mudslides), the collapse of slope has the frequent, widespread and catastrophic features and is a serious threat to national property and people's lives [2]. To ensure the security and stability of the slope, the monitoring must be carried out during the construction and operation of slope engineering [3]. Through the reasonable monitoring, the engineers can get all kinds of information and the state of slope stability [4].

Facing various methods and diverse information, the engineers can not consult books and make project efficiently. Based on the objective of safe construction, a database system including a comprehensive range of information about monitoring design, construction technology and equipment is built by achieving the design ideas of rapid and concise. By utilizing the development tools of Visual Basic and database platform of Access, the monitoring guidance system is developed with the consultation, editing, and analysis functions. The system provides a complete slope monitoring information platform to guide the engineering staff to quickly and accurately develop the design of slope monitoring.

## The guidance system composition

The core of this system design is to establish a comprehensive slope monitoring information database and rapidly and accurately guide the slope monitoring. In the guidance system, database system that has the largest amount of information is the core module and the most important part of the slope monitoring application. Database system consists of four modules: slope type module, monitoring content module, equipment module, and specification file module. The interface of the system is shown in figure1.

**Slope type module.** According to the thickness of slope, the scale of slope, hydrological conditions, structural types of rock mass, the deformation and failure modes of slope, we classify different types of slope in detail, recommend monitoring items and introduce the engineering examples.

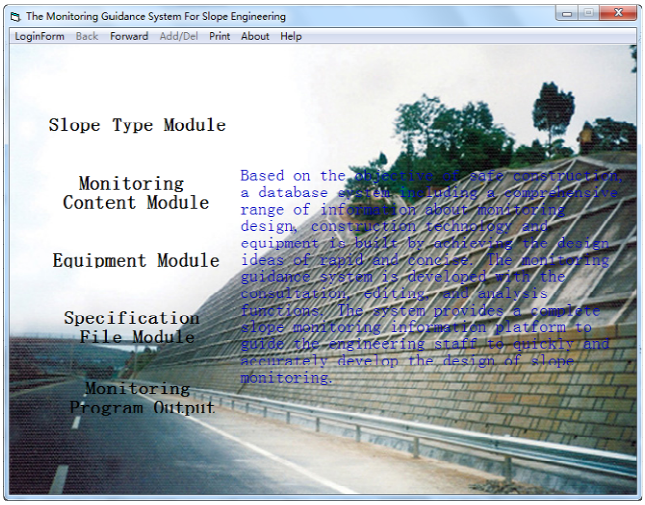


Fig. 1 The interface of the system

The slope failure classification and its influencing factors is the basis of slope treatment. Different slope failure types have the corresponding different monitoring method. According to the movement forms soil slope deformation and failure can be divided into collapse, overturning and sliding, lateral extension, flow and complex. The main types of rock slope failure includes wedge landslide, circular arc sliding surface landslide, the plane sliding of the landslide, collapse, accumulation landslide and so on. Therefore, this system is mainly described all these types of slope damage and monitoring techniques in detail [5]. The classification of slope type is shown in figure 2. And introduce of tractive slope is shown in figure 3.

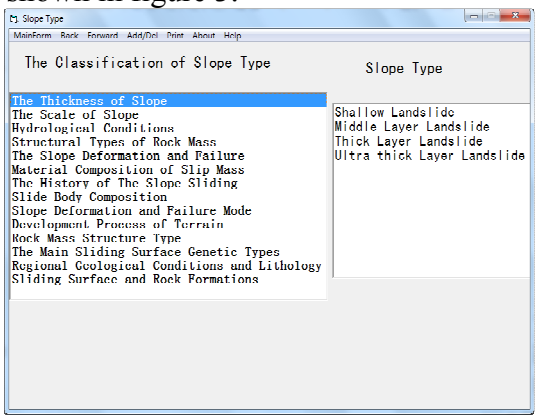


Fig .2 The classification of slope type

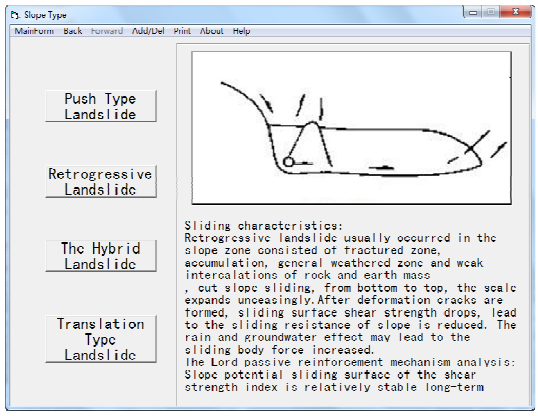


Fig .3 The introduce of tractive slope

**Monitoring contents module.** Geology factors are the foundation of creating landslides; and the non-geological factors will induce and speed up the development of landslides. Therefore, during slope monitoring, we need to grasp the main geological factors, and to carry out specific analysis on various inducing factors. Based on this view, monitoring content module divides the main monitoring items, such as the displacement monitoring, stress and strain monitoring, subsidence monitoring, groundwater monitoring [6].

In monitoring method, the system shows the measured parts, measuring point arrangement and monitoring period, monitoring frequency and early warning system and so on.

**Equipment module.** At present a lot of techniques and methods are used in the slope safety monitoring, from the traditional total station, inclinometer tube, pressure gauge, rain gauge and displacement meter, to the new type of GPS, TDR, laser range finder and so on [7].

So this equipment module introduces primarily detection equipment which has been widespread used in monitoring. This module also shows each instrument appearance, function, method of

application, manufacturer, and instrumental assessment. CX-6C fiber-optic gyroscope is introduced in figure 4.

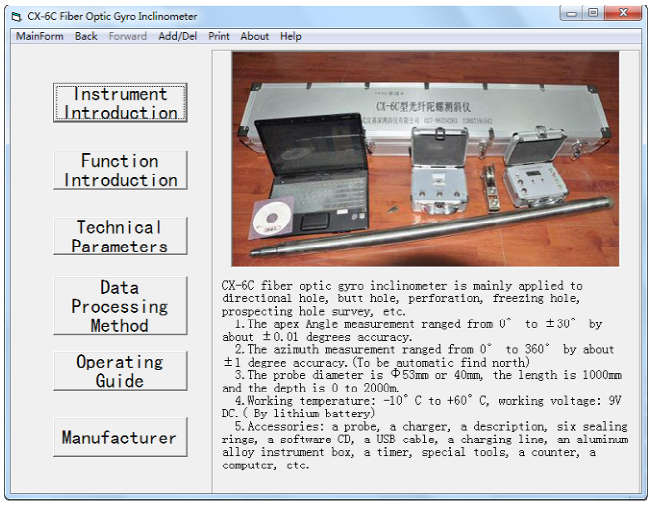


Fig. 4 The introduce of CX-6C fiber-optic gyroscope

**Specification file module.** We collected various specifications and regulations to make the users manage the download tasks more conveniently. And the system provides the monitoring program output and print to help engineers.

## Engineering application

Chaancun super-huge landslide in Dalian City of Liaoning Province was accelerating to slide since 2006. The human engineering activities led to the partial resurrection of the old landslide, and then the new landslide formed. The Chaancun landslide is a trust load caused landslide.

According to the collected landslide information, this system software recommends some monitoring programs and through the comparison with monitoring programs in practical engineering which shown in table 1. We can see some monitoring projects, equipment, and many other categories is approximately same, so the system has good guidance, auxiliary function and practical value. But some of the projects are not given, so this system is not perfect, which also needs follow-up improvement.

Table.1 Correlation Programs

| Monitoring contents | The actual monitoring programs | the system recommendation |
|---|---|---|
| The surface monitoring | Displacement monitoring of landslide surface (Scaling meter monitoring, GPS and total station monitoring) | The surface deformation monitoring (total station, theodolite, telescopic, GPS) |
| displacement monitoring | Deep displacement monitoring | Deep displacement monitoring |
| The water monitoring | Rainfall monitoring | Environmental factors monitoring(Measuring rainfall) |
| The pressure monitoring | Anti-slide pile rock pressure monitoring | |
| Hydrological monitoring | Groundwater dynamic monitoring | Hydrological monitoring |
| Others | change the surface crack, human engineering activities | Seam underground deformation monitoring |

## Conclusions

(1) In the face of all kinds of slope monitoring methods and monitoring information, to improve labor productivity, the author who utilizes the development tools of Visual Basic and database platform of Access, develops the monitoring guidance system for slope engineering with characteristics of reliability, versatility and scalability.
(2) The establishment of this system has the Open permissions, so engineers can create accounts; add new information of engineering tests. The system provides a complete slope monitoring information platform to guide the engineering staff to quickly and accurately develop the design of slope monitoring.
(3) The engineering application shows that the system has a beneficial effect on guiding engineering monitoring project, determining the monitoring scheme. But this system information is still insufficient, and the function is not perfect, so it still need to improve in the future.

## References

[1] NIE lei, WANG Ri-xu. GIS-Based landslide monitoring and forecasting system and its application in the landslide of fushun west open-Pit. Journal of Jilin University: Earth Science Edition,2010,40 (6)：1359-1364. (In Chinese)

[2] ZHANG Zhen-hua, FENG Xia-ting, ZHOU Hui, et al．Research on dynamic early warning method of slope deformation monitoring during excavation based on designed safety factor and failure mode. Rock and Soil Mechanics, 2009, 30(3):603-612. (In Chinese)

[3] WANG Jin-song, CHEN Zheng-yang, LIANG Guang-hua．Study of real time monitoring system of highway steep slopes based on GPS with multi-antenna. Rock and Soil Mechanics，2009, 30(5):1532-1536. (In Chinese)

[4] TAN liang. Three-dimensional Critical Slip Filed of Slope Stability Analysis and Its Application. Beijing: North China University of Technology，2007. (In Chinese)

[5] YE shui-sheng, YUAN xin. Further development and application of geosciences synthetic information maps database Management system. Journal of Jilin University: Earth Science Edition, 2010, 40（3）：726-732. (In Chinese)

[6] XIE Quan-min, DING Bao-yan, WU Ding-hong , et al．Study on case-based decision support system for selection of slope treatment schemes[J]. Rock and Soil Mechanics，2008, 29（5）：1353-1360. (In Chinese)

[7] GAO Jie, SHANG Yue-quan, SUN Hong-yue, et al. Application of CCD micro-deformation monitoring technology to slope remote monitoring. Rock and Soil Mechanics，2011, 32（4）：1269-1272. (In Chinese)

*Applied Mechanics and Materials Vols. 580-583 (2014) pp 823-826*
*© (2014) Trans Tech Publications, Switzerland*
*doi:10.4028/www.scientific.net/AMM.580-583.823*

# The application of BP artificial neural network in geotechnical engineering

Na Zhao

Department of Construction Engineering, Jinan Engineering Vocational College, Jinan, China

zhao_na00@163.com

**Keywords:** Time sequence; Forecasting; BP artificial network

**Abstract.** Based on MATLAB, the article apply BP artificial neural network theory on the forecasting problem of time sequence in geotechnical engineering, and find it is an effecting way to solve the forecasting problem of time sequence in geotechnical engineering.

## Introduction

Mechanical behavior of geotechnical engineering is a very complex system. The stress state of the whole system and rock mechanical properties are unclear. [1] However, a good mathematical model can correctly reflect the real relationship between the input (output) and the state of the real system. The artificial neural network is just to meet these characteristics. Artificial Neural network algorithm does not have superiority compared with the classical, but a distinct advantage when the conventional methods can not solve or poorly. It is often an effective tool especially on the mechanism question and laws do not understand, or the system can not be expressed with mathematics formula expressing. The artificial neural network can find rules contained in samples through the study and analysis of samples. Provided by MATLAB toolbox for professional field, users can focus on algorithm, and complete the programming with a few lines of a simple statement.

## Basic Principles

BP artificial neural network consists of input nodes, output nodes, and one or more layers of hidden nodes. The guiding ideology of network learning is the correction in the network weights ($W_{ij}$, $T_{li}$) and threshold (θ), so that the error function (E) along the gradient descent. Three layer BP artificial neural networks are represented as input nodes $X_j$, hidden nodes $Y_j$, and output nodes $O_l$. The network weight between the input nodes and hidden nodes is $W_{ij}$ the weight between the hidden nodes and output nodes is $T_{li}$. When the desired output of the output node is $t_l$, BP artificial neural network model computation formula is:

The hidden nodes output formula is:

$$y_i = f(\sum_j w_{ij} x_j - \theta_i) = f(net_i)$$
$$net_i = \sum_j w_{ij} x_j - \theta_i \quad (1)$$

The output node calculating formula is:

$$o_l = f(\sum_i T_{li} y_i - \theta_l) = f(net_l)$$
$$net_l = \sum_i T_{li} y_i - \theta_l \quad (2)$$

The weight of output layer correction formula is:

$$T_{li}(k+1) = T_{li}(k) + \eta\delta_l y_i$$
$$\delta_l = (t_l - o_l)\cdot o_l \cdot (1 - o_l) \quad (3)$$

The common transfer functions in MATLAB are Tansig, logsig and purelin. As an output layer, linear function (purelin) output value maybe any size, so the linear function can be used as a transfer function between the hidden layer and output layer in tunnel engineering time series prediction.

**The realization of MATLAB neurons**

The initial weights and thresholds of neurons are 0. The artificial neural network can be trained after the initialization of weights and threshold. During the training, network weights and threshold should be adjusted constantly to reduce the value of network performance function (net.perform.fcn), so that it reaches the predetermined requirements. The default value of the artificial neural network performance function is the MSE (network output and target output mean square error). BP artificial neural network minimizes the network performance function by calculating of the performance function gradient, and then adjusts the weights and threshold along the negative gradient direction.

The k-th loop adjustment formula:

$$x_{k+1} = x_k - \alpha_k g_k \quad (4)$$

Where:

$x_k$ ——the current weights and thresholds,

$g_k$ —— the current gradient,

$\alpha_k$ —— the learning rate.

To train the network by using the momentum of gradient descent function is not only faster convergence rate and the introduction of a momentum, but also effectively avoids local small problems in the network training.

$$\Delta W(k+1) = -a_k g_w(k) + mc \times \Delta W(k-1)$$
$$\Delta\theta(k+1) = -a_k g_b(k) + mc \times \Delta\theta(k-1) \quad (5)$$

Where:

$g_w(k)$, $g_b(k)$——the weights and threshold gradient of current performance function,

$a_k$——the learning rate,

$mc$——the momentum coefficient，value between 0 ~ 1.

**Engineering applications**

The rock classification surrounding Guanyin Temple tunnel of Yunfang highway is more, the change is much. As the density of exploration is limited, so that the actual tunnel rock classification may be different with the rock information provided by survey report used when the design, and could be occur many cases like the bad geological condition and surrounding rock large deformation which can not be proved. Tunnel structure is the outcome of combined action of surrounding rock and tunnel support. In order to give full play to the self bearing capacity of surrounding rock on the premise of rock and support safety, and to achieve the purpose of the

security in the economic and reasonable support conditions, the site must be achieve information construction by monitoring and measuring.

Monitoring group conducted a month of ZK175 +800 uninterrupted continuous observations, and forecasted by input BP artificial neural network after inputting new data everyday. Through the analysis of the dynamic data and forecast for a few days, the group analyzed surrounding rock stress change and forecast the future situation, and then got the following data in Table 1.

Table 1 ZK175+800 section peripheral displacement measurement value

| time ( d ) | value ( mm ) | time ( d ) | value ( mm ) | time ( d ) | value ( mm ) |
|---|---|---|---|---|---|
| 1 | 0.250 | 10 | 1.778 | 19 | 1.870 |
| 2 | 0.510 | 11 | 1.793 | 20 | 1.871 |
| 3 | 0.889 | 12 | 1.813 | 21 | 1.878 |
| 4 | 1.222 | 13 | 1.849 | 22 | 1.878 |
| 5 | 1.415 | 14 | 1.871 | 23 | 1.878 |
| 6 | 1.665 | 15 | 1.809 | 24 | 1.880 |
| 7 | 1.599 | 16 | 1.843 | 25 | 1.883 |
| 8 | 1.650 | 17 | 1.854 | 26 | 1.880 |
| 9 | 1.776 | 18 | 1.862 | 27 | 1.882 |

The group fitted the artificial neural network established in the construction process, predicted the later displacement around the tunnel by training the network, and continuously trained network with the emergence of new measurement data. In the process of network learning new data, we found that basic network could found the tunnel peripheral displacement convergence regularity basically. The prediction would be more accurate with the increase of learning data. The 10th, 14th, 20th, 25th days learning prediction error curve as Figure 1.

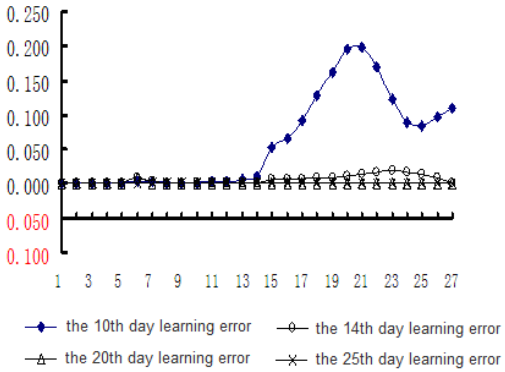


Figure 1 Simulation error curve

## Conclusions

Based on the monitoring data learning and prediction of Guanyin Temple tunnel, the comparison results of the forecast data and subsequent measurement showed that: BP artificial neural network has the characteristics like broad applicability, learning ability, can quickly grasp the regularity between input and output, etc. With the increase of the amount of information and ongoing training, multilayer BP artificial neural network can not only better fitting of the known data, but also has good prediction function. With the help of practical toolbox in MATLAB, the user can no longer consider complex programming process and more focused on algorithms, and more easily achieve the requirements of the different neural networks. In addition MATLAB has a powerful graphics functions, users can directly find the changing rule of the physical system. In short, it is an effective

way for the tunnel measurement data processing and prediction by using the MATLAB-based BP artificial neural network.

Table 2 The 10th, 14th, 20th, 25th days of data learning and prediction

| Time（d） | actual displacement（mm） | the 10th day learning error（mm） | the 14th day learning error（mm） | the 20th day learning error（mm） | the 25th day learning error（mm） |
|---|---|---|---|---|---|
| 1 | 0.250 | 0.00003 | 0.00000 | 0.00000 | 0.00015 |
| 2 | 0.510 | 0.00013 | 0.00002 | 0.00001 | 0.00106 |
| 3 | 0.889 | 0.00020 | 0.00008 | 0.00013 | 0.00030 |
| 4 | 1.222 | 0.00013 | 0.00000 | 0.00003 | 0.00104 |
| 5 | 1.415 | 0.00011 | 0.00135 | 0.00185 | 0.00237 |
| 6 | 1.665 | 0.00371 | 0.00762 | 0.00785 | 0.00070 |
| 7 | 1.599 | 0.00293 | 0.00254 | 0.00108 | 0.00021 |
| 8 | 1.650 | 0.00185 | 0.00221 | 0.00041 | 0.00016 |
| 9 | 1.776 | 0.00173 | 0.00176 | 0.00015 | 0.00183 |
| 10 | 1.778 | 0.00000 | 0.00014 | 0.00042 | 0.00002 |
| 11 | 1.793 | 0.00354 | 0.00000 | 0.00022 | 0.00041 |
| 12 | 1.813 | 0.00382 | 0.00008 | 0.00001 | 0.00038 |
| 13 | 1.849 | 0.00612 | 0.00001 | 0.00067 | 0.00004 |
| 14 | 1.871 | 0.01239 | 0.00000 | 0.00162 | 0.00085 |
| 15 | 1.809 | 0.05322 | 0.00711 | 0.00089 | 0.00048 |
| 16 | 1.843 | 0.06548 | 0.00504 | 0.00002 | 0.00010 |
| 17 | 1.854 | 0.09309 | 0.00627 | 0.00000 | 0.00001 |
| 18 | 1.862 | 0.12702 | 0.00794 | 0.00000 | 0.00008 |
| 19 | 1.870 | 0.16193 | 0.00953 | 0.00000 | 0.00002 |
| 20 | 1.871 | 0.19483 | 0.01245 | 0.00000 | 0.00002 |
| 21 | 1.878 | 0.19803 | 0.01388 | 0.00005 | 0.00001 |
| 22 | 1.878 | 0.16983 | 0.01654 | 0.00001 | 0.00000 |
| 23 | 1.878 | 0.12201 | 0.01839 | 0.00002 | 0.00000 |
| 24 | 1.880 | 0.08958 | 0.01790 | 0.00017 | 0.00002 |
| 25 | 1.883 | 0.08306 | 0.01418 | 0.00046 | 0.00005 |
| 26 | 1.880 | 0.09691 | 0.00834 | 0.00131 | 0.00001 |
| 27 | 1.882 | 0.11122 | 0.00110 | 0.00183 | 0.00003 |
| Error Sum | | 1.60288 | 0.15449 | 0.01921 | 0.01034 |

**Acknowledgements**

In this paper, Mr. Xu Rundong, China Zhongtie Major Bridge Reconnaissance & Design Institute Co.,Ltd. and Mr. Zhu Ningning, Water Conservancy Bureau of Shandong Province provided a large number of project examples and careful coordination, many relevant experts also gave lots of great support for the paper, in this thank you.

**References**

[1] Shengjun Zhang，Ye Xue, Jinan Tao. Prediction of Stable Displacement and Unstable Time on Tunnel and Slope[J], Chinese Journal of Geotechnical Engineering,1996,18(1):39~45. (In Chinese)

[2] Wei Gao. Discussion on "study on deformation behavior characteristics and modeling of slope system [J]. Chinese Journal of Geotechnical Engineering, 2002, 24(2): 260-. (In Chinese)

[3] Xin Wen, Lu Zhou. Simulation and application of MATLAB neural network[M]，Beijing: Science Press,2003. (In Chinese)

[4] Defeng Zhang. Simulation and application of MATLAB neural network[M]，Beijing: Publishing House of Electronics Industry：2009. (In Chinese)

*Applied Mechanics and Materials Vols. 580-583 (2014) pp 827-830*
*© (2014) Trans Tech Publications, Switzerland*
*doi:10.4028/www.scientific.net/AMM.580-583.827*

# Numerical simulation of slope excavation in highway renovation and expansion project

Genchaun Luo[1, 2,a], Zhongming He[1,b] , Xin Luo[1,c] and Qingguo Hu[1,d]

[1]School of Traffic and Transportation Engineering, Changsha University of Science & Technology,Changsha Hunan 410004, China

[2]Guanxi Communication Investment Group CO.,LTD , Nanning Guangxi 530028,China

[a]luogenchuan@163.com, [b]hezhongming45@126.com, [c]369991799@qq.com, [d]huqg204@126.com

**Keywords:** renovation and expansion project; Numerical Simulation; Slope excavation; Stability

**Abstract** Slope stability analysis requires detect and control the stress and strain timely. Familiar with the slope‘s stress and strain changes in excavation process has important guiding significance for the actual construction. In this paper, choose a slope in Guangxi freeway renovation and expansion process as the research object. Use FLAC3D to analysis the stress and displacement simulation results of this slope excavation step by step. Summarize the excavation regular pattern.

## Introduction

Slope excavation and unloading change the stress state of rock, it have a greater impact on the stability. Many scholars do research on excavation and slope stability. Luyu Zhang et al[1] use strength reduction calculated slope safety factor; Haichen Hu[2] use slope software analysis slope excavation stability; Yuhui Xiao et al[3] studied the deformation mechanism of slope excavation; Jian Zeng et al[4] and Hongmei Tang et al[5] use laboratory experiments to simulate the rock slope excavation process; Minghui Yang et al[6] analysis the stress and strain about multi-stage slope excavation simply. On the basis of these studies, analysis of the shear strain increment contours, main stress contours and displacement contours in each excavation step basis on the slope in Guangxi freeway renovation and expansion project. And set up a series of monitoring points to monitor displacements to provide a reference for the actual construction of slope excavation

## Numerical model

The slope is mainly by gravelly silty clay, strongly weathered layer and mid-weathered layer. The main mechanical parameters are shown in Table 1.

Table 1 Mechanical parameters table

| Lithology | Heavy ($KN/m^3$) | Cohesion (KPa) | Angle of internal friction ( ° ) | The bulk modulus （MPa） | The shear modulus （MPa） |
|---|---|---|---|---|---|
| gravelly silty clay | 18.5 | 28 | 18 | 33 | 20 |
| Strongly weathered layer | 21 | 35 | 23 | 370 | 243 |
| Mid-Moderately weathered layer | 24 | 80 | 40 | 5200 | 4800 |

The slope model as shown in Figure 1. It has three level slope(10m each), length of 75m, the rate of three level slopes are: 1:1,1:1.25 and 1:1.5, 2m platform. The model is total of 4147 nodes and 3430 units. Setting horizontal constraints on both side of this model, the bottom set of rigid constraints, fixed all the nodes in the y-direction deformation. The material of this model select Mohr-Coulomb elastic-plastic material, yield criterion using Mohr-Coulomb criterion, the convergence criterion using the relative convergence criterion(Calculate termination when the maximum unbalanced force and the typical internal force ratio is less than 10-5) .

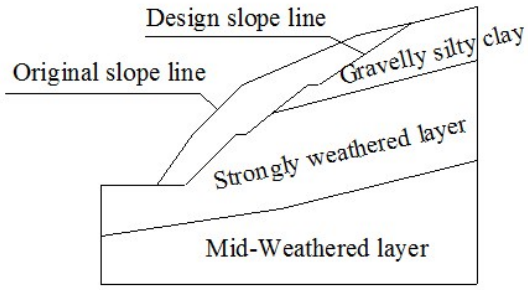


Figure 1 Schematic of slope

## The simulation results analysis

Before the slope excavation, use strength subtraction to get the slope safety factor. It's 1.16,which less than the slope stability boundary value of 1.20. The potential landslide include excavation parts. The slope safety factor is 1.29 after excavation completely, which in a stable state, so only need to take general ecological protection. Analysis the stress and strain contours of three steps of the excavation respectively.

## Numerical analysis of the first step in slope excavation

When the first excavation step is done, the safety factor is up to 1.26. The shear strain increment contour shows that the third layer do not appear the shearing deformation slope area. Potential sliding surface is transfer to the first and second slope. The shear strain increment value of the first level slope midpoint is the largest. Figure 2 and Figure 3 show the third and the first principal stress contour after first step excavation. Only the slope surface presented tensile stress, the maximum tensile stress up to 17.7 KPa in Figure 2. And in Figure 3, the maximum tensile appear in the second slope up to 9 KPa.

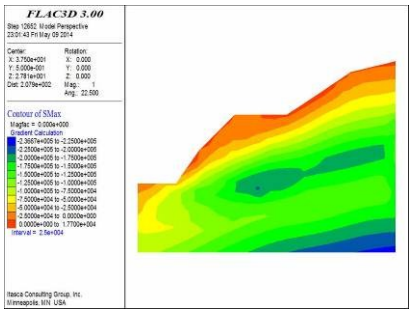


Fig.2 The third principal stress contour

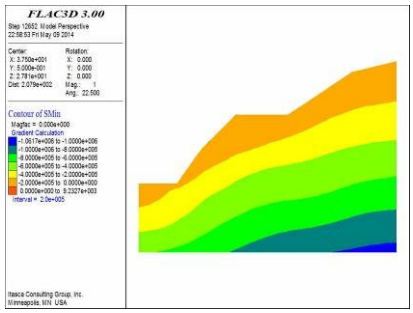


Fig.3 The first principal stress contour

Figure 4 and Figure 5 are the horizontal and vertical displacement contour. And the strain is mainly concentrate on the first and second slope. Figure 4 shows the biggest increment of the shear strain, which the horizontal displacement is also the biggest, up to 18.6cm. From figure 5, top of the second slope area get the maximum 12.5cm, the whole slope top also deformed 4cm.

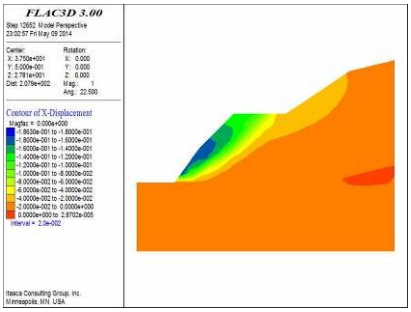


Fig.4 Horizontal displacement contour

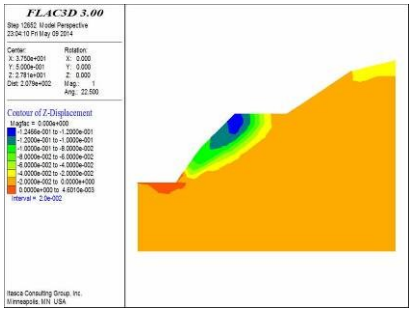


Fig.5 Vertical displacement contour

### Numerical analysis of the second step in slope excavation

When finished the second step excavation, the safety factor of slope increased to 1.42. Internal of the third level slope has appeared shear stress. Figure 6 and Figure 7 show the third and the first principal stress contour after the second step. We can see the maximum tensile stress value is 31.8 KPa appeared in the first and third level from figure 6. And figure 7 show us the maximum tensile stress increased to 46.4 KPa, the distribution is increase too.

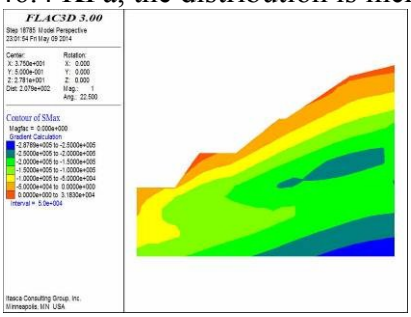


Fig.6 The third principal stress contour

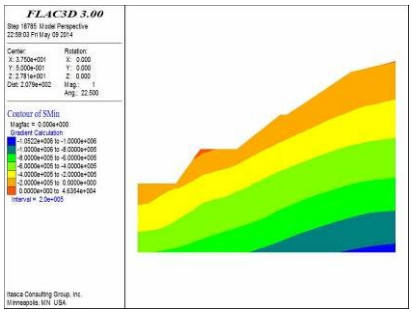


Fig.7 The first principal stress contour

Figure 8 is horizontal displacement contour. It shows bigger displacement area and the maximum 11.5cm appeared in the second and third level slope. It's decreasing in both sides. Figure 9 is vertical displacement contour. Top of the third level slope reaches a maximum value 14.3cm.

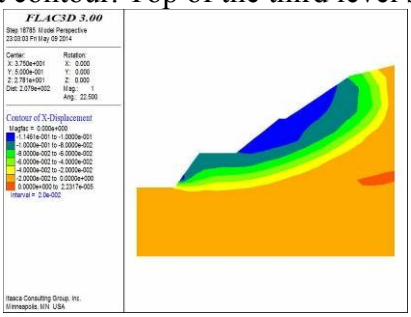


Fig.8 Horizontal displacement contour

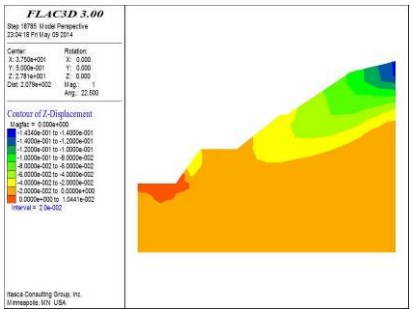


Fig.9 Vertical displacement contour

### Numerical analysis of the third step in slope excavation

The slope safety factor dropped to 1.29 after this step. But it is still larger than the slope stability boundaries. So it doesn't need special supporting. The distribution of shear strain increment and principal stress are the same, but the third principal stress value doesn't. The maximum tensile stress value dropped to 18.6KPa.

Figure 10 and Figure 11 are displacement contours. Figure 10 tells the area of the maximum horizontal displacement move downward, and the value is increased to 18.4cm. The maximum vertical displacement is 19.7cm from figure 11.

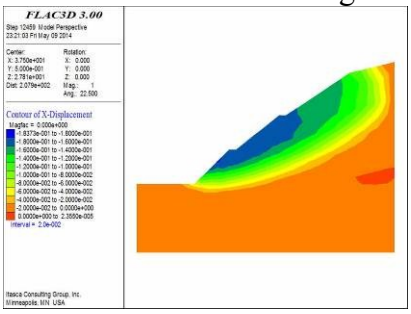


Fig.10 Horizontal displacement contour

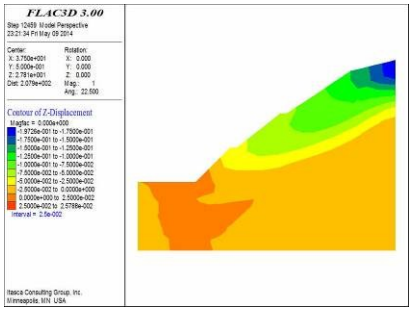


Fig.11 Vertical displacement contour

### Changes in displacement about monitoring points during excavation

Set a monitoring point in the toe and crest and waist of the slope at each level. Also in the top of the whole slope and pavement near the toe set up monitoring points. Figure 12 and Figure 13 are various monitoring points change in slope excavation process.

With the excavation proceeds, the constitutive relation rock mass deterioration, resulting in reduced rock strength and increased deformation. From the view of figure 12, the horizontal displacement of all monitoring points up to the maximum when the excavation is complete. Monitoring points show the shape of a parabola. From the view of figure 13, with the excavation proceeds, displacement of the first to the fifth monitoring points has increase, the sixth to the last monitoring points do not reflect the obvious regular pattern. But they still exhibit resilience characteristics.

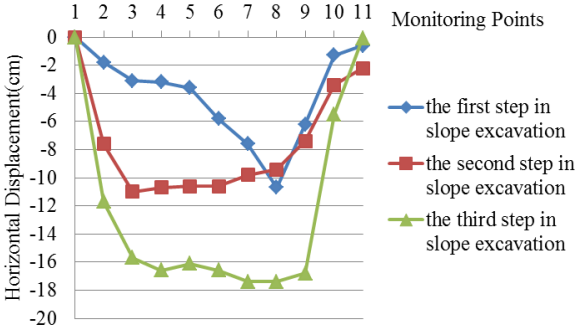


Fig.12 Monitoring points horizontal displacement

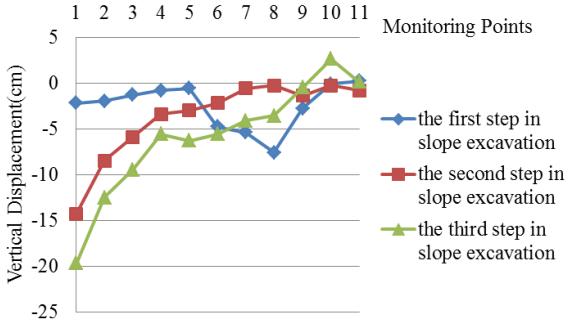


Fig.13 Monitoring points vertical displacement

## Conclusions

(1) Stress in the initial excavation is vary greatly, with the excavation progresses, the stress distribution will stabilize, but the stress of change still occurs.

(2) Strain increases in whole excavation slope. Every excavation will produce a potential sliding surface and horizontal displacement around the surface shear export is much larger. The export is generally appears in the recently completed excavation slope toe or waist. Vertical displacement showed resilience characteristics.

(3)In multi-level slope excavation process, early should be control the original slope stability. Reinforce monitoring the original potential export. In the late should be noticed the completed slope stability. Reinforce monitoring the completed slope toe area and take support measures appropriately.

## Acknowledgement

This project obtained the funding of the scientific research and technology development projects of Guangxi(1298011-2) and Hunan Science and Technology Project (2014FJ3067)

## References

[1] Luyu Zhang, Yingren Zheng, Shangyi Zhao, et al. The feasibility study of strength-reduction method with FEM for calculating safety factors of soil slope stability[J].Journal of Hydraulic Engineering,2003,21-27

[2] Haichen Hu. Highway excavation of soil slope stability analysis[J].Science & Technology Vision.2013,264-265

[3] Yuhui Xiao, Zhencun Li, Jin Duan et al. Mechanism and caculation research on excavation deformation of high layered dip rocky slope. Journal of Changsha University of Science & Technology(Natural Science), 2013,10(2):22-27

[4] Jian Zeng, Zhencun Li, Xin Guo. Mountainous Expressway bedding rock slope excavation process model test[J]. Highways & Automotive Applications, 2013,5:153-156

[5] Hongmei Tang, Hongkai Chen, Weiwen Cao. Model experiment in excavation of rock bedding slope[J].Rock and Soil Mechanics, .2011,32(2):435-439

[6] Minghui Yang, Bo Kuan, Zechang Zhou. Numerical simulation of excavation and support and Stability Analysis of a freeway cutting high slope[J]. Journal of China & Foreign Highway,.2011,31(1):25-29

*Applied Mechanics and Materials Vols. 580-583 (2014) pp 831-834*
*© (2014) Trans Tech Publications, Switzerland*
*doi:10.4028/www.scientific.net/AMM.580-583.831*

# On Fire Severity of Flammable Gas

WU Wen-zhong

Xi'an University of Science and Technology, China

E-mail: wuwenzhong@tju.edu.cn

**Keywords:** coalmine fire; flammable gas; fire severity; fire severity coefficient

**Abstract.** Flammable gases's fire need more attention in spontaneous combustion study of coalmine. Their premixed combustion is modeled to deduce the corresponding temperature-time function. Basing on this function curve and Simon Ingberg's early reports, their fire severity classification theory is established, including definition and equation of their fire severity, and definition of fire severity coefficient along with calculation of those coefficients of ordinary flammable gases. Applying this theory to a certain coalmine, calculate and audit fire severity of its 6 designed fire scenarios, in servitude to guidelines for fire protection technology there, and references for fire severity comparison among similar coalmines.

## Introduction

Undermine fires, a kind of severe incidents, burn much coal source, and also release flammable gas, to induce gas or coal dust explosions. Every year many such incidents are reported of much property and personnel loss in coalmines[1-3]. However, current research status of mechanism and extinguishing methods of spontaneous combustion of coal mine focus on its spontaneous combustion propensity, temperature rise, and little attention has been paid to flammable gas fire, and few reasonable fire protection measures are taken for the fight against this kind fires during the spontaneous combustion.

At normal Oxygen percent, coal oxidizes with CO, $CH_4$, $C_2H_4$, $C_2H_6$, $C_2H_2$ etc. flammable gases products too. During coal oxidization and temperature rise, CO first appears at 32℃, $C_2H_4$ first appears at 100.9℃[4]. $CH_4$ releases before, during and after mining. US EPA reported that the methane release from coalmine amounts to 8% of total methane release in mankind activity worldwide[5,6].

At undermine, existing CO, $CH_4$, $C_2H_4$, $C_2H_6$, $C_2H_2$ etc. flammable gases, mix with sufficient Oxygen at reasonable temperature, and light to fire or explosion, therefore, except for preventing inner-reason fires, coalmine fire protection should audit CO, $CH_4$, $C_2H_4$, $C_2H_6$, $C_2H_2$ etc. flammable gases fire and their severity, and design fire protection system, in order to hinder or delay severity state coming, and control fire evolution, to ensure miner evacuation success and coal lane structure safety.

We start from a mathematical model for flammable gas premixed combustion, and calculate its temperature-time function; basing on the function and Simon Ingberg's fire severity definition, establish fire severity classification theory for flammable gas, including: calculation equation of its fire severity, definition of its fire severity coefficient and their calculations of common flammable gases; apply this theory to audit flammable fire severity in a certain coalmine, suppose fire protection measures to prevent most severe flammable fires, in servitude to guidelines for fire protection and extinguishing in this mine.

## Temperature-time function for flammable gas premixed combustion

CO, $CH_4$, $C_2H_4$, $C_2H_6$, $C_2H_2$ etc. may mix with Oxygen, and cause fire or explosion lighted by a spark or at enough temperature. Suppose a flammable gas (Fuel, F) mixes with Oxygen (Oxygen, O) in a closed mining area of fixed volume (Fig.1), and burns at appropriate temperature (Temperature, T) into a transient fire[7]. The properties of the gaseous mixture are uniform in the area, and constant and equal specific heats. We adopt a control volume enclosing the burning area of the constant

volume, fixed mass, with ambient temperature, and there exists the following energy conservative equation

$$mc_v \frac{dT}{dt} = \dot{Q}_R - \dot{Q}_L = \alpha t^2 \tag{1}$$

where: $\dot{Q}_L$ -conductive heat loss, $\dot{Q}_R$ -chemical energy release rate of gaseous mixture, $\alpha$ -fire performance coefficient, $kW/s^2$ . And gets temperature-time function for flammable gas premixed combustion

$$T(t) = \frac{\alpha}{3mc_v} t^3 + constant \tag{2}$$

where: $t_0$ -initial time of burning, s; $T_0$ -initial temperature of mixture; $m$ -mass of mixture; $c_v$ -specific heat.

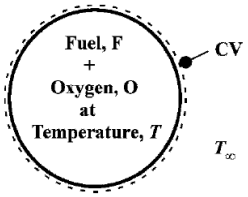


Fig.1 Flammable gas premixed combustion model.

**Flammable gas fire severity**

From the known temperature-time function for its premixed combustion in undermine, we can define and calculate flammable gas fire severity following Simon Ingberg, and then define its fire severity coefficient, and calculate those of common flammable gases out of their thermal property, for reference in auditing fire scenario and designing fire protection system.

In the 1920s Simon Ingberg defined fire severity as an area under the time-temperature curve above a base temperature, and the fire severity in two fires is equal when the areas under their time temperature curves are equal[8-10]. Denote flammable gas fire severity as $R_g$ , fire time $t$ , temperature-time function $T(t)$ as Eq.(2), the base temperature line $t_0 = 0$ , and initial temperature $T_0$=0 , then we have flammable gas fire severity and its coefficient $r_g$ :

$$R_g = \frac{\alpha}{12mc_v} t^4 = r_g t^4 \tag{3}$$

At assumption that a flammable gas performs a fast fire with a stoichiometric reaction and neglected diffusion effects, and those known specific heat capacities of common gases[11,12], specific heat capacity and mass of mixtures of Oxygen and 1mol gases, from Eq.(3) we calculate coefficients of 1mol common flammable gases fire severity as Tab.1.

TABLE 1. FIRE SEVERITY COEFFICIENTS OF COMMON GASES

| Gas[a,b] | $r_g$ (K•s$^{-3}$) | Gas[a,b] | $r_g$ (K•s$^{-3}$) |
|---|---|---|---|
| $H_2$ | 0.084 | CO | 0.083 |
| $CH_4$ | 0.031 | $C_2H_2$ | 0.021 |
| $C_2H_4$ | 0.015 | $C_2H_6$ | 0.012 |
| $O_2$ | 0.183 | | |

a. Normal atmospheric temperature and pressure: 1atm, 25℃; b. Mass of gas is 1mol.

## CASE STUDY: AUDIT FLAMMABLE GAS FIRE SEVERITY IN A CERTAIN COALMINE

Out of a certain coalmine, adopt its coal sample 1500 g for oxidization test at stable 30 ℃ with air flow 50 ml/min and continually rising temperatures, and record those indicative gases release in the process of spontaneous combustion for predicting coal fire[4]:

CO: at 32℃, first appears 5ppm; before 66.5℃, CO releases slowly within 19-135ppm; at 66.5℃, CO jumps to 279ppm; at 73.5℃, CO reaches to 324ppm; inside 73.5-113.4℃, CO release rises greatly from 200ppm to 1300ppm.

$C_2H_4$: first appears at 100.9℃, and releases slowly before 176.8℃, then rises greatly up to 330.61ppm from 199.9℃.

$C_2H_2$: at 262.8℃, first appears 39ppm; at 269.2℃, $C_2H_2$ releases its maximum 75ppm, which drops gradually to 0ppm at 326.3℃.

At 457.0℃, CO, $CH_4$, $C_2H_4$, $C_2H_6$, $C_2H_2$ release 14115, 19928, 270.61, 2906.2, 0ppm respectively.

We calculate and compare fire severity of these gases by Eq.(3) as Tab.2 out of this record with fire time about 50s[13]:

TABLE 2. FIRE SEVERITY COEFFICIENTS OF COMMON GASES IN THE DISCUSSED COALMINE

| Temperature level | fire severity (K•s) |
|---|---|
| 406-440℃ | $R_{C_2H_2} = 7.797\times10^{-7}$ |
| 520-630℃ | $R_{C_2H_4} = 2.841\times10^{-7} > R_{C_2H_6} = 1.969\times10^{-8}$ |
| 641-750℃ | $R_{CO} = 2.733\times10^{-8} > R_{CH_4} = 4.058\times10^{-9}$ |
| >750℃ | $R_{g,\,total} = R_{C_2H_2} + R_{C_2H_4} + R_{C_2H_6} + R_{CO} + R_{CH_4} = 1.115\times10^{-6}$ |

Table 2 shows that fire prevention measures at this coalmine can be divided into two categories: (1) should keep coal temperature below 32℃ to prevent its oxidization releasing flammable gases; (2) after the coal oxidization, should extract gases to deduce the concentrations of those flammable gases, and keep temperature below 406℃ to prevent their ignition.

## CONCLUSIONS

We establish fire severity classification theory for flammable gas, and apply it to audit flammable fire severity in a certain coalmine, for guidelines to fire protection in this coalmine and other coalmines too.

1) The mathematic model for flammable gas mixed combustion is founded, and its fire temperature-time function is derived from the energy conservation law inside this combustion;

2) From this fire temperature-time function and Simon Ingberg's early fire severity definition, fire severity classification theory is established for flammable gas, including definition and equation of its fire severity, and definition of its fire severity coefficient along with calculation of those coefficients of ordinary flammable gases;

3) Applying this theory to a certain coalmine, calculate and audit fire severity of its 6 designed fire scenarios in oxidization. Fire prevention measures at this coalmine directly come from the oxidization test and fire severity calculation of the indicative flammable gases.

## References

[1] XU Man-gui, XU Jing-cai, WEN Hu. Current research status of mechanism and extinguishing methods of spontaneous combustion of coal mine [J]. Journal of Xi'an University of Science and Technology, 2001, 21 (1):4-7.

[2] DENG Jun, XU Jing-cai, RUAN Guo-qiang. Review of the prediction and forecastion techniques of coal self heating both at home and abroad [J]. Journal of Xi'an University of Science and Technology, 1999, 19 (4):293-295.

[3] JIN Yong-fei, DENG Jun, XU Yan-hui, SUN Hai-he. Application of random detection method in detecting of underground coal fire [J]. Journal of Xi'an University of Science and Technology, 2010, 30 (6):647-650.

[4] SU Cai-quan, WANG Gang, ZHANG Rui, YU Yan-bin. Experimental Study on Indicative Gases of Temperature Rise with Self-ignition of Coal Samples in Liangbaosi Colliery [J]. Journal of Shandong University of Science and Technology (Natural Science), 2009, 28 (4):87-92.

[5] US EPA. Assessment of the worldwide market potential for oxidizing coal mine ventilation air methane [R]. United States Environmental Protection Agency, EPA 430-R-03-002; July 2003.

[6] ZHU Hong-qing, LIU Xing-kui. Numerical simulation of heating up of coal spontaneous combustion in gob area under tail roadway methane drainage pattern [J]. Journal of Xi'an University of Science and Technology, 2012, 32 (1):1-7.

[7] Li Yinqing. Performance-based design in building fire protection design [M]. Beijing: Chemical Industry Press, 2005.

[8] Ingberg, S. H. Tests of the severity of building fires [R]. NFPA Quarterly, Col. 22, No. 1, July 1928.

[9] Ingberg, S. H. The severity of fires in buildings [R]. Architectural Engineering and Building, May 1929.

[10] Robert W. Fitzgerald. Building Fire Performance Analysis [M]. England: John Wiley & Sons, Ltd., 2004.

[11] James G. Quintiere. Fundamentals of Fire Phenomena [M]. England: John Wiley & Sons Ltd, 2006.

[12] Drysdale, D. Introduction to Fire Dynamics [M]. England: John Wiley & Sons, Ltd, 1999, 2nd edn.

[13] Shanghai Municipality on Construction of Engineering Projects. Technical specification for building smoke control (DGJ 08-88-2006) [S].

*Applied Mechanics and Materials Vols. 580-583 (2014) pp 835-838*
*© (2014) Trans Tech Publications, Switzerland*
*doi:10.4028/www.scientific.net/AMM.580-583.835*

# Study on Cover Backfilling of Open Pit to Underground Basing on Natural Classification

Chao Chen [1,3, a], Deqing Gan [1,3], Chaoqun Yu[2], Aidong Song[2], Sen Wang[1,3], Hongjian Lu[1,3], Weihang Zhang[1,3]

[1]Hebei United University, Tangshan,063009

[2] Hebei Iron and Steel Group Mining Co.,Ltd, Tangshan,063009

[3]Mining Development and Safety Technology Key Lab of Hebei Province, Tangshan, 063009

[a]cclsy@sohu.com

**Keywords:** open pit to underground; covered rock; backfill; natural classification.

**Abstract.** The cover of the open pit to underground natural phenomena on the use classification of the mine caving mining ventilation, temperature, dilution and other indicators of ore loss have a more significant impact, but when the coating in the filling to form a reasonable natural grading, domestic research is still in the blank stage. In this paper, the background for the study of Shougang iron ore Xingshan, using theoretical analysis, physical simulation, field trials and other research tools, the coverage of the open pit to underground layer of backfill laws of the natural classification system for in-depth analysis of the results come Miaogou iron waste rock dump using artificial backfill to form a reasonable hierarchical structure and thickness of the natural cover is feasible.

## Introduction

At present there are many methods to form the cover of open pit to underground, to the Miaogou, it is are the most suitable method by backfilleding with waste dump[1,2].

There are mines into underground mining.Zhang Guojian[3] through the experimental confirmed that natural phenomenon of classification is objective existence in loose rock overburden of sublevel caving mining. Based on the loose rock mass characteristics and analysis of flow mechanics theory, Zhang zhijun[4,5]studied the ore loose rock overburden moving law in the process and reveals through physical simulation.The loose body of overburden rock flows naturally graded phenomenon, and then he provided theoretical of gradation composition for the formation of rock overburden.

## Influence factors of cladding backfill natural classification analysis

Backfill powder in the gravitational potential energy and movement will produce natural grading, the degree of natural grading and distribution of grain group will be restricted by the followed factors.

- Influence of the packing of the abandoned and dumping height abandoned
- Back to the filler particle size composition
- Rough and hard degree of the initial slope surface

## Back to the filler natural hierarchical physical simulation experiment research

### *Experimental Model*

Physical model is shown in Fig. 1, and scale model is 1:50.

**Ratio of the sample.**After the screening test material is a mixture of different size stones, the total number of stone 1000kg. Size ratio shown in Table 1.

**Simulation program.**Analog scraper shovels in the model 30m, 40m, 50m elevation backfill material simulation test.

### *Natural Classification Thickness Analysis*

Backfill different thickness grading down unloading height simulation shown in Table 2.

**Fig.1 Test model**

**Table 1 Size ratio of material**

| No. | Particle diameter mm | Percentage sieve | Cumulative percentage sieve |
|---|---|---|---|
| 1 | >20 | 13.40% | 13.40% |
| 2 | 16-20 | 2.80% | 16.20% |
| 3 | 10-16 | 26.00% | 42.20% |
| 4 | 5-10 | 33.00% | 75.20% |
| 5 | 2-5 | 23.20% | 98.40% |
| 6 | <2 | 1.60% | 100.00% |

**Table 2 Backfilling height of the natural grading**

| Backfilling height | | Particle size | | | Particle simulation size | | |
|---|---|---|---|---|---|---|---|
| MH/cm | SH /m | Fine /cm | Medium /cm | Coarse /cm | Fine /m | Medium /m | Coarse /m |
| 60 | 30 | 15.5 | 26 | 18.5 | 7.75 | 13 | 9.25 |
| 80 | 40 | 22 | 37 | 21 | 11 | 18.5 | 10.5 |
| 100 | 50 | 41.5 | 27 | 31.5 | 20.75 | 13.5 | 15.75 |

In the simulation process, Initial backfill poor mobility, natural classification is not obvious. After reaching a certain size, graded phenomenon is very obvious. Down by the backfill unloading height simulation of different thickness grading backfill different tables and pour unloading height simulate the final result can be seen naturally hierarchical classification is divided into three parts, fine-grained, medium-grained, coarse-grained. With the backfill down unloading height increases, the fine and coarse backfill layer thickness showed a rising trend, medium grain backfill layer thickness decreased after the first growth trend.

***Natural Classification Particle Size Analysis***

Physical simulation test backfill height of 50m analogue reverse unloading at 30m, 40m on the basis of, only the natural classification particle size analysis simulation 50m height were analyzed. Backfill naturally graded fine, medium-grained, coarse three-part feature such as shown in Table3-5.

**Table 3 Fine ratio after grading in test**

| No. | Particle diameter mm | Sieve | Percentage sieve | Cumulative percentage sieve |
|---|---|---|---|---|
| 1 | >20 | 26 | 2.60% | 2.60% |
| 2 | 16-20 | 22 | 2.20% | 4.80% |
| 3 | 10-16 | 268 | 26.80% | 31.60% |
| 4 | 5-10 | 386 | 38.60% | 70.20% |
| 5 | 2-5 | 292 | 29.20% | 99.40% |
| 6 | <2 | 6 | 0.60% | 100.00% |

According to backfill naturally graded fine, medium-grained, coarse ratio of three parts can be seen in Table:

- **Fine Fraction.**Particle size less than 5mm accounted for 29.8%, 5 ~ 16mm is 65.4%, 16 ~ 20mm of 4.8%.
- **Medium-grained.**Part.Particle size less than 5mm accounted for 10.6%, 5 ~ 16mm is 75.8%, 16 ~ 20mm is 13.6%.
- **Coarse Fraction.**Particle size less than 5mm accounted for 0%, 5 ~ 16mm is 44.8%, 16 ~ 20mm is 55.2%.

**Table 4 Grain ratio after grading in test**

| No. | Particle diameter mm | Sieve | Percentage sieve | Cumulative percentage sieve |
|---|---|---|---|---|
| 1 | >20 | 110 | 11.00% | 11.00% |
| 2 | 16-20 | 26 | 2.60% | 13.60% |
| 3 | 10-16 | 402 | 40.20% | 53.80% |
| 4 | 5-10 | 356 | 35.60% | 89.40% |
| 5 | 2-5 | 104 | 10.40% | 99.80% |
| 6 | <2 | 2 | 0.20% | 100.00% |

**Table 5 Coarse ratio after grading in test**

| | | | | |
|---|---|---|---|---|
| 1 | >20 | 456 | 45.60% | 45.60% |
| 2 | 16-20 | 96 | 9.60% | 55.20% |
| 3 | 10-16 | 428 | 42.80% | 98.00% |
| 4 | 5-10 | 2 | 2.00% | 100.00% |
| 5 | 2-5 | 0 | 0.00% | 100.00% |
| 6 | <2 | 0 | 0.00% | 100.00% |
| 1 | >20 | 456 | 45.60% | 45.60% |

***Nature dump site grading test analysis***

Process of forming a cover layer of artificial backfill and dump is rock row down the principle is the same, this paper do this scene 20m high dump were naturally graded field test, field test model shown in Fig.1.

**Natural Classification Thickness Analysis.**Dump site naturally graded fine, medium-grained, coarse obvious effect of three parts, field measurements after dump toe point elevation natural grading and classification conversion obtained after fine grading thickness 7.5m, medium grain 6.7 m, coarse 5.8m.

**Table 6 Fine ratio after grading**

| No. | Particle diameter mm | Sieve | Percentage sieve | Cumulative percentage sieve |
|---|---|---|---|---|
| 1 | >100 | 22 | 2.20% | 2.20% |
| 2 | 60-100 | 20 | 2.00% | 4.20% |
| 3 | 40-60 | 48 | 4.80% | 9.00% |
| 4 | 20-40 | 101 | 10.10% | 19.10% |
| 5 | 10-20 | 206 | 20.60% | 39.70% |
| 6 | 5-10 | 342 | 34.20% | 73.90% |
| 7 | <5 | 261 | 26.10% | 100.00% |

**Table 7 Grain ratio after grading**

| No. | Particle diameter mm | Sieve | Percentage sieve | Cumulative percentage sieve |
|---|---|---|---|---|
| 1 | >100 | 108 | 10.80% | 10.80% |
| 2 | 60-100 | 126 | 12.60% | 23.40% |
| 3 | 40-60 | 272 | 27.20% | 50.60% |
| 4 | 20-40 | 197 | 19.70% | 70.30% |
| 5 | 10-20 | 138 | 13.80% | 84.10% |
| 6 | 5-10 | 88 | 8.80% | 92.90% |
| 7 | <5 | 71 | 7.10% | 100.00% |

**Natural Classification particle size analysis.**Natural classification of different size rock select a representative sample of 3 points, depending on the circumstances of each sampling point sampling 1000kg. The rock samples were sieved turn over 100mm, 60mm, 40mm, 20mm, 10mm, 5mm, 5mm smaller than the sieve, sieve diameter, respectively, after weighing the rock, and recording weight; 100mm above the rock with ruler to measure, and then ,they are recorded and weighed. Screening results are shown in Table 6-8.

**Table 8 Coarse ratio after grading**

| No. | Particle diameter mm | Sieve | Percentage sieve | Cumulative percentage sieve |
|---|---|---|---|---|
| 1 | >100 | 260 | 26.00% | 26.00% |
| 2 | 60-100 | 281 | 28.10% | 54.10% |
| 3 | 40-60 | 162 | 16.20% | 70.30% |
| 4 | 20-40 | 101 | 10.10% | 80.40% |
| 5 | 10-20 | 82 | 8.20% | 88.60% |
| 6 | 5-10 | 61 | 6.10% | 94.70% |
| 7 | <5 | 53 | 5.30% | 100.00% |

According to the natural grading dump fine, medium-grained, coarse three-part matching table can be seen: the fine fraction less than 5mm diameter accounted for 26.1%, the grain diameter portion and a coarse fraction is greater than 100mm 36.8%.

Through physical simulation test and field test dump can be seen in the natural grading backfill reasonable physical simulation of natural thickness and particle size effects and hierarchical structure.Miaogou Iron status pit cover into the desired structure and thickness of the coating layer to determine the step height of the backfill 50m.

## Conclusions

In the paper, the forming by natural grading of Miaogou‘s cover is studied and the conclusions is obtained.

- Main factors affecting natural classification are the dumping height, the backfilling particle sizes, the degree of rough and hard slope.
- The natural grading process, initial natural classification is not obvious. After reaching a certain size, grading phenomenon is very obvious.It is divided into three parts, fine-grained , medium-grained , coarse-grained. With the backfill down unloading height increases, the fine and coarse backfill layer thickness increasing trend in grain backfill layer thickness decreased after the first growth trend.
- Through simulation test, Backfilling method by natural classification to form a high-level cover is simple , reliable, short construction period and good economic returns .

## Acknowledgements

This work was financially supported by Hebei Province Natural Science Foundation (E2013209328), and funded by Hebei Iron and Steel Group Mining Co.,Ltd.

## References

[1] Yang fu Jun,Gao Hai chuan. *Research and practice from open pit to underground mining technical problems of the transition period* [J], metal mining, 2006,356 (2) :18-21. In chinese.

[2] Lu Wang Jian,high Yong tao,WU Shun chuan. *Shi ren gou iron ore production scale open pit to underground mining optimization* [J], Beijing University of Technology, 2008,30 (9) :967-11. In chinese.

[3] Zhang Jian, Xu Guo quan. *Caving loose rock cover the impact of the natural grade of the ore loss and dilution* [J], metal mining, 2010,407 (5) :21-25. In chinese.

[4] Zhang Zhi jun, Shi-Ming Cheung, Song hong Yong. *Caving stope loose rock movement law cover research* [J], mining technology, 2008,8 (2) :11-13. In chinese.

[5] Pat Lam, Zhao Bing, Zhang Si wei. *Mine dump Rolling movement of its disaster prevention* [J], Chinese Journal of Geological Hazard and Control, 1998,9 (S) :127-135. In chinese.

# CHAPTER 2:

# Geological Engineering

*Applied Mechanics and Materials Vols. 580-583 (2014) pp 841-846*
*© (2014) Trans Tech Publications, Switzerland*
*doi:10.4028/www.scientific.net/AMM.580-583.841*

# A New Geometrical Model of Fluid Flow in Rock Fractures for Valid Application of the Cubic Law

Hongguang ZHU [1, a], Yaodong JIANG [1, b], Cheng YI [1, c], Heping XIE [2, d]

[1]State Key Laboratory of Coal Resources and Safe Mining, CUMT, Beijing, China;

[2]Sichuan University, Chengdu, Sichuan, China

[a]uu_gr@qq.com,[b]147026595@qq.com,[c]yicheng312@tom.com, [d]yorsel@163.com

**Keywords:** Rock fracture; Fluid flow; Local cubic law; Geometrical discrete-equivalent model

**Abstract.** The cubic law (CL) is one of the most commonly applied physical laws for flow through rock fractures and fractured media, but many studies indicate that the CL is often not adequate. We investigate the establishment conditions of valid applying the "cubic law" to flow in fractures. A dimensional analysis of the N-S equations yields three conditions for the applicability of cubic law, as a leading order approximation in a local fracture segment with parallel walls. These conditions may not be met in many natural rock fractures as whole and demonstrate that the "cubic law" should be exactly applied in local segments (local cubic law, LCL). In this way, a new 2D discrete equivalent model for natural rough fractures is introduced, and its equivalent aperture and flow formulation are derived. By comparing the developed model and experimental results of different fractures, good accuracy was found, and the model was validated. The model could be useful for theory studies of flows through real rock fractures.

## Introduction

In natural crust, the matrix permeability is negligible compared to the permeability of fractures, and the rock mass' hydraulic behavior is controlled by fractures. In such situations, the development of realistic and robust predictive models of flow and transport requires a thorough understanding of the physical processes that govern flow in individual fractures. Understanding and quantification of fluid flow through fractured rocks are important for several industrial activities and research topics, such as reservoir exploitation for water supply, petroleum, geothermal research, heat storage, and the safe design of disposal sites for domestic, industrial, and nuclear waste [1].

Traditionally, single fractures have been idealized as a set of parallel plates to obtain a tractable mathematical description of fluid flow, namely, the cubic law (CL). Because of its simplicity, the CL has been studied extensively and has become the primary governing law for flow in rock fractures [2, 3]. In a rigorous sense, the CL works the best for fluid flow in a highly idealized fracture with smooth and parallel fracture surfaces, such as saw tooth and stepped profiles [4]. In these cases, the fracture hydraulic behavior is expressed by the effective aperture term. However, field observations show that natural fractures are very unlikely to have smooth and parallel surfaces [5], and many laboratory experiments [6] and field measurements [7] indicate that the classical view is not adequate for describing flow. It is difficult to establish the CL in rock fractures that are rough-walled conduits with tortuose paths. Although more advanced conceptual models [8, 9] have been introduced in recent years, an alternative model for flow in fractures has yet to be generally accepted.

In light of the above discussion, we re-address the entire issue and begin by examining the conditions of applying the CL directly from the Navier-Stokes equation. Section 2 presents an order-of-magnitude analysis based on 2-D cross sections of a fracture. In section 3, we propose a new 2-D discrete-equivalent model for natural rough-walled fractures on the basis of CL conditions and develop its equivalent aperture and flow formulation. Finally, in section 4, we evaluated the model with the experimental results of fractures with different geometries.

**A Study of Applicable Conditions for the CL**

The incompressible flow of Newtonian fluid in rock fractures can be described by mass and momentum conservation equations. In 2-D fractures, for example, the fracture in Fig. 1, those Equations is written as follows:

$$\frac{\partial u}{\partial x}+\frac{\partial v}{\partial y}=0, \tag{1}$$

$$\rho\left(u\frac{\partial u}{\partial x}+v\frac{\partial u}{\partial y}\right)=-\frac{\partial P}{\partial x}+\mu\left(\frac{\partial^2 u}{\partial x^2}+\frac{\partial^2 u}{\partial y^2}\right), \text{ and} \tag{2a}$$

$$\rho\left(u\frac{\partial v}{\partial x}+v\frac{\partial v}{\partial y}\right)=-\frac{\partial P}{\partial y}+\mu\left(\frac{\partial^2 v}{\partial x^2}+\frac{\partial^2 v}{\partial y^2}\right) \tag{2b}$$

where $u$, $v$ is the flow velocity, $\mu$ is the fluid viscosity, $\rho$ is the fluid density, and $P$ is the hydrodynamic pressure. The Eq. (2) is called the Navier-Stokes equation.

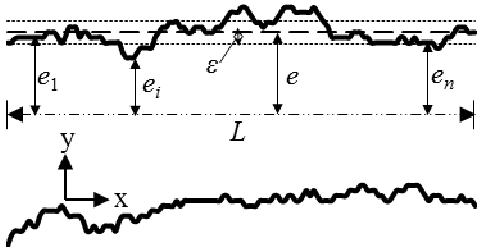


Fig 1 A rock fracture with aperture 2$e$ and length $L$.

In Fig. 1, $e_i$ is the test point aperture in a fracture, with $i$ from 1 to $n$. For a typical value of $e$ to be representative, the variation of $e_i$ must be limited over the length $L$, as follows:

$$e_i = e + o(\sum e_i). \tag{3}$$

$o(\sum e_i)$ is the infinitesimal of $\sum e_i$. It can be regarded as a very small amount here, $o(\sum e_i) \ll e$, so $(e_i - e)/e \ll 1$. We can include the roughness of the upper and lower walls:

$$\varepsilon = \max\left(\frac{\sigma_u}{e}, \frac{\sigma_l}{e}\right) \ll 1, \tag{4}$$

where $\varepsilon$ is called the non-dimensional roughness parameter, and $\sigma_u$ and $\sigma_l$ are the root mean square ( rms ) roughnesses (i.e., the rms deviations from the means) of the upper and lower walls, respectively, averaged over the length $L$ (Figure 1). This is the first and basic condition for valid application of the CL.

With the first condition (4), we can denote a typical velocity by $U$. Using (1), we can obtain the following:

$$v = \int_0^y \frac{\partial u}{\partial x} dy \tag{5}$$

Performing an order-of-magnitude analysis of (5), we obtain the approximate relations that $v$ is an order of $U\frac{e}{L}$. If the ratio of $e$ and $L$ is such that

$$\delta = \frac{e}{L} \ll 1, \tag{6}$$

And $u$ is an order of $U$, then $v \ll u$, $v$ is negligible relative to $u$, and (2b) can be written as follows:

$$\frac{\partial p}{\partial y} = 0 \Rightarrow p = p(x). \tag{7}$$

We can analyze the ratio of inertia and viscosity stress in (2a):

$$\frac{|\text{Inertia}|}{|\text{Viscosity}|}=\frac{\rho\left|u\frac{\partial u}{\partial x}+v\frac{\partial u}{\partial y}\right|}{\mu\left|\frac{\partial^2 u}{\partial x^2}+\frac{\partial^2 u}{\partial y^2}\right|}=\frac{\rho\left|u\frac{\partial u}{\partial x}\right|}{\mu\left|\frac{\partial^2 u}{\partial x^2}+\frac{\partial^2 u}{\partial y^2}\right|}\sim\frac{\rho}{\mu}\frac{U\frac{U}{L}}{\frac{U}{L^2}+\frac{U}{e^2}}=\frac{\rho Ue}{\mu}\frac{\delta}{\delta^2+1}=\text{Re}\times\delta \tag{8}$$

where $\text{Re}=\rho Ue/\mu$ is the Reynolds number in the fracture. From (8), we know $\frac{\partial^2 u}{\partial x^2}\Big/\frac{\partial^2 u}{\partial y^2}=\delta^2/1$ and $\frac{\partial^2 u}{\partial x^2}\ll\frac{\partial^2 u}{\partial y^2}$. Therefore, the condition

$$\text{Re}\times\delta\ll 1\ , \tag{9}$$

makes both terms on the left-hand side of (2a) negligible; thus, (2a) can be written as follows:

$$-\frac{\partial P}{\partial x}+\mu\frac{\partial^2 u}{\partial y^2}=0\ . \tag{10}$$

By combining (7) and (10) and integrating $u$ along the cross section, the CL is gotten as follows:

$$q=\int_e udy=-\frac{e^3}{12\mu}\frac{\partial P}{\partial x}=-\frac{e^3}{12\mu}\frac{\Delta P}{L} \tag{11}$$

where $\Delta P$ is the pressure drop across the fracture. In this case, the rough-walled fracture can be approximated as a pair of smooth parallel plates, and its aperture is the distance of parallel plates.

With the above conditions (4), (6), and (9), we can obtain the condition for the application of the CL in rock fractures:

$$\begin{cases}\max(\varepsilon,\delta)\ll 1 & (a)\\ \text{Re}\times\delta\ll 1 & (b)\end{cases} \tag{12}$$

The two geometric conditions (for $\varepsilon$ and $\delta$) in (12a) are somewhat dependent upon each other. On one hand, the length may not be too long because as we extend it, $\varepsilon$ will increase. On the other hand, we cannot minimize $\varepsilon$ by making the length shorter because of the condition on $\delta$. In fact, the geometric condition (12a) may be hardly met by many real rock fractures as a whole because of their long length and wall roughness, which is why researchers[6,7] conclude that the CL is not adequate for fluid flows in rock fractures. Our experiment also confirms this view [10].

Otherwise, it is obvious from (12b) that the Reynolds number and fracture roughness are coupled. The smaller $\delta$ is, the more assurance there is of the applicability of the CL for high Reynolds numbers. Similarly, the smaller the Reynolds number is, the more applicable the CL is for rough-walled fractures. Obviously, for smooth parallel plates, as long as the fracture is long enough ($\delta\to 0$), the CL will be very applicable for laminar flow ($\text{Re}\le 2300$). Usually, the length is long, and the aperture is small in natural rock fractures, which ensures a sufficiently small $\delta$; the Reynolds number is also not large, so condition (12b) can be met.

## A Discrete-Equivalent Model for Fluid Flow in 2-D Rock Fractures

To effectively use the CL, we must develop a geometric model suitable for analyzing the fluid flow behavior in fractured rough rock based on the applicable conditions. The analysis in the previous section shows that the CL is not applicable for fluid flow in rough-walled fractures because their rapidly varying wall geometry and long lengths mean condition (12a) cannot be met. To solve this problem, we 'break down' the fracture to shorter segments. As long as the discretizing method is appropriate for ensuring a reasonable length and roughness in each segment, then CL condition (12a) can be easily satisfied. In addition, if the Reynolds number is not large (say, ~100), condition (12b) is also met easily. Thus, the CL can be applied to the flow in each fracture segment. It is implied here that CL behavior should not be assumed correct or incorrect for the entire fracture; rather, it should be

studied on a local basis (segment), and the CL may be applicable only locally for natural rock fractures, hence the name local cubic law (LCL).

Based on the above principle, we derived a more general method for discretizing fractures. First, we divide the fracture equally along its flow direction into short segments with possibly appropriate lengths, ensuring every location with a rapidly varying aperture is 'broken down'; then, we assemble adjacent segments whose apertures vary gently as one segment, as shown in Fig. 2. The entire fracture is discretized as a stepped profile (dashed line), and the aperture of the 'break down' location is presented as a jump. In this case, conditions (12) is easily met in each segment, and we can apply the LCL to analyze the flow behavior in fractures.

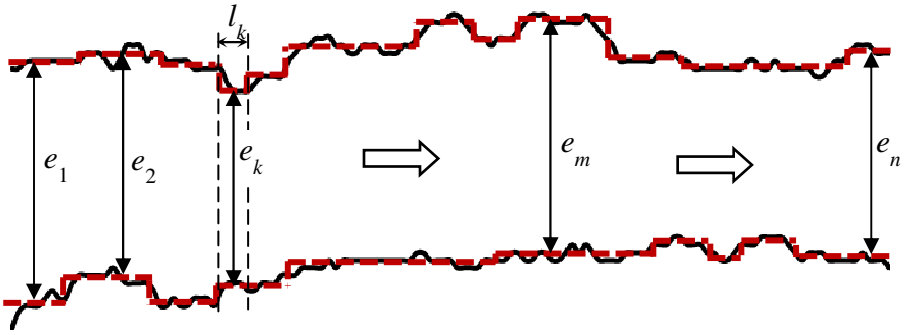


Fig. 2. 2-D discrete-equivalent model for rough-walled fracture

The flux through each segment in Fig. 2 can be calculated as follows:

$$q_k = \frac{e_k^{\,3}}{12\mu}\frac{\Delta P_k}{l_k},\ k = 1,2,\cdots,n, \tag{13}$$

where $\Delta P_k$ is the pressure drop of the $k$th fracture segment due to $q_k$, and $l_k$ and $e_k$ are the length and aperture, respectively.

For each segment fracture, the Mass Balance equation leads to the following:

$$q_1 = q_2 = \cdots = q_n = q. \tag{14}$$

Combining (13) and (14),

$$\Delta P_k = 12\mu q\frac{l_k}{e_k^{\,3}},\ k = 1,2,\cdots,n. \tag{15}$$

The total $\Delta P$ of the main fracture is the sum of $\Delta P_k$ for all segments, but it is obtained by ideal assumptions, and we need to consider the tortuosity effect; thus, we introduce a tortuosity factor $\tau$:

$$\Delta P = \sum_{k=1}^{n}\Delta P_k = 12\mu q\tau\sum_{k=1}^{n}\frac{l_k}{e_k^{\,3}}. \tag{16}$$

By comparing Eq.(11) and (16), and considering $L \simeq \tau\sum_{k=1}^{n} l_k$, the effective aperture can be calculated as follows:

$$e_{eq} = \sqrt[3]{\sum_n l_k \Big/ \sum_n \frac{l_k}{e_k^{\,3}}}. \tag{17}$$

From Eq. (16), the flow through main fracture can be calculated as follows:

$$q = \frac{1}{12\mu}\frac{\Delta P}{\tau\sum_n l_k / e_k^{\,3}}. \tag{18}$$

If a fracture is discretized by the same size $l$, Eq. (18) can be written as follows:

$$q = \frac{1}{12\mu}\frac{\Delta P}{\tau l}\frac{1}{\sum_n 1/e_k^3}. \quad (19)$$

## Discussion

To illustrate the reasonableness of our model, we completed physical experiments of fluid flow in some rough-walled fractures. The typical rough curve-JRC profiles in rock mechanics is used in the test. We selected the first, third, sixth and ninth curves and combined each of them with a plate to form 4 types of two-dimensional fractures; each fracture length is 100 mm, and the minimum aperture is 0.51 mm. By using experimental results, our model and the previous classical CL are analyzed and compared, as shown in table 1. The error of the average aperture method compared to the measured results is large, whereas our method is comparatively good. However, in the case of a large Reynolds number, the error increases significantly because the applicability of the LCL in flows with high Reynolds numbers is poor (condition (12b)). The correction and application of our model to flows with high Reynolds numbers needs to be studied further.

Table 1 Comparative analysis of test results according to classic CL and our model

| No. | $P_s$/Pa | $q_s/10^{-3}m^3/s$ | $e_p$/mm | $q_p/10^{-3}m^3/s$ | Error($q_p$) | $e_d$/mm | $q_d/10^{-3}m^3/s$ | Error($q_d$) | Re |
|---|---|---|---|---|---|---|---|---|---|
| 1-P | 486.5 | 0.165 | 0.91 | 0.26799 | **62%** | 0.82 | 0.18208 | **10 %** | 278 |
| | 98.2 | 0.035 | 0.91 | 0.05409 | **55%** | 0.82 | 0.03675 | **5%** | 59 |
| 3-P | 147.5 | 0.0969 | 1.35 | 0.26528 | **174%** | 1.02 | 0.10782 | **11%** | 170 |
| | 49.2 | 0.034 | 1.35 | 0.08849 | **160%** | 1.02 | 0.03596 | **6%** | 60 |
| 6-P | 290.2 | 0.187 | 3.3 | 7.62348 | **3977%** | 1.03 | 0.23181 | **24%** | 328 |
| | 149 | 0.106 | 3.3 | 3.91419 | **3593%** | 1.03 | 0.11902 | **12%** | 186 |
| 9-P | 49.8 | 0.12 | 4.37 | 3.03800 | **2432%** | 1.59 | 0.14633 | **22%** | 207 |
| | 29.9 | 0.0812 | 4.37 | 1.82402 | **2146%** | 1.59 | 0.08786 | **8%** | 140 |

Note: the subscripts *s*, *p* and *d* stand for results measured by physics experiment, calculated by the CL of the average aperture and by formulas (18) of the equivalent aperture, respectively.

## Conclusions

Based on the presented results, the following conclusions were obtained:

(1) By performing an order-of-magnitude analysis on the Navier-Stokes equation for a general rough-walled fracture, we obtain three conditions under which the CL is an adequate approximation of the flow: a) the fracture must be long enough relative to its aperture so that $\delta = e / L \ll 1$; b) over its length, the relative roughness parameter $\varepsilon$ must be limited to $\varepsilon \ll 1$; and c) inertial effects must be limited via $\mathrm{Re}\times\delta \ll 1$.

(2) According to these conditions, it follows that it is difficult to apply the cubic law for rock fractures as a whole; the law is only applicable in local segments of fractures (as local cubic law). When analyzing fluid flow in rock fractures through the cubic law, the matter should be discussed not simply from a global perspective but also from a local one.

(3) To make the cubic law effectively applicable for fluid flow in rough-walled rock fractures, we developed a new discrete-equivalent model and deduced the expression of an equivalent aperture and flow-calculating formula from 2-D perspectives. Compared with the experimental results of different rough-walled rock fractures, this model was validated. The model can effectively provide flow analysis in real rock fractures.

**Acknowledgements**

This work was financially by the National Program on Key Basic Research Project of China (973 Program, Grant No. 2010CB732002 and 2011CB201201).

**References**

[1] Neuman, S.P. Trends, prospects and challenges in quantifying flow and transport through fractured rocks. Hydrogeology Journal, 2005, 13(1): 124-147.

[2] Amadei, B., Illangasekare, T.. A mathematical model for flow and solute transport in non-homogeneous rock fractures, International Journal of Rock Mechanics and Mining Sciences & Geomechanics, 1994, pp. 719-731.

[3] Nazridoust, K., Ahmadi, G., Smith, D.H.. A new friction factor correlation for laminar, single-phase flows through rock fractures, Journal of Hydrology, 2006, pp. 315-328.

[4] Bear J, T.C.F., De Marsily G. Flow and Contaminant Transport in Fractured Rock., Academic Press, San Diego. 1993.

[5] Meheust, Y., Schmittbuhl, J.. Geometrical heterogeneities and permeability anisotropy of rough fractures, Journal of geophysical research, 2001, pp. 2089-2102.

[6] Durham, W.B., Bonner, B.P. Self-propping and fluid-flow in slightly offset joints at high effective pressures, Journal of Geophysical Research-Solid Earth, 1994, pp. 9391-9399.

[7] Novakowski, K.S., Lapcevic, P.A., Voralek, J., Bickerton, G.. Preliminary interpretation of tracer experiments conducted in a discrete rock fracture under conditions of natural flow, Geophysical Research Letters, 1995, pp. 1417-1420.

[8] Lee, H.-B., Yeo, I.W., Lee, K.-K.. The modified Reynolds equation for non-wetting fluid flow through a rough-walled rock fracture, Advances in Water Resources, 2013, pp. 242-249.

[9] Javadi, M., Sharifzadeh, M., Shahriar, K.. A new geometrical model for non-linear fluid flow through rough fractures, Journal of Hydrology, 2010, pp. 18-30.

[10] Hongguang Zhu, Heping Xie, Cheng Yi, et al.. Properties of fluid flow in rock fractures. Chinese Journal of Rock Mechanics and Engineering, 2013, 32(4):657-663. (In Chinese)

*Applied Mechanics and Materials Vols. 580-583 (2014) pp 847-850*
*© (2014) Trans Tech Publications, Switzerland*
*doi:10.4028/www.scientific.net/AMM.580-583.847*

# Control function of corrosion of calcareous sandstone over rock mass quality in one hydroelectric station on the Jinsha River

Shuqiang Lu[1,2,3,a], Peng Zhu[1,2,b *]

[1] Collaborative Innovation Center for Geo-Hazards and Eco-Environment in Three Gorges Area, Yichang, Hubei, 443002, China

[2] National Field Observation and Research Station of Landslides In Three Gorges Reservoir Area of Yangtze River, Yichang, Hubei, 443002, China

[3] State Key Laboratory of Geohazard Prevention and Geoenvironment Protection (Chengdu University of Technology), Chengdu, Sichuan, 610059, China

[a]Lsq2197@163.com, [b] zzhsp9058@163.com (*Corresponding author)

**Keywords:** rock mass quality classification; calcareous sandrock and conglomerate rock; elastic wave velocity; corrosion

**Abstract.** The hydro-electrical power station is planned to be built on the Jinsha River. The regional geologic structure is complex. On the basis of the geological engineering conditions and rock mass quality classification, the change of wave velocity of rock mass is used to analyze systematically the control function of corrosion of calcareous sandstone over rock mass quality. The modificatory standard of rock mass quality classification and the system of rock mass quality classification in the hydroelectric station have been carried out. The main results can be taken as the basic data and the theoretical proofs to evaluate the engineering rock mass stability.

## Introduction

The hydro-electrical engineering is planned to be built on the Jinsha River， with its damheight of 156m and installed capacity of 3000MW. The regional geologic structure is complex. The rock mass is mainly composed of Jurassic sandrock and conglomerate. The calcareous sandrock and conglomerate rock in the understratum will be corroded by the effect of groundwater. The corrosion depresses the rock mass strength, which influences the stabilization and deformation of dam foundation. Therefore, it is extremely important to make the rock mass quality classification correctly and reasonably in evaluating anti-slide stability of rock mass of dam foundation, making full use of utilizable rock mass and developing appropriate engineering measures.

Many methods on the classification of rock mass quality have been proposed at home and abroad since the middle of last century, but they are all specific to the non-soluble rock. In recent years, with the development of engineering construction in karst areas, rock mass quality little of these areas also has been studied [1,2]. However, the studies are mainly focused on carbonate rock, and pay little attention on sandrock and conglomerate [3].

In this paper, based on the geological engineering conditions and rock mass quality classification, the velocity of elastic wave in rock is used to analyze the control function of corrosion of calcareous sandstone over rock mass quality. The modified standards of rock mass quality classification and the system of rock mass quality classification of the hydroelectric station has been carried out. The main results can be taken as the basic data and the theoretical proofs to evaluate the engineering rock mass stability.

**Basic engineering geological conditions of the dam area**

The rock mass in the dam is mainly composed of Jurassic sandstone, conglomerate, siltstone and pelitic siltstone. The conglomerate fine sandstone and pebbled fine sandstone which are on the understratum of the dam will generate corrosion in the direction of stratification or steep-dipping fissure under the effect of groundwater. The results are large karst cave, calcium loss, semi-bonded sandy soil and white soft plastic kaolin in the fissure or levels.

Fracture structure is poorly developed in the dam site, and the main structure consists of fold, compresso-crushed zone and minor fault, with illtrastfatal-shearing belts and tectonic joints companion fold.

**Basic rock mass quality classification and corrosion degree**

Rock mass quality evaluation are the basis of rock mass stability analysing. Many classification methods of domestic and overseas consider the following factors of rock hardness, intactness of the rock, structure plane and its permeability as the basis of comprehensive evaluation.

The surrounding rock engineering geological classification of hydroelectricity, Standard for engineering classification of rock masses and RMR-system have been used in the rock mass quality classification.

According to the engineering geological properties of rock mass and references after the paper, the corrosion of sandstone and conglomerate can be divided into four grades (Table 1). The intensity grades of corrosion development is shown in Table 1.

Tab. 1 The intensity grades of corrosion development

| Corrosion | Line corrosion ratio (%) | Engineering geological properties |
|---|---|---|
| Highly corroded | 10~20 | Distributed mainly of solution pipe，crack-shape karst cave and cave. |
| Moderately corroded | 5~10 | Distributed mainly of solution fissure，pore and groove. |
| Slightly corroded | 0~5 | Distributed mainly of geodes, solution pores and solution pockmarked face. |
| Uncorroded | 0 | Rock mass was uncorroded and rock was well cemented. |

**Control effect of calcareous sandstone dissolution on rock mass quality**

Corrosion reduces rock mass integrity and wave velocity. And the quantitative analysis of the control effect of sandstone dissolution on rock mass quality is the problem. And the method of rock mass elastic wave velocity is analysed below.

The value of elastic wave velocity is a synthetic index to rock mass quality which depends on rock property, rock mass structure and rock mass existing condition. Therefore it is widely used in hydroelectric project.

The varying curve of wave velocity of rock mass in figure 1 presented that the change of wave velocity correlates with not only rock weathering and character (highly weathered is greater than slightly weathered, sandstone is greater than aleuvite and mudstone), but also rock corrosion.

Based on the adits datas, the results are reflected in table 2 from the datas of the relationship of wave velocity, rock weathering, rock character and corrosion.

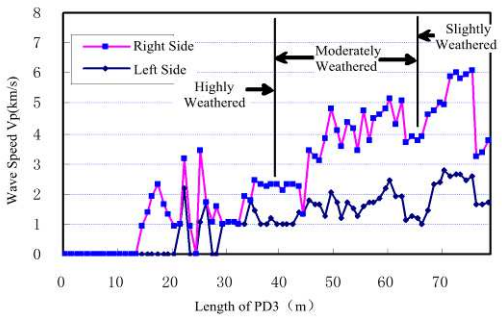


Fig. 1 Change of wave velocity of rock mass

Tab.2 The relationship of wave velocity, rock character and corrosion

| Weathering | Highly weathered | | | Slightly weathered | | | |
|---|---|---|---|---|---|---|---|
| rock character | sandstone | aleuvite | conglomerate | sandstone | | aleuvite | |
| corrosion | uncorroded | uncorroded | uncorroded | uncorroded | Slightly corroded | uncorroded | Slightly corroded |
| Length of adits | 5 | 6 | 2 | 9 | 3 | 14 | 3 |
| Average wave velocity (Km/s) | 1.34 | 1.41 | 2.06 | 2.79 | 1.46 | 2.36 | 1.37 |
| maximum | 1.58 | 1.97 | 2.08 | 3.54 | 1.47 | 3.37 | 1.43 |
| minimum | 1.08 | 1.09 | 2.03 | 2.07 | 1.45 | 1.18 | 1.33 |

Figure 2 indicates that few exploration adits are highly weathered or slightly weathered, and most of them are not corroded. And on the whole, it reflects good corresponding among rock property, weathering degrees and longitudinal wave velocity.

The datas of rock mass classification systems can be used to analyse the relationship with wave velocity. Figure 2 indicates the two aspects correlates very well.

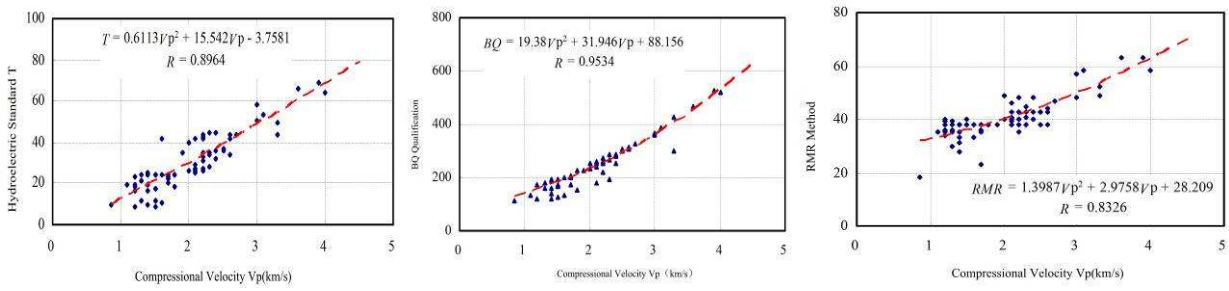


Fig.2 The relationship map of wave velocity and classification data

Combine the relationship of corrosion and wave velocity in table 2 with the formulas of rock mass quality classification systems and wave velocity, the influence of corrosion on rock mass quality classification can be achieved.

The relationship of wave velocity and rock mass quality classification systems in figure 2 can be presented by the following formulas:

$$T = 0.6113V_p^2 + 15.542V_p + 3.7581$$

$$BQ = 19.38V_p^2 + 31.946V_p + 88.156$$

$$RMR = 1.3987V_p^2 + 2.9758V_p + 28.209$$

From the formulas, the variation tendency of corrosion ratings on rock mass quality can be achieved. Table 3 lists the analytical datas of conglomerate and sandstone (take BQ qualification for example).

Tab.3 The influence of corrosion ratings on rock mass quality

| rock character | corrosion | Length of adits | Average wave velocity (Km/s) | BQ rating | Decreased rating | BQ class |
|---|---|---|---|---|---|---|
| conglomerate | uncorroded | 11 | 2.52 | 291.73 | | Ⅳ |
| | Slightly corroded | 3 | 1.90 | 218.82 | 24.99% | Ⅴ |
| | Moderately corroded | 5 | 1.46 | 176.11 | 39.63% | Ⅴ |
| | Highly corroded | 1 | 1.00 | 139.48 | 52.19% | Ⅴ |
| sandstone | uncorroded | 65 | 2.15 | 246.42 | | Ⅳ |
| | Slightly corroded | 11 | 1.68 | 196.52 | 20.25% | Ⅴ |
| | Moderately corroded | 14 | 1.44 | 174.34 | 29.25% | Ⅴ |
| | Highly corroded | 14 | 1.40 | 170.87 | 30.66% | Ⅴ |

The result shows that rock mass quality is decreased obviously due to the corrosion of rock cement. And on the whole it decreased one order of magnitude.

## Conclusion

Corroded rock have great differences with uncorroded rock. Corrosion will reduce integrity of rock. This is extremely unfavorable in dam foundation deformation and stability against sliding. Besides, the increases of corrosion degree will reduce the wave velocity and rock mass quality. The analysing of the change of wave velocity of rock mass is used to analyze systematically the control function of corrosion of calcareous sandstone over rock mass quality. It not only has carried out the relationship between rock mass quality and wave velocity, but also has achieved the quantitative evaluation of rock mass quality. It shows that the rock corrosion will lead to a distinct weakening of rock quality, and on the whole it decreased one order of magnitude. The main results can be taken as the basic data and the theoretical proofs to evaluate the engineering rock mass stability.

## Acknowledgements

This work was financially supported by Opening fund of State Key Laboratory of Geohazard Prevention and Geoenvironment Protection (Chengdu University of Technology) (SKLGP2012K032), Hubei Province Department of Education Science and Technology Research Project (D20121304) and Hubei Province Natural Science Fund project (2012FFA040, 2012FFB03804).

## References

[1] Zou Chengjie: *Water resources and hydropower engineering geology in karst areas*. China WaterPower Press, Beijing (1994). (In Chinese)

[2] Wang Jiajun: *Engineering geological classification for rock mass quality of dam foundation in karst terrain*. Carsologica Sinica, Vol. 11(1992), p.105–117 (In Chinese)

[3] Li Zhengkun, Zuo Chonghui: *Study on the weathering characteristics of Cretaceous red conglomerate*. Advances in Science and Technology of Water Resources, 21(2001), p.80–82 (In Chinese)

[4] Xiong Daokun, Fu Ronghua: *Vertical zonation method for intensity of karst development*. Geotechnical Engineering Technique, 19(2005), p.113–117 (In Chinese)

*Applied Mechanics and Materials Vols. 580-583 (2014) pp 851-856*
*© (2014) Trans Tech Publications, Switzerland*
*doi:10.4028/www.scientific.net/AMM.580-583.851*

# Dynamic Mechanism Research on the Tectonic Activation of Anninghe Rift

Junqi Liu [a], Yusheng Li [b]

State Key Laboratory of Geohazard Prevention and Geoenvironment Protection (Chengdu University of Technology), Chengdu, Sichuan, 610059, P. R. China

[a]610866672@qq.com, [b]liyusheng@cdut.cn

**Keywords:** Rift, Activation, Lithosphere, Mantle convection, Plastic flow, Dynamic mechanism

**Abstract.** Anninghe rift is located on the western edge of Yangtze Block next to Tibetan Plateau, along the axis of a continental paleorift zone, Panxi paleorift. Recent studies have found that an upward mantle convection system existed since the late Pliocene in the deep lithosphere of a long and narrow area controlled by Anninghe fault. Lithospheric temperature distribution in the area has characteristics similar to that in Baikal and other modern rifts. A mantle upwelling area was in a constant state of "pull-subsidence." Brittle rock mass of the shallow crust cracked into the new secondary subsidence blocks. A thick lacustrine sedimentary sequence of continental subsidence type developed. These all indicate that Anninghe rift is in an obvious tectonic activation state. It is believed that the tectonic activation of Anninghe rift has been produced by both horizontal squeeze from a plastic flow of the upper crust and expansion from mantle uplift. The pressure from the plastic flow of the upper crust is slightly greater than the expansion stress from the uplifting of lithosphere. Under this specific geodynamic environment, whether the tectonic activation of Anninghe rift can continue depends on the thermal motion rate of deep mantle materials and the eastward migration of the crustal materials of Tibetan Plateau.

## Introduction

During an international geophysical year and upper mantle planning in the 1950s, it was not only affirmed that oceanic rifts and continental rifts formed a worldwide unified system, but also found that the formation and function of the rifts were associated with some universal effects deep in the earth[1].

Anninghe rift is located on the western edge of Yangtze Block next to Tibetan Plateau (Fig. 1), along the axis of a continental paleorift zone, Panxi paleorift. Accompanied by Permian Emeishan basalt overflow, the earthen crust was drastically tensioned and ruptured. This continental rift with dome-shaped volcano pattern had sustained development during the Indo-Chinese epoch. During the late Pliocene when activities gradually weakened of the lithosphere, a main fracture system in the paleorift zone closed up[2]. Recent studies indicate that there have been mantle uplift and heat convection accompanied by significant crustal expansion in Anninghe rift. It is not clear if this phenomenon means that the paleorift was activated from a dormant state[3]. Comprehensive geological and geophysics investigations as well as earthquake-structure and crustal deformation measurements were researched to study tectonic rift activation and to put forward a new dynamic mechanism of rift activation.

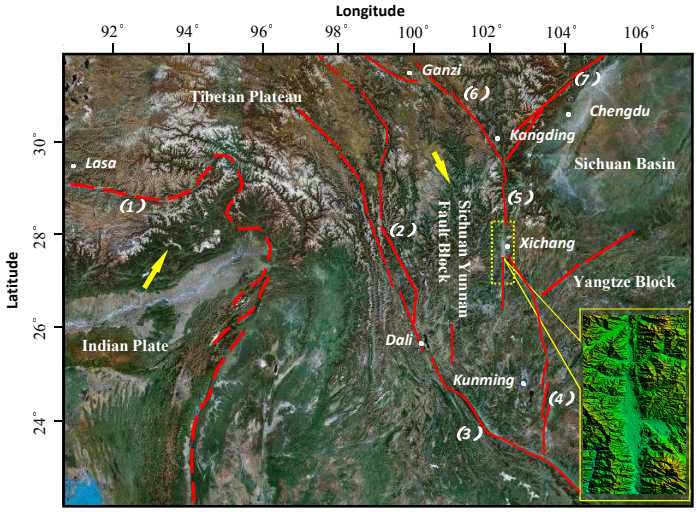


Fig. 1 Regional location map of Anninghe rift
((1) Yarlung Zangbo struture zone, (2) Jingshajiang River fault zone, (3) Honghe River fault, (4) Xiaojiang River fault, (5) Anninghe River fault zone, (6) Xianshuihe River fault zone, (7) Longmenshan Mountain fault zone.)

## Regional geophysical field and deep structure

According to crustal rock's electrical, magnetic and density data[4] (Fig. 2 left), the lithospheric electrical structure in Anninghe main tectonic belt is considerably different from that on either side of the belt. The low-resistivity layer of the crust and upper mantle is thinner and shallower and even disappears in some places. The shallowest low-resistivity layer in the upper mantle is only 80 km.

Regional crustal thickness varies from 39 ~ 43 km in Sichuan basin to 60 ~ 70 km in Tibetan Plateau. There is a north-south trending mantle uplift belt in the center of Anninghe rift[5] (Fig. 2 right). A high gravity anomaly zone is centered on Xichang. Massive high density basic and ultrabasic abnormal substances exist in the lithosphere.

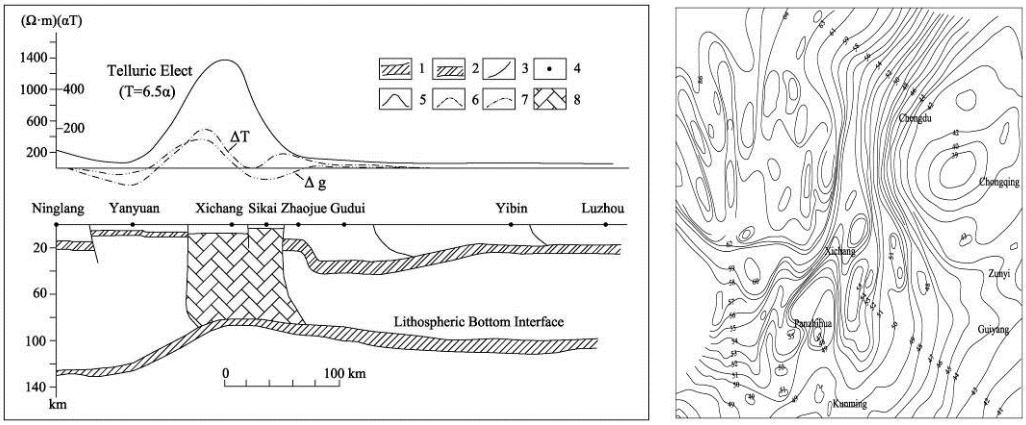


Fig. 2 Magneto telluric sounding profiles in Anninghe rift (left) and regional crustal thickness (right)
(left: 1- Shell low resistance layer, 2- The upper mantle low-resistivity layer, 3- Faults, 4- Magneto telluric sounding points, 5- The resistivity curve, 6- Voyage ΔT curve, 7- Δg curve, 8- High resistance anomaly.)

## Activity characteristics of the main boundary faults of Anninghe rift

We found an active main boundary fault developed along the eastern side of the valley via geological surveys, very low frequency electromagnetic method (VLF) and micro-dose α radiation measurement. According to crustal deformation data from leveling measurements of nearly 30 years (Table 1), the

main boundary fault is left-lateral strike-slip with strong compression as a whole. But it is not to be ignored that some sections had pull - normal fault activities (Fig. 3). Based on analysis of GPS data from a crustal movement monitoring network, the fault left-lateral slip rate is 2.5 ~ 6.0 (±1.8) mm/yr while the horizontal pull rate is 0 (±2) mm/yr[6].

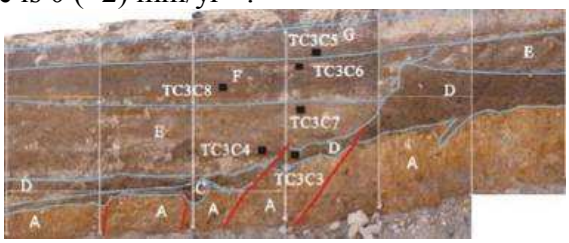


Fig. 3 Trench in northern section of main boundary fault

Table 1 Slip rate of main boundary fault

| Fault | Geological Survey (mm/a) | | GPS and Levelling (mm/a) | |
|---|---|---|---|---|
| | Left-lateral dislocation rate | Vertical dislocation rate | Left-lateral dislocation rate | Vertical dislocation rate |
| North Section (Shimian - Mianning) | 4.0~6.2 | 0.9~1.4 | 2.54~3.58 | 0 (±2) |
| North Section (Mianning - Xichang) | 5.0~7.2 | 1.8~0.73 | 5.3～6.0 | |

**Rift type fault basin of late Pliocene**

The Pan-Xi paleorift began a new round of rift expansion in the late Pliocene ($N^3_2$) after a lengthy "dormant" closing process from late Cretaceous (K) to Pliocene ($N_2$). Under control of the north-south trending boundary faults, Xigeda formation ($Q_{1x}$) was deposited in the fault basin with primarily lacustrine sediments of clay - silt layers in a strip along the Mianning – Xichang – Panzhihua within 120 km. The "fault-deposition" process lasted until the early Middle Pleistocene ($Q_2$) which successively deposited fluvial-lacustrine-swamp sediments of Dajingliangzi formation ($Q^1_{2d}$) on Xigeda formation. Crust settlement at this stage reached more than 2000 m in total or a rate of more than 1.30 mm/yr.

During the late Middle Pleistocene ($Q_2$) the rift zone crust turned into a "squeeze-closing" state from a "pull–subsidence" state. Boundary fault activities turned into "compression-reverse fault" from "pull-normal fault" (Fig. 4 left). Folding deformation also occurred in Xigeda formation ($Q_{1x}$) within the rift (Fig. 4 right).

During the early Late Pleistocene ($Q_3$), the rift was active again. Strong normal fault activities occurred along the boundary fault. The crust continued "pull–subsidence" and it lasted until the early Holocene ($Q_4$). Total "pull-subsidence" at this stage is more than 300 m with a subsidence rate of approximately 1.94 mm/yr.

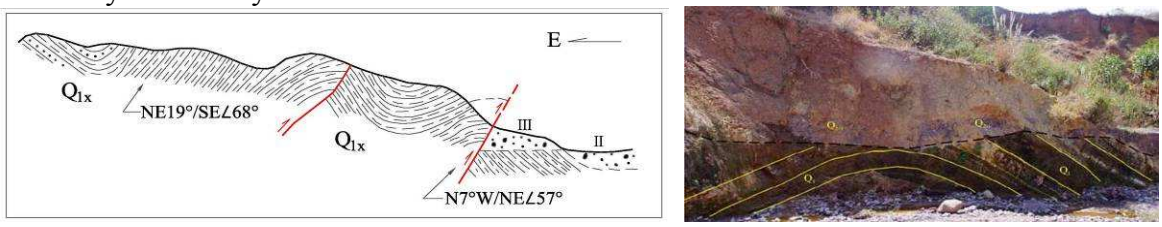


Fig. 4 The reverse fault activity of boundary fault of Anninghe rift (left) and the fold deformation in Xigeda formation ($Q_{1x}$) (right)

**Characteristics of tectonic rift activation and dynamic mechanism**

**Characteristics of Anninghe tectonic rift activation.** The deep lithosphere is still an upwelling system within mantle convection of Anninghe rift. Terrestrial heat flow measurements of this region

indicate that temperatures of 1100 ~ 1200 ℃ at the 80 ~ 90 km depth (Fig. 5 left) have reached the critical value of a molten mantle rock. When lithospheric temperature distribution of Anninghe region is compared to that of Baikal rift[7], shallow crust temperatures of Anninghe rift are lower than those of Baikal rift, but deep geothermal temperatures are approximately the same. This suggests that the deep crust of Anninghe rift still has similar characteristics with a modern rift, which is an important indication of rift activation.

Mantle upwelling caused changes in regional stress field, resulting in the upwelling area to be in a continuous crustal "expansion–pull–subsidence" state and the brittle rock mass of the shallow crust cracked into the new secondary subsidence blocks (Fig. 5 right). Recent measurements (Table 2) indicate that Anninghe rift is still in a state of continuous subsidence with a crust subsidence rate of 3.9 ~ 5.6 mm/yr. Obviously the rift zone was in a constant state of tectonic activation.

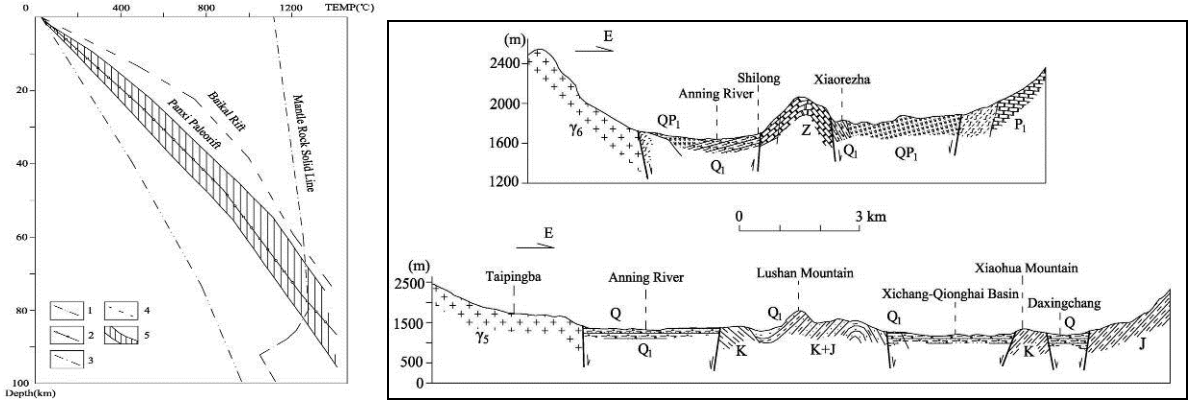


Fig. 5 Lithosphere temperature of Anninghe rift (left) and geologic structure profile (left: 1- Global average of geologic body with the same age, 2- Lithospheric temperature distribution of Aninghe rift, 3- Mantle rock solid line, 4- Lithospheric temperature distribution of Baikal rift, 5- Lithospheric temperature range in Anninghe region.) (right: Above - northern section of rift. Below - southern section of rift.)

Table 2 Vertical crustal deformation measurement results of Anninghe rift

| Measuring Position | | Deformation Rate (mm/yr) | Deformation Gradient (mm/km) |
|---|---|---|---|
| Measuring Section | Length (km) | | |
| Mianning-Shimian | 126.4 | + 4.7 | + 0.3 |
| Xindian-Mianning | 139.5 | - 4.4 | - 0.3 |
| Mianning-Dechang | 150.0 | - 5.6 | - 0.4 |
| Xichang-Dechang | 79.0 | - 4.7 | - 0.6 |

**Crustal dynamics mechanism of rift activation.** Regional P-wave and S-wave tomographic image cross section (Fig. 6 left) indicates that presence of an obvious Vp and Vs lower abnormal layer at a depth of approximately 16-26 km in the crust. This low-velocity layer is separated by a high speed and therefore high density rock mass in Anninghe valley. Those have some association with upper crust's block movement and mantle thermal motion.

Previous studies[8] have confirmed that a widespread southeastward plastic flow exists in the crust at this depth on the eastern edge of Tibetan Plateau including Anninghe valley. This flow drove an oblique collision of the west Sichuan-Yunnan fault block to the east Yangtze Platform, maintaining high compressive stresses in Anninghe fault at the contact zone. Focal mechanism solutions of modern earthquake reflect the existence of the stress state (Table 3). On the other hand, upward moving high temperature molten mantle rock is constantly penetrating through the lower crust into the shallow crust of the brittle fault zone, generating high fluid pressures and stresses. After moving into higher mantle, the molten rock gradually cooled to normal temperatures of the lithosphere and its temperatures dropped below the solid limit of a pyrite. Thus the rock lost characteristics of low speed seismic waves associated with a molten mantle rock. A high density rock mass was formed with high speed seismic wave characteristics in Anninghe valley and blocked the continuation of the

low-velocity layer at a 16 ~ 26 km depth. This condition also greatly increased stress accumulation in the crustal rock mass.

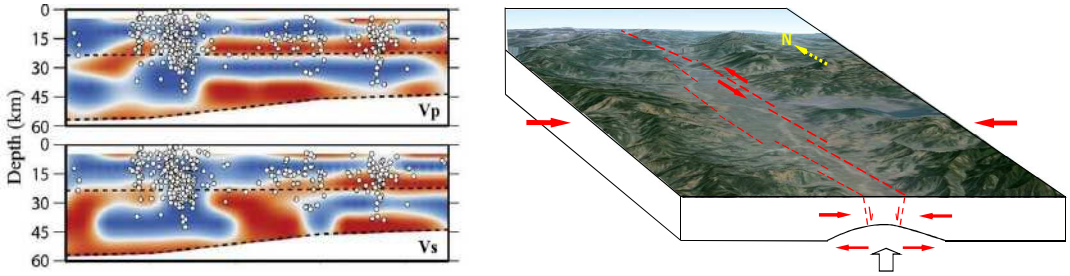


Fig. 6 Cross section of regional P-wave and S-wave tomographic image (left) and power source model of rift activation
(left: White dots indicate earthquakes. Red indicate low-speed. ANF – Anninghe rift. SY - Sichuan-yunnan fault block. YT - Yangtze Platform)

Table 3 Focal Mechanism Solutions of Anninghe Rift

| Time | Epicenter | | Ms | Nodal Plane A | | | Nodal Plane B | | | P | | T | | N | |
|---|---|---|---|---|---|---|---|---|---|---|---|---|---|---|---|
| | | | | Strike | Dip | Dip Angle | Strike | Dip | Dip Angle | Azimuth | Elevation | Azimuth | Elevation | Azimuth | Elevation |
| 1952.9.30 | 28°18′ | 102°12′ | 6.7 | 65 | NW | 75 | 354 | NE | 40 | 128 | 21 | 13 | 45 | 235 | 36 |
| 1962.2.27 | 27°36′ | 101°54′ | 5.5 | 65 | NW | 61 | 356 | NE | 87 | 301 | 18 | 45 | 23 | 183 | 61 |
| 1972.5.7 | 27°58′ | 101°19′ | 4.8 | 91 | N | 80 | 4 | E | 76 | 138 | 3 | 47 | 17 | 235 | 73 |

Based on the above analysis, tectonic activation of Anninghe rift was produced by both horizontal squeeze from a plastic flow of the upper crust and a tensile stress from the mantle uplift (Fig. 6 right). This pull - squeeze effect from the deep and shallow crusts has been in constant development and adjustment since the late Pliocene. It has not reached equilibrium at present time.

## Conclusions

Mantle uplift and heat convection exist in Anninghe rift along the axis of the Pan-Xi paleorift zone. The nearly north-south trending paleorift tectonic system is completely included in modern plate movement because of the movement between the crustal blocks. Especially the NWW trending compressive stress from the crustal material of Tibetan Plateau eastward drifting is slightly larger than the expansive stress from the present lithosphere uplifting. Under the specific geodynamic environment, whether the tectonic activation of Anninghe rift can continue its development depends on the thermal motion rate of deep mantle material and the eastward migration state of the crustal material of Tibetan Plateau. It is not impossible for the magma activity and crustal rifting to reappear in tectonic activation with Anninghe rift as the center.

## References

[1] D. Ravat, Z. Lu, L.W. Braile. Velocity–density relationships and modeling the lithospheric density variations of the Kenya Rift[J]. Tectonophysics, Vol. 302 (1999), p. 225-240.

[2] Weizhou Fu, Yubao Wu. Characteristics of the recent the recent tectonic stress field of Panxi rift valley zone and its vicinity[J]. Journal of Changchun College of Geology, Vol. 3 (1986), p. 95-102. (In Chinese)

[3] Jiwen Teng. Panzhihua-Xichang ancient rift and “activated” geophysical features[J]. Acta Geophysica Sinica, Vol. 30 (1987), p. 581-593. (In Chinese)

[4] Li Li, Guoyuan Jin. Telluric electromagnetic sounding study of crust and upper mantle in the Panxi “rift zone” and the Longmenshan faulted zone[J]. Geophysical & Geochemical Exploration, Vol. 11 (1987), p. 161-169. (In Chinese)

[5] Xianfu Yan. The deep geological structure of Yunnan and its adjacent areas[J]. Acta Geologica Sinica, Vol. 1 (1981), p. 20-28. (In Chinese)

[6] Jia Cheng. Western Sichuan area geodesy observational studies of present-day crustal movement [D]. Institute of Geology, China Earthquake Administration, (2008). (Iin Chinese)

[7] M. Jolivet, S. Arzhannikov, A. Chauvet, et al. Accommodating large-scale intracontinental extension and compression in a single stress-field: A key example from the Baikal Rift System[J]. Gondwana Research, Vol. 24 (2013), p. 918-935.

[8] Nelson, K.D., Zhao, W., Brown, L.D., et al. Partially molten middle crustbeneath southern Tibet: synthesis of project INDEPTH results[J]. Science, Vol. 274 (2001), p. 1684-1687.

*Applied Mechanics and Materials Vols. 580-583 (2014) pp 857-861*
*© (2014) Trans Tech Publications, Switzerland*
*doi:10.4028/www.scientific.net/AMM.580-583.857*

# SEARCHING FOR THE SHORTEST SEEPAGE PATH OF 3D NETWORK IN FRACTURED ROCK MASSES

Bin Pan[a], Yangsong Zhang[b,*]

Department of Civil Engineering, Nanjing University of Science and Technology, Nanjing,China

[a]bin_pan@163.com,[b]zysnj318@126.com

*Corresponding author. E-mail address: zysnj318@126.com (Yangshong Zhang)

**Keywords:** Fractured rock；Rock mass hydraulics；Discrete Fracture Network Model；Shortest seepage path.

**Abstract:**Fractured rock is a combination of rocks and fractures,the fractures which are ubiquitously distributed in fractured rock mass often constitute the flow and migration path of underground fluid and radionuclide.Discrete Fracture Network Model (DFN) was built with in-situ observations to evaluate the hydraulic conductivity tensor of rock masses.The fractures relation pattern with corresponding algorithm is given on the basis of computational geometric,and then the graph theory is employed as the mathematical model to represent the mutual positional relation of fractures.And then,with the use of Dijkstra algorithm, the hydraulic conductivity tensor could be obtained.

## Introduction

There are many different fractures,which,as with rocks, form a complex fracture network,in the rock masses.The permeability of the rock masses is very important to a pre-selected area for high-level radioactive waste repository.As the computer technology develops,the fractures relation pattern with corresponding algorithm is given on the basis of computational geometric,and then the graph theory is employed as the mathematical model to represent the mutual positional relation of fractures in 3D space[1](Wang and Yang,1992).And then,discrete mathematics was introduced to the research on the connectivity of the fractures in the rock masses[2](He and Liao,1995).The connectivity of fractures and permeability of volcanics were obtained though Discrete Fracture Network Model with the application of graph theory[3](2002,Park and Kim).In this paper,on the basis of graph theory,the relations between fractures were got by spatial geometry,and Dijkstra algorithm was applied to obtain the shortest seepage path in the rock masses.

## Spatial relationships between fracture disks

Getting the spatial relationships between fracture disks is the first step to this study.In the case of fracture is treated as a flat disk,there are many different spatial relationships between fractures.It is essential to get the intersecting line between each two related fracture disks,and the coordinates of the intersecting line can be obtained by Spatial geometry.

**Parallelism of two fracture disks.**Whether there is a intersecting line between every two disks depends on the coordinates of the centers and the normal directions of the fracture discs.But,if they parallel to each other,it indicates that there are no intersecting line between the selected fractures,and if not,further works should be done to get the coordinates of the intersecting line.

**Intersection of two fracture disks.**When solving the intersection of non-parallel fracture disks,the disks are assumed to be planes.But the size of fracture disk is limited indeed,even the planes of the fracture disks intersect,the real fracture disks may have no intersecting line(Fig 1).

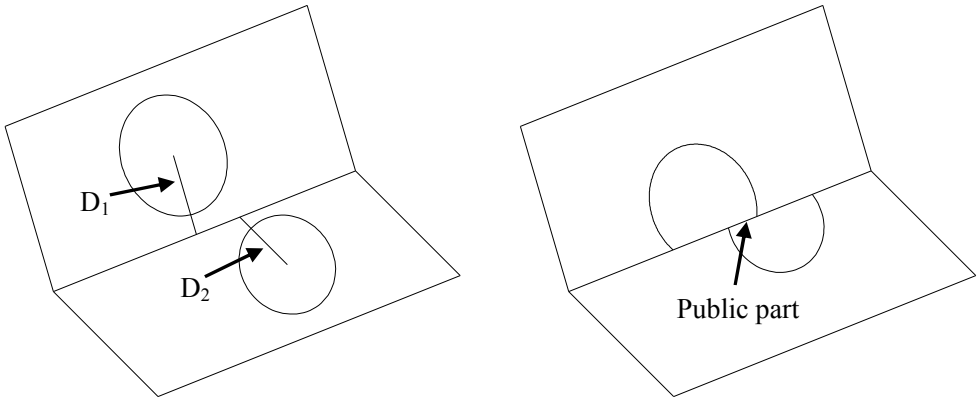


Fig.1 Planes of the fracture disks intersect

Then the $D_1$ and $D_2$,as shown in figure 1,are applied to judge the intersection of the two disks,if $D_1 \le r_1$ and $D_2 \le r_2$ ($r$ is the radius of the fracture disk),the the public part of the intersection line is the intersection line of the fracture disks.

**The real intersection line.**If the intersection points of the line L and the disk are assumed to be $(x_{11}, y_{11}, z_{11})$ and $(x_{12}, y_{12}, z_{12})$,then L can be written, in a general form, as

$$L_{p1} : \frac{x - x_{11}}{x_{12} - x_{11}} = \frac{y - y_{11}}{y_{12} - y_{11}} = \frac{z - z_{11}}{z_{12} - z_{11}} = t \tag{1}$$

Similarly

$$L_{p2} : \frac{x - x_{21}}{x_{22} - x_{21}} = \frac{y - y_{21}}{y_{22} - y_{21}} = \frac{z - z_{21}}{z_{22} - z_{21}} = t \tag{2}$$

Solve equation (1) and (2) with simultaneous equation approach.If the simultaneous equation has two different solutions,the fracture disks have real intersection line,otherwise not.

**Storage and representation of graph**

There are two different methods to store the graph—adjacency matrix and adjacency list.Adjacency matrix is a method that represents the graph as two arrays,but since the model has huge number of fractures inside,the arrays are too large to operate for the computer,adjacency list takes up less storage space(Fig 2).In this paper,adjacency list is used to store the relations of each two fracture disks.

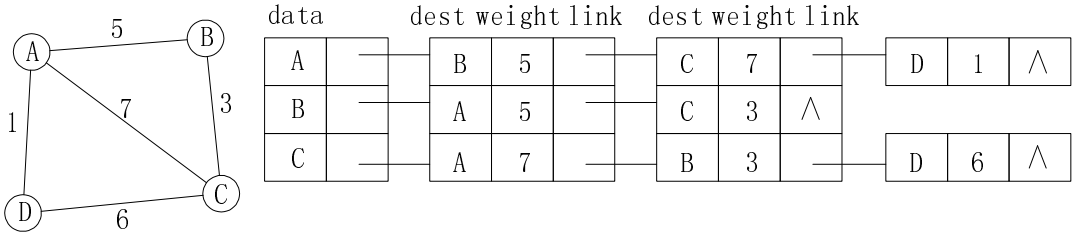


Fig.2 Adjacency list to store the graph

The weight in the adjacency list represents the time $T$ that water flows from one fracture disk to another.

$$T = \frac{L}{v} \tag{3}$$

According to Darcy's law

$$v = k \cdot i \tag{4}$$

Then

$$T = \frac{L}{k \cdot i} \tag{5}$$

According to Fig 3,the shortest time that water flows between two connected fracture should be written as

$$T = T_1 + T_2 = \frac{L_1}{K_1 \cdot i} + \frac{L_2}{K_2 \cdot i} \tag{6}$$

Where $L_1$ , $L_2$ represent the distances between the centers of the disk and the center of the intersection line. $K_1$ , $K_2$ corresponds to the permeability coefficient of $L_1$ , $L_2$ .

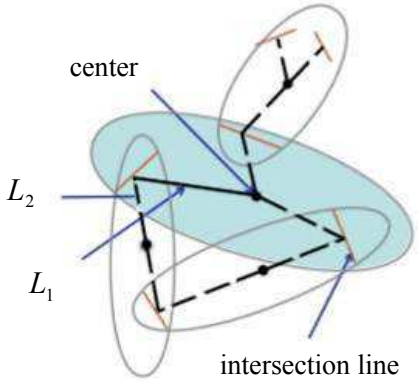


Fig.3 Water flows between fractures

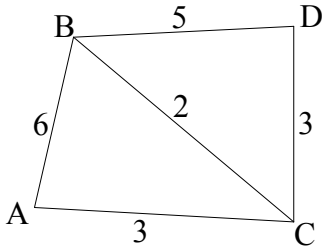


Fig.4 Data network structure

**Search for the shortest seepage path**

When all the time that water flows between each intersected fractures are obtained,the graph of the fractures of the DFN model is built up.Dijkstra algorithm is applied to search the shortest seepage path between two specified fracture disks.The Dijkstra algorithm can get the nearest node(fracture disk) that intersects the node specified each time,until the path reach the specified terminal point,if the terminal point is reachable.It is based on the ascending order,and is correct unless the weight of every node in the graph can be negative.Table 1 shows the operations Dijkstra algorithm takes to process the graph of Fig 4.

Table 1 Detailed algorithm process of Dijkstra algorithm

| step | S set | T set |
|---|---|---|
| | | T=<B, C, D> |
| | Take A,S=<A> | A→B=6 |
| 1 | The shortest:A→A=0 | A→C=3 |
| | Set A as specified node, | A→D is unreachable |
| | | Shortest path:A→C=3 |
| | Take C,S=<A, C> | T=<B, D> |
| 2 | The shortest:A→A=0,A→C=3 | Shortest path:A→C→B=5(A→B=6) |

| | | |
|---|---|---|
| | Set C as the specified node,A→C=3 | Now A→B=5 |
| | Take B,S=<A, C, B> | T=<D> |
| 3 | The shortest:A→A=0, A→C=3, A→C→B=5 | Shortest path:A→C→B→D =10（A→C→D =6） |
| | Set C as the specified node,A→C→B=5 | Now A→C→D=6 |
| | Take D,S=<A, C, B, D, > | |
| 4 | The shortest:A→A=0,A→C=3,A→C→B=5, A→C→D=6 | T is empty,done |

## Engineering Application

In this paper,the DFN model was built with datas got though in-situ observations of Jijicao district,Beishan,gansu,China.All the 5125 fractures,in the model,are divided into three sets(Table 2&Fig.5).

Table 2 The parameter of the fractures

| set | Direction/° | Dip/° | Volume density/ $m^3$ |
|---|---|---|---|
| 1 | 48.4 | 87.24 | 0.01441 |
| 2 | 220.09 | 3.16 | 0.00374 |
| 3 | 300.04 | 87.13 | 0.026646 |

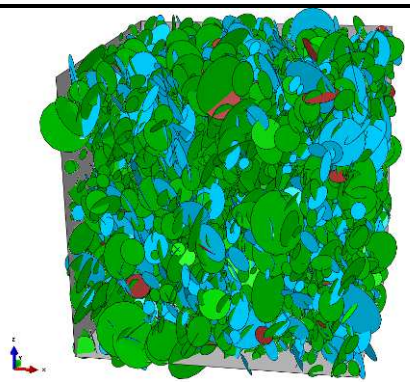

Fig.5 Water flows between fractures

As the the permeability coefficient of the closed fractures,compared with opening fracture, is quite small,the closed fractures and filled fractures are deleted.After getting all the intersection lines of each two fracture disks,the graph of the fractures in the model is obtained.Then,the shortest path of every two fractures is available by using Dijkstra algorithm.Fig 5 shows three different shortest path in three different directions.

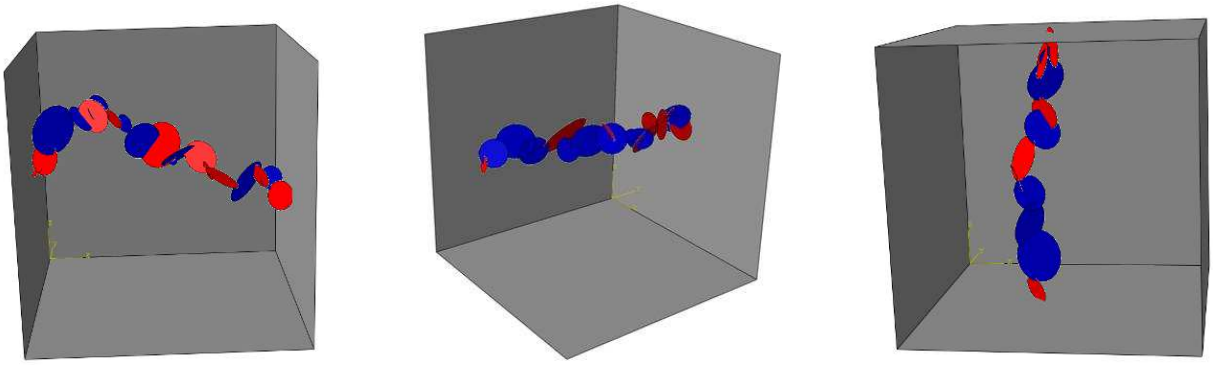

a) W—E a) S—N a) T—B

Fig.6 The shortest paths of three different directions

West to East:1475→623→3541→4088→1230→5080→74→1930→3501→202→3063→1999→798→1693→906→3365→604→2064→1473,go though 19 fractures.
South to North:1334→4476→3565→4370→641→2702→4922→2621→1343→3425→3769→4423→355→1255→1666→1354→2424→614,go though 18 fractures.
Top to Bottom:708→3051→963→2021→1689→3465→1707→439→3102→4102→3674→1563,go though 12 fractures.

## Conclusion

Discrete Fracture Network Model,based on the in-situ observations,is a very useful method to evaluate the hydraulic conductivity of rock masses.The intersections of each two fracture disks is the precondition to build the graph of the fractures in the model.And the Dijkstra algorithm is a very affective algorithm to obtain the shortest seepage path between the specified fractures,it helps a lot to get the equivalent direction permeability coefficient

## Acknowledgements

This research presented in this paper has been supported jointly by National Natural Science Foundation(NNSF) of China(40872172), National basic research program of China (973 Program: 2013CB036001)and State Administration of National Defense Science and Technology industry (Department Two-2012-491).

## References

[1] Zhi'en Wang, Chentian Yang. Numerical study of the fracture network model of groundwater flow and non-flow fracture network connectivity. Hydrogeology and Engineering Geology, 1992, 19(1): 12-14.

[2] Shaohui He, Guohua Liao. Study of Fractured rock flow model with initial fractures. Journal of Southern Institute of Metallurgy, 1995, 16(2): 27-35.

[3] Park B Y, Kim K S, Kwon S, et al. Determination of the hydraulic conductivity components using a three-dimensional fracture network model in volcanic rock[J]. Engineering geology, 2002, 66(1): 127-141.

*Applied Mechanics and Materials Vols. 580-583 (2014) pp 862-865*
*© (2014) Trans Tech Publications, Switzerland*
*doi:10.4028/www.scientific.net/AMM.580-583.862*

# Development features and fractal research of fault structure of No.5 coal seam in Chenghe-Second coal mine

Xicheng Xue[1, a], Jia Wang[2, b]

[1]College of Geology and Environment Xi'an University of Science and Technology Xi'an, China

[2]College of Geology and Environment Xi'an University of Science and Technology Xi'an, China

[a]xuexc331@163.com, [b]1051490786@qq.com

**Keywords:** Chenghe-Second coal mine, No.5 coal seam, fault structure, fractal theory

**Abstract.** Based on the collected geological exploration and underground mining data, this thesis has analyzed the development feature of faults of No.5 coal seam in Chenghe-Second coal mine and obtained fractal law of fault structure by fractal statistics. The result shows that the faults have a good self-similarity on the plane distribution and obvious fractal characteristics and that the larger the fractal dimension, the higher the complex degree of fault structures.

## Introduction

Chenghe-Second coal mine is located in western Chenghe mining area of Shaanxi province and its approved production capacity has reached 0. 69 million tons per year after several transformation and expansion. So far, the mine has fully formed mechanized mining pattern. The main mining area is third mining area of second level, the two working faces of which are both mined mechanically, and the main coal seam is No.5 coal seam in Taiyuan Formation of Upper Carboniferous Series. With the increasing strength of mining and extent of mechanization, mine geological structure , especially fault structure has a more obvious influence on production and construction of mine. This thesis has researched fractal features of No.5 coal seam of Chenghe-Second coal mine and summarized its development laws according to the result, which has a certain guiding significance for safety production of the mine.

## Chenghe Mining Area Survey

Chenghe mining area across Chengcheng and Heyang counties of Shaanxi Province, is a medium-sized mining area located in eastern Weibei coal field [1]. The mining area is 67 km long, 30 km wide, and covers an area of 1718 square meters [2]. The coal seams formed in the Carboniferous-Permian and geological reserves is 8.58 billion tons. Among them, the main coal seam is No.5 coal seam, the quality of which mostly is lean coal, partly meager coal.

In terms of plate motion, The mining area lies on the border of Erdos plots and Weihe basin and is bounded on the east by Lvliang uplift and Taihang uplift, Fenhe graben system developes between which, on the south by Qinling folded belt and on the west by thrust structural belt and Liupanshan structural belt. This geotectonic background determines that the structural feature of the mining area on the whole is a monoclinal structure sloping towards the north with east-west and north-west faults and secondary folds along the strike and lean.

## Fault Feature of Chenghe-Second coal mine

The basic structural feature of Chenghe-second coal mine is a monoclinal structure with strike EW, dip to N and dip angle 20°. The large and medium-seized faults are relatively fewer, and small-seized faults comparatively develop.

**Large and medium-sized faults.** Within the range of mining right of Chenghe-second coal mine, 4 large and medium-seized faults that are all normal faults and located in the north of the coal mine have been discovered, including 1 EW strike fault and 3 NE strike faults. The four faults are Fangjiahe

fault, Mjiahe fault, Duanzhuang fault and Nanyao fault from west to east. Among them, Mjiahe fault and Duanzhuang fault are a set of en echelon faults, and the southern side of Fangjiahe fault and Majiahe fault, strike NE, both turn into near EW.

**Small-sized faults**. Within the range of mining right of Chenghe-second coal mine, 101 small-seized faults have been discovered in coal series and also 200 small-seized faults in mined area of No.5 coal seam.

Main strike of the small-seized faults in coal series is NW (about 315°) and the faults along near NE (about 40°) comparatively develop (Fig. 1).

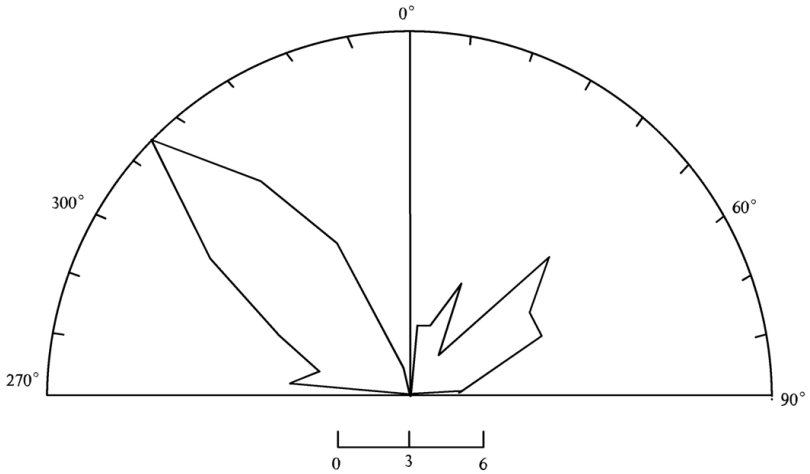


Fig.1 Statistics on strike of small-seized faults of No.5 coal seam

Main lean of the small-seized faults in No.5 coal seam is SW (about 225°), the faults along NE (about 55°) and SE (about 140°) comparatively develop, and along NW (about 315°) are fewer (Fig. 2).

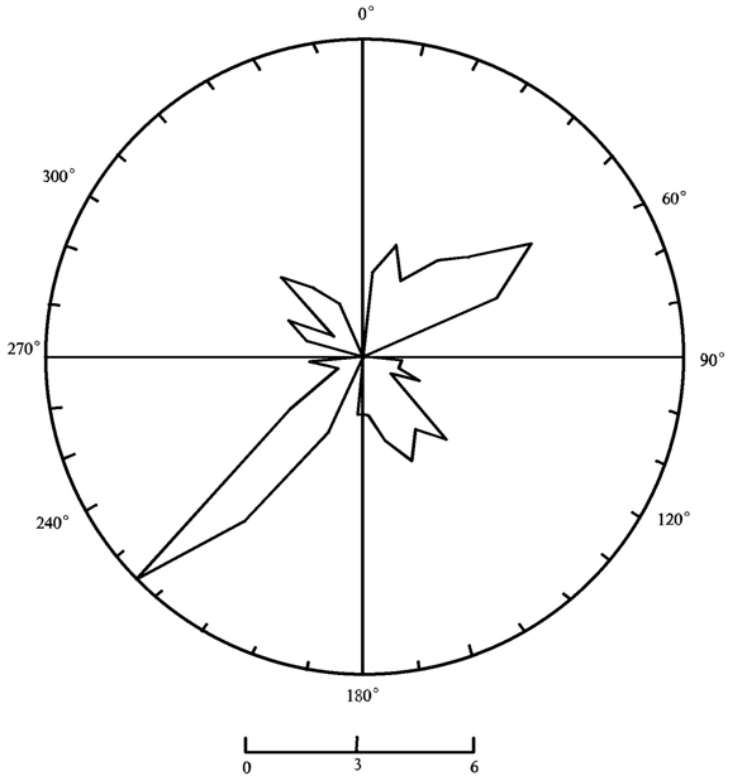


Fig.2 Statistics on lean of small-seized faults of No.5 coal seam

**Fractal Research of Fault Structure**

Based on the existing maps and data, this thesis has researched fractal features of No.5 coal seam of Chenghe-Second coal mine by input editing and spatial analysis two subsystems and scatter diagram module of Microsoft Office Excel.

First, dividing the coal mine into several grids with side length r and counting the total number of grids in which faults develop as reducing it with the ratio of 0.5 [3]. In order to attain fractal goal, the side length in this thesis is $r_0$=1000m, $r_1$=500m, $r_2$=250m and $r_3$=125m.

If the statistical result meet the following formula:

$$N(r)=Cr-D. \quad (1)$$

Where, it can be shown that fault structure has self-similarity within a certain range if C is a constant, and D is the fractal dimension.

And then, calibrating the numerical points in double logarithmic coordinate system. If fault structure has self-similarity, a fitting line can be getten from Ln(N(r))-Ln(r)scatter diagram, whose slope is -D and formula is:

$$Ln(N(r))=a+(-D)\ln(r). \quad (2)$$

Thus, the fractal dimension D and correlation coefficient R can be derived.

The correlation coefficient R of fault structure of each mining level is larger than 0.992 and the fractal dimension D is 1.6243, 1.684 and 1.0577 respectively, namely the fractal dimension of second level is largest, then first level and third level's is smallest. It can be concluded that complex degree of fault structures of second level is highest, followed by first level and third level's is lowest (Table 1).

Table 1 The fractal dimension D and correlation coefficient R of fault structure of each level

| Level | Fractal dimension D | Correlation coefficient R |
|---|---|---|
| First level | 1.6243 | 0.9985 |
| Second level | 1.684 | 0.9986 |
| Third level | 1.0577 | 0.9923 |

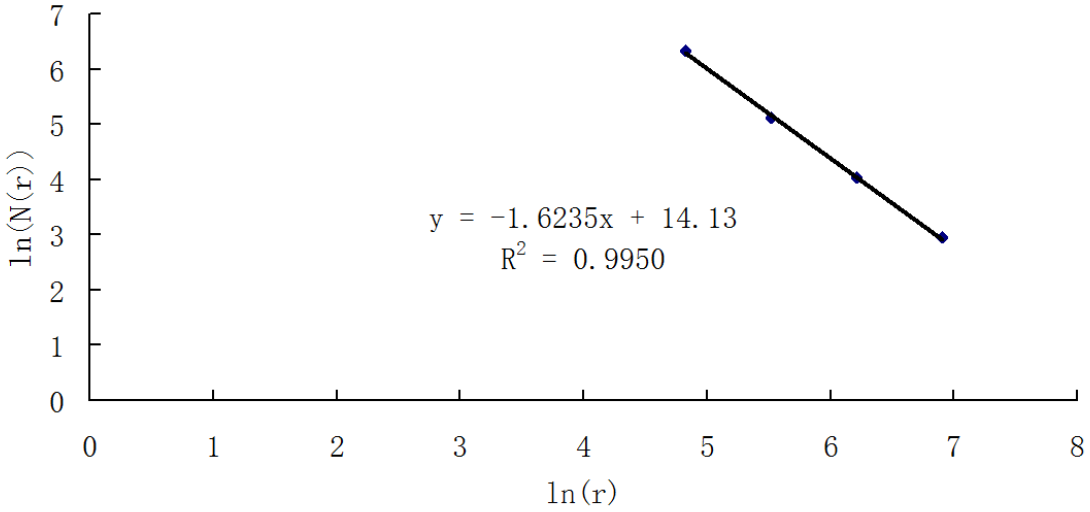


Fig.3 The Ln(N(r))-Ln(r) fitting line and fractal dimension of fault structure of No.5 coal seam

The result that the fractal dimension D of fault structure of No.5 coal seam is 1.6235 and the correlation coefficient R is 0.995 shows that fault structure of Chenghe-Second coal mine has good a self-similarity and meets fractal laws (Fig. 3).

## Conclusions

Bsed on structure features and fractal theory, the following conclusions could be obtained.

(1) 4 large and medium-seized faults have been discovered, which are all normal faults and have a obvious directivity.

(2) 200 small-seized faults in mined area of No.5 coal seam have been discovered, which are almost normal faults. Their main strike is NW, then near NE.

(3) The fractal dimension D of fault structure of No.5 coal seam is 1.6235 and the correlation coefficient R is 0.9950, which shows that fault structure of Chenghe-Second coal mine has a good self-similarity and obvious fractal features.

(4) The fractal dimension D of each level: second level > first level > third level, and the correlation coefficient R is larger than 0.9923, which shows that the larger the fractal dimension, the higher the complex degree of the structure [4] and the more the influence on safety production.

## Acknowledgements

This work was financially supported by Shaanxi Nature Science Fund Project (SJ08-ZT08-3).

## References

[1] Chenghe Mining Bureau: Shaanxi Meitan Jishu, p.64, 1992. In Chinese.

[2] Bingtai Ma etc: *The chronicle of Chenghe Mining Bureau* (Coal Industry Press, China 1999). In Chinese.

[3] Kun Wang, Lianwu Chen, Yueqiang Chen etc: Science and Technology of West China, Vol.7, No.26, p.18-19, 2009. In Chinese.

[4] Yucheng Xia, Huanren Fan, Mingxing Hu etc: Journal of Xi'an University of Science & Technology, Vol.1, No.7, p.22-43, 1997. In Chinese.

*Applied Mechanics and Materials Vols. 580-583 (2014) pp 866-869*
*© (2014) Trans Tech Publications, Switzerland*
*doi:10.4028/www.scientific.net/AMM.580-583.866*

# The Application of Reservoir Geo-modeling Technology in Section07, Ticleni Oilfield

Lingyun Pang

Postdoctoral Programme of China Industrial Economic Security Research Center,

Beijing Jiaotong University

**Keywords**:Geo-modeling, Section07, Stochastic Modeling, Lithofacies Model

**Abstract:** In the study of reservoir geo-modeling in Ticleni oilfield, structural model, the spatial framework of the geo-model was firstly constructed based on seismic and petrophysical data and integrated geological background analysis. Then the variogram function was analyzed based on petrophysical data and sedimentary setting analysis, and the litholofacies model was established. Finally, the property models were constructed with reservoir physical property controlled by lithofacies model. Therefore, the quantification of geological study achievements and the distribution of reservoir physical property are effectively combined, which provides the foundation for the sequent reservoir development of Section07.

## Introduction

Ticleni Oilfield was discovered in 1950, and section07 is one of the sections of the field. Totally 18 wells has been drilled in section07 up to Year 2013, among which 10 are function wells and only 2 are producing wells currently. The oilfield has entered the Middle-Later Period of development and transferred from high water-cut stage to full water cut stage, reserve-production balance to out of balance. Remaining oil mainly distributes in the place with poor porosity and permeability of reservoir, which make it much more difficult to be discovered. All the problems above are mainly due to the inner heterogeneity of reservoir. The traditional geological study, which focused on the qualitative description on reservoir, can't satisfy the command of reservoir description at Middle-Later stage of oilfield development. In order to tap potential of old oilfield and improve the exploration and exploitation level, fine description on reservoir is of great necessity [1]. 3 Dimension geo-modeling technology- a method closely combining of mathematics and reservoir geology, can quantify the shape, structure and parameters of reservoir, and thus well characterize subsurface condition of reservoir [2].

## Geological Background

Section07 is about 4.95km$^2$ and situated in the western side of Getic Depression, Dacic Basin, Romania. The structure characteristics of the basin are controlled by contractional movement in Middle to Late Miocene and extension movement in Paleogene to early Miocene. Oil reservoirs in Section 07 are mainly occurred in faulted monocline structural trap, and the whole stratigraphic units incline to southwest generally. Sandstone and mudstone are major lithology developed in shoreland facies. There are totally 18 wells in this section, among which 10 wells with petrophysical and production data were used in geo-modeling (Fig.1) The target formations are Sarmatian Formation and Helvetian Formation in Miocene, which are divided into 7 layers totally from top to bottom-Sa_VI, He_tr He_I, He_II, He_III, He_IV, He_V and He_VI (Sa is short for Sarmatian, He is short for Helvetian). History production occurred in geo-zones of He_tr, He_I and He_II.

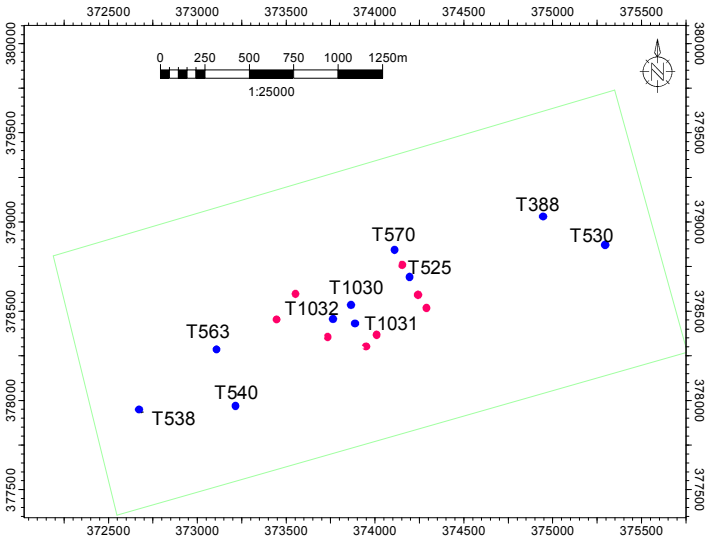


Fig. 1 Well Position of Section 07, Ticleni Oilfield

## Structure Model

Structure model is the basis of reservoir modeling, which provides the 3 dimensional spacial framework for the property modeling [3]. The fault model and the horizon model compose the structure model. The 60m×60m×10m gridding density for scaled geo-model and 30m×30m×1m for fine geo-model were adopted based on well density in the work area. The details of the process are as follows: firstly, fault model was constructed with interpreted seismic fault data and breakpoint data penetrated in wells; secondly 8 horizons were made through well tops data and controlled by seismic surface; finally the structural model of this section was constructed with Kriging (Fig.2). The structural model shows that the whole structure of the section is an NW-SE trend monoclinal structure with the structural high near well T1032.

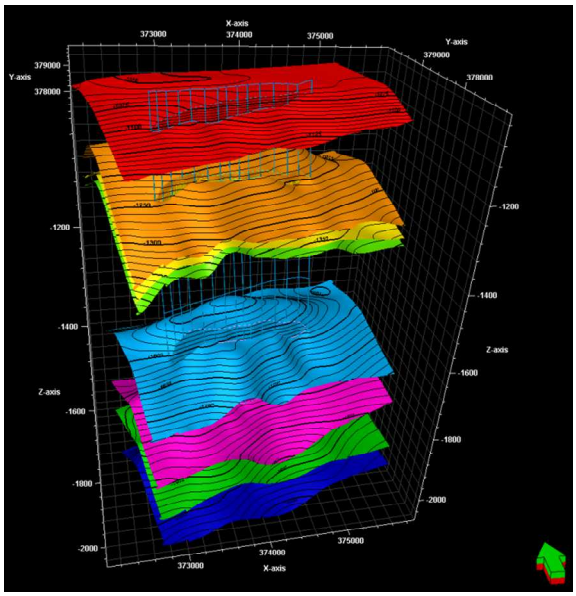


Fig. 2 Fault Modeling of Section 07, Ticleni Oilfield

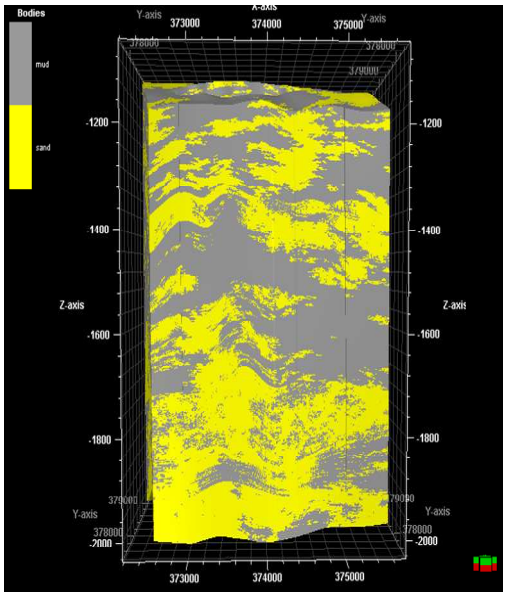


Fig. 3 Fault Modeling of Section 07, Ticleni Oilfield

## Lithofacies Model

According to the sedimentary setting and petrophysical analysis, the reservoir sandbodies in Section07 are mainly shoreland sands. The reservoirs of shoreland sedimentary environment are mainly composed of sand stone. The single sand body is of great thickness and multi-bed sand bodies superimposed. The distribution of sand bodies as well as the macroscopic heterogeneity of reservoir

are controlled by the sedimentary facies[4], while the spatial distribution of porosity and permeability etc. is mainly up to the spatial distribution of lithology. The property modeling in this paper is constrained by litholofacies model.

The sedimentary environment of section07 is shoreland and the provenance direction is NW-SE, therefore, the sand bodies of shaoreland are supposed to distribute along NE-SW strike across the provenance direction. The azimuth then is determined as NEE, and the lithofacies model is established based on the analysis above with well logging interpretation achievements of 10 wells (Fig.3).

## Property Model

The ultimate purpose of reservoir geo-modeling is to construct the model of reservoir parameters [5] (porosity, permeability, oil saturation and net to gross ratio), which can reflect the physical property of subsurface reservoir. Due to the heterogeneity and aeolotropy of reservoir physical property, deterministic modeling couldn't reflect the spatial variation of reservoir physical property [6]. Therefore, the stochastic modeling technology is adopted during this study. The property models, including porosity model (Fig.4), permeability model (Fig.5), water saturation model(Fig.6) and net to gross ratio (NTG for short) model (Fig.7), are constructed under the control of lithofacies with sequential Gaussian.

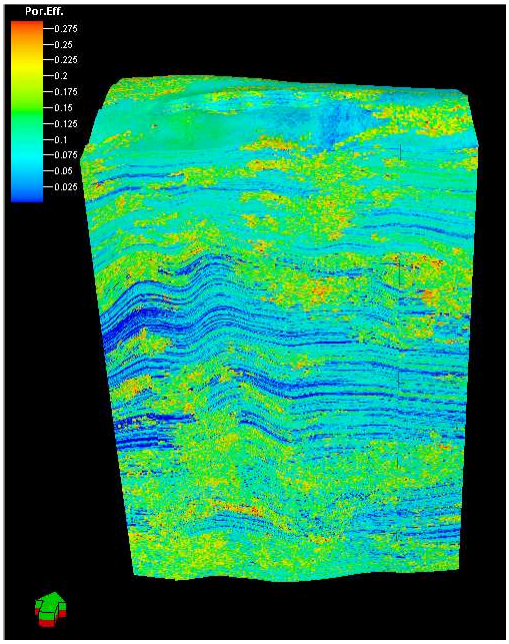

Fig.4 Porosity model

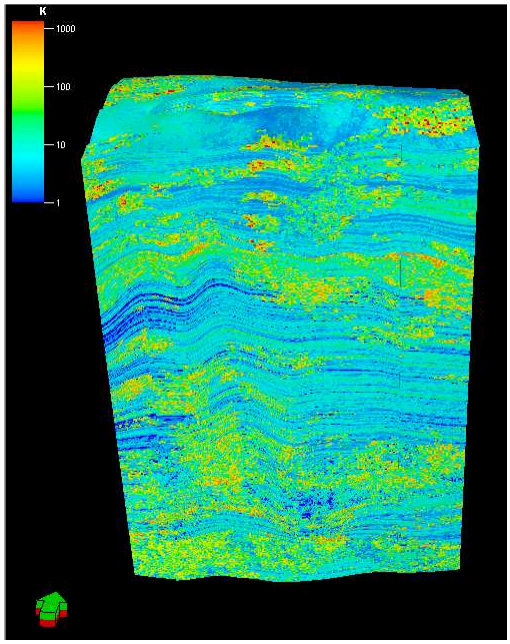

Fig.5 Permeability model

## 5.Reserv Match

Oil and gas reserve is related directly to the static parameter of the reservoir geo-model, and the distribution of porosity, permeability, water saturation and shale content determines the spatial distribution of the hydrocarbon in reservoirs. The heterogeneity and uncertainty of these parameters causes the uncertainty to reserve distribution and volume. Based on the geo-model of section07, the oil reserve was calculated by gridding with volumetric method. The influences of reservoir heterogeneity were fully considered in the reserve calculation, which greatly enhanced the accuracy. The reserve match showed that the relative tolerance of stock tank of STOIIP (147.5MMbbl ) to stock tank of original oil in place (STOOIP for short, value is141.4 MMbbl) 4.3%, which indicates the STOIIP matches well with STOOIP and the geo-model of section07 is relatively reliable.

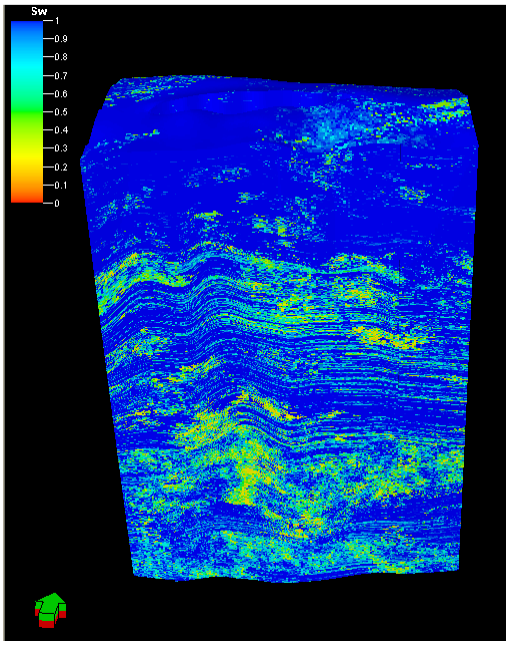


Fig.6 Water saturation model

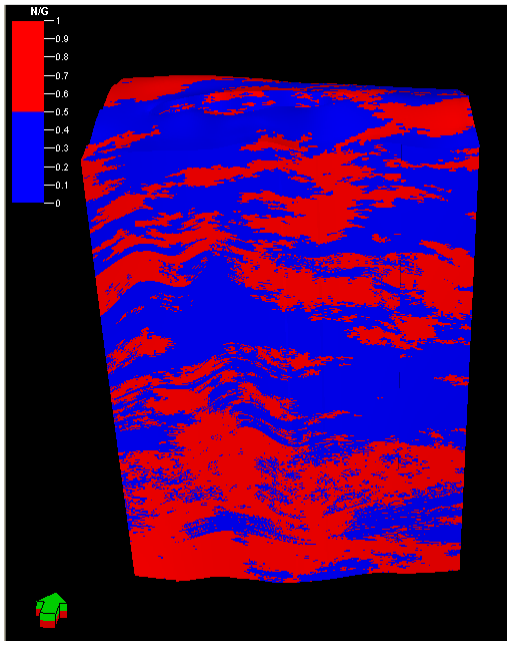


Fig.7 NTG model

## 6. Conclusion

1) There are many algorisms in the modeling software of Petrel, and suitable algorisms should be chosen to construct geo-model according to the real characteristics and data of different section.
2) Seismic, well logging and geologic data are synthetically applicated during the geo-modeling. Multiple data combine and constrain with each other, which as a result greatly improved the accuracy of the model and well characterized the reservoir.
3) The sedimentary microfacies wasn't divided in this study due to the lack of necessary data. The study about sedimentary facies need to be done deeply in the future, which would constrain the model make it much more close to the real geology and more reliable.

## References

[1]Y.N.Qiu, in:Ten years of reservoir geo-modeling, Journal of Acta Petrolei Sinica (1991), Vol.12, P.55-62.

[2] H. Haldorsen, R. Damsleth. *Stochastic Modeling*. JPT (1990),Vol.42, P.404-412.

[3]S.H.Wu, Z.K.Jin, C.X.Huang, et al.: Rerservoir modeling (Petroleum Industry Press,Beijing, 1999)

[4] S.H.Wu, Y.W.Zhang, S.J.Li, et al., in:The Geological Constrain Rules Improving the Accuracy of Reservoir Stochastic Modeling, Journal of China University of Petroleum (2001), Vol.25, P.55-58.

[5]Y.S.Sun, S.B.Guo, Y.L.Shao, in:The Application of Reservoir Physical Property Modeling in the Reservoir Description of Lianhua Oil-bearing Sand in Gao 2 Block, Journal of Gaosheng Oil field. Lithologic Reservoris (2010), Vol.22, P.27-30.

[6]X.G.Lv, D.F.Wang, in:Reservoir Geo-Modeling and Stochastic Modeling Technology. Journal of Petroleum Geology & Oilfield Development in Daqing (2000), Vol.19,P.11.

*Applied Mechanics and Materials Vols. 580-583 (2014) pp 870-874*
*© (2014) Trans Tech Publications, Switzerland*
*doi:10.4028/www.scientific.net/AMM.580-583.870*

# The Classification and Quality Evaluation of Rock-mass Based on Limited Geological Information

WU Xiao-guang[1,3,a] YANG Zhi-qiang[1] GAO Qian[1,b] BA Duo-heng[2]

[1] Key Laboratory of High Efficient Mining and Safety of Metal Mine Ministry of Education University of Science and Technology Beijing, Beijing, China

[2] Jinchuan Group Co. LTD Jinchuang Gansu Province，China

[3] Category Institute of Chinese People's Armed Police Force, Beijing China

[a] wuxiaoguang1981@126.com, [b]gaoqian@ces.ustb.edu.cn

**Keywords:** Rock masses classification;Geological evaluation; RMR; The 3rd mining area of Jinchuan.

**Abstract.** This paper takes the No. 1 ore body of Jinchuan 3rd mining area as an example, obtains the corresponding relation of surrounding rock quality evaluation index and spatial location.Through RMR rock classification method , using Rockware modeling system and limited geological informations, the statistical analysis of RMR and RQD showed that the rock of No. 1 ore body belongs to III~V type. Its rock mass is between normal to unstable. Through Rockware modeling system, we established the 3D rock properties model of UCS, RQD and RMR, and found that in the 5 to 6 rows of east hanging wall exists rock not conducive to the block caving method which belongs to the type of V. Finally, Statistical analysis was made based on the numerical model of strata. We find that , basically ,the rock block has good cavability because it belongs to the IV type of rock masses. However when design blocks and manage drawing, we must pay particular attention to the III type of rock, which is of moderate stability, and the V type of rock, which is less stable. All of these make a useful exploration for the research of key technology in the field of the interior of the earth.

## Introduction

We always want to fully describe the characteristics of deep rock mass. However there is no good method for comprehensive description of underground rock mass because of the unpredictability of the underground rock. So, when we want to classify or evaluate the quality of underground rock mass, the geological information is gained often based on sampling or drilling such as roadway joint investigation, geological exploration drilling and so on. There are two questions. For one, except for the number of quantitative information, there is so much qualitative information, such as the roughness of joints, the waviness of rock formation, the filling in the rock fractures and the description of the groundwater. When we carry on geological exploration or drilling logging, we must quantify the qualitative factors with certain technology to provide the basis for the classification of surrounding rock. The characteristics of these qualitative descriptions play an important role in the quality evaluation of the rock mass. For another, in order to obtained the predict result of the ore rock quality, we must obtain the quality evaluation index of surrounding rock and the corresponding relations between the space position and the rock mechanics parameters of ore body. All of information obtained through drilling need to be treated by stages and also comprehensively.

Jinchuan copper nickel sulfide deposit is a large scale deposit located in Jinchang, Gansu province. The ore grade is low in the 3rd mining area of Jinchuan, so the plan is to adopt the block caving method to mine ore. This methos has lower production cost and higher production efficiency. Because the block caving method has certain requirements for the quality of surrounding rock and ore body (The ore body has characteristics as the following: full of crannies, instable, large thickness, large inclination angle, good stability of the surrounding rock).As the resuilt the classification and the quality evaluation of the rock mass has special significance for the cavability, caving blocks and the mining management etc. Based on the survey data, JIA Ming-tao et al [2] speculated the RMR at the

regional of above 1554m level using geostatistical estimation method. They think that the ore rock cavability is mainly grade III. The collapsibility is good to very good. LIU Ye-ke[3], XIE Ben-xian[4] and their groups, from the Central South University, amend the RMR method, to reflecting characteristics of deep underground rock mass. YU Wei-jian, GAO Qian[5,6] from University Of Science and Technology Beijing conducted micro experimental study of deep rock mass in the 3rd mining area of Jinchuan. When analyzing the mechanical properties and the rheological law of tectonic zone of surrounding rock, they found that the rock mass has low strength because there are so many mineral crystal structures in the rock mass .The paper further points out that part of the rock is of high porosity, and easily expanse when touching and mud. These cases show that adopt caving method in the 3rd mining area of Jinchuan is suitable, but we need pay close attention to the problem of argillization when ore drawing management. The conclusion has an important guiding significance for our research.

So many literature shows that the cavability of the rock mass of the 3rd mining area of Jinchuan is good, however there are many disadvantage to the block caving method through careful study. So, how do we evaluate the quality of rock mass in a scientific way, and to provide some guidance for mining design and drawing management? This paper takes the No. 1 ore body of Jinchuan 3rd mining area as an example, uses the method of RMR surrounding rock classification, Rockware modeling tool and so on, introduces the classification and quality evaluation of rock-mass based on limited geological information.Capitalizing on these conclusions, we can take concrete technical response, to ensure that the ore mining more scientific and efficient in the premise of safety.

## Statistical Analysis of The Partial Drilling Mining

**RMR surrounding rock classification.** After the method of RMR surrounding rock classification was introduced in the year 1973~1975[8], it continued to add data and widely spread in the world. It uses the 6 indicators as the basic parameters.They are the uniaxial compressive strength of rock, rock quality designation(RQD), joint spacing, joint conditions, groundwater conditions and the correction coefficient. These indicators are determined by the relationship between the joint surface range to the foundation, together with the slope and the excavation direction. Among those parameters, there are quantitative parameters such as the uniaxial compressive strength, rock quality designation etc, and qualitative parameters such as joint conditions, groundwater conditions etc. RMR is a method which combins both qualitative and quantitative information. It can fully reflect the importance of qualitative indicators to the quality evaluation. The method of RMR is so flexible and simple that it meets the demand of qualitative information. As a result, when referring to the statistical analysis of the drilling mining, we use RMR surrounding rock classification.

**Analytical results.** The statistical analysis mainly described in detail the classifi-cation index of RMR changes along the borehole of the 12 bore-holes. Figure 1 shows the relationship between the surrounding rock quality RMR with depth, which from the borehole of Zk02. Table 1 shows the analysis results of RMR and RQD, from 10 boreholes.

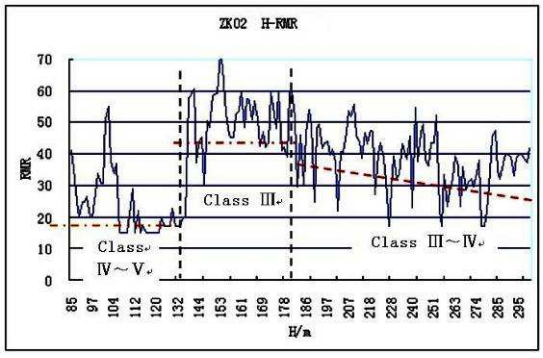


Fig. 1 The change relationship with depth of the surrounding rock quality which from the borehole of Zk02(lin5, Hanging Rock)

Table. 1 The statistical analysis results of the RMR and RQD from the 10 new drilled hole of the 3rd mine

| Line | | 5 | | 6 | | | 8 | 9 | 10 | | 11 |
|---|---|---|---|---|---|---|---|---|---|---|---|
| Boring number | | Zk01 | Zk02 | Zk03 | Zk04 | Zk05 | Zk12 | Zk07 | Zk08 | Zk09 | Zk10 |
| Position | | Footwall | Hanging wall | Footwall | Central | Hanging wall | Hanging wall | Central | Footwall | Hanging wall | Footwall |
| RQD | Mean | 57 | 9 | 14 | 6 | 40 | 21 | 9 | 46 | 37 | 53 |
| | SD | 35 | 6 | 6 | 5 | 32 | 26 | 6 | 30 | 34 | 30 |
| | CV | .605 | .657 | .406 | .737 | .794 | 1.262 | .675 | .649 | .914 | .577 |
| RQD Classification | | IV | V | V | V | V | IV | V | IV | IV | III |
| RMR | Mean | 47 | 37 | 49 | 32 | 39 | 29 | 38 | 43 | 39 | 46 |
| | SD | 10 | 14 | 10 | 11 | 14 | 11 | 11 | 12 | 13 | 11 |
| | CV | .218 | .361 | .204 | .345 | .371 | .385 | .293 | .282 | .330 | .243 |
| RMR Classification | | III | IV | III | IV | IV | IV | IV | IV | IV | III |

## Statistical modeling based on drilling cycle

In order to research the spatial variation of rock mass quality and cavability of the lean ore that comes from the No. 1 ore body of the 3rd mining area in detail, we adopted statistical analysis of drilling hole data, used Rockware modeling system, and established the three-dimensional characteristics model of UCS,RQD and RMR(or cavability). Figure 2 shows the 3D distribution model of UCS, Figure 3 shows the 3D distribution model of RQD and figure 4 shows the 3D distribution model of RMR.

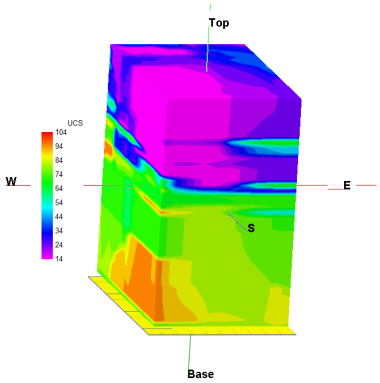


Fig. 2 The UCS model of the rock from No. 1 ore

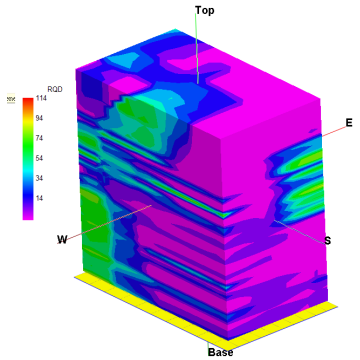


Fig. 3 The RQD model of the No. 1 ore

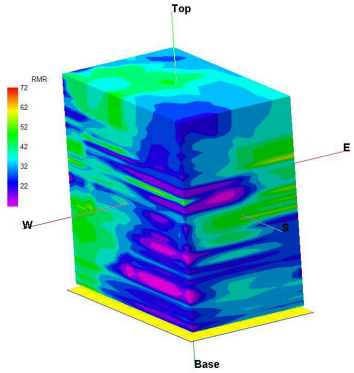


Fig. 4 The RMR model of the No. 1 ore

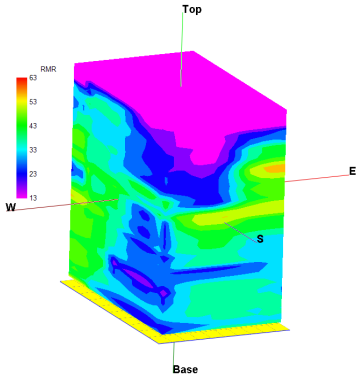


Fig. 5 The RMR ore block model

## Segment statistics of drilling and the three dimensional cavability model

In order to analyze and predict the cavability of the ore rock, we built Cavability evaluation model using Rockware modeling system according to the data of segment statistics of drilling. Figure 5shows the RMR ore block model which is based on rock drilling section. It clearly shows a stable

state of mining of No. 1 orebody rock, that is the eastern 5 ~ 6 of hanging wall which affected by the fault F8 belongs to class V. When block design and drawing management, we must pay attention to this kind of broken surrounding rock.

## The results of formation statistical analysis

In order to established numerical analysis model, we need to perform statistical analysis according to the formation that is divided the stratigraphic for the hanging wall rock, lean ore and the footwall rocks. Statistical analysis results of drilling the formation in Table 2. Table 2 shows the results of statistical analysis of surrounding rock and ore body.

Table. 2 Drilling statistics results according to the formation

| Boring number | Zk01 | | | Zk02 | | | Zk03 | | | Zk04 | | | Zk05 | | |
|---|---|---|---|---|---|---|---|---|---|---|---|---|---|---|---|
| | Depth | | RMR | Depth | | RMR | Depth | | RMR | Depth | | RMR | Depth | | RMR |
| | Top | Bottom | | Top | Bottom | | Top | Bottom | | Top | Bottom | | Top | Bottom | |
| Hanging Rock | 0 | 86 | 31 | 0 | 161 | 27 | 0 | 55 | 29 | 0 | 108 | 27 | 0 | 171 | 30 |
| Central lean ore | 86 | 206 | 51 | 161 | 302 | 38 | 55 | 213 | 51 | 108 | 260 | 31 | 171 | 414 | 25 |
| Footwall rocks | 206 | 240 | 35 | | | | 213 | 225 | 42 | | | | | | |
| Boring number | Zk07 | | | Zk08 | | | Zk09 | | | Zk10 | | | Zk12 | | |
| | Depth | | RMR | Depth | | RMR | Depth | | RMR | Depth | | RMR | Depth | | RMR |
| | Top | Bottom | | Top | Bottom | | Top | Bottom | | Top | Bottom | | Top | Bottom | |
| Hanging Rock | 0 | 124 | 31 | 0 | 80 | 32 | 0 | 126 | 31 | 0 | 125 | 36 | 0 | 191 | 34 |
| Central lean ore | 124 | 206 | 40 | 80 | 173 | 33 | 126 | 248 | 39 | 125 | 180 | 46 | 191 | 238 | 44 |
| Footwall rocks | 206 | 211 | 26 | | | | | | | | | | | | |

Table. 3 Statistics results based on the formation RMR

| Hanging Rock | | | Central lean ore | | | Footwall rocks | | |
|---|---|---|---|---|---|---|---|---|
| Mean | SD | CV | Mean | SD | CV | Mean | SD | CV |
| 31 | 2.8 | .092 | 40 | 8.5 | 0.214 | 34 | 8.0 | 0.234 |

## Conclusion

We can obtain the following conclusion based on the analysis results of drilling to statistics:

(1)The RMR of drilling change relationship with depth is complex. Besides individual drilling, the change is not very obvious, need to be further analysis.

(2) Generally speaking, the classification of rock mass that comes from the No. 1 orebody in the 3rd mining area, belongs to class III~V. Its stability ranges from the general to the unstable rock mass.

(3) Using the line eighth as a boundary line, we can divided the No. 1 orebody into two ore block. One is the eastern block and the other is the western block. The eastern block belongs to class III,IV, and the western block belongs to class IV (only the footwall rock of line 11 belongs to class III). Thus the eastern block rock mass is slightly better than the west ore block.

(4)The hanging rock is worse than the footwall rock of the eastern block. The hanging rock belongs to class IV, and the footwall rock belongs to class III.

(5)The rocks of western block are basically the same, both belong to class IV

Based on the RMR model which established by the classified data of drilling section, we can reach the conclusion that the line 5~6 of hanging wall in eastern block belongs to class V. When performing

block design and drawing management, we must pay attention to this kind of broken surrounding rock.

Through the establishment of numerical model, and the statistical analysis performed according to the formation, we can reach the conclusion that

(1) Generally speaking, there is a difference between hanging wall to the footwall. The surrounding rock in the hanging wall (RMR=31) is worse than in the footwall(RMR＝34). They both worse than the lean ore body（RMR=40）.The RMR mean value of the whole rock mass is 35, wchih belongs to the class IV. The whole rock has good cavability.

(2) The statistical analysis results based on the 10 holes shows that there are some variability exists among the hanging rock, the footwall rocks and the ore body. The variability of hanging rock is the minimum ($V$=0.092),and the footwall is the maximum($V$=0.234) while the variability of the lean ore body is smaller than footwall($V$=0.214).

(3)Generally speaking, the surrounding rock classification of the No. 1 orebody in the 3rd mining area belongs to the class IV. Ore body belongs to the upper of class IV, and the hanging wall and footwall rock belongs to the mean of class IV.

(4)Although the quality of the whole rock belongs to the type of class IV, from the RMR contour map we can see that there are some rock belongs to the medium stable rock (belongs to class III)in the footwall rock of line 5~6 (e.g. zk01 and ZK03 drilling in the table 2, RMR＝51) while he hanging wall belongs to instable rock(classV). It's unfavorable for the block caving of the eastern block in the No. 1 orebody, we must pay attention to this situation.

**Acknowledgements**

This work was financially supported by The national basic research program of china （2010CB731500)

**References**

[1] Information on http://bjwb.bjd.com.cn/html/2013-01/21/content_42239.htm

[2] Mingtao JIA and Liguan WANG:submitted to Rock and Soil Mechanics(2010),In Chinese.

[3] Yeke LIU, Ping CAO, Yongliang YI et al: submitted to Journal of Central South University:Science and Technology(2010) ,In Chinese.

[4] Benxian XIE, Yuanjiang CHEN and Xiuzhi SHI: submitted to Journal of Central South University:Science and Technology(2007) ,In Chinese.

[5] Weijian Yu, Qian Gao, Zhouping Zhang et al: submitted to Journal of Central South University:Science and Technology(2009) ,In Chinese.

[6] Weijian YU, Qian GAO, Shuhua ZHAI, et al: submitted to Engineering Sciences(2008)

[7] Jianwei WEI, in: The research of rock fragmentation prediction technology of block caving method in Jinchuan Mine No.3. Thesis, China: Central South University(2006) ,In Chinese.

[8] Bin Cai, Yong Yu and Xiaoming Wu: submitted to Chinese Journal of Rock Mechanics and Engineering (2001) ,In Chinese.

*Applied Mechanics and Materials Vols. 580-583 (2014) pp 875-878*
*© (2014) Trans Tech Publications, Switzerland*
*doi:10.4028/www.scientific.net/AMM.580-583.875*

# The genesis mechanism analysis of Qinglong landslide in the central region of Yunnan Province water source diversion reservoir area of the Jinsha River

Tengjiao Song[a], Jianping Chen[b], Xinjie Li[c], Jiyu Yan[d]

(College of Construction Engineering, Jilin University, Changchun 130026, China)

[a]695073389@qq.com, [b]249531952@qq.com, [c]326402830@qq.com, [d]821607099@qq.com

**Keywords:** Jinsha River area, Qinglong landslide, genesis mechanism

**Abstract.** Qinglong landslide is a very typical landslide in the central region of Yunnan Province water source diversion reservoir area of the Jinsha River. The geological background of the landslide region is introduced,including Landform, stratum lithology and geological structure and hydrogeological condition. Based on the collected geological data and according to the results of site investigation, the complete picture of Qinglong landslide is provided. Then the image of 3d vision is made. The longitudinal profile and cross-sectional profile are drawn. At last, The genesis mechanism of Qinglong landslide is analyzed from the point of landform, Rock mass structure and Geological structure. The study is helpful to understand the status of other landslides and can provide the basis of appraisal of reservoir bank stability.

## Introduction

QingLong Landslide is located in the upper reaches right bank in the central region of Yunnan Province water diversion of the Jinsha River. The distance between QingLong landslide and Aluogong dam site is about 34.537km. The volume of QingLong landslide is about $0.38 \times 10^8 m^3$.This landslide is a very typical one in the area. The genesis mechanism analysis of this landslide is very helpful to understand the status of other landslides and can provide the basis of appraisal of reservoir bank stability [1, 2].

## Geological Background of the Landslide

**Landform** The reservoir region is located in the north of Hengduan Mountains and the upper reaches of the Jinsha River. The main mountain ranges and river system are about north-south distributed, and the development is obviously controlled by regional structures. High mountains, deep valleys, and steep topography are the main characteristics of the global topography. The landform is extremely high relief extra-high zone of mountain and extremely high relief high zone of mountain. The relative height difference in the reservoir region is higher than 1000m, and the biggest height difference is higher than 2,800m. The elevation in most of the region is between 2200m to 4200m.

**Stratum Lithology and Geological Structure** The stratum in the reservoir region is South China strata. The exposure stratum in the reservoir are Gerong Formation, Qiongcuo Formation, Ranlang Formation, Gangdagai Formation, Qugasi Formation,Bolila Formation, Adula Formation, Dongwang Formation and other Formations. The outcropped lithologies are magmatite, metamorphic rocks and sedimentary rocks.

In addition, the S-N trending fracture structures in the reservoir are extremely developed, and the scales of these fault fractures are quite differently [3].

**Hydrogeological Condition** In the reservoir, tectonism is very strong. Wrinkles and fractures are well developed. The neotectonic activity is very active. The fractures, strata and rock, landform and climate are obviously different between the south, central and north regions. These conditions have

immediate impaction for the occurrence, distribution, enrichment and supply, runoff, excretion and hydrochemical characteristics, geothermal activity of underground water.

The supply of the underground water in the reservoir region mainly depend on rainfall. the pore water in loose rocks and the Karst ground water also can accept the supplement of the underground water in adjacent aquifers and surface water. The routes of underground water runoff are very short. The recurring cycles effects are strong. It has the characteristics of supplying from near areas and excreting in the near regions. The dynamic changes of springs are obviously impacted by seasons.

## Geological Characteristics of the Landslide

Qinglong landslide is located in Qinglong village which is situated in the right bank of the reservoir tail upper reaches. The shortest distance from the leading edge to the Jinsha River is 132m. The plane form of the landslide is the shape of irregular rectangle. The length is 1284m, and the width is 840m. The distribution elevation range is between 2100 and 2390m. The area is 86.3×104 m2. the average thickness is about 45m. the main trend is S24°W. The trend of bank slope in upper reaches is about S54°E. The trend of leading edge bank slope is S47°W.

Fig.1 Qinglong Landslide complete picture

Qinglong landslide mainly develops in the stratum of the first section of Lower Permian (west part). Site investigation shows that the bed rock of the landslide is Greenschist. The degree of weathering of the bed rock is moderate to intense. The joints in the rock mass are well developed, and the rock mass is broken relatively. The earth surface is smooth. The grain size of the deposition is mainly between 20 cm to 30 cm, and the content is about 80%. The maximum grain size is 50cm, and the content is about 5%. Fig.1 shows the complete picture of Qinglong landslide.

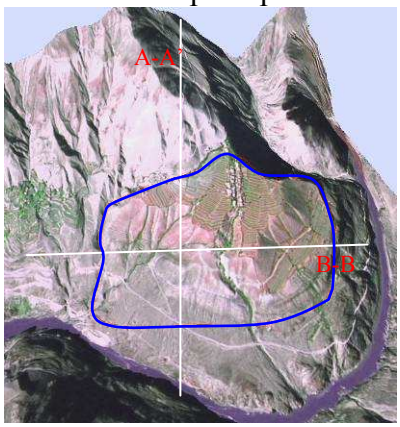


Fig.2 The image of 3d vision
of Qinglong Landslide

The Digital three-dimensional images of Qinglong landslide are established using the remote sensing images in the range of the landslide and combining DEM digital information [4, 5]. Then, the representative profiles of the landslide are arranged as shown in Fig.2.

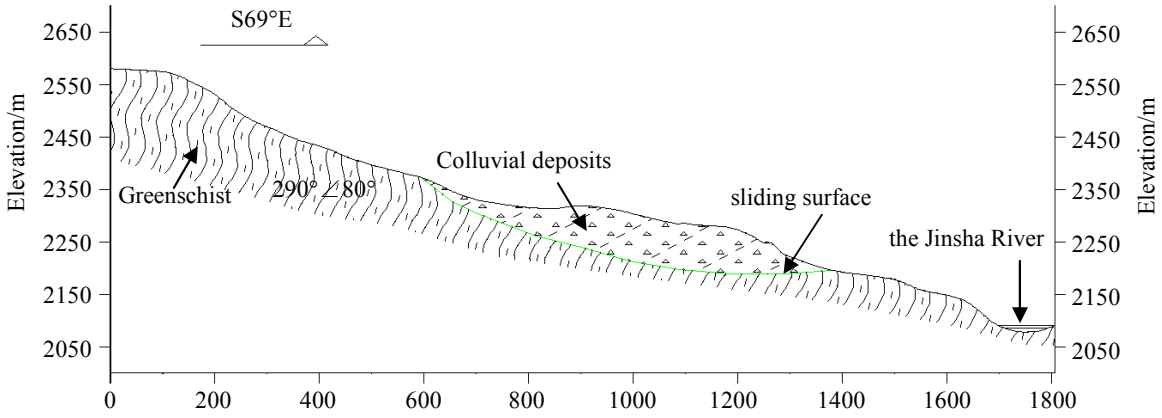


Fig.3 Qinglong longitudinal profile

Based on the 3D digital model of the landslide, the longitudinal section of the landslide is built from the bed rock in the trailing edge to the leading edge along the main distribution trend of Qinglong landslide as shown in Fig.3. The transverse section is built along the normal direction as shown in Fig.4.

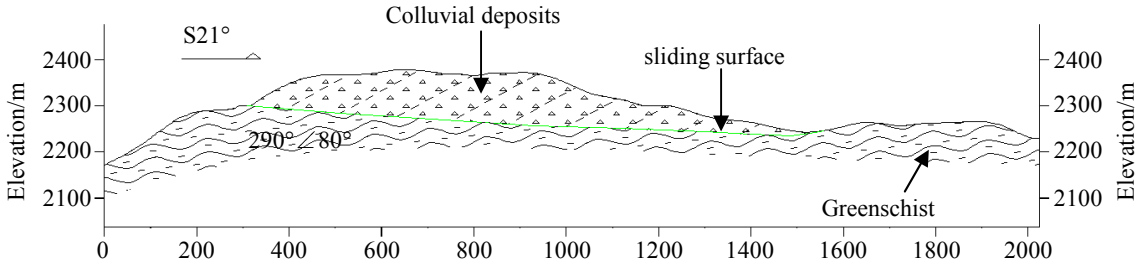


Fig.4 Qinglong cross-sectional profile

Fig.3 shows that the terrain of the trailing edge area of the landslide where the bedrock outcropped is very steep. There is a platform in the back of the landslide and its gradient is very small. Since its front part is seriously eroded, the leading edge of the landslide is steep. The elevation of the leading edge is 2198m, and the elevation of the trailing edge is 2374m. The relative elevation is 176m. The average thickness is about 45m, and the thickest part is about 89m. According to the arranged reservoir water level which is 2090m, the landslide will not be submerged after impounding.

Fig.4 shows that topographic undulation of the landslide is relatively sharp.

## Conclusions

The main features of Qinglong landslide are shown above. Then the buckling failure conditions of QingLong Landslide will be analyzed.

(1) Landform

Fig.3 shows that the relative elevation between the leading edge and the trailing edge is 176m. Both the top slope and the bottom slope are very steep. In addition, both boundaries of upper and lower reach are gullies. So the upper, lower and front boundaries are free. Furthermore, there is a river bend near the landslide. This geomorphology is beneficial to unload. To sum up, there are advantages for the slope's deformation and movement to the free surfaces under the effect of gravity.

(2) Rock mass structure

The bed rock of the landslide is mainly greenschist in the stratum of the first section of Lower Permian (west part). According to the results of site investigation, the degree of weathering is moderate to intense, and the output pattern is medium-thin. The stratum is trend to the inside of the slope steeply. In addition, the joints and cracks are well developed. The most rock masses in the accumulation zone are comparatively broken. Toppling deformation of the stratified rock mass to the

outside of the slope in the leading edge and upper reach under the gravity is found in the site investigation. The angle between the trend of the slope in the leading edge and the trend of the stratum is 27°. This condition is the base of the bed rock's toppling deformation. The two gullies in the upper and lower boundaries release the rock mass's constraint to the rock in the accumulation zone. This is an advantage of the bed rock's deformation. To sum up, the combination of the layer dipping toward to the inner slope steeply and the well developed joints in the rock mass is harmful to the stability of the slope rock mass.

(3) Geological structure

Some small faults are found in several districts in site investigation, and these faults are very short. The results show that tectonic stress impacts slightly the roc mass stability in accumulation zone.

In conclusion, we infer the mode of Qinglong slope failure is bend-rip failure.

**Acknowledgements**

This work was financially supported by the National Natural Science Foundation of China (41330636).

**References**

[1] H.z. Li, W.f. D., T.l. W.: Resources Environment & Engineering. Vol. 19 (2005), p. 57(in Chinese).

[2] R.q. H.: Chinese Journal of Rock Mechanic and Engineering Vol. 03 (2007), p. 433-454(in Chinese).

[3] R.j. K., S.c. Z., F.t. Y.: Chinese Journal of Geophysics Vol. 02 (1977), p. 96-109(in Chinese).

[4] J.s. S., R.c. X., L. S.: Earth science frontiers Vol. 06 (2007), p. 119-128(in Chinese).

[5] F.X. Study on the Relationship between Mechanism and Control Project for the Typical Giant Landslides in southwest China [D]. Chengdu Univerisity of Technology, Chengdu.(2010) (in Chinese).

*Applied Mechanics and Materials Vols. 580-583 (2014) pp 879-882*
*© (2014) Trans Tech Publications, Switzerland*
*doi:10.4028/www.scientific.net/AMM.580-583.879*

# Experimental investigation on the physical and mechanical features of clay shale in Bayingobi Basin of Inner Mongolia

Haian Liang [1,a], Qingrui Lu [2,b], Shijun Chen [2,c] and Haiyang Hu [2,d]

[1] State Key Laboratory Breeding Base of Nuclear Resources and Environment, East China Institute of Technology, Nanchang, 330013, China

[2] Architectual College, East China Institute of Technology, Nanchang 330013, China

[a]alianghaian@foxmail.com, [b]qingrui_lu@ecit.cn, [c]csjchen@ecit.cn, [d]1067673225@qq.com

**Keywords:** Clay shale, Triaxial tests, Mechanical strength, Rock mechanics

**Abstract.** The basic physical and mechanical characteristics of Clay shale in Bayingobi Basin of Inner Mongolia have been investigated by using supersonic testing system, rock mechanical testing system, and rock triaxial testing system. The results indicate that the deep clay shale of this region is characterized by high density, high mechanical strength, low deformation and strong brittleness. More specifically, according to the tests, because of their relative small particle size, the carbonate grains of clay rocks in this region are distributed more uniformly, and the average clay mineral content is comparatively low, as a result, the deep clay shale of this region are featured by large internal friction angle and high mechanical strength.

## Introduction

Clay shale, as one generally-accepted type of the important candidate surrounding rocks for underground waste disposal, is characterized by good self-healing and low permeability features. Currently, Amann studied the brittle behavior of deep clay shale of Opalinus, Switzerland [1-2], and almost simultaneously, Brapi carried out the investigation on the fracture mechanics characterization of clay shale in this region[3]. Liu Yuemiao conducted relevant research on the basic physico-mechanical behavior and time-temperature effects of crystalline rocks in Beishan district, Gansu province[4]. It is noteworthy that great achievements have been made by foreign researchers for the study on the physico-mechanical properties of clay shale taken as the waste disposal surrounding rock [5-9], however, much less relevant research has been carried out in China. In view of this, a series of research on the physical and mechanical characteristic of clay shale Baiyingobi Basinnde has been performed in this paper, which is intended for providing valuable information and technical supports for the construction of waste disposal repository and computational analysis of deep rock mechanics.

## Distribution of seriously destroyed dams in Wenchuan earthquake

## Physical property of clay shale

The amount-product method was adopted to measure the natural density of clay shale rock mass in this region, with the sample sizes taken as φ50×100 and Φ50×25 respectively. Figure 1 shows the natural density of deep clay shale rock mass in Bayingobi Basin varying with depth. It is shown that the density ranges from 2.26 to 2.6 g/cm3. The density of clay shale with the depth range of 570m-650m is relatively high, concentrating within the scope of 2.4 and 2.6 g/cm3. Generally the density of clay shale increases with depth.

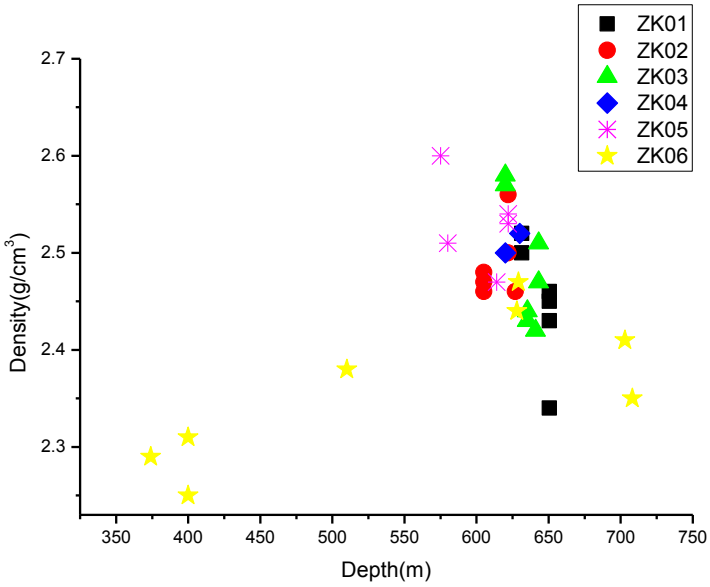


**Fig.1 Bulk density (in natural condition) varying with depth**

By making use of RSM-SY5 intelligent acoustic testing machine, the acoustic wave penetrative method was adopted to measure the compressive wave velocity of the rock samples with the size of φ50×100. Figure 2 indicates that the compressive wave velocity of clay shale in Bayingobi Basin, not closely related to the depth of rock, ranges from 3226 to 5263 m/s. Even at the same depth, the compressive velocities of clay shale differ largely from each other. The clay shale in this region is considered as anisotropic material, due mainly to that the compressive wave velocity is widely dispersed. From figure 3 it is shown that the compressive velocity increases with the increasing density of rock mass, nevertheless, affected by the composition, structure and fabrics of sedimentary rock, the clay rocks even with the same wave velocity take on certain scattering features.

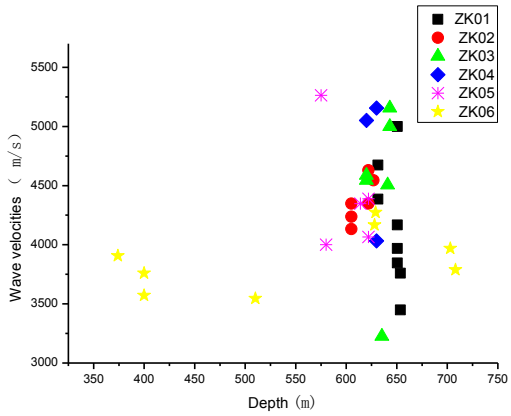


**Fig.2 Wave velocities varying with depth**

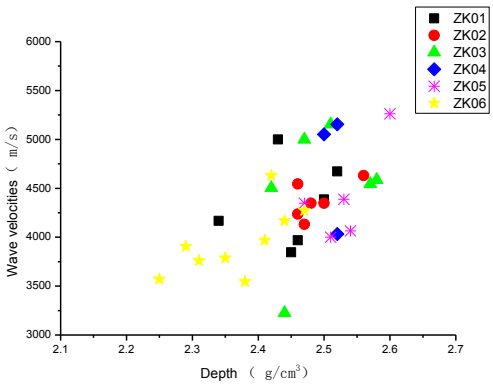


**Fig. 3 Wave velocities varying with bulk density**

## Mechanical properties of clay shale

Brazilian split tests were conducted to measure the tensile strength and uniaxial compressive strength of the rock samples with the size of φ50×25and φ50×100 respectively. Figure 4 shows the tensile strength of clay shale varying with density. It is indicated that the distribution of tensile strength is strongly scattered, within the range of 5MPa~16MPa. Besides, the tensile strength of clay shale in this region increases with the increasing density, and a positive correlation is shown between these two parameters.

The clay shale of this region is rich in carbonate composed mainly by calcareous cement, which leads to its relative high tensile strength. By analyzing the chemical cements of the clay shale in this region, we found that the carbonate content ranges from 12.51% to 17.19%； through microscope it can be

observed that the particle sizes of carbonate grains are relatively small, most concentrating on about 40μm, and the grains are distributed more uniformly, which probably leads to the higher strength of clay rocks in this region than that of other clay rocks of the similar type.

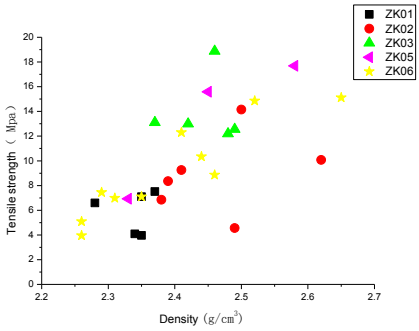


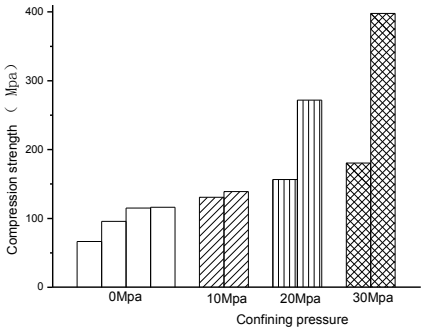


**Fig.5 Compression strength under confining pressure** **Fig.4 Tensile strength varying with bulk density**

Large rock triaxial testing system was adopted to measure the triaxial compressive strength of rock samples of the size φ50×10, with the confining pressures set as 10Mpa, 20Mpa and 30Mpa respectively. The testing results are shown in Figure 5.

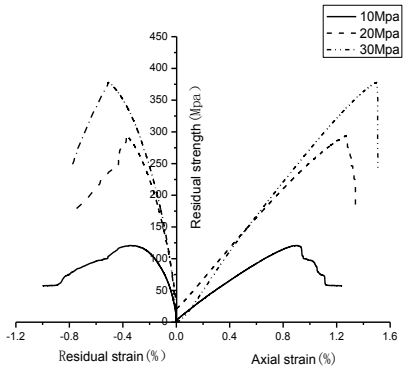


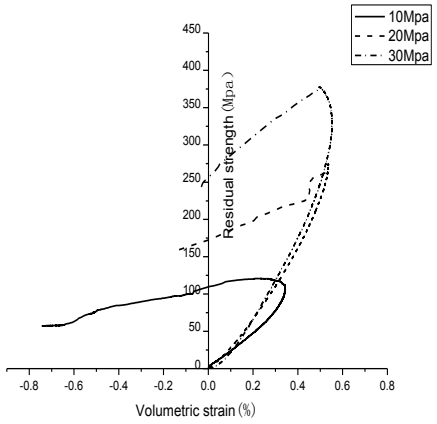


**Fig.6 Stress-strain curves of clay rock under different confining pressure** **Fig.7Stress-volumetric strain curves**

As shown in Figures 6, 7, with the increase of confining pressure, the axial breaking strength and residual strength of clay shale gradually increase. It is shown from the stress-strain curves that under different confining pressures, the clay shale takes on brittle failure characteristics after the peak stress. The stress-strain curves after the peak stress show that this type of clay shale can be considered as unsteady rupture propagation, that is, the peak stress dramatically declines, accompanied by the phenomenon of rapid volume expansion, so that the strain softening characteristics can be reflected. With the increasing confining pressure, the failure modes of rock transform gradually from brittle tensile failure, tensile-shear failure to shear failure. Under the confining pressure of 10Mpa, the clay shale shows brittle tensile failure mode, which belongs to the wedging tensile-shear failure modes. Many micro-cracks in the samples gradually form small longitudinal fractures, and are assembled into two sides of the wedge block by tensile forces. When the confining pressure increases up to 30Mpa, the clay shale of Bayingobi Basin shows weak-plane shear failure mode, also called single inclined-surface shear failure modes, in which many micro cracks form gradually small tensile cracks, and are interconnected and assembled into shear fractured zone by ultimate loads . according to the above testing results the strength envelope and Mohr-Coulomb strength curves of clay shale in Bayingobi Basin can be obtained, as shown in Figure 8, from which the cohesion and inner frictional angle are respectively obtained as 1.52Mpa and 59° .

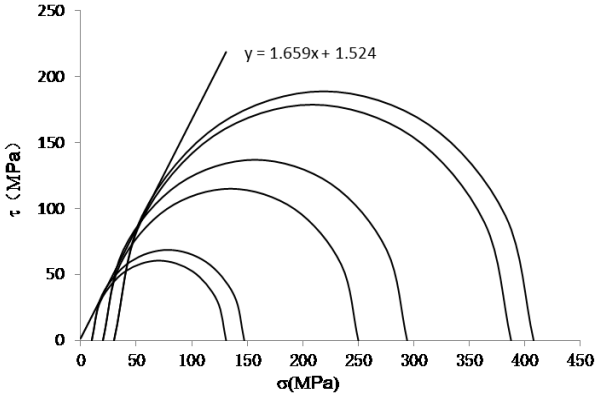


**Fig.8 Mohr-Coulomb strength curve**

## Conclusions

The deep clay shale of Bayingobi Basin, Inner Mogolia is characterized by such physical properties as high density, large compressive velocity and intact rock structures. The testing results show that the tensile strength and uniaxial compressive strength of the clay rocks in this region are relatively high. With the increasing confining pressures, the triaxial compressive strength, elastic modulus and passion ratio gradually increase. Under different confining pressures, the clay shale rock takes on the brittle failure modes after the peak stress. However, with the increasing confining pressures, the failure modes of clay rocks gradually transform from brittle tensile failure to shear failure modes.

## Acknowledgements

This work was financially supported by Special Scientific Found (DHBK2013103), and grants from the State Key Laboratory Breeding Base of Nuclear Resources and Environment (NRE1325).

## References

[1] Florian, Amann, Edward, Alan, Button. Experimental Study of the Brittle Behavior of Clay shale in Rapid, Rock Mech Rock Eng, Vol. (44) (2011), p. 415-430.

[2] Florian Amann. Peter Kaiser. Edward Alan Button. Experimental Study of Brittle Behavior of Clay Shale in Rapid Triaxial Compression, Rock Mech Rock Eng, Vol. (45) (2012), p. 21-33.

[3] F. Barpia, S. Valentea, M. Craverob, G. Iabichinob, C. Fidelibusb.Fracture mechanics characterization of an anisotropic geomaterial, Engineering Fracture Mechanics, 2012, 84: 111-122. Vol.10(84) (2012), p. 111-122.

[4] Hugman III RHH, Friedman M. Effects of texture and composition on mechanical behavior of experimentally deformed carbonate rocks , Assoc of Petro Geologists Bull, Vol.63(9) (1979), p. 1478-1489.

[5] Onodera T F, Asoka KHM. Relation between texture and mechanical properties of crystalline rocks,Bull Int Assoc Eng Geol,Vol. (22) (1980), p. 173-177.

[6] Robertson E C.Experimental study of the strength of rocks, Bull Geol Soc Am, Vol. (66) (1995), p. 1275-1314.

[7] Paterson M S.Experimental deformation and faulting in Wombeyan marble,Geol Sco Am Bull,1958,69:465-475. Vol. (69) (1958), p. 465-475.

*Applied Mechanics and Materials Vols. 580-583 (2014) pp 883-886*
*© (2014) Trans Tech Publications, Switzerland*
*doi:10.4028/www.scientific.net/AMM.580-583.883*

# Growth and Mechanics of Brittle Fault Systems in Rock Mass: An Example of Baihetan Hydropower Dam area

Wanqiang Cheng[1,2,a], Shengjie Di[1,b], Xueyong Xu[1,c], Gang Song[1,d]

[1]HydroChina, Huadong Engineering Corporation, Hangzhou, Zhejiang 310014, China

[2]Institute of Geology and Geophysics, Chinese Academy of Sciences, Beijing 100029, China

[a]Wanqiangcug@126.com, [b]di_sj@ecidi.com, [c]Xu_xy@ecidi.com, [d]Song_g@ecidi.com

**Keywords:** geometry characters, fault system, fault growth, mechanics .

**Abstract.** Architectures of fault systems play important role in stability and mechanics of rock mass. While growth mechanism of faults is intrinsic controler for architectures of fault systems. This paper presents a case on faulting in the dam area of an oversized hydropower in Southwestern China. The faults in this area are mostly strike-slip faults with shallow brittle deformation characters, extending tens to hundreds of meters. These faults can be divided into four groups which are formed during two generations corresponds to two periods of tectonic events. Growth model of these faults have been built based on geologic and mechanic data. The first generation of faults was formed based on preexisting joints. While the secondary generation emerge only if the existing faults become critically misaligned during rotation of the primary stresses. The criterion laws for formation of secondary faults are suggested. According to the growth model, we can predict placement of secondary faults in space. Conversely, when geometry and space characters of the fault systems are known, we can estimate mechanic parameters and tectonic environments of the rock mass.

## Introduction

Fault systems are first order structure surfaces which separate natural rock mass to be discontinuities [1, 2]. Architectures of fault systems are essential factors for stability and mechanics of rock mass [3]. Generally, faults derived from joints, cracks or secondary small faults. These fractures grow by linkage of neighboring ones through splay faults [4]. Succedent tectonic events may restart existing faults for they have lower cohesion. Whereas new fault will form when the primary fault becomes critically misaligned with the rotating principal stresses [5]. All above processes strictly comply with certain mechanics and geometry rules [2]. This makes it possible to quantitative predict 3D architecture of fault systems if the mechanics parameters and tectonic background of rock mass are known. It proved to be a difficult process for geometry data of fault systems are hard to obtain. Great or oversized geologic engineering area, however, provide excellent places for Quantitative analysis of fault systems because of large scale engineering excavation.

This paper presents plenty of geometry data of 261 fault traces in dam area of an oversized geologic engineering in Southwestern China, and contributes to give a quantitative analysis of the growth mechanism of these faults.

## Geological setting

The Baihetan dam area locates in downstream of Jinshajiang River between Ningnan county, Sichuan province and Qiaojia county, Yunnan province in southwestern China. This area belongs to western margin of Yangtze plate. Sediment records represent relatively stable shallow sea environment since Paleozoic with several uplifting movements. It transformed to foreland environments during Jinshajiang orogen events in Mid Triassic, and was activated by New Tethys events during Quaternary.

Continuous subduction of Indin Plate to Tibet caused lateral extrusion of Tibet terranes during Neogene. The Xianshuihe fault zone (Fig. 1, $F_1$) is the northeastern boundary of the extrusion and

presents left-lateral strike-slip with an average rate of ~10 mm/yr. The $F_1$ extends southeastward to Yangtze plate along Anninghe fault ($F_3$), Zemuhe fault ($F_4$) and Xiaojiang fault ($F_6$). All above 4 faults are restarted ancient faults, and now are seismogenic ones. The $F_3$ and $F_4$ composes folding lines which will increase sliding resistance of the fault zone. The Daliangshan fault zone ($F_5$) links the $F_1$ and $F_6$ directly and forms a perfect arc together with $F_1$ and $F_6$. Geological data indicate that the non-seismogenic $F_5$ is composed of six fault segments (Fig. 1). These segments are separated by spacers and compose left-lateral right-stepping echelon fault systems despite Yuexi fault (Fig. 1, No. ③) which shows reverse sense. Remote and field data suggests that the $F_5$ was a developing younger fault which will replace the $F_3$ and $F_4$ and is a potential seismogenic zone [6].

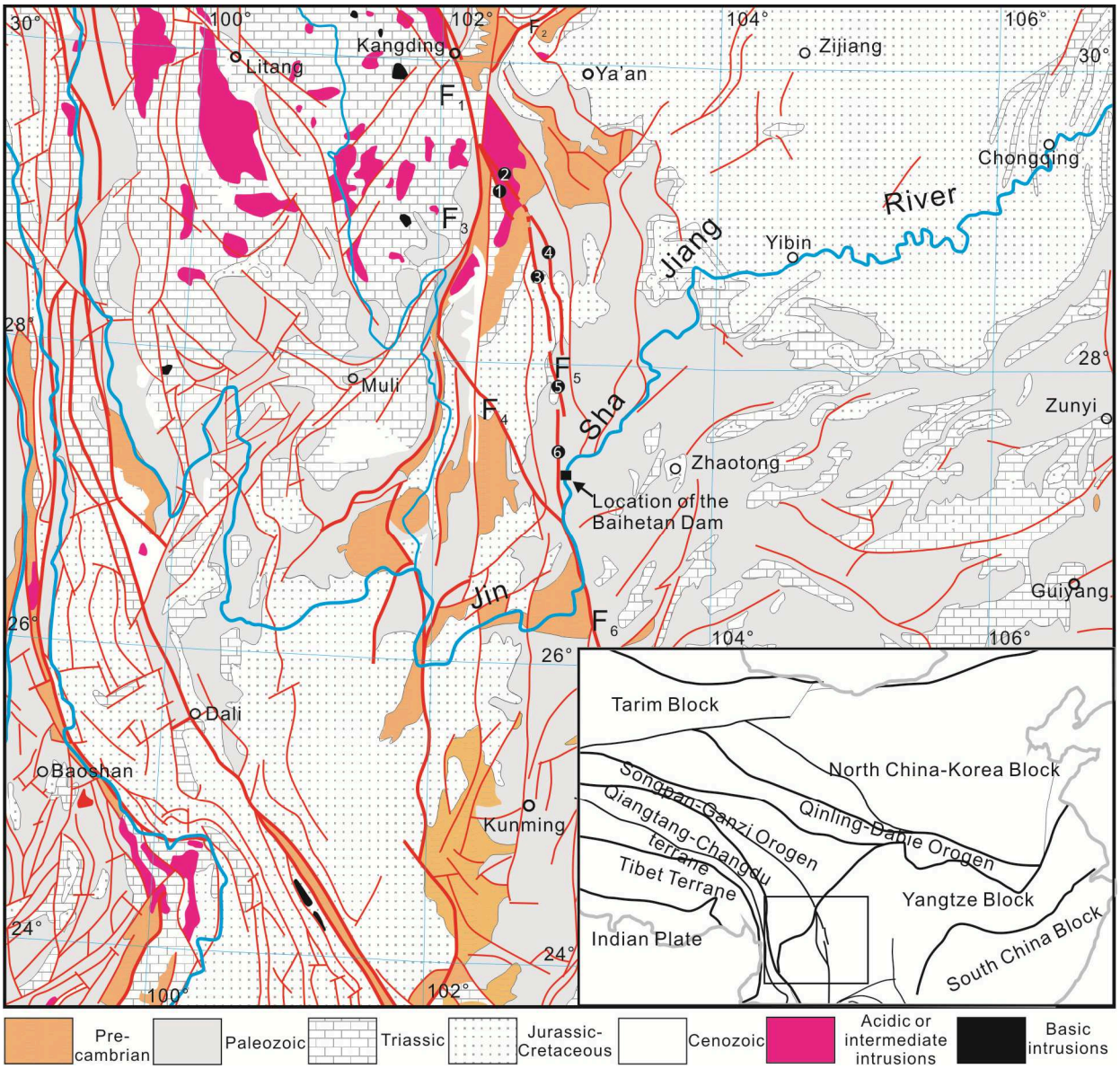


Fig. 1 Sketch tectonic map of Baihetan area and its neighborhood
($F_1$, Xianshuihe fault; $F_2$, Longmenshan fault; $F_3$, Anninghe fault; $F_4$, Zemuhe fault; $F_5$, Daliangshan faultl; $F_6$, Xiaojiang fault; Black number represent different segments of $F_5$)

## Geometry data

The Dam area is ~5 km away from Daliangshan fault which constraints structural processes of this area. Strata in this area are mainly Permian basalt eruption sequences that are covered by Triassic clastic rocks with an unconformity surface. The beds dip to 130° with an angle of 15~20°. Faults extending tens to hundreds meters are abundant while large faults are rare. The faults in this area are

mostly strike-slip ones with shallow brittle deformation characters. Four groups of faults, trending N55°-59°, N32°W, N33°E and SN respectively, can be observed, all with steep dipping.

About 53% faults strike N55°-59° (simplified as G1). These faults extend hundreds of meters while spacing 50~60m. Breccias and gouge can be seen in fault zones of 0.5~5m width. Two phase of shear sense can be seen in G1. Earlier shear sense show left-lateral transpressional sense, and was superposed by later right-lateral transtensional sense. The N33°E-trending ones (about 10%, G2) also record two periods of shearing, right lateral transpressional shearing in early stage and left lateral transpressional shearing sense in later stage. The G1 and G2 cut each other and show conjugate characters.

Another dominated group of faults strikes N32°W (G3), occupying 31% of total. These faults extend tens to hundreds of meters, and are smaller than G1. The G3 mainly presents left-lateral transpressional shearing, while a small part show two periods of movements similar as G1. The G1 faults constrains and terminates G3 ones. Geologic data indicate that G3 may secondary faults of G1.

The SN-trending faults (G4) are rare and constitute 2% of total faults. Generally, the G4 extends less than 300 m with 10~40 cm in width. These faults show reverse sense and superposed to tension in late stage. The G4 was cut and reformed by G1, indicating that the G4 was older than G1.

Joints and other fractures can also be grouped to four groups, corresponding to G1 to G4.

## Growth and mechanics of fault systems

According to former studies, two periods of tectonics can be identified after Triassic, namely Yanshanian Events (YE) and Xishanian Events (XE), respectively. The YE caused during Jinshajiang orogen event with major stress of W-E in late Mesozoic. While XE caused by southeastern extrusion of Tibet with a clockwise rotation of primary stress in late Quaternary.

**YE period.** Although frequency of fissures of N55°-59° (G1) and N33°E (G2) faults are quiet different, they have the same scales, corresponding kinematic processes, and opposite shearing sense. Especially they cut each other. All above evidences suggest flat conjugate characters. The acute angle 2θ between G1 and G2 is about 90°. According to Coulomb Criteria Eq.1, the angle of internal friction φ is close to zero. The rock mass show quasi-plastic characters. It means that the failure developed in high confining pressure. The maximum principal stress points to N79°E, approaching to W-E.

$$\theta = 45^{\circ} - \frac{\varphi}{2} \tag{1}$$

The SN-trending faults (G4) are also formed during this period, for they were cut and rebuilt by left-lateral G1 faults locally. The G4 dips to W steeply and shows reverse characters. These faults parallel with regional fold axis, and formed under W-E compression. They are initial products of regional folding event.

A small part of N32°W-trending (G3) faults present as fastigiate splay faults of G1. This part of G3 has the same kinematic patterns with G1. These faults are formed during shearing of G1 and are contrasted by G1.

**XE period.** The Indian plate subducted below to and collided with Tibet terranes in ~65Ma. Succedent continuous convergence of these two blocks cause a rapid uplift and southeastwards extrusion of Tibet in recent 10 Ma. The stress field rotated in clockwise accordingly. New stress may firstly restart existing faults for they have lower cohesion. G1 faults transformed to right-lateral transtensional ones during this period, for the $\sigma_1$ rotated to parallel with the G1. Whereas new faults G3 are formed when the primary fault G1 becomes critically misaligned with the rotating principal stresses.

The critical rotation angle of stress field is calculated by Coulomb failure criteria. According to rock mechanics, the angle of residual friction is equal to angle of internal friction and the cohesion of faults approaches to 0. The Coulomb criteria for forming a new fault and for sliding on a preexisting fault are given in Fig. 2. New faults can be formed only if the $L_1$ is catched not later than $L_2$.

The θ is the angle between maximum principal stress ($\sigma_1$) and fault. φ is internal friction angle of rock mass. $C_0$ is cohesion of the rock mass. and the $\theta_0$ without rotation equals to φ. Assuming that and the rock mass is isotropic. The critical angle of rotation, α, can be decided by Eq.2.

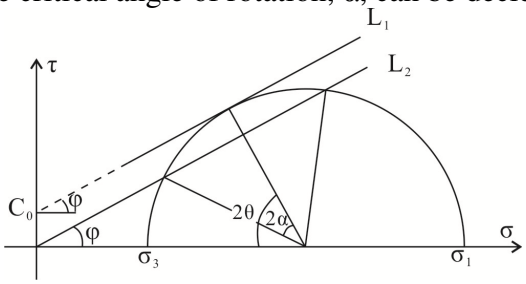


Fig. 2 A Mohr diagram with two failure criteria: $L_1$ for new faults and $L_2$ for preexisting faults

$$\alpha = \arcsin[\frac{C_0}{(\sigma_1 - \sigma_3)}\cos\varphi]^{\frac{1}{2}} \tag{2}$$

According to stress test by hydraulic fracturing method, the $\sigma_1$ of G3 points to N45°W. Thus, the θ and φ of G3 are about 13° and 64° respectively. The φ is similar with modern measured values in lab. Thus, an apparent uplift of research area happened during G1 to G3, and the G3 should be formed recently. According to in situ mechanic test data of the dam area, the $C_0$ and ($\sigma_1$-$\sigma_3$) are 1.7 Mpa and 5 Mpa respectively. Accordingly, the α is about 23°. The α' in field is 23~25°, and is consistent with α. The presents of G3 concerns with ($\sigma_1$-$\sigma_3$), thus the G3 may firstly formed in the base of G1 ones.

## Conclusions

1.Four groups of faults can be observed, trending N55°-59°W, N32°W, N33°E and SN respectively. N55°-59° trending and N33°E trending faults are conjugated ones originated from existing conjugate joints in late Mesozoic, and restarted during late Quaternary during tectonic extrusion of Tibet. The N32°W trending faults composes two genesis. A small part of the faults are splay faults of N55°-59° trending faults, while most of N32°W ones are second generation faults which are formed recently because of the rotation of the stress field.

2. According to Eq.2, the critical angle between G1 and G3 is 23°, which is consistent with field survey. The G3 may firstly formed in the base of G1 ones. Mechanic parameters and tectonic environments of the rock mass can be estimated when geometry and space characters of the fault systems are known.

## References

[1] E. Hoek and E.T. Brown, Underground excavations in rock. Institution of Mining and Metallurgy (1980).

[2] A. Gudmundsson, Rock fractures in geological processes. Cambridge University Press Cambridge, Vol. 592 (2011).

[3] D.G. Price and M. De Freitas, Engineering geology: principles and practice. Springer(2009).

[4] C. Mansfield and J. Cartwright, Fault growth by linkage: observations and implications from analogue models. Journal of Structural Geology, Vol.23(2001), p. 745-763.

[5] C.H. Scholz, R. Ando and B.E. Shaw, The mechanics of first order splay faulting: the strike-slip case. Journal of Structural Geology, Vol.32(2010), p. 118-126.

[6] H.L. He, Y. Ikeda, Y.L. He, M. Togo, J. Chen, M. Tajikara, T. Echigo and S. Okada, Newly-generated Daliangshan fault zone—Shortcutting on the central section of Xianshuihe-Xiaojiang fault system. Science in China Series D: Earth Sciences, Vol.51(2008), p. 1248-1258.

*Applied Mechanics and Materials Vols. 580-583 (2014) pp 887-892*
*© (2014) Trans Tech Publications, Switzerland*
*doi:10.4028/www.scientific.net/AMM.580-583.887*

# Sleeve Valve Pipe and Steel Pipe Micropile fractured tensile reinforcement in combination with the application of a mined-out area

Shengli Tang[1,a*], Liang Yang[1,b], Lihai Sun[1,c] and Xiongwei Li[2,d]

[1]College of Geology and Environment, Xi'an University of Science & Technology, Xi'an, P.R. China

[2]Xi'an Research Institute of China Coal Technology & Engineering Group Corp,

Xi'an , P.R. China

[a]drilling@163.com, [b]812157317@qq.com,[c]704352085@qq.com,

[d]693855091@qq.com

**Keywords:** Sleeve valve tube, Micropile, Gob, Stretching fractured zone

**Abstract.** Due to the early years of mining makes Gob fracture zone, the deformation of rock fracture zone, and gradually developed through. Located in the mined-out area causing tension within fractured zone of discontinuous deformation region arsenal varying degrees of ground and walls to crack, great security risk to the normal operation of the arsenal caused. Project uses Sleeve Valve Pipe and Steel Pipe Micropile reinforcement scheme. This paper describes the details of the reinforcement mechanism, the construction process, technical requirements and quality assurance measures. Practice has proved that the joint reinforcement program can continue to crack the wall of effective governance to ensure the safe operation of the security arsenal.

## Introduction

The object of reinforcement is arsenal, the north side of the mountain was originally cut from artificially, overall terrain located south than in the north end, located in a mining area of tension cracks band of discontinuous deformation region. The mine is fully mechanized coal mining methods and more, because of early mining makes mining district fracture zone, the deformation of rock fracture zone, and gradually developed through. Result in powder keg on the west side, the north and other areas with varying degrees of ground and walls to crack, great security risk to the normal operation of powder keg, shown in Fig. 1. Preliminary analysis of the region's mining area is a typical tensile fracture with discontinuous deformation Engineering venue. Because crack is not fully developed, reinforced area undulating terrain, lush vegetation surrounding the building, the use of surface coverage or lime slurry formed loess cover, then slip through the flower tube grouting body ineffective. Therefore, using the Sleeve Valve Pipe and Steel Pipe joint reinforcement methods Micropile to governance in the deformation of mining area.

Fig. 1. Arsenal wall cracking case

**Reinforcement Design**

Scholars has already to study Sleeve Valve Pipe equipment, materials and technology and other engineering applications technology [1, 2], or the mechanism of Splitting Grouting soil [3].The project has been the precedent for using Micropile in reinforce landslide areas, mechanism and failure mode of bearing micropiles. More for scholars to study the effect of pile group, load distribution, In practice [4, 5, 6, 7]. But the first time to use Sleeve Valve Pipe and Steel Pipe micro-piles in mining area reinforcement works of stretching fractured zone, with engineering practice.

This design is determined that the scope of grouting based on the size and distribution of the surface cracks, and arranged drilling and grouting in the walls of the arsenal outside. According to the cracks arsenal to determine the scope of this grouting in the northwest corner of the wall, the grouting regions as shown in Fig. 2.

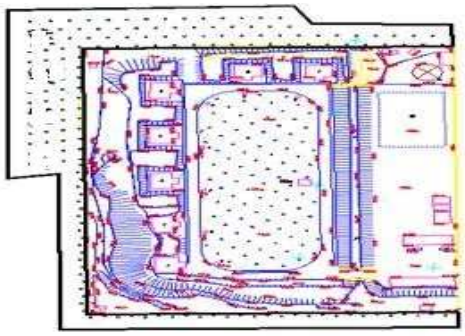

Fig. 2. Reinforcement Design

As shown in Fig. 2, grouting holes are arranged in a powder keg west, south and north wall of three side walls, which are arranged outside the northwest corner of the 4-row drilling, and north of the northwest corner of the location of the hole spacing of 7m, was plum-shaped layout, arranged two rows in the south and the southwest corner of drilling. North and south of the hole spacing 10m, row spacing of 1m, designed from the inside to the outside hole depth was 37m, 61m, 84m and 108m. Greater than 40m deep hole drilling the first hole aperture Φ89mm, secondary sweep the hole diameter is Φ130mm, adjustable hole depth is greater than the 40m Φ89mm and less than 40m deep hole drilling hole aperture Φ89mm until the final hole. Were arranged grouting hole of 168, with a total footage of 9922m, wherein the outer row of grouting holes 63, footage 4461m, the row of grouting holes of 105, footage 5461m.

When drilling depth, hole depth greater than 40m under way to take a top-down sub-grouting grouting, in principle two sections, the upper section using Sleeve Valve Pipe. Sleeve Valve Pipe tip, shown in Fig. 3, after grouting, 72 hours to sweep holes under the section with the orifice closed grouting, down into the PVC pipe flowers, flower tube from the bottom of the hole shot pulp mouth is not greater than 0.5m. When the hole depth is less than 40m, into full-bore Φ76mm using welded steel modded Sleeve Valve Pipe. After the completion of all grouting pipe, no longer pull.

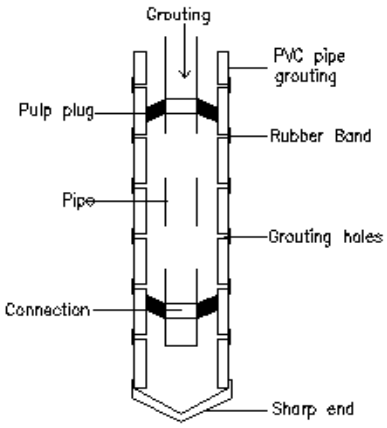


Fig. 3. Sleeve Valve Pipe Schematic

**Joint reinforcement mechanism**

**Sealing surface water.** As shown in Fig. 4, using of the sleeve valve pipe grouting technology can effectively solve the fractured zone take slurry grouting common problem, forming a slurry pulp to cover the surface, filling fractured zone to prevent infiltration of surface water increased arsenal slip, wall cracking.

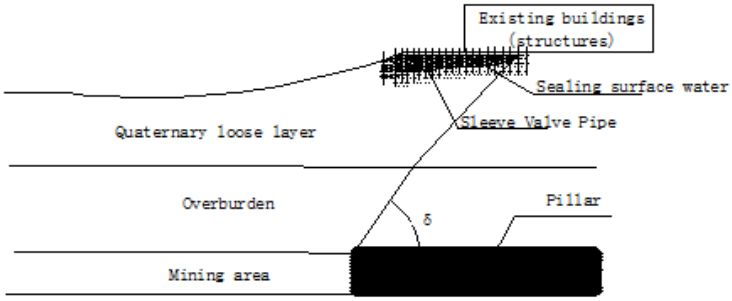


Fig. 4. Sealing surface water

**Moving angle increases.** Sleeve Valve Pipe and Steel Pipe Micropile combined to make mining area stretching fracture belt soil, rock to form a whole, improve friction belt slippage, while steel insert stable rock, but also raise bring slip friction resistance, increasing the angle of the mining area to move the angle shown in Fig. 5.

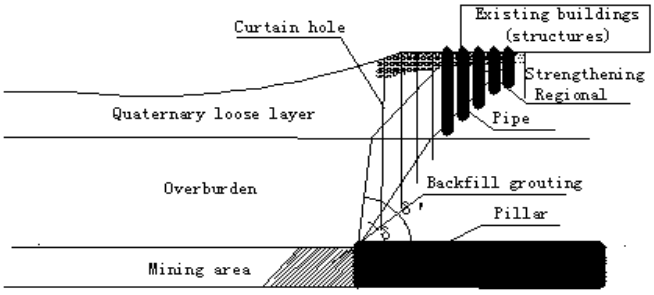


Fig. 5. Moving angle increases

**After moving angle shift.** Steel Pipe Micropiling through the deep slip reinforcement to improve the strength of the rock, while part of the slurry through the cracks into the mining area, filling a part of the mining area, the mobile angle mining area after the shift, as shown in Fig. 6.

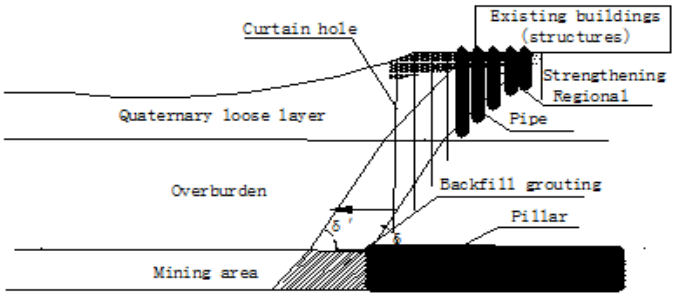


Fig. 6. After moving angle shift

**Construction technical requirements**

**Technical Requirements of Drilling.** Drilling structure: Aperture of drilling which depth more than 40m is ϕ89mm, when swept the hole diameter is ϕ130mm and more than 40m adjust to ϕ89mm; if depth of drilling less than 40m ,drilling aperture is ϕ89mm until the final.

Ending standard: depth of the final hole is less than 944m elevation, and drilled into the stable bedrock 1m.

Inclined requirements: Hole deviation should be less than 1 °. In the drilling process hole inclination measurement and calibration should be carried out to ensure that drilling is vertical, in order to create good working conditions for normal grouting.

Washed requirements: All holes are drilled by use of water. And holes are washed to make crack to flow and protect the best grouting effect before grouting.

sealing: Using cement mortar that water-cement ratio is 0.5:1 or 1:1 block all drilling after grouting. Greater than 40m drilling, method of the upper sealing using sets of shell material, lower segment seal by use of chuck (DN125mm flange), and using grout seal from 5 to 8m in hole. If depth of drilling is less than 40m, the way of sealing is sets of shell material. As shown in Fig.7.

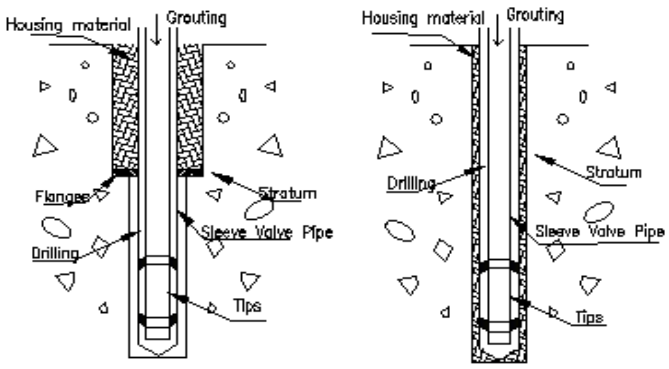


(a) Hole depth>40m (b) Hole depth<40m

Fig. 7. Sealing structure

**Technical requirements of grouting.** Pressure: At the beginning of grouting, test should be implemented that water is pressurized and time of test is not less than 10min, then converted into static pressure grouting. Pressure of orifice is controled not less than 1.5Mpa in the end.

Parameters: Water-solid ratio: 1:1 to 1:1.2, solid ratio (cement: fly ash): 3:7. Before grouting materials should be done a slurry mixture ratio test in the laboratory (with ratios of 1:1; 1:1.1; 1:1.2). It should be tested that dry material content per unit slurry, slurry density, initial and final setting time and stones rates.

The end standard of grouting: The final grouting pump pressure gradually increased.when grouting pressure is 1 ~ 1.2MPa , pump the amount is 15L/min, and stable 10 ~ 15min, grouting ends.

If a large number of surface cracks run pulp and adjacent drilling collusion, intermittent grouting should be taken immediately, intermittent time is not less than 48h, no more than 72h. When reached the end standard of grouting, grouting stops.

**Quality assurance measures.** Grouting holes are constructed in accordance with from the outside to the inside. Each row of holes sharing I, II. Isequence hole first are construct, II construction sequence hole again

In the grouting process , ground-based observations and underground observation are conducted. Ground-based observations include units grout, grouting, pressure, concentration of slurry and time. Underground observation Including plasma leakage and changes of underground water inflow.

## Conclusions

Existing buildings which is located at tensile fracture in mining area are regarded as objects. The width of gap with tensile fractured zone is small, and slurry is resist to flow. Forming a complete set of construction technology reinforce existing buildings which is located at tensile fracture in mining area. Advanced and innovative technology embodied in the following:

Sleeve Valve Pipe Technology effective solve the problem that when using the traditional method of grouting pulp run, pulp.

Joint reinforcement approach highlights the economic "green green philosophy and overcomes that the existing range of traditional grouting reinforcement is not clear, conservative design, the consumption of pulp, and higher project cost defects.

**References**

[1] Yong-Hua He, Zhiguo Li. Construction Technology, 2008,37 (Suppl 1) :254-256. (In Chinese).

[2] Lina Ma, Songhong Yan. Subgrade, 2010 (5) :67-69. (In Chinese).

[3] Yun Bai, Xueyuan Hou. Geotechnical Engineering, 1991,13 (2) :89-93. (In Chinese).

[4] Jinkai Yan, Yueping Yin, Yuming Men. Civil Engineering Journal, 2011, 44 (4): 120-128. (In Chinese).

[5] Jinkai Yan, Yueping Yin, Yuming Men. Journal of Engineering Geology, 2009, 17 (5): 669-674. (In Chinese).

[6] Shuwei Sun, Benzheng Zhu, Huimin Ma. Rock Mechanics and Engineering, 2010, 29 (Suppl 1) :3039-3044. (In Chinese).

[7] Shuwei Sun, Benzheng Zhu, Huimin Ma. Geotechnical Engineering, 2009,31 (10) :1564-1570. (In Chinese).

*Applied Mechanics and Materials Vols. 580-583 (2014) pp 893-896*
*© (2014) Trans Tech Publications, Switzerland*
*doi:10.4028/www.scientific.net/AMM.580-583.893*

# Evolution Characteristics of Permeability and Porosity of Mudding Weak Permeability Media with Nonlinear Flow

Yinger Deng[1, a], Jing Yu[2, b], Xin Peng[2, c]

[1]State Key Laboratory of Geohazard Prevention and Geoenvironment Protection, Chengdu University of Technology, Chengdu 610059, China;
[2]College of Environment and Civil Engineering, Chengdu University of Technology, Chengdu 610059, China

dengye6789@sina.com, [b]1225965177@qq.com, [c]2250656391@qq.com

**Keywords:** evolution characteristics, permeability, porosity, mudding weak permeability media, nonlinear flow, geological engineering.

**Abstract.** Concepts of flow permeability, flow permeability coefficient and flow porosity were presented to investigate changes of permeability and porosity of mudding weak permeability media with nonlinear flow. Formulas of flow permeability, flow permeability coefficient and flow porosity were presented to study the evolution characteristics. Results show that permeability and porosity of mudding weak permeability media nonlinear flow increase with pressure gradient or hydraulic gradient of nonlinear flow, while permeability and porosity of high permeability media Darcy flow are constant. The results can provide a test and calculation of micro porosity with a new method and can provide engineering safety of mudding weak permeability media nonlinear flow with scientific basis.

## Introduction

Groundwater can flow through all kinds of rock and soil media [1-3] and is an important factor inducing geological disasters [4]. Permeability and porosity are important physical property parameters of rock and soil materials. Several researchers have investigated permeability or porosity of porous media such as Collins [1] and Scheidegger *et al*. [2]. Brace *et al*. [3] discussed permeability of granite under high pressure. Fox *et al*. [4] discussed engineering geological problems. Bai *et al*. [5] described water resource characteristics. Neuman *et al*. [6] estabilshed conceptual models of flow and transport in the fractured vadose zone. Kong *et al*. [7] presented problems of advanced mechanics of fluids in porous media. Peng *et al*. [8] analyzed permeability of sandstone under different confining pressures.

The present work has been undertaken in order to analyze the evolution characteristics of permeability and porosity of mudding weak permeability media nonlinear flow. Concepts of flow permeability, flow permeability coefficient and flow porosity are presented to investigate the evolution characteristics. Influence of nonlinear flow of fluid on the permeability or the porosity is considered in the concepts to provide prevention of geological disasters with scientific basis.

## Physical Model

Mudding weak permeability media are assumed to be made up of capillaries. An equivalent model of porous media seepage is used to study mudding weak permeability media.

## Mathematical Model

**Mathematical Model of Pore Radius.** A partial differential equation for groundwater flow is given by equation (1) provided that the coordinate axes are assumed oriented parallel to the principle axes of the media.

$$r_{\mathrm{a}} = 2\left(\frac{2K}{n}\right)^{1/2} \tag{1}$$

where $r_a$ is average pore radius of porous media, $K$ is absolute permeability of porous media, $n$ is porosity of porous media. Change rate of average pore radius of porous media is

$$\dot{r}_K = \left(\frac{2}{nK}\right)^{1/2} \tag{2}$$

Correlation for permeability of porous media and permeability coefficient is

$$k = \frac{K\nu}{\mathrm{g}} \tag{3}$$

where $k$ is permeability coefficient of porous media system, $\nu$ is Kinematic viscosity of water, g is acceleration of gravity. So there are

$$r = 2\left(\frac{2k\nu}{n\,\mathrm{g}}\right)^{1/2} \tag{4}$$

and

$$\dot{r}_k = \left(\frac{2\nu}{n\,\mathrm{g}\,k}\right)^{1/2} \tag{5}$$

where $\dot{r}_k$ is Change rate of average pore radius of porous media.

**Formulas of Flow Permeability and Flow Porosity.** Flow in mudding weak permeability porous media is nonlinear flow as equation (6), which is different from Darcy flow [Deng, 2004].

$$\mathbf{v}\left(a_1 + \frac{a_2}{1 + a_3 v}\right) = -(\nabla p - \rho \mathbf{g}) \tag{6}$$

where $v$ is flow velocity of fluid in mudding weak permeability porous media, $a_1, a_2, a_3$ are coefficients respectively, $\nabla p$ is pressure gradient, $\rho$ is fluid density. Flow permeability of mudding weak permeability porous media is defined as

$$K_\mathrm{d} = \mu v / |\nabla p| \tag{7}$$

where $K_\mathrm{d}$ is flow permeability of mudding weak permeability porous media, $\mu$ is dynamic viscosity coefficients. Flow permeability coefficient of mudding weak permeability porous media is defined as

$$k_\mathrm{d} = \rho g v / |\nabla p| \tag{8}$$

where $k_\mathrm{d}$ is flow permeability coefficient of mudding weak permeability porous media. Flow porosity of mudding weak permeability porous media is defined as

$$n_\mathrm{d} = n\left(\frac{K_\mathrm{d}}{K}\right)^{1/2} \tag{9}$$

where $n_\mathrm{d}, n$ are flow porosity and porosity of mudding weak permeability porous media.

**Results and Discussion**

Changes of $r_a$ and $\dot{r}_a$ with $K$ are shown in Fig. 1. Changes of $r_a$ and $\dot{r}_a$ with $k$ is shown in Fig. 2. Schematic diagram of nonlinear flow and Darcy flow is shown in Fig. 3. Nonlinear flow curve is shown in Fig. 4. Changes of $K_d$ with $i$ is shown in Fig. 5. Changes of $k_d$ with $i$ is shown in Fig. 6. Changes of $n_d$ with $i$ is shown in Fig. 7.

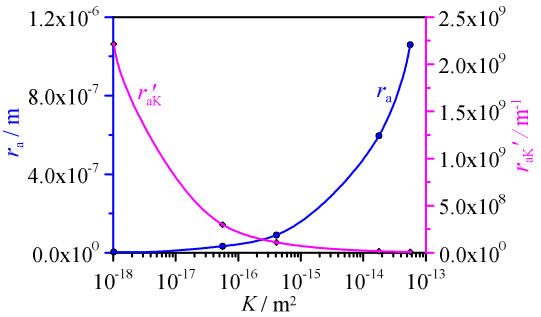


Fig. 1 Changes of $r_a$ and $\dot{r}_a$ with $K$

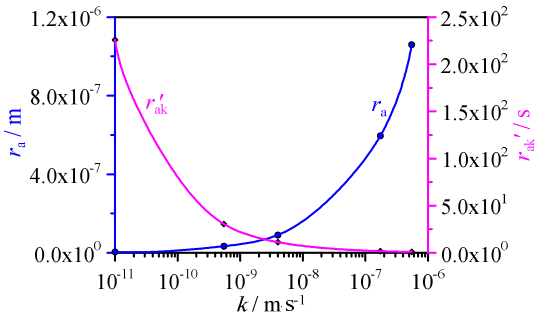


Fig. 2 Changes of $r_a$ and $\dot{r}_a$ with $k$

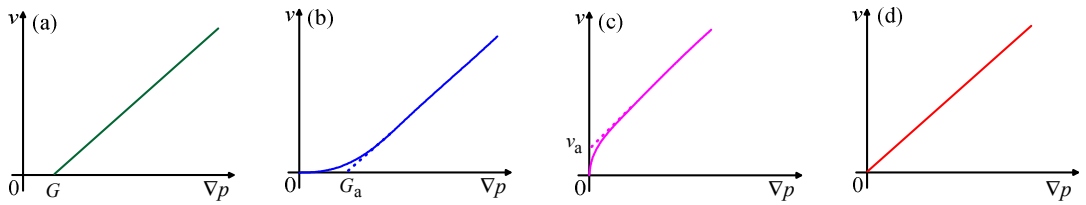


Fig. 3 Schematic diagram of nonlinear flow and Darcy flow

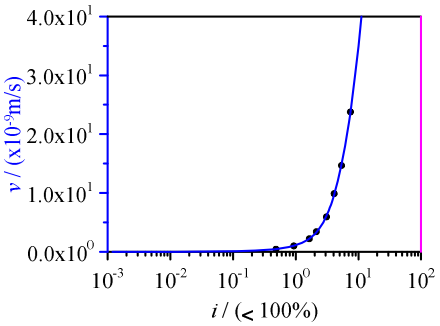


Fig. 4 Nonlinear flow curve

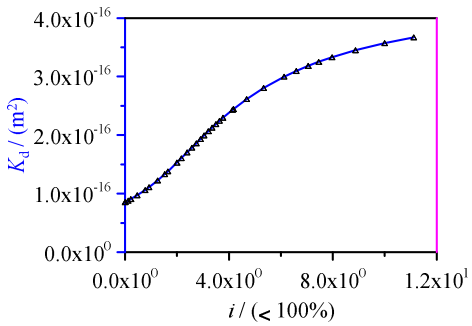


Fig. 5 Changes of $K_d$ with $i$

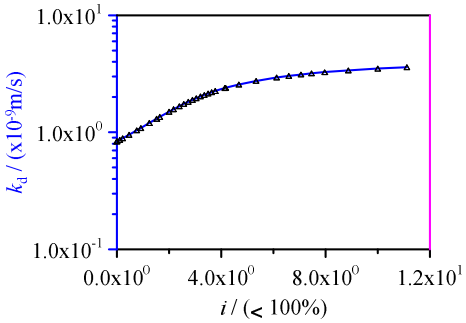


Fig. 6 Changes of $k_d$ with $i$

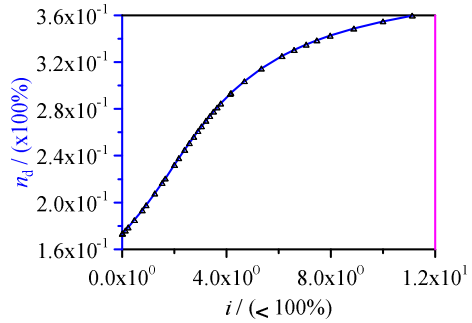


Fig. 7 Changes of $n_d$ with $i$

Fig. 1and Fig. 2 show that average pore radius of porous media decreases significantly with permeability and permeability coefficient. Pore channels of mudding weak permeability porous media are fine and the specific surface area is great so that solid-liquid interface molecular interaction is strong. Nonlinear flow has different kinds of possible flow curves different from Darcy flow curve in Fig.3. Nonlinear flow curve of mudding weak permeability porous media in Fig. 4 is similar to

schematic diagram (b) of nonlinear flow in Fig. 3. It is well known that permeability, permeability coefficient and porosity of Darcy linear flow in porous media do not change with hydraulic gradient changing. But Fig. 5, Fig. 6 and Fig. 7 show that permeability, permeability coefficient and porosity of nonlinear flow in mudding weak permeability porous media increase with hydraulic gradient respectively. Formulas of flow permeability, flow permeability coefficient and flow porosity provide micro and nano-scale pore of mudding weak permeability porous media with calculation method.

## Conclusions

In this work, concepts of flow permeability, flow permeability coefficient and flow porosity were presented to investigate changes of permeability and porosity of mudding weak permeability media with nonlinear flow. Formulas of flow permeability, flow permeability coefficient and flow porosity were presented to study the evolution characteristics. Permeability and porosity of mudding weak permeability media nonlinear flow increase with pressure gradient or hydraulic gradient of nonlinear flow, while permeability and porosity of high permeability media Darcy flow are constant. The results can provide a test and calculation of micro porosity with a new method. The results can provide engineering safety of mudding weak permeability media nonlinear flow with scientific basis.

## Acknowledgements

This work was supported by the National Natural Science Foundation of China (under Grant Nos. 41172277, 40202036, 40572163), Sichuan Provincial Found for Replacement of Academic and Technical Leader (under Grant No. 2009), the Specialized Research Fund for the Doctoral Program of Higher Education of China (under Grant No. 20095122110006) and the Key projects of Sichuan Provincial Department of Education (under Grant No. 07ZA009). The authors would like to thank Professors S. Y. Jia, X. J. Yu and X. M. Fu for their help.

## References

[1] R.E. Collins: *Flow of Fluids through Porous Materials* (The Petroleum Publishing Company, Tulsa 1976).

[2] A.E. Scheidegger: *The Physics of Flow through Porous Media* (University of Toronto Press, Toronto and Buffalo 1974).

[3] W.F. Brace, J.B. Walsh and W.T. Frangos: Journal of Geophysical Research Vol.73 (1968), p.2225.

[4] P. P. Fox, E. C. Mc: Bulletin of the Association of Engineering Geologists Vol.21(1984), p.101

[5] M. Bai, D. Elsworth, J.C. Roegiers: Water Resour Res Vol. 29 (1993), p.1621.

[6] S.P. Neuman, W.A. Illman, V.V. Vesselinov, D.L. Thompson, G. Chen, and A. Guzman: *Conceptual Models of Flow and Transport in the Fractured Vadose Zone* (National Academy Press, Washington, D.C. 2001).

[7] X.Y. Kong: *Advanced Mechanics of Fluids in Porous Media* (Press of University of Science and Technology of China, Hefei 1999) (in Chinese).

[8] S.P. Peng, Z.P. Meng and H. Wang: Chinese Journal of Rock Mechanics and Engineering Vol.22 (2003),p.742 (in Chinese).

*Applied Mechanics and Materials Vols. 580-583 (2014) pp 897-902*
*© (2014) Trans Tech Publications, Switzerland*
*doi:10.4028/www.scientific.net/AMM.580-583.897*

# Stability analysis of gypsum mine goaf surface based on discrete element method

Xiumin Liu, Congxin Chen, Kaizong Xia, Pinglu Huang

（State Key Laboratory of Geomechanics and Geotechnical Engineering, Institute of Rock and Soil Mechanics, Chinese Academy of Sciences, Wuhan 430071, China）

Xiuxiu8311@163.com

**Keywords:** gypsum mine, pillar, filling method, caving goaf, discrete element method

**Abstract:** Considering rock joints, the discrete element method was used to study gypsum mine surface short-term and long-term stability. Filling method and caving method were selected as the surface treatment. Through comparison, Caving method is more suitable for handling the gob of gypsum mine. Surface movement angle and subsidence angle were obtained on the basis of the plastic zone, surface tilt rate and surface horizontal strain, and whereby draw a goaf risk areas to guide residential relocation. The research methods and conclusions in this paper can provide reference for the study of the empty area stability in gypsum mining currently.

## Introduction

Gypsum mine generally use room and pillar mining method leaving in continuous pillars [1]. For water softening, the carrying capacity of gypsum mine is greatly reduced and result in gob roof collapse layer by layer, which can easily lead to a wide range ground subsidence .

Currently, a lot of research about the mechanism of ground subsidence has conducted caused by mining gypsum[2-5], and numerical simulation methods [6-8] has been widely used in mining engineering. Relative to the finite element method and finite difference method, discrete element method is adapted to calculate joints developed rock mass, so it is more suitable to Simulate and analyze the rock loose caused by mining and caving and other mechanical behavior.

In this paper, the discrete element method (UDEC) was used in Jing-Hua gypsum mine numerical simulation to analyze the goaf short and long term surface stability. By comparing the treatment effect of filling method and caving method, put forward some reasonable proposals to handling gob geological disasters. It has great significance in mechanism study and ground subsidence prevention of gypsum mine gob.

## Engineering background

Jing-Hua gypsum mine located in Jingmen, Hubei province. Ore is layered, flat seam occurrence, to 150°, tendency to 240° , inclination of 8 ~10°, seam thickness average 10.4m. It mainly contains lump ore and mud quality gypsum. The rock deposit upper is siltstone containing cream, low-intensity, easily to softening, relax in water.

The ore-body is medium thick and stable tilt. It is design to use the room and pillar mining method according to the ore-body occurrence conditions and engineering geological conditions. By design, the mine geometric parameters of room and pillar are: stope long axis generally 50m, width

7m, pillar size 4 m × 4m, Gob height 7m. There is left 2.5m thick gypsum as a protective top layer in gob top.

The geological section is shown in Figure 1. Cross-sectional is width 923.5m horizontal, 208m in vertical direction from surface to -100m.

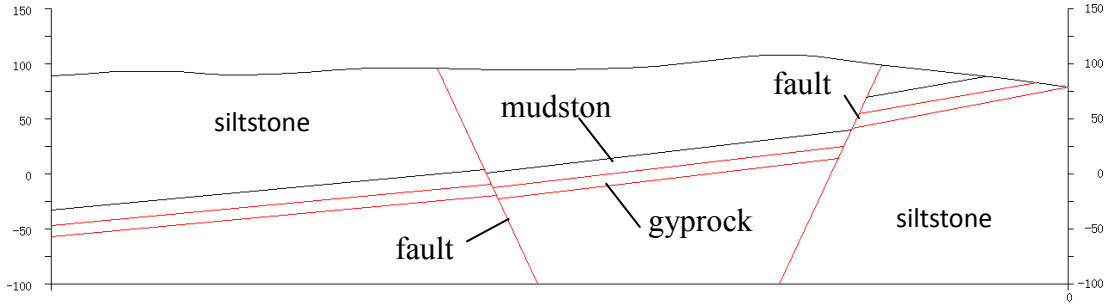


Fig. 1 Geological Sketch of Calculation Cross Section

Considering the lithology, bed thickness, rock quality, and its influence of surface deformation in gypsum mining process, the rock mass is mainly divided into siltstone, mudstone and gyprock three categories eventually. Mine rock mechanical parameters used in calculation is shown in Table 1.

The rock surface structure was considered in the calculation, and its parameters was selected based on similar geological structure of surface in gypsum mine, as shown in Table 2. About the filling method using in gypsum mine management, the physical and mechanical parameters of filling body was selected in accordance with related engineering experience, as shown in Table 3.

Tab.1 Mechanical Parameters of Rockmass

| Lithology | density KN/m$^3$ | E GPa | compressive strength MPa | Tensile strength MPa | cohesion MPa | Φ(°) | Softening Coefficient | μ |
|---|---|---|---|---|---|---|---|---|
| Siltstone | 24 | 3 | 22.3 | 0.74 | 1.86 | 48.5 | 0.588 | 0.28 |
| Mudstone | 24 | 2 | 16.6 | 0.18 | 0.5 | 45 | 0.5 | 0.3 |
| Plaster Rock | 23 | 4 | 27.6 | 0.81 | 2.8 | 40 | 0.825 | 0.28 |

Tab. 2 Rock Interface Parameters

| Tensile strength of joints (N/m) | Normal stiffness of joints (N/m) | Shear stiffness of joints (N/m) | Joints friction angle (°) | Joints adhesion(N/m) |
|---|---|---|---|---|
| $1.0\times10^6$ | $1.0\times10^9$ | $1.0\times10^9$ | 40 | $1.0\times10^6$ |

Tab. 3 Mechanics Parameters of Filling-body

| Lithology | Density KN/m$^3$ | E GPa | Compressive strength (MPa) | Tensile strength (MPa) | Cohesion (MPa) | Φ(°) | Softening Coefficient | μ |
|---|---|---|---|---|---|---|---|---|
| | 10 | 1 | 22.3 | 0 | 0 | 40 | 0.588 | 0.15 |

**Calculation model and scheme**

In order to analyze gob surface deformation and get rock movement law, covering the long-term stability of the overburden after taken caving method or filling method goaf treatments, it is arranged to calculate the following four scenarios:

Option One: calculate the short term stability based on the average pillar size (6.0m × 4.0m), ore room size (8.0m × 7.0m).

Option Two: calculate the long-term (several years after closure) empty area stability according to the average pillar, stope size of gypsum gob.

Option Three: Calculate the stability of the goaf after caving method.

Option fore: Calculate the stability of the goaf after filling method.The calculated cross section meshing grid were shown in Figure 2.

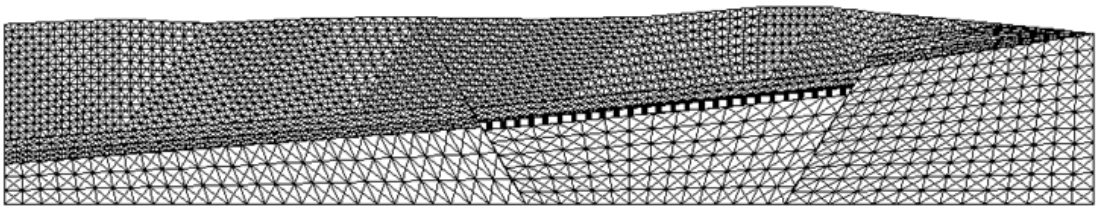

Fig. 2 Calculation Model

**Results analysis**

Plastic zone and total displacement contour were obtained by calculating under the fore program a, as shown in in Figure 3 to Figure 10 specificly. Analysis of the results shows that:

(1) Underground mining causes some extent deformation of the surface in Jinghua gypsum mine in the short term. According to the plastic zone(Fig.3), it can be seen there is no overall damage on the gob overburden. But 2m ~ 3m thick (Fig.7) of the top - safeguarding layer came into plastic losing the protective effect of the mined area. In addition, mining has resulted in tensile or shear plastic deformation of local surface area , it means there will be generating cracks and other geological disasters.

（2）According to the long-term stability analysis, years later JingHua underground mined-out area will be filled with water, so the top of the pillar and protective top - layer will soften due to flood damage, and the strength will be greatly reduced. The existence of faults is in control of the gob rock movement pattern.The overburden will have overall slip along the fault(Fig.4). The displacement contour (Fig.8) shows that the maximum horizontal displacement of the surface is0.53m, the maximum vertical displacement is 2.2m, and the maximum total displacement is 2.2m.

（3）If adopted caving goaf method, it can cause a huge overburden deformation and large-scale ground subsidence (Fig.5). The maximum displacement of the surface is 0.71m, the maximum vertical displacement is 2.75m, the maximum total displacement is 3.0m (Fig. 9)

（4）After filling the mined area, the overburden also has some distortion(Fig.6). The maximum horizontal displacement of the surface is 0.25m, the maximum vertical displacement is0.78m, the maximum total displacement is 0.80m (Fig. 10). But it will not cause massive surface collapse.

(5) Through the gypsum gob plastic zone graph after caving method applying, the ground movement angles on both sides of the border can be calculated, which are basically the same with the fault dip angle.

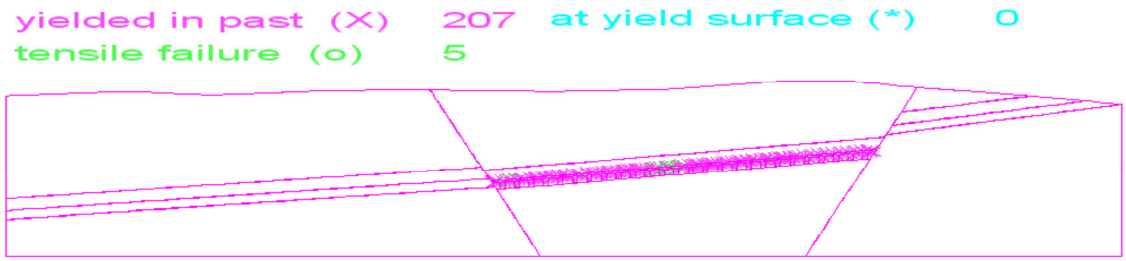


Fig.3 Plastic zone of gob in short term

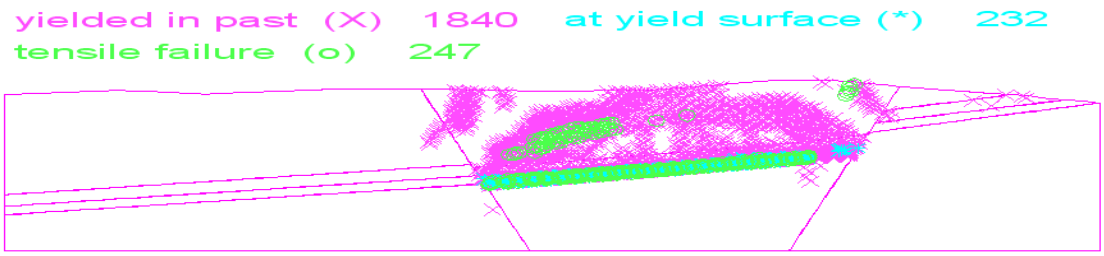


Fig.4 Plastic zone of gob in long term

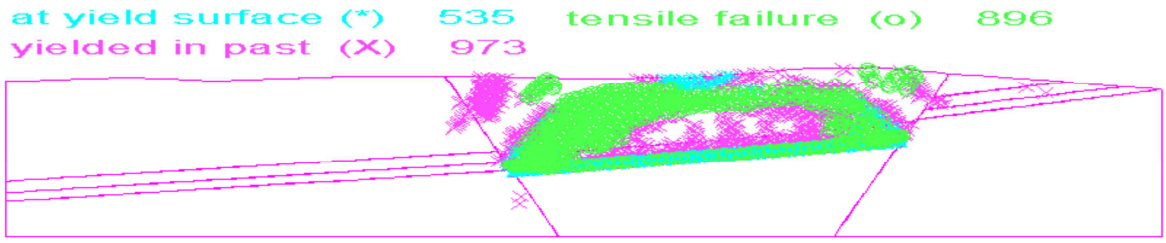


Fig.5 Plastic zone of gob after caving treatment

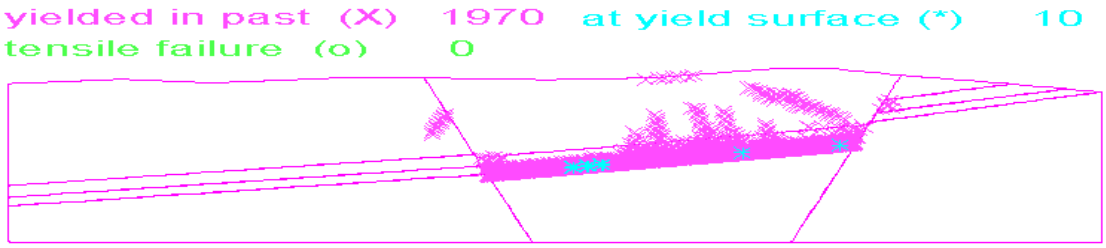


Fig.6 Plastic zone of gob after filling treatment

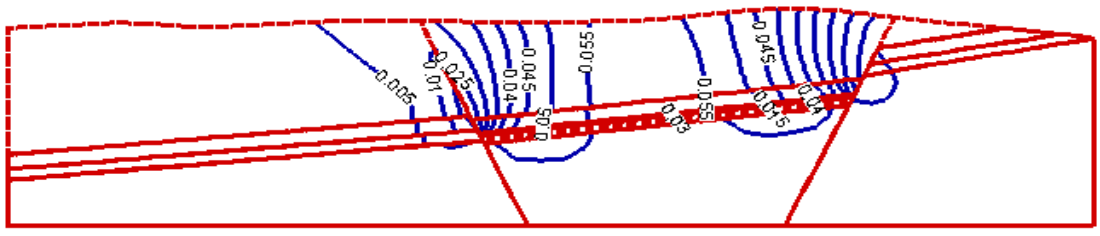

Fig.7 Displacement contours of gob in short term

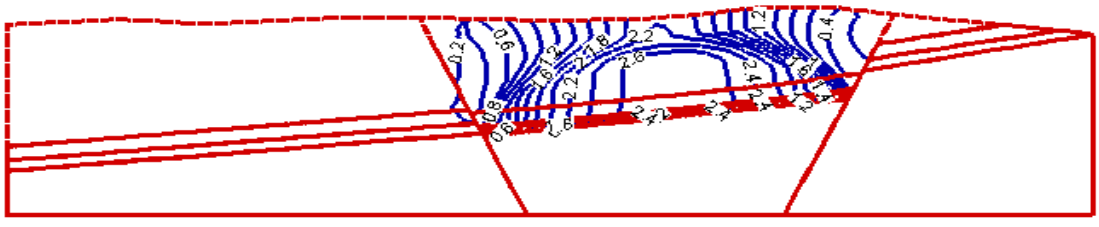

Fig.8 Displacement contours of gob in long term

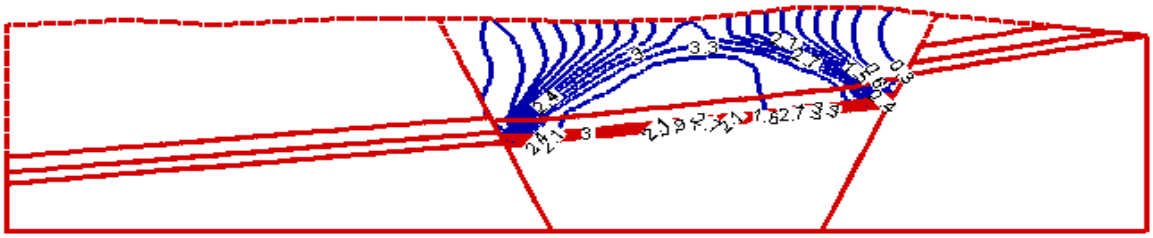

Fig.9 Displacement contours after caving treatment

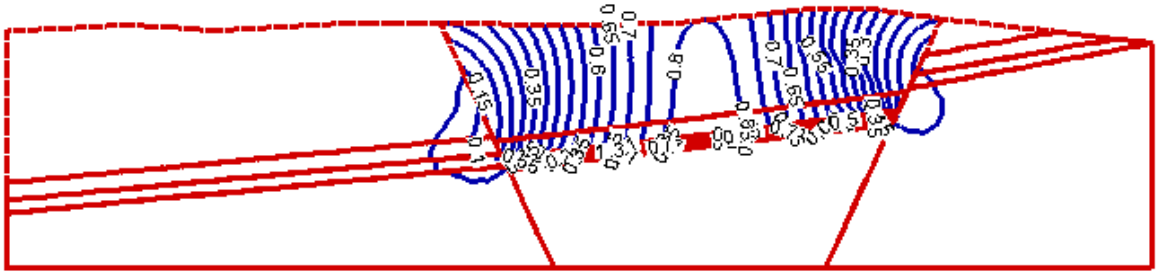

Fig.10 Displacement contours after filling treatment

## Conclusions

The results show that JingHua gypsum mine gob will not occur overall damage of overburden in the short term, only small local regional pillar roof may occur collapse. However, if not remediate, the gob will become a long-term source of potential dangers. According to the geological conditions ， underground mined-out area will be filled with water, and the top of the pillar and the upper protective claystone layer will soften, eventually the strength will be greatly reduced and lead to a wide range of surface subsidence.

Caving method and backfill are two effective treatment methods. It is recommended forced caving treatment for JingHua gypsum mine goaf, with Comparing the calculated effects the two Control Methods, and considering the gob treatment cost, technical, economic feasibility, and experience at the successful application of the caving method.The residents within the moving angular range should be relocated also.

## Acknowledgements

This work was financially supported by the National Natural Science Foundation of china (No. 51274188)

## References

[1] Jinan Wang, Xinchun Shang，Haitao Ma. Investigation of catastrophic ground collapse in Xingtai gypsum mines in China [J]. International Journal of Rock Mechanics & Mining Sciences，2008，45 (8):1480-1499.

[2] Yanjin1HAO, Lixin WU, Huayang DAI. Establishing a ground settlement prediction model with elastic slab theory[J]. Chinese Journal of Rock Mechanics and Engineering, 2006,25(1):2958-2962.

[3] Jinan WANG，Dazhong LI，Haitao MA. Study of rheological mechanical model of pillar-roof system in mined-out area[J]. Chinese Journal of Rock Mechanics and Engineering, 2010, 29(3):577-582.

[4] Shuo Yang. Mechanical Prediction for Mining Damage[M].Beijing：China Coal Industry Publishing House，1994.(in Chinese))

[5] Castellanza R, Gerolymatou E，Nova R. An attempt to predict the failure time of abandoned mine pillars[J]. Rock Mechanics Rock Engineering[J]，2008，41(3):377-383.
[6] Heping Xie, Hongwei Zhou, Wang Jinan, etc. Application of flac to predict ground surface displacements due to coal extraction and its comparative analysis[J]. Chinese Journal of Rock Mechanics and Engineering, 1999, 18(4):397-401.
[7] Changbin Yan，Guoyuan Xu，Xibing Li. Stability analysis of mined-out areas influenced by blasting vibration with flac3d[J]. Chinese Journal of Rock Mechanics and Engineering, 2005, 24(16):2894-2899.
[8] Xueliang1Jiang, Hui Yang, Ping Cao. FLAC3D analysis of interaction between goaf and open cut mining slopewith 3D geological model using SURPAC[J]. Rock and Soil Mechanics,2011,32(4):1234-1240.

*Applied Mechanics and Materials Vols. 580-583 (2014) pp 903-906*
*© (2014) Trans Tech Publications, Switzerland*
*doi:10.4028/www.scientific.net/AMM.580-583.903*

# Automated Analyzer，LOI and Other Methods for determination of Soil Organic Carbon

Yiyu Zhang[1, a *],Weihua Zhang[1,*]

[1]College of Resources and Environment, Southwest University, Chongqing, China
[a]email,948223274@qq.com; *Corresponding Author:swuwater@126.com

**Keywords:** SOC determination, Automated Analyzer, LOI, Comparison

**Abstract.** SOC as a significant quantity for the global carbon cycle, makes great sense in soil management and future climate scenario. With more and more researches carried out on SOC, methods used to the determination of SOC have being formed: automated analyzer, LOI and some others, such as using climate change information and remote sensing technique. The objective of this paper is to discuss advantages and disadvantages of automated analyzer (C-N analyzer) and LOI, and provide some references in selecting the appropriate measuring methods of SOC for the readers.

## Introduction

Soil, as the largest carbon pool in the terrestrial biosphere, plays a significant role in the global carbon cycle and climate change. Minor changes in soil organic carbon (SOC) storage can impact atmospheric carbon dioxide concentrations [1]. Estimates of SOC stock are required to assess the role of soil in the global carbon cycle[2]. Moreover, SOC is not only a vital parameter for administering soil fertility and erosion resistance[3], but also is essential for the calculation of future climate scenarios and to detect the potential for C sequestration or emission[4].

Laboratory methods for the determination of SOC demand to consider several factors, including the ease of use, health and safety concerns, cost, sample throughput and comparability to standard reference methods[5].The measurement methods which are prevalently adopted in laboratory can be divided into two general approaches of spatial extrapolation, which are described as: “measure andmultiply” and “paint by numbers” by Schimel[6]. In this paper, we put emphasis on the former one, comparing Loss-on-ignition (LOI) with an elemental analyzer and several other methods of the determination of SOC.

Compared to time-consuming and costly elemental analyzers, LOI as an inexpensive and reliable technique is more likely to be carried out in general laboratories and has being widely used in laboratory by soil scientists, geographers, geologists and limnologists for decades. Actually, some other methods are also applied varying with different circumstances of the determination of SOC, such as in situ methods[7] or climate change[8].

Our objective in this paper is 1) to discuss advantages and disadvantages of these major methods and 2) to provide some references in selecting the appropriate measuring methods of SOC for the readers.

## Automated analyzer

For the determination of SOC, A C-N analyzer is usually carried out. The automated technique is simple and accurate, and can not only be used for the automated analysis of 15N or 13C in plant and soil samples, but can also determine %N and %C on weighed samples. During carbon determination, the factors which have impacts on the rate of sample throughput can range from a matter of seconds for gravimetric measurements to minutes for the other techniques. Where a multi-sample autoloader is available, it allows a batch of samples analyzed simultaneously. Moreover, analyses can be carried out and then perform other sample preparations while the first batch of samples are analyzed [5].

Despite the simple and accuracy, it has been shown that automated methods yield more precise results than methods quantified manually [9]. Resulting from the initial purchase of the instrument

which can range up to $20,000 or more, the cost is high and may not be feasible. What's more, for some soil samples, the approach often involves pretreatment with acid to remove carbonate for calcareous soils, which may erode the instrument and interfere with C analysis in soil samples. It also leads to a time-consuming and cost for the machines [10].

## LOI

With increasing consciousness of environmental conservation, compared with the possible effects of dichromate on the environment produced by the traditional Walkley-Black method, LOI has been proposed to be an inexpensive and convenient method which is being widely used to measure soil organic carbon (SOC) and soil organic matter (SOM). LOI involves the two main procedures: combustion of samples at high temperatures and measuring weight loss after ignition[11,12], avoiding chromic acid wastes efficiently.

While in practical application, summarized by Konen, a significant factor limiting the comparability of results is that some investigators converted their LOI measurements to SOC concentration while others estimated SOM[12]. Tab.1 shows some consequences of the determination of SOC by different investigators.

Tab.1 Comparison of LOI Methods to Determine SOC

| LOI Equation | Region | Land Use | Soil Type | Depth | Combustion Temperature | Time |
|---|---|---|---|---|---|---|
| LOI = $W_{dry\ soil}$ - $W_{soil\ after\ combustion}$)/$W_{dry\ soil}$×1000[12] | USA | variously cultivated, uncultivated | clay, sand (more) | A Ap AB | 360℃ | 2h |
| Organic C%=-1.054+0.508LOI[13] | Scotland | natural profile, cultivated soils | 6 soil sub groups | 247mm | 800-900℃ | 30min |
| $LOI_{550}$=2.51+1.67TOC<br>$LOI_{550}$=-0.232+1.72TOC +0.0851C (C-%clay)[14] | New Zealand | cultivation permanent grassland | sand loam clay | 0~136cm | 550℃ 450℃ | 5h |
| $SOC_{LOI}$=($SOM_{LOI}$-4.189)/1.792[15] | China | dessert, shrub, cropland, grassland | brown desert Soil | 5 layers | 375℃ | 17h |

From the table, it is apparently to find that factors vary from temperatures and time of LOI to the expression of results in response to the Konen's viewpoint. In reality, in 1982 the problems had been noted by Nelson and Sommers that the wide range of factors used to convert SOC to SOM [16]. With the increased interest in C sequestration and the quantification of soil C, we believe it is critical to use LOI predictive equations for SOC, not SOM [12].

The LOI method measures the organic matter capacity of soils, but it seems difficult to transition the organic matter to a C basis, owing to the C content of organic matter not consistent and variations with vegetation type, degree of decomposition, age, and other factors[17]. In some specific horizons, overestimates organic matter may result from heating to temperatures above 150℃ driving off hygroscopic and interlayer water from clays and allophane. Other overestimation errors can be caused by CO2 release from carbonates in calcareous soils and possible decarboxylation of organic function groups, and the loss of water from hydroxyl groups in sesquioxides and octachedral sheets in phyllosilicate layers[15].According to many researches , Salehi concluded that LOI method has been widely used for estimating SOM in a muffle furnace at 360℃ for 2 h[18,19,20] and at 300, 450, and 600℃ for 2 h[21].This can be taken as a reference to choose temperatures and time of LOI.

As the distribution and conversion of SOC, relationships between LOI and SOC are developed differing in mineralogy (Carbonates are investigated more) and use of soils. For the LOI method, soil is oxidized at a high temperature (500-575℃), and the mass loss is proportional to the organic

matter content of the soil, Carbonates remain stable at temperatures used for analysis and will not be measured by the LOI method[22,23]. Thus LOI method should be maintained below 440℃, to avoid the destruction of any inorganic carbonates that may be present in the samples. Moreover, another concern with LOI is that under the temperatures used to combust the samples, some clay minerals may lose structural water or hydroxyl groups, which will increase the total sample weight loss leading to an overestimation in organic matter content. Optimum as it burnt most organic carbon destroyed less inorganic carbon, caused less clay structural water loss, and used less electrical energy. A combination of temperature around 375℃ and 16-17 hours results in a good LOI-SOC relationship, thus providing accurate estimates of SOC in many soil groups [15].

While inadequate for measurement where high accuracy is required, we can take advantage of determination of organic carbon through LOI for exploratory soil surveys where rough estimation of organic matter is required [24]. Furthermore, LOI when published datasets that tend to contain abundant information on LOI but fewer data on directly determined organic C%, by establishing regional relationships between LOI and C%[13].

## Other methods

Soil organic carbon stock is a significant proportion for the total organic carbon pool, and thus any small change in SOC may have great impact on atmospheric CO2 concentration. Many models, such as the DNDC (DeNitrification-DeComposition) or Daisy and RothC, were developed to predict the relationships between SOC change and climate change[8], which can be applied to the determination of SOC.

Based on remote sensing and spectroscopic measurements in the field, new in situ soil C methods are proposed where sample processing time and their subsequent analysis are absent or discontinuous[7].Certainly, many techniques in other fields can also be introduced to measure the soil organic carbon

## Conclusion

The approaches, automated analyzer, LOI and others, to estimate SOC , dominate in different areas. When accurate measurement is required and adequate fund are available, automated analyzer can be applied.LOI may be more appropriate when rough SOC estimation is needed, cost is limited and certain values (such as LOI information) are provided. We can also combine techniques and factors in other fields with determination of SOC, for instance, the meteorology and the remote sensing.

## References

[1]C.A.Johnston, D.D.Breshears and Z.G.Gcardon: Froniters in Ecology and Environment, Issu. 2(2004), P. 522-528.

[2]J.Gregory, J.James and J.Russell: submitted to African Journal of Agricultural Research (2010).

[3]B.Jankauskas and M.A.Fullen: Soil Erosion in Europe (2006).

[4]J.Wiesmeier, J.Spцrlein and J.Geu†:Global Change Biology. Issu. 18(2012), P.2233-2245.

[5]M.A.Suchmacher: Methods for the determination of the total organic carbon (TOC) in soils and sediments. Ecological Risk Assessment Support Center, (2002):1-23.

[6]D.S.Schimel and C.S.Potte:Blackwell Science. (1995)p.358-383.

[7]A.Chatterjee, L.Wielopolski and M.Z.Martin: Critical Reviews in Plant Science, Vol.28(2009), P.164-178.

[8]X.Xu, W.Liu and G.Kiely: Modeling the change in soil organic carbon of grassland in response to climate change Agriculture, ecosystems & enviroment, Vol.140(2011),P. 372-381.

[9]Y.K.Soon and S.Abboud: A comparison of some methods for soil organic carbon determination. Commun. Soil Sci.Plant Anal, Vol.22(1991),P.943-954.

[10]S.C.Byers, E.L.Mills, and P.L.Stewart: A comparison of methods of determining organic carbon in marine sediments, with suggestions for a standard method. Hydrobiologia, Vol.58(1978), P.43-47.

[11]C.A.Cambardella, A.M.Doran and J.W.Wienhold: Estimation of particulate and total organic matter by weight loss-on-ignition.In Lal,R. et al. (eds.) Assessment Methods for Soil Carbon. Adv. Soil Sci. CRC Press, Boca Raton. p.349-359 (2001).

[12]M.E.Konen, P.M.Burras and C.L.Talaga: Equation for predicting soil organic carbon using loss-on-ignition for north central U.S. soils. Soil Sci. Am. J.66: 1878-1881 (2002).

[13]A.Leon and R.L.Gonzalez: Predicting soil organic carbon percentage from loss-on-ignition using Bayesian Model Averaging. Soil Research, Vol.47(2010),P.763-769.

[14]K.S.Grewal, G.D.Buchan and R.Sherlock:A comparison of three methods of organic carbon determination in some New Zealand soils. Journal of Soil Science,Vol. 42(1991),P.251-257.

[15]X.Wang, J.Wang and J.Zhang:Comparisons of Three Methods for organic and inorganic carbon in calcareous soils of northwestern China.PLOS one, Vol.7(2012), P.1-6.

[16]D.W.Nelson and L.E.Sommers: Total carbon, organic carbon, and organic carbon matter. p.539-580.

[17]J.S.Batti and I.E.Bauer: Comparing loss-on-ignition with dry combustion as a method for determining carbon content in upland and lowland forest ecosystems. Commun. Soil Sci. Plant Anal, Vol.33(2002),P.3419-3430.

[18] G.Brunetto, G.W.Melo and J.Kaminski: Evaluation of loss-on-ignition method in the organic matter analysis in soils of the Serra Gaucha of the Rio Grande do Sul. Cienc. Rural, Vol.36(2006),P.1936-1939.

[19] P.A.V.Escosteguy, K.Galliassi and C.A.Ceretta: Soil organic matter determination by weightloss-on-ignition samples from the state of Rio Grande do Sul. Rev. Bras. Cien. Solo, Vol.31(2007),P.247-255.

[20]O.A.Yerokun S.Chikuta and D.Mambwe: An evaluation of spectroscopic and loss-on-ignition methods for estimating soil organic carbon in Zambian soils. Int. J.Agr. Res., Vol.2(2007),P.965-970.

[21]S.R.Abella and B.W.Zimmer: Estimating organic carbon from loss-on-ignition in northern Arizona forest soils. Soil Sci. Am. J., Vol.71(2006),P.545-550.

[22]M.C.Rabenhorst: Determination of organic and carbonate carbon in calcareous soils using dry combustion. Soil Sci. Soc. Am J., Vol.52(2006),P.965-969.

[23]E.E.Schulte and B.G.Hopkins: Estimation of soil organic matter by weight loss-on-ignition.Soil organic matter: analysis and interpretation, 21-31 (1996).

[24] M.H.Salehi, O.H.Beni and H.B.Harchegani: Refining soil organic matter determination by Loss-on-ignition.Pedosphere, Vol.21(2011),P. 473-482.

*Applied Mechanics and Materials Vols. 580-583 (2014) pp 907-911*
*© (2014) Trans Tech Publications, Switzerland*
*doi:10.4028/www.scientific.net/AMM.580-583.907*

# Determination of volumetric joint count based on 3D fracture network and its application in engineering

Jinliang Wu [a], Ji He [b*]

State Key laboratory of Water Resources and Hydropower Engineering Science, Wuhan University, 8 Donghu South Road, Wuhan 430072, PR China

[a]292960696@qq.com, [b]jihechn@gmail.com

**Keywords:** fractured rock mass; volumetric joint count; fracture spacing; stochastic fracture network; Monte Carlo method

**Abstract:** Volumetric joint count $J_v$ is an important parameter to evaluate the development of fractures. It is a fundamental representative for the strength and permeability of rock masses. However, $J_v$ cannot be directly measured in field. In this study, an indirect method is applied for its estimation. The main procedures are as follows: firstly, the volumetric joint frequency $f_i$ is assumed for $i$ th fracture set, and then a series of 3D stochastic discrete fracture networks (DFNs) are generated using the Monte Carlo method according to $f_i$ ; secondly, a survey line is drawn perpendicular to the fracture set in the each fracture network generated, the fracture spacing is measured along the survey line, then the average fracture spacing and its variance coefficient are calculated from all the DFNs; thirdly, by repeating the above two steps for different $f_i$ assumed, the relevant average fracture spacing and its variance coefficient are obtained, and two relation curves are built up between $f_i$ and the average fracture spacing (or its variance coefficient); fourth, the exact $f_i$ is estimated through this relation curve between $f_i$ and the average fracture spacing according to the exact fracture spacing measured in situ; finally, $J_v$ is calculated by summing the exact $f_i$ of all fracture sets up. In this study, this indirect method is applied in the rock masses of Xiaowan Hydropower Station. The result shows that the fracture spacing will reduce and its variation coefficient becomes stable as $f_i$ increases.

## Introduction

In nature, a rock mass usually contains a large quantity of fractures with complicated distribution. Therefore, its strength and permeability are quite different from an intact rock. Due to being the weakness, fractures are the key to control the strength and permeability of fractured rock masses[1,2]. As a result, the fracture growth level becomes an important indicator to value the quality of rock masses in engineering.

Volumetric joint count $J_v$ is generally adopted to quantitatively evaluate the fracture growth level at present. But owing to the restriction of surveying on site, $J_v$ only can be deduced from limited boreholes and limited exposures (e.g. slope surfaces or underground caverns). So far, scholars[3-6] have published a series of papers on the above issues. But these methods are mostly based on analytical formulas and experience coefficients, and the calculation results for $J_v$ may have large difference to the exact $J_v$ in situ. Therefore, Zhang et al. (2012) [7] used 3D fracture network to solve the problem, from which the relation curve between the line frequency and $f_i$ for each fracture set can be built and the $J_v$ can be calculated by summing the calculation $f_i$ of all fracture sets up.

In this paper, 3D fracture network is applied to build up two relation curves for each fracture set: the first one is between $f_i$ and the average fracture spacing, and the other one is between $f_i$ and the variance coefficient of spacing. The exact $J_v$ can be evaluated according to the first curve. By using 3D fracture network the indirect method is applied in the rock masses of dam foundation of Xiaowan

hydropower station based on field surveying data, which shows that the indirect method is feasible and has attractive advantages in practical engineering projects.

## Monte Carlo method

Monte Carlo method[8], also known as random sampling method, is based on probability and statistics theory, from which some complex problem can be solved by using electronic computers. Along with the rapid development of electronic technology, Monte Carlo method is widely applied in the areas of mathematics, physics and engineering technology.

In this paper, Monte Carlo method is used to generate stochastic parent DFNs, the procedure for the calculation of $J_v$ can be formulated in Fig 1:

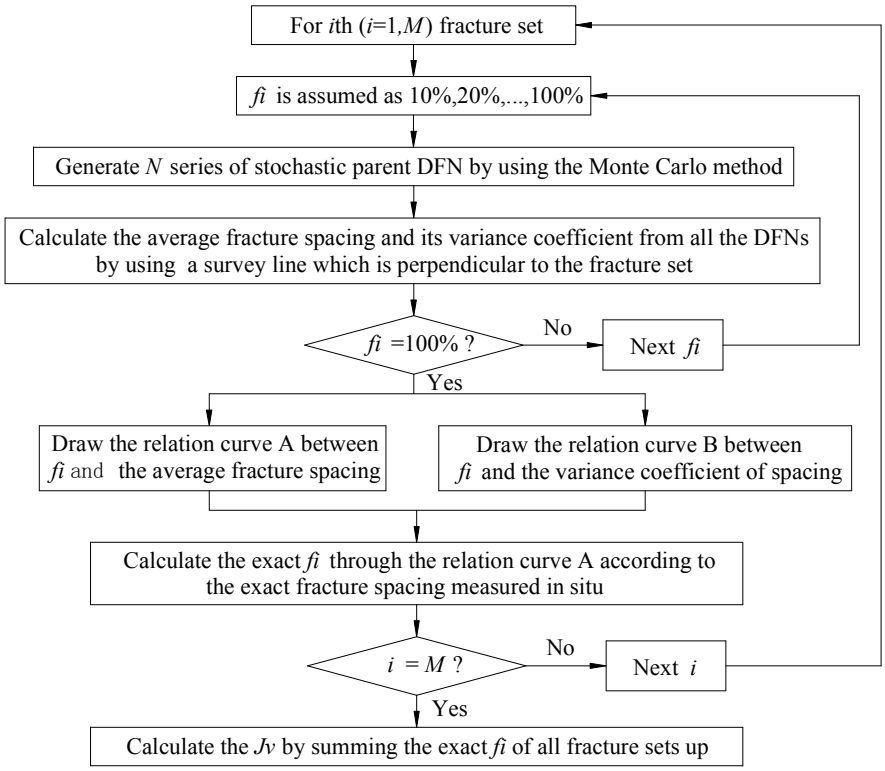


Fig. 1 The determination of $J_v$ flowchart

In Fig.1, the variance coefficient is used to measure the variance of the average fracture spacings calculated from N series of DFNs. The equation for the variance coefficient can be obtained as

$$\alpha_i = v_i / m_i \tag{1}$$

where, $\alpha_i$ is the variance coefficient; $v_i$ is the sample variance of the average fracture spacings from N series of DFNs; $m_i$ is the average fracture spacing from N series of DFNs.

## Calculation of fracture spacing

This part mainly focuses on how to determine the fracture spacing by using 3D fracture network. Based on the probability models of fractures measured in field, *M* sets of stochastic discrete fractures are generated in a large region of size $am \times am \times am$, in which the *o-xyz* coordinate system is built as follow: the origin is in the surveying center; the x-axis towards east, the y-axis towards north and the z-axis towards upright.

The number of fractures for the *i*-th fracture set is determined according to

$$N_i = f_i \times V \tag{2}$$

where, $f_i$ is the volumetric joint frequency for the i-th fracture set; $V$ is the volume of the survey region.

In order to measure the facture spacing for the i-th fracture set, a survey line is built up in the region, which includes the following main requirements: (1) the survey line takes the length of $L_i = a/3$ for avoiding the boundary effect; (2) the survey line has a midpoint at the origin $(0,0,0)$ and it should be perpendicular to the fractures as well. The equations for describing the survey line can be expressed as

$$\begin{cases} x_i = \sin\theta_i \times \sin\varphi_i \\ y_i = \sin\theta_i \times \cos\varphi_i \\ z_i = \cos\theta_i \\ \sqrt{(x_i^2 + y_i^2 + z_i^2)} \le (L_i / 6) \end{cases} \tag{3}$$

where, $L_i$ is the length for the *i*-th survey line; $\varphi_i$ is the average dip direction for the *i*-th fracture set; $\theta_i$ is the average dip angle for the i-th fracture set.

The fracture shape is assumed to be a disc, and the equations for describing any fracture can be formulated as

$$\begin{cases} A(x-x_0) + B(y-y_0) + C(z-z_0) = 0 \\ (x-x_0)^2 + (y-y_0)^2 + (z-z_0)^2 \le D^2/4 \end{cases} \tag{4}$$

where, $(x_0, y_0, z_0)$ is the center coordinates of a fracture; $D$ is the diameter of the fracture; $A, B, C$ is the coefficients for the equation.

The number of intersections between the i-th survey line and the i-th fracture set can be determined by solving the equations（3）and（4）simultaneously. Then, the average spacing[9] for the i-th fracture set can be calculated as

$$d_i = L_i / N_i \tag{5}$$

where, $d_i$ is the average spacing for the i-th fracture set; $N_i$ is the number of intersections.

## Engineering application

Xiaowan Hydropower Station is located at the upper reach of Mekong River. This paper takes the rock masses with weak weathering in the left bank as a research object. There are three main fracture sets in the rock masses: the first set is steep dip along the river, the second set is steep dip across the river, and the third set is low-angle dip along the river. According to the in-situ investigation and measurement, the probability models and relevant parameters of fractures are listed in Table 1. The *o-xyz* coordinate system is built as follow: the origin is in the surveying center; the x-axis towards east, the y-axis towards north and the z-axis towards upright.

Table 1 Probability models and relevant parameters of fracture sets

| Fracture set | Spacing | | | Dip direction | | | Dip direction | | | Trace length | | | Central point | Aperture (mm) |
|---|---|---|---|---|---|---|---|---|---|---|---|---|---|---|
| | Probability model | μ (m) | σ (m) | Probability model | μ (°) | σ (°) | Probability model | μ (°) | σ (°) | Probability model | μ (m) | σ (m) | | |
| 1 | Logarithm normal | 0.37 | 0.57 | Normal | 95.60 | 13.49 | Normal | 89.35 | 6.37 | Normal | 2.01 | 0.37 | Uniform | 0.16 |
| 2 | Negative exponent | 0.47 | 0.47 | Uniform | 11.09 | 7.96 | Normal | 79.64 | 10.08 | Logarithm normal | 2.23 | 1.48 | Uniform | 0.02 |
| 3 | Negative exponent | 0.60 | 0.74 | Uniform | 270.3 | 18.62 | Logarithm normal | 39.91 | 8.82 | Logarithm normal | 2.08 | 1.41 | Uniform | 0.16 |

For each fracture set, $f_i$ is assumed from 10% to 100%. For each $f_i$, M=50 DFNs are generated in a large region of size 60 m×60 m×60 m. According to the relevant parameters for the fracture sets (Table 1), three survey lines are built up using the equation (3). Then the average spacing and its variance coefficient for M=50 DFNs can be calculated.

Fig. 2 shows the relation curve between $f_i$ and the average fracture spacing for all fracture sets. Based on the the exact fracture spacing (Table 1), the exact $f_i$ for the three fracture sets can be calculated from the relation curve (Fig 2):

$$f_{j1} = 0.512\,; \quad f_{j2} = 0.174\,; \quad f_{j3} = 0.210 \tag{6}$$

Then $J_v$ can be calculated as

$$J_v = f_{j1} + f_{j2} + f_{j3} = 0.896 \tag{7}$$

Fig. 3 shows the relation curve between $f_i$ and the variation coefficient for all fracture sets. These results show that:

(1) The larger $f_i$ is, the smaller the average fracture spacing is.

(2) When $f_i$ is equal to 50%, the variation coefficient of fracture spacing tends to be stable.

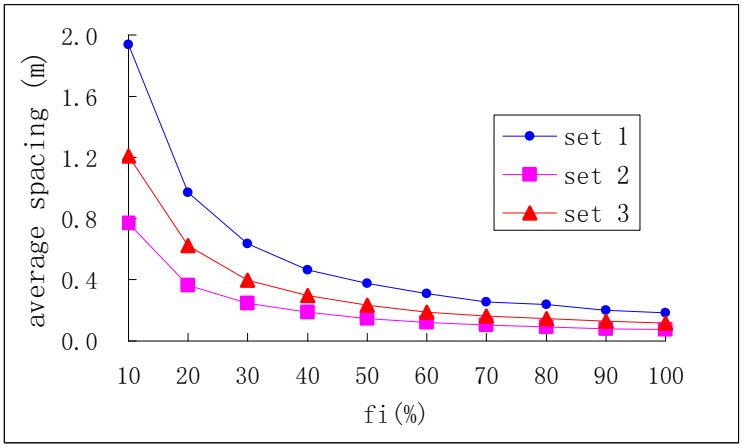


Fig. 2 The relation between $f_i$ and the average fracture spacing

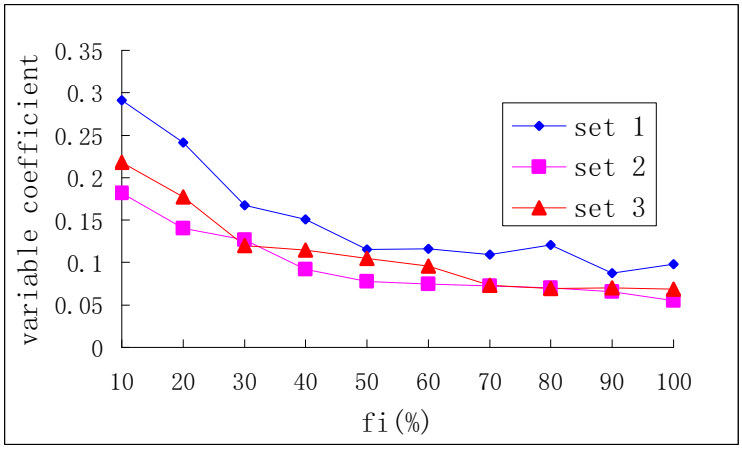


Fig. 3 The relation between $f_i$ and the variation coefficient

## Summary

This paper shows an indirect way to determine $J_v$ of fractured rock masses using Monte Carlo method. The engineering application shows that the fracture spacing will reduce and the variation coefficient becomes stable as $f_i$ increases. The suggested method is feasible and worth to be popularized in practical engineering projects.

## Acknowledgements

This project is supported by Research Fund for the Doctoral Program of Higher Education of China (No.20130141120013)

**References**

[1] Gang Liu, Jian Zhao, Hongwei Song,et al. Physical modeling of effect of joint density on deformation and failure of surrounding rocks[J]. Chinese Journal of Geotechnical Engineering, 2007, ,29（11）:1737-1741.(in Chinese).

[2] Jinliang Wu, Ji He, Shenghong Chen. Estimation of representative elementary volume and three-dimentional permeability tensor for fractured rock masses. [J]. Chinese Journal of Rock Mechanics and Engineering，2014,33（2）：309-316. (in Chinese).

[3] Chunhe Yang, Hongtao Bao, Guibin Wang, Tao Mei. Estimation of mean trace length and trace midpoint density of rock mass joints. China Journal of Rock Mechanics and Engineering,2006,25（12）：2475-2480. (in Chinese).

[4] Feng Lin, Runqiu Huang, Sheng Wang, et,al. Evaluation of in-situ measurement methods for counting volumetric joints of rock mass. Journal of Engineering Geology, 2008,16(5):663-667. (in Chinese)

[5] Panfeng Li, Jianhong Yang, Jian Yang,et al. New formulate for volumetric joint cont JV of jointed rock m ass. Journal of Engineering Geology, 2009,17（2）：240-243. (in Chinese).

[6] Xiuwen Hu, Shengming Hu, Yang Lu, et al. Measurement of volumetric joint count and its application in surrounding rock classification. Journal of Yangtze River Scientific Research Institute, 2010,27（6）：30-34. (in Chinese).

[7] Guangcheng Zhang, Huazhang Li, Ye Lin, et al. Assessment of joint volume frequency in rock mass and its application in engineering[J]. Journal of Engineering Geology, 2012,20（4）：585-590. (in Chinese).

[8] Lucheng Pei, Zhongqi Wang. The Monte Carlo method and its application[M]. Beijing：Ocean Press，1998：3-9. (in Chinese).

[9] Eissa Elsayed A, Zekai Sen. Probabilistic simulation of rock quality designation(RQD) [J]. Bulletin of the International Association of Engineering Geology, 1991,43:31-40.

*Applied Mechanics and Materials Vols. 580-583 (2014) pp 912-918*
*© (2014) Trans Tech Publications, Switzerland*
*doi:10.4028/www.scientific.net/AMM.580-583.912*

# Relations between paleoclimatological conditions and mineralogical characteristics of clays in Miocene sediments at Linxia basin, China

Na Yu[1, 2, a *],Hanlie Hong[3,b],Zhaohui Li[4,c],Kexin Zhang[3,d],Rongbiao Li[3,e]

[1]College of Earth Sciences, University of Jilin, Changchun, Jilin,130021,China

[2]Faculty of Prospecting and Surveying, Changchun Institute of Technology, Changchun, Jilin, 130021, China

[3]Faculty of Earth Sciences, China University of Geosciences, Wuhan, Hubei, 430074, China

[4]Geosciences Department, University of Wisconsin – Parkside, Kenosha, WI 53140, USA

[a]65277622@qq.com, [b]honghl8311@yahoo.com.cn, [c]li@uwp.edu

**Keywords:** Clay minerals; Linxia basin; Paleoclimate; Palygorksite

**Abstract.**Linxia basin is a late Cenozoic fault-block basin along the border between the Tibet plateau and the Loess plateau in Northwestern China. Its formation and sediments' record may be directly affected by the structural dynamics and the uplift of the Tibet Plateau. For this reason, we studied the mineral characteristics of the Maogou formation of Miocene sediments using X-ray diffraction (XRD) and scanning electron microscopy (SEM). The XRD results showed that quartz, chlorite, illite, calcite, plagioclase, orthoclase, kaolinite, and trace palygorskite are present throughout the sequence of the cross-section in Linxia basin. In contrast, gypsum and ankerite occur occasionally in the upper portion of the Miocene deposits. The content of calcite varied with layers in the profile and was relatively concentrated in mudstone. Chlorite and illite were observed transforming into palygorskite under SEM observation. Based on the mineral characteristics and the change of mineral composition, especially the clay minerals, it could be inferred that an arid environment prevailed in the region with warm and cold intervals during Miocene time.

## Introduction

Located on the northeastern margin of the Tibetan plateau, the Linxia basin is a late Cenozoic fault-block basin along the border between the Tibet plateau and the Loess plateau. The formation and uplift of the Tibet Plateau has a profound influence on its origin and evolution.Because of its unique geological location and complete lithologic sequences, the Linxia Basin has been studied extensively recently. Most of these studies were focused on paleomagnetism, pollen, fossils, and particle size distribution of the sediments. Significant achievement has been made on determination of stratigraphy, ages of rock formation, as well as the environmental markers related to low resolution paleoclimate (Chen et al., 1996; Fang et al., 1997; Zhong et al., 2001; Cao et al., 2004; Qiu et al., 2004; Deng, 2004; Song et al., 2005). These results show that the basin was formed about 30 Ma. As a paleo-lake basin, it was in a closed system in Quaternary and most part of Tertiary. The mineral components of the sediments are made of clay minerals, feldspar, quartz, calcite, and gypsum. Clay minerals formed from weathering on the surface will change as the sedimentation and burial processes proceeded. The formation of new clay minerals as well as the transformation of previously formed clay minerals was closely related to the environment.Thus,by studying the mineral association of the clay minerals,their relative ratios, their structural characteristics,and the transformation of different clay minerals, we could deduce the source region of the clay minerals, the type of weathering, and the climate and the geo-environment when these minerals were formed. Using the clay mineral assemblage and detailed mineral characteristic analyses, Hong et al. (2007) studied the paleoclimatic evolution subsequent to the initial-stage of uplift of the Tibetan plateau using Oligocene sediments in Linxia basin. Their results suggested relatively small fluctuations in climate conditions during the Oligocene epoch while an increased erosion of soils and poorly weathered parent rock in

more elevated or high-relief source areas might occurred in the late Oligocene. In the current study, we investigated the mineralogical characteristics of the clay minerals in the Miocene sediments of Linxia Basin using XRD, SEM and other techniques in order to extend our discussion with our sister paper (Hong et al., 2007) on the study of paleoclimate and geologic environment in this basin.

## Geology of the area

Geographically, the Linxia basin is located in Linxia, Gansu province, northwestern China. The study area is a mountain front fault depression basin among Leijishan fault, south Qinling fault, and Mt. Mahanshan (Fig. 1).

The Maogou cross section is located in a stream valley in Dongxiang County, Linxia basin (Fig. 1). The total thickness of the strata is 443 m. The sediments are Tertiary red deposits. The sediments of Zhongzhuang, Shangzhuang, Dongxiang, and Liushu formations were deposited at 21.8 – 5.41 Ma. Based on their lithologic units, the cross section can be divided into three sedimentary sequences. Conglomerate, sandstone, and siltstone derived from river deposits occur on the bottom of each sequence. The top of each sequence is made of massive mudstone, reflecting a progressive wet environment. Among the three sequences, the mineral composition of the mudstone in the lower sequence is more uniform. Vertical gypsum veins or spotted gypsum can be found in the lacustrine mudstone in the middle sequence. Within the mudstone of the upper sequence, micrite bands of different thickness with bluish gray color are often seen.

Based on the lithologic characteristics, the Maogou cross section can be divided into 17 layers (Shi et al., 1998) ,Based on field geological observation and the trend in lithologic changes, we decided to choose samples from layers 2, 3, 11, 15, and 17 for further study. The samples are named b-2, b-3, b-11, b-15, and b-17.

## Materials and methods

**Sample preparation.**amples were collected based on their lithological characteristics. Each sample is split into three portions. The first portion is used for mineral composition analysis by XRD. The second portion was used for clay mineral analyses. The samples were soaked with distilled water, stirred and the clay fraction was separated from the coarser particles by sedimentation methods. Both oriented samples and ethylene glycol saturated samples were prepared.

**Instrumental analyses**.X-ray analysis was performed using a Rigaku Dmax-IIIA X-Ray Diffractometer, with a CuKα radiation, Ni filter, a voltage of 35 kV and current of 30 mA. The slits were 1º for divergence and anti-scattering slits, 0.3 mm for receiving slit. X-ray diffraction patterns were recorded using continuing scan at a speed of 4º/min and a 2θ resolution of 0.02º.

Representative pelite samples were selected and then platinum-coated. The analyses were undertaken on a JSM-5610 SEM at an accelerating voltage of 20 kV and a beam current of 1–3 nA.

## Results and discussion

**XRD analyses.**The XRD patterns of the natural pelite samples from the Miocene sediments at Linxia basin is shown in Fig. 2. The major minerals are quartz (Q), calcite (C), chlorite (Ch), illite (I), mixed layer of illite/smectite (I/S), feldspar (F), ankerite (An), and gypsum (Gy). Their characteristic diffraction peaks are 3.34, 3.03, 14.26, 10.00, 15, 3.19, 2.90, and 7.60 Å.Oriented XRD patterns of the clay fractions before and after ethylene glycol (EG) saturation are plotted in Fig. 3. For the peaks of 10 and 14 Å, no shift in position was found after glycerol saturation, indicating that the clay minerals are illite and chlorite. Also, a shift of peaks after EG saturation is indicative of mixed layered (I/S) or smectite. Furthermore, trace amount of palygorskite (Pa), whose characteristic diffraction peak (110) is 10.53 Å, is seen in some samples. Semi-quantitative analyses were carried out using internal standard methods (Brindley, 1980; Zhang et al., 2003) to determine the mineral content of present clay minerals. The results from the five representative samples are listed in Table 1. The relative

amounts of clays minerals in clay fractions are listed in Table 2. The kaolinite contents varied from 10 to 15%, illite from 42 to 53%, chlorite from 11 to 23%, while I/S from 15 to 30%. Sample b-11 had the highest amount of chlorite and lowest amount of I/S (Table 2). Illite and chlorite are characteristic of cold regions and deserts marked by very low rates of weathering and areas of steep relief where mechanical erosion interferes with soil formation (Robert and Kennett, 1994; Pandarinath et al., 1999). The fact that all layers in the section contain chlorite and illite indicates that the climatic environment in Linxia basin didn't have much fluctuation during the Miocene epoch and the area was dominated by dry climate. In addition, the trend of chlorite content varied from low to high, and then from low to high again, indicating that the climate environment experienced two cycles from cold and dry to mild and wet. Gypsum precipitation is a good indicator of dry climate, while sample b-11 contains 35-40% gypsum. These results showed that the overall transition of the climate in the region was from cold and dry to wet climate. In the course of transition, there was an episode of even dryer climate condition. Sample b-17 contained about 5% ankerite, indicating that the lake water was rich in iron when the carbonate sediments were deposited. Considering that palygorskite is formed from hydrolysis of chlorite in sediments, the excess iron in solution derived from hydrolysis of chlorite could be responsible for ankerite precipitation, which again indicating dry climate condition. Geochemical studies along the Maogou section showed that the Linxia basin had a relatively cold and wet climatic condition in Miocene (Zhong et al., 1998), which agrees well with this study using mineralogical properties of the clay minerals as an indicator of climate changes. An et al. (2001) identified three stages of evolution of Asian climates with the first stage characterized by enhanced aridity in the Asian interior (Including Linxia basin) and onset of the Indian and east Asian monsoons, about 9±8Myr ago. However, an increase in sedimentation rate influenced by climate change and erosion rates occurred in Linxia basin at the beginning of Pliocene (Zhang et al., 2001).

**SEM analyses.**Observation of electron microscopic images reveals that individual crystals of the clay minerals form curvy thin plates, while the aggregates of the minerals showed random orientation of the platy minerals. On the edges of the platy clay minerals, fibrous minerals of 1-2 μm long can be observed (Fig. 4a). Some of these fibers appear curvy (Figs. 4b, c). Fibrous minerals can also be found on the edges of many sheet-like and platy mineral grains. EDS analyses showed that the major chemical composition of the platy minerals were Si, Al, and K. Thus, the host platy minerals are illite (Fig. 4d), whose presence is verified by X-ray diffraction analyses. The sheet-like minerals have chemical composition of Si, Al, Mg, and Fe, indicating that the minerals are of chlorite type (Figure not shown). Well developed fibrous minerals are present in aggregates. Each individual mineral is 4-6 μm long and 0.1 μm in diameter. They are twisted and mingled in all different directions, showing the characteristics of palygorksite (Fig. 4c). Their EDS analyses showed that the major chemical composition was Si, Al, Mg, and Fe with trace amount of K, in compliance with the chemical composition of palygorskite (Fig. 4e). In the X-ray diffraction patterns, a minor 10.52 Å diffraction peak, caused by (110) reflection of palygorskite can be seen, confirming the presence of palygorskite. Clay minerals as secondary minerals are commonly present in all types of sedimentary rocks. Their chemical composition and mineral association are very sensitive to the changes in climate and environment (Manalt et al., 2001; Médard, 2000; Perederij, 2001). Most of these clay minerals in the sediments are produced from chemical weathering on Earth's surface and settled out with the sediments. However, their chemical composition as well as crystallinity will change during burial and lithification processes. The changes are strongly affected by the geochemical and geothermal environment (Meng et al., 2005). In addition, the formation of clay minerals are also affected by the pH and salinity of the solution, the surface temperature as well as the chemical composition of the parent rocks, among which solution pH and temperature will strongly affect the hydrolysis process (Lu, 1997). Thus, the characteristics of crystal structure, crystal morphology, and mineral association will reflect the geo-environmental conditions when these minerals were formed to certain degrees.

Illite is a relatively stable mineral commonly found in the sediments. It is formed at an environment that has a higher $K^+/H^+$ ratio, under strong physical weathering, weak leaching, and weak alkaline conditions. As most illite was derived from weathering of K-feldspar, it is commonly used as an

indicator of neutral to weak alkaline terrestrial environment (Chen and Miu, 1996). The SEM (Fig. 4a) revealed growth of fibrous palygorskite (1-2 μm in length) along the edges of the illite. This phenomenon is produced in aqueous solution under a surficial sedimentary environment.

Palygorskite is a fibrous phyllosilicate. The basic structure of palygorskite can be described as being composed of 2:1 ribbons that are linked to each other laterally by single basal oxygen. It is formed in desert environment under arid or semiarid condition (Tateo et al., 2000; Khadkikar et al., 2000) and is a characteristic mineral found in eolian loess deposits as well as in the weathered product of micrite in arid and semiarid region, thus could be used as an indicator mineral for arid and semiarid environment (Singer, 1984). It is produced by authigenesis from solutions having high $SiO_2$ and MgO activity, low $Al_2O_3$ activity, and at pH 8–9 (Chen, 1991). Sedimentary-type palygorskite is commonly associated with other sedimentary minerals such as sepiolite, carbonate minerals, sulfate minerals, montmorillonite, cherts, quartz, serpentine, chlorite, and is found in the transition zone in a depositional basin. (Wang et al., 1993).

From the electron microscopic images (Fig. 4c) we can see that aggregates of fibrous crystals are found in the pore space of particles in the sediments. The crystals are about 6 μm long, have well developed faces, form radial growth pattern. Intergrowth can be seen in between different particles. These fibrous palygorskite grow and replace the platy clay minerals on the edges. In some places where the replacement was more thorough, the crystals are complete made of palygorskite crystals. However the aggregates of the palygorskite crystals still preserve the shape of original mineral grains. Some grains showed complete transition to palygorskite. From the shape of the aggregates of the fibrous palygorskite and the replacement of palygorskite crystals for clay mineral grains, it can be seen that the palygorskite was of authigenic origin (Verrecchia and LeCoustumer, 1996). Furthermore, from the fact that dolomite was found in the sediments in sample b-17, it can be seen that the soil environment in the area was high in Mg activity, thus promoting the formation of palygorskite(Bozkaya and Yalçin, 1995).

The fine characteristics found on quartz surfaces are also an important indication for the analysis of depositional environments and sedimentary facies (Chen et al., 1996). Many dissolution etches were found on the surface of quartz crystals under the observation of electron microscopic observation. The etches showed regular patterns, most of them form a triangular shape (Fig. 4f). As the dissolution of quartz occurred at media having a higher solution pH, it can be inferred that the water in the sedimentary basin was somewhat alkaline. Under such alkaline environment, the silicon derived from quartz dissolution can facilitate the formation of palygorskite.

Due to hydrolysis, chlorite is converted into palygorskite along the edges and in the factures. The presence of palygorskite showed that the environment was alkaline, similar to the observation of quartz dissolution. The silicon and magnesium produced from hydrolysis of chlorite and quartz provided the chemical condition for the formation of palygorskite. The authigenic palygorksite found in the sediments showed that the climate of the region was dominated by dry climate in late Miocene epoch, in agreement with the observation from clay mineral association study.

## Conclusion

Results from X-ray diffraction analyses of the sediments in Linxia geologic section showed that the mineral composition was made of chlorite, illite, orthoclase, plagioclase, quartz, calcite, and small amount of gypsum. Among these minerals, the illite content could be as high as 53%, and I/S as high as 30%, indicating that the climate of the source region of the sediments was dominated by semi-arid climate with occasional warm or cold periods. Sample b-11contains 35-40% of gypsum. The presence of gypsum provides a solid evidence of the regional climate change and reveals a graduate transition of the environment to arid condition. The study showed that in Miocene epoch Linxia basin was dominated by arid climate. Although short intervals with warm and cold climatic conditions were documented in the sediment, overall the climatic condition was relatively stable.

Palygorskite is a good indicator mineral formed in arid and semiarid environment. The magnesium released from hydrolyses of chlorite provides the necessary chemistry for palygorskite to form. Fibrous minerals were also found around the edges of illite in the sediments, again showing that extensive hydrolyses among the clay minerals in the sediments. The wide presence of authigenic palygorskite in the sediment of Linxia basin confirms that the climate in the region was dominated by arid climate in Miocene time.

**Acknowledgements**

The work was supported by funding from the China Geological Survey (No.1212010610103) and the Natural Science Foundation of China (No.40621002).

TABLE 1. Results of XRD quantitative analysis of the sediments

| ***Sample ID*** | *Mineral composition and contents ($W_B$/%)* | | | | | |
|---|---|---|---|---|---|---|
| | Q | C | CLAY | F | GY | AN |
| B-2 | 25–30 | 10–15 | 35–45 | 5–10 | – | – |
| B-3 | 25 | 10 | 60 | 5 | – | – |
| B-11 | 20–25 | 10 | 15–20 | 10 | 35–45 | – |
| B-15 | 25 | 15 | 50 | 10 | – | – |
| B-17 | 10 | 5–10 | 60–65 | 10 | – | 5 |

TABLE 2. Results of XRD quantitative analysis of clay fractions

| ***Sample ID*** | *Mineral composition and contents ($W_B$/%)* | | | |
|---|---|---|---|---|
| | KAOLINITE | CHLORITE | I/S | ILLITE |
| B-2 | 25–30 | 10–15 | 35–45 | 5–10 |
| B-3 | 25 | 10 | 60 | 5 |
| B-11 | 20–25 | 10 | 15–20 | 10 |
| B-15 | 25 | 15 | 50 | 10 |
| B-17 | 10 | 5–10 | 60–65 | 10 |

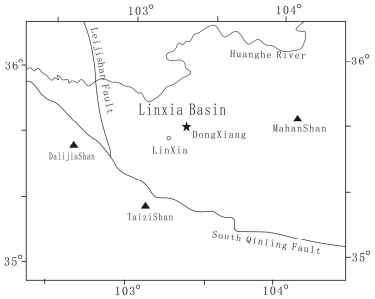


FIG.1. A generalized map showing the location of study area.

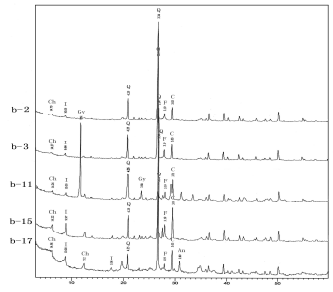


FIG.2. X-ray diffraction patterns of samples from the section.

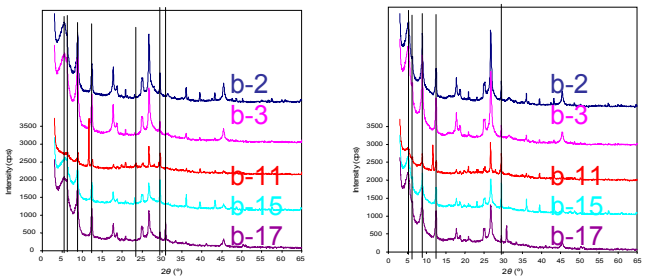


FIG.3. X-ray diffraction patterns of oriented (left) and EG saturated (right) samples from the section.

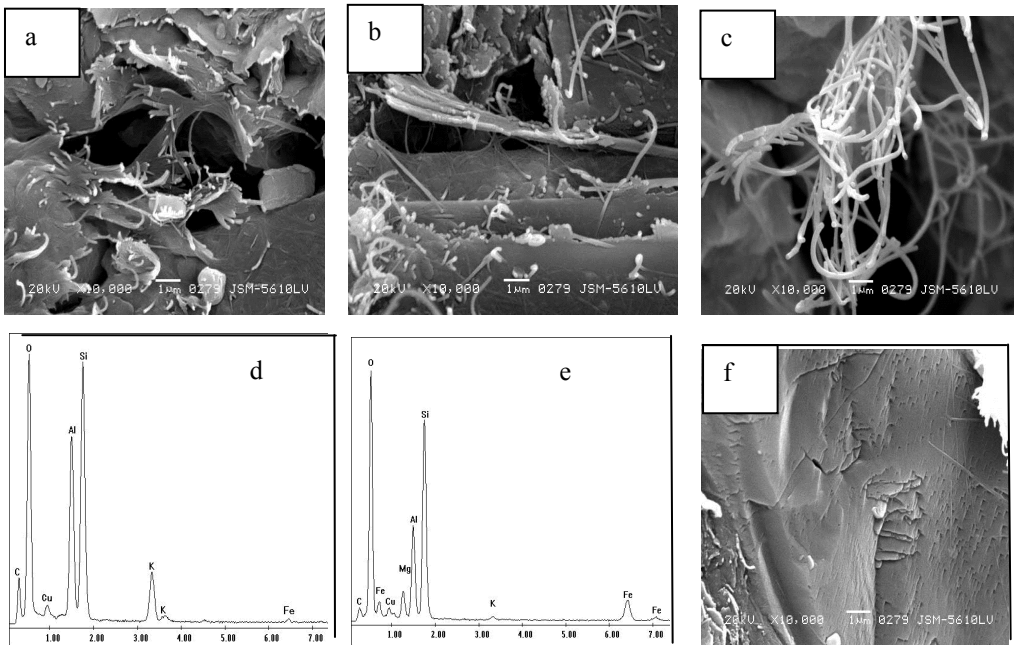


FIG.4. SEM images of the sediments from Linxia basin a. Sample (b-11), b and c. Sample (b-15), d. EDS of illite, e. EDS of palygorskite, f. Sample (b-2)

## References

[1] An, Z., Kutzbach, J.E., Prell, W.L., Porter, S.C.. Evolution of Asian monsoons and phased uplift of the Himalaya–Tibetan plateau since Late Miocene times. Nature 411（2001）62–66.

[2] Brindley, G.W.. Quantitative X-ray mineral analysis of clays: 1980,Pp. 411-438

[3] Chen, L.H., Miu, X. The Application of scanning electron microscopy on geological. Science Publishing Press, Beijing, 1996. (in Chinese).

[4] Chen, Z.G.. Genetic types of palygorskite clay. Geological Science and Technology Information 10,3, 24–28(1991).

[5] Fang X. M., Li J. J., Zhu J. J., Chen H. L., Cao J. X Division and age dating of the Cenozoic strata of the Linxia Basin in Gansu, China. Chinese Science Bullentin, 42(1997)1457–1471 (in Chinese).

[6] Hong, H., Li, Z., Xue, H., Zhu, Y., Zhang, K., Xiang, S.. Oligocene clay mineralogy of the Linxia basin: evidence of paleoclimatic evolution subsequent to the initial-stage uplift of the tibetan plateau. Clay Clay Miner. 55(2007)491–503.

[7] Li, J.J., Feng, Z.D., Tang, L.Y.. Late quaternary monsoon patters on the loess plateau of China. Earth Surface Processes and Landforms. 13（1988）125–135.

[8] Médard, T.. Palaeoclimatic interpretation of clay minerals in marine deposits: an outlook from the continental origin. Earth Sci. Rev. 49 ,14, 201–221.(2000)
[9] Perederij, V.I.. Clay mineral composition and palaeoclimatic interpretation of the Pleistocene deposits of Ukraine [J]. Quaternary International 76, 113-121.(2001)
[10] Robert C., Kennett J.P.. Antarctic subtropical humid episode at the Paleocene-Eocene boundary: Clay-mineral evidence. Geology 22, 211–214(1994).
[11] Shi, Y.F., Li, J.J., Li, B.Y.. Late Cenozoic Uplift and Environmental Change of Qinghai-Tibet Plateau. Guangzhou: Guangdong Science & Technology Press, 1998,pp.463. (in Chinese)
[12] Singer, A.. The paleoclimatic interpretation of clay minerals in soil and weathering-a review. Earth Sci. Rev. 21: 251-293(1984).
[13] Tateo, F., Sabbadini R., Morandi N. Palygorskite and sepiolite occurrence in Pliocene lake deposits along the River Nile: evidence of an arid climate. J. African Earth Sci. 31 ,324, 633–645.(2000)
[14] Verrecchia, E.P., LeCoustumer, M.N.. Occurrence and genesis of palygorskite and associated clay minerals in a Pleistocene calcrete complex, SDE Boqer, Negev desert, Israel. Clay Miner. 31, 183–202.（1996）
[15] Wang, H.Z., Li, J.F., Wang, Y.H., Shi, G.H.. New Development in research of crystal-chemistry and genesis of palygorskite. Geological Science and Technology Information 12 ,4, 51–55.（1993）
[16] Xi, X.X., Mu, D.F., Fang, X.M., LI, J.J.. Climatic change since the late Miocene in west China: evidence from anion chlorine in the Linxia red Basin. Acta Sedmentologica Sinica 16, 155–160. (1998)
[17] Zhang, P., Molnar, P., Downs, W.R.. Increased sedimentation rates and grain sizes 2–4 Myr ago due to the influence of climate change on erosion rates. Nature 410(2001)891–897.

*Applied Mechanics and Materials Vols. 580-583 (2014) pp 919-922*
*© (2014) Trans Tech Publications, Switzerland*
*doi:10.4028/www.scientific.net/AMM.580-583.919*

# Research about control factors and early warning system of early warning system in Song Fangtun Oilfield

Nan Lv[1, 2, a], Yueming Wang[3, b], Hongyu Liu[2, c]

[1] Northeast Petroleum University, Daqing, Heilongjiang, 163318, China

[2] The 2rd Oil Production Plant, Daqing, Heilongjiang, 163000, China

[3]The 9rd Oil Production Plant, Daqing, Heilongjiang, 163000, China

[a]lvnan1120@126.com, [b]wym815@126.com, [c]liuhongyu8516@126.com

**Keywords:** Geologic factor；development factor；early warning system；monthly average decline range

**Abstract.** The development effect of Song Fangtun Oilfield is mainly restricted by two factors which are geology and exploitation. In view of the main control factors in oilfield development, we selected two indexes,monthly average decline range and water content escalating rate to establish early warning system of blocks development effect. The system which has great practical application value, is sensitive to reflecting the monthly variation process of block development effect, and plays a certain guiding role in the development effect during the whole year.

## Introduction

Song Fangtun oilfield is located in Sanzhao Depression area at the the central of the northern is on the Songfangtun nose structure, and the southern is on the Mofantun nose structure. These two nose structure are developed in the process of Songliao Basin occurrence and development, under the background of the base rock appendices on the ancient central uplift zone, at a long time. The formation thickness is getting thinner from the north to the south. Song Fangtun oilfield belongs to the eight plant of the Daqing oilfield,which has been put into the early development,parts of the block have entered the high-water exploration period. The reservoir rocks in Song Fangtun oilfield is hybird sandstone with shale high content,upper cement contant.Since 1983, through four development phases such as experiment exploration, fast production, stable yields and technical tackle, the oilfield development effect continue to be improved, because the oil development is more delicate and scientific. So far, Song Fangtun oilfield is divided into 30 development block, the cumulative recovery degree is 11.6%, composite water cut reaches 57.14%.

## The main control factors of oilfield development

**Areal structure.**The early production of the wells at the top of the structure is relatively high, the water content is smaller, while those at the lower part of the structure the early production is relatively low, the water content is larger. This is due to gravitational differentiation, most water injection drives from the higher structure part to the lower part, and the larger difference is the greater driving force. For example Fang 76-103 located in the higher tectonic area of Song Fangtun oilfield produced 7.5 tons oil per day in the early stage, the composite water cut is 2%, while Fang 82-92 located in the lower part produced 2.7 tons oil, the composite water cut reached 3.4%.

The sand deposition in Song Fangtun oilfield mainly controlled by the northern provenance sedimentary system, developes three kinds of sedimentary types: channel sand, body sand sheet and sand sheet of non-subject. Both in the vertical and plane, the underwater distributary channel sand has the strongest water intake intensity and liquid production, followed by delta body sand sheet and sand sheet of non-subject (Table 1). The microfacies differences caused the reservoir development effect imbalance in the profile and plane[1].

Table 1 Comparison between water intake intensity and liquid production per unit thickness of different sedimentation types in Song Fangtun Oilfield

| Sedimentation type | Hygroscopic intensity ($m^3$/m.d) | Liquid production per unit thickness ($m^3$/m.d) |
|---|---|---|
| Channel sand | 2.84 | 7.41 |
| Body sand sheet | 2.10 | 5.23 |
| Sand sheet of non-subject | 1.81 | 4.71 |

**Reservoir physical property.** The oilfield development effect, especially the oil production situation of well, all have inseparable connection with reservoir physical property[2]. Under the same degree of reserve recovery, if reservoir physical property is better, and the thickness is greater, the oilfield development situation is better. Compared three development blocks in the Song Fangtun oilfield, we can see that under the same degree of reserve recovery, the greater the permeability, the higher the oil production rate (Table 2).

Table 2 Correlation table of reservoir physical property

| Block | Porosity (%) | Permeability (mD) | Effective thickness (m) | Degree of reserve recovery (%) | Oil production rate (%) |
|---|---|---|---|---|---|
| F407 | 20.98 | 114.92 | 7.9 | 8.12 | 0.87 |
| F3 | 19.77 | 53.39 | 4.0 | 8.49 | 0.70 |
| F148 | 19.42 | 45.44 | 2.4 | 8.44 | 0.16 |

**Well pattern.**Song Fangtun oil field used square pattern, pattern water flood area of inverted nine spot injection pattern, injection-production well ratio is 1:3. This water injection is more flexible, if absorbing capacity of input wells is high, which can meet the needs of oilfield development, we can carry out this way. If asorbing capacity of input wells is lower, which can not meet the needs of oilfield development, then the number of input wells can be properly increased in the suitable place to make injection-production well ratio kept at 1:3.

**Water content escalating rate.**Water content escalating rate is is the central index to evaluate the oilfield development effect, only fully understand rules of oilfield water content escalation, find out which factors are inevitable, which factors are artificial, which can be adjust by later measures, then we can provide scientific and reasonable base for adjustment decision and oilfield development, to lay a solid foundation for high production and stable yields of oilfield[3].

## Early tracking and warning system of development effect

**Selecting principle of early-warning index.**During the selection of index, there are three principles to be insisted: (1)Accurate sensitive principle, early warning indexes should be able to reflect the

main aspects of block development effect change accurately and sensitively. (2)Fully reliable principle, the authority and statistical caliber of early-warning indexes should be consistent, meanwhile the number of statistical data samples should be large enough to meet the needs of the forecast and adjustment. (3)Match principle, early-warning indexes should be matched with the specific elements and warning method.

**Production decline rate.** Production decline rate is the percentage of production decline in unit time, and is an important index to evaluate oilfield development effect. Therefore, to realize the effective control of production decline, is an important work for oil field to improve development effect[4]. There are mainly four aspects to analyze influence factors of Song Fangtun oil field production decline over the years: firstly improvement of well spacing density can slow down production decline rate; secondly the adjustment of water flooding regime in proper time can effectively slow down production decline; thirdly if the initial oil production rate is higher,the water line advances faster and cause the high decline, finally is high deliverability can bring high decline, and high deliverability for several years, will exacerbate subsequent years of oil decline[5].

**Monthly average decline range.** Monthly average decline range: the average decline range every month which is compared withe annual decline rate of peak production in last year.

$$Qn=Qo\times(1-D)^{n} \quad (1)$$

$$d=1-(1-D)^{1/12} \quad (2)$$

Among them: D—Annual decline rate of peak production till some year, %; d—Monthly decline of peak production by the end of some year, %; Qn—Annual output of oil, $10^4$t; Qo—Peak production, $10^4$t; n—Decreasing fixed number of year, year.

The monthly average decline range of block A in Song Fangtun oilfield was 1.63%, since January 2012, and the block development effect began warning. The development effect continue to be worse in the February. We began to take measures in March, the decline rang fall below 1.66%. The decline rang continue to decrease in the April, the development effect fell below the warning area, even got in the good area(Table 3).

Table 3 Alternation of monthly average decline range in block A between January to May in 2012

| Block | Monthly average decline range in 2012(%) | | | | |
|---|---|---|---|---|---|
| | January | February | March | April | May |
| | 1.63 | 3.45 | 1.65 | 1.01 | 0.7 |
| A | Monthly development effect in 2012 | | | | |
| | January | February | March | April | May |
| | warn | bed | warn | good | good |

**Monthly average water content increase.** Monthly average water content increase is the difference between the monthly average water content in certain month and the annual average water content in last year. Supervise the monthly average water content increase, especially analyze and adjust the block which water content increase is more than 5%, make a warning signal to the block which water content increase between 3% and 5%, to control the increase of water content.

The annual average water content rate of block B in Song Fangtun oilfield was 54.8%, since January 2012, the monthly average water content rate was 2.6% more than the annual average water

content rate in 2001. The increase rate reached 4.5% in the February (Table 4),and the block development effect began warning. The water content escalating rate fell back to 3% in May, the development effect turn better.

Table 4 Alternation of water content increase in block B between January to May in 2012

| Block | Monthly water content increase in 2012(%) | | | | |
|---|---|---|---|---|---|
| | January | February | March | April | May |
| | 2.6 | 4.5 | 6 | 4.1 | 2.8 |
| B | Monthly development effect in 2012 | | | | |
| | January | February | March | April | May |
| | good | warn | bed | warn | good |

## Conclusions

The main geologic factors that influence the development effect of Song Fangtun oilfield are structure, sedimentary system reservoir physical property and so on. Different development feature different geologic feature. The block located in the high structural part and developing well reservoir condition, will occupy the vantage ground in the process of development.

The main development factors that influence the development effect of Song Fangtun oilfield are well pattern, development mode, production decline rate, water content escalating rate and so on. The final development effect of oilfield will be improved by choosing appropriate well pattern type and development mode and emphasizing the control of decline rate and water content increase in the process of development.

Select two indexes, monthly average decline range and water content escalating rate to establish early warning system of blocks development effect, which has great practical application value, is sensitive to reflecting the monthly variation process of block development effect, and plays a certain guiding role in the development effect during the whole year.

## References

[1]Jun Hou,Lihai Cao,Yadong Liu,etal. Influence factors of water flooding and study of development scheme in Tai 105 area[J].Special Type Reservoir,2003,10(5):47-50.(In Chinese)

[2]Daopin Li.Decision theory of high efficiency development in low permeable sublayer oilfield [M].Beijing:Petroleum Industry Press,2003.(In Chinese)

[3]Jifeng Zhang,Xiaodong Tian,Weiqi Guo,et al. Discussion and application of the water cut increasing law of in water-flooding oilfield [J].Drill-Pluck Technology,2011,34(3):49-51.

[4] Yunfeng Zhang,Guoqiang Wang,Baoli Fu,etal. The diagenesis and the origin of abnormal high porosity zone in the deep clastic reservoir in Changling fault depression [J].Journal of Jilin University:Earth Science Edition,2011,41(2):372-376.(In Chinese)

[5] Yifa Ren,Xiaohua Zhao,Peijin Tian,Huijie Ma.The rupture structure and reservoir character in south Songliao basin in Changling Sag Yaoyingtai area [J].Natural gas geoscience,2005,16(2):206-209.(In Chinese)

*Applied Mechanics and Materials Vols. 580-583 (2014) pp 923-926*
*© (2014) Trans Tech Publications, Switzerland*
*doi:10.4028/www.scientific.net/AMM.580-583.923*

# Stability Analysis of Puzi Landslide in Chongqing

Kai He [a], Chun-li Chen [b]

Department of Geological Engineering, Chang'an University, Xi'an, 710054, China

[a]hekai2005@163.com, [b]chen_chunli@126.com

**Keywords:** geohazard, landslide, stability analysis, rainstorm condition

**Abstract.** The boot-shaped landform is steep for upper part and gentle for lower part, which is suffering from serious landslide and collapse hazards, and the Puzi landslide studied in this paper is in boot-shaped landform. Stability analysis of Puzi landslide was taken on the detailed analysis of the tectonic setting, formation lithology and the meteorological hydrological conditions. The result demonstrates that the Puzi landslide is on the critical to unstable state. And it is possible to integral slide under the influence of rainstorm or continuous rainfall and has higher risk of geohazard. It is recommended that people settled in the landslide area should be relocated and early warning monitoring should be carried out immediately. The results will offer technical support to prevent and relieve of geohazard in mountainous areas of southwest China.

## Introduction

Puzi landslide is located in Jinfo Mountains in Toudu town, Nanchuan district of Chongqing. Because of the special geological conditions in Jinfo Mountains, there is boot-shaped landform, which is steep for upper part and gentle for lower part, hardness-upward and softness-downward[1,2]. In such geological conditions, the area of gentle slope in front of the cliff is in face of serious landslide disaster besides dangerous rocks collapse from steep cliff behind. This kind of landslide is one of the typical geologic hazards all over the southwest China. Based on the Puzi landslide, the stability analysis of this kind of landslide was carried on in this paper. The results will offer technical support to prevent and relieve of geohazard in southwestern mountainous areas of China.

## Geology setting

Jinfo Mountain located in Nanchuan district of Chongqing. There is horizontal layered limestone which is easy to form cliff landform. In such special geological conditions, with precipitation, earthquake and increasing human activities, Jinfo Mountain is one of the areas with serious collapse and landslide geohazard [3-5].

**Geologic structure.** Puzi landslide is near the east wing of Jinfo syncline. The axis of Jinfo syncline is in the direction of NE~SW, the dip direction of west wing is 106～115°, the dip angle is 40~50°; while the dip direction of east wing is 290～310°, and the dip angle is 4～11°. It is typical partition wall style structure with broad and gently syncline core. As a result there are approximately horizontal stratums in study area.

**Strata and lithology.** The strata in Jinfo area from top to bottom are the Quaternary colluvium and diluvium ($Q_4^{col+dl}$), elurium and diluvium ($Q_4^{el+dl}$), made land ($Q_4^{ml}$), Changxing formation limestone of upper Permian ($P_2c$), limestone of Longtan formation ($P_2l$), Maokou formation limestone of lower Permian ($P_1m$), limestone of Qixia formation ($P_1q$), limestone of Liangshan formation ($P_1l$) and Hanjiadian formation silty shale of middle Silurian period ($S_2h$).

The main lithology is limestone, shale and clay rock (bauxite). The cliff is limestone with bauxite at the bottom. The lower slope is weak shale covered by the Quaternary colluvium and diluvium, formed the landform hardness-upward and softness-downward that easy to landslide.

**Climate and hydrology.** The landslide area has a subtropical warm and humidity climate and the vegetation is well developed. The region is blessed with plentiful rain and a mild climate, it is mostly

foggy and less sunshine. The climate possesses distinct vertical zonation that the mean annual temperature decreased with the decreasing of altitude, while the rainfall increased. According to the weather data of Nanchuan District, the mean annual temperature of this area is 14.3℃, the maximum and minimum temperature are 36℃ and -10℃. The annual frost-free period is 200 days. The annual average precipitation is 1170.2mm and the annual evaporation is 1134.9mm. The rainfall is intense and the maximum of the daily rainfall is 112.78mm. But rainfall of each season are very uneven season, May to August is the rainy season, in which period the rainfall is 80% of the whole year, and December -through-February is the dry season. Surface river is not developed, the Bozhi river flow from east to west 3km south of the Puzi landslide is the main river in this area and its river bed is the lowest datum of erosion with elevation of 720～780m. The concentrated and abundant rainfall becomes one of important factors of the landslide.

## Stability Analysis of the Landslide

**Landslide characteristic.** The toe of repture surface of the Puzi landslide is located in the the common border of the cliff and flat ground, bounded by gully and a small ridge on the two sides. The landslide is 800m long and 350m wide. The thickness of the landslide body is 10～40m. The slope angle of is 10° at the top and 20° at the lower part, and the slope aspect 120°. The landslide is large thrust load caused landslide with volume $700\times10^4 m^3$ and the damage scope $0.366km^2$(Fig.1). The elevation is 1260m at the top and 1000m at the toe, the relative difference in elevation is 260m.

The deformation characteristics are cracks 1～5cm wide appear in the rooms on the top of the slope, horizontal displacement at 0.5～10m and vertical displacement at 20～30cm. There are subsidence and deformation every year. It's very hard to preserve water for the paddy fields and there are varying degrees of collapsing on the slope. The cracks grown in width and depth recently, and the deformation of the rooms became violent. Some of the construction became dangerous substandard house.

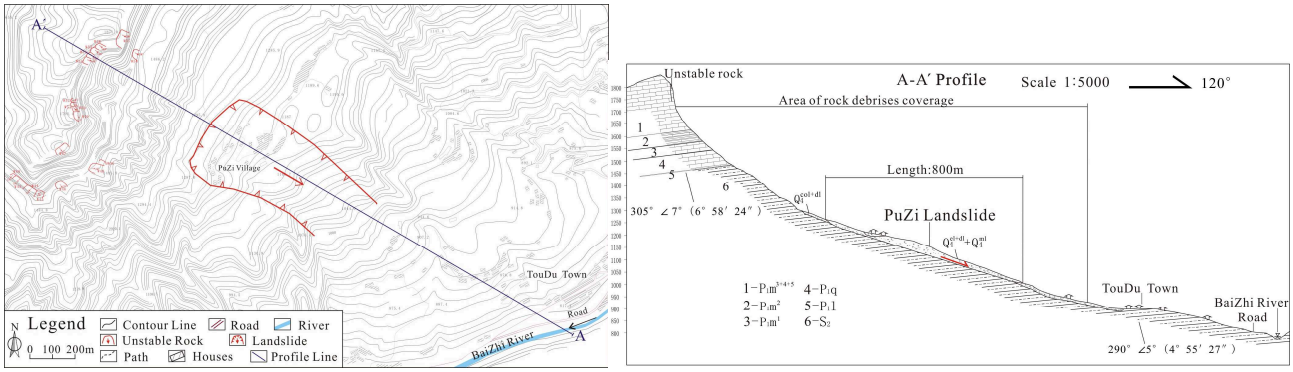


Fig.1 Plan view and A-A' profile of Puzi landslide

**Stability calculation of landslide.** The sliding surface of Puzi landslide is approximately broken-line type. According to the transfer factor method recommended by *China code for investigation of prevented and cured engineering of geological hazard* (DB50/143-2003), a stability calculation was carried out (Fig.2). Computation formulas are as follows.

$$Fs = \frac{\sum_{i=1}^{n-1}\left(R_i\prod_{j=i}^{n-1}\Psi_j\right)+R_n}{\sum_{i-1}^{n-1}\left(T_i\prod_{j=i}^{n-1}\Psi_j\right)+T_n} \quad (1)$$

$$\Psi_j=\cos(\theta_i-\theta_{i+1})-\sin(\theta_i-\theta_{i+1})\tan\varphi_{i+1}. \quad (2)$$

$$\prod_{j=i}^{n-1}\Psi_i = \Psi_i\times\Psi_{i+1}\times\Psi_{i+2}\ldots\Psi_{n-1} \quad (3)$$

$$R_i=N_i\tan\varphi_i+C_iL_i. \quad (4)$$

$$T_i=W_i\sin\theta_i+Z_i\cos\theta_i+D_i\cos(\beta_i-\theta_i). \quad (5)$$

$N_i=W_i\cos\theta_i-Z_i\sin\theta_i+D_i\sin(\beta_i-\theta_i)$. (6)

$D_i=\gamma_w h_i l_i \cos\theta_i \sin\beta_i$. (7)

$Z_i=W_i\omega$. (8)

Where,

Fs—Stability factor;

$W_i$—Gravity of block *i* (kN/m), including self-weight and additional load;

$R_i$—Force for anti-sliding of the block *i* (kN/m);

$N_i$—Normal component of force on the sliding surface for block *i* (kN/m);

$\varphi_i$—Internal friction angle for block *i* (º);

$C_i$—Cohesiveness for block *i* (kPa);

$L_i$—Length of the sliding surface for block *i* (m);

$T_i$—Sliding component of force on the sliding surface for block *i* (kN/m), $T_i$ can be negative when its direction is of opposite to sliding direction;

$\Psi_j$—Transfer factor of surplus sliding force transfers from block *i* to block *i+ 1*(j=i);

$Z_i$—Seismic force of block *i* (kN/m);

$D_i$—Hydrodynamic pressure of block *i* (kN/m);

$\beta_i$—Hydraulic gradient of block *i* (º);

ω—Seismic factor, the factor value is 0.05;

$h_i$—Height between underground water level to the sliding surface for block *i* (m).

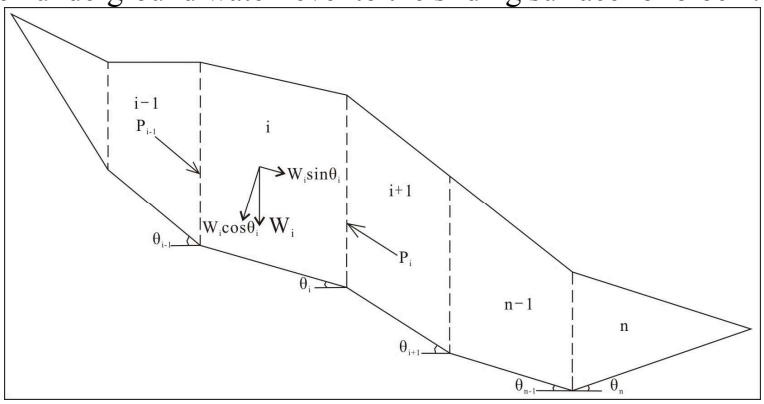


Fig.2 Schematic of landslide stability analysis.

All parameters in Fig.2 have the same meanings as Eq.1~Eq.8

The value of C and φ for potential sliding surface are hard to determined, so the regional empirical value was referred to. The unit weight of sliding mass is 21kN/m$^3$ for natural condition and 21.50kN/m$^3$ for saturated condition. C and φ of sliding zone is 19.1kPa and 17.23° respectively for natural condition, 18.00kPa and 16.90° respectively for saturated condition.

This calculation aimed to provide basis for landslide stability evaluation. Calculation load was composed of self-weight, the building load, hydrodynamic pressure and seismic force.

(1) Load.

Self-weight: The weight of the slide mass. Under the nature condition, The part above the underground water level use natural unit weight, while under the underground water level use buoyant unit weight.

The building load: There were little construction in this calculation section, so ignore the building load in calculation.

Hydrodynamic pressure: $D_i=\gamma_w h_i l_i \cos\theta_i \sin\beta_i$, Its direction is the same with the hydraulic gradient, calculate with different underground water level in each conditions.

(2) Calculation condition

According to the loading combination, landslide stability calculation could be divided into two working condition:

Condition No.1: Natural condition, self-weight + groundwater load in current situation.

Condition No.2: Rainstorm condition, self-weight + groundwater load in rainstorm situation.

Based on the project above-mentioned, Puzi landslide stability evaluation was carried out as requested by the *China code for investigation of prevented and cured engineering of geological hazard*. According to the computed results, stability factor for Puzi landslide is 1.019 under natural condition (condition No.1), while the Landslide stability factor is 0.963 under rainstorm condition (condition No.2). Contrasted the $F_s$ with table 1, it is shown that Puzi landslide is on the critical to unstable state in current situation, and instability in rainstorm situation.

Table 1 Partition of Landslide stability state

| Landslide stability factor $F_s$ | $F_s \geqslant F_{st}$ | $F_{st} > F_s \geqslant 1.05$ | $1.05 > F_s \geqslant 1.0$ | $F_s < 1.0$ |
|---|---|---|---|---|
| Landslide stability state | Stable | Metastable | Understable | Unstable |

Note: $F_{st}$ is landslide stability safety factors. The value for Puzi landslide is 1.15.

Because of the loose structure of sliding mass and poor strength, the stagnant water zone would be formed on the surface between bed rock and soil after rainwater infiltrated by rainstorm or continuous rainfall [6]. Silty shale prone to soften by groundwater soaked, as a result, strength of sliding zone reduction steeply, promoting the slope sliding. Puzi landslide could threaten 17 families (more than 90 people) which settled in the influence area of this landslide. It is advised that people settled in the landslide area should be relocated and early warning monitoring should be carried out immediately.

## Conclusions

Based on the research result, the following understanding and conclusions have been got.

(1) The China southwest mountainous area with boot-shaped landform steep for upper part and gentle for lower part is vulnerable to collapse and landslide hazards.

(2) As known from calculation, the stability factor of Puzi landslide is 1.019 and the landslide on the critical to unstable state under natural condition; the stability factor of Puzi landslide is 0.963 and the landslide is unstable under rainstorm condition. It is possible to slide under the influence of continuous rainfall or rainstorm, and there are high disaster risk.

(3) Considering the twofold impact of collapse and landslide, it is recommended that people lived in Puzi landslide area should be relocated and disaster monitoring and warming should be made as soon as possible.

## References

[1] RQ HUANG: Advance in Earth Sciences, in Chinese. Vol. 3 (2005), p. 292

[2] L.K.A. DORREN: Progress in Physical Geography, Vol.27 (1), 2003, p. 69

[3] Rainer POISEL. Martin BEDNARIK, Rudolf HOLZER, et al: Journal of Mountain Science, Vol. 3 (2005), p.211

[4] HT HU: Journal of Railway Engineering Society, in Chinese. Vol. 0 (2005), p.387

[5] L.K. A. Dorren: Progress in Physical Geography, Vol.27 (1), 2003, p. 69

[6] Huo-zhen WU, Mei-guo FENG, Yu-yong JIAO, et al.: Rock and Soil Mechanics, in Chinese. Vol.31 (Supp.1), 2010, p.324

*Applied Mechanics and Materials Vols. 580-583 (2014) pp 927-934*
*© (2014) Trans Tech Publications, Switzerland*
*doi:10.4028/www.scientific.net/AMM.580-583.927*

# The landslides developed with the evolution of the river terraces in the loess plateau, China

Xianli Xing[1, a *], Xiaokun Hou[2,b], Tonglu Li[3,c] and Ping Li[4,d]

[1]Department of Geological Engineering, Chang'an University, Xi'an, Shaanxi, 710054, China

[a]xianli626@126.com, [b]865694962@qq.com, [c]dcdgx08@chd.edu.cn, [d]dcdgx07@chd.edu.cn

**Keywords:** Tectonic movement, river terrace, loess plateau, loess landslide, landslide cycle.

**Abstract.** Landslide investigation in the center part of loess plateau reflects that most of large-scale old and ancient landslides lie on river terraces at different heights, but the small ones usually occur along the sides of V-shaped loess valleys, which implies that there is an inherent connection between the landslides and the erosion action. Since river terraces were formed by intermittent uplift of the crust, which controls the features of river erosion and the thickness of loess on the terraces. The analysis of typical loess landslides in this region shows that during relative static period, lateral erosion was dominated, so river valley was widened, which induced some large-scale landslides because the toe of slope was strongly eroded. While during the uplift period, vertical erosion was dominated, and the loess began to deposit on the terraces above water level, with the downcutting of the river, a narrow V-shaped valley formed, and then small loess landsides occurred on both sides of the rivers. Therefore, intermittent crustal uplifts not only led to the formation of multi-degree of terraces, but also induce alternative occurrence of large-scale and small loess landslides.

## Introduction

The northern Shaanxi is located in the center part of the Loess Plateau, with the total area of 92,521 $km^2$. The rivers here are the tributaries of the Yellow River as shown in Fig.1, which formed a river network cutting the Loess Plateau into the landform of ridges and domes penetrating with wide valleys and narrow gullies [1]. With the evolution of the landform, loess landslides become a serious geological hazard frequently occurring in this region, which not only caused huge losses of lives and property to local residents, but also restricted the sustainable development of local economy. In recent years, we carried out systematic investigations on landslides in northern Shaanxi, and the analysis for the geomorphic features of landslides shows that there is internal relation between the formation of landslides and the evolution of river terraces and gully. For example, there are about 30 ancient landslides distributing on the third terrace along the sides of Dazhuanghe River, Ganquan County. Landslides mainly occurred on the second terrace, on the south side of the Koujiahe River in Huangling County. On the south side of Jinghe River, landslides mainly developed on the first terrace. And a great many of new landslides and collapses occur on both sides of deep ditches on the edge of Luochuan loess platform. Based on the observations above, the paper intends to discuss the correlation among landslides, river terraces, and tectonic movement so as to reveal the temporal-spatial law of the formation of loess landslides in this region.

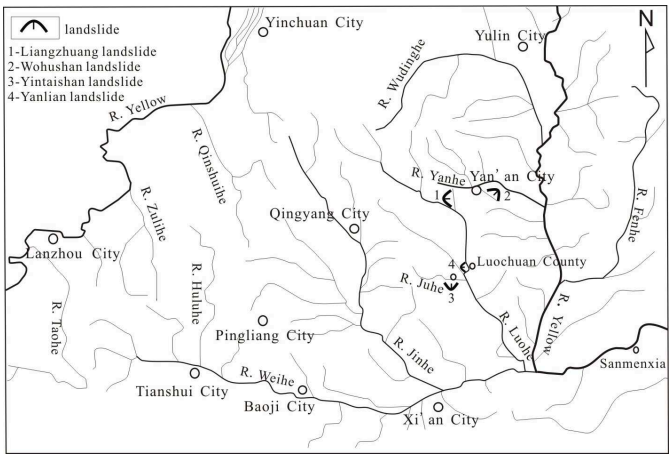


Fig.1 River system on the Loess Plateau (Accorrding to Lei X.Y, 2006)

**The stratum structure of the loess and the evolution of river terraces in loess plateau**

Loess is a kind of wind blown sediment, which only deposits on the stratum above the underground water level. The northern Shaanxi is located in the center of the Ordos basin in the Mesozoic era, where deposited a set of thick clastic material of river-lake facies. During the early Tertiary, crustal uplift led to the close of the lake-basin sediment. In the early to middle Pliocene ($N_2$), subsidence of the basin created a favorable condition for the deposit of the huge thickness of red mudstone and sandstone formation. At the end of Pliocene, the uplift of the loess plateau, including the northern Shaanxi, ended the lake-basin environment. Because of unequal uplift within the basin, secondary basins were created and the modern pattern of the Yellow River system formed. The original basins have being received a relative broad and thick loess deposit, where were manifested as the modern loess platforms (high lands with flat top). Luochuan loess platform is the largest one in northern Shaanxi, of which has a successive loess sediment of Quaternary. A loess profile in Potou village, Luochuan County, locating at the west side of Heimugou gully, has been accepted as the Luochuan standard loess section, on which the Quaternary paleoclimate and stratigraphic studies have been carried out in detail. In the early of the last century, according to the field characters, Liu D.S. (1984) divided the loess strata into three lithostratigraphic units. Those are Malan loess, Lishi loess, and Wucheng loess from upper to lower, traditionally known as $Q_3$, $Q_2$ and $Q_1$ respectively[2]. Beside the three typical units, A thin layer of 1-2m thick Holocene deposit($Q_4$) coves on the top, which consists of a layer of dark brown bed down and a brown-yellow bed up, of which, the former is called loam($S_0$) and the later is called Holocene loess($L_0$).

Because of frequent changes of climate in the Quaternary, the sediment are not uniform in composition and structure in the whole, but occurs as that the brown-yellow loess bed and the brown-red paleosol bed interbeded, reflecting the interchange of the climate. Loess represents the product of dry-cold climate, while paleosol, as well as the loam, represents that of warm-wet climate. Loess strata on Potou profile is made up of more than thirty loess-paleosol sequences reflecting that there had been more than thirty climatic fluctuations in Quaternary. Malan loess is the first layer of typical loess on the top, which is a set of uniform loose material, light in color, corresponding to last glaciations. Lishi loess includes the the first paleosol to the fifteenth loess sequences. Of the above loess, the ninth ($L_9$) and fifteenth ($L_{15}$) loess layer having a relative higher thickness and coarse particles represent the deposition under abominable climatic conditions, and the fifth paleosol ($S_5$) is a quite thick layer consisting of three sub-paleosols with two thin loess beds among them. So $L_9$, $L_{15}$ and $S_5$ are considered as the marked beds for identification of the loess stratigraphy in the field. Wuchen loess is consisted of frequently interbeded paleosol and loess beds with high content of calcium and stiff of properties, so it is called as lithoid loess. Below the Wuchen loess underlies the Neocene red clay.

Since 1980s，by radio active $C_{14}$ measurement, paleo-magnetism age and correlation of the isotope curves among the oceanic core holes and the loess sections, a detail dating has been made for the loess strata. According to result, the loess in Quaternary is divided into Holocene ($Q_4$), upper Pleistocene ($Q_3$), middle Pleistocene ($Q_2$) and lower Pleistocene ($Q_1$) Series. The boundary of Holocene and upper Pleistocene is located at the bottom of the black loam, aged at about 11 thousand years. That of upper and middle Pleistocene is located at the bottom of the first paleosol ($S_1$) aged at 128 thousand years. And that of middle and lower Pleistocene is located in the eighth loess ($L_8$) aged at 730 thousand years corresponding to B/M boundary of paleomagnetism. The boundary of lower Pleistocene and upper Pliocene is located on the top of red clay or bottom of the loess, a little higher than the B/M boundary of paleomagnetism. The age of M/G boundary is 2.47 million years, so the boundary of the Quaternary and Tertiary is considered as 2.50 million years or so. It ca be seen that the early lithologic units and the present chrono-stratigraphic units do not agree with completely. A composite stratigraphy of the Luochuan standard loess section is shown in Table 1.

The loess deposit is continuous on the loess platforms while that on river terraces depends on their uplift age. The older and higher the terrace is, the thicker and more loess beds the terrace undertaken.

In the Quaternary, the Loess Plateau uplift intermittently and the multi-level terraces developed. The evolution process of a terrace generally consists of two phases: lateral erosion phase and down cut phase[3]. During the static tectonic period, a river has lateral erosion and the riverbed is widened, while during the uplift period, it cut down vertically to form a new narrow riverbed and the original riverbed and floodplains become a terrace. The new riverbed would be the next terrace in the forth coming static-uplift cycle. In northern Shaanxi, the intermittent uplift of tectonic movement leads to the development of terraces distributing along the riversides. The surfaces of the terraces have been entirely covered by loess. Yue L.P, Lei X.Y, et. al (1997), who have studied the Luohe River terraces in northern Shaanxi, suggested that generally there are terraces ranging from first to fifth in this region with sandstone in Triassic Period as the bases[4]. Among the terraces, the base of the fifth terrace ($T_5$) is 55m above the riverbed, on which lies the loess-paleosol sequences from $L_0$ to $S_{11}$ with the total thickness of 78m. The base of the fourth terrace ($T_4$) is 20m above the riverbed, on which lies the loess-paleosol sequences from $L_0$ to $S_9$ with the total thickness of 60m. The base of the third terrace ($T_3$) is 10m above the riverbed, on which lies the loess-paleosol sequences from $L_0$ to $S_7$ with the total thickness of 45m. The base of the second terrace ($T_2$) is 5m above the riverbed, on which lies the loess-paleosol sequences from L0 to S2 with the total thickness of 10m. The base of the first terrace ($T_1$) is a layer of cultivated soil with the thickness about 1m and the underlying is the black loam, as figure 2 shows[5].

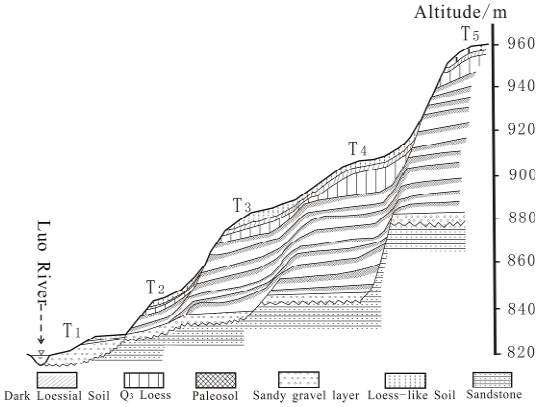


Fig.2 Loess section of the terraces of the Luohe River(According to Lei X.Y, 2001)

Correlating the loess or paleosol on the terraces in Fig.2 and their ages in table 1, the uplift time of the each terrace corresponding to the crustal uplift and static time has been determined as shown in table 2. It can be seen that the northern Shaanxi experienced seven times of the crustal uplift during the quaternary corresponding to seven times of erosion. The first uplift built up the outline of the loess plateau. With the rivers flew out the area, modern pattern of the river system formed. The second to

sixth uplift correspond to the formation of the first to fifth terraces while the seventh uplift corresponds to the rise of the high floodplain and the formation of modern river bed.

Table2. Correlation between crustal movement and the stratum structure of loess on the river terraces in Loess Plateau

| Absolute Age/10000a | Crust Movement | Formation | Erosion Period |
|---|---|---|---|
| 0-0.4 | River bed | MS | 7 |
| 0.4-1.0 | High flood plain | | |
| 1.0-2.3 | $T_1$ uplift | $L_0$ | 6 |
| 2.3-12.0 | $T_1$ widen | $S_0$ | |
| 12.0-17.0 | $T_2$ uplift | $L_1$ | 5 |
| 17.0-62.0 | $T_2$ widen | $S_1$-$S_2$ | |
| 62.0-66.0 | $T_3$ uplift | $L_2$ | 4 |
| 66.0-82.0 | $T_3$ widen | $S_3$-$S_6$ | |
| 82.0-85.0 | $T_4$ uplift | $L_7$ | 3 |
| 85.0-123.0 | $T_4$ widen | $S_8$-$S_9$ | |
| 123.0-127.0 | $T_5$ uplift | $L_{10}$ | 2 |
| 127.0-170.0 | $T_5$ widen | $S_{10}$-$S_{11}$ | |
| 170.0-178.0 | River formation | $Q_1$ | 1 |
| 178.0-250.0 | Loess deposit | $Q_1$ | |
| 250.0 | Overflowing of the paleo- lake | | Plantation surface |

**Correlation between landslides and the river terraces**

Landslides mostly occurred on the sides of the rivers. Investigation in the northern Shaanxi shows that most of old and ancient landslides shear out on different stages of the terraces, commonly on the first to third terraces, while the small loess landslides and collapses occur on the sides of V-shaped loess gullies [6,7].

The ancient landslides on the third terrace formed in 170-620 thousand years ago, which are generally large in size, clear in boundary, round and steep in back scarp with a armchair form. At present, this type of landslide is in an extra-stable state, the main reason is that after a long time of erosion, the residual sliding deposits have left a little, even the most sliding bed are outcropped, therefore, there are no material for revival. In addition, high position of the landslides keeps them from the extensive action by rivers or human engineering activities. Therefore, they have no threat to the life and activities of the people.

The Liangzhuang landslide is illustrated as the typical example mentioned above. The landslide is located on the right bank of the Dazhuanghe River in Liangzhuang Village, Shimen Town, Ganquan County (Fig.1). The boundary of landslide is obvious, and the sliding bed is almost bare (Fig.3). There is three terraces (T1-T3) on the river side here, where the first is about 2m above the riverbed to the top; the second is about 5m from above the riverbed to the base; the third terrace is about 12m above the riverbed to the base on which the landslide lies (Fig.4).

Fig.3 Overview of Liangzhuang landslide

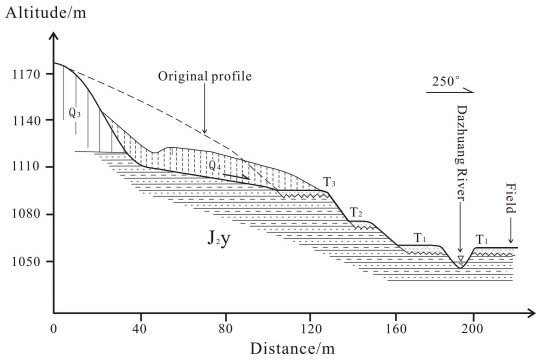


Fig.4 Main section of Liangzhuang landslide

The landslide occurred after the third terrace had been formed. During this period, the tectonic movement tended to be stable, so the riversides were eroded while the space of the second terrace was widening, as a result, the loess deposited on the third terrace slipped along the bedrock of the terrace base.

The landslides lying on the second terrace formed during 23-120 thousand years before present. They are usually large in scale and have multiple scarps. Most of the landslide deposits are remained on which gullies, sinkholes and cracks developed by long term erosion, so they allow amount of surface water seepage in. In addition, the toes of the landslides are usually cut for housing and road construction, so the landslides often revive.

The Wohushan landslide, located on the east side of the Wohushan Mountain, is a typical case for this type of landslide. left bank of the Nanchuan river, about 2 kilometers to the south of Yan'an railway station (Fig.1), with a dust-pan shape in plane view and about 280m in length, 260m in width, $105\times10^4 m^3$ in volume, multiple back scarps(Fig.5). The landslide had at least twice down sliding (Li T.L, 2006). There are three terraces ($T_1$-$T_3$) developed on the left bank of Nancuan River. The first terrace is flat and broad, and the widest part is about 200m. The second and the third are covered by loess deposit, which were revealed by the boreholes on the landslide (Fig.6). The bed rock base of the second terrace is 10-13m above the riverbed on which the landslide sheared out. The third terrace is buried deep in the slope.

Fig.5 Overview of Wohushan landslide

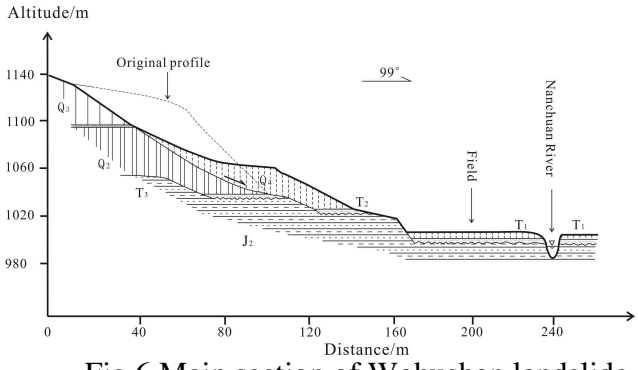


Fig.6 Main section of Wohushan landslide

The old landslides locating on the first terrace occurred during 4-10 thousand years before the present time. They are large in scale, clear in boundary and complete in form. Many villages distributed on the landslides since the terrain gets to be flatter after sliding, as a result, a great deal of domestic or irrigation water penetrates in or along fractures on the deposits, which causes the landslide being easily revival.

Yintaishan landslide is a typical example of such one, which is located at west side of the Yintai Mountain, and the left bank of the Juhe River, in Yintai Village, Qiaoshan Town, Huangling County (Fig.1). It is an old landslide of Early Holocene, with a length of 150m, a width of 300m, and a thickness of 10-12m in the toe and 25-30m in middle. Surprisingly, the whole Yintai Village is located on the landslide, which lies on the first terrace of the left Juhe river bank(Fig.7). The

interbedded sandstone and mudstone under the terrace deposit exposes at the both sides of the river (Fig.8).

Fig.7 Overview of Yintaishan landslide

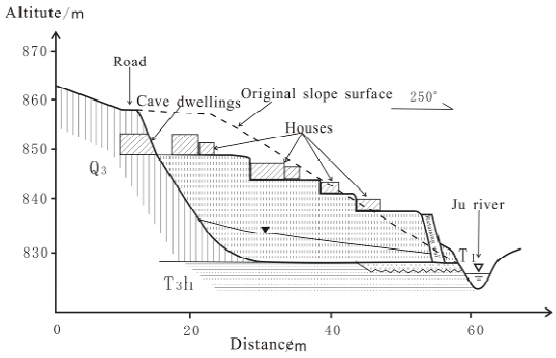


Fig.8 Main section of Yintaishan landslide

Small-size landslides are usually developed on both sides of the V-shaped deep gully with clear boundaries and steep back scarps. The landslides make the margin of the loess platform move backward and threaten the nearby residents and infrastructures. Meanwhile, the gullies are easy to be dammed by the landslide deposits. Take the landslide in Luochuan Oil Station as an example. It is located in the former Luochuan Oil Station (Fig.1), which lies on the top of a V-shaped valley side. The valley is 50m in depth and 100m in width (Fig.9 and Fig.10). In January 2009, when the landslide occurred, the main facilities of the oil stations slipped into the gully, resulting in 1.5 million yuan RMB of direct economic losses. The landslide has a steep back scarp and a height of 8m, a width of 65m, and thickness of 15m.

Fig.9 Overview of Old gas station landslide

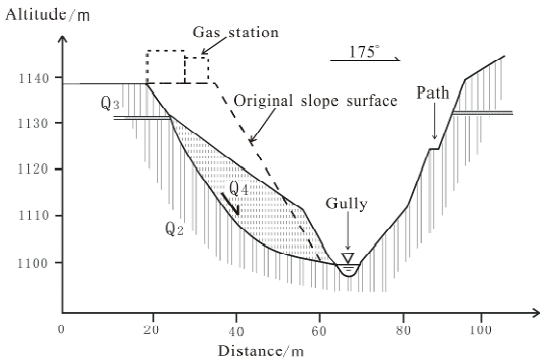


Fig.10 Main section of Old gas station landslide

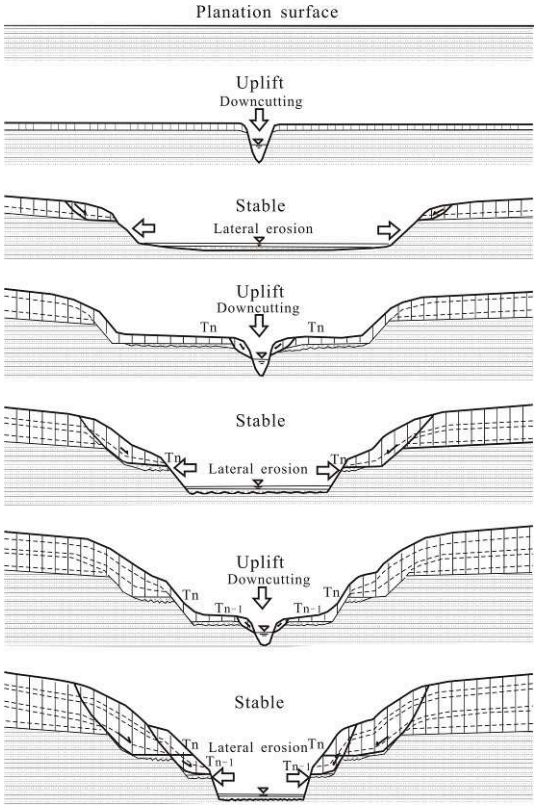


Fig.11 The relationship between the periodicity of landslide and terraces

The typical cases of landslides on different terraces in northern Shaanxi described above, under the control of tectonic movement, show that there is inherent connection between river terraces and landslides. In the first period of tectonic uplift, gullies and rivers emerged with the down cutting and the loess deposited on the plantation surface. Then after, with coming of the relative stable period, lateral erosion broadened the space of riverbed; meanwhile, as the result of the washout or pullout to the front of the bank slope by running water, the small landslides of the early loess on the plantation came into being. With the next cycle of tectonic uplift, the rivers cut down again to form a new narrow riverbed within the primary one, and then the highest terraces were formed and received the loess deposit. With continuous down cutting, the bank walls became higher and steeper, where V-shaped deep gully appeared and small landslides or collapses of the loess on the top of the terrace occurred. As tectonic movement tends to be stable, the lateral erosion worked again, and then the highest terrace retrogressed backward by the erosion, at the same time, large-scale landslides turned out on the top of the terrace. With multi-level terraces emerging by intermittent uplift, the centralized occurrences of large-scale and small-scale landslides turned out periodically. The whole cycle processes was shown in Fig.11.

## Conclusion

Landslides, in loess plateau, mainly occurred on the terraces along the erosion sides of the rivers and their tributaries. There are significant relations among the tectonic movements, the river terraces, and the landslides. During stable tectonic period, the rivers took the lateral erosion mainly and the river channels were widened, large-scale landslides on the terraces occurred. During the period of tectonic uplift, rivers eroded vertically, terraces of the next level began to come into being, small loess landsides and collapse occurred dominantly. Therefore, the landslides in loess region occurred periodically controlled by the tectonic movement.

**Acknowledgements**

This work was financially supported by the Natural Science Foundation of China (No. NSFC-41372329) and National "973" Project (2014CB744701). The supports of these agencies are gratefully acknowledged.

**References**

[1] Xiangyi Lei. Models of loess stratigraphical structure on the terraces in the Loess Plateau of China. Marine geology & quaternary geology, 2006, 26(2), 113-122. [In Chinese]

[2] Dongsheng Liu, Mengin Ding. A tentative chronological correlation of early human fossil horizons in China with the loess-deep sea records. Acta anthropologica, 1984, 3(2), 93-101. [In Chinese]

[3] Quanwei Wei, Lihua Tan, Suiji Wang. Formation and evolution of river terrace and environment responses. Progress in geography, 2006, 25(3), 55-61. [In Chinese]

[4] Leping Yue, Xiangyi Lei, Hongjun Qu. The age of terrace development in the middle reaches of the Yellow river. Geological review, 1997, 43(2), 186-192. [In Chinese]

[5] Xiangyi Lei. Geological hazards and human activity on the Loess Plateau, Geological Press, Beijing, 2001.[In Chinese]

[6] Tonglu Li, Jianhui Long, Xinsheng Li. Types of loess landslides and methods for their movement forecast. Journal of engineering geology. 2007,15(4),500-505. [In Chinese]

[7] Changliang Zhang, Adan Wang, Xianli Xing, Changye Wang, Tonglu Li, Ping Li. Research on mechanism of loess landslides caused by erosion. Rock and Soil Mechanics. 2012, 33(5), 1585-1592.[In Chinese]

*Applied Mechanics and Materials Vols. 580-583 (2014) pp 935-939*
*© (2014) Trans Tech Publications, Switzerland*
*doi:10.4028/www.scientific.net/AMM.580-583.935*

# Application of self-drilling anchor on coal gangue slope treatment

CHEN Tailin[1,a], ZHOU Jin[2,b], WANG Anming[2,c], LI Huan[2,d]

[1]Henan Vocational College of Water Conservancy and Environment, Zhengzhou 450011, China

[2]North China University of Water Conservancy and Electric Power, Zhengzhou 450045,China

[a]talent29@163.com, [b]zhoujin@ncwu.edu.cn, [c]463077840@qq.com,[d]349812919@qq.com

**Key words:** Coal gangue hill；High fill slope；Self-drilling type hollow bolt；Construction；Safety factor

**Abstract.** In the reinforcement of coal gangue slope treatment, it is difficult for hole and construction with traditional method, self-drilling anchor method was adopted, Slope stability safety factor was calculated with slope stability analysis software under coal gangue slope and self drilled anchor reinforcement coal gangue slope, and finally the anchor pipe processing technology, construction methods and the production of grouting process and framework were introduced, which provided the practice for similar engineering.

## Intorduction

As a new construction technology, self-drilling hollow anchor bar has been gradually promoted and applied in the slope reinforcement engineering in recent years. Integrating drilling, grouting and anchoring, it is an advanced anchoring system and overcomes easy-to-hole collapse and hard-to-pore-forming problems in the anchor bar construction in extremely loose and broken soil-rock mass. Combined with successful comprehensive application of network-attached grouting, drain hole and various support measures, the grouting effects under complicated geological conditions can be guaranteed. On the basis of engineering practice, this paper carried out the calculation and analysis on the self-drilling hollow anchor bar-reinforced coal gangue slope and then gave specific construction technology, providing reference for similar engineering.

## Engineering background

The proposed field is one western modern artificially accumulated slag platform and its terrain is smooth, with small ground elevation difference. It is a new factory district of coal gasification and supporting project of one Coal Industry Group. After site formation, 2 platforms are formed and the elevation difference between two platforms is about 20 meters, belonging to soil slope. Due to the changes of terrain, one fill embankment slope and one site slope of excavation are formed. Because the up and down devices of the slope are far from the side slope, the normal production activities in the factory district can be free from the destroy of the side slope. Considering the elevation of soil slope, its security level is defined as the second level. It needs reinforcement and protection processing to guarantee security. The project work life of the side slope is 50 years.

## Geological conditions

According to the analysis results of drilling, in-situ test and consolidation test, in the field 46.5m exploration depth range, the stratum is divided into 8 engineering geology unit layers according to genetic type, lithological characters and engineering geologic characters. Details are described as follows. ① layer (Q4ml): strong-weathered sandstone and coal gangue. In the drilling process, hole collapse and leakage are common. Its mean layer thickness is 7.2m. ② layer (Q4ml): strong-weathered sandstone and coal gangue, with mean layer thickness of 8.03m. ③ layer (Q2dl):

silty clay, with mean layer thickness of 4.92m. ④ layer (Q2d1): silty clay, with mean layer thickness of 5.17m. ⑤ layer (Q2d1): silty clay, with mean layer thickness of 5.73m. ⑥layer (Q2d1): pebble, with mean layer thickness of 1.89m. ⑦ layer (T): mudstone, with mean layer thickness of 5.86m. ⑧layer (T) with mean layer thickness of 2.18m. ⑨ layer (T): soft rock, with mean layer thickness of 3.50m.

**Coal gangue slope reinforcement stability calculation of self-drilling hollow anchor**

Known from the results of scene geological exploration and exploration report, this slope belongs to high slope, with about 75°slope angle. It is possible for landslide. Bishop Simplified and Janbu Simplified in slide software are used for stability calculation.

Before the slope reinforcement, stability coefficient calculated by Bishop Simplified is 0.491, shown as Figure 1 and that by Janbu Simplified is 0.459, shown as Figure 2. Through calculation, it is obvious to see this slope is unstable and its stability coefficient is less than 1. Thus, it needs reinforcement processing.

Through analysis, the anchor bar is adopted for reinforcement processing plan of the slope. The hollow anchor bar is selected and its extreme tension bearing capacity is no less than 220kN/ piece. The included angle between it and horizontal direction is 20°, shown as Figure 3. After the calculation, it is known that this slope is stable, with stability coefficient calculated by Bishop Simplified of 1.261 (Figure 4) and stability coefficient calculated by Janbu Simplified of 1.062 (Figure5). The calculation results show it is safe.

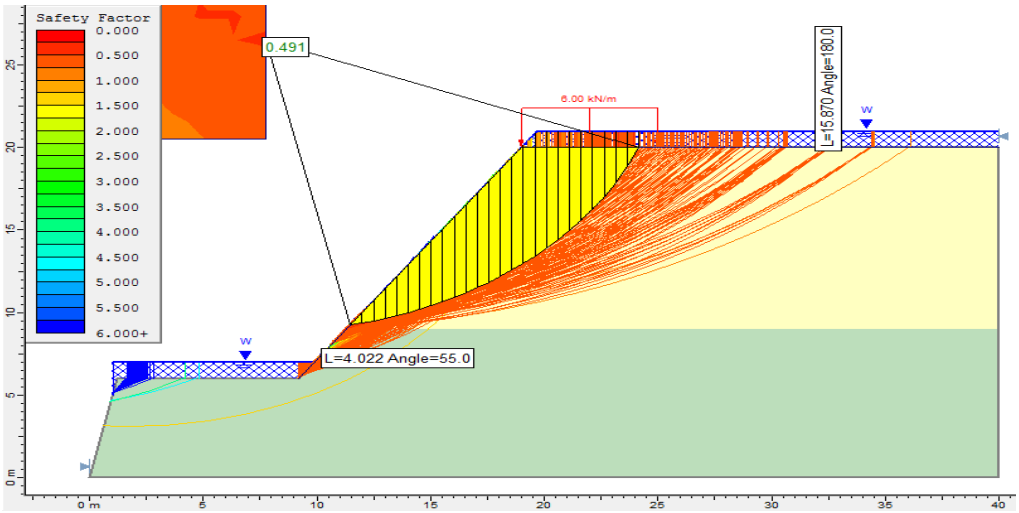


Fig.1 Calculating results of Bishop method

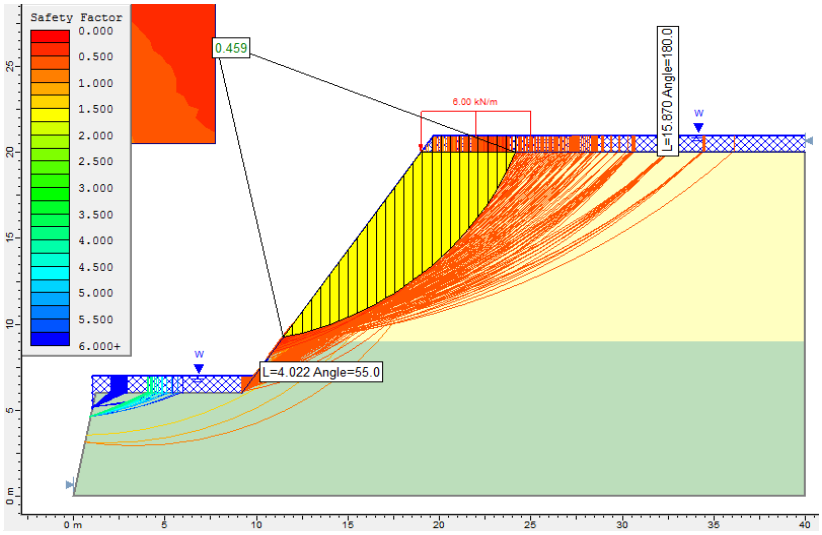


Fig.2 Calculating results of Janbu method

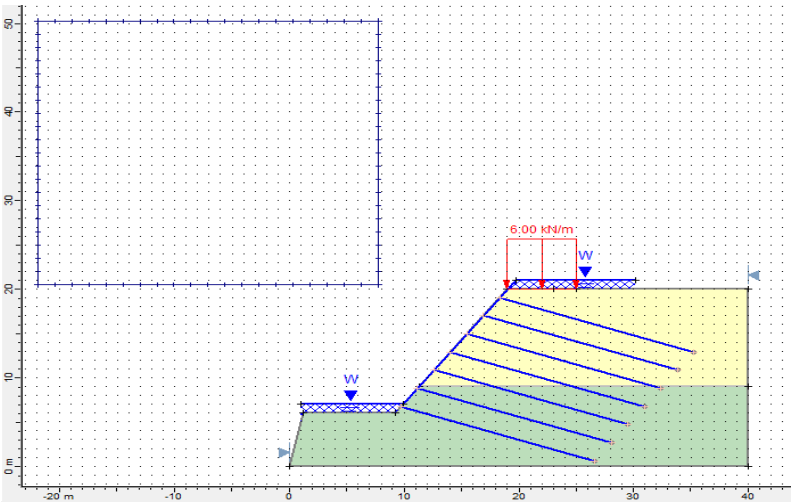


Fig.3 Reinforced slope analysis model

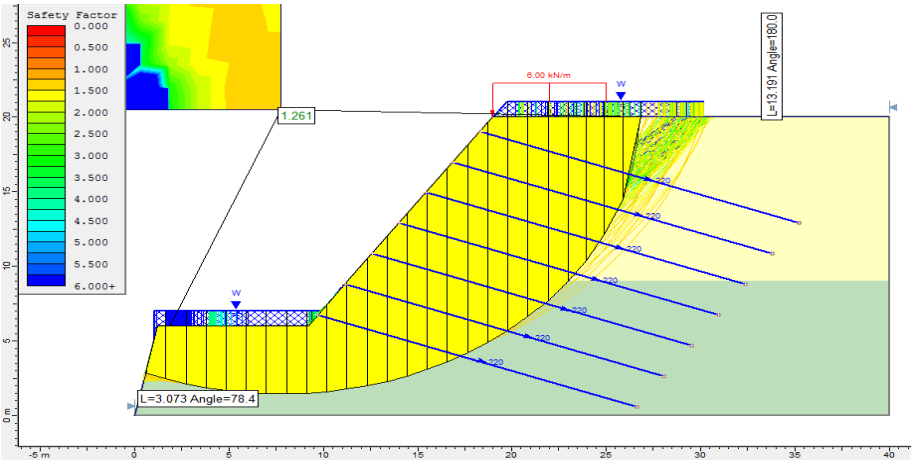


Fig.4 Calculating results of Bishop method with self-drilling hollow anchor

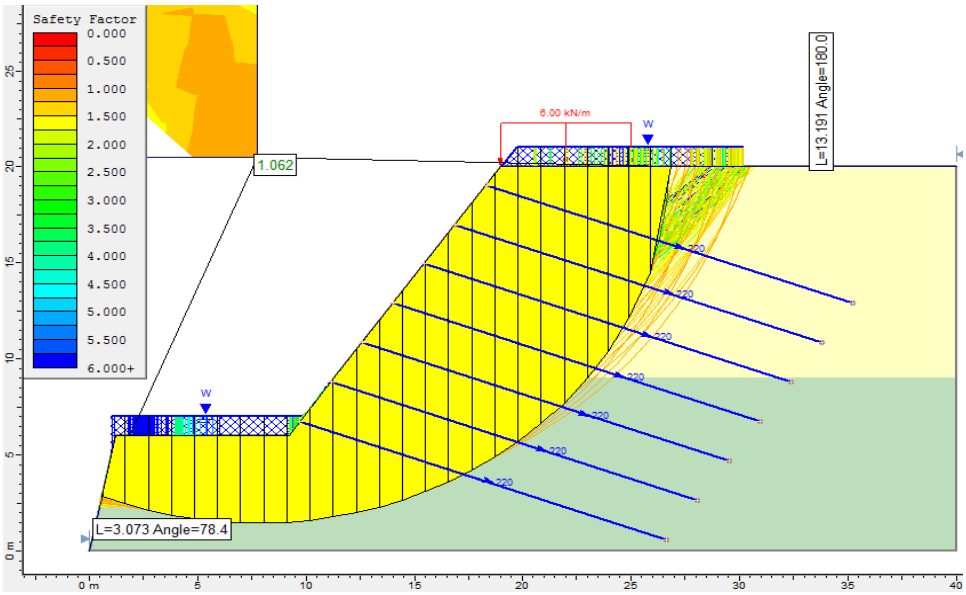


Fig.5 Calculating results of Janbu method with self-drilling hollow anchor

**Major construction technology**

### 5.1 Installation of self-drilling hollow anchor

(1) Excavate the contour line along arch and mark the position of anchor bar according to toroidal spacing. (2) Check anchor bar and whether foreign matter blocks the water pore of the drill and clean it. Connect the drill with anchor bar and anchor bar with drill pipe connection set. (3) Aim anchor bar at the anchor eye and wind or water shall be firstly provided by the hammerdrill. Then drill. (4) After the designed depth is reached, water or high-pressure blast washes the holes to check whether the hole is unblocked. Then discharge the drill pipe connection set. The exposed porthole of anchor bar is 10cm~15cm long. (5) Press the stop-grouting plug from the exposed end of anchor bar into the porthole about 30cm. If the anchor bar needs lengthening, connect the anchor bar in the connecting hole of anchor bar connection set with another anchor bar. Then keep drilling until it reaches the designed depth.

### 5.2 Grouting of self-drilling hollow anchor

(1) Make preparations and check whether the equipment is ready and the materials meet the requirements. Quickly connect the anchor, grout line and pump with quick coupling. (2) Open the pump and grout. The whole process shall be continuous and non-stop and complete at one single time. Stop pumping until the grout flows out from the edge of porthole cap or the pressure meter reaches the design value. (3) After completing the grouting of one piece of anchor bar, the coupling between the grouting flexible pipe and anchor bar. Clean and install another anchor bar and then grout. (4) In the grouting process, quick coupling shall be timely cleaned and the continuity of the grouting process shall be guaranteed. After completing the whole grouting process, timely clean and maintain the pump.

### 5.3 Treatment measures of coal gangue slope

#### 5.3.1 Drainage design

On the basis of the overall plan of landslide preventive treatment, drainage engineering design adopts the plan in consideration of the surface drainage, subsurface drainage or both. Drainage ditch and intercepting drain are set around and drainage system is set on the slope body, forming spatial three-dimensional drainage system.

### 5.3.2 Ecological restoration engineering

Coal gangue slope engineering has serious influences on the environment. Thus, ecological restoration shall be carried out. At present, the most commonly-used method is slope vegetation protection technology. The water-retaining property of coal gangue slope is poor and lacks nutrition, which is not beneficial to the vegetation growth. Thus, the layered compacted coal gangue slope is designed to be covered with mellow soil of 800mm. Shrubbery and grasses with dry resistance, developed root system and strong growth ability are planted. The planting season is spring.

## Conclusion

Self-drilling hollow anchor bar adopts thick-walled seamless steel pipe, surface thread forming process and complicated and refined parts to realize the integration of drilling, grouting and anchoring. By no aid of casing pipe wall protection and pre-grouting mortar and other special means, anchor eye can be formed quickly and the hollow rod grouting is used to guarantee the anchoring effect. In the coal gangue high fill slope treatment, self-drilling hollow anchor bar construction technology is adopts, which not only overcomes easy-to-hole collapse and hard-to-pore-forming problems in the anchor bar construction in extremely loose and broken soil-rock mass, but also achieves sound engineering benefit.

## Acknowledgments

This research had been financed by National Natural Science Foundation of China(51004049,41202246); Foundation for University Key Teacher of Henan province(2010GGJS-129); 2010 Natural Science Research Program of Henan Province Department of Education (2010a480002); the sincere gratitude were given to them!

## References

[1] Zhu Ruichen, Huang Yihui. Application of self-drilling anchor on the support of Los hydropower station collapse slope[J]. Zhejiang water conservancy science and technology, 2009, (6): 20-21

[2] Liang JiongJun. Anchoring and Grouting technology for Manual [M]. Beijing: China electric power press, 1999.

[3] Cheng Liangkui, Fan Jinglun. Geotechnical anchorage[M]. Beijing: China architecture and building press, 2003.

[4] Su Shaohua, Hu Haijun. Application of self-drilling anchor on the support of loose talus slope[J]. Western exploration, 2009, (3): 40-41

[5] Shi Guihe. Application of self-drilling anchor on Gao Mozan dam rock support loose talus slope[J]. northeast of water conservancy and hydropower, 2011 (6): 14-16

*Applied Mechanics and Materials Vols. 580-583 (2014) pp 940-946*
*© (2014) Trans Tech Publications, Switzerland*
*doi:10.4028/www.scientific.net/AMM.580-583.940*

# Researches on Slope Treatment Technologies under Complicated Geological Conditions in High Temperature and Rainy Regions

Rongxiang Shan[1,2,a] Haiping Li[1,2,b]

[1]China Merchants Chongqing Communications Research & Design Institute Co., Ltd. Chongqing, China;

[2]Chongqing Laboratory for Mountain Road Engineering and Disaster Prevention and Mitigation Engineering, Chongqing, China;

[a]email:shanrongxiang@cmhk.com, [b]email:lihaiping@cmhk.com

**Keywords:** Slope, Hot and Rainy, Phase of Deformation, Unloading Loose

**Abstract**. The appearance and development of deformation and loss of stability in the slope of cut is closely related with such interior causes as the qualities of layer rocks. Some external incentives like meteorological conditions, hydrology and process of construction are the main factors leading to the deformation of slope and its development. Three problems of deformation of slope, which is one of the common geographical hazards. The thesis, making an analysis of the geographical environment, the process of deformation and mechanism of destruction on slope of the right cut in Guangle Road K142+320～K142+740, reveals the key factors of deformation and damages of slope and proposes a reasonable realignment methods about slopes, which has achieved a good engineering effect and set a good example for the other similar slopes to be strengthened and improved.

## Introduction

The appearance and development of deformation and loss of stability in the slope of cut is closely related with such interior causes as the qualities of layer rocks. Some external incentives like meteorological conditions, hydrology and process of construction are the main factors leading to the deformation of slope and its development. With a shifting tendency to building more highways in mountain areas, under the conditions of complicated topography, ground features and geographical hydrology, highway construction is facing to a variety of slope problems and the deformation and damages of slope in cut is always one of the crucial factors that exert many influences on the highway construction and normal operation later. The problem of deformation of slope under complicated geographical conditions in rainy and hot areas has become one of the common geographical hazards in highway construction in mountain and hilly areas,

The thesis, taking the improvement of slope of right cut on Guangle Road K142+320～K142+740 as the example, gives a detailed introduction to the analysis of mechanism of deformation and process of improving design under the conditions of complicated geographical environment , high temperature and many rains, especially the process control in the period of slope improvement , which offers some experience to the hazard of slope deformation in the same type.

## The condition of slope and geographical environments in the project

### 1.1 the condition of slope

A section of highway K142+320～K142+740 is located in Shanghuang village, Shakou county, the city of Yingde, Guangdong Province. The slope, extending along the one side of a hill, is an excavated slope with a height of 29.34m ,the original slope rate of 1:1.25 in the design and an arch framework to protect it. Early in 2012, slope began to be excavated, and the method of protecting in unison after excavation is employed. In the period of rainy season from May to July in 2012, because of continuous rains, before the work of protection, the sliding and collapsing of rocks and soils happens on the surface of slope, and develops into the back and two sides, which brings the dangers into the slope of the possibility of loss of stability as a whole that is a threaten to the safety of the iron tower on the top of the slope.

Figure 1 Slope construction and its deformation

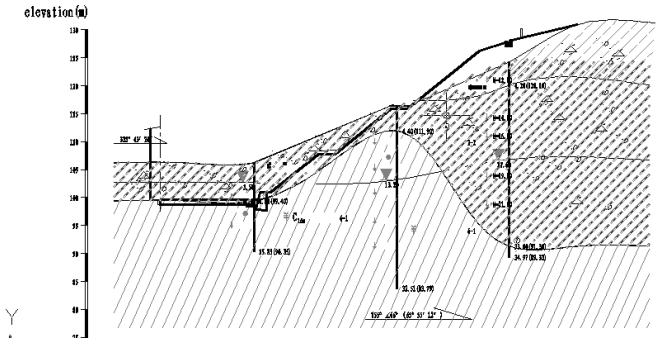


Figure 2 Typical geographical profile of the slope

**1.2 geographical environments in the project**

**1) Meteorology and hydrology**

This area is seated on tropical and sub-tropical monsoon zone. Influenced by the monsoon, it is warm and humid with an abundant waterfall. The summer is wet and hot with many typhoons and storms, but the winter is dry with cold air. In the rainy season from April to August, the waterfall covers the 70% of the yearly waterfall, but in the dry season from October to the next February, about 16%. According to the observation materials of waterfalls during 47 years in the station of Yingde Beijiang, the maximum waterfall in one hour is 320mm and the average waterfall in many years is 1982.4mm. The average temperature is about 20.9℃ in a year with an extreme high temperature 40.12℃. The average evaporation is 1666.7 mm in a year. The stereoscopic climate is distinct and the severe weather, rainstorm in particular, is frequent, which often happens from April to August.

There is no developed gully on the site. At present, ponding can be seen in the lower part of excavated zone. In the rainy season, little ground water, controlled by the rain, can be observed on the foot of slope.

**2）Topography and terrain**

The overall topography on site is shallow hill landform. Micro-

topography is shallow-hill slope, which is relatively mild with the slope of 10°～15°,ground elevation 100.3～118.6m and relative elevation difference 18.3m. It is straight alongside the longitudinal line, on several places of which exists gullies.

**3) Stratum lithology**

According to what the outdoor survey and misering of the topography revealed, exposed stratum lithology in cutting zones is mainly composed of powder slay of Q4dl and Q1el, while subterrane C1ds shale under charcoals. Its features and distribution are separately described as follows:

**(1) Q4dl:** light yellow, hard plastic, poor viscous, non-uniform, containing a small quantity of crushed stone, complicated components in each stratum, and 20%-30% of which are broken rubble with graits. It appears only at the top of the side slope, thickness of each stratum is not uniform, 4.20～10.80m.

**(2) Q2el:** reddish brown or taupe, local part being yellow, hard plastic, after weathering of shale being residual soil, inside which the structure is still visible, the rock core of which mainly comprises powder clay granule, and local part of which mixes weathered broken rubble, ordinary viscosity and 20%-30% of which are broken rubble with graits. It appears all along the slope, and thickness is 0.80～28.80m.

**(3) C1ds**

Weathered shale: taupe or reddish brown, earth structure, flaked formation, mineral components being mainly composed of clay, earth is viscous, weathering is strong, rock core appears like soil column, original rock structure is apparently clear, soft rock property so that it is of easy decomposition when encountering with water. It appears all along the slope, and buried depth, 0.80～33.00m, and stratum thickness are not uniform

Medium weathered shale: offwhite, aphanitic structure, stratified structure, joint crack greatly developed, flaked core and a little stumpy columns. It appears only 45.13m right from K142+640.

**4) Hydrogeology**

According to components of stratum rock and storage of underground water in this zone, the underground water on site can be divided into two kinds: pore phreatic water in loose rock mass and the weathered basement rock strip fracture water.

**An analysis of the mechanism of slope deformation**

**2,1 The qualities of material structures on the slope**

The upper part of the slope is mainly made up of powder-like clay from incomplete slopes, with the changing thickness of 0.8~28.8m, uneven distribution, great variation and lose structure. The rest part is all the weathering shale that under the influence of the structure is rather broken with many dense cracks among jointing and the space of the cracks range from 5cm to 20cm, so the rocks possesses the qualities of broken stones. Because the shale is mainly made up of clay minerals, full of the elements of montmorillonite and Kaolin, the wholly weathered shale and its weathered products also own the features of high liquid limit soiland can swell a little. Under the normal conditions, the performance of the project is OK, but many times of alternative of dryness and wetness, mechanical properties drop quickly. Meanwhile, the weathered shale with the qualities of broken rocks makes the passage of the penetration, evaporation and drainage of the rain smooth. So sliding and deformation is easy to be into existence in a depth that can be influenced by meteorology. The bottom of the slope is made up of uncomforted contact layer limestone with an uneven surface that changes a lot and is distributed in parts [3,4].

**2.2 slope construction and the history and features of deformation**

Excavation of the slope began in early 2012, and went into Phase-II in May, which was about 10m to the designed roadbed and the framework protection was out of operation. The slope is almost uncovered. The rainy season brings frequent and massive rains. To July of 2012, during the period of continuous rainfalls, sliding and collapsing happens on the part of slope K142+480, with a 30m wide , 11.5m tall and 30m thick body of sliding and collapsing. The sliding surface is an arc. The 30cm cracking and dropping happens close to the top of the slope was cut in a swollen shape of about 5- 10cm. The deformation of sliding and collapsing was formed many times and the scale of deformation tended to extend to the back and two sides of the slope. At the same time, there are many cases of sliding and collapsing on the surface of first-class slope that is adjacent to the deformed slope, whose deformation has obvious destructive features of soil-like slope. The development of deformations of rocks will have a heavy damage on the middle of the slope and the safety of electricity tower on the top of it.

In September, 2012, to avoid the above damages, an emergent improvement was operated: piles with three lines of steel pipes were cast on the top of the slope, in the front of the tower. After the improvement, the tendency to develop into the back is controlled. According to the detailed situation on site, by a comprehensive analysis, the surface of the slope is adopted the anchor-sticks grid beam to consolidate., and the first-class slope is placed the anti-sliding to support and defend with a foot-fixed defending wall. According to the adjusted design plan, the construction side completed the third-class and second-class slope anchor-sticks grid beam and anti-sliding pile on the first-class platform and defending wall from October 0f 2012 to May 0f 2013. Because of the coming of the rainy season and the frequent rainfalls, protection cannot be conducted in time, the surface of the first-class slope after being excavated appears the sliding of the rocks and it is hard to take a shape of slope. But the wholly stability is under control with no sign of a wholly stability and crack as a whole.

**Figure 3 Deformations before protection methods taken in july,2012**

**Figure 4 Scene of carrying out protections in july 2013**

**2.3 An analysis of deformation mechanism and influential factors**

The slope is mainly made up of the weathered shale and its weathered products. The rocks of the slope are controlled by the structure and weathering factors, which have dense joint cracks and broken rocks, classified into the category of broken rocks. The deformation of slopes can de divided into two phases according to the construction and process of deformation: Phase I is the superficial problems, which include the areas influenced by the excavation, or excavated unloading loose areas. Phase I can also be the deformation of rocks in the depth influenced by the meteorological conditions. Both of these are called the superficial deformation of slope Phase. Phase II is the wholly sliding and loss of stability of the whole slope, in which the deeper sliding caome into existence. Analysis is as follows respectively:

**1) Phase I----the superficial deformation of the slope**

According to the above analysis, because at the beginning of the excavation, there is no protection and the surface of the slope is exposed, it is easy for the rainfalls to penetrate into it and for the ground water to evaporate and drain. The stability of the slope is controlled by the geographical conditions, materialistic structures and rainfalls. On the basis of that the slope is mainly made up of weathered shale and its weathered products, the deformation macroscopically bears the features of destructive points in soil-like slope deformation----- the potential sliding surface is arc, and microscopically of cracks alongside the joints, and zigzag- like or stair-like layer, because of the control of the structural joint cracks and layers. If we take into the consideration the common existence of the massive rainfalls, strong sunshine, heavy evaporation, a tense alternatives of dryness and wetness on the superficial rocks, and a quick loss of rigid index of the meteorologically influenced rocks, the deformation often happens in a depth influenced by the meteorological conditions. In a word, the areas of deformation of the slope is mainly located in the areas influenced by the excavation, often 3-5m from the excavating ling. The features of deformation on this Phase are as follows: 1. the tensioning crack is often on the surface of the slope or near to the mouth line of the slope. 2. the cutting mouth is at the foot of the slope and the first-class surface of the slope. The preliminary deformation of the slope and the first-class slope deformation operated by anti-sliding piles are in such Phase.

**2) Phase II -----the formation of the deeper sliding and the wholly loss of stability**

Besides the influential factors in Phase I, the deformation of slope in Phase II has its own characteristics. With accumulation of the deformations, the areas of deformation must be extended in the width and broadness. Without the restriction and support in the superficial skidding soil, the depth of the deformation must be further developed. The enlargement and development of the deformation must result in that deformation is aggravated in the deep and back------a wholly loss of stability of the slope. The corresponding deformation features in this phase is: 1. the tensioning cracks and sliding appear in far back. 2. swell and deformation appears at the foot of the slope and

roadbed. 3. the depth of the deformation is over 5m, bigger than Phase I in the terns of the scale. If no effective consolidation is conducted, this phase is also the ultimate tendency of the deformation of the slopes.

**An analysis of the stability**

**3.1 Calculating method**

In recent days, the methods of calculating the stability of the slope can be categorized into 3[5]: limit balanced analysis,2 data analysis, 3. Probability theory. The limit balanced analysis is often employed and is also the most mature.

On the basis of the above analysis, blended with the soil-like sliding features of the deformation of the slope, according to the limit balanced theory and taking into account the loose structure of the weathered shale, the author adopts the arc sliding method to mimic the on-site situation and fold-line sliding theory to repeatedly perform the process of the deformation of the slope under the help of the figures from the survey to make an analysis of its deformation and tendencies.

**3.2 Soil Parameter**

The value of soil parameter was confirmed synthesizable by depending on geological survey reports and combining regional experience and back analysis cases. Below is the soil parameter lists of the slope in details.

**Sheet 1 The soil parameter lists of the slope**

| Name of the Geotechnical | density | | C(KPa) | | φ(°) | |
|---|---|---|---|---|---|---|
| | Degree of natural | Degree of saturation | Degree of Natural | Degree of saturation | Degree of Natural | Degree of saturation |
| Silty clay | 1.88 | 2.00 | 25.07 | 23.82 | 14.83 | 15.32 |
| Completely weathered shale | 1.96 | 2.15 | 22.98 | 26.98 | 15.87 | 15.08 |

**3.3 Computational analysis**

According to the excavation of the slope, in view of the slope deformation,model analysis was used under the continuos rain circumstance.In July 2012,the slope K142+480,stability coefficient of the section Fs=0.927 (superficial sliding) ~0.974 (deeper sliding). The slope is in poor stability and geotechnical landslide would be induced by continuous rainstorm.Refer to figure 5.

Simulation analysis of the overall slope stability after protection based on the adjusted protection schemes according to the design, and the stability coefficient Fs=1.569 (K142+480 section，under the continuous rainstorm circumstance)of rock slope after retaining wall was set. Refer to figure 6.

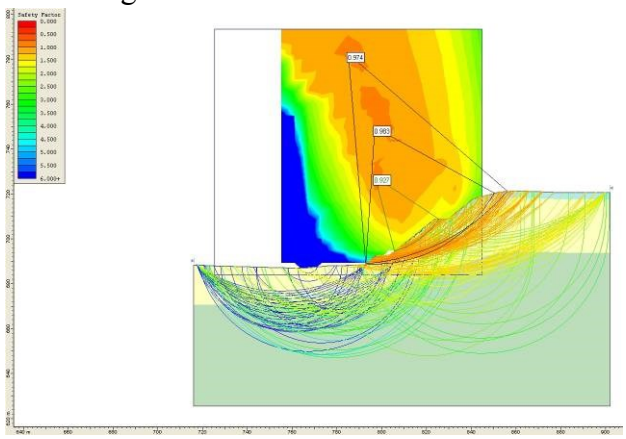

**Figure 5 Stability analysis of slope deformation(sectionK142+480 satus in July 2012)**

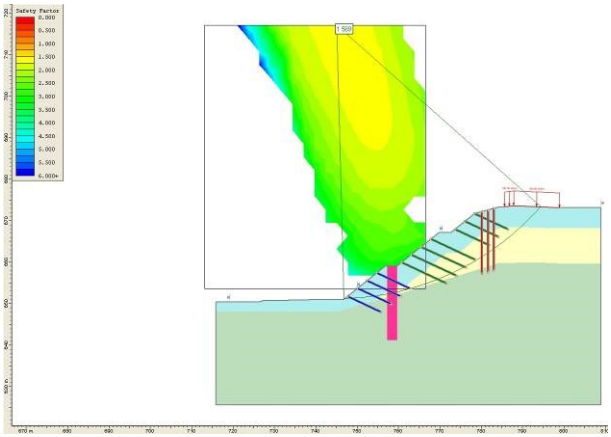

**Figure 6 Stability analysis of slope retaining structure**

According to the results of model analysis,the overall stability of the slope in the sliding surface was analyzed by polygon method. And K142+480 is taken as example:

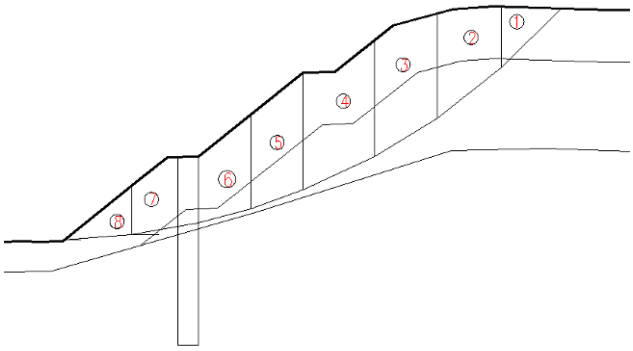


**Figure 7 Slice graph of the overall stability analysis of the slope (K142+480)**

Profile surplus sliding force under natural condition T=268.61kN, under continuos rain circumstance T=391.07kN; downslide force of designed retaining wall under continuos rain :805.83kN/km

**Improvement plan**

This slope has two features as follows:

**(1)** The geographical condition of the slope is complicated. The rocks have some unique qualities, like high limit of liquid and weak expansible ness, and at the same own the features of broken-stone soil and broken rocks. So its mold of destruction is controlled by the above features, which have the different destructive mold in different phases, especially in the later period when the situation is more complicated and the destructive mold is more various.

According to it, the general design plan of consolidating the slope adopts the phase-control and installment operation. That is to say, a preliminary and temporary method of placing steel pipe piles and casting to prevent the deformation from developing into the back, and the following method of taking anti-sliding piles as the main supporting structure to control the deep sliding and deformation. Anchor-sticks grid beam blended with planting grass on the surface of the slope controls the superficial deformation of the rocks in the slope.

**4.1 Improvement design plan in emergency**

To avoid that the deformation developed into the back and guarantee the safety of the tower before conducting the consolidating methods, placing steel pipe piles to support and enhancement of casting in the soil on the top of the slope through the holes of the piles, which improves the external environment of the slope, controls the speed of the deformation and create the conditions for the operation of the improvement methods.

Steel pipe piles placed on the inside of the intercepting dike on the top of the slpoe are arranged rectangularly in 3 rows, with 1.5m distance. The pipe pile's bore diameter is 130mm, with a steel tube(108mm*6mm) in it to be poured into cement mortar, Refer to figure 8.

**4.2 Treatment of the sliding slopes**

In accordance with the excavation condition of the side slope, and in combination with the features of the construction, the ratio of the consolidated part of the slope still abide by 1:1.25, the stepped height 8m. The dome of the side slope shall be consolidated by anchor lattice beam, with greenbelt in lattice, 3m between anchors. 1Φ32 anchors, whose bore diameter is 90mm, shall be adopted to be poured into M30 cement mortar. 3m C15 flag concrete barricade, with 1.2m top width and 3.0m wall height, is placed at the foot of Level one slope. Slide-resistance pile is placed at Level one platform to support the deep sliding down force. The slide-resistance pile is 1.5m*2.0m in section, 18m length, 6m in between, poured into by C30 concrete, placed in the K142+480-K142+580 at the higher part of the side slope of the tower area. See figure 9.

With the superficial rocks weathered and badly loose, collapsing appears on the firs-step slope because of the continuous rainfalls. The consolidation includes: removing the skidding soil from the surface, restoring surface of the slope by filling plant growth bags, casting the framework and afforesting the slope.

Drainage- intercepting system takes into consideration the interception and diversion of the surface precipitation to prevent rainwater permeating into the slope as well as the enhancement of the white-out of the underground water in the interior of the side slope. 60cm*60cm trapezoid catch water is placed at the outer edge of the side slope, and 40cm *40cm rectangular catch water is placed at the platform to divert the surface rainwater. The catch water is constructed by M7.5 mortar rubble. Level one and level three side slope is set with oblique outlet holes, and the holes' bore diameter are 110mm withΦ100 drainage pipes, 15m length and 12m in between. See figure9.

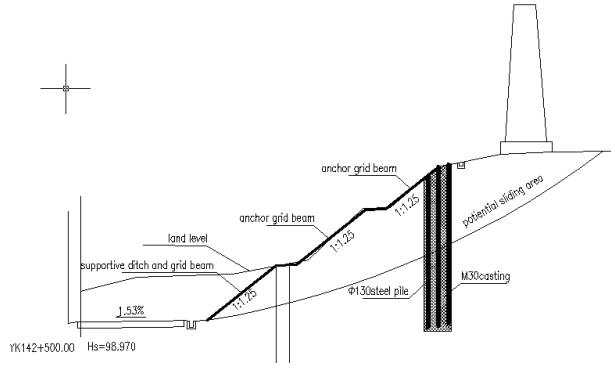


**Figure 8 Section Design of Section in Emergency**

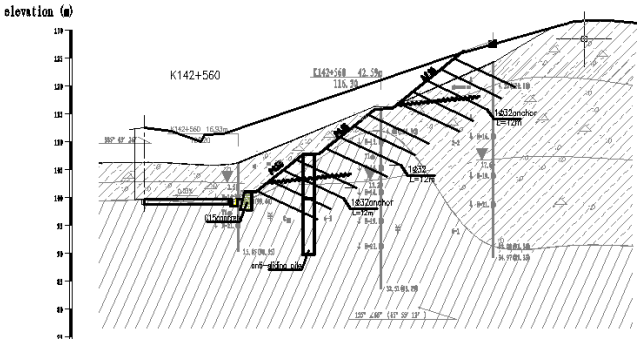


**Figure 9 Slope-consolidation section design (K142+560)**

## Conclusion

The slope on the right cut of Guangle Road K142+320～K142+740 located in a hot and rainy area with a complicated geographical conditions, is a mixed slope controlled by many kinds of factors. The author employs the limit balanced theory to analyze its stability on the basis of make a full analysis of its deformation mechanism and influential factors. According to its features, the consolidation of the slope adopts the ideas of phase-control and comprehensive methods mixed a lot of approaches to harness the slope. In the process of it, the whole slope remained stable and the tower on the top of it ran well, which realize the design ideas.

A successful harness of a slope must meet such requirements as "safety, economic, and environmentally-friendly". From the above analysis, it is known that, the deformation after the excavation is a constantly accumulated process and people's recognition of its deformation mechanism is a gradually deeper and deeper process. On the basis of strengthening the phase-control, timely adjusting with the change of the external condition (like the weather, the adjustment of the order of construction),according to the different phase of the deformation, a targeted improvement and a suitable time for consolidation are crucial to an effective improvement.

**An Introduction to Author**: Rongxiang : Shan (1980- ), Male, born in Dongming, Shandong, Associated professor, Senior Engineer, Main Academic and Practical Focus: Bridge Engineering, Geographical Hazards, Survey, Study and Treatment on the Problems and Damages of Highways. E-mail：shanrongxiang@ccrdi.cmhk.com。

## Literature References

[1]. Zhang zhaoyuan, Wang Shitian, Wang Lansheng. *The Theories of Geographical Analysis in Engineering* [M]. Being: Geography Publisher, 1981.

[2]. Xiao Shufang, Yang Shubi. Mechanics of Rocks [M]. Being: Geography Publisher, 1987.

[3]. Merchants Chongqing Transportation Research and Designing Institution Co.Limited,Chongqing. A Geographical Survey on Section T18 of from Zhangshi to Huadong on Lechang to Guangzhou Highway （K142+320～K142+700slope）[R]. Chongqing, 2008

[4]. Merchants Chongqing Transportation Research and Designing Institution Co.Limited,Chongqing. A Modification Design of YK142+320~YK142+740 right slope on Section T18 of from Zhangshi to Huadong on Lechang to Guangzhou Highway [R]. Chongqing，2008

[5]. Chen Zuyu. A Stability Analysis of Soil-like Slope (Axiom, Methods, Process) [M]. Beijing: Chinese Water Conservancy and Hydropower Publisher, 2003.

*Applied Mechanics and Materials Vols. 580-583 (2014) pp 947-953*
*© (2014) Trans Tech Publications, Switzerland*
*doi:10.4028/www.scientific.net/AMM.580-583.947*

# Research on two-dimensional landslide model control system based on support vector machine modeling

Zhong-tao LIU[1,a*], Zheng-hua FENG[2,b]

[1]Institute of Electrical Engineering & New Energy, China Three Gorges University, Yichang City, Hubei Province, China, 443002

[2]Institute of Electrical Engineering & New Energy, China Three Gorges University, Yichang City, Hubei Province, China, 443002

[a]2367185122@qq.com,[b]zhfeng@ctgu.edu.cn

**Key words:** Two-dimensional landslide model, least squares support vector machine (LS-SVM), Predictive control.

**Abstract.** Two-dimensional landslide model system is an important experimental platform for studying geological disaster, landslide behavior in different conditions are achieved by controlling the hydraulic pump drive model platform uplifting cabinet inclination. During the process of automation transformation of the two-dimensional landslide model system, control system based on computer is used to achieve a smooth lifting and precise angle of landslide model platform. Thanks to predictive control algorithm of least squares support vector machine (LS-SVM) model used in this paper, random real-time change of equivalent load applied on the hydraulic cylinder system effectively solved. The control system of the two-dimensional landslide model effectively eliminated crawling effect and pulse lifting in the condition of low speed and high load conditions of hydraulic system.

## Introduction

Our nation is one of the countries where the geological disaster happens frequently, such as landslide and debris flow. According to the various geological disasters derived from the Chinese investigations, landslide is as high as 68% in the proportion. Landslide disaster has caused huge losses to human life and property, which has brought the serious influence to the engineering construction[1~2] as well. The landslide slope stability is its natural adjustment, what influence the steady state effect factors are natural and human activities. One of the effective ways to study geological disasters of landslide gets through the landslide model design specific [3]. Model test of landslide belongs to the category of geomechanical model test. At present, the structure model test is the resource of the theory. The geomechanical model test commonly used in domestic and overseas are mainly made of framework model test and centrifugal model test. Frame type model test adopt the similarity model materials and the criteria in the framework by making model in normal gravity, and measure its deformation, stress and other factors in the model satisfying the boundary conditions of similar cases, and then reveal the formation mechanism of the landslide prototype[4]. The two-dimensional model realize the different characteristics in different dip angle by loading in consistent original soil and sand in the landslide box like actual study and lift a certain angle. The hydraulic system is the mainly lifting device of the landslide model. Because of the landslide model experiment box's large size and load and the random

changes of the center of gravity in the actual process, how to realize the exact stationary angle control of landslide model experiment box is the key of the landslide experimental case research.

## Mechanics Analysis Model of 2D Landslide

### 1.1 Landslide Experimental Platform

The landslide model test is destructive test, testing platform lifting control system can ensure the final break of uplift movements of the landslide model, which reveals the deformation characteristics of landslide and calculates the stability coefficient. As shown in figure 1, we can observe the two dimensional landslide model experiment platform.

Testbed frame is 8 meters length, 2 meters width and 5 meters high. The designing capacity is 700 *kN*, which lifted one end supported by a hydraulic cylinder designed to load 25*t*, the platform maximum tilt angle is 25*°*. The platform can install the water test system, non-contact measurement system of displacement field and multi physical quantity testing system (including water, soil pressure and displacement), the upper part of the platform roof installed artificial rainfall system. The test bench is a large comprehensive test platform which can simulate a variety of slope boundary conditions and multi physical quantity measured. The test platform of landslide is under the condition of rainfall and reservoir water, where the experiment box has sediment debris of the simulated landslide and the water of simulated rainfall.

Fig.1 Appearance and interior photos of two-dimensional landslide experiment platform

### 1.2 Landslide experimental platform lifting device

The hydraulic landslide control system transforms automatically mainly based on the original manual hydraulic control. Using a hydraulic cylinder supports one end of the landslide model, the stretch and shrinker of hydraulic cylinder control the inclined angle of the landslide model experiment box, the principle has been shown in figure 2. In order to provide the enough support moment, the hydraulic cylinder has a larger sectional area, so the flow of the solenoid valve should be improved accordingly, if the flow is too low, the speed of the hydraulic cylinder lifting may be very slow. We can control the elevation angle in a certain range, but the large section hydraulic cylinder will appear crawl phenomenon when it is in the low great pressure, thus causing pulsating torque when the hydraulic pressure lifting the landslide model box, and the pulsating torque will affect the landslide model experiment. The lifting speed cannot be too slow, and the accuracy of lifting angle measurement should be controlled, so it is necessary to analyze the movement and force of experimental model during uplift process. In figure 2, *BC* segment refers to hydraulic support device, *A* is the hinge, *G (x, y)* stands for the center of gravity of the sand, the rainfall and walls are simulated in the model. *L*, *H* is respectively defined as the high and long of the landslide model body.

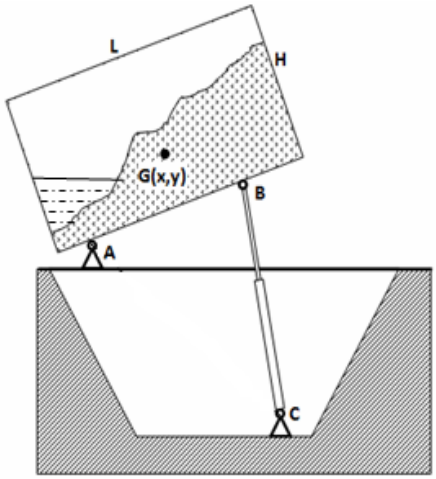


Fig.2 Motion control diagram of landslide experiment platform

**The motorial analysis of 2D landslide model**

**2.1 The geometric relation model in the process of model's movements**

From the analysis of landslide model diagram in figure 2, a schematic diagram model of uplift has shown in figure 3. *BC* refers to hydraulic support device, *A* is the rotating hinge of landslide model in the uplifting process, *F* stands for the lifting force of the hydraulic support device; *G* makes up the monolithic gravity of the model; *AG* is the cables between fulcrum *A* and model's center of gravity. The $\alpha_1$ is the intersection angle between *AC* and the horizontal, which will not change in the lifting process. The $\alpha_2$ is the intersection angle between *AG* and the direction of the box body length will not change as well. The $\alpha$ is the intersection angle between the landslide model and horizontal, changing according to the length of *BC* in the lifting process. The $\beta_1$ is the intersection angle between *BC* and the horizontal will change in the lifting process. The $\beta_2$ is the intersection angle between the length of box body and *BC* will change in the lifting process.

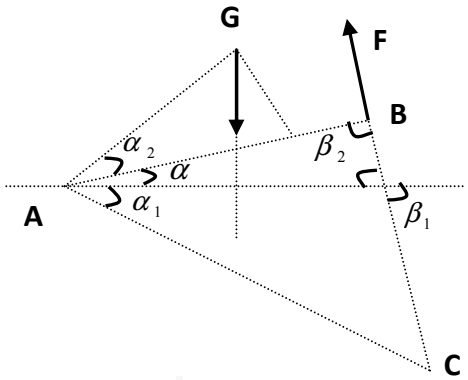

Fig.3 Sketch map of landslide model uplift movement

$$L_{BC}=\sqrt{L_{\mathrm{AB}}^2+L_{AC}^2-2L_{AB}L_{AC}\cos(\alpha+\alpha_1)} \quad .(1)$$

$L_{AB}$, $L_{BC}$ and $L_{AC}$ are the length *AB*, *BC* and *AC*. Known by the law of cosines variant:

$$\beta_2=arc\cos\left(\frac{2L_{AB}^2-2L_{AB}L_{AC}\cos(\alpha+\alpha_1)}{2L_{AB}\sqrt{L_{\mathrm{AB}}^2+L_{AC}^2-2L_{AB}L_{AC}\cos(\alpha+\alpha_1)}}\right) \quad .(2)$$

So we can get the moment that landslide model box gravity gives to fulcrum *A* in the lifting process:

$$T_1=G\times L_{AG}\times\cos(\alpha+\alpha_2) \quad .(3)$$

**2.2 Mechanical analysis in lifting process**

Hydraulic support force relative to the fulcrum of torque for the *A*:

$$T_2=F\times L_{AB}\times\sin(180-\alpha-\beta_2)\times\cos(\alpha) \quad .(4)$$

According to the moment balance:

$$F=\frac{GL_{AG}\cos(\alpha+\alpha_2)}{\sin(180-\alpha-\beta_2)L_{AB}\cos(\alpha)} \quad .(5)$$

Putting (1), (2) into (5) can get F that is the function of angle $\alpha$.

The lifting force is mainly provided by the hydraulic device, the control system adopts the original hydraulic system which provided oil to solenoid valve using a constant current hydraulic

cylinder, the export of solenoid valve is the hydraulic cylinder, considering the whole process of lifting, supposing the entrance constant pressure of hydraulic valve is $P_0$, so the valve flow is:

$$Q = \mu S(\frac{2(P_0 - \frac{F}{S})}{\rho})^{\frac{1}{2}} \tag{6}$$

The $S$ stands for the cylinder section area; $dl$ is the changed length of $BC$ in the lifting process:

$$dl = \frac{Q \times dt}{S} \tag{7}$$

During the lifting process of $BC$, according to (1), the support length differential coefficient of the hydraulic cylinder is:

$$dl = \frac{L_{AB}L_{AC}\sin(\alpha_1 + \alpha) \times d\alpha}{\sqrt{L^2{}_{AB} + L^2{}_{AC} - 2L_{AB}L_{AC}\cos(\alpha_1 + \alpha)}} \tag{8}$$

According to (7), (8):

$$\frac{d\alpha}{dt} = \frac{Q\sqrt{L^2{}_{AB} + L^2{}_{AC} - 2L_{AB}L_{AC}\cos(\alpha_1 + \alpha)}}{L_{AB}L_{AC}\sin(\alpha_1 + \alpha)S} \tag{9}$$

The $dt$ is the open time of valve. According to (5), the $F$ is the only variable in $Q$, and it is a function about $a$, if the center of gravity does not change in the lifting process, the $a$ is the only variable on the right side of (9). It is very difficult to seek the expression of a directly with the change of open time. From the above analysis:

(1) During the lifting process of model box, if the center of gravity of the box body does not change, the $\alpha_2$ and the $L_{AG}$ would not change; and we can get it in the lifting process by measuring α and solenoid valve opening time, and then get the $\alpha_2$ and the $L_{AG}$ of the box body's center of gravity by calculating;

(2) In the condition that the center of gravity of the landslide model body does not change, the tilt angle of landslide model can be controlled accurately by controlling the hydraulic cylinder valve open time.

According to the analysis of equation (9) can get the relationship between electromagnetic valve opening time and the angle of the landslide body. But in the process of time landslide experiment, due to the artificial rainfall added in the landslide experimental box, it causes the sand in the box containing water, and there is a lot of ponding in the box body. In the lifting process ,the the center of gravity of rain ponding is changing in real time, rain water in real time changes, and because of the change of elevation angle, both soil water flow and mudflow will cause the change of gravity center G. Changeable factors associated with water, soil water and soil factors such as landslide movement. Therefore, in order to realize

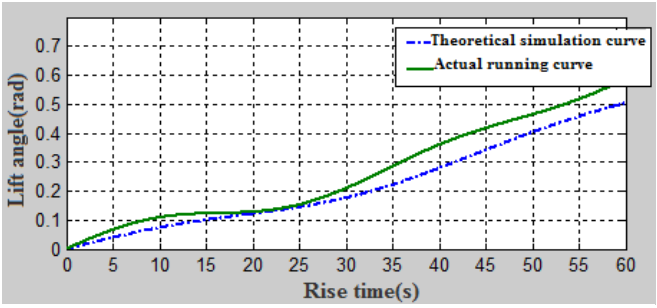


Fig.4 Lifting curve comparison of landslide model experiment box

the precisely control of box body's lifting angle by opening valve flow, we need acquire control system model of the entire landslide experimental box in real-time online. As shown in the figure 4, we can see the theoretic simulation curve and the actual running curve. Due to the parameters changes of the center of gravity in the lifting process, there is a big error between them.

## Control system modeling and predictive control

### 3.1 Support vector machine model

For the two landslide model experiment box, because of the constant changes of the center of gravity in the lifting process , and its changes are unpredictable, so it is a must to know the center of gravity parameters of the current model if want to obtain accurate angle control. This paper realizes to model the current model experiment box during lifting process in real-time by basing on the method of support vector machine rolling window regression modeling ,adopt the predictive control method to realize the control of the accurate angle. Support vector machine control technology is based on the object input and output, the prediction model of the principle of support vector regression direct nonlinear belongs to the nonlinear predictive control，which include predictive model, rolling optimization, feedback correction of basic characteristics[5~7]. The predictive control is a kind of optimal control algorithm, it determines the control effect in the future by optimizing a performance indicator, the index expect the model's predicted output as far as possible approaches to the reference trajectory, the characteristic index system related to behavior in the future[8]. The process of optimization is a rolling optimization in finite time, in every sampling time, the optimization performance index only refers to the limited time from the moment to the future , and in the next sampling time, the optimization period of time also brings forward[9]. Therefore the rolling optimization performance is: online optimization with the elapse of time, each moment repeated times without number; the optimization goal only care about dynamic performance prediction in the time domain system. In the predictive control, the optimization is not an off-line, it is repeated online, this is the fundamental point that the prediction controls is different from the traditional optimal control[10~12].

Suykens and Vandewalb proposed the least squares support vector machine (least-square SVM), the optimized index adopts the square, restrain equation only and have no inequality of C-SVM, then push out a series of different restrainable equations instead the quadratic programming problem[13~14]. The problem is expressed as:

$$\begin{aligned} &\min_{\omega,b,\xi,\rho} \frac{1}{2}\|\omega\|^2+\frac{1}{2}r\sum_{i=1}^{l}\xi_i^2 \\ &s.t. \quad \mathrm{y}_i\left(\omega^T\varphi\left(X_i\right)+b\right)=1-\xi_i \\ &i=1,...,l \end{aligned} \tag{10}$$

In the formula, the r is the regularization parameter.

Linear equation group can be obtained:

$$\begin{bmatrix} 0 & y^T \\ y & Q+r^{-1}I \end{bmatrix}_{(l+1)\times(l+1)} \begin{bmatrix} b \\ a \end{bmatrix} = \begin{bmatrix} 0 \\ e \end{bmatrix} \tag{11}$$

Kernel function adopts the RBF kernel function:

$$K\left(x,x_i\right)=\exp\left(-\left\|x_k-x_i\right\|^2/2\sigma^2\right) \tag{12}$$

The $\sigma$ is the RBF kernel parameters in the formula. In the condition where have no prior knowledge of the problem, the model trained by this kind of kernel function have a superior overall performance than other kernel and model. The $a$ and the $b$ can be solved via the least square method, the result of the application of LS-SVM to nonlinear regression functions is:

$$f(\mathrm{x}) = \sum_{i=1}^{l} a_i K(\mathrm{x}, \mathrm{x}_i) + \mathrm{b} \qquad .(13)$$

The prediction results can be measured by the error indicators: equal coefficient:

$$EC = 1 - \frac{\sqrt{\sum_t \left[T_{pred}(t) - T_{real}(t)\right]^2}}{\sqrt{\sum_t T_{pred}(t)^2} + \sqrt{\sum_t T_{real}(t)^2}} \qquad .(14)$$

The $EC$ express the fit between the prediction value and the real value, in general the fit is great if it is more than 0.90. The biggest advantage of least squares support vector machine is that can significantly improve the training speed of the standard support vector machine, simplify the computation complexity[15]. Adopt the means of literature [14] which proposed a rolling window algorithm, read a tilt sensor results in short-time interval, and regard it as the new sample into the predictive control algorithm model. During the comparative experiment process of support vector machine model, adopt the function theory analysis in it ,and use the numerical analysis method to obtain the needed time of required control angle ,then get a group of direct flow control angle data, the error between the actual setting angle and lifting angle is the direct control error, the support vector machine modeling error is between the setting control error of inclined angle and the error of inclined angle after prediction control, as shown in figure 5.

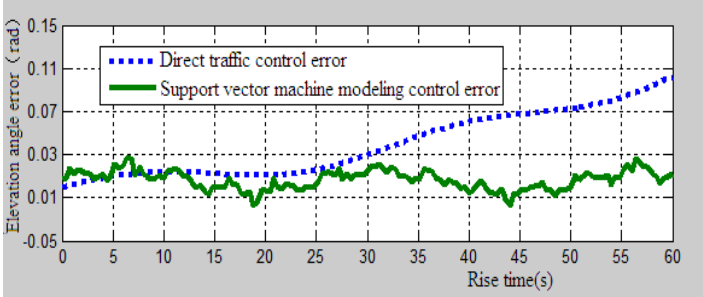


Fig.5 Inclination error curve comparison of landslide model experiment

**Summary**

The two - dimensional experimental box of landslide requires great puissance, because of the large area of hydraulic cylinder, we adopt the original circuit and hydraulic system in order to avoid the influence of the load which gave by the lifting process of the landslide model experiment in slow speed creeping. It needs adopt the control valve with large flow, the large flow makes the control of angle become the main problem in the control system, at the same time, because of the ponding water level's changes of simulated rainfall in the lifting process, the soil water content's transfusion makes the control object is a nonlinear dynamic system. This paper adopt the predictive control method of the support vector machine model as the two experimental box landslide model lift angle control algorithm, it effectively solves the title angle problem brought by the changes of box body in the actual operation. And programming the control software runs on the host computer. The system has been running for more than 2 years, the actual operation shows that the system can effectively control the landslide model lifting angle.

**References**

[1] Li Zhongkui, Lu Darong,Zhong Shanyuan, etal. Development and application of new technology for 3D geo-mechanics model test of large underground houses[J]. Chinese Journal of Rock Mechanics and Engineering, 2003，22(9):1430-1436.

[2] Cheng Shengguo,Luo Xianqi,Fang Kunhe.The test and design theory of the similar materials of soil-type landslide and the study on its assessment method[J].Water Power,2002,(4):21–22.

[3] Luo Xianqi,Liu Defu, etal. Model test study on landslide under rainfall and reservoir water fluctuation. Chinese Journal of Rock Mechanics and Engineering,2005,24(14):2476-2483

[4] Zhang Hao-Ran, Han Zheng-Zhi, Li Chang-Gang. Support vector machine based unknown systems identification and control[J].Journal of Shanghai Jiao Tong University,2003,37(1): 927-930

[5] Alexei Pozdnoukhov, Mikhail Kanevski. Multi-scale support vector algorithms for hot spot detection and modelling[J],2008.

[6] Si Wu,Shun-Ichi Amari. Conformal Transformation of Kernel Functions: A Data-Dependent Way to Improve Support Vector Machine Classifiers[J],2002.

[7] Lu Min,Zhang Zhanyu. Application of Support Vector Machine in Runoff Forecast[J],China Rural Water and Hydropower,2006,(2):47-49.

[8] Zhuo Sushuang,Su Guoshao,Yuan Qincheng.Long-term Forecast Method for Runoff Based on SVM[J]. Enterprise Science and Technology & Development, 2009,(18):88-92.

[9] Qu Zhongyi,Chen Yaxin,Shi Haibin,etal. Structure and algorithm of BP Network for underground hydrology forecasting[J]. Journal of hydraulic,2004,35(2):88-93.

[10] Liu Guodong,Ding Jing. Discussion on problems of BP neural networks applied to hydrological prediction[J]. Journal of hydraulic, 1999,30(1):65-70.

[11] Feng Guozhang. An analysis of effects of artificial neural network structures on precision of stream folw forecasting[J]. Journal of natural resources,1998,13(2):169-174

[12] Xing Zhenxiang. Application of modified genetic algorithm and back propagation artificial neural to water resource projects[D].Northeast Agricultural University.2004.

[13] Vapnik V N. The nature of statistical learning theory[M]. New York: Springer,1995.

[14] Wang Yuhong,Huang Dexian,Gao Dongjie,Jin Yihui. Nonlinear Predictive Control Based on Support Vector Machine[J]. Information and Control,2004, 33(2):133-137.

*Applied Mechanics and Materials Vols. 580-583 (2014) pp 954-957*
*© (2014) Trans Tech Publications, Switzerland*
*doi:10.4028/www.scientific.net/AMM.580-583.954*

# Uncertainty analysis and monitoring of earth dam

YANG Ling Qiang [1,a] , GAO Rui [1.b], and Wang Yan[1,c]

[1]School of Civil engineer and architecture, University of Jinan, Jinan, Shandong province, China

[a]cea_yanglq@ujn.edu.cn,[b]cea_gaor@ujn.edu.cn, [c]cea_wangyan@ujn.edu.cn

**Keywords:** earth dam; Uncertainty analysis; monitoring.

**Abstract.** Monte Carlo simulation provides a probabilistic method to evaluate the physical behavior of earth dam. Therefore, the behavior could be got in a more realistic manner. Based on the theory, an innovative software program code is developed by combining the Monte Carlo and finite difference methods to predict the performance of earth dams after impounding. In order to assess the efficiency of the method, the case study of earth dam, located at Southeast of China, has been studied in detail. The performance of this dam is predicted and compared with the field monitoring by using the monitoring data. The results shows the robustness of the proposed method.

## Introduction

Dams provide significant social and economic benefits, however risks made by the unstable dams could threat the life and property of the people who live in the downstream area. The safety assessment of a dam is a complex problem that needs to be analyzed and evaluated comprehensively by using different methods. Therefore, it is required to analyze the monitoring information, which is a key subject in the field of dam engineering. A typical dam contains various types of piezometers as total stress cells, settlement devices, triaxial deformation tubes, inclinometers and extensometers, all are installed during construction [1]. These sensors face uncertain inputs, which are originated from the physical uncertainties and human errors. It can be expected that the combination of these unknown parameters leads to an unreliable design [2]. Uncertainty analysis by mathematical and statistical softwares can be then used to evaluate the risks. Other uncertain events affecting dam's behavior and then its modeling are water inflow, reservoir level, earthquake magnitude and etc. They are used as input to the uncertain models, leading to probability distribution of response values (deformation, stresses, etc.). These consequences are expressed as the probability of occurrence functions. In this process, dam safety can be then assessed by mathematical models using the monitoring data [3].

Monte Carlo simulation is a very useful method for modeling the problems with uncertainty in the inputs data. This simulation method is based on input parameters those reflect the probability density function (PDF) of every parameter. Thus, the repetitive calculations take into account the randomly selected combinations of the inputs, generating a PDF or cumulative density function(CDF) for the outputs. Based on these CDFs, a risk level representing the high end (e.g. 95%), central tendency (median or mean), or any other desired level of probability can be obtained [4].

## Methodology

Dam behavior is conventionally evaluated by models of deformation, seepage, stress, and crack opening by using the complex and nonlinear functions. As the consequences of dam failure are serious, monitoring the behavior of dams is needed in the early stages of the impounding. It is also important to validate the assumptions made at the design step, particularly to control seepage phenomenon. Therefore, long-term monitoring of dam performance and regular measurements are improved during the operation period to ensure that the dam structure is functioning well. If the results of monitoring are in good consistency with the model estimations, it shows that the method of analysis has been carried out in a practical manner.

Monte Carlo and other probabilistic analytical techniques are relatively straightforward when applied to a case with parameter variability, the natural heterogeneity of a system and also parameter

uncertainty. On the other hand, model uncertainty represents a lack of knowledge concerning variables and their interactions to each other and thus constitutes uncertainty about whether a model approximates a real-world process or not. In brief, the Monte Carlo simulation is a numerical method to solve problems through stochastic simulation, and in this research the framework of study can be explained as follows: (1) The values of each stochastic variable are generated. The generations are based on the lognormal distribution for permeability variable and the normal distribution for density of foundation soil. (2) The pore pressures are obtained by using the finite difference model. (3) The steps described in points (1) and(2) are repeated until a statistically valid numbers of pore pressures are obtained. (4) The statistics of pore pressures are obtained like the mean, variance, CDFs and PDFs. (5) Finally, the results of Monte Carlo finite difference simulation and those of the monitoring are compared to figure out how the predication is correlated with the real observations.

## Case study

In order to implement the new concept, a case study of earth dam has been considered, which is vital for the life of people and ecology in its area. This dam is located in Shandong province of China.

In this study, only the data of piezometers are used, then the pore water pressure is utilized to demonstrate the capability of the proposed method. There are some hypotheses. First, soil properties are considered to be random variables in the Monte Carlo simulation process along with repetitive numerical analysis. As already discussed the lognormal distribution is assumed for the permeability random variable and normal distribution for the density of foundation soil. Finally, vertical coefficient of permeability, Ky, is taken as random variable and the permeability ratio, Kx/Ky is assumed to be 9. A summary of the field data including the coefficients of permeability and density is presented in Table 1.

In this case study, the piping event is considered the most serious failure mode of the dam. To evaluate the dam safety, 16 locations are considered to monitor the pore pressures. Some piezometers do not work well because of the bad installation. Considering the length of the dam, physical facts and boundary conditions, only some of them can be taken into account. To find the safety measure in the piping failure mode, the most of the evaluations are focused in the downstream area and near the drains. Therefore, 13 piezometers (as shown in Fig. 1) are considered and the summary of the monitoring results are presented in Fig. 2 shows the observed CDFs for all of the monitoring sites.

Table 1 Value of used parameters

| | Specifications | Maximum | Minimum | Average | Standard deviation | Coefficient of variation |
|---|---|---|---|---|---|---|
| Coefficient of permeability (cm/s) | First layer | 0.0072 | $1.540\times10^{-6}$ | $6.210\times10^{-4}$ | $13.6\times10^{-4}$ | 220 |
| | Second layer | 0.0031 | $1.540\times10^{-6}$ | $3.870\times10^{-4}$ | $7.22\times10^{-4}$ | 187 |
| | Third layer | 0.0032 | $1.5840\times10^{-6}$ | $5.270\times10^{-4}$ | $7.51\times10^{-4}$ | 167 |
| Saturated density (kN/m3) | | 18.4 | 14 | 15.38 | 0.77 | 5 |

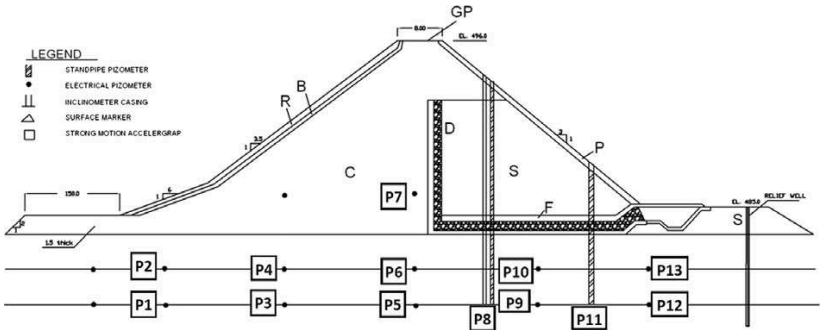


Fig. 1. The locations of the monitoring instruments in cross-section of earth dam

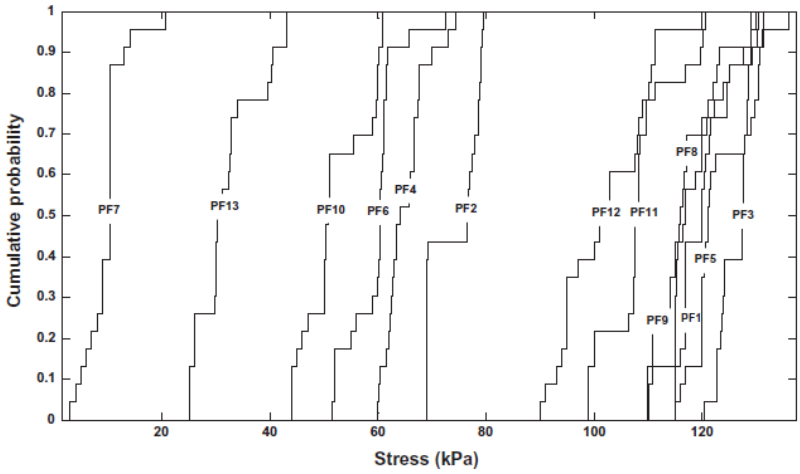


Fig. 2. The CDFs of the monitoring data at all points.

## Calculations by Monte Carlo finite difference method

In order to get an acceptable simulation, a large number of samples should be first produced. Nowak and Collins presented the required number of random samples as

$$N = \frac{1 - P_f}{(CoV)^2 P_f} \quad (1)$$

where Pf is the approximate failure probability and COV is the coefficient of variation. By using Eq. (1), if the failure probability and COV is considered $10^{-4}$ and 2, respectively, the required number of samples should be around 2750. Therefore, in this study, 2750 simulations were performed. In a precise study, the convergence of the statistics should be tested by performing a multiple number of samples. The finite difference grids of earth dam, modeled with FLAC is presented in Fig. 3. Because the dam's geometry is somewhat regular, the most elements are modeled as rectangular, to reduce the calculation time and the complexity of model.

The results of Monte Carlo simulation by using the new code are given in Fig.4. If the coefficient of variation is less than 10%, in this research it is assumed an appropriate output data. These predictions are useful in determining the critical points. The efficiency of the developed algorithm can be now assessed by comparing the observed results (Fig. 4) and those obtained by using the new method (Fig.4). Of course, due to some installation problem with piezometers, in some points (like in P7 and P13) a few errors are reported. Nevertheless, the general outputs indicate a very good fitness, indicating the effectiveness of the developed model in handling this problem and it will be shown by using a statistical test.

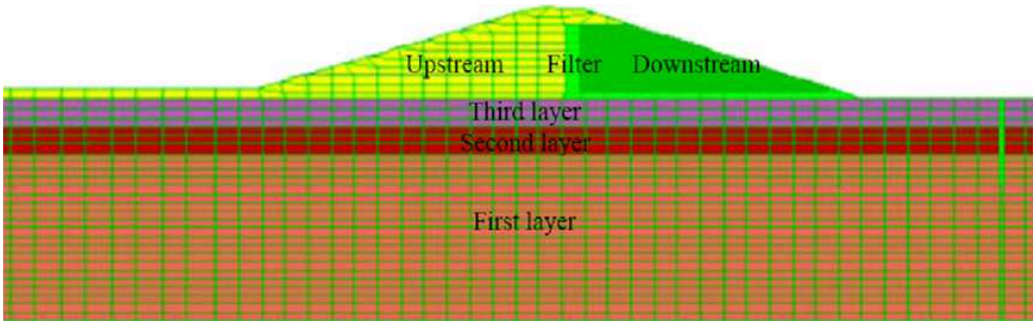


Fig. 3. The finite difference model of earth dam, modeled with FLAC.

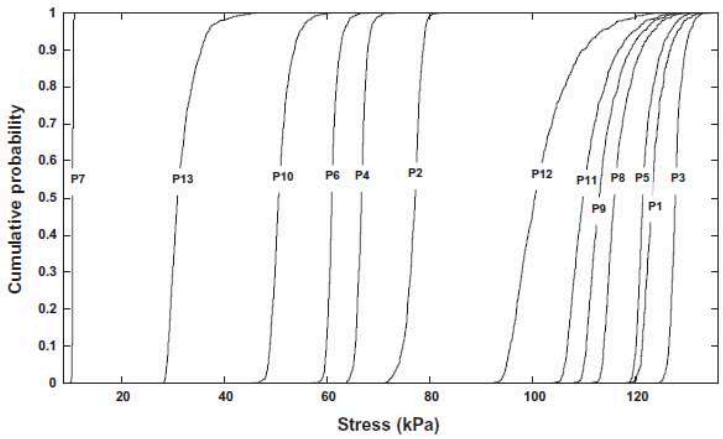


Fig. 4. The simulation results of the CDFs in all points

## Conclusions

There is a growing tendency to assess the safety levels of the dams, either under design or under operation. The risk of dam behavior is however a complex problem and cannot be evaluated just by the observed data. Considering the advantages of the probabilistic finite difference analyses, a new model was applied to predict the behavior of a dam during its impounding stage. According to the results, the predictions were in good fitness with the monitoring outputs. This concept of applying Monte Carlo simulation with a finite difference model resulted in interesting outcomes. However its performance depends on the simulation framework, the nature of the inputs, the nature of the loading conditions, the evidence used to characterize the distribution of the inputs and the extent to which the varied inputs can be considered independent. It is desired by using this method, the risk of dam failure to be reduced and decision-makers could better manage the uncertainties.

## Acknowledgements

This work was financially supported by Natural Science Foundation of Shandong province(No : ZR2012EEM025 and ZR2012EEL24).

## References

[1] Stewart M, Tsakiri M. The application of GPS to dam surface monitoring. J Geospat Eng 2001;3:45–58.
[2] Stewart RA. Dam risk management. In: Proc Geo Eng Conf, Melbourne; 2000. p.19–24.
[3] Jinping H, Yuqun S, Guhuai L. Comprehensive assessment method for large dam safety. In: 5th Int Symp Saf Sci Technol; 2006. p. 2351–2358.
[4] Darbre GR. Probabilistic safety assessment of dams. In: Proc XX Congr. ICOLD; 2000.

*Applied Mechanics and Materials Vols. 580-583 (2014) pp 958-961*
*© (2014) Trans Tech Publications, Switzerland*
*doi:10.4028/www.scientific.net/AMM.580-583.958*

# Study on rock strength characteristic by point load test

WANG Ruihong [1a]， JIANG Yuzhou[2b],GUO Jinlong[3c],TANG Tiancai[4d]

[1]Key Laboratory of Geological Hazards on Three Gorges Reservoir Area，China Three Gorges University，Ministry of Education，Yichang，Hubei 443002，China;

[2]Key Laboratory of Geotechnical Mechanics and Engineering of the Ministry of Water Resources，Yangtze River Scientific Research Institute，Wuhan，Hubei 430010，China

[3]China Three Gorges University,Yichang，Hubei ，China

[4]China Three Gorges University,Yichang，Hubei ，China

[a]43604258@qq.com , [b]jiangyuzhou5586@163.com, [c]125317331@qq.com, [d]444136942@qq.com

**Key words:** Rock specimen; Mechanical test; Point load; Uniaxial compressive strength

**Abstract**：Test point load test requires relatively small load, its instrument is portable, it can be easily applied to on-site testing,which may pave the way for the development of the fieldstrength of rock mechanics test, widely promoted in engineering construction, has a large space for development. When selecting the uniform rock do the load and saturation points uniaxial compression test respectively, and comparing the analysis of the two trials correlation between the results obtained by the method, the results showed that: point load test as a qualitative and semi-quantitative indicators are needed to meet the requiement of project, but if we put it as a fully quantitative indicators ,which will lead to large errors,and even lead to sweeping errors.

## Introduction

The mechanical strength of rock is an important parameter for rock engineering designing, constructing, its accuracy directly affects the security and stability of the construction and operation, as well as the economic rationality of construction[1-5]. The test load is relatively small and the instrument is portable in the point load test, which can be applied to field test. But the result is diversity, the accuracy is highly dependent on the number of test and related empirical formulas[6-9]. Point load test is mainly used for the estimation of rock uniaxial compressive strength or tensile strength, and classification of rock. Study on the correlation between rock point load strength and uniaxial compressive strength, many domestic and foreign scholars have done some research work. The results show that the Rc and $Is_{(50)}$of rocks have good correlation, and the table 1 lists some representative achievements.

## point load test instruments and methods

### 2.1 test instrument

Rocky Point Load Test uses SD-1 type of rock digita l point load tester, shown in Figure 1.

**Fig.1 SD-1 Point load instrument**

**Table1 The laws of Rock Rc and Is (50)**

| author | emprical formula |
|---|---|
| Broch & Frankln | Rc=29.07 Is（50） |
| International Society for Rock Mechanics | Rc=（20~25）Is（50） |
| Chengdu College of Geology | Rc=（18~19）Is（50）(minor axis) Rc=23.7Is（50）(macroaxis) |
| Northeast Institute of Technology | Rc=65+17.4 Is（50） |
| Second survey and Design Institute of Railways | Rc=22.819Is（50）0.745 |
| 2003,Quane and Russel | sterosome Rc =24.4Is50 weak rock Rc =3.86（Is50）2+5.65Is50 |
| In 2004Tsiambaos and Sabatakakis | Rc =7.3（Is50）1.71 Rc =23Is50 |
| In 2005 Fener | Rc =9.08Is50+39.32 |
| In 2009 Sabatakakis | Point load <2Mpa Rc =13Is50 Point load 2~5Mpa Rc =24Is50 Point load >5Mpa Rc =28Is50 |
| S.Kahraman ·O.Gunaydin | weak rock ：Rc =8.20Is+36.43 metamorphic rock：Rc =18.45Is-13.63 sedimentary rock ：Rc =29.77Is-51.49 |
| 《Test procedures of physical and mechanical properties of rocks》 | Rc=22.77 Is（50） |
| 《Standard for engineering classification of rock mass》GB50218-94 | Rc=22.82Is（50）0.75 |
| Rock test specification for Railway Engineering(TB 10115-98) | Rc=24.3382Is（50）0.7333 |

### 2.2 Test method and steps

（1）To ensure the same set of samples has a better uniformity, we take the rock samples into groups and each groups should not be less than 10.

（2）The samples can be,core samples, regular or irregular rock samples, which have different shapes for the corresponding size requirements. Test specimen shape and dimensions of the point load shown in Figure 2.

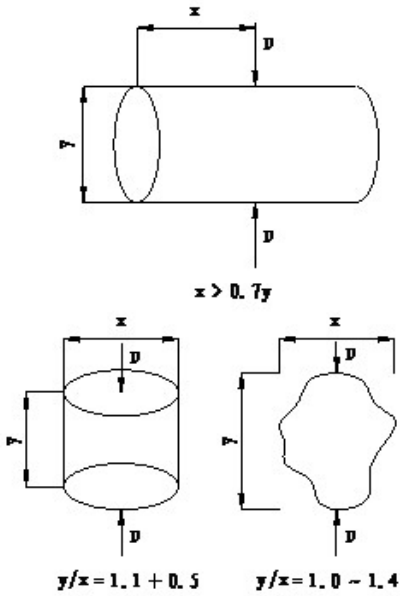


**Fig.2 The requirements of size for different shape specimens**

（3）To describe the rock lithology, we focus on structural characteristics of its structure, such as grain thickness, arrangement and joints, bedding and other developmental characteristic and degree of weathering, etc.

（4）When measuring the strength of the surface structure, we should ensure the two load connection point in the same structural level and uniform the applied load, the rate per second 0.05-0.1MPa.

### 2.3 Test documentation

The failure load of rock point load test is calculated in accordance with the formula (1) :

$$P = C \cdot F \tag{1}$$

The failure of specimens area and the equivalent circle diameter are calculated according to (2)(3):

$$A_f = D \cdot W_f \tag{2}$$

$$D_e^2 = 4A_f \cdot W_f / \pi \tag{3}$$

Rock point load strength formulaed according to (4), (5) .

$$I_s = P / D_e^2 \tag{4}$$

(Is as the unmodified point load strength index (MPa).)

$$I_{s(50)} = I_s \cdot F \tag{5}$$

$$F = \sqrt{\frac{D_e}{50}} \quad (6)$$

At the process of measuring data , deleting the maximum and minimum value, and then listing the rest of the measured value of the arithmetic mean value as the strength of rock point load test group.

**test results analysis**

In order to reduce the influence of rock heterogeneity, the test samples of point load strength and saturated uniaxial compressive strength have used homogeneous processing. We selected some typical magmatic rocks, sedimentary rocks and metamorphic rocks as the research samples, which with high, medium and low strength, as the research object.

The typical saturated uniaxial compression test curve of testing samples is shown in Figure 4.

The test results as shown in table 3. A set of experimental results of table rock point load strength and compressive strength of saturated average are listed, at the process of choosing data we take out a maximum and a minimum, and average value.

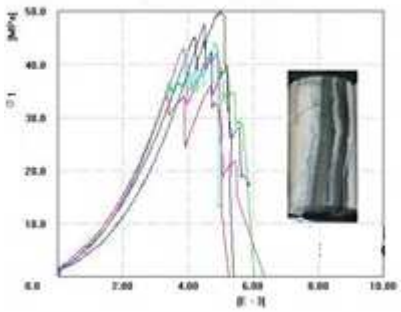

**Fig.3 The typical curves of uniaxial tests**

**Table 3 The results of tests and some parameters**

| types | names | $Is_{(50)}$(MPa) | Rc(MPa) |
|---|---|---|---|
| pyrogenic rock | granite | 9.99 | 198 |
| sedimentary rock | malmstone | 2.34 | 64.2 |
| metamorphic rock | marble | 4.29 | 175 |
| The green schist and marble interbed | Parallel to the bedding | 2.88 | 44.2 |
| | Vertical bedding | 3.73 | 68.8 |

Compared Fig.4 and Table3, the test samples adopted in both homogeneous sample and samples containing bedding rock both have good uniformity, so the same lithologic sample test results is comparable. Combined the domestic and foreign research results with the test results, a comprehensive analysis of different rock can be obtained, through the origin or not after the slope change range linear formula fitting the origin is very wide,nonlinear regression fitting parameters based on amplitude is also larger, with a unified formula ,to accurately summarize rock Rc and $Is_{(50)}$ relationship is difficult to achieve.

**Conclusion**

Point load strength test is a simple, fast speed, low-cost test, the sample size required can be the low and high-volume repeat tests, etc. This method has a good prospect for development and application. The current procedures and specifications of point load strength test on the discussion and provisions still defect, in practical geotechnical applications, it often can not be completely in accordance with standards and regulations to carry out the provisions. The shape and dimensions of the sample, lithology and structure factors directly affect the Rc and $Is_{(50)}$ the relationship. For the

different types of rocks ,whether linear or non-linear equation functions were fitted intensity interval value or whether it is different lithology types segmented partitions individually fitted, it is difficult to reunificate with one or several sub-partition function formula which can accurately describe the Rc and $Is_{(50)}$ related laws of all the rocks . Point load strength index and its conversion saturated uniaxial compressive strength value as the initial classification of rocks, and rock weathering zone or a selected point in the planning and engineering exploration and feasibility study initially estimated half of the compressive strength of rock quantitative indicators, the superiority of its fast economic and other test methods are incomparable. However, due to its accuracy is not enough, in practical the test data engineering are not using point load method to design, should be indoors, on-site testing machines the results obtained mainly in reliable comparative information for the next scene to do a small part of the point load test data, but in major projects or the best method used in all of rock testing machine to test the compressive strength of rock.

**Acknowledgements**

This work was financially supported by The national natural science fund project (51109120), The national natural science fund project (51109014) ,The China institute of water resources and hydropower research open fund (IWHR-SKL-201218),The Yangtze river open academy of sciences research fund(0720132214) ,Yichang city science and technology research and development project in 2012(A2012-302-04)and The three gorges university fund project talent research began in 2010(KJ2010B006).

**References**

[1] Broch E, Franklin JA. Point-load strength test[J]. Int J Rock Mech Min Sci, 1972, 9(6):669–697.

[2] Bieniawski ZT. Point load test in geotechnical practice[J]. EngGeol, 1975, 9(1):1–11.

[3] Forster IR . The influence of core sample geometry on the axial point-load test[J]. Int J Rock Mech Min Sci, 1983, 20: 291–295.

[4] ISRM. Suggested method for determining point-load strength[J]. Int J Rock Mech Min Sci, 1985, 22:53–60.

[5] Wei Ke He. Research of the quantitative evaluation on the granite weathering degree by point load [J]. Hydrogeology engineering geology，1982，2:16–21.

[6] Xiang Guifu ,Liang Hong. On the statistical analysis of Date and Strength Determinnation in Point Load Test of Rock[J]. Journal of rock mechanics and engineering，1986，5(2)：173–186.

[7] Li Maolan etc. Application of point load test to determine the rock uniaxial compressive strength, tensile strength report and accessories [R], the second survey design institute of the ministry of railways，1989.

[8]Tsiambaos G, Sabatakakis N. Considerations on strength of intact sedimentary rocks[J]. Eng Geol, 2004,72:261–273.

[9] Fener M, Kahraman S, Bilgil A, Gunaydin O. A comparative evaluation of indirect methods to estimate the compressive strength of rocks[J]. Rock Mech Rock Eng, 2005, 38(4): 329–343.

*Applied Mechanics and Materials Vols. 580-583 (2014) pp 962-965*
*© (2014) Trans Tech Publications, Switzerland*
*doi:10.4028/www.scientific.net/AMM.580-583.962*

# Research on the mechanical and thermophysical properties of frozen soil in cretaceous formation

Huadong Dai[1,a], Minglun Yin[1,b],Tianyu He[1,c],Kang Liu[1,d], Tie Li[1,e], Tieqi Zheng[1]

[1]School of mechanics & civil engineering, China University of Mining and Technology (Beijing), Beijing, 100083, China

[a]13811591874@163.com, [b]yml2323@163.com, [c]191763050@qq.com

[d]1047203232@qq.com, [e]604462706@qq.com

**Keywords:** Cretaceous formation. Artificially frozen soil. Elastic modulus. Specific heat.

**Abstract.** Through the test of artificial frozen soil of cretaceous formation soil sample, study the mechanical properties and thermophysical properties of cretaceous formation artificial frozen soil with different soil properties and subzero temperatures. Results indicate that, uniaxial compressive strength of artificial frozen soil of cretaceous formation soil sample linearly increases accompanied with drop in temperature, with identical soil properties and water content; with decreasing temperature, elastic modulus increases and Poisson's ratio decreases, in the case of the identical soil and ambient temperature; with decreasing temperature specific heat of artificial frozen soil decreases and thermal conductivity increases.

## Introduction

Artificial ground freezing, freezing method for short, have applied in China more than 40 years. Coal industry have built up a more perfect test system of frozen soil frozen soil and thermophysical properties. The result of test can directly and reliably guide the frozen design and construction [1-4].

## Elastic Modulus of Cretaceous Formation Frozen Soil

**Test Preparation.** Considering the representative soil sample, it different test point in cretaceous formation, and collect undisturbed soil and remoulded soil during Ling-dong Mine's excavation.

**Collection of Undisturbed Soil Sample.** Undisturbed soil means the sample's physical properties, as particle, water content, density, cementation, structure, remain unchanged.

Process of Undisturbed soil collection, including selection of collection devices, collection, field identification of sample, package storage and transportation of sample, referring to the Standard system of PRC, Technical standard for sampling of undisturbed soils.

Soil sampler. Φ89 penetration soil sampler, it met standard requirements. Field drilling meets depth requirement, Using rotary.

The sample field inspection and process need be done after the sample collection, as shown in Fig. 1 and Fig. 2. Package and transport the samples to laboratory.

Fig. 1. Sample process

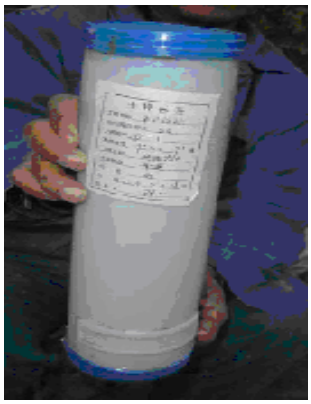

Fig. 2. Sample tag

**Collection and Process of Remoulded Soil Sample.** Remoulded soil sample means sample's physical properties, as particle, water content, density, cementation, and structure, changed after preparation.

The collection package transport and process reference to Artificial frozen soil physics mechanics performance test-Part 1: Artificial frozen soil experiment sample and specimen preparation method (MT/T 593.1).

According to requirement, it collect sample from undisturbed soil layer when shaft excavation reach preset position. In lab, under room temperature, it record sample's color, smell, other and so on, then test the water content and density of representative samples. Soil sample chops, and dry at 105~110°C with constant temperature, then cool to room temperature in the dryer. Chop the dry cool sample, sieve through 2mm standard soil screen. In the experiment, In accordance with the design requirements of moisture, water added to dry soil, stirred uniformly, sealed and put in moist chamber for more than 24h.

**Main Experiment Device.** In the experiment of this paper, uniaxial strength test include making sample, constant temperature maintenance and loading. Madding sample need compaction Jane, cutting ring, cut disc, oven, moist chamber, dryer, wooden mallet, rubber plate, aquarium, modification knife, hacksaw, Vaseline, wrap, plastic bags, sample tags and other containers. Constant temperature maintenance uses high accuracy XT5402 incubator, Meeting the temperature requirements of 0 ~ 60°C. The loading device include MTS-815 digital hydraulic servo machine, LC-127D road material strength machine, and CSS-1120 electronic multifunction machine.

**Test Method and Process.**

**Preparation of Soil Sample**. The test use remoulded soil sample. The sample meet requirements of Standard for soil test method- GB/T50123-1999. Put soil into dryer after screen. During the test, set ingredients in accordance with the required amount of soil moisture.

The sample prepared with pressure by layers. According to Volume, dry density, water content, it could calculate the mass of wet soil of each sample required. Divide the wet soil into 5 parts and press them into container by layer. In the test, a Φ60mm×H120mm ferruginous Cylinder with 5 loop lines is used to make sure same thickness of every layer. Difference between the measured value of density and theoretical value no more than 0.01g/cm3, water content no more than ±1%. The sample uniformity mainly presented in uniformity of density and water content, and the requirement of density and water content will decrease the discreteness of result.

**Test procedure**. There are four procedures in the frozen soil uniaxial compression test, which are develop hardware, constant temperature, lading and data acquisition.

Develop hardware and constant temperature: Configure the soil contains the water content that experimental designed, and put them in the clay for 24h, then in the sand soil for 6~8h. Coat a thin layer Vaseline in the brass test modes, and put the soil into the test modes delimitative, at last sand the test modes into the refrigerator. It is time to dismantle the test modes when they are frozen, Measuring soil sample size and weighed and recorded, and sand into thermostat for 24~48h after the test modes are Waterproofed

Lading: the frozen soil uniaxial compression test applies the way of controlling the strain rate, the loading rates of test machine are 1, 8, 1mm/min when the temperature are -5, -10, -15°C, and the strain rate are 0.013333, 0.106667, 0.013333%/s, the Temperature fluctuation range controls in ±0.2°C.

Data acquisition: Displacement sensors record the soil displacement, and loading sensors record the soil loads, sanding the results in the design documents which can be calculated as the stress-strain curve.

**Test Results**. The test results are shown in Table 1.

## Cretaceous System Stratum Frozen Soil Thermo-physical Properties

Table 1 Test of soil mechanical properties

| NO. | Temperature (°C) | Clay samples | | | Mudstone single axis compressive strength |
|---|---|---|---|---|---|
| | | Single axis compressive strength | Elastic modulus | Poisson's ratio | |
| 1 | -5 | 1.38MPa | 69MPa | 0.36 | 2.34MPa |
| 2 | -10 | 2.06MPa | 98MPa | 0.29 | 4.07MPa |
| 3 | -15 | 3.14MPa | 201MPa | 0.23 | 6.11MPa |

Frozen soil is a plurality mixture which contains Mineral particles, ice, unfrozen water and gas, there is a big difference between frozen and unfrozen soil, which directed by the water difference phase state or changing phase state. The main index of thermo-physical properties are specific heat, coefficient of heat transmission, temperature transfer coefficient, thermal capacity, latent heat of phase change. Specific heat capacity per unit of mass (λ) is called the per unit area soil conduct the temperature when the temperature gradient is 1°C /m in the direction of heat flow. It reflects the frozen soil conducting heat property. Soil thermal diffusivity is an index of the ability to change their temperature when the nearby soil's temperature is changing. It is a Basic indicator of study the process of unstable heat conduction. The soil heat capacity is the total heat of soil send out per volume when the temperature change range from initial temperature to frozen temperature. Latent heat of phase change is a sending out heat of water or a liquid change from liquid-state to Solid-state under a temperature state.

The test results are shown in Table 2. The frozen temperature of clay and mudstone are -0.56, -1.72°C.

Table 2 Specific heat of soil samples

| NO. | Temperature (°C) | Fine sand coefficient of heat transmission (w/(m·K)) | Clay samples | | Mudstone samples (kJ/(kg·K)) | |
|---|---|---|---|---|---|---|
| | | | Specific heat (kJ/(kg·K)) | Coefficient of heat transmission (w/(m·K)) | Specific heat (kJ/(kg·K)) | Coefficient of heat transmission (w/(m·K)) |
| 1 | -5 | 2.977 | 1.132 | 1.727 | 0.982 | 1.936 |
| 2 | -10 | 3.163 | 1.089 | 1.796 | 0.967 | 1.983 |
| 3 | -15 | 3.536 | 1.066 | 1.821 | 0.935 | 2.105 |

## Conclusion

Here are the main conclusions of cretaceous System stratum frozen soil Mechanical properties and thermal physical characteristics under the different properties of soil and temperature through a range of cretaceous System man-made frozen tests.

The single axis compressive strength of cretaceous System man-made frozen soil linearly increase with the temperature decreases under the same properties of soil and moisture content, The calculation ,σ-frozen soil short single axis compressive strength, MPa; a and b-the constants of soil property; θ-frozen temperature, °C.

The elastic modulus of cretaceous System man-made frozen soil increase with the temperature decrease under the same properties of soil and temperature. The Poisson's ratio decrease with the temperature decrease.

The specific heat of cretaceous System man-made frozen soil decrease with the temperature decrease. The coefficient of heat transmission increase with the temperature decrease.

**References**

[1] Chongxian Wang. Experimental Study on Physical and Mechanical Properties of Silty Permafrost [J]. Coal Science and Technology, 2000, Vol.28, No.8: 9~12.

[2] Wanwei Peng. Freeze Relations with Loess Tensile Strain Rate and Temperature [J]. Chinese Journal of Geotechnical Engineering, 1998, Vol.20, No.3: 31~33.

[3] Benliang Fan, Boyang Ding, Jifeng Wang. Uniaxial Compressive Strength Properties of Artificial freezing of Saturated Soft Soils of Hangzhou [J]. Journal of Zhejiang University of Technology, 2000, Vol.28, No.4: 319~325.

[4] Chunlei Wang, Qiang Xie, Chongxi Jiang. Experimental Study on Salt Unconfined Compressive Strength of Permafrost [J]. Subgrade Engineering, 2005, No.5: 58~60.

*Applied Mechanics and Materials Vols. 580-583 (2014) pp 966-970*
*© (2014) Trans Tech Publications, Switzerland*
*doi:10.4028/www.scientific.net/AMM.580-583.966*

# Coordinate transformation and the volume covering fractal algorithm of rock surface morphology

Ke MAN[1,2, a]，Yang ZHAO[3, b]，Hefei LI[3, c]

[1.] Division of Environment Engineering, Beijing Research Institute of Uranium Geology, Beijing 100029, China;

[2.] Key Laboratory of China National Nuclear Corporation on high level radioactive waste geological disposal, Beijing 100029, China;

[3.] Institute of Rock Mechanics and Fractals, China University of Mining and technology, Beijing 100083, China

[a.] thepopman@sina.com, [b.] zhaoyang@sina.cn, [c.] lihefei@sina.cn

**Keywords:** Coordinate transformation; surface morphology; fractal;

**Abstract.** The mechanics characteristics of the rock are mainly subjected by the joint and the fractures of the rock mass. For the joint, the surface morphology is especially the dominant influence factor. In order to describe the nature physics of rock surface, the surface morphology embarked on a fractured granite rock is described. And use the fractal dimension to calculate the volume of covering rock fracture surface, the relationship between fractal dimension and physical characteristics of rock surface.

## Introduction

Granite is a fractured rock. Deep underground of the granite tend to be able to form a complex fracture network, resulting in a huge seepage system. The fissures and groundwater seepage stress each other, which affects the safety of the role of deep nuclear waste disposal. However, getting the measured value is somewhat difficult. Complex fracture surface is rough surface, you want to use or evaluate the measured data to express the need for a fractured face every part of the fracture surface were measured. If you insist on using the method of measurement to express an artificial fracture surface, the workload is far too large. The actual measurement operation projects will encounter many unexpected trouble. It is difficult to measure the rough rock surface in a point of the projection height and the slope of the projection, followed by the desired distance between any two levels of access is also easy to do accurately, the common measurement tool furthermore error often can't be ignored. Statistical methods are complex and have a degree of objectivity; the results of statistical methods may be affected by the measuring instrument to measure the actual operation of the measurement accuracy. Therefore, many scholars began to characterize the surface morphology of exposure to the joint surface is different from the statistical methods. So far, it has reason to believe that the rock fracture surface morphology is very exploring, and has been getting many meaningful results [1-4].

Fractal methods have been applied to joints and fissures. Fractal dimension approach is still immature, through the tireless efforts of scholars have found that if the fractal dimension of the surface and the slope of the bosses will be able to combine, it will be more objective characterization of the physical characteristics of the rock surface .

Currently there are four kinds of methods for measuring. Fractal measurement of fracture surfaces, respectively perimeter-area relationship method (Kojima law-silt island method), bit -shaped cross-section method (Profile or Vertical section method), power-law spectrum method and self- affine fractal methods, but these methods are difficult to accurately express the rough section anisotropy and local features on the spatial distribution [5]. Calculation methods currently used to estimate the fractal dimension of real rock section, the most representative is triangular prism surface area method [6] , covering projection method [7,8] , covering cube method [9] as well as used herein, the volume of new overlay method. Because you can't change the nature of the approximate calculation of the fractal dimension, it is still not perfect with many errors, but the method of fractal geometry to the study of surface topography of rock brings new ideas and breakthroughs [10-13].

## Coordinate transformations

Normally, the test data is measured to obtain the coordinate conversion, which is not required. The calculation of the average value will not be affected. But in the study of rock surface morphology characteristics, often resulting scan data directly are not suitable for direct calculation. It requires some processing. Among these treatments, the method often requires the use of coordinate transformation, the transformed position of the original data to another new coordinate system to form a new set of position data. The new coordinate system is more conducive to our calculation processing of data can be analyzed better explored. Coordinate conversion process is actually a variation of the method of the coordinate system. The key is not how to calculate mathematical knowledge, but rather the transformation of the original scan data into what kind of a new coordinate system.

Then point to the distance formula based on surface scan data to transforming the old coordinate the new coordinates, we get the scan data of rock samples in the new coordinate system. The 99 data points are show Fig.1. The points that need to be transformed are show in Fig.2.

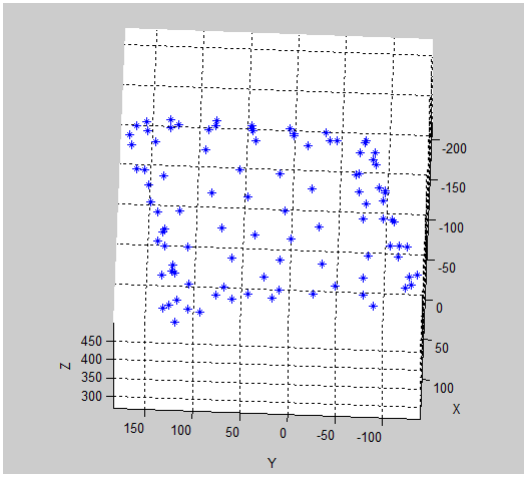


Fig.1. 99 Figure bit data

Fig.2. 29 points to be converted

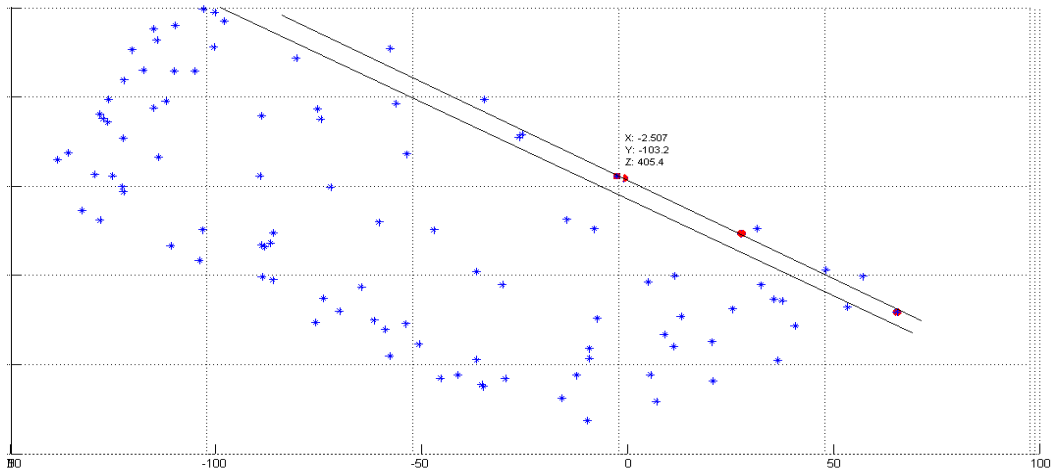


Fig.3. Select the datum

The method of this paper is easy to understand. First, establish benchmarks 3:00 X-Y plane. Select three data points XY plane parallel surfaces in red dots data. The three points are show in Fig.3. They are,

No. 48 data point (0.5797 14101 404.3);

No. 36 data point (66.76 121.6 329.3);

No. 89 data point (-2.507 -103.2 405.4);

Calculate the plane,

$$X - 0.0087Y + 0.88Z - 357 = 0 \tag{1}$$

Easily calculated parallel to the plane and has No. 17 data point (-85.79 -95.13 373.6)

For the new datum,

$$X - 0.0087Y + 0.88Z - 243.8 = 0 \tag{2}$$

The second step, seeking X_Z datum, as over

No. 19 (-130.8 147.4 386.2)

No. 26 (-11 124 294)

With two data points and vertical X_Y, it gets that

$$X + 9.237Y - 1.045Z - 827.18 = 0 \tag{3}$$

Readily calculated parallel to the surface and the data points over the 17th plane,

$$X + 9.237Y - 1.045Z + 1355 = 0 \tag{4}$$

The third step, seeking Y_Z datum,

Over 17 data points and perpendicular to the first two faces, it gets that

$$X - 0.2371Y - 1.1387Z + 488.689 = 0 \tag{5}$$

## Fractal

Classing the definition prism (see Fig.4), the bottom surface of the upper and lower triangular or quadrangular, the remaining faces are quadrilateral, and the quadrilateral are parallel to each of the two mutually adjacent common sides, surrounded by the surface of the polyhedron.

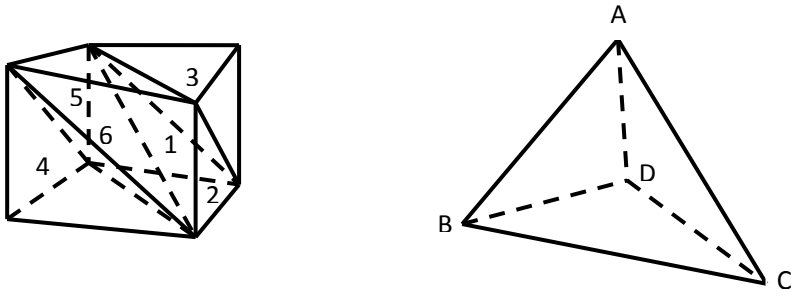


Fig.4. Schematic splitting prism class

Any class prism can be divided into six arbitrary tetrahedrons; accumulating six tetrahedral volumes can be obtained at any volume class prism. Volume formula for an arbitrary tetrahedron

$$V = \frac{1}{6}\begin{vmatrix} 1 & 1 & 1 & 1 \\ x_1 & x_2 & x_3 & x_4 \\ y_1 & y_2 & y_3 & y_4 \\ z_1 & z_2 & z_3 & z_4 \end{vmatrix} \tag{6}$$

Where (x1, y1, z1), (x2, y2, z2) (x3, y3, z3) (x4, y4, z4). Coordinate values are arbitrary tetrahedron of four vertices A, B, C and D.

Changing observation scales covering recalculated to cover the entire surface roughness required total, if the rough surface fractal nature. According to fractal theory, the following relationship is,

$$N(\delta) \sim c\delta^{-s} \tag{7}$$

S is called the fractal dimension, c is the volume per unit $R^3$. Calculated at different scales corresponding to the total volume of coverage, you can get a logarithmic scale with the total relationship, thereby calculating the fractal dimension.

## Conclusions

Scanning data often can't be directly used, the need for coordinate transformation in order to fit the required research, coordinate transformation explored in this paper is based on the selected plane carried, can fit to calculate the fractal dimension, with the presentation of the practical aspects of rock surface topography.

Volume covering method shows a good linear relationship with the volume. The method describing rough surface is feasible. Volume covering method directly adopt the laser scanner elevation data to calculate without regard to whether the scanning errors and other problems caused by the pitch, effectively avoiding the interpolation error.

## Acknowledgements

This work was financially supported by the Chinese National Science Research Fund (41202207).

**Reference**

[1] Bradshaw A D． Restoration of mined lands－using natural process[J]． EcolEng，1997，( 8) : 255- 269．

[2] Wang, YS Cui, YT Dong. Phytoremediation-An effective approach of heavy metal cleanup f QR rom contaminated soil[J] Acta Ecologica Sinica，2001， 21( 2) : 326 -331．(in Chinese)

[3] YH Wang, XJ Chen, YL Zhao. Remediation Technology of Contaminated Soils in the Metal Mine[J]． Journal of China University of Mining & Technology，2007，36 ( 4 ) :487 - 493．(in Chinese)

[4] JIANG Y，KOYAMA T，LI B，et al. Numerical modeling of fluid flow in single rock fracture during shear with special algorism for contact areas[J]. Journal of the Mining and Materials Processing Institute of Japan，2008，124：129-136.

[5] He-ping XIE. Fractals-rock mechanics [M]. Beijing: Science Press, 1996. (in Chinese)

[6] CLARK K C. Computation of the fractal dimension of topographic surfaces using the triangular prism surface area method [J]. Computers & Geoscience, 1986, 12(5): 713-722.

[7] H XIE, J A WANG, STEIN E. Direct fractal measurement and multifractal properties of fracture surface [J]. Phy Lett A, 1998, A 242: 41-50.

[8] H XIE, J A WANG, KWASNIEWSKI M A. Multifractal characterization of rock fracture surfaces [J]. Int J Rock Mech Min Sci, 1999, 35(1): 19-27.

[9] H W ZHOU, H XIE. Direct estimation of the fractal dimensions of a fracture surface of rock[J]. Surface Review and Letters, 2003, 10(5): 751-762.

[10] He-ping XIE, Xiu-qian XUE. Mathematical foundations and methods in fractals[M].Beijing: Science Press, 2005. (in Chinese)

[11] Clark K C. Computation of the fractal dimension of topographic surfaces using the triangular prism surface area method[J]. Computers and Geoscience, 1986 12(5):713-722.

[12] H Xie, H W Zhou, Feng Z. Further research on the Projective Covering Method [J]. International Journal of Solids and Structures, 2000, 37(33): 4627-4630.

[13] DJ Xue, HW Zhou. Algorithm of fractal dimension of rock fracture surface based on volume estimation [J]，Chinese Journal of Geotechnical Engineering，2012，34：1256-1262(in Chinese)

*Applied Mechanics and Materials Vols. 580-583 (2014) pp 971-976*
*© (2014) Trans Tech Publications, Switzerland*
*doi:10.4028/www.scientific.net/AMM.580-583.971*

# Study on control technology of slope in mountainous areas of southwest China under complex geological conditions

Wei Yang[1 2, a], Haiping Li[1 2, b]

[1]China Merchants Chongqing Communications Research & Design Institute Co., Ltd., Chongqing 400067, China

[2]National Engineering & Research Center for Highways in Mountain Area, Chongqing 400067, China

[a]dlyangwei@cmhk.com, [b]lihaiping@cmhk.com

**Keywords:** slope; deformation; geological structure; cataclastic rock; construction control

**Abstract.** Deformation process of slope has been controlled by a variety of factors due to the unique geological, hydrological and meteorological conditions. And southwest mountain areas of China has been become high incidence areas of slope diseases during highway construction and operation. According to Wendu Road K55+590 ~ K55+670 left slope engineering geological environment, the deformation process and mechanism analysis, The key factor of the slope deforming destruction is proposed. the appropriate engineering treatments and the construction control measures are also proposed based on analysis.

## Introduction

Deformation process of cutting slope is controlled by a variety of factors in addition to its internal geological control factors during the high grade highway construction and operation, but the external agency is the key factors affacting ing the development of slope deformation[1, 2]. Take the left side slope of the second grade highway Wenshan to Dulong（K55+590~K55+670）reconstruction project as an example, the detail introduction about slope deformation and treatment process under the complex geological condition southwest mountainous area is provided, especially the control process during the implementation of slope treatment. It provides some experiences for slope disease treatment for similar area or similar conditions.

## Characteristic and geological environment of the slope

**Characteristic of the slope.** Original design height of slope is 22.5m, slope ratio is 1:0.75, each grade heights is 10m. The slope collapsed several times during the construction, then slope ratio was adjusted to 1:1.5, and the total height of slope reached 32.5m. The excavation reached the design elevation in April of 2010. Tensile cracks appeared on the three-stage of the left side slope mouth and first-order platform after several days of continuous rain. And anterior border of slope extendeded outward significantly, soil and rock of first-order side slope collapsed partly. The stability of slope is bad and instability phenomenon appeared. Huge security risk is formed for highway construction and traffic and normal construction of roadbed is seriously affected. The complete picture and cross-section of the slope was shown in fig.1 and fig.2.

Fig.1 Slope construction and deformation

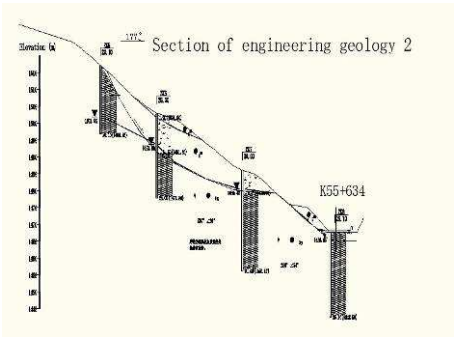


Fig.2 Typical geological cross-section of the slope

**Geological environment of the slope.** The slope located at a transitional zone between a temperate climate and tropical monsoon climate of Nanpan river, with warm, dampness climate, rainy in general. The annual maximum temperature is 22.9℃, minimum temperature is 6.3℃, and the average temperature is 16.7℃. The average annul precipitation was 1366.13mm.The rainy season is from June to September, dry season is from December to the next April. A v-shaped gully developed in southwestern and northern areas near the slope, there is flood flowing through during the rainy season, and with no large surface water near the site. Regional landform unit of the slope belongs to denuded low-middling mountain areas, the slope is located in anterior mid-part of the southern slope, and the nature slope is about 20°to 30°. There formed a three-stage cut slope with 36m heigh and 33°~53° grade. Its main formation lithology consists of the quaternary eluvial slope wash of gravelly silty clay(Qel+dl), Pojiao group argillaceous shale of lower devonian system(D1p), and carbonaceous shale [3]. The slope is located in the "Wenshan Yangliu well broom-like structure "influence zone. The seismic peak ground acceleration is 0.05g, the reflection of characteristic period of ground motion is 0.35s, the basic seismic intensity is six degree. Influenced by two compresso-shear fault belt, the rock secondary folds of the slope developed well, the jointed and fractured of bedrock developed and rock is broken. Based on lithologic combination and groundwater storage, the site groundwater is mainly consists of the loosened rocks pore-water of quaternary and the weathering mesh fissure water in bedrock.

## Deformation and failure mechanism of slope

**Structural characteristic of the slope.** The main formation lithology consists of the quaternary eluvial slope wash of gravelly silty clay (Qel+dl), pojiao group argillaceous shale of lower Devonian system(D1p),and carbonaceous shale. The quaternary eluvial slope wash composed of silty clay, brown red, brown yellow, little humid, hard plastic and mixed with strong weathering brecciated shale ,the thickness is about 1.00, Pojiao group of lower Devonian system composed of argillaceous shale and carbonaceous shale, the characteristics of argillaceous shale are yellow, shale structure and thin-bedded construction; the characteristics of carbonaceous shale are dark grey, black, compact structure and thin-bedded construction. The rock-formation attitude is 230°∠24°, the rock trend to be larger angles with left side artificial slope of the planned road, which belongs to tangential slope, and the attitude of rock formation is favorable for slope stability. Due to the influences of structure, there are crashed rock structures, and with intensive developed joint fissures. the main distance is about 5cm～20cm.The rock has the characteristics of gravel soil, because of argillaceous shale and carbonaceous shale mainly contain clay mineral, rich smectite and kaolin, completely decomposed shale and its weathered products has the character of high liquid limit soil, dry shrinkage and wet expansion characteristics, under normal circumstances the engineering performance is available, but after several alternation of drying and wetting its mechanical properties decrease, because of weathered rock mass has the character of cataclasite, so it's easy for rainwater infiltration ,evaporation and discharge. The slip and deformation problem is easy to occur within atmosphere influence depth (According to the local data, generally about 3m).

**The slope construction.** Original design height is 22.5m, slope ratio is 1:0.75 and each grade heights is 10m. Slope construction began in October 2009, during the construction, the slope collapsed several times, after clear away earthwork, the slope ratio was adjusted to 1.5, and the total height of slope is 32.5m. In mid-April 2010, the cutting excavation reached the design of pavement elevation, The basic shape of the cutting excavation formed. After several days of continuous rain, tensile cracks appeared on the three-stage of the out side slope groove and first-order platform; in the next several days, crack increased and became broad, the lower part of the secondary slope and near the toe of slope zone appeared phenomenon of obvious dilatancy, linear creep circumstances occurred in toe of the slope and middle lower part of secondary slope, part rock soil of first stage slope appeared slip and slump phenomenon. the stability of slope is very low and very easily distorted, under condition of continuous rainfall or Improper clear away earthwork, slope issue has become a engineering landslide problem. The slope deformation was shown as two independent rock and soil deformation and instability situation, which called: H1, H2 landslide.

**analysis of deformation mechanism.** The main material components of slope were completely decomposed shale and its weathered products, controlled by structure and weathering factors, joint fissures of the slope rock mass intensive developed and rock structures are crashed, it belongs to the category of cataclastic rock mass. On the basis of the failure mode controlled by preferred structure planes, and has the gravelly soil type slope failure characteristics at the same time. Based on slope construction and slope deformation process, the deformation of slope was clearly divided into two phases: Phase One is the problem of shallow surface, mainly scope of slope excavation or called slope excavation unloading and relaxation range. And also has the atmosphere influence depth of rock and soil deformation phase--called the shallow surface of slope deformation phase; Phase two is the formation of deep sliding surface, the instability phase of whole sliding slope[4].

## Analysis of stability for the Slope

**Calculation method.** The current calculating method of the stability of the landslide is mainly divided into three categories [5]: limit equilibrium analysis method, digital analysis method, and probability method. Limit equilibrium method is the ripest, and most widely used calculating method in engineering. Combined with the slope characteristics of the disease, based on the limit equilibrium theory, meanwhile taking the weathering rock mass structure is loose and the slope deformation has characteristics of soil landslide into account. We used the circular sliding method analyze the present model situations, and at the same time combined with the survey data we used the sliding broken line method inverse the slope deformation process, simulation and analysis of its deformation, and predicts the future trend of deformation.

**Parameters of rock or soils.** Geotechnical parameter was comprehensive determined by the basis of the geological survey report and combined with regional experiences and back analysis. See table 1 for specific parameters of slope geotechnical parameters [4].

Table 1 Slope geotechnical parameters

| Rock Name | Density(kN/m$^3$) | | C(kPa) | | φ(°) | |
|---|---|---|---|---|---|---|
| | natural | saturate | natural | saturate | natural | saturate |
| completely weathered shale | 22.5 | 23.00 | 8.5 | 7.5 | 24.0 | 23.5 |
| strongly weathered shale | 23.5 | 24.0 | 31.5 | 30.0 | 28.0 | 27.5 |

**Calculation results.** According to slope excavation situation, and in the light of progress on simulation analysis of slope deformation under continuous rainfall condition, in April 2010, section stability coefficient of the slope (K55+634) is Fs=0.953[4], the slope stability is poor, and the sliding instability phenomenon of rock soil will happen under continual heavy rainfall, The calculation results were represented in figure 3. According to the results of simulation analysis, analyzed the overall stability by using the sliding broken line method along with slipping surface. Still used the section (K55+634) as example, the strip of calculation was shown as figure 4.

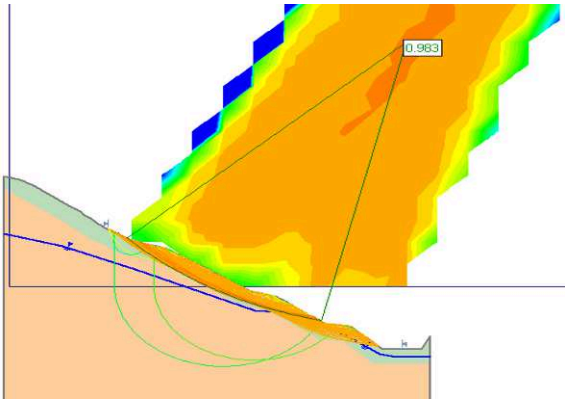


Fig.3 Stability analysis of the slope deformation (the section K55+634 in April 2010)

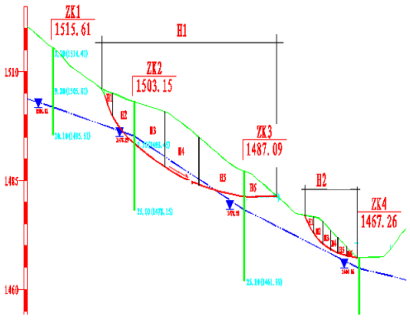


Fig.4 Slice of stability analysis of overall slope (the section K55+634 in April 2010)

Under natural condition the stability coefficient of residual sliding force of slope H1 was Fs=1.05, the residual sliding force is T=1345.95kN, under continuous rainfall condition the stability coefficient is Fs=0.975, the residual sliding force is T=1635.90kN, the landslide H2 was mainly loose rock mass sliding formed, the scale is small, so take the results of the calculation results of the landslide H1.

## Treatment schemes and dynamic design of the slope

Based on the specific characteristics of the slope, considered the bad stability of rock and soil mass of the slope, and the tendency of partial slope sliding, slumping and whole instability, at beginning of slope deformation has used the scheme of purge earthwork for the slope treatment. But after purge earthwork, the slope deformation region continuous extend to trailing edge, and the scale is continually expanding, to avoid further expansion of the slope deformation, this treatment scheme did not reconsider the scheme of purge earthwork. But considering the deformation of surface structure of rock and soil has been completely destroyed, and the loose structure, after saturated with water it is easily slumping under continuous rainfall condition, and it is difficult to add effective support, therefore, used appropriate clearing process for the shallow deformation, the demonstration of reinforcement scheme mainly focus on considering the basis to ensure the overall stability of the slope and taken the stability principle of shallow rock and soil of the slope into account. Used the anti-slide pile as the main supporting engineering, the relative steep slope used hanging net sprayed concrete and closed anchorage to control local deformation of soil slope, the relative gentle slope used the supporting seeping grooves combined with skeleton planting protection ,and assisted with interception and discharge comprehensive treatment.

During the anti-slide pile construction, the process of hole digging appeared extrusion failure and cracking phenomenon at the starting point and the middle parts of the slope, according to the dynamic design principles, steel pipe piles were added in the hierarchical platform for emergency supporting and retaining, at the same time set up temporary back pressure engineering in the lower to ensure the safety of construction, controlling the development rate of slope deformation. After the implementation of emergency measures, main project of the anti-slide pile basically completed. The specific design was shown in figure 5.

Because groundwater is very developed, the rock mass of first stage slope weathering serious, after repeated disturbances, the phenomenon that the poor slope stability, soil slippery and slumping is prominent, and controlled by setting up protective covering retaining wall of the road cut, as shown in figure 6.

After finished the later anti-slide pile construction of slope, the monitoring data shown that the anti-slide pile deformation of the middle of third grade and the fourth grade is large, due to the developed groundwater the first degree appeared severe collapse, to ensure the reinforcement effect, the anchor cable frame beam reinforcement was added to the third grade of slope K55+590-K55+656 and fourth grade of slope K55+608-K55+644, added steel pipe pile retaining to the platform of first

slope and added retaining wall protection to the surface of first slope respectively, as shown in figure 5 and figure 6.

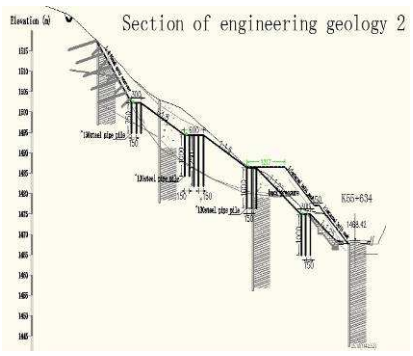


Fig.5 Section design of emergency management

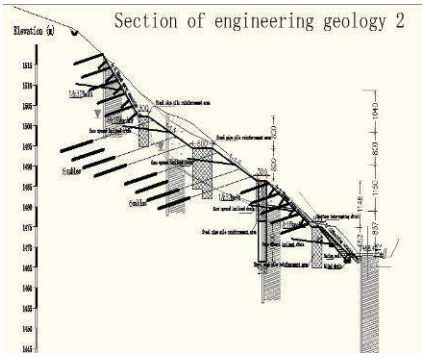


Fig.6 Section design of slope reinforcement （the section K142+560）

After implementation of the above scheme, slope deformation can be effectively controlled; Monitoring data show that, since completed the treatment engineering about 3 years, the various measures of stress and strain are in the design range, slope performances well.

## Conclusions

(1) In southwest mountain area the structure is developed, the rock in fractured zone and its influence zone belong to cataclasite, the slope failure mode on the basis of the controlled preferred combination structure planes, has the gravel soil slope failure characteristic at the same time.

(2) In southwest mountain area, the process of deformation development under complex geological conditions can be divided into two stages, stage one is the problem of shallow surface layer, namely the incidence of slope excavation or called slope excavation unloading relaxation incidence, concurrently with the rock soil mass deformation phase in atomspheric influence depth, stage two is the formation of slip surface, and the whole slope sliding phase.

(3) Adopted the treatment thought of stage control implementation to reinforce the left side slope of Wendu road k55+590~670, and combined with a variety of measures for comprehensive treatment. During slope treatment, the whole slope is stable, the tunnel construction is safe, and the design is realized.

(4) The standard of successful slope treatment is “Safe, economic, and environment-friendly”, the deformation development of slope excavation is a continuously accumulation process, cognition of its deformation mechanism is also a gradually perfected process, strengthen the stage control, with the change of external conditions (Such as weather, adjustment of the construction process and so on), the targeted treatment measures on the slope is proposed, according to the deformation stage, select the appropriate reinforcement time is the key to successful treatment of the slope.

## Acknowledgements

This work was financially supported by the Science and Technology Project of Western Traffic Construction (2009 318 740 99) and the Chongqing Natural Science Foundation (cstc2012jjA30008).

## References

[1] Zhang Zhuoyuan, Wang Shitian, Wang Lansheng. Analysis principles of engineering geology [M].Beijing: Geological Publishing House, 1981. (in Chinese)

[2] Xiao Shufang, Yang Shubi. Rock soil mechanic [M].Beijing: Geological publ. House, 1987. (in Chinese)

[3] Geological Engineering Investigation Institute of Kunming Building Materials. The report of engineering geological exploration of the left slope engineering of the second highway reconstruction project Wenshan to Dulong K55 +590 ~ K55 +670[R].Kunming Yunnan, 2010.(in Chinese)

[4] Chongqing Communications Research and Design Institute of China Merchants. Left side slope treatment construction design of Wenshan to Dulong second highway reconstruction project K55 +590 ~ K55 +670 [R]. Chongqing, 2011(in Chinese)

[5] Chen Zuyu. Analysis of the soil slope stability (Principle, Method and Program)[M].Beijing: China WaterPower Press, 2003.(in Chinese)

[6] Hu Hao. Research and prevention of landslide disaster in the mountain road[D].Hunan, Central south university, 2010.( in Chinese)

*Applied Mechanics and Materials Vols. 580-583 (2014) pp 977-980*
*© (2014) Trans Tech Publications, Switzerland*
*doi:10.4028/www.scientific.net/AMM.580-583.977*

# Anisotropic Bounding Surface Model in ABAQUS Software

Qin Yazhou[1,2,a], Chen Qi [3]

[1] School of Transportation ,Nantong University, Jiangsu Nantong 226019, China

[2] Xinglin College, Nantong University, Jiangsu, Nantong 226019, China

[3] Guangdong Hydropower Design Institute, Guangzhou, 510635 , China

[a] yazhouqin2008@163.com

**Keywords:** Dynamic Properties ,Soft Clay , Anisotropic Bounding Surface, UMAT Subroutine.

**Abstract.** This paper presents an improved anisotropic bounding surface model which is based on Wheeler's elastoplastic model (S-CLAY1). The developed model is programmed in ABAQUS software by writing UMAT subroutine, which is integrated in Return Mapping Algorithm. The parameters sensitivity analysis is implemented on plastic modulus. The study shows that the developed anisotropic bounding surface model is capable of describing the dynamic properties of soft clay.

## Introduction

Natural soft clays are generally anisotropic. Most dynamic properties of soft clay are associated with certain preferred orientation in space. Anisotropy of soft clay can be classified into two components, one is inherent anisotropy and the other is stress-induced anisotropy by Casagrande [1]. There have been generally two ways to quantify the anisotropy of soft clay, one is based on micromechanical concept and is called fabric tensor[2,3],the other is based on macroscopic response of soft clay and is named anisotropic tensor[4].

Wheeler[5] proposed an anisotropic elastoplastic model for soft clay from Finland(S-CLAY1). The model is an extension of the critical state model and can describe the change of yield curve inclination with plastic strain.

This paper proposed the new constitutive model of soft clay based on S-CLAY1 model and the bounding surface theory, which is capable of describing anisotropy and dynamic properties of soft clay.

## The anisotropic bounding surface model

### Bounding surface equation of the model

$$F=\frac{3}{2}(\overline{s}_{ij}-\overline{p}\alpha_{ij})(\overline{s}_{ij}-\overline{p}\alpha_{ij})-(M^2-\frac{3}{2}\alpha_{ij}\alpha_{ij})(p_0-\overline{p})\overline{p}=0 \tag{1}$$

where $\overline{s}_{ij}$ and $\overline{p}$ are the mean effective stress and deviatoric stress on bounding surface, respectively, $\alpha_{ij}$ is anisotropic tensor defining the inclination of the yield curve, $M$ is the critical state value of the stress ratio, $p_0$ defines the size of the yield curve.

### Hanrdening laws

The model incorporates two hardening laws. The isotropic hardening law describes change of size of the yield curve, which is assumed to be related to the change of pre-consolidation pressure $P_0$,

$$\dot{p}_0=\frac{v_0}{\lambda-\kappa}p_0\dot{\varepsilon}_v^p \tag{2}$$

where $\lambda$ is the slope of the post-yield compression curve in the $e-\ln p$ plane, $\kappa$ is the slope of elastic swelling lines in the $e-\ln p$ plane, $v_0=1+e_0$, $e_0$ is initial void ratio.

The rotational hardening law describes the change of inclination of the yield curve produced by plastic strain, include plastic volume strain $\varepsilon_v^p$ and plastic deviatoric strain $\bar{\varepsilon}_s^p$

$$\dot{\alpha}_{ij}=\mu[\left(\frac{3s_{ij}}{4p}-\alpha_{ij}\right)<\dot{\varepsilon}_v^p>+\beta\left(\frac{s_{ij}}{3p}-\alpha_{ij}\right)\dot{\bar{\varepsilon}}_s^p] \tag{3}$$

where the soil constant $\beta$ controls the relative effect of plastic deviatoric strains on the rotation of the elliptical surface, the soil constant $\mu$ controls the rate at which the deviatoric fabric tensor heads toward their current target values.

**Mapping rule**

Radial mapping rule has been adopted in the developed mode[6,7].

**Elastic modulus**

Elastic modulus incorporates two components, the elastic shear modulus *G* and the elastic bulk modulus *K*. The elastic shear modulus *G* is related to the elastic bulk modulus *K* by assuming a constant value of Poisson's ratio *v*,

$$K=\frac{v_0}{\kappa}p\ ,\quad G=\frac{3K(1-2v)}{\left[2(1+v)\right]} \tag{4}$$

The relationship between the elastic increments of volumetric and deviatoric strain is

$$\dot{\varepsilon}_v^e=\frac{\dot{p}}{K}\ ,\quad \dot{e}_{ij}^e=\frac{\dot{s}_{ij}}{2G} \tag{5}$$

**Plastic modulus**

The developed model obeys the associated flow rule. Therefore the yield function also serves as the plastic potential function. According to the consistency conditions, the bounding plastic modulus $\bar{K}_p$ is obtained as

$$\bar{K}_p=-\left(\frac{\partial F}{\partial p_0}\dot{p}_0+\frac{\partial F}{\partial \alpha_{ij}}\dot{\alpha}_{ij}\right)/\dot{\Lambda} \tag{6}$$

Where $\Lambda$ is plastic loading index.

The plastic modulus at image stress state in the proposed model is

$$\begin{aligned}\bar{K}_p=&bp\left[\frac{v_0}{\lambda-\kappa}p_0\left(M^2-\frac{3}{2}\alpha_{ij}\alpha_{ij}\right)+3\mu\left(bs_{ij}-p_0\alpha_{ij}\right)\left(\frac{3s_{ij}}{4p}-\alpha_{ij}\right)\right]\\ &\times\left[\left(M^2-\frac{3}{2}\alpha_{kl}\alpha_{kl}\right)(2bp-p_0)-3b\left(s_{kl}-p\alpha_{kl}\right)\alpha_{kl}\right]+3b^2p\mu\beta\\ &\left(bs_{ij}-p_0\alpha_{ij}\right)\left(\frac{s_{ij}}{3p}-\alpha_{ij}\right)\left[6\left(s_{kl}-p\alpha_{kl}\right)\left(s_{kl}-p\alpha_{kl}\right)\right]^{\frac{1}{2}}\end{aligned} \tag{7}$$

The plastic modulus at current stress state in the proposed model is obtained by interpolation method as

$$K_p=\bar{K}_p+\frac{v_0}{\lambda-\kappa}p_A R_{ij}R_{ij}\left(\frac{l}{<r_0-sb>}\right)^W \tag{8}$$

Where $P_A$ is variable related to the value of plastic modulus, $R_{ij}$ is gradient of plastic potential, *s* denote the size of elastic zone, *W* is positive constant[8].

**The parameter sensitivity analysis**

The proposed model involves 9 material parameters. The parameters $\lambda$， $\kappa$， $\nu$， $M$, $p_0$ can be determined in a standard process from triaxial and oedometer tests, bounding surface configurations($W$, $P_A$), these parameters can be determined as proposed by Ling, anisotropic parameters($\beta$， $\mu$) can be determined as proposed by Wheeler. Various value of variable $P_A$ was taken($P_A$=200，$P_A$=2.0E4) to investigate the function of $P_A$.

The required model parameters are listed in Table 1.

Table1. Parameters in simulations of undrained triaxial cyclic test

| $\lambda$ | $\kappa$ | $\nu$ | $M$ | $\mu$ | $\beta$ | $W$ | $p_0$/kpa | $P_A$ |
|---|---|---|---|---|---|---|---|---|
| 0.17 | 0.034 | 0.3 | 1.1 | 15 | 0.6 | 2 | 600 | 200/2.0E4 |

The dynamic load in simulations is the positive and negative alternating load, as shown in Fig.1.

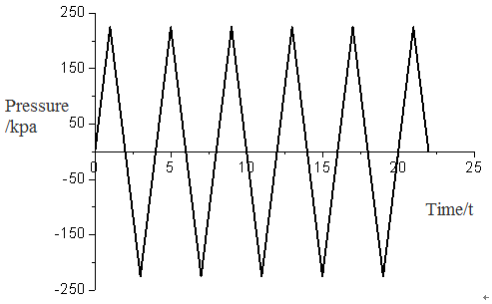


Fig.1 The dynamic load in test

If $P_A$=200，the effective stress path curve and stress-strain curve of soft clay of the simulations are shown as Fig.2 and Fig.3.

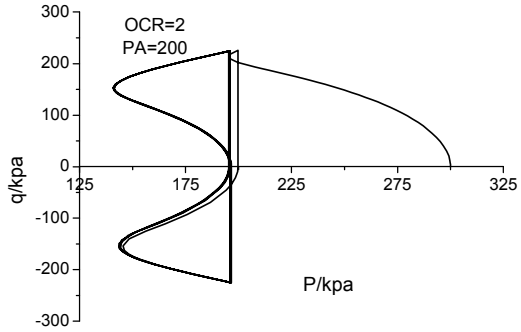


Fig.2. Numerical simulation of the effective stress path of soft clay ($P_A$=200)

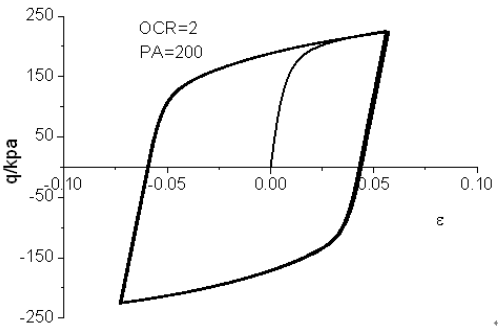


Fig.3. Numerical simulation of the stress-strain of soft clay ($P_A$=200)

Fig.2 and Fig.3 show the results of numerical simulations of undrained triaxial cyclic test on soft clay with $P_A$=200. According to equation (10), the simulation results show the plastic modulus of soft clay is small and the hysteresis loops is large. Larger strain of soft clay is produced compared with the actual deformation of soft clay. So the simulation results do not reproduce the actual dynamic characteristics of the soft clay with $P_A$=200.

If $P_A$=2.0E4，the stress path curve and stress-strain curve of soft clay of simulations are shown as Fig.4 and Fig.5.

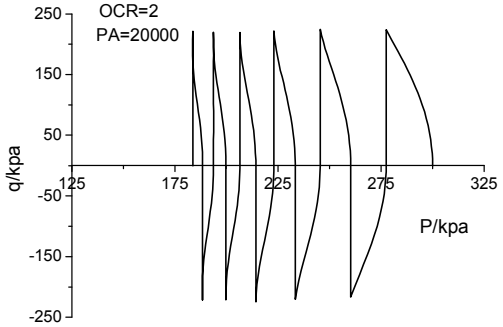


Fig.4. Numerical simulation of the effective stress path of soft clay ($P_A$=2.0E4)

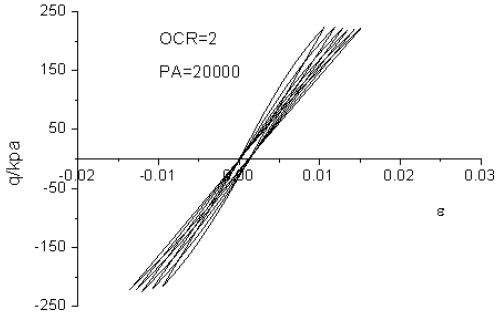


Fig.5. Numerical simulation of the stress-strain of soft clay ($P_A$=2.0E4)

Fig.4 and Fig.5 show the results of numerical simulations of dynamic properties on soft clay with $P_A$=2.0E4. The simulation results show the effective mean stress decrease and inclination increase of hysteresis loops of soft clay. It means the stiffness of soft clay decrease and soft clay become softening. It can be seen the simulation results reasonably agree with practical response behavior of soft clay under dynamic load with $P_A$=2.0E4.

## Conclusions

An anisotropic constitutive model, based on the critical state concept and bounding surface plasticity, has been developed to simulate the dynamic properties of soft clay under cyclic loading. The proposed model is programmed in ABAQUS software by writing UMAT subroutine, which is integrated in Return Mapping Algorithm. The parameter sensitivity analysis is implemented on plastic modulus. The proposed model is suitable to reproduce dynamic behavior of soft clay.

## Acknowledgements

This work was financially supported by the PhD early development program of Nantong University (03080672) and Research foundation of education and teaching of Xinglin College, Nantong University. (0312520142).

## References

[1] Casagrande A, Carrillo N. Shear failure of anisotropic materials[J]. Journal of Boston Society of Civil Engineers, 1944, 31(4): 74–81.

[2] Anandarajah A, Dafalias Y F. Bounding surface plasticity.Ⅲ: application to anisotropic cohesive soils[J]. Journal of Engineering Mechanics, 1986, 112(12): 1292–1318.

[3] Liang R Y, Ma F G. Anisotropic plasticity model for undrained cyclic behavior of clays[J]. Journal of Geotechnical Engineering, 1992, ASCE, 118(2): 227–265.

[4] Whittle A J. Evaluation of a constitutive model for overconsolidated clays[J]. Geotechnique, 1993, 43(2): 289–313.

[5] Wheeler S J, Naatanen A, Karstunen M, et al. An anisotropic elastoplastic model for soft clays[J]. Canadian Geotechnical Journal, 2003, 40: 403–418.

[6] Dafalias Y F. Bounding surface plasticity. Ⅰ: mathematical foundation and hypoplasticity[J]. Journal of Engineering Mechanics, 1986, 112(9): 966–987.

[7] Dafalias Y F, Herrmann L R. Bounding surface plasticity. Ⅱ: application to isotropic cohesive soils[J]. Journal of Engineering Mechanics, 1986, 112(12): 1263–1291.

[8] Ling H I, Yue D Y, Kallakin V N, et al. Anisotropic elastoplastic bounding surface model for cohesive soils[J]. Journal of Engineering Mechanics, 2002, 128(7): 748–758.

# CHAPTER 3:

# Tunnel, Subway and Underground Facilities

*Applied Mechanics and Materials Vols. 580-583 (2014) pp 983-986*
*© (2014) Trans Tech Publications, Switzerland*
*doi:10.4028/www.scientific.net/AMM.580-583.983*

# Construction Methods for Long-span and Bifurcation Tunnel Structure

Chunlei Xin[1,a], Bo Gao[1,b]

[1]Key Laboratory of Transportation Tunnel Engineering, Ministry of Education, Southwest Jiaotong University, Chengdu, Sichuan 610031, China

[a]raymond_xin@qq.com, [b]prgaobo@home.swjtu.edu.cn

**Keywords:** Tunnel Engineering, Long-span Tunnel, Bifurcation Tunnel, Numerical Simulation, Construction Methods.

**Abstract.** Long-span and bifurcation tunnel engineering is not very common in underground engineering field. It is difficult to construct this complicated structure because of numerous influencing factors. In order to find out the optimum construction method for long-span and bifurcation tunnel to guarantee construction security and stabilization of this project, six construction methods were compared and analyzed by using numerical simulation. The results show that: (1) The excavation of confluence segment and small interval tunnel can affect each other but the confluence segment is the crucial part of the whole project. (2) The vertical brace determines the stabilization of surrounding rock and preliminary support in confluence segment. (3) The central concrete between main tunnel and ramp tunnel is the key point to guarantee the construction security and stabilization of small interval tunnel. The above results certainly contribute to research and develop new types of construction methods for long-span and bifurcation tunnel engineering.

## Introduction

Tunnel and underground structures excavation can cause surrounding rock geostress redistribution. Therefore, construction methods of tunnel structures have significant effects on tunnels stabilization and ground subsidence [1]. Normally, tunnel cross-section is divided into several parts to excavate. Thus, different construction procedures can lead to surrounding rock loads acting on tunnel structures in different ways [2]. Ground subsidence and ground buildings destruction may happen after tunnel excavation, especially for the complicated long-span and bifurcation tunnel structures [3]. Therefore, it is of great significant for researching the tunnel structures excavation stabilization. Currently, a great many research results about construction methods mostly base on ordinary tunnel structures [4]. It is quite rare to see the research results about construction methods for long-span and bifurcation tunnel structures. This paper introduces and compares six construction methods for long-span and bifurcation tunnel structures and selects the best one. The key procedure of the best construction method is pointed out and optimized. Finally, the surrounding rock plastic zone and geostress together with preliminary support deformation characteristics are analyzed and the corresponding technical countermeasures are put forward.

## The project background and characteristics

This research bases on the Chongqing Renhechang highway tunnel project and focuses on the bifurcation segment. The bifurcation tunnel ichnography is shown in Fig.1. The bifurcation segment is composed of separation tunnel, small interval tunnel, confluence segment, amplification cavern and main tunnel. The main features of this bifurcation tunnel project are as follows: (1) The fragmentized granite is the main surrounding rock and it has bad self-stabilization; (2) This project is shallow buried tunnel structure, the buried depth of the whole tunnel is approximately 14.2-24.5m; (3) The maximum required ground subsidence is 30mm but it is difficult to achieve because of the complicated construction methods and the poor engineering geologic conditions; (4) The excavation span changes greatly in the construction process. The main tunnel excavation span is 16.23m; the

ramp excavation span is 10.50m; the confluence segment excavation span is 27.80m. The cross-sectional profile of bifurcation tunnel is shown in Fig.2.

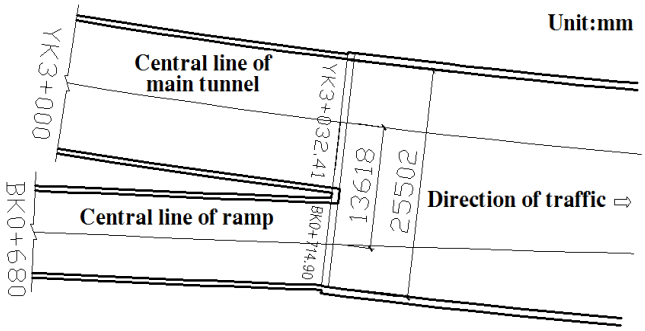


Fig.1 Ichnography of bifurcation tunnel

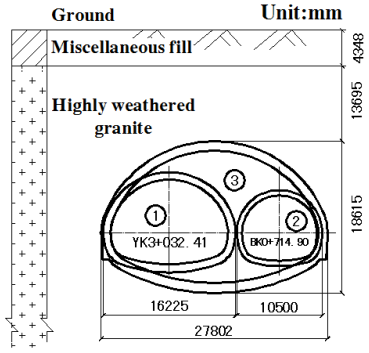


Fig.2 Cross-sectional profile of bifurcation tunnel

## Comparison and selection for construction methods

Bifurcation segment construction is the emphases and difficulty of this tunnel project. In order to ensure construction security, six construction methods are proposed to optimize. Fig.3 shows these six construction methods and construction procedures are followed by numerical sequence.

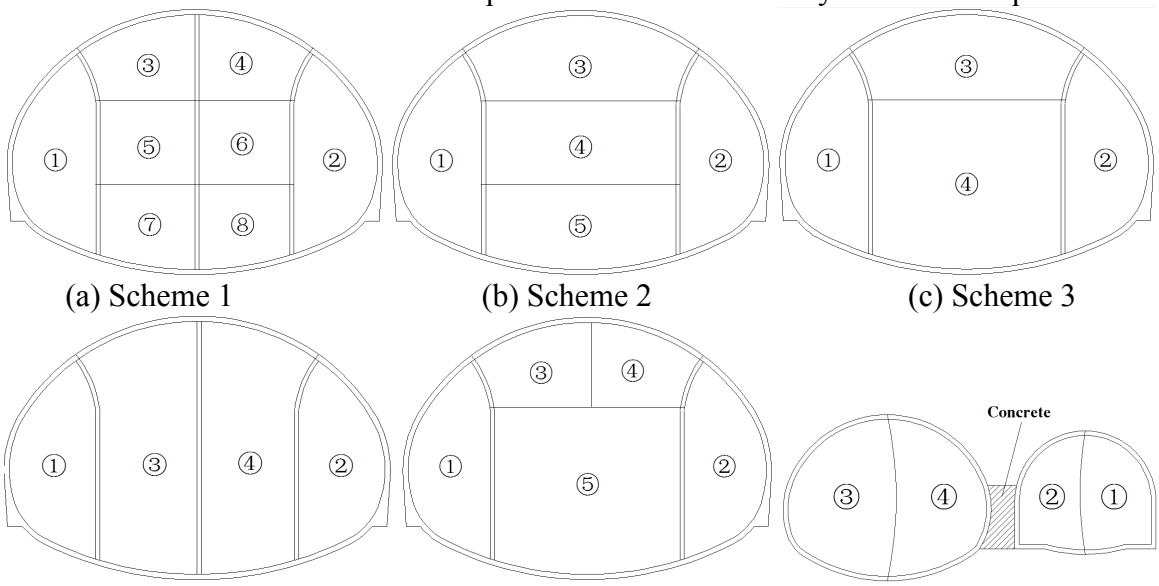


(a) Scheme 1 (b) Scheme 2 (c) Scheme 3

(d) Scheme 4 (e) Scheme 5 (f) Scheme 6 (small interval tunnel)

Fig.3 Different construction methods and construction sequence

**3-dimensional numerical model.** The entire numerical model size is X×Y×Z = 300×50×120m$^3$ (shown in Fig.4). Moreover, the scope of small interval separation tunnel is Y=0-25m and the scope of confluence segment is Y=25-50m (shown in Fig.5). The distance between tunnel central point and left or right boundary is more than 3-5 times as long as the tunnel diameter. The upper boundary is ground and the distance between bottom boundary and tunnel central point is 80m. All these boundaries setting can guarantee the accuracy of calculation results. The whole numerical model is comprised of 163600 solid elements and 181818 nodes.

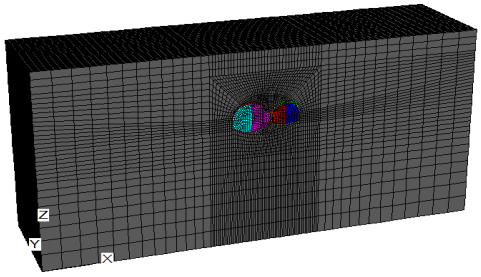

Fig.4 The entire numerical model

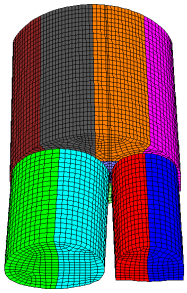

Fig.5 Numerical model of bifurcation segment

**Calculation parameters.** The physics and mechanics parameters of surrounding rock are listed in Table 1. Where, *B* is bulk modulus, *S* is shear modulus, *F* is friction angle, *C* is cohesive strength and *D* is density.

Table.1 Physics and mechanics parameters of surrounding rock

| Surrounding Rock | *B*/MPa | *S*/MPa | *F*/° | *C*/MPa | *D*/kgm$^{-3}$ |
|---|---|---|---|---|---|
| Miscellaneous fill | 5.6 | 1.23 | 20 | 0.005 | 2000 |
| Highly weathered granite | 1100 | 400 | 25 | 0.1 | 2500 |

## Calculation results analysis and construction method optimization

**Plastic zones of surrounding rock.** The scope and position of surrounding rock plastic zones can be used to evaluate the effects of construction methods. After using different construction methods to excavate, plastic zones around tunnel structure are shown in Fig.6.

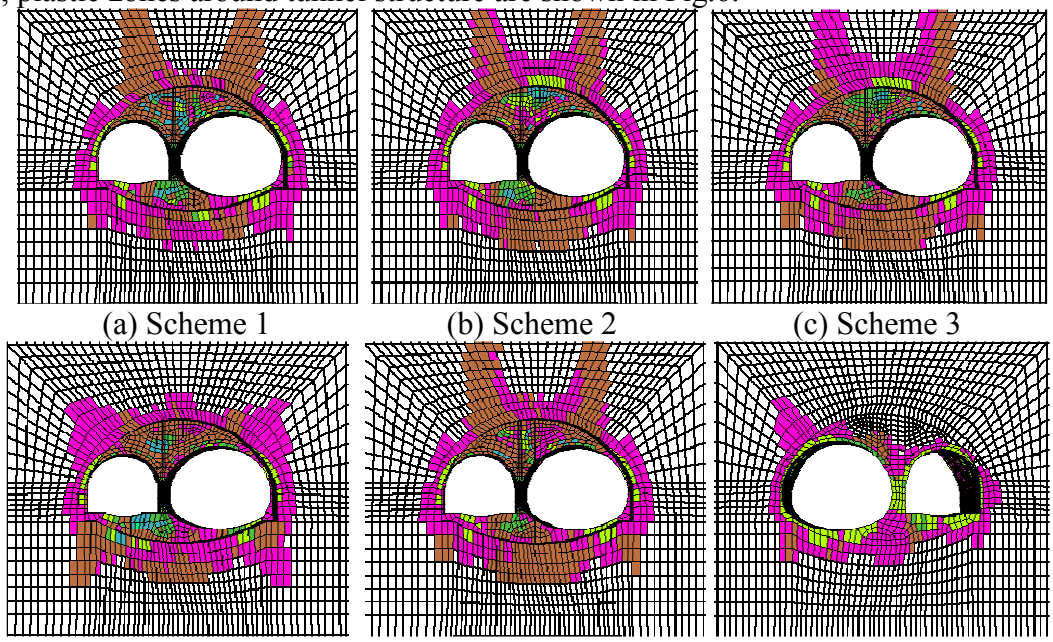

(a) Scheme 1 (b) Scheme 2 (c) Scheme 3

(d) Scheme 4 (e) Scheme 5 (f) Scheme 6 (small interval tunnel)

Fig.6 Plastic zones of excavated tunnel by using different construction methods

The plastic zone of scheme 4 is obviously smaller than other schemes, especially at tunnel crown place. But plastic zone on tunnel arch shoulder is approximately 5-6m. However, plastic zones of other schemes are quite similar. There are quite obvious plastic zone belts at crown place of main and ramp tunnel. As for the small interval tunnel, large plastic zone appears on central concrete wall.

**Geostress of surrounding rock**. Fig. 7 is maximum principal stress isolines of surrounding rock around confluence segment.

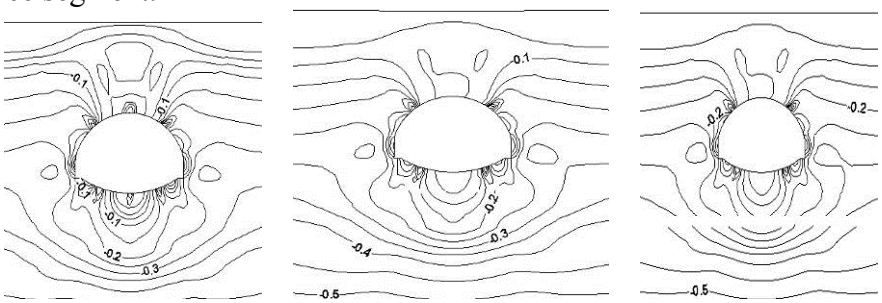

(a) Scheme 1 (b) Scheme 2 (c) Scheme 3

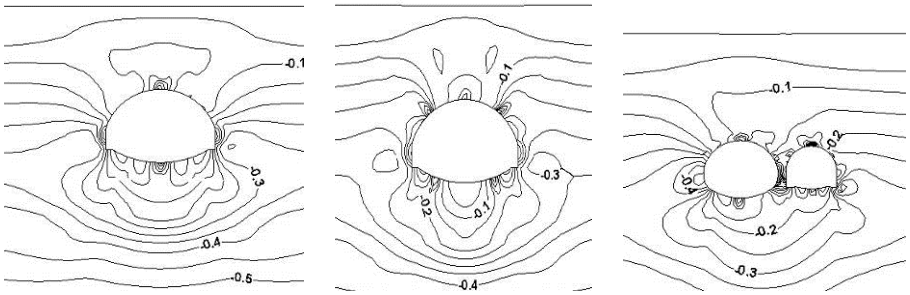

(d) Scheme 4 (e) Scheme 5 (f) Scheme 6 (small interval tunnel)

Fig.7 Maximum principal stress of tunnel by using different construction methods (Unit: MPa)

Stress concentration appears on tunnel side wall and arch springing, regardless of which method is used. Therefore, it is necessary to strengthen support of these parts during the process of construction. However, stress concentration appears on tunnel crown and invert when scheme 4 is used, because the vertical brace hinders surrounding rock deformation. Moreover, it is quite obvious that stress concentration appears on central concrete of small interval tunnel. It means that tunnel stabilization can be obtained by enlarging scope of central concrete and strengthening advanced support.

**Deformation characters of preliminary support.** Table 2 shows deformation characters of preliminary support when using different construction methods. Although preliminary support deformation largely unaffected by construction methods, the advantage of scheme 4 is obvious.

Table 2 Maximum preliminary support displacement by using different construction methods

| Displacement of prelimenary support | Scheme 1 | Scheme 2 | Scheme 3 | Scheme 4 | Scheme 5 |
|---|---|---|---|---|---|
| Maximun vertical displacement/mm | -37 | -39 | -38 | -32 | -39 |
| Maximun convergence displacement /mm | 11 | 11 | 11 | 10 | 11 |

## Conclusions

The excavation of confluence segment and small interval tunnel can affect each other but the influence of confluence segment excavation plays a dominant role. Scheme 4 is more suitable for confluence segment construction than other schemes, because plastic zone is smaller and geostress is lower than using other schemes. The vertical brace in scheme 4 determines stabilization of surrounding rock and preliminary support. The central concrete between main tunnel and ramp tunnel is the key point to guarantee the construction security and stabilization of small interval tunnel.

## Acknowledgments

The research was funded by the National Natural Science Foundation of China (No. 51178398).The authors also gratefully acknowledge the financial provided by China Scholarship Council.

## References

[1] de Farias, MM; Moraes, AH; de Assis, AP. Displacement control in tunnels excavated by the NATM: 3-D numerical simulations. Tunnelling and Underground Space Technology, 2004, Vol.24, No. 4, pp.376-389.

[2] Bo Wu, Bo Gao, Taiyue Qi. Optimization analysis of excavation sequence of tunnel groups between metro stations. China Railway Science, 2003, Vol.24, No. 5, pp.23-28 (in Chinese).

[3] Bo Wu, Bo Gao, Xiaoming Suo. Mechanical Simulation and Analysis of Construction Behavior of Urban Metro Tunnelling with Small Interval. China Journal of Highway and Transport, 2005, Vol.18, No. 3, pp.84-89 (in Chinese).

[4] EISENSTEIN Z.D. Larger undersea tunnels and progress of tunneling technology. Tunnelling and Underground Space Technology, 1994, Vol.9, No. 3, pp.283-292.

*Applied Mechanics and Materials Vols. 580-583 (2014) pp 987-990*
*© (2014) Trans Tech Publications, Switzerland*
*doi:10.4028/www.scientific.net/AMM.580-583.987*

# Effect of Time-varying on Shield Tunnel Lining Structure

Fengjun Liu[1, a], Junfang Chen[1,b]

[1] School of Civil Engineering, Henan University of Science and Technology, 471023, Henan Luoyang, P.R.China

[a]lfjhaust@163.com , [b]chenjunfang0726@163.com

**Keywords:** Shield tunnel method; time-varying effect; shrinkage and creep effect; displacement

**Abstract.** In order to survey the time-varying effect on shield tunnel lining structure, rigidity reduce in the Homogeneous Ring Design Theory is introduced. There are three methods to evaluate the rigidity reduction caused by the aging effect. The first is the bending rigidity analysis method, which considers that the bending rigidity changes with the time-dependent stress and strain. The second is the method named the equivalent moment of inertia; the last is aging coefficient method. With the Homogeneous Ring Design Theory, the internal forces and displacement of the shield tunnel segment lining can be calculated. Based on the preliminary results, using the 1st method, the reduced rigidity and the long-time displacement at different instants of time can be calculated. It is found that the concrete shrinkage and creep effect can't be ignored in the segment design. The survey is beneficial to monitor the deformation of tunnel lining, and the maintenance of the segments. It will make the tunnel work steadily and safely during the using period.

## Introduction

With the economy developing, technology improving and urban land decreasing, underground structures are rocketing. The construction of the shield tunnel has stepped into a peak stage in China. Shield tunnel design theories are also developing rapidly. How to make the design model in line with the actual situation is a research hot spot [1].

Shield tunnel lining structure is composed of concrete segment. As we all known, the shrinkage and creep effect is a general characteristic of concrete, which have great influence on the structure. It has both positive aspects and the negative aspects. For the beneficial aspects, in some cases the shrinkage and creep effect is helpful to prevent the formation of crack, reduce the stress concentration phenomena and the temperature stress, etc. For the negative aspects, it will make the structural deformation and flexural deflection increase. In the prestressed concrete, the effect will cause the loss of prestress[2]. So it becomes very necessary to define the degree of the adverse effect to the segment ring structure. The creep and shrinkage of concrete is closely related to the time and environment, and the creep is in connection with load age and the cross section stress. For the reinforced concrete structure, the creep is also influenced by the reinforcement ratio [3].

## Method of the Long-term Stress and Strain Calculation

**Internal force analysis of tunnel lining structure.** As known to all, the stress is a response of the external force. So if we want to make it clear that how the stress and strain will distribute under the long-term load, the first thing we must do is to calculate the inner force on the structure. According to the characteristics of underground structure design in China, the tunnel design model is divided into four kinds: the experience analogy model, the load-structure model, the stratum structure model, the convergence limit model. Among all these models, the load-structure model is the most widely used. For it is featured by less complexity or effort. What's more, it has clear mechanical concepts and clear safety factor evaluation method [4,5,6]. The homogeneous ring method is one representative of the load-structure model, and it is the most commonly used. It defines the lining structure as a uniform circle, and it does not consider the location of the joint. Curved beam element is applied to simulate the lining ring. All of the assumptions make the calculation of the model simpler and more convenient. Not only the method has those advantages, but also the calculation results can meet the

needs of the project. All the characters make the method widespread in the segment design [7]. The inner force of the structure that calculated by the homogeneous ring method can be consulted in the *Tunnel Standard Specification (on Shield tunnel)* [8].

**Long-term stress and strain of eccentrically compressed members.** As the specification above described, the inner force loaded on every section is a combination of bending moment $M$ and axial force $N$. This type of the load effect will make the curved beam element bearing eccentric force. So we consider the tunnel lining structure as an eccentric compression member. The paper titled *the long-term effect of creep and shrinkage of reinforced concrete structures* [9]mainly studies on the calculation of long-term stress and strain in different structure forms bearing different loading forms. The article describes detailedly what effect creep and shrinkage have on the eccentric component. The general idea is that the force of eccentric component separately be treated as a superposition of the axis force and pure bending moment, as shown in Fig.1. We can easily calculate the stress $\sigma(t_0)_N$ , $\sigma(t_0)_M$ and strain $\varepsilon(t_0)_N$ , $\varepsilon(t_0)_M$ for the initial loading times. As to the calculation of the stress and strain with a long-term load, the author established the strain full amount recursive expression which bases on the theory of creep recovery. In the process of analysis and calculation, we can obtain the increment of the stress and strain step by step at the time of $t_i = t_1, t_2, t_3 \cdots\cdots$. The changed value of stress and strain at different times can be calculated at last.

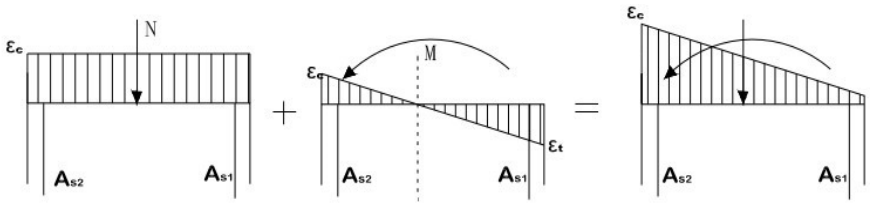


**Fig.1 Strain superposition of section**

## Example Analysis

**Background and engineering conditions of the project.** Shanghai Yangtze river tunnel project is one of the major infrastructure construction projects in Shanghai or even in China. The design reference period is 100 years. It is designed according to the standard of two-way six-lane highway, and constructed by shield method. The inner diameter of the tunnel is 13.7 meters, outer diameter is 15.0 meters. Each ring is composed of 10 pieces of segments, the width of which is 2 meters. The inside reinforcement area $A_{s1} = 11084mm^2$, $\rho_1 = 0.85\%$, outside $A_{s2} = 5458mm^2$, $\rho_2 = 0.42\%$. In order to validate the bearing capacity and stability of the lining segment to assurance the stress and deformation under construction loads, Tongji University conducted a test on the whole ring with a scale of 1:1. The test applied loads on the model, which simulated the different buried depth and different pressure coefficient. At the same time, the experimenters measured the internal force and bending moment value under various working conditions[10].

**Internal force and deformation based of the lining structure.** The working condition of the structure is as follow. The thickness of earth-fill cover is 29 m, and the coefficient of horizontal pressure is 0.68. As the load and the structure are symmetrical, we can just do mechanical analysis on a quarter of the circle structure. We use straight beam (shell) unit to simulate the segment ring.The strength classes of concrete is C50, whose elastic modulus $E_c = 3.45 \times 10^7 kPa$. According to the computing theory of homogeneous circle model, we obtain the curve of internal force diagram as shown in Fig.2.

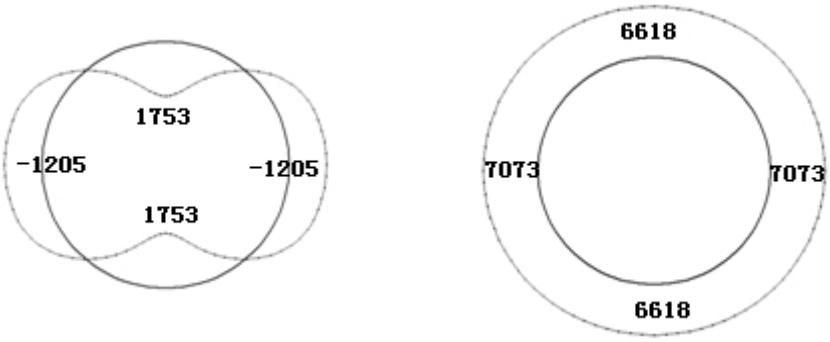


a) Bending moment /kN·m b) Axial force /kN

**Fig.2 Internal force based on homogeneous circle theory**

**Time-depend bending rigidity and deformation.** Seeing the results of the internal force, we know that the tunnel structure belongs to the eccentrically compressed members**,** so we can use the analysis method mentioned above to analyze the performance of shield lining under long-term load. According to the principle of minimum stiffness theory and the result of bending moment, the lining structure can be divided into two parts-the positive bending moment part and the negative bending moment part, which differ from the bending rigidity. The rigidity of the section, which accords with the maximum positive bending moment ( $M^{+}_{\max}$ ), is regarded as the rigidity of the positive bending moment part. The rigidity of the section, which accords the corresponding of the minimum negative bending moment ( $M^{-}_{\max}$ ),is regarded as the rigidity of positive bending moment part. Considering the different rigidity we can calculate the corresponding total vertical deformation $\Delta_v$ and total horizontal deformation $\Delta_h$ at the moment of 1 year, 3 years and 10 years. The equivalent rigidity coefficient $\eta^t$ can be obtained comparing the theoretical deformation value with the calculated deformation using different reduction factor values (0.8, 0.7, 0.6……) on the base of the principle of minimum stiffness theory. The results are shown in Table 1. (The relative humidity is 75%).

**Table 1. Total Deformation and Rigidity Coefficient**

| Time | Bending rigidity [$\times 10^{14}$N·mm$^2$] | | $\Delta_v$ [mm] | $\Delta_h$ [mm] | Rigidity coefficient $\eta^t$ |
|---|---|---|---|---|---|
| | $M^{+}_{\max}$ | $M^{-}_{\max}$ | | | |
| $t_0$ | 11.16 | 15.14 | 46.20 | 37.44 | 0.80 |
| t=1 year | 10.11 | 13.77 | 50.75 | 41.56 | 0.74 |
| t=3 years | 9.68 | 13.13 | 52.93 | 43.54 | 0.70 |
| t=10 years | 9.58 | 13.00 | 53.46 | 44.00 | 0.69 |

**Stiffness degradation effect and the deformation analysis.** Based on the results shown in Table 1, the curve of the flexural stiffness and total deformation respectively are shown in Fig.3.

Fig.3 suggests that the cross section rigidity's degenerate, which is the negative impact of shrinkage and creep effect. It shows that the rigidity tends to be basically stable a decade later. In order to take this negative condition into account, we introduce a rigidity reduction factor, whose value is 0.69, in the design of homogeneous ring method. The factor is a comprehensive one, which not only considers the joint's weakening effect on the ring, but also considers the rigidity degradation caused by the shrinkage and creep effect. The displacement diagram shows that the shrinkage creep deformation of shield tunnel lining structure grows rapidly in the first three years and much slowly later. The shrinkage and creep deformation will accomplish in 10 years and remain basically stable then. From the deformation results we find that the increased deformation, which caused by the concrete creep and shrinkage effect, will reach 16.5% of the initial deformation.

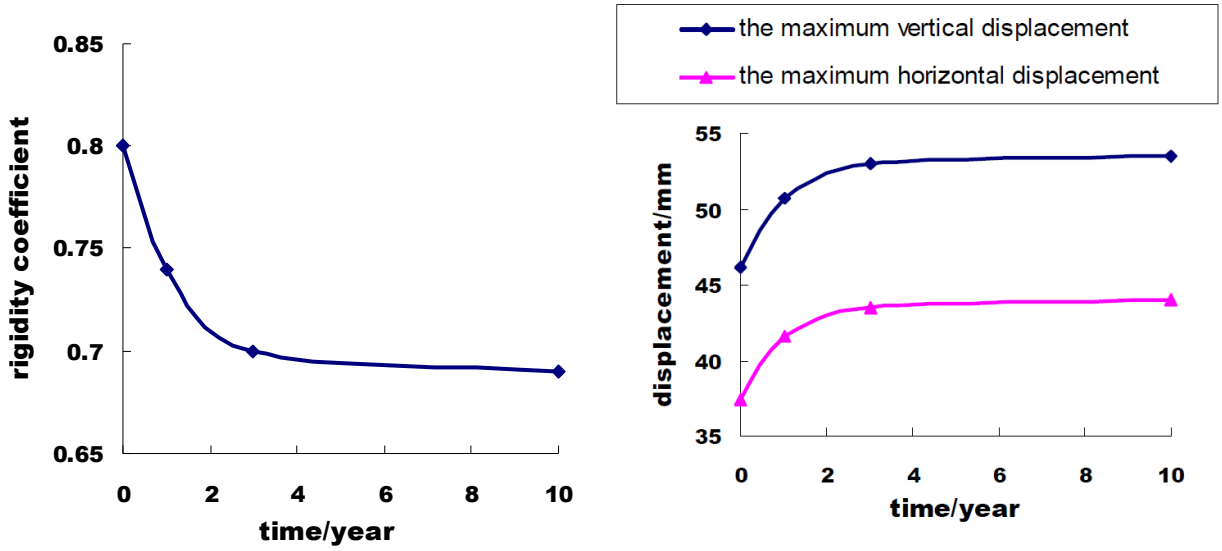


**Fig.3 Changed rigidity and displacements with time**

## Conclusions

1. The concrete shrinkage and creep's influence on segment deformation is large. It is one of the main factors contributing to the increase of the deformation, and can't be ignored in design.

2. The deformation of the first three years will achieve 98.87% to the final deformation. The deformation curve shows that the shrinkage and creep effect has bigger impact on the structure in the first three years. The influence is basically stabilizing later.

3. The shrinkage and creep effect will weaken the rigidity.To match the design result with actual situation up more closely, we recommend using the value of the rigidity at the tenth year in the design of homogeneous ring method.

4. In the first 3 years, we should monitor the deformation of the segment frequently, especially in the vertical and horizontal location. In order to guarantee the tunnel operates safely, measures should be taken to avoid a large displacement.

## References

[1] Jianhang Liu and Xueyuan Hou: *Method of shield tunnel* (China Railway Publishing House, Beijing 1991).(In Chinese)

[2] Lv Zhou and Yongchun Xu: *Shrinkage and Creep* (China Railway Publishing House, Beijing 1994). (In Chinese)

[3] Neville A.M. and Dilger W.H. ect.: *Creep of Plain and Structural Concrete* ( Constructions Press, London 1983).

[4] W.Q. Ding and Z.Q. Yue, et al:Todd Harper ashimoto: *The International Journal for Numerical and Analytical Methods in Geomechanics* Vol.28 (2004),p.57

[5] H. Mashimo and T. H. Ishimura: *Tunneling and Underground Space Technology* Vol.18 (2003), p.233

[6] Hehua Zhu and Maoyu Cui, etc: J*ournal of geotechnical engineering* Vol.22 (2) (2000), p.190

[7] Jianming Huang: *Railway Construction* Vol.6 (2004) p.29 (In Chinese)

[8] JSCE. *Tunnel Standard Specification and Explanation (on Shield tunnel)* (China Architecture and Building Press, Beijing 2001). (In Chinese)

[9] Can Sun: Long-term creep and shrinkage effect research and application. *Harbin Industrial University,* 2010. (In Chinese)

[10] Liang Lu and Dong OuYang et al, in: *Proceedings of the 17th National Conference on Structural Engineering*, In 2008. (In Chinese)

*Applied Mechanics and Materials Vols. 580-583 (2014) pp 991-996*
*© (2014) Trans Tech Publications, Switzerland*
*doi:10.4028/www.scientific.net/AMM.580-583.991*

# Analytical Hierarchy Process Based Post-earthquake Health Diagnosis Method for Tunnel in South of China

Hao Huang[1,a], Wei Zhang[2,b], LuFeng Yang[2,c], Zhen Chen[2,d]

[1] Guangxi Polytechnic of Construction, Nanning, 530003, China

[2] School of Civil Engineering & Architecture, Guangxi University,Nanning, 530004, China

[a] hhouse@126.com, [b] zh.ei@163.com, [c] lfyang@gxu.edu.cn, [d] 464785706@qq.com

**Keywords:** Tunnel in south China; Health diagnosis; Post-earthquake; Analytical hierarchy process

**Abstract:** In order to evaluate the health condition of the tunnel in South China and give advices on reinforcement and maintenance scheme, a post-earthquake health diagnosis method is presented. After a comprehensive investigation on failure modes of tunnel, a four-level ranking method and a index system for post-earthquake health diagnosis of highway tunnel are proposed. Besides, analytical hierarchy process (AHP) is introduced into for determining the post-earthquake health diagnosis mode. Case study manifests the validity of the proposed method, which can provide valuable guide to the post-earthquake health diagnosis and relief work.

## Introduction

Many tunnels have been built across the mountains in south of China, and would be important lifeline if earthquake happens for its outstanding aseismatic performance. However, some damage appearances are also found in some tunnels after earthquake [1, 2]. In order to avoid hidden danger, it is necessary to provide a valid post- earthquake health diagnosis method for tunnel.

The health condition of those tunnels in the region of South China is affected by high temperature, heavy precipitation and special geology and geomorphology. However, there is no diagnosis method on post-earthquake health diagnosis for these tunnesls. In this paper, an analytical hierarchy process (AHP) based health diagnosis method is established, in which the index limits were decided by norms and engineering experience.

## AHP for post-earthquake health diagnosis of tunnel

The procedure of health diagnosis method for tunnel in South China is presented in Fig. 1, which is based on AHP method. The key steps are consisted of construction of hierarchy analysis, determination of index weight, redistribution of index weight, comprehensive grading and health level judgment.

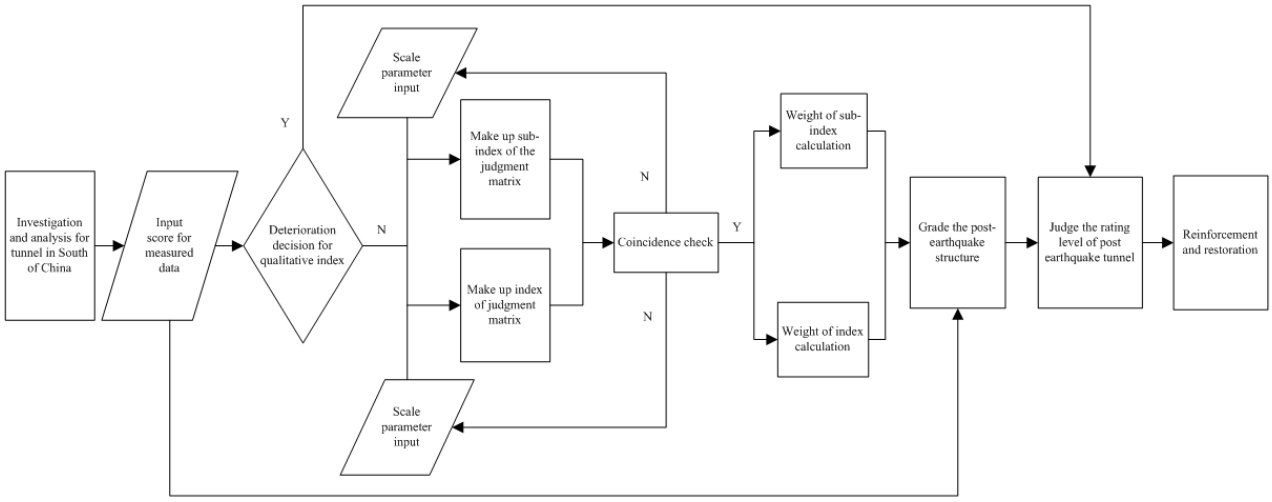


Fig. 1 Procedure of the health diagnosis

## 2.1 Hierarchy analysis structure

According to the tunnel characteristics in South China, an AHP structure is established, in Fig. 2. It is composed of four levels: the target, the index level; the sub index level, scheme level.

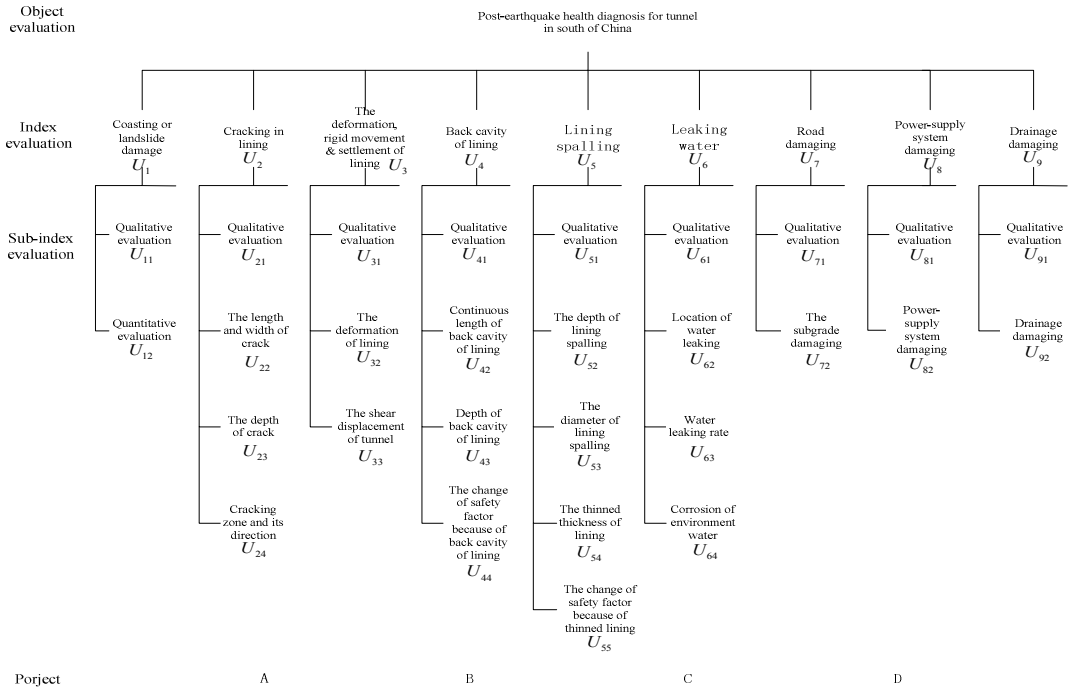


Fig. 2 Analytical hierarchy structure

## 2.2. Index weight

Index weight and sub index weight can be achieved by formulating judgment matrix, calculating its max eigenvalue and the corresponding eigenvector. The judgment matrix can be developed through comparison of each element in the same level and decision of the importance relative to superior level using scaling method. Now, the 10/10~18/2 scaling method is adopted to construct the judgment matrix [3].

$$A=\begin{bmatrix} W_1/W_1 & W_1/W_2 & \cdots & W_1/W_n \\ W_2/W_1 & W_2/W_2 & \cdots & W_2/W_n \\ \vdots & \vdots & \ddots & \vdots \\ W_n/W_1 & W_n/W_2 & \cdots & W_n/W_n \end{bmatrix} \quad (1)$$

Post-multiply the weight W by matrix A and the weight W of each element in matrix A can be derived

$$AW = nW \tag{2}$$

Where, $n$ is the matrix order. The maximum of the eigenvalue in Eqn. (2) is $\lambda_{max}=n$ except that all the other eigenvalues equal zero. In order to guarantee the rationality of the health diagnosis result, the consistence of judgment matrix A should be checked, which can be realized by introducing random consistence ratio CR.

$$CR = CI / RI \tag{3}$$

Where, $CI$ is the index for matrix consistence judgment, $CI = (\lambda_{\max} - n)/(n-1)$, $\lambda_{\max}$ is the maximum of all eigenvalues, $n$ is the order of judgment matrix; $RI$ is the average random consistence index of the same level, as shown in Table 1.

Table 1 Random consistency index

| n | 1 | 2 | 3 | 4 | 5 | 6 | 7 | 8 | 9 |
|---|---|---|---|---|---|---|---|---|---|
| RI | 0.00 | 0.00 | 0.58 | 0.90 | 0.12 | 1.24 | 1.32 | 1.41 | 1.45 |

According to the investigation conducted by Huang[4], the index weight and sub index weights are proposed as follows.

(1) Index weight

$$W = (W_{u1} \quad W_{u2} \quad W_{u3} \quad W_{u4} \quad W_{u5} \quad W_{u6} \quad W_{u7} \quad W_{u8} \quad W_{u9})$$
$$= (0.0715 \quad 0.2860 \quad 0.1907 \quad 0.0715 \quad 0.0715 \quad 0.1226 \quad 0.1226 \quad 0.0318 \quad 0.0318)$$

(2) Sub index weight

Coasting or landslide damage: $W_{u1} = (W_{u11} \quad W_{u12}) = (0.5000 \quad 0.5000)$

Cracking in lining: $W_{u2} = (W_{u21} \quad W_{u22} \quad W_{u23} \quad W_{u24}) = (0.2000 \quad 0.3000 \quad 0.2000 \quad 0.3000)$

The deformation, rigid movement & settlement of lining:

$W_{u3} = (W_{u31} \quad W_{u32} \quad W_{u33}) = (0.3333 \quad 0.3333 \quad 0.3333)$

Back cavity of lining: $W_{u4} = (W_{u41} \quad W_{u42} \quad W_{u43} \quad W_{u44}) = (0.2222 \quad 0.3332 \quad 0.2222 \quad 0.2224)$

Lining spalling: $W_{u5} = (W_{u51} \quad W_{u52} \quad W_{u53} \quad W_{u54} \quad W_{u55}) = (0.1666 \quad 0.2498 \quad 0.2498 \quad 0.1669 \quad 0.1669)$

Leaking water: $W_{u6} = (W_{u61} \quad W_{u62} \quad W_{u63} \quad W_{u64}) = (0.2999 \quad 0.2999 \quad 0.2001 \quad 0.2001)$

Road damaging: $W_{u7} = (W_{u71} \quad W_{u72}) = (0.4000 \quad 0.6000)$

Power-supply system damaging: $W_{u8} = (W_{u81} \quad W_{u82}) = (0.4000 \quad 0.6000)$

Drainage damaging: $W_{u9} = (W_{u91} \quad W_{u92}) = (0.4000 \quad 0.6000)$

### 2.3. Redistribution of index weight

In consideration of labor and equipment, some judgment indexes cannot be obtained. Accordingly, their weights have to be eliminated; that is to say the index weight should be redistributed as follow.

$$W_{ij} = W_{ij} / \sum_{j=1}^{n} W_{ij} \tag{5}$$

### 2.4. Total score with multi-index and evaluation of health level

The total score is acquired by adding each element multiplied by its index weight:

$$S_{sum} = \sum_{i=1}^{n} \sum_{j=1}^{m_i} W_i \times W_{ij} \times S_{ij} \tag{6}$$

Where, $S_{sum}$ is the total score; $n$ is the number of index; $m_i$ is the number of sub index for each index; $W_i$ is the index weight; $W_{ij}$ is the sub index weight; $S_{ij}$ is the score of sub index.

The sub index grading rules are that the range of $S_{ij}$ is from 1 to 4 for the four conditions: extremely serious condition, serious condition, relative serious and ordinary condition. When the sub index $U_{ij}$ cannot be obtained, $S_{ij}$ is 0. The total score $S_{sum}$ is directly set to be 1 when a tunnel is evaluated to in extremely serious condition by those qualitative indexes.

The health level can be determined according to the value of $S_{sum}$, *as* shown in Table 2.

Table 2 Health level according to $S_{sum}$

| Level | Extremely serious | serious | relatively serious | Ordinary |
|---|---|---|---|---|
| $S_{sum}$ | $1.0 \le S_{sum} \le 1.5$ | $1.5 < S_{sum} \le 2.5$ | $2.5 < S_{sum} \le 3.5$ | $3.5 < S_{sum} \le 4.0$ |

## Health classification

Four-level health classification (shown in Table 3) is adopted with considering of characteristics of tunnel in South China.

Table 3 Four-level health classification

| Level | Conclusion |
|---|---|
| A (extremely serious) | Damage condition is extremely serious. Tunnel should be stopped and reconstructed immediately. |
| B (serious) | Damage condition is serious. Tunnel may be removed or reconstructed according to its importance and service demand. |
| C (relatively serious) | Damage condition is relatively serious Tunnel can be is improved by rehabilitation |
| D (ordinary) | Damage condition is relatively minor. Tunnel can serve normally after rehabilitation. |

Health diagnosis should be conducted according to indexes. There are 9 indexes in the first floor, including coasting or landslide damage, cracking in lining, the deformation & rigid movement & settlement of lining, back cavity of lining, lining spalling, leaking water, road damaging, power-supply system damaging, drainage damaging, as shown in Fig.2. Among these indexes, the universal diagnosis indexes consist of lining crack width and length, lining thickness, lining deformation, displacement, sedimentation, lining back cavity, qualitative evaluation of lining delamination or spalling, quantitative evaluation of lining cross-section strength degradation, lining delamination or spalling, qualitative evaluation of leakage, water intrusion, water and sand emission on road surface[5, 6]. Meanwhile, with regard to the characteristics of tunnel in South China and its destruction mode after earthquake, special diagnosis indexes including qualitative and quantitative evaluation of entrance landslip and collapse, the deformation & rigid movement & settlement of lining, the shear displacement of tunnel, depth of back cavity of lining, the change of safety factor because of back cavity of lining, the thinned thickness of lining, the change of safety factor because of thinned lining, location of water leaking, location of water leaking, leakage flow rate, corrosion of environment water, qualitative evaluation of road damaging, quantitative evaluation of the subgrade damaging, qualitative and quantitative evaluation of power-supply system damaging, are added.

## Indexes and standards of characteristic diagnosis

The indexes and corresponding limits of diagnosis are as follows. For the index of entrance landslip and collapse, its evaluation index and standard can be achieved by statistics data of the cases including entrance landslip and rock collapse[5]. For the lining crack index, the crack depth evaluation index can be defined as the ratio k of crack depth[6]. Meanwhile the influences of lining thickness and the crack position and trend on the structure health should be considered during the establishment of evaluation index[7]. For the ultimate capacity index after earthquake, its evaluation index can be calculated through tunnel experiment data[8]. For the index of lining deformation, displacement, sediment, the evaluation index of lining displacement rate and shear displacement can be obtained depending on the related trade norm and model experiment[7]. For the lining back cavity index, the evaluation index of continuous length of back cavity of lining and cavity depth can be

determined depending on the related trade norm[9] and model experiment[10]. For the leakage index after earthquake, the evaluation index of leakage position can be determined through relevant studies[7], and the leakage flow rate index can be determined according to the Construction Industry Research and Information Association[11]. For road damage index, qualitative evaluation index can be acquired in reference with the emission of water and sand on the road surface[12] and qualitative evaluation of roadbed[13]. While the quantitative evaluation index can be determined based on *The restore guide for post-earthquake road in Wen Chuan* [14]. For the power supply and drainage index, the power supply evaluation index can be determined by the drop of rated voltage, and the sediment index[15] can be determined from the drainage index.

## Case study

Using the proposed diagnosis method, the Wendou highway tunnel survived from the Wenchuan earthquake was selected and evaluated. The health index marks are listed in Table 5.

Table 5 Grade for the health diagnosis parameters of Du-Wen highway tunnel

| Characteristic of earthquake damage [16] | | | Health index mark | | | | | |
|---|---|---|---|---|---|---|---|---|
| Dujiangyan head tunnel entrance | Wenchuan head tunnel entrance | Tunnel body | | | | | | |
| The shotcrete on side and face upward slope cracks, the crack width is about 30~100mm, (has not been construction) | The original entrance slope was strengthened with vertical anchor beams. The protection structures were not damaged seriously，but the vertical beam and the ground cracked generally. The right part without strengthening collapsed locally. | The lining cracks a lot which were mainly transversal and circular. The crack width is about 10~20mm, and some cracks were crisscrossed. The construction joints cracked, and its width were about 5~30mm. The inverse arch and filled part cracked and dislocated a lot. One inverse arch and filled part in the left and right tunnel respectively bugled and cracked, whose length reached 60m and the hump height was about 60cm | $S_{11}$ 2 | $S_{41}$ 0 | $S_{61}$ 0 | | | |
| | | | $S_{12}$ 0 | $S_{42}$ 0 | $S_{62}$ 0 | | | |
| | | | $S_{21}$ 2 | $S_{43}$ 0 | $S_{63}$ 0 | | | |
| | | | $S_{22}$ 1 | $S_{44}$ 0 | $S_{64}$ 0 | | | |
| | | | $S_{23}$ 0 | $S_{51}$ 0 | $S_{71}$ 2 | | | |
| | | | $S_{24}$ 1 | $S_{52}$ 0 | $S_{72}$ 1 | | | |
| | | | $S_{31}$ 1 | $S_{53}$ 0 | $S_{81}$ 0 | | | |
| | | | $S_{32}$ 2 | $S_{54}$ 0 | $S_{82}$ 0 | | | |
| | | | $S_{33}$ 1 | $S_{55}$ 0 | $S_{91}$ 0 | | | |
| | | | | | $S_{92}$ 0 | | | |

Substitute the each of the index mark $S_{ij}$ into equation(6), then the tunnel health condition mark can be calculated, as shown in Table 6.

Table 6 Health diagnosis for the post-earthquake Du-Wen highway tunnel

| Information about Douwen highway[16] | | The health diagnosis for tunnel in South China | | |
|---|---|---|---|---|
| Start and end stake number | Earthquake damage degree | Comprehensive mark | Evaluation level | Health evaluation |
| K13+385~K17+445（right line） | Serious damage | 1.43 | B | Serious |

The tunnel damage condition in Table5 are concluded from the field studies carried out by the authors and the documents given by Road Design Institution of Sichuan and Communications Design Institute of Sichuan. The evaluation results diagnosed by the health diagnosis for tunnel in South China coincides with the results given documents mentioned.

## Conclusion

The post-earthquake diagnosis indexes are established in consideration of the characteristics of the tunnel in South China. Using the AHP method, the comprehensive post-earthquake evaluation for highway tunnel in South China can be appropriately done. The traditional AHP method is improved by judging the stop factor to give the conclusion and redistributing the weight, which can fit the practical condition for the post-earthquake diagnosis of tunnel in South China. The evaluation results of Duwen highway tunnel diagnosed coincides with the results given by some survey documentations. The example shows that the proposed method can provide valuable information and advice for relief work.

## Acknowledgement

This research was supported by the National Natural Science Foundation of China (51168003, 51169003), the Major Projects of Guangxi Natural Science Foundation (2012GXNSFEA053002), the Systematic Project of Guangxi Key Laboratory of Disaster Prevention and Structural Safety (2012ZDX05).

## Reference

[1] W.L. Wang, T.T. Wang, J.J. Su: Assessment of damage in mountain tunnels due to the Taiwan Chi-Chi Earthquake Vol. 16(2001), p. 133–150.

[2] Z.Z. Wang, B. Gao, Y.J. Jiang: Investigation and assessment on mountain tunnels and geotechnical damage after the Wenchuan earthquake Vol. 52(2009), p. 546–558.

[3] Y.J. Guo, F.M. Zhang, P.T. YI: Rationality analysis on different scales and comprehensive evaluation result sensitivity Vol. 30(2008), p. 1277–1280.

[4] H. Huang: Post-earthquake health diagnosis method for tunnel in south of China (2012).

[5] W.X. Xiao, Y. Kuang, J.J. Chen: *Anlysis for collapse case of tunnel* ( Southwest Jiaotong University Press, Chengdu 2002).

[6] X. Luo: Study of Dianosis Method and system for health condition of highway tunnel (2007).

[7] W.H. Huang, L. Chen, Q.F. Hu: *Tunnel and underground engineering life-cycle risk management* (Science Press, Peking 2010).

[8] M. Li, H.K. Chen: Experimental research on tunnel health criterion of deficiency in lining thickness Vol. 32(2011), p. 570–577.

[9] D.W. Zhang: Safety assessment for railway tunnel Vol. (2004), p. 77–84.

[10] M. Li, H.K. Chen, F.W. Xiong: Test research on health criterion of cavities behind the lining Vol. 30(2011), p. 398–402.

[11] J.X. Zhu, P. Zhang: Waterproof grade standard and detection of tunnel engineering Vol. 38(2009), p. 22–24.

[12] JTC H12-2003 Highway Tunnel maintenance technical norm. Beijing: China Building Industry Press (2003).

[13] Z.Q. Li, J.B. Li, H.R. Zhang: Earthquake damage characteristics and safety assessment of post-earthquake working status of road subgrade Vol. 28 (2011), p. 57–62.

[14] Ministry of Transport of the People's Republic of China: *The Restore Guide for Post-earthquake Road in Wen Chuan* (China Communications Press, Beijing 2008).

[15] DB31/T444-2009 Evaluation procedures for drainage pipe through TV and sonar monitoring. Shanghai: Shanghai Bureau of Quality and Technical Supervision (2009).

[16] T.B.Li: Failure characteristics and influence factor analysis of mountain tunnels at epicenter zones of great Wenchuan earthquake Vol. 16(2008), p. 742–750.

*Applied Mechanics and Materials Vols. 580-583 (2014) pp 997-1000*
*© (2014) Trans Tech Publications, Switzerland*
*doi:10.4028/www.scientific.net/AMM.580-583.997*

# Numerical Analysis of Construction Method in Shallow-buried Large-section Loess Tunnel

Zhijie Sun[1, a]

Shanxi Key Laboratory of Highway Construction & Maintenance Technology in Loess Region, Key Lab of Highway Construction & Maintenance Technology in Loess Region, Shanxi Transportation Research Institute, Shanxi, Taiyuan, 030006

[a]chinasunzhijie@163.com

**Keywords:** Loess tunnel; Large-section; Construction Method; Deformation; Plastic Zone.

**Abstract.** To research the deformation regularity of large section loess tunnel in construction procession with different construction methods, 3D Numerical Simulation is applied and the large-section loess tunnel of highway is taken as an example. Comparing deformation regularity of surrounding rock in three types of construction method conditions, the research results show that: The CRD method takes precedence in the condition of the convergence of surrounding rock is large. The both sides heading method takes precedence in the condition of ground surface settlement is large.

## Introduction

Because of the large span highway tunnel's large cross section, the support structure will be under greater pressure of surrounding rock, which under the influence of more complex load condition and many other factors such as many processes interact during construction, repeated disturbance of surrounding rock and lining of supporting non-simultaneous construction. Which easily lead to surrounding rock collapse and tunnel lining crack. So the construction technology of highway tunnel with large cross section in a major research project shall be implemented at home and abroad.

Because of Bearing capacity of loess layer its own, while tunnel excavating can lead to large deformation easily, particularly when you first entered the cave complex geological condition of shallow-buried portal section not only, most of the time, with shallow, bias and other problems, which brought much risk to the construction safety[1,2].

According to the current construction techniques, excavation of tunnel with large cross section the choice of method is as follows: benching stepping method, CRD method, both sides heading method. This paper discusses the three types of whole process simulation of excavation scheme for construction, during excavation of tunnel surrounding rock deformation studies to find optimal construction method.

## Engineering Example

Tunnel stratum is the fourth group of upper Pleistocene Malan silt ($Q_{3m}$), In the lower strata is the fourth middle Pleistocene Lishi silty clay ($Q_{2l}$). The lower part of the Pleistocene Lishi is in the fourth group (Q2l) silty clay. The tunnel passes through the bottom of silty clay($Q_{2l}$). The

surrounding rock is classified as class V and class VI by Chinese national standard. The entrance of tunnel placed in the v-class surrounding rock on the hillside slopes in poor geological conditions, which stratum is Lishi loess and Quaternary group, Malan group recent deposits. The stability of surrounding rock is very poor, the construction is difficult and the design uses a pair of side wall heading method.

## Numerical Modeling

Plate elements simulate primary support of sprayed concrete. Solid elements simulate surrounding rocks and reinforced area. Beam elements simulate bolts. The numerical models with different construction methods are as follow in Fig.1.

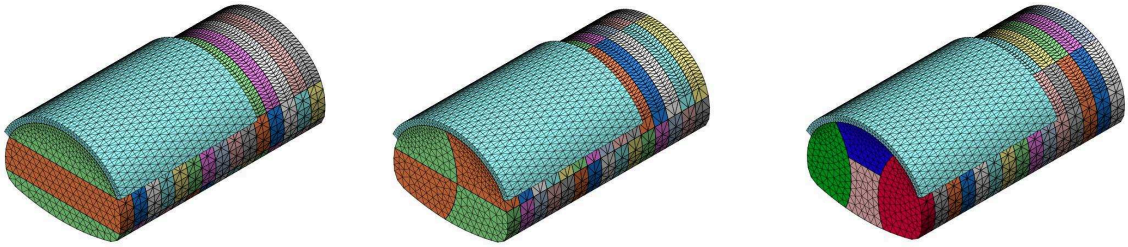

(a)Benching stepping method (b)CRD method (c) Both side heading method

Fig.1 Three-dimensional simulation model

The constitutive model for rock and reinforced rock are all Mohr-Coulomb models. The primary support of sprayed concrete is elastic material. All material parameters are shown in Tab.1[3,4].

Tab.1 Material Parameters in Model

| Material | Modulus(GPa) | Poisson's | Density ($kg/m^3$) | Cohesive(kPa) | Internal friction angle($^o$) |
|---|---|---|---|---|---|
| Class Ⅴ Rock | 0.15 | 0.3 | 2120 | 91.8 | 35.24 |
| Reinforced Rock | 1 | 0.25 | 2300 | 200 | 45 |
| Primary Support | 27.4 | 0.2 | 2332.84 | — | — |

## Analysis Results

In order to simulate the clearance displacement regularity of surrounding rock with different construction methods, the displacement of the key points with the key parts of the different working conditions were monitored through the whole construction process.

The key points of tunnel section are as follow in Fig.2, in which the point A, B, D is vertical displacement points and the point B, C are horizontal displacement point.

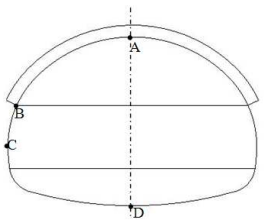


Fig. 2 The key displacement points diagram

The vertical displacement and horizontal displacement curves through the whole construction process of key points with surrounding rock through the whole construction process in different

construction methods are shown in Fig.3. The position value means surrounding rock settlement, while the negative value means surrounding rock uplift.

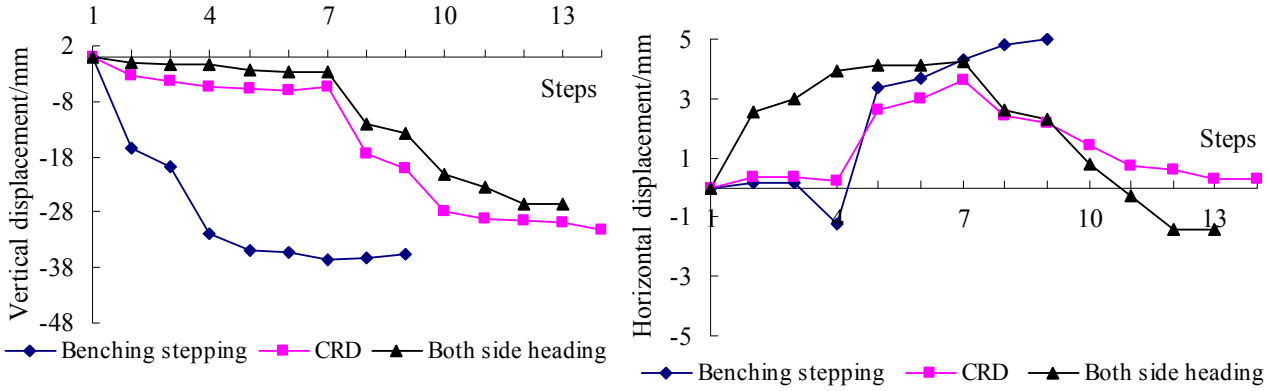


(a) Vertical displacement of point A (b) Horizontal displacement of point C

Fig. 3 The displacement curves through the whole construction process

As shown in Fig.3(a), in the construction of benching stepping method, vault subsidence caused by excavating is growing fast, arch settlement occurs most before primary support. The vault subsidence caused by upper bench construction accounts for 46 percent of total settlement value.

As shown in Fig.3(a), in the construction of CRD method, vault subsidence caused by left side heading excavating is very small, while right upper side heading excavating it growing fast. After right lower side heading supported, the arch settlement tended to be stable. The vault subsidence caused by right side heading construction accounts for 37 percent of total settlement value.

As shown in Fig.3(a), in the construction of both sides heading method, vault subsidence caused by both sides heading excavating is very small, while middle upper side heading excavating it growing fast. After middle lower side heading supported, the arch settlement tended to be stable. The vault subsidence caused by middle side heading construction accounts for 55 percent of total settlement value.

The value of vault subsidence in the construction of both sides heading method is minimum, benching stepping method is maximum.

As shown in Fig.3(b), the regularity of horizontal displacement between CRD method and two-side heading method is similar, both are increase at first and reduce at last. Because of the level of the binding to support the surrounding rock, the horizontal displacement of CRD method is minimum. Because of a free surface is large caused by excavation for bench method, the horizontal displacement of benching stepping method is maximum.

The ground settlement curves in different construction methods are shown in Fig.4.

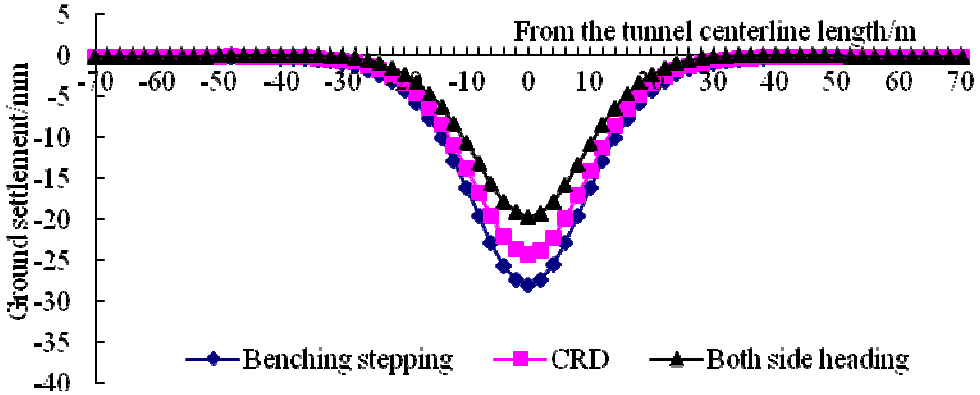


Fig. 4 The ground settlement curves in different construction methods

As shown in Fig.4, the max ground settlement with benching stepping method is 28mm, it decreases 24mm with CRD method, it decreases 20mm with both side heading method.

So while ground surface settlement is large, the both sides heading method takes precedence compare with the other two construction methods.

The final plastic zones in different construction methods are shown in Fig.5.

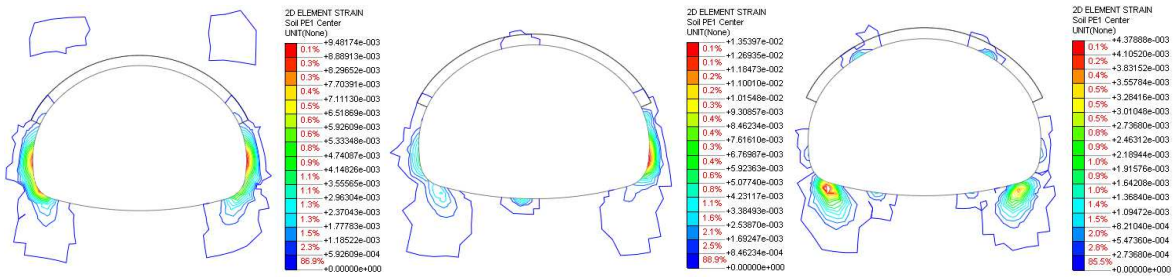


(a)Benching stepping method (b)CRD method (c) Both side heading method

Fig. 5 The plastic zone in different construction methods

As shown in Fig.5(a), in the construction of benching stepping method, the plastic zone occurred around from arch corner to wall side, also vault occurred. The surrounding rock's maximum plastic strain occurred in wall side. As shown in Fig.5(b), in the construction of CRD method, the main plastic zone occurred around from arch corner to wall side, also invert occurred. The surrounding rock's maximum plastic strain occurred in right wall side which construction later. As shown in Fig.5(c), in the construction of both sides heading method, the main plastic zone occurred around invert, stress concentrations appeared small plastic zone. The surrounding rock's maximum plastic strain occurred in both sides invert.

## Conclusions

Comparing deformation regularity and plastic zone of surrounding rock in three types of construction method conditions, the research results show that. The CRD method takes precedence in the condition of the convergence of surrounding rock is large. The both sides heading method takes precedence in the condition of ground surface settlement is large.

## Acknowledgements

This work was financially supported by the Shanxi Traffic Science and Research Project (Research and Application of Supporting Structure Mechanical Properties of Large Section of Loess Tunnel), (2012-1-1).

## References

[1] Jinwen Li: *Shanxi Science & Technology of Communications.* Vol. (216) (2012), p. 37-38.

[2] Hongyue Zhan and Qicai Wang: *Journal of Water Resources Architectural Engineering.* Vol.7(4) (2009), p. 117-120.

[3] China Merchants Chongqing Communications Research & Design Institute: *Code for Design of Highway Tunnel (JTG D70-2004)* (China Communications Press publications, Beijing 2004).

[4] Shichun Wang: *Classification of Tunnel Rock* (Southwest Jiaotong University Press publications, Chendu 2007).

*Applied Mechanics and Materials Vols. 580-583 (2014) pp 1001-1007*
*© (2014) Trans Tech Publications, Switzerland*
*doi:10.4028/www.scientific.net/AMM.580-583.1001*

# Numerical Simulation of Effect of Foundation Pit Excavation on Underlain Shield Tunnel

Wei Gang*, Hu Ling-wei, Chen Kai-lei

Department of Civil Engineering, Zhejiang University City College, Hangzhou 310015, China

weig@zucc.edu.cn (*Corresponding author)

**Keywords:** foundation pit excavation; shield tunnel; finite element method; uplift

**Abstract:** In the background of a foundation pit excavation project on Yanan Road in Hangzhou City, this study simulated the excavation of foundation pit above an underground tunnel using 3D MIDAS/GTS software. The combined action of foundation pit, ground and tunnel were considered. The influence of foundation pit excavation on the deformation of underlain shield tunnel was evaluated and simulations were carried out on the effectiveness of different strengthening and control approaches. Results from the research showed that during the stages of piling and ground strengthening, settlement occurred at the tunnel; with the excavation of foundation pit, uplift deformation at the bottom of the foundation pit and the tunnel increased; with stricter strengthening and control techniques employed, the magnitude of uplift at the tunnel and bottom of the foundation pit reduced, suggesting that various control procedures were effective to some extent.

## Introduction

As the arterial traffic in modern cities, the safety of subways is significant. However, with the development of the city, subway tunnels would be inevitably affected by underground construction during service period. The excavation and unloading of the foundation pit and dewatering measure would apply vertical and horizontal displacement on the underlain shield tunnel, causing significant disturbance. On the other hand, there is strict limit on the deformation of subway tunnels. In Shanghai for example, the maximum displacement in normal condition shall not exceed 20 mm; the radius of curvature of deformation shall be bigger than 15000 m; the relative deflection shall not exceed 1/2500 [1]. Therefore, it is significant to investigate the influence of foundation pit excavation on the underlain tunnel. A number of studies had been conducted in recent years regarding this issue and the key methodologies include: actual measuring and analysis [2], empirical modelling [3], analytic solution modelling [4] and finite element simulation [5-7] etc. However, the majority of current studies focused on the geological conditions in Shanghai, studies based on the geological conditions in Hangzhou are rare.

This study simulated the excavation of foundation pit above an underground tunnel using 3D MIDAS/GTS software. The influence of foundation pit excavation on the deformation of underlain shield tunnel and the effectiveness of different strengthening and control approaches were evaluated.

## Project summary

This study used an underground pedestrian crosswalk as in Hangzhou as the background. The plan of the foundation pit appeared to be a ‘Z’ shape. The main channel was located in west-east direction with 30 m in length, 10 m in width and 3.8 m in height. The main body of the crosswalk was constructed using box concrete structure. The section of Hangzhou Subway line 1 between Hubin Station and Longxiangqiao Station lay right under the underground crosswalk in a square cross position. The clear distance between the excavation surface of the foundation pit and the tunnel was 8.1 m. Open cut method was used to construct the crosswalk by dividing large foundation pit to small ones. The relative positions of the crosswalk and surround area were given in Figure 1. This study investigated a small foundation pit located at the east side at stage one of the project.

The distribution of rock and soil layer in construction area was: ①1 miscellaneous fill, ①2 plain fill, ②2 silty clay, ②3 sandy silt, ③1 mud and muddy clay, ③2 muddy clay mixed with silt, ③3 muddy and silty clay mixed with silt, ④ silty clay, ⑤1 muddy and silty clay, ⑤2 (muddy) silty clay, ⑥1 silty clay, ⑥2 clay. Based on the actual excavation depth and distribution of ground condition, the western part of the excavation surface was sandy clay and the eastern part muddy clay. The sectional view of the foundation pit was shown in Figure 2.

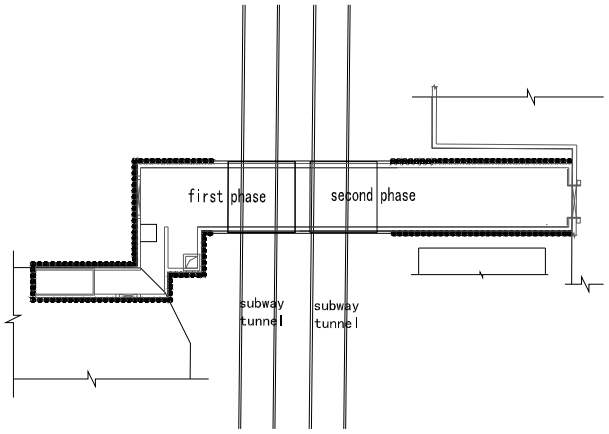


**Fig.1 Plan view of foundation pit and tunnel showing relative positions**

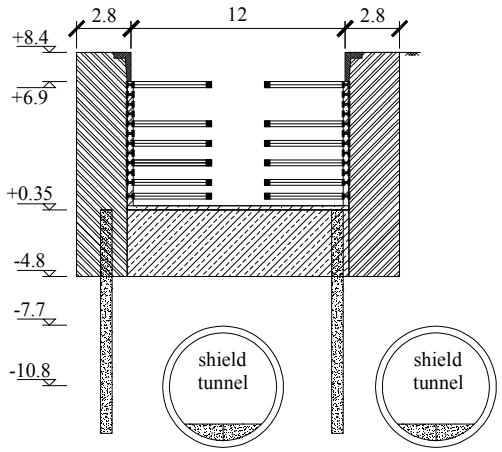


**Fig.2 Sectional view of foundation pit**

The exterior protective structure of the foundation pit consisted of four rows of Φ800@600 high-pressure jet grouting piles. Portal uplift piles with a dimension of Φ600@1500 were bored and grouted using C30 concrete. Steel circuit purlins and steel supports were used as support system. The steel had an 'H' section with a dimension of 300×300×10×15 mm. A total of 6 steel supports were constructed and layered excavation was adopted.

## 3D finite element simulations

### Model establishment and calculation of parameters

The foundation pit had a length in south-north direction of 12 m, a width in west-east direction of 11.4 m and a depth of 8 m. The four rows of high-pressure jet grouting piles with a diameter of 800 mm was replaced by walls (called sidewalls) with a thickness of 2600 mm during simulation. The side wall was 17.2 m in length, 16.6 m in width and 13.2 m in depth. The bored and grouted piles with 600 mm in diameter were replaced by walls (called uplift piles) with 600 mm in thickness and 12 m in length. The steel supports was converted to solid columns with a specific weight of 10.2 $kN \cdot m^{-3}$ and an elastic modulus of 26 GPa. The sidewalls, uplift piles and steel supports were modelled by solid elements and linear elastic materials. The strengthened ground located underneath the excavating ground was modelled by solid elements and Mohr-Coulomb constitutional model with a thickness of 5.2 m, a length of 12 m and a width of 11.4 m. Plane plate elements and linear elastic material were used for the bottom. The bottom was modelled by C15 concrete with a thickness of 0.1 m.

The shield tunnel was modelled with plane plate elements and linear elastic material with a wall-thickness of 0.35 m and an outer diameter of 6.2 m. The depth of the axis of the tunnel was 19.2 m. C50 concrete was used to model the tunnel. To simplify the simulation process, the ground was defined as homogeneous soil and modelled with solid elements and Mohr-Coulomb constitutional model. The parameters were calculated using the weighted average value of each layer. The physical and mechanical parameters of each material were listed in Table 1.

**Table 1 Physical and mechanical parameters for materials**

| | Elastic modulus (MPa) | Poisson's ratio | Specific weight (kN/m$^{3)}$ | Cohesion (kPa) | Angle of friction (º) | $K_0$ |
|---|---|---|---|---|---|---|
| Ground | 24 | 0.33 | 18.9 | 17 | 18 | 0.53 |
| Strengthen ground | 200 | 0.2 | 20 | 30 | 40 | 1 |
| Sidewalls | 10000 | 0.2 | 23 | | | 1 |
| Uplift piles | 30000 | 0.2 | 25 | | | 1.5 |
| Steel supports (original) | 200000 | 0.3 | 78.5 | | | 1.5 |
| Steel supports (converted) | 26000 | 0.3 | 10.2 | | | 1.5 |
| Tunnel | 34500 | 0.2 | 25 | | | |
| Bottom | 22000 | 0.2 | 25 | | | |

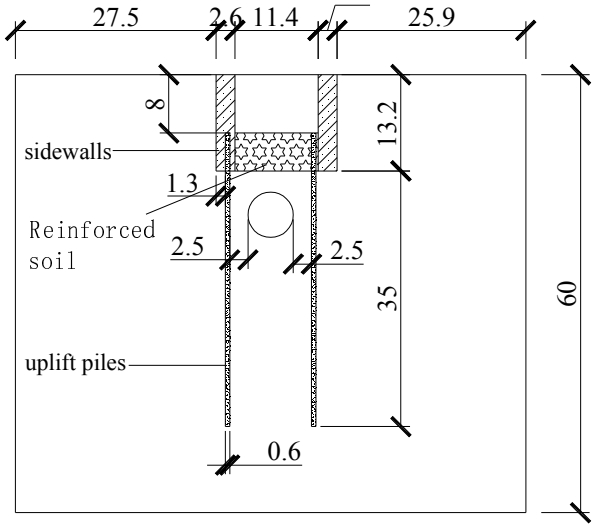


**Fig.3 Longitudinal section diagram of foundation pit**

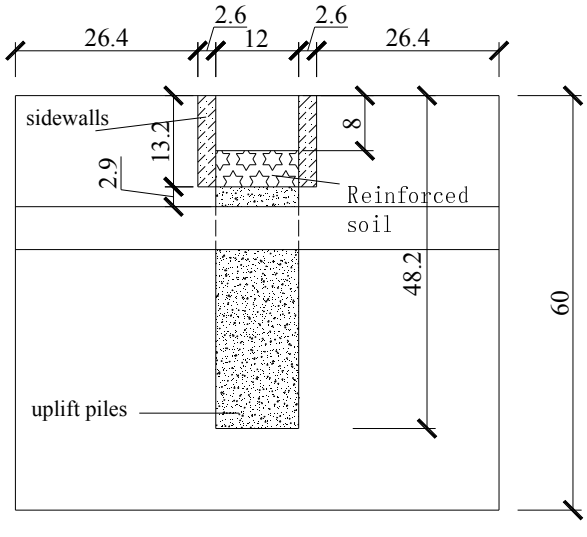


**Fig.4 Horizontal section diagram of foundation pit**

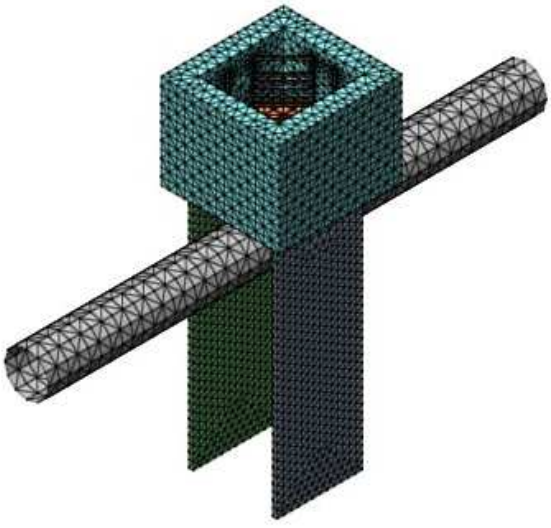

**Fig.5 Models of foundation pit and tunnel**

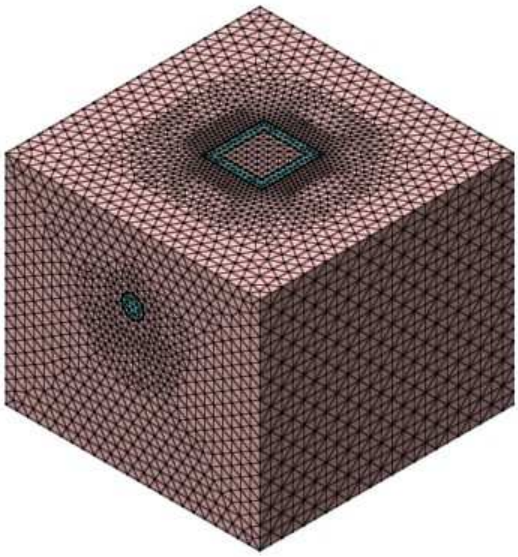

**Fig.6 Overall models**

The model had a length of 70 m in horizontal direction, 70 m in longitudinal direction and 60 m in vertical direction. The longitudinal section and horizontal section of the foundation pit and tunnel was shown in Figures 3 to 4. The meshing of the model was demonstrated in Figures 5 and 6.

**Simulation of excavation process of foundation pit**

The study assumed: (1) The permeation effect of underground water was ignored and the deformation of ground was irrelevant with time; (2) the ground was a homogenous and continuous elasto-plastic material which obeys Mohr-Coulomb yield criterion; (3) Perfect contact existed

between the tunnel, sidewalls, uplift piles and bottom of the foundation pit and the surrounding ground; no slipping or separation occurred during deformation; (4) it was assumed that the deformation of tunnel was zero before the excavation of foundation pit; only the additional deformation of tunnel due to excavation of foundation pit was studied.

Simulation procedures: (1) activate the ground, apply boundary conditions and self-loads, zero clearing the displacement; (2) start the excavation of tunnel ground after the initial stress state was acquired; (3) generate the tunnel and zero clearing the displacement; (4) modify the element attributes for sidewalls and uplift piles; (5) modify the element attributes of strengthened ground; (6) excavate the ground; (7) modify the element attributes of steel supports; (8) generate the bottom.

A total of 6 different excavating manners, and strengthening and control techniques were simulated in ascending order of stricter strengthening and control techniques employed to simulate the effect of different excavation techniques on the tunnel. Setting the actual construction condition as standard, the detailed simulation plan is given in Table 2.

**Table 2 Plan of different excavation, strengthening and control techniques**

| Condition | Detailed plan |
|---|---|
| Condition 1 | One excavation, one support, no uplift pile, no ground strengthening |
| Condition 2 | One excavation, one support, uplift piles, no ground strengthening |
| Condition 3 | One excavation, one support, uplift piles, ground strengthening |
| Condition 4 | Two excavations, four supports, uplift piles, ground strengthening |
| Condition 5 | Three excavations, six supports, uplift piles, ground strengthening (standard condition) |
| Condition 6 | Three excavations, six supports, uplift piles, ground strengthening, distributed load of 20 kPa applied temporarily on the bottom |

## Results of finite element simulation

### Analysis of standard working condition (condition 5)

The excavation of foundation pit was achieved via 6 stages during simulation: (1) construct the sidewalls and uplift piles; (2) strengthen the ground at pit bottom; (3) excavate the first layer of ground and setup the first and second steel support; (4) excavate the second layer of the ground and setup the third and fourth steel support; (5) excavate the second layer of the ground (until the bottom is reached), and setup the fifth and sixth steel support; (6) construct the bottom.

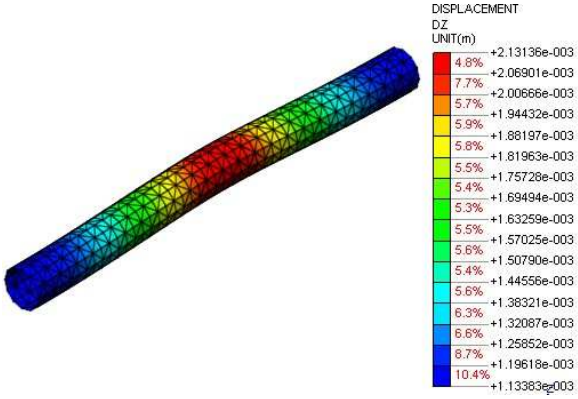


Fig.7 Vertical displacement diagram of tunnel

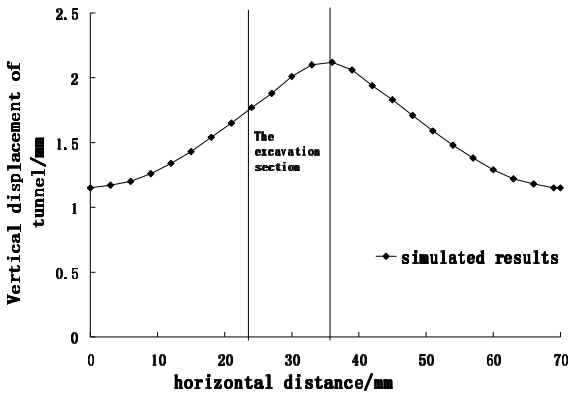


Fig.8 Vertical displacements at each point of tunnel

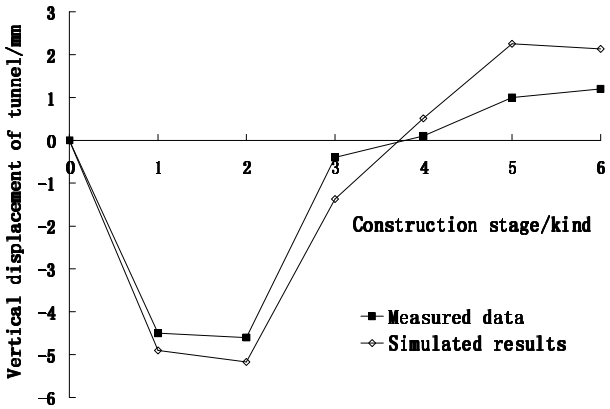


**Fig.9 Maximum vertical displacements for tunnel in different construction stages**

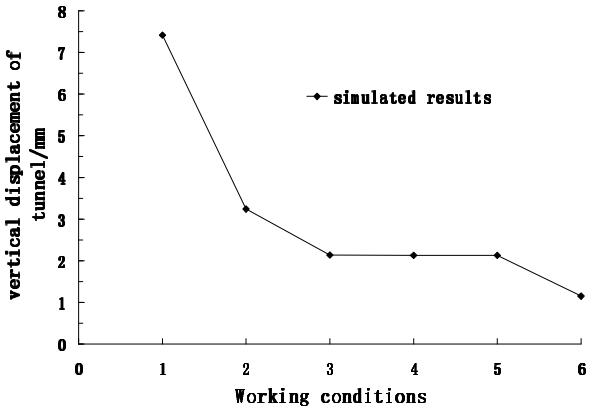


**Fig.10 Ultimate vertical displacement of tunnel under different conditions**

Figure 7 shows the ultimate vertical deformation of tunnel in standard condition. Figure 8 shows the vertical displacement of each point at tunnel in standard condition with a positive value representing humping. The position of foundation pit in the figure ranged from 29 m to 41 m. It can be seen from the figure that the vertical displacement of tunnel appeared to be normal distribution where the maximum uplift located in the middle of the foundation pit; the vertical uplift reduced with the increase of distance to the foundation pit centre; the overall uplift exceeded 1 mm, suggesting that the excavation of foundation pit affected the underneath shield tunnel in a large range.

Figure 9 shows the maximum vertical displacements for tunnel in different construction stages, wherein the negative value in Y coordinate represents settlement and positive value represents uplift. It can be seen from the diagram that: (1) the results from finite element analysis matched favourably with the measured value. Although there were discrepancies in value, the trends were extremely close, which suggests that the simulation was reliable; (2) settlement occurred at the stages of piling and ground strengthening led by downward force induced by the friction between the pile and ground during piling. The measured maximum settlement of tunnel during piling was -4.6 mm and the simulated value was -5.17 mm, which was very close to the measured value; (3) uplift occurred at the tunnel after the excavation of foundation pit. The reason for uplift is that the tunnel floated when the applied pressure reduced due to the excavation. Uplift reached the peak when the excavation was completed (at the fifth construction stage). The value of uplift reduced slightly when the bottom was cast, suggesting that casting the bottom reduces the amount of uplift. The simulated maximum vertical uplift was 2.13 mm which was slightly larger than the measured value, 1.2 mm; (4) Qi [8] discovered the trend of first settlement then uplift during piling and excavation of foundation pit, which matches the findings of this study.

**Analysis of impact factors**

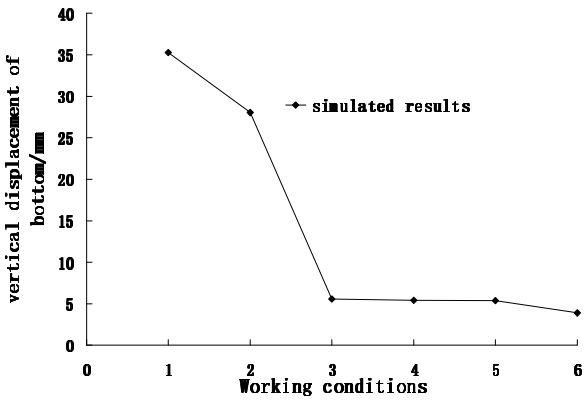


**Fig.11 Ultimate vertical displacement of bottom under different conditions**

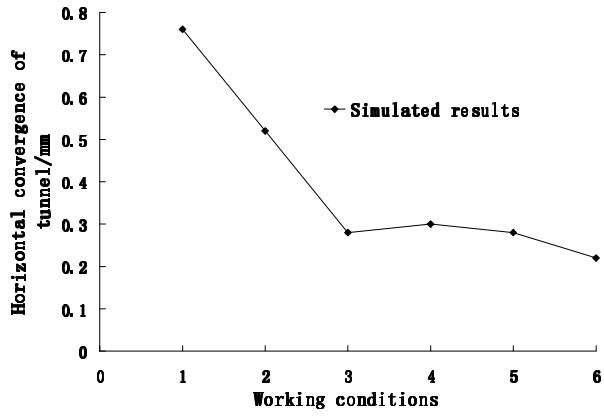


**Fig.12 Ultimate horizontal convergence of tunnel in different conditions**

Figures 10 and 11 demonstrate the ultimate vertical displacement of tunnel and bottom under different conditions with positive value being upward displacement. As shown in the figures: (1) the maximum uplift in the tunnel was 7.42 mm which was smaller than the alarm value (10 mm). This suggests that the effect of excavation of foundation pit on the tunnel is not significant due to the fact that the ground cover above the tunnel was thick (16.1 m) and the distance of excavation surface of foundation pit from the top of the tunnel was large (8.1 m), resulting to a large pressure, and thus, the unloading effect of excavation was not significant; (2) with stricter strengthening and control techniques, the ultimate uplift of tunnel and bottom reduced; (3) the descending rate of the curve was fast in the first three conditions which suggests that the uplift of tunnel and bottom could be significantly reduced with the employment of uplift piles and strengthening of pit bottom ground; (4) the variation of curve in the last three conditions was smooth which suggests that steel supports, layered excavation and temporary load had a certain level of effect on controlling the uplift of tunnel of bottom, but not obvious; (5) in conclusion, multiple strengthening and control techniques can be used to effectively control the floating of tunnel and pit bottom ground when excavating foundation pit on top of an existing shield tunnel.

Figure 12 showed the ultimate horizontal convergence of tunnel in different conditions with positive value being inward converge. It can be seen from the figure that: (1) the excavation of foundation pit reduced the pressure above the tunnel but the horizontal pressure remained the same. Therefore the convergence deformation of tunnel shifted from 'horizontally tension and vertically compression' to 'horizontally compression and vertically tension', suggesting that the additional horizontal convergence was inward (positive value); (2) the horizontal convergence value was small for tunnel with a maximum value of 0.76 mm. The amount reduced with stricter strengthening and control techniques which shows that the techniques had certain effect on convergence control.

## Conclusions

This study used MIDAS/GTS software to conduct 3D finite element simulations to analyse the deformation of existing tunnel using a foundation pit project on Yanan Road in Hangzhou City as background. The efficiency of different strengthening and control techniques was simulated using the software to provide support for similar projects.

The following conclusions were drawn: (1) the tunnel first settled then uplifted during piling and excavation stages. The excavation of foundation pit affected the underneath shield tunnel by a great range: the vertical displacement of the tunnel appeared to be normal distribution with maximum value of humping located at the middle of the pit. With the increase in distance to the centre of the pit, the amount of vertical uplift reduced; (2) with stricter strengthening and control techniques, the uplift in the tunnel and bottom reduced, suggesting that uplift piles, strengthening of pit bottom ground, layered excavation, steel support and surcharge had certain effect on controlling the deformation of tunnel and bottom and the effect was more obvious for uplift piles, ground strengthening and surcharge. Optimisation of project plan could be carried out using finite element analysis in actual constructions.

## Reference

[1] CHEN Yu, ZHANG Dongmei. Analysis of monitoring data on tunnel heaving due to unloading of foundation pit excavation. Underground Space, 2004, 24(5): 748－751. (in Chinese)

[2] ZHENG Gang, LIU Qingchen, DENG Xu, et al. Field measurement and analysis of effect of excavation on existing tunnel boxes of underlying metro tunnel in operating. Rock and Soil Mechanics, 2012, 33(4):1109－1116, 1140. (in Chinese)

[3] LI Zhigao, LIU Hao, LIU Guobin, et al. Influence analysis of deep-dip excavation on down tunnel based on the measured displacement. Chinese Journal of Underground Space and Engineering, 2005, 1(4): 619－623. (in Chinese)

[4] CHEN Yu, LI Yongsheng. Calculation of tunnel heaving due to unloading of pit excavation. Chinese Journal of Underground Space and Engineering, 2005, 1(1): 91－94. (in Chinese)
[5] ZHANG Zhiguo, ZHANG Mengxi, WANG Weidong. Two-stage method for analyzing effects on adjacent metro tunnels due to foundation pit excavation. Rock and Soil Mechanics, 2011, 32(7): 2085－2092. (in Chinese)
[6] HUANG Hongwei, HUANG Xu, Schweiger F Helmut. Numerical analysis of the influence of deep excavation on underneath existing road tunnel. China Civil Engineering Journal, 2012, 45(3): 182－189. (in Chinese)
[7] ZHANG Junfeng, WANG Jianhua, CHEN Jinjian, et al. 3-D FEM back-analysis of an over size and deep excavation. Journal of Shanghai Jiaotong University, 2012, 46(1): 42－46, 52. (in Chinese)
[8] QI Kejun, WANG Xudong, JIANG Gang, et al. Analysis of deep pit excavation adjacent to tunnel. Chinese Journal of Rock Mechanics and Engineering, 2005, 24(Supp.): 5485－5489. (in Chinese)

*Applied Mechanics and Materials Vols. 580-583 (2014) pp 1008-1012*
*© (2014) Trans Tech Publications, Switzerland*
*doi:10.4028/www.scientific.net/AMM.580-583.1008*

# On karst water inrush( gushing) geological environment in Pingyang tunnel

Zhu Qing-qing[1,2,a]， Miao Qiang-qiang[2,3,b] , Jiang Shu-ping[3,c]

[1]College of Chemical Engineering,Northwest Minority University,Lanzhou 730000,China；

[2]Key Laboratory of Exogenic Mineralization and Mine Enivronment,Chongqing 400042, China

[3]Chongqing Communications Research and Design Institute, Chongqing, 400067,China.

[a]zqq520@163.com, [b]miaoqiang2008@qq.com, [c]jiangshuping@ccrdi.cmhk.com

**Keywords:** karst area, water inrush( gushing),tunnel, geological environment

**Abstract.** According to Pingyang tunnel karst complex groundwater environment ， This paper carried out thorough theoretical analysis and field observation from Pingyang tunnel stratum rock properties, engineering geology, hydrogeology, the surrounding patch, runoff and drainage and the changes of surface water environment, as well as tunnel excavating. The complex formation mechanism has given in the Pingyang tunnel karst water . Some effective references had put forward for the engineering treatment, provided some valuable references for other similar underground engineering construction.

## Introduction

According to incomplete statistics[1], the tunnels were previously built 1992 in China. There are 80% water inrush disaster in construction. There are more than 30% cases of large water. The total water amount exceeds10000$m^3$/d. A lot of water inrush tunnel is not only affecting the project construction and the project progress. But the extensive and profound impact on the ecological environment closely related, including water environment, soil environment, biological habitat environment etc[2].

Influence factors of karst water movement is more complex. Hydrogeological conditions are mostly related to the incomplete quantitative, even the random, fuzzy, it is difficult to use a deterministic model to describe. karst system open, Among the various factors in the system is through interaction. Therefore this article from the karst area of Chongqing Pingyang tunnel excavation were analyzed by the surrounding water environment change.

## Project background

Pingyang tunnel is located in Xiushan County of Chongqing, For double hole four lane highway tunnel, the separation arrangement form according to the uplink and downlink. Tunnel left and right two hole axis maximum distance is 16.5 ~ 43.5m. Tunnel import and export section are restricted by terrain to small spacing tunnels. Tunnel right line is full-length 3315m, Tunnel left line is full-length 3309.949m, the maximum depth is 400m in the middle.

The tunnel site exposed strata mainly carbonate sedimentary, sandwiched between the small continental sedimentary clastic rock. Tunnel exposed strata mainly sedimentary carbonate sedimentary, sandwiched between the small continental sedimentary clastic rock. Fracture is more developed. That development mainly individual form,such as karst fissure, Karst depression, stone bud, karren, solution groove, sinkholes, Karst funnel, Karst valley.The Karst in underground karst mainly forms were karst fissures, karst cavities and underground rivers. In addition, the Pingyang tunnel is passing through the Pingyanggai syncline, in Figure 1.The syncline core formed some longitudinally underground rivers. Existing underground river and cave provided space and favorable remotion channels for groundwater runoff, occurrence and tunnel water irrush(gushing). In general, the main tunnel adverse geological phenomena were weak interlayer and karst.

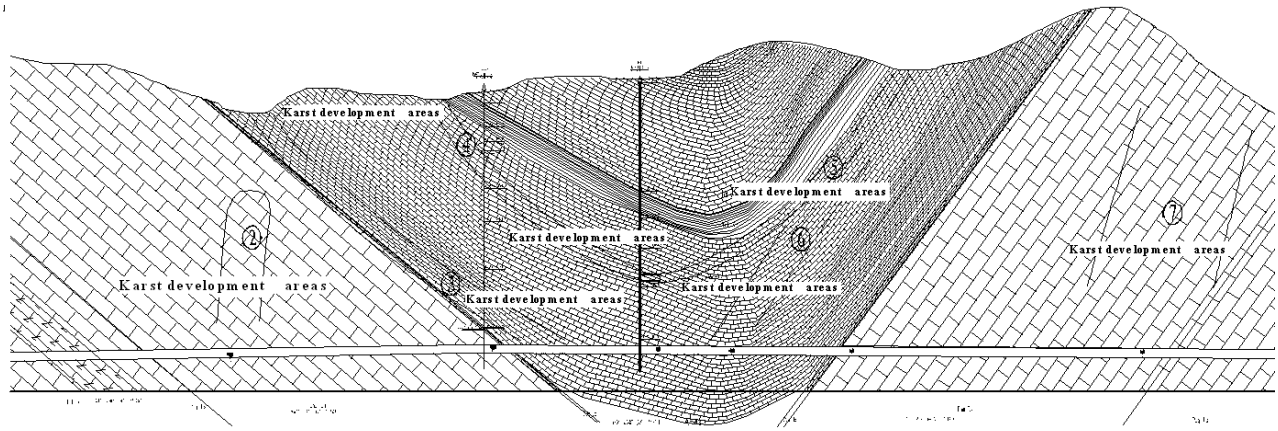


Fig. 1 The left tunnel engineering geological profile

**Pingyang tunnel karst development mechanism**

3.1 The shape and characteristics of karst development

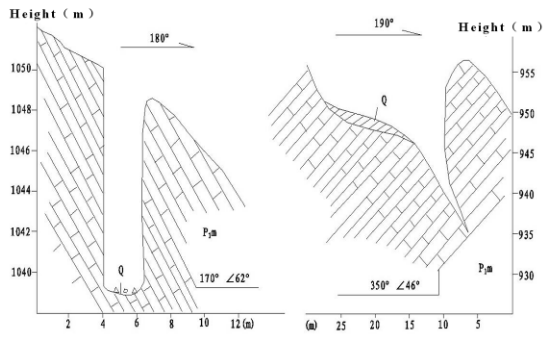


Fig. 2 Sinkholes and funnel section

The tunnel site karren, solution groove, stone teeth can be seen everywhere on the surface. The karst depression, sinkholes or funnel and cave in this area only survey to 234, sinkholes or funnel has 116. Sinkholes hole was circular or ellipse, 3-8m in diameter, general development depth 5-15m, A few depth can not see the bottom, bottom filling clay gravel, main silt, shaft shape less(See Figure 2). Most of them distributed in valley or depression, funnel in the slope zone. That often affected by topography were saucer shaped funnel inclined. Mainly affected by Stratum, terrain and crack control level development, depth in 1-3m.

3.2 Karst development law

There are four levels of planation surface in this region development. The elevation is a large class of mountain stage1200-1300m, 900-1100m and 700-800m mountain basin stage, 400-500m canyon stage.

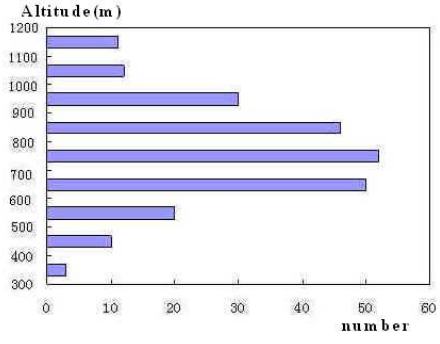


Fig. 3 Karst form distribution

Due to karst development change has closely related to the crustal rise, pause and karst water, the different karst development period with different karst morphology, A layer characteristics formed karst forms in the region, statistics of Pingyang cover area karst depression, sinkholes, caves funnel, as shown in Figure 3. The karst individual form concentrated in three, four and five grade in the karst surface. At the same time, when the crust rise and the pause time interval frequent, At the same time also has a characteristic of karst layer.

3.2.2 Inhomogeneity of karst development

That has inhomogeneity of karst development in this region. In the plane, Karst surface are concentration developed in the lower planation areas of valley and depression. And valley and depression concentrated in the central development part or underground cave distribution development section.Karst individual form number was less in the slope zone, scale small. From the structural point view, Karst centralized development in anticline， syncline core ， fracture zone and the rock faces change belt near. From the view of karst development stratum, large depressions seen area, sinkholes, karst caves, ect. that Karst individual form in the lower Permian, Dazhi group and Changxin group of Permian and Maokou group of Permian distribution area can be seen everywhere, As shown in Figure 4. While in other strata distribution area, Karst individual form relatively less and small.

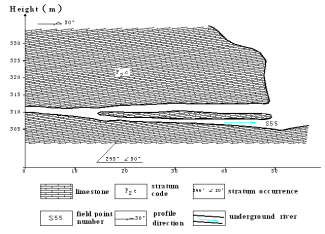


According to field investigation, the depression, sinkholes, funnel, cave Developed in the $T_{1d+j}$ formation reached to 46. The average surface karst rate K=3.2, P1m thick layer limestone reached to 75, K=6.82. $P_{2c}$ K=6.3, $P_{2w}$ K=2.8, $P_{1q}$ stratum k＝1.7, At the same time, both sides of tunnel line in the range of 2km ,the average surface karst rate was as high as K=5.8. But in this range, concentrated in Pingyanggai syncline core that fully reflect the inhomog- eneity of the karst development.

Fig. 4 Longdong underground river discharge geological profile

3.2.3 Karst development to the deep

Karst development characteristics that is karst sharply to the deep crust development. In the new tectonic movement under the action, large area of intermittent intense crustal rising, the base level of erosion and erosion datum also cut down sharply, but the cutting speed of the former quicker than the latter. The formation of deep high gorge, the karst ground cutting must be reduced to fragments, the modern karst landform formatted.

Groundwater to meet the falling drainage datum plane, sharply to deep runoff, the vadose zone with gradual thickening. Leading to erosion gully region, Trough valley set the depression that stacked sinkholes, funnel phenomenon everywhere, full description of the karst development in succession and to the deep features. At the same time, part of the underground river or karst springs cave pipeline in order to adapt to different periods base level of erosion that led to multilayer cave. That is real reflection the karst development to depth. As developed in the solution crack cave spring at Runxi town Shiban village Chayuan. The spring of early discharge is its left side cave. With the crustal uplifting, groundwater along the advantages water flowing fracture corrosion cut. The intermittent spring discharge point formatted as shown in Figure 5.

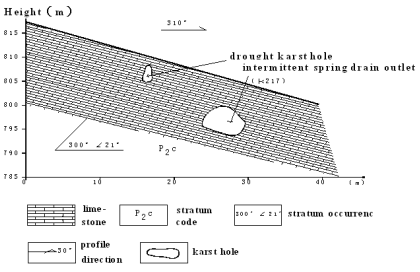


Fig. 5 Intermittent spring discharge geological profile

3.2.4 Karst development vertical zonality

Since the quaternary period, Because the region is a large area crust intermittent uplift. The rate of karst development is less than crustal rise speed. This caused the pattern of karst development with

the increasing depth decreased, karst water alternating cycle severe, karst very development, karst cave large scale, a number of. But in the underground depths, groundwater movement is very slow. Only developed some dissolved pore and karst crack. The vertical zonation of karst development has been formatted, from the surface to the underground can be divided into three zones ( see Figure 6).

(1)Vertical hole gap band (vadose zone): Located in the zone between below the surface to water table. Vertical karst caves are well developed, Include sinkholes, shaft, funnel and soluble gap etc.

(2)Horizontal pipe band (including seasonal fluctuation zone and saturated zone): Karst pipeline horizontal direction is very developed, including the cave and underground river, Groundwater in the cave passage runoff to the nearby drainage datum surface.

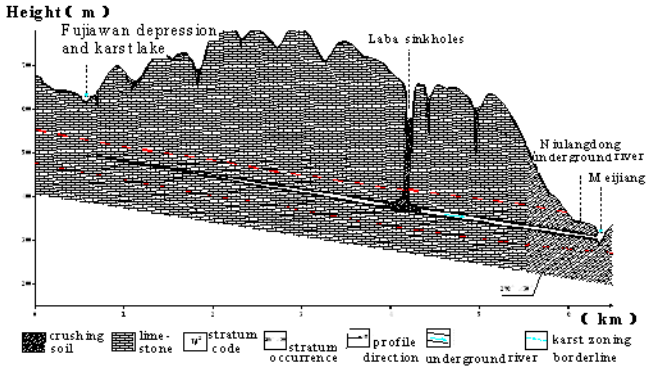


(3)Deep pore zone (deep circulation zone): this band only developed a small dissolved pore and gap. In the meantime the groundwater slowly flow to discharge area or rarely influenced by the drainage area. This region buried depth different, In the valley, general 10 meters to tens meters. In the mountains can be hundreds of metres deep.

Fig.6 Fujiawan depression and karst lake

3.2.5 Recharge, runoff, discharge and dynamic characteristics of karst water

Karst water is mainly recharged by rain in this area. Some local sections mutually transformated between surface water and groundwater. Atmospheric precipitation intensity recharge of groundwater level is mainly controlled by three factors as following in this area. The first is the intensity of karst development. Due to rainfall infiltration groundwater recharge is realized through the rock inside the cave. Especially the development of karst in vertical valley, depression area, is not only in the terrain conducive to precipitation collected, but after the rain quickly into different sizes of sinkholes, funnels. Therefore, the development of karst, the infiltration recharge amount is higher. The second is limited in fissures that controlled by fracture development direction, the overall present reticular runoff.

According to the groundwater discharge point exposed position can be divided into different overflow, drop and water blocking type excretion and other categories. Drop discharge refers to the distribution in the slope gully in the discharge point. These springs are mostly occurred in the structural fracture or weathering fissure groundwater. Because limited water bearing fractured size, The occurrence water is also very limited, In favorable slope or valley edge collection and excretion. Water blocking type and overflow type excretion is that part of the underground river, spring in the valley on both sides of the steep excretion. Discharge point is generally higher than the water surface 5-10m, This difference is due to the distribution of water resisting layer resistance effect or controlled by the base level of erosion . As mentioned before Niulangdong, Longdong underground river were overflow type. Water blocking type excretion refers to the groundwater to downward flow discharge process by lower non soluble rock resisted that forced runoff to cause by cutting terrain excreted springs, rivers on the earth's surface. Such as investigated rock doorway, water cave, Shendong rock underground river and ash soil, Miaolongtang spring point is the best proof.

3.3 The dynamic change characteristics of the karst water

Atmospheric precipitation to surface infiltration or punctate perfusion method into the underground, A linear relation between the groundwater dynamic change and rainfall variability. Such as the investigation on Pingyanggei preliminary prospecting hole (ZK48-1) water table were randomly observed. In the sunny half months later, drilling water depth is 110m, If reduced the level of 8-15 hours, The water level immediately rises to 70m, that fully reflects the correlation. Generally , the karst water recharge area has relatively larger, the underground runoff path lengther, the pressure gradient smaller, The underground river more development. When discharge point and local erosional surface height difference is small, groundwater discharge point flow and the water level variation is small; otherwise.

## Conclusion

(1)Pingyanggai syncline core formed longitudinally some underground rivers , these underground river and cave existed，to groundwater runoff，to occurre and tunnel water inrush provides space and good migration channel. Weak intercalation distribution when the tunnel after excavation, under the action of surrounding rock prone to fall in, subsidence, collapse and other.

(2)According to the occurrence of karst groundwater migration space，karst water excretion point size，The karst development intensity and strata water abundance，the characteristics of groundwater movement that the karst water divide into water abundant karst conduit water system, Content rich water karst gap and karst cave water system, water second abundant Karst fissure water system, and discusses three major systems distribution of 42 groundwater water points. At same time development, recharge, runoff, discharge characteristics and its relationship with tunnel were carried out.

(3)Most of tunnel section in the strongly developed karst belt that groundwater recharge runoff and deep circulation zone. Therefore, encounter water gushing and mud brust are the main site of K38+420 , K39+ 050,K39+175～K39+350,K39+425,K39+965. This should become the focus of prediction water gushing in construction stage. In case of a stock like water and muddy, flow not reduction, It should take drainage or other control measures.

（4）Tunnel Excavation would formated large catchment channel that will cause both sides of tunnel the large range of surface water omission and underground water level to reduce.

## Acknowledgements

This work was financially supported by 53 batch China postdoctoral science foundation funded project, Supported by Chongqing Land and Housing Administration Bureau 2011 Annual third batch of geological disaster prevention special fund project (120301)，the Fundamental Research Funds for the Central Universities.

## References

[1] WANG Hai-bin.Regulation and prevention and cure motheds to groundwater in mountain tunnel [D]. Chengdou:Southwest jiaotong university master degree thesis,2003.

[2] MA Jian-qin.The Corrosive groundwater types and its occurrence environment around underground works [J] Modern Tunnelling Technology, 2001, 38(1):56-60.

*Applied Mechanics and Materials Vols. 580-583 (2014) pp 1013-1018*
*© (2014) Trans Tech Publications, Switzerland*
*doi:10.4028/www.scientific.net/AMM.580-583.1013*

# Preliminary Ideas of the Metro Station Constructed by Shield Tunneling Method Combined with Prefabricated Method

Huifeng Su[1, 2, a],Weining Liu[1,b] and Fuchun Liu[3, c]

[1]School of Civil Engineering, Beijing Jiaotong University, Beijing 100044,China

[2]Shandong University of Science and Technology, Qingdao, Shandong 266590,China

[3]China Railway 19th Bureau Group 2nd CO., LTD, Liaoyang, Liaoning 111000, China

[a]shf7521@163.com,[b]wnliu@bjtu.edu.cn,[c]545896556@qq.com

**Keywords:** Shield method, Prefabricated, Metro station, Joint, Standardize

**Abstract.** Confronting with the difficulties of the construction metro station in the Northeast of China, a new idea of shield method combined prefabricated method is put forward. In the paper the research status of the underground engineering precast assembly technology was analyzed and classified firstly. The method of single round interval shield combined with open-cut(or covered excavation) prefabricated sections and on the basis of shield tunnel to build single arch station is especially worth studying and promotion. Then the key prefabricate theory needing to deal with such as how to calculating the spring stiffness and so forth of the calculating model. The key technology such as joint formation, waterproof and the other of shield method combined with prefabricated method was discussed.

## Introduction

During the construction of the Metro Station, the Risk of the shallow mining method is much high. The time of cast-in-place on the basis of the method of open cutting is long and will bring about many difficulties for the traffic. In winter of the Northeast China, the method of cast concrete is difficulty also. Using prefabricated part will not only insure the good quality of the concrete, but also reduce some technology. Meanwhile, it will improve the environment and lower the construction cost.

More and more metro tunnel takes shield method during the construction. For the sake of reducing the mutual interference between station and space interval shield construction, improving the once forward distance of the shield and reducing the abandoned segment and the construction cost, combining with shield tunneling method is a good idea.

So the metro station constructed by shield tunneling method combined with prefabricated method has extensive application prospects.

## Research Status of the Underground Engineering Precast Assembly Technology

### 1.1 Foreign Application Status of the Prefabricated

In foreign the underground engineering precast assembly technology has obtained the certain development and pre-engineer's standardization is one of the underground engineering's principal characters, but it is mainly applied to the open cut metro tunnel[1,2]. For example, Toshkent Shahri city of UZ adopted widespread rectangular "into sections lining structure" in the 1970s, Rotterdam city of Netherlands adopted "shell type tunnel" in Metro East-West Line, Sendai Subway of Japan used prefabricated double span box structure and single span structure of prefabricated rectangle in double-lane vehicular tunnel and large precast arched concrete with its maximum span is 12m in Expansion Project of road by Japan alliance with France. Etc.

The Former Soviet Union has some applied cases about the metro station's prefabricated method[3,4], such as multilayer single arch metro station made of big block fabricated member in Minsk city of Belarus. In Russia the first double-deck interchange station was built on the principle of

the single arch structure and its characteristic, thus is Olympic Green Station. In addition, The Soviet Union has the cases of prefabricated members in shaft and the place between shaft and gallery.

### 1.2 Application Status of the Prefabricated Metro Station of Our Country

Research and application about underground fabricated of our country is not too much. The fabricated technology about underground engineering is mainly used in the metro tunnel constructed by shield and mainly round structure.

During the construction of long tunnel we also have taken the technology of precast slab and template, inverted arch and padding poured by RCC so as to accelerate progress and improve the quality of the inverted arch and the padding concrete[5]. In the construction of the Qinling Tunnel(18.4Km), inverted arch was made of precast unit and abutment wall of cast-in-situ[6].

Compare with the foreign metro station's prefabricated unit research and the successful applications, the study of the metro station's prefabricated unit is in its infancy.

## Research Status of Building the Station Combined with Shield Method

In foreign, countries such as Former Soviet Union[7-10], Japan[11-13], Germany[14] and so forth have studied the method of building metro station combined with shield. Three methods of building the station combined with shield are as follows:

### 1.3 Enlarging the Station on the Basis of Full Diameter Shield

(1)Shield combined with cross aisle to build station

The station was made by two or three parallel circular tunnels with the help of cross aisle and the difficulty is cross aisle's design and construction.

(2) Method of shield combined with semi-shield(roof shield) to build station

In this way both sides of the tunnel was built parallel with two shields. Under cover of one semi-shield the office station was built later which was an island platform typical.

(3)Method of shield combined with mining method or open cut method to build station

### 1.4 On the Basis of Space Interval Shield to Enlarge the Station

Fist the vehicular tunnel was cut-through by the interval shield(OD 5.5m), then the segment on the side of near the platform was removed to enlarge the station. With this method the stations were spread in Russia Saint Petersburg city(about 10 ) which was called three arch wall column station.

(1)Single round shield combined with semi-shield to construction closed platform station

(2)Single round shield combined with open cut method(covered excavation) to construction column station

### 1.5 Single Arch Station

The station was constructed based on the shield tunnel which means through both sides of the travelling tunnel finished by shield filled with concrete as the base of arch abutment to enlarge the station. There are some successful examples of this type of station in the Former Soviet Union.

In China about the project in construction or the planned in Beijing metro, Guangzhou line 1 and 5, Chengdu line 1, professor Weining Liu of BJTU and professor Chuan He of SWJTU each leads his team having done some research on the designing and construction methods of combining with shield to building the station. They also have acquired some good effects[15-20]. The main idea is that the shield transits the station first, removing or keeping part segment to open door providing the condition of loading and unloading, which is using the method of undermining or open cutting cast-in-place. Make a general survey of the method of combining with shield to build the station, it is mainly in research stage of numerical simulation and similar model test and special segment, but no project example and mainly is cast-in-situ station combining with shield and Open Cut(NATM).

In view of our technology and economic capability and applications, the method of single round interval shield combining with open-cut(or covered excavation) prefabricated sections and on the

basis of shield tunnel to build single arch station is especially worth studying and promoting. The shield tunnel is used as the lane and the structure can be prefabricated entirely or partly of the former method which fits the large span station. Of the latter method the arch foundation needs cast-in-site which fits the smaller station.

## the Principle Design Philosophy of Prefabricating

At present, there are many studies of shield tunnel's prefabricated lining. Japan is active in the field of technology about shield method and has published a great quantity papers of numerical calculation[21]. Many domestic experts and scholar have studied in this field in recent years and have achieved some consequence[22-27].

The same point of these model patterns is simulating the property of joint by spring. Now the model pattern can simulate longitudinal joint, girth joint, bedding joint and so forth simultaneously.

Making a general survey of the study history of segment joint, the joint models develop is shown in fig. 1.

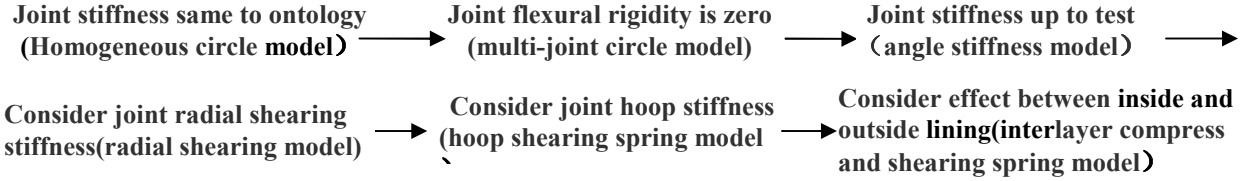


**Fig.1 The Development of the Joint Model**

These types of model are on behalf of the prefabricated lining tunnel's trend probably, although are flaws such as how to think the stiffness of spring and how to simplify the calculating method to improve the efficiency and so forth.

For our country there is no use of the station's prefabricating, and only papers[28-30] are about analyzing the standard section of station. In these papers longitudinal rigidity was not considered and related joint' tectonic pattern and model test of waterproof project was lack, but also there were no further analysis for the detailed dimension and prestressed constructions of rib shape. These also have no discussed the staircase and related gallery's joint which is changed in structural section. In addition, with regard to open cut prefabricated station the anti-seismic is needed to study to analyze the character in earthquake.

## Key of the Prefabricated Method

There are defects of prefabricated concrete structure such as complex structure of joint, low integration, a poor performance in earthquake of joint etc. from the existing project, in the development of the large precast technology; the following for topics need to be resolve.

### 1.6 Study of the Component's Standardization

Prefabricating and Standardization is closely connected. If the components of the metro is standardized or not is the precondition of the component of prefabricated and is also related with benefit. Achieving the standardization means achieving the scale of production and benefit model change. For example, the machine determines the basic configuration in shield tunnel construction. The round section gives the quite advantage of components standardization. So the technology of circular precast segments develops rapidly. For the open cut metro station, the section is mainly rectangular or arched. But how to divide the components is one key of making the components standardized to use the prefabricated parts.

### 1.7 Precast Construction Type to Choose and Structural Parts to Divide

Judging from the application examples there are four types of the prefabricated structural element, that is two types of Rectangular frame and two arch structure also, as fig. 2 shows.

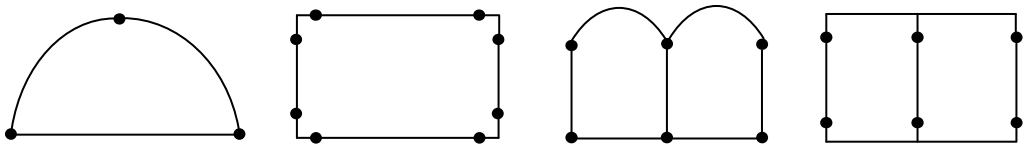


**Fig. 2 Structure Form and Connector Station Sketch Map**

For type (a) and (b), base slab can be adopt when the span is lesser and when the span is larger the slab should be made to inverted arch. For type (c) and (d), base slab can be adopt because of the mid-board can decrease the slab' span.

After the form has been determined, the components' division not only the structure rational condition but also the probability of the components' manufacture and assembling should be considered. Prefabricated parts should be request light for manufacture and assembling. Besides, reducing the types of components so as to scale manufacture is important principle for the components' division. The way of common division is shown in fig.2 and the joint is located at the part of smallest bending moment.

**1.8** Joint Formation and Waterproof

Joint formation and waterproof work is one of the key to the component prefabricated which will affect the service environment and durability.

*5.3.1 Joint Formation*

Like the joint of segment, according to the joint property it can be divided into rigid joint and flexible joint; according to the function it can be divided into longitudinal joint and transverse joint. Longitudinal joint and transverse joint can be in one type and different. Judging from the adopting joint, it probably has the following types:

(1) using concrete joint cast-in-place

It is a simple, economic, reliable and perfect rigidity that can be used in longitudinal direction and transverse direction.

(2) using bolted joint with prestressed tighten

The type of it is similar to concrete segment joint except the prestressed is taken place by push of jack. It is flexible and through PN BW installed between the components to sealing up.

(3) using joint with commercial bolt

It is simple in structure and construction which is major applied to fabricated segment. It can be adapt to a certain error because of its reservation bolt hole is 5-10mm larger than bolt. Besides, bolt hole can be reserved in component in order to assembling conveniently.

(4) using joggle fastener itself

This type of joint is so much that has broad development prospects.

(5) the others type

There are mainly embedded steel plate joints and curved bar bolt joint etc.

The joint should meet the following conditions: has the function of resisting shear; has the function of water proofing requested; connected and located easily; has certain popularity and durability.

According to the above request, the form of transverse joint should be selected commercial bolt with handspike in metro and station' prefabricated part. The joint is simple in structure and construction convenient to save cost. Besides, joggle joint can be selected to joggle the prefabricated part. The joggle joint also can guarantee the accurate position of the flank wall and roof and baseboard without its complex structure.

*5.3.2 Waterproof of joint*

The main reason of leakage for the prefabricated part is its environment, structure, sealing material, construction and etc. Section waterproof can be selected waterproof concrete to sealing itself for its prefabrication can ensure is quality. It is important for the joint sealing because of the main leakage comes from joint and seam. Waterproof process in plane joint is probably pasting rubber waterstop on the side of the wall rock and setting up ring washer in bolt and grouting.

1.9 manufacture and install of component

Success or failure of component is in supervision. Strict and good management specifically manifested in the manufacture and installation work for these reasons the two segments should be pay great attention.

For the manufacture of component, the principle is production precision. In order to guarantee the precision the template should be designed carefully. The other key point is the installation work in engineer especially the effect of waterproof.

**Summarize**

Shield tunneling method combined with prefabricated method to build station is a systematic project. Something such as how to connect segment with prefabricated part, waterproof property of clip ring joint with station's structure and earthquake resistant capability and durability and so forth should be worth studied deeply. Preliminary studies and application should be taken as soon as possible in some good conditions so as to put forward the development of its technology.

**References**

[1] ITA-Working Group Research: Japan Tunneling Association. p. 1-26,1988

[2] Chi Zhang, in: The Tunnel, 1997(2):10-18. In Chinese.

[3] Qihu Qian, Chengzhi Qi, in: Essence of the Russia subway construction (China Railway Press, Beijing, 2002). In Chinese.

[4] Urban Rapid Rail Transit, 1994, Vol. 2: 42-46. In Chinese.

[5] Guihong, in: Highway, 2004(11):145-148. In Chinese.

[6] Construction Techniques Summarization of Xi'an-Ankang Railway Qinling Tunnel TMB, in: The ministry of railways engineering management center(China Railway Press. Beijing, 2004). In Chinese.

[7] . Dailing Hong, in: Tunnel and Underground Engineering, 2000(l):33-39. In Chinese.

[8] Subway Investigation Reports in Russia, in: Urban Rail Transit Research Center of Beijing Jiaotong University. Beijing,2003. In Chinese.

[9] Taihui Li, in: Subways and Light Rails. 1994(4):45-46. In Chinese.

[10] Hiroyuki KAMATA, Yoshio MATSUMOTO. in: Conceptional Design and Feasibility Study of a New Tunneled Station with Multi- Circular Face Shield(MF Shield)(Quarterly Report of RTRI, 1992, 33(2): 115-123)

[11] Dexiang Zhang, in: Underground Space, 1993, 13(2): 145-151. In Chinese.

[12] Mingqi Xian, in: Tunnel translations, 1992(9): 50-57. In Chinese.

[13] George D. Moir, Yunxin Ma, in: Municipal Engineeing Technology, 2004.6:196-199. In Chinese.

[14] Kanglin Wei, Wei Huang, Hongnv Huang. In: Journal of haihe river university. 2001(Supplement): 157-161. In Chinese.

[15] Meili Lu. In: Study on Schemes and Risk Analysis of the Expanded Metro Station under Shield Running Tunnel(Beijing jiaotong University PhD dissertation, Beijing, 2007). In Chinese.

[16] Weining Liu, Meili Lu, Xinjin Zhang, Zhaoping Li. in: Chinese Journal of Rock Mechanics and Engineering, 2009, 25(8): 1629-1639. In Chinese.

[17] Xinjin Zhang, Weining Liu, Meili Lu, Ting Guo, Xiaolin Li, Deyou Guo.in: Journal of the China Railway Society, 2009, 31(6): 53-90. In Chinese.

[18] Xinjin Zhang. In: Study on Key Technologies of the Metro Station Constructed by Shield Tunneling Method Combined with Mining Method(Beijing Jiaotong University PhD dissertation, Beijing, 2010). In Chinese.

[19] Wei Li. in: Study on Schemes and Applied Technology Problems of Metro Stations Constructed with Shield-driven Method and Mining Method(Southwest Jiaotong University Doctor Degree Dissertaton, Chengdu, 2006). In Chinese.

[20] Chuan He, Jianlong Ding, Wei Li. in: Journal of Southwest Jiaotong University, 2005, 40(3) : 293-297. In Chinese.

[21] Mamort M, Makoto K Yuzo K. in:Study Oil limit state design method for tunnel lmingsp(JSCE Proceedings, No. 445, 1995: 141-149)

[22] Hongsheng Jiang,Xueyuan Hou. In: Chinese Journal of Rock Mechanics and Engineering, 2004.23(9). 1574-1577. In Chinese.

[23] Dongyang, Chuan He. in: Journal of the China Railway Society. 2005.27(4).90-95. In Chinese.

[24] Ning Yu, Yanhui Bai, Hehua Zhu. in: Chinese Journal of Underground Space and Engineering. 2009.5(3).439-444. In Chinese.

[25] Houmei Zhang. In: Research and Construction Practice of the shield tunnel(China Building Industry Press, Beijing, 2010). In Chinese.

[26] Chuan He, Jiangang Zhang, Zongxian Su.in: The Mechanics Character of the Underwater Shield Tunnel with Large Cross-Section(Science Press, Beijing, 2010). In Chinese.

[27] Yujie Li. in: Application of Discontinuous Contact Computational Model in Mechanical Behavior of Shield Lining(Beijing jiaotong University PhD dissertation, Beijing, 2012). In Chinese.

[28] Yonggang Jia. in: Study of Mechanics Characteristic of the Fabricated Railway Tunnel(Southwest Jiaotong University Master Degree Thesis,Chengdu, 2003). In Chinese.

[29] Huimin Liu. In: Study on the Mechanics Characters of the Fabricated Linings in the Subway Constructed by Open-cut Method(Southwest Jiaotong University Master Degree Thesis, Chengdu, 2003). In Chinese.

[30] Jianhong Liu. In: Study on the Design Optimization of the Fabricated Structure of the Subway Stating Constructed by Open-cut Method and the Mechanical Behavior of Construction(Southwest Jiaotong University Master Degree Thesis, Chengdu, 2007). In Chinese.

*Applied Mechanics and Materials Vols. 580-583 (2014) pp 1019-1023*
*© (2014) Trans Tech Publications, Switzerland*
*doi:10.4028/www.scientific.net/AMM.580-583.1019*

# Pre-stressed Reinforcement and Security Analysis of Tunnel Lining with Dislocation and Cracks

Jingwei Zhang[1,a]

[1]Civil Engineering School, Southwest Jiaotong University, Chengdu 610031, Sichuan, China

[a]496521718@qq.com

**Keywords:** Tunnel lining, lining split, pre-stressed reinforcement, numerical simulation, security analysis.

**Abstract.** Security of secondary lining is of utmost importance to tunnel engineering quality as the main bearing structure and the last water-prevent line for rock types I, II, III. Tunnel lining with dislocation and cracks is one of the most serious defects to secondary lining. Based on the case of Goujiagou tunnel, the potential threat is listed. The pre-stressed regulation scheme is designed, and the parameters are determined. The loose surrounding rock pressure on lining is calculated by P's theory. Based on the results, the numerical simulation model is build by means of FES code ANSYS; and the internal pressure before and after the reinforcement is analyzed. According to the above-mentioned research results, this paper calculated the safety factor, and checked the structure strength. Research results indicate that the regulation design is feasible and the pre-stressed parameters are appropriate. The results will provide reference to design for dislocation and cracks of tunnel lining.

## Introduction

With the time goes by, there will be all kinds of defects of existing tunnel. The lining breach which will leads to water leakage of tunnel and lining collapse is one of the main defects of hidden troubles. It will have some impact on using performance of tunnel directly, even though driving safety and useful life. We should pay more attention to treatment of tunnel lining with dislocation and cracks. Because this defect frequently proves surrounding rock pressure had redistributed and there are some other defects.

Since the 1960s, many experts did the research work in this filed and got a lot of research achievements. Among them, Zhi-xiong Qian created finite element model, calculated structure security and finally recommended treating method according to detection results [3]. Yong Wang used engineering criterion to analysis safety factor of liner sections [4]. Ting-jin Liu created finite element model for cavity behind primary lining, and investigated the influence of cavity on bearing capability [1]. Yong-hua Liu used load-structure model and statistical parameter to discuss structure security with vault cavity lining thickness and cracks [5].

This paper mainly discussed the research and analysis on regulation scheme and the parameters of pre-stressed resin anchored bolt, and the structure security during construction which based on practical engineering.

## Engineering Situation

This is a double-track railway tunnel in speed of 160km/h mixed passenger and freight. Most of surrounding rock isⅣ and other is Ⅴ.The rock type is mudstone and sandstone.

There are two longitudinal symmetrical concrete cracks on the arch crown in the section of 9m (K0+435～+444) of tunnel body, and the pressure replacement of right wall occurred due to geological conditions and construction methods etc. The results of detection indicate that left obviously(crack of high slump concrete),right hidden; the left longitudinal crack width is 15mm,depth is about 20mm,and there are different period cement slurry at both ends of cracks; the other crack width

is about 2mm since 0.5m below long span of K+438.5 to lower mileage, and the angle between cross section is 30 extending to right haunch circular construction joint, and it cross to the left arch crown crack, which almost make the lining under dangerous ,and cantilever fracture may be occurred any time.

## Pre-stressed Reinforcement Scheme

The main reasons of the left arch crown longitudinal crack are as follows:

1) There are two intermittent joint both left and right (K0+435～+444) .2) The collapse pressure due to cavity behind liner of left arch crown.3) Additional load on structure because of slight expansion of mudstone .

Based on the above-mentioned reasons and existing engineering experience, the pre-stressed reinforcement scheme was designed. Fig. 1 shows the design of regulation measure.

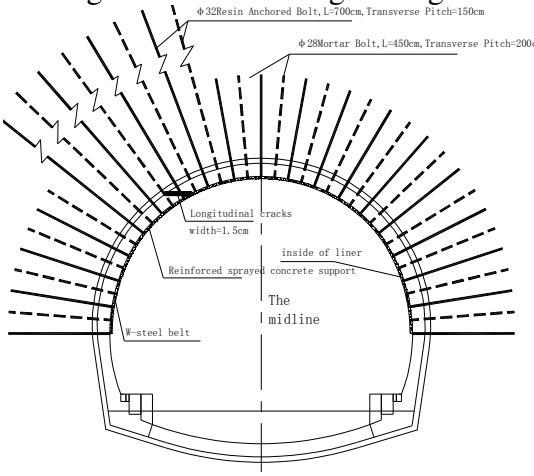


Fig. 1 Design of regulation measure

1) Decorating two rows of pre-stressed Φ32resin anchored bolt up and down along the direction of crack on left lining. The spacing of tangential and longitudinal is 1.5m; then applying 200KN pre-stressed on the anchored bolt to strengthen the liner.2) Decorating W-steel belt and longitudinal decoration is 1.5m above maximum span. Expecting using drill nail or shorter anchor to fixed W-steel belt within the scope of crack 2.5m up and down; others using 4.5m Φ28mechanical anchor bolt and the space is 2m.3) Laying Φ6,10cm×10cm steel fabric in area of W-steel belt.4) Spraying polypropylene fiber concrete and the depth is 8cm.

## Determination of Reasonable Parameters

**Calculation Pattern.** This paper adopts the pattern of conventional load - structure to calculate. The formation and lining function is considered as formation spring without pulling; the force transmission between the primary and second lining is considered as composite beam; the connection of spring is compression or tension in calculation, and broken phase method is adopted in the process.

**Physical and Mechanical Parameters.** The surrounding rock class is V in disease section. Table. 1 shows physical and mechanical parameters of surrounding rock and structure.

Table. 1 Physical and mechanical indexes of surrounding rock and structure

| Structural style | E(GPa) | ν | γ(KN/m$^3$) | Φ ($^o$) | K(MPa) |
|---|---|---|---|---|---|
| Intense weathering mudstone | 2.0 | 0.40 | 22 | 46 | 300 |
| Moderate weathering mudstone | 6.0 | 0.33 | 23 | 55 | 400 |
| C25 concrete | 29.5 | 0.20 | 23 | / | / |

**Calculation Model.** This is a deep tunnel and the depth is 36.95m; the excavation width is 12.98m.According to《Code for design on tunnel of railway》and P's theory to calculate the loose rock pressure:

$$q_1 = \gamma b = \frac{\gamma a_1}{f} \tag{1}$$

$$e_1 = \gamma b tg^2(45° - \frac{\varphi}{2}) \tag{2}$$

$$e_2 = \gamma(b+h)tg^2(45° - \frac{\varphi}{2}) \tag{3}$$

Where b is the maximum height of natural balance arch; $a_1$ is the biggest span arch of natural balance, and $a_1 = a + htg(45° - \frac{\varphi}{2})$ ; $f$ is P's coefficient.

This paper used beam element to simulate second liner, and spring element to the foundation. The left crack is replaced by hinge joint. Fig. 2 a) shows the calculation model before reinforcement and b) shows the calculation model after reinforcement. Fig. 2 shows the calculation model of structure.

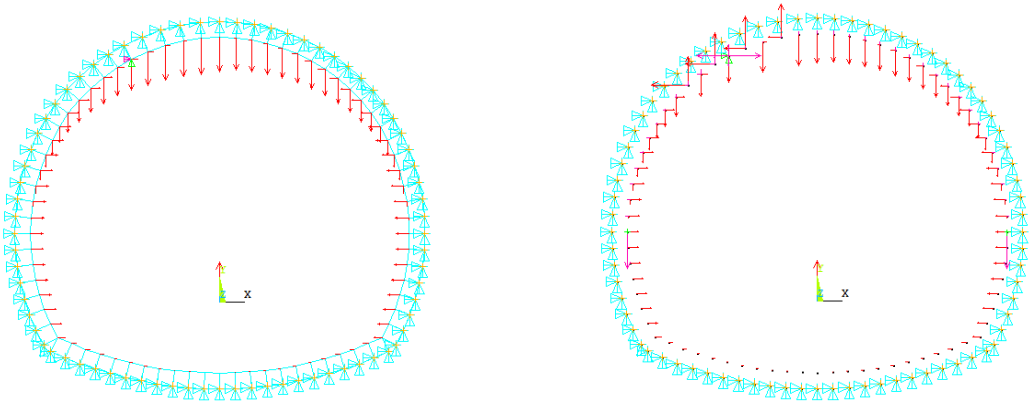

a) Original state b) Reinforcement state

Fig. 2 The calculation model of structure

**Calculation Results**. Fig.3 shows the axial force in original state, and Fig.4 shows the bending moment in original state; Fig. 5 shows the axial force in reinforcement state, and Fig.6 shows the bending moment in reinforcement state.

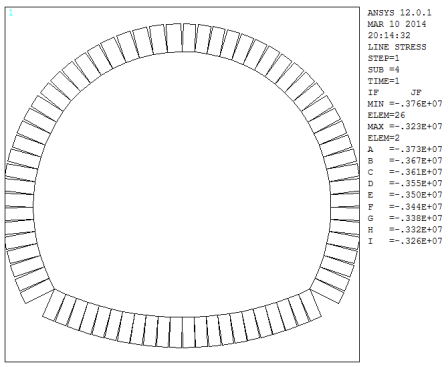


Fig. 3 The axial force in original state (N)

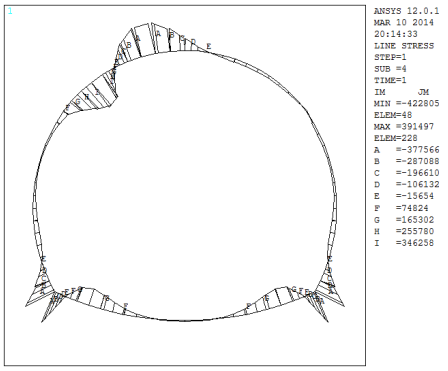


Fig. 4 The bending moment in original state (N.m)

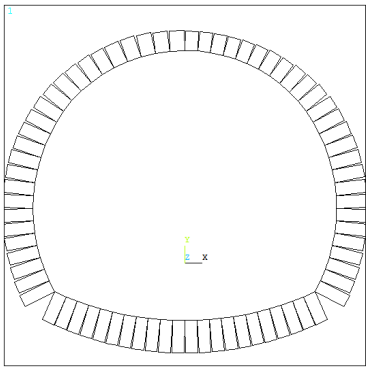


Fig. 5 The axial force in reinforcement state (N)

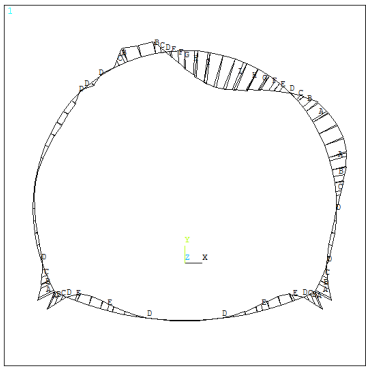


Fig. 6 The bending moment in reinforcement state (N.m)

## Evaluation of Structure Security

Based on the above-mentioned research results, the security factor of control lining section was calculated to evaluate the structure strength by comparing difference between the two states. According to the 《Code for Design of Road Tunnel》 (JTJ D70 -2004) and theory of failure stage, the eccentric compression concrete strength calculation are as follows.

$$K = N_L / N \geq K_P \tag{4}$$

When controlled by the compressive strength. $e = M / N \leq 0.2h$:

$$N_L = \varphi \alpha R_a bh \tag{5}$$

Where $\varphi$ is the coefficient of vertical component, $R_a$ is the ultimate compressive strength of concrete, $\alpha$ is the eccentricity influence coefficient of the axial force, and $\alpha = 1 - 1.5 \cdot e / h$, $b$ is the breadth of section, $h$ is the thickness of section.

When controlled by the tensile strength. $e = M / N \geq 0.2h$:

$$N_L = \varphi \frac{1.75 R_l bh}{\frac{6e}{h} - 1} \tag{6}$$

Where $R_l$ is the ultimate tensile strength of concrete.

Table. 2 shows the security coefficient of control sections before regulation and Table.3 shows the security coefficient of control sections after regulation. Fig. 7 shows the tendency and contrasting relations of the structure security between original and reinforcement state.

Table. 2 Security coefficient of control sections before regulation

| Location | Bending Moment (N·m) | Axial Force (N) | Eccentric Distance $e_0$ (m) | Safety Factor | Note |
|---|---|---|---|---|---|
| Left Arch Crown | -445249 | -3.38E+06 | 0.132 | 1.6 | N |
| Left Arch Haunch | 328814 | -3.46E+06 | 0.095 | 2.1 | Y |
| Side Wall | -445249 | -3.93E+06 | 0.113 | 1.6 | N |
| Inverted Arch | 156800 | -3.77E+06 | 0.042 | 2.5 | Y |

Table. 3 Security coefficient of control sections after regulation

| Location | Bending Moment (N·m) | Axial Force (N) | Eccentric Distance $e_0$ (m) | Safety Factor | Note |
|---|---|---|---|---|---|
| Left Arch Crown | 1.91E+05 | -6.90E+05 | 0.276 | 2.0 | Y |
| Left Arch Haunch | -2.32E+05 | -1.62E+06 | 0.144 | 4.3 | Y |

| Location | Bending Moment (N·m) | Axial Force (N) | Eccentric Distance $e_0$ (m) | Safety Factor | Note |
|---|---|---|---|---|---|
| Side Wall | -2.13E+05 | -1.83E+06 | 0.117 | 4.5 | Y |
| Inverted Arch | 1.05E+05 | -1.72E+06 | 0.061 | 6.1 | Y |

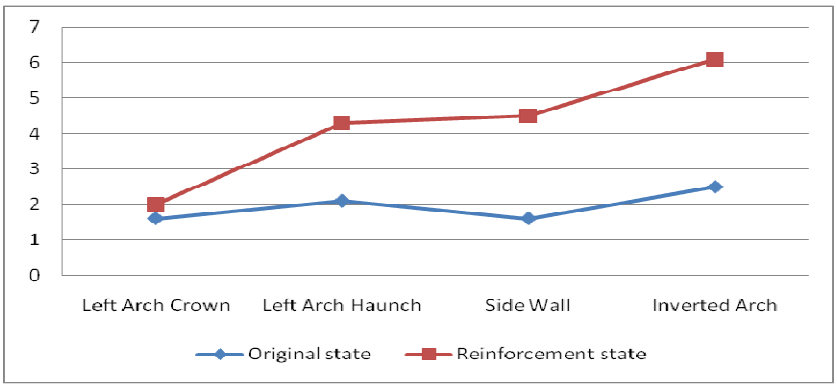


Fig. 7 Security coefficient of structure compared with original and reinforcement state

## Conclusions

The lining cracks result in stress concentration significantly especially the 149 point, and the structure strength greatly reduced. Especially the left arch security coefficient is lower than the standard value 2; at the same time, it results in surrounding rock pressure distribution. The stress concentration of other control nodes also obviously. The security margin of structure is low. Cantilever fracture may occur at any time, and it is unpredictable.

The area of stress concentration moving to the right arch that lining is in good condition and also reinforced, after using 200KN pre-stressed resin anchored bolt and reinforcement measure. Based on the above-mentioned research results, the control section security coefficient has obviously improved than original state, and the security factor of several key nodes meets the specification values. It indicates that pre-stressed reinforcement scheme is feasible, and 200KN parameter selection is appropriate.

## References

[1] Tingjin LIU, Hehua Zhu, Wenqi Ding. Chinese Journal of rock mechanics and engineering Vol23 (2), 75-78. (in Chinese)

[2] Zhi-ping Nie, Shaohua Zhu, Wenguang Zhao, et al. Journal of Huazhong University of Science and Technology: Urban Science Edition,2003 (9) :42—45.(in Chinese)

[3] Zhixiong Qian, Yongxiang Yang, Ying-ren Zheng. Chongqing Construction,2001 (3):13-17.(in Chinese)

[4] Yong Wang. Geotechnical Engineering Technique, 2004(10):258~262.(in Chinese)

[5] Yong-hua Liu. Study on safety estimation of express-way tunnel [D]. Chengdu: Southwest Jiaotong University , 2004.

[6] Chuning Wang, Mingfeng Lei, Li-min Peng. Journal of Railway Science and Engineering,2011,8(3) :53—58.(in Chinese)

[7] Mingfeng LEI, Li-min Peng, Cheng-hua Shi, et al. Chinese Journal of Underground Space and Engineering ,2008 , 4 (7):1 357—1 362.(in Chinese)

*Applied Mechanics and Materials Vols. 580-583 (2014) pp 1024-1028*
*© (2014) Trans Tech Publications, Switzerland*
*doi:10.4028/www.scientific.net/AMM.580-583.1024*

# Research on Layout of Measurement Points in Tunnel Lighting Experiment

Qiang YANG[1,], Bo LIANG[2,a],Guobing PAN[2], Shiyong HE[2], Wei CHEN[2], Xiaoyu DANG[2], Zhiwei WU[2]

[1] Yunnan Highway Development & Investment CO, LTD, Yunnan of China

[2] Chongqing Jiaotong University, Chongqing of China.

[a] liang_laoshi@126.com

**Keywords:** Layout Mode, Measurement Area, DIALux, Range of Light Effects, Tunnel Lighting Experiment .

**Abstract.** Based on the measured data of the tunnel lighting, this paper is focusing on the arrangement of measured points in the experiment of tunnel lighting. Through the way of changing the location of measured area and the arrangement of measured points, comparing the simulation from the software DIALUX and the actual measurement in a repetitive region, the best position of measured area and the corresponding layout mode can be found. Analysis shows that, the larger the lamp distance is, the more similar the experiment and simulation results are. Before the experiment, the analysis of the light distribution curve is required, then, the simulation of software can help to find out the best position of lamp interval, measured area and layout mode, in order to ensure the authenticity of the results and to avoid too large or too small lighting evaluation, layout mode must include the maximum measured points and the minimum measured point.

## Introduction

In recent years, the number of tunnels is increasing year by year, traffic safety problems have become increasingly prominent. In the process of a driver passing across the tunnel by car, traffic safety and the tunnel lighting environment are closely related, Reasonable evaluation of traffic lighting environment have important meaning for enhancing the quality of lighting, ensuring traffic safety, conserving energy, protecting environment, maintaining and improving lighting facilities.

Currently, traffic lighting environment evaluation mainly adopt the method of static measurements of the tunnel lighting parameters; luminance or illumination parameters are the most commonly used parameters [1]. Although with the advancement of technology, measurement tool constantly upgrading [2], the measurements are always measured using the method of drawing line and getting points in the measured area[3] to get illuminance or luminance of each points to evaluate the quality of lighting. For the layout measured point, the distribution is disposed generally rectangular, square etc; according to different requirements of measurement and evaluation, the rational design for the density and location of the points is required.

Due to the high tunnel lighting requirements, the way of reflecting inside of the tunnel is complex [4], and how to choose the right way of distribution, lighting measurement, tunnel lighting quality evaluation, is not explicitly given in the specification. How to choose a rational way of distributing the measured points in a limited area, realistically reflect the actual lighting situation, and provide a reference for tunnel lighting illumination measurement experiment is the main task of this paper. In this paper, DIALux software is used to model and analysis the actual tunnel lighting environment, and carry out the research for tunnel lighting illuminance measurement experiment of measured points distribution, thus finding a suitable distribution of measured points by comparing.

## Tunnel Lighting Evaluation

### 2.1 The Index of Tunnel Lighting Evaluation

The index of highway tunnel generally includes the luminance (illuminance), glare restriction, induction etc, where glare and induction have clear rules in the specification, and the brightness (average brightness, uniformity, luminance range etc.) affect the driver's visual contrast sensitivity and luminance contrast of the road object relative to the visual background, so this paper selects the brightness as a basic index to evaluate the quality of tunnel lighting. Related information shows: selecting the appropriate brightness index do good for improving RP (revealing power) [5], which is conducive to driving safety.

For the highway tunnel in which traffic flow have a larger proportion of motor vehicle, direction and distance of driver's observation is relatively fixed, and the layout of the environment presents a unified, so the road luminance and illuminance distribution in the field of view is corresponding[6]; Also in the actual measurement process, the measurement of illuminance measurements is more convenient and easy in operation compared with the luminance measurements. therefore this paper selects illumination as the research target to evaluate the quality of tunnel lighting.

### 2.2The Method of Tunnel Lighting Measurement

Tunnel lighting evaluation changes with the method of measurement and distribution of measured points; based on the measurement of illuminance and distribution of measured points, this paper mainly introduces the two ways of the illuminance measurement: the center point method which regard the center point of rectangle grid as the basic point; the four-point method which regard the four vertices of rectangle grid as the basic points. According to the different distribution of measured points, in Fig.2-1, 2-2, the calculation formula[1] of corresponding average illuminance is as follows:

$$E_{hav} = \frac{1}{4MN}(\sum E_{\theta} + 2\sum E_0 + 4\sum E) \tag{1}$$

$$E_{hav} = \frac{1}{MN}(\sum E) \tag{2}$$

Where:

$E_{hav}$ —The average horizontal illuminance; Unit: lx; M /N—The number of vertical / transverse grid

$E_0$ —The measured illuminance of four vertices in measured area; Unit: lx;

$E_{\theta}$ —Except $E_0$， the measured illuminance of four outer edges； Unit: lx;

E—The measured illuminance inside of the four outer edges; Unit: lx;

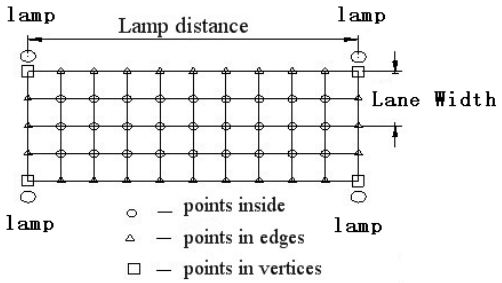


**Fig.2-1 Layout mode of the four point method**

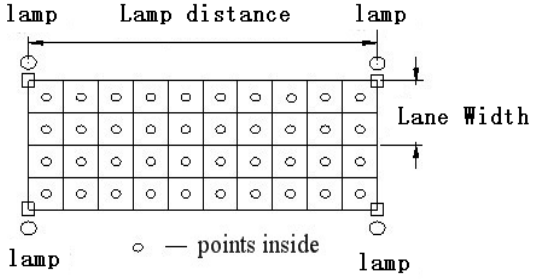


**Fig.2-2 Layout mode of the center point method**

Calculation of the tunnel illumination uniformity:

$$U_1 = E_{\min} / E_{\max} \tag{3}$$

$$U_2 = E_{\min} / E_{hav} \tag{4}$$

Where:

$U_1$ —Illumination uniformity (range); $U_2$ —Illumination uniformity (average deviation);

$E_{\min}$ —Minimum illumination; Unit : 1x; $E_{\max}$ —Maximum illumination; Unit: 1x;

$E_{hav}$ —average illumination； Unit: 1x.

## Evaluation of DIALux Simulation Results Based on the Measured Data

### 3.1 Overview of Physical Measurement

Physical measurements are carried out in the only 1:1 entity tunnel in China located in " Key Laboratory of Tunnel Construction & Maintenance Technology, Ministry of Communications, PRC, " of CCRDI: Tunnel length 200m, width 10m, height 7.15m. Adopting parameters is shown in Table 3.1:

**Table 3.1 Adopting tunnel parameters**

| | |
|---|---|
| Reflection coefficient of tunnel wall | Wall/0.3 , ceiling /0.1, pavemen/0.3 |
| Lamp distance /m | 3、4、5、6、7 |
| Lamp height /m | 5 |
| Sidewall height /m | 5 |

Physical measurements adopt the four-point method which the distance between two points is 1m ×1m, the measured data, test the reliability of the results of the simulation software.

### 3.2 Overview of Software Simulation

DIALux is a professional lighting calculation software developed by the German software company, which can carry out simulation and calculation of lighting design, and has wide support of lamp parameters. Due to its calculations is carried out in strict accordance with CIE140, and built Europe and America standard road values[7], in order to get appropriate parameter modification in the simulation process, and achieve the best effect of simulation, it is necessary to test Lamp light intensity.

### 3.3 Comparison of Analytical Results

In the same location of entity tunnel and simulated tunnel, their illumination indicator parameters are Comparative analysis using the four-point method. In view of the large number of illumination analysis indicators. This paper uses the Origin software to draw and analysis relevant data, as shown in Fig.3-1,

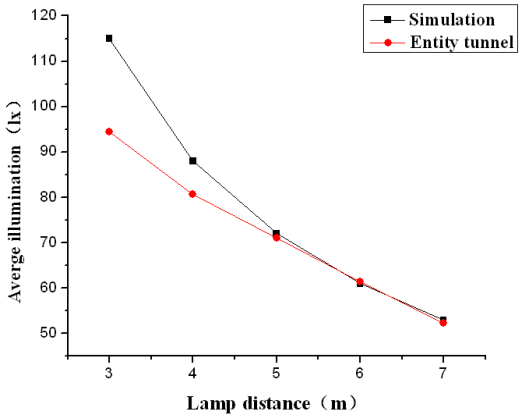


**Fig.3-1 The contrast of average illuminance between entity tunnel and simulation model in different lamp distance**

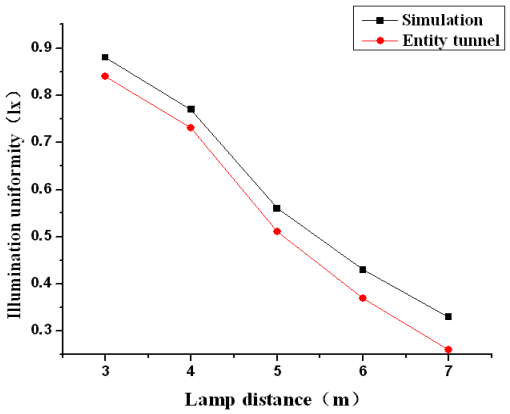


**Fig.3-2 The contrast of illumination uniformity($U_1$) between entity tunnel and simulation model in different lamp distance**

Fig.3-1 shows that the analog value calculated by the simulation model are gradually equal to the measured value of the entity tunnel with the decrease of the lamp distance. And Fig.3-2 show that with the decrease of the lamp distance, the illumination uniformity increase, furthermore the analog value become more and more close to the measured value.

From the comparison above we found that, due to the differences between the reality and ideal experimental conditions, the analog value had some deviation with the measured value, however, they had the same trends with the lamp distance change and their deviation are getting smaller. It is say that we can simplify the evaluation method of measuring the road tunnel lighting quality, and in this method we can had a reasonable assessment to the tunnel lighting.

## Study for Distribution of the Measured Point Based on the DIALux

### Introduction of the Simulation Analysis

Based on the theory above we use the DIALux to analysis the simulation model in this paper, in order to analysis the lighting situation for the entity tunnel.

Ideal parameters was adopted to built the simulation model, and the lamp parameter was based on the LED which was verified by appropriate tool.

The basic rule for layout the measuring point is: the point must be in the lateral lane and between the two vertical lamps; the area for measure should be convenient for the post-processing. According to different circumstances, the pattern of point layout is changed as follows: l×w — 0.5m×0.5m,0.5m×1m,1m×1m,1m×0.5m; Meanwhile translate the measurement area: the spacing area between two lamps is translated to half area on each side. The region of Horizontal line where the midpoint between lamps is the reference position: i.e 0m, and the others is by shift, the largest shift is half the lights spacing. The simulation model is shown in Fig.4-1:

**Fig.4-1 Simulation model**

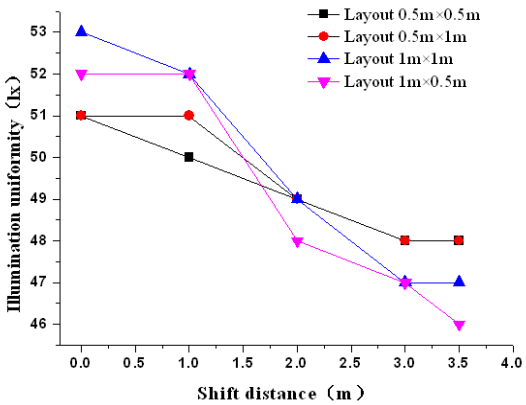


**Fig.4-2 Under different ways of layout, the trend of the average illumination varies with the shift**

### Measurement Position, Layout Can Influence the Calculation Result

The calculation results of Lamps spacing 7m is shown in Fig.4-2, 4-3:

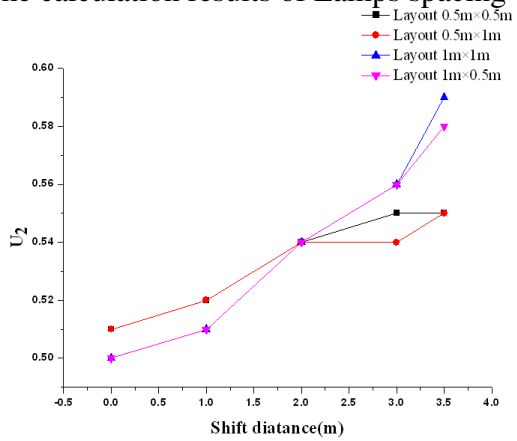


**Fig.4-3 Under different ways of layout, the trend of illumination uniformity ($U_2$) varies with the shift**

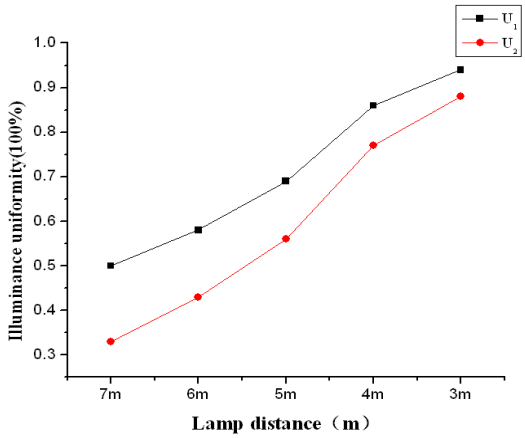


**Fig.4-4 The trend of $U_1$ and $U_2$ as the lamps spacing change**

Diagram result shows that: with the change of measurement region, the average value has a diminishing trend, but $U_2$ increases, the range is 0.08. Meanwhile axial spacing is 1m, whose value is greater than the axial spacing is 0.5m, and the average measurement value of the square layout way with 0.5m×0.5m changes least. which demonstrates more intensive distribution, more effective of the data. From the fig.4-2, 4-3, whether the average or mean difference, they both intersect in the 2m shift. Therefore, under the parameter of this tunnel, measurement area which shift 2m is more reasonable.

**The Impact of Measurement Lamp Spacing**

The Fig.4-4 shows that： with the decrease in lamp spacing, the illuminance uniformity increases, illuminance uniformity increases gradually, and with the illuminance uniformity increase, the measurement point can be appropriately reduced, select 1m×1m points layout may be a better choice.

For the simulation of the other lamps spacing, the measured value change trends are similar to that of 7m, the extremum value is almost not change, the average is changed more, and their change magnitude is different.

**The Impact of Lamps Distribution Curve**

From the measurement data, the lamp distribution curve is asymmetric, which is reflected on the longitudinal points, and the value is asymmetrical, which similar to the distribution of the actual measurement data. The maximum point of the simulated data is below the horizontal lamps and the minimum point is mainly on the weakness side of the axial lamp distribution curve. Therefore, in the case that lamp spacing is 5m, 6m and 7m, the layout average value is minimum without arrange the measurement points below the lamp, and it will low rating the tunnel lighting. On the contrary the layout average value is maximum when arrange measurement points include the points below the lamp, and that will overestimate the road lighting. Therefore, in order to find minimum value, the lamp distribution curve should be considered when arrange the meansurement points to ensure the evaluation data is accurate.

**Conclusions**

Through the comparison of software simulation and the real value, we concluded as follows:

(1) More dense the measurement points, more useful the result in evaluate the tunnel lighting quality.

(2) The best measurement layout of different lamp spacing is different, the smaller lamp spacing, the higher uniformity, the measurement points can decreased appropriately;

(3) Due to the nature of the lamp, the location and layout should consider the lamp distribution curve: the measurement region should contain the maximum and minimum values;

(4) Due to the lamps and design factors of the actual tunnel, we should make software simulation of the entity tunnel, and find the appropriate regions and layout under the different lamps spacing, type and actual tunnels, so that we can have a reasonable evaluation of tunnel lighting.

**Acknowledgement**

This research is financially supported by the Doctoral Fund of Ministry of Education (20115522110003) , Science and Technology Research Projects of Yunnan Communications Department (YJK2010 (B) 16-B), Project Foundation of Chongqing Municipal Education Committee (KJ120402), and Open Fund of the State Key Laboratory Breeding Base of Mountain Bridge and Tunnel Engineering(CQSLBF-Y14-8).

**References**(All In Chinese)**:**

[1]GB/T 5700-2008. Measurement methods for lighting [S]. Standards Press of China，2008

[2] FANG Bo, CAO Gang: China Light＆Lighting. 2008,12

[3] CHEN Zhonglin, WENG Ji, HU Yingkui: Light and Lighting. 2005.5

[4]PAN Guobing, LIANG Bo, PI Yuhang: Journal of Highway and Transportation Research and Development.2012,9

[5] CUI Hanjing: Journal of Highway and Transportation Research and Development. 2012.8

[6] WANG Wei, HUI Zhao, YIN Jun: Journal of Tianjin Polytechnic University.2012,8

[7] TUO Fu. Performance evaluation of Lighting simulation tools by comparing physical and digital measurements[D]. Department of Industrial Engineering, Tsinghua University. 2011.5

*Applied Mechanics and Materials Vols. 580-583 (2014) pp 1029-1032*
*© (2014) Trans Tech Publications, Switzerland*
*doi:10.4028/www.scientific.net/AMM.580-583.1029*

# Study of Life Safety on the Fire Accidents in the Subway Station

Hua Xie[a], Yanying Xu, Xu Zhang and Jian Chen

School of Safety Engineering, Shenyang Aerospace University, Shenyang 110136, China

[a]email: tedalanchong@163.com

**Keywords:** Life safety, Fire accidents, Subway station.

**Abstract.** Subway station fire can easily cause many calamities that lead to a large amount of social and public problems, because the smoke spread moves in the same direction as the personnel evacuation. Therefore, life safety issues caused by the subway station fire and relevant investigation should be comprehensively taken into account in the fire safety design in order to minimize the fire accident loss. Here previously reported fire accidents in the subway station are reviewed in detail and some research on the life safety of the subway station fire are presented, which could be helpful for the accident prevention and provide guidance to future study on the safety design in the subway station fire.

## Introduction

With the rapid development of economy in China, the urban transportation system faces new opportunities as well as challenges [1, 2]. The subway is one of the most common vehicles and also bears heavy work of transiting large passenger progressively. So, amount of subway stations are built in order to meet the demand of the city development. In the event of subway fire, a lot of smoke are produced and rapidly spread to overall subway stations because of stack effect and space limitation. In particular, the smoke spread direction mostly coincides with the evacuation path of the passenger, which could reduce passengers' visibility and result in the mishaps caused by the asphyxiation and stampede. Large amounts of statistical data show that calamitous fires in the subway station can usually cause heavy fatalities [3]. Additionally, the arson, terrorism attack and other accidental fire may also give rise to the disaster since there are a large number of passengers in the subway station every day.

Emergency evacuation in the subway station fire is very difficult due to the complexity of the smoke spread, the twists and turns of the evacuation route, the dense and chaos of the passengers. Therefore, study of life safety on the fire accidents in the subway station has attracted much attention and becomes an interesting topic in the field. Currently, the reported investigations focus on the evacuation time and human behavior [4], which is limited by the data collection of survivors in the tragedy. In recent years, more and more attentions have been paid to the establishment and development of evacuation models with the fast development of the electron technology, which marks that the fire life safety enter into a new stage of the performance-based design. FDS+Evac is one of the most common evacuation softwares that is developed by VTT Technical Research Center of Finland and National Institute of Standards and Technology (NIST) together [5]. This software has been widely used to investigate life safety issues caused by the subway station fire for offering the theoretical guidance of safety study on further the urban transportation. King's Cross (1987), Zürich (1991), Daegu (2003) and Burnley (2007) have been present in this work, some accidents have been discussed in brief and the suggestion has been provided in order to avoid this type of calamity happen again.

## Fire Accidents

The study on fire accidents in the subway station can provide meritorious information to life safety in the subway station fire, which is used to improve safety design to prevent similar miseries in the future.

The three well known fire subway accidents (King's Cross, Zürich and Daegu) are selected and introduced because they associate with human behavior in fire [6]. All these accidents have a significant impact on life safety, which also urge people to more think about the safety practice in the subway.

**King's Cross, 1987.** On November 18, 1987, a fire accident happened in one escalator at the King's Cross subway station in London, UK [7]. A passenger set fire to a mixture of detritus and dust under the escalator and thus led to the fire. The fire spread quickly to the major ticketing hall on the top of the escalator, where smoke gathered and resulted in a flashover in the end. The fire brigade arrived at the King's Cross subway station after 15 minutes. At the moment, the flashover had already turned into the combustion, so firefighters mainly rescued the passengers trapped in the fire instead of putting out the subway station fire. At last, this fire accident led to 31 fatalities and some others injured [7].

The fire incident at the King's Cross subway station is a typical case, which explained how to escape at a subway station by applying the role-rule model and illustrated the behavior characteristics in the fire [6].

**Zürich, 1991.** On April 16, 1991, a fire started on a subway train in Zürich, Switzerland [8]. The fire accident was due to the arson, which was firstly found by a staff member of the subway station and a conductor in the other train. However, both of them did not report this emergency situation to the subway driver. Then, the subway was forced to stop in the middle of the 1.2 kilometers long Hirschengraben tunnel since a passenger drew the emergency break of the subway. Finally, no casualties and injuries were fortunately reported in this fire accident even if the fire was not stamped out immediately.

The Zürich subway fire [8] is also the other example that can be deciphered by using the human behavior theories.

**Daegu, 2003.** On 18 February 2003, a mentally ill patient ignited a subway train with the gasoline at Jungangno Station in Daegu, South Korea. The fire spread rapidly to all carriages within 60 seconds on account of the flammability of interior materials in the subway. Two trains were burnt down in the fire, which led to 192 fatalities and 148 injuries because the overall subway station was quickly filled with smoke [9].

The fire accident of the Daegu subway station emphasized the importance of life safety design in subway station fire and the necessity of improving smoke control system so as to retain a safe evacuation passageway. A rational and potential way that study life safety issue is to simulate the evacuation behavior of human in the subway station by applying the computer models. Such method may avoid real crowd evacuation experiment in the subway station and ensure the safety of passengers.

## Human Behaviors in Fires

A discussion about human evacuation behavior in the fire accident of the subway station should be carried through, which can provide helpful information for the life safety design of the subway station.

Canter et al. developed the behavior sequence model [10], which contributed to explaining the human behavior in the fire, as shown in Fig.1. The model is established on the basis of the systematic research of the human behavior in a variety of fires, which include household, multiple occupancy and hospital fires. Needed information was collected through talking with survivors of the fires about the escape behaviors taken. Among these behaviors, how to discover the fire and get out of the fire was the research emphasis.

Fig. 1 shows that the human escape behavior in a fire accident may be divided into three different stages, which is the interpret stage, prepare stage and act stage, respectively. Each stage is constituted with a series of behavior sequence, which is a sequence of the spontaneous behavior that human takes in the fire accident. In addition, this figure also proves that the potential behavior of human in the fire

becomes diversity due to the behavior sequence opened up, which can afford a more businesslike evacuation planning [10].

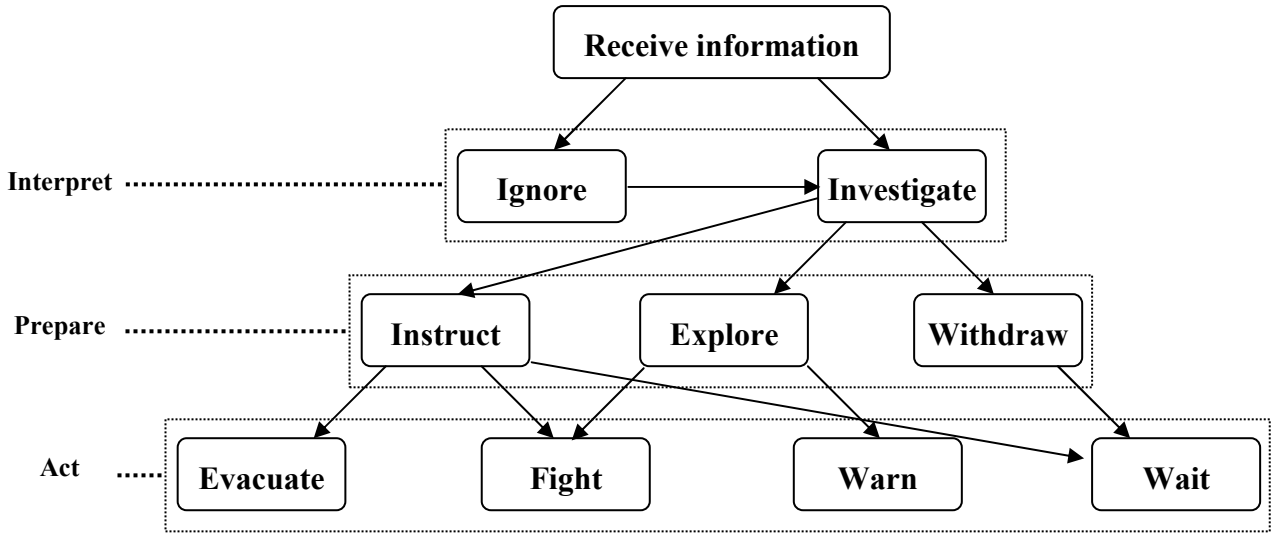


Fig. 1. The behavior sequence model developed by Canter et al. [10], which is helpful for understanding the human behavior in a fire.

In the fire initial stage, the information about the fire is lacking. So, the human behavior is indeterminate because people can not obtain the information needed. That is to say, once persons get enough information for the fire, they can take reasonable action. When people get the original fire cue, they could ignore or investigate the information and then search others information. Therefore, the interpretation stage is the same to all evacuation processes of the fire accident, which could be helpful for reducing the total evacuation time [6].

## Effect of Smoke on Human Behaviors

Smoke spread in the subway station has been investigated, but there has been still a lack of research on the effect of smoke on human behaviors in the subway fire. It is well known that the human behavior in the smoke is different from the in the smokeless environments. In other words, the greater the smoke density is, the lower the visibility of persons is, the longer the evacuation time is and the more dangerous life safety is. Additionally, many toxic gases generated in the fire has also the irritation of human eyes, people can not thus open their eyes, which leads to the extension of the evacuation time [6]. Therefore, study of effect of smoke on human behaviors should be very necessary for the life safety design in the fire accident.

## Summary

People do not pay close attention to the life safety when they travel convenience with the subway. Therefore, the fire accident in the subway station makes it necessary for any countries to re-examine their safety design towards the life safety, which should be tried from the emergency evacuation behaviors of persons.

Additionally, it should be noted that the unreasonable design of the subway path would aggravate fire accidents, and make the subway station more easily to the disaster happens. Smoke control is also an important effect factor subway fire accident becoming calamity. Great effort have been made to carry out the research on the human evacuation behavior in fires by some models, future investigation should thus devote to integrate existing evacuation models with future theoretical framework, which contributes to the rapid development of the urban transportation system.

**Acknowledgements**

This work was financially supported by the Youth Optional Subjects Foundation of Shenyang Aerospace University (201202Y).

**References**

[1] X. Hua, X. Zhang and H.C. Niu: Advanced Materials Research Vol. 663 (2013), p. 17

[2] H. Xie, X. Wang, Z. Wang, Y.Y. Xu, X. Zhang and J. Chen: submitted to Applied Mechanics and Materials (2014)

[3] S. Gwynne, E.R. Galea, M. Owen, et al: Fire and Materials Vol. 3 (1999), p. 383

[4] C.K. Chen: Physica A Vol. 1 April (2012), p. 2408

[5] Y.F. Li, X.X. Lin, X. Feng, C. Wang and J.M. Li: Proedia Engineering Vol. 42 (2012), p. 741

[6] K. Fridolf, D. Nilsson and H. Frantzich: Fire Technology Vol. 49 (2013), p. 451

[7] Information on http://www.nationalarchives.gov.uk/doc/open-government-licence/ open-government- licence.html

[8] Information on http://www.lotsberg.net/artiklar/andersen/en_table_1.html

[9] J.S. Roh, H.S. Ryou and S.W. Tooh: Journal of Mechanical Science and Technology Vol. 24 (2010), p. 937

[10] D. Canter, J. Breaux and J. Sime, in: *Domestic, multiple occupancy, and hospital fires*, edtied by D. Canter Fires and human behaviour Wiley, Chichester (1980), pp. 117

*Applied Mechanics and Materials Vols. 580-583 (2014) pp 1033-1036*
*© (2014) Trans Tech Publications, Switzerland*
*doi:10.4028/www.scientific.net/AMM.580-583.1033*

# Study on Emergency Evacuation in the Subway Fire Accidents

Hua Xie[a], Yanying Xu, Xu Zhang and Jian Chen

School of Safety Engineering, Shenyang Aerospace University, Shenyang 110136, China

[a]email: tedalanchong@163.com

**Keywords:** Emergency evacuation, Fire accidents, Subway.

**Abstract.** The fire accident is a substantial risk in the subway due to the complexity of the underground construction confined space, which can cause a large number of human fatalities. Therefore, some effort should be made to promote the public security in subway fire accidents. Among of them, the establishment of emergency evacuation plan is very important in fire safety design and should be paid enough attention because it can provide beneficial help to life safety. The evacuation strategy including the evacuation route and evacuation safety zone are detailedly discussed in this paper, which lays the foundation for future studies of safe evacuation in the subway fire accidents.

## Introduction

In recent years, the subway construction in Mainland China has obtained the unprecedented development [1, 2]. By the end of 2009, the total length of the subway lines were 950 km, which can be used to the transportation in Chinese Mainland. Additionally, a number of cities (for example, Beijing, Shanghai, Guangzhou, Tianjin, Chongqing, Shenyang, Xian, Chengdu, Nanjing, Hangzhou, Suzhou and Dalian) are building subway lines, which the overall length reaches 1154 km. And then, others cities (such as Qingdao, Shijiazhuang, Jinan, Changsha, Hefei, Kunming, Lanzhou, Fuzhou, Ningbo, Xiamen, Dongguan, Urumqi, Nanning, Taiyuan, Yantai, Wuxi, Zhengzhou, and Guiyang) are planning them. As of August 20, 2009, the total plan length of the subway construction is 2260 km and the total investment budget is 882.003 billion RMB. By 2015, the overall length of the subway lines will extend to 4189 km in Chinese Mainland [3]. Therefore, the emergency evacuation in the subway fire accidents has attracted more and more attentions because it has the relation with the life safety of people. Currently, the computer simulation method is one of the most commonly used measures and is able to model the safe evacuation behavior in the subway fire during the subway design. Shi et al established the safety evacuation strategy by applying the agent-based model on the basis of the experimental data, which results will contribute to the study on the safety design of the subway evacuation [3].

It is well known that the smoke is the most dangerous factor in the fire accident and not flame and high temperature. Many substances in the fire smoke have highly toxic and irritating effects. Among of them, carbon monoxide (CO) is the most dangerous, which can cause carbon monoxide poisoning and the additive effects of hydrogen cyanide (HCN) and phosgene ($COCl_2$). The inhalation of the fire smoke also can result in incapacitation and loss of consciousness. In addition, sulfur oxides ($SO_x$), hydrogen chloride (HCl) and hydrogen fluoride (HF) when wet may transform into sulfuric, hydrochloric and hydrofluoric acid, which has strong corrosion resistance to the human body and material [4]. It should be noted that smoke can reduce the visibility and prevent people get out of the fire safely. In fact, the poor visibility caused by the dense smoke is a hinder to emergency evacuation and fire escape, which can lead to death by suffocation [5]. Therefore, the smoke flow should be taken into account in the investigation of emergency evacuation in the subway fire accidents. Both the subway evacuation strategy and related research progress in the fire accident have been discussed in the present work, and the recommendation has been provided to give some reference about the safety design of the subway.

## Research Progress

With the rapid development of the economy, the evacuation capability designed according to the previously predicted passenger traffic volume can not meet the requirement of the evacuation once the subway fire is really, which hinders the personnel safe escape. Many subway fire accidents around the world have shown that the errors of the emergency evacuation strategies will lead to a large number of casualties [2]. Therefore, the establishment of the emergency evacuation plan has been paid much attention because it is a critical question that we must think about in the design of the subway safety. The influence of some factors has also been analyzed and discussed, which focuses more on the behavioral and psychological characteristics of passengers in the subway, the evacuation plan and evacuation time, etc.

The behavior characteristics of passengers in emergency circumstances of Chinese subway have been investigated by He et al [6]. The organization question of the subway operation has also been researched under the circumstances of unexpected excessive passenger flows [7]. In addition, the traffic congestion characteristics at the floor stairs of the subway station have been studied in the evening peak hours [8].

With the progress of electronic science and technology, the computer is widely used to explore the evacuations behavior in the subway fire accident. For example, Helbing et al. quantified the passenger psychological response and obtained some typical passenger evacuation behaviors on the basis of the social force model [9]. Up to now, more than 20 kinds of the evacuation models have been established based on the modeling framework of the network model, fine grid model and continuous vector model. These proposed models are also segmented into different types in accordance with the practical application of the subway evacuation, such as modeling type, risk assessment type and optimization type [10]. Li et al. applied the evacuation modeling to evaluate the harm of smoke diffusion on life safety when the subway interchange station fired [11]. They concluded that fire smoke would impede the evacuation process, extends the evacuation time and obviously influence physical and psychological state, which ultimately results in a large number of deaths in the subway fire accident.

It should be noted that the subway in some countries are constructed in different eras, which results in the difference of the emergency evacuation strategy between the different countries. Therefore, the emergency evacuation strategy is not universal for the subway of different countries, which should be formulated on the basis of different standards and the actual situation in different countries.

Currently, most of the investigation work reported focus mainly on the crowd evacuation behavior of different buildings. Little attention is given to the subway evacuation strategy, especially the subway of Mainland China. Consequently, a systematic study of the emergency evacuation strategy about China subway is very necessary and helpful for guiding the life safety design of the subway in China. However, how to unify and optimize the safe and economic project is still an urgent issue, which results from the lack of understanding of establishing the evacuation strategy and the limit of applying of appropriate engineering calculation [3].

## Subway Evacuation Strategy

A comparison study found that the evacuation situation in the subway and building had many similarities, but there were also significant difference that needs to be carefully taken into account during designing and constructing the subway. Additionally, many research results about human behaviors in the fire accident may also be applied to the study of the evacuation strategy in the subway fire.

Subway evacuation strategy should comprehensively think over many aspects, such as the geometrical construction of the subway station, the location of a fire, the passenger flow volume, the evacuation route, the evacuation safety zone, and effective evacuation time, etc. The evacuation route and the evacuation safety zone are detailedly discussed in the establishment of emergency evacuation strategy in this work.

**Evacuation Route.** When the subway station fires and people are evacuated, the main escape passages include the platform screen door, the automatic gate, the train door, the escalator and staircase, the entrance and exit passages, the side door These passages with the state of emergency are different from their normal operation state, which is referred to as the emergency evacuation state of the passage [3].

- Opening strategy of the platform screen door. When a fire happens in the subway, the platform screen door and train door should be completely opened for the emergency evacuation of the passenger. However, when the subway train is the emergency shut down and the location of the train door is not in the correct position, the emergency exit of the platform screen door should be opened for the emergency evacuation of the passenger. Such is able to effectively reduce personnel casualties.
- Escalator operating strategy. When the fire happens and the passenger is evacuated, all the upward escalators from the platform to the station hall should be kept in upward operating state. In this case, the downward escalators have two emergency strategies that can be carried out. One strategy is to turn the downward escalators to the upward escalators, another strategy is to stop the downward escalators and use it as the fixed staircase, both of which help the passenger emergency evacuation. However, once the fire in one escalator, and then this escalator can not be applied for the passenger evacuation.
- Automatic gate strategy. And when the fire happens, all the automatic gates should be opened for the emergency evacuation of the passenger, which contain the entire entrance and exit automatic gates.
- Entrance or exit passage strategy. If the subway fire breaks out in an entrance or exit passage, then this access will not be applied to evacuate urgently since the passageway has been very dangerous.

**Evacuation Safety Zone.** When a fire breaks out, the identification of the evacuation safety zone is determined on the availability of the smoke control and exhaust system. The smoke removing system can be applied to efficaciously prevent the smoke from spreading the upper storey and prolong survival time for the various subway platform fires. Under this circumstance, the upper storey of the subway platform is able to be regarded as the evacuation safety zone. It should be noted that the upper storey of the subway platform may not be the storey of the station hall, which could be the storey of the passage or equipment.

When a fire happens in the station hall of the subway station, the storey of the station hall may not always be the evacuation safety zone, which mainly depends on whether or not the smoke control system on the storey of the station hall can efficiently prevent the smoke spreading. Under normal conditions, the evacuation safety zone in a fire of the station hall is the entrance and exit of the station hall.

## Future Prospects

With the improvement of people security awareness, the subway safety has aroused general concern of the society. Therefore, How to ensure the safety of the subway travel is very important and becomes a safety topic. In this paper, the research progress about the emergency evacuation of the subway fire has been reviewed, and the evacuation strategy (includes the evacuation route and the evacuation safety zone) is discussed on the basis of the behavior characteristics of passengers, which can be helpful for the safety design of the subway construction.

In addition, up to now, the emergency evacuation behavior of the disabled people is paid little attention, these efforts should be thus strengthened in order to meet the requirements of travel and safety of the disabled people, which is also a future research direction about the life safety of the subway. All these investigation are for the life safety of human, when the subway offers great convenience to people.

**Acknowledgements**

This work was financially supported by the Youth Optional Subjects Foundation of Shenyang Aerospace University (201202Y).

**References**

[1] H. Xie, X. Zhang and H.C. Niu: Advanced Materials Research Vol. 663 (2013), p. 17

[2] H. Xie, X. Wang, Z. Wang, Y.Y. Xu, X. Zhang and J. Chen: submitted to Applied Mechanics and Materials (2014)

[3] C.L. Shi, M.H. Zhong, X. Z. Nong, L. He, J.H. Shi and G.g. Feng: Safety Science Vol. 50 (2012), p. 1319

[4] Information on https://en.wikipedia.org/wiki/Smoke

[5] J.S. Roh, H.S. Ryou and S.W. Tooh: Journal of Mechanical Science and Technology Vol. 24 (2010), p. 937

[6] L. He, M.H. Zhong, C.L. Shi, J.H. Shi, H.C. Chen and Q.X. Xu: Fifth International Conference on Pedestrian and Evacuation Dynamics (PED), Gaithersburg, MD, USA (2010)

[7] Y.N. Wang: Beijing Jiao Tong University, Master degree thesis (2008)

[8] C.S. Jiang, Y.F. Deng, C. Hu, H. Ding and W.K. Chow: Safety Science Vol. 47 (2009), p. 931

[9] D. Helbing, L. Buzna, A. Johansson and T. Werner: Transportation Science Vol. 39 (2005), p. 1

[10] E.D. Kuligowski and R.D. Peacock: Technical Note 1471 Vol. 6 (2005), p. 153

[11] Y.F. Li, X.X. Lin, X. Feng, C. Wang and J.M. Li: Proedia Engineering Vol. 42 (2012), p. 741

*Applied Mechanics and Materials Vols. 580-583 (2014) pp 1037-1041*
*© (2014) Trans Tech Publications, Switzerland*
*doi:10.4028/www.scientific.net/AMM.580-583.1037*

# Study on Fire Smoke Movement of Urban Traffic Link Tunnel

Xiaolin Yao [1,2, a] and Zhigang Zhang [2,3,a]

[1]Luzhou Vocational and Technical College, Luzhou, Sichuan, 646005, China

[2]Faculty of Geosciences and Environmental Engineering, Southwest Jiaotong University, Chengdu, Sichuan, 610031, China

[3]China Electronics Technology Group Corporation 26th Research Institute，Chongqing, 400060, China

[a]402162972@qq.com

**Keywords:** Urban traffic link tunnel, Fire smoke, Semi-transverse ventilation, numerical simulation.

**Abstract.** Fire simulation software (FDS) was employed to simulate the fire smoke movement of urban traffic link tunnel (UTLT) under the semi-transverse ventilation. Numerical simulation and theoretical analysis were used to analyze the fire smoke movement in three fire scenarios. The analytical results show that: semi-transverse ventilation can effectively control the spread of fire smoke. When the exhaust air rate is certain, the exhaust port interval of 20 m and 50 m has little effect on function of smoke control. The research results provide references for the design of smoke control measures in UTLT.

## Introduction

Most UTLT made up of a main circular tunnel and some connective tunnels are built in underground space of downtown area [1]. UTLT often linked to the underground parking lot and business district is different from regular tunnels. The multiple points of entry and exit, high traffic and narrow section are its most striking feature. Therefore, it's a possibility for a fire. The fire smoke in circular tunnel spreads quickly with great potential fire and harm hazard [2, 3].

So far, the research has focused on longitudinal ventilation and transverse ventilation in UTLT fire that draws most attention from many scholars at home or abroad [4-6]. Until recently, there is little information available in literature about the effect on smoke management and movement under semi-transverse ventilation. In this paper, UTLT has been taken as a research subject. Three fire scenarios are presented and simulated by FDS. Through theoretical and numerical methods, the impacts of exhaust port interval and semi-transverse ventilation on smoke movement are analyzed. The results of the research can provide reference for design of fire control in UTLT under semi-transverse ventilation.

## Model of UTLT

**UTLT Description.** UTLT taken as a research subject runs 2400 m under the municipal road. Each side of UTLT is about 600 m with 4 m high and 8 m wide. The main tunnel with one-way counterclockwise is two lanes. The 560 m long exit ramps is about 4 meters high and 4 m wide.

**Fire Model of UTLT.**

(1) Model of FDS.

In this paper, UTLT has been taken as a research subject. According to the design size, the fire model of UTLT is built by the FDS software, as shown in Fig.1.

(2) Heat Release Rate.

Based on functions and features of UTLT, the frequency of fire is considered once in the same time because it allows only sedan car to drive and it is closed for other cars to traffic. The heat release rate is $t^2$ growth pattern and the maximum is 20MW. This is equivalent to the heat release rate of 3-4 cars ignited.

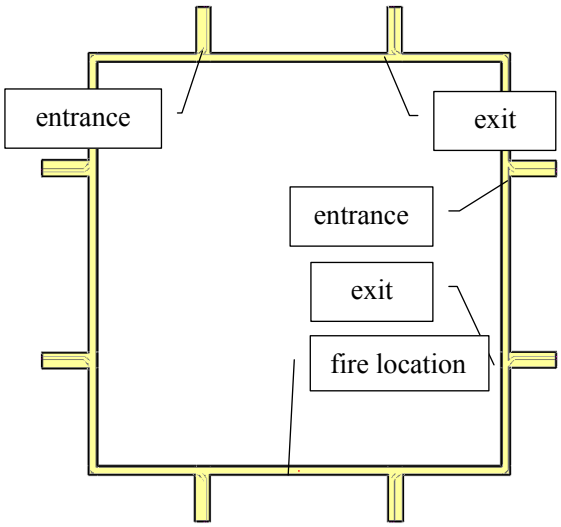


Fig.1 FDS model of UTLT

(3) Smoke Management System.

The size of fire source is 2.0m x 2.0m x 2.0m situated in central tunnel. The exits of UTLT are considered as natural ventilation openings. The simulation time is 1200s.

The smoke zone is set up on every 100 m in main circular tunnel. The exhaust port can be set on request under the semi-transverse ventilation. Smoke screen is 0.5 m high. According to the specification requirements [7], interval of emergency evacuation path is 250-300 m. Therefore, 300 m range is managed as smoke prevention and exhaust area which contains burning smoke zone and its two adjacent sites. The smoke management system works properly when the fire happens. According to the < Specifications for Design of Ventilation and Lighting of Highway Tunnel >, exhaust air rate is 12 air changes per hour determined by way of the specification.

**Scenarios Design.** In order to research the influence of exhaust port and semi-transverse ventilation on the fire smoke movement, three fire scenarios are presented and simulated by FDS, as defined in Table 1.

Table 1 List of fire scenarios

| fire scenarios No. | exhaust port interval (m) | semi-transverse ventilation system |
|---|---|---|
| A | - | failure |
| B | 50 | normal |
| C | 25 | normal |

## Analysis of Simulation Results

**Simulation Results of Fire Scenarios A**. Semi-transverse ventilation system has been failure in fire scenario A. The simulation results indicate that the fire smoke can spread out of the smoke prevention and exhaust area at 290s. The total distance of fire spread can reach 865 m in the range of main circular tunnel at 1200s, as shown in Fig.2. The temperatures exceed 60 ℃ at right-and-left distance of 150m to fire location at 1140s. The poor visibility at right-and-left distance of 150m to fire location can only be 10 meters at 335s.

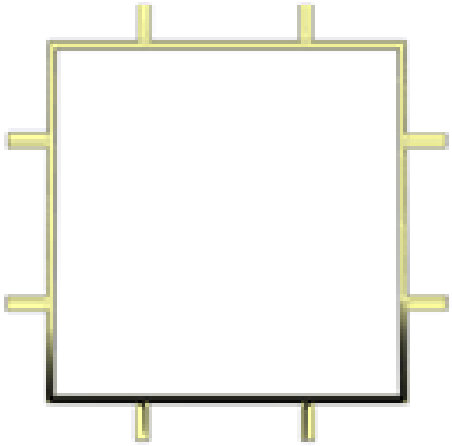

Fig.2 Smoke spread pattern at 1200s

**Simulation Results of Fire Scenarios B.** It is two exhaust ports in one smoke zone interval of 50 m in fire scenario B. The simulation results indicate that the fire smoke can spread out of the smoke prevention and exhaust area at 410s. The total distance of fire spread can reach 430 m at 1200s. The temperatures are always below 60 ℃ at right-and-left distance of 150m to fire location within a period of 1200s. The poor visibility at right-and-left distance of 150m to fire location can only be 10 meters at 583s. The distribution of visibility field on the height of 2 m at 900s is presented, as shown in Fig.3.

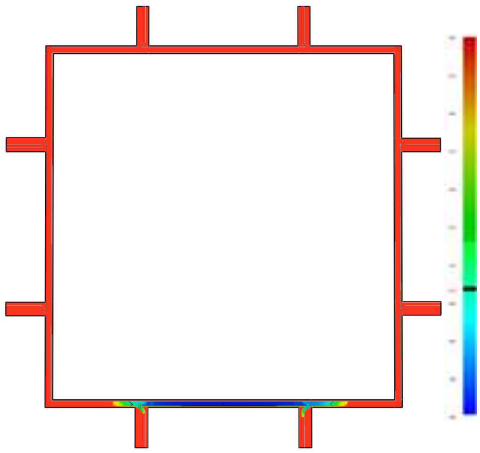

Fig.3 The distribution of visibility field on the height of 2m at 900s

**Simulation Results of Fire Scenarios C.** The exhaust air rate is 12 air changes per hour determined by way of the specification. It is four exhaust ports in one smoke zone interval of 25 m in fire scenario C. From simulation results, the fire smoke can spread out of the smoke prevention and exhaust area at 410s. The total distance of fire spread can reach 425 m at 1200s, as shown in Fig.4. The temperatures are always below 60 ℃ at right-and-left distance of 150m to fire location within a period of 1200s.

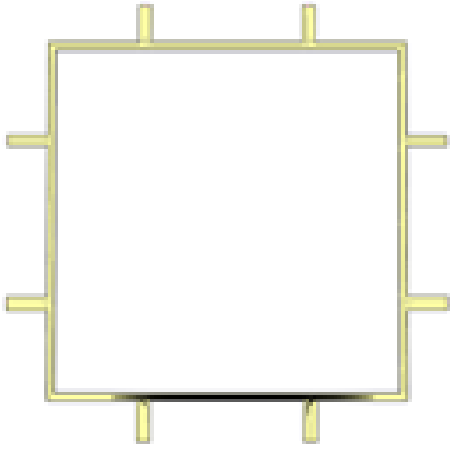

Fig.4 Smoke spread pattern at 1200s

**Influence of Semi-transverse Ventilation System on Simulation Results.** Table 2 describes the distance of smoke spread in scenario A and B. Comparison of the results, when semi-transverse ventilation system operates properly, distance of smoke spread can be as short as about 435 m. The temperature variety curve at 90m is presented as shown in Fig.5. When semi-transverse ventilation system fails, temperatures in the same place are higher than in normal conditions. Because the hot smoke with large amount of heat is being taken out by semi-transverse ventilation system. Semi-transverse ventilation system has a significant effect on smoke control, improvement of visibility and reduction of temperature.

Table 2 Distance of smoke spread in scenario A and B

| fire scenarios No. | distance of fire spread in left side(m) | distance of fire spread in right side(m) | Total distance of fire spread(m) |
|---|---|---|---|
| A | 405 | 460 | 865 |
| B | 195 | 240 | 435 |

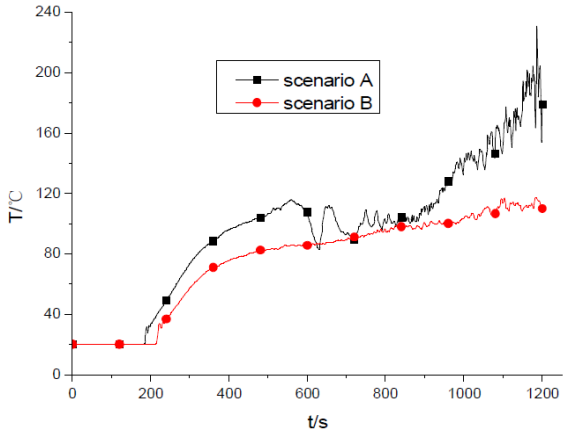


Fig.5 Temperature variety curve at 90m from fire source

**Influence of Exhaust Port Interval on Simulation Results.** Table 3 lists the distance of smoke spread in scenario B and C under the semi-transverse ventilation. The temperature variety curve at 90m is presented as shown in Fig.6. The exhaust port interval has a less influence on smoke control.

Table 3 Distance of smoke spread in scenario B and C

| fire scenarios No. | distance of fire spread in left side(m) | distance of fire spread in right side(m) | Total distance of fire spread(m) |
|---|---|---|---|
| B | 195 | 240 | 435 |
| C | 195 | 235 | 430 |

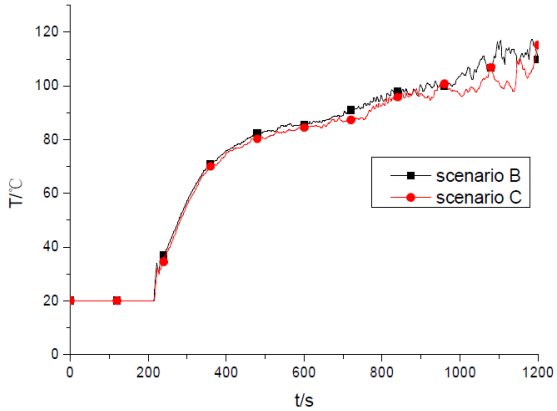


Fig.6 Temperature variety curve at 90m from fire source

## Conclusions

In this paper, UTLT has been taken as a research subject. Three fire scenarios are presented and simulated by FDS. Through the analysis of distance of smoke spread, visibility and temperature, this paper draws the following conclusions:

(1) When semi-transverse ventilation system operates properly, distance of smoke spread can be as short as about 435 m. Semi-transverse ventilation system has a significant effect on smoke control, improvement of visibility and reduction of temperature.

(2) When the exhaust air rate is certain, the exhaust port interval under the semi-transverse ventilation has a less influence on smoke control.

In order to ensure that semi-transverse ventilation system operates properly, it must be periodic examine and maintenance. The settings for exhaust port should be made as economy as possible.

## References

[1] Gaoying Hua, Wei Wang, Yaohu Zhao a, et al: Building Science Vol. 24 (2008), p. 15.

[2] Jie Zhu, Junyu Dai, Jianbo Wu, et al: Journal of Safety and Environment Vol. 13 (2013), p. 240.

[3] Zhigang Zhang: Southwest Jiaotong University Master Degree Thesis. (2013)

[4] C. Lin, Y.K. Chuah: Tunnelling and Underground Space Technology Vol. 23 (2008), p.522.

[5] Yuchun Zhang, Chuan He, Yanhua Zeng, et al: Journal of Disaster Prevention and Mitigation Engineering Vol. 29 (2009), p. 663.

[6] Lei Li, Wenli Liu, Hai Tang, Wandi Wang: Science & Technology Review Vol. 26 (2008), p. 40.

[7] PRC Ministry of Construction: *Code of Design on Building Fire protection and prevention* (China Planning Press, Beijing 2006).

*Applied Mechanics and Materials Vols. 580-583 (2014) pp 1042-1050*
*© (2014) Trans Tech Publications, Switzerland*
*doi:10.4028/www.scientific.net/AMM.580-583.1042*

# Research on the regional stress field of underground powerhouse at the right bank of Baihetan hydropower station

Qing Zhao[1], Xianlun Leng[2], Xiang He[1]

[1]School of Civil Engineering and Architecture, Wuhan Polytechnic University，Wuhan，430023,China

[2]State Key Laboratory of Geomechanics and Geotechnical Engineering,

Institute of Rock and Soil Mechanics, Chinese Academy of Sciences, Wuhan 430071, P. R. China

**Keywords**：Baihetan hydropowerstation, regional stress, distribution rules, regression analysis.

**Abstract.** According to the analysis results about the distribution rules of tectonic regional stress in China mainland, the distribution rules of tectonic regional stress in Chuandian and the tectonic movement of Baihetan , the distribution rules of regional stress in Baihetan were preliminary analysed. Based on measured results of geostress and the statistical analysis of the measured results about the geostress of the shallow crustal magmatic in China mainland,the distribution rules of regional stress in underground powerhouse at the right bank of Baihetan hydropower station were studied. In general,the maximum and the minimum horizontal principal stresses and the vertical stresses increase linear with depth . In dam abutment $\sigma_H > \sigma_h > \sigma_v$ .while in the underground powerhouse $\sigma_H > \sigma_v > \sigma_h$ .Based on the measured results of geostress,the dispersed point charts of the ratio among the maximum horizontal stress ,the minimum horizontal stress and the vertical stress with depth in China were established, using the method from the statistical analysis of measured results about the shallow crustal geostress in China mainland and the corresponding regression analysis was studied.

## Introduction

Rock stress is an important factor in rock mass stability and engineering operations, and the geostress is one of the most important fundamental factors that influence the stability of many projects such as underground caverns . The stress field has complicated origin and is influenced by many factors. In recent decades, geostress data measurement and theoretical analysis show that the formation of geostress is related to many kinds of geodynamic processes, among which the movement and extrusion of crustal plate and gravity are the main factors constituting the geostress.In-situ test of the geostress is the most direct method to provide regional geostress data. However, due to high cost, space restriction, geological conditions complexity and so on, the in-situ test is not suitable for a large number of measurements. In addition, the test result of geostress of each point can only reflect the characteristics of local ground stress, which results in the high discreteness of test results[1].Therefore, based on the measured data of ground stress field, geological conditions and the effective mathematical-mechanical inversion methods, the ground stress field can be obtained more accurately. This method has wide application and used widely in engineering to analysis the distribution of ground stress field.

Our country is located in the eastern part of the Eurasian plate. Due to the subduction of the Pacific plate in the east, the push of the Philippine Sea Plate in the southeast and the collision of the Indian plate in the west, the new tectonic movement in the region is particularly active. Especially, since nearly 45 Ma, the strong collision and squeezing resulted from the movement of Indian subcontinent to the Asian continent have changed the topography of western China greatly. With the Indian plate moving northward continuously, Himalayas and Tibetan Plateau uplift rapidly since the middle Miocene(16~10Ma), which generate combined extrusion to the surroundings[2].Because the Chinese mainland is controlled by the interaction of surrounding plates ,the maximum principal

stress decreases from west to east, and tectonic activity is intense in the west, while relatively weak in the east[3].In present, the strike of the maximum principal stress axes in China mainland is distributed radially in generally toward the center of the Tibetan Plateau[4],from west to east, which is rotating clockwise gradually from the direction of nearly NS to the directions of NNE, NE, NEE, and SE; the horizontal stress is dominated in the tectonic stress field, while the maximum and minimum principal stress axes are nearly horizontal. The direction of the maximum principal stress appears obvious regional characteristic, which can be roughly divided into the west region, the north and northeast China region, the south part and Sichuan-Yunnan region [5].

Baihetan hydropower station is constructed on the east of the Sichuan-Yunnan rhombic block, the geostress field is not only influenced by the tectonic movement of itself, but also influenced by the geostress field of china and Sichuan-Yunnan area. Therefore, the geostress field distribution in the engineering site of Baihetan hydropower station can be fitted effectively according to the statistical regularity of stress field and the test results of Baihetan hydropower station. In this paper, the distribution rules of the regional stress in underground powerhouse at the right bank of Baihetan hydropower station will be researched using the method of regression fitting, based on the China regional tectonic stress analysis results and the measured data.

## The analysis about the geological tectonic origin of Baihetan regional stress

Baihetan hydropower station is constructed within the downstream of Jinshariver which links Qiaojia County of Yunnan Province and Ningnan County of Sichuan Province. The Ningnan area is located in the east of the Chuandian rhombic block, where the geostress field is not only influenced by the plate movement but also influenced by the faults in the surrounding area of the Sichuan-Yunnan. In addition, the tectonic movement of the Baihetan area makes the geostress field more complicated .Underground powerhouse cavern group are located within the mountain valley area with strong earthquake activities, where the basic earthquake intensity is Ⅷ degree. The topography of engineering area is complicated, which has higher regional stress , complex geological conditions, developed F14, F16 and F-17 faults, various faulting belts, columnar joints and other adverse geological structures.

**Statistics and analysis of the measured geostress of the shallow crust magmatite in China mainland.**The basement of Baihetan Hydropower Plant is mainly the Emei Mountain Basalt of Permian system, which is typical spray-type magmatic rock.Jingfeng[5] collected the measured geostress from more than 400 drill holes, according to the “in-situ stress field data compiled in the world”[6]by Chen Pengnian, “studies of Chinese mainland crustal stress environment”[7] by XieFuren and other published books and papers . The measured range involves almost the whole area of Chinese mainland. Based on the lithology of the underground powerhouse area in Baihetan right bank, he studied the distribution rule of the geostress field of the shallow magmatic rocks in China mainland by statistical method. Stress relieving methods and hydro-fracturing methods are the primary test methods, while a small number of caving methods is adopted. The distribution of the shallow magmatic rocks with depth in china mainland is shown in Figure 1.As shown in Figure 1, the magnitude of the vertical stress has a linear relation with the buried depth in general .The relationship can be fitted with linear regression method and the fitting formula is shown as Equation (1).

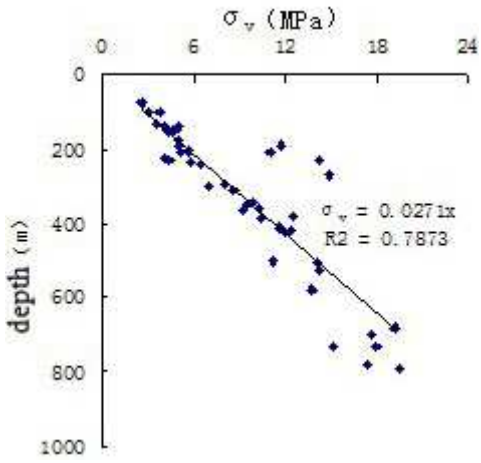


Fig.1.Curve of magmatite's $\sigma_v$ vs. depth in China

$$\sigma_v = 0.0271H \qquad (R^2 = 0.7201) \tag{1}$$

Where $H$ is buried depth, $R$ is linear relative coefficient

The distribution of the maximum and the minimum horizontal principal stresses with depth in the shallow magmatic rocks in China mainland are shown in Figure 2.which shows that the maximum and the minimum horizontal principal stresses has a linear relation with the buried depth in general. The linear regression fitting is adopted, and the fitting formula is shown as Equation (2).

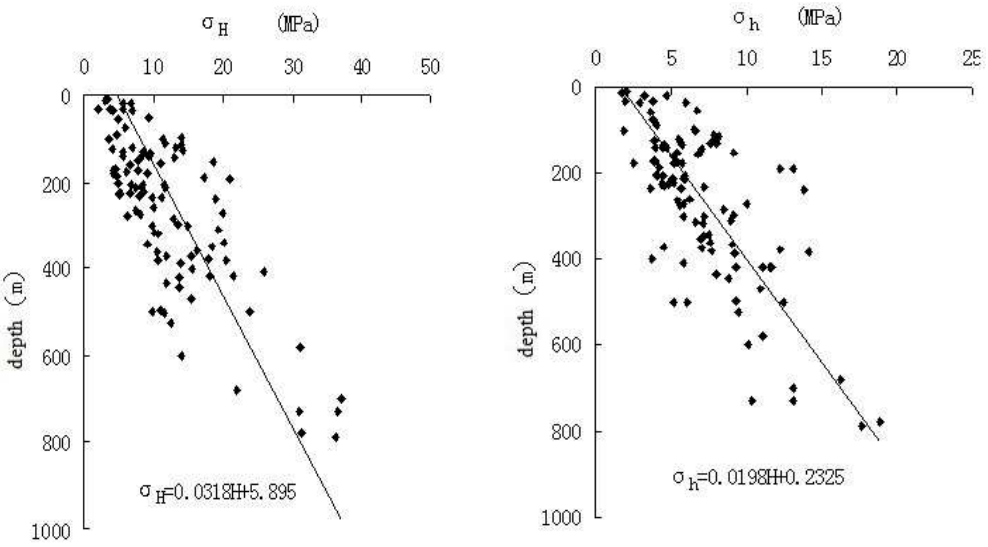


Fig.2. Curve of magmatite' horizontal principal stress vs.depth in China

$$\begin{cases} \sigma_H = 0.0318H + 5.895 & (R^2 = 0.7111) \\ \sigma_h = 0.0198\ H + 0.2325 & (R^2 = 0.5534) \end{cases} \tag{2}$$

**The study on the modern tectonic stress field in Sichuan-Yunnan region.** Sichuan-Yunnan region is one of the four tectonic stress areas in China, located in the southeastern edge of Qinghai-Tibet plateau, which is the edge of the interaction converge contact zone between the Eurasian plate and Indian plate. As the strong earthquake activity area in China, its tectonic stress field is relatively complicated. The direction of the principal compressive stress has great change,

where the direction of the principal compressive stress rotates clockwise from north to south[8].In Longmenshan fault zone ,Xianhuihe fault zone, and the north area, the direction of the principal compressive stress of geologic structure stress field is nearly east-west; In Sichuan-Yunnan rhombic block, the principal compressive stress directs between north and north-west[9]; in the east of Sichuan-Yunnan rhombic block, the direction of the principal compressive stress appears mainly north- west; while in the west of Sichuan and Yunnan rhombic block, the principal compressive stress directs between north and north- east.

By the mechanism of the inversion of focal, Cui classified the tectonic stress field of China mainland into 3 zones[10], which is southwestern Yunnan stress zone, Sichuan-Yunnan stress zone and Mabian-Zhaotong stress zone. In southwestern Yunnan stress zone, the distribution orientation of the maximum horizontal principal stress is mainly NNE - SSW trending ( azimuth angle20°);in Sichuan-Yunnan stress area, the distribution orientation of the maximum horizontal principal stress is mainly NNW-SSE trending(azimuth angle340°)； in Mabian-Zhaotong stress area， the distribution orientation of the maximum horizontal principal stress is mainly NWW-SEE trending. In general, in the Sichuan-Yunnan region the direction of the maximum principal stress of the three stress zones appears the characteristic of the rotation clockwise from east to west.

**The analysis of Baihetan regional tectonic movement.** Since the basalt eruption of Permian Emeishan, the project area of Baihetan hydropower had experienced mainly Himalayan movement and Yanshan movement .After the basalt eruption ,the geological evolution history of this area is divided into Himalayan period and Yanshan period. There are Sichuan movement, Himalayan movement and the Neotectonic movement in Himalayan period, in which the latter two geological tectonic movements are the main affecting factors for the formation of the geostress field in Baihetan dam area.

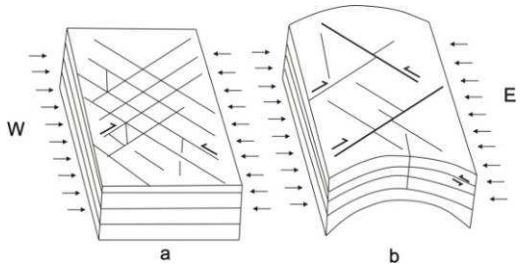


Fig.3.Sketch map of the direction of development and movement of fault in Stage of Yanshan

Formed in the late Yanshan period, the fault structures in Baihetan hydropower station dam area include four groups of faults, which are N60 º W, N20 º W, N40 º E and near NS faults. Under the nearly east-west extrusion stress field, the NW trending faults mainly acted as left-lateral slippage, while the NE trending faults acted as right slippage(Fig. 3 b), and the near NS trending faults acted as reverse faults. In the Xishan period, the Himalayan Indian Plate squeezed the Chinese continental plate along the NNE trending , where the main features of the tectonic stress field were nearly horizontal NS shortening and EW extension. The dam site area did not form a new fault system, and mainly the pre-existing four group faults moved again. In this period, the NW trending faults mainly acted as right-lateral slippage, while the NE trending faults acted as left-lateral slippage, and the NS trending faults mainly acted as normal faults. Neotectonic movement refers to the tectonic movement after the Sichuan-Yunnan rhombic block formation (about 5 Ma).In this period, the Tibetan plateau extrused eastward, leading to the separation of Sichuan-Yunnan rhombic block Yangzi landmass, with the movement to the south and clockwise rotation. Based on the earthquake mechanism, the measured stress condition in-situ and the distribution rule of the present tectonic stress field in southwestern China, the basement of Baihetan hydropower station is located in the east of the Sichuan-Yunnan rhombic block. Due to the Indian plate pushing northward, the crust in China is shortened in the north-south direction and extended in the south-west direction. The lithosphere substance of the Tibetan plateau is extruded to the east, which forms a NWW trending

compressive stress field in Xichang-Ningnan area. Therefore, according to the analysis of Baihetan regional tectonic movement, the principal compressive stress direction is NW-NWW trending [11].

**The analysis of the measured geostress in the right bank of Baihetan hydropower station**

In order to measure the accurate magnitude and the direction of the geostress field in the Hydropower Station, 8 drill holes are distributed in the slope of the right side bank, while 6 in the plant area , as shown in Fig 4.

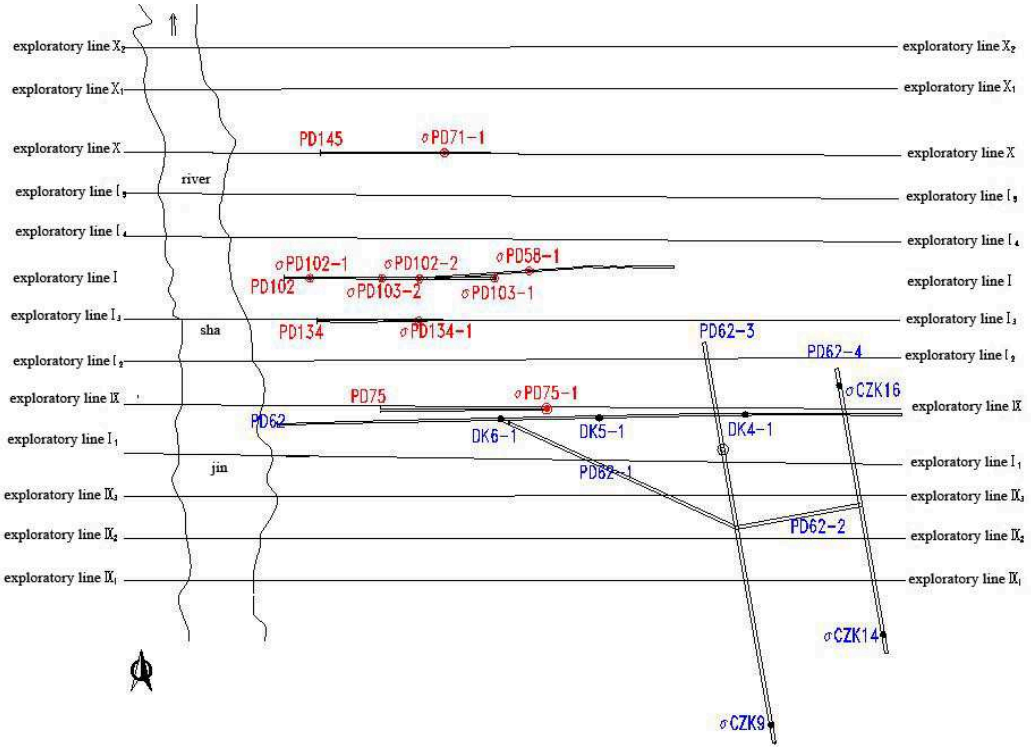


Fig.4.Sketch map of measuring points

From the test results, the value range of the maximum principal stresses of the slope at the right bank is approximately 3.8～14.2MPa, with the average of 8.7MPa. The main direction is NNE trending, with a few direction being NNW and NW and the average value being about N7°E, the dips being given priority to gently dips with a small amount being nearly level. The value range of the minimum principal stresses is 3.5~6.0MPa, with the direction being NWW trending and the dips changing greatly. In the factory of the right bank, the value range of the maximum principal stresses is19.2~24.6Mpa, with the average value being 21.8Mpa, the main direction being NEE trending, and the dips being nearly level. The value range of the minimum principal stresses is 5.2~11.5MPa, giving priority to NNW trending, and the dips are middle steep. There is large deflection between the direction of the measured principal stress and regional structure analysis. According to the current preliminary analysis, the main reasons are the river erosion, the geological movement of bank slope and so on.

**The deduction analysis of the stress field in the engineering area based on the statistics of the measured data**

**Regression fitting of the measured geostress.** The geostress field of the engineering area can be denoted by the three orthogonal principal stresses .The direction of $\sigma_2$ is nearly vertical, which can be expressed by $\sigma_v$;The direction of $\sigma_1$ and the minimum principal stress $\sigma_3$ are nearly horizontal, which can be expressed by $\sigma_H$ and $\sigma_h$ separately. Based on the measured geostress data of Baihetan hydropower station area and the distribution rule of the geostress field of the shallow magmatic rocks in China mainland, the distribution rule of the geostress field of the underground

powerhouse at the right bank of Baihetan hydropower station is studied by the method of linear regression fitting without considering the maximum and minimum horizontal principal stress direction, which is shown in figure 5.

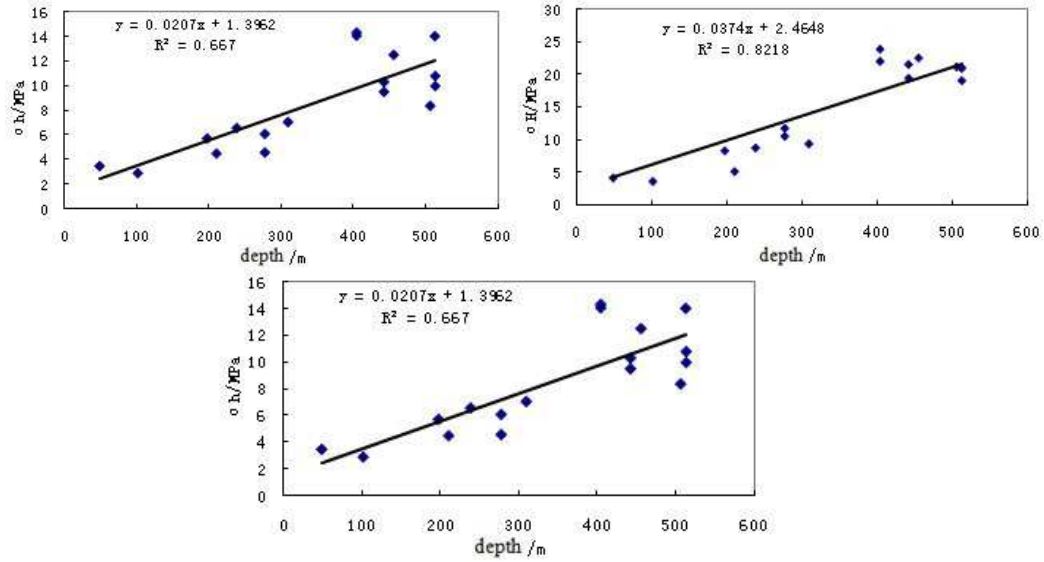


Fig.5. Curve of the verticalstresses,the maximum and minimum horizontal principal stress vs.depth in underground powerhouse of the right bank of Baihetan hydropower station

As shown in fig 5 , in generally, $\sigma_v$ , $\sigma_H$ and $\sigma_h$ increase with the burial depth, scatters change within a near parallel band. $\sigma_v$ , $\sigma_H$ and $\sigma_h$ show the linear relationship with the buried depth, and the result of the linear regression fitting formula is following Equation (3)

$$\begin{cases} \sigma_v = 0.0254H & (R^2 = 0.708) \\ \sigma_H = 0.0374H + 2.4648 & (R^2 = 0.822) \\ \sigma_h = 0.0207H + 1.3962 & (R^2 = 0.667) \end{cases} \quad (3)$$

In the depth range of the test, the change trend of the geostress with depth of the underground powerhouse area at the right bank of Baihetan hydropower station is similar to the statistic distribution of the stress of the shallow continental in China, while there are some errors in the magnitude. This is because that it is affected by the factors such as geomorphology, rock weathering and so on.

**The analysis of the measured geostress and the verification of fitted stress.** The change laws of the average lateral pressure coefficient $(\sigma_H + \sigma_h)/2\sigma_v$ , lateral pressure coefficient $\sigma_H/\sigma_v$ and $\sigma_h/\sigma_v$ with buried depth at the right bank of Baihetan hydropower station can reflect properly the differences of horizontal stress and the role of the horizontal tectonic stress, and also can be applied to the practical engineering more conveniently. The comparison between the measured stress and the principal stress obtained by fitting formula(3) is shown in table 1,and the profile of $\sigma_H/\sigma_v$ , $\sigma_h/\sigma_v$ and $(\sigma_H + \sigma_h)/2\sigma_v$ with buried depth are shown in figure 6.

Figure 5 and 6 illustrate that , in the depth range (48~309m) at right bank slope, the value range of the vertical stresses $\sigma_v$ is about1.22~7.85MPa ,the value range of the maximum horizontal principal stresses $\sigma_H$ being about4.26~14.02MPa, the value range of the minimum horizontal principal stresses $\sigma_h$ being about 2.39~7.79MPa. The ratio of the average horizontal principal stress and the vertical stress $(\sigma_H + \sigma_h)/2\sigma_v$ is about 1.42~2.73,and the ratio of the maximum horizontal

principal stress and the vertical stress $\sigma_H/\sigma_v$ is about 1.79~3.49,that is to say, the lateral pressure coefficient of the maximum horizontal principal stress direction is about 1.79~3.49,andthe ratio of the minimum horizontal principal stress and vertical stress $\sigma_h/\sigma_v$ is about 0.99~1.96, that is to say, the lateral pressure coefficient of the minimum horizontal principal stress direction is about 0.99~1.96. Generally, the horizontal stress of the abutment area stress field in shallow ground of the earth crust dominate ,the numerical size of the above three stresses is $\sigma_H > \sigma_h > \sigma_v$. In the depth range of the underground powerhouse in right bank (404～513m), the value range of the vertical stresses $\sigma_v$ is about 10.3~13MPa ,the value range of the maximum horizontal principal stresses being $\sigma_H$ about 17.57~21.65MPa, the value range of the minimum horizontal principal stresses $\sigma_h$ being about 9.76~12MPa.The ratio of the average horizontal principal stress and vertical stress $(\sigma_H+\sigma_h)/2\sigma_v$ is about 1.29~1.33,the ratio of the maximum horizontal principal stress and vertical stress $\sigma_H/\sigma_v$ is about 1.66~1.71,that is to say, the lateral pressure coefficient of the maximum horizontal principal stress direction is about1.66~1.71 ,and the ratio of the minimum horizontal principal stress and vertical stress $\sigma_h/\sigma_v$ is about0.92~0.95, that is to say, the lateral pressure coefficient of the minimum horizontal principal stress direction is about 0.92~0.95. generally, the numerical size of the above three stresses is $\sigma_H > \sigma_h > \sigma_v$.

From Table 1, when the depth is less than 100m, the stress value obtained by fitting formula (3) appears a large jump, which is not consistent with the actual condition .This is because the geostress in the shallow rock stress field is mainly affected by the poisson effect and rock weathering .Therefore, fitting formula (3) must be modified. The method of piecewise fitting is adopted, and the result is shown as equation(4).

Table1. Comparison between measured stresses and stresses got in the fitting analysis

| Location | Drilling | The depth of gallery (m) | Altitude (m) | Burial depth (m) | $\sigma_H$(MPa) | | $\sigma_h$(MPa) | | $\sigma_v$(MPa) | |
|---|---|---|---|---|---|---|---|---|---|---|
| | | | | | measured | fitted | measured | fitted | measured | fitted |
| the right bank underground powerhouse | σCZK9 | 586 | 642.9 | 404 | 23.8 | 17.57 | 14.1 | 9.76 | 8.6 | 10.3 |
| | | | | | 22 | 17.57 | 14.3 | 9.76 | 10.8 | 10.3 |
| | σCZK14 | 689 | 644.9 | 442 | 19.4 | 19 | 9.51 | 10.5 | 11.7 | 11.2 |
| | | | | | 21.5 | 19 | 10.3 | 10.5 | 12.4 | 11.2 |
| | σCZK16 | 673 | 644.3 | 513 | 19 | 21.65 | 9.98 | 12 | 10.3 | 13 |
| | | | | | 20.9 | 21.65 | 10.8 | 12 | 12.5 | 13 |
| | DK4 | 562 | 622 | 506 | 21.1 | 21.39 | 8.38 | 11.9 | 5.3 | 12.9 |
| | DK5 | 383 | 626 | 512.4 | 21.1 | 21.63 | 14 | 12 | 12.5 | 13 |
| | DK6 | 262 | 625 | 455.4 | 22.5 | 19.5 | 12.5 | 10.8 | 10.8 | 11.6 |
| the right bank slope | σPD71-1 | 150 | 735 | 278 | 5 | 12.86 | 4 | 7.15 | 4.6 | 7.06 |
| | σPD102-1 | 30 | 683 | 48 | 4.12 | 4.26 | 3.48 | 2.39 | 4.3 | 1.22 |
| | σPD102-2 | 160 | 683 | 238 | 8.72 | 11.37 | 6.58 | 6.32 | 8.1 | 6.05 |
| | σPD103-2 | 60 | 780 | 101 | 3.59 | 6.242 | 2.91 | 3.49 | 3.1 | 2.57 |
| | σPD58-1 | 130 | 930 | 210 | 5.1 | 10.32 | 4.5 | 5.74 | 5.3 | 5.33 |
| | σPD134-1 | 120 | 739 | 197 | 8.27 | 9.833 | 5.73 | 5.47 | 9.8 | 5 |
| | σPD103-1 | 200 | 784 | 309 | 9.34 | 14.02 | 7.06 | 7.79 | 10.9 | 7.85 |
| | σPD75-1 | 200 | 830 | 277 | 11.7 | 12.82 | 4.59 | 7.13 | 6.9 | 7.04 |
| | | | | | 10.5 | 12.82 | 6.1 | 7.13 | 7.5 | 7.04 |

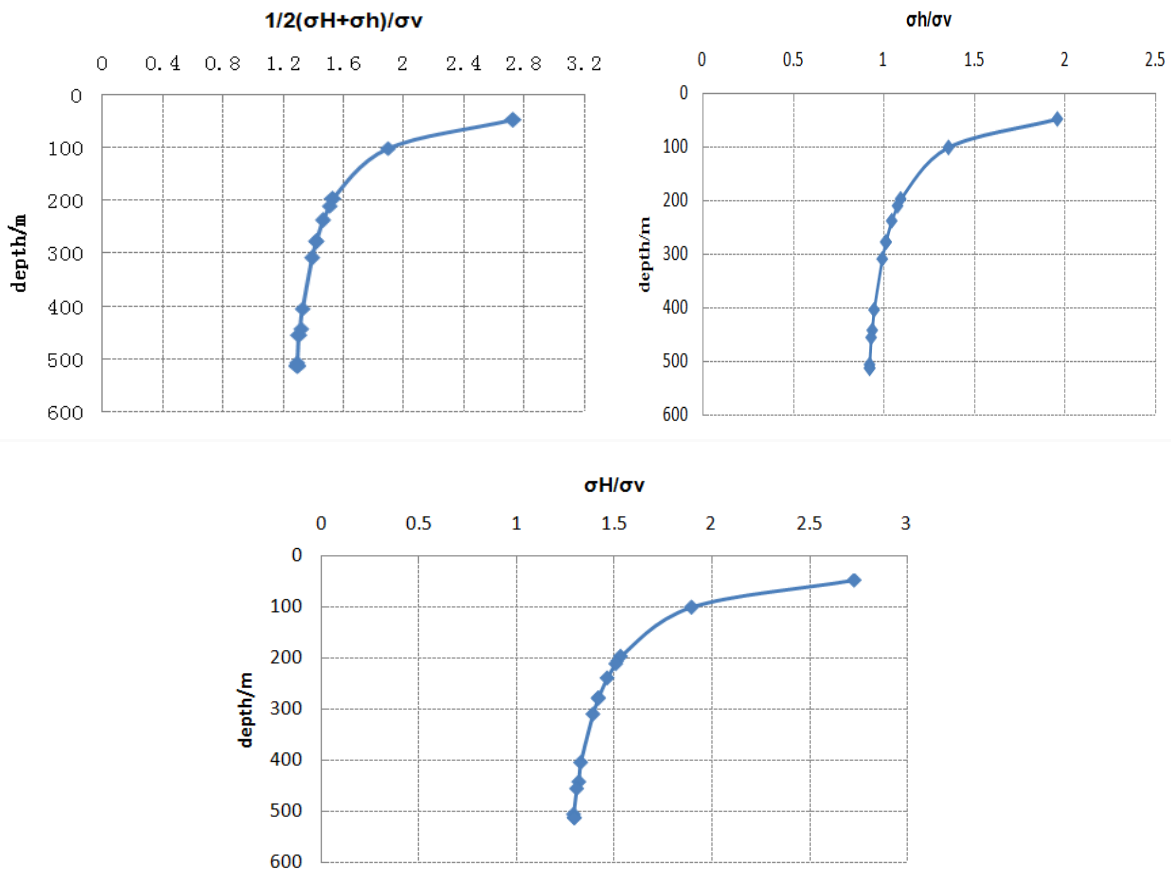


Fig.6. Curves of $\sigma_H/\sigma_v$, $\sigma_h/\sigma_v$, $(\sigma_H+\sigma_h)/2\sigma_v$, vs.depth in baihetan

## Conclusions

By analyzing the distribution of the geostress field in Chinese mainland, Sichuan-Yunnan region and the tectonic movement of Baihetan area, preliminarily conclude the direction of the principal compressive stress field of the underground powerhouse area in Baihetan hydropower station is concluded preliminarily as NW ~ NWW trending. Based on the geostress measurement, the method of the statistical analysis about the measured data of the shallow crustal geostress in China mainland is adopted. The regression formulas of the distribution law of the geostress with depth at the right bank underground powerhouse area are fitted .Then the fitting result is analyzed, and the distribution law of the geostress field in the right bank underground powerhouse of Baihetan hydropower station is studied:

(1) In the right bank slope area, the average direction of the maximum principal stresses is about N7 ° E trending, the dips being given priority to gently dips, a small amount being nearly level; The direction of the minimum principal stresses is NWW trending, the dips changing greatly in the right bank factory. The main direction of the maximum principal stresses is NEE trending, the dips being nearly level, while the main direction of the minimum principal stresses is NNW trending,the dips being middle steep.

(2) $\sigma_v$, $\sigma_H$ and $\sigma_h$ generally present the linear relationships with buried depth generally, which is similar to the distribution of the stress at the shallow continental in China, but there are some errors in magnitude. The numerical size of the above three stresses is $\sigma_H > \sigma_h > \sigma_v$ in the dam abutment ,while $\sigma_H > \sigma_v > \sigma_h$ in the underground powerhouse .

(3) In the right bank slope area, the change range of $(\sigma_H + \sigma_h)/2\sigma_v$, $\sigma_H/\sigma_v$ and $\sigma_h/\sigma_v$ are large in the shallow area, and decrease rapidly with the increase of buried depth. In the depth range of the right bank underground powerhouse(404～513m),the value of $(\sigma_H + \sigma_h)/2\sigma_v$, $\sigma_H/\sigma_v$, and $\sigma_h/\sigma_v$ is smaller.

**ACKNOWLEDGMENTS**

This work was financially supported by the National Natural Science Foundation of China, General Program (Nos.91215301).

**References**

[1] JING Feng, YINJian-min, ChenHao, et al..The inversion of ground stress field of Considering the complex geologic origin in engineeringarea. Journal of Yangtze River Scientific Research Institute.26(2009)51-54.

[2]XIE Fu-ren, ZHANG Shi-min, DOU Su-qing, et al..The evolution characteristics of the quaternary tectonic stress environment in north and east edge Qinghai-Tibet plateau .ActaSeismologicaSinica21(1999)501-512.

[3]CHEN Lian-wang, YANG Shu-xin, XIE Fu-ren,et al.. Numerical simulation of The modern annualvariation characteristics of tectonic stress-strain field in China mainland .Earthquake Research In China 21（2005）341-349.

[4]YANG Shu-xin, CHENLian-wang,XIE Fu-ren. A study of regression analysis and numerical simulation on modern tec-stress field in China mainland. Rock and Soil Mechanics24(2003)257-260.

[5]JING Feng.Research on the distribution rule of the shallow crustal geostress field in the china mainland and engineering disturbance characteristics.WuHan: Institute Of Rock And Soil Mechanics Chinese Academy Of Sciences.(2009)

[6]CHEN Peng-nian,CHEN Hong-de,GAO Li-qing. World-situ stress measurement data compilation. Beijing: Earthquake Publishing House.(1990)

[7]XIE Fu-ren,CHEN Ce-qun,CUI Xiao-feng.The study of the crustal geostress environment in the china mainland. Beijing :Geological Publishing House.(2003)

[8]WANG Shao-jin, LONG Xiao-fan,YU Qing-kun.The analysis of modern tec-stress field in Kunming area. Journal Seismological Research28(2005)178-184.

[9]CHEN Wan-zheng, DIAO Gui-ling, LV Yi-pei,et al..The focal mechanics mechanism, the rate of movement and activity modes of Sichuan-Yunnan block.Seismology And Geology25(2003)71-86.(in Chinese)

[10]CUI Xiao-feng,XIE Fu-ren,ZhANG Hong-yan.Recent tectonic stress zoning in Sichuan-Yunnan region and its dynamic interest. Journal OfSeismological Research28(2006)451-460.(in Chinese)

[11]JIN Chang-yu, FENG Xia-ting,ZHANG Chun-sheng. Research on initial stress field of Baihetan hydropower station. Rock and Soil Mechanics31(2012)846-855.

*Applied Mechanics and Materials Vols. 580-583 (2014) pp 1051-1055*
*© (2014) Trans Tech Publications, Switzerland*
*doi:10.4028/www.scientific.net/AMM.580-583.1051*

# Study on the Blasting Excavation Method of Urban Shallow Tunnel

Ziqiang Li[1,a], Zheng Li[1,b]

[1]Southwest Jiaotong University, Chengdu, Sichuan 610031, China

[a]lzq1102dd@163.com, [b]lizheng212@vip.qq.com

**Keywords:** Urban Tunnel, Shallow-underground Cut Method, Blasting Construction, CD Method, Bench Method with Reserved Core Soil.

**Abstract.** The construction method requires careful consideration in order to reduce impact of tunnel on the surface of the building in the city. It can have great significance in choosing appropriate blasting excavation method for the poor surrounding rock conditions and complicated ground constructions of shallow buried tunnel. This paper combines the Guanhui urban railway transport projects which the shallow buried tunnel through the dense residential areas, research on the influence of CD method and bench method with reserved core soil when use blasting excavation method on the surface buildings by finite element method. The suitability of two kinds of blasting excavation method in the urban shallow tunnels is analyzed and compared, eventually determine the CD method with blasting excavation is more suitable for the urban shallow tunnel construction, it provides reference and suggestion for future similar construction methods that tunnel construction under the city.

## Introduction

With the development of the national economic, a large number of various types of city tunnel have been constructed, its environment is usually complex such as the buried depth is shallow, too many surface buildings, road facilities and underground pipeline planted densely, it is inevitable to impact the surrounding environment during tunnel construction[1]. Take the mechanical excavation can effective reduce the impact of urban tunnel construction on the environment. But due to the high cost, slow construction progress, narrow working space, blasting excavation is usually chosen in the city shallow tunnel[2].

Seismic effect is an important factor affecting the safety of blasting during the city tunnel blasting excavation. The harm of excavation vibration of underground structures on the ground facilities, especially on the urban surface buildings has attracted the attention of engineering field, domestic and foreign researchers have done a lot of research on this. Glenn gets the relationship between blasting vibration frequency and structural damage degree by the study[3]. Shibo Liu put forward that by the blasting construction environment more and more complex, the resident reaction near the blast area response more strongly[4]. Shigen Fu analysis the seismic effect of blasting vibration principle and point out the blasting vibration velocity is an important quantity that leads to destruction of building structure, it can also make normal work of buildings affected[5]. From the existing research results, the research for the influence of blasting construction on the surrounding environment have achieved certain results, but the choice of blasting construction method has no definite conclusion when shallow buried tunnel underpass densely populated areas.

This paper is based on the Guanhui urban railway transport projects which the shallow buried tunnel through the dense residential areas as the research background, combined with the actual engineering environment and use numerical simulation method to analyze the vibration velocity and surface subsidence of the adjacent buildings above the tunnel what are caused by CD method or bench method with reserved core soil. This paper analyzes the suitability of construction method when the tunnel through the dense residential areas, and provide reference and recommendations for similar engineering.

## Research Background

**Safety Criteria of Blasting Vibration.** According to the relevant provisions of China *Blasting Safety Regulations*[6], the safety velocity of blasting vibration is determined as $V$=2cm/s, combined with the actual geological conditions and surface structures of the Guanhui urban railway transport projects, specified the safe and permitted standard value of blasting vibration is 1.5cm/s for the V~VI class surrounding rock.

**Construction Method Introduction.** Depending on the nature of each segment surrounding rock of Guanhui urban railway, mainly choose CD method and bench method with reserved core soil for the V~VI class surrounding rock.

**Bench Method with Reserved Core Soil.** Using circular excavation with reserved core soil can reduce the amount of one-off surrounding rock excavation and prevent squeezing out the tunnel face in the city shallow buried tunnel, the excavation method is as: reserved the core soil platform in upper heading curved section → primary support → excavate the central core soil → excavate the lower bench → carry out combined bolting and shotcrete for the side wall → concrete filling the secondary lining and inverted arch. Combining with actual situation of engineering, the longitudinal size of core soil should be more than 4m, the area of core soil should be more than half of the upper section.

**Middle-wall Method (CD Method).** CD method is mainly used in the rock mass which the geological conditions is poor and the steady ability is low, it also applies to underground engineering construction when surface subsidence must be strictly controlled. The excavation method is as: excavate one side of the tunne → construct the temporary middle-wall → after a certain distance in advance excavation side, partially excavate the other side of the tunnel. To support each part after the excavation so making each part to be an independent closed structure.

**The Determination of Blasting Load.** This paper assumes that blasting load on the excavation boundary surface and face of tunnel by the triangular load method. Taking rise time as 0.012s and time of descent segment as 0.100s on the basis of numerous investigations. Total duration of the simulation takes 2.0s in order to understand the situation of surrounding rock-supporting system after the blasting load.

The peak stress $P_{\max}$ of blasting load uses the following empirical formula to solve:

$$P_{\max} = \frac{139.97}{Z} + \frac{844.81}{Z^2} + \frac{2154}{Z^3} - 0.8034 \,(\text{kPa}) \tag{1}$$

$$Z = R^* / Q^{1/3} \tag{2}$$

where, $Z$ = reduced distance; $R^*$ = the distance from explosion center to the load acting surface (m); and $Q$ = explosive charge (kg), take the total explosive charge when simultaneous blasting, take the maximum period of explosive charge when segmented blasting.

## The Establishment of the Finite Element Model

**Project Profile.** The Guanhui urban railway transport projects in close proximity to above many important ground buildings and underground pipelines clouds. Most foundation of the ground building above tunnel are natural foundation and man-power hole pile foundation, Most building are the framework structure and masonry structure. It is strict with the ground surface settlement when the section tunnel passes through large area of residential areas and factory. Tunnel sits mostly on completely-weathered migmatitic gneiss, it is belongs to the urban shallow tunnel that the minimum thickness of covering soil on the vault is only 8m.

**Establishment of the Model.** In this calculation, the surrounding rock is simulated by using the bilinear elastic-plastic model, sprayed concrete and middle wall is simulated by using the elastic model. The blasting load value of CD method and bench method are both 1.2MPa on the basis of the f Eq. 1 to Eq. 2. Apply the no reflection boundary in the X, Y and Z considering that seismic wave reflects at the boundary will affect the accuracy of the results during the blasting process, at the same time, enlarge the model appropriately in order to a better research on the change rules of surface

velocity during blasting excavation. Specific size is as follows: Z = 76m, X = 80m, Y = 61.45m, the finite element model as shown in fig. 1.

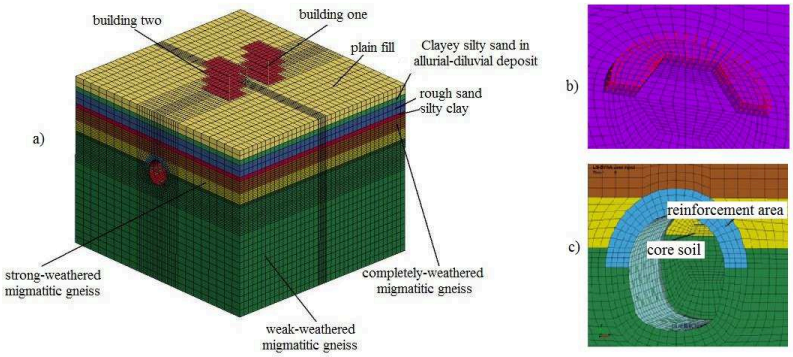


Figure 1. Schematic diagram of the finite element model where they act as valves: a) Full finite element model; b) Bench method; c) CD method with reserved core soil

The selection of surrounding rock parameters is according to the 7 section field test and support parameters refer to Dongguan other similar projects and relevant codes.

Table 1. The parameter of numerical simulation.

| Designation | Elasticity modulus(Pa) | Poisson's ratio | Yield strength(Pa) | Failure strain | Density(kg/m³) |
|---|---|---|---|---|---|
| Weak-weathered migmatitic gneiss | 1e9 | 0.28 | 1e6 | 0.02 | 2500 |
| Strong-weathered migmatitic gneiss | 0.4e9 | 0.32 | 0.8e6 | 0.02 | 2300 |
| Completely-weathered migmatitic gneiss | 0.1e9 | 0.33 | 0.5e6 | 0.02 | 2200 |
| Silty clay | 0.26e9 | 0.35 | 0.2e6 | 0.02 | 1950 |
| Rough sand | 0.20e9 | 0.35 | 0.5e6 | 0.02 | 1900 |
| Clayed silty sand in allurial-diluvial deposit | 0.14e9 | 0.36 | 0.1e6 | 0.02 | 1850 |
| Plain fill | 0.05e9 | 0.37 | 5e4 | 0.02 | 1800 |
| Sprayed concrete | 2.8e10 | 0.2 | - | - | 2300 |
| Middle wall | 2.8e10 | 0.2 | - | - | 2500 |

This paper simulates four conditions as shown in Table 2. Furthermore, tunnel vault and settlement of ground surface are monitored as follows: every 2m to set up a monitoring site in the tunnel axial direction and the horizontal direction of tunnel face.

Table 2. Calculated work condition.

| Work condition | Construction method | Blasting excavation position | Surface condition |
|---|---|---|---|
| 1 | Bench method with reserved core soil | The upper arc heading | No buildings |
| 2 | Bench method with reserved core soil | The upper arc heading | Buildings |
| 3 | CD method | The upper left section | No buildings |
| 4 | CD method | The upper left section | Buildings |

**The Analyses of the Results of Model Calculation**

With the help of computer simulation, get the influence of different blasting excavation methods on the tunnel and surface building by the $V_{ymax}$ change curve of tunnel horizontal and longitudinal monitoring sites. Set monitoring site as the origin, the abscissa negative value of X direction indicates

the left side of the origin, the positive value indicates the right side, the abscissa negative value of Z direction indicates the front of tunnel face, the positive value indicates behind tunnel face.

**The Analysis of Work Condition 1 and 2.** Fig. 2 shows each monitoring site $V_{ymax}$ change curve of X direction in work condition 1 and 2. Fig. 3 shows each monitoring site $V_{ymax}$ change curve of Z direction in the work condition.

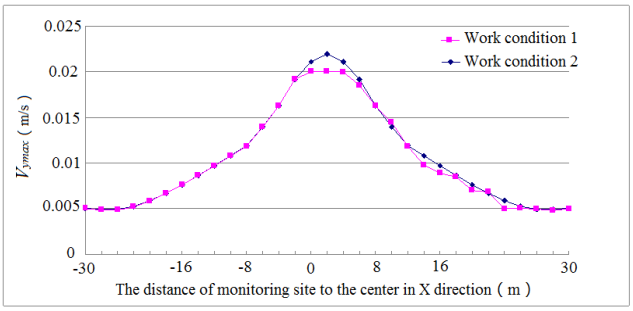


Figure 2. Comparison of work condition 1 and 2 monitoring site in the X direction

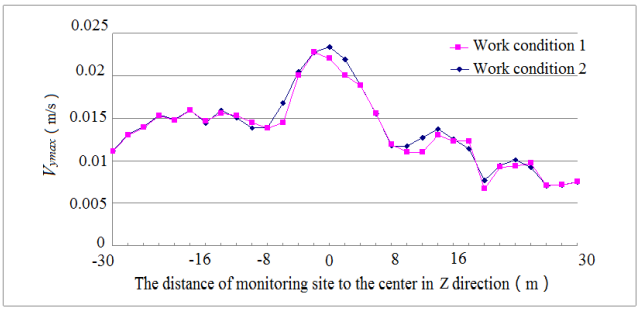


Figure 3. Comparison of work condition 1 and 2 monitoring site in the Z direction

As shown in Fig. 2, the maximum vertical velocity $V_{ymax}$ of the working condition 1 and 2 have appeared in the upper part position of tunnel face (X = 0) what are 2.19 cm/s and 2.04 cm/s. Contrast work condition 1 with 2: 1. Both the change rule of $V_{ymax}$ curve are consistent: $V_{ymax}$ gradually decreases with the increase of distance from the center and its ratio of decline tends to slow, $V_{ymax}$ changes gradually stable and show a converging trend when the distance is about 22m from the center. The result shows that effects of blasting no longer increase when the horizontal distance from the center of the tunnel excavation over 22m and that is the range of influence by bench method with reserved core soil. 2. Surface velocity appeared certain reduced because of the existence of the building structure (cylinder nodes at X = 0m and X = 13.75m) and performance more obvious but varied little near the X = 0 m and X = 12.

As shown in Fig. 3, the maximum vertical velocity $V_{ymax}$ of the working condition 1 and 2 have appeared in the front of tunnel face what are 2.34 cm/s and 2.27 cm/s. Contrast work condition 1 with 2: 1. Both the change rule of $V_{ymax}$ curve is consistent: The velocity attenuates quickly within the range of 10m in front of tunnel face to 6m behind tunnel face and finally decreased about 50%. Velocity remained unchanged during 10m-24m in front of tunnel face and 6-16m behind tunnel face. 2. The velocity in front of tunnel face is always greater than that behind tunnel face and the influence of blasting vibration in front of tunnel face is also bigger in the same distance from center position.3. Surface velocity appeared certain reduced because of the existence of the building structure (cylinder nodes at Z = -8m, Z = 0m, Z = 10m and Z = 18m).

**The Analysis of Work Condition 3 and 4.** Fig. 4 shows each monitoring site $V_{ymax}$ change curve of X direction in work condition 3 and 4. Fig. 5 shows each monitoring site $V_{ymax}$ change curve of Z direction in the work condition.

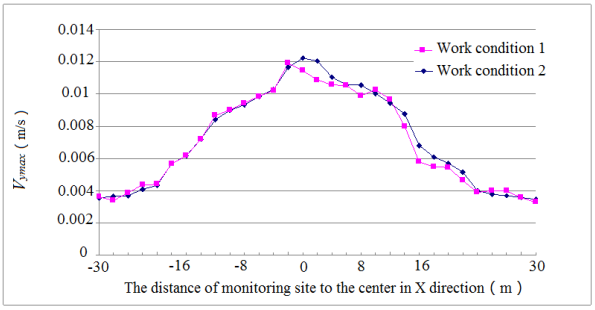


Figure 4. Comparison of work condition 3 and 4 monitoring site in the X direction

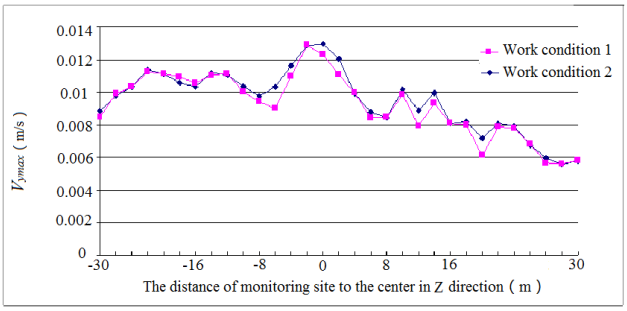


Figure 5. Comparison of work condition 3 and 4 monitoring site in the Z direction

As shown in Fig. 4, the maximum vertical velocity $V_{ymax}$ of the working condition 3 and 4 have appeared near the center point what are 1.226 cm/s and 1.245 cm/s. Contrast work condition 3 with 4: 1. Both the change rule of $V_{ymax}$ curve are consistent: $V_{ymax}$ gradually decreases with the increase of

distance from the center and its ratio of decline tends to slow, $V_{ymax}$ changes gradually stable and show a converging trend when the distance is about 22m from the center. The result shows that the influence of blasting excavation is very weak when the horizontal distance from the center of the tunnel excavation over 22m. 2. Surface velocity appeared certain reduced because of the existence of the building structure (cylinder nodes at X = 0m and X = 13.75m) and performance more obvious but varied little near the X = 0 m and X = 12.

As shown in Fig. 5, the maximum vertical velocity $V_{ymax}$ of the working condition 3 and 4 have appeared near the center point what are 1.296 cm/s and 1.287 cm/s. Contrast work condition 3 with 4: 1. Both the change rule of $V_{ymax}$ curve are consistent: The velocity attenuates quickly within the range of 8m in front of tunnel face to 4m behind tunnel face and finally decreased about 30%. Velocity remained unchanged during 8m-26m in front of tunnel face and 4-22m behind tunnel face. 2. The velocity in front of tunnel face is always greater than that behind tunnel face and the influence of blasting vibration in front of tunnel face is also bigger in the same distance from center position. 3. Surface velocity appeared certain reduced because of the existence of the building structure (cylinder nodes at Z = -8m, Z = 0m, Z = 10m and Z = 18m).

**The analysis of work condition 1 and 3.** By comparing the pictures above, the general regularity of the vibration velocity of CD method and bench method are the same, the maximum velocity appears on the surface near the tunnel face. From the vibration velocity values, bench method is much higher than that of CD method and the biggest value difference reached about 1 cm/s. This is mainly due to the area of excavation section of bench method is bigger and explosive payload is more compared with CD method.

## Conclusion

This paper simulates the different blasting construction methods when shallow buried tunnel underpassing densely populated areas by numerical analysis, analysis different blasting construction methods on the impact of tunnel and surface buildings and come to the conclusions as follows:

1. By contrasting two kinds of blasting excavation method, the surface vibration velocity attenuation regularity consistent. But the vibration velocity caused by bench method is significantly higher, the area of excavation section is bigger and explosive payload is more compared with CD method. Given the facts, the bench method is much better than CD method when buried tunnel underpassing densely populated areas.

2. The vibration velocity of the excavation section caused by two methods gradually decreases with the increase of distance from the center, the influence of blasting is no longer increasing when the horizontal distance from the center is more than 22m, the tow methods show similar laws.

3. The extreme value of tunnel longitudinal vibration velocity both appear in the front of tunnel face at the same position from the center point. The range of influence by bench method on the rear is about 18m and that is about 24m caused by CD method. Although the influence range of CD method is greater, but the value has been far less than the control value.

4. During the process of two kinds of blasting construction methods, surface velocity appeared certain reduced because of the existence of the building structure, but the magnitude and range of influence are small.

## References

[1] J.J. Luo: Rock and Soil Mechanics. Vol.7(2007), p. 83-87.

[2] G. I. Taylor: *Analysis of Explosion of a Long Cylindrical Bomb Detonated at one end*. Chapam and Hall(1941).

[3] S.B. Liu: Railway Engineering. Vol. 12(2006), p. 63-65.

[4] S.G. Fu: *Test and Evaluation of Tunnel and the Blasting Vibration.* Vol. 6(2006), p. 45-48.

[5] China. *Blasting Safety Regulations*. GB6722-2003.

*Applied Mechanics and Materials Vols. 580-583 (2014) pp 1056-1060*
*© (2014) Trans Tech Publications, Switzerland*
*doi:10.4028/www.scientific.net/AMM.580-583.1056*

# The Monitoring and Numerical Simulation Analysis on the Construction of a Shallow Underpass

Lisheng Liu [1, a], Jie Zhao [1,b]

[1] The R&D Center of the Civil Engineering Technology, Dalian University, Dalian 116622, China

[a]liulis1230@163.com, [b]zhaojie_gd@163.com

**Keywords:** monitoring measurement; stress release; numerical simulation; underpass.

**Abstract.** Based on the dynamic monitoring project of one underpass in Dalian, this paper tries to validate the control effect of the ground settlement on the stability of tunnel surrounding rocks during construction of underground passage under urban arterial road by means of analyzing the vertical ground settlement curves, convergence curves of tunnel inner perimeter and vault displacement curves. With the numerical calculation tool of the software FLAC, it also analyzes the construction of XS- 2 # cross-section which was in the south side of the whole construction section at different stages by adopting the plane-strain model. Therefore, we can get the influence curves of ground settlement under different construction stages with considering the release of stress. The simulation results are basically consistent with the measured data, which has a great significance for the subsequent design and construction of underground projects with similar geological conditions.

## Introduction

In consequence of the losses of the stratum and changes in groundwater levels during excavation of underground tunnel, formation stress of a certain range of cavern excavation area is adjusted and changed from the cavern invading to deep geological formations, resulting in the subsidence and displacement of ground surface and buildings [1]. When the surface movement and deformation exceed a certain limit, it will affect safety and proper usage of the tunnel and the ground buildings. Therefore, it requires more stringent for the design and construction of the tunnel and the control on the surrounding environment [2].Based on the dynamic monitoring project of one underpass in Dalian, the field measurements and numerical simulation analysis which are two different means are used to investigate the influence on surface subsidence and crown settlement in various stages of construction. This dynamic information is an important reference data of information construction to guide the construction progress and ensure the safety and efficiency of construction.

## Project Overview

The project is located in interchange of Wuhui Road and Zhongshan Road, which is the rare city underground without effect of traffic during construction. And shallow mining method is adopted for the main channel Construction. The Underpass passes through Zhongshan Road and Wuhui Road.

Engineering site belongs to gentle slope belt, and the ground level changes from 25.76 m to 26.98 m. As the survey data is shown, the top-down of site strata: plain fill (layer thickness is 3.4-5.4m), silty clay (layer thickness is 1.6-4.0 m), sidewall rock (layer thickness is 2.0-2.6m), and bed rock which is mainly strongly weathered lime stone. It is only a small amount of groundwater in the drilling depth, and the main source is atmospheric precipitation.

## Construction Monitoring Program

According to the project monitoring program, the main monitoring content includes: Surface subsidence monitoring, crown settlement monitoring and clearance convergence monitoring.

Three survey lines of surface subsidence monitoring were located along the Zhongshan road: XN - 1#, XN - 2#, XN – 3 are located on both sides of road and pat respectively and the interval is 5m.Three survey lines of Wuhui Road were established : XS -1#, XS- 2#, XS - 3#, which are consistent with the north side. Each survey line from the west to the east is arranged five measuring points (as shown in Figure1); Convergence clearance section is for each surface subsidence monitoring sections below and a total of six monitoring sections and each section has three survey lines (as shown in Figure 2); Vault subsidence monitoring puts clearance convergence points as the monitoring points and each section sets up one monitoring point.

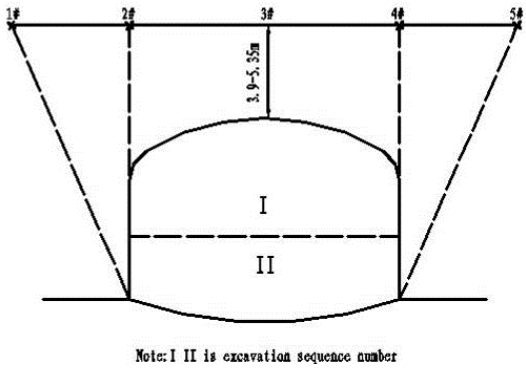


**Fig. 1** Surface Subsidence Monitoring of Cross-section Diagram

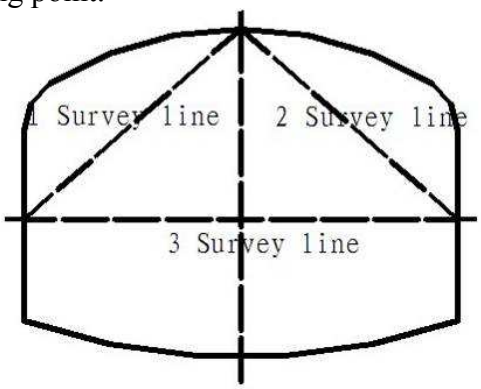


**Fig. 2** The Diagram of Deformation Monitoring Convergence

## The Analysis of Construction Monitoring Data

**The Analysis of Longitudinal Settlement.** The underpass project taskes the excavation foundation pit of Hope Square as the center. Then it is excavated in both sides of the direction and the construction period of three months in the cave. Surface subsidence monitoring uses six monitoring sections which located north and south and the monitoring frequency is once a day. Choose two of the six lines, the monitoring results are shown in Figure 3.

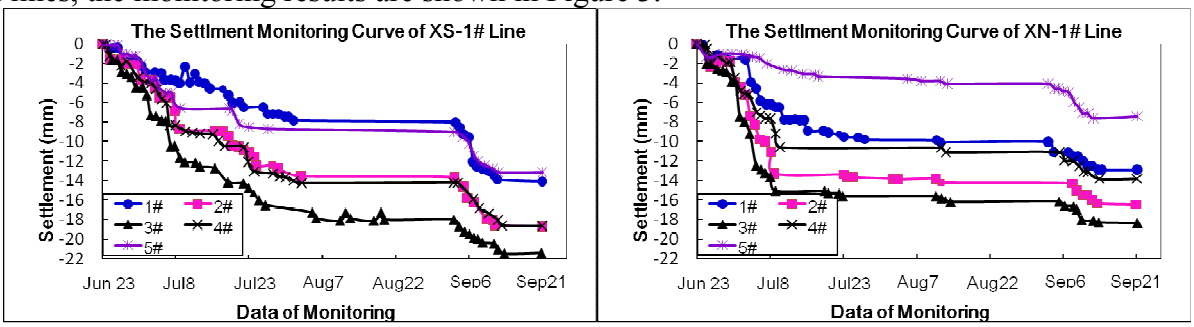


**Fig. 3** Longitudinal Monitoring of Ground Subsidence Curves

By the curves of monitoring in Figure 3 and combining the construction site conditions, we pair the data of inspection to analyze as follows:

(1) Owing to the sudden release of the stress, surrounding rock generates unbalanced force in the initial excavation of the tunnel, resulting in a larger surface subsidence ( of the total settlement amount of 50%~ 80% ) and rapid sedimentation rate(maximum sedimentation of 2. 6mm/d) at this stage, moreover, the sedimentation rate with long duration is greater than zero. With the completion of stress redistribution and the initial support system, pavement settling tends to zero.

(2) Since the cross-section roof surrounding are plain fill with poor uniformity and high compression , resulting in a sudden increase in road subsidence ,it have brought a safety hazard to underground construction and road traffic.

(3) The second step of the excavation is from mid-July 2009 to early August 2009,and vertical ground subsidence curve shows the second step of the excavation of the tunnel surrounding rock has a significant impact on stability , resulting in 10 ~ 12mm ground subsidence.

**The Data Analysis of Clearance Convergence.** Tunnel displacement monitoring data can better reflect the surrounding conditions (including rock lithology and disturbance), so by dynamically monitoring the displacement of the tunnel, the state of the tunnel deformation can be understood to determine the stability of surrounding rock. The monitoring result of XS-1 # headroom displacement is shown in Figure 4 and Figure 5.

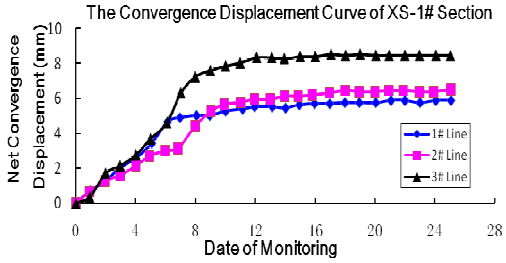


**Fig. 4** XS-1 # Cross-section Convergence Curve

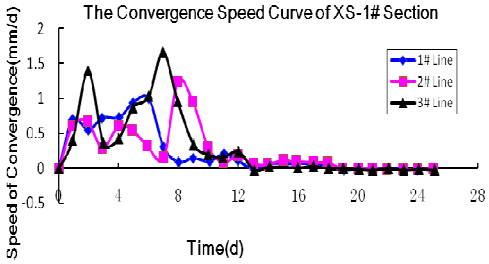


**Fig. 5** XS-1 # Cross-section Convergence Rate Curve

The convergence monitoring data curve shows that it has three stages:

The first phase (after excavation 10d) is increased dramatically Stage: the convergence rate is three times of average rate throughout the monitoring period and convergence reaches more than 80% of a cumulative amount of convergence.

The second phase (after excavation 11 ~ 20d) is slow growth phase: the cumulative amount of convergence grows slowly and convergence rate is only 25 to 30% of average convergence rate .Surrounding rock deformation has not yet reached a steady state.

The third phase (after excavation 21 ~ 26d) is stabilization phase : When the convergence rate with continuous 3 ~ 5 d is zero and convergence is no longer growing ,it can be considered as a steady state and can be secondary lining construction.

**The Data Analysis of Vault Subsidence**. Since vault subsidence monitoring as a reflection of overlying soil is an important cave monitoring project. It can timely reflect of cave excavation and support for overlying soil disturbances. Vault subsidence monitoring curve of sections XS-2 # # is shown in Figure 6.

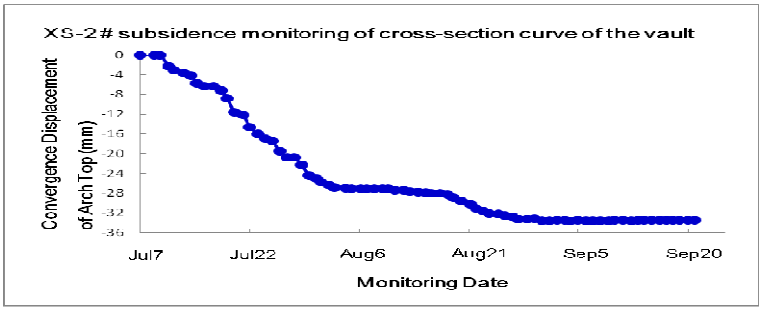


**Fig. 6** XS-2 # Subsidence Monitoring of Cross-section Curve of The Vault

As can be seen from the figure 6, vault subsidence and the ground settlement almost simultaneously generate and the impact factor is basically the same. Vault final subsidence is (33.6mm) slightly larger than the maximum surface subsidence (32.4mm), which is due to the overburden excavation makes overlying soil produce a certain amount of Ta areas resulting in vault settlement slightly larger than the amount of surface subsidence.

## Numerical Simulation of Cross Section XS-2# Excavation

In order to further verify that the observed results in construction site, it is analyzed using numerical simulation method for the deformation of tunnel surrounding rock. According to the prospecting data and actual excavation, the numerical simulation for XS–2# section by adopting plane strain model is carried out based on the numerical simulation software–FLAC2D. In order to simulate the excavation

space effect on changes in the surrounding rock stress better, the stress release method is adopted for numerical simulation of the whole process of excavation.

Stress release method, which is also called Reverse Stress method or Reverse Stress Release method ,was first put forward by Duncan and Dunlop (in 1969)[3]. The excavation of tunnel engineering problem is analyzed by De-an Zhao[4], Zhe Hao[5], Qing-an Hu[6], Linsheng Xu[7] and so on, who adopted the method removing unit to produce the node force vector of release load to extract equivalent load vector for the release, respectively.

**Calculation Model.** Due to the channel length is greater than the height and width of its cross section, the plane strain model is adopted to analyze to simplify the calculation. The balance of the accuracy of the calculation and calculation for engineering should be considered to determine the calculation area. In order to guarantee the reliable data, the distance between the edge of the area calculation model and the perimeter of the tunnel should be greater than three times of the largest span tunnel. At the same time, the error caused by the size of the calculation area can be ignored. Therefore the size of the model can be taken as 64X39m. The FLAC Lagrange finite difference method is adopted in the numerical simulation. Calculation model is established by using Mohr - Coulomb criterion as the yield criterion of soil, as is shown in figure 7.

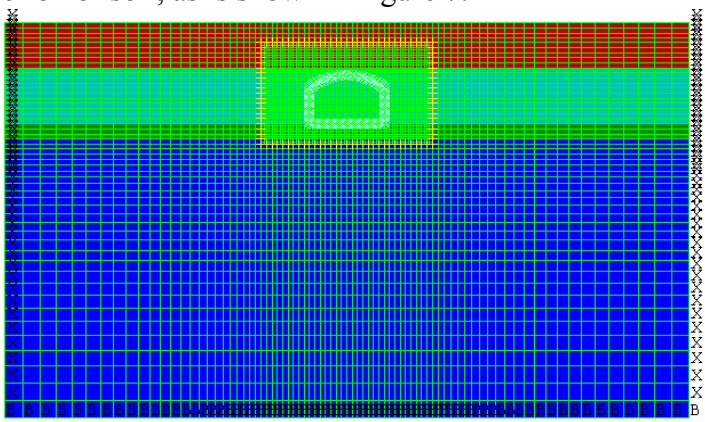

**Fig. 7** Model of Cross Section XS-2#

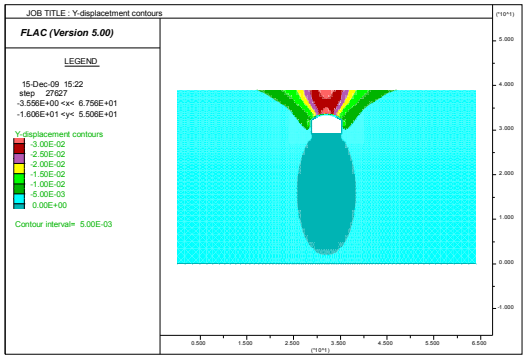


**Fig. 8** The Displacement Fringe of cross section XS-2#

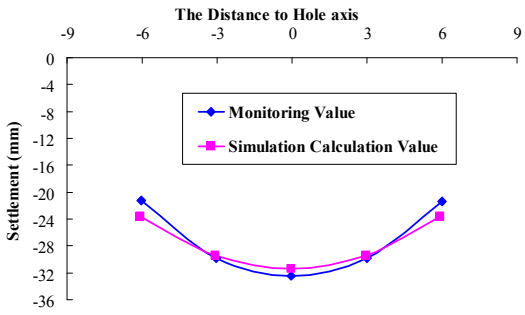


**Fig. 9** The calculated results of surface settlement trough curve compared with the monitoring of cross section XS-2#

**The Analysis of Simulation Results.** From the simulation results, stability of tunnel can be guaranteed during being excavated under the condition of the existing supporting, we can draw the following conclusions through calculation:

(1) The vertical displacement contours of the section XS-2# is shown in figure 8 and the largest vertical displacement of the section is occurred in the vault (32.6 mm), which is consistent with vault subsidence of field monitoring (33.3 mm).

(2) From figure 9, the calculated results of surface settlement trough curve compared with the monitoring of cross section XS-2#, we can conclude that the two curves are similar to normal

distribution curve. and is basically consistent with each other either on the change law or on the maximum which makes clear that FLAC finite difference method will reflect the excavation affect the ground settlement better.

(3) Although the ground last subsidence of tunnel axis in both the detection result and numerical simulation result are larger than the vigilance values 30 mm, surrounding rock is still keep the steady state and do not undergo plastic yield.

## Conclusion

Through the analysis of the field monitoring data about one of the underground tunnel engineering in Dalian and combining with the finite difference numerical in software–FLAC, the stress release method is adopted to XS–2# section for numerical simulation of the excavation.

Therefore, through the comparison of field monitoring and the results of numerical simulation we can draw the following conclusion:

(1) It should highly pay attention to the influence of rainfall on ground settlement during the construction process in rainy season, especially for area with more backfill soil. Meanwhile, the most efficient way to eliminate potential frustrations caused by rainfall should be adopted, such as increasing the frequency of monitoring when rain falls, builders and monitoring personnel is required to be present at all times and pumping-exhaust the accumulated water in the tunnel immediately.

(2) The stress release method can simulate the effect of tunnel excavation space influence on change of surrounding rock stress under the plane strain condition very well. Meanwhile, the best construction simulation period of the secondary lining is given according to the reflect curve of the underlying stress controlling the process of stress release during tunnel excavation.

(3) By comparing the calculation result of numerical simulation software–FLAC with field monitoring data, when the ground last subsidence is slightly larger than the vigilance values 30 mm, it can be proved that surrounding rock might not lose stability either on the observation in the construction site or the convergence of the max unbalance force in the numerical simulation.

## References

[1] Mengshu Wang. Genera l theory of shallow underground[M]. H efei Anhui Education Press, 2004. (In Chinese)

[2] Zhaowei Liu, Yunchen Zhao. Urban underground construction monitoring and inform ation feedback [M]. Beijing: Science Press, 2004. (In Chinese)

[3] Wenfeng Duan, Leixiao Wang, Xionghua Liao. Discussions about problems of construction mechanics in geotechnical engineering and its numerical simulation approaches [J]. Journal of Jilin Architectural and Civil Engineering Institute, 2003, 20( 2): 16-22. (In Chinese)

[4] De-an Zhao, Xiaolin Cai, Zhimin Chen,etal. Influence of side-pressure coefficient on mechanical behavior of tunnel lining [J].Chinese Journal of Rock Mechanics and Engineering, 2003, 22( Supp. 2): 2 857-2 860. (In Chinese)

[5] Zhe Hao, Wei Li, Bin Liu. Study on numerical simulation of excavation process in Hanjialing large span tunnel [J].West-China Exploration Engineering, 2005, (2):96-99. (In Chinese)

[6] Qing-an Hu, Gang Cui, Lijun Jiang. Simulating of tunnel excavation by means of spatial opposite loadingmethod[J].Tunnel Construction, 2006,26(4):3-5. (In Chinese)

[7] Linsheng Xu, Jun Sun, Shuping Jiang. Numerical simulation of dynamic CRD construction process in Yangpeng tunnel [J]. Journal of Geological Hazards and Environment Preservation, 2001, 12(1):58-67. (In Chinese)

*Applied Mechanics and Materials Vols. 580-583 (2014) pp 1061-1064*
*© (2014) Trans Tech Publications, Switzerland*
*doi:10.4028/www.scientific.net/AMM.580-583.1061*

# Metro Station Deformation Caused by Deep Foundation Pit Construction

Chunlei Xin[1,a], Bo Gao[1,b]

[1]Key Laboratory of Transportation Tunnel Engineering, Ministry of Education, Southwest Jiaotong University, Chengdu, Sichuan 610031, China

[a]raymond_xin@qq.com, [b]prgaobo@home.swjtu.edu.cn

**Keywords:** Underground Engineering, Deep Foundation Pit, Metro Station, Numerical Simulation, Structural displacement.

**Abstract.** Many excavation and backfill methods can be used to construct a deep foundation pit, but foundation pit construction will undoubtedly affects security of existing metro station. This research based on a transfer station of Chengdu Metro, three-dimensional numerical simulation method was used to analyze the deformation of metro station by changing construction methods of foundation pit. The results show that: (1) Both excavation and backfill methods of foundation pit have a significant effect on connection segments of metro station. (2) The main body of metro station is largely unaffected by foundation pit construction but it has been in the process of subsidence. (3) The more the construction steps of foundation pit are, the more slowly the displacement of metro station changes. The above results certainly contribute to research and develop new types of construction methods for complicated metro station.

## Introduction

It is common that a deep foundation pit engineering is close to a metro station in operation, especially in this extensive development era of urban underground space. The excavation of deep foundation pit can certainly lead to redistribution of geostress field, thereby causing deformation of metro station [1]. However, the structural deformation requirement of operating metro station is quite stringent. Therefore, many deformation control measures must be used in the process of foundation pit excavation [2]. Obviously, it is of great significance to resolve a contradiction between urban construction and existing metro protection [3]. Currently, many scholars have done some research on similar issue but each real project has their own features and solutions [4]. Many construction methods are put forward but they may not be suitable for another projects. This paper bases on Chengdu Metro Chunxilu station project. Numerical simulation method is used to analyze deformation features of metro station by changing excavation and backfill methods of deep foundation pit. Finally, the best foundation pit construction method is put forward for this project.

## Background and features of project

Chunxilu station is a transfer station on Chengdu Metro line two and line three. This project includes two sections, one is No.1 transfer hall and the other is No.2 entrance. The transfer hall is a new construction and the entrance needs to be reformed. According to the design requirements of this transfer station, the relative position between transfer hall and existing entrance is shown in Fig.1. The length of transfer hall is 28.2m, the width is 14.1m and the height is 7.5m. There is a ventilation channel connected with transfer hall and its cross-section dimension is 14.8m×10.3m.

The transfer hall and the ventilation channel are constructed simultaneously by using cut and cover method. Construction procedures include foundation pit excavation, soil reinforcement, lining construction and soil backfill. Each construction procedure can affect the structural deformation of existing metro station. The subsection excavation method is used to excavate transfer hall. Along the vertical direction of transfer hall, the soil mass is divided into two layers to excavate. Meanwhile, the soil mass is divided into four equal parts along the length direction of transfer hall. Bored piles are constructed around the foundation pit before soil mass excavation and steel braces are made

immediately after excavation. After constructing the lining structures, the steel braces are removed and soil mass is backfilled in four equal parts. The excavation method is shown in Fig.2 and Fig.3.

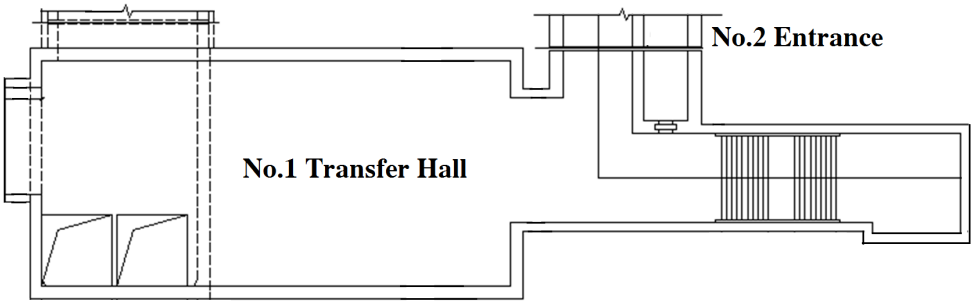


Fig.1 Relative position between transfer hall and existing entrance

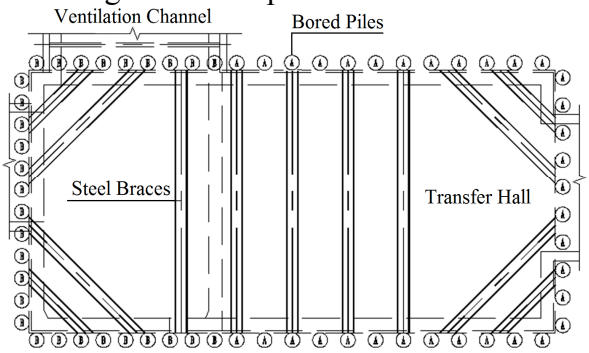


Fig.2 Ichnography of transfer hall excavation

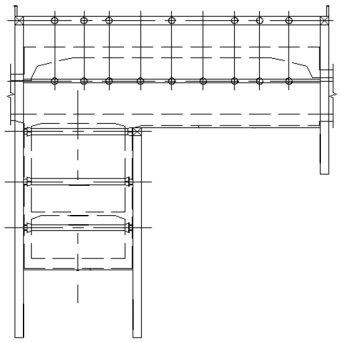

Fig.3 Profile of transfer hall excavation

## General situation of numerical simulation

**3-dimensional numerical model.** According to the tunnel mechanics theory and border theory, the entire numerical model size is X×Y×Z = 65×50×100m$^3$ (shown in Fig.4). Specifically, the model system is composed of existing metro station, civil defense section, passageway section and transfer hall (shown in Fig.5). All these boundaries setting can guarantee the accuracy of calculation results. The whole numerical model is comprised of 207,000 solid elements.

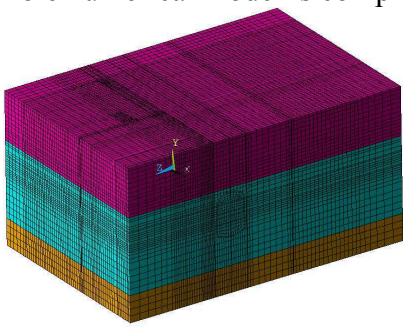

Fig.4 The entire numerical model

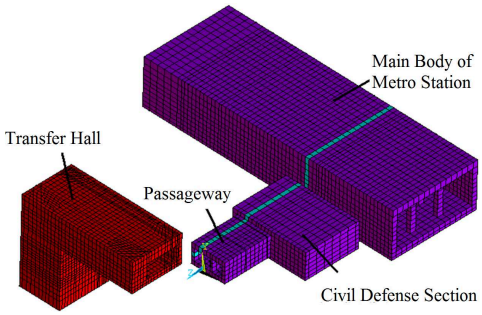


Fig.5 Numerical model of research system

**Calculation parameters.** The physics and mechanics parameters of soil mess and foundation pit are listed in Table 1. Where, $\gamma$ is bulk density, $E$ is elastic modulus, $\mu$ is Poisson's ratio, $C$ is cohesive strength and $\varphi$ is friction angle.

Table.1 Physics and mechanics parameters of model system

| Position | $\gamma/(kNm^{-3})$ | $E/MPa$ | $\mu$ | $C/kPa$ | $\varphi/(°)$ |
|---|---|---|---|---|---|
| Soillayer 1 | 17.3 | 15 | 0.35 | 10 | 21 |
| Soillayer 2 | 20.9 | 50 | 0.35 | 22 | 38 |
| Soillayer 3 | 21.5 | 80 | 0.35 | 15 | 48 |
| Bored piles | 21 | 800 | 0.3 | 100 | 39 |
| Lining | 24 | $3.15\times10^4$ | 0.25 | -- | -- |
| Steel braces | 25 | $8\times10^4$ | 0.2 | -- | -- |

## Analysis of calculation results

**Influence of foundation pit excavation on metro station displacement.** After excavating the foundation pit, the existing metro station displacement nephograms are shown in Fig.6 and Fig.7.

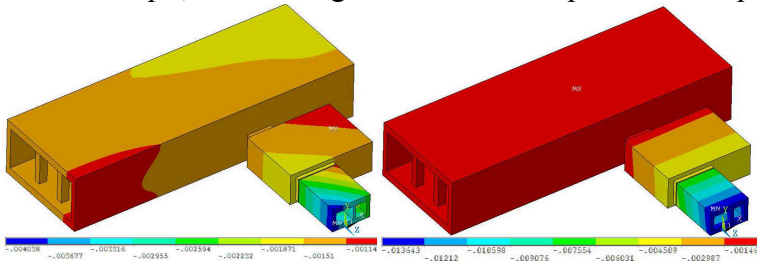

Fig.6 Vertical displacement Fig.7 Horizontal displacement

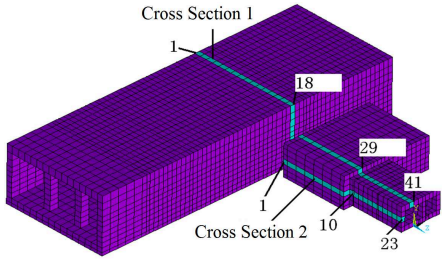


Fig.8 Monitoring sections and spots

The horizontal displacement of existing metro station is larger than vertical displacement. The main body of metro station is largely unaffected by foundation pit excavation. However, foundation pit excavation has a significant effect on both passageway section and civil defense section. The shorter the distance between metro station and foundation pit is, the more obvious the displacement of metro station is.

In order to further study on displacement features of metro station, monitoring spots are chosen to analyze the vertical and horizontal displacement separately (shown in Fig.8).

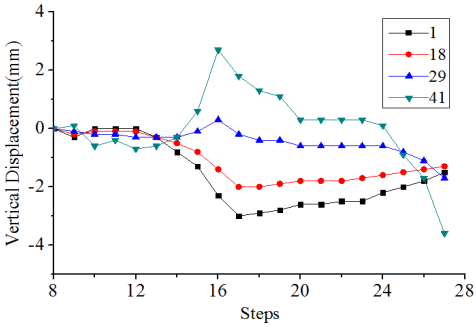


Fig.9 Vertical displacement of monitoring spots

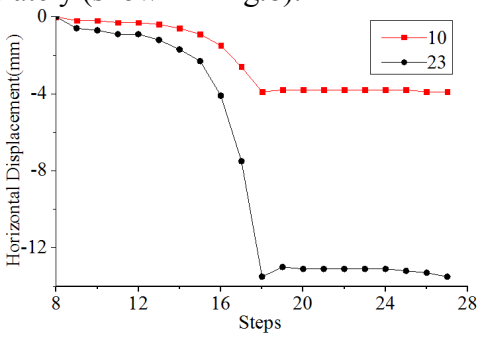


Fig.10 Horizontal displacement of monitoring spots

Fig.9 shows that a bulge phenomenon happens in passageway and civil defense section in the process of foundation pit excavation. Moreover, the shorter the distance between metro station and foundation pit is, the more obvious the upheaval is. The main body of metro station has been in the process of subsidence. Fig. 10 shows that the horizontal displacement mainly happens in the process of foundation pit excavation.

**Influence of excavation methods on metro station displacement**. Fig. 11 and Fig.12 show the vertical and horizontal displacement curves with different excavation methods separately.

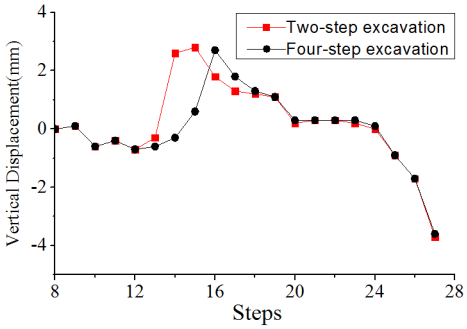


Fig.11 Vertical displacement of metro station with different excavation methods

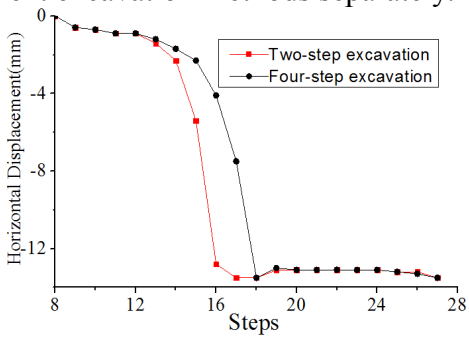


Fig.12 Horizontal displacement of metro station with different excavation methods

The final displacement of metro station is largely unaffected by different excavation methods of foundation pit. The major influence of excavation methods on metro station displacement is in the process of excavation. The more the excavation steps of foundation pit are, the more slowly the displacement of metro station changes. Thus, the metro station is not vulnerable to large displacement.

**Influence of backfill methods on metro station displacement.** Fig. 13 and Fig.14 show the vertical and horizontal displacement curves with different backfill methods separately.

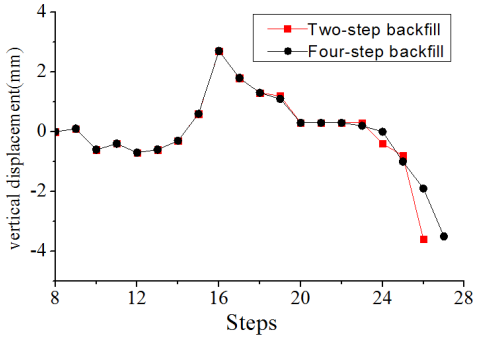


Fig.13 Vertical displacement of metro station with different backfill methods

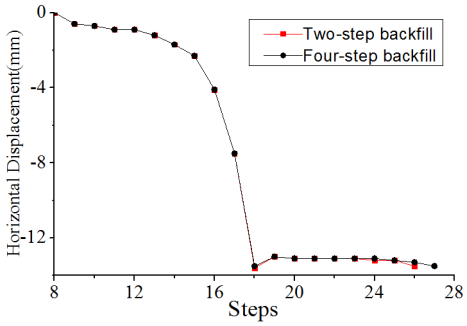


Fig.14 Horizontal displacement of metro station with different backfill methods

The final vertical displacement of metro station is not affected by backfill methods of foundation pit and backfill methods merely affect the subsidence velocity of metro station. When using four-step backfill method, the subsidence velocity is slower than using two-step backfill method. Moreover, the more slowly the displacement of metro station changes, the more secure the metro station is. Since the horizontal displacement is mainly determined by foundation pit excavation methods, backfill methods have little effect on horizontal displacement of metro station.

## Conclusions

Both excavation and backfill methods of foundation pit have significant effects on connection segments such as passageway section and civil defense section. However, the main body of metro station is largely unaffected by foundation pit construction but it has been in the process of subsidence. The shorter the distance between metro station and foundation pit is, the more obvious the displacement of metro station is. The more the construction steps of foundation pit are, the more slowly the displacement of metro station changes.

## Acknowledgments

The research was funded by the National Natural Science Foundation of China (No. 51178398).The authors also gratefully acknowledge the financial provided by Southwest Jiaotong University and China Scholarship Council.

## References

[1] Kontogianni, VA; Stiros, SC. Induced deformation during tunnel excavation: Evidence from geodetic monitoring. Engineering Geology, 2005, Vol.79, No. 1-2, pp.115-126.

[2] Kontogianni, V; Tzortzis, A; Stiros, S. Deformation and failure of the Tymfristos Tunnel, Greece. Journal of Geotechnical and Geoenvironmental Engineering, 2004, Vol.130, No. 10, pp.1004-1013.

[3] Meng Gao, Guangyun Gao, Shijin Feng. Control of deformation of operating subway station induced by adjacent deep excavation. Chinese Journal of Geotechnical Engineering, 2008, Vol.30, No. 6, pp.818-823 (in Chinese).

[4] Xiangpeng Kong, Guobin Liu, Shaoming Liao. Influence of construction of Shanghai stadium transverse station of pearl line phase II on station of metro line No.1. Chinese Journal of Rock Mechanics and Engineering, 2004, Vol.23, No. 5, pp.821-825.

*Applied Mechanics and Materials Vols. 580-583 (2014) pp 1065-1071*
*© (2014) Trans Tech Publications, Switzerland*
*doi:10.4028/www.scientific.net/AMM.580-583.1065*

# New Developments and Applications in Rail Transit Construction Technology

Runjun Li[1,2,a] , Renliang Shan[1,b], Qiulin Liao[2 ,c], Fumei Wu[2,d]

[1]School of Mechanics & civil engineering, China University of Mining & Technology, Beijing, 100083, China

[2]Beijing urban construction design & development group co., Limited, Beijing, 100088, China

[a]1161036851@qq.com,[b]srl@cumtb.com.cn,[c]27878587@qq.com,[d]2505170221@qq.com

**Keywords:** rail transit, new technology, shallow mining method, new construction equipment, risk source;

**Abstract.** Combining with the practical engineering case, the paper summarizes the shallow mining method construction mechanism, construction methods and auxiliary technology. Aiming at the problems in the shield construction, the paper introduces the shield machine equipment's latest comprehensive construction and technology, especially the shield technology dealing with the conglomerate stratum where the water and boulders is rich. It fills the domestic blank; Deep grouting and pipe roof reinforcement technology are aimed at the specific sources of risk; Whole cross-section of pallet trucks, electric vehicles, automatic metering and other new equipment have been widely applied to the construction site.

## Introduction

Now the development of urbanization is in high-speed in China, as a key part of urban transportation , rail transit, which has the merits of large capacity, punctuality, shortcut, safety and high efficiency, low carbon environmental protection, etc. is the focus of the big cities' development in the current and future. The rail lines, often along the main roads in the cities, inevitably will through a lot of underground pipelines, lakes and the surrounding building structures. So it constitutes a potential threat that the track traffic construction exerts negative influences on nearby existing architectural environment. On the other hand, the lines, which are often difficult to avoid water-rich sand pebbles, silty sand stratum and other undesirable formation, tend to restrict its construction. Together with the emerging of new technologies, equipments and processes, the rapid development of the theory about the design of rail transit construction brings the fast-developing track traffic.

## The rapid development of shallow mining method

In 1948, L.V.Rabcewicz, an Austrian expert, designed the safe and economic tunnel excavation method and support structure basing on the use of new building materials. And a theory named "New Austrian Tunnel Construction Method" was formed in 1963, or "New Austrian Tunneling Method" (NATM) for short[1]. In the 1980s, the principle of NATM was first used to study and test the shallow mining method in the loess stratum near the portal of the double-line tunnel in Jundushan railway. Then this new technology was successfully applied in the return section building of Fuxingmen subway in Beijing in 1986. The shallow mining method was widely introduced in Beijing subway Fu-Ba line in the 1990s, resulting in the construction of the Metro section of 13.5 km approximately and 4 underground digging stations, including Xi'dan, Tian'anmen West, Wangfujing and Dong'dan[2]. It created a set of new technologies, processes and methods about underground excavation construction of urban metro works that the successful construction of Fu-Ba line enriched and developed the shallow mining method.

Due to the different excavation methods, the shallow mining method can be divided into a number of specific construction methods, such as the full-face method, the positive step method, the method of circular excavation with core soil, the single side heading method, the double side heading method,

the center diaphragm method, the cross diaphragm method, the center drift method, the side drift method, the column-hole method, etc. According to the geological and hydrological conditions, the size and shape of the cross-section, the length of the tunnel, the engineering support form, the buried depth, the construction technology and equipment, the project duration and other factors, underground construction projects have a variety of construction methods. Especially the new technology of "one-time supporting arches covered cut and reverse approach", it is shown in Fig 1 that research of " one-time supporting arches" has formed new technology of design and construction. It has obtained the national invention patent, and realized the new breakthrough of underground construction methods of underground engineering[3].

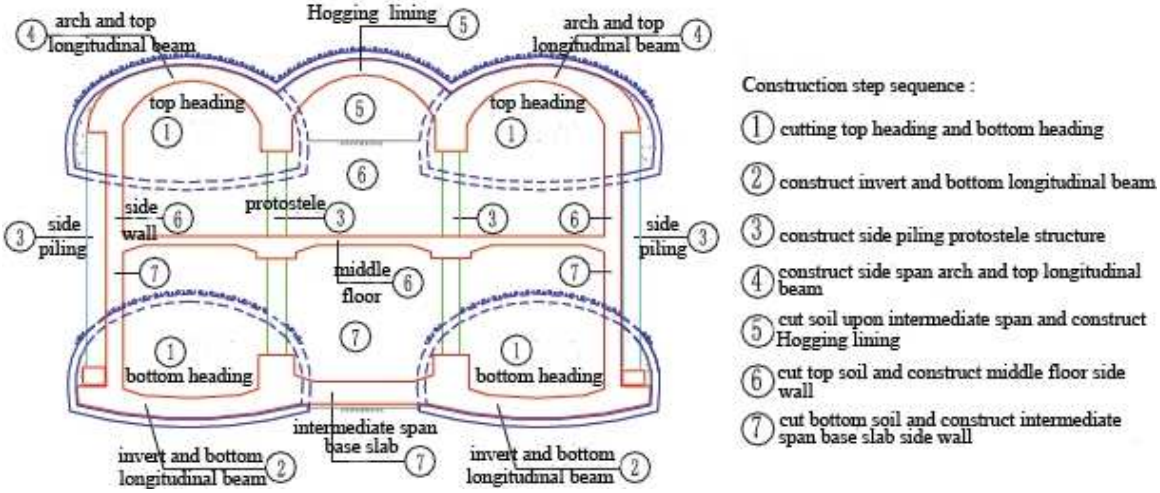


Fig.1 One-time supporting arches covered cut and reverse approach

**The extensive use of Shield Technology**

The construction technology of shield in China was first used in the late 50's of twentieth Century. In the year of 1957, Beijing constructed its city sewer by hand dug type shield diameter of 2.0m and 2.6m, systemic and comprehensive shield test was started in Shanghai Tang'qiao in 1963. In the year of 1996, the subway line 8 introduced knife type shield, and the shield construction technology was first substantively used in subway engineering in Beijing. After entering 21st century, with the large-scale construction of rail transit, the shield construction technology has been widely used and developed indifferent depth of shallow buried stratum. Taking the construction of Beijing subway as an example, since the shield construction of subway line 5 in 2000, subway line 5, line 4, line 10, airport Line, line 9, Daxing line, line 6, line 8, Yizhuang lines have started construction. At present, the new lines under construction such as line 6 (phase two), line 7, line 14, Changping line (phase two) and line 16 extensively used earth pressure balance shield technology to construct tunnel, for example, the 7 intervals of line 6 (phase two) are all constructed by shield method. The upcoming construction of subway line 8 phase three, line 6 west extension, line 3, line 12, line 17 and Yanfang line north extension section will extensively use shield technology to construct interval tunnel[4].

Shield construction technology is a tunnel construction method of high degree of mechanization and automation, its basic working principle is a cylinder of steel component along the tunnel axis forward while to dig soil. The shell of the cylinder components is shield, it plays a role of temporary support in the unlined tunnel bearing the soil pressure, and sometimes it bears the pressure of underground water and keeps the underground water outside. Mining, row soil and lining operations work under the cover of a shield.

Shield construction consists of 3 parts, they are stabilizing the excavation face, mining and rowing soil, lining (backwall grouting). Shield machine is made up of excavation system, propulsion system, soil system, the segment assembling system, hydraulic, electrical, control systems, attitude control device, guide system, the grouting device, rear trolley, centralized lubrication device, advanced drilling and grouting, articulated device, ventilation, muck improvement device and some other

important devices such as shield shell, stabilizer and entry gate. Shield machines used in subway construction are mainly imported from Japan and Germany, domestic equipments and equipments imported from other countries are less. With the development of domestic shield, shield (such as railway equipment and railway heavy) has begun the application in the subway. And this percentage will be further improved in the subway shield tunnel construction in the future; it is expected to become the mainstream of subway construction equipment in the future.

Shield construction is divided into air, mud, earth pressure balance of different types according to different soil and working mode. Shield construction has many characteristics such as high degree of automation, saving manpower, fast speed of construction, excavate at once, and not affected by climate, can control the ground settlement, reduce the impact on ground buildings, the underwater excavation does not affect the water transport, in the tunnel under the condition of long, large buried depth, shield in subway construction is more economic and reasonable. As the optimization of cutter head, the update of soil improvement method and modified agent, especially the appearance of real-time information management system of shield construction, shield technology will be widely used in railway construction[5].Under the shield of Beijing subway line 9 in Yuyuantan east lake project, a large diameter high-strength boulder-rich conglomerate formation is very difficult water-rich, through scientific research, exploration summary, under the successful wear, to fill the domestic blank.

**Over-seat single-track Transit Systems**

Straddled-type monorail refers to the single track to support, keep stability and guide, the car ride on track beam of the railway. In China, the Chongqing metro line two was first imported from Japan, from opening the trial operation in 2004; it has been running 19 km. In the near future, Chongqing will build two city backbone lines and two branch lines, the newly built lines will be totally 100km. The city of Beijing will also start the two straddle type monorail, the length will be approximately 60 km, and the two lines will be in the form of the viaduct. Straddled-type monorail is characterized by strong adaptability, low noise, small turning radius and strong climbing ability[6]. Similar to the "air train", the speed of straddled-type monorail can reach 60 kilometers per hour, and it is especially suitable for the ground and elevated city rail transit line. Straddled-type monorail, for example, the use of special track will not cause derailment; the use of air springs and rubber wheel makes passengers feel superior; Powered by electricity does not produce air pollution; low noise and low vibration; it has simple structure and short construction period, saving construction and repair cost[7].

**The methods for ground reinforcement and supporting surrounding rock are keeping update**

In recent years, the traditional ground reinforcement and rock support of grouting, pipe roof, advanced small catheter reinforcement, anchors and other methods in terms of technology, construction methods, equipment, etc. have made great strides[8].

Grouting generally pre-grout proceeding from the vertical face of soil, mainly static pressure grouting, chemical grouting and fracture grouting, respectively, for sand and gravel, sand and silt soil of different porosity strata; from the grouting way of advancing and retreating deep grouting technology. In addition to the tunnel excavation grouting can be carried from the ground, but also horizontally or diagonally levels grouting from the tunnel face and vault Excavation outside. In terms of grouting materials, in addition to general grout, modified silicate slurry, there are some expansion of the slurry, the slurry as TGRM, no shrinkage slurry, WSS and ultrafine grout slurry, MS slurry and so on. In particular, in recent years, the construction of the subway emerging deep drilling equipment by injecting grouting process improvement, process optimization grouting, grouting equipment improvements and slurry flow and pressure control, well played strata reinforcement, sealing effect, substantially increased the risk of various types of subway construction safety management and control source are shown in Fig 2.

Fig.2 Grouting slurry injection volume and pressure dual control

Fig.3 Pneumatic down the hole hammers managed drilling pipe shed construction

General methods for bassoon shed construction: before the tunnel excavation, using horizontal drilling rigs in the arch area drill horizontal according to holes, spacing and depth by design, bury pipe with pre-drilled hole wall and pre-drilled through the wall hole injecting grout to reinforce and increase the stiffness of the soil pipe so that to perform an arch tunnel umbrella steel shed. The structure itself is a shear behavior, which can effectively carry partial load of overlying soft soil, and so was reinforced soil shear strength has dramatically increased, resulting in tunnel excavation has started but the arch support did not construct or not play a role in the casing body to provide the required support force, to reduce or eliminate the pipeline near ground subsidence and deformation caused by tunneling, tunneling to ensure safety. Mature engineering methods are: aqueous drilling method, pneumatic hammer drilling method and hosting DTH drilling method (for the heart with pipe DTH) and so on. As shown in Fig 3, to solve pipe roof power in large-size pebble layer and other issues, from the impact of the power drill, impact configure and slag, and other aspects of the drill torque constantly update and improve the pneumatic DTH drilling method as custodian double drill large diameter wind slagging DTH drilling hosting new technology, to achieve a structure of 50m long bassoon studio in large-size sand and gravel formations.

Advanced small catheter is a kind of process during bored tunnel of tunneling excavation, mainly for handling formation fracture zone, ultra-shallow construction support, arch safety. Small catheter tip tapering to be easy inserted and hit and prevent slurry to kick ahead. The middle of a small catheter should be diamonded grout vent hole with φ6 ~ 8mm, which was plum-shaped layout[9]. Currently advanced small pipes are mainly water gas pipes with outside diameter φ32mm, wall thickness 3.25mm, tube length 2 ~ 4.0m, different strata using ultra-fine grout or cement-silicate double slurry, strictly control the pressure of grouting process, grouting amount and gelling time and other parameters, all these measures achieved good results. according to the different strata ,when setting a small catheter ,we can choose to set it in front of shotcrete or after shotcrete , Methods for setting up small catheter have fight the rig method, blowpipe law, hammering method and wind pipe jacking method. Advanced small pipes have advantages such as obvious initial support effect, good construction and high security; it can greatly improve the safety of Shallow mining method[10].

**Establishing real-time monitoring system for construction information**

Monitoring of the construction process has not only the construction monitoring but also the introduced the third-party monitoring. Construction Monitoring is mainly construction units monitor all the construction process monitoring project. Third-party monitoring is a third-party monitories part of the construction monitoring project, the frequency of this kind monitoring is generally lower than the construction monitoring. In recent years, management at all levels attached great importance to the monitoring and management during construction process and the control of the work surface, put a lot of manpower, material resources, in the establishment of network platform system. It has played a good role in the construction of the security risk management process. For example, the establishment and operation of Beijing city track traffic engineering construction security monitoring system can effectively implement the risk management and control, reduce the frequency and the probability of risk source induced accidents[11].

In addition, Building information modeling (BIM) technology is introduced into the construction of subway engineering, exploring the implementation mechanism and mode of action of technology

of building information modeling in the subway construction management. Turning the traditional 2D static design drawings into the text for computer manipulation of virtual procedures, through the system platform can effectively integrate information of the project construction which realize the three-dimensional size of real (3D) method of construction simulation and construction progress of image interactive display organic combination ( 4D), and contribute to correct all kinds of display the complex construction information and guidance for construction security through environmental risk source give full play to the role of information model[12].

**Special risk source engineering process technology**

Subway line in city, which is inevitable that among housing, building and foundation of buildings and roads, pipelines, subway, railway and other structures near, side wear or wear, namely the proximity between the building (structure). In order to ensure the construction safety of Metro and the adjacent buildings safety, generally taken in isolation or protection way for scientific disposition. Approaching construction of buildings should be detailed investigation of engineering conditions, geological conditions, both the current situation and structure safety requirements, and implementation plan protection measures for analysis and prediction, on the basis of the investigation; the construction process by monitoring feedback to guide construction and ensure the safety of existing structures.

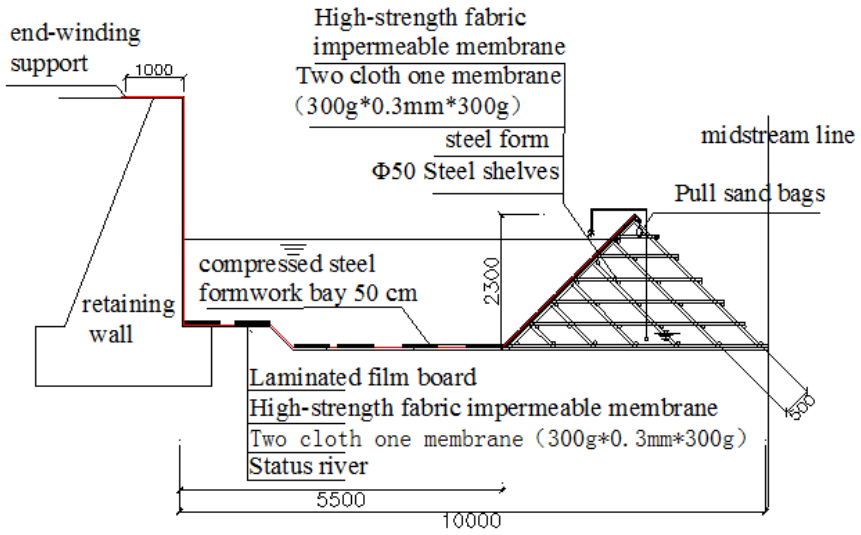


Fig.4 Pile cofferdam

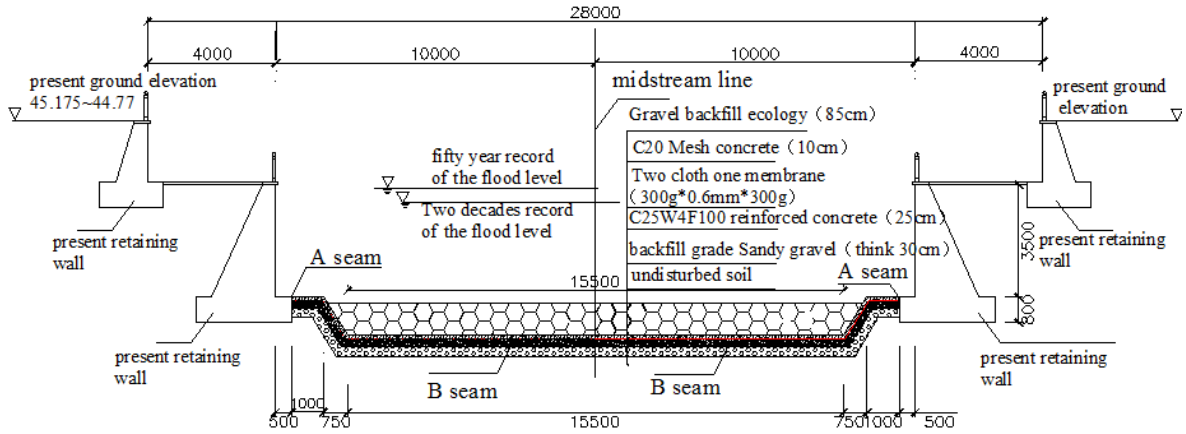


Fig.5 Two cloth of a film with reinforced concrete rigid flexible and economic structure

In recent years, in Hangzhou, Tianjin, Beijing and many, the construction of subway line under construction in rivers and lakes in the accident, causing huge losses, therefore, formation reinforcement of the tunnel pass below the rivers and the reinforcement technology is concerning. At present, from the construction management and technical measures have some new progress, such as

pre grouting and freezing of the soil reinforcement, can significantly improve the safety of excavation construction of Shield Crossing Rivers, As shown in Fig 4, the use of new technology of river diversion pile cofferdam construction is simple, detachable, material recycling, short time limit and no pollution to the river; As shown in Fig 5, new technology channel seepage "two Cloth one Membrane" is better than the reinforced concrete rigid flexible and economic structure seepage, with higher properties; stronger resistance to deformation, little affect the river ecological.

**Special equipment in Metro Construction**

Subway construction mostly is underground construction. The project safety, personnel safety and environmental protection have become the focus of the industry gradually. To this end, around quickly closed, low pollution, the respect such as mechanical operation appeared a lot of new type of special equipment.

As shown in Fig 6, The formwork jumbo for standard tunnel should be combined with the characteristics of linear engineering design to power driven walking mechanism to drive the trolley running tunnel concrete molding, the use of cylinder and screw jack adjustment in place and the template die machine; formwork jumbo in shallow tunnel large amount of use, has the advantages of safety, convenience, high work efficiency[13]. Tunnel primary support structure in the construction process according to the mixing ratio of cement, sand, gravel, accelerating agent, according to the proportion of weighing mixing can be used only for the spraying operation. Through the design of metering, automatic lifting, stirring devices to achieve the shotcrete material automatic metering, mixing, As shown in Fig 7, namely the development of automatic metering mixing device for mixing concrete, high efficiency, low dust, to ensure that the excavation work quickly closed, improve the construction risk controllability.

Fig.6 Formwork jumbo

Fig.7 Automatic metering and mixing equipment

In addition, with the improvement of mechanization operation level, many small jobs independent research and development of new machinery and equipment appeared in the cave. Excavation operations tunneling machine to improve the high-risk mechanized tunneling earthmoving operations, as shown in Fig 8, efficiency and operational safety improved significantly; As shown in Fig 9, construction materials hole transport vehicles with electric vehicles relative to gasoline or diesel fuel, greatly reducing air pollution; multi-hole guide the beginning of the formation of branched structures need to be rid of jobs, high-power hydraulic shears, avoiding artificial rid of security risks, but also significantly improve the effectiveness.

Fig.8 Tunneling machine

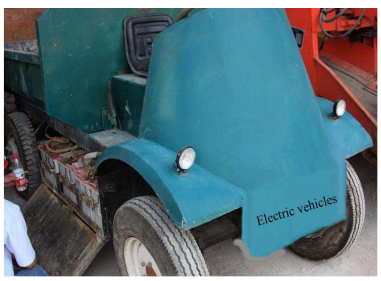


Fig.9 Electric vehicles

## Conclusion

With the development of urbanization, urban land space getting smaller and smaller, environmental conditions getting more complex, the construction of rail transit is growing more difficult, more and more high risk, and construction method, technology, process, equipment, etc are required innovating to adapt to the needs of social development.

## References

[1] Changjun He, Zhongyong Jiang , and Changyong Liu. Development of Shallow Tunnel Construction Method[J]. Municipal Engineering Technology, 2009,27(3):273-279.(In Chinese)
[2] Mengshu Wang. Outline of Tunnel Construction by means of Method of Undercutting with Shallow Overburden[J]. Tunnel Construction, 2006,26(5):1-4.(In Chinese)
[3] Meiqun Huang. Technology of Top-down Bored Excavation with Cast-in-situ Arch for MetroStation Construction[J]. Urban Rapid Rail Transit, 2009,22(6):66-71.(In Chinese)
[4] Guohua Cui. Current Study Status and Developing Prospect of the Tunnel Boring Machine[J]. Mining & Processing Equipment, 2006,34(6):24-27.(In Chinese)
[5] Wenfeng Wang, Dezhi Liu, and Junning Yang. Technique of EPBM through Existing Railway. Essay Collection of fifth China International Seminar on Tunnel Engineering[C]. Underground Traffic Engineering and Engineering Safety, 2011(11):507-514.(In Chinese)
[6] Jianhua Zhong. Straddle Type Monorail in Chongqing[J]. Urban Rapid Rail Transit, 2004,17(5):17-22.(In Chinese)
[7] Lin Li. The Guideway Beam Design for Chongqing Monorail System[J]. Urban Mass Transit,2003(6):88-93.(In Chinese)
[8] Zerong Li. The Mechanism of Small Conduit Injection Process and it's Application in Tunneling[J]. Technology and Innovation Management, 2009,30(3):399-401.(In Chinese)
[9] Guoqiang Wang. Research on Application of Advanced Small Ducts Grouting Technology in Shallow Excavation Loess Metro Tunneling. Essay Collection of the Third National Underground and Underwater Engineering and Technical Exchanges. Construction Technology, 2011,40: 253-257.(In Chinese)
[10] Chuanguo Cheng. Application of Advanced Small Ducts in Shield Tunnel Going through Huanghe out of the Hole in South-to-North Water Diversion Project. Essay Collection of the fifteenth China Civil Engineering Society and the Seventeenth Tunnel and Underground Works Branch[C].Construction Technology, 2012,49:563-568.(In Chinese)
[11] Furong Luo. Study on Safety Risk Control System and Monitoring System in Construction of Beijing Metro[D]. Beijing ,Beijing Jiaotong University, 2011.(In Chinese)
[12] Zhaoqiu Liu, Yungui Li. The Development of BIM and Its Application in Design of Project[J]. Building Science, 2009,25(1):96-108.(In Chinese)
[13] Xuyang Liu. Discussion on the Design of Tunnel Lining Trolley Template[J]. China Construction Metal Structure, 2007,(2):42-46(In Chinese)

*Applied Mechanics and Materials Vols. 580-583 (2014) pp 1072-1075*
*© (2014) Trans Tech Publications, Switzerland*
*doi:10.4028/www.scientific.net/AMM.580-583.1072*

# Numbering Analysis of Ground Settlement by Shield Method Based on the Model of Corrected 'Equivalent Circle Zone'

Zhou Zelin[1,a], Chen Shougen[1]

[1] The College of Civil Engineering, Southwest Jiaotong University, Chengdu, 610031, China

[a]zhouzelin2016b@163.com

**Keywords:** Shield tunnel; Equivalent circle zone; Ground settlement; Numbering analysis; Back analysis

**Abstract.** Through the analysis of 'gap parameter' and ground movement pattern in shield tunnel, this paper researched and corrected the model of 'equivalent circle zone' proposed by predecessors. The 'equivalent circle zone', which is a comprehensive reflection of shield gap, grouting filling and stratum perturbation, is considered to be unequal thickness in this paper. With the measured data of practical shield tunneling, the unknown parameters of corrected 'equivalent circle model' can be obtained by back analysis through numbering analysis. The back analysis of Shen Zhen line-5 is carried out to validate the rationality of the method proposed in this paper. Research shows that: the corrected model can reflect the feature and values of ground settlement more factually than the previous model and can offer a reference to predict ground deformation during shield tunneling.

## Introduction

It is unavailable to disturb the stratum in shield tunneling, so predicting and controlling the ground settlement effectively are always a research hotspot in tunnel community. The factors, such as soil conditions, construction technology and workmanship parameters are hard to be analyzed quantitatively. So, how to reflect the influence of those factors on the ground settlement is an important problem to be resolved.

Researches on the ground settlement of shield tunneling are as follows: Perk (1969) [1] imposed the famous perk formula to predict the ground settlement, this theory assumes that the volume of curve of ground settlement is equal to the volume of ground loss; Rowe& Kack (1983) [2] proposed the concept of 'gap parameter ' to reflect the ground loss caused by overbreak of shield cutter, deformation of excavation face and the gaps between the shield shell and soil layer; Zhu Zhonglong (2001) [3] performed a formula to calculate the settlement on the vertical section based on the theory of stochastic medium; Wang Huihui (2001) [4] predict the trend of ground movement using the method of neural network. ; Wei Gang (2006) derived a ground deformation formula based on the Mindlin solution of elastic mechanics. These researches based on analytical method, stochastic medium and neural network have strict theoretical basis, but cannot consider the influence of workmanship and the nonlinear character of soil.

Compared with theoretical studies, numerical modeling provides a convenient, economical approach to study the settlement of ground. Based on the model of 'equivalent circle zone' proposed by Zhang Yun (2002) [5], this paper carried out a numbering model to analysis the ground settlement. The corrected 'equivalent circle zone' are proposed in numbering analysis. Based on actual project, ground settlement predicted by this method is been compared with actual measured data.

### ‘Gap parameter’ and movement model of ground

Shield tunneling is a complex mechanic process. Overbreak of shield cutter, deformation of excavation face, gaps between the shield machine and soil, and workmanship are most important factors to induce the ground settlement, Rowe & Kack (1983) proposed ‘gap parameter’ to equivalent the impact of these factors. The ‘gap parameter’ is:

$$g = G_p + U_{3D} + w \tag{1}$$

Where, $g$ means the ‘gap parameter’; $G_p$ is the physical gap; $U_{3D}$ is the elastoplastic deformation of excavation face; $w$ means the level of workmanship.

Shield gap will induce ground movement. For the flowing reasons: (*i*) shield machine in construction usually keep the posture of pitching up to avoid bowing down; (*ii*) the gravity of shield machine and segments applied on the soil layer below the tunnel. So the movement model of soil around segment is unevenly factually. Lee (1992) proposed unevenly movement model of ground. Lee’ theory is consistent with the case in practical tunneling and has been applied extensively.

### Numbering method

**Corrected equivalent circle zone.** The shield gap, ground movement and distribution pattern of synchronous grouting are hard to be analyzed quantified in numbering simulation. To address this issue, Zhang Yun (2002) presented the concept of ‘equivalent circle zone’, as shown in Fig. 1. The factors above are generalized to be an orbicular ‘equivalent circle zone’ which distribute evenly around the segment. The ‘equivalent circle zone’ can be reflected by three parameters: Young’ modulus $E$, Poisson's ratio $u$ and thickness $\Delta$. With the measured data, these parameters above can be obtained by back analysis.

Through the analysis of ‘Gap parameter’ and movement model of ground above, the distribution forms of shield gap and movement of ground, which are closely related to the shape and distribution pattern of ‘equivalent circle zone’, are unevenly back around the segment. So, the distribution pattern of ‘equivalent circle zone’ is uniform actually too, and its’ shape is not a ring strictly. Based on these cognitions, this paper present a model of corrected ‘equivalent circle zone’, as shown in Fig. 2. In this model, the displacement of soil upper the tunnel is largest under gravity, while the soil below the tunnel is smallest with little resilience deformation of ground.

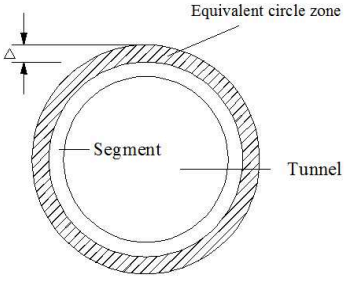


Fig. 1 Model of “Equivalent circle zone”

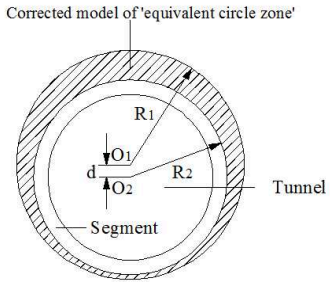


Fig. 2 Corrected model of “Equivalent circle zone”

In Fig. 2, $R_2$ is the outside diameter of segment. To reflect the scope and changes of thickness of corrected ‘equivalent circle zone’, two parameters are introduced as following: $R_1$ and $d$. Among these two parameters, $R_1$ is the radius of equivalent circle zone, which can reflect the scope of corrected ‘equivalent circle zone’; d is the distance from the center of equivalent circle zone to the center of shield tunnel, which can reflect the changes of thickness.

**The method of back-analysis.** In numbering analysis using the model proposed in this paper, there are four parameters to be assured: $R_1$, $d$, $u$ and $E$. To determine the values of above four parameters, the optimized back analysis are used in this paper according to the measured data, and the objective function for these unknown parameters is shown as follows:

$$J(x)=\sum_{j=1}^{D}\sum_{i=1}^{N}[u_{ij}(x_i)+u(x_i)'_{ij}]^2 \tag{2}$$

where, $u_{ij}(x_{ij})$ and $u_{ij}(x_{ij})'$ mean the settlement of monitoring point $i$ after the excavation stage $j$, respectively; $x_k$ denote parameter vector $x_k=[R_1,d,E]$. The value range of $x_k$ is shown as follows:

$$R_2 \le R_1 \le R_2+0.2;\quad 0\le d\le 2(R_2-R_1);\quad E_{\text{soil}}\le E\le E_{cement};\quad 0\le u\le 0.5 \tag{3}$$

where, $E_{soil}$ and $E_{cement}$ denote the Young' modulus of soil and cement respectively. In back analysis, the objective function *J(x)* is a complex functions with high nonlinearity and the method of 'corrected Powell' is employed to back-analyze the unknown parameter vector $x_k$.

## Numbering analysis of practical shield tunnel

**General situation of practical tunnel.** Numbering analysis is conducted based on project of Shen Zhen line-5. The metro tunnel between Qian Haiwan station and Lin Hai station was constructed by shield method. Designed inner-diameter of segment is 5.8m, thickness of segment is 0.36m, strength of segment is C50, value of 'gap parameter' is 8.5cm. The stratums from top to bottom are artificial fill-back, clay, silt clay and sand, hard clay and sand. The mechanical parameters of stratums and segments are shown in Table 1.

Table 1 The mechanical parameters of soil and segment material

| Materials | $E_0(M\text{pa})$ | Poisson's ratio | Unit weight (KN/m$^3$) | Cohesion (kPa) | Friction (°) |
|---|---|---|---|---|---|
| Artificial fill-back | 3.1 | 0.3 | 18.0 | 16.0 | 11.0 |
| Clay | 8.5 | 0.32 | 19.5 | 31.0 | 15.0 |
| Silt clay and sand | 11.6 | 0.32 | 19.5 | 32.1 | 16.5 |
| Hard clay and sand | 20.0 | 0.3 | 21.0 | 33.4 | 20.0 |
| Segment | 30000 | 0.2 | - | - | - |

**Numbering modeling.** A three-dimension numbering model is carried out by Flac3D to analyze the ground settlement in tunneling. The results obtained this method will be compared with the results obtained by Zhang Yun' model and Perk formula. Numbering model and grid mesh is shown in Fig. 3. The sizes of model are as follows: horizontal width 25m, high 32m and with a longitudinal length of 30m. The displacements are constrained in vertical direction at the bottom, while the zero displacements are imposed at the later boundary. The soil behavior is described to be an elastic-plastic model based on Mohr-Coulomb criterion.

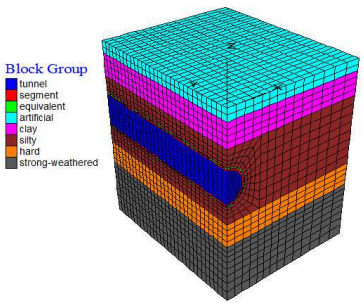


Fig. 3 Numbering model and grid mesh

**Result of analysis.** According to the back analysis, the parameters' value of corrected 'equivalent circle zone' are as follows: $R_1$=3.112m, d=4.6cm, u=0.21, E=1.58Mpa. To compare the results, this paper also carry out the back analysis using the method of 'equivalent circle zone', and the values of parameters are as follows: E=1.46MPa, u=0.21，and $\Delta$=12.4cm .

The results of ground settlement on tunnel' cross-section is shown in Fig. 4. As can be seen, the settlement curves obtained through the corrected 'equivalent circle zone' proposed is the most consistent with the measured data compared with other methods. The result of "equivalent circle zone" is larger than measured data, which means that the distribution pattern of equivalent circle of zone has an important influence to ground settlement. The result of Perk formula is the largest, that's because Perk formula hasn't consider the elimination of synchronous grouting to the shield gap in calculation; The changes of ground settlement curves on tunnel' longitudinal-section in Fig. 5. Because the deformation of the excavation face' soil caused by the supporting force applied on the working face, the ground located at about two-diameter in front of the shield machine occurred uplift deformation, the maximum value of uplift is about 0.25cm. Measured data of ground settlement is very consistent with the calculation data, which verified the rationality of the method proposed in this paper.

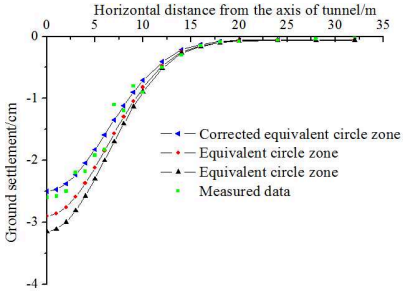


Fig. 4 Ground settlement curves on cross-section

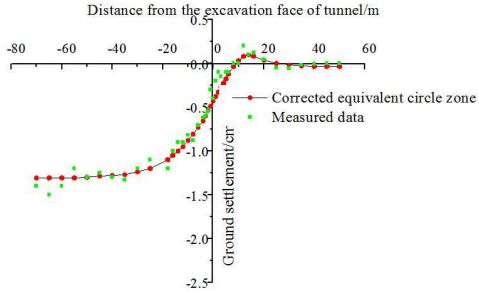


Fig. 5 Ground settlement curves on longitudinal-section

## Conclusion

In this paper, a model of corrected 'equivalent circle zone' is proposed to predict the ground settlement. Some conclusions are drawn as flows:(1) The distribution forms of shield gap and movement of ground are closely related to the shape and distribution pattern of 'equivalent circle zone', and its' distribution pattern back around the segment is unevenly;(2) In numbering analysis, the distribution pattern of equivalent circle of zone has an important influence to ground settlement. The results of ground settlement obtained by using the method proposed in this paper are very consistent with measured data, which verified the rationality of the method proposed in this paper.

## Reference

[1] Perk R B. Deep excavations and tunneling in soft ground [C] State of the Art Report. Proceedings of 7th International Conference on Soil Mechanics and Foundation Engineering . Mexico City: [s.n.], 1969: 225-290.

[2] Rowe R K, Lo K Y, Kack G J. A method of estimating surface settlement above tunnels constructed in soft ground [J]. Canadian Geotechnical Journal, 1983, 20(8):11-22.

[3] Suihui Wang, Guorong Pan. Applying Theory of Artificial Neural Network to Deformation Prediction of Ground Deformation During Tunnel Excavation[J]. Journal of Tongji University, 2001，29(10):1147-1151. (In Chinese).

[4] Zhonglong, Zhu, Qinghe Zhang, Hongwei Yi. Stochastic theory for predicting longitudinal settlement in soft-soil tunnel[J]. Rock and Soil Mechanics, 2001， 22(01): 56-59. (In Chinese)

[5] Yun Zhang, Zongze Ying, Yongfu Xu. Analysis on Three-Dimensional Ground Surface Deformations Due to Shield Tunnel[J]. Chinese Journal of Rock Mechanics and Engineering, 2002, 21(3): 288-392. (In Chinese)

*Applied Mechanics and Materials Vols. 580-583 (2014) pp 1076-1080*
*© (2014) Trans Tech Publications, Switzerland*
*doi:10.4028/www.scientific.net/AMM.580-583.1076*

# Numerical Analysis on Interaction Induced by Crosswise Tunneling

Penglu Gan[1,a], Xiaowu Tang[2,b], Wenming Shen[3,c] and Hengyu Wang[4,d]

[1]Research Center of Coastal and Urban Geotechnical Engineering, Zhejiang University, Hangzhou 310058, China

[2]Research Center of Coastal and Urban Geotechnical Engineering, Zhejiang University, Hangzhou 310058, China

[3]China Railway Eryuan Engineering Group Co. ltd, Hangzhou 310004, China

[4]Research Center of Coastal and Urban Geotechnical Engineering, Zhejiang University, Hangzhou 310058, China

[a]email: dennis19900828@gmail.com, [b]email: tangxiaowu@zju.edu.cn,

[c]email: swm240203@163.com, [d]email: why303433506@gmail.com

**Keywords:** Numerical simulation; Tunnel intersection; Vault settlement; Reinforcement measure

**Abstract.** A position conflict exists between Harbin Urban Rail Transit Line No.1 and the branch tunnel of "7381" civil air defense tunnel. Intense tunnel interaction occurs when Line No.1 is perpendicularly tunneled across the branch tunnel. The investigation of the interaction is necessary. A 3D numerical simulation is established using FLAC$^{3D}$ and the vault deformation around the tunnel intersection is analyzed. The vault settlement of Line No.1 increases by 1.4 times during crosswise tunneling, while the vault settlement of branch tunnel increases 21.0mm in addition. The affected region of the tunnel intersection is further revealed. The affected length of the vault of Line No.1 and branch tunnel is 7.5 times the diameter and 6 times the width respectively. In combination with monitoring data, the reinforcement effect is studied at last. Both the vault settlement and surface settlement are well controlled in the tunnel intersection.

## Introduction

As the development of urban cities in China, underground tunnels for various purposes appear and experience rapid expansion. Meanwhile, the phenomenon of overlapped tunnels frequently occurs[1,2]. In the recent years, the issues related to overlapped tunnels arouse the attention of many researchers as the potential danger remains uncertain and the ground deformation is complicated. For the purpose of structure protection, the influence of a new bored tunnel on an existing tunnel is widely studied in the overlapped region[3,4]. Through in-situ monitoring, Zhang et al.[5] revealed the ground movement induced by the construction of overlapped tunnels using shallow buried-tunnelling method. Huang[6] obtained the values of surface deformation induced by excavation and water drawdown respectively on the basis of numerical results of overlapped tunnels. The complicated procedures of staged excavation were simulated in FLAC$^{3D}$. Liu et al. [7] analyzed the vault settlement of the existing tunnel under different excavation sequences. However, a new bored tunnel is either excavated beyond an existing tunnel, or excavated beneath an existing tunnel in these researches about overlapped tunnels. The overlapped situation that a new bored tunnel is excavated across an existing tunnel at same buried depth is rarely encountered. For the related study is insufficient, many risks exist during the crossing construction. This paper takes the tunnel section from the Ammeter Factory Station to Coast Park Station in Harbin Urban Rail Transit Line No.1 as background. Through 3D numerical simulation, the influence of the tunnel intersection on vault settlement is analyzed, and the affected value and region of vault settlement are both discovered. Furthermore, the feasibility of corresponding supporting measures is certified. The results of this paper have guiding significance for the design of other similar tunnel construction.

## Engineering Situation

The Ammeter Factory Station to Coast Park Station in Harbin Urban Rail Transit Line No.1 lay beneath at the west side of Xizhimen Street. Line No.1 consists of two single circular tunnels with an average diameter of 6.5m. The buried depth is about 14.0m~17.0m. The start-end mileage of tunnel section is CK6+129.4~CK7+116.5. Shallow buried-tunnelling method is adopted in the construction. And the typical cross section of the single circular tunnel is excavated by benching tunneling method. Before the excavation of metro tunnel, a civil air defense tunnel ("7381" Tunnel) which has been constructed in earlier years already exists underground. The paper abbreviates the civil air defense tunnel to *CAD* tunnel in the following sections. The No.1, No.2 and No.3 branch tunnel of the *CAD* tunnel has a geographical location conflict with the metro line abovementioned. The branch tunnel and Line No.1 perpendicularly intersects. The plan of overlapped intersection is presented in Fig.1. Fig.2 indicates the profile of tunnel intersection.

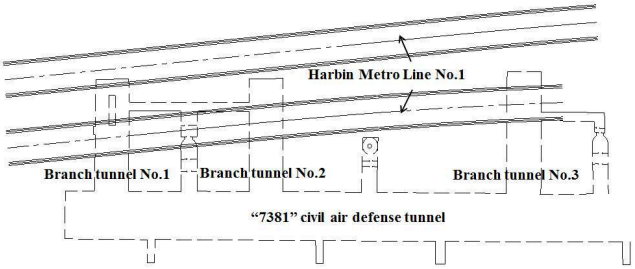


**Fig.1** Plan sketch of tunnel intersection

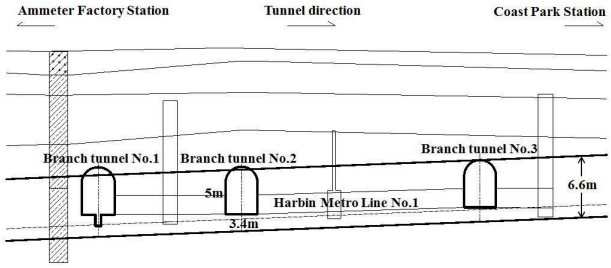


**Fig.2** Profile diagram of tunnel intersection

## Numerical Simulation

**Engineering Simplification.** The proposed up line of metro tunnel intersects almost perpendicularly with the branch tunnel No.1, branch tunnel No.2 and branch tunnel No.3 of the civil air defense tunnel in spatial terms. During the construction crossing each branch tunnel, the soil is greatly disturbed and the stress of soil is complicated around tunnel intersection. Accidents may occur and the existed *CAD* tunnel will be damaged if not taking the right supporting way. Considering the engineering conditions that the up line tunnel excavated across three branch tunnels are similar, the research can be simplified as a problem that the up line is excavated across one branch tunnel. The following analysis is conducted on the basis of this typical condition and vault settlement induced by excavation is analyzed using FLAC$^{3D}$.

**FLAC$^{3D}$ Model.** The numerical model of the tunnel intersection is shown in Fig.3. The whole model consists of 18036 elements and 18748 grid points. As Fig.3 shown, the length of the model in x, y, z direction is 80m, 40m and 40m respectively. The metro tunnel is a single circular tunnel with the diameter of 6.6m and the height and width of the branch tunnel is 5m and 3.4m respectively. The Mohr-Coulomb elasto-plastic constitutive model is employed for the soil in this analysis. Pre-grouting and concrete lining of the tunnels are simply modeled by shell element. According to the geotechnical investigation report between Ammeter Factory Station and Coast Park Station, the mechanic parameters of soil and shell elements are given in Table 1 and Table 2.

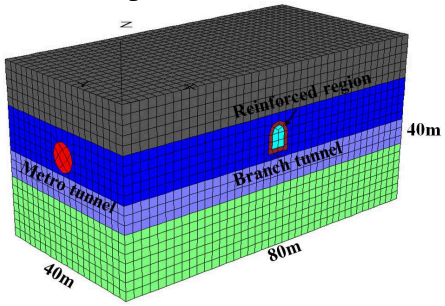


(a) Global mesh model

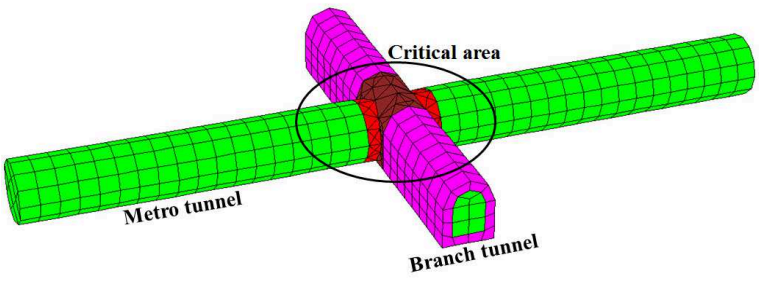


(b) Internal tunnel intersection

**Fig.3** Finite difference model

**Table 1** Mechanic parameters of soil

| Soil Type | $\gamma$ (kN/m$^3$) | $E$ (MPa) | $C$ (kPa) | $\varphi$ ($^o$) |
|---|---|---|---|---|
| Silty clay | 18.4 | 33.6 | 63 | 10.7 |
| Silty clay | 18.9 | 36.0 | 66 | 15.0 |
| Medium sand | 18.9 | 45.6 | 6 | 28.7 |
| Reinforced soil | 20.0 | 72.0 | 300 | 50.0 |

**Table 2** Parameters of shell elements

| Shell Type | $E$ (MPa) | $d$ (m) | $v$ |
|---|---|---|---|
| Branch tunnel | 120 | 0.3 | 0.25 |
| Reinforced branch tunnel | 200 | 0.6 | 0.25 |
| Metro tunnel | 500 | 0.3 | 0.25 |
| Reinforced metro tunnel | 600 | 0.6 | 0.25 |

**Sequences of simulation.** Step1: Obtain initial stress field under gravity; Step2: Excavate and support the branch tunnel; Step3: Excavate and support the metro tunnel when tunnel intersection is unreinforced; Step4: Excavate and support the metro tunnel when tunnel intersection is reinforced.

## Result Analysis

**Vault settlement without reinforced measures.** Vault settlement around the intersection of the metro tunnel and branch tunnel is the research emphasis in this paper. First, we assume that no reinforced measures are adopted in the intersection. The metro tunnel is excavated according to benching tunneling method. After calculation of FLAC$^{3D}$, the vault settlement curves of metro tunnel and branch tunnel are shown in Fig.4 and Fig.5 respectively. As Fig.4 shown, the settlement curve performs like V-shape which consists of two parabolas. The maximum vault settlement is 21.0mm which occurs at the crossing point of metro tunnel and branch tunnel (X=40m). Vault settlement gradually decreases to 15.1mm from the center to the edge in X direction. The maximum differential settlement is 0.45mm/m. The reason for increasing settlement is great stress concentration around tunnel intersection. In Fig.4, the vault settlement curve induced by individual excavation of metro tunnel is also presented so that the tunnel interaction can be clearly revealed. The vault settlement is basically uniform and there won't be any great differential settlement. However, due to the existence of branch tunnel, vault settlement around the tunnel intersection is obviously larger. The affected region reaches from X=15m to X=65m. This length equals to 7.5 times the diameter of metro tunnel.

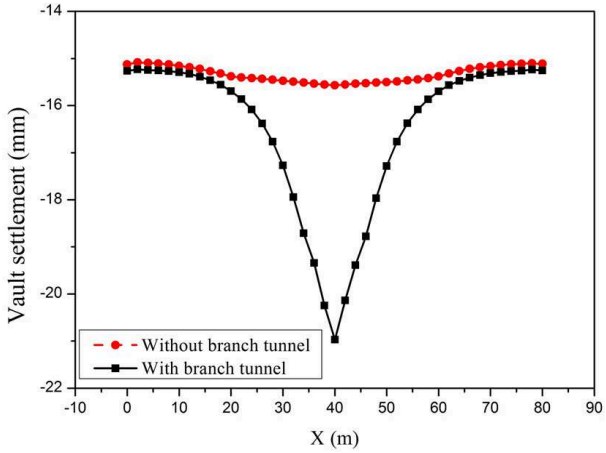


**Fig.4** Vault settlement of metro tunnel

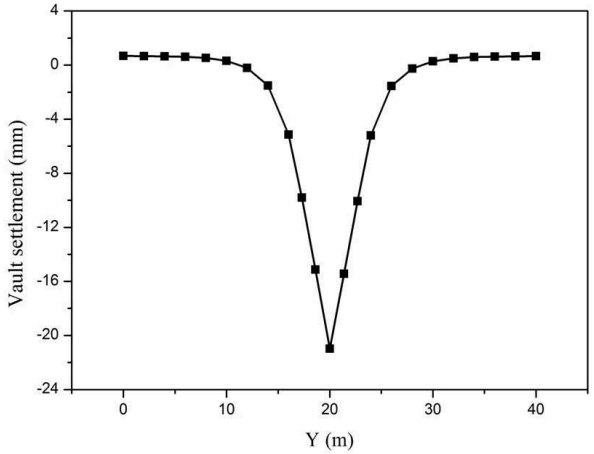


**Fig.5** Vault settlement of branch tunnel

As Fig.5 shown, a similar V-shape settlement curve of branch tunnel is induced by the tunneling of metro tunnel. The position where maximum vault settlement occurs is the same as metro tunnel. However, the vault settlement almost drops to 0 at the edge of branch tunnel. The maximum different settlement is 2.92mm/m which is much larger than metro tunnel. Thus the branch tunnel is more dangerous than metro tunnel during the crossed tunneling. The affected region of branch tunnel during tunneling reaches from Y=10m to Y=30m. This length equals to 6 times of the width of branch tunnel. Therefore, the affected region in the tunnel intersection is very big in both metro tunnel and branch tunnel. For reducing vault settlement around the tunnel intersection, the surrounding soil needed to be mainly reinforced.

**Reinforced measures and analysis.** As above mentioned, the tunneling will lead great vault settlement around the tunnel intersection and cracks may occur. Therefore, before the excavation of up line, pipe umbrella grouting is employed behind the lining of branch tunnel around the intersection. After grouting, I-steel (I45b) frame is installed inside the branch tunnel at the up line location to reinforce the intersection. I22a steel is used in the junctions of steel frame at the vault, sidewall and inverted arch part. The distance between two steel frames in the longitudinal direction is 0.5m. In addition, for the uncompacted places between steel frame and lining of branch tunnel, steel plates are employed to pad and weld the gaps. What's more, double-layer welding steel net ($\Phi$6.5@150×150) and C20 shotcrete are employed at the gap of the vault and inverted arch of steel frame. Detailed reinforced measures of branch tunnel No.1 is shown in Fig.6.

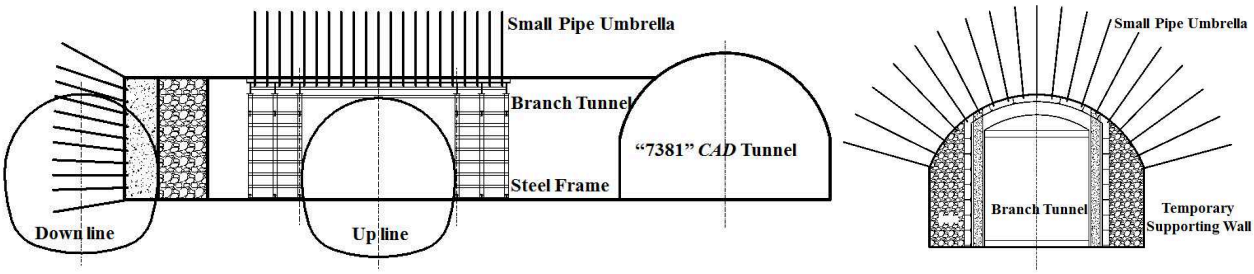


(a) Longitudinal view (b) Transverse view

**Fig.6** Reinforced scheme diagram

According to the practical supporting condition, soil parameters of the reinforced region and shell element are updated to the value in Table 2 at a 12m range of tunnel intersection in both transverse and longitudinal direction (X=34m~X=46m, Y=14m~Y=26m). For the lack of relevant date of grouting and steel reinforcement, the parameters in Table 2 are quoted from the paper of Queiroz[8]. After the calculation under reinforced measures, vault settlement curves of metro tunnel and branch tunnel are drawn in Fig.7 and Fig.8 respectively. The numericla results are similar to the monitoring data. As Fig.7 shown, the previous maximum vault settlement drops to 13.2mm after reinforcement. And the vault settlement in the reinforcement region is even smaller than other region. In Fig.8, the vault settlement of branch tunnel also decreases after reinforcement. All the final settlement stabilizes in a safe range. Thus, the reinforced measures are effective for the safety of the tunnel intersection.

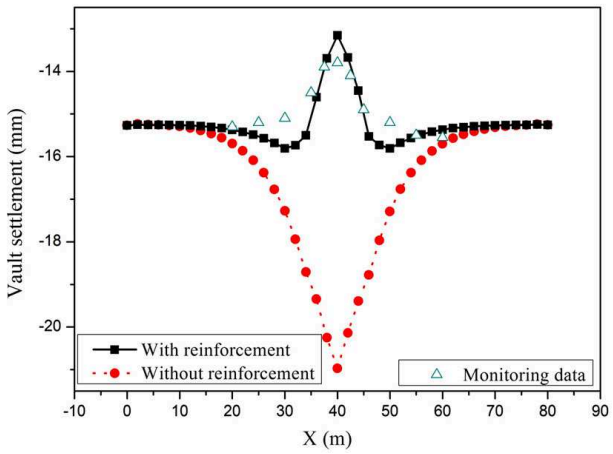


**Fig.7** Reinforcement effect on vault settlement of metro tunnel

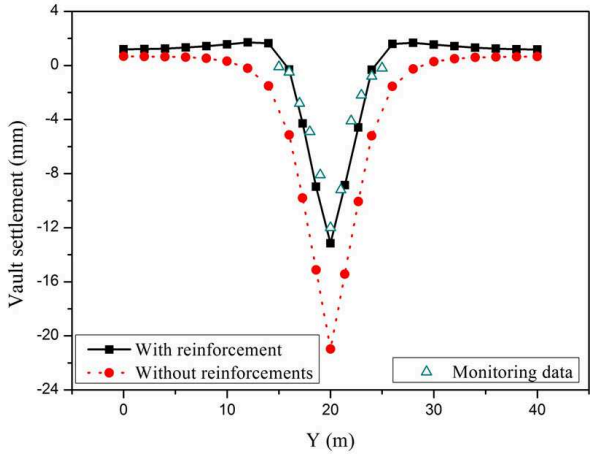


**Fig.8** Reinforcement effect on vault settlement of branch tunnel

Besides, the surface settlement is investigated. The surface settlement curve right above the axis of metro tunnel is drawn in Fig.9. Before reinforcement, the settlement curve fits the gauss distribution. After reinforcement, the maximum surface settlement changes from 6.1mm to 3.1mm. The decline degree in settlement reached to 50%. The surface settlement in the reinforcement region obviously reduces and the entire settlement becomes more even. Fig.10 shows the surface sttlement right above

the axis of branch tunnel. The entire surface settlement has also been reduced by reinforcement. From the view of surface settlement, the reinforced measures are still effective and needed.

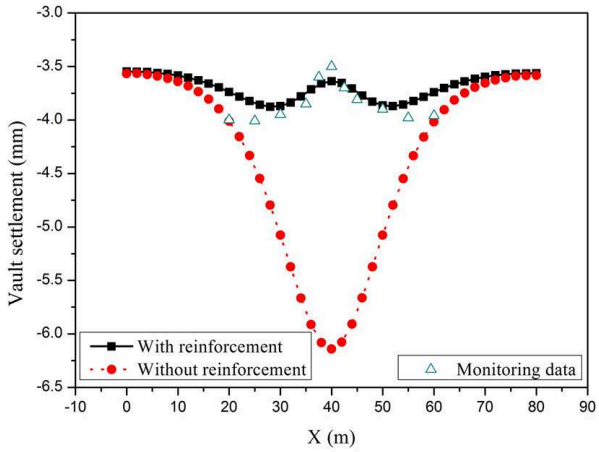


**Fig.9** Reinforcement effect on surface settlement right above axis of metro tunnel

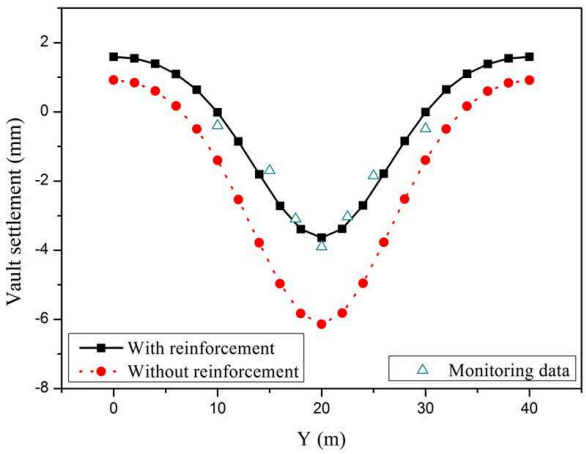


**Fig.10** Reinforcement effect on surface settlement right above axis of branch tunnel

## Conclusions

A numerical simulation of crosswise tunneling is conducted by FLAC$^{3D}$ in this paper. The following conclusions can be drawn:

(1) Without any reinforced measures, the vault settlement in the tunnel intersection will increase significantly during the metro tunneling across the branch tunnel.

(2) Due to existence of branch tunnel, a large region of vault will be affected in the tunnel intersection. The length of affected region of metro tunnel is 7.5 times diameter and the length of affected region of branch tunnel is 6 times width.

(3) Reinforced measures including grouting, steel frame and shotcrete decrease the vault settlement and ground settlement effectively in the tunnel intersection. The reinforcing method employed in the construction is the reference to other similar engineering.

From the conclusions mentioned above, an existing tunnel has significant influence on vault settlement during a new tunnel excavated across. Detailed research need to be conducted in the future.

## References

[1] F.G. Li: Tunnel Construction Vol. 30 (2010), p. 554

[2] J. Zhao and Y.H. Li: Tunnel Construction Vol. 30 (2010), p. 138

[3] Z.X. Cao: Modern Tunnelling Technology Vol. 42 (2005), p. 57

[4] X.R. Tan, S.G. Chen and J.X. Wang: Tunnel Construction Vol. 29 (2009), p. 415

[5] C.P. Zhang, D.L. Zhang and M.S. Wang: Chinese Journal of Rock Mechanics and Engineering Vol. 27 (2008), p. 3244

[6] J. Huang and D.L. Zhang: Chinese Journal of Rock Mechanics and Engineering Vol. 24 (2005) p. 2176

[7] H.L. Liu, P. Li and J.Y. Liu: Tunnelling and Underground Space Technology Vol. 26 (2011) p. 276

[8] P.I.B. Queiroz, R.N. Roure and A. Negro, In: Proceedings, International Symposium on Geotechnical Aspects of Underground Construction in Soft Ground, London, 15–17 June. Taylor and Francis/Balkema, Leiden, The Netherlands. pp. 211–217 (2006)

*Applied Mechanics and Materials Vols. 580-583 (2014) pp 1081-1087*
*© (2014) Trans Tech Publications, Switzerland*
*doi:10.4028/www.scientific.net/AMM.580-583.1081*

# Research on Key Technology of Shield Machine Main Drive Sealing

Runjun Li[1,2,a], Renliang Shan[1,b], yixiong Gui[2,c]

Jinzhong Yang[2,d], Jian Liu[1,e]

[1]School of Mechanics & civil engineering, China University of Mining & Technology, Beijing, 100083, China

[2]Beijing urban construction design & development group co., Limited, Beijing, 100088, China

[a]1161036851@qq.com, [b]srl@cumtb.com.cn, [c]364844365@qq.com, [d]986087848@qq.com,

[e]960875409@qq.com

**Keywords:** shield machine, main drive sealing, fracture failure, installation forms, platen method

**Abstract.** Due to poor bonding of a shield machine main drive leading to seal failure sealing fracture failure occurs, the proposed installation forms of adhesive sealing method is replaced by platen method, and seal material NBR replaced by a fluorine rubber, so that the combination of the housing seal is more reliable, avoiding the fracture caused by discontinuity of local sealing. Construction process increases the injection of three different oils enhancing the sealing effect. Through the application of practical project, no failure appears after sealing transformation.

## Introduction

Shield machine main drive system called Shield "heart", the main drive sealing is the "heart of the diaphragm", and so the main drive sealing crucial role. On the one hand, Complete and reliable main drive seal through the lubrication grease injection and maintain a certain pressure, provide a good working environment for the main drive bearing; on the other hand, grease with a certain pressure to force out the shield machine kokura side, can effectively prevent silt soil compartment into the main drive inside, causing parts to wear out and fail. While the shield machine main drive seal forms a seal with other mechanical devices are basically the same, but because of the shield tunneling machine in the underground construction, the sealing system cannot be replaced in the tunnel cave interior, if the seal is damaged due to the construction of the gap is too big or worn and other problems caused by the main bearing gear oil leak or silt particles into the gearbox, causing damage to the main bearings or gears, resulting in paralysis of the shield machine, very serious economic losses immeasurable impact and will shield project. Shield Construction of such incidents occurred both at home and abroad, such as: 2007 send in East Gas Pipeline crossing the river to the 360m tunnel shield construction, the shield machine cutter head main bearing oil seal oil pressure drops, the inspection shield structure cutter head pressure plate bolt main bearing seal all broken, deformed outward pressure plate, dual-sealed damaged and must be repaired in order to continue the excavation. The final choice of methods for slurry pipeline from TBM cutter heading to face pressure injection of modified mud on the heading face for closure sealing, maintenance personnel with pressure for entrance, replace the seal and the pressure plate. The direct cost of 179,000 Yuan is needed to repair it with a time of 13 days [1]. Another example: in 2010 a company in the construction of Beijing metro line in a bid to promote the use of the shield machine in the process due to seal wear, a lot of sediment into the main drive gear box, resulting in paralysis of the shield machine. Approach is to clean up the soil positions, removal of the main drive motor reducer, the seal cavity clean sediment, unable to disassemble the main drive, it cannot replace the main drive seal, before finally taking a Kokura face seal bulkhead installation and continued into the seal grease to make the completion of the tunnel shield machine construction, maintenance took a month or so. After completion of the shield tunneling machine construction receives disintegration, the main driver for almost scrapped eventually is replaced as a whole, huge economic loss.

Causes of these accidents are due to the main drive seal design, installation, and use of the material, resulting in the main drive seal due to the presence of certain defects or maintenance is not

in place. The units used a shield machine for some period after the completion of tunneling construction, repair and maintenance base for the maintenance process; we found broken main drive seal failure problem occurs. After we analyze the reasons for breaking the seal on the main drive seal a technical research to improve and achieved good effect in the subsequent construction of the shield to avoid the risk of seal failure because the main drive and cause serious accidents shield machine.

## The main drive seal design of shield machine

**The main drive sealed design of factory.** The current domestic market of shield machine brand is more, but the form of main drive seal is very much the same. Seal structure of the design shall ensure that the sealing lip has a good follow, keep the best contact Angle with the axis of rotation. Ensuring dynamic sealing effect while reducing the contact area of the seal, reducing friction and heat sealing lip wear to the maximum extent, so that it can be used for pressure conditions (such as EPB working condition)[2][3]. EPB shield machine main drive seal is generally divided into the inner periphery seal and the outer periphery seal, both are combined seal, respectively combined by lip seals and seal combination VD. Lip seals are Multi-lip seal with the effect of static, dynamic, self-sealing effect and better toughness. VD seal is a seal-ring side of the V formed by the thick lip, VD ring is applicable to the axis of rotation dynamic seal, the sealing lip has good mobility and adaptability, can compensate the larger tolerance and angular deviation[4].

The shield machine original factory design of main drive seal form is shown in figure 1, The inner periphery and the outer periphery seal sealing lip seals are combined by one Multi-lip seal (hereinafter referred to as lip seal) three VD seals. The materials used in making the VD seal of shield machine Lord drive seal is nitrile butadiene rubber ,called NBR. The surface roughness Ra of the seal is 3.2μm, the roughness Ra of the metal surface which is in contact with the lip is 1.6μm.

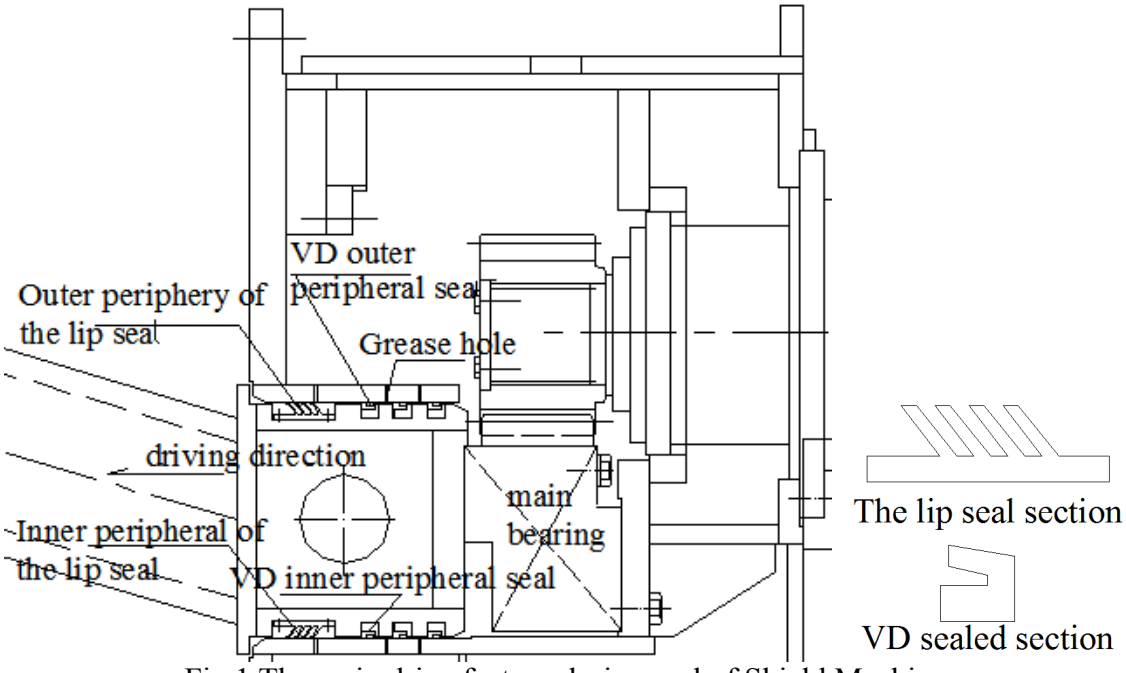


Fig.1 The main drive factory design seal of Shield Machine

**The installation of the main drive seal.**

(1)The installation form of the lip seal

The form of lip seal is circular, LORD Corporation LORD produced using 305 two-component epoxy adhesive bonding with the metal mounting surface plate bolts tightened before use, after the installation is complete, the top spot of the platen bolts fixed to prevent bolts loose. Figure 2: The lip seal installation.

Fig.2 The lip seal installation

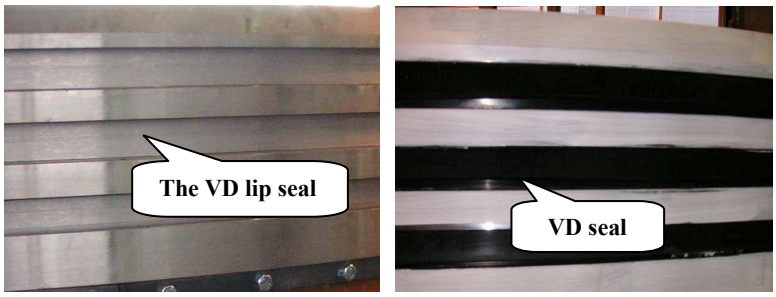


Fig.3 VD the lip seal installation

(2)The installation form of the VD seal

The form of the VD seal is band, the Joint use instant dry adhesive , then embedded it into the drive seal groove, and before embedding seal groove in metal groove, daub a two-component epoxy Lord LORD305 adhesive. Adhesive solidifying time is around 24 hours. As shown in figure 3: VD the lip seal installation.

**The working principle of main drive seal.** Using concentrated lubrication equipment inject EP0 lubricating grease in the cavity between the two sealing，Design the outer periphery of each cavity injection volume was 20ml/min, within weeks of each chamber is 16ml/min, a total consumption of about 2000ml / m when the shield tunneling was working. VD seal may remain in the cavity to produce a lubricating grease pressure when the pressure exceeds a certain range of a forward cavity grease leakage, while the former can ensure that the grease lubrication of the cavity does not flow. Lubricants grease injection device with a certain pressure to squeeze a steady stream to the main drive end face plate and spacer transfer surface soil positions to prevent silt soil compartment under the action of earth pressure inside the sealed into the main drive, which in turn has to the sealing effect.

## The problems of Shield Machine Main Drive Sealing

**The general situation of shield tunneling construction.** In the second phase of Beijing Metro Line 10, Chedaogou Station to Changchun Bridge Station tunnel section is located in Haidian District, Beijing. This tunnel section runs north-south. The length of the right line tunnel is 749.374m and the length of the left line tunnel is 742.44m. Interval line profile design average grade is 14.47 ‰. The thickness of covering soil is 10～12m. The section of shield tunnel crossing strata is mainly composed of sandy pebble with size of 20 ~ 40 mm. Maximum particle size is not less than 170 mm and particle size is greater than 20 mm pebble accounted for over 60% of the total mass.

The main technical parameters of shield machine in the process of tunneling construction include, the upside soil pressure is 40~50KPa, the knife rotating speed is 1.4 rpm, the cutter torque is about 2850kN·m (50%), the total thrust is about 20000kN, the advance rate is between 40~60mm/min.

**The problems of Shield Machine Main Drive Sealing.** After completion of the above construction, we found that the Shield Machine Main Drive Sealing appeared the following two issues when we repaired shield machine. One is the VD sealing fracture failure. Second, the lip seal and seal liner worn metal surface.

(1) The VD sealing fracture failure

The VD sealing fracture failure as shown in figure 4, the third DVD sealed fracture length of about 10 cm. The reason of fracture is the VD sealing installed in the form of adhesive. Local bonding strength is not uniform. While seals and sealing bushing sliding relative rotation, sealing bushing to seal tangential tensile force along the circumferential direction. Seal bonding strength with low position under the action of tensile force does cause gradual sealing glue. And then to form stress concentration. Eventually lead to seal fracture failure.

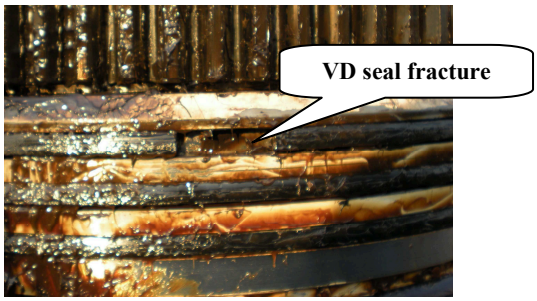


Fig.4 VD seal fracture

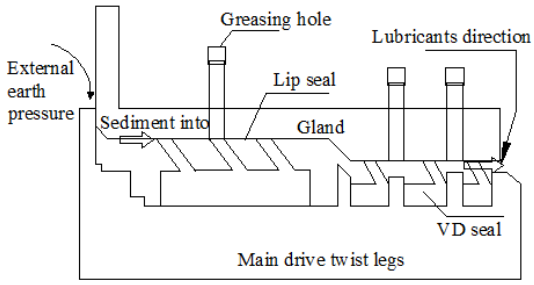


Figure.5 Diagram of sand invasion after VD seal fracture

The VD sealing fracture failure consequence is the grease inside the sealed cavity leakage to the big gear system and bearings in the box due to the loss of seal block. At the same time due to loss of pressure seal back and front-end existing earth pressure, resulting the mud invasion led to the lip seal wear and then the failure, as shown in figure 5. But also can make the lubricating oil consumption increase. By measuring, in the later stages lubricating grease for construction usage increased about 1000 ml/m compared with the previous. More serious is that mud into the large gear box and main bearing lead to wear retarding mechanism of Shield Machine Main Drive. Fortunately, due to the interval in short driving distance has not caused serious failure of shield machine downtime.

(2) Lip seal and the sealing bushing wear

Lip seal wear. After the collapse of the main driver, we check found lip seal four lip all have different degree of abnormal wear. Especially the lip seal the outside piece, due to the direct contact with the mud, the wear is most serious. In the process of shield tunneling in normal, the knife rotating speed is 1.4 rpm, peripheral lip seal linear velocity $V=2\pi rn/60=0.23m/s$, the temperature can reach 50℃, and cannot ensure that the lubricating oil supply is adequate, the seal is easy to wear. As shown in figure 6 was the state of the lip seal maintenance after the excavation of shield machine is about 1.5 km. The first and second sealing lip has damage failure. If promote longer distance will have serious consequences as shield machine downtime.

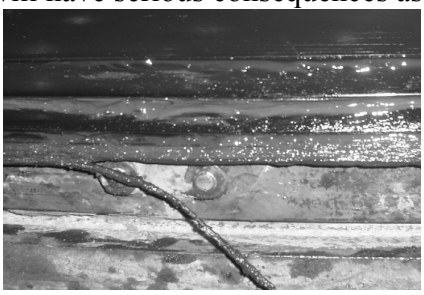

Fig.6 The lip seal wear

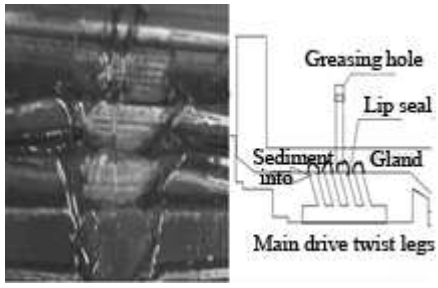


Fig.7 Gland sealing position corresponding to the wear of the lip

According to the design requirements, for the reason of sealing bushing wear, the amount of compression of the sealing lip is 7mm, to ensure the reliability of the seal. Shield machine in use after a certain period of time, as a result of the main bearing sealing lip and mud -normally the first sealing lip only direct contact with mud-and sealing bushing relative rotating slide for a long time. Lip seal in grinding out a liner circumferential direction of the bushing about 3~5 mm groove(The depth of the groove mark according to the length of the run time and external when excavating soil storehouse to the pressure of the sealing lip)[5]. In a sealed bushing and sealing lip seal and VD sealing contact position there are varying degrees of wear. As shown in figure 7.

Because this kind of wear and tear of the clearance groove will reduce the main bearing sealing lip seal performance and accelerated wear of the sealing lip. Although there is continuous lubricating grease filling, when the wear reaches a certain degree, amount of compression seal cannot compensate for wear. Still can cause the main bearing seal chamber lubricating grease in the body can't establish a certain pressure, lead to external mud invasion, causing the main driving gear,

main bearing roller, roller and cage damage[5]. If you do not eliminate the dangers caused by the groove marks, even change the new seal, due to the uneven groove mark, lip and fitting clearance of bushing cannot meet the design requirements, the sealing effect is also not ideal. So you need to repair or replace the seal.

## Retrofit scheme of main drive sealing

According to the analysis of the above problems, wear and tear of VD seal and wear of sealing bush can lead to serious consequences, in order to avoid the problems and enhance the reliability of sealing, it is essential to improve the material and installation form of the three seal.

**Material improvement of the three seal.** As the three seal is near the gear box, the temperature of the seal is high when the main drive is running and, the maximum can reach 60℃, the seal prone to accelerated aging and the binder may fail in the environment. The solution is to change the material of the three seal outside and inside, replace Nitrile butadiene rubber with Synthetic rubber containing fluorine. Fluorine rubber has excellent properties such as high temperature resistant performance, corrosion resistance, hot water resistance and hot steam resistance[6]. Characteristics of various rubbers are shown in Table 1.

Table 1 Characteristics of various rubber sheets

| Varieties / Characteristic | | Natural rubber | Styrene buta-diene | Nitrile buta-diene | Butyl chloride | silicone | Fluorine rubber |
|---|---|---|---|---|---|---|---|
| operating temperature | Min | -50 | -40 | -25 | -35 | -60 | -15 |
| | Max | 80 | 100 | 130 | 130 | 280 | 250 |
| hardness | | 20-90 | 30-90 | 30-90 | 30-90 | 10-80 | 60-90 |
| tensile strength MPa | | 10-30 | 10-25 | 8-25 | 10-25 | 6-11 | 8-20 |
| Tear resistence KN/m | | 30-100 | 20-70 | 20-80 | 20-80 | 10-35 | 15-60 |

**Modification installation form of VD seal.** Most seal fractures are caused by bad bonding and local uneven stress change the installation from Cementation method to platen method. Process plate according to the mounting surface radian inside and outside the main drive sealing; reorder the VD seal with crimping edges. The seal plate is annular after installation, then, fixes the plate with bolt. The seal renderings are shown in Fig. 8.

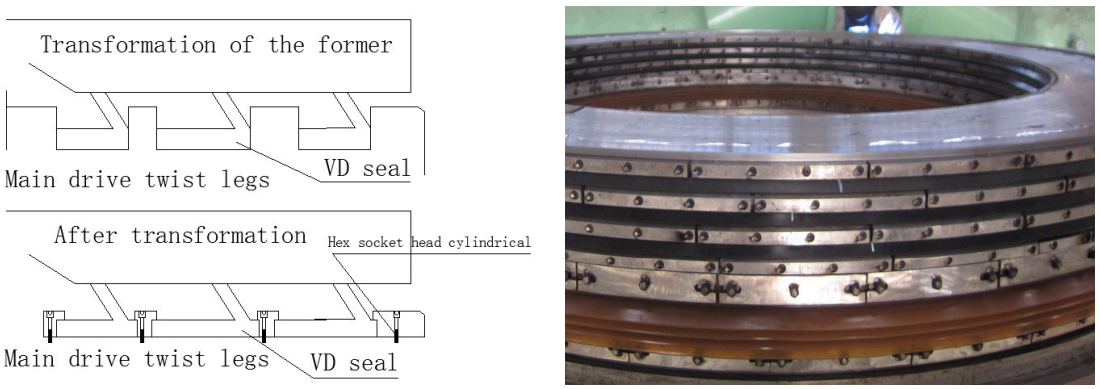


Fig.8 Seal after renovation renderings

Transformation process and main points:

(1) Process the bracket by vertical lathe machine, then, drill and thread at the design location. Process plate is according to the surface radian of the processed bracket and drill.

(2) The bolts must be new ones, totally 832. The bolt strength grade 8.8.

(3) Coat the surface of VD seal uniformly with cementing agent in case the grease reflows from the mounting surface gap.

(4) The pressure of bolt must be uniform when install the plate in case the plate deformed.

(5) Weld the connection point of bolt and plate after tightening the bolt in case the Screwed off. In the process of welding, care must be taken not to make the high temperature welding slag welding with seal and damage the sealing. In order to prevent failures, fireproof cloth must be used to protect the seal, preventing the contact of welding rod and seal.

**The application effect after the transformation of the main drive seal**

After the transformation of the main drive seal, this shield machine was used in the sixth engineering contract section of Beijing metro line 9, between Diaoyutai East station to Baishiqiao South station, and switched to the construction of 404 meters along the right line after tunneling a distance of 651 meters to Baishiqiao South station along the left line, total 1.05km in distance. Geological conditions across the range: pebble and conglomerate layers, partially mixed with fine sand and silt. The state of the shield machine, whose main technical parameters: the rotation speed of the disk cutters was 1.4rpm, tunneling speed was about 50mm/min, the cutter head torque about 60% (about 3462kN.m), was relatively stable.

During the excavation of the 1.05 km-long project, through continuous monitoring on lubricating oil, the consumption of lubricating oil was about 2.20 ml/m and pressure and consumption of lubricating oil were kept within the threshold set by the design. After the tunnel was completed, when the main drive seal was dismantled and checked again, no rupture phenomenon of inner and outer VD seal had been discovered. It was not found looseness occurred or Silt invaded when checking the seal plate at the same time. Figure 9：The wear of the contact place between the sealing lip and cartridge decreased and was about 0.6 ~ 0.8mm.

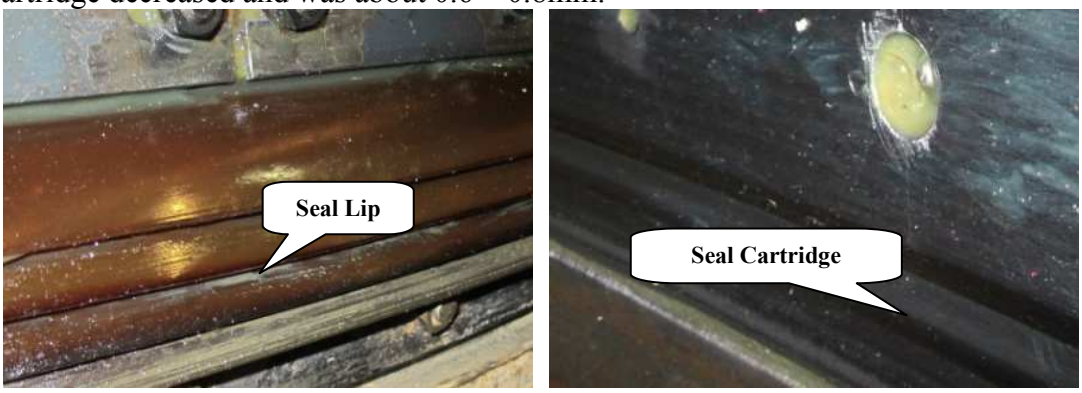


Fig.9 Main drive seal using renderings

**Conclusion**

After the technical reconstruction of the main drive seal, shield machine with favorable effects did not fracture again; Roughness Ra value, elasticity and other properties of the fluorine rubber seal complied with the design requirements, and its high-temperature aging performance had increased compared with nitrile butadiene rubber. This ensured that the shield machine was reliable in underground construction.

The pressure plate type, the installation form of this main drive seal, made the combination of seal and shell more reliable, avoiding failure caused by the seal fracture owing to local uneven stress. After modification, through the engineering application test, it achieved the desired effect of modification technology research of the seal, accumulated rich experience for the design and manufacture of shield machine.

At the same time, we should draw lessons from the main drive seal system of shield machine of other brands, such as main drive sealing system of NFM shield, which is injected three kinds of oil to achieve the purpose of sealing and lubrication and designed mechanical labyrinth seal in the side of soil storehouse to further enhance the sealing effect, consists of five lip seals specially designed.

In the course of excavation, the monitoring of lubricating grease should be strengthened, including consumption, oil pressure, etc. to enhance the ability to predict failures.

In short, shield tunneling will be more and more safe and reliable with continuous improvement and innovation of the technical performance of shield equipment; shield equipments are also easier to maintain; this tunneling technology will be continually applied to various fields in underground engineering construction.

**References:**

[1] Li Shengxin. Repair Methods of Shield Tunneling in the main Bearing seal. Petroleum Engineering Construction, 33 (5):65~66.(In Chinese)

[2] Tao Jian-jun. Heavy Machinery on the Sealing Technology [J] . Maschinen Markt, 2003(27): 112~113.(In Chinese)

[3] Gao Wei-xian, Deng Li-ying, Zhang Rui-lin. Research On the Seal Structure of main Bearing for Shield Machine [J]. Mining & Processing Equipment.2008(13):21~23(In Chinese)

[4] Sealing Technology Network.http://www.mfw365.com /: VD Rubber seal definition.(In Chinese)

[5] Liu Ju-ning. Adjustment and Replacement of main Shaft Seals of Shield Machine[J]. Construction Machinery 2006.09(The semimonthly):101~102.(In Chinese)

[6] Liu Ling-mei. Summary of the Performance and Application of Fluorine Rubber[J]. Organo-Fluorine Industry, The second phase: 5~6.(In Chinese)

[7] Miao Nan.Treatment Measures for Wearing of main Drive Sealing Slide of EPB Shield[J]. Tunnel Construction, 2013, 11:977-981.(In Chinese)

[8] Ling Bo.Trouble removal of shield main driving gear oil leaking[J]. Construction Mechanization,2012, 06:92-93.(In Chinese)

[9] Su Peng-cheng , Zhang Rui-lin ,He En-guang.FEA on strength of main driving bearing of Shield Machine[J].Mining &Processing Equipment ,2010,15:13-17.(In Chinese)

[10] Yang Ming-jin. Analysis and Transformations for the Gearbox of the Main Drive System of NFM Shield[J]. Modern Machinery, 2012,02:66-68. (In Chinese)

[11] Guo Xi-qin.Trouble shooting of main Driving System for Soil Pressure Balance Type Shield Machine [J] .Construction Machinery,2007,19:103-104+107.(In Chinese)

[12] Liu Wen-xi, Hu Hong-xing,Zhuang Yuan-shun. Maindrive seal system analysis of tunnel machine[J] .Machinery,2013,06:76-80.(In Chinese)

[13] SUN Ling-qiao. causes and preventive measures of the Shield Machine main drive seal failure [J]. Mechanical Engineer, 2012, 07:207-209.(In Chinese)

[14] Counter measures for Malfunctions of Drive Sealing Of Screw Conveyors of Shield Machines[J].Tunnel Construction,2012,01:134-138.(In Chinese)

[15] Han Feng-hong. Analysis on Consumption of Lubrication Grease, HBW Grease and Tail SkinSealing Greas:Case Study on Herrenknecht Shields and NFM Shieldss[J]. Tunnel Construction, 2011, 03:405-410.(In Chinese)

*Applied Mechanics and Materials Vols. 580-583 (2014) pp 1088-1091*
*© (2014) Trans Tech Publications, Switzerland*
*doi:10.4028/www.scientific.net/AMM.580-583.1088*

# Review of Testing and Analysis on Metro-Induced Vibration

Jiwei Li [1, 2,a]

[1] School of Engineering and Transportation, South China University of Technology, Guangzhou 510641, Guangdong, China

[2] Application Center of Engineering and Measurement, Guangzhou Institute of Measuring and Testing Technology, Guangzhou 510663, Guangdong, China

[a] email: jilinlijiwei@163.com

**Keywords:** metro; environmental vibration; vibration measurement; vibration mitigation measuremen

**Abstract.** With the rapid development of metro, the vibration induced by metro is the more and more common and widely concerned. In this paper, test and analysis of vibration induced by metro is discussed, and the five aspects of the research status at home and abroad are emphasized, which are the analysis of the vibration causes, the analysis of vibration influence, the summary of vibration test technology, the analysis of the relevant theoretical results and the analysis of vibration reduction application measures. This paper will provide the theory basis and the practice reference for the vibration design of environmental vibration induced by metro.

## Introduction

Since twentieth Century 60-70 years, the world economy rapidly develops, the number of vehicles sharply increase, which led traffic conditions to more and more worsening[1]. Metro become aware of an effective way to solve the traffic problems, which has a lot of advantages such as saving land, large transport capacity, stable running time, small investment, safety and environmental protection.

With the rapid development of metro, while bringing a lot of convenience to people, it also causes a lot of problems. Usually, the subway traffic throughout the city downtown area, its impact on the surrounding environment can not be ignored. Among the complaints about the metro, the vibration induced by metro is the most common and most widely concerned. Because vibration induced by metro is long-term and repetitive, may cause the shedding and cracking of decorations, deformation or subsidence of foundation, thus it will affect the safety of buildings and service life; vibration will affect physiology and life[2]; in addition, it is bound to affect the normal operation of precision instrument[3]. As in Czech, some of masonry structures near rail cracked, which is caused by vibration of the vehicle through them, and in some place the ancient church collapsed because of the expanding crack[4]; some walls of the Guta lie in China Xi'an city and many pagodas of Beijing have different degree damage by the traffic vibration[5]; the some tile murals of Beijing Metro Line 2 falled off which is caused by vibration not only affect the appearance but also affect traffic safety in certain degree[6].

## Analysis of the causes of vibration induced by metro

In the metro system, the train is due to interact between the wheel and rail, the vibration energy is produced; it is transferred to the tunnel hrough the bed, then the vibration of the tunnel and surrounding rock is caused; the vibration is transferred to the foundation near the building through the surrounding soil and rock, further it will transfer along the column, beam, wall and floor; at last the vibration of people and equipment lieing on the floor is caused[7].

The vibration induced by metro mainly experiences 3 stages, vibration source, propagation in the medium and the environment vibration, which constitute a system including of train-support structure- soil - building - people. The vibration system is composed of the source, propagation path and the vibrating body, the vibration source is mainly composed of a train, rail supporting structure and fundation, the important affecting factors include of characteristics of vehicle types, marshalling,

dynamic characteristics, speed, bearing structure and its foundation; the propagation path, namely, ground and underground soil, including bearing structure foundation soil interaction, the upper and the building, vibration in soil spread; vibration bodys include of building, equipment and people[8].

From the metro vibration process, while the train moves as a certain speed, there are a lot of causes of vibration induced as the following [7,9]: 1) the wavefront of moving loads; 2) the discrete support sleeper or fastener; 3) the change of track stiffness caused by changing stiffness of subgrade; 4) the cyclic loading of trains; 5) the collision impact force while train moves through rail joint or switch; 6) the continuous irregularity generated by eccentric wheels; 7) the uneven pulse irregularity caused by wheel tread wear; 8) the deformation of embankment system under wheel pressures; 9) the horizontal gap between wheel and axle deformation. Among these the train's wheel pressure is the main reason.

**Analysis of the influence of vibration induced by metro**

1) vibration impact on the structural safety

Compared to the earthquake and explosion that can cause severe damage, the impact of metro vibration on the building is not due to get instant results, because its vibration energy is smaller, but as the result of long-term accumulation, the dynamic fatigue and stress concentration will be caused, which will mainly be appearance of structure and function loss, damage and short service life.

2) vibration impact on the use of instrument

Precision instruments have high requirements for storage and use, every type of equipment has its own normal indicators of control. While the value of the vibration transfered by the running subway exceeds its allowable indicators, the work system and dense instrument will swing or tremble, which leads to cause error of measurement system. Serious when causing the precision instrument failure, or even destroy, more serious condition is that the instrument can't be used. So, when the subway line is planned, it must be inspected whether there are precision instruments where the line runs through, it must take reasonable measures to avoid causing immeasurable loss.

3) vibration impact on human life

Vibration impact on people's daily life is very extensive, especially the large noise is often accompanied by vibration. So the vibration mainly generate interference and influence for people's life, work, study and rest, the main performance is unable to efficiently concentrate, to study or work.

4) vibration impact on human health

The long time metro vibration will have great effects on the human body and psychological reaction, including of impaired visual sense, vomiting, fainting, heart sick, nervous disorders and limb activity decreases. The impact on psychology is that people sometimes feel fear, pain, sensitivity, insomnia and nightmares. It is visible that the long-term vibration impact on human daily life can not be ignored.

**Summary of metro vibration testing technology**

At present, there are contact and non-contact vibration test methods, contact test method is more common. The former has two types: one is magnetoelectric speed sensor, its working principle is when the magnetic flux changes through a coil, the electromotive force will be produced, velocity output electromotive force and the coil is proportional; the other is piezoelectric acceleration sensor, its working principle is using certain substances such as piezoelectric effect of quartz crystal, while the accelerometer vibrates, the force of the mass on the piezoelectric elements will change, when the measured vibration frequency is much lower than the natural frequency of the accelerometer, the change of force and the measured acceleration is proportional.

The data extracted by piezoelectric acceleration sensor is more intuitive, more convenient. But this method can not realize long distance real time monitoring, there are some shortcomings such as the piezoelectric sensor is still the traditional connection mode, when the number of measuring point is more, the test operation time will be in short [10]; and like that only one sensor can be arranged in a cross section, which can only measure the parameters of a specific section of real-time monitoring,

but the long distance real-time changes of the parameters along the line is in need; moreover the data processing must be carried on after the end of the test, which can not monitor in real time.

The development of science and technology provides the possibility for solving the above defects, the distributed optical fiber sensing technology with its unique advantage is particularly worthy of esteem[11]: it can realize remote measurement and monitoring; it can carry on the long distance test, it has high performance ratio; the optical fiber can all become sensitive element, which can acquire the distribution information of measured the sensing area in real time; it can process data in real time, and it can achieve truly real-time monitoring, timely finding and solving the potential problems and harm.

## Analysis of related theoretical results of metro vibration

There are many relevant theories about metro vibration, which mainly consists of the theoretical analysis method, the experimental method, and the numerical calculating method.

The theoretical analysis method is an analytic method, which directes mainly against the train load, the rule of vibration transmission, vibration prediction and affecting of the buildings and so on.

But the theoretical analysis method has its limitations, it is difficult to meet the harsh application environment, so numerical finite element method, boundary element method and the two mixed method are widely applied. Among them, the finite element method is a kind of modern computational methods with the development of computer technology and the rapid development of the solution domain. Boundary element method is more suitable for the infinite medium, and it is not suitable for study on vibration problems with irregular shape, therefore, usually the finite element and boundary element are jointed to use[12].

The experimental method obtains data through tests, analyzes vibration propagation and environmental impact through the data. So the conclusion is more direct, more reliable[13].

## Application and analysis of reducing vibration measures

1) controlling vibration source measures

The vibration source is track structure, the elastic support is instead of rigid links to reduce energy transfer. There are many research results and engineering practice case, as shown in Table 1 [14].

Table 1 Comparison of several common rail structure

| Structure / Project | III track absorber fasteners | LORD fasteners | Vanguard fasteners | Elastic holistic beds | Rubber floating slab | Steel floating slab | Ladder track system |
|---|---|---|---|---|---|---|---|
| Damping [db] | **≤8** | **≤8** | **≥12** | **8~12** | **10~18** | **≥25** | ≥20 |
| Cost [mil./km] | **1.2** | **1.2** | **7** | **1** | **7.5** | **10** | 6.3 |
| Service-life[year] | **10** | **30** | **50** | **30** | **50** | **Long** | Long |
| Maneuverability | Mature technology | Mature technology | High precision | complex processes | Cast in situ | High precision | Uneasily control |

2) controlling vibration transmission measures

Vibration spreads through tunnel wall and soil, the control measures mainly barrier the vibration transmission through them. Cutting vibration propagation can be employed to optimize the roadbed, bridge, tunnel, soil structure and increase the strata thickness, commonly the most used methods include excavation damping ditch and setting the isolation wall and the isolation barrier [15].

3) vibration receptors control measures

The building installation damper is one of the most common measures, the components and materials of vibration isolation commonly used are steel springs, air springs, rubber, liquid spring, cork and felt. Among all, the most widely used is metal rubber composite shock absorber.

During the choice of building materials, it is necessary to choose some greater rigidity material, such as while selecting the materials of the ground, the hard materials can be chosen, such as cement floor and terrazzo floor, which have good vibration reduction effect.

**Summary**

In this paper, test and analysis of vibration induced by metro is discussed, and the five aspects of the research of home and abroad are emphasized, which are the analysis of the vibration causes, the analysis of vibration influence, the summary of vibration test technology, the analysis of the relevant theoretical results and the analysis of vibration reduction measures. This paper will provide the theory basis and the practice reference for the vibration design of environmental vibration induced by metro.

**Acknowledgements**

This work was financially supported by the Postdoctoral program of Guangzhou.

**References**

[1] Li Jiwei: *Estimation and prediction of link travel time for urban trunk and secondary streets* (JiLin university, Changchun 2012).

[2] U.S. Department of Transportation Federal Transit Administration (FTA)， Manual for high-speed ground transportation noise and vibration impact assessment(2005).

[3] Hsiao HuiHung, Yeong: A review of researches on ground-borne vibrations with emphasis on those induced by trains. Proceeding of the National Science Council, Vol. 25 (2001), p. l-16.

[4] Bata M: Effects on buildings of vibrations caused by traffic. Building Science, Vol.6(1971), p. 221-246.

[5] Chen Jianguo: *Prediction and Parameters Research on Viaduct Train-induced Environmental Vibrations* (BeiJing JiaoTong university, BeiJing 2009).

[6] Chen Jianguo, Xia He, Xiao Junhua, Cao Yanmei: Experimental study of ground vibrations induced by moving train. Rock and Soil Mechanics，Vol. 29 (2008), p. 3113-3118.

[7] Li Shouji: *Study on Subway-Induced Environmental Vibration and Floating Floor lsolation* (Tong Ji university, ShangHai 2008).

[8] Wei Pengbo: *Prediction and Assessmen tfor Urban Train-induced Environmental Vibration* (BeiJing JiaoTong university, BeiJing 2009).

[9] Shi Lianxu: *Research on Vibration of Nearb yMuseum Induced by Chengdu Metro Line 2* (BeiJing JiaoTong university, BeiJing 2011).

[10] Ji Guoyi, Zhao Chunsheng: Summary of Vibration Testing and Analysis. Machine Building and Automation，Vol. 39 (2010), p. 1-5.

[11] Wei Liangbin: *The Software Design and Realization of Distributed Optical Fiber Vibration Sensor* (Huazhong University of Science & Technology, WuHan 2007).

[12] L. Auersch: The excitation of ground vibration by rail traffic: theory of vehicle- track- soil interaction and measurements on high- speed lines. Journal of Sound and Vibration，Vol. 284 (2005), p. 103- 132.

[13] Zhai Jiequn: *Test and Analysis of Vibration Propagation caused by the Subway train* (Tong Ji university, ShangHai 2007).

[14] Zhang Huihui: Summary on Vibration-noise Controls of Rail System. Railway Construction Technology，Vol. (2011), p. 171-175.

[15] Liao,S,Sangrey DA: Use of Piles as isolation barriers. Journal of the Geotechnieal Engineering Division，Vol.104 (1978), p. 1139-1152.

*Applied Mechanics and Materials Vols. 580-583 (2014) pp 1092-1095*
*© (2014) Trans Tech Publications, Switzerland*
*doi:10.4028/www.scientific.net/AMM.580-583.1092*

# Stability Analysis of Wall Structure which its Depth is over thousand m

Yinghao Wang[1,a] Xiaochen Fu [1,b] Xiaohong Jing[1,c]

[1]The school of Architecture and Civil Engineering, Inner Mongolia University of Science & Technology, Baotou 014010, China

[a]wyh1978@sina.com, [b] 461329321@qq.com, [c] 790540500@qq.com

**Key words:** concrete; wall structure; deformation coordination; strength check

**Abstract:** According to the monitoring result of wall structure which its depth is over thousand, analyzed the strain of inner and outer edges of concrete and inner steel; Neglect construction factors, by comparing the strain of inner concrete and inner steel, it shows that their deformation is consistently; Using the average strain of inner and outer edges of concrete to check strength adopting method of concrete structure design code, shows that they can meet the requirement.

## Introduction

In China, after decades of development of coal industry, shallow resources both in quantity and quality appear degradation trends. The forecast shows that by 2020 China's key coal mining depth will reach an average of 1200 m.

Shaft is important thoroughfare of mine underground engineering contact with the ground, and it is first built in mine construction. But deep engineering confronts complex stress, temperature and seepage, there was no theoretical formula on wall design with super km; According to current "Code for design of coal mine shaft and chamber" [1], 1200 m deep shaft design shows that both concrete strength and thickness of the wall is greater than the real results or appears failure. But in reality face similar projects using engineering analogy method. There is no theoretical basis of its security. So the super km wall stability analysis has practical significance.

## Project profile

This mine lays Hebei province. The wellbore diameter is 8.0 m; its depth is 1340 m. From top to bottom, wellbore cut across the Cenozoic quaternary strata, tertiary alluvium with189 m, Mesozoic Triassic strata with 331 m, the upper Permian series of strata with 840m; Bedrock section full of mudstone and powder, fine, medium and thick sandstone. Under - 1100 m, wall structure is single-layer steel concrete which concrete strength grade is C60; - 1100~1200 m, wall thickness is 80 cm; under -1200 m is 90 cm.

## Monitoring program

According to the progress of the project, the whole monitoring is divided into two levels: first level located at - 1208 m, the second level is located at - 1306 m.

The selected principles of measured vertical position: (1) can monitor deformation of different lithology. (2)According to the requirement of the design institute， near the horsehead (-1309 m) set up a monitoring level.

The selected principles of measured plan position: (1) to avoid all kinds of conflicts such as with sinking equipment layout, the permanent equipment and guide. (2) Measuring point layout accord with suitable density, focused, avoid duplication and reduce cost.

Tests include: radial, tangential and vertical strain of concrete in outer margin; tangential and vertical strain in inner margin; stress changes of circular and longitudinal reinforcement in outer margin.

Monitoring equipment include vibrating sensor, multi-point measurement system by microcomputer control, vibrating concrete strain meter, reinforcement meter and soil pressure box.

First level sensors were embedded in a vertical wellbore 1208 m deep. The basic on behalf of the wellbore wall force and deformation of shaft wall, and the first level of embedding location in northeast, north to west 58° and east to south75°, a total of 27 sensor, there are 26 normal work, have the effect of 21 sensors, reflect the mechanical response characteristics of borehole wall lasted 288 days. This paper only analyzes monitoring results of the first level.

### Average strain analysis on outer margin concrete

Outer margin strain includes hoop strain, vertical strain and radial strain; the average strain varying with time as shown in figure 2.1.

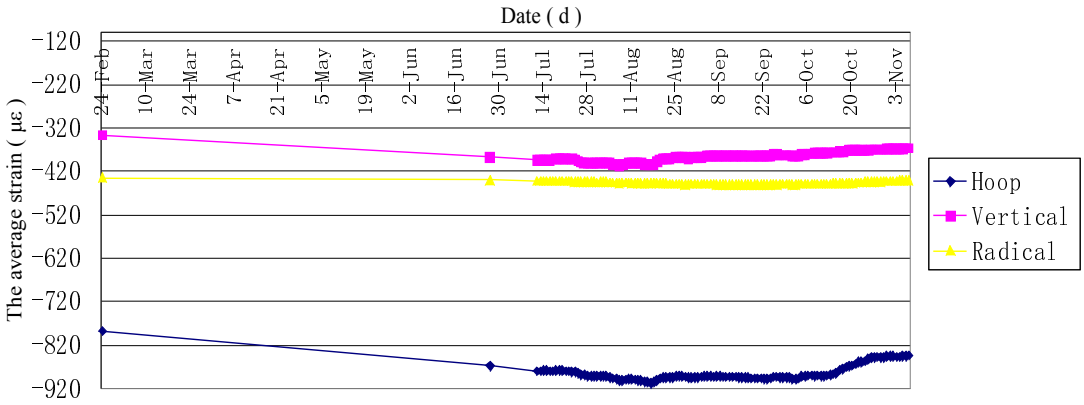


**Fig.2.1 The average strain of outer margin concrete**

The figure 2.1 shows that concrete strain has the following features:

(1)Overall, hoop strain is the largest, the second is vertical strain and radial strain is minimum, shows that the maximum principal stress appear in hoop; the minimum principal stress appear in radial; their strain increase all the time, show the obvious creep properties;

(2)Deformation of inner margin basically includes instantaneous deformation and creep deformation; creep deformation is divided into decay creep and steady creep stage; On June 27, begin to construct horsehead (-1309 m); because the influence of the construction, the vertical and hoop deformation of outer margin show the obvious phenomenon of load shedding after middle of August.

### Average strain analysis on inner margin concrete

Outer margin strain includes hoop strain and vertical strain; the average strain varying with time as shown in figure 2.2.

The figure 2.2 shows that concrete strain has the following features:

(1)Because taking no reinforcement measures around the borehole wall, so the radial strain near the zero (even producing strain, relative to the ring and vertical should be very small and negligible), then only monitor the ring and vertical strain; Overall, the ring strain is greater than the vertical strain; they increase all the time, show the obvious creep properties;

(2) Two direction deformation basically includes instantaneous deformation and creep deformation, creep deformation is divided into decay creep and steady creep stage; the vertical and hoop

deformation of inner margin show the obvious phenomenon of load shedding after middle of August.

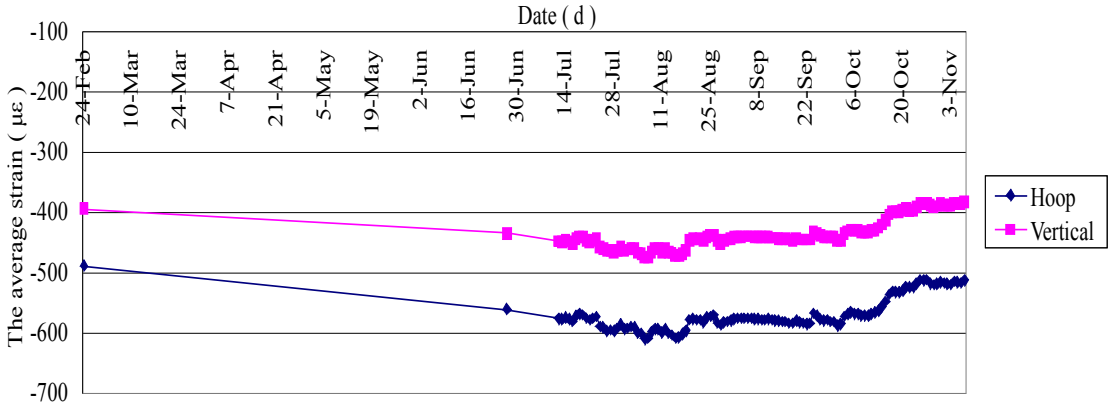


**Fig.2.2 The average strain of inner margin concrete**

**Average stress analysis on inner margin reinforcing bar**

Inner margin reinforcing bar stress directions include the ring and the vertical; The average stress varying with time as shown in figure 2.3.

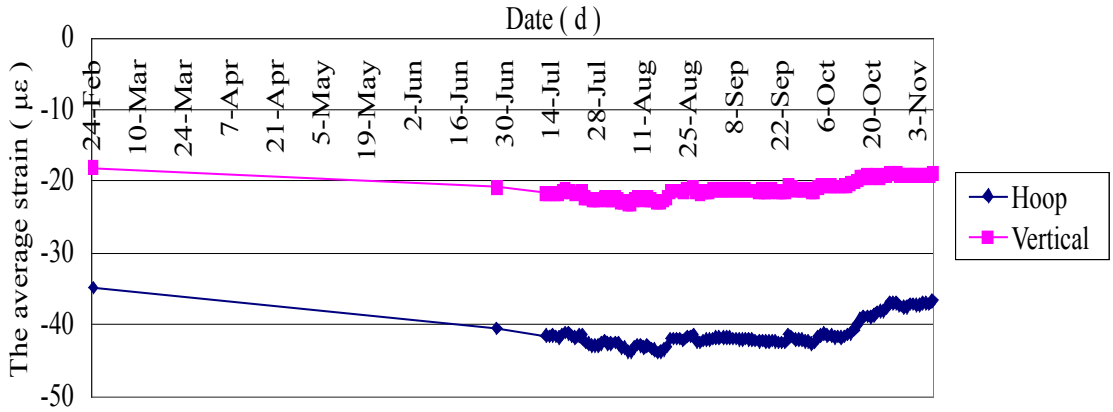


**Fig.2.3 The average stress of inner margin reinforcing bar**

The figure 2.3 shows that inner margin reinforcing bar has the following features:

(1) For inner margin reinforcing bar stress include the ring and the vertical, its increasing regularities is same as the concretes either outer margin or inner margin;

(2) Around the steel bar and concrete strain should be coordinated: reinforced elastic modulus E is 2.0 x $10^5$ MPa, the maximum hoop strain of steel was - 576.69με, the average strain was - 541.96με, compare with the inner margin concrete strain, reach to the maximum - 608.30με,same to the average -568.01με ; the maximum vertical strain of steel was -305.31με, the average strain was - 276.77με; compare with the inner margin concrete strain, either maximum - 474.68με or average -434.61με, has a gap.

**Stability judgment on borehole wall**

Due to the depth is much greater than the thickness, inner or outer radius, and monitoring the wall rock deformation with time change is main target, therefore can be considered as a plane strain problem.

According to the average concrete strain of inner and outer margin, to calculate the average stress using the generalized Hooke's law [2], the result was shown in table 2.1.

**Table 2.1 Three dimensional stress average value of inner and outer edge concrete**

| location | hoop stress $\sigma_1$ （MPa） | vertical stress $\sigma_2$ （MPa） | radial stress $\sigma_3$ （MPa） |
|---|---|---|---|
| Inner margin | 24.56 | 20.56 | 0 |
| Outer margin | 39.47 | 32.58 | 29.21 |

**Stability judgment on outer margin**

By the calculation rules on strength of concrete under multi-axial stress state which comes from the current code for design of concrete structure [3], the stress ratio of $\sigma_2 / \sigma_1 = 0.84$, find concrete compressive strength increase coefficient is 1.2; C60 concrete compressive strength design value is 27.5 MPa, the $\sigma_1 = 24.56 < 27.5 \times 1.2 = 33$MPa, so meet the strength requirements of concrete.

**Stability judgment on inner margin**

By the calculation rules on strength of concrete under multi-axial stress state which comes from the current code for design of concrete structure, the stress ratio of $\sigma_2/\sigma_1 = 0.83$, $\sigma_3/\sigma_1 = 0.74$, find concrete compressive strength increase coefficient is 3.0; C60 concrete compressive strength design value is 27.5 MPa, the $\sigma_1 = 39.47 < 27.5 \times 3 = 82.5$MPa, so meet the strength requirements of concrete.

**Conclusions**

(1) By average strain on inner and outer margin concrete, the hoop strain is the largest, vertical strain is second and radial strain is the smallest. So the maximum and minimum principal stress direction is hoop and radial.

(2)The gap between the hoop strain of concrete and steel is smaller, shows that their deformation is coordinated; Due to the horsehead construction factors, the gap between the vertical strain of concrete and steel is greater, but their stress direction is the same. Therefore, regardless of construction factors, steel and concrete strain is coordinated;

(3) Based on three position concrete strain average of outer and inner margin, to calculate three principal stress direction strain average, then using the generalized Hooke's law to calculate the principal stress, at last using the first rule of strength to check concrete strength, meet the strength requirements.

**References**

[1]GB 50384-50384, Code for design of coal mine shaft and chamber[S].Beijing: China planning press, 2007, in Chinese.

[2] Hongwen Liu. Material mechanics [M].Beijing: Higher education press, 2004,in Chinese.

[3] GB50010-2010, Code for design of concrete structures [S]. Beijing: China architecture & building press, 2010, in Chinese.

*Applied Mechanics and Materials Vols. 580-583 (2014) pp 1096-1099*
*© (2014) Trans Tech Publications, Switzerland*
*doi:10.4028/www.scientific.net/AMM.580-583.1096*

# Design of high speed railway tunnel and its construction method in abrupt slope with loose rockmass

Zhou Xiaojun[1,a], Jiang BO[2,a], Yang Rui[1,b] and Ning Chao[1,c]

[1]Key Laboratory of Transportation Tunnel Engineering, Ministry of Education, Southwest Jiaotong University, Chengdu, 610031, China

[2]The 1st Design Institute of Civil Engineering and Architecture, China Railway ErYuan Engineering Group Co. Ltd., Chengdu 610031, China

[a]Zhouxjyu69@163.com, [b]253477813@qq.com, [c]1195664687@qq.com

**Keywords:** Railway tunnel, tunnel portal, loose rockmass, four bench cut method, pipe roof protection, friction pile

**Abstract.** This paper mainly deals with the structural design of high speed railway tunnel and its driving method in abrupt slope with loose rockmass, meanwhile summarizes the connection between tunnel portal and bridge abutment in loose rockmass according to complicated landform and geology. The anti-slide piles are adopted to retain the stability of abrupt slope near the tunnel portal. In order to eliminate the risk and cost in tunnel construction, four bench cut method is invented to satisfy the safe excavation of loose rockmass in the tunnel. Composite fiber rockbolt is also employed to keep the stability of working face while driving the tunnel. The innovative tunneling method presented in the paper can be applied to guide the rational design and economical construction of high speed railway tunnels in loose surrounding rock under harsh geological conditions.

## Introduction

The land in southwestern China teems with high mountains with harsh landform and geology [1]. So a great amount of tough technical problems may be encountered when designing and building transportation lines such as expressways and high speed railways [2]. In order to expedite the social and economic development of western China, a new railway line entitled as Chengdu-Lanzhou railway is now concurrently under construction in Sichuan and Gansu province of China, its whole line is 457.59km long, in which tunnels and bridges account for 86.06% of its total length. The average altitude of the railway line in these regions ranges from 500m to 1800m. The longest tunnel is called Ping'an tunnel with an entire length of 28km. Since the most lands in Southwestern China is covered by mountains, so there are countless valleys and slopes in this terrain. Another tough problem is that the region had been struck by the magnitude 8 seism that took place in 2008. This shows that most slopes and precipices are very weak and its rockmass haven been loosened by the seism, especially rockmass in shallow layer of mountain slopes. If tunnels are designed to pass through the mountains in transportation lines at this terrain, the connection between tunnels and bridges in the same line still becomes another key problem. This paper focuses on the design and connection of tunnel portal and bridge in steep slopes, meanwhile, dissect the construction method for tunnels in abrupt slope with loose rockmass. According to the planning of the Chengdu–Lanzhou railway line, it consists of two main lines, i.e., right line and left one. One typical of its tunnels is named Mao Xian tunnel, it is 9910m long, its two exit portals lie on a steep slope of a mountain and its aerial view is depicted in Fig.1.

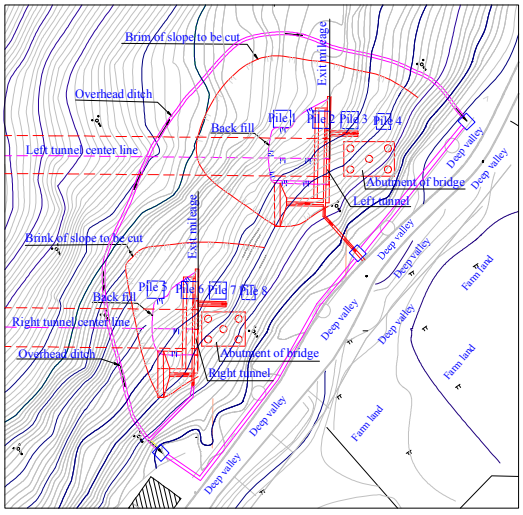


Fig.1 Aerial view of railway tunnel

It is seen from Fig.1 that the landform of the slope exists in oblique form; its inclination angle reaches 36°. The two tunnels pass through the mountain with an angel of 22° against the contour line of the slope. Since the slope of the mountain exists in curved surface, so the mileage of the tunnel portal is different from each other. The exit mileage of left portal is greater than that of the right one. So there is 10 meters distance between left portal and right one. According to the general extension of Chengdu–Lanzhou railway line, two bridges will be upbuilt to concatenate the tunnel portals, as there is much less place to lay the bridge in front of the portals, so the bridges and their abutments must be placed closely to the portals and the detailed location of the bridge abutments are also shown in Fig.1.

## Geological Condition of the Tunnel Portals

It has been testified that geological condition of slope and lithology of surrounding rock always essentially affect the design and selection of tunnel structure and its tunneling method [3, 4]. In order to effectuate rational and economical design of the tunnel, reconnaissance and survey on the geological conditions of the slope have been carried out in advance. The obtained results show that the surrounding rock lithology falls into two types, namely the Quaternary period and the Triassic system. The surface layer of the slope mainly consists of gravel soil ($Q_4^{dl+col}$) and sandy gray ($Q_4^{dl+col}$), but the lower strata comprises phyllite with embedded sandstone ($T_3^x$). The obtained physical and mechanical parameters are listed in Table 1.

Table 1 Physical and mechanical parameters of surrounding rock

| Surrounding rock | Density/(g/cm$^3$) | Cohesion/(kPa) | Internal friction/(°) | Load bearing capacity (kPa) |
|---|---|---|---|---|
| Gravel soil ($Q_4$) | 2.10 | 8.0 | 40.0 | 250 |
| Sandy clay ($Q_4$) | 1.95 | 13.0 | 18.0 | 150 |
| Phyllite ($T_3^x$) | 2.20 | 20.0 | 25.0 | 300 |

It's deduced from Table 1 that both sandy clay and phyllite possess low shear strength. This connotes that if the loose surrounding rock is not treated, then it easily collapses during tunneling. According to the basic load bearing capacity of surrounding rock, the front and side slope around tunnel portals should be also enhanced. Thus it is deduced that before building tunnels and bridges in the railway line, subsidiary measures must be taken to augment the strength of surrounding rock and slope [5, 6].

## Tunnel Portal and Its Design

According to the designed velocity of passenger train in this new railway line, its travelling speed reaches 200km/h. meanwhile, in view of the line extension; two separated tunnels must be built at this site, namely the right tunnel and the left one in its corresponding line. The clear spacing between the two tunnel center lines is set within 30m. Fig.1 additionally shows that the exit mileage of right tunnel is 10m smaller than that of the left one. Concurrently, in consideration of the oblique slope, bench portal is employed to satisfy the abrupt slope of the mountain [4]. Bench portal may readily consort with its inclined landform, thus they are applied to the separated tunnels. In addition to the tunnel portal, there are two railway bridges in front of them so that rail tracks on the bridges can be linked with those in the tunnels. Moreover, since a deep valley exists in front of the portals, in order to diminish the influence of flood and solifluction on the bridge piers in the valley where there is a heavy rainfall, thus bridge piers must be laid near the portals. So their abutments and piers will occupy the patch where tunnel portals stand. The relationship between tunnel portals and bridge abutments is still plotted in Fig.1. The four red rectangles in front of portals in Fig.1 illustrate the concrete location of bridge abutments in the railway line. The designed portals and abutments of bridges are concisely illustrated in Fig.2 and Fig.3 respectively. In order to ensure the stability of left slope with higher height, four anti-slide piles with depth of 30m are placed at each left side of the slope by means of finite element analysis, so there are 8 anti-slide piles altogether placed in the left slopes. In addition, prestressed tensile cables are set in the surrounding rock so as to exalt the stability of slopes during

tunneling and future operation of the bored railway tunnels [5, 6]. Fig.2 also shows the relationship between left tunnel and right one. Since the exit mileage of left tunnel is longer in comparison with that of the right tunnel, so the transection of right tunnel is shown in Fig.2. However, the transection of right tunnel is not picturized in Fig.3.

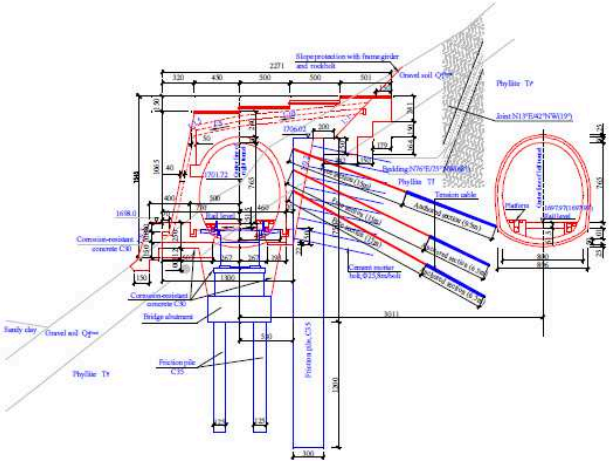

Fig.2 Front view of right tunnel portal (Unit: cm)

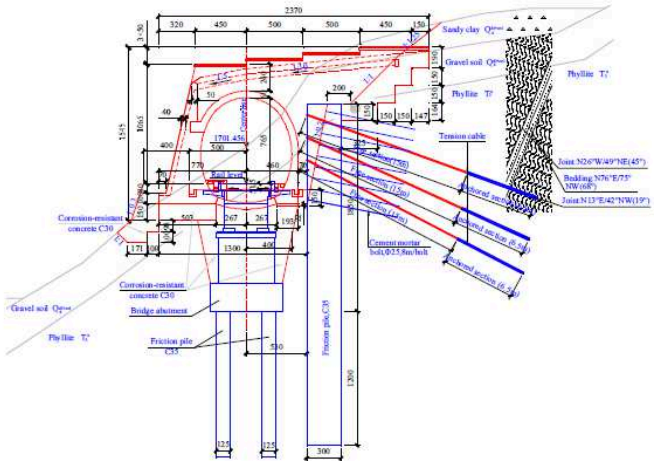

Fig.3 Front view of left tunnel portal (Unit: cm)

**Tunneling Process and Its Design**

In order to eliminate ground settlement and abrupt collapse generated by excavation of the tunnels and their portals, the key task is to choose feasible and economical tunneling procedure before excavation. According to the geological condition of surrounding rock, the slope and surrounding rock must be treated in advance; therefore, friction piles and pipe roof protection have been implemented. Only the treatment and reinforcement of surrounding rock have been accomplished begins the excavation of tunnel portals. The treatment scheme is picturized in Fig.4. Since the surrounding rock in the front working face is loose, if full face cut method is used then collapse may easily occurs during tunneling, this does not only affect the safety of working staff, but thwart the construction progress as well. Therefore partial excavation is considered [4, 5]. Furthermore, composite fiber rockbolt is applied to fortify the strength and stability of working face [6]. The application of fiber rockbolt is conducted in terms of 1bolt/m$^2$. Its length reaches 5m in front of working face. The detained layout and distribution of fiber rockbolt in working face is clearly depictured in Fig.4.

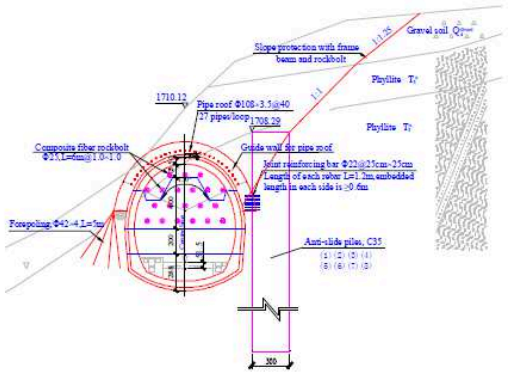


Fig.4 Ground treatment for tunnel portals (Unit: cm)

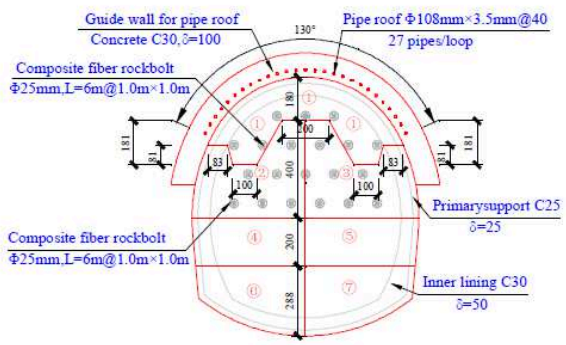


Fig.5 Four bench cut method (Unit: cm)

On the basis of the loose surrounding rock and its mechanical parameters, four bench cut method is proposed, according to this tunneling method, the whole working face of the tunnel including its portal is divided into four drifts, and in order to banish the mutual disturbance on excavation of loose rock in each working face, a short distance of about 7m to 8m must be maintained among them. The

tunneling procedures for the bored tunnels are explicitly depicted in detail in Fig.5 and Fig.6 separately. Fig.5 shows the division of working face in the tunnel, and Fig.6 illustrates the longitudinal profile of the tunneling method.

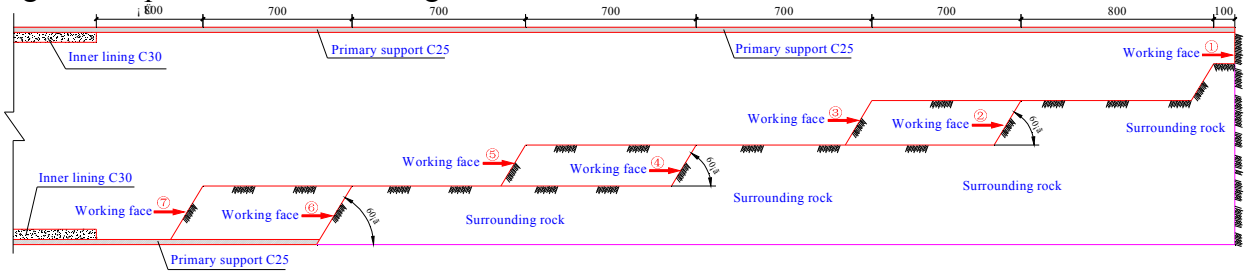


Fig.6 Profile of four bench cut method (Unit: cm)

The numbers circumscribed with red-hued circles in Fig.5 and Fig.6 betokens the principal driving steps in loose surrounding rock. According to this method, primary support must be established in time because it is used to resist all rock pressure or soil thrust during tunneling and long-term operation. The permanent reinforced beton lining must be cast in time when the fourth bench has been bored. The minimum distance must be kept within 7m between every two working faces.

## Conclusions

If drill and blast method is used to bore railway tunnel in steep slope with loose rockmass in mountainous area, four bench cut method (FBCM) is effective in reducing construction risk and cost in comparison with such tunneling methods as center diaphragm method (CD method), cross diaphragm method (CRD method) and two side drift method. In order to abate the collapse of surrounding rock during tunneling, composite fiber rockbolt is a useful mean to enhance the stability of working face. With respect to inclined slope, anti-slide piles are also efficient in retaining its stability. If loose soil and rockmass is treated with rational technical measures, then abutment of bridge in railway line can be closely laid to the tunnel portal. The method presented in this paper is a useful one to guide the design and construction of high speed railway tunnels in complex strata.

## Acknowledgements

This work is financially supported by the National Natural Science Foundation of China (No.51378436) and the technical development program of the China Railway Corporation (No.2010G018-C-1-3). The authors extend sincere thanks to their financial support.

## References

[1] Zhou Xiaojun, Wang Jinghe, Lin Bentao. Study on calculation of rock pressure for ultra-shallow tunnel in poor surrounding rock and its tunneling procedure. ***Journal of Modern Transportation***. 2014, 22(1): pp:1-11.

[2] Zhou Xiaojun, Wang Jinghe, Hu Hongyun, Wang Xiaofeng. Structural Design of Highway Tunnel in Loose Surrounding Rock and its Tunneling Procedure. *International Conference on* Transportation, 2013, pp:80-87

[3] Zhou Xiaojun, Zhou Jiamei. ***Urban Metro and Light Rail Transit*** (in Chinese). Chengdu: Southwest Jiaotong University Press, 2012.

[4] Zhou Xiaojun, Yang Changyu, Wang Jinghe, Yu Xueying. Study on Structural Design and Construction Procedure for a Triple Arch Railway Tunnel. *The 4th International Conference on Digital Manufacturing & Automation*, 2013, *IEEE computer society*, pp:1299-1301.

[5] Zhou Xiaojun, Guo Rui. Design of Structure and Its Enclosure for Subaqueous Tunnel to Cross River in Urban Highway Line. *Applied Mechanics and Materials*, 2014, Vols: 488-489: pp: 390-393.

[6] Zhou Xiaojun, Hu Hongyun, Wang Xiaofeng. Design of a Subway Station Crossing Urban Trunk Road by Open Cut and Tunneling method. *The 4th international Conference on Digital Manufacturing & Automation*, 2013, *IEEE computer society*, pp: 457-460.

*Applied Mechanics and Materials Vols. 580-583 (2014) pp 1100-1104*
*© (2014) Trans Tech Publications, Switzerland*
*doi:10.4028/www.scientific.net/AMM.580-583.1100*

# Numerical Simulation for Construction Process Large-span Flat Tunnel Under the Condition of Shallow Buried

JunJie Li[1, a], Li Tuo[1,b] GuanJun Zhang[1,c]

[1] College of architecture and civil engineering, Xihua University, China

[a]18903911619@163.com, [b] 13980883865@163.com, [c] 15208214048@163.com

**Keywords:** numerical simulation; shall large span tunnel; benching with a small pilot tunnel tunneling method; surrounding; rock deformation; construction method

**Abstract.** The thesis takes a three-lane tunnel construction in Zhejiang as an example. Simulating the course of dynamic construction of large- span tunnel on geology condition of four- grade rock mass and shallow buried by FLAC 3D software ,it carries out comparative and stress situation in the runnel surrounding rocks .Getting the displacement and stress changes rule of the construction by using benching with a small pilot tunnel tunneling method can guide the construction scientifically.

## Introduction

Along with the increasing traffic demand and the continuous development of tunnel construction technology, there are more and more large-span tunnel engineering. Large-span tunnel has a flat shape, the characteristics of large span, so it is easy to affect the stability of surrounding rock in the process of construction. At the same time, Large-span tunnel's surrounding rock stress will be converged more easily, relaxation pressure will be bigger, the bearing capacity of the supporting structure will be relatively smaller. Large span tunnel out of hole construction must be not only ensure the construction safety, but also guarantee the progress of construction because great potential risk exist [1]. So it is necessary to do research on large-span flat tunnel under the condition of shallow buried way out of the hole.

## Project summary

The tunnel is a separated tunnel in Zhejiang , in accordance with the level of highway and urban road design standard, speed of 60 km/h, the width of 14.5 m, clear height of 5.0 m. Left hole is 646 meters long and right hole is 699 m long. Hole right out of the mouth of the cave is hilly slope landforms, weak rock weathering, through strong breeze ~ rock tunnel,as the same time the tunnel was buried of depth above 20 m, groundwater activity is stronger.There are drench and dripping water When it is excavated,The surrounding rock belongs to the Ⅳ level which stability is poor. This paper, by using FLAC 3D program , simulate for benching with a small pilot tunnel tunneling method through numerical analysis method.

## Finite element model and calculation parameters

Modeling selection scope is the inverted arch tunnel to the lower tunnel below 50 m, length of 129.1m, width at 149m,tunnel length 80 m.Model boundary condition are as follows: the bottom adopt displacement boundary conditions,both of the vertical and horizontal displacement are imposed constraint, the horizontal displacement lateral is imposed constraint, only the top for the free surface, not imposed any constraint.

The early bolting shotcrete primary support (thickness 20 cm) ,bolting and steel arch shelf are converted into the shotcrete in Stiffness contribution way in modeling[1].The surrounding rock used Mohr coulomb model ,according to geological exploration data,surrounding rock and supporting material parameters such as Table 1, calculation model is shown in Fig. 1.

Considering time and space effect, the construction process simulation of tunnel excavation release stress by 30%, 70% after tunnel primary support and the stress release. By only considering the stability of surrounding rock in the construction process, so it is simulated without the second lining[1].

Table 1 Model parameters

| | ρ/kg/m³ | E /GPa | μ | c /MPa | ϕ /° |
|---|---|---|---|---|---|
| Ⅳ | 2200 | 5 | 0.3 | 0.5 | 35 |
| Ⅲ | 2400 | 15 | 0.25 | 1.2 | 45 |
| Primary lining | 2500 | 21 | 0.2 | | |

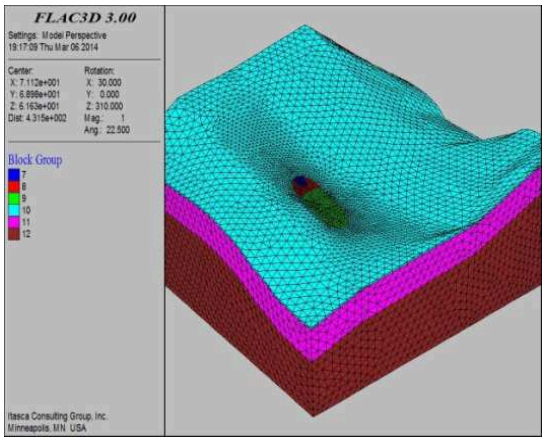


Fig. 1 Numerical simulation mode

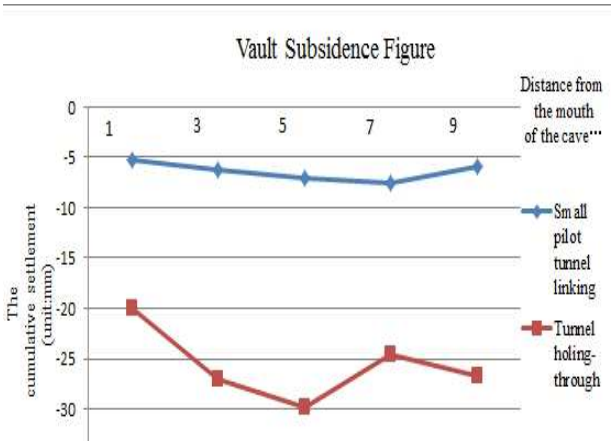


Fig.2 Vault subsidence (unit: mm)

**The analysis of numerical simulation results**

FLAC 3D software was used to calculate respectively the stress and displacement of surrounding rock and supporting structure in excavation process to get the stress and strain rules of surrounding rock when up and down the steps small pilot tunnel method applied.

As shown in figure 2,the surface range,vertical displacement and the vertical stress of surrounding rock of small pilot tunnel excavation are smaller,especially the data section of the surface subsidence after small pilot tunnel breakthrough is 2mm while the total settlement after the tunnel is 29.5mm,which shows that up and down the steps of small pilot tunnel method is a relatively safe method of out of the hold,which caused the relatively small disturbance to surrounding rock during construction.

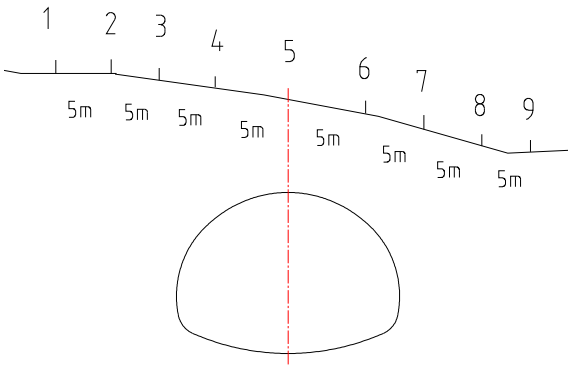


Fig. 3 The settlement measurement point of the surface

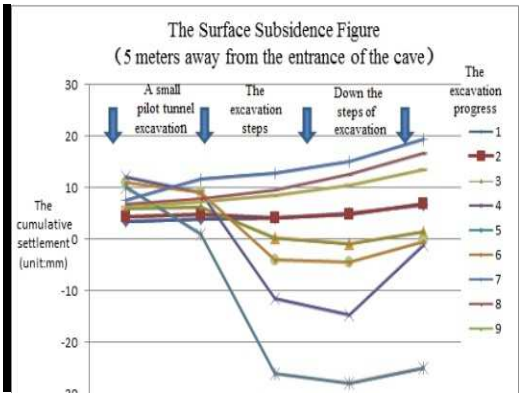


Fig. 4 Surface subsidence (5 meters away from the mouth of the cave) (unit: mm)

We can learn from figure 4 that the impact of small pilot tunnel excavation to ground surface settlement is small, but deformation increases significantly after step excavation. This is due to the large span on the steps which result in the stress concentration and cause settlement increases. The subsidence area is stable after supporting in bottom bench excavation, which states that the tunnel supporting closed loop can greatly improve the stability of surrounding rock.

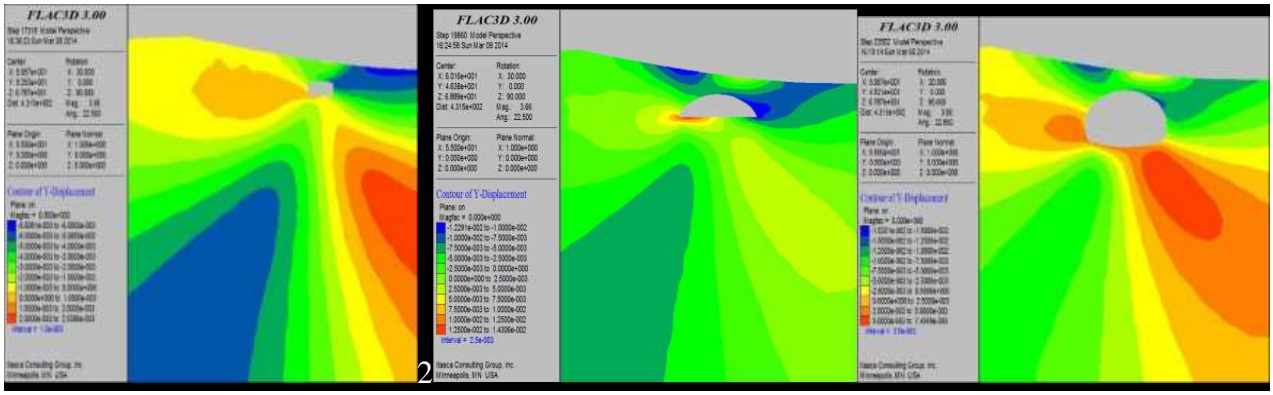


a) Small pilot tunnel linking b） Linking up the stairs c） Down the steps through

Fig. 5Hoeizontal deformation of surrounding rock
(5 meters away from the mouth of the cave) (unit: mm)

Fig.5 shows that sidewall astringed after small pilot tunnel linking, deep side of the arch foot parts astringed inward 2.54 mm, shallow buried side arch of astringed outward 6.6 mm, as shown in figure 6 a.Due to bias, after the up and down the steps through, the most obvious convergence is in deep side arch on shallow buried and side inverted arch and the largest amount of convergence is 7.5 mm.

Select 5 meters away from the mouth of the cave, buried depth of 6.9 meters of cross section to study.

Fig.6 shows that a small pilot tunnel excavation area is lesser, the disturbance of surrounding rock after excavation is smaller, the surrounding rock mass stress concentration phenomenon is not obvious. All excavation complied caused stress redistribution, the arch foot of surrounding rock exhibited obvious stress concentration phenomenon after up and down the steps excavation,local failure may occur in the practical construction this part, hence the construction of the arch foot foot bolt lock should be strengthened. The maximum vertical stress should be in the vicinity of a wall after tunnel linking.

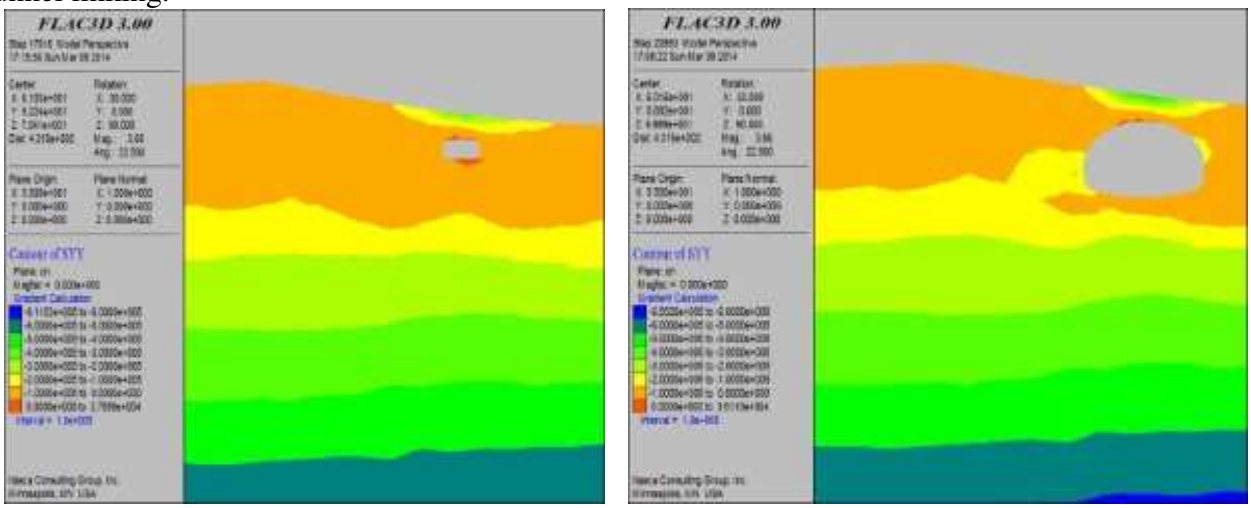


a) Small pilot tunnel linking b) Down the steps through

Fig.6 The stress cloud of surrounding rock (unit: kN / ㎡)

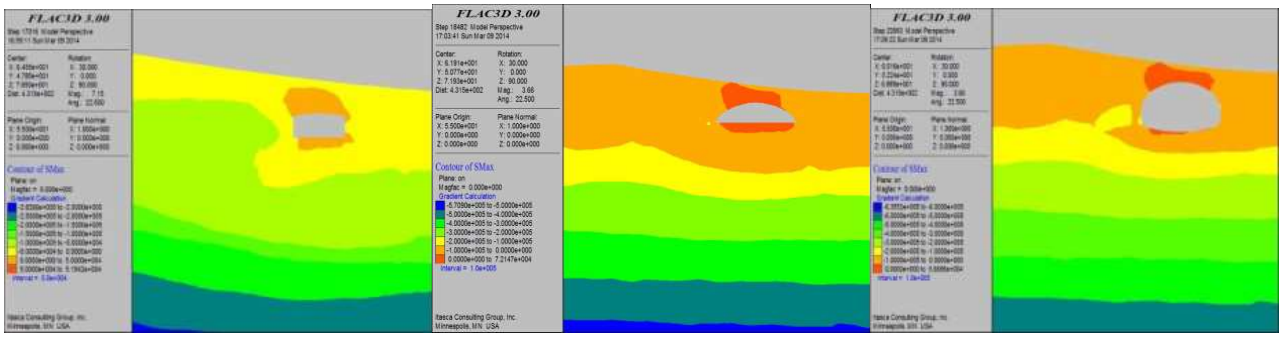

a) Small pilot tunnel linking b） Linking up the stairs c） Down the steps through

Fig.7 The first principal stress of surrounding rock (unit: kN/㎡)

Fig.7 shows that 0.05MP tensile stress produced on the top after small pilot tunnel excavation, along with the up and down the steps of excavation, tensile stress gradually increased to 0.06 MP.

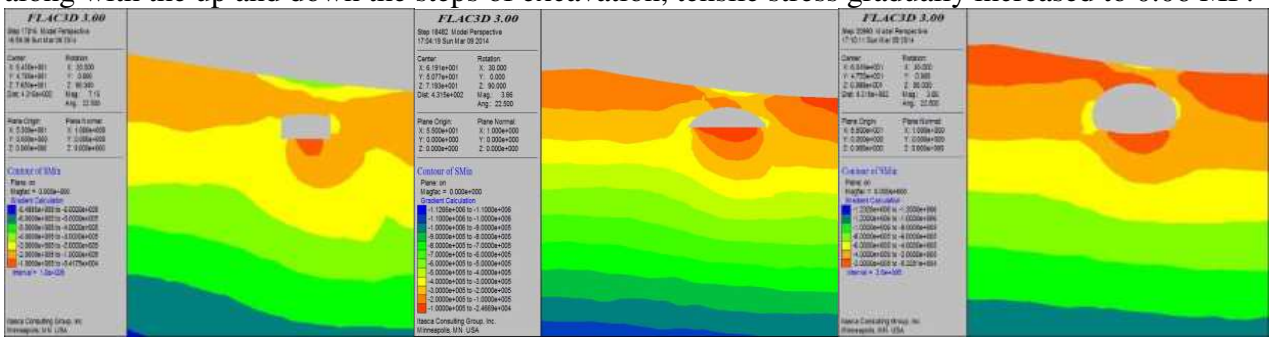

a) Small pilot tunnel linking b） Linking up the stairs c） Down the steps through

Fig.8 The third principal stress of surrounding rock (unit: kN/㎡)

Fig.8 shows that the third principal stress are mainly as follows:due to the influence of the bias effect,after small pilot tunnel breakthrough,surrounding rock stress distributed asymmetry, main stress direction from deep side to shallow buried side.Along with the excavation, on both sides of the arch waist has emerged the phenomenon of stress concentration, reached 0.04 MP and deep side stress concentration range is larger than shallow buried side, covering the arch foot position.so construction quality of lock foot bolt should be noticed during construction.

## Conclusion

The tunnel in Zhejiang province is simulated by using the FLAC 3 d software, there are some conclusions through analyzing stress ,displacement of surrounding rock and surface settlement of shall large span tunnel on condition of shallow buried .

1）Under the condition of shallow buried shall large span tunnel, the impact on surrounding rocks is little by using benching with a small pilot tunnel tunneling method, the rock surface range , vertical displacement and the vertical stress of surrounding rock are relatively small, relatively safe.so it is a good method .

2）The surrounding rock pressure will redistribute when a small pilot tunnel and up the step are excavated,there is tensile stress in the top of the tunnel , arch foot of deep-buried and arch arch crown of shallow-buried have a phenomenon of compressive stress concentration of different levels. Feet-lock bolt is paid special attention to strengthen the construction because the rocks near the feet-lock bolt may be failure

3）The benching with a small pilot tunnel tunneling method is better than others at construction resource utilization, schedule, the construction difficulty , process transformation and cost if the surrounding rock is better,and it can ensure the efficiency of the construction, speed and and safety .

4）The crown settlement and peripheral convergence change completely in the process of excavation, it needs to strengthen the monitoring , the real-time data from the monitoring guide the construction of scientifically

Supported by the Innovation Found of Postgraduate Xi Hua University

**References**

[1] Longxiang Huang and Hongyuan Yang:C*omparative Analysis and Application of The Construction Method in Shallow Large Span Tunnel*. (Highway Engineering,in china2011)

[2] Xiong Shi :*Study on stability of the VI-class surrounding rock of large-span shallow tunnel under unsymmetrical pressure*. Hunan University of Science and Technology, in china (2011)

[3] Xu Wang: *Three—steps-seven—footwork Tunnelling Method and Risk Analysis* Central South University, in china (2011)

[4] Dongping Zhao and Mingnian Wang: S*tudy on Construction Method of Large- span Tunnels by Numerical Simulation*.Chinese Journal of Underground Space and Engineering, in china (2011)

[5]Gao Wenxue and Sun Wenlong: Numerical Simulation and Monitoring Analysis for Construction Process of Shallow Tunnel Under Unsymmetrical Pressure. Construction Technology, in china (2011)

*Applied Mechanics and Materials Vols. 580-583 (2014) pp 1105-1111*
*© (2014) Trans Tech Publications, Switzerland*
*doi:10.4028/www.scientific.net/AMM.580-583.1105*

# Study on FEM Numerical Simulation and Strain Monitoring of Tunnel Secondary Lining

Yingna Li[1, a], Meng Liu[1, b], Sheng Wu[1, c], Hao Liu[2], Jiankun Su[2], Zhilin Zhang[2], Chuan Li[1, d]

[1]Faculty of Information Engineering and Automation, Kunming University of Science and Technology, Kunming 650500, Yunnan, China

[2]Yunnan Aerospace Engineering Geophysical Exploration Co., Ltd., Kunming 650217, Yunnan, China

[a]l_m1105@163.com, [b]529311411@qq.com, [c]lmkm1988@163.com, [d]boatriver@eyou.com

**Keywords:** tunnel engineering, separated tunnel, secondary lining, FEM numerical simulation, strain on-site monitoring

**Abstract.** Safety of secondary lining is of utmost importance to tunnel engineering quality as the main load-bearing structure and the last waterproof line of rock tunnel under type III. The comparative study of strain state results from FEM numerical simulation and on-site monitoring in Yunnan Tianxin Tunnel was conducted to obtain the stress regularity of tunnel lining. The results showed that except vault, the strain states of secondary lining obtained by numerical simulation and on-site monitoring were consistent. The strain value of on-site monitoring was approximately 60%~70% to the simulation value. And the strain value of right side was greater than the value of the corresponding location on the left side. It's noticed that high strain were found in tunnel haunch and arch springing. Great attention should be paid to arch springing for the largest strain value. The strain monitoring value of vault (309.83με~327.23με) has been detected larger than simulation value (209.37με), which matches well the crack phenomenon of vault. Therefore it's significant to focus on the long-term monitoring of vault. The defects of single on-site monitoring method such as poor predictability were made up effectively by comparative study. The results achieved can be recommended for similar projects.

## Introduction

With the increasing development of economy, more and more highway tunnels are constructed [1]. Nowadays composite lining structure is prevailing of the high-grade highway tunnel construction, which consisted of primary support, secondary lining and the waterproof layer between them [2]. For rock tunnel under type III, safety of secondary lining is of utmost influence on tunnel engineering quality as the main load-bearing structure and the last waterproof line of tunnel. Thus the stress monitoring and analysis of secondary lining are of great significance for the tunnel [3]. As an important part of NATM, tunnel monitoring measurement plays a vital role in guaranteeing the construction safety, optimizing the support structure and reducing the materials consumption. However the limited results and poor predictability can be obtained from on-site monitoring owing to the restricted field condition and measuring method, measurement error and data deficient [4-7]. FEM numerical simulation is widely employed as aid in tunnel monitoring measurement result from the merits of perceptual intuition, fast, economical and experiment repeatedly [6,8]. The combination of the FEM numerical simulation and on-site monitoring is beneficial to understand the stress regularity of secondary lining in construction process comprehensively, and also the defects of single on-site monitoring method such as poor predictability can be made up effectively [7,9]. It's therefore significant for the combination method in realizing tunnel information construction.

In this study, taking Yunnan Tianxin Tunnel as the research object, FEM numerical simulation and long-term on-site monitoring of secondary lining strain were conducted. And the stress state of

secondary lining was analyzed through the comparative study which can be recommended for similar projects.

**Tianxin Tunnel Engineering Situation**

TianXin Tunnel is a two-tube, two-lane separated tunnel which is the control project of Yunnan Yi Egao second-class highway. Its beginning and ending stake numbers are shown as follows: Left K47+100~K49+220 (total 2120 meters); Right K47+073~K49+345 (total 2272 meters). The maximum buried depth of tunnel is 257meters. And the midlines distance between left range and right range is 30meters approximately. The tunnel is located in medium low mountain gentle slope area that makes a shallow cut, outcropping Mesozoic "red rock", with 1500~1900 meters above sea level and the relative height difference of 100~500 meters. With accordance of summit levels the mountaintop is rounded. And the slope gradient is about 20 degrees with shape "V" valleys. The lithological characters of the tunnel area are mainly mud rock, mingled with sandstone, argillaceous sandstone and conglomerate. The tunnel mainly passes through the class IV and V surrounding rock. The supporting structure of the tunnel designed by NATM is composed of primary lining and secondary lining. And inner contour is designed to the single-center circle curved wall lining structure of which radius is 5.5 meters with 11 meters wide and 7.10 meters high, as shown in Fig.1.

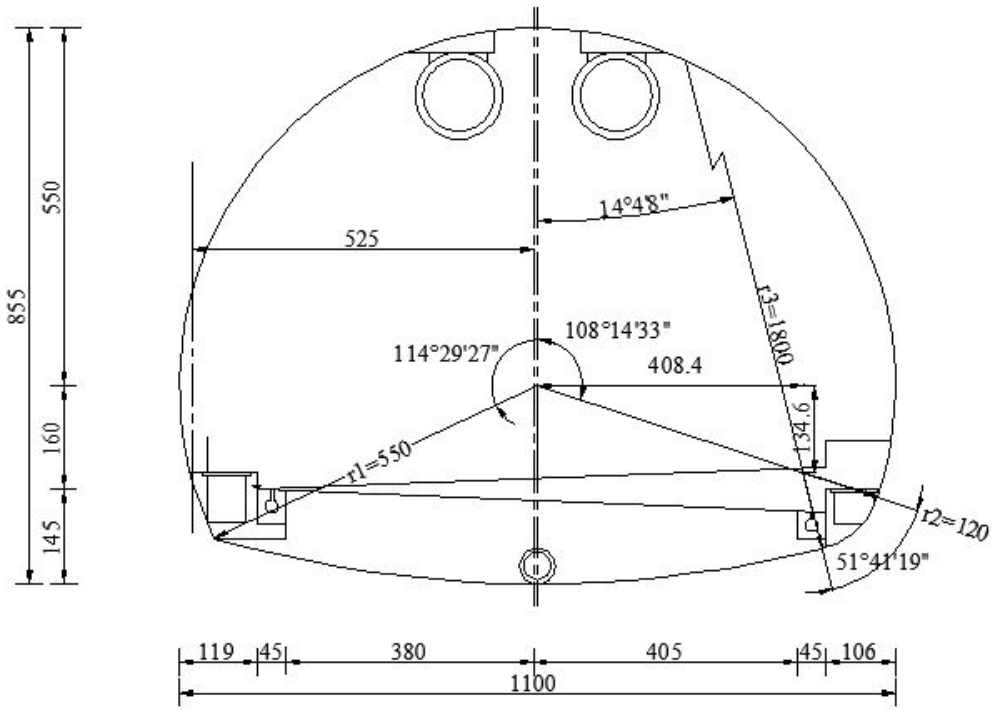


Fig.1 Inner contour drawing of the tunnel (unit: cm)

**Finite Element Model of Tunnel Structure**

The FEM numerical simulation and analysis on secondary lining strain state of right Section K47+808 were conducted by using ANSYS FEM analysis software in this part.

**Ansys Finite Element Model and Simplification.** Right section K47+808 that using type S5b composite lining structure is located in class IV (type III) surrounding rock with about 158.2 m burial depth. Its primary lining and secondary lining thickness are 25 cm and 50 cm respectively. The plane strain model of elastic theory was built in which element Plane42, Beam3 and Link1 simulated the surrounding rock and primary lining, secondary lining and anchor separately. Utilizing the method of improving the rock mechanical parameters of reinforcement area of which reinforcement range was 3.5 m (the length of anchor bolt) simulated the supporting effect of advanced small pipe, steel mesh reinforcement and structural steel support [10]. Based on Saint Venant's principle, the left and right

calculating boundary was 5 times the width of the tunnel, and the lower and upper calculating boundary was 3 times and 2 times the height of the tunnel respectively. Meanwhile the vertical uniform loads (3350.41kPa) were applied to the upper boundary. The benching tunneling method was simulated by the technique of "birth and death of element". The stress releasing was simulated by the method of applying virtual support force to release the stress step by step [11]. The coefficient of stress releasing was 0.6 when the primary lining was built. After secondary lining built, the stress released entirely. The FEM computation model and mesh generation were presented in Fig.2.

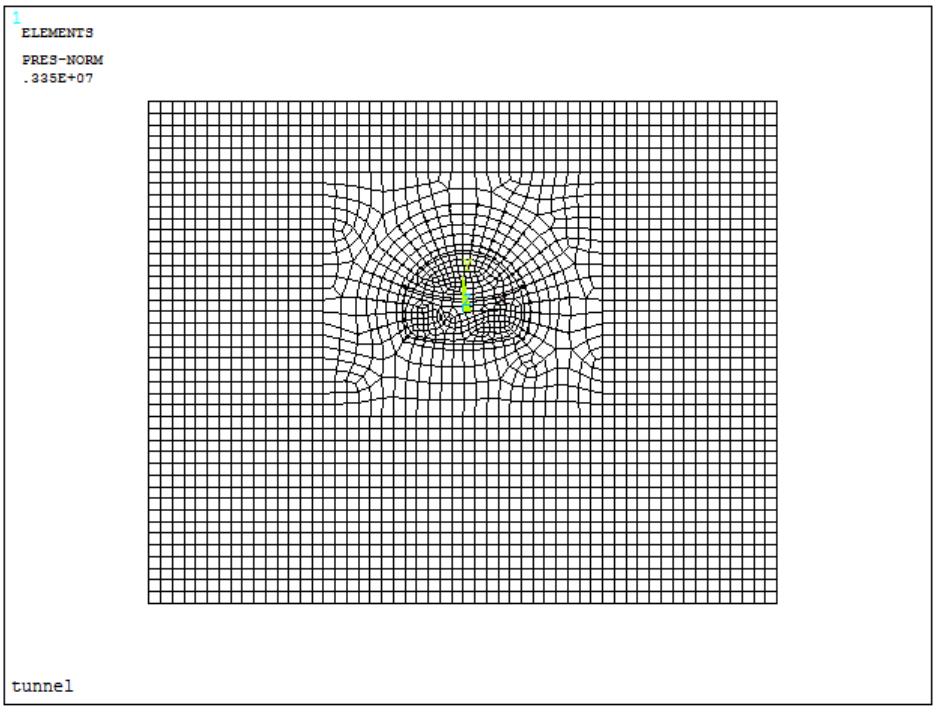


Fig.2 The FEM computation model and mesh generation

**The Parameters of Tunnel Model.** According to Code for Design of Road Tunnel (JTG D70-2004) [2], Code for Design of Concrete Structures (GB 50010-2010) [12] and Technical Regulations for Hollow Bolt (TB/T 3209-2008) [13], the material parameters of surrounding rock, support structure and anchor bolt were selected in Table 1.

Table 1 The parameters of materials in computation model

| Materials | Elastic Modulus E[GPa] | Poisson Ratio μ | Density γ[kN/m$^3$] | Cohesion c[MPa] | Frictional Angle φ[$^o$] |
|---|---|---|---|---|---|
| Surrounding rock(IV) | 6 | 0.35 | 23 | 0.7 | 39 |
| Reinforcing ring(III) | 10 | 0.3 | 25 | 1.5 | 50 |
| Primary lining | 28 | 0.2 | 25 | - | - |
| Anchor bolt | 206 | 0.3 | 78.5 | - | - |
| Secondary lining | 28 | 0.2 | 25 | - | - |

**Analysis of Strain Simulation Results.** The simulated secondary lining axial strain of Tianxin Tunnel right Section K47+808 was shown in Fig.3.

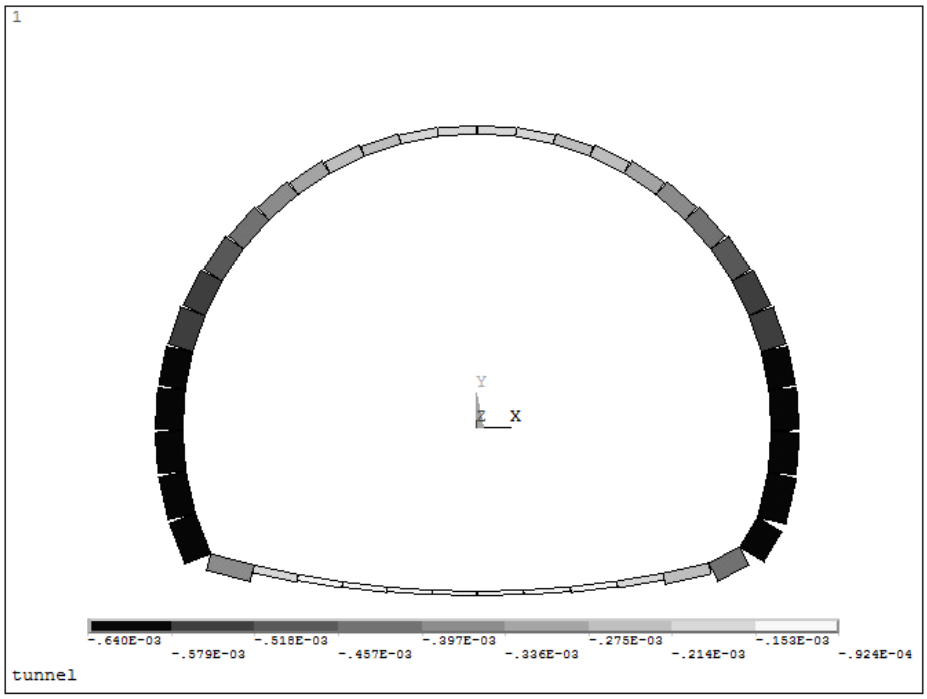


Fig.3 Axial strain of the secondary lining on Section K47+808 (unit: με)

It was observed from the simulation result that the secondary lining strain of this section was compression strain and the strain value of right side was greater than the value of the corresponding location on the left side. The strain gradually increased from vault to arch springing. It was noticed that high and low strain values were found in the position from haunch to arch springing and the inverted arch respectively. The strain varied from 92.40 με to 639.87 με. The minimum strain (92.40 με) occurred in the middle of inverted arch (element 5810) and the maximum strain (639.87 με) occurred in right arch springing (element 5841). The strain (613.50 με) of left arch springing (element 5827) was also large. The values of haunches, spandrels and vault were 483.15 με (left haunch), 522.42 με (right haunch), 373.29 με (left spandrel), 441.77 με (right spandrel) and 209.37 με (vault) separately. Great attention should be paid to the position from haunch to arch springing after secondary lining built.

## Tunnel Monitoring Scheme

For the purpose of monitoring the secondary lining stress state of Tianxin Tunnel for long time, 10 representative sections were respectively selected in the left and right holes according to the progress and defect of the project. The spacing of sections was 20 meters. The monitoring mileage of left hole were K47+770, K47+790, K47+810, K47+830, K47+850, K47+870, K47+890, K47+910, K47+830, K47+950 and the monitoring mileage of right hole were K47+810, K47+830, K47+850, K47+870, K47+890, K47+910, K47+930, K47+950, K47+970, K47+990. Based on the strain distribution of the numerical simulation, the embedded FBG strain sensors were installed on the secondary lining main reinforcement of the sections above, as shown in Fig.4.

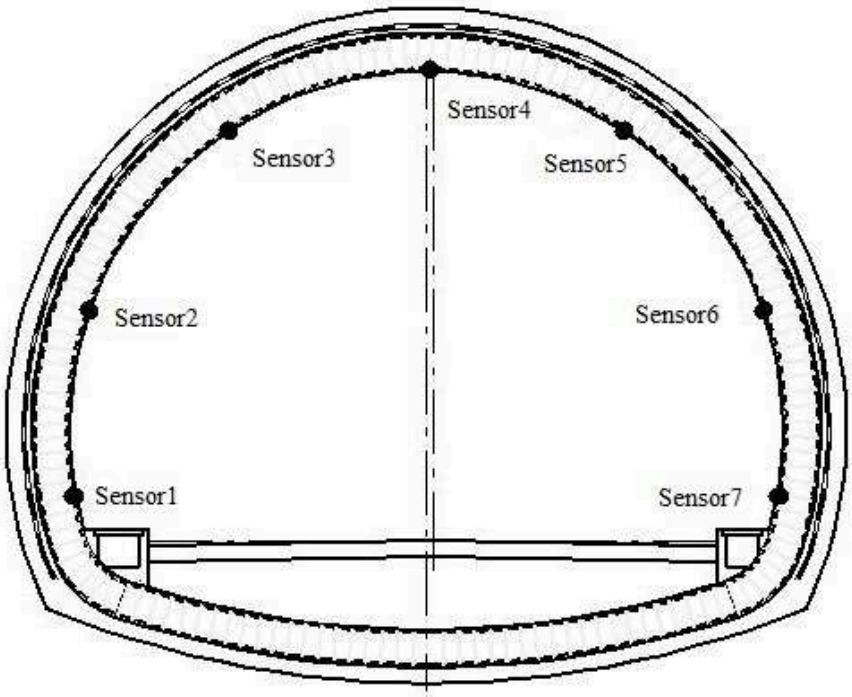


Fig.4 Layout of the strain monitoring point in secondary lining

The embedded FBG strain sensors were installed from August 1, 2011 to April 29, 2012. The collection frequency of the strain data was provided in Table 2.

Table 2 Collection frequency of the strain data

| Measurement Item | Instrument Equipment | Collection Frequency | | | |
|---|---|---|---|---|---|
| | | 1-15d | 16-30d | 30-90d | >90d |
| Strain of Secondary lining | The Embedded FBG Strain Sensor | 1time/d | 1time/2d | 1-2times/7d | 1-3times/30d |

The strain formula of the embedded FBG strain sensor used in monitoring was as follows:

$$\varepsilon = K * \left[ \lambda_1 - \frac{(\lambda_{t1} - \lambda_{t0}) * K_t}{K_w} - \lambda_0 \right] \tag{1}$$

Eq.(1), $K$ was the strain sensing coefficient of FBG strain sensor( $\mu m / nm$ ); $K_t$ was the temperature sensing coefficient of FBG strain sensor( $C / nm$ ); $\lambda_1$ was the current wavelength of FBG strain sensor( $nm$ ); $\lambda_0$ was the initial wavelength of FBG strain sensor( $nm$ ); $K_w$ was the temperature sensing coefficient of FBG temperature sensor( $C / nm$ ); $\lambda_{t1}$ was the current wavelength of FBG temperature sensor( $nm$ ); $\lambda_{t0}$ was the initial wavelength of FBG temperature sensor( $nm$ ).

**Analysis of Strain Monitoring Data**

Strain monitoring of secondary lining had been conducted on right Section K47+808 for sixteen months. The variation of secondary lining strain on time was presented in Fig.5.

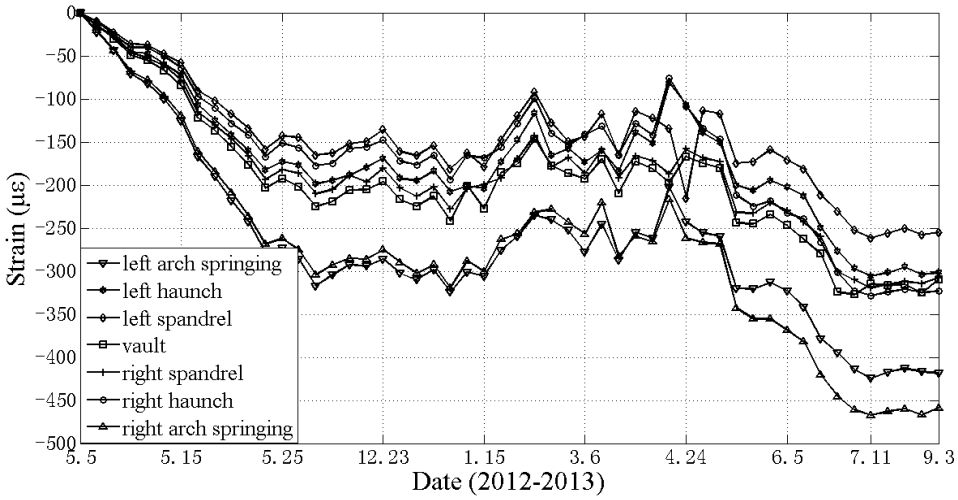


Fig.5 The space-time diagram of secondary lining strain on right Section K47+808 of Tianxin Tunnel

The monitoring results showed that the stress of secondary lining was asymmetric compression state. And the strain of right side was greater than the value of the corresponding location on the left side. The arch springing value was larger than haunch and spandrel. During June 2013 to September 2013, the monitored strain value of secondary lining had been basically stable. The maximum strain reached to 472.44 με occurred in the right arch springing, which was in the range of the safety variation. The stress state of right section K47+808 was in line with the stress regularity of tunnel secondary lining. Great attention should be paid to the changes in arch springing of secondary lining due to its greater strain monitoring value.

According to the buried position of embedded FBG strain sensors on right section K47+808, the simulated strain value of corresponding position on the finite element model was selected to be analyzed compared to monitoring value, as listed in Table 3.

Table 3 Comparison of the on-site strain monitoring data and simulation results on right Section K47+808 of Tianxin Tunnel

| Positions | Strain Variation Range of Monitoring Stable Value (2013.6~2013.9) | Strain Simulation Value |
|---|---|---|
| left arch springing | -424.27με~-413.08με | -613.50με |
| left haunch | -306.07με~-294.88με | -483.15με |
| left spandrel | -261.66με~-250.47με | -373.29με |
| vault | -327.23με~-309.83με | -209.37με |
| right spandrel | -319.73με~-307.78με | -441.77με |
| right haunch | -328.61με~-320.84με | -522.42με |
| right arch springing | -467.31με~-458.78με | -639.87με |

Comparison of monitoring data with simulation results showed that except vault the simulation results coincided with the monitoring data quite well. However the strain value of on-site monitoring was smaller than simulation results and was approximately 60%~70% to the simulated value. This is mainly because the on-site strain monitoring of this section started with the sixth measurement value (May 5, 2012) and the monitoring value later was based on it. The whole strain of secondary lining couldn't be measured, which resulted in smaller monitoring value. The strain monitoring value of

vault had been detected larger than simulation value, which matched well the crack phenomenon of vault on this section. Therefore it's significant to focus on the long-term monitoring of vault.

## Conclusions

The comparative study of strain states resulted from FEM numerical simulation and on-site monitoring on right section K47+808 of Tianxin Tunnel was conducted. The results showed that:

(1)Except vault, the strain states of secondary lining obtained by numerical simulation and on-site monitoring were consistent. The strain value of on-site monitoring was approximately 60%~70% to the simulated value. The stress of secondary lining was asymmetric compression state. And the strain value of right side was greater than the value of the corresponding location on the left side. It's noticed that high strain was found in tunnel haunch and arch springing. Great attention should be paid to arch springing for the largest strain value.

(2)The strain monitoring value of vault (309.83 με~327.23 με) has been detected larger than simulation value (209.37 με), which matches well the crack phenomenon of vault. Therefore it's significant to focus on the long-term monitoring of vault. The defects of single on-site monitoring method such as poor predictability were made up effectively by comparative study, which proved that this method was effective in the process of tunnel construction.

## References

[1] Keguo Sun, Shucai Li, Qingsong Zhang, et al. Chinese Journal of Rock Mechanics and Engineering, 2007, 26 (z2):4465-4470

[2] JTG D70-2004, Code for Design of Road Tunnel[S], 2004

[3] Tingjin Liu, Hehua Zhu, Wenqi Ding. Chinese Journal of Rock Mechanics and Engineering,2004, 23(2):75-78

[4] Tai Bao, Yue Shui. Journal of Guizhou University(Natural Sciences), 2009, 26 (4):131-133

[5] Yongqiang Yu, Yaobang Lu, Weinian Zhong, et al. Highway Engineering, 2011, 36 (4):1-3

[6] Zhe Hao, Wei Li, Bin Liu. West-China Exploration Engineering, 2005, (2):96-98

[7] Zhewen Xu. Journal of Transportation Systems Engineering and Information Technology, 2008, 8(4):127-131

[8] Changxiang Liu, Changxin Lu. Chinese Journal of Underground Space and Engineering, 2007, 3(4):688-692

[9] Xiaowang Zhang, Jinsheng Nie. Highway Engineering, 2008, 33(5):99-103

[10] Yang Zhao, Weibi Wang, Changneng Yang. Central South Highway Engineering, 2005, 30(2): 181-184

[11] Feng Gao, Chang-xin Sun. China Journal of Highway and Transport, 2010, 23(4):70-77

[12] GB 50010-2010, Code for Design of Concrete Structures[S], 2010

[13] TB/T 3209-2008, Technical Regulations for Hollow Bolt[S], 2001

*Applied Mechanics and Materials Vols. 580-583 (2014) pp 1112-1115*
*© (2014) Trans Tech Publications, Switzerland*
*doi:10.4028/www.scientific.net/AMM.580-583.1112*

# Study on Simulation Analysis of Excavation Deep Foundation Pit in Qingnian Road Station of Tianjin Subway Line 2

Yang Bai[1, a], Pengbo Cui[1,a] , Jingbo Wu[2,a] and Lei Wu[3,a]

[1] JiangSu JianZhu Institute, China

[2]Hangzhou city housing and urban construction bureau, China

[3] CCCC First Highway Consultants Co., China

[a]1106162187@qq.com

**Keywords:** MIDAS GTS,deep foundation pit,analogue simulation, retaining structure,Tianjin Subway

**Abstract.** On the basis of hydrogeology data,Mohr-Coulomb constitutive model in software MIDAS GTS was employed to simulate excavation deep foundation pit in Qingnian Road station of Tianjin subway line 2 after each excavation step of different construction procedures.It is positive scinentifcity for simulating excavation pit ahead of time and predicting its deformation and displacement characteristics in the foundation pit,and it is significant for the timely revision of the schemes in the next construction process.

## Introduction

With the development of economy of China,subway plays a vital role in overall arrangement of a city,such as city planning,traffic,economy and environment and so on.The primay task in constructing subway is to maintain the stability of enclosure structure of subway station.Deep excavation is fundamental basis of subway station.To ensure its security is significant economic and social benefit. The excavation of the subway station has great influence on the surrounding environment,which may affect the safety of the adjacent constructions and the underground pipelines.Moreover water gushing and collapse accidents may occur when shield tunneling entering or leaving the well.In order to avoid or mitigate these harmful effects,it is necessary to study the variation laws of the stress and deformation of supporting system and the ground surface during the excavation.

## The General Situation of the Project

The QingNian Road station of Tianjin subway line 2 is located near a junction of Huanghe Avenue,Qingnian road and Yuci road in Nankai district, Tianjin. The station start stop mileage is DK7+931.203～DK8+122.803, the mileage of the station center is DK8+022.003.The length of Qingnian station is 191.600m, the main structure is double-story and double-span frame structure (island style), the length of deep foundation pit of the station is 191.600m,the width of the standard section is 21.00m,the depth of the standard section is 16.000m. Retaining structure of foundation pit is diaphragm wall with reinforcement concrete and steel struts,the width of diaphragm wall is 0.8m. the standard width of the diaphragm wall is 6m, Adjusted the width according to external situational changed, the joint of continuous wall is aligned with the induction joint. Constructed the reinforcement concrete top beam and the size of beam section is $b \times h$=1.0m×0.8m. The main station steel strut is φ 600 × 14 steel pipe, the steel struts are assembled on site according to the width of the foundation pit and the deviation of center line must be less than 20mm, The steel struts moving end and fixing end are required to meet the force and setted the jack to support the pre axial force in the steel side.The parameters of strata are shown in Table 1 and the parameters of supporting measures are shown in Table 2.

Table 1.Parameters of strata

| Stratigraphics | Elastic modulus /kpa | Poisson ratio | Weight /( $KN \cdot m^{-3}$ ) | Cohesion /kpa | Frictional angle /( ° ) | Initial stress parameter $K_0$ |
|---|---|---|---|---|---|---|
| Filling soil | 5000 | 0.42 | 20 | 15 | 15 | 0.63 |
| Silty clay | 18000 | 0.36 | 20 | 9 | 9 | 0.42 |
| Mud limestone | 500000 | 0.24 | 28 | 300 | 36 | 0.36 |

Table 2.Parameters of supporting measures

| Title | Elastic modulus /Mpa | Poisson ratio | Weight /( $KN \cdot m^{-3}$ ) | Section types |
|---|---|---|---|---|
| Diaphragm wall | 30000 | 0.2 | 25 | 0.8m thickness |
| Reinforced concrete support | 30000 | 0.2 | 25 | 0.8m width, 1.0m height, square |
| Steel support | 200000 | 0.25 | 78 | 0.6m diameter，pipe wall thickness 0.012m ，pipe |

**The excavation procedures**.The foundation pit is excavated from top to bottom and the main station foundation pit excavation is divided into 5 layers, the excavation procedures are as follows:

Step 1, analyzing initial earth stress, earthwork excavation began in the consolidation settlement of soil under the action of self weight in the construction;

Step 2,diaphragm wall construction;

Step 3,diaphragm wall construction and concreted the first reinforced concrete support;

Step 4,Excavated 4.8 meters below the surface and constructed the second steel support;

Step 5,Excavated 8.8 meters below the surface and constructed the third steel support;

Step 6,Excavated 12.8 meters below the surface and constructed the fourth steel support;

Step 7,Excavated to the bottom of the pit (16.0 meters below the surface) ,as is shown in Fig.1.

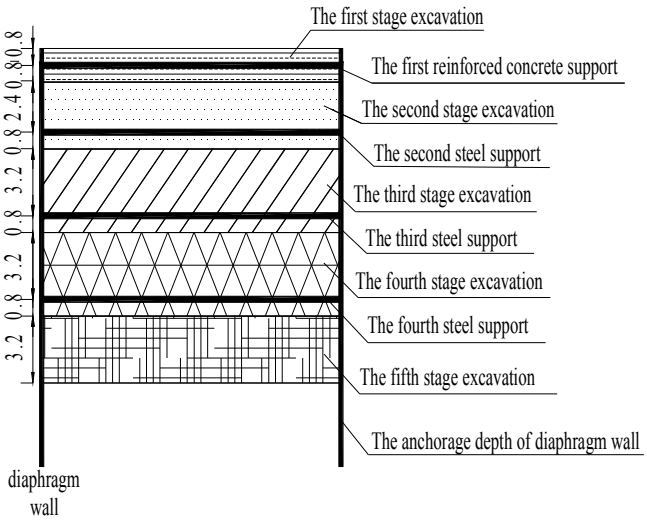


Fig.1 Schematic diagram of excavation sections

Fig.2 Schematic diagram of excavation sections in midas gts

Then established the model of schematic diagram of excavation by using Mohr-Coulomb constitutive model in software Midas (As is shown in Fig.2).

The grade of deformation-control foundation pit:

1.The safety grade of the main station foundation pit support structure is the first degree.

2.The Maximum ground surface settlement≤0.1%H.

3.The horizontal shifting of the diaphragm wall $\delta_h \leq 0.14\%H$， and $\delta_h \leq 30mm$ .

**Basic assumptions.**Being satisfied with the conditions of the calculation accuracy and making correct conclusions, basic assumptions to simplify the calculation are as follows:

1.The materials are homogeneous and isotropic,
2.The soil is considered as the perfect elastic-plastic material,
3.Ignores the stiffness change caused by diaphragm wall segmental construction,
4.Steel and concrete supports are considered as linear elastic materials.

**Analysis of numerical results.**

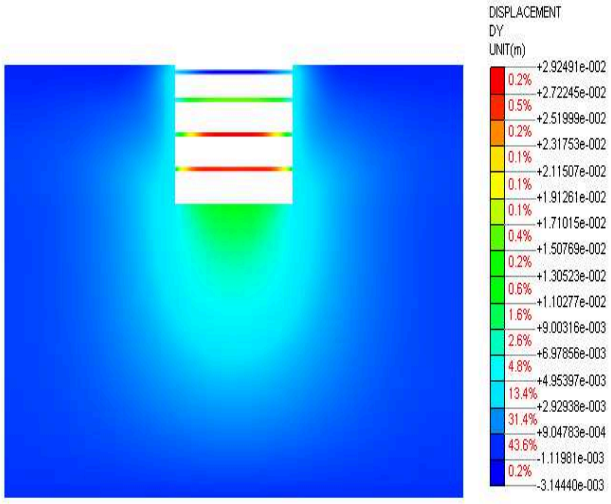


Fig.3 Displacements in *y* direction

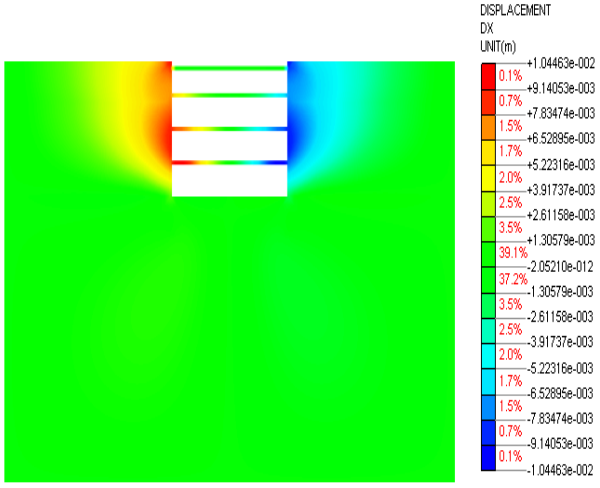


Fig.4 Displacements in *x* direction

As is shown in Fig3.The maximum of uplift of the bottom of foundation pit is 11.8mm where occurs in the central regions of the bottom of foundation pit.The maximum of uplift of the top of foundation pit is 4.8mm. The figures are less than the specified value of the grade of deformation-control foundation pit ,so that the excavation process is safe and reliable.

As is shown in Fig4.The maximum of horizontal deformation of the diaphragm wall is 9.13mm, The figures are less than the specified value of the grade of deformation-control foundation pit ($\delta h \leq 0.14\%H=22.4mm$ and $\leq 30mm$) .Along with the increase of the depth of excavation, horizontal displacement of steel support restraint decreases gradually. Therefore, in the process of excavation, it's need to increase the other auxiliary supporting structures.

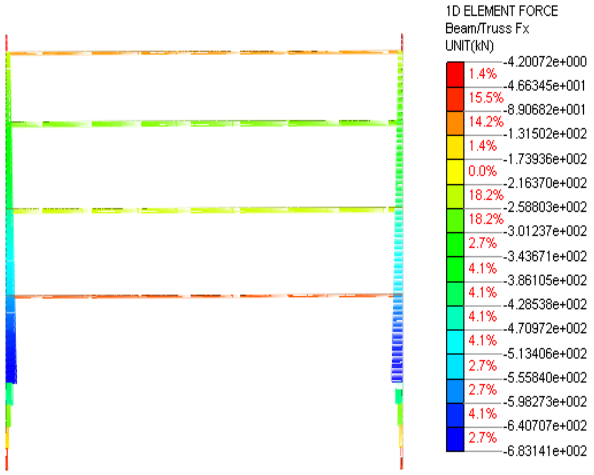


Fig.5 Axial force of retaining structure

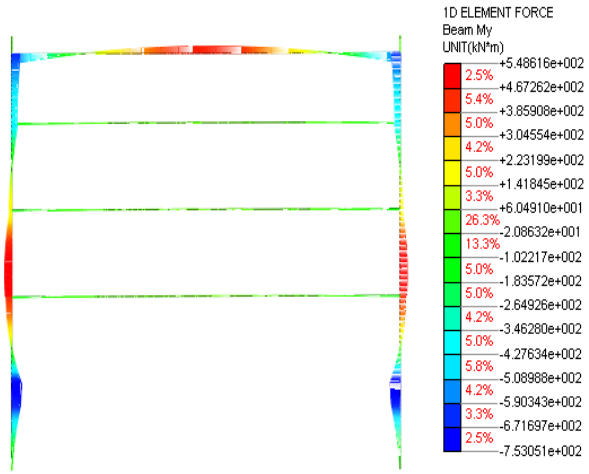


Fig.6 Bending moment of retaining structure

The axial force of the diaphragm wall increases along with the depth of excavation according to the *x* direction of axis of the retaining structure of foundation pit(as is shown in Fig.5) and the maximum of axial force is $6.67*10^2 KN$. While with anchorage depth of the diaphragm wall (4 metres) increases the axial force goes down.The axial force of the first,second and the third supports are high and the forth support is low for the strength of lower layer of soil is more higher.

For the first reinforced concrete support,the diaphragm wall can be considered to a beam structure.As is shown in Fig.6,the bending moment of the upper part and lower part of the wall is

$6.41*10^2 KN•m$ and $5.33*10^2 KN•m$， the maximum bending moment is $7.53*10^2 KN•m$ at the bottom of the deep foundation pit. The first reinforced concrete support can be considered as two fixed ends beam , the maximum bending moment of the first reinforced concrete support are $4.56*10^2 KN•m$ and $6.61*10^2 KN•m$ at the fixed ends and the middle of the support.The bending moment of three steel supports are very small.

Through the numerical simulation analysis of the excavation deep foundation pit in Qingnian Road station of Tianjin subway Line 2, the design of retaining structure of the deep foundation pit is safe and reliable, the construction of the layer-step method excavation is safe and feasible. The foundation pit is stable, numerical simulation can predict the displacement and internal force of important parts of retaining structure of the deep foundation pit which can guide the correction of foundation pit scheme.As for the foundation pit, soil is the main source of load, and a part of the support system , the deformation of supporting structure not only influences the stability of foundation pit, also can make the load and the distribution of soil are changed; as the foundation of inner soil have been digging pit, which reduces the supporting role of inner soil continuous wall.

## Conclusions

Deep foundation pit of subway station is a systematic project, due to the complexity of the soil medium and timeliness, and the diversity of the support and the environment, so the use of numerical simulation of the finite element method can more fully from the space, time, reflecting a variety of factors on the supporting structure and surrounding soil stress and displacement effects.By using Mohr-Coulomb constitutive model in software Midas,the numerical simulation was carried out to research the deep excavation of subway station in Qingnian Road station of Tianjin subway line 2. Analysed the deformation of foundation pit which includes the displacement of supporting structure,the deformation of soil in the pit and near the pit, the internal force of the retaining structure with struts .And the theoretical basis and guidance are provided to actual engineering and these can contribute to improve the structutre design and construction level and safety.Valuable design,construction and scientific research experiences are accumulated and provided to the similar engineering.

The excavation of foundation pit has obvious spatial effect, exposure time after excavation has great influence to the deformation of foundation pit. The construction procedures of foundation pit excavation should be reasonably arranged by the principle of “the first support then slotting,the first support then excavation,excavates layer by layer, avoid excessive excavation”.

## Acknowledgements

This work was financially supported by the Shaanxi Natural Science Foundation (2007E232), and Shaanxi Provincial Department of Education natural science research project (08JK334).

## References

[1] LIU Jian-hang,HOU Xue-yuan.Excavation Engineering Handbook.Beijing,China Architecture and Building Press,1997( in Chinese)

[2] YANG Xue-qiang,LIU Zu-de,HE Shi-xiu.Research about spatial Effect of Deep Pit Supporting.Chinese Journal of Geotechnical Engineering,1998,20(2):74-78(in Chinese)

[3] SUN Kai,XU Zhen-gang,LIU Ting-jin,et al.Construction Monitoring and Numerical Simulation Analysis of a Foundation Pit.Chinese Journal of Rock Mechanics and Engineering, 2004, 23(2):293-298.(in Chinese)

[4] GAO Wen-hua,YANG lin-de,SHEN Pu-sheng.Influencing Factors of the Space-Time Effect on the Timbering Structure Internal Force and Transmutation of Soft Clay Deep Foundation Pit.Journal of Civil Engineering,2001,34(5):90-96.(in Chinese)

*Applied Mechanics and Materials Vols. 580-583 (2014) pp 1116-1121*
*© (2014) Trans Tech Publications, Switzerland*
*doi:10.4028/www.scientific.net/AMM.580-583.1116*

# The Application of Getting $R_c$ Value from Point Load Test and Rebound Test by Tunnel Surrounding Rock Classification System

Rixu Wang[1, a], Zhongchen Yuan[2,b]

[1]Shenyang Jianzhu University,Hunnan East Road 9th, Hunnan Region, Shenyang, China

[2]Shenyang University of Technology,Guanghua Road 30th, Hongwei Region, Liaoyang, China

[a]alsun1010@163.com, [b]yuanzhongchen@163.com

**Keywords:** POINT LOAD; REBOUND; TUNNEL SURROUNDING ROCK; ROCK CLASSIFICATION; MATLAB TECHNOLOGY.

**Abstract.** The point load test and rebound tests were part of a simple rock testing methods, which together with a user-friendly, work environment characterized by less demanding test, so test the application of rock in the tunnel are very broad. Obtained by these two tests of rock uniaxial compressive strength Rc saturation level for the characterization of rock hard quantitative indicators, in the rock classification has a high status. With the computer technology in tunnel works in the field of application that can batch test data to establish the tunnel surrounding rock classification system. Article is based on two kinds of test in the same tunnel project in contrast to the use, through the rock classification system to analyze and evaluate both.

## Introduction

Tunnel is one kind of chamber architecture built in rock mass which has stress history and tectonic signs. Thus, correct classification on the rock level is related to tunnel design, construction program, construction costs, etc.. In recent decades, tunnel surrounding rock classification is regarded as one of the most important research contents in tunnel technique all over the world. In China, the classification should be a combination of qualitative and quantitative methods, so rock grading sections are generally determined by field experience. Undoubtedly, various tests in the surrounding rock mass must be accurate enough so that the consistent results of field observations and field test can finally judge the level of surrounding rock. The main index like $R_c$(rock uniaxial saturated compressive saturated compressive strength), however, can greatly influence the result of level classification. Indeed, this kind of indexes need combination of unified factors and artificial intelligence system[1-2], and point load test and rebound test offer the possibility for $R_c$ as an example.

## The Theory of Reflecting the Rock Mass by $R_c$

By the standard of Engineering classification of rock mass(GB50218-94, China), there has the following correspondence between rock uniaxial compressive strength and rock hardness divided qualitatively in Table 1.

**Table 1 The corresponding relationship between Rc and qualitative division of rock hard degree**

| *Rc* [MPa] | >60 | 60~30 | 30~15 | 15~5 | <5 |
|---|---|---|---|---|---|
| Rigidity | Hard Rock | Subhard Rock | Subsoft Rock | Soft Rock | Extremely Soft Rock |

Commonly used index BQ represents the basic quality of rock, and it is determined by rock uniaxial compressive strength and rock mass integrity index. Their relationship is shown as Eq. 1.

$$BQ = 90 + 3R_C + 250K_V \quad (1)$$

(Restrictions: when $R_C > 90K_V + 30$, $R_C = 90K_V + 30$, and when $K_V > 0.04R_C + 0.4$, $K_V = 0.04R_C + 0.4$)

## The Achievement of $R_c$ Value in Grading System for Tunnel Surrounding Rock

Based on the MATLAB technology, grading system for tunnel surrounding rock relying on GB50218-94 can be built. There are qualitative classification, quantitative classification and BQ correction three modules step by step in order to establish the ultimate level of the rock mass and guide engineering[3-5]. Combined with point load test data and rebound test data, field parameters analysis opens up a path to get $R_c$ and BQ at the investigation stage.

Point load test data needs to entry D[cm], L[cm], P[kN] as the format at the input, and the data of single test block forms a row. Files at the input must be EXCEL format so that they can form tabular database. On the other hand, rebound test data needs to enter two tables at the input, namely rebound value table and bulk density data table. In the rebound value table, rebound number N [no unit] and modified angle · [°] are input as the column, while a single measurement point data forms a row. In the bulk density data table, the mass m [g] and the volume V [$cm^3$] of single test block are input as the column, while a single test block data forms a row. Naturally, the two tables are EXCEL file format at the input.

After multi-step formula calculations, the core program of point load data processing module formed a principal formula, which is in an unprecedented way. The $R_c$ of a single test block is obtained as Eq. 2 and Eq. 3:

$$R_c[\mathrm{MPa}] = 22.82I_{s(50)}^{0.75} = 58.5 \cdot \frac{P[\mathrm{kN}]^{0.75}}{D[\mathrm{cm}]^{0.375} L[\mathrm{cm}]^{0.375}} \quad (2)$$

And then the values for each row are averaged and output[6].Similarly, the rebound data processing module core program is the following formula:

$$R_c[\mathrm{MPa}] = 10^{0.0088\bar{N}\cdot\gamma+1.01}, \gamma = \frac{m}{V} \quad (3)$$

Here $\bar{N}$ is the average of $\Delta N_\alpha$ (rebound correction value). In practical engineering, the rebound hammer frequently can not be kept horizontal test situation. Thus, ±15°, ±30°,±45°,±60°, ±90° angles are chosen in actual use. Different rebound test angle correction of internal procedures formulas are shown in Table 2.

**Table 2 The use of rebound correction formula for different testing angles**

| Angle | Correction formula |
|---|---|
| 90° | $\Delta N_\alpha = -0.0012N^2 + 0.1725N - 8.975$ |
| 60° | $\Delta N_\alpha = -0.0003N^2 - 0.0289N + 3.64$ |
| 45° | $\Delta N_\alpha = 0.05N - 5$ |
| 30° | $\Delta N_\alpha = 0.05N - 4$ |
| 15° | $\Delta N_\alpha = -0.0005N^2 + 0.055N - 2.4$ |
| −15° | $\Delta N_\alpha = -0.0003N^2 + 0.0005N + 1.395$ |
| −30° | $\Delta N_\alpha = -0.0005N^2 - 0.0162N + 2.294$ |
| −45° | $\Delta N_\alpha = -0.0003N^2 - 0.0289N + 3.64$ |
| −60° | $\Delta N_\alpha = 0.05N + 4.5$ |
| −90° | $\Delta N_\alpha = 0.05N + 5$ |

In the system, weight options are set up rock hardness qualitative survey, as shown in Table 3.

**Table 3 Qualitative survey of the rock hard degree**

| Qualitative survey of the rock hard degree | |
|---|---|
| Hammering sound | 1. Crisp; 2. Subcrisp; 3. Uncrisp; 4. Dumb; |
| Reboundstrength | 1. Rebound; 2. Slight rebound; 3. None; |
| Hand touchfeeling | 1. Shock hand; 2. Slightly shock hand; 3. Not shock the hand |
| Degree ofcrushed difficulty | 1. Hard to crush; 2. Difficult to crush; 3. Sub-Easily crushed; 4. Easily crushed; 5. Can be crushed by hands |
| Water reaction | 1. None; 2. Slight water reaction; 3. Nails can carve prints; 4. Hand can break apart; 5. Can be shaped into groups |

So, as long as the intuitive investigation ends, operator of the system can add the option values have been selected[7], then the range of $R_c$ can be got. The setting is:

(1)When the sum is in the range of 0-6, $R_c$ >60;

(2)When the sum is in the range of 7-11, 30< $R_c$ <60;

(3)When the sum is in the range of 12-15, 15< $R_c$ <30;

(4)When the sum is in the range of 16-18, $R_c$ <5.

This structure is characterized in that large quantities of data can be done in one process[8]. As Matlab program is relatively simple and operation time is very short, computational efficiency can be greatly improved[9]. Meanwhile, the structure takes into the condition that only one kind of the two test can be obtained when the other one does not have a case[10]. But when both tests have been carried out, there has a comparison module. Module interface is shown in Fig.1.

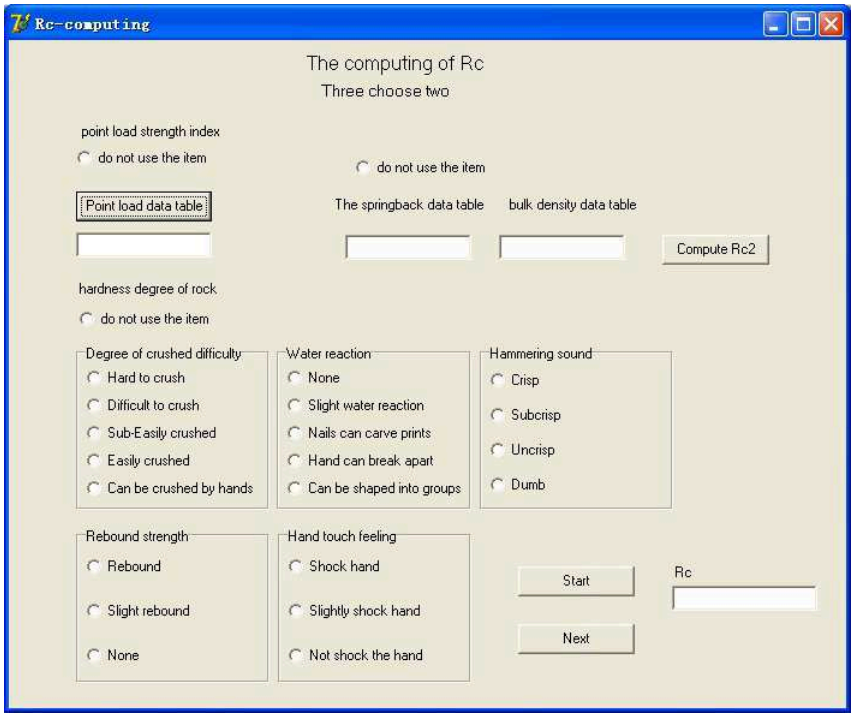


**Fig.1 The interface of Rc value determination in Matlab tunnel surrounding rock classification system**

## Comparison of the Two Tests in Actual Projects

**Changbanpo Tunnel in Jingyu County, Jilin Province, China.** Changbanpo tunnel is located at the west side of Yanping village, Sandaohu township, Jingyu county in Jilin province of China, which belongs to two-lane separate tunnel from west to east. The surrounding rock is mainly brown

and gray, weak andesite. Joints and fractures mostly exist in a fault zone in the RK248 +593-565 section that will be discussed here. Overall, the rock here is cracked structure and poor stability. Fig.2 is the scene photo of tunnel surrounding rock graphed during the tunneling process, which needs accurate and step-by-step rock classification.

**Fig.2 The broken rock mass of Changbanpo tunnel**

Table 4 is the result of tunnel analyze using the grading system for three times.

**Table 4 The rock classification results of Changbanpo tunnel RK248+593-565 bid section**

| Section | $R_C$ value(point load test) | $R_C$ value(rebound test) | Difference | Relative error | Final rock classification |
|---|---|---|---|---|---|
| RK248+590.6 | 20.79MPa | 22MPa | 1.21MPa | 5.82% | IV |
| RK248+588.2 | 26.82MPa | 27MPa | 0.18MPa | 0.67% | IV |
| RK248+576.3 | 28.19MPa | 30MPa | 1.81MPa | 6.42% | IV |

**Liuhuangqian Tunnel in Anhui Province, China.** Liuhuangqian tunnel is in southwestern Anhui province, and the tunnel is an important component of the Xizong highway in Anhui province. The ZK47+355-267 section being analyzed lies on the Meizi checkpoint. The surrounding rock here is subhard rock, and hammering sound is crisp, and hands have shocked feeling. The structure is between crack blocks and thick layers.

Table 5 is the result of tunnel analyze using the grading system for four times.

**Table 5 The rock classification results of Meiziguan tunnel ZK47+355-267 bid section**

| Section | $R_C$ value (point load test) | $R_C$ value (rebound test) | Difference | Relative error | Final rock classification |
|---|---|---|---|---|---|
| ZK47+355 | 56.35MPa | 42MPa | 14.35MPa | 25.47% | III |
| ZK47+325 | 67.98MPa | 61MPa | 6.98MPa | 10.27% | III |
| ZK47+287 | 57.23MPa | 45MPa | 12.23MPa | 21.37% | III |
| ZK47+267 | 76.49MPa | 70MPa | 6.49MPa | 8.48% | III |

From the above two examples of engineering analysis, it can be shown that $R_c$ reflects the rock rigidity[11]. It has obvious correlation between point load test and rebound test. However, there are some other features of the two tests:

(1)The difference and relative error between the two tests become larger when the rock is harder. Inversely, the difference and relative error between the two tests become smaller when the rock is softer. This maybe because there are larger difference between rock strength and structural plane strength in hard rock.

(2)When the rock is hard, the point load test data is more often larger than the rebound test data. When the rock is soft, the point load test data is more often smaller than the rebound test data. The reasons may be these: first, the risk of point load test obtaining in a weak rock structure is less than the risk of rebound test obtaining in a weak rock structure; second, if the rock hardness is poor, rebound hammer is not sensitive to the value of 10 or less, then rebound hammer will get no data, and the operator will often classify this condition as a test failure condition, thus smaller number will may be filtered.

(3)Compared to rebound test, point load test data can obtain more significant figures, the results are more accurate.

In summary, the point load test and rebound test effectively reflect the degree of rock hardness. If more precision is required, point load test can be chosen. But the rebound test is convenient and needs lower time and space condition, thus it can be considered using rebound test instead of point load test (especially in soft rock).

## Conclusion

In view of the above described, the following conclusions can be maked:

(1)Quick surrounding rock classification can not be ignored in tunnel construction. The using of computer software technology and artificial intelligence system is necessary so that the efficiency of grading will be effectively improved.

(2)The rock uniaxial compressive strength Rc is an important parameter in the tunnel surrounding rock classification. Through the point load test data and rebound test can meet the engineering requirements because of their own advantages. In the actual project, they can be chosen under the circumstances or combined in AI system.

## References

[1] R. Wang, L Nai: Landslide Prediction In Fushun West Open Pit Mine Area With Quadratic Curve Exponential Smoothing Method Geoinformatics 2010, China, Beijing(2010), June 18–20, p. 1-6.

[2] R. Wang, L. Nai: The design and application of time prediction and spatial prediction in Fushun west open pit landslide monitoring and prediction system, GCIS 2010 Symposium(2010), p. 391-396.

[3] H. Wen: A Study on Intelligence System supported by GIS and its Application of Landslide-Forecast, Doctor Degree Dissertation of Chongqing University(2004), p. 52-54.

[4]. L. Nai, R. Wang: GIS Based Landslide Monitoring and Forecasting System and its Application in the Landslide of Fushun West Open Pit, Journal of Jilin University(Earth Science Edition) Vol. 40 No.6(2011), p. 1359-1364

[5] C. Zhao, D. Cui, Z. Liu, et al.: GIS data for complex three dimensio nal limitequilibrium slope stability analysis, Rock and Soil Mechanics, vol.30(3).(2009), p. 707-711.

[6] D. Word: Fundamentals of Data Structures, Algorithms and Performance, MA: Addison Wesley(1993).

[7] D.E.Knuth: The Art of Computer Programing, Vol. 1/Fundamentals. and Vol.3/Sorting and Searching. MA: Aderson Wesley(1973).

[8] J. D. Ullman: *Principles of Database*(Computer Science Press, New York,1998)

[9] M A. Jackson : *Principles of Program Design*(Academic Press, Houston, 2000).

[10] Z. Manna: *Mathematical Theory of Computation*( McGraw Hill, New York,1974).

[11] B. Langefors: *Theoretical Analysis of Information Systems*.(Studentlitteratur, Lund, 1973).

*Applied Mechanics and Materials Vols. 580-583 (2014) pp 1122-1126*
*© (2014) Trans Tech Publications, Switzerland*
*doi:10.4028/www.scientific.net/AMM.580-583.1122*

# The dynamic response of shallow buried structure under the action of explosion load

Qian Zhang[1, a *], Haibing Wei[1, b], Junhai Zhao[1,c]

[1] Chang'an Road No.161, Chang'an University, Xi'an 710064, China

[a]563178082@QQ.com, [b]1583576542@QQ.com, [c]zhaojh@chd.edu.cn

**Keywords:** ground explosion; shallow buried structure; dynamic response

**Abstract.** Simulating and analyzing the dynamic response of the shallow underground structure under the ground explosions by LS-DYNA. The results show that the ground shock under ground explosions contains two different forms, one is direct impact ground shock and the other is indirect impact ground shock; with the increasing of depth, the ground shock decreases. The effective stress of the upper part of the roof is larger than other parts of the shallow underground structure; the effective strain of the corner of the roof is larger than other parts of the shallow underground structure.

## Introduction

Because of the underground structures (such as subway station, underground passage) are crowded and not easy evacuation, they often become the first choice for the terrorist attack[1]. Once the terrorist attack occurring, it is difficult to measure the serious consequences, so improving the ability of physical protection of underground structures is extremely important.

The ground shock under ground explosions contains two different forms, one is direct impact ground shock and the other is indirect impact ground shock. When designing the underground protective structure, it mainly considers the load causing by the ground shock. This paper simulated and analyzed the distribution of the wave field and the dynamic response of the shallow underground structure under ground explosion by using finite element software LS-DYNA. The research achievements on the issue at home and abroad are as follow. Junyu Fan[2] analyzed the wave field distribution of the shallow ground under the ground explosion; simulated the load distribution of the shallow buried underground structure, when the dynamite did not hit the structure directly. Jinchun Liu[3] putted forward the practical calculation method of the impact induced wave in soil, they analyzes the experimental data and the results of numerical simulation of the explosive induced wave under the contact explosion. Literature [4] putted forward the calculation method of ground motion parameters of the shallow surface shock induced by explosives, when the ground and the soil is given for homogeneous medium.

## The calculation model and material model

### The calculation model

The calculation model is shown in Fig1, the size of the explosives is 0.4 m * 0.4 m * 0.4 m, the charge is 104.3kg.The distance between the structure and the explosive is h = 3.5 m. The thickness of the air layer in the calculation model is 0.9 m, the thickness of soil layer is 8 m, the structure in the model is reinforced concrete structure, the strength grade of concrete is C30, the steel strength grade is HRB300,the height of structure is h = 4.1m, the span is L=7 m, the thickness of the roof is h1 = 0.5 m, the thickness of the bottom is h2 = 0.5 m, the thickness of the side wall is h3 = 0.5 m.

In this paper, the model of finite element analysis used a quarter model, the attribute of the unit are SOLIDE164, the boundary adopted no reflection boundary.

This paper will be divided into two kinds of working condition. One is without underground structures; it is mainly used to study the field distribution of the explosion shock wave under the ground explosions. The grid of the explosive and the air, the solid are meshing into Euler grid in the model. The algorithm used multiple material ALE algorithms; this algorithm allows the same grid

contains different materials. The other condition has the underground structure; it is mainly used to study the dynamic response of underground structures under ground explosions. The grid of the explosive and the air, the solid are meshing into Euler grid in the model. The grid of the reinforced concrete structure is divided into Lagrange; it used the algorithm of fluid-structure interaction. Finite element model and the meshing of the model is shown in Fig2.

The unit system adopts cm, g, us in this article.

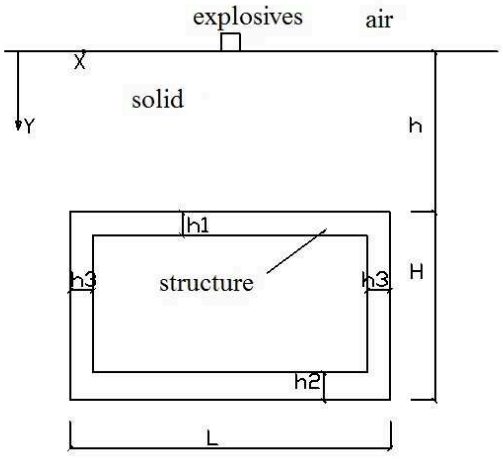


Fig1.The calculation model

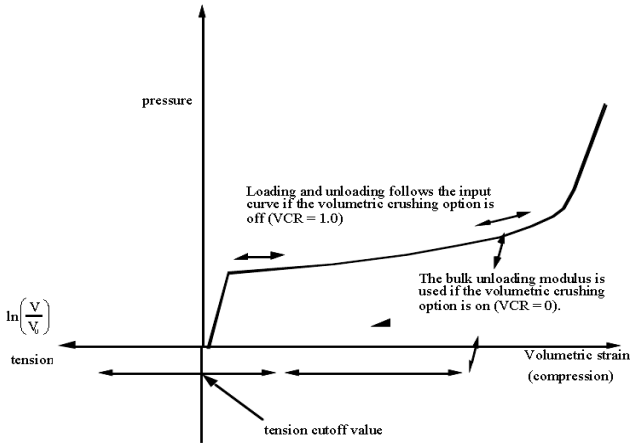


Fig3.The relationship

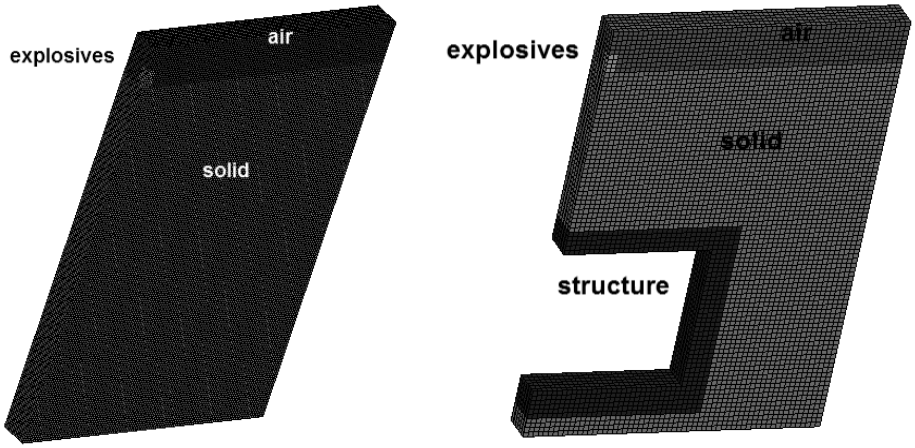


Fig2. The finite element model and the meshing

**The model and parameters of material**

(1)The material model and parameters of the air

In this paper, the air was described by material model of * MAT_NULL and state equation of LINEAR_POLYNOMIAL. This article takes:

$C_0 = -1E-6, C_1 = C_2 = C_3 = C_6 = 0, C_4 = C_5 = 0.4, V_0 = 1.0\ E_0 = 0.25E-5$

(2) The material model and parameters of the explosive

In this paper, explosives was described by material model of *MAT_HIGH_EXPLOSIVE_BURN and the state equation of JWL. The value of material parameters are shown in Table1.

Table1.parameters of JWL and*MAT_HIGH_EXPLOSIVE_BURN

| A | B | R1 | R2 | ω | E0 | V0 | R | D | PCJ | BE-TA | K | G | SI-GY |
|---|---|---|---|---|---|---|---|---|---|---|---|---|---|
| 3.737 | $7.33e^{-2}$ | 4.15 | 0.95 | 0.3 | 0.043 | 1.0 | 1.63 | 0.693 | 0.21 | 0 | 0 | 0 | 0 |

(3)The material model and parameters of the soil

In this paper, soil was described by material model of *MAT_SOIL_AND_FOAM, the relationship between pressure and volume strain is shown in Fig3.the values of material parameter are shown in Table2.

Table2.The parameters of the soil

| R0 | G | BULK | A0 | A1 | A2 | PC | VCR | REF |
|---|---|---|---|---|---|---|---|---|
| 1.8 | $6.4E^{-4}$ | 0.3 | $3.4E^{-13}$ | $7E^{-7}$ | 0.3 | $-6.9E^{8}$ | 0 | 0 |

(4) The material model of the structure

This article used the * MAT_BRITTLE_DAMAGE to describe the reinforced concrete. This kind of material contains the option of reinforcement ratio. It is a composite material of concrete and steel. The value of parameter is: density $\rho$=2.5, Poisson's ratio $\nu$=0.2, elastic modulus E=0.3, reinforcement of volume percentage is 0.02, the yield stress of reinforced is 0.003.

**The results and analysis of calculation**

**The ground shock under ground explosions**

Fig 4 is the propagation of stress wave with time under the ground contact explosion. We can see the ground shock of the shallow ground can be divided into direct impact and indirect impact in the figure. In Fig5, indirect impact almost has no effect on cell c, At the moment, the value of angle $\beta$ is about 61° ($\beta$ is the angle between radial of blasting center and the plumb line of the ground). Below the surfer of ground, when $\beta$ is between 0°to 61°, compression wave is mainly caused by direct impact shock. The area is called central region. When the value of $\beta$ is about between 61°to 90°, compression wave is a mixture of direct and indirect wave. The region is called surface region. The result is in accordance with the conclusion of literature [5].

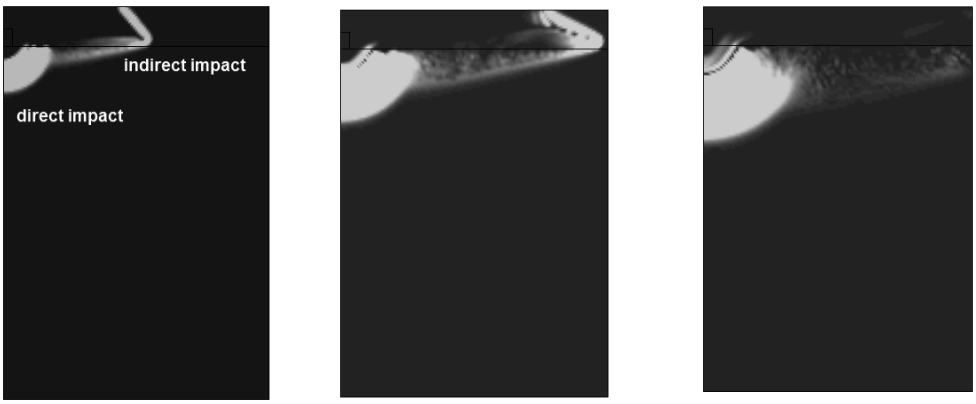


Fig4.The propagation of stress wave

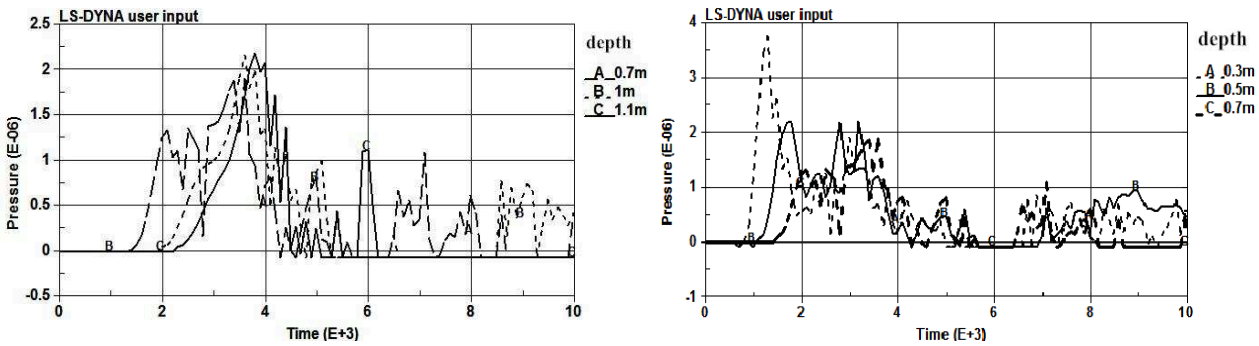


Fig5.The horizontal distance to the explosion center is 2m

In the surface region, the cell has two pressure peaks, showing in Fig5. At the first time, pressure peak was caused by the indirect impact; the second was caused by the direct impact. With the increasing of the depth, the values of two peaks are reducing. With the increasing of the depth, the

effect of indirectly impact is diminishing. Cell B in the figure, the values of two peaks are equal. At the moment, the value of angle β is about77°. When the beta is greater than 77°, indirectly impact played the leading role, namely the value of the first peak is greater than the second peak. The area is called near surface region. When β between 61°to 77°, the directly impact played the leading role, namely the value of the first peak is less than the second peak, the area is called the surface area. The result is in accordance with the literature [5].

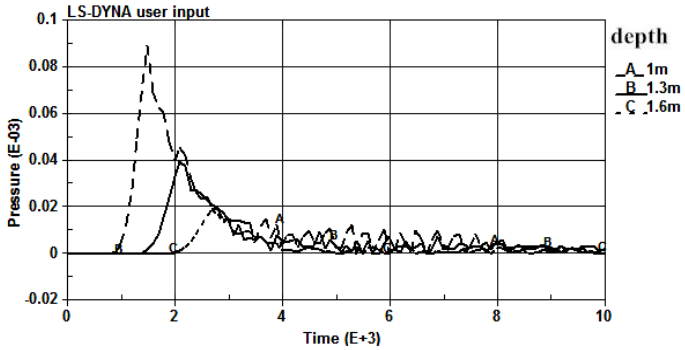


Fig6.The horizontal distance to the explosion center is 0m

In the central region, we can see in figure 6, with the increasing of depth, the value of overpressure decreasing, and the rising time increasing.

To sum up: 1.The ground explosion will cause the ground impact .The ground shock of the shallow ground can be divided into direct impact and indirect impact.

2. When β≤61°, it is called the central region. In the region, compression wave is mainly caused by direct impact shock. When 61°≤β≤77°, it is called the near surface region . In the region, compression wave is a mixture of direct and indirect wave; the directly impact played the leading role. When 77°≤β≤90°,It is called the surface region . In the region, compression wave is a mixture of direct and indirect wave; the indirectly impact played the leading role.

3. With the increasing of depth, directly and indirectly impact shocks were decreasing.

## The load-bearing characteristics of the shallow buried underground

In this article, the explosive hit structure directly. Structure is in the region of the β≤61°, where the directly impact played the leading role on the structure. In Fig 8, 9, we can see that the effective stress of the upper part is larger than other parts of the shallow underground structure; the effective strain of the corner of is larger than other parts .The destruction of the structure starts from the central and the corner of the roof.

Figure 7, 8 for biggest moment of the effective stress and effective strain, respectively, unit # 1456 has the maximum effective stress, the value is 0.35 Mpa; unit # 21271 has the maximum effective strain, the value is 8.49e-6. The effective strain is less than 0.025, the structure has not cracked, and it was not destroyed.

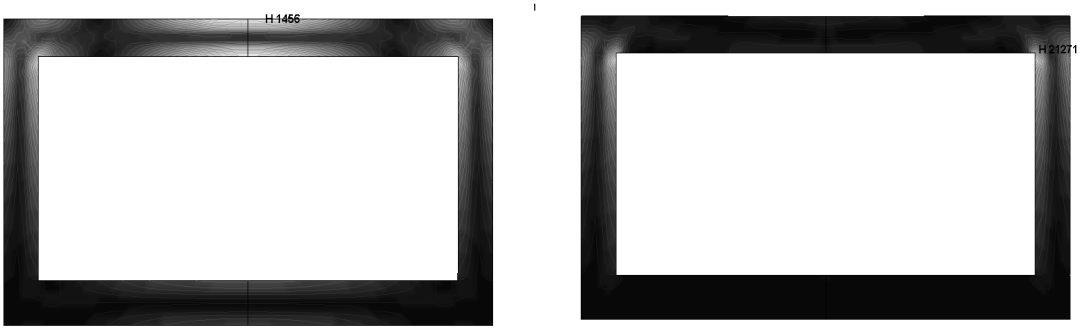

## Conclusions

This paper studies the form of propagating and the classification of compression wave, and dynamic response of underground structures under the ground contact explosion by LS-DYNA. The conclusion is as follows:

(1) The compression wave field under the contact explosion is divided into three regions. They are the central region $0°\leq\beta\leq61°$, the surface area $61°\leq\beta\leq77°$, the shallow surface region $77°\leq\beta\leq90°$.

(2) The directly impact has mainly effect on central region, the directly impact and the indirect impact has the effect on the surface area and the shallow surface area. The directly impact played the leading role on the surface area, the indirectly impact played the leading role on the shallow surface area

(3) In the shallow buried underground structure, the peak of effective stress appears in the central of roof, the peak of effective strain appears in the corner of the roof. In the condition, the structure has not cracked, not destructed.

## Acknowledgements

This work was financially supported by Natural Science Foundation of China (41202191), China Postdoctoral Science Foundation (2012M520079, 2013T60868), Doctoral Fund of Ministry of Education of China (20110205130001, 20120205120001) and Natural Science Foundation of Shannxi Province of China (2011JM7002).

## The Reference

[1] Guomin Zhao. The risk evaluation methods of the subway station in a terrorist attack [J]. JOURNAL OF BASIC SCIENCE AND ENGINEERING,2006,14:312~317.In Chinese.

[2] Junyu Fan. Characteristics of loads on shallow-buried structures under the ground explosions[J]. Journal of PLA University of Science and Technology,2008,6:676~680.In Chinese.

[3] Jinchun Liu. Practicable calculating method of indirect ground shock in soil at surface contact explosions[J]. Journal of PLA University of Science and Technology,2010,2:121~124.In Chinese.

[4] U S Department of the Army, the Navy and the Air Force. Structures to Resist the Effects of Accidental Explosions[M]. TM5-1300. Washington DC: Department of Army, the Navy and the Air Force, 1990.

[5] ALEKSEENKO V D. Experimental Investigation of a Dynamic Stress Field in soft Soil Produced by an Explosion[J]. No.5, AH CCCP. 1963.

*Applied Mechanics and Materials Vols. 580-583 (2014) pp 1127-1133*
*© (2014) Trans Tech Publications, Switzerland*
*doi:10.4028/www.scientific.net/AMM.580-583.1127*

# Discussion On Highway Tunnel Monthitoring Measurement Control Standards

Long Jin Tan[1] , Hong Qing Zhou[2] ,Kai Sheng Chen[1]

Long Jin Tan, Male, born in 1979, is mainly engaged in teaching and research of road engineering and geotechnical engineering.Civil Engineering School,Guizhou University Guiyang Guizhou China

Hong Qing Zhou, Male, born in 1959, is mainly engaged in teaching and research of geological engineering and geotechnical engineering.Resource and Enviornment School,Guizhou University Guiyang Guizhou China

Kai Sheng Chen, Male, born in 1975, is mainly engaged in teaching and research of road engineering and geotechnical engineering. Civil Engineering School,Guizhou University Guiyang Guizhou China

E-mail: 375408600@qq.com, zjff@qq.com,chen_kaisheng@163.com

**Key Words:**Tunnel construction; Monthitoring and Measurement; Control standards; Surrounding rock stability

**Abstract:**Tunnel monthitoring reference value is an important indicator to determine the stability of surrounding rock. Existing tunnel specification vault settlement and surrounding convergence gives some guidance views, But in the actual project also found a number of problems, And no indication of surface displacement control reference value specification in. Based on the analysis of relevant norms, In practical engineering, for example, Monthitoring and Measurement standards for construction tunnel some meaningful discussion.

Design and construction of highway tunnels are increasingly using NATM. In order to grasp the extent of the construction of rock stability and support force, Dynamic mechanical deformation or information, To determine the design, construction, safety and economy, After the tunnel excavation site shall be in accordance with the design requirements and the actual situation of immediate distribution and monthitoring, Feedback so as to achieve the design, construction instructional purposes. But control standards is not an easy thing to determine, There is no uniform standard at home and abroad, Although the current specification gives some guiding opinions for surrounding tunnel displacement and vault settlement,there are also some problems, so individual scholars have done some researches on surface subsidence control standards for some particular projects.

This paper focuses on monthitoring and measuring the surrounding tunnel displacement and vault settlement as well as surface subsidence control standards,for the purpose to throw away a brick in order to get a gem.

## Existing tunnel monthitoring measurement control standards specification

### 1.1 The projects must be measured in existing tunnel measurements norms

The projects must be measured are current measurement to ensure the stability of surrounding rock in the design and construction.Then by judge the stability of the rock to guide design and construction. Such kind of tests are simple, low cost, high reliability, but it plays a vital role in monthitoring rock stability and guiding the design and construction.

Table 1 Tunnel site monthitoring measurements will test the project

| No. | Project Name | Methods and Tools | Arrange | Test accuracy | Measurement interval | | | |
|---|---|---|---|---|---|---|---|---|
| | | | | | 1 ～ 15[d] | 16[d] ～ 1[month] | 1 ～ 3[month] | ＞ 3[month] |
| 1 | Inside, outside observation | Field bservations, geological ompass | After the initial excavation and shoring | | After blasting each | | | |
| 2 | Peripheral displacement | the various types of convergence | Each 5 ~ 50[m] a cross-section, each section of the measured points 2-3 | 0.1[mm] | 1 to 2 times / [d] | 1times / 2[d] | 1 to 2 times / [week] | 1 to 2 times / [month] |
| 3 | Vault settlement | Method of leveling, level, ruler, etc. | Each 5 ~ 50[m] a section | 0.1[mm] | 1 to 2 times / [d] | 1times / 2[d] | 1 to 2 times / [week] | 1 to 2 times / [month] |
| 4 | Surface subsidence | Method of leveling, level, ruler, etc. | Hole section, Shallow segment(h0≤2b) | 0.5[mm] | Before and after the excavation face distance measurement section <2b, the 1 or 2 times / [d] | | | |
| | | | | | Before and after the excavation face distance measurement section <5b, the 1/2 ~ 3[d] | | | |
| | | | | | Excavation face from the front and rear sections measuring> 5b, the 1/3 ~ 7[d] | | | |

Note: b——Tunnel excavation width.

$h_0$——Tunnel depth.

**1.2 Existing Monthitoring and Measurement tunnel specification control standards**

Measured displacement value should not exceed the limits of the tunnel displacement, then must be constructed follow the requirements in Table 2 of displacement management level. Under normal circumstances, it is better to set the designed tunnel reserved deformation as the ultimate displacement. The tunnel excavation contour should be reserved for the deformation according to the requirement, if there is no such a requirement, Table 3 is a reference, and the adjustments could be made based on monthitoring and measurement information.

Table 2 Displacement management level

| Management Level | Management displacement [mm] | Construction Status |
|---|---|---|
| Ⅲ | $U<(U_0/3)$ | Construction may be normal |
| Ⅱ | $(U_0/3)\leq U\leq(2U_0/3)$ | Should strengthen support |
| Ⅰ | $U>(2U_0/3)$ | Special measures should be taken |

Note: U—Measured displacement value;

U0—Design limits displacement value.

Table 3 Outlines reserved deformation of excavation

| Rock level | Set aside the amount of deformation [mm] | | Rock level | Set aside the amount of deformation [mm] | |
|---|---|---|---|---|---|
| Ⅰ | Two lanes | — | Ⅳ | Two lanes | 50～80 |
| | Three lanes | — | | Three lanes | 80～120 |
| Ⅱ | Two lanes | — | Ⅴ | Two lanes | 80～120 |
| | Three lanes | 10～50 | | Three lanes | 100～150 |
| Ⅲ | Two lanes | 20～50 | Ⅵ | Two lanes | Field measurements to determine |
| | Three lanes | 50～80 | | Three lanes | |

According to the Specification, to determine whether the tunnel ceiling unstable or failure,the maximum displacement value is a standard, the upper limit of construction management control standard is the 2/3 of the ultimate displacement in the displacement level management table .

### 1.3 Discussion control standards

In the monthitoring and measurement, it is not proper to tell whether the tunnel is relatively unstable or failure occur to compare the measured maximum displacement with limit displacement . The reasons are:

（1）In the tunnel excavation process it is hard to precise the limit displacement due to the engineering geological conditions, environmental conditions, Excavation method, complex support forms of tunnel and underground. So the comparison of measured maximum displacement with ultimate displacement is difficult to operate.

（2）Design drawings or related specification has the deformation of the initial reservation tunnel support.In order to ensure the secondary lining support space can't be invaded by the surrounding rocks and initial support and to ensure the accurately of tunnel construction clearance after the secondary lining, you can take the designed reserved deformation as the ultimate displacement and control it and can not guarantee that whether the tunnel will be destroyed when the secondary lining support space being invaded.In the actual project, The surrounding rocks have already damaged although the measured displacements are far from the limit displacements.(table 4 for reference)

（3）Specifications did not clearly pointed out in the end is the ultimate displacement vault settlement or the surrounding convergence displacement is controlled vault settlement is based on the convergence or in the surrounding displacement control based norms seem vague, actually vault settlement and surrounding convergence displacement is not the same (see Table 4).

（4）There is no value of the reference surface displacement control in the specification, it is difficult to guide the construction of the actual project.

Table 4 Den Cao Tang pond tunnel section measured maximum displacement

| Section Stake | Rock level | Vault settlement [mm] | Surrounding convergence [mm] | Ultimate displacement [mm] | Remark |
|---|---|---|---|---|---|
| K4+334[mid] | VI | 4.39 | 5.36 | 200 | Appear mud |
| K4+403[mid] | VI | 15.76 | 29.76 | 200 | Cracking vault |
| YK4+315 | V | 26.84 | 27.67 | 180 | Two lining cracking, falling concrete |
| YK4+339 | V | 30.89 | 31.93 | 180 | |
| ZK4+225 | VI | 20.02 | 26.06 | 200 | Vault cracking and seepage |
| The first platform（exit）surface | | 208.68 | | Reference value specification does not surface displacement | Severe ground subsidence, the emergence of local slump, some cross beam broken, damaged or deformed serious anchorage |
| The second platform（exit）surface | | 248.14 | | | |
| The third platform（exit）surface | | 89.11 | | | |
| The fourth platform（exit）surface | | 255.81 | | | |

### The domestic and foreign relevant specifications to determine deformation standards

（1）Relevant normative standards in France

France M.Louis proposed maximum allowable displacement increases with increasing depth, the depth of about 1/1000. Tunnel displacement reference values established by the French Ministry of Industry Table 5 (tunnel section 50 ~ 100 ㎡). The reference value can be used as a reference displacement reference primary election, it is more important is to rely on engineering experience accumulation.

Table 5 French crown and surface subsidence of different allowable depth

| Tunnel depth/[m] | Inside the vault allowed to settlement/[mm] | | Allow the surface to settlement/[mm] | |
|---|---|---|---|---|
| | Hard Rock | Soft Rock | Hard Rock | Soft Rock |
| 10~50 | 10~20 | 20~50 | 10~20 | 20~50 |
| 50~100 | 20~60 | 100~200 | 20~60 | 150~300 |
| 100~500 | 50~100 | | 50~100 | 200~400 |
| 500~750 | 40~120 | 200~400 | 40~120 | 300~600 |

Can be seen from Table 5,①This standard takes the conditions of rock and effects of the depth into account, without considering the impact of the shape of the tunnel excavation;② soft rock allowed more vault settlement than hard rock when buried in the same depth;③ under the same condition of surrounding rocks, allowing vault settlement increases with depth .

（2）Japan related normative standards

A Japanese company proposed to determine the threshold of vault sinking according to rock compressive strength, as shown in Table 6. Analysis can be obtained from the table. It considered the effect of the strength of the rock and the requirements of the different levels of alert, but it did not consider the effect of tunnel depth and the shape of the tunnel. Similarly, the lower the alert level, the lower the compressive strength, the greater the allowable vault settlement; while at the same compressive strength, the higher alert level, the smaller the allowable vault settlement.

Japan《NATM construction design draft guidelines》made in accordance with the value of the total displacement monthitoring (or monthitoring the displacement has been estimated based on the final displacement value) to typed the rocks, and then, in accordance with the rock category to determine the appropriate support systems. The relationship of Clearance change value and rock categories are shown in Table 7. In-depth analysis of the table shows, ① It considered the impact of two factors :that is the tunnel span and the rock categories , without considering the impact of the depth of tunnel; ② With the same span, the worse the rock, the greater Clearance change value allowed ; ③ rock under the same conditions, the greater the span, the greater the Clearance change value allowed.

Table 6 Vault subsidence

| Alert level | Uniaxial compressive strength(MPa)/Settlement/cm | | |
|---|---|---|---|
| | Rc＞100 | Rc=5~100 | Rc=0.5~5 |
| Ⅰ | 0.3~0.5 | 0.5~1 | 1~3 |
| Ⅱ | 1~1.5 | 1.5~4 | 4~9 |
| Ⅲ | 3~4 | 4~11 | 11~27 |

Table 7 Clearance change and the relationship between the rock category

| Rock type | The value of clean air/mm | |
|---|---|---|
| | Single line | Double line |
| Ⅰ~Ⅱ | ＞75 | ＞150 |
| Ⅱ~Ⅲ | 25~75 | 50~150 |
| Ⅲ~Ⅴ | ＜25 | ＜50 |

(3) The country of the relevant norms or regulations

To determine whether the tunnel is relatively unstable or failure occurs,you can judge it by comparison of the measured maximum displacement with the limit displacement as well as according to the displacement rate of change or the trend rate of displacement to judge.

To determine according to the displacement rate of change:

(1) the rapid growth phase of deformation: the deformation rate is greater than 1.0mm / d ;

(2) slow growth stages of deformation: the strain rate 1 ~ 0.2mm / d ;

(3) stable phases: the deformation rate of less than 0.2mm / d

The above strain rate deformation clearance standards are measurements for general tunnels Clearance change and vaults settlement. If it is for measuring high stress, karst, swelling, squeezing rock, etc, you should make specific standards for determining the specific circumstances.

To determine according to the trend rate of displacement:

Since the rheological properties of rock, rock deformation before damaged is a curve process which can be divided into three stages:

(1) Basically stable region: the main indicator is the displacement rate gradually decreased, namely: $\frac{d^2u}{dt^2} < 0$ ,rock are stable .

(2) Transition zone: displacement rate remains unchanged, namely $\frac{d^2u}{dt^2} = 0$ , Showing that the rocks are becoming unstable, need to warn, to strengthen support systems.

(3) Damage zone: displacement rate gradually increases, namely $\frac{d^2u}{dt^2} > 0$ , Showing that the rock in danger, must immediately stop construction, to take effective measures to control the deformation.

《Technical Specification for monthitoring and measuring the tunnel railway TB 10121-2007》 take the allowed relative displacement values to determine the ultimate displacement.

Further analysis to regulate shows that: ① The table considers the two factors:tunnel depth and rock types.Didn't consider the size of the span of the tunnel or excavated cross-section; ② rock under the same conditions, the greater the depth, the larger relative convergence allowed; ③ the same depth, the worse rock conditions , the greater the relative convergence allowed.

（4）Compare domestic and foreign relevant provisions of the subway project

In Beijing, Guangzhou, according to local experience, we recommend the appropriate monthitoring and control standard for subway construction.See Table 8 Table 9 Table 10.

Table 8 Beijing subway shield law, construction law Shallow control reference monthitor

| Method | Monthitoring Project | | Reference value/[mm] | Average and maximum displacement speed control value/([mm]/[d]) |
|---|---|---|---|---|
| Shield | Surface subsidence | | 20 | Average value of 1, a maximum of 3 |
| | Vault settlement | | 20 | Average value of 1, a maximum of 3 |
| Shallow law | Surface subsidence | Interval | 30 | Average value of 2, a maximum of 5 |
| | | Workshop | 60 | |
| | Arch bottom bulge | Interval | 10 | |
| | | Workshop | 10 | |
| | Vault settlement | Interval | 60 | Average value of 2, a maximum of 5 |
| | | Workshop | 120 | |
| | Horizontal convergence | Interval | 20 | Average value of 2, a maximum of 3 |
| | | Workshop | 20 | |

Table 9 Guangzhou subway construction baseline monthitoring and control

| Monthitoring Project | Reference value/[mm] | Control reference |
|---|---|---|
| Surface subsidence/[mm] | Ⅰ, Ⅱ Country rock,Ⅲ, Ⅳ Country rock | 30 |
| | | 19 |
| Vault settlement/[mm] | Ⅰ Country rock, Ⅱ Country rock,Ⅲ, Ⅳ Country rock | 50 |
| | | 30 |
| | | 19 |
| Deformation rate /([mm]/[d]) | Ⅰ, Ⅱ Country rock,Ⅲ, Ⅳ Country rock | 5 |
| | | 3 |
| Buildings tilt/‰ | Whole line | 3 |

Table10 Monthitoring benchmarking countries, both inside and outside the subway project deformation

| Standard | Ground largest settlement/[mm] | Ground subsidence trough curvature inflection | Formation loss coefficient/% | Inside Sidewall horizontal convergence/[mm] | Inside the dome settlement/[mm] |
|---|---|---|---|---|---|
| Japan, France, Germany, comprehensive specification | 50 | 1/300 | 5 | 20~40 | 75~229 |
| Our management standards | 30 | 1/500 | 5 | 20 | 50 |

**Explore the tunnel deformation monthitoring measurement control standards**

Tunnel monthitoring deformation control benchmark are an important part of the tunnel construction risk assessment,and it is also the premise of monthitoring the risk ,besides it is the maximum allowable value to ensure the safety of monthitored object. During monthitoring process, once the monthitoring data exceeds the reference value control, monthitoring department must mark it out in the monthitoring reports prominently and call the police, and do research and analysis jointly with the relevant departments , the reference value can be adjusted to control if necessary. Generally according to the following principles to determine the control reference:①should meet requirements of existing regulations related to design and construction, specifications and guidelines. jointly determined by the construction, design, supervision, construction and other related departments ,then being included in monthitoring programs. ③The monthitoring and control ling reference value should ensure the safety and normal use of the tunnel adjacent structures and to consider the requirements proposed by the competent authorities of the neighboring structures.④monthitoring and control reference value should have the feasibility of construction projects, to meet the premise of safety, you should consider increasing the speed of construction and reducing construction costs.⑤some monthitoring projects whose baseline values is not yet clearly defined at present, the monthitoring data can be reference to similar projects abroad.⑥to analyze the stability of the surrounding rock and supporting structure condition and the safety of the surrounding environment, you should correct the predetermined allowable displacement according to specific engineering field monthitoring results and engineering experience.

**Conclusion**

During the construction phase of the tunnel, in order to measure the Changes of surrounding rock (Such as surface subsidence, vault settlement, circumference displacement and so on) and the working state of the supporting structure ,we often use the total station, level meter, instrument and so on .Timely provide the information like the stability of rock degree and reliability and safety of the supporting structure,to anticipate accidents and danger, as the basis for adjustment and modificator of support design.To settle down the time for the second lining construction according to the measured results in the Composite lining,to monthitor the surrounding rock displacement of retaining structure of prestress shall not exceed the design standard.Therefore, it is very important to determine the reference value of monthitoring and measurement. The paper analyzed the existing tunnel monthitoring measurement specification, domestic and foreign relevant specifications, and some practical engineering projects, aiming to throw away a brick in order to get a gem.

**Acknowledgements**

This work was financially supported by Guizhou province excellent scientific and education qualified people governor special funds projects（Qiansheng zhuan he zi(2010)6 hao）and Guiyang scientific and technological research projects in the field of social development ([2010] building science and agriculture contract the first - social –No 47 )

**References**

[1] Technical Specifications For Construction Of Highway Tunnel（JTG F60-2009）

[2] Highway Tunnel Construction Technology Conditions（JTG/T F60-2009）

[3] Specification for Design of Highway Tunnel (JTG D70-2004)（JTG D70-2004）

[4] Technical Specification of Railway Tunnel Monthitoring Measurement (TB 10121-2007)

[5] People's Republic Of China Ministry Of Railways.TB10108－2002 Railway Tunnel Construction Method Gunite Technical Specifications [S]. Beijing：China Railway Press,2002.

[6] National metallurgical industry bureau.GB50086－2001 Concrete Anchor Spray Supporting Technical Specifications [S]. Beijing: China planning press, 2001.

[7] Xuan De YAO, Meng Su Wang.. Statistical Analysis Of Shallow Tunneling Method Subway Construction Caused Surface Subsidence Control Standards [J]. Rock Mechanics And Engineering,2006, 25(10):2030-2035.

[8] Jiang Wen Li,Chun Zhi Liu,Quan Yong Zhu. Excavation Tunnel Under The Railway Station Benchmarking Study Of Surface Subsidence Control [J]. Rock And Soil Mechanics,2005,26(7):1165-1169.

[9] Rui Liang. Statistical Analysis And Prediction of Surface Subsidence Caused by Beijing Subway Tunnel Construction [D]. Beijing: Beijing Jiaotong University,2007.

[10] Li Ding Zhang,Jun Huang. Analysis And Prediction Of Vault subsidence value by Metro Tunnel Construction [J].Rock Mechanics And Engineering,2005,24(10):1073－1077.

[11] Yu Jian Wang. Discussion On the Issues of Tunnel Project Monthitoring And Measurement [J]. Modern Tunnelling Technology,2008,( Supplement):7-14.

*Applied Mechanics and Materials Vols. 580-583 (2014) pp 1134-1137*
*© (2014) Trans Tech Publications, Switzerland*
*doi:10.4028/www.scientific.net/AMM.580-583.1134*

# Research on Early Concrete Crack Control of Shijiazhuang Subway Construction in Winter

Xiangmei Yu[1,a] Lijun Cao [1,b] and Dongyang Geng[1, c]

[1] Shijiazhuang University of Economics NO.136 Huai An East Road, Shijiazhuang City, Hebei Province, P.R.China 050031

[a] yuxiangmei6606@163.com,[b] caolijun2000@163.com,[c]15200012621@139.com

**Keywords:** subway.concrete; cracking. construction quality.

**Abstract.** The control of concrete cracking is a complicated and difficult problem for civil engineering. It is more difficult to control the cracking of the concrete poured in the winter. Thorough the analysis of the construction of the Shijiazhuang subway in winter, several methods are integrally applied. Frost proof and decreasing the temperature stress of concrete is considered together. The construction quality of the concrete arrive a satisfied level and the cracking of the concrete is successfully handled.

## Introduction

Concrete crack control has long been a complicated and difficult subject in both engineering and academic circles. To solve this difficult problem, engineering technologists and researchers of many institutions have carried on long-term and large amount research and exploration work on construction technology, concrete admixtures, concrete mixture ratio, raw materials for concrete and many other aspects and made many achievements and gained valuable experience]. HanSufang and others] put forward that the comprehensive measure combining prevention, release and resistance, as well as the method combining design, material and construction should be adopted to control the concrete crack. However, concrete crack control is a complicated system problem and when it comes to the specific measure to control the crack, and different scientists hold different academic and technical opinions]. Especially, since the late 90s of last century, with the updating national cement standard, concrete products have developed towards high fineness and strength with fast growing speed, and early strength grinding aid, which has brought more serious problem to concrete crack control [1-2].

## Mechanism of concrete crack

The early cracks on concrete with large volume appear mainly due to the thermal shrinkage caused by hydration heat, as well as drying shrinkage, plastic shrinkage and autogenous shrinkage. Plastic shrinkage control is relatively simple that is to say common construction measures can better avoid it, but to avoid other kinds of shrinkage, research on mechanism is needed to get the countermeasures.

The greater the volume of concrete, especially in the subway station construction, the more difficult the diffusion of the heat produced by hydration of cement, the higher the temperature, and the greater the volume change caused. The most fundamental reason led to the crack is the large volume change caused by risen temperature due to the hydration. The adiabatic risen temperature inside the concrete caused by concrete hydration heat is Eq. 1 [3-6]:

$$T_{max} = \frac{W \cdot Q}{\gamma_h \cdot C} \tag{1}$$

In the formula: $T_{max}$ -- The highest adiabatic risen temperature (℃)

Q-- hydration heat （KJ/kg）

$\gamma_h$ -- density of concrete （Kg/m3）

C-- specific heat of concrete (KJ/(kg. ℃))

Thus, the adiabatic temperature produced by the concrete can rise highly, and when the environment temperature change is great and subway station wallboards of large volume adopts temperature control measures rather than computing according to thermal engineering, the difference between inside and outside temperature of concrete will rise and be more than 25 ℃, which will generate considerable temperature stresses (cause cold shrinkage) leading to the crack. At the same time, the risen temperature of concrete also accelerates the evaporation on concrete surface, leading to drying shrinkage.

The interior of large volume concrete has free water, bound water, combined water,interlayer water and a variety of forms of water, and they have different losing processes of internal and external moisture gradient. In early period, first, big pores and big capillary pores lose water, but the loss of this kind of water will not cause shrinkage. Then, pores with radius less than 1000A start to lose water. The kind of water loss will generate shrinkage due to capillary pressure. After losing some water, concave surface will be formed in the capillary pore. Capillary pore pressure formula of single pore is Eq. 2:

$$P=2\sigma/r \tag{2}$$

In the formula, $\sigma$ represents the surface tension, the lower temperature of surroundings, the smaller the radius of the concave surface, the greater the capillary pressure. The relation among capillary pressure, surface tension and relative environment humidity is determined by the following type Eq. 3:

$$P=2\sigma/r=1300\ln(1/\phi) \tag{3}$$

In the formula, $\phi$ represents relative humidity and pores distribute randomly to all directions inside concrete, leading to the shrinkage of all directions inside concrete due to the pressure. As the humidity lowers further (less than 60%), the water adsorbed on the surface of hydrated calcium silicate gel will evaporate, leading to the closer distance between the gel and finally the irreversible shrinkage. When the humidity is reduced to 45%, the interlayer water of hydrated calcium silicate gel structure will lose, and the loss of this kind of water will cause great and irreversible shrinkage of concrete.

Table 1 Concrete materials proportion

| *No.* | *Structure position* | *Concrete number* | *Cement content kg/m³* | *Sand content kg/m³* | *Stone content kg/m³* | *Water kg/m³* |
|---|---|---|---|---|---|---|
| 1 | Station flank | $C_{40}$ | 310 | 773 | 1082 | 165 |
| 2 | Station flank | $C_{40}$ | 281 | 832 | 1018 | 170 |
| 3 | Station flank | $C_{40}$ | 362 | 713 | 1069 | 180 |
| 4 | Station flank | $C_{40}$ | 330 | 713 | 1069 | 180 |
| 5 | Station roof | $C_{40}$ | 340 | 720 | 1079 | 180 |

Concrete autogenous shrinkage mechanism is quite complex, and mature theory has not been formed yet. By so far, capillary tension theory is accepted widely. According to the definition, autogenous shrinkage presents more obviously in high performance concrete with low water-binder, because the gel material that do not hydrate needs water to continue the hydration process, and when there is no water or the water consumption rate is faster than the outside water migration rate, moisture migration inside concrete will occur and concave surface be formed inside pores. The

formation of this kind of concave surface will generate tension inside concrete, resulting in shrinkage and this kind of shrinkage is autogenous shrinkage.

## Practical project analysis

Shijiazhuang subway line No.1 has a total length of 22.14km, 7028m of which adopts mine construction method, 749m open digging method and the rest shield driven method. We research the subway station constructed in winter, detailed summary the concrete crack situation of the subway station constructed in winter, select 5 typical stations to describe, and the concrete construction materials proportion of the investigated stations is on Table 1. After the concrete cracks were found in former sections, we have adopted appropriate and adjusted the materials proportion reasonably, and then continue to observe concrete construction of the later sections.

## The generation reason and control analysis of concrete crack

The concrete crack factors influenced by the subway construction in winter are quite complicated, involving design, material, construction craft and many others. Therefore, we comprehensively analyze the concrete crack problem of the subway stations and the main reasons are as follows:

Both the floor and roof of the subway station are commonly of large volume. The thickness of flank is 600 mm, and if the lateral widened part is considered, the thickness is about 700 ~ 800 mm. The hydration heat of concrete causes the appearance of the cracks. Wind resistance, heat preservation, stove or steam anti-freezing measures are adopted. Site concrete after pouring concrete has been in a state of normal temperature, about 10 ℃, and the early strength of concrete develops very fast. Under such circumstance, the relatively dry condition in shed is harmful to the moisture retention and maintenance. The initial setting time of concrete of the two sections poured in December 2006 is about 5 hours, the concrete hydration hardening speed is quite fast, and the hydration heat is quite concentrated. The initial setting time of concrete poured between January and March, 2007 is about 11 hours, which is conducive to the delay of the concrete heat release speed and can lower the concrete hydration heat peak.

Due to the vertical flank concrete structure, on the one hand, it is difficult to reserve the moisture and maintain. After removing from the mold, the moisture loses quickly, further speeding up the drying shrinkage and autogenous shrinkage of concrete. The dosage of crack-resistance waterproofing agent needs to be increased, by raising the limit expansion ratio of concrete to eliminate the shrinkage influence brought by the negative maintenance conditions. On the other hand, the flank concrete is restricted by the foundation concrete, and shrinkage stress is not easy to release. When comprehensive value of the temperature shrinkage stress caused by concrete hydration heat, the autogenous shrinkage stress and drying shrinkage stress by concrete early strength and other shrinkage stresses exceeds the tensile strength of concrete, the concrete can produce cracks. However, the early tensile strength of concrete is very low. About 3 days or so, the expansion value of the compensation shrinkage concrete is not high, less than 1.5 x 10-4, which can only compensate the early drying shrinkage and autogenous shrinkage of concrete, and if there is a large temperature stress at this point, it is impossible to completely compensate. The thermal expansion coefficient of concrete is about one over one hundred thousand. According to the theory of linear expansion, the reduction of every 10 ℃ will produce 1 x 10-4 shrinkage value. The wall structure is different form the floor structure, after removing from the mold, the heat loses quite fast, and in a very short period of time to environment temperature inside the shed can be reached. Considering the temperature measuring situation of the project, the difference between the environment and the internal concrete temperature is about 40 ℃, temperature shrinkage 4 x 10-4, and the ultimate tensile strain rate of concrete only 2.5 x 10-4. Therefore, concrete crack problem of this project is mainly caused by the temperature stress.

According to theoretical analysis, experiment and practice experience, the following measures are adopted in the subsequent subway construction in winter: reduce the cement dosage appropriately, in order to reduce the amount of hydration heat; increase the fly-ash dosage appropriately; adjust the

CSA crack-resistance waterproofing agent dosage from 9% to 11%, in order to increase the expansion of the concrete; fully retard, retarding the setting time of concrete from 5 hours to 11 hours, to slow the rate of hydration heat. Through the implementation of the above countermeasures, the highest temperature inside the concrete is controlled to 35 ℃, environment and the internal concrete temperature lower to 25 ℃, so that no crack is found in the concreted constructed in January to march 2007.

**Winter construction suggestions on Shijiazhuang subway station concrete**

Try to reduce the dosage of cement, but the minimum dosage of silicate cement should not be less than 300 kg/m3; Water cement ratio should be controlled in 0.45, not higher than 0.55. Secondary fly ash dosage should be increased, generally between 15% to 30%; Add high efficiency water reducing agent, or compound admixture with high efficiency water reducing function, retarder, and etc; Appropriately choose silicate cement of strength grade 42.5, with area of no more than 350 m2 / kg, the measured C3A content of cement should not be more than 5%;The anti-cracking water-proofing agent used should accord with JC476-2001 and JC474-1999, and higher technical requirements should be put forward (7 d limit inflation rate in water should not be less than 0.030%, 7 d in water turning to dry air 21 d limit inflation rate not less than - 0.010%, exudation rate not more than 50%, penetration height ratio not more than 35%).

**Conclusion**

Although adding anti-cracking water-proofing agent is an effective method to control concrete crack, but it is not a panacea. The concrete crack control is a complicated system problem, to solve which comprehensive measures are needed. Especially for the winter construction of large volume and long line concrete, in order to prevent concrete from enduring the cold , heat preservation, heat storage and adding mixed antifreeze and other measures should be adopted, to help concrete set and harden as soon as possible, which is construction standard requirements in winter. However, from the perspective favorable to crack control, hydration heat release process of concrete should be slowed down, so as to decrease the difference between the highest temperature inside the concrete and the environment temperature. Antifreeze and reducing the temperature stress of concrete must be considered coordinately to ensure that the quality control of concrete can reach the satisfactory level.

**References**

[1]J.B. Martino， N.A. Chandler， International Journal of Rock Mechanics & Mining Sciences 41 (2004) .

[2]Michael Tsesarsky ，Yossef H. Hatzor， Tunnelling and Underground Space Technology 21 (2006) .

[3]Doolin,D,Sitar, N, ASCE 128 (11),1158–1168. 2002

[4] P.Klmar. Infi Elements for Numercal Anslysis of Underground Excavation[J].Tunnel and Underground Technology，2000,15.

[5] Cai M,Kaiser P K . Tunnelling and Underground Space Technology,2005,20(4)

[6] Shahidi A R, Vafaeian M. Tunnelling and Underground Space Technology, 2005, 20(7)

*Applied Mechanics and Materials Vols. 580-583 (2014) pp 1138-1142*
*© (2014) Trans Tech Publications, Switzerland*
*doi:10.4028/www.scientific.net/AMM.580-583.1138*

# Response of the Spiral Conveyor Spewing in Water-rich Sand

Yirong SONG[1,a], Jia HE[2,b], Guangfeng CHEN[3], Min HONG[4], Pengbo LI[5]

[1]Department of Geological Engineering, Qinghai University, Xining, 810016, China

[2]School of Civil Engineering, Lanzhou University of Technology, Lanzhou, 730050, China

[3]School of Earth and Space Sciences, Peking University, Beijing, 100087

[4]Beijing Branch of China Railway Construction Engineering Group, Beijing, 100070, China

[5]Tangshan Railway Vehicle Co., LTD, Tangshan, 063035, China

[a]email: songyirongqh@163.com, [b]email: hejia0537@foxmail.com

**Keywords:** Shield Construction; Spiral Conveyor Spewing; Response Measures

**Abstract.** Spiral conveyor spewing is a serious danger when the shield tunneling machine crosses water-rich sand stratum. It will lead to the malfunction of dregs discharging and the failure of soil pressure's effective control. It will be a chief reason to influence construction progress and even cause secondary disaster, which led to the serious destroy of the survival environment, such as ground collapse, water leakage in the tunnel. The danger of spiral conveyor spewing and the countermeasures and the method of the project can be stated by the construction experience in some sections, in order to give some suggestion and references to similar engineering.

## Introduction

The stratum is made of grain filling soil, silty clay and fine sand, coarse sand, gravel, sand and gravel in order from top to bottom, see Pig1. According to the exploration report the shield machine is in the gravel sand and gravel stratum [1].

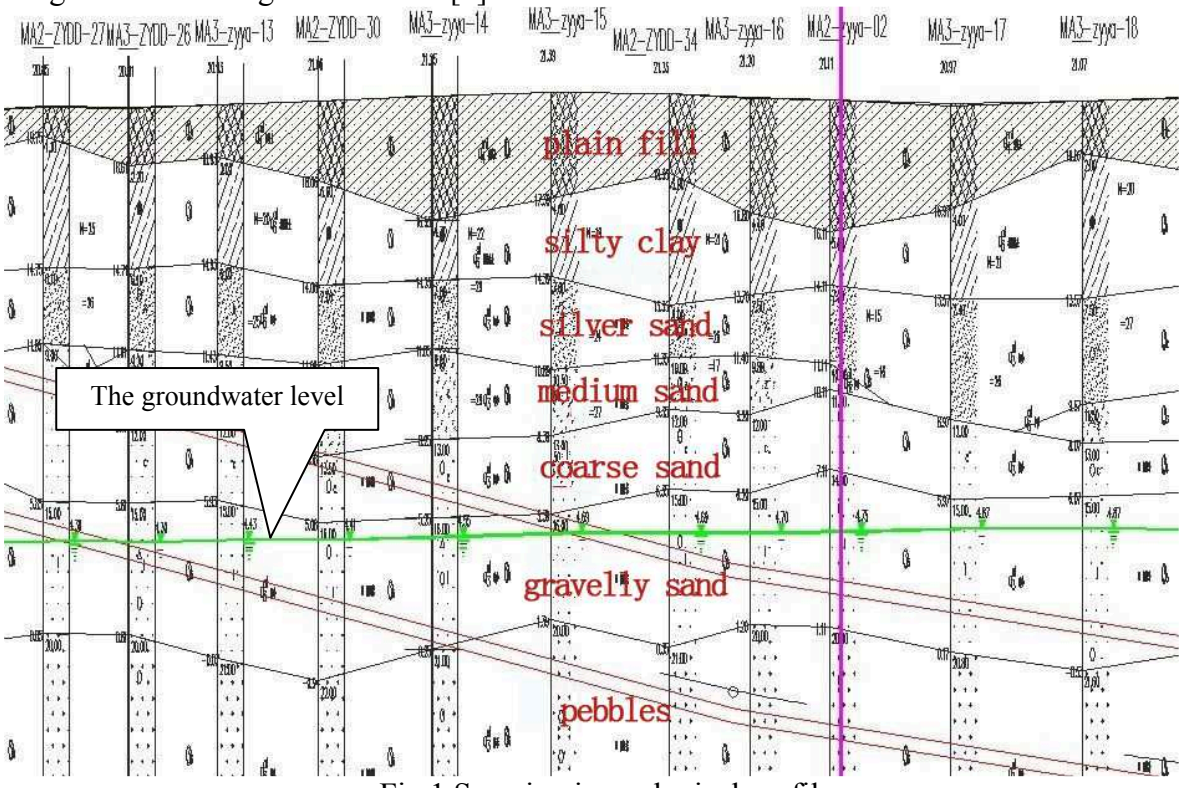


Fig.1 Spewing in geological profile

Gravelly sand: saturated, moderate density, good permeability. Its mechanical properties have obvious thixotropy and liquidity. Its penetration is medium. Under the dynamic water pressure, it has the possibility of soil flowing or piping. On the basis of the Technical Manual on Municipal Soft soil underground construction (in 1990, compiled by Shanghai municipal engineering), the

flowing sand is easy to be caused in gravelly sand layer. Circular gravel: saturated, moderate density, mixed grain size, poor uniformity. The largest diameter of the circular gravel can be 4cm~5cm. The lithological composition in this layer is complicated, it is mainly composed of quartz and sandstone, a little siliceous rock. Roundness of round gravel is better, most of them are sub round ~ round. Permeability is good in this layer. It is rich in water and has high hydraulic permeability. These traits can also cause water gushing and bursting during the construction, thus influencing directly on the safety of construction. The stability of the surrounding rock is poor, so it is easy to collapse and easy to be damaged. Above the underground water level 4.70m is the whole section water rich sand layer.

## The Harm Caused by Spewing and the Mechanism of It

**The Harm Caused by Spewing.** Firstly, a lot of mud is squirted from the screw machine's slag notch, see Pig 2 and Pig 3. It seriously affect construction environment in the connection bridge area and even affect the shield tail and the whole car. So the screw machine must be stopped to clean the waste residue. The waste residue cleaning is time-consuming by manpower. Secondly, when the shield machine stops driving, slag notch of the screw machine is closed, the mud in the soil bin quickly fill the whole screw machine. Once the gate is started again, another spewing will happen, this will form a vicious circle. Then the diving speed should be slow down. It will take a long time to clean the muck. These will seriously influence Shield construction progress. Lastly, due to the uncontrollable quantity of soil slag in the process of spewing, it is difficult to establish the real earth pressure balance. So the perturbation to the stratum will be dramatic and even cause secondary quality accidents, such as surface subsidence [2].

Fig.2 The segment assembling area construction environment after spewing

Fig.3 Construction environment trolley region after spewing

**Spewing Mechanism.** The mechanism of EPB shield tunneling (Pig 4) stabilization is that sand which is left over after the process of cutter cutting is filled with soil warehouses, equilibrating pressure between earth in the soil warehouses and out of the soil warehouses; in the process of digging, screw conveyor is for adjusting speed and amount of excavated soil, equilibrating amount between entering soil and excavated soil, which can ensure stabilization of shield tunneling. If excavation surface exists high pore pressure and permeability coefficient is high, muck at excavation surface will become thin with tremendous mobility [3-7].

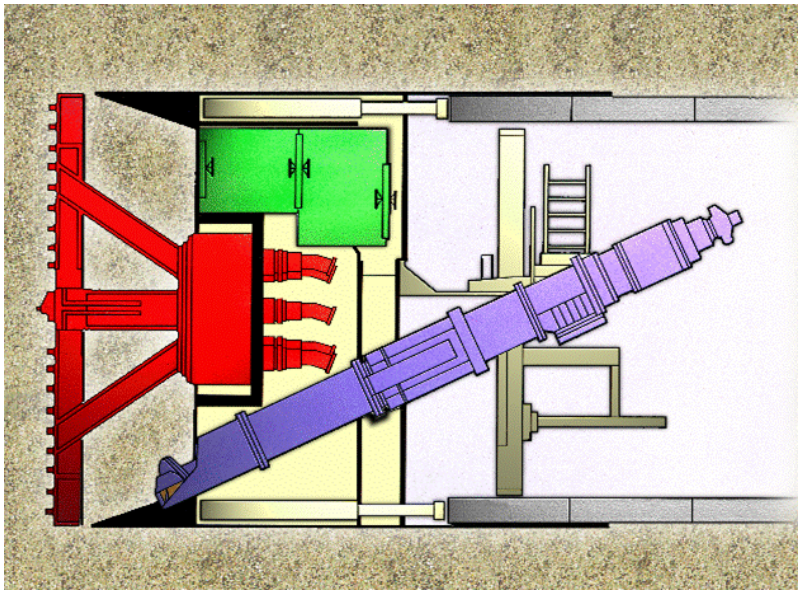

Fig.4 EPB Shield Tunneling

Water body under high pressure which flows soil warehouses and spiral conveyor collects, which will increase pressure in the soil warehouses and back brake of spiral conveyor, cutter torque, and slow down driving speed. When the gate is open, pressure in the soil warehouses decreases; while the gate is closed, water in the strata is soon filled with the soil warehouses, as a result, earth pressure will increase and mud water spurts after opening screw conveyor, which causes that shield fails to work [8-10].

## Reason Analysis

- This location is negative terrain which is easy to collect surface water, and silty clay under plain fill as water-resisting layer, as a concave shape, it is easy to collect the groundwater. If the perched groundwater of plain fill leakage occurs through silty clay, spewing may arise.
- Survey data indicate that, in this section, the plain fill of MA2-ZYDD34 hole, MA3-zyya2 hole, MA2-zyya2 hole and MA3-zyya17 hole is loose, with the clay, sand and a small amount of gravel. This plain fill backfill recently, the permeability and water storage performance in this section are relatively well. It is Easy to form the upper perched water and generate spewing conditions.

- There are drainage pipes above the shield axis surface buried in the region. If the pipes leak, sewage will be gathered in the plain fill, it will be another water leakage conditions. In the process of construction, the tunnel operators can smell peculiar smell which indicates that between spewing water and surface water connections exist.
- Silty clay as water-resisting layer, if it is not serious disturbance or destruction, the leakage will be very weak. In ordinary it can not constitute the spewing conditions, but the exploration drilling penetrates water-resisting layer. If the sealing is not good, it will become a juncture of the perched water and the lower part of the phreatic water. After a certain period of time, there will be form the funnel-like pressure water between the silty clay and phreatic water, the pressure formed by the pressure water acting on the top of the shield. After a certain disturbance in the shield machine construction process, spewing will occur.

**The Countermeasures**

During shield construction process, if the spewing is not treated in a timely and appropriate manner, the water or mud gush was easy to happen. sandy soil around excavation surface and shield tunnel segment will be taken out. These easily lead to construction accidents, such as ground collapse, the seepage of shield tunnel.

Effective measures should be taken to eliminate the spewing as soon as possible, in order to avoid these construction accidents. Construction control measures are listed as following:

- Inject the polymer materials into soil bin after the field engineer testing. Strengthen the workability of residue. Then inject Polymer solution into soil bin after been mixed in the bentonite tank.
- Innovate screw machine slag not, in order to avoid a lot of water and soil flow from belt conveyor. Then the artificial cleaning time will be reduced and ergonomics will be improved.
- To strengthen the surface subsidence monitoring, 24 hours on duty.
- optimize tunneling parameters，adopt the mode of high earth pressure, high thrust tunneling.
- Before tunneling, we should inject polymer into soil bin，then start the cutter. After mixing muck and high-molecular polymer up, the shield machine works again.
- Stop using foaming agent during the tunnel digging. Just use it occasionally in order to avoid the pipe block.
- Do the second grouting in the area which is about the tenth ring around the gushing area to block the water behind shield machine flowing into the soil bin(Fig 5).
- Add a circle of bubbles and the quilt to the outer surface of segment which is assembled in the subsequent steps, to stop the rear water(Fig6).

Fig.5 Secondary grouting

Fig.6 Add a circle of Quilts and foam

## Conclusions

These measures can successfully govern the gushing of screw machine and make the shield machine bail out as soon as possible. Many harmful factors are caused by screw machine spewing, but now quite limited measures can be taken to solve this problem. So we can only try to avoid it in the shield construction. Try to avoid rainwater and sewage pipe lines in the planning the subway route. In the stratum where the spewing easily happens, shield machine should go through as soon as possible. Machines should not stay a long time for the hidden danger increasing.

## References

[1] Zhu Wei, Qin Jian-she and Wei Kang-lin. Research on the Mechanism of the Spewing in the EPB Shield Tunnelling[J]. Chinese Journal of Geotechnical Engineering, vol.26 No.5, 2004.

[2] Kang Hong-xin. Waterproof Technique in Tunneling of Earth Press Balancing Shield Machine[J]. Construction Mechanization, vol.27 No.3, 2006.

[3] Xue Ru-jing, Chen Dong and Wu Jing-shu. The Analysis of Discharging Amount of Earth in EPB Shield Tunnelling. Industrial Construction, 2008,38(S1):974-976.

[4] Jiang Yu-sheng, Wang Chun-he, Chen Dong and so on. A Mechanical Model of Earth Pressure Balance Shield Screw Conveyor[J]. Mechanics and Engineering, 2007, 29(5):52-55.

[5] Qin Jian-she and Zhu Wei. Study on Flowing Through Screw Conveyor During Excavation With EPB Shield[J]. Rock and Soil Mechanics, 2004, 25(10):118-122.

[6] Zhang Min, Zheng Zhi-min and Deng Zong. EPB shield Tunnelling Expansion in Water-saturated Strata[J]. Tunnel Construction, 2003, 23(2):7-9,25.

[7] Hu Guo-hua, Hu Shao-hua, Gong Guo-fang and so on. The Analysis of Dumping of Earth Pressure Balance Shield Screw Conveyor[J]. Construction Machinery and Equipment, 2008, 39(4):6-7,43-46.

[8] Chen Hui-fang, Chen Guang-feng, Cheng Qian-yuan and so on. Application of Vertical Local Freezing Method in the Construction of Shield Entering Cave[J]. Construction Technology, 2012,41(8):84-87.

[9] Chen Hui-fang, Chen Guang-feng, Cheng Qian-yuan and so on. Safety Measures for Shields Passing Soft Muddy Soil Strata Containing High Pressure Methane[J]. Construction Technology, 2012, 41(7):75-76,81.

[10] Chen Guang-feng, Chen Hui-fang, Zhao Rong and so on. Application of Numerical Simulation in Pumping Tests for Metro[J]. Journal of Railway Engineering Society, 2010, 7:77-82.

*Applied Mechanics and Materials Vols. 580-583 (2014) pp 1143-1147*
*© (2014) Trans Tech Publications, Switzerland*
*doi:10.4028/www.scientific.net/AMM.580-583.1143*

# Study on deformation prediction of the tunnel surrounding rocks based on non-equal time-interval grey model

Pengfei Geng[1,a] , Changmin Yang[2,b],Weidong Guo[2,c], Peng Wang[3,d]

[1,2]College of Civil Engineering and Architecture, Hebei University, Baoding 071000, Hebei, China;

[3]Hebei construction group co., LTD

[a]liuyefeifei001@163.com,[b]changmyang@163.com,[c]hbugwd_2008@126.com,[d]8121693@qq.com

**Key words:** grey system; GM (1, 1);deformation; non-equal time-interval

**Abstract:** The thesis develops an non-equal time-interval GM (1, 1) model to forecast the deformation of the tunnel surrounding rock. A program is compiled via MATLAB 7.1 platform to implement the model. With the assistance of the program and the monitoring record of the convergence, the deformation is predicted and the error is analyzed. The numerical results indicate that the non-equal time-interval GM (1, 1) model does well in predicting the deformation of tunnel surrounding rock and is worthy to put into use in tunnel engineering.

## Introduction

As is well known, it is difficult to measure or forecast the deformation in tunnel engineering due to unknown of rock formation condition, rock attitude, different geologic progress. In addition, excavation sequence and method, supporting time and method, supporting rigidity etc, also have effects on the stability of the surrounding rock[1]. Thus make the tunneling progress a grey system [2-4] . In order to avoid injured and master the behavior of the rock, develop a effective model to exactly predict the deformation may be necessary.

At present, there are many methods to forecast rock deformation such as regression analysis model, data smoothing processing, time series model, grey model, artificial neural network model, etc. Among these models, the grey system model is widely used in projects and does a good performance with few amount of monitoring data[5-6].

The target of the grey model is a differential equation according to a few data. The demand is the utilizing, developing and processing of the dynamic information.

The primary research object is intrinsic grey system which need a discrete function to simulate the behavior characteristics of grey system. The main task of the grey system is to establish a differential equation dynamic model with discrete sequence, which is known as the grey model GM. [7]

GM(1,1) model is the core content of the grey model, its prerequisite is the equality of the sample period time distance and its main means to processing is to rule the original data to find the relationship.[8] The most commonly methods used is additive. This approach is called number generation.

Generally, the original sequence $x(i)$ shows no regularity but considerable randomness. After its implementation of the accumulated generating:

$$x^{(1)}(i) = \sum_{k=1}^{i} x^{(0)}(k) \tag{1}$$

the new sequence series $x^{(1)}(i)$ can weaken the randomness of the data and make it shows significant feature regularity. Taking the new series $x^{(1)}(i)$ into the grey model GM and then the model was conducted to inverse operation to restore the original sequence.

As we can see, in this process, the time distance are equal. This type of grey system is called equal time-interval grey model. But in the observe progress, because of the weather and construction order and other factors, the sample period time distance are not easy to keep equal.

For a number of issues in many fields, due to changes in conditions or influence of various factors, the time distance is unequal so that it would resulted in large error when use such models. Therefore, constructing an non-equal time-interval grey model has some real needs and theoretical significance.[9]

In view of this, this paper use the non-equal time-interval GM(1,1) model to forecast the convergence of the surrounding rock combining with the data measured from Zhangzhuo expressway Linli tunnel project and confirm the reliability and validity of the model[8].

**Modeling GM (1, 1)**

Based on the time series $t(i)$, a grey progress's original sequence $x_0^{(0)}(i)$ meets the condition:

(1) $t(i)-t(i-1)>0$;

(2) $\exists i, j \in [1,n]$,

$t(i)-t(i-1) \neq t(j)-t(j-1)$ ,

where $1 \le i \le n$, we call it non-equal time-interval grey progress.

Set $\Delta t = t(i)-t(i-1)$, when $\Delta t$ is small, we can construct a new set of time series $t_n(i)$.

$$t_n(i) = b_0 + b_1(i) \tag{2}$$

where $i \in N, b_0, b_1$ are constant.

As we can see $t_n(i)$ and $t(i)$ are very close.

$$\text{Set} \quad \sum_{i=1}^{n}[t_n(i)-t(i)]^2 = \min \tag{3}$$

By Lagrange interpolation principle, we can conclude that:

$$x_1^{(0)}(i) = x_0^{(0)}(i) + \frac{[x_0^{(0)}(i+1)-x_0^{(0)}(i)][t_n(i)-t(i)]}{t(i+1)-t(i)} \tag{4}$$

Throw formula (4), we can get a new series sequence $x_1^{(0)}(i)$ related to $t_n(i)$. The new series is liner and satisfied with the GM (1, 1) model.

According to the principle of least squares and (1),(2),(3),it can be deduced that:

$$\left.\begin{aligned} b_0 &= \frac{\sum t_n(i)}{n} - \frac{b_1 \sum i}{n} \\ b_1 &= \frac{n\sum i t_n(i) - \sum i \cdot \sum t_n(i)}{n\sum t_i^2 - \sum i^2} \end{aligned}\right\} \tag{5}$$

$$\frac{dx^{(1)}(i)}{di} + a_1 x_1^{(1)}(i) = a_2 \tag{6}$$

$$\text{Set} \quad B = \begin{bmatrix} -[x_1^{(1)}(1)+x_1^{(1)}(2)]/2 & 1 \\ -[x_1^{(1)}(2)+x_1^{(1)}(3)]/2 & 1 \\ \cdots & \cdots \\ -[x_1^{(1)}(n-1)+x_1^{(1)}(n)]/2 & 1 \end{bmatrix}$$

Then $a_1$ and $a_2$ meets:

$$[a_1 a_2]^T = (B^T B)^{-1} B^T y^n \tag{7}$$

Thus, we can have the following equation:

$$x^{(1)}(k) = (x^{(0)}(1) - \frac{a_2}{a_1}) e^{a_1(1-k)} + \frac{a_2}{a_1} \tag{8}$$

The equation (8) is an equal time interval grey model. After taking formula (2) into (8) we can draw the non-equal time-interval GM (1, 1) model responsive equation as:

$$x_0^{(1)}(t) = [x^{(0)}(1) - \frac{a_2}{a_1}] e^{a_1(1-\frac{t-b_0}{b_1})} + \frac{a_2}{a_1} \tag{9}$$

Calculate the value of each point in $x_0^{(1)}(t)$ and regressive reduction to get the fitted value related to the original data. The reduction formula for generating is:

$$\hat{x}_0^{(0)}(t) = \frac{(x_1^{(0)}(1) - \frac{a_2}{a_1})(1 - e^{a_1}) e^{a_1(b_0 + b_1 - t)}}{b_1} \tag{10}$$

**Model accuracy test**

(1) Residual test

Absolute error of the prediction is:

$$\varepsilon^{(0)}(k) = X^{(0)}(k) - \hat{X}^{(0)}(k) \text{ ,k=1,2,…,n} \tag{11}$$

The relative error of prediction is:

$$q = \left| \frac{\varepsilon^{(0)}(k)}{X^{(0)}(k)} \right| \times 100\% \tag{12}$$

(2) Posterior error test

$$S_1 = \frac{1}{n} \sum_{k=1}^{n} [x^{(0)}(k) - \bar{x}]^2 \quad \bar{x} = \frac{1}{n} \sum_{k=1}^{n} x^{(0)}(k)$$

$$S_2 = \frac{1}{n} \sum_{k=1}^{n} [\varepsilon^{(0)}(k) - \bar{\varepsilon}]^2 \quad \bar{\varepsilon} = \frac{1}{n} \sum_{k=1}^{n} \varepsilon^{(0)}(k)$$

The posteriori error ratio is:

$$c = S_2 / S_1 \tag{13}$$

Small error probability is:

$$p = p\{|\varepsilon(k) - \bar{\varepsilon}| < 0.6745 S_1\} \tag{14}$$

**Table 1 Accuracy class reference table**

| | posteriori error ratio C | Small error probability P | Result |
|---|---|---|---|
| Ⅰ | c≤0.35 | P≥0.95 | Excellent |
| Ⅱ | c≤0.50 | P≤0.95 | Good |
| Ⅲ | c≤0.65 | P≤0.80 | Pass |
| Ⅳ | c＞0.65 | P＜0.70 | Fail |

According to the descending order of P and C, the prediction accuracy can be divided into four categories as the Table1 shows.

## Engineering practice

The model developed above was used to predict the convergence of the surrounding rock in Linli tunnel, Zhangzhuo expressway engineering. The data was measured by JSS30A type digital device. The method to note the record is to read three value each time, the final record is the average of the three reading records. Because of the construction and human factors, the records were noted in non-equal time distance. In order to improve the prediction accuracy, the record was intercepted; the middle section was used to the prediction. The prediction program was compiled via MATLAB 7.1 platform.

Table 2 is the YK79+010-section convergence monitoring records after temperature correction. Table 3 is the contrast of monitoring and predicted value.

**Table 2 YK79+010 section convergence-monitoring record**

| | 1 | 2 | 3 | 4 | 5 | 6 | 7 | 8 | 9 | 10 | 11 |
|---|---|---|---|---|---|---|---|---|---|---|---|
| **Time distance/hour** | 23.5 | 25 | 22 | 26 | 24.5 | 23.5 | 24 | 24.5 | 24.5 | 25 | 23.5 |
| **Convergence value/mm** | 7.23 | 7.26 | 7.27 | 7.32 | 7.33 | 7.35 | 7.38 | 7.43 | 7.46 | 7.51 | 7.51 |
| | **12** | **13** | **14** | **15** | **16** | **17** | **18** | **19** | **20** | **21** | **22** |
| **Time distance/hour** | 26 | 23.5 | 24 | 25 | 23.5 | 25.5 | 21.5 | 22 | 23.5 | 24 | 24.5 |
| **Convergence value/mm** | 7.57 | 7.63 | 7.66 | 7.72 | 7.78 | 7.82 | 7.86 | 7.90 | 7.95 | 7.98 | 8.04 |

**Table 3 Contrast of monitoring and predicted value**

| | 1 | 2 | 3 | 4 | 5 | 6 | 7 | 8 | 9 | 10 | 11 |
|---|---|---|---|---|---|---|---|---|---|---|---|
| **Time distance/hour** | **23.5** | **25** | **22** | **26** | **24.5** | **23.5** | **24** | **24.5** | **24.5** | **25** | **23.5** |
| **Convergence value/mm** | **7.23** | **7.26** | **7.27** | **7.32** | **7.33** | **7.35** | **7.38** | **7.43** | **7.46** | **7.51** | **7.51** |
| **Predicted value/mm** | **7.21** | **7.25** | **7.29** | **7.32** | **7.36** | **7.40** | **7.44** | **7.48** | **7.52** | **7.56** | **7.60** |
| **Relative error/%** | **0.37** | **0.23** | **0.28** | **0.10** | **0.48** | **0.76** | **0.82** | **0.65** | **0.90** | **0.74** | **1.25** |
| | **12** | **13** | **14** | **15** | **16** | **17** | **18** | **19** | **20** | **21** | **22** |
| **Time distance/hour** | **26** | **23.5** | **24** | **25** | **23.5** | **25.5** | **21.5** | **22** | **23.5** | **24** | **24.5** |
| **Convergence value/mm** | **7.57** | **7.63** | **7.66** | **7.72** | **7.78** | **7.82** | **7.86** | **7.90** | **7.95** | **7.98** | **8.04** |
| **Predicted value/mm** | **7.64** | **7.68** | **7.72** | **7.77** | **7.81** | **7.85** | **7.89** | **7.93** | **7.98** | **8.02** | **8.06** |
| **Relative error/%** | **0.92** | **0.68** | **0.89** | **0.66** | **0.31** | **0.43** | **0.39** | **0.39** | **0.36** | **0.41** | **0.21** |

The non-equal time-interval GM (1, 1) model responsive equation is

$$\hat{x}_0^{(0)}(t) = (7.235 - \frac{7.1508}{-0.0053})(1 - e^{-0.0053})e^{-0.0053(1-t)}$$

Absolute percentage error is 0.041786%; posteriori error ratio $c = 0.136734$ ; small error probability P=0.9545; excellent rate for Ⅰ.

The results indicate that the non-equal time-interval GM (1, 1) model is considered exactly accurate. The predicted value coincides perfectly with the measured data.

## Conclusions

1.This article developed an non-equal time-interval GM(1,1) model, predicted the convergence of the surrounding rock in Linli tunneling engineering with a small amount of data, provided a theoretical basis on deformation prediction.

2. The accuracy test of the model shows the excellent rate for, I ,which ensure the predicted value reliable and truthful.

3. With the utilizing of measured data and MATLAB 7.1 platform, the paper demonstrated the rationality of taking tunnel deformation as a grey model and the feasibility of using the model to forecast the value.

4. The engineering example confirmed that the non-equal time-interval GM (1,1) model shows a good performance in short time distance. However, the model is in an exponential form, when the time distance become longer, its predictive ability remains further proof.

## Acknowledgements

Foundation item: supported by Bureau of Transportation science and technology project Hebei Province China, Project(Y-201031)

## References

[1] Wang Y.G.,Han A.M., & Wang J.,etc, (2009),Optimization Analysis on Tunnel Surrounding Rock Deformation Prediction Based on GM (1,1), Modern Transportation Technology,Vol.6 No.5,Oct. 47-51

[2] DENG J.L.(1990),Grey system theory tutorial, HuaZhong University of Science and Technology Press,428

[3] LIU S.F.,& DENG J.L.(2000),The Range Suitable for GM (1, 1), Systems Engineering-theory & Practice, (5),121-124

[4] LIU S.F., & Lin, Y.(1998),An introduction to grey systems, PA, USA: IIGSS Academic Publisher.

[5] HAO Z.(2004),Displacement Prediction and Stabilization Forecast of Surrounding Rock of Highway Tunnel Excavation, HIGHWAY, No.8,Aug.197-203

[6] Erdal Kayacan, Baris Ulutas, & Okyay Kaynak.(2010),Grey system theory-based models in time series prediction, Expert Systems with Applications 37 1784–1789

[7] SUN H.Y,(1996),Non-equalTime-interval Grey Model and its APPlication, Journal of Basic Science andEngineering, Vol.4, No.4 December.407-411

[8] ZOU S.G., ZHANG K.L., & ZHANG S.P., etc ,(2012),Application on grey system in the tunnel monitoring measurement, Yangtze River,Vol.43 ,Supplement(1),June.62-64

[9] DAI W.Z. &LI J.F. , (2005), Modeling Research on Non-equidistance GM(1,1) Model, Vol.9, Sep.89-93

*Applied Mechanics and Materials Vols. 580-583 (2014) pp 1148-1152*
*© (2014) Trans Tech Publications, Switzerland*
*doi:10.4028/www.scientific.net/AMM.580-583.1148*

# Mechanical calculation for collapse mechanism of surrounding rock on shallow tunnel

Ying Peng[1] , Junsheng Yang[2] , Yanhua Shen[1] , Jianhua Liu[1,a]

[1]School of Civil Engineering,Hunan University of Technology, Zhuzhou 412007, China

[2]School of Civil and Architectural Engineering, Central South University, Changsha 410075, China

Corresponding author, Jianhua Liu, [a]email:liujh070601@sohu.com

**Keywords:** shallow tunnel, surrounding rock pressure, limit analysis

**Abstract.** The upper bound method of limit analysis is used for surrounding pressure calculation of shallow tunnel. Two rigid-block translational collapse mechanisms are assumed for shallow tunnel and the corresponding formulas are deduced. The earth pressure of shallow tunnel has been transformed into a mathematic optimization problem, we can get optimization solutions for the surrounding rock pressure by corresponding calculating program. It is concluded that the upper bound method of limit analysis is a feasible approach for the determination of surrounding pressures on shallow tunnel.

## Introduction

As the tunnel designing, the core problem is how to determine the reasonable supporting parameters of tunnel surrounding rock, and the failure modes are determined by the supporting parameters of tunnel surrounding rock failure mode,so the research is of great significance for the structural design of tunnel. Because of the model test uses the real material in reality, it can reflect the spatial relationship between geological structure and engineering structure at the basic principle in similar conditions, so it more intuitively reflects the overall characteristics of geotechnical engineering mechanics, deformation and failure characteristics.

## The collapse mechanism of shallow buried tunnel surrounding rock

There are many factors influencing the surrounding rock pressure of shallow tunnel, we only consider the surface as level here, and it simplified as a plane strain problem, and we make the following Basic assumption:

(1) The tunnel with circular cross section is simplified as a rectangular section which highs H, span of 2b, and H and 2b are diameter, irregular shaped section can also be simplified to rectangle, to do so doesn't lose generality. (2) We suppose the surrounding rock of tunnel is elastic perfectly plasticity body, the c-material obeys the Mohr Coulomb yield criterion. (3) The overburden thickness of tunnel is h, the subjected uniform supporting force of tunnel roof is q, the horizontal uniform supporting force of side wall is e, e=Kq, K is parameters.(4) The side walls moving inwards is allowed in the deformation of the tunnel mode, the vertical of roof moves downward. At the same time, the movement of side wall and roof dosn't affect from each other, the support structure may be appropriate to move in order to adapt to the deformation of surrounding rock, and the mutual friction of surrounding rock in the deformation process of mutual is ignored.

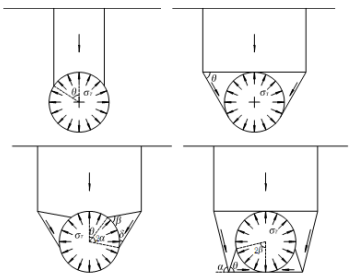

Fig.1 Collapse mechanisms of shallow tunnel in cohesive material

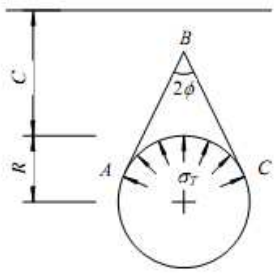


Fig.2 Collapse mechanism of shallow tunnel in cohesionless material

Formulating a suitable structure of shallow tunnel surrounding rock failure mode is the key to calculate the surrounding rock pressure by upper bound method, usually through the analysis of engineering example, model test or numerical calculation methods. Usually collapse mechanism includs rigid block rotation and translation, translation and rotation combined form. In practical application, the translational collapse mechanism is the one most commonly used [1]. Figure 1 is the four kinds of failure modes of [2] clay of shallow buried tunnel proposed by Davis E H. Figure 2 is a cohesionless soil and shallow buried tunnel surrounding rock collapse mechanism proposed byAtkinson J H and Potts DM[3].

Collapse mechanism that figure1 and figure2 showing basicly reflects the main collapse forms of cohesive and cohesionless soil about shallow buried tunnel, but still rough. Therefore,to the shallow buried tunnel constructed by the new Austrian Tunneling Method, the C-φ materials as surrounding rock, two kinds of collapse mechanism is presented in Figure3, shown in Figure4 (based on the mode A and mode B) in translational mode, and assuming that the tunnel roof and side wall support force are uniformly distributed, but it's not the same.

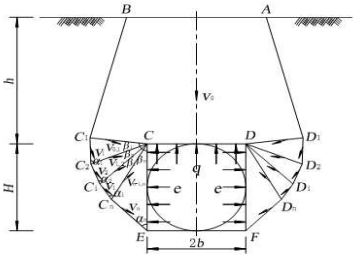

Fig.3 Collapse mechanism A

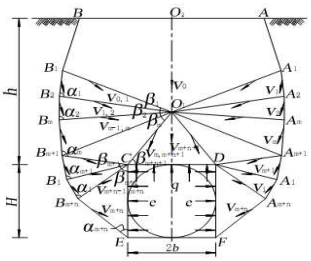

Fig.4 Collapse mechanism B

According to the associated flow rule, speed rigid slider between discontinuous velocity vector line and discontinuous line is the angle $\varphi$, and the velocity vector should satisfy the vector closure, then can get the tunnel overall buckling collapse mechanism A the corresponding velocity field as shown in figure5. The velocity of the roof above the wedge $ABC_1CDD_1$ is $\nu_0$, vertical downward. Speed at the side wall of the triangular block from top to bottom is $\nu_0$ in turn, their relative speed is $\nu_1 \cdots \nu_i \cdots \nu_n$, the relative velocity in each triangular shape followed and the determined by the angle $\alpha_1 \cdots \alpha_i \cdots \alpha_n$ and $\beta_1 \cdots \beta_i \cdots \beta_n$ , (Fig. 3).

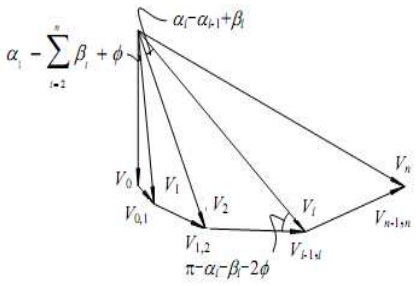

Fig.5 Velocity field for collapse mechanism A

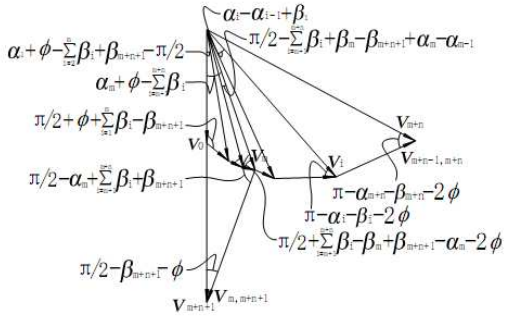

Fig.6 Velocity field for collapse mechanism B

The velocity field figure 6 for the collapse mechanism to the corresponding B. The velocity of the wedge $AO_2BB_1O_1A_1$ is $\nu_0$, vertical downward. The wall above the speed of the triangular block from top to bottom $\nu_1 \cdots \nu_{m-1}$ in turn, the relative velocity between the order, quadrilateral slider velocity $B_mB_{m+1}CO_1$ between side wall and roof top is $\nu_m$ ,form and collapse mechanisms of side wall is similar to the A slider, slider velocity from top to bottom $\nu_{m+1} \cdots \nu_i \cdots \nu_{2,m+n}$ in turn, roof top triangle slider $CDO_1$ velocity is $\nu_{m+n+1}$, direction vertical downward, and the relative speed of slide $B_mB_{m+1}CO_1$ is $\nu_{m,m+n+1}$. The collapse mechanism is determined by $\alpha_1 \cdots \alpha_i \cdots \alpha_{m+n}$ and $\beta_1 \cdots \beta_i \cdots \beta_{m+n}, \beta_{m+n+1}$ (Fig. 4).

**Maximum limit analysis method**

Maximum limit analysis theorem can be stated as:to the plasticity strain rate field $\dot{\varepsilon}_{ij}^{*}$ and velocity field $v_i^{*}$ of arbitrary movement permit, the limit load $F_i$ determined by the virtual power equation (1) is same or greater than the limit load of the real $F$ [4]:

$$\int_S F_i v_i^{*}\,\mathrm{d}S+\int_A \gamma_i v_i^{*}\,\mathrm{d}A=\int_A \sigma_{ij}\dot{\varepsilon}_{ij}^{*}\,\mathrm{d}A+\int_{S_D}(\tau-\sigma_n\tan\phi)\Delta v_i^{*}\,\mathrm{d}S \qquad (1)$$

The limit load in type (1)is the load prompting system damage. Assuming the material obeys the Mohr Coulomb yield criterion and associated flow rule [4], for two-dimensional problems, velocity discontinuity lines as power dissipation is:

$$D=cv\cos\phi \qquad (2)$$

**Mechanical calculation**

Mechanical calculation according to the collapse mechanism A. The calculation of velocity field to movement permission. According to the permissive condition that rigid sliding should meet, The velocity vector should meet the closure conditions[4] , According to figure 3 , figure 5,each velocity should satisfy the following recurrence relationseach:

$$v_1=\frac{\sin\left(\sum_{i=1}^{n}\beta_i+\phi\right)}{\sin(\pi-\alpha_1-\beta_1-2\phi)}v_0 \qquad (3)$$

$$v_{0,1}=\frac{\sin\left(\alpha_1-\sum_{i=2}^{n}\beta_i+\phi\right)}{\sin(\pi-\alpha_1-\beta_1-2\phi)}v_0 \qquad (4)$$

$$v_{i+1}=\frac{\sin(\alpha_i+2\phi)}{\sin(\pi-\alpha_{i+1}-\beta_{i+1}-2\phi)}v_i \quad (i=1,\cdots,n-1) \qquad (5)$$

$$v_{i,i+1}=\frac{\sin(\alpha_{i+1}-\alpha_i+\beta_{i+1})}{\sin(\pi-\alpha_{i+1}-\beta_{i+1}-2\phi)}v_i \quad (i=1,\cdots,n-1) \qquad (6)$$

The calculation of the gravitational power. As it is shown in Figure 3,when the shallow buried tunnel suffers destruction , gravity power is equal to all rigid blocks' gravity power.So,we need calculate the rigid block area and their speed in the vertical direction component.The recursive relations of each velocity discontinuity length are as follows：

$$BC_1=\frac{1}{\cos\phi}\left(h-CC_i\cdot\cos\sum_{j=1}^{i}\beta_j\right) \qquad (7)$$

$$CC_i=\frac{\sin\alpha_i}{\sin(\pi-\alpha_1-\beta_i)}CC_{i+1} \quad (i=1,\cdots,n-1) \qquad (8)$$

$$CC_{i+1}=\frac{\sin\beta_i}{\sin(\pi-\alpha_i-\beta_i)}CC_{i+1} \quad (i=1,\cdots,n-1) \qquad (9)$$

$$CC_n=\frac{\sin\alpha_n}{\sin(\pi-\alpha_n-\beta_n)}CE \quad (i=1,\cdots,n-1) \qquad (10)$$

$$C_nE=\frac{\sin\beta_n}{\sin(\pi-\alpha_n-\beta_n)}CE \quad (i=1,\cdots,n-1) \qquad (11)$$

Each rigid block area respectively is as follows：

$$\Delta CC_iC_{i+1}=\frac{1}{2}CC_i\cdot C_iC_{i+1}\cdot\sin(\pi-\alpha_i-\beta_i) \quad (i=1,\cdots,n-1) \qquad (12)$$

$$\Delta CC_nE=\frac{1}{2}CC_n\cdot C_nE\cdot\sin(\pi-\alpha_n-\beta_n) \qquad (13)$$

$$\frac{1}{2}\square ABC_1CDD_1=\frac{1}{2}BC_1\cdot CC_1\cdot\sin\left(\sum_{i=1}^{n}\beta_j-\phi_n\right)+\frac{1}{2}\left[2b+CC_1\cdot\cos\left(\sum_{i=1}^{n}\beta_i-\frac{\pi}{2}\right)-BC_1\sin\phi\right] \quad (14)$$

According to equation (3) - (14) and the rigid block velocity vector together with the vertical angle,we can get half of the failure mode of gravity power called $P_\gamma$:

$$\int_S P_\gamma=\int_A\gamma_i v_i^*\,\mathrm{d}A=\frac{1}{2}\square ABC_1CDD_1\cdot\gamma v_0+\frac{1}{2}\Delta CC_nE\cdot\gamma v_n\cdot\cos(\alpha_n+\phi)+\gamma\cdot\sum_{i=1}^{n-1}\left[\Delta CC_1C_{i+1}\cdot v_0\cdot\cos(\alpha_i+\phi)-\sum_{j=i+1}^{n}\beta_j\right]\frac{n!}{r!(n-r)!} \quad (15)$$

The calculation of dissipation power. The dissipation power can be calculated according to equation (2), half of the total power dissipation called Pe also can be calculated according to the following equation:

$$\int_S P_e=\int_{S_D}(\tau-\sigma_n\tan\phi)\Delta v_t^*\,\mathrm{d}s=c\cdot\cos\phi\left[\sum_{i=1}^{n-1}\left(C_iC_{i+1}\cdot v_i+CC_i\cdot v_{i-1,i}\right)+BC_1\cdot v_0+C_nE\cdot v_n\right] \quad (16)$$

The calculation of Supporting force power. The power of vertical supporting force of tunnel roof called q and horizontal side wall supporting force called e can be calculated as following:

$$P_T=\int_S F_i v_i^* dS=-bqv_0-HKqv_n\cdot\sin(\alpha_n+\phi) \quad (17)$$

The calculation of support reaction force. Throug feding equation (15)-(17) into equation (1),we can get the tunnel roof vertical support reaction called q:

$$q=\frac{p_\gamma-p_c}{bv_0+HK\cdot\sin(\alpha_n+\phi)v_n} \quad (18)$$

The optimization of the upper limit solution to surrounding rock pressure. For the collapse mechanism A,assuming that the tunnel side wall of the triangle number is n,so we can determine its shape according to a group of angle $\alpha_1\cdots\alpha_i\cdots\alpha_n$ and $\beta_1\cdots\beta_i\cdots\beta_n$, correspond to an upper bound solution called Q at the same time ,that is $q=f(\alpha_1,\cdots,\alpha_i,\cdots,\alpha_n,\beta_1,\cdots,\beta_i,\cdots,\beta_n,)$. According to the upper bound theorem, maximum q that meet the licensing conditions is corresponding to an optimal solution to this collapse mechanism. So the problem changes:On condition of meeting physical constraint conditions,seek the maximum value of the objective function. From Figure 4,the angle between the velocity vector must be positive.Then, the constraints to collapse mechanism called A are as bellow:

$$\begin{cases}\alpha_1-\sum_{i=2}^{n}\beta_i+\phi>0\\ \pi-\alpha_i-\beta_i-2\phi>0 \quad (Among\ them\ i=1,\cdots,n)\\ \alpha_i-\alpha_{i-1}-\beta_i>0 \quad (Among\ them\ i=1,\cdots,n)\end{cases} \quad (19)$$

As for the failure mode of B,according to the above steps we can calculate each speed recursive relationship.

## Conclusions

(1) The objective function and constraint conditions of the upper bound method of limit analysis for surrounding rock pressure are get by two collapse mechanisms of shallow tunnel. after that optimization solutions for the surrounding rock pressure can be gotten by corresponding calculating program and an optimization method. (2) For the upper bound method of limit analysis, we need to determine K value of the ratio of the level of uniform support reaction force e and the vertical uniform supporting reaction force q. We should choose multiple K values in practical application so it can get a set of e and q , and then them are checked as structure load. (3) It may form a sliding surface through the earth's surface after Shallow tunnel wre excavated and leading to produce a wide range of plastic area. It is concluded that the upper bound method of limit analysis is a feasible approach for the determination of surrounding rock pressures on shallow tunnel.

**Acknowledgements**

This work was financially supported by the Hunan Provincial Natural Science Foundation of China (14JJ2117)

**References**

[1] A. Drescher, E. Detournay: Geotechnique, Vol. 43 (1993), p. 443-456
[2] E.H. Davis, M.J.Gunn, R J.Mair: Geotechnique, Vol. 30 (1980), p.397-416.
[3] J.H. Atkinson, D.M.Potts :Geotechnique, Vol. 27 (1977), p. 203-215
[4] W. F.Chen: *Limit analysis and soil mechanics*(Elsevier Scientific Publishing Company, New York 1975).

*Applied Mechanics and Materials Vols. 580-583 (2014) pp 1153-1160*
*© (2014) Trans Tech Publications, Switzerland*
*doi:10.4028/www.scientific.net/AMM.580-583.1153*

# The research on environment vibration due to Subway with rail pads of frequency-dependent stiffness

Fan Yang[1, 2, a], Kai Wei[1, 2, b] and Yanchen Song[1, 2, c]

[1] Key Laboratory of High-speed Railway Engineering, Ministry of Education, Chengdu, China, 610031.

[2] School of Civil Engineering, Southwest Jiaotong University, Chengdu, China, 610031.

[a] 15928078353@163.com, [b] wei_mike@163.com, [c] yanchen_songjiaoda@163.com

**Keywords:** Subway tunnel; Environment vibration; Frequency-domain method; Rail pad; Frequency-dependent stiffness.

**Abstract:** Based on Vehicle-Track Coupling Dynamics and the spectrum analysis technique of the Finite Element Method, a frequency-domain method of environment vibration due to subway is put forward and frequency-range distribution of ground acceleration is discussed. Compared with the measured data, the result shows that after considering frequency-dependent stiffness of rail pad, the error is less than 0.3dB in the frequency range of 0-30 Hz, but it is up to 11.8 dB in the frequency range of 50-100 Hz. And the frequency-domain distribution of ground vibration changes too. Thus, the frequency-dependent stiffness of rail pads is not negligible in the prediction of environment vibration generated by subway.

## Introduction

The vibration and noise induced by subway recently troubles people a lot. To reduce their influence, the vibroisolating material is adopted such as the rail pad, the damping pad under track sleepers or beds and so on. In this paper, the rail pad generally made of viscoelastic rubber material is focused on.

In the past, the stiffness was treated as a constant when dynamic characteristics was analysed. However, the viscoelastic material's dynamic constitutive behavior relies on frequency, temperature and amplitude. So its dynamic performance changes with the frequency. And the wheel-rail force has a wide frequency band. Therefore it's not reasonable to treat the stiffness as a constant.

According to Vehicle-Track Coupling Dynamics and Finite Element Method, the random vibration response of subway system in which the viscoelastic material's stiffness changes with frequency is analysed.

## The Frequency-domain Method of Environment Vibration due to Subway

First, the spectrum of the dynamic random load acting on the fastening system is achieved. Then it's processed to be the linear load which acts on the two dimensional finite element model of the tunnel and foundation. Through the direct integral method of finite element model, the environment vibration level around the subway tunnel can be calculated.

### 1.1 The spectrum feature of the force acting on the subway fastening system

#### 1.1.1 Vehicle-track coupling dynamic model [1]

**(1)Vehicle model**

Subway car can be simplified as a half vehicle system with doubled suspension systems. It has ten freedom degrees including the vertical and nodding motion of the vehicle and the bogies, and the vertical motion of the wheelsets.

**(2)Track model**

The subway common track structure is the monolithic track bed with short sleepers embedded, which is composed of rail, fastener, perforated concrete sleeper and concrete ballastless track bed.

For the sleeper is encastred into the track bed and the mass of the base is big, the vibration mainly reflects on the rail. Thus, the rail is simplified as an Euler beam supported by discrete points.

**1.1.2 The amplitude spectrum of the fastening force**

The vehicle-track vertical system is simplified as a linear spring-damper system. And the response spectrum of freedom degrees is achieved by the classic analysis method of linear random vibration. The specific calculation steps are as follows.

The vibration differential equation of Vehicle-Track Coupling Dynamic System is expressed below.

$$[M]\{\ddot{q}\}+[C]\{\dot{q}\}+[K]\{q\}=\{Q\}=\left[K_f\right][Z_0] \tag{1}$$

Where: $[M]$ is the mass matrix of the system; $[C]$ is the damping matrix of the system; $[K]$ is the stiffness matrix of the system; $[K_f]$ is the transformation matrix of the system; $\{Q\}$ is the generalized force vector of the system; $\{q\}$ is the generalized displacement vector of the system; $\{Z_0\}$ is the irregular displacement vector.

If $\{Z_0\}=[I]e^{-j\omega t}$, then $[q]=[H(\omega)]\ e^{-j\omega t}$. $[H(\omega)]$ can be solved by Eq. (1).

$$(-\omega^2[M]+i\omega[C]+[K])[H(\omega)]=\left[K_f\right][I] \tag{2}$$

The transfer function considering the frequency-dependent stiffness can be solved by Eq. (2).

$$(-\omega^2[M]+i\omega[C_\omega]+[K_\omega])[H(\omega)]=\left[K_f\right][I] \tag{3}$$

The relationship between the input and output power density function is achieved by random vibration theory and the transfer function:

$$[S_{out}(\omega)]=\left[H^*(\omega)\right][S_{in}(\omega)][H(\omega)]^T \tag{4}$$

Where: $[H(\omega)]$ is the vibration transfer function matrix of the system; $[H^*(\omega)]$ is the conjugate function matrix of $[H(\omega)]$; $[H(\omega)]^T$ is the transposed matrix of $[H(\omega)]$. To simplify the power spectrum of the output response, the transfer function matrix of the single input-output system with multiple degrees of freedom is put forward.

$$[H_s(\omega)]=[H_1(\omega)]e^{-j\omega\tau_1}+[H_2(\omega)]e^{-j\omega\tau_2}\quad\cdots+[H_n(\omega)]e^{-j\omega\tau_n} \tag{5}$$

Where: $[H_s(\omega)]$ is the transfer function matrix of the response of all freedom degrees in the system with the excitation of n wheelsets.

$$\tau_1=0\qquad\tau_i=\Delta l/v \tag{6}$$

Where: $\Delta l$ is the distance between the first wheelset and the $i$th wheelset (m); $v$ is the speed of the vehicle (m/s).

Then the response power spectral density of different freedom degrees is achieved by calculating the transfer function matrix $[H_s(\omega)]$.

$$S_{qi}(\omega)=\left|H_s(\omega)\right|^2 S_{11}(\omega) \tag{7}$$

$$\ddot{S}_{qi}(\omega)=\omega^4 S_{qi}(\omega) \tag{8}$$

Where: $S_{qi}(\omega)$ is the power spectral density of the displacement response of the $i$th freedom degree; $\ddot{S}_{qi}(\omega)$ is the power spectral density of the acceleration response of the ith degree of freedom; $S_{11}(\omega)$ is the power spectrum density of the track irregularity under the wheelset 1; $H_{s(i,1)}(\omega)$ is the transfer function matrix of the frequency response of the $i$th freedom degree.

Assuming the vehicle speed is 80 km/h and the track irregularity comes from the fifth grade track irregularity PSD of U.S. railways (wavelength ranging from 0.1 to 100 meters), the power spectral density amplitude spectrum of the force acting on the fastener whose stiffness is 40 or 50 kN/mm is shown in Fig. 1.

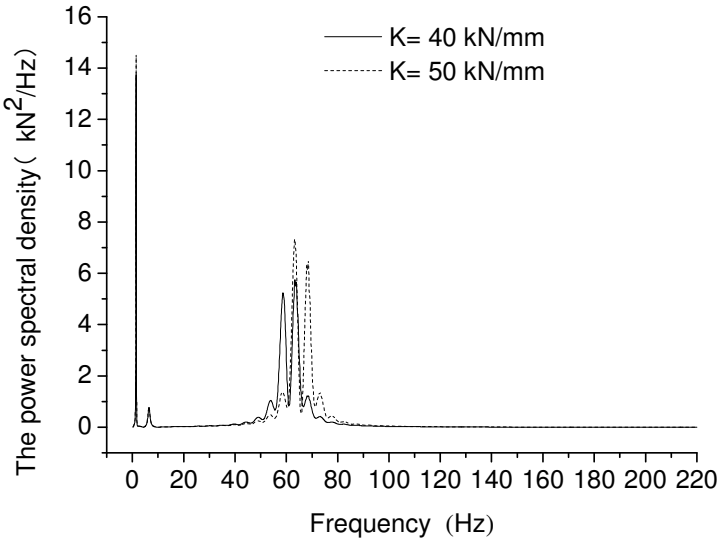


Fig. 1 The power spectral density of the force acting on the fastener

As shown in Fig. 1, the frequency-domain distribution and the amplitude of the dynamic random load change with the fastener stiffness. And the dynamic load is especially sensitive to the fastener stiffness changing. Thus, the frequency-dependent stiffness must be taken into consideration in the analysis of wheel-rail dynamic system.

Usually, the stiffness of rail pad increases with the frequencies raising. But it's a pity few researchers study the frequency-dependent stiffness of rail pads. Some research conclusions show the stiffness was linear with the frequency under the logarithmic coordinate, to see the Eq. (9). The approximate frequency-stiffness curve of the rail pads in the test line can be given based on the Eq. (9) when treating $f$ as 4 Hz and taking $K$ as 40kN/mm.

$$\log_{10}^{y} = 0.1306(\log_{10}^{x} - \log_{10}^{f}) + \log_{10}^{K} \tag{9}$$

Based on the above analysis and the frequency-dependent stiffness of the rail pad being 40kN/mm at 4 Hz. Then the spectrum of the dynamic random load is shown in Fig. 3 after considering the frequency–dependent stiffness of rail pad.

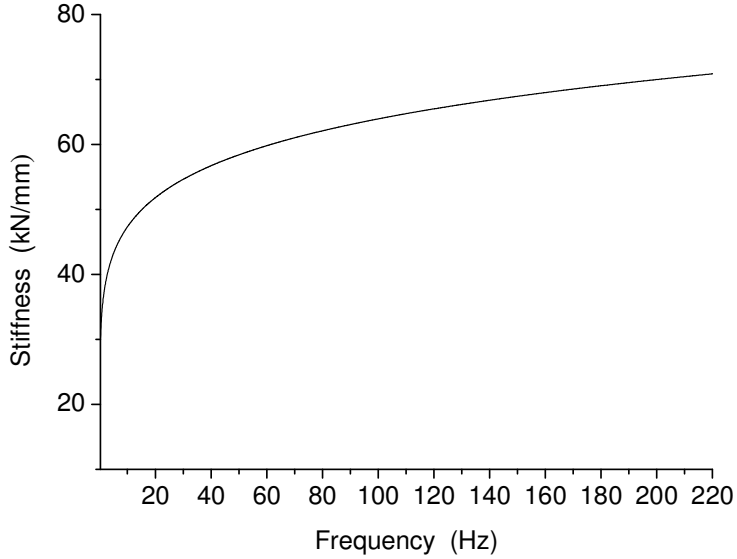


Fig. 2 The relationship between the stiffness of rail pad named **DT VI 2** and the frequencies based on the tested fitting curve

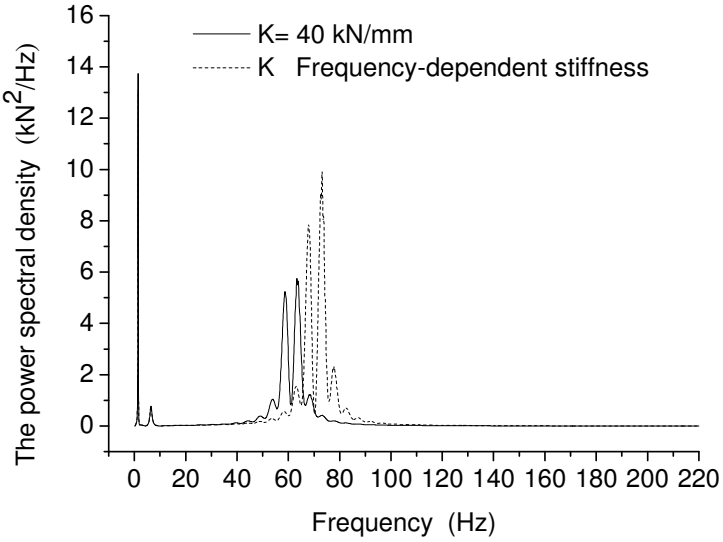


Fig. 3 The dynamic random load acting on the fastener whether considering the frequency-dependent stiffness of the rail pad

### 1.1.3 The simulation of the equivalent linear load about the force acting on the subway fastener

The dynamic random load acting on the subway fastener should be processed to be equivalent linear load so that the subway tunnel can be simplified as the two-dimensional tunnel-foundation model to solve. The Ref. [2] puts forward an equivalent linear load formula(Eq. (10)) whose calculation accurancy depends on $K_0$. But $K_0$ ranges from 0.6 to 0.9, so the calculation error is a little large and the fastener's stiffness and the fastener spacing are not considered.

$$L_F(t) = K_0 \cdot \frac{P(t) N_b n_w}{L_{car}} \tag{10}$$

Where: $L_F(t)$ is the linear load evenly distributed along the center line of the track (kN/m); $P(t)$ is the measured vertical load acting on the rail(kN); $N_b$ is the number of the bogies of one vehicle ($N_b$=2); $n_w$ is the number of the wheelsets of one bogie ($n_w$=2); $L$ is the length of one carriage ($L$=22.1m).

The noise and vibration evaluation ideas put forward by the Federal Railroad Administration in 2006 introduced the concept of force density. The force density means the traffic load per meter(N/m) which is averaged in the length of one car. The result will be treated as the equivalent linear load. According to the static calculation, it's found one wheel force can be supported by at least 3 fasteners whose spacing is about 1 meter. In one meter range, the equivalent uniformly distributed load seems the ratio between $P(t)$ (the fastener force) and $d$(the fastener spacing). In this method, the fastener's stiffness can be taken into consideration, to see Eq. (11).

$$F(t)=\frac{2P(t)N_b n_w}{L} \tag{11}$$

Where: $F(t)$ is the linear load evenly distributed along the center line of the track; $P(t)$ is the fastening force.

Because of the symmetry, half of the tunnel structure and load ($F(t)$/2) are analysed in this paper. So the equivalent load of the amplitude of the spectrum by Eq. (11) is used in this paper to study on the influence of the stiffness of the fastener.

### 1.2 The finite element model of the tunnel and foundation

#### 1.2.1 The model parameters and boundary conditions

Researches show that the precision of the dynamic calculation will be sufficient when the width of the soil model is 15 times the width of the tunnel diameter and the depth is 7 times the depth of the tunnel depth[3,4]. At the test site, the diameter is 6.2 meters and the depth is 6 meters.So the model is made 100 meters wide and 50 meters deep.

Moreover, the minimum size of the soil layer should be 1/12 times the stratigraphic shear wavelength to obtain sufficient accurancy($\lambda_s=C_s/f$). For the vibration frequency range which has great effect on the human body is 1-80 Hz and the shear wave velocity is shown in Table 1, the minimum size of the soil layer is at least 0.2 meter.

A horizontal displacement constraint is applied at the axis of symmetry and fixed constraint is applied on the bottom. To guarantee precision, the free boundary is applied in the far-field region .

#### 1.2.2 The dynamic parameters of the soil layer

**(1)The dynamic shear modulus**

The Martin-Davidenkov Model can be used to compute the dynamic shear modulus in Eq. (12).

$$\frac{G_d}{G_{\max}}=1-\left[\frac{\left(\frac{\gamma_a}{\gamma_0}\right)^{2B}}{1+\left(\frac{\gamma_a}{\gamma_0}\right)^{2B}}\right]^A \tag{12}$$

$$G_{\max}=x\rho V_s^y \tag{13}$$

Where: $G_{max}$ depends on Eq. (13); $G_{max}$ is the maximum dynamic shear modulus; $G_d$ is the dynamic shear modulus; $\gamma_0$, $A$ and $B$ ($\gamma_a=10^{-5}$) is shown in the Ref. [5]; $x$ and $y$ is the curve fitting constants whose values are suggested in Ref. [6] and [7]. To clay soil: $x$=20.9, $y$=1.28; To sand: $x$=30.0, $y$=1.29.

The relationship between shear modulus and elasticity modulus is shown in Eq. (14).

$$E_d=2G_d(1+\mu) \tag{14}$$

**(2)The dynamic damping**

The dynamic damping ratio D is calculated according to Eq. (15) where $\varphi$ and $D_{\max}$ come from Ref. [5]. In the finite element model, rayleigh damping matrix is adopted. The proportional damping coefficient $\alpha$, $\beta$ is calculated assuming $f_1$ and $f_2$ is 10 and 80 Hz respectively.

$$D = D_{\max}(1-\frac{G}{G_{\max}})^{\varphi} \tag{15}$$

Table 1 Soil Parameters

| Soil category | The thickness of soil layer (m) | Density (kg/m$^3$) | Shear wave velocity(m/s) | Dynamic modulus (MPa) | Damping ratio | Poisson's ratio |
|---|---|---|---|---|---|---|
| Silty clay | 12.5 | 1740 | 190 | 75.0 | 0.01 | 0.3 |
| Silty-fine sand | 30 | 1860 | 340 | 250.3 | 0.014 | 0.3 |

**Analysis of the Results**

**2.1 The test site of Nanjing subway in tunnel**

Nanjing Metro Line 1 begins from Bridge Maigao and ends to China Pharmaceutical University. It's 39.7 kilometres long. There are 27 stations along it. The subway train are marshaled by six Vehicle A whose highest speed is 80 km/h. The test site between the Station Zhongsheng and the Station Xiaoxing is so spacious that the background vibration is very small. In addition, the soil layer is obviously divided into two layers where the upper layer is silty clay and the lower layer is silty-fine sand.

The track structure consists of 60kg/m rail, Fastener DT VI2(shown in Fig. 4) and the monolithic concrete bed. The static stiffness of the fastening system is composed of the fastening element stiffness $K_c$ and the rail pad stiffness $K_p$. The static stiffness $K$ is 30kN/mm. But $K_c$ is only 0.5~1.2kN/mm. So $K_p$ is approximately equal to $K$. Moreover, the dynamic and static stiffness ratio of the Fastener DT VI2 is 1.2-1.4 at the frequency of 4 Hz. So the dynamic stiffness is about 36kN/mm~42kN/mm. The value was set as 40kN/mm at 4 Hz.

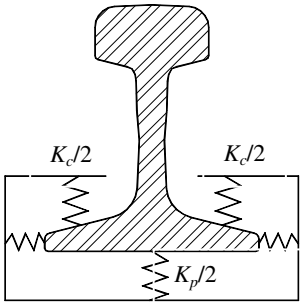


Fig. 4 The mechanical model of the fastener

**2.2 The influence of frequency-dependent stiffness of rail pads on environment vibration**

Under the condition: the speed-80km/h, $K$-40kN/mm and the irregularity-the fifth grade track irregularity PSD of U.S. railways. The vertical ground vibration acceleration in 1/3 octave at the position 5m away from the tunnel center is extracted to compare with the measured data.

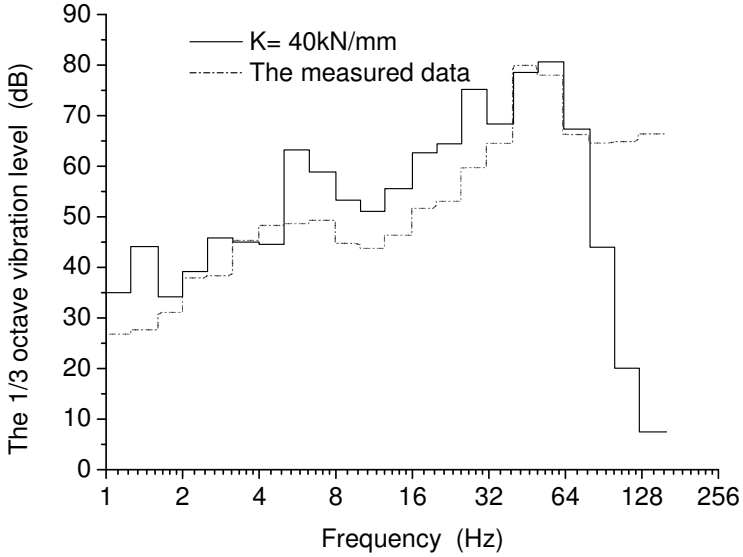


Fig. 5 The comparison of the measured data and the results with *K* being 40kN/mm

Compared with the measured data, they agree well on the whole. And the gaps between them are 1.3dB and 2.6dB at the center frequency 50 Hz and 63 Hz. But the gaps are 7-14 dB at the center frequency 1.6 Hz and 6.3-31.5 Hz.

For the load peak calculated from the fifth grade track irregularity PSD of U.S. railways appears at 1.6 Hz and 6.3 Hz. It means the actual irregularity of the track is different from the fifth grade track irregularity PSD of U.S. railways at the wavelength $V/f$=50m and 12.7m.

In conclusion, the method put forward in this paper agrees with the measured data well.

**2.3 The influence of frequency-dependent stiffness of rail pads on environment vibration**

The environmental vibration is calculated according to whether taking the frequency-dependent stiffness into consideration. Compare their 1/3 octave vibration level as follows.

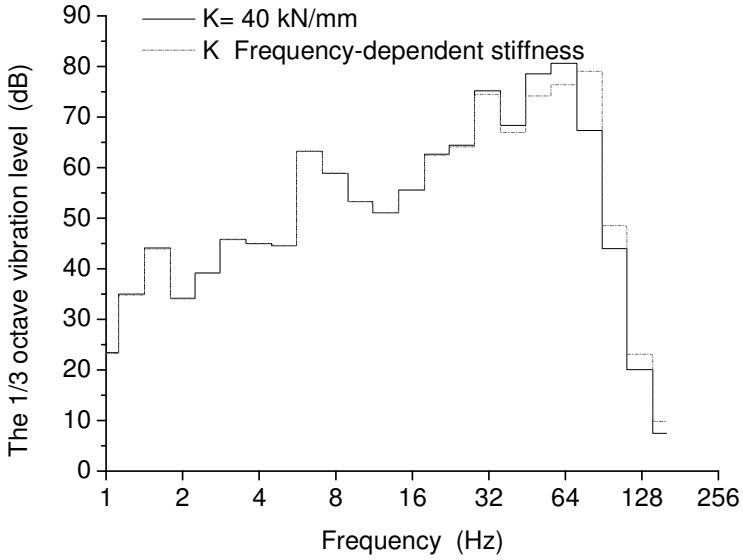


Fig. 6 The result of K being 40kN/mm and the frequency- dependent stiffness

As shown in Fig. 6, the difference of the response in the low frequency range can be ignored. In the range of frequency less than 30 Hz, the difference is less than 0.3dB. But the difference is a little large

when the frequency is more than 30 Hz. And the gap is up to 11.8dB at 80 Hz. The gap decreases when the frequency is more than 80 Hz. Given all these, the frequency-dependent stiffness of rail pads in the analysis of environmental vibration induced by subway must be considered, especially in the project where a lot of rubber material is used.

## Conclusions and Suggestions

**(1)** The calculated results agree with the measured data well, so the calculation model and the selection of parameters are reasonable. The accurancy and the efficiency of frequency-domain solution are high.

**(2)** By comparing the 1/3 octave vibration level of vertical ground acceleration after considering the frequency-dependent stiffness of rail pad, the result shows:

The gap is less than 0.3dB in the center frequency range of 0-30 Hz;

The maximum gap is 11.3dB at the center frequency more than 30 Hz and the frequency-domain distribution also changes;

In a word, if the frequency-dependent stiffness of rail pads in wheel-rail dynamic system is ignored, the prediction accurancy of environment vibration in the frequency domain is hard to ensure.

## References

[1] W.M. Zhai: Vehicle-Track Coupling Dynamics (Science Press, China 2007)(In Chinese)

[2] H. Xia: Traffic Induced Environmental Vibrations and Controls(Science Press, China 2010) (In Chinese)

[3] B.C. Zhang: Practice and analysis of vibration control for shallow embedded underground works with relative system. D. Beijing: China Academy of Railway Sciences, 2002(In Chinese)

[4] A.Z. Lu, B.S. Jiang and C.A. You:Research on Range of Mesh about Finite Element for Back Analysis of Displacement. J. China Civil Engineering Journal, 1999, 32(1): 26-30(In Chinese)

[5] G.X. Chen: Geotechnical Earthquake Engineering (Science Press, China 2007) (In Chinese)

[6] Z.B. Gao, Y.F. Gao and H.M. Tan: Lab and In-situ Tests on Maximum Dynamic Shear Modulus of Saturated Clay Soils. J. Chinese Journal of Geotechnical Engineering, 2010, 32(5): 731-735(In Chinese)

[7] Z.B. Gao, H.M. Tan and X.S. TAO: Comparative Analys is on Dynamic Shear Modulus of Saturated Sandy Soils in Laboratory and Field Tests. J. Journal of Disaster Prevention and Mitigation Engineering, 2010, 30(1):53-57(In Chinese)

*Applied Mechanics and Materials Vols. 580-583 (2014) pp 1161-1167*
*© (2014) Trans Tech Publications, Switzerland*
*doi:10.4028/www.scientific.net/AMM.580-583.1161*

# Tunnel collapse treatment technique Research in Xinjiang Tianshan high-altitude, low-temperature Mountain

ZHU Chun-sheng[1],YANG Xiao-hua[1]

(Key laboratory for Special Area Highway Engineering of Ministry of Education,

Chang'an University,Xi'an 710064,China)

**Keywords:** Tunnel Collapse Treatment technique

**Abstract:** Based on YuXiMoLeGai tunnel in G217 Cholma to the Nalati highway, aiming at the outlet section of K723+911~K723+919 collapse, through model experiment and numerical calculation combined with on-site measurement, the article studies tunnel collapse treatment technique and technical effect in xinjiang tianshan mountains in the geological conditions of high altitude, low temperature, crushing of rock mass and rock rich in water. The results show that after the CRD method, expanding the scope of the grouting construction, increasing the number of small duct grouting lock foot, strengthening methods of supporting parameters are adopted, vault subsidence deformation rate is 0.4-1.5 mm/d, peripheral convergence deformation rate is 0.5-2.2 mm/d, stress the most unfavorable right hance monthly increase in stress and strain amplitude is 3.97% and 2.35% respectively.The treatment controls the land slide body deformation and stress well.

## 0 Introduction

Along with the accelerating of the construction of the highway transportation in Xinjiang , Urumqi-WeiLi,WenSu-ZhaoSu highway project through the Tianshan mountains will be on the agenda step by step.The highway tunnels will grow up to be project control engineering.

At present, the number of highway tunnel operation in Xinjiang is not much, mainly along the highway such as G30, G217 in the TianShan mountains. In such a complex environment with high altitude, low temperature, crushing rock and rich groundwater, it is less experience to build a road tunnel in Xinjiang even no reliable reference in domestic. The operated SaiLiMuHu tunnel in G30 line built alongside lake has encountered water gushing in its build progress. The project targetly studied the tunnel waterproof material and system. Haxilegen tunnel in G217 line studied the segregation and void treatment technology for dealing with lining seepage, local deformation, cracking and other diseases. The tunnel old G217 was built through Tianshan mountains scrapped soon due to improper collapse treatment coursed forming hollow water into ice frozen. Visibly, recent research focuses on the tunnel waterproof and drainage system, percolating water treatment technology,but it is less for collapse treatment technology research.

In 2009, the reconstruction of G217 Yuximolegai tunnel. Along the full tunnel especially the K723 + 600 ~ K724 + 038 period is surronded by broken rock and rich water, which brought great difficulties to the project. This paper takes K723 + 911 ~ + 919 section of collapse as support, studies tunnel collapes treatment technology in Tianshan mountain in Xinjiang high altitude, cold mountain. This paper can provide technical support for the project land slide treatment and engineering experiences to the construction of highway tunnel in the Tianshan mountains.

## 1 The geological conditions and the land slide

### 1.1 The geological conditions

The exit of Yuximolegai tunnel through 385m fault fracture zone, which is compression and scissor fault derived from Awulela bruchfalten zone, distributed at the top of Yuximolegai. Tunnel cave itself is developed through the formation of joints, groundwater flow, moderate water-rich area. Tunnel entrance is mileage of K722 +095, entrance elevation is about 3200m,and the exit mileage of K724 +038, exit elevation is about 3230m, throughing fault fracture zone at K723 +600 ~ K724 +038, the total length of the tunnel is 1943m. K723 +910 ~ K723 +940 section of tunnel hole body is Ⅴ grade rock, weathered seriously, extremely broken, wet, integrity is poor. The segment with strong chlorite schist ~ weak weathered, soft, easy to soften water, rock Ⅴ grade level. At which K723 +911 chlorite schist right tunnel face by softening effect of groundwater is extremely weak broken.

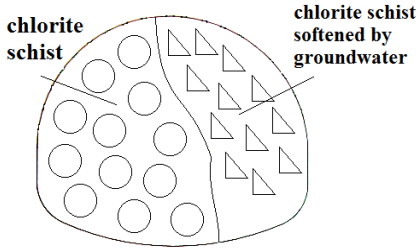


Figure 1 K723 + 911 geology sketch

1.2 Original construction plan and landslides case

The method of large section tunnel construction is in accordance with the usual "three-step seven-step excavation" construction way, and method of pre-grouting small pipe supporting to against rock weak and rich in water. Flault fracture zone segment is Ⅴ Grade Rock , the main support parameters shown in Table 1:

Table 1 The main supporting parameters

| Rock type | Bolt | The grid steel frame | Steel mesh | Shotcrete thickness | Second lining thickness |
|---|---|---|---|---|---|
| V grade | The arch of 120°φ42×3.5， l=3.0m advance grouting pipe, ring distance 0.4m ， side wall hollow grouting anchor diameterφ25，L=3.5，ring, vertical spacing of 1.0×0.5m, plum blossoms. | The 0.5m/ pin spacing | Full set HPB235 phi 6 steel mesh, mesh of 15 x 15cm | 25cm C25 | 50cm C30, S8 Reinforced concrete ， The main reinforcement spacing:20cm |

According to on-site monitoring and measuring, the vault cumulative subsidence curves (Fig. 2) of K723 +911 section from 27 th to 29th of July sedimentation rate accelerated. So at 2:00 on the 29th, at the right side of arch start peeling off and cracking at exit of K723 +911 ~ K723 +919 Yuximolegai tunnel, after that a small amount of sprayed concrete block out. At 5:00 pm, the part sprayed concrete falling off the block, 5:36 ection landslided at the right location demi, the landslides amount of 200 ~ 300m$^3$. Subsequently, landslides off the block has been continued, about 8:00 am, the collapse of the cavity has a small amount of water gushing, 8:50 emerged a large landslide, collapse the entire body will be closed tunnel section, landslides volume 600 m3 ~ 700m3. 9:15 slump continued with plenty of water gushing cavity (Figure 3).

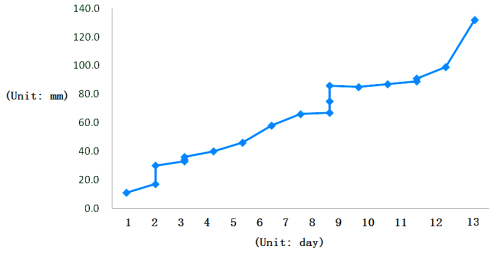


Figure 2 K723 + 911 section of soil slip before vault settlement curve

Figure 3 Tunnel K723 + 911 ~ + 919 section of land slide K723 and running water

According to the engineering geological conditions and soil slip situation description, watering, broken surrounding rock are the major causes of soil slip, the construction plan did not meet the requirements of practical engineering in construction may be a fall-in internal cause. To carry out the groundwater seepage field analysis and broken effect on lining structure stress analysis of surrounding rock is the main research content of this article.

## 2 Numerical analysis of groundwater seepage field changes

The Thermal Seepage model is established (temperature) module adopting the software ADINA, grouting water plugging the water-resisting layer model, the mountain rock using four-node isoparametric plane entity unit (2D - Conduction) Seepage material (Seepage) definition.

Table 2 Geotechnical permeable classification table

| Permeability grade | Standard | | The character of rock mass |
|---|---|---|---|
| | k（cm/s） | q（Lu） | |
| Extremely permeable | K<10-6 | q<0.1 | The intact rock, rock mass containing equivalent opening <0.025mm fracture |
| Medium permeability | 10-4≤K＜10-2 | 10≤q＜100 | Rock containing equivalent opening 0.1-0.5mm fracture |

Take K724 K723 + 500 - + 500 tunnel profile for calculating object (range of about 700 m × 600 m), the water-bearing media of the tunnel area is strong to the weak chlorite schist, soft, easy under the influence of water softening, joint fissure development, crushing of rock mass, see table 2 for rock and soil permeability scale, permeability coefficient $8\times10^{-3}$ cm/s, the grouting body permeability coefficient of $1\times10^{-8}$ cm/s, failure to take 30 kN/m$^3$. A small amount of breccia layers of mountain surface is neglected.

Seepage head pressure and the results of equipotential line distribution, the analysis results are as follows:

Atmospheric precipitation and snow melt water infiltration through strata cranny migration within the mountain, general mountain gradually loss from the left ridge to the right. K723 + 911 in 42.5% of the total water area, the minimum head appeared near the tunnel, as shown in figure 4, head pressure are uniformly distribution of equipotential line and seepage field in the condition of basically stable.

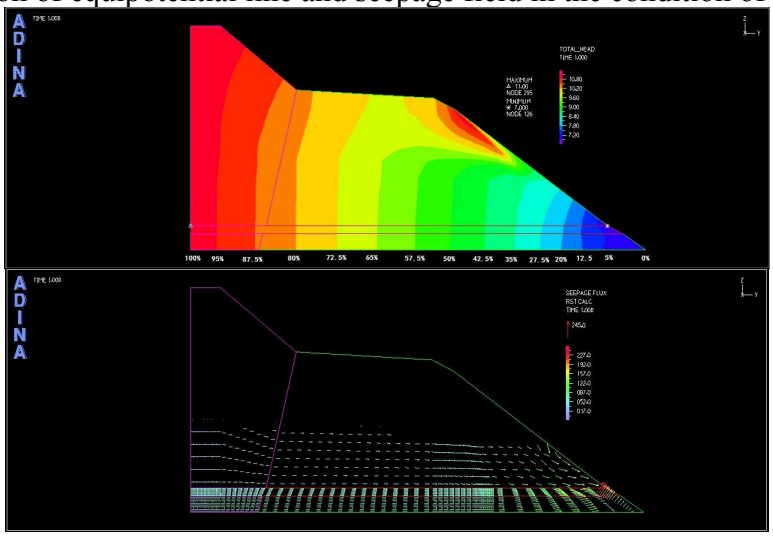


Figure 4 Initial seepage water head distribution and flow distribution

After tunnel cavern excavation, groundwater seepage field of mountain change, as shown in figure 5, constraints K723 + 911 in 67.5% head pressure area, before the excavation increased 58.8%; Tunnel excavation constraints to exit, head pressure distribution of equipotential line more tightly, change is more compact, 240m from K723 +911 to the exit,water head pressure decreased from 67.5% to 0%, that of tunnel excavation change mountain of groundwater seepage field distribution, exacerbating the groundwater flocked to the trend of the tunnel. Constraints value maximum seepage line, seepage flow maximum velocity of 581.0 m/d, a mountain of initial seepage field maximum flow velocity of 245.0 m/d increased by 137.1%.

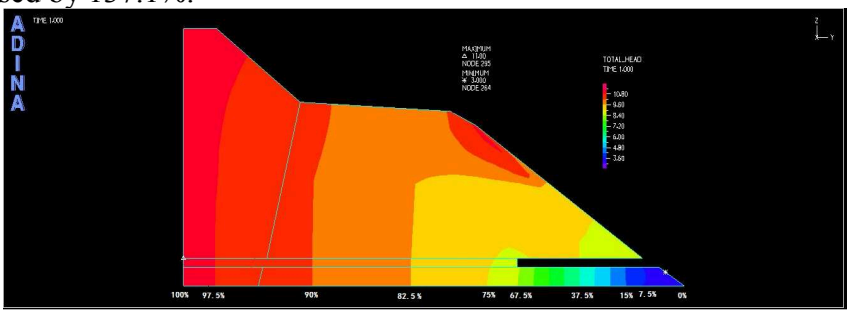

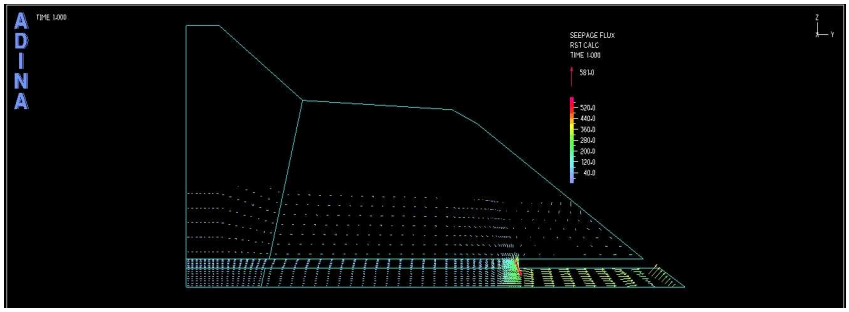

Figure 5 Tunnel after excavation of the seepage water head distribution and flow distribution

Grouting to the surrounding rock within 10M of Constraints, groundwater seepage velocity is less than 0.04 m/d in scope of grouting, water inflow fell dramatically, but through the calculation results can be seen, the groundwater in the grouting body water-resisting layer below a lot of concentration.

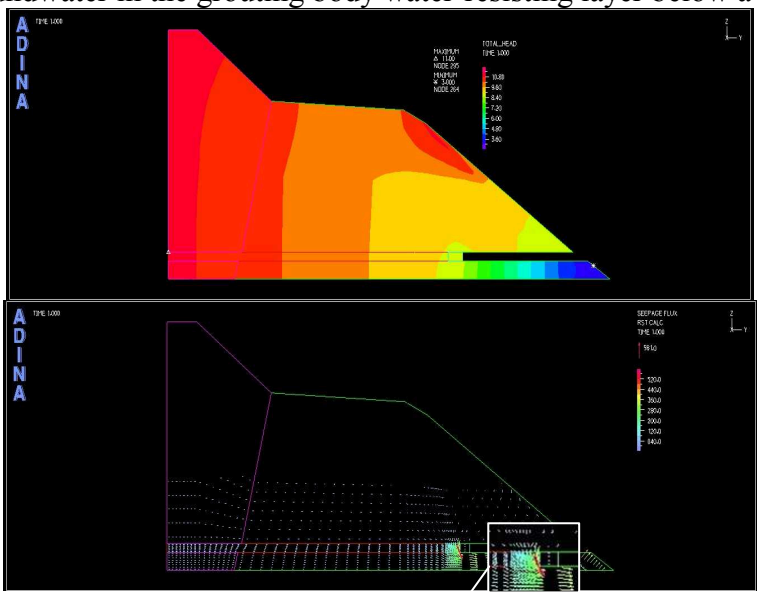

Figure6 After grouting seepage water head distribution and flow distribution

Analysis showed that: firstly, mountain tunnel excavation leads to groundwater seepage field change, in the role of head pressure, ground water to the tunnel portal area where and gushed out; Secondly, after grouting water plugging, grouting body can form good sealing effect, but the groundwater along the grouting water-resisting layer formed by the peripheral (below), suggest that area should be increased when water plugging grouting to ensure sealing ability of water-resisting layer or set drainage tunnel drainage facilities such as channel.

**3 Land slide tunnel lining stress model experiment and the simulation analysis**

3.1 Model experiment

3.1.1 Parameter Settings

The PYD - 50 three to plane strain loading geomechanics model experiment device for horizontal loading experiment, the model size is 70 cm X 50 cm × 20 cm. Barite powder：quartz sand：gypsum model: water = 1:1:0. 27:0. 45 simulate weakly weathered limestone (equivalent to Ⅴ class rock),with angle of internal friction for 19 °,cohesive for 0.09MPa, the elastic modulus of 210 MPa, poisson's ratio of 0.35. the water: dosage of gypsum=1:1 simulate model of concrete material, the modulus of elasticity of 3.5 GPa.

In order to simulate K723 + 911 geological situation, using the quartz sand simulating soften chlorite schist of the right constraints. Considering the original construction scheme adopt the arch of 120 ° grouting failed to effectively curb the abuse of the surrounding rock collapse, the experiment adopt whole grouting scheme.

The experiment simulate in-situ stress on the tunnel structure in the way of loading step by step,observating and recording pressure of surrounding rock and lining structure of tangential stress changes. Experimenting process includes two stages: the first stage starts from the experiment load to tunnel lining to crack limit load condition. Crushed surrounding rock of tunnel on the right side make lining structure be under non-uniform pressure of surrounding rock, observating and recording lining disease occurrence and distribution characteristics.The second stage, after whole grouting scheme, the lining structure eventually achieve full damage state by the ground stress

Table 2 The parameter value selection

| Media type | E(GPa) | \μ | φ（°） | C（MPa） |
|---|---|---|---|---|
| Rock | 1.5 | 0.35 | 24 | 0.1 |
| Shotcrete | 30 | 0.167 | / | / |
| Second lining | 30 | 0.167 | / | / |
| Soften rock | 0.15 | 0.35 | 22 | 0.01 |
| Grouting reinforcement | 30 | 0.167 | / | / |

3.1.2Model experimental results

As shown in figure 8,analysising from the characteristics of time: before grouting, left arch feet first crack and extending to the left side-wall, then right hance and side-wall occurs serious cracks, the last is the left hance disease. Analysising from characteristics of location: affected by crushed on the right side of the weak surrounding rock, the lining of the diseases are mainly distributed in the upper half of the arch ring. Measured stress on the left arch foot is the most serious, the tensile stress is 3.36 Mpa. secondly, tensile stress is 1.79 Mpa at right side of the wall and right hance compressive stress is 1.09 MPa. That crushed surrounding rock of tunnel on the right side of distribution of weak bias effect, making the left arch foot force the most unfavorable, and drive the arch ring right side to produce torque, which does not favor the structure safety. After grouting, from the time characteristics: left arch and left foot arch waist firstly crack, gradually extending upward to the vault and downward to the inverted arch, eventually crack at the vaul. From the spatial characteristics: the distribution of diseases from main upper arch ring transferring to the left arch ring.Diease in the second quadrant area inclouding vaule and left arch waist is most serious. Comparison with before and after grouting to load the plane x, y, - x, -y four direction stress as followe: except the y direction stress changing from tensile to compressive, the other three direction of the lining under stress value increased by 193%, 193% and 193% respectively.

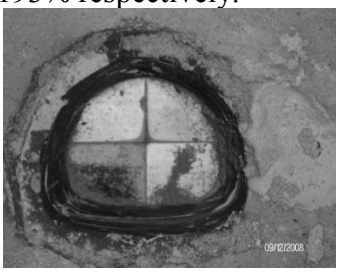

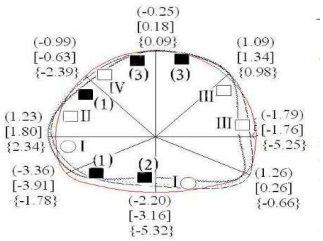


Figure 7 Experimental model Figure 8 Lining structure distribution of tangential stress and disease

3.2 The simulation analysis

3.2.1 Timulation model

Using ANSYS finite element software, the calculating model with four node isoparametric plane entity unit (PLANE42) simulates the surrounding rock (including grouting period).Two node isoparametric plane beam element (BEAM3) simulates the initial supporting structure.Four node isoparametric plane entity unit (PLANE42) simulates of the secondary lining.The parameter value is according to table 1, by adjusting the parameters of surrounding rock modulus to simulate grouting measures.

3.2.2 the simulation analysis results

The simulation calculation shows that:before grouting,arch feet lining under negative bending moment is maximum（4.459 kN） and maximum axial force distribution on the left arch foot 649.37 kN. From the overall, the upper arch ring under high axial force，which in vault and arch waist is 585.36kN. After grouting, bending moment and axial force distribution are reduced, the bending moment of the right side wall reduce from 1.159 kN close to zero, on the right side of the wall axial force is 439.114 kN, decreased by 32.4% before the grouting. After grouting, moment extremum at arch feet increase by about 92%.Bending moment of the inverted arch extreme value increase by about 115%, sidewall axial force extreme value increase by about 36%.

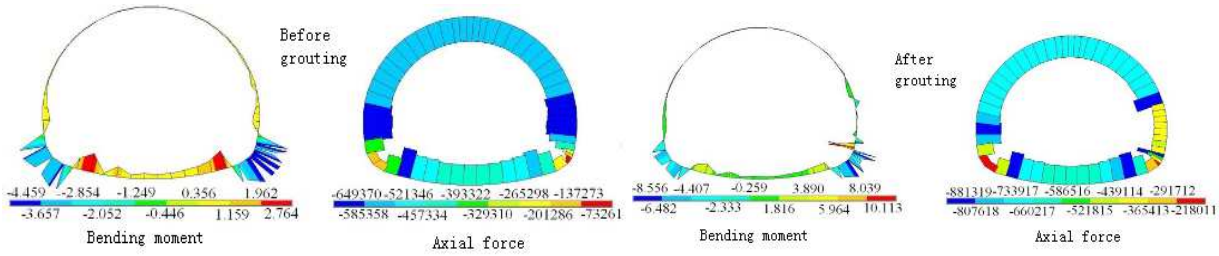


Figure 9Lining bending moment (unit kN, m) and axial force (unit: N)

3.3 Comprehensive analysis

Comprehense model experiment and finite element calculation, analysis results are as follows:

First is the mechanical properties: in experiment，stress on ±x, ±y directions of arch ring plane increase by 1.0 to 2.0 times, which is consistent with the simulation calculation results： the bending moment and axial force of lining reflected by 0.3 to 1.0 times.It suggests that increase scope such as the whole grouting is to improve the force distribution of arch ring, and improve the lining structure stress performance.

Secondly, disease characteristics, as shown in table 4, in the experiment model, the tunnel arch waist and sidewall inherit the maximum axial force that influence the safety of the structure. It is suggested that in addition to the supporting parameters improve lining.Adding beam to improve horizontal and vertical resistance is necessary.

Table 4 Results contrast

| | Model test | Simulation analysis |
|---|---|---|
| Arch half amplitude | Before grouting, large area crack | Bear huge axial force on the half range |
| The left half ring | after grouting, large area crack | On the left side wall bear huge axial force |
| The arch foot | Before and after the left arch foot grouting are the first to crack | Arch subjected to a great moment |

Thirdly, after grouting,by bias effect of surrounding rock, arch feet especially on the left become adverse stress area.It is suggested besides improving constraints in weak rock,reinforcement measures should also pay attention to the measures such as anchor pipe with lock foot.

4. The cause analysis and treatment plan

4.1 Collapse cause analysis as following

(1) Hydrogeological: tunnel site in central area of rock joints and fissures is developed, connective and of rich groundwater groundwater.On the right side of tunnel face at K723 + 911,chlorite schist in water is softened serious, the stability of surrounding rock capacity reductions beyond lining bearing expectations, which is the direct cause of land slide.

(2) Reinforcement measures: collapse section surrounding rock is main of strong weathering chlorite schist.Integrity is poorer.The lack of stability to of surrouding rock make support bear a huge pressure cause arch feet, arch waist buckling deformation. Fault zone pre-reinforcement take arch department 120 ° setting 3.0 m long lead small duct grouting measures parameters is too low to control the deformation of the surrounding rock.

**4.2 Treatment scheme**

(1)Adopting the advanced small pipe grouting is to reinforce stratum.Using Φ42 cm 3.5 m lone small duct grouting forepole, along the upper half arch ring, ranging from the original plan 120 ° to 150 °, improve the ability of the surrounding rock stability.

(2) For hance and sidewall are greatly under axial force, the CRD method is suggested to adopte, to establish the relation between beam, increasing the bearing capacity, hance, sidewall bearing.

(3) The grid steel frame adopts Φ42 small duct grouting (length of 3 m) lock foot which set two each nodes.

(4) The primary support use C25 Sprayed concrete thickness changed from 25 cm to 30 cm.

(5) The second lining:encryption lining steel ring space, which changed from 20 cm to 15 cm.

4.3 Site measurement

(1) K723 + 920 vault subsidence curve and peripheral convergence curves are as shown in figure 10 and 11: vault subsidence deformation rate is 0.4 -- 1.5 mm/d, peripheral convergence deformation rate

is 0.5 -- 2.2 mm/d.It indicates that after the treatment land slide body tends to be stable, not continues to expand.

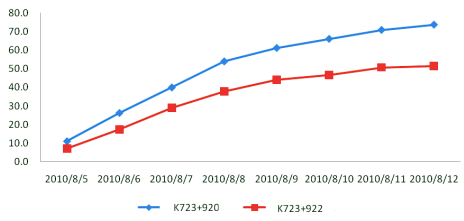


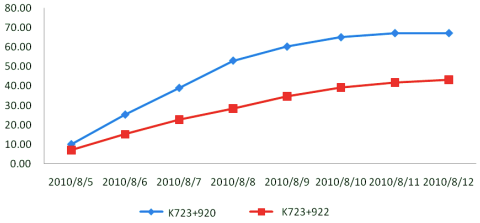


Figure 10 K723+ 920 vault subsidence curve Figure 11 K723 + 920 peripheral convergence curves

(2)The lining stress and strain comparison no August and September are as shown in figure 12. The stress and strain monthly increase rate were 3.97% and 2.35% respectively at the right hance which is seriously pressed.It indicates the treatment make the land slide body deformation and stress get better control, treatment scheme is reasonable.

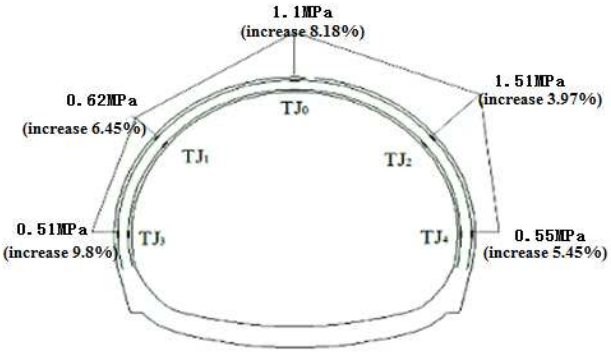


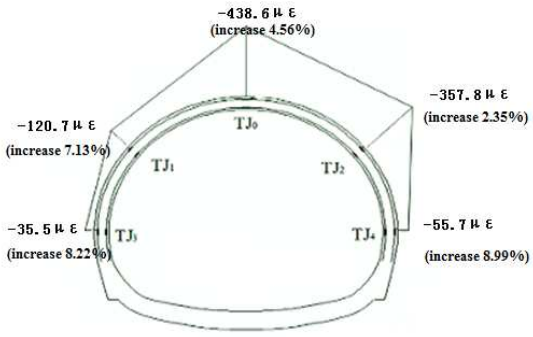


A: distribution and changes of pressure B: the distribution and variation of strain (negative tension)

Figure 14 K723+915 section two lining stress, strain distribution

## 5 Conclusion

(1)The tianshan mountain area affected by the snow melt water and atmospheric precipitation.The groundwater is relatively rich. Excavation make groundwater seepage field change and the groundwater collecting at the tunnel face cause water disease.Grouting have good water plugging effect, but should be combined with hydrology geology determine reasonable grouting scope to ensure the sealing ability of water-resisting layer.

(2) The ground water make the right crushed rock soften cause bias.Experiment shows the arch foot force is disadvantageous, in addition to improve grouting range，treatment should also pay attention to complementary with anchor pipe and lock foot.

(3) The model experiment and simulation analysis results shows：In the arch ring plane ±x, ±y principal directions except the y direction, the other three direction of the lining under stress value increased by 193%, 90% and142% respectively. Whole grouting measures can obviously improve the arch ring stress, improve safety lining structure.

(4)By adopting CRD construction scheme for the soil slip K723 + 919, expanding the scope of the grouting construction to 150 °, and adding small duct grouting lock foot, strengthen lining supporting parametersm, tunnel collapse is controlled in the normal range. Treatment scheme is reasonable with vault subsidence deformation rate is 0.4 -- 1.5 mm/d, peripheral convergence deformation rate is 0.5 -- 2.2 mm/d

## References

[1] Dj.M. Maric, P.F. Meier and S.K. Estreicher: Mater. Sci. Forum Vol. 83-87 (1992), p. 119
[2] M.A. Green: *High Efficiency Silicon Solar Cells* (Trans Tech Publications, Switzerland 1987).
[3] Y. Mishing, in: *Diffusion Processes in Advanced Technological Materials*, edtied by D. Gupta Noyes Publications/William Andrew Publising, Norwich, NY (2004), in press.
[4] G. Henkelman, G.Johannesson and H. Jónsson, in: Theoretical Methods in Condencsed Phase Chemistry, edited by S.D. Schwartz, volume 5 of Progress in Theoretical Chemistry and Physics, chapter, 10, Kluwer Academic Publishers (2000).
[5] R.J. Ong, J.T. Dawley and P.G. Clem: submitted to Journal of Materials Research (2003)
[6] P.G. Clem, M. Rodriguez, J.A. Voigt and C.S. Ashley, U.S. Patent 6,231,666. (2001)
[7] Information on http://www.weld.labs.gov.cn

*Applied Mechanics and Materials Vols. 580-583 (2014) pp 1168-1173*
*© (2014) Trans Tech Publications, Switzerland*
*doi:10.4028/www.scientific.net/AMM.580-583.1168*

# Tunnel lining microstructure and mechanical properties of evolutionary analysis

Yundong Ma[1, a], Shuang Liang[1,b]

[1]Dalian Jiaotong University, Dalian, Liaoning,China

[a] yundongma@126.com, [b]liangsflai@126.com

**Keywords:** Tunnels, Mesoscopic Model, Strain, Fracture.

**Abstract.** For the tunnel lining microstructure, mechanical properties evolve analyzed. This paper have established and meshed microstructural model and got the situation under its force structure loads, the cracking strain as a criterion for its application fracture criterion to get a good cracking and expansion of the tunnel lining meso model. The results of the case under the macrostructure of the model compared with the microstructure results can get the adventage of the microstructure in using tunnel lining.

## Introduction

In the course of the tunnel lining mainly by internal stress of the mountain came load, temperature and humidity changes caused. Temperature and humidity are the main factors that cause cracking and failure of the tunnel lining. Any strength suffered a load of tunnels are lower than the fracture failure of the concrete lining, The failure of tunnel lining is due to repeated loads of concrete damage, lower intensity, thus causing cracks to appear concrete lining failure[1].

At present, China is taking most of the tunnel concrete lining macro model to analyze the forces. Due to increase the degree of importance of tunnel security, this macro model is no longer able to meet the demand for the safety of the tunnel, concrete lining microstructure model can better analyze the real force, the improved security[2].

## Concrete microstructural model's establish

Concrete on Meso usually seen as a composite consisting of coarse aggregate, cement mortar and interface consists of a three-phase medium. Research shows that two-dimensional numerical simulation method is a static circular aggregate distributed simulation method, which have high efficiency and good usability. Table 1 is a microscopic model properties of various materials and concrete materials.

Table 1 Material parameters

| Material | Modulus of elasticity$(GPa)$ | Poisson's ratio | Bulk density$(kN/m^3)$ |
|---|---|---|---|
| Aggregate | 50 | 0.2 | 27 |
| Curing cement morta | 25 | 0.2 | 21 |
| Bonding interface | 22 | 0.2 | 21 |
| Concrete | 28 | 0.2 | 21 |

In this paper,with the aid of Fuller proposed maximum density ideal grading curve, taking the Monte Carlo method, using a formula Guevara text, making three-dimensional model into a two-dimensional plane of concrete conduct. Using the random aggregate model to do the stress of the tunnel under the effect of load analysis.Figure 1 is a micromechanical model of tunnel.

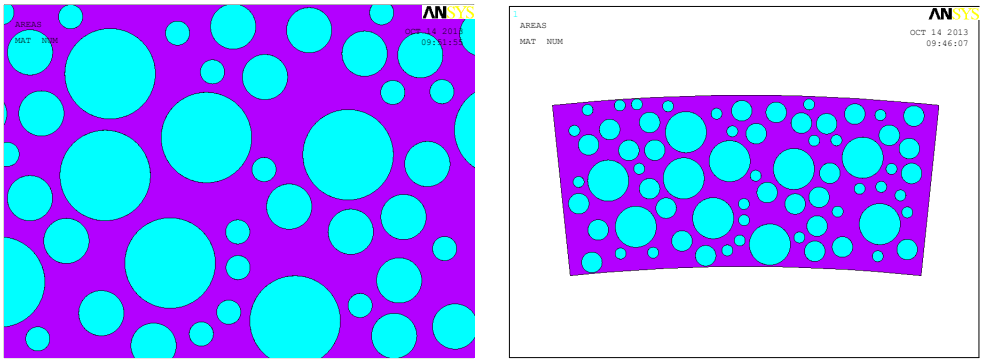

Fig.1 A micromechanical model of tunnel lining concrete

According to the properties of various materials to mesh[3], mesh diagram is shown in Fig.2:

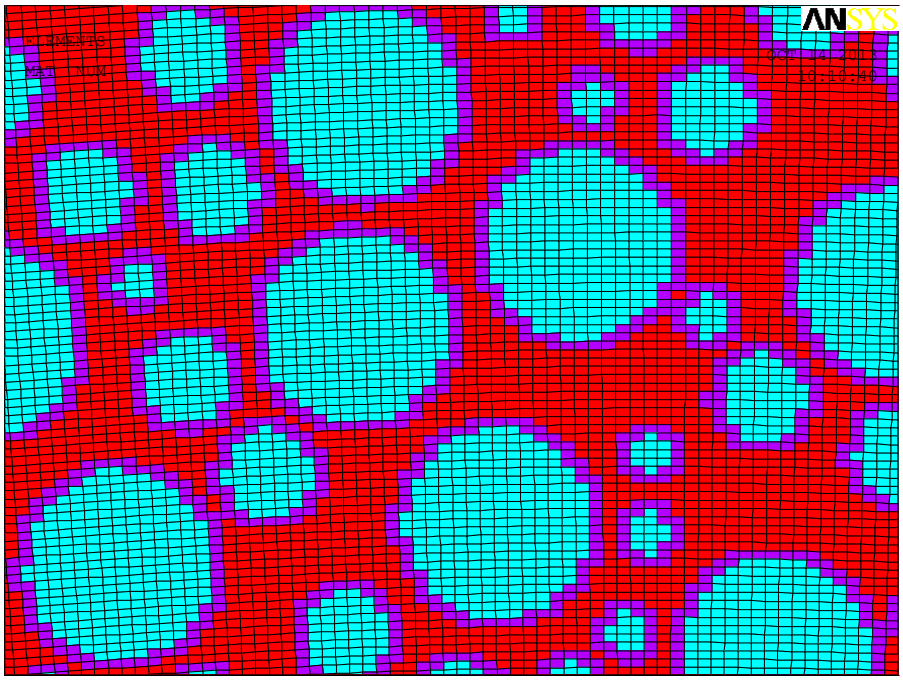

Fig.2 Meshing figure

**The establishment of a fracture criterion**

Based on the concrete mesoscopic mechanics method is to continuum mechanics, damage mechanics and computational mechanics to analyze the combination of meso-scale deformation, damage and failure process. Basic idea is to regard concrete as aggregate, cement mortar and curing of the interface between the three-phase heterogeneous composite material, choose the appropriate concrete mesoscopic structure model, considering the aggregate unit, curing cement mortar and interface materials mechanical properties of different units, as well as the failure criterion and simple tension and compression damage model reflect the stiffness degradation, using finite element method (fem) simulation of concrete crack propagation process of the specimens and the failure pattern, intuitively reflect the damage fracture failure mechanism of the specimens.

Concrete is a kind of quasi brittle material, after carrying on the macroscopic stress-strain curve of nonlinear because of micro crack initiation and extension, and is not caused by the plastic deformation. Therefore, can be described by elastic constitutive relation of damage mechanics and mechanical properties of concrete mesoscopic unit of each phase. Damaged material constitutive relation by the relationship between the nominal stress $\sigma$ and the strain $\varepsilon$ nondestructive material

$$E = E_0(1-D)\ \sigma = E\varepsilon\ (0 \le D \le 1) \tag{1}$$

$E_0$ is the initial elastic modulus in formula, $E$ is modulus of elasticity after injury,D isdamage variable. This paper argues that when the unit of the maximum tensile stress reaches its limit value of the given when the cell starts tensile damage. This article uses the double line damage evolution model, the equation asbelow and stress strain graph as Fig.3

$$D=\begin{cases} 0 & \varepsilon_{\max}<\varepsilon_0 \\ 1-\dfrac{\eta-\lambda}{\eta-1}\dfrac{\varepsilon_0}{\varepsilon_{\max}}+\dfrac{1-\lambda}{\eta-1} & \varepsilon_0<\varepsilon_{\max}\le\varepsilon_r \\ 1-\lambda\dfrac{\varepsilon_0}{\varepsilon_{\max}} & \varepsilon_r<\varepsilon_{\max}\le\varepsilon_u \\ 1 & \varepsilon_{\max}>\varepsilon_u \end{cases} \tag{2}$$

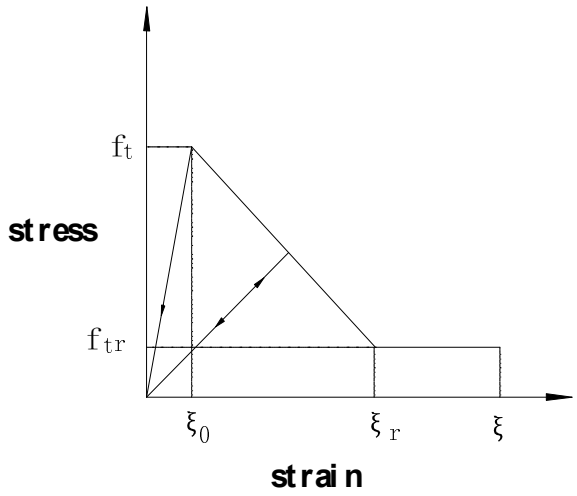


Fig.3 Double broken line model of concrete meet each phase

$f_t$ is the tensile strength of concrete material in; $f_{tr}$ for each phase damage unit tensile residual strength, $f_{tr}=\lambda f_t$, $\lambda$ is residual strength coefficient, $0\le\lambda\le1$; $\varepsilon_0$ as a unit stress reaches tensile strength of the principal tensile strain; $\varepsilon_r$ with tensile residual strength of the corresponding residual strain, $\varepsilon_r=\eta\varepsilon_0$, $\eta$ for residual strain coefficient, for concrete material in general scope of $1<\eta\le5$; $\varepsilon_u$ as the ultimate tensile strain, $\varepsilon_u=\xi\varepsilon_0$, $\xi$ as the ultimate strain coefficient, $\xi>\eta$; $\varepsilon_{\max}$ as a unit in the maximum principal tensile strain loading history[4].

Fracture criterion is measured by strain, due to the micromechanical model is a combination of three kinds of materials, so using three different critical strain. This article take the fracture strain of the aggregate is 0.002, the fracture strain of the slurry was 0.0012, the interface fracture strain of 0.001. And macroscopic model is a kind of material, the fracture strain value through weighted arithmetic is 0.0015.

**The mesoscopic model and macroscopic model for comparative analysis**

Because the model of the tunnel is very big, the whole model of mesoscopic models are used to analysis, has a high requirement on the computer, and will take a long time to operations, so we take the part of the largest stress tunnel is analyzed, namely the top of the tunnel. Due to the tunnel radius is big, can take the top analysis similar to rectangle concrete blocks, so this article simulated by rectangular concrete blocks.

This article selects 2000 mm long and 600 mm high concrete two-dimensional model as an example for analysis. In this model distribute with uniformly load, load is increased, Until the concrete bear not the fracture load. Fig.4 is the micromechanical model of concrete at various stages

in the process of gradually loading, strain and fracture in the diagram in (a) - (d) the load is increased, it is concluded that the stress at the same time also has been increased.

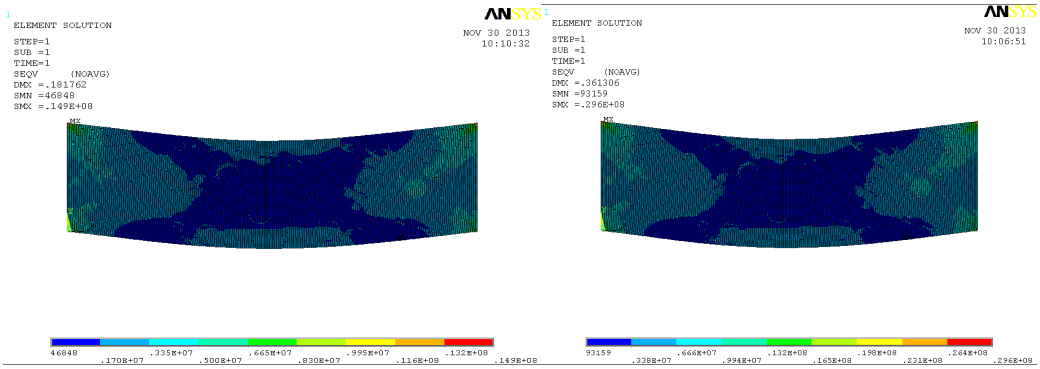


(a) Load for $1\times10^8\,N$ stress nephogram (b) Load for $2\times10^8\,N$ stress nephogram

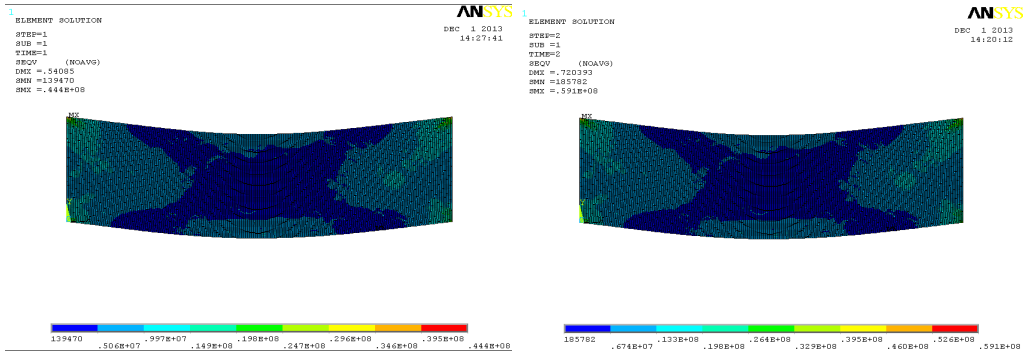


(c) Load for $3\times10^8\,N$ stress nephogram (d) Load for $4\times10^8\,N$ stress nephogram

Fig.4 Mesoscopic model the forces of the concrete loading

Compared to concrete mesoscopic model, macroscopic model is as the same material of the concrete under the same load should be trying to get as shown in fig.5:

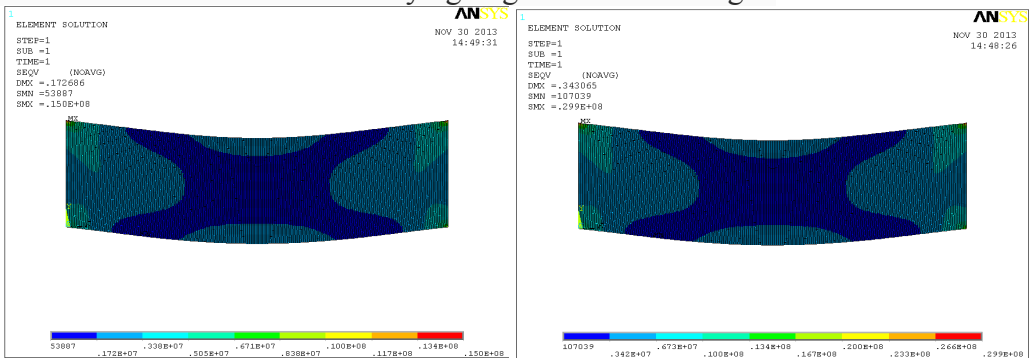


(a) Load for $1\times10^8\,N$ stress nephogram (b) Load for $2\times10^8\,N$ stress nephogram

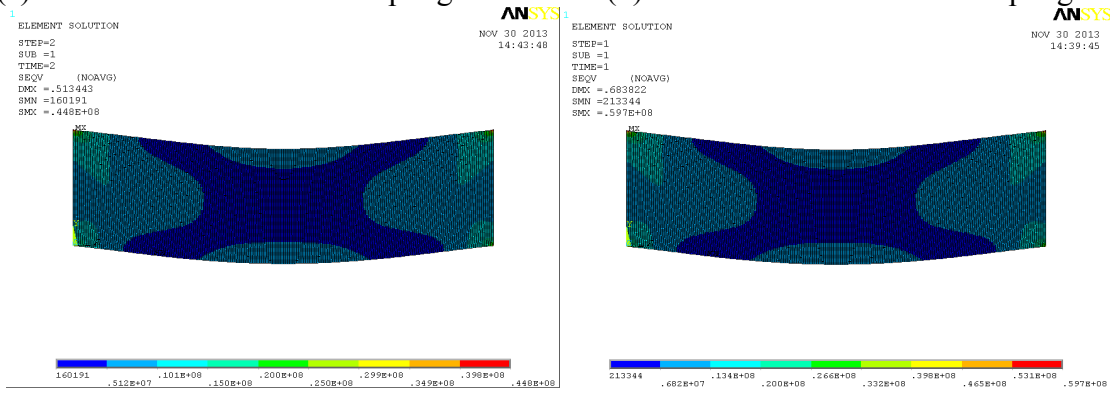


(c) Load for $3\times10^8\,N$ stress nephogram (d) Load for $4\times10^8\,N$ stress nephogram

Fig.5 Macromodel the forces of the concrete loading

Fig.6 is application of a fracture criterion of crack, (a) is a mesoscopic mechanics model of concrete fracture diagram, it can be seen that the fracture of concrete is not regular, accord with the actual situation. (b) is the model of concrete as the same kind of material, this case model is completely symmetrical, although on the mechanics analysis is set up, but with the actual situation is different, so the mesoscopic model is more accurate.

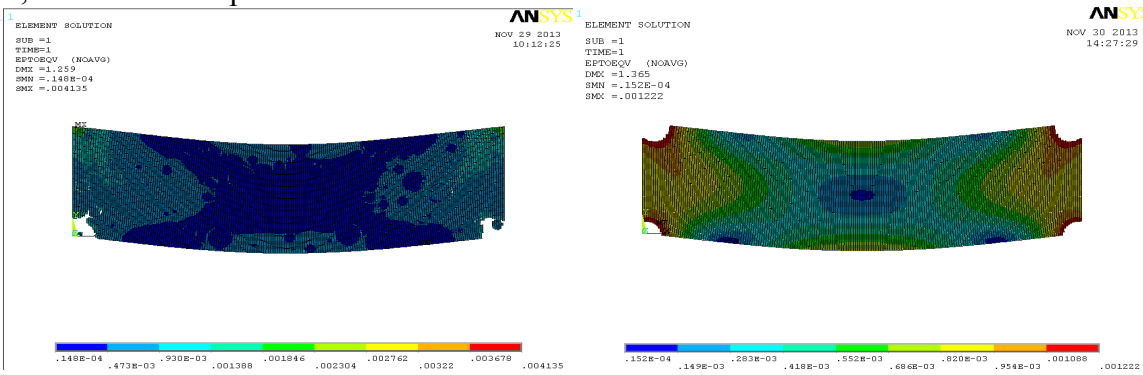


(a) The fracture in mesoscopic mechanics model (b) The fracture in macroscopic mechanics model

Fig.6 The comparison of concrete fracture

Figure 7 is the two forms of concrete strain increases with the load together, although looks gap is not very big, but because of the fracture strain of the concrete as the same kind of material is bigger than the actual, so have led some to achieve the ultimate strain unit without failure, lead to error will be larger and larger

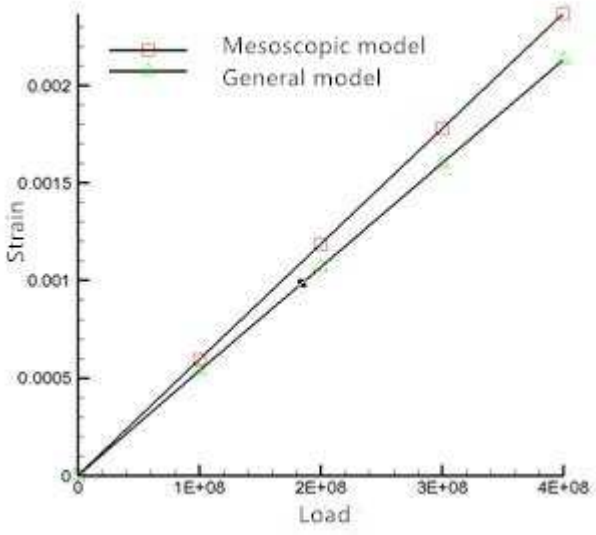


Fig.7 Under various stages of the loading strain contrast.

## Conclusions

Through the above analysis and comparison, in the process of load increasing, the difference between the two models are gradually revealed. We can see from fig.4 to fig.6 mesoscopic model is more close to reality, because the concrete itself is uneven, but the latter obvious symmetry is clearly is inconsistent with the actual, the micromechanical model of crack position is consistent with the actual situation. Two models are begin when load for cracks, but the position of the cracks, and extend the degree are different, micromechanical model of crack is more close to actual. Mesoscopic model the crack propagation of concrete in the trend of faster and faster, and the macro model belongs to a steady state, is at odds with the theory of what we know.

To sum up, Mesoscopic model is more accurate compared to the macroscopic model in the analysis of the mechanical properties, the micromechanics of concrete will be our future development direction.

**References**

[1] An Chun,Wangcheng Zhu. Damage and fracture of concrete, numerical experiments[M], Science press.Beijing2003(in chinese)

[2] Huaifa Ma,Houqun Chen,Baokun Li.,2004，2(2)：124-130(in chinese)

[3] Zongmin Wang,Zhizhang Qiu. 2005，22(6)：728-732(in chinses)

[4] Jile Xue,Jiabao Huang.Guangdong Water Resources and Hydropower, 2004,8(4) (in chinses)

*Applied Mechanics and Materials Vols. 580-583 (2014) pp 1174-1177*
*© (2014) Trans Tech Publications, Switzerland*
*doi:10.4028/www.scientific.net/AMM.580-583.1174*

# BIM technology Used in underground subway station planning simulation

Hongke Pu[1, a*], Qingchao Wei[1,b]

[1] School of Civil Engineering, Beijing Jiaotong University, Beijing 100044, China

[a]peakhill@163.com, [b]qcwei@bjtu.edu.cn

**Keywords:** BIM technology, underground station, planning, cooperative design, cost.

**Abstract.** This paper studied the underground subway station planning depend on BIM technology. The existing 3D buildings' information was processed by computer technology. Using the information and planning based on constraints on the space station, the simulation of the actual situation in 3D view way constantly, adjust planning position, compare each project calculation cost, obtain the optimal line position. We can carry cooperative design plan the subway station by the restrictive conditions and achieve the optimal line layout.

## BIM technology Introduction

BIM is a Building Information Model, a combination of all of the geometry Model Information, functional requirements and component performance, will be a construction project throughout the life cycle with information including the construction schedule, construction, maintenance and management of the process of information [1]. The simulation with the real information of building digital information integration of all kinds of information related to project data model is a detail expression of relevant information about the project. Building information model is a direct application of digital technology in architectural project, but it is also a kind of application to the design, construction, management of the digital method. This method supports the construction project integrated management environment, can significantly improve efficiency and reduce risk in the process of its life[2,3].

BIM is using digital technology to the process of the construction project design, construction, operation and its process results is an information rich multi-dimensional project model - named the BIM model. Different cooperated parties use different software to solve their problems to complete the project construction and operation method of work is a production line, with information creation, management and share。 The purpose of BIM is to make the information on this production line coherence, error elimination, increased efficiency in advance.

Through the analysis of the BIM overall solution in traffic planning, project cost control, data sharing on the application of multiple directions, successfully overcome people and traffic with pedestrian safety problems that may arise, collaborative underground space, and with the perfect blend of the whole region.

## BIM application in underground engineering

Domestic well-known experts and scholars in the field of underground space make "ideas and technology leading the urban underground space in the future the development" as the theme, put forward the concept and technology direction of the development and utilization of urban underground space[4]. Though the construction of urban underground space in China has made rapid development, there are larger gap between our cities and the development and utilization of historic, economic strength of the city in the developed countries.

Therefore, urban underground space development and utilization in our country is facing the huge opportunity and challenge situation, need to lead the future development of urban underground space in China with advanced ideas and technology. First is in terms of concept, to promote resource

conservation and environment friendly urban construction as the basis, comprehensive exploitation and utilization should be forward-looking strategic planning, integration of underground space on the ground, strengthen the modernization of urban underground space atmosphere, improve the quality of internal environment. According to different area can adhere to the principle of focus, in view of the underground space of rail transit around development can adopt flexible planning. Second, in terms of technology research and application, study ways to establish urban underground space building integrated design methods and standards. Strengthen the urban underground construction comprehensive disaster prevention technology research. System of urban underground space construction standards, perfect the relevant standard specification. Internal environment protection technology measures were put forward. Strengthen research and development of urban underground construction management information platform based on BIM technology. To strengthen all kinds of construction technology research and popularize advanced technology.

Using BIM technology in civil engineering, construction and management of underground space, realize the underground engineering design, plan approval, construction, daily management full cycle of information, intellectualization. It is important to promote construction of underground space development and utilization, and management level, and it is the modern city construction management direction.

The characteristics of underground space: the poor geological conditions, surrounding environment complex, shallow buried structure, the stability of surrounding rock. Urban underground engineering construction lags behind the urban construction, especially the urban subway projects are often built under the buildings in highly concentrated area, and through a variety of the vicinity of the pipeline under the road in the city. Construction often causes ground deformation and surface subsidence. The inherent deformation and settlement of neighbor buildings and facilities damage cannot be ignored. Urban underground pipe network facilities, street, parking and other structures with influence each other, restrict each other, it may create many special problems in design and construction technology.

BIM technology can provide better solutions [5] on the collision coordination management with other buildings and pipelines, quantity control, performance analysis, and design efficiency.

## Subway station planning and BIM Technology

Underground station layout, especially under the environment of existing structures should follow certain principles [6].

- Station hall layer partition should be arranged clear, management room and equipment room should meet the technological requirements of each system.
- Determine platform type based on alignments and transfer requirements.
- Station entrances should be set on the road outside red line or surrounding the city square, and consider the transfer and connection with other traffic.

The station layout needs to analyze the influencing factors, and determines the boundary conditions. The surrounding environment; Building demolition and pipeline moving conditions; The construction method; Traffic source; The conditions of the comprehensive development.

After determining the limiting conditions and influence factors, plan the location of the space station. Station surrounding by existing facilities such as shopping malls, residential, roads, parks, power pipe trench, fire pipeline, rain water pipe, water pipe, gas pipe, communications net, heat pipe network, need to be considered in space layout, whether the construction is convenient, and save on economy. Collaborative design is very important in the design of underground station. Collision detection is the key to the collaborative design, including hard collisions and soft collision. Hard collision is direct contact. Soft collision is two entity's distance within limits. In this case, BIM technology combined with related 3D software can efficiently deal with this kind of problem. Calculated the corresponding project cost: earth quantity, demolition costs etc.

Station planning process as follows:

- Through the existing conditions of information processing, extraction size, location and other specific information and data from pipes, facilities, buildings, etc., save to the database.
- On drawing software AutoCAD and REVIT for secondary development, stereo display all information.
- According to the principle, design specification and input constraints, design program for the station planning.
- If do not conform to the requirements, repeat last step, to achieve the optimal design scheme.

## Case analysis

FaTou station of one metro line no.7 is taken as an example to analyze application of BIM technology. The metro line is near to parks, schools, community (Fig. 1). Follow is the case of FaTou station planning analysis.

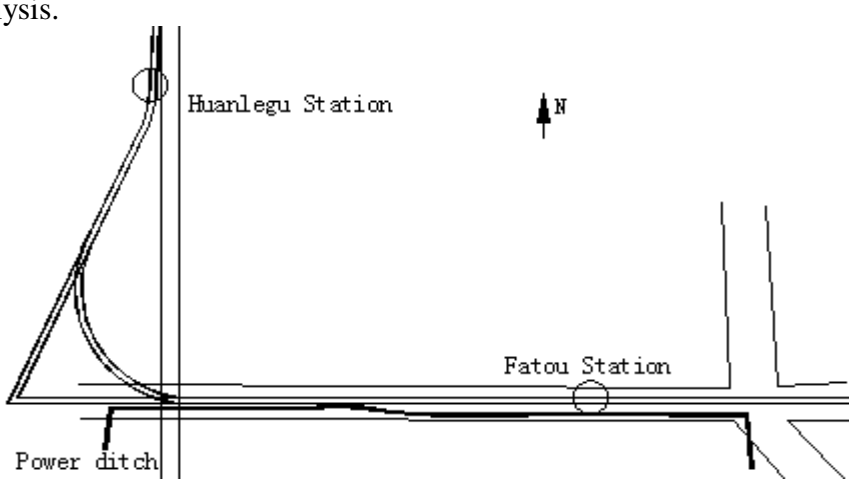


Fig. 1 Fatou station planning position

- **Status**

Road and traffic status: the station site in FaTou south road on the east side with FaTou road intersection. The station has JinFa stance on the east side road and vertical FaTou road intersection. The road traffic flow is not big.

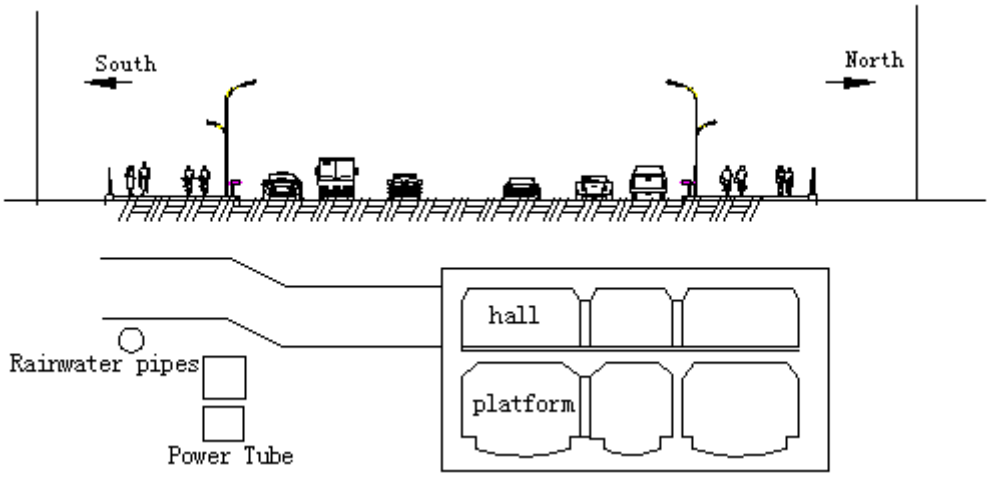


Fig. 2 Section of pipe, road and station

Present situation of underground pipeline: pipeline lays under the road, near the rain water, telecommunications, electricity, water pipes, etc. FaTou south road under rain sewage, electricity pipeline,(Fig 2).

- **Analysis**

Line main control points: One is residential buildings located on FaTou south road on the west road corner. Another is along the south road of FaTou buried two parallel power channel. FaTou station is located in influence scope of the power channel. Because power trench has many ground manholes, the left hand lane and Fatou line station at the top of the heat pipe can not be achieved through the ditch. If pass from the bottom, then the requirements of the line as a whole buried deeper and the part of heat pipe near Fatou local station needs to be moved. To solve above problems focus on the line flat position, Fatou station's selection need to be optimize and to choose.

1. Set the corner radius of the curve R350m, line and station are located beneath the power trench, the left side of the center line distance to residential 10.5m, requires diversion of large power line, entrances lift height is large, poor conditions

2. Move the Fatou South line southward 5m, subway line and FaTou station deviate power pipe trench. FaTou station stands below the part position in the south planning green space, add a set of R1200m curve. The center of the left line distance to apartment can be adjusted to 21m. Due to adjust line to the power line south, the line needs to pass two times through power trench. After adjusting for the underground station, two layers of island platform station along the west. Station has three channels, three entrances, and two sets of four wind pavilion, northwest three entrances in FaTou south road. Construction of open-cut method is simple, is easy to carry out.

3. Move FaTou south route northwest 20m, the line and FaTou station deviate power line range, reduce the construction's change and impact on the pipeline. But due to the line moving north, FaTou station is within the scope of residential land, and the circular curve radius is adjusted to R300m, adjust center line of left subway line distance to house boundary to 8m. The station is close to the north of FaTou south road red line. Construction of open-cut method is simple, is easy to carry out.

After several adjustments and comprehensive evaluation, get the optimal solution.

## Summary

Through the analysis of the underground station, using BIM technology, combining with computer automated processing, convenient man-machine interaction, collaborative design with the original facilities and building, choose the right station and line and put forward the optimal solution. In urban rail line planning, using BIM in the whole line network planning, automation line network planning, adjustment, it will improve efficiency and save cost.

## References

[1] Li Xiao. Green BIM in the Building Life Cycle Application Prospects of the Domestic Construction[J]. Journal of information Technology in Civil Engineering and Architecture. 2012, 4(2), p.52 (in Chinese)

[2] CHEN Qian, ZHANG Yuan. Discussion on the Conception and Application of BIM[D]. Value Engineering.2012,(2), p.61 (in Chinese)

[3] Chen Qiang. BIM Adoption Risk Study in Building Design Project[J]. Journal of information Technology in Civil Engineering and Architecture.2012,4(1), p.22 (in Chinese)

[4] Hu Song，Feng Dongpo，Li Donghao， Hu Hanyu. Application of BIM in the Piping System in Infrastructure Project[J]. C0NSTRUCTION TECHNOLOGY.2012,,41(371), p.22 (in Chinese)

[5] XUAN Yun-gan. BIM in the Building Life Cycle Application Prospects of the Domestic Construction Implementation of Parametric Building Modeling[J]. Jiangsu Architecture.2012,(6), p.11 (in Chinese)

[6] Mao Baohua. Planning and design of city rail transit[M], China Communications Press, the second edition,2011 (in Chinese)

*Applied Mechanics and Materials Vols. 580-583 (2014) pp 1178-1183*
*© (2014) Trans Tech Publications, Switzerland*
*doi:10.4028/www.scientific.net/AMM.580-583.1178*

# Comfortable Quality Analysis of Subway Station Vibration Induced by Multiple Trains

Bingqing Zhang[1,a*]

[1]Key Laboratory of Road and Traffic Engineering of Ministry of Education, Tongji University, 4800 Caoan Road, Shanghai, China

[a]zhangbingqingjane@gmail.com

**Keywords:** multiple trains; subway; comfortable quality of vibration

**Abstract.** With more and more subway lines in cities, people have pay much attention to the comfortable quality of subway vibration, especially in transfer stations or stations that have more than one line which platform and floor have much violent vibration. The paper bases on a subway station with multiple trains, builds the finite model, puts measured wheel-rail force as the load and gets the dynamic responses. Then it accords conventional international standard of comfortable quality which uses weighted root mean square acceleration as index to evaluate the comfortable quality of platform and floor or other areas. The result shows: The station could meet the requirement of comfortable quality.

## Introduction

With the fast development of urban railroad transportation and the need of city traffic network, the phenomenon of more than one line goes through a station is more and more. Multiple trains' operations must have much stronger influence on the station's vibration, especially the people who are on the platform. The noise and vibration induced by trains could beyond people's comfortable field and do harm to people's health [1,2]. So, it's necessary to evaluate the comfortable quality of vibration when multiple trains run at the same time.

## Evaluation method of vibration comfortable quality

### Existing research and specification

There are many factors relate to body comfortable quality, such as vibration frequency, direction, exposure time, distance , human posture and so on. The vibration ergonomics expert Griffin[3-6] have done a series of indoor test in the field and made a lot of contribution. Domestic scholar have done some theoretical researches, put forward some evaluation methods and put them into engineer practice[7-12].But now there is still no mature and global standard or method at home and abroad.

The paper accords to the methods in ISO10137:2007[13], it includes base evaluation method and additional evaluation method. When ACC PEAK/weighted root mean square acceleration value<6, using weighted root mean square acceleration value as the evaluation index, the value is compared with the multiplied base curve. When ACC PEAK/weighted root mean square acceleration value>6, using vibration dose as the evaluation index in order to consider the influence of load impact effect on the vibration comfort. Then the value is compared with the multiplied base curve. The base curve is shown in Fig.1, for the continuous and intermittent vibration, the multiplying factors are shown in Table 1.

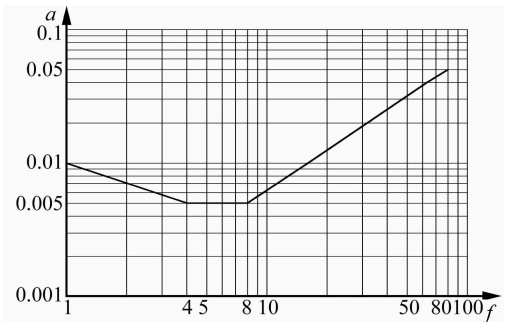


(a)Building vibration Z-axis base curve for acceleration (foot-to-head vibration direction)

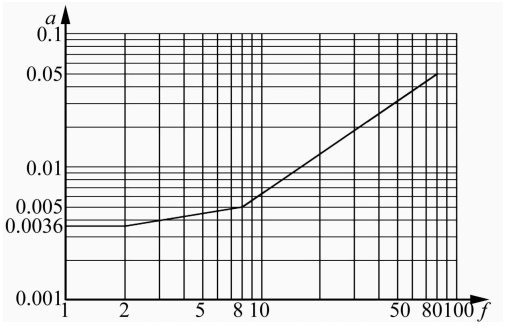


(b) Building vibration combined direction(x-, y-,z- axis) acceleration base curve

Fig.1 Vibration acceleration base curves

Tab.1 Multiplying factors in the standard of ISO10137:2007

| Place | Time | Multiplying factors |
|---|---|---|
| Critical working areas（e.g. some hospital operating-theatres, some precision laboratories, etc） | Day | 1 |
| | Night | 1 |
| Residential(e.g. flats, homes, hospitals) | Day | 2~4 |
| | Night | 1.4 |
| Quiet office, open plan | Day | 2 |
| | Night | 2 |
| General office (e.g. schools, offices) | Day | 4 |
| | Night | 4 |
| Workshops | Day | 8 |
| | Night | 8 |

## The calculation method

According to former evaluation index and method, the evaluation can be divided into the following steps:

(1) Determine working environment, which determine the multiplying factor;

(2) Build the finite model, get acceleration-time curve of measuring points;

(3) Transfer time value to frequency-domain value of acceleration with the use of Fourier Transform, get the root mean square acceleration values of 1/3 octave;

(4) Get the weighted root mean square acceleration values as the weight coefficient (specific coefficients and ways according to ISO2631[14]);

(5) Calculate the value of ACC PEAK/weighted root mean square acceleration value, in order to make sure choose base evaluation method or additional evaluation method;

(6) Compare the weighted root mean square acceleration values or vibration does with the multiplied base curve, then evaluate the comfort degree of different areas in the station.

## The calculation model of station

The station with a single pole and double spans structure. It has station hall floor, ground floor first floor and second floor, three floors in total. The elevation of station hall floor is -2.5m, the elevations of platforms are -9.5m and -17.7m. On the left side and right side of ground floor first floor and second floor are line 4, the left, right line and line 6, the left, right line, 4 lines in total. The cross section of station is shown in Fig.2, the calculation model is shown in Fig.3.

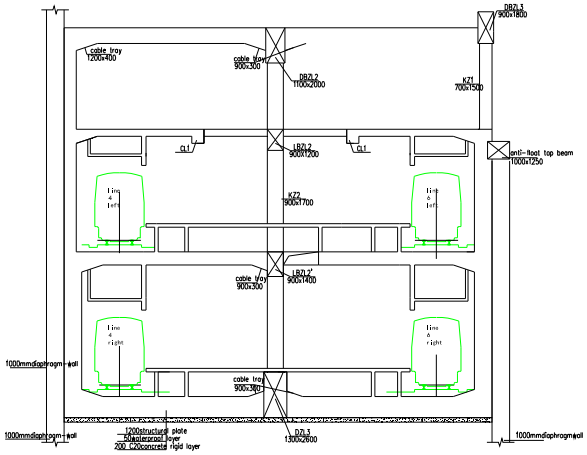


Fig.2 The cross section of station

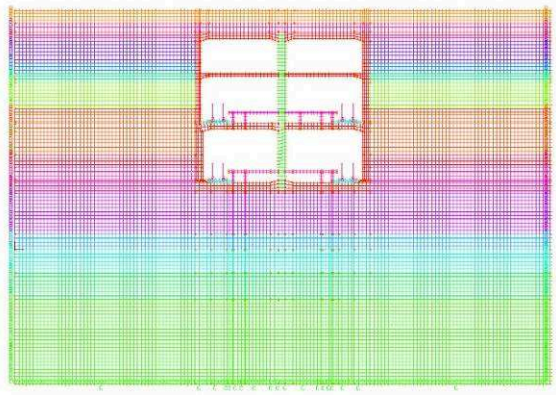

Fig.3 The finite calculation model of station

## Acceleration calculation and comfortable quality evaluation

The object in the paper is a subway station, which belongs to noisy regions with dense population. So, it regards the station as the 4th kind place is enough according to Tab.1, makes the multiplying factor as 4.0, then the limit acceleration should be: only consider vertical vibration is $4\times5.0\times10^{-3}=2.0\times10^{-2}$ m/s$^2$; consider three directions' vibration is $4\times3.6\times10^{-3}=1.44\times10^{-2}$ m/s$^2$. Because the influence of train's vibration on environment mainly in the vertical direction, so following analysis only consider vertical vibration, which means $2.0\times10^{-2}$ m/s$^2$ is the evaluation standard.

It needs to evaluate the comfortable quality of station hall and two platforms respectively. During modelling, it regards station structure as train-station structure and uses structure-load model which puts measured wheel-rail force on the foundation bed as external force. The wheel rail force-time curve is shown as Fig.4. According to the condition of trains' running, it have two most dangerous conditions, first condition is that: Line 4 left and right trains go through at the same time, no trains of Line 6; second condition is that: Line 4 and Line 6 left and right trains go through at the same time. The distribution of the measured points in station hall floor and platforms is shown in Fig.5.

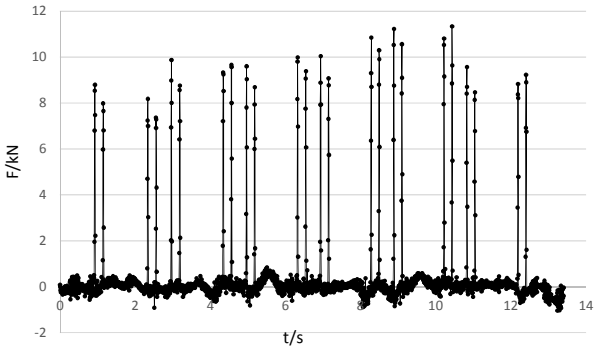


Fig.4 The wheel rail force-time curve

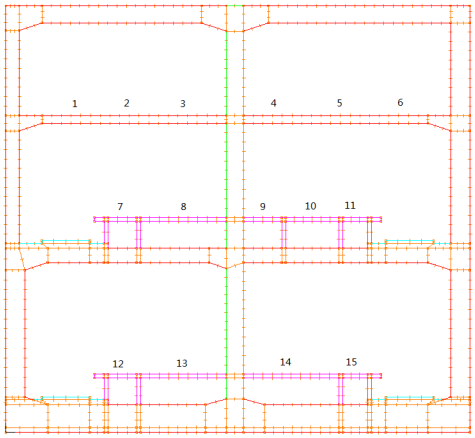


Fig.5 Distribution of the measured points

Through the calculation of 2 conditions, it can get acceleration-time curve of measuring points, as shown in Fig.6,7,8,9(only list several points);then transfer time value to frequency-domain value of acceleration with the use of Fourier Transform, finally get the weighed root mean square acceleration values with the method in ISO2631.

**Station hall floor**

*Condition 1*

In the condition 1, the acceleration- time curve of point 2 is shown in Fig.6, the weighed root mean square acceleration values $a_w$ of every point in station hall floor are in Table 2.

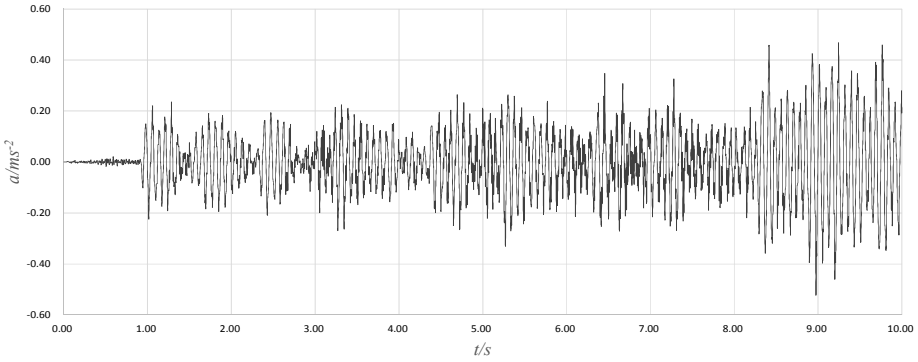


Fig.6 The acceleration- time curve of point 2 in condition 1

Table 2 The weighed root mean square acceleration values of every point $a_w$

| Node number | 1 | 2 | 3 | 4 | 5 | 6 |
|---|---|---|---|---|---|---|
| $a_w$/mm.s$^{-2}$ | 0.098 | 0.100 | 0.063 | 0.212 | 0.200 | 0.054 |

*Condition 2*

In the condition 2, the acceleration- time curve of point 2 is shown in Fig.7, the weighed root mean square acceleration values $a_w$ of every point in station hall floor are in Table 3.

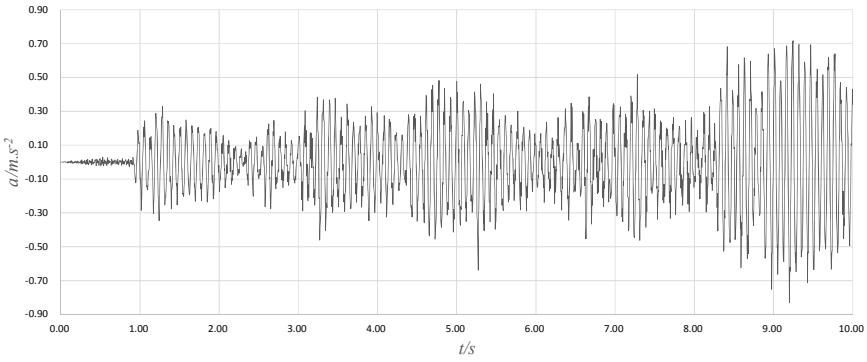


Fig. 7 The acceleration- time curve of point 2 in condition 2

Table 3 The weighed root mean square acceleration values of every point $a_w$

| Node number | 1 | 2 | 3 | 4 | 5 | 6 |
|---|---|---|---|---|---|---|
| $a_w$/mm.s$^{-2}$ | 0.112 | 0.215 | 0.135 | 0.140 | 0.276 | 0.091 |

From Table 2 and Table 3, we can see the maximum of weighed root mean square acceleration values $a_w$ of every point in platform is 0.276mm/s$^2$, which is less than 20 mm/s$^2$, it shows that the station hall floor could meet the need of comfortable quality. At the same time, it shows that condition 2 has much influence on the platform's vibration.

**Platform**

*Condition 1*

In the condition 1, the acceleration- time curves of point 8 and 13 are shown in Fig.8, the weighed root mean square acceleration values $a_w$ of every point in station hall floor are in Table 4.

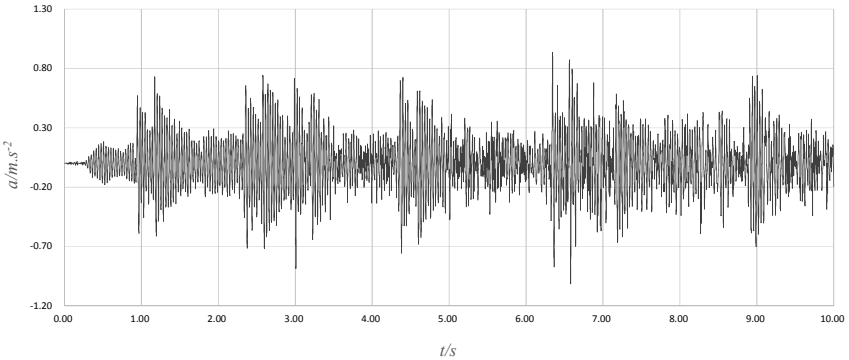


(a) the acceleration- time curve of point 8 in condition 1

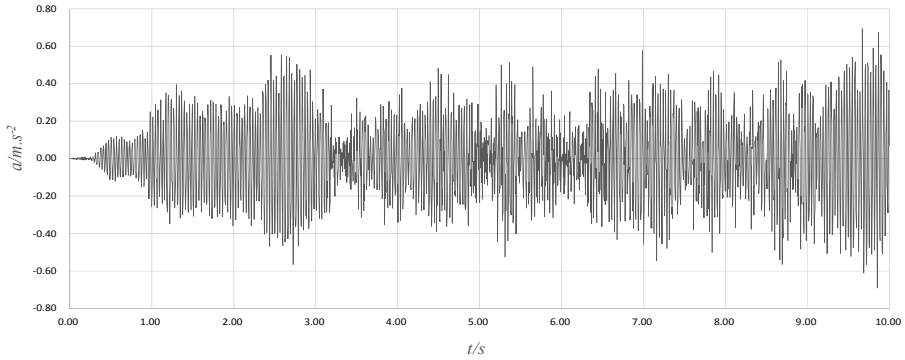


(b) the acceleration- time curve of point 13 in condition 1

Fig 8. The acceleration- time curves of point 8 and 13 in condition 1

Table 4 The weighed root mean square acceleration values of every point $a_w$

| Node number | 7 | 8 | 9 | 10 | 11 | 12 | 13 | 14 | 15 |
|---|---|---|---|---|---|---|---|---|---|
| $a_w$/mm.s$^{-2}$ | 0.126 | 0.234 | 0.130 | 0.143 | 0.263 | 0.094 | 0.123 | 0.251 | 0.044 |

*Condition 2*

In the condition 2, the acceleration- time curves of point 8 and 13 are shown in Fig.9, the weighed root mean square acceleration values $a_w$ of every point in station hall floor are in Table 5.

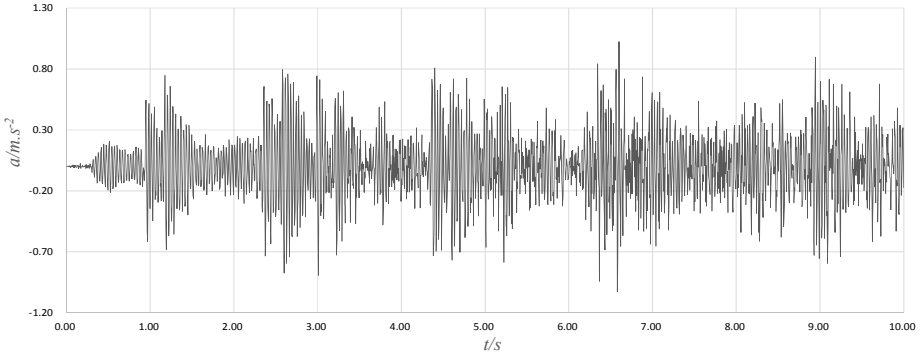


(a) the acceleration- time curve of point 8 in condition 2

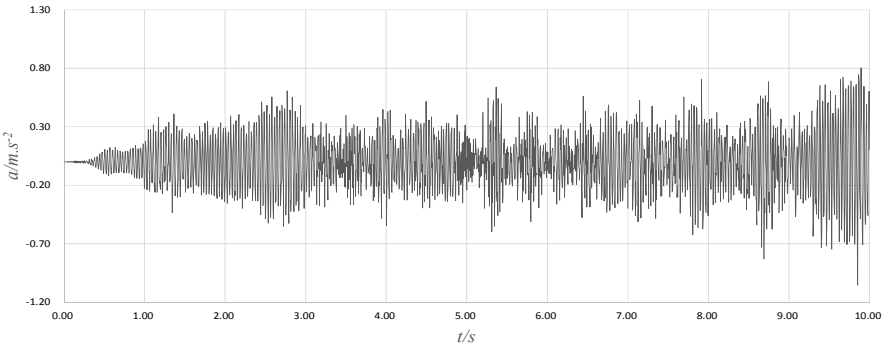


(b) the acceleration- time curve of point 13 in condition 2

Fig 9. The acceleration- time curves of point 8 and 13 in condition 2

Table 5 The weighed root mean square acceleration values of every point $a_w$

| Node number | 7 | 8 | 9 | 10 | 11 | 12 | 13 | 14 | 15 |
|---|---|---|---|---|---|---|---|---|---|
| $a_w$/mm.s$^{-2}$ | 0.073 | 0.139 | 0.045 | 0.080 | 0.084 | 0.049 | 0.118 | 0.081 | 0.039 |

From Table 4 and Table 5, we can see the maximum of weighed root mean square acceleration values $a_w$ of every point in platform is 0.263mm/s$^2$, which is less than 20 mm/s$^2$, it shows that the platform could meet the need of comfortable quality. At the same time, it shows that condition 1 has much influence on the platform's vibration.

## Conclusions

From the results above, we can see the maximum of weighed root mean square acceleration values $a_w$ of every point in station is 0.276mm/$s^2$, which is less than 20 mm/$s^2$, it shows that the station could meet the need of comfortable quality. Weighed root mean square acceleration values of every point varied differently, and floors don't have much relation with weighed root mean square acceleration values.

The paper gives the way of evaluating comfortable quality of vibration in projects according to ISO10137-2007 and ISO2631-1997, it evaluates the floors' comfortable quality in a station when multiple trains go through. It shows that the station could meet the comfortable quality need of vibration.

## References

[1] He Xia, Yanmei Cao:submitted to Journal of Railway Science and Engineering(2004), in Chinese
[2] Tong Jiang, Xin Zhang:submitted to Journal of Tongji University(2004), in Chinese
[3] Parsons K C, Griffin M J:submitted to Journal of Sound and Vibration( 1988)
[4] Griffin M J: *Handbook of human vibration* (Academic press, 2012).
[5] Ahn S J,Griffin M J: submitted to Journal of Sound and Vibration(2008)
[6] Morioka M, Griffin M J: submitted to Journal of sound and vibration(2008)
[7] Zhigang Song,Weiliang Jin: submitted to Journal of Basic Science and Engineering(2002), in Chinese
[8] Zhigang Song,Weiliang Jin: submitted to Journal of Vibration Engineering(2005), in Chinese
[9] Haoxiang He,Weiming Yan,Ailin Zhang: submitted to Journal of Vibration Engineering(2008), in Chinese
[10] Jianguo Chen, He Xia, Jinbao Yao: submitted to Journal of Vibration and Shock(2011), in Chinese
[11] Jinxu Pan, Shaofeng Yu: submitted to Low Temperature Architecture Technology(2013), in Chinese
[12] Guobo Wang, Weiping Xie, Yanli Yu: submitted to Journal of Vibration and Shock(2010), in Chinese
[13] International Standard 10137：Bases for Design 0f Structures—Serviceability of Buildings and Walkways against Vibration[S].2007
[14] International Standard 2631-2: Evaluation of Human Exposure to Whole-body vibration: Continuous and shock-induced vibration in buildings [s]. 1997

*Applied Mechanics and Materials Vols. 580-583 (2014) pp 1184-1187*
*© (2014) Trans Tech Publications, Switzerland*
*doi:10.4028/www.scientific.net/AMM.580-583.1184*

# Optimization of tunnel support type through fault zone

Ke Li[1, a,*], Han Guo[2, b,*]

[1]Natinoal Engineering laboratory for highway tunnel construction technology, China Merchants Chongqing Communications Research & Design Institute, China

[2]College of Civil Engineering, Chongqing University, China

[a]nick.88@163.com, [b]brankoilic14@gmail.com, [*]These authors contributed equally to this work

**Keywords:** tunnel, finite element method, fault zone, support type.

**Abstract.** The mechanical properties of tunnel surrounding rock in fault zone is usually quite weak, and the support pressure and displacement are larger than other sections, so the support type in fault zone is a critical issue for tunnel safety. Three types of tunnel support through fault zone were analyzed by finite element method (FEM): ①Reinforced concrete support, ②bolting-shotcreting and reinforced concrete support, ③grouting and reinforced concrete support. The result shows that support stress and surrounding rock displacement with grouting and reinforced concrete support is quite smaller than the other support types.

## Introduction

For mountain tunnel, fault zone is a weak section in construction, because of the weak physical and mechanical properties of surrounding rock mass. After excavation, the displacement of surrounding rock is larger than other sections, which causes larger stress for support structure[1-3], the stability of tunnel rock in fault zone is difficult to be ensured[4].

As the important influence of fault zone on tunnel construction, prediction of the location of fault zone and dynamic response of tunnel in fault zone were investigated by researchers[5,6], which provided theoretical basis for engineering practice. But in actual tunnel engineering through fault zone, the support type is reinforced by experience, the quantitative calculations of typical support results are not conducted in design.

In this paper, three typical tunnel support types are analyzed in a mountain tunnel project through fault zone, the calculation results by 3D-FEM are compared to quantitatively study the effects of the three support types and identify the proper support type.

## Engineering Background

A mountain road tunnel in western China is a double line tunnel penetrating a fault fractured zone. The left line tunnel is chosen as the research tunnel, it is designed as a 3 lane tunnel, its excavation area is 113.93 $m^2$. The length of the tunnel is 1567m and the maximum buried depth of the tunnel is 188.91m. The width of fault zone is 70~360m, the mountain rock is mainly consists of limestone, dolomitic limestone, and sandstone.

## FEM model

To focus on the support effect in fault zone, some assumptions are made in the FEM calculation:
(1) The earth surface is smoothed;
(2) The rock is homogeneous and isotropic except in fault zone;
(3) Only the major fault zone is considered.

A 100m wide, 900m long model is established (see Fig.1), the middle fault zone is 300m long. The bottom is constrained in three directions, the earth surface is free, and the other surfaces are constrained in normal direction. The rock constitutive model is Mohr-Coulomb model. The initial stress is obtained by regression analysis:
Stress in $y$ direction is 1.24 times gravity, normal stress in $x$ direction is 20.4MPa, normal stress in $z$ direction is 22.2MPa, shear stress $\tau_{xy}$ is 0.13MPa, $\tau_{yz}$ is 1.2MPa, $\tau_{xz}$ is 0.33MPa.

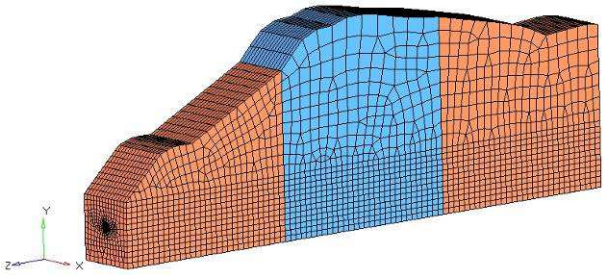

Fig.1 3D-FEM model of tunnel

The calculation parameters of rock and structure is shown in Table 1, $t$ is the thickness of support, $E$ is elastic modulus $\mu$ is Possion ratio, $\rho$ is density, $c$ is cohesion, $\varphi$ is frction angle.

Table1 Calculation parameters of FEM tunnel model

| Support structure | | | Rock in fault zone | | | | | Rock out of fault zone | | | | |
|---|---|---|---|---|---|---|---|---|---|---|---|---|
| $t$ | $E$ | $\mu$ | $\rho$ | $E$ | $\mu$ | $c$ | $\varphi$ | $\rho$ | $E$ | $\mu$ | $c$ | $\varphi$ |
| 0.6m | 28 GPa | 0.2 | 2400 kg/m$^3$ | 4.03 GPa | 0.38 | 3.25 MPa | 32° | 2680 kg/m$^3$ | 11.29 GPa | 0.27 | 7.6 MPa | 45.2° |

**Three support types**

Three typical tunnel support types are calculation in FEM model (see Fig.2): ①Reinforced concrete support(type I), ②bolting-shotcreting and reinforced concrete support(type II), ③grouting and reinforced concrete support(type III).

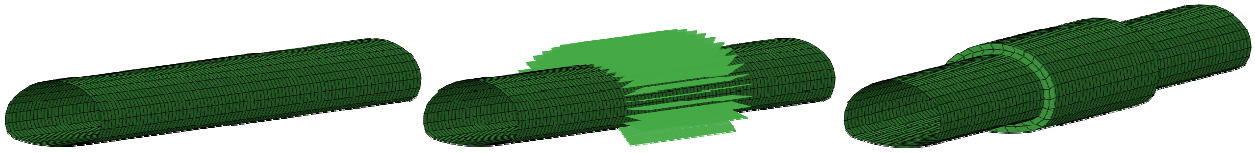

(1) Reinforced concrete support

(2) Bolting-shotcreting and reinforced concrete support

(3) Grouting and reinforced concrete support

Fig.2 Three support types of the tunnel

Other calculation parameters:
(1) Bolt: spacing 0.6m×0.6m, 4m long, diameter 25cm, $E$=206GPa, $\mu$=0.3;
(2) Grout: thickness is 2m, $E$=21GPa, $\mu$=0.24, $c$=3.25MPa, $\varphi$=32°.

**Comparison of three supporting effects**

**Calculation Results**. The horizontal, vertical displacement of tunnel surrounding rock and the Mises stress of the tunnel support structure with three support types are shown in Fig.3.

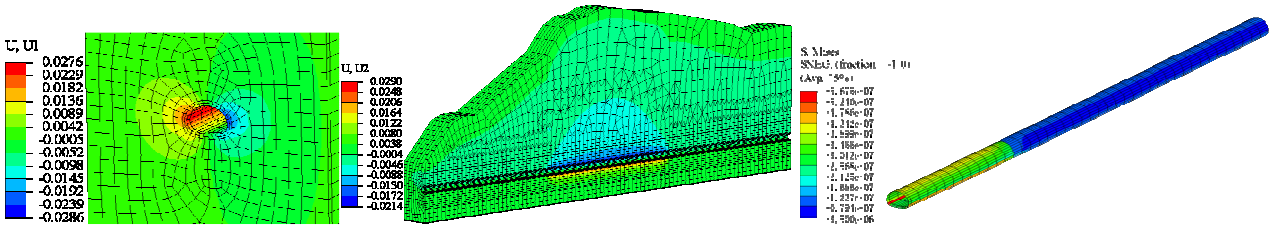

(1) Horizontal displacement (2) Vertical displacement (3) Mises stress of support structure

Fig.3 Calculation result of reinforced concrete support(type I)

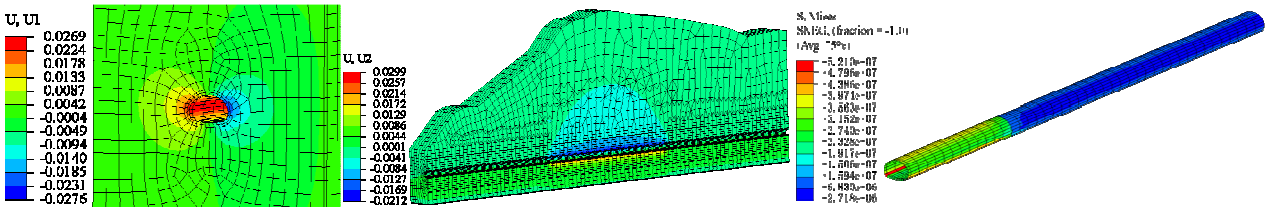

(1) Horizontal displacement (2) Vertical displacement (3) Mises stress of support structure

Fig.4 Calculation result of bolting-shotcreting and reinforced concrete support(type II)

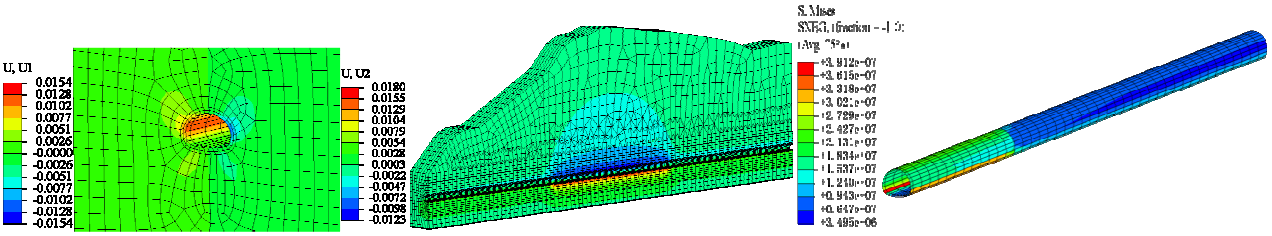

(1) Horizontal displacement (2) Vertical displacement (3) Mises stress of support structure

Fig.5 Calculation result of grouting and reinforced concrete support(type III)

It is shown that rock displacement and structure stress in fault zone are much larger than the other sections. The displacment in fault zone is more than 10mm larger than common zone, so the reinforcment of structre is necessary. The maximum stress of structure is at the bottom of side wall, more attention should be paid in design.

**Comparison of results**. The maximum horizontal displacement of surrounding rock, maximum settlement of valt, maximum uplift of inverted arch with three support types are compared in Fig.6.

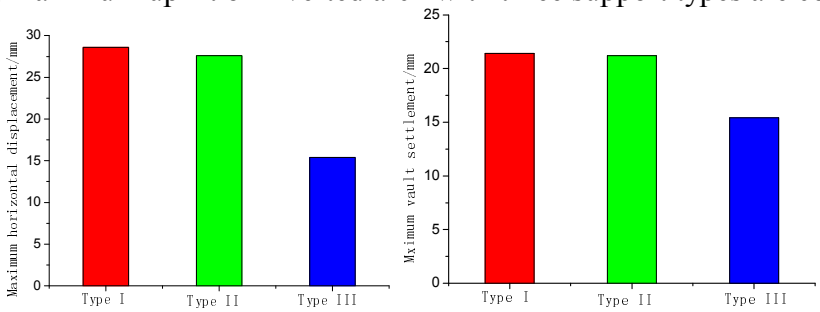


(1)Maximum horizontal displacement (2)Maximum vault settlement

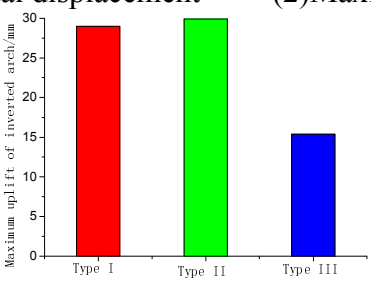


(3)Maximum uplift of inverted arch

Fig.6 Maximum displacement of surrounding rock with three support types

The comparison of maximum support structure stress is shown in Fig.7.

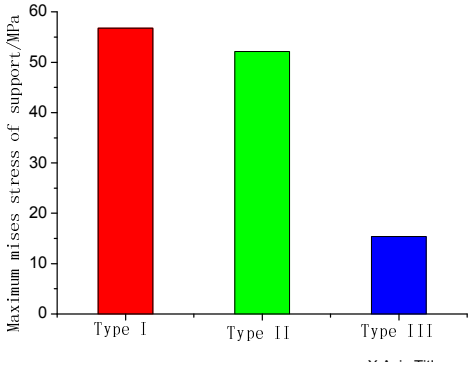


Fig.7 Maximum mises stress of support structure with three support types

The results shows that the displacement of surrounding rock and support stress with support type I is the largest, and the displacement and stress with support type III is the lowest. The maximum horizontal displacement with three support types are 27.6mm, 26.9mm, 15.4mm respectively, and the maximum support structure stress with three support types are 56.75MPa, 52.10MPa, 39.12MPa, respectively.

## Summary

Three tunnel support types in fault zone are compared:①Reinforced concrete support(type I), ②bolting-shotcreting and reinforced concrete support(type II), ③grouting and reinforced concrete support(type III). The FEM calculation shows that the surrounding rock displacment and structure stress with type III is the lowest, on other hands, type III is the most effective tunnel support type for fault zone.

## Acknowledgements

This work was financially supported by the Chongqing Science and Technology Project (cstc2012gg-yyjs30002), Chongqing Science and Technology Project (cstc2013yykfB0230).

## References

[1] Süleyman Dalgıç. Tunneling in squeezing rock, the Bolu tunnel, Anatolian Motorway, Turkey[J]. Engineering Geology, 2002, 67(1-2): 73–96.

[2] Mete Kun, Turgay Onargan. Influence of the fault zone in shallow tunneling: A case study of Izmir Metro Tunnel[J]. Tunnelling and Underground Space Technology, 2013, 33: 34–45.

[3] J.S. Yang, L. Yan, S.J. Deng, G.L. Li. Interactions of four tunnels driven in squeezing fault zone of Wushaoling Tunnel[J]. Tunnelling and Underground Space Technology, 2006, 21(3-4): 359.

[4] P.H.S.W. Kulatilake, Qiong Wu, Zhengxing Yu, Fuxing Jiang. Investigation of stability of a tunnel in a deep coal mine in China[J]. International Journal of Mining Science and Technology, 2013, 23(4): 579-589.

[5] Luan T. Nguyen, Maria Datcheva, Tamara Nestorović. Identification of a fault zone ahead of the tunnel excavation face using the extended Kalman filter[J]. Mechanics Research Communications, 2013, 53(3): 47-52.

[6] Xiang Zhao, Jiang Shuping, Yi Yi. Study on Shaking Table Model Test Scheme of Tunnel Subjected to Near-Fault Pulse-Like Ground Motions[J]. Modern Applied Science, 2014, 8(3): 126-139.

*Applied Mechanics and Materials Vols. 580-583 (2014) pp 1188-1191*
*© (2014) Trans Tech Publications, Switzerland*
*doi:10.4028/www.scientific.net/AMM.580-583.1188*

# Force Analysis of the Middle Wall in Multi-arch Tunnel under Central Hole + CRD Method

Li Jun, Wang Zong Lin

School of Transportation Science and Engineering, Harbin Institute of Technology, Harbin 150090, China

hitlij@yeah.net

**Keywords:** Multi-arch Tunnel, Force Analysis, Middle Wall, Mechanical Properties

**Abstract.** arch tunnel construction in the presence of construction mechanics often unclear, the lack of systematic design and construction of the theory can learn. Harbin Clinic Road thesis double-arch tunnel project as the basis, the construction process through its hole + CRD using the finite element simulation analysis and on-site monitoring measurement data processing, engineering arch tunnel song used in the wall study the mechanical properties.

## Introduction

In the design and construction of the arch of the tunnel, is still a lack of effective projects can draw analogies can be, there are more problems, in addition to even itself be perfect arch tunnel structure type, another important factor is the mechanics of the arch tunnel no in-depth study of the characteristics, especially the position of the wall in the arch of the tunnel, the tunnel of this site is the place where stress concentration, the force is very complex, tension, compression, bending, twisting, cutting both, while the wall mechanics behavior and its displacement and settlement indicators directly related to the overall stability of the arch of the tunnel. In subway construction, although open-cut construction method is most convenient, but in the bustling city traffic arteries, intensive commercial construction zone, due to traffic conditions, geographical conditions, open-cut construction can not be implemented, and the cover lid down construction dig dug along the building need traffic relief, to some extent, affect traffic. Therefore, it is necessary to combine the mechanical properties of the actual project arch tunnel in the wall for further analysis, which is an important reference and guidance for total construction of double-arch tunnel.

## Project Overview

Health Road Bridge project is located in Nangang District, Harbin and Xiangfang District, Ha Ping Road starting point for the design and finish of the street through the village, project length of 3500 meters. East-west road red line width of 60m. Associated with the Arboretum area to consider wearing Ha Ping Road tunnel form, Province Forest Botanical Garden and triple road. This project is parallel to the Ring Road, a city main road between the Third Ring Road, Ring Road and the Third Ring Road and 3.5 km spacing are also supporting road between the two loops. After the project is completed effectively triage and Hing, dynamic road traffic coming up with triple road through rural road network formed Street, the main road to form a new system. Tunnel "middle hole + CRD" method of construction, the use of soft soil Shallow Large Span Tunnel and the Urban Design Study hole + CRD method, that is, first excavated in the hole, and then the outside of the two main tunnel excavation has three pilot tunnel , followed successively by the main tunnel excavation inside the left lane of the three guide hole in the wall, and finally has the right line of the main tunnel excavation construction technology on the inside of the walls of the three-hole lead, materials and energy savings, effective control of costs, maximize social, economic efficiency. The construction method for the construction method similar to existing industry or national labor law innovation and development, the formation of patented technologies, and supporting construction method.

**The wall structure type double-arch tunnel**

Arch tunnel's arch tunnel wall is load-bearing force transmission and key parts, is to maintain the overall stability of the central arch of the tunnel, but also anti-drain key positions. In the double-arch tunnel structure, the importance of the wall can be said pivotal. Corresponding to the four double-arch tunnel section type, the structure type also has four walls, the walls are straight overall layered straight in the wall, the whole song in the wall, and three songs in the wall, the basic section type shown in Fig.1. Harbin Clinic Road tunnel wall in the form of a curved wall.Tunnel "middle hole + CRD" method of construction, the use of soft soil Shallow Large Span Tunnel and the Urban Design Study hole + CRD method, that is, first excavated in the hole, and then the outside of the two main tunnel excavation has three pilot tunnel , followed successively by the main tunnel excavation inside the left lane of the three guide hole in the wall, and finally has the right line of the main tunnel excavation construction technology on the inside of the walls of the three-hole lead, materials and energy savings, effective control of costs, maximize social, economic efficiency. The construction method for the construction method similar to existing industry or national labor law innovation and development, the formation of patented technologies, and supporting construction method.

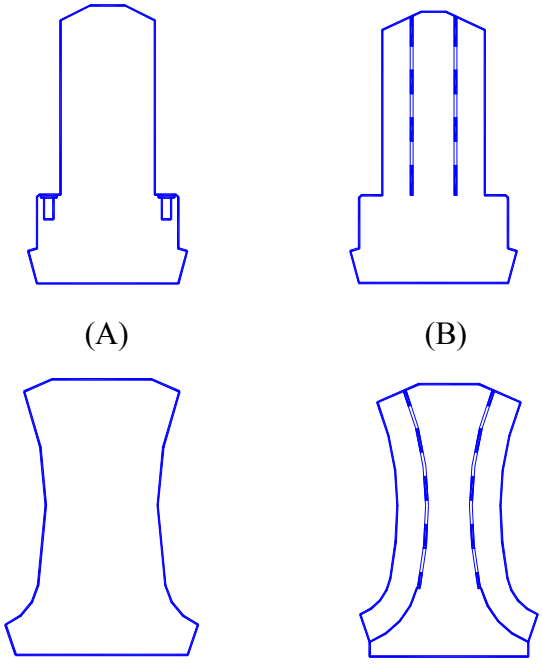


A whole wall directly, B layered straight in the wall,

C whole song in the wall, D three-song in the wall

Figure.1 Basic types of double-arch tunnel wall

**Force process variation in middle wall construction**

Arch tunnel in the wall by the time the two main tunnel construction in all directions repeatedly loads and loads vault over the role of the force is very complex, pressing, pulling, bending, shear are internal forces are constantly changing, mainly five distinct converting the internal forces, shown in Figure 2. (1) before the main tunnel excavation: the guide hole equivalent to one-way tunnel, the walls to withstand the pressure from the main dome of the rock to produce relaxation, belonging axial compression structure, since the wall section is relatively large, at this stage by force is relatively stable. If the tunnel bias exists, the wall is also biased loads role. (2) the right hole before excavation support: excavation hole left, destabilizing the pilot tunnel excavation in rock formation, the whole tunnel produces bias. The walls are eccentric compression structure, this time in the main wall shear

and bending. (3) When the hole is not left right after the cave excavation support: Supporting the right tunnel surrounding rock deformation is suppressed, while the right footing to set the initial support of the top hole on the right side of the wall. At this point, only the left hole in the wall on the same side of the pressure to produce, and bear right tunnel initial support to pass pressure. (4) when the left does not support tunnel excavation: excavation hole left and right holes in the wall to form a bias. Early (5) support on both sides of the main tunnel after the completion of: the left and right holes are formed, the wall is mainly exposed to the vertical force, force and stability. The wall by the force process also closely related to geological factors and construction. If the tunnel overall bias exists, or the side of the main tunnel collapse occurred a great impact, the force will give the wall construction.

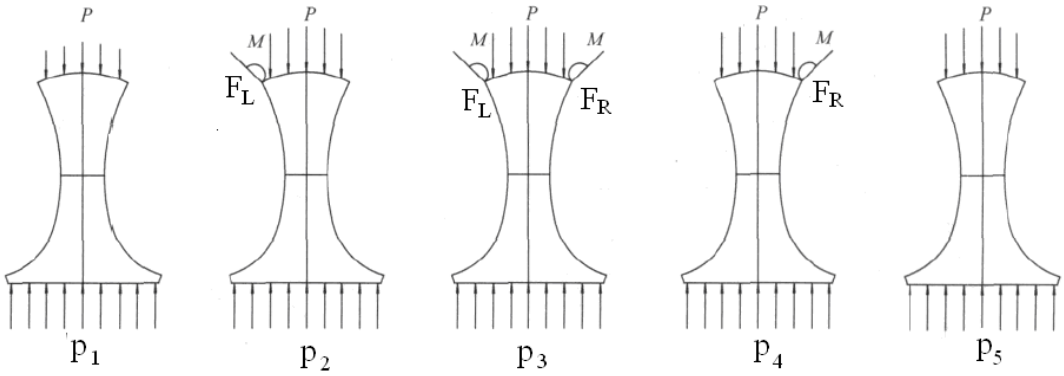


Figure.2 Wall force convert in the construction process

**Middle wall stress analysis**

As an important load-bearing walls in the double-arch tunnel structure, which is closely related to the force in the form of the construction process, the analysis of the wall in both the construction process, the wall construction process with effective stress changes, shown in Figure 4-4 - 7,4-4-8 shown by comparative analysis because the first step of an excavation hole left, then the right excavation hole in the wall left, right uneven stress concentration in the excavation process, the maximum stress 14.2Mpa, and with a significant reduction in stress during the excavation, the final state of total stress contours significant concentration phenomenon (Figure 3). As the excavation process step 2 symmetry, the main form of stress distribution is relatively symmetrical relative terms during the excavation process a maximum stress in the wall of a small 8.1Mpa, and the construction process in the wall left and right small differences, the force uniform and stable (Fig.4).

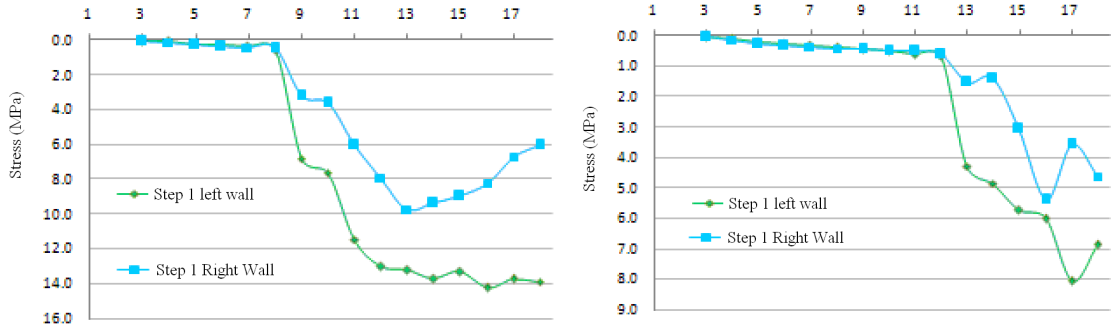


Wall stress in Step 1 Wall stress in Step 1

Figure.3 The results of the wall stress data

Middle wall stress analysis As an important load-bearing walls in the double-arch tunnel structure, which is closely related to the force in the form of the construction process, the analysis of the wall in both the construction process, the wall construction process with effective stress changes, shown in Fig.3 and 4 shown by comparative analysis because the first step of an excavation hole left, then the

right excavation hole in the wall left, right uneven stress concentration in the excavation process, the maximum stress 14.2Mpa, and with a significant reduction in stress during the excavation, the final state of total stress contours significant concentration phenomenon (Fig.3). As the excavation process step 2 symmetry, the main form of stress distribution is relatively symmetrical relative terms during the excavation process a maximum stress in the wall of a small 8.1Mpa, and the construction process in the wall left and right small differences, the force uniform and stable (Fig.4).

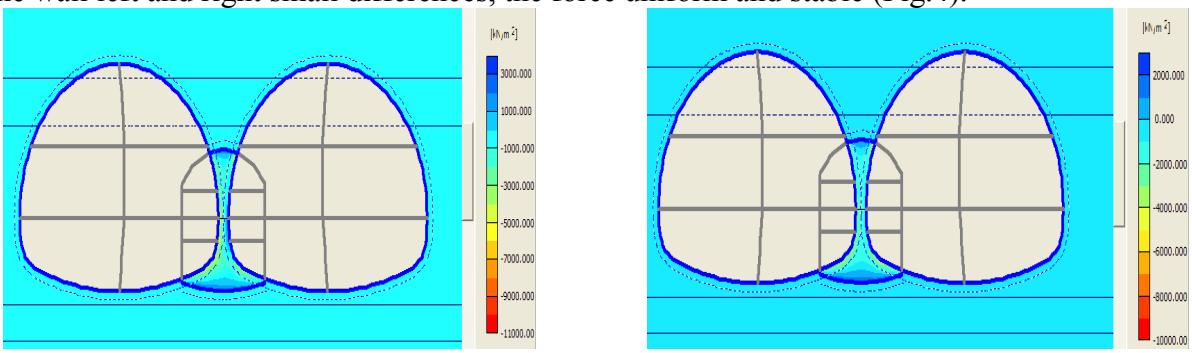

Tunnel wall stress in Step 1 Tunnel wall stress in Step 2

Figure.4 Tunnel wall stress

Excavation processes impact on the wall by the force of a large, asymmetrical when excavation process, the wall will withstand the horizontal force and overturning moment, especially in the first cavern while construction is completed, the other side of the cavern cave hair only when the wall will be in the most dangerous state, according to this time the forces should be as the wall design.

## Conclusion

In the process of dismantling temporary support will encounter break the balance of the original architecture of the risks arising from excessive deformation or structural instability, but as long as removal of temporary support scheme selection is reasonable, and strictly control the construction process, the removal of temporary support to strengthen monitoring during the measurement, so that monitoring and feedback to guide the construction, tunneling structure can ensure the temporary removal process does not produce too large deformation, fully able to ensure formation occurred within the scope of the displacement can be controlled. This is mainly due to the loose soil belongs to the medium, not a homogeneous elastic medium, adjustments due to the stress caused by unloading obvious, stress of soil material is mainly due to their own gravitational mass and the accompanying stress field. This shows that the theoretical calculations and underground engineering can not be fully consistent with the actual situation, resulting in major reason for this is because of the complexity of the decision geotechnical conditions. In actual engineering practice, we must pay attention to measurement, based on the actual situation to choose the right parameters and appropriate supporting construction methods.

## References

[1] C. Zhang, X. T. Feng, H. Zhou: International Journal of Rock Mechanics and Mining Sciences, Vol.52 (2012), p.139-162
[2] A. Thurston: Orthopaedics and Trauma, Vol.27 (2013), p.332-341
[3] F. M. P. Leclère, F. Unglaub: Neurochirurgie, Vol.58 (2012), p.309-313
[4] W. Feng, R. Huang: Tunnelling and Underground Space Technology, Vol.32 (2012), p.190-197
[5] L. Jing: International Journal of Rock Mechanics and Mining Sciences, Vol.40 (2003), p.283-353
[6] D. Chowdhury: Physics Reports, Vol.529 (2013), p.1-197
[7] C. Zangerl: International Journal of Rock Mechanics and Mining Sciences, Vol.45 (2008), p.1195

*Applied Mechanics and Materials Vols. 580-583 (2014) pp 1192-1196*
*© (2014) Trans Tech Publications, Switzerland*
*doi:10.4028/www.scientific.net/AMM.580-583.1192*

# Force State of Country Rock and Supporting Structure in Multi-arch Tunnel under Central Hole + CRD Method

Li Jun, Wang Zong Lin, Zhong Jun Fei

School of Transportation Science and Engineering, Harbin Institute of Technology, Harbin 150090, China

hitlij@yeah.net

**Keywords:** Engineering Mechanics, Construction Mechanics, Tunneling, Rock Stress

**Abstract.** The reason situ stress is very complicated, and it is still not very clear question. In this paper, the construction process through practical engineering analysis on a variety of construction methods and steps arch tunnel to study the effects of different excavation methods and deep anchor support large section tunnel under guard by theoretical analysis of surrounding rock stress field, strain field and variation of the displacement field, analysis of different rock excavation methods, supporting stress state characteristics, in order to optimize the choice of tunneling method provides a theoretical basis. Under the conditions all kinds of rock reasonable steps to secure construction methods put forward and lay the foundation for long-term safety arch tunnel.

## Introduction

In the process of tunnel excavation, the surrounding rock, and the walls supporting the force, such as the state of research is necessary. By the beginning of the lining between the support and the soil pressure cells buried early lining, second lining, buried in wall reinforcement meter measured the actual rock, initial support, the walls of the excavation force size , always comparing initial support, second lining, the wall by the condition of the actual force with the theoretical value of the support is within the control of the controllable range of safety analysis of the progress of each step with the various parts of the excavation of the force changes in the analysis that is located in various parts of the rock vaults, arches back (lumbar arch left and right arch waist), invert (invert left and right side invert, invert the bottom) of the rock stress conditions, peri with the dynamic effects of stress in rock excavation face advance to determine the shortest distance between the excavation face the stress of the surrounding rock, excavation for the introduction of the Act, in which the accumulation of geological conditions for construction data, and construction. The use of soft soil Shallow Large Span Tunnel and the Urban Design Study Cave + CRD method, that is, first excavated in the hole, and then has two main tunnel excavation outside the three-hole lead, followed successively by the main tunnel excavation in the left lane the inside wall of the three-hole lead, finally has the right line of the main tunnel excavation by construction technology inside the walls of the three-hole lead, materials and energy savings, effectively control costs and maximize social and economic benefits. The construction method for the construction method similar to existing industry or national labor law innovation and development, the formation of patented technologies, and supporting construction method.

## Rock stress state of the construction process

Refers to the surrounding rock tunnel tunnel certain range, have an impact on the stability of the rock tunnel . From the perspective of mechanical analysis point of view, the boundary should be drawn in rock stress changes caused by tunneling negligible place , or on the border due to the excavation of the tunnel surrounding rock displacement should be zero in this range should be 6 to 10 times the hole diameter on the cross section. In Weak Rock , joints and fissures are well developed , very broken rock was cut , structural deformation and failure of rock face have no effect , so the

characteristics of the rock mass and structure characteristics of the rock is not fundamentally the difference between , for example, soil can be considered as a special kind of severe weathering broken rock . Soil conditions can be classified according to particle size clayey soil, sandy soil, gravel soil . Soil plasticity index greater than 10, becoming clayey soil, which plasticity index greater than 10 and less than or equal to 17 for the powder soil clayey soil, soil plasticity index greater than 17 is clay. Particle size greater than 2mm content does not exceed 50% of the total mass of fine particles and particle size greater than 0.075mm content of more than 50% of the total mass of the soil is sandy soil . Particle size greater than 2mm content of more than 50% of the total mass of soil is gravelly soil . Thus, the mechanical properties of the rock mass is the result of the inevitable effects of many factors , but some rock is rock mechanical properties from the control action , and some rock mechanical properties of structural plane is dominant . Description and determine the level of construction rock The tunnel is the beginning of large-span Shallow silty clay rock lining double, two separate tunnel lining, excavation width of 26.4m, excavation height of 9.812m, the roof covering the soil around 7 ~ 8m. Rock level can be calculated are V-class rock. Construction using the middle hole + CRD construction method, and this method has been optimized to realize that both sides of the hole and the hole while the main tunnel excavation, on both sides of the hole, the pilot tunnel excavation method has under construction excavation.

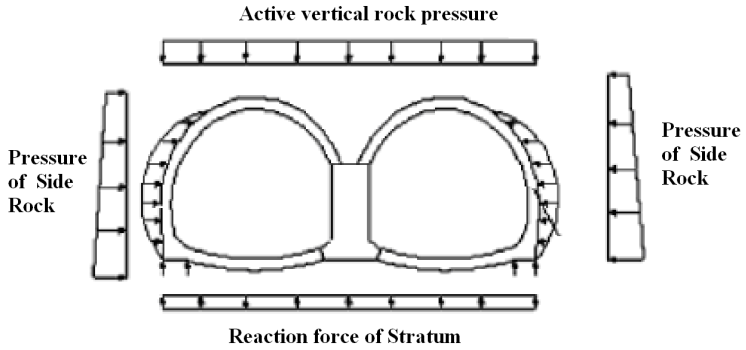


Figure.1 Composite lining rock pressure analysis

When architecture design of the tunnel, there are two computing models, one is the main supporting structure as the bearer, rock deformation from the supporting structure of a constraint, called load - structure model. Another rock was carrying in the body, supporting structure to limit the tunnel rock deformation, supporting structure and surrounding it as a single unit, as co-hosts of the tunnel structure system, called strata - load model. Before the tunnel excavation, rock in the initial stress state, the tunneling induced redistribution of rock stress, and natural rock "arching" form a natural arch. According to the two models can be considered: the arch tunnel in shallow, so to load - structural model to analyze its force. So in the process of double-arch tunnel excavation in rock stress changes are as follows: 1. In the pilot tunnel excavation, the destruction of the initial rock stress state, causing the cavern and initial support deformation stress redistribution, the formation of new stress field - rock secondary stress field. 2. When the right tunnel excavation, rock stress redistribution roof also formed three rock stress state. 3. When the left tunnel excavation, rock stress redistribution roof also formed four rock stress state. 4. Set "second lining", due to some of the deformation front has not completely stopped, so there will still be part of the force, such as residual deformation of rock, and reduce the physical and mechanical properties of rock after construction, etc., still "second lining" to commitments. This "second lining" stress state of the rock should be called double-arch tunnel surrounding rock stress state five times.

**Rock Pressure Calculation**

Calculation of shallow buried even the top of the vertical uniform Jacobsson Arch Tunnel dynamic pressure consists of two parts, namely:

$$q = \gamma H$$
$$q_z = \gamma(H_1 - H) \tag{1}$$

Where: q-tunnel vertically uniform pressure (kN/m$^2$); qz-as between the walls and the sides of the triangular block sandwiched arch weight (kN/m$^2$); γ-rock density (kN/m$^3$); H-tunnel depth, refers to the top of the tunnel to the distance (m) the ground. The role of rock pressure levels on both sides of the tunnel lining is:

$$e_1 = \gamma H \tan^2(45^\circ - \frac{\phi}{2})$$
$$e_2 = \gamma(H + h)\tan^2(45^\circ - \frac{\phi}{2}) \tag{2}$$

Where: e1, e2-tunnel vault and horizontal rock pressure at the bottom; γ-rock density (kN/m3); H-tunnel depth, refers to the top of the tunnel to the distance (m) the ground; h-tunnel excavation height (m); Φ-rock to calculate the friction angle (°).

Rock pressure can be calculated during construction due to rock stress five double-arch tunnel construction process of re-distribution, the more complex nature of the rock, but a lot of changes, human factors, such as excavation and support methods great influence on rock nature, can not be estimated in advance. In theory it should be analyzed to determine the combination of experience, to guide the construction of double-arch tunnel.

**Charged to guard the construction process study the stress state**

Before the body hole tunneling, rock for relatively low-level implementation of advance support to enhance the strength and stability of surrounding rock. Body in the hole tunneling process, also in order to maintain a stable rock, must immediately apply for initial support. Support form the tunnel is: a bolt, steel mesh, shotcrete and steel as the primary support and supplemented necessary to mold build advance support for the secondary lining of reinforced concrete lining composition, initial support and the secondary set between the arch lining waterproof barrier.

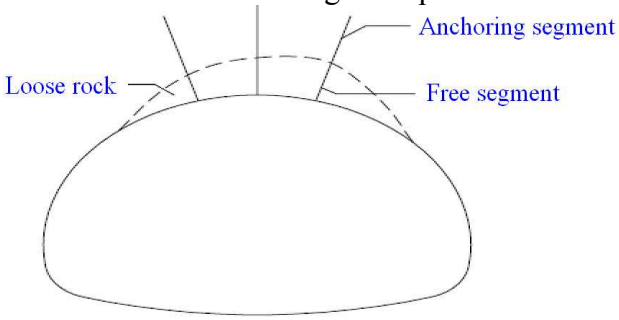


Figure.2 Schematic of rock tunnels bolt action

Through on-site testing of soft soil tunnel anchor stress and statistical analysis to study the effects and mechanisms supporting soft soil tunnel anchor, the following main conclusions: (1) Through the anchor stress test data meta-analysis, found arch compression bolt to the main arch of the foot anchors in tension-based, skirting the foot of the lock bolt has a tensile stress is also compressive stress; locking bolt stress is generally greater than the foot arch anchor stress. In soft soil tunnel system bolting obvious. (2) analysis that the tunnel excavation of shallow tunnels in soft soil arch occurred overall settlement, there is no anchor anchoring section. Deep soft soil tunnel excavation soil mass produce a larger plastic zone, and the system is currently anchor of "short and tight" is not used to set principles through the plastic zone, there was no anchoring segment. In addition, anchor and soil using cement mortar or adhesive roll poor anchoring agent, thus arch tunnel in soft soil anchor system protective role in not charged.

From the analysis of the deformation of soil mechanics state arch tunnel in soft soil anchor system, analysts believe that because the anchor is anchored to the initial support and into the soil, the soil from inside the deformation constraint in the early after applying for support, with respect to the subsequent deformation of the soil, the anchor is stationary, so the big tunnel in soft soil deep loess Shallow tunnels or plastic zone, arch system bolt down by the soil the frictional resistance, which is equivalent to withstand negative skin friction piles, which anchors the arch system pressure.

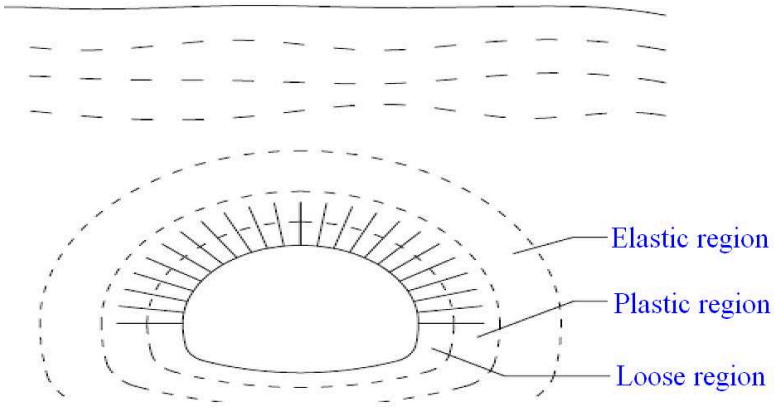


Figure.3 Produces of plastic tunnels in deep loess area

Description and determine the level of construction rock The tunnel is the beginning of large-span Shallow silty clay rock lining double, two separate tunnel lining, excavation width of 26.4m, excavation height of 9.812m, the roof covering the soil around 7 ~ 8m. Rock level can be calculated are V-class rock. Construction using the middle hole + CRD construction method, and this method has been optimized to realize that both sides of hole while the main tunnel excavation, on both sides of the hole, the pilot tunnel excavation method has under construction excavation.

**I-beam gantry study the stress state**

When measured using surface-type strain gauge steel top and bottom flange steel support indirect test strain, then by Hooke's law to calculate the stress test point, and then assume that the steel support in the state without regard to flexible working beam web site shotcrete force, you can get the steel support inverse mechanical method based on the actual internal forces as follows:

$$\sigma_1 = \frac{N}{A} - \frac{M}{I}h$$
$$\sigma_2 = \frac{N}{A} + \frac{M}{I}h \tag{3}$$

$$N = \frac{A(\sigma_1+\sigma_2)}{2}$$
$$M = \frac{I(\sigma_2-\sigma_1)}{2h} \tag{4}$$

wherein: $\sigma_1, \sigma_2$ is the upper beam of I-beam, a lower edge of the test stress (MPa); N is calculated beam axial force (kN), M for the beam bending moment calculated value (kN * m); A is the beam cross-sectional area ($m^2$), I is the moment of inertia beam ($m^4$); h is a surface-type steel beam horizontal strain (X-axis) of the distance (m) meter away.

It is prone to collapse during excavation, so depending on the circumstances when applying for advanced small pipe excavation, excavation contour play reinforcement and soil pipe roof reinforcement area of effect. In the long tube, and a small catheter together, even rock stress relaxation, the initial relaxation small, can effectively achieve the maintenance of rock, rock reinforcement purposes, to provide a reliable guarantee safe excavation. As can be seen from the results of the analysis that the beam erection short, stress increases rapidly, visible beam earlier play

its carrying capacity, can play a role in supporting timely rock. Beam stress lasts about 2-4 months before gradually stabilized, the same description of weak and fractured rock, the rheological properties of the original rock stress release, and verify the correctness of the foregoing analysis. Beam overall state of compression, bending moment is small, in line with the theoretical analysis of the law, but its material properties play a limited, in contrast to shot Crete stress state, the proposed design phase should be appropriately reduced beam model, increasing jet concrete thickness, material properties, and give full play to project cost savings.

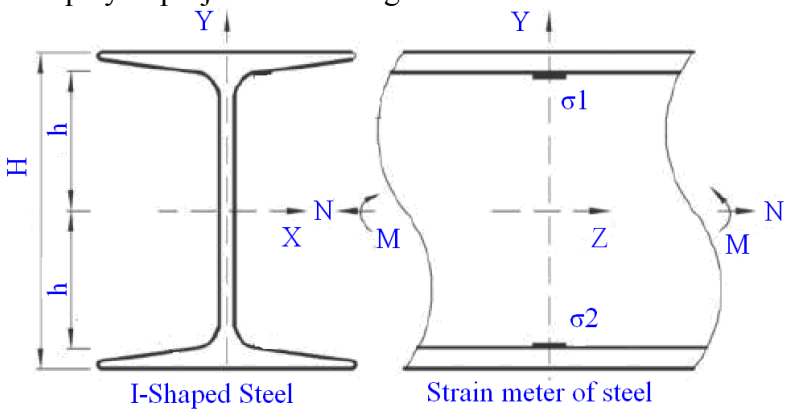


Figure.4 Steel strain gauge layout and internal force calculation icon

## Conclusion

During the design calculation of the external load is considered as rock pressure, ignoring the role of rock reinforcement and self-supporting capability bolt, the calculation model is safer. Through the entire shell of reinforced mesh shelf space calculation shows that steel compression deformation is synchronous, while unit internal forces reinforced curve indicates the middle of the reinforced to withstand a greater load for the main bearing bars. According to the mechanical characteristics of steel lattice shell structures, we arranged some reinforcement strain test section. About ten days or so deformed shell from installing network supporting structure is large, the future network shell and rock interactions stabilize.

## References

[1] J.Lai, H. Fan, B. Liu, T. Liu: Procedia Engineering, Vol.15 (2011), p.5473-5477

[2] C. Zhang, X.Feng, H.Zhou: International Journal of Rock Mechanics and Mining Sciences, Vol.52 (2012), p.139-162

[3] C. Zangerl, K.F. Evans, E. Eberhardt, S. Loew: International Journal of Rock Mechanics and Mining Sciences, Vol.45 (2008), p.1195-1210

[4] P. G. C. Prazeres, K. Thoeni, G. Beer: Computers and Geotechnics, Vol.40 (2012), p.160-173

[5] F. Huang, X.L. Yang: Tunnelling and Underground Space Technology, Vol.26 (2011), p.614-618

[6] W. Feng, R. Huang, T. Li: Tunnelling and Underground Space Technology, Vol.32 (2012), p.190-197

[7] Y. Cai, T. Esaki: Tunnelling and Underground Space Technology, Vol.19 (2004), p.607-618

[8] N. Barton: International Journal of Rock Mechanics and Mining Sciences, Vol.39 (2002), p.185-216

[9] J.S. Lee, M. Sagong, G.C. Cho, S.Y. Choo: Tunnelling and Underground Space Technology, Vol.25 (2010), p.518-525

*Applied Mechanics and Materials Vols. 580-583 (2014) pp 1197-1202*
*© (2014) Trans Tech Publications, Switzerland*
*doi:10.4028/www.scientific.net/AMM.580-583.1197*

# Key Construction Technology of Shield Machine Passing Through the Airport Apron in Shallow Soft Soil

Li Runjun[1,2,a], Shan Renliang[1,b], Li Runsheng[2,c], Lv Jinyang[1,d], Song Yongwei[1,e]

[1]School of Mechanics & civil engineering, China University of Mining & Technology, Beijing, 100083, China

[2]Beijing urban construction design & development group co., Limited, Beijing, 100088, China

[a]lirunjun2@sina.com, [b]srl@cumtb.com.cn, [c]453396753@qq.com, [d]897616010@qq.com, [e]895027891@qq.com

**Keywords:** shield machine in shallow soil, airport apron, sedimentation control, soil pressure control, deep splitting grouting

**Abstract.** It is a hard engineering problem for the shield machine passing through the capital airport apron in shallow soft soil. Tunneling parameters were obtained from the 50m simulation test section ahead the apron. The shield machine kept tunneling steady and balanced by optimizing the control technology of soil pressure and grouting. According to the monitoring results, the secondary and repeated grouting technology was applied timely. The deep splitting grouting technology was used when the monitoring value exceeding control standards. The settlement value was effectively controlled.

## Introduction

The shield machine past through the Capital Airport apron in T2 branch line of Beijing Capital International airport. It is a super risk source, on the one hand, to ensure the safety of aircraft taxiing and parking, airport apron surface deformation is very hard to control; On the other hand, the tunneling of shield machine in shallow soil make great disturbance to the surface, it's hard to control the deformation of the surface, which makes construction more hard[1], so effective measures must be taken to ensure the safety and success.

## Engineering situation

**Design overview.** The underground section of the shield interval in T2 branch line need to pass through the Capital Airport apron[2] before reaching the T2 Airport terminal. As shown in Fig.1, the length is 376m. The thickness of the covering soil above the tunnel is 8.6-10.2m, line spacing is 12m, internal diameter of shield tunnel is 5400mm, thickness is 300mm, width is 1200m. Construction used earth pressure balance shield machine[3].

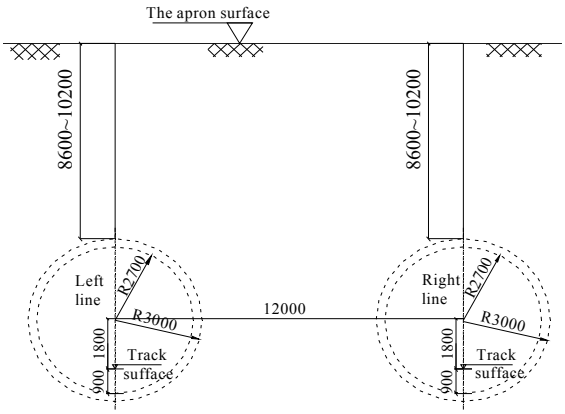


Fig.1 Shield tunnel under apron profile sketch

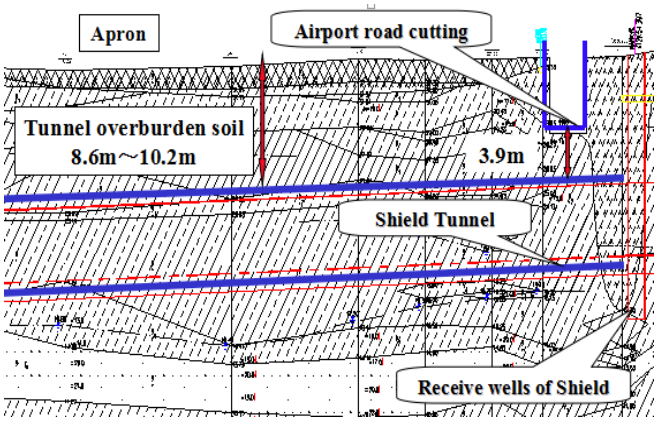


Fig.2 Geological section of shield crossing the apron

**Geological and hydrological conditions.** As shown in Fig.2, the shield machine mainly cross the silty clay④, clay④second layers, some local cross silty sand④third layers, which belong to soft soil layer. The water which tunnel shield crossed involved two layers: The one is perched water, buried depth of groundwater is 3.46-3.80m; The other one is Interlayer diving, buried depth of groundwater is 15.7-19.5m. Water is larger.

## Engineering characteristics

(1)The control of ground subsidence is very strict, which leads the difficult construction. Due to the particularity of the airport apron, especially the plane taxiing area have a high demand to the sedimentation value of surface, the control standard of sedimentation value by airport management department is: the maximum subsidence control values allowed by surface should no more than 20mm, which made it very hard to control the surface sedimentation for double lines shield tunnel crossing.

(2) Covering soil is shallow, which has large disturbance to the formation.

(3) The formation is mainly saturated silty clay, and has a high level of underground water.

## Soil pressure management techniques of tunnel shield excavation

**Working soil pressure setting of tunnel shield.** The soil pressure value could calculate according to "Static soil pressure+ hydraulic pressure+ the reserved pressure" [4], but the static soil pressure value is difficult to determine, under the general, we can make the measured value of the soil pressure gage on excavation face when the shield stop approximately as the target soil pressure set point. According to the calculation and initial tunneling debugging, the target soil set point is 55~70 Kpa.

**Keep excavation surface soil pressure balance.** In order to control surface stability, we must keep formation soil pressure P and soil pressure in the sealed cabin P0 for a dynamic balance by the management of target soil pressure. This balance, can realize by adjust and control the dump soil mass of screw conveyer.

As shown in Fig.3, it is the relationship between excavation surface pressure difference $|P-P|$ and the dump soil mass of screw conveyer when tunneling. It is clear that the value and range of change of soil pressure is an important factor for excavation surface stability. In order to make the screw conveyer dump regularly, and ensure the soil pressure of excavation surface, target of soil

pressure management also contained mud add amount (mud property involved), Jack advancing speed, Cutting knife plate speed control etc. Therefore, the target work pressure management actually is an integrated management of technology. As shown in Fig.4, through the adjustment of soil pressure above, soil pressure stability was realized.

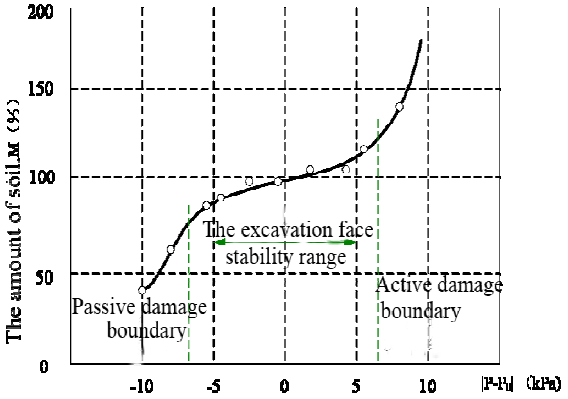


Fig.3 The relationship between pressure change and the amount of soil

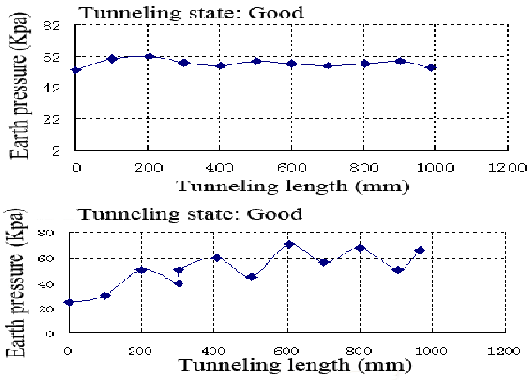


Fig.4 Variation graph of soil pressure in indoor soil which excavating a ring indoor

**The management of excavation soil mass.** Whether there is a balance between excavation soil mass and dump soil mass has a big impaction to excavation surface soil pressure[5]. Fig.5 shows the relationship between excavation soil mass and dump soil mass of one circle when tunneling. As shown in Fig.5, if excavation soil mass bigger than dump soil mass, the soil pressure has a tendency to rise, or the soil pressure has a tendency to reduce.

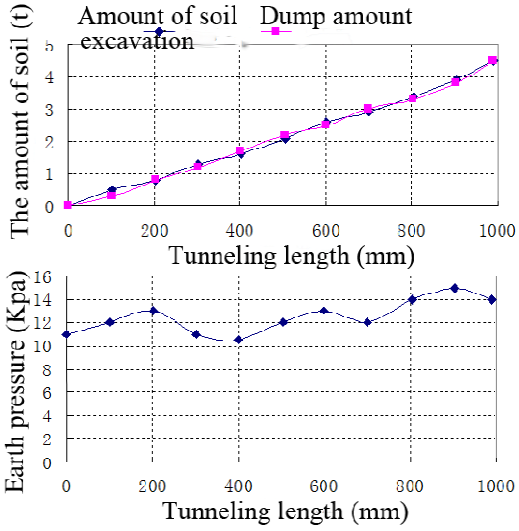


Fig.5 The relationship between the amount of excavated soil, soil volume and soil pressure

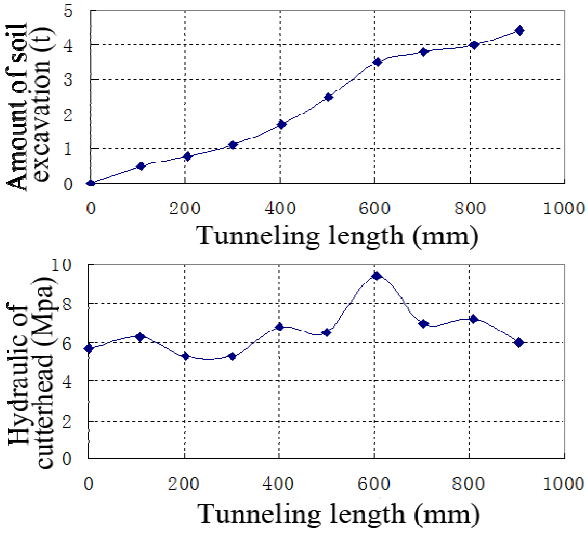


Fig.6 The relationship between excavated soil volume and hydraulic cutter

As shown in Fig.6, the tunnel shield excavation soil mass management requirements is to make the amount of soil digging and dump equal volume of soil Through adjust oil pressure of cutter head and screw conveyer when construction to realize the balance of excavation soil mass and dump soil mass. But these parameters are changing constantly as the shield tunneling, so, it's too hard to make excavation soil mass and dump soil mass strictly equal to each other, there are some fluctuation between them in engineering practice.

### Synchronous grouting and multiple supplement grouting

**Synchronous grouting.** Synchronous grouting use double(A,B) slurry, when the shield advance about 100 mm, send the A and B slurry respectively through the two grouting pumps on the trolley, and intensively mixed in the hybrid tube of the machine head then outpoured by the grouting lines on the shield shell, the synchronous grouting would begin, When pushed over 900 mm then the synchronous grouting completed. After every synchronous grouting the grouting lines should be cleaned by the high pressure water pipe in the head.

In this engineering, the pressure of the synchronous grouting inlet was chosed 1.1 ~ 1.2 times of static soil pressure, grouting pressure≤0.28Mpa. Synchronous grouting quantity was nearly about 140％ of the theory of clearance, which was 1300L per circle; Synchronous grouting began meanwhile with lining away from shield tail and tunneling, and should complete before one circle driving completed.

**Twice (or more times) grouting.** Twice (or more times) grouting mainly make up for the inadequacy of synchronous grouting, Therefore the slurry property are obviously different from synchronous grouting slurry. The fineness of slurry material should be smaller and fluidity of slurry should be better, it was necessary to adding retarder to prolong the setting time. Meanwhile, in order to increase the strength of slurry, bentonite must be abandoned. The grouting pressure should be some smaller, the time might extend appropriately, which is long time and low pressure. Twice grouting: 700L/2 loop, grouting pressure ≤0.3Mpa；Three times grouting: 500L/2 loop, grouting pressure ≤0.35Mpa.Twice, three times supplement grouting use the injected hole on the 4 ~ 6 slices with loop after the tunnel shield to complete.

### Deep hole fracturing grouting technology inside the tunnel hole

In order to control the surface subsidence value of the airport apron, after the shield machine went through, the deep hole fracturing grouting technology[6] was introduced to compact and split the soil with disturbance, to jacking and strengthen formation a little to ensure the final settlement of apron was controlled within the allowable range.

Specific practices are as follows: reserved grouting hole at its top segment, each loop is 2-3 ones, mainly upward direction, as shown in Fig.7, the depth of grouting in this engineering is 6m; Grouting hole diameter 84 mm. Slurry was double grout and grouting volume and pressure should be adjusted according to monitoring data timely.

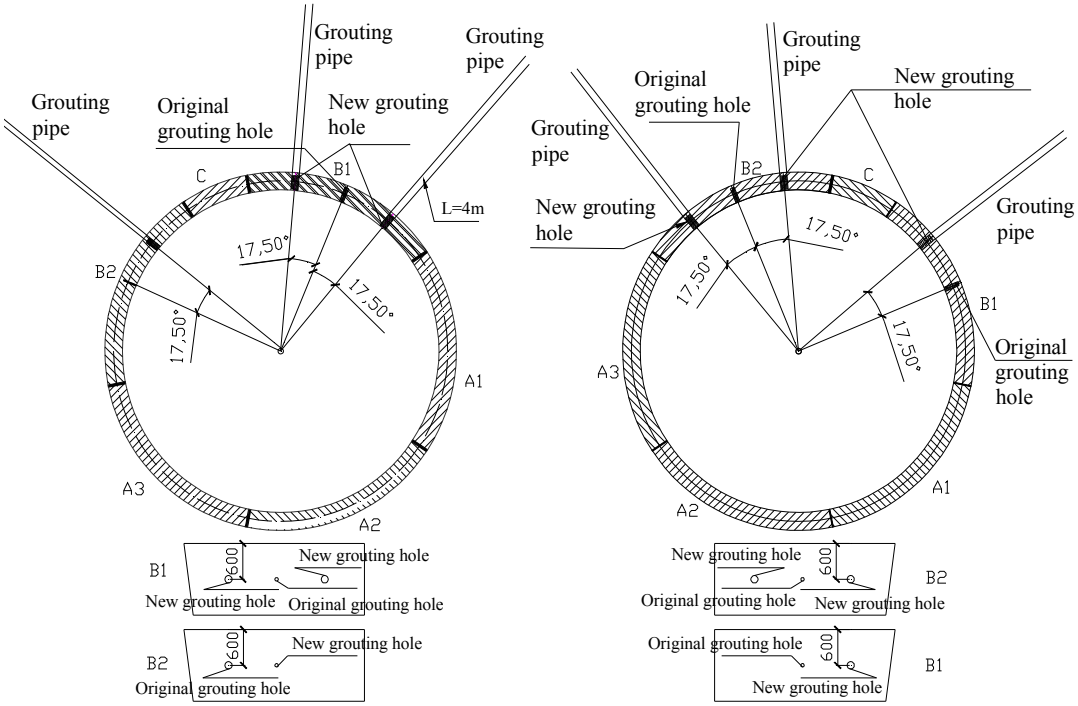


Explanation:
1, the new grouting hole locations acrossing the tube sheet steel can be adjusted.
2, the new grouting hole diameter 84mm. Grouting pipe depth is 4m.

The distribution map of the added grouting hole on B1, B2 segment

Fig.7 Schematic diagram of deep hole grouting

**Other technology measures**

1) Before entering the apron 50 meters as the apron simulation period, completely simulated tunneling according to the operation requirement when tunnel shield cross the apron[7], strengthened the monitoring, summarized the construction parameters to provide the basis for the formal construction of crossing the apron.

2) Verify each control point coordinates and elevation in detail, especially on curve and vertical curve, determined shield tunneling line based on design curve deviant and vertical curve modification value and control the tunneling posture of shield machine to avoid deviation.

**Monitoring results**

Based on the data analysis of whole process crossing, and due to limited space, monitoring results of midcourt line which through the right line were chosed was shown in Fig.8.

Monitoring results showed that the maximum subsidence of right line is18 mm, which means taking these effective technical measures ensure the safety of apron when shield machine crossing.

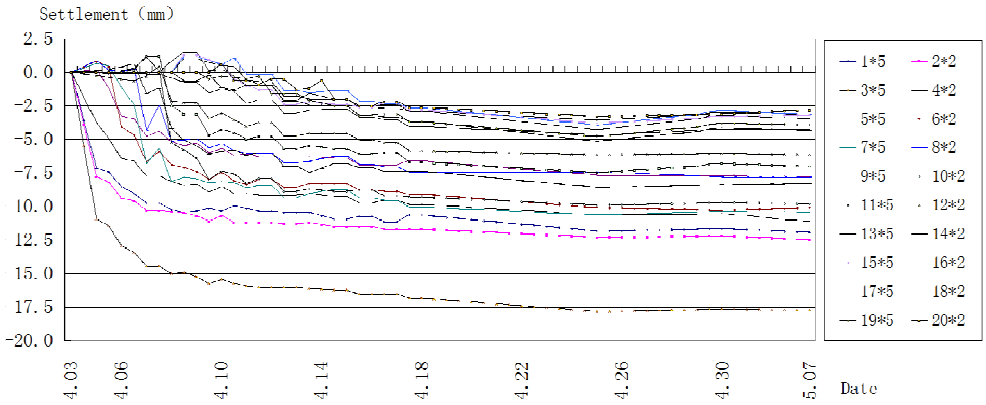


Fig.8 Settlement graph of right tunnel centerline monitoring points

## Conclusion

1) When advanced in shallow overburden soil and saturated silt and silty clay (local of sand layer) , because of the low strength of soil, the stability is poor, formation displacement increases, surface subsidence control is difficult, and airport management requirements of the surface control values is very strict, during the construction process, based on optimizing shield tunneling parameters, taking dynamic soil pressure control technology, secondary grouting technique and deep hole fracturing grouting technology, sedimentation valve was controlled within the target value, to ensure the safety and speed when the shield crossing.

2) Due to the particularity of the airport apron, In order to ensure the safety of the aircraft taxiing and parking, strengthen the construction of monitoring, monitoring data timely feedback operation surface to ensure the safety of apron during the shield crossing.

## References

[1] Gao Ailin, Ma Xuemei, Jin Huai, ect. Deformation of airport apron caused by shield tunnel passing[J]. Urban Rapid Rail Transit, 2010, 01:74-77.(In Chinese)

[2] Wang Ning, Zhou Shuming, Song Chaoye. Numerical simulation analysis for tunnel construction beneath adjacent parking apron [J]. Shanxi Architecture, 2010, 15:329-330.(In Chinese)

[3] Li Xinggao, Yuan Dajun, Yu Jiao. Study on construction method of tunnels underneath airport[J]. Science and Technology Innovation Herald. 2013,31:2-3. (In Chinese)

[4] Mei Lesheng. The excavation simulation analysis of the tunnel pass through the airport running[D]. Chongqin, Chongqin transport University, 2012.(In Chinese)

[5] Zhou Linshen, Chen Xuejing. The construction of shield machine pass through the airport arpon[J]. BeiJing, Special Structures, 2008,03:76-79.(In Chinese)

[6] Song Chaoye, Zhou Shuming, Wang Ning. Design and construction of shield tunnel beneath adjacent parking apron and u-shaped groove. Construction Technology, 2007, 36(11): 75-77+92.(In Chinese)

[7] Wu Xingliu, Liu Huimin. Study on the surface subsidence of metro shield tunnel passing through the apron. Journal of Shijiazhuang Tiedao University(Natuar Science). 2013, S2: 77-80.(In Chinese)

*Applied Mechanics and Materials Vols. 580-583 (2014) pp 1203-1206*
*© (2014) Trans Tech Publications, Switzerland*
*doi:10.4028/www.scientific.net/AMM.580-583.1203*

# Optimization of construction method for Shijiazhuang Xinbai Subway Station

Chunyan Gao[1, ,2,a], Jianguang Niu[2,b] and Dongyang Geng[2,c]

[1]School of Mechanics & Civil Engineering,China University of Mining & Technology(Beijing),China

[2]School of management science and Engineering,Shijiazhuang University of Economics,China

[a]gaochunyan2010@163.com, [b]niujianguang10@163.com, [c]15200012621@139.com

**Keywords:** subway, scheme, model.

**Abstract.** To choose an appropriate construction scheme for subway, it's feasible to use fuzzy optimization theory and comprehensively consider the security of four construction methods as well as such factors as environmental influence, construction period, construction difficulty and construction cost, etc. to set up a mathematical model for the construction method of subway station. An analysis is made on the impact of group-effect in the excavation construction of pilot tunnel presented in PBA construction method on arch crown settlement and ground surface settlement, and a study is made on the arch crown settlement and ground surface settlement caused by the four construction methods in construction process. In addition, a contrastive analysis is made to draw a conclusion that PBA construction method is the most suitable construction method for Xinbai Square Subway Station in Shijiazhuang.

## The establishment of multi-objective fuzzy model

The establishment of a decision set, that is, a tentative construction scheme for Xinbai Square Subway Station is as follows:

$$D=\{d1，d2，d3，d4\}. \tag{1}$$

In the set, d1 refers to PBA construction method, d2 refers to twin-side heading method, d3 refers to center drift excavation method, and d4 refers to NTR construction method.

The following is the factor set affecting the construction methods for subway:

$$U=\{u1，u2，u3，u4，u5\}. \tag{2}$$

In the set, u1 refers to safety influence; u2 refers to environmental influence; u3 refers to impact of construction duration; u4 refers to impact of construction difficulty; u5 refers to impact of construction cost.

After the above is summed up, the fuzzy optimization matrix R of alternatives for five indicators is shown below:

$$R=\begin{pmatrix} r_{11} & r_{12} & r_{13} & r_{14} \\ r_{21} & r_{22} & r_{23} & r_{24} \\ r_{31} & r_{32} & r_{33} & r_{34} \\ r_{41} & r_{42} & r_{43} & r_{44} \\ r_{51} & r_{52} & r_{53} & r_{54} \end{pmatrix} \tag{3}$$

## Comparison of security

As per field measured data, the final arch crown settlement value of each construction method is extracted for comparison, as shown in Table1.

Table1 Comparison of arch crown settlement

| Construction methods | Final arch crown settlement (mm) |
|---|---|
| PBA construction method | -40.2 |
| Twin-side heading method | -73.9 |
| Center drift excavation method | -68.2 |
| NTR construction method | -11.3 |

The values in Table1 show that NTR can minimize the value of arch crown settlement, and the value of settlement doesn't increase suddenly in each simulated construction procedure. For the sake of safety, among the four construction methods, NTR construction method is the most suitable one for the complex environment of Xinbai Square Subway Station Work, followed by PBA construction method, with twin-side heading method at the bottom.

As for safety influence, NTR construction method is a little better than PBA construction method, rather better than center drift excavation method, and significantly better than twin-side heading method, so the following is worked out:

$$1r = (1r1,\ 1r2,\ 1r3,\ 1r4) = (0.818, 0.429, 0.538, 1). \quad (4)$$

**Comparison of the impact on the surroundings**

Measured value shows that NTR can minimize the value of ground surface settlement upon the completion of construction, the construction method can reduce the value of ground surface settlement to 0.3 and 1.4 in the places ±14m away from the symmetric axis of subway station; When PBA construction method is used, the value of ground surface settlement in each observation point is greater than that when NTR construction method is used, and the value of ground surface settlement is only 187 and 18.6 in the places ±14m away from the symmetric axis of subway station; compared to NTR construction method and PBA construction method, twin-side heading method and center drift excavation method cause a much larger value to ground surface settlement. As per the contrast analysis of the four construction methods, NTR construction method is the best one, while center drift excavation method is the worst one, from the perspective of the impact on the surrounding buildings.

In addition, the size of ground surface settlement can also reflect the impact of construction on underground utilities to a certain degree, that is to say, the smaller the size of ground surface settlement is, the weaker the impact of the settlement on underground utilities will be. Anhydrous operation is essential for PAB construction method, twin-side heading method and center drift excavation method, namely, underground water level must fall below working face. This will cause consolidation and shrinkage to soil void, and very precocious and large-scale deformation and settlement to earth surface, which will produce a particularly great impact on environments. However, NTR construction method includes a perfect waterproof design, which is conducive to soft foundation and water-rich sandy land. Construction precipitation is not available, lest surface subsidence should occur. In conclusion, from the perspective of an impact on environment, NTR construction method is optimal and center drift excavation method is worst.

Environmental impact serves for a qualitative index, and the method for the determination of the relative superiority of qualitative index is adopted. As for environmental impact, NTR construction method is a little better than, rather better than twin-side heading method, and significantly better than center drift excavation method, so the following is worked out:

$$2r = (2r1,\ 2r2,\ 2r3,\ 2r4) = (0.818, 0.538, 0.429, 1). \quad (5)$$

**Comparison of construction difficulty**

When PBA construction method is adopted, heading construction should be implemented in advance; afterwards, in the pilot tunnel, construction should be implemented for fender post, middle column,

floor beam and head beam. However, operating conditions are poor and construction space is small inside the tunnel, so it's very difficult to implement construction. After beam column is completed, vault construction will be implemented. The section size of Shijiazhuang Xinbai Subway Square is very large, which adds to the difficulty of arch crown construction.

In spite of the fairly mature construction technique for twin-side heading method and center drift excavation method, both construction methods adopt partition excavation, and use grill steel frame, wire mesh, and pneumatically placed concrete flexible supporting system to implement construction timely, so that fracture surface should be closed as soon as possible and construction should be simple. However, due to the impact of preliminary bracing and cross strut, before second lining is established, it's necessary to explode preliminary bracing and dismantle cross strut, for stress transformation is needed for the lining. In this process, it's necessary to ensure the safety and stability of preliminary supporting system. If only part of second lining is established, the quality of concrete and waterproofing layer can't be guaranteed. If the full section is established, there will be a great potential safety hazard when preliminary bracing and supporting system is dismantled.

For NTR construction method, construction should be implemented inside steel tube. However, due to the limited space and more joints of reinforcement inside a steel tube, a great many connectors are needed. In the same time, second lining concrete can't be tamped but can only be processed as per pouring sequence and pouring measures in construction process. Also because of the features of NTR construction method, the construction for each of its tube awnings is an independent working plane. During the construction period for tube awnings, in each steel tube there should be separately set ventilation and lighting facilities; in addition, such facilities as transport rail, etc. are needed as well, which adds to the difficulty of engineering construction. Therefore, a conclusion can be drawn that twin-side heading method is the same to center drift excavation method concerning the impact of construction difficulty. Twin-side heading method is a little better than PBA construction method and significantly better than NTR construction method, so the following is worked out:

$$4r = (4r1,\ 4r2,\ 4r3,\ 4r4) = (0.667,\ 1,\ 1,\ 0.333). \tag{6}$$

**Comparison of construction cost and duration**

As a quantitative index, construction cost and duration are represented by determined values. Detailed value of partial costs and construction duration should be offered to the designing institute and construction side. The value of partial costs is shown in Table 2.

Table2 Value of partial costs (unit: ten thousand yuan)

| Partial costs | PBA construction method | Twin-side heading method | Center drift excavation method | NTR |
|---|---|---|---|---|
| Cost of labor | 2058.27 | 1743.63 | 1848.51 | 2932.71 |
| Cost of materials | 11052.8 | 9363.2 | 9926.4 | 15748.48 |
| Cost of construction machinery | 1441.26 | 1220.94 | 1294.38 | 2053.57 |
| Disposal costs | 785 | 665 | 705 | 1118.5 |
| Management cost | 362.67 | 307.23 | 325.71 | 516.75 |
| Total | 15700 | 13300 | 14100 | 22370 |

The time limit for the project will be 32 months for PBA construction method; 30 months for twin-side heading method; 30 months for center drift excavation method; 36 months for NTR construction method.

Both construction cost and construction duration are a quantitative index, and the following is obtained based on the method for the determination of the relative superiority of quantitative index:

3r =(3r1， 3r2，3r3，3r4)=( 0.67, 1 ,1, 0). (7)

5r =(5r1， 5r2，5r3，5r4)=( 0.735, 1 ,0.912, 0). (8)

After the above is summed up, the fuzzy optimization matrix R is worked out:

$$R_{4\times5}=\begin{pmatrix} r_{11} & r_{12} & r_{13} & r_{14} \\ r_{21} & r_{22} & r_{23} & r_{24} \\ r_{31} & r_{32} & r_{33} & r_{34} \\ r_{41} & r_{42} & r_{43} & r_{44} \\ r_{51} & r_{52} & r_{53} & r_{54} \end{pmatrix}=\begin{pmatrix} 0.818 & 0.429 & 0.538 & 1 \\ 0.818 & 0.538 & 0.429 & 1 \\ 0.67 & 1 & 1 & 0 \\ 0.667 & 1 & 1 & 0.333 \\ 0.735 & 1 & 0.78 & 0 \end{pmatrix}. \quad (9)$$

**Calculation of weighted value**

Determine a judgment value for the comparison of each two factors

Create a judgment matrix

e11=1;e12=1; e13=3; e14=5;e15=5.

A judgment matrix is created:

$$E=\begin{pmatrix} e_{11} & \cdots & e_{1m} \\ \vdots & \ddots & \vdots \\ e_{m1} & \cdots & e_{mm} \end{pmatrix}=\begin{pmatrix} 1 & 1 & 3 & 5 & 5 \\ 1 & 1 & 1 & 3 & 5 \\ \frac{1}{3} & 1 & 1 & 1 & 3 \\ \frac{1}{5} & \frac{1}{3} & 1 & 1 & 1 \\ \frac{1}{5} & \frac{1}{5} & \frac{1}{3} & 1 & 1 \end{pmatrix}. \quad (10)$$

**Fuzzy synthetic evaluation system**

The compound operation of weight matrix A and fuzzy relation matrix B works out:

D= A ×R={0.773，0.648，0.645，0.703}. (11)

The computation result shows that NTR construction method, though better than other construction methods in the aspect of settlement control, is inferior to other ones in the aspect of construction duration, construction difficulty and construction cost. The computation result shows that the synthesis score of PBA construction method is 0.773, higher than that of other construction methods, which indicates that PBA construction method is the most suitable method for Xinbai Square Subway Station after such factors as environmental impact, construction duration, construction difficulty and construction cost, etc are taken into overall consideration.

**Acknowledgments**

This work was financially supported by The Doctoral program of Higher Education Research Foundation (20120023110007), Technical Economics and Management of Academic Discipline Project of Hebei .

**References**

[1] Wanbo QU,Xinrong LIU, Ruijin HUANG and Mingzhong LIU, in： Railway Engineering,(2012).in Chinese.

[2] Ruijie CHANG, in：Urban Rapid Rail Transit,(2010).in Chinese.

[3] Wanying HUANG,Jianxin LIU, in： Journal of Guangdong Communications Polytechnic,(2013).in Chinese.

*Applied Mechanics and Materials Vols. 580-583 (2014) pp 1207-1211*
*© (2014) Trans Tech Publications, Switzerland*
*doi:10.4028/www.scientific.net/AMM.580-583.1207*

# Study on Classification and Regulation for Defects on Railway Tunnel

Jingwei Zhang[1,a],Shuai Wang[2,b],Huixuan Huang[2,c]

[1]Civil Engineering School, Southwest Jiaotong University, Chengdu 610031, China

[2]Dacheng Headquarters, the Xibei Company, the Tenth Bureau Group, CREC, Nanchong637000, China

[a]jwzhang1990@yeah.net,[b]16099305@qq.com,[c]408420228@qq.com

**Keywords:** Railway tunnel, quality defects, regulation classification, project design, treating techniques.

**Abstract.** Quality defects and diseases will happen to railway tunnel after it in operation four to five years later, such as lining split, water leakage and landslide of second lining. Based on the case of Goujiagou tunnel located at Ⅳ surrounding rock with mudstone and sandstone, the regulation for this tunnel is put forward; the causes and characteristics of all kinds of defects are analyzed by studying on the particularity of railway tunnel construction. Based on different extend of injury, the classification of the same type defect is proposed. Research results indicate that the regulation design is feasible and the treating technique is appropriate by using new technology, methods and materials. The results will provide reference to design for the same type tunnel regulation.

## Introduction

Quality defects mainly include lining thickness, imperfect, hollow behind the lining, bad waterproof system and so on; disease mainly include lining split, morphology and seepage which caused by quality defects and other external factors. There is a causal connection between defects and disease, and the former is the cause of the latter. Yinming LU analyzed the classification of tunnel disease and the reasons on the existing tunnel [1]; Xiaojun XIANG determined the different regulation schemes, and introduced the construction technology according to Longquanshan tunnel [2].

These studies are too simple to solve tunnel defects and lacking of creativity so that it could not be able to governance defects timely and effectively. Also regulation should be different because the same defects vary in degree, and research work in this field is not enough. We should improve the treating techniques and adopt new technologies and materials because of the limitation of existing construction in span time.

## Engineering Situation

This is a double-track railway tunnel in speed of 160km/h mixed passenger and freight. Most of surrounding rock isⅣ and other is Ⅴ.The rock type is mudstone and sandstone.

By using ground penetrating radar to identify the causes of detects in further development of nondestructive testing. The biggest density in the section of 105m（K0+000~+105）, 31cavities in arch lining; 2 insufficient lining thickness; 14 less dense of concrete; 6 lining split without seepage; 17 water leakage etc.

## Analysis of Causes of Defects

In terms of this tunnel, there are basically the following several aspects:

**The Geological Reasons**. The tunnel through the hill with denudation and groove valley landform where distribute of powder clay. Some tunnel diseases are caused by the geological reasons which have effect on tunnel lining, such as lining deformation and split. The surrounding rock is poor and loose. Vertical load of loosely pressure on arch will lead to tensile crack along the longitudinal easily;

horizontal strata structure will lead to plastic extrusion and gravity collapsing possibly in loose rock mass; the swelling soil pressure will lead to horizontal cracks on side wall or spandrel etc.

**The Construction Reasons.** This tunnel constructed by means of Center Diaphragms (CD).According to the confirmation with drilling, some cavity behind lining split caused by over-break. Poor quality of compaction of concrete leads to less dense of lining; improper handling measures of waterproof and drainage will lead to expansion joint seepage etc; thus it can be seen that imperfect quality of control system is the main causes of quality defects.

**Underground Water Development.** When there are cavities behind lining, groundwater will be deposited in the formation of cystic fluid, increase the pressure of surrounding rock and lead to lining damage; loosing bearing capacity or happening plastic flow will lead to lining pressure increasing because of surrounding rock mudding or softening in mudstone and sandstone. Rock discontinuities and weak surrounding rock instability because of water will also lead to loss bearing ability of surrounding rock, thus increasing lining pressure. These factors are likely to destroy the structure.

**Other Reasons.** Tunnel lining is prone to be damaged in earthquake, because it belongs to support rigidity, and bending shear capacity is lower. Gas is another cause.

## Regulation Design

### Design Principle.

1）Using general, dynamic design, in line with safe, practical, reliable quality, reasonable economy, the principle of advanced technology

2） Try to use the existing lining structure performance, and repair damage areas timely and efficiently

3） Ensure safety and reduce the impact on line operation

4） Method and the process should be operability and safety

5） All of the empty and imperfect area behind the lining must be grouted

**Design Scheme.** The main reference resources are as follows: 1) investigation data 2) tunnel nondestructive testing report 3) topography, landform and geological conditions 4) completion data 5) related specifications. This paper analyzes the cause of defects and disease. The regulation design is based on the experience of the past. Table. 1 shows the characteristics of the regulation and classification.

Table. 1 The characteristics of the regulation and classification

| Package type | Regulation measure | Suitable objects | Process method | Level |
|---|---|---|---|---|
| Structure reinforcement | Chisel and repair-DCBZT-03 （as shown in Fig.1） | Thickness of plain concrete lining | Break lining --setΦ42Grouting and slurry pipe etc—implant shear rebar--Φ28 mechanical anchor bolt -- Steel fabricΦ6@10×10cm --sprayed Polypropylene fiber concrete support--24h grouting. | I |
| | W-Steel belt reinforcement-DCBZT-04 （as shown in Fig.2） | Thickness of lining between 10cm and 20cm;or staggering or crack length＞10m,width ＞2mm | W-Steel belt along the ring to decorate---spacing of 1m,Φ28mechanical anchor bolt -- Steel fabricΦ6@10×10cm -- sprayed Polypropylene fiber concrete support | II |
| | Combination structure-DCBZT-05 | Thickness of lining between 20cm and 30cm;or fracture development and cross distribution | W-Steel belt along the ring to decorate --Φ28mechanical anchor bolt at both ends—expansion bolt M20×200 -- Steel fabricΦ6@10×10cm -- sprayed Polypropylene fiber concrete support | Ⅲ |

| Package type | Regulation measure | Suitable objects | Process method | Level |
|---|---|---|---|---|
| | Straddle anchor-DCBZT-06 | Vertical or diagonal crack length＞5m, width＞0.5mm | Φ28mortar bolt along cracks—spacing of bolt is2 times the thickness of the lining -- Steel fabricΦ6@10×10cm -- sprayed Polypropylene fiber concrete support | IV |
| Leakage water treatment | Grouting behind lining-DCBZT-07（as shown in Fig.4） | Cavity and less dense of concrete | Cement mortar P.O.32.5;water cement ratio under0.38;FDN water reducer; stone rate ＞98%; detection compactness(sampling rate20%); | I |
| | Drainage by grooving-DCBZT-08 | Arch seepage or side wall water jetting | U-notch along ring direction to side ditch –laying rubber tube and fixed steel—cement paste and BR-2waterproof agent-- brushing area within two sides of cracks with waterproof coating. | II |
| Others | grouting and plugging-DCBZT-09 | Micro-flaws on the surface of Reinforced concrete lining | Grouting mouth--polish--wash—installation of grouting valve—plugging flaws—checking air pressure--grouting | I |

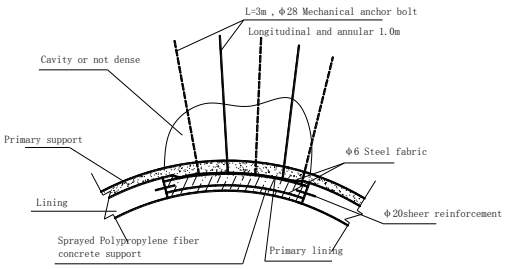


Fig. 1 Design of lining removing and repairing

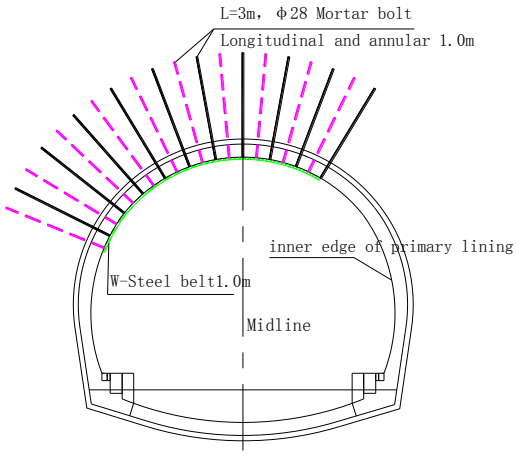


Fig. 2 Design of reinforcing with W-steal belt

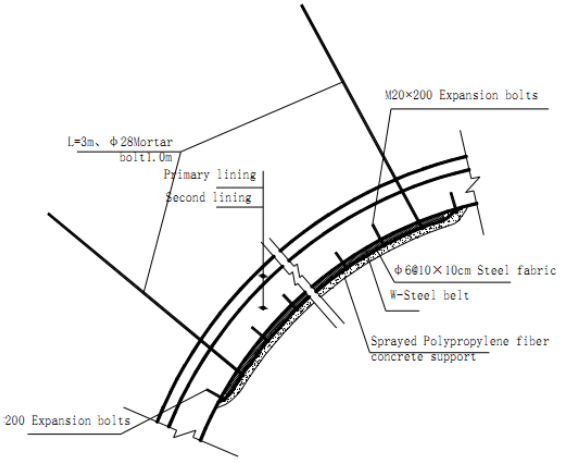


Fig. 3 Design of composite reinforcement

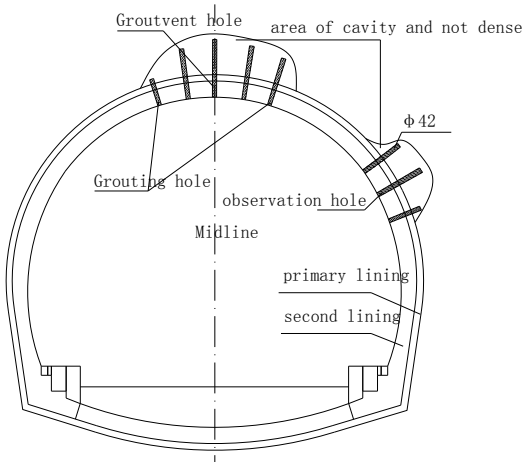


Fig. 4 Design of hollow grouting

## Classification and Treating Measures

Table 2 shows the classification and treating measure of lining thickness; Table 3 shows the classification and treating measures of defects behind lining; Table 4 shows the classification and treating measures of lining split and leakage.

Table 2 Classification and treating measures of lining thickness

| Grade of quality defects | A | B | C | Note |
|---|---|---|---|---|
| Classification basis | h＜10cm | 10cm≤h＜20cm | 20cm≤h＜30cm | |
| Parallelism measure | DCBZT-03 | DCBZT-04 | DCBZT-05 | |

**Where** h is the thickness of tunnel lining.

Table 3 Classification and treating measures of defects behind lining

| Grade of quality defects | | A | B | C | D | Note |
|---|---|---|---|---|---|---|
| Classification basis | Cavity | a＜20cm<br>or L≥5m<br>or P≥20cm | 20cm≤a＜35cm<br>or 3m≤L＜5m<br>or 11cm≤P＜20cm | 35cm≤a＜50cm<br>or 1m≤L＜5m<br>or 5cm≤P＜10cm | a≥50cm<br>or L＜1m<br>or P＜5cm | |
| | Not dense | —— | a＜30cm<br>or L≥8m<br>or P≥25cm | 30cm≤a＜60cm<br>or 3m≤L＜8m<br>or 10cm≤P＜25cm | a≥60cm<br>or L＜3m<br>or P＜10cm | |
| Parallelism measure | | DCBZT-07 | | | | |

**where** a is defects location begin with initial lining;
L is length of defects;
P is depth of defects.

Table 4 Classification and treating measures of lining split and leakage

| Grade of quality defects | A | B | C | D | Note |
|---|---|---|---|---|---|
| Classification basis | L≥10m<br>or W≥2mm | 5m≤L＜10m<br>or 1mm≤W＜3mm | 2m≤L＜5m<br>or 0.2mm≤W＜0.5mm | L＜2m<br>or W＜0.5mm | |
| Parallelism measure | DCBZT-04 | DCBZT-06<br>（side wall） | DCBZT-04（arch） | No processor<br>（plain concrete） | |
| | DCBZT-09（where leakage of water） | | | DCBZT-09（reinforced concrete） | |

**where** L is the length of cracks;
W is the width of cracks.

## Controlling Techniques of Construction

**Process of Grouting.** The process of grouting behind lining: according to the area of cavity and not dense, ensure hole location; grouting, observation and spout hole are from low to high to internal surface of cavity; spout hole could also play the role as grouting in sometimes; It is important in process of grouting to determine the length and opening size of notch, and it should be between primary and second to fill in the both lining by the way.

**Polypropylene Fiber Concrete.** The main difficulty of this process is that it should avoid populating railway track and track bed during concrete. So it is important to do the best to protect the structure with open tube and agricultural cloth. Lining Surface should be chiseled before concrete.

## Conclusion

The load model of tunnel structure is changeable. Surrounding rock change with time and development of groundwater and external disturbance; the cause of tunnel disease is various, and the limitation of non-destructive testing with geological radar, such as the limited Survey Line, The strong

interference of steel arch to testing results. For the above reasons, we can't find out the situation of quality defects and disease fully.So we should adjust the design according to the site condition.

There is a large quantity of leakage. The application effect of "combine caulking with draining" in the treatment is good, but it remains to be further tested during the rainy season; the carbon fiber cloth was not adopted,and the reason is that zone of Tension and compression is Not easy to be determined and it is poor durability; the final solution of W-Steel belt combined with sprayed Polypropylene fiber concrete support not only achieved, but also belongs to flexible support;the construction technology of mortar bolt has reference significance for existing railway for the speediness of pore-forming and good effect of grouting.

The research results were adopted in the remaining 11 tunnel.

**References**

[1] Yingming LU, Liwei CHEN. Both the phenomenon of tunnel disease classification and the reason analysis [J].Railway Engineering, 2010(11),46-49.(in Chinese)

[2] Xiaojun XIANG. Treatment of defects in Longquanshan tunnel[ J]. Modern Tunneling Technology, 2005(2), 65—71. (in Chinese)

[3] Guang HUANG, Wenge QIU, Huijian ZHANG. The level of tunnel rock failure mechanism and the construction countermeasures [J]. Pioneering With Science & Technology Monthly, 2012（10）, 188-190.(in Chinese)

[4] Livei CHEN. Discussion on die investigation methods of tunnel defects and their countermeasures[J]. modern tunneling technology, 2004(2) 53—57. (in Chinese)

[5] Changchun ZHU . Reparation technology of Road tunnel lining crack[J]. geotechnical word, 2004(9), 67~68.(in Chinese)

[6] Hai-jing LIU, Cai-chu XIA, He-hua ZHU. Studies on Tunnel Damage[J].Chinese Journal of Underground Space and Engineering,2007（3）,947~953. (in Chinese)

[7] Baoshu GUAN . Focus of maintenance and management of Tunnel Engineering [M].People's Communication Press, Beijing 2004. (in Chinese)

[8] The Working Bureau in Ministry of Railway, the handbook of railway operation(tunnel)[M].the Railway Press of China Beijing 1997. (in Chinese)

[9] Xin Luo, Zhibin Li, Jiayan Zheng. Study on defects behind the lining of road tunnels[J].Modern Tunnelling Technology 2006(supp):79—82.(in Chinese)

*Applied Mechanics and Materials Vols. 580-583 (2014) pp 1212-1217*
*© (2014) Trans Tech Publications, Switzerland*
*doi:10.4028/www.scientific.net/AMM.580-583.1212*

# The dynamic response of Zhengyangmen gate tower induced by Beijing metro line 2

Song Qi[1, a], Guo Jiaqi[2,b], Chen Wenhua[3,c], Guo Ping[4,d]

[1] School of Civil Engineering, Beijing Jiaotong University, Beijing 100044, China

[2] China Datang Technologies & Engineering Co.,Ltd., Beijing 100097, China

[3] School of Civil Engineering, Beijing Jiaotong University, Beijing 100044, China

[4] Civil Engineering Postdoctoral Station, Beijing University of Technology, Beijing 100124, China

[a]songqi2012@gmail.com, [b]jqguo@sohu.com, [c]whchen@bjtu.edu.cn, [d]zdhuagp@163.com

**Keywords:** Zhengyangmen gate tower; subway vibration; vibration velocity; vibration displacement

**Abstract.** Zhengyangmen gate tower is a national emphasis cultural relic unit along the north-south axis of Beijing, which is above the Beijing metro line 2. Based on dynamic analysis model of gate tower and the position of gate tower and subway, the dynamic response characteristics of gate tower induced by Beijing metro line 2 are calculated, and compared with the in-site vibration test data.

## Introduction

With the development of metro, the vibration caused by subway train has negative effects on people's life, the normal use of equipment, and the safety of buildings, especially the ancient architectures.

The ancient architectures are much fragiler as time passes, and the subway vibration will make it worse. So, the dynamic research of the ancient architectures induced by subway vibration becomes more and more important. The in-site vibration test is widely used to direct the dynamic response of the ancient architectures under the effect of existing subway vibration, and the theory research are not mature.

In this paper, taking Zhengyangmen gate tower (as shown in Fig.1) for example, the dynamic characteristics of gate tower are calculated by theory method.

Fig.1 Zhengyang Men gate tower

**Vibration of subway train**

The dynamic equation is set by the dynamic model of subway train, and the vibration of subway train is calculated by solving the equation (Eq.1).

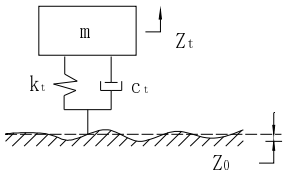


Fig.2 Dynamic model of train

$$m\ddot{Z}(t) + c_t[\dot{Z}(t) - \dot{Z}_0)] + k_t[Z(t) - Z_0)] = 0 \quad (1)$$

where m is 11048kg,$k_t$ is 1050kN·m$^{-1}$,ct is 24000kN·m$^{-1}$.

The vibration displacement and velocity of subway train are shown as Fig.3and Fig.4.

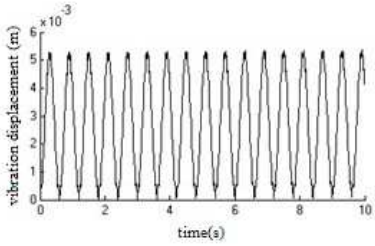


Fig.3 Displacement time history of irregular excitation of train

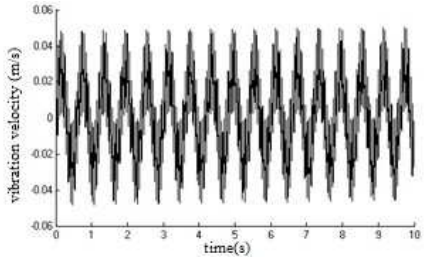


Fig.4 Velocity time history of irregular excitation of train

**Dynamic model of gate tower**

The space coordinate (Fig.5) is set by the position of gate tower and metro line 2, and simplified into2-D plane problem (Fig.6).

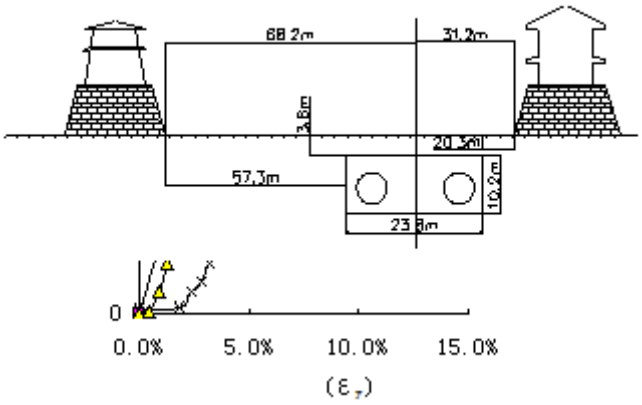


Fig.5 The position of gate tower and metro line 2

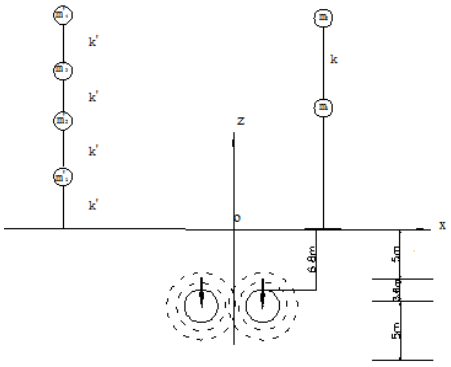


Fig.6 Dynamic model of gate tower under the action of subway

As shown in Fig.6, the propagation distance of the vibration of subway train is short in silt strata, so it is assumed that the propagation route of train vibration is direct and the vibration is spread as wave P. When the vibration reaches the bottom of gate, the direction of propagation can be decomposed into two, one is along X axis and the other is along Z axis.

The dynamic equation of gate tower is set as follow:

$$M\ddot{u} + C\dot{u} + Ku + MI\ddot{u}_p(t) = 0 \quad (2)$$

Where M is mass matrix of gate tower, C is damping matrix of gate tower, K is rigidity matrix of gate tower, I is unit vector, u is the vibration displacement of gate tower, $\ddot{u}_p(t)$is the vibration acceleration of subway train.

## Dynamic response of gate tower

### 3.1 under right tunnel subway train vibration

The dynamic characteristics of gate tower are calculated as follow (Fig.7-Fig.10), when the gate tower is affected by right tunnel subway train vibration.

When the vibration propagates along X axis, the gate tower vibrates along X axis.

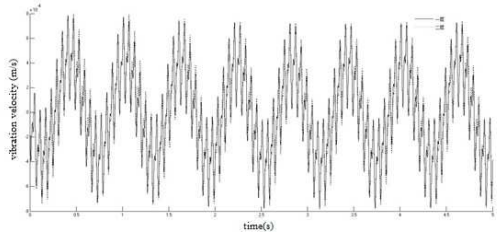


Fig.7 Velocity time history of gate tower along X axis

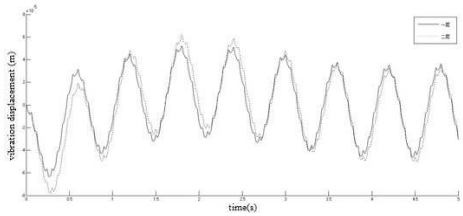


Fig.8 Displacement time history of gate tower along X axis

When the vibration propagates along Z axis, the gate tower vibrates along Z axis.

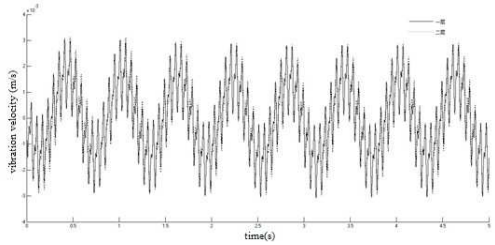


Fig.9 Velocity time history of gate tower along Z axis

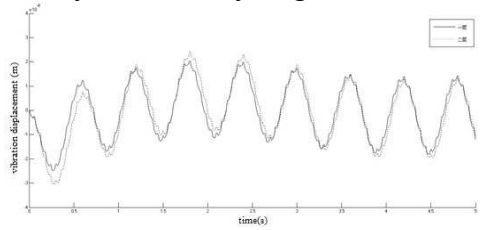


Fig.10 Displacement time history of gate tower along Z axis

### 3.2 under left tunnel subway train vibration

The dynamic characteristics of gate tower are calculated as follow (Fig.11-Fig.14), when the gate tower is affected by left tunnel subway train vibration.

When the vibration propagates along X axis, the gate tower vibrates along X axis.

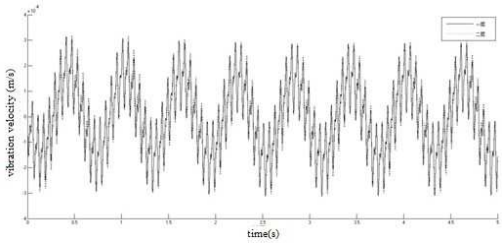


Fig.11 Velocity time history of gate tower along X axis

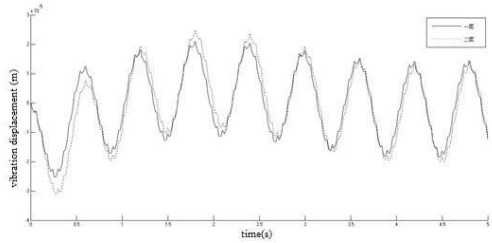


Fig.12 Displacement time history of gate tower along X axis

When the vibration propagates along Z axis, the gate tower vibrates along Z axis.

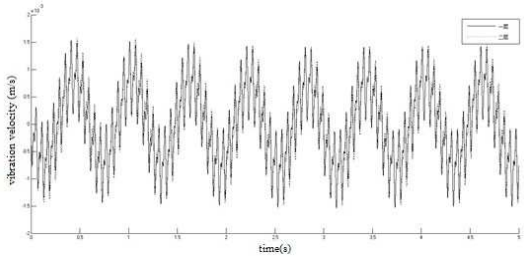


Fig.13 Velocity time history of gate tower along Z axis

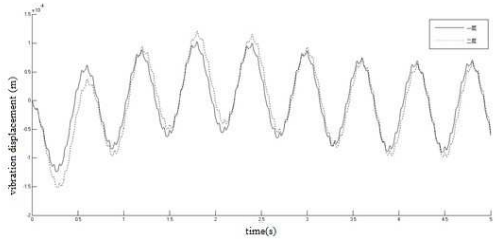


Fig.14 Displacement time history of gate tower along Z axis

### 3.3 under two tunnels subway trains vibration

The dynamic characteristics of gate tower are calculated as follow (Fig.15-Fig.18), when the gate tower is affected both by right and left tunnel subway train vibration.

When the vibration propagates along X axis, the gate tower vibrates along X axis.

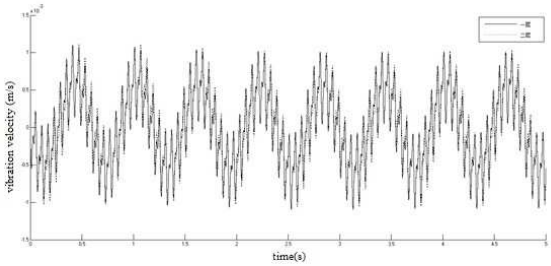


Fig.15 Velocity time history of gate tower along X axis

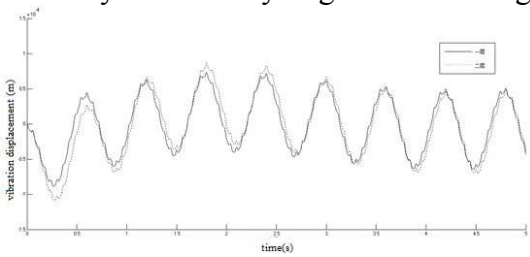


Fig.16 Displacement time history of gate tower along X axis

When the vibration propagates along Z axis, the gate tower vibrates along Z axis.

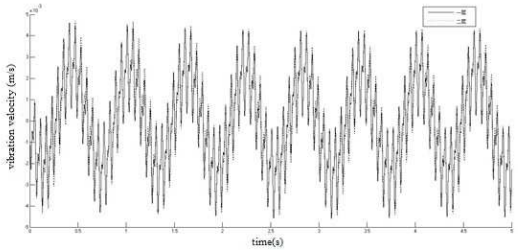


Fig.17 Velocity time history of gate tower along Z axis

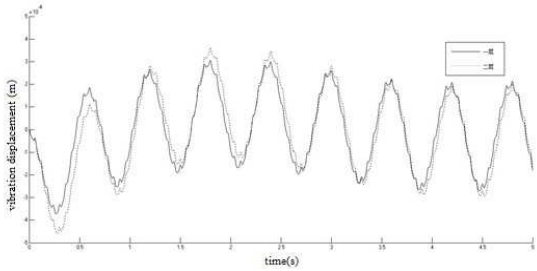


Fig.18 Displacement time history of gate tower along Z axis

### Summary

The vibration velocity of gate tower is analyzed by the spectral analysis method, and spectrogram is shown in Fig.19.

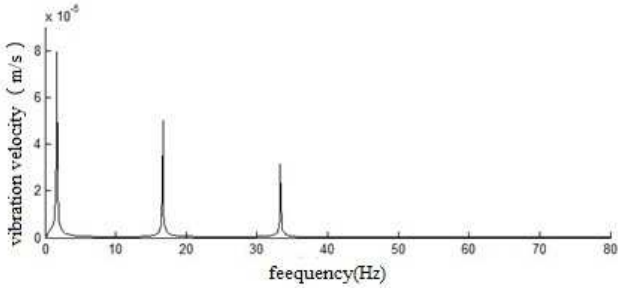


Fig.19 Vibration velocity frequency analysis of gate tower

The dynamic response characteristics of gate tower can be summarized as follow:

(1) The vibration displacement of gate tower increases with height, but the vibration velocity is almost same;

(2) The vibration displacement under the effect of two tunnel subway train is nearly double of one tunnel's, the vibration displacement maximum along X axis is 0.11mm,and the vibration velocity maximum is 1.15mm/s, which are a little bigger than the value of in-site test.

(3) The main vibration frequencies of gate tower are focus in three different frequencies, 1.8-2.1Hz, 15-17Hz, and 32-34Hz, which are same as the in-site test.

## References

[1] Song Qi. Dynamic Response of Zhengyangmen Ancient Architectures Induced by the Vibration of Subway and Ground Traffic[D]. Beijing Jiaotong University ,2014.

[2] Chen Guo, Zhai Wanming. Numerical Simulation of the Stochastic Process of Railway Track Irregularities[J]. Journal of Southwest Jiaotong University, 1999,34(2):138-142.

[3] Zhang Yu'e, Bai Baohong. The method of identifying train vibration load acting on subway tunnel structure[J].JOURNAL OF VIBRATION AND SHOCK,2000,19(3):68-76.

[4] Wang Xiangqiu, Yang Linde, Gao Wenhua. In-situ vibration measurement and load simulation of the raising speed train in railway tunnel[J]. JOURNAL OF VIBRATION AND SHOCK,2005,24(3):99-102.

[5] Qin Yazhou, Xu Jiancong. Numerical Simulation of Train Load by Time Domain Method[J]. Henan Science,2010,28(6):701-704.

[6] Feng Junhe, Yan Weiming. NUMERICAL SIMULATION FOR TRAIN STOCHASTIC VIBRATING LOADS[J]. JOURNAL OF VIBRATION AND SHOCK,2008,27(2):49-52

*Applied Mechanics and Materials Vols. 580-583 (2014) pp 1218-1222*
*© (2014) Trans Tech Publications, Switzerland*
*doi:10.4028/www.scientific.net/AMM.580-583.1218*

# Study on Investigation and Analysis of ExistingTunnel Diseases

Dongping Zhao[1,a], Xinrongtan[2,b], Lingli Jia[3,c]

[1]Research Division of Science and Technology Engineering, China Railway Eryuan Engineering Group Co. LTD, Chengdu 610031, China

[2]School of Civil Engineering, Southwest Jiaotong University, Chengdu 610031, China

[3]School of Architecture, Southwest Jiaotong University, Chengdu Sichuan 610031, China

[a]dpingzhao@163.com, [b]xy.tan@163.com, [c]jialingli@163.com

**Keywords:**Investigation, Analysis, Existing Railway, Tunnel Disease

**Abstract:** Due to the impactofgeological condition, climate condition, design, construction and other factors, the existing railway tunnelappears some diseases more and more, and even some diseases have serious influence to the normal use of tunnels and traffic safety. To eliminate these dangers, we should understand the typeof diseases and their causes. Based on the existing tunnel disease investigation and analysis,tunnel diseases were classified, the reason of tunnel diseases were analyzed, which can provide a reliable basis for the tunnel disease treatment. The result indicates that railway tunnel diseases include lining water leakage, lining structure disease, lining concrete disease, foundation disease, lining off block and so on. All kinds of diseases of tunnel lining are often interrelated, so the tunnel disease usually is a result of multiple factors.

## Introduction

Nowadays, the tunnel construction and operation scale of China are all at the first place of the world. By the end of 2012, in mainland, 10,100 railway tunnels with a total length of about 7600 km were operating, about 3800 railway tunnels with a total length of about 7300 km were constructing, and 5100 railway tunnels with a total length of about 10800km were planning[1].With the increasing number of tunnels, tunnel diseases become increasingly prominent after tunnel operation, the number of tunnel diseasesis increasing year by year, and some diseases have seriously affected the normal use of the tunnel structure and traffic safety[2][3].

In fact, the tunnel disease exists in the whole process. Some tunnel diseases have been existed before being used[4][5]. The causeof tunnel diseasesis very complex. Different diseases affect tunnel'sservice life differently.Therefore, many scholars have made a lot of researches work on the tunnel disease[6]~[11]. Most of the existing research works are mostly limited to a particular disease and specific engineering conditions, and the understanding of the tunnel disease mechanism is not deep enough. So, the reliability improvement measures and their operabilityare not satisfied.

Based on the existing tunnel disease investigation and analyzed, the author classifies tunnel diseases, and analyzes causes of tunnel disease generation, the result can provide a reliable basis for the tunnel disease treatment.

## Railway Tunnel Diseases Investigation

The range ofdisease survey covers 1995 tunnels, with a total length of 1397 km, all these tunnels are within the scope of jurisdiction of Chengdu Railway Bureau. As it can be seen from the survey results, regardless of their construction period, the number of tunnel with disease is more than 50% of the total number of tunnels, some even up to 100%, as shown in Figure 1.

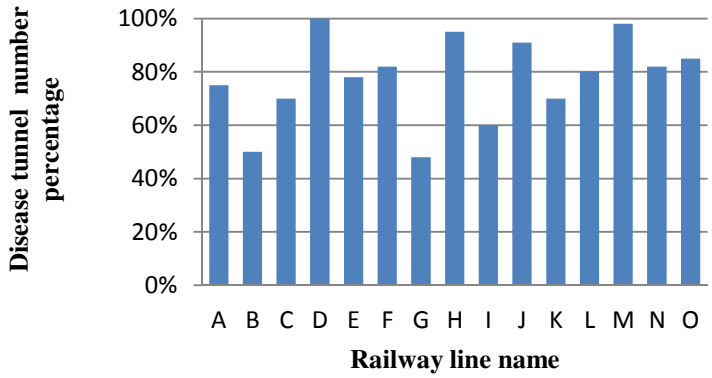


Fig. 1 Proportion of Disease Tunnels' number in Each Railway Line

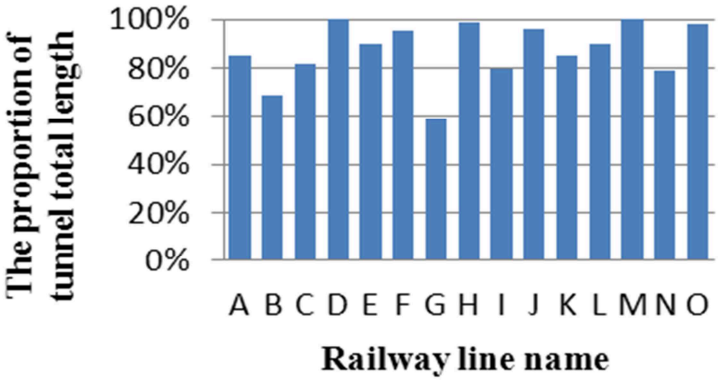


Fig. 2 Proportion of Disease Tunnels' total length in Each Railway Line

In Figures 1 and 2, the abscissa represents the letter name of the line, which are described in Table 1.

Tab. 1 The correspondence between letters and the name of the railway line

| CODE | RAILWAY LINE NAME |
|---|---|
| A | Hukun the first line |
| B | Hukun the second line |
| C | Xiangyu the first line |
| D | Xiangyu the second line |
| E | Baocheng the first line |
| F | Baocheng the second line |
| G | Yuhuai line |
| H | Qiangui line |
| I | Chengkun line |
| J | Chengyu line |
| K | Neiliu line |
| L | Chuanqian line |
| M | Dacheng the first line |
| N | Dacheng the second line |
| O | Dawan line |

Judging from the surrounding rock of diseased tunnel, the worse surrounding rock conditions, the higherfrequency of the tunnel disease occurrence.Conversely, the better rock conditions, the lower frequency of occurrence of disease phenomenon.Generally, the disease phenomenon occurs in IV-class surrounding rock, V-class surrounding grade rock area, accounting for about 83% of the total disease section, as shown in Figure3.

Judging from the type of damage, water leakage and lining cracks are two main types, accounting for about 84% of the total number, followed by facilitiedamage, lining corrosion, arch bottom deformation, as shown in Figure 4.

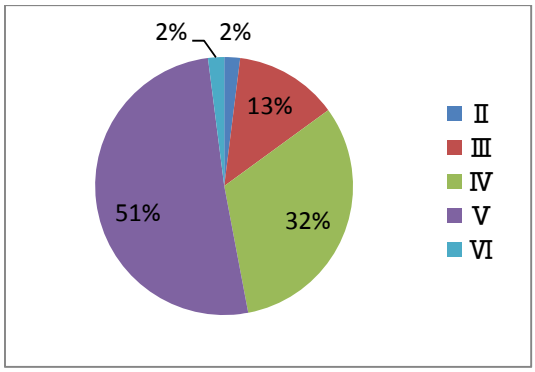


Fig.3 Relationship between Disease Tunnel and Surrounding Rock Grade

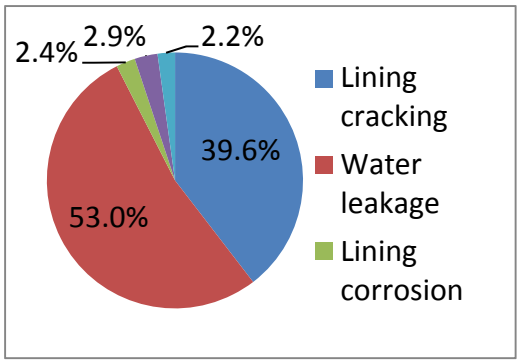


Fig. 4 Proportions of Various Types of Disease

Based on an investigation of 226 tunnels in the range of Shenyang railway Bureau, the tunnel disease can be summed up four types, namely, lining cracks,water leakage and seepage, freezing injury, lining corrosion and so on.The statistic result of tunnel disease characteristic was shown in table 1.

Tab. 1 Statistic of Tunnel Disease Characteristics

| Disease Characteristics | Tunnel Quantity | Diseases Quantity | Total Length/m |
|---|---|---|---|
| Lining Crack | 120 | 894 | 6115 |
| Water Leakage or Seepage | 156 | 1595 | 9061 |
| Freezing Injury | 33 | 109 | 2279 |
| Lining Corrosion | 112 | 722 | 3684 |
| Drainage Facilities Damage | 26 | 69 | 6037 |

## The Typeand Cause of Railway Tunnel Diseases

Study results indicate that China railway tunnel diseasequantity is more, and tunnel disease type is rich, and the cause of tunnel disease is complicated. The railway tunnel disease types include lining water leakage, lining structure disease, lining concrete disease, foundation disease and so on.

The tunnel lining water leakage includes tunnel leaks, gushing water, subsurface flow, lining corrodible water and freezing injuryetc. Underground water from tunnel surrounding rock or earth's surfaceenters the tunnel directly and indirectly by the type of seepage,leakage or drip, which will form lining water leakage disease finally.The chemical composition of underground water from tunnel surrounding rock, including salts, acids and alkalies, which will corrodes lining concrete, the water erosion disease will be formed. In cold region, if underground water or surface water enters the tunnel and freezes into ice, tunnel lining structure will be damaged seriously. In general, tunnel water leakage disease in the non-electrified railways does not directly interfere with traffic and is easily overlooked. However, along with the time growth, the various water damages may cause lining erosion,rail corrosion, sleeper decomposition, subgrade pumping mud. In the electrified railways, it may endanger the traffic. In cold region, it may induce freezing injury or the glazed ice invasion.The tunnel water leakage mainly has five reasons:①tunnel waterproof and drainage system failure; ②outlet pipes formation because of lining concrete density insufficient; ③chemical corrosion of

lining concrete by underground water; ④lining concrete construction defect, including uneven mix of concrete,improper construction methods,etc.⑤lining cracks.

Tunnel lining structural diseases mainly include lining deformation, lining movement and lining crack damage. Deformation of tunnel lining is divided into lateral deformation and vertical deformation, and the lateral deformation is the main deformation. Movement refers to the lining of the tunnel lining whole or part of a rotation (tilt), translation and sink. The movement of lining is divided into vertical movement and lateral movement. The crack of tunnel lining is refers to the lining surface is the result of the deformation of the lining. Tunnel lining crack is usually is visible on the surface of the inner lining, this is the main cause of concrete damage.The main reasons for the formation of tunnel lining structural disease are following severalaspects.First of all is geological impact,it makes rock pressure too large or uneven distribution and even more than lining actual strength and stiffness.The second is the impact of the terrain, the tunnel near the water in the hillside prone to bias, when the roof covering layer is thin, easily leads lining cracking.The third is the impact of groundwater. The fourth is the impact of the lining structure. Because there is difference between actual stress and assumedstress when the tunnel be designed, which may leadthe lining cracking. The fifth is the impact ofconstruction methods and construction qualities. When the tunnel be built in loose rock, the pressure increases, and the lining thickness is not enough, lack of strength, backfill behind the lining not dense, and there will be structural deformation and cracking after tunnel operation. The sixth is the impact of operation and maintenance. The lining strength will be affected by train vibration, soot, steam, etc. which will also produce lining cracks.

Tunnel lining concrete disease is the phenomenon of lining concrete strength decline, concrete lining cracking, corrosion, porosity, surface off or off blocks etc. which is caused by physical or chemical factors. Thereby itwill reduce the durability of structure, and cause other types of diseases, directly reduce the service life of tunnels.Tunnel lining concrete disease mainly damage are as follows. ①Reduce the bearing capacity of lining structure on the same surrounding rock. ② The tunnel clearance area becomes small, the running safety of vehicle be affected③Arch lining off, affecting traffic and personal safety④The crack water Leakage, causing the facilities corrosion, roadbed frost heave. ⑤The bedding and inverted breakage.The main reason for the formation of tunnel lining concrete diseaseismainlyfollowing severalaspects. First,lining concrete subjected to various chemical erosion, such as solubility (or soft) erosion, decomposition (or acid) erosion, salt corrosion, oil erosion and biologyerosion.Second, concrete alkali aggregate reaction products cause swelling of concrete cracking. Third, carbonation or chloride contamination destruction the passive film of reinforced concrete, steel corrosion, concrete smooth muscle bursting, the protective layer and some corners take off. Fourth, concrete micro pores water, at a temperature of alternating positive and negative effects, the formation of ice inflation pressure and fatigue stress combined effects of osmotic pressure, at the role of this fatigue stresses concrete produced denudation outside to the inside, thereby reducing the strength of concrete. Fifth,the lining concrete deformation cracks caused by factors such as temperature, shrinkage, swelling, uneven settlement, etc. reduce the strength and durability of concrete.

Tunnel foundation disease mainly refers to subsidence, cracking, and mud pumping caused by base disease and water leakage. Tunnel foundation diseases easily lead to difficultly maintain the geometric lines, restrict train speed-up and derail in the tunnel seriously.Tunnel foundation disease has three reasons. Firstly, when the base is weak layer, such as weathered bedrock, fracture zone, over break section, it is easily soaked and softens by water because of its low intensity and loose structure. Secondly, cyclic action of the dynamic train loads to the track bedforms mud pumping. Thirdly, the expansion of soft rock usually leads toTunnel foundation diseas.

## Summary

The railway tunnel disease include lining water leakage, lining structure disease, lining concrete disease, foundation disease, lining off block and so on. All kinds of diseases of tunnel lining are often interrelated, which is a result of multiple factors.Lining water leakage is the first class. Lining

structure disease is the second class. Lining concrete disease is the third class. Foundation disease is the fourth class. Moreover, some accident happens occasionally, like landslide squeezing tunnel lining making lining damage, rock cavity where tunnel pass through karst strata, lining collapse, landslide in the opening of the tunnel and rockslide, and is still dangers to traffic.

All kinds of diseases tunnel lining are often interrelated, is a result of multiple factors. Lining Leakage is the first category of disease, the disease is the second largest category of structural lining diseases, diseases of concrete lining is the third largest category of disease, the disease is the fourth largest category of subgrade disease. In addition, landslides caused by squeezing the tunnel lining Lining Crack, tunnel through lava rock formations formed cavity lining collapse, landslides and rockfall at the entrance and other small incidents have also occurred, and endanger traffic safety.

**References**

[1]FengJimeng, Qiu Wenge, Wang Yusuo, Wang Haiyan. Study of Defect Distribution Regularity in Existing Tunnelsand the Classification of Tunnel Environments[J]. Modern TunnellingTechnology, 2013, Vol.50, No.4, p. 35-41.

[2]Li Xiaokun, Shi Chenghua, Lei Mingfeng. Defect Classification of Tunnel Structures in Sulfate Environments[J]. Modern TunnellingTechnology, 2011, Vol.48, No.4,p.19-24.

[3]Guan Baoshu. Collection of Key Points for Maintenance Management of Tunnel Engineering[M]. Beijing: China CommunicationsPress, 2004

[4]Pei Taotao, Chen Liwei, Shi Xianming, Shi Yalong. Study on treatment measures of cracks in lining of existing railway tunnel[J]. Railway Engineering, 2013, No.4, p. 76-79.

[5]Li Wei, Yang Dan, Li Qing. Application of Capillary Drain Pipe in Leakage Treatmentof Existing Tunnel[J]. China Building Waterproofing, 2013, No.4, p. 30-33.

[6]Wang Qingguo. Discussion on Defect Treatment Technology of Existing Tunnel Lining[J]. Northern Communications, 2010, No.10, p.55-57.

[7]Wang Haiyan, Qiu Wenge, Feng Jimeng. Research on the Construction Solutions to Increase the Lining Concrete Durability of MountainsTunnel under Aggressive Environments[J]. Modern Tunnelling Technology, 2011, Vol.48, No.6, p.17-22.

[8]Yang Huilin. Analysis of Fault Reasons of Qijia Mountain Tunnel and Strengthening Schemes[J]. Highway, 2004, No.8,p.187-190.

[9]Luo Xin,Xia Caichu. CurrentSituationandProblemsofClassificationofTunnelDiseases[J].Chinese Journal of Underground Space and Engineering, 2006, Vol.2, No.5, p.877-880.

[10]Liu Haijing, Xia Caichu, Zhu Hehua, Luo Xin.Study on Tunnel Damage[J].Chinese Journal of Underground Space and Engineering, 2007, Vol.3, No.5, p.947-943.

[11]WengBishi, Li Xiaokun, Long Gungcheng, Xie Youjun. Investigation on dederioration of lining concrete of railway tunnel suffering sulfate ambient[J]. Journal of railway science and engineering, 2010, Vol.7, No.3, p.91-93.

*Applied Mechanics and Materials Vols. 580-583 (2014) pp 1223-1226*
*© (2014) Trans Tech Publications, Switzerland*
*doi:10.4028/www.scientific.net/AMM.580-583.1223*

# Development States and Existing Problems Research of Nondestructive Testing of Bolt

Xiankai Bao[1, a], Huanhuan Liu[2,b], Lijuan Liang[3,c]

[1]College of Architecture and Civil Engineering, Inner Mongolia University of Science andTechnology, Baotou, Inner Mongolia 014010

[2]College of Architecture and Civil Engineering, Inner Mongolia University of Science andTechnology, Baotou, Inner Mongolia 014010

[3]Shanghai Jianke Engineering Consulting Co,Shanghai 200032 China

[a] E-mail:bxkzlm@163.com, [b]404708815@qq.com,[c] E-mail:lianglijuan@jkec.com.cn

**Key words:** anchor, Nondestructive testing,The research progress, detector.

**Abstract.** As the primary technique to offer safety and productivity improvement s for under-ground project s , rock bolt s have been widely used in t he construction of t raffic and hydro-power stations. The quality of the rock bolt s is of great importance and has been paid a lot of at tention to. This paper reviewed the history of some techniques used for the inspection of rock bolt s and analyzed their t heory and application. It point sout that the t heoretic p roblem is t he primary problem existed in t hese techniques.Nondestructive testing of bolt develops quickly with plenteous accomplishments and experiences.And we state these accomplishments mainly and look into the future.

## Introduction

Anchoring technique is applied widely in large construction projects such as tunnel,mine and slope strengthening now.Anchering technique in geotechnical engineering will reduce support structure weight greatly, save meterial and guaratee construction safety and stability by using fully rock-soil self-strength and self bearing capacity.There is a urgent need of an easy, economical, reliable anchoring quality testing method to meet all kinds anchoring engineer testing requirements further and offer a reliable method for construction quality control and engineer reliability testing in engineering. Drawing testing of anchoring quality with hydraulic jack in our country due to various reasons will desturb anchor solid greatly,which is a destructive method. Applying dynamic testing method is necessary and is important for engineer in remedy of static load testing.

It's hard to discover quality problems and manage accidents due to anchoring imperceptibility. So bolt testing is necessary in anchoring engineering. The improvements of testing quality and result reliability will guarantee the anchoring engineering quality and safety.

There are many problems to solve both in theory and practice in the complicated systems engineering Traditional testing method depends mainly on pulling resistance testing which is suitable for some occasions with many deficiencies. First, it's a destructive testing method with limited sample numbers which may take a part for the whole and can't guarantee anchoring quality. Secondly, its operation is troublesome with high cost. So Non - destructive Testing of Bolt becomes the research point. But it is possible to solve the problem with wave theory because of the theory application widely in rock-soil engineer. Anchor rod body fits elastic rod wave theory on aspects, geometry form, material and stress conditions, so stress wave method can be applied in anchoring quality testing.

## Development states

### Development states abroad

H.F.Thurner[1] proposed ultrasonic testing method in mortar bolt anchoring and trial-produce Bultmer detector in 1988. But there are two problems to solve. Ultrasonic testing is just suitable for short bolt and in simplex anchoring medium due to serious ultrasonic attenuation.And the piezo-electric crystal can make ultrasonic emission into bolt under the strict conditions of bolt end re-machining and polishing on the scene.

Minerals Management Service exploited ultrasonic apparatus in 1990's for bolt strain and length, but it can't evaluate construction quality[2]. It adopted ultrasonic principle and the deficiencies are that it's not suitable for long bolt because of serious ultrasonic attenuation, strict excitation condition can't make quantification evaluation, and bolt end polishing on the scene for better ultrasonic signal is not applicable.

Doctor M．D．[3]Beard in London University made use of Guided Wave Ultrasonic Technique for bolt testing. He got the most ideal Ultrasonic excitation frequency and developed specialized Vibration sensor by analyzing dispersion curves of signal rate, energy rate, attenuation coefficient and taking the influences of rock modulus, Epoxy layer modulus and anchoring quality into consideration.40 kHz is the most ideal low excitation frequency and 2MHz is on the contrary. And the testing is just for 3.0m max combining low excitation frequency and high excitation frequency.

### Development states at home

Non - destructive Testing of Bolt applied to anchoring quality in 1980's and developed quickly in these years. In the end of 1980's, the bolt detector M-7 developed by china academy of rall way sciensces and Institute of technology and methods increased effective testing length by use of mechanical im pact excitation with relative accordant energy.The bolt detector LX 一 10E can make comprehensive analysis with pulling resistance testing, which is developed by Wuhan creative high-tech Co., ltd, and mainly used in anchoring quality testing in slope engineering. The model test using audio frequency stress wave to test anchoring quality and estimate anchoring force by Wang Mingwu studied the non-destructive drawing testing and can make applications of results to practical engineering.

Xu Ming in Chongqing University[4] applied sonic wave technique into non-destructive anchoring engineering integrity testing based on sonic wave principle and estimated bolt integrity by using artificial neural network of non-linear dynamics into the grey system quality testing and acquired certain effects.

Lv Fu[5] raised a new non-destructive bolt testing method based on magnetostrictive guided wave technology in 2010. And developed bolt testing system on the basis of magnetostrictive guided wave testing principle and guided wave characters in bolt.And with the system he accomplished bolt length and deficiency testing experiment in air and concrete structure and realized contactless non-destructive bolt testing by stimulating L(0,1) model guided wave.
And the result indicated that the method can be applied into bolt quality testing with easy process, high detection precision and bolt imperceptibility testing.

Li Yi, Wang Cheng and Liu Haifeng[6] in Taiyuan University of Technology raised anchoring comprehensive parameter dynamic nondestructive testing with laboratory studies and field measurements. The ultimate principle is that the sensor installed on the top of bolt accepts reflected signal from The transient impact load applied to the bolt end and makes signal proceeding and frequency domain analysis to get_essential parameters of effective anchoring length, anchoring quality, working load and ultimate bearing capacity (drawing force) which reflects anchoring characters. And the method meets the requirements of construction quality security detection and support parameter optimization design.

## Existing problems

There are many problems in nondestructive testing in theory, apparatus, signal processing and inversion imaging although many scientific and technical workers preceded much theory researches.

In theory wave propagation law in anchoring, stimulating method of some model wave in favor of anchoring quality testing and effective wave identification and extraction technology are the problems. So many testing workers may handle affairs by experiences in practices.

Wave propagation theories are on the solutions of One-dimensional non-homogeneous wave equation under different boundary and initial conditions. Its results are not important for testing apparatus system design and effective wave application although it decreased mathematical calculation. Taking the testing solution as a one-dimensional project is just based on longitudinal wave propagation in bolt and ignored medium influences. The coupled effect of the bolt, anchoring medium and surrounding rock should be took into consideration for theory application in practice.

In apparatus and software, some manufactures and institutes at home and aboard developed non destructive testing and apparatus depending on small strain foundation pile integrity detection technology with the progress of electronic technique and detection technical[7]. There are many nondestructive detectors such as the multifunction rock anchoring detector of SRB-MATS-P/B/S/P, the mineral anchor cable intrinsic safety type detector of CMSW6(A),the bolt quality detector of LHMG-V8,the bolt detector of MT-1by Wang Mingwu and the portable bolt detector by institute of rock and soil machenics,chinese academy of sciences. However, these detectors have disadvantages of low sampling rate and defection effect.The portable intrinsic safety type non destructive detector based on guided wave by Wang cheng can test effect anchoring length and anchoring force accurately and verdict anchoring quality. It is proved by repetitive tests the detector has application potential in underground coal mine because it meets intrinsic safety anti-explosion requirements with its stable and reliable property. Non destructive detector will be more accurate result, easy operation, perfect function and high effect with science and technology development and researchers study.

## Thoughts and suggestions to solve problems

According above analysis, the problem demanding prompt solution in nondestructive anchoring quality testing is in theory which apparatus and software development problems will be solved on. We should solve the wave equation under cylindrical multi-layer elastic medium model, calculate different guided wave dispersion characteristics and find out deficiency testing model wave so that to solve wave propagation characters theories in anchoring system. Meanwhile we exploit processing and imaging software on the theoretical forward modeling results, extract effect signals specially and remove noise wave, and use joint time frequency analysis for processing and imaging which will work well. Theoretical forward modeling difficulty is great without a doubt. So model test for Theoretical forward modeling will be necessary for anchoring quality sonic wave testing. And the results of model test can checkout theoretical forward modeling results validity as well as remedy theory deficiencies. More useful we can establish standard gallery with a certain model test workload, deal with measured data by using pattern recognition and neural network technique. and this is another solution. In all, model tests benefit for the nondestructive anchoring quality testing.

## Conclusions

Nondestructive anchoring testing has a great progress and also huge development space at home. These nondestructive testing methods have deferent deficiencies and limitations. Thorough analysis and researches in theory and enough engineering practices will ensure a perfect application of the nondestructive anchoring testing. I believe that the technique will promote engineering creation development greatly with its improvement.

**Acknowledgements**

This work was financially supported by the Inner Mongolia University of Science and Technology Youth Innovation Foundation (2010NC049).

**References:**

[1] Thurner, H.F.Boltometor-Instrument for Non-destructive Testing of Grouted Rock Bolts[A].In: Proceedings of the2nd International Symposium on Filed Measurements in Geomechanics[C].Rotterdam:A.A.Balkema,1988.135-143.

[2] Tadolini S C, Dyni R C, Transfer Mechanics of Full-column Resin-grouted Roof Bolts, The US Bureau of Mines, Denver, CO, 1990.

[3] Beard M D，Lowe M J S, Non～destructive testing of rock bolts using guided ultrasonic waves[J],International Journal of Rock M mechanics and Mining Sciences，2003，40.

[4] Xu Ming, Zhang Yongxing, Li Yan. Anchor Dynamic Tests Numerical Solution ,World Earthquake Engineering 2003, 9, in volume 19, （3）, 68～72.

[5] Lv Fuzai, Wang Fei, Xiang Yiqiang, Tang Zhifeng, Zhu Ran. Design of New Anchor Test Method Based on Magnetostrictive Guided Wave Technology [J]. Journal of Engineering Design. 2010(06)

[6] Li Yi, Wang Cheng. The Experimental Research of Anchoring Quality by Stress Reflection Wave Method, Journal of China Coal Society, 2000, 4, in volume 25, No. 2, 160～164.

[7]Zhong Hongwei, Hu Xiangyun, Xiong Yonghong, Xiao Boxun, Status Analysis of Bolt Anchoring Quality Acoustic Detection Technology, Chinese Journal of Engineering Geophysics, 2005,2, in volume 25（1），50～54.

*Applied Mechanics and Materials Vols. 580-583 (2014) pp 1227-1231*
*© (2014) Trans Tech Publications, Switzerland*
*doi:10.4028/www.scientific.net/AMM.580-583.1227*

# Identification of Surrounding Rock Parameters Based on MSVR

LI Xiaolong[1, a], ZHANG Junjing[1,b], WANG Fuming[1, c] and ZHANG Bei[1,d]

[1] College of Water Conservancy and Environment Engineering, Zhengzhou University, No.100 of Science Road, Zhengzhou, China, 450001

[a]zzulxl1977@163.com, [b]junjinzhang@126.com, [c]fuming573@126.com, [d]beizhang@126.com

**Keywords:** rock parameter, identification, MSVR, PSO.

**Abstract.** An inversion method based on multi-output support vector regression (MSVR) is proposed for identifying the mechanical parameters of surrounding rock. This method considers the surrounding rock as a multi-output system during excavation, and the surveyed rock deformations of each monitoring section as its output. First, perform numerical experiments based on the principle of orthogonal test to obtain the calculated deformation values corresponding to different rock parameter combinations, and use them as the samples for training the model of MSVR as reflecting the nonlinear mapping relationship between rock and its deformations. Second, use the PSO to seek the optimal rock parameters based on measured deformations of rock mass. An example is employed to test the presented inversion method. The results showed that compared with the inversion method based on single-output support vector regression (SSVR), the proposed one is more inclined to reach the global optimization goals and achieve more reliable inversion results due to its consideration of the inherent correlativity among the measured deformations of each monitoring section.

## Introduction

Due to high inhomogeneity of stratum, the rock parameters obtained by means of laboratory or field test are short of representativeness and therefore can't meet the requirements of numerical analysis of underground engineering. The back analysis technique developed in recent decades is regarded as a kind of relatively ideal method to determine the wanted parameters.

Zhao et al. used SVM for geo-material parameters back analysis[1]. Xu et al. developed the joint inversion method of SVM and simulated annealing algorithm (SA) for identifying the rock mechanic parameters of underground grotto of Suofengying Hydraulic Power Plant[2]. Liu et al. successfully identified the three-dimensional elastoplastic model parameters in tunnel engineering by using improved GA-SVR algorithm[3].

However, by far almost all back analysis methods based on SVM employ single output SVM, and this means that the individual regression model should be established for the deformation data of each monitoring point or line. But in fact, during excavation for each monitoring section, usually more than one survey points or lines are set and so more than one array of deformation data are got. In the other words, these data are the outputs corresponding to same monitoring section. So during excavation the surrounding rock is in essence a multi-output system and using MSVR to identify the geo-material parameters maybe be more reasonable and perhaps can lead more ideal results. Based on such consideration, a inversion method based on MSVR is presented in this paper. The method first establishes the MSVR model reflecting the nonlinear mapping relationship between rock and its deformations, then applies PSO to seek the optimal rock parameters. Finally, an inversion example is selected to investigate the method's applicability.

## Multi-output Support Vector Regression

SVM is a new type of general machine learning method proposed by Vapnik in 1990s under the framework of Statistical Learning Theory (SLT)[4]. Based on structural risk minimization principle (SRM), SVM possesses powerful nonlinear mapping and generalization ability, and has become a new hot topic after artificial neutral network (ANN). SVM was initially developed for handling

pattern recognition problem, and later, the SVM for regression was also put forward by Smola and Schoelkopf, also called support vector regression (SVR), which can approximate to any nonlinear function by an arbitrary accuracy and is widely used in practical projects[5].

Soon after that, multi-output support vector regression (MSVR) was proposed by Perez-Cruz[6]. The MSVR provides a new regression algorithm for the problem that the output variable of a system is a vector. Suppose we are given a training data set, $\{x_i, y_i\}$ $(i=1,\ldots,l)$, where $x_i \in R^d$ denotes the space of the input, $y_i \in R^m$ denotes the corresponding output. The object of MVSR is to generate a set of regression functions,

$$f^j(x) = (w^j, x) + b^j, \quad j = 1,\ldots,m \tag{1}$$

to minimize the structural risk. By using a hyper-spherical insensitive zone, the structural risk function can be defined as follows:

$$\min \sum_{j=1}^{m} \left\| w^j \right\|^2 + C \sum_{i=1}^{l} \xi_i \tag{2}$$

subject to

$$\left\| \boldsymbol{y}_i - \boldsymbol{\Phi}^T(x_i)\boldsymbol{w} - \boldsymbol{b} \right\| \le \varepsilon + \xi_i \quad i = 1,\ldots,l \tag{3}$$

where $\xi_i \ge 0$, $\boldsymbol{y}_i = \left(y_i^1, y_i^2, \ldots, y_i^m\right)^T$, $\boldsymbol{w}_i = \left(w_i^1, w_i^2, \ldots, w_i^m\right)^T$, $\boldsymbol{b} = \left(b^1, b^2, \ldots, b^m\right)^T$, and $\boldsymbol{\Phi}(\cdot)$ is a function vector to realize nonlinear transformation to a higher dimensional space.

In order to solve the MSVR, we first introduce the constrains (3) into (2), making use of the Lagrange multipliers, leading to the minimization of

$$L_P = \min \sum_{j=1}^{m} \left\| w^j \right\|^2 + C \sum_{i=1}^{l} \xi_i - \sum_{i=1}^{n} \alpha_i (\varepsilon + \xi_i - \left\| \boldsymbol{y}_i - \boldsymbol{\Phi}^T(x_i)\boldsymbol{w} - \boldsymbol{b} \right\|^2) - \sum_{i=1}^{n} \mu_i \xi_i \tag{4}$$

With respect to $w^j$, $b^j$ and $\xi_i$ and its maximization with respect the Lagrange multipliers, $\alpha_i$ and $\mu_i$. Then using the Karush-Kuhn-Tucker Theorem, the above optimization problem can be converted into solving the following equation system:

$$\begin{bmatrix} \mathrm{K} + \mathrm{D}_{\alpha}^{-1} & 1 \\ \alpha^T \mathrm{K} & \alpha^T 1 \end{bmatrix} \begin{Bmatrix} \beta^j \\ b^j \end{Bmatrix} = \begin{Bmatrix} y^j \\ \alpha^T y^j \end{Bmatrix} \tag{5}$$

**Execution of the Back Analysis Method Based on MSVR**

As in any conventional approach to the displacement back analysis, the objective function,is defined as the sum of absolute value of deviation between the calculated displacement and the measured one of each point or line, and is expressed as the following Eq (6).

$$f = \sum_{i=1}^{n} \left| u_{im} - u_{ic} \right| \tag{6}$$

Where *f* represents objective function value, *n* is the total number of monitoring points (or lines), $u_{im}$ is the measured displacement of the *i*th point (or line), and $u_{ic}$ is the calculated displacement of the *i*th point (or line).

The execution of the inversion method comprises such steps as follows:

(1) Estimate the valuing range of rock mass mechanical parameters to be recognized according to the practical engineering problems and determine the scheme of numerical experiments in line with the principle of orthogonal or uniform experimental design.

(2) Establish a reasonable numerical model of underground engineering. Use the model to calculate the corresponding displacement of key points for each set of tentative geomechanical parameters. Each set of geomechanical parameters and corresponding displacement of key points compose a training example.

(3) Based on the learning examples obtained in the previous step, use PSO[7] for optimal selection of the MSVR model parameters, and establish the MSVR model with best approximation ability.

(4) Substitute MSVR model for the numerical model of underground engineering to calculate the surrounding rock deformations corresponding to every group of parameters, and again, use the PSO to search for optimal rock mass parameters till the inversion results meet the precision requirement are find.

**Verification of the Back Analysis Method**

To verify the back analysis method presented in this paper, a certain deeply buried tunnel is considered. The tunnel's excavation section and arrangement of survey lines are depicted in Figure 1. Suppose the surrounding rock is isotropic and homogeneous, the initial vertical ground stress is $\sigma_y = 2.34\text{MPa}$, lateral pressure coefficient is $\lambda = 0.57$, the elastic modulus is $E = 7\text{GPa}$, Poisson's ratio is $\mu = 0.25$, cohesive stress is $C = 0.6\text{MPa}$, and internal friction angle is $\phi = 30^\circ$. FEM is used to establish the numerical model of the tunnel and Drucker-Prager yield criterion is employed for elastoplastic analysis.

As rock deformation is insensitive to Poisson's ratio, the elastic modulus of surrounding rock, cohesive stress and internal friction angle are selected as the parameters need to be identified. According to related engineering geological data, the valuing ranges of the three parameters are estimated as 20°≤$\varphi$≤40°; 4GPa≤$E$≤9GPa; 0.3MPa≤$C$≤0.9MPa, respectively.

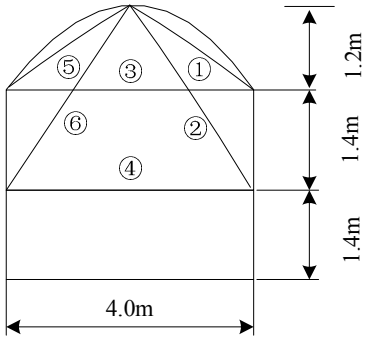


**FIG. 1. Tunnel section and layout of measured lines**

Each parameter is divided into 6 levels as illustrated in Table 1. The orthogonal experiment principle is used to design the learning sample, and there are 36 groups of parameter combination altogether. Uniform design method is used to construct test sample and there are 6 groups of parameter combination. For each group of parameters, use the established finite element model to calculate the corresponding deformation values of survey line 1, 2, 3 and 4 (the calculated values of survey line 1 and 5, 2 and 6 are identical, respectively, due to the symmetrical structure). Each set of geomechanical parameter with its corresponding deformations of the monitoring lines is considered as a training sample.

**Table 1. Factors for tests on orthogonal table and their levels**

| levels | 1 | 2 | 3 | 4 | 5 | 6 |
|---|---|---|---|---|---|---|
| $E$/GPa | 4 | 5 | 6 | 7 | 8 | 9 |
| $C$/MPa | 0.3 | 0.42 | 0.54 | 0.66 | 0.78 | 0.9 |
| $\varphi$/° | 20 | 24 | 28 | 32 | 38 | 40 |

To compare the inversion precision of SSVR and MSVR, suppose the computed deformations of survey line 1, 2, 3 and 4 as measured values corresponding to predetermined parameters, and use the two methods to identify them, respectively. The MSVR model parameters was set as: choosing RBF function as Kernel function, $\sigma = 0.35$, $c = 50$, $\varepsilon_m = 0.006$. For SSVR, to make hypercube and 3-dimensional hyper-sphere have the same volume, the width of insensitive zone is set as $\varepsilon_s = 0.7435\varepsilon_m$, and the other parameters are same as SSVR. The particle swarm optimization

parameters are selected as: acceleration factors $c_1 = 0.5$, $c_2 = 0.5$, $\omega$ applying linear inertia weight, population size $N = 20$ and the maximum iterations $t_{max} = 40$.

The parameters' inversion results are shown in the following table 2 and table 3. It can be seen that compared with standard SSVR, the proposed method using MSVR obviously possesses higher inversion precision. For MSVR, its maximum relative error of inversion parameter is 1.74%, and its final object function is 0.02, while for SSVR, the maximum relative error reaches 9.33%, and the object function is just 0.07. The reason maybe explained by the surrounding rock is regarded as a multi-output system and the inherent correlativity among the measured deformations of different survey lines of the same section is considered when using MSVR.

**Table 2. Result of back analysis**

| | theoretical value | MSVR | | SSVR | |
|---|---|---|---|---|---|
| | | inverse value | relative error % | inverse value | relative error % |
| *E*/GPa | 7.0 | 6.88 | 1.71 | 7.16 | 2.28 |
| *C*/MPa | 0.6 | 0.592 | 1.33 | 0.612 | 2.2 |
| *φ*/° | 30 | 29.7 | 1.0 | 27.2 | 9.33 |

**Table 3. Comparison of back analysis results with measured displacements**

| survey line | 1 | 2 | 3 | 4 | $f$ min |
|---|---|---|---|---|---|
| theoretical value/mm | 1.73 | 3.37 | 3.22 | 5.57 | |
| MSVR/mm | 1.73 | 3.36 | 3.23 | 5.57 | 0.02 |
| SSVR/mm | 1.72 | 3.39 | 3.24 | 5.59 | 0.07 |

## Conclusion

By substituting the multi-output support vector machine (MSVR) for standard singe-output support vector machine (SSVR), a novel inversion method of MSVR is proposed for identifying the mechanical parameters of surrounding rock. An example of back calculating tunnel rock's elastoplastic parameters was employed to test the method's practicality and reliability. The results showed that, compared with the back analysis method based on standard SSVR, the presented method is more inclined to reach the global optimization goals and thus could achieve more reliable inversion results with higher precision.

## Acknowledgements

The authors appreciate the support of the National Natural Science Foundation of China (Nos. 51179175 and 51008285), the Plan For Scientific Innovation Talent of Henan Province（No:124200510020）, and the science and technology research project of Education Department of Henan province（No:13B580377）

## References

[1] Zhao Hongbo, Feng Xiating. Study on Genetic-support Vector Machine in Displacement Back Aanalysis[J]. Chinese Journal of Rock Mechanics and Engineering, 2003, 22(10): 1618-1622.

[2] Xu Chuan-hua, Ren Qing-wen, Zhou Qing-hua. Displacement back analysis based on support vector machine and simulated annealing[J]. Chinese Journal of Rock Mechanics and Engineering, 2005, 24 (22): 4134-4138

[3] Liu Kaiyun, Qiao Chunsheng, Liu Baoguo. Intelligence identification of three-dimensional elastoplastic model parameters in tunnel engineering based on improved GA-SVR algorithm[J]. Chinese Journal of Rock Mechanics and Engineering, 2007, 26(6): 1164-1172

[4] VAPNIK V. Statistical Learning Theory. New York: Wiley. (1998).

[5] Smola A J, Scholkopf B. A Tutorial on Support Vector Regression[R] NeuroCOLT2 Technical Report Series NC2-TR-1998030, 1998.

[6] PEREZ-CRUZ F, CAMPS-VALLS G, SORIA-OLIVAS E, et al. Multi-dimensional function approximation and regression estimation[C] // Proc of Int Conf on Artificial Neural Networks. Berlin: Springer-Verlag, 2002, 2415: 757 – 762.

[7] Kennedy J, Eberhart R. Particle swarm optimization[C]// Proceedings of IEEE International Conference on Neural Network. Piscataway: NJ IEEE Service Center, 1995: 1942-1948.

*Applied Mechanics and Materials Vols. 580-583 (2014) pp 1232-1237*
*© (2014) Trans Tech Publications, Switzerland*
*doi:10.4028/www.scientific.net/AMM.580-583.1232*

# Kinematics analysis of working edge point for gauge disc cutter in cutterhead of tunneling machine

Qixing Wu[1,2, a], Guanfeng Tian[1,2, b] Lin Chen[1, c] and Hongwei Ma[1,2,d]

[1] Department of Mechanics and Civil Engineering, Jinan University, Guangdong Guangzhou, China

[2]The Key Laboratory of Disaster Forecast and Control in Engineering, Ministry of Education of China, Jinan University, Guangdong Guangzhou, China

[a]wqx510632@126.com, [b]tiangf126@126.com, [c]1823326357@qq.com,[d]tmahw@jnu.edu.cn

**Keywords:** motion equation, cutterhead, gauge disc cutter, tunneling machine

**Abstract.** Based on the analysis of movement characteristics of gauge disc cutter in cutterhead of tunneling machine, the motion equation to describe the working behavior of the edge point of gauge disc cutter in tunneling process is deduced by using the method of space coordinate transformation matrix. The motion equation has the advantages of considering more parameters, such as position variables of disc cutter, cutter radius, cutterhead rotating speed and advance speed.

## Introduction

Disc cutter is the main component of tunneling machine, which is also an important and wearing part for breaking rock. Relevant statistics data[1,2] shows that cutter tools are the largest amount of consumables in the boring process of tunneling, and their costs are often one-third of the whole price of the machine. Since the tool life directly determines the number of tool changes and downtime, the operating efficiency and construction costs of the tunneling machine will be affected seriously. Therefore, the kinematics analysis of working edge point for disc cutter of tunneling machine will be helpful to analyze cutter wear and rock breaking mechanism further, which will be the theoretical basis for cutter life prediction and cutterhead design of tunneling machine.

## Movement characteristics of disc cutter

Movement state of disc cutter in cutterhead of tunneling machine can be thought as the synthetic motion of two fixed axis rotations[3,4]. As shown in Fig.1, relative to the frame OAB, the rigid body rotates around the fixed shaft $Z_1$ with angular velocity $\omega_1$, while the fixed shaft $Z_1$ rotates around the fixed axis $Z_2$ with angular velocity $\omega_2$. Taking the framework OAB as a moving reference system, the former moving pattern is relative motion and the latter is implicated motion. When $\angle AOB = 90°$, the rotating rigid body corresponds to a disc cutter of the tunneling flat cutterhead, whose mounting axis $OZ_1$ intersects with rotation center axis $OZ_2$ of the cutterhead. Then the disc cutter advances together with the cutterhead along axis $OZ_2$.

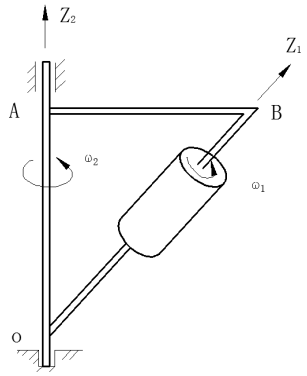


Fig.1 General model of the disc cutter motion

Because the movement state of any edge point of disc cutter affects the degree of cutter wear and rock breaking, it is necessary to study the trajectory equation of any disc cutter edge point for analyzing the rock breaking course, which includes the process from the contacting moment of edge point with rock to the time of its maximum penetration. The process of breaking rock by disc cutter is the aggregate of numerous edge points which break rock through penetrating[5-7].

## Motion equation of working edge point of gauge disc cutter

As discussed earlier, when the disc cutter goes ahead along the excavation axis, it revolves around the central axis of cutterhead and rotates around its mounting shaft at the same time. It is showed that the motion state of disc cutter is three-dimensional. Therefore, spatial kinematic analysis method[8] is suitable to be used to analyze the motion of disc cutter.

The cutters of tunneling machine cutterhead include two styles: inner and gauge disc cutters, as showed in fig.2. The kinematics analysis of working edge point for inner disc cutter in cutterhead of tunneling machine has been finished[9]. So the relatived analysis for gauge disc cutter especially will be carried out as following.

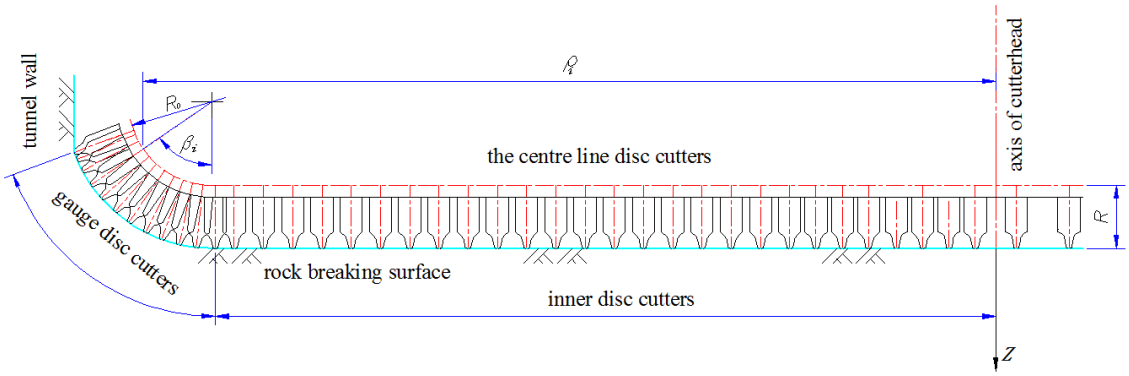


Fig.2 Arrangement of disc cutters on cutterhead of Herrenknecht EPBΦ6280 shield

**Matrix method of spatial coordinate transformation**[8, 10]**.**Spatial coordinate transformation is the coordinate relations of any spatial point $P$ between two spatial systems $o_m x_m y_m z_m$ and $o_n x_n y_n z_n$, as shown in Fig.3. Let coordinate arrays of point $P$ in coordinate system $o_m x_m y_m z_m$ and $o_n x_n y_n z_n$ are $r_m$ (refer with: Eq.1) and $r_n$ (refer with: Eq.2) respectively. The movement of origin $O_n$ in $m$ coordinate system can be expressed by vector $\overrightarrow{O_m O_n}$ with coordinate array $R_m^{(O_n)}$ (refer with: Eq.3).

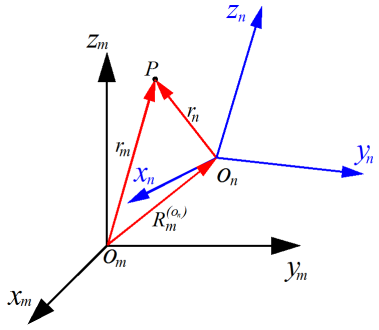


Fig.3 An sketch of coordinate transformation of a spatial point

$$r_m = [x_m, y_m, z_m]^T . \tag{1}$$

$$r_n = [x_n, y_n, z_n]^T . \tag{2}$$

$$R_m^{(O_n)} = \left[x_m^{(O_n)}, y_m^{(O_n)}, z_m^{(O_n)}\right]^T . \tag{3}$$

From point $O_m$, the vector relationship of point $P$ is expressed as Eq.4.

$$\overrightarrow{O_mP} = \overrightarrow{O_mO_n} + \overrightarrow{O_nP}. \tag{4}$$

By coordinate transformation , the Eq.4 becomes Eq.5.

$$r_m = R_m^{(O_n)} + C_{mn} r_n. \tag{5}$$

Wherein $C_{mn}$ is $3 \times 3$ transformation matrix from $n$ coordinate system to $m$ coordinate system. Each matrix element is cosine of the angle corresponding to the two coordinate axes, namely the direction cosine. So matrix $C_{mn}$ is also called the direction cosine matrix, expressed as Eq.6.

$$C_{mn} = \begin{bmatrix} \cos(x_m \hat{} x_n) & \cos(x_m \hat{} y_n) & \cos(x_m \hat{} z_n) \\ \cos(y_m \hat{} x_n) & \cos(y_m \hat{} y_n) & \cos(y_m \hat{} z_n) \\ \cos(z_m \hat{} x_n) & \cos(z_m \hat{} y_n) & \cos(z_m \hat{} z_n) \end{bmatrix}. \tag{6}$$

**Establish trajectory equation of working edge point of gauge disc cutter.**The measurement sensors installed in copy tool can be used to determine the position of cutterhead rotation angle of tunneling machine. When the copy tool is at the bottom the rotation angle is generally defined as zero degree. And then the rotation angle increases from 0° to 360° in a counterclockwise direction viewing from the front of the cutterhead.

Fixed coordinate system *OXYZ*: plane *XOY* is tunnel excavating face which is parallel to the cutterhead plane and *OX* axis is consistent with the position of copy tool when it is at the bottom (i.e. the cutterhead rotation angle is 0° ). Viewing from the rear of cutterhead, rotation angle increases when cutterhead rotates in clockwise, and *OZ* axis is the cutterhead rotation center axis with the excavating direction forward positive, as shown in Fig.4.

Moving coordinate system $o_1xyz$: point $O_1$ is the center of disc cutter; $o_1y$ axis is the mounting shaft of disc cutter and the direction away from the cutterhead center is positive; $o_1z$ axis connects the center of disc cutter and the maximum penetration point of cutter edge and the direction to penetrate rock is positive; the direction of $o_1x$ axis is positive at which the disc cutter rotates forward, as shown in Fig.4.

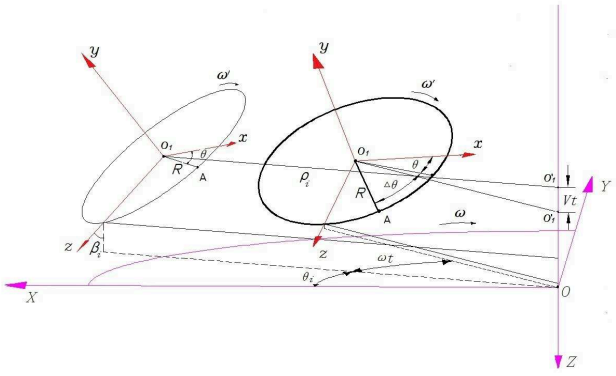


Fig.4 An analytical sketch of the rock-breaking movement of the gauge disc cutter

In fixed coordinate system *OXYZ* shown in fig.3 and fig.4, among all the positional parameters for the number $i$ disc cutter, installation dip $\beta_i$ and gauge installation radius $R_i$ need to be considered besides installation radius $\rho_i$ and polar angle $\theta_i$.

In moving coordinate system $o_1xyz$ showed in fig.4, the polar coordination of working edge point $A$ of gauge disc cutter in plane $xo_1z$ is $(R,\theta)$, in which $R$ is the radius of the disc cutter and $\theta$ is the initial polar angle of working edge point $A$ of gauge disc cutter.

Therefore, the coordinate array of the moving coordinate system origin $O_1$ in the fixed coordinate system can be expressed as Eq.7.

$$r_O^{(O_1)} = \begin{bmatrix} \rho_i \cos\theta_i \\ \rho_i \sin\theta_i \\ -R - R_0(1-\cos\beta_i) \end{bmatrix}. \tag{7}$$

The coordinate array of working edge point $A$ of gauge disc cutter in the moving coordinate system can be expressed as Eq.8.

$$r_{O_1}^{(A)} = \begin{bmatrix} R\cos\theta \\ 0 \\ R\sin\theta \end{bmatrix}. \tag{8}$$

According to the method of spatial coordinate transformation matrix, the point $A$ in the moving coordinate system can be transformed into the fixed coordinate system by two transformation.

(1) Turn dip $\beta_i$ to positive position of disc cutter around negative direction of $o_1x$ axis with the coordinate system origin $O_2$, then the direction cosine matrix $C_{O_2O_1}$ is Eq.9.

$$C_{O_2O_1} = \begin{bmatrix} 1 & 0 & 0 \\ 0 & \cos\beta_i & \sin\beta_i \\ 0 & -\sin\beta_i & \cos\beta_i \end{bmatrix}. \tag{9}$$

（2）Transform the positive position of disc cutter into fixed coordinate system $OXYZ$, then the direction cosine matrix $C_{OO_2}$ is Eq.10.

$$C_{OO_2} = \begin{bmatrix} -\sin\theta_i & \cos\theta_i & 0 \\ \cos\theta_i & \sin\theta_i & 0 \\ 0 & 0 & 1 \end{bmatrix}. \tag{10}$$

After above transformation, the coordinate array of working edge point $A$ of gauge disc cutter at the initial moment in the fixed coordinate system can be expressed as Eq.11.

$$r_O^{(A)} = r_O^{(O_1)} + C_{OO_2} C_{O_2O_1} r_{o_1}^{(A)}. \tag{11}$$

The Eq.7, Eq.8, Eq.9, Eq. 10 are substituted into the equation Eq.11 , Eq.12 can be obtained.

$$\begin{aligned} r_O^{(A)} &= \begin{bmatrix} \rho_i \cos\theta_i \\ \rho_i \sin\theta_i \\ -R - R_0(1-\cos\beta_i) \end{bmatrix} + \begin{bmatrix} -\sin\theta_i & \cos\theta_i & 0 \\ \cos\theta_i & \sin\theta_i & 0 \\ 0 & 0 & 1 \end{bmatrix} \begin{bmatrix} 1 & 0 & 0 \\ 0 & \cos\beta_i & \sin\beta_i \\ 0 & -\sin\beta_i & \cos\beta_i \end{bmatrix} \begin{bmatrix} R\cos\theta \\ 0 \\ R\sin\theta \end{bmatrix} \\ &= \begin{bmatrix} \rho_i \cos\theta_i - R\sin\theta_i\cos\theta + R\sin\beta_i\cos\theta_i\sin\theta \\ \rho_i \sin\theta_i + R\cos\theta_i\cos\theta + R\sin\beta_i\sin\theta_i\sin\theta \\ -R - R_0(1-\cos\beta_i) + R\cos\beta_i\sin\theta \end{bmatrix} \end{aligned}. \tag{12}$$

Then the coordinate of point $A$ at the initial moment in the fixed coordinate system can also be expressed as Eq.13

$$\begin{cases} X_A = \rho_i \cos\theta_i - R\sin\theta_i \cos\theta - R\sin\beta_i \cos\theta_i \sin\theta \\ Y_A = \rho_i \sin\theta_i + R\cos\theta_i \cos\theta - -R\sin\beta_i \sin\theta_i \sin\theta \\ Z_A = -R - R_0(1-\cos\beta_i) + R\cos\beta_i \sin\theta \end{cases}. \tag{13}$$

Let rotation angular velocity of shield cutterhead is $\omega$ and advance speed is $V$, then after time $t$, the cutterhead rotation angle is $\omega t$ and the azimuth of disc cutter becomes ($\theta_i$+$\omega t$), the coordinate array of origin $O_1$ of the moving coordinate system in the fixed coordinate system becomes into Eq.14.

$$r_O^{(O_1)} = \begin{bmatrix} \rho_i \cos(\theta_i + \omega t) \\ \rho_i \sin(\theta_i + \omega t) \\ -R - R_0(1-\cos\beta_i) + Vt \end{bmatrix}. \tag{14}$$

The direction cosine matrix $C_{O_2O_1}$ keeps unchanged, while $C_{OO_2}$ changes to Eq.15.

$$C_{OO_2} = \begin{bmatrix} -\sin(\theta_i + \omega t) & \cos(\theta_i + \omega t) & 0 \\ \cos(\theta_i + \omega t) & \sin(\theta_i + \omega t) & 0 \\ 0 & 0 & 1 \end{bmatrix}. \tag{15}$$

Suppose the rotation of disc cutter is pure rolling, the Eq.16 will be satisfied.

$$(\rho_i + R\sin\beta_i) \cdot \omega t = R \cdot \Delta\theta. \tag{16}$$

After time $t$, rotation angle of gauge disc cutter rolling is Eq.17

$$\Delta\theta = \frac{\rho_i + R\sin\beta_i}{R} \omega t. \tag{17}$$

So after time $t$, the coordinate array of point $A$ in the moving coordinate system becomes Eq.18.

$$r_{O_1}^{(A)} = \begin{bmatrix} R\cos(\theta + \frac{\rho_i + R\sin\beta_i}{R} \omega t) \\ 0 \\ R\sin(\theta + \frac{\rho_i + R\sin\beta_i}{R} \omega t) \end{bmatrix}. \tag{18}$$

And the coordinate array of point $A$ in the fixed coordinate system becomes Eq.19.

$$r_O^{(A)} = \begin{bmatrix} \rho_i \cos(\theta_i + \omega t) - R\sin(\theta_i + \omega t)\cos(\theta + \frac{\rho_i + R\sin\beta_i}{R} \omega t) + R\sin\beta_i \cos(\theta_i + \omega t)\sin(\theta + \frac{\rho_i + R\sin\beta_i}{R} \omega t) \\ \rho_i \sin(\theta_i + \omega t) + R\cos(\theta_i + \omega t)\cos(\theta + \frac{\rho_i + R\sin\beta_i}{R} \omega t) + R\sin\beta_i \sin(\theta_i + \omega t)\sin(\theta + \frac{\rho_i + R\sin\beta_i}{R} \omega t) \\ -R - R_0(1-\cos\beta_i) + Vt + R\cos\beta_i \sin(\theta + \frac{\rho_i + R\sin\beta_i}{R} \omega t) \end{bmatrix}. \tag{19}$$

Thus, at time $t$, the equations of motion parameters of point $A$ in the fixed coordinate system is also represented by the following Eq.20.

$$\begin{cases} X_A = \rho_i \cos(\theta_i + \omega t) - R\sin(\theta_i + \omega t)\cos(\theta + \frac{\rho_i + R\sin\beta_i}{R} \omega t) - R\sin\beta_i \cos(\theta_i + \omega t)\sin(\theta + \frac{\rho_i + R\sin\beta_i}{R} \omega t) \\ Y_A = \rho_i \sin(\theta_i + \omega t) + R\cos(\theta_i + \omega t)\cos(\theta + \frac{\rho_i + R\sin\beta_i}{R} \omega t) - R\sin\beta_i \sin(\theta_i + \omega t)\sin(\theta + \frac{\rho_i + R\sin\beta_i}{R} \omega t) \\ Z_A = -R - R_0(1-\cos\beta_i) + Vt + R\cos\beta_i \sin(\theta + \frac{\rho_i + R\sin\beta_i}{R} \omega t) \end{cases}. \tag{20}$$

When $\beta_i$=0, which means inner disc cutter, the formula (20) will change into the same as the motion equation of inner disc cutter in file [9]. So the motion of inner disc cutter can be thought as a special case of gauge disc cutter.

At last, when all the parameters of $R$, $\rho_i$, $\theta_i$, $\beta_i$, $R_0$, $\theta$, $\omega$ and $V$ are determined, the spatial motion position of working edge point of gauge disc cutter at any time can be calculated accurately.

## Conclusion

On the basis of the analysis of movement characteristics of gauge disc cutter in cutterhead, the motion equation of working edge point of gauge disc cutter is deduced in tunneling process by using the method of space coordinate transformation matrix, which provides theoretical basis for analyzing tool wear and rock breaking mechanism.

## Acknowledgements

This work was financially supported by the Key Laboratory of Disaster Forecast and Control in Engineering, Jinan University, Ministry of Education of China (No.21613406) and the National College Students' Innovation and Entrepreneurship Training Program(No.201310559005,Jinan University).

## References

[1] Mengshu Wang: Rock Tunnel Boring Machine (TBM) Construction and Engineering Examples ( China Railway Publishing House, Beijing 2004 ).

[2] Zhichang Wan, Mingyuan Sha and Yanling Zhou: Mod. Tunn. Techno.Vol.39(2002(5)),p.1 (in Chinese)

[3] Zhaohuang Zhang: Construction Mach. Equip. (1995(06)), p.15(in Chinese)

[4] Zhaohuang Zhang: Full face rock tunnel boring machine and rock breaking theory of tools ( China Railway Publishing House, Beijing 2003).

[5] Zhaohuang Zhang, Changming Ji: J. Basic Sci. Eng. Vol.17(2009(02)), p.265(in Chinese)

[6] Zhaohuang Zhang: Construction Mach. Equip. (1998(02)), p.9(in Chinese)

[7] Dongsheng Tian, Zhaohuang Zhang: Construction Mach. Equip. (2000(02)), p.11(in Chinese)

[8] Chunlin Zhang: Advanced Theory of Mechanisms (Beijing Institute of Technology Press, Beijing 2005).

[9] Qixing Wu, Hongwei Ma: Appl. Mech. Mater. Vols.405-408(2013),p.3293

[10] Yimin Xia, Zhiyong Ji, Xiwen Zhou and Changfeng Tu: J. Wuhan Univ. Technol. Vol.32(2010), p.78(in Chinese)

*Applied Mechanics and Materials Vols. 580-583 (2014) pp 1238-1242*
*© (2014) Trans Tech Publications, Switzerland*
*doi:10.4028/www.scientific.net/AMM.580-583.1238*

# Mechanism analysis and prevention method for tunnel fire

Jing Wu[1,a],Feimin Shen[1,b], Ping Jiang[1,c]

[1]College of Civil Engineering, Fuzhou University, Fuzhou, Fujian 350108, China

[a]wujingcqu@163.com, [b]1003474815@qq.com, [c]13696867456@163.com

**Keywords:**Tunnel fire; Spontaneous combustion; Ambient temperature; Ventilation; Combustibles

**Abstract:**By analyzing the typical fire casesand tunnel fire statistics during 2008 to 2013 in Fujianprovince of China, results shows that the main causesfor the fire were vehicle accidents and spontaneous combustion. By the investigation, there are three approaches to prevent the tunnel fire exposed to different combustibles. For flammable solid, an effective method to prevent fires is to decrease the maximum environment temperature and the product concentration.For flammable liquid, adjusting the ambient temperature and enhancing ventilation can prevent or reduce the fire accidents.For flammable gas, the effective method to prevent the fire is to decrease the fuel density and the ambient temperature.So, for long tunnels or busy tunnels,it must strengthen the management of the vehicles. Moreover, in the hot season and rush hour it should control the ambient temperature inside the tunnels.

## Introduction

In recent years, with the rapid development of the transport industry, tunnels are emerging and the trafficsare increasing.The number and the frequency of vehicles which carrying all kinds of combustible material through tunnel is growing, and also the frequency of tunnel fire is increasing year by year.

According to statistics, the frequency of road tunnel fire is 10 to 17 times per million kilometers, which average frequency is 13.5 times per million kilometers,and the road tunnel fire risk is 20 to 25 times the railway tunnel[1]. Take an example of FujianProvince in China, the special topography as "eight mountains one waterand one field", the total number of expressway tunnels and the total length of single-hole tunnelsare all more than 470 and 470 kms in 2010. With the construction of the highway extending from the coastal areas to the inland mountains, the highway mileage will reach 6,100 kms, and the total length of single-hole tunnels will be more than 1000 kms till2020 inFujianProvince [2]. According to the data of Traffic Police Corps Public Security Bureau of Fujian Province, the highway tunnel accidents caused the number of deaths is nine in 2009 from the whole province, the death toll in 2010 and in 2011 is respectively ten and seven.Until October 2012, the number is six.

## Causes of tunnel fire

Through the typical cases, the various causes to the tunnel fire are as below [3~6]:

**1.1 Traffic accidents.**After vehicle occurred rear-end, scratch, collision (against wall), digression in the tunnel, fires take placed by the overturning derailment or the explosion. For example, the most serious tunnel accident up to nowwas happened in Salang tunnel of Afghanistan in 1982, a truck crashed into a tanker, causing an explosion, and resulting 200 deaths and hundreds of vehicles damaged. And just before author finalized the paper, two tankers carrying hazardous chemicals took rear-end collision in Yanhou tunnel of Shanxi province in China on March 1st, 2014, the front vehicle leaked out methanol, and the methanol caughtfire in the driver's disposal, then the rest vehicles and coal and other flammable goods ignited an explosion inside the tunnel, which caused 31deaths, and 9persons missing. The fire burned for 73 hours, 42 vehicles were damaged.

**1.2 Vehicles and cargo spontaneous combustion.**There are varieties of vehicles through the tunnel, some of them carrying combustible cargo or flammable items, which meet open flame or the road beating or in high temperature environment,then cargo mutual friction was burning or

spontaneous combustion occurred. Take an example: the earliest recorded tunnel accident was in 1949, the truck equipped with carbide and sulfide caught fire in Holland tunnel of New York in U.S.A, large amounts of carbon monoxide and sulfide were produced which led to 66 persons poisoned and 23 vehicles damaged. The tunnel was nearly severely damaged 200 meters.

**1.3 Vehicles own faults.**It was caused by power overheating, electrical circuit overload, short circuit and flash fire, and the wheel, rail, brake friction gave out heat. For example, a large truck caught fire due to friction tire burst in Spa tunnel of Beijing-Zhuhai expressway on March 21st, 2006, which caused tunnel lighting and fire-proofing seriously damaged, and the tunnel was maintained for 11 days before opening to traffic.

**1.4 Tunnels aging and failuresof electrical facilities.**Generally the tunnel useful life is very long. And it is dark, damp, dusty, electric and wiring facilities are easy to be aging and failure, equipment maintenance and overhaul are weak, which easily leads to fires. Such as on September 21st, 1987, the high-voltage wire spit fire in Ikoma Railway tunnel of Japanese, the broken power lines and the traveling train (the front) sparked firesin the tunnel, resulting 49 casualties.

**1.5 Arson.** Such as terrorist activities, take revenge on society, mental illness tolead man-made fires. As Daegu subway fire of Korea in 2003, a man ignited a plastic bottle which contained 2L gasoline, and then thrown to the carriage, resulting the entire cars and the train traveling across on fire, eventually leading to 196 deaths and 147 persons injured.

**1.6 Illegal use of fire.** It was caused by throw fire (cigarettes) and the use of unprotected fire. Such as: combustible gas explosion occurred inDaegu subway construction of Korea in 1995, killing 101 persons on the spot and injuring 143 ones.

**1.7 Other factors.** The earthquake, tornado, outside fire or other external hazards lead to vehicles or facilities in the tunnel on fire. For example in 2008, the train derailed due to Wenchuan earthquake and caught fire in the 109 tunnel of Baocheng railway inChina.

Table 1 shows the cause classification of railway, highway and subway tunnel fires in recent years.

Tab.1 Cause classification of tunnel fires in recent years[4]

| Classification of tunnels | The number of fires | Tunnel facilities spontaneous combustion | Vehicles and cargo ignition | Traffic accidents | Illegal use of fire | Arson | Others |
|---|---|---|---|---|---|---|---|
| Railway tunnels | 16 | 2 | 4 | 7 | 1 | 0 | 2 |
| Highway tunnels | 46 | 0 | 25 | 20 | 1 | 0 | 0 |
| Subway tunnels | 27 | 4 | 11 | 3 | 2 | 6 | 1 |

From Tab.1, for highway tunnels and subway tunnels, vehicle ignition is the main reason, followed by traffic accidents and arson. For railway tunnels, traffic accidents as the leading cause, followed byvehicles ignition. The resultis consistent with the tunnel fire statistics during 2008 to 2013 inFujianwhichwas acquired from Fujian Fire Brigade of China, as shown in Table 2 and Table 3.

Tab.2 Statistics of tunnel fires in Fujian province on January 2008 to May 2013

| Fires types | Number | Proportion |
|---|---|---|
| Failures of electrical facilities | 24 | 19.67% |
| Illegal use of fire | 1 | 0.82% |
| Vehicles and cargo ignition | 17 | 13.93% |
| Arson | 1 | 0.82% |
| Vehicles own faults | 0 | 0.00% |
| Traffic accident | 64 | 52.46% |
| Other | 15 | 12.30% |
| Total | 122 | 100.00% |

Tab.3 Statistics of tunnel fires in Fujian province in 2012

| Fires types | Number | Proportion |
|---|---|---|
| Failures of electrical facilities | 5 | 11.11% |
| Illegal use of fire | 0 | 0.00% |
| Vehicles and cargo ignition | 9 | 20.00% |
| Arson | 1 | 2.22% |
| Vehicles own faults | 2 | 4.44% |
| Traffic accident | 22 | 48.89% |
| Other | 6 | 13.33% |
| Total | 45 | 100.00% |

**Mechanism analyses of tunnel fires**

According to the tunnel fire causes investigation and Fujian tunnel fire statistics, the tunnel fire was mainly caused by trafficaccidents and spontaneous combustion. Due to the causesof traffic accidentsaremore complex, some scholars such as ShenAizhong[5], Kang Xiaolong[7] have studied, and the author would not repeat them again. This article focused on the combustion mechanism of some combustibles lead to vehicles ignition, and using this method to prevent the tunnel fire.

Combined with the types of flammable materials and combustion state, the tunnel fires classificationsare shown in Table 4. Generally, tunnel fires primarily are Class A, Class B and Class C fires. The following details describe these three types of fire burning mechanism.

Tab.4 Classifications for tunnel fires

| Items | Types | Definitions or features |
|---|---|---|
| Classified by the type of combustibles | Class A fire | Caused by carbonaceous solid combustibles such as wood, cotton, paper and so on. |
| | Class B fire | Caused by TypeA, B, C liquids, such as gasoline, diesel, methanol, etc. |
| | Class C fire | Caused by the flammable gases, such as coal gas, natural gas, acetylene, hydrogen, etc. |
| | Class D fire | Caused by flammable reactive metals, such as potassium, sodium, magnesium, aluminum-magnesium alloyand so on. |
| | Class E fire | Refers to the fire burning still live from electrical components and equipments, such as electronic components, electric and electronic wires and cables |
| Classification by burning state | Smoldering combustion | Smoldering fires burning, no flame |
| | Naked flame | The fire burning has a long flame |

**2.1 Flammable solid (Class A fire).**Before solid fuel caught fire, it usually had occurred pyrolysis due to heating, by melting, sublimation, cracking, pyrolysis and other gasification reaction, released flammable gas, which mixed with the oxidizer, and resulted in fire. It formed gas flame first.

At high enoughtemperature, common solid combustibles in the vehicle (such as: wood, coal, plastics, rubber, etc.) would occur pyrolysis and gasification reaction, and release flammable gases. Usually the volatile gases releasingorder is: $H_2O$, $CO_2$, $C_2H_6$, $C_2H_4$, $CH_4$, tar, CO, $H_2$, etc. At last, the productis the porous carbon. Determining how much the amount of carbon depends on fuel types, heating rate and the final temperature of heating. In particular, some solid combustibles rapidly increase alargenumber of flammable gases when the temperature reaches a certain value(flash temperature),such as the flash temperature of woodis 260℃, then the weak spark can ignite them, thus it must strictly monitor the ambient temperature.

In addition, smoldering combustion caused fires in many countries has a large proportion of the total, it should be much concerned. Smoldering is the only gas-solid interface burning, no gas-phase flame. Smoldering temperature is low, slow burning, and involves high levels of CO gas. The plume is explosive and flammable, not easy to discover, but great danger.

Compared with naked flame, smoldering fires' characteristics are: in the small heat strength, it can also occur smoldering.When the heat dissipation conditions are poor, the heat is likely to accumulate, and it would be benefit to spread.Smoldering would spread in low oxygen concentration environment.When the oxidation reaction rate is slow, and the corresponding maximum temperature is low, alsothe spread velocity is very slow.Using short high-speed airflow is difficult to blow smoldering.When the combustion zone expands, it could turn into flame fire.

In short, the maximum temperature and the product concentration in the reaction zone are the key parameters when solid combustible turn into the fire. These analyzes are consistent with scholars' experiment results[8].

**2.2 Flammable liquid (Class B fires).**Before burning, combustible liquids evaporated first, followed by the diffusion of fuel vapor, and mixed air to form a combustible mixture, at last formed the premixed flame or diffusion flame in space somewhere after ignition (the flame is not close to the surface, but in the location of space).

Therefore, the ignition characteristics are related to the evaporation of combustible liquids. And the flash point is an important parameter indicating the evaporation characteristics. Table 5 shows the flashpoint values of flammable goods which vehicles contained in the tunnel. The lower the flash point is, the more easily to be vaporized. From the table, most petroleum products have low flash point, even like diesel fuel, engine oil, etc. They may have a high concentration after a long period.Once within the firingrange, they are in the risk of combustion.

Tab. 5 Flash points of some flammable liquids

| Combustibles' name | Ethanol | N-butanol | Acetone | Petroleum | Engine oil | Cylinder oil | Gasoline | Lubricants |
|---|---|---|---|---|---|---|---|---|
| Flash point (℃) | 10 | 34 | -20 | 30 | 196 | 215 | 10 | 285 |

The morethe combustible liquidis likely to evaporate, the more the vapor concentration easily reaches the ignition ranges, and fire hazard is more danger. The evaporation characteristics are affected by temperature, thus it must monitor the ambient temperature and ventilation, and then the flammable vapors'concentration can't reach the firingrange.

As seen from above, the temperature is still an important factor. In order to prevent or reduce the tunnel fire, it should strengthen monitoring of liquid fuel in high-temperature environment.

**2.3 Flammable gas (Class C fire).** The combustible gas mixed with the oxidant (air or oxygen) in the space, when the mixture concentration reached the firingrange, under certain external conditions the reaction intensely accelerated, and the space instantaneously arriveda high temperature(on fire), then the external conditions called fire condition.It can be expressed asEq. (1):

$$f(T_0, P_0, h, d, u_\infty, T_\infty, x_i) = 0. \quad (1)$$

Where,

$T_0$: initial temperature of the combustible mixture. $P_0$: initial pressure of the combustible gas mixture. h:convective heat transfer coefficient of the system and the environment.d:the characteristic size of the system. $u_\infty$: the relative speed of the system and the environment. $T_\infty$: ambient temperature.$x_i$: ignition distance.

From Eq. (1), when the flammable gas and the system are constant, ambient temperature, wind speed and ignition distance play a vital role in the fire conditions.

In this system, the chemical-reactiongeneration heat and losing heat to environmentalare two main considerations. If the exothermic chemical-reaction plays a dominant role, the system must be on fire.Otherwise it can not be. Thus, the critical condition can be expressed asEq. (2):

$$\frac{VEP_c}{hFR^3T_\infty^4} Q_i k_{oi} X_A \cdot X_B \exp(-\frac{E}{RT_\infty}) = 1. \quad (2)$$

Where,

V - volume of the system, $m^3$

F - surface area of the system, $m^2$

$P_c$ - pressure, Pa

h - convective heat transfer coefficient, $W/(m^2 \cdot K)$

R - universal gas constant, J/(mol·K)

E - activation energy, J/mol

$T_\infty$ - ambient temperature, K

$Q_i$ - the heat of reaction, J/mol

$k_{oi}$- reaction constant

$X_A$, $X_B$- mass percentage of fuel and oxidant (concentration),%.

When $X_A$ and $X_B$ are constant, we can obtain the relationship between critical temperature and critical pressure.When $P_c$ is constant, we can get the relationship between critical ignition temperature and the concentration of combustible gas mixture. When $T_\infty$ is unchanged, we can gain the relationship between critical ignition pressure and the concentration of combustible gas mixture.

From Eq. (2) the firingrange curve can be drawn.And the curve shows that controlling fuel concentration and ambient temperature is an effective way to prevent ignition.

In fact, only one combustible during the burning in the fire is rare. Most of the fires are simultaneously burning several combustible materials.

## Conclusions

Combine the typical fire cases with tunnel fire statistics in Fujian, it shows spontaneous combustion and vehicle accidents are the two main causes.

To analyze the mechanisms of different combustibles leading to the tunnel fire, the following conclusions can be obtained:

(1) For solid combustibles, controlling the maximum environment temperature and the product concentration are the most effective measures to prevent fires.

(2) For the combustibleliquid, adjusting the ambient temperature and enhancingventilation can reduce the incidence of fires.

(3) For the combustible gas, monitoring fuel concentration and ambient temperature are still an effective way to prevent ignition.

## Recommendations

(1) For long tunnels or busy tunnels, it must strengthen the management of the vehicles to reduce the frequency of tunnel fires and the risk of accidents. Such as: set fast and effective equipments to detect inflammable and explosive goods at the tunnel entrances.The vehicles catching large amount or large-scale Class A fire hazard are ban or restricted through the tunnel.Tunnel traffic management department staff should regulate flammable product packing and transport, when the vehicles do not meet the packaging requirements and transport condition, they need to be corrective in the parking lot or go back to repackage and load, and to hang an obvious mark of dangerous cargo.

(2) In the hot season and rush hour it should control the ambient temperature inside the tunnel. Such as: install temperature probes.Once the temperature exceeds the critical value, they would start fans for ventilation.In addition to ventilation, it can also carry out other cooling measures.Under the traffic jam, it should control the number of vehicles entering the tunnel, and keepa requirement safe distance.

## References

[1] Deng Tian, Jian Zhang, Zhi Han:China ITS Journal. Vol.11 (2009), p.104-106 (in Chinese)
[2] Information on http://www.zgjtb.com
[3] JianQiang, HehuaZhu, ZhiguoYan, JianYao: Modern Tunnelling Technology (Supplement). Vol. 26 (2006), p.608-612 (in Chinese)
[4] Hao Hu, Liang Yi, Yang Yang: Chinese Public Security (Academic Edition).Vol.18 (2010), p.55-58 (in Chinese)
[5] AizhongShen: Road Traffic Management. Vol.17 (2002), p.40-41(in Chinese)
[6] Yaqiong Wang: Study on fire safety countermeasures in Single highway tunnel for subtended traffic.Xi'an: Chang'an University(2009), p.15 -17 (in Chinese)
[7] Xiaolong Kang, WeiWang, Yaohua Zhao, Gaoying Hua: Chinese Safety Science Journal.Vol.17 (2007), p.110-116(in Chinese)
[8] WeichengFan, QinganWang, Fenghui Jiang, Jianjun Zhou: Fire Science Concise Guide. China Science and Technology University Press,Hefei (1995), p.110-145(in Chinese)

*Applied Mechanics and Materials Vols. 580-583 (2014) pp 1243-1248*
*© (2014) Trans Tech Publications, Switzerland*
*doi:10.4028/www.scientific.net/AMM.580-583.1243*

# Metro construction safety risk assessment based on the fuzzy AHP and the comprehensive evaluation method

Xin Zheng[1, a], Fenghai Ma[1,b]

[1]College of Civil and Architectural Engineering, Dalian University, Dalian, 116622, China

[a]jasmine150@163.com, [b]xkb@vip.163.com

**Keywords:** Subway construction, Risk management, Risk assessment

**Abstract.** Facing with a variety of risks in the process of the metro construction, the metro construction needs to carry on the risk management. The risk assessment is the main link of the metro project risk management also the foundation of the decision analysis. This paper introduces the basic concept of the subway risk management, as a case study of Changchun No.1 subway construction risk assessment using the fuzzy AHP and the comprehensive evaluation method. The results show that Changchun subway station work sites exist many risk factors and the risk level difference is big. The major attention should be paid to the geological risks, the environment risks and the construction technical risks, while the environment risks and the construction technical risks are the focus of the risk analysis.

## Introduction

The adverse consequences or influence in the process of the subway and the underground engineering construction stands a big chance, whose main types include: economic losses, schedule delays, casualties, environmental impacts and social impacts. The implementation of the subway and underground engineering risk management should be reasonable and feasible to reduce the adverse consequences or adverse effects[1,2].

The project risk management refers to the project participants through risk definition, risk identification, risk estimate, risk evaluation and risk decision-making and control, optimizes the combination of various risk management techniques, the engineering implementation of effective risk control and tracking process properly. The project risk assessment is an important content and step in the process of the risk management. On the basis of project risk identification, with methods of risk assessment, it assesses overall risks of the project. According to the results of the risk assessment, take risk control measures, carry on the effective management of risk, make every stage of the project construction risk reduce to the lowest level[3].

The risk analysis of subway construction has quite a few achievements at the present stage, but still no in accordance with the risk of underground engineering construction to specific analysis. This paper, under the premise of the brief introduction of the risk management, combined with Changchun metro engineering construction, clearly puts forward all kinds of the risk source in Changchun subway construction, and a quantitative classification on the basis of this, the corresponding control measures are put forward.

## Risk Management

**The definition and classification of risk management.** The risk management is the economic unit of the possible risks to predict, identify, assess, analyze, and on this basis to effectively dispose of the risk at the lowest cost to achieve scientific management methods of the largest security .

Risk management is mainly divided into two categories:

(1) Business management risk management mainly study the political, economic, social change, the management risk which all enterprises face.

(2) Insurance risk management mainly regards insurable risk as an object of risk management, puts the insurance management at the core position, security management as a supplementary means.

**The objectives of risk management.** The basic goal of risk management is the minimum economic cost to obtain maximum security benefits. That is the least amount of the risk management to maximize dispersed expenses, transfer, eliminate the risk in order to achieve economic benefits and safeguard people's basic purpose of social stability.

**The content of risk management.** The content of the risk management includes the following four parts:

(1) Risk identification. The risk identification is the first step in project risk management. It refers to identify the principal risks affecting project quality, progress, investment and security objectives successfully achieved.

(2) Risk assessment. Risk assessment is the quantification of the project risk process after risk identification. Risk assessment can be used in an integrated evaluation method, AHP analytic hierarchy process and fuzzy evaluation method, etc.

(3) Risk analysis. Risk analysis is based on the previous work in the process of the project management about the consequences of any events that may occur, in order to determine the probability of the event and the potential impact of the project related to the possible consequences.

(4) Risk Control. Risk control is the use of certain techniques to try to avoid or control risks, eliminate or reduce the risk of loss caused by the incident. Focus on risk control is to eliminate the risk factors and reduce the risk of loss.

## Subway Construction Risk Assessment

Yikuang Street station in Changchun No.1 subway project as an example, uses the AHP and the fuzzy comprehensive evaluation method for the risk assessment, in order to solve possible safety hazards in Changchun subway construction, ensuring the safety of the subway construction.

**Project overview.** Yikuang street station is located at a street intersection of the Yikuang street and the people's street, along the people's street to the north-south layout. The standard segment of the main structure of the station is two-floor cross- island platform, the effective platform length is 118m and the total width of the standard segment is 19.0m. The station floor depth is of 16.0m~19.0m and the roof cases 3.0m ~ 4.35m. The main station and the station interval structure use the open cut method construction. The retaining structure is in the form of bored piles combined with steel support while soil between piles is under the protection of the net-suspended spray concrete. In the main scope of the station underground are many pipelines. The site formation is composed of the quaternary holocene artificial filling soil layer, the quaternary alluvial cohesive soil and sandy soil, the cretaceous mudstone. Two layers of groundwater exist in the interval formation. The foundation pit precipitation method of the main structure uses tube well dewatering.

**Risk identification.** Through access to a large number of the station construction materials, taking the actual needs of the project and the operational risk assessment into account, do the systems analysis. The risk of the Yikuang street station Construction(A) are divided into the geological risk($B_1$), the construction technology risk($B_2$), the environment risks($B_3$). The geological risk($B_1$) has subordinate levels: the poor stability silty clay layer($C_1$); the construction technology risks($B_2$) have subordinate levels: the bored piles construction risks($C_2$), the erection of steel support is not timely($C_3$), the net sprayed concrete and the waterproof mortar is not timely($C_4$), the pit heap dynamic load is too large($C_5$), the winter construction risks($C_6$); the environment risks($B_3$) have subordinate levels: the adjacent buildings($C_7$), the power lines under the precincts of the mainland($C_8$), the venue feedwater supply cast iron DN300($C_9$). According to these three risk factors as the criterion, set up 3-class hierarchy model, use fuzzy analytic hierarchy process(AHP)[4] to the subway station construction risk identification[5,6]. The process is as follows.

(1) Establish hierarchical structure model. As is showed in fig.1.

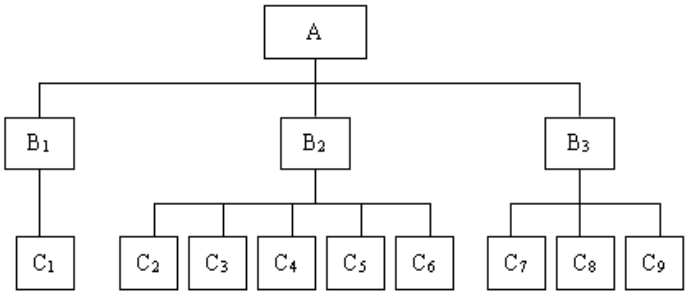


Fig.1 The structure model of hierarchical levels

(2) Priority of judgment matrix. In Yikuang street station construction risk pass class hierarchy model with more than one layer of each element layer elements as a criterion, establish fuzzy preference relation matrix.

$$A^K = (a_{ij}^k)_{n\times n}, k = 1,2,\cdots,m \tag{1}$$

In the above formula, $a_{ij}^k$ stands for the precedence relations coefficient evaluated between the object i and j. When the evaluation object i is better than j, $a_{ij}^k = 1$; when the evaluation object i is the same as j, $a_{ij}^k = 0.5$; when the evaluation object i is worse than j, $a_{ij}^k = 0$. The results of the judgment optimizing the relationship between numerical value is shown in Tab.1, Tab.2 and Tab. 3.

Tab.1 A~$B_{1\text{-}3}$ precedence relations determined matrix

| A | $B_1$ | $B_2$ | $B_3$ |
|---|---|---|---|
| $B_1$ | 0.5 | 0 | 0 |
| $B_2$ | 1 | 0.5 | 0.5 |
| $B_3$ | 1 | 0.5 | 0.5 |

Tab.2 $B_2$~$C_{2\sim6}$ precedence relations determined matrix

| $B_2$ | $C_2$ | $C_3$ | $C_4$ | $C_5$ | $C_6$ |
|---|---|---|---|---|---|
| $C_2$ | 0.5 | 0 | 0 | 0 | 0 |
| $C_3$ | 1 | 0.5 | 0.5 | 0.5 | 1 |
| $C_4$ | 1 | 0.5 | 0.5 | 0.5 | 1 |
| $C_5$ | 1 | 0.5 | 0.5 | 0.5 | 1 |
| $C_6$ | 1 | 0 | 0 | 0 | 0.5 |

Tab.3 $B_3$~$C_{7\sim9}$ precedence relations determined matrix

| $B_3$ | $C_7$ | $C_8$ | $C_9$ |
|---|---|---|---|
| $C_7$ | 0.5 | 1 | 1 |
| $C_8$ | 0 | 0.5 | 0.5 |
| $C_9$ | 0 | 0.5 | 0.5 |

(3) Construction of fuzzy judgment matrix. Numerically transform the above priority of judgment matrix according to the following formula.

$$r_{ij} = \frac{r_i - r_j}{2n} + 0.5 \tag{2}$$

$$R = r_{ij} = \begin{pmatrix} r_{11} & r_{12} & \cdots & r_{1n} \\ r_{21} & r_{22} & \cdots & r_{2n} \\ \cdots & \cdots & \cdots & \cdots \\ r_{n1} & r_{n2} & \cdots & r_{nn} \end{pmatrix} \tag{3}$$

In the above formulas, $r_{ij}$ stands for the relative importance of element i compared with j. You can get fuzzy judgment matrix as $R^{A}_{B_{1-3}}$, $R^{B_1}_{C_1}$, $R^{B_2}_{C_{2-6}}$, $R^{B_3}_{C_{7-9}}$.

$$R^{A}_{B_{1-3}} = \begin{pmatrix} 0.617 & 0.417 & 0.417 \\ 0.417 & 0.667 & 0.667 \\ 0.417 & 0.667 & 0.667 \end{pmatrix} \qquad R^{B_1}_{C_1} = (1)$$

$$R^{B_2}_{C_{2-6}} = \begin{pmatrix} 0.100 & 0.400 & 0.400 & 0.400 & 0.200 \\ 0.400 & 0.700 & 0.700 & 0.700 & 0.300 \\ 0.400 & 0.700 & 0.700 & 0.700 & 0.300 \\ 0.400 & 0.700 & 0.700 & 0.700 & 0.300 \\ 0.200 & 0.500 & 0.500 & 0.500 & 0.300 \end{pmatrix} \qquad R^{B_3}_{C_{7-9}} = \begin{pmatrix} 0.833 & 0.583 & 0.583 \\ 0.583 & 0.333 & 0.333 \\ 0.583 & 0.333 & 0.333 \end{pmatrix}$$

(4) Single -level sorting. Using the square root to calculate Yikuang street station hierarchical structure model, the indicators relative to the upper layer of the criteria weights. The calculation results obtain as follows.

$\partial^{A}_{B_{1-3}} = [0.222 \;\; 0.389 \;\; 0.389]^{T}$ $\qquad \partial^{B_1}_{C_1} = [1]^{T}$

$\partial^{B_2}_{C_{2-6}} = [0.126 \;\; 0.235 \;\; 0.235 \;\; 0.235 \;\; 0.168]^{T}$ $\qquad \partial^{B_3}_{C_{7-9}} = [0.445 \;\; 0.278 \;\; 0.278]^{T}$

(5) The total level sorting. Synthesized according to the relative weigh, calculate the element C level relative to A weights of hierarchy elements, in order to achieve overall level sorting. The results are shown in Tab.4.

Tab.4 The hierarchy total sort

| Level | $B_1$ | $B_2$ | $B_3$ | $\partial^{A}_{C}$ | Sort |
|---|---|---|---|---|---|
| | 0.222 | 0.389 | 0.389 | | |
| $C_1$ | 1.000 | 0.000 | 0.000 | 0.222 | 1 |
| $C_2$ | 0.000 | 0.126 | 0.000 | 0.049 | 6 |
| $C_3$ | 0.000 | 0.235 | 0.000 | 0.091 | 4 |
| $C_4$ | 0.000 | 0.235 | 0.000 | 0.091 | 4 |
| $C_5$ | 0.000 | 0.235 | 0.000 | 0.091 | 4 |
| $C_6$ | 0.000 | 0.168 | 0.000 | 0.065 | 5 |
| $C_7$ | 0.000 | 0.000 | 0.445 | 0.173 | 2 |
| $C_8$ | 0.000 | 0.000 | 0.278 | 0.108 | 3 |
| $C_9$ | 0.000 | 0.000 | 0.278 | 0.108 | 3 |

Obtained from Tab.4, according to the geological risk, the construction technology risk and the environment risk, the order of importance for the risk factors effected on Changchun Yikuang Street subway station construction is $C_1$, $C_7$, $C_{8,9}$, $C_{3\text{-}5}$, $C_6$, $C_2$.

**Risk Assessment.** Metro station construction risk assessment is on the basis of identifying the source of the metro station construction risk, establishing a model comprehensively considering the risk probability and the risk assessment. According to the relevant risk acceptance criteria and

evaluation standards, evaluating the metro station construction risk, which will provide a scientific basis for the risk response and monitoring, could ensure the metro station project smoothly.

In this paper, Yikuang street station construction risk acceptance criteria and evaluation criteria applied the relevant provisions of grade adopt the rules of the urban rail transit construction risk management of underground engineering (GB50652-2011). Using comprehensive evaluation method, first of all, according to the identified risk factors list the risk questionnaires, then please experienced experts to evaluate the possible risk factors and risk events, and then integrate and conclude that the overall level of risks, the risk classification are shown in Tab.5.

Tab.5 Yikuang street station risk classification

| Risk Type | Risk Factors | Risk events | Risk Level | The overall risk level |
|---|---|---|---|---|
| Geological risk($B_1$) | $C_1$ | Disturbed by the construction of large deformation | Ⅳ | Ⅲ |
| Construction technology risk($B_2$) | $C_2$ | Split between pile, piles intrude into structure limits | Ⅲ | |
| | $C_3$ | Maintenance of structural deformation | Ⅲ | |
| | $C_4$ | Leakage of water | Ⅲ | |
| | $C_5$ | Excessive local deformation | Ⅲ | |
| | $C_6$ | Concrete frostbite , support prestressing loss | Ⅲ | |
| Environment risk($B_3$) | $C_7$ | Settlement deformation | Ⅲ | |
| | $C_8$ | Mechanical construction, easy to break | Ⅱ | |
| | $C_9$ | Subsidence deformation, easy water leakage | Ⅲ | |

## Conclusion

Subway construction technology is now quite mature, but due to the construction market confusion, the expansion of construction scale, resulting in a subway construction is still accident-prone subway construction phase, and targeted to construction risk analysis is quite necessary. Yikuang street station construction risk assessment as an example, assess the construction risks of the every work site in Changchun No.1 subway. The following conclusions can be drawn:

(1) Changchun subway construction risk analysis is focused on the construction technology risk and the environment risks, while the geological risk of the construction risk related to the influence of the environment risks and the construction technology risks is relatively weak.

(2) The supporting process of the foundation pit excavation phase is the main part of the risk of construction technology, taking reasonable support method and strict construction quality control is the key to solve this problem.

(3) On the ground along Changchun subway line existing a mass of buildings and large structures and the underground pipe network are the main factors causing the environment risk.

**Acknowledgment**

This work is supported by the National Natural Science Foundation of China (51174038).

**References**

[1] Shengli Zhu, Wenbin Wang, Weining Liu. Subway construction risk management[J]. Urban Rail Transit. Vol. 21(2008), p.56 (In Chinese)

[2] Jing Wang, Pengfei Wang, Tanyue Hu. Risk Management subway tunnel construction project[J]. Underground Space and Engineering. Vol. 5(2009), p. 385 (In Chinese)

[3] Youjie Lu, Jiayi Lu. Project Risk Management[M]. Beijing: Tsinghua University Press(1988) (In Chinese)

[4] Jijian Xie, Chengping Liu. Fuzzy mathematical methods and its applications[M]. Wuhan: Huazhong University and Technology Press(2006) (In Chinese)

[5] Xunjie Guo, Fenghai Ma, Qingyuan Yang, etc. Hefei subway station construction risk analysis[J]. Liaoning University of Engineering and Technology. Vol. 31(2012), p. 300 (In Chinese)

[6] Xiaohao Li, Yongfa Song. CIM model in the construction of the subway security risk assessment[J]. Engineering Management Journal. Vol. 24(2010), p. 513 (In Chinese)

*Applied Mechanics and Materials Vols. 580-583 (2014) pp 1249-1253*
*© (2014) Trans Tech Publications, Switzerland*
*doi:10.4028/www.scientific.net/AMM.580-583.1249*

# Monitoring and Analysis for the Deformation of SMW Retaining Structures in Subway Station

Jiangtao Xia[1, a], Shaofei Zhang[2], Huarong Shen[1], Zejun Liu[1], Shiqing Huang[3, b]

[1]School of Civil Engineering, Huaiyin Institute of Technology, Huai'an 223001,China

[2] Department of Mechanics and Civil Engineering, Jinan University, Guangzhou 510632, China

[3] MOE Key Lab of Disaster Forecast and Control in Engineering, Jinan University, Guangzhou 510632, China

[a]xjthyit@163.com, [b]thuangsq@jnu.edu.cn

**Keywords:** Deep Foundation Pit; SMW; Monitoring; deformation; Subway Station.

**Abstract.** The monitoring is carried out for deformation of the soil-mixing-wall structures used in Baijihu subway station. The horizontal displacement of deep soil is obtained, as well as the ground subsidence around the edges of the foundation pit. Their variation rules under the influence of some factors, such as soil excavation and support settings etc, is analyzed. The results show that during the process of SMW construction, it is necessary to monitor the horizontal displacement of deep soil and the ground subsidence around the edges of the foundation pit, especially during the early stage of excavation.

## Introduction

Soil-Mixing-Wall (SMW) construction method is a relatively new flexible retaining technology for deep foundation pit. It have some advantageous characteristic in terms of social and economic efficiency compared with other retaining structures. However, its working mechanism and design theory remains immature yet. Therefore, it's limited from a wide range of applications for deep foundation engineering.[1-2] With the advent of the era of the subway, it is particularly urgent to strengthen the research in the field of how to accurately predict the deformation of SMW retaining structures in deep foundation pit, in order to take measures to control the loading and deformation in the process of design and construction of subway.[3]

In recent years, various kinds of practical methods have been put forward to improve the performance of SWM retaining structures. Osamu et al.[4] introduced the soil-cement mixed wall technique for excavation support and groundwater control. Anderson[5] introduced an innovative retaining wall technique utilizing a deep soil mixed cutoff wall system with an architectural concrete facing. Nicholson et al.[6] presented a design for a new deep mixing method wall system using deep mixing techniques with an array of soil/cement mixed columns arranged in the native soil to creates a gravity block. Kim et al.[7] proposed a novel retaining wall system employing the soil-cement mixing technique which can be applied at urban excavation sites. David et al.[8] described the construction of the cement deep soil mixed wall for the earth retention system.

In this paper, the monitoring is carried out for the horizontal displacement of the maintenance structures in the deep soil, as well as the surrounding ground subsidence, for the Baijiahu station. Meanwhile, the variation of the horizontal displacement in deep soil and the ground subsidence under the influence of some factors, such as soil excavation and support setting etc, is analyzed. As a result, the deformation rules of SMW retaining structures are found when it is applied for the deep foundation pit during the construction of subways stations.

## Overview of the Project and its Monitoring

**Project overview.** Baijiahu station belongs to the south extension of Line 1 of Nanjing subway. It is located in the north from intersection of Ningli Road and Tianyuan Road, near the north-south axial of

Phoenix Port. Baijiahu station is designed as a box-like structure with two layers and three spans lying underground. The first layer underground is the station hall and the second layer is platform, which has an island-like form and a width of 12 m.

The geological conditions in this project is very complicated, which can be described as follows. From top to bottom, ①-1 miscellaneous fill, ③-1b1-2 silty clay (hard-plastic), ③-1c2-3 silty soil (slightly-medium density), ③-2d2-3 silty sand (slightly-medium density), ③-2b2-3 silty clay (plastic), ③-4e silty sand mixed gravel, k1g-1 strong weathered argillaceous conglomerate, k1g-2 moderately weathered argillaceous conglomerate, the based floor located on ③-2d2-3 silty sand.

The open-cut and sequential construction technique is adopted for the main structures. The depth of the foundation pit varies from 14.494m to 14.834m. Thus, φ850@600 cement -soil three-axis mixing piles with interpolation of HN700×300 steel are applied in the retaining structures. According to the depth of excavation and geological data, the interpolation steel is arranged in two ways: two h-shaped steel interpolated with one ignored, and one ore ignored. All of the h-shaped steels will be recycled after the construction of main structures is completed.

The layout of the station is mainly symmetric along the direction in the plane. At the corner of the pit, moderate amount of diagonal braces are set down to stabilize the walls of the foundation pit. The excavation of the pit is symmetrically carried out, layer by layer and segment by segment. The depth of each layer of excavation is about 3m. Before the support and the waist beam are installed, the excavation should be extended down to about 0.3m below them. The supports in the walls of the main foundation is divided into four groups distributing in the vertical direction. The length of vertical intervals between each group are 4.1m , 3.0m and 4.1m, respectively. And the horizontal intervals between each support is 3.5m.

**Monitoring Scheme.** According to some general characteristics of Baijiahu station, such as engineering geology and construction, etc., the plain layout of the monitoring points of the foundation pit is shown in Fig. 1. Herein CX1–CX8 denote the monitoring points for the horizontal displacement of the deep soil; $Z_{1\text{-}1}$–$Z_{6\text{-}4}$ denote the monitoring points for the axial forces in the steel supports; $d_i$ ($i$ = 1–22) denote the monitoring points for the surrounding ground subsidence.

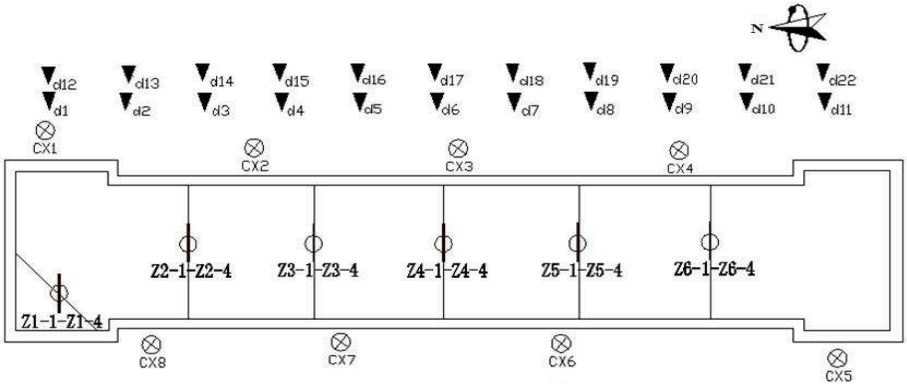


Fig.1 Layout diagram of the monitoring points

The main monitoring points are distributed as follows: In order to measure the horizontal displacement of the deep soil, four monitoring points are set up in the measurement holes on each side of the station's section. And 8 inclinometers are buried in the inclinometers holes, which are drilled by the light drilling rig. Each hole has the depth of 30m, numbered from CX1 to CX8. Twenty-two monitoring points for the surrounding ground subsidence are located on the road near the east of the station. Each monitoring point is numbered as $d_i$ ($i$ = 1–22). In the 6 typical sections of foundation pit, a steel-string type axial force meter is arranged at one end of each steel pipe support in order to monitor the supporting force. There are four support on each typical section. All of the 24 monitoring points are numbered as $Z_{i\text{-}j}$ ($i$ = 1–6, $j$ =1–4), where $i$ represents the No. of sections, and $j$ represents the No. of supports on each section. For example, "$Z_{3\text{-}2}$" represents the second supporting axial force monitoring points from top to bottom in the third section.

## Monitoring Results and Analysis

**Monitoring and analysis of deep soil horizontal displacement.** The whole process of the excavation of the foundation pit can be divided into six steps. In Step 1, the excavation is extended to the location near the first support. In Step 2, the first support is installed and the first layer of the foundation pit is excavated. In Step 3, the second support is installed and the second layer of the foundation pit is excavated. Step 4 and Step 5 can be deduced from this. In Step 6, the main structures of the station is poured, as well as the foundation cushion.

The horizontal displacement of deep soil varies continuously along with the steps. The monitoring results obtained from point CX8 is shown in Fig. 2. In Step 1, the horizontal displacement is relatively small. From Step 2 to Step 3, the maximum horizontal displacement increases rapidly from 3.5mm to 17.7mm. It is mainly resulted from the quick release of the loading during the process of the excavation. And the rate of load releasing is the fastest at the beginning of excavation.

As the first two support is set up timely, the stiffness of the retaining structures becomes higher. As a result, there is no notable variation in the horizontal displacement from Step 3 to Step 4. It is obvious that the first and second support have significant restriction on the horizontal displacement of retaining structures. In Step 6, the maximum horizontal displacement is 29.3mm, which does not exceed the alarm value (30mm). The maximum value occurs at the depth of 10.5 m, about 3/4 depth of the pit.

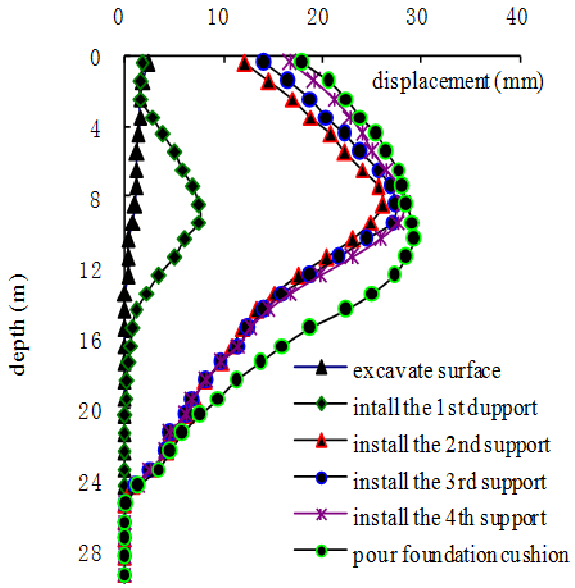


Fig.2 Curves of horizontal displacement of retaining structure in CX8.

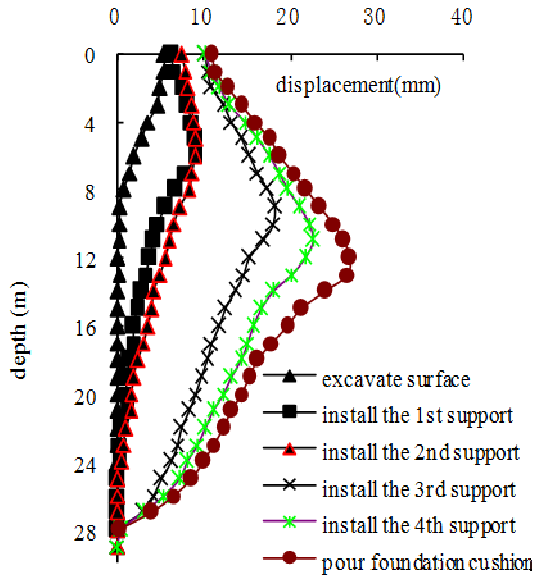


Fig.3 Curves of horizontal displacement of retaining structure in CX2.

The monitoring results obtained from point CX2 is shown in Fig. 3. Its variation tendency is similar with the one in CX8. Only the maximum horizontal displacements at the pile head are slightly different: CX8 is 18.0mm, while CX2 is 10.7mm. It is maybe caused by storing of the steel supports near the west side of CX8 monitoring point. Therefore, during of the process of construction, the heaped load around foundation pit should be strictly controlled. Moreover, the load near the edges of the foundation pit should be reduced as much as possible to minimize the impact on the deformation of the foundation pit. The maximum value of the deep soil's horizontal displacement in CX2, close to the one in CX8, does not exceed the alarm value either. It can be concluded that temporary heaped load has less influence on the maximum value of the deep soil's horizontal displacement.

**Monitoring and analysis of surrounding ground subsidence.** There are no important buildings around the project. The subsidence curves at surface monitoring points ($d_1$–$d_5$) located in a row near the east side of the foundation pit are shown in Fig. 4. As it can be seen from the Fig. 4, the ground subsidence at all monitoring points is relatively small. The maximum occurs at the point $d_4$ with the value of only -3.4mm, where the minus sign denotes the downward subsidence.

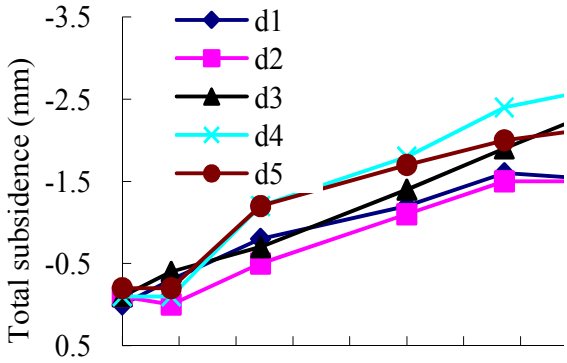


Fig.4 Ground subsidence curves at monitoring points $d_1$-$d_5$.

During the process of SMW construction, the soil is cut and mixed, which cause a relatively small disturbance in the soil around the foundation pit. It is shown from the theoretical analysis that the ground subsidence curves are groove-like. At the monitoring point closer to the edges of the pit, the subsidence is larger, and vice versa. It is shown, from the Fig. 4, that there is a similar developing trend of the subsidence at all monitoring points. The maximum subsidence was detected on October 14th, when the excavation was extended to the location near the forth support. All of the ground subsidence curves can be divided into three stages obviously. In the first stage, the subsidence develops rapidly during the Step 1 of the excavation. The vertical deformation is mainly led by the lateral deformation of the support structures, which accounts for about 34% of the total subsidence. As mentioned above, the fast rate of the subsidence is mainly resulted from the quick deformation of the support structures during the initial process of the excavation. In the second stage, the pre-stressed steel supports provide an enough lateral supporting force to reduce the lateral displacement. Thus, the further subsidence is prevented and the downward subsidence becomes slow. In the third stage, the cushion was poured, and the foundation pit tended to be almost stable. Therefore, the subsidence gradually became stable and slow.

The final total ground subsidence at all monitoring points are listed in Table 1. It can be found that there is an obvious space effect in the around ground subsidence. The ground subsidence at most monitoring points has a trend of downward subsidence. Exceptionally, in the initial process of the excavation, there is slightly rising at the north points $d_1$, $d_2$, $d_{12}$, $d_{13}$, due to the temporarily stacked materials around the foundation pit.

The SMW retaining structures are somewhat flexible. When the excavation is fairly deep, and the soil is relatively soft, a considerable plastic flow would occur in the soil. As the soil near the support structures deviates to the interior and the bottom of the foundation pit, the stresses in the soil behind the retaining walls are released, and the ground subsidence occurs.

Tab. 1 Final total ground subsidence at all monitoring points

| | | | | | | |
|---|---|---|---|---|---|---|
| Monitoring points | $d_1$ | $d_2$ | $d_3$ | $d_4$ | $d_5$ | $d_6$ |
| Subsidence (mm) | -1.5 | -1.5 | -2.5 | -2.7 | -2.2 | -10.2 |
| Monitoring points | $d_7$ | $d_8$ | $d_9$ | $d_{10}$ | $d_{11}$ | $d_{12}$ |
| Subsidence (mm) | -29.7 | -29.9 | -17.4 | -20.7 | -18.7 | -1.2 |
| Monitoring points | $d_{13}$ | $d_{14}$ | $d_{15}$ | $d_{16}$ | $d_{17}$ | $d_{18}$ |
| Subsidence (mm) | -2.9 | -4.1 | -3.4 | -3.3 | -7.0 | -38.9 |
| Monitoring points | $d_{19}$ | $d_{20}$ | $d_{21}$ | $d_{22}$ | | |
| Subsidence (mm) | -79.2 | -21.1 | -19.4 | -14.1 | | |

As it can be seen from Table 1, the subsidence at points $d_{18,}$ $d_{19,}$ $d_{20}$ is relatively large. The underground pipelines around the pit are damaged during the process of construction, which caused the leakage accident occurring in the southeastern section of the foundation pit. As a result, the ground subsidence at the corresponding points around the pit is increased. The subsidence at the monitoring points of $d_{18,}$ $d_{19}$ and $d_{20}$ exceeds the alarming value.

Herein, some measures, such as gravity grouting, dewatering well, are timely taken to prevent the subsidence from increasing. When the sidewalls in the leakage section are poured completely, the dewatering wells stop working. The downward subsidence becomes slower, even has a rising trend with the recovery of groundwater level. Finally, the subsidence is controlled.

## Conclusions

Through monitoring and analysis for the deformation of the SMW structures used in Baijiahu station, it can be concluded that:

(1) The soil-mixing-walls (SMWs) are flexible retaining structures. During the excavation, the maximum value of horizontal displacement appears at about 3/4 depth of the foundation pit.

(2) The axial forces in the support structures vary with the depth of excavation. During the process of excavation of foundation pit, it is necessary to strictly control the preloading around the edges of pit to reduce its influence on the deformation of foundation pit.

(3) During the early stage of excavation, the ground subsidence is obvious (about 34% of the total subsidence), which need strict monitoring. When the pouring of cushion is finished, the ground subsidence around the foundation pit becomes gradually stabilized.

(4) It is necessary to enhance the monitoring during the construction, which will contribute to the quick feedback of construction information. Informational construction is an effective means for the smooth implementation of SMW construction method. It is helpful to promptly find the problem and adopt the optimal countermeasure.

## Acknowledgement

The support of this work from the National Natural Science Foundation of China (Grant No. 10902043 and 11032005), the Specialized Research Fund for the Doctoral Program of Higher Education of China (Grant No. 20094401120005), Foundation for Distinguished Young Talents in Higher Education of Guangdong, China (Grant No. LYM09027) is acknowledged.

## References

[1] H. Chen. Research on Interaction of Shaped Steel and Cement-Soil of SMW Engineering Method [D]. Tianjin: Tianjin University School of Civil Engineering, 2003. (in Chinese)

[2] X.J Wu. G.B. Liu. Application of SMW method in a deep foundation pit of under-zhangyang Rd, Pudong South Road. Underground Engineering and Tunnels. Vol. 24 (2005), p. 27 (in Chinese)

[3] D.Q. Wu. Research on calculation means and application of retaining structure in SMW engineering method [D]. Xian: Xian University of Science and Technology, 2006. (in Chinese)

[4] O. Taki, D.S. Yang. Excavation support and groundwater control using soil-cement mixing wall for subway projects. Proceedings - Rapid Excavation and Tunneling Conference. (1989), p. 156.

[5] T.C. Anderson. Anchored deep soil mixed cutoff/retaining walls for Lake Parkway project in Milwaukee, Design and Construction of Earth Retaining Systems. Vol. 83 (1998), p.1.

[6] P.J. Nicholson, J.K. Mitchell, E.W. Bahner, Y. Moriwaki. Design of a soil mixed composite gravity wall. Geotechnical Special Publication. Vol. 81 (1998), p. 27.

[7] Y.S. Kim, Y.S. Cho. A case study of retaining wall with soil-cement mixing reinforcement for Korean Urban site. Geotechnical Special Publication. Vol. 206 (2010), p. 70.

[8] W. David, Z. Daren. Deep soil mixed wall and jet grouting for an excavation retention system at museum of fine arts, Boston. Geotechnical Special Publication. Vol. 228 (2012), p. 379.

*Applied Mechanics and Materials Vols. 580-583 (2014) pp 1254-1257*
*© (2014) Trans Tech Publications, Switzerland*
*doi:10.4028/www.scientific.net/AMM.580-583.1254*

# Approach on Pollution gases Diffusion Path of small Spacing Tunnel Entrance Based on CFD

Yanying Xing

Research Institute of Highway Ministry of Transport, RIOH Transport Consultants Ltd, Kuangyi Building,No.15 East Huayuan Road,Haidian Distric,Beijing,China 1001911

zdxyy@vip.sina.com

**Keywords:** Small spacing tunnel. Diffusion path.CFD. Treatment program

**Abstract.** Small spacing tunnel due to the special structure form and two tubes are only separated by a thin wall. This structure form is likely to cause secondary pollution, pollution gas discharged into the adjacent tunnel. This phenomenon will lead to increased ventilation system energy consumption. This paper analysis gas diffusion path between two adjacent tunnels, using CFD (Ansys Fluent). To relieve the pollution gases secondary pollution of tunnel portal area, using CFD analyzed gas diffusion path under different circumstances, for opening hole on the top of sunshades, extended of the wall between two adjacent tunnels and other programs, and identify more comprehensive disposal program.

## Introduction [1,2,3]

Due to the special structure form of small spacing tunnel, two tubes are only separated by a thin wall. Two-tubes can't be staggered in the longitudinal direction (refer with: Fig. 1). This structure form is likely to cause secondary pollution pollution gases on tunnel entrance area, reducing the efficiency of the ventilation system.

This article relies on a small spacing tunnel, using CFD software to analyze the gas diffusion path .Based on the analysis results, take appropriate measures to alleviate secondary pollution polluting. Using CFD software analyze the spread of pollution gases under taken different treatments and put forward the corresponding counter measures.

Fig.1 Schematic of small spacing tunnel portal (Sketch map)

## Description of small spacing tunnel

Tunnel with two-tubes
One-way traffic
Six-lane (two-way)
Small spacing with sunshades
Jet fan longitudinal ventilation (normal operation case)

## Numerical simulation model [4,5,6]

Establish the actual tunnel size ratio of 1:1 numerical model.

Using CO as tracer gas.

Viscous model: k-ε

Component transport model

The actual model by using a three-dimensional model of the tunnel 1:1 numerical simulation as following:

Tunnel model length is 20m. Cave sunshades length is 90m.

Tunnel exit section length 100m, width 80m, 50m high cubes simulation outside atmosphere.

In order to simplify the problem, the model made the following assumptions:

1) Made in the tunnel the tracer gas inlet CO with maximum concentration 150ppm.

2) Considered contaminated gas flow rate and concentration at the exit of the tunnel are evenly distributed.

3) Don't consider the impact of motor vehicle pollution in the tunnel gas diffusion.

## Pollution gases diffusion path under original model [5,6]

At the exit of the tunnel ( no wind on the sunshades tunnel exit )， pollution gases diffusion path were simulated, CO concentrations are shown below(refer with: Fig. 2).

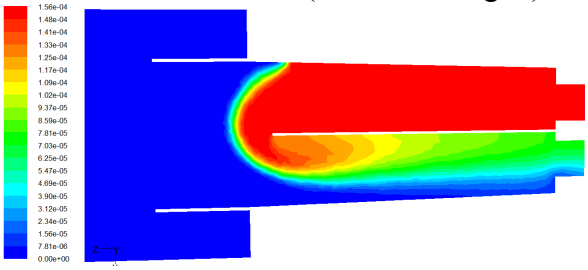


Fig.2 Pollution gases diffusion path near tunnel portal (original model)

As can be seen from the Fig.2, CO concentrations of downstream tunnel entrance is higher. Pollution gas diffusion along the tunnel entrance area into the adjacent tunnel with the piston wind action. It causes pollution gases such secondary pollution between two tubes.

By analyzing the simulation results, CO concentrations of upstream and downstream tunnel entrance tunnel exit were 150ppm, 55.3pmm. Approximately 30% of pollution gases from upstream tunnel come into the downstream tunnel. To reduce secondary pollution between two tubes, it's necessary to take measures to intervene contaminated gas diffusion path. Combined with engineering practice, ready to adopt the following three options: " increase the length of the wall between two tubes", "open holes on top of sunshades " and " increase the length of the wall between two tubes combined with open holes on top of sunshades " .Analyzed pollution gases diffusion path for three scenarios, using CFD software and identify the optimal technology solutions.

## Pollution gases diffusion path under improve model [5,6]

Creat numical simulation models based on on the actual size of the tunnel and analyze pollution gaes diffusion path under different case.The results of pollution gaes diffusion path under three kind of program conditions ,as following:

- **Lengthen the wall between the two tubes**

Under no wind conditions outside, lengthen the wall between the two tubes (Length increased is 20m), CO diffusion path as shown below (refer with: Fig. 3).

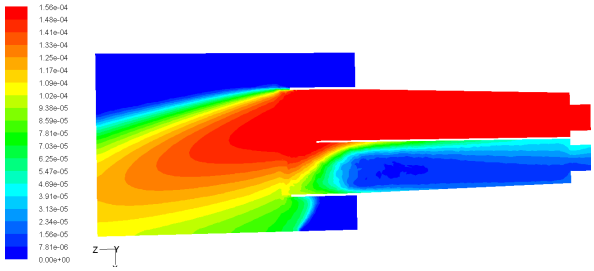

Fig.3 Pollution gases diffusion path near tunnel portal (lengthen the wall between two tubes)

As can be seen from the Fig 3, the concentration of pollutant gases downstream of the tunnel is relatively small and the polluted gas diffusion in the horizontal direction. Compared with the original model, contaminated gas stream to get a better suppression. This is due to the growth in the length of the wall, so that the interaction between two tubes is relatively small.

After analyzing the results of numerical simulation, concentration of CO is 150ppm on tunnel exit portal, and concentration of CO is 23.6ppm on adjacent tunnel entrance. Pollution gases upstream of approximately 15.6% in the tunnel into the downstream tunnel. Compared with the original scheme, polluted gas stream between two tubes has been greatly improved.

- **Open holes on top of tunnel sunshades** [5,6]

Under no wind conditions outside, open holes on top of tunnel sunshades, CO diffusion path as shown below (refer with: Fig. 4).

At the top of sunshades opening size of its opening is 3m × 3m. No wind tunnel exit conditions, the gas stream pollution case sunshades top opening program was simulated, and its CO diffusion path as shown below.

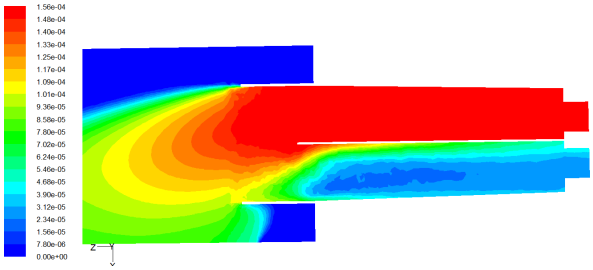

Fig.4 Pollution gases diffusion path near tunnel portal (open holes on top of tunnel sunshades)

As can be seen from the Fig.4, the concentration of CO in the tunnel portal region, respectively, compared with the original plan, the change is significantly. Concentration of pollutant gases and down the tunnel entrances CO were 150ppm, 54.6ppm, and program two gas streams contaminated hole inhibition effect is basically the same.

- **Lengthen the wall between the two tubes combination open holes on top of tunnel sunshades** [5,6]

The scheme 1 and 2 together, namely lengthen the wall and open holes on top of tunnel sunshades.

The tunnel exit windless condition, the scheme 1, 2 combinations of polluted gas stream is used to simulate the CO diffusion path, as shown below (refer with: Fig. 5).

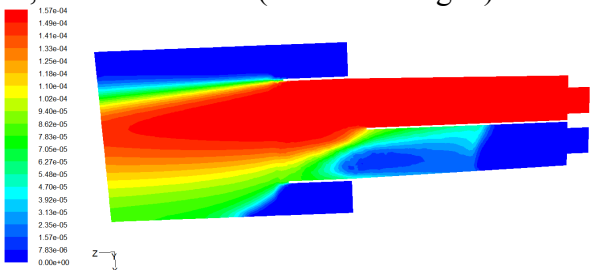

Fig.5 Pollution gases diffusion path near tunnel portal (Combination scheme)

As can be seen from the Fig.5, the concentration of pollutant gases downstream of the tunnel is relatively small, and the polluted gas diffusion in the horizontal direction in the hole. Concentration of pollutant gases and down the tunnel entrances CO were 150ppm, 20ppm. The scheme to curb pollution gas stream is more advantages than the front two schemes.

Above three kinds of schemes to alleviate pollution gas stream is efficiently. which kinds of scheme can be used depending on operation condition.

**Acknowledgements**

In this paper, use the CFD(Ansys Fluent )software to analyze pollution gas diffusion path on the small spacing tunnel portal area, by CO as tracer gas. Through numerical analysis with different intervention programs, we have found the way to control tunnel polluted gas stream of small spacing tunnel and to improve the efficiency of ventilating system.

The tunnel portal also by restricting the tunnel lighting, landscape and other factors, the scheme also needs to integrate various factors. It need achieve the unity of function and landscape.

**References**

[1] Shaozhang Chen, Yue Chen, Immersed tunnel design and construction [M] Beijing: Science Press, 2002.(in chinese)

[2] PIARC COMMITTEE ON ROAD TUNNELS ,“ROAD TUNNELS:VEHICLE EMISIIONS AND AIR DEMAND FOR VENTILATION”，1995

[3] PIARC COMMITTEE ON ROAD TUNNELS ,“ROAD TUNNELS:VEHICLE EMISIIONS AND AIR DEMAND FOR VENTILATION”，2004

[4] ISAO YOSHIZAWA, KOOSAKU IIMURA, “Atmospheric dispersion characteristics of polluted air from the portal of an urban road tunnel” 8Th International Conference on Aerodynamic and Ventilation of Vehicle Tunnel，1994（791-808）.

[5] Wangyi Wu, Fluid mechanics [M] Beijing: Beijing university press,2004.(in chinese)

[6] Fujun Wang, Computational fluid dynamics analysis - The principle and application of CFD software[M] Beijing: Tsinghua University press,2004.(in chinese)

*Applied Mechanics and Materials Vols. 580-583 (2014) pp 1258-1263*
*© (2014) Trans Tech Publications, Switzerland*
*doi:10.4028/www.scientific.net/AMM.580-583.1258*

# Influence of Foundation Pit Excavation on Existing Shield Tunnel and its Protection Range

Xin Wen[1, a], Chenrui Pang[1,b]

[1] The Key Laboratory of Road and Traffic Engineering, Ministry of Education, Tongji University, Shanghai 200092, China

[a]jorjordan@sina.com, [b]chrvpang@163.com

**Keywords:** foundation pit excavation; tunnel displacement; numerical simulation; protection range

**Abstract.** Taking a foundation pit in Nanjing as the background, a numerical model was established to simulate the dynamic process of foundation excavation by 2D finite element software. The influences of different factors on the displacement of the lateral shield tunnel during the foundation pit excavation are studied. The research indicates: when a foundation pit excavation is needed on the side of a shield tunnel, we should select the area in which the tunnel is buried deeper, control both the excavation volume and the distance between tunnel and pit, and try to avoid the excavation depth close to the buried depth of the tunnel. On the basis of numerical calculation, the protection range of the shield tunnels is determined according to different excavation depth of the foundation pits and different buried depth of the tunnels.

## Introduction

Among the 48 Chinese cities with over 1 million inhabitants, more than 30 cities have carried out preparatory work for rail transit. By 2015, it is predicted that 79 rail transit lines will be built in 22 cities, with a total length of 2259.84km.

With the open of the subway, the areas along the line usually become the gold land for commercial development and residential buildings, which leads to a growing number of foundation pits near the existing subway tunnels. In recent years, the scale of the foundation pits near tunnels has a trend of "deep, big and near"[1]. While the underground space today is getting much tighter, the protection of the surrounding environment has gradually become the dominant controlling factor when referring to the design and construction of foundation pits. The influence of the foundation pit construction on surrounding environment should be controlled within an allowable range. The key point of the foundation pit design is gradually shifted to deformation control[2]. As for subway tunnels, the requirements of Shanghai Metro are as follows: under normal circumstances, the maximum of the structure cannot exceed 20mm; the radius of curvature of the line curve after deformation must be larger than 15000m; the relative bending must be smaller than 1/2500. Under such strict conditions, the influence of the foundation pit excavation on nearby tunnels has become an important issue which attracts a great deal of attention in engineering.

Some research on the calculation of foundation pit has been carried out. Yu Chen[3] and Zhiguo Zhang[4] deducted the calculation method of longitudinal deformation of the tunnel caused by foundation pit excavation by analytical method. By taking time-space effect into consideration, Zhigao Li[5] conduced a practical calculation method of tunnel displacement and deformation. Jiaping Li[6] and Lijuan Zhang[7] analyzed the tunnel deformation caused by foundation pit construction, respectively, with the help of numerical simulation. And they both proposed effective technical measures after analysis. Overall, analytical method cannot take the complexity of the construction border into consideration, while the study is only about the tunnel's longitudinal deformation, instead of cross section deformation. What's more, the deformation of only one or two items can be estimated by the empirical or semi-empirical formulation in which not much factors is contained. The numerical method can comprehensively consider the interaction of soil, surrounding structures and excavation.

However, the soil parameters cannot be selected accurately because it's affected by many factors, which is also the important and difficult part of numerical simulation.

This paper is based on the background of a foundation pit in Nanjing. A numerical model is established to simulate the dynamic process of foundation excavation by 2D finite element software. The influences of different factors on the displacement of the lateral shield tunnel during the foundation pit excavation are studied. On the basis of numerical calculation, the protection range of the shield tunnels is determined in order to provide some reference for similar constructions.

## Analysis about the influence of the foundation pit excavation on shield tunnel

The process of foundation pit excavation is the process of foundation pit unloading. The unloading volume gradually increases during the excavation process. Foundation pit unloading may cause the upward bulge at the bottom of the pit, the lateral deformation of the envelope and the deformation of the soil layer, which leads to the ground settlement and the deformation of the nearby subway tunnel as well[8].

The stress state changes both inside and outside the foundation pit during the excavation. The original earth pressure at rest may turn into active or passive earth pressure, which makes envelope to withstand loads and then deformation occurs. So the displacement field may change and pass to the adjacent tunnels. And as a result, deformation of the tunnel will be developed. As for shield tunnels, partial displacement of the tunnel may cause the tunnel axis deviation, which leads to such problems as the open of the longitudinal joints, the leakage of the longitudinal seams and the cracks in the segments, thus affecting the security of the tunnel structures. The deformation problems of the tunnels caused by deep foundation pit excavation are particularly severe in soft soil areas.

In recent years, there's a growing trend in both size and depth of foundation pit. Engineering practice has shown that the area and the amount of the ground settlement caused by deep large foundation pit are much larger than those of the past narrow pit because of the bigger unloading volume, long construction time and complicated construction condition. Also, the influences on the adjacent subway structures and other municipal facilities are much more sophisticated.

## Establishment of the model

A numerical model is established by 2D Plaxis based on a foundation pit in Nanjing. In order to study the influence laws of the foundation pit on the displacement of the lateral shield tunnel, following factors should be contained in the simulation process: the buried depth h of shield tunnel, the excavation width l, the excavation depth H and the horizontal distance d between tunnel and foundation pit.

In practical engineering, the effect of building foundation pit excavation on existing shield tunnel is a complicated three-dimensional problem. In this engineering, taking the fact into consideration that not only the direction of the length of the pit is consistent with the direction of the tunnel line, but also the length is relatively longer, the problem can be simplified as a plane problem. The cross section which is perpendicular to the tunnel axis is selected. The schematic diagram of the simplified calculation model is shown in Fig.1.

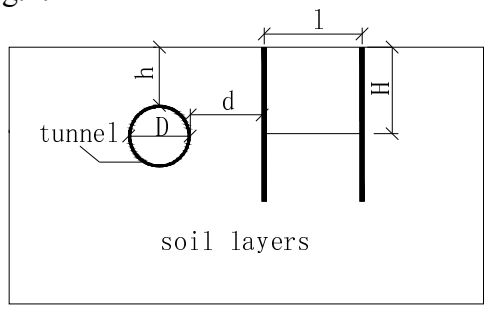


Fig.1 Schematic diagram of simplified calculation model

The width of the model varies with the excavation width and the distance between the tunnel and pit. A distance of two times the excavation width is left on the side of the structures. The depth of the model is 80m. The soil elements obey the elastic-plastic yield criterion of Hardening-soil. The tunnel's segments and the diaphragm walls are simulated by linear elastic plate elements, while the support in the foundation pit is simulated by bolt elements. The insertion ratio of the diaphragm is set as 1:1. The interactions between the segments and the walls with the soil are simulated by setting Goodman contact surface elements on the surfaces of the segments and walls, along with appropriate virtual thickness factor and strength reduction factor. Fully fixed constraints are applied at the bottom of the model. Vertical sliding constraints are applied on both sides. The top of the model is set as a free boundary. The calculation model is shown in Fig.2.

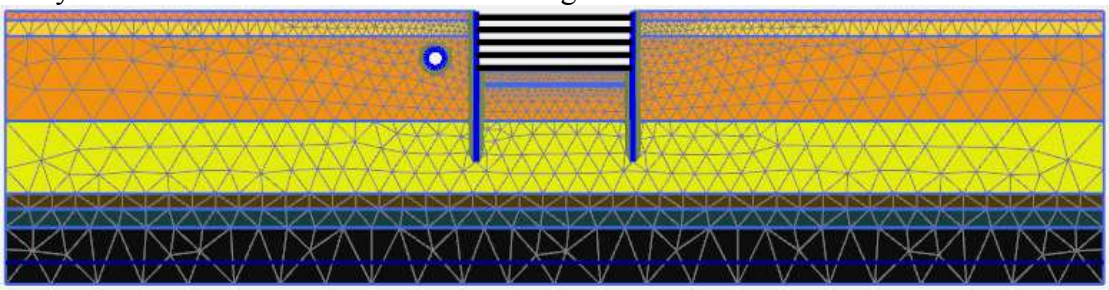

Fig.2 Plaxis model

**Selection of the Parameters**

According to the practical engineering, the outer diameter of the tunnel is 6m, the thickness of the segments is 0.35m. The young's modulus of the concrete used in the segments is 34.5GPa and its density is 2500kg/m$^3$. The segments are viewed as an elastic homogeneous ring, while the parameters of the segments are altered according to the actual situation. The envelope used in the foundation pits of different depth varies, so the equivalent thickness of the diaphragm wall in the model is set different accordingly.

The soil parameters refer to the geological survey report of this engineering, which is shown in Table 1.

Table 1 Soil properties

| Soil layer | $\gamma$[kN/m$^3$] | $c$[kPa] | $\Phi$[°] | $E_s$ [MPa] |
|---|---|---|---|---|
| ① | 18.0 | 16 | 8 | 6.10 |
| ②-2 | 17.9 | 25 | 12 | 3.50 |
| ②-3 | 17.3 | 18 | 9 | 2.95 |
| ③-1 | 18.6 | 5 | 33 | 11.60 |
| ③-2 | 20.7 | 2 | 40 | 16 |
| ④ | 20.0 | 20 | 36 | 15 |
| ⑤-1 | 21.0 | —— | —— | 45 |

**Analysis of the calculation result**

The key point of finite element calculation is to study the law by which the factors affects the displacement when the foundation pit excavation take place near the existing tunnel. In the calculation, the standard values of the factors are set by the following way: the buried depth of shield tunnel h=2D, the excavation width l=50m, the excavation depth H=18m and the horizontal distance between tunnel and foundation pit d=10m. The control variable method is used to find how different factors influenced the displacement of the shield tunnel, which means when one of the factors is under study, the others should be considered as invariable. How these factors influence the tunnel displacement is shown in Fig.3~Fig.6 (the horizontal displacement towards the pit is set as positive value; the vertical displacement upward is set as positive value).

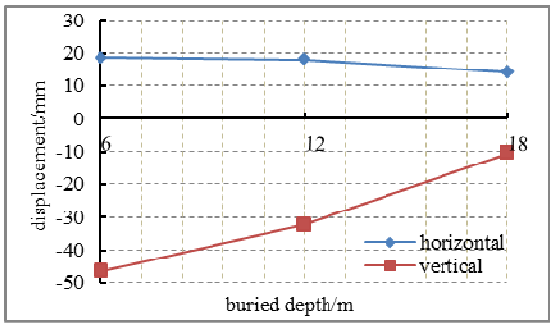


Fig.3 Displacement variation along with buried depth h

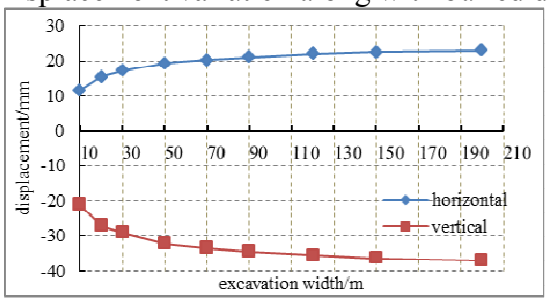


Fig.4 Displacement variation along with excavation width l

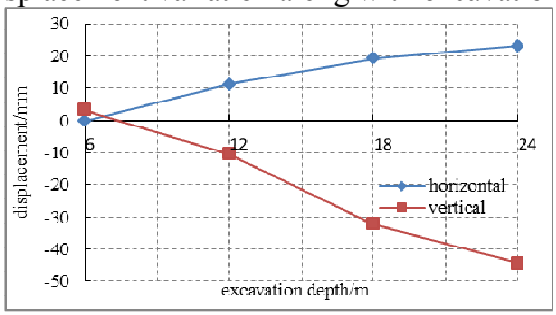


Fig.5 Displacement variation along with excavation depth H

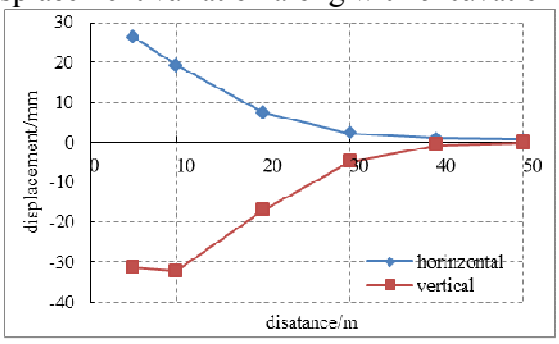


Fig.6 Displacement variation along with the distance between tunnel and pit d

The horizontal and vertical displacement of the tunnel both decrease as the buried depth increases. The tunnel displacement increases with the increasing excavation width. When the excavation reaches 50m, the rate of increase gets smaller and presents a convergence trend. Similarly, the tunnel displacement increases with the increasing excavation depth and the rate of increase has a trend of convergence. As the horizontal distance between the foundation pit and the tunnel gets larger, both the horizontal and the vertical displacement gradually approach 0. But unlike the horizontal displacement which decreases monotonously, the vertical displacement first increases and then decreases. That is because when the tunnel and the foundation pit are too close, the existence of the tunnel hindered the downward development of soil displacement to some extent. The maximum tunnel displacement occurs when the horizontal distance is 10m.

In addition, when the excavation width l is 50m, how the horizontal and vertical displacement of the tunnel varies with the distance between the tunnel and foundation pit d under the circumstance of different buried depth h and excavation depths H is shown in Fig.7~Fig.9.

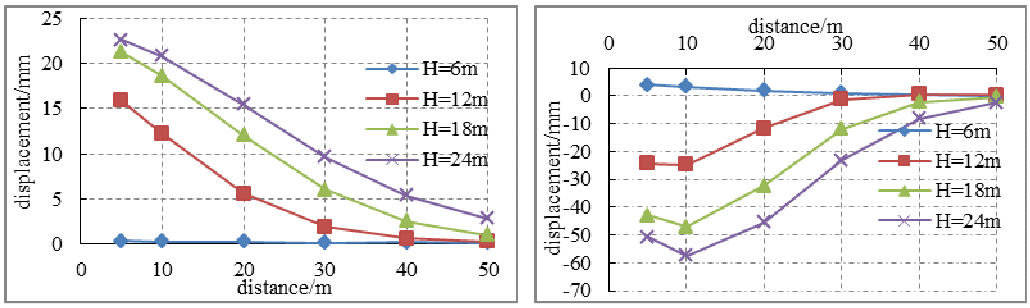


(a) horizontal displacement (b) vertical displacement

Fig.7 Displacement variation along with distance d (h=1D)

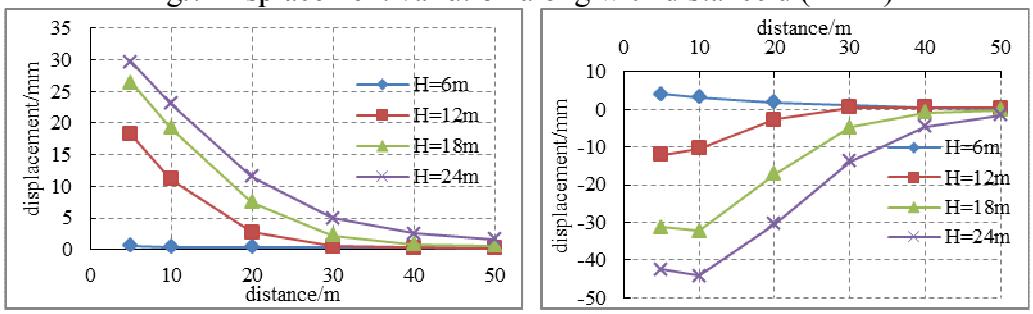


(a) horizontal displacement (b) vertical displacement

Fig.8 Displacement variation along with distance d (h=2D)

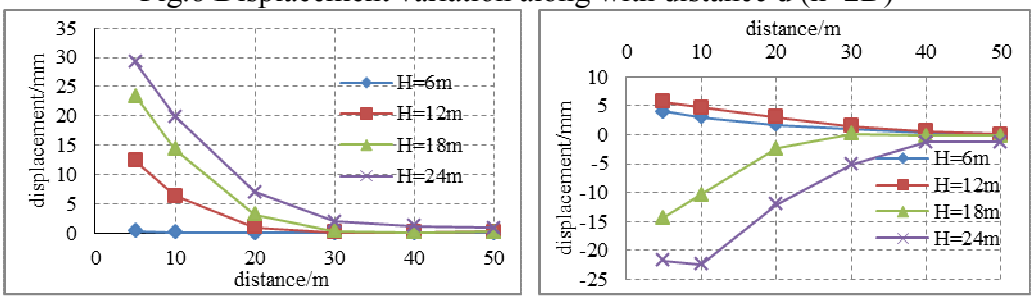


(a) horizontal displacement (b) vertical displacement

Fig.9 Displacement variation along with distance d (h=3D)

When the settlement of the tunnel occurs, the amount of the horizontal displacement is usually about 36%~59% of that of the vertical displacement. It's worth noting that when the buried depth of the tunnel is close to the excavation depth, the horizontal displacement may be larger than the vertical displacement. As an example, when the excavation depth is 12m and the buried depth is 2D(12m), the amount of the horizontal displacement is 107% of that of the vertical displacement; when the excavation depth is 18m and the buried depth is 3D(18m), the amount of the horizontal displacement is 138% of that of the vertical displacement. The reason for this phenomenon is that where the maximum horizontal displacement of the diaphragm wall takes place happens to meet the buried depth of the tunnel, which makes the horizontal displacement relatively larger.

Specially, when the excavation depth is 6m, the vertical displacement of the tunnel comes in the form as bulge, but by a small amount. When the excavation depth is 12m and the buried depth is 3D, the tunnel may bulge as well.

**Protection range of tunnel**

As we can learn from the calculation result by finite element methods in previous chapter, when the excavation volume is very large, the tunnel displacement cannot meet the requirements of Shanghai Metro. So the control and protection of the foundation pit excavation is necessary on both sides of the tunnel within a certain range. Based on the calculation above, to control the tunnel displacement less than 20mm, the minimum distance between the tunnel and the foundation pit——the protection range of tunnel——is determined according to different excavation depth and buried depth, as is shown in Table 2.

Table 2 Protection range of tunnel

| Excavation depth / Buried depth | 6m | 12m | 18m | 24m |
|---|---|---|---|---|
| 1D | **5m** | **20m** | **30m** | **40m** |
| 2D | **5m** | **5m** | **20m** | **30m** |
| 3D | **5m** | **5m** | **10m** | **20m** |

## Conclusions

The close excavation on the side of the existing tunnel may cause the displacement of the lateral tunnel. Taking a foundation pit in Nanjing as a background, this paper discussed the influence of several factors on the tunnel displacement. The following conclusions can be drawn:

1. As the buried depth increases, both the horizontal and the vertical displacement decrease gradually. Selecting the area in which the tunnel is buried deeper helps to reduce the impact of the excavation on tunnel.

2. The tunnel displacement increases with the excavation width and depth, which represent the excavation volume. When conducting a foundation pit excavation, the excavation volume should be controlled. Dividing the foundation into several areas is a proper way when it comes to a pit of large size, while the specific dividing method remains to be further studied.

3. As the horizontal distance between the foundation pit and the tunnel gets larger, both the horizontal and the vertical displacement gradually approach 0. The horizontal displacement decreases monotonously, while the vertical displacement first increases and then decreases.

4. When the buried depth of the tunnel is close to the excavation depth, where the maximum horizontal displacement of the diaphragm wall takes place happens to meet the buried depth of the tunnel, which makes the horizontal displacement relatively larger. Such circumstance should be avoided as much as possible in engineering.

5. On the basis of numerical calculation, the protection range of the shield tunnels is determined according to different excavation depth of the foundation pits and different buried depth of the tunnels. The excavation within the protection range should be strictly controlled.

## References

[1] Weidong Wang, Jiangbin Wu, Shaoming Huang: Chinese Journal of Underground Space and Engineering. Vol.1 547-553 (2005) (in Chinese)

[2] Xueyuan Hou, Guobin Liu, Yuanxiong Huang: Construction Technology. Vol.29 5-7(2000) (in Chineses)

[3] Yu Chen, Yongsheng Li: Chinese Journal of Underground Space and Engineering. Vol.1 91-94(2005) (in Chineses)

[4] Zhiguo Zhang, Mengxi Zhang, Weidong Wang: Rock and Soil Mechanics. Vol.32 2085-2092(2011) (in Chinese)

[5] Zhigao Li, Hao liu, Guobin Liu, et al: Chinese Journal of Underground Space and Engineering. Vol.1 619-623 (2005) (in Chinese)

[6] Jiaping Li: Chinese Journal of Underground Space and Engineering. Vol.5 1345-1348,1360 (2009) (in Chinese)

[7] Lijuan Zhang, Wei Sun, Ming Xie, et al: Chinese Journal of Underground Space and Engineering. Vol.6 1409-1412 (2010) (in Chinese)

[8] Jian Jia, Xiaolin Xie, et al: Journal of Shanghai Jiaotong University. Vol.42 1005-1010 (2009) (in Chinese)

*Applied Mechanics and Materials Vols. 580-583 (2014) pp 1264-1267*
*© (2014) Trans Tech Publications, Switzerland*
*doi:10.4028/www.scientific.net/AMM.580-583.1264*

# LS-SVM-Markov Model for Tunnel Deformation Prediction

Cai Gaotang[1,a] , Hu Sujuan[2,b,*]

[1]Nanchang Inst Technol, Coll Water Conservancy & Ecol Engn Nanchang 330099, Peoples R China

[2]Jiangxi Tourism and Commerce vocational college, Nanchang 330099, Peoples R China

[a]chaigt12345@sina.com

**Keywords:** Tunnel deformation analysis, LS-SVM; Markov chain, displacement prediction.

**Abstract.** In order to effectively predict aspects of tunnel deformation, taking effective and timely measures against the problem to ensure the safety of tunnel ,LS-SVM-MC model is proposed . Namely, Markov chain based on LS-SVM corrects the error, and ultimately improves the accuracy of prediction. By the analysis and calculation of deformation prediction of a tunnel , you can find that the method is more in line with the actual situation, showing predictive superiority and a high prediction accuracy.so the method can serve as a new ways of tunnel deformation prediction,some promotional value can be gained in later work.

## Introduction

In tunnel safety monitoring, analysis and processing of tunnel deformation monitoring data is very significant.. Least squares support vector machine (LS - SVM) is an extension of a standard support vector machine, which is different from the conventional method using equality constraints, LS-SVM can convert the SVM quadratic programming problem into solving linear equations ,not only makes a significant reduction in the workload, but also improves the computing speed. Markov chain has nothing to do with the past state, has certain advantages in forecast of the displacement series affected by many factors . In order to make tunnel deformation monitoring work more accurate, text combine these two predictive methods, namely the LS-SVM - Markov chain model is introduced into the tunnel deformation forecast, the results show that the model prediction accuracy is high, can be extended . in engineering practice.

## LS-SVM-MC Model Construction

### The theory of LS-SVM model

while adhering to the principle of structural minimization, in high-dimensional space, dot product operation is replaced by kernel function of the former space, as a result, the calculation can be simplified. LS-SVM[1-2] is a nonlinear, black-box regression method, which is a modified vision of standard SVM regression. The LS-SVM training procedure involves the selection of a kernel parameter, which should be chosen carefully because it defines the structure of the high dimensional feature space, and thus controls the complexity of the solution.

Given the data set $(X_i, Y_i)$ ,i= 1,2,...,1, consider the regression model:

$$y_i = F(x_i) = w^T \varphi(x_i) + b \tag{1}$$

$$\min_{w,b,\varepsilon} J(w,b,\varepsilon) = \frac{1}{2} w^T w + \gamma \frac{1}{2} \sum_{i=1}^{l} \varepsilon_i^2 \tag{2}$$

$$y_i = F(x_i) = w^T \varphi(x_i) + b + \varepsilon_i \tag{3}$$

where $\varepsilon$ is slack variable of error, $b$ is constant deviation and $\gamma$ is referred as the regularization constant. In order to solve this constrained optimization problem, the Lagrangian corresponding to Eq. (2) can be constructed

$$L(w,b,\varepsilon,a) = J(w,e) - \sum_{i=1}^{l} a_i [w^T \varphi(x_i) + b + \varepsilon_i - y_i] \tag{4}$$

Any function satisfying Mercer's condition can be used as the kernel function. And there are three typical kernel functions, they are, Linear Kernel, Polynomial Kernel and Radial Basis Function (RBF) Kernel.

The LS-SVM model can be obtained at a new point $x_i$ by:

$$y(x) = \sum_{i=1}^{l} \alpha_i K(x, x_i) + b \tag{10}$$

.

In addition, Corresponding changes are made through specific issues, in order to derive the best predictive models.

**Markov correction model**

MC is released by Markov in the early 20th century, because of it has strong applicability is actively promoting in various fields [4-6].such as geotechnical, transportation, construction. Namely, the error of between the observed value and the predicted value is divided into several intervals, and each interval is named. For $S_m \quad (m = 1,2,3.....l)$, the state probability of relative error state $S_m$ transfered into state $S_n$ from time step k is

$$P_{mn}^{(k)} = \frac{C_{mn}^{(k)}}{C_m} \qquad (m,n = 1,2,3.....) \tag{11}$$

Where, $C_{mn}^{(k)}$ represents the number that $C_m$ transfers to $C_n$, $C_n$ represents the number of states for the relative error in a number of intervals. But in the calculation of the number of $C_n$. Because they do not know what the future state of development. The last k states need to be eliminated.

The probability of each state will be in statistics, in which the probability is maximum, then the predicted value is in the corresponding state. This paper argues that the midpoint of the range is the most likely relative error of the predicted value. the following formula can be predictive value: of the most probable timing displacement .

$$U(x) = (1+\overline{\Delta})u(x) = \left[1+\frac{(\Delta_U + \Delta_D)}{2}\right]\times u(x) \tag{13}$$

Where(12), $U(x)$ is the final prediction value obtained by the MC model, $u(x)$ is the initial predicted value obtained by LS-SVM. $\Delta_U$, $\Delta_D$ is the upper and lower limits. $\overline{\Delta}$ is The average relative error..

**Project**

To test the LS-SVM-Markov model in tunnel displacement prediction results, a tunnel literature displacement time series of observations of this paper gives are verified. Due to be affected by various factors, the tunnel has a certain displacement,According to accordingly its deformation prediction, LS-SVM --- Markov model makes predictions of a vertical displacement of the measuring point ,and compare with prediction results of the sole LS-SVM. Firslyt, the state transition probability matrix is listed:

$$P(1) = \begin{bmatrix} 0.67 & 0.33 & 0 & 0 \\ 0.01 & 0.84 & 0.15 & 0 \\ 0.02 & 0.18 & 0.74 & 0.06 \\ 0 & 0 & 0.43 & 0.57 \end{bmatrix} \qquad P(2) = \begin{bmatrix} 0.50 & 0.33 & 0.17 & 0 \\ 0.01 & 0.74 & 0.24 & 0.01 \\ 0.04 & 0.3 & 0.58 & 0.08 \\ 0 & 0.14 & 0.57 & 0.29 \end{bmatrix}$$

$$P(3) = \begin{bmatrix} 0.33 & 0.50 & 0.17 & 0 \\ 0 & 0.66 & 0.31 & 0.03 \\ 0.08 & 0.35 & 0.49 & 0.08 \\ 0 & 0.29 & 0.57 & 0.14 \end{bmatrix} \qquad P(4) = \begin{bmatrix} 0.17 & 0.50 & 0.33 & 0 \\ 0 & 0.61 & 0.33 & 0.06 \\ 0.09 & 0.38 & 0.47 & 0.06 \\ 0 & 0.57 & 0.43 & 0 \end{bmatrix}$$

Taking the predicted displacement of 2011/3/, shown in fig. 1. For example, extract the four date values of LS-SVM [3]which is closed to it in order to predict vertical displacement by Markov.

The results is shown in the following table 1.

Table1. COMPARING THE PREDICTION OF LS-SVM AND LS-SVM-MARKOV MODEL

| Date | Original value （mm） | Fitted values of LS-SVM （mm） | Erroe (%) | Fitted values of LS-SVM-MC modle （mm） | Erroe （%） |
|---|---|---|---|---|---|
| 2011/3/7 | 49.00 | 49.1475 | 0.30 | 49.08 | 0.16 |
| 2011/3/8 | 48.74 | 48.9520 | 0.44 | 48.89 | 0.31 |
| 2011/3/9 | 48.55 | 48.7662 | 0.43 | 48.69 | 0.29 |
| 2011/3/10 | 48.01 | 48.5608 | 1.15 | 48.50 | 1.02 |
| 2011/3/11 | 48.20 | 48.3717 | 0.36 | 48.31 | 0.22 |
| 2011/3/12 | 47.94 | 48.1846 | 0.51 | 48.12 | 0.37 |

| | | | | | |
|---|---|---|---|---|---|
| 2011/3/13 | 47.79 | 48.0003 | 0.44 | 47.94 | 0.31 |
| 2011/3/14 | 47.60 | 47.8625 | 0.55 | 47.80 | 0.42 |
| 2011/3/15 | 47.31 | 47.7089 | 0.84 | 47.65 | 0.71 |
| 2011/3/16 | 47.24 | 47.5544 | 0.67 | 47.49 | 0.52 |

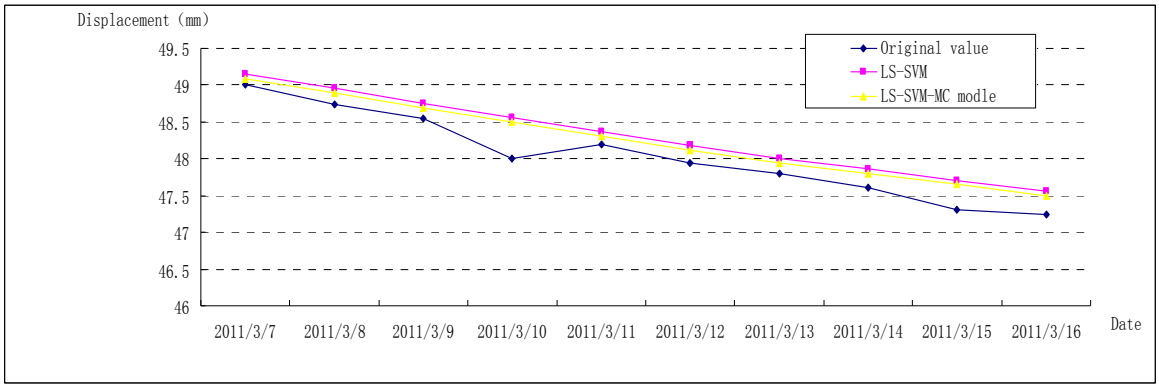


Fig.1 Fitting Curves of LS-SVM and LS-SVM—Markov

## Conclusion

On the basis of tunnel displacement prediction of the LS-SVM, this paper proposes a new method, namely LS-SVM-MC model. Markov chains can furtherly correct data which LS-SVM treated, thereby improving the accuracy and effectiveness. Through this project example, you can know, LS-SVM-Markov model is closer to the actual value than a single LS-SVM model, the tunnel displacement prediction has promotional value.

## References

[1] LIU Zun Xiong, Zhong Hua-lan, Zhang Yun.Least squares support vector machine multi-scale short-term load forecasting model [J]. Xi'an Jiaotong University School newspaper, 2005,39 (6): 620-623.

[2] Jia Rong, Cai Zhenhua, Kang Rui .System Marginal Price Forecasting based on least squares support vector machine [J]. High Voltage Engineering, 2006, 32 (11) :145-148

[3] SONG Zhi Zi, Li Junjie squares support vector machines in tunnel deformation prediction [J]. Water Resources and Power, 2006, 24 (6): 49-52.

[4] Weiguo Xiao, Li Wenhua .university faculty prediction method based on Markov chain model [J]. Ningxia University (Natural Science Edition), 2004, 25 (4) :309-310.

[5] Joseph Wong, Markov chain in the long term load combination forecasting, [D]. Changsha: Hunan University, master's thesis, 2010.

[6] Huteng Bo, YE Jian Castanopsis, Markov chain model in GIS data prediction [j]. Applied Technology, 2008 (8) :90-93

*Applied Mechanics and Materials Vols. 580-583 (2014) pp 1268-1272*
*© (2014) Trans Tech Publications, Switzerland*
*doi:10.4028/www.scientific.net/AMM.580-583.1268*

# Optimization of Stope Structural Parameters in Phosphorite Mine and Its Stability Analysis

Li Xiangxing [1, a], Li Kegang*[1, b]

Faculty of Land Resource Engineering, Kunming University of Science and Technology, Xuefu Road No253, Kunming, China

*likegang_78@163.com

**Keywords:** room-and-pillar mining; structural parameter optimization; stope stability; numerical simulation

**Abstract.** A mine plans to exploit the low dip thin phosphate deposit by room-and-pillar mining. But a township highway is just above the orebody, and its distance is only 80m, in order to better control the ground pressure in stopes and ensure the operation security, the size of room and pillar must be reasonably designed to maintain the stability of stopes and surrounding rock. The 3D-σ numerical simulation method was applied to analyze the surrounding rock stability in different stope structure parameters. The results show that when holding the size of pointed prop unchanged, the surrounding rock stability would decline with the increase of room width and pillar spacing, for security, the mining plan, the pointed prop is 3×3 m, the stope width and pillar spacing is not more than 9 m, were considered to be one of the optimal. In addition, it is important to emphasize that if the mining depth exceeds 300m, some methods, such as decreasing the spacing of stope and pointed props or increasing the pillar size, need to be taken to avoid the stope instability caused by greater ground pressure.

## Introduction

For underground mine which applied open-stope method, the stope stability is directly related to the safety of the production and ore recovery rate [2-3]. Therefore, to reasonable confirm the stope's structure parameters on span of the room, the pillar size etc, has a very important theoretical and guiding significance to maintain the stability of the overlying rock and ensure the safe, efficient and sustainable production of mining enterprises. Based on the background for underground mining of phosphate rock in Yunnan province, on the basis of rock mechanics parameters, taking the finite element numerical method for simulating analyzing the stability of different stope mining methods is to reach the aim of through the optimization of stope structure parameters to ensure that the purpose of mine safety production and provide theoretical basis for the mine production.

## Engineering situation

The Deng ganshu phosphate ore is monoclinic structure, orebody thickness is 3~4m, dip angle is between 20° and 40 °, ore body part exposed on the surface, and the tendency to extend along nearly 400 meters deep. Formation lithology is relatively single, roof and floor of ore bodies are in thick bedded dolostone, and the difference of rock engineering geological characteristics is not big. The rock has hard dense, high mechanical strength, and good stability. Mining area terrain elevation has not big difference, there are not major surface water bodies; the surface of roadway is relatively dry, water has not the big impact on mining. As the ore body and surface topography is anti-dip occurrence and does not have the open-pit mining conditions, therefore, the room and pillar mining method is determined to use for underground mining of phosphate body. In addition, there is also a village road through the upper part of the phosphate rock body. In order to guarantee the normal production of the mine and highway operation safety, it is necessary to optimize the stope structure parameters when mining the phosphate rock body.

**Establishment of the model**

According to the occurrence conditions of Jinsha phosphate rock and the select principle of drawing boundaries [4-8], combining with the theory of mechanics, a three-dimensional finite element model is built. The Model along the ore body strike direction is 400 m (x direction), cross ore body strike direction is 500 m (z direction), and the vertical direction is 420m (y direction). It is divided more than 299250 nodes and 70,006 20-node three-dimensional isoparametric element units. Using the horizontal displacement constraint the Model, then the bottom is fixed boundary constraints, and the Mohr - Coulomb plastic failure criteria is adopted. The research section of the ore body buried shallow, according to the relevant experience , in-situ stress changes in the shallow levels is relatively complex and horizontal stress is small, so this calculation use $\lambda=\mu/(1-\mu)=0.43$ as the basic calculation scheme. Figure 1 is the resulting grid computing model.

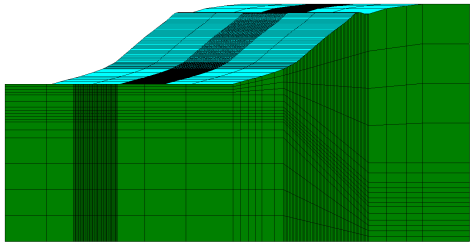

Fig. 1 The result of grid computing model

**Value of rock mass mechanics parameters**

Rock mass is complex organism which is made up of rock and structural plane. Due to the differences of nature and stress conditions, rock breaking can be divided into brittle failure and the plastic failure, its strength characteristics is influenced and controlled by the intensity of the rock and structural plane, rock mass structure factors and so on. Based on this, getting accurate mechanical parameters of rock mass is not realistic, but the follow-up calculation still need to make the accurate solution of the analysis and rock mass mechanics parameters in line with the actual as far as possible. On the basis of the rock mass structure statistical analysis, indoor rock mechanics test, and combining with Hoek Brown - experience formula, it is able to determine rock mass mechanics parameters. Due to the limitation of space, the concrete solving process can refer to reference [9]. Table1 is physical mechanics parameter values of rock mass by reduced and inversed.

Table 1 Physico-mechanical parameters of rock mass

| Rock type | density/g·cm$^{-3}$ | Elastic modulus/GPa | Poiss-on ratio | Tensile strength/MPa | Cohesion /MPa | Internal friction angle/° |
|---|---|---|---|---|---|---|
| orebody | 2.81 | 35.35 | 0.338 | 1.34 | 1.87 | 37.42 |
| direct roof | 2.72 | 27.51 | 0.251 | 0.93 | 1.46 | 38.47 |
| direct floor | 2.72 | 27.51 | 0.251 | 0.93 | 1.46 | 38.47 |
| Indirect roof | 2.74 | 45.22 | 0.305 | 1.74 | 2.25 | 41.35 |
| Indirect floor | 2.74 | 45.22 | 0.305 | 1.34 | 1.87 | 37.42 |

**Determination of analysis methods**

For the mine exploitation used room and pillar methods, the content of the stope structure parameter optimization is rich, if we consider the overall amount of computation together, the calculation is very large and not easy to realize, therefore, the computational study is divided into the following two steps:

The first step: According to the orebody occurrence conditions, on the premise of preliminary determine the point column size, the different room span size affect on the stope stability is analyzed;

The second step: Based on the results of research in the first step, exploring the stability of the roof, pillars, roof and bottom pillar point at different points column spacing, and finally achieving the goal of stope structure parameters optimization.

**Analysis of stope stability of different room span**

Because the ore body of Deng ganshu ore block is thinner, and when the point column is 3 x 3m, the ratio of height to width is close to 1:1, which can fully meet the requirements. Therefore, in the process of simulation, the point column is determined primarily to adopt 3 x 3 m. On this basis, using the following four schemes simulates and analyses mining stope stability of different room spans:

Option one: Point column is 3 × 3m, stope span is 6m; Option two: Point column is 3 × 3m, stope span is 9m;

Option three: Point column is 3 × 3m, stope span is 12m; Option four: Point column is 3 × 3m, stope span is 15m.

The calculation results are analyzed from the aspects of stress distribution, safety factor and plastic zone. Due to the limitation of space, the results are only presented in part. Figure 2, Figure 3, are respectively orebody ceiling and point column plastic layout of part schemes after excavation, Figure 4 is the change curve of safety coefficient of different orebody's roof and point column.

(1)In the aspect of stress distribution, orebody roof in scheme 1 and 2 did not appear tensile stress, but the value in scheme 3 and 4 had reached 1.581 MPa, is greater than the tensile strength of rock mass itself, which can cause large area roof caving. Therefore, the room span should not be too big in the mining process, which should be controlled about 9 m. The point spacing also should not be too big, otherwise, the point column pressure is too big to favor the stope stability.

(2)In plastic zone distribution, when the room span is 12 or 15 m (scheme 3 and 4), the direct roof after orebody mining almost completely access into plastic state (fig.2a), the minimum safety coefficient is less than 1, only 0.984 and 0.963. When the room span is reduced to 9m (scheme 2), the plastic area of direct roof is decreasing obviously (fig.2b). The plastic zone near the excavation body exists in the independent form, and there is no contiguous phenomenon, although the partial failure of direct roof is possible, it won't appear the total collapse, the minimum safety factor of roof increases to 1.173. From scheme 1 to 4, the variation of plastic zone and safety coefficient from point column, pillar, roof and bottom pillar are as same as that of roof (fig.3). Therefore, to control the room span about 9 m is favorable to mining security.

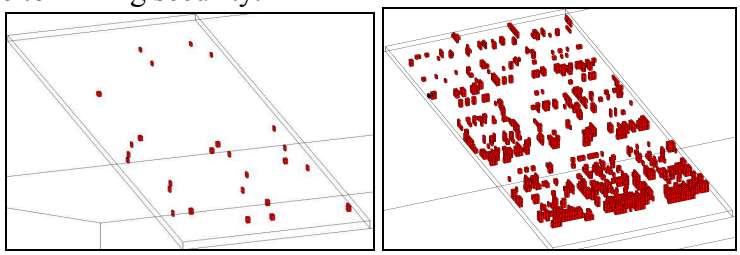

(a) scheme 2 (b) scheme 4

Fig. 2 The plastic zoo distribution range of the roof of different room span

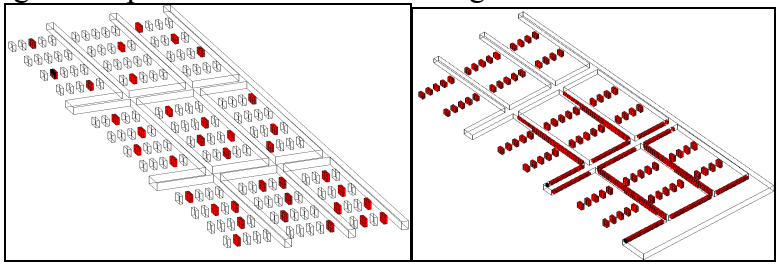

(a) scheme 2 (b) scheme 4

Fig. 3 The plastic zone distribution range of point pillar, roof and bottom pillar of different room span

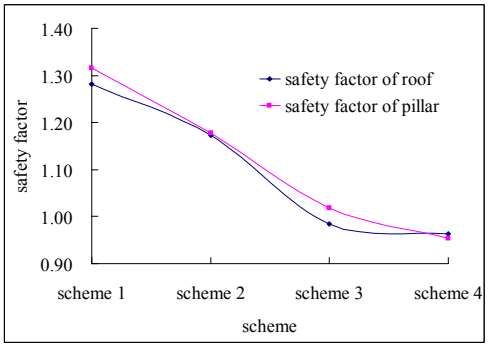


Fig. 4 The safety factor curve of roof and pillar of different schemes

**Stability analysis of different pillar column spaces**

According to the previous calculation results, for Deng ganshu ore block, the ore room span should be controlled about 9 m is reasonable if the point column is reserved 3x3 m. On this basis, using simulation analysis of the following four pillar spacing tries to find out the reasonable numerical value to guide production.

Scheme 5: point column is 3 x 3m, ore room span is 9m, point spacing is 6 m;
Scheme 6: point column is 3 x 3m, ore room span is 9m, point spacing is 9 m;
Scheme 7: point column is 3 x 3m, ore room span is 9m, point spacing is 12 m;
Scheme 8: point column is 3 x 3m, ore room span is 9m, point spacing is 15 m;

From the calculation results of four schemes, three schemes except scheme 5 appeared roof tensile stress. when the pillar spacing exceeds 9 m, the roof tensile stress exceeds the strength of rock mass itself, the stope lacking of stability. In safety factor of the roof, pillar, roof and bottom pillar, the minimum value in scheme 5 and 6 is respectively 1.149 and 1.144, other solutions are less than 1. As well, the distribution of plastic zone is smaller in scheme 5 and 6, better stability (Fig. 5a, Fig. 6a). So, the best point column spacing is controlled within 9m, and the mining security can be guaranteed.

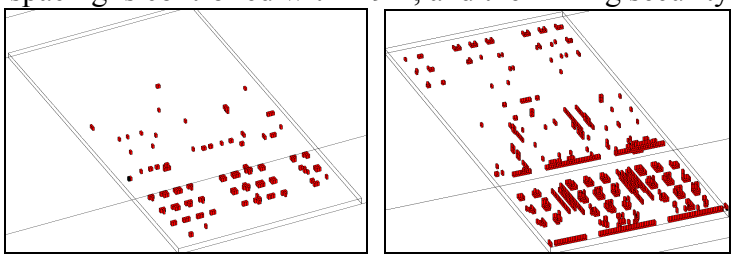

(a)Scheme 5 (b) Scheme 8

Fig. 5 The roof plastic zone distribution range of different pillar spacing

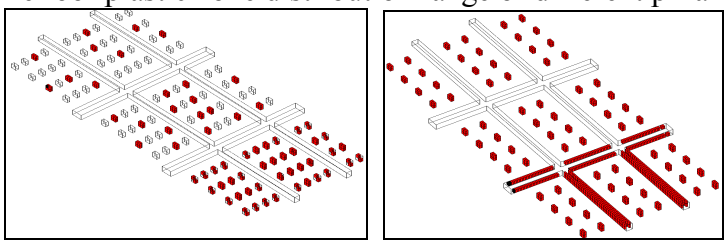

(a) Scheme 5 (b) Scheme 8

Fig. 6 The plastic zone distribution range of point pillar, roof and bottom pillar of different pillar spacing

**The final suggestion and optimization of stope structure parameters**

Due to the limitation of computing grid unit, the simulation only analyzed three sections along the tendency of the orebody, a total of nine stopes' stability, not considered change rule of continuing deep mining of the ore bodies. But through the investigation of the calculation results, it can be found, the mining is deeper, the pressure of the roof, pillar spacing and the roof and bottom pillar is greater;

the plastic zone is wider, the safety factor is smaller. It also shows that the stability of the stope field and the overlying rock is worse. Therefore, if the buried depth of ore body is bigger, stope structure parameters should be adjusted. According to the engineering practice, we recommend:

(1)If the mining depth is less than 200 m, mining can be in accordance with the point column 3 x3 m, ore room span 9 m, pillar column spacing 9 m;

(2)when the mining depth exceeds 200 m, in the premise of maintaining the point column 3x3 m, room span and point column spacing should be decreased (e.g. 6 m), or increase the point column (e.g. 5x5 m), which can continue to ensure mine safety production.

## Conclusions

The result analysis of the 3D-σ numerical simulation technology is shown below:

(1) For shallow mining, if mining point column size is within 3x3m, controlling the room span and point spacing about 9m is more reasonable.

(2)As mining is deeper, the stope structure parameters should adjust, or pillar size still maintain 3x3m, but the room span and the point column spacing is reduced to 6 m, or increase point pillar size, only in this way can we guarantee the stability of the overlying rock mass.

(3)The mining is a dynamic process, blasting damage will reduce continually the mechanical strength of rock mass, therefore, the subsequent production should be based on the actual condition of stope stability, repeated analyses and verifications, in order to achieve the purpose of safe and efficient mining.

## Acknowledgements

This work was financially supported by the National Natural Science Foundation of China (41362013).

## References

[1] Guangxu Tong. Higher hard rock mining. Metallurgical Industry Press. 1995 (In Chinese)

[2] Jian Chang. The analysis and parameter optimization of Western hubei slow thin hematite stope stability [D]. Wuhan University of technology. 2010.5 (In Chinese)

[3] Jiamian Ye, Jingming Jiang, Liguan Wang, Xinglong Feng . The numerical simulation study of Stope structure parameters optimization [J]. Journal of China mining. 2010 (03) ( In Chinese)

[4] Runqiu Huang, Zhuoyuan Zhang, Shitian Wang. Numerical simulation and matching of engineering geology [J]. Hydrogeology engineering journal, 1991, 18 (5): 7-10. ( In Chinese)

[5] Xiangui Zhou, Jinguo Cao. Rock and soil mechanics numerical method research [J]. Building Technique Development, 2002, (8): 15-18. ( In Chinese)

[6] Dongyuan Jia. A study of synthetical analysis method by finite element for rock slope stability [D]. Chongqing: Chongqing University. 2003, 6. ( In Chinese)

[7] Luyu Zhang, Yingren Zheng, Shangyi Zhao etc. The feasibility study of strength-reduction method with FEM for calculating safety factors of soil slope stability[J]. SHUI LI XUE BAO. 2003, (1):21-27(In Chinese)

[8] Xiaochun Gu. The development and utilization of mineral resources plan of Yongshan Jinsha mining Limited Liability Company [R]. Mining technology. 2009 (01) (In Chinese)

[9] Ze Yang, Kepeng Hou, Kegang Li etc. The determination of YunXi DaTun tin rock mass mechanics parameters [J]. Rock and soil mechanics, 2010, 31 (6): 1923-1928. (In Chinese)

*Applied Mechanics and Materials Vols. 580-583 (2014) pp 1273-1278*
*© (2014) Trans Tech Publications, Switzerland*
*doi:10.4028/www.scientific.net/AMM.580-583.1273*

# Research of the key control parameters standard for shield tunnel under-crossing high speed railway

LIU Zhe [1, a *], HE Ping [2,b]

[1]PhD Student, Tunneling and Underground Engineering Research Center of Ministry of Education,Beijing Jiaotong University, Beijing,China

[2]Professor, Tunneling and Underground Engineering Research Center of Ministry of Education,Beijing Jiaotong University, Beijing,China

[a]liuzhe.youxiang@163.com, [b]phe@bjtu.edu.cn,

**Keywords:** shield tunnel; long-wave irregularity; settlement trough; numerical simulation; control standards

**Abstract.** This paper takes a new shield tunnel as the research object, which intends to cross a section of a high speed railway. Based on design specifications and the existing monitoring data to analyze the change rule of track irregularities, this article proposes the control of wavelength and relevant amplitude in the above case, following the design specifications and long-wave irregularity management demands of high-speed highway. And the controlling values of wavelength and amplitude required are presented with the outcome of the range of the settlement trough, drawn out of the under-crossing process. And it also uses large-scale non-linear finite element analysis software to simulate the high speed railway track deformation in actual constructions, to test whether the deformation meet the requirements of the control standards and deformation law. The results can provide reference for the construction measure when shield tunnel under crosses the high speed railway in the future.

## Introduction

With the rapid progress of China's urbanization, it has the urgent needs to the rapid development of urban transport. In the development of a new round of transportation, the railway will undoubtedly become one of the spotlight。Among these, The safe, fast, efficient, low-carbon quality make the high-speed railway become the object of focus on the development of China's transportation construction.

Meanwhile, the great development of high-speed railway has gradually bring some engineering problems. Domestic and foreign scholars have done a lot of research to explore such issues.[1].Some scholars do research by choosing stratum reinforcement proposal in different geological conditions.Depend on the different geological conditions,Xu [2] made a research to choose the ground reinforcement program.Zhu[3] calculate the surface subsidence by two-dimensional finite element method.

The focus and problems of the research at home and abroad include the following aspects: 1):Most of the study at present is the general railroad, Since the standard of the high-speed railway considerably stricter than the general railroad,we need to be discussed in depth study of the high-speed rail.2): Control indicator is the core of the control standards, the control indicators of the high-speed rail can not meet the needs of the actual operation largely. 3): Most of the current study of the tunnel under-crossing the railway are mostly concentrated in the choice of reinforcement, then prove its feasibility by calculating. But this method can not quantify the value of the specific construction control and has little effect to guide the construction in different backgrounds.

Based on the need to solve the above problems, in this paper, considering the settlement after construction and the settlement after the operations of the high-speed railway. Emphasis on the effects of long-wave irregularity to the high-speed rail, proposed the waveform control indicator to improve the indicator system of tunnel under-crossing high speed railway. Hope to provide a reference to construction of the tunnel under-crossing high speed railway in the future.

## Project overview

The paper do the research about the section of the subway under-crossing high speed railway, the right section of the subway under-crossing the railway with oblique 61 °. The length of Intersection is 33 m. the left section of the subway under-crossing the railway with oblique 64 °. The length of Intersection is 32 m.。

The field area strata including 2.2m of miscellaneous fill soil; The plain fill layer is 0.63m ; The sand and gravel formations is 5.86m; The clayey silt is 2.23m; The following layer is pebble layer. The subway is mainly under-across the gravel layer formation.

## Track irregularity management control indicators of high-speed railway

The high-speed railway roadbed, bridges, rail and other design and construction standards are much higher than the general railroad, The fundamental reason is due to the high-speed railway track must ensure the smoothness of the track lasting stability. Because the train track irregularity increased mainly by vibration, wheel and rail movement. When the smoothness of the track in high stage, The dynamic force in vibration and movement of trains between wheel and rail is relatively small.Traffic safety, stability and comfort can be guaranteed. On the contrary,even when track, roadbed and bridge structure are fully meet the requirements of strength, and the smoothness of the track is poor,vehicle vibration and wheel-rail forces caused by track irregularity will significantly increase under the conditions of high-speed trains is running. It make the smoothness,comfortable and security of the train seriouly deterioration, there may even lead to the train derailment. Therefore, the countries which has developed technology of high-speed railway,for example, Japan and Germany have been established the relatively perfect high-speed rail irregularity management standards that adapt their national conditions. Table 1 is the Japanese Shinkansen irregularity management's value.

With the development of China's high-speed railway undertakings is growing fast, China is also focus on the harm of train track irregularity. At present, the high-speed rail irregularity management standards of China mainly do reference to foreign standards,at the same time, there are many scholars achieved research results in the field of Irregularity Management that adapt our country. Table 2 is a the vertical smoothness of longwave amplitudes management control indicators in different speeds.

Table 1: Japanese Shinkansen management objectives index value

| Category | | | Unit | Accepta -nce | Planned maintenance | Comfort management | Security management | Speed management |
|---|---|---|---|---|---|---|---|---|
| Unsmo-othness of the track | 10m string method | Vertical | mm | ≤4 | 6 | 7 | 10 | 15 |
| | | Along the track | mm | ≤3 | 4 | 4 | 6 | 9 |
| | | Gauge | mm | ≤±2 | +6，-4 | +6，-4 | +6，-4 | |
| | | Level | mm | ≤3 | 5 | 5 | 7 | |
| | | Planarity | mm/2.5 | ≤3 | 4 | 5 | 6 | |
| | 40m string method | Vertical | mm | 10（＞210Km/h） | | | | |
| | | Along the track | mm | 7（＞210Km/h） | | | | |
| | The raised and concave unsmoothness of the track | | mm/m | 0.30 | 0.60 | | | |

Table 2: Long-wave spiky management amplitude under each speed

| Number | Speed (Km/h) | Wavelength management of the level（m） | Wavelength management along the track (m) | Ⅰclass(mm) | Ⅱclass(mm) | Ⅲclass(mm) |
|---|---|---|---|---|---|---|
| 1 | 200 | 70 | 100 | 7 | 11 | 15 |
| 2 | 250 | 90 | 120 | 7 | 10 | 14 |
| 3 | 300 | 110 | 150 | 7 | 10 | 14 |
| 4 | 350 | 120 | 180 | 7 | 10 | 14 |
| 5 | 400 | 140 | 200 | 7 | 10 | 14 |

## Irregularity status and analysis

**An existing field trials.** According to the geological conditions of the parameters involved in this article, set the measured data of a high-speed railway foundation testing work sites as an example. [4] Analysis of its regularity.

The test points are in DK1472+052.3 ～ +167.3section. Select32 sections for text,such as DK1623+051,DK1623+57, DK1623+512 and so on. Set the settlement monitoring instrument under the subgrade surface in all types of monitoring section. And planted settlement monitoring instrument in all section of center and the left and right sides of embankment.

**The analysis of irregularity data.** With the train operating speed increased, people focus the attention of high-speed railway irregularity. The researchers found that not only the shortwave irregularity controlled by 10m chord will cause the train shake, Long-wave irregularity also makes the strong resonance of train. This is the "1Hz problem"occurred in Japan and France. Long-wave irregularity caused by tunnel under-crossing high speed railway is the key of this article. Set the magnitude of the irregularity as the function of the mileage. Graphed to facilitate the analysis of its irregularity wavelength, use the irregularity wavelength to contrast with the irregularity management standards.

Use the mileage-irregularity amplitude value chart to represent the subsidence of test cross section in different test section. The chart can use to analysis the irregularity wavelength and amplitude of track,and prepare for propose the control chart of settler waveform. Use the monitoring data of [4] to established coordinate chart by mileage - irregularity amplitude value.The results are Fig 1.

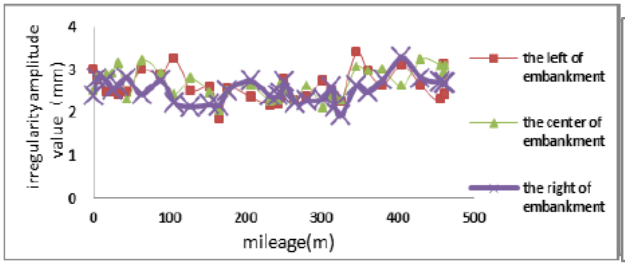


Fig 1: The maximum settlement test by settlement observation pile

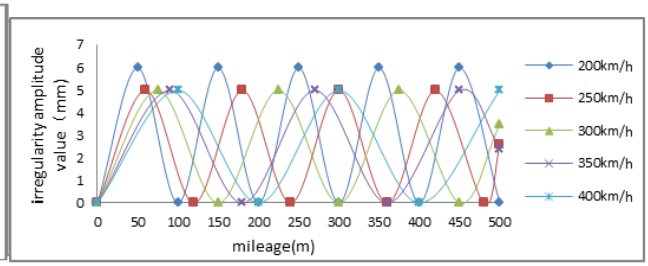


Fig 2: Net operating under standard conditions of comfort settlement irregularity amplitude (comfort standards)

According to Ⅱ class in Table 2,the comfort standard, reserved 5mm as the settlement in the period of train operation by the regulatory requirements. Draw the maximum amplitude chart under the conditions of 200km/h ~ 400km/h controled wavelength.(Fig2)

The sum of the track settlement after constration and the settlement caused by under-crossing high speed railway should less than control standards of high speed railway track amplitude. According to this idea, long wave irregularity control index value caused by tunnel under-crossing high speed railway is the difference value between long wave irregularity control index value of high speed railway with the actual longwave irregularity value of track settlement after constration.

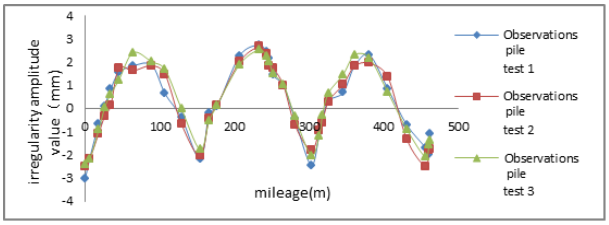


Fig3: Comfortable waveform control standards of under-crossing high speed railway (300km / h)

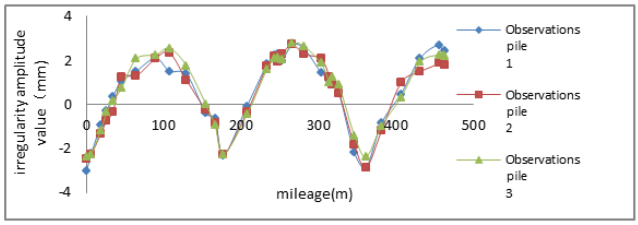


Fig 4: Comfortable waveform control standards of under-crossing high speed railway (350km/h)

And concern about the high speed railway, focus the two situation of 300km/h and 350km/h. The irregularity amplitude of the two speed that deduct the settlement during operation time in Fig 2 subtract the maximum settlement of the observation test pile in figure 1, then obtained the 300km/h

irregularity waveforms in Fig 3. And obtained the 350km/h irregularity waveforms in Fig 4 by the same way.

According to the safety standards of III level in Table 2, and set 5mm settlement for the settlement during train operations. drawing maximum amplitude diagram under the wavelength control conditions by 200km/h ~ 400km/h. (Fig 5).

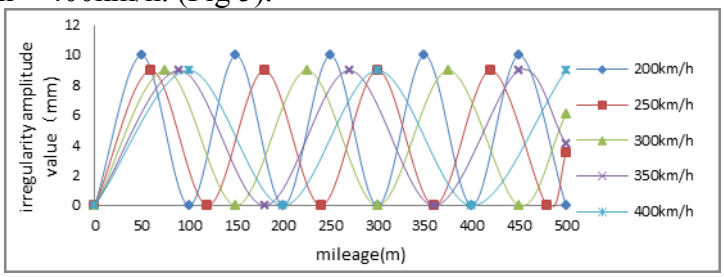


Figure 5: 200 km/h ~ 400km/h, net operating under standard conditions of safety settlement irregularity amplitude(safety standard)

The irregularity amplitude of the two speed that deduct the settlement during operation time in Fig 5 subtract the maximum settlement of the observation test pile in Fig 2,then obtained the 300km/h irregularity waveforms in Fig 6. And obtained the 350km/h irregularity waveforms in Fig 7 by the same way.

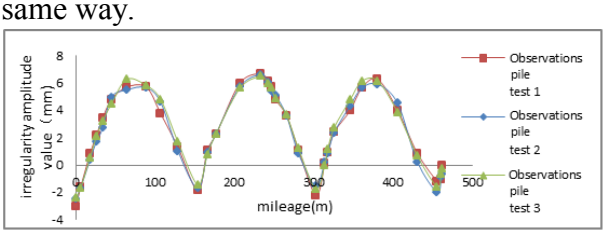


Fig6:Safety waveform control standards of under-crossing high speed railway(300km/h)

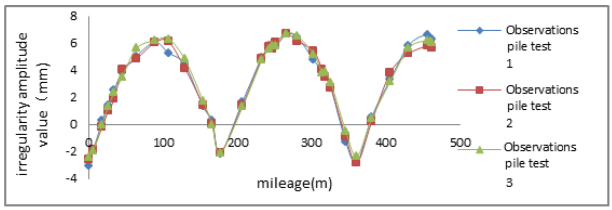


Fig7:Safety waveform control standards of under-crossing high speed railway(350km/h)

Through the analysis above, the minimum cosine waveform can be the control standard for sedimentation trough by tunnel under-crossing high speed railway. Invert the cosine waveform, then the control waveform of sedimentation trough has been created. The control waveform of sedimentation trough is the key indicators by tunnel under-crossing high speed railway.

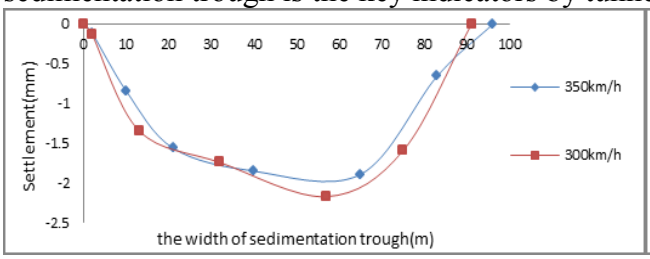


Fig 8:The control waveform of sedimentation tank(comfort standards)

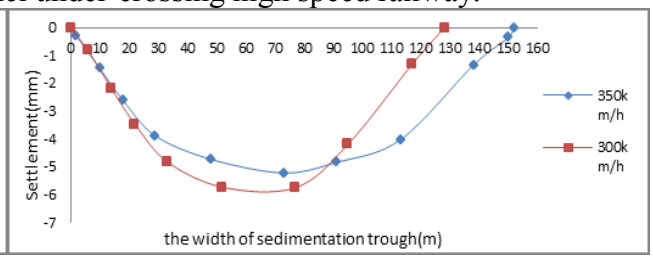


Fig 9:The control waveform of sedimentation trough (safety standard)

According to the comfort standard (Fig 3-4), the control waveform of sedimentation trough by tunnel under-crossing high speed railway gived in Fig 8; According to the safety standard (Fig 6-7), the control waveform of sedimentation trough by tunnel under-crossing high speed railway gived in Fig 9. The waveform control chart of sedimentation trough can define the range of sedimentation trough by tunnel under-crossing high speed railway. Use the width of the settlement trough limited the irregularity management of longwave values. The maximum settlement value of sedimentation trough limited the magnitude of longwave irregularity management. In other words, if you want to meet the comfort requirements of the high-speed railway during operation, the sedimentation trough graph caused by tunnel under-crossing high speed railway must inside the waveform control diagram of sedimentation in fig8.If you want to ensure the safety requirements of high-speed railway,then the sedimentation trough graph caused by tunnel under-crossing high speed railway must inside the waveform control diagram of sedimentation in fig 9.

Long-wave irregularity of the track means that the uneven settlement will cause the vehicle resonance at a specific wavelength . So the sedimentation tank formed by the tunnel under-crossing high-speed railway should be less than or greater than this wavelength range. And because this particular wavelength is longer, in order to make it easy to control, so choose the control targets of settlement trough width less than this particular wavelength. According to this idea, the next Fig 8 to 9 summarized the control waveform of tunnel under-crossing high-speed railway according to the comfort and safety indicators respectively. It has been shown in Table 3.

Table 3:The control indicators of sedimentation trough by tunnel under-crossing high-speed railway

| Category \ v | 300（km/h） | 350（km/h） |
|---|---|---|
| Comfort index | maximum settlement 2.17mm | maximum settlement 2.01mm |
| | The maximum width of the sedimentation tank 91m | The maximum width of the sedimentation tank 96m |
| Safety index | maximum settlement 5.94mm | maximum settlement 5.21mm |
| | The maximum width of the sedimentation tank 126m | The maximum width of the sedimentation tank 149m |

**Numerical simulation of tunnel under-crossing high-speed railway**

Numerical simulation using finite element analysis software, the overall model is shown below in Figure 10. In order to reduce the influence of boundary effects, the model along the tunnel axis (Z direction) taking 78m, vertical (Y direction) taking 36m, a horizontal plane perpendicular to the tunnel direction (X direction) to take 108m. Since the tunnel Oblique under-crossing the high-speed railway, in order to facilitate the calculation of excavation, take the tunnel perpendicular to XOZ plane, and the tunnel has 32.5 degrees to XOZ plane. The track length is 110m. Model boundary conditions are displacement boundary conditions, where the soil and the bottom around the vertical restraint on the free surface of the soil constraints embankment also used two vertical constraints.

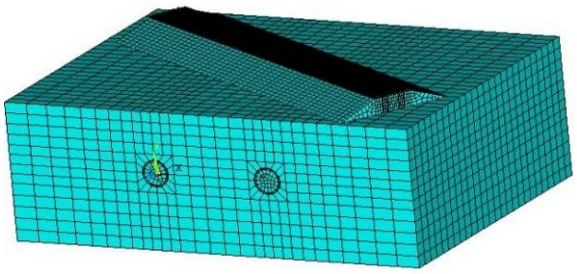

Fig 10: Overall model figure

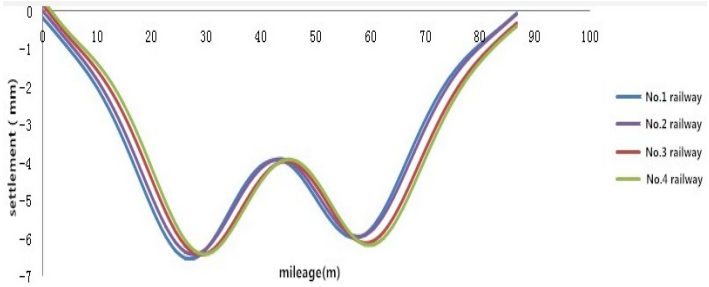


Fig11: 1 to 4 Track sedimentation trough

**The parameters of each material in Numerical simulation.** According to the geological survey report, simplified the soil into layers.The parameter has been shown in Table 4-5.

Table 4:The basic physical and mechanical properties of the foundation soil

| Soil | $\gamma(N/m^3)$ | CohesionC($Pa$) | friction $\varphi$ (°) | Poisson's ratiom | Modulus E(kpa) | Thickness (m) |
|---|---|---|---|---|---|---|
| plain fill soil | $1.85\times10^4$ | $1.5\times10^4$ | 10 | 0.3 | $1.5\times10^7$ | 2 |
| silt soil | $1.90\times10^4$ | $2.2\times10^4$ | 10.2 | 0.3 | $2.5\times10^7$ | 22 |
| pebble | $2\times10^4$ | $1.02\times10^4$ | 18.7 | 0.3 | $6.0\times10^7$ | 12 |
| embankment soil | $1.95\times10^4$ | $6\times10^4$ | 7.4 | 0.3 | $3.0\times10^7$ | 4 |

**Calculation process and the analysis of the results.** Soil, lining, concrete slabs, are using solid elements, use the contact elements between the concrete slab and the embankment soil , the miscellaneous and embankment soil.

Table 5 The parameters of tunnel lining, rails and concrete slab structure

| Name | g(N/m3) | E(kpa) | m | inside diameter (m) | outside diameter(m) | thickness (m) |
|---|---|---|---|---|---|---|
| tunnel lining | $2.5\times10^4$ | $2.76\times\times10^{10}$ | 0.2 | 3 | 3.3 | 0.3 |
| rail | $7.83\times10^4$ | $2.1\times10^{11}$ | 0.3 | — | — | — |
| concrete slab | $2.5\times10^4$ | $2.76\times\times10^{10}$ | 0.2 | — | — | 0.5 |

Tunnel excavation, the disturbed ground has already been completed in this consolidation settlement, the settlement will be cleared during the simulation strata and orbit. The left side of the tunnel has been excavated first, and then the right side of the tunnel . Make a two-dimensional figure of the sedimentation trough accroading to the mileage and settlement results. And the mileage as the X-axis, Y-axis as a settlement. sedimentation trough were drawn 1-4. As shown in Fig 11.

Fig 11 shows that the largest settlement on the 1st rail tunnel under the left side of the under-crossing is caused at the 3rd largest settlement of the track 6.33mm,cause the 4th largest settlement was 6.32 mm.The right side of the rail caused by tunnel under-crossing is 5.88mm; the 2nd largest settlement of the track 5.91mm; the 3rd largest settlement of the track 6.12mm; the 4th largest settlement of 6.15mm.

because of the left side of the tunnel should excavate first,and the sedimentation trough caused by right side of the tunnel excavation will superimpose the sedimentation trough caused by the left side of the tunnel.It will cause top of the left side tunnel greater settlement. The settlement in the left side of the tunnel is 0.2 ~ 0.3mm larger than the settlement in the right side. Formed the largest settlement in the upper left position of the track on the 1st tunnel.

We can judged by the 11 figure that irregularity wavelength caused by lane tunnel is about 86m, therefore, the sedimentation trough caused wavelength must satisfy the control value of long-wave irregularity at 300km / h, 350km / h speed conditions. The lane tunnel caused maximum subsidence is 6.36mm. Basically satisfy the control standards of 300km / h herein,and a little larger than the control standards of 350km / h .

## Conclusions

1.Reference to the National norms long-wave uneven amplitude. Proposed the comfort and safety indicators of tunnel long-wave irregularity and its corresponding limited amplitude under-crossing high-speed railway. Proposed the limited value of respectively.

2. Use the finite element simulations the tunnel under-crossing the railway. The results show that the safty requirements achieved both of the irregularity wavelength control value and amplitude control values.but the comfort requirements is only achieved the irregularity wavelength control value,and the amplitude of the control targets is not achieved . This shows that we need to strictly control the level of construction technology in the construction process. Focusing on the use of support measures to ensure the comfort requirements of high-speed passenger.

## Reference

[1]S. Gupta, Y. Stanus, G. Lombaert. Influence of tunnel and soil parameters on vibrations from underground railways[J]. Journal of Sound and Vibration，327 (2009) 70–91.

[2]XU Gan Cheng,LI Cheng Xue ,WANG Hou Yu. Analysis of influence of metro shield tunneling crossing underneath high speed railway [J]. ROCK AND SOIL MECHANICS，2009，30:269～273.

[3]ZHU Zhengguo, LI Bingbing, LI Wenjiang. Study on Ground Surface Settlement Control Standard Induced by Construction of New-Built Railway Tunnel Under-Passing Existing Railway [J]. China Railway Science，2011，32(5)：78～82.

[4]DUN Hao. The analysis of soft handle high-speed rail technology and sedimentation. Huazhong University of Science and Technology Master Thesis，Wu han,2012

*Applied Mechanics and Materials Vols. 580-583 (2014) pp 1279-1282*
*© (2014) Trans Tech Publications, Switzerland*
*doi:10.4028/www.scientific.net/AMM.580-583.1279*

# Research on defects of tunnel portals during the operation

Kuzhu Zhu[1, a *],Jianhang Luo[1,b]

[1]Guangxi Key Laboratory of Geomechanics and Geotechnical Engineering, College of Civil Engineering and Architecture, Guilin University Of Technology, Guilin, Guangxi, 541004, China

[a]wuzhu3u@126.com, [b]luokehang@163.com

**Keywords:** operation tunnel; tunnel portal; defects; mechanics analysis.

**Abstract.** Through the site investigation of defects on a secondary highway tunnel portal in Guizhou Province and survey data, this paper aims to analyze the detection mechanism of all defects. Controlled by bias effect of tunnel portals, the defects of portal lining cracking and leakage are pretty serious. A fully understanding of these mechanisms can help to improve and fine design and construction of tunnel portal, reducing the production of defect.

## Introduction

Surveys [1~3] indicate that dehiscence, deformation, peeling, water leakage and other defects in a substantial proportion of the lining. It will affect traffic, the safety of tunnel and shorter the time of intervals service life. As the complicated natural environment and other factors around the portals, result in the evaluation of the health status of the tunnel a world-class problem. According to the present experience, the defects treatment lack of exact system and scientific research on tunnel defect theories, methods and procedures. This will inevitably lead to unreasonable and wrong defect management programs and measures. Thus, it is necessary to conduct a comprehensive research on defects of tunnel portals. Through site investigation, detection data, this paper will take a tunnel in Guizhou Province as an example to evaluate the health of the portals, and make some suggestions about design, construction and maintenance of the tunnel portal of this kind.

## Project overview and main defects of the tunnel

**Project overview**. A secondary roads tunnel is 656m long. It has two lanes whose width and height are namely 9 and 6.5 meters. The entrance is between K45+862~K45+872, exit is K46+505~K46+518.Tunnel portals are designed with wing wall forms while the hole body support in the form of curved wall. This tunnel construction started in 1991 and opened to traffic in late 1992. Tunnel has simple geological structure, no fault, and rocks clear hierarchy. Near in tunnel entrance, vertical rock weathering is 20m deep, with the weathered rock crushing, unstable joint development. Destruction of rock structures directly lead to a large tunnel structure defects, and even endanger the safe operation of the tunnel. Tunnel have opened to traffic since 1992, there has been a large area of seepage water and some structural cracks and other defects. On export segment structure the problems like settlement deformation, damage cracking appeared in 2003.

**Site survey.** In order to grasp the current situation of the tunnel, ensure the reasonability of management and maintenance of the tunnel defects, we need to carry out a detailed survey on tunnel. Finally, we can make a comprehensive evaluation of the security situation about tunnel. In terms of these factors, following are investigation and analysis on tunnel,(1) The site detailed survey of cracks and water leakage and other defects;(2) Measure the tunnel contour by tunnel laser

profiler;(3) Measure the lining thickness, defects and intensity of lining through high-frequency radar, ultrasonic.Based on site surveys tunnel disease, the main defects are as follows: cracks (As shown in Fig.1), water leakage, the surface of the lining of disease, deform. As shown in Table 1. Defect of the tunnel entrance sketching are shown in Fig.2.

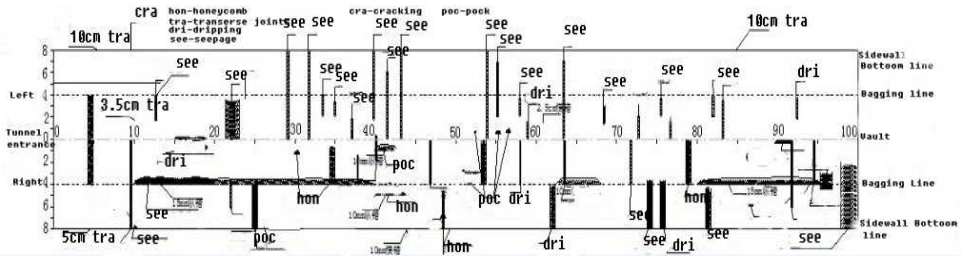


Fig. 1 Cracks on tunnel portal Fig.2 Lining defects sketch

Table1 Statistics tunnel disease site survey

| Types Of Defects | Lining Disease（quantity） | | | Deform | | | | Leakage of water （quantity） | Crack （quantity） |
|---|---|---|---|---|---|---|---|---|---|
| | Honeycomb | Pock | Peel off | Dislocation | | Concave | Convex | | |
| | | | | Transverse | Longitudinal | | | | |
| left | 0 | 0 | 0 | 6 | 8 | 0 | 5 | 119 | 54 |
| right | 49 | 51 | 84 | 56 | 58 | 15 | 35 | 197 | 83 |
| Total | 49 | 51 | 84 | 62 | 64 | 15 | 40 | 316 | 137 |

**Detect of tunnel portal.** Combined tunnel survey data, the completion of the design documents and a comprehensive analysis to detect cross-section of the tunnel contour, The lining section outlines the characteristics of temple tunnel entrance can be inferred in the cross section K45+862 shown in Fig.3 and the reasons are as follows: (1) Section K45+862~K46+072: The overall outline of lining is over break. That is to say, the actual measurement segment is larger than design section on the cross-sectional contour, and has no significant local deformation. (2)Section K46+452~K46+518: lining hasn't significant deformation. But the lining segments are serious due to cracks, because the mold has been built concrete to reinforce lining, the actual measurement segment does not reflect the state before reinforcement.

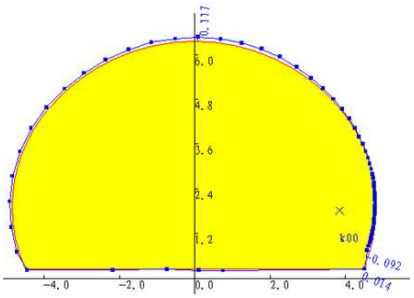


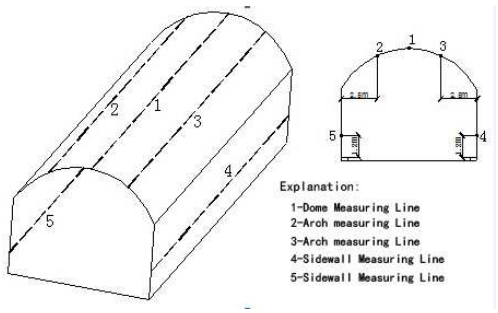


Fig.3 Tunnel transect contour - K45+862 section Fig.4 Schematic geological radar line lay out

**Geological radar detects.** Five survey lines were arranged longitudinally along the tunnel, one arranged on vault; two on arch waist, other two on side walls. Particular arrangements are shown in Fig.4. According to detecting the lining quality on the import and export by geological radar, rebar spacing comply with regulatory requirements completely, and early and secondary lining concrete lining are relatively dense. Due to space limitations, this paper did not attached to specific test data.

**Strength tests of concrete lining.** According rock category lining forms and disease characteristics, strength testing of each section, respectively, use the rebound method, ultrasonic and rebound combined method in strength. Combining with the results of geological radar, strength testing of concrete lining is carried out on the basis of water leakage and crack investigative work in

the tunnel. Taking into account the actual characteristics of the tunnel project, strength testing work to the tunnel treats cross-section as the research object, especially in key positions of export segment, it should be encrypted to ensure the reliability and precision of research.

Rebound method is a basic method of nondestructive testing, which is based on direct hammer rebound values to obtain the concrete surface compressive strength of concrete.

Ultrasound combined rebound method use low-frequency ultrasound measurement instrument and a standard kinetic energy 2.207J 's Hammer to test same area of structure or component through rebound speed of sound and in situ testing. By using of national unity strength curve which has been built up, it can calculate concrete compressive strength of the survey area.

In order to compare the results of measuring strength of different detection methods, the test results of rebound method, ultrasonic and combined rebound method are summarized in Table 2.

Table 2 Strength test results

| Sectional position | Lining concrete strength（M Pa） | | | | |
|---|---|---|---|---|---|
| | Rebound Method | | Ultrasonic combined method | | Comprehensive estimated value |
| | Left wall | Right wall | Left wall | Right wall | |
| K45+862(K000) | 34.2 | 23.9 | 35.4 | 30.4 | 23.9 |

**Causes of defects**

**Influenced by bias effect.** There are 205 defects in the section K45+862~K45+962, in a density of 2.05 per meter. From the number of defects, we can draw that the defects on right side of the tunnel are more severe than that on left. According to the analysis of the geological data, the main reasons are: (1) rock tilted from right to left, causing the right side of the tunnel withstand greater pressure than the left and formed the bias effect; (2) rock groundwater vulnerability in the lining behind the right side of collection, (3) underground tunnel in which the lining has some erosion [4].

**Leakage water.** Surface water is mainly main ditch water from Dashibao Dam, and its exposure position is higher than the entrance; tunnel's exit section go through a length of 100m coal-strata which has been mined largely. Inside the cave, it's filled, semi- filling or unfilled, which could easily lead to the accumulation of groundwater; Lots tunnel entrance near vertical rock weathering a depth of 20m, with the weathered rock crushing, which formed a tunnel seepage water channel; Outlet sections of the tunnel more than 100 meters occurred within the scope of collapse several times; construction unit when the original footage from the outlet end to more than 40 meters, the tunnel arch was larger leaks, the cave was saturated with water after a long plastic state, the body is completely collapse loss of self-supporting capability. These adverse conditions provide the conditions for the production of leakage water; however, the gaps between the lining, improper water-proof measures of arch and side walls on the same lining, cause of leakage water [5].

**Lining cracks of entrance-portal.** There are ring-cracks of the entrance-portal lining. It is in the haunch section which formed an angle of 45° with the plumb line, in a length of about one meter. Both the side has cracks, presenting a symmetrical shape. There are also cracks in the vault. Meanwhile, there is a radial crack on the left, developed tracking the building blocks until the top of the portal. And there are small cracks in the peak of the arch. Portal on the right side there are cracks in development. According tunnel portal near the surface cracks and circumstances, there is a gallery portal segment slipped body, resulting in bias. The side slope in the entrance-portal is stable. Due to the bias effect, there are cracks on the portal and other defects in gallery portal segment.

**Lining cracks of exit-portal.** There are wide cracks in the exit-portal, as is shown in Fig 5, and it also shows that the tunnel has no obvious bias. Exit-portal has an about 13 meters gallery portal. Since gallery portal of lining segments has many cracks, reflecting that the lining has been

damaged. Based on the above analysis, because the upper covering of the gallery portal and the adjacent surrounding rock are poor, therefore, pressure acting on the lining is huge. Moreover, the lining material's strength and thickness is smaller than the original design, making the peak of the arch sink too much, thus, the lining is cracked. The mechanism is shown in Fig 6, the destruction of gallery portal segment and adjacent surrounding rock has grown to the surface.

Fig.5 Cracks on the exit -portal

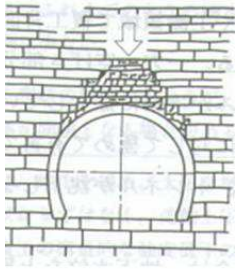

Fig.6 Mountain Temple tunnel portal collapse mechanism

**Conclusions of tunnel health evaluation and Suggestion**

**Cracks and water leakage.** (1) From the point of defects severity, the entrance-portal is more serious than the exit- portal and the right side of tunnel is more severe than the left side;(2) From the point of defects distribution, the defects are mainly in K45+862~K45+962, K46+062~K46+162, K46+362~K46+462, K46+462~K46+518.

**Fracture surface contour of the tunnel and surface deformation.** The actual fracture surface contour of section: K45+862 ~ K46+072 of the tunnel is larger than its design, the outer of lining is in a whole external expansion.

**Tunnel portal and side slope.** (1) Side slopes of the tunnel's entrance and exit are steady;(2) There are cracks in the entrance-portal and gallery portal; grouting slippage massif above the gallery portal: K45+862~K45+872 of the entrance-portal, and behind the lining;(3) Exit-portal has been severely damaged; the lining of its gallery portal has been damaged, cracks have developed to the earth's surface. Grouting and reinforcing the gallery portal:K46+505 ~K46+518 of exit-portal, setting a thick of 20cm concrete arch cover, injecting Epoxy slurry to the cracks.

**Acknowledgement**

This work was supported by the National Natural Science Fund of China(No.41102202), Guangxi Natural Science Foundation(No.2010GXNSFB013012 & No. 2012GXNSFGA060001) .

**References**

[1] Bureau o f Jilin railway, handbook of railway tunnel maintenance [M]. 1980, Press of People's Railway.(in Chinese)

[2] Jiangbin Wu, Dingli Zhang, etc. Current damage situation of railway operation tunnels and their inspection and evaluation [J]. 2003, China Safety Science Journal ,13 (6):45-52. (in Chinese)

[3] Haijing Liu, Caichu Xia, Hehua Zhu. Studies on tunnel damage [J]. 2007, Chinese Journal of Underground Space and Engineering, 3(5):947-953. (in Chinese)

[4] Chunjing Wang. Operations highway tunnel construction safety assessment and integrated disease treatment technique[D]. 2010,Central South University, Changsha. (in Chinese)

[5] Gaofei Dai, Hehua Zhu, Caichu Xia. Study on Causation of Highway Tunnel Defects and Their Countermeasures [J]. 2005,China Safety Science Journal, 15(12):89-92.(in Chinese)

*Applied Mechanics and Materials Vols. 580-583 (2014) pp 1283-1287*
*© (2014) Trans Tech Publications, Switzerland*
*doi:10.4028/www.scientific.net/AMM.580-583.1283*

# Study on Risk Trend Assessment of Metro Tunnel crossing underground pipeline Based on Partial Connection Number

Hongtao Xie[1, a], Bo Li[2,b] and Yunsheng Zhao[3,c]

[1,2,3] Faculty of Engineering, China University of Geosciences Wuhan 430074, china

[a]hongtao_xie@126.com, [b]libomxd@163.com, [c]yshzhao@cug.edu.cn

**Keywords:** risk trend assessment; underground pipeline; set-pair analysis (SPA); partial connection number

**Abstract.** A model of risk trend assessment for metro tunnel crossing underground pipelines is proposed in this paper based on the partial connection number. This paper fully considered the certainty and uncertainty of the index and used "partial connection number method" to analyze the risk developing trend and its sort of metro tunnel crossing underground pipelines. A case study was performed on a metro tunnel engineering of Shenzhen Line 9. The results showed that this model considered the dynamic characteristics of risk, enriching the contents of risk assessment of underground engineering, which can provide a reference for the risk management.

## Introduction

There are a variety of underground pipelines in urban cities, such as gas pipe, water mains, thermal pipeline, cable conduit communication, etc. These guarantee the normal life of the urban residents. Metro lines usually emplace along city arterial road, thus, metro tunnel construction will inevitably pass through a variety of urban underground pipelines. The available risk assessment methods which focus on risk state assessment lack of analysis for risk dynamic trends [1, 2]. Based on the partial connection number of set-pair analysis (SPA), this paper proposes a risk trend analysis method of the metro crossing underground pipeline to comprehensively analyze the development trends of risk, which provides a new way to evaluate the impact of urban metro tunnel on underground pipeline.

## Risk Trend Assessment Model

Set pair analysis is a theoretical method based on identical discrepancy contrary (IDC) analysis proposed by Chinese scholar Keqin Zhao, which made to study theory uncertainty problem. It takes connection number to reflect the uncertainty and uncertainty of systems, and their mutual conversion rule [3]. Connection number is represented by $U$:

$$U = a + bi + cj \tag{1}$$

The letters $a$, $b$ and $c$ are identical degree, discrepancy degree and contrary degree under the studied question of two sets, and $a+b+c=1$. $i$ is discrepancy coefficient, $i \in [-1, 1]$; $j$ is contrary coefficient, $j=-1$. Five-element connection number is an extension of three-unit connection number, expands from $bi$ to get the mathematical expression of five-element connection number:

$$U = a + bi_1 + ci_2 + di_3 + ej \tag{2}$$

**Connection Degree.** After form a set pair with each index and its risk level, calculate the connection number between them. Taking the fuzzy division of risk level standard into account, the formula of fuzzy connection degree is formed. The connection degree between the smaller-better indexes and its risk level standard is:

$$\mu_l = \begin{cases} 1+0i_1+0i_2+\cdots+0i_{K-2}+0j & x_l \le s_1 \\ \dfrac{s_2-x_l}{s_2-s_1}+\dfrac{x_l-s_2}{s_2-s_1}i_1+0i_2+\cdots+0i_{K-2}+0j & s_1 < x_l \le s_2 \\ 0+\dfrac{s_3-x_l}{s_3-s_2}i_1+\dfrac{x_l-s_2}{s_3-s_2}i_2+\cdots+0i_{K-2}+0j & s_2 \le x_l \le s_3 \\ \vdots & \\ 0+0i_1+0i_2+\cdots+\dfrac{s_K-x_l}{s_K-s_{K-1}}i_{K-2}+\dfrac{x_l-s_{K-1}}{s_K-s_{K-1}}j & s_{K-1} < x_l \le s_K \\ 0+0i_1+0i_2+\cdots+0i_{K-2}+1j & x_l > s_K \end{cases} \tag{3}$$

The connection degree between the greater-better indicators and its risk level standard is:

$$\mu_l = \begin{cases} 1+0i_1+0i_2+\cdots+0i_{K-2}+0j & x_l \ge s_1 \\ \dfrac{x_l-s_2}{s_1-s_2}+\dfrac{s_1-x_l}{s_1-s_2}i_1+0i_2+\cdots+0i_{K-2}+0j & s_2 \le x_l < s_1 \\ 0+\dfrac{x_l-s_3}{s_2-s_3}i_1+\dfrac{s_2-x_l}{s_2-s_3}i_2+\cdots+0i_{K-2}+0j & s_3 \le x_l < s_2 \\ \vdots & \\ 0+0i_1+0i_2+\cdots+\dfrac{x_l-s_K}{s_{K-1}-s_K}i_{K-2}+\dfrac{s_{K-1}-x_l}{s_{K-1}-s_K}j & s_K \le x_l < s_{K-1} \\ 0+0i_1+0i_2+\cdots+0i_{K-2}+1j & x_l < s_K \end{cases} \tag{4}$$

**Risk level**. If considering indexes weight, the comprehensive connection degree between index and its risk level can be expressed as:

$$u = \sum_{m=1}^{n}\omega_m a_m + \sum_{m=1}^{n}\omega_m b_{m,1} i_1 + \cdots \sum_{m=1}^{n}\omega_m b_{m,K-2} i_{K-2} + \sum_{m=1}^{n}\omega_m c_m j \,. \tag{5}$$

Wherein $\omega_m$ is the weight of index $m$ ($m$ = 1,2,…$n$).

Evaluate the risk level of factors through confidence.

$$h_k = (f_1 + f_2 + \cdots + f_k) > \lambda \,, \quad k = 1,2,\cdots K \tag{6}$$

Wherein: $f_1 = \sum_{m=1}^{m}\omega_m u_{m1}$ ; $f_2 = \sum_{m=1}^{m}\omega_m u_{m2}$ ; $f_3 = \sum_{m=1}^{m}\omega_m u_{m3}$ ; $f_4 = \sum_{m=1}^{m}\omega_m u_{m4}$ ;… $f_k = \sum_{m=1}^{m}\omega_m u_{mk}$

$\lambda$ is confidence level, when it remains constant, if $h_k > \lambda$ and $h_{k-1} < \lambda$, the risk level is $k$. In general, its value is in a range of [0.50, 0.70].

**Partial connection number.** Partial connection number is an adjoint function reflecting the system's development trends of connection state, which characterizes the strength of risk trends. Partial connection number of five-element connection numbers is defined as follows:

Partial positive connection number:

$$\partial u^+ = \partial a + \partial b i_1 + \partial c i_2 + \partial d i_3 \,. \tag{7}$$

Partial negative connection number:

$$\partial u^- = \partial b^- i_1 + \partial c^- i_2 + \partial d^- i_3 + \partial e^- j \tag{8}$$

Wherein: $\partial a = \dfrac{a}{a+b}, \partial b = \dfrac{b}{b+c}, \partial c = \dfrac{c}{c+d}, \partial d = \dfrac{d}{d+e}; \partial b^- = \dfrac{b}{a+b}, \partial c^- = \dfrac{c}{b+c}, \partial d^- = \dfrac{d}{c+d}, \partial e^- = \dfrac{e}{d+e}$

Partial positive connection number reflects the degree of positive risk trends; Partial negative connection number reflects the degree of risk negative trends. The actual development trend of risk is the synthetic action of positive and negative trends. Therefore, the definition of total partial

connection number is $\partial^{+}_{-}u = \partial u^{+} - \partial u^{-}$. If $\partial^{+}_{-}u > 0$, which means a potential decreasing trend of risk; If $\partial^{+}_{-}u < 0$, it means a potential improving trends of risk; If $\partial^{+}_{-}u = 0$, it means a critical state of system, the system trend may be negative or positive.

## Risk Index System of Metro Construction crossing Underground Pipelines

Stratum settlement by metro tunnel excavation may cause joint pipeline deformation. If the deformation is too large, the damage of the pipeline will be caused, The impact between metro tunnel construction and the adjacent underground pipeline is mutual, which is not only associated with pipeline type, damage condition, pipeline materials and joint type, but also about construction methods, construction technology and management, engineering and hydrogeological conditions[4, 5]. Based on available research achievements and influence of various parties, risk indexes of metro tunnel crossing adjacent underground pipeline are shown in Table 1.The risk index is divided into five levels: level 1(secure), level 2(comparatively secure), level 3(general secure), level 4(comparatively dangerous) and level 5(dangerous).

Table 1 Risk indicators and classification of metro tunnel crossing underground pipelines

| | index layer | Level 1 | Level 2 | Level 3 | Level 4 | Level 5 |
|---|---|---|---|---|---|---|
| underground pipeline situation/$u_1$ | pipeline type/$u_{11}$ | heat-supply pipeline | water supply pipeline | waste pipeline | gas pipeline | cable conduit |
| | pipeline materials/$u_{12}$ | flexible pipe(PVC) | steel pipe | reinforced concrete pipe | concrete pipe | cast-iron pipe |
| | pipeline size/$u_{13}$ | 1800(mm) | 1500(mm) | 1000 (mm) | 500 (mm) | 200 (mm) |
| | joint type/$u_{14}$ | flexible pipe(PVC) | Steel pipe | cast-iron pipe | reinforced concrete pipe | concrete pipe |
| | damage condition/$u_{15}$ | intact | basically intact | general intact | damaged | severely damaged |
| | pipeline depth/$u_{16}$ | 1(m) | 2(m) | 3(m) | 4(m) | 5(m) |
| tunnel engineering conditions /$u_2$ | formation conditions/$u_{21}$ | Ⅵ | Ⅴ | Ⅳ | Ⅲ | Ⅱ, Ⅰ |
| | tunnel depth/$u_{22}$ | 30(m) | 25(m) | 20(m) | 15(m) | 10(m) |
| | tunnel cross-sectional dimension/$u_{23}$ | 6(m) | 9(m) | 12(m) | 15(m) | 18(m) |
| | construction environment/$u_{24}$ | excellent | good | general | poor | bad |
| | level of construction techniques and management/$u_{25}$ | richful similar construction experience,powerful technical force,high management level | comparatively richful similar construction experience,comparatively powerful technical force,comparatively high management level | general richful similar construction experience,general powerful technical force,general high management level | scanty similar construction experience,weak technical force,lower level of management | no similar construction experience,shortage of technical force,poor level of management |
| | construction method/$u_{26}$ | shield,reasonable cross-sectional shape and force conditions,no stress concentration | shield,comparatively reasonable cross-sectional shape and force conditions,no stress concentration | mining,comparatively reasonable cross-sectional shape and force conditions | mining, poor cross-sectional shape and force conditions | open excavation, poor force conditions,large stress concentration |
| | construction time effect/$u_{27}$ | losse | comparatively losse | progressive | tight | grab duration |
| pipelines adjacenct to tunnel/$u_{31}$ | | non-adjacent | comparatively adjacent | adjacent | very adjacent | extremely adjacent |
| security measure/$u_{41}$ | | excellent | good | general | poor | bad |

## Application Example

A tunnel engineering under construction of Shenzhen metro Line 9 crosses multiple urban underground pipelines. Four underground pipelines were selected to investigate their type, material, joint type, depth, damage condition, as well as plane location relation with tunnel. The parameters are shown in Table 2.

Table 2 Pipelines risk parameters

| Index | pipelines parameter | | | |
|---|---|---|---|---|
| | A | B | C | D |
| pipeline type | flexible cable conduit | gas steel pipeline | concrete sewer | steel water supply pipe |
| pipeline materials | PVC | steel | concrete | steel |
| pipeline size | diameter 300(mm) | diameter 400(mm) | diameter 1200(mm) | diameter 1000(mm) |
| pipeline depth | 1.86(m) | 1.31(m) | 3.24(m) | 0.99(m) |
| damage condition | basically intact | basically intact | general intact | basically intact |
| joint type | PVC pipe | steel pipe | concrete pipe | steel pipe |
| surrounding rock level | Ⅳ | Ⅳ | Ⅲ | Ⅲ |
| tunnel depth | 14.25(m) | 13.30(m) | 11.56(m) | 12.60(m) |
| tunnel cross-sectional dimension | 6(m) | 6(m) | 6(m) | 6(m) |
| construction method | shield | shield | mining | shield |
| plane location relation between pipeline and tunnel | pipeline and tunnel parallel /horizontal distance 2.3m | Pipeline and tunnel vertical | pipeline and tunnel intersect | pipeline and tunnel intersect |

The quantitative indexes can be directly put into equation (3) and (4) to solve connection degree. But qualitative indexes must be combined with engineering practice to contrast the value of risk index to risk rating criteria. Expert evaluation method was used to measure coincidence degree between them, respectively assign value: level 1(90 points), level 2(80 points), level 3(70 points), level 4(60 points), level 5 (50 points). the risk parameters value of each pipeline was shown in Table 3.

Table 3 Risk parameters value of pipelines

| index | $u_{11}$ | $u_{12}$ | $u_{13}$(mm) | $u_{14}$ | $u_{15}$ | $u_{16}$(m) | $u_{21}$ | $u_{22}$(m) | $u_{23}$(m) | $u_{24}$ | $u_{25}$ | $u_{26}$ | $u_{27}$ | $u_{31}$ | $u_{41}$ |
|---|---|---|---|---|---|---|---|---|---|---|---|---|---|---|---|
| weight | 0.15 | 0.20 | 0.10 | 0.20 | 0.20 | 0.15 | 0.10 | 0.10 | 0.10 | 0.05 | 0.30 | 0.30 | 0.05 | 0.20 | 0.15 |
| A | 50 | 90 | 300 | 90 | 76 | 1.86 | Ⅳ | 14.25 | 6 | 68 | 85 | 83 | 68 | 56 | 83 |
| B | 60 | 80 | 400 | 80 | 84 | 1.31 | Ⅳ | 13.30 | 6 | 76 | 85 | 83 | 68 | 50 | 84 |
| C | 70 | 60 | 1200 | 50 | 68 | 3.24 | Ⅲ | 11.56 | 6 | 65 | 85 | 69 | 68 | 50 | 76 |
| D | 80 | 80 | 1000 | 80 | 75 | 0.99 | Ⅲ | 12.60 | 6 | 66 | 85 | 77 | 68 | 50 | 79 |

Professional system and Analytic Hierarchy Process (AHP) were used to determine relative importance of index and index weight, as shown in Table 3. Comprehensive connection number for each pipelines are:

$u_A$=0.294+0.300$i_1$+0.082$i_2$+0.163$i_3$+0.160$j$;

$u_B$=0.226+0.405$i_1$+0.048$i_2$+0.099$i_3$+0.222$j$;

$u_C$=0.075+0.149$i_1$+0.258$i_2$+0.227$i_3$+0.291$j$;

$u_D$=0.328+0.471$i_1$+0.133$i_2$+0.055$i_3$+0.014$j$;

According to confidence 0.60, the risk level of pipelines A, B, C and D are “general secure”, “comparatively secure”, “comparatively dangerous” and “comparatively secure”. The order of security is D>B>A>C, minimum risk of D, followed by B and A, the highest risk of pipeline is C. Pipeline C needs intensive monitoring and corresponding control measures during construction.

Put five-element connection number of each pipelines into the formula to solve partial positive and negative connection number, and then make them normalized. According to the definition of five-element connection number, i1,i2,i3∈[-1,1], j=-1. Partial connection number method of proportional parts is applied to discrepancy coefficients.

Discrepancy coefficients of first-order partial positive connection number are:

$i_1=\partial a/(\partial a+\partial b)$, $i_2=\partial b/(\partial b+\partial c)$, $i_3=\partial c/(\partial c+\partial d)$

Discrepancy coefficients of first-order partial negative connection number are:

$i_1=\partial c^-/(\partial b^-+\partial c^-)$, $i_2=\partial d^-/(\partial c^-+\partial d^-)$, $i_3=\partial e^-/(\partial d^-+\partial e^-)$

Calculation results and pipeline risk development trend analysis are shown in Table 4. The total partial connection numbers of pipeline A, B and C are less than zero, the risk trend is positive; the total partial connection numbers of pipeline D is greater than 0, the risk trend is negative. Comparing the total partial connection numbers of each pipeline, the risk trend ranking of them can be determined. The result shows that the trend of D is the best, followed by A and C, B is the worst. Based on the level "comparatively secure", the risk of pipeline B has a significant tendency to the level "general secure".

Table 4 The correlation degree and risk level of pipelines

| | partial positive connection number | $i_1$ | $i_2$ | $i_3$ | $\partial u^+$ | partial negative connection number | $i_1$ | $i_2$ | $i_3$ | $\partial^- u$ | $\partial^+ u$ | risk trend | rank |
|---|---|---|---|---|---|---|---|---|---|---|---|---|---|
| A | $0.234+0.371i_1+0.158i_2+0.238i_3$ | 0.260 | 0.472 | 0.268 | 0.468 | $0.269i_1+0.114i_2+0.354i_3+0.263j$ | 0.201 | 0.510 | 0.288 | 0.478 | -0.0095 | positive | 2 |
| B | $0.190+0.474i_1+0.173i_2+0.163i_3$ | 0.187 | 0.478 | 0.336 | 0.416 | $0.304i_1+0.050i_2+0.319i_3+0.327j$ | 0.094 | 0.571 | 0.335 | 0.491 | -0.0755 | positive | 4 |
| C | $0.200+0.219i_1+0.318i_2+0.262i_3$ | 0.333 | 0.284 | 0.382 | 0.464 | $0.286i_1+0.272i_2+0.201i_3+0.241j$ | 0.335 | 0.291 | 0.374 | 0.491 | -0.0271 | positive | 3 |
| D | $0.152+0.289i_1+0.263i_2+0.296i_3$ | 0.257 | 0.391 | 0.351 | 0.433 | $0.452i_1+0.169i_2+0.224i_3+0.155j$ | 0.217 | 0.456 | 0.327 | 0.404 | 0.0297 | negative | 1 |

## Conclusions

Based on existing research, this paper proposed a risk evaluation index system of metro tunnel construction crossing adjacent underground pipeline. The impact of various aspects is taken into consideration during selecting index, which is more realistic, the assessment result is more reasonable. From the perspective of development, the partial connection number was used to analyze risk trends of metro tunnel crossing underground pipeline in this paper based on the static risk assessment, which comply with the requirements of the project dynamic risk management. Introducing partial connection number of set pair analysis into analysis of risk trends riches the risk assessment content of underground engineering risk assessment.

## Acknowledgements

This work was financially supported by Key Project of the Hubei Province Natural Science Foundation (No.2013CFA110), Teaching laboratories Open Foundation in China University of Geosciences (Wuhan) (No.SKJ2013107) and BT project of Shenzhen Metro Line 9.

## References

[1] J.H. Bi, W. Liu and Z.F. Jiang: Rock and Soil Mechanics. Vol. 27(2006), p.1317 (in Chinese).

[2] X.G. Wu, T.M. Zeng, L.M. Zhang, et al: Journal of Railway Engineering Society. Vol. 30(2013), p.127 (in Chinese).

[3] K.Q. ZHAO: *Set Pair Analysis Method and its Primary Application* (Scientific and Technical Press, China 2000), (in Chinese).

[4] K. Wang, C.P. Zhang and M.S. Wang: "Safety evaluation and control on underground pipeline influenced by metro construction", International Conference on Management and Service Science, MASS 2011, Wuhan, China 2011.

[5] F. Sun, R. Pan and T.L. Chen: "Study on grouting heave for pipeline underground in urban tunnel engineering", 2nd International Conference on Applied Mechanics and Materials, Switzerland, p.492, 2014.

*Applied Mechanics and Materials Vols. 580-583 (2014) pp 1288-1292*
*© (2014) Trans Tech Publications, Switzerland*
*doi:10.4028/www.scientific.net/AMM.580-583.1288*

# Water Inrush Risk Evaluation into the Tanjiaba Tunnel

SUN Yibo[1, a], FENG Manyao[2,b]

[1]Jinan Urban Construction Group, Ji'nan, China

[2]FENG Manyao, Licheng, Ji'nan City Highway Bureau, Ji'nan, China

[b]fengmany@163.com

**Keywords:** Risk measurement; Water inrush; Karst tunnel; Fuzzy comprehensive mathematics; Tanjiaba mountain tunnel.

**Abstract.** The Tanjiaba tunnel lies in Hurongxi highway in Hubei Province. There are some middle karstified soluble rocks and a fish pool above the tunnel. To avoid the disaster of water inrush into the tunnel, risk evaluation is necessary to guide the construction. Fuzzy mathematics model is put forward to distinguish potentially dangerous parts along the tunnel. Use the fuzzy mathematics model differentiated the tunnel into 4 ranks of dangerous parts according to risk index. It is applied in the Tanjiaba tunnel and practice approves that the model are useful.

## Introduction

In the industrial revolution of 18th century, Hneri Fyaol introduced risk management thought into enterprise management field. Until 1950s, risk management is developed to a subject in American and risk management is developed rapidly in western countries. In 1970s, risk analysis was introduced into tunnel and underground projects study by Einstein. H. H. Since 1990s, risk of tunnel construction was paid more attention than ever before for more and more amazing tunnel collapse accidents occurred. Risk analysis came to use rapidly in tunneling engineering. The ITA committee was also paid much attention to tunnel risk analysis and published the book "Guidelines for Tunneling Risk Management" as standard and reference for risk analysis and management for tunneling engineering at 2002.

In China, the fuzzy analysis approach has been used in project by YANG Jian-ping at 1998. In recent years, LIU Dan, BAI Ming-zhou, LI Bing, ZOU Chong-feng and etc have been studied water inrush risk. However, theory on water inrush risk and evaluation is not mature yet now. The main controlling factors need to be refined. Application of fuzzy comprehensive evaluation method must help development of risk analysis technique of water inrush into karst tunnel significantly.

## Risk measurement

## Main controlling factors of water inrush into karst tunnel

**Lithology.** According to lithology, karst aquifers can be grouped into 4 categories: intensively, middle, weekly karstified aquifer and aquifuge of insoluble rocks.

**Groundwater.** Groundwater level (h) is an important factor governing of water inrush into karst tunnel. In the case when $h \geq 60$m above tunnel floor at the time of excavation, water inrush disaster may cause severe damages of property and person safety. If $30 < h \leq 60$m, the severe property damage may be occur but generally the safety of person may not be caused. If $0 < h \leq 30$m, only the construction may be influenced. If there is no drainage in time, collapse may be caused. If $h < 0$, there will be no water inrush.

**Geostructure surface.** The open surfaces such as fault, fracture, joint and migration pathway serve for ground water. The secondary dissolution pipeline mainly formed at surface. Large karst cave systems always following tenso-shear faults, lager fracture, bedding plane and unloading fracture

along the quayside. Practice shows that the structure surface of fracture does more contribute to the cave, pipeline and strong development than bedding plane.

**Occurrence of strata.** Rock karstification is inhibited considerable in case strata occur horizontally as a result of anisotropy of rock body broking infiltration of rain and surface water. Karstification of rocks is limited as well in the case when strata occur vertically, as outcrop area of soluble rock in this case will be the smallest and subsequently function of the feedback loop of karst differentiation discussed by WANG Shitian in 1962 will be significantly limited. The most favorable conditions for kastification would take place when strata occurs 20ºto 60º inclined, for example, in a monocline structure or in the wing parts of a syncline or anticline.

**Ancient denudation (paleoerosion) surface.** The ancient denudation surface consists of discontinuity surface, the continental deposit upon the surface and the dissolution zone under the surface. In China, according to the sort of the continental deposit, ancient denudation surface used to be divided into 3 types which are Fe-Al type, phosphate type and coal type. In the south of China, one of the most popular ancient denudation surfaces of coal type is one at the top of Maokou limestone ($P_{1m}$) and in most areas in south western China a intensively karstified zone with large open cavities had always been recognized in lime stone beds right beneath the denudation surface.

**Landform.** Surficial karst feature is taken as parts of the underground river systems on the ground. Depression, sinkhole (doline) and swallow hole are actual inlets or reliable indicator of trunk or tributary of underground river systems and their water input depends on the surficial catchment area. Karst shaft and swallow hole are located in unsaturated zone. They are formed not only by dissolution but also by gravitational collapse.

**Rainfall.** Groundwater level in karst region fluctuates with time greatly. The amplitudes of fluctuation depend on water recharge amount from surface water. If there is a strong rainfall during construction, the water level will rise rapidly and may reach 100m even more in annual amplitudes in conduits. A high water level increases water inrush risk. While in fissure zone surrounding conduits surfacial water into ground slowly and they obtain little water from unsaturated zone, but much water may receive laterally from conduits and water level here also rises although slowly. When water level in conduits rapidly dropping, water in fissures comes to flow to niebering conduits and this makes water level in conduits drops at a lower rate than rising one.

**Table . 1.** Controlling factors of water inrush

| factor rank | $D_1$ | $D_2$ (m) | $D_3$ | $D_4$ (º) | $D_5$ | $D_6$ |
|---|---|---|---|---|---|---|
| I | strong | >60 | strong | 20－60 | strong | strong |
| II | middle | 30<h<60 | middle | 0<a<20<br>60<a<90 | middle | middle |
| III | weak | 0<h<30 | weak | 0, 90 | weak | weak |

## Fuzzy comprehensive evaluation model

**Determining influence factors.** At first, the influence factors are determined. Secondly, the factor set D is conformed. The D is defined as D={$D_1$，$D_2$，……$D_7$}.

Where, $D_1$－lithology, $D_2$－groundwater, $D_3$－geostructure surface, $D_4$－strata occurrence, $D_5$－paleoerosion surface, $D_6$－landform and $D_7$－rainfall.

**Giving evaluation set.** For the risk of water inrush was divided into 4 ranks, the evaluation set is given as V={$V_1$, $V_2$, $V_3$,$V_4$}. Where, $V_1$ - the risk of rank I, $V_2$ - rank II, $V_3$ - rank III, and $V_4$ - rank IV.

**Forming the mathematical model.** As mentioned above, each factor has 4 index or state sets and is denoted by $V_1$， $V_2$， $V_3$，$V_4$. Where $V_i$＝ {$V_{i1}$，$V_{i2}$，…，$V_{i7}$} (i＝1，2，3，4). Then Table 1 can be expressed by the following matrix V.

$$V = V_{ij}\begin{bmatrix} V_{11} & V_{12} & \cdots & V_{17} \\ V_{21} & V_{22} & \cdots & V_{27} \\ \vdots & \vdots & & \vdots \\ V_{41} & V_{42} & \cdots & V_{47} \end{bmatrix}$$

Where, V is the matrix of the state or index of water inrush risk and it is considered as the mathematical model of water inrush. The row vector of V is called class vectors and the column vector of V is called state vector.

**Determining weight value.** The weight value is the experience of the referee and has greatly fluctuation. The different weight values of the same factor are given by different experts and the weight average is considered as the value of the factor. As each of the factors of the water inrush has different status and function, the weight is different. The weight value of all the factors is defined as A. Where, A =( $a_1$， $a_2$， …， $a_7$).

According to the properties and internal relations of the factors and the weight given by the experts, all the weight is given as following.

Without the aquifer of karst, there is no water inrush. So $D_1$ is regarded as the first important factor and the weight is the maximum, $a_1$=1. The underground water level is the second important factor and $a_2$ is 0.9. $D_3$ and $D_4$ are the factors influence the migration of the water and generally looked as the important factors, ($a_3$, $a_4$)=(0.8, 0.7). $D_5$ is less important than $D_4$, $a_5$=0.6. $D_6$ and $D_7$ are the secondary factors and ($a_6$, $a_7$) = (0.4, 0.2). By substitution of the data obtained into A, A= $1/D_1$+$0.9/D_2$+ $0.8/D_3$+$0.7/D_4$ + $0.6/D_5$+$0.4/D_6$+$0.2/D_7$. Normalized A, then (a1， $a_2$， $a_3$， $a_4$， $a_5$， $a_6$， $a_7$) = (0.22， 0.20， 0.17， 0.15， 0.13， 0.09， 0.04).

The weight value of $D_1$ is the maximum and account for 22%, so petrofabric is the main controlling factor. If add $D_1$ to $D_5$, the sum accounts for 87%, so these 5 factors compose the basic factor of water inrush.

**Model of fuzzy comprehensive evaluation.** To evaluate the risk rank of water inrush, the fuzzy relation is introduced,

$$V = V_{ij}\begin{bmatrix} a_1p_1 & a_2p_1 & \cdots & a_7p_1 \\ a_1p_2 & a_2p_2 & \cdots & a_7p_2 \\ a_1p_3 & a_2p_3 & \cdots & a_7p_3 \\ a_1p_4 & a_2p_4 & \cdots & a_7p_4 \end{bmatrix}$$

Where, V is called the matrix risk rank indices of water inrush.

The value of $p_i$ is given by the experience or the expert. Using the arithmetic progression with the difference of 1/8 and 3/8 which multiplies by 100 correspond to $p_i$, the pi value of water inrush ranks is given in Tab**le 2.**

**Table 2.** The risk rank indices of water inrush

| factor rank | $D_1$ | $D_2$ | $D_3$ | $D_4$ | $D_5$ | $D_6$ | $D_7$ | $P_i$ |
|---|---|---|---|---|---|---|---|---|
| I | 19.25 | 17.5 | 14.875 | 13.125 | 11.375 | 7.875 | 3.5 | 87.5 |
| II | 13.75 | 12.5 | 10.625 | 9.375 | 8.125 | 5.625 | 2.5 | 62.5 |
| III | 8.25 | 7.5 | 6.375 | 5.625 | 4.875 | 3.375 | 1.5 | 37.5 |
| IV | 2.75 | 2.5 | 2.125 | 1.875 | 1.625 | 1.125 | 0.5 | 12.5 |

**Table 3.** Interval of the rank value

| Risk rank | Interval of $P_i$ value |
|---|---|
| I | 75～100 |
| II | 50～ 75 |
| III | 25～50 |
| IV | 0～25 |

According to the factors of the tunnel section, $\sum D_{ij}$ can be obtained. Compare $\sum D_{ij}$ to the interval of the ranks value (Table 3), and then the rank is obtained.

## Engineering Application

**Engineering situation.** In the area mainly lies formation outcrop: Zhengyangzu($K_{2z}^1$). The tunnel passes two pass areas.

**The sample of the risk evaluation.** The interval YK224＋380-YK224＋400 occurs $K_{2z}^{1}$. Underground water level is about 25m above the bottom of tunnel when recharge is sufficient. There is no geostructure and the stratium inclined at about 20º. There is no paleoerosion surface. This part of tunnel route lies beneath a trough valley and the construction take place in rainy while the condition of seepage of the surface water is quite well. The index of water inrush factors and the risk value are given in Ta**ble 4.**

**Table . 4.** The risk index of the rank of water inrush

| factor | $D_1$ | $D_2$ | $D_3$ | $D_4$ | $D_5$ | $D_6$ | $D_7$ | $\sum D_{ij}$ |
|---|---|---|---|---|---|---|---|---|
| state | middle | 0<h<30 | \ | 20－60 | \ | strong | strong | |
| value | 8.25 | 12.5 | 2.125 | 13.125 | 1.625 | 5.625 | 3.5 | 46.75 |

As $\sum D_{ij}$ =46.75, so the risk of this section is rank Ⅲ.

**Verification.** When tunneling, there are a water inflow at YK224＋398. And the results show that there is underground water at the place. Several outflow points occur, the largest outflow of water is about 50m$^3$/h, the hydrops is about 100m (Figure 1), and the construction is iffuluenced by that. The water inflow shows that the risk evaluation model is fit for dividing the water inrush rank.

**Fig. 1.** Hydrops after water inrush when excavation

(1) In this paper, Factors controlling water inrush risk are analyzed and proposed.
(2) With the help of fuzzy mathematic，a fuzzy comprehensive evaluation model for dividing the rank of water inrush into karst tunnel risk has been put forward. The evaluation procedure and criteria are given for evaluation.
(3) Risk evaluation model is used in Tanjiaba tunnel of Hurongxi highway. And the excavation result shows that the model is reasonable and correct.

## References

[1] Einstein H. H., Viek S. G., Geologic model for a tunnel model[C]. Proceedings of Rapid excavation and tunneling conference. 1974, pp. 1701-1720.

[2] Einstein.H.H., Risk and risk analysis in rock engineering[J], Tunnelling and Underground Space Technology, 1996,Vol.11, no. 2, pp. 141-155.

[3] D. R. S. van Hasselt, V. Hentschel, M. Hutteman, et al, Amsterdam's North/South Metroline [J], Tunnelling and Underground Space Technology, 1999,Vol. 14, No. 2, pp. 191-210.

[4] B. Nilsen, A. palmstrom, H .Stille, Quality control of a sub-sea tunnel project in complex ground conditions[J]. Challenges for the 21st century, 1992, pp.137-145.

[5] Heinz Duddeck, Challenges to Tunnelling Engineers[J], Tunnelling and Underground Space Technology, 1996,11(l), pp.5-10.

[6] Reilly. J and J. Brown, Management and control of cost and risk for tunneling and infrastructure projects[C], Proceedings of the 30th ITA-AITES World Tunnel Congress,22-27 May 2004, Singapore.

[7] YANG Jianping, DU Duanfu, Fuzzy Analysis Approach to Project Risk[J], Journal of Beijing University of Aeronautics and Astronautic, 1998, Vol.24, No.1,pp.71-74. (in Chinese)

[8] BAI Ming-zhou, XU Zhao-yi, WANG Lian-jun, et al, Study on Water Outburst Geological Disaster of Tunnel Construction at Complicated Karst Zone, China safety Science Journal, 2006,Vol.16,No.1, pp.114-118. (in Chinese)

*Applied Mechanics and Materials Vols. 580-583 (2014) pp 1293-1296*
*© (2014) Trans Tech Publications, Switzerland*
*doi:10.4028/www.scientific.net/AMM.580-583.1293*

# Numerical Analysis of Two Structural Schemes of the HK-Zhuhai-Macau Immersed Tunnel

Yajiao Dai[1, a *], Mengjia Zhou[1], Yufei Kong[1], Xiaodong Liu[2] and Zhigang Zhang[2]

[1]Department of Civil Engineering, Tsinghua University, Beijing 100084, China;

[2]CCCC Highway Consultants CO., Ltd., Beijing 100088, China;

[a]daiyajiao@163.com

**Keywords:** Immersed tunnel; FE simulation; Structural design;

**Abstract.** Two structural schemes of the Hong Kong-Zhuhai-Macau Immersed Tunnel were compared. In Scheme 1, the prestressed reinforcing bars were to be cut off after installation. And in Scheme 2, the prestressed reinforcing bars will be kept there as they were after installation. A finite element model for sections E12~E15 was built by using the finite element software PLAXIS with consideration to the construction process and different loading conditions to analyze both schemes. The calculation results show that they both meet the design requirements.

## Introduction

The immersed tunnel of the Hong Kong-Zhuhai-Macao Bridge (or HK-Zhuhai-Macau Immersed Tunnel) is a great project that has attracted worldwide attention. Its is about 6 km in length and most of the tunnel is buried deep in the seabed. The immersed tunnel consists of 33 sections, namely E1~E33, in which E1, E2, E32 and E33 are 135m long and others are 180m in length. Each section contains several segments of 22.5 meters long.

The segments are connected by shear connecters at their joints and the Ω Gasket (Rubber Waterstop) is used for water prevention. Eight or six segments are connected as a whole by prestressed reinforcing bars at both the top and the buttom during the floating transportation and immersing. After being laid onto the foundation trench in the sea, adjacent sections are connected by the GINA Gasket as well as the Ω Gasket and compressed by water pressure. Two designing schemes were proposed during the design and discussion.

Scheme 1(Flexible Design): In the original structural design, all the prestressed reinforcement were to be cut off after installation of the tunnel. In this way, the GINA Gasket at *section joints* (or immersion joints) would be compressed once more and the *segment joints* (or expansion joints) could deform more freely after the relaxation of reinforcement. The Flexible Design allows certain deformation at segment joints to make the tunnel adapted to differential settlement and earthquake.

Scheme 2: The second scheme proposed by CCCC Highway Consultants required prestressed reinforcement be kept during the tunnel's usage period. It was aimed to overcome some disadvantages of the Flexible Design, where flexibility of segment joints would increase the risk of water leakage when considering differential settlement or seismic activity[1]. The original design referred to the famous Oresund Tunnel. However, geological and loading conditions here are more various than that in the Oresund strait. Moreover, cutting off reinforcement would change the internal force of the whole tunnel and the sudden relaxion of the prestress might possibly introduce damage to the structure. So, Scheme 2 was put forward to reserve prestressed reinforcement, the same as they were for transportation. The second scheme tended to tie the eight or six segments in a section more firmly. It still differed from traditional rigid designs since the prestress was not so large.

The main objectives of this paper are to analyse the two structural schemes and to checking out which one is more suitable. A finite element model is made, including four neighbouring segments. Sections in the numerical model include E12S4~E12S8, E13S1~E13S8, E14S1~E14S8, and E15S1~E15S5. Dead loads, live loads, temperature loads and basement unevenness are considered in the calculation.

## The Numerical Model

The calculation is completed in the famous FEM software PLAXIS 3D 2012. Staged construction in the software is used, including excavation, ground improvement, tunnel immersion, rubble filling and long-term muck siltation in the next decades. Figure 1 shows 2D sketches of four main calculation steps. Figure 2 shows the shape of the tunnel's cross section and a side view of the model.

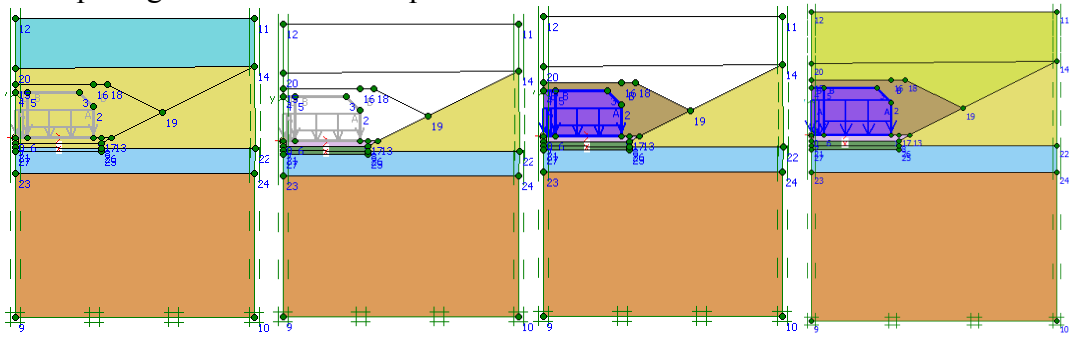

Figure 1. Four main construction steps: 1. inatial phase, 2. excavation and mat layer pavement, 3. tunnel immersion and rubble filling, 4. muck siltation.

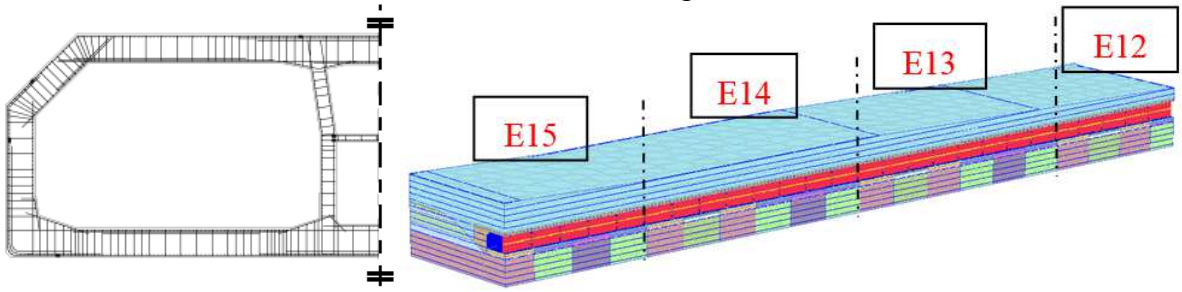


Figure 2. Left: cross section of the tunnel(half), the tunnel is 37.95m in width and 11.45m in height; Right: 3D FE model in PLAXIS.

**Soil Parameters.** According to the geological investigation report, there are mainly four soil layers. Some are excavated first. Before installing the tunnel, soils beyond the tunnel would be replaced by dynamic compacted rubble fill. After tunnel installation, more rubble would be filled in the foundation trench. The Hardening Soil Model [2] is used for soils and soil parameters come from geological reports and experiments. Parameters for HSM are listed in Table 1.

In order to reflect uncertainties in the ground improvement, the unevenness of foundation stiffness is considered in this model. We change the modulus of subsoils manually to let it vary like a sine function within the range of each section (180m). The amplitude of the variation is 30%. The unevenness of muck siltation has also been taken into account. The height of the muck siltation over E14 is 20m and that over E13 changes from 20m-16m linearly.

Table 1. Parameters of soils in Hardening Soil Model

| Number of soil layers | Soil | $\gamma$ (kN.m$^{-3}$) | $c$ (kPa) | $\varphi$ (°) | $E_{50}^{ref}$ (MPa) | $E_{oed}^{ref}$ (MPa) | $E_{ur}^{ref}$ (MPa) | $m$ |
|---|---|---|---|---|---|---|---|---|
| 11 | Muck and mucky soil | 16.2 | 9 | 6 | 2.50 | 1.25 | 7.50 | 0.76 |
| 31 | Clay | 18.1 | 43 | 20 | 9.65 | 4.88 | 28.95 | 0.90 |
| 32 | Clay with sand | 18.5 | 36 | 24 | 15.25 | 7.63 | 45.75 | 0.60 |
| 44 | Medium sand | 20.3 | 0 | 37.8 | 42.42 | 42.42 | 127.3 | 0.60 |
| / | Compacted rubble fill | 20 | 0 | 40 | 100 | 100 | 300 | 0.60 |
| / | Mat layer rubble fill | 20 | 0 | 40 | 10 | 10 | 30 | 0.60 |
| / | Rubble fill over tunnel | 20 | 0 | 40 | 10 | 10 | 30 | 0.60 |
| / | Muck siltation | 15 | 9 | 6 | 2.5 | 1.25 | 7.50 | 0.76 |

Note: the first four soils are in-situ soils; four original layers in Figure1-1 are 11, 31, 32 and 44 from top to buttom.

**Jiont modelling.** It's quite important to model the joints properly. We proposed a method for joint modelling, where the mechanical behavior of segment joints in both schemes can be reflected by changing material properties.

As is shown in Figure 3, an imagined gap of 0.8m is reserved between two segments. Horizontal springs (node-to-node anchors) connect both sides to transmit axial pressure and bending moment (Figure 3-c). These node-to-node anchors are 0.2m long. And they are elasto-plastic in segment joints to allow tension cut-off. There are also some springs connecting vertical and horizontal shear connecters to transmit shear force and allow shear deformation(Figure 3-a,b). As is mentioned above, sections are connected by the GINA Gasket and Ω Gasket. Segments are connected by shear connecters as well as the Ω Gasket at their joints. GINA Gasket used here is *GINA seal TB G-320/370*. The *EA* of each spring is calculated from the GINA Gasket, Ω Gasket or the concret that this spring stands for.

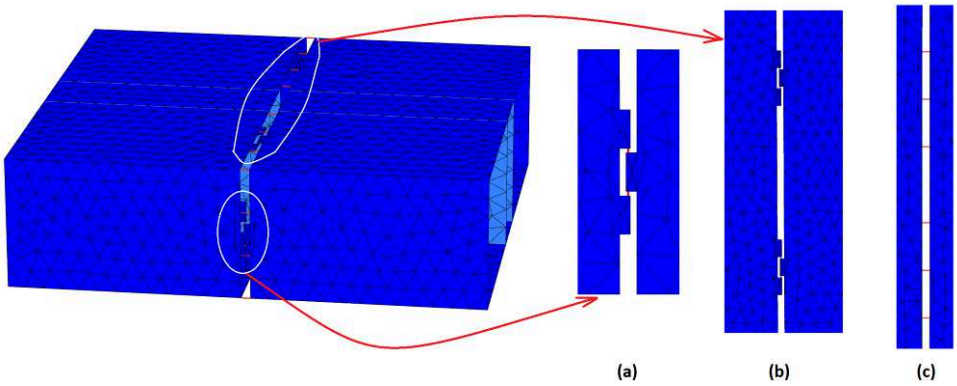


Figure 3. Section joint simulation, (a) vertical shear connecter, (b) horizontal shear connecter, (c) springs to transmit axial pressure and bending moment.

**Loading.** Dead loads of the tunnel include: 1. Self-weight of the structure, 26.023kN/ m³; 2. Dead load of road surfaces and equipments, 30kPa on the floor; 3. Hydrostatic pressure, mean sea level +0.54m is used for determining water pressure on the walls and floors; the axial force induced by water is about 158323kN, considering the relaxion of GINA, it is reduced to 158323*0.6=94994kN; 4. Rubble filling and muck siltation, calculated automatically in the spftware; 5.Concret shrinkage and creep, equivalent to 4.65˚C cooling; 6. Prestress, totally 191578k. Live loads considered here include: 1.Traffic load, 8.4kPa on the floor; 2. Temperature load, ±10˚C.

The loading conditions include: (1) Basic condition: dead loads with out shrinkage and creep, as well as traffic loads; (2) Cooling condition: the basic one with shrinkage and creep and temperature decrease. (3) Warming condition: the basic one with shrinkage and creep and temperature increase. The partial factor of live loads is 0.8.

As the software cannot simulate temperature change directly, an axial force equalling $EA\alpha\Delta t$ is applied to each segment instead. This method is accurate in calculating deformation and joint forces.

## Calculation and Results

The main difference between two design schemes is whether to cut off the prestressed reinforcing bars. The difference should also be expressed in our model. The axial force resulted from prestress and water pressure are simulated by axial load define in the model. If the prestressed bars are cut off, the axial force will change with it.

The axial force in segment joints introduced by prestressing is 191578kN. The axial water pressure for hydraulic compression is 158323kN, which make the prestress reduce a little; as a result, the increment of axial force is 157433kN, and the compressive deformation of GINA is 154mm in hydraulic compression. If the prestress is relaxed in Scheme 1, GINA will be compressed by 2.9mm more. The axial force in segment joints reduces by 176197 kN. Taking into account GINA's relaxion, the axial force at different position is adjusted, shown in Table 2.

Table 2. Initial axial compressive force at different positions before loading

| | Reinforced concrete and segment joints (kN) | Prestressed bars(MPa) | GINA(kN) |
|---|---|---|---|
| Scheme 1: Flexible Design | 191578+157433*0.6 -(190697-14500*0.6)=104041 | -- | (158323+14500)*0.6 =103693.8 |
| Scheme 2: | 191578+157433*0.6=286038 | 1209-5.56*0.6=1205.664 | 158323*0.6=94993.8 |

Table 3. Main results of calculation

| | Max bending moment of segment joints (kN*m) | | Max axial force increment of segment joins (kN) | Max shear force of segment joints (kN) | Max shear force of section joints (kN) | Max opening of section joints (mm) |
|---|---|---|---|---|---|---|
| Scheme 1 | +552512 | -542868 | +95861 | 23816kN | 21234 | 12.6 |
| Loading condition | Basic | Warming | Cooling | Basic | Basic | Cooling |
| Scheme 2 | +749981 | -726393 | +136358 | 28773 | 27940 | 18.0 |
| Loading condition | Warming | Cooling | Cooling | Cooling | Basic | Cooling |

Note: 1.positive bending moment means concret at the top has bigger compressive stress; 2. axial force increment should be added to the axial force in Table 2 to get the total axial force force, tension positive; 3. the opening of section joints is a increment value on the basic of primary compression, around 155mm.

Obviously, the deformation of segment joints in Scheme 2 would be smaller than that in Scheme 1. As worries for Scheme 2 include larger internal forces at segment joints and larger deformation at section joints(GINA Gasket), we list results of joint stress and section joint opening in Table 3.

It can be seen from Table 3 that, for Scheme 2, even though deformation at section joints are bigger that the Flexible Design, the GINA Gasket is still safe for water prevention. The bending moment and axial force in both schemes meets the requirement of structural design.

Due to the axial force provided by prestress, the minimum axial force of segment joins in Scheme 2 is 149680kN. To be conservative, we use the coefficient of friction of concret as 0.3 to estimate the maximun shear capacity: 149680*0.3=44904kN. This is much bigger than the maximum shear force, 28773kN. It is the same with the Flexible Design in Basic and Warming Conditions. However, for the Flexible Design in Cooling condition, where the shear force is 11276kN, the minimum axial force is too small to provide enough friction, so the shear capacity depends on the concret shear connecter, 16000kN. From this perspective, Scheme 2 has more emergency capacity.

## Conclusions

The calculation of static loads presented above shows that, both design schemes can meet the design requirements and have enough capacity. Considering possible risks for cutting prestressed bars off and the fact that Scheme 1(Flexible Design) not being suitable for seismic activities, we recommend Scheme 2 for the Hong Kong-Zhuhai-Macau Immersed Tunnel.

## Acknowledgement

This work is completed under the guidance of Prof. Erxiang Song from the Department of Civil Engineering, Tsinghua University.

## References

[1] R.S. van Oorsouw. Behaviour of segment joints in immersed tunnels under seismic loading(TU Delft, Netherlands 2010).

[2] T. Schanz, P.A. Vermeer and P.G. Bonnier. The hardening soil model: Formulation and verification[C]// Beyond 2000 in Computional Geotechnics-10 Years of Plaxis, 1999.

*Applied Mechanics and Materials Vols. 580-583 (2014) pp 1297-1300*
*© (2014) Trans Tech Publications, Switzerland*
*doi:10.4028/www.scientific.net/AMM.580-583.1297*

# The deformation characteristics analysis of metro tunnel in complicated geological conditions

QIU Dao Hong[1, a], LI Shu Cai[1,b], XUE Yi Guo[1,c] and XIE Fu Dong[1,d]

[1] Research Center of Geotechnical and Structural Engineering, Shandong University, jinan 250061, China

[a]qdh2011@126.com, [b]lishucai@sdu.edu.cn, [c]36913565@qq.com, [d]869694632@qq.com

**Keywords:** metro; deformation characteristics; monitoring and measuring; numerical simulation

**Abstract:** Qingdao Metro Line 3 is the first subway line in Shandong province, some tunnels need to cross water-rich sandy layers. At the time of passing through the water-rich sandy layers, how to maximum the deformation characteristics of the tunnel during excavation becomes the critical problem of the design and construction. This paper studies Qingdao Metro Line 3, directs at water-rich sand layer section YK16+382, with the use of on-site monitoring and measuring instruments, analyses the characteristics of ground deformation of the cross section. And we calculated the deformation by Flac3D numerical simulation in YK16+382 cross section, studied the arch and surface subsidence and convergence deformadon variation of convergence. Finally compare site monitoring measurement with numerical computational results and then we can get the convergence of arch and surface subsidence and convergence deformadon, provide theoretical guidance for the actual construction.

## Introduction

Metro as a new means of transport in plays a vital role in easing urban traffic congestion, serve the general public with a safe, convenient, comfortable, clean form of transport. By the end of 2012, including Beijing, Shanghai, Tianjin and other 12 cities have opened metro[1]. Subway tunnel built on the place that has accumulated soil and geological complex, underground pipeline dense, narrow tunnels, heavy traffic, busy shopping center, and the construction and development along the subway tunnel will due to urban vertical deposition. A certain degree of settlement can be regarded as normal phenomenon[2]. But if the settlement amount exceeds a certain limit, it will cause deformation of subway tunnel construction, settlement and displacement on the surrounding environment, even unimaginable accidents. In order to ensure the safety of subway tunnels main structure and surroundings, the subway tunnel construction must be carried out settlement monitoring, timely analysis of the monitoring data and feedback, as well as to forecast future settlement[3-5].

This paper study on the subway project under complex formation in Qingdao Metro line 3, analysis of arch and surface subsidence and convergence deformadon and numerical simulation for the convergence of data, by comparison to get some useful conclusions.

## Project overview

Qingdao metro line 3 first-stage project west since Shinan District Qingdao railway station, to east along Guangxi road, and Taiping road, and Wendeng road, and Hong Kong Road, to municipal government and then turn into Nanjing Road to North, entere Harbin road, and Heilongjiang road, and Wannianquan Road to licun, to west along Jingkou road, and Zhenhua road to end at Qingdao North Station, total length about 25.1km, all for underground line.

Qingdao metro line 3 first-stage project of He-He section is single-hole single lane, the interval is underground excavation, from the Hexi station, through Zhangcunhe, tunnel starting mileage is K16+149.875, ending mileage is the K17+24.969.The tunnel go through the formation of water -rich sand layers, depth 2.5~10.5M,line spacing is 13~36.35m. Hexi station ~ Hedong station tunneling section is single hole single horseshoe-shaped structure that tunnel through the formation of water -rich sand layers, maximum depth of the tunnel is 10.5M.

## Field monitoring and measuring

3.1 Field monitoring data

The major monitoring of He-He interval is arch and surface subsidence and convergence deformadon. Select YK16+382 monitor to study, for example, the monitoring surface subsidence have 6 monitoring stations, arch settlement has 2 monitoring stations, and convergence deformadon has 4 monitoring stations. Monitoring data measured points as shown in table 1 below.

Table 1 The accumulative total settlement of the measuring points

| Number of measuring points | Accumulative total settlement (mm) | Number of measuring points | Accumulative total settlement (mm) |
|---|---|---|---|
| DC02-68 | -5.34 | DC02-71 | -6.76 |
| DC02-69 | -6.55 | DC02-72 | -6.45 |
| DC02-70 | -7.38 | DC02-73 | -4.84 |

3.2 Analysis on ground settlement data

According to monitoring YK12+660 from May 13, 2012 to September 16, 2012, 5 months of monitoring data curves. From figure 2, the largest settlement appear in the measuring points 10DC02-70 between the two tunnel, has a maximum cumulative amount of change of -7.38mm. Axle wire of the right line and peripheral point of the left line measuring points 10DC02-69, 10DC02-71, and 10DC02-72 are slightly less than the settlement of intermediate points, the average settlement is -6.5mm. Measuring points on both sides of the tunnel have the smallest settlement, about -5.3mm and -4.8mm. According to the curve, we can get that the surface begins to subside after tunnel excavation, there might be some rebound .Then subsidence rate become faster, finally plateaued.

Above the tunnel right line YK16+382 cross section,6 points settlement changes at different times are showed in Figure 3 , the data curve is a sedimentation tank. From the line charts we can clearly see that there is maximum surface subsidence above the tunnel centre line, reaching 7-8mm, and diminishingly along the tunnel centre line, the settlement is very small about 10 meters away from the center line. The settlement can basically be ignored. According to the settlement curve we can reveal the excavation sequence of the two tunnels. The right line tunnel excavat early, measuring point 10DC02-69 settled clearly, with the excavation of the left lane, other measuring points also have a significant settlement. Eventually reaches a steady state.

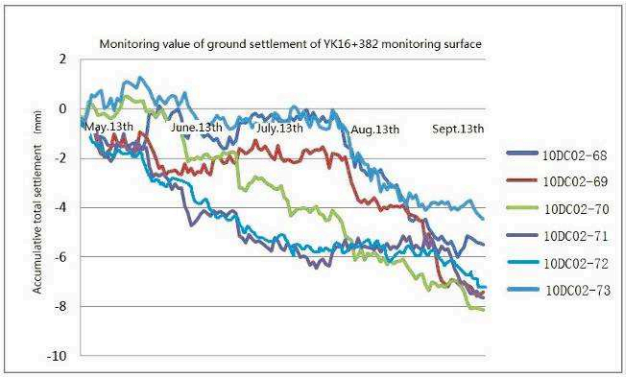


Fig 2 The cumulative curve of ground settlement of YK16+382 section

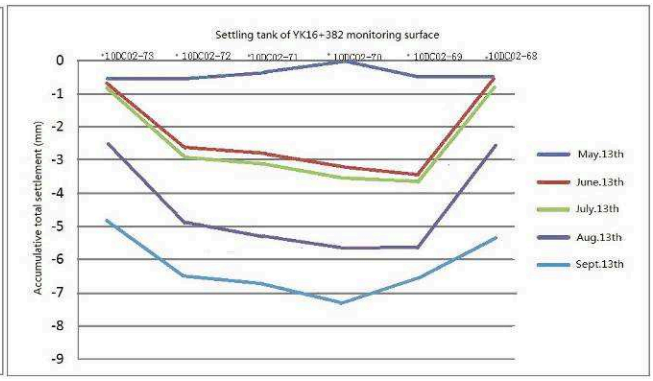


Fig 3 Settling tank analysis of YK16+382 section

**Numerical simulation and comparative analysis of ground settlement**

Numerical simulation is presented using Flac3d. The left and right sides of the model are imposed X-direction horizontal constraint, the front and back sides are imposed Y-direction constraint, the bottom of the model is imposed Z-direction constraint, and all borders are imposed self-weight stress of rock and soil mass. The calculation model is shown in figure 4.

By comparing the curve obtained from measured data with the one obtained from numerical simulation, we obtain the curve shown in figure 6. In the figure, YK16+382 actually measured settling tank is obtained from the latest settlement record in the monitoring data table, and settlement from numerical simulation is obtained after the final settlement is stable. Through the comparison of the curves, at the axes and both sides of the tunnel, the settlement of monitoring surface obtained from numerical simulation can virtually satisfy with the one obtained from actual measurement, however, in the middle of the two tunnels, the actually measured settlement is different from the numerically simulated one. The former is slightly smaller than the later.

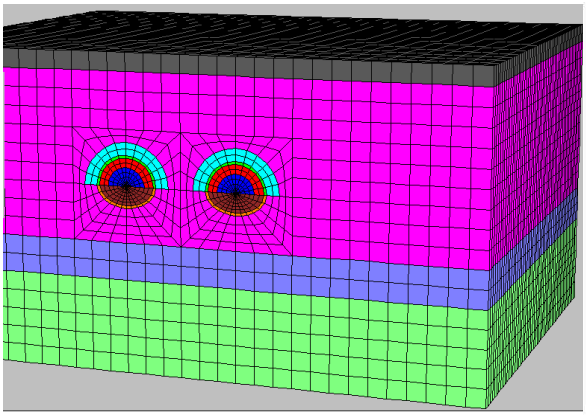

Fig 4 Numerical simulation

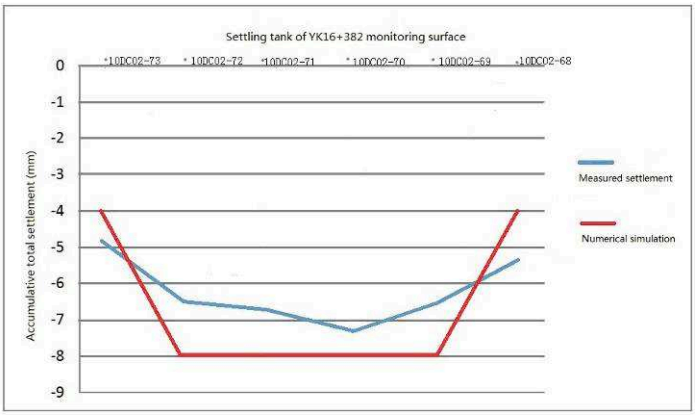


Fig 5 Comparison between actual measurement and numerical simulation of settling tank

The following points can be summarized by comparing the actually measured ground settlement with the numerically simulated one of YK16+382 monitoring surface.

1. The curves of both actually measured ground settlement and numerically simulated one of YK16+382 monitoring surface can virtually satisfy the calculation of settling tank in experience method. The settlement at the tunnel axes and the middle of the two tunnels is large and decreases gradually towards both sides.

2. The reason why the numerically simulated settlement is larger than the actually measured one is that the former is obtained after the layer is finally stable, however, the monitoring surface is monitored within 6 months, when the layer is not stable, which makes the simulation value lager than actual settlement.

## Conclusion

This paper comparatively analyzes the actual measurement and numerical simulation of ground settlement, vault settlement and convergence of the tunnel in watery sand section of Qingdao metro line 3, making the following conclusions and recommendations.

1. The settling tank of Hehe tunnel virtually satisfies the experience method prediction, which means the settlement at tunnel axes is the largest and decreases towards both sides. However, since the distance between the two tunnels is less than 3D (D means the width of the tunnel), there is a superposition to the settlement between the two tunnels. It can be proved by both numerical simulation and actual measurement that after the superposition, the settlement of the layer between the two tunnels is close to the one of tunnel axis.

2. The displacement nephogram of numerical simulation and settlement curve tendency virtually satisfy the monitoring situation in practical engineering. Thus numerical simulation is helpful to site construction and measurement and can provides theoretical and data bases to raise the accuracy and efficiency of ground settlement control.

## Acknowledgements

This work was financially supported by National Natural Science Foundation of China (51309144), Shandong Provincial Natural Science Foundation(ZR2013EEQ024), Independent Innovation Foundation of Shandong University (2012TS063, 2012TS061).

## References

[1] Barry M.New，M.P.0 Reillyy Tunneling indueed ground movement:predicting the magnitude and effeets,in: James D Geddes eds.Proc.4 International Conference on Ground Movement and Stucture,Pentech Press，London，1992，671-697.

[2] ZHU Zhonglong,SUN Jun,ZHANG Qinghe. Study of ground deformation control in construction under shield tunnelling based on intelligent fuzzy logic control method[J].Rock and Soil Mechanics, 2005,26(6):896-900(In chinese).

[3] JIANG Yiliang,CUI Yi,LI Yuan.Measurement and simulation of ground settlements of Tianjin subway shield tunnel construction [J].Rock and Soil Mechanics,2005,26(10):1612-1616(In chinese).

[4] JIA Jianbo,JIAO Cang.Analysis of ground deformation for shallow tunnel in Tianjin Metro [J].Tunnel Construction, 2006,26(1):18-21(In chinese).

[5] SONG Kezhi,WANG Mengshu.Reliability Analysis of ground settlement with shield tunnel construction based on Peck Formula [J].Journal of Northern Jiaotong University,2004, 28(4):30-33(In chinese).

*Applied Mechanics and Materials Vols. 580-583 (2014) pp 1301-1305*
*© (2014) Trans Tech Publications, Switzerland*
*doi:10.4028/www.scientific.net/AMM.580-583.1301*

# Auger Bored Piles Application Works in the Subway

Wu Yang

(Hunan Urban Construetion College ,Xiangtan, 411103 ,China)

**Keywords:** Long spiral; pile; metro; construction applications

**Abstract:** Pile Foundation Construction jobs are usually wet process has contaminated a large, long duration, the pile of inconsistent quality, cost out. And long bored piles to adapt to a variety of complex geological conditions, but not the impact of water table, is widely used in various projects of the foundation engineering, this according to subway construction in Kunming, the application of experience, a brief description length screw pile construction anti-interpolation technology.

## Project profile

Chenggong Station of Kunming Rail Transit is located at the crossing of Caiyunnanlu Road and Liandalu Road, arranged along the Caiyunnan Road. It is an underground double-layer and three-span island station and it is the transfer station of Line 1 and Line 4. It has four entrances, named No.1, 2, 3, 4 respectively, as well as No.1, 2, 3 fire evacuation exits and No.1, 3 air ducts. The east side of the station entrances, air ducts and other ancillary structures will be constructed by using open-cut construction, part of the west side of No.1 2 entrances and No.1 fire evacuation exit will be constructed by using underground tunneling. The building envelope of open-cut ancillary structures adopts a diameter of Φ800@1000～@1100 drilling interval pile + internal bearing support system, local channel adopts using 40C U-bar @ 1000 supporting. There are six types of retaining piles, 800mm in diameter, 5 to 16 meters in length, with a total number of 804 piles, 9,361 linear meters. The project demands a large number of ancillary envelope piles, short period and high construction requirements, traditional wet construction process will lead to long pore-forming period, bring difficulties in slurry wall, cause great pollution and piles unstable, as well as high construction cost. Through projects optimization, the Project Department has selected a long spiral auger to conduct pore-forming. Long spiral auger pumping superfluid concrete inserting steel reinforcement cage technology is evolved from the Japan CIP construction method. It uses a dedicated long spiral auger drill machine to a predetermined depth, continuously injects superfluid concrete through the drill valve until the pile-top, and then inserts the steel reinforcement cage to form the pile. It is a new pile foundation construction method. Superfluid concrete bored pile technology is widely used, because it is not restricted by underground water level, adopting the concrete with low friction coefficient, strong liquidity and good aggregate dispersion, the auger can drill as well as press-grouting concrete, easily to handle and concrete pouring fast, good pile quality and reduce cost. Remarkable results have been achieved. Engineering geological conditions are listed below:

| Table 1: Geological conditions | | | |
|---|---|---|---|
| Level No. | Name of rock-soil | Characteristics of Rock-soil | Thickness of the level |
| 1 | Plain fill | Containing clay, crushed stones; compaction slightly | 2～5.5m |
| 1-2 | Silty clay | Isabelline; grayish yellow; plastic | 1.5～3m |
| 2-2 | Clay | Grayish yellow; grey; plastic | 5m |
| 3-3 | Organic clay | Ash black; plastic | 0.5～5m |
| 4-3 | Organic silt | Black; plastic | 0.5～3m |
| 5-4 | Silt | Grey, dark grey; saturated and dense | 6m |
| 11-3 | Round grave soil | Grey, yellowish-brown; saturated and dense | 0.5～4m |

**Construction process**

Superfluid concrete bored pile uses long spiral auger drill machine to design elevation, after stop drilling as lifting the auger as pressure injecting the superfluid through the concrete holes on the inner pipe bit, continuously injecting until reaches the top of design elevation, then removes the drill pipe and inserts the steel reinforcement cage into pile. When pressing the concrete to the top of the pile, poured concrete should exceed 50cm to the top to ensure the concrete strength of the pile-top. The construction process is as follows:

Leveling the ground → lofting pile → mounting equipment → place steel casing→ drilling machine in position → drill to the design elevation then stop → as lifting the auger as pressure injecting the superfluid through the concrete holes on the inner pipe bit → lift the drill pipe and insert the steel reinforcement cage → pile-forming → pile-top protection.

**Construction scheme**

3.1 Construction technology preparation

According to the survey report of geotechnical engineering, grasp the geological and hydrological conditions; jointly examine the pile foundation construction drawings and other drawings; investigate the underground pipelines, underground structures and adjacent dilapidated buildings around the construction site and adjacent areas, in order to take appropriate measures to secure and protect, thereby ensure the smooth construction of the piles; level the ground, site pay-off, assemble equipments; detect the pile elevation and determine the drilling depth.

3.2 Construction raw materials preparation

The raw materials used in the project must be re-inspected and qualified; use Portland cement and ordinary Portland cement, strength grade is not less than 32.5Mpa, water-cement ratio should be 0.5 to 0.6; stone diameter should be 5 to 16cm; adopt medium sand, clay content$\leqslant$2%; tap water.

3.3 Construction mechanical equipments

Superfluid concrete pile construction should use auger boring machine, depending on the types of pile to select appropriate models and rig drilling parameters. The project uses 2 sets of CFG-32 long auger, the electrical power 200kw, drilling speed 2m/min and 81r/min, 20 piles forming everyday.

3.4 Master operation construction scheme

3.4.1 pore-forming

(1) Re-inspect the pile location before point leading drilling in place, the drill should align the pile points when construct, stabilize the drilling, control the auger drill center and verticality by using leveling instrument and plummet to ensure the drilling steady during the construction, the drilling lower should be 10 to 20cm away from the ground, aligned with the pile location and buried in the ground, making the pile center deviation is less than 10mm required by the specifications and design.

(2) Using wire pendant to measure pile frame verticality during the drilling process, use leveling instrument to measure the level of the chassis to ensure that the drill pipe verticality (≤0.5%), meanwhile, clean the muck beside the hole as rotate the drill to prevent the muck falling when lift the drilling.

(3) When touch underground obstructions or hard formations, slow down the drilling speed to avoid sticking.

(4) Check the drill bit and blade diameter every shift to ensure pile aperture not less than the design value.

(5) Drill to the design depth, rotate 0.5 to 1min, wait for all bottom soil entering leaves and then stop rotating to ensure the thickness of bottom soil less than 10cm.

(6) Directly use the drill pipe to measure the depth of pore, i.e. mark the drill pipe to measure before construction.

3.4.2 Concrete injecting

(1) Drill to the design depth and make all soil into the blades, then lift the drill bits off the bottom of the pore 20 to 30cm to ensure the superfluidity drill discharge to open flexibly.

(2) Inject concrete to bury drill bit 50 to 100cm, then begin to lift the drill. When lift the drill to inject concrete pumping, strictly control the lifting speed, making sure the lifting speed matches the speed of the concrete injecting. Before lifting the drill pipe, the concrete in the drill pipe is required to be above the ground. At the same time, to calculate each pile pumped concrete square volume, adjust the drill speed depending on the lift force that concrete pumping exerts to the drill pipe, ensuring the drill pipe and blades to exert squeezing effect on the concrete, lift the drill as injecting, until reach the design elevation of the pile-top.

3.4.3 Lift steel reinforcement cage making machine

(1) Steel reinforcement cage shall be welded strictly in accordance with the requirements of design drawings, ensure the lap length and welding quality as required, in order to prevent that vibration subsidence leads to the cage sealing off and falling apart.

(2) The Steel cage should be stocked for certain amount before construction. The finished cage must be submitted to the commissioner to inspect and accept. A qualifying signage should be hung on the qualified cage to mark the information such as the cage type, location and length.

(3) The cage production should be arranged on a relatively level area to guarantee the cage straight. During the process, manual tumbling and lifting must strictly protect the steel cage from deformation and sealing off.

(4) Before laying down the steel cage, alignment and centering should be conducted; when lifting the cage, reasonably arrange the lifting point, lift the head of the cage as workers lift the bottom of the cage; in the process of hanging straight, at least two technicians should control and command far away in the vertical direction; prohibit to hit the hole wall to make sure the protective layer of the cage is 70 to100mm; The cage should continuously sink depend on the weight of itself, if the

sinking resistance is too large, remove the steel cage promptly, re-insert into the bore; the reinforcement sink until the exposing part is less than 1m away from the ground, then use the vibrator to press it into the bore, and monitor top of the pile with a level elevation.

**Quality standards**

Test the steel and other raw materials before the construction to ensure the quality in line with national standards; inspect the bores, concrete injecting, the steel reinforcement cage production and installation in the whole construction process; examine the concrete strength and pile quality after the construction; master control project quality should satisfy the standards in Table 2.

Table2: Master control project quality standards

| No | Content | Allowable deviation |
|---|---|---|
| 1 | Space between the main reinforcements of the cage | ±10mm |
| 2 | Pile position | Supporting pile side foundation pit side direction 100mm; vertical foundation pit side direction 150mm; |
| 3 | Bore depth | 0，+300mm |

**Pile foundation detection**

5.1 Pile quality inspection

(1) Superfluid concrete mixing should inspect the raw materials quality, measuring, concrete mixing proportion, admixtures, slump, and concrete strength;

(2) The steel reinforcement cage producing should inspect the reinforce specifications, welding specifications, variety, weld length, weld appearance quality, main reinforcement and stirrups producing deviation;

(3) During the construction, it is required to inspect the hole center location, hole depth, diameter, verticality, the actual position of the steel cage, and fill in the appropriate quality inspection records;

(4) Test the concrete strength grade after pile-forming;

(5) When excavate the pile-top, it is required to inspect the number of piles, position and pile-top appearance quality promptly.

5.2 Pile Integrity Test

Piles will be tested according to *Technical specification for testing of building foundation piles"* (JGJ106-2003). This project uses low strain to test the pile integrity. There are 804 envelope piles in the project and 20% of them, i.e. 17 piles will be tested in accordance with the design and specification.

**Conclusions**

Superfluid concrete pile construction technology is of high degree of mechanization, fast construction progress, economic efficiency; compared with wet pile-forming filling pile, although he concrete filling factor is slightly higher, but in the same geological conditions, it is able to

remove the demand for mud wall, thus the comprehensive cost will be saved 15%～20%. This technology has the function of wall self- protection with pile materials, without any additional measures to protect the wall, basically save the work of mud contamination, mud treatment, and mud outward transport, exerting little effects on the environment; In the process of planting the cage, due to the energy of vibration equipment is small, and the force is exerted in the flow plastic concrete, therefore, it will not produce intense vibration and shock response, and the vibration and noise is fully controlled in the range allowed by construction, thus it can be confirmed that the construction method has less impact on the environment, so it is a environment friendly green construction method. Placed the cage in plain concrete pile is helpful to improve the load-bearing and pullout resistance capacity; simplify the construction program will improve the efficiency and reduce the cost.

The key technology of the steel reinforcement cage piles applied in metro construction has yet to be thorough investigation, research, testing, evaluation and application. Through continuous accumulation, progress and creation, make the technology reach high engineering application level.

**References**

[1]. Technology specification for excavating piles bored with long auger inserted reinforcing steel cage after jacked concrete. DB11/T582－2008. Beijing Municipal Construction Committee. 2008.

[2]. Deng Minghua. Application of Long Auger Boring Filling Pile in Soft Foundation Treatment of Dongting Lake Area. Hunan Hydro ＆ Power. 2005 (06).

*Applied Mechanics and Materials Vols. 580-583 (2014) pp 1306-1310*
*© (2014) Trans Tech Publications, Switzerland*
*doi:10.4028/www.scientific.net/AMM.580-583.1306*

# Impact of Urban Rail Transit on Residential Property Values in Hangzhou

Lianfa Ruan[1, a], Jingping Yin[1, b]

[1] Institute of Construction Management of Zhejiang University, Hangzhou, China, 310058

[a]lianfa@zju.edu.cn, [b]yin193193@163.com

**Keywords:** urban rail transit; residential property value; hedonic pricing

**Abstract.** This research investigates the impact of the first metro line (Line 1) in Hangzhou on its station-area residential property values. A hedonic pricing model shows that Line 1 had a statistically significant and positive effect on residential prices in its operation period. Compared with its construction phase, the impact did not change significantly, indicating that metro rail transit had a long-term positive influence on the station-area property values. These findings suggest that such capitalization is likely to lead to high-density and transportation-oriented development. While planning the urban rail transit system, such impact should be fully considered.

## Introduction

There is no doubt that urban rail transit greatly improves the accessibility to urban spatial location, and is convenient for people to travel. A survey in Shanghai showed that in three major factors that have effects on the housing price (along the rail transit, around the large green areas, along the river), along the rail transit is the first factor to consider for 88% of buyers while buying houses [1].

## The literature review

Empirically, urban rail transit plays an important or even a guiding role on urban spatial planning and layout. In theory, most of quantitative researches around the world especially in western developed countries use asset value method. This method is based on the capitalization hypothesis theory that the benefits brought by social infrastructure will be fully reflected in the increasing of the land price or real estate price finally [2]. Existing researches home and abroad, except for a few studies that concluded the impact of rail transit on the surrounding properties is not significant or even negative [3], most studies supported the conclusion of the hypothesis. Knaap et al. (2001) used data on vacant land sales in Washington County, Oregon. They found that plans for light rail investments have positive effects on land values in proposed station areas. These findings suggested that such capitalization is likely to discourage the development of low-density housing in station areas and encourage high-density, transportation-oriented development [4]. Bae (2003) investigated the impact of the construction of a new subway line (Line 5) in Seoul on nearby residential property values. The results showed that distance from a Line 5 subway station had a statistically significant effect on residential prices only prior to the line's opening [5]. Most other studies had shown that urban rail transit stations had positive multiplier effects on property values. And from the city center area to the peripheral zone, the impacts of rail transit on land prices or housing prices gradually expand [1, 2, 6, 7, 8]. Therefore, while planning the urban rail transit system, designers should fully think of such impact.

Metro Line 1 is the first line of the urban rail transit lines construction in Hangzhou, total length 53 km (including xiasha extension) with 34 stations, of which 31 underground stations, 3 elevated stations. It is the main backbone line in Hangzhou rail transit network, connecting the main city zone with the suburb areas. The project started construction on March 28, 2007 and its opening date is November 24, 2012 (excluding xiasha extension). Yang Hong (2010) had examined the effects of Hangzhou Metro Line 1 on house prices, finding that the properties which are less than 500 meters away from the rail station had a significant premium of 9.4%, while those in the 1500 meters range didn't show any increment [8].

Yang's research was during the construction phase of Line 1 and didn't cover the operation period. So studying the multiplier effect on the property of Metro Line 1 in its operation phase is conducive to explore long-term impacts of urban rail transit on its surrounding properties. If the multiplier effect during the operational phase is still significant, urban rail transit can be considered to have a long-term effect on property values, thus leading to a high-density development in station area and thereby affecting the design of urban planning.

In this paper we try to deepen Yang's study to examine the impact on the operation phase, and focus on the residential properties with a distance of 500 meters from Line 1. More important, by comparing with Yang's results, we try to figure out whether the Hangzhou urban rail transit contributes to transportation-oriented development or not.

## Variables selected

The affected area of rail transit on the real estate values is generally limited to a certain area, and Yang's study showed that significantly affected area by Metro Line 1 during the construction phase is in the range of 500 meters. So in order to facilitate comparison, the paper determines the radius of 500 meters from the station as research area. In addition, the impact of rail transit on different types of properties is very different. This paper focuses on the commercial residential houses, which is consistent with Yang's research.

**Variables.** Factors that affect the housing price are complex. In order to control the other variables, and to focus on the rail transit factor, this paper intends to use the common factor controlling method: hedonic pricing method. Hedonic pricing method usually controls factors through three aspects: characteristics of the house and property itself, characteristics of the neighborhood and community, and environmental characteristics (accessibility characteristics). Based on the results of previous researches, as well as the availability of the data, here we choose the average sale price of a residential project (donated as Pr) as the dependent variable. And also we select eight independent variables from the above three aspects, where there are one property characteristic, three accessibility characteristics and four neighborhood characteristics. The definitions of these variables and the expected sign of each variable are shown in Table 1. The major purpose of this paper is to investigate the impact of Line 1 on residential prices, so we list the metro rail transit variable separately from accessibility characteristic vector.

Table1 Quantification and the expected sign of the residential characteristic variables

| Variable | Definition | Unit | Expected sign |
|---|---|---|---|
| Pr | The average price per square meter of a project | yuan/$m^2$ | |
| Metro | Dummy variable, distance from the Line 1 station (less than 0.5Km = 1, otherwise = 0) | | + |
| Age | The average age of residential houses | year | - |
| D_WCBD | Straight-line distance from the traditional CBD Wulin Square | Km | - |
| D_QCBD | Straight-line distance from the new CBD Qianjiang New City | Km | - |
| D_WL | Straight-line distance from the pleasant landscape : West Lake | Km | - |
| BL | The number of bus lines around the project within 1Km | | + |
| SCH | Distance from the nearest primary school | Km | - |
| SCH_Q | Dummy variable, quality of the nearest primary school (very good=3, good=2, ordinary= 1) | | + |

**Data collection and processing.** In this paper, the main city of Hangzhou is chose as research area. The real estate industry in this region is relatively mature. Take project as the basic unit of

analysis, and data sample contains a total of 660 projects in Hangzhou. Use the average transaction prices in April 2014 as housing prices, which are obtained directly from the real estate company. In addition, from a variety of real estate search sites (such as SouFun etc.) we complement the residential own characteristics data, such as the average age of residential project, so that the data is more complete. Use Google Maps to measure the distance variables, including the distance to Hangzhou traditional CBD (Wulin Square), the distance to new CBD (Qianjiang New City), and the straight-line distance to the pleasant landscape West Lake. Before put these variables into the model, we preprocess the data to eliminate abnormal values, and finally get a valid sample of 603 projects.

Conducting all variables correlation analysis before build the model can provide an intuitive point of view to determine the relationship between the sequences. The results show that the correlation coefficient between BL and D_WCBD is statistically significant, with value of -0.786. The correlation coefficient between D_WL and D_WCBD is also significantly, up to 0.756. This phenomenon is not out of expectation. Wulin Square as the traditional CBD, is the center of public transport system, the closer to Wulin Square, the more bus lines. West Lake is near to Wulin Square, so their correlation is high. Therefore here we intend to select variables BL and D_WL into the model rather than selecting D_WCBD to prevent collinearity problems.

## Empirical Analysis

**Model building.** Hedonic pricing model has three forms: logarithmic form, semi-log form and direct form. Because both real variables and dummy variables are in this paper, we choose the semi-log form that in addition to the dummy variables, the other variables are in the form of logarithm. Model equation is expressed as Eq. 1.

$$\text{InPr}=\beta_0+\beta_1\text{Metro}+\beta_2\text{In Age}+\beta_3\text{ In D_QCBD}+\beta_4\text{In D_WL}+\beta_5\text{ BL}+\beta_6\text{ In SCH}+\beta_7\text{SCH_Q}+\varepsilon. \quad (1)$$

OLS is used to estimate the model with all variables entering the regression equation directly. The overall indexes of regression results are shown in Table 2.

Table2 Results of overall indexes

| Model | $R^2$ | Adjusted $R^2$ | Std. Error | F | Sig.F |
|---|---|---|---|---|---|
| 1 | 0.448 | 0.442 | 0.203 | 60.521 | 0.000 |

From Table 2, we can see $R^2$ of the regression is 0.448, indicating that the model has a certain degree of explanatory power. And F statistic value is 60.521, much larger than 2, rejecting the assumption that all variable coefficients in the model are 0, which means the overall regression is statistically significant. The estimation of hedonic pricing model is shown in Table 3.

Table 3 Estimation of hedonic pricing model

| Model | B | Beta | t | Sig. | VIF |
|---|---|---|---|---|---|
| Constant | 10.532* | | 163.259 | 0.000 | |
| InSCH | -0.016 | -0.026 | -0.833 | 0.405 | 1.086 |
| SCH_Q | 0.060* | 0.180 | 5.668 | 0.000 | 1.084 |
| InD_WL | -0.261* | -0.562 | -13.806 | 0.000 | 1.790 |
| InD_QCBD | -0.051* | -0.102 | -3.037 | 0.002 | 1.216 |
| BL | 0.001 | 0.037 | 0.932 | 0.352 | 1.684 |
| InAge | -0.089* | -0.219 | -6.285 | 0.000 | 1.309 |
| Metro | 0.060* | 0.098 | 2.972 | 0.003 | 1.174 |

Note: *donate significant level at 1%.

As we can see from Table 3, VIF values of all variables are less than 10, indicating that there is no significant multi-collinearity. When put D_WCBD variable into the equation, all variable VIF values

are still less than 10, but the VIF values of D_WL and BL increase significantly. So it is reasonable not to put D_WCBD variable into the model.

Comparing the results of this paper with Yang's results, the result is shown in Table 4.

Table 4 Comparison of the results in operation phase (2014) and construction phase (2010)

| Variable | Operation phase (2014.4) | Construction phase (2010.3) |
|---|---|---|
| Constant | 10.532* | |
| InSCH | -0.016 | |
| SCH_Q | 0.060* | |
| InD_WL | -0.261* | -0.340* |
| In D_QCBD | -0.051* | -0.105* |
| BL | 0.001 | |
| InAge | -0.089* | -0.018* |
| Metro | 0.060* | 0.090* |

Note: *donate significant level at 1%.

**Result analysis.** From Table 3 we can see that the coefficient of Metro variable is 0.06, significantly positive and consistent with our expectation, indicating that Line 1 on its operational phase has a positive effect on the surrounding residential prices, with a premium of 6%. The Metro coefficient value (0.06) is almost the same as that of InD_QCBD (-0.051), while smaller than InD_WL coefficient value (-0.261). This suggests that Line 1 plays an important role in guiding residential development in the view of comparison with CBD's impact on poverty values.

Take a closer look at comparison of the results in operation phase (2014) and construction phase (2010) shown in Table 4. Because the selected variables and the samples in the two papers are not the same, the absolute values of the coefficients in the two aren't able to compare. However, the basic condition for a qualified econometric model is its applicability, which means the estimations of different scientific equations on a same issue won't be completely different without any rational reasons. The coefficient signs of D_WL, D_QCBD and Age are the same in the two models, and the difference between these coefficient values are small. So we have reasons to believe that the coefficients of Metro in the two models are comparable. Both Metro variable coefficients are significantly positive, and the values are only of a small gap (0.09 to 0.06). The explanation of this result is as follow.

In construction phase, metro rail transit did not bring substantial convenience to people. But most of commercial houses in Hangzhou are pre-sale, so the value of convenience brought by rail transit for travel had been partly reflected in property prices in advance. In addition, buyers for the investment purpose also contributed to the increase. When it comes to the operation phase, the actual rail transit convenient features appeared. Those people waiting to see the substantial convenience no longer hesitate to purchase, thereby further contributing to transfer the benefit value brought by metro rail transit to property price.

## Conclusions

Metro Line 1 has a significantly positive effect on residential prices in its operation phase (2014). Compared with the impact on its construction phase (2010), there is no significant change, indicating that metro rail transit has a long-term positive influence on the station-area property values. The result is consistent with most previous studies, and contributes to adding evidence to verify the assumption that capitalization of convenience brought by urban rail transit is likely to lead to high-density and transportation-oriented development. So we suggest that while planning the urban rail transit system, such impact should be fully considered.

**References**

[1] H.X. Pan, B.H. Zhong: Urban Planning Forum, (2008), p. 62-67
[2] X.F. Ye, W. Cai: Journal of Tongji University(Natural Science),Vol. 30 (2002), p. 432-436
[3] J.Zhang: Research on the Spatial Variation of the Urban Housing Land Prices Based on Geographically Weighted Regression Model—A Case Study of Hangzhong, published MS dissertation, Zhejing University (2012).
[4] Gerrit J. Knaap, C.D.L.D.: Journal of Planning Education and Research, Vol. 21(2001), p. 32-39
[5] Bae, C.C., M. Jun and H. Park: Transport Policy, Vol. 10(2003), p. 85–94
[6] X. Wang, D. L. Zhu, and M. Zhang: Urban Problems (2004), p. 39-42
[7] C. Nie, H. Z. Wen, and X.F.Pan: Geograhical Research (2010), p. 801-809
[8] H.Yang: Effects of urban rail transit on housing prices: A case study of Hanzhou subway, published PhD dissertation, Zhejing University (2010).

*Applied Mechanics and Materials Vols. 580-583 (2014) pp 1311-1314*
*© (2014) Trans Tech Publications, Switzerland*
*doi:10.4028/www.scientific.net/AMM.580-583.1311*

# Dynamic accumulation damage characteristics of initial cracks for the lining of high-speed railway's tunnel

Xiangqiu Wang[1,a], Bin Cai[2,b]

[1] Dept. of Civil Engineering, Foshan University, Foshan,528000, China

[2]Faculty of Civil Engineering of Guangdong University of technology ,510006，China

[a]tongji_wxq@163.com,[b]864353786@qq.com

**Keywords:** tunnel of high railway, initial damage of lining structure, mechanism of cumulative damage, theory of linear elastic damage

**Abstract:** After have been analysed the initial dynamic cumulative damage mechanism of lining structure of the high speed railway tunnel,the conclusions have been gained that, under the effect of the long-term vibrating load of high speed train, When the damage energy accumulation reached a limit values, the damage zone caused by the initial crack which has been existed in the tunnel lining will be expansed further more. for the more, based on the accumulation damage theory linear elasticity and the analysis method dynamic finite element, The extension characters and calculation method of initail crack in the tunnel lining structures for the high railway have been proposed.

## Introduction

The lining of high speed railway's tunnel belongs to the steel reinforced concrete structure, Inevitably there are initial cracks or defects in the process of tunnel construction, under the effect repeatedly on the vibration loadings of the running train, the initial cracks will be expanded and evoluted,the dynamic damage of tunnel structure will also continue to accumulate and deepen. When the damage is accumulated to a certain extent, it may lead to local failure of tunnel structure and overall instability. The research is very rarely about the dynamic damage mechanism of tunnel structure at home and abroad. The current representative research on the dynamic damage characteristics of tunnel structure mainly includes that the spectral analysis techniques based on the Hilbert-Huang transform had been used to analyse the spectral characters of inputting seismic waves by Wang Zhengzheng etc. in refrences [1,2], according to the principle of energy, the energy responsing equation was derived out under the principle of damage conditions, and based on the damage energy equation the nonlinear seismic responsing characteristics of tunnel structure had been analysed. Based on the theory of fatigue cumulative damage, The train loads of ordinary railway tunnel bed structure fatigue life and damage degree had been studied by Peng Limin, Shi Chenghua etc. in refrences [3]. The method of finite element and the indoor model test had been used to research the vibration responsing characteristics and fatigue life of the tunnel structure for the high-speed railway by Huang Juan etc.in refrences [4],and this study had founded a new researching field on the damage of structural tunnel.

The engineering practice shows that the initial damage exists inevitably in the concrete lining structure of high railway's tunnel because of the particular construction environment. under the effect of the long-term vibrating load of high speed train, the initial damage will be continuously accumulated, leading to mechanical characteristics of tunnel lining structure inevitably becomes cumulative damage weakening. In this paper, based on the concrete damage theory, the evolution regularities of fatigue damage discussed for the initial crack of the high-speed railway tunnel, and

then, the foundation was laid to study on the long-term dynamic stability of the structure of high speed railway's tunnel.

**Dynamic damage mechanism of tunnel structure of high-speed railway**

According to the existing design theory and specifications of railway tunnel, the lining structrue is usually composed by two supportings,and the second lining structure is generally in elastic state. If the initial crack is not exsited in the second lining structure, even though the vibration loads of high-speed train effect for a long-term, the new dynamic crack will theoretically not produce,and the dynamic damage or destruction will not take place in the lining structure.but there are so many of unfavorable factors such as the construction quality problems, the groundwater seepage of surrounding rock induced by the vibration of train, The damage of initial lining, the redistribution of surrounding rock stress and so on,the initial cracks usually exists in the key parts of tunnel such as the roof , the arch waist and other Location. The vibration energy would be accumulated in the initial damage region around those initial cracks,with the long-term effect of high-speed train vibration loads. When the accumulation of damage energy reaches a limit value, It will lead to the stable growth of damage crack, and ultimately leads to the damage destruction of tunnel lining structure.

**Stress intensity factor of initial Damage crack**

The engineering practice shows that the initial cracks of tunnel lining mainly belongs to the tension crack, even though the forms of them are complex and diverse. The growth direction of crack is generally perpendicular to the surface of the lining structure,and the destructive force is also the strongest,So this paper mainly focus on the development law of these cracks. In order to simplify the calculation, the lining structure of high speed railway's tunnel is regarded as the problem of plane strain. for an initial damage crack of tunnel lining structure, the tip of this initial damage crack is regarded as the origin of coordinates to establish a corresponding coordinate system.based on the linear elastic theory, The displacement field around the finite region of crack's tip can be obtained as following as[5]:

$$\left.\begin{aligned} u &= \frac{K_I}{8G}\sqrt{\frac{2r}{\pi}}\left[(2\lambda-1).\cos\frac{\alpha}{2}-\cos\frac{3\alpha}{2}\right] \\ v &= \frac{K_I}{8G}\sqrt{\frac{2r}{\pi}}\left[(2\lambda+1).\sin\frac{\alpha}{2}-\sin\frac{3\alpha}{2}\right] \end{aligned}\right\} \quad (1)$$

In which, $\lambda$ is the elastic coefficient of material, for the problem of plane strain, which equals to $3-4\mu$. $G$ is The shear modulus of the material, $\mu$ is the Poisson's ratio, $K_I$ is the stress intensity factor of crack's tip, r is the distance from the calculation point to the crack's tip.

By the refrence [5], for the equation of [1],suppose to $\alpha=\pi$ ,the vertical displacement near to the crack's tip can be obtained as following as:

$$v = \frac{4(1-\mu^2)}{\sqrt{2\pi}E}K_I\sqrt{r} \quad (2)$$

In which,E is the elastic modulus of material.

When $r \to 0$ ,the tensile stress intensity factor at the tip of initial damage crack can be expressed as following as:

$$K_I = \lim_{r \to 0} \left( \frac{\sqrt{2\pi} E v}{4(1-\mu^2)\sqrt{r}} \right) \quad (3)$$

Because of the stress intensity factor varies with the displacement field of crack's tip, In order to consider the vibration loadings of high-speed train and the dynamic interaction between the surrounding rockmass and the tunnel's structure effect on the stress intensity factors of crack's tip, a model of finite element can be established to simulate the dynamic interaction between the surrounding rockmass and the tunnel's structure,and applying the vibration loadings of high-speed train on the model to analyse the changing regularity of the stress intensity factor for the initial damage crack's tip in different times.

**The propagation criterion for the initial damage crack**

As is mentioned before, When the damage energy accumulation reaches a limit values at the initial crack's tip in the lining structure of tunnel, which caused by the external forces such as the vibration of train and so on.it can be said that if the stress intensity factor at the tip of initial damage crack reach the fracture toughness of concrete,the new expansion will be generated at the initial crack,and the damage degree will be continued until the unstable fracture of concrete lining structure. According to the criterion of fracture mechanics of concrete structure[6], the criteria for crack propagation can be expressed as followings as:

When $K_I < K_{IC}^S$, the crack will not be extended.when $K_{IC}^S \le K_I \le K_{IC}^E$, the crack will be extended steadily.and when $K_I > K_{IC}^E$, the crack will be in the unstable growth stage. Where, $K_{IC}^S$ is the fracture toughness of concrete, $K_{IC}^E$ is the unstable fracture toughness of concrete. These parameters can be obtained by the method of three point bending beam, the splitting test of cube and so on.

**The cumulative damage calculation of tunnel lining structure**

The dynamic loadings caused by the high speed railway's train is a random vibration.the dynamic stress caused by the vibration loadings can be considered to be composed with a number of different amplitude vibration cycles, and the cumulative damage effect caused by the vibration of high speed railway's train can be calculated by the method of numerical integral which based on the linear cumulative damage theory.

Supposing that the crack length of tunnel's lining at some moment is $a_i$,the dynamic stress amplitude is $S_i$, so the amplitude of stress intensity factors can be expressed as:

$$\Delta K_i = C S_i \sqrt{\pi a_i} \quad (4)$$

In which, $C$ is the flexibility coefficient of materail, the increment of crack growth, is also called as $da$ can be obtained by the fatigue damage characteristic curve of tunnel's lining that is $da/dN - \Delta K$ , so we can get $a_{i+1} = a_i + da$ , for the more, if the damage cracks are superposited,which caused by several different amplitude of the vibration cycle ,the dynamic accumulation damage crack can be expressed as followings as:

$$a = a_0 + \sum_{i=1}^{N} (da_i) \quad (5)$$

## Analysis of examples

A high-speed railway's tunnel with composite lining those average thickness of the second lining is 50cm, The straight wall arch was adopted for the section of tunnel, the buried depth of tunnel is 10.6m, the concrete grade of tunnel is C25, there exists an initial crack with depth of 20mm In the part of tunnel's vault Center because of construction reasons. It has known that the fatigue damage curve of tunnel's lining structure can be expressed as $da/dN = 3.2\times10^{-3}.(\Delta K)^{4.23}$, the elastic modulus of concrete lining $E$ equals to $2.55\times10^{4}Mpa$, the poisson's ratio of concrete lining $\mu$ equals to $0.20$, the fracture toughness of concrete lining $K_{IC}^{S}$ equals to $0.348Mpa/m^{1/2}$,and the unstable fracture toughness of Concrete lining $K_{IC}^{E}$ equals to $1.16Mpa/m^{1/2}$.The method of dynamic finite element as shown in the refrence [7] is adopted to analyse the dynamic response characteristics of tunnel's lining structure,and the equations as metioned as before are adopted to analyse the damage characteristics of tunnel's lining structure. The maximum stress intensity factor of tunnel lining arch top position of the initial crack tip, it is also called $K_{\mathrm{Im}ax}$ can be obtained to $0.396Mpa/m^{1/2}$.it is satisfied to the Stable growth conditions of crack.for the more,we can calculate out the fatigue life of tunnel's lining structure is $3.52\times10^{6}$ under the vibration loadings of high-speed train. The calculation results accord with the practical engineering[8].

## Conclusions

The crack of initial damage has enormous influence on the fatigue damage of high-speed railway's tunnel, its impact on the long-term life of tunnel's lining structure can not be ignored. Based on the cumulative damage theory of the linear elastic fracture mechanics and combined with the finite element method which can consider the dynamic interaction between the surrounding rockmass and the lining structure of tunnel, the fatigue cumulative damage characteristics of tunnel's lining structure can be calculated reasonably and its results can satisfied to the practical engineering.

## Acknowledgements

This work was financially supported by the project of National Natural Science Fund (51278121).

## References

[1]WANG Zheng-zheng,GAO Bo,JIANG Yuan-jun:Science in China,Series E:Technological Sciences,2009,Vol.52(2009),P.546

[2] WANG Zheng-zheng, Tan yong-gang, zhang zhan:Journal of dalian university of technology, Vol.51(2011),P.861

[3] PENG Li min, SHI Cheng-hua, HUANG Juan. Journal of the china railway society,2007,Vol.29(2008),P.28

[4]Huang Juan:*Study on the vibration response and fatigue life of high-speed railway tunnels based on damage theory*[D]. Central south university,2010

[5]ZHU Bo-fang. *The finite element method*[M].China waterpower press,the press of China WaterPower,1998.

[6] XU Shi-lang Zhao Guo-fan. *the research of fracture mechanics for concrete*. Dalian:The press of dalian university of technology,1991

[7]WANG Xiang-qiu, YANG Li-de,GAO Wen-hua: Chinese Journal of Rock Mechanics and Engineering,Vol.24(2005),P.1746

[8]CHUI Yu-ping,Sun Wei-zhe,DONG Jun.highway,2003(1),P.284

*Applied Mechanics and Materials Vols. 580-583 (2014) pp 1315-1320*
*© (2014) Trans Tech Publications, Switzerland*
*doi:10.4028/www.scientific.net/AMM.580-583.1315*

# A Numerical Investigation on Time-Dependent Failure of Tunnels Based on the Long-Term Strength Characteristics of Rocks

Lianchong Li [1, a], Meng Xing [1, b]

[1] School of Civil Engineering, Dalian University of Technology, Dalian 116024, China

[a] li_lianchong@163.com, [b]xingmeng0923@foxmail.com

**Keywords:** Rock tunnel; Strength degradation; Time-dependent deformation; Numerical simulation

**Abstract.** How to establish the proper rheological model to describe and simulate the relationship between rock mechanic characteristics and time is one of the difficulties in the tunnel long-term stability analysis. In this paper, a numerical model to replicate the time-dependent deformation of rock mass was presented. In the model, the time-dependent deformation is described in terms of degradation of intrinsic physical and mechanical properties of rock and accumulation of mesoscopic damage inside the rock. Based on the model, uniaxial numerical experimentation and tunnel numerical model test are numerically constructed and investigated respectively. The model well reflects the initial creep, steady creep of rock and accelerated creep, which preliminary prove the validity of the proposed model. The results of the tunnel numerical model test show that the displacement curves from the numerical simulation were generally consistent with those from physical model tests. Furthermore, the macroscopic failure modes and local mesoscopic damage evolution of the tunnels were simulated.

## Introduction

The long-term stability is the key to the design of tunnel engineering in rock masses; nevertheless, rheological properties have a variety of adverse effects on the long-term stability of engineering. Previous studies have proved that time-dependent deformations of rock play an important role in the design and construction of tunnels in rock masses with time-dependent strength and deformation properties [1]. In general, when the load reaches the instantaneous strength of the rock (usually refers to the rock uniaxial compressive strength), the rock is destroyed. When load is lower than the instantaneous strength, such as continuous action for a long time, rock damage may also occur due to the rheological effect. So, measuring the stability of permanent and long lived rock engineering should not be in terms of long-term strength rather than the instantaneous intensity as the calculation index of rock strength. In this study, a rheological model based on a simple strength-degradation law was employed in RFPA [2] to study the mechanism of time-dependent deformation and damage evolution of rock tunnels, which was attempted to gain an insight into the long-term stability of rock tunnels.

## The relationship of the rock long-term strength and time

Long-term strength is an important mechanics index of rock rheological mechanics properties. The long-term strength of rock refers to strength with time is reduced, and gradually tend to be a stable convergence value [3]. According to the creep experiment, Chen illustrated the concept of long-term strength of rock, there was a critical strength $f_c$, when the load was less than the $f_c$, deformation was stable creep; when the load was greater than the $f_c$ for accelerating creep, and $f_c$ is the long-term strength of the rock, and pointed out that the long-term stability of the roadway after excavation mainly depended on the long-term strength of surrounding rock [4]. Shao, in terms of the perspective of material mechanical properties degradation over time, carried on the simulation study on characteristics of rock creep [5]. And based on the characteristic of the long-term strength, a series of studies on the long-term stability of tunnels have been widely carried out [6].

In this work, in view of degradation of intrinsic physical and mechanical properties of rock and accumulation of mesoscopic damage inside the rock, the strength degradation model of mesoscopic representative element is employed in the mesoscopic elastic damage model. As is shown in Fig.1, the strength degradation model assumes the strength of the mesoscopic elements degrades with time, and the degradation rate depends on a combination of factors, such as stress, environment, etc., and finally reached a stable long-term strength. The strength degradation model of the mesoscopic representative element can be described as the following equation [7]:

$$f_t = f_\infty + (f_0 - f_\infty)e^{-at} \quad (1)$$

Where $f_0$ is the initial strength of the element; $f_t$ is the element strength at time t; $f_\infty$ is the long-term strength of the element, when $t \to \infty$, $f_t \to f_\infty$; $a$ is the factor of the strength degradation, reacting the speed of intensity attenuation. The values of $f_\infty$ and $a$ depend on the environment factors around rock mass and can be determined by experiments and field calibration. The above model has been achieved in RFPA$^{2D}$, and this work makes use of RFPA$^{2D}$ to conduct corresponding numerical analysis investigations. The introduction of RFPA$^{2D}$ can be found in the literature [8].

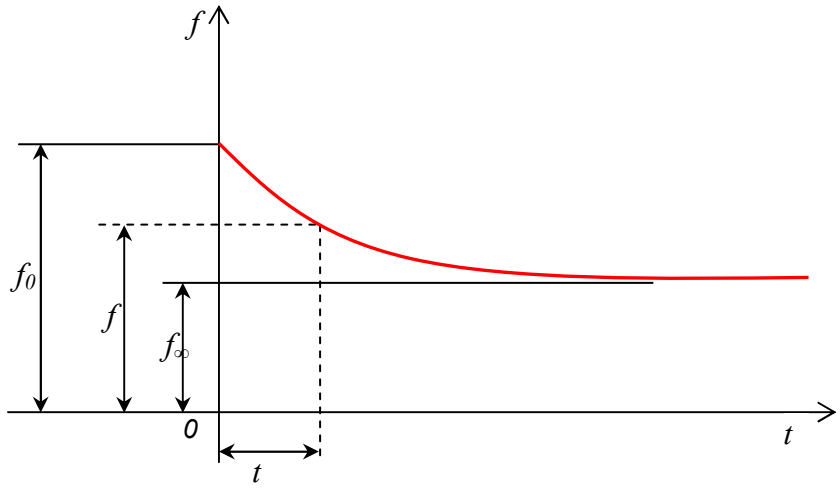


Fig.1 Strength degradation model of mesoscopic representative element

## Model validation and creep damage analysis

**The rock creep numerical experimentation under uniaxial loading.** In the section, characteristics of creep damage of rock under uniaxial loading are analyzed. The literature [9] implemented uniaxial compression creep test of some argillaceous slate, and based on the creep test results under different stress level, the time-dependent behaviors of strength and elasticity modulus of weak rock are discussed. The uniaxial numerical experimentation, based on above the physical experiment, establishes a two-dimensional numerical sample, the mechanical properties of which are of are listed in Table 1. And its geometrical dimension is 50mm×100mm, divided into 125×250, 31250 units. Then numerical samples are applied loads, $P$=5.08MPa, 10.10MPa and 15.82MPa, respectively. The creep curves of physical and numerical experimentations are showed in Fig.2.

Table 1 Parameters employed in uniaxial numerical test

| Parameter | Homogeneity index($m$) | Young's modulus($E$/ MPa) | Compressive strength($\sigma_c$/ MPa) | Tensile strength ($\sigma_t$ /MPa) | Friction angle ($\varphi$/°) |
|---|---|---|---|---|---|
| Rock | 3.5 | 5880 | 108.5 | 10.85 | 45 |
| Parameter | Unit Weight ($\gamma$/ KN·m$^{-3}$) | Poisson's ratio ($\mu$) | Ratio of long-term strength to instantaneous strength | | Coeff. of strength degradation ($a$) |
| Rock | 22.8 | 0.25 | 0.49 | | 0.05 |

As shown in Fig.2, the simulations agree well with the experimental results. And, according to either physical or numerical results, load stress level has great effect on creep properties of rock.

When load stress ($P$=5.08MPa, 10.10MPa) is less than the long-term strength, the creep stage 1 and 2 occur, and in the first phase of the creep, duration is within 75 d with large deformation and the strain rate continues to decay; to stage 2, strain rate keeps on constant with small deformation and duration is very long, specimen without damage, so they belong to the stable creep. When load stress ($P$=15.82MPa) is greater than the long-term strength, the model well reflects the initial creep, steady creep of rock and accelerated creep, and both experimental and numerical simulation results show significantly accelerated creep stage. The strain rate changes acceleration after attenuation firstly, belonging to the unstable creep. Research on the creep properties laws of rock accords with the creep basic laws got by experiment, which preliminary prove the validity of the strength degradation model.

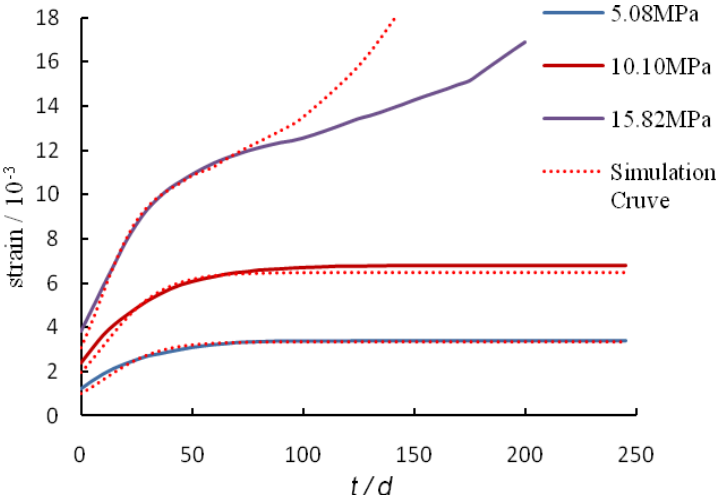


Fig.2 The creep curves of physical and numerical tests under different stress level

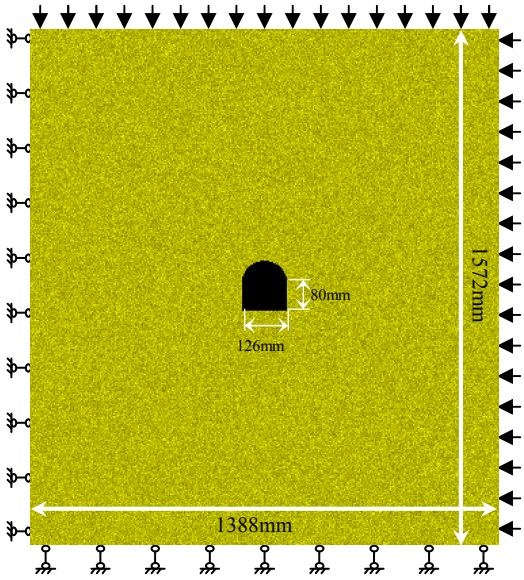


Fig. 3 The numerical simulation model

**Creep damage analysis of rock surrounding tunnel.** As a representative form of rock engineering, tunnel is widely used in mining engineering, traffic engineering, etc., and rheological properties have more adverse impacts on the long-term stability. How to establish the proper rheological model to describe and simulate the relationship between rock mechanics characteristics and time, relevantly describing deformation and failure characteristics of rock mass, have been one of the difficult problems in the tunnel long-term stability analysis [10]. In view of the uniaxial numerical experimentation in the above section, the strength-degradation model was employed to study the mechanism of time-dependent deformation and damage evolution of rock tunnel by the reproducibility of the scale model experimentation.

The literature [11] studied the creep properties of tunnel surrounding rock, not setting lining, after the excavation. The reproducibility of the scale models was examined by comparing the results of model experiments with the numerical analysis. The numerical simulation model and the properties of the trial material are described in Table 2 and Fig. 3 respectively. On the basis of model experiment, the surrounding rock pressure (Vertical: $P$=150KPa, Horizontal: $\lambda P$=52KPa) is defined as $\sigma_o$, and the numerical model are applied loads in sequence, $2\sigma_o$, $3\sigma_o$, $3.5\sigma_o$, by multi-stage loading. Fig. 4 compares displacement of floor heave, roof subsidence and wall convexity under multi-stage loads in the model tests with the displacement in the numerical simulation. From the comparison, we can see that the displacement curves from the numerical simulation shows a good agreement with that in the physical model tests. After the tunnel model is loaded (the excavation of the tunnel, in practice), the tunnel surrounding rock stress occurs redistribution and there will be a rapid initial instantaneous elastic deformation in surrounding rocks at this time. After the experiences of stress redistribution and the initial deformation of tunnel surrounding rock, under the long-term load, the destructions of both of side walls, roof and floor focus on creep, and its creep displacement is slow, with deformation rate lower than the previous stage; this phase is called the transient creep stage.

Table 2 Parameters employed in tunnel numerical model test

| Parameter | Homogeneity index($m$) | Young's modulus($E$/ MPa) | Compressive strength($\sigma_c$/ MPa) | Tensile strength ($\sigma_t$ /MPa) | Friction angle ($\varphi$/°) |
|---|---|---|---|---|---|
| Rock | 3 | 110 | 2.4 | 0.24 | 32 |
| Parameter | Unit Weight ($\gamma$/ KN·m$^{-3}$) | Poisson's ratio ($\mu$) | Ratio of long-term strength to instantaneous strength | | Coeff. of strength degradation ($a$) |
| Rock | 27.2 | 0.44 | 0.7 | | 0.1 |

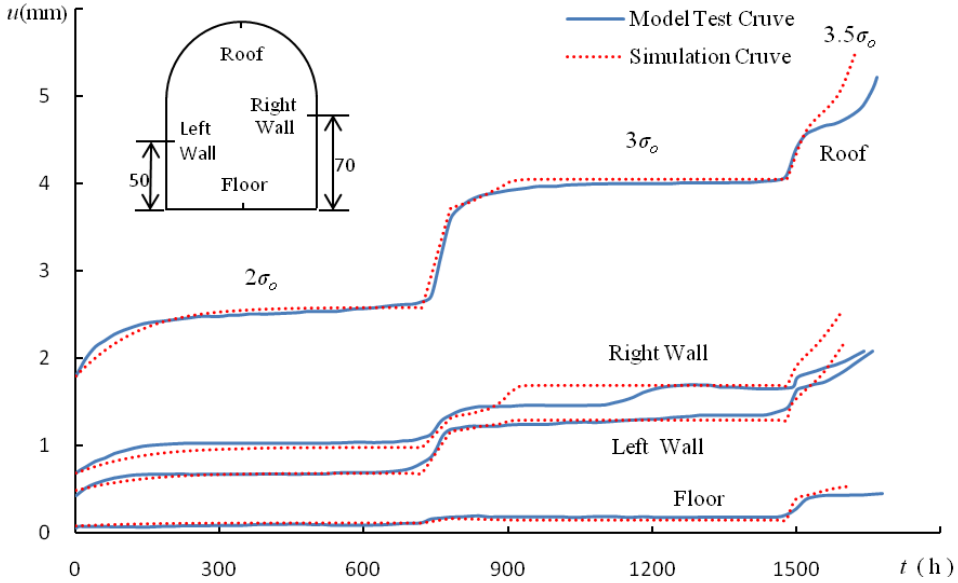


Fig. 4 The displacement curves of model and numerical tests

In the numerical simulation, the distribution of failure zone was used to represent the failure pattern of the tunnel. The calculation results are described in Fig. 5. Fig. a and Fig. b, respectively, shows elastic modulus and the maximum stress figures numerically obtained, and the dark elements represent the nucleated flaw. In Fig. b, the elements with lighter shade of grey have relatively higher stresses. During applying the first-stage load, high stress concentration occurs in the two side walls, showed in Fig. b(1); in spite of strength degradation over time, since tunnel surrounding rock suffer less pressure, damage does not occur. Because of second-stage load applied, higher stress concentration occurs and the initial cracks generate in the two side walls, illustrated in Fig. a(2) and Fig. b(2). As time goes on, the rock mass strength attenuates with time constantly and cracks cut-through in the side walls and extend into the tunnel gradually, described in Fig. a(3) and Fig. b(3). Eventually, according to Fig. a(4) and Fig. b(4), under the time and third-stage load, both of side walls generate the overall destruction and cracks extend into two shoulders of the tunnel.

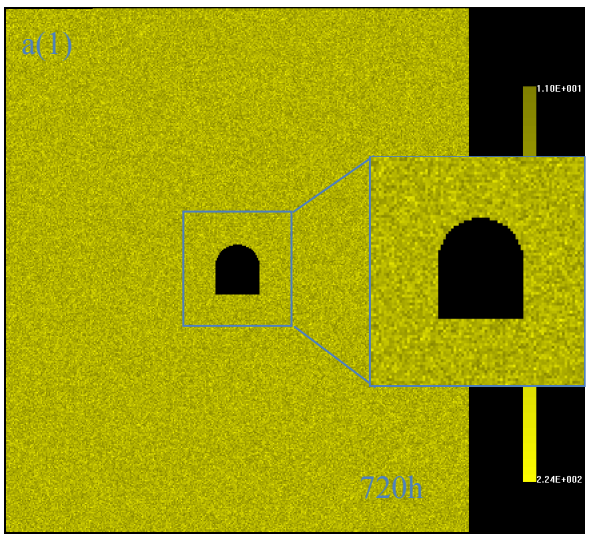


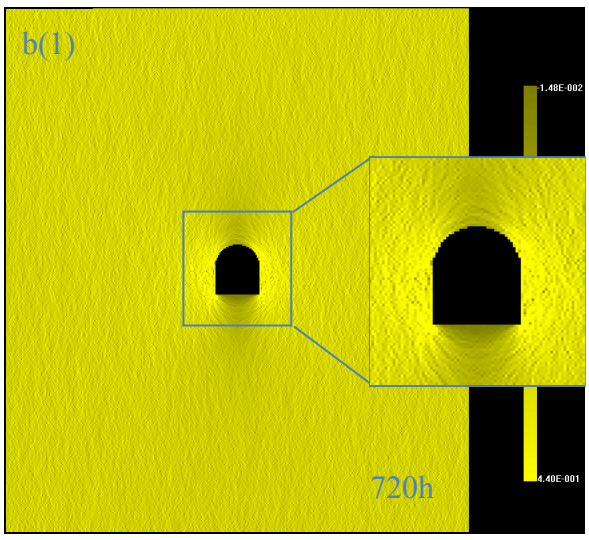

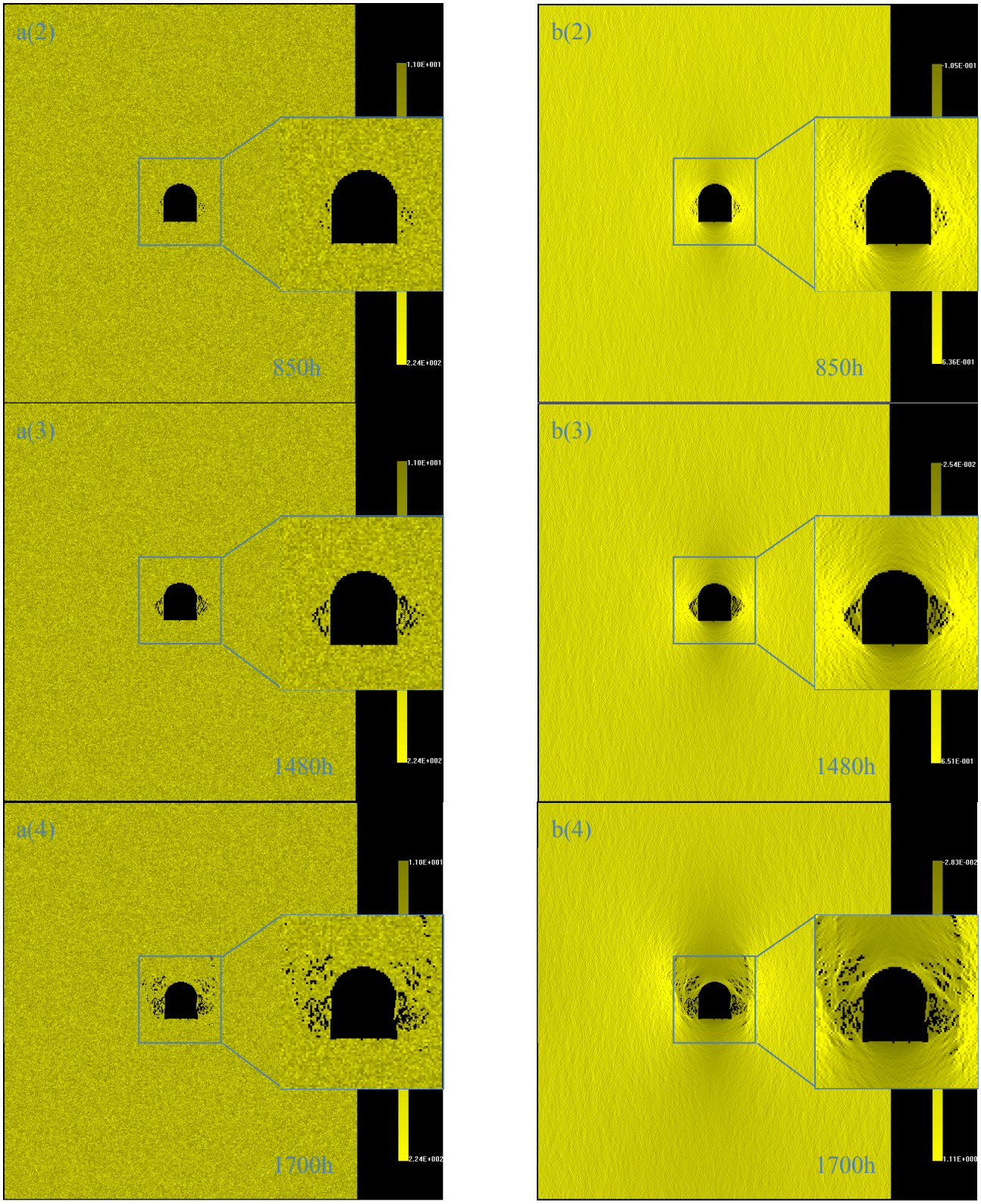


Fig. 5 Numerically obtained time-dependent failure mode of tunnel, (a) failure mode shown with modulus, (b) maximum shear stress evolution

## Conclusions

In this study, a numerical model in an attempt to replicate the time-dependent deformation of heterogeneous rock mass was presented. In the model, the time-dependent deformation is described in terms of degradation of intrinsic physical and mechanical properties of rock and accumulation of mesoscopic damage inside the rock.

Using this model, implemented in the RFPA$^{2D}$, uniaxial numerical experimentation and tunnel numerical model case are numerically constructed and investigated respectively. It is shown that the long-term features of rock mass can be accurately modeled with the proposed approach:

(a) The results of the uniaxial numerical experimentation show that the strain laws agree well with the experimental results and the model well reflects the initial creep, steady creep of rock and accelerated creep. These preliminary prove the validity of the strength degradation model;

(b) In view of the application of the strength-degradation model in the reproducibility of the tunnel scale model experimentation, we can see that the displacement curves from the numerical simulation shows a good agreement with that in the physical model tests. After the tunnel model is loaded, the tunnel surrounding rock stress occur redistribution and there is a rapid initial instantaneous elastic deformation. Then under the long-term load, the destructions of both of side walls, roof and floor focus on creep, with deformation rate lower than the previous stage; this phase is called the transient creep stage. As the rock mass strength attenuates constantly, or environmental factors change, such as load change, the displacement may increase rapidly, and then creep damage occurs.

**Acknowledgements**

This work was jointly supported by the National Natural Science Foundation of China (Grant No. 51279024) and the National Basic Research Programme of China (Grant No. 2014CB047100). The authors are grateful for these supports.

**References**

[1] J. Kemeny: International Journal of Rock Mechanics & Mining Sciences Vol. 42(2005), p. 35–46

[2] C.A. Tang: International Journal of Rock Mechanics & Mining Science Vol. 34(1997), p. 249–261

[3] J. Sun: Chinese Journal of Rock Mechanics and Engineering Vol. 26(2007), p. 1081-1106 (in Chinese)

[4] TAN Tjongkie: Chinese Journal of Rock Mechanics and Engineering Vol. 1(1982), p. 1–8 (in Chinese)

[5] J.F. Shao: Computer and Geotechnics Vol. 30(2003), p. 549-555

[6] L.C. Li, C.A. Tang, Z.Z. Liang, T. Xu, X.X. Zhai: Progress in Mining Science and Safety Technology, Pts A and B, In: International Symposium on Mining Science and Safety Technology (2007), p. 373-378

[7] M.F. Cai, M.C. He, D.Y. Liu: Rock Mechanics and Engineering (Science Press, Beijing, 2002) (in Chinese)

[8] L.C. Li, C.A. Tang, W.C. Zhu: Computers and Geotechnics Vol. 36(2009), p. 1246-1258

[9] H.F. Xu: Chinese Journal of Rock Mechanics and Engineering Vol. 16(1997), p. 246 - 251

[10] S.Q. Yang: Doctoral Dissertation (Hohai University, Nanjing, 2006) (in Chinese)

[11] D.P. Zhou: Journal of Southwest Jiaoyong University Vol. 3(1993), p. 15-20 (in Chinese)

*Applied Mechanics and Materials Vols. 580-583 (2014) pp 1321-1326*
*© (2014) Trans Tech Publications, Switzerland*
*doi:10.4028/www.scientific.net/AMM.580-583.1321*

# Measurement and Research on Broken Zone of Surrounding Rock in Cha Zhen Tunnel

Wang Rui[1,2] Liang Yan[2] QIN Wei[2]

([1.]School of Civil Engineering and Architecture, Xi'an University of Technology Xi'an 710048, China [2.]School of Civil and Architecture Engineering , Xi'an Technological University, Xi'an 710032, China)

19185877@qq.com,429014646@qq.com,304752234@qq.com

**Keywords:** Surrounding Rock; Broken rock zone; Elastic-plastic analysis; Multi-point displacement meter;

**Abstract.** The use of the Analysis and calculation with elastic-plastic theory and Deep displacement of surrounding rock measurement determine the distribution range on broken zone of surrounding rock in Cha Zhen tunnel ; it verifies The stability of surrounding rock and the design rationality of bolting parameters ;Providing a theoretical base for the setting on broken zone of surrounding rock supporting parameters.

## Introduction

As the rapid development of highway tunnel construction and the continuous renewal of tunnel construction technology in China, the introduction of various kinds of modern construction machinery possibly makes Blasting excavation replaced by Mechanical excavation. However, drilling and blasting method is still the main method of tunnel excavation in the mountains. In engineering practice, In order to optimize the design scheme, it's essential to minimize the disturbance of rock and drill blasting excavation on the surrounding rocks as much as possible, and to play the bearing capacity of surrounding rock to maximum. In the construction of Cha Zhen Tunnel, it unites the elastic-plastic theory with deep displacement monitoring method to determine the range of the broken zone of surrounding rock ,which offers a more reliable basis in the design of surrounding rock bracing.

In recent years, many scholars have studied a lot on broken zone of surrounding rock. GUO Liang,LI Jun-cai ,who used ground penetrating radar to determining the broken zone about bias tunnel and get the range of the bias tunnel's broken zone(GUO Liang et al.,2011).LI Ning,DUAN Xiaoqiang, Who used The process of tunnel's working face and monitoring data, by using the analysis of plastic theory， acquiring the rock parameters of the real state(LI Ning et al.,2006).

Li Zheng Lin, Wu Ruixiang using bilinear stress injury model and the Stress equivalence principle to obtain the analytical solution of theoretical analysis， and Validated it through projects(Li Zhenglin et al.,2011). Dong Fangting and other scholars put for forward the Detailed method of support theory of Broken Zone of Surrounding Rock Through a large coal mine tunnel testing and laboratory testing(Dong Fangting,2001;GONG Jian-wu,2007).

## Project Overview

Cha Zhen Tunnel, with the total length of 1496m, which is located between Yufeng village and Chazhen village of Xixiang County has one-way two lane.Lithology is mainly moderate and intense weathering metamorphic andesitic basalt, and the surrounding rock is mainly IV class, V class. The main groundwater is bedrock fissure water,structural fissure water， and little layer pore water spread over its surface.

The construction clearance of Cha Zhen Tunnel is: clear width of 10.25m, clear hight of 6.8m. The inside radius of the arch wall of the designing inner contour is 5.0m, of the inverted arch is 15.0m. The biggest excavation line is 12.88m. Construction adopts NATM and Composite lining support. The initial support uses sprayed concrete of C25, steel fabric and hollow grouting anchor rod whose length is 3.5m; the secondary support adopts C30 overall model of reinforced concrete lining and Core-keeping Ring Cut blasting Method.

**Adopt elastic-plastic analysis to determine Broken Zone of Surrounding Rock**

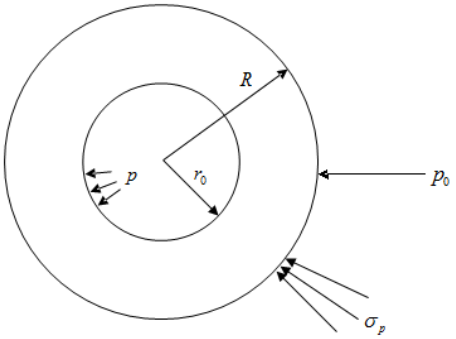


Fig . 1 Elastic-plastic area of tunnel

The method of elastic-plastic mechanics can establish equation on the basis of the character that elastic stress is equal to the plastic stress between the plastic zone and the elastic zone interface(REN Qingwen,2001), and deduce the computational formula of the surrounding rock's radius. It is regarded as axisymmetric problem and assumes that initial ground stress is ,inner pressure is,lateral pressure coefficient is 1, cohesion is,angle of internal friction is,radius stress ishoop stress is,As shown in picture 1, the excavation radius of the tunnel is,the plastic zone's radius is,and the thickness of the broken zone of surrounding rock is:

$$\mathrm{B} = R - r_0 \tag{1}$$

Regardless of the volume strength in the plastic zone, the differential equation of equilibrium of axisymmetric problem is:

$$\frac{\mathrm{d}\sigma_r}{\mathrm{d}r} + \frac{\sigma_r - \sigma_\theta}{r} = 0 \tag{2}$$

The yield criterion adopts Mohr-Coulomb yield criterion:

$$\tau_f = c - \sigma_n \tan\varphi \tag{3}$$

Or it could be expressed as $\sigma_1(1+\sin\varphi) - \sigma_3(1-\sin\varphi) = 2c\cos\varphi$ (4)

When we adopts $\sigma_1, \sigma_2, \sigma_3$ ,($\sigma_1 \geq \sigma_2 \geq \sigma_3$) for principal stress

If $\sigma_1 = \sigma_r, \sigma_3 = \sigma_\theta$, we can acquire the equation (5) and then (6):

$$\sigma_r(1+\sin\varphi) - \sigma_\theta(1-\sin\varphi) = 2c\cos\varphi \tag{5}$$

$$\sigma_\theta = \frac{\sigma_r(1+\sin\varphi)-2c\cos\varphi}{1-\sin\varphi} \tag{6}$$

Put equation(6)into equation (2), and we can reach:

$$\frac{\mathrm{d}\sigma_r}{\mathrm{d}r} - \frac{2\sigma_r\sin\varphi}{r(1-\sin\varphi)} = -\frac{2c\cos\varphi}{r(1-\sin\varphi)} \tag{7}$$

integrate equation (7), and we can get $\sigma_r = c\cot\varphi + c_1 r^{\frac{2\sin\varphi}{1-\sin\varphi}}$, in the boundary condition: $(\sigma_r)_{r=r_0} = -p$, and we can also reach: $c_1 = \frac{-p-c\cot\varphi}{r_0^{\frac{2\sin\varphi}{1-\sin\varphi}}}$, and

$$\sigma_r = c\cot\varphi - (p+c\cot\varphi)(\frac{r}{r_0})^{\frac{2\sin\varphi}{1-\sin\varphi}} \tag{8}$$

Substituting the equation (8) into equation (6), we can get the plastic zone's stress:

$$\sigma_\theta = c\cot\varphi - \frac{1+\sin\varphi}{1-\sin\varphi}(p+c\cot\varphi)(\frac{r}{r_0})^{\frac{2\sin\varphi}{1-\sin\varphi}} \tag{9}$$

In the elastic zone($r \geq R$) according to Lame Answer of elastic mechanics, we can assume that stress at $r=R$ is $\sigma_p$, initial ground stress in the distance is , we can get:

$$\left\{\begin{array}{l}\sigma_r = -\frac{R^2}{r^2}\sigma_p - (1-\frac{R^2}{r^2})p_0 \\ \sigma_\theta = \frac{R^2}{r^2}\sigma_p - (1+\frac{R^2}{r^2})p_0\end{array}\right\} \tag{10}$$

Add the equations of (10) together, we can get: $\sigma_\theta + \sigma_r = -2p_0$, at the same time, this equation can meet the requirement, and then combine it with equation (8) and (9), we can reach:

$$\sigma_r = c\cos\varphi - p_0(1-\sin\varphi) \tag{11}$$

Because of $(\sigma_r)_{r=R} = \sigma_p$, equation(8) is equal to equation(11), and then combine them eliminating , finally we can get Fenner formula to determine the scope of the broken rock zone.

$$\frac{R}{r_0} = [\frac{(c\cot\varphi+p_0)(1-\sin\varphi)}{p+c\cot\varphi}]^{\frac{1-\sin\varphi}{2\sin\varphi}} \tag{12}$$

This paper chooses the tunnel's left hole ZK225+527 as an example. The depth of tunnel is 150m, natural stress ratio =1.This paper assumes $\sigma_h \approx \sigma_v = \sigma_0$, the initial ground stress is caculated as geostatic stress, and $p_0$=3.672, The selection of rock parameters is shown in table1.

Tab . 1 The parameter selection

| rock grade | elasticiy modulus E MPa | Bulk density V KN/m$^3$ | Friction Angle $\varphi$ ° | Cohesive force $c$ MPa |
|---|---|---|---|---|
| Ⅴ | 15 | 24.48 | 31 | 0.67 |

Combined with the tunnel's monitoring measurement data, at the vault of tunnel section ZK225+527, the contact pressure between the surrounding rock and the initial lining at the angle of 45°,90°,135°.is 32.7215 k Pa， 22.7035 k Pa， 24.5672 k Pa .

Put the parameters into the equation(12), the tunnel's excavation radius is $r_0$ =5.0m

$p$ =32.7215 k Pa , we can reach： $R/r_0$ = 1.393，and then B= $R-r_0$ =1.965 m；

$p$ =22.7035 k Pa ， we can reach: $R/r_0$ = 1.399，and then B= $R-r_0$ =1.995 m；

$p$ =24.5672 k Pa ， we can reach： $R/r_0$ = 1.398，and then B= $R-r_0$ =1.990 m.

Above all, we can get the scope of the broken rock zone $1.965 \le B \le 1.995$

**Measure the displacement of the deep surrounding rock to determine the broken rock zone**

Cha Zhen tunnel adopts multiple position extensometer to measure the rock's displacement in different depths, and then according to the displacement measurements and temporal curve we can get displacements measurements within the rocks in different depths. Ideally, the displacement of the deep surrounding rock is more smaller when it is more farther from the excavation contour surface, and it's Generally linear with depth. If there is displacement mutation between adjacent two points, it shows that the surrounding rock's interface exists between these two points. When adjust the supporting parameters it needs anchor stock overstep these points. If the displacement between adjacent two points changes on average and meanwhile there exists larger displacement in the deepest point, it'll show that the surrounding rock's disturbed scope is larger, it's not enough only to adjust the length of anchor stock but needs further comprehensive measures.

This paper chooses the typical section ZK225+527 as the monitoring section, respectively bury three groups of multiple position extensometer at vault and both sides of the arch waist place, each of them has three points respectively monitoring the surrounding rock's displacement at hole's depth of 1m,2m,3m. Multi-point displacement meter embedded graph is shown as picture 2.

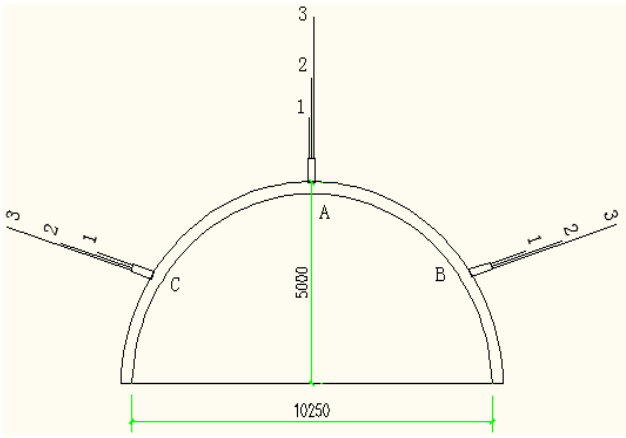


Fig . 2 Multi-point displacement meter embedded graph

This monitoring lasts 60 days, the frequency of the monitoring is twice a day from day1 to day15. once for two days in 16—30days, twice for two weeks in 30—60days, and choose accumulative data of multiple position extensometer as analytic object. The data of multiple position extensometer which is monitored is shown in table2.

Tab . 2 Multi-point displacement meter test results

| Measuring point | | Hole depth m | displacement mm |
|---|---|---|---|
| A | 1 | 1.0 | 23.36 |
| | 2 | 2.0 | 3.31 |
| | 3 | 3.0 | 1.52 |
| B | 1 | 1.0 | 16.98 |
| | 2 | 2.0 | 1.18 |
| | 3 | 3.0 | 0.95 |
| C | 1 | 1.0 | 25.42 |
| | 2 | 2.0 | 2.64 |
| | 3 | 3.0 | 2.20 |

From the table, three groups of displacements tend to be smaller along with the depth,but don't have linear relation. The displacement of point 1 is lager while point 2 and point 3 are smaller, and there is a mutation between point1 and point 2. Above all, we can get the thickness of the broken rock zone :1.0<B<2.0m.

## Conclusions

①Combining the result of elastic-plastic theory with the analysis of the measured data, we can get that the scope of broken rock zone of Cha Zhen tunnel is between 1.9m and 2.0m.Actually, the designed length, which is 3.5m, can meet the needs of practical engineering and ensure the surrounding rock's stability.

②This paper verifies that Elastic plastic formula has high accuracy when it calculates the scope of broken rock zone, especially the tunnel with circular section, but should have higher accuracy for initial ground stress.

③It seems intuitive using multiple position extensometer to monitor the surrounding rock's deformation, but the result is not so accurate because of many disturbing factors and changeable rock conditions. So it should consider theoretical analysis to better determine the scope of broken rock zone.

④The broken rock zone is an important parameter for tunnel's design and construction , and the important parameter to assess the stability of the surrounding rock.Cha Zhen tunnel's using of method which combines theoretical analysis with measurement at the job site lays the foundation for supporting system's optimization and provides a strong guarantee to ensure the safety of tunnel construction .

**References**

[1]GUO Liang，LI Jun-cai，ZHANG Zhi-cheng，et al. Research on Surrounding Rock Broken Zone of Tunnel under Unsymmetrical Loading with Ground Penetrating Radar and Its Application[J]. Chinese Journal of Rock Mechanics and Engineering，2011,30(Z1)：3009. ( in Chinese)

[2]LI Ning，DUAN ,Xiao-qiang，CHEN Fang-fang. A Back Analysis Method for Elastoplastic Displacement of Broken Rock Zone around Tunnel[J]. Chinese Journal of Rock Mechanics and Engineering，2006, 25 (7)：1304.( in Chinese)

[3]LI Zheng-lin，WU Rui-xiang，LI Long-jian，et al. Method for Defining the Broken Zone of Tunnel Surrounding Rock Based on Damage Theory[J].Chinese Journal of Underground Space and Engineering，2011,7（6）：1060.( in Chinese)

[4]DONG Fang-ting et al. Support Theory and Application Based on the Broken Rock Zone in Surround Rock[M].Beijing：China Coal Industry Publishing House，2001.( in Chinese)

[5]GONG Jian-wu, XIA Cai chu, GONG Jian-wu, XIA Cai chu, ZHU He-hua. Measurement and Analysis on Releasing Zone of Surrounding Rock in Heshang Tunnel[J].Chinese Journal of Underground Space and Engineering，2007,3(3)：475.( in Chinese)

[6]REN Qing-wen，ZHANG Hong-chao.A Modification of Fenner Formula[J]. Journal of Hohai University 2001,29(6)：109. ( in Chinese)

*Applied Mechanics and Materials Vols. 580-583 (2014) pp 1327-1330*
*© (2014) Trans Tech Publications, Switzerland*
*doi:10.4028/www.scientific.net/AMM.580-583.1327*

# Numerical simulation study on three-step method Construction for Neighborhood tunnel

Cai Lingling, Yang Xiuyuan, Guo Ning

Center for Hydrogeology and Environmental geology, CGS , Baoding, Heibei,China

caill00@163.com

**Keywords:** neighborhood tunnel, numerical simulation, stress field, displacement field

**Abstract.** When crossing difficult terrain or extreme regional geological conditions encountered, there are difficulties in laying road routes, the spacing between two adjacent tunnels is limited. Neighborhood tunnel is a form of tunnel structure between separate and arch ones, less affected by the topography. It is more conveniently and easier to control the cost. Surrounding rock deformation mechanism with construction of three-step method is more complex, and therefore a reasonable means of construction technology and support is essential. Taking a certain neighborhood tunnel highway engineering background, aimed to provide guidance for follow-up monitoring and support, we use numerical simulation software FLAC$^{3D}$ on three-step method excavation construction. Rational creep analysis of geotechnical model and calculation parameters is selected. It helps to calculation and analysis the mechanical response of tunnel surrounding rock characteristics and clarify the tendency of displacement and stress fields.

## Introduction

When complex terrain or extreme regional geological conditions encountered, difficulties of laying road routes arise. In this case the construction of the tunnel project, about road width is difficult to form a separate lane distance, requiring the use of neighborhood tunnel or arch tunnel [1]-[2]. Neighborhood Tunnel is a tunnel in the form between separate tunnel and arch tunnel. It is more conveniently and less affected by topography. In recent years, many scholars have carried out research associated with it[3]-[5]. Here we take Shi-Man expressway project which was constructed with three-step method as the example, and analysis of the mechanical response characteristics after excavation by numerical simulation calculation FLAC$^{3D}$ .

## Project profile

Shi-Man Expressway crossing region is located in the Qinba mountainous hinterland, at an altitude between 100 ~ 1596.2m, belonging to mountainous terrain. Route strides over four types of landscapes, as follows: tectonic erosion of the low mountains, tectonic denudation of the hilly, mountain basin tectonic denudation and erosion valley accumulation. The area attributes South Qinling miogeosyncline fold belt on tectonics, complex lithology and fissure karst water groundwater mainly water -based.

## Calculation model and simulation program

### 3.1 Tunnel construction and model selection

The study takes neighborhood tunnel to the highway as the main object. To facilitate the simulation, the three- step method excavation can simplify to four major procedure, as follows: construction in right steps →construction in the upper left and middle right steps →construction in middle left and lower right steps →construction in left steps.

If the country rock condition is complex in engineering practice, it will show various characteristics of composite or overlay after excavation. FLAC$^{3D}$ can simulate the creep properties of the material which is related to the time. But a single model can not reflect the actual deformation.

Burgers model and Mohr-Coulomb model is combined here to be a viscoplastic model (Fig.1), it can better reflect the deformation characteristics of soft rock. Rock in the tunnel appears viscoelastic performance before the yield, and viscoplastic performance after entering the yield, with a clear three-stage creep curve.

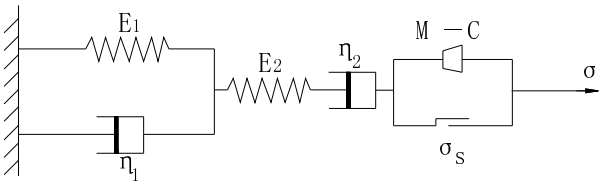


Fig.1 Modified Burgers creep model

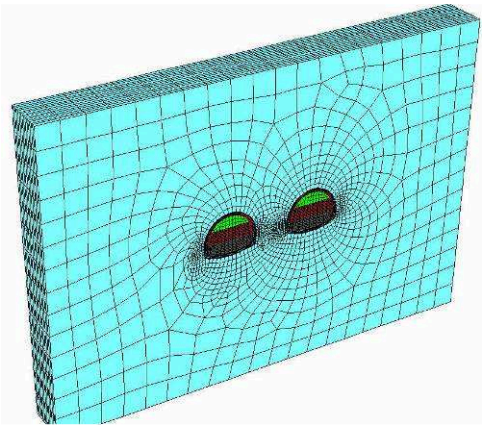

Fig.2 Tunnel model

3.2 Computing model

According to the terrain conditions, the maximum depth of the tunnel is 47m. Due to poor mechanical properties of rock, large rock deformations occur easily. Rock Classification is mostly at level Ⅳ～Ⅴ. By simplifying the geological model, the model boundaries is rather than three times the effective diameter of the neighborhood tunnel, namely the horizontal length of 100m, vertical height of 70m, vertical take 10m that a construction cycle. Model set boundary conditions that limit the model in addition to the five ground surface boundary edge interface, based on the model of the surface terrain conditions under its own weight load stress. Bearing on the bottom plus a fixed model to restrain all degrees of freedom, and in parallel to the sides of the tunnel plus sliding bearings, only restrain degrees of freedom in the X-axis direction. In summary, through the above modeling requirements, a three-dimensional tunnel model (Fig.2) is established, containing 37,335 units and 40,384 nodes.

3.3 Calculation parameters selected

Rock relaxation and destruction after tunnel excavation is a dynamic process, affecting by many factors and complex mechanism of action. Tunneling-induced rock initial stress release and adjusting is finally bound to form elastic and plastic zones in the tunnel. The strength and deformation characteristics of rock within the range will deteriorate. Considering structural surface, interlayer and other uncertainties inside the rock, its mechanical properties are very different from experimental rock mechanical parameters. In order to reflect the deterioration of the mechanical parameters as much as possible, we appropriately reduce the mechanical parameters , the parameters used in the simulation is then reduced : $E_M$＝1.17GPa,$E_K$＝0.98GPa,$\eta_M$＝$16.5\times10^3$GPaS,$\eta_K$＝$4.57\times10^3$GPaS,E＝1.8GPa,μ＝0.3,C＝0.3MPa,Φ＝23º, the tensile strength = 0.32MPa.

## Simulation results

4.1 Analysis of the displacement field

After excavation and initial support in three-step method construction for neighborhood tunnel, the vertical displacement and horizontal displacement field distribution changes (shown in Fig.3). According to the simulation results, when construction in right steps is finished, vault settlement is 2.80mm; when construction in the upper left and middle right steps is finished, vault settlement is 25.49mm; when construction in middle left and lower right steps is finished, vault settlement reaches 36.31mm; when construction in left steps is finished, which means all sections are completed, vault settlement reaches the maximum of 65.77mm.

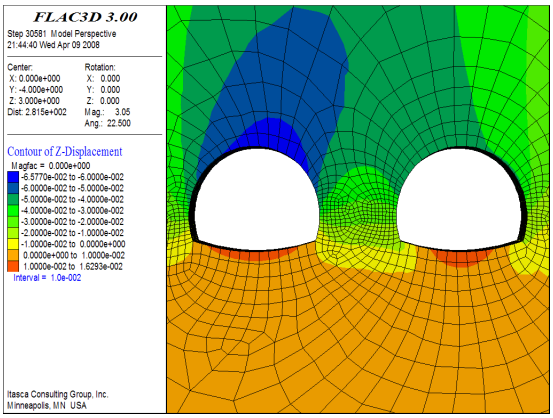


Fig.3a The final Z direction displacement

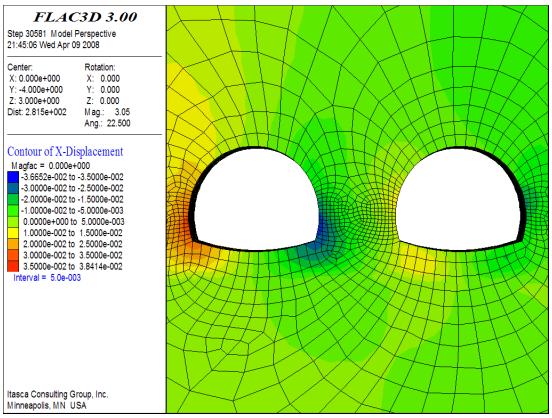


Fig.3b The final X direction displacement

In terms of horizontal displacement, when construction in right steps is finished, the maximum convergence is 0.5mm; when construction in the upper left and middle right steps is finished, the maximum horizontal displacement is 11.39mm, located in the right steps outside the cave wall with horizontal displacement of the inner sidewall of 11.34mm and the inside on the left stepped buttresses maximum horizontal displacement of 7.5mm; when construction in middle left and lower right steps is finished, the maximum horizontal displacement is 17.27mm, located in the right steps outside the cave wall; when construction in left steps is finished, the maximum horizontal displacement gets 38.41mm, located in the left side wall parts.

4.2 Stress field analysis

After excavation and initial support in three-step method construction for neighborhood tunnel, maximum and minimum principal stress distribution changes (shown in Fig.4). According to the simulation results, when construction in right steps is finished, principal stress σ1 maximum compressive stress is 2.70MPa and tensile stress is 0.02MPa, located in the right steps outside the cave wall; principal stress σ3 maximum compressive stress is 0.97MPa and tensile stress is 0.14MPa, having a small amount of the distribution at the top of the arch and the bottom on the steps. When construction in the upper left and middle right steps is finished, principal stress σ1 maximum compressive stress is 9.56MPa and tensile stress is 0MPa, focused on top of the arch of the right hole. When construction in middle left and lower right steps is finished, principal stress σ1 maximum compressive stress is 11.04MPa and tensile stress is 0MPa, located in both arch of two holes, but the maximum value is found in right hole. There also has a small distribution at the right side of the right hole. Principal stress σ3 maximum compressive stress is 1.0MPa and tensile stress is 0.10MPa, located at the bottom of both two hole. When construction in left steps is finished, principal stress σ1 maximum compressive stress is 15.97MPa and tensile stress is 0MPa, principal stress σ3 maximum compressive stress is 1.26MPa and tensile stress is 4.98MPa, concentrated on both sides of the right holes' foot.

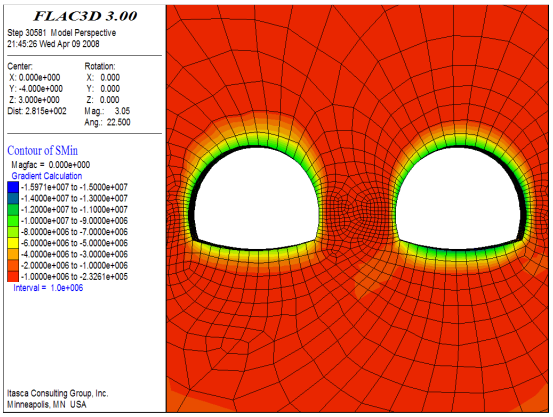


Fig.4a The maximum principal stress

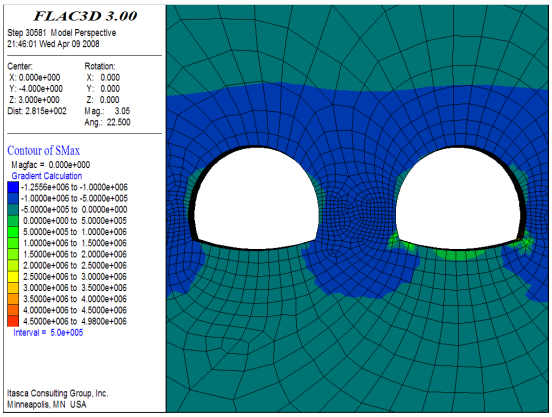


Fig. 4b The minimum principal stress

Neighborhood Tunnel excavation at each step of the maximum displacement and the maximum / minimum principal stress is shown in Table 1.

Table 1 Comparison of the displacement and principal stress

| step | maximum displacement (cm) | | maximum / minimum principal stress (MPa) | | | |
|---|---|---|---|---|---|---|
| | | | $\sigma_1$ | | $\sigma_3$ | |
| | Z | X | press | tense | press | tense |
| 1 | 2.80 | 0.5 | 2.70 | 0.02 | 0.97 | 0.14 |
| 2 | 25.49 | 11.39 | 9.56 | 0 | 1.43 | 0.06 |
| 3 | 36.31 | 17.27 | 11.04 | 0 | 1.00 | 0.10 |
| 4 | 65.77 | 38.41 | 15.97 | 0 | 1.26 | 4.98 |

## Conclusion

It can be learned from numerical simulation on the three-step neighborhood tunnel construction methods, after construction is completed the vault maximum settlement value is up to 65.77mm, the maximum horizontal displacement value is up to 38.41mm (located in the left bottom part of the left hole); principal stress $\sigma_1$ maximum compressive stress is 15.97MPa and tensile stress is 0MPa； σ3 maximum compressive stress is 1.26MPa and maximum tensile stress is 4.98MPa, concentrated on both sides of the arch foot in the right hole. In the excavation and construction, it should be the importance of these parts above-mentioned and strengthen the monitoring and measurement together with lining for the tunnel timely.

## References

[1] YI Xiaoming,ZHANG Dingli,CHEN Tielin: Stratum Deformation Monitoring and Mechanism Analysis of Xiamen Subsea Tunnel , edited by Chinese Journal of Rock Mechanics and Engineering(2007).

[2] LV Ming,GRØV E,NILSEN B: Norwegian experience in subsea tunnelling. edited by Chinese Journal of Rock Mechanics and Engineering(2005).

[3] LIU Yanqing, ZHONG Shihang, LU Rusui: Experimental Study on Mechanical Characteristics of Twin Tunnels with Small Spacing, edited by Chinese Journal of Rock Mechanics and Engineering(2000).

[4] YANQi xiang, HE Chuan, YAO Yong: Study on Construction Characteristic and Dynamic Behavior of Soft Rock Tunnel, edited by Chinese Journal of Rock Mechanics and Engineering( 2006).

[5] JIN Xiaoguang, LIU Wei, ZHENG Xuegui: Optimization of Excavating Sequence for Closely Spaced Bias Double tube Tunnels, edited by Journal of Highway and Transportation Research and Development( 2005).

*Applied Mechanics and Materials Vols. 580-583 (2014) pp 1331-1334*
*© (2014) Trans Tech Publications, Switzerland*
*doi:10.4028/www.scientific.net/AMM.580-583.1331*

# Study on Pressure Observation of Fully Mechanized Caving Faces in Coal Seams with Rock Burst Danger in Xiagou Coal Mine

Zhichao Tian [1, a], Yejiao Liu [1, b], Wencai Wang [1, c], Yuhui Ren [1, d]

[1]Inner Mongolia University of Science and Technology, Baotou, Inner Mongolia, 014010, China

[a]bailey280@163.com,[b]liuyejiao408@163.com, [c]wencai99999@163.com, [d]rnyhui@163.com

**Keywords:** fully mechanized caving face, pressure appearance law, pressure observation, mining roadway

**Abstract.** Taking the first fully mechanized caving face in Xiagou coal mine as research background, through the pressure observation on the scene field of fully mechanized caving face with rock burst danger, this essay reveals the pressure appearance law of coal seams rock burst danger and concludes that the field roof structure of fully roof mining is more conducive to the release of coal rock stress compared to layered mining structure and this method plays a mitigation role on moving pressure shock of coal rock. The fully mechanized caving faces can be explored fast under safety conditions. The research results are of great theoretical and practical significance to the mining production with similar geological conditions.

## Introduction

ZF4401 working face is the first caving fully mechanized caving face in Xiagou coal mine and it is located on the western flank of three down hills in 404 mining area. The non-mining district is on the western end of the face and the three down hills coal pillars are on the eastern end, leaving 2.5~3.5m at the bottom of the face. The inclined length of the face is 186m, and the inclination of its first 77.8m is 25 ° as well as the inclination of its last 108.2m is 7 °.

## Layout of measuring points on the working face

The comprehensive pressure observation on 4401 face was carried out through laying out three key measuring areas to do "three volume" observation. I test area was on the 15, 16 frame, Ⅱ test area was on the 50, 51 frame and III test area was on the 85, 86 frame. At the same time the chart recorder observation was done on the 50 frame [1]. The layout schematic diagram of working surface area is shown in Fig.1.

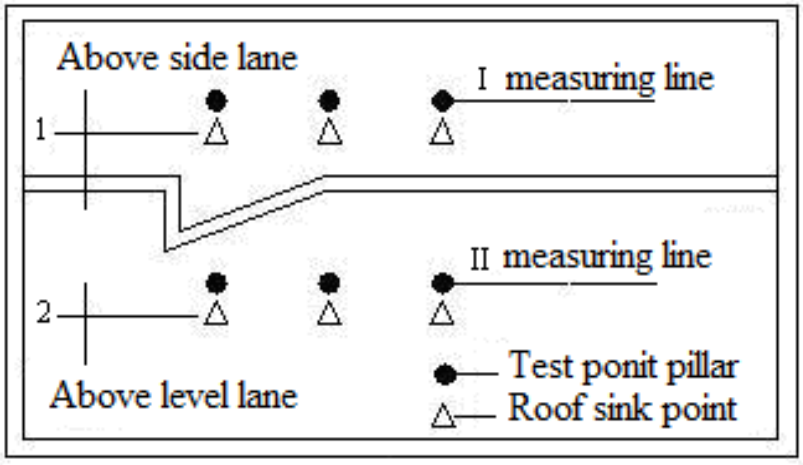


Fig.1 Layout of test areas on the working face

We used the roof dynamic method to observe the pressure distribution law of advanced support. Seven dynamics detectors were laid out in track, the space of which was five meters, as shown in Fig. 2.

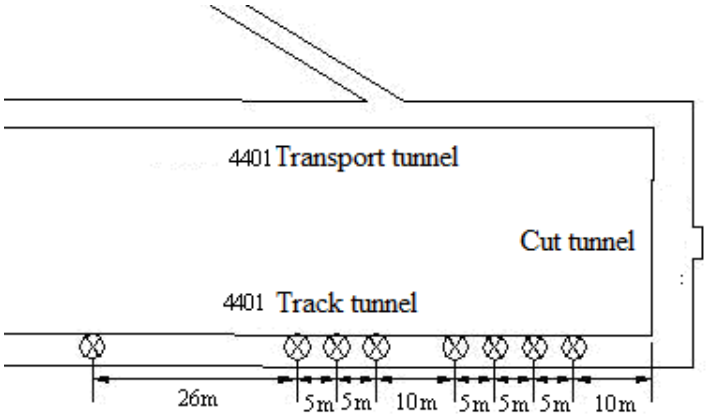


Fig.2 Layout of Roof dynamic detectors

**Initial and periodic pressure**

The push-production of 4401 face began on April 28, 2005. When the above push mining distance reached 20m, the direct roof of 4401 face felled without any water spray on the face and its gob-sides. During the period of direct roof initial collapse, the pressure increase of face frame was not apparent; however, the caving phenomenon of face side and local top coal appeared. But, when the above push mining distance reached 27m, meanwhile when the bellow push mining distance reached 35.5m to the western side of cut hole, the basic top initial pressure in working face began, as shown in Fig.3.

The number of coal cannons before initial pressure increased up to more than 10 times with a modest sense of vibration in the central. The working resistance of support increases were not obvious and some reduced, in which 70~74 frames spelled with the depth of 0.4m, 82~87 frames spelled with the depth of 0.8m, 63~64 frames spelled with the depth of 0.5m and 42～45 frames spelled with the depth of 0.3m.These data showed that the initial pressure was biggest at coal wall[2].

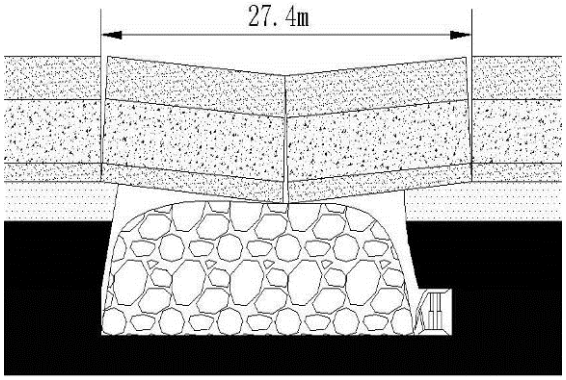


Fig.3 First pressure rock structure on working face

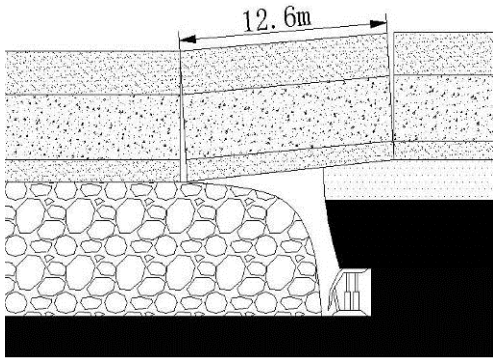


Fig.4 Periodic pressure rock structure on working face

It could be drawn from the comparison and statistics results of support resistance around the appearance of face periodic pressure that the pressure increased little when the face main roof periodic pressure came. The increase range of support resistance was around 4.9MPa on average and the safety valve did not opened, as shown in Fig.4.

**Laws of mining face pressure appearance**

The measured initial supporting force of bracket during the observation was 25.87MPa on average while the design support force was 31.5MPa, which was only 82.1% of rated initial support force. The initial supporting force of bracket during pressure was 26.12MPa on average, which was 82.9% of rated initial support force. The frequency distribution of initial supporting force is shown in Fig. 5.

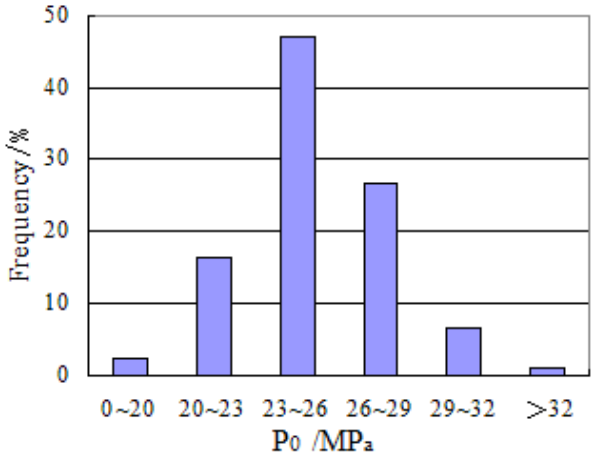


Fig.5 Frequency distribution histogram of initial supporting force ($P_0$)

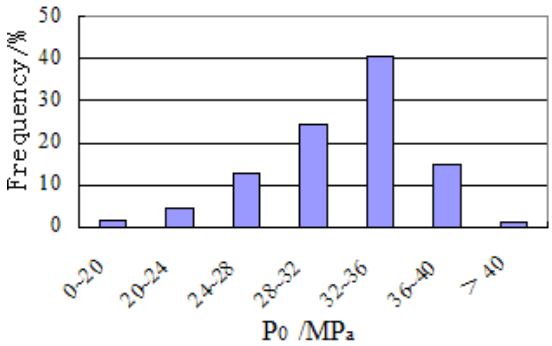


Fig.6 Frequency distribution histogram of working resistance ($P_0$)

Fig.5 shows that the initial supporting force between 23MPa and 26MPa accounted for 46.9%, while the same force between 23MPa and 29MPa accounted for 73.7%. And the conclusion can be drawn from the measured average initial support force and its distribution characteristics that the initial support force of bracket is relatively high so that it can meet the practical requirements.

The measured working resistance of bracket during the observation was 32.7MPa on average while the design working resistance was 38.0MPa, which was only 86.1% of rated working resistance. The working resistance of bracket during pressure was 35.92MPa on average, which was 94.5% of rated working resistance. The frequency distribution of working resistance is shown in Fig. 6.

Fig.6 shows that the working resistance between 24.0MPa and 36.0MPa accounted for 77.8%. The percent of working resistance above 32.0MPa is near 60% while the percent above 28.0MPa exceeds 80.0%.

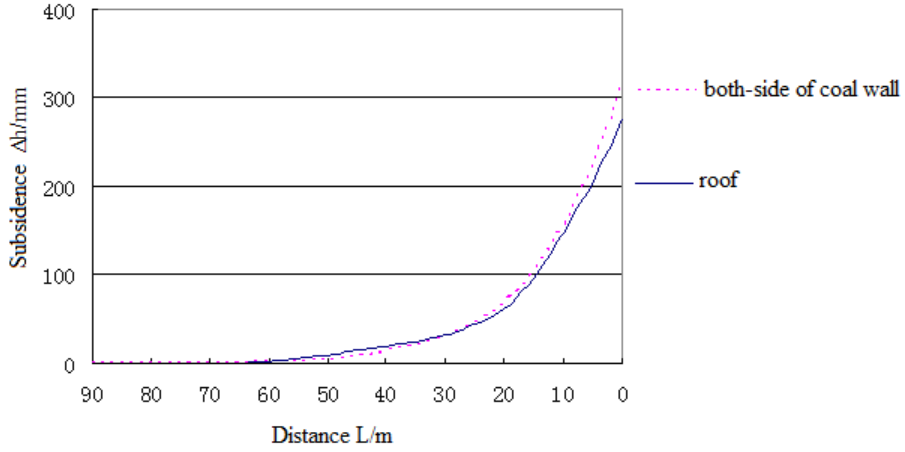


Fig.7 Curve of the relationship between displacement and distance on both-sides of tunnel

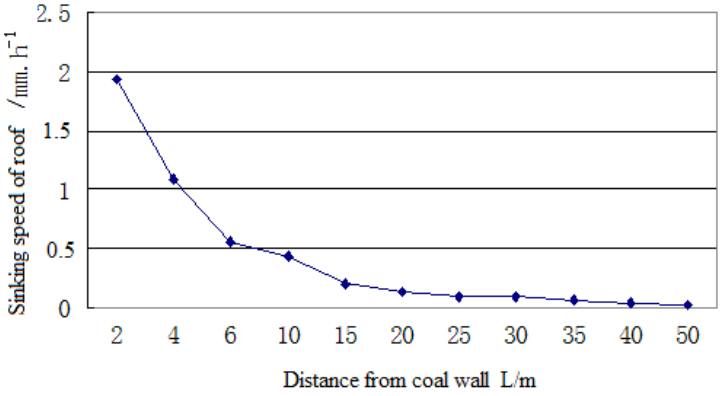


Fig.8 Curve of the relationship between velocity and distance on roof

**Pressure appearance laws of mining tunnel**

We can make the surface displacement curve of surrounding rock and the displacement velocity curve by sorting out the observation data, as shown in Fig.7 and Fig.8. Based on the roadway displacement curve, the mining influence on tunnel can be analyzed [3-4].

From the above analysis, it can be concluded that the pressure appearance of transportation tunnels is significant when the working face advance support distance is 50m; meanwhile the phenomenon of bottom drum and roof local fracture occurs at the advanced support pressure zone. But the moving speed of tunnel sides is faster than the roof subsidence during the coal mining influence stage. The coal body roof outburst distance is between 150mm and 200mm while the lower part distance is between 20mm and 60mm when the mining distance is at the range of 5m to 40m close to the working face export. And the bending deformation of anchor steel appears at the same time. Also from the observation results it can be seen that the design of tunnel support can basically meet the support requirements.

**Conclusions**

•The direct roof of 4401 fully mechanized caving face in Xiagou coal mine belongs to the second kind of roof, the initial caving step distance of which is 11.3m. The initial roof caving step distance of old roof is 27.4m and the periodic pressure step distance is 12.6m on average. So its roof stability is jugged as medium, that is II level and its pressure appearance is obvious.
•The geological mining condition of 4401 working face is stable and the step sink of coal roof will not happen.
•The field roof structure of fully mining is more conducive to the release of coal rock stress compared to layered mining structure and this method plays a mitigation role on moving pressure shock of coal rock.

**Acknowledgements**

This work was financially supported by Chinese National Natural Science Foundation (NO. 51364028) and Innovation Program of Inner Mongolia University of Science & Technology in China (2010NC050 and 2011NCL033).

**References**

[1]Yunliang Tan, Fangcheng Li, Hui Zhou, et al.: Chinese Journal of Rock Mechanics and Engineering, vol.19, No.4 (2000), pp.425-428, in Chinese.

[2]Liyou Pan, Lijun Zhang, Xiangui Liu: *Rock burst Prediction and Control Technology*, China University of Mining and Technology Press, Xuzhou, Jiangsu, (2006), in Chinese.

[3]Zhenqi Song: *The Utility of Mine Pressure and Control,* China University of Mining and Technology Press, Xuzhou, Jiangsu, (1998), in Chinese.

[4] Minggao Qian: *Ground pressure and its control,* China Coal Industry Publishing House, Beijing, (1984), in Chinese.

*Applied Mechanics and Materials Vols. 580-583 (2014) pp 1335-1341*
*© (2014) Trans Tech Publications, Switzerland*
*doi:10.4028/www.scientific.net/AMM.580-583.1335*

# Research on Geostatic Stress and Optimization of Bolt Support for Tilted Strata Roadway

Renliang Shan, Liang Tian, Wenfeng Zhao, Jinyang Lv, Yuhang Xiao, Longfei Wei, Xianyong Hao

School of Mechanics & Civil Engineering, China University of Ming & Technology, Beijing, 100083, China

cumtbtianl@126.com

**Keywords:** roadway; original rock stress; sight instrument; ultrasonic test; bolt support; numerical simulation

**Abstract.** In order to tunnel safely, efficiently and economically, we carried out the study on geostatic stress characters and optimizing bolting support parameters in 2# coalbed of Zijin Colliery. Based on the surveys of geological conditions, original rock stress, broken rock zone measurement and analysis of roadway deformation, characters and mechanism of roadway failure is figured out. According to existent problems, normal support theories were used and a variety of numerical computations were carried out by FLAC$^{3D}$.New support methods of bolt installed vertically in tilted roof and strengthen support of sidewalls and corners of roadway were figured out. Monitoring of convergence meters and roof separation were followed to know effects of new design timely. The research was carried out for 600 meters The monitoring results proved that the optimized support design was viable and the new bolting parameters were reasonable.

## Introduction

Due to the complicated geological conditions and existence of the tectonic stress, rock failure and stress distribution of the roadway[1,2], which is located in tilted strata, present asymmetry. Meanwhile for the existence of soft rocks, the range of broken rock zone is quite wide[3], and traditional symmetrical support is difficult to control rock formation effectively[4]. So many scholars have carried out extensive research on failure mechanism and its support measures[5].

Taking advantage of stress sensor[6] , ultrasonic test[7] and sight instrument[8], the maximum principal stress, thickness of broken rock zone and rock fissures situation of surrounding rock of 2# coalbed in Zijin mine can be got .The reasons of rock deformation and failure is analyzed. On this basis, according to the theory of strengthening sidewall support and corner support[9], the original support design and many optimized support designs are compared and analyzed by FLAC $^{3D}$[10]. In these ways, support problems of 3024 workface can be effectively solved.

## Geological conditions

Zijin Colliery is located in Huozhou city, Shanxi Province, 2# coalbed in Shanxi formation is mainly mined in 3204workface. The coal is mainly made up of semibright coal and durain comes second. The structure is layered and the dip angle of the coalbed is 8°~10°.The coalbed is medium strength ,f<1.5. The joint and stratification are medium developmental. The fracture is uneven and brittle. The striation is black. The thickness of coalbed is 2.04~2.06m. The roof is made up of black mudstone with a thickness of 0.2m, and sometimes becomes to grey sandy mudstone. The joint and stratification are both developmental. The floor is made up of sandy mudstone and the stratification is developmental. , Fig 1.shows rock formation of surrounding rock. The gas emission of 3204 workface is 2.63m$^3$/min. Mine inflow mainly comes from K8 fracture aquifer of sandstone. The estimated normal water inflow during driving is 6m$^3$/h and the maximum water inflow is 15m$^3$/h.

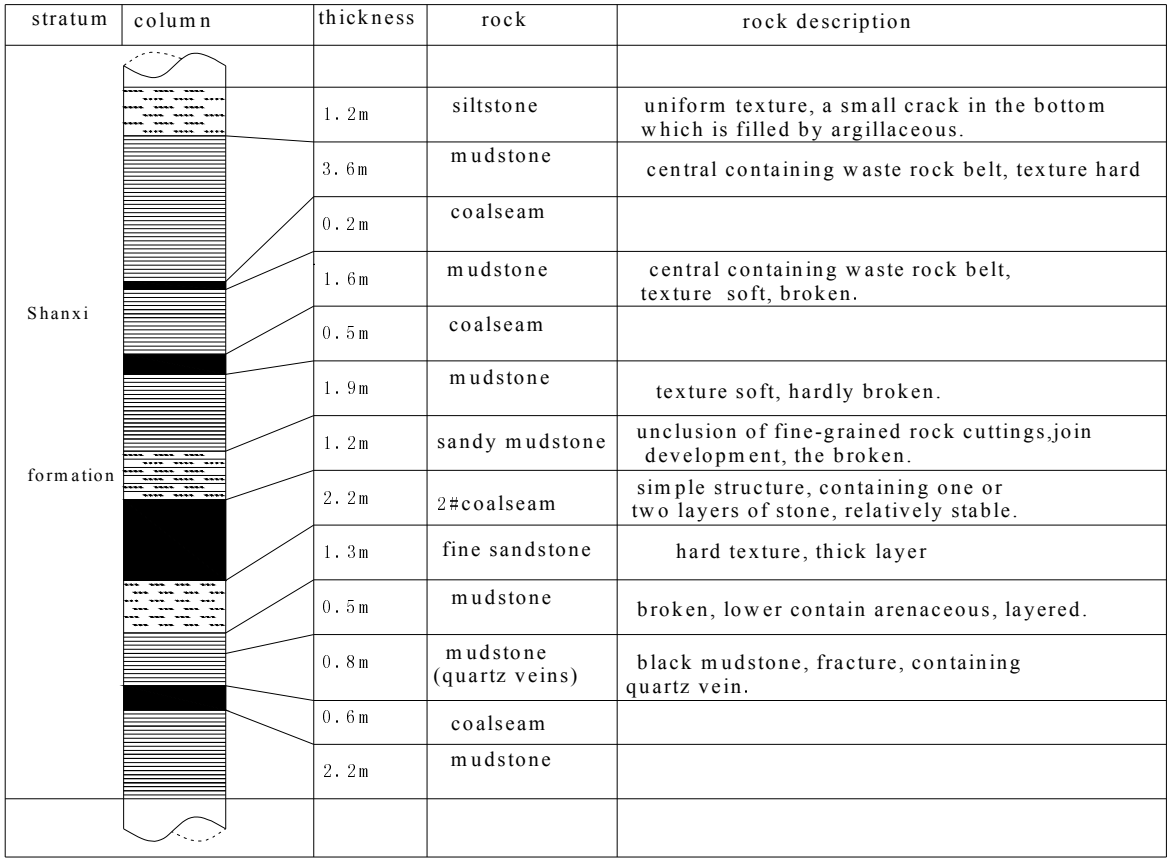


Fig 1 Rock formation of 2# coal bed

**Original rock stress**

Stress relief method was used in our test, the instrument is CSIRO HI stress sensor,which is made in Australia. There were two monitoring position, once is in right sidewall of 3201-1 roadway ,the other is in left sidewall of west airway. There were holes , the length of them were totally 76.6m.Tab 1 shows the parameters and test results.

Tab 1 Parameters of holes and results of original rock stress

| position | rock | azimuth angle [°] | dip angle [°] | length [m] | $\sigma_{hmax}$ [Mpa] | $\sigma_{hmin}$ [Mpa] | $\sigma_v$ [Mpa] | $\sigma_{hmax}/\sigma_v$ |
|---|---|---|---|---|---|---|---|---|
| 3201-1 | siltstone | 95 | 55 | 15.25 | 15.76 | 8.25 | 8.30 | 1.90 |
| | mudstone | 92 | 31 | 15.50 | 9.34 | 0.41 | 8.30 | 1.13 |
| | fine sandstone | 67 | 4 | 15.30 | 20.75 | 6.61 | 8.30 | 2.50 |
| west airway | siltstone | 355 | 45 | 15.45 | 16.00 | 6.87 | 8.05 | 1.99 |
| | mudstone | 355 | 14 | 15.10 | 11.70 | 1.15 | 7.96 | 1.47 |

We come to a conclusion that horizontal stress is major principle rock stress, its azimuth angle is 85º～101º.Horizontal principal stress is greater than vertical stress,it's 1.13 to 2.50 times the level of vertical stress, horizontal principal stress has big effect to north-south roadway, but small to east-west roadway.

**Broken rock zone measurement**

Sight instrument and ultrasonic test were used for broken rock zone measurement. The four pictures in Fig 2 show the result of sight instrument in roof rock. The hole is 2.5 m, probe location was counted by 2.5 minus the number on steel rule. We can see clearly that there is a fracture at 2m in Fig 2(a), its width is about 8mm. When it reached about 1.4 m, shown in Fig 2(b) and Fig 2(c), anther two

fractures appeared. Finally the probe reached nearly to 0.5m, the upper-left wall in the hole dropped out for rock stress. We come to a conclusion that zone of broken rock in roof is 2.0m deep.

(a)2.0m (b)1.45m (c)1.37m (d)0.5m

Fig 2 Roof hole of roadway

We carried out ultrasonic test in order to get more accurate range of broken rock zone. The principle of ultrasonic test is that the wave velocity is different in different kind of rocks. With the development of fractures, its velocity will lower. We chose three positions and there are 14 holes in all. The result shows that the thickness of broken rock is 1.4m~2.2m.

## Characters and mechanism of roadway formation and failure

**Characters.** A survey of roadway formation and failure was done in roadway of 1201 and 3201 workface, we found the failure characters as follows. Fig 11 shows the deformation and failure of roadway.

(1) Surrounding rock was unbroken early days. With the excavation of roadway, it became hardly broken because of the effect of weathering and water supply, bearing capacity of rock reduced badly.

(2) The deformation of right sidewall was larger than left. After a period of time, bulking force results in large deformation in surrounding rock, especially in the lower coal. The deformation of roof and sidewalls was extremely broken near fault

(3) Large deformation of support components occurred. The mesh changed into shape of pocket, most of metallic belts change into waves pattern, wall caving were severe and there's no belt in sidewall support.

(4) Size of roadway shape was definitely changed because of complicated strata and construction. The height of middle roadway enlarges from 2.8m to 3.3 m, while its width enlarges from 4.2m to 4.4m.The height of sidewalls also increase obviously.

**Mechanism.** (1)High horizontal tectonic stress has big effect to north-south roadway.

(2) The coal and its roof is too soft and fractures in rock are fully developed. The existence of fault aggravates bearing capacity of rock.

(3) Force analysis of pre-stressed anchor is shown in Fig 3,when anchor is perpendicular to roof, the effective component force $F_1$ is smaller than $F'$ , while the component force $F_2$ is harm to roof stability.

Fig 4 shows two kinds of shear stress in different sections, when anchor is perpendicular to roof, the section is circular *abcd*, while it is vertically set, the section is elliptical $a'b'c'd'$.With the effect of the same shear force Fs, the maximum of shear stress in circular section is Eq 1, while in elliptical, the value is Eq 2. The dip angle of gently inclined seam is $\theta$=8°~25°, $\tau'_{\max} = 0.99 \sim 0.91\tau_{\max}$ , so setting anchors vertically can enhance shear resistance.

$$\tau_{\max} = \frac{4F_S}{3\pi r^2} \tag{1}$$

$$\tau'_{\max} = \frac{4F_S}{3\pi r^2}\cos\theta \tag{2}$$

(4) The value of torque is 120 N·m , which is too low to blot support in broken roadway. Some pressure gages were lost or destroyed, it also led to low prestress.

(5) Rigidity of meshes are not enough.

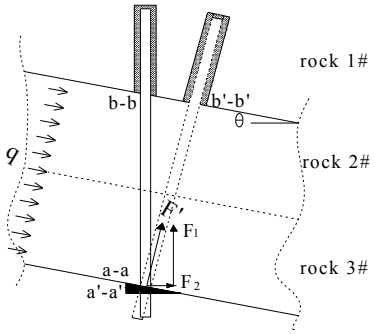


Fig 3 Force analysis of pre-stressed anchor in roof

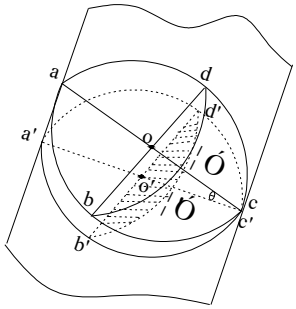


Fig 4 Sketch map of shear stress

**Numerical analysis by FLAC$^{3D}$**

The numerical model is shown in Fig 5. The length, height, width of the model is 30 m, its parameters are all based on field rock formation. Shape of roadway is excavated once, the length of numerical roadway is totally 14.4m with nine times to complete.

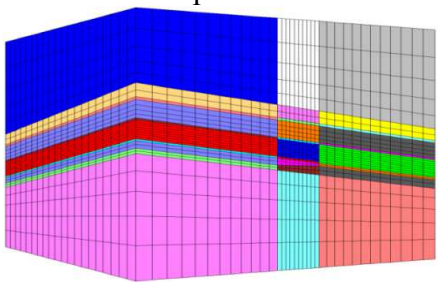

Fig 5 Numerical model of rock stratum

Fig 6 shows two mechanical models of different support designs. The optimized design change 6 anchors into 5 in roof, its new row space is 1000×800mm. We change position of cables and its row space to 1600 m, some of anchors in sidewalls are also changed.

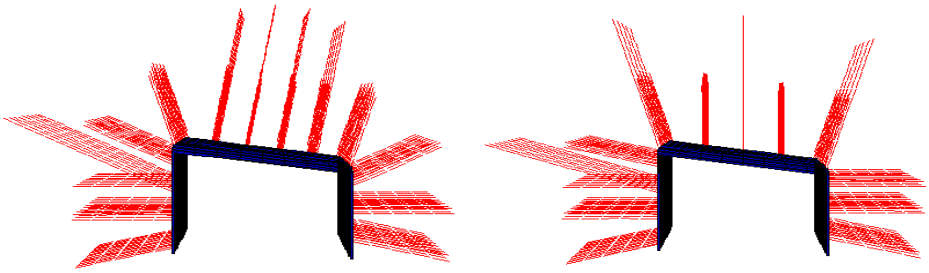

(a) (b)

Fig 6 Mechanical model of different support designs

Fig 7 shows plastic zone of different support designs. The yellow area means plastic zone of surrounding rock. Compared Fig 7(b) with Fig 7(a), we can find that yellow area in left sidewall become smaller, while larger in right wall. The yellow area also reduces in roof and floor.

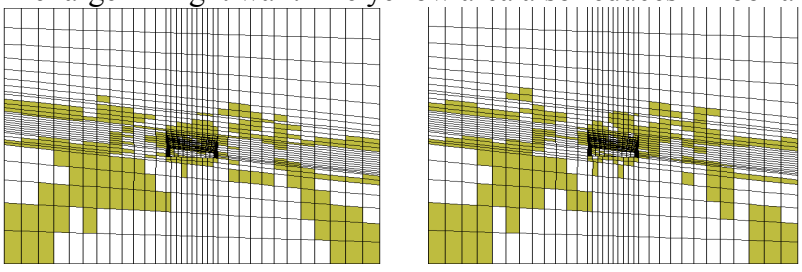

(a) (b)

Fig 7 Plastic zone of different support designs

Displacement of different support designs are shown in Fig 8, the number means z-displacement. The blue area is the maximum of z-displacement

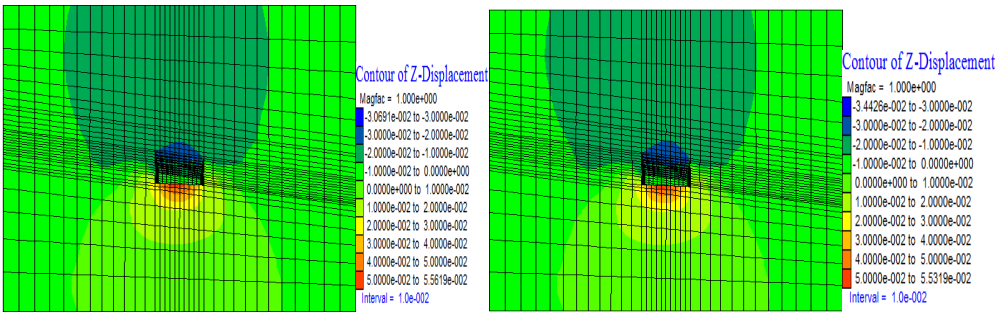


(a) (b)

Fig 8 Displacement diagram of different support designs

The displacement of surrounding rock is shown in Tab 2. In this table, the effect of two designs, including roof, sidewalls and floor is Compared with original design, the displacement of roof increase 0.95%, while displacement of sidewalls and floor decrease all. By increasing the yielding deformation of roof properly, the stress in sidewalls and floor can lower, it do good to stability of roadway.

Tab 2 Displacement of surrounding rock

| supporting design | | roof | left sidewall | right sidewall | floor |
|---|---|---|---|---|---|
| original design | displacement[mm] | 23.912 | 33.531 | 43.141 | 44.248 |
| optimized design | displacement[mm] | 24.138 | 33.326 | 42.181 | 43.998 |
| | variation[%] | 0.95↑ | 0.61↓ | 2.22↓ | 0.56↓ |

## Control technology of tilted strata roadway

**Optimized support design.** Based on theory of strengthening sidewall support and corner support and theory of anchors set vertical, we determine the final support design with technicists of Zijin colliery after ten designs were completed by FLAC$^{3D}$. Fig 9 shows the optimized settlement of anchors and cables.

(1) Anchors in roof should be set vertically. For roof support, the number of anchors decrease from 6 to 5. Its size is Ø20×2400 mm. Row space changed for 1000×800 mm, the dip angle of anchors in corner is 75°.The cables in roof are Ø 17.8×5400 mm and set vertically, its row space is 2000×800 mm. Fig 9(b) shows the location.

(2)Anchors in sidewalls and corner should be strengthened. Anchors used in sidewalls should be lengthened from 2.0 m to 2.4 m. Its row space is 850×800 mm There are four anchors of Ø20×2400mm in left sidewalls and three in the right side. The first row should be tilted upward 15°in left side. The fourth row anchors in both side are tilted 15°down. The cable is Ø 17.8×4500 mm combined with belt. it's dip angle is 20°.

(3) There is one K2355 resin and one CK 2355 resin for each anchor, and each cable is matched with one CK 2355 resin and two K2355 resin. Gridding of meshes is 150×150 mm. The thickness of tray is 12 mm.

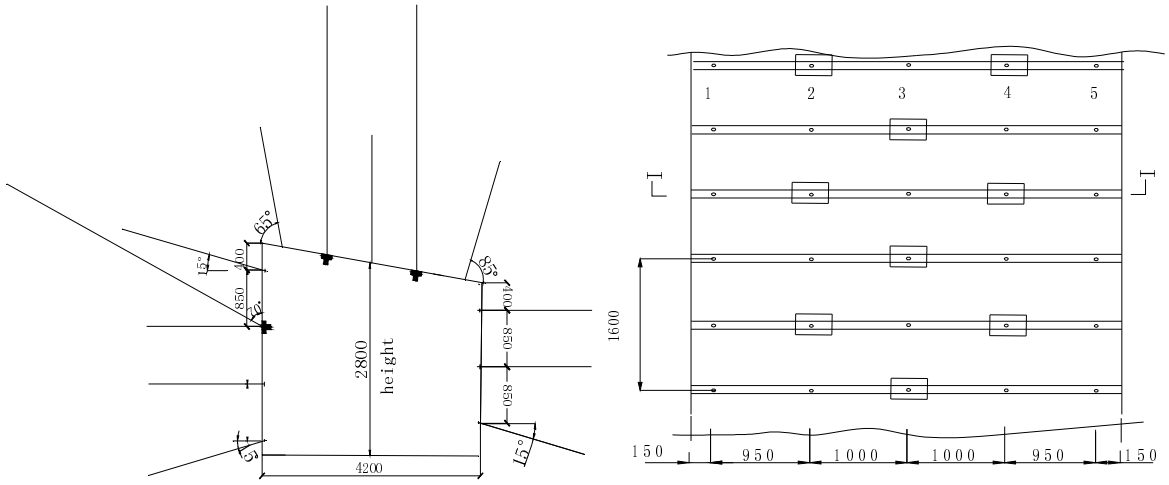


(a) (b)

Fig 9 Optimized support design

**Support effect.** In order to monitor the surface displacement and roof separation of surrounding rock, we chose four sections as shown in Fig 10. Original support design was used for section 2, optimized design was used for section1, 3 and 4. Monitoring work began from Apr 16, 2010 to May 28.It lasted for 43 days, the optimized design was applied to support for 600m.

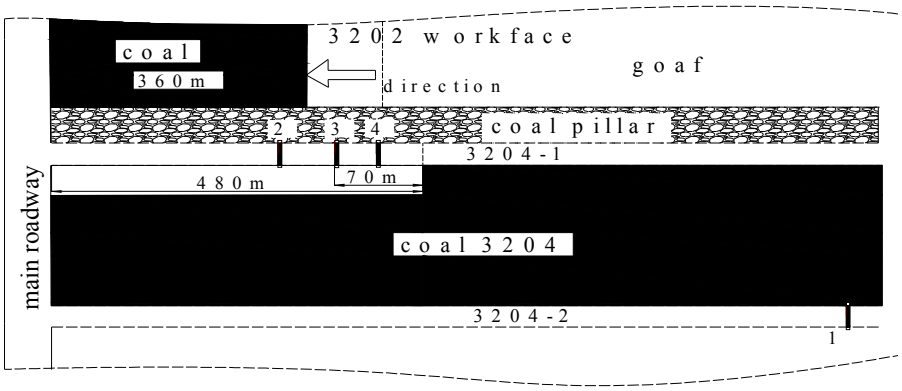


Fig 10 Sketch map of monitoring sections and excavation in 3204 workface

Fig 12 is the optimized support effect of roadway on May.28, 2010.Compared with Fig 11, we can see that deformation and failure of roadway is well controlled. According to monitoring results, the maximum of roof separation is 181mm at section 2, the average separation is 69 mm, it's very close to numerical result. And the average convergence of sidewall is 83mm, and average convergence between roof and floor is 87 mm. All the values are less than original design effect.

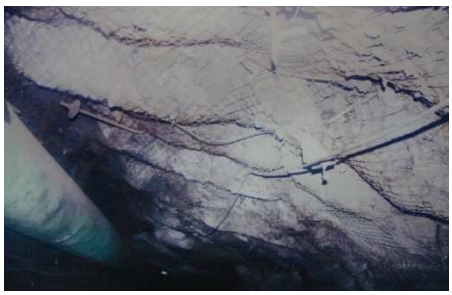

Fig 11 Failure of surrounding rock

Fig 12 Support effect of optimized support

## Conclusions

(1)Horizontal stress is major principle rock stress, its azimuth angle is 85º～101º. It's 1.13 to 2.50 times the level of vertical stress. Horizontal principal stress has big effect to north-south roadway, but small to east-west roadway.

(2)The broken rock zone of roof and two sidewalls in 2# coal seam are both greater than 1.5m, the stability of the roadway is so bad that it's really difficult to control deformation.

(3)Settling anchor and cable vertically can make the prestress of anchor (cable) get more effective, meanwhile horizontal component force with side effect can be reduced.

(4)By these measures, such as lengthening anchor and cable of sidewall, increasing its diameter or intensity, can improve the strength and rigidity of sidewall in coal roadway to restrain roof deformation.

**References**

[1] Xiaoming Sun, Guofeng Zhang and Feng Cai: Chinese Journal of Rock Mechanics and Engineering, Vol.28 (2009), p. 1137~1143(In Chinese)

[2] Hai Wu, Nong Zhang and Weijun Wang: Journal of Hunan University of Science and Technology (Natural Science Edition). Vol. 28(2013), p. 6-12. (In Chinese)

[3] Mingjian Zhang, Jinhai Gao and Shiyi Wei: Chinese Journal of Rock Mechanics and Engineering. Vol. 29(2010), p. 3259~3254. (In Chinese)

[4] Hongwei Wang, Jianhua Zhang and Youfu Zeng: Coal Engineering, Vol (2012), p. 72~75. (In Chinese)

[5] Hongwei Wang, Yongping Wu: Shanxi Coal. Vol. (2012), p. 1~4. (In Chinese)

[6] Jianxin Liu, Zhongming Zhao and Yishun Zhang: Coal Engineering. Vol (2003),p. 33~34. (In Chinese)

[7] Renliang Shan, Xiangsong Kong and Zhenting Wei: Chinese Journal of Rock Mechanics and Engineering. Vol. 32 (2013), p. 1304~1314. (In Chinese)

[8] Renliang Shan, Xiangsong Kong, Liang Tian: Method of strong support for sidewall and corner of coal roadway: China, ZL 201010243094.7[P]. 2010–12–15. (In Chinese)

[9] Jijun. Zhou, Renliang. Shan, Hui. Wang and Kai. Yin: Ming Research and Development. Vol. 3(2010), p. 30-33. (In Chinese).

[10] L. R. Alejano, A. Rodriguez-Dono and E. Alonso: Tunneling and Underground Space Technology. Vol. 24(2009), p. 689-705.

*Applied Mechanics and Materials Vols. 580-583 (2014) pp 1342-1346*
*© (2014) Trans Tech Publications, Switzerland*
*doi:10.4028/www.scientific.net/AMM.580-583.1342*

# Construction Monitoring Technology Analysis for Railway Tunnel

Jinfang Hou [1, a], Ju Chen [2,b], Rongli Wang[3,c]

[1] CCCC Tianjin Port Engineering Institute, Ltd., Key Laboratory of Port Geotechnical Engineering, Ministry of Communications, PRC, Key Laboratory of Geotechnical Engineering of Tianjin, Dagu South Road No.1002, Tianjin, China

[2] CCCC Tianjin Port Engineering Institute, Ltd., Key Laboratory of Port Geotechnical Engineering, Ministry of Communications, PRC, Key Laboratory of Geotechnical Engineering of Tianjin, Dagu South Road No.1002, Tianjin, China

[2] CCCC Tianjin Port Engineering Institute, Ltd., Key Laboratory of Port Geotechnical Engineering, Ministry of Communications, PRC, Key Laboratory of Geotechnical Engineering of Tianjin, Dagu South Road No.1002, Tianjin, China

[a] jinfanghou@163.com, [b] chenju@tepi.com.cn, [c] wangrongli@tepi.com.cn

**Keywords:** Crown Settlement; Clearance Convergence; Ground Settlement; Wall Rock; Tunnel

**Abstract.** Based on the railway tunnel engineering, the research on comprehensive technological for the monitoring of tunnel construction is performed. It is shown that the deformation of wall rock would mainly suffer the comprehensive influence of multiple factors like type of the wall rock, construction method and supporting measures, size of the excavated section, etc. through the monitoring of the crown settlement, clearance convergence and ground settlement. The wall rock will be stable within 20d and 40d after the tunnel excavation. And the secondary tunnel lining could be constructed. Numerical simulation method was also adopted to analyze the deformation and stress of the wall rock. It is presented that the construction interval shall not be too long for the stability of wall rock. Therefore, the numerical analysis method and site monitoring method could be used together to achieve more comprehensive and reliable monitoring of tunnel construction.

## Introduction

In recent years, the railway tunnel engineering is gradual developed and the tunnel construction technology is increasingly improvement. New Austrian Tunneling Method has been widely recognized as the most advanced method in the current tunnel construction. However, the technical level of new Austrian Tunneling Method application is still not matured in the design and construction of the mountain tunnel in our country[1], and the site monitoring and measurement especially needs further improvement. Dynamic design and construction based on the site monitoring and measurement have become the development direction for the design and construction of current tunnel engineering[2]. With the basis of one railway tunnel, the clearance convergence and crown settlement of tunnel were measured in this paper. And then the wall rock was evaluated, the influencing factors was analyzed. Last, the effective monitoring technology for railway tunnel construction was also researched.

## Project Overview

The geologicl structure of the tunnel region is relative complicate, and the levels wall rock mainly include level III, level IV, level V and etc. The underground water is also relative sufficient. The construction methods were full face tunnel construction method and benching tunneling method. The monitoring and measurement items mainly included: observation within and outside of cave, clearance change, crown settlement of tunnel and ground settlement. All items were all placed on single test section and the single test section was arranged in lengthwise along the tunnel. The density of observation points at the central line of the tunnel was increased appropriately. Fig 1 is the picture of measurement lines and the measurement points placing the end of line. One test section of the full

face tunnel construction method would have two lines with three points. The benching tunneling method would have three lines and five points.

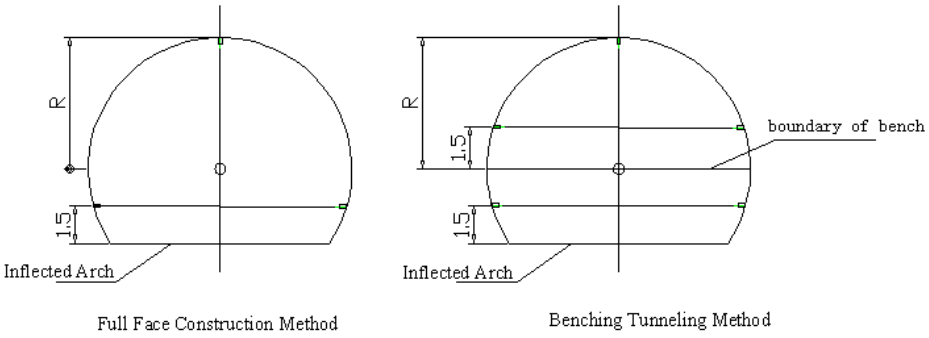


**Fig.1 Arrangement Diagram for the Measurement Lines and Points**

The initial reading data were completed within 24 hours after the excavation and before the excavation of the next cycle. The ending time for the monitoring was the following. After the wall rock stability, the measure frequency was one time per three days for two weeks. The measurement work could be completed if no obvious deformation had been detected. The measurement should be continued if any obvious deformation had been detected. The measurement could only be finished when no obvious deformation had been detected.

## Monitoring Results and Analysis

**Crown Settlement.** Fig.2 is the classic crown settlement curve, which is often shown on the exit and entrance of tunnel, class III wall rock, benching tunneling method. It is also named as 'perfect and smooth deformation curve'. The curve was relative smooth. After the excavation, the crown settlement was relatively even, the settlement speed was gradually decreased, and the curve of crown settlement was demonstrated in a logarithm function curve. The settlement speed of the crown is maintained at the level of 0.07mm/d at 16 days and the crown settlement was maintained at 24mm. It was shown that the wall rock was basically stable.

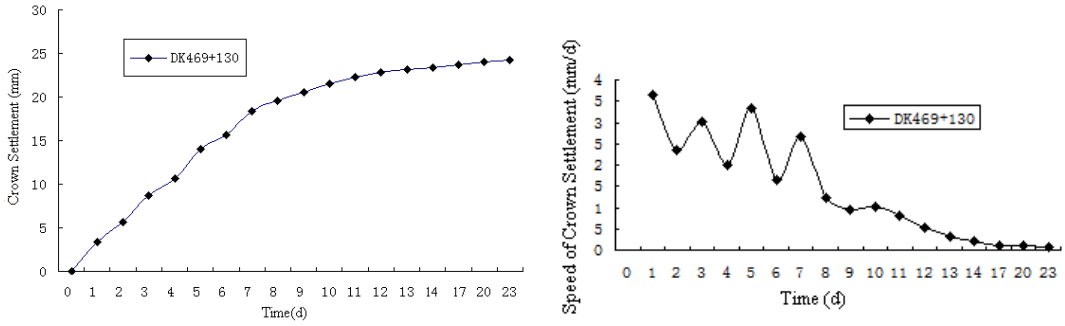


(a) Crown Settlement (b) Crown Settlement Speed

**Fig.2 Perfect and Smooth Deformation Curve**

At the exit of the tunnel of class IV wall rock, full face tunnel construction metho,the crown settlement curve demonstrated in the similar shape of 'step' as being shown in Fig.3. This type of curve could be generally divided into four stages: 1) High-speed increasing stage: the time of duration was 4d and the average rate of variation was between 2.5mm/d and 3.0mm/d; 2) Slow increasing stage: the time of duration was 6d, and the average rate of variation was between 0.2mm and 0.8mm/d; 3) Second high-speed increasing stage: the time of duration was 2d, the settling velocity increased quickly and the crown settlement speed was 3mm/d; 4) Gradual stable stage: the time of duration was 17d, and the average rate of variation was 0.1mm/d. The second high-speed increasing stage was occurred because of the influence of the excavation of steps. It is necessary to increase the monitoring and the observation within the cave.

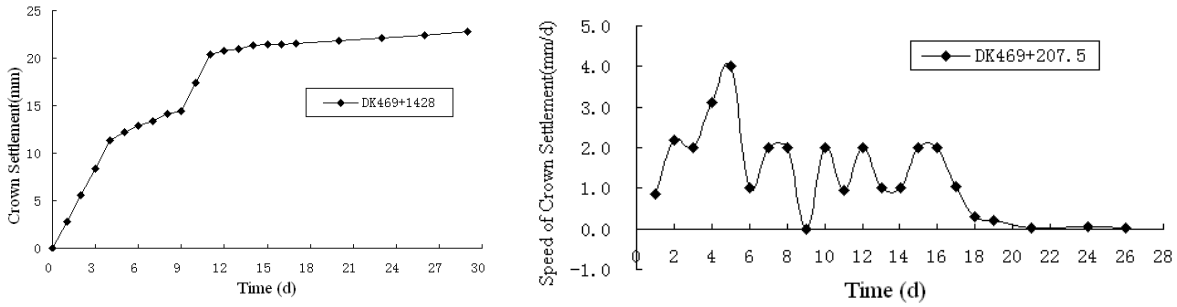


(a) Crown Settlement (b) Crown Settlement Speed

**Fig.3 Deformation Curve Similar to the Shape of Step**

The curve showing in Fig.4 would generally demonstrated in shallow-buried section. The deformation of the crown at the early stage was relative quick. The wall rock was basically stable at the time of 18d. For such curve, it is necessary to strengthen the monitoring and measurement, especially strengthening the monitoring density and observation within cave when the settlement speed was high.

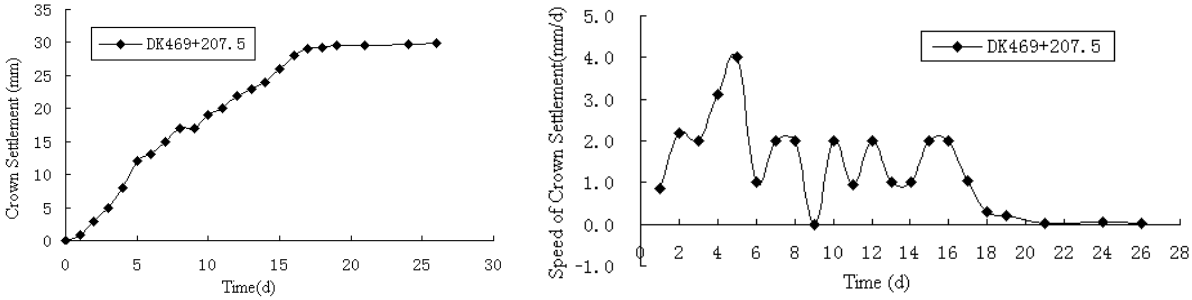


(a) Crown Settlement (b) Crown Settlement Speed

**Fig.4 Deformation Curve in Shallow-buried Section**

**Clearance Convergence.** The classic Clearance Convergence curve is shown on Fig.5. Fig.5(a) is the most common curve with small excavation. The clearance convergence was maintained at 2.6mm after 10 days. Fig.5(b) is shown in some measurement section with big excavation. Due to the influence of the surrounding construction, the convergence speed at the time of 16d was very high. However, the wall rock was not damaged. The wall rock is basically stable at the time of 40d. It should be strengthened the monitoring for the test section with the curve like Fig. 5(d).

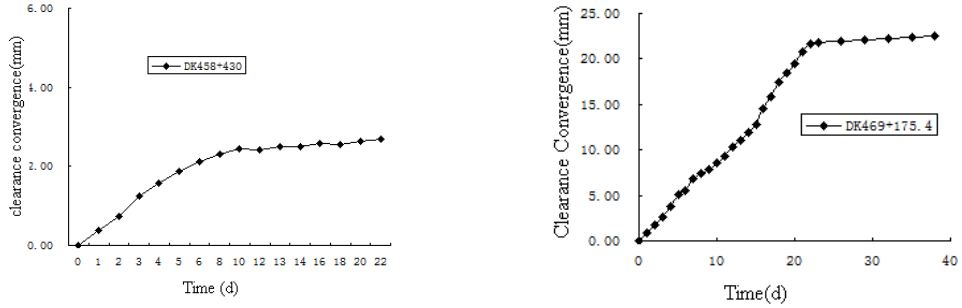


(a) Smooth Type (b) Other Type

**Fig.5 Clearance Convergence Curve**

**Ground Settlement.** Eight observation points of ground settlement were placed at each section. Fig.6 was the settlement curve. 1# observation point was located at the center and 4# observation point was located far away from the center. The ground settlement of 1# observation point was greater than that of 4# observation point. They were respectively 4.9mm and 2.7mm. However, the trends of two cuvers were basically same. Both of them had demonstrated slow settlement at the beginning, and the settlement was stopped at the time of 13d.

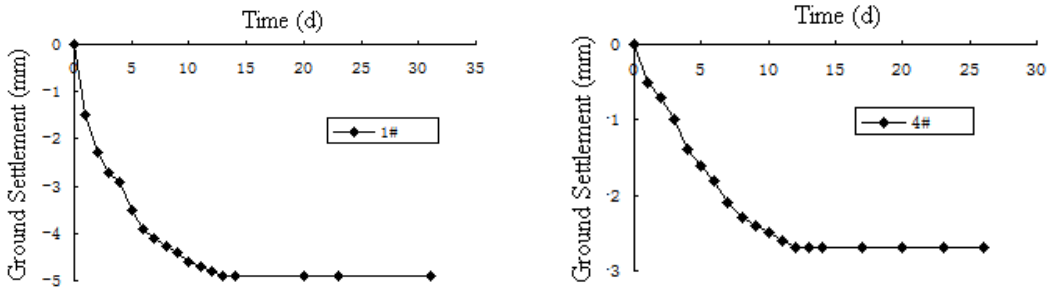


**Fig.6 Ground Settlement Curve**

Above all, the main influencing factors to wall rock deformation included: (1)Wall rock type: along with the decrease of the types of wall rock, the deformation of rock wall would increase and the stable time would also become longer; (2) Construction method and supporting measures: the excavation method and supporting measures of the tunnel construction would directly influence the release of the stress of wall rock; (3) size of the excavation section: the deformation displacement of small excavation section was relative small. Therefore, it is necessary to comprehensively consider the influencing factors of various aspects to effectively guide the tunnel construction.

## Deformation Calculation Analysis of Wall Rock

**Calculation Section.** A classic section locating at class IV wall rock area was as the typical calculation section. And the construction method was benching tunneling method. FE analysis software PLAXIS3D was adopted with M-C constitutive model. According to the construction procedure, the construction could be simplified into three work conditions. They were excavation and supporting of upper steps; excavation and preliminary supporting of sinus and side wall; the excavation and preliminary supporting of inflected arch. The height of tunnel model was 12.9m, the maximum span was about 14.7m, the length was 103m and the burial depth was 100m. The upper border was free border, the left and right border demonstrated lateral displacement, and both the vertical and lateral displacement on the lower border were restricted. The elements were solid[3,4].

**Material Parameters.** The parameters of the materials selected are shown in Table 1.

**Table 1 Material Parameters**

| Material | Unit Weight | Cohesive force | Friction angle | Expansion angle | Elasticity modulus | Poisson's ratio | Burial Depth or Thickness |
|---|---|---|---|---|---|---|---|
| | $\gamma$ (kN/m$^3$) | c (kPa) | $\varphi$(°) | $\psi$ | E (GPa) | $\nu$ | $H$ (m) |
| Wall Rock | 27 | 10 | 50 | 0 | 80 | 0.25 | 100 |
| Preliminary Supporting | 26 | - | - | - | 40 | 0.2 | 0.27 |

**Calculation Results.** The results showed the excavation and supporting of tunnel changed the stress distribution of the wall rock, and stress concentration appeared at the connection area between the preliminary supporting and wall rock. Therefore, the time interval between the construction of the upper steps and lower steps shall be not too long. Otherwise, the stress concentration would result in the instability of the wall rock.

Fig.7 is the comparison of the calculation results and the actual measured data.

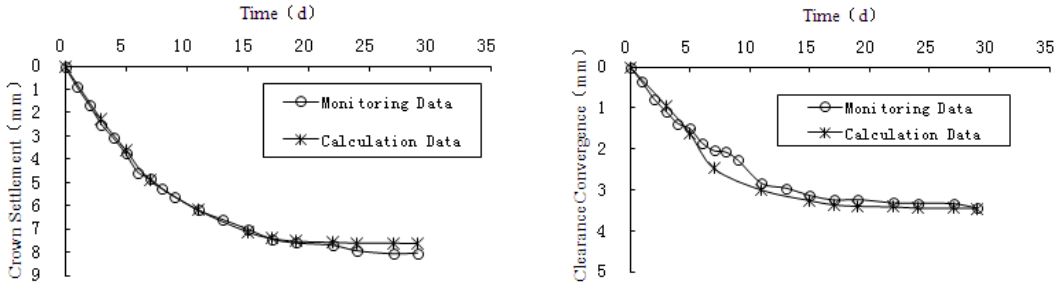


(a) Crown Settlement (b) Clearance Convergence of Upper Step

**Fig.7 Comparison between Actual Measured Data and Calculation Results**

It could be seen from Fig.7 that the trends of the calculation results and the actual measure data are basically similar. The crown settlement calculation result was stabilized at 20d after the construction. The actual measured data was slightly larger than the calculation, which was stabilized at 28d after the construction. It was because that the errors were resulted from the differences between the complicate construction environment and the ideal status of numerical analysis. The clearance convergence calculation value of upper step was slightly higher than the actual measured value, and the wall rock was stable after 25d. Therefore, numerical analysis method could be used to perform forecast for the wall rock in the construction process, and evaluate the safety of wall rock with the site construction monitoring.

## Conclusion

(1) The wall rock deformation of the tunnel was mainly suffered the comprehensive influence of many factors like wall rock type, construction method, supporting measures, size of the excavation section, and etc.(2) At the time between 20d and 40d after the excavation of the tunnel, the surrounding convergence, crown settlement and the ground settlement met the requirements, which could support the construction of second lining. (3) After the excavation and supporting construction of the wall rock of upper steps, the stress concentration was appeared at the joint area of steps. Therefore, the interval between the construction of upper step and lower step should not be too long. (4)The numerical analysis method and site monitoring method could be used together to establish a much more comprehensive monitoring technology for tunnel construction.

## References

[1] Wu Mengjun, Chen Zhanggui, Xu Xibin, etal. The Present and Prospect of Highway Tunnel Surrounding Rock Stability[J]. Journal of Chongqing Jiaotong Institute, 2003,22(2):23-28.(In Chinese)

[2]GuoQiliang,Wu Faquan,Qian Weiping, Zhang Yanshan. Study on Relationship between Deformation of Surrounding Rock and in-situ Stress in Wushaoling Deep-burried Railway Tunnel[J]. Chinese Journal of Rock Mechanics and Engineering, 2006, 25(11):2194-2199. (In Chinese)

[3] Kumar P. Infinite Elements for Numerical Analysis of Underground Excavations [J]. Tunneling and Underground Technology 2000, 15(1):117-124.

[4] Liu Yunfang, Zhong Zuowu,Wang Jie. Interpretation of Three-dimensional Geostress Results Measured by Hydraulic Fracturing Technique[J]. Chinese Journal of Rock Mechanics and Engineering, 2002, 21(6):833-838. (In Chinese)

*Applied Mechanics and Materials Vols. 580-583 (2014) pp 1347-1351*
*© (2014) Trans Tech Publications, Switzerland*
*doi:10.4028/www.scientific.net/AMM.580-583.1347*

# Application of Grouting Reinforcement Technology in Pingshan Shaft Station

Liang Tian[1,a], Jing Yi Xi[1], Jian Liu[1],Xiao Dong Liu[1], Feng Shang[2,b], Xun Dong[3,c]

[1]School of Mechanics & Civil Engineering, China University of Ming & Technology, Beijing 100083, China;

[2] Poly Energies Holding Co., LTD: Beijing 100010, China;

[3]POSCO E&C China Co., LTD: Beijing 100102, China

[a]cumtbtianl@126.com, [b]346687885@qq.com,[c]58730180@qq.com

**Keywords:** shaft station; soft rock; sight instrument; grouting; cable anchor support

**Abstract:** Support of soft rock is a big challenge in all mines at home and abroad. Soft rock is of different kinds of rheological property for geological conditions, mine ground pressure and so on. It brings about really difficult problem to roadway support. In order to ensure safety application and prolong usage, shaft station need to be reinforced. Sight instrument was used to analyze broken conditions. The results show that the broken depth in roof rock is 5~6 m, and greater than 4 m in sidewalls. According to failure characters and sight results, we determine that rock of shaft station belongs to high geo-stress and jointed soft rock. On this basis, technology of grouting reinforcement combined with cable anchor support is carried out. Monitoring results of surface convergence and cable force show that bearing capacity of surrounding rock increases obviously, roadway contraction and floor heave are well controlled.

## Introduction

Pingshan Colliery is located in Qinshui County, Shanxi Province. Most existing roadways in 3# coalbed were broken. Flash coat fractured[1], lining broke for being extruded[2], partial floor fractured, contraction of roadway section was large[3]. All those deformation characters belonged to high stress soft rock [4], it easily expanded for rock dilatation[5], it was of strong rheological property[6]. In order to solve those problems and keep prosperous production, this paper introduces grouting reinforcement technology in Pingshan shaft station and nearby chamber.

## Characters and mechanism of roadway failure

**Geological conditions.** 3# coalbed is mainly mined, burial depth is about 460 m, the thickness of coalbed is 3.70~6.30 m, the average thickness is 5.22 m, the average dip angle is 10°. False roof is sandy mudstone, joint and fracture is fully developed, it easily weathering to sheet structure. Main roof is siltstone, it's about 5.25 m thick. Upper roof is fine sandstone it is 9.55 m thick and stable, protodyaknove's number is 4~6. The floor is mainly made up with mudstone and sandy mudstone, its thickness is 3.55 m, fracture is fully developed with bad integrality. Fissure water in sandstone is the main runoff in roof of 3# coalbed, normal water inflow is 25.21 $m^3$/h, and the maximum is 38.75 $m^3$/h.

**Sight instrument.** In order to test the range of broken zone and internal deformation of surrounding rock, four stations were chosen in shaft station roadway. Take pictures of station 3 for example to explain our test, as is shown in Fig 1 and Fig 2.

Station 1 was located at loopway. Fractures were well developed within 5.5 m in roof, the rock was extremely broken in 2.7 m~5.5 m, roof separation was obvious at 4.8 m, and the rock was of good integrality outside 5.9 m. Broken rock in sidewalls mainly concentrated upon 1.5 m, the rock beyond 1.5 m was of good integrality.

Station 2 was located at heavy lane near auxiliary shaft. The result showed that surrounding rock in this roadway was severely damaged, the broken depth of roof reached to 6.2 m, multiple crushed zone appeared in that range, and fractures were fully developed.

Fig 1 shows roof hole and Fig 2 shows sidewall hole. Station 3 was located at light lane. Roof rock was damaged severely within 4.7 m, fractures were fully developed, especially in 2.2 m~2.8 m, roof separation was obvious. The broken length of sidewall was at least 4 m, because drilling was stopped at 3.95 m. Continuous crushed zone appeared in 1~2.4 m, fractures were well developed in 2.5~3.2, coal was badly broken in 3.4~3.9 m, and there was also shuttered zones.

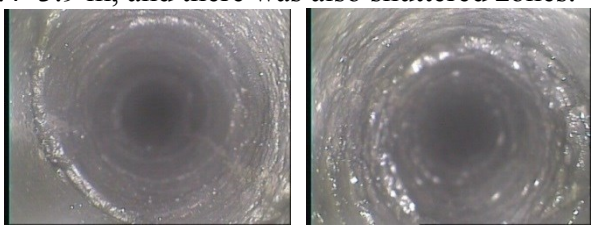

(a) 0.8 m (b) 4.3 m

Fig 1 Roof hole of station 3

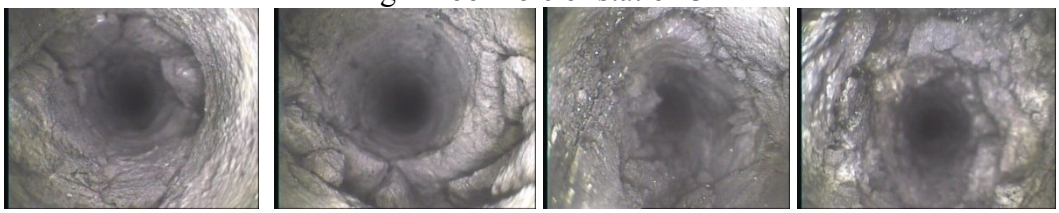

(a) 0.9 m (b) 1.0 m (c) 3.4 m (d) 3.9 m

Fig 2 Sidewall hole of station 3

Station 4 was located at heavy lane. The result showed that joint and fractures were fully developed within 5 m, especially that consecutive crushed zone appeared in coal, hole collapse occurred at 4.9 m.

By analysis results of four stations, we came to a conclusion that the broken depth is 5~6 m in roof of shaft station, multiple large fractures exist within that range. The broken depth in sidewalls can even reach to 4 m, crushed zone in coal is consecutive.

Through representation of roadway failure, geologic structure and lithology, we can figure out that surrounding rock of 3# coalbed belongs to high geo-stress and jointed soft rock, it is composite type. This type of soft rock expands easily for dilatation, and is of strong rheological behavior. Main deformation and failure phenomenon of roadway is broken rock, large contraction and floor heave.

## Reinforce measurements

Mechanism of grouting reinforce is by filling fractures in rock to improve bearing capacity of surrounding rock itself, then the stability of roadway can increase. The process of reinforce is grouting, shaping roadway, support and shotcrete, the order is grouting floor first ,then the sidewalls and roof grouting at last. Take roadway reinforcement in loopway for example, we explain the process of reinforcement construction.

**Reinforce materials.** Cement-based inorganic grouting material was mainly used for reinforce, and high strength polyester would be used in special position. 525# ordinary portland cement mixed with XPM additive was used to compound cement paste. Cement- sodium silicate grout would be used if large-scale mud leakage happened. XPM additive was 8%~10% of cement weight, water cement ratio of cement paste was 0.8:1~1:1.

Keep cement ratio when double grout was used, concentration of sodium silicate was 48~55Be, modulus was 2.8~.2, bulk factor of cement paste and sodium silicate was 1:0.4~1:0.6.

**Grouting parameters of vault and sidewalls.** Both roof grouting holes and sidewall holes are in rows, the row space in loopway is 1600 mm, 1335 mm in waiting chamber, 1300 mm in light lanes and 2400 mm for all the others. Fig 3 shows the sketch map of grouting holes in loopway, diameter of

each hole was Ø36 mm, length of each hole was 8000 mm. Angle of the lowest holes tilted 5° downward, and all the other holes were perpendicular to roadway surface, pre-embedded pipe was used for later grouting, grouting pipes were all 7000 mm long, it grouted all length once, grouting pressure was 4~6 MPa.

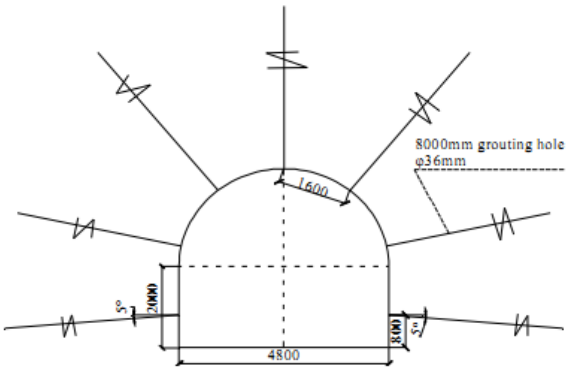


Fig 3 Sketch map of grouting holes

Grouting pressure must be guaranteed during construction, take appropriate measures when leakage occurred, such as, leaking stoppage and regrouting. New grouting holes should be constructed if leakage was severe.

**Grouting parameters of floor.** Grouting holes in floor were in rows, the average row space was 2000mm. Fig 4 shows the sketch map of floor holes. Length of floor holes was 4m, it diameter was 56mm, 3.5 meters long grouting pipes were pre-embedded after drilling construction, at the same time, all puissant cables, 4.3 meters long and diameter 22 mm ,were pre-embedded too, it grouted all length once, grouting pressure was 3 MPa.

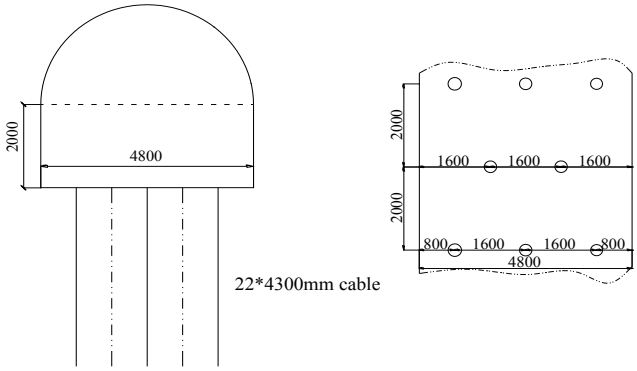


Fig 4 Sketch map of grouting holes and cables in floor

## Support design

Fig 5 shows the sketch map support parameters of cables and anchors in loopway.

**Anchor parameters.** Specification of anchors was Ø22×2400 mm, they were made by high strength deformed steel bar. Two low viscosity resins were used for each anchor, it was K2335 type and Z2360 type, diameter of bolt holes was 28 mm, column space was 800 mm, and row space 1000 mm. All anchors were rectangular and perpendicular to roadway surface, and pre moment of force was 400N·m. Specification of high strength trays was 150×150×10 mm. Steel meshes were welded by Ø6.5 mm steel, grid size was 100×100 mm, specification of meshes was 2.9 m×1.1 m, and steel beams were welded by Ø14 mm steel.

**Cable parameters.** Cables position was rectangular, row space was 2000 mm and column space 1600 mm. They were set between anchor rows, one K2335 resin and two Z2360 resins were used for each cable. Specification of roof cables, made of 1×19 steel strand, was Ø22×8300 mm, they were perpendicular to roadway surface and their preload was greater than 250 kN. Specification of sidewall cables was Ø17.8×5800 mm, they were also perpendicular to roadway surface and their preload was greater than 150 kN.

**Shotcrete.** Strength grade of shotcrete was C20, the thickness of roof and sidewalls concrete was 150 mm. Strength grade of floor concrete was C10.

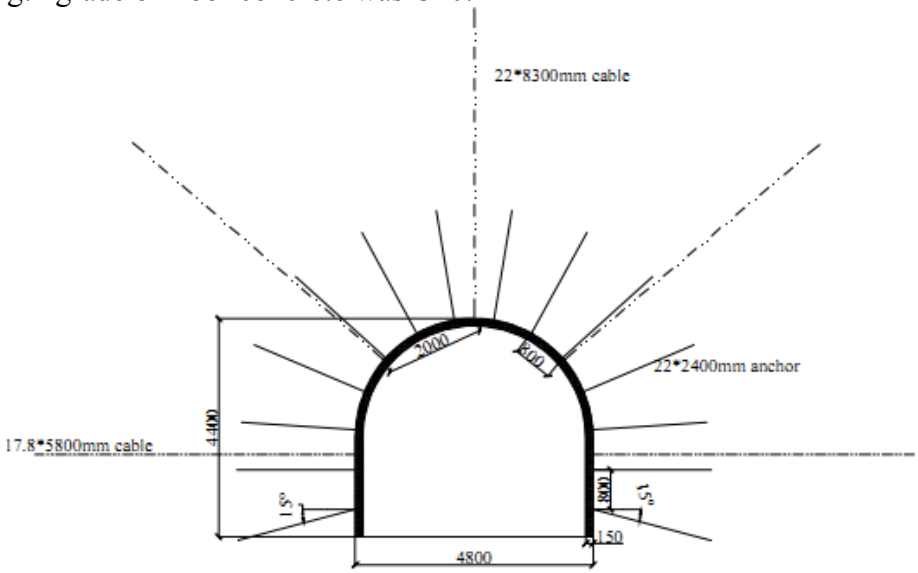


Fig 5 Sketch map of support in loopway

**Floor support parameters.** Sketch map of floor support is shown in Fig 4. Beam steel, diameter 20 mm, were combined with pre-embedded cables after grouting. Specification of floor cables was Ø22×4300 mm, it was made of 1×19 high strength preloaded steel strands. Cables were pre-embedded in grout holes in rows, their preload was greater than150 kN, it would grouting overall length by cement paste. Specification of high strength tray was 300×300×16 mm.

## Rock pressure monitoring

**Analysis of roadway displacement.** Fig 6 shows monitoring section of surface convergence using Cross point method, measuring nails made of wood were 400 mm, their diameter was 32 mm. Measurement accuracy was 1 mm.

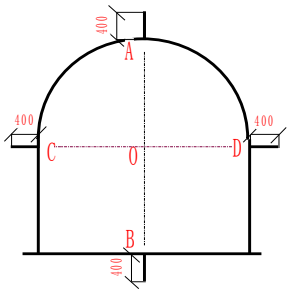


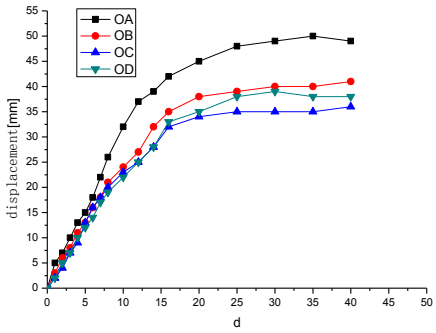


Fig 6 Sketch map of displacement monitoring Fig 7 Curve of roadway displacement

Fig 7 shows curve of roadway displacement with construction days, it's 40 days totally. We can see that in early age, roadway deformation grow faster, until 25 days later deformation become stable. The maximum displacement is roof, it's about 50 mm. Displacement of left sidewall is minimum, it's 37 mm. Convergence of roof-floor is about 87 mm, convergence of sidewalls was about 79 mm, deformation of roadway is small, obvious floor heave and wall caving never appeared, support effect is desired.

**Analysis of cable force.** Fig 8 shows the MGH instrument made in Shandong University of Science and Technology. Fig 9 shows curve of cable force in loopway, it lasted for 28 days, 22# curve shows curve of roof cable, while 17.8# curve shows curve of sidewall cable.

Fig 8 Vibrating wire dynamometer for cable

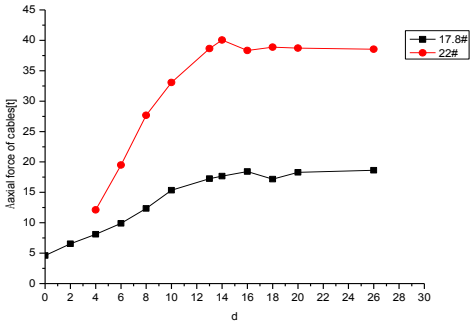


Fig 9 Curve of cable force

Fig 9 shows that roof cable is greater than that of sidewall cable and it grow faster, it tend to stable at 38t after 12 days. The maximum force is about 40 t, so construction quality of cable must be guaranteed. Force of sidewall cable grow gently, it's stable at 14 t after 16 days.

## Conclusions

It has been four years since Pingshan shaft station was reinforced. Roadway of shaft station is of good integrality and stable, its deformation is quite small so far.

(1) Failure area of roof is 5~6 m and greater than 4m of sidewalls, fracture developed fully, the surrounding rock belongs to high geo-stress and jointed soft rock.

(2) Grouting is an effective technology to fracture-developed roadway in soft rock, grouting can fill fractures inside rock, improve its carrying capacity and increase rock integrality, then carrying capacity of rock itself can be made full use of.

(3) Axial force of roof cable is greater than that of sidewall cable, it illustrates the vertical stress of surrounding rock is greater, construction quality of cable should be guaranteed.

## References

[1] Guinan Xu, Guangyao Hou. Zhongzhou Coal, Vol. (2010), p. 68~69 (In Chinese).

[2] Lizhi Cui, Shichao Lu and Jiang Lu: Coal Engineering. Vol. (2005), p. 28-29 (In Chinese).

[3] Baoquan Cao, Guohua Guo and Shichao Lu: Journal of Wuhan University of Technology (Information and Management Engineering). Vol. 29(2007), p. 55~56. (In Chinese).

[4] Xiang Kong. Modern Mining. Vol.(2011),p12~15.(In Chinese)

[5] Chengen Wang, Jihong Hu and Yongjie Liu. China Coal Vol.33 (2007),p 27~30.(In Chinese)

[6] Wenping Li, Jicheng Wang and Kaiping Wang. Chinese Journal of Rock Mechanics and Engineering, Vol.23 (2004), p 79~85.(In Chinese).

*Applied Mechanics and Materials Vols. 580-583 (2014) pp 1352-1357*
*© (2014) Trans Tech Publications, Switzerland*
*doi:10.4028/www.scientific.net/AMM.580-583.1352*

# Research Status and Development Trends of Roadway Surrounding Rock Stability Classification

Renliang Shan[1, a], Xiangsong Kong[1, b], Jian Liu[1, c], Jianfang Li[1, d], Yao Bai[1, e], Yongwei Song[1, f]

[1]School of Mechanics and Civil Engineering, China University of Mining and Technology, Beijing 100083, China

[a]srlcumtb@163.com, [b]suihan555@126.com, [c]ljcumtb@163.com, [d]ljfcumtb1@163.com, [e]bycumtb@163.com, [f]sywcumtb@163.com

**Keywords:** roadway surrounding rock; stability classification; classification index; classification method; research status.

**Abstract.** Stability classification of roadway surrounding rock is of great significance as the prerequisite of safe production in roadway engineering. Based on a great number of issues analysis, the research status of roadway surrounding rock stability classification has been dissected from aspects of classification indexes and methods. At the end, it has put forward that choosing scientific and reasonable indexes, applying combined technology with more than three methods, using new technology and new methods are the three development trends of roadway surrounding rock stability classification research.

## Introduction

The roadway field conditions are changeable and uncontrollable, as the main channel it plays an important role in engineering production. Therefore, making out scientifically stability classification become an important subject for industry experts and scholars. Many achievements have been obtained in this area recent years, mainly on classification indexes and methods. The research status of roadway surrounding rock classification has been studied, and the development trends have been analyzed.

## Research status of classification indexes

The selection of roadway surrounding rock stability classification indexes can directly affect the discriminated accuracy of stability type. Based on the influence extent and selection principles, classification index is the main influencing factors extracted from a great many influence factors. The influence factors are roughly divided into natural factors and mining technical factors. Natural factors are mainly the magnitude and direction of ground stress, the strength and characteristics of rock and coal seam, etc., mining technical factors are mainly roadway width and height, the coal pillar width and service life, etc., as shown in table 1.

The selection of roadway stability classification indexes should follow the principles as below:

(1) Importance: when choosing indexes, the more important factors should be considered while the factors with less affect ignored, and the importance of each index must on the same level.

(2) Independence: each index is independent, revealing a certain property with low correlation to others.

(3) Distinguish ability: the sample data of each index should have obvious difference.

(4) Easy availability: the index can be acquired in field or laboratory, and quantitatively assessed.

(5) Definiteness: the index should be fundamental, with simple meaning, not be confused.

(6) Foresight: the index can be obtained by exploration, to providing roadway support references.

Considering the influence degree and the index selection principle, the most commonly used classification indexes are shown in table 2.

Table 1 The influence factors of roadway surrounding rock stability

| Natural factors | | Mining technical factors | |
|---|---|---|---|
| Surrounding rock strength | Roof strength | The roadway section | Roadway width |
| | Seam strength | | |
| | Floor strength | | Roadway height |
| Ground stress | Self-weight stress | | |
| | Maximum principal stress | Mining size | The ratio of mining to caving |
| | The angle between maximum Principal stress and roadway | | |
| Geological characteristics of coal seam | Thickness of coal seam | | Mining height of coal seam |
| | Angle of coal seam | | |
| | Buried depth of coal seam | | |
| Thickness of roof(floor) | Thickness of immediate floor | | The ratio of immediate roof and mining height |
| | Thickness of immediate roof | | |
| | Thickness of main roof | | |
| Integrity of surrounding rocks | Index of rock Integrity | | |
| | Rock quality designation (RQD) | | The ratio of mining height to roadway height |
| | Structural plane(joint fissure) | | |
| | The angle between structural plane orientation and roadway axis | | |
| Characteristics of strata behavior | First caving span of immediate roof | Other factors | Width of coal pillar |
| | First caving span of main roof | | |
| | Periodic weighting span of main roof | | Service life |
| Role of water | Inrush water | | Coal-mining method |

Table 2 The stability classification indexes of roadway surrounding rock

| | |
|---|---|
| Natural index | Roof strength, Seam strength, Floor strength, Buried depth of coal seam, RQD, |
| | Angle of coal seam, First caving span of immediate roof, Inrush water |
| Mining technical index | Roadway width, Roadway height, The ratio of immediate roof and mining height, |
| | Width of coal pillar |

## Research status of classification methods

There are three system methods in roadway surrounding rock stability classification: classification with single index, classification with comprehensive indexes and classification with multi-index, as shown in Fig.1.

**Classification with single index.** Protogyakonov's coefficient of rock strength is defined in protodyakonov's theory based classification method, as shown in formula (1). The roadway surrounding rock is divided into 15 types in the method. Protodyakonov's theory based classification method is simple to use, but could not specify the surrounding rock integrity.

$$f = \frac{\sigma_c}{10} \tag{1}$$

Where $f$ is Protogyakonov's coefficient, $\sigma_c$ is uniaxial compressive strength.

RQD is the short name of rock quality designation, the RQD value is defined in RQD classification method, as shown in formula (2). This method can reflect the surrounding rock integrity, dividing the surrounding rock into five types. It has better practicability, but could not reflect the influence of jointed rock mass.

$$\mathrm{RQD} = \frac{L_1}{L_2} \tag{2}$$

Where RQD is rock quality designation, $L_1$ is the accumulation length of more than 10 cm core, $L_2$ is the length of the drilling.

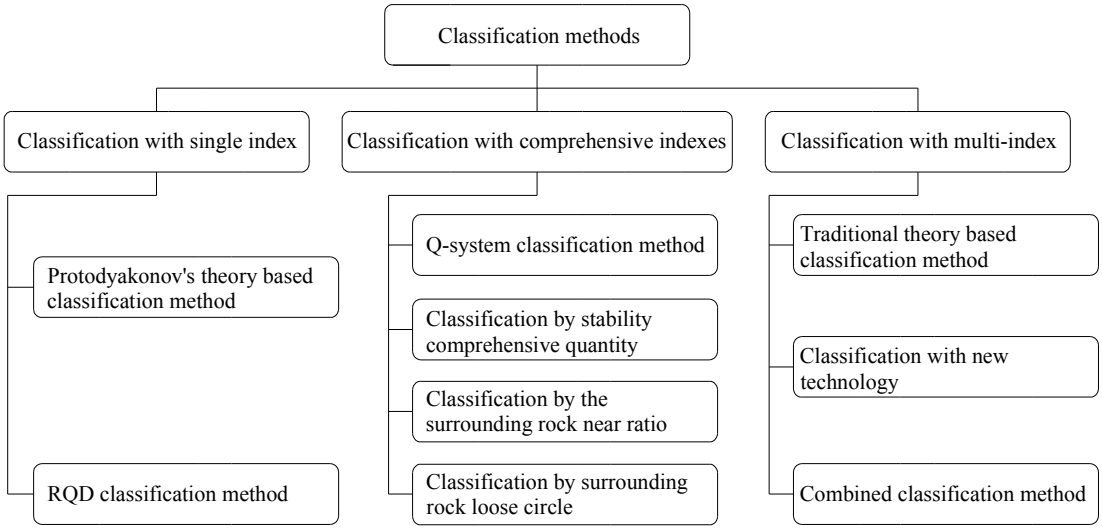


Fig. 1 The stability of roadway surrounding rock classification method

It can be seen that, classification with single index method is simple and easy, widely applied with strong practicability. However, the roadway has complex geological conditions, affected by so many factors that rock joints and fissures, hydrological factors cannot be taken into account with single physical and mechanical index, thus the surrounding rock stability could not be accurately reflected.

**Classification with comprehensive indexes.** The surrounding rock is divided into 9 types by the Q-system classification method, the joint effect is analyzed emphatically, and the comprehensive index Q value is calculated by formula (3). The classification accuracy is improved greatly by the method, as the joint and the ground stress are reflected, but there is some subjectivity in quantitative determination of each index.

$$\mathrm{Q}=\frac{\mathrm{RQD}}{J_{\mathrm{n}}}\times\frac{J_{\mathrm{r}}}{J_{\mathrm{a}}}\times\frac{J_{\mathrm{w}}}{\mathrm{SRF}} \tag{3}$$

Where RQD is quality designation, $J_{\mathrm{n}}$ is the joint number, $J_{\mathrm{r}}$ is the joint roughness, $J_{\mathrm{w}}$ is the joint reduction coefficient of water, $J_{\mathrm{a}}$ is the metamorphic degree of the joint, SRF is the stress reduction coefficient of water.

The stability is divided in to five levels by stability comprehensive quantity method. The surrounding rock comprehensive quantity formula is shown as formula (4).

$$\mathrm{S_g}=\frac{R_{\mathrm{ef}}}{\gamma\times H\times k\times a\times b} \tag{4}$$

Where $\mathrm{S_g}$ is the stability comprehensive quantity, $R_{\mathrm{ef}}$ is effective rock strength, γ is surrounding rock bulk density of, $H$ is buried depth, $k$ is stress concentration factor, $a$ is show coefficient, $b$ is damage coefficient.

The formulas about classification by the surrounding rock near ratio method are shown as formula (5) and (6). It determines the appropriate supporting scheme by the roadway relatively near ratio.

$$\mathrm{K}=0.066H+4.3S_{\mathrm{V}}\times M+24.3\sqrt{G_{\mathrm{L}}}-78\pm0.03 \tag{5}$$

$$\mathrm{U}=2.3\mathrm{K}+3.5 \tag{6}$$

Where K is the relatively near ratio of roof and floor, U is the relatively near ratio of sidewalls, $H$ is buried depth, $S_V$ is filled coefficient, $M$ the mining height, $G_L$ is floor strength coefficient.

Classification by roadway surrounding rock loose circle method divides surrounding rock stability into 6 types according to the loose circle size. The method is easy to operate and widely used, yet there is no analytic expression about the relationship between loose circle size and the influencing factors.

From the analysis above, it can get that with representation and practicability, many influence factors can be comprehensively considered in the composite index of surrounding rock classification method, and a single quantitative comprehensive index is obtained. But in most kinds of the classification with comprehensive indexes method, the indexes focus on several main influence factors that not all the influence factors can be reflected, also, some factors decided by experience would affect the surrounding rock stability judgment.

**Classification with multi-index.** Classification with multi-index method mainly contains traditional theory based classification, classification with new technology and combined classification method, each method consists of variety classification methods, detailed in Fig. 2.

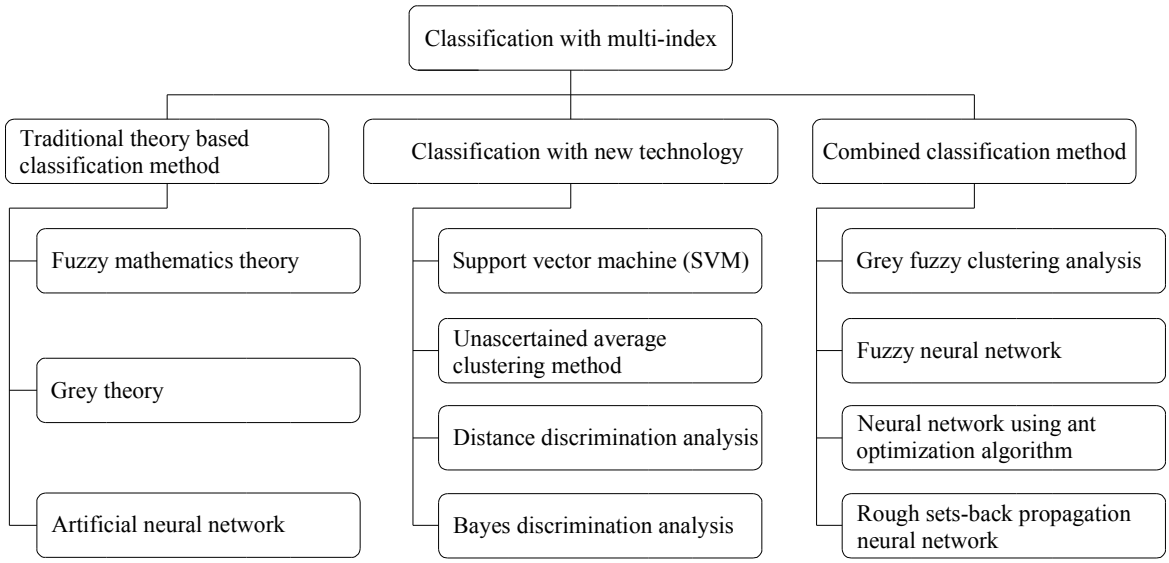


Fig. 2 The multi-index classification method

Traditional theory based classification method contains fuzzy mathematics theory method, grey theory method and artificial neural network method.

With the development of fuzzy mathematics theory, the methods applied in stability classification of roadway surrounding rock are mainly fuzzy cluster analysis, fuzzy discriminatory analysis and fuzzy comprehensive evaluation. First, the seven indexes including dynamic load coefficient were determined, then the surrounding rock stability type in Shenhuo mining was determined base on fuzzy cluster analysis method [1]. The surrounding rock stability fuzzy recognition model was established, and the application instance was studied [2]. The fuzzy comprehensive evaluation was divided into two giant steps, six small steps, with good applicability in Zhengzhou coal group mines [3].

The grey theory is composed by three systems, as shown in figure 3. The grey theory in the stability classification study can be divided as: grey relation analysis, gray model (GM), grey forecasting analysis. Grey relation analysis method is applied to verify the stability classification in Xuzhou mining, and satisfying results were got [4]. The grey model (GM) were established in three steps, on this basis, the new information model GM (1, 1) was got by reducing or increasing new array data, with higher prediction accuracy[5].

Artificial neural network is a highly nonlinear dynamic system with its weights dynamically adjusted by learning and training. The most widely applied one in stability classification of surrounding rock is BP network model, the second widely applied is RBF network model. BP network model is a kind of forward feedback artificial neural network, as shown in Fig. 4. In

Shendong mining roadways, after selecting five classification indexes, the three-layer BP network model was established with its accuracy higher than 95% [6]. RBF network model is three-layer forward artificial neural network, as shown in Fig. 5. In Huangbaici mining engineering, the RBF network classification model was built and expected results gained [7].

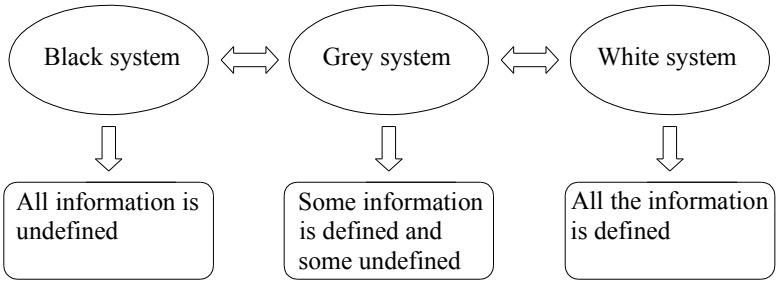


Fig. 3 Three kinds of system

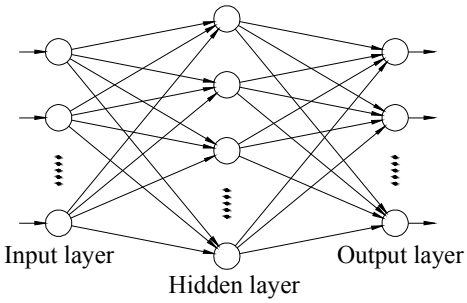


Fig. 4 The structure of BP network model

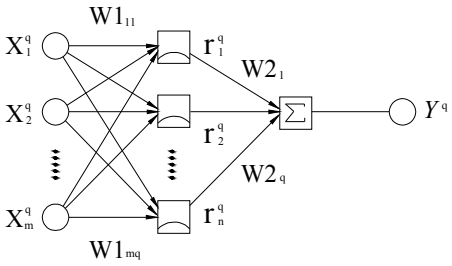


Fig. 5 The structure of RBF network model

Classification with new technology method mainly includes support vector machine (SVM), unascertained average clustering method, distance discrimination analysis and bayes discrimination analysis method. The support vector machine (SVM) classification of one-to-one model was established to classify the mining roadways in Pingdingshan mining [8]. The unascertained average clustering model was established, and the roadway types was accurately predicted [9]. Based on theory of distance discriminant analysis, the corresponding model was built, and practical application showed it had high accuracy in roadway classification [10]. Roadway bayes discriminant model was set up, and the recognition rate was 100% [11].

Combined classification method mainly includes grey fuzzy clustering analysis, fuzzy neural network, neural network using ant optimization algorithm and rough sets-back propagation neural network method. The grey fuzzy clustering analysis model for roadway type identification was established, and applied to the stability classification practice in Jixi mining roadways [12]. The fuzzy neural network model was established, and the practical application proved that the model had faster calculating speed with more accurate classification ability [13]. The neural network model using ant optimization algorithm based on heuristic global optimization was set up, and the stability type of surrounding rock was accurately predicted [14]. The rough sets-back propagation neural network model had high coincidence and tolerance with fast convergence speed, which had been improved in engineering application [15].

The above analysis illustrates that many factors influence the surrounding rock stability, and each one represents a certain property, therefore, choosing main factors as the stability classification indexes is essential for evaluating the surrounding rock stability comprehensively. Classification index is the basis of surrounding rock stability classification, although there is a complicated nonlinear relationship between each index and the surrounding rock stability, the multi-index classification method adopted by the more and more advanced theory technology with high mapping precision, especially the combined methods can foster strengths and circumvent weaknesses, accelerate the operation speed and improve the classification precision.

**Development trends**

(1) Because the stability classification indexes are commonly used as the input part with great importance in stability classification, scientific and reasonable index selection is bound to be one of the development trends in roadway stability classification studies.

(2) Because in the combined methods technology, all the methods can play their advantages and make up the shortcomings of others, ideal classification results can get, what's more, there are still limitations in combined methods that with only two kinds at present, thus combined methods with more than three kinds will become an important development trend in roadway surrounding rock stability research in the future.

(3) With the development of mathematical methods and the improvement of technology, there will be more new technology and methods with more advantages than the traditional, and applying these new technology and methods to surrounding rock stability classification study is the future development trend.

**Acknowledgements**

The study is supported by the Fundamental Research Funds for the Central Universities (No.2010YL09), the National Natural Science Fund Committee & the Shenhua Group Co., Ltd. jointly funded project (No.51134025) and Ph. D top-notch innovative talents' cultivation fund project of China University of Mining and Technology, Beijing.

**References**

[1] F Cao, Y. Cheng: Coal Mining Technology. Vol. 11 (2006), p. 65-70(in Chinese).

[2] X. D. Xiang: Journal of Liaoning Technical University (Natural Science). Vol. 20 (2001), p. 17-20(in Chinese).

[3] J. P. Wei, Z. C. Li, P. M. Sang: Coal Engineering. 5 (2010), p. 69-72(in Chinese).

[4] T. Y. Qi, X. Z. Zou: Journal of Mining & Safety Engineering. 2 (1990), p. 49-54. (in Chinese)

[5] J. B. Shen, J. G. Qu, Z. W. Zhan: Coal Mining Technology. Vol. 16 (2011), p. 22-24(in Chinese).

[6] Y. J. Zhu, T. Feng: Journal of China Coal Society. Vol. 37 (2012), p. 565-570(in Chinese).

[7] J. S. Zhang, Z. W. Wang, R. Z. Wang: Modern Mining. 12 (2010), p. 84-86(in Chinese).

[8] Y. D. Zhu, W. T. Ma: Journal of Mining & Safety Engineering. Vol. 23 (2006), p. 362-365. (in Chinese)

[9] L. J. Dong, G. Y. Zhao: Journal of PLA University of Science and Technology (Natural Science Edition). Vol. 10 (2009), p. 575-579(in Chinese).

[10] Z. H. Zhu, T. Feng, D. H. Xie: Mineral Engineering Research. Vol. 25 (2010), p. 6-9(in Chinese).

[11] C. P. Li, H. B. Hao: Journal of China Coal Society. Vol. 36 (2011), p. 304-307(in Chinese).

[12] Y. C. Ning, Z. G. Xing: Systems Engineering-Theory & Practice. 8 (1997), p. 117-124. (in Chinese)

[13] G. X. Song, Z .Y. Yang, X. Sun: Geotechnical Engineering Technique. Vol. 18 (2004), p. 224-229(in Chinese).

[14] J. Sun, X. Y. Liu: Microelectronics & Computer. Vol. 25 (2008), p. 117-119(in Chinese).

[15] A. L. Jiang, Y. L. Qi: Journal of Central South University (Science and Technology). Vol. 42 (2011), p. 3189-3194(in Chinese).

*Applied Mechanics and Materials Vols. 580-583 (2014) pp 1358-1363*
*© (2014) Trans Tech Publications, Switzerland*
*doi:10.4028/www.scientific.net/AMM.580-583.1358*

# Analysis on Changes of Mechanical Properties of Lining of Tunnels in Huangtu Regions Taking Account of Loess Cavity by Using ADINA

Heping Zhou[1,a], Enyong Wang[2,b], Yuxia Hu[3,c], Zhiqiang Liu[4,d] , Jianbo Cui [5,e]

[1] Educational Center of Gansu, Lanzhou, China, 730030

[2]. Lanzhou City University, Lanzhou, China, 730070

[3]. Lanzhou City University, Lanzhou, China, 730070

[4]. Lanzhou Jiaotong University, Lanzhou, China, 730070

[5]. Lanzhou City University, Lanzhou, China, 730070

[a]gyzhp@126.com, [b]595262628@qq.com, [c]huyuxia586@126.com, [d]lzqiang@mail.lzjtu.cn, [e]1539761114@qq.com

**Keywords:** lining of tunnel, loess cavity, finite element.

**Abstract.** In this article, we focused on changes of mechanical properties in lining of tunnel caused by loess cavity. We established a corresponding model and carried out numerical analysis by using finite element analysis software ADINA, considered the effect of different locations, different size of the cavity and depth of the tunnel. The results showed that change of the mechanical properties has the largest effect on the lining at the arch foot nearby the loess cavity, and it grows with the growth of the cavity‘s size and depth of the tunnel.

## Introduction

A notable feature of the loess in Loess Plateau is the wet collapsibility. When wetted by water, it is likely to collapse. A lot of loess cavities formed by the collapsed loess after rain water infiltration. These loess cavities seriously affect nearby buildings or tunnels. It will be followed by a significant decreased in their mechanical strength. The survey also found that the main factors of tunnel‘s diseases in loess area are the effect of water, especially these cavities changed the force on the lining, severely, it will lead it to deformation, cracking or buckling. For loess tunnel, its lining plays a crucial role.Therefore, analysis changes of mechanical properties of lining of the tunnels in Huangtu Regions taking account of loess cavity is very importent. We focused on changes of mechanical properties in tunnel's lining caused by loess cavity. We established a corresponding model and carried out numerical analysis by using finite element analysis software ADINA, considered the effect of different locations, different size of the cavity and depth of the tunnel.

## Model and Parameters

Calculating model is based on the general loess tunnel, Fig.1 is a cross sectional view of the tunnel. Figure 2 is its finite element model and cell division. The tunnel depth is 12m, lining material of the tunnel is C30 concrete, and the average thickness is 20cm. Mechanical parameters of the lining and loess are shown in Table. We used four-node plane strain parameter unit on the rock, a total of 4,695 units. Lining is divided into 117 beam units. We use cell life and death technology of the finite element method to simulate the appearance of cavity. In the calculation, we assume that the cavity appeared at top, shoulders, waist and arch foot of the lining in the loess (area marked in Fig.2) respectively, and consider the size of the cavity were four grades (25 ~ 30cm, 45 ~ 55cm, 70 ~ 80cm and 95 ~ 100cm).

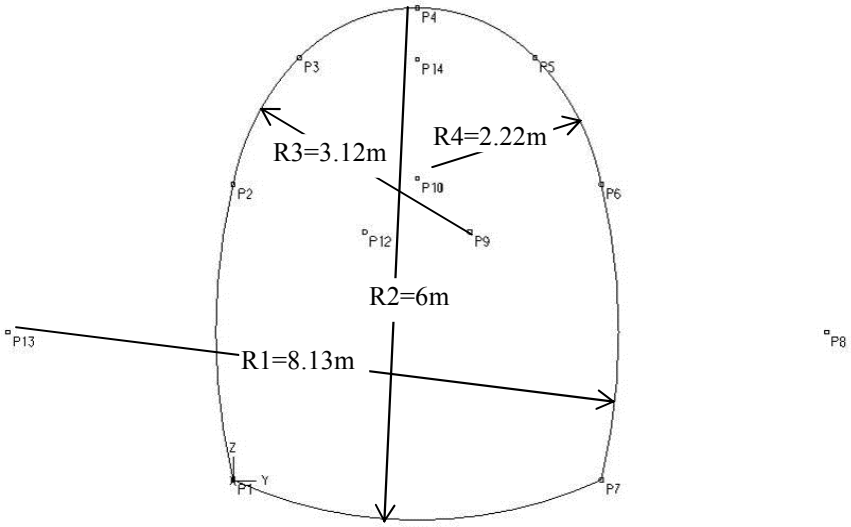


Fig.1 Tunnel section

Table Material Parameters

| | Modulus of elasticity(Pa) | Density($kg/m^3$) | Cohesion (Pa) | Angle of internal friction ($\varphi$) |
|---|---|---|---|---|
| Rock and Soil | 1.5e9 | 1800 | - | - |
| Concrete(C30) | 28.5e9 | 2500 | 0.16e6 | 28 |

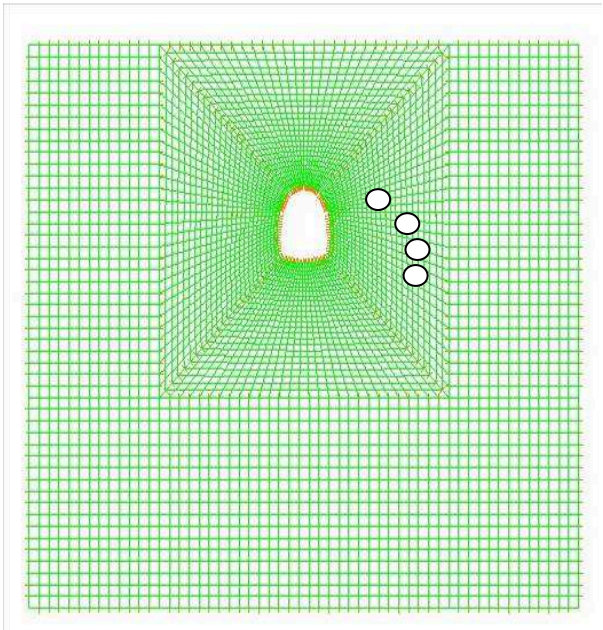

Fig.2 The finite element grids of the model

## Analysis

The results of calculation showed that the appeared cavity destroyed the original force balance on the lining. The internal forces (axial force and bending moment mainly) in the lining has undergone great changes.

**Changes of Internal Forces in the Lining Caused by Different Position and Size of the Cavity.** According to many studies, the main disadvantage of cavity generated is the additional negative axial force and bending moment. The distribution of the additional axial force and bending moment when a cavity appeared at the top of the lining is shown in fig.3.

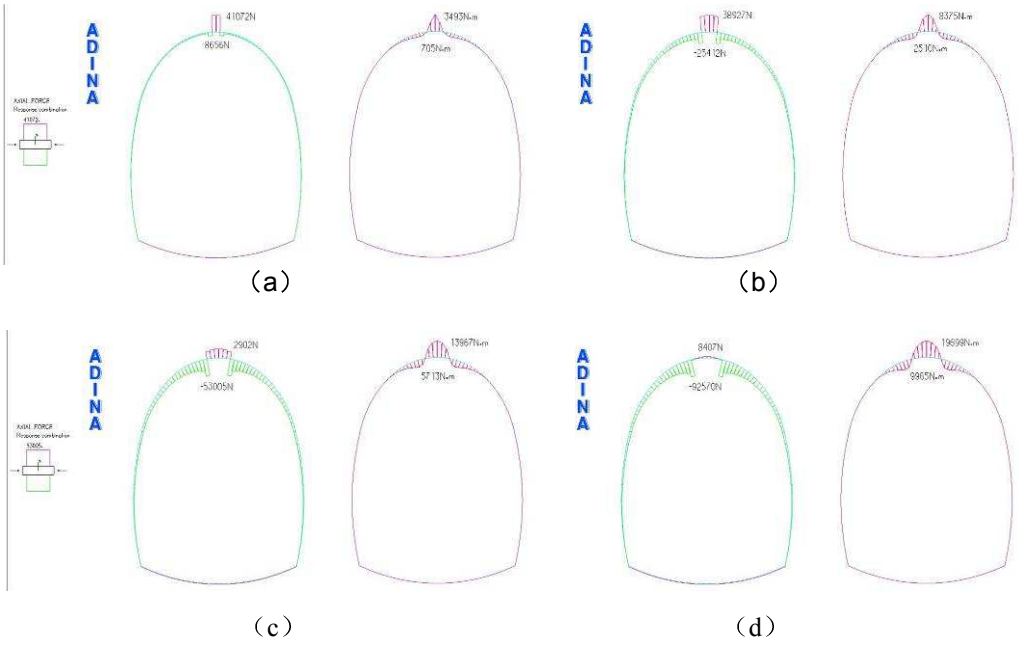


Fig.3 Cavity appeared at the top of the lining

As can be seen, major changes of the internal forces in the lining occur in the vicinity of the cavity. Positive axial force (pressure) occurs in the region appeared cavity, with negative axial force (pull) on sides of it, and negative axial force decreases with the increase of distance of cavity. Additional negative axial force and bending moment are the main disadvantages of the cavity generated.

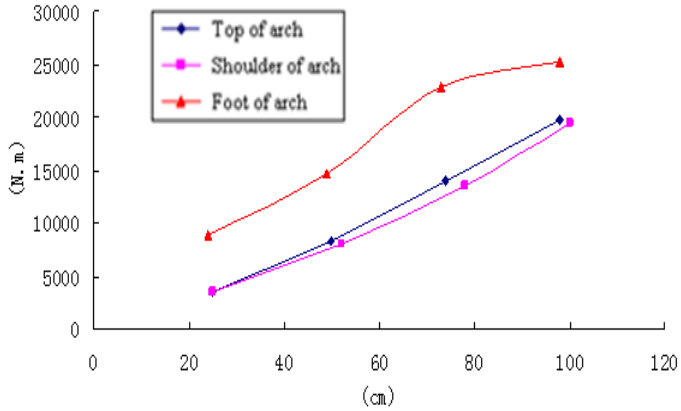


Fig.4 The relationship between additional moment and cavity size at different locations

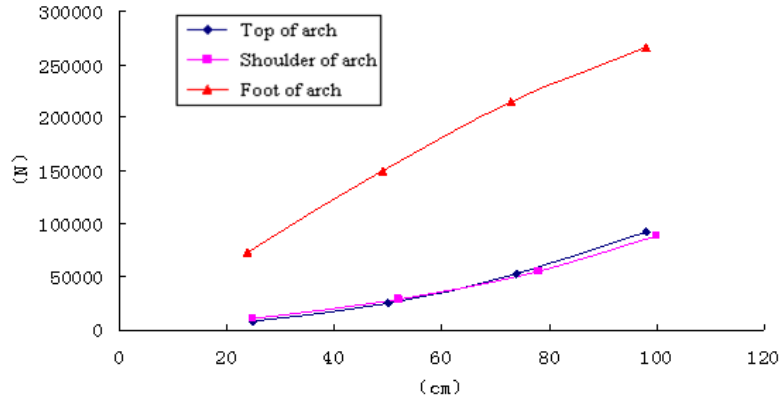


Fig.5 The relationship between additional axial force (pull) and cavity size at different locations

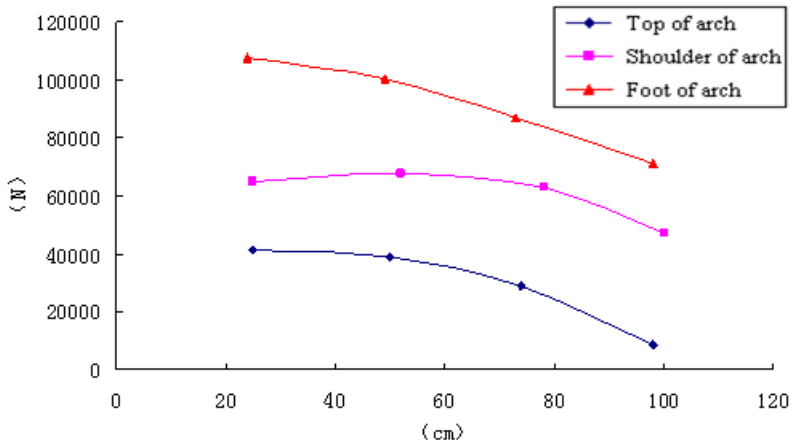


Fig.6 The relationship between additional axial force (compress) and cavity size at different locations

Fig.4, 5 and 6 illustrated that the additional moment and negative axial force (pull) are increased with the increases of the cavity, but a positive axial force (compress) is the opposite. It can be seen, the larger the hole, the more unfavorable for tunnel's safety. It also can be seen the additional internal forces at lining vault, spandrel and foot of the arch generated by the cavity are more than arch waist, bottom of the arch. This point should be noted.

**Changes of Internal Forces in the Lining Caused by Different Depths of the Tunnel.** Considering the tunnel depth at 12m, 20m, 30m, 40m and 50m, and the size of cavity appeared at the top of lining is 50cm. Changes of internal forces in the lining caused by different depths of the tunnel is shown in Fig.7.

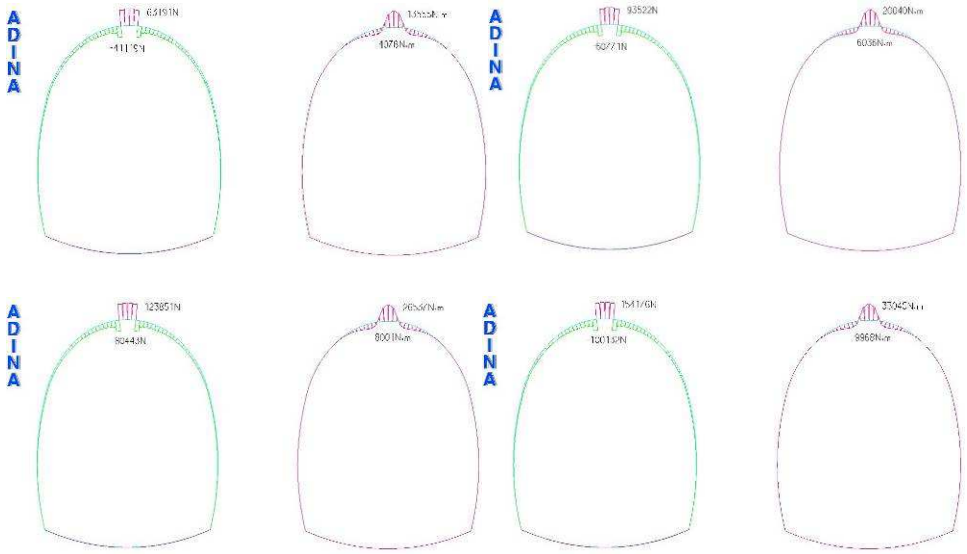


Fig.7 Changes of internal forces in the lining caused by different depths of the tunnel

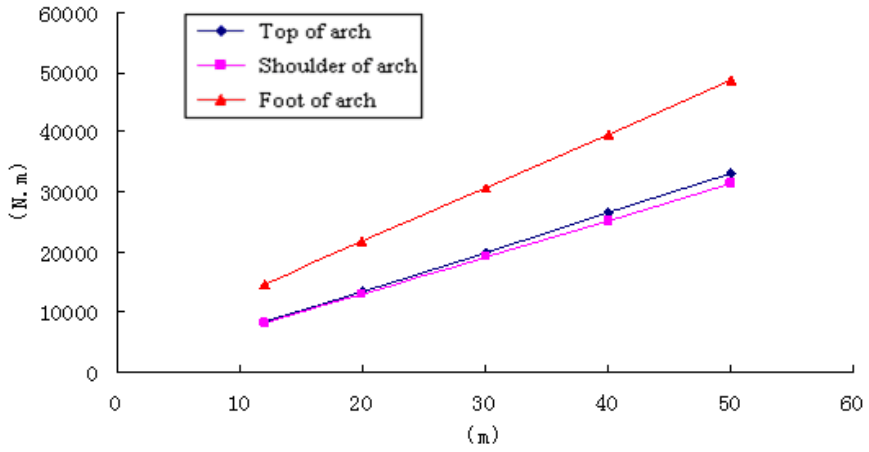


Fig.8 The relationship between additional moment and depths of the tunnel at different locations

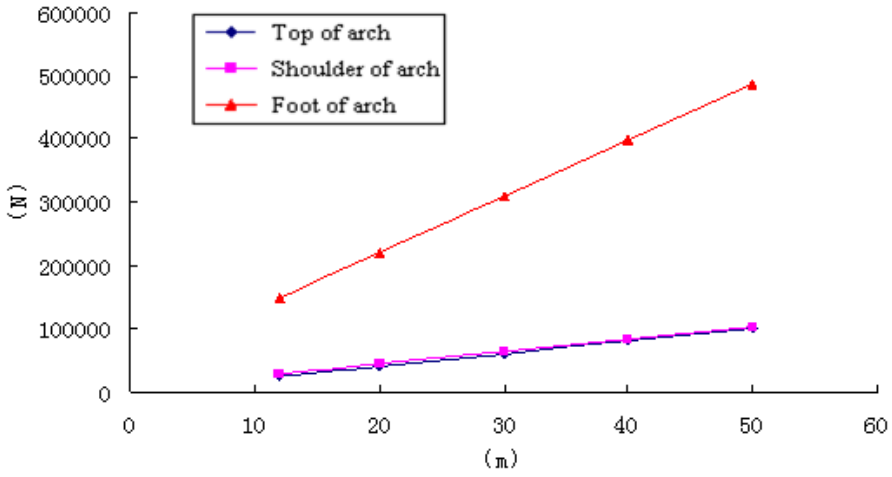


Fig.9 The relationship between additional axial force (pull) and depths of the tunnel at different locations

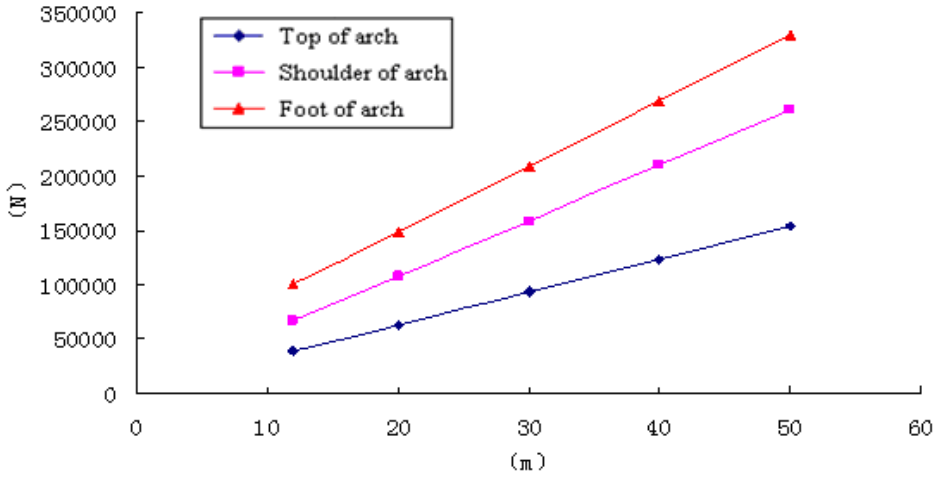


Fig.10 The relationship between additional axial force (compress) and depths of the tunnel at different locations

We can see that the relationship between maximum of additional internal forces and depth of the tunnel is substantially linear, and effect of depth of the tunnel is basically the same when cavity at the dome and spandrels, but with a greater impact on the foot of the arch.

## Conclusion

Due to the loess's nature of the wet collapsibility, it is easy to collapse to produce cavity behind the lining of the tunnel. Cavity changed the mechanical properties of the lining. Through the analysis, we found that different locations, size of the cavity and depth of the tunnel are the main factors affecting the mechanical properties of the lining, and the larger the cavity, the greater the depth of the tunnel, and the lower location of the cavity, the greater the mechanical effects of the cavities on the lining of the tunnel.

## References

[1] Theory and Modeling Guide Volume Ⅰ: ADINA, 2004. ADINA R&D, Inc.

[2] Ding Zhaoming,Yang Xiaohua: Analysis of Disease Causes and Treatment Measures of Highway Tunnel in Loess, *Journal of Engineering Geology*, 2009，17(1):p.138-144. "In Chinese"

[3] Jing Ren, Wang Yonggang: Mechanical Behavior during Construction Process and Construction Control for Collapsing Stratum of Collapsible Loess Tunnel, *HIGHWAY*, Feb.2009, No.2. "In Chinese"

[4] Ji Wujun, Investigation and Analysis of Engineering Problems for Loess Tunnels, *Rock and Soil Mechanics*, Vol.30 Supp.2, Dec. 2009. "In Chinese"

[5] Qiao Chunsheng, Guan Zhenxiang, Teng Wenyan, Study on Deformation of Tunnel Excavated in Saturated Loess, *Rock and Soil Mechanics*, Vol.24 Supp. Oct. 2003. "In Chinese"

[6] Zhao Zhanchang, Xie Yongli,Yang Xiaohua, Ll Youyun, Observation Research on the Mechanical Characteristic of Highway Tunnel Lining in Loess, *China Journal of Highway and Transport*,Vol.17 No.1,Jan.2004. "In Chinese"

*Applied Mechanics and Materials Vols. 580-583 (2014) pp 1364-1368*
*© (2014) Trans Tech Publications, Switzerland*
*doi:10.4028/www.scientific.net/AMM.580-583.1364*

# Research of fractured surrounding rock physical and mechanical characteristics in Shuguang mine No.2 mining area

Huajun Xue[1,a], Junlong Xue[1,b], Minglun Yin[1,c], Jie Kong[1], Zongming Gao[1]

[1]School of mechanics & civil engineering, China University of Mining and Technology (Beijing), Beijing, 100083, China

[a]296504206@qq.com, [b]799216685@qq.com, [c]yml2323@163.com

**Keywords:** Surrounding Rock Deformation. Fractured Surrounding Rock. Physical and Mechanical Characteristics. Supporting of Roadway.

**Abstract.** Since the excavation of roadway in Shuguang mine No.2 mining area, shotcrete layer has fallen off and the surrounding rock deformation was serious. For studying big deformation of roadway in Shuguang mine No.2 mining area, the paper analyzed fractured surrounding rock physical and mechanical characteristics of No.2 mining area. The results show that the uniaxial compressive strength, uniaxial tensile strength, cohesion, internal friction angle of fractured surrounding rock were very low. And the whole physical and mechanical characteristics were poor. It is the basic reason of big deformation of roadway surrounding rock physical and the important basis of late supporting of roadway.

## Introduction

The design length of rail roadway in Shuguang mine No.2 mining area is 4000m. The service life is 30a. The buried depth is about 500m. The section shape of roadway is vertical wall-round arch with drivage width 4.94m, clear width 4.7m, vertical wall height 1.6m, drivage circular arch radius 2.47m, clear width 2.35m, drivage sectional area 16.99m$^2$, clear sectional area 15.72m$^2$. The purpose of roadway drivage is to meet raw coal transportation, ventilation, traffic, pipeline laying. Due to sedimentary environment, the variation in thickness of 2# upper coal seam is bigger in 1.27~2.48m. The average is 1.73m. The 2# lower coal seam that the thickness is 0~0.94m is local seam. The average is 0.40m. The thickness of mudstone which is parting is 0.8~1.25m. The floor of coal seam is fine sandstone, mudstone or shale. The dip of 2# coal seam is 0~10º and the coefficient of hardness f is 0.6.

Since the excavation of roadway in Shuguang mine No.2 mining area, due to 2# coal of roadway sides with low strength, shotcrete layer has fallen off and the surrounding rock deformation was serious. Surrounding rock of rail roadway damaged diagram is shown in Fig. 1 In order to optimize the support scheme of roadway, reduce the deformation of roadway surrounding rock, maintain the stability of roadway, to physical and mechanical properties test of crushed surrounding rock of roadway, the paper tested and analyzed fractured surrounding rock physical and mechanical characteristics for solving the problem of big deformation of surrounding rock of roadway fundamentally.

Fig. 1. Surrounding rock of rail roadway damaged diagram

## Experimental Preparation

**Experiment Content.** The experiment tests the density, uniaxial compressive strength, elastic modulus, Poisson ratio, uniaxial tensile strength, cohesion, internal friction angle of roadway surrounding rock of immediate roof, sides, immediate floor, and old floor.

**Sample collection.** Sample collection is according to the national standard "Methods for determining the physical and mechanical properties of coal and rock-Part 1: General requirements for sampling" GB/T 23561.1 2009.

The samples used in the experiment were taken from immediate roof, sides, immediate floor, old floor of rail roadway in Shuguang mine No.2 mining area. Due to high ground pressure, the drilling core forming difficulty, we collected uniform mechanical properties, appropriate size, complete block samples to the lab and made into standard specimen [1].

**Specimens Fabricating.** Sample fabricating is according to the specimen processing standard of the national standard "Methods for determining the physical and mechanical properties of coal and rock" GB/T 23561.1-2009 ~ GB/T 23561.16-2010.

Standard specimen fabricating equipment are diamond machine, stone sawing machine, grind stone machine. We has made 45 specimens that 20 specimens for uniaxial tensile test with φ50mm×25mm size and 25 specimens for uniaxial compressive test and triaxial compressive test with φ50mm×100mm size.

**Experimental Instruments.** The main experimental instruments have diamond machine, stone sawing machine, grind stone machine, grinder, vernier caliper, PGC-753e electronic balance, extensometer, XTYE-2000 hydraulic pressure tester.

## Experimental Scheme

Specimen density: The actual diameter and the actual height of the specimen were measured with a vernier caliper. The mass of the rock samples were measured with Adem PGC-753e electronic balance. Then using the formula to calculate density of each test piece, so the average density of the sample was

Uniaxial tensile strength, uniaxial compressive strength, triaxial compressive strength: The uniaxial tensile strength of the specimen were tested by the XTYE-2000 type of hydraulic pressure experiment machine. The loading method was displacement loading. The speed of it was 0.002mm/s, and the interval of experimental data acquisition was 5ms.

## Experimental Process

All the specimens was checked the name and number packets, and checked the machining accuracy and measurements before measured. The specimen color, grain, bedding, joints, cracks, degree of weathering, moisture status and processing problems was described.

**Testing Density of Specimen.** The actual diameter and the actual height of the specimen were measured with a vernier caliper. The mass of the rock samples were measured with electronic balance. Each specimen tests three times, calculating the average.

**Testing Uniaxial Tensile Strength of Specimen.** Uniaxial tensile strength was measured by split tests.

Through both ends of the specimen diameter, draw a straight line along the axis parallel to each other as two loads at baseline, the two pads of the load along the baseline with a rubber band fixed at both ends of the specimen.

Starting pressure testing machine and adjust the pressure system to a working state. The pad assembly of the specimen placed in a pressure plate bearing test machine center, and adjust the spherical seat, so that uniform bearing the specimen, of the pad, the center line of the centerline of the specimen and pressure testing machine in a straight line, and in the specimen plus the protector.

Starting pressure experiment machine, testing machine using displacement control. Pressure is applied to the specimen 0.1kN~0.5kN, and then the speed 0.002mm/s and uniformly loaded continuously until the destruction of the sample up. Specimens should eventually destroy the plane by two pads of the decision, or should be considered invalid experiment.

After the experiment is completed, immediately remove the specimen failure, and sealed with a plastic bag. Fig. 2 (a) shows destroyed specimens after split test loaded.

a. Uniaxial tensile test b. Uniaxial compressive test c. Triaxial compressive test

Fig. 2. Failure sample after pressure experiment

**Testing Uniaxial Compressive Strength of Specimen.** The extensometer to measure the axis and radial strain when loading on the specimen should be properly installed.

Starting the pressure testing machine, and adjusting the pressure system to a working state. The specimen should be placed at the center of the bearing plate of the pressure testing machine, and adjusting the spherical seat to make sure that the centerline of the pressure testing machine, the upper and lower bearing plate, and the specimen are in a straight line, not eccentric. We should make sure the specimen's upper and lower are exerted by uniform force, meanwhile adding a protector outside the specimen. The experimental loading method is as same as the splitting experiment.

After the experiment is completed, immediately removing the damaged specimen, and sealed with a plastic bag. The destroyed specimens under the uniaxial compressive test are shown in Fig. 2 (b).

**Testing Triaxial Compressive Strength of Specimen.** Wiping the two end surface of cushion block. The specimen is placed between the upper and lower pads, so that the three centers was in a straight line. Then the specimen and cushion block were put on Anti - oil sets. The specimen were sealed with a rubber band or sealing tape. The extensometer that measuring specimen axis and radial strain during the loading were properly installed on the specimen. The pad is then placed in the lower part of the center of pressure chamber base, having a good piston pressure chamber cover. Then put the pressure chamber of the specimen placed on a material testing machine, and between the platen, and to the upper and lower pressing plate axis coincides with the axis of the pressure chamber.

Starting pressure testing machine, and applying pressure 0.1kN~0.5kN to fixed specimens. Then open the pressure chamber vent, start side pressure pump, oiling the pressure chamber, exhaust air while oiling, when the air pressure chamber drain and tighten the vent.

Axial loading, when the pressure is stable between 2kN~10kN, extensometer readings to make adjustments to 0, the starting point as a contingency measure. And then 0.5MP/s loading rate longitudinal load is applied stability until the specimen damage, note the failure load values. After unloading the specimen was removed, and record the damage situation then sealed with a plastic bag. Fig. 2 (c) shows the failure specimens after loading triaxial compression [2-3].

## Experimental Results

Through testing, the basic physical parameters of specimen are shown in Table 1.

Through testing, the test load-vertical displacement curves are shown in Fig. 3. The uniaxial tensile strength of specimen are shown in Table 1.

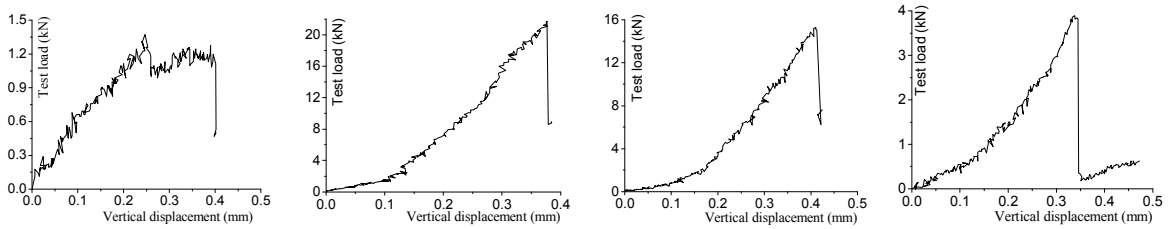


a. 2#coal of sides b. sandy shale of immediate roof c. sandy shale of immediate floor d. sandy shale of old floor

Fig. 3. Test load-vertical displacement curves of some samples

Through testing, the complete stress-strain curves under uniaxial pressure are shown in Fig.4. The uniaxial compressive strength, elastic modulus, Poisson ratio of specimen are shown in Table 1.

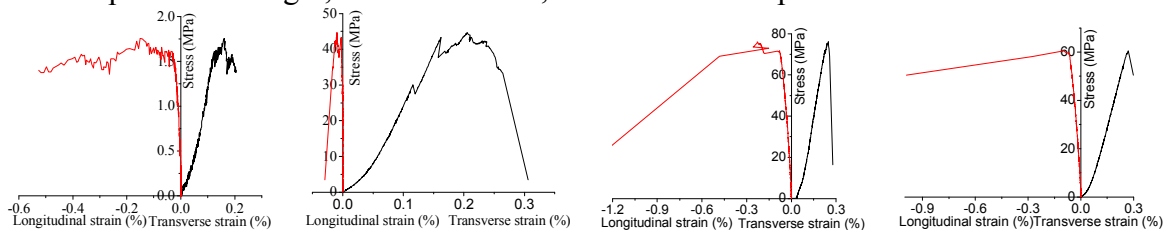


a. 2#coal of sides b. sandy shale of immediate roof c. sandy shale of immediate floor d. sandy shale of old floor

Fig. 4. Complete stress-strain curves under uniaxial pressure of some samples

Through testing, the Mohr's circle are shown in Fig.5. The triaxial compressive strength, cohesion, internal friction angle of specimen are shown in Table 1.

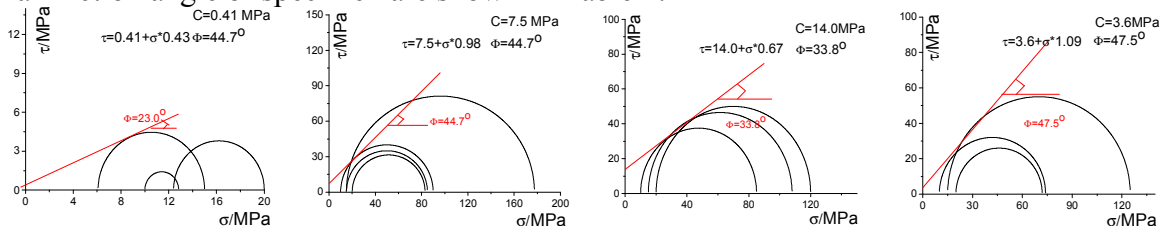


a. 2#coal of sides b. sandy shale of immediate roof c. sandy shale of immediate floor d. sandy shale of old floor

Fig.5. Mohr's circle

## Conclusions

Through laboratory test, the paper analyzed fractured surrounding rock physical and mechanical characteristics of No.2 mining area. The physical and mechanical parameters of surrounding rock are shown in Table 1. The Table 1 shows that the strength of coal of sides is poor and very fractured. And it is the key of the roadway supporting. The roadway support strength should be strengthened overall, especially the sides in late supporting.

Table 1 Physical and mechanical parameters of surrounding rock of No.2 mining area rail roadway in Shuguang mine

| Lithology | Position | P(kg/m³) | σ(Mpa) | $\sigma_t$(Mpa) | E(Gpa) | μ | Φ(°) | C(Mpa) |
|---|---|---|---|---|---|---|---|---|
| Coal | Sides | 1.521E+03 | 4.720 | 0.355 | 4.250 | 0.310 | 23.0 | 0.4 |
| Sandy shale | Immediate roof | 2.628E+03 | 106.614 | 9.277 | 41.743 | 0.432 | 44.7 | 7.5 |
| Sandy shale | Immediate floor | 2.658E+03 | 78.037 | 7.594 | 42.918 | 0.456 | 33.8 | 14 |
| Sandy shale | Old floor | 2.628E+03 | 68.004 | 1.544 | 39.481 | 0.367 | 47.5 | 3.6 |

**References**

[1] Bo Liu, Renshu Yang, Dongming Guo etc. Burst-Prone Experiments of Coal-Rock Combination at -1100m Level in Suncun Coal Mine [J].Chinese Journal of Rock Mechanics and Engineering, 2004, 23(14): 2402-2408.

[2] Standardization Administration of the People's Republic of China. GB/T 23561.1-2009~GB/T 23561.16-2010. People's Republic of China Standard. Beijing: Coal Industry Publishing House, 2009.04.

[3] D. M. Guo, H. J. Xue, L. J. Li, et al. Research on Bursting Liability and its Preventive Measures of -906m Deep Coal and Rock in Zhuji Coal Mine [C]. 2nd International Conference on Civil Engineering, Architecture and Building Materials, Yantai, 2012.

*Applied Mechanics and Materials Vols. 580-583 (2014) pp 1369-1376*
*© (2014) Trans Tech Publications, Switzerland*
*doi:10.4028/www.scientific.net/AMM.580-583.1369*

# Finite Element Analysis on Causes of Crack in Large Underground Garage

Bin SHU[1] and Jianhe PENG[2]

[1,2]Anhui and Huaihe River Water Resources Research Institute, Bengbu Anhui, China

492582452@qq.com

**Keywords:** underground garage; crack; finite element method; underground water; expansive soil

**Abstract:** The paper aims to solve the serious and regular crack problems in underground garage. ANSYS finite element software is applied to set up the overall finite element model on floor-foundation and foundation coupling beam-foundation soil in underground garage. Combined with engineering field detection, factors influencing underground garage floor like underground water level, soil expansion caused by water content change in expansive soil, soil poisson ratio, foundation settlement are taken into consideration to find out the causes of cracks. The study is expected to provide reference for similar cases in other projects.

## Introduction

At present, numerical methods like finite element methodand finite difference method, which can deal with complicated boundary and work out high nonlinear problems, have been widely applied to concrete crack analysis. In recent years, due to relatively accurate analysis of the whole process of concrete structure from loading to failure, finite element method can be used to fix the important data like cracking loadand failure load. It can help to do performance evaluationwhen macro cracks exist in present structure, and help to describe and predict propagation characteristicsof the cracks as well[1]. ANSYS finite element software has been applied to do static calculation for the workshopstructure of a power plant, to get the stress and displacement responseof concrete members in generator floorand finally help to analyze the causes of cracks in generator floor of the workshop. Taking reference from the case, this study adopts large general finite element software ANSYS[4-6] to analyze the static force of the running underground garage, to calculate the strain, stress and displacement response with interaction of different loads under running condition, and to explore the causes of concrete cracks in underground garage. The study is expected to provide reference for designing and engineering of similar garages.

## Engineering survey

### 1.1 Site engineering geologic conditions

The geomorphic units of the site are hilllock and clough landform, with mainly clay of late quaternary renewal period（Q3）and partly silty clay of shorter depositional time on clough landform. The whole overburden layer is 28m in thickness, and bedrock strong-weathered zone is 7m in thickness. The engineering site is originally farmland with a fish pond in, featured with soft soil and rich underground water. From top to bottom, the stratum distributes in the following way: ①miscellaneous fill； ② powder clay; ③ clay; ④ clay.

### 1.2 Structure layout

The underground garage is round in shape. The base coupling beam at the bottom of the floor is formed by circumferential ring beam and radial coupling beam.The separate base under the poles is directly connected with base coupling beam and floor. The thickness of the floor is 300mm, and it changes to 400mm when the radius turns more than 57.8m. As for the structure layout of the floor, base and base coupling beam, see Fig 1.

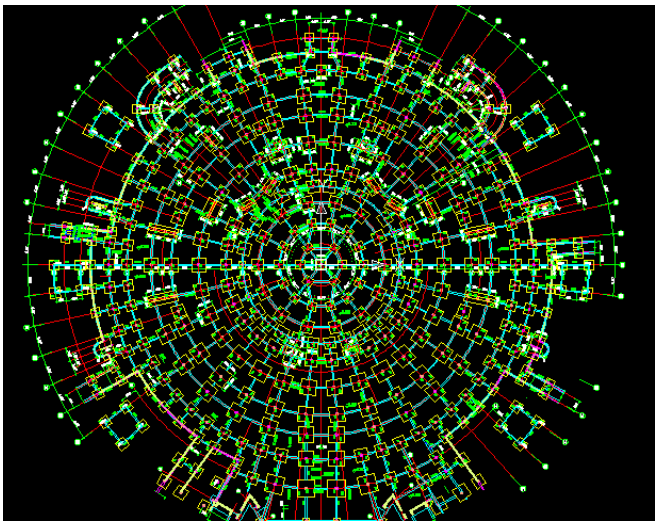

Fig 1 Structure layout of the floor, base and base coupling beam

## Field detection

### 2.1 Crack description

Through detection, there is no crack on poles and beams of first layer. Stripping cracks on wall body of the basement, it can be found that it is surface powder layer that cracks.

Cracks are common in leveling blanket on floor surface, and the most serious cracking lies in the area with radius between 44.6m and 57.8m. Cracks distribute in circumferential and radial way, and most lie in the middle of the floor. The width of crack surface ranges from 0.05mm to 0.2mm.

Through field straddle coring detection, it can be found that cracks are broad on the top and narrow in the bottom. Of 14 sample cores, 12 belong to sloping layer cracks and 2 extend to structure layer of the floor. From sample core surface, he width of cracks in structure layer is less than 0.05mm.

### 2.2 Structure testing

(1) The size of cross section of sampled frame beam can basically meet the design requirement. The appearance is in good condition with no defect like bare bars, voids or pores.

(2) The inferred value of concrete strength of the sampled basement poles ranges from 35.6MPa to 44.5MPa, which meet the requirement of design strength level C35. The inferred value of concrete strength of the sampled beams in first floor ranges from 31.5MPa to 45.4MPa, which meet the requirement of design strength level C30.

(3) The main bars configuration of sampled poles and frame beams, as well as the stirrup configuration in both encryption area and non-encryption area of poles and beams, all meet the design requirement.

### 2.3 Field monitoring

(1) According to the field situation, 3 water-level monitoring holes, namely, hole 1#, hole 2#, hole 3# are set up outside the underground garage. Throughout a rainy season, the water level of hole 1#

becomes 3.38~4.15m higher than the floor, the water level of hole 2# becomes 3.62~4.06m higher, and the water level of hole 3# becomes 2.81~3.78m higher. Monitoring result indicates that underground water level has relationship with surface water.

(2) In cracking area, select some frame poles and floor sample to take settlement observation. No settlement phenomenon is found, which indicates that the construction has been stable in settlement. The deformation of the basement floor has no obvious relationship with the changes of underground water level.

## Establishment of finite element analysis model

On the basis of engineering quality testing result, in order to further analyze the causes of floor cracks, ANSYS software is applied to take simulation analysis for floor-base and coupling beam-soil body structure system. Proper elements are selected to set up a 3d integral model. Factors like head pressure, poisson ratio, expansion ratio and expansion thickness of expansive soil, etc. are taken into consideration. Under different engineering conditions, the stress and strain state of the structure system is analyzed to explore the causes of floor cracks.

### 3.1 Calculation parameters

The physical and mechanical parameters of the floor, base, coupling beam and bottom soil are listed in Table 1.

Table 1 Physical and mechanical parameters of materials

| Item | Bulk density KN/m$^3$ | Elastic modulus MPa | Poisson ratio | Tensile strength MPa | Compressive strength MPa |
|---|---|---|---|---|---|
| C35 Concrete | 23 | 31500 | 0.27 | 1.57 | 16.7 |
| ③$_2$ Clay | 19.5 | 17.5 | 0.2~0.35 | / | / |

Partial coefficients are not considered in load. Pulling stress is positive while compressive stress is negative. The model adopts cartesian right coordinate with x and y as horizontal coordinate axis and z as vertical coordinate axis.

### 3.2 Calculation cases

（1）Underground water level: calculate the head pressure when water level reaches 1m, 2m, 3m, 4m, 5m respectively.

（2）Expansive soil: consider the combination of different values of volume expansion ratio, expansive thickness and poisson ratio: (1)when volume expansion ratio reaches 1%, 1.5%, and 3% ; (2)when the expansive thickness of clay layer ③2 reaches 1.5m, 3m, and 5m; (3)when poisson ratio of clay layer ③2 reaches 0.35, 0.3, 0.25, and 0.2.

### 3.3 Foundation settlement

Loaded by upper structure, the foundation settles with the floor and presses the ground. Therefore, convert the upper structure load on top of foundation as 150 KN/㎡.

### 3.4 Model specification

In this project, floor, foundation, coupling beam and soil body all adopt 3d 4 nodes tetrahedron element. The bottom of ③2 clay layer is constrained in three directions, and the surrounding boundary of ③2 clay layer is constrained in-plane.

## Calculation result analysis

### 4.1 Effect of foundation settlement

Through calculation and analysis, the max value of principal stress of floor is around 0.6MPa, with larger value in the range of 0.35MPa to 0.55MPa. The result can be seen in Fig 3. Therefore, according to the principal stress, under the single influence of structure gravity, foundation settlement has slight possibility to cause floor cracks.

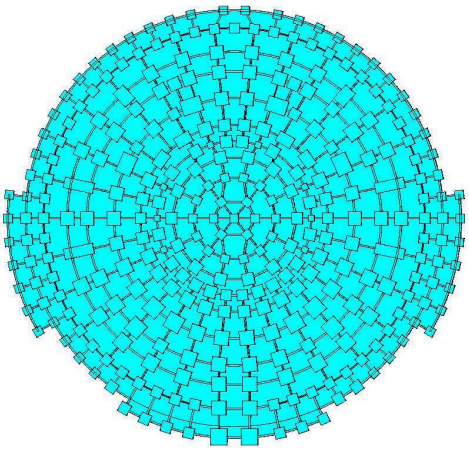

Fig 2 Structure model of floor, foundation and foundation coupling beam

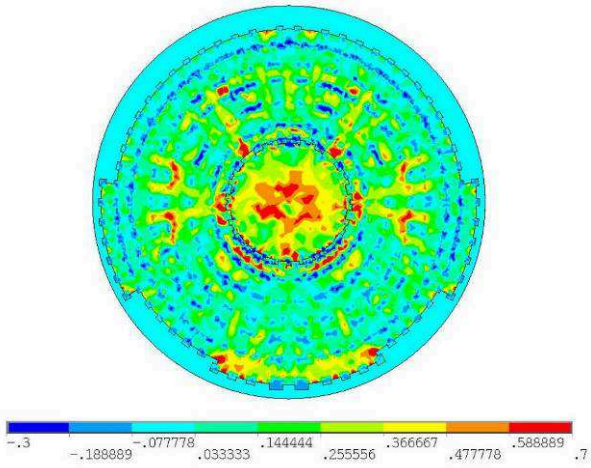


Fig 3 Distribution map of principal stress of floor structure $\sigma_1$ in foundation settlement

### 4.2 Effect of underground water on underground garage

Underground water is an important factor to influence the force on floor. Set the designed water level as 1m, and in engineering, take dewatering measure if water level reaches higher than 1m. Through testing underground water, it is found that underground water can reach as high as 4.15m, which is far beyond the designed level.

Five water heads are considered in calculation. The extreme value of floor stress under different engineering situations can be seen in Table 2.

Calculation result shows: under different underground water pressure, the maximum pulling stress in x, y direction and the maximum of principal stress $\sigma_1$ mainly lie in the middle part of the floor divided by coupling beams with radius between 44.6m and 57.8m. When water head is higher than 4m, the maximum of principal stress $\sigma_1$ reaches beyond 1.57MPa in some areas, which is beyond C35 concrete tensile strength. Detailed results can be seen in fig 4. When water head is higher than 5m, the maximum of principal stress $\sigma_1$ reaches beyond 1.57MPa in many areas. Detailed results can be seen in Fig 5.

Table 2 Extreme values of floor stress under different engineering situations

| Engineering situation / Results | | | 1m Water head | 2mWater head | 3mWater head | 4mWater head | 5mWater head |
|---|---|---|---|---|---|---|---|
| Extreme values of floor stress (MPa) | Pulling stress | $\sigma_{xx}$ | 0.42(few) | 0.6 | 0.9 | 1.1 | 1.5 |
| | | $\sigma_{yy}$ | 0.46 | 0.6 | 0.9 | 1.1 | 1.5 |
| | | $\sigma_{zz}$ | 0.12 | 0.15 | 0.25 | 0.4 | 0.5 |
| | compressive stress | $\sigma_{xx}$ | 0.46 | 0.9 | 1.4 | 1.8 | 2.3 |
| | | $\sigma_{yy}$ | 0.5 | 1.0 | 1.6 | 2.2 | 2.5 |
| | | $\sigma_{zz}$ | 0.25 | 0.5 | 0.8 | 1.0 | 1.4 |
| | Principal stress | $\sigma_1$ | 0.6 | 0.7 | 1.0 | ⩾1.57 (few) | ⩾1.57(many) |
| | | $\sigma_2$ | -0.55 | -1.1 | -1.8 | -2.5 | -3.0 |

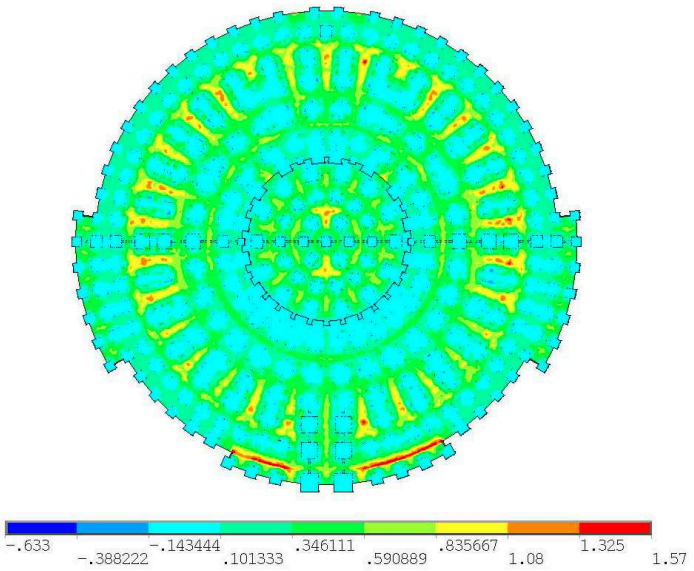


Fig 5 Distribution map of principal stress of floor structure $\sigma_1$ in 5m water head

### 4.3 Effect of expansive soil on underground garage floor

Different expansive ratio, expansive thickness and possible poisson ratio of the soil are considered. The extreme values of principal stress under different engineering situations can be seen in Table 3. Detailed analysis is as follows:

（1）When the floor structure is under the effect of expansive force with different expansive ratio, the maximum pulling stress in x, y direction and the maximum principal stress mainly locate in the middle part of the floor divided by coupling beams with radius between 44.6m to 57.8m. When the poisson ratio is 0.35 and the volume expansive ratio of the floor becomes 1.5%, in many areas the maximum value of principal stress $\sigma_1$ becomes over 1.57MPa; when the expansive ratio reaches 3%, in most areas the maximum value of principal stress $\sigma_1$ becomes over 1.57MPa. The areas where the principal value is beyond C35 concrete compressive strength(1.57MPa) mainly locate in the middle part of the floor divided by coupling beams and many locate in the floor with radius between 44.6m to57.8m. When the poisson ratio is 0.3 and the volume expansive ratio of the floor becomes 1.5%, cracking tales place in a few areas; when the expansive ration reaches 3%

cracking tales place in many areas. When poisson ratio is or less than 0.25 and the expansive ratio is 1.5%, most principal stress is less than 1.57MPa with little possibility to crack; when the expansive ratio is 3%, in many areas of the middle part of the floor divided by the coupling beams, the principal stress is over 1.57MPa with more possibility to crack.

（2）Displacements in x, y directions of the floor structure are slight. Displacement in z direction is comparatively more obvious, with maximum value between 0.7mm to 2mm locating in the floor of radius between 44.6m to 57.8m. Displacement in z direction may cause concrete cracking in upper leveling blanket.

Above all, if expansive soil pressure is only considered, when the volume expansive ratio reaches 1.5% to 3%, the floor structure may crack in some parts or in most areas.

Table 3 Extreme values of principal stress under different engineering situations

| Item \ Engineering situation | | | Poisson Ratio | | | |
|---|---|---|---|---|---|---|
| | Expansive thickness | Expansive ratio | 0.35 | 0.3 | 0.25 | 0.2 |
| Extreme values of principal stress (MPa) | 5m | 1% | ≥1.57 few | 1.1 | / | / |
| | | 1.5% | ≥1.57 many | ≥1.57 a few | ≥1.57 few | 1.4 |
| | | 3% | ≥1.57 many | ≥1.57 many | ≥1.57many | ≥1.57 many |
| | 3m | 1% | ≥1.57 few | 1.0 | / | / |
| | | 1.5% | ≥1.57 many | ≥1.57 a few | ≥1.57 few | 1.3 |
| | | 3% | ≥1.57 many | ≥1.57 many | ≥1.57 many | ≥1.57 many |
| | 1.5m | 1% | ≥1.57 few | 1.0 | / | / |
| | | 1.5% | ≥1.57 many | ≥1.57 a few | ≥1.57 few | 1.25 |
| | | 3% | ≥1.57 many | ≥1.57 many | ≥1.57 many | ≥1.57 many |

### 4.4 Effect of foundation settlement, water head pressure and expansive soil on underground garage floor

Through calculation and analysis, water head pressure and soil expansion caused by water content change in ③2 clay layer are possible reasons for cracks in underground garage floor. The rise of underground water level causes the increase of water head pressure, which further leads to the increase of water content in ③2 clay layer. These elements are mutual influenced to take effect. Meanwhile, the effect of the foundation settlement and pressure on foundation soil as loaded by upper structure can be neglected.

Therefore, it is of necessity to take integral consideration of foundation settlement, water head pressure and soil expansion caused by water content change in clay layer to study the strain and stress of underground garage floor and foundation in skirt building. In the calculation, the upper structure load on foundation top is converted to 150KN/m2; foundation floor is supposed to be subjected to 5m water head pressure; in 1.5m under foundation floor the volume ratio of the soil is supposed to be 1%. Calculation result can be seen in Fig 6. The result shows, the principal stress in many areas of the floor with radius between 44.6m to 57.8m is over 1.57MPa, which may cause cracking in many areas.

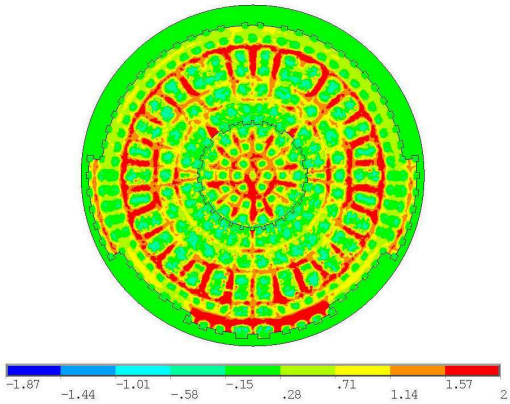


Fig 6 Distribution map of $\sigma_1$ in the floor with co-effect of foundation settlement, underground water pressure and expansive soil (1% expansion ratio)

### 4.5 Integral analysis

Integral analysis under different engineering situations shows, under the single effect of foundation settlement caused by the dead weight of upper structure, it is of slight possibility to crack in larger area of the floor; under the co-effect of foundation settlement caused by the dead weight of upper structure and higher water pressure, the foundation floor cracks; besides foundation settlement and higher water pressure, with extra effect of expansive soil, even if the expansion ratio is only 1%, cracks would become common. The calculation result coincides with the field testing result in distribution rule and position of cracks. The floor cracking has intimate relationship with rich underground water and higher water level, which is the main reason for floor cracking.

## Conclusion

The engineering quality of underground garage is a complicated problem with practical significance. This paper starts from practical engineering background, through field quality testing, adopts finite element method to study the mechanical properties of floor-foundation and foundation coupling beam-foundation soil structure system. It studies the strain and stress of the floor in different engineering situations with effect of underground water level, soil expansion caused by water content, poisson ratio and foundation settlement, and it analyzes the causes of the cracks in underground garage floor. Through calculation and analysis, the following conclusion can be drawn:

1. Effect of underground water on underground garage structure system. As it takes a long span for large underground engineering, usually through wet and dry seasons, with drastic change in water level, the dewatering measure has great effect on engineering quality of underground garage.

2. Effect of expansive soil on underground garage structure system. For the infiltration of the surface water makes the foundation clay expand to produce vertical thrusting force to lead to cracks, engineering investigation and designers need pay special attention to it.

## References

[1] Yin Zheng-gang. 3D Finite Element Method Static Analysis on Qiaogong Powerhouse[J]. Enterprise Science and Technology & Development, 2008( 10) : 130-131.

[2] XUE Jingjing; ZHANG Zhenhua. Static Cause Analysis of Floor Cracks for Powerhouse of Hydropower Station with 3D Finite Element Method [J]. Water Resources and Power, 2011(2): 72-75.

[3] WANG Xizhong. ZHANG Zhenhua. Analysis of slope stability of Boarixile Open-pit Mine with ANSYS [J]. Journal of Liaoning Technical University(Natural Science), 2008, 27(3): 342-345.

[4] MA Xian-chun; WANG Lei; ZHAO Fa-suo. SENSITIVITY ANALYSIS ON FACTORS INFLUENCING LANDSLIDE STABILITY AND DISCUSSION ON ITS TREATMENT DESIGN [J]. Journal of Geomechanics, 2008, 14(4): 381-385.

[5] XU Yu-jing; SUN Ke-li; HUANG Fu-cai. Application of ANSYS in the Earth dam seepage flow stability computation[J]. Water Power, 2003, 29(4): 69- 71.

[6] WANG Xizhong. ZHANG Zhenhua. Analysis of slope stability of Boarixile Open-pit Mine with ANSYS [J]. Journal of Liaoning Technical University(Natural Science), 2011(2): 72-75.

*Applied Mechanics and Materials Vols. 580-583 (2014) pp 1377-1381*
*© (2014) Trans Tech Publications, Switzerland*
*doi:10.4028/www.scientific.net/AMM.580-583.1377*

# The Application of Fracture Mechanics in Highway Tunnel Lining Cracking

Songzhou Chen[1,a]

[1]Road & Bridge International Co.Ltd.,South Branch Co.Ltd.,Beijing 101121,China

[a]305934042@qq.com

**Keyword:** Fracture mechanics Highway tunnel Stress intensity factors Cracks

**Abstract**.Lining cracks of highway tunnel has a very important effect on the healthy operation of the tunnel. Establishing the model for concrete fracture mechanics evaluation, we could identify the tunnel lining cracking situation. By using Linear elastic fracture mechanics method we could calculate the stress field of crack in the lining. Separately by different depth we have calculated crack stress intensity factor. We get that growing rates of variation of stress intensity factor as the crack depths increase. So lining tunnel health operations severely cracked.

## Introduction

As a branch of solid mechanics, fracture mechanics is a science and studies the strength of the materials or structures with crack and crack extension rule. According to the mechanical characteristics of the object, fracture mechanics can be divided into the linear elastic and elastic-plastic fracture mechanics [1]. The fracture mode of engineering components can be classified into three basic types: I fracture type (open), II fracture type (slip), III fracture type (tear). From the point of view of mechanics of elasticity, fracture type can be considered to be respectively the plane stress problems, plane strain problems and constant cross-section rods reverse problems (actually belong to the two-dimensional problem). When the fracture problems are in research, the stress intensity factor K is one of the important concept. It is a major determinant of the crack tip stress field strength, is the crack area public factor of stress component value and it also is the important parameter of the crack in engineering component wether it is damaged or not .When the stress intensity factor K is not greater than the material fracture toughness Kc, we think the buckling does not destroy; On the contrary, the engineering materials will lose their job functions.

Because the highway tunnel's geological condition is more complicated, the tunnel design and construction technology development are not yet perfect, during the tunnel service they usually appear all sorts of diseases, such as: water leakage, lining crack and so on. Among them, the healthy operation of the tunnel is mostly affected by the tunnel lining cracking. Groundwater along the inside lining crack seeps into the tunnel and causes corrosion of the internal auxiliary facilities such as ventilation, lighting and the others, at the same time it damages the pavement. If lining crack is not timely and accurate processed, it is likely to affect the normal operation of the tunnel. In this paper, based on the lining cracking problem of a tunnel of Chongqing, We calculate and analyze the theory of fracture mechanics to judge the change of the crack effect on lining structure.

## Concrete Fracture Mechanics

Crack of concrete structure has a decisive influence. Since 1961, when the fracture mechanics were introduced in the research of concrete material, we have been studying the formation, development and characteristics of concrete crack. A branch of the fracture mechanics, concrete fracture mechanics [6] is produced .

Stress environment and crack of concrete structure have direct relation, quantitative description of the instability criterion and model of concrete crack is one of the important research content of concrete fracture mechanics. Because concrete fracture mechanics characteristics mainly include the following[1]: (1) At the crack tip, concrete material has different from metal micro crack zone and it is the decision of the evolution process of concrete crack; (2) Whether in a plane stress problem or a plane strain problem, the load of concrete crack can be easily unified to analysis and research; (3) the fracture toughness of concrete Kc has the very strong scale effect; (4) the cracking of concrete material area and crack area strain are essentially different. The application of fracture mechanics of concrete in tunnel project is mainly reflected by studying the stability of the lining of serious cracks, analyzing the necessity of strengthening and treatment methods.

Fracture mechanics of concrete can be divided into the linear elastic fracture mechanics of concrete and concrete nonlinear fracture mechanics. Through studying the linear elastic fracture mechanics, concrete fracture state can use two kinds of methods: stress field method and energy method.

**Tunnel Lining Crack Analysis**

2.1 Project summary

The tunnel buried depth and its geological conditions is complicated, geological location is longer than the other. For area with poor geological conditions (such as IV, V class of surrounding rock), we adopt Φ 25 hollow grouting anchor spray, spray concrete, steel fiber concrete, the grid steel frame construction support, mold injection of concrete and reinforced concrete lining. In the early stages of the tunnel lining.

2.2 Lining crack type

(1) According to the relationship of fracture strike and tunnel towards, lining crack can be divided into longitudinal crack, ring to crack and oblique crack.

Longitudinal cracks are the lining cracks which parallel to the tunnel axis and they are the most harmful cracks; the ring cracks almost occurred in bad geological location and the mouth of the cave; Oblique belongs to structural cracks. The causes are that tensile stress of inclined section of the tunnel concrete is more than tensile strength and shear stress is more than the shear strength.

(2) According to the fracture fissure feature, lining crack can be divided into a mouth crack (figure1 (a)), silent type, fault type (figure1 (b)) and shrinkage ring type.

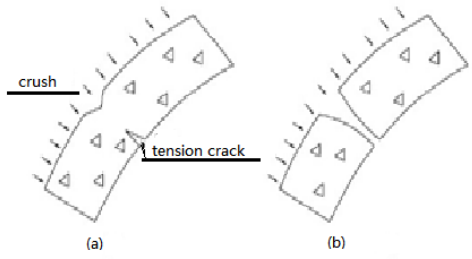


Fig.1. Characteristics diagram of lining fracture

2.3 The detection method and statistics of Lining crack

（1）The field detection techniques of lining crack

At present, the main method of detection of tunnel lining crack' s situation is: the length and width of the cracks were measured with a ruler, the depth of the cracks were mainly determined by drilling or ultrasonic method. The detection methods of development and change of the crack

mainly has: marking grey piece, marking metal plate, marking drill nail and the measuring method of the crack meter and strain gauge.

（2）Lining crack statistics

Lining crack statistics and detection of a highway tunnel's left hole in Chongqing is as follows: On the left side of the wall, there have been 77 arch loin vertical cracks , cracks generally range from the ground to hance, individual crack extended upward to the vault, a total of 17 cracks' width is greater than 0.4 mm; On the left side of the wall, hance, the part of the vault appeared the levels of article 7 of the longitudinal crack, a total of five cracks' width is greater than 0.4 mm. The position with the right side of the wall and hance appears 65 vertical cracks, including 10 cracks craze after fracture closed, 14 cracks have been closely processed. Cracks generally range from the ground to hance, individual crack extended upward to the vault, only 1 crack width is greater than 0.4 mm; At right side of the wall, hance and the vault, there were eight longitudinal cracks and the cracks are about 1.5 m from the ground, individual crack extended upward to the vault, only a crack's width is greater than 0.4 mm. Among them, the longest length of the crack is 1150 cm, the shortest is 10 cm. The typical pictures are shown in Fig.2,Fig.3,Fig.4..

Fig.2Rightarch lumbar transverse cracks on K8+775

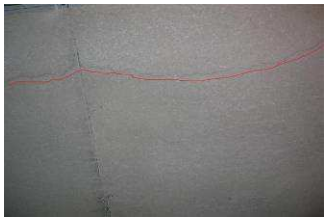

Fig.3 Arch vertical cracks on K10+339

Fig.4 Rightarch lumbar inclined cracks

2.3 Lining crack reason analysis

The cracking reasons of tunnel lining are various: design, construction and service environment and many other factors which could lead to a lining cracks. When tunnel lining appears cracking condition, this explains that the service environment of the tunnel is much more severe than expected design, so the analysis of the causes of cracks on the lining of tunnel is good for maintenance. The major effect of the lining cracking reasons [2, 3, 6] are as follows:

(1) Design reason

According to the error of the hierarchy of surrounding rock' s type, lining option is not adapt to the environment of the surrounding rock, and the actual load of lining caused by the actual under design load is greater than the expected value; Corresponding measures didn't be taken in areas of complex geological situation, as the swelling wall rock section did not take the curved wall of inverted arch lining.

(2) The construction

The hydration of cement, the temperature stress of concrete material itself, improper restrictions, construction method, construction technology, construction organization and management and so on are almost likely to lead to the cracking of concrete lining.

(3) Geological environmental reasons

Bad geology area, geological surrounding rock without surveying and groundwater exploration are likely to cause the cracking of concrete lining.

**Lining structure fracture mechanics calculation**

The situation of cracking of tunnel lining is the large number of longitudinal cracks, arch cracking is in severe cases. Based on the linear elastic fracture mechanics state of knowledge , this paper analysis and research state of lining structure cracks to calculate the stress intensity factor of the concrete through the stress field method and to judge state of concrete crack extension through the change of the stress intensity factor.

3.1 Lining structure fracture mechanics calculation model [2], [3]

When calculating the lining concrete fracture mechanics, the first time is to determine fracture external mechanical environment, the tunnel vault crack force situation can be simplified as working together between vault bending moment $M_d$ and arch axial force $N_d$. Because at the beginning of the tunnel lining adopt single heart round piece of lining structure, so the calculation formula of the vaults of the internal force is shown in Eq. 1:

$$\left.\begin{aligned} M_d &= M_{hp} + \sigma_d M_{d\sigma} \\ N_d &= N_{hp} + \sigma_d N_{d\sigma} \end{aligned}\right\} \quad (1)$$

Respectively, $M_{kp}$ and $N_{kp}$ are the arch structure of bending moment and axial force; $M_{d\sigma}$ and $N_{d\sigma}$ are the arch elastic resistance of bending moment and axial force; $\sigma_d$ is the elastic resistance.

Simplified calculation mode of the vault lining crack fracture mechanics is shown in Fig.5:

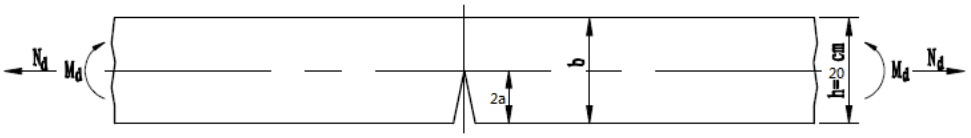


Fig.5 The calculatianal model of fracture mechanics

The thickness of the tunnel initiative lining is 20 cm. Based on the calculation of the different depth of crack fracture mechanics , this paper analyzes the influence of cracks on the lining structure. Taking 2 a = 2~18 cm, vault cracks whose width is b are infinite long slat.

3.2 Stress intensity factor calculation [1], [6], [7]

For the sake of safety, lining crack stress intensity factor were calculated according to the type I fracture; Under the condition of elastic fracture mechanics, the arch axial force and bending moment are regarded as the external load of stress intensity factor. $K_1$ is obtained by linear elastic superposition principle, That is to say as Eq. 2 :

$$K_1 = K_{1M} + K_{1N} \quad (2)$$

I loading stress intensity factor is available type (3) :

$$K = y\sigma\sqrt{\pi a} \quad (3)$$

Among them, y is the shape of the crack factors or load conditions, such as type (4) and (5):

$$y_M = \sqrt{\frac{2b}{\pi a}\tan\frac{\pi a}{2b}}\,\frac{1+0.2(1-\sin\frac{\pi a}{2b})^4}{\cos\frac{\pi a}{2b}} \quad (4)$$

$$y = \sqrt{\frac{2b}{\pi a}\tan\frac{\pi a}{2b}}\,\frac{0.8+\frac{2a}{b}+0.4(1-\sin\frac{\pi a}{2b})^3}{\cos\frac{\pi a}{2b}} \quad (5)$$

$$\sigma_M = \frac{6M}{b^2} \quad (6)$$

$$\sigma_N = \frac{N}{A} \quad (7)$$

Respectively, substitute (6) and (7) into type (3):

$$K_{1M} = 6y_M \frac{\sqrt{\pi a}}{b^2} \cdot M \quad (8)$$

$$K_{1N} = y_N \frac{\sqrt{\pi a}}{A} \cdot N \quad (9)$$

Substitute(8) and (9) into type

$$K_1 = 6y_M \frac{\sqrt{\pi a}}{b^2} \cdot M + y \frac{\sqrt{\pi a}}{A} \cdot N \quad (10)$$

The depth of crack is taken different values between 4 to 18 cm, the change of the stress intensity factor come to the conclusion, such as Tab. 1.

Tab.1 Calculation results of stress intensity factor

| Crack depth: 2a | 2a=2 | 2a=4 | 2a=6 | 2a=8 | 2a=10 | 2a=12 | 2a=14 | 2a=16 | 2a=18 |
|---|---|---|---|---|---|---|---|---|---|
| $K_1$ | $56.5M_d$ $+1.7N_d$ | $68.9M_d$ $+2.0N_d$ | $84.5M_d$ $+2.8N_d$ | $101.1M_d$ $+3.7N_d$ | $120.4M_d$ $+4.9N_d$ | $142.9M_d$ $+6.1N_d$ | $177.2M_d$ $+9.3N_d$ | $212.5M_d$+ $10.6N_d$ | $320.9M_d$ + $18.9N_d$ |

3.3 The result analysis

See from table 1, at the beginning of the lining cracking, stress intensity factor of crack extension grows slowly, but with the increase of crack depth and the change of the stress intensity, the cracks are becoming more and more sensitive. This suggested that the deeper crack depth of tunnel lining structure is most harmful.

## Conclusions

The crack of tunnel lining concrete have very big effect on the healthy operation of the tunnel, particularly because concrete crack was born and the tunnel is in the mountain, once the cracks penetrate the lining, it will cause the seepage water diseases. Effect of corrosion on the lining of steel bar is caused by groundwater. Eventually great influence on the healthy operation of the tunnel comes out. So the calculation of the tunnel lining fracture mechanics plays an important role in the lining of health.

## References

[1] Qichao Hong. Engineering fracture mechanics foundation[M].Shanghai jiaotong university press, 1986

[2] Shun jun. Underground structures[M], science press, Beijing, 1991

[3] Renhun Jia. Tunnel engineering[M].Chongqing university press, 2005

[4] Zhiguo Li, Yujun Zhang. Bearing capacity analysis of cracking of tunnel and governance technology.Tunnel construction, 2003, 23 (4)

[5] Leckie F A, Hayhurst D R. Constitutive equations for creep rupture[J]. Acta Metall, 1977(25)

[6] MinYao Xu.Application of fracture mechanics theory in highway tunnel lining cracking research[D]. Chongqing jiaotong university, master's thesis,2008

[7] Zhijian Yi. A new method for finding the solutions of stress intensity factor[J]. Journal of Chongqing jiaotong institute .1991(10)

*Applied Mechanics and Materials Vols. 580-583 (2014) pp 1382-1387*
*© (2014) Trans Tech Publications, Switzerland*
*doi:10.4028/www.scientific.net/AMM.580-583.1382*

# Studies on Damage Distinguishing of Underground Tunnel Structure based on BP Neural Network

ZUO Xi[1,2,a], CHEN Guo-xing[2,b], LI Wei-qian[2,c]

([1.] Institute of Architectural Engineering, Jinling institute of technology, Nanjing, 211169

[2.] Institute of Geotechnical Engineering, Nanjing University of Technology, Nanjing, 210009)

[1]School of Architectural Engineering, Jinling institute of technology, China

[2] Institute of Geotechnical Engineering, Nanjing University of Technology, China

[a]zxjit@jit.edu.cn, [b]gxchen@njut.edu.cn, [c]liwq@126.com

**Key words:** BP neural network; underground engineering structure; damage identification; change rate of curvature

**Abstract:** With the expansion and development of scale of construction on metro engineering, the damage diagnosis and the safety evaluation on underground engineering structure have become vital problems to be solved. This paper raised an idea to distinguish underground engineering structure based on BP neural network: define change rate of curvature of structure, and recognize it as the input scalar of BP neural network, using a reducing unit elastic modulus method to simulate damage location and damage degree, through various set of underground structure extent of damage, recognize the first four order curvature structure change rate as input of BP neural network. The results show that the method using BP neural network can identify the damage degree of underground engineering structure accurately and can solve the damage identification problem of underground engineering structure conveniently and effectively.

## Introduction

During the use of process, due to fatigue load, environmental corrosion, material aging, defect and other reasons, underground structure produce damage accumulation gradually, which reduces structure's bearing capability and the ability to resist natural disasters,so existing structure may have serious damage especially when suffering earthquakes. Hence the analysis of dynamic damage degree of underground structure, then the earthquake damage characteristics of it is particularly important to evaluate. The seismic damage evaluation of the eventual establishment of underground structure damage quantitative evaluation standard under the effect of earthquake, and provide a theoretical basis for the seismic design and seismic rehabilitation of underground structure.

In the recent 30 years, domestic and foreign scientific workers work very fruitful researches in structural damage identification technology. Cawley confirmed that identification of damage existence can be improved according to reduce the frequency and damping structure. Biswas studied structure damage localization according to the structure changes of natural frequency and vibration mode. Mannan studied that using the measured frequency response function of structure can diagnose damage. Cassiots introduces a method using only frequency variation of structure to identify local stiffness reduction. Kunihiko used the finite element calculation model to train BP neural network model,and identify the damage state and damage degree in known strain condition. Xie will use the SVM to the damage detection of composite structures, the results show that the

support vector machine method has a high recognition accuracy. Yu detected structural damage, using the method of dynamic response analysis and the eigenvalues of the perturbation theory.

In this paper, based on a large number of domestic and international relevant damage identification and neural network literature, according to the development prospect of damage identification and artificial neural network, using the finite element ABAQUS program, it combines the modal analysis theory and BP neural network for damage identification of underground structure engineering, meanwhile realizes the identification of damage location and the degree of damage.

**Damage identification of underground structure method based on BP neural network**

Due to dynamic characteristics and physical parameters of the structure are related directly, damage of underground structure will change the dynamic characteristics. But the damage identification method only using dynamic parameters is to identify structure, which often needs math to solve complex inverse problems, and is difficult to be applied to practical engineering. Due to the neural network for its excellent nonlinear mapping ability can make the inverse problem positive, we can combine the dynamic parameter analysis method with neural network technology, and recognize structural damage indicator with kinetic parameters as the characteristic parameters of neural network input to identify structure damage.

BP neural network with its good nonlinear mapping ability becomes the most widespread neural network in the field of application of structure damage diagnosis. BP neural network is multilayer network which makes W-H learning rules general, and can weight train nonlinear differential function, and is also a multilayer feedforward neural network. Transform function of its neurons is S type function, so the outputs is continuous variables between 0 to 1, and this function can realize the arbitrary nonlinear mapping from input to output. The basic BP algorithm includes two aspects: signal propagation and error back propagation. That is to say that the calculation direction of actual output is from the input to the output, while the weights and threshold corrections direction is from the output to the input. The network structure and the algorithm flow chart are as shown in Figure 1 and Figure 2. In the graph, $x_j$ represents the j-th node input in the input layer, j=1,2,⋯,m; $w_{ij}$ represents the weight between the i-th node in the hidden layer and the j-th node in the input layer; $\phi(x)$ represents the driving function in the hidden layer; $w_{ki}$ represents the weight between the k-th node in the output layer and the i-th node in the hidden layer, i=1,2,⋯,q; $a_k$ represents the K-th node threshold in the output layer, k=1,2,⋯, L; $\varphi(x)$ is the driving function of output layer; $O_k$ says the output of the K node in the output layer.

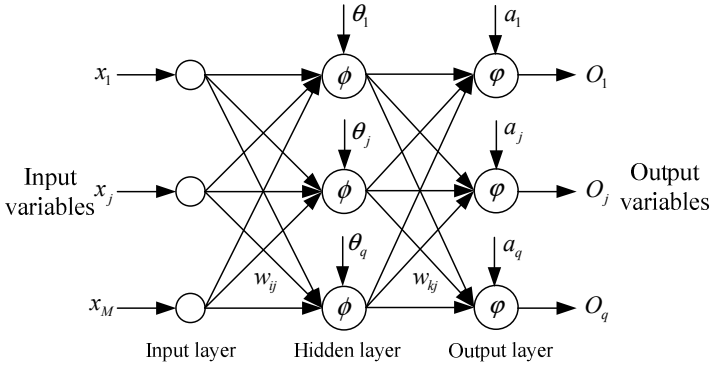


Fig.1 Structure of BP network

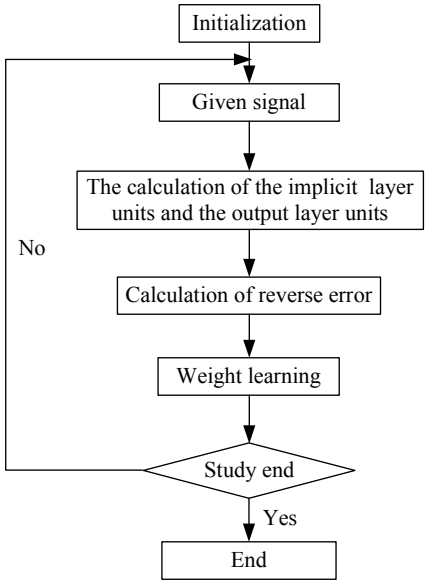


Fig.2 Process of BP algorithm

Considering the input vector of the neural network has a direct impact on the recognition performance of the network, physical quantities of damage location should be the parameters sensitive to the structure of local damage, and are on the trend of monotonous change with the increase of structural damage degree. This paper chooses the curvature change rate as input of neural network, recognizes the damage location and extent as output, to identify the damage location and extent. In this paper, the definition of frequency change rate: suppose the i-th order curvature value of the point k is $\delta_{i,k}$ when the structure has no injury, the curvature value under the i order mode of vibration is $\delta_{i,k}^{*}$ after injury mode, then the curvature change is $\Delta\delta_{i,k} = \delta_{i,k}^{*} - \delta_{i,k}$, and then define relative change rate of the curvature is the sum of change rate of i order curvature $\varepsilon = \sum_{0}^{i} \left| \Delta\delta_{i,k} / \delta_{i,k} \right|$. This paper focuses on studying the influence of structural damage on the change rate of curvature, and effectively predict the structural damage through the change rate of curvature.

In this paper, during the damage identification process, BP network model structure uses three-layer network, and the neurons number in the input layer is 4, and the number of the hidden layer neurons is 6, and output layer neurons number is 4, and the transfer function of the hidden layer neurons uses S type tangent function tansig, and the output layer neuron transfer function uses S type logarithm function logsig. The network training process is a process revising the weights and thresholds constantly, and make the input error of network reach the minimum error by adjusting, and the final training error of this article is 0.0015, so iterating until the network converge.

## Damage identification of underground subway structure

2.1 Analysis model of damage identification of underground structure

Taking Nanjing Metro as the research background, the typical underground tunnel structure as the research object, structure of underground tunnel is simulated by beam element, and the foundation soil were simulated by solid element, and the computational domain foundation width is 120m, and the finite element of grid soil underground tunnel structure system is divided as shown in Figure 3, and the node of underground tunnel structure is as shown in Figure 5. The mechanics material parameters of structure:elastic modulus E=$3\times10^{10}$ Pa, density ρ= 2500kg /$m^3$, Poisson's ratio μ= 0.2. The mechanics material parameters of soil: elastic modulus E =$8\times10^{6}$ Pa, density

$\rho$=1800kg/m$^3$, Poisson's ratio $\mu$=0.35. We can analysis the finite element modal and get the input of the neural network.

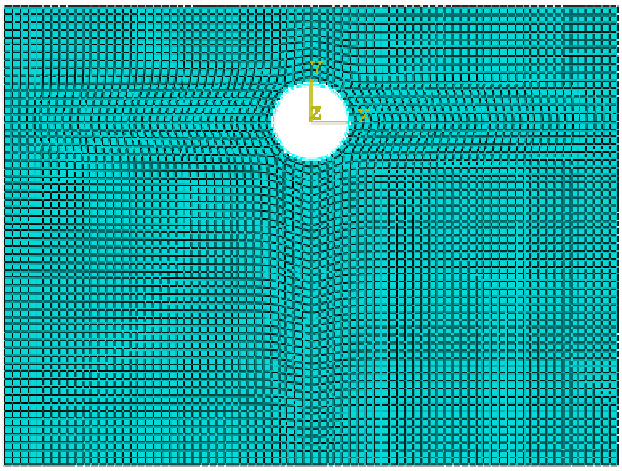

Fig.3 Finite element mesh of soil-underground structure system

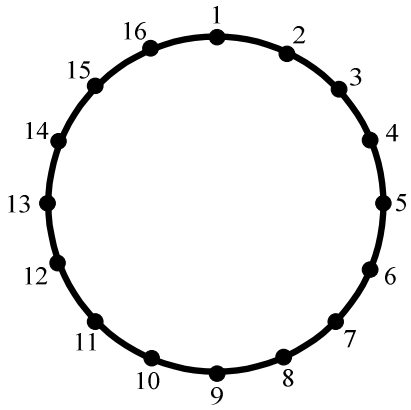


Fig.4 Node diagram of underground structure

2.2 Damage identification of underground subway structures

Damage of structure in essence is local structural stiffness loss, so the analysis on the dynamic damage characteristics of the structure can simplify calculation, assuming the structural damage can be simulated by reducing the elastic modulus of elements. The damage at one position can be simulated with the reduce of the elastic modulus,and the damage degree of the structure can be simulated with the reducing degree of the elastic modulus.

According to the existing research we can know that circular tunnel structure damage in the plane of tunnel about $45^0$ position is the most serious,so we should study No. 3, No. 7, No. 11 and No. 15 node among finite element models for the damage identification of circular underground tunnel structure. Assuming that underground structure around the unit of No.3 node causes damage of 30%, drawing a curve as shown in Figure 6 which shows node changes with the first 4 order change rate of curvature. It can be seen that the curve peak appears in the 3 node position, the change rate of curvature is very sensitive to the damage location, and is not affected by the symmetric structure, therefore we can determine the location of the damage of underground structures according to the rate of 4 order curvature changes in the structure.

In order to determine the variation characteristics of damage degree of underground structure, by calculating the change rate of curvature about the unit in different damage cases, Figure 7 is the curve of the change rate of curvature nodes around No.3node when the damage degree is 10%, 30%, 50%, 70% and 90%. It can be drawn from the chart, the change rate of curvature of structure is sensitive to the damage degree of underground structure, namely in the same damage location, with the increase of the damage degree, numbers of curvature change rate increases.

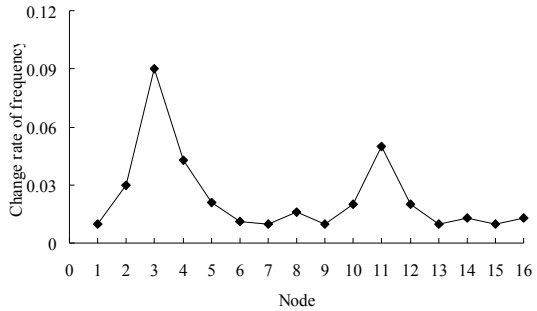


Fig.5 Curve of change curvature rate

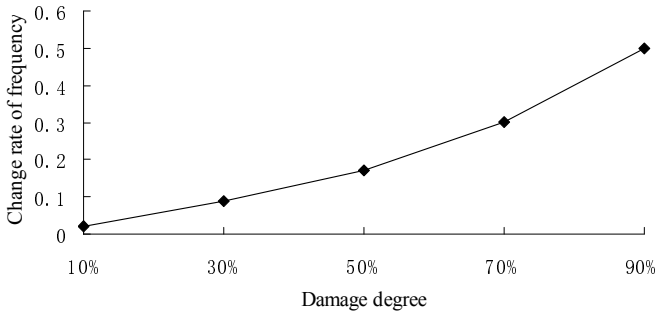


Fig.6 Change curvature rate of node 3

Recognizing a total of 20 sets of data of modal change rate when the damage degree of No.2,No.5,No.8,No.11 node respectively are 10%, 30%, 50%, 70%, 90% as training samples for BP neural network. The output of the neural network (Y1, Y2, Y3, Y4) respectively represent damage situation above 4 units, such as network output (0, 0.5, 0, 0) No.5 on behalf of 50% of the injury on the unit. To train sample, plus the change rate of curvature on the 40% and 80% damage degree as the test sample of the neural network, which is used to test the adaptability of recall memory, interpolation and extrapolation of neural network.

Neural network training error is 0.001398 after BP neural network training 20000 times, then the training halts. Input the test sample set into the trained neural network, and the test results are shown in Table 1, and the errors between the theoretical value and the predicted value are as shown in Figure 7. It can be found that the error between the theoretical value and the predicted value is relatively small, and the predicted values can reflect the damage degree completely based on BP neural network.

Table.1 Damage identification results based on BP Neural Network technique

| Sample | Ideal output of network | | | | Actual output of network | | | |
|---|---|---|---|---|---|---|---|---|
| 3 node | 0.1 | 0 | 0 | 0 | 0.110 | -0.001 | 0.015 | -0.002 |
| | 0.3 | 0 | 0 | 0 | 0.334 | 0.001 | -0.001 | -0.002 |
| | 0.5 | 0 | 0 | 0 | 0.546 | -0.008 | 0.002 | 0.001 |
| | 0.7 | 0 | 0 | 0 | 0.737 | 0.000 | -0.007 | 0.001 |
| | 0.9 | 0 | 0 | 0 | 0.943 | -0.005 | 0.010 | 0.009 |
| 7 node | 0 | 0.1 | 0 | 0 | 0.007 | 0.120 | 0.000 | -0.009 |
| | 0 | 0.3 | 0 | 0 | 0.004 | 0.325 | 0.006 | 0.001 |
| | 0 | 0.5 | 0 | 0 | -0.009 | 0.526 | 0.005 | 0.010 |
| | 0 | 0.7 | 0 | 0 | 0.005 | 0.741 | 0.002 | -0.009 |
| | 0 | 0.9 | 0 | 0 | -0.007 | 0.956 | 0.001 | 0.005 |
| 11 node | 0 | 0 | 0.1 | 0 | -0.004 | 0.007 | 0.101 | 0.006 |
| | 0 | 0 | 0.3 | 0 | 0.006 | 0.005 | 0.321 | -0.006 |
| | 0 | 0 | 0.5 | 0 | 0.002 | -0.002 | 0.530 | 0.013 |
| | 0 | 0 | 0.7 | 0 | -0.013 | 0.011 | 0.732 | 0.004 |
| | 0 | 0 | 0.9 | 0 | 0.008 | -0.001 | 0.933 | -0.004 |
| 15 node | 0 | 0 | 0 | 0.1 | 0.001 | 0.001 | -0.009 | 0.112 |
| | 0 | 0 | 0 | 0.3 | 0.014 | 0.010 | 0.003 | 0.320 |
| | 0 | 0 | 0 | 0.5 | -0.005 | 0.009 | -0.009 | 0.522 |
| | 0 | 0 | 0 | 0.7 | 0.021 | 0.006 | 0.009 | 0.727 |
| | 0 | 0 | 0 | 0.9 | -0.009 | 0.002 | 0.014 | 0.920 |

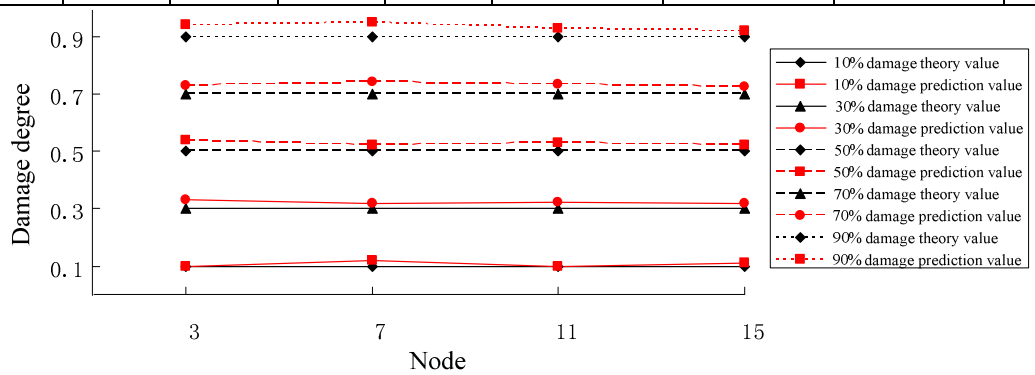


Fig.7 Prediction error curve between the predicted value and the theoretical value under different damage degree

## Conclusions

This paper introduces the method of underground tunnel structural damage identification based on BP neural network method, and analyses metro tunnel structure through ABAQUS finite element computing platform, and combining with the damage identification model of structure BP neural network, we can draw the following conclusions:

(1)it is reasonable to recognize the first 4 order change rate of curvature of underground engineering structure as the damage signature, because the signature is not only sensitive to the damage location, but damage degree is monotone function, and using it as input parameters of BP neural network can obtain the damage identification results.

(2) The trained BP neural network has good associative memory, good interpolation and extrapolation abilities, so that it can accurately identify the damage degree of underground engineering structure, and has high accuracy.

(3) Based on the BP neural network, underground engineering structure damage identification method only needs to consider the structure of the first 4 modes, and it is easy to acquire data, and has high precision, and can simply and effectively determine the damage degree of underground tunnel engineering structure.

## Acknowledges

This work was funded by Chinese Postdoctoral Science Foundation under Contract No. 2013M540442, Nature Science Foundation of Jinling institute of technology under Contract No. Jit-n-201202.

## References：

[1] CAWLEY P, ADAMS R D. The location of defects in structures from measurements of the natural frequencies. Journal of strain analysis, 1979, 14(2): 49-57

[2] BISWAS M, PANDEY A.K et al. Diagnostic experimental spectral modal analysis of a highway bridge. Journal of modal analysis, 1990, 5(1): 33-42

[3] MANNAN M A, RICHARDSON M H. Detection and location of structure cracks using FRF measurement. Proceeding of the 8th international modal analysis conference, Orlando, U.S.A, 1990, 652-657

[4] GASSIOTS S, JEONG G. D. Identification of stiffness reduction using natural frequencies[J]. Journal of engineering mechanics, ASCE, 1995, 121(5): 1106-1113

[5] KUNIHIKOTANAKA, ALANR.HARGENS. Wavelet Paeket transform for R-R interval ariability Medical. Engineering & Physies，2004, (26): 313-319

[6] XIE J H. APPlieation of Hilbert Transform and LS-SVM to Aetive Damage Monitoring for Composite Materials. The Proeeeding of 4th China-Japan-US Symposium on Struetural Control and Monitoring, 2006

[7] YU L., CHENG L., YAM L.H., YAN Y.J. Application of eigenvalue perturbation theory for detecting small structural damage using dynamic responses. Composite Structures, 2007, 78: 402-409.

[8] Zuo Xi, Yang Shu-cai, Chen Guo-xing. Analysis on Evolution of Nonlinear Seismic Damage of Subway Station Structure. Earthquake Resistant Engineering and Retrofitting, 2010, 32(1): 110-116

*Applied Mechanics and Materials Vols. 580-583 (2014) pp 1388-1391*
*© (2014) Trans Tech Publications, Switzerland*
*doi:10.4028/www.scientific.net/AMM.580-583.1388*

# Non-linear free vibration of submerged floating tunnel tether

Zhibin Su [1], Shengnan Sun [1,a]

[1] School of Architecture & Civil Engineering, Liaocheng University, Liaocheng, Shandong, 252059, China

[a] sunshengnan1982@163.com

**Keywords:** submerged floating tunnel; tether; non-linear free vibration; sag; initial tension

**Abstract.** Taking the free vibration system of a submerged floating tunnel tether as research object, the non-linear free vibration equation was set up. By means of Galerkin method, the partial differential equation was transformed into a set of ordinary ones. The damping ratios of the first four modes were obtained after complex eigenvalue analysis. Subsequently, effects of inclination, sag, initial tension force and length of tether on its modal damping ratios were analyzed. The results show that inclination and sag of tether merely affect the damping ratio of first in-plane mode; they have no effect on the damping ratios of higher order in-plane modes and out of plane modes; the first in-plane modal damping ratio of tether is in direct proportion to its inclination, whereas in inverse proportion to its sag; the first modal damping ratio of tether (both in-plane and out of plane) is in direct proportion to its length, whereas in inverse proportion to its initial tension.

## Introduction

Submerged floating tunnel (SFT), suspending in the water at some convenient depth and fixed to the seabed by means of a suitable anchoring system, is an innovative concept for crossing deep waterways. Compared with long span cable-stayed and suspension bridges, the increase of cost with span length is generally much better for submerged floating tunnels .

Vibration of tether was studied by many experts and scholars. Ge *et al.* [1] investigated the effect of tunnel surge motion on the dynamic response of a tether by considering the forcing and parametric excitations. Chen *et al.*[2] set up vortex-induced oscillation equations of tether and discussed its maximal dynamic shearing force and bending moments. Ge *et al.* [3] investigated vortex-induced vibration of submerged floating tunnel tube-tether coupled model. Luo *et al.* [4] established a nonlinear dynamic model equation of tether and solved it by the secondary development of finite element software. To solve the dynamic response of submerged floating tunnel under current, Xiang and Chao [5] studied the vortex-induced vibration and parametric vibration of tube and tethers.

In this paper, taking the free vibration system of a submerged floating tunnel tether as research object, the non-linear free vibration equation is set up. By means of Galerkin method, the partial differential equation is transformed into a set of ordinary ones. The modal damping ratios of the first four modes are obtained after complex eigenvalue analysis. Subsequently, effects of inclination, sag, initial tension force and length of tether on its modal damping ratios are analyzed.

## Non-linear free vibration model of tether

Fig. 1 shows the nonlinear analytical model proposed for the free vibration analysis of tether. Let $\boldsymbol{Z}=[x(s)\ y(s)]^{\mathrm{T}}$ denote the static configuration of tether, $s$ being a curvilinear abscissa. The dynamic configuration subjected to dynamic loading is described by the displacement $\boldsymbol{U}=[u(z,\ t)\ v(z,\ t)]^{\mathrm{T}}$ measured from the static equilibrium position. $t$ is time and $x$, $y$, $z$ are Cartesian coordinates shown in Fig. 1.

The governing differential equations of the tether motion can be derived using the Hamilton principle

$$\delta\int_{t_1}^{t_2}\int_0^L (Q-V)\mathrm{d}s\mathrm{d}t+\int_{t_1}^{t_2}\int_0^L \delta W\mathrm{d}s\mathrm{d}t=0 \tag{1}$$

In which, $\delta$ is the symbol for variation; $t_1$ and $t_2$ are the limits of the time interval; $L$ is the unstretched length of tether; $Q$ is the kinetic energy density, $Q=\frac{m}{2}(\dot{\boldsymbol{U}})^{\mathrm{T}}\dot{U}$ ; $V$ is the elastic strain energy density, $V=V_i+\frac{EA}{2}\varepsilon^2+T_0\cdot\varepsilon$ , $\varepsilon=(\boldsymbol{Z}')^{\mathrm{T}}\boldsymbol{U}'+\frac{1}{2}(\boldsymbol{U}')^{\mathrm{T}}\boldsymbol{U}'$ ; d$t$ is the differential of time; $\delta W$ is the virtual work density associated with the gravity, dynamic loading and damping force, $\delta W=\delta\boldsymbol{U}^{\mathrm{T}}\left[\gamma_{\mathrm{f}}V_{\mathrm{S}}\cos\theta-\boldsymbol{c}\dot{U}+F_{\mathrm{D}}\right]$.

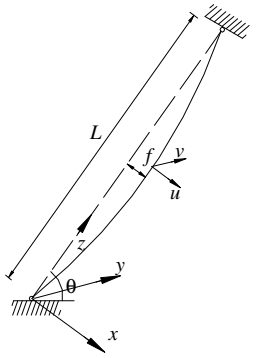


Fig. 1 Non-linear free vibration model of tether

Where $E$, $A$ and $m$ denote the modulus of elasticity, the cross-sectional area and the mass per unit length of unstretched tether respectively; $V_{\mathrm{i}}$ is the elastic strain energy density held in the initial (static) configuration; $T_0$ is the tether tension in the static configuration; $\varepsilon$ is Lagrangian strain; $\gamma_{\mathrm{f}}$ is the buoyant unit weight of tether; $V_{\mathrm{S}}$ is the volume per unit length of unstretched tether; $\theta$ is the tether inclination with respect to the horizontal level; $\boldsymbol{c}$ is viscous damping coefficient of tether, $\boldsymbol{c}=\mathrm{Diag}[c_x \quad c_y]$; $F_{\mathrm{D}}$ is the acting force applied by water per unit length when the tether vibrates.

The static equilibrium position of the tether is approximated by the quadratic parabola, $x=4f\frac{z}{L}\left(1-\frac{z}{L}\right)$.

Simlifying equation (1), omitting balance items under static loads, higher order small amount and small amount of $z$-direction motion, the following non-linear partial differential equation is obtained.

$$m\frac{\partial^2 u}{\partial t^2}+c_x\frac{\partial u}{\partial t}-EA\frac{\partial}{\partial z}(\varepsilon\frac{\partial x}{\partial z})-T_0\frac{\partial^2 u}{\partial z^2}=-F_{\mathrm{D}} \tag{2}$$

$$m\frac{\partial^2 v}{\partial t^2}+c_y\frac{\partial v}{\partial t}-T_0\frac{\partial^2 v}{\partial z^2}=-F_{\mathrm{D}} \tag{3}$$

In which, $H_0$ is the $z$-direction component of tension and $T_0\approx H_0$; $L_{\mathrm{E}}$ is the tether length in the static configuration; $f$ is the static displacement in the middle of tether.

Equation (2) and equation (3) are in-plane vibration equation and out of plane vibration equation of tether respectively. Due to these two equations are similar, here only equation (2) is analyzed in detail.

According to Morison equation, when the tether vibrates, the total acting force induced by water per unit length may be expressed as the sum of the damping force and the additional inertial force

$$F_{\mathrm{D}}=\frac{1}{2}C_{\mathrm{D}}\rho_{\mathrm{w}}D_{\mathrm{t}}\sqrt{\frac{8}{\pi}}\sigma_{\dot{u}}\dot{u}+C_{\mathrm{m}}\frac{\pi D_{\mathrm{t}}^{\ 2}}{4}\rho_{\mathrm{w}}\ddot{u} \tag{4}$$

Where, $D_{\mathrm{t}}$ is the diameter of the tether; $\rho_{\mathrm{w}}$ is the water density and $\rho_{\mathrm{w}}$=1028 kg/m; $C_{\mathrm{m}}$ is the additional mass coefficient and $C_{\mathrm{m}}=1$; $C_{\mathrm{D}}$ is the drag force coefficient and $C_{\mathrm{D}}=0.7$ , In which, $\sigma_{\dot{u}}$ is variance of $\dot{u}$ .

By means of Galerkin method, the partial differential equation is transformed into a set of ordinary ones

$$[\boldsymbol{M}]\ddot{u}+[\boldsymbol{C}]\dot{u}+[\boldsymbol{K}]u=0 \tag{5}$$

Where, $[\boldsymbol{M}]=[\boldsymbol{M}_1]+[\boldsymbol{M}_2]$, $[\boldsymbol{M}_1]$ and $[\boldsymbol{M}_2]$ are mass matrix and added mass matrix of tether respectively; $[\boldsymbol{C}]=[\boldsymbol{C}_1]+[\boldsymbol{C}_2]$, $[\boldsymbol{C}_1]$ and $[\boldsymbol{C}_2]$ are damping matrix of tether and damping matrix provided by water respectively; $[\boldsymbol{K}]=[\boldsymbol{K}_1]+[\boldsymbol{K}_2]$, $[\boldsymbol{K}_1]$ and $[\boldsymbol{K}_2]$ are equivalent stiffness matrix provided by initial tension and dynamic tension respectively.

## Numerical analysis and Results

For the convenience of discussion, the following dimensionless parameter which reflects the sag and tensile property of tether is introduced [6].

$$\lambda^2 = \left(\frac{\gamma_f V_s L\cos\theta}{H_0}\right)^2 \cdot L/[H_0 \cdot L_E/(EA)] \tag{6}$$

Basic parameters [7] of tether are shown in Table 1.

Table 1 Basic parameters of tether

| Length (m) | Diameter (m) | Mass per unit length (kg/m) | Density (kg/m$^3$) | elastic modulus (Pa) | Initial disturbance (m) | Initial tension force(N) |
|---|---|---|---|---|---|---|
| 161.66 | 0.489 | 1474.23 | 7850 | $2.1\times10^{11}$ | 0.001 | $2.572\times10^{7}$ |

**Effect of tether sag on its modal damping ratios.** Changing sag of tether by changing its inclination, effect of tether sag on its modal damping ratios are shown in Fig. 2. It is shown that when tether sag increases, the damping ratio of first in-plane mode decreases, whereas the damping ratios of two to four in-plane modes and first four out of plane modes keep constant. That is to say, similar to tether inclination, tether sag merely affects the damping ratio of first in-plane mode.

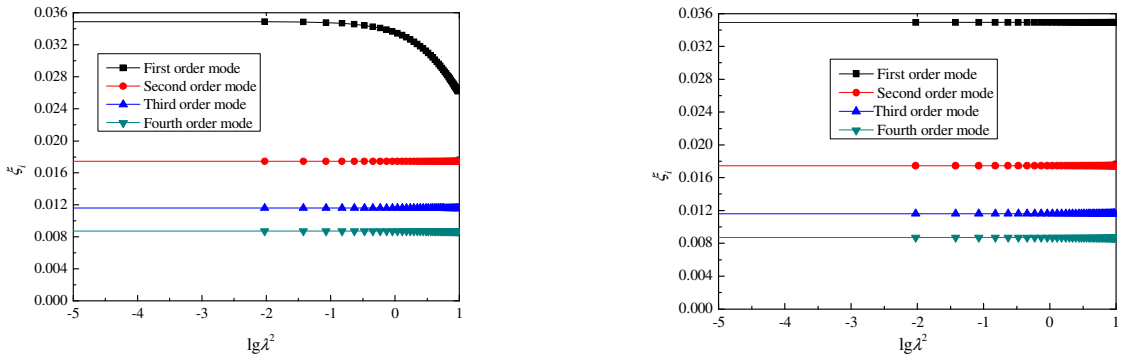


(a) in-plane (b) out of-plane

Fig. 2. Relationship between modal damping ratios and sag of tether

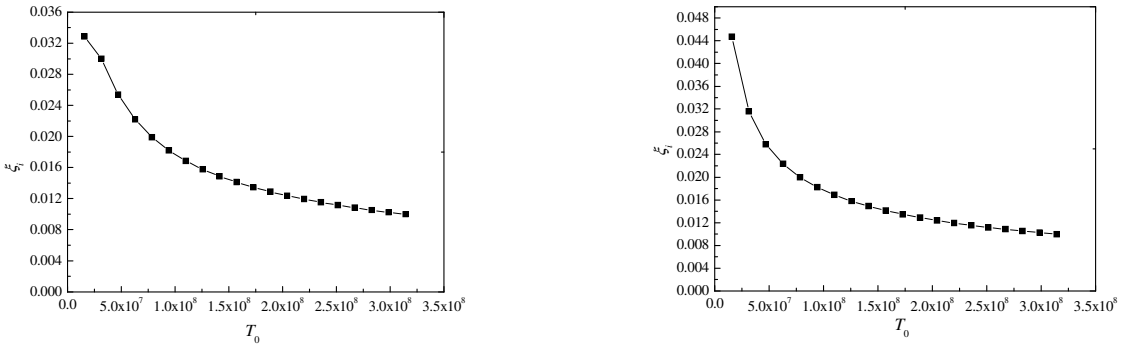


(a) in-plane (b) out of-plane

Fig. 3. Relationship between modal damping ratios and initial tension of tether

**Effect of tether tension on its modal damping ratios.** Effect of tether tension on its modal damping ratios of the first mode (both in-plane and out of plane) are shown in Fig. 3. It can be seen that, due to the influence of tether tension on its vibration period, when tether sag increases, the damping ratios of first in-plane and out of plane modes decrease.

**Effect of tether length on its modal damping ratios.** Effect of tether length on its damping ratios of the first mode (both in-plane and out of plane) are shown in Fig. 4. It is shown that, when tether

length increases, the damping ratios of first in-plane and out of plane modes increase. However, the curve of the first in-plane modal damping ratio is non-linear, whereas that of the first out of plane modal damping ratio is linear.

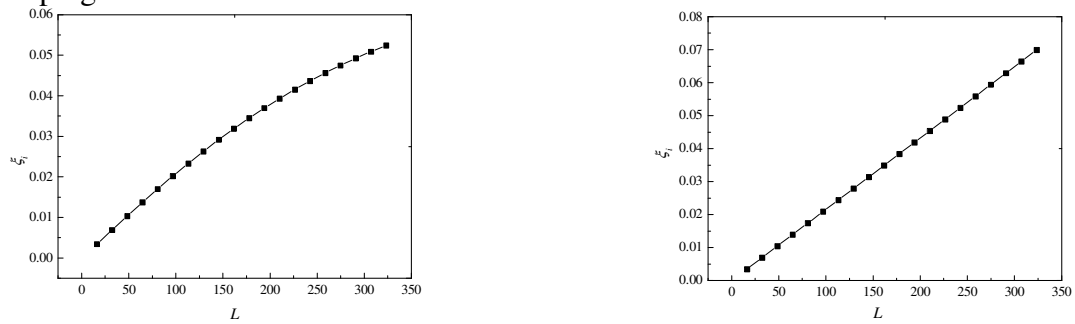


(a) in-plane (b) out of-plane

Fig. 4. Relationship between modal damping ratios and length of tether

## Conclusions

(1) Inclination and sag of tether merely affect the damping ratio of first in-plane mode; they have no effect on the damping ratios of higher order in-plane modes and out of plane modes.
(2) The first in-plane modal damping ratio of tether is in direct proportion to its inclination, whereas in inverse proportion to its sag.
(3) The first modal damping ratio of tether (both in-plane and out of plane) is in direct proportion to its length, whereas in inverse proportion to its initial tension.

## Acknowledgements

This work was financially supported by National Natural Science Foundation of China (Grant No.51 108224) and Shandong Provincial Natural Science Foundation, China (Grant No.ZR2013EEL006).

## References

[1] Ge, F., Dong, M. S., Hui, L. and Hong, Y. S., Vortex-induced vibration of submerged floating tunnel tethers under wave and current effects [J], Engineering Mechanics, 2006, **23**(S1): 217~221. (in Chinese)

[2] Chen, J. Y., Sun, S. N. and Wang, B. G., Dynamic analysis for the tether of submerged floating tunnel, Chinese Journal of Computational Mechanics, 2008, **25**(4): 488~493. (in Chinese)

[3] Ge Fei, Long Xu, Wang Lei, Hong Youshi. Study of vortex-induced vibration of submerged floating tunnel tube-tether coupled model [J]. China Journal of Highway and Transport, 2009, 22(3): 83-88. (in Chinese)

[4] Luo, G., Shi, Y. Y., Shen, Q. and Li, H., Lateral dynamic characteristics analysis for cable of submerged floating tunnel in water [J] , Journal of Changan University, 2012, **32**(3): 73~78. (in Chinese)

[5] Xiang, Y. Q. and Chao, C. F., Vortex-induced dynamic response for combined action of tube and cable of submerged floating tunnel [J], Journal of Zhejiang University, 2012, **46**(3): 409~415. (in Chinese)

[6] Irvine, H. M., Cable structures. Cambridge: Massachusetts Institute of Architectural and Civil Engineering [M], 1981.

[7] Faggiano B, Landolfo R and Mazzolani F M. Design and modelling aspects concerning the submerged floating tunnels: an application to the Messina strait crossing [C]// Krobeborg. Strait Crossing 2001. Swets & Zeitlinger Publishers Lisse, 2001: 511-519.

*Applied Mechanics and Materials Vols. 580-583 (2014) pp 1392-1397*
*© (2014) Trans Tech Publications, Switzerland*
*doi:10.4028/www.scientific.net/AMM.580-583.1392*

# Numerical Simulation Method Utilization in Water Gushing Yield Forecasting of Paoziling tunnel in Hunan province, China

Yanna YANG[1,a], Qiang ZHANG[1,b,*], Mo XU[1,c]

[1] State Key Laboratory of Geohazard Prevention and Geoenvironment Protection (Chengdu University of Technology), Chengdu, Sichuan, 610059, China;

[a]yangyanna@cdut.cn, [b,*] zhangqiang-cdut@qq.com, [c]xm@cdut.edu.cn(*Corresponding author)

**Keywords:** Paoziling tunnel; water-bursting accident; railroad tunnel engineering; numerical simulation method; water gushing yield forecast;

**Abstract.** Empirical analytic method and theoretical analytic method are usually applied to calculate and predict water gushing yield in the tunnel engineering in the past but have much limitations and errors. Ample water source, hydrodynamic conditions and expedite channels are essential for water-bursting accidents in railroad tunnel engineering. From a lot of study of fractal geometry in rock mass, it is found that the multi-dimension value of fissure network is colligate reflection of the length, the direction, space and the number of fissures, so the value can be used to describe the complicated frameworks in rock mass. But it is a sound tackle to quantities the complicated frameworks. Numerical simulating method is convinced to be applied to calculate and predict water gushing yield of tunnel and underground engineering. It focuses on analyzing texture characteristics of water-containing medium, building hydro-geological conceptual model, and modeling long-term hydrodynamic field development. An experimental application in Paoziling tunnel under-crossing mountain reservoirs in Hunan province was presented in this article, and long-term hydrodynamic field development had been obtained under the condition of drainage from the tunnel, and the gush yield in the tunnel during the process of storing water in the reservoir was also predicted.

## Introduction

Water gushing yield calculation and forecast was one of the fatal problems in constructing process of tunnel and underground engineering. The complexity of texture characteristics of water-containing medium of underground rock mass makes water gushing yield calculation and forecast much more difficult in practice [1]. Two kinds of analytic methods, empirical analytic method and theoretical analytic method were always applied to calculate and forecast water gushing yield in the tunnel engineering in the past but had much limitations and errors [2, 3]. On the other hand, hydro-geological numerical simulating method was seldom used in the past, and, now it was trying to be applied in the tunnel and underground engineering to calculate and forecast water gushing yield [4,5].

The Paoziling railway tunnel in Hu'nan province was a large and deep-buried tunnel with 6640m long. The tunnel passed through the north end of a synclinorium. Danjiang River flows through the nucleus part of the synclinorium. By view of the aspect of physiognomy, the tunnel passed through the surface watershed of Danjiang River, and the river was being cut off for the construction of a reservoir. The reservoir water storage and river seepage might lead to a comparatively large quantity of water gush during the process of excavation and operation of tunnel, prediction and calculation of the water gush in the tunnel under such circumstances was a prominent geological issue for this project.

## Methods

Based on the systematic and theoretical research of the basic geological conditions of the tunnel site, the stress had been laid on the research into the hydro-geological characteristics of the tunnel surrounding rock medium, and hydro-geological physical models had been built up for the construction site. The hydro-geological boundaries and hydro-geological parameters of the

surrounding rocks had been analyzed synthetically, and 3D-Modflow(Modular Three-dimensional Finite-difference Ground-water flow model) by utilizing finite-difference and the equilibrium principle of ground water was carried out on the characteristics of the underground seepage field changing under different influential factors where the tunnel passed, and quantities of water gush at this section of tunnel under the influence of various factors was predicted and calculated.

## Geological conditions of the tunnel site

The tunnel site was situated at the middle section of the southern mountain ridges, in terms of physiognomy. It was an area of low-and-middle hills. The strata were mainly sandstone, siltstone and cleaving stone of the Ordovician system $O_31$, Devonian system $D_2t$ at the tunnel site, having a serious weathering. The thick sandstone and intermediate-thick quartz sandstone were the main water-containing medium, and the fissures were relatively well-developed at the base, having a fine permeability in the horizontal direction, but bad in the vertical direction. The fissures were better-developed in the sandstones than the cleaving stone that was soft and being weathered, with around 0.30m thick. The cleaving stone was a relative water-resisting layer. The 4th stratum was complete-new pluvial, $Q_4^{al+pl}$, slide rock, eluvium, heterogeneous in terms of thickness, the maximum thickness could reach 275m.

The tunnel site was in the sub-tropical area, over the years, the average temperature was 17.60℃, average rainfall 1337mm, average evaporation amount 1536.3mm. The main source of ground water at the site was rain, at the same time, there were seepages from the river and the reservoir to be built and put into operation. Danjiang River passed in direction of NW-SE through the nucleus of the synclinorium, crossing the tunnel axis at D1K73+165 in a bevel angle of 40°, at the left side of the line, with dam 70m high, elevation (at the top of the dam)of 323m, and normal water level of 317.50m(elevation at the top of weir ). The trailing tunnel passed 560m far away from the edge of Danjiang reservoir, and road shoulder elevation was about 245m. The drilling at the river bottom revealed that, because Danjiang River was at the nucleus of the synclinorium, the steep, slant and vertical structural fissures were intensively developed comparatively, especially in the sandstones, thus they had a strong capacity for guiding water.

## The establishment of 3D spatial geological model

3D Spatial Numerical Model was established to forecast the quantity of water gushing yield of the tunnel, with emphasis laid on the characteristics of various factors of the underground seepage field.

## The model region and water flow boundaries

The simulation area took the water divides at the two sides of the river as its flow boundaries which had no water supplies to the computation area. If the upper and lower reaches of the river had side underground inflow and outflow, it would be regarded as the first category of boundary condition, i.e. water-head-fixed boundary. In the vertical direction, the model bottom was selected the position 50m lower than the tunnel axis at the connection with the valley. Therefore, it could be regarded that the place where the tunnel lied as an independent hydro-geological unit. The model, after being established, was illustrated on plane in Fig.1.

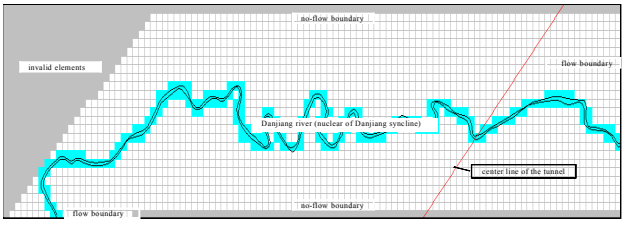


Fig.1 3D spatial numerical model and the types of boundaries

## The Generalization and discrete of the model

It had to be considered the influential factors to the underground water supply resources such as rivers, reservoirs, rainfalls, the seasonal dynamic changes in evaporation amount [6,7].

To partition in accordance with the alteration characteristics of the water-containing medium in vertical direction as revealed in the zone-survey, site-survey materials and drilling materials, the ground surface super stratum was the first layer, taking the nucleus of the synclinorium as the elevation of the emersion of the 2nd base rock above the ground, to partition downward in turn according to different lithological features. In consideration of the limited capacity of computer and speed of computation, the size of the model on plane was 5250×1250m$^2$, subdivided by the use of equipage network grid, each grid was 50×50m$^2$ in size. In the vertical direction, it had been totally delaminated into 10 layers. The whole mode had been totally subdivided into 105×25×10=26250 units, in which the amount of invalid units was about 1/10, as indicated in the Table 1.

Tab.1 The state of delaminating and lithological features of every layer

| Delaminating No. | Average Thickness[m] | Layer-top Elevation of Each Layer[m] | Lithologic Features |
|---|---|---|---|
| 1 | 0.5~275.0 | 322.0 | The Fourth-System of ploluvial, slide rock, strong-air slaked quartz-sand stone |
| 2 | 8.0 | 211.0 | Fresh-weak air slaked thick siltstone, relatively intact |
| 3 | 19.5 | 203.0 | Fresh quartz-sand stone, fissure well-developed |
| 4 | 23.0 | 183.5 | Fresh, intermediate, interbedding of thick quartz-stone and siltstone |
| 5 | 15.0 | 160.5 | Fresh, thick quartz-sand stone, fissure developed |
| 6 | 16.1 | 145.5 | Fresh, intermediate, interbedding of thick quartz-sand stone, fissure relatively developed |
| 7 | 11.2 | 129.4 | Fresh, thick and super-thick siltstone, core intact |
| 8 | 11.0 | 118.2 | Fresh quartz-sand stone, fissure relatively developed. |
| 9 | 10.0 | 108.2 | Fresh siltstone, relatively intact |
| 10 | 20.0 | 88.2 | Fresh quartz-sand stone, fissure relatively developed. |

## The hydro-geological parameters of the water-bearing stratum

(1)Permeability Coefficient *K*

In the whole simulation computation, the determination of the medium permeability coefficient was extremely important [8]. In respect of fissure medium, when most part of fissures was filled up, the permeability coefficient of fissure medium depended on the particle composition and particle size of the medium itself more than being affected by the fissure width [9].

Snow computation method was adopted to seek the permeability coefficient of the rocks through synthetic computation, and to make modifications to the computation results by referring the site or field drilling and water-pumping test results, and the penetration coefficient in vertical direction and taking value was listed in the Table 2.

Tab.2 The values of the water-bearing stratum transmissivity in heterosphere

| Parts | Lithologic Features | Kxx[m/d] | Kyy[m/d] | Kzz[m/d] |
|---|---|---|---|---|
| Nucleus area of the synclinorium at river valley | Siltstone | 0.260 | 0.260 | 0.0260 |
| | Interbedding of sandstone and siltstone | 0.269 | 0.269 | 0.0269 |
| | Sandstone | 0.280 | 0.280 | 0.0280 |
| Two-wing area of the synclinorium at the two sides of the river valley | Siltstone | 0.256 | 0.256 | 0.0256 |
| | Interbedding of sandstone and siltstone | 0.261 | 0.261 | 0.0261 |
| | Sandstone | 0.272 | 0.272 | 0.0272 |

(2) Valid cavity

The rock stratum was taken to the scope of depth 0-90, the part of it with depth larger than 90m.

(3) Make up strength and evaporation strength

In consideration of the impact of topographic gradient, ground-surface plantation, soil towards rain seepage and evaporation strength, made a discount and decrease to the measure value by the corresponding experience coefficient 0.6, so as to be in conformity with the actuality.

(4) Simulation Stress Periods

In accordance with the difference between the rainfall and evaporation amount during different periods, the simulation could be divided into different stress periods, and the duration of simulation was one year, which were totally divided into 12 different migration periods. The parameters of every period of stress were listed in the Table 3.

Tab.3 The evaporation and recharge values in every stress periods

| Stress Periods | Stress Period Ⅰ (month of 12-1) | Stress Period Ⅱ (month of 2-3) | Stress Period Ⅲ (month of 4-6) | Stress Period Ⅳ (month of 7-8) | Stress Period Ⅴ (month of 9-11) |
|---|---|---|---|---|---|
| Evaporation Intensity(mm/d) | 0.000371 | 0.000385 | 0.000821 | 0.001328 | 0.000723 |
| Rainfall Intensity(mm/d) | 0.000592 | 0.001156 | 0.002324 | 0.00171 | 0.000867 |

## Simulation Computing Schemes

Simulation computation mainly took three types of factors that affect the tunnel gush into consideration, and the specific scheme was listed in the Table 4.

Tab.4 The fundamental circumstances of simulating process

| Computation Schemes | Status of ground water current | Duration | Stress Period | Amount of Time Slots | Aim of Simulating Operation |
|---|---|---|---|---|---|
| Ⅰ | Steady current | One year | 10 | 12 | Parameter Checking |
| Ⅱ | Non-steady current | One year | 5 | 12 | Prediction of the gush yield upon excavation under natural status |
| Ⅲ | Non-steady current | One year | 5 | 12 | Prediction of the gush yield upon excavation under the status that the reservoir is at operation. |
| Ⅳ | Non-steady current | One year | 5 | 12 | Prediction of the gush yield upon excavation under heavy rainfall. |

## Results

### Flowing field features of the site and tunnel gushing yield prediction under natural condition

The simulation results of the underground seepage field under the natural state prior to the construction of tunnel had primarily reflected the topographic features of ups-and-downs in the construction area of the tunnel, as Fig.2 shown, which indicated that the parameters selected in the model schemes were reliable.

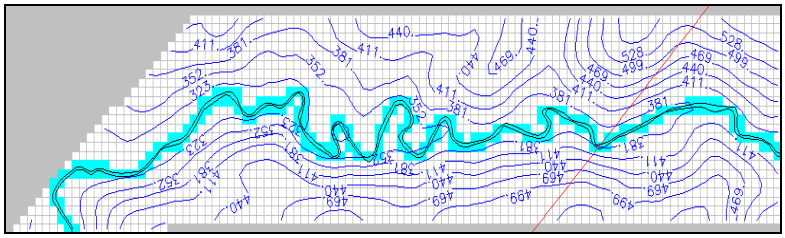

Fig.2 The distribution of natural groundwater seeping field (unit:[m])

Under the natural condition, along with the continuation of the time of water drainage in the tunnel, the depth contours of ground water would gradually shift towards the two sides of the tunnel axis, as Fig.3 shown. The seepage fields had relatively great changed in respect of integral configuration, and depth contours became sparse and the ground water divide occurred. The drainage of water inside the tunnel had greatly lowered down the groundwater position at the two sides of valley. Through the simulation of a complete water year, the gush of water inside tunnel at different periods under natural condition was around 1.614~2.936×$10^4$$m^3$/d.

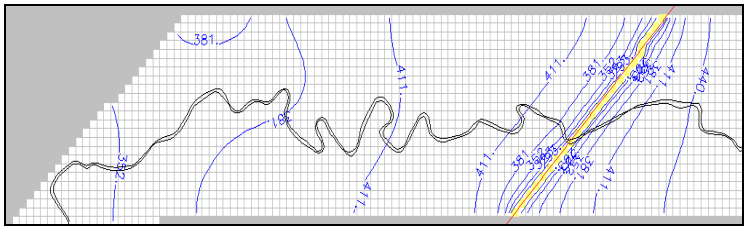

Fig.3 The distribution of ground-water flowing field after 365 days' draining (unit:[m])

**Tunnel gush yield prediction after the completion and putting-into-operation of reservoir**

Along with the continuation of the time of drainage in the tunnel, under the impact from the reservoir, the position of the groundwater divide would gradually shift towards the reservoir. 365 days after the tunnel drained, the impact would reach the rear or tail of the reservoir, as Fig.4 shown. Due to the existence of the ground water divide, the water level of reservoir would not be lowered down at great extent, i.e. the span, scope of the impact of tunnel drainage towards the water storage in reservoir would be limited, and it would not seriously or materially decrease the water volume of reservoir water storage and even dried the storage. The gush inside the tunnel after to the completion and putting-into-operation of reservoir was 2.458～3.208×$10^4$$m^3$/d.

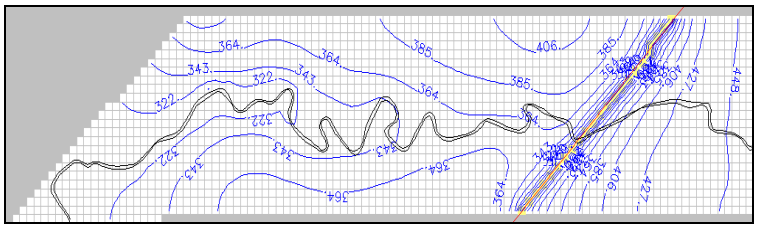

Fig.4 The distribution of ground-water flowing field after 365 days draining with the reservoir running (unit:[m])

**3.3 Tunnel gush yield prediction under the operation of reservoir and heavy rain**

After the completion and putting-into-operation of the reservoir, and under the condition of heavy rain, along with the continuation of time, the depth contours of groundwater would gradually shift towards the two sides of the tunnel, and the scope of influence due to tunnel drainage would be further decreased The extent and scope of impact towards reservoir water storage would be further decreased compared with that in normal years (Fig. 5). Under such condition, the gush in tunnel was 2.522～3.938×$10^4$$m^3$/d.

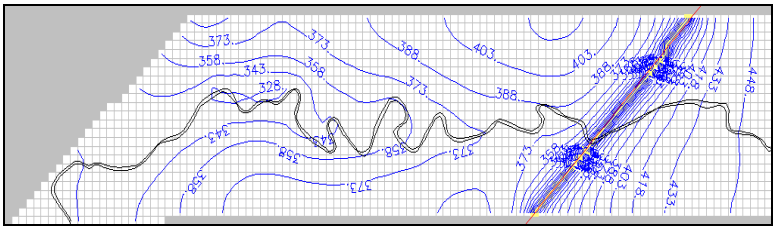

Fig.5 The distribution of ground water field after draining 365 days with the reservoir running and abnormal recharge (unit:[m])

The comparison of the simulation results data and the groundwater flowing fields was shown that, after the completion and putting-into-operation of reservoir, the gush in the tunnel, under the condition of heavy rain, would be increased by 638 $m^3$/d（dry season）～7296 $m^3$/d（rain season）for the different time intervals compared with that in normal years. The operation of reservoir and the heavy rain condition would have a relatively significant impact to the gush yield in this section of tunnel. It was needed to do a good job of the measures of prevention of water gush and water drainage.

## Discussion

By utilizing the numerical simulation method, through medium generation, establishment of spatial physical models, and the determination of boundary conditions, the gush yield of the tunnel has been predicted through simulation during the construction of reservoir. The simulation results have shown the spatial and temporal alteration characteristics of the groundwater seeping fields at the tunnel draining area under the impact of various factors. The numerical simulation method, as a method for predicting and calculating the gush yield in the underground tunnel, is worthy of further research and promotion.

## Acknowledgements

This work was financially supported by Natural Science Foundation of China (NO. 41202213), independent research topic of Characteristics of geological resources and geological engineering disciplines of State Key Laboratory of Geohazard Prevention and Geoenvironment Protection (Chengdu University of Technology).

## References

[1] Jin-Hung Hwang, Chih-Chieh Lu, 2007. A *semi-analytical method for analyzing the tunnel water inflow*. Tunnelling and Underground Space Technology, 22: 39–46.

[2] Goodman, R., 1965. *Groundwater inflows during tunnel driving*. Engineering Geology, 2 (2), 39–56.

[3] Zhang, L., Franklin, J.A., 1993. *Prediction of water flow into rock tunnels: an analytical solution assuming and hydraulic conductivity gradient*. International Journal of Rock Mechanics and Mining Sciences and Geomechanics Abstracts, 30 (1), 37–46.

[4] Chen Suozhong, 1999. *The Principle of Modflow 3D Finit-difference Ground Water Seeping Models*. Jiangsu Geological and Mineral Information (in Chinese).

[5] El Tani, M., 2003. *Circular tunnel in a semi-infinite aquifer*. Tunneling and Underground Space Technology 18, 49–55.

[6] Pan Guoying, 1994. *Comments on the Fitting Results of Ground Water Numerical Simulation Models*. Journal of Jiaozuo Institute of Mine Industry,13(2) (in Chinese).

[7] Li Junting, Wang Yuji and etc, 1987. *Ground Water Dynamics*. The Publishing House of Geology (in Chinese).

[8] Chen Chongxi, Tang Zhonghua and etc, 1989. *The Numerical Method for Ground Water Fluidity*. The Publishing House of Wuhan Institute of Geology (in Chinese).

[9] Chen Chongxi, 1985. *Research into the Computation Methods for Gush Yield in Adits.* The Publishing House of Wuhan Institute of Geology (in Chinese).

*Applied Mechanics and Materials Vols. 580-583 (2014) pp 1398-1401*
*© (2014) Trans Tech Publications, Switzerland*
*doi:10.4028/www.scientific.net/AMM.580-583.1398*

# Reliable Design and Study on HighwayTunnel Lining Structure

Zelin Niu [1,2,a], Qi Yanbo[2, b],Huang Jiesheng[3,c],Wang Chao[3,d],Li Junlin[3,e]

[1]School of Civil Engineering,Xi'an University of Achitecture and Technology 710055, Shaanxi, P. R. China

[2]China Railway 13th Bureau Group Co.,LTD 300308,Tianjin City , P. R. China

[3]The 2nd Engineering Co.,Ltd.of the 13th Bureau Group of China Railway 518083,Guangdong Province, P. R. China

[a]nzl109109@163.com,[b]wht@163.com,[c]hjs@163.com,[d]wc@163.com,[e]ljl@163.com

**Keywords:** Lining,Structure Reliability,Rock-Mechanics Model,Monte Carlo Finite Element, Statistical.

**Abstract.** The article proposed the reliability calculation method for tunnel lining design combining Rock-Mechanics model and Monte Carlo finite element method.The reliability calculation model of tunnel lining structure design was established considering tunnel character. The types of the statistical characteristics and distribution of axial force for the big cross section of the loess tunnel structure had been summarized. The study result stated that the method is feasible. It has important theoretical guiding significance to the practice structure reliability design of tunnel and underground engineering.

## Introduction

Based on the fixed value of structure design and the traditional safety coefficient method are used to evaluate the reliability of tunnel lining structure design, the practice proved this method is reliable, but it is based on the fixed parameter, which means can't consider any and the safety of the structure calculation and check computation of uncertainty factors and the variability of design variables, this give accurate evaluation of tunnel lining structure design is safe and reliable planted unable to eradicate the hidden trouble. At the same time, it can also cause waste of construction materials. Professor Guan baoshu in 1989 by quantification theory and fuzzy mathematics method, proposed the railway tunnel surrounding rock classification of forecast and decision criteria [1]; Xie jinchang in 1988, the first professor of single railway tunnel surrounding rock collapse height and lining on the relaxation of load probability and statistics analysis, and its probability distribution function is the best fitting [2]; in 1996 professor Jing shiting experiments on bias of concrete component and puts forward the concrete influence coefficient of eccentric compression member of statistical parameter calculation formula, and the fuzzy reliability and reliability of composite lining is studied [3]; In 2005, the railway tunnel design code (TB1007-2005) [4] lists the probability limit state design method and the meaning of the relevant parameters; 2010 Yang Jianguo, Xie Yongli [5] is introduced about the development direction of tunnel structure reliability theory at present, the main is to develop in the direction of research and the dynamic time-varying structural system.Choose what kind of easy to implement in the field of practical application, however, the theoretical model of? Calculation method and means come from? A random variable how to reasonable value? These are the key problems about the structural reliability theory in the practical engineering application. For this reason, the article will take the loess railway tunnel as the engineering background, and studies loess tunnel lining structure reliability design ,and puts forward a practical method of tunnel lining structure reliability design and calculation method.

## Calculation Model and Calculation Method

Among the four calculation model of tunnel lining structure, the calculation model Rock-Mechanics is a very mature theory calculation model, its famous is simple and reliable numerical data. Therefore,

on the basis of the model and the Monte Carlo method and K-S test,this article calculates and studies the distribution laws of lining structure effect and the mathematical characteristics. About the the parameters and variables of the random number,the paper adopts the relevant datas of based on the theory of the reliability safety evaluation and analysis method of the loess tunnel lining structure [6].

## Lining structure reliability calculation

**The Calculation of Lining Structure Effect.** Based on Hei Shansi tunnel lining finite element mesh Graph(in figure 1) and summary table random numbers' calculating parameters on loess tunnel [6], the paper uses calculating program of a Monte-Carlo finite element to get the 100000 times calculation on structural effect of calculation.At last, the numerical results of the loess tunnel lining structure effect is got. The axial force data of the loess tunnel lining structure arch cross-section is summarizes in table 1.

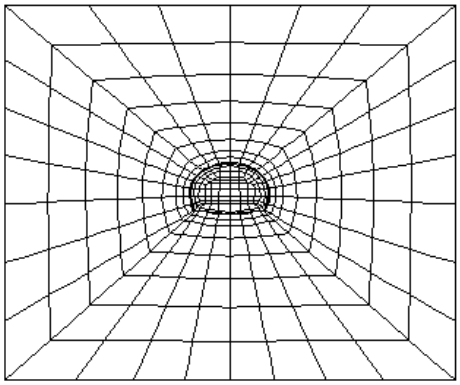

Fig.1 Finite Element Mesh

Tab.1 Summary table on axial force of tunnel arch-top

| The number of iterations | Axial force (kN) | The number of iterations | Axial force (kN) | The number of iterations | Axial force (kN) |
|---|---|---|---|---|---|
| 1 | 934.73 | 6 | 569.56 | 11 | 362.85 |
| 2 | 852.83 | 7 | 619.48 | 12 | 583.28 |
| 3 | 683.58 | 8 | 536.57 | 13 | 536.57 |
| 4 | 585.25 | 9 | 514.18 | 14 | 443.52 |
| 5 | 525.91 | 10 | 623.18 | 15 | 763.27 |
| ⋮ | ⋮ | ⋮ | ⋮ | ⋮ | ⋮ |
| 99986 | 525.64 | 99991 | 563.61 | 99996 | 934.73 |
| 99987 | 362.85 | 99992 | 851.17 | 99997 | 852.83 |
| 99988 | 583.28 | 99993 | 536.57 | 99998 | 683.58 |
| 99989 | 536.57 | 99994 | 548.98 | 99999 | 585.25 |
| 99980 | 461.68 | 99985 | 860.68 | 100000 | 652.36 |

Note: because this page is limited, some data have been slight.

**The Numerical Statistical Analysis.**The paper applies distribution hypothesis and statistical test for numerical results of 100000 effect on Hei Shansi loess tunnel lining structure,and makes the right judgment. To illustrate the calculation method of this article, at the same time, in consideration of the characteristics of the tunnel lining structure, the paper select100000 times axial force datas in the most unfavorable position (vault location) tunnel structure for an example to illustrate that how does the numerical results of the structure effect with the probability distribution assumption and K-S test.

**Drawing Frequency Histogram.**First, the data is sorted through by artificial simple method, then the SPSS statistical software [7] is used to group the 100000 vault section axial force datas to the 13

intervals,finally it draws the loess tunnel lining structure effect results of the numerical frequency histogram, namely the vaults section axial force of loess tunnel lining structure frequency histogram, as shown in figure 2. From figure 2, that obeying positive skewness distribution can be concluded about the vault section axial forces(N) on the loess tunnel lining structure.

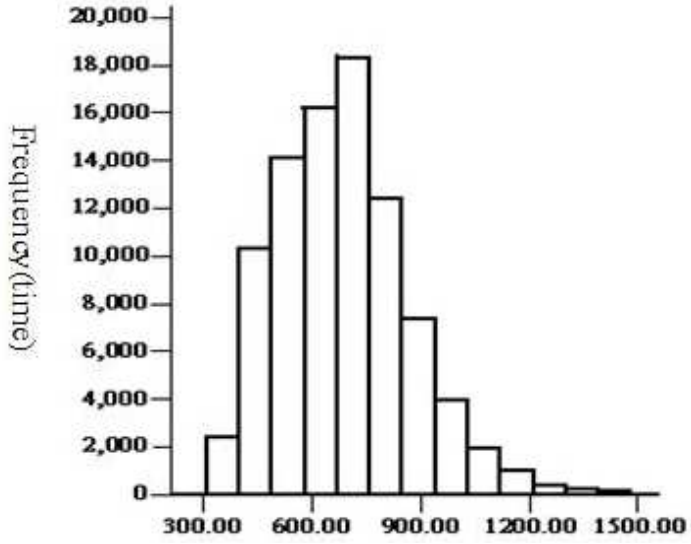


Fig.2 Distribution histogram on axial force of tunnel arch-top in loess tunnel

**The Distribution Rule of Statistical Tests.**According to the general distribution of the article drawing the axial force frequency histogram of tunnel lining structure,combined with previous commonly used type of probability distribution,this paper makes the loess tunnel lining structure arch cross-section function distribution law of axial force (N) approximate to logarithmic normal distribution assumption,and K-S inspection. Arch cross-section (Dn) of the axial force statistics calculation result of 0.0049 is less than the critical value of 0.005, (D100000,0.005),0.0051,therefore it could prove that the axial force of Hei shansi loess tunnel lining structure vault cross section obeies logarithmic normal distribution hypothesis is true. Similarly all axial forces of lining applies logarithmic normal hypothesis test, as shown in the table 2. Through table 4, this hypothesis is accepted, so the distribution types of each section axial force the loess tunnel lining obey the lognormal distribution.

Tab. 2 The hypothesis testing of tunnel each axial force 's distribution types

| Lining section number | statistic | Lining section number | statistic | Lining section number | statistic | Assuming distribution | The critical value | The critical value test results |
|---|---|---|---|---|---|---|---|---|
| 1 | 0.0046 | 12 | 0.0046 | 23 | 0.0046 | Logarithmic normal distribution | 0.0051 | All accepted |
| 2 | 0.0045 | 13 | 0.0047 | 24 | 0.0004 | | | |
| 3 | 0.0043 | 14 | 0.0004 | 25 | 0.0044 | | | |
| 4 | 0.0048 | 15 | 0.0045 | 26 | 0.0046 | | | |
| 5 | 0.0049 | 16 | 0.0048 | 27 | 0.0044 | | | |
| 6 | 0.0046 | 17 | 0.0049 | 28 | 0.0004 | | | |
| 7 | 0.0047 | 18 | 0.0046 | 29 | 0.0046 | | | |
| 8 | 0.0046 | 19 | 0.0044 | 30 | 0.0045 | | | |
| 9 | 0.0044 | 20 | 0.0049 | 31 | 0.0043 | | | |
| 10 | 0.0004 | 21 | 0.0047 | 32 | 0.0048 | | | |
| 11 | 0.0046 | 22 | 0.0045 | 33 | 0.0049 | | | |

## Conclusion

Through the analysis and study of lining structure reliability design in loess tunnel, the paper put forward the concrete method that using the " Rock-Mechanics " model and Monte Carlo finite element method to study structural reliability of the tunnel lining, considering of the successful practice, it greatly promotes the structural reliability theory in the practical application and developmentin the field of tunnel structure reliability design.

According to the analysis results ,this paper put forward that the axial force distribution type of lining structure in Hei shansi loess tunnel obey the lognormal distribution, for the future this provides the theory basis for the design of the other size tunnel lining structure.

In this study, the method of realizing the statistical analysis of data and hypothesis test in terms of tunnel structure reliability theory is practical, for the future there is important significance to the statistical analysis of large amounts of data engineering.

## References

[1] Guan Baoshu.Quantitative Study for Rock Masses Classification of Railroad Tunneling Engineering , In Chinese, 1996.

[2] Xie Jinchang,Tan ZhongSheng.Optimum Fit for the Probability Distribution Function of Loosened Rock load on Railway Tunnel Lining in China. Proceedings of the International Congress, In Chinese,1990(2):627-632.

[3] Jing Shiting. Underground Structure Reliability Analysis Research Progress.Shijiazhuang Railway Journal, In Chinese, 1995(2):13-19.

[4]The Second Survey and Design Institute of Railway .TB10003-2005Code for Railways Tunnel Design.Beijing: China Railway Press, In Chinese, 2005.

[5]Xie Yongli. Progress in Research on Tunnel Structural Reliability.Modern Tunnelling Technology, In Chinese, 2009(6):1-7.

[6] Niu Zelin .Analysis and Study on the Safety Reliability of the Loess Tunnel Lining Structure Chang 'an University Library: Chang 'an University, In Chinese, 2012.

[7]Gu Rongyan.*SPSS 12.0 for Windows Practical tutorial and operation skills*.Shanghai: Shanghai Science and Technology Literature Press, In Chinese, 2005,123-142.

*Applied Mechanics and Materials Vols. 580-583 (2014) pp 1402-1407*
*© (2014) Trans Tech Publications, Switzerland*
*doi:10.4028/www.scientific.net/AMM.580-583.1402*

# The Example Analysis of the Transfer Stations of Subway

Lijie Yu[1,a *], Yongling Li [2,b], and Kuanmin Chen [3,c]

[1]Traffic engineering, School of Highway, Chang'an University, Xi'an 710064, China
[2]Technology Department, Xi'an Metro Co. Ltd, Xi'an 710018, China

[3]Traffic engineering, School of Highway, Chang'an University, Xi'an 710064, China

[a]1175595323@qq.com, [b]79456682@qq.com, [c]623567515@qq.com

**Keywords:** traffic engineering; choice of transfer manner; example analysis; transfer station of subway

**Abstract.** Two lines intersection is the common transfer manner of the subway. In order to analyze the characteristics and applicability of the two lines transfer manner, this paper analyzes different transfer stations of subways at home and abroad, and evaluate the current use of them, in the views of the form of the intersection of the lines (parallel and intersection), and the relative location between the lines and the stations. Then it summarizes the characteristics and applicability of the transfer manner. Finally, it gives advices of the choices of the two lines transfer stations in different situations.

## Introduction

Transfer station is located at the junction of different subways in the rail transit net. The basic manners of the transfer stations are one-platform-interchange station, station hall transfer station, channel transfer station, and transfer out of the station.

Nowadays, the studies of the transfer stations were mostly in the following areas: The analysis of the basic transfer manners and the method of choice[1]; the summary of the current situation of the built-up transfer stations in a city[2]; or the design forms of the transfer stations[3]. These studies also analyzed the transfer manners and the current situations. They focused on analyzing the basic transfer manners in theory, but lacked in summarizing the transfer manners in concrete metro interchange manners.

Two lines intersection is the common transfer manner of the subway. This paper analyzes different two lines transfer stations of subways at home and abroad, and evaluate the current use of them, in the views of the form of the intersection of the lines (parallel or crossed), and the relative location between the lines and the stations. Then it summarizes the characteristics and applicability of the transfer manner. Finally, it gives advices of the choices of the two lines transfer stations in different situations.

## Parallel Form

The parallel form can be divided into two types: the lines located in the same elevation, the lines located in different elevation.

**The Lines Located in the Same Elevation**

(1) When the platforms of the lines are independent, they must be related by the change of the height. So the station hall transfer and channel can be chosen.

Sihui Station in Beijing is a station hall transfer station( in figure 1), because of the difference of the engineering standard and the long interval building time. The transfer height is high, and the transfer passenger flow influence the enter and exit flow.

Sanyuanqiao Station in Beijing is a channel transfer station( in figure 2), because of the long distance and the difference of the ticket system. The distance of the transfer is long, but it can disperse the passenger flow.

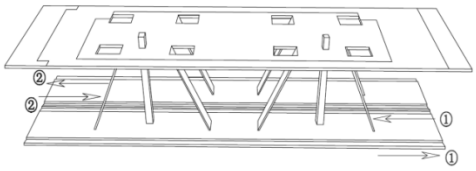


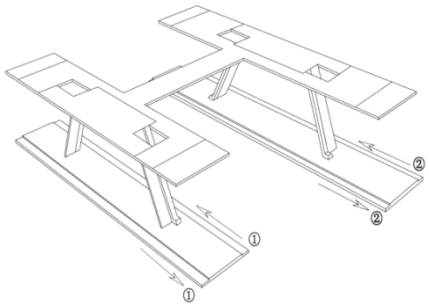


Fig.1 Sihui Station in Beijing Fig.2 Sanyuanqiao Station in Beijing

(2) When the different lines are in the same platform because of the previous reservation, the one-platform-interchange can be chosen.

Victory Park Station in Moscow makes up with two parallel island platforms[4]. And the lines in every platform have the same direction but different name. The platforms are connected by the channel in the middle( in figure 3). Most passengers can transfer in the platform, and other direction can transfer through the channel.

Nanchang Station in Hong Kong makes up with 2 is land platforms and a side platform( in figure 4). Most passengers can transfer in the platform, and other direction can transfer through the station hall. The composition of the flow in the station hall is complicated.

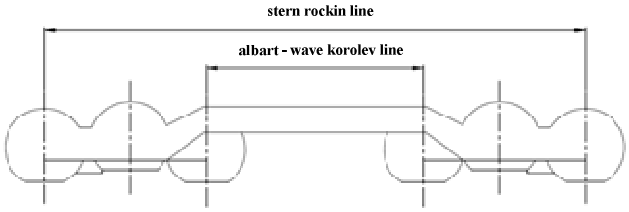


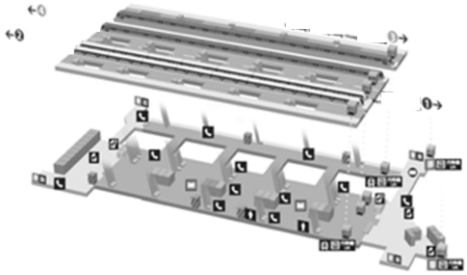

Fig.3 Victory Park Station in Moscow Fig.4 Nanchang Station in Hong Kong

**The Lines Located in Different Elevations**

(1) When the platforms of the lines are independent, the passengers can transfer by the stairs. But the transfer passengers in different directions are not separated, the efficiency of transfer is low.

(2) When different lines are built in the same platform because of the previous reservation, the one-platform-interchange can be chosen.

Laojie Station in Shenzhen can achieve one-platform-interchange because the different lines are located in the same platform.And other transfer can be achieved by stairs( in figure 5)[5]. The passenger flow of different kinds and different directions can be separated.

Andoni Station in Paris is designed malposed( in figure 6)[6]. This form of platform can separate the transfer flow of the different directions, and at the same time it can shorten the detouring transfer time.

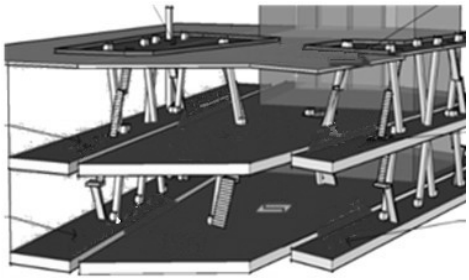

Fig.5 Laojie Station in Shenzhen

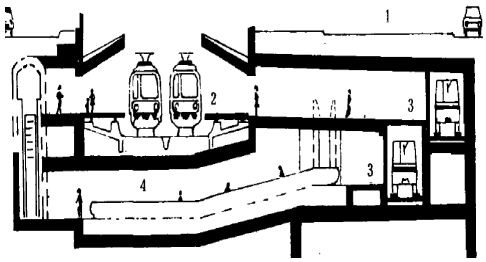


Fig.6 Andoni Station in Paris

**Summary of two Parallel Lines**

The summary of the two parallel lines is shown in Table 1.

Table 1 The summary of the two parallel lines

| Situation of lines | Transfer manner | Applied condition | Advantage | Disadvantage |
|---|---|---|---|---|
| In the same elevation | Station hall | Interval of the built time is long. The standard of the projects is different. The previous reservation is not made. | The two lines can be designed independently. Reservation can be made conveniently. | The transfer height is big. The transfer passenger flow and the enter and exit flow are mixed in the station hall. |
| | Channel | Interval of the built time is long. The standard of the projects is different. The previous reservation is not made or the lines are far. | The two lines can be designed independently. Reservation can be made commodiously. The distance of the transfer is long, and passengers can be dispersed. | The distance of the transfer is long. |
| | Platform & channel | Interval of the built time is short. The previous reservation is made but the lines are far. | One direction of transfer is conveniently; others can evacuate the passengers. | The two lines must be designed dependently. Reservation must be made. |
| | Platform & station hall | Interval of the built time is short. The previous reservation is made. | One direction of transfer is conveniently. | The two lines must be designed dependently. Reservation must be made. |
| In different elevations | Platform | Interval of the built time is long. Or the previous reservation is not made. | The two lines can be designed independently. Reservation can be made conveniently. | The transfer height is big. The transfer flows in different directions have conflicts |
| | Platform & station hall/channel | Interval of the built time is short. The previous reservation is made. | One direction of transfer is conveniently. | The two lines must be designed dependently. Reservation must be made. |

**Crossed Form**

When the subways are crossed, a node is appeared. If the station is located at the node, the relatively convenient transfer can be realized. But if the station can't be located at the node, the relatively convenient transfer can also be realized by reasonable transfer manners.

**Stations Located at the Node**

(1) When the station is located at the node, the most usual transfer manner is the platform-interchange. With the help of the stairs, it make the passengers complete transfer in the platform.

Lianglukou Station in Chongqing has two island platforms, and transfer flow can go to the other lines by stairs( in figure 7). The transfer is very convenient, but the transfer node is few, and the transfer flow in different directions is not separated. The efficiency is low.

(2) When the station is located at the node, the combination transfer manners can enhance the efficiency of the transfer.

Beidajie Station in Xi'an is "十" island-side crossed form. Metro Line 1 to Metro Line 2 is platform-interchange by stairs. Metro Line 2 to Metro Line 1, the transfer flow must pass the station hall( in the figure 8). When the transfer flow is large, the transfer node of side platform can be enlarged, such as Zhongshan Station[7] in Nanchang and Tianfuguangchang Station in Chengdu.

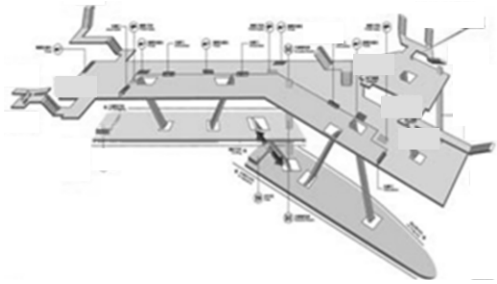

Fig.7 Lianglukou Station in Chongqing

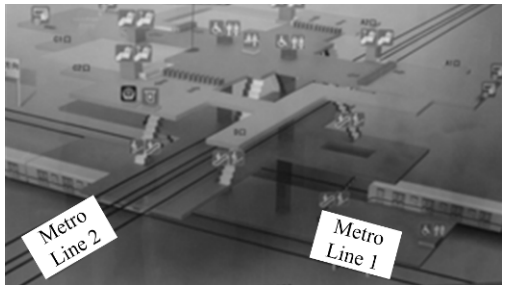


Fig.8 Beidajie Station in Xi'an

Haidianhuangzhuang Station in Beijing is also "十" island-side crossed form, and by setting transfer channel, the transfer nodes are added up to 4( in figure 9). The transfer nodes can scatter the transfer flow, and the efficiency of transfer is enhanced.

Xinjiekou Station in Nanjing is "十" island-island crossed form. Metro Line 2 to Metro Line 1 is platform-interchange by stairs. Metro Line 1 to Metro Line 2, the transfer flow must pass the transfer channel( in the figure 10). This manner separate the transfer passenger flow and the enter and exit flow, and also separate the transfer passenger flow in different directions. But it has only one transfer node, the transfer flow which route is shorter may jam when the flow is large.

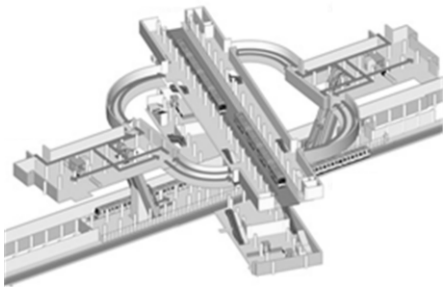

Fig.9 Haidianhuangzhuang Station in Beijing

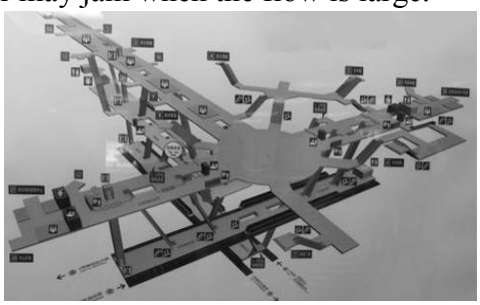

Fig.10 Xinjiekou Station in Nanjing

(2) When the station is located at the node, if the reservation is done, the most convenient transfer manner is the two-direction-platform transfer manner.

Gongyuanqian Station in Zhuangzhou is "十" crossed form, and the platforms is distributed in two flours. In ever flour, there is an island platform and two side platforms, which are separated by

rails(in figure 11). The transfer passengers go to the island platform of the other line from the middle of side platform. Passengers go out of the station from the ends of the side platforms, and the island platforms only allow passengers to get on the trains.

Central Station in Hong Kong is the transfer station of Tsuen Wan Line and MTR Island Line. The island platform of Tsuen Wan Line is on the second floor , in the middle of the side platforms of MTR Island Line( in figure 12). All the directions of the transfer passengers can accomplish transfer in the platforms.

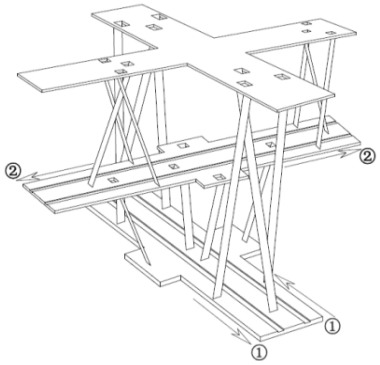


Fig.11 Gongyuanqian Station in Zhuangzhou

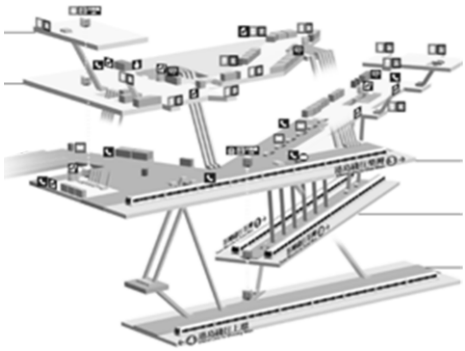

Fig.12 Central Station in Hong Kong

**Stations did not Locate at the Node**

Whether one station or two stations are not located at the crossed node, the transfer channel is employed.

Kowloon Tong Station in Hong Kong is made up of two separated platforms. The side platform of MTR East Rail Line and the island platform are at right angles. The stations has three station halls, and are connected with channel( in figure 13). This transfer manner can separated the transfer passenger flow and the enter and exit flow. But the transfer distance is long.

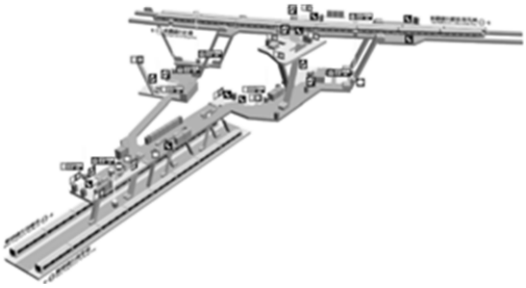

Fig.13 Kowloon Tong Station in Hong Kong

**Summary of two Crossed Lines**

The summary of the two crossed lines is shown in Table 2.

Table 2 The summary of the two crossed lines

| Situation of lines | Transfer manner | Applied condition | Advantage | Disadvantage |
|---|---|---|---|---|
| Stations located at the node | Platform | Interval of the built time is short. The previous reservation is made. | Transfer is conveniently. | The transfer nodes are few. The transfer flows of different directions are not separated. Reservation must be made. |
| | Platform & station hall | The previous reservation is made | One direction of transfer is conveniently. The transfer flows of different directions are separated. | The transfer passenger flow and the enter and exit flow are mixed. The flow in station hall is complex. |

| | | | | |
|---|---|---|---|---|
| | Station hall & channel | | The transfer flow can be dispersed because the transfer nodes are more | |
| | Platform & channel | | One direction of transfer is conveniently. The flows of different properties are separated completely. | The transfer nodes of platform are few, and easy to be jammed. |
| | Bidirectional platform | Interval of the built time is short. The previous reservation is made. | Transfer is the most conveniently. | Reservation must be made. Construction is difficult. |
| Stations did not locate at the node | Channel | Interval of the built time is long. The standard of the projects is different. The previous reservation is not made. | The flows of different properties are separated. The two lines can be designed independently. | The distance of the transfer is long. |

## Conclusion

This paper analyzes different two lines transfer stations of subways at home and abroad, and evaluate the current use of them, in the views of the form of the intersection of the lines (parallel or crossed), and the relative location between the lines and the stations. Then it summarizes the characteristics and applicability of the transfer manner. In the practical design, the transfer manner must be chosen according to specific circumstances.

## References

[1] Zhenhua Gao, Baoming Han, Xianghui Ru: Planning study of transfer stations of urban rail transit( In Chinese), Integrated Transportation, 2003, pp. 50-51.

[2] Yong Zhou: Ponders on transfer stations of rail transit( In Chinese), Urban Mass Transit, 2004, pp. 42-44.

[3] Ning Bao: Primary investigations on building design of transfer stations of urban rail transit( In Chinese), Beijing Transportation University, 2009.

[4] С.Г. Ye M Karyev, И.Л. Zhukov: New construction of subsurface excavation stations( In Chinese), Urban Rapid Rail Transit, 2002, pp. 51-55.

[5] Jiwei Lu, Yi Wang,Xiaokun Lu: System of urban transport and integration of space: urban design of Laojie Station in Shenzhen( In Chinese), Urban Planning Forum, 2001, pp. 4-7.

[6] Min Li: Exploration of the building design of Zhongshan Station of Metro Line 1 and Metro Line 3 in Nanchang( In Chinese), Underground Engineering and Tunnels, 2010, pp. 18-21.

[7] Jinsheng Liu: Design of transfer stations of two light rail stations in Paris( In Chinese), Urban Planning, 1991, pp. 52-53.

*Applied Mechanics and Materials Vols. 580-583 (2014) pp 1408-1411*
*© (2014) Trans Tech Publications, Switzerland*
*doi:10.4028/www.scientific.net/AMM.580-583.1408*

# Subway station group decision and evaluation of fire emergency

Lijun Cao [1,a] Xiangmei Yu [1, b] and Dongyang Geng[1,c]

[1] Shijiazhuang University of Economics NO.136 Huai An East Road, Shijiazhuang City, Hebei Province, P.R.China 050031

[a] caolijun2000@163.com, [b] yuxiangmei6606@163.com, [c] 15200012621@139.com

**Keywords:** Tunnel.Different sections.Numerical analysis.

**Abstract.** In order to build subway station fire emergency group decision-making system, Aim at the subway station fire characteristics in this paper, analyze the problems of emphasis from emergency decision, and group decision method is proposed to use to solve this problem. The method can avoid failure of the overall decision making mistakes because a single decision maker. Found of decision-making group consist of experts, academics, policy-makers, considering several key factor such as professional, academic, expert ratings, weight, to build group decision model .At the same time, evaluation of the subway station fire emergency group decision effectiveness to build subway station fire emergency response system, Ultimately improve the efficiency of emergency response and level of decision-making for subway station.

## Introduction

Project Overvie In China, the cities, where subway has been built and put into operation, include Beijing, Shanghai, Guangzhou, Tianjin, Shenzhen, Hong Kong and Nanjing; meanwhile, in such eight cities as Chongqing, Shenyang, Xi'an, Wuhan, Chengdu, Harbin, Hangzhou and Shijiazhuang subway is under construction. Various countries' experience in developing rail transit shows that China's underground railway traffic will enter an unprecedented period of rapid construction and development after network volume operation is realized for subway[1-2].

## Emergency group decisions on subway fires

In traffic-free times, emergency fire evacuation drills can be conducted in the mid of the car body in the tunnel, to simulate the implementation of local group decisions of evacuation planning. When a fire breaks out in a train in a tunnel, in principle, the train should be driven into the front station as far as possible, where passengers can be evacuated; or else, the train need be pulled up in the tunnel for emergency disposals. Since a lot of smoke will be released during combustion, passengers' tolerance degree of the smoke determines whether to conduct timely evacuation. If the fire starts at the middle of the train, it's feasible to adopt unidirectional evacuation or bidirectional evacuation, thereby to accelerate evacuation velocity[3-5]. Under the condition of bidirectional evacuation, ventilating system should exhaust air towards the driving direction of the train, to ensure that the draught should be selected as an ideal evacuation direction. In the choice of evacuation modes, it's feasible to organize evacuation for the passengers according to the emergency condition, or evacuate them all at the same time to shorten evacuation time. But in the meantime, it's necessary to bear such accident risks as stampede caused by panicky passengers. In view of the above, for the preceding subway fire accident, we work out a set for emergency evacuation planning $S^* = \{S_1, S_2, \cdots, S_7\}$, in which planning $S_1$ expresses that bidirectional and simultaneous evacuation is adopted for the passengers after the train is driven into the front station.

**The implementation of emergency group decisions on subway fires**

In view of the domain knowledge involved in the accident, the emergency command center selects four domain experts to make emergency decisions $D=\{D_1,D_2,D_3,D_4\}$, letting them take part in the evaluation of the emergency evacuation planning. The emergency evacuation planning is mainly described by several attributes, including: Security $(d_1)$ expresses that this plan will be adopted to evacuate the passengers and to expect the possible casualties in the end; Evacuation cost $(d_2)$ refers to the sum of manpower, material resources and financial resources to be needed in the process of the evacuation when this plan is adopted; Accident loss $(d_3)$ refers to the financial loss to be caused and social impact to be produced in the end when this plan is adopted to evacuate the passengers.

**The evaluation of emergency group decisions on subway fires**

According to each expert's domain knowledge, the emergency command center distributes the emergency evacuation plans, to determine the relation between the decision-making experts and the local group decision of the emergency plans. $D_1$ participates in evaluating such planning sets $\{S_1,S_2,S_3\}$, $D_2$ participates in evaluating such planning sets $\{S_1,S_4,S_5,S_6,S_7\}$, $D_3$ participates in evaluating such planning sets $\{S_2,S_3,S_4,S_5,S_6\}$ and $D_4$ participates in evaluating such planning sets $\{S_1,S_6,S_7\}$. Based on the preceding relation of evaluation, all the experts respectively provide the local weights of the evaluation planning $a_{ij}^k\ (k=1,2,3,4)$ for the various attributes $d_i\ (i=1,2,3)$.

Aiming at attribute $d_1$, decision-making expert $D_1$ makes a comparison between $S_1,S_2,S_3$, the plans he participates in evaluating, to assess their performance on security, thinking that $S_3>S_1>S_2$, thus working out that $a_{11}^1=0.312$, $a_{12}^1=0.118$ and $a_{13}^1=0.487$; for attribute $d_2$, expert $D_1$ offers his assessment of the three plans on evacuation cost, thinking that $S_2>S_3>S_1$, thus working out that $a_{21}^1$=0.147, $a_{22}^1$=0.449 and $a_{23}^1=0.287$; in the end, for attribute $d_3$, decision-making expert $D_1$ makes a comparison between these three plans concerning accident losses, thinking $S_3>S_2>S_1$, thus making a preference judgment that $a_{31}^1=0.100$, $a_{32}^1=0.189$ and $a_{33}^1=0.557$. Similarly, the other three decision-making experts respectively make a preference judgment on their own evaluation plan under all properties.

$$x_1=(x_{11},x_{12},\cdots,x_{17})^T=(0.138,0.109,0.257,0.075,0.1778,0.110,0.075)$$

According to the above local weight $a_{ij}^k$, we integrate the opinions of all the experts, to obtain the group weight of such various plans as $S_1,S_2,\cdots,S_7$ under all the properties like $d_1,d_2,d_3$. Decision group $D=\{D_1,D_2,D_3,D_4\}$ thinks that on security, the performance of emergency evacuation plans $S_1,S_2,\cdots,S_7$ is manifested as:

$x_1=(x_{11},x_{12},\cdots,x_{17})^T$ = (0.138, 0.109, 0.257, 0.075, 0.1778, 0.110, and 0.075)

That is, decision group D thinks that on security, all the plans should be sorted this way: $S_3>S_5>S_1>S_6>S_2>S_4>S_7$. Accordingly, decision group D has also given out its group preference about all the decision schemes under such two properties as evacuation cost and accident loss.

According to the result of the group weight of the plans $x_i=(x_{i1},x_{i2},\cdots,x_{i7})^T$, i = 1, 2, 3, we also work out the experts' weight vectors $\sigma_i=(\sigma_i^1,\sigma_i^2,\cdots,\sigma_i^k)^T$, i = 1, 2, 3, under all properties, that is, based on the experts' judgment on the plans' local weight $a_{ij}^k$, we work out each expert's weight, see Tab.4.5. For instance, according to the evaluation of all the experts $D_1,D_2,D_3,D_4$ on emergency

evacuation plans $S_1, S_2, \cdots, S_7$ on security, it's worked out that expert $D_1$ 's weight $\sigma_1^1$ = 0.518, expert $D_2$ 's weight $\sigma_1^2$ = 0.623, expert $D_3$ 's weight $\sigma_1^3$ = 0.699 and expert $D_4$ 's weight $\sigma_1^4$ = 0.320. Similarly, according to each expert's judgment on the weight of evacuation cost and accident loss, the distribution outcomes of the experts' weights are arrived at, as is shown in Tab.1. In addition, we normalize the experts' weights under all properties in Tab.1. The objective function value Z is equal to 0.02679.

Table 1 Emergcntdecision except weights under each attribute

| Property | σ i1 | σ i2 | σ i3 | σ i4 |
|---|---|---|---|---|
| d1 | 0.518 | 0.623 | 0.699 | 0.320 |
| d2 | 0.520 | 0.432 | 0.687 | 0.285 |
| d3 | 0.432 | 0.519 | 0.873 | 0.247 |

**The judgment on the weight of emergency group decisions on subway fires**

After obtaining group weights for the plans, the four decision-making experts $D_1, D_2, D_3, D_4$ respectively use indeterminate information to make a pairwise comparison between the properties $d_1, d_2, d_3$ concerning their degree of importance, to get interval number reciprocal judgment matrixes $\tilde{B}^1, \tilde{B}^2, \tilde{B}^3, \tilde{B}^4$.

Table 2 Weight interval judegement of emergency scenario attributes

| Decision Expert | d1 | d2 | d3 |
|---|---|---|---|
| D1 | [0.362, 0.497] | [0.081, 0.100] | [0.188, 0.217] |
| D2 | [0.435,0.550] | [0.107,0.152] | [0.139,0.231] |
| D3 | [0.344,0.430] | [0.213,0.287] | 0.154,0.187] |
| D4 | [0.280,0.375] | [0.131,0.132] | [0.475,0.413] |

According to the relative formula, we work out that $j^{1'} = j^{2'} = j^{3'} = j^{4'} = 0$, which shows that all the above judgment matrixes $\tilde{B}^1, \tilde{B}^2, \tilde{B}^3, \tilde{B}^4$ are consistent reciprocal judgment matrices. In addition, according to $d_{ij}^{k-} = d_{ij}^{k+} = 0$, we work out the judgment of all the experts $D_1, D_2, D_3, D_4$ on the weight ranges of all the properties $d_1, d_2, d_3$, as is shown in Tab.2. To take decision-making expert $D_1$ for example, the comparison of his three properties' importance can be expressed by interval numbers as [0.362, 0.497,[0.081, 0.100]，[0.188, 0.217] after being calculated.

After normalizing the expert weights under each property, put them into the formula and work out finally that the mean estimated value of attribute weights is that $\overline{w}_1 = 0.473, \overline{w}_2 = 0.137, \overline{w}_3 = 0.179$.

**Result analysis on emergency group decisions on subway fires**

At last, based on the calculations of the plans' group weights and attribute weights, we compute the decision group members' group evaluation value $G_j$ of alternative set. After making a local preference judgment on the scheme set $S^* = \{S_1, S_2, \cdots, S_7\}$, experts $D_1, D_2, D_3, D_4$ gather group's opinions, thinking plan $S_3$ is the best one according to their ordering of optimization preference for all the plans: $S_3 > S_5 > S_2 > S_1 > S_6 > S_4 > S_7$.

Besides, according to the relative formula, we obtain the decision group members' individual local evaluating value $R_j^k$ for alternative offer, as is shown in Tab.3. According to the experts' calculations of the individual local evaluating value in Tab.3, expert $D_1$ sorts his emergency plan set $\{S_1, S_2, S_3\}$ as $S_3 > S_2 > S_1$ according to his own individual preference; expert $D_2$ sorts his emergency plan set $\{S_1, S_4, S_5, S_6, S_7\}$ as $S_5 > S_4 > S_1 > S_6 > S_7$ according to his own individual preference; expert $D_3$

sorts his emergency plan set $\{S_2, S_3, S_4, S_5, S_6\}$ as $S_3 > S_5 > S_2 > S_6 > S_4$ according to his own individual preference; expert $D_4$ sorts his emergency plan set $\{S_1, S_6, S_7\}$ as $S_1 > S_6 > S_7$ according to his own individual preference.

By gathering the experts' individual partial evaluations, we get a group evaluation result basically the same to the experts' individual local evaluation result, only that the group sorts plans $S_6$ and $S_4$ differently from the individual preference of expert $D_2$. When making an analysis on this problem, we find that expert $D_3$ has also participated in evaluating plans $S_4$ and $S_6$. By comparing the weights of expert $D_2$ and expert $D_3$, we find that the group members agree with expert $D_3$ who has greater degrees of importance in sorting and opinions. So here we can view that the group preference is rational.

In addition, the reckoning in Tab.3 also indicates that if consulting expert $D_1$, emergency evacuation plan $S_3$ should be selected for the fire accident. Accordingly, if we only use the individual opinions of experts $D_2, D_3, D_4$ for references, then emergency evacuation plans $S_5, S_3, S_1$ will separately serve as the basis for emergency response. However, such individual decisions of the experts are obvious incomplete. On the one hand, each expert just makes a local decision on the scheme set dependent on his domain knowledge, so there is lack of integral comparability between all the schemes in the set; on the other hand, since we don't gather the individual preferences of the decision experts, the preceding evaluation results have failed to integrate the opinions of the decision group, so individual decision making is lack of effectiveness.

Table 3 Partial pretenence values and ranking of emergency decision expert individual

| proposal | $R_j^1$ | Sort | $R_j^2$ | Sort | $R_j^3$ | Sort | $R_j^4$ | Sort |
|---|---|---|---|---|---|---|---|---|
| $S_1$ | 0.127 | 3 | 0.198 | 3 | —— | | 0.387 | 1 |
| $S_2$ | 0.153 | 2 | —— | | 0.166 | 3 | —— | |
| $S_3$ | 0.387 | 1 | —— | | 0.323 | 1 | —— | |
| $S_4$ | —— | | 0.197 | 2 | 0.109 | 5 | —— | |
| $S_5$ | —— | | 0.189 | 1 | 0.217 | 2 | —— | |
| $S_6$ | —— | | 0.134 | 4 | 0.153 | 4 | 0.353 | 2 |
| $S_7$ | —— | | 0.148 | 5 | —— | | 0.210 | 3 |

## Conclusion

According to the local group decision model presented by this paper, the expert group has made an emergency decision on the subway fire accident, thinking emergency evacuation plan $p_3$ should be adopted, that is, the train should be pulled up in the tunnel and ventilation system should be opened to protect the passengers from poisonous smoke, and the passengers shouldn't be evacuated for the time being.

## References

[1]Coppola D P. Oxford Burlington, Oxford：Butterworth-einemann Publications, 2007.

[2] Abouelnaga A E. Nuclear Engineering and Design, 2010, 240(7).

[3]Meeks H N. Environmental Toxicology & Chemistry, 2009, 28(9).

[4] Roh J S. Tunneling & Underground Space Technology, 2009, 24(4).

[5]Kauffman J. Pullic Relations Review, 2005, 31(2).

*Applied Mechanics and Materials Vols. 580-583 (2014) pp 1412-1416*
*© (2014) Trans Tech Publications, Switzerland*
*doi:10.4028/www.scientific.net/AMM.580-583.1412*

# Based on effect coefficient method of metro tunnel collapse risk evaluation model and its application

Penglin Cai [1, a], Jia Wang[1,b] and Shuwen Tian[1,c]

[1] Construction Engineering College，Jilin University，Changchun， Jilin 130026， China

[a]450344284@qq.com, [b] 1067715199@qq.com, [c] 597758449@qq.com

**Keywords:** Metro; collapse; risk; effect coefficient method; TSP203.

**Abstract.** Tunnel collapse is one of the most common accidents in the tunnel construction of city subway, and risk assessment is a method to measure the magnitude of the collapse risk. In order to effectively identify in advance the risk category of tunnel collapse, an identification method is put forward based on entropy weight method and efficiency coefficient method. On the basis of a comprehensive analysis of factors that affect the collapse, 6 main factors including rock level, tunnel depth, tunnel span, the surrounding conditions, groundwater and construction factors are selected as the evaluation indexes. Through a quantitative description of the evaluation indexes by using the TSP203 geological prediction system, and based on the basic principles of ideal point method, a comprehensive and intelligent evaluation model which can identify the tunnel collapse risk in subway construction is established. Finally, the model is applied to practical engineering, and it shows that the result of risk assessment is consistent with the actual construction conditions, which provides a new perspective on the advancing identification of tunnel collapse risk in subway construction.

## Introduction

With the rapid development of China's urban rail transit construction. The engineering geological conditions become increasingly complex and confronting problem is increasingly challenging . collapse is common disaster in construction of the subway tunnel, most of the domestic construction subway tunnel have occurred collapse more or less.It is not only to bring hinder tunnel construction, but also seriously threat to the safety of equipment and person. Due to the complexity of the surroundings in the city, the tunnel collapse would also have a significant social impact.So the tunnel collapse risk assessment study has important significance.

For subway tunnel collapse risk assessment, the method is generally used engineering experience analogy. That is, by comparing with similar collapse in engineering and engineering-related information to predict the subway tunnels along the route, there are some scholars adopt comprehensive evaluation method for collapse-related information on a comprehensive analysis to analyze different sections of collapse risk. Such as the risk index method, fault tree analysis, Monte Carlo simulation method, AHP, fuzzy evaluation method, influence diagram method,LECD and so on. These methods are more subjective, there are a lot of inconvenience in practice .The collapse risk assessment results are often inconsistent with the actual situation.

## The basic principle of efficacy coefficient method

Efficacy coefficient method also can be called as efficacy function method, based on the principle of multi-objective planning, According to the multi-grade standards, the evaluation index can translate into measurable evaluation scores through conversion function, and then an overall evaluation is obtained according to the evaluation objects , and judge the merits based on the final score, This method is used to evaluate the object with comparison, ordering, and rarely used for classification.We have a new try to apply it to grade the risk .Calculate the maximum and minimum efficiency coefficient for each classification. to determine the efficiency coefficient demarcation point, and make the classification more reasonable. the improved evaluation steps as follows:

2.1 Set the classification standard

Classification standard is the max and min value of corresponding evaluation of some category, the max limit value is the max standard of one category, and the min value is the min standard. set evaluation standard vector is $Y=(y_1,y_2,\ldots,y_m)$ , classification number is m, and standard value number is m+1, classification standard value is $k_j(j=0,1,2,\ldots,m+1)$

2.2 Indentify standard coefficient of standard value

Standard coefficient is the level coefficient of corresponding standard value, Objectively reflect the different levels of evaluation criteria value, it is used to calculate the index of the actual value corresponds to the standard value, the standard value for each category, there is a corresponding coefficient. Standard coefficients is represented with number ranged between 0-1 , record as $\lambda_j$ $(j=1,2,\ldots,m+1)$ .Calculate formulation as follows:

For efficiency index that the larger value is the better:

$$\lambda_j=\begin{cases}1 & k_j \geq x_{\max}\\ \dfrac{k_j-x_{\min}}{x_{\max}-x_{\min}} & x_{\min}<k_j<x_{\max}\\ 0 & k_j \leq x_{\min}\end{cases} \tag{1}$$

For cost-type index that the smaller value is the better:

$$\lambda_j=\begin{cases}1 & k_j \leq x_{\min}\\ \dfrac{x_{\max}-k_j}{x_{\max}-x_{\min}} & x_{\min}<k_j<x_{\max}\\ 0 & k_j \geq x_{\max}\end{cases} \tag{2}$$

In the formulation, $\lambda_j$ is the standard coefficient; $k_j$ is the standard value; $x_{max}$ is the max index; $x_{min}$ is the min index.

2.3 Determine the weight of each index

Entropy method is used here. "Entropy" has been widely used in many fields. In information theory, the information is a measurement of the ordering degree , the information entropy is defined as:

$$e_j=-k\sum_{i=1}^{m}p_{ij}\cdot\ln p_{ij} \quad p_{ij}=r_{ij}\Big/\sum_{i=1}^{m}r_{ij} \tag{3}$$

In the formulation, $k=1/\ln m$ ,$r_{ij}$ is the evaluation of i term under j index， $e_j$ is the confusion degree of j evaluation index, that is, entropy value.

The entropy of the evaluation index j is:

$$w_j=(1-e_j)\Big/\sum_{j=1}^{n}(1-e_j) \tag{4}$$

2.4 Determine the effective coefficient of individual indicators

Efficacy coefficient e single index includes two parts, one is basis score,it is calculated by the standard values of some index.The other one is adjusted score ,it is calculated by the extra part that the index actual value exceed standard values.

The computational formula of basis score is: $b_i=\omega_i\lambda_j$,the computational formula of adjusted score is

$$\varepsilon_i=w_i(\lambda_{j+1}-\lambda_j)\left(\frac{x_i-k_j}{k_{j+1}-k_j}\right) \tag{5}$$

So the effective coefficient of individual indicators is:

$$e_i = b_i + \varepsilon_i = w_i(\lambda_j + (\lambda_{j+1} - \lambda_j)(\frac{x_i - k_j}{k_{j+1} - k_j})) \tag{6}$$

$k_{j+1}$ is upper standard value, $k_j$ is bottom standard value, $\lambda j_{+1}$ is upper standard coefficient,$\lambda j$ is bottom standard coefficient. $\omega_i$ is the weight .$x_i$ is actual value.

2.5 Calculate the total efficiency coefficient

The total efficiency coefficient is the summation of each individual indicators efficacy coefficient. The formula is:

$$E = \sum_{i=1}^{n} e_i \tag{7}$$

2.6 Get the total score in each category and the classification of evaluation object

Plugge the various categories of standard efficiency coefficient values into the formula (1), calculate for total efficiency coefficient corresponding to each category, Determine the classification criteria, and then determine the cave belong to which category.

## Index system in advance of subway tunnel collapse risk evaluation

TSP203 system is Switzerland Ann's measurement technology companies to develop a new generation of advanced geological forecast system. In comprehensive consideration of TSP203 can detect effectively on the basis of the data and the factors influencing the subway tunnel collapse.

This paper selected surrounding rock classification, buried depth, span and surrounding environment, the influence of groundwater and construction management of six major factors as tunnel collapse risk evaluation index. The level of the surrounding rock and groundwater development situation based on TSP203 advance geology forecasting system, tunnel buried depth, span, surrounding environment and construction factor obtained by site investigation.

Based on the experience and the results of previous studies, the tunnel collapse risk is divided 5 Levels, very dangerous, dangerous,normal, safe,very safe, and corresponding risk levels are as follows: I Level, II Level, III Level, IV Level and V Level . The classification of the division of each evaluation is shown in Table 1

Table 1 Indices and criterion for collapse risk assessment

| Collapse risk level | I | II | III | IV | V |
|---|---|---|---|---|---|
| Vp/km/s | 0-1.5 | 1.5-2.5 | 2.5-3.5 | 3.5-4.5 | 4.5-6.0 |
| burial depthH/m | 0-5 | 5-10 | 10-15 | 15-20 | 20-30 |
| spanD/m | 21-30 | 15-21 | 9-15 | 5-9 | 0-5 |
| Groundwater | 0.8-1.0 | 0.6-0.8 | 0.4-0.6 | 0.2-0.4 | 0-0.2 |
| surroundings | 0.8-1.0 | 0.6-0.8 | 0.4-0.6 | 0.2-0.4 | 0-0.2 |
| Construction management | 0.8-1.0 | 0.6-0.8 | 0.4-0.6 | 0.2-0.4 | 0-0.2 |

## Engineering Applications

4.1 Project overview and the tunnel collapse risk classification

Project of Qingdao Metro ( 3 Line) route Shinan District, Shibei District, Sifang District, and Licang District, approx 24.9km. All underground lines, to Qingdao subway's first line, societies that are significant. This paper has the station underground line to licun part of Hexi, include 5subway station and 5 interzone tunnel. The tunnel is single holes and single horseshoe-shaped structure, distance between two hole is 12m, and expanding the section construction of air defense section. According to the survey of geological data, the section thickness of Quaternary 10.1~17.9 metres, mainly consisting of Quaternary holocene artificial filled soil (Q4ml), the flood-alluvial (Q4al+pl) and upper

Pleistocene alluvium (Q3al +PL). Sites dominated by coarse-grained granite bedrock, interspersed with granitic porphyry vein-in the meantime, part of the tunnel under water-rich Sandy layers, construction risk is significant.

4.2 Standard coefficient of standard value of categories

In the establishment of the index system for evaluation of surrounding rock stability, span, groundwater surroundings, construction management belong to the benefit indicators, that is,the higher the value, the lower the stability of the surrounding rock, the greater the risk of collapse in tunnel. The rest indicators are cost index, that is, the lower the value, the lower the stability of the surrounding rock, the greater the risk of collapse in tunnel. The standard value and standard coefficients of each indicators is showen in Table 2.

Table 2 Standard value and standard coefficient of each classification

| level | Vp | | Burial depth | | Span | | Groundwater | | Surroundings | | Construction management | |
|---|---|---|---|---|---|---|---|---|---|---|---|---|
| | SV | SC | SV | SC | SV | SC | SV | SC | SV | SC | SV | SC |
| I | 0 | 0 | 0 | 0 | 30 | 0 | 1.0 | 0 | 1.0 | 0 | 1.0 | 0 |
| II | 1.5 | 0.25 | 5 | 0.17 | 21 | 0.30 | 0.8 | 0.2 | 0.8 | 0.2 | 0.8 | 0.2 |
| III | 2.5 | 0.41 | 10 | 0.33 | 15 | 0.50 | 0.6 | 0.4 | 0.6 | 0.4 | 0.6 | 0.4 |
| IV | 3.5 | 0.58 | 15 | 0.50 | 9 | 0.70 | 0.4 | 0.6 | 0.4 | 0.6 | 0.4 | 0.6 |
| V | 4.5 | 0.75 | 20 | 0.67 | 5 | 0.83 | 0.2 | 0.8 | 0.2 | 0.8 | 0.2 | 0.8 |

4.3 Engineering application

To test the reliability of the model, apply the model to post 4 different hole recognition tunnel collapse risks.TSP203 combined field data and field research to determine evaluation parameters of the tunnel section, as Table 3 below:

Table 3 Assessment of collapse risk factors

| number | $V_p$ | Burial depth | span | Groundwater | Surroundings | Construction management |
|---|---|---|---|---|---|---|
| 1 | 0.91 | 11 | 6.2 | 0.71 | 0.7 | 0.5 |
| 2 | 2.4 | 16 | 11.2 | 0.41 | 0.8 | 0.45 |
| 3 | 3.2 | 13 | 8.1 | 0.26 | 0.3 | 0.5 |
| 4 | 0.37 | 9.5 | 6.2 | 0.82 | 0.95 | 0.3 |

After determining the risk evaluation index of the cave.Carry out dimensionless processing of each index to eliminate size disparity. According to formula (3), establish evaluation cave collapse risk assessment matrix. Based on the theory of entropy formula (4),we can calculate the weighted values for each indicator.The evaluation index weight value are : 0.51, 0.04, 0.07, 0.19, 0.15, 0.04.

Combine standard values ,standard coefficient , each weights and calculation formula(6)(7),we can get the total efficiency coefficient range of collapse risk rating.We can get that level I total efficiency coefficient range is 0~0.2313. Similarly to other levels of total efficiency coefficient range, level II is 0.2313~0.4093, level III is 0.4093～0.5928,level IV is 0.5928～0.7714 ,level V is 0.7714～1.

According to equation (6) and Table 7 for each index value of the evaluation section cave,we can calculate the collapse risk of the evaluation cave.Taking hole 1 as an example for illustration purposes. TSP wave velocities measured to 0.91from table 2 shall have a level II risk, and then from table 4 to its standard value is 0 , standard coefficient is 0, upper standard value is 1.5, upper standards coefficient is 0.25, its weight is 0.51.Thought equation (6) the individual indicators efficiency coefficient of rock wave velocity is:

$$e_{1\cdot} = 0.51\left[0.25 + (0.25-0)\frac{0.91-0}{1.5-0}\right] = 0.0765 \tag{8}$$

In a similar way we can get the rest individual indicators efficiency coefficient. Thought formula (7) we can get that total efficiency coefficient is:

$$E = \sum_{i=1}^{5} e_i = 0.26653 \tag{9}$$

So cave 1 belongs to level I (0.2313～0.4093).The result is showed in table 4.

Table 4 Comparative results of surrounding rock

| number | individual indicators | | | | | | total | level | actual |
|---|---|---|---|---|---|---|---|---|---|
| | $V_p$ | depth | span | groundwater | surroundings | management | | | |
| 1 | 0.0765 | 0.01456 | 0.05537 | 0.0551 | 0.045 | 0.02 | 0.26653 | II | II~III |
| 2 | 0.20094 | 0.02136 | 0.05411 | 0.1121 | 0.03 | 0.022 | 0.44051 | III | III |
| 3 | 0.26979 | 0.01728 | 0.0511 | 0.1406 | 0.105 | 0.02 | 0.60377 | IV | III~ IV |
| 4 | 0.0306 | 0.01256 | 0.05537 | 0.0342 | 0.0075 | 0.028 | 0.16823 | I | I |

## Conclusions

1. This paper presents a method that grade the risk of collapse in front of the subway tunnel face in advance ,which is based on the results of a probe TSP203 and the use of intelligent rock mechanics method. Engineering applications show that the method is practical, workable.It provides a new idea for subway tunnel collapse risk assessment . The idea is universal in solving complex problems in geotechnical engineering.

2. This article apply entropy weight method and effect coefficient method to the subway tunnel collapse risk assessment ,and the risk level compared with the actual results show that this method is accurate. This method is after all just an evaluation and analysis methods, in practical application process, taking into account the factors that affect the risk of subway tunnel collapse, should further improve the evaluation system, and try to adopt a more scientific approach to determine the weight of each index to improve the accuracy.

## References

[1] LI Shucai，SHI Shaoshuai，LI Liping,etc.Attribute Recognition Model and Its Application of Mountain Tunnel Collapse Risk Assessment [J]. Journal Of Basic Science And Engineering，2013,21(1):147-158.

[2] LI Shu-cai, XUE Yi-guo,ZHANG Qing-song,etc. Keytechnology study comprehensive prediction and earlywarningof geological hazards during tunnel constructionin high-risk karst areas[J]. Chinese Journal of Rock Mechanics and Engineering, 2008, 27(7): 1297-1307.

[3] You Pengfei，Mou Ruifang. Research on Landslide Risk Assessment model about Subway Tunneling Based on Set Pair Analysis [J]. Journal of Wuhan University of Technology(Transportation Science & Engineering)，2012，36(5)：1009–1012.

[4] MENG Fan-qi, LI Guang-jie, WANG Qing-bing, et al. Research on early warning of debris flow based on efficacy coefficient method[J]. Rock and Soil Mechanics, 2012, 33(3): 835－840

[5] Chen Jiejin，Zhou Feng，Yang Junsheng，et al． Fuzzy analytic hierarchy process for risk evaluation of collapse during construction of mountain tunnel［J］． Rock and Soil Mechanics ，2009，30( 12) : 3622-3626

[6] WANG Ying-chao，SHANG Yue-q uan，SUN Hong-yue，et al. Research and application of rockburst intensity prediction model based on entropy coefficient and ideal point method[J]. Journal of China Coal Society，2010，35(2)：218-221.

[7] QIU Dao-hong, LI Shu-cai, ZHANG Le-wen, et al. Prediction of surrounding rock classification in advance based on TSP203 system and GA-SVM[J]. Chinese Journal of Rock Mechanics and Engineering，2010，suppl(1)：3221-3226.

[8] XU Zhenhao，LI Shucai，ZHANG Qingsong，et al. Reflection characteristic of seismic wave in TSP advance geological prediction[J]. Chinese Journal of Underground Space and Engineering，2008，4(4)：640–644.

# CHAPTER 4:

# Seismic Engineering

*Applied Mechanics and Materials Vols. 580-583 (2014) pp 1419-1425*
*© (2014) Trans Tech Publications, Switzerland*
*doi:10.4028/www.scientific.net/AMM.580-583.1419*

# Application of FEM strength reduction dynamic analysis in the seismic design of reinforced earth-retaining wall with geo-grid

Xiaosong Tang[1,2,a], Yingren Zheng[2,3,b] and Lai Jie[2,c]

[1]School of Civil Engineering, Chongqing University, Chongqing, China

[2]Logistical Engineering University University, Chongqing, China

[3]Engineering and Technology Research Center of Geological Hazard Prevention and Treatment, Chongqing, China

[a]hnm97@163.com, [b]zhengl32@163.com, [c]454501543@qq.com

**Keywords:** geo-grid; reinforced earth-retaining wall; stability analysis; FEM strength reduction; dynamic analysis

**Abstract.** Due to the special mesh structure, geo-grid material can avoid local subsidence of filling material, reduce uneven settlement of soil mass to the largest degree and improve the whole stability of soil mass, so the reinforced earth-retaining wall with geo-grid is widely used in engineering. Meanwhile, researches on its dynamic characters are not enough and it is hard to judge the whole stability of reinforced earth-retaining wall under seismic condition. When unstable failure happens, the location of failure surface can hardly be identified. These disadvantages have seriously limited the development of this supporting method and cause unsafe potentials for engineering. Based on the FEM strength reduction dynamic analysis and combined with practical engineering, the paper conducts stability analysis on the reinforced earth-retaining wall of geo-grid under seismic condition and the research achievements provide a new thinking for the seismic design of reinforced earth-retaining wall with geo-grid.

## Introduction

With the rapid development of the economy in China, the application and the scales of reinforced earth-retaining wall with geo-grid are both increasing. The design should satisfy not only the requirements of static safety but also the requirements of seismic design. The researches corresponding to static condition are comparatively enough relatively mature [1~4]. Studies on the seismic design are few and there is no reasonable standards accepted in engineering. Only a few of research achievements are focused on the stress and deformation characteristics, and the inner stability of the structure of reinforced earth-retaining wall under seismic condition. It is hard to judge the whole stability of reinforced earth-retaining wall dor dynamic loads. When unstable failure happens, the most dangerous failure surface cannot be identified [5~8]. These disadvantages have seriously limited the development of this supporting method and caused unsafe potentials for engineering.

So based on FEM strength reduction dynamic analysis [9,10] and combined with the traditional pseudo-static method, seismic analysis on a certain engineering with high reinforced earth-retaining wall with geo-grid has been conducted in the paper. The calculation results show that the dynamic performance of reinforced earth-retaining wall with geo-grid in the engineering is satisfactory and can reach the requirements of seismic design. The research achievements provide a new thinking for the seismic design of reinforced earth-retaining wall with geo-grid.

## Theory of FEM strength reduction dynamic analysis

①Theories of FEM strength reduction dynamic analysis

Under static condition, FEM strength reduction respectively reduces the parameters of shear strength c and tan φ by c/ω and tan φ/ω till ultimate equilibrium state. The reduction coefficient at the moment

is the safety factor of the slope. At present, the stability analysis under static condition through this method is very mature[11,12].

Under seismic condition, the dynamic magnifying coefficient of slope would increase and the slope is becoming closer to the unstable failure with the reduction of material parameters. And the failure mode of slope under seismic condition is mostly tensile-shear failure, so the reduction of tensile strength should be considered during the strength reduction, that is $\sigma_t'=\sigma_t/\omega$.

②Discussions on the failure conditions

The criteria of unstable failure should be clear if adopting FEM strength reduction to calculate the safety factor. At present, three criteria of unstable failure under static condition are: (1) the transfixion of plastic zone or the equivalent plastic strain from the slope foot to slope top; (2) the mutation of strain and displacement of sliding place in soil mass; (3) the non-convergence of static equilibrium calculation. In static calculation, the transfixion of plastic zone is not sufficient but necessary condition for whole failure of slope [11, 12], so the non-convergence in the calculation is often taken as the criterion of unstable failure.

In the dynamic analysis under seismic condition, the above three criteria can also be used to judge the unstable failure in principle: (1)the transfixion of failure surface (tensile-shear failure surface); (2)the mutation of the displacement of the potential sliding mass. Considering the load is always changing with time under seismic condition, so the displacement would change at any time. Different with the static condition, the mutation of the displacement at a certain moment cannot judge the unstable failure. If the final displacement after dynamic effects mutates, the mutation of the relationship curve between reduction coefficient and the displacement can be identified as the criterion of unstable failure; (3)the non-convergence of displacement or speed can be regarded as the failure criterion. Due to the complication of the dynamic analysis under seismic condition, all the above three criteria should be used to judge the unstable failure under seismic condition.

Compared with other methods, FEM strength reduction dynamic analysis possesses the following advantages: (1)as a complete dynamic method, it does not need to search the failure surface and evaluate dynamic load empirically. The seismic wave can be used directly to evaluate the stability under dynamic condition so as to reduce the influence of artificial assumption; (2) the practical tensile-shear failure surface under seismic condition can be obtained directly; (3) it can take the interaction between rock and soil mass and the supporting structure into consideration to fully reflect the dynamic properties of rock and soil mass, so more reasonable safety factor under dynamic effects can be worked out.

## Practical engineering

In a high embankment engineering in a certain airport, reinforced earth-retaining wall with 60 meters high is constructed. The retaining wall composes of four stages. Each stage is 15 meters high with an inclining angle of 70° . The lengths of geo-grids from the bottom to the top are respectively 45 meters, 37 meters, 30 meters and 25 meters. The vertical interval between geo-grids is 0.4 meters. The platform with 3 meters wide is set every 15 meters along the retaining wall vertically. The comprehensive gradient is 1:2.5, as shown in Figure 1.

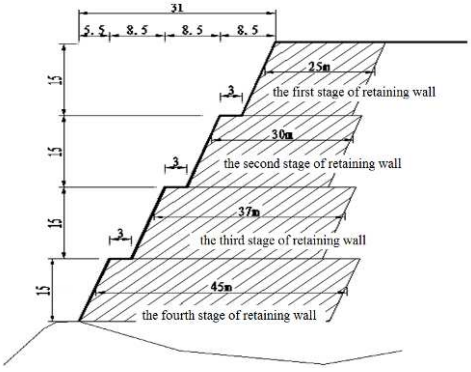


**Fig. 1 Layout of reinforced earth-retaining wall with geo-grid**

The interaction between geo-grid and the soil is simulated through setting coupling spring and the stress transfer satisfies the Mohr-Coulomb criterion. Except press, only tension is considered for the geo-grid material, which is flexible material without flexural rigidity. So the constitutive relationship of the geo-grid element can be simplified as linear elasticity and regarded as one-dimensional element deforming along the axial direction, as shown in Figure 2. If only considering displacement in the horizontal direction, the relationship between the stress and the displacement of node is $\{p\}=[k]^e\{u\}$, where $\{p\}$is the stress on node,$\{p\}=\begin{Bmatrix} p_i \\ p_j \end{Bmatrix}$;$\{u\}$ is the displacement of node,$\{u\}=\begin{Bmatrix} u_i \\ u_j \end{Bmatrix}$; $[k]^e$ is the matrix of element stiffness; $[k]^e=\frac{AE}{L}\begin{bmatrix} 1 & -1 \\ -1 & 1 \end{bmatrix}$; A is the cross section area; L is the element length. The mechanic properties in the shear direction of the geo-grid is shown in Figure 3, where $c_{inter}$ and $\varphi_{inter}$ are the strength parameters of geo-grid and soil interface. The mechanic and physical parameters of rock and soil mass and geo-grid material are shown in Table 1.

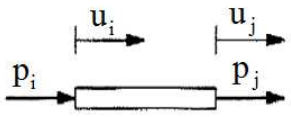


**Fig. 2 Element of reinforced material of geo-grid**

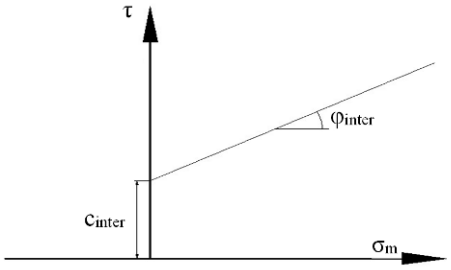


**Fig. 3 Failure line of shear strength**

**Table 1 Physical and mechanic parameters of the materials**

| Material | Unit weight of soil/kN·m$^{-3}$ | Elastic modulus /MPa | Poisson ratio | Cohesion /kPa | Inner friction angle/° |
|---|---|---|---|---|---|
| Backfill soil | 20 | 45 | 0.3 | 10 | 30 |
| Bed rock | 23 | 1600 | 0.14 | 1000 | 33 |
| Geo-grid | - | - | - | 7.0 | 24.23 |

The input seismic wave is Linghe Wave(Linghe, 1995, NS direction) and the peak acceleration is 0.17g, which is larger than the basic fortification intensity 7 degree, but less than 8 degree. In the numerical simulation, bidirectional input is used where the peak acceleration in the vertical direction is 2/3 of that in the horizontal direction. The slope sites is free boundary, which can prevent the reflection of seismic wave on the boundary to simulate the condition of infinite field boundary under seismic condition. Local damping is used to satisfy the requirements on precision of general engineering and the damping coefficient is 0.157.

Through intercepting the major energy section, the duration of inputting seismic wave is 10 seconds. The filtered seismic wave after correcting the baseline is shown in Figure 4. The FEM strength reduction dynamic analysis mentioned above is used to analyze the stability of reinforced earth-retaining wall.

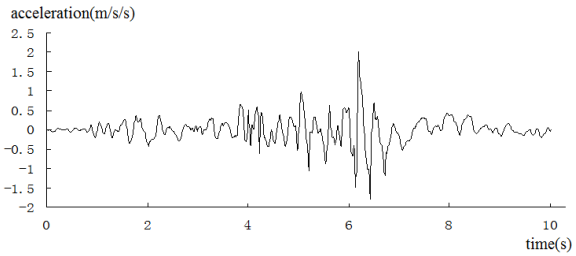


**Fig. 4 Inputting seismic wave**

Stability analysis should be conducted under dead weight condition first to judge whether it can satisfy the design requirement. The mesh of model and the location of data points A~H are shown in Figure 5.

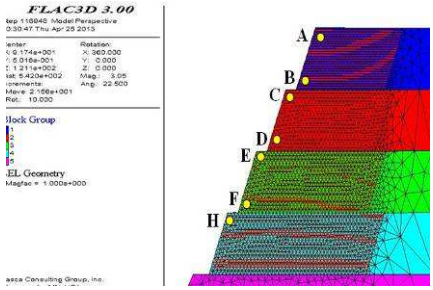


**Fig.5 The mesh of reinforced earth-retaining wall and the location of data points**

The engineering is carried out stage by stage to ensure the safety requirement during construction. The safety factor of each construction stage is obtained through calculation stage by stage, which are shown in Table 2. Under dead weight condition, the safety factor of the engineering is 1.39. At the moment, the maximum stress on the geo-grid is 92.54kN/m and the strength reservation of geo-grid itself is 2.18, which can satisfy the design requirement.

**Table 2 Safety factor of each stage of engineering under dead weight condition**

| Stage | The 4th stage | The 3rd stage | The 2nd stage | The 1st stage |
|---|---|---|---|---|
| Safety factor | 1.75 | 1.58 | 1.45 | 1.39 |

Then the stability analysis under stress field of dead weight and seismic condition is carried out to identify the dynamic safety factor. By adopting FEM strength reduction dynamic analysis, mutation happens in the accumulated displacement after dynamic effects in data point A when the reduction coefficient is 1.17, as shown in Figure 6. Unstable failure can be judged initially and the dynamic safety factor is between 1.14 and 1.18.

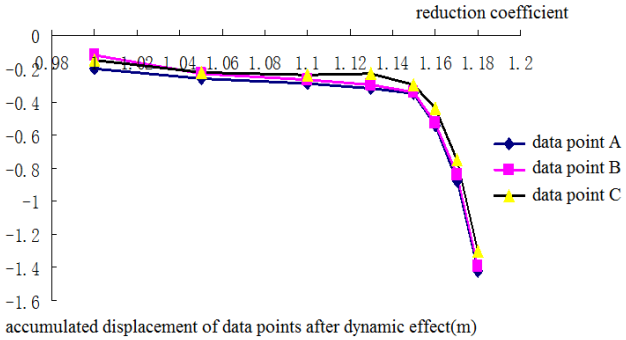


**Fig. 6 Relationship curve between displacement and reduction coefficient of data points after dynamic effect**

When the reduction coefficient is 1.15, convergence of the displacement after dynamic effect appears in the calculation and the structure can still bear loads. Failure has not happened on the retaining wall, as shown in Figure 7(a). When the reduction coefficient is 1.17, convergence of the displacement does not happen after seismic effects in the calculation and failure happens on the retaining wall, as shown in Figure 7(b).

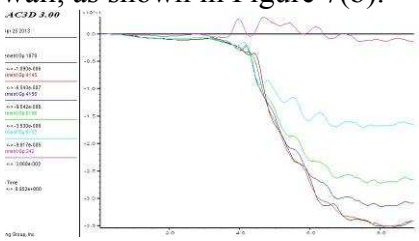

**(a) Reduction coefficient is 1.15.**

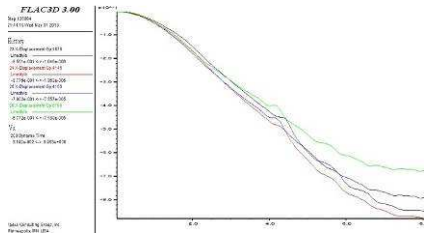


**(b) Reduction coefficient is 1.17.**

**Fig.7 Time-history curve of horizontal displacement of each data point under different reduction coefficient**

When the reduction coefficient is 1.15, shear plastic zone transfixes. The max shear strain of the plastic zone is within 3% and most parts are less than 1%, which implies it has the tendency of failure and failure has not happened, as shown in Figure 8(a). When the reduction coefficient is 1.17, the maximum of shear strain is up to 6.8% and the plastic zone transfixes, so failure happens on the retaining wall, as shown in Figure 8(b). In conclusion, the dynamic safety factor of this engineering is about 1.16.

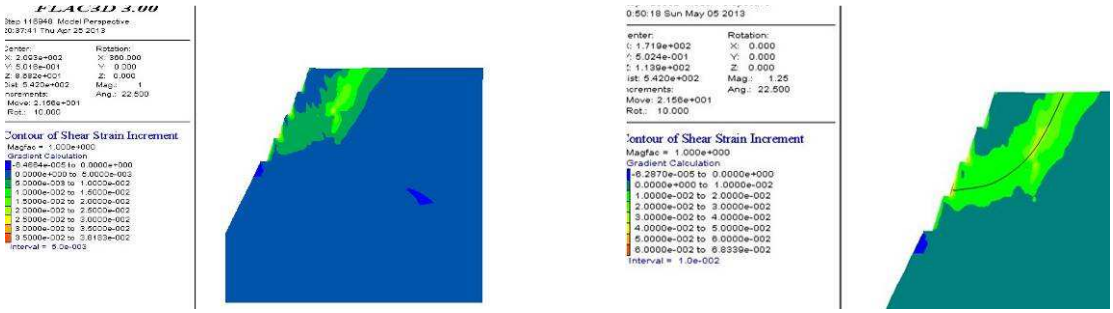


**(a) Reduction coefficient is 1.15.** **(b) Reduction coefficient is 1.17.**

**Fig. 8 Nephogram of shear increment under different reduction coefficient**

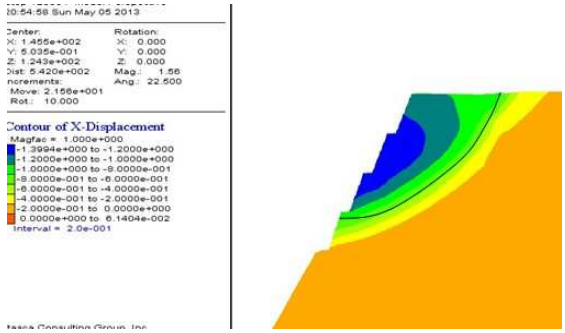


**Fig. 9 Nephogram of horizontal displacement(Reduction coefficient is 1.17)**

The location of failure surface can be identified through the mutation of plastic strain or displacement when unstable failure happens, especially the mutation of plastic strain which is more obvious. The mutation of plastic strain is usually on the point where the max plastic strain is. So the location and morphology of the failure surface can be identified through this principle. If connecting the points where the plastic strain increases in Figure 8(b) , the curve would be the location and morphology of failure surface, as the black curve in Figure 8(b) shows. The change of contour line of displacement in Figure 9 can also illustrate the failure surface. The failure surface identified through these two methods are basically the same, which slides out along the bottom of the third stage of retaining wall.

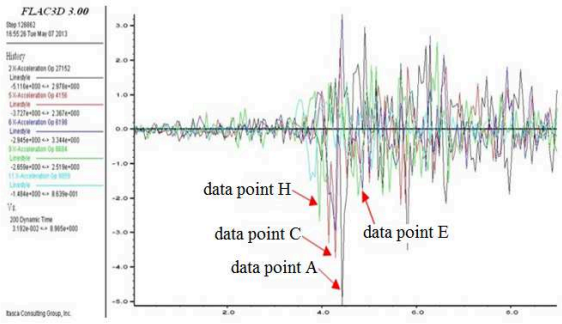


**Fig. 10 Time-history curve of acceleration of each data point**

Figure 10 is the time-history curve of acceleration of the data point on the top of each stage of reinforced earth-retaining wall, which shows the higher the data point, the larger the peak acceleration, the more obvious the magnifying effect is. If defining the ratio of peak acceleration to

the peak value of input seismic wave (0.17g) as the magnifying coefficient of acceleration, it is about 1.29~2.95 under seismic condition.

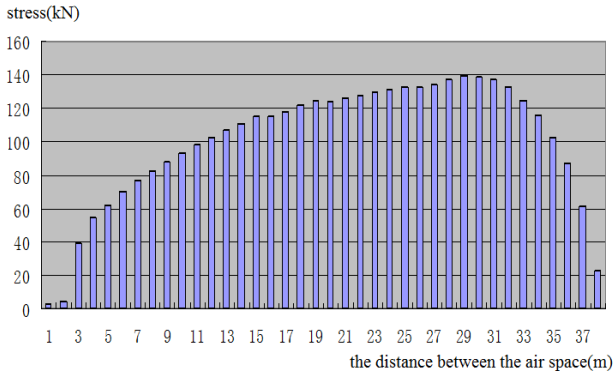


**Fig. 11 Layout of stress on the bottom of the third stage of earth-retaining wall (Reduction coefficient is 1.16)**

Figure 11 is the layout of stress on the bottom of the third stage of earth-retaining wall. The stress on the geo-grid increases linearly from the air space to a certain depth and then reduces gradually. The max tension of the reinforced bar is 139.8kN/m, which is less than the ultimate tension of the reinforced bar (200 kN/m). The strength reservation of the reinforced bar itself is about 1.43 ,so the design requirements of geo-grid under seismic condition can be satisfied.

## Summary

The paper introduces FEM strength reduction dynamic analysis into the seismic design of reinforced earth-retaining wall with geo-grid. Combined with practical engineering, the safety factor, the dynamic response of earth-retaining wall and the location of failure surface of unstable failure under seismic condition can be worked out. The research achievements can provide a new thinking for the seismic design of reinforced earth-retaining wall with geo-grid.

## Acknowledgment

The research has been completed under the financial support of the China 973 National Key Basic Research and Development Project(Grant No.2011CB710606).

## References

[1] TATSUOKA F, TATEYAMA M, KOSEKI J. Behavior of Geogrid-reinforced soil retaining walls during the Great Habshin-Awaji Earthquake [C]// Proceedings of 1st International Symposium on Geotechnical Earthquake Engineering. 1995: 55-60.

[2] Leshchinsky D, Han. J. Geosynthetic reinforced multitiered walls [J]. Journal of Geotechnical and Geoenvironmental Engineering，ASCE，2004，130(12): 1225-1235.

[3] LV Wen-liang, YAN Shu-wang, LIU Run. Application of Finite Element Method in Reinforced Soil Retaining Wall[J]. JOURNAL OF TIANJIN UNIVERSITY,2002,35(5): 596-600.

[4] GAO Jiang-ping,YU Mao-hong,HU Chang-shun,et al. Study on the distributive rule of the earth pressure and its coefficient of the reinforced earth wall[J]. Chinese Journal of Geotechnical Engineering, 2003,25(5): 582-584.

[5] Seed H B, Whitman R V. Design of earth retaining structures for dynamic loads. In: ASCE Specialty Conference. Ithaca,1970,103-147.

[6] LIU Hua-bei. Analysis on seismic behavior of geogrid-reinforced retaining wall subjected to horizontal and vertical excitations[J]. Chinese Journal of Geotechnical Engineering, 2006,28(5):594-599.

[7] LING H I, LIU H, MOHRI Y. Parametric studies on the behavior of reinforced soil retaining walls under earthquake loading[J]. Journal of Engineering Mechanics, ASCE, 2005, 131(10): 1056－1065.

[8] Yang Guolin，Wang Yonghe. MODEL TESTING AND DYNAMIC RESPOND ANALYSIS ON REINFORCED EARTH WALL UNDER REPEATED LOAD[J]. Chinese Journal of Rock Mechanics and Engineering, 2002,21(10): 1541-1546.

[9] ZHENG Yingren，YE Hailin，HUANG Runqiu. Study on the seismic stability analysis of a slope [J]. JOURNAL OF EARTHQUAKE ENGINEERING AND ENGINEERING VIBRATION, 2010,30(2): 173-180.）

[10] ZHENG Yingren， YE Hailin， HUANG Runqiu. Analysis and Discussion of Failure Mechanism and Fracture Surface of Slope under Earthquake [J]. Chinese Journal of Rock Mechanics and Engineering, 2009, 28(8):1914-1723.)

[11] ZHENG Y R, TANG X S, and ZHAO S Y, “Strength reduction and step-loading finite element approaches in geotechnical engineerin”, ournal of Rock Mechanics and Geotechnical Engineering, 2009, pp.21-30.

[12] ZHENG Yingren, and ZHAO Shangyi, “Discussion on safety factors of slop and landslide engineering design”, Chinese Journal of Rock Mechanics and Engineering, 2006, pp.1937-1940.

*Applied Mechanics and Materials Vols. 580-583 (2014) pp 1426-1429*
*© (2014) Trans Tech Publications, Switzerland*
*doi:10.4028/www.scientific.net/AMM.580-583.1426*

# Damage Mechanism of Yiliang Earthquake on September 7, 2012

Zhuo Lin[1, 2,a], Ming Tian[3,b], Dongbai Chen[1,c] and Chunfeng Li[1,d *]

[1]Earthquake Administration of Shanxi Province, PR. China

[2]Institute of Earthquake Engineering for Shaanxi Province, PR. China

[3]Earthquake Administration of Hefei City, PR. China

[a]55951485@qq.com, [b]402894041@qq.com, [c]371486556@qq.com, [d]635546550@qq.com

**Keywords:** Yiliang Earthquake, Low-cycle Fatigue, Damage Mechanism

**Abstract.** According to the analysis of the structure, topography, earthquake sequence, and earthquake hazards in September 2012 earthquake of Yiliang County, Yunnan Province, the mechanism of the earthquake damage is given. The low-cycle fatigue, shallow source, topography, population density, seismic capacity of the structure and seismic awareness of the residents is the main damage factor. This research provides a reference to the seismic design of analogous regions.

## Introduction

At 11:19(Beijing time) on September 7, 2012, Yiliang County, Yunnan Province, 5.7 earthquake occurred, with focal depth of 14.0 km. At 12:16 on September 7, 5.6 earthquake occurred, with focal depth of 10.0 km. By 18:00, in Zhaoyang-Yiliang area there had been 72 earthquakes in which 16 ranged from 0 to 0.9 ML, 26 from 2.0 ML to 2.9 ML, 6 from 3.0 to 3.9 ML, 2 from 4.0 to 4.9 ML and 2 from 5.0 to 5.9ML. As at 11:00 on the 9th, a direct result of the earthquake is that 81 people were

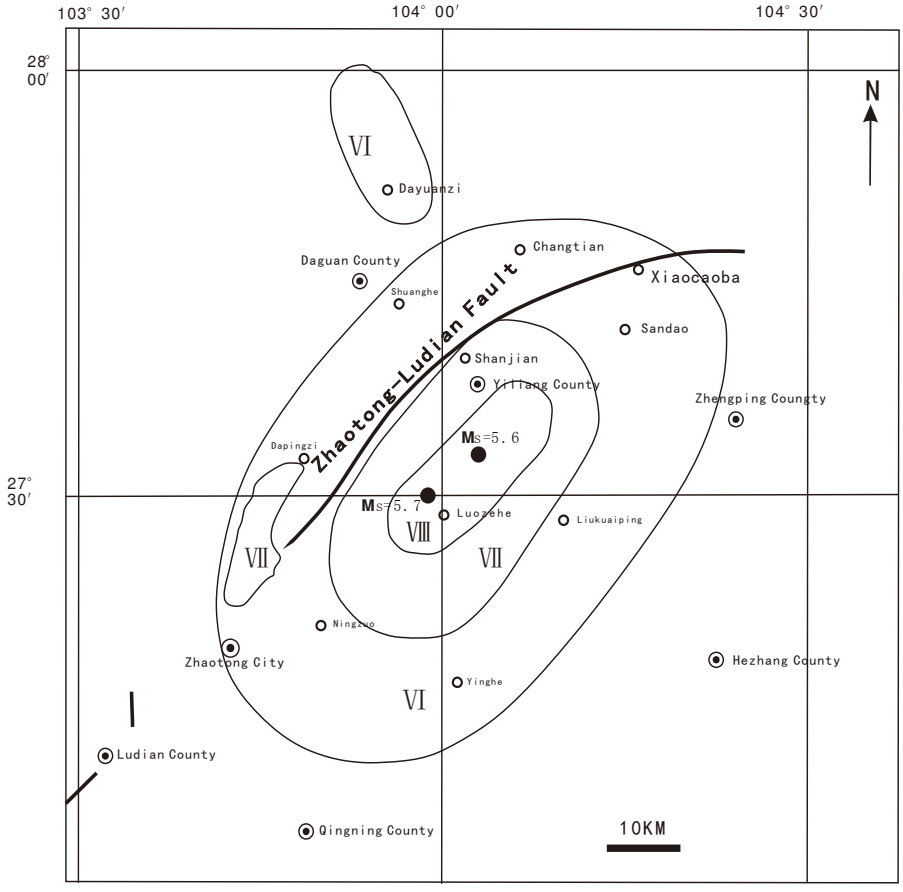


Fig.1 Yunnan Yiliang seismic intensity distribution

killed. On 4 October, triggered secondary disasters caused 19 people to be killed, and the affected population is over 740,000. The earthquake caused direct economic losses of 8.279 billion yuan. In order to clarify the mechanism of damage, in this paper, structure characteristics, topography, and earthquake sequences are analyzed. Figure 1 shows the Yunnan Yiliang seismic intensity distribution.

**Geology and Geomorphology of Yiliang County.** In the disaster area, the terrain shows that the south-west is higher, and the northeast is lower; and that the west-east is narrower and the north-south is wider. The terrain slopes from southwest to northeast, indicating the landforms of deep canyon. The most areas were eroded mountain cut by rivers, and gulling is evident. The peak elevation is 2780m, the lowest elevation 520m, and relative elevation reaches 2260m. There is no doubt that the terrain can help the occurrence of secondary earthquake disaster (Fig.3). After the earthquake, at part of the road on both sides of the mountain in Yiliang County, collapse occurred and huge stones from the mountain slided down. This led to the very serious traffic congestion, and the rescue teams can only go forward on foot, slowing the rescue process. As figure 2 shows, the zone with seismic intensity Ⅷ is located in low-lying valley.

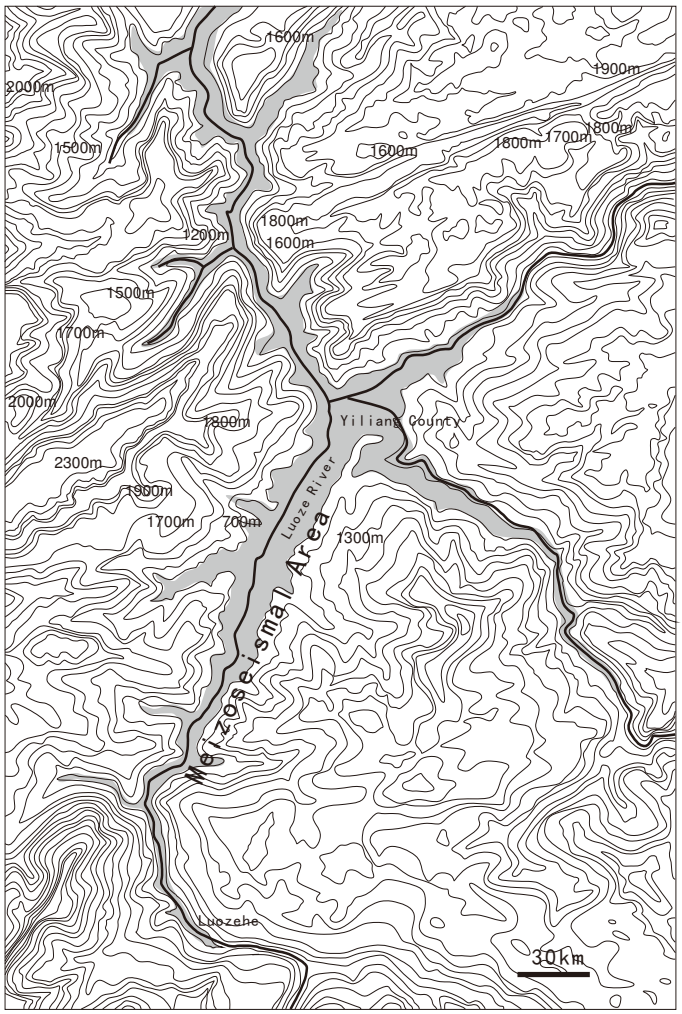


Fig. 2 Topographic maps in disaster area

Fig. 3 Secondary damage

**Structure Features.** In the disaster area, the structure is that of stone concrete, wood and concrete, brick wood, brick concrete, and frame structure (Fig. 4). Generally speaking, the seismic performance of the structures is weak. The reason of poor performance of anti-seismic structure is that the economy is relatively uncultured, and people's awareness is very weak.

Fig. 4 Destruction of wood and concrete structure

**Shallow Earthquake.** The 5.7 magnitude earthquake focal depth is 14 km, and 5.6 earthquake focal depth is 10 km. For shallow earthquake, the focal depth is also shallow. So, although the magnitude of the earthquake is not high, because of the shallow focal depth, the damage is evident.

**The Population Density.** Klose town is 33 km away from the epicenter of Zhaotong City, and 15 km from Yiliang County, and the population density is 205 people per square kilometer, which is twice the average population density of Yunnan Province. Coupled with the time when the earthquake occurred at noon, many people are in the house, and some houses collapsed, causing casualties.

**Low-cycle Fatigue.** When the earthquake make structure vibrate a few to dozens times, a low-cycle fatigue can occur, and lower seismic force can make the structure damage. Low-cycle fatigue is the result for micro cracking to jointly produce significant rupture after many vibrations, thereby destroying the structure.

At 11:19(Beijing time) on September 7, 2012, Yiliang County, Yunnan Province 5.7 earthquake occurred, with focal depth of 14.0 km, and at 12:16 on September 7, 5.6 earthquakes occurred, with focal depth of 10.0 km. Figure 5 is the strong motion records of 5.7 earthquake, recorded in Zhaotong Jing Staion. The peak acceleration of two horizontal components are 51cm/s$^2$ and 56.6cm/s$^2$ respectively. The effective duration about the components was 20 seconds. Figure 6 is the strong motion records of 5.7 earthquake, recorded in Zhaotong Jing Staion. The peak acceleration of two horizontal components are 277.9cm/s$^2$ and196cm/ s$^2$ respectively. The effective duration is much shorter than that of 5.7 earthquake. However, the peak acceleration is very bigger. The difference may

be due to different focal depths, and the focal depth has also effect on duration. Although the peak acceleration of 5.7 earthquake is small, the effective duration is longer, making the structure produce low-cycle fatigue. The effective duration of 5.6 earthquake is small, but peak acceleration is big, so it has great potential for destruction. And that the earthquake of magnitude 5.6 occurred after the 5.7 earthquake is equivalent to increasing the time for earthquake to effect on structure. The superposition of two earthuakes appears more conducive to resulting in low-cycle fatigue. Of course, it is necessary to pay attention to that Zhaotong Jing Station be located in the zone with seismic intensity Ⅶ, and epicentral distance over 20km. It is possible that in epicentral area (with seismic intensity Ⅷ) , the peak acceleration could be higher (no seismic station in epicentral area), the pulse-type ground motion can appear, and the destructive force may be greater. In addition, the two 4 earthquake and many 3 earthquake in the area [1] also help create low-cycle fatigue (3 earthquake often has the power to destroy).

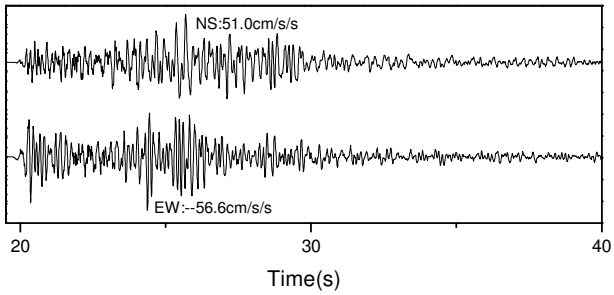


Fig. 5 Strong motion records of 5.7 earthquake in Zhaotong Jing'an Station (the distance of epicenter is 23.52km, and the focal depth is 14km)

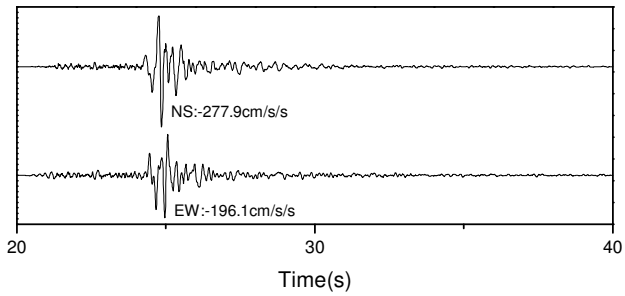


Fig. 6 Strong motion records of 5.6 earthquake in Zhaotong Jing'an Station (the distance of epicenter is 29.35km, and the focal depth is 10km)

## Conclusion

In September 2012 earthquake of Yiliang County, Yunnan Province, the mechanism of the earthquake damage is the low-cycle fatigue, shallow source, topography, population density, seismic capacity of the structure and seismic awareness of the residents.

## Acknowledgements

This work was financially supported by Earthquake Technology Spark Program (XH12045) and Shanxi Provincial Natural Science Basic Research Program (2013JM5014).

## References

[1] J. Lu, X.F. Zheng, J. Xiao, Z.J. Xie, X.F. Zeng, B. Li, F.F. Dong: Chinese Journal of Geophysics Vol.56(2013), p.2645

*Applied Mechanics and Materials Vols. 580-583 (2014) pp 1430-1434*
*© (2014) Trans Tech Publications, Switzerland*
*doi:10.4028/www.scientific.net/AMM.580-583.1430*

# Deformation and energy-based seismic damage evaluation of Steel reinforced concrete and reinforced concrete Piers

Jiajue Lin[2,a], Airong Liu[1,2,b*], Qicai Yu[2,c], Jiangdong Deng[2,d]

[1]Guangzhou University-Danjiang University Join Research Center for Engineering Structure Disaster Prevention and Contro, Guangdong Guangzhou 510006 P.R.China;

[2]School of Civil Engineering of Guangzhou University; Guangzhou 510006, China

[a]285143797@qq.com, [b]Liu-a-r@163.com, [c]Yuqicai @163.com, [d]dengjdong@163.com

*Corresponding author: Airong Liu (1972-), Professor, Doctor. [b]Liu-a-r@163.com

**Keywords**: Deformation; Hysteretic energy; Steel reinforced concrete piers; Reinforced concrete bridge pier; Multi-modal; Cyclic pushover

**Abstract:** The method of MMCP (modified modal cyclic pushover) which can reflect the dual criterion of deformation and energy was used to make an assessment on seismic performances of the steel reinforced concrete piers and reinforced concrete bridge piers. Then the calculated results were analyzed comparing with the results of dynamic time historical analysis and quasi static test. To some extent, the MMCP analysis may simulate the seismic action. In addition, the MMCP method can also be associated with the design response spectrum, making the evaluation results to be reliable and safe. The results indicate that MMCP applicability analysis also exists in the steel reinforced concrete structure, and the seismic capacity of steel reinforced concrete bridge piers is better than reinforced concrete bridge piers.

## Introduction

In earthquake damage there is a phenomenon: a lot of bridges only got damaged badly without collapse after the first stage of earthquake. However with the repeatedly low intensity of aftershocks, they collapsed. It is generally believed that with the repeated actions of earthquake, a structure will constantly dissipate energy and produce new plastic deformation which will eventually lead to collapse. The cause of the damage of a bridge is it emerges certain deformation and experiences certain process of energy consumption at the same time [6].

This text adopts the type of Ghobarah model:

$$D_G = 1 - \frac{k_f}{k_0} \tag{1}$$

where, $k_0$ and $k_f$ are respectively lateral stiffness of the structure before and after the earthquake.

## The basic principle of Modified modal cyclic pushover[4]

### 1.1.Aseismic maximal displacement evaluation for the multi degree of freedom (MDOF） system

According to the principle of energy spectrum, the result of ESDOF displacement can be obtained. And then according to the principle of energy, ESDOF spectrum displacement can be obtained:

$$S_{d,n} = \sum \Delta S_{d,n} = \sum (\Delta E / \sum_{i=1}^{i=m} F_{i,n}) \tag{2}$$

The transformation based on energy criterion is more stable and the capacity curve reverse problem that neglected model probably can be eliminated.

### 1.2 Assessment for hysteretic energy dissipation of multi-degree of freedom (SDOF) system

Khashaee[1]established the calculation methods based on statistical analysis of a large number of seismic waves on hysteretic energy dissipation of a single degree of freedom system :

$$\frac{E_h}{m} = 0.72(1-\mu^{-1})^{0.7} E_i \tag{3}$$

## Analysis of examples

### 2.1 The numerical example design and finite element model

The model size and reinforcement details are as shown in Table.1 and Fig.2.

**Table.1 Pier design parameters**

| Specimen number | Section size (mm×mm) | Concrete | Axial compression ratio | Steel bone model | Stirrup | Longitudinal reinforcement of column | Reinforcement ratio（%） |
|---|---|---|---|---|---|---|---|
| SRC | 300×300 | c35 | 0.15 | 100x125x6x10 | φ8@100 | 4Φ12 | 3.55 |
| RC | 300×300 | c35 | 0.15 | ------ | φ8@100 | 6Φ25 | 3.27 |

**Fig.2 Example models and fiber section**

### 2.2 The contrastive analysis between the calculation results and the dynamic time history

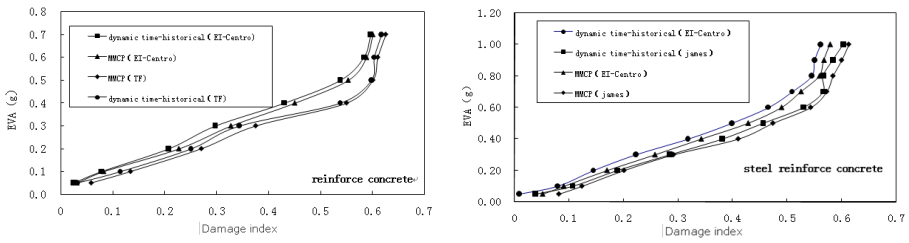


**Fig.3 Whole structure damage evaluation with MMCP method**

It can be seen from the Fig.3, under the influence of El Centro wave, when the earthquake intensity are the same, the damage degree of reinforced concrete bridge piers is smaller than that of the steel encased concrete ones :when the overall damage indexes reach 0.6 (close to collapse [2]), the steel reinforced concrete bridge piers can withstand the EPA 0.89 g of seismic action, and reinforced concrete is only 0.61 g. When the overall damage index is 0.3 (repairable), corresponding

earthquake PGA of steel reinforced concrete bridge piers is 0.41 g, while that of the reinforced concrete bridge piers is only 0.28 g. So the overall seismic capacity of steel reinforced concrete bridge piers is better than the reinforced concrete bridge piers.

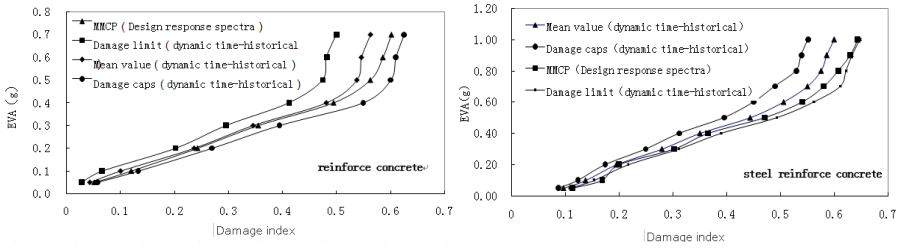


**Fig.4 Analysis for degree of safety with MMCP method using design response spectrum**

Fig.4 gives the calculation result according to MMCP method of the design response spectrum [3]. We can see from the picture, the structural damage values using the MMCP method of design response spectrum in each stage of fortification level are greater than the mean values of dynamic time historical analysis results. Although in most of the range, it is still less than the upper limit of dynamic time historical analysis, but it has a certain degree of safety and economy. The degree of safety and economy depends on the design response spectrum, so the evaluation results are in harmony with the specification. In addition, Fig. 8 also reflects that the seismic resistance of steel reinforced concrete bridge piers is far stronger than reinforced concrete bridge piers.

### 2.3 comparative analysis of calculation and pseudo static test

In ref. [5], Yu Huijun and other scholars have completed the pseudo static test on the ordinary reinforced concrete (RC) and steel reinforced concrete (SRC) column pier model, the test used the loading method of force-displacement hybrid controlled. Every level load has a repeated cycle; Change to the loading method of displacement controlled after the pier enters the yield phase , the hysteresis curves of the two components can be got according to the method that load repeatedly cycles three times per level . They respectively are:

**Table 4 The comparison of test and MMCP**

| By using mathematical analysis software originpro, conduct the hysteresis curve of each level loading for integral to get hysteretic energy dissipation. According to the test process and phenomenon mentioned in the article and the method of MMCP that combined with the design response spectrum in section 3.1 , the results | Slight damage (repairable) | | Secondary damage (repairable) | | Damaged beyond repair | | Serious damage | |
|---|---|---|---|---|---|---|---|---|
| | Vertex displacement | Hysteretic energy dissipation | Vertex displacement | Hysteretic energy dissipation | Vertex displacement | Hysteretic energy dissipation | Vertex displacement | Hysteretic energy dissipation |
| RC(test) | 17.1 | 1746 | 34.2 | 9552 | 51.4 | 19526 | 68.5 | 35629 |
| RC（ MMCP） | 18.3 | 1582 | 36.9 | 8765 | 54.9 | 18624 | 71.7 | 33458 |
| Error （%） | 7.0 | -9.4 | 7.9 | -8.2 | 6.8 | -4.6 | 4.7 | -6.1 |
| | | | | | | | | |
| SRC（test） | 16 | 1896 | 32 | 8832 | 64 | 27156 | 80 | 50789 |
| SRC（MMCP） | 17.2 | 1771 | 35.1 | 8462 | 66.9 | 24837 | 87.2 | 46926 |
| Error（%） | 7.5 | -6.6 | 9.7 | -4.2 | 4.5 | -8.5 | 9.0 | -7.6 |

It can be seen in the table 4: in this paper, the method can accurately predict the hysteretic energy dissipation of structure; For the same damage, error value of MMCP method and pseudo static test result is maintained at below 10%, on the overall, the alignment of the two results appears to be good. Reinforced concrete bridge piers are better at the aspect of ductility and energy dissipation capacity compared with the steel reinforced concrete bridge piers , and they also reflects the better earthquake resistance.

## Conclusions

This paper puts forward the improved multimodal reciprocating pushover (MMCP) method for structural seismic damage assessment. After analysis the following conclusions can be summarized:

(1) MMCP method introduces the structural maximum deformation and hysteretic energy dissipation under earthquake at the same time, and it embodies the reciprocating motion characteristics of structure under seismic action.

(2) MMCP method simulates the seismic effect to some extent, and it can accurately evaluate the structural seismic displacement and the hysteretic energy dissipation demand.

(3) Ductility and deformation capacity of steel reinforced concrete piers is greater than the reinforced concrete ones.

At the same time, this method can also be combined with the design response spectrum, eliminating the problem of selecting wave while analyzing the dynamic time history, which can make the evaluation result universal and reliable.

**Acknowledgments**

This study was sponsored by national natural science foundation of China(No.11272095, 51378133), science and technology planning project of Guangdong Province(No.2012B040302005), science and technology planning major project of Guangzhou City(No.2011Y2-00006), and key technological innovation program of Guangdong Ministry Education (No.2012CXZD0028).

**References**

[1] Khashaee P. *Energy-based seismic design and damage assessment for structures*. Dallas, Texas: Southern Methodist University, 2004.

[2] Chopra A K, Goel R K. Earthquake Engineering and Structural Dynamics, 2002, 31(3):561-582

[3] GB 50011—2001 Code for seismic design of buildings. Beijing: China Architecture & Building Press, 2001( in Chinese)

[4] QiMeng YU, Ping Shao, Jing Wu. Journal of civil engineering, 2011, 44 (5):16-23. ( in Chinese)

[5] HuiJun Yu, Qicai Yu, Airong Liu: *Method based on energy theory and experimental study on seismic performance of long-span arch bridge*. Guangdong, Guangzhou: Guangzhou University, 2012. ( in Chinese)

[6] Ai-rong Liu, Ren Xiong, Qicai YU, Junping Zhang and Yong Xu: *Deformation and energy seismic damage model considering the impact of strong aftershock.* Journal of shenzhen university science and engineering, 2011, 28(3):189-194. ( in Chinese)

*Applied Mechanics and Materials Vols. 580-583 (2014) pp 1435-1438*
*© (2014) Trans Tech Publications, Switzerland*
*doi:10.4028/www.scientific.net/AMM.580-583.1435*

# Experimental Study on Dynamic Mechanical Properties of Galvanized Iron Wire under Seismic Strain Rate

Hao Zhang[1, a], Jiahe Zhang[2, b], Debin Wang[3, c] and Xu Li[2, d]

[1] School of Civil Engineering, Shenyang Jianzhu University, Shenyang 110168, China

[2] China Architecture Design & Research Group, Beijing 100044, China

[3] Faculty of Infrastructure Engineering, Dalian University of Technology, Dalian 116024, China

[4] School of Civil and Safety Engineering, Dalian Jiaotong University, Dalian 116028, China

[a]hzhang_sjzu@hotmail.com, [b]reounald@gmail.com, [c]wdb1215@163.com, [d]lx3818262@163.com

**Keywords:** Galvanized iron wire, Dynamic tensile test, Strain rate, Dynamic constitutive relationship, Shaking table test

**Abstract.** This paper focuses on the mechanical properties of galvanized iron wire under various conditions of earthquake-type strain rate. The dynamic tensile test of galvanized iron wire was conducted on MTS New 810 electro-hydraulic servo-controlled testing system. The dynamic tensile constitutive relationship of galvanized iron wire was proposed under seismic strain rate. The accuracy of the proposed constitutive relationship of galvanized iron wire was verified by comparing with reinforcing steel.

## Introduction

The galvanized iron wire are widely used in shaking table test, and it is often simulated the reinforcing steel in reduced scale model which also affected by strain rate under seismic action. Dynamic mechanical properties of reinforcing steel are widely illustrated and discussed in literature [1-2]. However, no comprehensive studies are available, aimed at quantifying strain rate effect on galvanized iron wire. The dynamic tensile constitutive relationship of galvanized iron wire should be used in numerical simulation of shaking table test with strain rate effect. Nevertheless, there is no practical model related to this kind of material. In this paper, the dynamic tensile test of galvanized iron wire was carried out under the range of seismic strain rate. The dynamic mechanical properties of galvanized iron wire were investigated. Based on the test results, the dynamic tensile constitutive relationship of galvanized iron wire was obtained.

## Description of the dynamic tensile test of galvanized iron wire

MTS New 810 electro-hydraulic servo-controlled testing system was used to investigate the dynamic properties of galvanized iron wire, under the approximate seismic range of strain rate between $2.5\times10^{-4}$/s and $2.5\times10^{-1.4}$/s (0.1/s), that $2.5\times10^{-4}$/s as the quasi-static strain rate.

Fig. 1 Test equipment.

Monotonic tensile loading was adopted with the strain rate being kept as constant during loading conditions. Three types of specimen were selected that the diameters were (a) D=1.6mm, (b) D=2mm and (c) D=2.8mm, respectively.

**Dynamic tensile test program on galvanized iron wire**

The tensile stress-strain curves of galvanized iron wire are illustrated in Fig. 2. The stress-strain relationship is quite similar under the different strain rate. Results of yield strength, ultimate tensile strength and yield strain are list in Tab. 1 to Tab. 2.

Based on the test results, Young's modulus has no obvious change under different strain rate, in which the mean values of the different conditions are 72023MPa, 71371MPa and 73235MPa. The mean yield strength and ultimate strength increased by 9.14%-20.69% and 3.15%-8.72% respectively when the strain rate increased from $2.5\times10^{-4}$/s to $2.5\times10^{-1.4}$/s . Yield strain increases first and decreases afterwards, it was also recognized that strain rate had negligible effect. Therefore, the mean values of the different conditions are $0.794\times10^{-2}$, $1.701\times10^{-2}$ and $0.671\times10^{-2}$. The ultimate tensile strain also have no obvious strain rate dependent, which the mean values of the different specimens are $22.84\times10^{-2}$, $21.11\times10^{-2}$, $18.29\times10^{-2}$.

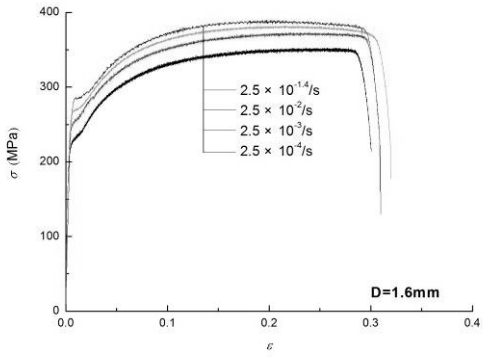


(a)

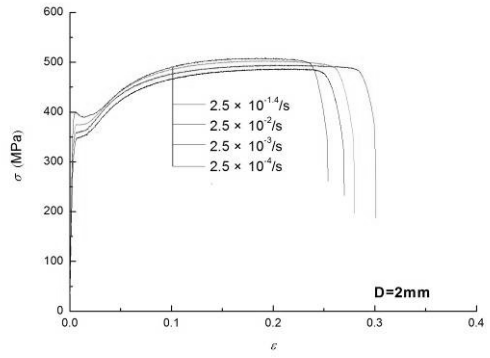


(b)

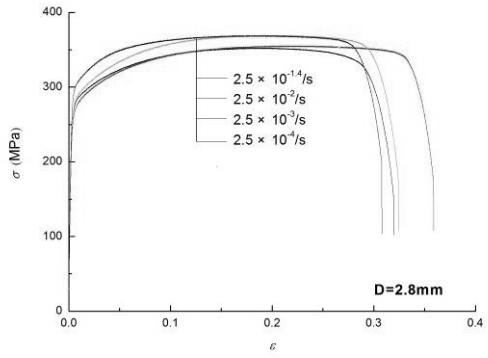


(c)

Fig. 2 Stress-strain curves of galvanized iron wire

The results of the three types of galvanized iron wire indicate that yield strength and tensile strength increase linearly with logarithmically increasing strain rate. The empirical relationships are the following:

$$\frac{f_{yd}}{f_{ys}} = 1.0 + 0.0456\lg\left(\frac{\dot{\varepsilon}_w}{\dot{\varepsilon}_{w0}}\right) \quad (1)$$

$$\frac{f_{ud}}{f_{us}} = 1.0 + 0.0212 \lg\left(\frac{\dot{\varepsilon}_w}{\dot{\varepsilon}_{w0}}\right) \quad (2)$$

Where $\dot{\varepsilon}_w$ represents the strain rate, $\dot{\varepsilon}_{w0}$=2.5×10$^{-4}$/s is the quasi-static stain rate, whilst $f_{ys}$ and $f_{yd}$ are the quasi-static and dynamic yield strength, $f_{us}$ and $f_{ud}$ represent the quasi-static and dynamic tensile strength.

Tab. 1 Yield strength of galvanized iron wire at different strain rates

| Diameter (mm) | Strain rate (s$^{-1}$) | $f_{y1}$ (MPa) | $f_{y2}$ (MPa) | $f_{y3}$ (MPa) | Mean value (MPa) |
|---|---|---|---|---|---|
| 1.6 | 2.5×10$^{-4}$ | 237.32 | 240.09 | 238.25 | 238.55 |
| | 2.5×10$^{-3}$ | 247.14 | 254.59 | 252.44 | 251.39 |
| | 2.5×10$^{-2}$ | 268.42 | 257.49 | 267.28 | 264.40 |
| | 2.5×10$^{-1.4}$ | 297.52 | 280.45 | 285.72 | 287.90 |
| 2 | 2.5×10$^{-4}$ | 358.09 | 354.66 | 351.26 | 354.67 |
| | 2.5×10$^{-3}$ | 366.18 | 363.06 | 355.69 | 361.64 |
| | 2.5×10$^{-2}$ | 372.90 | 377.36 | 377.09 | 375.78 |
| | 2.5×10$^{-1.4}$ | 398.06 | 393.76 | 401.04 | 397.62 |
| 2.8 | 2.5×10$^{-4}$ | 269.71 | 273.58 | 277.34 | 273.54 |
| | 2.5×10$^{-3}$ | 279.65 | 279.91 | 278.66 | 279.41 |
| | 2.5×10$^{-2}$ | 289.60 | 283.20 | 284.60 | 285.80 |
| | 2.5×10$^{-1.4}$ | 310.01 | 296.09 | 289.51 | 298.54 |

Tab. 2 Ultimate tensil strength of galvanized iron wire at different strain rates

| Diameter (mm) | Strain rate (s$^{-1}$) | $f_{u1}$ (MPa) | $f_{u2}$ (MPa) | $f_{u3}$ (MPa) | Mean value (MPa) |
|---|---|---|---|---|---|
| 1.6 | 2.5×10$^{-4}$ | 353.38 | 355.12 | 360.53 | 356.34 |
| | 2.5×10$^{-3}$ | 356.18 | 370.53 | 373.66 | 366.79 |
| | 2.5×10$^{-2}$ | 382.98 | 375.13 | 373.45 | 377.19 |
| | 2.5×10$^{-1.4}$ | 393.46 | 378.61 | 390.18 | 387.42 |
| 2 | 2.5×10$^{-4}$ | 488.71 | 485.82 | 484.53 | 486.35 |
| | 2.5×10$^{-3}$ | 501.45 | 494.75 | 487.77 | 494.66 |
| | 2.5×10$^{-2}$ | 496.59 | 504.25 | 500.90 | 500.58 |
| | 2.5×10$^{-1.4}$ | 517.41 | 509.11 | 519.89 | 515.47 |
| 2.8 | 2.5×10$^{-4}$ | 351.65 | 352.72 | 353.20 | 352.52 |
| | 2.5×10$^{-3}$ | 352.74 | 355.55 | 353.29 | 353.86 |
| | 2.5×10$^{-2}$ | 352.42 | 365.70 | 369.67 | 362.60 |
| | 2.5×10$^{-1.4}$ | 367.27 | 365.37 | 358.25 | 363.63 |

**Comparison of dynamic tensile properties between galvanized iron wire and reinforcing steel**

Li's model [3], Lin's model [4] in China and CEB model [5] in Europe are the several typical dynamic tensile constitutive models of reinforcing steel. Li's model was obtained by dynamic tensile test of reinforcing steel (HPB235, HRB335 and HRB400) under the range of seismic strain rate (2.5×10$^{-4}$/s-2.5×10$^{-1.4}$/s). This model is suitable for the yield strength of reinforcing steel with the range of 235MPa≤$f_{ys}$≤430MPa. Lin's model was obtained by dynamic tensile test of reinforcing steel (HPB235, HRB335 and HRB400) under a higher range of strain rate (2/s-80/s). The model can extrapolate to the range of strain rate less than 2/s which can be proved. CEB model was obtained by dynamic tensile test of reinforcement which the design yield strength is 420MPa under the range of

strain rate less than 10/s. The quasi-static strain rate is $5\times10^{-5}$/s. The proposed model is suitable for the yield strength of galvanized iron wire with the range of 239MPa$\leqslant f_{ys} \leqslant$355MPa.

In order to verify the accuracy of the proposed dynamic tensile constitutive model of galvanized iron wire, Li's and Lin's models of reinforcing steel were selected to compare. The CEB model is only suitable for the yield strength of reinforcement with 420MPa which is not used to compare. The comparing results can be observed in Fig. 4 and Fig. 5. Results show that the dynamic tensile properties of the models are quite similar. Hence, the galvanized iron wire is suitable for repalcing reinforcing steel in shaking table test.

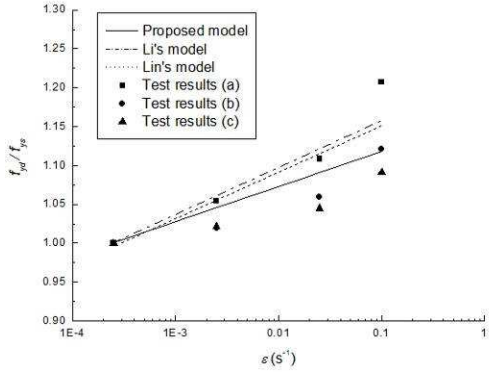


Fig. 4 Comparison of yield strength increasing factor of the proposed model and the other models

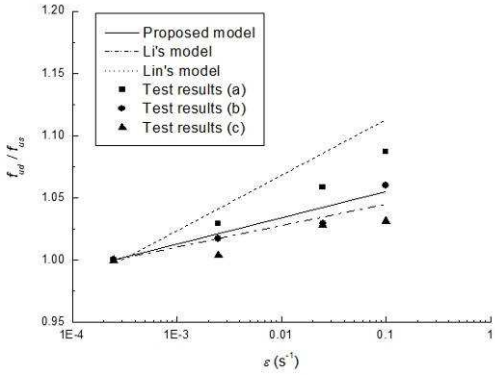


Fig. 5 Comparison of tensile strength increasing factor of the proposed model and the other models

## Conclusions

Based on the previous test results obtained, the following observations can be drawn on the earthquake-type strain rate on the dynamic mechanical properties of galvanized iron wire.

(1) The stress-strain relationships galvanized iron wires were quite similar under various conditions of seismic strain rate. The effects of strain rate causes moderate increases in the yield strength and the ultimate tensile strength. The yield strain, ultimate strain and Young's modulus do not appear to be affected by strain rate.

(2) The dynamic tensile constitutive relationship of galvanized iron wire was proposed. The dynamic mechanical properties of galvanized iron wire are similar to reinforcing steel. Consequently, the galvanized iron wire is suitable for repalcing reinforcing steel in shaking table test.

## Acknowledgements

This work was financially supported by the National Natural Science Foundation of China (Grant No: 51308356) and Shenyang Municipal Science and Technology Program of China (Grant No: F13-158-9-00).

## References

[1] L. J. Malvar, C. A. Ross: ACI Material Journal. Vol. 95 (1998), p. 735.

[2] D. Asprone, R. Frascadore, M. D. Ludovico, A. Prota and G. Manfredi: Engineering Structures. Vol. 35 (2012), p. 29.

[3] M. Li, H. N. Li: China Civil Engineering Journal. Vol. 43 (2010), p. 70.

[4] F. Lin, X. L. Gu, X. X. Kuang, X. J. Yin: Journal of building materials. Vol. 11 (2008), p. 14

[5] J. EIBL: Dubrovnik, Comite Euro-lnternational du Beton, 1988.

*Applied Mechanics and Materials Vols. 580-583 (2014) pp 1439-1442*
*© (2014) Trans Tech Publications, Switzerland*
*doi:10.4028/www.scientific.net/AMM.580-583.1439*

# Peak Story Drift of a Building Structure Subjected to Earthquakes

Jeng-Hsiang Lin[1, a]

[1] Department of Architecture, Hwa Hsia Institute of Technology, No. 111, Gongjhuan Rd., Jhonghe District, New Taipei City 23568, TAIWAN

[a]hsiang@cc.hwh.edu.tw

**Keywords:** Earthquake ground motion, Building, Peak story drift, Random vibration theory.

**Abstract.** Many studies have demonstrated that the story drift is the critical parameter that is best correlated with damage in buildings. In this study, an approximate solution for mean value and standard deviation of peak story drift at each story of a building structure under earthquake motions was derived, based on random vibration theory. The accuracy was demonstrated by the Monte Carlo simulation solutions. Comparison of the computed results with the available simulation results indicates that the proposed solution is satisfactory. The results of numerical examples show that the period of a building structure plays a major role that affects the peak drift at each story. The peak drift at each story increases as the period of the structure increases.

## Introduction

Conventional building codes emphasize that the methods of seismic-resistant design have the objectives to provide for life safety and damage control [1]. It is not economically feasible to give complete protection to buildings in the event of a worst-case earthquake; it is tacitly accepted that structural damage should be prevented and nonstructural damage minimized in the occasional moderate earthquake and that serious damage or collapse should be prevented in the much rarer severe earthquake [2]. Modern building codes emphasize the philosophy in which the design criteria are expressed in terms of achieving specified performance objectives when the structure is subjected to specified levels of seismic hazard [3]. Performance objectives can be related to the level of damage to the building, and the level of damage can be related to structural response parameter. The performance target can be the structural response parameter attached to a certain threshold. Many studies [4,5] have concluded that the story drift ratio is the critical parameter that is best correlated with damage to buildings. The peak story drift ratio can be used as an indicator representing the structural demands.

Recent developments in earthquake engineering indicate that probabilistic evaluation has been performed increasingly to ensure building performance under earthquakes. The need to evaluate statistical characteristics of peak drift of a building structure during earthquakes is quite apparent.

## Peak Story Drift Analysis

For the analytical procedures presented herein, earthquake excitations were considered as a stationary Gaussian random process with zero mean. Although an earthquake motion is not stationary, during the time of strong motion a typical earthquake is approximately stationary, and good estimates of structural responses can be made using random vibration theory [6]. Thus, the story drifts of a building structure will be stationary Gaussian random processes with zero mean.

**Peak Story Drift.** If $y_i(t)$ and $y_{i+1}(t)$ are, respectively, the lateral displacement time histories at the $i^{\text{th}}$ and $i+1^{\text{th}}$ degree of freedom (or at story floor level *N-i+1* and *N-i*) and $S_i(t)$ is the relative story displacement time history between these two story floor levels, then $S_i(t)$ can be expressed as

$$S_i(t) = y_i(t) - y_{i+1}(t), \qquad i = 1 \quad to \quad N-1 \tag{1.a}$$

$$S_N(t) = y_N(t), \tag{1.b}$$

where $N$ is the number of degree of freedom or the number of stories in the structure. The peak drift at each story of the structure during earthquake motions may be defined as

$$\Delta_i = \sup(S_i(t)), \qquad i=1 \quad to \quad N \tag{2}$$

where "sup" implies the maximum value of the entire range of the relative displacement time history. Thus, $S_i(t)$ may be evaluated once the displacement time histories $y_i(t)$ and $y_{i+1}(t)$ are determined.

**Ensemble Mean Squares of Relative Displacement and Relative Velocity Processes.** For the linear structure systems, the power spectral density function $S_{S_iS_i}(\omega)$ for the relative story displacement process $S_i(t)$ can be given by [7]

$$S_{S_iS_i}(\omega) = S_{aa}(\omega)\left\{\sum_{j=1}^{N}\sum_{k=1}^{N}\frac{1}{M_jM_k}\left(\varphi_{i,j}\varphi_{i,k}+\varphi_{i+1,j}\varphi_{i+1,k}-2\varphi_{i,j}\varphi_{i+1,k}\right)\left(\sum_{l=1}^{N}\sum_{m=1}^{N}m_lm_m\varphi_{l,j}\varphi_{m,k}\right)\mathrm{Re}\left[H_j(\omega)H_k(-\omega)\right]\right\}, \quad i=1 \quad to \quad N-1 \tag{3.a}$$

$$S_{S_NS_N}(\omega) = S_{aa}(\omega)\left\{\sum_{j=1}^{N}\sum_{k=1}^{N}\frac{\varphi_{N,j}\varphi_{N,k}}{M_jM_k}\left(\sum_{l=1}^{N}\sum_{m=1}^{N}m_lm_m\varphi_{l,j}\varphi_{m,k}\right)\mathrm{Re}\left[H_j(\omega)H_k(-\omega)\right]\right\}, \tag{3.b}$$

where $H_j(\omega) = 1/(\omega_j^2 + i2\xi_j\omega_j\omega - \omega^2)$ (4)

$$\mathrm{Re}\left[H_j(\omega)H_k(-\omega)\right] = \frac{(\omega_j^2-\omega^2)(\omega_k^2-\omega^2)+(2\xi_j\omega_j\omega)(2\xi_k\omega_k\omega)}{\left((\omega_j^2-\omega^2)^2+(2\xi_j\omega_j\omega)^2\right)\left((\omega_k^2-\omega^2)^2+(2\xi_k\omega_k\omega)^2\right)} \tag{5}$$

and $f_i(t)$ is the $i^{th}$ component of external force vector. $\omega_j$, $\xi_j$, and $M_j$ are the $j^{th}$ modal undamped natural frequency, damping ratio, and mass of the structure, respectively.

The ensemble mean squares of the relative story displacement process $S_i(t)$ and of the relative story velocity process $\dot{S}_i(t)$ are related to the spectral density function $S_{S_iS_i}(\omega)$ by the equations

$$\sigma_{S_i}^2 = \int_{-\infty}^{\infty} S_{S_iS_i}(\omega)d\omega \tag{6}$$

and $$\sigma_{\dot{S}_i}^2 = \int_{-\infty}^{\infty} \omega^2 S_{S_iS_i}(\omega)d\omega \tag{7}$$

Substituting Eqs. (3.a) and (3.b) into Eqs. (6) and (7) with the assumptions that the one-sided power spectral density function of the input ground motion is relatively smooth with no sharp peaks and the modal damping ratios of the building is small, gives

$$\sigma_{S_i}^2 \cong \sum_{j=1}^{N}\frac{G(\omega_j)}{M_j^2}\left(\sum_{l=1}^{N}\sum_{m=1}^{N}m_lm_m\varphi_{l,j}\varphi_{m,j}\right)(\varphi_{i,j}-\varphi_{i+1,j})^2\frac{\pi}{4\xi_j\omega_j^3} \quad i=1 \quad to \quad N-1 \tag{8.a}$$

$$\sigma_{S_N}^2 \cong \sum_{j=1}^{N}\frac{G(\omega_j)}{M_j^2}\left(\sum_{l=1}^{N}\sum_{m=1}^{N}m_lm_m\varphi_{l,j}\varphi_{m,j}\right)\varphi_{N,j}^2\frac{\pi}{4\xi_j\omega_j^3} \tag{8.b}$$

$$\sigma_{\dot{S}_i}^2 \cong \sum_{j=1}^{N}\frac{G(\omega_j)}{M_j^2}\left(\sum_{l=1}^{N}\sum_{m=1}^{N}m_lm_m\varphi_{l,j}\varphi_{m,j}\right)(\varphi_{i,j}-\varphi_{i+1,j})^2\frac{\pi}{4\xi_j\omega_j} \quad i=1 \quad to \quad N-1 \tag{9.a}$$

$$\sigma_{\dot{S}_N}^2 \cong \sum_{j=1}^{N}\frac{G(\omega_j)}{M_j^2}\left(\sum_{l=1}^{N}\sum_{m=1}^{N}m_lm_m\varphi_{l,j}\varphi_{m,j}\right)\varphi_{N,j}^2\frac{\pi}{4\xi_j\omega_j} \tag{9.b}$$

**Statistics of Peak Drift at Each Story.** For a zero-mean stationary Gaussian story drift process, Lin [7] had shown that mean and standard deviation of the peak drift $\Delta_i$ can be expressed by the approximate relation

$$\bar{\Delta}_i \cong \left(\left(2\ln(\upsilon T)\right)^{0.5} + 0.5772/\sqrt{2\ln(\upsilon T)}\right)\sigma_{S_i} \tag{10}$$

and $$\sigma_{\Delta_i} \cong \pi\sigma_{S_i}/\sqrt{12\ln(\upsilon T)} \tag{11}$$

in which $$\upsilon = \sigma_{\dot{S}}/\pi\sigma_S \tag{12}$$

## Numerical Examples

**Earthquake Power Spectrum.** The smooth earthquake power spectrum, $G(\omega)$, used in Eqs. (8.a), (8.b), (9.a), and (9.b) can be represented by the Kanai-Tajimi expression as follows:

$$G(\omega) = (\omega_g^4 + 4\xi_g^2\omega_g^2\omega^2)G_0 / ((\omega_g^2 - \omega^2)^2 + 4\xi_g^2\omega_g^2\omega^2) \quad (13)$$

where $G(\omega)$ reflects the frequency content during the most intense part of the ground motion and is a one-sided power spectrum, $\omega_g$ is the predominant ground frequency, $\xi_g$ is the ground damping and $G_0$ is a measure of ground intensity. The values $\omega_g = 4\pi$ and $\xi_g = 0.6$ have been suggested for firm ground sites and $G_0$ can be related to the peak ground acceleration, $a$, by

$$G_0 = 0.1461\xi_g a^2 / \omega_g(1 + 4\xi_g^2) \quad (14)$$

**Studied Parameters.** There were 3 cases of building structures having different height and story number, including 4, 8, and 12-story building, to be investigated. For each case, the mean value and the standard deviation of peak story drift at each story of the structure under the Kanai-Tajimi excitations were determined from Eq. (10). The corresponding parameter values of each building are given in Table 1. In each building, the story heights, the story masses, and the modal damping ratios were kept the same. The elastic stiffness of the first story, $Ke_1$, was selected by trial and error method to produce the desired fundamental periods, shown in Table 1. The stiffness ratios of the $i+1^{\text{th}}$ story to the $i^{\text{th}}$ story, $Ke_{i+1} / Ke_i$, were equal to 0.95. The story masses and heights were taken as 454545 kg and 320 cm, respectively. The earthquake intensity, expressed by the peak ground acceleration (PGA), is taken as 0.1g. Time duration equals 30 seconds. The parameters of the Kanai-Tajimi model (Eq. (13)), namely $\omega_g$ and $\xi_g$, are taken as $4\pi$ and 0.6, respectively.

Table 1. Parameter values of buildings investigated in this study

| Story number of building | Fundamental period, T (s) | Stiffness, (*kN/cm*) | Damping (%) |
|---|---|---|---|
| 4 | 0.575 | 4708 | 5 |
| 8 | 0.967 | 6288 | 5 |
| 12 | 1.311 | 7900 | 5 |

**Numerical Results and Accuracy of the Proposed Solutions.** Fig. 1 shows the numerical results of the proposed solutions. As shown in Fig. 1, for each building, the peak drift of a structure under earthquake motions varies with story. Fig. 1 also shows that the peak drift at each story of a building structure increases as the period of the building increases. To demonstrate this observation, the effect of period distribution of a building on the peak drift at each story was investigated.

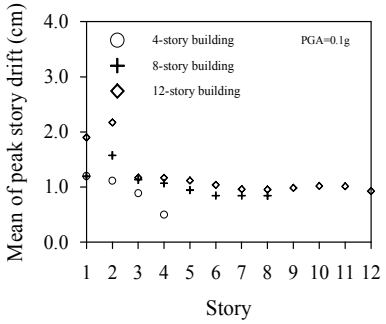


Fig. 1. Story distribution of peak drift.

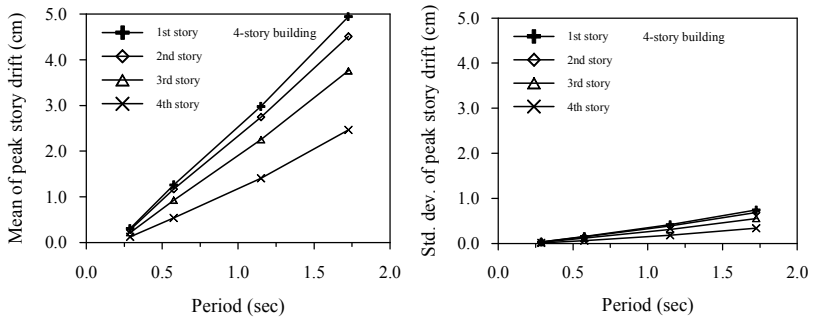


Fig. 2. Effect of period distribution on peak story drift.

To investigate the effects of period distribution on the peak story drift, a 4-story building was studied. Fig. 2 shows the peak drift at each story of the 4-story building increases as the period increases. Thus, the periods of buildings play a major role that affects the peak story drift of buildings. It is noted that the numerical results may change with different buildings and earthquake models. The emphasis is on the approach to evaluate the peak drift at each story of a building structure.

Simulation is frequently applied to estimate extremes or other descriptors of random processes. The accuracy of the proposed solutions was demonstrated by comparing the computed results with the simulation results. For the case of the 4-story building having a fundamental period of 0.575 s, the computed mean values and standard deviations of the peak story drifts are shown in Figs. 3(a) and 3(b), respectively, and the results obtained by the Monte Carlo simulation method are shown also in the figures for comparison. Figure 3 shows that the presented results, as computed from Eqs. (10) and (11), agree well with the simulation results.

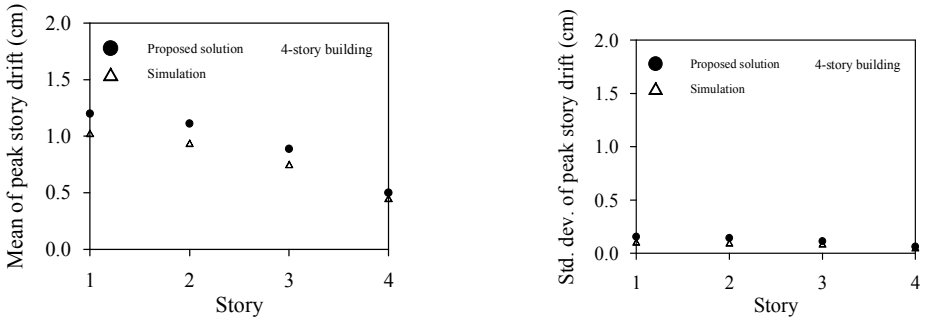


Fig. 3. Comparisons of proposed results and simulation results for peak story drift.

## Concluding Remarks

Based on the assumption of linear elastic structure responses, the spectral approach presented in this study yields a simple closed-form solution for mean value and standard deviation of peak drift at each story of a building structure. From the viewpoint of probability-based design, the need to evaluate the mean value and standard deviation of peak drift at each story of a building structure during earthquake motions is quite apparent and the presented results may be helpful to researchers or practicing engineers for fragility analysis and investigation of possibility of structural malperformance. Detailed procedure of the proposed approach and some numerical examples are presented in this paper. The results of numerical examples show that the period of a building structure plays a major role that affects the peak drift at each story. The peak drift at each story of a building structure increases as the period of the structure increases.

The proposed solution for evaluating the peak drift at each story of a building structure is based on the assumption of linear elastic responses. However, since the responses of structures subjected to major earthquakes may easily proceed to the inelastic range, one must carefully examine the applicability of the presented solutions.

## References

[1] V.V. Bertero, J.C. Anderson, H. Krawinkler, E. Miranda: Design guidelines for ductility and drift limits: Review of state-of-the-art in ductility and drift-based earthquake- resistant design of buildings, Report No. EERC 91-15. Earthquake Engineering Research Center, (1991).

[2] V.V. Bertero, J.C. Anderson, H. Krawinkler, E. Miranda: Design guidelines for ductility and drift limits: Review of state-of-the-art in ductility and drift-based earthquake- resistant design of buildings, Report No. EERC 91-15. Earthquake Engineering Research Center, (1991).

[3] FEMA: NEHRP guidelines for the seismic rehabilitation of buildings, Report No. 273, Federal Emergency Management Agency, Washington, D.C. (1997).

[4] B. B. Algan: Drift and damage considerations in earthquake resistant design of reinforced concrete buildings, Ph.D. thesis, Univ. of Illinois, Urbana-Champaign, (1982).

[5] J.P. Moehle: Seismic drift and its role in design, Proc., 5th U.S.–Japan Workshop on the Improvement of Building Structural Design and Construction Practices, San Diego, (1994), p. 65–78.

[6] K. David: Earthquake design practice for buildings. Thomas Telford, London, (1988).

[7] J.H. Lin: Seismic fragility analysis of frame structures, International Journal of Structural Stability and Dynamics, Vol. 8 (2008), p. 451-463.

*Applied Mechanics and Materials Vols. 580-583 (2014) pp 1443-1448*
*© (2014) Trans Tech Publications, Switzerland*
*doi:10.4028/www.scientific.net/AMM.580-583.1443*

# Research Advances in Seismic Behaviors of Shear Wall with Opening

Liyan Gong[1,a] ,Jianwei Chen[1, b] and Youpo Su[1,c]

[1] College of Civil and Architectural Engineering, Hebei United University, Tangshan 063009, China

[a]lygong2012@163.com, [b]heuu2010@163.com, [c]suyoupo@126.com

**Keywords:** shear wall, opening, seismic performance, prefabricated

**Abstract.** In order to meet the requirements for using function of structure, openings are often needed to be laid out in shear wall, and the mechanical behaviors of the wall will be significantly influenced. The experimental analysis, establishment of simplified mechanical model and numerical simulation researches on shear wall with opening were reviewed, the research findings on shear wall with opening at home and abroad were summarized, and the seismic behaviors were induced and analyzed. The problems about seismic behaviors of shear wall with opening which need to be solved urgently were pointed out.

## Introduction

Site construction, as a traditional mode of production, is widely applied to the concrete construction in our country for a long time, whose level of industrialization is low, loss of building materials and amount of construction garbage are large, quality of construction is unstable and whole life cycle energy consumption is high, all these disadvantages can't conform to national energy-saving and environmental protection policy. With the rapid development of our country's urbanization and urban modernization, the contradiction between energy and lack of resources is becoming more and more prominent, and the situation of ecological construction and environmental protection is increasingly serious. Housing industrialization, which adopts prefabricated construction methods, is one of the most important ways to realize building energy conservation and emissions reduction. It is estimated that green construction methods can make energy consumption reduced by 20%, water consumption reduced by 63%, timber formwork consumption reduced by 87%, the quantity of construction refuses reduced by 91% per square meter[1]. To realize housing industrialization, the theoretical study related to it must be taken seriously, which can provide theoretical basis for developing prefabricated structure system. Over the past decade , more and more Chinese researchers have paid attention to the study of prefabricated concrete building, lots of relevant technical researches have been carried out by such institutions like Number of units China Academy of Building Research, Tsinghua University, Harbin Institute of Technology, Beijing University of Technology, Southeast University, Hefei University of Technology etc, and also get demonstrated and applied in some real estate development projects of a certain size in Shenyang, Shenzhen, Changsha and other places[2] (refer with: Fig. 1[3]).

Common shear wall often need to be opened in order to meet the requirements for using function and vertical layout in building structures (refer with: Fig. 2[4]). On the one hand, strength and stiffness of the shear wall will be reduced due to the decrease of concrete area and discontinuity of steel bars around the opening, moreover stress concentration can be easy to appear at the corners of opening, which will cause cracks at an earlier stage of loading process and affect using functions. On the other hand, ultimate bearing capacity analysis of shear wall is the main content of RC structures' ultimate bearing analysis and seismic performance evaluation. Ultimate capacity-deformation characteristics of sheer wall are the essential structure parameters in the nonlinear push-over analysis and dynamic time-history analysis, however, in Chinese "Code for design of concrete structures"(GB50010-2010), only strength checking formulas for RC shear wall with openings are listed, rather than ultimate bearing capacity formulas[5,6].Therefore, the effects that openings have on bending strength, shear strength and other seismic performances must be considered when the openings are relatively large or at important parts.

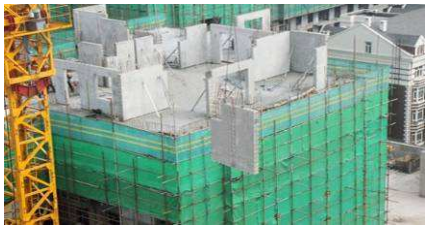

Fig.1 Prefabricated structure site of Brilliance Group

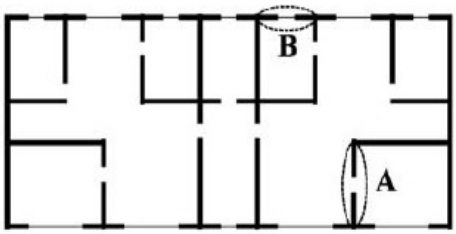


Fig.2 Plane graph of shear wall with openings

For prefabricated composite shear wall with concrete filled steel tube columns, not only the effects that openings have on ultimate bearing capacity, failure mechanism, energy dissipation capacity and other seismic performances need to be considered like common wall, but also it need to take the cooperative performances of prefabricated concrete filled steel tube columns working together with concrete shear wall into consideration. So cooperative working performances of all this structural members when existing openings ought to be further researched, in order to design prefabricated composite shear wall optimally, consequently, this new structure system will have multiple seismic fortification lines indeed.

## Analysis of research status and development in seismic performance of shear walls with opening

Shear capacity and lateral stiffness of the sheer wall are reduced because of the openings, whereas, the ductility and energy-dissipation capacity can be improved effectively when the openings are arranged properly. Bearing mechanism, energy-dissipation capacity, failure mode and other characters of the wall will become extremely complicated due to the impacts of many factors, such as the frame constraint, thickness of wallboard, the size, the position and the form of opening etc. A large number of researches related to this issue are conducted in China and abroad, which have obtained many achievements mainly in three aspects, which lie in experimental analysis, establishment of simplified mechanical model and numerical simulation.

Finite element analysis and experimental research on sheer wall with opening were performed by C.Y.Lin and C.L.Kuo[7](1988). Thirteen 2/3 scale models of shear walls had been tested in order to investigate the effects of different opening sizes and layouts of steel bars along the opening on ultimate strength and performance parameter design after the wall cracking. Test results indicate that the steel bars around the opening have a significant effect on ductility and shear strength of the wall. The shear capacity coming from oblique steel bars can achieve 40% of the yield strength, while the shear capacity coming from the horizontal bars and vertical bars can just achieve 20%. What's more, the paper also points out that shear strength of the sheer wall with opening is affected not only by the width of opening, but also by the height of opening.

A shear wall with an opening was designed according to JASSS by Daisuke Kato, Toshimi Kabeyasawa etc [8] (1995). Strength reduction factors and stiffness reduction factors of the wall with opening provided by JASSS are based on elastic theory or simplified equilibrium equation, which are not suitable for the conceptual design of ultimate strength. Therefore, a seismic design method for shear wall with opening based on ultimate capacity is proposed, and the experimental data of 35 walls coming from seven literatures are compared and analyzed. The results indicate that the data and suggested formula for calculating shear strength are in good agreement, and the formula can be used for structural design.

Present situation of tests on shear wall with RC frame containing opening was summarized by Zhonghan Chen[9](1997). Regularities of this issue are obtained on the basis of rearranging numerical analysis results, and the current simplified calculation formula for strength reduction factor of shear wall with opening was modified. In addition, it also shows that if the openings are off-centren, the shear strength will be further reduced.

Tests and theoretical analysis results of two shear walls with opening at the bottom were summarized by Christopher P. Taylor, Paul A. Cote etc [10] (1998).Two 1/4 scale specimens were

tested under cyclic horizontal loading and constant axial pressure, in order to evaluate the effects of choosing transverse boundary bars depending on displacement-based design method and the effects of choosing horizontal shear bars depending on strut-and-tie model. Test results indicate that the specimens will have stable energy-dissipation capacity and good ductility when designed adopting both of the two methods above, in addition, it also points out that the strut-and-tie model can be an effective tool for designing the discontinuous region of specimens.

The static analysis and dynamic analysis on shear wall with opening was performed by H.-S. Kim and D.-G. Lee using super elements[4](2003).This method was developed on the basis of matrix compensation and had no limit for the quantity , size and location of openings. Through the analysis of engineering examples, it can be concluded that this method is an effective way to analyze the mechanical behavior of the shear wall with opening, which has a high calculation accuracy and can save both computing time and occupancy of computer capacity greatly.

The strain-stress constitutive model for concrete and steel bar under monotonic and cyclic loading on shear walls with opening was established by Mengpu Wang, Xiyuan Zhou etc[11](2005) . In this model, the plane-strain 4-node quadrilateral parametric element was adopted, and also the concrete and the steel bar were considered as a whole unit, in which the bars were dispersed. The cracking, yielding, failure and other nonlinear characteristics of reinforced concrete were also reflected in this model. Meanwhile, on the basis of this model, dynamic equation was solved by using renewal precise time step integration method, in this way, time-history analysis of the shear wall with opening was completed. The calculation results indicate that the time-history curve of top floor displacement based on this method matches well with the curve based on dynamic nonlinear analysis, in addition, this new method takes less computing time.

Tests on 7 specimens of steel reinforced concrete (SRC) low-rise shear walls with opening (one specimen used for comparative analysis is without opening) had been conducted by Lumin Zhou, Jin Gong etc[12](2006). Parameters that investigated in the test were the size of opening and the form of steel skeleton concealed bracing (herringbone and splayed). The test results indicate that the seismic performance of SRC low-rise shear walls is good, and the openings have an influence on the shear strength, the ductility and the energy-dissipation capacity of the walls. Furthermore, with the opening dimensions increasing, the shear strength of the walls decreases but the ductility and the energy-dissipation capacity increase, and the failure characteristics expressed in the tests have a similarity with frame structure. Besides, it also points out that stress concentration is easy to occur around the opening, which leads to the appearance of the first cracks and stiffness reduction, thus the service performance of components are affected. As a result, structural measures like concealed beams and columns are advised to be set around the opening for strengthen.

The accuracy of a manual method for calculating horizontal stiffness of shear walls with opening had been studied by A. Neuenhofer [13](2006). The investigative parameters were the location, the change of height-width ratio and the size of opening. A finite element equation was established and the calculation analysis was conducted combining with Matlab. Through comparing the results of finite element analysis with the results of the manual calculation, it knows that although the manual calculation is complicated, the calculation results are well consistent with horizontal stiffness of shear wall with opening.

By taking the RC shear walls with opening based on shear resistant mechanism (“M-M” model) as the research objects, the existing “M-M” model was modified and the calculating equations for ultimate bearing capacity of the walls were derived by Huailiang Chen and Dachang Zhang etc[14](2007). The experimental values and calculated values for ultimate strength of two models were compared and analyzed on 23 specimens of different reinforcement, sizes and stress statuses. It shows that the calculation results depending on the modified “M-M” model match well with the test results and have high calculation accuracy. The modified “M-M” model can simulate the ultimate strength of RC shear wall with opening very well.

Pseudo-static tests on 1/4 scale shear walls with and without opening were studied by István DEMETER, Tamás NAGY-GYÖRGY etc[15](2008), in order to investigate the seismic behaviors of

prefabricated shear wall with opening and strengthened with fiber reinforced polymer (FRP). The variable parameters were the position of opening and the location of steel bars. On the aspect of axial load, standardized axial stress $v$ (the ratio of induced stress $v_0$ and concrete characteristic strength $f_{ck}$) was referenced, ranging from 0.01 to 0.2 and the horizontal load was controlled by displacement.

Elastic finite element analysis for steel frame-reinforced concrete infill shear walls with opening was performed by Qingjiang Zhang, Yinquan Yu etc[16](2009). According to the principle that lateral displacements will be equal when the structures are under the same lateral force, the shear wall was simplified into a model of cross steel brace. In this case, the distribution of stress and deformation under mono lateral loading were calculated. The calculation results show that the lateral stiffness of steel frame-reinforced concrete infill shear walls with opening can be simulated accurately by the model of cross steel brace, and some measures are proposed to be taken to prevent the concrete in the corner from cracking or crushing prematurely, which will affect the functions of structure.

A large number of tests and finite element analyses on shear walls with large eccentric openings were performed by Dr.Jiyang Wang's team[17-21] (2009~2012). A reduction factor was applied to calculate ultimate lateral bearing capacity and shear stiffness. Results show that the changes of stress transfer mechanism, failure mode, bearing capacity and shear stiffness of walls are all significantly affected by the large eccentric openings. Tests on seismic behavior of two shear walls with single row of steel bars and openings were conducted by professor Wanlin Cao's team[22-24] (2008~2010). The failure mechanisms of walls with different structural measures and forms were studied, and the calculation model on sheer capacity was found by his team. The experimental results are consistent with calculation results. Experimental research on seismic performance of RC composite shear wall with opening was performed by Dr. Zijun Wang's team[25-26] (2011~2012). The results show that the loading process and failure mode of the composite shear walls with opening are similar to those of shear walls with opening, while the prefabricated RC cover for the thermal insulation layer can improve the bearing capacity about 7% and reduce the stiffness degradation. What's more, the shearing frame can make the prefabricated parts and the cast-in-place concrete parts of the RC composite shear wall with opening work together very well.

From the above analysis, it can be seen that researches on seismic behaviors of RC shear wall with opening are relatively active, and lots of achievements have been obtained, which can provide important theoretical bases for the optimization design of the shear walls.

## Conclusions

Though many results on shear wall with opening are obtained, some problems also need to be solved.

1) Although shear capacity and lateral stiffness of the sheer wall are reduced because of the openings, the ductility and energy-dissipation capacity can be improved. And the seismic behaviors of the shear wall will be influenced by the frame constraint, the size, the location of opening etc. However, further researches are still needed to find out the effects of various factors on shear wall with opening.

2) Compared with common shear wall, the researches on prefabricated composite shear wall with boundary frames and openings are relatively less. More researches about the effects that opening has on seismic behaviors of this composite shear wall are required to popularize and apply this structure.

## Acknowledgements

Funding for the research was provided by National Natural Science Foundation (51278164).The author would like to thank to the authors of pertinent references to present data and suggestions.

**References**

[1] Baoxing Chou, Housing Industry. 4 (2010) 11-15. (In Chinese)

[2] Xiaoqing Liang, Housing Industry. 7 (2012) 20-23. (In Chinese)

[3] Information on http://www.vuhui.com/ProductShow.asp?ID=175

[4] H.-S. Kim, D.-G. Lee, Engineering Structures. 25 (2003) 981-991.

[5] Dachang Zhang, Huailiang Chen, Zhongqiang Lu, China Civil Engineering Journal. 41 (2010) 44-50. (In Chinese)

[6] GB 50010-2010: China Architecture and Building Press, 2010. (In Chinese)

[7] C.Y.Lin, C.L.Kuo, Proceeding of Ninth World conference on Earthquake Engineering. 8 (1988) 535-540.

[8] Daisuke Kato, Toshimi Kabeyasawa, et al, ACI Structural Journal. 92 (1995) 495-501.

[9] Zhonghan Chen, Building Structure. 12 (1997) 33-36. (In Chinese)

[10]Christopher P. Taylor, Paul A. Cote, and John W. Wallace, ACI Structural Journal. 95 (1998) 420-433.

[11]Mengpu Wang, Xiyuan Zhou, LiZhong Huang, Journal of Earthquake Engineering and Engineering Vibration. 25 (2005) 47-54. (In Chinese)

[12]Lumin Zhou, Jin Gong, et al, Sichuan Building Science. 32 (2006) 108-112. (In Chinese)

[13]A. Neuenhofer, Journal of Structural Engineering. 132 (2006) 1846-1851.

[14]Huailiang Chen, Dachang Zhang, Xudong Zhang, Journal of Nanjing University of Technology. 29 (2007) 95-101. (In Chinese)

[15]István DEMETER, Tamás NAGY-GYÖRGY, Valeriu STOIAN, et al, 12th WSEAS International Conference on SYSTEMS. 7 (2008) 813-819.

[16]Qingjiang Zhang, Yinquan Yu, et al, Building Structure. 39s (2011) 493-495. (In Chinese)

[17]Jiyang Wang, Wenjuan Lou, Hitoshi TANAKA, Journal of Building Structures. s2 (2009) 41-46. (In Chinese)

[18]Jiyang Wang, Masanobu SAKASHITA, Susumu KONO, et al, Journal of Zhejiang University SCIENCE A (Applied Physics & Engineering) . 11 (2010) 202-211.

[19]Ying Jiang, Jiyang Wang, Wenjuan Lou, Journal of Shenyang Jianzhu University (Natural Science) . 26 (2010) 1066-1072. (In Chinese)

[20]Jiyang Wang, Wenjuan Lou, Hitoshi TANAKA, Journal of Building Structures. 44 (2011) 35-41. (In Chinese)

[21]Jiyang WANG, Masanobu SAKASHITA, Susumu KONO, et al, Struct. Design Tall Spec. Build. 21 (2012) 669-681.

[22]Wanlin Cao, Jianwei Zhang, Yabin Yang, Journal of Beijing University of Technology. 36(2010) 1186-1192. (In Chinese)

[23]Wanlin Cao, Min Wang, Shaohe Wang, Earthquake Engineering and Engineering Vibration. 28 (2008) 85-90. (In Chinese)

[24]Wanlin Cao, Bin Zeng, Min Wang, Journal of Beijing University of Technology. 35 (2009) 603-610. (In Chinese)

[25]Zijun Wang, Weiqing Liu, Jisong Lu, Journal of Nanjing University of Technology (Natural Science Edition). 33 (2011) 5-11. (In Chinese)

[26]Zijun Wang, Weiqing Liu, Yanhua Ye, Building Structure. 33 (2012) 156-163. (In Chinese)

[27]Youpo Su, Lin Gao, Haibin Chen, Jianwei Chen, Guoqiang Xu, CN. Patent 202466890U. (2012)

[28]Jianwei Chen, Youpo Su, World Earthquake Engineering. 29 (2013) 51-62. (In Chinese)

*Applied Mechanics and Materials Vols. 580-583 (2014) pp 1449-1457*
*© (2014) Trans Tech Publications, Switzerland*
*doi:10.4028/www.scientific.net/AMM.580-583.1449*

# Response modification factor for Y-eccentric-braced steel frame structures designed based on Chinese Code

YANG Wen-xia [1,3, a], GU Qiang [2,b] ,CAO Ping-zhou[3,c] and SHI Rong-jin[1,4]

[1] Jiangsu Huning Steel Structure and Machinery CO.LTD , Wuxi 214231, China

[2] School of Civil Engineering, Suzhou University of Science and Technology , Suzhou 215011, China

[3] School of Civil and Transportation Engineering,Hohai university, Nanjing,210098 China

[a]darky1978@163.com, [b]guqiang383@163.com, [c]zhensen@163.com, [d]jshngj@vip.163.com,

**Keywords:** Y-eccentric braced steel frames; response modification factor; pushover analysis

**Abstract.** In current seismic design procedure, structure base shear is calculated according to the linear elastic response spectra divided by the response modification factor, which accounts for ductility and overstrength of a structural system. In this paper, the response modification factors of Y-eccentric braced steel frames (**YECBF**)designed based on Chinese Code were evaluated by an improved pushover analysis on 12 examples with various stories and spans lengths. According to the analysis results, the effects of fundamental periods, storey numbers, and spans of frames on the behavior factor were studied. In the end, an appropriate response modification factor was proposed for YECBF designed base on Chinese Code.

## Introduction

For building structure remaining elastic during a severe earthquake, it must be designed for large forces; a structure is expected to experience inelastic deformation during a strong earthquake. In most seismic codes such as the ATC (1995) and FEMA (2008)[1-3], the seismic design forces are established by applying a response modification factor R to the earthquake forces that would develop if the structure were to respond elastically. However, the expected inelastic deformations should be limited within an acceptable range to prevent structure failure. Therefore, proper earthquake resistant design requires that the ductility capacity of the structure exceeds the ductility demand imposed by the design earthquake load. In other words, the value of response modification factor $R$ should reflect the capability of a structure in dissipating energy.

Many scholars found that the response modification factor relates to the ductility and overstrength of a given structure [4-10].In the well-known documents such as ATC(1995), he response modification factor was calculated as the product of three factors: overstrength factor, ductility factor, and redundancy factor. FEMA695 (2008) points out that the redundancy factor becomes unity for structures designed using an ultimate strength method. In this case the response modification factor is determined as the product of the ductility factor $R_\mu$ and the overstrength factor $R_\Omega$.

$$R = \frac{V_e}{V_d} = \frac{V_e}{V_y} \cdot \frac{V_y}{V_d} = R_\mu \cdot R_\Omega \tag{1}$$

Figure1 represents a typical structural response, the horizontal axis is lateral roof displacement and the vertical axis is the base shear. The term, $V_e$, represents the force level that would be developed in the seismic-resisting system, if the system is remained entirely linearly elastic for the design earthquake. The term, $V_y$, represents the yield strength of the ideal system. And the term, $V_d$, is the seismic base shear required for elastic design. The terms, $\Delta_e$， $\Delta_y$ ,and $\Delta_d$， are the roof displacements corresponding to the base shear.

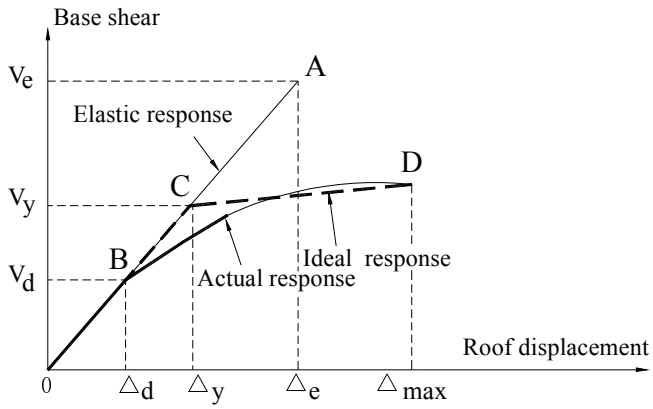


**Figure .1** Illustration of response modification factor

The latest seismic design philosophy in China is reflected in the active Code GB50011-2001(2001) with a cryptical *R* value of 2.8125 disregarding of the ductility capacity of different structures [11-12]. It is very clear that the reserve strength and the ductility of code-compliant buildings vary wildly as a function of building type and building height. Values for response modification factor must address these variations. The objective of this paper is to quantify the *R* values of Y-eccentric braced steel frame system (**YECBF**) complying with Chinese seismic code.

In this paper, a new method for defining the response modification factor was proposed from an improved inelastic pushover analyses considering loading effects and high mode effects. Twelve YECBF examples with different stories and different ratios of storey height to spans were established to evaluate the effects of different design parameters on the response modification factor. Based on the findings, a tentative R value was proposed for the YECBF designed according to Chinese Code.

**Proposed pushover analysis**

Figure 1 shows that the response curve is most important in the quantification of *R* in which inelastic behavior of the building should be explicitly considered. To obtain the response curve of a given structure, the incremental dynamic analysis (**IDA**) is the most rigorous method, but it's computationally demanding and time consuming. Current civil engineering practice prefers to use the pushover analysis method to estimate seismic demands. However, in a typical pushover analysis, both the force distribution and target displacement are based on the assumption that the response is controlled by the fundamental mode and that the mode shape remains unchanged after the structure yields. Obviously, after the structure yields, both assumptions are approximate, especially for high rise building. None of the invariant force distribution can account for the contribution of high modes to response, or for a redistribution of inertia forces because of structure yielding and the associated changes in the vibration properties of the structure.

To overcome these limitations, an improved pushover analysis procedure was proposed: The advised pushover analysis is an approximate adaptive force distribution that attempt to follow more closely the time-variant distributions of inertia forces. The detail of this improved pushover analysis procedures are introduced as follows:

①Recurring to time history analysis, calculate the vertical distribution of horizontal inertial force and the relevant maximum top displacements under three earthquake levels: minor earthquake (**ME**: earthquake have an average return period of 50 years), design earthquake (**DE**: earthquakes have an average return period of 475 years.), and rare earthquake (**RE**: earthquakes have a 2 %~3% probability of being exceeded in 50 years or an average return period of 2475 years). In this course, at least ten appropriate ground motion records should be chosen for each building.

②Adopting the inversed triangle vertical distribution, push the structure until the top displacement ΔME arrived.

③Follow the second step, change the pushover force to the vertical distribution of the horizontal inertial force under ME, push the structure until the top displacement $\Delta_{DE}$ arrived.
④Follow the third step, modify the pushover force as the vertical distribution of the horizontal inertial force under DE, push the structure until the top displacement $\Delta_{RE}$ arrived.
⑤Follow the forth step, calibrate the pushover force as the vertical distribution of the horizontal inertial force under RE, push the structure until the unstable condition is reached.
Mark down the base shear force and top displacement during the entire pushover process. The response curve is then obtained by plotting the base shear value against the roof displacement.

**Method for determining R**

According to Figure 1 and the well known ductility factor theory proposed by Newmark N.M. and Hall W.J. (1982)[13], for a long period structure whose fundamental period is larger than 1.0 second, if the inelastic displacement demand $\Delta$ under DE is determined, the seismic base shear $V_e$ can be easily quantified with the assumption that the elastic displacement $\Delta_e$ equal to the inelastic displacement demand $\Delta$. When $V_e$ of a given structure is determined, the $R$ can be easily determined by Eq.1.In this paper, the inelastic displacement demand $\Delta$ under DE of YECBF is determined by CSM (capacity spectrum method recommended by ATC (1995)). It requires both capacity curves and demand curves be converted in response spectral ordinates firstly.
**Capacity curves.**The displacement and force values of the structural capacity curves obtained from pushover analysis are converted to spectral values as follows:

$$S_{ai} = \frac{V/G}{\alpha_i} \tag{2}$$

$$S_{di} = \frac{\Delta}{\gamma_i X_{i,roof}} \tag{3}$$

Where, $V$ (base shear) and $\Delta$(displacement) represent any point at the pushover curves, $S_a$ and $S_d$ are the corresponding spectral acceleration and displacement values respectively. $\alpha_i$ and $\gamma_i$ are modal mass coefficient and participation factors for the $i$-th natural period. $X_i$, roof is the roof-level amplitude of the $i$-th natural period.
**Demand curves.**The design acceleration response spectrum, which is given in standard $S_a$ (spectral acceleration), versus $T$ (period) format is converted into acceleration-displacement response spectra format (generally known as ADRS format) with the following well-known equation:

$$S_{di} = \frac{T_i^2}{4\pi^2} S_{ai} g \tag{4}$$

Where, $S_{di}$ is the spectral displacement at any point on the acceleration-response spectrum in Chinese Code represented by $S_{ai}$ and $T_i$. Plotting $S_{ai}$ against $S_{di}$ results in the demand curve for the design. Then, the design spectrum is reduced to an inelastic spectrum based on the $R_\mu$-$\mu$-$T$ relationship proposed by Newmark N.M. and Hall W.J. (1982) and Peter Fajfar (1999)[13-14]. For a given level of displacement ductility, Figure 2 shows how to obtain the inelastic design response spectrum (**IDRS**) starting from a linear elastic design response spectrum (**LEDRS**).

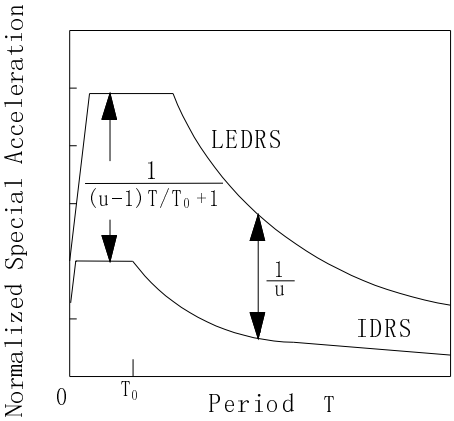


**Figure .2** The Relationship between IDRS and LEDRS

In Figure 2, $\mu$ is the displacement ductility level. $T_0$ is the transitional period, which can was defined by the site character period $T_g$ and displacement ductility level $\mu$( $T_0 = 0.65\mu^{0.3} T_g \le T_g$).

**Displace demand $\Delta$.**When one *i*-th modal capacity curve is graphically superimposed onto a set of demand curves obtained from different ductility levels, one intersection point called the performance point under *i*-th mode is obtained. The corresponding roof displacement $\Delta_i$ under the *i*-th mode can be gained according to Eq.3 .According to the MPA procedure proposed by Anil K.Chopra and Rakesh K.Goel (2002)[15], the demand displacement $\Delta$ of the structure under DE can be calculated as Eq.5:

$$\Delta = \sqrt{\sum_i \Delta_i^2} \tag{5}$$

## R of YECBF

**Model design.**To get a creditable value of response modification factor for the YECBF structures complied with Chinese Code, two groups of analysis models are designed: one group with the same span (6.0 meters) and different storey number of 8, 12, 16 and 20 marked as "Y1-total floors", and the other 8-, 16-storey group with different spans of 5.4m, 6.0m, 6.6m, 7.2m and 7.8m marked as "Y2-total floors-spans". The story height of each model was fixed to 3.6m and the length of all short links which dissipate energy by yielding essentially in shear is 800mm. One important to be mentioned is that in the top floor, all the structure was designed with V-center-braced seismic-resisting system. The plan and elevation configurations for the models are similar to Y1-12 shown in Figure 3 and Figure 4 respectively. All buildings were designed for an eight intensity region with the first design group, and soil conditions were assumed to be a general stiff soil defined as Site Class II in the Code GB50011-2001.The braces were designed to resist all lateral seismic loads. The structural design was carried out using the program SAP2000. Due to space limitations, the quantification procedure of *R* for model Y1-12 was only enumerated. The structural members selected for this model are listed in Tab.1.

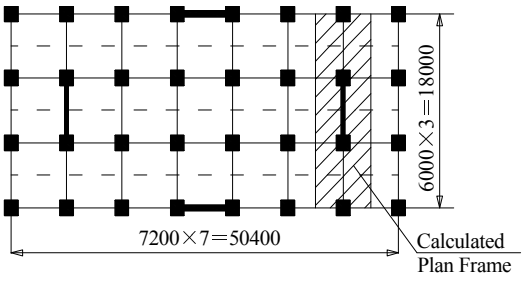


**Figure .3** Plan layout of the model (units: *mm*)

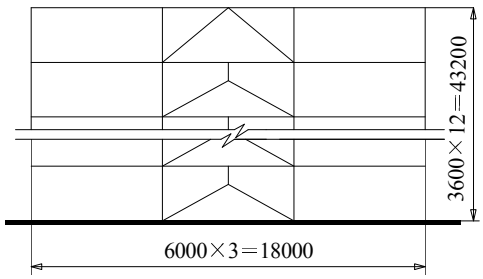


**Figure .4** Configuration of the model (units: *mm*)

**Table .1** Sections of 12-story structure (Q345)

| Story | Interior col. | Links | Exterior col. | Beams | Lean brace |
|---|---|---|---|---|---|
| 1~3 | H650×500×24×30 | H550×200×16×18 | H400×300×12×20 | H450×250×10×14 | H450×300×16×20 |
| 4~6 | H550×400×16×28 | H500×200×16×18 | H400×300×12×20 | H450×250×10×14 | H450×300×16×20 |
| 7~9 | H400×400×12×20 | H400×200×14×18 | H400×300×10×18 | H500×300×10×14 | H400×300×16×18 |
| 10~12 | H400×300×12×18 | H400×200×12×16 | H400×300×10×18 | H500×300×10×14 | H400×300×16×18 |

**Nonlinear dynamic analysis of Y1-12.**To establish the response curve based on the proposed pushover analysis, the force distribution and target displacement under the ME, DE and RE must be defined. Therefore, nonlinear time history analyses were carried out firstly. To avoid event bias, ten ground motion records were chosen from the Pacific Earthquake Engineering Research Center database on the sites located greater than or equal to 10 km from fault rupture. The background information and mean beta spectrum are included in Tab.2 and Figure 5 respectively. In dynamic analyses P-Δ effect was considered by (1.0dead +0.5live), and the equivalent damping is assumed to be 3.5% under ME and DE, but under RE, the damping is defined as 5%. Based on the nonlinear dynamic analyses results, the mean vertical distribution of horizontal inertial force under three earthquake levels for the ten ground motions were picked out. For comparative patency, the horizontal inertial forces were normalized to the same roof value as unit one and plotted in Figure 6. The details of numerical model for nonlinear analysis can be seen in document [16].

**Table .2** Ground motion records for 12-story modal structure

| No. | Records | Station | Durations/Sec. | DT/Sec. | PGA/g |
|---|---|---|---|---|---|
| 12-1 | Coyote Lake 1979 | 57383 Gilroy Array #6 | 27.1 | 0.005 | 0.146 |
| 12-2 | Kocaeli Turkey 1999 | Mecidiyekoy | 44 | 0.005 | 0.054 |
| 12-3 | Loma Prieta 1989 | 57064 Fremont - Mission San Jose | 39.95 | 0.005 | 0.124 |
| 12-4 | Northridge 1994 | 24278 Castaic - Old Ridge Route | 40 | 0.02 | 0.568 |
| 12-5 | Northridge 1994 | 24157 LA - Baldwin Hills | 40 | 0.02 | 0.239 |
| 12-6 | Northridge 1994 | 90015 LA - Chalon Rd | 31.07 | 0.01 | 0.225 |
| 12-7 | Northridge 1994 | 24396 Malibu - Point Dume Sch | 40 | 0.02 | 0.13 |
| 12-8 | Northridge 1994 | 24088 Pacoima Kagel Canyon | 40 | 0.02 | 0.301 |
| 12-9 | Northridge 1994 | 90049 Pacific Palisades - Sunset Blvd | 25 | 0.01 | 0.179 |
| 12-10 | Northridge 1994 | 13123 Riverside - Airport | 26 | 0.02 | 0.024 |

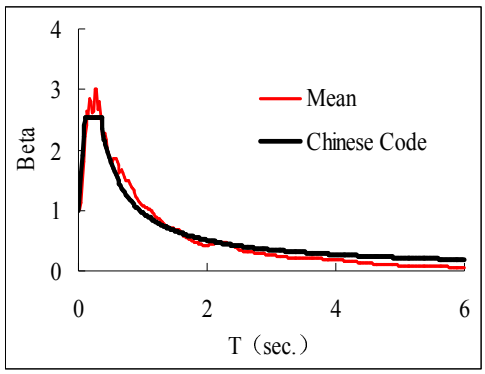


**Figure .5** Mean beta spectrum and Chinese Code beta spectrum

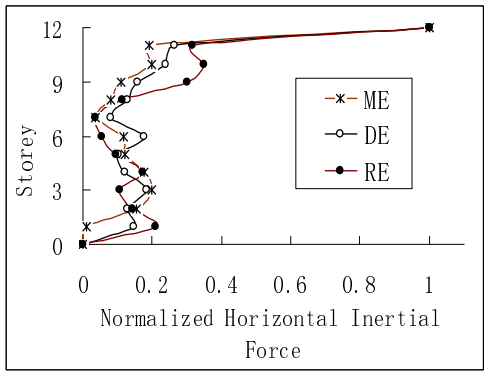


**Figure .6** Distribution of horizontal inertial forces for 12-story model

**R of Y1-12.** According to the proposed pushover analysis in this paper, the actual response curve was plotted in figure Figure 7. Based on the initial stiffness and the energy dissipation equality law, the yield base shear force and yield roof displacement were obtained as 3601kN and 286.9 mm, respectively. According to CSM mentioned above, the ductility factor $\mu$=2 under DE was assumed firstly, step-by-step iterative procedure was carried out until the ductility level is infinitely close to a fix value of μ=1.355.In the end the actual performance point under the first three modes were found as shown in Figure 8( $S_{d1}$=356.5mm， $S_{d2}$=167.6mm and $S_{d3}$=127.8mm, respectively, total mass coefficient is 0.945). Then the demand displacement $\Delta$ was established as 390.8mm according to Eq.3 and Eq.5.

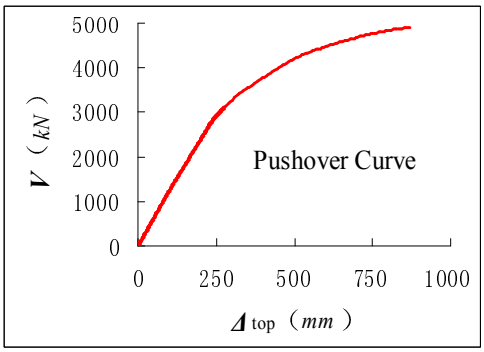


**Figure .7** Response curves of the 12-storey model

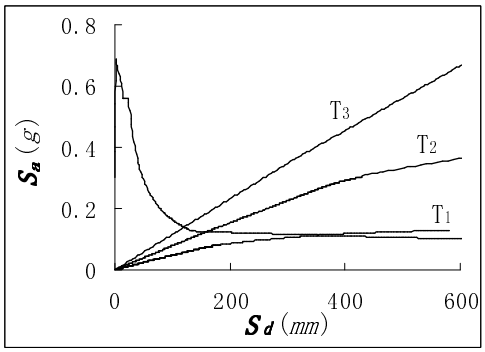


**Figure .8** Performance points for the first three modes under the actual ductility factor $\mu$=1.355

***R* of all models.**The response modification factors of all models were estimated by the same method as illustrated in Y1-12. For space limitations, the detail process were omitted, and only three key base shears $V_d$, $V_y$ and $V_e$ were presented in Table3 along with the response modification factors for each model.

**Table .3** $V_d$, $V_y$ ,$V_e$ and $R$ of all models

| Models | Y1-8 | Y1-12 | Y1-16 | Y1-20 | Y2-8-5.4 | Y2-8-6.6 |
|---|---|---|---|---|---|---|
| $V_e$ (kN) | 4104 | 4916 | 6728 | 7337 | 3635 | 4794 |
| $V_d$ (kN) | 1167 | 1442 | 2027 | 2201 | 1031 | 1362 |
| $V_y$ (kN) | 2350 | 3601 | 4548 | 4941 | 2055 | 3229 |
| $R$ | 3.517 | 3.409 | 3.319 | 3.333 | 3.526 | 3.520 |
| Models | Y2-8-7.2 | Y2-8-7.8 | Y2-16-5.4 | Y2-16-6.6 | Y2-16-7.2 | Y2-16-7.8 |
| $V_e$ (kN) | 5200 | 5287 | 6220 | 7362 | 8325 | 9028 |
| $V_d$ (kN) | 1453 | 1418 | 1773 | 2222 | 2452 | 2647 |
| $V_y$ (kN) | 2848 | 2654 | 4637 | 4916 | 5616 | 6126 |
| $R$ | 3.579 | 3.729 | 3.508 | 3.313 | 3.395 | 3.411 |

Table3 shows that all the response modification factors of YECBF models are larger than the value cryptically prescribed in Code GB50011-2001(2001), the minimum value is 3.313 and the maximum is 3.729 which exceed the Code value about 18% and 33% respectively. The reason is that the fixed $R$ value of 2.8125 in Chinese Code was obtained mainly based on studies of reinforced concrete structures. The ductility capacity and the energy dissipating capacity through inelastic behavior of YECBF is better than reinforced concrete structure, so the Code value disregarding of the ductility capacity of different structures is too little for the Y-eccentric braced steel frame.

## Result analysis

To evaluate the effects of some key design parameters such as fundamental period, storey number and the span length on $R$, response modification factors of the 12 models were plotted in Figure 9~Figure 11 versus the nominalzed periods $T/T_g$ ($T$ is the fundamental period, and $T_g$ is the site character period), the total number of building floors $N$, and the ratios of storey height to spans $\lambda$, respectively. Figure 9～Figure 11 shows that the modification factors of YECBF designed based on Chinese Code decrease as the fundamental period and total storey number increase, but the decrease trend is not obvious. However, for 16-storey buildings $R$ decreases as $\lambda$ increases, but the 8-storey ones just has the opposite trend. Figure 11 also shows that the response modification factors for 16-storey buildings are somewhat smaller than those obtained in 8-storeys ones, but the differences become smaller as the ratios of storey height to spans increase.

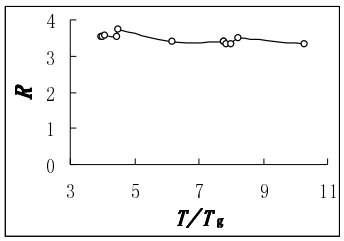


**Figure .9** $R$ versus normalized period

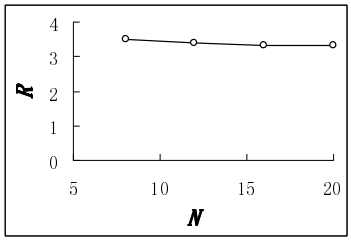


**Figure .10** $R$ versus storey number

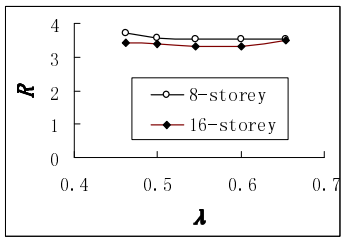


**Figure .11** $R$ versus the ratio of storey height to span

## Summary

(1)In this paper an improved pushover analysis was utilized in quantification of $R$ for YECBF. The proposed pushover analysis is an approximate adaptive force distribution and attempts to follow more closely the time-variant distributions of inertia forces, in which the contribution of high modes to response and the redistribution of inertia forces because of structure yielding and the associated changes in the vibration properties of the structure were considered approximately.

(2)To evaluate the response modification factor of YECBF, a new method for defining the behavior factor was proposed according to the general definition of the behavior factor. The elastic design

earthquake force level $V_e$ was determined by an improved capacity spectrum method based on modal pushover analysis procedure proposed by Anil K.Chopra and Rakesh K.Goel (2002) and well known ductility factor theory proposed by Newmark N.M. and Hall W.J. (1982).
(3) To get a creditable value of response modification factor for the YECBF structures complied with Chinese Code, twelve models were designed: one group with different storey number and the other with different spans. Based on the analysis results, the effects of some key design parameters such as fundamental period, storey numbers and the spans length on the response modification factors were evaluated.
(4) In the end, a reasonable $R$ value of 3.5 for the YECBF designed based on Chinese Code was advised.

**Acknowledgements**

This research is sponsored by a Grant (No. 2013M531295) from the China Postdoctoral Science Foundation. This support is gratefully acknowledged. The authors also acknowledge the Hohai University (China) and the Jiangsu Huning Steel Structure and Machinery CO.LTD. for providing facilities for this research.

**References**

[1]ATC. Structural response modification factors. ATC-19, applied Technology Council, Redwood City, California, 1995, p.5-32.

[2]ATC. A critical review of current approaches to earthquake-resistant design. ATC-34, Applied Technology Council, Redwood City, California, 1995, p.31-36.

[3]FEMA, Quantification of building seismic performance factors. FEMA-695, Federal Emergency Management Agency, Washington, D.C., 2008.

[4]Chopra A K, Ernesto F C . Evalutaion of building code formulas for earthquake forces[J]. Journal of Structural engineering, 1986,112(8):1881-1899.

[5] Uang Chia-Ming.Establishing R（or Rw）and Cd factors for building seismic provisions[J]. Journal of Structural Engineering, 1991,117(1):19-28.

[6]Uang Chia-Ming. Deflection Amplification factor for seismic design provisions[J]. Journal of Structural Engineering, 1994,120(8):2423-2436.

[7]Maheri M R, Akbari R. Seismic behavior factor R for steel X-braced and Knee-braced RC buildings[J]. Engineering Structures, 2003, 25:1505-1513.

[8]Marino R. Comparison of European and Japanese seismic design of steel building structures[J]. Engineering Structures, 2005,27: 827–840.

[9]Daneshjoo M F F, Melchers R E . A method for determining the behavior factor of moment-resisting steel frames with semi-rigid connections[J].Engineering Structures, 2006,28:514-531.

[10]Nohenmy G , Peter T . Performance of steel moment-frame building deigned according to the Colombian code NSR-98[J], Engineering Structures, .2007,29:2274-2281.

[11]GB50011-2001. Code for seismic design of buildings. Beijing City, 2001,P.R.China.

[12]SHAO Jian-hua. Structural Influencing Coefficient and Deflection Amplification Factor of Moment-Resisting Steel Frame-Steel Plate Shear Wall as a Dual Lateral Load-resisting System[D]. Nanjing: Hohai University, 2008,(in Chinese).

[13]Newmark N.M., Hall W.J.. Earthquake Spectra and Design[M]. Berkeley, CA. ,Earthquake Engineering Research Institute Monographs , 1982.

[14]Fajfar P. Capacity spectrum method based on inelastic demand spectra[J]. Earthquake Engineering and Structure Dynamics, 1999,23: 979-993.

[15]Chopra A K, Goel R K. A model pushover analysis procedure for estimate seismic demands for buildings[J]. Earthquake Engineering and Structure Dynamics, 2002, 31:561-582.

[16]YANG Wen-xia, LI Chun-yan, Gu Qiang. The Sap2000 nonlinear analysis model of eccentrically braced steel frame with Y-links[J]. Journal of Lanzhou University of Technology, 2010.(in Chinese).

*Applied Mechanics and Materials Vols. 580-583 (2014) pp 1458-1462*
*© (2014) Trans Tech Publications, Switzerland*
*doi:10.4028/www.scientific.net/AMM.580-583.1458*

# Seismic Performance of the Reinforced Concrete Frame Structures with Infilled Walls of Different Configuration

Minsheng Guan[1,2,3, a], Hongbiao Du[3,b], Wei Chen[1,c] and Yuhua Wu[1,d]

[1] School of Civil and Transportation Engineering, Guangdong University of Technology, Guangzhou 510006, China

[2] State Key Laboratory of Subtropical Building Science, South China University of Technology, Guangzhou 510640, China

[3] College of Civil Engineering, Shenzhen University, Shenzhen 518060, China

[a]msguan@gdut.edu.cn, [b]du_hongbiao@126.com, [c]417410418@qq.com, [d]925368712@qq.com

**Keywords:** infilled wall frame structure; bare frame structure; configuration; seismic performance; time-history analysis

**Abstract.** Using the three-strut model, five types of frame structures, i.e., without infilled walls, with full infilled walls, without bottom-storey infilled walls, without middle-storey infilled walls and without top-storey infilled walls, were studied. The mode analysis and nonlinear time-history analysis were carried out on each model. In order to investigate the effects of infilled walls with different configurations on the seismic behavior of reinforced concrete frame structures, the structural periods, the ratio of $T_t$ to $T_1$ and the maximum interstorey drifts were analyzed. The results indicate that the infilled walls enhance the lateral stiffness of frames, and the configuration of infilled walls has little influence on the calculation of structural periods. It also shows that the weaker storey is formed due to the unreasonable layout of infilled walls, thus leading to the collapse of the whole structures under the seismic action.

## Introduction

The infilled wall frame structures are widely used in practical engineering projects for the advantages of flexible configurations and acquiring more space in buildings. However, there are still some weaknesses existing in the utilization of the infilled wall structures. For example, the irregular configurations of infilled walls are often used for building functions, which would easily form a weak storey due to large difference of lateral stiffness among adjacent stories of structures. Thus, the structures would be damaged under earthquake actions, since the plastic deformation concentrates only in one storey. On the other hand, the irregular configurations of infilled walls would yield large torsional responses, which bring a great damage to the safety of the structures. In practical design, the infilled walls are regarded as non-structural components that their weights are added to the frames. The structural natural period is reduced to consider the impact of stiffness of infilled walls on the seismic behavior of structures. It's illustrated from many earthquake disasters that this approach is too simple to consider the interactions between the infilled walls and frames, which will result in the collapse of the buildings [1-3].

In this paper, five finite element analysis models of the frame structures with infilled walls of different irregular configurations are established adopting the three-strut model. The elasto-plastic time-history analysis is carried out on each model. Taking the structural periods and interstorey drifts as index, the impacts of the infilled wall and its configuration on the seismic behavior of frame structures are studied by comparing with the bare frame structure and can be helpful in practical engineering applications.

**The Mechanical Model of Infilled Wall**

Extensive research were conducted to simulate the mechanical behavior of infilled walls. In 2003, El-Dakhakhni [4] proposed the three-strut model on the basis of the improvement of the equivalent brace model (Fig. 1). The infilled wall is equivalent to three braces that is pinned with the frame. The location and geometric parameters of the three-strut are calculated from the contact length among braces, beams and columns, the area of brace.

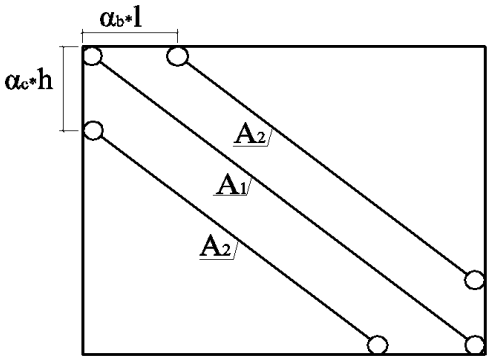


Fig.1 Three-strut model

The parameters, including the coefficient of the contact length $\alpha_b$ and $\alpha_c$ among the infilled wall, beams and columns, and the area of the brace $A_d$ , are the key to the determinations of the location and geometric size of the three-strut model. Due to the mechanical behaviors of the structure changing under the earthquake actions, there are difficulties in the quantification of the parameters. However, the changes can be ignored when only considering the overall seismic response of the structure.

The parameters of infilled walls are calculated by applying the following equations(1)~(6).

$$A_d = \frac{(1-\alpha_c)\alpha_c h_c t_w \frac{\sigma_c}{f_c} + \alpha_b l_b t_w \frac{\tau_b}{f_c}}{\cos\theta} \tag{1}$$

$$\alpha_c h_c = \sqrt{\frac{2(M_{pj} - M_{pc})}{t_w \sigma_{c0}}} \le 0.4 h_c \tag{2}$$

$$\alpha_b l_b = \sqrt{\frac{2(M_{pj} - M_{pb})}{t_w \sigma_{b0}}} \le 0.4 l_b \tag{3}$$

$$\sigma_{c0} = \frac{f_c}{\sqrt{1+3\mu^2 r^4}} \quad , \quad \sigma_{b0} = \frac{f_c}{\sqrt{1+3\mu^2}} \quad , \quad \tau_b = \mu\sigma_b \tag{4}$$

$$A_c = r^2 \sigma_{c0} \alpha_c (1 - \alpha_c - \mu r) \ , \quad A_b = \sigma_{b0} \alpha_b (1 - \alpha_b - \mu r) \tag{5}$$

$$\text{If } A_c > A_b, \ \sigma_b = \sigma_{b0}, \ \ \sigma_c = \sigma_{c0} \frac{A_b}{A_c}; \text{ if } A_c < A_b, \ \sigma_b = \sigma_{b0} \frac{A_b}{A_c}, \sigma_c = \sigma_{c0} \tag{6}$$

where, $h_c$ is the height of the frame column, $t_w$ is the thickness of the infilled wall, $\sigma_c$ and $\sigma_b$ are the normal stress of the contact surface among the infilled wall, beam and column, respectively, $f_c$ is the compression strength of infilled wall, $l_b$ is the calculation span of frame beam, $\tau_b$ is the shear stress of the contact surface between infilled wall and beam, $\theta$ is the angle between the diagonal of the

three-strut and frame beam, $M_{pc}$ is the yield moment of column, $M_{pb}$ is the yield moment of beam, $M_{pj}$ is the minimum value among the yield moment of column, beam and joint, $\mu$ is the coefficient of fraction between infilled wall and frame, the value is 0.7, $r$ is the length ratio of column to beam.

## The Analysis Model of Infilled Wall Frame Structures

A 7-story reinforced concrete frame structure is selected as an example. The height of structure is 3.6 m (see Fig.2). The cross section of the beam is 0.3m×0.5m, and the cross section of column is 0.5m×0.5m. The thickness of the cast-in-place concrete floor slab is 0.1m. The concrete strength is C30, and the longitudinal steel bar of all the beam and column is HRB335, and slab reinforcement and links are HPB235. The thickness of infilled wall is 0.24m. The site fortification intensity is Grade 8; the type of site is Ⅱ; the basic design acceleration is 0.1g; the design earthquake group is the second group; the characteristic period of site is 0.4s. The dead loads are self-weight of structure, and the live loads of floor and roof are 2.0KN/m$^2$.

Five types of analysis models are established according to the requirements of common architectural features and spatial arrangement. Model A represents a bare frame structure. Model B represents a full infilled walls frame structure. Model C represents a frame structure without infilled walls in the first storey. Model D represents a frame structure without infilled walls in the fourth storey. And model E represents a frame structure without infilled walls in the top storey.

The three-strut model is used to capture the mechanical behavior of infilled walls[4,5]. The wall materials are common fried brick. The material physical parameters of the infilled walls are as follows: the elastic modulus is 2.4×103 Mpa, the grade of mortar strength is M5, the grade of masonry strength is MU10, and the weight density is 18 kN/m3. Typical El Centro E-W wave is selected for the time-history analysis with peak ground acceleration of 220 gal according to the code for seismic design of buildings[6].

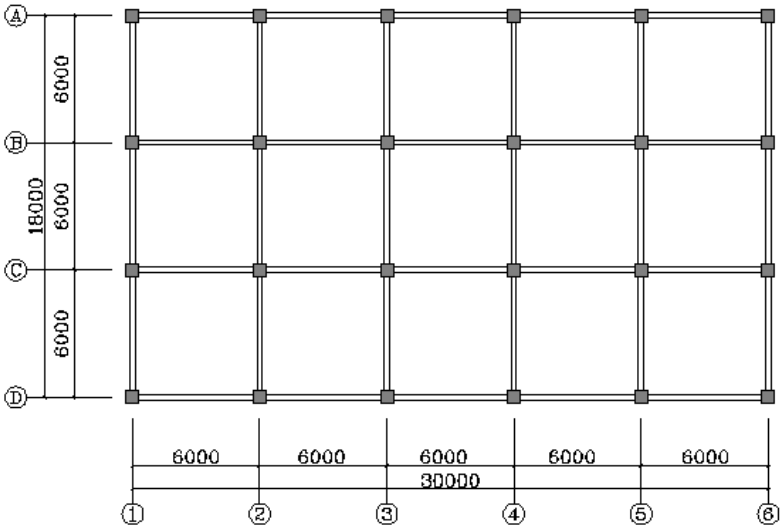


Fig.2 The plan of model

## The Analysis of Numerical Results

**The Analysis of Structural Periods.** The natural periods and the ratio of the first torsional period to the first translational period are calculated through the modal analysis on the five models A-E. The impact of the configuration of the infilled walls on the lateral stiffness and torsional effects of structures are studied, which can be seen in Table 1 and Fig. 3.

Table.1 The periods of frames with masonry infilled walls(S)

| Period \ Type | Model A | Model B | Model C | Model D | Model E |
|---|---|---|---|---|---|
| $T_1$ | 1.058 | 0.612 | 0.688 | 0.688 | 0.602 |
| $T_t$ | 0.944 | 0.538 | 0.610 | 0.608 | 0.529 |
| $T_t/T_1$ | 0.892 | 0.878 | 0.886 | 0.883 | 0.879 |

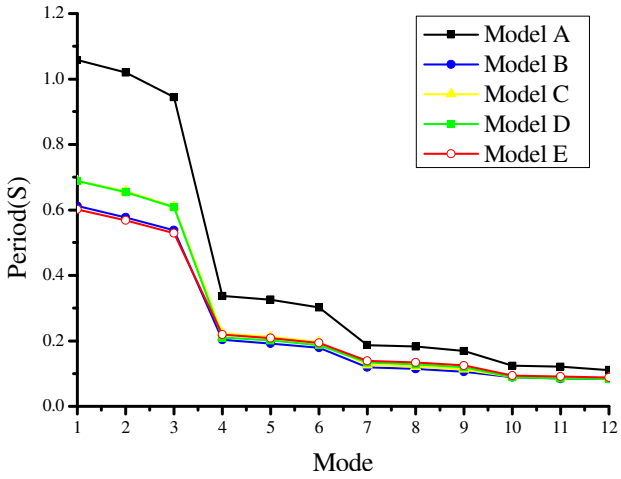


Fig. 3 The periods of frames with masonry infilled walls

It can be seen that the lateral stiffness of the frame structure is significantly enhanced from the contributions of infilled walls. The natural periods of Models B-E are obviously less than that of Model A. For the first three modes, the periods of infilled walls frame structures are 0.5-0.7 times than that of model A. In addition, the natural periods of Models B-E are approximated to each other. Among them, the period of Model B is almost the same to that of Model E. It indicated that the configuration has minor influence on the natural periods of the structures.

It also presented that the ratio of the first torsional period ($T_t$) to the first translational period ($T_1$) should be controlled to ensure that the structures have sufficient torsional stiffness. The ratios of $T_t$ to $T_1$ of Models A-E are less than 0.9, which meet the requirements of the code. Model A has the largest value of 0.892, and Model B has the smallest value of 0.878. The ratios of $T_t$ to $T_1$ of Models C-E have a increasing trend comparing with that of Model A. The torsional effects of structures increase with the ratios of $T_t$ to $T_1$ increasing. It showed that the torsional effects of structures would be exacerbated by the irregular configuration of infilled walls, which would lead to a damage of structure under the earthquake actions.

**The Analysis of Interstorey Drifts of Structures.** Fig. 4 shows that the maximum interstorey drifts of each model under the major earthquake of Grade 7 for the El Centro accelerogram. It can be seen that the configurations of infilled walls have significant impact on the structural interstorey drifts. There is a similar trend for the interstorey drift curves of Model A and Model B. The interstorey drift of Model B is significantly less than that of Model A due to the lateral stiffness of structure is enhanced by the infilled walls. The maximum interstorey drifts of the two models are located at the second storey, and the value of Model B is 0.66 times of that of Model A. The uniform distributions of the interstorey drifts reflect that the distribution pattern of the energy dissipation along the height of the structure is even. Thus, the structure has good ductility. The interstorey drifts of without infilled walls storeys have sudden changes. The structural deformation concentrates in the first storey of Model C, fouth storey in Model D and top storey of Model E. The interstorey drifts of the deformation concentrated storeys of each model are larger than that of the corresponding storey of Model A. For Model E, the interstorey drift of the deformation concentrated storey has grown large by 64%. However, the interstorey drifts of other storeys are significantly smaller than that of Model A. There

are sudden changes in the lateral stiffness of the storey with no infilled walls, leading to the formation of weak storey of the structure. Thus, the structure would be easily damaged under the earthquake action.

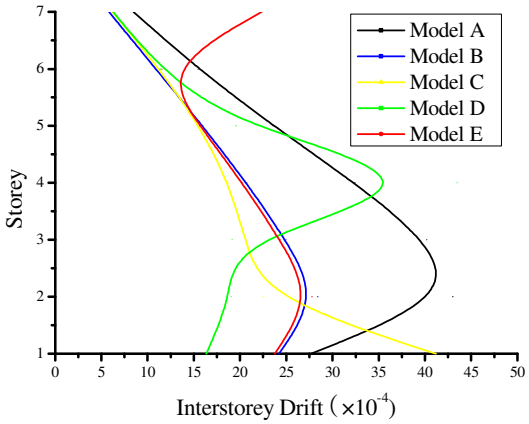


Fig.4 The maximum interstorey drifts of structure with masonry infilled walls

## Conclusions and Suggestions

Five types of RC frame structures are analyzed though the modal analysis and the nonlinear dynamic time-history analysis. Some conclusions are as follows:

(1)The infilled walls enhance the lateral stiffness of the structures. The natural periods of infilled walls frame structures are significantly 0.5-0.7 times less than that of the bare frame structure.

(2)The configurations of infilled walls have minor influence on the natural periods of the structure. The periods of Models B-E are close to each other.

(3)The irregular configurations of infilled walls have major influence on the interstorey drifts of the structure. Due to sudden changes in the lateral stiffness of the structure, the weak storey is formed. As a result, the structures are destroyed during the earthquake. Such structural damages should be avoided in the seismic design.

(4)For the seismic design of the frame structures with infilled walls in irregular configurations, the interaction between the infilled walls and frames should be taken into considered instead of adopting a simplified approach according to the code.

## Acknowledgements

This work was financially supported by the Intellectual Innovation Program of Shenzhen Science and Technology Innovation Committee (JCYJ20130329142338934) , the Open Foundation of State Key Laboratory of Subtropical Building Science, South China University of Technology (2014KB27) and the Youth Science Foundation of Guangdong University of Technology(13QNZD007).

## References

[1] J.G.Zhang, T.Z.Huang, W.Z.Lei and B.F.He: Geological Bulletin of China, Vol.28 (2009), p.1079 (in Chinese)

[2] S.Hou and W.Yang:Journal of Dalian University of Technology, Vol.49 (2009), p.754 (in Chinese)

[3] M.Z. Zhang: China Civil Engineering Journal, Vol.42 (2009),p.21 (in Chinese)

[4] W.W.El-Dakhakhni, M.Elgaaly and A.A.Hamid: Journal of Structural Engineering-ASCE, Vol.129 (2003),p.177

[5] L.Koutromanos, A.Stavridis and P. B.Shing: Computers&Structures, Vols.11-12 (2011),p.1026

[6]Code for Seismic Design of Buildings (GB50011-2010), Beijing: China Building Industry Press, 2010 (in Chinese)

*Applied Mechanics and Materials Vols. 580-583 (2014) pp 1463-1466*
*© (2014) Trans Tech Publications, Switzerland*
*doi:10.4028/www.scientific.net/AMM.580-583.1463*

# Shaking table test analysis of bottom-business multi-story masonry structure in small and middle towns in the southward

Yongduo Liang[1, a], Xun Guo[2,b], Huawei Yi[3,c], Yongzhen Li[1,d] and Jinzheng Jiang[1,e]

[1]Earthquake Administration of Liaoning Province, Liaoning Shenyang, 110034, China

[2]Institute of Disaster Prevention, Hebei Sanhe, 065201, China

[3]Saint King Architectural Design And Consultancy Co，.Ltd, Shandong Yantai, 264000, China

[a]liangyongduo1437@163.com, [b]guoxun@iem.ac.cn, [c]tingyudd@163.com,

[d]ldztlyz@163.com, [e]aboyjjz@163.com

**Keywords:** bottom-business multi-story masonry structure, winged column, earthquake simulation shaking table test, seismic resistant capacity

**Abstract:** Bottom-business multi-story masonry structure is widely used in small and middle towns in the southward in China. In the downtown of Beichuan county which affected by Wenchuan earthquake, more than 80% of this kind of building collapsed. But the Apartment of Beichuan Telecommunication Bureau behaved well earthquake resistant capacity with a moderate damage in the earthquake. The obvious difference between this building and others is the setting of winged columns in the front longitudinal wall of the first floor. For proving the influence of these members in the structure seismic capacity, the earthquake simulation shaking table test of 2 1/5 reduced scale models were designed and carried out. The models dynamic response, acceleration, displacement and strain were measured and collected, that model with winged columns behave well was testified. And the reinforcement method of balancing stiffness and increasing ductility is put forward. The results provide a foundation for the retrofitting design of the existing houses.

## Introduction

For economy limits and weak disaster prevention consciousness, building seismic capacity is low lead to “weak earthquake vs sever disaster” is a predominant characteristic in China. The bottom-business multi-story masonry structure which is more popular and cause severe damages in small and middle towns in the south of China. According to inadequate statistics, there are about two million such buildings existing in China, and 120 million residents are involved. There are no relative codes in “Seismic Code for Buildings (GB 50011-2010)” of China and no relative research in other countries. But this kind of structure can’t disappear in China because of its advantages. So in this paper, the different elements capabilities between the Apartment of Beichuan Telecommunication Bureau (Fig.1) which behaved well in earthquake and others will be studied by shaking table test.

(a) Face view (b) Back view

Fig.1 Apartment of Beichuan Telecommunication Bureau

**Shaking table test**

Based on prototype of the Apartment of Beichuan Telecommunication Bureau, test models C and D were designed. The models plane view as shown as fig.2. The tests were carried out in key laboratory of earthquake engineering and engineering vibration, Institute of Engineering Mechanics, China Earthquake Administration.

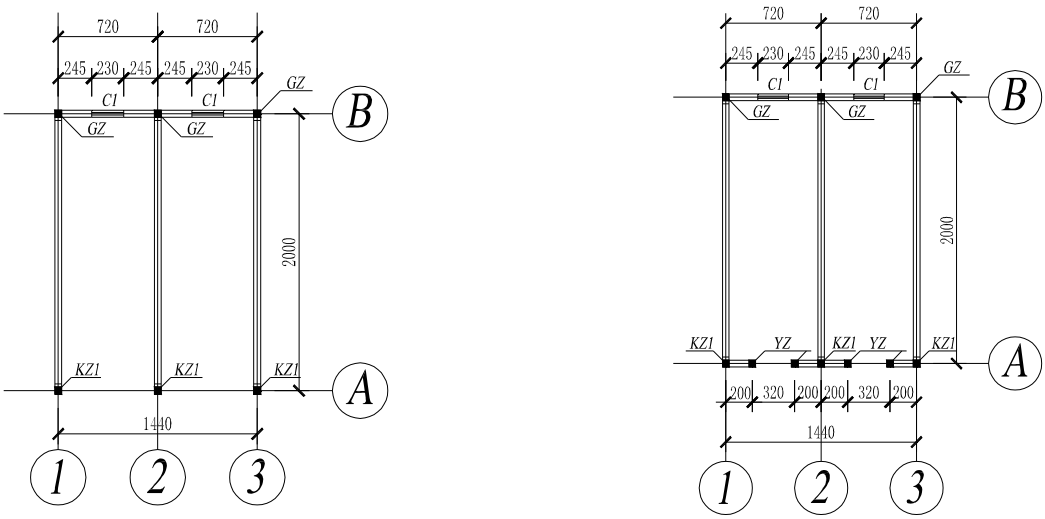


(a) Model C (b) Model D

Fig.2 Model plan view

According to test aim and content, 16 acceleration sensors were placed on vibration table-board and the top of the models; 4 displacement meters were correctly placed and 22 strain gauges were beam column joint, wall pier, area around doors and windows.

Considering the prototype is in Wenchuan, Wolong wave was used in the shaking table tests. The character of the Wolong wave is as shown as fig.3. During the testing, 4 classes earthquake wave were used, the details as shown as table 1.

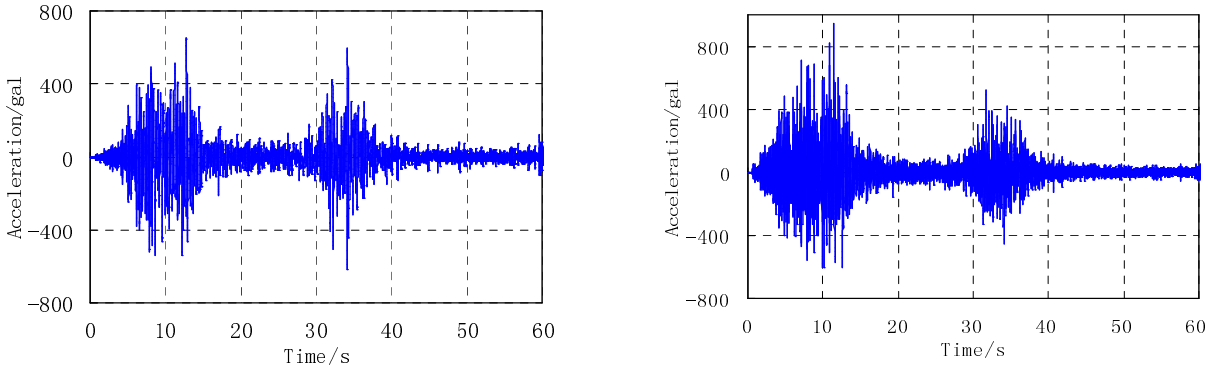


(a) Y (b) Z

Fig.3 Wolong groud motion

Table.1 Model test operation condition schedule

| | input earthquake motion | input acceleration peak/g | | output acceleration peak/g | |
|---|---|---|---|---|---|
| | | Y(longitudinal) | Z(vertical) | Y(longitudinal) | Z(vertical) |
| 1 | Wolong wave | 0.1 | 0.1 | 0.07 | 0.04 |
| 2 | Wolong wave | 0.2 | 0.1 | 0.14 | 0.05 |
| 3 | Wolong wave | 0.4 | 0.1 | 0.31 | 0.15 |
| 4 | Wolong wave | 0.8 | 0.1 | 0.66 | 0.38 |

**Test analysis**

When PGA=0.08g, two models all in the elastic working condition, the frame cooperate with walls and no cracks appeared.

When PGA=0.14g, fine cracks $45^0$ with the horizontal appeared on two window holes of model C back wall.

When PGA=0.31g, fine cracks also appeared on the frame of model C and the same thing occurred on the two outward lateral walls. The preexist cracks run to radiate cracks around the window. And some reticulate cracks appeared under the window. Boundary cleared block come into being on the wall pier. Whereas, no visible cracks on the frame of model D.

When PGA=0.66g, model C collapse, model D inclined obviously, the degree of inclination reached 1/12. The models suffered four accumulative earthquakes as shown as fig.4.

Fig.4 Model C, D suffered earthquake PGA=0.66g

Before load, after second load (0.14g) and third load (0.31g), longitude natural frequencies were attained, the results as shown as fig.5. From the chart, after 0.31g, the natural frequency of model C reduced about 60%, whereas model D changed a little.

The former three tests acceleration results of models were measured and comparison figure as shown as fig.6. The acceleration amplification first increased and then decreased along with earthquake emotion input. When natural frequency approximately equal to input earthquake emotion, the acceleration amplification reached its maximum values, they are 2.43 and 1.64.

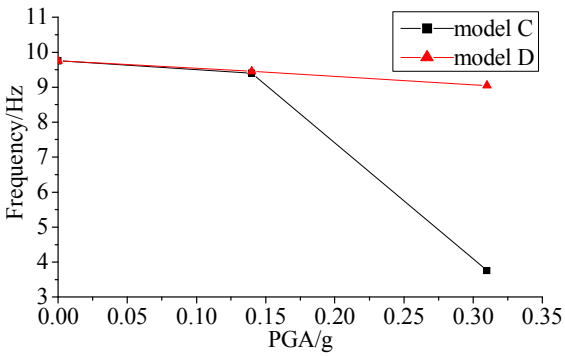


Fig.5 Longitude natural frequency

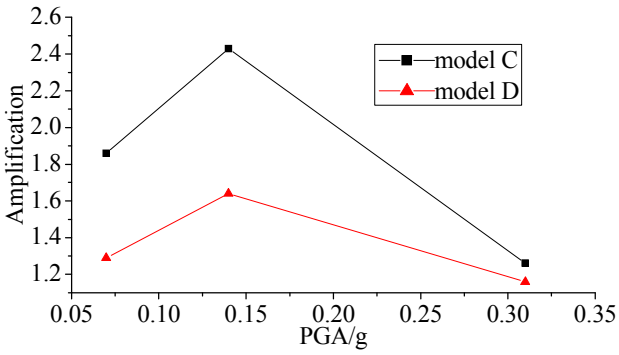


Fig.6 Acceleration amplification

The displacement of platform and model top after each loading were measured and recorded. The relative displacement results after three loading as shown as fig.7. The max relative displacement of model C is 17.87mm and here the degree of relative displacement reached 1/43, that is say bottom-business multi-story masonry structures have some ductility in certain circumstances.

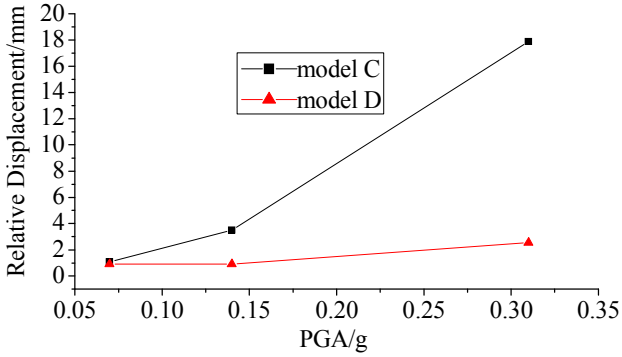


Fig.7 Relative displacement

Strain values of two models on the back longitudinal wall and window upside were attained, as shown as fig.8. From the chart, the strain value on the model C back longitudinal wall (7# and 9#) always higher than model D corresponding place (15# and 19#). And after second load (PGA=0.14g), 9# was damaged and out of work, 7# approach its ultimate compressive strength after third load (PGA=0.31g). It testified the back longitudinal wall of normal bottom-business multi-story masonry structure destroied severely than with winged columns.

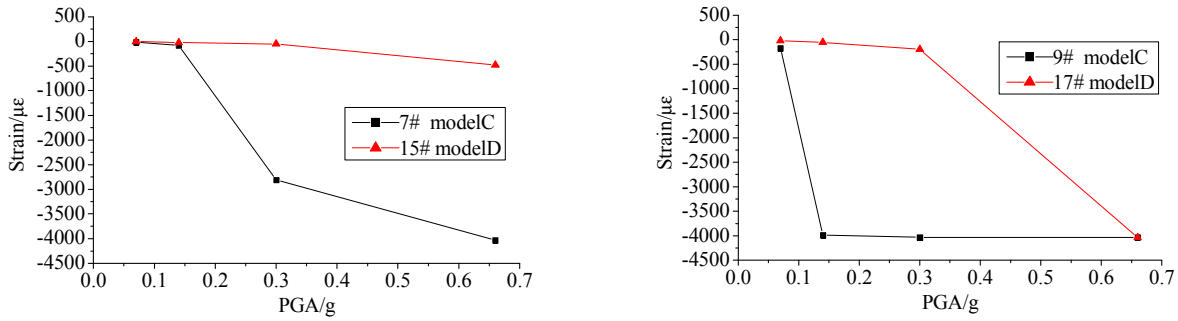


(a) 7#, 15# (b) 9#, 17#

Fig.8 Strain contrast of model C and model D

## Summary

The front longitudinal wall with winged columns or not may influenced seismic capacity of total structure greatly. Under the same grade earthquake motion, the damage of with winged columns obviously lightly than normal.

From normal model shaking table test phenomenon and results analysis, the back longitudinal wall firstly failure, then the vertical load was bear by other walls, finally the whole building collapsed due to exceeded limit bearing capacity.

Considering with winged columns in front longitudinal wall may provide stiffness, what can balance earthquake inertial forces come from other walls. So, the idea of balancing stiffness between front and back longitudinal walls and increasing the ductility of back longitudinal wall may be a good retrofitting method for bottom-business multi-story masonry buildings.

## Acknowledgements

This work was financially supported by the Doctoral Fund of Liaoning Earthquake Administration (L NDZBSJJ002) and Ministry of Science and Technology (2012A04).

## References

[1] “Seismic Code for Buildings (GB 50011-2010)”, China Architecture Press, Beijing, 2010.

*Applied Mechanics and Materials Vols. 580-583 (2014) pp 1467-1470*
*© (2014) Trans Tech Publications, Switzerland*
*doi:10.4028/www.scientific.net/AMM.580-583.1467*

# Shaking Table Test of Reinforced Concrete Frame-wall Model

Hao Zhang[1, a], Bing Li[1,b], Xu Li[2,c] and Debin Wang[3,d]

[1] School of Civil Engineering, Shenyang Jianzhu University, Shenyang 110168, China

[2] Faculty of Infrastructure Engineering, Dalian University of Technology, Dalian 116024, China

[3] School of Civil and Safety Engineering, Dalian Jiaotong University, Dalian 116028, China

[a]hzhang_sjzu@hotmail.com, [b]Cebli@sjzu.edu.cn, [c]lx3818262@163.com, [d]wdb1215@163.com

**Keywords:** RC frame-wall, Shaking table, Dynamic characteristics，Seismic responses, Strain rate

**Abstract.** A 1/5 scaled three-story RC (reinforced concrete) frame-wall model was modeled in microconcrete and fine wire and carried out on the shaking table. The main objective of this paper aimed to investigate the dynamic characteristics, the seismic responses, and the failure mechanisms of the model, also concentrated on the strain rate of concrete on structural members under seismic action. Based on the test results, some significant conclusions are obtained for engineering practice.

## Introduction

The Shaking table test plays an important role in earthquake-resistant design, seismic response analysis and failure mechanisms of structures, and it is capable of reproducing the whole process of earthquake response by various seismic waves [1-2]. Hence, it is important to understand the overall straructural behavior under earthquakes. In this article, a 1/5 scaled RC frame-wall model shaking table test was carried out.

## Description of the model

The model was made of microconcrete and fine wires as shown in Fig.1. The main parameters of the model are illustrated in Fig. 2 and Fig. 3. The total height of the model is 1.98m. The material properties of microconcrete were tested with 18 specimens which were 70mm×70mm×70mm with the mean ultimate compressive strength of 8.41Mpa. The main reinforcing steel in columns and beams were 3mm fine wires. The 0.9mm fine wires were adopted for stirrups in the beams and columns. The 2mm fine wire mesh was used as the reinforcement in two orthogonal directions in walls and slabs.

## Similitude relationship

Generally, in order to make sure that the model behaves the similar dynamic properties to prototype, The model design should according to dynamic similitude theory [3-4]. Based on the capacity and size limit of the shaking table, the main similitude relationships are shown in Tab. 1.

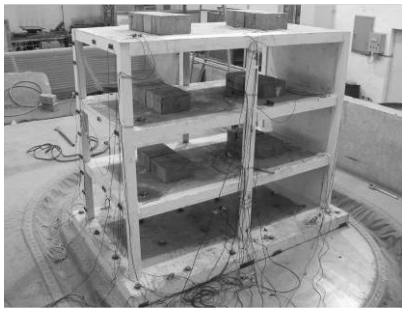

Fig. 1 Test model on shaking table.

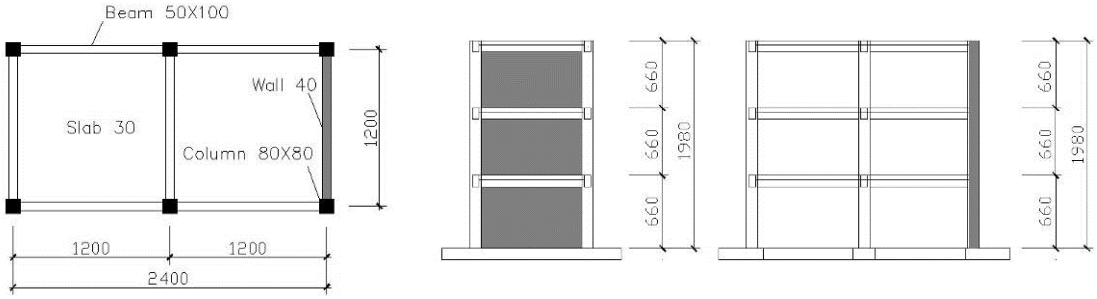


Fig. 2 Parameters of the test model

Tab. 1 Similitude relationship of the model

| Physical quantity | Similarity relationship | Coefficient |
|---|---|---|
| Length | $l_r$ | 0.2 |
| Elastic modulus | $E_r$ | 0.25 |
| Equivalent density | $\overline{\rho_r} = \frac{m_m + m_a + m_{om}}{l_r^3 (m_p + m_{op})}$ | 1.26 |
| Stress | $\sigma_r = E_r$ | 0.25 |
| Deflection | $r_r = l_r$ | 0.2 |
| Time | $t_r = l_r / \sqrt{E_r / \overline{\rho_r}}$ | 0.447 |
| Velocity | $v_r = \sqrt{E_r / \overline{\rho_r}}$ | 0.44 |
| Acceleration | $a_r = E_r / (l_r \overline{\rho_r})$ | 1 |
| Frequency | $\omega_r = \sqrt{E_r / \rho_r} / l_r$ | 2.237 |

**Ground motion input and instruments**

The typical ground motion El Centro wave (N-S component and vertical component) was selected, that the maximum accelerations were 341.7cm/s$^2$ and 206.3cm/s$^2$. The time interval of the records was compressed according to Tab. 1. The target input peak ground accelerations (PGA) of horizontal direction are illustrated in Tab. 2, and the target input peak value of vertical direction was compressed according to the real ratio of the ground motion.

Tab. 2 Test program

| Test No. | Input PGA of x direction (g) | Direction |
|---|---|---|
| WN-1 | 0.05 | x |
| EC-1 | 0.16 | x/z |
| EC-2 | 0.24 | x/z |
| EC-3 | 0.33 | x/z |
| EC-4 | 0.40 | x/z |
| EC-5 | 0.45 | x/z |
| EC-6 | 0.50 | x/z |
| EC-7 | 0.54 | x/z |
| EC-8 | 0.58 | x/z |
| EC-9 | 0.60 | x/z |
| EC-10 | 0.66 | x/z |
| EC-11 | 0.70 | x/z |
| EC-12 | 0.73 | x/z |
| EC-13 | 0.86 | x/z |

Note: WN and EC denote White noise and El Centro records, respectively.

Furthermore, the instrumentation is installed so that overall and local responses of the model could be measured, like accelerations measured by accelerometers, displacements measured by LVDTs and strain rate measured by fiber bragg grating strain sensor.

## Test results

The effective frequencies and damping ratio were obtained from the test as shown in Fig. 3 and Fig. 4. The frequency decreases and damping increases when the model damage progresses. Cracks were found on the column and at the end of the beam of the second story after the EC-3 (PGA=0.33g). The previous cracks spread and new cracks were occurred on other beams and columns after the EC-6 (PGA=0.5g). Finally, some connections of beam and column were almost completely damage, the crushing of microconcrete and buckling of fine wire were observed after the test.

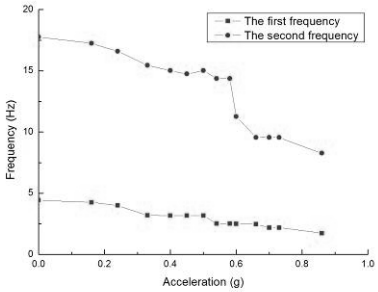


Fig. 3 Effective frequencies

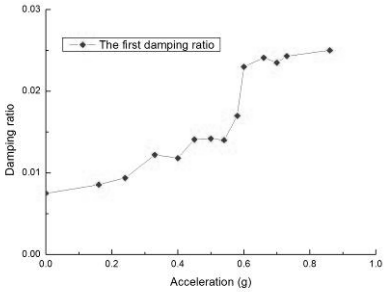


Fig. 4 Damping ratio

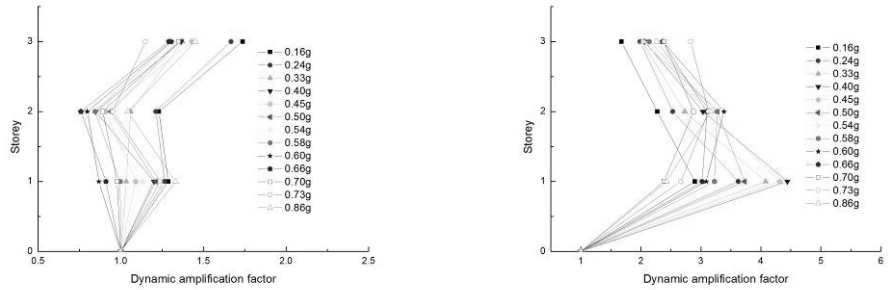


(a) Horizontal direction (b) Vertical direction

Fig. 5 Dynamic amplification factors of stories

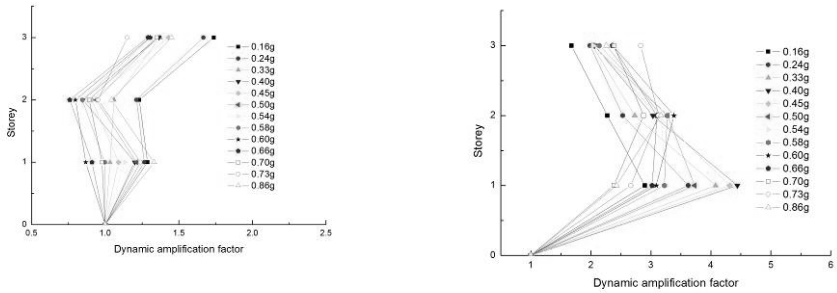


(a) Horizontal direction (b) Vertical direction

Fig. 6 Maximum displacement of stories

The horizontal and vertical dynamic amplification factors of stories can be observed in Fig. 5. The maximum displacement of stories can be observed in Fig. 6. It was observed that the dynamic amplification factor of stories decreases when the input acceleration increases, the maximum values

of the horizontal and vertical direction are 1.74 and 4.44, which were located on the top and the first floor, respectively. In other hand, the maximum displacement of stories increases when the input acceleration increases. The maximum strain rate of concrete on structural members of the test model can be observed in Tab. 4.5. The strain rate of concrete increases with the increasing input peak value. The range of strain rate of concrete on beams and columns are $2.0\times10^{-3}$/s to $2.7\times10^{-2}$/s and $6.5\times10^{-3}$/s to $6.8\times10^{-2}$/s under moderate to extrem earthquake action.

Tab. 3 Maximum strain rate of concrete on structural members

| Input PGA of principal direction (g) | Story | Maximum strain rate of concrete on beams ($s^{-1}$) | Maximum strain rate of concrete on columns ($s^{-1}$) |
|---|---|---|---|
| 0.16 | 1 | $2.0\times10^{-3}$ | $1.7\times10^{-2}$ |
| | 2 | $3.2\times10^{-3}$ | $6.9\times10^{-3}$ |
| | 3 | $3.5\times10^{-3}$ | $6.5\times10^{-3}$ |
| 0.40 | 1 | $2.8\times10^{-3}$ | $3.0\times10^{-2}$ |
| | 2 | $6.6\times10^{-3}$ | $1.2\times10^{-2}$ |
| | 3 | $6.8\times10^{-3}$ | $1.7\times10^{-2}$ |
| 0.60 | 1 | $6.1\times10^{-3}$ | $5.1\times10^{-2}$ |
| | 2 | $1.7\times10^{-2}$ | $1.2\times10^{-2}$ |
| | 3 | $8.2\times10^{-3}$ | $2.6\times10^{-2}$ |
| 0.70 | 1 | $9.6\times10^{-3}$ | $5.8\times10^{-2}$ |
| | 2 | $2.7\times10^{-2}$ | $1.5\times10^{-2}$ |
| | 3 | $1.0\times10^{-2}$ | $3.5\times10^{-2}$ |
| 0.86 | 1 | $9.0\times10^{-3}$ | $6.8\times10^{-2}$ |
| | 2 | $2.5\times10^{-2}$ | $1.5\times10^{-2}$ |
| | 3 | $1.9\times10^{-2}$ | $4.5\times10^{-2}$ |

## Conclusions

Based on the shaking table test results obtained, the following observations were drawn:

(1)The frequency decreases and damping increases when the model damage progresses. The dynamic amplification factor decreases and maximum displacement when the input acceleration increases.

(2) The strain rate of concrete increases with the increasing input acceleration. It was observed that the strain rate of concrete are $10^{-3}$ to $10^{-2}$/s under earthquake action.

## Acknowledgements

This work was financially supported by the National Natural Science Foundation of China (Grant No: 51308356) and Shenyang Municipal Science and Technology Program of China (Grant No: F13-158-9-00).

## References

[1] X. L. Lu, Y. Zhou, W. S. Lu, B. Zhao: Earthquake Engineering and Structural Dynamics. Vol. 36 (2007), p. 439.

[2] P. Martinelli, F. C. Filippou: Earthquake Engineering and Structural Dynamics. Vol. 38 (2009), p. 587.

[3] M. Zhang: Earthquake Engineering and Engineering Vibration. Vol. 7 (1997), p. 52.

[4] G. M. Sabnis, H. G. Harris, R. N. White, M. S. Mirza: *Structural Modeling and Experimental Techniques* (Prentice Hall, New Jersey 1983).

*Applied Mechanics and Materials Vols. 580-583 (2014) pp 1471-1476*
*© (2014) Trans Tech Publications, Switzerland*
*doi:10.4028/www.scientific.net/AMM.580-583.1471*

# Analysis on Self-centering Capacity of Prefabricated Frame Joints

Yun ZOU[1,a], Hui LIN[2,b], Wei-qiang MA[1,c]

[1]School of Environment Civil Engineering, Jiangnan University, Wuxi Jiangsu 214122, China;
[2]School of Civil Engineering, Tongji University, Shanghai 20092, China.

[a]zouyun@Jiangnan.edu.cn;[b]469404346@qq.com ;[c]mwqiang_95@163.com

**Keywords:** self-centering; prefabricated frame joints; finite-element analysis; seismic behavior

**Abstract:** In order to research the self-centering capacity of prefabricated frame joints, this paper designed analysis models of prefabricated frame joint with the finite element software ABAQUS, contrastively analyzed seismic behavior of joint applied pretention and joint without pretention. Joint applied pretention is found to have better self-centering capacity. Then the paper calculated and analyzed the factors of stretching control stress, number of post-tensioned steel. The results show that number of post-tensioned steel has a greater influence on the seismic behavior of the structure, and the stretching control stress has influence in a certain range. The results have some degree of guiding significance for the popularization of prefabricated frame.

## Introduction

The seismic performance of prefabricated structure largely depends on joint's construction[1]. Joints are divided into strong connection and ductile connection. Strong connection usually splices prefabricated component together in the way of cast-in-place and can achieve similar or equivalent strength with the cast-in-place structure. China, Japan and New Zealand mostly use strong connection. Self-centering prefabricated frame adopts ductile connection. By reasonable node structure design, joint acquires well rotation capacity. And when earthquake happens, elasto plastic deformation of the structure is mainly concentrated in the joint, beam and column maintains elastic deformation, residual deformation is small because of self-centering capacity provided by post-tensioned steel's resilience, the structure is easy to repair after earthquake. This paper built one prefabricated frame joints with self-centering capacity and analyzed various influence factors of self-centering capacity and seismic behavior.

## Finite element analysis model

### The basic information about the model

According to current research achievements in China and overseas[2]-[6], adding prestressed tendon in prefabricated frame joint beam can improve self-centering capacity of joint and reduce residual deformation. This paper designed one self-centering prefabricated frame joint JD-1. Prefabricated components buried bellows in column and beam, weared 4 prestressed steel strands in it, stretched strand in post-tensioned method with tension stress of 1000Mpa then grouted the holes. Longitudinal reinforcement and stirrup also used connection method of reserving channel then grouting. Size and reinforcement of analysis model is shown in Fig 1.

## Material constitutive model

The concrete constitutive model uses a damage constitutive model of concrete in ABAQUS program which assumes that the destruction of concrete material is mainly for the cracking and crashing. Yield and damage evolution are controlled by stretching the equivalent plastic strain and compression of the equivalent plastic strain. At the same time, the model also has better convergence.

Longitudinal reinforcement and stirrup uses the ideal elastic-plastic model, poisson ratio of 0.3. The strength of steel will remain the same after steel in tension reaches the yield strength. The finite element model does not consider the bond-slip effect between steel and concrete.

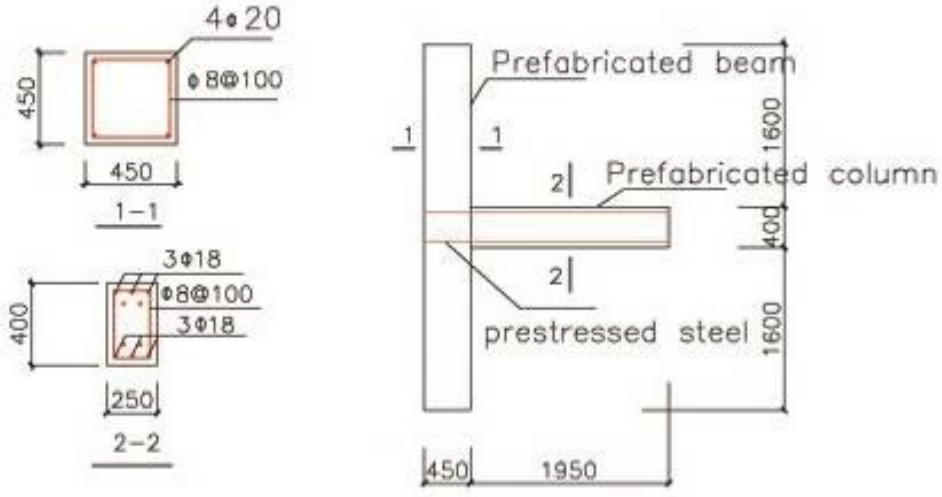


Fig 1 Size and reinforcement details of JD-1

**Boundary conditions and load mode**

Due to frame is statically indeterminate structure, the boundary condition of simulation is very important when study the performance of the beam-column joints. This paper referred to self-centering steel frame joint experiment in Tsinghua University, and adopted "Horizontal column vertical beam" in convenience. The model set hinge supports in both column ends to simulate inflection point of frame column and connected the supports to ground, applied bidirectional horizontal load to simulate seismic action at the top of beam which was seen as free end. The load mode is shown in Fig 2.

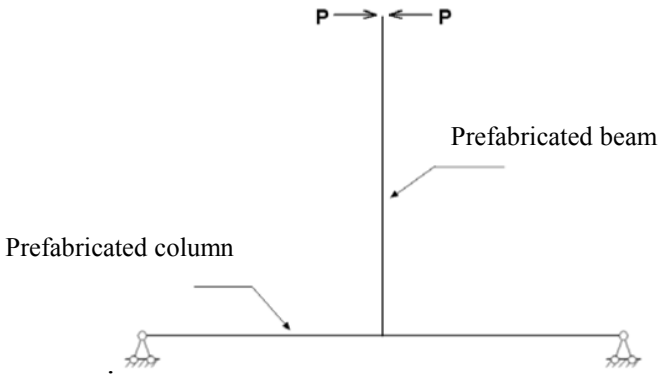


Fig 2 Loading diagram

**Finite element analysis model**

Take specimen JD-1 in the previous section as specimen BASE. Considering the structure's significant influence factors of the stretching control stress and number of post-tensioned steel, this paper designed 3 series of 7 prefabricated frame joints to analyze the influence on joint force property.

**Contrast analysis of joints with prestress and without prestress**

Based on specimen BASE, this paper designed a finite element model JD-BZL without prestress to study the influence of applying prestress on prefabricated frame joints mechanical property.

Specimens under monotonic loading load - displacement curve is shown in Fig 3. Specimens under cyclic loading hysteresis curve is shown in Fig 4, hysteretic loop is shown in Fig 5, skeleton curve is shown in Fig 6.

Fig 3 shows, specimen JD – BZL's initial stiffness and bearing capacity decreases obviously while the yield displacement is larger, specimen BASE's initial stiffness and bearing capacity is larger while the yield displacement is smaller. Fig 4 shows, specimen JD – BZL's self-centering capacity is significantly worse than specimen BASE during Several smaller loading cycle. Fig 5 shows, specimen JD – BZL's dissipation capacity is a little lower than BASE for without prestress. Fig 6 shows, skeleton curve of two specimen are close to load - displacement curve, and specimen JD - BZL stiffness decreases obviously.

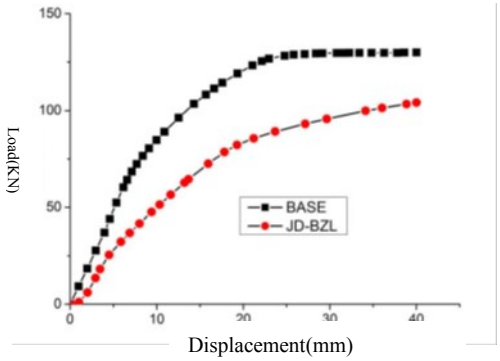


Fig 3 Load-displacement curves of BASE and JD-BZL

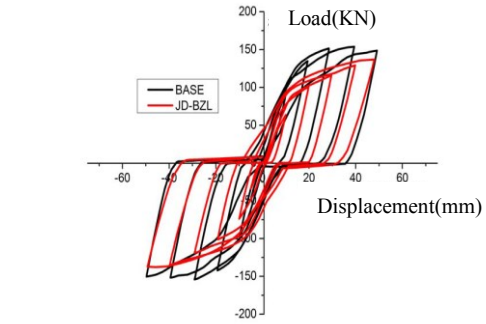


Fig 4 Hysteresis curves of BASE and JD-BZL

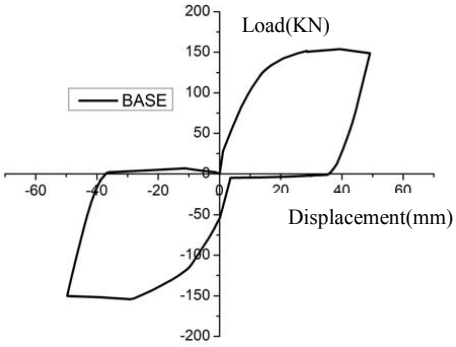


(a) Hysteretic loop of specimen BASE

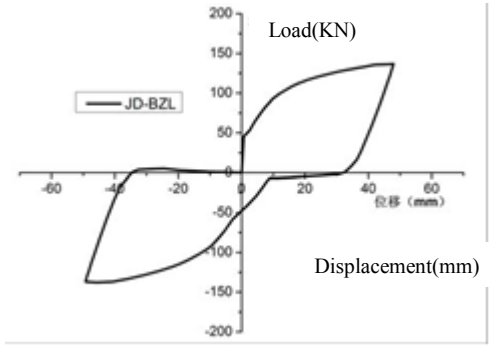


(b) Hysteretic loop of specimen JD-BZL

Fig 5 Hysteretic loops of BASE and JD-BZL

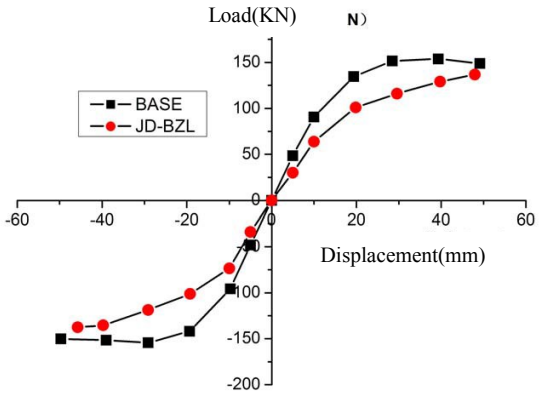


Fig 6 Skeleton curve of BASE and JD-BZL

It can be concluded from the former two chapters, increasing stretching control stress in a certain range can enhance self-centering capacity joint's ultimate strength, stiffness and elf-centering capacity, but it will not work when beyond the range.

**Stretching control stress on the influence of prefabricated frame joints force property**

Based on specimen BASE, this paper designed finite element models JD-1500 and JD-2000 to study the different stretching control stress caused prefabricated frame joints force property. Take specimen BASE as JD-1000 with stretching control stress 1000Mpa. The stretching control stress of specimen JD-1500 is 1500Mpa and the stretching control stress of specimen JD-2000 is 2000Mpa. Specimen under cyclic loading hysteresis curve is shown in Fig 7.

As can be seen in Fig 7, hysteresis curve tracks of three joints are in good agreement with each other except stiffness is slightly different when unloading. In addition, ultimate strength of three joints are mostly the same. This suggests that when stretching control stress came to 1000Mpa, ultimate strength of joint would not increase, and the stiffness and self-centering capacity would not change too much.

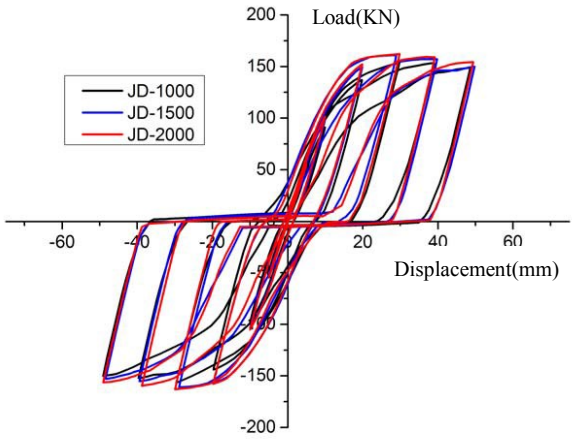


Fig 7 Hysteresis curves of specimens in different stretching control stress

**Number of prestressed steel on the influence of prefabricated frame joints force property**

Based on specimen BASE, this paper designed finite element models JD-2G and JD-6G to study the different number of prestressed steel caused prefabricated frame joints force property. Specimen BASE still had 4 prestressed steel strands, specimen JD-2G had 2 prestressed steel strands and specimen JD-6G had 6 prestressed steel strands. The stretching control stresses of 3 specimens are all 1000Mpa.Specimens under monotonic loading load-displacement curve is shown in Fig 8. Specimen under cyclic loading hysteresis curve is shown in Fig 9, hysteretic loop is shown in Fig 10, skeleton curve is shown in Fig 11.

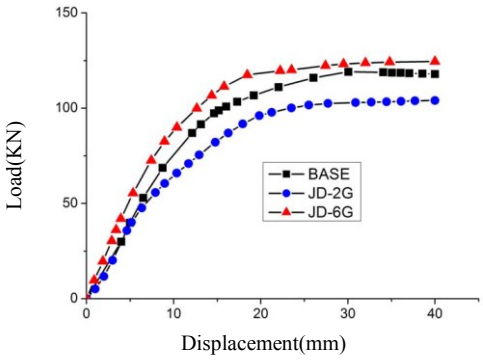


Fig 8 Load-displacement curves of specimens in different number of prestressed steel

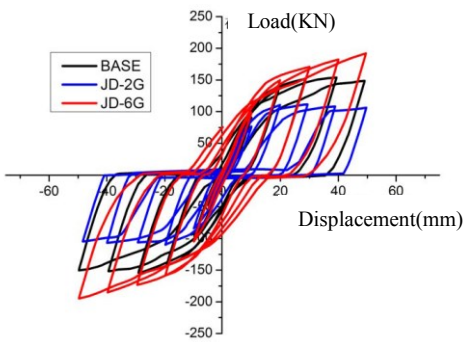


Fig 9 Hysteresis curves of specimens in different number of prestressed steel

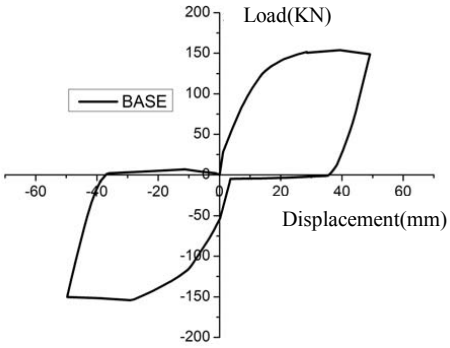


(a) Hysteretic loop of specimen BASE

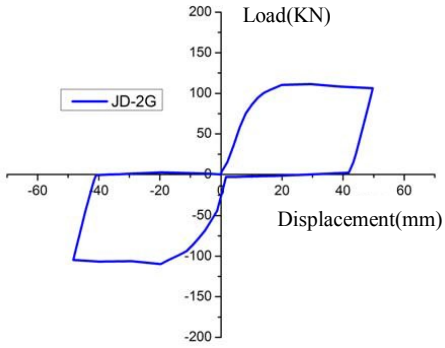


(b) Hysteretic loop of specimen JD-2G

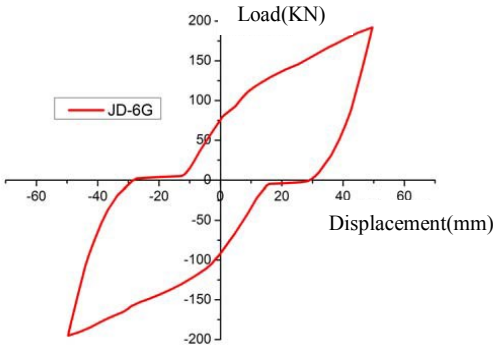


(c) Hysteretic loop of specimens JD-6G

Fig 10 Hysteretic loops of specimens in different number of prestressed steel

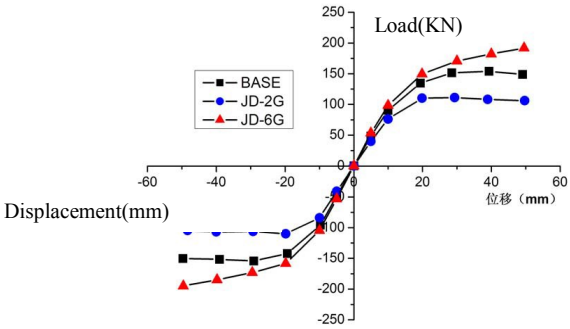


Fig 11 Skeleton curves of specimens in different number of prestressed steel

As can be seen in Fig 8 and Fig 9, specimen JD-2G's bearing capacity and self-centering capacity have a certain decline while JD-6G's have a certain increases. Initial stiffness of 3 joints has a little difference. Fig 10 shows, the number of prestressed steel has a great influence on joint's dissipation capacity, the more post-tensioned steel joint has, the better dissipation capacity joint obtains. Fig 11 shows, JD-2G's initial stiffness is less due to reducing prestressed steel and the joint enters yield phase earlier. JD-6G's initial stiffness is larger and skeleton curve trends slow.

## Conclusions

In this paper, non-linear finite element analysis on self-centering prefabricated frame joint with the finite element analysis software ABAQUS under static load and low-cycle reciprocating load, the main conclusions are as follows:

1) Stretching prestressed steel in prefabricated frame joint can enhance joint self-centering capacity, and increase joint strength and stiffness at the same time, but decrease joint yield displacement.

2) Increasing stretching control stress of self-centering prefabricated frame joint has a significant impact on joint force property. Increasing stretching control stress of joint in a certain range can enhance joint's strength, stiffness and elf-centering capacity, but it will not work when beyond the

range. Ensure that prestressed reinforcement keeps elastic working state in the whole process increasing stretching control stress.
3) With the number of post-tensioned steel in self-centering prefabricated frame joint increasing, self-centering capacity of joint obviously increases, and joint strength, stiffness and dissipation capacity increases at the same time.

**Acknowledgements**

This work was financially supported by National Natural Science Foundation of China through Grant 51378240.

**References**

[1]Weichen XUE: Research progress and application of precast concrete frame structure system[J](In Chinese). Industrial Building.2002,32(11):47-50.

[2]Lieping YE, Xuchuan LIN, Xunliu WANG: Self-centering performance and seismic performance of prestressed concrete structures[C](IN CHINESE)."Development of green technology, construction managing structure "academic of the 14th national conference on concrete and prestressed concrete.2007.

[3]Zhenhua PAN: Research on self-centering capacity of steel frame system[D](IN CHINESE). Tsinghua University.2010.

[4]Zhenhua PAN, Peng PAN, Lieping YE: Finite element simulation and parameter analysis on self-centering capacity of steel frame joint.[J](IN CHINESE). Journal of building structures.2011,32(3):35-42.

[5]Zhenhua PAN, Peng PAN, Fawei QIU: Research on self-centering capacity of steel frame system[J](IN CHINESE). China Civil Engineering Journal.2010, 1(43):403-410.

[6]Xiaoning CAI, Shaoping MENG, Weiwei SUN: Experimental research on self-centering frame side joint’s seismic performance[J](IN CHINESE).China Civil Engineering Journal. 2012, 45(12):29-37.

*Applied Mechanics and Materials Vols. 580-583 (2014) pp 1477-1480*
*© (2014) Trans Tech Publications, Switzerland*
*doi:10.4028/www.scientific.net/AMM.580-583.1477*

# The Effect of Damping on Seismic Performance of Steel Frame

Xinwu Wang [1,a] ,Changjiao Hu [2,b]

[1] Department of Civil Engineering, Luoyang Institute of Science and Technology, 471023, China

[2] School of Civil Engineering,Henan University of Science and Technology,471000, China

[a] wxw197100@sina.com,[b]1246686577@qq.com

**Keywords:**Damping, Steel frame,Seismic performance

**Abstract.**To study the effect of damping on seismic performance of steel frame, using the pseudo dynamic test by inputting damping and no damping to analyze the seismic performance of semi-rigid steel frame. Analysis was focused on the effect of damping on the panel zone strain, story drift and interlayer force.The conclusion was that under the more severe earthquake, the structural damping had effects on the seismic performance of semi-rigid steel frame.

## Intruduction

Damping was a kind of features during free vibration which was due to external influence or structural effect that decreased amplitude of structure and was one of the important characteristics that formed the seismic performance of structure.In the process of the amplitude decreasing, vibration system dissipated energy through different mechanisms of action.When researchers analyzed the seismic performance of steel frame, they often idealized the damping through setting linear viscous dampers or shock absorber in the steel frame that could't reflect the real implication of the damping to the structure.Calculating the damping coefficient of the semi-rigid steel frame and inputting damping value and undamped in the pseudo dynamic test, the variations about displacements ,strains and loads for the semi-rigid steel frame were analyzed. It was concluded that under the more severe earthquake, the structural damping had effects on the seismic performance of steel frame with semi-rigid connection..

## The Calculation Formulas of Structural Damping Coefficient [1,2]

In structural dynamic analysis, through the reasonable selection of damping coefficient, the energy that the mechanism of action dissipated and the energy dissipation by vibration were equal.Before the calculation of damping coefficient, it was necessary to determine the damping ratio that was the ratio of damping coefficient and critical damping coefficient.Viscous damping model was adopted in the practical engineering, and the damping ratio was defined as a constant.The paper employed 0.02 as the damping ratio of steel frame. The Rayleigh damping coefficient method was used to calculate the damping coefficient.

Damping matrix was calculated according to Eq. 1:

$$[C]=\tau_M[M]+\tau_K[K]. \quad (1)$$

$$\tau_M=2(\lambda_i\omega_j-\lambda_j\omega_i)\omega_i\omega_j/(\omega_j-\omega_i)(\omega_j+\omega_i). \quad (2)$$

$$\tau K=2(\lambda i\omega j-\lambda j\omega i)/(\omega j-\omega i)(\omega j+\omega i). \quad (3)$$

In which[C],[M],[K]were mass matrix,damping matrix, stiffness matrix of the structure respectively;$\omega_i$,$\omega_j$ were the circular frequency of vibration mode i,j respectively;$\lambda_i$,$\lambda_j$ were damping ratio of modal i,j respectively, $\lambda_i = \lambda_j = 0.02$.

Circular frequency were solved according to the structural dynamic Eq. 4:

$$[M]\{\ddot{u}\}+[C]\{\dot{u}\}+[K]\{u\}=[M]\{\ddot{u}g\}. \quad (4)$$

Assuming $u_1=\varphi_1\sin(\omega t+\theta)$; $u_2=\varphi_2\sin(\omega t+\theta)$. (5)

Inputting Eq. 5 into homogeneous equation,then got Eq. 6, Eq. 7:

$$-m_1\omega^2\varphi_1+(k_1+k_2)\varphi_1-k_2\varphi_2=0. \quad (6)$$

$$-m_2\omega^2\varphi_2-k_2\varphi_1+k_2\varphi_2=0. \quad (7)$$

$\omega_i$,$\omega_j$ were solved.

Substituting circular frequency $\omega_i$, $\omega_j$ and 0.02 damping ratio Eq. 2 and Eq. 3,$\tau_M$ and$\tau_N$ were solved.Then put them in Eq. 1 to get [C].

## Pseudo-dynamic Test

**Experiment.** The pseudo dynamic test of semi-rigid steel frame (as shown in Fig. 1)which had a scale ratio of 1:2 with two layers, single span and studio was carried out. The steel frame was designed according to the specifications for design of steel structures (GB 50017-2003)[3].The underlying height was 2.2 m, the top height was 2.0 m, span and studio were both 3.0 m.The steel used were Q235 steel, and beams ,columns and subdivision T steel were hot-rolled H steel.Fitting M16 and 10.9 high strength bolts to connect beams ,columns and T steel. The cross section sizes of specimen were followed:

Column:HW175mm×175mm×8mm×11mm;Beam:HW194mm×150mm×6mm×9mm;

T steel: HW500mm×200mm×10mm×16mm.

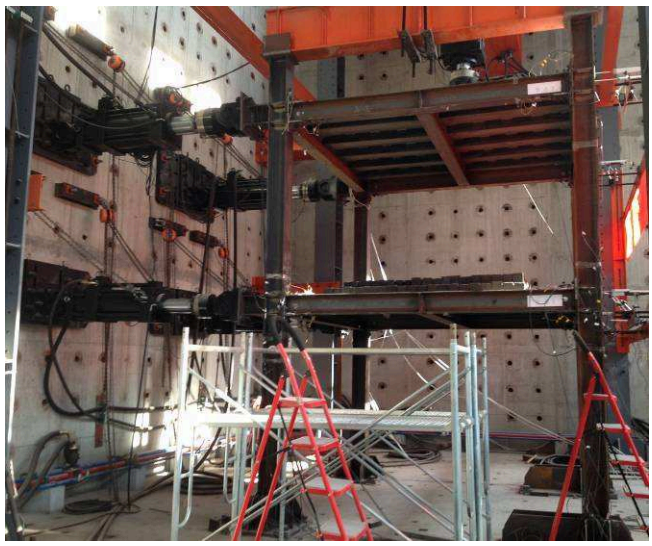

Fig. 1.Test site of steel frame with semi-rigid connection

**Test Procedure.** Literature [4] introduced the principle of pseudo-dynamic test.Test equipment included reaction wall, stents, the electro-hydraulic servo loading system and data acquisition system (DH-3816N static signal acquisition instrument).Test loading device equiped four horizontal actuators that two 100t horizontal actuators were at the top story and the underlying frame

decorated two 50t horizontal actuators. The seismic wave of test was EIcentro wave selected according to the "regulations of buildings seismic test method" (JGJ-96) and adopted 70 gal seismic acceleration peak value.Test used mixed load displacement control, and firstly to determine the stiffness matrix, mass matrix and damping matrix of steel frame,m1 = m2 = 5200 kg.Putting the stiffness matrix[K] and mass matrix[M] into the Eq. 1, got the damping matrix [C].Then the specimen was loaded by inputting the damping coefficient and without damping. Using static signal acquisition instrument and displacement meters to measure the panel zone strain and the node displacement and using force sensors and displacement sensors to get load feedback and displacement feedback of steel frame.

## The Analysis of Test Results

**Panel Zone Strain.**The time history curve of panel zone strain was shown in Fig. 2. (a), (b), (c), (d) diagrams respectively showed the strain at beam end flange, T steel web, the bottom of the column and T steel flange in the undamped and damped.It got that the undamped strain variation amplitude was slightly greater than the damped strain amplitude, but the difference was minor that the damping had little effect on the strain.

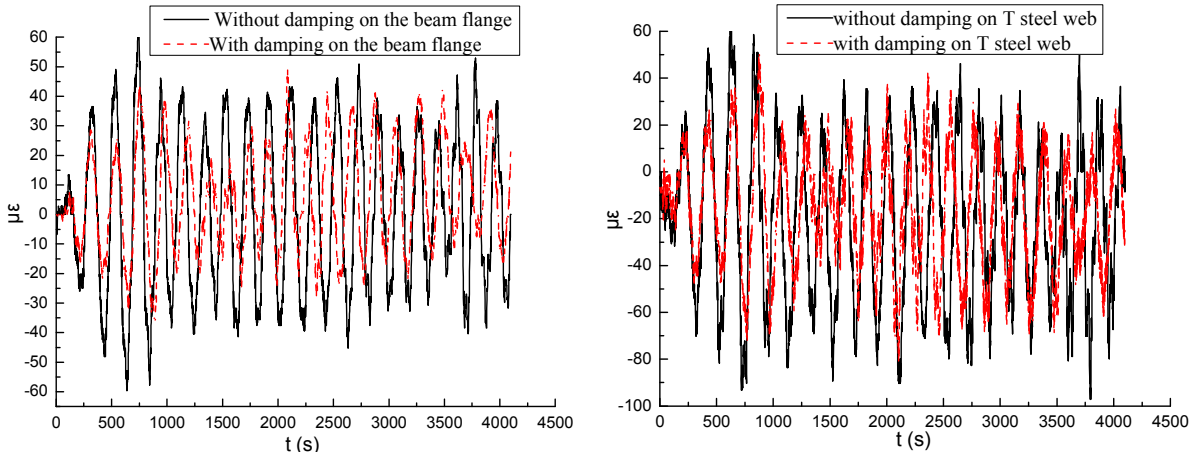


(a) Strain on the beam flange




(b) Strain on T steel web

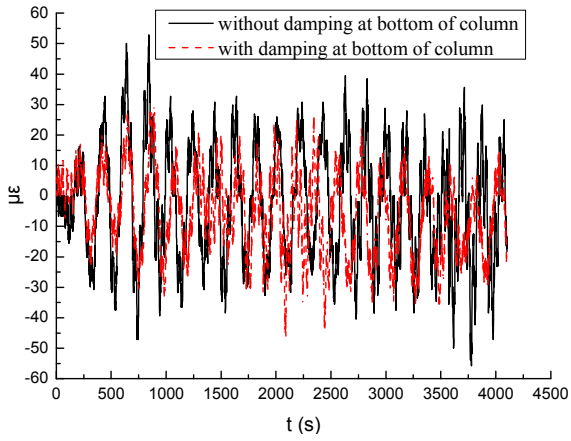


(c) Strain at the bottom of column

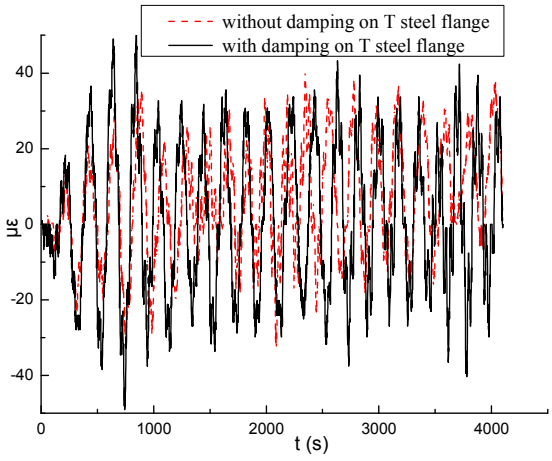


(d) Strain on T steel flange

Fig. 2 .Panel zone strain with and without damping

**Story Drift.**Time history curve of displacement was shown in Fig. 3.It showed that the the peak value of story drift undamped was greater than that with damping, and steel frame without damping had larger sidesway and the response amplitude was bigger.

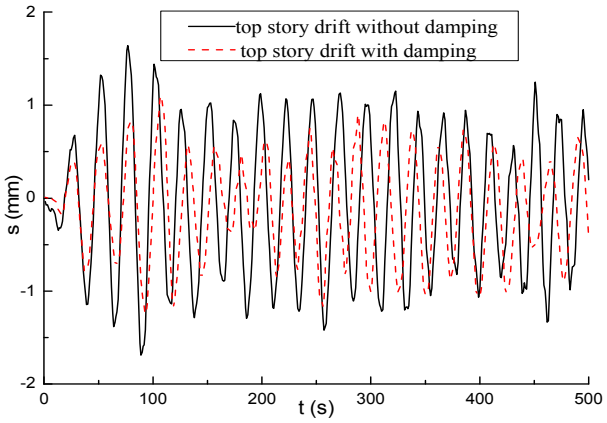


Fig. 3. Story drift

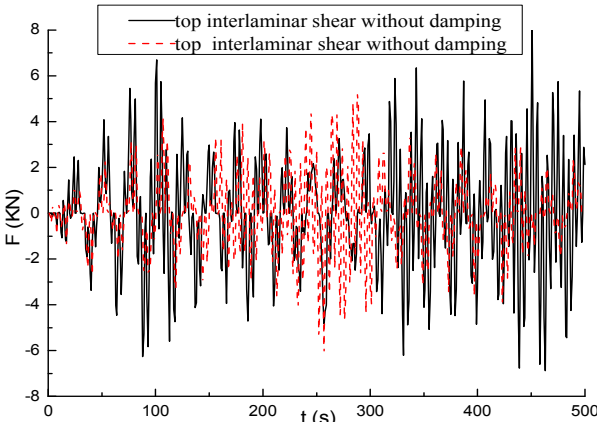


Fig. 4. Interlaminar shear

**Interlaminar Shear.**The time history curve of interlayer shear was shown in Fig. 4 that the load feedback peak of frame with damping was less than undamped frame which showed the maximum of interlayer shear decreased under the influence of damping .

## Conclusions

Through analyzing the test results, it concluded that:

(1) The structural damping had little effects on the strain ,but it had impact on the story drift and interlaminar shear which was in keeping with literature [5].

(2)It also showed that the displacement of steel frame under dynamic loading not necessarily decreased as the stiffness of nodes increasing, and the factors included damping.

(3)Under the effect of damping, the story drift and interlaminar shear peak of the semi-rigid connection steel frame decreased which was contributed to the structural seismic.

## Acknowledgement

The experiment was carried out by the Science and Technology Research Project of Henan Province (Project No.122102210550) in the structure lab of Luoyang Institute of Science and Technology .

## Reference

[1]Yu Chen, Shimin Dong, Liping Li.The introduction for pseudo-dynamic test method in the regulation of seismic test method. Building science.In Chinese(1995)

[2]Shizhu Tian, Tong Zhao. Research on seismic pseudo-dynamic test.Earthquake engineering. In Chinese (2001)

[3]GB50017-2003.Steel Structure Design Specification[S].Beijing:China Building Industry Press. In Chinese (2003)

[4]Fawei Qiu,Jia-ru Qian,Zhipeng Chen.The Structural Seismic Experimental Methods [M]. Beijing: Science Press. In Chinese (2000),P:119-127

[5]Peng Yu.The effect of P-Δ and damping on the dynamic behavior of steel frame with semi-rigid connection.Master degree paper of Guangdong university of technology. In Chinese (2011)

*Applied Mechanics and Materials Vols. 580-583 (2014) pp 1481-1485*
*© (2014) Trans Tech Publications, Switzerland*
*doi:10.4028/www.scientific.net/AMM.580-583.1481*

# The Influence Analysis of Mechanical Behavior between Pile and Soil on End Bearing Pile Foundation's Dynamic Characteristic

Wei Hu[1,a], Yahui Zhang[1,b],Ying Zhang[1,c]

[1] School of Civil Engineering and Architecture, Hainan University, Renmin Road 58#, Hai kou, Hainan, P.R. China 570228

[a] yilukuangben1982@163.com, [b] junhui901125@qq.com, [c] 527738149@qq.com

**Keywords:** end bearing pile; finite-infinite element; dynamic interaction; interface's mechanical behavior

**Abstract:** Dynamic structural model of saturated soil was introduced, and combining with the finite element program, the finite-infinite element models of end bearing pile foundations was established. Four models of interface between pile and soil including absolutely jointed, slippage, crack, both slippage and crack were considered to study the interface's effect on pile foundation's dynamic characteristics. The results were as follows: the interface's mechanical behavior has a little influence on the distributions of pile section's shearing stress and horizontal displacement. Pile section's shearing stress reaches the maximum near the ground surface when interface is slippage or crack, and reaches the minimum ones when interface is absolutely jointed. Horizontal displacement could be divided into two phases and the ground surface is the dividing line. The interface's behavior greatly changes the distribution of acceleration time-history curve. To different models, the maximum acceleration all appears at the ground surface. On the whole, the interface's behavior has significant influence on end bearing pile, which should be pay attention in the design from now on.

## Introduction

In pile-soil-structure system, for the big difference of material properties between pile and soil on two sides of interface, the deformation and displacement of pile and soil are usually not coordinate with each other. The property of interface has great influence on the dynamic characteristics of pile-soil-structure system under earthquake. However, most of researches are based on the hypothesis of absolutely jointed between pile and soil, or only slippage and no crack. These researches have some extent reasonable for system under small earthquake, but the reaction of system is no longer in elastic stage under moderate and strong earthquakes. The reaction of free field and the interaction of interface will generate permanent deformation in soil, with the inconsistency of movement between pile and the surrounding soil, and the lower tensile strength of soil itself, crack will appear in the normal direction between pile and soil besides the slippage along the tangent direction. In fact, the phenomena of separation between pile and soil, pile sinking or uplifting are very common in earthquake. In addition, the mechanical mechanisms of these two kinds of phenomena are interactional itself. Crack occurred in shallow place will significantly decrease the later resistance of pile and will has adverse effect on vertical bearing capacity of pile when crack occurs in the depths. Both cases will trigger greater slippage of interface, which will affect the extent of crack with dissipating energy at the same time.

On the base of dynamic structural model of saturated soil, finite-infinite element model of single end bearing pile foundation was established in this paper, and to investigate the influence of slippage and crack mechanism between pile and soil on the pile foundation's dynamic characteristics. Four types of interface models will be considered, and the law of influence will also be summarized based on the comparison of the results at last.

**Dynamic structural model of saturated loess**

To consider the structure of saturated loess, the dynamic model that had been put forward by Hu, W.(2008) will be used in this paper. the basic constructed steps of which are as follows: on the base of stain hardening stress-stain relationship of completely remolded loess, the degradation of initial shearing modulus and un-drained strength, which consider the effects of supper pore pressure and the structure's changing, are used to model the cyclic degradation of saturated loess under dynamic loading; The stress share ratio is introduced to describe the structure, and the dynamic model of saturated loess which consider the structure is constituted at last. The physical meanings of other parameters are also presented in Hu, W.(2008). On the base of ABAQUS' redevelopment platform, the structural dynamic model of saturated loess is implemented by Fortran language, e.g., Hibbitt et al.(2002), Xu, Y. J. et al.(2004).

**The finite-infinite element models and estimation of parameters**

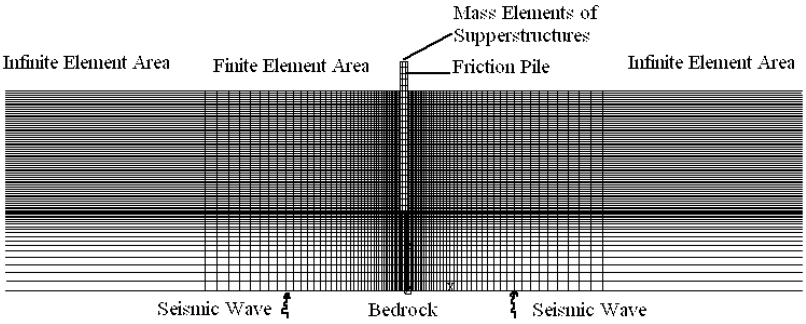


Fig.1 The finite-infinite element model of pile-soil-structure system

The prototype of pile-soil-structure's finite-infinite model is a single column pier which is always used in viaduct. The typical finite-infinite element model of friction pile-soil-structure system is showed in Fig.1. Where the pile is concrete bored pile or manual excavation pile and is treated as elastic, where $E = 20GPa$, $\nu = 0.25$, $\rho = 2.3g/cm^3$. The value of parameters in dynamic model of saturated loess are as follows: $\beta = 1.0$, $\nu = 0.45$, $\phi = 25$, $c = 13kPa$, $c_c = 0.1638$, $c_s = 0.0234$, $K_0 = 1.0$, $K_p = 174.49$, $n_p = 0.9626$, $k_{urp} = 1.6$, $\mu = 2.0$, $H = 0.925$, $\chi = 23.1$, $t = 2.06$, $\Lambda_0 = 0.634$, $\zeta_{\max} = 0.8$, $e_{i\max} = 1\%$, $e_{iult} = 10\%$, $a = -0.4343$, $b = -1$, $\gamma_{sat} = 19.6kN/m^3$, void ratio $e = 1.0$. Pile's length is 30m and the thickness of soil is 50m. The area within a distance of 100m from pile's two sides is finite element region, the outside area is infinite one. The supper-structure is predigested as mass element on the top of pile. In this analysis, the total mass of supper-structure is 200t. The adjusted Koyna horizontal acceleration time-history is imported at bedrock, and the peak value is 100gal.

**Interface model between pile and soil**

The attribute of contact between pile and soil contains two parts [4], tangential effect and normal effect. The former obeys the Coulomb's law to simulate bond-slip between pile and soil, which is showed in Fig.2 and it's expression is as follows,

$$\tau_{crit} = \mu p \tag{1}$$

Where $\tau_{crit}$ is the critical shear stress, $\mu$ is the friction coefficient and $\mu = 0.5$ in this paper, $p$ is the normal contact pressure. The latter adopts exponential pressure-overclosure relationship to model the crack- closure mechanism. It means that when the clearance between pile and soil is large than $c_0$, $p$ is zero; once it's less than $c_0$, the interface begin to transfer pressure. In the calculation, $c_0$ is equal to 0.001m. Along with the diminishment of clearance, $p$ increases in exponential form.

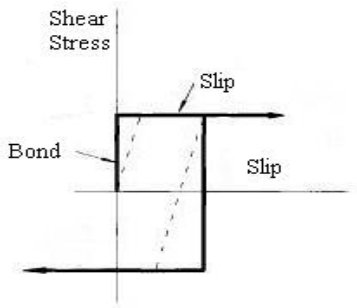


Fig.2 Bond-slip model

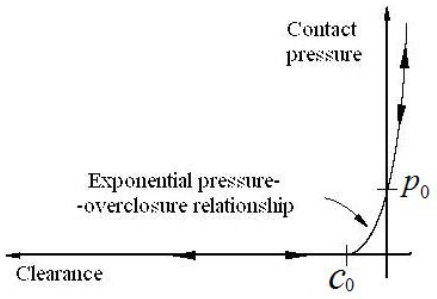


Fig.3 Crack-closure model

**The influence of interface model**

Figure 4 to 6 represent the absolute maximum of pile section's shear stress, horizontal acceleration and horizontal displacement along the depth respectively. Fig.4 shows that the interface's behavior has a little influence on the distributions of pile section's shear stress but has influence on it's value. Shear stress distributes as wavy style from the bottom to the up of pile, and reaches the maximum at ground surface, which reflects the traveling wave effect of earthquake. The reason of it is because of the different propagation velocity of earthquake wave in pile and soil, which gives rise to relative displacement between them, and results to varying pressure. When the interface is absolutely jointed, the pressure at ground surface reaches the minimum 108.6kPa, and for the model of slippage and crack, the pressure reaches the maximum 121.8kPa at the same place, which increases about 12.2%. The cases of only slippage and only crack are between the former two situations, whose value increases about 6.69% and 7.37% than the minimum respectively.

What we can see from the Fig.5 is that the interface's behavior greatly changes the distribution of end bearing pile's acceleration time-history curve. For different interface models, the maximum all appears at ground surface, the value of which is the biggest for absolutely jointed and is the smallest for slippage and crack. At the end of pile, acceleration has the minimum both for absolutely jointed and slippage only, but for the slippage and crack, it has the maximum. The reason may be that the separation between pile and soil cuts off the transfer path of horizontal load when considering crack.

Fig.6 shows that the interface's behavior has a little influence on both of the distribution and value of horizontal displacement. The distribution can be divided into two phases and the ground surface is the dividing line. In the first phase, displacement is almost in line increase with the depth from the bottom. The second phase presents nonlinear increase from the ground surface to the top, and reaches the maximum at the top of pile. The table 1 indicates that when the interface is both slippage and crack, horizontal displacement reaches the maximum and reaches the minimum when the interface is absolutely jointed, with the other cases are among them.

What the Fig.7 shows is the pile's horizontal acceleration time-history curve at -0.5m corresponding with different interface's behavior, which has a great influence on it's distribution learned from the picture. When the interface is absolutely jointed, the acceleration reaches the maximum and reaches the minimum when the interface is both slippage and crack, which is less 25% than the former. This is because of the pile passing through a discontinuity surface of stiffness, the strong constraint of the end is more likely to lead to the interface's relative displacement, which give rise to a big difference between the cases of both slippage and crack and absolutely jointed. Moreover, the interface's bond-slip also reduces the peak acceleration.

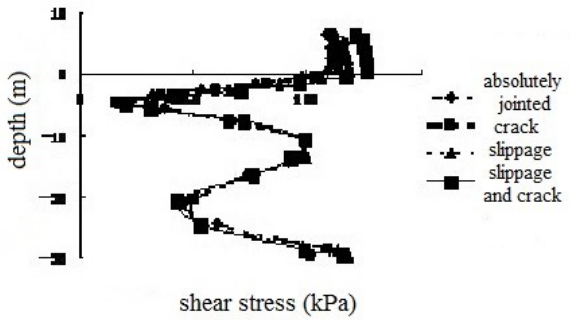


Fig.4 Distribution of shear stress

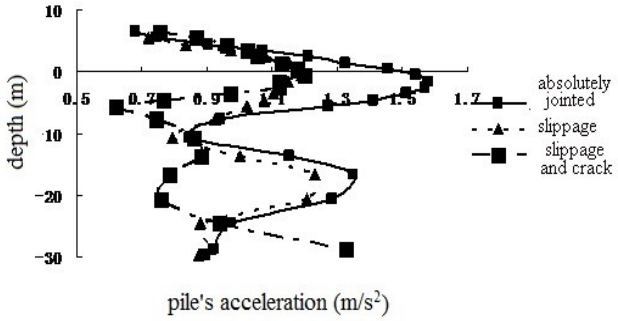


Fig.5 Distribution of horizontal acceleration

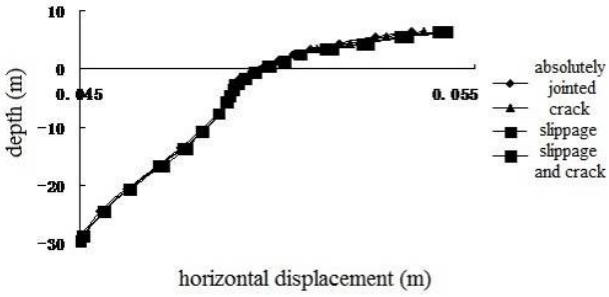


Fig.6 Distribution of horizontal displacement

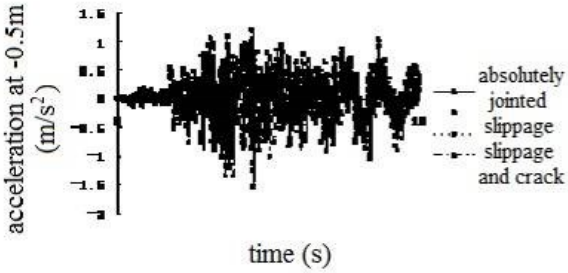


Fig.7 Time-history of horizontal acceleration

## Conclusion

Combining dynamic structural model of saturated soil with finite element program, the finite-infinite element models of end bearing foundations were established. Four situations of interface between pile and soil including absolutely jointed, slippage, crack, both slippage and crack were considered to study the interface's effect on pile foundation's dynamic characteristics. The results were as follows:

1 The interface's mechanical behavior has a little influence on the distribution of pile section's shear stress but has effect on it's value. Shear stress reaches the maximum when the interface is both slippage and crack and arrived at the minimum when the interface is absolutely jointed.

2 The interface's behavior greatly changes the distribution of end bearing pile's acceleration time-history curve. To different kinds of interface, pile's maximum acceleration arrives at the earth's surface, and reaches maximum when interface is absolutely jointed and reaches minimum when interface is both slippage and crack.

3 The interface's mechanical behavior has a little influence on the pile's horizontal displacement, which could be divided into two phases. In the first phase, displacement is almost a straight line up from the end of the pile to the earth's surface. In the second phase, displacement is in an accelerated nonlinear increase from the earth's surface to the top of the pile, and reaches maximum at the top. Horizontal displacement reaches maximum for both of slippage and crack, and reaches minimum for the absolutely jointed.

4 The interface's behavior has serious influence on end bearing pile's dynamic characteristic, which should be emphasized in the studies from now on.

**Acknowledgments**

The author sincerely acknowledges the financial supports from the "Twelve Five-Year" Plan key projects supported by National Science and Technology (No.2013BAK05B00), Hainan Provincial Natural Science Foundation Project (No.513144), and the Midwest Key Areas Construction Project Plan of Hainan University which made the present study possible.

**References**

[1] Hu Yujia, Cheng Changjun, Yang Xiao. Nonlinear Dynamical Characteristics of Piles Under Horizontal Vibration. Applied Mathematics and Mechnics, 26(6):645-652. (2005)

[2] Xian Xiaochun. Numerical Simulation of Soil-pile-structure's Dynamic Interaction under Earthquake. Da Lian, Dalian University of Technology. (2003)

[3] Chen Bo. Simulation and Analysis of Soil-pile foundation-Structure's Dynamic Interaction. Shang Hai, Tongji University. (2002)

[4] Tara Crystal Hutchinson. Characterization and evaluation of the seismic performance of pile-supported bridge structures. California, The University of California. (2001)

[5] Hibbitt, Karlsson, Sorensen. Inc. ABAQUS/Standard User's Manual; ABAQUS/CAE User's Manual; ABAQUS Keywords Manual; ABAQUS QUS Theory Manual. American: HKS Company. (2002)

[6] Wang Jinchang, Chen Yekai. ABAQUS'Application in Civil Engineering. Han Zhou, Zhe Jiang University Press. (2006)

[7] Zhang Zhuo, Zhang Fan, Cen Song. ABAQUS Non-linear Finite Element Analysis and Examples. Bei Jing, Science Press. (2005)

[8] Hu Wei. Saturated Loess'Dynamic Model and It's Application to the dynamic interaction of pile-soil-structure system under earthquake. Xi'an University of Architecture and Technology. (2008)

[9] Zhu Xiang-rong, Wang Jin-chang. Introduction to partly soil models in ABAQUS software and their application to the geotechnical engineering. Rock and Soil Mechanics, 25(Supp.2):144-148. (2004)

[10] Xu Yuan-jie, Wang Guan-qi, Li Jian, Tang Bi-hua. Development and implementation of Duncan-Chang constitutive model in ABAQUS. Rock and Soil Mechanics, 25(7):1032-1036. (2004)

*Applied Mechanics and Materials Vols. 580-583 (2014) pp 1486-1489*
*© (2014) Trans Tech Publications, Switzerland*
*doi:10.4028/www.scientific.net/AMM.580-583.1486*

# The Present Situation of Rural Housing and the Seismic Performance Analysis

Han Li[1, a]

[1] Graduate School of Shandong University of Science and Technology, Qingdao, Shandong, China 266590

[a]309083602@qq.com

**Keywords:** security, masonry structure, dangerous point, typical masonry building, seismic time history analysis, system with ring beam and structural concrete column

**Abstrat.** In recent years, the security of rural building has attracted more and more attention. The analysis of the existing problems of rural building summarized the distribution of dangerous points, and the use of finite element analysis method was carried out on the typical farmhouse seismic time history analysis to find out seismic weak places in the masonry structure buildings. Then the study also shows that the system with ring beam and structural concrete column has good reinforcement effect. This study plays an important role in improving the rural housing construction measures and the seismic performance of the building.

## Introduction

In recent years, many earthquakes had taken place in China, and only in 2013, there had happened 23 times that over 5.0 magnitude. The sudden earthquake brought huge economic losses and casualties to the state and local residents. By the analysis, the heavy casualties and losses were mainly caused by the unreasonable details of seismic design. According to preliminary statistic[1], the applicable masonry buildings account for more than 90% in residential buildings, especially in the villages, because of the structures' convenient materials, simple construction and low cost, it become one of the most common structures. Restricted by economic and technical conditions, the rural buildings prone to damage than urban housing. So the seismic analysis of the existing rural housing has very importance practical significance.

Our purpose is aimed at analyzing and summarizing the existing problems of rural buildings in the earthquake, and finding out the dangerous points, then on the basis of the theory of finite element analysis, selecting a typical rural resident structure system for numerical analysis to observe the rural housings' damage that under different details of seismic design. But because there is currently no special rules for the constitutive relations and failure criteria of masonry structure, to a certain extent the accuracy of finite element analysis is limited.

## The present situation of Rural housing

First of all, the rural housings mostly use local materials which their strength is low and lack of cohesiveness, so the integrity of walls is poor, and leads to the structures prone to overall damage or severe local failure in the earthquake. Second, most rural masonry buildings built in before 1989[2], their construction mostly rely on experience and lack of earthquake consciousness, the buildings generally do not set ring beams and structural concrete columns, and most directly to put walls as bearing structures, the lap length of roofs, roof panels, purlins and walls is insufficient, nodes anchoring unreliable, the contact area between structures is small, roofs and roof panels are easy to damage during earthquake and cause casualties. Third, most rural housings' design according to owner's requirements, so the rate of hole is high and leads to the insuffient bearing capacity of walls. Finally, the connection between vertical and horizontal wall is unreliable, it leads to the poor integrity of walls, so it is also one of the main causes of walls that easy to damage.

**The finite element analysis**

**The masonry building plan.** ANSYS has a powerful modeling and solving ability, the ways of modeling are divided into integral and separated ways, our main purpose of modeling is to analyze the damage of integral building and focus on the macro calculation, so we choose integral modeling. Here we do numerical simulation on a typical farmhouse. The farmhouse prototype is shown in fig.1, for the convenience of modeling, we have to simplify the model, main structure dimensions are shown in fig.2.

**Fig.1** Farmhouse prototype

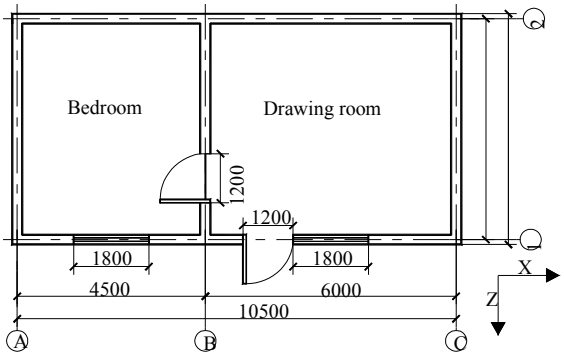


**Fig.2** The masonry building plan

**Finite element models for the masonry buildings.** Because the majority materials of rural house roof are sintering tiles, soils, plant straw, etc., their load through beam purlins pass to the wooden structures, finally to load bearing walls, roof stiffness is smaller than wall rigidity, so in this article, the roof load and purlin load by MASS21 convered on the corresponding position of walls. The self-weight of roof is 2.4kN/m2, structural concrete columns and ring beams are in accordance with the structural requirements for reinforcement, They are reinforced with HRB335, the wall with fired common brick, mortar with M7.5, concrete with C25, modulus of elasticity with 2.7×103MPa, Poisson's ratio with 0.15

The constitutive relation about Masonry structure is not yet clear, and because the masonry compression yield strength is greater than tensile yield strength, so the yield criterion of modeling by means of the criterion of Drucker-Prager[3], it is commonly used in soil mechanics , masonry is assumed to be the ideal elastic-plastic state. Modeling uses Solid45, it can reflect the model of stress and strain under seismic action, and the bottom of the structure is fixed, the finite element model is shown in fig.3.

**(a)** The original structure **(b)** The structure with reinforcement

**Fig.3** Two finite element models of the masonry

**Modal analysis.** By extracting the first 40 modal with the Block Lanczos [4] and analyzing the mode of model, we find that masonry structure maybe occur translation and torsion in the lower order diagram, so the masonry building in less absorption of seismic energy maybe occur vibration even damage, vibration is given priority to with torsion of the gables, then followed by the vertical translation of walls. And through the analysis we find that after setting up the structural measures the natural vibration period significantly improved. The original structure's cycle is 0.15s, and the reinforced structure's cycle is 0.2s. The curve of vibration periods are shown in fig.4 (series 1 from the original structure, series 2 from the structure with reinforcement).

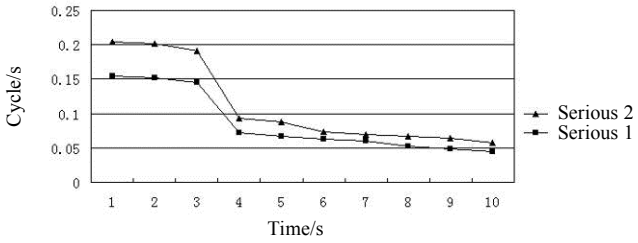


**Fig.4** Curve of vibration periods

**The seismic time history analysis.** In the time history analysis, we select the acceleration from EL-CENTRO earthquake as X, and select the top 20s acceleration, a total of 1000 points, time interval is 0.02s, peak acceleration occured in 3.14s, 3.417m/s2, the curve of acceleration is shown in fig5. According to the peak acceleration of frequent earthquake[5] in 8 degree, we adjust the peak acceleration from EL-CENTRO earthquake.

After constraint all nodes at the bottom of the structure, we get the absolute displacement. By observing the node of gable top, we find the node's displacement is reduced after reinforced. In the first case the maximal displacement is 24.3mm, but the latter is 17mm, so it proves that the structure of the constructional column and ring beam has limited the translational displacement. But while details of seismic design were taken, gable's displacement is still relatively large. Because gables alone connected with purlins, it equivalents to a cantilever structure and prones to whiplash effect[6]. It is visible that gable is still a weak link in seismic strengthening, so during the reinforcement of rural housing, it is necessary to set the annular ring beam on the gables. The curve of gable top displacement is shown in figure 6( series 1 from the original structure, series 2 from the structure with reinforcement ).

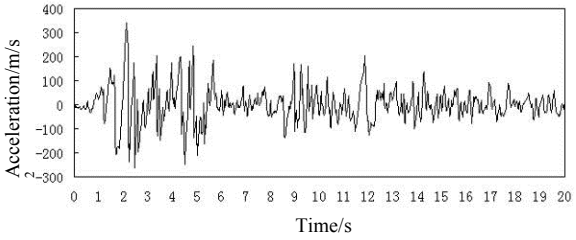


**Fig.5** Acceleration from EL-CENTRO earthquake

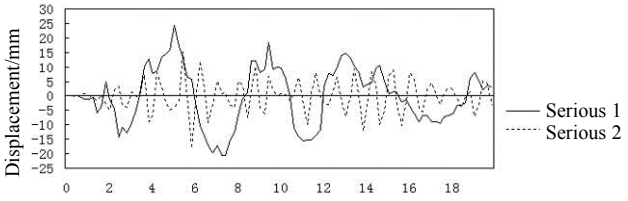


**Fig.6** The curve of gable top displacement

After the time history analysis, we found that under horizontal earthquake action the original structure's stress concentration phenomenon mainly exist in the bottom of the housing and the junction between vertical and horizontal walls. With the earthquake acceleration inputting, the overall stress value increases, in 0.02s, the maximum is $1.2\times10^{-3}$MPa,in 3.14s, the stress reaches 4.47MPa, and the lintel and wall stress value is large different from other places, these places are prone to damage and produce the v-shaped cracks. The damage location and form are as same as the actual seismic building damage locations, it verifies the feasibility of using finite element software simulation. After setting details of seismic design, the phenomenon of stress concentration are significantly reduced, and it mainly appears in the structural column and ring beam, it is visible that the system has good binding effect for masonry wall. The integral framework that they formed can limit the horizontal displacement of structure, enhances the integrity of masonry structure, reduces the appearance of cracks, and effectively makes up for the shortcoming of low wall shear strength. When an earthquake occurs, it can effectively reduce the damaging effect of the structure. However, there are stress concentration occur in structural columns and ring beam, this phenomenon indicates that

these place prone to damage during an earthquake, so it is necessary to strengthen the link between ring beams, structural columns and walls. The concrete nephogram of stesses are shown in fig.7.

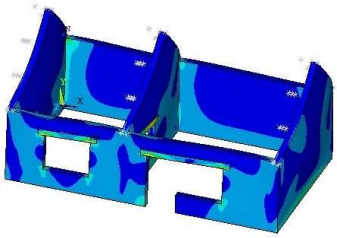

**(a)** The initial stress nephogram of original structure

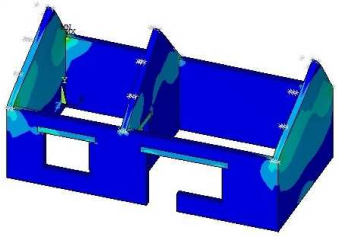

**(b)** The 3.14s stress nephogram of original structure

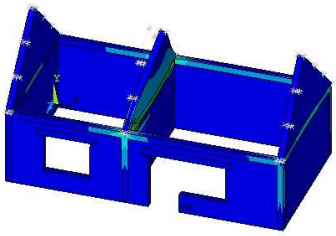

**(c)** The initial stress nephogram of the structure with reinforcement

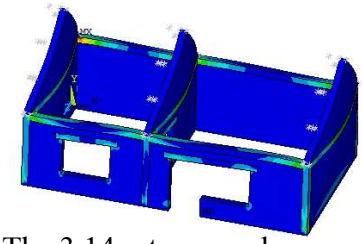

**(d)** The 3.14s stress nephogram of the structure with reinforcement

**Fig.7** The nephogram of stesses

## Conclusion

1)Rural masonry structure houses are destroyed mainly due to the low strength of materials, insufficient bearing capacity of walls, weak connection between the components, and unreliable connection between vertical and horizontal walls, those problems lead to poor housing integrity, so the structure prone to occur serious damage;

2)Through modal analysis we conclude the basic cycle and vibration mode map, and find out that the farmhouse is given priority to gable torsion, followed by the vertical translation. The structure's cycle significantly increased after reinforcement. The original structure's cycle is 0.15s, but the reinforced structure's cycle is 0.2s, the system with ring beam and structural concrete column improved the structure's rigidity, and enhanced the seismic capacity.

3)By the time history analysis we found that ring beam and structural concrete column can form a good framework and effectively limit the horizontal displacement of the structure. Structure's stress concentration was significantly reduced. So we should promote the system with ring beam and structural concrete column, it has very important significance.

## References

[1] Chuanzhi Xu. Numerical Simulation under Reinforcing Masonry Building of Menhanical Seismic Action Based[D]. Hebei United University, 2012. (In Chinese)

[2] Jinpeng Yao, Chang Peng. Seismic Analysis of Engineering Structure[M]. Beijing:Tsinghua Univer- sity Press, Beijing Jiaotong University Press, 2012. (In Chinese)

[3] Yingmin Li, Han Jun, Liu Liping. Application of ANSYS to Finite Element Analysis for Nonlinear Masonry Structures[J].Journal of Chongqing Jianzhu University. 2006, 28(5): 90-96. (In Chinese)

[4] China Academy of BuildingResearch.GB50011-2010, Code for Seismic Design of Buildings. Beijing:China Architecture &Building Press, 2010. (In Chinese)

[5] Xinmin Wang. ANASYS Numerical Analysis of Engineering Structure[M].China Communications Press, 2007. (In Chinese)

[6] Ke Xu. Analysis of Some Types of Structural Damages in Wenchuan Earthquake[J].Earthquake Resistant Engineering and Retrofitting, 2009, 30(6): 19-23. (In Chinese)

*Applied Mechanics and Materials Vols. 580-583 (2014) pp 1490-1493*
*© (2014) Trans Tech Publications, Switzerland*
*doi:10.4028/www.scientific.net/AMM.580-583.1490*

# Geotechnical Seismic Isolation System - Further Experimental Study

Wei Xiong[1,a], Mingren Yan[1,b], and Yaozhuang Li[1,c]

[1]Institute of Disaster Prevention and Safety Technology, College of Civil Engineering, Central South University, China

[a]bbbear2002@gmail.com, [b]sinymr@sina.com, [c]liyz@csu.edu.cn

**Keywords:** geotechnical seismic isolation (GSI) system, rubber-sand mixture (RSM), experimental study, shaking-table test

**Abstract.** The isolation effectiveness of the Geotechnical Seismic Isolation (GSI) system was further investigated via a series of prescribed shaking-table tests. The dynamic response of GSI system was also evaluated in detail of this work. A parametric study for assessment of the isolation performance of GSI was conducted by varying experimental key parameters, such as rubber percentage of rubber-sand mixtures (RSM), configuration of the foundation, storey number of the superstructure, and different kinds of seismic acceleration inputs. From the parametric survey, it can be concluded that the GSI system can to some extent attenuate the dynamic response of the superstructure under big earthquake shakings.

## Introduction

Earthquake is one of the most devastating natural hazards on our planet. From the beginning of 21st century, earthquakes have occurred increasingly frequent. In 2008 Wenchuan Earthquake, about 80,000 people lost their lives. The 2010 Haiti Earthquake has caused death toll up to 220,000. About 690,000 lives have died by reason of earthquakes in the first decade of the 21st century.

In order to counterstrike the severe earthquake hazard worldwide, scientists and seismologists have endeavored their abilities to bringing more efficient anti-earthquake methods and ways. Some seismic isolation techniques have been proposed by professionals in these dedications. Zhou *et al*. [1] investigated the dynamic performance of an inter-storey seismic isolation application through analytical simulation on a frame structure. Zhang *et al*. [2] evaluated the seismic isolation behavior of the rubber particles via a series of cyclic shear and shaking-table tests. Tsang [3] proposed an innovative Geotechnical Seismic Isolation (GSI) system facilitating rubber-sand mixtures (RSM), which is especially suitable for the developing countries. The GSI system was then experimentally studied by Xiong and Li [4]. Tsang illustrated the GSI system in [5].

In this paper, the seismic isolation performance of the GSI system was further investigated via a series of shaking-table tests conducted on a 1/3-scale steel frame. A parametric study, for assessing the optimal configuration of the GSI system, was performed in the experiments by varying the key parameters such as rubber percentage of rubber-sand mixtures (RSM), configuration of the foundation, storey number of the superstructure, and different kinds of seismic acceleration inputs. The remainder of this paper has the details.

## Shaking-table experiments on the GSI system

**The Superstructure** As shown in Figure 1, a steel-frame structure was constructed to represent the superstructure, and the scaling factor was determined as 1/3. The detailed information of the model structure was given in Table 1. The structure was designed that it can be assembled/dissembled into one storey or three storeys. The basemat measures 2.7 m × 2.7 m × 0.45 m.

Table 1. The detailed information of the model structure

| Number of storeys | Column and beam | Inter-storey height | Overall height |
|---|---|---|---|
| 1 or 3 | 150 mm ×150 mm | 1.5 m, 1.2 m, 1.2 m | 3.9 m |

**The Soil Box** The dimension of the soil box was 4 m × 4 m × 1 m. In order to lessen the boundary effect of the seismic wave, four plates of sponge, each of which was 0.3 m thick, were pasted against the inner soil box.

**Instrumentation** Vertical and horizontal accelerometers were instrumented within the structure to capture the dynamic response. The instrumentation is given in Figure 1.

**Testing Scheme** A parametric study was carried out to evaluate the dynamic behavior of the GSI system by varying the experimental key factors. These factors include: rubber percentage of rubber-sand mixtures (RSM), configuration of the foundation, storey number of the superstructure, and different kinds of seismic acceleration inputs. Table 2 presents the detailed testing scheme.

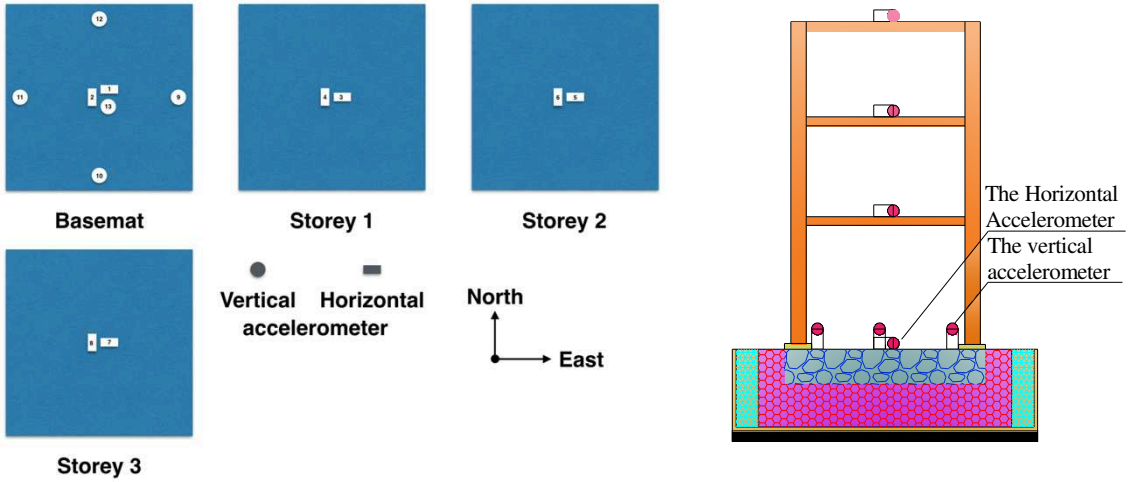


Figure 1. Instrumentation and layout of the structure

Table 2. Detailed testing scheme

| RSM percentage | Foundation configuration | Storey number | Input seismic wave | Case number |
|---|---|---|---|---|
| 0%<br>25%<br>50% | Fixed base<br>Pure sand<br>GSI | 1<br>3 | Kobe<br>Northridge<br>Turkey | 24 |

## Experimental results and its analysis

After processing the experimental data, the comparison between acceleration time histories of different scenarios is presented in Table 3. The selected comparison between acceleration time histories of different scenarios under Northridge seismic wave input is illustrated in Figure 2. The following phenomena can be observed in these experimental results:

1. The pure-sand foundation exhibits the best seismic isolation within the three foundation types (25% RSM, 50% RSM, and pure-sand). Under both Northridge and Kobe shakings, the pure-sand layer has fair attenuation on dynamic response of the superstructure in EW and NS directions.
2. GSI system can reduce the dynamic response of the structure in EW direction under Northridge shakings, yet the isolation performance is inferior to that achieved by the pure-sand foundation. In NS direction, GSI even amplifies the acceleration of the structure, which is in contrast with the pure-sand foundation. The amplitude factor of the GSI system on the horizontal acceleration of the structure is in the range between 4% and 36%. The maximal amplification factor occurred in scenarios with 50% RSM foundation, which is 36%. While for Kobe input, the dynamic response of the structure in both directions is preferably decreased by GSI foundation. Nevertheless the reduction by GSI is lower than that obtained by the pure-sand foundation. The dynamic response of the structure in both directions is magnified with GSI layer when the structure is shaken by Turkey seismic wave. The corresponding amplification factor is within 1.5% to 98.1%.

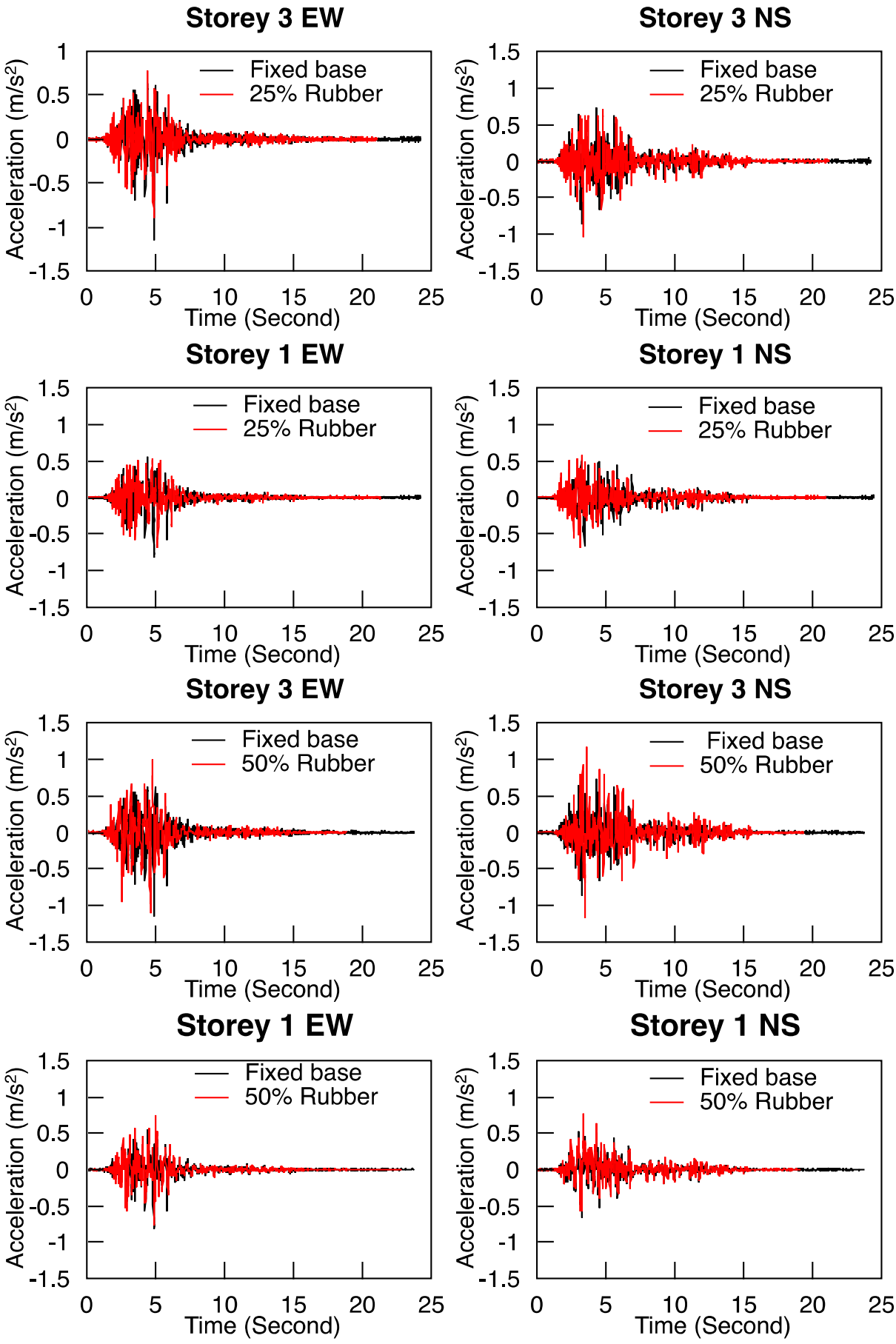


Figure 2. The comparison of different acceleration time-histories, Northridge input.

Table 3. Comparison between the acceleration amplitudes of different scenarios

| Horizontal acceleration amplitude ($m/s^2$) | | FB | Pure sand | % | 25%RSM | % | 50%RSM | % |
|---|---|---|---|---|---|---|---|---|
| Northridge EW | Storey 1 | 0.81 | 0.55 | -32.1% | 0.69 | -14.8% | 0.78 | -3.7% |
| | Storey 3 | 1.16 | 0.67 | -42.2% | 0.89 | -23.3% | 1.10 | -5.2% |
| Northridge NS | Storey 1 | 0.66 | 0.49 | -25.8% | 0.69 | +4.5% | 0.77 | +16.7 |
| | Storey 3 | 0.86 | 0.62 | -27.9% | 1.04 | +20.9% | 1.17 | +36.0% |
| Kobe EW | Storey 1 | 1.04 | 0.77 | -26.0% | 1.04 | 0% | 0.85 | -18.3% |
| | Storey 3 | 1.45 | 1.17 | -19.3% | 1.06 | -26.9% | 1.14 | -21.4% |
| Kobe NS | Storey 1 | 0.95 | 0.64 | -32.6% | 0.77 | -18.9% | 0.78 | -17.9% |
| | Storey 3 | 1.57 | 0.98 | -37.6% | 1.09 | -30.6% | 1.15 | -26.8% |
| Turkey EW | Storey 1 | 0.46 | 0.46 | 0% | 0.80 | +73.9% | 0.56 | +21.7% |
| | Storey 3 | 0.53 | 0.59 | +11.3% | 1.05 | +98.1% | 0.80 | +50.9% |
| Turkey NS | Storey 1 | 0.46 | 0.44 | -4.3% | 0.60 | +30.4% | 0.69 | +50.0% |
| | Storey 3 | 0.66 | 0.63 | -4.5% | 0.67 | +1.5% | 0.97 | +47.0% |

3. In scenarios with Kobe input, the accelerations of the structure are more or less decreased with all three-foundation types. This is due to the relatively large acceleration amplitude of the Kobe seismic wave.

## Conclusions

From the analysis of the experimental data, it can be seen that the pure-sand layer had some attenuation effect on the seismic response of the superstructure. The seismic isolation performance of the GSI system varied noticeably from one seismic acceleration to another. From the investigation of the experimental results, the following conclusions can be made:

1. The seismic isolation performance of GSI is generally inferior to the pure-sand foundation during earthquake shakings, for the RSM layer is too thin in the experiments. The response attenuation of GSI with larger rubber content is greater than that with smaller rubber content.

2. The seismic isolation of GSI is not evident in small earthquakes.

3. The dynamic response attenuation is more prominent in Storey 3 of the structure than that in Storey 1, in both cases of the GSI and pure-sand foundation.

4. The GSI layer must be thicker (up to minimum 5 m, optimum to 10 m or thicker, here to 1.5 m in this experiments) as to achieve more ideal results.

## Acknowledgements

National Science Foundation of China (Grant Number 51108467), Fundamental Research Funds for the Central Universities (Grant Number 2011QNZT118), the Open-End Fund for the Valuable and Precision Instruments of Central South University, and scientific research & developing scheme project sponsored by the China Railway Corporation (No.2013T001).

## References

[1] F. L. Zhou, Y. Zhang, and P. Tan: China Civil Eng. J. Vol. 8 (2009), p. 1 (In Chinese)

[2] C. Zhang, R. Wang, and Z. R. Lin: Eng. Earthq. Mitig. Retro. Vol. 33(20012, p. 52 (In Chinese)

[3] H. H. Tsang: Earthq. Eng. Struct. Dyn. Vol. 37(2008), p. 283

[4] W. Xiong, Y. Z. Li: Earthq. Eng. Struct. Dyn. Vol. 42(2013), p. 2187

[5] H. H. Tsang, in: *Earthquake Engineering*: *New Research*. Nova Science Publishers, Inc., New York, U.S. (2004).

*Applied Mechanics and Materials Vols. 580-583 (2014) pp 1494-1498*
*© (2014) Trans Tech Publications, Switzerland*
*doi:10.4028/www.scientific.net/AMM.580-583.1494*

# Seismic Response Analysis of Deep Water Bridges with Pile Group Foundations

Dongxiao Zhao[1, a], Junjie Wang[1,b] and Junsheng Su[1,c]

[1]Dept of Bridge Engr, Tongji Univ., 1239 Siping Rd, Shanghai, China

[a]zhaodong.g888@163.com; [b]jjqxu@tongji.edu.cn, corresponding author; [c]sujunsheng@yeah.net

**Keywords:** Seismic dynamic response, fluid-structural interaction, Morison equation, finite volume method, dynamic mesh

**Abstract.** In this paper, we intended to replace the fluid-structure interaction of deep water bridge piers with acceleration-dependent forces during an earthquake. The hydrodynamic pressure on bridge pier groups under seismic excitation is studied using the finite volume method. Different seismic waves with various spectrum components are selected in order to cover frequently encountered cases. The calculated forces of these cylinders are fitted into the Morison equation, and by calculation, the drag force term is negligible, thus the effect of fluid is converted into one added mass term. The paper further calculated the dynamic response of a continuous beam bridge with pier groups in water to check the validity of our proposed method.

## Introduction

With the advancement of communication and transportation, long-span bridges and cross-continent bridges are frequently built, and many of their piers lay in water. The dynamic behavior of these bridges would be different because of the fluid-structure interaction. However, we currently possess no thorough understanding of quantitative details due to the complex nature governing FSI problems, this is particularly true if we were to calculate the seismic response of deep water bridges for the random factors involved. Many scholars seek simplified ways to deal with this problem. Karadeniz[1] analyzed the coupling of seismic ground motion and deepwater waves using spectrum method while assuming the seismic wave as simple random processes. Etemad and Gharabaghi[2] adopted the Nogami model to analyze the joint dynamic effect of earthquakes and waves with same and opposite directions on structures. Bai De-gui[3] implemented the 3D finite element method to model the pier-piles-soil system, they also use Stokes wave theory and Morison equation to analyze the effect of waves and currents. Wei Kai and Wu Yong-ji[4] studied the water-group pile foundation interacted modeling using potential-fluid element in ADINA, and further investigated the relationship between the hydrodynamic influence and geometry of the piles. There are two main topics concerning previous research: analytical methods and numerical methods. Because of the many assumptions, analytical methods would fail to predict accurately in many cases. The numerical methods are powerful tools in analysis and prediction, however, previous research treated the fluid too simply regardless of viscous and turbulence factors. In this paper, we give the detailed CFD analysis of cylinders moving in water according to seismic input, and then present a method suitable for practical usage.

## CFD analysis of cylinders moving in water

In this section, we simplify the piers as rigid cylinders moving in water, and then calculate the pressures on these cylinders using finite volume method. Finite volume method resembles the finite difference method, only differs in that it is more versatile and automatically fluxes conservation.

In order to satisfy the stability condition for the finite volume method, the CFL condition needs to be met:

$$C = \Delta t \sum_{i=1}^{3} \frac{u_i}{\Delta x_i} \le C_{max} . \tag{1}$$

Where $\Delta t$ is the time step, $u_i$ and $\Delta x_i$ is the velocity magnitude and grid length in the i direction, $C_{max}$ usually takes 1 for explicit schemes. In calculation, we need only concern the average CFL number among cells.

For CFD analysis, viscous model is also an important factor which affects the calculating results. Here we choose the k-epsilon model, the requirement for first wall layer grid size of the model can be determined by an empirical formula:

$$y^+ = 0.172\frac{\Delta y}{D}Re^{0.9} \approx 30. \tag{2}$$

Our CFD model is a $24m \times 24m \times 8m$ tank filled with 6.5m deep water and air at the rest part, so it is a two-phase flow. A cylinder with 2m diameter is located at the center. In the calculation, the cylinder is moving according to the velocity input (we calculated input cases of sine waves and six seismic waves), thus the grid should be updated per time step, which is essentially a dynamic mesh problem and could be realized by smoothing the mesh using diffusion equation. Due to the requirement of dynamic mesh, two grid zones, one with rigid motion and the other with deforming, is separated. Taken into consideration the above factors and the constraints of CFL number and viscous model, our discretization of the model is shown in the Fig1.

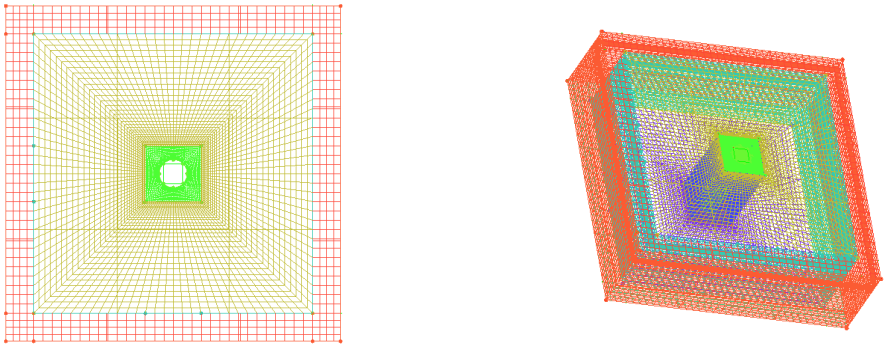

(a) vertical view of grids (b) isometric view of grids

Figure 1: Spatial discretization of calculation domain

In the grid discretization shown in Fig1, there are 367094 elements and 340680 nodes. The grid is refined near the cylinder wall and at the free surface of the water. The boundary conditions at the bottom and the sides are mirror symmetry, and at the top is pressure outlet boundary condition. We use the second order upwind scheme for momentum equation, and the PISO scheme for pressure-velocity coupling term.

6 seismic velocity inputs of various spectrum components were calculated, the typical resulting forces on the cylinder is shown in Fig2.

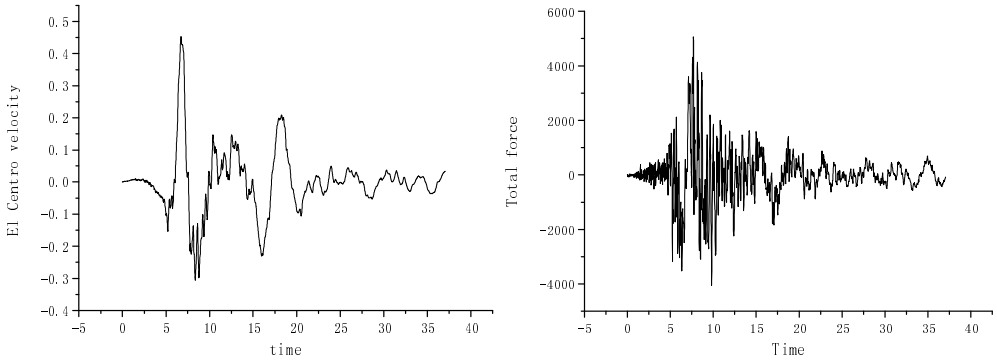


(a) El Centro velocity input (b) forces of El Centro wave

Figure 2: Typical resulting forces

Having obtained the hydrodynamic forces on these cylinders, we fit the data into the Morison equation, which is initially designed to estimate wave loads on offshore structures [5]. The equation gives the force along the flow direction on unit length cylinders:

$$F_t = F_m + F_d = \frac{\pi}{4}\rho D^2 C_M \dot{u}(t) + \frac{1}{2}\rho C_D D u(t)|u(t)|. \quad (3)$$

The first term in Eq3 is an inertial force term, and the second term in the formula is a drag force term. Denote the calculated hydrodynamic forces as $F_t$, we use the least square method to calculate coefficients $C_M$ and $C_D$. The calculated coefficients for input waves is shown in Tab1.

Table 1: Least square fit of seismic wave input

| | Coyote | Olympia | El Centro | Parkfield | Gengma1 | Gengma2 |
|---|---|---|---|---|---|---|
| $C_M$ | 0.779 | 0.767 | 0.853 | 0.799 | 0.778 | 0.765 |
| $C_D$ | 3.63 | 5.16 | 2.09 | 3.78 | 19.17 | 18.13 |
| $\|\|F_M\|\|_2/\|\|F_t\|\|_2$ | 97.19% | 95.56% | 97.45% | 98.48% | 95.45% | 94.01% |

From Tab1 we can observe that $C_M$ is approximately 0.8, and $C_D$ fluctuates randomly. Additional calculation of sine waves shows similar results. However, if we compare the force components, the drag force is negligible compared to the inertial force in all cases, and the inertial force term alone is adequate to represent the calculated hydrodynamic force. Two typical graphs of Morison inertial force and Morison drag force in the time domain are shown in Fig2.

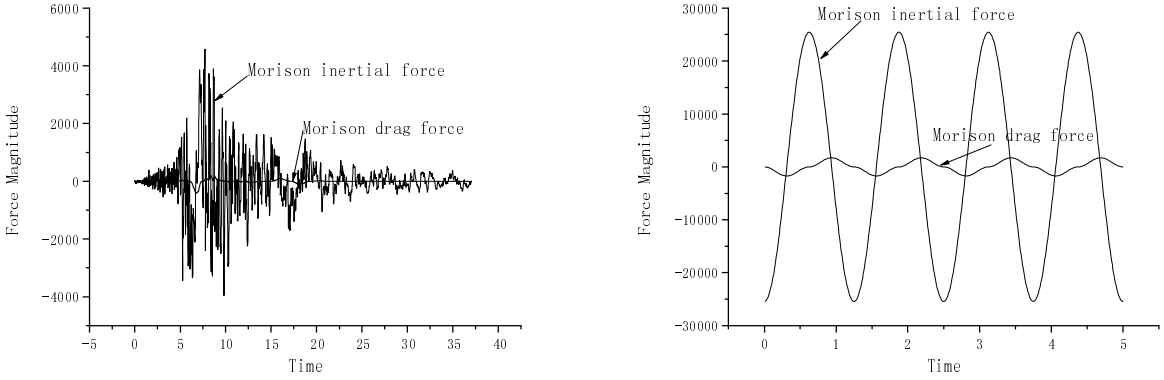


(a) Force decomposition of El Centro wave (b) Force decomposition of sine wave

Figure 3: Typical resulting forces

In case of pier groups, we analyzed two piers, four piers, five piers, and nine piers, to take into account the mutual coupling effect between cylinders. We also modeled and calculated block pile caps. The result is similar: Morison drag force is negligible, and Morison inertial coefficient is approximately 0.8, with 10% accuracy. The result accords with the experiments conducted by Sarpkaya [6] Thus, it is concluded that for peer groups, the unit length hydrodynamic force can be approximated as:

$$F(t) = 0.8\frac{\pi D^2}{4}\rho\dot{u}(t) \ . \quad (4)$$

The force direction is opposite to the input pier velocity.

**Hydrodynamic force in structural dynamic equation**

For deep water bridge excited by seismic waves, in the finite element representation of structural dynamics, the uniformly distributed hydrodynamic force is converted to nodal force. The structural dynamic equation can be written as:

$$M\left(\ddot{u} + R\ddot{u}_g\right) + C\dot{u} + Ku + M_w\left(\ddot{u} + R_1\ddot{u}_g\right) = 0 \ . \quad (5)$$

In which $R_1$ is a column vector consists of 1, and $M_w$ is the added mass matrix.

The added mass matrix is a diagonal matrix, and its nonzero terms correspond to the hydrodynamic forces in Eq4. The above structural equation can be arranged as:

$$(M+M_w)\ddot{u}+C\dot{u}+Ku=-(MR+M_wR_1)\ddot{u}_g. \tag{6}$$

From Eq6, we can see that the fluid changes the structural dynamic properties by adding terms in the mass matrix, which decreases structural natural frequencies. If more structural volume is immersed in water, the change would be more drastic.

Eq6 can be computed by direct integration or modal superposition. It should be noted that in modal superposition, due to changes in the mass matrix, the system cannot be decoupled by real modal. The common practice is to transform the quadratic eigenvalue problem $(\lambda^2(M+M_w)+\lambda C+K)\phi=0$ to the state space:

$$(\lambda A+B)s=0. \tag{7}$$

In which $A=\begin{pmatrix}0 & M+M_w\\ M+M_w & C\end{pmatrix}$, $B=\begin{pmatrix}-(M+M_w) & 0\\ 0 & K\end{pmatrix}$.

The computed eigensystem can decouple A and B, and can further be transformed to the original dynamic equation.

## Numerical simulation and analysis

A continuous beam bridge with piers in water is modeled into 417 nodes and 415 beam elements, which is shown in Fig4. The pier groups consist of 4 concrete cylinder piers of 1.2m diameter.

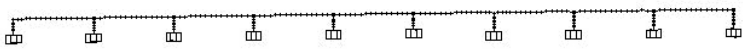

Figure 4: Finite element discretization of a beam bridge

Natural frequencies are calculated with and without water, and the first 20 results are shown in Fig5. From the figure we can see that clear differences occur at the 5th, 6th, and 11th~19th frequencies, which is corresponding to the bending and torsional modes.

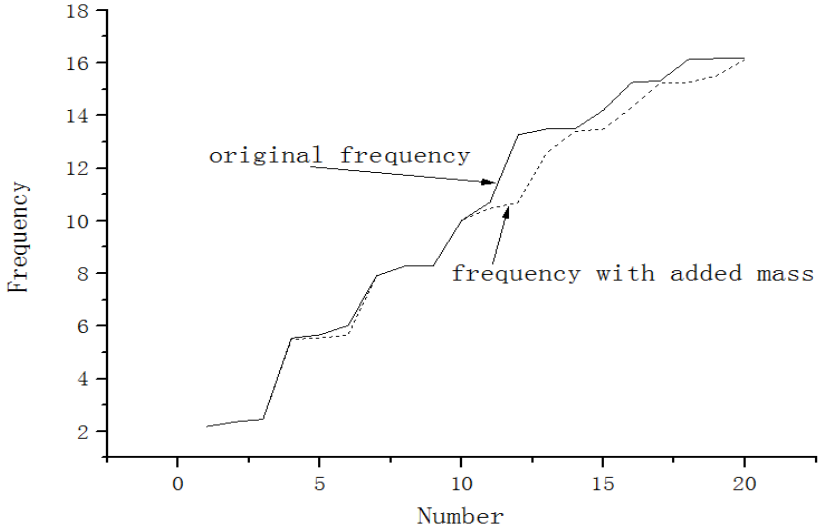


Figure 5: Frequency contrast of structure with and without water

The displacement of this beam bridge excited by the El Centro seismic wave is calculated both in the original structure and in the structure with water, and the maximum displacement in three directions is contrasted for the two cases, which is shown in Tab3.

Table 3: Maximum displacement contrasts on certain DOFs

| | $2^{nd}$ mid-span y | $6^{th}$ mid-span y | $9^{th}$ mid-span x | $9^{th}$ mid-span y |
|---|---|---|---|---|
| Disp, no water[m] | 0.0959 | 0.0937 | 0.0896 | 5.75E-5 |
| Disp, water[m] | 0.0834 | 0.0937 | 0.0831 | 4.990E-5 |
| Relative diff | 14.93% | 0 | 7.8% | 15.16% |

According to the figure , the difference between these two results is not negligible, thus the existence of fluids would change the dynamic property and the response of structures.

## Conclusion

From the above calculation and analysis, we draw the following conclusions:

1. Fluid effect is not negligible in structural seismic response.
2. When the hydrodynamic pressure of vertical structures from seismic excitation is decomposed according to the Morison equation, the drag force term would be negligible compared to the inertial force term.
3. For seismic waves and sine waves, the Morison inertial coefficient for one pier, pier groups, and bridge caps is approximately 0.8. Thus we can approximate the hydrodynamic effect as the time history of forces dependent on structural acceleration.

Further research direction is the direct fluid-structural interaction modeling of bridges to get a more detailed understanding of this problem. Furthermore, a more complicated problem is the joint action of seismic waves, waves and currents, which appears frequently in deep water conditions.

## References

[1] Karadeniz H. Spectral analysis of offshore structures under combined wave and earthquake loadings[C]. The Proceedings of the International Offshore and Polar Engineering Conference. International Society of Offshore and Polar Engineers, 1999.

[2] Etemad A K, Gharabaghi A R M, Chenaghlou M R. Nonlinear Dynamic Behavior of Fixed Jacket-Type Offshore Platforms Subjected to Simultaneously Acting Wave and Earthquake Loads[C] ASME 2004 23rd International Conference on Offshore Mechanics and Arctic Engineering. American Society of Mechanical Engineers, 2004.

[3] Bai Degui., Seismic response analysis of bridge pier supported by pile foundation considering the effect of wave and current. Nanjing University of Technology, 2008.

[4] WEI Kai, WU Yong-ji, XU Can et al. NUMERICAL DYNAMIC ANALYSIS FOR WATER-PILE GROUP BRIDGE FOUNDATION INTERACTED SYSTEM [J]. Engineering Mechanics, 2011, 28(Supplement I): 195-200. (In Chinese)

[5] Morison J R, Johnson J W, Schaaf S A. The force exerted by surface waves on piles[J]. Journal of Petroleum Technology, 1950, 2(05): 149-154.

[6] Sarpkaya T. Force on a circular cylinder in viscous oscillatory flow at low Keulegan-Carpenter numbers [J]. Journal of Fluid Mechanics, 1986, 165: 61-71.

*Applied Mechanics and Materials Vols. 580-583 (2014) pp 1499-1505*
*© (2014) Trans Tech Publications, Switzerland*
*doi:10.4028/www.scientific.net/AMM.580-583.1499*

# Analysis of strong ground motion characterization in the 2013 Lushan earthquake

Tian Yu[1, a], Ming Lu[2,b] and Xiaojun Li[3,c]

[1,2]Institute of Crustal Dynamics, China Administration, 1 Anningzhuang Road , Beijing 100085, China.

[3]Institute of Geophysics, China Administration, 5 Minzu Xueyuan Nan Road , Beijing 100081, China.

[a]yutian0721@yeah.net, [b]Luming6@yeah.net, [c]beerli@vip.sina.com

**Keywords:** Lushan earthquake, ground motion, hanging wall effect, topographic effect, directivity effect.

**Abstract.** Lushan earthquake on 20th April, 2013 was another thrust fault earthquake occurred at Longmen Mountain Fault Zone after 2008 Wenchuan Ms8.0 earthquake. Based on ground motion attenuation model, this paper has chosen 45 strong motion records with rupture distance less than 200km, to analyze the hanging wall effect, topographic effect and rupture directivity effect of Lushan earthquake. The results show that hanging wall effect in Lushan earthquake was not obvious as 2008 Wenchuan earthquake; ground motion in mountain areas attenuated with increasing rupture distance more quickly than that in plain areas; rupture directivity effect is obvious for two components of horizontal ground motion, which are fault-perpendicular and fault-parallel components. PGA in the forward rupture area is larger than those in the backward rupture area. With the period increased, the gap between backward and forward rupture area become small, and finally PGD in backward rupture area is greater than those in the forward rupture area.

## Introduction

The Lushan Ms 7.0 earthquake on 20 th April, 2013 caused 188 casualties, 25 missing, 10,000 wounded and tens of billions of economic losses. Lushan earthquake was another big thrust fault earthquake occurred at Longmen Mountain fault zone after the 2008 Wenchuan Ms 8.0 earthquake [1]. In this earthquake, the National Strong Motion Networks Center of China obtained a wealth of strong motion records. Based on ground motion attenuation model, this paper uses ground motion records in Lushan earthquake to analyze the hanging wall effect, topographic effect and directivity effect. The results can provide a scientific basis for ground motion prediction in Southwest China.

Because of the geological characterization of seismogenic fault, directivity of seismic wave propagation process, crustal structure and site effect, hanging wall effect, topographic effect and directivity effect appear in the spatial distribution of ground motion in great earthquakes. Those effects not only complicate the spatial distribution of ground motion, but also influence the various frequency component of ground motion differently, which have increased the bias and variability of ground motion prediction.

Hanging wall effects of ground motion refers to that the ground motion in the hanging wall is greater than that in the footwall with the same rupture distance, which is mainly present in the near-fault areas of dip-slip earthquakes. Earthquake Engineering scientists generally believe that site in the hanging wall is closer to the rupture plane than site in the foot wall with the same rupture distance, and this is the substance of hanging wall effect. Hanging wall effect was discovered very earlier. However, it was not verified until Abrahamson and Someville [2] found a clear hanging wall effect in the strong motion records of Northridge earthquake. Thereafter Yu, Wang[3,4] used the strong motion records in 1999 Chi-Chi earthquake and 2008 Wenchuan earthquake to verify the hanging wall effect again. Then, Chang[5] quantitatively analyzed the hanging wall effect of Chi-Chi earthquake and came up with amplification factor of hanging wall effect on peak acceleration and acceleration response spectrum.

Topographic effect of ground motion generally refers to amplification of the terrain on high frequency component of ground motion, which is closely relative to the shape of the mountain. Ground motion on the ridge is greater than that on the foothills. On the other hand, another topographic effect has attracted the attention of earthquake engineering scientists. For the big earthquake, seismic intensity contour in mountain areas is denser than that in plain area, and seismic intensity in mountain areas attenuate more quickly than that in plain area. This phenomenon has been verified by Hua County Earthquake in 1556 and Wenchuan Earthquake in 2008.

Rupture directivity effect of ground motion refers to that ground motion in the forward rupture area has an accumulated effect and its high frequency component will be greater than usual. However, the sub-source of seismic wave in the backward rupture area arrive at different time, and the long period component will be abundant, which will increase the duration of ground motion. Rupture directivity effect cause spatial variations in ground motion amplitude and duration around fault. Somervile [6] had used strong motion data to build a empirical relations of rupture directivity on ground motion attenuation relations. Liu made a detailed explanation about rupture directivity effect by using dislocation theory.

**Strong motion Data**

Lushan Ms 7.0 earthquake (Epicenter location :30.3 ° N, 103.0 ° E; focal depth: 15 km), occurred in the southern section of the Longmen Mountain fault zone. Chinese Academy of Sciences and Institute of Geophysics both had inverted the focal mechanism of Lushan earthquake, and the two results are similar[7,8]. This paper used the result of Institute of Geophysics , China Earthquake Administration(CEA): Nodal plane Ⅰ, strike 34 °, dip 55 °, slip angle 87 °; nodal plane Ⅱ, strike 220 °, dip 35 °, slip angle of 95 °. As soon as the earthquake happened, CEA had organized a scientific expedition to investigate the outcrop of seismogenic fault, and finally proved there isn't an obvious outcrop. Combined with inversion result and geological evidences, this paper supposed that the length of the seismogenic fault is 60km, its center is the epicenter.

In Lushan earthquake, 83 state strong motion stations in Sichuan province got strong motion records, 45 of which were with fault distance less than 200km. Most state strong motion station were equipped with SYSCOM or ETNA digital accelerographs with full scale of ±2g and band width of 0 ~ 80Hz. Fig.1 displays the location of the 45 state strong motion stations with fault distance less than 200km. According the fault geometry and topographic map of Sichuan province, 45 state strong motion station are classified as four groups, which are hanging wall(mountain area) stations, footwall (plain area)stations, forward rupture area stations and backward rupture area stations. Table 1 shows the classification results. There are more stations in the hanging wall area and forward rupture area than footwall and backward rupture area. Based on the classification, this paper analyzes the strong motion characteristics of Lushan earthquake.

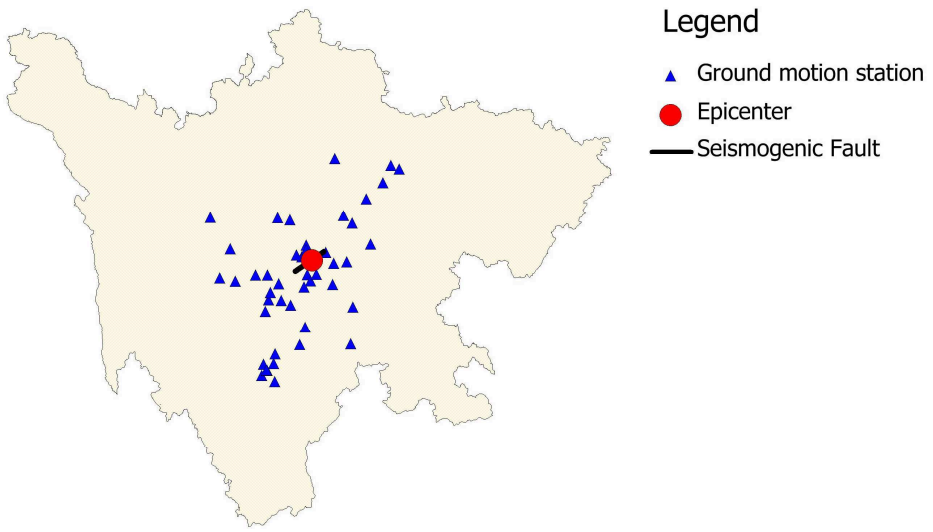


Fig. 1 Location of the 45 state strong motion stations with fault distance less than 200km in Lushan earthquake.

Table 1 Classification of the state strong motion station.

| Number | Haning wall （Mountain area） | Foot wall (Plain area) | Forward rupture area | Backward rupture area |
|---|---|---|---|---|
| 1 | 51AXT | 51CDZ | 51BXD | 51AXT |
| 2 | 51BCD | 51GLQ | 51BXM | 51BCD |
| 3 | 51BXD | 51HYQ | 51DFB | 51BXY |
| 4 | 51BXM | 51HYT | 51DFT | 51BXZ |
| 5 | 51BXY | 51HYW | 51GLQ | 51CDZ |
| 6 | 51BXZ | 51HYY | 51HYQ | 51DJZ |
| 7 | 51DFB | 51LDG | 51HYT | 51HSS |
| 8 | 51DFT | 51LDJ | 51HYW | 51JYH |
| 9 | 51DJZ | 51LDL | 51HYY | 51PJD |
| 10 | 51HSS | 51LSF | 51KDG | 51PJW |
| 11 | 51JYH | 51LSL | 51KDT | 51PXZ |
| 12 | 51KDG | 51MCL | 51KDX | 51QLY |
| 13 | 51KDT | 51MNA | 51KDZ | 51SFB |
| 14 | 51KDX | 51MNC | 51LDG | 51XJD |
| 15 | 51KDZ | 51MNH | 51LDJ | 51XJW |
| 16 | 51PXZ | 51MNJ | 51LDL | |
| 17 | 51SFB | 51MNT | 51LSF | |
| 18 | 51XJD | 51MNW | 51LSL | |
| 19 | 51XJW | 51PJD | 51MCL | |
| 20 | | 51PJW | 51MNA | |
| 21 | | 51QLY | 51MNC | |
| 22 | | 51TQL | 51MNH | |
| 23 | | 51XDM | 51MNJ | |
| 24 | | 51YAD | 51MNT | |
| 25 | | 51YAL | 51MNW | |
| 26 | | 51YAM | 51TQL | |
| 27 | | | 51XDM | |
| 28 | | | 51YAD | |
| 29 | | | 51YAL | |
| 30 | | | 51YAM | |

## Ground motion attenuation model

In order to study the hanging wall effect, topographic effect and rupture directivity effect of ground motion in Lushan earthquake, we derives ground motion attenuation model from strong motion data by using statistics method. The ground motion parameters used in this paper are peak ground acceleration (*PGA)*, peak ground velocity (*PGV)*, and spectral acceleration (*SA*) with damping ratio of 5%. Since the mounting azimuth of digital accelerographs has impact on amplitude of ground motion, Boore's method[9] has been introduced. Horizontal acceleration is decomposed into two orthogonal components in any angles, and geometrical mean of the *PGA*, *PGV* and spectral acceleration of two orthogonal components are defined as *GMROTD50(*$T_i$*)*. A penalty function is defined as follows:

$$Penalty(\theta) = \frac{1}{N_{per}} \sum_{i=1}^{N_{per}} [sqrt(Y_1 \times Y_2)/GMROTD50(T_i) - 1]^2 \quad (1)$$

Where,$Y_1$,$Y_2$ are the *PGA*, *PGV* and spectral acceleration of two orthogonal components. $N_{per}$ is the number of period used in the calculation. $T_i$ is the period.

Select the specific mounting azimuth angle θ to minimize the penalty function, and defined the *GMROTD50* atθas *GMROTI50(*$T_i$*)*. *GMROTI50* of *PGA*,*PGV*,*SA* are used to regress the ground motion attenuation model parameters.

Ground motion attenuation model used in this paper is as follows:

$$\log_{10}(Y) = C_0 + C_1 \log_{10}(R + C_2) \quad (2)$$

Where, *Y* are the ground motion parameters, such as the *GMROTI50* of *PGA*,*PGV* and *SA*； *R* is the fault distance; $C_0$, $C_1$, $C_2$ are the regression parameters.

## Strong motion characterization of Lushan earthquake

### 4.1 Hangingwall effect and topographic effect

Strong ground motion data with fault distance less than 200km are used to regress the ground motion attenuation model in equation 2. Fig.2 and Fig.3 demonstrate the fitting of ground motion attenuation model for *PGA* and *PGV*. Fig.4 displays the comparison of attenuation relation curves between hanging wall (Mountain area) and foot wall (Plain area) on *PGA*, *PGV* and Spectral acceleration at period of 0.5 second.

In the near-fault range(fault distance less than 50km), there were 4 strong motion stations in the hanging wall (Mountain area), and 8 stations in the footwall(Plain area).The four stations in the hanging wall were all located in Baoxin county. In comparison of *PGA*, *PGV*, ground motion in the hanging wall didn't looks greater than that in the footwall, except for the station 51BXD. 51BXD is the nearest station to the fault in the hanging wall and *PGA* in 51BXD was greater than 1G. Wen[10]believed that the topographic effect was the main reason for the huge PGA in 51BXD. 51QLY is the nearest station to the fault in the foot wall, with the fault distance of only 3 km. Since it was located in the end part of the seismogenic fault, the ground motion was relatively small.

Overall, hanging wall effect in Lushan earthquake was not obvious as 2008 Wenchuan earthquake, though they both occurred at Longmen Mountain fault zone and with similar focal mechanism. There might be two main reasons for the difference. Firstly, the stress accumulated in the Longmen mountain fault zone had been well released after the Wenchuan earthquake. As a result, the energy and fault size of Lushan earthquake was relatively small. Secondly, according to the investigation of scientific expedition, there was not an outcrop of seismogenic fault in Lushan earthquake, which would weaken the high frequency component of ground motion.

Through the comparison of ground motion in mountain areas and plain areas, amplification effect of terrain was not obvious. In the range of fault distance between 50km to 200km, ground motion in mountain areas attenuated more quickly versus fault distance and was smaller than the ground motion

in plain areas. *PGA* Attenuation relation curves of mountain area and plain area had a junction point at the fault distance of about 40 kilometers, which was similar to the result of Li Xiaojun[11] on the 2008 Wenchuan earthquake.

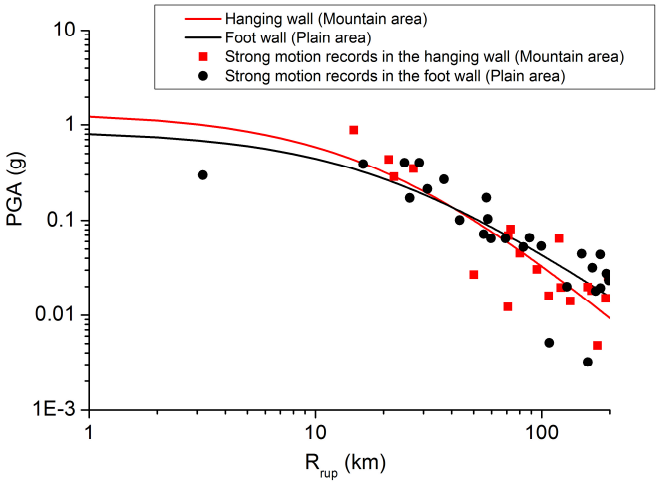


Fig.2 Fiting of attenuation relation curves on PGA

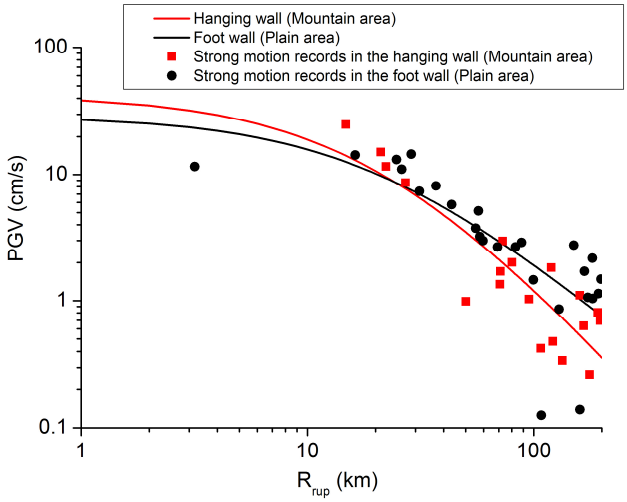


Fig.3 Fiting of attenuation relation curves on PGV

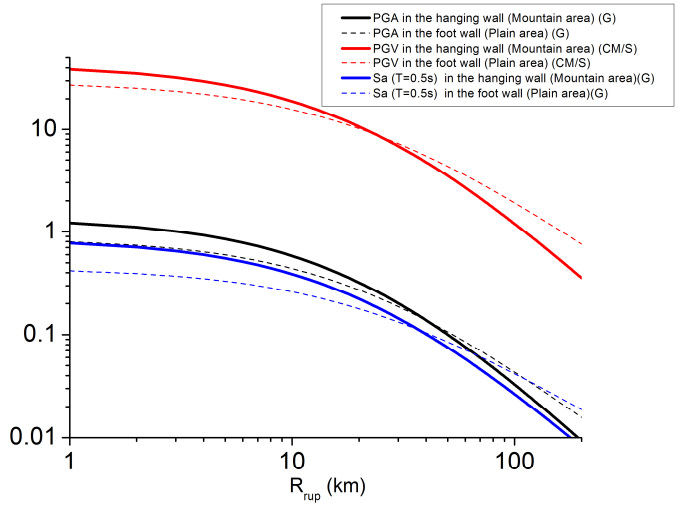


Fig.4 Comparison of attenuation relation curves between Hanging wall (mountain area) and Foot wall (Plain area) on PGA, PGV and Sa (T=0.5s)

### 4.2 Rupture directivity effect

Horizontal component of ground motion has been decomposed into two components, which are fault-perpendicular and fault-parallel components separately. According to the distribution of aftershocks, the rupture direction of Lushan earthquake was southwest. Fig.5 and Fig.6 show the comparison of attenuation relation curves along the rupture direction of *PGA*, *PGV*,*PGD* and spectral acceleration (T=0.5 seconds) between the two horizontal components. Rupture directivity effect on both components is obvious. For *PGA*, the amplitude in the forward rupture area is considerably greater than that in backward rupture area. With period increasing, long period ground motion in backward rupture area is raising, and become equivalent to that in forward rupture area for *PGV*, finally exceed for *PGD*. Both horizontal components have shown this trend.

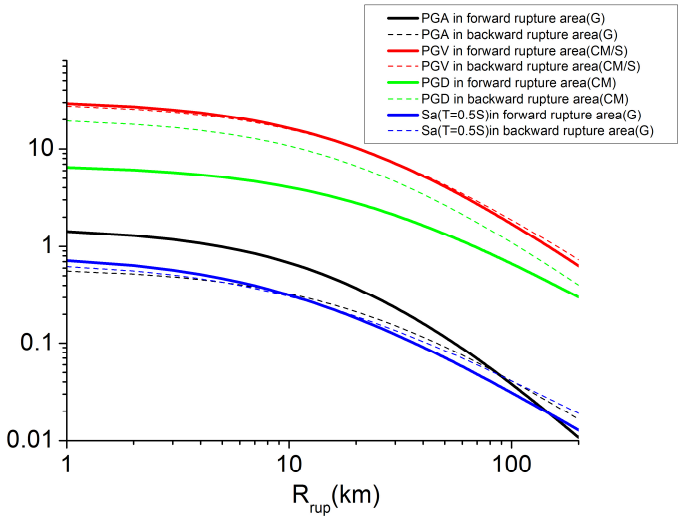


Fig.5 Comparison of attenuation relation curves for fault-parallel component between forward and backward rupture area on PGA, PGV, PGD and SA(T=0.5 s)

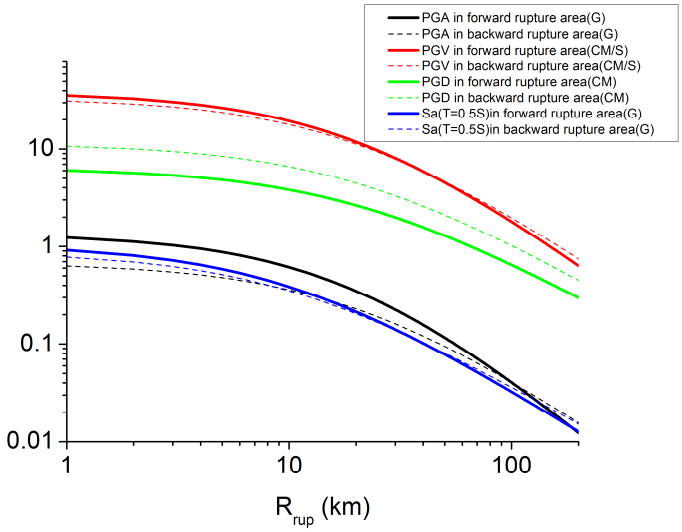


Fig. 6 Comparison of attenuation relation curves for fault-perpendicular component between forward and backward rupture area on PGA, PGV, PGD and SA(T=0.5 s)

### Conclusion

Through statistical analysis of strong motion data, hanging wall effect, topographic effect and rupture directivity effect in Lushan earthquake have been studied in this paper. It is found that:

1. Hanging wall effect is not obvious. From the comparison of *PGA*,*PGV*, ground motion in the hanging wall is not greater than that in the footwall. However, if inferred from attenuation relation curves, ground motion in the hanging wall has a potential of being larger than that in the foot wall.

2. Ground motion in the mountain area attenuated versus fault distance more deeply than that in the plain area.
3. Rupture directivity effect is obvious. In the forward rupture area, high frequency component of ground motion get accumulated and is considerably greater than that in backward rupture area. And in the backward rupture area, ground motion generated by sub-fault arrive at different time , which enlarge the duration of ground motion and increase the long period component of ground motion. This trend has been shown in fault-perpendicular and fault-parallel components of horizontal ground motion.

**Acknowledgements**

The records used in this study are provided by the National Strong motion Networks Center of China. We give our thanks to the National Strong motion Networks Center of China and all of the relevant managers and experts. This work was financially supported by the National Natural Science Foundation of China (51278469), and National Basic Research Program of China (ZDJ2013-04).

**References**

[1] X.W. Xu, G.H. Chen, G.H. Yu, et al. Seismogenic structure of Lushan earthquake and its relationship with Wenchuan earthquake. Earth Science frontiers, Vol.20(3)(2013), p.11

[2] N. A. Abrahamson, P.G. Somerville. Effects of the hanging wall and footwall on ground motions recorded during the Northridge earthquake． Bull Seism Soc Amer,Vol.86(1B)(1996),P.93

[3] Y.X. Yu, M.T. Gao. Effect of the hanging wall and footwall on peak acceleration during the Chi-Chi earthquake, Taiwan. Acta Seismologica Sinica(in Chinese),Vol. 23(6)(2001),P.615

[4] D. Wang, L.L. Xie.Geometric effects resulting from the asymmetry of dipping fault：Hanging wall/footwall effects. Acta Seismologica Sinica(in Chinese), Vol.30(3)(2008), P.271

[5] T.Y. Chang, F. cotton, Y.B. Tsai et al. Quantification of hanging—wall effects on ground motion：Some insights from the 1999 Chi-Chi earthquake．Bull Seism Soc Amer，Vol.94(6)(2004), P.186

[6] P.G. Somerville, N.F. Smith and R.W.Graves. Modification of empirical strong ground motion attenuation relations to include the amplitude and duration effects of rupture directivity. Seismological research letters,Vol.68(1)(1997),P.199.

[7] Y. Zhang, L.S. Xu and Y.T. Chen. Rupture process of the Lushan 4.20 earthquake and preliminary analysis on the disaster-causing mechanism. Chinese J. Geophys (in Chinese),Vol.56(4)(2013), P.1408

[8] C.L. Liu, Y. Zheng, C. Ge et al. Rupture process of the 2013 Lushan Ms 7.0 earthquake. Science China: Earth Sciences, Vol.43(6)(2013), P.1020

[9] D.M. Boore, J.W. Lamprey and N.A. Abrahamson. Orientation-Independent measures of ground motion. Bull Seism Soc Amer,Vol.96(4A)(2006), P.1502.

[10] R.Z. Wen, Y.F. Ren, W.H. Qi et al. Maximum acceleration recording from Lushan earthquake on april 20, 2013. Journal of Southwest Jiaotong University(in Chinese), Vol.48(5)(2013),P.783

[11] X.J. Li, L. Liu, Y.S. Wang et al. Analysis of Horizontal Strong-Motion Attenuation in the Great 2008 Wenchuan Earthquake. Bull Seism Soc Amer,Vol.100(5B)(2010), P.2440.

*Applied Mechanics and Materials Vols. 580-583 (2014) pp 1506-1510*
*© (2014) Trans Tech Publications, Switzerland*
*doi:10.4028/www.scientific.net/AMM.580-583.1506*

# Development and Prospect of China's Bridge Seismic Bearing

Long Zhang[1, a], Canhui Zhao[2,b], Liang Li[3,c] and Bingbing Fan[4,d]

[1]School of civil engineering of Southwest Jiaotong University, Chengdu,Sichuan province,China

[a]13658087657@163.com, [b]ll19890219@126.com, [c]wudifan90_05@163.com

**Keywords:** seismic bearing , earthquake-reduction and seismic-isolation, hysteretic characteristic

**Abstract:** Since entering the new century, bridge techniques are developing rapidly in our country. When bridge seismic techniques had not reached a certain degree, seismic design of bridge bearings was rarely involved. However, since the amount of the bridges that had collapsed in earthquakes due to the bearings damage were becoming larger, in the design of bridges, seismic design in current bridges has been taken seriously.This paper mainly introduces several widely used seismic bearings and analyzes the structures and hysteretic characteristics of them and forecasts the development direction of seismic bearings.

## Introduction

In the seismic design of bridge, the seismic design of bridge bearings cannot be ignored, and it has been considered to be one of the parts that have comparatively weak seismic performance in the system of bridge. A great part of the damage of bridges that have occurred in earthquakes is the result of the destruction of the bridge bearings. In the survey of the great Hanshin earthquake, Japan found that the number of the bridges' damage, as a result of the destruction of the bridge bearings, has reached twenty-eight percent of the total destruction number.

Bridge bearings will generate varying degrees of damage in earthquake, which may lead to damage of upper structures and bridge piers, and then the beam will slip away or fall down. Bearings will appear tensile damage, shearing damage or the surrounding concrete will generate cracks when the earthquake force is greater than that the bearing can support. It is found that numerous bridges are damaged due to the bearing damage in the survey of the 5.12 earthquake in China.

Bearing damage may lead to transformations of the force transferring path in system of structures, and the transformations have great influence on bridges. In recent years, earthquake-reduction and seismic-isolation techniques are developing very fast. Due to the view of the previous "stiff resistance" approach was no longer applicable, the new opinion of "shock absorption and isolation" was born. Based on the energy concept, using the active control and the passive control or the combination of both, trying to extend the natural vibration period to avoid the energy concentration range, the structure and the ground motion can be separated to reduce the incoming seismic energy and make the energy-dissipating capacity of the structure stronger.

## The Development of Bearings

The world bridge building techniques are changing rapidly, and the types of bridge bearings are also increasing. From steel bearings before the twentieth century 60's to rubber bearings and to teflon plate plane sliding bearings and to spherical bearings, the development shows that seismic performances of bearings and attentions to the design of bearings are increasing.

**Rubber Bearing (RB)**

Rubber bearing is a kind of plate rubber bearings. Plate rubber bearings are divided into unstiffened bearings and stiffening bearings. Unstiffened bearing is made of pure rubber, and its compression deformation under the action of vertical force is too large, and the rubber has lateral expansion. So it is rarely used in the bridge structure.While what plate rubber is more wildly used is the stiffening bearing which is also named rubber bearing.

Laminated rubber bearing is constituted by multilayer thin rubber sheet (5, 8, 11, 15 mm) and thin steel sheet (2, 3, 4, 5 mm),and the two are layered cross each other. It has top flange plate and bottom flange plate, and its shape of plane is circular or rectangular. Its structure is shown in Fig. 1.

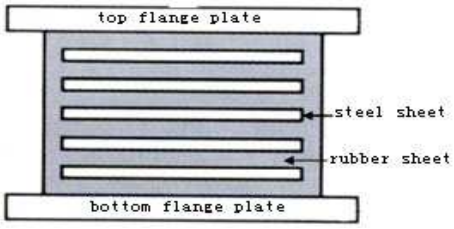


Fig.1 Rubber bearing

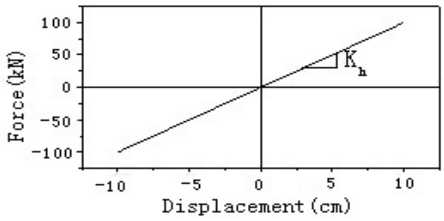


Fig.2 Calculation model of restoring force

The steel sheet in rubber can enhance the bearing stiffness under vertical load and the stability of the bearing under the action of horizontal force.The number, shape and design of the bearing are mainly determined by the size of the vertical load.

Massive experiments show that the hysteretic curve of laminated rubber bearing is long and narrow, and it can be approximately as a linear process. Its calculation model of restoring force is shown in Fig.2.

It shows that laminated rubber bearing almost has no ability of energy dissipation under shear deformation, so when it is used in actual engineering, it must work with other energy-consuming devices.

**Pot Rubber Bearing**

Pot rubber bearings have a rubber plate in a steel pot which can bear pressure and rotation, and use the low coefficient of friction between the stainless steel plate and the teflon to adapt to the request of the displacement of bridge. The bearing capacity of rubber has been actually improved due to the lateral restraint,which can make the rubber in a three-way compression state.

Compared with plate rubber bearings, pot rubber bearings have the advantages of better vertical bearing capacity, allowing larger displacement and flexible rotation. Pot rubber bearings not only have the advantages of low sliding friction coefficient, simple structure and compact structure, but also have the advantages of light weight, low building height, easiness of processing and saving steel,compared with general cast steel roller bearing.

**Lead Rubber Bearing(LRB)**

LRB is formed by inserting a lead rod vertically in the middle of rubber bearing. Lead has good elastic and plastic properties, so it has the ability to dissipate seismic energy during an earthquake. LRB 's structure is shown in Fig.3.

Fig.3 Lead rubber bearing

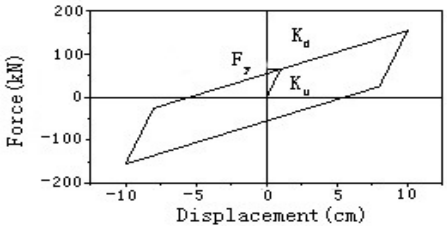


Fig.4 Force - displacement hysteretic model

The yield strength of lead is only 10Mpa, relatively low, but its initial shear stiffness can reach 130Mpa, and its fatigue characteristic is very well under the condition of plastic deformation. Lead rubber bearing has two kinds of stiffnesses,the one is initial stiffness($K_1$) and the other is yield stiffness($K_2$). The value of $K_1$ equals the sum of the value of shear stiffness of lead and rubber, and the value of $K_2$ just equals the value of shear stiffness of rubber.

LRB has excellent hysteretic characteristics, and it has high initial stiffness (more than 10 times of ordinary laminated rubber bearings') .But the resistance caused by temperature and creep is very low. The force - displacement hysteretic model of LRB can be expressed by the bilinear model shown in Fig.4. The area of hysteretic curve increases with the increasing of diameter,the number of lead, and the deformation. This shows that the energy of bearings deformation is higher than the energy which is released when unloading, and the other energy was absorbed by bearings. And that can makes the design of the LRB become very flexible.

**Friction Pendulum System(FPS)**

FPS takes use of the concept of pendulum to extend the natural vibration period to resist earthquake. The sliding surface is a curved surface so that we can utilize the restoring force required by the weight of the structure to make the structure have an effect of automatic resetting and reducing the maintenance work after earthquake. FPS was first proposed by Dr Victor Zayas in 1985. It has developed widely due to having solved the shift problems of many other bearings after earthquake,simple structure and cost-saving.

At present, China has developed six kinds of seismic isolation devices with automatic recovery capability. Among them friction pendulum isolation (FPI) and double spherical aseismic bearings are widely used. Their structures are shown in figure 5 and Fig.6.

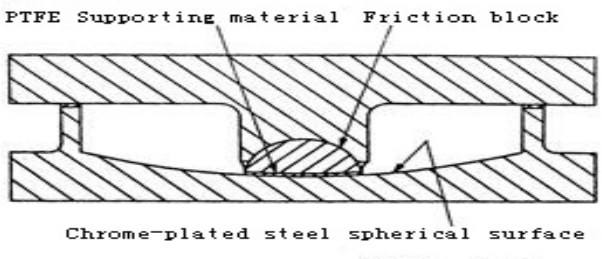


Fig.5 FPI

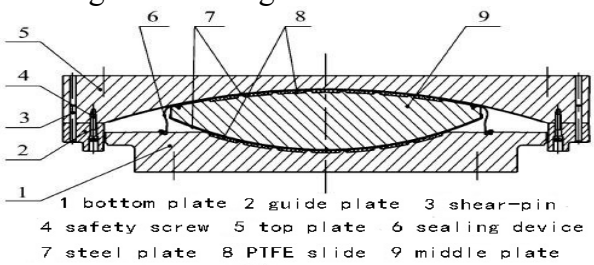


Fig.6 Double spherical aseismic bearing

FPI is shown in Fig.5, which is a lower sliding device and contains a slider with an aspherical surface and a ball type cast steel sliding surface. Both of the surfaces have the same curvature so that they are completely well tangent. Based on this, the compressive stress of the surface under vertical load is uniform. Bearing can slide in any direction, and its size is mainly controlled by the maximum design displacement.

Double spherical aseismic bearing is shown in Fig.6, which is an upper sliding device. Its working principle is similar to FPI's. It has a double spherical ball, a spherical cast steel sliding surface and a steel ball rotation surface. The spherical cast steel sliding surface and the steel ball rotation surface have the same curvature so that they can be also tangent to each other very well. Based on this, the compressive stress of the surface under vertical load is uniform. Bearing can slide in any direction, and its size is mainly controlled by the maximum design displacement.

The force-displacement model of FPS can be described by a bilinear model shown in Fig.7.

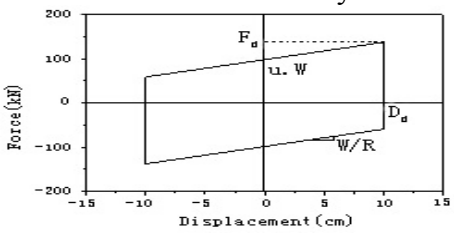


Fig.7 Force-displacement model

**Friction Roller Bearing**

Friction roller bearing is designed according to the phenomenon that the settings of rubber bearing and damper will make the integrated intensity of the structure decreased. For rubber bearing, the tensile strength is not high, when earthquake occurred, steel plate and rubber will be separated. Vertical ground motion will reduce the anti-slip ability of bearings. Rubber bearings don't have the device to limit relative displacement. Therefore, the increase of some relative displacement between beam and pier may lead to the increase of the stress of other piers.The structure of roller friction bearing is shown in Fig.8.

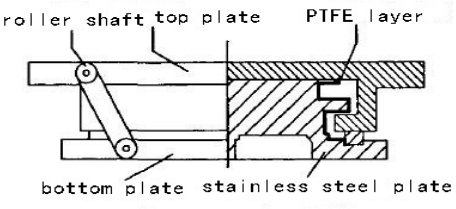


Fig.8 Friction roller bearing

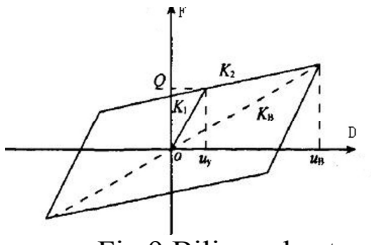


Fig.9 Bilinear hysteretic model

It contains an upper bearing plate and a lower bearing plate, and between the two plates there is a stainless steel plate. And there is a PTFE layer between the stainless steel plate and the bearing plate. The working mechanism of roller friction bearing is that the upper and lower bearing plates generate relative slip with the stainless steel plate to consumes the earthquake energy via sliding friction. Because of the roller, relative slip keeps in a certain range, which is easy to be reset and repaired after earthquake.

Using the bilinear model to simulate the hysteretic characteristics of friction roller bearing and adopting $K_1$(initial stiffness), $K_2$(yield stiffness) and Q(yield strength) as the bearing mechanics parameters,the bilinear hysteretic model of RFB is shown in Fig.9.

**Cable Damping Bearing**

Cable damping bearing is based on pot rubber bearing with additional limiting device. Pot rubber bearing shows the advantages of high vertical bearing capacity and large horizontal displacement, having good energy dissipation properties. However, it does not have the ability of automatic recovery under strong earthquake, which causes that the relative displacement of the main girder and pier is difficult to control. If this situation can not be controlled, after the earthquake the bearing will produce a great deal of residual deformation, which may even lead to falling girder. Based on this, the cable damping bearing under small earthquake and medium earthquake uses the bolt fixed function and utilizes shear bolts to consumpt energy and a cable machine to limit beam's displacement in great earthquake. Cable bearing's structure is shown in Fig.10.

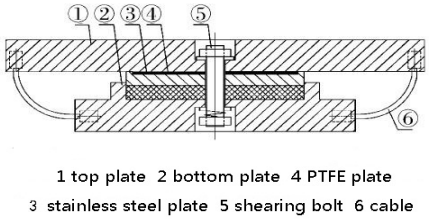


Fig.10 Cable damping bearing

Cable damping bearing belongs to sliding isolation bearing in nature. So it is not sensitive to seismic wave frequency relative to other supports.

Cable damping bearing has advantages of pot rubber bearing and high horizontal sliding ability, for small friction coefficient between PTFE plate and stainless steel plate of upper support. What's more, the cable successfully overcomes the weak horizontal limitation, making the bridge easy to reset after earthquake.

**Elastic-Plastic Falling-Off Prevention Ball Steel Bearing**

Elastic-plastic falling-off prevention ball steel bearing is jointly developed by Fengze Engineering Rubber Technology Development Stock Company.LTD and tongji university. Its structure is shown in Fig.11. The sliding surfaces between the top(base) bearing plate and the ball core can make the bearing meet the need of larger rotation.

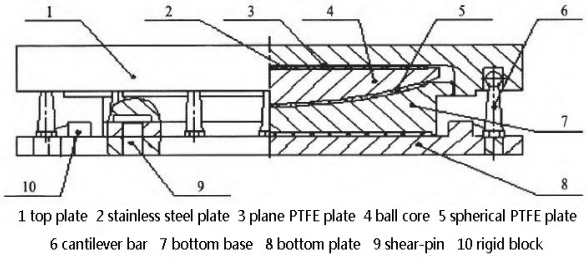


Fig.11 Elastic-plastic falling-off prevention ball steel bearing

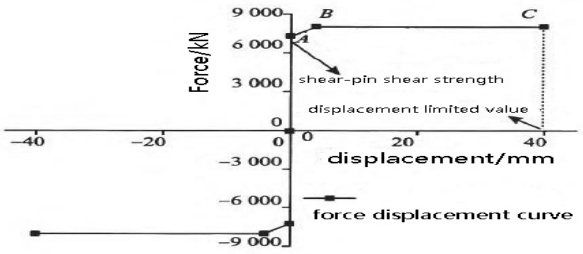


Fig.12 Force - displacement curve

The force - displacement curve of elastic-plastic falling-off prevention ball steel bearing is shown in Fig.12 . The "A" point in the Figure corresponds to the shearing strength of the shear pin (10% of the vertical force), and when the earthquake force is less than the shearing strength,the earthquake force is supported by the shear pin. If the earthquake force is greater than the shear strength, shear pin was cut,and the earthquake force is bearing by the cantilever bar. Cantilever bar has elastic and plastic phase. And when reached the plastic phase,the cantilever bar can dissipate energy.When the

displacement reached to the “C” point, it means that it has reached the ultimate state,and at that time the rigid block can limit the displacement of beam to prevent the girder falling.

## Summary

(1) There are also a large amount of other bearing types, such as height adjustable pot rubber bearing, tension-compression bearing, guide bearings,concrete hinge bearing, cylindrical bearings etc.. In addition, for earthquake-reduction and seismic-isolation,there are lots types of dampers, such as E-type steel damper, arc-shaped steel damper, short arm steel damper, elastic-plastic steel damper, fluid viscous dampers etc.. Some seismic measures may be jointly used to achieve better results.
(2) The seismic design of bearings is one of the most difficult parts in the seismic design of bridges.From the result of the destruction of the bridge in earthquake,there are also a large amount of bridges that were damaged due to the bearing failure. For the existing seismic bearings, their seismic principles are mainly "reduction and isolation", abandoning the thought of "stiff resistance" , and earthquake can be resisted by changing the natural vibration period and adding energy dissipation devices.
(3) Cliffide Flower, maintenance-free after the earthquake (good function of recovery), application of new materials, and simple-reliable structure must be considered together in the seismic design of bearings, and they are the development directions of bearing design. Although seismic bearings have been very mature, it’s very difficult to ensure that the bearing is completely reliable in earthquake. Materials are very important to bearings, and there is no time to delay for finding more powerful and more comprehensive materials. So, it must be the new material bearings that will change the bearing age.

## References

[1] Lichu Fan. Bridge Seismic(in Chinese) [M]. Tongji University Press, 1997

[2] Aijun Ye, Zhongguo Guan. Bridge Seismic(in Chinese) [M]. China Communications Press, 2011

[3] Junshen Zhuang. Bridge Bearing(in Chinese) [M]. China Railway Publishing House, 2010

[4] Junshen Zhuang. Bridge Aseismic Bearings And Device(in Chinese) [M]. China Railway Publishing House, 2012

[5] Dongsheng Wang. Damage to highway bridges during Wenchuan Earthquake(in Chinese) [J]. Journal of Earthquake Engineering and Engineering Vibration, 2009

[6] Wenzheng Zhu & Jianxin Liu. Influence of lead rubber bearing on earthquake resisting behavior of bridges(in Chinese) [J]. Journal of Chang’an University, 2004

[7] Hongmei Tang, Rongcan Liu & Hongkai Chen. A Study on Seismic Isolation Response of Bridges Friction Roller Bearings [J]. Highway Communication Science Technology, 2010

[8] Wancheng Yuan & Binbin Wang. Numerical Model and Seismic Performance of Cable-sliding Friction Aseismic Bearing(in Chinese) [J]. Journal of Tongji University, 2011

[9] Liying Nie & Guangpu Zhu. Application of Elastic-Plastic Falling-Off Prevention Ball Steel Bearings in Seismic Design of Bridge(in Chinese) [J]. Journal of Jiangnan University, 2013

*Applied Mechanics and Materials Vols. 580-583 (2014) pp 1511-1514*
*© (2014) Trans Tech Publications, Switzerland*
*doi:10.4028/www.scientific.net/AMM.580-583.1511*

# Feasibility Analysis of Applying Biomechanical Properties of Human Body to Seismic Design of Building Structure

Shasha Wu [a], Guanchang Kang [b], Shao Wang, Junying Lian [c]

School of Environment and Civil Engineering, Jiangnan University, Wuxi, China, 214122

[a] qushuishangshang@126.com, [b] weilaiweiran@126.com, [c] lindalianjunying@126.com

**Keyword:** high-rise building；anti-seismic；human spine；deformation；reset

**Abstract:** With the rapid development of high-rise buildings in our country, the seismic design of structures is becoming more and more important. And the seismic performance of traditional seismic system is not perfect, there are still some room for improvement. This article points out the advantages of the human body vertebra seismic system by comparing the characteristics of the current building aseismic system with the deep analysis of the human body vertebra seismic system and the application of the seismic characteristics of the human body vertebra in seismic design of building structure application foreground is prospected.

## Preface

The human body is like a building, and the bones of the human body is similar to the structural skeleton of the building. The human bones is formed for adapting to the different living environment during the long history. The morphology and structure of the bones are associated with their forces, meeting the most optional design principles. Skeleton has the abilities of anti-vibration, shock resistance and keeping its own balance, so it can provide a good reference for the modern seismic design of building. While the traditional ergonomics in the research of building design is mainly involved in anthropometry, environmental physiology and environmental psychology and so on, which usually takes the morphological features of the human body, human perception, and human response as the objects to study its application of the usage features of buildings, it seldom involves the application of human biomechanical properties in the seismic design of building. For now, our country's building structure design is a very important area in seismic design of building. With the development of high-rise buildings, seismic design of building structure is becoming increasingly important. Our current major seismic components in building earthquake-resistant structures are damper and seismic isolation rubber bearings. Seismic isolation rubber bearings are mainly used for base-isolated. It can significantly reduce the natural frequency of the structure, and is applicable to short period of low-rise and rigid structure. And the deformation damping capacity of the "damper" can only play a role when the structure is at a low speed movement. It is limited when the speed or the acceleration is over the corresponding value.

## Biomechanical properties of human bones.

The functions of human bones are movement, support and protect the body. It is a strong support for human body, functioning as leverage and anchor plates for movements. Human spine is the central axis of the bone of the body which is hard and flexible, also is the activity center of body and the transfer hub of force, enjoying good biomechanical properties. It could be able to bear the stress of squeeze, stretch, bend and rotation.

There are mainly three ways to realize the body vertebra's anti-shock, impact resistance as well as keep its structural balance and stability.

(1)Physiological curvature of the spine: the spine is the connection of vertabrae, intervertebral disc and ligaments. Seeing it from the side, it forms four physiological curves with neck and waist bent forward, chest and sacral backward. And by this, the spine is like an elastic fender which can adjust itself. Other four curves are conducive to maintaining the strength and stability of the intervertebral joints and increasing the adaptability and ability to absorb the impact of the spine.

(2)The elastic deformation of the intervertebral disc: intervertebal disc is a elastic cushion made up of fibrous cartilage, playing the cushion role between the intervertebral body. Under different load, it can absorb shocks and stabilize the spine by generating corresponding deformation.

(3) The elastic deformation of ligament: there are strong ligaments around the spine, which can stand the most tension load of it. By the mutualism between each ligament, it can limit the excessive deformation of the spine and reset the after deformation of the spine.

Support
Damping
Anti-cut

Cushion
Deformation and energy absorption
Stable spine

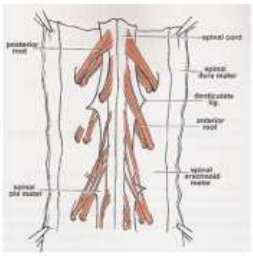

Bear tension load
Elastic deformation
Shrink back

**Morphology and mechanical properties of human bones conform to the requirements of building shape and structure performance**

Buildings shape aspect: in order to meet the needs of people's life or production, buildings should have a stable building space firstly. But, speaking of the human thorax, it is a conical bone cage which is flat at both the front and back parts with short front wall and long back wall for adults. It is just like a solid container, playing a role in supporting and protecting chest, abdomen and viscera. Its huge accommodation and perfect body can be a good choice for architectural bionic body.

Building structure: a good building should have good damping characteristics of energy dissipation and could maintain its stability. And the skeleton is the support frame of the body, in addition to support body weight, to protect the internal organs' function, bone in the spine also has the property of resisting to shock, pound and sustaining the balance of human body structure and stable features. Its seismic performance is adapted to the structure of the seismic demand.

**A preliminary attempt to apply the biomechanical properties of human bones in seismic structure design of building.**

**(1) Imitation of spinal shock absorber**

By abstracting the shock absorption of the human body, we apply it to the building structure seismic design. Thus, we designed the imitation of the human body vertebra shock absorber model, which has a kind of ideal seismic performance. See the Fig.1,Fig.2,Fig.3:

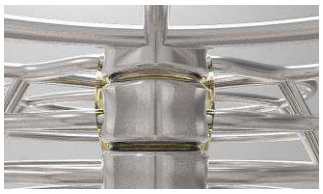

Fig.1

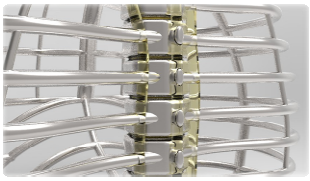

Fig.2

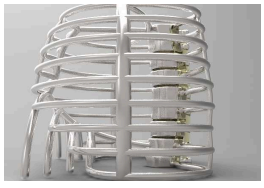

Fig.3

Fig.1, Fig.2, Fig.3 shows the main features of the structure:

1) Imitation of the spine internode shock: the force bearing pole in the middle is similar to the human body's vertebra, and the link between each section is like the joints. Every section is an

absolute rigid body that no distortion occurs. But the internode material has certain elasticity, and could have a small deformation. Between the adjacent internode, it has the cushion effect. Under the different load, it produces the corresponding deformation and it can absorb the shock and keep the integral structure in stable.

2) Imitation of the ligament flexibility reset: the elastic fibers, run through up and down, is similar to human body's ligaments. It can bear the most tension load of the spine and limit the excessive deformation of the spine, making the spine can be reset after the shock absorption of the spine deformation. At the same time, it can also absorb the suddenly imposed enormous amounts of energy and can effectively absorb the shock in the fast loading environment.

3) Imitation of the spinal flexion shock: internode connection and ligaments can realize "spine" as a force rod, which has greater rigidity and can form tiny curvature. Such "spine" is like an elastic curved bar, and is beneficial to maintain the stability of the gravity center of the building and reduce the shocks. Its small curvature increased the adaptability and ability of absorbing the pound of the spine.

**(2) The imitation of human body earthquake-resistant structure**

As mentioned before, the thorax of the human body not only has a large accommodation space, but also has a perfect body, which can accommodate and protect the vital organs. Its function is similar to the peripheral guardrail of the building. Therefore, we use human thoracic model in the shape design of the building, apply the structure and construction of the human spine in design of anti-seismic structures of building and imagine a human-like seismic structure through improvement and innovation.

**Holism**: the whole structure is consists of two bilateral "thorax" and "spine", and the total weight of "thorax" is borne with three parts. The first part is passing from the thorax to the progressive transformation of the four big arches, and most load is borne by the arch; the second part is from the vertical bar at the two sides to the ground; the third part is from the three poles at the top to the "spine". Among them, in the middle of the bilateral structure, a shockproof seam is set up in order to prevent the two of them influence each other in an earthquake.

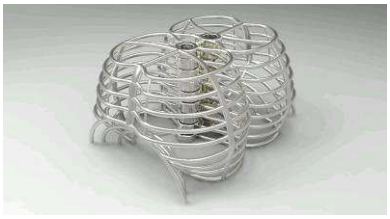

Fig.4

**Forecasting the prospect of applying the human sciences to the seismic design of building**

With the development of bionics, the bionics structure has been more and more widely used in structural design of the building. The common applies are hive-like structure, bamboo-like structure, spider web-like structure and the bird's nest-like structure, etc. But so far, the attention of the human skeleton-like structure is still very low in the construction industry.

In our country, building aseismic level has been developed to a certain stage. At present, the most commonly used domestic seismic components are dampers and rubber isolation bearing. People usually think the damper on the building is similar to the human body joint connection, has the function of deformation and damping; and the shape of the prestressed reinforcement is similar to the shape of the human body's ligament. But it must be stressed that the current damper damping device is much less perfect than the human body's shock absorption system.

First of all, the damper's abilities of deformation and damping are limited by structural motion state, not yet reaching the effect of human joints' damping layer by layer. Second, the damper a poor ability to reset after deformation of shock absorbing, but the ligaments around the human spine can effectively reset after the deformation. In addition, the current dampers and design of building structure is separate, and this make the structure cannot bear the vertical load when it is damping.

While the human's spine is the combination of load and suspension, it can achieve damping under vertical load at the same time, and can effectively reset. It is needed to be clear that the prestressed reinforcement in building is looked as same as the spine, but the load and damping theory of them are totally different. Human's spine is only depend on its own elastic property, allowing a certain deformation of the spine and can also collect rally energy to reset after the deformation of the spine.

## Conclusion

Through the above analysis, we know that it is completely feasible to apply the biomechanical properties of human bones in the seismic design of building structure. The shock absorption mechanism of human's absorption system still has a lot for the seismic building structure to learn from. For example, we can make use of spinal flexion damping principle to study what kind of curvature can maintain the stability of the structure and conducive to the structural damping at the same time. We can also dig the body joints' advantages in shape, structure, etc. And apply to the improvements of the damper damping performance. We can also invent a kind of prestressed elastic reset function according to the principle of elastic reset of the human body's ligament. Human body structure's potential is much far than this in terms of seismic design of building structure. It is like a huge treasure, holding so many secrets waiting for our civil engineer to discover. I believe in the future, the development and utilization of the seismic system of human body structure will make great contribution to the buildings' earthquake prevention and disaster reduction in the 21st century.

## Reference

[1] Changjiang Jiang,Yuquan Liu. China's high-rise building seismic design methods and prospect(in Chinese). Spread of science and technology, 2010 (18)

[2] Jingyu Su, Demin Zeng. The research and application of building structure vibration isolation technology in China(in Chinese). Earthquake engineering and engineering vibration, 2001 (S1)

[3] Chunfu Jin. introduction to building structure seismic design method(in Chinese). The China science and technology information, 2006 (01)

[4] Gaofeng Wei, Chengtao Wang. human skeletal muscle system(in Chinese). Study of the biomechanical modeling and simulation analysis of Shanghai jiaotong university, 2010

[5] Chengtao Wang. Mechanical virtual people [J]. China medical biomechanics, 2006

*Applied Mechanics and Materials Vols. 580-583 (2014) pp 1515-1520*
*© (2014) Trans Tech Publications, Switzerland*
*doi:10.4028/www.scientific.net/AMM.580-583.1515*

# A Method for Checking Eccentricity of Solid Concrete Piers with Low Longitudinal Reinforcement Ratio under a Minor Earthquake

Xingchong Chen[1, a],Zunwen Liu[1, b],Yongliang Zhang [1,c]and Lu Pei[1, d]

[1]School of Civil Engineering, Lanzhou Jiaotong University, Lanzhou, Gansu, 730070, China

[a]chenxingchong@263.net, [b]lzjtulzw@163.com, [c]zhangyong_L@126.com,[d]493968244@qq.com

**Keywords:** concrete with low longitudinal reinforcement ratio; solid pier; minor earthquake; checking parameters

**Abstract.** Solid concrete piers with low longitudinal reinforcement ratio are extensively used in high-speed railway in China. However, how to check such structures is not specified in current technical codes. Checking these structures by eccentricity and stress indexes is discussed hereby. The moment-curvature relationships for piers of various reinforcement ratios are presented by employing the software UCfyber and these moments are compared with moments calculated by allowable stress approach, moments corresponding to the code-specified permissible eccentricity, moments corresponding to the allowable reinforcement stress and stabilizing moments induced by tensile reinforcement and self weight of the piers, respectively. The results show that the allowable stress approach could be used to check the strength and eccentricity of solid concrete piers with low longitudinal reinforcement ratio in high-speed railway; the restriction on permissible eccentricity may be to a proper extent relaxed for such piers, based on the fact that tensile reinforcement provides an additional stabilizing moment and the reinforcement contributes to the pier's bearing capacity.

## Introduction

Nowadays, high-speed railway is developing rapidly around the world. As for concrete piers used in high-speed railway bridges, there are a variety of types. Solid round-ended slab-type piers, circular piers and rectangular piers are usually used in small-span bridges in Germany, France and other western European countries. And, due to the seismic intensity of western European countries being comparatively low, the seismic action is generally not a controlling factor.[1] In Japan, continuous reinforced concrete rigid-frame bridges with a span of approximately 10 meters and a high reinforcement ratio are extensively used. In China, solid concrete piers are characterized by a reinforcement ratio less than 0.5% in most cases, even in areas of high seismic intensity.[2]. With the strict limitations on longitudinal force induced by rail breaking and transverse stiffness, the section size, stiffness, and weight of bridge piers used in high-speed railway are comparatively great, resulting a large seismic force. Without a proper seismic design, these piers would be prone to damage.

Unfortunately, how to check solid concrete piers with low longitudinal reinforcement ratio under a minor earthquake is not specified in current technical codes. Alternatively, checking method for masonry or common reinforced concrete structures are adopted in practical design, which is not reasonable. The checking method for masonry structures is too conservative for such piers while the checking method for common reinforced concrete structures needs to be further verified. Yanzhong Ju performed pseudo-static testing on ten scale-modelled piers with low longitudinal reinforcement ratios of 0.1% and 0.2%, exploring the relationship between the pier's ductility and shear span ratio, longitudinal reinforcement ratio and hooping reinforcement ratio[3]. Lizhong Jiang, et. al. conduted pseudo-static testing on solid round-ended piers with low longitudinal reinforcement ratios, concluding that the hysteretic curve being of dramatically pinched shape[4]. Shiqiaozhongliang, et.al. performed low-cycle fatigue testing on scale-modelled railway piers with low longitudinal reinforcement ratio varying from 0.12% to 1.66%, and worked out the formulas of displacement ductility coefficient of the piers[5,6]. However, the above mentioned studies focus on energy dissipation capacity and deformability of concrete piers with low longitudinal reinforcement ratio

under a major earthquake, not concerning the problems under a minor earthquake. In this paper, the seismic checking of solid concrete railway bridge piers with low longitudinal reinforcement ratios under a minor earthquake is to be studied.

**Analysis process**

As far as the minor earthquake condition is concerned, the current seismic code requires checking on strength and stability for reinforced concrete piers, and requires checking on eccentricity, strength and stability for plain concrete piers. For reinforced concrete piers, the allowable stress approach is adopted to check the tensile stress of reinforcement and the compressive stress of concrete to ensure they are within a permissible value. For plain concrete or masonry piers, eccentricity design is the major consideration since the pier is prone to cracking under eccentric loading, due to the low tensile strength of plain concrete and masonry. If the cracking is severe, the plain concrete and masonry are vulnerable to moisture erosion. Meanwhile, a large tension zone on the section is not favorable to the stability of the pier. The eccentricity checking is to ensure crack resistance and stability.

However, how to check solid concrete piers with low longitudinal reinforcement ratios is not specified in current technical codes. .This paper is to deal with this problem by performing analysis of the strength, stability and sectional moment-curvature relationship of the pier. The detailed work is listed below.

(1)Analysis of the moment at pier-bottom section by the allowable stress approach

It is well known that the allowable stress approach involves the following basic assumptions:.

a.The assumption of plane section, which means that a plane section before bending remains a plane section after bending.

b.The assumption of elastic body, which means that the stress is proportional to the strain (in the compression zone).

c.The tensile strength of the concrete is neglected.

(2) Analysis of the moment corresponding to the code-specified permissible eccentricity.

For a rectangular section, the permissible eccentricity is specified to be 0.8S, where S is the distance between the centroid of the cross section and the extremely compressed fiber. The corresponding moment is M=N×0.8S. The vertical force N at the pier bottom is a resultant force of the concentrated force applied at the pier top and the self weight of the pier.

(3)Analysis of the stabilizing moment

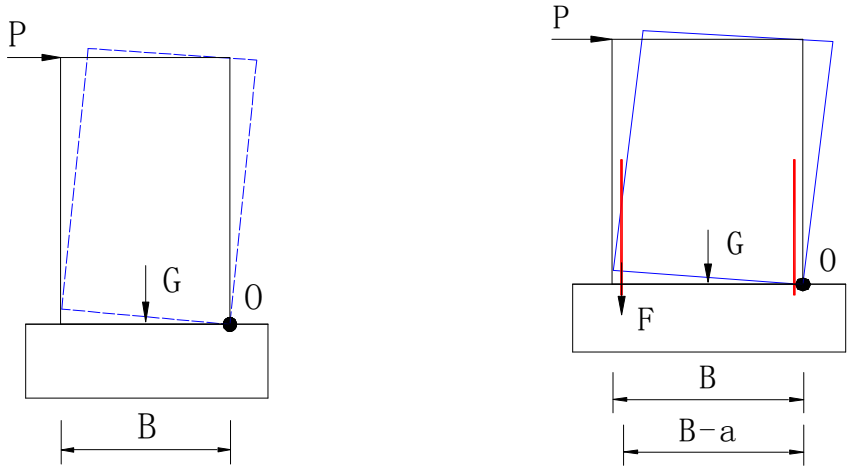


(1) Stabilizing moment produced by the pier’s self weight

(2) Stabilizing moment produced by the tensile reinforcement and the pier’s self weight

Fig.1 Stabilizing moment

The stabilizing moment offered by the pier’s self weight can be calculated as follows:

$$M=G\bullet\ 0.5B \tag{1}$$

The stabilizing moment offered by the tensile reinforcement and the pier’s self weight can be calculated as follows:

$$M=G\bullet\ 0.5B+F\bullet\ (B-a) \quad (2)$$

$$F=n\bullet\ fy\bullet\ As \quad (3)$$

where, F means tensile force of the reinforcement in the tension zone; fy means the yielding stress of the reinforcement; As means the sectional area of a single steel bar; n means the number of the reinforcement bars in the tension zone; a means the thickness of concrete cover; B means the sectional dimension along the direction of horizontal loading.

Overall analysis of the moment-curvature relationship at the pier bottom

The UCfyber software is employed to obtain the moment-curvature relationship of the pier-bottom section. The Mander model is applied in the stress-strain relationship of the concrete while a parabola model is adopted as the stress-strain relationship of the reinforcement.

## Numerical examples

### 2.1 Rounded-ended piers

A double-line simply-supported box-girder bridge is chosen, which has round-ended piers. The pier section comprises a linear segment of 3.4m and two circular segments with a diameter of 2.6m. The weight of the girder over a single span is 14379kN. C30 concrete is adopted for the bridge. The reinforcement ratios of 0.05%, 0.1%, 0.2%, 0.3%, and 0.4% are selected for the pier, respectively. The height of the pier's straight-section is 11m.

#### 2.1.1 The case of longitudinal reinforcement being HRB335

With the longitudinal reinforcement being HRB335, the eccentricity magnification coefficient is shown in Table 1 and Table 2. From the tables, we can see:

(1)For solid concrete piers with low longitudinal reinforcement ratio, the restriction on permissible eccentricity may be to a proper extent relaxed, based on the fact that tensile reinforcement produces an additional stabilizing moment and the reinforcement contributes to the pier’s bearing capacity. With the safety factor being unchanged, the eccentricity of the pier with reinforcement ratios of 0.1%, 0.2%, 0.3%, and 0.4% may be relaxed to 0.90S, 1.0S, 1.1S, 1.2S, respectively.

(2)For the pier with reinforcement ratio less than 0.4%, it is too conservative to base the seismic design on an eccentricity of 0.8S. It is applicable to check the pier’s strength through allowable stress approach, which actually ensures both its strength and stability.

Tab. 1 Results for eccentricity magnification coefficient of pile-bottom section(controlled by stabilizing moment)

| reinforcement ratio /% | moment corresponding to code-specified permissible eccentricity (0.8S)/kN·m | stabilizing moment induced by pier's weight/kN·m | safety factor corresponding to code-specified permissible eccentricity | stabilizing moment induced by tensile reinforcement and pier's weight/kN·m | Inversely computed permissible eccentricity | eccentricity magnification coefficient |
|---|---|---|---|---|---|---|
| 0.05 | 19354 | 23608 | 1.22 | 25600 | 0.87S | 1.08 |
| 0.1 | 19354 | 23608 | 1.22 | 27609 | 0.94S | 1.17 |
| 0.2 | 19354 | 23608 | 1.22 | 31694 | 1.07S | 1.34 |
| 0.3 | 19354 | 23608 | 1.22 | 35456 | 1.20S | 1.50 |
| 0.4 | 19354 | 23608 | 1.22 | 39502 | 1.34S | 1.67 |

Tab. 2 Results for eccentricity magnification coefficient of pile-bottom section(controlled by moment corresponding to allowable stress)

| reinforcement ratio /% | moment corresponding to code-specified permissible eccentricity (0.8S)/kN·m | stabilizing moment corresponding to allowable stress/kN·m | stabilizing moment induced by tensile reinforcement and pier's | Correspondi-ng safety factor | Inversely computed permissible eccentricity | eccentricity magnification coefficient |
|---|---|---|---|---|---|---|
| 0.05 | 19354 | 20300 | 25600 | 1.26 | 0.84S | 1.05 |
| 0.1 | 19354 | 21800 | 27609 | 1.27 | 0.90S | 1.13 |
| 0.2 | 19354 | 24700 | 31694 | 1.28 | 1.02S | 1.28 |
| 0.3 | 19354 | 27200 | 35456 | 1.30 | 1.12S | 1.41 |
| 0.4 | 19354 | 30200 | 39502 | 1.31 | 1.25S | 1.56 |

### 2.1.2 The case of longitudinal reinforcement being HRB400

With the longitudinal reinforcement being HRB400, the eccentricity magnification coefficient is shown in Table 3 and Table 4. From the tables, it can be seen that with the increase of the reinforcement strength, the allowable eccentricity of the pile-bottom section may be further improved. For the pier with reinforcement ratios of 0.1%, 0.2%, 0.3%, and 0.4%, the eccentricity may be relaxed to 0.90S, 1.0S, 1.2S, 1.3S, respectively. For the pier with reinforcement ratios between 0.1% and 0.4%, the permissible eccentricity may be determined by the method of linear interpolation.

## 2.2 Circular piers

A 32m double-line simply-supported box-girder bridge is chosen, which has circular piers. The diameter of the pier's section is 4.0m. The weight of the girder over a single span is 12898kN. C30 concrete and HRB400 reinforcement are adopted for the bridge. The height of the pier is 10m. The results are shown in Tab.5 and Tab.6.

Tab. 3 Results for eccentricity magnification coefficient of pile-bottom section(controlled by stabilizing moment)

| reinforcement ratio /% | moment corresponding to code-specified permissible eccentricity (0.8S)/kN·m | stabilizing moment induced by pier's weight/kN·m | safety factor corresponding to code-specified permissible eccentricity | stabilizing moment induced by tensile reinforcement and pier's weight/kN·m | Inversely computed permissible eccentricity | eccentricity magnification coefficient |
|---|---|---|---|---|---|---|
| 0.05 | 19354 | 23608 | 1.22 | 26410 | 0.89s | 1.12 |
| 0.1 | 19354 | 23608 | 1.22 | 29407 | 1.00s | 1.25 |
| 0.2 | 19354 | 23608 | 1.22 | 35099 | 1.19s | 1.49 |
| 0.3 | 19354 | 23608 | 1.22 | 40163 | 1.36s | 1.70 |
| 0.4 | 19354 | 23608 | 1.22 | 46088 | 1.56s | 1.95 |

Tab. 4 Results for eccentricity magnification coefficient of pile-bottom section(controlled by moment corresponding to allowable stress)

| reinforce-ment ratio /% | moment corresponding to code-specified permissible eccentricity (0.8S)/kN·m | stabilizing moment corresponding to allowable stress/kN·m | stabilizing moment induced by tensile reinforcement and pier's weight/kN·m | Correspon-ding safety factor | Inversely computed permissible eccentricity | eccentricity magnification coefficient |
|---|---|---|---|---|---|---|
| 0.05 | 19354 | 21160 | 26410 | 1.25 | 0.87s | 1.09 |
| 0.1 | 19354 | 22800 | 29407 | 1.29 | 0.94s | 1.18 |
| 0.2 | 19354 | 26000 | 35099 | 1.35 | 1.07s | 1.34 |
| 0.3 | 19354 | 29200 | 40163 | 1.37 | 1.21s | 1.51 |
| 0.4 | 19354 | 32300 | 46088 | 1.42 | 1.34s | 1.67 |

Tab. 5 Results for eccentricity magnification coefficient of pile-bottom section(controlled by stabilizing moment)

| reinforcement ratio/% | moment corresponding to code-specified permissible eccentricity (0.7S)/kN·m | stabilizing moment induced by pier's weight/kN·m | safety factor corresponding to code-specified permissible eccentricity | stabilizing moment induced by tensile reinforcement and pier's weight/kN·m | Inversely computed permissible eccentricity | eccentricity magnification coefficient |
|---|---|---|---|---|---|---|
| 0.05 | 24737 | 35339 | 1.42 | 38155 | 0.75S | 1.08 |
| 0.1 | 24737 | 35339 | 1.42 | 40969 | 0.81S | 1.16 |
| 0.2 | 24737 | 35339 | 1.42 | 46667 | 0.92S | 1.32 |
| 0.3 | 24737 | 35339 | 1.42 | 52342 | 1.03S | 1.48 |
| 0.4 | 24737 | 35339 | 1.42 | 57419 | 1.13S | 1.62 |

Tab. 6 Results for eccentricity magnification coefficient of pile-bottom section(controlled by moment corresponding to allowable stress)

| reinforcement ratio /% | moment corresponding to code-specified permissible eccentricity (0.7S)/kN·m | stabilizing moment corresponding to allowable stress/kN·m | stabilizing moment induced by tensile reinforcement and pier's weight/kN·m | corresponding safety factor | Inversely computed permissible eccentricity | eccentricity magnification coefficient |
|---|---|---|---|---|---|---|
| 0.05 | 24737 | 27800 | 38155 | 1.37 | 0.78S | 1.12 |
| 0.1 | 24737 | 29600 | 40969 | 1.38 | 0.83S | 1.19 |
| 0.2 | 24737 | 33100 | 46667 | 1.41 | 0.93S | 1.33 |
| 0.3 | 24737 | 37000 | 52342 | 1.41 | 1.04S | 1.49 |
| 0.4 | 24737 | 40400 | 57419 | 1.42 | 1.14S | 1.63 |

From Table 5 and Table 6, it is clear that for the circular pier with reinforcement ratios of 0.1%, 0.2%, 0.3%, and 0.4%, the eccentricity may be relaxed to 0.8S, 0.9S, 1.0S, 1.1S, respectively. .For the pier with reinforcement ratios between 0.1% and 0.4%, the permissible eccentricity may be determined by the method of linear interpolation.

## Conclusions

（1） The solid concrete pier with a reinforcement ratio less than 0.1% can be handled as a plain concrete pier, due to the fact that the permissible eccentricity is increased just to a very limited extent.

（2）For the solid pier with reinforcement ratio between 0.1% and 0.4%, the permissible eccentricity .may be to a proper extent relaxed, based on the fact that tensile reinforcement provides an additional stabilizing moment and the reinforcement contributes to the pier's bearing capacity.

（3）For the circular or rectangular piers with reinforcement ratio between 0.1% and 0.4%, strength checking can be developed through allowable stress approach, which would ensure the sectional strength and the stability of the pier as well.

## Acknowledgments

This work is supported by the National Natural Science Foundation of China (Grant No.: 51268027) and by the Program for Changjiang Scholars and Innovative Research Team in University (Grant No.: IRT1139), Ministry of Education, China. The authors wish to express theirs thanks for the support.

## References

[1] ZHENG Jian. High-speed railway bridges in China [M]. Beijing: Higher Education Press, 2001. (In Chinese)

[2] GB50111—2006, Code for Seismic Design of Railway Engineering [S]. China Planning Press, 2009. (In Chinese)

[3] JU Yanzhong, YAN Guiping, LIU Lin. Experimental Study on Seismic Behavior of Large-scale RC Round-ended Piers with low longitudinal reinforcement ratio [J]. China Civil Engineering Journal, 2003, 36(11): 65-69. (In Chinese)

[4] JIANG Lizhong, SHAO guangqiang, JIANG jingjing, WANG hui. Experimental Study on Seismic Performance of Solid piers with Round-ended Cross-section in High-speed Railway [J]. China Civil Engineering Journal, 2013, 13 (3): 86-95. (In Chinese)

[5] LIU Qinghua, YAN Guiping, CHEN Yingjun. Experimental Studies on Seismic Behavior of Reinforced Concrete Bridge Piers [J], Journal of Northern Jiaotong University, 1996, 20(5): 517-521. (In Chinese)

[6] FAN Lichu, ZHUO Weidong. Seismic Ductility Design of Bridges [M]. Bei Jing: China Communication Press, 2001. (In Chinese)

*Applied Mechanics and Materials Vols. 580-583 (2014) pp 1521-1527*
*© (2014) Trans Tech Publications, Switzerland*
*doi:10.4028/www.scientific.net/AMM.580-583.1521*

# Application of the Jerk Feedback on the Shaking Table

Fangfang LI [1, a], Jinbao JI [1,b], Xiaojun LI [1,c] and Na LI [1,d]

[1] Beijing Key Laboratory of Earthquake Engineering and Structural Retrofit, Beijing University of Technology, Beijing, China

[a]fangfangbjut@126.com, [b]jinbao@bjut.edu.cn, [c]beerli@vip.sina.com, [d]lina15275166945@163.com

**Keywords:** shaking table, jerk, multi-variable control, system simulation

**Abstract.** For the shaking table system, the $90^o$ phase shift frequency of the servo valve system is close to the oil column resonance frequency, the bandwidth under the influence of servo valve features was so narrow that it cannot meet requirements. Multi-variable control is presented in this paper by introducing the jerk feedback on the basis of the three-variable control. The theoretical derivation and the system simulation show that: the jerk feedback can reduce the oil column resonance frequency, and decrease the influence of the system performance caused by the servo valve characteristics.

## Introduction

The shaking table is the most direct and the most effective research tool of the engineering seismic field. Since 1890, the Japanese started using mechanical devices to attempt to simulate earthquake[1,2], The United States, Japan, China, Britain and other countries built hundreds of different scale shaking table[3]. At the same time, as the developments of the hydraulic, electronic, automation, sensors, signal processing, control technology, the shaking table realized the transition from analog control to digital control, and the transition from displacement PID control to the acceleration feedback control, then the three-variable control (displacement, velocity and acceleration) become the basic control algorithm of the shaking table[4,5]. The three-variable control of shaking table uses the feedback of displacement, acceleration and the velocity synthesized from acceleration integral and displacement differential to realize a closed loop control. The studies of the domestic and foreign scholars have shown that the actuator cylinder could be positioned by the displacement feedback, the range of the using frequency could be extended by the velocity feedback, and the stability of the system could be improved by the acceleration feedback[6~8]. However, when the $90^o$ phase shift frequency of the servo valve system is close to the oil column resonance frequency, the system characteristics are seriously influenced by the characteristic of servo valve, at the same time the influence caused by the characteristic of servo valve could not be removed by changing the control gains of the three-variable control. The bandwidth of the system is narrow and it could not meet requirements.

In order to solve this problem, the present paper puts forward a multi-variable control algorithm. The multi-variable control algorithm is formed by adding the jerk feedback on the basis of the three-variable control algorithm. The jerk feedback can reduce the oil column resonance frequency, and decrease the influence of the system performance caused by the servo valve characteristics.

## System analysis

### System analysis with the jerk feedback

Jerk, the physical quantity to describe the acceleration's variation, is determined by the acceleration's variation and time. The jerk feedback is introduced in the open loop transfer function of the electro-hydraulic servo system. The system block diagram is shown in the Fig. 1.

In the Fig.1, $u$ is the input signal of the system, $x$ is the output signal of the system, $E$ is the control-error signal, $k_q$ is the flow gain of slide valve near the static working point, $K_c$ is the flow

pressure coefficient of the slide valve near the steady state motion point, $C_c$ is the total leakage coefficient, $v$ is the oil cylinder equivalent volume, $\beta$ is the oil bulk modulus of elasticity, $P_L$ is the load pressure, $A_p$ is the effective pressure area of piston, $M$ is the mass of load, $K_j$ is the gain of the jerk feedback.

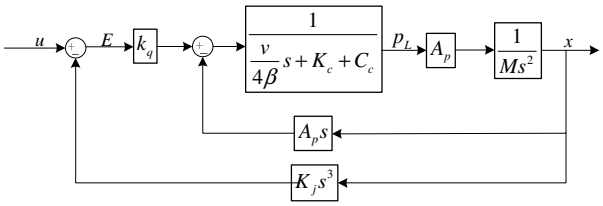


Fig.1 The transfer function diagram with the jerk feedback

The transfer function diagram of the system is：

$$\frac{x}{u}=\frac{k_q}{A_p}\frac{1}{\left(\frac{1}{n_j^2}s^2+\frac{2D_j}{n_j}s+1\right)s} \tag{1}$$

Where

$$\begin{cases}\dfrac{1}{n_j^2}=\dfrac{1}{n_0^2}+\dfrac{k_q k_j}{A_p}\\ \dfrac{2D_j}{n_j}=\dfrac{2D_0}{n_0}\end{cases} \tag{2}$$

$$\begin{cases}n_0^2=\dfrac{4\beta A_P^2}{MV}\\ \dfrac{2D_0}{n_0}=\dfrac{M(K_C+C_C)}{A_P^2}\end{cases} \tag{3}$$

Where $n_0$ is the oil column resonance frequency of the actuating cylinder, $D_0$ is the damping ratio, $n_j$ is the oil column resonance frequency of the system with the jerk feedback, $D_j$ is the damping ratio of system with the jerk feedback.

The equation(2)shows that when the jerk feedback is negative feedback, $k_j>0$, $n_j<n_0$, $D_j<D_0$, the oil column resonance frequency and the damping ratio are decreased, and when the jerk feedback is positive feedback, $k_j<0$, $n_j>n_0$, $D_j>D_0$, the oil column resonance frequency and the damping ratio are improved.

**System analysis with multiple feedback control**

The system with multiple feedback control is formed by introducing the jerk feedback into the three-variable control (the displacement feedback, the velocity feedback and the acceleration feedback). The system block diagram is shown in the Fig.2.

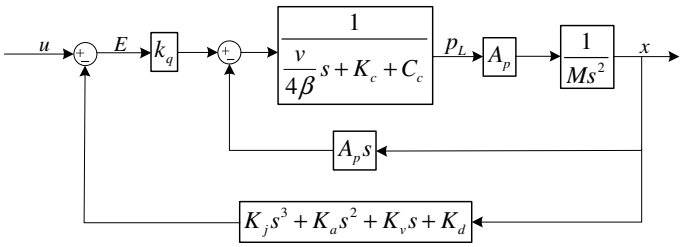


Fig.2 The transfer function diagram with the multiple feedback control

According to the Fig.2, the transfer function diagram of the system is：

$$\frac{x}{u_0}=\frac{k_q A_d}{A_p}\frac{1}{\frac{s^3}{n_0^2}+\frac{2D_0 s^2}{n_0}+s+\frac{k_q}{A_p}(K_{j0}A_j^{'}s^3+K_{a0}A_a^{'}s^2+K_{v0}A_v^{'}s+K_{d0}A_d^{'})} \tag{4}$$

Where $u_0$ is the command signal, $A_d$ is the gain of the displacement input, $A_d^{'}$ is the gain of the displacement feedback, $A_v^{'}$ is the gain of the velocity feedback, $A_a^{'}$ is the gain of the acceleration feedback, $K_{d0}$ is the normalized sensitivity of the displacement feedback, $K_{v0}$ is the normalized sensitivity of the velocity feedback, $K_{a0}$ is the normalized sensitivity of the acceleration feedback, $K_{j0}$ is the normalized sensitivity of the jerk feedback.

Equation（4）can be simplified as

$$x=\frac{A_d}{K_{d0}A_d^{'}}\frac{1}{\frac{1}{k'}\left(\frac{s^2}{n^2}+\frac{2Ds}{n}+1\right)s+1}u_0 \tag{5}$$

Where

$$\begin{cases} A_d^{'}=\dfrac{kA_p}{k_q K_{d0}}=\dfrac{k'A_p}{k_q K_{d0}}\dfrac{k}{k'} \\ A_v^{'}=\dfrac{A_p}{k_q K_{v0}}\left(\dfrac{k}{k'}-1\right) \\ A_a^{'}=\dfrac{A_p}{k_q K_{a0}}\left(\dfrac{2D}{n}\dfrac{k}{k'}-\dfrac{2D_0}{n_0}\right) \\ A_j^{'}=\dfrac{A_p}{k_q K_{j0}}\left(\dfrac{1}{n^2}\dfrac{k}{k'}-\dfrac{1}{n_0^2}\right) \end{cases} \tag{6}$$

$$\frac{1}{n^2}=\frac{\left(1+\frac{k_q K_{j0}A_j^{'}n_0^2}{A_p}\right)}{1+\frac{k_q}{A_p}K_{v0}A_v^{'}}\frac{1}{n_0^2} \tag{7}$$

$$\frac{2D}{n}=\frac{1}{1+\frac{k_q}{A_p}K_{v0}A_v^{'}}\left(\frac{2D_0}{n_0}+\frac{k_q K_{a0}A_a^{'}}{A_p}\right) \tag{8}$$

The equation(7) shows that：

（1）when $K_{v0}A_v^{'}=K_{j0}A_j^{'}n_0^2$, $n=n_0$

（2）when $K_{v0}A_v^{'}>K_{j0}A_j^{'}n_0^2$, $n>n_0$

（3）when $K_{v0}A_v^{'}<K_{j0}A_j^{'}n_0^2$, $n<n_0$

The equation(8) shows that：

When without velocity feedback nor jerk feedback

$$\frac{2D}{n}=\left(\frac{2D_0}{n_0}+\frac{k_q K_{a0}A_a^{'}}{A_p}\right) \tag{9}$$

As the existence of the velocity feedback, thus

$$\frac{1}{1+\frac{k_q}{A_p}K_{v0}A_v^{'}}<1 \tag{10}$$

The introduction of jerk is no influence on the system damping, so we can adjust $A_a^{'}$ to reach the needed damping ratio, increase the damping ratio of system, which can improve the oil column resonance frequency and improve the system stability.

**System analysis with different bandwidth of servo valve**

In the control of multiple s with the jerk feedback, analysis was made using the shaking table system with different bandwidth of servo value (40Hz, 60Hz, 80Hz and 100Hz). The frequency responses of the system are shown in figure 3(a, b, c, d).

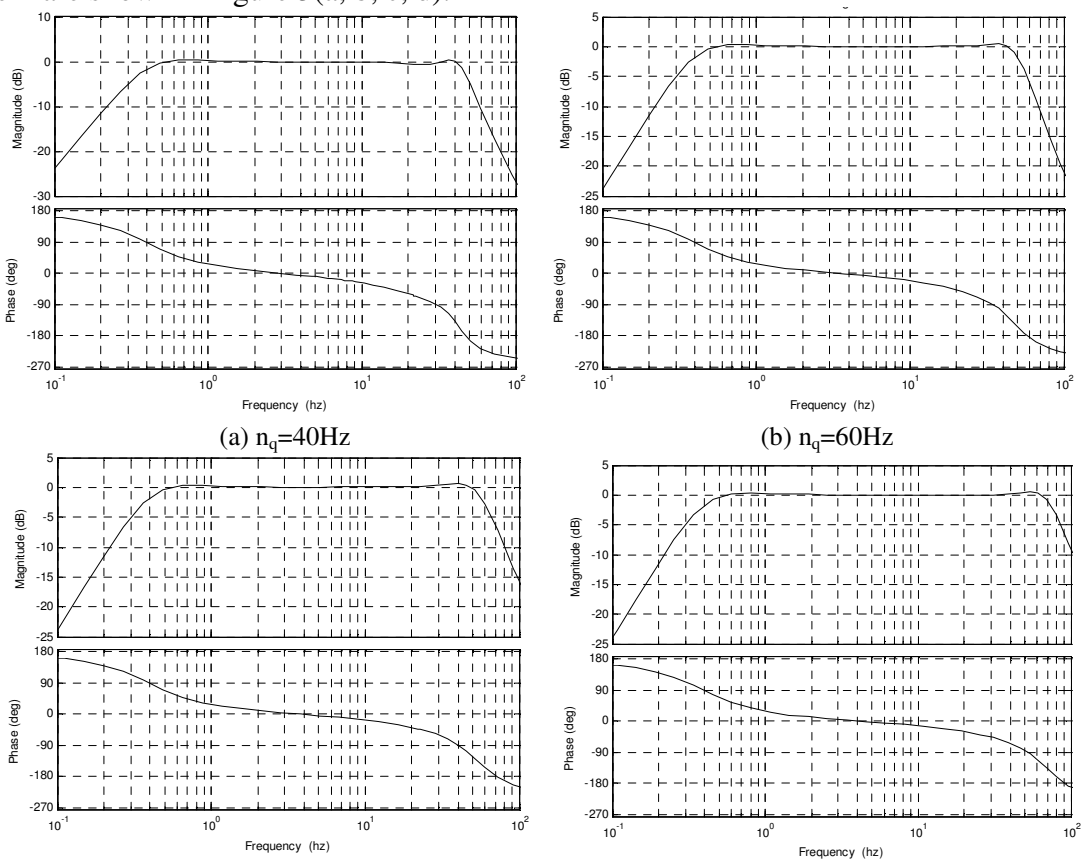


(a) $n_q$=40Hz (b) $n_q$=60Hz

(c) $n_q$=80Hz (d) $n_q$=100Hz

Fig.3 The frequency responses of the system with different bandwidth of servo valve

The Fig.3 shows that the oil column resonance frequency is decreased by the jerk feedback, and the influence of system performance caused by the servo value is reduced. With the multiple control, the system bandwidth is from 0.4Hz to 40Hz when the servo valve frequency is 40Hz, the system bandwidth is from 0.4Hz to 50Hz when the servo valve frequency is 60Hz, the system bandwidth is from 0.4Hz to 65Hz when the servo valve frequency is 80Hz,and the system bandwidth is from 0.4Hz to 75Hz when the servo valve frequency is 100Hz. Obviously, compared with the three-variable control, the jerk feedback can decrease the oil column resonance frequency, reduce the influence of shaking table performance caused by the servo value, thus broaden the system bandwidth.

**System analysis with the interaction between specimen and mesa**

Regarding the specimen as a single degree of freedom, we analyze the system considering the interaction between specimen and mesa on the basis of multi-variable control. We take the system which the $90^o$ phase shift frequency of the servo valve system is 60Hz as an example. The parameters of the system are, $A_d=0.375$ , $A_v=3.01\times10^{-2}$ , $A_a=1.08\times10^{-2}$ , $A_v^{'}=0$ , $A_a^{'}=1.1\times10^{-2}$ , and $A_j^{'}=1.0\times10^{-2}$. The natural vibration frequency of the specimen is 3Hz, 6Hz, or 9Hz. The

damping ratio is 0.05 or 0.02, and the masses of the specimens are different. The frequency responses of the system considering the specimen as a single degree of freedom are shown in figure 4(a, b, c, d).

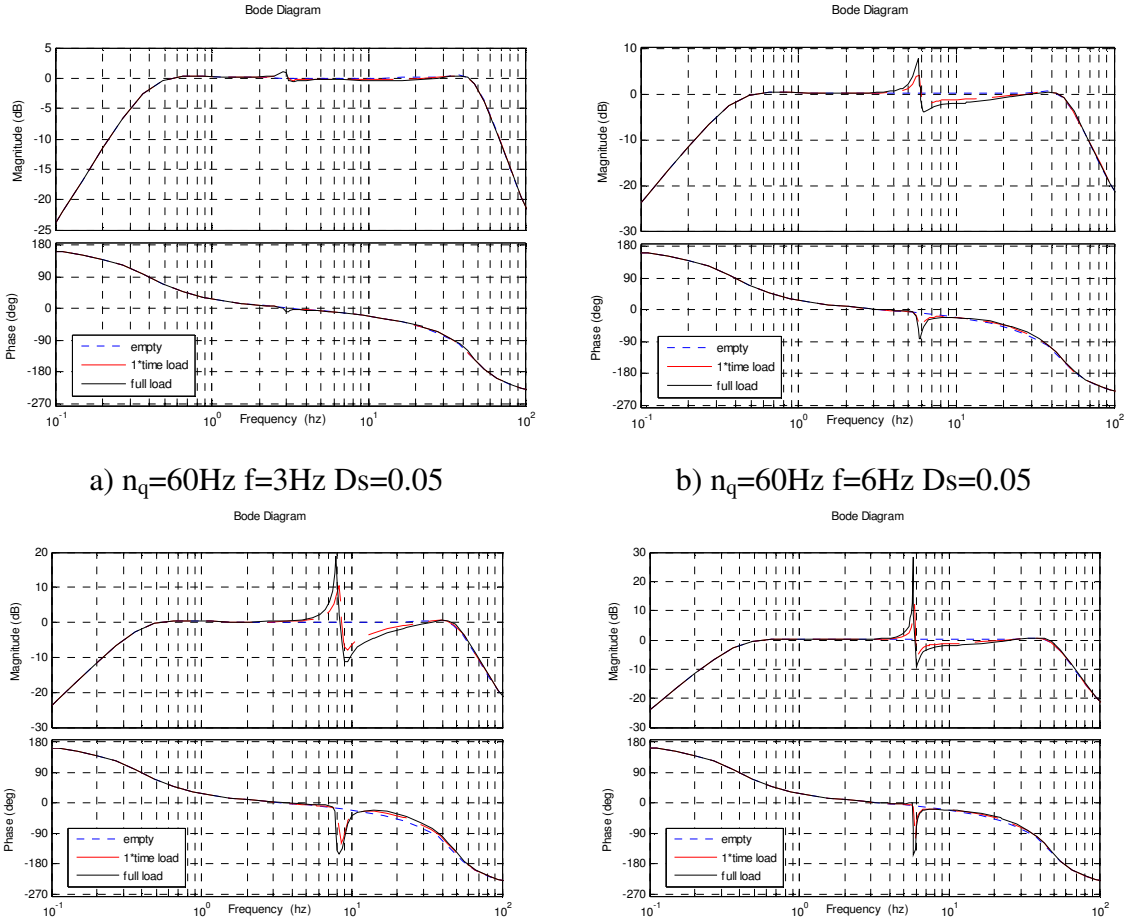


a) $n_q$=60Hz f=3Hz Ds=0.05 b) $n_q$=60Hz f=6Hz Ds=0.05

c) $n_q$=60Hz f=9Hz Ds=0.05 d) $n_q$=60Hz f=6Hz Ds=0.02

Fig.4 The frequency responses of the system with different specimens

The Fig.4 shows that

(1)Due to interact between specimen and mesa, the system produced a resonance which can impact the signal output of the mesa. The size of the peak is proportional to the quality and the frequency of specimen, and inversely proportional to the damping ratio of specimens.

(2) The oil column can be reduced by adding the jerk feedback, the influence of the system performance caused by the servo valve characteristics can be decreased, and the frequency band of the system can be broadened.

(3) With the multi-variable control, the system in the high frequency region is stable.

## Simulation of shaking table with multi-variable control

According to the transfer function of the shaking table with the multiple control and the shaking table (3m×3m) of the key laboratory of earthquake engineering and structural retrofit(the shaking table performance is shown in table 1), build the control system simulation model in the MATLAB / Simulink, take the wave of El-centro for an example to simulate. The result of simulation is shown in figure 5. Under the multiple control with jerk feedback, the response waveform of shaking table and the expected waveform are in good agreement, its control effect is better than three-variable control. Multi-variable control is very good to improve the control precision of the system.

Table 1 Shaking table performance

| | | | |
|---|---|---|---|
| Platform size | 3m×3m | Counter weight | 6Ton |
| Peak load | 10Ton | Maximum displacement | ±10cm |
| Maximum speed | 60cm/s | Maximum acceleration | 2.0g（Full load）<br>0.9g（empty） |
| Frequency range | 0.1～50Hz | Control mode | acceleration control |
| Working mode | One-way of the level | Wave | Sine、Random、seismic wave |

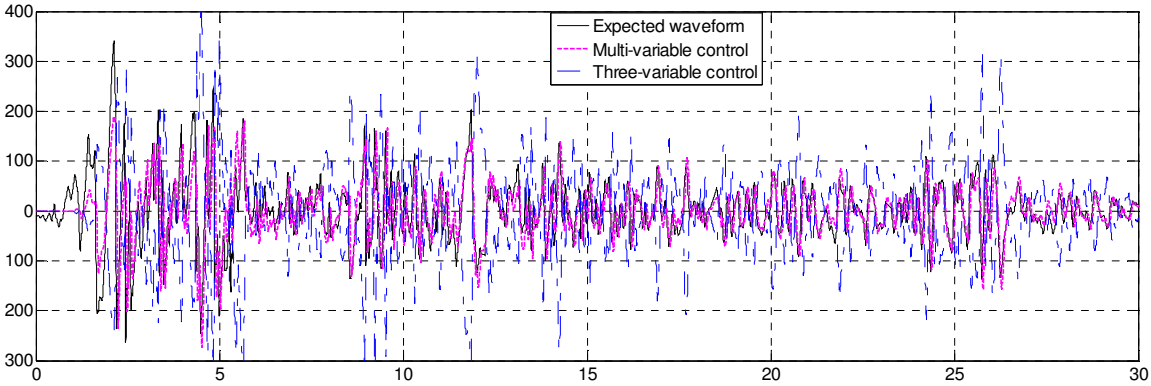


Fig.5 Acceleration time-history curve of the shaking table with multi-variable control

## Conclusions

The influence of the performance of the shaking table system caused by the bandwidth of servo valve was analyzed in this paper. The shortcomings of the existing three-variable control were pointed out. We have put forward a multi-variable control by adding the jerk feedback. Considering the interaction between specimen and mesa, we analyzed the shaking table with the multi-variable control. We draw the following conclusions.

(1) The multi-variable control system was formed by adding the jerk feedback to the three-variable control system. For the system which the $90^{o}$ phase shift frequency of the servo valve system was close to the oil column resonance frequency, the oil column can be reduced by adding the jerk feedback, the influence of the system performance caused by the servo valve characteristics can be decreased, and the frequency band of the system can be broadened.

(2) Considering the interaction between specimen and mesa, the feature of the system in the high frequency area was still relatively ideal. The system was in steady state with the multi-variable control.

(3) Based on the application of the jerk feedback on the shaking table, we have carried on the theoretical derivation and simulation analysis, however, the application still need much testing in practice.

## Acknowledgements

The authors are grateful to acknowledge that this paper is partially financially supported by the National Natural Science Foundation of China under Grant No.51278013 and the open foundation of Beijing Key Lab of Earthquake Engineering and Structural Retrofit. Moreover, the retired expert Haohua HUANG had offered lots of valuable suggestions on this paper, heartfelt thanks for him too.

**References**

[1] Severn R.T.：Earthquake Engineering in Europe, Garevski M, Ansal A, Springer Netherlands, Vol. 17 (2010), p. 383.

[2] Severn R.T.: EARTHQUAKE ENGINEERING & STRUCTURAL DYNAMICS, Vol. 40 (2011), p. 195.

[3] Haohua, HUANG: *Design and application of the shaking table* (Seismological Press, Beijing 2008). (in Chinese)

[4] Zhenyun, TANG, Zhenbao, LI. Jinbao, JI and Weiming, YAN: Journal of Earthquake Engineering and Engineering Vibration, Vol.29(6), p. 162-169. (in Chinese)

[5] Jinbao JI, Fangfang LI, Zhenbao LI and Lijuan SUN: Structural Engineers,Vol.28(2012),p.96 (in Chinese)

[6] Junwei HAN, Liming YU, Hui ZHAO and Zhongyi WANG: Journal of Harbin Institute of Technology, Vol.31(1999),p. 21-23.(in Chinese)

[7] Tagawa Y, Kajiwara K:Proceedings of the Institution of Mechanical Engineers. Part I: Journal of Systems and Control Engineering. Vol.221(2007),p. 171-181.

[8] Yanhua WANG, Wenrang CHENG:Journal of Vibration and Shock. Vol.2(2010),p. 99-102. (in Chinese)

*Applied Mechanics and Materials Vols. 580-583 (2014) pp 1528-1532*
*© (2014) Trans Tech Publications, Switzerland*
*doi:10.4028/www.scientific.net/AMM.580-583.1528*

# Data Processing and Preliminary Analysis of Strong Motion Records from the Ms7.0 Lushan, China Earthquake

Haiying YU[1, a], Baofeng ZHOU[1, 2,3,b], Wenxiang JIANG[1, c], Cheng YANG[1, d], Quancai XIE[1, e], Pingyu TAN[1, f], Siming XU[1, g], Xiaofen ZHAO[1, h]

[1] Institute of Engineering Mechanics, China Earthquake Administration, Harbin 150080, China

[2] Heilongjiang Construction Group, Harbin 150080, China

[3] Harbin Institute of Technology, Harbin 150080, China

[a]haiyingyu@126.com,[b]zbf166@126.com,[c]jwx_iem@163.com,[d]bjsmoc@gmail.com,

[e]xiequancai@163.com,[f]tpingyu@163.com,[g]xusiming512@163.com,[h]929921908@qq.com

**Keywords:** Lushan Ms7.0 earthquake, data processing, baseline correction, attenuations of PGAs

**Abstract.** At 8:02 a.m. Beijing time on April 20, 2013, an Ms 7.0 earthquake shook the city of Ya'an, China. Until 24:00:00 on 20 July 2013, a total of 339 strong-motion records from 113 free-field stations, 21 records from 1 strong-motion structure array and 1123 groups of aftershock records have been collected, processed and analyzed preliminarily by the China Strong Motion Network Center (CSMNC) in this paper. There are more than 26 stations located within Longmenshan fault zone and all peak ground acceleration (PGA) of records is larger than 50gal. The PGA of Baoxingdiban station reaches 1005.4 gal after zero-line initialization, which firstly breaks through 1g in the mainland of China. Based on the mainshock records, shakemaps of those PGAs are plotted and attenuation relationships of PGAs are presented in this article.

## Introduction

The Lushan earthquake occurred at 8:02 on April 20, 2013 in Sichuan, China, which caused a highly destructive and shallow source earthquake(Ms7.0) with hypocenter located at 30.3°N and 103.0°E at a depth of 13km after "5.12" Wenchuan earthquake. Positioning and earthquake focal mechanisms results show that the earthquake occurred on the Longmenshan fault zone belonging to thrust earthquakes. The fault zone is the boundary line between Plateau block in intense activity and Sichuan Basin blocks in weaker activity, which cuts along the northwestern margin bottom of the Sichuan Basin with 400km in width and 60km in length. And it is a huge tectonic belt with complex scale type. Longmenshan fault zone is constituted by four major faults, which is respectively after the Longmenshan fault (Wenchuan-Maowen fracture), the central fracture (Kitagawa-Yingxiu fracture), the former Hill fault (Guanxian-Jiangyou fracture) and Piedmont buried fault from west to east[1].It is in the southern tip of the Longmenshan fault zone which controls the rupture of Lushan earthquake. The location did not rupture slip when the Wenchuan earthquake occurred. And it is the strongest earthquake have occurred in the Longmenshan fault zone since Wenchuan earthquake[2] . Mainshock and aftershocks distributed in the Pengxian-Guanxian fault lying in the southwestern tip of the Longmenshan fault zone, also located in Coulomb stress increasing region after the Wenchuan earthquake, and both focals are of the similar nature with the major of thrust[3].

Until July 20th, 2013, there has been a total of 114 stations obtaining strong motion records in Lushan earthquake, which distributed in Sichuan, Yunnan, Gansu and Shaanxi province, 83 groups of records are obtained in Sichuan, 27 groups in Yunnan included 7 groups of structure array records, 8 groups in Shaanxi and 2 groups in Gansu, and there were 177 earthquakes which triggered strong motion stations, including 18 times lower than M3.0, 109 times between M3.0 and M4.0, 45 times between M4.0 and M5.0, 4 times between M5.0 and M6.0, and only once of M7.0. There were four times for M5.4 aftershocks within 33 hours after the mainshock. Earthquake sequences distribution is shown in Fig.1, and Lushan earthqukes distribution is shown in Fig.2.

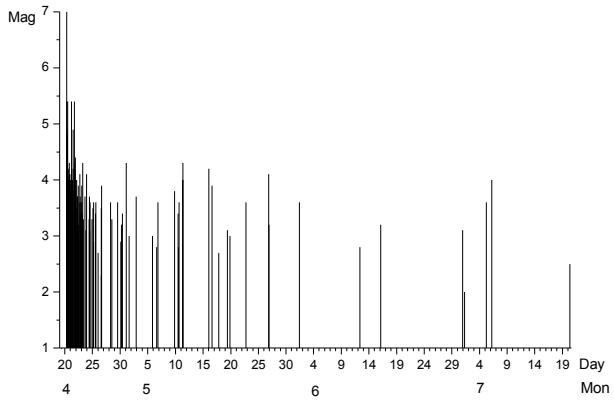


Fig.1 Lushan Earthquake mainshock and aftershocks sequence records

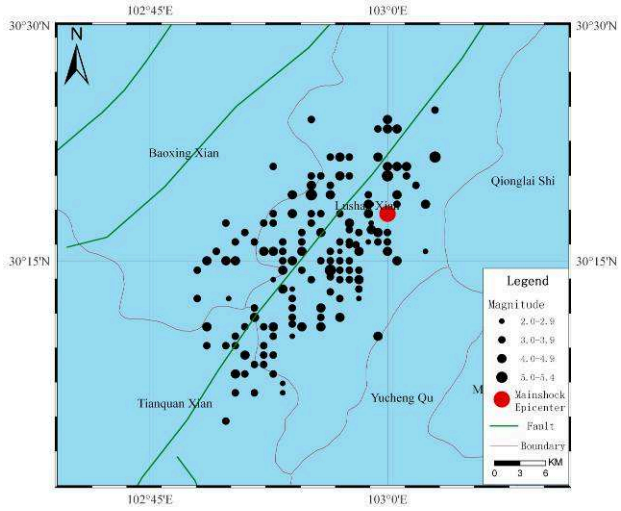


Fig.2 Lushan mainshock and aftershocks epicenter distribution with strong motion

## Collection, Arrangement and Statistical Analysis of Acceleration Records

In Lushan Ms7.0 earthquake, there were totally 120 groups of strong motion events with epicentral distance from 18.5 to 771.2km, which were obtained from Sichuan, Yunnan, Gansu and Shaanxi province. Fixed stations distribution obtaining records is shown in Fig.4. Baoxingdiban strong motion station received the maximum peak ground motion 1005.4gal, and this is the first strong motion record in excess of 1g in the mainland of China. There were 339 strong motion records obtained by strong ground motion station, and the static of peak ground motion is shown in Fig.3. There are totally 22 strong motion records with PGA above 200gal, and 238 strong motion records with PGA below 25gal. There are totally 21 strong motion records obtained by structure array. And there are 21 strong motion records with epicentral distance within 50km shown in table 1. All these stations are equipped with digital instruments with Etna, K2, GSR-18 or MR-2002 type. And most of these instruments apply the SLJ-100 type force-balanced-accelerometer sensors, only few Etna-type strong-motion seismographs are equipped with the ES-T type force-balance-accelerometer sensors. In the records, the frequency range of these seismographs is 0-80Hz, and the sampling rate is 200sps generally. 20 seconds is regarded as pre-event time[4].

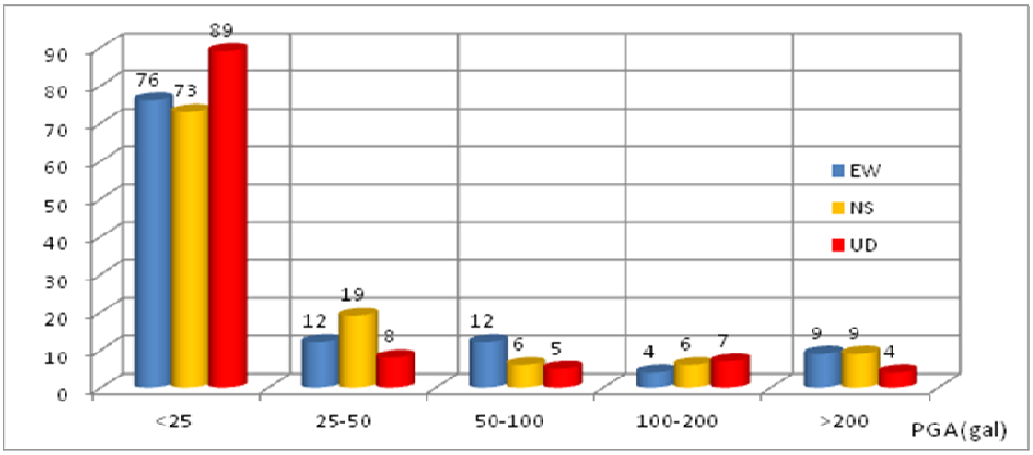


Fig.3 Peak ground acceleration statistics in strong ground motion stations

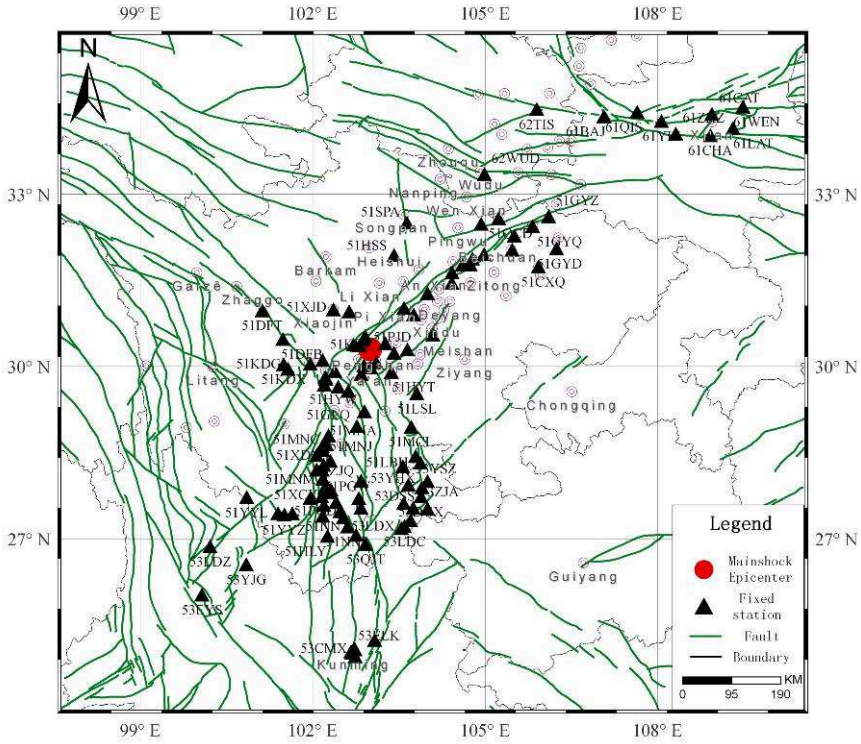


Fig.4 Fixed stations distribution with records obtained from the Lushan $M_S$7.0 Earthquake

when the short-term and imminent prediction of a large earthquake has been released or an earthquake has occurred, the emergency response of the mobile strong ground motion observation is required, which will be essential for capturing the mainshock or the aftershock records[5].After the occurrence of the Lushan earthquake, Sichuan Province Seismological Bureau, Yunnan Province Seismological Bureau (Southwest Regional Strong Motion Network Center) and Hubei Provincial Seismological Bureau carried out 9 strong motion mobile observation points rapidly, while they kept adjusting mobile stations position based on aftershocks distribution and trend so as to obtain strong motion records as precious as possible.

Until July 20, 2013, the National Strong Motion Network received a total of 1123 groups of three -component aftershocks strong motion records from fixed and mobile observation stations. There are 965 groups of strong motion records obtained by Sichuan Province fixed strong motion stations in 91 aftershocks. Southwest Regional Strong Motion Network Center and Hubei Provincial Seismological Bureau has obtained 144 and 14groups of acceleration records respectively in mobile observation stations. Epicentral distances of these aftershocks are from 0.85 to 312.10km. The maximum peak ground acceleration reaches 576.9gal in Lushanfeixian station.The number of strong motion records between M4.0 and M5.0 has reached 48.9 % of total records, while the number of strong motion records more than M5.0 only reaches 12.2 % of total records.

## Data-Processing of Strong Motion Records

The data-processing of strong motion records from this earthquake is carried out by CSMNC, which establishes the conventional procedure: recycling strong motion records and records report card from provincial bureau, preliminary sorting, transition and unification of data-format, metadata entry, zero-line correction of the original strong motion records and uncorrected acceleration time histories plotted in uniform-format routinely. Specifically, the correction process includes Fourier spectrum, response spectrum and the signal to noise ratio of the spectrum analysis. The steps of zero-line correction are as follows:

1. Calculate the average acceleration of the pre-event time of the original acceleration record;
2. The average acceleration is removed from the original acceleration record.

### The Attenuation Relationships of PGAs in Lushan Mainshock

The focal mechanism and finite-fault model for the Lushan earthquake released by Wang Weimin[3] are adopted in this article to calculate the rupture distances (the shortest distance between the station and the fault plane) of 83 stations. Based on the records and the corresponding rupture distances, the attenuation relationships of PGAs can be developed. The ground motion model used in this article is as Equation 1:

$$\log_{10}(PGA) = a + b * \log_{10}(D_{rup} + c) \quad (1)$$

Where PGA denotes the peak ground acceleration in gal; Drup denotes the rupture distance in km; a, b and c are the coefficients to be determined using the method of least-squares and the values of them are listed in Table 1, where σ denotes the regression standard deviation. The corresponding regress curves of three-component PGAs for Lushan earthquake are plotted in fig.5.And comparations of PGAs for three components in the Lushan mainshock are shown as fig.6. With the fault distance increasing, ratios of horizontal PGAs to vertical ones grow larger. However, ratios of EW PGAs to vertical ones are in attenuation trend. For fault distance within 135.3 km, PGAs in EW direction are larger than ones in NS direction. And ratios distributions for horizontal PGA to vertical ones for near-fault stations are shown in fig.6.

Table 1 The list of regression parameters

| direction | a | b | c | σ |
|---|---|---|---|---|
| EW | 4.73016 | -1.52593 | 14.13163 | 0.29422 |
| NS | 4.64835 | -1.48638 | 15.10284 | 0.32145 |
| UD | 4.49273 | -1.54794 | 15.05708 | 0.27166 |

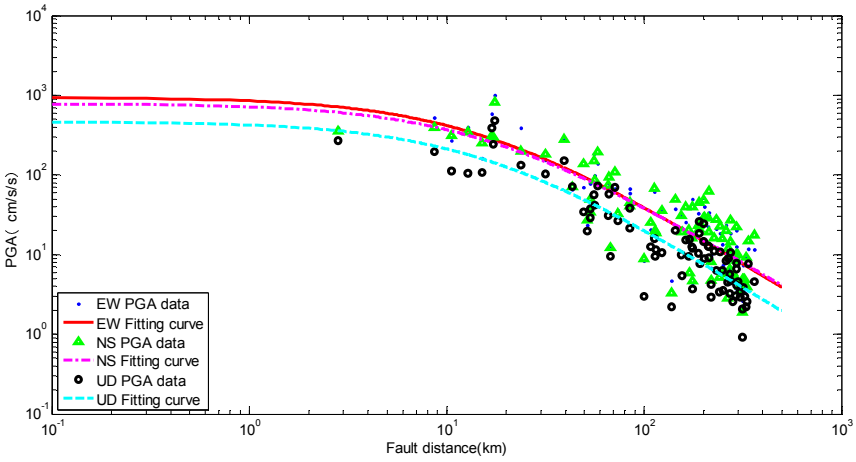


Fig.5 The Lushan earthquake specific regress curves of PGA for the three components

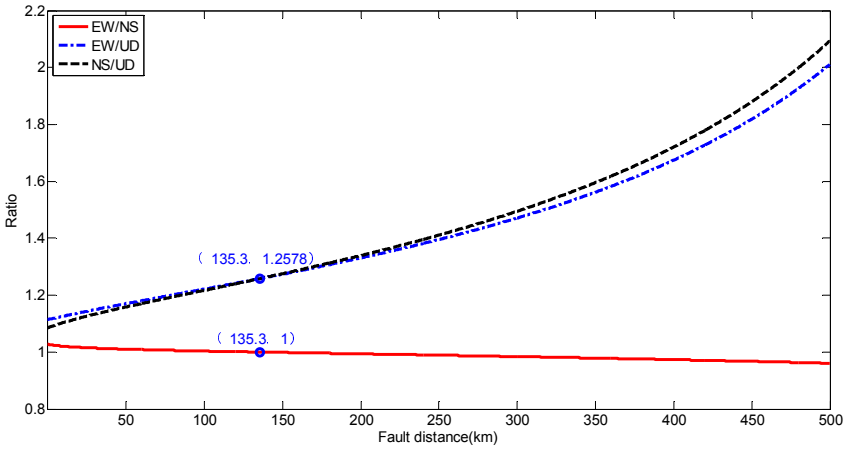


Fig.6 Regress curves comparations of PGA for three components in the Lushan mainshock

## Conclusions

There was another higher magnitude earthquake occurred in Longmenshan fault after the Wenchuan earthquake, and a amount of strong ground motions were obtained by fixed and mobile strong motion stations, which provide an unprecedented opportunity to study the attenuation relationships of strong motion parameters, to revise the seismic ground motion parameter zonation map, and to re-determine the design ground motion parameters. Based on the preliminary analysis in this paper, the following conclusions can be drawn:

1. In the Lushan mainshock, there are totally 120 groups of strong motion records with epicentral distance from 18.5 to 771.2km, among which there are 21 strong motion records obtained by structure station. And a total of 1123 groups of three-component strong motion records from fixed and mobile observation stations in aftershocks.
2. PGA from Baoxingdiban strong motion station reaches 1005.4 gal after zero-line initialization, which fills in the domestic gap in the near-fault strong motion records breaking through 1g.
3. With the fault distance increasing, ratios of horizontal PGAs to vertical ones grow larger, however, ratios of EW PGAs to vertical ones are in attenuation trend. For fault distance within 135.3 km, PGAs in EW direction are larger than ones in NS direction.
4. The large number of records obtained in this event greatly enriches strong motion resourses in Longmenshan and enlarges the database of strong motions in China.

## Acknowledgements

The authors are very grateful to the substantial support from the Department of Seismic Disaster Prevention, China Earthquake Administration. We also hope to express our deepest gratitude to Prof. Zhou Yongnian and Li Shanyou for their valuable suggestions. Thanks to the strong motion observed personnel from the Seismological Bureau of Sichuan, Yunnan, Gansu, Shaanxi and Hubei provinces/municipalities and those from Institute of Engineering Mechanics, China Earthquake Administration for their hard works of strong motion observation and the collecting of records. This work was financially supported by Nonprofit Industry Research Project of CEA Fund (201208014), Specific Item of Fundamental Scientific Research in Institute of Engineering Mechanics Fund (2010C02), National Natural Science Foundation of China Fund (51308517), National Natural Science Foundation of China Fund (41174161).

## References

[1] Haiying Yu, Dong Wang, Yongqiang Yang, Quaicai Xie, Wenxiang Jiang, Baofeng Zhou, Jian Yang, Xiang Cheng: Technology for Earthquake Disaster Prevention, Vol.3, Issue.4(2008), p.321-336. (In Chinese)

[2] Weimin Wang, Lianfeng Zhao, Juan LI, Zhenxing Yao: Chinese Journal of Geophysics, Vol.51, Issue.5(2008), p.1403-1410. (In Chinese)

[3] Weimin Wang, Lianfeng Hao, Zhenxing Yao:Chinese Journal of Geophysics, Vol.56, Issue.4 (2 013), p. 1412-1417. (In Chinese)

[4] Haiying Yu, Wenxiang Jiang, Quancai Xie:Earthquake Engineering and Engineering Vibration, Vol.29, Issue.6(2009), p. 1-12. (In Chinese)

[5] Ruizhi Wen, Zhenghua Zhou, Xiaojun Li, Cheng Yang, Yuhuan Wang,Quan Liu, Xiaotao Yin, Mindu Zhou, Jianwen Cui:Earthq Sci, Vol.22 (2008), p.181−187.

*Applied Mechanics and Materials Vols. 580-583 (2014) pp 1533-1537*
*© (2014) Trans Tech Publications, Switzerland*
*doi:10.4028/www.scientific.net/AMM.580-583.1533*

# Permanent Displacement Identification Analysis in 2011 Mw9.0 Tohoku Earthquake, Japan

Baofeng Zhou[1,2,3,a], Tingsu Song[4,b], Ruizhi Wen[1,c] and Lili Xie[1,3,d]

[1] Institute of Engineering Mechanics, China Earthquake Administration, Harbin 150080, China

[2] Heilongjiang Construction Group, Harbin 150080, China

[3] Harbin Institute of Technology, Harbin 150080, China

[4] Yunnan Seismological Bureau,Kunming,650041, China

[a]zbf166@126.com,[b]saviour_sts@163.com, [c]ruizhi@iem.net.cn, [d]llxie@ iem.net.cn

**Keywords:** Mw9.0 Tohoku Earthquake, baseline correction, permanent displacement, Hermit interpolation.

**Abstract.** Permanent displacement identification is one of key topics in near-fault ground-motion research. A new method based on Hermit interpolation and flatness technique is proposed to determine permanent displacements, since the Iwan law is not applicable in Mw9.0 Tohoku earthquake permanent displacement recognition. The method is then tested by coseismic displacements resulted from GPS station nearby. Results show that: the causes for strong motion record baseline drift are very complex so that Iwan method is not suitable for permanent displacements identification in the Mw9.0 Tohoku Earthquake, while the new baseline correction method combining Hermit interpolation and flatness technique is suitable for permanent displacement analysis of near-fault ground motion in 2011 Mw9.0 Tohoku Earthquake.

## Introduction

Japan was struck by a magnitude 9.0 earthquake off its northeastern coast of Honshu at 05:46:23 UTC on March 11, 2011. This is one of the large earthquakes that Japan has ever experienced. The earthquake off the Pacific coast reached Mw9.0 with a focal depth of 24km, and the epicenter was located at latitude 38.1° and longitude 142.9°, which is called Mw9.0 Tohoku Earthquake by Japan Meteorological Agency (JMA) [1]. Obvious horizontal and vertical coseismic displacements received by GPS stations are found by Japanese scholars. In addition, when a strong earthquake happens, engineering structures will suffer from damages due to the permanent ground displacements which have been confirmed in 1999 Chi-Chi earthquake, 2008 Wenchuan earthquake, 2010 Chile earthquake and 2010 New Zealand earthquake.

Due to mutual compression deformation, dislocation or base damage, structures and lifeline system will suffer from damage, collapse or fracture[2]. And even soil liquefaction will occure[3]. The most active and effective measure is to make good seismic design of construction projects in order to reduce future earthquake disaster[4]. Jonathan has analysed earthquake damage on structures, and pointed out that permanent displacements were associated with shallow underground fault dislocation closely. Therefore, in order to discuss the earthquake disaster, permanent displacement associated with strong ground motion is an important research topic. Reasonable theory should be adopted in combination with strong motion data to identify permanent ground displacements to provide necessary reference for the study of earthquake focal mechanisms and engineering seismology.

Baseline correction on near-fault acceleration records has to be applied before further study. Baseline correction methods have been studied by many scholars. Graizer[5] was the first one to advocate the use of least-square fit of baseline correction. Iwan[6] applied a two-point method improved by Boore[7] and Boore & Bommer[8]. Chiu[9] used high-pass filter before integrating acceleration.Wu[10] has also made some improvements on Iwan method to process Chi-Chi

earthquake strong-motion data. Boore & Akkar[11] discussed and presented a new baseline correction scheme based on Monte Carlo technique, and used the noise model to simulate baseline changes. Wang Guoquan[12] offered a new way to correct baseline on the 1999 Chi-Chi mainshock. HaiYing Yu[13] made baseline correction repeatedly on the Wenchuan earthquake near-fault strong motion records. Zhao[14] also proposed a new baseline correction method by using excel spreadsheet. Most baseline correction methods assume that change occurs in limited time points, but it is not easy to automate, and often requires human intervention so as to cause the data processing results vary with different researcher. Therefore, it is the core that how to eliminate baseline drift in strong motion records and give a reasonable approach to identify permanent displacements for the near-fault strong motion data processing. Strong motion stations within 5km away from GPS stations are selected to conduct the study of permanent displacements in the 2011 Mw9.0 Tohoku Earthquake[15]. Iwan law is studied for permanent displacements analysis, and a new identification method is presented to conduct the comparative study with GPS data offered by JPL and California Polytechnic ARIA research team.

**Reasons for Baseline Drift**

One of the fundamental topics on the near-fault earthquake data processing is how to determine the reasonable position and the extent of the baseline drift in acceleration, velocity and displacement so as to provide theoretical basis for correction methods. So much in-depth research on baseline drift has been carried out by many scholars. Hudson[16] agreed that digitization of records, bending and lateral deformation of the recording paper mainly affects middle-period and long-period strong motion records. Trifunac[17] has found that the baseline drift in analog records would occur and the fixed baseline would no longer be a straight line if the recording paper was in irregular lateral movement. Then a fixed baseline waveform reflects the relative lateral recorder irregular movement, which formed strong motion acceleration noise. The development of digital strong motion accelerometers promotes the rapid development of data processing. Although strong motion instruments have been improved greatly on sensitivity, dynamic range, and stability, which has promoted a significant improvement in data quality, however, Chiu [9] has believed that most of the baseline error in analog records still exists in the data with high resolution and high sampling rate. These errors include a constant acceleration baseline drift, low-frequency instrument noise, low-frequency background noise, the initial value in acceleration and velocity, and human error. In summary, the digital strong motion records baseline drift is due to inaccurate response from the instrument, fatigue electromagnetic noise, sensor material, background noise and ground tilt or rotate and bring the pollution of ground vibration signal[12]. But, in fact, reasons for baseline drift are often uncertain. The mechanism of baseline drift is not clear as well adequate tests and the theoretical basis are not enough, therefore, the baseline correction is still an important topic in strong motion data processing.

**Iwan Method**

In 1985, Iwan and other researchers studied PDR-1 and FBA-13 series digital strong motion instruments through experiment and found that baseline drift of acceleration records came from sensor hysteresis with a hysteresis threshold 50gal[18]. Accordingly, the acceleration process was divided into three parts, i.e., the first part which starts from the record beginning till the first reach of greater than50gal; the third part from the last reach of greater than 50gal till the end of the record; and the middle strong motion part in between. Each part of the baseline offset was a constant while the baseline drift occurred in strong vibration stages. The recording process is comprised of two offsets representing the average changes. The physical basis of which is initial acceleration, velocity and displacement is zero; the average velocity should be close to zero at the end of ground motion, the displacement should be zero if no permanent displacement occurred in strong motion stations, on the contrary, displacement should end with the trend of paralleling to the time axis approximately. This method is the first used to test methods determining the cause of baseline drift for digital strong

motion record with great objectivity systematically. Therefore, we apply the method in making baseline correction on 2011 Mw9.0 Tohoku Earthquake strong motion records selected from the k-net Network within 5km from GPS stations. Related data is shown in Table 1. It is not difficult to find that permanent displacements and coseismic displacements are not satisfactorily consistent and even opposite sign appears. For data in Table 1, the permanent displacement extracted from station AKT006 is well consistent with coseismic displacement from GPS stations nearby, however, the east-west permanent displacement is 33.6cm while the coseismic displacement reaches 50.21cm, leading to a relative displacement error 33.08%. The north-south permanent displacement is only -30.71cm, but the coseismic displacement recorded by GPS station reaches -43.68cm, and the relative displacement error is 29.69%. Related displacement time history is shown in Fig. 1.

Since the vertical peak acceleration does not exceed 50gal, the Iwan method is not used. For most strong motion stations, the displacement relative error is too high as to 296% with respect to the GPS stations nearby. Therefore, Iwan law does not apply to permanent displacement identification in Japan M9.0 near-fault strong motion record.

Table 1 Coseismic displacements and permanent displacements for 2011 Tohoku earthquake(Iwan)

| No. | Measure Direction | GPS station code | Coseismic Displacement [cm] | Strong motion Station code | Permanent displacement [cm] | Sphere Distance [m] | Displacement Error（%） |
|---|---|---|---|---|---|---|---|
| 1 | EW | 183 | 50.21 | AKT006 | 33.6 | 26.40 | 33.08 |
| | NS | | -43.68 | | -30.71 | | 29.69 |
| | UD | | 2.90 | | / | | / |
| 2 | EW | 928 | 152.94 | AKT023 | 65.67 | 166.60 | 57.06 |
| | NS | | -79.31 | | -19.86 | | 74.96 |
| | UD | | -4.51 | | 8.86 | | 296.45 |
| 3 | EW | 158 | 36.98 | IWT001 | 2.05 | 726.80 | 94.46 |
| | NS | | -42.06 | | -14.22 | | 66.19 |
| | UD | | -3.08 | | 0.2 | | 93.51 |

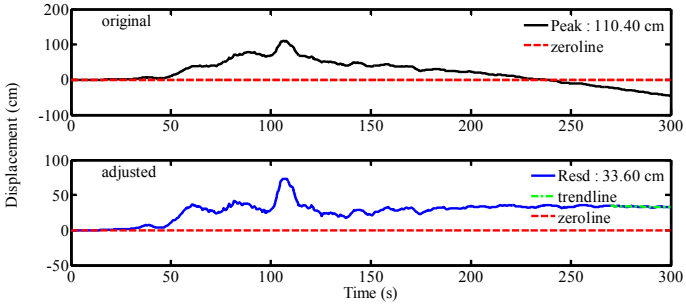


Fig.1 Displacement time history before and after correction(Iwan)

## Hermit Interpolation Baseline Correction Method

In order to prevent the loss and distortion of related time history information, baseline correction methods instead of filtering methods have to be applied for strong motion data processing. Due to complicated acceleration baseline drift with rich high-frequency components, it is very difficult to determine the location and extent of baseline drift accurately in acceleration time history, instead velocity time history can be used. Generally, the baseline of velocity time history is not in linear trend.. Moreover, the baseline trend is more complex in strong shock, so it is difficult to determine its basic shape. One thing is certain that the process of baseline change was continuous, that is, the time history is continuous and derivative. The change process of baseline is smooth instead of abrupt. In order to ensure a better interpolation polynomial approximation to target function, some constraints should be made that interpolation polynomial junction should have the same derivative values with the objective function. As a polynomial interpolation, cubic interpolation function is enough, since

Runge phenomenon is likely to occur with high power number. Therefore, the two-points cubic Hermite interpolation method is used for n+1 orders interpolation problem. And then a piecewise linear interpolation curve connecting two line segments is used to make the transition point continuous and first-order derivative.

In addition, the following assumptions are made:(1) the end and beginning value should be zero or close to zero for acceleration and velocity time histories, and there should not be a obvious baseline drift; (2) PGD does not appear at the end of displacement time history, which located corresponding to the time of PGA or PGV substantially; (3) the displacement trend will tend to approximately parallel to the time axis. The flatness is selected as the judgment parameter to determine the final permanent displacement reasonably as Wu and Wu [19].

Calculation results are shown in Table 2. Relative error is less than 15% for East-West component. Taking staion AK006 for example, the permanent displacement is 46.86cm while the coseismic displacement of GPS station nearby is 50.21cm, that is, the displacement error is only 6.67%. The displacement time histories is shown in Fig. 2. Of course, the vertical permanent displacement is relatively large, which is possibly related to the observed vertical GPS observation defects greatly.

Table 2 Coseismic displacements and permanent displacements for 2011 Tohoku earthquake(Hermit)

| No. | Measure Direction | GPS station code | Coseismic Displacement [cm] | Strong motion Station code | Permanent displacement [cm] | Sphere Distance [m] | Displacement Error（%） |
|---|---|---|---|---|---|---|---|
| | EW | | 50.21 | | 46.86 | | 6.67 |
| 1 | NS | 183 | -43.68 | AKT006 | -49.13 | 26.40 | 12.48 |
| | UD | | 2.90 | | 8.69 | | 199.66 |
| | EW | | 152.94 | | 169.59 | | 10.89 |
| 2 | NS | 928 | -79.31 | AKT023 | -73.06 | 166.60 | 7.88 |
| | UD | | -4.51 | | -2.90 | | 35.7 |
| | EW | | 36.98 | | 31.89 | | 13.76 |
| 3 | NS | 158 | -42.06 | IWT001 | -52.90 | 726.80 | 25.78 |
| | UD | | -3.08 | | -16.92 | | 449.35 |

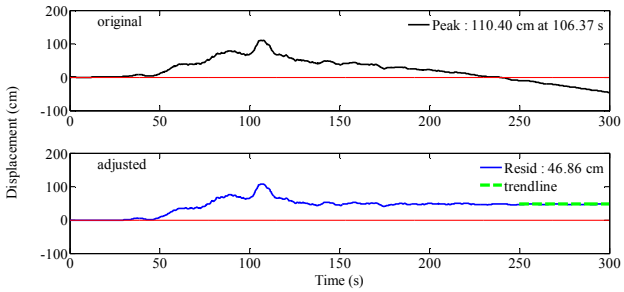


Fig.2 Displacement time history before and after correction(Hermit )

## Conclusions

Through analyzing the causes for strong motion records baseline drift using the strong motion records obtained from within 5km from GPS stations in 2011 Mw9.0 Tohoku Earthquake, we found that the Iwan I law is inapplicable to recognize the permanent displacement so that a combining method of Hermit law and flatness technique is proposed. Main points can be outlined as below.

1. The baseline drift mechanism of record is complex and presently still difficult to determine.
2. The Iwan law is only suitable to analyze the near-fault strong motion records for PDR-1 and FBA-13 stations while it is unable to identify the permanent displacement in 2011 Mw9.0 Tohoku Earthquake.
3. The Hermit interpolation baseline correction method combined with flatness technique has been proved to be efficient to recognize the permanent displacement in Japan.

**Accreditation**

Preliminary GPS time series provided by the ARIA team at JPL and Caltech. All original GEONET RINEX data provided to Caltech by the Geospatial Information Authority (GSI) of Japan.

**Acknowledgements**

This work was financially supported by Specific Item of Fundamental Scientific Research in Institute of Engineering Mechanics Fund (2013B20), National Natural Science Foundation of China Fund (51308517), Heilongjiang Postdoctoral Fund(LBH-Z13178), National Natural Science Foundation of China Fund (51208234).

**References**

[1] Ruizhi Wen, Baofeng Zhou, Dacheng Shi, Yefei Ren: Recent Developments in World Seismology, Vol. 388, Issue. 4 (2011), p. 1-7. (In Chinese)

[2] Baofeng Zhou: China Civil Engineering Journal, Vol. 46(2013), p. 135-140. (In Chinese)

[3] Zhaoyan Li,Yongzhi Wang, Xiaoming Yuan: Chinese Journal of Geotechnical Engineering, Vol. 35(2013), p. 140-145. (In Chinese)

[4] Hongbiao Liu, Xun Guo: China Civil Engineering Journal, Vol. 45, Issue.12(2012), p. 18-28. (In Chinese)

[5] V.Graizer: Earth Physics, Vol.12, Issue. 15 (1979), p. 875-885.

[6] W.D.Iwan, M.A.Moser and C.-Y.Peng: Bulletin of the Seismological Society of America, Vol.75, Issue.5 (1985), p.1225-1246.

[7] D.M.Boore: Bulletin of the Seismological Society of America, Vol. 91, Issue.5 (2001), p.1199-1211.

[8] D.M. Boore, J.J.Bommer: Soil Dynamics and Earthquake Engineering, Vol. 25 (2005), p.93-115.

[9] Hung-Chie Chiu: Bulletin of the Seismological Society of America, Vol. 87, Issue.4 (1997), p. 932-944.

[10] Yih-Min Wu, Chien-Fu Wu: J Seismol, Vol. 11 (2007), p. 159-170.

[11] S.Akkar, D.M. Boore: Bulletin of the Seismological Society of America, Vol.99(2009), p.1671-1690.

[12] Guoquan Wang: Seismology and Geology,Vol.26, Issue.1 (2004), p.1-14. (In Chinese)

[13] Haiying Yu, Wenxiang Jiang, Quancai Xie: Earthquake Engineering and Engineering Vibration, Vol. 29, Issue.6 (2009), p.1-12.(In Chinese)

[14] John X. Zhao, John Beavan: Proceedings of the Ninth Pacific Conference on Earthquake Engineering Building an Earthquake-Resilient Society, 2011.

[15] Information on http://www.k-net.bosai.go.jp/k-net/quick/index_en.html.

[16] D.E.Hudson, A.G.Brady, M.D.Trifunac: Earthquake Engineering Research Laboratory, Report No.EERL 69-20, (1969).

[17] M.D.Trifunac: California Institute of Technology Earthquake Engineering Research Laboratory ,Report No.EERL 70-07, (1970).

[18] D.M.Boore: Open-file report 99-545,version 1.0(1999), p.5-6.

[19] Yih-Min Wu, Chien-Fu Wu: J Seismol, Vol.11 (2007), p.159-170.

*Applied Mechanics and Materials Vols. 580-583 (2014) pp 1538-1544*
*© (2014) Trans Tech Publications, Switzerland*
*doi:10.4028/www.scientific.net/AMM.580-583.1538*

# Research on Shaking Table Control Parameter Tuning Technology Based on System Identification

Jinbao JI[1, a] , Lijuan Sun[1, b] , Pengyun Zhan[1, c] ,Juke Wang [1, d] and Linlin Song[1, e]

[1]Beijing Key Laboratory of Earthquake Engineering and Structural Retrofit, Beijing University of Technology, Beijing, China

[a]jinbao@bjut.edu.cn, [b]sunlijuan2007yan@163.com, [c]zhanpengyun@126.com,

[d]wangjuke2013@163.com, [e]577070636@qq.com

**Keywords:** shaking table, Parameter Tuning, System Identification, Simulation Validation

**Abstract.** The control parameter of shaking table is one of the key elements which significant influence on the system control performance. An algorithm which uses the model of system identification to theoretically calculate the control parameter is put forward, and then obtains the optimal three-parametric control parameter based on theoretical calculation. Tuning algorithm can get more ideal control parameter and could be applied in shaking table TVC parameter self-tuning.

## Introduction

Shaking table is one of the reliable key instruments in the field of Earthquake Resistant Engineering[1]. The tuning of shaking table control parameter is an important link during its debug process. In general, shaking table often adopts three-parametric control algorithm, thus the rational setup of three-parametric control parameter is essential for shaking table to give play to its control performance[2]. Rational three-parametric control parameter combination can broaden effective bandwidth for a system; on the contrary, it will be very hard to get preconceived control effect and it's possible to lead to shaking table's self-excitation and the damage of equipment[3]. The tuning of shaking table control parameter includes theoretical tuning and empirical tuning. Theoretical tuning calculates controller's control parameter with theoretical derivation based on mathematical model of controlled object. Yang Zhidong[4] employs root-locus method, with graphic mode, to describe all the six parameters' numerical relationship of shaking table closed-loop system pole with feedforward and feedback, but practical system model is very different from theoretical model, and the calculation process is complicated and tedious, which often results in big deviation of the parameter obtained through this method. empirical tuning is concluded by engineering technicians through lots of practice and is based on existing experience. Han Junwei[5] utilizes matching principle of practical frequency characteristic to shaking table system control parameter to conduct theoretical and experimental research. The result shows that tuning principle can guarantee the optimal working state of shaking table; but the tuning process needs a mass of repeated tuning, which is time-consuming and energy-consuming. For a particular control system, a series of tuned control parameters are only suitable to certain working condition, while the practical working condition is changing following the change of controlled object and environmental factors. Therefore, this paper makes use of least square method identification system parameter and combines with theoretical calculation method to gain the optimum control parameter.

## System analysis

### Control principle of shaking table

The system composition of shaking table under the three-parametric control is shown in the Fig. 1 that the displacement, speed and acceleration signal generated by the earthquake wave through three-parametric generators, along with the displacement, acceleration feedback signal collected by sensor, and acceleration feedback signal compounded by the aforementioned two signals form

closed-loop system, which converts electrical signal into hydraulic signal through servo valve, and then drives hydraulic servo cylinder and propels table-board of shaking table and model specimen to vibrate according to the expected signal law[6]. On account of hydraulic control theory, the open-loop transfer function of shaking table can be shown in formula (1).

$$G(s)=\frac{K_v}{s(\frac{s^2}{n_0^2}+\frac{2D_0 s}{n_0}+1)} \tag{1}$$

where, $n_0$ is inherent frequency of hydraulic system; $D_0$ is camping ratio of hydraulic system.

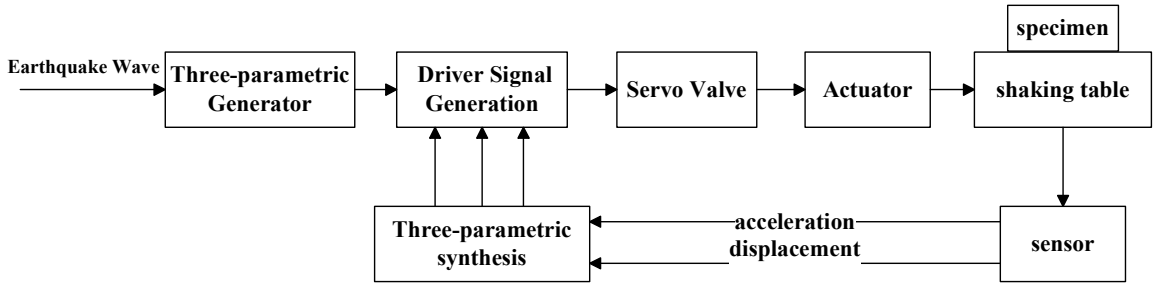


Fig.1 System Composition of Shaking Table

Three-parametric controller is an important constituent part of shaking table control system. Three-parametric control algorithm is to offset the disadvantages of limited bandwidth and damping of shaking table in simple displacement control, so as to better realize acceleration, speed and displacement control in different frequency bands. In three-parametric control, displacement controls low-frequency stage, speed commands mid-frequency stage and acceleration controls high-frequency stage, fulfilling the aim of enlarging system stamping and broadening system frequency band[7,8].

Controller is composed of three-parametric feedback control and feedforward control. Three-parametric feedback controller increases system stamping ratio and resonant frequency, broadens system frequency's sphere of application and strengthens system stability through regulating three feedback coefficients of $k_{af}$, $k_{vf}$ and $k_{df}$. Three-parametric feedforward controller adjusts three feedforward parameters of $k_{ar}$, $k_{vr}$ and $k_{dr}$ to get the cancellation of pole near imaginary axis in closed-loop transfer function, which can further broaden system working bandwidth. Three-parametric control principle schematic diagram is shown in the Fig.2. In the chart, $d_0$ and $v_0$ are two parameters of rejector, and VelSyn is speed synthesizer module.

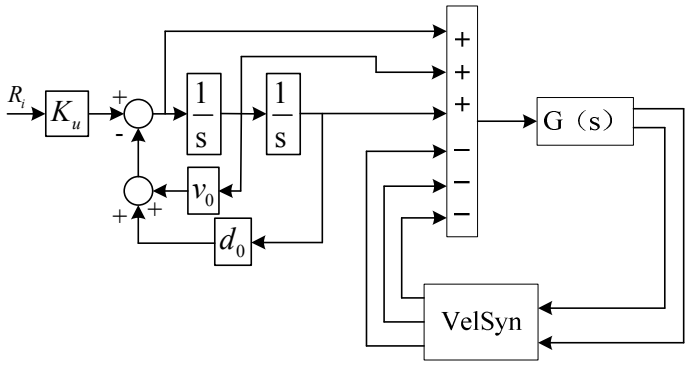


Fig. 2 Three-parametric Control Principle Schematic Diagram

**System analysis Self-tuning based on system identification**

**System analysis under the single influence of displacement feedback**

Since the shaking table adopts acceleration control method, the system can not locate in the situation of open-loop, traditional PID parameter tuning algorithm can not be directly applied in the tuning of shaking table system, thus, under mere feedback of displacement, the block chart of the system is shown in Fig.3. Transfer function corresponding to chart Fig.3 is shown in formula (2).

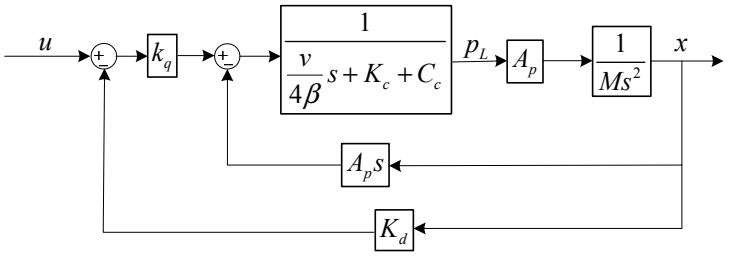


Fig.3 System Transfer Function under Displacement Feedback

$$\frac{x}{u}=\frac{1}{K_d}\frac{1}{\frac{A_p}{k_q K_d}(\frac{s^2}{n_0^2}+\frac{2D_0 s}{n_0}+1)s+1}=\frac{K_v}{s(\frac{s^2}{n_0^2}+\frac{2D_0 s}{n_0}+1)+K_d K_v} \tag{2}$$

where , $u$ is the input signal of the system, $x$ is the output signal of the system, $k_q$ is flow gain of slide valves near steady stale working point, $K_c$ is flow pressure parameter of slide valves near steady state operating point, $C_c$ is sum leakage coefficient, $v$ is volume equivalent to oil cylinder, $\beta$ is oil bulk modulus, $P_L$ is loading pressure, $A_p$ is feasible pressure bearing area of piston, $M$ is loading mass, $K_v$ is open-loop gain, $K_d$ is displacement feedback gain.

**Least Square Method Parameter Identification Principle**

In practical industrial control, control parameter uses theoretical calculation to get original value, and conducts manual regulation in trial test. But control parameter only aims to changeless system model, which is time-consuming without high accuracy[9]. In order to obtain more precise system control parameter, it is necessary to get more accurate system parameter to make use of real system input and output signal, so as to get the optimum system parameter. Least square method is popularly applied into various fields by virtue of its briefness, strong applicability, which can help get better object model. Discrete transfer function of the system can be shown in formula (3). Dynamic procedure mathematical model of the system is shown in formula (4).

$$G(z^{-1})=\frac{b_1 z^{-1}+b_2 z^{-2}+\ldots+b_n z^{-n}}{1+a_1 z^{-1}+a_2 z^{-2}+\ldots+a_n z^{-n}} \tag{3}$$

$$u(k)G(z^{-1})+e(k)=y(k) \tag{4}$$

Further get the following relation:

$$y(k)=-a_1 y(k-1)-a_2 y(k-2)-\ldots-a_n y(k-n)+b_1 u(k-1)+b_2 u(k-2)+\ldots b_n u(k-n)+e(k) \tag{5}$$

where, $u(k)$ and $y(k)$ are input and output quantities during the process, $e(k)$ is noise, $a_k$ and $b_k$ are unknown vector quantities, $k=1,2,...n$ .

The primary idea of Least Squares is to set minimized criterion function as formula (6) shows.

$$J(\theta)=\sum_{k=1}^{N}(y(k)-\varphi^{T}(k)\theta)^{2} \tag{6}$$

where, $\varphi^{T}(k)=\left[-y(k-1)\ \ldots -y(k-n)\ \ u(k-1)\ \ \ldots\ \ u(k-n)\right]^{T}$

$\theta=[a_1\quad a_2\quad \ldots\quad a_n\quad b_1\quad b_2\quad \ldots\quad b_n]$

With minimized criterion, estimated value $\hat{\theta}$ of smallest $\theta$ in the aforementioned function $J(\theta)$ can be obtained so as to confirm system transfer function.

**Tuning Algorithm Principle**

As system parameter calculated by shaking table is very different from practical system parameter, this paper adopts identification method to fit practical mode of the system with identification model being third-order system. The transfer function through identification is shown in formula (7).

$$G(s)=\frac{b}{a_3s^3+a_2s^2+a_1s+a_0} \tag{7}$$

With formula (2) and formula (7), system practical parameter $K_V$, $n_0$ and $D_0$ can be deduced as formula (8) shows.

$$\left.\begin{array}{ll} K_d=\dfrac{a_0}{b} & K_v=\dfrac{b}{a_1} \\ n_0=\sqrt{\dfrac{a_1}{a_3}} & D_0=\dfrac{a_2}{2\sqrt{a_1a_3}} \end{array}\right\} \tag{8}$$

System control parameter can be Related algorithm of document [10] can get system control parameter. Parameter tuning formula is shown in table 1. Procedure of tuning algorithm is shown in Fig.4.

Table 1 Control Parameter Gain

| Three-parametric Feedback Gain | | Three-parametric Feedforward Gain | |
|---|---|---|---|
| Displacement Feedback Gain | $A_d'=\dfrac{k'k_v}{K_d}\dfrac{n^2}{n_0^2}$ | Displacement Feedforward Gain | $A_d=A_d'$ |
| Speed Feedback Gain | $A_v'=\dfrac{k_v}{K_v}\left(\dfrac{n^2}{n_0^2}-1\right)$ | Speed Feedforward Gain | $A_v=\dfrac{2D_cA_d}{\alpha n_c}$ |
| Acceleration Feedback Gain | $A_a'=\dfrac{k_v}{K_a}\left(\dfrac{2Dn}{n_0^2}-\dfrac{2D_0}{n_0}\right)$ | Acceleration Feedforward Gain | $A_a=\dfrac{A_d}{\alpha\beta n_c^2}$ |

where, $k'=\dfrac{n_bn_c}{n_c+2D_cn_b}$; $D=\dfrac{n_b+2D_cn_c}{2n_c\sqrt{1+2D_c\dfrac{n_b}{n_c}}}$; $K_d$, $K_v$, $K_v$ are respectively displacement, speed and sensitivity coefficient; $\alpha$, $\beta$, $C_1$, $C_2$ are integral gain fixed parameters in artificial circuit. $n_c$, $D_c$ are determined by parameter itself.

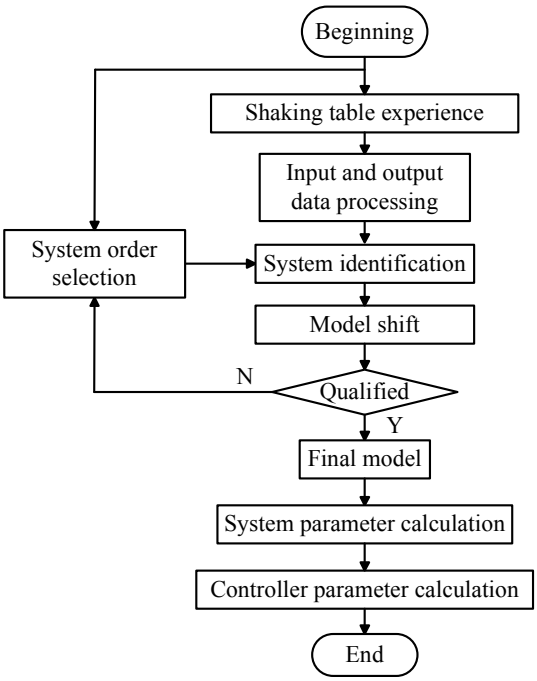


Fig.4 Tuning Algorithm Flow Chart

**Simulated of Parameter Self-tuning Algorithm**

This paper researches on shaking table with the size of 3m×3m . Its performance index is shown in table2. The transfer function of shaking table selected in the consideration of the influence of servo valve and sensor's second order characteristic is presented as formula (9).

$$H(s)=\frac{G(s)G_q(s)}{1+G(s)G_q(s)G_a(s)} \tag{9}$$

where, $G_q(s)=\dfrac{1}{\dfrac{s^2}{n_q^2}+\dfrac{2D_q s}{n_q}+1}$ is transfer function of servo valve; $G_a(s)=\dfrac{1}{\dfrac{s^2}{n_a^2}+\dfrac{2D_a s}{n_a}+1}$ is transfer function of sensor.

The simulation time of this experiment, the interval of sampling time is 0.001s, the input signal is white noise signal of 0.1-50Hz, the maximum acceleration amplitude is 0.1g, the system transfer function of the shaking table in displacement close-loop (neglect servo valve and sensor's second order characteristic) is shown in formula (10).

Table 2 Performance Index of Shaking Table System

| Project | index | Project | index |
|---|---|---|---|
| Platform size | 3m×3m | Counter weight | 6Ton |
| Peak load | 10Ton | Maximum displacement | ±10cm |
| Maximum speed | 60cm/s | Maximum speed | 2.0g（Full load）<br>0.9g（empty） |
| Frequency range | 0.1～50Hz | Control mode | acceleration control |
| Working mode | One-way of the level | Wave form | sine wave, random wave, earthquake wave |

$$G(S)=\frac{1928000}{s^3+26.3s^2+21210s+289300} \tag{10}$$

The transfer function corresponding to the open-loop system is like formula (11):

$$G(s)=\frac{1928000}{s^3+26.3s^2+21210s} \tag{11}$$

Formula (4) can deduce $K_V$=90.9005 , $n_0=145.637$ , $D_0=0.0903$ . The gain calculated values via theoretical calculation are $A_d=A_d'=0.375$ , $A_v'=0$ , $A_v=3.1073\times10^{-2}$ , $A_a'=1.7150\times10^{-2}$ , $A_a=1.1944\times10^{-2}$ .The parameter after being adjusted with the influence of servo valve and sensor's second order characteristic on control parameter values being taken into consideration are $A_d=A_d'=0.375$ , $A_v'=0$ , $A_v=3.3\times10^{-2}$ , $A_a'=1.1\times10^{-2}$ , $A_a=0.9\times10^{-2}$ , system frequency response curve is shown in the Fig.5, which shows within the scope of 0.4-50Hz, amplitude is controlled within ±3dB. This states that within working frequency bandwidth, output signal can well recur input control signal.

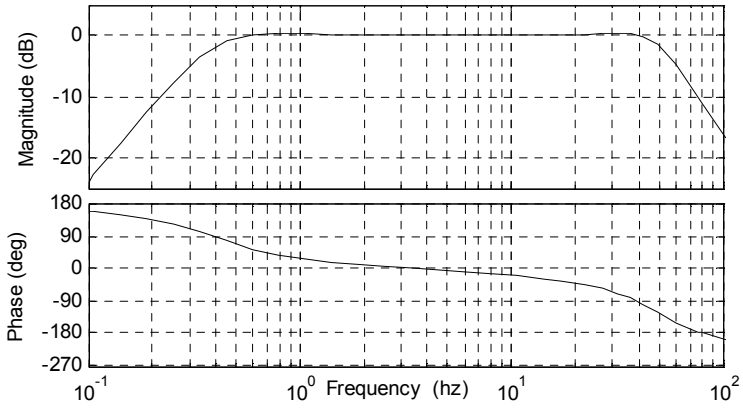


Fig 5: Frequency-response Curve with Regard to Servo Valve and Sensor's Character

## Conclusions

This paper adopts system identification and theoretical calculation method to get three-parametric control system's control parameter, system identification employs least square method, which identifies and gets close-loop transfer function of the system under the single influence of displacement feedback. As the identification method is easy to reach and system property is the real property of practical system, the control parameter obtained by such an identification method is highly precise with good control effect. Simulation calculation shows the control parameter got through system identification fits well with the control parameter got through simulated practical system, which verifies the validity of parameter tuning algorism put forward in this paper. Meanwhile, this method needs fewer debugging times with higher accuracy, and it is very easy to conduct programming realization, thus this is an effective shaking table parameter self-tuning algorism.

## Acknowledgements

The authors are grateful to acknowledge that this paper is partially financially supported by the National Natural Science Foundation of China under Grant No.51278013 and the open foundation of Beijing Key Lab of Earthquake Engineering and Structural Retrofit. Moreover, the retired expert Haohua HUANG had offered lots of valuable suggestions on this paper, heartfelt thanks for him too.

**References**

[1] Hironaka K, Miura J and Horiguchi K:Transactions of the Japan Society of Mechanical Engineers: Vol. 75(2009),p. 2909

[2] Stoten D P and Shimizu N. Proceedings of the Institution of Mechanical Engineers, Part I: Journal of Systems and Control Engineering. Vol. 221(2007),p. 423

[3] Chengshun FAN, Weiqing CUI, Shijie LI，in: Proceedings of the 2010 International Conference on Information Technology and Scientific Management ,edited by Scientific Research Publishing, Tianjin, China(2010). (in Chinese)

[4] Zhidong Yang.: *Research on control technologies of simulation of vibration environment using hydraulic vibration table* (Haerbin Institute of Technology， 2009). (in Chinese)

[5] Junwei HAN, Baosheng HU, Mingdong ZHOU and Liming YU: Earthquake Engineering and Engineering Earthquake Vibration. Vol. 1 (1997),p. 116. (in Chinese)

[6] Zhangwei CHEN, Pan TIAN and Wei JING. Automobile parts. Vol.8(2010),p.79 (in Chinese)

[7] Zhenbao LI, Zhenyun TANG and Jinbao JI: Journal of vibration and Shock. Vol.10(2010),p. 211.(in Chinese)

[8] Junwei HAN, LIming YU, ZHAO Hui and Zhongyi WANG: Journal of Harbin Institute of Technology. Vol. 3(1999),p. 21 .(in Chinese)

[9] Zhenyun Tang, Zhenbao LI, Jin-bao JI and Hua MA: Technology for Earthquake Disaster Prevention. Vol. 1(2010),p. 20. (in Chinese)

[10] Haohua HUANG. *The design and application technology of shaking table*( Seismological Press, Beijing 2008) .(in Chinese)

*Applied Mechanics and Materials Vols. 580-583 (2014) pp 1545-1550*
*© (2014) Trans Tech Publications, Switzerland*
*doi:10.4028/www.scientific.net/AMM.580-583.1545*

# Research Summary of Vibration Reducing Performance for Infilled Wall

Mingshe Sun[1,a] , Shuying Qu[2,b] , Fanbo Meng[3, c] and Cuiling Li[4,d]

[1] Department of Civil Engineering, Yantai University, Yantai, China 264005

[2]Department of Civil Engineering, Yantai University, Yantai, China 264005

[3]Department of Civil Engineering, Yantai University, Yantai, China 264005

[4]Department of Civil Engineering, Yantai University, Yantai, China 264005

[a]sunmingshe2012@126.com, [b]qsy_qu@163.com, [c]mfbo@163.com, [d]lcling627@163.com

**Keywords:** Infilled Wall, Passive Control, Energy-dissipation, Shock Absorption

**Abstract.** Infilled wall is always regarded as a nonload bearing element, its energy-dissipation capacity and impact for the frame structure under earthquake have not been taken seriously. In this paper the function of infilled wall for frame structure was discussed, energy-dissipation capacity of different measures were analysed and compared from the point of passive control theory. This paper provides the reference for the further research of filler wall.

## Introduction

Infilled wall is an important part of frame structure, but it is regarded as outside load in progress of designing. In fact the mechanism between the infilled wall and frame structure is quite complicated, especially under the action of earthquake. As the application of new wall materials and damper, it is more important to do research on performance of new damping infilled wall, and it would provide important reference for promotion of the new wall.

## Research Situation of Energy-dissipation Capacity for Infilled Wall

**Infilled Wall Is Leaved out of Account in Structure Design.** Frame structure is one of the most popular building types in industrial and civil construction. It serves as separate and containment structures in frame structure, and always be regarded as a non-structural element. Since the collaborative working mechanism between infilled wall and frame structure is complex, in the concrete structure design, horizontal and vertical load resistance response of frame is analysed without the consideration of infilled wall, the infilled wall is regarded as a uniformly distributed load and input structure calculation software. The effect that infilled wall works has been considered by simply use of cycle time reduction, such as structure design clear specified, Under the vertical load, internal forces of the frame can be calculated though the layer method. Under the action of wind load and horizontal seismic, internal forces of the frame can be calculated though the D method. High-rise frame structures can be calculated through the matrix displacement method respectively according to the planar frame and space frame by using computer.

However, earthquake damage happened at home and abroad proved that as a non-structural element, infilled wall is still involved in the seismic action. Frame infilled wall's influence on the structure response under seismic action mainly displays in the following two aspects, firstly, existence of the infilled wall changed stiffness of the empty frame and the overall stiffness of the structure level. If the infilled wall was distributed along the vertical direction uniformly, the vertical weak layer would appear at the less infilled wall floor. Under the action of horizontal seismic wave, the weak floor would break firstly, as is shown in Fig.1.

Fig1. Vertical stiffness are uneven, sidesway is large, collapse happened

Similarly, if the infilled wall was distributed along the horizontal direction uniformly, stiffness center of the structure would shift, which would finally amplify the torsion effects of the structure and torsion failure would be inevitable when the quake hit, as is shown in Fig.2.

Fig2. Infilled wall was distributed uniformly, stiffness center shifted, torsion failure happened.

Secondly, infilled wall would restrain beams, columns, walls of the structure. Especially, when there is a large window between adjacent columns. Existance of the infilled wall restrains the deformation of the bottom of the columns and effective length will be shortened, short column will appear, This kind of short column destruction caused structural damage has been confirmed by previous disasters, as is shown in Fig.3.

Fig3. Short columns damage

So the role of infilled wall in frame structure can be summed up in the following two aspects in general. Firstly, infilled wall dissipate the energy that inputed into the structure under earthquake through its own deformation which will finally protect the body. Secondly, along with the seismic

action, frame wall crack gradually, stiffness will reduce, the wall will fall out and collapse. It is often seen that under medium earthquake, main body frame structure has not yet been destroyed while infilled wall has suffered serious damage. The destruction of the infilled wall not only affect the building's using function , increase the repair cost, but also endanger life safety or affect the emergency evacuation when seriously damage. So in the practical engineering, damage of the infilled wall is often regarded as a judgment for structure function under normal play and life safety in earthquake. In current design theory under the background of seismic performance, it is necessary for earthquake engineering to re-examine the infilled wall frame structure seismic shock absorption performance [1,4].

**Measures to Improve the Energy Dissipation Performance of Infilled wall**

Traditional structural anti-seismic concept is using the resistance of the structure to resist seismic action, includes bearing capacity of its own and plastic deformation ability. With the development of society and related disciplines, more reasonable and effective anti-seismic technology [5,6] have been explored, structure control design appears. Structure control design is to inhibit response of structure caused by dynamic load by install energy consumption or damping device on the structure. Structural control [7] is mainly divided into passive control, active control, semi-active control, mixed control, and the intelligent control developed in recent years.

Structure passive control is to point to add a subsystem in certain parts of the structure, or make constructional change on some component of structure in order to change the dynamic performance of the structure system. Passive control has the advantages of simple construction, low cost, ease of maintenance and without external energy support, etc. currently, passive control techniques are widely used in practical engineering, for example, some kind of energy dissipation device is set up between structure and foundation to reduce upwards transport of the seismic energy, finally reduce the vibration of the structure. Passive control of infilled wall has been applied in the following several aspects.

**Make Constructional Change on the Structure to Improve Dissipation Capacity.** On one hand, integrity of the structure that resisting seismic action can be improved by enhance the strength of the component or strengthen the connections between components, as prescribed by seismic code in Clause 3.3.7 [8] paragraph 3, non-structural element attached to the building or roof and nonbearing wall of stairwell should be reliably connected or anchored with the main structure, in case of collapsed hurt or broken during the earthquake. In paragraph 4, as for enclosure wall and partition wall of the frame structure, the adverse impacts on the structure during the earthquake should be estimated unreasonable setting of the main structure caused damage should be avoided. In practical engineering, the masonry structure reinforcement method is mainly used to solve the above problems, for example, Increased aseismic performance of outsourcing wall reinforced concrete facing, Steel mesh and cement mortar layer reinforcement method, Increase the structural integrity by using pressure grouting method, Add ring beam,(constructional column) reinforcement method. Besides in accordance with the design specifications for the corresponding ring beam and constructional column set. The following Rachel steel reinforcement method is used to reinforce the infilled wall. In the process of structure construction, bar is embedded in beams and columns, surrounding reinforced is set in the wall, embedded bar and surrounding reinforced should be twisted together or welded, as is shown in Fig. 4. "L", the distance between reinforcing steel bar, should be considered according to the actual needs. Generally, it is 300 ~ 600 mm. After the house built, wall beams and columns can be directly decorated.

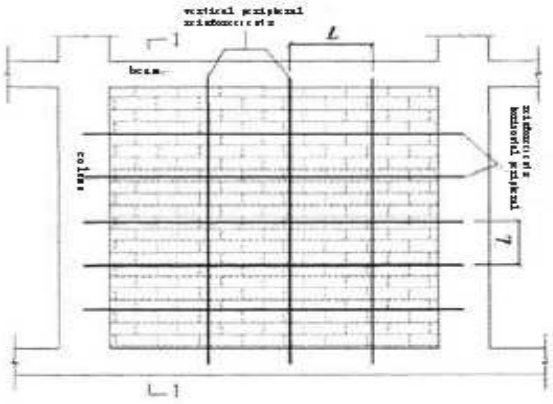

Fig.4 Wall with surrounding reinforcement

**Cooperative Use of Construction Measures and Energy Consumption Components.** It is true that infilled walls of reinforced concrete structure should be released or flexible connected with columns as is advised by Earthquake Resistant Design Code in 13.3.3.2 [9]. But the specification does not give specific practice. Academia rarely does relatively research. Flexible connection has the advantage of reducing the adverse effect that infilled wall acted on frame structure under seismic loading, but, it also undermines the beneficial effects infilled wall acted on the frame under the normal using condition. Energy consumption flexible connection is a new type of connection between the infilled wall and frame, which is improved on the basis of flexible connection method. The specific approach is to release clearance in the upper, left and right part between the wall and main body framework. Put specified damping device or damping in upper, left and right sides of the gap, or both of them. The gaps should also be filled with soft mortar, and connected by active connection plate fixed on the main structure, as is shown in Fig.5 to Fig.7. Through the reasonable design, the damping device (components) can provide a certain amount of connection stiffness to ensure good stiffness for frame structure under normal use condition. Under the action of the earthquake, the relative displacement appears between the wall and the main body frame, then damping device yield energy, stiffness reduce significantly, Thus the negative impact of the infilled wall stiffness for main body frame can be reduced, earthquake energy and earthquake response can also be reduced.

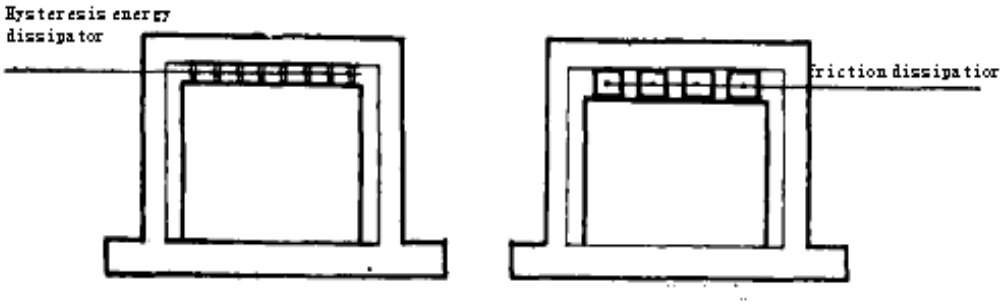


Fig.5 Energy dissipation device set in the crack of the wall

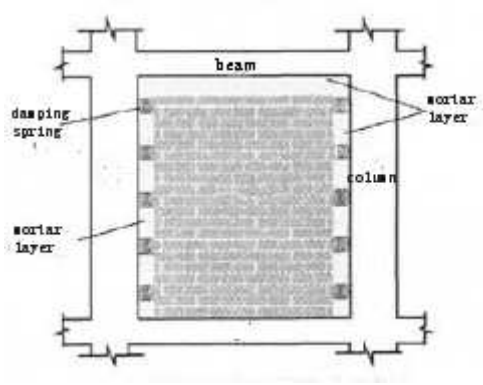


Fig.6 Wall with gaps

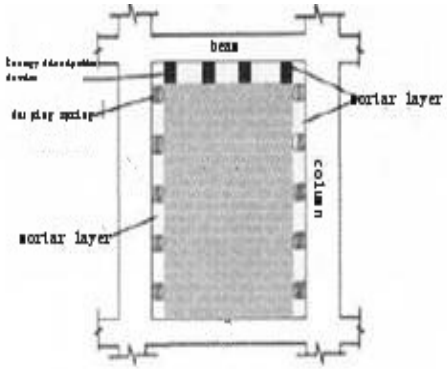


Fig.7 Wall with gaps and damping devices

**Improve the Wall Itself Structure, Make the Wall Itself Become a New Type Damping Wall.** According to the previous earthquake damage of infilled wall, some scholars proposed damping infilled wall frame system. Damping infilled wall frame is to divide a piece of infilled masonry wall into several masonry units; Viscoelastic material layers are set between masonry units. The forming layer is just similar to the viscoelastic damper, which is formed by one layer of steel plate and one layer of viscoelastic material layer. There are gaps between masonry units and frame columns filled with soft article mortar or viscoelastic materials. Viscoelastic damper and new damping infilled wall are shown in Fig.8 and Fig.9. When the frame is acted by earthquake, masonry units of different location will produce relative displacement, viscoelastic material layer shear deformation, absorb and consume the earthquake energy. Finally the wall damage will be reduced or avoided.

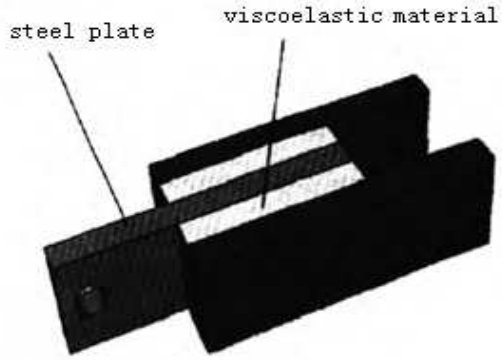


Fig.8 Viscoelastic damper

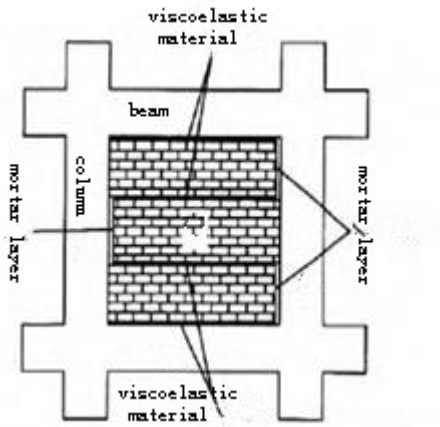


Fig.9 New damping infilled wall

This new framework damping wall has many advantages, the infilled frame wall itself is a damper, and it can improve the energy consumption capability of infilled wall. And it doesn't require additional damping energy dissipation device, viscoelastic layer is added in the middle of the horizontal mortar joint of infilled walls, it will not add difficulty to the construction.

## Conclusion

According to the damage characteristics of infilled wall frame structure, research Situation, need of wall policy and development trend of modern seismic design concept, Research on new type shock absorption performance of the masonry infilled wall is the urgent needs of the engineering practice and environment sustainable development, and will provide a scientific basis for further aseismic design code revision in China.

As we can see from the theoretical and experimental research on infilled wall frame in recent years, because of the existence of infilled wall, there are obvious difference on Mechanical performance between frame structure and empty frame. Stiffness, bearing capacity and energy-dissipating capacity

of the frame structure are also improved compared with empty frame. At the same time, due to the big stiffness the infilled wall cracks earlier and easily when earthquake comes. In view of the advantages and disadvantages of the infilled wall effect on framework, the theory and experimental study has made certain achievement but still not perfect. It is difficult to consider the impact in the design progress. The improvement of the design theory and the reform of wall materials also require further research work. And along with the application of new masonry materials, solid clay brick infilled wall materials used in frame structure are replacing by new masonry materials, But because of a lack of related research on performance of new masonry infilled wall frame structure , At present the rules of the clay brick are still mainly used in the design of infilled wall. Advantage of the performance of new wall materials can not be given full play, and it will hinder the application of new type masonry infilled wall. New damping components and dissipative damping elements based on energy theory have been used in frame wall more and more. Research on Energy dissipation performance of damping and mechanism become more and more urgent. This also provides a new direction for the experimental study on the theoretical analysis and numerical simulation. Carry out research on new aseismic performance of masonry infilled wall frame and designing method will provide the basis for the future new infilled wall frame structure anti-seismic design, and help promoting new wall policy and application of new materials.

**References**

[1] Yun Zhou, Shuilin Peng, Congyong Wu, Qingli Yin, Yangzhao Guo. Earthquake Resistant Engineering and Retrofitting, 2011, 33(4): 79-84. (In Chinese)

[2] Lixue Jiang, Qiaowen Zheng. Industial Construction, 2009, 39(10): 40-47. (In Chinese)

[3] Zixiong Guo, Yibin Wu, Qunxian Huang. Journal of Earthquake Engineering and Engineering Vibration, 2008, 28(6):172-177.

[4] Yun Zhou, Shuilin Peng, Yangzhao Guo, Zhengmin Zou, Qingli Yin. Journal of Disaster Prevention and Mitigation Engineering, 2011, 5(31): 469-476. (In Chinese)

[5] Yongfeng Du, Jifang Geng. Earthquake Resistant Engineering and Retrofitting, 2011, 33(1): 38-42. (In Chinese)

[6] Tingting Guo, Jihua Yu, Xiwei Xu. Earthquake Resistant Engineering and Retrofitting, 2010, 32 (4): 125-133. (In Chinese)

[7] Weiming Yan, Fulin Zhou, Ping Tan. World Information on Earthquake Engeering, 1997, 13(2):8-19. (In Chinese)

[8] National Standards of the People's Republic of China, Code of Aseismic Design of Buildings (GB50011-2010).

[9] National Standards of the People's Republic of China, Code for Design of Concrete Structures (GB50010-2010).

*Applied Mechanics and Materials Vols. 580-583 (2014) pp 1551-1554*
*© (2014) Trans Tech Publications, Switzerland*
*doi:10.4028/www.scientific.net/AMM.580-583.1551*

# Analysis on Seismic Performance of Beam and Plate Converter Floor

Gentian Zhao[a], Xuting Kou[b],

School of Architecture & Civil Engineering,

Inner Mongolia University of Science & Technology, Baotou 014010, P.R. China

[a]zhaogentian93110@sina.com, [b]408949009@qq.com

**Keywords:** thick transferring plate; seismic design; frame and shear wall structure; overall structure calculation

**Abstract:** With the project case, the seismic performance of girder transfer floor member and the plate transfer floor member were discussed. Contrast calculation was carried out in girder transfer floor member and the plate transfer floor member with SATWE method to analyze its reasonable and unreasonable places. Based on overall structure calculation of a high rise building, the seismic design requirements for buildings applying thick transferring plate have been presented. The conclusion is that the seismic performance of girder transfer floor member is more advantageous and affordable, more convenient and more economical in ingredients.

## Introduction

Today, high-rise building has been developing toward the complex body, and being versatile and comprehensive. A building along the height direction pursues very complex functions as residential, office, entertainment, shopping and other functions. The bottom arranged shopping malls; intermediate floors can be as shops, restaurants and entertainment facilities; upper floors are used for hotel, residential; top floor, also can be designed into the garden, or even a stadium. Such a building has become a complex, which needs to really achieve different structural forms to make these functions come true.

This complex also faces many problems. Central is a small space or medium-sized. The lower requires large column grid, large bays. From a structural and the stress, because of the lower by force, stiffness, requiring multi-wall, column grid density; into the upper part of the force will be reduced, the wall can be reduced, reducing the number of columns, column grid to expand. Such a structure is the structural requirements and building requirements contrary, therefore, the structure must be designed to be "anti-conventional design" [1], that is in accordance with the requirements of the upper column grid building dense, small space, the lower column grid sparse, large space. In order to achieve this arrangement, it leads to a new concept of "conversion structural elements" [2], to set the conversion component of floors, called the conversion layer.

This article focuses on beam conversion structure and plate transfer structure for discussion. Transfer Beams are most widely used because of its simplicity of design and construction, the force clear. And converting the beam layout is very casual, portrait or landscape can be a two-way arrangement. But if and when the column grid to stagger down very much, when used in many places difficult to directly supporting beams, you need to make a plate suspended deck conversion layer. Flexible plate lower column grid conversion layer can be arranged, it doesn't need to be aligned with the upper structure. But it is heavy, and many materials are used.

## Project overview

This works for A sugar mill district revitalization group A city building, building a total height of 52.60 meters (outdoor ground to the eaves), basement (ceiling height of 3.90 m) and 16 floors (one, two-storey 4.50 m, three to sixteen layers of height 3.00 m); gross floor area of 15,619.66 square meters; retail floor area of 3,301.62 square meters; residential portion of the area of 12,318.04 square

meters. The basic wind pressure: W0 = 0.55 kN/m2. Basic snow pressure: S0 = 0.50 kN/m2. Venue Category: Ⅱ class, in the form of building structures: Part frame supported shear wall structure. Floor Structure: Reinforced Concrete Floors cast reasonable service life of 50 years, seismic fortification intensity is 6 degrees; basic design earthquake acceleration: 0.05g, site soil type: supporting layer of soil is soft ground soil, seismic design groups: the first group; class C buildings.

Residential conversion layer above as wall structure, shear seismic rating of four (five layers - the top) level, the conversion layer below the mall for the frame shear wall structure, the framework for the two seismic level, level of seismic shear walls three (-1 layers to four layers).

Figure 1 is architecture elevation.

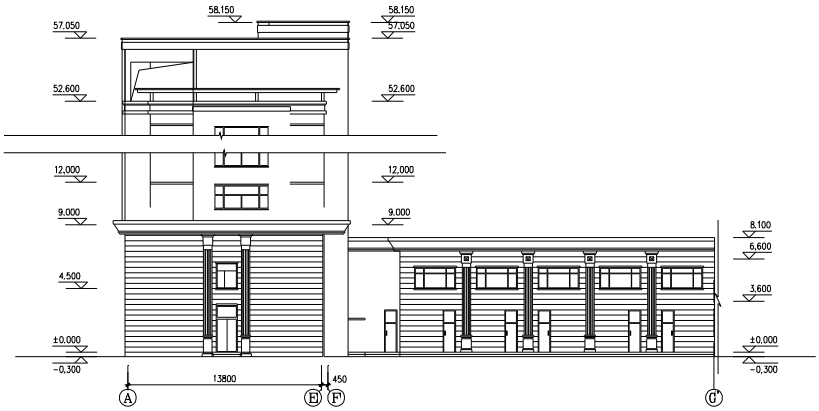


Fig.1 Architecture elevation

**Model selection**

According to architectural requirements, the second layer is determined to convert the ground floor, it is designed for the conversion layer in three cases, the first one is the beam conversion layer (Ⅰ), the second is the 1500mm conversion layer thick (Ⅱ), the third is 1200mm thick slab conversion layer (Ⅲ). In order to ensure a clear contrast to the various programs, so consistent conversion layer superstructure and substructure, but it does not affect the conversion layers thick high.

Program Ⅰ, the main transfer beam breadth is 400mm and height is 1300mm. Select a building expansion joint on the left of the beam layout (Figure 2).

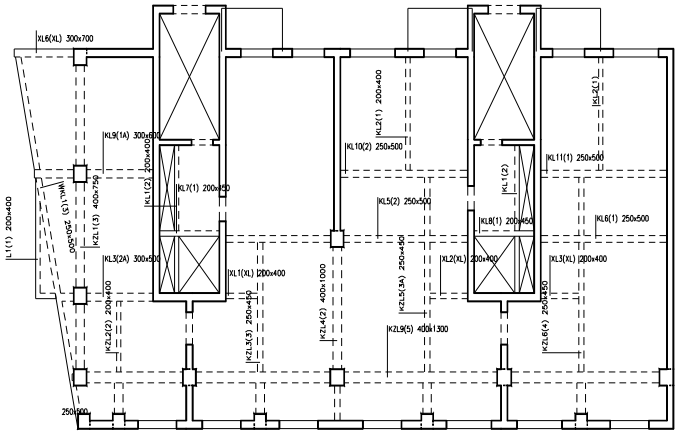

Fig.2 The left of the beam layout

Program Ⅱ, beam in the program Ⅰ will be converted component beam, its breadth is 300mm and height is 600mm. and the floor slab thickness to 1500mm. A building expansion joint is selected on the left of the beam layout.

Program Ⅲ, beams arrangement is the same program Ⅱ, thick slabs only changes to 1200mm.

**Seismic performance analysis and comparison**

Under the current prevailing norms of seismic, in plans for 6 degrees of seismic intensity vertical seismic forces are negligible [3], the project area is located 6-degree, area so is used here only two-way horizontal seismic force is calculated. In this paper, SATWE modeling, rigid floor is assumpted, the overall structure of the lateral deformation resistance between structural displacement and story drift angle OK. Bi-layer average displacement and maximum drift are showed in Table 1.

Table1 Bi-layer average displacement and maximum drift

| The average displacement X direction layer | | | | The average displacement Y direction layer | | |
|---|---|---|---|---|---|---|
| Floor | Program Ⅰ | Program Ⅱ | ProgramⅢ | Program Ⅰ | Program Ⅱ | ProgramⅢ |
| 15 | 5 | 5.06 | 5.05 | 4.14 | 4.19 | 5.05 |
| 14 | 4.68 | 4.73 | 4.72 | 3.79 | 3.84 | 4.72 |
| 13 | 4.33 | 4.38 | 4.37 | 3.44 | 3.48 | 4.37 |
| 12 | 3.97 | 4.01 | 4 | 3.08 | 3.12 | 4 |
| 11 | 3.59 | 3.63 | 3.62 | 2.72 | 2.76 | 3.62 |
| 10 | 3.2 | 3.24 | 3.23 | 2.37 | 2.4 | 3.23 |
| 9 | 2.8 | 2.83 | 2.83 | 2.02 | 2.05 | 2.83 |
| 8 | 2.39 | 2.43 | 2.42 | 1.69 | 1.72 | 2.42 |
| 7 | 1.99 | 2.02 | 2.01 | 1.37 | 1.39 | 2.01 |
| 6 | 1.58 | 1.61 | 1.61 | 1.06 | 1.09 | 1.61 |
| 5 | 1.2 | 1.22 | 1.22 | 0.78 | 0.8 | 1.22 |
| 4 | 0.83 | 0.85 | 0.85 | 0.54 | 0.55 | 0.85 |
| 3 | 0.49 | 0.51 | 0.51 | 0.36 | 0.36 | 0.51 |
| 2 | 0.27 | 0.28 | 0.28 | 0.22 | 0.23 | 0.28 |
| 1 | 0.12 | 0.13 | 0.12 | 0.1 | 0.11 | 0.12 |
| X direction maximum displacement Angle between the layers | | | | Y direction maximum displacement Angle between the layers | | |
| Floor | Program Ⅰ | Program Ⅱ | ProgramⅢ | Program Ⅰ | Program Ⅱ | ProgramⅢ |
| 15 | 1/7865 | 1/7681 | 1/7721 | 1/7383 | 1/7227 | 1/7254 |
| 14 | 1/7401 | 1/7235 | 1/7271 | 1/7215 | 1/7064 | 1/7090 |
| 13 | 1/7048 | 1/6904 | 1/6934 | 1/7103 | 1/6959 | 1/6984 |
| 12 | 1/6807 | 1/6686 | 1/6711 | 1/7077 | 1/6941 | 1/6965 |
| 11 | 1/6629 | 1/6532 | 1/6552 | 1/7126 | 1/6999 | 1/7022 |
| 10 | 1/6577 | 1/6499 | 1/6514 | 1/7265 | 1/7143 | 1/7166 |
| 9 | 1/6638 | 1/6573 | 1/6584 | 1/7517 | 1/7396 | 1/7420 |
| 8 | 1/6651 | 1/6592 | 1/6601 | 1/7825 | 1/7699 | 1/7724 |
| 7 | 1/6769 | 1/6708 | 1/6718 | 1/8248 | 1/8106 | 1/8135 |
| 6 | 1/7021 | 1/6949 | 1/6961 | 1/8885 | 1/8711 | 1/8746 |
| 5 | 1/7416 | 1/7324 | 1/7340 | 1/9911 | 1/9678 | 1/9725 |
| 4 | 1/8230 | 1/8112 | 1/8131 | 1/9999 | 1/9999 | 1/9999 |
| 3 | 1/9999 | 1/9999 | 1/9999 | 1/9999 | 1/9999 | 1/9999 |
| 2 | 1/9999 | 1/9999 | 1/9999 | 1/9999 | 1/9999 | 1/9999 |
| 1 | 1/9999 | 1/9999 | 1/9999 | 1/9999 | 1/9999 | 1/9999 |

It can be seen from the table1, in the X, Y bidirectional seismic force, the average displacement scheme floor maximum 5.31mm, than 5.37mm and program two of the two 5.36mm are small. It is not difficult to see that a middle drift, drift and the total displacement is less than scheme two and three, and the scheme three and slightly better than scheme two. It means that the beam layer for seismic performance is better than the transfer plate layer conversion, but also can determine the initial plate thickness increased after the displacement of the structure will also increase. Therefore, the thick plate is not conducive to seismic.

By contrast, also found that each variable change plan model is smaller, and the scheme two and three are the variables. Conversion layer above three models are used for shear wall

structure, stiffness mutation are evident. Also found in the transfer floor layer displacement three schemes are the same, this is due to their stricter torsion, with conversion layers structure will have stiffness mutation in conversion layer, and it is the stiffness mutation will cause the reverse occurred. This type of housing ductility is poor, once the earthquake occurs, torsion failure is sudden failure, and secondary disasters caused are immeasurable.

In the earthquake, due to the existence of the plate, so here to focus a great deal of stiffness and mass, increases suddenly here earthquake, earthquake response will be strong. Not only the thick plate transition layer itself large force, but also because the vertical stiffness of the mutation, adjacent layers has also been considerable force, once the earthquake, and earthquake damage adjacent layer can not be ignored. The plate test showed that, the interaction of vertical force and earthquake force, plate punching failure not only possible, but also may cause shear failure, plate must be three to reinforcement. [4]

## Conclusions

For seismic design, building with the conversion layer transfer can be used in the area of the seismic intensity 6 in transfer slab and beam, but the thick plate transfer should not be used for 7 degrees and 7 degrees above high-rise building. And at 8 degree, for conversion layer the vertical earthquake should be considered. Conversion layer should not be used at 9 degrees. The paper draws the following conclusions:

As long as the structures with transfer, stiffness mutation will happen. The maximum design conversion is required to control the stiffness mutation, and beam transfer layer can better mutation stiffness, the thick plate transition, in fact, the thickness of the plate on the structural displacement change is not significant. The reduced stiffness mutation of the most basic idea is to strengthen the lower, weakening the upper. While the strong column and weak beam is impossible, it is important to ensure the conversion layer stiffness, to ensure the smooth realization of conversion.

The great stiffness, displacement of each scheme in the conversion layer of the interlayer and the interlayer displacement angle will be significantly reduced. For the plate transition layer, although in accordance with the norms of vertical seismic force can be neglected, but the vertical earthquake does exist, one of which is the main reason of seismic performance moderator system is not good, so the conversion layer below the column must strengthen structure, and strictly control the axial compression ratio of column.

The seismic performance of comprehensive analysis of the three models, the girder transfer floor seismic most superior performance, whether it is from the angle of displacement and inter story displacement point of view, is one of the minimum displacement solution. In practical engineering, with thick plate transition layer construction should avoid as far as possible, can also change the architectural layout, let the thick plate structure into beam structure. The thick plate transition is still a big problem in seismic design. Except the design difficulty, the construction is very complex, and the amount of materials and the cost is higher than the girder transfer floor.

## References

[1]Tang Xingrong. Design of Special and Complicated High-rise Building Structures[M].Beijing: China Machine Press,2006.6-90.

[2]JGJ3-2010, Technical specification for concrete structures of tall building[S]. Beijing: China Building Press,2009.

[3]GB50011-2010, Code for Seismic Design of Building[S]. Beijing: China Building Press, 2010.

[4]Cai long,Du hongbiao,Jin renhe. Influence of Lateral Stiffness Ratio on Seismic Behavior of Shear Wall Structures Supported on Frames under Horizontal Seismic Action [J], Earthquake Resistant Engineering and Retrofitting , 2012，34(1) : 1-6.

*Applied Mechanics and Materials Vols. 580-583 (2014) pp 1555-1558*
*© (2014) Trans Tech Publications, Switzerland*
*doi:10.4028/www.scientific.net/AMM.580-583.1555*

# Ultimate State of Bridges with Rocking Isolation under Extreme Earthquakes

T.Y. Lee [1,a], M.Y. Huang [2,b] and K. J. Chung [3,c]

[1] Associate Professor, Dept. of Civil Engineering, National Central University, Taiwan

[2] Graduate Student, Dept. of Civil Engineering, National Central University, Taiwan

[3] Graduate Student, Dept. of Civil Engineering, National Central University, Taiwan

[a]tylee @ncu.edu.tw, [b]vi60113@hotmail.com, [c]100322016@cc.ncu.edu.tw

**Keywords:** ultimate state, rocking isolation, bridge, spread foundation, extreme earthquakes

**Abstract.** This study is aimed to analyze the ultimate state of bridges with rocking isolation of spread foundations under extreme earthquakes. The Vector Form Intrinsic Finite Element method (VFIFE) is adopted to simulate the failure procedure of bridges with and without rocking isolation. To simulate the highly nonlinear behaviors between soil and foundations, Winkler-based models are established in the VFIFE in this study. A practical five-span bridge with spread foundations is chosen to study the effect of rocking isolation and discuss the influence of altering parameters of bridges. The analytical results are compared between linear soil springs and nonlinear soil springs. Furthermore, the ultimate state of bridges is simulated to realize the dynamic behaviors of bridges under extreme earthquakes.

## Introduction

The rocking of bases resulted in lesser structural internal forces and deformations. Kawashima and Nagai[1] analyzed a five-span bridge with rocking response under three directional ground excitations. The analytical results show that the effect of rocking isolation is significant in reducing the plastic deformation of the plastic hinges at the bottom of columns, whereas it increases the displacements of deck and column. Although some studies show that the spread foundations do not overturn even if the spread foundations are subjected to ground motions with peak acceleration much larger than the equivalent accelerations in the traditional static analysis[2]. The issue of overturning is still critical in spread foundation when exhibiting rocking response. Therefore, this research is aimed to clarify the overturning instability and the isolation effect through ultimate numerical simulation when rocking response occurs in spread foundations.

It is difficult to analyze the ultimate situation of bridges under extreme earthquakes by using the traditional finite element method. Therefore, Vector Form Intrinsic Finite Element method (VFIFE), a new computational method, is selected to be the computational method in this study. The VFIFE developed by Ting et al.[3] is superior in managing the engineering problems with material nonlinearity, discontinuity, large deformation, large displacement and arbitrary rigid body motions of deformable bodies.

## Vector Form Intrinsic Finite Element

The Vector Form Intrinsic Finite Element has been developed based on theory of physics to simulate failure response of a structural system due to applied loads. The first step in the VFIFE analysis is to establish a discrete model for a continuous structure by using a lumped-mass idealization. It is noted that all lumped masses are connected by deformable elements without mass. The equations of motion at each mass or so-called node for all degrees of freedoms are constructed by applying Newton's Second Law of Motion. Assume that a structural system consists of a finite number of particles. A particle designated as $\alpha$ has a mass matrix $\mathbf{M}^{\alpha}$ and a displacement $\mathbf{d}^{\alpha}(t)$ at time $t$. The equations of motion for particle $\alpha$ are

$$\mathbf{M}^{\alpha}\ddot{\mathbf{d}}^{\alpha}(t) = \mathbf{P}^{\alpha}(t) - \mathbf{f}^{\alpha}(t) \quad (1)$$

Where $\mathbf{P}^{\alpha}$ is the applied force or equivalent force acting on the particle; $\mathbf{f}^{\alpha}$ is the total resistance force exerted by all the elements connecting with the particle, or the internal resultant force. Each element without mass is in static equilibrium.

Since the failure progress of structures involves changes in material properties and structural configuration, discrete time domain analysis is essential to solve the equations of motion, Eq. (1). In calculating the internal forces, a set of deformation coordinates is defined for each element and for each time increment. Compared to the traditional finite elements, the unique of the VFIFE is to calculate rigid body motion and element deformations through the de-formation coordinates in each time increment. By doing so, the VFIFE can deal with large displacement, deformation and rigid body motion simultaneously.

## Target Bridge and Analytical Model

The target bridge is a five-span continue bridge with rigid bearings, as shown in Fig. 1. The total length is 5@40 m = 200 m and a width of 12 m, which is supported by four reinforced concrete columns with a height of 12 m in each and two abutments. Spread foundations are designed to support the abutments and columns. The bearings installed on the abutments and columns are roller bearings and hinge bearings, respectively. After hinge bearings rupture, the dynamic friction coefficient in the interface is assumed to be 0.4. The friction coefficient of the roller bearings is assumed to be 0.1.

The spread foundations are embedded in sandy soil with N-value of the standard penetration test over 50. Based on seismic design codes, the spread foundations are 2 m thick, 6.5 m long in longitudinal direction and 7 m wide in the transverse direction. Underlying soils are idealized by soil springs as shown in Fig. 2 to simulate the interaction of soils and foundations. The Winkler springs [4] are used to simulate the nonlinear soil behavior as shown in Fig. 3. The elastic part simulates the far-field behavior while the plastic part simulates the near-field permanent displacement. Figure 4(a) is the analytical model of the vertical and horizontal soil springs while Fig. 4(b) is the model of shear soil springs. Note that the vertical soil springs is of compression only.

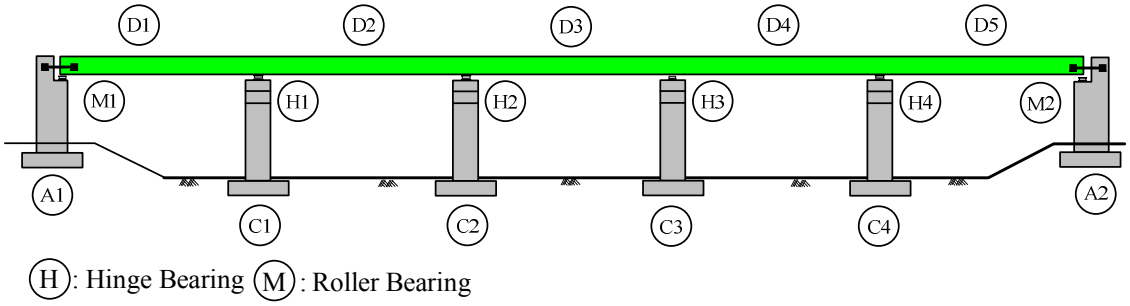


Figure 1. Five-span continuous bridge with roller and hinge bearings

In simulation, the target bridge is subjected to the near-field ground motion recorded at JMA Kobe station in the 1995 Japan Kobe earthquake. In order to observe when the bridge will collapse, the ground acceleration is amplified from 100% to 250% at an increment of 10%.

## Numerical Simulation Results

From the simulation results, the demanded ductility of columns in the analysis case with rocking isolation is smaller than that in the analysis case without rocking isolation shown as fig. 5. The target bridge collapses at smaller ground motion when the rocking of foundation is not considered in analysis. Figure 5 presents the rotation of plastic hinge at the bottom of column C1 in the analysis cases by using linear and nonlinear soil springs, both of which include rocking isolation. It is observed

that the maximum rotation of plastic hinge in the case by nonlinear soil springs is larger than that in the case by linear soil springs.

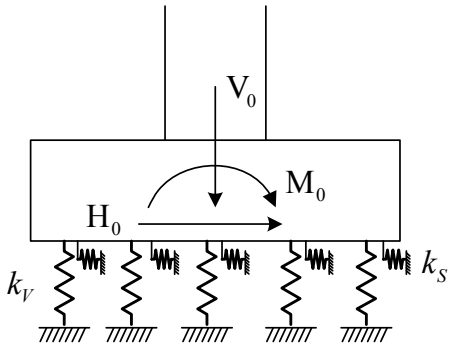


Figure 2. Analysis model of spread foundation

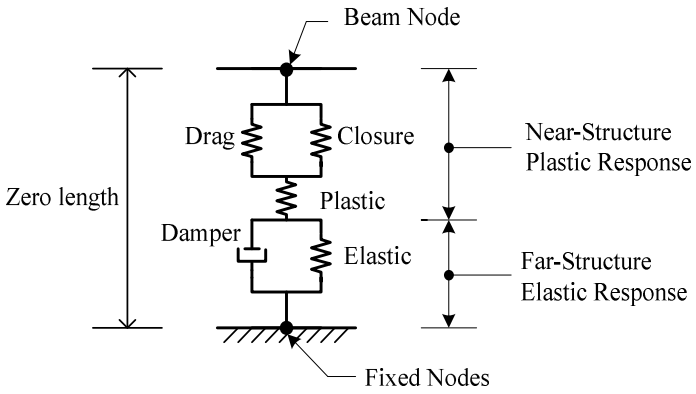


Figure 3. Winkler-based model

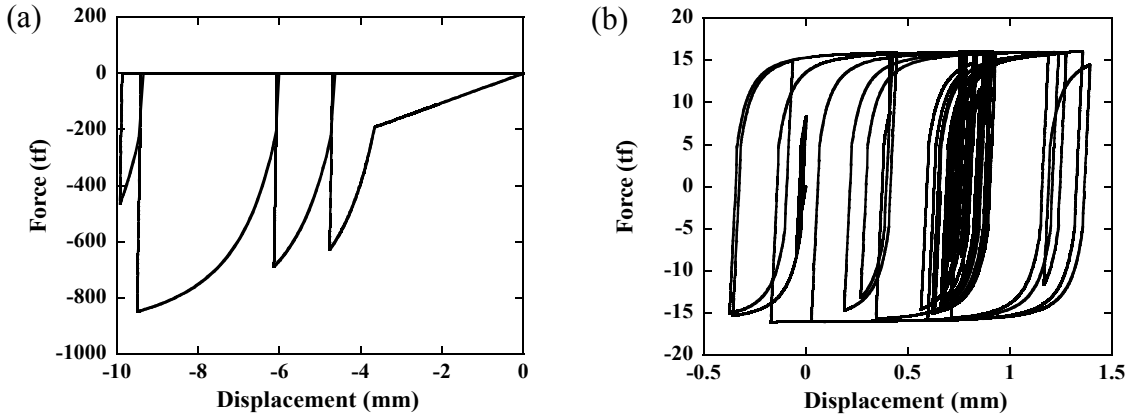


Figure 4. Hysteretic loops of nonlinear (a) vertical soil spring (b) shear soil spring

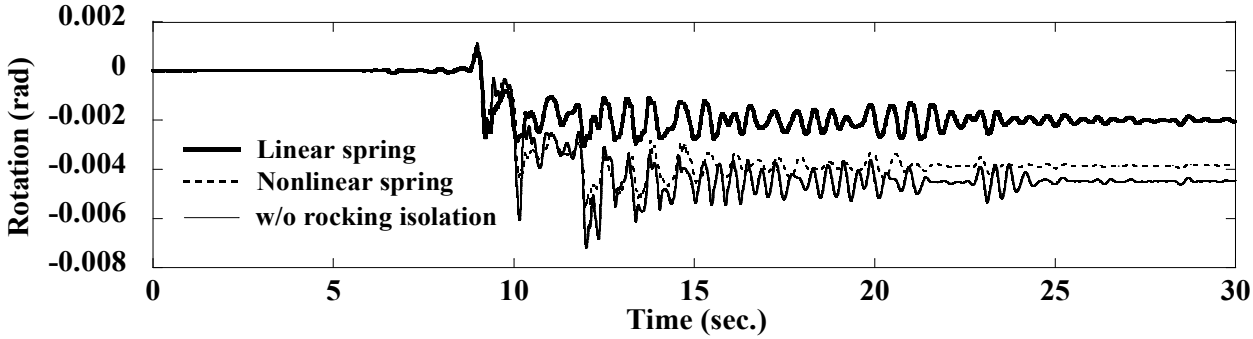


Figure 5. Rotation of plastic hinge at the bottom of column C1

Figure 6 shows the failure procedure of the target bridge with rocking isolation under 180% of the JMA Kobe records. All hinge bearing fracture first. Plastic hinges occur at the bottom of the columns. After the column reaches the ultimate ductility, the column loses the capacity of moment resistance and finally collapse. The deck fall downs with the collapse columns and then unseats from the abutment A1.

## Summary

The effect of rocking isolation of spread foundation for bridges was studied through ultimate analysis by using the Vector Form Intrinsic Finite Element method. A typical five-span viaduct under near-field ground motions was analyzed. The numerical simulation successfully predicts the failure

process of the bridges with rocking isolation under extreme earthquakes. The following conclusions may be obtained from the simulation results presented herein.

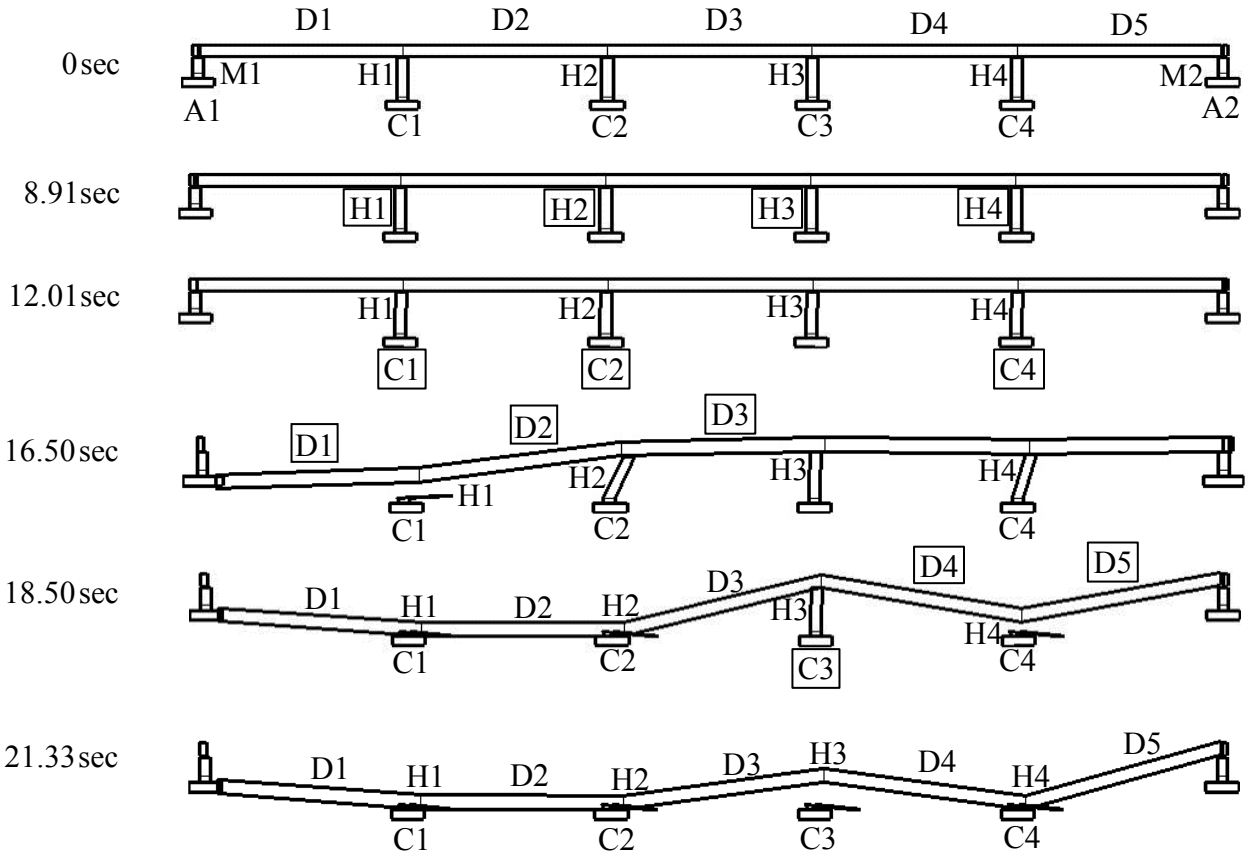


Figure 6. Failure procedure of the target bridge with rocking isolation under 180% JMA G.M.

(1) Compared with the bridge without rocking isolation, the bridge with rocking isolation performs better and collapses at smaller ground motion. It is beneficial to allow the spread foundation to rock for mitigating the seismic response of bridges under strong ground motion.

(2) While adopting linear soil springs to simulate the soil-structure interaction, the displacement of deck would be more conservative and the plastic hinges of columns will be overestimated.

(3) Rocking isolation dissipates the seismic-induced energy of structures to mitigate the damage. However, the permanent deformation of soil after earthquake is another issue for safety of bridges.

**References**

[1] Kawashima, K. and Nagai, T. 2006. Effectiveness of rocking seismic isolation on bridge. 4th International Conference on Earthquake Engineering, Taipei, Taiwan.

[2] Kawashima, K., Unjoh, S. and Mukai, H. 1994. Inelastic rock-ing of direct foundation during an earthquake. Civil Engi-neering Journal 36(7) : 50-55.

[3] Ting, E. C., C. Shih and Y. K. Wang. 2004. Fundamentals of a vector form intrinsic finite element: Part I. basic procedure and a plane frame element, Journal of Mechanics (20): 113-122.

[4] Raychowdhury P, Hutchinson TC. Performance evaluation of a nonlinear Winkler-based shallow foundation model using centrifuge test results. Earthquake Engng Struct. Dyn. 2009; 38: 679-698.

*Applied Mechanics and Materials Vols. 580-583 (2014) pp 1559-1563*
*© (2014) Trans Tech Publications, Switzerland*
*doi:10.4028/www.scientific.net/AMM.580-583.1559*

# Verification of LSSRLI-1 Applicability on Soft Sites Using Exact Solution

Ruishan Li [a], Xiaoming Yuan [b]

Key Laboratory of Earthquake and Engineering Vibration, Institute of Engineering Mechanics, China Earthquake Administration, 29 Xuefu Road, Harbin 150080, China

[a]lrshan22@hotmail.com, [b]yxmiem@163.com

**Keywords:** seismic analysis; exact solution; LSSRLI-1; soft sites; deficiency.

**Abstract.** LSSRLI-1 is an equivalent linear program which is used for seismic ground response analysis. Since the LSSRLI-1 was proposed by Xiaojun Li in 1989, it played very important role in seismic safety evaluation, solved the inputting problem for dynamic response analysis of structure. Some deficiency was found in the practice, especially when the layered site is soft. Linear exact solution is deduced in the frequency domain.based on the engineering wave theory. A program is compiled in the MATLAB environment, which is used to compare with the LSSRLI-1 results, including the ground response spectrum and the soil strain distribution.

## Introduction

Seismic response analysis of soil deposits is a part of geotechnical earthquake engineering, which deals with the site effects on the propagated seismic wave in the ground. Seismic ground response analyses provide researchers with important results, including design response spectrum, liquefaction susceptibility estimation and seismic slope stability assessment [1]. Available seismic ground response analysis methods are categorized into linear, equivalent linear and non-linear methods that perform the analysis in the time or the frequency domain. These methods defer in their modeling of soil behavior under earthquake loading. The equivalent linear method considered the shear modulus and damping ratio as constants for the whole duration of the earthquake. Compared to the equivalent linear method, the non-linear is mainly dependent on the dynamic constitutive model which is out of complex. Because of its advantages, the equivalent linear method is mostly used in the practice.

In China, the siesmic response analysis is carried out, using the LSSRLI-1 program which was proposed by Xiaojun Li in the 1989. In twenty years of practice, many deficiencies were found, especially when the site is soft.

In this paper, the linear exact solution is deduced based on the engineering wave theory and was compiled into a computer program in the MATLAB environment. To compare with the exact solution, the non-iteration results of LSSRLI-1 were calculated. The comparation includes the ground surface acceleration response spectrum and the soil strain distribution. The dynamic non-linear parameters are dependent on the shear strain of the previous iteration. Thus, the shear strain affects the ground motion, and vice versa.

## Models

The simplified single-layer and double-layer models are demonstrated in Fig.1. In the two kinds of models, the local coordinate of each layer is downward direction, with the origin at the layer top. Each layer is homogeneous and isotropic, and characterized by the thickness, h, mass density, $\rho$, shear wave velocity, $v_s$, and damping ratio, $\xi$. In this paper, three acceleration time histories (Fig.2), with each amplitude regulated to 0.1g, 0.2g, and 0.4g respectively, was used as the input motions. There are totally 4 models with different thickness and shear wave velocity are chosen. Two of them are single-layer model, and the remaining two are double-layer model. The specific parameters of these models are listed in the table 1. The nonlinear curves of shear modulus decreasing and damping ratio increasing with the shear strain, used in this paper was depicted in Fig.3 [2].

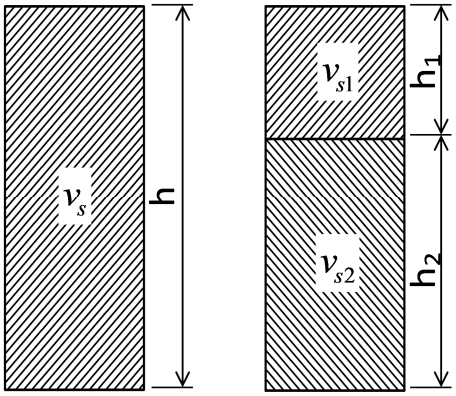


Fig.1 Simplified models of single-layer and double-layer

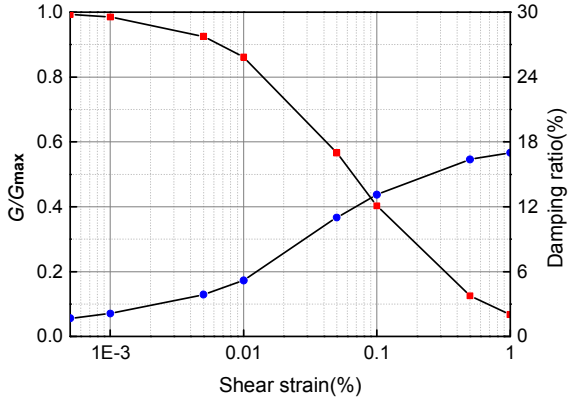


Fig.3 Dynamics non-linear curves

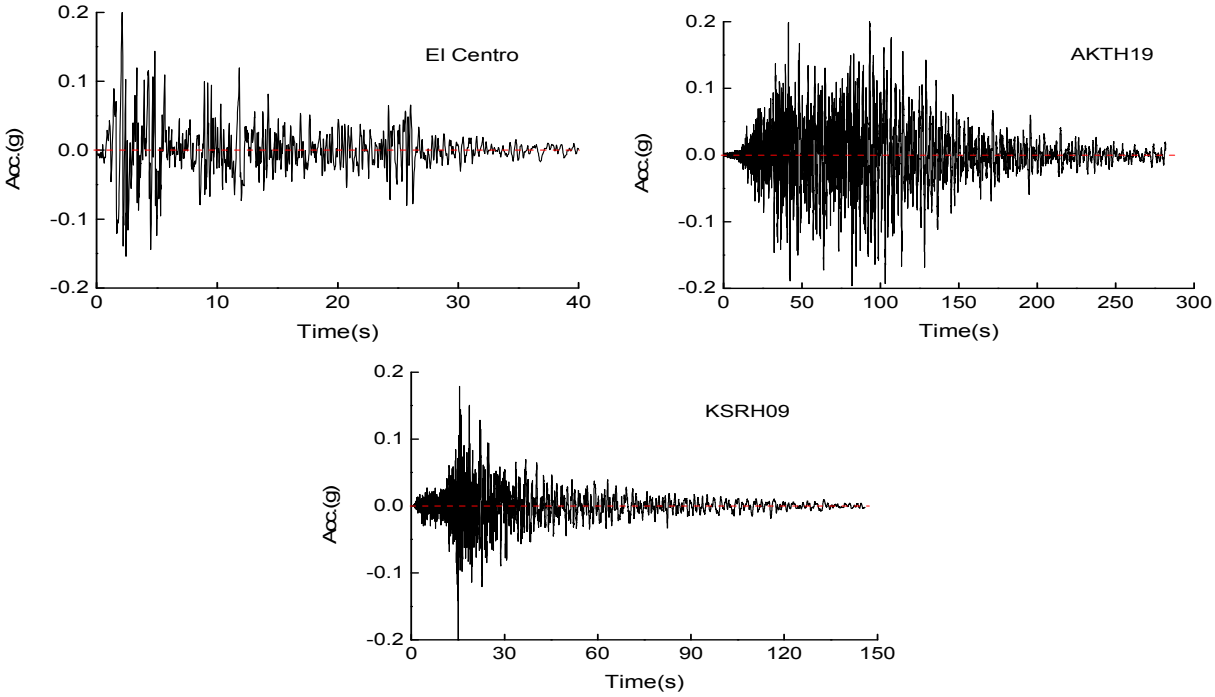


Fig.2 Input accelerations for 0.2g case (El Centro, AKTH19 and KSRH09)

Table 1 Specific parameters of calculation models

| | | | | | |
|---|---|---|---|---|---|
| Single-layer models | No. | $v_s$(m/s) | | H(m) | |
| | 1 | 120 | | 100 | |
| | 2 | 90 | | 120 | |
| Double-layer models | No. | $v_{s1}$(m/s) | $h_1$(m) | $v_{s2}$(m/s) | $h_2$(m) |
| | 3 | 120 | 30 | 180 | 70 |
| | 4 | 90 | 40 | 150 | 80 |

**Exact solution**

Consider the wave equation of motion as:

$$\frac{\partial^2 u}{\partial t^2} = v_s^2 \frac{\partial^2 u}{\partial z^2} + \frac{2\xi v_s^2}{\omega} \frac{\partial^3 u}{\partial z^2 \partial t} \tag{1}$$

A harmonic displacement occurs due to a harmonic load can be express as [1]:

$$u(z,t)=U(z)e^{i\omega t} \tag{2}$$

Using the stationary solution of elastic stress wave propagating in a homogeneous material, considering the complex modulus for hysteretic damping, the transfer functions H($\omega$) of shear strain in soil from the input accelerations can be expressed as follows, as well as the amplification ratio R($\omega$) of ground surface outputs to the inputs [3, 4].

For single-layer models:

$$H(\omega)=\frac{k^*\sin(k^*z)}{\omega^2\cos(k^*h)} \tag{3}$$

$$R(\omega)=\frac{1}{\cos(k^*h)} \tag{4}$$

For double-layer models:

$$H_1(\omega)=\frac{k_1^*\sin\left(k_1^*z_1\right)}{\omega^2\left[\cos\left(k_1^*h_1\right)\cos\left(k_2^*h_2\right)-\alpha\sin\left(k_1^*h_1\right)\sin\left(k_2^*h_2\right)\right]} \tag{5}$$

$$H_2(\omega)=\frac{k_2^*\left[\cos\left(k_1^*h_1\right)\sin\left(k_2^*z_2\right)+\alpha\sin\left(k_1^*h_1\right)\cos\left(k_2^*z_2\right)\right]}{\omega^2\left[\cos\left(k_1^*h_1\right)\cos\left(k_2^*h_2\right)-\alpha\sin\left(k_1^*h_1\right)\sin\left(k_2^*h_2\right)\right]} \tag{6}$$

Where ω is frequency of incident wave; h is the thickness of soil layer; $v_s$ is the shear wave velocity of soil layer; ξ is the damping ratio. They all specifically demonstrated in the Fig.1. $k^*$ is the wave number, which can be obtained from the following formula.

$$k^*=\frac{\omega}{v_s^*}=\frac{\omega}{v_s(1+i\xi)} \tag{7}$$

## Results and Conclusions

The main purpose of seismic response analysis is to obtain the ground surface motions, while what can be used by the engineers directly is the response spectra. So here first shows the ground surface response spectra, calculated by LSSRLI-1 and the exact solution.

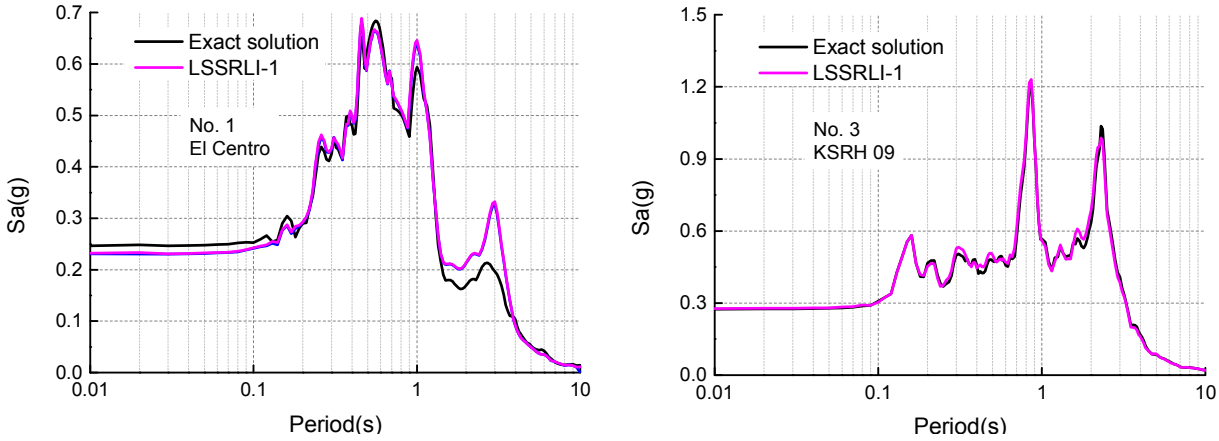


Fig.4 Response spectra of ground surface under 0.2g peak inputs

Fig.4 shows that the response spectra of different models, calculated by exact solution and LSSRLI-1, under different input conditions, agree well with each other. The consistency is independent with soil models and input conditions.

As mentioned before, the soil shear strain distribution affects the ground motion seriously, because the soil dynamic non-linear parameters are dependent on the shear strain. The shear strain distribution, without iteration, were dipicted in Fig.5. To demonstrate how the shear strain affects the ground motion, the program was run for one more time. The dynamic parameters were interpolated from Fig.3, according to the equivalent shear strain.

$$\gamma_{eq} = 0.65\gamma_{max} \tag{8}$$

In equation (8), the $\gamma_{mas}$ is the peak value of shear strain time history. The updated ground response spectrum is illustrated in Fig.6.

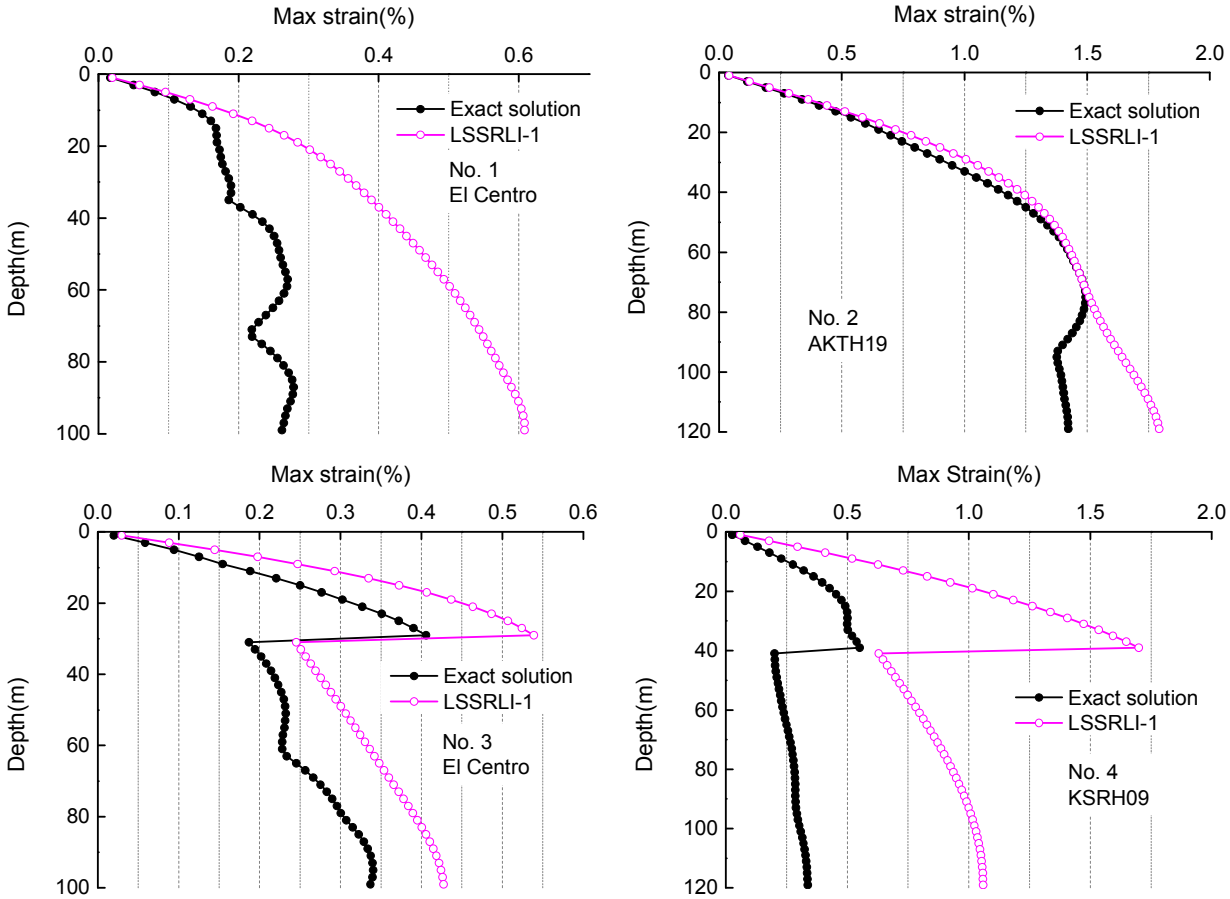


Fig.5 Distribution of shear strain in soil under 0.2g peak inputs

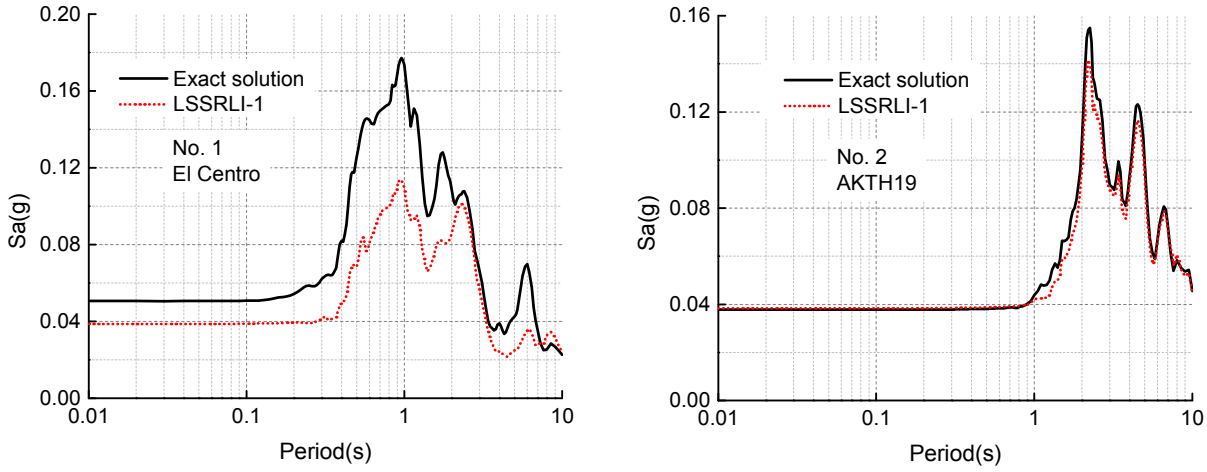

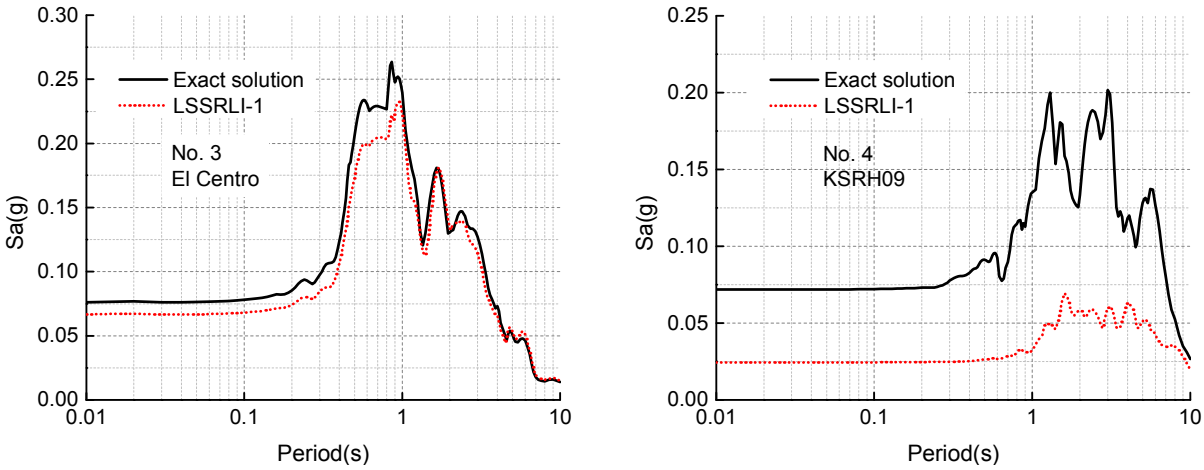


Fig.6 Updated ground response spectrum under 0.2g peak inputs

Fig.5 clearly indicates that the shear strain distributions, calculated by LSSRLI-1 and exact solution separately, differ from each other seriously. In some cases, the LSSRLI-1 results may reach 2.5 times of that of exact solution. Depending on the shear strain distribution in Fig.5, we calculated a series of new dynamic non-linear parameters, using equation (8) and Fig.3. One more iteration was carried out based on the updated parameters. Fig.6 shows that two group of response strctrum curves have much difference, which can not be ngelected. The explaintaton of this phenomenon is that the shear strain affects the ground motion seriously.

We can get a clear conclusion easily that LSSRLI-1 is not suitable for soft sites any more. Its main problem is the calculation method of shear strain distribution, but its ground motion transfer function is correct. This provieds us with a direction for developing the soil seismic response analysis program.

## Acknowledgements

This research is supported by Fundamental Research Funds of Institute Engineering Mechanics and Earthquake (201408020-03) and the Chinese National Science Foundation (51278472, 41272357, 51208477).

## References

[1] Kramer, S. L. *Geotechnical earthquake engineering*. Upper Saddle River, NJ: Prenticl Hall. 1996

[2] R. Sun, H.J. Chen, X.M. Yuan. Uncertainty of non-linear dynamic shear modular ratio and damping ratio of soils. Chinese Jounal of Geotechnical Engineering. 2010(08):1228-1235

[3] L. Chen, W. Wang and X. Yuan: Advanced Material Research Vol. 446-449 (2012) 1404-1407.

[4] Z.P. Liao: Wave Propagation Theory in Engineering Practice, Seismic Press, Beijing, 1996.

*Applied Mechanics and Materials Vols. 580-583 (2014) pp 1564-1569*
*© (2014) Trans Tech Publications, Switzerland*
*doi:10.4028/www.scientific.net/AMM.580-583.1564*

# Controls on material and mesh for structural nonlinear time-history analysis

Chen Xiaoming[1a], Duan Jin[1b], Qi Hu[1c], Li Yungui[1d]

[1]China state construction technical center, Beijing, China

[a]Chenxiaoming00@tsinghua.org.cn

[b]Duanjin@cscec.com, [c]Qihu@cscec.com, [d]Liyungui@cscec.com

**Keyword:** Elastic-plastic, Time-history analysis, Concrete constitutive relation, Damping, Mesh

**Abstract.** In order to improve the solution of nonlinear time-history analysis for high-rise buildings, the concrete constitutive relation of Chinese code has been modified by using Najar damage theory, and based on the limitation of stable time increment in explicit dynamic analysis, a simplified Rayleigh damping form with tiny stiffness proportional damping is proposed to decrease the damage induced by those high frequencies, at last, the influence of mesh size on stress and damage is also discussed. The numerical results show that these principles are workable for more accurate results.

## Introduction

To ensure the structural performance under expected rare earthquake, deformation verification must be made to avoid overall collapse. On the other hand, the damage time-history and damage level of the main members are also very important for the structural optimization.

Analysis of nonlinear time-history is the most useful tool for the results mentioned above. Due to the nonlinear problems—those with large deformations and/or nonlinear material response, especially the complex nonlinearity of concrete, it is very difficult to obtain an ideal solution. At the same time, the efficiency of analysis is also a key point because of the large volume of high buildings. Limited by these two factors, explicit dynamic method has more advantages than the implicit dynamic method. Compared to the implicit dynamic analysis procedure, each increment in explicit method is relatively inexpensive because there is no solution for a set of simultaneous equations, and it would not suffer from the convergence of iterations needed for implicit method. Even like this, it would still take more than dozens of hours to analysis a high-rise building under a one-minute seismic wave by using parallel solvers. So the engineers may have to confront the balance between reliability of solution and efficiency.

By using the explicit method presented in software for nonlinear time-history analysis, reliable definition of materials, suitable selection of elements and reasonable meshing scheme may be the most important works for solving the questions discussed before, thus the nonlinear time-history analysis was made for a high-rise building combined with Abaqus/Explicit for achieving more reasonable FEA model.

## Constitutive model of concrete

Different with researchers, engineers prefer to use those constitutive models of concrete which are more simply and reliable to ensure the mechanical reliability, such as Mander model[1] and the model in the Chinese 'Code for design of concrete structures'[2].

For the constitutive model presented in Chinese 'Code for design of concrete structures', in which the tension skeleton curve of concrete is as follows:

$$\sigma = (1- d_t) E_c \varepsilon \tag{1}$$

$$d_t = \begin{cases} 1-\rho_t[1.2-0.2x^5] & x \le 1 \\ 1-\dfrac{\rho_t}{\alpha_t(x-1)^{1.7}+x} & x > 1 \end{cases} \tag{2}$$

The compression skeleton curve of concrete is：

$$\sigma = (1- d_c) E_c \varepsilon \tag{3}$$

$$d_c = \begin{cases} 1-\dfrac{\rho_c n}{n-1+x^n} & x \le 1 \\ 1-\dfrac{\rho_c}{\alpha_c(x-1)^2+x} & x > 1 \end{cases} \tag{4}$$

By these equations, the damage curve is also defined together with the skeleton curve. According to the performance in engineering, this definition may lead to excessive concrete damage though the skeleton curves are reasonable. Compared with this, the damage definition of Najar[3] based on energy is more suitable [Fig.1].

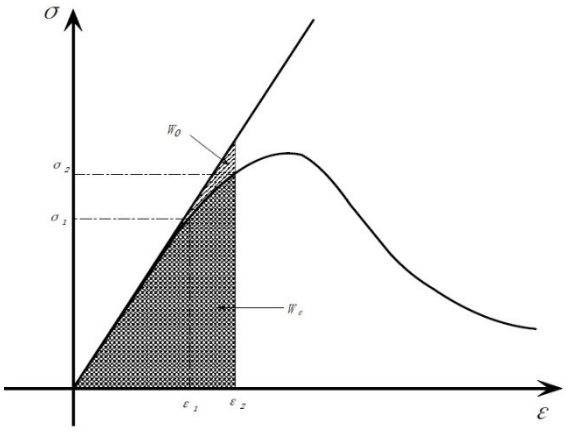


Fig.1 Najar's damage theory

Combined the skeleton curve with Najar's damage definition, a new concrete constitutive model can be formulated out. As an example, the curves of C40 for these two models are shown in Fig.2.

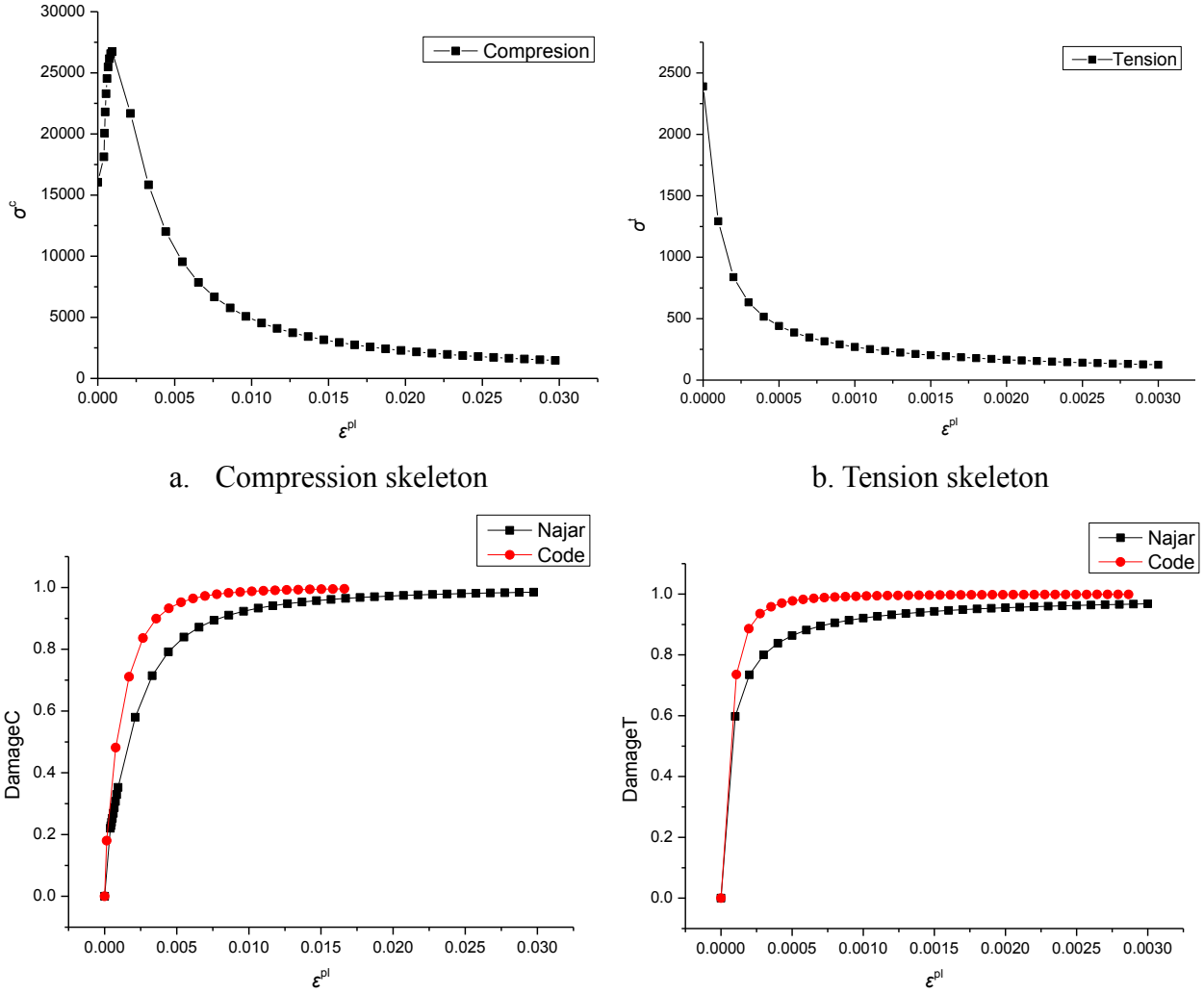


a. Compression skeleton b. Tension skeleton

c. Compression damage d. tension damage

Fig.2 Constitutive model of concrete

**Damping model**

Modal damping has the merit of simulating the damp of each mode accurately in a large range of frequency. On the other hand, for the merit of longer time increment, Rayleigh damping is still used as the main damping form of many software especially for the nonlinear direct integration method. In Abaqus/Explicit, users have to choose Rayleigh damping instead of modal damping which is not available, it can be written as:

$$\mathbf{C} = \alpha\mathbf{M} + \beta\mathbf{K} \tag{5}$$

Where $\alpha$ is the parameter of mass proportional damping and $\beta$ is the parameter of stiffness proportional damping.

By the fundamental frequency $\omega_1$ and an important high frequency $\omega_i$, a low level damping can be achieved by Rayleigh damping between these two frequencies, for those frequencies higher than $\omega_i$, the vibration can be damped by the monotonically increasing damping level.

Because of the relationship between damping and stable time increment in explicit method as follows：

$$\Delta t \le \frac{2}{\omega_{\max}}\left(\sqrt{1+\xi_{\max}^2}-\xi_{\max}\right) \tag{6}$$

It can be derived that the influence on stable time increment of $\alpha$ is nearly negligible, but even a small $\beta$, which is the same order of magnitude as the initial stable time increment without damping, may make the stable time increment reduce by about 50%[4]， so usually it is advised to neglect the stiffness proportional damping in explicit method， for engineering applications, by neglecting $\beta$， a simplified damping model can be expressed only with $\alpha$.[5]：

$$\alpha = \frac{4\pi\xi}{T} \tag{7}$$

This simplified damping model is an inverse ratio function about periods. If using the fundamental period to formulate $\alpha$, it cannot damping the high frequencies efficiently, especially for the vertical vibrations. From the numerical results, although these vibrations cannot affect horizontal response significantly, but the damage induced by vertical vibration will be different more or less.

A suitable stiffness proportional damping without more loss of efficiency can be taken into account as shown in Fig.3

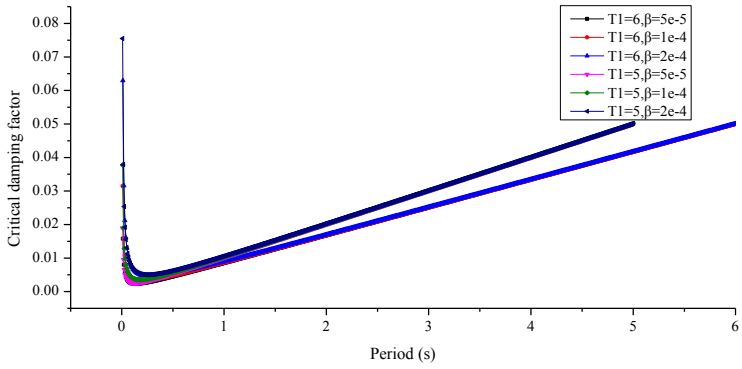


Fig.3 Rayleigh Damping model

**Mesh control**

Limited by the results transfer between Abaqus/Standard and Abaqus/Explicit, shell element S4R or S3R can be used for simulating wall and plate. Reduced integration usually provides more accurate results and significantly reduces running time. But when reduced integration is used with first-order (linear) elements, hourglass control should be required， Therefore, when using first-order reduced-integration elements, hourglass must be checked through the artificial strain energy. A finer mesh not only can reduce the artificial strain energy but also can achieve smooth solution and more accurate damage results.

Engineers are used to design the building structures with meshes larger than 1m. With coarse meshes, the results of structural global response such as displacement angle and base shear are precise enough, but the numerical error of shell stresses usually cannot be neglected especially for those elements in wall-beams and short-leg walls. The variation of reinforcement induced by mesh size may not be significant because of the adjustments and combinations of internal forces require by national code. For the nonlinear time-history analysis under expected rare earthquake，the results of damage depend on the stress precision seriously and different mesh size may lead to different final results.

**Numerical example**

Nonlinear time-history analysis of a high-rise building shown in Fig.4 has been performed with Abaqus/Explicit, comparison of global indexes, energy curves and damage of members has also been made to verify these principles discussed in this paper.

From the results listed from Fig.6 to Fig.9, Different mesh size may achieve similar displacement history, but the numerical error of damage in shell elements may not be negligible and a small stiffness proportional damping can decrease the stiffness degradation of plates significantly.

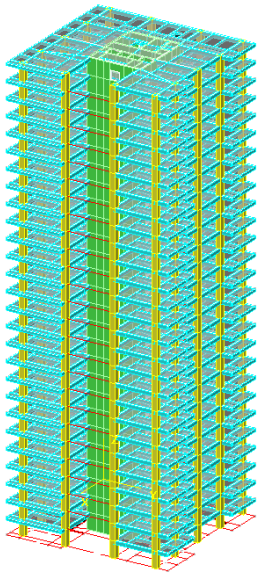

Fig.4 Model of high-rise building

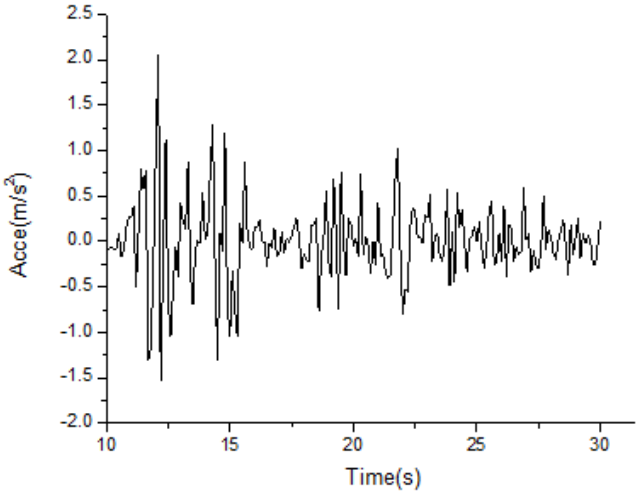


Fig.5 Seismic wave

The seismic wave with the peak acceleration equal to 220gal is shown in Fig.5.

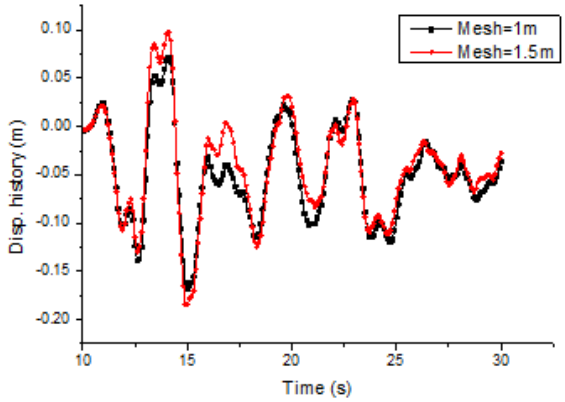


Fig.6 Top displacement history

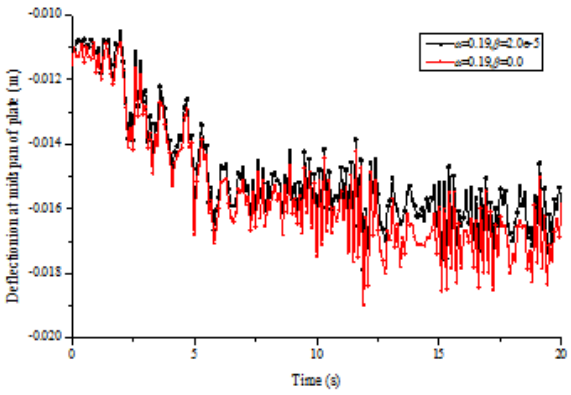


Fig.7 Deflection history of one plate

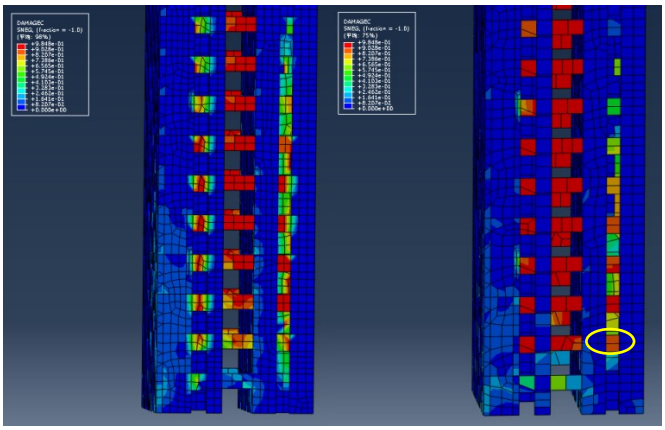

Fig.8 DamgeC of walls(1m vs 1.5m)

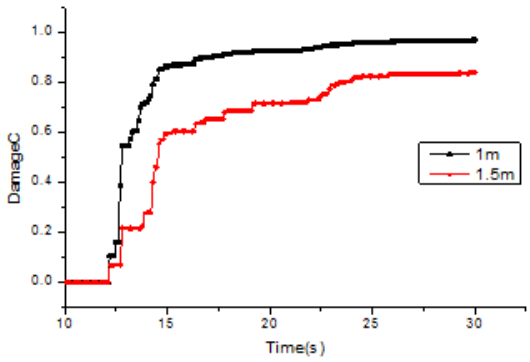


Fig.9 DamageC of selected wallbeam

**Summary**

In order to achieve reasonable solutions of nonlinear time-history analysis for high-rise structures, at first, Najar damage definition has been introduced into the concrete constitutive relation presented in Chinese code. Secondly, although it will decrease the stable time increment dramatically, suitable stiffness proportional damping still can ameliorate the damage without more less of efficiency. And at last, finer mesh size is usually needed more than elastic analysis for hourglass control and precise stress and damage results.

**Reference**

[1] Mander, J.B., Priestly, M.J.N., Park, R., Theoretical Stress—Strain Model for Confined Concrete. Journal of Structural Engineering, ASCE，1988, 114(8): 1804～1826.

[2] Code for design of concrete structures (GB50010-2010). China architecture & building press, Beijing.

[3] J Najar, D Krajcinovic, J Lemaitre. Continuous damage of brittle solids. ,in: D. Krajcinovic, J. Lemaitre (Eds.),Continuum Damage Mechanics, Theory and Applications, Springer, Wien (1987), p. 233.

[4] ABAQUS Inc. ABAQUS User Manual, V6. 5. 5, 2006.

[5] Yang Xianqiao，Fu Xueyi，Huang yongjun. Elastic-plastic time history analysis of Pingan Finance Center. The 21th national academic conference of high-rise building structure，NanJing China. 2010:807-818.

*Applied Mechanics and Materials Vols. 580-583 (2014) pp 1570-1573*
*© (2014) Trans Tech Publications, Switzerland*
*doi:10.4028/www.scientific.net/AMM.580-583.1570*

# Influence of saturation degree on deamplification of $P_1$ wave through multilayered porous media

Mehiaoui Hadjebar Mahdia Yasmina[1, a *], Hadid Mohamed.[1,b] and Berrah Mounir Khaled[2,c]

[1] National School of Public Works, Rue Sidi Garidi, Algiers, Algeria

[2] Department of Civil Engineering, Ecole Nationale Supérieure Polytechnique, 10 Avenue Hassan Badi, Algiers, Algeria

[a]mahdia_y@yahoo.fr, [b]hadid_mohamed2003@yahoo.fr, [c]mkberrah@yahoo.fr

**Keywords:** $P_1$ wave; deamplification; coherency; porous media; saturation degree.

**Abstract.** The deamplification model developed by Zendagui et al. has been adapted in this study for the case of $P_1$ wave propagation in porous media in order to investigate the effect of saturation degree on motion coherency at depth. The input wave amplitude distribution function is generated compatibly with the suitable free field coherency model and the top wave amplitudes are evaluated using the transfer matrix method following the Biot's theory. The results show that even if the saturation degree decreases slightly below the complete saturation, it influences the coherencies of horizontal and vertical motion due to $P_1$ wave incidences. Elsewhere, the generation process shows that in this case, the wave front content, necessary to produce a coherency identical to the Luco and Wong model at the free field, is more focus with less intensity than required in the case of a complete saturation.

## Introduction

Because most of seismic arrays are installed on the surface, spatial variability of seismic motion at depth is not directly observable. The approach consisting on estimating the statistical properties of seismic motion at any point in the half space on the basis of the statistical properties obtained on the surface is known as the stochastic deconvolution of earthquake motion. Its basic methodology has been established by Kausel and Pais [1]for the case of a half space. Later, Zendagui et al. [2,3] extended this formulation to the case of *P* and *SV* waves propagating in a multilayered soil.

The analysis of dynamic transient phenomena in fluid-saturated porous media is of great interest in earthquake geotechnical engineering and geophysics because of its relationship with soil liquefaction problems. According to the widely accepted Biot's theory [4] the wave propagation pattern is different comparing to standard wave elastic theory. Therefore, the deconvolution process must be adapted to the case of porous media. The deamplification approach is extended in this paper to the case of multilayered poro-elastic media excited by $P_1$ wave incidence. Elsewhere, the input wave amplitude distribution function is generated compatibly with the suitable free field coherency model. This is done in order to improve the original process. Furthermore, many studies [6-8] indicate the influence of the saturation degree on the porous media dynamic response. A parametric study investigating the effect of this parameter, on the motion coherency at depth, is presented.

## $P_1$ waves stochastic deamplification process

Supposing that $N$ trains of uncorrelated plane waves are propagating into a half-space with different incident angles $\theta_j$, the vertical and horizontal displacements induced are then

$$u(x,y,t)=\sum_{j=1}^{N}u(x,y,\theta_j,t) \quad ; \quad v(x,y,t)=\sum_{j=1}^{N}v(x,y,\theta_j,t). \tag{1}$$

The displacement field is supposed homogeneous, its free field cross-correlation can then be expressed in terms of the horizontal offset $\lambda = x' - x''$ and the temporal shift $\tau = t' - t''$ as follows

$$C_{uu}(\lambda,0,\omega) = E\left[\sum_{j=1}^{N} u(x',0,t')\, u^T(x'',0,t'')\right] \quad ; \quad C_{vv}(\lambda,0,\omega) = E\left[\sum_{j=1}^{N} v(x',0,t')\, v^T(x'',0,t'')\right]. \tag{2}$$

By Fourier transforming these functions with respect to temporal shift $\tau$, spatio-spectral cross density functions are obtained.

$$S_{uu}(\lambda,0,\omega) = \int_{-\infty}^{+\infty} C_{uu}(\lambda,0,t)\, e^{-i\omega t} d\omega \quad ; \quad S_{vv}(\lambda,0,\omega) = \int_{-\infty}^{+\infty} C_{vv}(\lambda,0,t)\, e^{-i\omega t} d\omega. \tag{3}$$

The power spectral density function is giving as [3]: $S_j(\omega)=g^2(\theta)S(\omega)$, with $g^2(\theta)$ being the relative amplitude of the wave trains which depends, in general, on the incidence angle [3]. The deamplification process consists on determining the cross-spectral density function at any depth $y$ from the surface ones.

$$S(\lambda,y,\omega) = \Im_k\left[\mathbf{T}\Im_\lambda[S(\lambda,0,\omega)]\mathbf{T}^T\right]. \tag{4}$$

This allowes to calculate soil motion coherency at any soil depth $y$.

$$\gamma(\lambda,y,\omega) = \frac{S(0,y,\omega)}{S(\lambda,y,\omega)}. \tag{5}$$

However, the relative amplitude of the wave trains $g^2(\theta)$ must first be determined. In 1996, Iguchi and Hanamura [9] presented a closed form solution for the amplitude estimation of incoming waves that corresponds to a coherency free field model. In this paper, the well known Luco and Wong [5] model is adopted and the following simple equation is adopted for the amplitude distribution function

$$g^2(\theta) = e^{-(\varphi-\theta)^2/\beta}. \tag{6}$$

$\varphi$ is the mean incident angle with respect to the vertical and $\beta$ is a coherency degree dependent parameter determined by an iterative process.

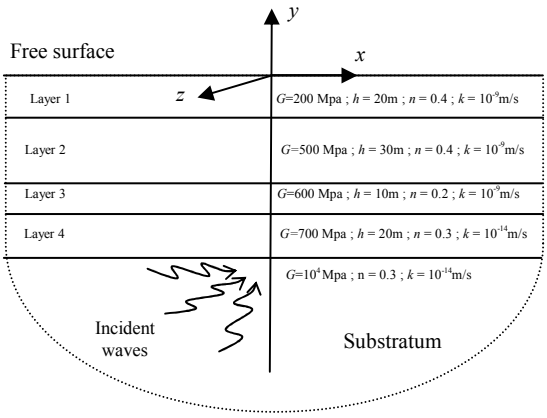


Fig. 1: Numerical example

Table 1 Common material properties of the soil layers

| | |
|---|---|
| $\rho_S$ Density of solid grains [kg/m$^3$] | 2610 |
| $K_s$ Bulk modulus of solid grains [Pa] | 36 $10^9$ |
| $K_w$ Bulk modulus of water [Pa] | 2.2 $10^9$ |
| $\upsilon$ Poisson ratio | 0.25 |
| $\xi$ Damping | 0.05 |

**Numerical example**

Let us consider a multi layered viscoelastic porous soil overlying a substratum as shown in Fig. 1. Each layer is characterized by its shear modulus (G), porosity (n) and permeability (k). All the soil layers are considered fully water saturated and their common geotechnical characteristics are

summarized in table 1. In the cas of $P_1$ wave incidence, the computed surface coherencies are plotted in fig. 2 for two values of the Luco and Wong incoherence parameters [5]. This procedure permits to generate the waves amplitudes intensity function as shown in figure 3. The values of parameter $\beta$ are found iteratively.

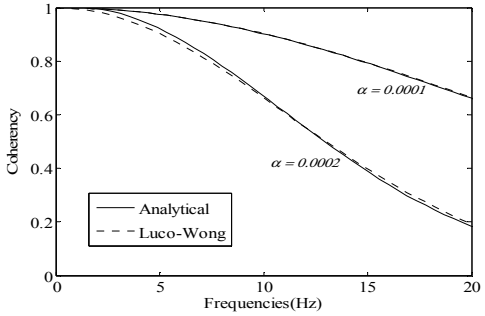


Fig. 2: Examples of coherencies computed at the free surface for $\lambda = 50$ m

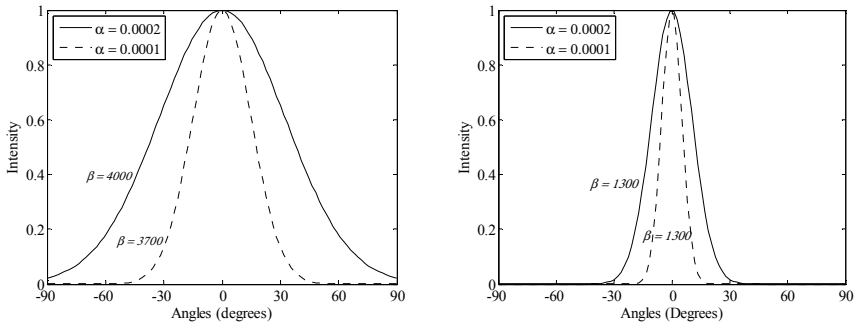


Fig. 3 : Examples of identified intensity function for $\varphi = 0°$ (a) $S_r = 100\%$ (b) $S_r = 98\%$

The deamplification procedure is executed in order to determine the spatio-spectral density function in depth. The transfer function between the soil surface and an elevation $y$ in the soil is evaluated using the exact stiffness matrix method. The coherencies at the top and the bottom of the multilayered soil are shown in figures 4 and 5.

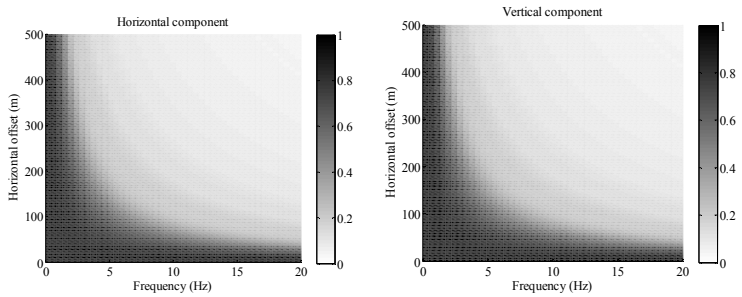


Fig. 4: Free field coherencies

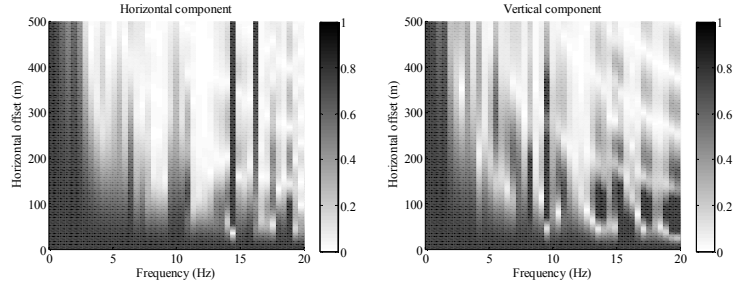


Fig. 5: Coherencies at 80 m depth for $S_r = 100\%$

Yang [6-8] indicates that a slight decrease in the saturation degree may have significant influence on soil dynamics responses. In this topic, coherency has been evaluated using the same example here before but for a different saturation degree *Sr* = 98% (see fig 3 and 6).

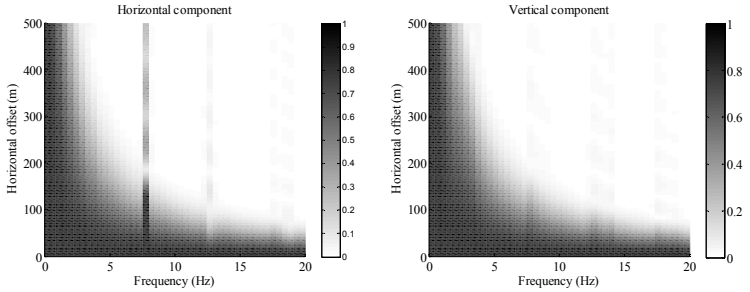


Fig. 6 : Coherencies at 80 m depth for Sr = 98%

## Conclusion

The deamplification process has been extended herein for the case of poro-elastic multilayered soil profile. Numerical example has been presented in the case of $P_1$ wave train incidence. The input wave amplitude distribution function has been generated according to the Luco and Wong coherency model and the coherencies have been calculated for complete saturation (*Sr*=100%) and fully saturation (*Sr*=98%). The results showed that saturation degree modifies both input wave amplitude distribution and coherencies. The generated wave front content is more focused with less intensity in the case of fully but not complete saturation whereas deconvoluated coherencies of complete saturation case are more important.

## References

[1] E. Kausel, A. Pais, Deconvolution of stochastic SH-waves motions in soil deposits. Research report N° R84-09, MIT, Depart. of Civil Engin., Cambridge, Massachusetts, USA. (1984)

[2] D. Zendagui, M.K. Berrah, E. Kausel, Stochastic deamplification of spatially varying seismic motions. Soil Dyn. and Earth. Engin. 18 (1999) 409-421.

[3] D. Zendagui, M.K. Berrah, Spatial variation of seismic motion induced by propagation of body waves. Soil Dyn. and Earth. Engin. 22 (2000) 805-811.

[4] M.A. Biot, Theory of propagation of elastic waves in a fluid saturated porous solid. Journal of Acoustic Society of America. 28 (1956) 168-191.

[5] Luco, J.E. and Wong, H.L., Response of a rigid foundation to a spatially random ground motion, Earth. Engin. and Struct. Dyn. 14 (1986) 891-908.

[6] J. Yang, T. Sato, Effect of hydraulic interface conditions on seismic reflection and transmission. 11th European Conference on Earthquake Engineering, Balkema, Rotterdam. (1998)

[7] J. Yang, Influence of water saturation on horizontal and vertical motion at a porous soil interface induced by incident P wave. Soil Dyn. and Earth. Engin. 19 (2000) 575-581.

[8] J. Yang, Saturation effects on horizontal and vertical motions in a layered soil-bedrock system due to inclined SV waves, Soil Dynamics and Earthquake Engineering. 21 (2001) 527-536.

[9] M. Igushi and M. Hanamura, Estimation of incident seismic waves based on spatial variation of surface ground motions. P N° 1230, 11th World Conf. on Earth. Engin., Acapulco, Mexico. (1996)

*Applied Mechanics and Materials Vols. 580-583 (2014) pp 1574-1580*
*© (2014) Trans Tech Publications, Switzerland*
*doi:10.4028/www.scientific.net/AMM.580-583.1574*

# Precise Integration Method of Pseudo-dynamic Testing of Structures

Haibo Wang[1,a], Rong Liu[2,b]

[1,2]School of Civil Engineering, Central South University, Changsha Hunan, China 410075

[a]haibarg@csu.edu.cn,[b]liurongcsu@sina.com

**Keywords:** pseudo-dynamic test of structures; precise integration method; predict-correct method; central difference method

**Abstract.** Based on nonlinear precise integration method, two new numerical integration methods of pseudo-dynamic test of structures are presented. One is explicit predict-correct, four order accuracy and multistep method avoiding calculating the inversion of the state matrix. The other is implicit predict-correct, four order accuracy and multistep method that need calculate the inversion of the state matrix. Since their accuracies are superior to the central difference method by enlarging time step and their stabilities are better, the structural systems of multi-degree of freedom could be well tested and the testing work would be largely reduced. Finally, a pseudo-dynamic test of combined tube structure has been executed with the explicit multi-step method.

## Introduction

Proposed for the first time by a Japanese scholar Professor M.Hakuno in1969, the pseudo-dynamic test method is a structural anti-seismic test method combining cybernation with structural test effectively. It can be used for the earthquake simulation test of large-scale structure. Then the structure restoring force can be measured directly from the specimen with no theoretic hypothesis. Different from numerical integration method, it does not require to assume restoring force behavior in advance that can get from the reaction force and displacement in actuator during the test. Since restoring force behavior is provided through test device synchronously, it avoids the errors originated from the behavior assumptions during the computer numerical simulation and improves the computer simulation accuracy of structural dynamic response. Advantage of the method is that it can be used to do anti-seismic experiment in large-scale, high-proportion models even the structural prototypes. And since the load process is gradual during the test, the structure destruction process can be observed in detail[1].

Numerical integration methods of pseudo-dynamic testing can be divided into two categories, explicit and implicit integration methods[2]. Explicit integration methods mainly include the central difference method, explicit Newmark method and modified Newmark method. Implicit integration methods mainly included Newmark- $\beta$ method and $\alpha$ - method. It is well known in the numerical analysis of the structure that the calculation accuracy of implicit methods is obviously better than explicit methods. In addition, explicit methods are conditionally stable and higher efficiency for each time step, but in order to ensure its stability the time step must be small. Implicit integration methods can be through appropriate choice of parameters to ensure the integration stability, so a larger time step can also be applied. Since explicit integration methods do not require iteration and are easy to operate in test, the majority of the current application is explicit integration methods, generally not the implicit methods. But researchers have been exploring to apply implicit methods to pseudo-dynamic testing. P.B. Shing and M.T. Vannan[3,4,5] have had detailed discussions on these issues such as the accuracy and error analysis of $\alpha$ - method for the pseudo-dynamic experiments. Qiu Fawei[6]has taken reinforced concrete frame structure as an example to study implicit $\alpha$ - method and its application in the substructure pseudo-dynamic test. Both in the theory and calculation disadvantages of these methods are not high precision, large artificial damping and that does not reflect the high frequency components.

Based on nonlinear precise integration method, combined the precise integration method[7] with the predict-correct Adams-Bashforth-Moulton multi-step method[8], two new numerical integration

methods of pseudo-dynamic testing are established. One is explicit predict-correct, fourth-order accuracy and multistep method avoiding calculating inversion of the state matrix, the alternative is implicit predict-correct, fourth-order accuracy and multistep method that need calculate the inversion. Due to the high calculating precision of these methods, pseudo-dynamic testing can be accomplished by enlarging time step and multi-degree of freedom structural systems could be well tested. Numerical examples show that these methods will largely reduce the testing work and have good practicality compared to central difference method. Finally, a pseudo-dynamic test of combined tube structure has been executed with the explicit multi-step method.

**Precise integration method of pseudo-dynamic testing**

There is a time interval for the processed earthquake record. It is usually 0.02s and difficult to express with continuous function. However, single-step method need to find an intermediate function value through continuous load function, therefore it can not be used for pseudo-dynamic test. And since the Adams method has poor stability and accuracy, it can not be though. The following discussion is how to apply multi-step predict-correct method with enlarged time step to numerical simulation examples of pseudo-dynamic testing.

The motion differential equation for Pseudo-dynamic test can be expressed as Eq. 1.

$$M\ddot{x}(t)+C\dot{x}(t)+r(x,t)=f(t) \tag{1}$$

Where $M$ and $C$ are $n\times n$ order mass matrix, damping matrix respectively and $\ddot{x}(t)$, $\dot{x}(t)$, $x(t)$ and $f(t)$ are $n$ order motion acceleration, velocity, displacement and load vector of particle respectively. $r(x,t)$ is $n$ order restoring force vector of particle.

In the pseudo-dynamic testing the mass matrix $M$ is known and the damping matrix $C$ is usually considered to be a given linear damping or ignored, so $f(t)=-M\ddot{x}(t)$ is known as $\ddot{x}(t)$ is the input ground motion acceleration.

Eq. 1 can be converted into a first-order differential equation as Eq. 2.

$$\dot{v}(t)=Hv(t)+R(v,t)+F(t) \tag{2}$$

Where

$$v(t)=\begin{Bmatrix} x(t) \\ M\dot{x}(t)+\dfrac{Cx(t)}{2} \end{Bmatrix},\quad R(v,t)=\begin{Bmatrix} 0 \\ -r(x,t) \end{Bmatrix},\quad F(t)=\begin{Bmatrix} 0 \\ f(t) \end{Bmatrix},\quad H=\begin{bmatrix} -\dfrac{M^{-1}C}{2} & M^{-1} \\ \dfrac{CM^{-1}C}{2} & -\dfrac{CM^{-1}}{2} \end{bmatrix}$$

Or when the initial stiffness $K_0$ has been considered, then

$$R(v,t)=\begin{Bmatrix} 0 \\ K_0x(t)-r(x,t) \end{Bmatrix},\quad H=\begin{bmatrix} -\dfrac{M^{-1}C}{2} & M^{-1} \\ \dfrac{CM^{-1}C}{2}-K_0 & -\dfrac{CM^{-1}}{2} \end{bmatrix}$$

This article is analyzed with the post form.

With the index matrix introduced, Eq. 2 can be turned into the same solution integral equation as Eq.3

$$v(t_{k+1})=e^{H\Delta t}v(t_k)+\int_{t_k}^{t_{k+1}}e^{H(t_{k+1}-\tau)}R(v,\tau)d\tau+\int_{t_k}^{t_{k+1}}e^{H(t_{k+1}-\tau)}F(\tau)d\tau \tag{3}$$

Where $v(t_{k+1})$, $v(t_k)$ are respectively the values of solving vector at time $t_{k+1}$ and $t_k$.

**The explicit method avoiding calculating inversion of the state matrix of pseudo-dynamic testing.**

As the first n terms of $R(x(t_{k+1}),t_{k+1})$ is 0, the precise integration multi-step solving process in Eq. 3 can directly be used for pseudo-dynamic test of structures then turn into explicit method. Specific implementation is as follows:

(1) Solve predetermined applying displacement $x(t_{k+1})$

$$v(t_{k+1}) = e^{H\Delta t}v(t_k) + \frac{\Delta t}{24}\left(19G(t_k) - 5G(t_{k-1}) + G(t_{k-2})\right) + w(t_{k+1}) \tag{4}$$

Where $G(t_k) = e^{H\Delta t}R(v(t_k),t_k)$, $G(t_{k-1}) = e^{2H\Delta t}R(v(t_{k-1}),t_{k-1})$, $G(t_{k-1}) = e^{3H\Delta t}R(v(t_{k-2}),t_{k-2})$

$w(t_{k+1})$ is the high precision integral formula Cotes [8], and it can be expressed as Eq. 5.

When $\Delta t = 2\Delta t"$ (note: $\Delta t"$ is the interval for seismic records, for example if $\Delta t"$ = 0.02s, then $\Delta t$ = 0.04s)

$$w(t_{k+1}) = \frac{\Delta t}{6}\cdot\left[e^{H\Delta t}F(t_k) + 4e^{H\cdot\frac{1}{2}\Delta t}F(t_k + \frac{\Delta t}{2}) + F(t_{k+1})\right] \tag{5a}$$

When $\Delta t = 3\Delta t"$

$$w(t_{k+1}) = \frac{\Delta t}{8}\cdot\left[e^{H\Delta t}F(t_k) + 3e^{H\cdot\frac{2}{3}\Delta t}F(t_k + \frac{\Delta t}{3}) + 3e^{H\cdot\frac{1}{3}\Delta t}F(t_k + \frac{2\Delta t}{3}) + F(t_{k+1})\right] \tag{5b}$$

When $\Delta t = 4\Delta t"$

$$w(t_{k+1}) = \frac{\Delta t}{90}\cdot\left[7e^{H\Delta t}F(t_k) + 32e^{H\cdot\frac{3}{4}\Delta t}F(t_k + \frac{\Delta t}{4}) + 12e^{H\cdot\frac{1}{2}\Delta t}F(t_k + \frac{\Delta t}{2}) + 32e^{H\cdot\frac{1}{4}\Delta t}F(t_k + \frac{3\Delta t}{4}) + 7F(t_{k+1})\right] \tag{5c}$$

It can be seen from Eq. 5 that the different values of $\Delta t / \Delta t^*$ are to select the different integration methods and actually it uses the each-step seismic wave information within $\Delta t$ to improve its calculating accuracy.

If time interval of the test is too long, the method accuracy will be decreased and the test points will also be reduced. Generally it can be based on the test accuracy requirements to take $2\Delta t" \sim 4\Delta t"$.

(2) Once $v(t_{k+1})$ has been solved, it means $x(t_{k+1})$ is known. The displacement $x(t_{k+1})$ can be exerted by the actuator, then the restoring force $r(x(t_{k+1}),t_{k+1})$ would be obtained in this step. $R(x(t_{k+1}),t_{k+1})$ is known then apply it to the following formula

$$v(t_{k+1}) = e^{H\Delta t}v(t_k) + \frac{\Delta t}{24}\left(9R(v(t_{k+1}),t_{k+1}) + 19G(t_k) - 5G(t_{k-1}) + G(t_{k-2})\right) + w(t_{k+1}) \tag{6}$$

Where the meaning of the parameters is the same to Eq. 4.

The whole process of pseudo-dynamic test could be completed with Eq. 4 to Eq. 6. Gauge head values (Note: the first three steps values after calculating) can be calculated by the linear assumption for displacement and the use of the initial stiffness. In the initial stage of the earthquake, the seismic wave peak is usually small so the assumption should be supposed to be feasible.

**The implicit method calculating inversion of the state matrix of pseudo-dynamic testing.**

Implicit pseudo-dynamic integration method calculating inversion of the state matrix can use the above explicit pseudo-dynamic integration method as the basis for estimates. Its steps of implementation are presented as follows:

(1) Firstly, the displacement $x^0(t_{k+1})$ can be calculated with Eq. 4 and estimated then achieved by using the actuator.

(2) Measuring the restoring force of the step $r(x(t_{k+1}),t_{k+1})$, you can get $R(x(t_{k+1}),t_{k+1})$ and computer $v(t_{k+1})$

$$\begin{aligned} v(t_{k+1}) = e^{H\Delta t}\Big[v(t_k) + H^{-1}c_0 + \left(\Delta t H^{-1} - H^{-2}\right)c_1 + \left(\Delta t^2 H^{-1} - 2\Delta t H^{-2} + 2H^{-3}\right)c_2 + \\ \left(\Delta t^3 H^{-1} - 3\Delta t^2 H^{-2} + 6\Delta t H^{-3} - 6H^{-4}\right)c_3\Big] - H^{-1}c_0 + H^{-2}c_1 - 2H^{-3}c_2 + 6H^{-4}c_3 + w(t_{k+1}) \end{aligned} \tag{7}$$

Where the expression of $w(t_{k+1})$ can get from Eq. 5 and

$$\begin{cases} c_0 = R_{k+1} \\ c_1 = \dfrac{-11R_{k+1} + 18R_k - 9R_{k-1} + 2R_{k-2}}{6\Delta t} \\ c_2 = \dfrac{2R_{k+1} - 5R_k + 4R_{k-1} - R_{k-2}}{2\Delta t^2} \\ c_3 = \dfrac{-R_{k+1} + 3R_k - 3R_{k-1} + R_{k-2}}{6\Delta t^3} \end{cases} \tag{8}$$

Where $R(v(t_i),t_i)$ is short for $R_i$.

Thus $x^1(t_{k+1})$ can be obtained.

(3)If $\left|x^1(t_{k+1}) - x^0(t_{k+1})\right| \le \varepsilon$ then take $x^1(t_{k+1}) = x^0(t_{k+1})$ and execute the next step; otherwise, use actuators to achieve $x^1(t_{k+1})$ then take $x^0(t_{k+1}) = x^1(t_{k+1})$ and perform the (2) step. ($\varepsilon$ is a smaller number to control accuracy and the desirable is 0.02mm.)

(4) $k = k+1$, if $k >$ the total number of steps, end the test; otherwise perform the first step.

Gauge head calculation of the implicit method is the same to the explicit method discussed previously in this article. Since this method is implicit, the test for each step may need multi-step to complete, thus the workload is increased.

## Analysis of examples

Due to various errors, the pseudo-dynamic test of structures is not repeatable. So the testing examples are difficult to select .The impact of round-off errors has been only considered in this paper. The accuracy for controlling the actuator displacement is taken as 0.01mm and the force is 0.01kN. Take the calculated value of refine segmentation direct integration method [7] as the ratio. Since the central difference method and the explicit Newmark-$\beta$ method are the same in essence, then the central difference method is compared with the explicit and implicit multi-step method mentioned in this paper about errors.

**Example 1:** For a structural system of single degree of freedom, the motion equation is Eq. 13

$$M\ddot{x}(t) + C\dot{x}(t) + r(x,t) = 0.4Mg\sin 2\pi t \tag{13}$$

Where $M = 50$t, damping ratio is 0.05, the initial elastic stiffness $K = 28.8$kN/mm, g = 9.80665. The earthquake lasts for 10s, displacement unit is mm and force unit is kN. Take the restoring force $r(x(t),t) = Kx(t)(1 - 0.0015x^2(t))$.

The controlled time step for the central difference method to calculate is 0.02s and the time step of the explicit multi-step method and the implicit method in this article is 0.04s. The actual calculated displacement and the calculated errors of the three methods are shown in Fig. 1and Fig. 2.

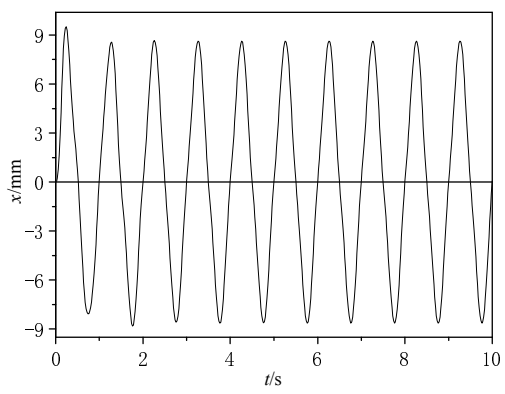


Fig.1 Displacement time-history curve of calculation

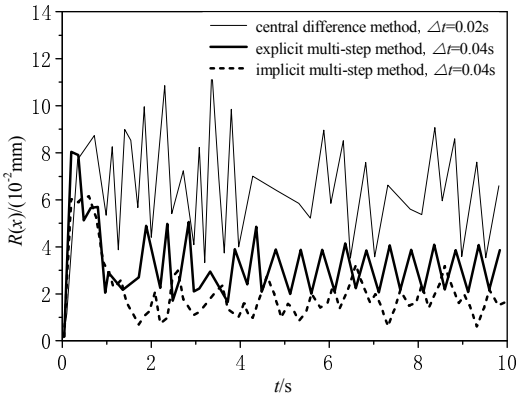


Fig.2 Enveloping diagram of displacement error

**Example 2:** The author has completed the steel tube-in-tube structure model of the equivalent two degrees of freedom without considering the impact of damping. The input seismic wave is a sine wave, the prototypical peak acceleration is 0.40g, the time lasts for 10s, the equivalent mass $m_1$ = 2016kg and $m_2$ = 1464kg; the time step $\Delta t$ can be solved by similarity coefficient, the prototypical time step is 0.02s and the time step $\Delta t$ = 0.00422s. Displacement unit is mm, force unit is kN. Assuming that its pseudo-dynamic test equation can be written as Eq. 14

$$10^{-3}\times\begin{bmatrix}2.016 & 0\\ 0 & 1.461\end{bmatrix}\begin{Bmatrix}\ddot{x}_1\\ \ddot{x}_2\end{Bmatrix}+\begin{Bmatrix}r_1\\ r_2\end{Bmatrix}=0.4\alpha g\sin(10\pi t)\times\begin{bmatrix}2.016 & 0\\ 0 & 1.461\end{bmatrix} \tag{14}$$

Where the restoring force is taken as Eq. 15

$$\begin{Bmatrix}r_1\\ r_2\end{Bmatrix}=\begin{bmatrix}28.9 & -12.0\\ -12.0 & 8.8\end{bmatrix}\left(\begin{Bmatrix}x_1\\ x_2\end{Bmatrix}-4\begin{Bmatrix}\sin(0.05x_1)\\ \sin(0.05x_2)\end{Bmatrix}\right),\quad \alpha=2.41,\quad g=9.80665,\quad \pi=3.14159. \tag{15}$$

The controlled time step for the central difference method to calculate is 0.00422s and the step of the explicit multi-step method and the implicit method in this article is 0.01688s. The actual calculated displacement and errors of the three methods are shown in Fig. 3, Fig.4 and Table 1.

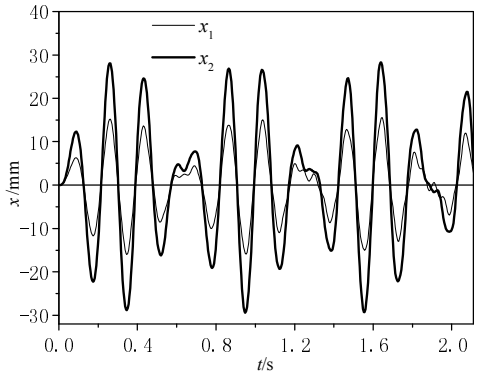


Fig.3 Displacement time-history curve of calculation

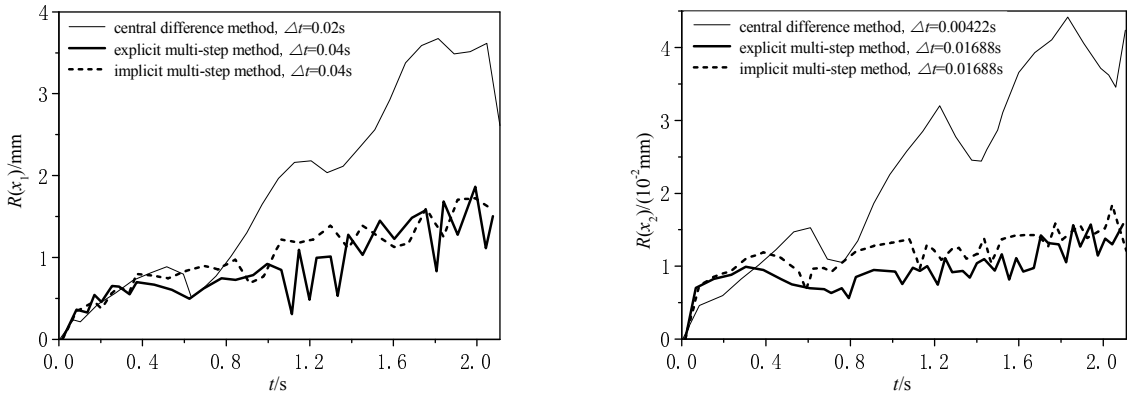


(*a*) $R(x_1)$ (*b*) $R(x_2)$

Fig.4 Enveloping diagram of displacement error

Table1 Displacement error of calculation (%)

| Example | Step (s) | Example 1 | Step (s) | Example 2 | |
|---|---|---|---|---|---|
| Relative error | | $R^*(x)$ | | $R^*(x_1)$ | $R^*(x_2)$ |
| The center difference method | 0.02 | 1.21 | 0.00422 | 22.92 | 15.0 |
| The explicit method | 0.04 | 0.85 | 0.01688 | 11.62 | 5.36 |
| The implicit method | 0.04 | 0.65 | 0.01688 | 10.75 | 6.34 |

Note: The above error is relative and $R^*(x_i) = \left|\max(R(x_i)) / \max(x_i)\right| \times 100\%$.

By comparing example 1with 2 (Figure 2, Figure 4 and Table 1) some conclusions can be drawn: (1) Whether it is for systems of single degree of freedom or two degrees, with the time step increased the accuracy of the explicit and the implicit multi-step method in this article is better than the central difference method; (2) The central difference method for a pseudo-dynamic testing system of single degree of freedom is high accuracy algorithm but poor for the system of two degrees of freedom; (3)For non-linear example1 since the displacement peak occurs in the initial stage , there will be large errors for the explicit and implicit multi-step method in this stage. During the actual pseudo-dynamic testing process, you can avoid this situation (The displacement peak in the actual seismic action is generally not presented in the initial stage); (4) For a system of single degree of freedom, the accuracy of the implicit method is obviously higher than the explicit method. But for a system of two degree of freedom, there is no advantage for the implicit method. Since the implicit method requires iterative to complete the test, the workload will be some increase. Therefore the explicit method is more practical.

## Applied research

Based on the above explicit numerical integration method of pseudo-dynamic testing, the pseudo-dynamic testing [10] of the steel-concrete composite tube-in-tube structure model of the equivalent two degrees of freedom has been completed by the author. Consider the linear Rayleigh damping. The input seismic wave is Elscentro N-S wave and the prototypical acceleration peaks are 0.62g, 1.00g respectively. The time lasts for 10s, the equivalent mass $m_1$ = 9413kg, $m_2$ = 6363kg; the time step $\Delta t$ can be solved by similarity coefficient and the prototypical time step is 0.02s and $\Delta t$ = 0.00546s.The acceleration similarity coefficient is1.34. Displacement unit is mm and load unit is kN. Its pseudo-dynamic test equation can get from Eq. 7. Where (before the acceleration reaches the peak (0.62g and 1.00g) the initial stiffness are $K_{01}$ and $K_{02}$ respectively)

$$C=\begin{bmatrix} 0.1385 & -0.04963 \\ -0.04963 & 0.05270 \end{bmatrix},\quad K_{01}=\begin{bmatrix} 45.983 & -20.093 \\ -20.093 & 16.284 \end{bmatrix},\quad K_{02}=\begin{bmatrix} 33.01 & -16.78 \\ -16.78 & 15.07 \end{bmatrix}$$

Time step of the explicit multi-step method is 0.02184s, namely the test points are 1/4 for the central difference method. At the height of testing load point the displacement time-history curve of the two acceleration peaks are measured as Fig.5.

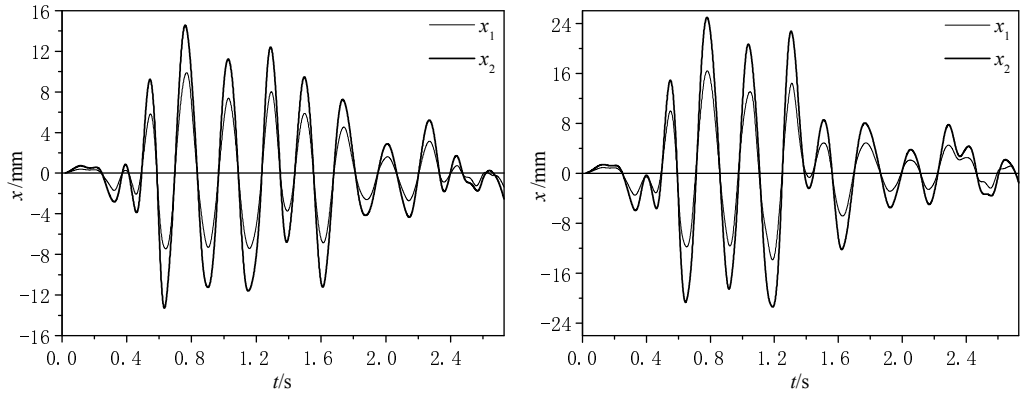


(*a*) 0.62g (*b*) 1.00g

Fig.5 Displacement time-history curve of test by two peak ground acceleration

## Conclusions

(1) Based on non-linear precise integration method, two numerical integration methods of pseudo-dynamic testing including explicit and implicit have been derived with four order accuracy. Both can be used for pseudo-dynamic testing system of multi-degree of freedom.

(2) Since the calculated precision of the methods is high, the pseudo-dynamic testing structural systems of multi-degree of freedom can be completed by enlarging time step. Analysis of the examples and applied research in the paper have shown that the workload in these methods will be exponentially less than the central difference method and more practical.

(3) Since the implicit method requires iterative to complete the test, it will increase the workload. Therefore the explicit method is higher value in practical.

## References

[1] Qiu Fawei, Qian Jiaru, Chen Zhipeng. Seismic test methodology for structures [M]. Beijing: Science Press, 20. In Chinese

[2] Tina Shizhu, Zhao Tong. World Information on Earthquake Engineering, 2001, 17(4):p60-66. In Chinese

[3] P. B. Shing, M. T. Vannan. Earthquake Engineering and Structural Dynamics, 1990, 19(2):p631-651.

[4] P. B. Shing, M. T. Vannan, E. Cater. Earthquake Engineering and Structural Dynamics, 1991, 20(2):p551-576.

[5] P. B. Shing, M. T. Vannan.Earthquake Engineering and Structural Dynamics, 1991, 19(3):p809-819.

[6] Qiu Fawei. World Information on Earthquake Engineering, 1995, 12(3):p44-48. In Chinese

[7] Zhong Wanxie. Journal of Dalian University of Technology, 1994, 34(2):p131-136. In Chinese

[8] Chu Dewen, Wang Yuanfeng. Engineering Mechanics, 2002, 19 (6):p115-119. In Chinese

[9] Qiu Chunhang, Lu Hexiang, Cai Zhiqin. Journal of Computational Mechanics, 2000, 17 (2): p127-132. In Chinese

[10] Chen Bowang. Study on method of pseudo-dynamic testing and theoretical analysis of tube structure[D]. Changsha: Hunan University, 2006. In Chinese

*Applied Mechanics and Materials Vols. 580-583 (2014) pp 1581-1590*
*© (2014) Trans Tech Publications, Switzerland*
*doi:10.4028/www.scientific.net/AMM.580-583.1581*

# Reliability Analysis In Performance-Based Earthquake Engineering

EL GHOULBZOURI Abdelouafi[1, a], EL ALAMI Zakaria[1, b], EL HANNOUDI Sabrine[1, c]

[1] National School of Applied Sciences of Al Hoceima, Civil engineering Dept., BP 03, Ajdir Al Hoceima, Morocco

[a]e.abdelouafi@hotmail.fr, [b] elalami.gc@gmail.com, [c] sabrina.elhnd@gmail.com

**Key words:** Performance-based engineering, RPS2000, Finite element, Nonlinear analysis, Seismic design, Finite reliability analysis.

**Abstract.** The performance-based engineering approach, as opposed to prescriptive rules of code-based design, is based on simulation of real structural behavior. Reliability of the expected performance state is assessed by using various methodologies based on finite element nonlinear static pushover analysis and specialized reliability software package.
Reliability approaches that were considered included full coupling with an external finite element code based methods in conjunction with either first order reliability method or importance sampling method. The building considered in the actual study has been designed against seismic hazard according to the Moroccan code RPS2000.

## Introduction

The finite element method is currently the dominating tool for simulating structural behavior. A coupling of this method with reliability analysis algorithms leads to the finite element reliability method described in this work. The first coupling between FORM (first-order reliability method) reliability analysis and the finite element method is found in Der Kiureghian and Taylor [10]. Since then, a number of advances have been reported, including those by Liu and Der Kiureghian [11], Gutierrez et al.[12], Zhang and Der Kiureghian [13], Der Kiureghian and Zhang [14], Sudret and Der Kiureghian [15], Imai and Frangopol [16], Haldar and Mahadevan [17], and Frier and Sorensen [18]. Such methods address the key issue in performance-based engineering. Based on performance criteria mandated by the client or the society, probability estimates for reaching specified structural performance thresholds are computed. In addition, sensitivity and importance measures for the model parameters are available.
Finite element reliability analysis (FERA) has been developed to account for uncertainties in structural analysis. The input parameters of the finite element model are provided as random variables to account for uncertainty in the material, geometry, and loading parameters. Subsequently, the probability of response events is computed. This is achieved by defining limit-state functions (also referred to as performance functions) in terms of response quantities of the finite element analysis.

Finite element reliability analysis using full coupling between a finite element code and reliability methods such as the FORM and Monte Carlo methods tend to be computational time consuming for practical problems which could include a large number of random variables. At each iteration, the limit-state function and its derivatives are to be evaluated through finite element computations. An effective method which combines FORM and subsequent importance sampling around the most probable failure point has been proposed by (Haukaas and Der Kiureghian [19]. The Importance Sampling Method (ISM) requires only a limited number of evaluations of the limit-state function (and its gradient with respect to the random variables) to find the approximation point, followed by efficient importance sampling analysis centered at this point. In this last reference, Haukaas and Der Kiureghian [19] have presented numerical examples involving comprehensive nonlinear finite element models with approximately 500 random variables were presented.

**Finite element seismic reliability analysis of buildings**

The performance-based engineering approach is based on simulation of real structural behavior. This feature sets it apart from classical prescriptive rules associated to code-based design. The client or government regulations prescribe desired performance objectives, which are translated into decision variables or functions and serve defining performance criteria.

Applying reliability analysis methods in the context of performance-based engineering uses the specified performance functions as performance criteria or limit-states. The term failure denotes then the event of not meeting a given performance criterion. It is then important to know how to translate such performance requirements into explicit performance functions attainable by finite element structural analysis.
In this work reference is made to the performance level introduced by the Moroccan seismic code RPS 2000, [20], which intends limiting the building roof displacement ratio. Other performance criteria introduced to distinguish performance-based engineering states with regards to earthquake events could be for example those defined according to the Federal Emergency Management Agency [21].In this case, the performance states include: operational performance for which the event does not affect the occupants or functioning of the building; immediate occupancy performance for which the occupants can immediately return to the building after the seismic event; life safety performance and collapse prevention performance.
The client or code regulations determine in general an acceptable hazard level for each of these performance requirements. For an earthquake event with probability, say, 50% in 50 years, immediate occupancy performance may be demanded. On the other hand, for an earthquake event with probability 2% in 50 years only life safety performance may be desirable. A formal similarity could be stated between the limit-state in the present work according to RPS 2000 and the collapse prevention limit-state according to FEMA.
In this work, finite element analysis was performed by means of OpenSees platform. The beam-column element used is a displacement-based element having the aptitude to take into account distributed plasticity that develops through fiber cross-sections. The element uses the stiffness formulation approach. A user-selected number of integration points along the element can be prescribed. The fiber cross-sections are composed of uniaxial material models.

Material models for steel, unconfined concrete in girders and column cover regions and confined concrete in column core regions that are used in the actual work correspond respectively to the uniaxial smoothed bi-linear steel material and uniaxial smoothed concrete material.

**Estimation of performance probabilities and response statistics**

The primary concern in structural reliability analysis is to estimate probabilities of failure to achieve predefined performance. In the simplest case of one performance function, the component reliability problem is formulated as

$$p_f = \int_{g(x)\leq 0} f(x)dx \tag{3.1}$$

Where $p_f$ is the probability of failure, $x$ is the vector of random finite element model parameters, $g(x)$ is the performance function and $f(x)$ is the joint PDF of $x$.Note that the integration is over the set of random variables $x$,which in finite element reliability analysis can be large. Closed-form solutions of Eq. (3.1) are unavailable except for a few special cases. For this reason, a number of methods have been developed for the purpose of solving the integral approximately. These include the first- and second-order reliability methods, FORM and SORM, sampling analysis, response surface methods and numerical integration schemes. The latter method is usually not a feasible

alternative when the number of random variables is greater than 3 or 4. Furthermore, in finite element reliability analysis, it is desirable to limit the number of evaluations of $g$ and its gradient. This makes methods such as FORM, SORM and importance sampling (IS) tractable, while it excludes the crude Monte Carlo sampling scheme for problems with small failure probabilities. A common aspect of FORM, SORM and IS is that they all employ the so-called design point. This is the most likely point in the failure domain, when the variables are transformed to the standard normal space. As such, this is the ideal point for approximating the limit-state surface separating the safe and failure domains. FORM
analysis estimates the failure probability by approximating the limit-state surface by the tangent hyper-plane at the design point. SORM analysis estimates the failure probability by approximating the limit-state surface by a quadratic surface tangent at the design point. An IS analysis may subsequently use the design point as the center of sampling to obtain an improved estimate of the failure probability. The options for FORM and IS analysis are implemented in OpenSees. The framework for SORM analysis is also implemented in OpenSees. However, this option is currently limited to a simple algorithm to estimate the ¯first principal curvature for the fitting paraboloid using a method developed by Der Kiureghian and DeStefano [22].

Before proceeding to discuss methods that address the probability integral in Eq. (3.1), the method available in OpenSees for computing second moments of response quantities are described. These statistics of the response describe the propagation of uncertainties through the finite element model.

**Form**

FORM analysis addresses the reliability problem in Eq. (3.1) by means of two key operations. Firstly, we find the design point in the transformed uncorrelated standard normal space. Secondly, we approximate the limit-state surface at this point and make use of the properties of the standard normal space to obtain the probability estimate. The first item can be a challenging task in nonlinear finite element reliability analysis.

The distance from the origin of the standard normal space to the design point, denoted $y^*$ ,istermed the "reliability index" and denoted $\beta$ .The first-order probability estimate is then found as

$$p_f \approx p_{f1} = \Phi(-\beta) \tag{4.1}$$

where $\Phi(.)$ denotes the standard normal CDF. It is common to define the "alpha vector" as the negative normalized gradient row vector at the design point, i.e.,

$$\alpha = -\frac{\nabla G}{\|\nabla G\|} \tag{4.2}$$

Where $\nabla G = \left[\frac{\partial G}{\partial y_1} \ldots \frac{\partial G}{\partial y_n}\right]$.In terms of $\alpha$ ,the reliability index is given by $\beta = \alpha y^*$.

Additionally, $\alpha$ is one of several parameter importance measures available as a by-product of FORM analysis. Such measures are valuable in practical engineering design. They can also be used to reduce the number of random variables in a model.

**Importance Sampling Analysis**

In the crude Monte Carlo method the sampling distribution is centered at the mean point. Since failure events tend to occur in the tail regions of probability distributions, this implies that a large

number of samples are required to obtain good failure probability estimates. A concern in finite element reliability analysis is that the large number of evaluations of the performance function may be computationally costly. This inhibits the use of crude Monte Carlo sampling in most finite element reliability applications. By centering the sampling distribution near the failure domain, a far more efficient sampling scheme is obtained. This is the basic idea behind the importance sampling method. By introducing an indicator function $I(y)$ such that $I(y)=1$ if $g(x)\le 0$ ,and $I(y)=0$ otherwise,we can rewrite Eq. (3.1) as follows (Ditlevsen and Madsen ) [23].

$$p_f = \int_{\Omega_y} I_y \varphi(y) dy = \int_{\Omega_y} \left( I(y) \frac{\varphi(y)}{f(y)} \right) f(y) dy \tag{5.1}$$

Where $\Omega_y$ denotes the entire standard normal space, $\varphi(.)$ is the joint standard normal PDF and $f(y)$ is a joint PDF which must be non-zero within the region where $I(y)=1$ .It is observed that the last integral in Eq. (5.1) is an expectation of the random variable $I(y)\frac{\varphi(y)}{f(y)}$ relative to the distribution $f(y)$ .This expectation can be estimated by generating statistically independent realizations of the random variable $I(y)\frac{\varphi(y)}{f(y)}$ derived from the distribution $f(y)$ .The average of this sample is an unbiased estimator of the expectation and, thus, of $p_f$ .Crude Monte Carlo sampling analysis results when $f(y)$ is selected identical to $\varphi(y)$ so that the distribution is centered at the mean point, i.e., the origin in the standard normal space. In IS analysis the center of the sampling distribution is shifted to a point selected by the user, e.g., the design point (Melchers ) [24].

The sampling analysis implemented in OpenSees evaluates Eq. (5.1) by repeatedly generating a vector $\bar{y}$ of independent and normally distributed random numbers with zero means and unit variances. $\bar{y}$ is then transformed according to $y = y_{center} + L\bar{y}$ where $y_{center}$ is a user-provided mean vector and $L$ is the Cholesky decomposition of a user-provided covariance matrix $\sum$ .The mean vector defines the center of the sampling density. The most effective choice is the design point. The covariance matrix is typically chosen as a unit matrix. Increasing (decreasing) the value of a diagonal element of $\sum$ leads to a broader (narrower) sampling density along the axis of the corresponding random variable. Off-diagonal elements may be added to make the sampling distribution elongated in preferred directions.
The vector $y$ is transformed back into the original space $x = x(y)$ where the performance function $g(x)$ is evaluated for this realization of the random variables. $I(x)$ is assigned a value based on the outcome of $g(x)$ .The variable $q(y) = I(x(y))\frac{\varphi(y)}{f(y)}$ is then evaluated with the following expressions for the joint PDF in the standard normal space, $\varphi(y)$ , and the sampling density $f(y)$ :

$$f(y) = \frac{1}{(2\pi)^{n/2}\sqrt{\det \sum}} \exp\left[ -\frac{1}{2}(y - y_{center})^T \sum^{-1} (y - y_{center}) \right] \tag{5.2}$$

$$\varphi(y) = \frac{1}{(2\pi)^{n/2}} \exp\left[ -\frac{1}{2} y^T y \right] \tag{5.3}$$

Where $n$ is the number of random variables.

The probability of failure is estimated as:

$$p_f \approx p_{f,sim} = \bar{q} = \frac{1}{N}\sum_{i=1}^{N} q_i \tag{5.4}$$

Where $q_i = q(y_i)$ and $N$ is the number of samples. A measure of accuracy of the probability estimate is the variance of $p_{f,sim}$ ,which noting that $q_i$ are statistically independent and identically distributed, is given by:

$$\mathrm{Var}\left[p_{f,sim}\right] = \sum_{i=1}^{N} \frac{1}{N^2}\mathrm{Var}\left[q_i\right] = \frac{1}{N}\mathrm{Var}\left[q\right] \tag{5.5}$$

Where $\mathrm{Var}\left[q\right]$ is the common variance, which is estimated from the generated sample using the well-known formula:

$$\mathrm{Var}\left[q\right] \approx \frac{1}{N-1}\left[\sum_{i=1}^{N} q^2{}_i - \frac{1}{N}\left(\sum_{i=1}^{N} q_i\right)^2\right] \tag{5.6}$$

Substituting Eq. (5.6) into Eq. (5.5), the variance of the probability estimate is:

$$\mathrm{Var}\left[p_{f,sim}\right] \approx \frac{1}{N(N-1)}\left[\sum_{i=1}^{N} q_i{}^2 - \frac{1}{N}\left(\sum_{i=1}^{N} q_i\right)^2\right] \tag{5.7}$$

Thus, we only need to store the sums of the $q_i$ and the $q_i{}^2$ values. In OpenSees, the coefficient of variation of the probability estimate

$$\mathrm{c.o.v}\left[p_{f,sim}\right] = \frac{\sqrt{\mathrm{Var}\left[p_{f,sim}\right]}}{p_{f,sim}} \tag{5.8}$$

is computed and monitored. The sampling is repeated a user-defined number of times, or until the above c.o.v. estimate falls below a specified target.

**Implementation in OpenSees**

OpenSees is regarded as a collection of software components rather than a packaged code. This software architecture is facilitated by an object-oriented programming approach. The developer creates objects, or, abstractly, classes, instead of focusing on the procedural attributes of the problem. The objects contain data members and member functions and may interact by calling each other's member functions. The member functions perform operations on the data members of its object, or on data that is passed to the member function at run-time.

Haukaas and Der Kiureghian [19] extended OpenSees with objects to perform reliability analysis in combination with finite element analysis. The analysis part of these implementations contains a number of analysis tools that are employed in our implementations. **Figure1** shows an overview of the reliability module, where the analysis-domain decomposition is emphasized. The analysis tools are shown with a particular symbol to be data members of the reliability analysis, while the various

analysis types are shown to be sub-classes of the generic reliability analysis. The reliability analysis performs operations on the reliability domain, which include random variables, correlation coefficients, and limit-state functions. Eight analysis types that facilitate FOSM, FORM, SORM, sampling analysis, parametric reliability analysis, system reliability analysis, out-crossing analysis, and visualization of the limit-state function were initially available.

The developments in this work benefit strongly from the organization of OpenSees into a collection of analysis tools. The existing analysis tools for reliability analysis in OpenSees include probability transformation, determination of search direction and step size in the search for the MPP, search algorithms to determine the MPP, random number generation, etc. These and others are listed in **Figure 2**, where it is emphasized that they are data members of the reliability analysis, which thereby can make use of them in the analysis.

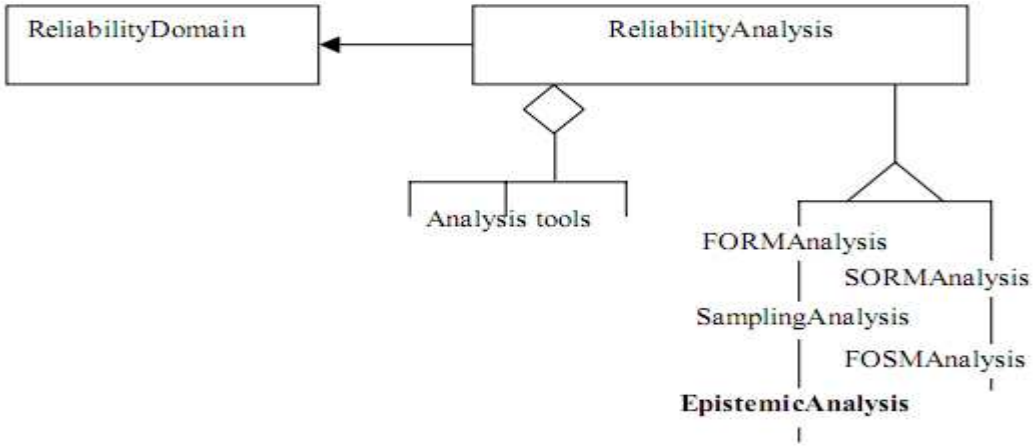


**Fig. 1**

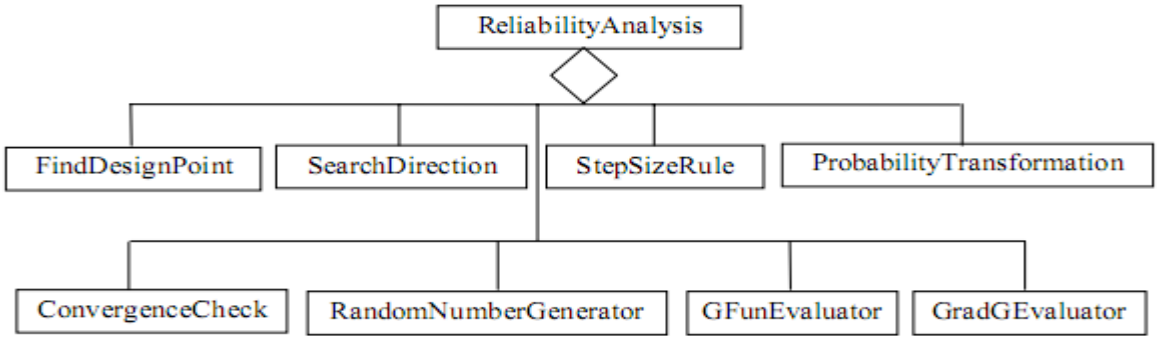


**Fig. 2**

**Numerical Example**

Consider the three-storey, two-bay reinforced concrete structure in **Figure 3**, **Figure 4** and **Table 1** for reliability analysis. The material properties of the concrete and reinforcement steel and load parameters are modelled as aleatory random variables, as detailed in **Table 2**, **Figure 5**, **Figure 6** and **Figure 7**. These are intended to model the inherent, irreducible uncertainty in the finite element model parameters.This limit-state function seeks the probability that the horizontal displacement at the roof of the structure exceeds 0.4% of the building height, when deterministic lateral seismic is evaluated according the Moroccan seismic code RPS2000 recommendations for a given geographic zone, soil site, ductility coefficient and building priority. The limit state function writes

$$g(x) = 0.004\,x9000 - u_4 \tag{7.1}$$

Where $u_4$ is the horizontal displacement, in units of mm, of node 4 from a static nonlinear pushover-type analysis. .Reliability analyses are performed with FORM and MCS for limit-state function in Eq. (7.1). The results are summarized in **Table 3**.

**Table 1: Applied vertical loads at the RC structural nodes**

| Nodes | Vertical seismic load (KN) |
|---|---|
| 2, 10 | $W_2 = W_{10} = 141.6$ |
| 3, 8, 11 | $W_3 = W_8 = W_{11} = 94.4$ |
| 4, 12 | $W_4 = W_{12} = 47.2$ |
| 6 | $W_6 = 283.2$ |
| 7 | $W_7 = 188.8$ |

**Table 2: Uncertainty modeling of the random variables of the reinforced concrete buildings**

| | Distribution | Mean | Coefficient of variation | Standard deviation |
|---|---|---|---|---|
| Steel reinforcement material parameters: | | | | |
| $f_y$ | Lognormal | 500 (MPA) | 0.05 | 25 (MPA) |
| E | Lognormal | 200000 (MPA) | 0.05 | 10000 (MPA) |
| $\alpha$ | Lognormal | 0.02 | 0.05 | 0.001 |
| Confined concrete material parameters: | | | | |
| $f'_{c,cc}$ | Lognormal | 44.24(MPA) | 0.15 | 6.636(MPA) |
| $f'_{cu,cc}$ | Lognormal | 35(MPA) | 0.15 | 5.24(MPA) |
| $\varepsilon_{c,cc}$ | Lognormal | 0.003 | 0.15 | 0.00045 |
| $\varepsilon_{cu,cc}$ | Lognormal | 0.015 | 0.15 | 0.00225 |
| Unconfined concrete material parameters: | | | | |
| $f'_{c,uc}$ | Lognormal | 30(MPA) | 0.15 | 4.5(MPA) |
| $f'_{cu,uc}$ | N/A | 0.0(MPA) | N/A | N/A |
| $\varepsilon_{c,uc}$ | Lognormal | 0.003 | 0.15 | 0.00045 |
| $\varepsilon_{cu,uc}$ | Lognormal | 0.006 | 0.15 | 0.0009 |
| Lateral loads: | | | | |
| P4 | Lognormal | 56.64 (KN) | 0.2 | 11.328 (KN) |
| P3 | Lognormal | 37.76 (KN) | 0.2 | 7.552 (KN) |
| P2 | Lognormal | 18.88 (KN) | 0.2 | 3.776 (KN) |

* Correlation coefficient ((P3,P4)=0.6 , (P2,P4)=0.6 and (P2,P3)=0.6)

**Table 3: Sampling analysis and FORM reliability results**

| Structure type | reinforced concrete structure |
|---|---|
| Limit-state function type | Displacement |
| Reliability index (FORM) | 1.57508 |
| Probability (FORM) | 0.0576184 |
| Reliability index (MCS) | 1.58821 |
| Coefficient of variation (MCS) | 5% |
| Probability (MCS) | 0.0561193 |

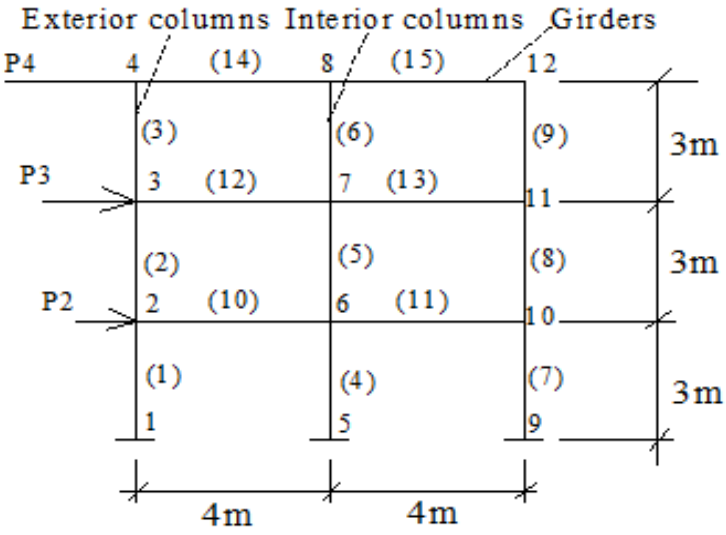


Fig. 3

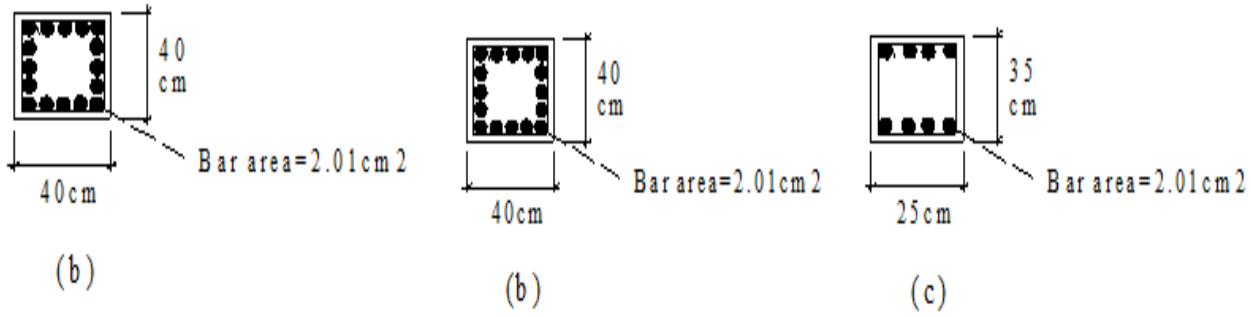


Fig. 4

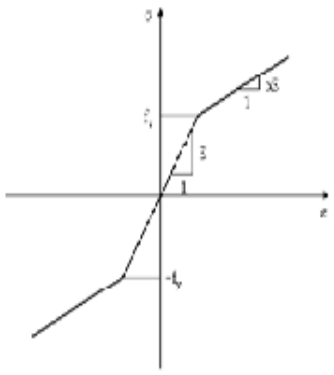

Fig. 5

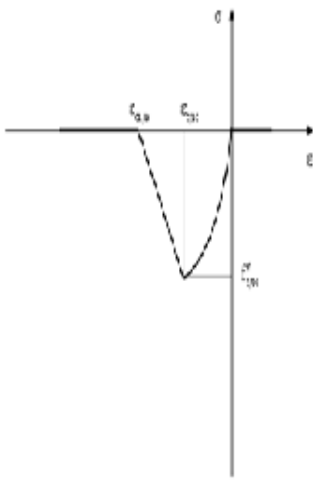

Fig. 6

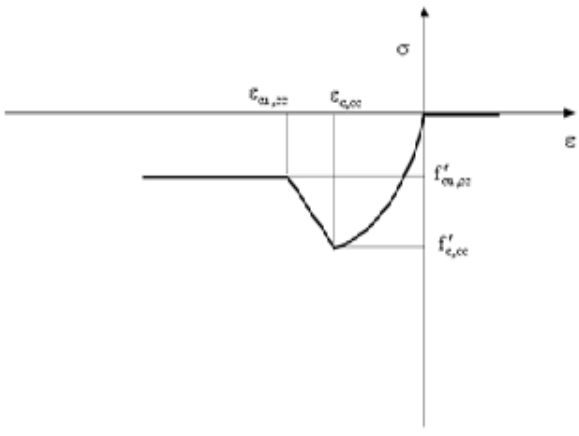

Fig. 7

## Conclusions

Within the framework of the same methodology of reliability analysis (either full coupling ), the approximate method FORM does not give the same results than the more precise modified Monte Carlo ISM Method. In general, FORM overestimates the probability of failure.The obtained results have shown that full coupling reliability analysis conducted with ISM is recommended because FORM analysis could exaggerate sometimes the probability of failure.Influence on reliability data of the chosen PDF's to model uncertainties is very significant when considering full coupling reliability analysis.

In order to perform reliability analysis of seismic performance based design, huge care should be given to selection of PDF's that model parameters uncertainties (these should be is general identified through experiments).These conclusions could not be generalized without precautions to other problems dealing with reliability analysis and thorough analysis is needed to assess performance of the various methodologies.

## Bibliography

[1] OC. Celik and BR. Ellingwood: Seismic fragilities for non-ductile reinforced concrete frames – Role of aleatoric and epistemic uncertainties. Structural Safety, Vol. 32 ( 2010), p. 1–12.

[2] BA. Bradley and DS. Lee: Accuracy of approximate methods of uncertainty propagation in seismic loss estimation. Structural Safety, Vol. 32 (2010), p. 13-24.

[3] D. Asprone, F. Jalayer, A. Prota and G. Manfredi: Proposal of a probabilistic model for multi-hazard risk assessment of structures in seismic zones subjected to blast for the limit state of collapse. Structural Safety , Vol. 32 ( 2010), p. 25–34.

[4] AB. Liel, CB. Haselton, GG. Deierlein and JW. Baker: Incorporating modeling uncertainties in the assessment of seismic collapse risk of buildings. Structural Safety, Vol. 31 ( 2009), p. 197–211.

[5] O. Möller, RO. Foschi, LM. Quiroz and M. Rubinstein: Structural optimization for performance- based design in earthquake engineering: Applications of neural networks. Structural Safety 2009,Vol. 31 ( 2009), p. 490–499.

[6] V. Piluso, G. Rizzano and I. Tolone I: Seismic reliability assessment of a two-story steel-concrete composite frame designed according to Eurocode 8. Structural Safety, Vol. 31 (2009), p. 383-395.

[7] RJ. Williams, P. Gardoni and JM. Bracci: Decision analysis for seismic retrofit of structures. Structural Safety, Vol. 31 (2009), p. 188-196.

[8] L. Berto, R. Vitaliani, A. Saetta and P. Simioni: Seismic assessment of existing RC structures affected by degradation phenomena. Structural Safety, Vol. 31 (2009), p. 284-297.

[9] J. Song and WH. Kang: System reliability and sensitivity under statistical dependence by matrix-based system reliability method. Structural Safety, Vol. 31 (2009), p. 148-156.

[10] A. Der Kiureghian and RL. Taylor: Numerical methods in structural reliability. In G. Augusti, A. Borri and G. Vannucchi, editors: Proceedings of the Fourth International Conference on Applications of Statistics and Probability in Civil Engineering. ICASP4, Bologna: Pitagora Ed.ITALIE, (1983),p. 36-225.

[11] PL. Liu and A. Der Kiureghian: Optimization algorithms for structural reliability. Structural Safety, Vol. 9(3) (1991), p. 78-161.

[12] M. Gutierrez, J. Carmeliet and R. de Borst: Finite element reliability methods using diana. In: Kusters GMA, Hendriks MAN, editors. Diana Computational Mechanics, Dodrecht: Kluwer Academic Publishers, (1994), p. 64-255.

[13] Y. Zhang and A. Der Kiureghian, in: Finite Element Reliability Methods for Inelastic Structures. Report No. UCB/SEMM-97/05, Berkeley: University of California, (1997).

[14] A. Der Kiureghian and Y. Zhang: Space-variant finite element reliability analysis. Computer methods in applied mechanics and engineering, Vol. 168 (1999), p. 173-183.

[15] B. Sudret and A. Der Kiureghian, in: Stochastic finite element methods and reliability. a State-of- the-Art report, Report No. UCB/SEMM-2000/08, Berkeley: University of California, (2000).
[16] K. Imai and DM. Frangopol: Geometrically nonlinear finite element reliability analysis of structural systems. i: theory, ii: applications. Computers and Structures. Vol. 77(6) (2000), p. 677-709.
[17] A. Haldar and S. Mahadevan, in: Reliability assessment using stochastic finite element analysis. New York: John Wiley and Sons, (2000).
[18] C. Frier and J. Sorensen: Stochastic finite element analysis of non-linear structures modelled by plasticity theory. In: A. Der Kiureghian, S. Madanat and J. Pestana. editors. Proceedings of the Ninth International Conference on Applications of Statistics and Probability in Civil Engineering, ICASP9, Rotterdam: Millpress. (2003), p. 90-283.
[19] T. Haukaas and A. Der Kiureghian, in: Finite Element Reliability and Sensitivity Methods for Performance-Based Earthquake Engineering. PEER Report 2003/14, Pacific Earthquake Engineering Research Center, University of California at Berkeley, (2004).
[20] Règlement de construction parasismique RPS 2000. Ministère de l'ATUHE, Secrétariat d'État à l'Habitat, Kingdom of Morocco, (2001).
[21] Federal Emergency Management Agency, FEMA-356. Prestandard and Commentary for the Seismic Rehabilitation of Buildings, ASCE, Federal Emergency Management Agency, Washington, DC, (2000).
[22] A. Der Kiureghian and M. DeStefano, in:"Efficient algorithm for second-order reliability." JOURNAL of Engineering Mechanics, ASCE. Vol. 117(12) (1991), p. 2923- 2904.
[23] O. Ditlevsen and H.O. Madsen, in: Structural Reliability Methods. Wiley, Chichester, New York: NY,(1996).
[24] R. E. Melchers, in: Structural Reliability Analysis and Prediction. John Wiley and Sons, Chichester: 2nd edition, (1999).
[25] T.V. Santosh et al: Optimum step length selection rule in modified HL-RF method for structural reliability. Pressure Vessels and Piping. Vol. 83 (2006), p. 742-748.

*Applied Mechanics and Materials Vols. 580-583 (2014) pp 1591-1594*
*© (2014) Trans Tech Publications, Switzerland*
*doi:10.4028/www.scientific.net/AMM.580-583.1591*

# An Energy Dissipation Device Based on Shape Memory Alloys for Frame Structures

Yun Chen[1,a*], Nailong Zhu[2,b] and Shuai Gao[3,c]

[1]College of Civil Engineering and Architecture, Hainan University, Haikou 570228, China

[2]China United Northwest Institute for Design and Research, Xi'an 710082, China

[3]Department of Civil Engineering, Tsinghua University, Beijing 100084, China

[a]email: chenyunhappy@163.com, [b]email: 460484489@qq.com, [c]email: 375988592@qq.com

**Keywords:** shape memory alloys; push-over analysis; time-history analysis.

**Abstract.** This paper proposes an energy dissipation device based on shape memory alloys（SMA）for frame structures. By setting anchorage device below and near the inflection point of the first storey columns, a set of force cable and energy dissipation cable using SMA are installed symmetrically in the anchorage device and the bottom of them fixed in the ground. Analytical study including the push-over and time-history analysis were investigated by ANSYS finite element program to a new CFST frame and an ordinary CFST frame. Studies have shown that the device can effectively control the structural displacement response and acceleration response, dissipating large amounts of earthquake energy. Therefore, the energy dissipation devices had a better value and prospects in engineering.

## Introduction

Frame structures are widely used in structural systems. In order to avoid the collapse of frame structures, the key structural components cannot be seriously damaged under strong earthquakes. Consequently, anti-seismic requirements are "strong column-weak beam", "strong shear-weak bending" and "strong node-weak elements". For frame structures, the design idea is to make the beam produce plastic hinges firstly, which can avoid the loss of stability of the structure, leading to collapse. However, practice has shown that plastic hinges, due to the uncertainty of earthquake action and some factors not fully taken into account in structural design, frequently occurred at the column end in frame structures. This phenomenon is caused by the fact that the overall shear force applied to the building by an earthquake is higher at the base (A. Plumier et al. 2005), in addition, as a result of the largest P-delta effects at the bottom storey of structures, the bottom storey columns is more prone to damage and their repair after an earthquake is very difficult.

As an attempt to provide an idea to solve this problem, the paper firstly presents an energy dissipation device based on shape memory alloys for frame structures. Later, Static push-over analysis and time-history analysis were calculated to investigate the seismic performance of the device. Calculation results shows that it is effective to mitigate the damage of frame columns by the device, which also has the advantage of some degree of energy-consuming and easiness to repair after the earthquake.

## Working Principle

For frame structures, under the seismic action, the structural column generally produces an inflection point, and usually one-way bending deformation occurred below the inflection point. According to the deformation of frame columns under earthquake, the paper proposes a new energy dissipation device, as was shown in Figure 1. By setting anchorage device below and near the inflection point of the first storey columns, a set of force cable and energy dissipation cable are installed symmetrically in the anchorage device and the bottom of them fixed in the ground.

Under an earthquake, columns generate deformation, but mainly one-way bending occurs below the inflection point. In this case, anti-torque is applied to the column by the tension force cables,

which can reduce the moment of the first storey columns. At the same time, the earthquake energy is dissipated through repeated non-linear deformation by the energy dissipation cables. Energy dissipation cables consisted of SMA ropes and force cables consisted of wire ropes.

SMA is a kind of super-elastic material and has been applied in many areas due to their high power density, solid state actuation, high damping capacity, durability and fatigue resistance. When integrated with civil structures, SMA can be passive, semi-active, or active components to reduce damage caused by environmental impacts or earthquakes（G. Song et al. 2006, Jin-Ho Roh et al. 2008, Qiang Pan et al.2007）.

In engineering applications, SMA generally has to go through repeated tensile cycle test until their performance stabilizes. The super-elastic strain of SMA is generally 8% ～10%, and its hysteresis loop is relatively full. By a device installed in the structure, SMA can dissipate lots of seismic energy under the earthquake with little residual deformation.

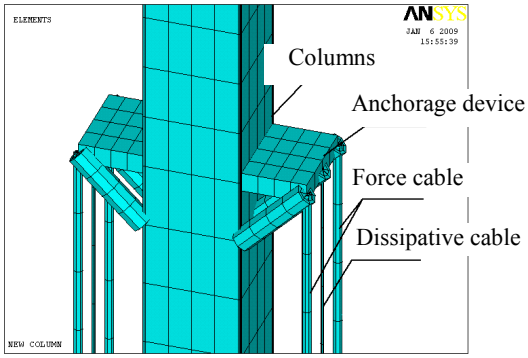


Fig.1 New Energy Dissipation Device

Fig.2 Tensile test site

**Analytical Model**

In the section, two one-span, one-storey CFST (concrete-filled steel tube) frames are investigated to validate the workability of the proposed design device. The first one is an ordinary CFST frame, while the second one is a CFST frame with a set of force cable and energy dissipation cable symmetrically installed. According to the working principle discussed above, ANSYS finite element program is used to carry out the push-over and time-history analysis of the two frames. The FEM model of new energy dissipation device is shown in Figure 1.The steel tube and steel beam used in the model is Q235 with yield strength of 235MPa, and the diameter of force cable is 28mm, with yield strength of 335MPa. The diameter of SMA bar is 10mm. The super-elastic deformation behavior of shape memory alloy was studied through material test, and its stress-strain curves were equivalent to multi-linear model (shown as Fig.2 and Fig.3).

Solid 65 elements are used to simulate concrete, and solid 45 elements are utilized in the modeling of steel tube and steel beam. The used steel was assumed to behave as an elastic plastic material. Link10 element was used to simulate wire ropes while Solid 185 element is adopted to simulate SMA. This kind of element is a special element of ANSYS to represent the material property of SMA.

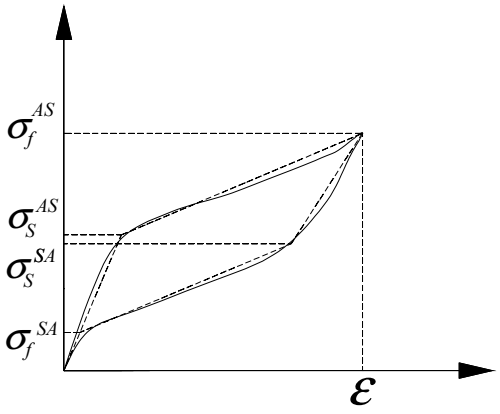


Fig.3 Equivalent linear stress-strain curves

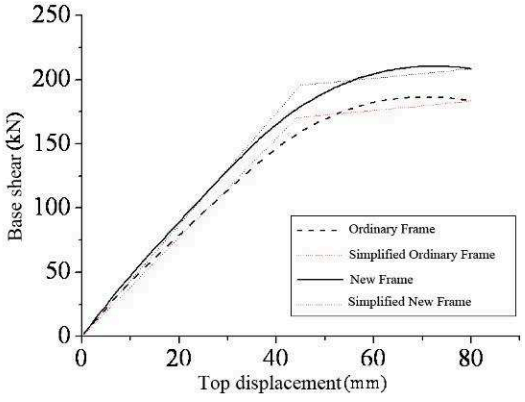


Fig. 4 Base shear-top displacement of common frames and new frames

### Static Analysis

For a detailed comparison of the performance of two frames, static push-over analysis and low cyclic loading analysis were conducted.

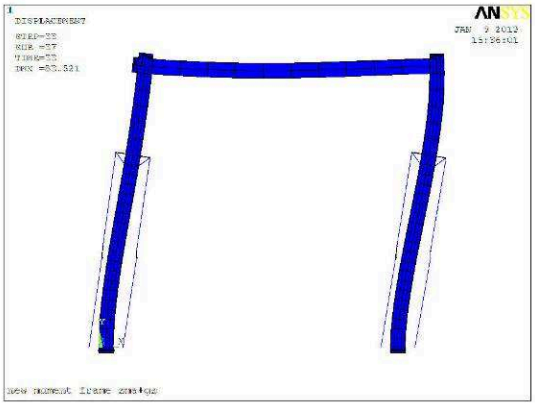

Fig.5 Deformation of new frame

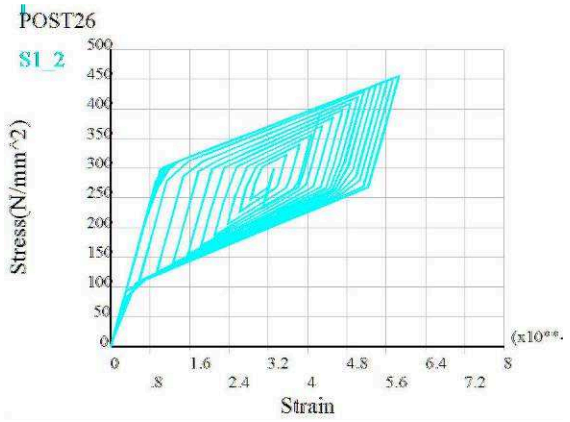


Fig.6 SMA Hysteretic energy curves

An axial load of 3480kN was first applied until the axial-load ratio of the CFST column reached 0.4. Then, displacement controlled load was applied with the level maximum displacement of 80mm until storey drift angles of both frame reached 1/73. In this case, both of frames have been yielding. The base shear-top displacement of common frames and new frames obtained from the analysis are shown in Figure 4 and the deformation of the new frame is shown in Figure 5.

From the base shear-top displacement curves, we can find the deformation of both frames is stable. Due to the action of force cable, maximum bearing capacity of the new frame is higher than the common one by 13%. To compare the yield shear force of both frames, the method proposed by FEMA-273 is used to calculate the base yield shear force of the two frames.

The yield shear force of the ordinary frame is 170.246kN, and the yield displacement is 44mm, while the yield shear force of the new frame is 195.672kN, with yield displacement of 45mm. In other words, the yield shear force of the new frame is 1.15 times higher than ordinary frame. And its yield displacement is also larger than ordinary frame. The Initial stiffness of new frame is 4.352kN/mm with the post-yield stiffness of 0.362kN/mm, and the stiffness degrading ratio is 8.3%; the initial stiffness of ordinary frame is 3.857kN/mm with the post-yield stiffness of 0.369kN /mm, and the stiffness degrading ratio is 9.6%. With the similar stiffness degrading ratio, the new frame has a higher bearing capacity. The SMA hysteretic energy curves is very full, which indicates that the SMA can dissipate a large amount of seismic energy(shown as Figure 6).

### Dynamic Time-history Analysis

In order to further study the effects of force cable and energy dissipation cable, and especially investigate the effects of energy dissipation cable, a dynamic time-history analysis was studied in this section. The El Centro waves were input as seismic waves. Seismic wave peak was 200cm/s$^2$.

In the section, a total of three kinds of structure were compared, the first for ordinary CFST frame, named Frame1; the second CFST frame only setting force cable, named Frame 2; the third CFST frame setting both force cable and energy dissipation cable, named Frame 3.

#### 5.1 Displacement Control Effect

As was show in the Figure 7 and Table 1, the displacement-time curve of three kinds of frame was compared. During the whole course of time history, Frame 1 has maximum displacement, and its maximum displacement reached 55mm, at the same time, its maximum inter-story drift angle reached 1/109; Frame 2 has maximum displacement of 42mm while Frame 3 has maximum displacement of 37mm, and their maximum inter-story drift angles reached 1/143 and 1/162 respectively. Frame 2 has control effects of 23.6%, while frame 3 has control effects of 32.7%. Hence, comparing with Frame 2, Frame 3 has the better control effects.

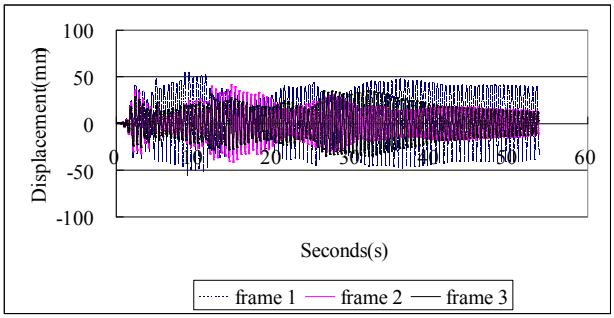


Fig. 7 Comparison of displacement-time curve

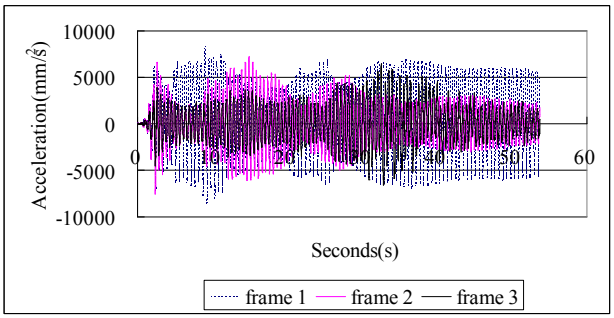


Fig.8 Comparison of acceleration-time curve

Table 1 Comparison of Displacement Control Effects

| Frame 1 | Frame 2 | Frame 3 |
|---|---|---|
| 55mm | 42mm | 37mm |
| Control effects | 23.6% | 32.7% |

Table 2 Comparison of Acceleration Control Effects

| Frame 1 | Frame 2 | Frame 3 |
|---|---|---|
| 8410mm/s$^2$ | 7245 mm/s$^2$ | 6497 mm/s$^2$ |
| Control effects | 13.9% | 22.7% |

5.2 Acceleration Control Effect

As was shown in the Figure 8 and Table 2, the acceleration-time curve of three kinds of frame was compared. During the whole process of time history, Frame 1 has maximum acceleration of 8410 mm/s$^2$; Frame 2 has a maximum acceleration of 7245 mm/s$^2$, while Frame 3 has a maximum acceleration of 6497 mm/s$^2$. Frame 2 has control effects of 13.9%, while Frame 3 has control effects of 22.7%. So, comparing with Frame 2, Frame 3 has the better control effects.

## Conclusions

This paper firstly proposed a new energy dissipation device to mitigate the damage of columns, by setting a set of force cable and energy dissipation cable symmetrically near and below the inflection point, the structural bearing capacity can be improved effectively. It should be noted that force cable has better control effects to the response of displacement and acceleration, but the control effects of energy dissipation cable was not remarkable, because it did not reached enough plastic strain. So, lots of work was still to be done to study the energy dissipation capacity of SMA. Another advantage of the new energy dissipation was that when the cable was damaged under strong earthquakes, it can be easily replaced.

## Acknowledgements

The authors acknowledge the support from Scientific Research Starting Foundation of Hainan University (kyqd1401), Hainan Natural Science Foundation, and the Midwest Key Areas Construction Project Plan of Hainan University.

## Reference

[1] Plumier, C. Doneux, L. Stoychev, T. Demarcot.(2005), "Mitigation of Soft Storey Failures of R.C. Structures Under Earthquake by Encased Steel Profiles," *Fourth International Conference on Advances in Steel Structures*,Pages 1193-1198

[2] G. Songa, N. Maa, H.-N. Lib. (2006), "Applications of shape memory alloys in civil structures," *Engineering Structures*, 28,1266–1274

[3] Jin-Ho Roh, In Lee and Jae-Hung Han. (2008), "Damping characteristics of SMA films and their application for passive vibration isolation," *International Journal of Applied Electro-magnetics and Mechanics,* 27,225–241

[4] Qiang Pan and Chongdu Cho. (2007), "The Investigation of a Shape Memory Alloy Micro-Damper for MEMS Applications,"*Sensor*s, 7, 1887-1900

*Applied Mechanics and Materials Vols. 580-583 (2014) pp 1595-1599*
*© (2014) Trans Tech Publications, Switzerland*
*doi:10.4028/www.scientific.net/AMM.580-583.1595*

# Analysis of the Influence of Mortise-tenon Joint Damage on Seismic Performance of Ancient Timber Structure

Xueliang Wang[1, a], Liang Jin[2,b]

[1] Hubei Key Lab. of Roadway Bridge and Structure Engineering, Wuhan University of Technology, Wuhan, Hubei, 430070, China

[2]School of Civil Engineering and architecture, Wuhan University of Technology, Wuhan, Hubei, 430070, China

[a]wxllhb@163.com, [b]491787602@qq.com

**Keywords:** Ancient timber structure, Damage of mortise-tenon joint, Energy dissipation, seismic performance.

**Abstract.** This research investigated the influence of mortise-tenon joint before and after damage on seismic performance of ancient lifted-beam timber structure. Dynamic responses of an ancient timber structure under various earthquake intensities were analyzed by ANSYS to extract the M-θ hysteresis loops of mortise-tenon joints before and after damage. The area of the largest hysteresis loop was taken as quantitative indicator to measure energy dissipation of mortise-tenon joints. The results shows that if some mortise-tenon joints were damaged, they dissipated much less earthquake energy decreasing by 31.8%-38.5%, and top displacement of structures increased by 1.79%-5.96% correspondingly. Moreover, the displacement under 8-degree-fortification, 7-degree-rare earthquake intensity increased most obviously. Therefore, energy dissipation of mortise-tenon joint is a main indicator to the assessment of seismic performance of a damaged ancient timber structure.

## Introduction

Chinese ancient timber structure is part of the cultural heritage of all human beings with great historical and cultural value. But centuries of exposure to the natural environment has destroyed existing ancient timber structures more or less. These damages will inevitably influence the structural bearing capacity, especially seismic performance. Seismic performance of ancient timber structure has been studied from several perspectives, seismic mechanism[1,2], shaking table test[3,4], restoring force model[5], and strengthening methods[6]. But there has not been any research on seismic performance of damaged ancient timber structure. Research has indicated that mortise-tenon joint is a major dissipative component in an ancient timber structure; therefore the damage of mortise-tenon joint has an important influence on the seismic performance of ancient structure. Studying this influence will provide a theoretical base for evaluating the seismic resistance of existing ancient timber structure.

In this research an ancient lifted-beam timber structure was simulated numerically as finite element model, the structural seismic response before and after damage were analyzed assuming some damage locations and extent in the structure. Then the areas of the hysteresis loop of mortise-tenon joint before and after damage were compared to measure the influence of damaged joints on the structural seismic performance.

## Finite Element Model of an Ancient Lifted-Beam Timber Structure

**Simulation of the ancient timber structure.** Jiayou Palace timber structure was modeled by finite element analysis software ANSYS shown in Fig. 1. In this model the mortise-tenon joint was simulated by element COMBINE39 with nonlinear generalized force-deflection capability which can be used to model the semi-rigid connection. 30% stiffness reduction is assumed to simulate mortise-tenon joint damage, the damage locations were shown in Fig. 2.

According to the parameter of mortise-tenon joint given by H.Y.Zhang[7] and Y.H.Yang[8], the M-θ model for the mortise-tenon joint before and after damage were shown in Fig. 3.

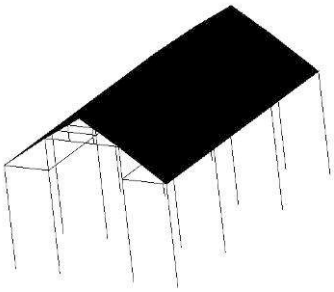

Fig. 1. FE model

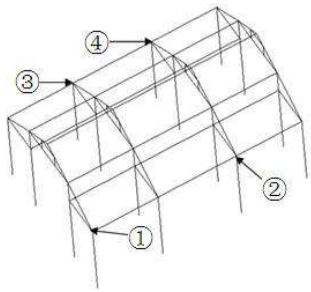


Fig. 2. Damage locations

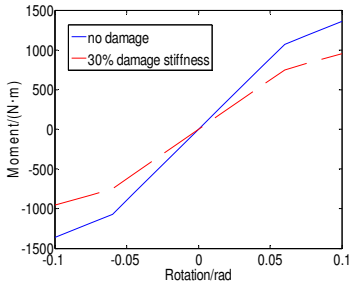


Fig. 3. The M-θ model

**Dynamic characteristic analysis.** Frequencies and mode shapes of original and damaged structure were extracted respectively. The results showed that structural modes before and after damage were almost the same, the 1, 2 and 3 modes are longitudinal, lateral translation, and torsional shape respectively, tiny changes in frequency were shown in Table 1.

Table 1: Frequencies before and after damage

| conditions | First order | Second order | Third order |
|---|---|---|---|
| original | 1.2193 | 1.4582 | 1.6984 |
| damaged | 1.2194 | 1.4580 | 1.6982 |
| Change rate | 0.008% | 0.014% | 0.012% |

Table 1 shows that Frequencies of the structure before and after damage change slightly, hence, the change of structural seismic performance is mainly due to the change of energy-dissipating capacity caused by joint damage.

## Seismic Response and Analysis of Energy Dissipation

To investigate the seismic performance of ancient lifted-beam timber structure, EL-CENTRO earthquake wave was chosen as input, shown in Fig. 4, to analyze the seismic response and energy dissipation of mortise-tenon joint under 7, 8 and 9-degree seismic fortification intensities. According to Code for Seismic Design of Buildings, the peak accelerations of EL-CENTRO wave under conventional earthquake, medium earthquake and rare earthquake were shown in Table 2.

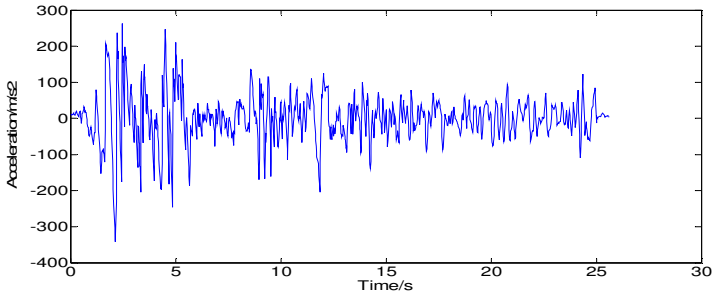


Fig. 4. EL-CENTRO earthquake wave

Table 2. The peak ground acceleration ($m/s^2$)

| Earthquake intensity | 7-degree | 8-degree | 9-degree |
|---|---|---|---|
| conventional earthquake | 0.35 | 0.7 | 1.4 |
| medium earthquake | 1 | 2 | 4 |
| rare earthquake | 2.2 | 4 | 6.2 |

Table 2 indicates the peak ground acceleration of 7-degree rare and 8-degree medium earthquake, and that of 8-degree rare and 9-degree medium earthquake were respectively closer. Hence, only the peak ground accelerations of 0.35, 0.7, 1.4, 2.2, 4.0 and 6.2 m/s$^2$ were taken into consideration. The seismic responses of the structure before and after damage were analyzed under different earthquake intensities. The M-θ curves of mortise-tenon joint ③ were extracted. Some results were shown in Fig. 5. Some top displacements time-history curve were shown in Fig. 6-7 as well.

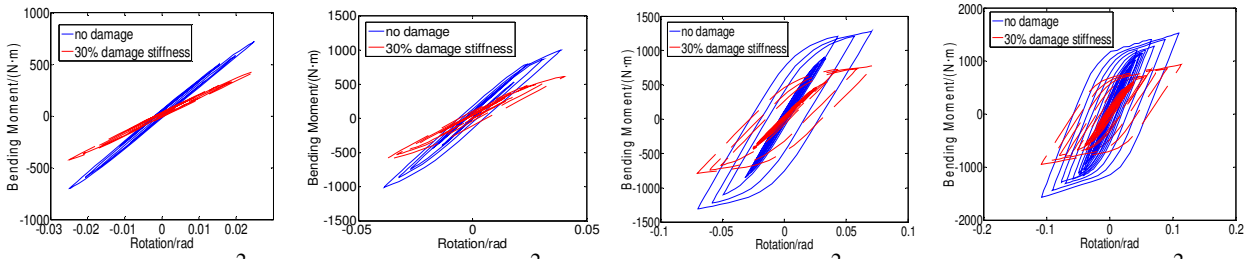


(a) 1.4 m/s$^2$ (b) 2.2m/s$^2$ (c) 4 m/s$^2$ (d) 6.2 m/s$^2$

Fig. 5. Hysteresis curves of mortise-tenon joints before and after damage under various accelerations

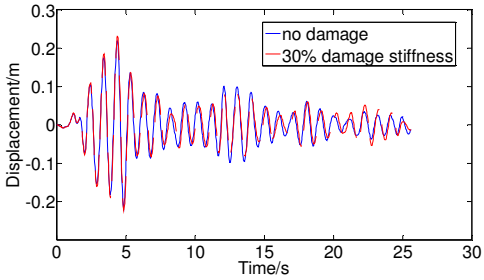


Fig. 6. Displacement curve at 2.2 m/s$^2$

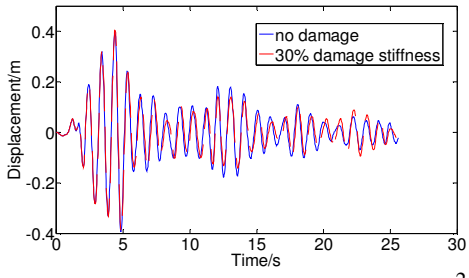


Fig. 7. Displacement curve at 4 m/s$^2$

Fig.5-7 showed when the peak acceleration of earthquake was less than 1.0 m/s$^2$, the structure works mainly in the elastic phase, mortise-tenon joint has hardly dissipated any earthquake energy, the only difference of the hysteresis curves before and after damage is stiffness reduction; When the peak acceleration were 1.4m/s$^2$, mortis-tenon joint started to work in elastic-plastic phase, long and narrow hysteresis loop has formed under earthquake, it has already begun to dissipate some energy, but not much, and the damaged mortise-tenon joint entered first into elastic-plastic phase; When the peak acceleration reached 2.2m/s$^2$, both mortise-tenon joints before and after damage functioned totally in elastic-plastic phase, quadrilateral hysteresis loop has formed under earthquake, and energy-dissipation increased apparently, the hysteresis loops of mortis-tenon joint before and after damage were similar, the comparison of their energy-dissipation needs further study; When the peak acceleration reached 4m/s$^2$, mortise-tenon joint entered elastic-plastic phase as soon as the structure started vibrating, the full hysteresis loop were formed, energy-dissipation brought into full play, joint rotation reached 0.08, structural top displacement was about 0.4m, displacement angle was 0.15, mortise-tenon joint would occur obviously looseness, structure would destroy in this phase; In the case of 9-degree rare earthquake, hysteresis loop of mortis-tenon joint was enlarged, and if the structure could work still, joint rotation will reach 0.12, the structural top displacement would reach 0.62m, tenon will dropped out, and structure will collapse completely.

## Results and Discussion

Since it is difficult to judge qualitatively the influence of mortise-tenon joint damage on seismic response, quantitative analysis is needed, the maximum displacements of structure under different earthquake acceleration were shown in Table 3, where $d_o$ and $d_d$ were the maximum top displacements of the original timber structure and damaged structure respectively, $e$ was the displacement change ratio, where $e=(d_d- d_o)/ d_o$.

Table 3 Maximum top displacement before and after damage

| peak ground acceleration[m/s$^2$] | 0.35 | 0.7 | 1.4 | 2.2 | 4.0 | 6.2 |
|---|---|---|---|---|---|---|
| $d_p$ [m] | 0.035 | 0.07 | 0.14 | 0.218 | 0.396 | 0.614 |
| $d_o$ [m] | 0.036 | 0.0723 | 0.148 | 0.231 | 0.409 | 0.625 |
| $e$[%] | 2.86 | 3.29 | 5.71 | 5.96 | 3.28 | 1.79 |

Table 3 showed that structural top displacement under different earthquake intensity rised slightly from 1.79% to 5.96% when stiffness of mortise-tenon joint reduced by 30%, which was because structural stiffness decreases resulted from the damage of mortise-tenon joint. The $e$ distribution indicated: when the peak ground acceleration values were 1.4m/s$^2$ and 2.2m/s$^2$, the top displacement increased most sharply, the change rates are 5.71% and 5.96% respectively; when the peak ground accelerations were 0.35m/s$^2$ and 0.7m/s$^2$, the top displacement increases by approximately 3%; when the peak ground acceleration values were 6.2m/s$^2$, the top displacement increased only by 1.79%.

The energy dissipation of mortise-tenon joint was measured by the area of hysteresis loops. The larger is area of hysteresis curves, the more energy dissipation there is. The hysteresis loop's area of mortise-tenon joint③ is shown in Table 4, where $A_{eo}$ and $A_{ed}$ is the hysteresis loop area of original and damaged mortise-tenon joints③ respectively, $e_A$ is the area change ratio, where, $e_A=( A_{ed} - A_{eo})/ A_{eo}$.

Table 4 Equivalent viscous damping coefficient

| peak ground acceleration [m/s$^2$] | 0.35 | 0.7 | 1.4 | 2.2 | 4.0 | 6.2 |
|---|---|---|---|---|---|---|
| $A_{eo}$ | 0.0490 | 0.1969 | 2.267 | 15.44 | 104.25 | 261.4 |
| $A_{ed}$ | 0.0302 | 0.1211 | 1.539 | 10.53 | 67.99 | 166.4 |
| $e_A$[%] | -38.4 | -38.5 | -32.1 | -31.8 | -34.8 | -36.3 |

Table 4 showed that with the increase of peak ground acceleration, energy-dissipation of mortise-tenon joint increased significantly no matter there's any damage or not. But compared to the original joints, damaged joints dissipated much less earthquake energy, the decreasing rate ranged from 31.8% to 38.5%.

## Conclusion

The research investigated the influence of mortise-tenon joint damage on seismic performance of ancient Lifted-beam timber structure. It is proved that structural top displacement increased slightly and energy-dissipation of mortise-tenon joints decreased by approximately 31.8-38.5% because of the damage of mortise-tenon joint, which affected the seismic capability of the ancient timber structure significantly. Therefore the energy-dissipation of mortise-tenon joints is a significant parameter to evaluate the seismic performance of damaged ancient timber structure.

## Acknowledgements

The work was financially supported by a grant from the National Science Foundation of China (51208399) which is gratefully acknowledged.

## References

[1]. M. H. Yu, ODA. Y and D. P. Fang: submitted to Advances in Mechanics (2006)
[2]. J. Y. Xue, H. T. Zhao and P. C. Zhang: submitted to China Civil Engineering Journal (2004)
[3]. Y. Sui, H. T. Zhao and J.Y. Xue: submitted to Journal of building structures (2010)

[4]. J.Y. Xue, F.L. Zhang, H. T. Zhao and Y. Sui: submitted to China Civil Engineering Journal (2012)
[5]. K. Yao, H. T. Zhao and H. P. Ge: submitted to Engineering Mechanics(2006)
[6]. H. P. Ge: Experimental study on seismic behavior of Chinese ancient wooden building with strengthened mortise-tenon( Xi'an University of Architecture and Technology, Xi'an, 2004)
[7]. H. Y. Zhang: Dynamic analysis of the Chinese historical timber buildings(Xi'an University of Architecture and Technology, Xi'an 2008)In Chinese
[8]. Y. H. Yang and J. X. Wang: submitted to Journal of Kunming University of Science and Technology (Science and Technology)(2009) In Chinese

*Applied Mechanics and Materials Vols. 580-583 (2014) pp 1600-1603*
*© (2014) Trans Tech Publications, Switzerland*
*doi:10.4028/www.scientific.net/AMM.580-583.1600*

# Demand diagrams based on inelastic spectra: a proposal for the implementation of the capacity spectrum method in the Romanian seismic design code

Iolanda-Gabriela CRAIFALEANU[1,2 a]

[1]Technical University of Civil Engineering Bucharest, Department of Reinforced Concrete Structures, Bd. Lacul Tei, nr. 122-124, Sector 2, Bucharest, Romania

[2]National Institute for Research and Development in Construction, Urban Planning and Sustainable Spatial Development "URBAN-INCERC", INCERC Bucharest Branch, Sos. Pantelimon, nr. 266, Sector 2, Bucharest, Romania

[a]i.craifaleanu@gmail.com, iolanda.craifaleanu@utcb.ro

**Keywords:** capacity spectrum method, inelastic spectra, strength reduction factors, Romanian seismic design code

**Abstract**. During recent years, an increasing number of studies advocate the application of the capacity spectrum method based demand diagrams computed directly from inelastic response spectra, as an alternative to the basic formulation of the method, which uses elastic spectra computed for single degree-of-freedom oscillators with modified characteristics to account for inelastic behavior. When demand diagrams are based on the code-specified elastic spectrum, inelastic spectra are typically determined by dividing the elastic spectrum by strength reduction factors. The paper presents the application of the method, based on strength reduction factors computed with a unified analytical expression, deduced by the author in previous studies. The expression and is valid both for broadband and narrow band ground motions. Taking as a starting point the newly-enforced elastic design spectra in the 2013 edition of the Romanian seismic design code, the method is exemplified for the capital city, Bucharest. It is shown that, for the analyzed case, the use of the proposed strength reduction factors leads to results that are very close to those obtained by the "classical" nonlinear static procedure used in the code. This suggests a good potential for the implementation of the capacity spectrum method in the Romanian code, based on these factors.

## Introduction

The Capacity Spectrum Method (CSM) is an important component of the present generation of seismic codes. Proposed by Sigmund Freeman in 1975 [1], the method combines the nonlinear static analysis of the structure and the nonlinear dynamic analysis of a set of linear-elastic single degree-of-freedom systems (SDOF) with modified characteristics to account for inelastic behavior effects. Due to its intuitive and relatively simple approach, the method is largely used, being also implemented in several regulatory or pre-regulatory documents. During recent years, several proposals have been made for the improvement of CSM, aimed to increase the accuracy of results and to enhance its applicability.

The paper investigates the possibilities of using CSM by ensuring compatibility with the new edition, enforced starting from January, 1, 2014, of the Romanian seismic design code, P100-1/2013 [2]. Even though the code includes the nonlinear static procedure among the prescribed analysis methods, CSM is still not included. Based on previous studies performed by the author [3, 4, 5], a proposal is formulated for CSM application in the new Romanian regulatory context.

## Brief presentation of the capacity spectrum method

The steps of CSM, as described in [6, 7], are briefly presented in the following.

1. The base shear – roof displacement relation is determined, by nonlinear static analysis, for the considered structure.

2. The resulting force and displacement values are converted into values for an equivalent SDOF system, by using the following relations:

$$D = \frac{D_n}{\Gamma_1 \Phi_{n1}}, \quad (1) \qquad A = \frac{Q_B}{M_1^*}, \quad (2)$$

where

$$\Gamma_1 = \left(\sum_{i=1}^{n} m_i \Phi_{i1}\right) \Big/ \left(\sum_{i=1}^{n} m_i \Phi_{i1}^2\right), \quad (3) \qquad M_1^* = \left(\sum_{i=1}^{n} m_i \Phi_{i1}\right)^2 \Big/ \left(\sum_{i=1}^{n} m_i \Phi_{i1}^2\right). \quad (4)$$

In the above equations, $n$ is the number of stories of the structure, $m_i$ – lumped mass at the $i$-th floor level, $\Phi_{i1}$ – the $i$-th floor element of the fundamental mode eigenvector ($i$=1, ..., $n$), $D_n$ – roof displacement of the structure, $M_1^*$ – effective modal mass for the fundamental vibration mode, $\Gamma_1$ – modal participation factor for the fundamental vibration mode. By this conversion, the "*capacity spectrum*" [7] or the "*capacity diagram*" [6] is obtained.

3. The 5%-damped linear acceleration spectrum is plotted in ADRS [7] (or "*A-D*" [6]) format, with the spectral (pseudo)accelerations, $A$, on the ordinate, and the spectral displacements, $D$, on the abscissa. The displacements are computed with the formula $D = [T^2/(4\pi^2)]A$, where $T$ is the vibration period. By this, the "*demand spectrum*" [7] or the "*demand diagram*" [6] is obtained.
4. The diagrams obtained in steps 2 and 3 are plotted on the same chart.
5. Dynamic nonlinear analyses are performed for a series of linear-elastic SDOF systems, with successively updated values of the equivalent eigenperiod, $T_{eq}$, and of the equivalent viscous damping, $\xi_{eq}$. The two characteristics are computed as functions of the period, damping, ductility and assumed hysteretic law. Based on their values, demand diagrams are determined, for various values of the ductility, μ. The target displacement (displacement demand) is found as the point for which the ductility value is the same, both on the capacity and on the demand diagram.
6. The displacement demand is converted back to roof displacement, with Eq. 1. Depending of the position of this value on the base shear – roof displacement diagram, the force and displacement demands for the structure are obtained.

**Use of inelastic spectra in the capacity spectrum method**

In order to improve the precision of the model, Chopra and Goel [6] proposed that, instead of modifying the characteristics of linear systems to account for nonlinear behavior, as in step 5 of the method, inelastic spectra computed for various values of ductility are used. If the demand diagrams are obtained based on linear-elastic code spectra, inelastic spectra can be determined by dividing elastic spectra with strength reduction factors. Strength reduction factors, $R_\mu$, are defined as in Eq. 5, by the ratio between the minimum yield strength, $F_e$, required in order that the systems behaves elastically under the considered seismic action and the yield strength $F_y$, corresponding to the attainment of a specified ductility, μ. In Eq. 5, $A$ and $A_y$ are the accelerations corresponding, respectively, to the two situations. Several analytical expressions have been proposed for these factors, among which those of Newmark and Hall [8], Miranda and Bertero [9], Vidic et al. [10].

$$R_\mu = \frac{F_e}{F_y} = \frac{MA}{MA_y} = \frac{A}{A_y}. \quad (5)$$

**Application of the CSM for compatibility with the new edition of the Romanian seismic code**

To apply CSM in its improved variant, described in the previous section, inelastic response spectra were determined, based on the elastic design spectra in the newly-enforced edition of the Romanian seismic design code, P100-1/2013. For this purpose, strength reduction factors were used, as determined in previous studies of the author [3, 4], from the analysis of ground motions recorded during the strong Vrancea (Romania) earthquakes of 1977, 1986 and 1990.

A analytical expression of $R_\mu$ was proposed in [3] (Eq. 6), where, for broadband motions, $\chi$ is the vibration period, $T$, while for narrow-band motions, $\chi$ is the ratio between $T$ and the predominant period of the ground motion, $T_g$:

$$R_\mu = \mu^{\frac{\chi^2 + C_1\chi + C_2}{C_3\chi^2 + C_4\chi + C_5}}. \quad (6)$$

In the following, the application of the method is illustrated for the capital city of Bucharest where, due to the soft soil conditions, a design spectrum with a corner (control) period, $T_C$, of 1.6 s is specified by the P100-1/2013 code. This period value was also found to characterize the predominant period of the ground motion, $T_g$, for strong earthquakes. The coefficients in Eq. 6, adequate, according to [3], for Bucharest (narrow frequency band motions, values with 10% probability of exceedance) are listed in Table 1.

Table 1. Values of the coefficients in Eq. 6

| $\chi = T/T_g$ | $C_1$ | $C_2$ | $C_3$ | $C_4$ | $C_5$ |
|---|---|---|---|---|---|
| 0.01...0.75 | 0 | 0 | 1 | 0.254 | 0 |
| 0.75...5 | -1.829 | 0.929 | 1.348 | -2.668 | 1.403 |

Inelastic spectral displacements, $D$, were computed, for various ductility values, with Eq. 7 and the demand diagrams in Fig. 1 were determined.

$$D = [T^2/(4\pi^2)]\, A\mu/R_\mu. \quad (7)$$

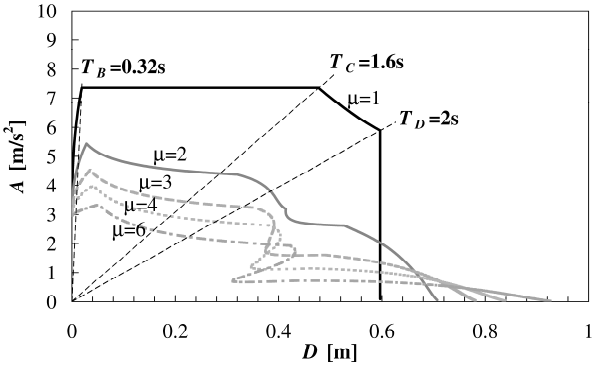


Fig. 1. Demand diagrams for Bucharest, determined based on the elastic design spectrum in the P100-1/2013 code

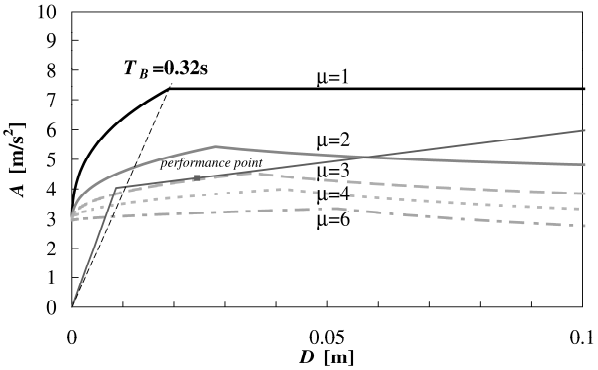


Fig. 2. Results of validation performed for a shear wall structure

In a first evaluation, the demand diagrams in Fig. 1 were used to determine the target displacement for a reinforced concrete shear wall building for which, previously, a nonlinear static analysis of the building was performed according to the P100-1/2013 provisions. The bilinearized base shear – roof displacement curve, as well as the performance point obtained according to the code are shown in Fig. 2, corresponding to a ductility $\mu = 2.84$. It can be noticed that this point is very close to the intersection between the capacity diagram of the building and the demand diagram for $\mu = 3$, which

shows a very good agreement between the results obtained by the two methods. Further systematical analyses are necessary to completely validate the adequacy of the proposed $R_\mu$ expression for use in the capacity spectrum method.

## Conclusions

An application of the improved variant of the capacity spectrum method, based on the use of inelastic spectra, was presented, aimed for compatibility with the newly-enforced Romanian seismic design code, P100-1/2013. By using a unified analytical expression of the strength reduction factors, proposed by the author in previous studies, demand diagrams were determined, for various ductility values, from the elastic design spectrum specified by the code. The encouraging results obtained by a preliminary validation against the "classical" nonlinear static procedure included in P100-1/2013 showed that the method could be successfully implemented in the code.

The application also pointed out the importance of developing reliable expressions of strength reduction factors, accounting for their variation with period, ductility and spectral content of seismic motion. This would allow, among others, enhancing the accuracy of results obtained by the capacity spectrum method and an easier implementation of its improved version in seismic design codes.

## References

[1] S.A. Freeman, J.P. Nicoletti, J.V. Tyrell: Evaluations of existing buildings for seismic risk – A case study of Puget Sound Naval Shipyard. Bremerton, Washington. Proceedings of the 1st U.S. National Conference on Earthquake Engineering, EERI, Berkeley, California (1975) 113-122.

[2] MDRAP: Code for the seismic design of buildings: Part I – Design prescriptions for buildings, P100-1/2013, Monitorul Oficial, Part I, No. 558 of 03.09.2013, Bucharest, 2013 (in Romanian).

[3] Craifaleanu, I.G.: Strength reduction factors: a unified analytic expression for narrowband and broadband ground motion records, Proceedings of the XIIth International Symposium "Acoustics and Vibration of Mechanical Structures", Timisoara, Romania, May 23-24, in: Applied Mechanics and Materials, 430: 367-371, Trans Tech Publications, Switzerland, 2013.

[4] Craifaleanu, I.G.: Strength reduction factors for Romanian Vrancea earthquakes: general characteristics and peculiarities, Proceedings of the 13th SGEM GeoConference on Science and Technologies in Geology, Exploration and Mining, Albena, Bulgaria, June 16-22, 2 (2013): 887-894.

[5] Craifaleanu, I.G.: Modern methods used in international prescriptions for the evaluation of the seismic performance of buildings and their implementation in Romanian codes, Buletinul AICPS, nr. 3 (2000):89-95 (in Romanian).

[6] A.K. Chopra, R.K. Goel: Capacity-demand-diagram methods based on inelastic design spectrum, Earthquake Spectra 15.4 (1999): 637-656.

[7] ATC: Seismic evaluation and retrofit of concrete buildings. Report ATC-40. Applied Technology Council, Redwood City, California, 1996.

[8] N.M. Newmark, W.J. Hall, Earthquake Spectra and Design, Earthquake Engineering Research Institute, Berkeley, California, 1982.

[9] E. Miranda, V.V. Bertero, Evaluation of Strength Reduction Factors for Earthquake-Resistant Design, Earthq. Spectra, 10: 2 (1994) 357-379.

[10] T. Vidic, P. Fajfar, M. Fischinger, Consistent inelastic design spectra: strength and displacement, Earthq. Eng. Struct. D., 23:5 (1994) 507-521.

*Applied Mechanics and Materials Vols. 580-583 (2014) pp 1604-1608*
*© (2014) Trans Tech Publications, Switzerland*
*doi:10.4028/www.scientific.net/AMM.580-583.1604*

# Research ofSoil Layers Amplification Effect Based on Strong SeismicRecords and Calculations

Liang Wang[1,a], YaSu[2,b]

[1]Key Laboratory of Earthquake Engineering and Engineering Vibration,

Institute of Engineering Mechanics, CEA, Heilongjiang, Harbin 150080, China

[2]CNBM International EngineeringCo.,LTD, Beijing, 100048, China

[a]wl_8395@126.com,[b]sophie.masako@gmail.com

**Keywords:**BoreholeArrays, Strong Seismic Records, Amplification Effect, Predominant Period.

**Abstract.**This paper states the comparison research of calculation results from program LSSRLI-1 and program SHAKE2000,with the strong seismic records as well asthe site soil conditions by using borehole arrays. The analytical results show thatthe site soil conditions havean amplification effect on the seismic PGA and response spectrum values, however, the actual seismic records are not consistent with the program calculations on the amplification effect.Besides,the site soil conditions also have an altering effect on the predominant period of seismic response spectrum, where actual seismic records and program calculation results of the altering effect are not the same either.

## Introduction

Seismic damage documents indicate that site soils havegreat impact on the seismic motion of bedrock. In comparison with the bedrock motion, the surface motionhas a big difference in the amplification and the spectral characteristics. This site soil impact on the amplification and spectral characteristics of the bedrock motion is called site effect, which has become earthquake expert's main concerns.

The most effective and direct method to study the site effect is to establishborehole arrays, which have strong-motion instruments set at different depth of the same site. In this way, the impact of site soils on the seismic motion can be analyzed by comparing strong seismic records of the surface with those ofthe bedrock [1]. The actual seismic records indicate that in general the amplification effect of the site soil on the earthquake exists [2].

When conducting risk analysis and determination design of the seismic motion, usually the input seismic motion of the bedrock is determined at first, thenthe site inner cover soil's impact on the input seismic motion is considered on the basis of the dynamic soil properties by using soil response analysis program to calculate the surface motion. The soil dynamic parameters arenormally obtained from in situ testing and indoor soil testing, but the soil testing will disturb the soil sample and make the soil's original stress statehard to recover, which has great impact on the dynamic parameters [3]. Meanwhile, due to the limitation of soil response program, the calculation results and the actual seismic records would have some difference.

Based on strong seismic records of Xiangtang-3 borehole array, calculations of the surface motionby program LSSRLI-1 and program SHAKE2000 have been carried out, and the comparison of the actual seismic records with the calculation results,as well as the corresponding analysis are reported in this paper.

## Introductionfor Xiangtang-3borehole array

Tangshan Xiangtanglocal site borehole arrayswere established in 1992, whileits No.3 borehole array was a newoneduring its renovation and expansion project in 2000. Xiangtang-3 borehole array was put into use in December, 2000 and has obtained several strong seismic records by now [4].

Xiangtangborehole array is located in Luan village, Hebeiprovince, and its location terrain is flat with quaternary stratigraphic soil and Archean metamorphic rock. With a total depth of 47m, the array goes across the entire soil layers reaching weakly weathered rock. It is determined to be type-II

through the drilling and shear wave velocity test, and correspondinghistograms and shear wave velocity diagram are shown inFig. 1.

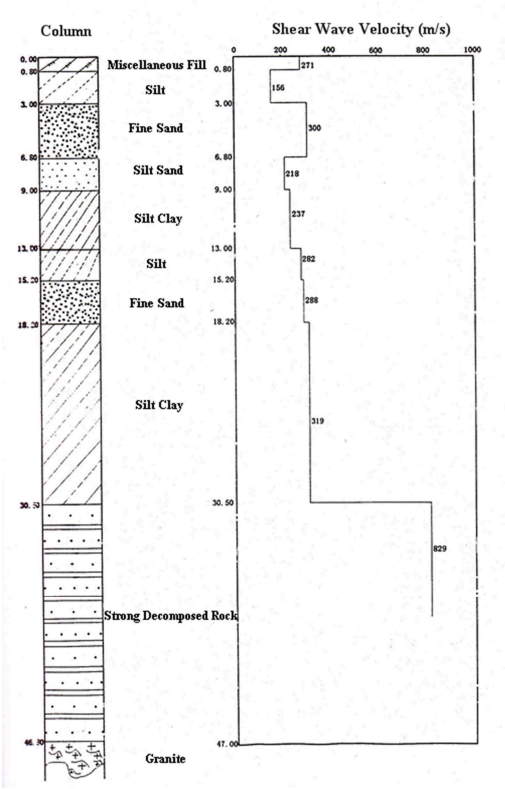


**Fig. 1**Site drilling histogram and shear wave velocity distribution diagram

**Table 1**Bulk density and consolidation pressure of soil samples

| Sample No. | Depth（m） | Density（g/cm$^3$） | Consolidation pressure |
|---|---|---|---|
| 1 | 1.0-1.2 | 1.84 | 0.5 |
| 2 | 3.8-4.0 | 1.94 | 1.0 |
| 3 | 7.8-8.0 | 1.96 | 1.0 |
| 4 | 10.1-10.3 | 1.87 | 1.0 |
| 5 | 14.1-14.3 | 2.08 | 1.5 |
| 6 | 19.0-19.2 | 1.94 | 2.0 |
| 7 | 23.4-23.6 | 1.98 | 2.5 |
| 8 | 27.5-27.7 | 2.01 | 2.5 |

Through the indoor soil testingof rock-soil samples, the bulk density, consolidation pressure, dynamic shear modulus ratio $G_d/G_{dmax}$, as well as the relationship between dampingratio and shear strain at different depths have been determined.

Table 1 shows the bulk density and the consolidation pressure of soil samplesat different depths of No.3 array. Table 2 and Table 3 show the nonlinear properties (dynamic shear modulus ratio and damping ratio)of soil samples.

**Table 2** Dynamic shear modulus of soil samples

| No. | Shear Strain（$10^{-4}$） | | | | | | | |
|---|---|---|---|---|---|---|---|---|
| | 0.05 | 0.1 | 0.5 | 1 | 5 | 10 | 50 | 100 |
| 1 | 0.97 | 0.941 | 0.763 | 0.616 | 0.243 | 0.138 | 0.031 | 0.016 |
| 2 | 0.979 | 0.959 | 0.825 | 0.702 | 0.32 | 0.19 | 0.045 | 0.023 |
| 3 | 0.98 | 0.96 | 0.828 | 0.707 | 0.326 | 0.194 | 0.046 | 0.026 |
| 4 | 0.988 | 0.976 | 0.89 | 0.802 | 0.447 | 0.288 | 0.075 | 0.039 |
| 5 | 0.978 | 0.956 | 0.814 | 0.686 | 0.304 | 0.179 | 0.042 | 0.021 |
| 6 | 0.979 | 0.959 | 0.825 | 0.703 | 0.321 | 0.191 | 0.045 | 0.023 |
| 7 | 0.985 | 0.97 | 0.866 | 0.763 | 0.392 | 0.244 | 0.061 | 0.031 |
| 8 | 0.973 | 0.948 | 0.785 | 0.646 | 0.268 | 0.155 | 0.035 | 0.018 |

**Table 3** Damping ratio of soil samples

| No. | Shear Strain（$10^{-4}$） | | | | | | | |
|---|---|---|---|---|---|---|---|---|
| | 0.05 | 0.1 | 0.5 | 1 | 5 | 10 | 50 | 100 |
| 1 | 0.016 | 0.029 | 0.051 | 0.066 | 0.098 | 0.105 | 0.112 | 0.113 |
| 2 | 0.004 | 0.007 | 0.022 | 0.033 | 0.065 | 0.074 | 0.085 | 0.087 |
| 3 | 0.012 | 0.017 | 0.035 | 0.045 | 0.067 | 0.073 | 0.079 | 0.08 |
| 4 | 0.011 | 0.015 | 0.033 | 0.044 | 0.074 | 0.084 | 0.096 | 0.097 |
| 5 | 0.018 | 0.024 | 0.047 | 0.06 | 0.086 | 0.093 | 0.099 | 0.1 |
| 6 | 0.004 | 0.007 | 0.029 | 0.049 | 0.106 | 0.125 | 0.146 | 0.149 |
| 7 | 0.007 | 0.011 | 0.027 | 0.038 | 0.067 | 0.077 | 0.087 | 0.089 |
| 8 | 0.018 | 0.024 | 0.049 | 0.062 | 0.088 | 0.094 | 0.101 | 0.102 |

## Introductionfor Program

In order to do the comparison analysis with Xiangtang-3 borehole array's strong seismic records, two kinds of soil response analysis programs, LSSRLI-1 and SHAKE2000, have been used to calculate the seismic response of site soils.

In 1989,LiaoZhenpeng[5] proposed the equivalent linear resolving method of surface soil response. Base on this method, Dr. LiXiaojun usedFORTRAN language to program the LSSRLI-1, which was then widely used in engineering applications of seismicrisk analysis and safety evaluation. Ascribed to its theoretical basis of the equivalent linear approach, the programcan be suitably applied to calculate the soil seismicresponse under strong motion.

In 1970, Dr. Per Schnabel and Professor John Lysmer[6]programmed SHAKE, which was officiallyissued in 1972 at the University of California, Berkeley Earthquake Engineering Research Center. The equivalent linear approachalso forms the theoretical basis of program SHAKE, which is nowadays the most popular program in the soil seismic response analysis. The program hasseveral modified versions and the latest version of SHAKE2000 has been applied in this paper.

## Selection of seismic records

Ever since the official implementationin Dec. 2000, Xiangdang-3 borehole array has recorded several strong motions, according to which is relevant researches have been done.

Selected fromChina National Strong Motion Network Center, the acceleration records of 47m underground and surfaceat Xiangtang-3 borehole array have been applied in this paper.These two seismic records both include 8200 points for the acceleration time history witha time interval of 0.005s. Table 4 shows the specific information of the selected seismic records.

**Table 4** Seismic record information

| Centre | Magnitude | Epicentral Position | Hypocenter Depth | Time |
|---|---|---|---|---|
| Luan-Village | 3.8 | 39:48'N 118:46'E | 30 | 2002/5/6 |

Fig. 2 and Fig. 3 are acceleration and Fourier spectrum of seismic records at 47m underground of Xiangtang-3 borehole array.

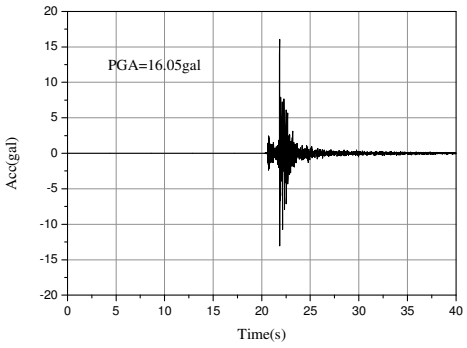


**Fig. 2**Acceleration of47munderground

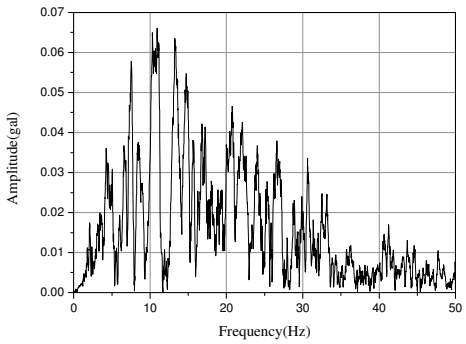


**Fig. 3** Fourier spectrum of 47m underground

## Calculation Analysis

Takingthe above seismic records of 47m undergroundat Xiangtang-3 borehole array as the input seismic motion and Xiangtang-3 borehole array's section as the calculation section, LSSRLI-1 program and SHAKE2000 program has respectively calculated the surface acceleration and response spectrum, which have beencompared with the actual surface records for consistence analysis in this paper.

Fig. 4, Fig. 5 and Fig. 6 separately shows the actual surface acceleration record, LSSRLI-1 program calculated surfaceacceleration and SHAKE2000 program calculated surface acceleration.

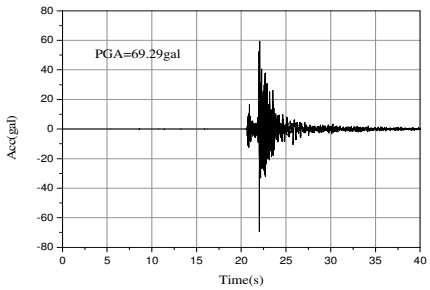


**Fig. 4**Actual surface accelerationrecord

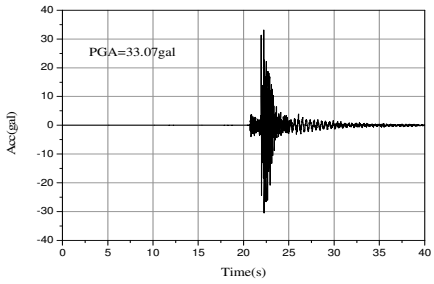


**Fig. 5** LSSRLI-1 calculated surface acceleration

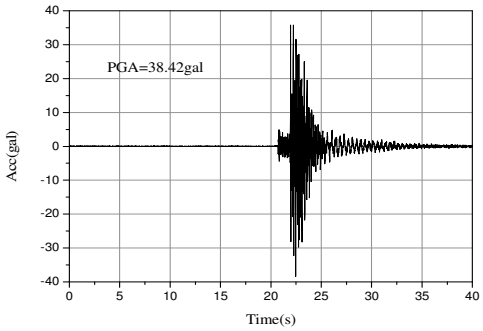


**Fig. 6** SHAKE2000 calculated surface acceleration

Seismic damage documents and borehole strong seismic records indicate the amplification effect of site soils on the seismic motion, whichis directly reflectedby PGA's amplificationof the seismic acceleration. By comparingthe input seismic motion of Fig. 2 with the output seismic motion of Fig. 4, Fig. 5 and Fig. 6,both actual seismic records and calculation results of LSSRLI-1 and SHAKE2000 show the amplification of PGA. However, the amplification effect shown by the actual seismic records is more significant rather than that shown by the calculations.

Fig. 7 shows the actual underground acceleration records of Xiangtang-3 borehole array.Fig. 8 shows the actual surface acceleration records of Xiangtang-3 borehole array, as well as the calculated response spectra of LSSRLI-1 and SHAKE2000.

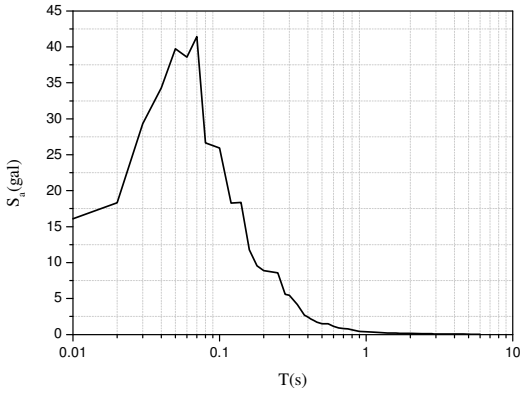


**Fig. 7**Input seismic response spectrum

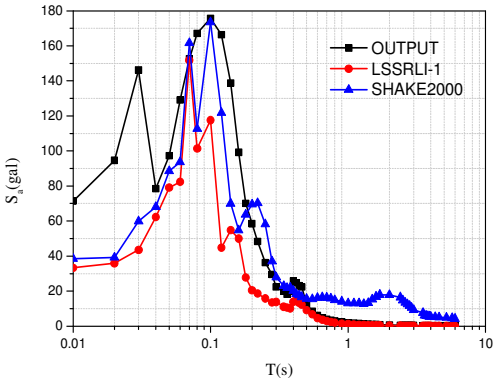


**Fig.8** Output seismic response spectra

Seen from Fig. 7and Fig. 8, site soils havean altering effect on the acceleration response spectrum but this altering effect shown bythe actual seismic records is not the same as that shown bythe calculation results of LSSRLI-1 and SHAKE2000, which is reflected on two aspects.Firstly, the actual seismic records and the calculation results of LSSRLI-1 and SHAKE2000 show different amplification effect on the response spectrum values;secondly, the altering tothe predominant periodof response spectrumshown bythe actual seismic records and the calculation results of LSSRLI-1 and SHAKE2000 are not the same.

## Conclusion

Through the comparison analysis between borehole array strong seismic records and the program' s calculation results, it is concluded that site soil conditions havean amplification effect on PGA, with the amplification effect shown by the actual seismic records being more significant. Besides, site soil conditions also havean amplification effect on the response spectrum values, though the amplification effect and the altering to the predominant periodof response spectrum shown by actual seismic records and program calculation results are different.

## References

[1] Lü Hongshan. Site coefficients suitable to china site category, Acta Seismologica Sinica(2007)
[2]ZHANG Wen-bo. Estimation of absolute site amplification, Earthquake Engineering and Engineering Vibration (2001)
[3]Chen Xueliang. Inversion of waveforms from Xiangtang borehole seismic array for soil dynamic property, Acta Seismologica Sinica(2007)
[4]XIE Li-li. A three dimensional array for site effects on strong ground motion, Earthquake Engineering and Engineering Vibration (1999)
[5]Liao Zhenpeng. Seismic microzonation(1989)
[6]User's manual for SHAKE91—A computer Program for conducting equivalent linear seismic response analyses of horizontally layered soil deposits(2002)

*Applied Mechanics and Materials Vols. 580-583 (2014) pp 1609-1612*
*© (2014) Trans Tech Publications, Switzerland*
*doi:10.4028/www.scientific.net/AMM.580-583.1609*

# RESEARCH ON PERFORMANCE-BASED SEISMIC LEVELS OF NONSTRUCTURAL COMPONENTS

Haihua Zhu[1, a], Guo Zhao[1,b]

[1]Institute of Civil Engineering, Henan University of Science and Technology, Luoyang, China 471023

[a]zhuhh010@163.com, [b]zhaofuture@163.com

**Keywords:** Non-structural components; Performance-based seismic design; Performance levels.

**Abstract.** By research of the functional classification, seismic fortification performance objectives and quantified targets of non-structural components, according to the case of earthquake destruction in non-structural components, analyzed the reasons for the destruction . proposed three functional classification;Based on performance-based seismic design theory, proposed four level seismic performance objectives division and quantify seismic indicators of inter story displacement angle.

## Introduction

With the social economic development and people's living standards improve, the demand for residential security needs to gradually shift to comfort. Thus, the cost proportion of nonstructural components in the total construction increase gradually. Analysis of the cost of building a pointed out: In recent years, due to the decoration technology improves, structural cost accounted for only about 30% of the total construction cost. The structural members of a house in the quake did not destruction, but nonstructural components destroyed, it means a loss of 70% -80% of the total cost of construction ,and very difficult to repair. So many countries in the world began to increasingly more attention to the seismic safety of nonstructural components.

## Destruction Analysis of nonstructural components

Investigation performance of non-structural components in the earthquake, summarizes the earthquake effects and the destruction laws on nonstructural components is the fundamental basis of seismic design of nonstructural components

## Non-structural wall

Nonstructural wall including partition wall ,enclosure wall, etc. .The main reason of the nonstructural wall is destruction during an earthquake is the main structure deformation, interlaminar lateral displacement, partition wall connections and seams are not reliable, reasons for itself material, uncoordinated of partition wall stiffness and the main structure stiffness etc.. Figure 1 is a common form of destruction to non-structural wall.

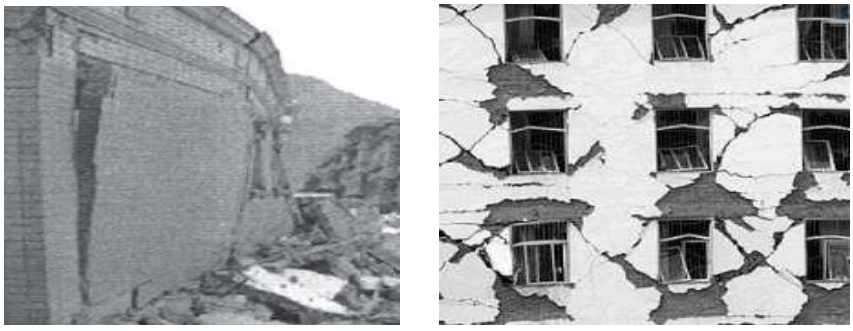

Figure 1 Nonstructural wall destruction

**Stairs**

The destruction of the stairwell is often serious than other parts, leading to evacuation difficulty, Cause secondary disasters. The main reason of the destruction is stair platform elevation is inconsistent with the adjacent room floor, different reactions between rigid stairwells and other parts of houses cause large relative movement. Figure 2 is a common failure form of stairs.

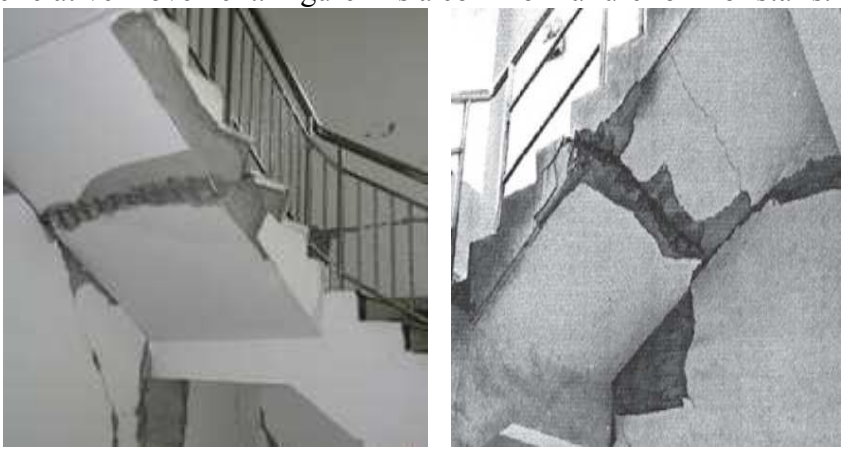

Figure 2 The destruction of the stairs

**Prominent roof components**

The main component is a prominent roof stairwell, the elevator, equipment room and other facilities。A lot of damage domestic and foreign showed, in the event of a strong earthquake, as "whiplash effect", the main structure has not destruction or minor damage, but the partial highlight structure has taken place serious damage or even collapse, which damage was generally more severe.

The main reasons of the destruction: the anchor is not firm or anchorage old failure; The second is due to seismic amplification by the large inertia force. Figure3 is a common failure form of non-structural components prominent roof.

Figure3 The destruction of non-structural components prominent roof

**The classification of nonstructural components**

Seismic design of nonstructural components usually include architectural nonstructural components and architectural affiliated mechanical and electrical equipments, The code for seismic design of buildings (GB 50011-50011 ) explained in detail to it. Just like for different types of buildings in different seismic performance objectives, these wide variety of nonstructural components in the seismic design can not be generalized to reach the same kind of seismic performance. In order to achieve the security requirements, while avoiding the waste due to the excessive demands of its safety

in design for all non-structural components, refer to the relevant specification[1,2], the non structural components in accordance with the functions are divided into three categories.

Class Ⅰ, In addition to nonstructural components class Ⅱ, Ⅲ. Such as partition walls, ceilings, furniture etc., These components can be easily removed or can be repaired within a short time in the devastation.

Class Ⅱ,Components maintain the main architecture function, and provides emergency escape. Such as stairs,evators,large air conditioning equipment etc. .

ClassⅢ,Components can bring secondary disasters. Such as gas pipelines, water tank, water pipelines etc..

**Seismic performance target of nonstructural components**

The performance levels is that in a certain probability of earthquake, performance level owners hope can achieve. Performance-based seismic design theory is first proposed at the twentieth century in the early 1990s by American scientists and engineers, aroused great interest in earthquake engineering researchers in Japan and Europe, and launched various studies. In recent years, Chinese scholars also started the research on this theory[3,4]. Compared with the traditional three earthquake goals "minor earthquake not damage, moderate earthquake can repair, strong earthquake not fall," the performance-based seismic design theory is more advanced, more flexible, more responsive to current needs

Table 1 does a comparison between conventional design and performance-based design process from the target performance, design methods ,the selection of test methods and finally achieve the performance level, etc. . [5]

Table 1 Comparison of conventional design and performance-based design

| | conventional design | performance-based design |
|---|---|---|
| performance level | Specifications give | Owner explicitly set |
| Design methods and test methods | Using specification design methods Meet the requirements of specification | Designers choose proper method |
| Performance achieved | The actual level of performance is not clear | The actual level of performance is clear |

In this paper, considering the seismic performance of different types of non-structural components, reference to the relevant information and in accordance with non-structural components, the seismic performance objectives are divided into four classes:

Class1-Full operation. Refers to the building's and equipment's function at the time of the earthquake or after earthquake can continue to maintain, structural components and nonstructural components may have minor damage, but the building structure intact.

Class2-Basic operation. The basic function of architecture is not affected, the key and important part of the structure and indoor items is not damaged, non structural components may be damaged, but after the general repair or without repair can continue to use.

Class3-Dysfunction.Refers to the basic functions of building are affected, damage to nonstructural components heavier but not completely lost the use of function, life safety can be guaranteed.

Class4-Loss of function. Refers to the basic functions of the building no longer exist, there is serious damage to nonstructural components, loss of function.

According to the different categories earthquake standards and nonstructural components division, Table 2 determines its basic performance levels of different types of non-structural components.

Table 2 Performance levelss of all nonstructural components

| | full operation | basic operation | dysfunction | loss of function |
|---|---|---|---|---|
| Multi-case earthquake | II , III | I | | |
| Design earthquake | III | II | I | |
| Rare case earthquake | | III | II | I |

**Quantitative design indicators of nonstructural components**

The above are qualitatively classified and described on the performance of the target, But for the actual project, the quantitative indicators and more aspects of designer use. From what we know of the connection form of nonstructural components and structural, Structural deformation where the nonstructural components location is the main cause of its destruction. Therefore, Using the inter story displacement angle as the damage index of non structural components is appropriate[6]. The literature suggests that when the interlayer lateral displacement angle reaches l / l000, non-structural elements likely to suffer damage, which have a certain reference value for us to Determinate elastic inter story displacement angle as the performance criterion of non structural components[7].

**Summary**

Nonstructural components is an important part of the building structure, its seismic performance has important effect on the seismic performance of building structure .in practical engineering, must attach great importance to them. In this paper, the performance levels and performance levels of non-structural components were studied, analyzed results are as follows:

According to non-structural components of damage cases presented its classification criteria.

Seismic performance levels suitable for non-structural components are proposed: full operation, basic operation, dysfunction, loss of function.

Suggested that using inter story displacement angle as a quantitative indicator of nonstructural components to do performance-based seismic design.

**References**

[1] K.Pao,Performance-Based Seismic Design Of Buildings Considering Architectural Elements (2002)

[2] Construction General Clauses of Performance Seismic Design(The trial), China Planning Press, (2004). In Chinese.

[3] Wang YaYong . China seismic design patterns in 2000, Building structure(1999). In Chinese.

[4] Zhou Yun,An Yu ,Liang XingWen.Study on The Theory and Methods of Performance - Based Seismic Design, World Earthquake Engineering,(2001), In Chinese.

[5] Yamanouchi Hetal. Performance-Based Design for Structural Design of Buildings.Building Research Institute,Japan,(2000)

[6] Guo ZiXiong.The Study of Elastic Enter Story Displacement Angle Limit in Building Seismic Deformation Analysis, Earthquake Engineering, No.2,(1998), In Chinese

[7] ScholI R E. Brace Dampers：An AIternative Structural System for Improving Earthquake Performance of Buildings［C］. Proc. Of the 8thWCEE，San Francisco VoI.5(1984)

*Applied Mechanics and Materials Vols. 580-583 (2014) pp 1613-1617*
*© (2014) Trans Tech Publications, Switzerland*
*doi:10.4028/www.scientific.net/AMM.580-583.1613*

# Research on Seismic Damage of Buildings in the Beichuan Earthquake

Fan Wang[1, a *], Chen Ning[2, b]

[1]State Key Laboratory of Subtropical Building Science, South China University of Technology, Guangzhou 510640, China

[2]Architectural Design and Research Institute, South China University of Technology, Guangzhou 510640, China

[a]33204981@qq.com, [b]1259769156@qq.com

**Keywords:** Seismic damage investigation; RC frame building; Pushover analysis; Seismic design

**Abstract.** This paper mainly discusses seismic damage of RC frame buildings in Beichuan county based on the investigation on the spot. The building damage forms are classified and component failures are analyzed. Applying finite element analysis software, the performance of RC frame buildings under severe earthquake is simulated and the components plastic hinge development is researched. The analysis results are made a comparison with real damage of buildings in this paper and some suggestions are proposed to seismic design.

## Introduction

On may 12, 2008, an 8.0 earthquake happened in Sichuan province. A mass of buildings damaged or destroyed during the earthquake. Beichuan county is one of major disaster areas, which located in northwest of Sichuan province, at approximately 104°E and 32°N. Its position is extremely close to the earthquake epicenter. According to The Chinese seismic intensity scale [1], the earthquake intensity of Beichuan county can be classified to 10 level or even higher. Under such big earthquake, the buildings tend to have elastic-plastic deformation. Through the analysis, the components failure and the development of hinges, this paper try to find the weak part of RC frame building and give some suggestions to reinforce it. Finite element analysis software PUSH of PKPM program is used to simulate buildings behavior in strong earthquake.

## Masonry Structures Seismic Damage Investigation

Masonry structure is commonly used in medium-and-small towns or countries. In Beichuan county, lots of apartment, schools, office buildings and shop stores are made of masonry. However, weak connection between mortar and blocks make masonry structures demonstrate brittleness. From the investigation results, masonry structure buildings damaged heavily in the earthquake. According to their failure characteristics, we classify damaged masonry buildings into 4 categories including collapsed buildings, overturned buildings, heavily damaged buildings with cut-through vertical fracture and partly damaged buildings with cross shear fracture in the wall.

The heavily damaged buildings failure mechanism can be attributed to supporting components failure for insufficient bearing capacity or oversized displacement. Usually, the weak storey of masonry structure is the first storey. Most buildings destroyed or overturned as a result of

supporting wall became invalid. The cut-through vertical fracture in some masonry buildings appeared mainly because these buildings didn't set ring-beams or tie-columns. This kind of structures usually have low integrity.

**RC Frame buildings Seismic Damage Investigation**

RC frame structure is also a common structure form in Beichuan county, which is applied in business-living building, office building, government building and factory. Contrasting to masonry structure, RC frame structure performs superior in major disaster area. Through the study on damaged RC frame buildings, we can find that heavily damaged frame buildings usually developed hinges at component ends in the 1st storey or the 2nd storey. Other damage forms contain enclosure structure failure and filler wall fracture. Few frame structures completely collapsed, basically achieving national standard "non-collapse during severe earthquake" requirement. However, it's far from satisfaction that most plastic hinges appeared at column ends prior to beam ends. It's obvious that the design of most frame structures hasn't accorded with strong column-weak beam requirement.

**Analysis of RC Frame Structure Seismic Performance**

Lately, static elastic-plasticity analysis (pushover analysis) is widely applied to evaluate seismic performances of structure. Based on it, the capacity spectrum method is used to get the structure performance point, which is the intersection point of structure acceleration-displacement response spectrum and structure demand spectrum. The point reflects the structure maximal displacement and maximal acceleration under certain seismic effect.

**Seismic Performance of Low-rise and Mid-rise Frame Structures**

In order to analyze structure seismic performance under severe earthquake, six frame structure building models are established applying EDPA&PUSH software of PKPM program. These models have the same typical floor and the number of storey for each model is from 2 to 7. Except for different storey number, the plan size and components of the typical storey are identical. One of 5-storey frame structure model abridged general view and its typical floor is showed in Fig.1.

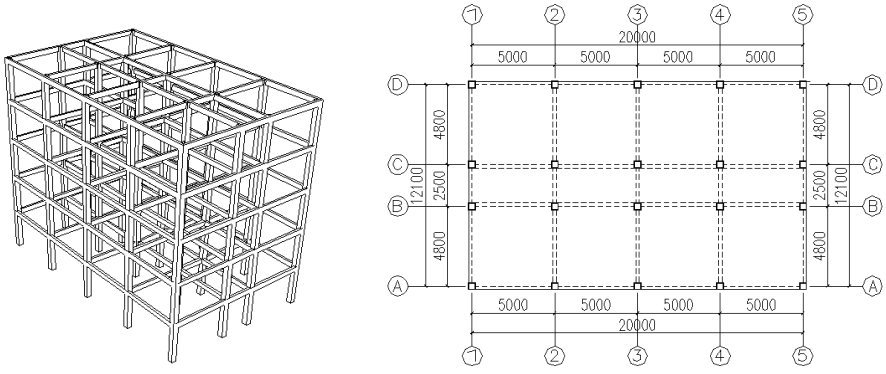


Fig.1 5-storey frame structure model and its typical floor (mm)

All models use 200mm×500mm RC beam and 300mm×300mm RC column. By pushover analysis on them, we obtain performance point of frame structures with various storey numbers under 8 level earthquake. In performance point status, structure model's base shear, peak displacement and maximal displacement angles are obtained (see Table 1).

Table 1 The seismic performance of frame structure under severe earthquake

| Model | Base shear (kN) | Peak displacement (mm) | maximal displacement angle | Storey of maximal displacement angle |
|---|---|---|---|---|
| 2-storey structure | 1996.2 | 41 | 1/156 | 2nd |
| 3-storey structure | 2019.3 | 62.6 | 1/127 | 2nd |
| 4-storey structure | 2043.1 | 88.1 | 1/113 | 2nd |
| 5-storey structure | 1980.8 | 118.6 | 1/101 | 2nd |
| 6-storey structure | 2256.5 | 155.1 | 1/93 | 2nd |
| 7-storey structure | 2530.6 | 214 | 1/77 | 2nd and 3rd |

It is showed from the table above that the 2nd storey has the maximal displacement angles for medium height frame structures at performance point. In the same earthquake, the amplification of base shear is not as remarkable as peak displacement while frame structure storey numbers increase. Maximal displacement angle appears steadily at the 2nd storey, almost unaffected by storey numbers. The 2nd storey should be paid more attention when designing a medium height frame structure.

**Research on Frame Structure hinge development**

Under gradually increasing lateral force, frame structure will come into elastic-plastic state. Hinges appear along with components continuous displacement. The first hinge positions of six frame structure models are showed in Fig.2. The solid line represent beam and column components, the black dot represent the first hinge positions under increasing lateral force.

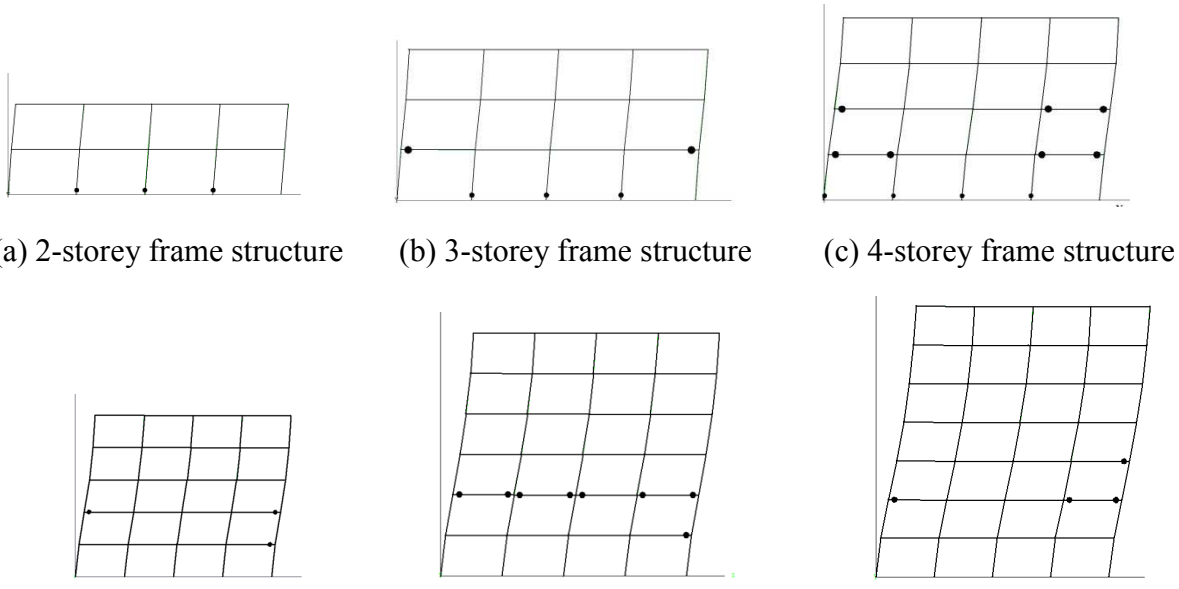

(a) 2-storey frame structure (b) 3-storey frame structure (c) 4-storey frame structure

(d) 5-storey frame structure (e) 6-storey frame structure (f) 7-storey frame structure

Fig.2 The first hinge positions under increasing lateral force

From pushover results of 2-storey frame structure to 7-storey frame structure, it is learned that low-rise buildings tend to develop hinges at column end firstly while mid-rise buildings tend to develop hinges at beam end. The 1st storey is usually the place where the hinges appear mostly for low-rise frame buildings. Unlike low-rise buildings, the first hinges appear mainly at beam end of 2nd or 3rd storey for mid-rise buildings. In addition, low-rise frame buildings present a bending failure under intensive seismic force, while for mid-rise buildings, a shear failure instead.

Through the analysis on place where hinges development firstly, we could find the weakest position of a frame building under severe earthquake. By strengthening these weak components, or adjusting components position, serious seismic damage may be relieved or avoided.

Except the results above, attention should be paid that many factors influence the development of hinges. On the one hand, fixed end of column is usually considered at foundation top, where surrounding soil will provide restraint to column footing because of buried depth from ground surface to foundation top. On the other hand, frame beams and concrete floor are concreted integrally, so the stiffness of beam is enhanced by floor board. Reinforced steel bars may enhance bearing capacity of beam end by 8% to 40%. Generally, the restraint from floor board is ignored when analysis and designing a frame structure, so many hinges developed at column end instead of beam end for column end lacking of lateral restraint. Also, the influence of filler wall in frame structure is not taken into account when we use a FEA software to analyze it. Under real seismic force, filler wall and floor board will restrict beam in two directions, which could improve bearing capacity of beams further. The damage situation in Beichuan county proved the analysis above.

## Conclusions

Based on building seismic damage investigation in Beichuan county and results of static elastic-plasticity analysis on multilayer RC frame structure buildings, some conclusions and suggestions are listed as follow.

(1) Masonry structure building has a low anti-seismic capacity. In area where earthquake happens frequently, this kind of structure should be carefully designed and constructed. Ring-beam and tie-column could improve integrity of masonry structure immensely.

(2) RC frame structure performs superior to masonry structure under seismic effect. Yet the strong beam weak column phenomenon is common based on investigation. The reinforced steel bar should improve relatively in column components when designing a frame structure.

(3) Maximal displacement angle of RC frame building usually appears steadily at the 2nd storey in performance point status. Under severe earthquake, the 1st storey or 2nd storey is usually the weakest position of RC frame structure. Constructed measures should be taken to enhance this part of structure.

**Acknowledgements**

This work was financially supported by the Open Foundation of the State Key Laboratory of Subtropical Building Science of South China University of Technology (2014KB29).

**References**

[1] GB/T 17742-2008: *The Chinese seismic intensity scale*. In Chinese.

*Applied Mechanics and Materials Vols. 580-583 (2014) pp 1618-1623*
*© (2014) Trans Tech Publications, Switzerland*
*doi:10.4028/www.scientific.net/AMM.580-583.1618*

# Seismic Analysis of 5-span High-speed Railway Continuous Girder Bridge

Jianhu Guo[1, a], Mingqi Lu[1, b]

School of Civil Engineering, Beijing Jiaotong University, Beijing, 100044, China

[a]598263599@qq.com, [b]593434137@qq.com

**Keywords:** High-speed Railway Continuous Girder Bridge; Vibration Mode; Seismic Effect; Performance Requirements.

**Abstract.** In recent years, with the development of high-speed rail in China，bridge has a higher proportion in the lines. Every year earthquake occurs many times accidentally in China. In order to ensure the target performance of bridges under earthquake action, we need to be based on the seismic analysis. Only have a deep knowledge of seismic effect discipline, can we enable to guide seismic design economically and reasonably and achieve predetermined target performance. Our study shows that the main vibration mode is a combination of the longitudinal or lateral translation or the revolution around Z axis. Under high-level earthquake, the maximal displacements of side piers and the fixed pier are larger, the maximal longitudinal pier shaft moment of the fixed pier (No.3) or No.5 pier in lateral direction is larger. But the value that exceeds the yield moment is small, which indicates that the development of plasticity is little. The longitudinal shear force of the bearings on the same pier are the same, bearings fixed longitudinally own the largest value. Even bearings whose lateral directions are fixed on the same pier own larger forces. Seen from average maximum values of bearings, all bearings are at the second stage, meeting the requirements that we don't need to repair or slightly repair the bridge to make it act normally once after an earthquake.

## Introduction

Earthquake is one of natural disasters which people have to be faced with. Earthquake disasters and their secondary disasters do enormous economic losses and casualties to human beings, and *seismic design of building structures is an active measure*. Nowadays, our country is devoted to building high-speed railways, the total mileage already built and under construction has reached tens of thousands of kilometers. Considering hydrology, geology, interchange, in order to ensure the line smooth, traveling comfortable and safe and reduce the occupancy of land, we choose bridges, which are taking a bigger percentage of the total length of railways being built. The proportion of bridges in the line has reached 70%-80% [1,2,3]. Therefore, study about the seismic effect discipline of high-speed railway bridges has the urgently realistic meaning. So we enable to guide the seismic design economically and reasonably and achieve the predetermined target performance. In this article, we take the 5-span high-speed railway continuous girder bridge in Tianjin-Qinhuangdao passenger dedicated line as an example, *the article analyses the discipline and characteristics of the bridge's seismic effect under high-level earthquake*.

## Establishment of the Finite Element Model

**Outlines of the Project and Layout Drawing.** The railway bridge is across Jingshan in Fengnan. The total length of beam body is 301.5 meters, the calculation spans of longitudinal girder from one side to another are, in order, 45 m, 70 m, 70 m, 70 m, 45 m. The following Fig. 1.1 shows the 5-span continuous girder bridge.

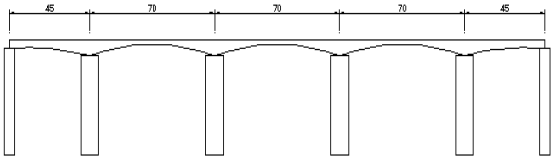


Fig. 1.1 5-span continuous girder bridge

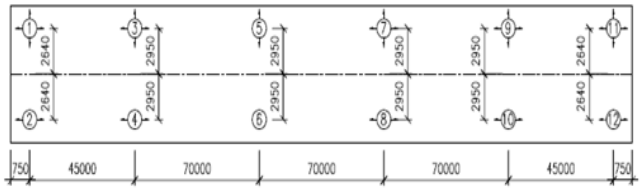


Fig. 1.2 The layout of the bearings

From left to right, the piers are, in order, No.1, No.2, No.3, No.4, No.5, No.6. The corresponding heights of piers are 12.75 m, 10 m, 10.5 m, 11 m, 13.5 m, 16.75 m. The No.3 pier is the fixed one, the site classification is the Second according to Code for seismic design of railway engineering.

Fig. 1.2 shows us the layout of all bearings. The No.5 bearing is laterally movable, the No.6 one is fixed in both directions, No.2, No.4, No.8, No.10, No.12 are longitudinally movable, No.1, No.3, No.7, No.9, No.11 are movable in both directions.

**Definition of Bearings.** While structure is under earthquake, different work stages are classified based on the damage of bearings [4,5]. Fig. 1.3 and Fig. 1.4 respectively give definitions of movable and fixed bearings.

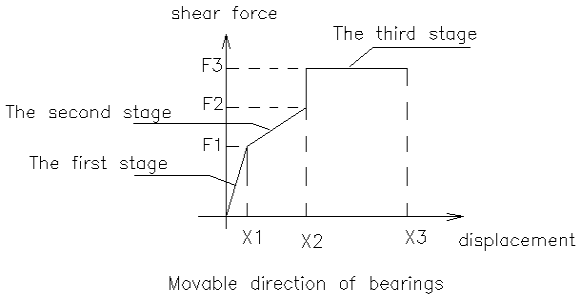


Fig. 1.3 The definition of movable bearings

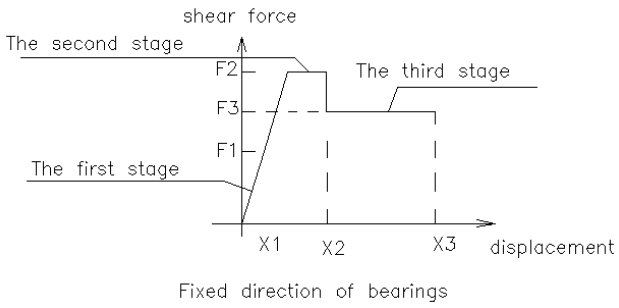


Fig. 1.4 The definition of fixed bearings

**Mode Analysis.** Through above works and analysis of engineering drawings, the finite element model of the whole bridge is created in SAP2000 [6,7,8,9,10,11]. In order to ensure accuracy, the model is further modified with considering the SSI effect [12]. By the calculation, spring stiffness is applied to each bottom of all piers. Carry out the analysis of mode and the 1st to 12th vibration modes and periods influence the structure greatly .The main vibration modes are shown in Fig.1.5.

Mode2，T=0.594s Mode4，T=0.452s Mode5，T=0.401s Mode6，T=0.380s

Fig. 1.5 Main modes and periods of the bridge

Seismic survey tells us the earthquake damage of bridges occurs in longitudinal or lateral direction, especially in longitudinal direction. The damage of bearing anchoring is mainly caused by clipping not by tugging, which indicates earthquakes' horizontal components play a role in vibration control. Consequently, we only consider the horizontal components in the seismic design [11].

The article calculates fifty modes, we conclude that the main vibration mode is a combination of the longitudinal or lateral translation or the revolution around Z axis. That is the second mode-the fixed pier bends longitudinally and the beam body drifts longitudinally, the fourth and sixth mode-the beam body vibrates antisymmetrically in lateral direction, the fifth mode- the beam body vibrates symmetrically in lateral direction.

### Analysis of Seismic Effect under High-level Earthquake

**Seismic Record Events.** Select 8 (ACHL, 1058, ASUL, FOR, L4B, LRIV, MEL and RIV) seismic record events from the Pacific Earthquake Engineering Research Center (PEER) database. The PGA of high-level earthquake is 0.38g .Through calculation, we adjust the amplitude modulation.

**Average Maximal Displacement of Pier Shaft and Beam Displacement (mm).** The following Fig. 1.6 and Fig. 1.7 respectively show the trends on average maximal displacements of pier shaft and maximal displacements of the beam in longitudinal and lateral directions.

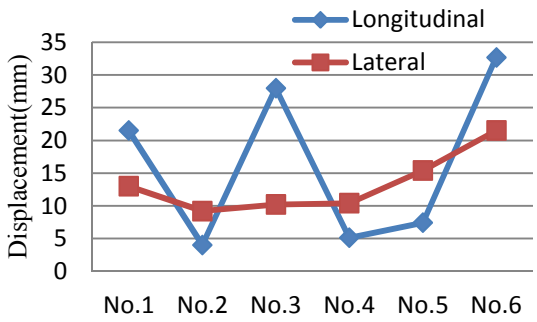


Fig. 1.6 The average maximal displacement of pier shaft

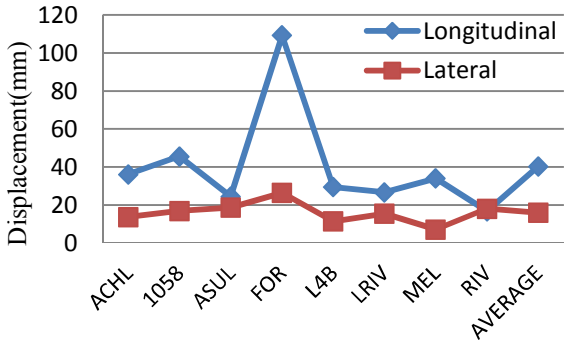


Fig. 1.7 The maximal displacement of the beam

From Fig. 1.6, it can be observed that the average maximal displacements of pier shaft in both directions have the same trends that decrease firstly and then increase from the fixed pier to side piers. In longitudinal direction the displacements of No.1, No.3 and No.6 piers are larger. The value of No.6 pier is the largest, which is relevant to the characteristics of side piers that their heights are taller and sections are smaller. The value of No.2 pier is smaller, which is 9.8% smaller laterally and 85.7% smaller in longitudinal direction than the No.3 pier. The value of No.1 pier, No.3 pier and No.6 pier are separately 39.5%, 63.6% and 34.3% longitudinally larger than that in lateral direction.

On the whole, the average maximal displacements of intermediate piers adjacent to the fixed one are smaller, whereas, the fixed and side piers have larger response. Therefore, we should not only pay attention to fixed piers but also the tall and slender side piers.

It can be seen from Fig. 1.7, the maximal displacement of the beam appears to be the largest when under FOR. Contrast with FOR, values of other 7 events seem to be small and approximate. This is closely related with its own characteristics of the event. Characteristics of the seismic waves are mainly affected by the amplitude, spectrum and duration time. While the spectrum is affected by the hypocenter, route of transmission and site condition, the article uses the Second site classification, and the PGA is 0.38g when imported in the software. Although these two parameters are consistent, there are lots of differences in respective characteristics among different events. The lateral value is 7.8% smaller than that in longitudinal direction except RIV. The longitudinal maximal displacement is 40.3 mm and 15.9 mm laterally, which will certainly influence the location of seismic side retainer, the size of expansion joint and requirements for bearings' deformation, with the implication that seismic designers must consider all the factors above.

**Average Maximal Moments of Pier Shaft (kN·m)**. In order to contrast clearly, Table 1.1 lists the piers' yield moments. Fig. 1.8 shows the maximal moments of pier shaft attached to each record event.

Table 1.1 The yield moments of pier shaft

| Piers No. | No.1 | No.2 | No.3 | No.4 | No.5 | No.6 |
|---|---|---|---|---|---|---|
| Longitudinal Yield Moment | 95030 | 394000 | 398400 | 405800 | 407400 | 95030 |
| Lateral Yield Moment | 195700 | 754300 | 769900 | 912200 | 911100 | 195700 |

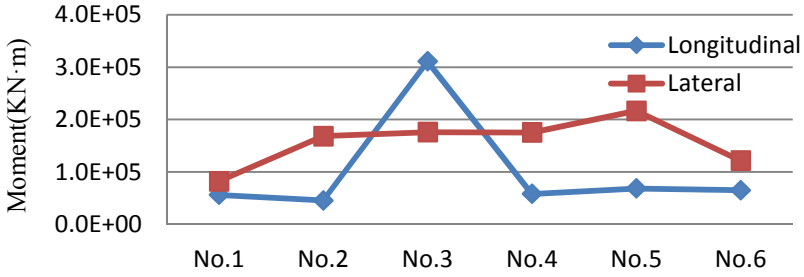


Fig. 1.8 The average maximal moments of pier shaft

From Fig. 1.8 we can see that the No.3 pier has the largest moment longitudinally which implies the bottom section of the fixed pier is the most dangerous. But the average value does not reach the yield point, which is 22% smaller than the yield moment. Other piers' values are closed to each other, the value of the No.2 pier is a little smaller and the No.5 a little larger. The value of No.6 pier is closed to its yield moment, it is 31.6% smaller. Looking laterally, the piers' average values appear to increase firstly and then decrease. The value of No.5 pier reaches the largest, the No.1 is the smallest and then the No.6. All values are smaller than the yield moments and the NO.6 pier is the most closed to the yield value.

From the above analysis of average values, we know *the bridge is in elastic phase under high-level earthquake*. The whole structure does not need to be repaired or to be slightly repaired.

**Maximal Longitudinal and Lateral Forces of Bearings (kN).** Fig. 1.9 shows us the maximal longitudinal forces of bearings under high-level earthquake. And Fig. 2.0 gives us forces in lateral direction.

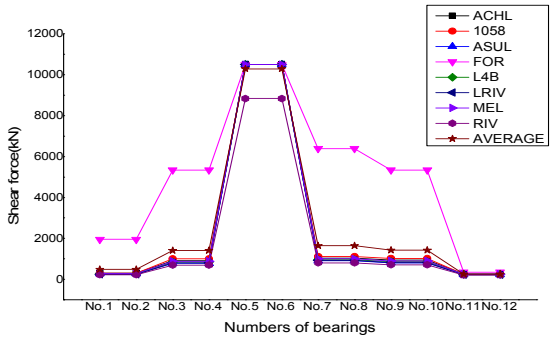


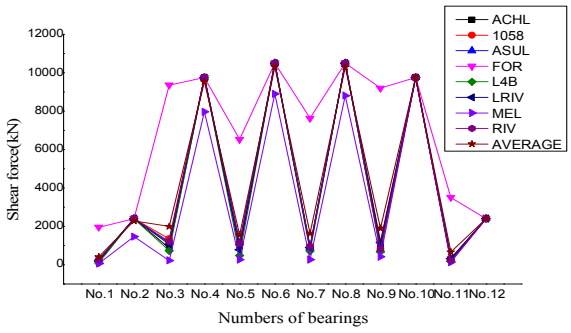


Fig. 1.9 Maximal longitudinal forces of bearings Fig. 2.0 Maximal lateral forces of the bearings

In Fig. 1.9, for longitudinal direction, the No.5 and No.6 bearings are fixed. When the beam body is drifting, the displacement is mainly caused by the No.3 pier's bending longitudinally. Besides, forces of No.5 and No.6 bearings are the largest, which are 6 to 49 times larger than others. Movable bearings transfer less shear force during strong earthquake events. Seismic energy mainly transfers from the substructure to the superstructure through the fixed bearing. The inertial force produced by the superstructure transfers to substructure by the fixed bearing as well [11].Therefore,

the longitudinal fixed bearing is the most easily being damaged. Once damaged, the beam body will easily move abnormally and begins to collide with the abutments, which we should focus on while designing. The two bearings on the same pier suffer the same forces in longitudinal direction. What is more, in this direction their shear forces and displacements curve are also the same, which indicates that the stress states of bearings are consistent and simultaneous. That is closely related to the setting conditions of bearings. The bending of fixed pier vibration mode provides the condition.

From Fig. 2.0, for lateral direction, values of bearings on side piers are smaller. Even number bearings own larger forces on the same pier and they are about 3.7 to 6.7 times than corresponding odd number bearings. Shear forces of odd number bearings are 2.4 to 4.7 times larger than bearings on side spans. It is related to the setting of even number bearings, for they are fixed laterally. No.6 and No.8 bearings are more easily being damaged, No.4 and No.10 bearings take the second place. So bearings of intermediate spans should be taken more care while designing.

**Maximal Longitudinal and Lateral Displacements of Bearings (mm).** Seen from Fig. 2.1, the

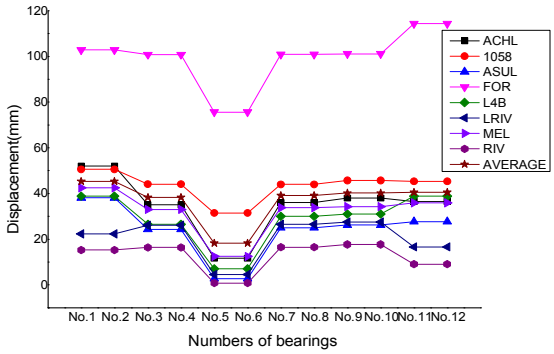


Fig. 2.1 The maximal longitudinal displacements of bearings

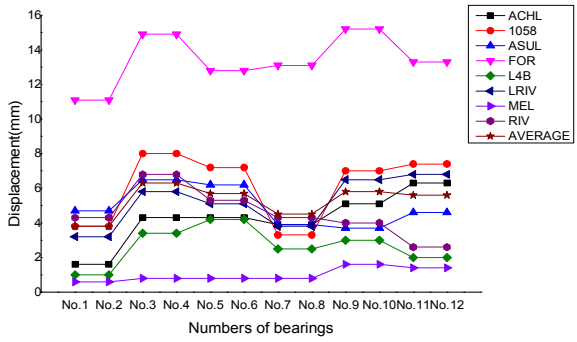


Fig. 2.2 The maximal lateral displacements of bearings

longitudinal view, No.5 and No.6 bearings own smaller displacements but larger shear forces so that the bearing bolts' stress will balloon and more easily be clipped. Besides, while under FOR event, all bearings go into the *third* stage except No.11 and No.12 bearings. This phenomenon indicates bearings are likely to be destroyed. Similarly, Fig. 2.2 considers response in lateral direction. Even number bearings' shear forces are larger because odd number bearings are movable and even number bearings are fixed laterally. While no matter in longitudinal or lateral direction, their displacements are the same. It is reasonable because each of the bearings is anchored in the pier top and the bottom of the beam whose stiffness are high enough. From *average views*, all bearings are at the *second* stage, meeting the performance requirements that bearings needn't to be repaired or slightly repaired after earthquake.

## Conclusions

Through our study, we draw some conclusions above, in short:

1. The main vibration mode is a combination of the longitudinal or lateral translation or the revolution around Z axis.

2. The average maximal displacements of the fixed and side piers have larger response. We should not only pay attention to fixed piers but also the tall and slender side piers.

3. The longitudinal maximal displacement is 40.3 mm and 15.9 mm laterally, which will certainly influence the location of seismic side retainer, the size of expansion joint and requirements for bearings' deformation, so seismic designers must consider all the factors.

4. As shown by the results of maximal moments of pier shaft, the bridge is in *elastic* phase under high-level earthquake. The whole structure does not need to be repaired or to be slightly repaired.

5. The longitudinal fixed bearing is the most easily being damaged. Once damaged, the beam body will easily move abnormally and begins to collide with abutments. The stress states of bearings on the same pier are consistent and simultaneous. Bearings' Shear forces in lateral direction on side piers are smaller. Even number bearings own larger forces on the same pier.

6. Through values of average displacements of bearings， we know bearings are all at the second stage, which indicates the bridge does not need to be repaired or to be slightly repaired. So *it exactly meets the performance requirements for important bridges.*

**Acknowledgements**

This research is supported by Research and Development of Science and Technology Plan Project of China Railway Engineering Corporation (2013G002-A-3), and the Fundamental Research Funds for the Central Universities (No. 2012JBM077).

**References**

[1] Baiyu Shan: *Seismic analysis of continuous girder bridge of Passenger Railway* (Southwest Jiaotong University 2009). (In Chinese)

[2] Jiakui Gong: submitted to Journal of West-china Exploration Engineering (2005).

[3] Kazuhiko KAWASHIMA and Shigeki UNJOH: submitted to Journal of Japan Association for Earthquake Engineering (2004).

[4] Huang Yong: submitted to China Civil Engineering Journal (2010).

[5] Sang-Hyo Kim: submitted to Journal of Engineering Structure (2006).

[6] Priestley M J N, Park R: submitted to ACI Structural Journal (1987).

[7] Paulay, T., Priestley, M J N: *Seismic Design of Reinforced Concrete and Masonry Buildings*, New York (1992), in press.

[8] YongDuo Liang, Zhiguo Sun, Dongsheng Wang: submitted to Concrete (2011).

[9] Lichun Fan: *Seismic ductile design of bridges* (The People's Communication Publishing Company, China 2001). (In Chinese)

[10] JTG/TB02-01-2008, *Guidelines for Seismic Design of Highway Bridges*, edtied by Ministry of Transport of the People's Republic of China (2008).

[11] GB5011-2006(2009), *Code for seismic design of railway engineering*, edtied by China Railway Ministry, M. E. Sharpe (2009).

[12] TB 10002.5-2005/J464-2005, *Code for design on subsoil and foundation of railway bridge and culvert* (China Railway Press, Beijing 2005).

*Applied Mechanics and Materials Vols. 580-583 (2014) pp 1624-1628*
*© (2014) Trans Tech Publications, Switzerland*
*doi:10.4028/www.scientific.net/AMM.580-583.1624*

# Seismic Performance Analysis of Steel Frame With Wedge Devices Based on the Energy Dissipation

Jinsong Lei[1,a], Wenxia Luo[2,b], Jialong Jiang[1,c] , Wen Zhang[1,d]

[1]College of Civil Engineering and Architecture, Southwest University of Science and Technology, Mianyang, Sichuan, 621010, China

[2]China Coal Technology and Engineering Group Chongqing Design and Research Institute, Yuzhong District, Chongqing ,621010, China

[a]173266820@qq.com, [b]420227158@qq.com, [b]584693592@qq.com, [d]447267477@qq.com

**Keywords:** Wedge Devices, Steel Frame, Low Cyclic Load, Energy Dissipation, Time History Analysis

**Abstract.** The steel frame with wedge devices is a kind of shock structure based on the node energy consumption. The seismic performances of steel frame with wedge and ordinary steel frame model under low cycle reciprocating load simulation analysis and time history analysis under earthquake loads are analyzed by using finite element software, compared the respective energy dissipation performance and seismic performance, the results show that the wedge spring damping device can effectively control story drifts of structure, reduce the seismic response of structure, and well consume the seismic energy, so the structure of the new column bases with wedge spring devices show better seismic performance.

## Introduction

Due to the steel has excellent toughness and ductility, making steel structure has the power and repeat resistance changes in the role of the good ability, so the steel structure building is generally thought to have a better seismic performance. With the severity of the damage from the earthquake, the shock energy research of steel frame has become more important, steel frame structure damping system to reduce seismic by energy consumption, according to the energy dissipation mechanism can be divided into the shock absorption system and the energy consumption damping system two stages of development.

External energy dissipation system is set up some extra energy dissipation devices in the steel, mainly seismic energy consumption by energy dissipation devices to achieve damping purposes. Some of the commonly used engineering measures is :(1)In the Beam-column joints set energy dissipation device to form energy dissipation nodal points, when the sides way of a structure produce angle changes, energy dissipation device participate in energy dissipation. By spring and wedge to screw up of a new type steel column base, the device through the sliding of the wedge, spring deformation and plastic elongation of the screw to control column base displacement, at the same time consume earthquake energy, to achieve the effect of dissipater of shock, this is a new technology researched by Japan. (2)Between the steel connection setting various Energy-dissipated brace, including ordinary center support, prevent buckling support, with the support of the damper etc. [1, 2]. Setting Energy-dissipated brace can form multiple resist lateral force system, under the effects of earthquake, support for all before destroying almost horizontal load happen axial deformation, and the frame that did not effected by horizontal load almost happened only bending deformation; After damage in support stiffness rapidly reduces the earthquake action reduced sharply, at this time the framework for horizontal load. So the support frame system support have the function of the fuse, make structure subject do not damage, and have good seismic performance. In this paper the new steel frame of the energy dissipation were analyzed with the method of finite element simulation, and the low weeks reciprocating load of the simulation analysis to the single wedge with steel frame have been down, and the deformation characteristics, the hysteretic curve and skeleton curve are analysed, through the comparative analysis of maximum displacement, relative storey displacement, inter-story

drift of five-story with a wedge of steel frame which are under the earthquake effect and figure out the displacement and accelerated speed of time history analysis curve.

## Wedge of Steel Frame Energy Dissipation Principle

Japan Kobe earthquake in 1995, a large number of steel structure column base have suffered serious damage, according to the damage characteristics, a new shock absorber that consist of bolt, spring and wedge block [3], make the column foot basis than the ordinary type column foot smaller layer between the corner, but the ability to absorb seismic energy is not reduced, the principle is shown in Fig. 1. Ordinary column foot slip caused by the bolt of plastic elongation, shown in Fig. 2. And wedge column foot can improve this slip-column foot by spring to push the wedge cut into the gap, every time the loading and unloading are for always origin, showing the no-slip-type hysteretic characteristics, shown in Fig. 3. The device through the wedge block sliding, spring deformation and screw plastic elongation to consume earthquake energy, achieved the effect of damping energy dissipation.

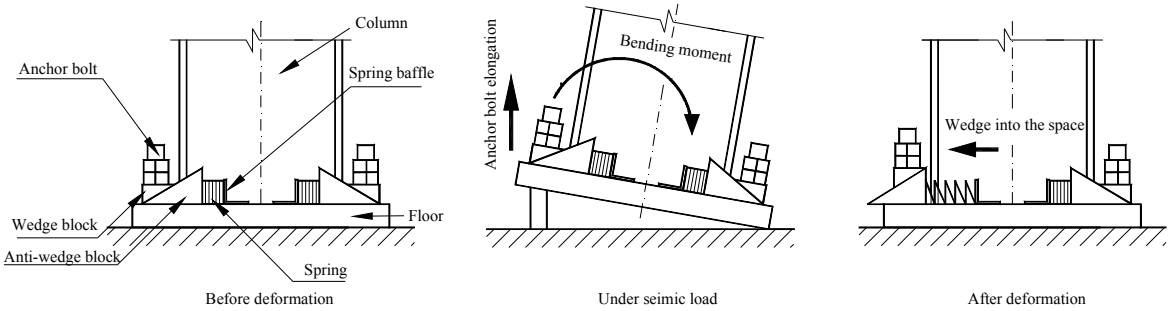


**Fig. 1** Wedge device principle diagram

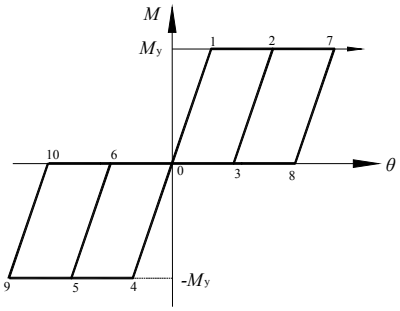


The route of hysteresis:
0⇒1⇒2⇒3⇒0⇒4⇒5⇒6⇒0⇒
7⇒8⇒9⇒10⇒0⇒11⇒12⇒13⇒
14⇒0⇒10⇒9⇒…

**Fig. 2** Ordinary exposed-column steel base

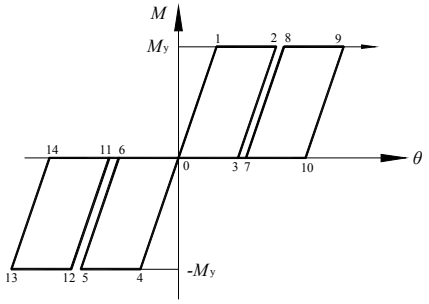


The route of hysteresis:
0⇒1⇒2⇒3⇒0⇒4⇒5⇒6⇒
0⇒1⇒7⇒8⇒0⇒4⇒9⇒10⇒
0⇒1⇒…

**Fig. 3** The exposed-column base with wedge devices

## Finite Element Analysis of Single Layer Non-slip Steel Frame

**Loading method.** Low cyclic loading test simulation analysis method is essentially a static nonlinear analysis. Compared with the static elastic-plastic analysis, the difference is that the horizontal loads is reciprocating direction, and each cycle load of amplitude is changing, each cycle by multiple load of steps, getting the bearing capacity of the structure component, stiffness, deformation capacity, the hysteretic curve, energy dissipation capacity and structure of failure mechanism, they apply to structure seismic performance analysis, especially the analysis of the structure of shock energy consumption [4].In this paper the simulation analysis for convenience, all adopt the displacement as loading control index, loading system shown in Fig. 4.

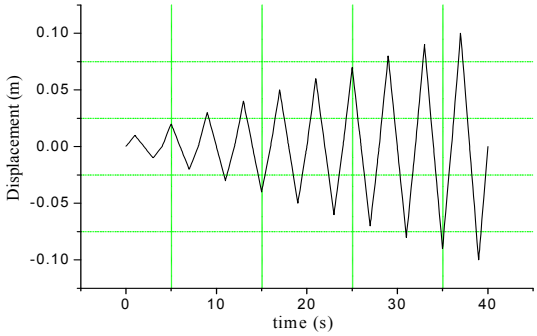


**Fig. 4** Load displacement graph

**Finite element analysis model.** This paper using the finite element software ANSYS to single wedge with steel frame, ordinary steel frame low cyclic reciprocating load of the simulation analysis,4 meters high, span of 6m,each frame beam-column is the same size, member section dimensions are shown in Table 1.

**Table 1** Member section dimensions

| Component type | Height (mm) | Width (mm) | Webs thickness (mm) | Flange thickness （mm） |
|---|---|---|---|---|
| Frame beams | 400 | 200 | 8 | 13 |
| Frame column | 400 | 400 | 13 | 21 |

**Load-displacement curve**. To compare the hysteresis characteristics of the steel frame with wedge and ordinary steel frame, when doing the experiment of low cyclic loading simulation analysis, horizontal displacement load imposed in the framework of vertex, and take the load point location of the load-displacement curves are analyzed, Fig. 5 and Fig. 6 are the two kinds of steel framework of the load-displacement curves.

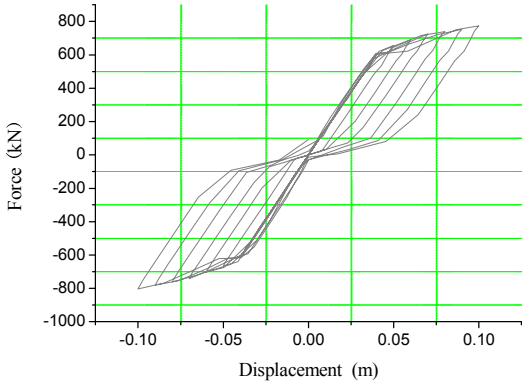


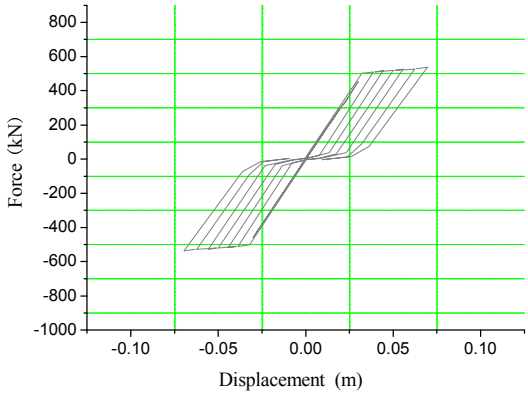


**Fig. 5** Wedge with steel frame load-displacement curve **Fig. 6** Ordinary steel frame load-displacement curve

The comparative analysis of load - displacement curve shows good ductility with a wedge of steel framework, stiffness than ordinary steel frame and carrying capacity is better also, due to cyclic loading, when the bolt was pulling up, there will be a space between the bolt and backplane, rebound after the spring compression, wedge immediately cut the gap generated by the plastic elongation of the bolt, so every time the loading and unloading are for always uninstall origin, present non-slip type characteristics, the hysteretic curve area of each significantly increased, better energy dissipation capacity and ordinary steel frame ductility is poorer, carrying capacity is also significantly smaller, since the loads, the gap made by bolts of plastic elongation is not restored, further increase of plastic deformation based on the original when re-loaded, therefore, each loading and unloading is not always origin and show the characteristics of Sliding, the hysteretic curve area is significantly reduced and then the consumption ability is bad. This shows that wedge with steel frame has better performance of energy consumption than the ordinary steel frame.

**Time History Analysis of Multi-layer Wedge Steel Frames Under Seismic Action**

**Model Design.** Two kinds of steel framework for 5 layers, storey height is 4m, total height 20m, horizontal three cross 6×3×6m, based on the plane of the truss model theory, take the transverse specimens of a framework for the establishment of the finite element model, section size, the material properties and analysis unit have the same simulation analysis with single-layer low-cycle reciprocating load. Because the plane model, boundary conditions are: The upper structure plane all constraint, only allowed to happen turn the motion in the plane. beam-column connections is rigid joints entity. Support and framework of the connection as hinges, two kinds of model and basic connections are embedded solid.

**Time History Analysis Under Earthquake.** According to 8 degrees fortification intensity, occurred earthquake, input EI Centro North-south seismic records [5], according to the <Code for seismic design of buildings> the am earthquake acceleration, adjusting the maximum acceleration of peak 4m/s$^2$, time interval 0.02s, take the first 20 s to the analog input seismic waves and take 0.05 to the damping ratio of the entire structure of the elastic-plastic analysis in the rare earthquake, comparative analysis of the results in Table 3-4, time history analysis and the acceleration time history analysis shown in Fig. 7 and Fig. 8.

**Table 3** Seismic response of the El Centro(NS)-wave under the action of ordinary steel framework

| Layer number | maximal displacement (cm) | relative storey displacement (cm) | Inter-story drift （rad） | acceleration (cm/s$^2$) |
|---|---|---|---|---|
| 1 | 1.1329 | 1.1329 | 1/353 | 218.935 |
| 2 | 2.6561 | 1.5232 | 1.5232 | 373.003 |
| 3 | 4.1808 | 1.5247 | 1/262 | 507.286 |
| 4 | 5.4034 | 1.2226 | 1/327 | 634.372 |
| 5 | 6.6389 | 1.2355 | 1/323 | 758.294 |

**Table 4** Seismic response of the El Centro(NS)-wave with a wedge of steel framework

| Layer number | maximal displacement (cm) | relative storey displacement (cm) | Inter-story drift （rad） | acceleration (cm/s$^2$) |
|---|---|---|---|---|
| 1 | 0.6237 | 0.6237 | 1/641 | 278.546 |
| 2 | 1.4679 | 0.8442 | 1/474 | 309.752 |
| 3 | 2.3647 | 0.8968 | 1/446 | 341.892 |
| 4 | 3.0626 | 0.6979 | 1/573 | 375.289 |
| 5 | 3.7411 | 0.6785 | 1/589 | 409.506 |

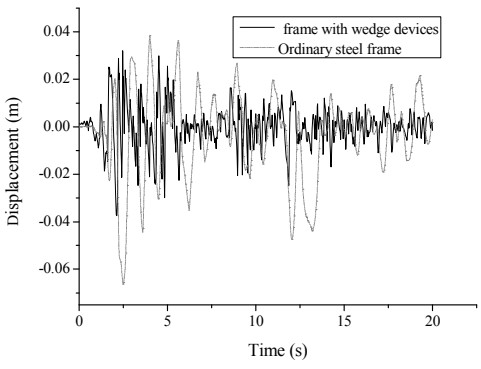


**Fig. 7** Top floor displacement-time curve

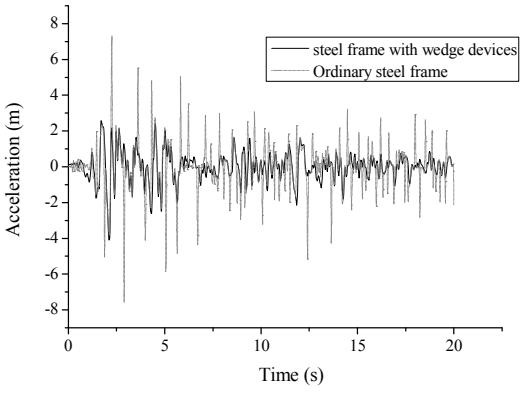


**Fig. 8** Top floor acceleration-time curve

From the comparison and analysis of the Table 3-4 and Fig. 7-8, the regularities are found: (1) As the floors increase, the maximum displacement of both the two steel frames are increase under rare occurrence earthquake. Compared with the ordinary steel frame, a wedge steel frame has a better performance on the maximum displacement, it shows the displacement reaction reduce about 44%; (2) The interlayer displacement of a wedge framework has been under control; (3) After analyze the Inter-story drift of models, we can get that the wedge with steel frame inter-story drift is smaller than

the ordinary steel frame because of the seismic control effects. According to the code for seismic design of buildings, the limit of elastic displacement angle between the layers is 1/300 of High-rise steel structure and the limit of elastic displacement angle between the layers is 1/50 of High-rise steel structure. But the limit of elastic displacement angle between the layers is 1/80 of energy dissipation device, ordinary frame cannot meet this requirement and the other two models can do; (4) The accelerated speed of the three steel frame reach the maximum. In the top storey, and the acceleration response reduce about 46% of the wedge block structure [6].

## Conclusions

Both the Simulation Analysis under low cycle reciprocating load effect and the time history analysis under the earthquake of wedge with steel frame and ordinary steel frame show that:
(1) The hysteric curve characteristics of ordinary steel frame is sliding, while the hysteric curve characteristics of wedge with steel frame is Non-slip type due to the spring-return and wedge block cut which made its uploading and downloading in the original point from the beginning to the ending.
(2) The energy dissipation of wedge with steel frame is excellent owe to the full hysteric curve. Comparing with ordinary steel frame, all the bearing capacity, stiffness, ductility deformability and energy consuming are better.
(3) The wedge device can strengthen the capacity to resisted earthquake of nodal point of wedge with steel frame, made it always under control and have an excellent anti-seismic performance under the rare earthquakes, but the higher deformation displacement and acceleration of ordinary steel frame made it can not meet the specification.
(4) Low cost, constriction convenient, and good anti-seismic performance all are the merits of wedge device. Therefore, it is a really good seismic node which should be researched deeply and used widespread.

## References

[1] Fulin Zhou: Vibration Control of Engineering Structure (Seismological Press, China 1997).

[2] Code for Seismic Design of Buildings (China Building Industry Press, China 2001).

[3] Takao Takamatsu: J. Non-slip-type Restoring Force Characteristics of an Exposed-type Column Base. Journal of Constructional Steel Research. Vol.61 (2005), p. 942-961

[4] QiaoLing Xian and Fulin Zhou: J. The Low Levels of Energy Dissipation Braced Frame Structure Weeks Reciprocating Load Test Simulation Analysis Method. Earthquake Engineering and Engineering Vibration,(2002) 22 (3). In Chinese.

[5] Xiangzhen Li, Hailong Ou and Guoliang Cheng: J. The Friction Energy Dissipation Support Steel Frame Structure of the Elastic-plastic Seismic Response Time History Analysis. Earthquake Engineering and Engineering Vibration, (2002) 22 (3).

[6] Hiroyuki Tamai and Takao Takamatsu: J. Cyclic Loading Tests on a Non-compression Brace Considering Performance-based Seismic Design. Journal of Constructional Steel Research. Vol.61 (2005), p. 1301-1317.

*Applied Mechanics and Materials Vols. 580-583 (2014) pp 1629-1632*
*© (2014) Trans Tech Publications, Switzerland*
*doi:10.4028/www.scientific.net/AMM.580-583.1629*

# Seismic performance analysis on single-storey masonryhousewith sliding damping technology

Kang Yuan[1, 2, a],Yingmin LI[1, b]and Bo Kuang[1, c]

[1]College of civil Engineering, Chongqing University, Chongqing 400045, China

[2]College of hydraulic and civil engineering, Shihezi University, Shihezi, Xinjiang 832003, China

[a]williamyuan1982@163.com, [b]liyingmin@cqu.edu.cn,[c]447341421@qq.com

**Keywords:** Masonry structure, Sliding damping, Rubber beam, Hysteretic curve, Seismic performance

**Abstract:** This paper presents a technology of sliding damping which could resist ground frost heaving. In the technology, setting the low-grade mortar bond of the upper and lower ring beams to achieve slip shock absorption, and setting the rubber beams to achieve shear deformation limiting. By rubber beam shear performance test,the shear strengthof the rubber beam has been acquired.In the paper, the finite element software has been adopted to simulate the seismic performances of common wall and sliding damping wall structures under low cyclic reversed loading, the hysteretic curves between the bottom shear and the top displacement of the walls. The researchresults show that sliding damping ring beam has the very good function on dissipatingseismic energy and reducing seismic action.

## Introduction

In recent years, with the aseismic attention'simprovement of rural building, some scholars began to research easy isolation and damping technology for village and town construction, such as Professor WanlinCao[1], [2]of Beijing University of Technologyhas developed a base isolation structure with double control device,the devicewas consist with upper and lower beam, graphite plate-glass cloth-graphite sliding isolation layer, and the limit steel bar.Professor ShoupingShang [3], [4] of Hunan University has developed a reinforced-asphalt compound isolation layer between foundation and ground ring beam, and Professor YingminLi [5]of Chongqing University has developed two simple seismicenergy dissipation technologies of arranging-rubberbeam inwalls and laying asphalt-sand cushion on foundation beam.

Based on the successful experiences of the related technology, in view of the high earthquake intensity and ground frost heave are the most important hazards for low-rise buildingin Xinjiang,a kind of sliding damping technology withbuilt-in rubber beam of ring beam has been put forward in this paper,which is not only achieve the effect of shock absorption, but also can eliminate ground frost heaving damage through the base ring beam. Its layout program is: Settings built-in rubber damping ring beam at the outdoor ground level, which consists of two layers are bonded as a whole by a mortar layer, as shown in Figure.1. The damping system working principle is: under the effect of small earthquakes, the low-grade mortar doesn't craze, the aseismic structure relies on its own aseismic capability to realize the fortification goal of "No damage with smallearthquake"; under medium and strong earthquakes, the ring beam divides into two parts, the main structure can slideintegrally with the upper ring beam, the rubber beam can limitshear deformation, the injuries of the upper structure mitigate effectivelyto achieve thefortification goal of'mendable in Moderate Earthquakes and no collapsing with strong earthquake". Through the base ring beam Settings, the danger of ground frost heaving force to the structure's integrity could be eliminated.

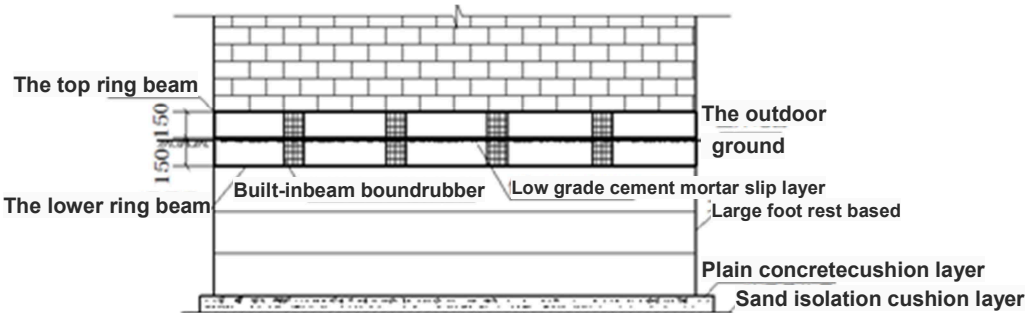


Fig.1Arrangement ofsliding damping system

Based on the study of the shear performance of the individual rubber beam and presupposing reasonableslippageof upper structure, theseismic performances of common wall pieces and slip damping wall pieces were analyzedby ABAQUS software, working principles of suspension system were verified, which could lay a foundation for subsequent experimental study.

## Experimental study on shear behavior of rubber beam

Rubber beam as an important damping element, its damping effect is mainly done through its shear deformation under horizontal earthquake action. Therefore, the shear properties of rubber beams were tested in this paper, the size of the upper and lower ring beam is $150\times240$, the thick of mortar in the middle layer is restricted at 10mm, rubber beam size is set as $310\times150\times80$, shear properties of two conditions withthree wire hoop and five wire hoop were studied, the results show as Fig. 2 (b).

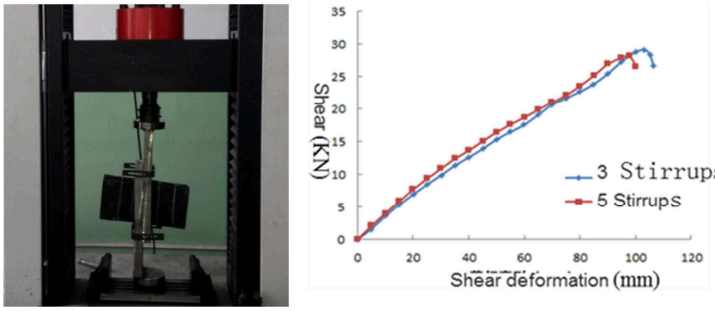


(a)Test loading device (b) Shear performance curves of rubberbeams

Fig. 2 Test loading device and test results

The following conclusions can be reached from the test results in Fig. 2: 1) There is little change of shear behaviorsbetween restricted by three and five wire hoop,in the overall, the shear strength is mainly decided by the shear stiffness of the cross-section, the rubber beam'slimiting amount of deformation is around 100mm, the ultimate shear capacity is about 30KN; 2) the shear P-Δ relationship embodied in a linear deformation before failure, after the shear failure, the intensity decreases rapidly. Therefore, rubber beam can be simplified as the level spring in the numerical simulation, each rubber beam's shear stiffness is taken as 300000N / m.

## Comparative Study of the monolithic wall seismic performance

**Modeling.** In this paper, the seismic performance of slip damping ring beam walls and common wall comparison were analyzed by ABAQUS software, thewall size of model is $240\times2800\times3000$, the structural columns on both sides are $240\times240$, the top was a pressure beam that analog upper load. Integrated model was used to simulate the upper wall, interior walls are simulated by 8-node hexahedral linear reduced integration unit (C3D8R), material constitutive used plastic damage model;spring unit were set at the both ends of the wall to simulated beam shear properties of rubber, mortar's slipping damping performance was simulatedthrough the friction surface (coefficient of

friction $\mu = 0.4$ ), This article used the coulomb friction model to analog slipping of the mortar layer, the main surface used the contacting property of "surface-to-surface contact" in interaction module to definite the masonry wall, the minor surface is the low-grade mortar layer [6] (Analysis model shown in Fig.3).

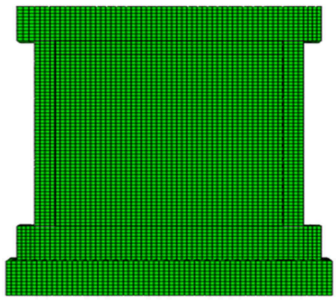

Fig. 3 Finite element analysis model

**Theloading system.**The low cycle alternating loading system was used, beginning with the force control loading stage,ending with the displacement loading control.For damping wall, the ultimate displacementwas 100mm,and for the common wall, the ending of loading was the appearance of severe pressure damage of wall.

**Experimental results and analysis.**Fig. 4 shows the hysteretic curvesof the base shear and the top displacement of the walls under two kinds of conditions, from the figure can draw the following conclusions:1)The hysteretic curve shape of common wallvaries from straight at the beginning to spindle gradually,it shows the three stages of Elasticity, cracking, and elastic-plastic. After entering the elastic-plastic stage, each loading cycle has some residual deformations,the hysteretic loop area increases gradually, The carrying capacity begins to declineafter reaching the ultimate load (300KN), the hysteretic loop area increases obviously shows that the wall damage is serious. On the other hand, in the damping wall, hysteresis curve shape is regular, each load cycle almost has no residual deformation, closing to the ideal energy consumption model, the hysteretic loop area is much larger than the ordinary wall; 3) The base shear of damping wall maintains at about 35KN, the base shear of damping wall is far less than common wall's,it shows that, under the condition of ensuring rubber beam limiting displacement. The sliding damping ring beam can achieve a good energy dissipation effect.

## Conclusion

This paper used research methods that combining experimental research and numerical simulation, the slip dampingwall and common walls' seismic performance were studied. Following conclusions could be drawn:

1) Rubber beam's shear capacity of the size $310\times150\times80$ is 30KN, the ultimate shear deformation is 100mm. Its shear strength and deformation capacity mainly related with Shear stiffness of the cross-section.

2) The damping walls reflect good ability of energy consumption under low cyclic loading. Compared with the common wall,the base shear of walls could be greatly reduced,the upper part of the structure could reciprocating sliding together with the ring beam,the upper structure almost keep the elastic state.

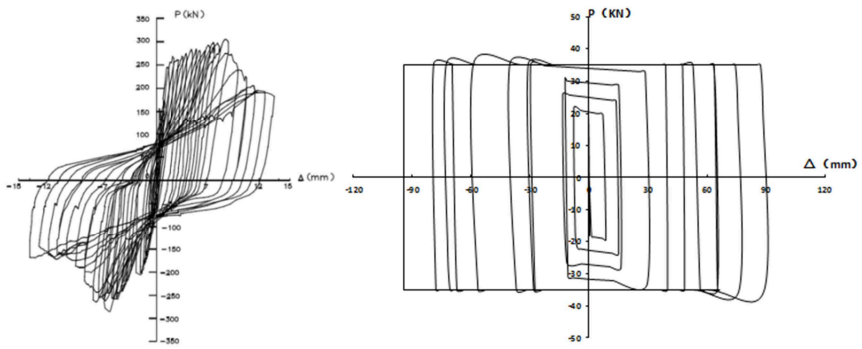


(a) Common wall (b) Damping walls

Fig. 4 Hysteretic curves

**Acknowledgment**

This work is supported by Natural Science Foundation of China (51368054), Science and Technology Plan Projects of Xinjiang Production and Construction Corps (2014AB053)and Talent Plan Projects ofShihezi University (2012ZRKXYQ17).

**References**

[1] Cao Wanlin, Zhou Zhongyi, Wang Qing et al. Experimental study on base vibration isolation and anti-seismicmasonry structure in rural areas by shaking table test. JOURNAL OF VIBRATION AND SHOCK, 2011,30(11):209-213.

[2] Zhou Zhongyi,Cao Wanlin, Wang Qing et al. Rural base isolation masonry structure building shaking table test research. Journal of Civil.Architectural & Environmental Engineering, 2010,32(S2):521-523.

[3] Shang Shouping, Yao Fei, Liu Ke.Study of the structure of a new type of isolation layer and shaking table test. CHINA CIVIL ENGINEERING JOURNAL, 2011,44(2): 36-41.

[4] Shang Shouping, Shen Rong. Research on Isolation Properties of Masonry Model. Journal of Hunan University (Natural Sciences), 2012, 39(9): 1-5.

[5] Li Yingmin, Bu Changming.Experimental comparative study on shaking table test of low-rise masonry wall with sliding absorption system and solid system. Journal of Central South University(Science and technology), 2012, 43(8): 3228-3236.

[6] ZhuoZhuang, Zhang Fan, Qin Song. ABAQUS Nonlinear Finite Element Analysis and Examples. Beijing：China Social Sciences Publishing House，2005.

*Applied Mechanics and Materials Vols. 580-583 (2014) pp 1633-1636*
*© (2014) Trans Tech Publications, Switzerland*
*doi:10.4028/www.scientific.net/AMM.580-583.1633*

# Seismic reduction and control analysis of hybrid structure with viscous dampers under strong earthquake

Sen Qiu[1,a], Shucheng Deng[2,b] and Zhaoquan Zhu[2,c]

[1] College of Construction Management, Jiangsu Jianzhu Institute, Xuzhou, 221116, China

[2] College of Civil and Transportation Engineering, Hohai University, Nanjing, 210098, China

[a]qiusennj@163.com, [b]dschhu@163.com, [c]zzq@hhu.edu.cn

**Keywords:** Hybrid structure, Viscous damper, Seismic reduction, Strong earthquake.

**Abstract.** This article focuses on the effect of viscous damper on seismic performance of steel-concrete hybrid structure under strong earthquake. The result shows that viscous damper has effect on seismic reduction and control. The story lateral displacement, story drift rotation and energy dissipation-seismic can be reduced effectively by viscous dampers. The maximum value of vibration-reduction ratio is 36.0%, 67.9%, 36.9%. It is different effect on seismic reduction by different earthquake ground motion. Response of earthquake amplifies under Pasadena earthquake wave than the others.

## Introduction

In recent years, steel-concrete hybrid structure for high-rise building has been widely used. This structure has many advantages on the plane layout and force defense system. But under strong earthquake this structure has been damaged seriously, such as two high-rise buildings in Japan in 1992 [1], so there is a debate on the seismic performance of the structure system.

The traditional methods were restricted by economy, construction and using spatial. This way will increase the stiffness of structure and also expand the seismic energy input the structure. The dampers can provide damping force for structures and the stiffness of structure isn't changed by viscous dampers. Compared with other dampers, the model of viscous dampers is relatively simple and widely used in practical projects [2]. Nonlinear time-history analysis method was used in this paper to study the anti-seismic performance. The effect of viscous damper on anti-seismic performance was analyzed under strong earthquake.

## General situation of the project and Computation models

**The project**. The project is a 15-storey steel-concrete hybrid structure of 60 m with steel framework and concrete shear wall [3]. The design basic acceleration of ground motion is 7 degree (0.1g). The measure grade of shear wall and frame is Ⅰ and Ⅱ respectively. The structural plane is shown in Fig. 1.

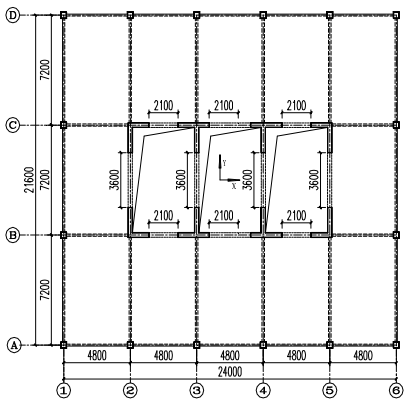


Fig. 1 Structural plane (mm)

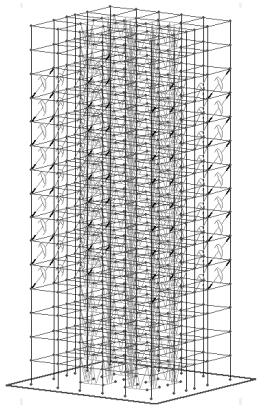

Fig. 2 3D model

The dead load on the floor and roof is 6.0 kN/m$^2$ and 7 kN/m$^2$ respectively. The live load on the floor and roof is 2.0 kN/m$^2$. The dead load on the beam is 1.5 kN/m.

**Computation models**. The nonlinear dynamic time-history analysis is carried out by CANNY program [4]. There are 720 beam elements, 300 column elements, 180 wall elements and 72 damper elements. The 3D model of structure is shown as Fig. 2. The dampers set up on the floor from 5 to 13, where the story drift rotation is much larger than that of the other stories.

## Earthquake ground motion and Analysis cases

**Earthquake ground motion**. In order to analyze the dampers' effect on seismic reduction under different earthquake ground motion, there are three earthquake waves selected: El Centro(1940), Pasadena(1952), San Fernando(1971). The maximum acceleration and occurrence time are shown as 341.7gal at 2.14s, 46.5gal at 6.9s, 137.86gal at 12.54s. Fourier frequency domain graphs (FFT) of the three earthquake waves are shown as Fig. 3.

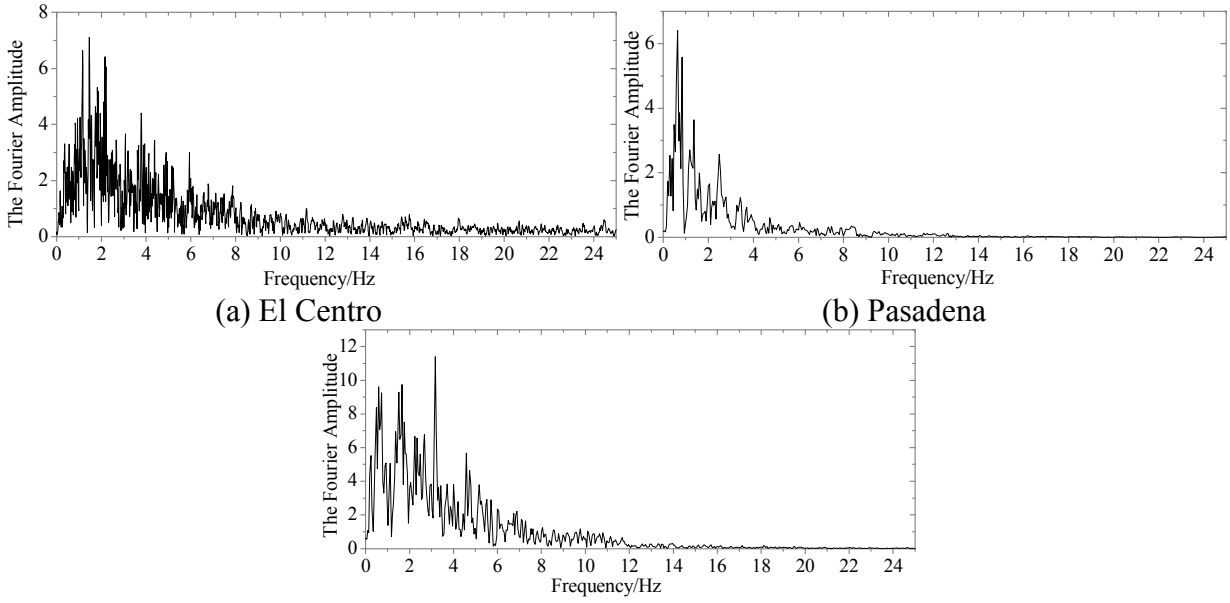


(a) El Centro (b) Pasadena

(c) San Fernando

Fig. 3 Fourier frequency domain graphs

From the Fig.3, it could be observed that the El Centro energy focus on 1.0-2.5Hz, the maximum energy at 1.4648Hz; Pasadena energy focus on 0.3-0.7Hz, the maximum energy at 0.6348Hz; San Fernando energy focus on 1-4Hz, the maximum energy at 3.1738Hz. Analysis of vibration modal, the structure's fundamental frequency is 0.6334Hz near the Pasadena's frequency of maximum energy. The structure resonance occurs under earthquake ground motion of Pasadena.

**Analysis cases**. The structure without and with viscous dampers are called non-control and additional damper structure. There are 4 analysis cases as shown in Table. 1.

Table. 1 Main analysis cases

| Number | Seismic intensity | Damper | Case |
|---|---|---|---|
| 1 | 8-degree seldom (0.40g) | Without | S8ND |
| 2 | | With | S8HD |
| 3 | 9-degree seldom (0.62g) | Without | S9ND |
| 4 | | With | S9HD |

**Analysis of different cases**

**The maximum story lateral displacement**. The maximum story lateral displacement in direction Y under different cases is illustrated in Fig. 4. In 9 degree seismic seldom intensity, the maximum story lateral displacement is too much under Pasadena earthquake wave. The components of structure are serious damaged. The story lateral displacement of stories with viscous dampers is reduced effectively under the other earthquake waves. The maximum value of vibration-reduction ratio is 36.0%.

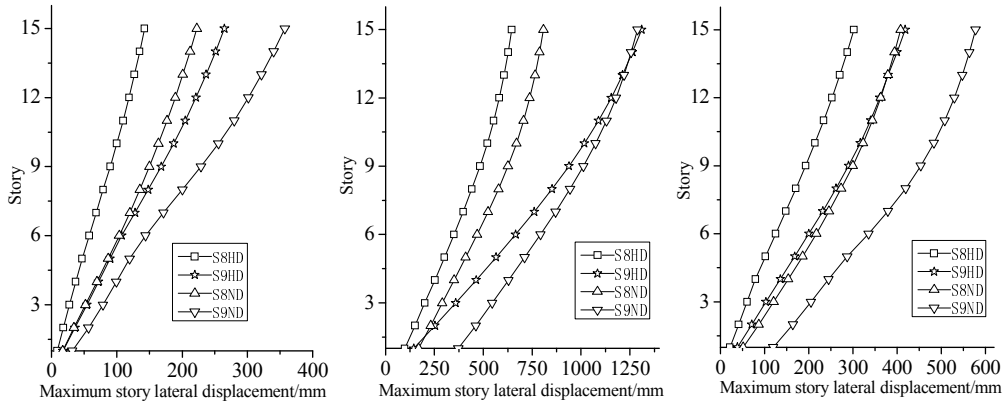


(a) El Centro (b) Pasadena (c) San Fernando

Fig. 4 The maximum story lateral displacement

**Story drift rotation.** The story drift rotation of non-control structure and additional damper structure are shown in Fig. 5. The first story drift rotation occurred saltation under Pasadena earthquake wave in 8, 9 degree seismic seldom intensity. It could be observed that the components of this story appeared nonlinear deformation. Seismic reduction and control are not evident only depend on increasing dampers. The story drift rotation of stories with viscous dampers is reduced effectively under the other earthquake waves. The maximum value of vibration-reduction ratio is 67.9%.

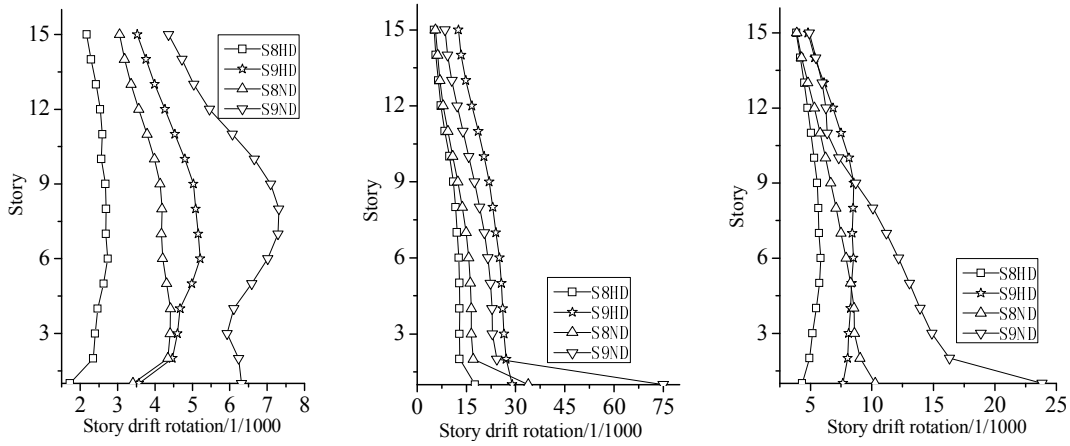


(a) El Centro (b) Pasadena (c) San Fernando

Fig. 5 Story drift rotation

**Acceleration amplification coefficient.** The story drift rotation of non-control structure and additional damper structure are shown in Fig. 6. In 8 and 9 degree seismic seldom intensity, the acceleration amplification coefficient changes a great deal in value. The maximum value of vibration-reduction ratio is 25.2% and 27.5% respectively.

**Analysis of energy**. The input energy and the balance with the system dissipated energy (strain energy, damping energy, damper energy and kinematic energy) under El Centro earthquake wave in 8 degree seismic seldom intensity are shown as Fig. 7. Under El Centro earthquake wave, the input energy of non-control structure is 3610kN·m and additional damper structure is 4090kN·m. In spite of

the input energy increases after additional damper, energy dissipation of the dampers is 1510 kN·m. The ratio of the dampers' energy is 36.9%.

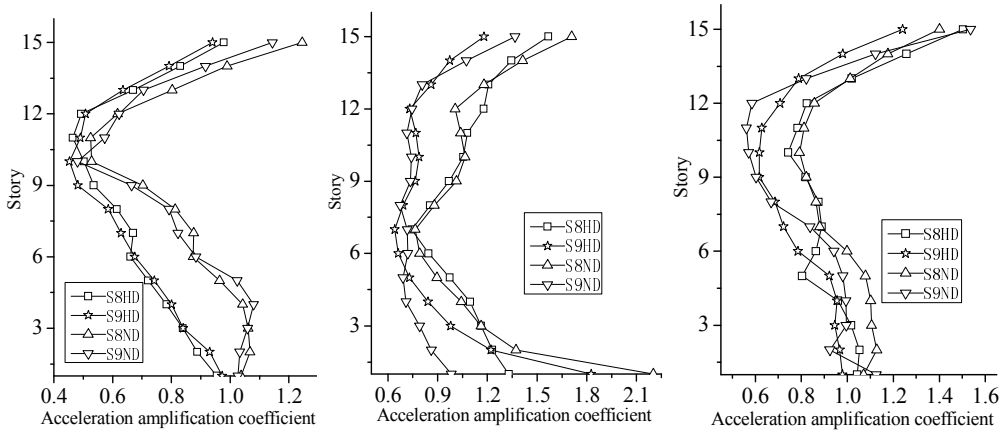


(a) El Centro (b) Pasadena (c) San Fernando

Fig. 6 Acceleration amplification coefficient

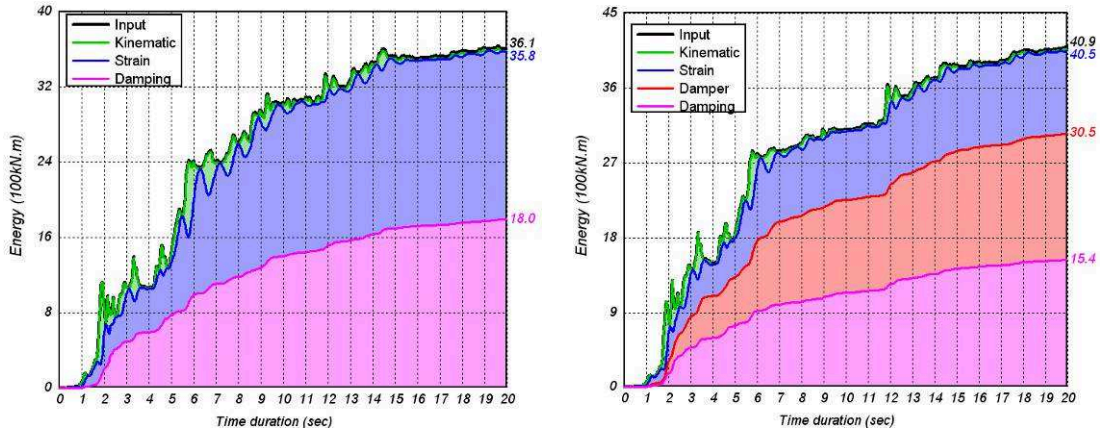


(a) No damper (b) Have dampers

Fig. 7 Analysis of energy under El Centro earthquake wave

## Conclusion

The seismic performance of uncontrolled structure and energy dissipation structure is analyzed. The main conclusions are summarized as follows:

(1)The viscous dampers can reduce the story drift rotation, the story lateral displacement and energy dissipation-seismic of structure.

(2) Under different earthquake ground motion, seismic performance of the structure is different. As the paper expound above, the maximum energy at 0.6348Hz of Pasadena. It is nearly 0.6334Hz of the structure's fundamental frequency. Response of earthquake amplifies under Pasadena earthquake wave than the others.

## References

[1] S.Morino. Recent developments in hybrid structures in Japan-Research, design and construction[J]. Engineering Structures,1998,20(4-6):336-346.

[2] BUILDING SEISMIC SAFETY COUNCIL. NEHRP guidelines for the seismic rehabilitation of buildings [R] . Washington D C:Federal Emergency Management Agency ,1997.

[3] Zhihua Huang, Xilin Lu , Ying Zhou and Yi Bo: JOURNAL OF TONGJI UNIVERSITY (NATURALSCIENCE), Vol. 38 (2010), p. 170 (In Chinese).

[4] Li K.N. CANNY2004 DATA-INPUT MANUAL. May.2004..

# CHAPTER 4:

# Seismic Engineering

*Applied Mechanics and Materials Vols. 580-583 (2014) pp 1639-1644*
*© (2014) Trans Tech Publications, Switzerland*
*doi:10.4028/www.scientific.net/AMM.580-583.1639*

# Simplified Dispersion Curves of Earthquake Love Wave for Rotational Seismic Motion Estimation

Yuewei Liu[a], Hongnan Li[b]

Faculty of Infrastructure Engineering, Dalian University of Technology, 116024, China

[a]wmhansen@163.com, [b]hnli@dlut.edu.cn

**Keywords:** phase velocity, dispersion, simplified dispersion curve, Love wave, rotational motion, stiffness matrix

**Abstract.** In the simulation of the rotational seismic ground motion, the apparent velocity of Love wave is always assumed to be equal to the S wave velocity of top layer of the site approximately, with the dispersion of surface wave not being fully considered. In this paper, the effect of the velocity structure to the Love wave dispersion is discussed based on the stiffness matrix theory. It shows that to assume the velocity to be equal to the S wave velocity of the top layer may greatly overestimate the low frequency rotational seismic motion. A simplified dispersion curve, is suggested for rotational seismic ground motion simulation. The shape of the bilinear curve is shaped by 3 parameters. They are the corner frequency, the minimum phase velocity and the velocity ratio. The parameters are affected by the velocity structure of the site.

## Introduction

The rotational ground motion is not considered directly due to lack of the recorded rotational ground motion. Some simplified theoretical methods were developed to simulate the rotational motion from the translation motion for rotational seismic design of structures[1]. The apparent velocity of the incidence wave is one of the key parameters in these methods.

The earthquake wave contains several types of components, such as the P wave, S wave, Rayleigh wave and Love wave. The apparent velocity of Love wave is dispersed. The transfer matrix theory and the stiffness matrix method are some of the way to research the wave dispersion[2,3]. The methods are widely applied in earthquake wave inverse, earthquake exploration and other fields. But the methods have not been introduced to the rotational earthquake motion simulation by civil engineers, because they are too complicated. The apparent velocity of Love wave is assumed to be equal to the S wave velocity of the upper layer of the site[4,5]. It is not reasonable. Li considered a two-layer space, a low-velocity layer above an elastic half-space, and derived calculation formulations of phase velocities with frequency dispersion[6]. The formulations are simple, containing no matrix operation. Since the wave velocities of earth's surface change distinctly along its depth, the two-layer space is too simple.

This paper will introduce the methods based on the stiffness matrix theory to calculate the phase velocities of Love wave in multi-layer half space, and present a simple way to determine the apparent velocities of surface waves that can be used for rotational seismic ground motion estimation.

## Stiffness matrix theory

Generally, the surface of earth is layered and the wave velocities of the medium are increasing along the depth of the layers. Thus, consider a multi-layer isotropic elastic half space shown as Fig.1 (a). In the figure, j is the layer number, $\lambda$ and $\mu$ are the Lame constants, $\rho$ is the density, d is the thickness of layer, u, v and w are the displacements of layer, $\sigma$ is the stress on the interface and F is the exterior force. Let the Love wave propagate along x, so the Love wave is in the x-y plane. In the layer j, the wave equation is (the subscript j is omitted if no confusion rises)[7]

$$\begin{bmatrix} F_{y,j-1} \\ F_{y,j} \end{bmatrix} = \mu_j b_j \begin{bmatrix} -cth(bd) & \csc h(bd) \\ \csc h(bd) & cth(bd) \end{bmatrix} \begin{bmatrix} v_{j-1} \\ v_j \end{bmatrix} \tag{1}$$

where

$$b = \sqrt{k^2 - k_\beta^2} \quad (k > k_\beta) \ , \ k = \omega / c \ , \ k_\beta = \omega / \beta \ , \ \beta = \sqrt{\mu / \rho}$$

in which c is the velocity of Love wave, k is the wave number, α and β are the velocity of P wave and S wave, respectively, and ω is frequency. The direction of displacement and force are shown in Fig. 1(b).

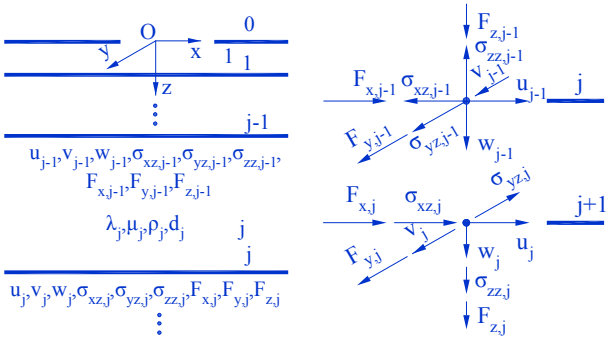


(a) (b)

Fig. 1. Multi-layer half space. (a) Layers. (b) Direction of displacement, stress and force

Subdivide the layers to ensure the thickness of the subdivided layers in the calculating process were small enough, so bd is small. Using the Taylor expansion, one has

$$cth(bd) \approx \frac{1}{bd} + \frac{bd}{3} \quad , \quad \csc h(bd) \approx \frac{1}{bd} - \frac{bd}{6} \tag{2}$$

At the same time, in the free condition, F=0, one has Eq. (4) after transmutation from Eq. (2)

$$\left( \begin{bmatrix} -\frac{\mu}{d} + \frac{\omega^2 \rho d}{3} & \frac{\mu}{d} + \frac{\omega^2 \rho d}{3} \\ \frac{\mu}{d} + \frac{\omega^2 \rho d}{3} & -\frac{\mu}{d} + \frac{\omega^2 \rho d}{3} \end{bmatrix} - k^2 \begin{bmatrix} \frac{\mu d}{3} & \frac{\mu d}{6} \\ \frac{\mu d}{6} & \frac{\mu d}{3} \end{bmatrix} \right) \begin{bmatrix} v_{j-1} \\ v_j \end{bmatrix} = 0 \tag{3}$$

If $[v_j, v_{j-1}]^T \neq 0$ , Eq. (4) must be satisfied as follows

$$\left\| \begin{bmatrix} -\frac{\mu}{d} + \frac{\omega^2 \rho d}{3} & \frac{\mu}{d} + \frac{\omega^2 \rho d}{3} \\ \frac{\mu}{d} + \frac{\omega^2 \rho d}{3} & -\frac{\mu}{d} + \frac{\omega^2 \rho d}{3} \end{bmatrix} - k^2 \begin{bmatrix} \frac{\mu d}{3} & \frac{\mu d}{6} \\ \frac{\mu d}{6} & \frac{\mu d}{3} \end{bmatrix} \right\| = 0 \tag{4}$$

Assembling Eq. (4) by layers, k and c can be obtained.

**Velocity of Love wave in some sites of China**

In some regions of China, the velocity structures, described by the statistic expressions as Eq. (5), are shown in Table 1[8].

$$\beta = q_1 H^{q_2} \tag{5}$$

where $q_1$ is β of the first layer, H is the depth of the layer, $q_2$ is the parameter which denote the increasing grades of β.

The dispersion curves are plot in Fig. 2.

**Simplified dispersion curve**

**Parameters.** For civil engineers who are engaged in structure rotational seismic design, the method above to calculate the dispersion curve of Love wave is so complicated that the reasonable simplification is needed. As shown in Fig.2, the dispersion curve can be simplified into a bilinear curve with a horizontal segment and a bias. The shape of the bilinear curve is controlled by 3 controlling parameters, $f_c$, $c_{\min}$ and $\zeta$. They are defined as follows:

Table 1 Distribution of S wave velocity in some regions of China and controlling parameters of the simplified curve

| NO. | region | soil type | $q_1$ / m/s | $q_2$ | $v_{s,30}$ (m/s) | $c_{\min}$ (m/s) | $\varsigma$ | $f_c$ (Hz) |
|---|---|---|---|---|---|---|---|---|
| 1 | Beijing | sandy soil | 110.0 | 0.309 | 240.4 | 187.8 | 2.2 | 2.7 |
| 2 | Beijing | clay soil | 104.0 | 0.407 | 295.1 | 220.9 | 3.6 | 2.1 |
| 3 | Tianjin | sandy soil and clay soil | 98.4 | 0.334 | 229.7 | 176.3 | 2.3 | 2.4 |
| 4 | Shanghai | sandy soil and clay soil | 111.7 | 0.198 | 182.8 | 146.3 | 1.4 | 3.6 |
| 5 | Tangshan | sandy soil and clay soil | 143.9 | 0.371 | 370.7 | 283.2 | 3.4 | 2.8 |
| 6 | Xi'an | clayey soil | 145.5 | 0.266 | 284.0 | 223.4 | 1.9 | 3.6 |
| 7 | Xi'an | paleosoil | 229.3 | 0.145 | 327.9 | 267.6 | 1.4 | 6.4 |
| 8 | Yingkou | sandy soil and clay soil | 116.1 | 0.260 | 223.1 | 175.4 | 1.8 | 3.1 |
| 9 | Haicheng | sandy soil and clay soil | 131.8 | 0.268 | 258.6 | 203.0 | 1.9 | 3.3 |
| 10 | Yantai | alluvial clay | 210.0 | 0.300 | 448.1 | 354.7 | 2.7 | 4.0 |
| 11 | Yantai | diluvial clay | 229.8 | 0.142 | 326.2 | 266.3 | 1.3 | 6.4 |
| 12 | Yantai | mud | 97.4 | 0.273 | 193.6 | 151.6 | 1.7 | 2.7 |
| 13 | Yantai | sandy soil and clay soil | 124.0 | 0.270 | 244.6 | 191.8 | 1.9 | 3.2 |
| 14 | Qinhuangdao | sandy soil and clay soil | 130.2 | 0.281 | 264.3 | 206.7 | 2.0 | 3.2 |
| 15 | Hebei | sandy soil and clay soil | 113.2 | 0.324 | 257.4 | 198.3 | 2.3 | 2.7 |
| 16 | Xiamen | clay soil | 109.1 | 0.223 | 190.5 | 151.4 | 1.5 | 3.3 |
| 17 | Xiamen | mud | 64.7 | 0.263 | 125.3 | 98.7 | 1.4 | 2.1 |
| 18 | Xiamen | sandy soil | 80.9 | 0.376 | 211.2 | 159.6 | 2.6 | 1.9 |
| 19 | Anyang | sandy soil and clay soil | 152.5 | 0.307 | 331.5 | 258.2 | 2.4 | 3.4 |
| 20 | Low Reach of Liaohe River Plain | sandy soil and clay soil | 76.0 | 0.403 | 213.3 | 159.6 | 2.9 | 1.7 |

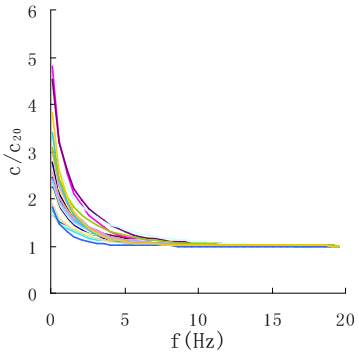


Fig.2. Dispersion curves ( $c_{20}$ in the figure is the velocity at where frequcy is 20Hz).

**Simplified dispersion curve**

**Parameters.** For civil engineers who are engaged in structure rotational seismic design, the method above to calculate the dispersion curve of Love wave is so complicated that the reasonable simplification is needed. As shown in Fig.2, the dispersion curve can be simplified into a bilinear curve with a horizontal segment and a bias. The shape of the bilinear curve is controlled by 3 controlling parameters, $f_c$, $c_{\min}$ and $\zeta$. They are defined as follows:

(1) $f_c$ is the corner frequency. It is the turning point of the bilinear curve. When the frequency is higher than $f_c$, the simplified dispersion curve is horizontal. When the frequency is lower than $f_c$, the simplified dispersion curve is declining.

(2) $c_{\min}$ is the minimum phase velocity. It is the velocity along horizontal line. It can also be regarded as the phase velocity at 20Hz since the range of earthquake frequency that the structure engineering takes into consideration is usually between 0.1Hz and 20Hz.

(3) $\zeta$ is the velocity ratio, defined as $\zeta = c_{0.1} / c_{\min}$, where $c_{0.1}$ is the phase velocity at 0.1Hz.

**Corner frequency.** It is shown in Fig.2 that the dispersion curve is smooth. There is no obvious turning point to distinguish the 2 segments. The corner frequency is determined by the following work:

As shown in Fig. 3, on the exact dispersion curve, let point A be (0.1, $c_{0.1}$), let point C be (19.6, $c_{\min}$) ($c_{\min} = c_{19.6}$, $c_{19.6}$ is the phase velocity at 19.6Hz). Find a point B ($m$, $c_{\min}$) to ensure the area $S_{ODABCE} = S_{ODĒE}$. The point B is considered as the turning point, $f_c$ is considered to be equal to $m$.

The corner frequencies are shown in Table 1. They are between about 1.7-6.4 Hz in these sites in Table 1. $f_c$ is related to $q_1$ tightly. The relation is shown in Fig.4. The fitting formula of $f_c$ with $q_1$ is as follows

$$f_c = 0.025q_1 + 0.06 \tag{6}$$

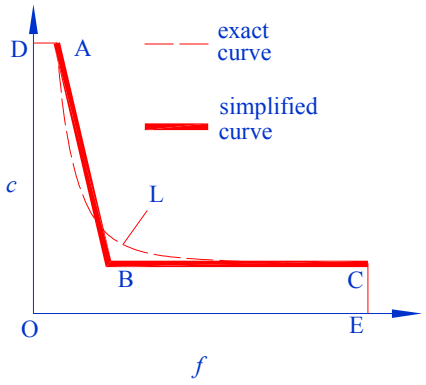


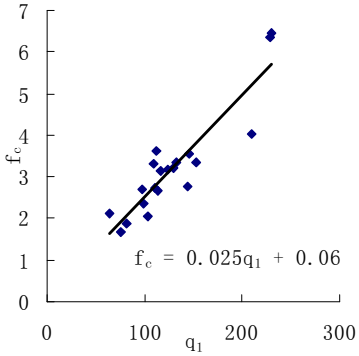


Fig.3. Determination of the corner frequency Fig.4. Corner frequency

**Minimum phase velocity.** $c_{\min}$ is close to the S wave velocity of the first layer, because in high frequency region, the phase velocity of Love wave is affected by the upper layers of earth's surface mainly. In civil engineering, $v_{s,30}$ is an effective S wave velocity of the layers between 0-30m, and is commonly used to distinguish the site type and to determine the seismic load of structures. It is defined by Eq. (7)

$$v_{s,30} = \frac{\sum d_i}{\sum (d_i / \beta_i)}, \sum d_j = 30m \tag{7}$$

It is practicably to find the relation between $c_{\min}$ and $v_{s,30}$ rather than the relation between $c_{\min}$ and the S wave velocity of the strict first layer. $c_{\min}$ and $v_{s,30}$ of the sites are shown in Table 1 and Fig.5. They show that $c_{\min}$ is close to $v_{s,30}$, as described by Eq.(8).

$$c_{\min} \approx 0.70 - 0.85 v_{s,30} \tag{8}$$

**Velocity ratio.** $\zeta$ are shown in Table 1. $\zeta$ is related to $q_2$ tightly. The relation is shown in Fig.6. The fitting formula of $\zeta$ with $q_2$ is Eq. (9) as follows

$$\zeta = 0.71 \exp(3.69 q_2) \tag{9}$$

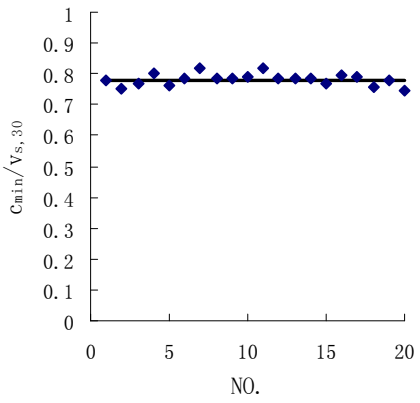


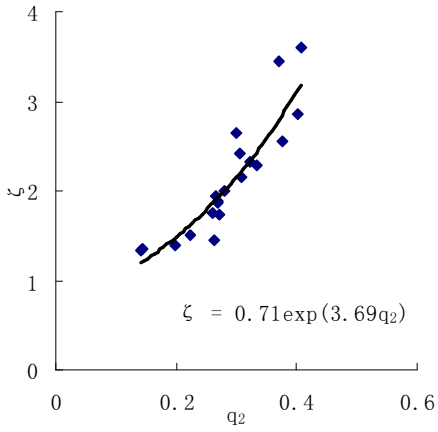


Fig.5. Minimum phase velocity Fig.6. Velocity ratio

## Conclusion

Based on the stiffness matrix theory, the effects of the velocity structure of site on dispersion curve are discussed in this paper. It shows that the dispersion curve can be simplified into a bilinear curve with a horizontal segment and a bias. The simplified dispersion curve is shaped by 3 parameters, $f_c$, $c_{\min}$ and $\zeta$. The parameters is suggested based on the statistic data of some sites in China.

## Acknowledgments

The research work in this paper was supported by the National Science Foundation of China under Grant No. 90815026 and 50638010 and the National Seismic Project under Grant No. 200808074. These supports are gratefully acknowledged.

## References and Notes

[1] A. Rutenberg and A.C. Heidebrecht, Rotational ground motion and seismic codes, Canadian J. of Civil Eng., 12 (3) (1985) 583-592.

[2] J.P. Wolf, *Dynamic soil-structure interaction*. Prentic-Hall, Inc., Englewood Cliffs, 1985.

[3] You-Hua Fan, Jia-Qi Liu and Bai-Xun Xiao, Faster vector transfer matrix method to calculate the dispersion of Rayleigh wave. Journal of Hunan university, 29(5) (2002) 25-29.

[4] V.W. Lee and M.D. Trifunac., Torsional accelerograms. Soil Dynamics and Earthquake Engineering. 4, (1985) 132–139.

[5] M.A. Bravo and F.J. Sanchez-Sesma, Seismic response of alluvial valleys for incident P, SV and Rayleigh waves. Soil Dynamics and Earthquake Engineering. 9 (1990) 132–139.

[6] Hong-Nan Li, Li-Ye Sun and Su-Yan Wang, Frequency dispersion characteristics of phase velocity in surface wave for rotational components of seismic motion. Journal of Sound and Vibration. 258(5) (2002) 815–827.

[7] Hua-You Chai et al., *Theory of surface wave in elastic space and its application in rock engineering*. Beijing: Science Press. 2008.

[8] Xi-Yuan Zhou, Guang-Jun Wang and Jing-Yu Su., *Site, basement and design earthquake*. Beijing: Seismological Press. 1991.

*Applied Mechanics and Materials Vols. 580-583 (2014) pp 1645-1648*
*© (2014) Trans Tech Publications, Switzerland*
*doi:10.4028/www.scientific.net/AMM.580-583.1645*

# Study on Seismic Behavior of Self-centering precast frame

Hui LIN[1, a], Tianqi LI[2,b], Qiang WANG[3,c]

[1]School of Civil Engineering, Tongji University, Shanghai 200092, China

[2]School of Environment Civil Engineering, Jiangnan University, Wuxi Jiangsu 214122, China

[3]School of Civil Engineering, Shenyang Jianzhu University, Shenyang, Liaoning 110168, China

[a]linhui_jnu@163.com, [b]Ltq_tiger15@126.com, [c]wangqiangsy@163.com

**Keywords:** self-centering; precast concrete frame; finite element analysis; seismic performance.

**Abstract.** Self-Centering structure is a kind of new structure, which aims for reducing the residual deformation of structure after the earthquake. In order to research the Seismic Behavior of Self-centering Prefabricated concrete frame, a new joint applied with prestressed tendons and a traditional joint are designed in this paper with the finite element software ABAQUS. The seismic performances of them are contrastively analyzed. The new joint is found to have better self-centering capacity. Then two plane frame models are analyzed. The result shows that the frame applied with prestressed tendons has some capacity of self-centering and enough energy dissipation effects.

## Introduction

Prefabricated construction is a construction structure of industrial production. It has advantages of high quality, fast construction and so on. Seismic behavior is the key point in the study of prefabricated structure. The seismic principles of "three standards and two phase" in China allow the structure to enter the stage of elastic-plasticity in moderate or major earthquake. It makes large residual deformation and high repairing cost after the earthquake, though it protects the people's safety [1-3].

Self-Centering structure is a kind of new structure, which aims for reducing the residual deformation of structure after the earthquake. The research of Self-Centering structure originated from the study on prefabricated prestressed concrete frame with unbonded tendons. A lot of research have been done on Self-Centering steel frame structure. Prestressing technique was first applied to steel frame to realize the capacity of Self-Centering by J.Ricles [3]. A new kind of steel frame joint was studied by Pan Peng [4-5], which uses post-tensioned (PT) high-strength steel to tie the beam on the column to resist moment and provide self-centering force. However, research achievements on Self-Centering concrete structure are not sufficient. A kind of new self-centering post-tensioned precast connections (PTED) was proposed by Meng Shaoping [6].

A new kind of precast concrete joint is studied, which has the capacity of self-centering. This new joint uses post-tensioned high-strength steel and dry joint method. The post-tensioned reinforcements tie the beam on the column to resist moment and provide self-centering force. In order to study the seismic performance of such joint and the overall frame structure, the finite element software ABAQUS is used to analysis the capacity of self-centering and seismic behavior.

## Study on Self-Centering joint

The current domestic and international research indicates that adding post-tensioned tendons in prefabricated concrete beams can improve displacement restoring capacity, and reduce residual deformation after the earthquake [7]. Therefore, a self-centering prefabricated prestressed concrete frame joint JD-1 is designed in this paper, as shown in Fig.1. And a common prefabricated concrete frame joint JD-2, which is late poured in joint core region, as shown in Fig.2. Dimensions and reinforcement of these two joints are identical. In order to make the finite element model truly reflect the stress state of the joints in the actual project, the paper model is designed as an exterior joint of a general frame.

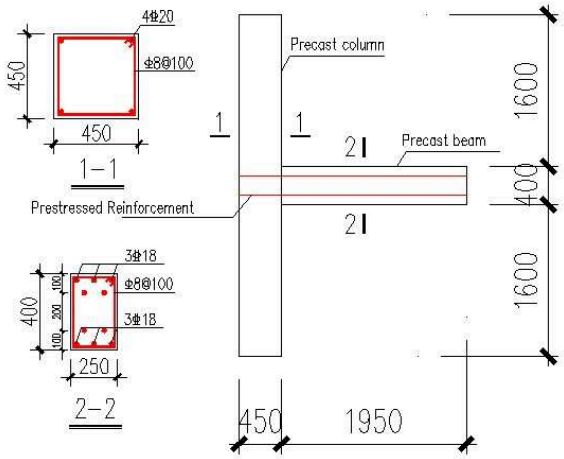


Fig.1 Size and reinforcement of JD-1

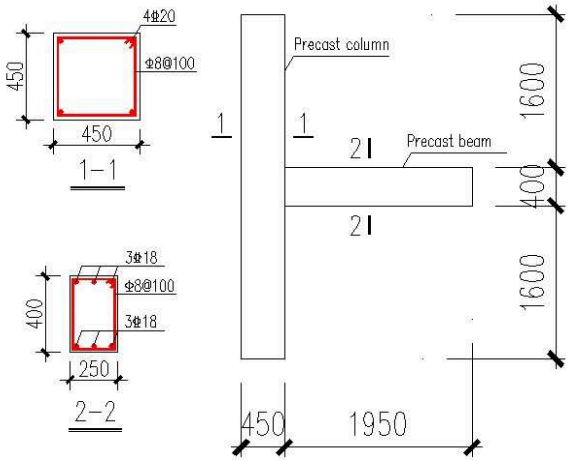


Fig.2 Size and reinforcement of JD-2

A dry method is used to splice joint JD-1. 4 steel strands are put in the corrugated pipe, which are buried in the joint before pouring the concrete. Then tendons are prestressed before hole grouting. Joint JD-2 is constructed by traditional method. A distance from the joint core region is left for cast-in-place.

Beam-column longitudinal reinforcement are HRB400 rebar, the stirrups are HPB335 reinforced, and the strength grade of concrete is C45. Nominal diameter of tendons are 15.2mm, tensile strength is 2000Mpa. 1000Mpa was applied to tendons in the pre-tensioning stage.

**Material constitutive relationships**

Concrete Damaged Plasticity model in ABAQUS program are selected as concrete constitutive model in this paper. The model assumes the destruction of the concrete material to crack and crush. Yield and failure surface evolution is controlled by tensile and compression equivalent plastic strains. The model also has better convergence. Therefore, this model is used to simulate the nonlinear behavior of concrete in this paper. The constitutive relationship proposed in Appendix C of GB 50010-2010 is used to describe the concrete stress-strain relationship.

The stress-strain relationship proposed in Appendix C of GB 50010-2010 is used for rebar and tendon in this paper. The slope of polygonal line's first ascent is the young's modulus of rebar and tendon. Rebar begin to enter Strengthen period after yield platform and the Strengthen period is simplified to a straight line. Maximum strain of the yield platform is assumed as $\varepsilon s=4\varepsilon y$. Ideal elastoplastic model is used only in tendon. Bond-slip effect is not considered in the paper.

**Boundary and loading conditions**

Since boundary conditions is very important to the performance of the frame joint, a "horizontal column and vertical beam" mode is used in this model, as shown in Fig.3. The loading procedure of JD-1 is divided into 2 stages. Firstly tendons are stretched, and then monotonic and cyclic load are applied to the edge of the beam. There is only one loading stage in JD-2. In these two analysis models, C3D8R element is used for concrete and T3D2 element for rebar and tendon, as shown in Fig.4.

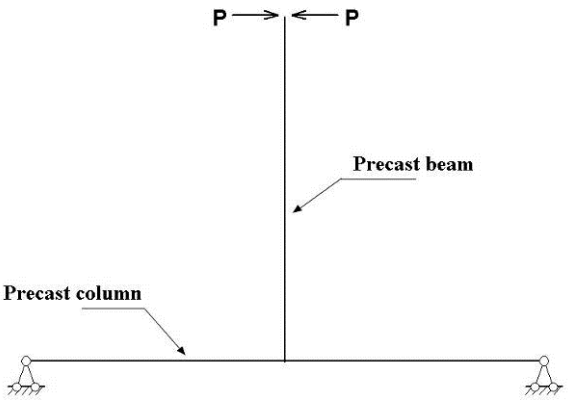


Fig.3 Loading diagram

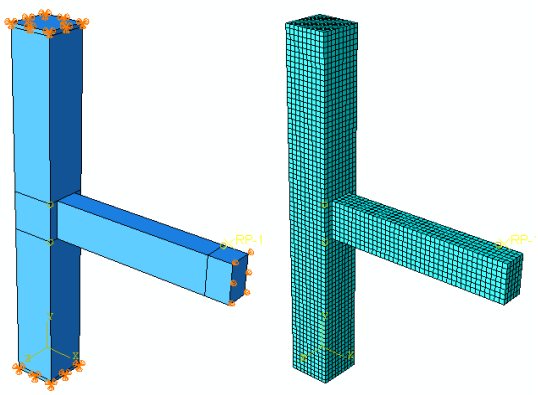

Fig.4 Finite element analysis model

**Analysis of load-displacement curve**

The load-displacement curves of JD-1 and JD-2 under monotonic load are shown in Fig.5. It can be seen that bearing capacity of JD-1 is higher than JD-2. in the path of the curves, JD-2 has larger initial stiffness, but firstly enter into the elastoplastic stage. Although JD-1 has a lower initial stiffness, it is still in the elastic stage when the displacement is 5mm. the yield displacement of JD-1 is 16.97mm, while JD-2 is 10.85mm.

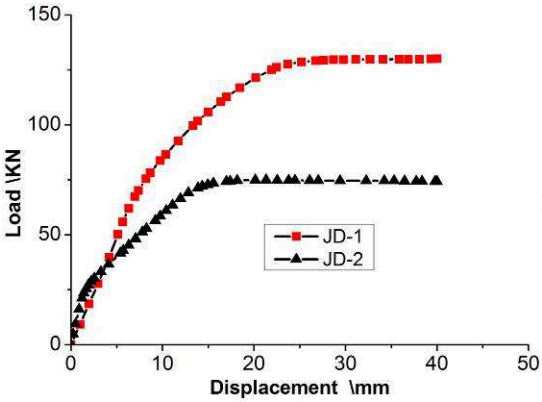


Fig.5 Load-displacement curve comparison

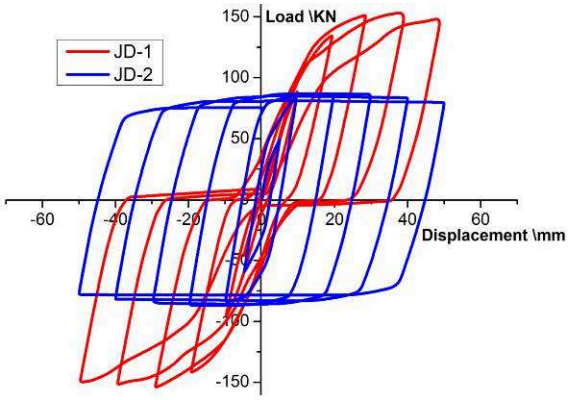


Fig.6 Hysteresis curve comparison

**Analysis of hysteresis curve**

The hysteresis curves of JD-1 and JD-2 are shown in Fig.6. It can be seen that the hysteresis curve of JD-2 is in spindle type under cyclic loading. This graphics type indicates large energy dissipation effects and good seismic performance. Although the curve of JD-1 is not as plump as JD-2, the displacement returned to zero after each cycle, indicating that JD-1 has a better displacement restoring capacity. On the other hand, the curve of JD-1 shows a clear "double flag" shape, which indicates good energy dissipation performance.

## Study on overall frame

In order to analysis the seismic performance of Self-Centering overall frame, a one-floor single-span Self-Centering plane frame model ZFW-F1 is built. Another one-floor single-span plane frame HJ-F1 is also built for comparison. All the parameters of these two frames are the same, except for the post-tensioned tendons in ZFW-F1. The span of the frame is 5m, and the storey height is 4m. The column section is 400mm×400mm, and the beam section is 250mm×500mm.the model of ZFW-F1 is shown in Fig.7.

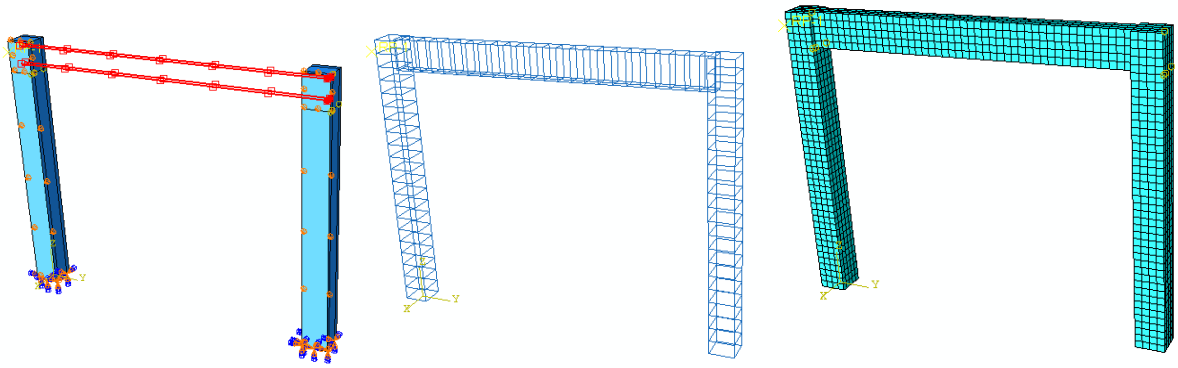

Fig.7 Finite element analysis model

The procedure of the analysis can be divided into 3 steps: Firstly, tendons are prestressed. Secondly, vertical force is loaded on the top of the columns. Then monotonic loading and low reversed cyclic horizontal loading are applied to the frame.

**Analysis of load-displacement curve**

Monotonic loading is applied to the two frame models to get the load-displacement curve, shown in Fig.8. It can be seen that the initial stiffness of ZFW-F1 is lower than HJ-F1, but the load capacity of ZFW-F1 is higher than HJ-F1.

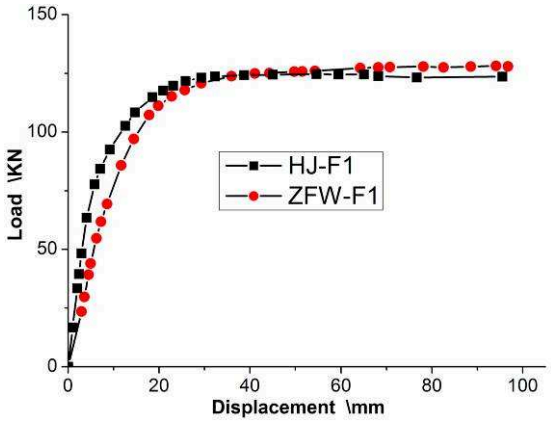


Fig.8 Load-displacement curve comparison

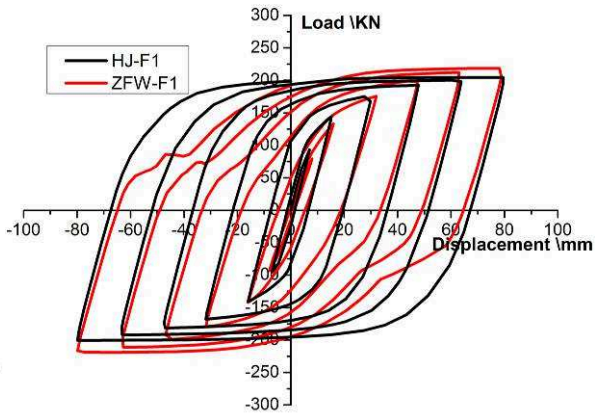


Fig.9 Hysteresis curve comparison

**Analysis of hysteresis curve**

The hysteresis curves of ZFW-F1 and HJ-F1 are shown in Fig.9. It can be seen that ZFW-F1 has some capacity of self-centering. The residual deformation of ZFW-F1 after each cycle is much lower than HJ-F1. On the other hand, the energy dissipation effects of both frame are similar.

## Conclusions

In this paper, a new kind of self-centering prefabricated prestressed concrete frame joint JD-1 is analysed by ABAQUS, compared with a prefabricated traditional joint JD-2. Then a Self-Centering plane frame ZFW-F1 is analysed, compared with a common frame HJ-F1. The conclusions are as follows:

1) Self-centering joint JD-1 performs better in bearing capacity than the traditional joint JD-2, but the initial stiffness of JD-1 is lower.

2) The hysteresis curve of JD-1 shows a clear "double flag" shape, indicating good self-centering characteristic and enough energy dissipation effects.

3) The initial stiffness of ZFW-F1 is lower than HJ-F1, but the load capacity of ZFW-F1 is higher than HJ-F1. ZFW-F1 has some capacity of self-centering and enough energy dissipation effects.

## Acknowledgements

This work was financially supported by National Natural Science Foundation of China through Grant 51378240 and "Twelfth Five" science and technology support program (2012BAJ16B05).

## References

[1] Lieping Ye, Xuchuan Lin, Xunliu Wang. Fourteenth National Conference of concrete and prestressed concrete. (2007), p.345-350

[2] Palermo A, Pampanin S, Calvi G M. Journal of Earthquake Engineering. Vol. 9(2005), p.899-921

[3] Garlock M M,Sause R, Ricles J M. Journal of Structural Engineering. Vol. 133(2007), p.239-299

[4] Zhenhua Pan. Study of Self-centering Steel Moment Frames[D]. Tsinghua University (2010)

[5] Zhenhua Pan, Peng Pan, Lieping Ye. Journal of Building Structures. Vol. 32(2011), p.35-42

[6] Cai Xiaoning, Meng Shaoping, Sun Weiwei. China Civil Engineering Journal. Vol. 45(2012), p. 29-37

[7] Priestley, MJNigel. PCI Journal. Vol.4(1991), p.50-57

*Applied Mechanics and Materials Vols. 580-583 (2014) pp 1649-1652*
*© (2014) Trans Tech Publications, Switzerland*
*doi:10.4028/www.scientific.net/AMM.580-583.1649*

# Study on Seismic Detection applied in Mine Advance and Side

Yunbing Hu[1,2,a], Yao Wang[2,b] ,Yanqing Wu [2,c] and Zixuan Liu[3,d]

[1]School of Geoscience and Info-Physics, Central South University, Changsha, 410083,China

[2]Chongqing Research Institute Co., Ltd., of China Coal Technology and Engineering Group, Chongqing ,400039,China

[3]Sinopec International Petroleum Exploration and Production Corporation,Beijing,100029,China;

[a]huybing@163.com, [b]742806027@qq.com, [c]wuyanqing9@163.com, [d]282577630@qq.com

**Keywords:** advanced detection; side detection; Radon transformation.

**Abstract.** This paper mainly discusses that the tunnel seismic advance detection is applied in mine geo-hazard detection. Separating the field seismic data of mine by radon transformation and migrating the data through advance way and side way, we accomplished advance and side detection simultaneously by one-time shot seismic data. Case study was carried on at Qinshui basin Yangmei No.5 mine field, and detection results mainly coincide with out-crops, demonstrating that our method can be one reference in mine geo-hazard detection.

## Introduction

Seismic exploration is an effective geophysical methods along with the development of petroleum industry, It has popularized and been effective in coal mine geological exploration recently. With the deepening depth of coal resources exploration, the resolution of seismic exploration has been difficult to meet the geological demands for safety and mining efficiency. The shortage mainly reflected in the detection of changes of coal bed thickness, imaging of subtle faults, small falls and columns, and discerning of denudation belt. In addition, data acquisition and processing will face many problems in the area of multiple seam and inclined coal mine. Due to its high resolution, detection distance, strong anti-interference ability, strong pertinence, mine seismic achieved more and more attention in recent years, and it has become a hot spot of mine geophysical research. Li modeled the elastic wave field stimulated by point-source or plane wave source in the coal mine roadway [1]. Seismic wave field and propagation characteristics of various wave patterns in different models were analyzed by Yang[2]. The principles and application of mine seismic data acquisition were studied by Hu[3]. The work above just focuses on advanced detection research, and has not considered the side geological conditions detection. Mine seismic data acquisition is mainly conducted for the tunnel advance detection, which often does not include the mine side, while the side information is also critical to the safety production of coal mine. In view of this, on the basis of previous research studies, the author uses one-time seismic data simultaneously to detect the mine advance and side.

## Principle of Mine Seismic Detection

The basic principle of seismic exploration is based on the difference of wave impedance of different medium. Generally it could be divided into three parts: acquisition, processing and interpretation.

Figure 1 illustrates how the mine seismic data is acquired. Seismic waves triggered from each shot point will be received as effective signal by geophones bringing along information of different interface's wave impedance. The following aspects should be considered in data acquisition process.

Selection of geometry parameters, including the sampling rate, group interval and the minimum offset. According to the past working practice, frequency of coal roadway seismic data and rock roadway data is generally no more than 3000Hz and 5000Hz respectively, with the sample rate

0.05ms and 0.08ms. The highest frequency of Nyquist frequency recovery is 6250Hz and 10000Hz respectively, which can meet the requirements of data acquisition. Small group interval will lose far offset data, while big interval will affect the consistency of events, also the geometry the actual mine should be considered. Minimum angle offset is set according to the angle between the direction of main and advance anomaly interface and the direction of the face tunneling. When the angle is small, converted wave can be induced due to small offset, and when the angle is large, you will need to increase minimum offset. The actual detection results shows bigger minimum offset will weaken the signal and then damage the resolution.

Geological conditions and geometry of mine may differ tremendously. Hence we can make the appropriate adjustments to the observation system according to the site, to ensure the smooth construction.

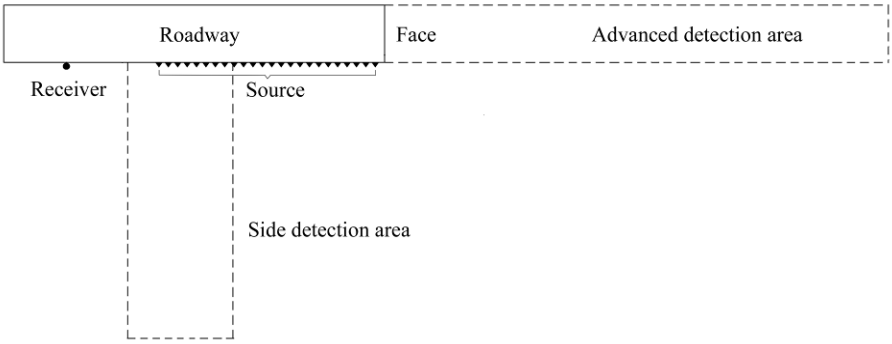


Fig.1 Sketch of seismic data acquisition

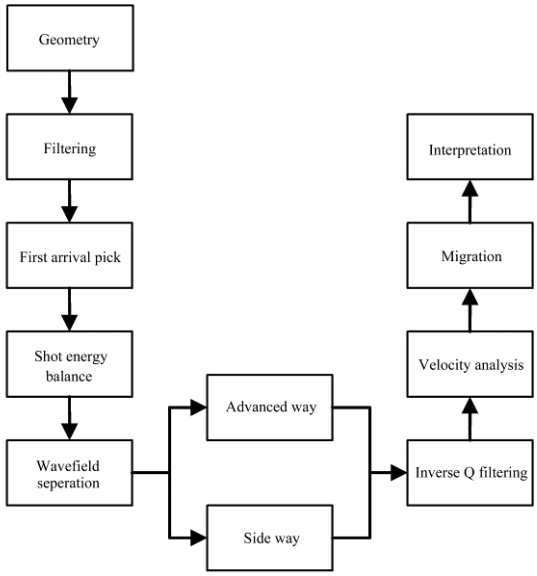


Fig.2 Seismic data processing flow chart

Mine seismic data processing includs 3 steps, the establishment of geometry, separation wave field and migration.The specific details of the process flow are shown in Figure 2. Firstly we establish geometry, input the group interval, receiver and roadway geometry information to the processing system, and then there will be filtering of seismic data applied in order to eliminate sound waves, surface waves and artificial noise. Then we pick up first arrivals of the filtered seismic data, using the least squares method for early correction of each channel seismic to calculate the direct wave velocity for subsequent processing and analysis. As the shots fired, the energy source may not be completely consistent in each channel, so we need to balance the data for the accuracy of processing. The wave field of the data is then separated, and the geophones receive the seismic signals from all directions of shod head in front, rear and side. The advance detection only need to use seismic reflection signals

from shod head front, and side may only need information from side direction to detect. There are 3 method for wave field separation: Radon transform, FK dip filtering and median filtering.Due to shortage of mine seismic data, the latter two methods are not effective. We use Radon transform to do wave separation. After that Q filtering processing is applied on the seismic wave field, to compensate the amplitude and frequency attenuation during propagation. Then migration will be carried out for advance and side seismic data. There are many seismic migration algorithm, due to the limitations of the mine seismic data, we selected Kirchhoff pre-stack depth migration. Finally, interpret the results, the geophysical results will be translated into geological information.

## Case study

To identify the geological conditions mine advance and side and provide reference for tunneling and mining face, we conduct mine seismic. Because the existence of The PVIs, we rigorously design the geometry. Also due to the relatively uneven north side and the gas discharge tube, we set up geometry on the south side. We have 24 shots, one geophone, a sampling rate of 0.05ms, sampling points of 6000, shots spacing of 1.5m, minimum offset of 18m. In order to prevent loosening of wall of roadway and surface wave interference, we have borehole depth of 1.5m, borehole with the wind and air pressure with seal mud of 1m to ensure process consistency.

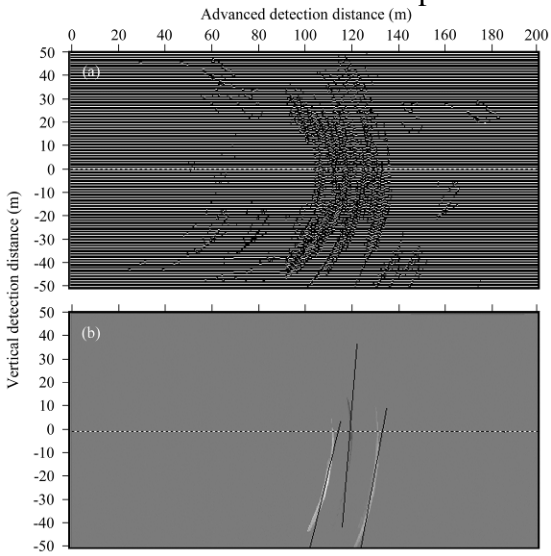


Fig.3 Advanced detection results

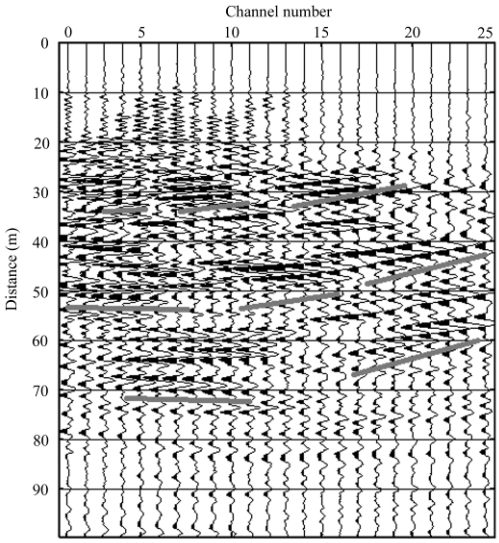


Fig.4 Side detection results

After mine seismic data processing we have results of Figures 3 and Figures 4, where Figure 3 (a) shows migration profile of mine advance, and Figure 3 (b) shows extracted amplitude anomalies interface. The horizontal-axis of Figure 3 represents the distance in the advance direction, the zero point means the geophone position, and the vertical axis represents the distance from the geophone to the top and the bottom plate in the vertical direction. During interpretation, position of the zero point will be moved to the shod head. There exists strong impedance area about40m-60m in front of shod head, with a very large impact scope and a chaos wave field. Figure (b) illustrates that 3 extracted high-amplitude interfaces can be observed, which shows the alternating impedance polarity from negative to positive and back to negative. Through geological analysis, a preliminary predict is made that the anomaly is a collapse column. Generally the column range will be smaller than the anomaly area, but here because the wave field collapse column is more complex and multiple waves are easy to generate, the anomaly range images larger. Figure 4 shows the result of mine side. By migration profile analysis, a strong wave impedance exists in the south mine side between 30m-70m within the detection area, but the continuity of the events is poor , so these anomalies are unlikely to be indicated as faults.

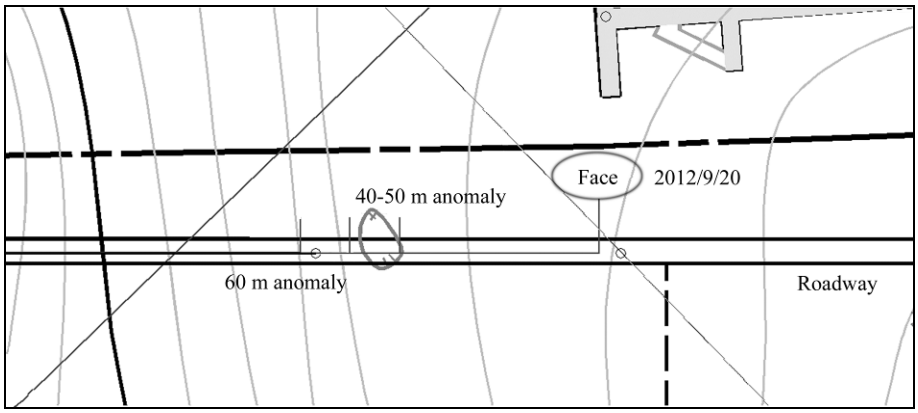


Fig.5 Geological plan

Verified excavation is done and shown in Figure 5. The marked the position of Face shows where the face of the roadway. A small flat oval-shaped collapse column is found at 38m-46m, which composed of limestone from the collapsed roof, well cemented and no water conductivity phenomenon. And it is the reason why the impedance is large and mutiple extist. Verified drilling in Southern side indicate a certain degree of fragmentation in 30m-60m range in coal formation, so the results match our prediction.

## Conclusions

Based on previous studies conducted on the mine seismic applied research, the following conclusions are made: The high resolution, strong anti-interference ability, highly targeted and reliable results of seismic mine detection do have some advantages on predicting fall columns and other geological anomalies in mine exploration. We did pioneer study on simultaneous detection of mine advance and side, by using Radon transform. We separated the seismic wave field of advance and side, and image the two at the same time through pre-stack time migration. The detection of mine advance mainly uses the experience of tunnel advance detection for reference, so there is a solid theoretical basis. But for the detection of mine side there are few studies. The small detection area and shallow detection depth are the focuses of improving direction.

## Acknowledgements

The project supported by National Science and Technology Major Project of the Ministry of Science and Technology of China (Grant No. 2011ZX05040-002).

## References

[1] Li guihua, Zhu guangming, Li guiliang. Wave field characteristics of seismic survey in coal mineroadway[J]. COAL GEOLOGY & EXPLORATION, 2009,37(5):54-57(in Chinese).

[2] Yang sitong, Cheng jiulong. Numerical simulation of fore detecting with seismic in coal roadway and study of wave field characteristics[J]. JOURNAL OF CHINA COAL SOCIETY,2010,35(10):1633-1637(in Chinese).

[3] Hu yunbing, Wu yanqing, Song jing. Analysis on Characteristics of Reflection Seismic Pilot Detecting Technology in Thin Layered Media[J]. JOURNAL OF HENAN POLYTECHNIC UNIVERSITY, 2006,26(6):469-473(in Chinese).

*Applied Mechanics and Materials Vols. 580-583 (2014) pp 1653-1657*
*© (2014) Trans Tech Publications, Switzerland*
*doi:10.4028/www.scientific.net/AMM.580-583.1653*

# Study on the Anti-seismic Performance of New Swing Structure System based on PUSHOVER

Liu Di[1, a]

[1] College of Architecture and Civil Engineering，Shangqiu Normal University，Shangqiu Henan 476000，China

[a]Liudi@sqnc.edu.cn

**Keywords:** Swing Structure System, Pushover, Opensees

**Abstract.** Swing structure is added to the current frame structure for forming the new swing structure system. In this paper, by taking the existing structure as an example, the anti-seismic performance of the new swing system is analyzed with pushover method and the current earthquake resistant design code, and influence of swing rigid frame with different stiffness ratios on the anti-seismic performance of the new structural system is discussed. According to the results, by setting swing rigid frame with different stiffness ratios, it can enhance the bearing capacity and ductility of the structural system remarkably, coordinate the deformation model of the structural system, give full play to the energy-dissipating capacity of the structure, and improve the anti-seismic performance of the structure.

## Introduction

During major disaster, the architectural structure should not only protect people's lives and properties, and some facilities, such as hospitals, fire control and communication command center, etc. should also be responsible for the rescue after disaster and recover the production. However, according to the statistical analysis of previous disasters, it is not difficult to discover that the destruction of construction structure usually exceeds the expected design target. Therefore, for a long time, mangy new structural systems, such as energy dissipation structural system, isolated structural system, recoverable functional structure system, etc. have been proposed successively on the basis of several traditional structural systems by domestic and foreign engineering technologist and scientific researchers. The basic thought is to enhance the safety degree of the agricultural system, to alleviate the damage to the main body of the structural element during the disaster, so as to avoid the severe damage and collapse of the architecture.

In this paper, new swing structural system design is proposed on the basis of previous studies. According to the current code for seismic design of building, the anti-seismic performance level of new swing structure system is discussed with PUSHOVER method, aiming to draw related conclusions for providing references for the judgment of post-seismic injury degree of the related new structural system, which will provide greater selection space for the decision makers and designer of engineering construction.

## Calculation model

According to the statistics of current earthquake damage, during the earthquake process, plastic hinge may occur easily in the top and bottom of the column in frame structural system, which may give rise to the destruction of weak story. Meanwhile, damages to the rest layers are within the expected range. Therefore, the new swing structural system design proposed in this paper is an auxiliary structure attached to the traditional structure system by taking the light strong steel or concrete filled steel tube as the main anti-seismic component of the structural system, and swing structural system is formed. In this paper, an existing reinforced concrete frame structure is redesigned on the basis of the original residential building with general structural design software

PKPM, according to the *Code for Design of Concrete Structures a*nd *Code for Seismic Design of Building*.

The residential building is a six-floor reinforced concrete frame structure. The first floor is a parking lot, with no filler walls, while the above floors are residences, with horizontal and longitudinal filler walls. Considering the influence of filler walls, the rigidity of the bottom layer is remarkably smaller than the upper floors. The earthquake fortification intensity of the building is 8, falling into the second group of Level II, the characteristic site period is Tg=0.4s, the story height is 3.0m, and the floor is 120mm in thickness. The overall effect of PKPM finite element model is shown in figure1. The dead load of the floor in the model is 5.0kN/m$^2$, the live load is 2.0kN/m$^2$, and the combination coefficient is 0.5. The strength grade of concrete is C30, and that of non-structural component if C25, the longitudinal bar is HRB335, the stirrup is HPB235, the transverse reinforcement and the tendon is HPB235.

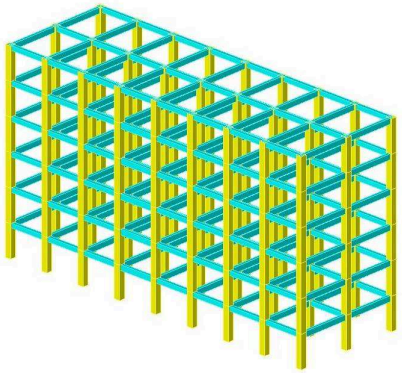

Fig. 1 PKPM Finite Element Model

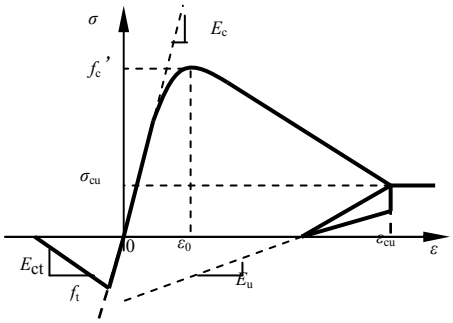


Fig. 2 Uniaxial Material Concrete 02

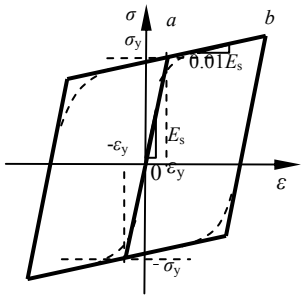


Fig. 3 Uniaxial Material Steel 02

The beam column of the reinforced concrete frame, as well as the beam column and support of the swing rigid frame is simulated with nonlinear Beam Column fiber unit, while the constitutive relation model is the uniaxial material concrete 02 of OpenSees, and the constitutive relation model is shown in figure 2. The constitutive relation model of the steel tube employed by the rebar and concrete filled steel tube is the uniaxial material steel 02 in OpenSees, and the constitutive relation model is shown in figure 3.

In this paper, the finite element method model of the reinforced concrete frame structure and light swing structure system is constructed respectively with the finite element software of Opensees. The finite element model is named as RC and modeli respectively, as shown in table 1.

Table 1 The Finite Element Model

| Stiffness ratio | 0.0100 | 0.1000 | 0.2500 | 0.5000 | 0.7500 | 1.0000 |
|---|---|---|---|---|---|---|
| Swing structure system | M1 | M2 | M3 | M4 | M5 | M6 |

**Model loading plan**

In this paper, the static elastic-plastic analysis of the self-adaption model is realized with Tcl/Tk based on the OpenSees calculation procedure. According to the loading of horizontal yawing force based on the displacement control, the side force is updated every five steps. The horizontal displacement increment takes the 0.02% structural height. Meanwhile, the P-Δ second-order effect is considered, but the interaction with the power of the structure is not considered.

**Selection of performance index**

Before the pushover analysis of static power based on displacement, the performance objective of the light swing structure system is determined according to the current earthquake resistant design code. The earthquake resistant design code of year 2010 takes the control objective of the interlayer

displacement angle under different collapse states aiming at the vertical component, and the maximum inter-layer displacement angle control objective under different collapse states corresponding to the reinforced concrete frame structure is taken as the basis of performance point selection.

According to the related requirements of the engineering practice and current seismic design of buildings in China, the performance objective of the light swing structural system is selected on the basis of the original frame structure, for further improving and guaranteeing the anti-seismic performance of the structure, namely it will not be destructed severely at 8.5 degree and collapse at 9 degree.

**Pushover result analysis**

According to the previous calculation method, the top displacement-base shear curve of the structural model can be achieved, as shown in figure 4.

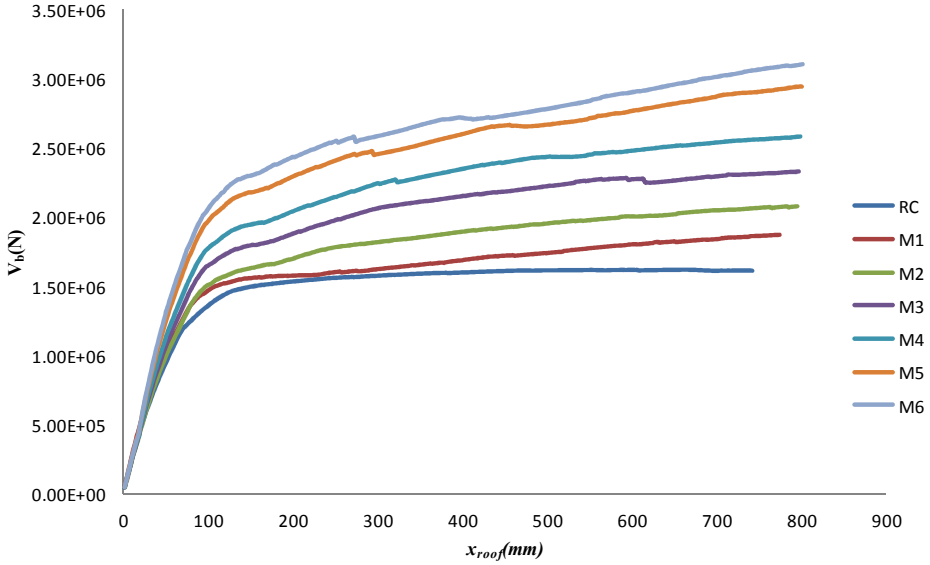


Fig. 4 The top displacement-base shear curve

After the pushover curve of each structural system is obtained, according to equation 1-2, it can be transformed as Sa-Sd curve, namely the relation curve of the spectral acceleration and spectral displacement.

$$S_a = \frac{V_b}{aW} \tag{1}$$

$$S_d = \frac{x_{roof}}{\Gamma \phi^{roof}} \tag{2}$$

According to equation 3, as well as the current anti-seismic code, the demand spectrum curve is established, and the two shall be combined for iteration, thus to achieve the performance point. According to the index of the performance point, if it reaches the anti-seismic performance objective can be achieved can be estimated.

$$S_d = \frac{T^2}{4\pi^2} S_a \tag{3}$$

The power spectrum and demand spectrum curve in A-D coordinate of the frame structure is shown in figure 5.

The earthquake demand spectrum of the reinforced concrete structure intersects as at 7 and 8 degree, and according to the performance point, it can be worked out that the spectrum displacement is 0.05019m, the equivalent damping ratio is 14.756%, and at this moment, it has already entered the plastic stage. At 8 degree, the spectrum displacement is 0.1082m, and the equivalent damping ratio is

21.409%. The maximum inter-layer displacement angle of the bottom at 7 degree is 1/188, and it is 1/52 at 8 degree.

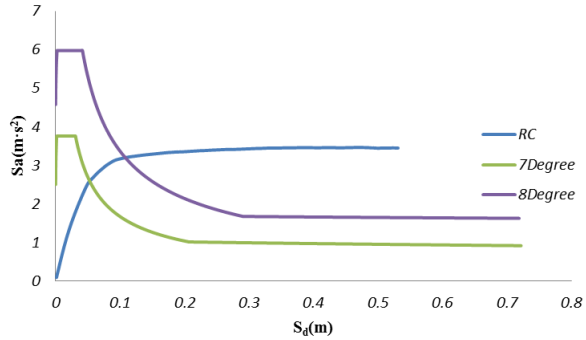


Fig. 5 The top displacement-base shear curve of RC

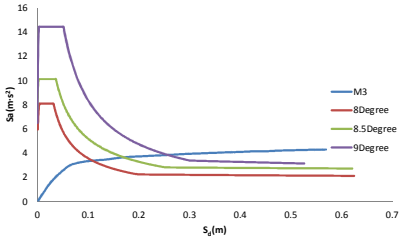


Fig. 6 The top displacement-base shear curve of M3 mode

After the pushover analysis of static force is conducted for M1-M6, it can be discovered that M3 has already reached the requirement of anti-seismic performance objective. The power spectrum and demand spectrum curve of M3 model in A-D coordinate is shown in figure 6. The earthquake demand spectrum of the light swing rigid structure system intersects as at 8, 8.5 and 9 degree. According to the performance point, it can be calculated at the spectrum displacement is 0.1178m, and the equivalent damping ratio is 24.559%. At this moment, it has already entered the plastic structure. At 8.5 degree, the spectrum displacement is 0.1737m, and the equivalent damping ratio is 28.829%. At 9.5 degree, the spectrum displacement is 0.2864m, and the equivalent damping ratio is 34.935%. The maximum inter-layer displacement angle of the bottom layer is 1/226 at 8 degree, 1/98 at 8.5 degree and 1/57 at 9 degree.

## Conclusion

It is not difficult to discover after the analysis of computing result based on the elastic-plastic pushover analysis that:

(1). The overall bearing capacity and ductility of the swing rigidity structure is better than that of the reinforced concrete frame structure.

(2). In major earthquake, more structural components of the swing rigid frame shall participate in the overall anti-seismic work of the structure, and more component may enter the plastic stage, which may result in the remarkable increase of damping ratio.

(3) The performance objective shall be selected rationally, and according to the performance objective, the parameters of the structural system shall be selected, for it can not only improve the anti-seismic performance of the structural system, but also consider the cost control and design requirements.

**References**

[1] CAO H Y, PAN P, YE L P: Pushover analysis of RC frame rocking wall structure[J]. Journal of vibration and shock, vol. 30, no.11(2011), pp.240-245.

[2] ZHOU Y ,LU X L:State-of-the-art on rocking and self-centering structures. Journal of Building structures, vol. 32, no. 9(2011), pp.1-10.

[3] HAN L H, TAO Z,YAN W B:Hysterics behaviors of concrete filled steel tubular beam-columns with circular sections. Earthquake Engineering and Engineering Vibration, vol. 21, no. 1(2001), pp.64-73.

[4] GB50011—2010 Code for seismic design of buildings [S]. Beijing: China Architecture and Building Press(2010)

[5] Yongfeng, Li Hui, Billie F.Spencer,Jr., Zhao Guofan: Real mode superpose-tion method for analysis of seismic response of non-proportionally damped isolated structures[ J] . Engineering Mechanics, vol. 20, no.4(2003), pp.24-32.

*Applied Mechanics and Materials Vols. 580-583 (2014) pp 1658-1661*
*© (2014) Trans Tech Publications, Switzerland*
*doi:10.4028/www.scientific.net/AMM.580-583.1658*

# Study on the seismic safety of the Qinghai traditional dwellings

Mengjie Zhang[1, a], Lianxin Liu[1,b] and Yanan Shi[1,c]

[1] Department of Civil Engineering, Qinghai University, Xining, 810016, China

[a]qin.uo@163.com, [b]qhdxllx@126.com, [c]tsshiyanan@126.com

**Keywords:** traditional dwellings; Zhuangke; field research; seismic issues

**Abstract.** Qinghai is a multi-ethnic region, mainly living in the eastern agricultural areas Han, Hui and Tu, mainly living in the southwest area of animal husbandry Tibetan and Mongol. In order to adapt to the cold, arid, windy and long sunshine time climate of Qinghai, people created a unique style of traditional vernacular dwelling, Zhuangke. This unique architectural form is mainly with wooden frame bearing, matching with brick walls or rammed earth walls. Such buildings are mostly villagers themselves built according to past experience; do not involve seismic design, resulting in a great security risk. Through the field investigation of ten natural villages, this article has a deep understanding of the seismic performance of Zhuangke. Based on survey data, this paper presents its structural safety and seismic performance problem.

## Introduction

Qinghai is a multi-ethnic region, the province with an average elevation of 3,000 meters, is a typical plateau continental climate, with dry, little rain, windy, alpine-cold and long sunshine time, etc. Qinghai inhabited by the Han, Hui, Tu and Salar ethnic groups. Traditional dwellings in Qinghai are affected by geographical position and local customs, and become a unique form of local-style dwellings, Zhuangke.

Zhuangke is the basic form of Han, Tu, Hui and Salar's local-style dwelling houses. It is a load-bearing wood frame construction. Combined with the national characteristics, Zhuangke made different decorative timber frame, as shown in Fig. 1. The main enclosure walls are rammed earth walls, adobe walls and brick walls (Fig. 2).

The research of Qinghai Zhuangke has begun in the 1970s. Most of the current studies are to explore the adaptability to natural environment from residential function, courtyard layout and construction technology, and do not involve the study of seismic performance. The ten natural villages for research involves Han, soil, back and Sala, including Huzhu County, Xunhua County and Ledu County. Through the field investigation of traditional dwellings for the three main ethnic in Qinghai, this article has a deep understanding of the seismic performance of Zhuangke. Based on survey data, this paper presents its structural safety and seismic performance problem. Detailed analysis of each question is as follows.

## Research Analysis

Through the analysis of field research found that currently there are the following seismic weaknesses of Zhuangke: the lack of connection measures for enclosure walls and roof trusses, the shallow embedment of column base, inadequate connections for columns and walls, without overlapping measures in vertical and horizontal wall junction, the big stiffness differences of walls and timber frame. Detailed analysis of each question is as follows.

Fig. 1 The national decoration of Zhuangke

(a) Traditional Zhuangke (b) Newly-built Zhuangke

Fig. 2 The different structure form of traditional and newly-built Zhuangke

**The lack of connection measures for enclosure walls and roof trusses.** There is no connection between roof and wall body, and nor between purlin and gable (Fig.3).The mechanical properties of wood components and walls are much different, and there is no valid connection between the two. In the earthquake, the two can't keep working together, leading to the knot in vertical and horizontal wall cracking and making wall into a monolithic wall. Due to the lack of effective connection between gables and purlins, gables are prone to out-of-plane instability. So the probability of gables' collapse is higher than the vertical wall.

Fig. 3 The connection measures for enclosure walls and roof trusses

**The shallow embedment of column base.** The survey finds poles mainly are placed directly on the base block, as shown in Fig. 4. Under earthquake, horizontal seismic action can only be transferred by friction of column's end face. This force's transfer road is easy to cause column foot sliding, even lead to column foot slipped from base blocks, and finally cause the timber frame collapsed.

Fig. 4 The embedment of column base

**Inadequate connections for columns and walls.** Some of Zhuangke's pillars are all wrapped by the wall, some are partly wrapped, and others separate from the wall (Fig. 5). It is obvious that there is no reliable connection between retaining walls and pillars, so under the earthquake action, the damage of walls would occur before the timber frame. Between a timber frame beams are usually joggle, so their joints' stiffness and strength are low. After the destruction of the wall, the building will lost the main component to resist lateral force. In the larger horizontal earthquake, the mortise-tenon joints start loosening, and then the building will appear lateral deformation in the direction of the weaker stiffness. When the lateral deformation is much larger, the whole structure will collapse.

(a) pillars are all wrapped (b) pillars are partly wrapped (c) pillars separate from the wall

Fig. 5 The relationship between the pillar and wall

**Without overlapping measures in vertical and horizontal wall junction.** The junctions of vertical and horizontal walls are rickety, which is prone to produce vertical cracks. Because of the lack of connection measures, the junction of gable walls and back walls will crack and damage. Especially when pillars are wrapped by walls (Fig.6), due to the pillars weaken the cross section of the wall, the walls' integrity decreases.

**The big stiffness differences of walls and timber frame.** The greater weight of the wall, its deformation is lower. The larger stiffness difference between the wall and the wooden skeleton makes the wall easily to collapse in the earthquake. Rammed earth walls are more likely to be collapsed in the earthquake, and the damage of brick walls is not serious. And the construction process of adobe walls and rammed earth walls are labor-intensive and time-consuming. Due to rainfall, walls would severe damaged (Fig. 6) and need regular repair. So the villagers prefer to use brick walls as enclosure walls. So in economically developed areas, new-built Zhuangkes mainly

use brick walls instead of rammed earth walls and adobe walls, which were widespread used. Although walls' material improved, but the block walls mainly do not take necessary seismic measures.

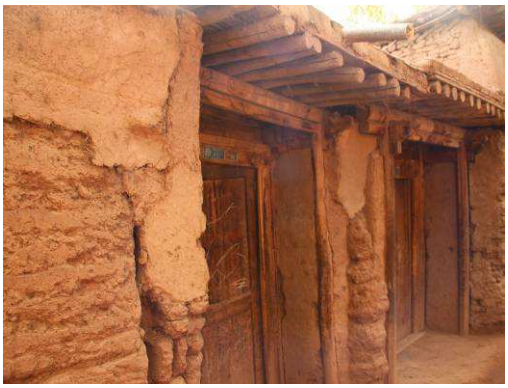

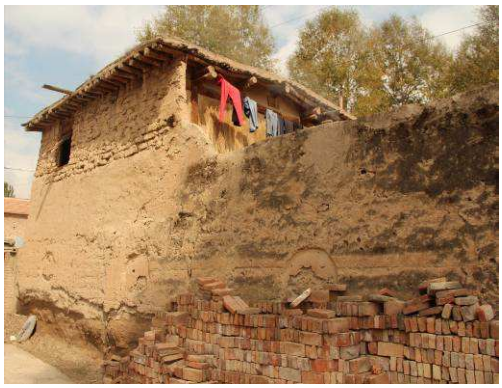

Fig. 6 The damage of walls

## Conclusions

In order to adapt to the cold, arid, windy and long sunshine time climate of Qinghai, people created a unique style of traditional vernacular dwelling, Zhuangke. Such buildings are mostly villagers themselves built according to past experience; do not involve seismic design, resulting in a great security risk. There are many seismic performance problems and seriously affect the structural safety. How to solve the questions, to improve the seismic performance and structural safety of Zhuangke is the main direction of the future research. Only by improving the seismic performance of Zhuangke, enhance the safety of traditional houses in Qinghai, and promote the long-term inheritance of the national characteristics.

## Acknowledgements

This work was financially supported by one of the National Science & Technology Pillar Program, the Integration demonstration of plateau ecological community planning and green building technology (2013BAJ03B03) and Study on current situation and improvement techniques about dwellings' seismic performance in Qinghai province (2013-QGY-9).

## References

[1] Shujia Cui. Eastern Qinghai Dwellings, Zhuangke[J]. Architectural Journal. 1963(01). （in Chinese）

[2] Jing Ha, Rui Pan. Analysis on The Regional Features of Qinghai "Zhuangke" Traditional House[J]. Architectural History. 2009(12). （in Chinese）

[3] Jun Guo, Tiansheng Zhong, Xiejun Zhou, Constrution Technology of Vernacular Dwellings Zhuangke in Qinghai[J], Industrial Construction. 2009(S1). （in Chinese）

[4] Nan Shao. Study on the Adaptability to natural geographic environment of Zhuangke[J]. Qinghai Science and Technology. 2010(01). （in Chinese）

[5] Junming Gu,Study on Seismic Performance of Timber Construction in Villages[D]. Kunming: Kunming University of Science and Technology. 2006.3. （in Chinese）

[6] Xuguang Lu, Experimental Study on Seismic Strengthing of the Timber Residence in Villages and Small Towns[D], Chang'an University, Xi'an. 2011.6. （in Chinese）

*Applied Mechanics and Materials Vols. 580-583 (2014) pp 1662-1666*
*© (2014) Trans Tech Publications, Switzerland*
*doi:10.4028/www.scientific.net/AMM.580-583.1662*

# A suggestion on uncertainty correction of ground motion attenuation in probabilistic seismic hazard assessment

Wang Chuanfang[1] *Tao Xiaxin[1,2,a] Anastasia Z[1] Zhao Kai[2] Jiang Wei[2]

[1] School of Civil Engineering, Harbin Institute of Technology, Harbin 150090, China

[2] Institute of Engineering Mechanics, China Earthquake Administration, Harbin, 150080, China

[a]taoxiaxin@aliyun.com

**Keywords:** Uncertainty correction; Ground motion; Attenuation; PSHA

**Abstract**. The uncertainty of ground motion attenuation and its correction in PSHA is deal with in this paper. Mean values and standard deviations of random errors of three attenuation relationships of NGA-west1 are analyzed statistically from the data base released by the project. The dependences of the mean and deviation on magnitude, distance and peak ground acceleration are checked by the data base. The fact of mean values varying with acceleration is revealed obviously. Ground motion parameter Y is adopted into the probability density function of random error in a form of subsection. Finally, a suggestion to improve the correction is presented as subsection correction in the paper. The result of a case study by suggested procedure shows that the corrected acceleration is slightly higher than that of the traditional correction at the start of hazard curve, and is significantly lower than that of the traditional correction at the end of the curve, if the mean of random error decreases with acceleration.

## Introduction

Due to the lack of the seismic and geological data and poor understanding of effect of focal mechanism, seismic wave transmission and the local site conditions on PSHA, there must be a lot of uncertainty in the result, in which the uncertainty of attenuation relationship is dominant. Corresponding correction naturally become an issue for people, and the large increase of risk in low probability has been controversial.

Probabilistic seismic hazard assessment, PSHA was founded more than forty years ago, and have been adopted in seismic hazard assessment world wide [1, 2], while it was queried on and off. The uncertainty process is one of the most focuses in the debates. Some researchers pointed out that overestimation happened in some PSHA projects come from unreasonable correction of uncertainty of ground motion attenuation [3-5]. Esteva revealed the fact that the distribution of the random error of motion attenuation was accord with Normal distribution, and developed a correction procedure. He mentioned that variation of the random error was obvious, so that to take into account the error in PSHA is especially important [6]. Ang and Der Kiureghian suggested a procedure to combine the uncertainty of the attenuation into inherent uncertainty of ground motion by means of total probability formula, after seismic hazard estimated from a mean attenuation relationship [7]. It is called as ‘correction’ now, and its rationality is queried since there are often some large increases on the corrected hazard especially at very low exceeding probability range.

As part work of an ongoing project of basic issues in seismic hazard assessment (51178151) supported by NSFC, the improvement of uncertainty correction have been deal with. This paper presents just a preliminary result.

**Ground motion attenuation relation and its uncertainty**

Attenuation relation predicts a ground motion parameter for given magnitude and distance with simplification on source mechanism, wave propagation and local site condition. Survey and analysis in several decades show the fact that there is always a quite large variation in ground motion, even if from similar magnitude, depth, distance and site condition, for whatever which motion parameter [8, 9]. In general, attenuation relationship of ground motion could be represented as following formula

$$\ln Y = f(M, R) + \varepsilon \tag{1}$$

where $Y$ is for motion parameter, e. g. peak ground acceleration; $M$ for magnitude, $R$ distance, f for a function form, $\varepsilon$ is for the difference between $\ln Y$ and $f(M, R)$, called as random error above. From the fitting principle, $\varepsilon$ must have a Normal distribution with 0 mean, i.e. the standard deviation $\sigma$ is the only numerical character. It is not hopeful to attempt reduce the $\sigma$ obviously by means of adding any more variable, or expending data base from accumulated observing data. The following figure shows that clearly [10].

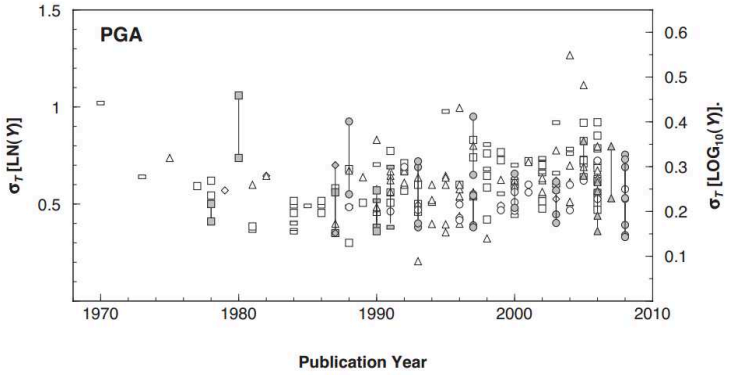


Figure 1 The variation of $\sigma$ with publication year

It is obvious that $\sigma$ represents the inherent randomness, error from simplification, and validity of the function form $f$, the latter could be considered as result of ignorance on attenuation [11].

NGA project released a good data base of ground motion, and worked out three attenuation relationships with $\sigma$ values of acceleration 0.52, 0.72 and 0.67. The corresponding distributions are shown in Fig. 2, where C-B is for Campell-Bozorgnia [12], C-Y for Chiou-Youngs [13] and Id for Idriss [14].

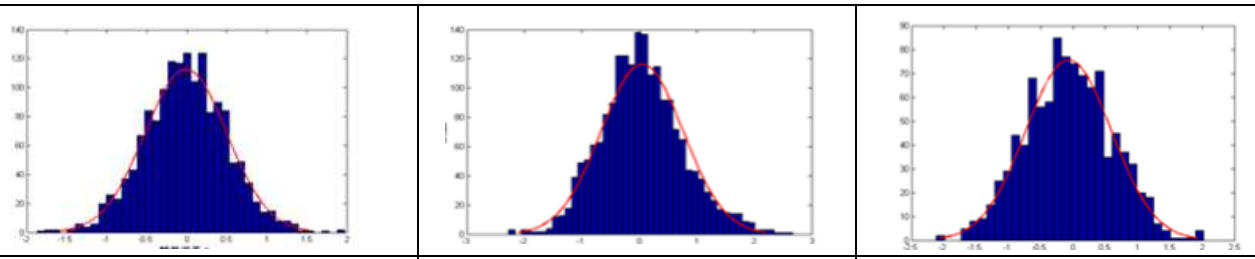

| C-B relation | C-Y relation | Id relation |
|---|---|---|

Figure 2 Histograms and the corresponding Normal distribution curves

The mean and $\sigma$ of $\varepsilon$ of the three relations in total and in three magnitude groups, are listed in table 1. In the table, there are three values in each grid separated by '/' respectively for C-B (left), C-Y (middle) and Id (right).

Table 1 The numerical characters of $\varepsilon$ of the three relations in magnitude groups

| Magnitude | Number of data | Percentage (%) | Mean | $\sigma$ |
|---|---|---|---|---|
| [4.5, 5.5) | 264/369/90 | 17/19/9.1 | -0.068/0.073/0.354 | 0.623/0.726/0.742 |
| [5.5, 6.5) | 349/995/603 | 22.5/51.3/61.1 | -0.103/0.064/-0.062 | 0.502/0.632/0.634 |
| [6.5, 8.0) | 938/576/294 | 60.5/29.7/29.8 | 0.037/-0.193/-0.210 | 0.481/0.566/0.645 |
| In total | 1551/1940/987 | 100 | -0.012/0.048/-0.067 | 0.516/0.715/0.666 |

The same values in four distance groups are listed in table 2, where * is for no data in that group.

Table 2 The numerical characters of $\varepsilon$ of the three relations in distance groups

| Distance (km) | Number of data | Percentage (%) | Mean | $\sigma$ |
|---|---|---|---|---|
| (0, 10] | 115/157/55 | 7.4/8.1/5.6 | 0.056/-0.074/-0.147 | 0.474/0.716/0.708 |
| (10, 50] | 680/1182/329 | 43.8/60.9/33.3 | -0.030/0.099/-0.018 | 0.543/0.715/0.664 |
| (50, 100] | 500/601/409 | 32.2/31.0/41.4 | -0.013/-0.021/-0.093 | 0.498/0.710/0.667 |
| (100, 200) | 256/*/174 | 16.6/*/17.6 | 0.008/*/-0.072 | 0.492/*/0.646 |
| In total | 1551/1940/987 | 100 | -0.012/0.048/-0.067 | 0.516/0.715/0.666 |

The same values in three acceleration groups are listed in table 3.

Table 3 The numerical characters of $\varepsilon$ of the three relations in acceleration groups

| Acceleration (g) | Number of data | Percentage (%) | Mean | $\sigma$ |
|---|---|---|---|---|
| (0.02, 0.1] | 971/1166/800 | 63/60.1/79.7 | 0.139/-0.132/-0.160 | 0.496/0.682/0.620 |
| (0.1, 0.4] | 500/673/171 | 32/34.7/17 | -0.233/0.280/0.237 | 0.457/0.673/0.729 |
| (0.4, -) | 80/101/33 | 5/5.2/3.3 | -0.474/0.584/0.596 | 0.435/0.646/0.525 |
| In total | 1551/1940/987 | 100 | -0.012/0.048/-0.067 | 0.516/0.715/0.666 |

From the tables, one can find that the numerical characters do not vary with magnitude and distance obviously, or no clear trend of variation with magnitude and/or distance, but the absolute value of mean decreases with acceleration very clearly while $\sigma$ is quite stable. This trend is clearer in Fig. 3.

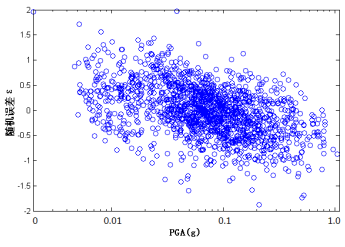


C-B

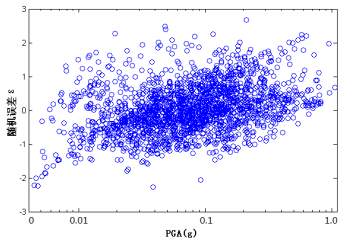


C-Y

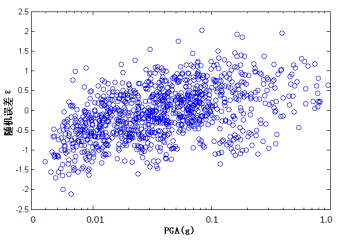


Id

Figure 3 The distribution of $\varepsilon$ with acceleration

An improvement to distribution of random error is suggested from the above findings as Normal distribution with same $\sigma$ and subsection mean, $f_y(\varepsilon)$. To define the $f_y(\varepsilon)$ in subsections from situation that a continuous function of the mean on acceleration can not be developed from the limited data at present

**Subsection correction of uncertainty of ground motion attenuation in PSHA**

From the total probability theorem, the correction formula with $f_y(\varepsilon)$ could be expressed as

$$P(Y_c > y) = \int_{-3\sigma}^{3\sigma} P(Y > ye^{-\varepsilon}) f_y(\varepsilon) d\varepsilon \tag{2}$$

where $Y_C$ is for the corrected ground motion parameter, e. g. acceleration; $Y$ is for the uncorrected one; $f_y(\varepsilon)$ the probability density function of $\varepsilon$ with a stable $\sigma$ and different means in some acceleration subsections.

For a given acceleration y, in the $i^{th}$ subsection among $(y_0, y_1], (y_1, y_2]\ldots\ldots(y_{n-1}, y_n]$, the correction formula could rewritten in detail as

$$\mathrm{P}(Y_C > y) = \int_{\mu_i-3\sigma}^{\mu_i+3\sigma} P(Y > ye^{-\varepsilon}) f(\varepsilon) d\varepsilon \tag{3}$$

where $\mu_i$ is the mean of $\varepsilon$ in the $i^{th}$ subsection.

For the purpose to get a set of more even subsections with their own detail mean, a statistics of in four acceleration groups are again worked out. The result from data without those with small acceleration is listed in table 4. The resulted hazard curves as an example are shown in Fig. 4.

Table 4 The mean values of $\varepsilon$ of C-B relation in four acceleration groups

| Acceleration (g) | Number of data | Percentage (%) | Mean | $\sigma$ |
|---|---|---|---|---|
| (0.01, 0.05] | 388 | 29.7 | 0.135 | 0.468 |
| (0.05, 0.1] | 442 | 33.8 | -0.006 | 0.390 |
| (0.1, 0.2] | 276 | 21.1 | -0.120 | 0.438 |
| (0.2, 1.0) | 201 | 15.4 | -0.231 | 0.442 |
| In total | 1307 | 100 | -0.027 | 0.452 |

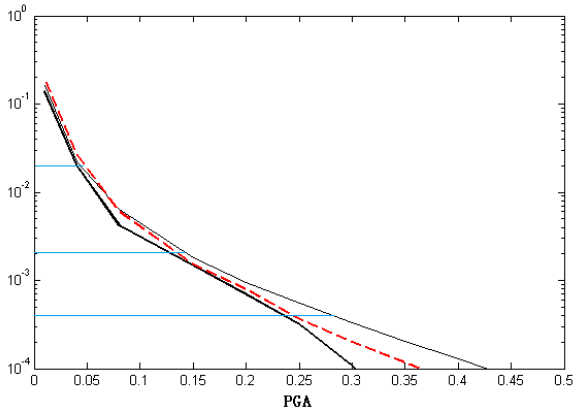


Figure 4 The hazard curves for an engineering site

One can see from the figure that the acceleration for a given exceeding probability by subsection correction is smaller than that by correction with mean 0, especially for the low exceeding probability.

## Conclusion

In order to improve the representation of random error of ground motion attenuation, three NGA-west1 relations are checked and analyzed statistically by their own data bases. The result shows that the error distributions are Normal with stable standard deviation and a varied mean. It is true but not sure for all attenuation relationship published up to know. To take the findings into account, a subsection probability density function is suggested in this paper, and a subsection correction of the uncertainty of attenuation relation in seismic hazard assessment is also presented. Result of a case study shows that hazard curve by subsection correction is lower than that by correction with mean 0, i. e. the acceleration for a low given exceeding probability by subsection correction is obviously smaller than that by correction with mean 0.

The NGA-west 2 data base was released in 2012, and then the attenuation from those data would published soon, therefore the contribution of the paper is just a preliminary suggestion, but is really interested.

## Acknowledgements

This paper is financially supported by the National Nature Science Foundation of China (51178151 and 51178435), International Science & Technology Cooperation Program of China (2011DFA21460), and KJ1343 of Special Scientific Research Fund of IWHR，China.

## References

[1] Cornell C A. Bulletin of the Seismological Society of America, 1968, 58(5): 1583-1606.
[2] Tao X X. Dissertation for Master degree in engineering. Institute of Engineering Mechanics, Academia Sinica. 1981 (in Chinese)
[3] Bommer J J, Abrahamson N A. Bulletin of the Seismological Society of America, 2006, 96(6): 1967-1977.
[4] Strasser F O, Abrahamson N A, Bommer J J. Seismological Research Letters, 2009, 80(1): 40-56.
[5] Stein S, Geller R J, Liu M. Tectonophysics, 2012.
[6] Esteva L, Villaverde R. Proceedings of Fifth World Conference on Earthquake Engineering. 1973, 2: 2586-2596.
[7] Der Kiureghian A and Ang A H-S. Bulletin of the Seismological Society of America, 67(4), 1977
[8] Tao X X. Journal of natural disaster，1992, 1(1)：101-111 (in Chinese)
[9] Tao X X. World Earthquake Engineering. 1987, (2): 17~26 (in Chinese)
[10] Douglas J. Earth-Science Reviews, 2003, 61(1): 43-104.
[11] Tao X X, Z R Tao, L Wang. Civil Construction and Environment Engineering, 2010，32（S2）:138-142 (in Chinese)
[12] Campbell K W, Y Bozorgnia. Campbell-Bozorgnia. PEER Report. 2007
[13] Chiou B, R R Youngs. PEER Report. 2008
[14] Idriss I M. Interim Report Issued for USGS Review. 2007
[15] Ancheta T D, Y Bozorgnia, R Darragh, W J Silva, B Chiou, J P Stewart, D M Boore, R Graves, N A Abrahamson, K W Campbell, I M Idriss, R R Youngs, G M Atkinson. 15WCEE N.5599, Lisbon, Span, 2012
[16] Campbell K W, Y Bozorgnia. 15WCEE N.2942, Lisbon, Span, 2012

*Applied Mechanics and Materials Vols. 580-583 (2014) pp 1667-1675*
*© (2014) Trans Tech Publications, Switzerland*
*doi:10.4028/www.scientific.net/AMM.580-583.1667*

# Average Damage Ratio and Earthquake Damage Matrix of Non- engineered Building in Seismogenic Provincial Regions in China

XING Juehui, LU Ming[a], ZHAO Yamin, YU Yan

[1]Institute of Crustal Dynamics, China Earthquake adminstration, Beijing100085,China

[a] luming6@yeah.net

**Keywords:** non-engineered building; seismic damage assessment; damage ratio; average damage ratio; earthquake damage matrix

**Abstract.** Non-engineered buildings are most of self-built house, which locate in rural area in China. The structural defect of non-engineered buildings could reduce seismic capacity. The damage of these buildings are the main cause of earthquakes casualties and economic losses. The main types of the building structures include the wooden house, soil and wood house, brick and wood house and masonry house. It is the seismogenic provincial regions for Xinjiang, Qinghai, Gansu and Yunnan in China. Based on the four type houses in the four regions, 104 earthquake disaster loss reports were selected from 1990 and 2013. This article focused on the analysis of house damage data. This article proposes "the average damage ratio" concept, which takes one provincial region as an area and studies the whole area data. Due to a combination of multiple and differenteffects of earthquakes within one provincial region, the average damage ratio can be on behalf of the damage ratio, and reflects the non-engineered building characteristics in the provincial region. And then the article demonstrates that the earthquake damage matrix of different house types in these four provinces area. The earthquake damage matrix provides a more reliable basis for the earthquake disaster evaluation in rural area.

## Introduction

Non-engineered buildings are not only informally designed and constructed, but also have much structural defect and high vulnerability. China should face and admit the facts that non-engineered buildings are widely used in the country, and the largest engineering group leading to huge losses and casualties in earthquakes. Most of the earthquakes and heavy disasters occurred in the western region in China, such as Xinjiang, Qinghai, Gansu, Yunnan and Sichuan. It is necessary to carry out seismic capacity study of non-engineered buildings in these regions.

The non-engineered buildings in China are mainly located in rural areas, and mainly self-built house. Because the national area is vast and the natural and the humanistic environments are much different, these same type houses have much different in various regions. The seismic damage ratio of buildings is the most direct performance of the quantitative seismic capacity. It is the basic work of the closest to the actual to research on the damage ratio of different types of buildings from earthquake survey data.

## Earthquake Survey Method and Data Sources

### *Site Survey Methods*

It has been more than 20 years for the earthquake disaster assessment to step into the scientific and standardized track in China. The earthquake disaster assessment explores in Datong-Yanggao earthquake in 1989. The first regulation of the earthquake damage assessment enacted in 1993. The earthquake damage assessment officially started as a responsibility of national and provincial earthquake administration bureaus since 1993. The assessment method in practical work continuously improved and refined. The earthquake damage assessment method has already become national standard since 2005[1].

Building damage survey is the core of China's earthquake disaster assessment. The site assessment method is summarized as follows:

a. Sample survey methods including restrictions regulations of survey path and sampling rate.
b. Identify structure type.
c. Assessment on the level of damage and construction area statistic.
c. Comprehensive assessment and classification of intensity area.
d. Calculation of various types of house and different levels of the damage ratio for each seismic intensity.
e. Calculate the total loss of all types of house by using the unit house area cost, different levels of damage loss ratio and the damage ratio of buildings.

The damage ratio just reflects house damage only one earthquake, because the damage ratio obtained from one seismic event. It can be analyze the seismic capacity of the houses in the affected areas.

In summary, the damage ratio of buildings contains four key elements, which are as house types and destruction grades, specific earthquake and its intensity area.

However, to understand the house seismic capacity and to establish the damage matrix in a greater area, the more information of the damage assessment data need to obtain, and more analysis need to finish.

*House Damage Data Sources*

This paper analyzes the house damage data of the 188 earthquake damage assessment reports from 1990 to 2013. Ultimately selected data are from the available, more reliable 104 reports, which earthquake events are shown in the Table1 to Table2.

**Table1 Xinjiang Earthquake Directory**

| Time | Place | Magnitude | Time | Place | Magni-tude | Time | Place | Magni-tude |
|---|---|---|---|---|---|---|---|---|
| 1993.12.1 | Kashen | 6.0 | 1998.6.25 | North of Akesu | 5.2 | 2003.2.24 | Bachu-Jiashi | 6.8 |
| 1995.5.29 | Jimunai | 5.0 | 1998.7.28 | Baicheng | 5.5 | 2003.5.4 | Jiashi | 5.8 |
| 1996.3.19 | Jiashi-Atushen | 6.9 | 1998.8.2 | Jiashi | 6.0 | 2003.9.2 | Aketao | 5.9 |
| 1997.1.21 | Jiashi | 6.4, 6.3 | 1998.9.18 | Aheqi | 4.4, 4.8 | 2003.12.1 | Zhaosu | 6.1 |
| 1997.3.1 | Jiashi | 6.0 | 1999.3.15 | Keche | 5.6 | 2005.8.26 | Moyu | 5.2 |
| 1997.4.6, 4.11, 4.16 | Jiashi | 6.3, 6.4, 6.6, 6.3 | 1999.6.17 | Baicheng | 5.3, 5.0 | 2008.3.21 | Yutian-Cele | 7.3 |
| 1998.3.19 | Atushen | 6.0 | 2001.3.24 | North-west of Hejing | 5.0 | 2011.11.1 | Nleke-Gongliu | 6.0 |
| 1998.5.29 | Pishan | 6.2 | 2003.1.4 | Jiashi | 5.4 | 2012.6.30 | Xinyuan-Hejing | 6.6 |

**Table2 Qinghai Earthquake Directory**

| Time | Place | Magni-tude | Time | Place | Magni-tude | Time | Place | Magni-tude |
|---|---|---|---|---|---|---|---|---|
| 1994.1.3 | Gonghe-Xinghai | 6.0 | 1995.7.9 | Gonghe-Xinghai | 5.3 | 2000.9.12 | Xinghai | 6.6 |
| 1994.2.16 | Gonghe-Xinghai | 5.8 | 1995.7.22 | Yongdeng (in Qinghai) | 5.8 | 2003.4.17 | Delingha | 6.6 |
| 1994.9.4 | Gonghe-Xinghai | 5.3 | 1995.12.18 | Maduo | 6.2 | 2010.4.14 | Yushu | 7.1 |
| 1994.9.24 | Gonghe-Xinghai | 5.5 | 1999.11.26 | Maqin | 5.0 | | | |
| 1994.10.10, 10.12 | Gonghe-Guinan | 5.3 | 2000.4.15 | Zaduo | 5.3 | | | |

**Table3 Gansu Earthquake Directory**

| Time | Place | Magni-tude | Time | Place | Magni-tude | Time | Place | Magni-tude |
|---|---|---|---|---|---|---|---|---|
| 1995.7.22 | Yongdeng | 5.8 | 2002.12.14 | Yumeng | 5.9 | 2004.9.7 | Min-Zhuoni | 5.0 |
| 1996.6.1 | Tianzhu-Gulang | 5.4 | 2002.12.14 | Yumeng | 5.9 | 2012.5.3 | Jiuquan – Alashan | 5.4 |
| 1999.4.15 | Wenxian-Wudu | 4.7 | 2003.10.25 | Minle-Shandan | 6.1, 5.8 | 2013.7.22 | Minxian-Zhangxian | 6.6 |
| 2001.7.11 | Sunan | 5.3 | 2003.11.13 | Minxian-Lintan-Zhuoni | 5.2 | | | |

**Table4 Yunnan Earthquake Directory**

| Time | Place | Magni-tude | Time | Place | Magni-tude | Time | Place | Magni-tude |
|---|---|---|---|---|---|---|---|---|
| 1993.1.27 | Puer | 6.3 | 1998.10.1, 10.27 | Ninglang | 5.3, 5.2 | 2003.7.21 | Dayao | 6.2 |
| 1993.5.30 | Jinggu-Lincang-Shuangjiang | 4.9, 5.0, 5.0 | 1998.11.19 | Ninglang | 6.2 | 2003.10.16 | Dayao | 6.1 |
| 1993.7.17 | Zhongdian | 5.6 | 1998.11.1 | Xuanwei | 5.1 | 2003.11.15 | Ludian | 5.1 |
| 1993.8.14 | Yaoan | 5.6 | 1999.11.25 | Chengjiang | 5.2 | 2003.11.26 | Ludian | 5.0 |
| 1994.9.19 | Jinggu | 5.2 | 2000.1.15 | Yaoan | 5.9, 6.5 | 2004.8.10 | Ludian | 5.6 |
| 1995.2.18 | Cangyuan-Lancang | 5.1 | 2000.1.27 | Qiubei-Mile | 5.5 | 2004.10.19 | Baoshan Longyang | 5.0 |
| 1995.7.12 | Menglian | 7.3 | 2000.8.21 | Wuding | 5.1 | 2004.12.26 | Shuangbai | 5.0 |
| 1995.10.24 | Wuding | 6.5 | 2000.10.6 | Longchuang | 5.8 | 2005.1.26 | Simao | 5.0 |
| 1996.2.3 | Lijiang | 7.0 | 2001.4.10 | Shidian | 5.9 | 2005.8.5 | Huize-Huidong | 5.3 |
| 1996.7.2 | Lijiang | 5.2 | 2001.5.24 | Ninglang-Yanyuan | 5.8 | 2005.8.13 | Wenshan | 5.3 |
| 1996.9.25 | Lijiang | 5.7 | 2001.6.8 | Shidian | 5.3 | 2012.6.24 | Ninglang-Yanyuan | 5.7 |
| 1997.1.25 | Mengla-Jinghong | 5.1 | 2001.7.10 | Chuxiong | 5.3 | 2012.9.7 | Yiliang | 5.7, 5.6 |
| 1997.1.30 | Jinghong-Jiangcheng | 5.5 | 2001.7.15 | Jiangchuang | 5.1 | | | |
| 1997.10.23 | Lijiang | 5.3 | 2001.10.27 | Yongsheng | 6.0 | | | |

## Non-engineered Building Types and Average Damage Ratio

*The Non-engineered Building Types*

According to the survey data, buildings can be divided into two categories, After earthquake-proof building and non-engineered building. The main types of the non-engineered buildings include wooden house, soil and wood house, brick and wood house and masonry house, shown in Table 5.

**Table 5 The non-engineered building types and code**

| | The non-engineered building types | code |
|---|---|---|
| 1 | wooden house | A1 |
| 2 | soil and wood house | A2 |
| 3 | brick and wood house | A3 |
| 4 | masonry house without seismic design | B |

The types and codes of each kind house consistent with The Chinese Seismic Intensity Scale[5].

*Average Damage Ratio*

Within an appropriate range of large area, the houses of the same type have no or a little change in the structure, the damage ratio of houses can be analyzed in quantitative combining multi-earthquake damage data. This article proposes " the average damage ratio " concept, which takes one provincial region as an area and studies the whole area data of under multiple and different earthquakes. Due to a combination of multiple effects of earthquakes within one provincial region, the average damage ratio can be on behalf of the damage ratio in the provincial region.

The average damage ratio is calculated as the Eq.1- Eq.2.

According to the The Chinese Seismic Intensity Scale [5], the damage ratio $\lambda_i$ is as follows,

$$\lambda_{ij} = A_j \Big/ S_j \tag{1}$$

$i$ --- damage level of house.

$j$ --- type of house structure.

$A$ --- the sum construction area of j type houses which damage level is i in a seismic intensity area.

$S$ --- the total construction area of j type houses in a seismic intensity area.

The calculation of average damage ratio considers damage ratio $\lambda_i$ of multi- earthquakes under one same seismic intensity area, $\overline{\lambda_i}$ is as follows,

$$\overline{\lambda_{ij}} = \frac{\sum_{k=1}^{n} \lambda_{ij}^{\ k}}{n}. \tag{2}$$

$i$ --- damage level of house.

$j$ --- type of house structure.

$k$ --- earthquake serial number.

$n$ --- earthquake occurrences for statistics.

$\overline{\lambda_i}$ --- average damage ratios under a certain damage level $i$.

$\lambda_i$ --- damage ratios under a certain damage level $i$.

*Average damage ratio of the 4 provincial regions*

According to the above definition, the average damage ratios are calculated for the various type house of non-engineered buildings. All of the data are from Xinjiang, Qinghai, Gansu and Yunnan in China. Fig.1-Fig.4 show that the average damage ratios of the same type house are much different in various provincial regions.

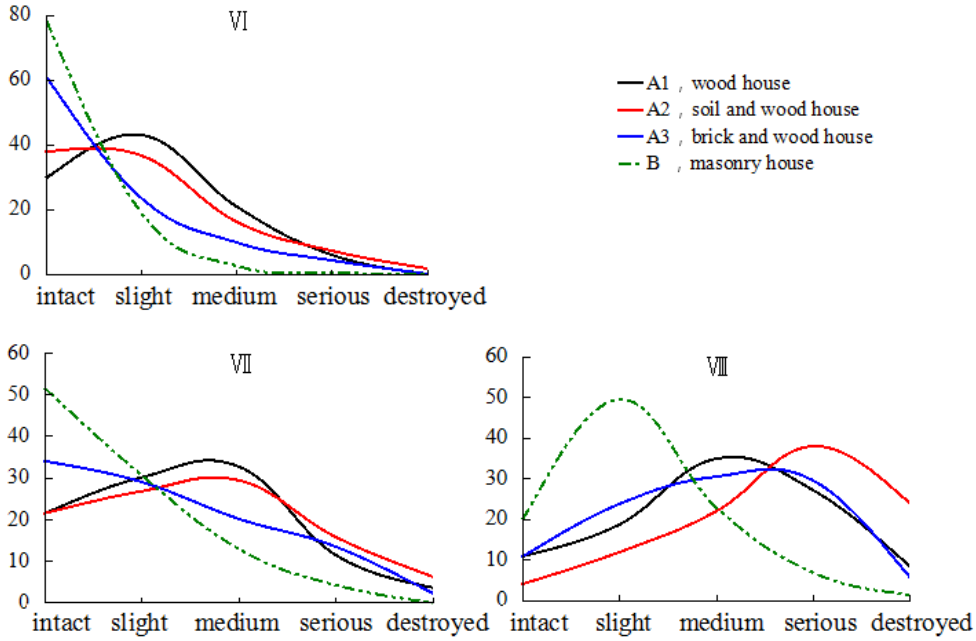


**Fig.1 Damage Ratio of House in Gansu**

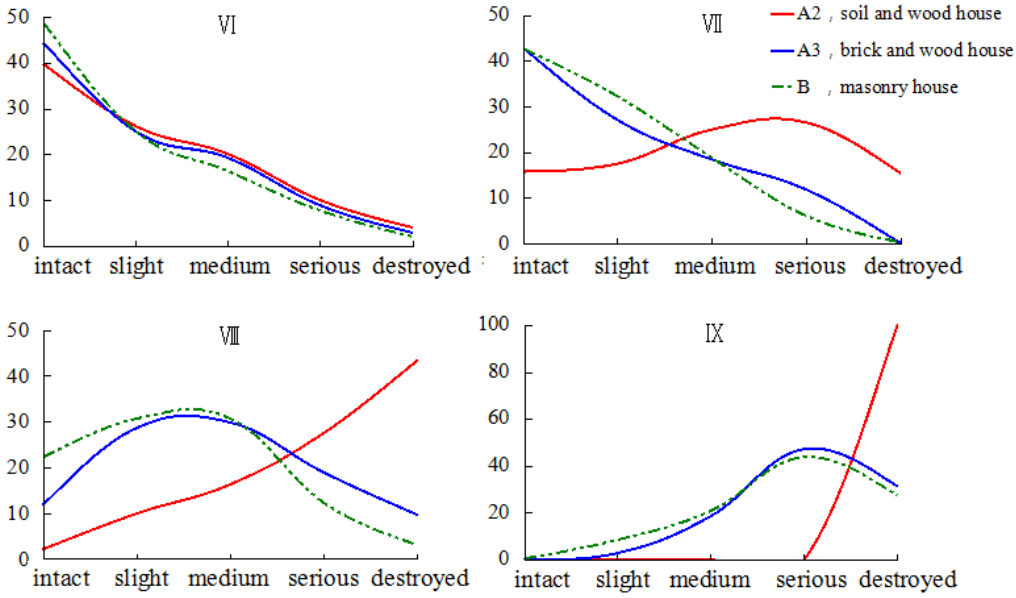


**Fig.2 Damage Ratio of House in Qinghai**

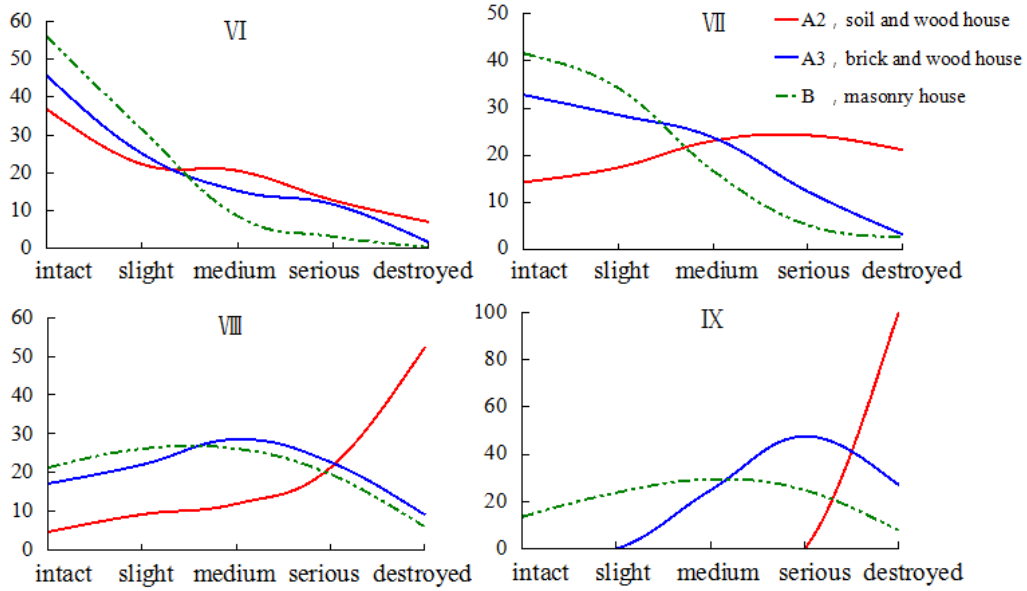


**Fig.3 Damage Ratio of House in Xinjiang**

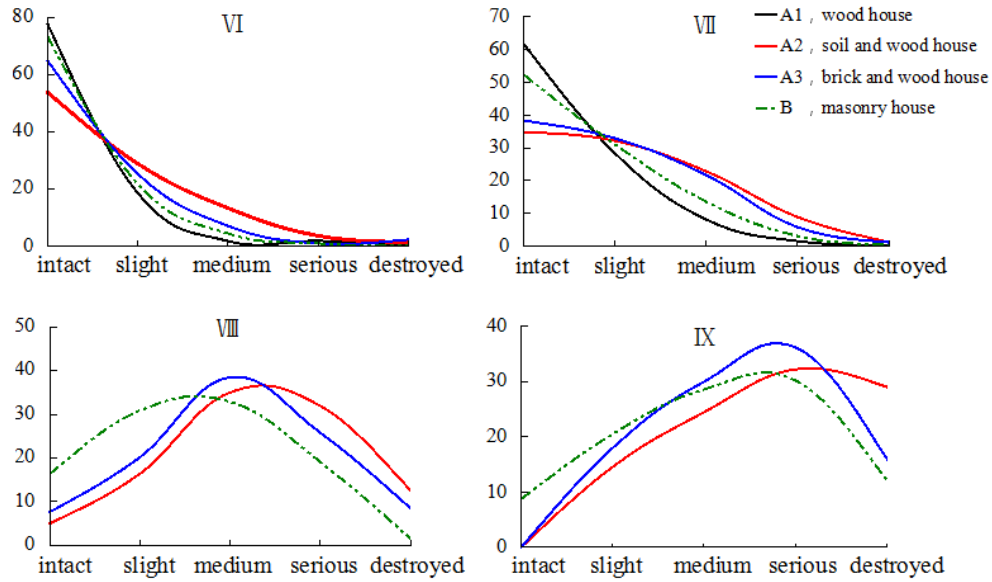


**Fig.4 Damage Ratio of House in Yunnan**

### Earthquake Damage Matrix of Non-engineered Building

The earthquake damage matrix can be obtained by analyzing a large number of building damage survey data of multi earthquakes. The matrix indicates the probabilities of different damage level of house under a seismic intensity.

Through earthquake damage matrix, it is objectively and reasonably to analyze the seismic capacity of various types of house, and evaluate or predict the extent of house damage.

According to the average damage ratio of the non-engineered buildings, earthquake damage matrix can be obtained, which reflects the house characteristics and the seismic capacity in Xinjiang, Qinghai, Gansu and Yunnan provincial region respectively, shown in Table 6-Table 9.

**Table 6 Xinjiang Earthquake Damage Matrix**

| housetype | damage / intensity | intact | slight | medium | serious | destroyed |
|---|---|---|---|---|---|---|
| soil and wood house | Ⅵ | 37.0 | 22.4 | 20.5 | 12.8 | 7.3 |
| | Ⅶ | 14.3 | 17.3 | 23.1 | 24.3 | 21.0 |
| | Ⅷ | 4.9 | 9.4 | 12.0 | 21.5 | 52.2 |
| | Ⅸ | 0.0 | 0.0 | 0.0 | 0.0 | 100.0 |
| brick and wood house | Ⅵ | 45.9 | 25.3 | 15.2 | 11.9 | 1.7 |
| | Ⅶ | 32.7 | 28.5 | 23.6 | 12.2 | 3.0 |
| | Ⅷ | 17.1 | 22.2 | 28.7 | 22.7 | 9.3 |
| | Ⅸ | 0.0 | 0.0 | 25.0 | 48.0 | 27.0 |
| masonry house | Ⅵ | 56.0 | 31.5 | 8.5 | 3.4 | 0.6 |
| | Ⅶ | 41.5 | 34.3 | 16.5 | 5.2 | 2.5 |
| | Ⅷ | 21.5 | 26.4 | 26.3 | 19.7 | 6.1 |
| | Ⅸ | 13.5 | 24.0 | 29.6 | 24.8 | 8.1 |

**Table 7 Qinghai Earthquake Damage Matrix**

| housetype | damage / intensity | intact | slight | medium | serious | destroyed |
|---|---|---|---|---|---|---|
| soil and wood house | Ⅵ | 39.6 | 26.1 | 20.1 | 10.1 | 4.1 |
| | Ⅶ | 15.8 | 17.5 | 25.2 | 26.3 | 15.2 |
| | Ⅷ | 2.3 | 10.1 | 16.6 | 27.6 | 43.4 |
| | Ⅸ | 0.0 | 0.0 | 0.0 | 0.0 | 100.0 |
| brick and wood house | Ⅵ | 44.1 | 25.1 | 19.2 | 8.8 | 2.8 |
| | Ⅶ | 42.6 | 27.1 | 18.6 | 11.7 | 0.0 |
| | Ⅷ | 12.1 | 28.9 | 30.1 | 18.9 | 10.0 |
| | Ⅸ | 0.0 | 2.7 | 18.6 | 47.3 | 31.4 |
| masonry house | Ⅵ | 48.6 | 25.1 | 16.5 | 7.8 | 2.0 |
| | Ⅶ | 42.8 | 32.2 | 18.6 | 6.1 | 0.3 |
| | Ⅷ | 22.4 | 31.0 | 30.9 | 12.6 | 3.1 |
| | Ⅸ | 0.5 | 8.0 | 20.5 | 43.7 | 27.3 |

**Table 8 Gansu Earthquake Damage Matrix**

| housetype | damage / intensity | intact | slight | medium | serious | destroyed |
|---|---|---|---|---|---|---|
| wood house | Ⅵ | 30.0 | 42.9 | 21.1 | 6.0 | 0.0 |
| | Ⅶ | 21.5 | 30.3 | 32.7 | 11.8 | 3.7 |
| | Ⅷ | 10.8 | 18.7 | 34.9 | 27.2 | 8.4 |
| soil and wood house | Ⅵ | 38.0 | 36.5 | 16.4 | 7.4 | 1.7 |
| | Ⅶ | 21.5 | 26.8 | 29.6 | 15.8 | 6.3 |
| | Ⅷ | 3.9 | 11.9 | 22.1 | 38.0 | 24.1 |
| brick and wood house | Ⅵ | 60.8 | 23.5 | 11.0 | 4.5 | 0.2 |
| | Ⅶ | 34.2 | 29.1 | 20.4 | 13.8 | 2.5 |
| | Ⅷ | 10.7 | 23.6 | 30.5 | 29.4 | 5.8 |
| masonry house | Ⅵ | 77.9 | 18.8 | 2.8 | 0.5 | 0.0 |
| | Ⅶ | 51.6 | 30.8 | 12.9 | 4.6 | 0.1 |
| | Ⅷ | 20.1 | 49.4 | 22.6 | 6.6 | 1.3 |

**Table 9 Yunnan Earthquake Damage Matrix**

| housetype | damage / intensity | intact | slight | medium | serious | destroyed |
|---|---|---|---|---|---|---|
| wood house | Ⅵ | 77.9 | 18.5 | 1.7 | 1.7 | 0.2 |
| | Ⅶ | 61.6 | 28.5 | 8.0 | 1.6 | 0.3 |
| soil and wood house | Ⅵ | 53.5 | 28.9 | 13.1 | 3.4 | 1.1 |
| | Ⅶ | 35 | 32 | 23 | 8.9 | 1.1 |
| | Ⅷ | 4.8 | 16.2 | 34.8 | 31.9 | 12.3 |
| | Ⅸ | 0.0 | 14.6 | 24.3 | 32.1 | 29.0 |
| brick and wood house | Ⅵ | 64.6 | 25.4 | 7.1 | 0.9 | 2.0 |
| | Ⅶ | 38.4 | 33.0 | 21.7 | 5.8 | 1.1 |
| | Ⅷ | 7.5 | 20.0 | 38.4 | 25.8 | 8.3 |
| | Ⅸ | 0.0 | 19.0 | 29.0 | 36.0 | 16.0 |
| masonry house | Ⅵ | 73.1 | 21.5 | 4.4 | 1.0 | 0.0 |
| | Ⅶ | 52.1 | 31.2 | 13.5 | 3.0 | 0.2 |
| | Ⅷ | 16.1 | 30.8 | 32.8 | 19.0 | 1.3 |
| | Ⅸ | 8.8 | 20.6 | 28.5 | 30.1 | 12.0 |

## Conclusions

The article studied non-engineered buildings in seismogenic provincial regions in China. What the features are that these buildings are not only informally designed and constructed, but also exist much structural defect and high vulnerability. Non-engineered buildings exist widely in China, and are the largest engineering group led to huge losses and casualties in earthquakes.

The damage data of the study are from 104 reports of earthquake damage assessment from the 1993 to 2013 in Xinjiang, Qinghai, Gansu and Yunnan in China.

This article proposes " the average damage ratio " concept, which takes one provincial region as an area and studies the data of earthquake damage assessments in the whole area. Due to a combination of different effects of earthquakes within one provincial region, the average damage ratio can be on behalf of the damage ratio in the provincial region. On the other hand, the damage ratio just reflects such house damage of only one earthquake.

The earthquake damage matrix indicates the probabilities of different damage degree of house under differential seismic intensity. The article gives respectively the earthquake damage matrixes of the non-engineered buildings in Xinjiang, Qinghai, Gansu and Yunnan of China, which provide a more reliable basis for the earthquake disaster evaluation in these rural areas.

## Acknowledgements

This work was financially supported by the National Natural Science Foundation Program (51278469,51108428), the Beijing Nova Program (Z121106002512059), the research grant from Institute of Crustal Dynamics, China Earthquake Administration (ZDJ2013-03, ZDJ2013-4), and the seismic industry special (200708047).

## References

[1] GB/T 18208.3-2000 *Post-earth field works-Part3: Code for field survey, Part4: Assessment of direct loss*[S]. Beijing: China Camera Standard, 2000 (in Chinese)

[2]*The Compilation of Disaster Losses Assessment in Chinese Mainland(1990~1995)*[M]. Beijing: Seismological Press, 1996. (in Chinese)

[3]*The Compilation of Disaster Losses Assessment in Chinese Mainland(1996~2000)*[M]. Beijing: Seismological Press, 2001. (in Chinese)

[4] T*he Compilation of Disaster Losses Assessment in Chinese Mainland(2001~2005)*[M]. Beijing: Seismological Press, 2010 (in Chinese)

[5] GB/T17742-2008 *The Chinese Seismic Intensity Scale*[S]. Beijing: China Camera Standard, 2008 (in Chinese)
[6] Zhiqian Yin. *Classification of Structural Vulnerability and Estimation of Earthquake Disaster in The Future*[J]. Earthquake research in China,1996,01:49-55.(in Chinese)
[7] Gansu Provincial Earthquake Bureau. Disaster Losses Asse*ssment of Yushu M7.1 earthquake.*[R]. Beijing: China Seismological Bureau,2010 (in Chinese)
[8] Xinjiang Provincial Earthquake Bureau. *Disaster Losses Assessment of Nileke-Liulian M6.0 earthquake.*[R]. Beijing: China Seismological Bureau,2011 (in Chinese)
[9] Yunnan Provincial Earthquake Bureau. *Disaster Losses Assessment of Ninglang-Yanyuan M5.7 earthquake.*[R]. Beijing: China Seismological Bureau,2012 (in Chinese)
[10] Xinjiang Provincial Earthquake Bureau. *Disaster Losses Assessment of Xinyuan-Hejing M6.6 earthquake.*[R]. Beijing: China Seismological Bureau,2012 (in Chinese)
[11] Xinjiang Provincial Earthquake Bureau. *Disaster Losses Assessment of Yutian M6.2 earthquake.*[R]. Beijing: China Seismological Bureau,2012 (in Chinese)
[12] Gansu Provincial Earthquake Bureau. *Disaster Losses Assessment of Jiu-Alashan M5.4 earthquake.*[R]. Beijing: China Seismological Bureau,2012 (in Chinese)
[13] Yunnan Provincial Earthquake Bureau. *Disaster Losses Assessment of Yiliang M5.7, M5.6 earthquake.*[R]. Beijing: China Seismological Bureau,2012 (in Chinese)
[14] Gansu Provincial Earthquake Bureau. *Disaster Losses Assessment of Zhangxian-Minxian M6.6 earthquake.*[R]. Beijing: China Seismological Bureau,2013 (in Chinese)
[15] Xinjiang Provincial Earthquake Bureau. *Disaster Losses Assessment of Nileke-Liulian M6.0 earthquake.*[R]. Beijing: China Seismological Bureau,2011 (in Chinese)

*Applied Mechanics and Materials Vols. 580-583 (2014) pp 1676-1679*
*© (2014) Trans Tech Publications, Switzerland*
*doi:10.4028/www.scientific.net/AMM.580-583.1676*

# Collapse-resistance measure for the bottom frame structure under earthquake

Duozhi Wang[1,2, a], Junwu Dai[1,2,b] , Ruochen Shan[1,2,c]

[1]Institute of Engineering Mechanics, China Earthquake Administration

[2]Key Laboratory of Earthquake Engineering and Engineering Vibration, CEA

[a]wangdz_iem@126.com, [b]junwudai@126.com, [c]498123190@qq.com

**Keywords:** collapse-resistance measure; the bottom frame structure; earthquake; collapse model

**Abstract.** The bottom frame structure, with serious earthquake damage, occupies a large proportion in the houses collapsed in earthquakes. However, because it is economic and practical, it is still widely used. Based on the understanding of the seismic performance of bottom frame structure, this paper determines to study seismic measures of the bottom frame structure. The current seismic measures can be divided into two major categories: strengthening key components and avoiding key components, therefore this paper adopts the method of strengthening parts which are easy to collapse for reinforcement, under the premise of meeting the stiffness ratio between reasonable layers, adds wing wall to improve the capacity of resisting collapse of the structure and pinpoints the efficiency of adding wing wall in the capacity of resisting collapse through quantitative analysis. Although there are differences in the improvement of the capacity of resisting collapse under different seismic waves, adding wing walls reasonably can greatly improver the anti-collapse capacity of the structure..

## Introduction

The structural collapse is the main cause of casualties caused by the earthquake. In Wenchuan Earthquake, the collapse of houses with bottom frame structures is a common phenomenon, and in Beichuan County, the rate of this structural collapse has reached 80%. Houses with bottom frame structures are universal in middle-sized and small cities in the south of Yangtze River in China, according to rough statistics, there exist more than 20 million houses of this kind and more than 120 million residential population at the present in China. Researches on seismic measures of this structure for the improvement in the anti-collapse capacity of houses with this structure have been an urgent social need. (Fig. 1)

(a) (b)

Fig. 1 Collapse of ground floor[1]

**Major characteristics of earthquake damage and suggestions on anti-collapse**

The main forms of the bottom frame structure collapse include collapses of the bottom frame layer, transition layer and the whole structure, among which, the collapses of the bottom frame layer and the whole structure are caused by the damage in the bottom frame layer. In addition, local damage of the structure occurs firstly in the bottom frame layer in most cases. Therefore, reducing the damage in the bottom frame layer is the major measure for avoiding the collapse of the bottom frame structure. Due to commercial purposes, the earthquake resistant wall of the bottom frame structure is usually arranged in the back facade of the structure, nearly no shear wall is set on the longitudinal side of the structure. Although this can meet needs in the commercial use, it is prone to lead to torsion failure of the structure in earthquakes. Therefore, taking commercial use into consideration, it is necessary to set up wing walls in the front of the structure as much as possible to reduce the eccentricity of the structure seismic damage to the structure. Therefore, based on quantitative analysis on the role of wing walls setting up on the front of the bottom frame structure, the following numerical analysis has been conducted.[2]

**The comparison analysis on the anti-seismic collapse of the bottom frame structure**

**Design information** According to the current design code, the shear wall structure on the 7°0.15g area of the first layer in the bottom frame is designed, the structure is located at the site of the second category with a total height of 4 layers, where, the bottom layer is 4.5m high, the rest layers are 3m high, the bottom frame column is 400 × 400mm2, the frame beam 300 × 600mm2, the thickness of the reinforced concrete earthquake resistant wall is 300mm, and the upper masonry structure is sintered brick MU10, the mortar is M10, mortar, the grade of concrete strength is C30, the longitudinal reinforcement is HRB335 and the stirrup is HPB300, comparison analysis on the earthquake response is conducted between cases with and without front wing wall. The structural plane layout is shown in Figure 2. Where, the lateral stiffness ratio between structural layers in the structure without wing wall is 1.93 and the lateral stiffness ratio of the structure with swing wall is 1.02. It can be found that the structural layout is more uniform and symmetrical after setting swing wall and the eccentricities of structural barycenter and steel center have been greatly improved, details can be seen table 1.

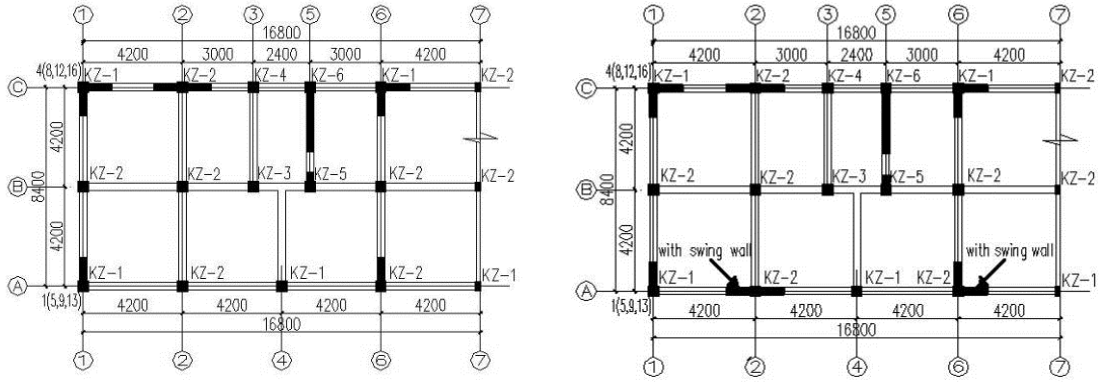


(a) Without Swing Wall (b) With Swing Wall

Fig.2 The structure arangement

Table 1 The eccentricity of the structure

| | Barycentric Coordinate | | steel center Coordinate | | Centroid Coordinate | | Barycentric Eccentricity | | Centroid Eccentricity | |
|---|---|---|---|---|---|---|---|---|---|---|
| | X | Y | X | Y | X | Y | X | Y | X | Y |
| Without Swing Wall | -0.0021 | 0.4805 | -0.0021 | 2.8302 | 0 | 0 | -0.0021 | 0.4805 | -0.0021 | 2.8302 |
| With Swing Wall | -0.0021 | 0.1694 | -0.0021 | 0.4600 | 0 | 0 | -0.0021 | 0.1694 | -0.0021 | 0.46 |

**Comparison analysis between finite elements** The bottom frame structure finite element model in ANSYS, multilinear isotropic model is adopted in concrete and masonry, multilinear isotropic model is adopted in steel to simulate, and the element type adopts SOLID65. The interaction between soil and structure is not taken consideration, while the material nonlinearity is not, the fixed form is used in the bottom structure and its finite element model is shown in Figure 3.

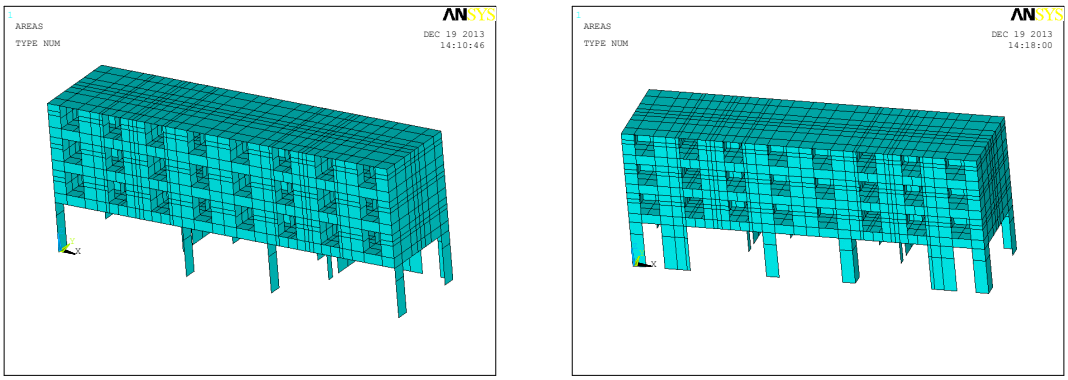


(a) Without Swing Wall (b) With Swing Wall

Fig.3 The FE model

311 seismic wave, the Wolong seismic wave and Ya'an seismic wave are input respectively and are conducted simulation. It is compared and found that there are the following improvements on the the seismic performance of the bottom frame structure after adding swing wall:

1. The displacement of the bottom frame structure decreases significantly, especially on the side adding swing wall.(Fig. 4(a), (b))
2. With the increase of layers, the trend of decrease in displacement declines gradually. (Fig. 4(b), (c))
3. There is a significant control effect on the vertical displacement and displacement on the side adding shear wall.
4. There are significant differences in anti-seismic effects caused by different seismic waves. (Fig. 4(b), (d) , (e))

It can be seen that adding shear wall on the front without affecting the commercial use has improved the seismic performance of the structure with lower cost. It is suggested that stipulating the minimum shear wall ratio on the back of the bottom frame structure in design, so as to reduce the seismic damage caused by the torsional deformation of the structure and improve anti-seismic capacity of the structure.

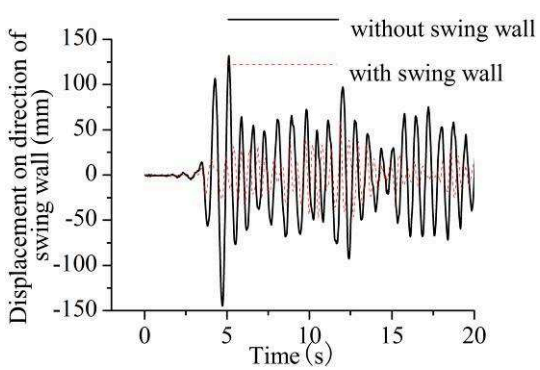


(a) Displacement on X of point 1 under 311 wave

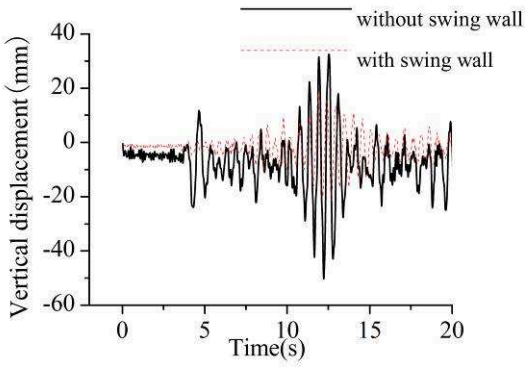


(b) Displacement on Z of point 1 under 311 wave

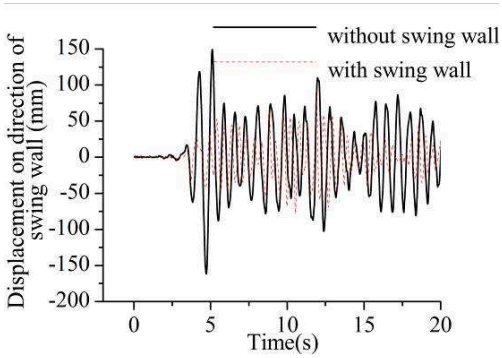


(c) Displacement on X of point 13 under 311 wave

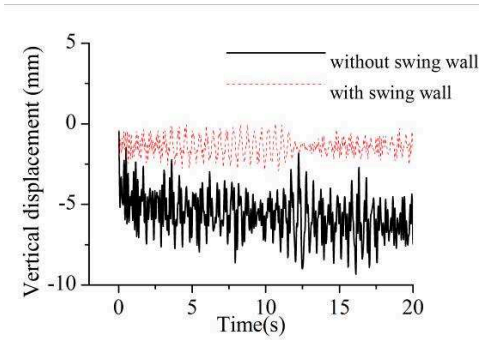


(d)Displacement on Z of point 1 under Wolong wave

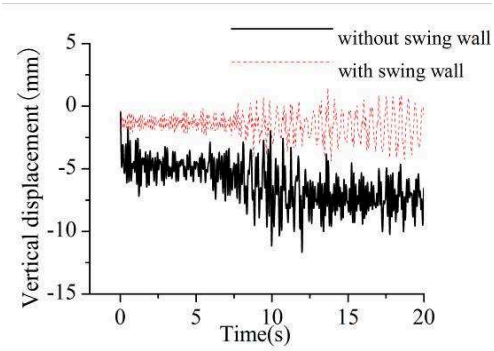


(e) Displacement on Z of point 1 under Yaan wave

Fig.4 The comparison of seismic performance of structure

## Conclusions

In view that the bottom frame structure is economical, practical and widely used with serious seismic damage, and its collapse rate is high in practical earthquake, and reinforcing the key part and adding swing wall in the bottom layer under the premise of meeting requirements in regulated and reasonable stiffness rate between layers, has achieved great anti-seismic effect. At the same time, analysis on anti-seismic effects of different seismic waves has been conducted, and it is found that though there are differences in the anti-seismic effect between different seismic waves, they have achieved better effect. The displacement of the bottom frame structure has decreased significantly, especially on the side adding swing wall; with the increase of layers, the trend of decrease in displacement declines gradually; There is a significant control effect on the vertical displacement and displacement on the side adding shear wall; and there are significant differences in the anti-seismic effects caused by different seismic waves.

## Acknowledgement

This work was financially supported by the China Natural Science Foundation (51108430, 91315301), and The Postdoctoral Science Foundation of Heilongjiang Province (LBH-Z12267).

## References

[1] Wang Duozhi, Dai Junwu, Zhang Chenxiao. seismic damage analysis for multi-story masonry building with RC frames on ground floor. Applied Mechanics and Materials, 2012, Vols. 204-208:2555-2558.

[2] Duozhi Wang, Zhang Chenxiao, Junwu Dai. Elaborate failure model and seismic response analysis for Multi-story Masonry Building with R. C. Frames on Ground Floor. Advanced Materials Research Vols. 753-755 (2013) pp 504-507

*Applied Mechanics and Materials Vols. 580-583 (2014) pp 1680-1686*
*© (2014) Trans Tech Publications, Switzerland*
*doi:10.4028/www.scientific.net/AMM.580-583.1680*

# Dynamic analysis of artificial boundaries in gravity dam-foundation rock interaction system

Wen Qiao[1,a], Guoming Liu[1,b]

[1]College of Civil Engineering, Fuzhou University, 2 Xue Yuan Road,

University Town, Fuzhou, Fujian, China 350108

[a]qiaowen1213@163.com, [b]lgm6379@163.com

**Keywords:** hydraulic structure, artificial boundary condition, gravity dam-foundation system, dynamic analysis, seismic wave

**Abstract.** ANSYS was used to focus on comparative analysis of several artificial boundary conditions that are widely used in engineering applications. The accuracy and stability of dynamic analysis results were then analyzed in details of a semi-infinite foundation with different artificial boundaries and different frequency input loads. Lastly, the seismic response of a gravity dam-foundation rock system was explored numerically. Experimental results revealed the simulation accuracy of artificial boundaries was closely related to the dynamic characteristics of input load and the elastic wave velocity. When the input load frequency was high, only the material with comparably higher elastic wave velocity could maintain the stability of the artificial boundary. Viscoelastic artificial boundary is practically simple and can better simulate the semi-infinite material elastic recovery ability and energy radiation outside the boundary.

## Introduction

Over the recent decades, the research of dynamic interactions of gravity dam-foundation under seismic action has made a certain progress. With the development of computer technologies and experimental techniques, the measurement data with respect to model test, earthquake monitoring and in situ observation has been accumulated continuously[1]. However, the better combination of structural dynamic response and seismic wave still needs further study. Nowadays, there exists quite a number of artificial boundary simulation techniques in the interaction analysis of dam-foundation rock, such as viscous boundary[2], viscoelastic boundary[3], transmitting boundary[4-5] and paraxial approximation boundary[6-7]. Nevertheless, under the condition of different materials, the simulation accuracy of different artificial boundaries vary, and there is rare comparison research of the simulation results under different calculation conditions for these artificial boundaries. For this reason, using ANSYS to simulate a semi-infinite foundation with different artificial boundaries, including viscous boundary, elastic boundary, viscoelastic boundary, fixed boundary and extended boundary, this paper conducted a comparative analysis of the dynamic responses under different frequency input loads, as well as the calculation accuracy and stability of these boundaries. Then, the seismic response of a viscoelastic boundary gravity dam-foundation rock system was analyzed in details, which thereby provided with a reference to anti-seismic analysis for similar engineering projects.

## Common Artificial Boundary Theory

**Viscous Boundary.** The viscous boundary, brought up by Lysmer et al[2], takes into consideration of impact of wave energy dissipation over soil dynamic properties. The setting idea of such

boundary is to set dampers at the boundary which absorb the energy of lay scattered waves, that is, to apply damping forces along the normal and tangential directions at the calculation area boundary, then to transform the damping forces to equivalent concentrated forces at the boundary nodes, eventually to calculate the damping forces along the two directions of every boundary nodes. The expressions they obtained of normal stress σ and tangential stress τ of the boundary nodes with relation to horizontal displacement u and vertical displacement w are shown as follows:

Bottom Boundary:

$$\left.\begin{aligned}\sigma &= a_H \rho v_p w \\ \tau &= b_H \rho v_s \dot{u}\end{aligned}\right\} \quad (1)$$

Side Boundary:

$$\left.\begin{aligned}\sigma &= a_v \rho v_p w \dot{u} \\ \tau &= b_v \rho v_s \dot{w}\end{aligned}\right\} \quad (2)$$

Where: $\dot{w}$ and $\dot{u}$ are the velocity components along normal and tangential directions of the boundary nodes; $v_p$ and $v_s$ are the velocity of compression wave and shear wave of the incident wave; $a_H$ , $b_H$ , $a_v$ , $b_v$ the non-dimensional numbers which reflect the non-damping characteristics; $\rho$ is the density of material.

In the case of viscous boundary, high accuracy of calculation results is achieved when the incident wave is normal to the artificial boundary; while it is not so satisfactory when the incident wave is close to parallel to the boundary. Because the viscous boundary has the advantages of clear physical meaning, simple to deal with and easy to realize in common software, it is therefore widely used.

**Viscoelastic Boundary**. By adopting a similar derivation method with viscous boundary, Deek derived the viscoelastic boundary based on the assumption that the two-dimensional scattered wave was cylindrical wave[3]. This boundary is equivalent to continuously distributed paralleling spring-damper systems set on an artificial truncated boundary, of which the parameters of spring module and damper module are expressed as:

$$\left.\begin{aligned}K_b &= 0.5\frac{G}{R} \\ C_b &= \rho c\end{aligned}\right\} \quad (3)$$

Where: $\rho$ is the material density; $G$ is the shear modulus; $R$ is the distance between scattered wave source and artificial boundary, which is the vertical distance to the boundary in this calculation model; $c$ is the wave velocity in the material; velocity normal to the boundary is compression wave velocity $c_p$, and that parallel to boundary is shear wave velocity $c_s$; $K_b$ and $C_b$ are the spring and damper forced on the artificial boundary.

Viscoelastic boundary is an elastic boundary when neglecting the damper, and in turns a viscous boundary when neglecting the spring. It can be seen from the viscoelastic boundary expressions that the boundary conditions is capable of simulating not only the propagation of scattered wave from finite field to infinite field, but also the elastic recovery ability of material. Besides, since the concept of viscoelastic boundary is clear and easy to realize using finite element, it is widely used for the interaction analysis of soil structure, as well as the modal analysis of such system[8-11].

## Dynamic Response and Analysis under Different Input Loads

### Calculation Model.

To verify the simulation results of different artificial boundaries under different frequency input loads, the dynamic response of a linear elastic semi-infinite foundation was analyzed under three different frequency triangle impulse loads. Figure 1 is a semi-infinite spatial model, where $-1.0 \le x \le 1.0\text{m}$, $0 \le y \le 2.0\text{m}$; the mesh size is $\Delta x = \Delta y = 0.05\text{m}$. 5 boundaries were applied on this artificial boundary, including viscous boundary, elastic boundary, viscoelastic boundary, extended boundary and fixed boundary, where *R* is the vertical distance from the input point to the artificial boundary. The whole calculation was realized in ANSYS and Newmark was adopted for time integral, which is unconditional stable[12]. The viscous boundary and viscoelastic boundary was simulated by COMBIN14 module, and the extended boundary took the calculation results of a 30-m side length model as exact solution. The material parameters of the calculation models are: elasticity modulus $E = 2.5\text{Pa}$, mass density $\rho = 1.0\,\text{kg}/\text{m}^3$, Poisson's ratio $\nu = 0.25$, load time step $\Delta t = 0.05\text{s}$, material damping is taken as 0 for better understanding of the adsorption of radiation damping to the energy around the boundary. Figure 1 shows the load action range, and Figure 2 is the curves of three different frequency triangle impulse loads.

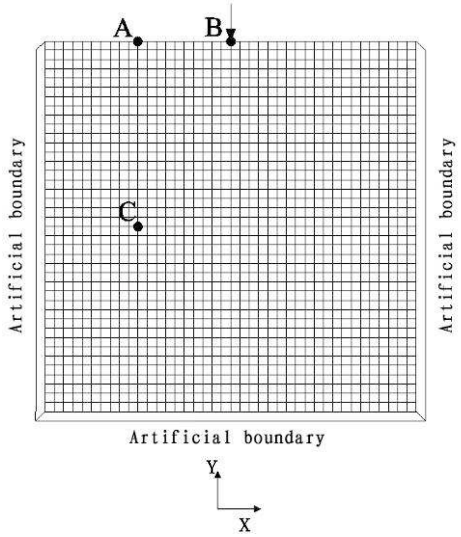


Fig.1 Input Seismic Source Load

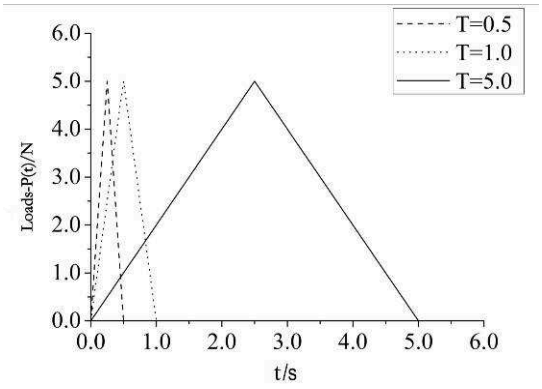


Fig.2 Finite Element Model

### Results and Analysis.

Figure 3 – Figure 6 are the displacement response time curves of five boundary conditions monitored from point *A*, *B*, *C* under different input load action timings and different material shear wave velocities. It can be seen from these 8 figures that the type of artificial boundary has an obvious impact on the displacement of monitoring point. The farther the distance from the boundary base is, the greater the impact becomes of the boundary type to the calculation results. Compared with other boundary conditions, the results of viscoelastic boundary are more close to accurate solution, and as response time increases, there exists drift phenomenon at the viscous boundary which is mainly determined by the characteristics of the damper itself. Under the conditions of fixed boundary and elastic boundary, there exist different levels of oscillation for the displacement of monitoring point, and it exhibits serious distortion in the case of fixed boundary. By comparing Figure 3, 4 and 6, it can be found that with a constant material spear velocity, by reducing the

frequency or increasing the period of seismic source load, the simulation results of viscoelastic boundary can be improved properly. From Figure 4 and 5, it can be seen that with constant seismic source frequency, the simulation results of viscoelastic boundary get worse by simply increasing the elastic wave velocity. In general, with higher frequency and higher material elastic wave velocity, the simulation results become better. Therefore, both seismic load frequency and material characteristics have critical impacts on dynamic response. It is important to select the frequency range properly as well as taking into consideration of impact of materials.

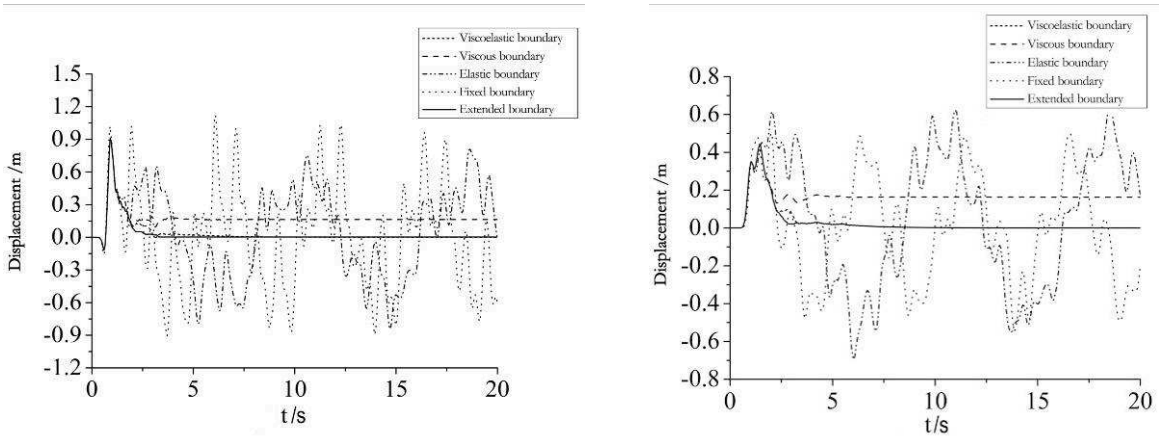


（a）Observation point A （b）Observation point C

Fig.3 Dynamic response of $T_p = 0.5\text{s}$， $C_S = 1$ at observation points

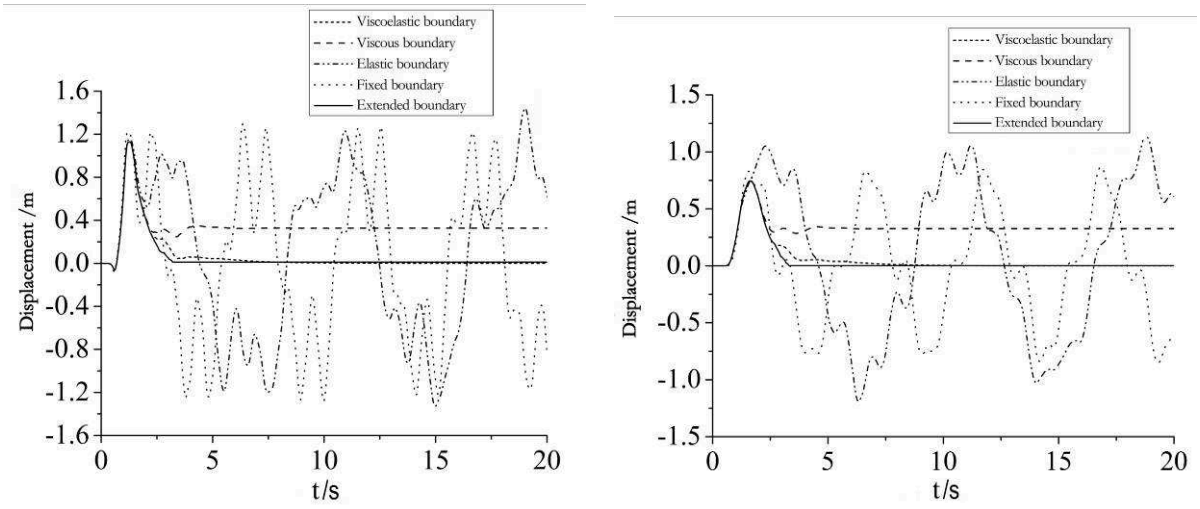


（a）Observation point A （b）Observation point C

Fig.4 Dynamic response of $T_p = 1.0\text{s}$， $C_S = 1$ at observation points

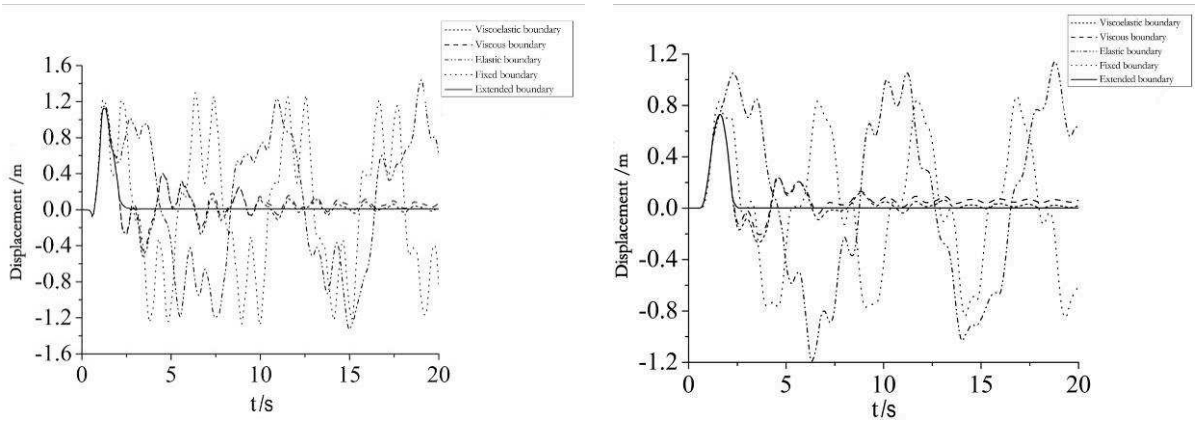


（a）Observation point A （b）Observation point C

Fig.5 Dynamic response of $T_p = 1.0\text{s}$， $C_S = 10$ at observation points

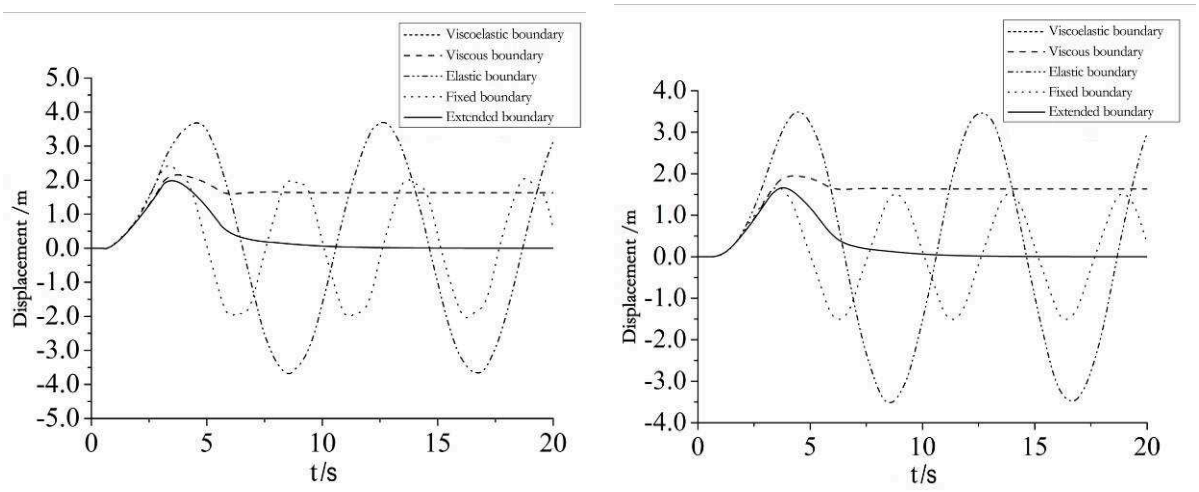


（a）Observation point A （b）Observation point C

Fig.6 Dynamic response of $T_p = 5.0\text{s}$， $C_S = 1$ at observation points

**A Dynamic Finite Element Example of Gravity Dam-Foundation System**

**Calculation Model.** A concrete gravity dam has the following parameters: height = 101m, crest elevation=74m， dam top width = 16m, upstream normal storage level = 64m, designed flood level = 63.88m, check flood level = 67.68m, and the shock strength = 7. The material parameters are: elasticity modulus of dam body concrete and dam foundation rock is 25.5 GPa and 18.0 GPa , respectively, Poisson's ratio are 0.167 and 0.2, respectively, concrete volume-weight is $24000\,\text{N/m}^3$ , and the foundation rock volume-weight is $29000\,\text{N/m}^3$ . In the case of dynamic analysis, dynamic elastic modulus is 30% larger than static elastic modulus. Figure 7 is a finite element model of gravity dam-foundation rock system simulated in ANSYS, with foundation depth of upstream, downstream, and dam foundation itself being twice of the dam height. With the design response spectrum regulated in *Hydraulic Structure Seismic Design Code* (DL5073 - 2000) being the target spectrum, an artificial seismic wave (time interval = 0.02s, acceleration peak = 0.1g, and duration = 30s) was synthesized using trigonometric series. During calculation, a horizontal

equivalent nodal force was applied at artificial boundary node in the bottom. Figure 8 are the acceleration - time, velocity - time and displacement - time curves of artificial seismic wave.

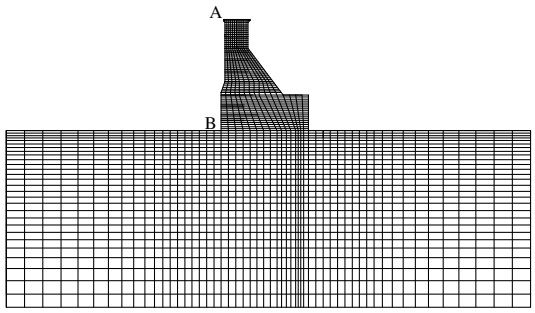


Fig.7 Dam-foundation system finite element model

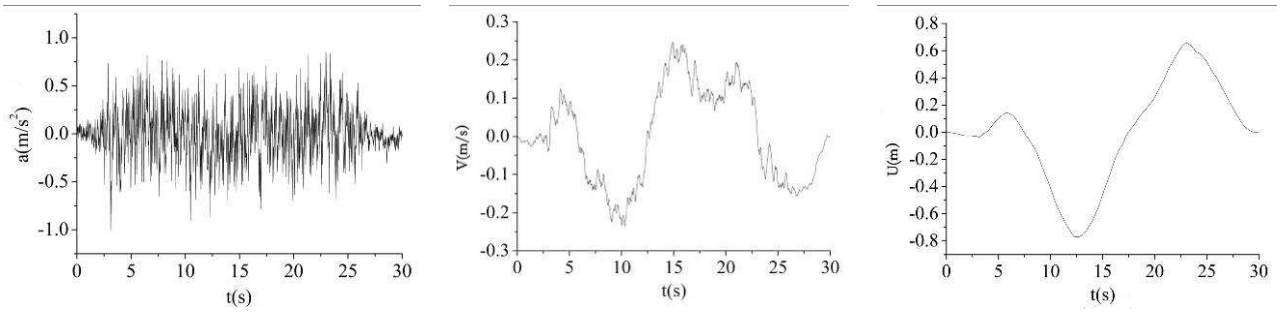


（a）Acceleration （b）Velocity （c）Displacement

Fig.8 Artificial seismic wave curves

**Results and Analysis.**

Figure 9 is the acceleration – time curve along X direction of dam top node *A* and dam foundation node *B* under viscoelastic and fixed boundary conditions.

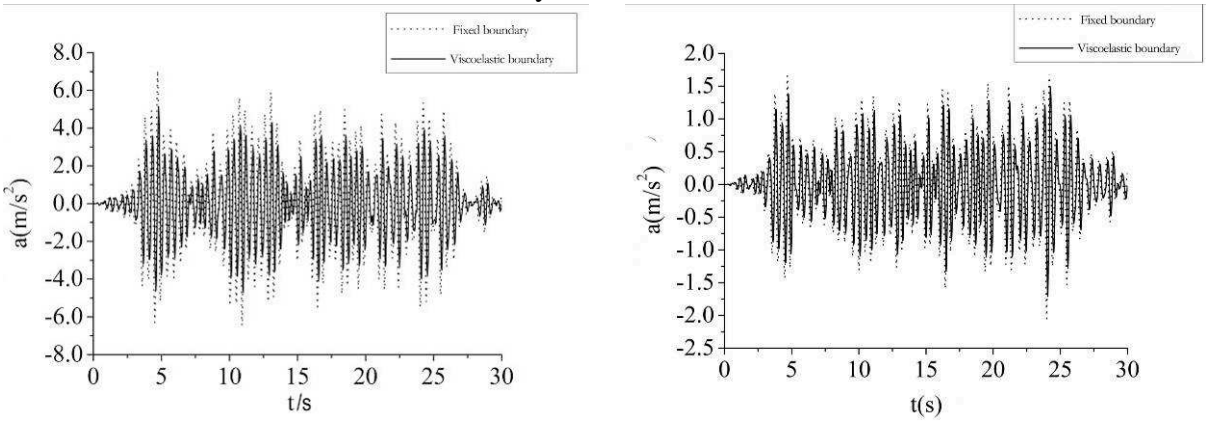


（a）Node A at the crest of dam （b）Node B at the bottom of dam

Fig.9 Acceleration time history curve under two boundary conditions at nodes A, B

From Figure 9, it can be seen that, comparing with conventional fixed boundary of massless foundation, the gravity dam – foundation rock system with viscoelastic artificial boundary that taking into consideration of foundation radiation damping shows a clear weakening in peak acceleration response of both dam top and foundation, with the weakening range being 20% ~ 30%. This method avoids the reflection of seismic wave on the fixed boundary and considers the impact of foundation radiation damping, which makes the dynamic analysis results more conform to the real situation.

## Conclusion

Using ANSYS, this paper analyzed the dynamic responses of a semi-infinite foundation under different artificial boundary conditions and their impact factors. The conclusions are as follows:

1）Different artificial boundary conditions directly impact the dynamic interaction results of structure – foundation. The accuracy of dynamic analysis results is directly influenced by the selection and simulation of artificial boundary conditions. Thereinto, the viscoelastic artificial boundary condition has the advantages of simple principle, easy to realize, fine simulation results and good stability.

2）The simulation results of viscoelastic artificial boundary are related to not only the material parameters, but also the frequency or period of the seismic source load. When the seismic source has a higher frequency, the corresponding higher material elastic wave velocity will result in a good simulation results under viscoelastic artificial boundary condition.

3）At last, a numerical analysis of seismic response over a concrete gravity dam – foundation rock was conducted, which proved the impact of infinite foundation radiation damping is not negligible.

## Acknowledgements

This work was financially supported by the Fujian Province Natural Science Foundation (2011J01309).

## References

[1] Xiaolu Gu, Hongjin Qian, Huishan Liu: Ground and foundation(Chinese architectural press, Beijing 2003)

[2] Lasmer J, Kuhlemeyer R L. Finite Dynamic Model for Infinite Media. Journal of the Engineering Mechanics Division, ASCE,Vol.95(1969),p:859-877

[3] Deek A J, Randolph M F. Axisymmetric Time-domain Transmitting Boundaries. Journal of the Engineering Mechanics,Vol.120(1994),p.25-42

[4] Wolf J P. Song C. Doubly Asymptotic Multi-directional Transmitting Boundary for Dynamic Unbounded Medium Structure Interaction Analysis. Earthquake Engineering and Structural Dynamics,Vol.24(1995),p.175-188

[5] Underwood P, Geers T L .Doubly Asymptotic Boundary Element Analysis of Dynamic Soil-structural Interaction. International Journal of Soils and Structure.Vol.17(1981),p.687-697

[6] Clayton R, Engquist B. Absorbing Boundary Conditions for Acoustic and Elastic Wave Equations.Bull.Seism.Soc.Amer.Vol.76(1977),p. 1529-1540

[7] Zhen Chen, Changyong Liu: Finite element analysis of high intake tower with oblique incident seismic waves. Yellow river. Vol.34(2012),p.131-133

[8] Pengcheng Fu, Gang Wang, Jianmin Zhang: A simplified analysis method for dynamic response of subway tunnel subjected to longitudinally propagating shear waves. Earthquake engineering and engineering vibration. Vol.24(2004),p.45-50

[9] Jingbo Liu, Zhenyu Wang, Kefeng Zhang:3D finite element analysis of large dynamic machine foundation considering soil-structure interaction. Engineering mechanics.Vol.19(2002),p.34-38

[10] Liuchao Qiu, Hua Liu, Feng Jin. Time-domain finite-element analysis of two dimensional seismic soil-structure interactions. Engineering mechanics.Vol.23(2006),p.114-119

[11] Denghong Chen, Chengbin DU, Juwei Yuan. Viscous-spring boundary element based on ABAQUS and application to dynamic analysis of a gravity dam. World earthquake engineering. Vol.26(2010),p.127-132

[12] Wen Qiao, Guoming Liu. Dynamic finite element analysis of levees based on viscoelasticity artificial boundary. Water resources and power.Vol3(2012),p.120-123

*Applied Mechanics and Materials Vols. 580-583 (2014) pp 1687-1691*
*© (2014) Trans Tech Publications, Switzerland*
*doi:10.4028/www.scientific.net/AMM.580-583.1687*

# Dynamic analyses of a Self-anchored Suspension Bridge under Seismic Excitations

Wang Cheng[1, a], Wang Yanxu[1,b]

[1] Roadway Construction Project Management Center of Beijing Municipal Roadway Administration Bureau, 100031, Beijing，China

[a]postwc@126.com, [b]postwyx@126.com

**Keywords:** self-anchored suspension bridge; response spectrum; time-history method; artificial seismic wave; seismic response.

**Abstract.** The seismic response of the Wusong bridge was analyzed though the response spectrum method and the time-history method by adopting the MIDAS/CIVIL. The analysis results show that the longitudinal displacement of the main girder is much larger under longitudinal seismic input, so some inhibiting device or dampers should be used to avoid impacting. There is not coupling between longitudinal and lateral seismic excitations, while the seismic response of moment and shear force at the bottom of the main tower is much larger. On the contrary the seismic response of main beam and the main cable should be calculated under the longitudinal and vertical seismic excitations because of the coupling between the both of them. Furthermore, the artificial seismic wave fitting standard response spectrum was generated to conduct the time-history analysis and the results are much larger than the results from the response spectrum method.

## Introduction

The development of self-anchored suspension bridge in China started in the last two decades. Through the engineering practice in the last ten years, the construction technology of it has reached the international advanced level. As the self-anchored suspension bridge has unique advantages of elegant, pleasing appearance in the form of medium-span city bridges, a large number of self-anchored suspension bridge have been built in recent years. At the same time, complete set of specialized research on the anchor suspension bridge was carried out. But research in the aspects of a long-span self-anchored suspension bridge anti-seismic and damping is relatively weak. At home and abroad, the existing codes for seismic design of bridges don't provide any detailed provisions about the seismic performance of this type of bridge; just treat them as distinct bridges and gives only seismic conceptual design principles. Although some research of the seismic performance of self-anchored suspension bridges has got some useful conclusions, most research was aimed at a certain bridge[1-5]. Generally speaking, the research of the seismic performance of self-anchored suspension bridges is relatively weak. Considering the differences between bridges, the regular pattern of the seismic response of this kind of bridges should be specially considered.

## Dynamic characteristic calculation

The finite element model of the bridge was built by MIDAS/CIVIL. The main girder and the main tower were simulated by space beam elements. Suspenders and the main cables were simulated by the cable element that only subjected to tension. The rendering of finite element model of the overall structure is shown in Figure 2. The dynamic characteristic analysis is shown in Figure 3.

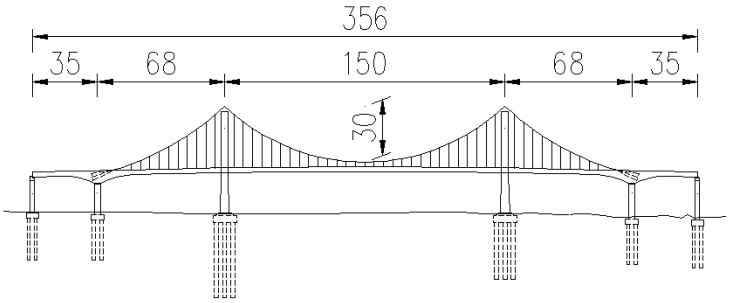


Fig.1 Layout of the bridge (Unit: m)

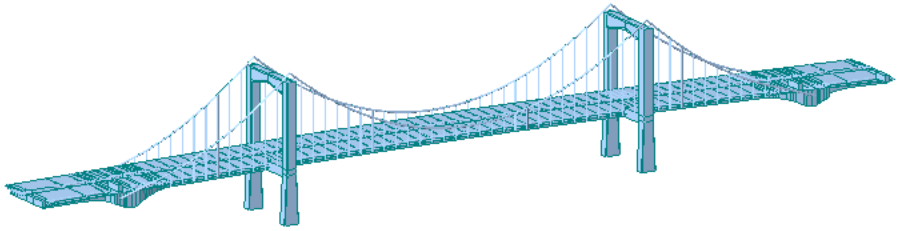

Fig.2 FE model of the Wusong bridge

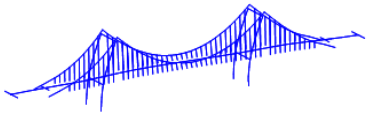

(a) f1=0.172Hz

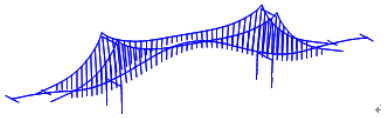

(b) f2=0.583Hz

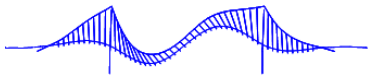

(c) f3=0.866Hz

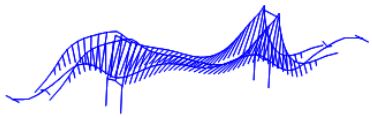

(d) f4=1.480Hz

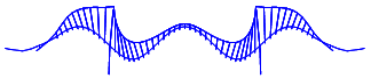

(e) f5=1.505Hz

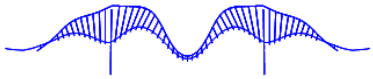

(f) f6=1.933Hz

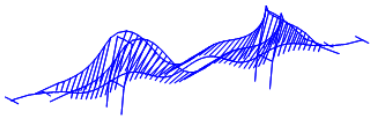

(g) f7=2.573Hz

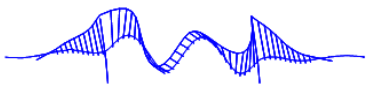

(h) f8=2.891Hz

Fig.3 The first eight modes

## Seismic response analysis

### Response spectrum analysis

Response spectrum method is simple and straightforward calculation. In the program stage, peak values of the bridge can be getting by a smaller amount of calculation under earthquake. For seismic calculation of bridge, the most important thing is the peak response of structure under earthquake. This is also the reason for that response spectrum method is widely favored by bridge designers.

The Wusong Bridge is located at Ⅶ degree area of the seismic intensity zoning map in China. The peak of ground motion acceleration is 0.1g in this area. Based on "Guidelines for Seismic Design of Highway Bridges", the bridge is divided into Class A, the intensity standard of seismic fortification is 7 degrees, and the peak of designed basic ground motion acceleration is taken as 0.10g in the horizontal direction. According to the Chinese "Guidelines for Seismic Design of Highway Bridges" promulgated in 2008, the designed horizontal maximum acceleration response spectrum is 0.296g from calculation, which is larger than the effect value of previous seismic code

Reference to the measured data of other long-span suspension bridges, such bridge the damping ratio of this type of bridge is small. So in this response spectrum analysis, the damping ratio is set to 0.02. Based on "Guidelines for Seismic Design of Highway Bridges " , the type of site soil of this bridge is Class Ⅱ. Figure 5 shows the horizontal design acceleration response spectrum of this bridge. The vertical design acceleration response spectrum is getting with the horizontal design acceleration response spectrum multiplied by a factor of 0.65. In order to satisfy the accuracy requirements, in this response spectrum analysis, the top 100 vibration modes are selected and combined with the CQC method.

Table 1 shows the seismic response of the main girder and the main cable under earthquake input, and table 2 shows the seismic response of the main tower under earthquake input. Under longitudinal seismic input, longitudinal and vertical vibration of the main tower and the main beam is very small, almost no lateral vibration. The structure deformation is performed with longitudinal drift of the main girder and longitudinal swing of the main tower. The larger longitudinal displacement of the main girder determines the design of connected components such as bearing. The design of concrete self-anchored suspension bridge is dominated by the bending moment of the root–section of the bridge tower. Under lateral earthquake input, the deformation is performed with lateral vibration of the main tower and main girder; the vertical and horizontal vibration of the main tower and main girder of this bridge is not obvious; and the earthquake action almost have no effect on the main cable internal forces. Under vertical earthquake input, the vertical, lateral and longitudinal vibration of the main tower and the main girder of this bridge are not obvious; structure deformation is performed with longitudinal swing of the bridge tower and vertical vibration of the main girder.

Tab.1 The dynamic response of the girder and main cable based on response spectrum method

| direction of input | internal forces of main beam | | | | | displacement of beam | | | force of cable |
|---|---|---|---|---|---|---|---|---|---|
| | $F_x$(kN) | $V_z$(kN) | $V_y$(kN) | $M_z$(kN.m) | $M_y$(kN.m) | longitudinal/m | lateral/m | Vertical/m | (kN) |
| longitudinal | 2006.6 | 1549 | 0 | 0 | 24776.8 | 0.157 | 0 | 0.007 | 2351.5 |
| lateral | 0 | 0 | 11539 | 252610 | 0 | 0 | 0.021 | 0 | 69.2 |
| Vertical | 3035.2 | 4343.2 | 0 | 0 | 42320.4 | 0.001 | 0 | 0.029 | 1348.7 |

Tab.2 The dynamic response of main tower based on response spectrum method

| direction of input | section position | internal forces of main tower | | | | | displacement of main tower | |
|---|---|---|---|---|---|---|---|---|
| | | Fx (kN) | Vy (kN) | Vz (kN) | My (kN.m) | Mz (kN.m) | longitudinal(m) | Lateral (m) |
| longitudinal | top | 1594.00 | 54.10 | 1855.00 | 5462.00 | 455.50 | 0.13 | |
| | bottom | 1330.80 | 114.00 | 2238.20 | 115930.60 | 653.40 | 0.00 | |
| lateral | top | 1677.10 | 814.20 | 2.10 | 10.60 | 22699.30 | | 0.03 |
| | bottom | 4277.00 | 4273.90 | 4.90 | 76.90 | 60124.60 | | 0.00 |
| Vertical | top | 284.10 | 288.10 | 150.10 | 750.70 | 2330.20 | 0.01 | |
| | bottom | 3572.60 | 557.90 | 315.00 | 8764.00 | 3181.70 | 0.00 | |

**Response spectrum analysis**

In this analysis, artificial seismic waves meeting the requirements of the codes, are generated with MATLAB, which are based on the trigonometric series superposition method. First, get the design acceleration response spectrum, according to the design code, the actual type of the bridge site and design intensity. Secondly, transform the design acceleration response spectrum into a power spectrum. Then artificial seismic waves can be generated from inverse Fourier transform of the

random phase of the Fourier amplitude spectrum, which is obtained from the power spectrum. After the artificial seismic waves generated, adjust its intensity values based on regulatory requirements. Finally, get artificial seismic waves matching the design response spectrum, which can be used for the bridge seismic analysis. The artificial seismic waves shown in Figure 4 are generated from the design acceleration response spectrum, which is matching the design response spectrum. The total duration is taken as 20s, and Δt is taken to be 0.01 s.

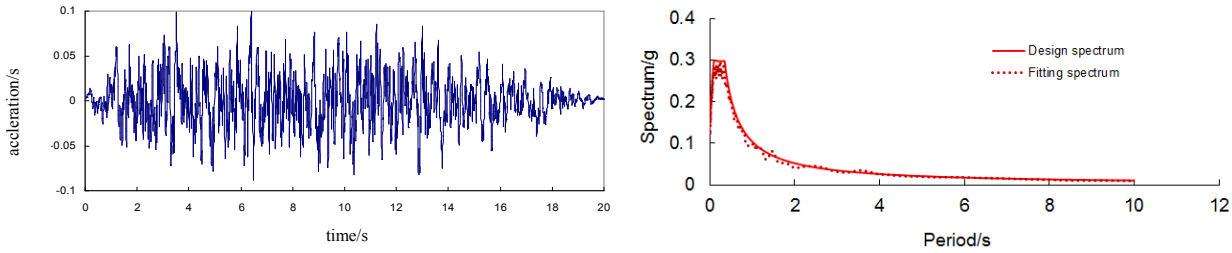


Fig.4 Artificial seismic wave matching the design response spectrum

Table 3 and Table 4 shows the seismic response of the main beam, the main cable and the main tower based on the time history analysis method. By comparing with table 1 and table 2, seismic response obtained from time history analysis method is consistent with the result of response spectra analysis method, but the peak value is slightly different. In general, response peak value get from time history analysis method is larger than the result of the response spectrum method. So the response spectrum method can be used for preliminary design, and time history analysis method is more reasonable and reliable for detailed design.

Tab.3 The dynamic response of the girder and main cable based on time-history method

| direction of input | internal forces of main beam | | | | | displacement of beam | | | force of cable |
|---|---|---|---|---|---|---|---|---|---|
| | $F_x$(kN) | $V_z$(kN) | $V_y$(kN) | $M_z$(kN.m) | $M_y$(kN.m) | longitudinal/m | lateral/m | Vertical/m | (kN) |
| longitudinal | 2930.3 | 2773.9 | 0.0 | 0.0 | 26184.4 | 0.155 | 0.0 | 0.010 | 2732.2 |
| lateral | 0.0 | 0.0 | 11068.4 | 243341.1 | 0.0 | 0.0 | 0.022 | 0.0 | 73.6 |
| Vertical | 4082.6 | 6618.5 | 0.0 | 0.0 | 57801.5 | 0.001 | 0.0 | 0.031 | 1633.4 |

Tab.4 The dynamic response of main tower based on time-history method

| direction of input | section position | internal forces of main tower | | | | | displacement of main tower | |
|---|---|---|---|---|---|---|---|---|
| | | Fx (kN) | Vy (kN) | Vz (kN) | My (kN.m) | Mz (kN.m) | Longitudinal (m) | Lateral (m) |
| longitudinal | top | 1879.4 | 80.2 | 1819.6 | 6021.8 | 667.6 | 0.13 | |
| | bottom | 1738.2 | 169.9 | 2342.7 | 121590.5 | 972.8 | 0 | |
| lateral | top | 1666.3 | 781.2 | 2.3 | 10.8 | 21908.7 | | 0.03 |
| | bottom | 4490.8 | 4036.8 | 5.8 | 99.1 | 57096.8 | | 0 |
| Vertical | top | 1951.8 | 302.4 | 189.7 | 1055.2 | 2466.1 | 0.01 | |
| | bottom | 4670.9 | 594.6 | 488.3 | 13398.4 | 3392.9 | 0 | |

## Summary

This article is based on a seismic response analysis of self-anchored suspension bridges, and the main results are as follows:

(1) Under longitudinal seismic input, concrete self-anchored suspension bridge is performed with longitudinal drift of the main beam and longitudinal swing of the bridge tower. Results show that the longitudinal displacement of the main girder is much larger so some inhibiting device or dampers should be used to avoid out-of- codes displacement and connective component's bad working.

Internal force doesn't control the design of the main beam and the main cable, and the root section is the main control section during the tower design.

(2) Under the lateral seismic component action, the performance of concrete self-anchored suspension bridge is dominated by lateral vibration, but the internal force and deformation of the bridge tower and main girder is small ,because of its gate type bridge tower with big lateral stiffness.

(3) Under the vertical earthquake component action, concrete self-anchored suspension bridge is characterized by vertical and longitudinal vibration. In this condition, the internal force and deformation of the bridge tower are little, having no decisive effect on design. Impact on the main beam is significant; peak of the vertical bending moment of the main beam is located near the pier top of the side span. Combined with the main cable anchorage zone with complex stress state, this area should be taken into consideration in the design.

(4) The time-history analysis results are much larger than the results from the response spectrum method. Response spectrum method is suitable for the preliminary design or the Plan formulation. And time history analysis results are advisable for component detailed design.

**References**

[1] ZHANG Zhe, ZHANG Hongjin, Q IU Wenliang. Research on experiments of concrete self-anchored suspension bridge model[J]. Journal of Dalian University of Technology, 2005, 45(4): 575~579.

[2] KANG Shibin, ZHU Yu, DENG Yulin. Dynamic Analysis of a Self-Anchored Suspension Bridge[J]. Structural Engineers, 2008,24 (4): 24~30 (in Chinese)

[3] Fang Hai, LiuWeiqing, Wang Rengu. Design method of energy-dissipating earthquake-reduction along longitudinal direction of self-anchored suspension bridge[J]. Earthquake Engineering and Engineering Vibration, 2006, 26(3): 222-224 (in Chinese)

[4] Liu Chuncheng, Zhang Zhe, Shi Lei. Application of pseudo excitation method to vertical seismic response analysis of self-anchored suspension bridges[J]. Journal of Southeast University ( Natural Science Edition), 2003, 33(4): 522-525(in Chinese)

[5] Zhang Hang, Li Li, Long Xiaohong. Seismic Response Analysis and Performance Evaluation of a Long-span Suspension Bridge [J]. Earthquake Resistant Engineering and Retrofitting，2007, 29(1): 85-93(in Chinese)

[6] YANG Meng-gang, HU Jian-hua, CHEN Zheng-qing. Seismic Response Analysis of self-anchored Suspension Bridge with Single-tower[J]. J.cent. South Univ. ( Science and Technology), 2005, 36(1): 133-137(in Chinese)

*Applied Mechanics and Materials Vols. 580-583 (2014) pp 1692-1695*
*© (2014) Trans Tech Publications, Switzerland*
*doi:10.4028/www.scientific.net/AMM.580-583.1692*

# Inertial Coefficient Adopted in Pile-pier Structure under Deep Water

Guoshuai Sun[1, a*], Chunguang Liu[2,b] , Jun Xie[3,c], Fangjing Ma[1,d]

[1]College of management, Liaoning University of Technology, Jinzhou 121001, China

[2]Faculty of Infrastructure Engineering, Dalian University of Technology, Dalian 116024, China

[3]College of Civil Engineering, Hebei University of Architecture, Zhangjiakou 075024, China

[a]gs.sun@aliyun.com, [b]liucg@dlut.edu.cn, [c]xiejun79@126.com, [d]xiaojing0024@126.com

**Keywords:** Morison equation; Inertial coefficient; Accurate algorithm; Approximation algorithm.

**Abstract.** In order to study the effect of hydrodynamic pressure acted on pile-pier structure in deep water, an investigation on the inertial coefficient is developed. Based on the Morison equation, the usual suggested value is analyzed, especially the noncircular slender cylinder is considered. Besides, the effect of scale of structure is studied, including accurate algorithm and approximation algorithm. Study results indicate that the Morison equation is also applied to noncircular slender cylinder, and the value of inertial coefficient is influenced by the scale of structure. Moreover, the calculated results of accurate algorithm and approximation algorithm are consistent within a certain range, so the choice of calculation method should be governed by the required precision.

## Introduction

In recent years, the mechanical property of submerged structure or component has been brought into researchers' sights[1]. When the earthquake occurs, the dynamic interaction between the submerged structure and surrounding water will cause the threats to the safety of bridge system. During the past decades, many theoretical methods and experimental studies have been performed to investigate the effect of hydrodynamic pressure for bridge or other structures under seismic excitation[2-4].

For the research purposes, this problem should be appropriated to simplify. Morison et al. introduced the Morison equation which has been widely used to estimate the hydrodynamic pressure on the small scale structures[5].

In this paper, an investigation on the effect of hydrodynamic pressure acting on pile-pier structure is developed, especially the main content focus on the inertial coefficient.

## Inertial coefficient

**Governing equations.** The Morison equation of unit cylinder can be expressed as:

$$f = C_M \rho A\ddot{u} - C_m \rho A\ddot{x} + C_D \frac{\rho}{2} D[\dot{u} - \dot{x}]|\dot{u} - \dot{x}| \tag{1}$$

Where, $f$ is defined as wave force; $C_M$ , $C_m$ and $C_D$ are, respectively, the inertial , added mass and drag coefficients; $\dot{u}$ and $\ddot{u}$ are , respectively, the in-line water particle flow velocity and acceleration; $\dot{x}$ and $\ddot{x}$ are , respectively, the in-line velocity and acceleration of cylinder.

There are two problems for the calculation of wave force by Morison equation, which are the appropriate wave theory and relevant hydrodynamic coefficient. Since the Morison equation was presented, many researchers have carried out a large number of model tests and field observation, but the data of hydrodynamic coefficient including inertial coefficient $C_M$ and drag coefficient $C_D$ show larger discreteness. In this paper, the inertial coefficient $C_M$ will be analyzed.

**Suggested value.**

For noncircular slender cylinder, the cross-sectional area is used to replace the area of circle in the Morison equation. Figure 1 shows the inertial coefficient $C_M$ which based on the test results of Zhu[6].

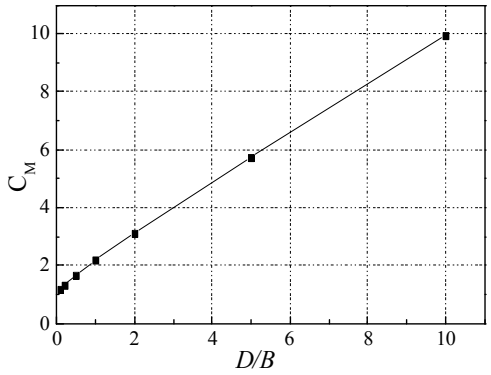


Figure 1 The correspondence between the rectangular cross-section with different length and width and inertial coefficient

Based on the curvilinear trend by the length-width ratio, the approximate formula of the equivalent inertial coefficient $C'_M$ can be obtained:

$$C'_M = 1.067 + 1.091 \times \left(\frac{D}{B}\right)^{0.909} \tag{2}$$

Based on the calculated results by Eq. 1 and *Code of Hydrology for sea Harbour*[6], the inertial coefficient used for several typical sections is listed in Table1.

Table 1 The inertial coefficient used for several typical sections

| Shape of cross-section | | Area | $C_M$ |
|---|---|---|---|
| Circle | Direction of motion, D | $\frac{\pi D^2}{4}$ | 2 |
| Square | Direction of motion, D, D | $D^2$ | 2.19 |
| Rectangle | Direction of motion, B, D | $DB$ | $C'_M$ |

**Effects of different factors**

**The sensitivity**. Based on the theoretical results of Ju[7] and Liaw[8] , the inertial force can be expressed as:

$$f_I = C_M \rho \frac{\pi D^2}{4} \frac{\mathrm{d}^2 \mathrm{u}}{\mathrm{dt}^2} \tag{3}$$

$$C_M = 1 + M_w \Big/ \frac{\rho \pi D^2}{4} \tag{4}$$

$$M_w(z) = \frac{p_1^I(z)}{\phi_1(z)} \tag{5}$$

$$p_1^l(z) = 4\rho_w D \sum_{m=1}^{N} \frac{I_{1m}}{(2m-1)} E_m(\lambda'_m, \frac{D}{2}) \cos(\alpha_m z) \tag{6}$$

$$E_m(\lambda'_m, \frac{D}{2}) = \frac{K_1(\lambda'_m, \frac{D}{2})}{K_0(\lambda'_m, \frac{D}{2}) + K_2(\lambda'_m, \frac{D}{2})} \tag{7}$$

$$I_{1m} = \int_0^{H_w} \phi_1(z) \cos(\alpha_m z) \mathrm{d}z \tag{8}$$

$$\lambda'_m = \alpha_m = \frac{(2m-1)\pi}{2H_W} \tag{9}$$

In Eq.7, $K_n$ is the modified Bessel function of order n of the second kind.

Based on Eq. 4- Eq. 9, the calculated results was shown in Figure 2. From the Figure 2, for small scale, when the height of water level remains constant, the distribution of $C_M$ along the height of structure is tending towards stability under water level. But the variance starts to get bigger with increasing diameter.

For the general seismic ground motion, in view of the excitation frequency, the effect of free surface wave and compressibility of fluid can be neglected when the inertial coefficient is analyzed.

**Approximation algorithm**. If the effect of mode of vibration may be neglected, the Eq. 5 can be simplified as:

$$M_w(z) = p_0^l(z) \tag{10}$$

The Eq.10 is equivalent to the $\phi_1(z)$ in Eq.8 replaced as $\phi_0(z) = 1$.The calculated results are shown in Figure 2.

By comparing with the accurate algorithm, for small scale, when the height of water level remains constant, the distribution of $C_M$ along the height of structure is tending towards consistent under water level. But the variance starts to get bigger with increasing diameter. The comparison among different diameter is shown in Figure 3. It indicates that the smaller scale and the more deviation from the suggested value.

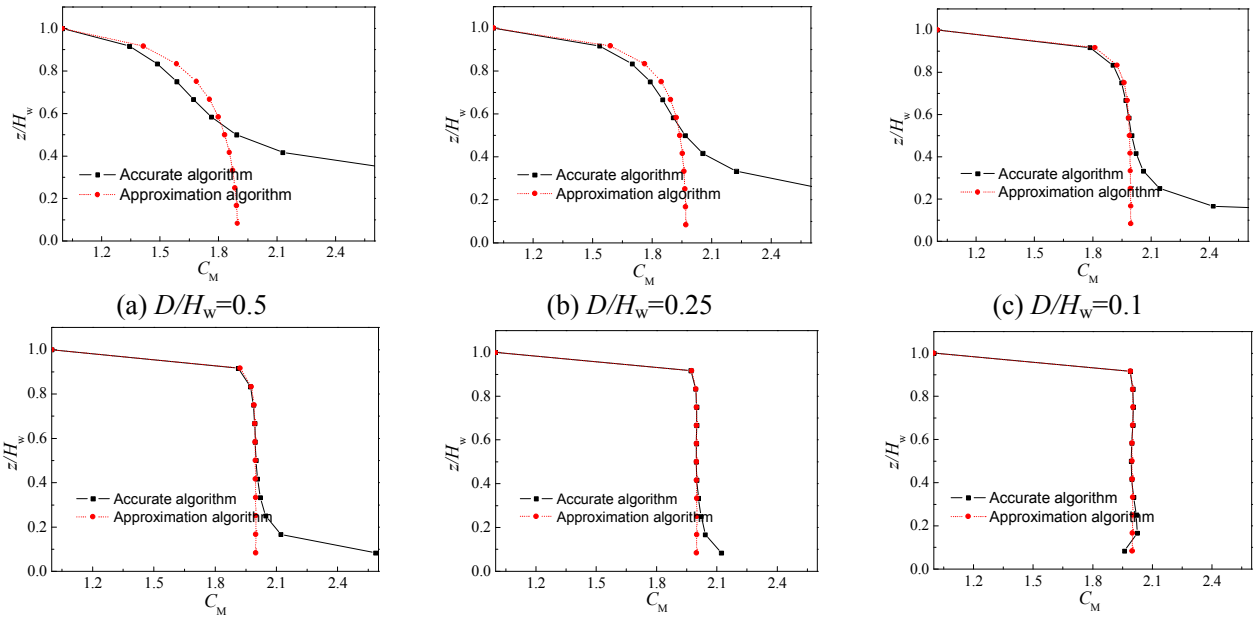


(a) $D/H_w$=0.5 (b) $D/H_w$=0.25 (c) $D/H_w$=0.1

(d) $D/H_w$=0.05 (e) $D/H_w$=0.025 (f) $D/H_w$=0.01

Figure 2 Comparison of distributions of inertial coefficient calculated by different algorithm

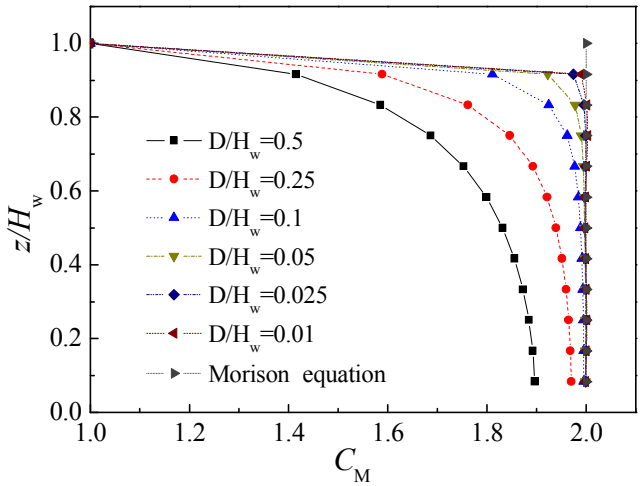


Figure 3 The distribution of inertial coefficient calculated by approximation algorithm

## Conclusion

This paper presents the investigation on inertial coefficient in calculating the hydrodynamic pressure acting on the deepwater structure. Based on the Morison equation, the usual suggested value is analyzed, especially the noncircular slender cylinder is considered. Besides, the effect of scale of structure is studied, including accurate algorithm and approximation algorithm. The conclusions deduced from the results of the investigation indicate that the Morison equation also applied to noncircular slender cylinder, and the value of inertial coefficient is influenced by the scale of structure. Moreover, the calculated results of accurate algorithm and approximation algorithm are consistent within a certain range, so the choice of calculation method should be governed by the required precision.

## References

[1] G.S. Sun, Y.H. Zhao, W. Gu. Stability of Concrete filled CFRP-steel tube under Axial Compression. Proceedings of the 12th International Symposium and IIW International Conference on Tubular Structures. 2009, pp.111-116.

[2] C.G. Liu, G.S. Sun, L. Han. Shaking Table Test of Pile-Water-Pier Superstructure. Transactions of Tianjin University, 2012,18(3), pp.188-193.

[3] M.G. Li, X. Li, R.B. Dong, ea al. Study on Model Tests and Hydrodynamic Force Models for Free Spanning Submarine Pipelines Subjected to Earthquakes. China Ocean Engineering, Vol.24(2), pp.305-320.

[4] G. S. Sun, C. G. Liu. Research on Hydrodynamic Pressure of Deep Water Bridge Structure. International Efforts in Lifeline Earthquake Engineering: pp. 465-472.

[5] J.R.Morison, J.W. Johnson, S.A.Schaaf. The Force Exerted by Surface Wave on Piles. Journal of Petroleum Technology, 1950, 2(05), pp.149-154.

[6] Y.R. Zhu. Wave Mechanics for Ocean Engineering. Tianjin University Press,1991.

[7] Code of Hydrology for sea Harbour(JTJ 213-98), Industry Standard of PRC.

[8] R.C.Ju, X.C. Zeng.Theory of Coupled Vibration between Elastic Structure and Fluid. Seismological Press,1983.

[9] C. Y.Liaw, A. K.Chopra. Dynamics of Towers Surrounded by Water. Earthquake engineering and structural dynamics, 1974, 3(1), pp.33-49.

*Applied Mechanics and Materials Vols. 580-583 (2014) pp 1696-1699*
*© (2014) Trans Tech Publications, Switzerland*
*doi:10.4028/www.scientific.net/AMM.580-583.1696*

# Numerical analysis of seismic behavior of a concealed bracing connection for precast concrete shear walls

Qiao Jin[1,a], Wannan Guo[1,b] , Weijian Zhao[1,c] , Bin Zhang [1,d], Depeng Zhang[1,e]

[1]School of Civil Engineering, Shenyang Jianzhu University, Shenyang, China

[a]goldenfss@163.com, [b]guownlove@126.com, [c]zhaoweijian75@hotmail.com, [d]18640341277@163.com, [e]zdpppa023@163.com

**Keywords:** precast shear wall structure; concealed bracing; hysteresis curve; seismic behavior; seismic ductility

**Abstract.** Aiming at the horizontal connection joint of the precast shear wall structure, this paper presents a new-type horizontal wall-to-wall connection. Based on the ABAQUS finite element analysis platform, an accurate finite element model of shear connection joints was built. By quasi-static numerical tests, the seismic behavior of the proposed connection of the precast shear wall system was analysed and compared with that of the traditional cast-in-place connection. The numerical results show that the seismic performance of the presented connection, such as deformability and energy-dissipation capacity, is slightly lower than that of its cast-in-place counterpart.

## Introduction

It is a basic trend of the building and housing industrialization, promoted by Chinese government, to develop precast concrete structures in order to realize the overall goal of low carbon, green, energy-saving and sustainable building. In consideration of the lack of knowledge of how the precast concrete shear wall system performs under seismic loading conditions, the use of this type of construction should be treated with caution in China, one of the most seismically active nations in the world. For precast concrete load-bearing shear wall panels, behavior of the connections greatly influences structural integrity of the entire structure. Therefore, in order for precast concrete shear wall panel systems to gain acceptance and be a competitive construction system in Chinese seismic regions, the anti-seismic behavior of the connections between the precast members must be studied. At present, many Chinese researchers, such as Jiaru Qian [1], Zhengxing Guo, etc. [2-4], are working to understand the seismic performance of such a system mainly by comparison with that of its equivalent cast-in-place system.

In this paper, An abaqus-based nonlinear finite element (FE) analysis under low-cyclic loading is implemented in order to understand the seismic performance of the proposed connection way of precast shear walls in comparison with that of the cast-in-place connection way.

## Description of FE modeling

The horizontal joint specimens are models of localized regions in the precast shear wall which contain the horizontal joint connections. Three kinds of FE models of horizontal joint specimens were considered. Specifically, the first one (PSW-2) was built to simulate the proposed wall-to-wall connections for precast shear wall structures, which was reinforced by using a herringbone concealed bracing with Φ16 bars between the upper and lower walls, as shown in Fig.1. The second one (CSW) was built to simulate its cast-in-place counterpart (Fig.2), which used the "*tie*" connection to link the upper wall with the lower ground base beam; the third one (PSW-1) was built

to simulate the conventional connection for precast shear wall, which had the same reinforcing bars as the CSW model, but used frictional contact elements to connect the upper wall with the ground base beam. The vertical reinforcement of all these wall models was deformed bars of grade HRB 335, while the stirrups of the boundary elements and the horizontal distributed reinforcement of the models were applied with grade HPB 300. The C35 concrete was used for the three models. The main material properties for steel and concrete are presented in Table 1.

Table 1 Elastic mechanical properties of materials

| Model type | Elastic modulus(Mpa) | Poissom ratio | Compressive strength（Mpa） | Tensile strength （Mpa） |
|---|---|---|---|---|
| Concrete | $2.648\times10^4$ | 0.167 | 16.7 | 1.57 |
| HRB335 | $2.0\times10^5$ | 0.3 | 300 | 300 |
| HPB300 | $2.0\times10^5$ | 0.3 | 270 | 270 |

There was a loading beam (rigid body) on the top of the upper wall for all these wall models, which was subjected to a vertical uniform load . For all models, the axial compression ratio was set to 0.15. The steel mesh arrangement for all the FE models are shown in Fig.3 and Fig. 4.

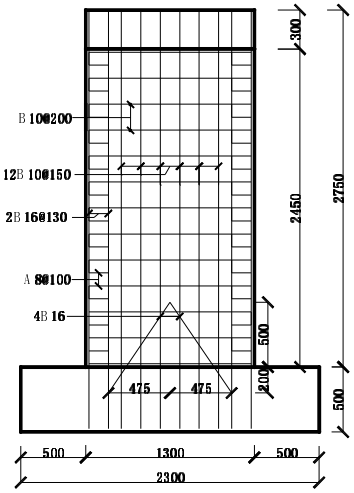


Fig.1 Reinforcement map of the PSW-2 model

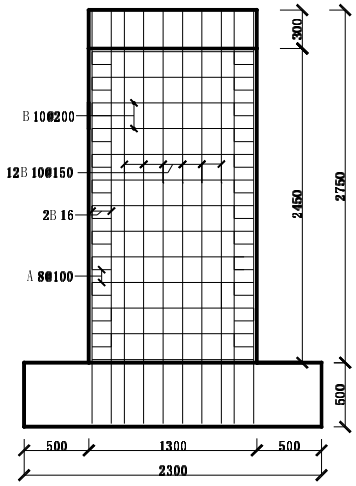


Fig.2 Reinforcement map of the CSW and PSW-1 model

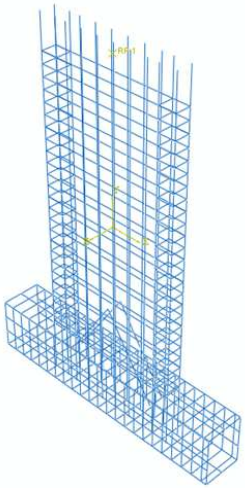

Fig.3 Steel mesh of the PSW-2 model

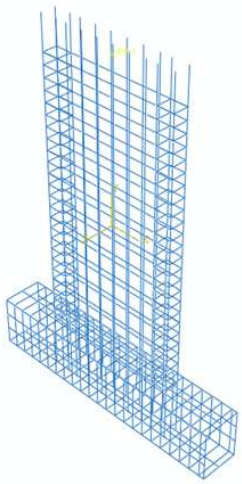

Fig.4 Steel mesh of the CSW and PSW-1 model

**Numerical results of the finite element analysis**

The area hysteresis curve encircles reflects the energy dissipation capacity of a structure. By applying cyclic loads on the three models, we obtained different hysteresis curves of the three

wall-to-wall connections, as shown in Fig.5, Fig.6 and Fig.7, and hence we drew the skeleton curves in Fig .8.

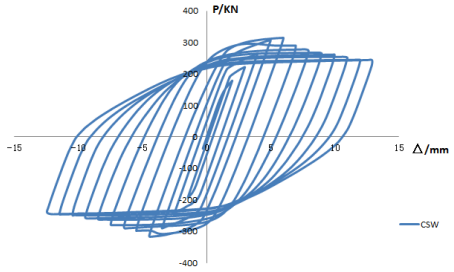


Fig.5 Hysteresis curves of CSW

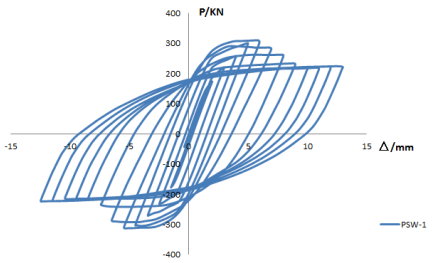


Fig.6 Hysteresis curves of PSW-1

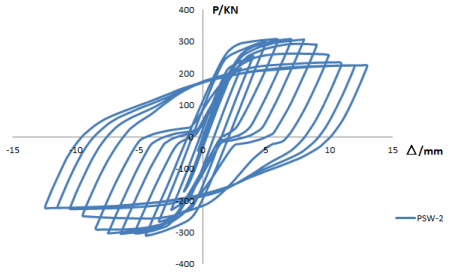


Fig.7 Hysteresis curves of PSW-2

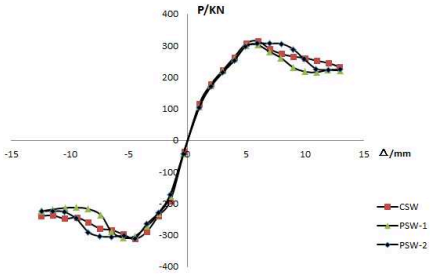


Fig.8 Skeleton curve comparison

Table 2.Hysteresis loop area

| Model Type | The area that hysteresis curve encircles |
|---|---|
| CSW | 3184 $mm^2$ |
| PSW-1 | 1969 $mm^2$ |
| PSW-2 | 2637 $mm^2$ |

Table 2 calculates the area that the hysteresis curve encircles for these models. The results show that the hysteresis curves for the CSW model encircles the largest area. But for the PSW-1 model and the PSW-2 model, the latter has a 30% area increase, compared with the former, which shows that the concealed bracing in the PSW-2 model takes a positive effect on energy dissipation performance of the model.

Table 3.Loading-displacement relation of the hysteresis curves [5-6]

| Model type | Yield load $P_y / KN$ | Yield displacement $\Delta_y / mm$ | Ultimate load $P_u / KN$ | $\Delta_o / mm$ | Ultimate displacement $\Delta_u / mm$ | Displacement ductility $\mu = \Delta_u / \Delta_y$ |
|---|---|---|---|---|---|---|
| CSW | 178.8 | 2.00 | 3151 | 5.99 | 8.98 | 3.97 |
| PSW-1 | 169.9 | 1.98 | 302.5 | 5.95 | 5.95 | 3.02 |
| PSW-2 | 172.9 | 1.97 | 307.2 | 5.89 | 7.17 | 3.63 |

Table 3 indicates the loading-displacement relation of the hysteresis curves for the three models. We can see from Table 3 that the CSW model has the best seismic performance, compared with the other two models. For the PSW-1 model and the PSW-2 model, the ultimate displacement of the latter has a 20.5% increase, which means that the concealed bracing in PSW-2 model makes a better deformation capacity.

Fig.9 shows the stiffness degradation curves of the models. It is easy to see that the initial stiffness of the CSW model is a little larger than that of the other two, but there is no obvious difference in the stiffness degradation trend of all the models.

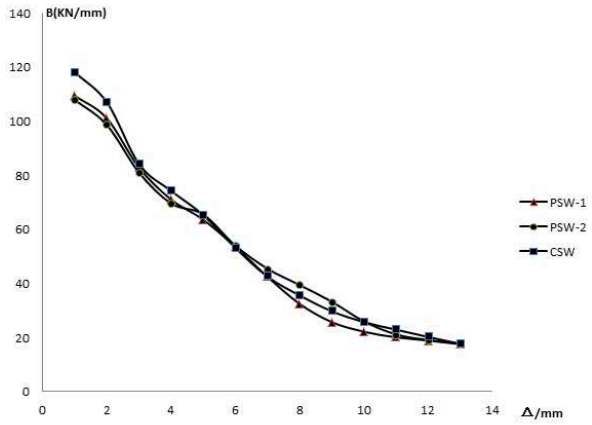


Fig.9 Stiffness degradation curve of the three models

## Conclusion

In this paper, we develop an ABAQUS-based three dimensional finite element method to study a new-type concealed bracing connection of precast shear wall structures. By comparison with the equivalent cast-in-place shear wall systems, the following conclusions can be drawn:

(1) The new connection by setting concealed bracings at the regions of joints has a good seismic performance, which can balance the easy and rapid assembly technology for precast shear wall systems, with the reliability of connection joints.

(2) Structural design of the concealed bracing connection for precast shear wall systems need to be further optimized. And some difficulties, such as reinforcement design and location set-up of concealed bracings under different axial pressure ratios, are still worth studying.

## Acknowledgements

This work was financially supported by the Science and Technology Plan Projects of MOHURD (2012-K4-06) and the Natural Science Foundation of China (No.51278312).

## References

[1] Jiaru Qian, et al. Journal of Building Structures. Vol. 32-6 (2011), p. 51-59 (in Chinese)

[2] Zhengxing Guo, Niancai Dong, Zhangfeng Zhu. Construction Technology. Vol. 40-11 (2011), p. 20-22 (in Chinese)

[3] Zhangfeng Zhu, Zhengxing Guo. China Civil Engineering Journal. Vol. 45-1 (2012), p. 69-76 (in Chinese)

[4] Zhangfeng Zhu, Zhengxing Guo. Journal of Earthquake and Engineering vibration. Vol. 31-1 (2011), p. 35-40 (in Chinese)

[5] GB 50011-2010. Code for seismic design of buildings. China Architecture & Building Press (in Chinese)

[6] GB 50010-2010.Code for design of concrete structures. China Architecture & Building Press (in Chinese)

*Applied Mechanics and Materials Vols. 580-583 (2014) pp 1700-1703*
*© (2014) Trans Tech Publications, Switzerland*
*doi:10.4028/www.scientific.net/AMM.580-583.1700*

# Seismic Performance of Base-isolation Building Subjected to Near-fault Ground Motion with Velocity Pulse

He Qiumei[1, a], Li Yaqi [1, b]， Zhao Yamin[2, c] and Yang Yu [3, d]

[1] Institute of Geophysics, China Earthquake Administration, Beijing, 100081, China

[2]Institute of Crystal Dynamics, China Earthquake Administration, Beijing, 100085, China

[3]Nuclear and Radiation Safety Center, Ministry of Environmental Protection of the People's Republic of China, Beijing, 100080, China

[a]heqiumei06@126.com, [b]lily@126.com，[C]zhaoyamin_icd@126.com，[d]alanayang1949@126.com

**Keywords:** Near-fault pulse-like ground motion, Base-isolation building, Seismic response, Nonlinear time history analysis.

**Abstract.** The seismic response of the base-isolated structure can be reduced significantly in the far-field region compared to the conventional seismic structure. However, near-fault ground motions with velocity pulse may cause the adverse influence on the seismic performance of the base-isolation building, which needs to be investigated deeply. In this paper 6 ground motions with velocity pulse are selected as the input, and the seismic response of a 9 layers conventional seismic RC frame building and comparative base-isolation building with lead-core rubber bearings are obtained by nonlinear time history analysis. The result indicates that base-isolation building with lead-core rubber bearings are of good aseismic performance under the near-fault ground motions with velocity pulse.

## Introduction

The basic characteristics of near-fault ground motion include the concentration of strong ground motions, surface rupture, rupture directivity effect, large velocity pulse and hanging wall effect [1]. For all of these basic characteristics, the large velocity pulse with very high energy has the greatest influence on the engineering structures, and the seismic responses (such as stress, displacement, ductility and etc.) of structures subjected to velocity pulse are much greater than those ground motions without velocity pulse[2]. In the far-field region, the seismic response of the base-isolated structure can be reduced significantly. However, near-fault ground motions with velocity pulse may cause the adverse influence on the seismic performance of the base-isolation building, which needs to be investigated deeply [3-7]. This paper established a conventional seismic building and a comparative base-isolation building with lead-core rubber bearings, input 6 typical strong motion records with velocity pulse, calculate dynamic response of aforesaid structures to analyze the seismic performance of the lead-core rubber bearings subjected to the near-fault ground motions with velocity pulse.

## Calculation models

The model of conventional seismic building is 9 layers reinforced concrete frame structure, the height is 32.4m, the material is C30 concrete, and the beam-column layout as figure1. The sizes of components are as follow: beam is 600mm×400mm, column is 650mm×650mm and floor thickness is 100 mm. Reinforced concrete beams and columns are equivalent to homogeneous rod units, the floor is equivalent to shell element, the material characteristics mainly on the characteristics of concrete. In the process of calculation, considering bending deformation, shear deformation of the beam element and bending deformation, shear deformation, axial deformation of the column element, assuming the floor absolutely rigid in its own plane and neglecting the out-of-plane stiffness.

35 lead rubber bearings GZY600 are putted between each column base and column to set up a base-isolation building model. In nonlinear analysis lead rubber isolation bearings are simulated by biaxial nonlinear hysteresis unit. Lead rubber isolation bearing GZY600 parameters are as follows:

vertical stiffness is 2614000 KN/m, equivalent stiffness is 1859 KN/m, equivalent damping ratio is 27.2%, stiffness before yield is 6519 KN/m, stiffness after yield is 1003 KN/m, and yield strength is 94.2 KN.

The first three natural vibration period of the conventional seismic building model are 1.066s, 1.034s and 0.962s. And the first three natural vibration period of the base-isolation building model are 1.980s, 1.712s and 1.593s.

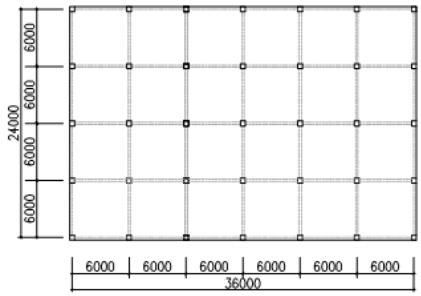


Fig1. Standard floor plan (mm)

## Algorithm

The algorithm of base-isolation structure nonlinear time history analysis is fast nonlinear analysis (FNA), FNA method is an effective method to nonlinear analysis, in this method, the nonlinear is treated as external load, considering the nonlinear load and correction the modal equation.

## Selected ground motions

Select 6 near-fault pulse-like velocity ground motions as input, the parameters are shown in table1, the acceleration and velocity time histories of the ground motions are shown in figure2.

Table1. Selected ground motions

| code | earthqueke | magnitude | station | component | site | duration |
|---|---|---|---|---|---|---|
| A1 | Northridge（1994） | 7.1 | Newhall-W.Pico Canyon Rd | comp046 | B/C | 20.48s |
| A2 | Imperial Valley(1979) | 6.5 | E07 | compSN | B/C | 20.48s |
| A3 | Imperial Valley(1979) | 6.5 | E04 | compSN | B/C | 20.48s |
| B1 | CHI-CHI（1999） | 7.6 | TCU75 | compEW | D | 40.96s |
| B2 | CHI-CHI（1999） | 7.6 | TCU76 | compEW | D | 40.96s |
| B3 | CHI-CHI（1999） | 7.6 | TCU129 | compEW | D | 40.96s |

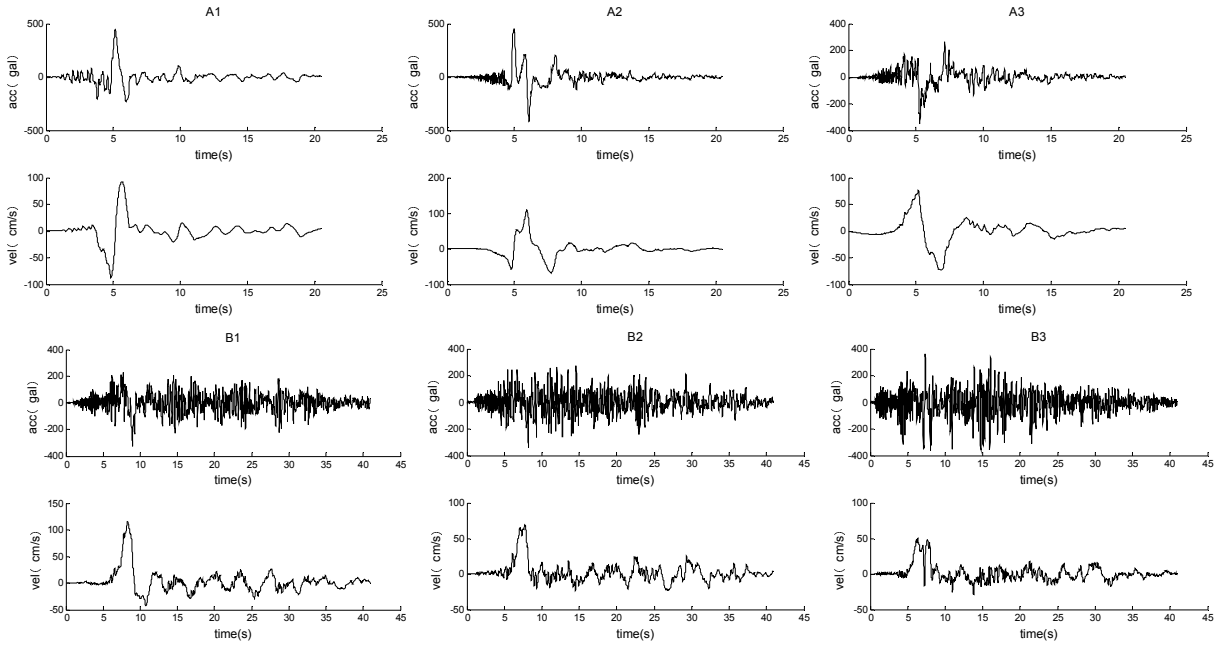


Fig.2 Acceleration and velocity time histories of the ground motions

## Acceleration response

Figure3 is the acceleration response time history of the base-isolation building model and the conventional seismic building model subjected to the ground motions of table1. Comparing with the conventional seismic building, the top story acceleration response is reduced significantly to 1/2-1/5. This means that the seismic action of the superstructure of the base-isolation building is greatly decreased.

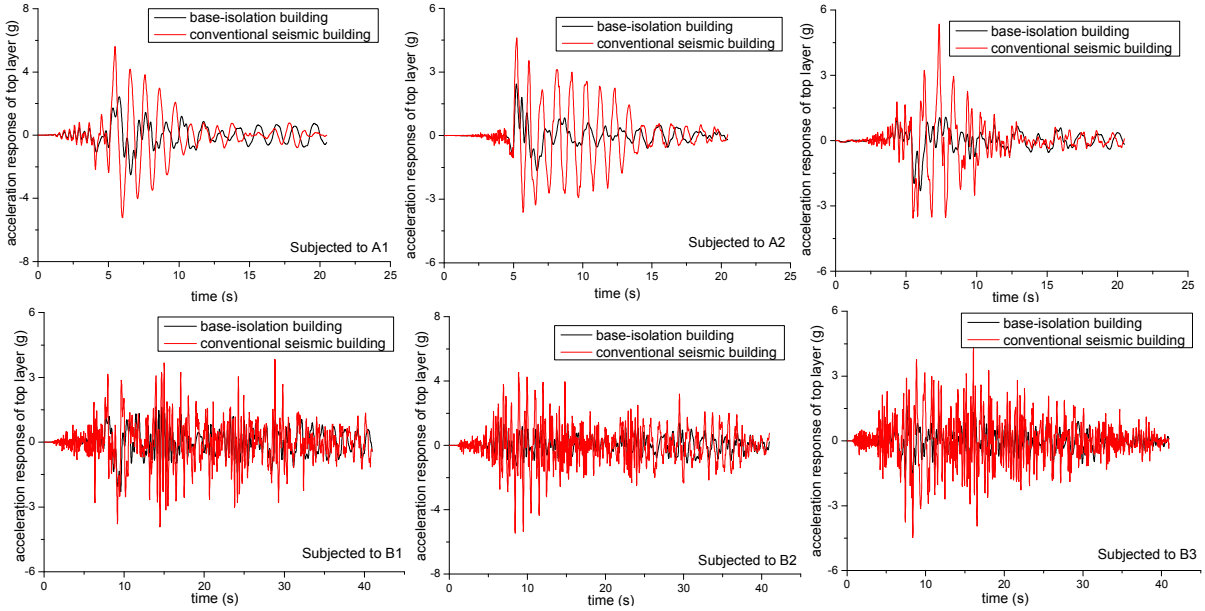


Fig.3 Acceleration response of top layer

## Base shear

Table2 is the X direction base shear of the base-isolation building and the conventional seismic building subjected to the pulse-like velocity ground motions in table1. It can be learned that the base bear of the base-isolation building model is obviously lower than the conventional seismic building model; the base isolation device reduces the structural base shear.

Table2. Maximum base shear of X direction

| Model | maximum base shear（KN） | | | | | |
|---|---|---|---|---|---|---|
| | A1 | A2 | A3 | B1 | B2 | B3 |
| Base-isolation building | 9129 | 6427 | 7559 | 8081 | 4433 | 4621 |
| Conventional seismic building | 15107 | 10371 | 11139 | 9881 | 8122 | 8128 |
| proportion（%） | 61% | 62% | 68% | 82% | 55% | 57% |

## Story drift response

Story drift response is an important index to represent the degree of structure seismic damage. Figure4 is the story drift response of the base-isolation building model and the conventional seismic building model subjected to 6 pulse-like velocity ground motions in table1. The story drift of the superstructure of the base-isolation building is effectively reduced comparing with the conventional seismic building. The horizontal displacement of the base-isolation building focuses on isolation floor bearing. The story drift of the 3-5 layer of the conventional seismic building are larger than the other layer.

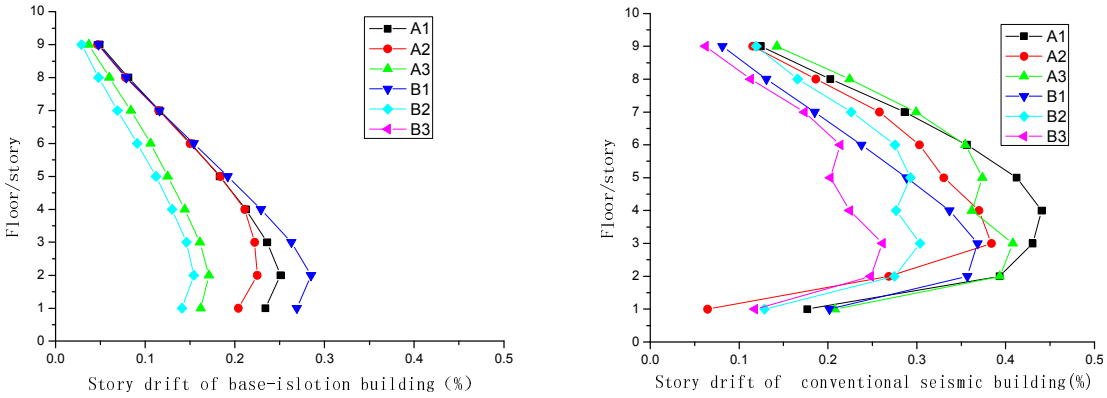


Fig.4 Story drifts response

## Conclusions

6 pulse-like velocity near-fault ground motions are selected as the input, and the seismic response of a 9 layers conventional seismic RC frame building and comparative base-isolation building with lead-core rubber bearings is obtained by nonlinear time history analysis. Compared with the conventional seismic building, the top floor acceleration response, the X direction maximum base shear and the story drift of base-isolation building significantly reduced. The result indicates that base-isolation building with lead-core rubber bearings are of good aseismic performance under the near-fault ground motions with velocity pulse.

## Acknowledgment

This work was supported by the National Natural Science Foundation of China(51108428), Beijing Nova Program (Z121106002512059)，and research grant from Institute of Geophysics, China Earthquake Administration（DQJB12B28）

## Reference

[1]LI Shuang, XIE Li-li. Progress and trend on near-field problems in civil engineering [J]. Acta Seismologica Sinica, 2007,29(1):102-111

[2] Hall J F, Heaton T H, Halling MW, et al. Near-source ground motion and its effects on flexible buildings [J]. Earthquake Spectra, 1995, 11 (4): 569-605.

[3]Makris N, Chang S P. Effect of viscous,viscoplastic and friction damping on the response of seismic isolated structures [J]. Earthquake Engineering and Structural Dynamics, 2000, 29: 85-107.

[4] Jangid R, Kelly J. Base isolated for near-fault motions [J]. Earthquake Engineering and Structural Dynamics, 2001, 30: 691-707.

[5]Yang Di-xiong， LI Gang, Cheng Geng-dong. Seismic analysis of base-isolated structures subjected to near-fault pulse-like ground motions[J]. Earthquake Engeering and Engeering Vibration,2005,25(2):119-124.

[6]LI Xiao-jun, HE Qiu-mei, QI Xing-jun. Seismic mitigation control effects of long-span cable-stayed bridges to ground motions with velocity pulse[J]. Journal of Basic Science and Engineering, 2012,20(2):272-285.

[7]HE Qiu-mei,LI Xiao-jun, Yang Yu. Displacement response analysis of base-isolated buildings subjected to near-fault ground motions with velocity pulse[J]. Journal of Basic Science and Engineering, 2014,22(1):1-13.

*Applied Mechanics and Materials Vols. 580-583 (2014) pp 1704-1707*
*© (2014) Trans Tech Publications, Switzerland*
*doi:10.4028/www.scientific.net/AMM.580-583.1704*

# Seismic Response Analysis of Free Long-Span Submarine Flexible Pipelines under Earthquakes

Yu Lin Deng[1, a], Yu Bian[1, b], Fan Lei[1, c]

[1]School of Transportation, Wuhan University of Technology, Wuhan 430063, China

[a]dengyulin2006@163.com, [b]bianyu0702@163.com, [c]leifan2008@163.com

**Keywords:** submarine flexible pipeline; seismic response; fluid-structure interaction; dynamic analysis

**Abstract.** Submarine pipelines are described as the lifeblood of offshore oil and it is crucial to ensure the seismic safety of the submarine pipelines. Based on the fluid-structure interaction numerical analysis method and by using finite element software ADINA, the analysis models of the free long-span submarine flexible pipelines under earthquakes were established. By employing dynamic time-history method, the influences of fluid-structure interaction on the seismic response of the submarine pipelines were researched. The results showed that the peak normal stress and the peak displacement of submarine pipelines' mid-span considering the influences of the fluid-structure interaction are greater than those without considering the influences, and the influences of the fluid-structure interaction on the seismic response of the submarine pipelines will increase with the increase of the submarine pipelines' diameter.

## Introduction

It's difficult to lay submarine pipelines, and maintenance is a burden as well. Submarine pipelines leakage will cause serious economic loss and marine environment pollution. Submarine pipelines are designed flat out on the bottom of the sea, but long span will occur due to the fact that current scour, submarine topography, pipeline stress concentration and so on [1,2]. And on dynamic performance, there is a big difference between land pipelines and submarine pipelines [3,4]. But there is no seismic design code of submarine pipelines at present [5]. In this paper, based on the fluid-structure interaction numerical analysis method and by using finite element software ADINA, the seismic response of free long-span submarine flexible pipelines has been studied, in order to explore the influences of the fluid-structure interaction on the seismic response of the submarine pipelines.

## Finite element model

### Model parameter

Four submarine pipelines whose diameters are 0.1m, 0.2m, 0.3m and 0.4 m were selected as the calculating model. Main parameters of the model are shown in Table 1.

Table.1. Main parameters of the model

| No | Main parameters | Unit | Value |
|---|---|---|---|
| 1 | Length of the pipe | $[m]$ | 30 |
| 2 | Density of the pipe | $[kg \cdot m^{-3}]$ | 7850 |
| 3 | Modulus of elasticity | $[GPa]$ | 200 |
| 4 | Diameter of the pipe | $[m]$ | 0.1~0.4 |
| 5 | Pipe wall thickness | $[m]$ | 0.01 |
| 6 | Poisson's ratio | – | 0.3 |
| 7 | Density of sea water | $[kg \cdot m^{-3}]$ | 1030 |

The whole calculation domain is a cylinder whose diameter is ten times more than submarine pipelines' diameter and both ends of submarine pipelines extended five meters. With infinite

boundaries to constrain the flow field, the Potential-based fluid element is used for the water and the number of Potential-based fluid is 49920. Consolidation is used to constraint the ends of submarine pipelines. The Shell element is used for submarine pipelines and the number of Shell is 2304. Calculation model is shown in Fig.1.

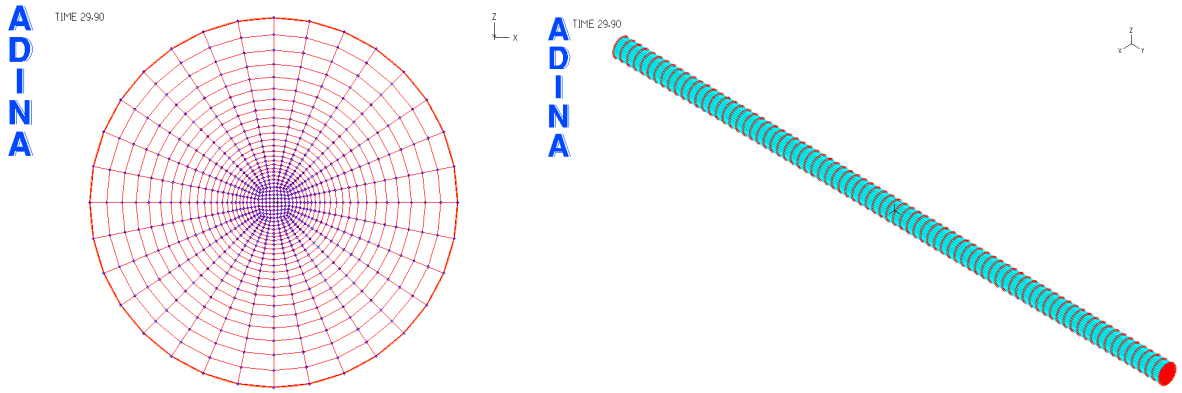


(a) Cross-section mesh (b) Whole mesh

Fig.1. Calculation model

**The earthquake wave input**

Three earthquake acceleration time-history curves were selected from PEER Ground Motion Database. Assuming that submarine pipelines are located in zone 9 degrees of seismic intensity, then each of the peak acceleration time-history curves were adjusted to 0.4g [6]. As shown in Table 2.

Table.2. Selected free-field ground motions

| No | earthquake record | location | PGA [g] | amplitude modulation index | interval |
|---|---|---|---|---|---|
| 1 | 1940 El Centro | Imperial Valley | 0.313 | 1.278 | 0.02 |
| 2 | 1994 Northridge | Hollywood | 0.245 | 1.633 | 0.01 |
| 3 | 1995 Kobe | Shin-Osaka | 0.212 | 1.887 | 0.01 |

**Calculated work condition**

The finite element model has been analyzed in the following two conditions: (1) considering the fluid-structure interaction, three types of earthquake load have been applied to submarine pipelines; (2) not considering the fluid-structure interaction, three types of earthquake load have been applied to submarine pipelines.

**Analysis of computing result**

According to the two kinds of working conditions, earthquake waves have been input along the X direction in the model. The seismic response time-history analysis has been completed. The normal stress and the displacement of the submarine pipelines' mid-span were the results which have been focused on.

The mid-span normal stress time-history curves and the mid-span displacement time-history curves of submarine pipelines which diameter is 0.2m under the action of three earthquake waves are shown in Fig.2~4.

Figure.2~4 indicated that: (1) whether to consider the fluid-structure interaction or not , the changing trends of the mid-span normal stress time-history curve and the mid-span displacement time-history curve are basically identical; (2) the peak normal stress and the peak displacement of submarine pipelines' mid-span appeared at different moment in two the situations which considering the fluid-structure interaction and not considering, also the peak normal stress and the peak displacement of submarine pipelines' mid-span considering the influences of the fluid-structure interaction are greater than those without considering the influences.

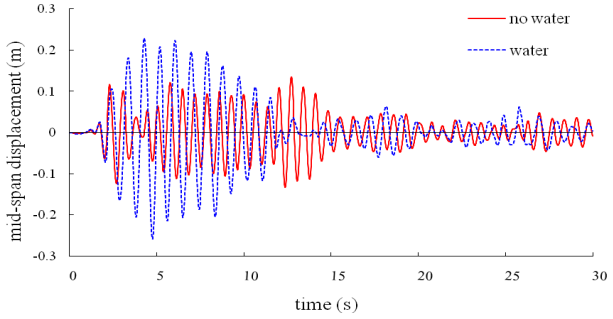


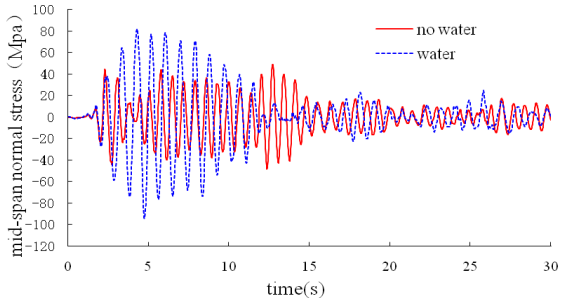


(a) The mid-span normal stress time history curve (b) The mid-span displacement time history curve

Fig.2. El Centro earthquake wave response

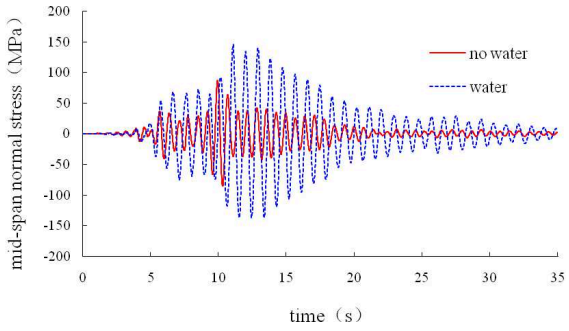


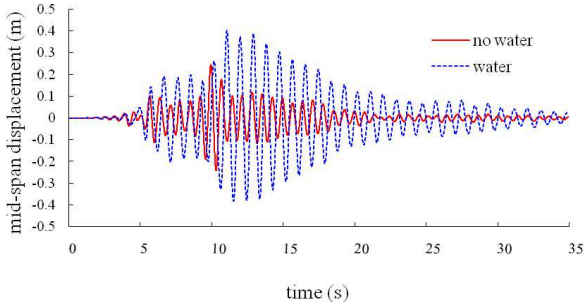


(a) The mid-span normal stress time history curve (b) The mid-span displacement time history curve

Fig.3. Northridge earthquake wave response

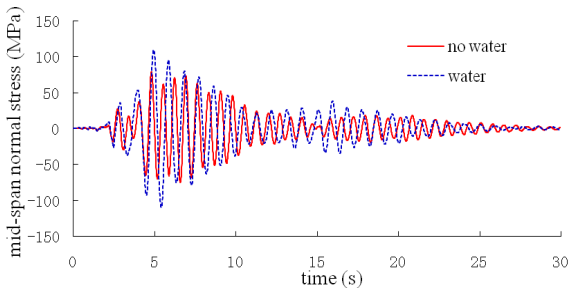


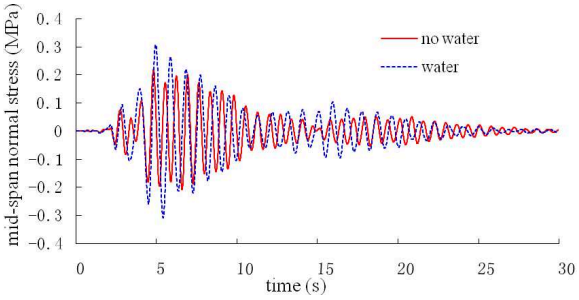


(a) The mid-span normal stress time history curve (b) The mid-span displacement time history curve

Fig.4. Kobe earthquake wave response

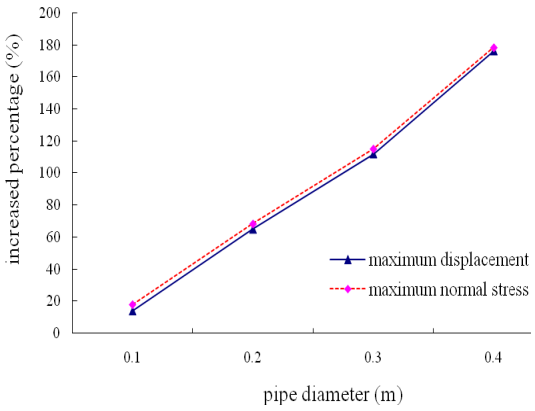


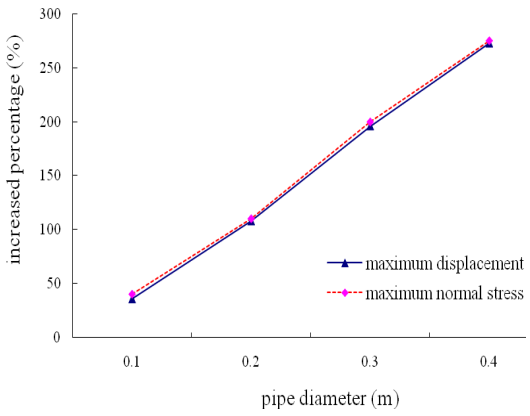


(a) EI Centro earthquake wave (b) Northridge earthquake wave

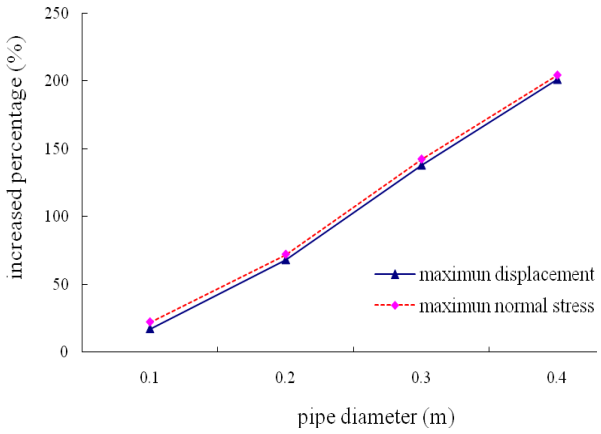


(c) Kobe earthquake wave
Fig.5. The increased percentage

The increased percentage of the maximum normal stress and the maximum displacement of submarine pipelines' mid-span considering the influences of the fluid-structure interaction were compared with the one that without considering the influences of the fluid-structure interaction are shown in Fig.5.

Figure.5 indicated that: the increased percentage of the peak normal stress and the peak displacement of submarine pipelines' mid-span showed growth trend with submarine pipelines' diameter. In other words, with the increase of the pipe diameter, the influence of the fluid-structure interaction on the seismic response of submarine pipelines will be greater.

## Conclusions

In this paper, based on the fluid-structure interaction numerical analysis method and by using finite element software ADINA, the seismic response of free long-span submarine flexible pipelines has been studied. The results showed that: (1) the peak normal stress and the peak displacement of submarine pipelines' mid-span considering the influences of the fluid-structure interaction are greater than those without considering the influences; (2) the influences of the fluid-structure interaction on the seismic response of the submarine pipelines will increase with the increase of the submarine pipelines' diameter.

## Acknowledgements

Supported by the "Fundamental Research Funds for the Central Universities (WUT: 2014-IV-110)".

## References

[1] Yansheng Luo, Fuzzy Fatigue Reliability Analysis on Vortex Induced Vibrations of Submarine Pipeline Span[D], China University of Petroleum, Beijing ,1999, In Chinese.

[2] Patel M H. Applied Ocean Research,2002,22(1):45-53.

[3] Yazdchi M, Crisfield M A, International Journal for Numerical Methods in Engineering, 2002, 54(9):1256-1308.

[4] Gao F P, Jeng D S, Wu Y, Journal of Transportation Engineering, 2006, 32(7):590-596

[5] Zhengce Sun, Menglan Duan and Wen Zhang, Journal of Vibration Engineering ,2004,17(3): 263-268.

[6] Guidelines for Seismic Design of Highway Bridges, JTG/T B02-02-2008, In Chinese.

*Applied Mechanics and Materials Vols. 580-583 (2014) pp 1708-1711*
*© (2014) Trans Tech Publications, Switzerland*
*doi:10.4028/www.scientific.net/AMM.580-583.1708*

# SRC Frame-RC Core Wall Hybrid Structures Collapse-resistant Design

Yuanyuan Wu[a], Zhenkun Cui[b], Qianqian Gong[c], Lei Zeng[d.*]

School of Urban Construction, Yangtze University, Jingzhou, 434023, P.R. China

[a]wuyuan9950@163.com, [b]cuizhenkun163@163.com, [c]simetime118@163.com, [d]zenglei28@126.com.

**Keywords:** SRC frame-RC core wall, Earthquake Collapse, Collapse-resistant Design

**Abstract.** To study Steel reinforced concrete frame-reinforced concrete core wall (SRC frame-RC core wall) hybrid structure earthquake damage evolution and collapse mechanism, this paper holds the earthquake collapse mechanism, seismic collapse analysis and collapse control strategies as the mainline, establishes performance degradation and collapse criterion characterization based on structure dynamic characteristics, adopts incremental dynamic analysis (IDA) method to complete the prototype structure collapse-resistant test and quantitative assessment of seismic collapse analysis and determine the main factors that affect the structure collapse-resistant properties. Through numerical analysis to reveals the mechanism of the earthquake collapse and obtains optimal collapse model, and proposes methods and measures of collapse-resistant design for such structure, which has practical significance for enhancing the ability of high-level hybrid structure to earthquake.

## Introduction

Collapsed buildings caused heavy casualties in the earthquake, how to integrate the ideas of collapse-resistant design, seek reasonable collapse model of structural and improve the structure seismic collapse-resistant capacity is important. Steel and concrete composite structure have been widely used in high-rise buildings in recent decades with its high carrying capacity, excellent performances of ductility, SRC frame-RC core wall hybrid structures are more used in High-rise building in China. However, a lot have been built SRC frame-RC core wall hybrid structure have not been tested in strong earthquake, the corresponding structural design specification does not have specific provisions and technical requirements to prevent collapse, and lacking of information and research related to earthquake damage. Based on the research abroad, the research status, problems of SRC frame-RC core wall hybrid structures collapse-resistant performance were reviewed, and future research directions are suggested in this paper, which can provided a reference for SRC frame-RC core wall hybrid structure collapse-resistant design and seismic design.

## Research Status

The SRC frame-RC core wall hybrid structures have attracted extensive attentions from many scholars around the world. Through seismic performance experiments and numerical simulation of hybrid structure, scholars researched the seismic response and failure characteristics, experimental model, seismic calculations, which can provide the basis for the seismic design criteria and construction requirements for seismic design. Xilin Lv et al. [1] and Peifu Xu et al. [2] conducted a lot of tall frame-core wall structure quasi-static test or simulated earthquake shaking table according to the actual project respectively.

David [3], Graham [4], Xinzheng Lu et al. [5] applied high-precision numerical finite element model to analysis structure seismic collapse, Park [6] proposed earthquake damage assessment model based on the principle of energy, Leiming Zhang et al. [7] put forward agency guidelines as a criterion for judging the structure collapse. Sasani [8] verified the capacity and the existing evaluation methods of structure to resistant progressive collapse by experimental method.

## Existing problems

Although many scholars' research had show that through rational design, SRC frame-RC core wall hybrid structure are fully able to meet current seismic requirements, but such structure engineering applications there have been some problems to be solved:

1) The lateral stiffness of the frame and the concrete core wall is difference, and the concrete core wall borne the most earthquake action. Under rare earthquake, plastic hinges mainly appear on the concrete core wall, the plastic hinge mechanism is unfavorable to seismic, once the core wall occurs large deformation and serious damage, the outer frame will cause instability or partial collapse of the entire structure.

2) Current research on the hybrid structure most contrary to a particular practical engineering structures, the existing research does not clearly reflect the collapse mechanism of such structures under earthquake, can not accurately assess the influence of various factors for collapse-resistant properties of such structure. With the refinement of experimental methods, to accurately reproduce the mechanical behavior of the structure during the earthquake, the damage evolution and the development process of collapse under destruction is an effective method, which is the foundation to propose effective and feasible strategy to control SRC frame-RC core wall structure failure mode.

3) Structural collapse is a complex numerical process from continuum to non-continuum, numerical models have high demands, most current numerical simulation research focused on the overall collapse of the seismic behavior, and more concentrated in SDOF frame structure on the overall level of collapse, for tall frame-core wall hybrid structures collapse simulation studies under earthquake are less.

4) Currently the judgment criteria and evaluation indicators suitable for SRC frame-RC core wall hybrid structure earthquake collapse are less, the existing guidelines can't reflect effects of the load magnitude and action path changes to structure cumulative damage, due to the structural collapse is a complex unstable problems, collapse criterion and damage assessment indicators of SRC frame-RC core wall hybrid structure should be identified in the overall hierarchy.

## Collapse-resistant design

Future studies on the collapse-resistant of SRC frame-RC core wall hybrid structure should hold the collapse mechanism of earthquakes, seismic collapse analysis and collapse-resistant design countermeasures as the main line, the research technology roadmap shown in Fig.1

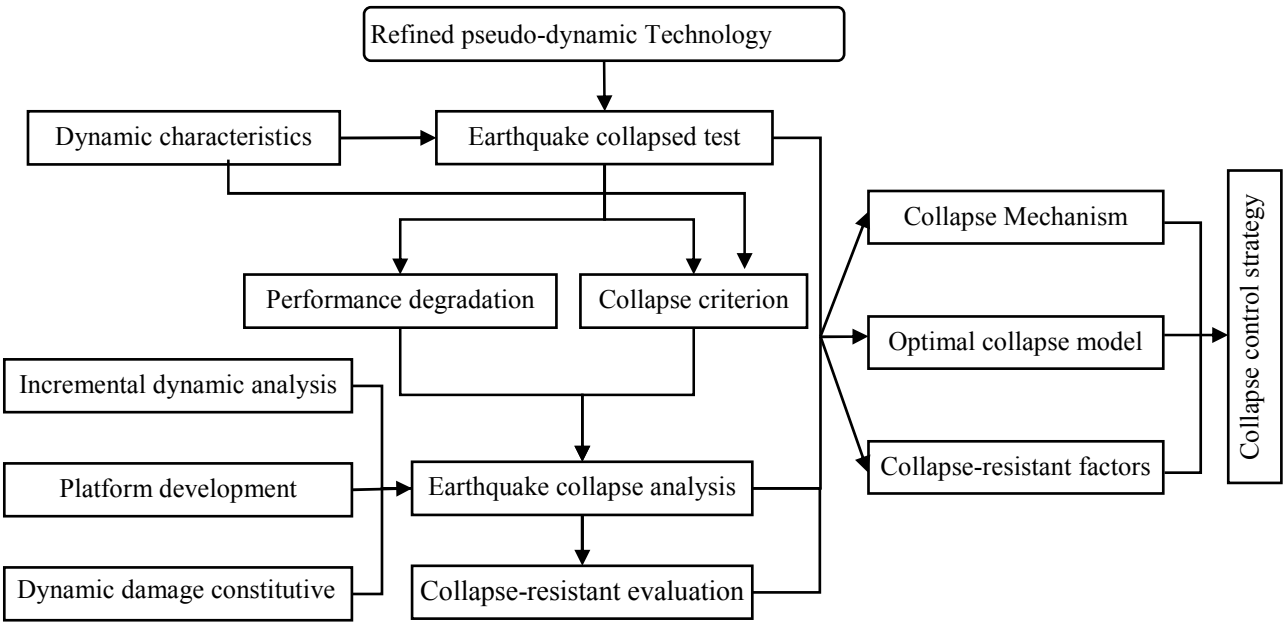


Fig. 1 The main line and research technology roadmap

**1) Conduct earthquake collapse experiment of SRC frame-RC core wall hybrid structure based on pseudo dynamic technology.** Conduct SRC frame-RC core wall hybrid structures scale model pseudo dynamic experimental study, to simulate complex mechanical behavior and collapse process of such hybrid structures under earthquake damage. By experiment to explore the structural damage path, the collapse mechanism and the collapse criterion under the earthquake, to study collaborative work performance of RC core wall and SRC frame under different ground motion parameters and different force stage.

**2) Establish structural seismic collapse criterion based on structural dynamic characteristics.** Structural collapse is a very complex nonlinear dynamic process, describe the structure damage performance and degradation characteristics under cyclic loading based on structure dynamic characteristics is the trend of future development. Through quantitative assessment by studying the changes of structural frequency from damage to collapse under earthquake, taking into account higher mode effects on seismic response, leading into modal participation factor, building relationships with structural degradation rate between the dynamic characteristics, further to establish characterization methods and collapse criterion to access the performance degradation based on the frequency of the vibration mode.

**3) Numerical analysis of seismic collapse of SRC frame-RC core wall hybrid structures.** Based on the finite element method, considering the element nonlinear numerical model (element birth and death) and the contact nonlinearity, considering the bond-slip behavior of steel and concrete according to preliminary basic research, by secondary development, introducing structural collapse criterion based on dynamic characteristics, to have a better results when the simulated structure from the continuous state to a fully discrete state status.

**4)Adopt incremental dynamic analysis (IDA) methods to assess the performance of collapse-resistant.** The structure elastic-plastic differential equation of motion is

$$[M]\{\ddot{x}(t)\}+[C]\{\dot{x}(t)\}+[K]\{x(t)\}=-[M][R]\{\ddot{x}_g(t)\} \tag{1}$$

where $[M]$, $[C]$, $[K]$ are the global mass matrix, viscous damping coefficient matrix, stiffness matrix respectively; $[R]$ is the unidirectional ground motion direction cosine column vector; $\{\ddot{x}(t)\}$, $\{\dot{x}(t)\}$, $\{x(t)\}$ are the acceleration, velocity, displacement of structure relative to the ground at t; $\{\ddot{x}_g(t)\}$is the ground motion acceleration at t. Formula (1)at $t+\Delta t$ moment also is established,

$$[M]\{\ddot{x}(t+\Delta t)\}+[C]\{\dot{x}(t+\Delta t)\}+[K]\{x(t+\Delta t)\}=-[M][R]\{\ddot{x}_g(t+\Delta t)\} \tag{2}$$

We can obtain the structure incremental motion equations with Formula 1 subtracts Formula 2,

$$[M]\{\Delta\ddot{x}\}+[C]\{\Delta\dot{x}\}+[K]\{\Delta x\}=-[M][R]\{\Delta\ddot{x}_g\} \tag{3}$$

Where $\{\Delta\ddot{x}\}=\{\ddot{x}(t+\Delta t)\}-\{\ddot{x}(t)\}$, $\{\Delta\dot{x}\}=\{\dot{x}(t+\Delta t)\}-\{\dot{x}(t)\}$, $\{\Delta x\}=\{x(t+\Delta t)\}-\{x(t)\}$, $\{\Delta\ddot{x}_g\}=\{\ddot{x}_g(t+\Delta t)\}-\{\ddot{x}_g(t)\}$

The IDA method based on the above equation(3), by inputting the gradually incremental seismic records intensity, until structural damage calculation model collapses, hold the ground motion intensity measures(IM) as indicators of structural collapse-resistant, to evaluate structure seismic collapse-resistant, When $N_c$ earthquakes recorded (the total number record is $N_t$) collapsed at a ground motion intensity, the $N_c/N_t$ called the structure collapse possibility under ground motion intensity. The ATC-63 Committee [9] suggests

$$IM=S_a(T_1)/S_a(T_1)_{MEC} \tag{4}$$

Where $S_a(T_1)$ is the structure first period spectral acceleration, $S_a(T_1)_{MEC}$ the structure first period design spectral acceleration to criterion under Maximal Considered Earthquake, for china seismic code

$$S_a(T_1)_{MEC} = \alpha(T_1)_{MEC} g \quad (5)$$

Where $\alpha(T_1)_{MEC}$ is the horizontal seismic influence coefficient to period $T_1$ under maximal considered earthquake (MCE), and $g$ is acceleration of gravity.

Apply IDA method based on nonlinear dynamic time history analysis, by introducing material dynamic damage constitutive, considering initial damage and damage evolution in the analysis process, to find out the SRC frame-RC core wall properties and response under different earthquake intensity. Through statistical analysis of structural response-seismic strength parametric curves and combining with structural collapse criterion, to determine the critical earthquake standards.

5)**Analysis of SRC frame- RC core wall hybrid structure collapse-resistant factors and collapse control.** Based on the seismic collapse test and IDA results, conducting local and global sensitivity parameters analysis for the overall structure collapse-resistant capability, to definite the Structure collapse-resistant capability under multi-parameter coupling, get the best collapse-collapse-resistant mode and put forward collapse-resistant design countermeasures for such structure

## Conclusion

In this paper, SRC frame-RC core wall hybrid structures collapse-resistant under earthquake, the research status and existing problems are analyzed. Through prototype structure model collapse-resistant test, the IDA method and numerical analysis to set up collapse mechanism, collapse criterion, reveal dynamic catastrophic failure mechanism, and propose quantitative evaluation method of collapse-resistant and collapse-resistant design measures.

## Acknowledgements

This work was financially supported by the National Natural Science Foundation of China (51108041), the Creative Experiment Program of National College Students (101048933) and the Hubei Natural Science Foundation (2011CDB009).

## References

[1] Xilin Lv, Yun Zou, Wensheng Lu, et al: Earthquake Engineering and Engineering Vibration, 2004, 24 (3): 57-63. (In Chinese)

[2] Peifu Xu, Yantao Xue, Congzhen Xiao, et al: Building Structures, 2005, 35(5): 3-8. (In Chinese)

[3] David Nbilow, Mahmoud Kamara. U. S: ASCE, 2004.

[4] Graham Powell. Progressive collapse: ASCE, 2005.

[5] Xinzheng Lu, Xuchuan Lin, Lieping Ye, et al: Engineering Mechanics, 2010, 27(11): 64-70. (In Chinese)

[6] Park Y. J.,Ang A. H. -S. and Wen Y. K: ASCE, 1985, 111(4): 740-757.

[7] Leiming Zhang: [Ph. D. Thesis]. Tsinghua University, 1999(In Chinese)

[8] Sasani M, Sagiroglu S: Journal of Structural Engineering, 2008, 134(3):478-488.

[9] ATC-63 Quantification of building seismic performance factors[S]. Applied Technology Council, 2008.

*Applied Mechanics and Materials Vols. 580-583 (2014) pp 1712-1717*
*© (2014) Trans Tech Publications, Switzerland*
*doi:10.4028/www.scientific.net/AMM.580-583.1712*

# Study on Seismic Performance of Irregular RC Frame with Specially Shaped Columns

Jian Tang[1, a] , Lang Wu [2,b]

[1]College of Civil Engineering, JiangXi Science&Technology Normal Univercity, Jiangxi Nanchang 330013, China

[2]College of Civil Engineering, Nanchang Institute of Technology, Nanchang 330044, China

[a] tjwmr@163.com,[b]wulang19812005@126.com

**Keywords:** specially shaped column; RC frame; nonlinear seismic response analysis; seismic performance

**Abstract:** According to the code and technical regulation, a irregular RC frame with specially shaped columns have been designed, which situated at the area of fortification intensity 7. Subsequently, the nonlinear dynamic analysis has been carried out for the structure by inputting ground motions in two directions. After summing up the calculation results, this paper have examined seismic performance of the structure under the rare seismic actions and given a primary evaluation on the structure to see if it achieves the predetermined seismic aims. It indicates that the structure designed the codes can achieve the predetermined seismic aims under the rare earthquake.

## Introduction

In recent years, a lot of experimental research and theoretical analysis have been done on the frame structure of special-shaped reinforced concrete columns, due to the urgent needs of engineering practice. Experimental studies were focused on special-shaped column member and the frame structure model shaking table tests. Although the small number of trials have been done on the overall structure, also obtained some of research results. Existed experimental studies show that the frame structure of special-shaped columns is in the elastic stage with the input of small earthquakes, the shape of deformation curve is a type of flexure-sheer, between the wall and the general framework. The structure of shaped column has better integral stiffness and self lighter. The frame with specially shaped columns lack of earthquake-resistant performance embody in some aspects that cross-section with a serious asymmetry, core region of the node is relatively weak, the section weakened severely after the concrete cover fall off, cross-section design needs improvement and so on.

However, due to experimental study under restriction of equipment and funding, it is unpractical to conduct a series larger size of over-all structure of dynamic or static tests. At present it is not deep enough for study that nonlinear analytical method of integral space of the frame with special-shaped columns. There is not a nonlinear analytical method and tool to reflect main stress characteristics of structure with reinforced concrete special-shaped columns and has been widely recognized. Elasticoplastic deformation of structure can not be practical, there is unclear to whether the design of structure can meet requirements for earthquake fortification of " no collapse under major earthquake". Therefore , it is necessary to carry out research for special seismic non-linear dynamic response analyses of the frame with shaped columns. This article use finite element flexibility method based on fiber model beam-column elements to adopt triaxial non-linear earthquake response analyses on the frame construction with irregular shaped columns under the action of mono directional lateral earthquake and inspect earthquake-resistant behavior of the frame in accordance with the specifications designed under the rare earthquake level.

## Analytical mode

According to the code and technical regulation in Chinese, a irregular RC frame with specially shaped columns have been designed, which situated at the area of fortification intensity 7(0.10g). Fundamental natural period of structure is 0.84 second. Figure.1 show layout of the structure and Reinforcement in columns and beams.

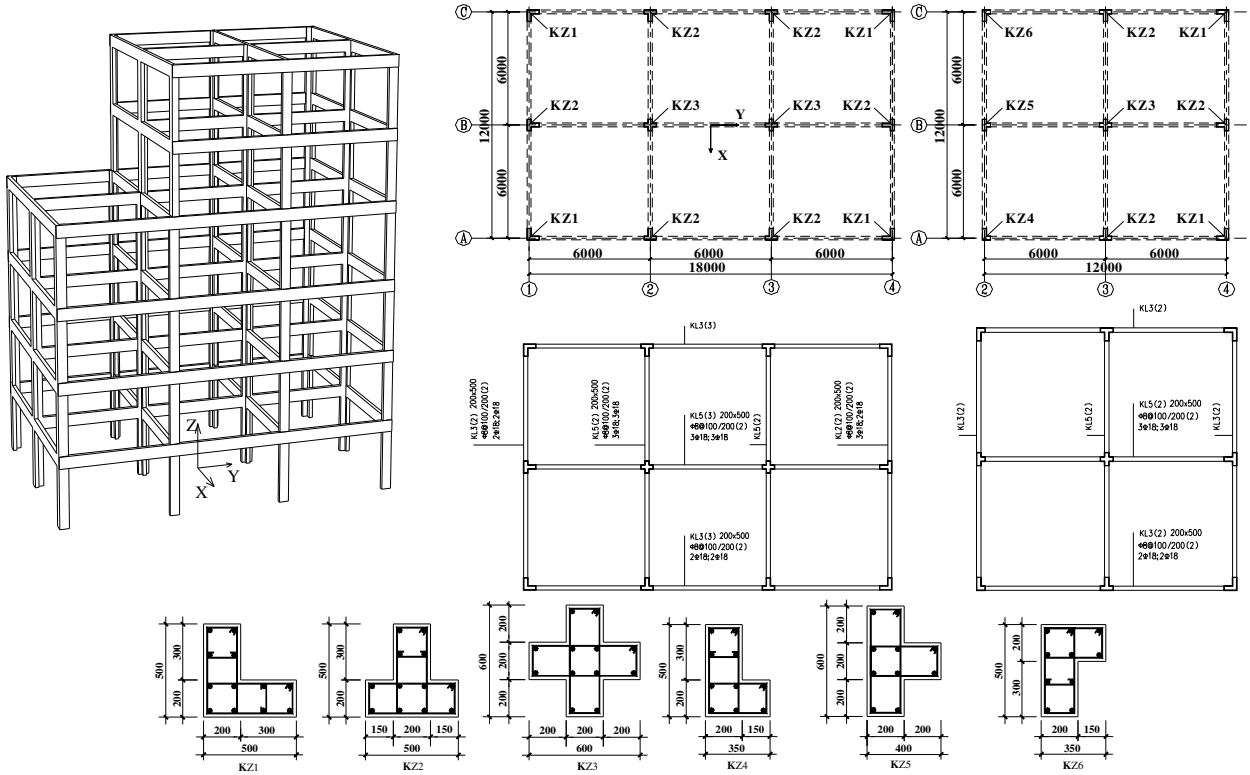


Fig.1 Layout of the structure and Reinforcement in columns and beams

Use SAP2000 to calculate elastic horizontal shift for structure. Maximum inter-story drift angle of the structure is 1/1181 under frequent earthquake, satisfy the requirement of design specification (1/550). And the calculative results show in the Table 2, which show that the structure is torsional irregularity.

Table 1 Ratio of the floor's maximum inter-story drift and the mean inter-story drift

| Floor | 1 | 2 | 3 | 4 | 5 | 6 |
|---|---|---|---|---|---|---|
| Ratio | 1.18 | 1.19 | 1.20 | 1.21 | 1.18 | 1.17 |

The axial-load ratio of L shaped,T shaped,cross-shaped column are 0.34,0.55,0.70, not in excess of the specified limits of the axial-load ratio 0.50,0.55,0.70.

This article adopt nonlinear dynamic analytic procedure of fiber model of beam-column elements formation based on flexibility method that cross-section of beam-column element is discretized into a number of vertical fiber, ignoring the shearing effect and considering each fiber in a unidirectional stress The fiber model also consider lateral constrained influence in the uniaxial stress-strain relationship, and use plane-section assumption to create beam-column element stiffness matrix for calculating the nonlinear relationship of force and deformation of the total cross section on the basis of uniaxial stress-strain relationship of corresponding fibrous materials. Analytical procedures used in this article has been verified efficiency and accuracy of analysis on the level of general rectangular column member and structure. This program not only can output stem end force and displacement of unit, but also output each specified internal force and deformation of section and the value of stress-strain of the fibers, which can fully examine response of macro and micro levels for structure.

This article select "3+1" waves, crude seismic wave which distinguish are USA00641, USA00707, IND00364, artificial wave is ACC5. Use SAP2000 to conduct response spectrum analysis and

elastodynamic time history analysis for structure, checking whether chosen seismic wave satisfy afferent requirement of criterion. The calculative results show in the Table 2, chosen seismic wave can well satisfy the requirement of criterion.

Since the structure of irregular layout , two horizontal directions on the selected seismic waves are input along the X and Y direction, while the amplitude ratio in X and Y direction is 1:0.85.

Table 2 Base shear by elastic dynamic analysis and modal analysis at seismic intensity 7(0.10g)

| wave | USA00641 | USA00707 | IND00364 | ACC5 |
|---|---|---|---|---|
| Shear of response spectrum analysis | | 206 | | |
| Shear of elastodynamic history analysis | 187 | 181 | 169 | 201 |
| Ratio | 0.91 | 0.88 | 0.82 | 0.98 |
| Average ratio | | 0.90 | | |

## Organization of the Text

In this paper, the response from the overall performance of the structure (such as inter-story drift angle, inter-story twist angle) to a single member state (such as the moment-curvature relationship of cross-section, the stress and strain of fiber) will be inspected. Since only input the ground motion along the X-axis under the rare earthquake, examine the response along X-axis of the structural response.

The maximum inter-story drift angel, inter-story twist angel and the maximum displacement are shown in Table 3, Figure.2 and Figure.3. The ratio of the maximum inter-story drift of the two edges and the mean inter-story drift are shown in Table 4. The moment-curvature of the column of the first floor and the beam of the second floor are shown in Figure.4(only USA00707) . The maximum strain of fiber structural beams and columns are shown in Table 5 after inputting four seismic wave(peek acceleration is 2.2m/s$^2$).

Table 3 Max inter-story drift angel, twist angel and the maximum displacement under the rare motion

| wave | USA00641 | USA00707 | IND00364 | ACC5 | average | max |
|---|---|---|---|---|---|---|
| Max inter-story drift angel of left edge | 1/259[2] | 1/273[2] | 1/273[2] | 1/290[2] | 1/273 | 1/259 |
| Max inter-story drift angel of right edge | 1/186[2] | 1/207[2] | 1/189[2] | 1/156[2] | 1/183 | 1/156 |
| Max inter-story twist angel | 0.00068[2] | 0.00067[2] | 0.00086[2] | 0.00077[2] | 0.00075 | 0.00086 |
| Max displacement (mm) | 53.7 | 51.3 | 56.9 | 60.7 | 55.7 | 60.7 |
| Max displacement/overall height | 1/335 | 1/351 | 1/316 | 1/297 | 1/323 | 1/297 |

[2]—the second floor

Table 4 Ratio of the maximum inter-story drift of the two edges and the mean inter-story drift of the structure under the rare motion

| | USA00641 | USA00707 | IND00364 | ACC5 |
|---|---|---|---|---|
| First floor | 1.17 | 1.19 | 1.10 | 1.26 |
| Secondfloor | 1.16 | 1.14 | 1.18 | 1.30 |
| Third floor | 1.16 | 1.12 | 1.22 | 1.32 |
| Fourth floor | 1.21 | 1.16 | 1.24 | 1.36 |
| Fifth floor | 1.03 | 1.06 | 1.04 | 1.09 |
| Sixth floor | 1.02 | 1.01 | 1.07 | 1.07 |

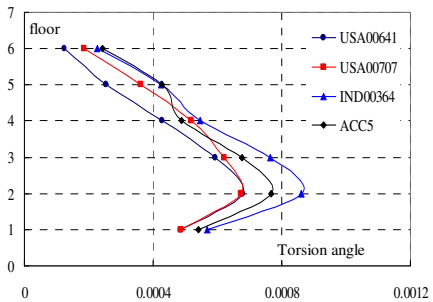


Fig.2 Maximum inter-story torsion angle of the structure under the rare

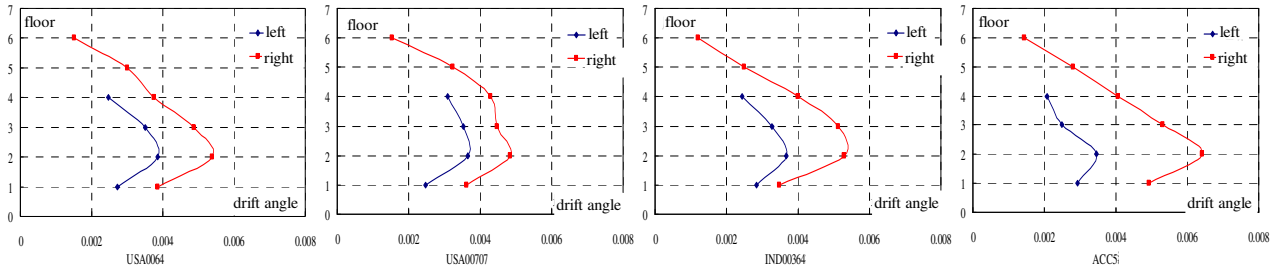


Fig.3 Maximum inter-story drift angle of the structure under the rare motion

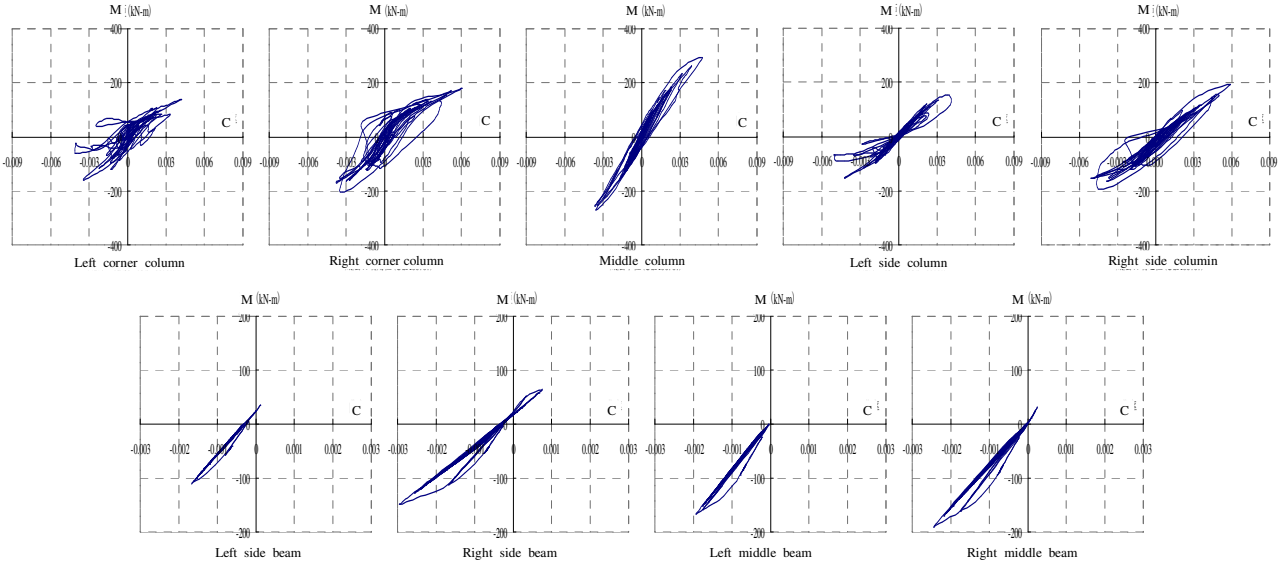


Fig.4 Moment-curvature of columns and beams under the rare motion

Table 5 Max strain of fiber structural beams and columns under the rare motion

| Location | | USA00641 | USA00707 | IND00364 | ACC5 | MAX |
|---|---|---|---|---|---|---|
| Max strain of concrete in columns | Left corner | -0.00112[1] | -0.00144[1] | -0.00116[1] | -0.00128[1] | -0.00144 |
| | Right corner | -0.00169[1] | -0.00182[1] | -0.00134[1] | -0.00168[1] | -0.00182 |
| | Middle | -0.00242[1] | -0.00329[1] | -0.00191[1] | -0.00244[1] | -0.00329 |
| | Left side | -0.00128[1] | -0.00199[1] | -0.00136[1] | -0.00163[1] | -0.00199 |
| | Right side | -0.00211[1] | -0.00262[1] | -0.00192[1] | -0.00195[1] | -0.00262 |
| Max strain of steel in columns | Left corner | 0.00201[1] | 0.00229[1] | 0.00159[1] | 0.00258[1] | 0.00258 |
| | Right corner | 0.00245[1] | 0.00226[1] | 0.00197[1] | 0.00204[1] | 0.00245 |
| | Middle | 0.00130[1] | 0.00211[1] | 0.00088[1] | 0.00170[1] | 0.00211 |
| | Left side | 0.00201[1] | 0.00240[1] | 0.00143[1] | 0.00195[1] | 0.00240 |
| | Right side | 0.00139[1] | 0.00256[1] | 0.00117[1] | 0.00082[1] | 0.00256 |
| Max strain of concrete in beams | Left corner | -0.00065[2] | -0.00071[2] | -0.00066[2] | -0.00068[2] | -0.00071 |
| | Righ corner | -0.00099[2] | -0.00091[2] | -0.00102[2] | -0.00097[2] | -0.00102 |
| | Left middle | -0.00091[2] | -0.00097[2] | -0.00091[2] | -0.00095[2] | -0.00097 |
| | Right middle | -0.00109[2] | -0.00103[2] | -0.00110[2] | -0.00114[2] | -0.00110 |
| Max strain of steel in beams | Left corner | 0.00087[2] | 0.00079[2] | 0.00078[1] | 0.00076[2] | 0.00087 |
| | Righ corner | 0.00139[2] | 0.00110[2] | 0.00129[2] | 0.00163[2] | 0.00163 |
| | Left middle | 0.00061[2] | 0.00065[2] | 0.00065[2] | 0.00082[2] | 0.00082 |
| | Right middle | 0.00086[2] | 0.00072[2] | 0.00088[2] | 0.00128[2] | 0.00128 |

[1]—the first floor [2]—the second floor

Table 3~5,Fig. 2~4 refer:

1. The maximum inter-story drift angel, twist angel and displacement of the structure on four waves: the inter-story drift of the both edges in each story is diffrernt, the maximum inter-story twist

angel of each story is 0.00086rad(as there is the difference of 15.48mm in the maximum displacement between two edges of the first floor at the same time); the maximum inter-story drift angel of left edge and right edge is 1/259 and 1/156, the maximum displacement is 60.7mm, equivalent 1/297 to the total height; the maximum ratio of the maximum inter-story drift of the two edges and the mean inter-story drift is 1.32, and occur in the fourth floor.

2. The moment-curvature of beams and columns: the beams all have not yielded during the process; the columns all have yielded, but each degree is not deep.

3. The strain of beam and column section: For the beams, either the maximum concrete compressive strain or maximum reinforced tensile strain occur in the second floor. The maximum compressive strain which is 0.0110 has a far distance from the ultimate compressive strain of concrete witch is 0.004. The maximum tensile strain of reinforced which is 0.00163, has a certain distance from the yield tensile strain of reinforced. For the columns, the middle column has a larger compressive strain than the side column and the side column has a larger compressive strain than the corner column. The maximum compressive strain which is 0.00329 has a certain distance from the ultimate compressive strain which is 0.004. But the corner column has a larger tensile strain of reinforced than the middle column and side column. The tensile strain of reinforced is 0.00258, which is 1.3 times of the yield tensile strain of reinforced.

## Conclusions

On the basis of the nonlinear seismic response analysis of reinforced concrete frame with shaped columns, refers to the relevant norms, procedures and documentation, the evaluation results of the overall seismic behavior are as following:

1. The evaluation of seismic behavior according to the general failure criteria:

For the fortified target “no collapsing with strong earthquake”, the overall evaluation of structural failure criterion adopts the allowance of inter-story drift angel is 1/65. Under the rare earthquake, the maximum inter-story drift angel of left and right edge is 1/259 and 1/156. Therefore, according to the general failure criterion, the structure accordance with the code and technical regulation in Chinese in 7(0.10g) degree zone can meet the target of “no collapsing with strong earthquake”.

2. The evaluation of seismic behavior according to the local failure criteria:

Under the rare earthquake action, the steel in the ground floor columns are different levels of yield, while the compressive strain of concrete has quite a distance from the ultimate compressive strain; the steel in all beams has not yielded.And the moment-curvature hysteretic curve of beams and columns has not yielded obviously. Therefore the structure can meet the “no collapsing with strong earthquake” request. But according to the sequence of the emergence of the hinges, the beam-hinge doesn’t emerge while the column-hinge emerges in the bottom of columns. So the sturcture can’t form a beam-column hinge energy dissipation mechanism of beam-hinge energy dissipation first, column-hinge energy dissipation secondary. The bearing capacity doesn’t reduce significantly under rare earthquake.

In summary, according to the current design specification and technical regulations in chinese, the reinforced concrete frame with shaped columns of fortification intensity 7(0.15) degree, site Ⅱ, first set of the classification of design earthquake can basically meet the request “ no collapsing with strong earthquake”.

## Acknowledgements

This work was financially supported by the National Natural Science Foundation of China (Grant No. 50478067“researches on 3D inelastic seismic response analysis methods and integrated seismic performance of reinforced concrete structure with specially shaped columns”) and University research projects (Grant No. Ky2012zy13“seismic response analysis of reinforced concrete structure with specially shaped columns under bidirectional earthquake”).

**References**

[1] Aurelio Ghersi and Pier Paolo Rossi. Influence of bi-directional ground motions on the inelastic response of one-storey in-plan irregular systems [J]. Engineering Structures,2001,23:579-591.
[2] E.Spacone, F.C.Fillippou and F.Taucer. Fiber beam-column model for nonlinear analysis of R/C frames:I.formulation [J]. International Journal of Earthquake Engineering and Structural Dynamics, 1996,25(7):711-725.
[3] Jian Tang, Pinwen Mao, Study on seismic performance of regular RC frame with specially shaped columns [J]. Advanced Materials Research, v243-249, p 5152-5156,2011.
[4] Mingdi Chen, Tao Chen, Jian Tang, Yaowei Wang, An investigation on inelastic responses of asymmetric structures to different ground motions [C]. 13th World Conference on Earthquake Engineering [A]. 2004,Paper No.1491

*Applied Mechanics and Materials Vols. 580-583 (2014) pp 1718-1722*
*© (2014) Trans Tech Publications, Switzerland*
*doi:10.4028/www.scientific.net/AMM.580-583.1718*

# Study on Seismic Response Characteristics of Step-Terrace Frame Structure on the Slope

Li-ping Liu[1,2,a], Ji-jin Liu[1,2,b], An-liang Li[1,2,c], Ming-zi Tan[1,2,d]

[1]College of Civil Engineering, Chongqing University, Chongqing 400045, China

[2]Key Lab of New Technology for Construction of Cities in Mountain Area, Chongqing 400045, China

[a]liuliping@cqu.edu.cn, [b]cquliujijin@gmail.com, [c]cqu_lianliang@163.com, [d]xiaozi.tmz@163.com

**Keywords:** Slope; Frame structure; Soil-structure interaction; Seismic wave; Seismic response

**Abstract:** The seismic response of step-terrace frame structure is affected by the slope. Considered soil parameters of slope, the floor numbers and span numbers of layers below the scarp, 45 step-terrace frame example structures were designed, and three excitations at bedrock were selected to analyze the example structures response with dynamic time-history analysis method. The research indicates that when the other conditions are the same, the soil becomes softer, or structure's span numbers on the slope becomes larger or the slope becomes higher, the dynamic interaction between slope and step-terrace frame structure becomes more obvious. When the inputted ground motion at slope foot is adopted and the slope soil is soft, the seismic response of structure without soil-structure interaction is smaller than that of with soil-structure interaction.

## Introduction

Step-terrace frame structure refers to the structure whose foundation is on two or more different elevations and the structure's bottom is connected to different level of foundations. This kind of structure makes good use of the slope height space, reduces the excavated slope volume and has some applications in mountain city. Compared with ordinary frame structures, step-terrace frame structures have particularities in seismic design. Liu Li-ping et al.[1] summarized the existing hillside building structure and put forward the problems we should pay attention to in seismic design of the hillside building. Wang Li-ping et al.[2] studied methods to control lateral stiffness in step-terrace structure and put forward some suitable norms of the lateral stiffness controlling for step-terrace structure, and design suggestions were given in the paper. Zhao Yao et al.[3] put forward a simplified analytical model for step-terrace structure and analyzed the problems of anti-overturning stability. Shan Zhi-wei et al.[4] preliminarily discussed whether there exist any differences on seismic response of step-terrace structure between the whole analytic model with the soil-structure interaction considered and the model with the bottom fixed, which showed that soil - structure interaction had a significant effect on the seismic response of step-terrace structure. The existing research about step-terrace structure focuses primarily on the seismic response and seismic performance control, etc. Step-terrace frame structure's seismic response is inevitably affected by slope, so it is necessary to regard the slope and step-terrace frame structure as a system to analyze the seismic response characteristics.

Focusing on the research and realization of step-terrace frame structure on the slope, this paper analyzed the seismic response characteristic of the step-terrace frame structure when soil parameters of slope and the floor number and span number of layers below the scarp changed, to provide theoretical basis for seismic design of step-terrace frame structures.

## Analytical Model

Slope and slope toe within 1 meter are assumed to be composed of soil mass, and bedrock below. Step-terrace frame structure crosses between the slope crest and slope toe. As shown in figure 1, an analytical model of step-terrace frame structure on the slope system was built. The sides of the analytical model used free boundary. In order to reduce the influence on seismic response by artificial boundary, the calculation range of both side boundaries was set to 1200m. The bottom used fixed boundary to simulate bedrock. Besides, the damping in analytical model used Rayleigh damping. The ground motion was inputted at the bedrock surface. In order to take consideration of the interaction between slope and Step-terrace frame structure under the seismic action, different heights of slopes and different soil parameters of slopes were designed. The total floors' number of structure remained constant, varying the floor number and span number of layers below the scarp was adapted to the variation on height of slope and scope influenced by slope.

According to the paper[5], USA00418, USA03011, USA03028(three bedrock waves) were chosen as inputted ground motion, besides, their amplitudes were modulated to 0.18m/s$^2$, as shown in figure 2.

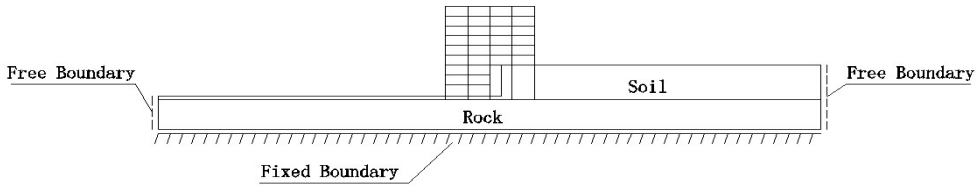


Fig. 1 Analytical model of step-terrace structure on the slope

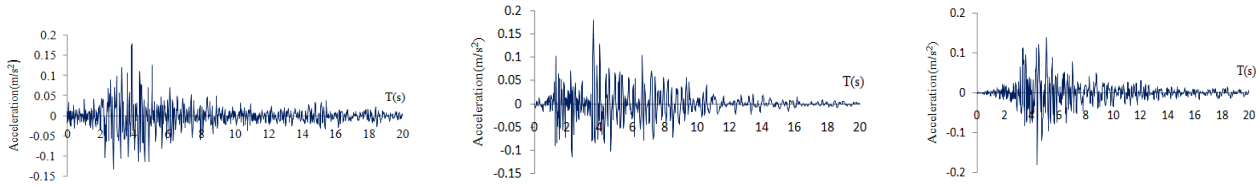


(a)USA00418 (b)USA03011 (c)USA03028

Fig. 2 Seismic acceleration time-history for the analytical model

## Example Design

Considered soil parameters of slope, the floor number and span number of layers below the scarp, 45 examples were designed which include 5 types of soil parameters and 9 types of structures. Soil parameters of slope are shown in Table 1. All of the structures are 9 floors. The number of layers below the scarp is 1, 3, or 5 respectively, and the span number of layers below the scarp is 1, 2 or 3respectively. Frame structures' parameters are shown in Table 2, where the beams' density is an adjusted density.

The thicknesses of frame structures' floor and roof plates are both 150mm. Live load on floors is 2kN/m$^2$. Live load on roofs is 0.5kN/m$^2$. Beams' bearing load width is 6m. Considered the contribution of dead load and live load on the bearing range of plates which was resulted by the seismic action, an adjusted density was used instead. T-shaped beams whose flange widths were 2m were used to take place of primary frame beams to consider the contribution made by floor plates to the stiffness of beams. The foundations of the frame structure used piles whose diameters were 800mm, and their strength grade of concrete was C30.

The examples were named as XX-X-X, which respectively represent the soil type of slope, the floor number of layers below the scarp and the span number of layers below the scarp. Soil types were written as TA, TB, TC, TD,D, which respectively represented the soil type A, B, C, D and rock. For example, TA-3-2 means the slope's soil type is A, its number of layers below the scarp is 3, and its span number of layers below the scarp is 2.

Table 1 Soil Parameter of Slope

| | Elasticity modulus (MPa) | Poisson's ratio | Density ($kg/m^3$) | Shear wave velocity(m/s) | Damping ratio |
|---|---|---|---|---|---|
| Soil A | 70 | 0.3 | 2000 | 116 | 0.05 |
| Soil B | 200 | 0.3 | 2000 | 196 | 0.05 |
| Soil C | 600 | 0.3 | 2000 | 339 | 0.05 |
| Soil D | 1400 | 0.3 | 2000 | 519 | 0.05 |
| Rock | 6500 | 0.3 | 2500 | 1000 | 0.05 |

Table 2 Material Parameters of Structure

| Type | Floor number | Section size (mm x mm) | Concrete's strength grade | Elasticity modulus ($10^4N/mm^2$) | Adjusted Density ($kg/m^3$) | Damping ratio |
|---|---|---|---|---|---|---|
| Columns | 1-4 | 650x650 | C30 | 3.0 | 2400 | 0.2 |
| Columns | 5-9 | 550x550 | C30 | 3.0 | 2400 | 0.2 |
| Roof beams | 9 | 500x250 | C30 | 3.0 | 11100 | 0.2 |
| Floor beams | 1-8 | 500x250 | C30 | 3.0 | 9600 | 0.2 |

**Seismic Response Analysis**

Three bedrock waves (in Fig.2) were selected to the 45 examples for the dynamic time-history analysis. The average results of the 3 wares were putted forward. The peak value of story shear and peak value of inter story displacement of 9 structures with different soil parameters were comparative analyzed.

**Story Shear**

The peak value of seismic story shear of 9 structures with different soil parameters are shown in Fig.3. From Fig.3a to Fig.3i, it is visible that the seismic story shears of the structures on the slope with different soil parameters which change from soft to hard has been gradually reduced. The peak value of seismic story shear of structure on the rock slope is small. It illustrates that when the other conditions are the same, if the soil of slope becomes softer, it can result the dynamic interaction between slope and step-terrace frame structure becomes more obvious. Compared among Fig.3a, Fig.3b and Fig.3c, it's shown that the more the structure spans' number on the slope is, the larger the seismic story shear is when the soil parameters of slope are the same. It illustrates that when the other conditions are the same, if structure's span number on the slope becomes more, it can result the dynamic interaction between slope and step-terrace frame structure becomes more obvious. Compared among Fig.3a, Fig.3d and Fig.3g, it's shown that the higher the slope is, the lager the seismic story shear is when the conditions of slope soil parameter and structural height are the same. It illustrates that when the other conditions are the same, if the slope becomes higher, it can result the dynamic interaction between slope and step-terrace frame structure becomes more obvious.

It is shown that the seismic story shear of the structure on rock slope is the smallest while the structure on soil slope is the largest when the inputted ground motion at slope foot is adopted. It illustrates that without considering the slope and structure's dynamic interaction the calculated seismic story shear becomes smaller when the ground motion is inputted at the slope foot, so it tends to be unsafe with this calculation method.

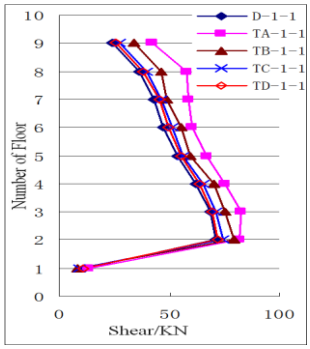


(a) 1 layer and 1 span below scarp

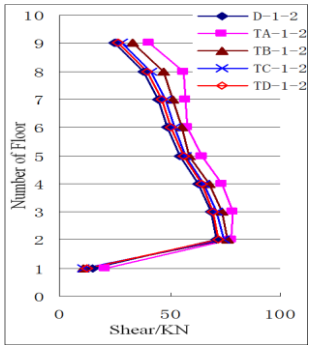


(b) 1 layer and 2 span below scarp

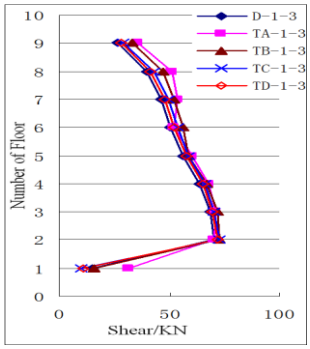


(c) 1 layer and 3 span below scarp

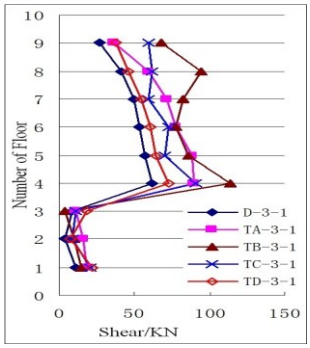


(d) 3 layer and 1 span below scarp

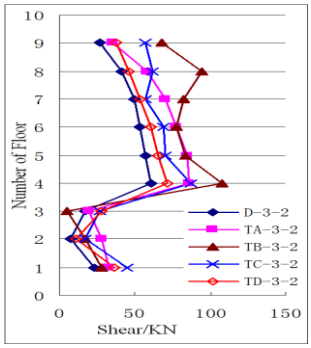


(e) 3 layer and 2 span below scarp

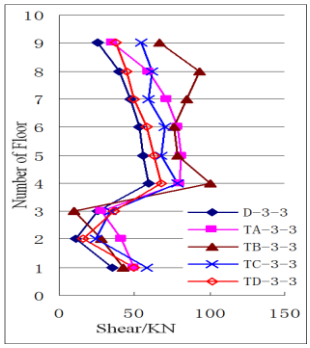


(f) 3 layer and 3 span below scarp

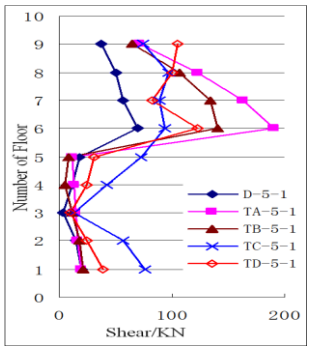


(g) 5 layer and 1 span below scarp

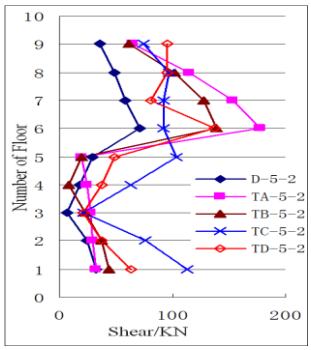


(h) 5 layer and 2 span below scarp

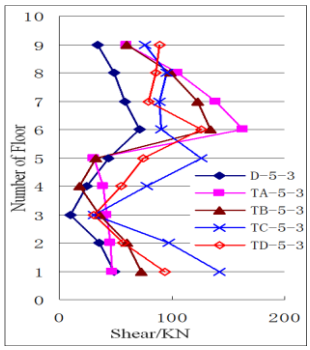


(i) 5 layer and 3 span below scarp

Fig. 3 Peak value of seismic story shear of 9 structures with different soil parameters

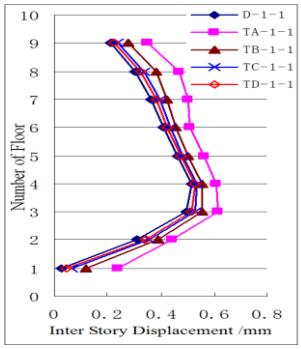


(a) 1 layer and 1 span below scarp

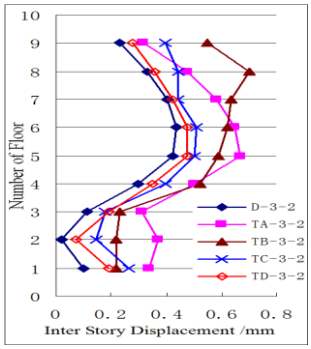


(b) 3 layer and 2 span below scarp

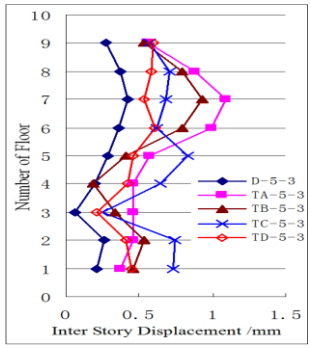


(c) 5 layer and 3 span below scarp

Fig. 4 Peak value of inter story displacement of those structures with different soil parameters

**Inter Story Displacement**

The peak value of inter story displacement of those structures with different soil parameters are shows in Fig. 4. The rules are similar to the structure example's seismic story shear in Fig.3. The softer the soil is, the larger the inter story displacement is when the structure is in the same condition. The larger the structure spans' number on the slope is, the larger the inter story displacement is when the soil parameters of slope are the same. The higher the slope is, the lager the inter story displacement is when the conditions of slope soil parameter and structural height are the same. Those further illustrate the interaction between slope and step-terrace frame structure can't be ignored under the seismic action.

## Conclusions

Through analysis of the 45 step-terrace structure on the slope examples, conclusions are as follows:

(1) When the other conditions are the same, if the soil of slope becomes softer, or structure's span number on the slope becomes more or the slope becomes higher, it can result the dynamic interaction between slope and step-terrace frame structure becomes more obvious.

(2) When the slope soil is soft, slope has a great effect on seismic response of the step-terrace frame structure, dynamic interaction between the slope and step-terrace frame structure can't be ignored.

(3) When the inputted ground motion at slope foot is adopted and the slope soil is soft, the seismic response of structure without soil-structure interaction is smaller than that of with soil-structure interaction.

## Acknowledgment

The paper was supported by Natural Science Foundation Project of Chongqing CSTC (2011BB0093).

## Reference

[1] Li-ping Liu, Shu-yan Ji, Ying-min Li: *Special Problems on a Seismic Design of Building Structures on the Slope*. The 11th high-rise building technology communication meeting(2007)(In Chinese).

[2] Li-ping Wang: *Design Ground Motion Input and Control Method of Lateral Stiffness for Building Structures on the Slope*, Chongqing University, Chongqing (2011) (In Chinese).

[3] Yao Zhao: *Study on Dynamic Characteristics and Overturning Stability for Structures Supported by Foundations with Different Horizontal Level*, Chongqing University, Chongqing (2010) (In Chinese).

[4] Zhi-wei Shan: *Study on the Seismic Performance of Step-Terrace Structure*, Chongqing University, Chongqing (2008) (In Chinese).

[5] Pu Yang, Ying-min Li, Ming Lai: *A New Method for Selecting Inputting Waves for Time-History Analysis*, China Civil Engineering Journal 2000, 33(6):33-37(In Chinese).

*Applied Mechanics and Materials Vols. 580-583 (2014) pp 1723-1728*
*© (2014) Trans Tech Publications, Switzerland*
*doi:10.4028/www.scientific.net/AMM.580-583.1723*

# Study on Simplification Conditions of Curved Regular Bridges under Seismic Effect

Taiyu Song[1, a], Yin Shen[1, b] and Guoping Li[1, c]

[1]Department of Bridge Engineering, College of Civil Engineering, Tongji University, Shanghai 200092, China

[a]songty1990@aliyun.com, [b]shenyin@tongji.edu.cn, [c]lgptj@mail.tongji.edu.cn

**Keywords:** curved girder bridges; seismic response; finite element model; regular bridge simplification conditionspublisher to produce a keyword index.

**Abstract.** A radius of curvature 20 times greater than the deck width of the bridge (R≥20b) is required as a specification in the regular bridge simplification conditions of the seismic response of curved girder bridges. Selecting benchmark bridges and employing parameter analysis method, this article studies on the effect of R/B value of the curved girder bridge on the response ratio of the seismic response calculated using the finite element model and that using a regular girder bridge. This study shows that on conditions that the deck width of the bridge is constant, the smaller the radius of curvature and the larger the B/R value (i.e., the smaller the R/B value) of the curved girder bridge are, the greater the difference between the seismic response of the curved girder bridge and the result calculated with a regular girder bridge is, and the difference is more significant under traverse seismic effect than that of longitudinal seismic effect. On conditions that the radius of curvature is constant, the impact of the change of B/R value due to the deck width change of the bridge on the difference between the seismic response of the curved girder bridge and the result calculated with a regular girder bridge is insignificant. Compared with the deck width of the bridge, the difference between the seismic response of the curved girder bridge and the result calculated with a regular girder bridge is more sensitive to the radius of curvature.

## Introduction

Curved girder bridges can well overcome the limits of topographical and ground object and satisfy the continuity of the overall route alignment, and they are extensively applied in urban viaducts, interchanges projects and high-grade highways both domestically and abroad. Due to the structural properties, curved girder bridges greatly differ from straight girder bridges when under stress. “Bending-torsion coupling” effect is dominant in curved bridges, and the greater the curvature is, the more significant the coupling effect becomes. In particular, such bending-torsion coupling effect is amplified by the ground motion, as to make the damage to the curve girder bridge duo to seismic effect more severe.

To date, studies on seismic response of curved girder bridges mainly focus on two aspects: the determination of the worst input angle of the seismic wave and the determination of the principles in the simplified anti-seismic computation of curved girder bridges [1~4], but there are fewer studies on the ratio of the radius of curvature to the bridge width [5~9].Regarding regular girder bridge simplification conditions in the seismic response of curved girder bridges, this article studies the effect of the ratio of the radius of curvature to the deck width of the bridge on the seismic response, employing as the benchmark the response ratio of the seismic response of the straight bridge finite element model to the result calculated with a regular girder bridge.

## The regular girder bridge simplification of the benchmark bridge

Straight girder bridges with deck width of 10.5 m, 5.25 m and 21 m respectively are chosen as benchmark bridges in this article.

Typical highway single-spaned concrete straight box girder bridges are chosen as benchmark bridges, and finite element modeling is performed using MIDAS. The elevation view, the cross sectional view and the main girder sectional view are shown in figures. 1, figures. 2 and figures. 3.

Setting B type as the bridge type, 0.45 s as the group characteristic period, type II as the ground type, level 7 as the fortification level, and 0.1 g as the peak value of the basic ground motion acceleration in horizontal design, the maximum of the acceleration response spectrum in horizontal design can be derived that $S_{\max} = 0.1g$ .

The piers are solid rectangular ones, with height of 11.7 m. The width of the pier bases is 1.3 m along the bridge and 2.8 m across the bridge. Two piles with diameter of 1.5 m and length of 43.5 m are chosen as the base. The total height of the pedestal and padstone is 0.3 m, the layout of pedestals are fixed ones and shifting ones along the bridge, and pedestals across the bridge are all fixed ones. The upper structure applies C50 concrete, the piles apply C40 concrete, and the deck pavement of the bridge adopts asphalt concrete with thickness of 10 cm.

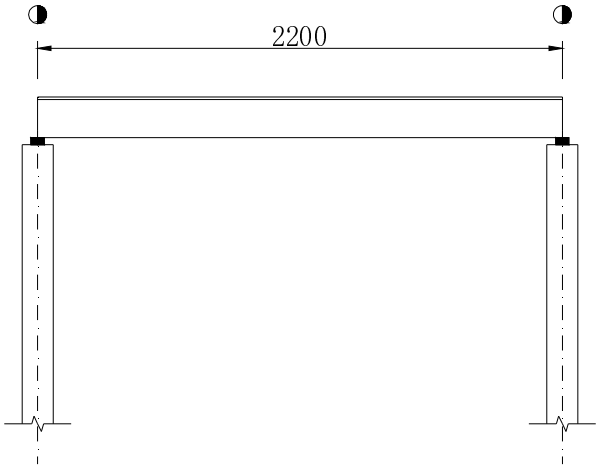


Fig. 1 Elevation view of the bridge (unit: cm)

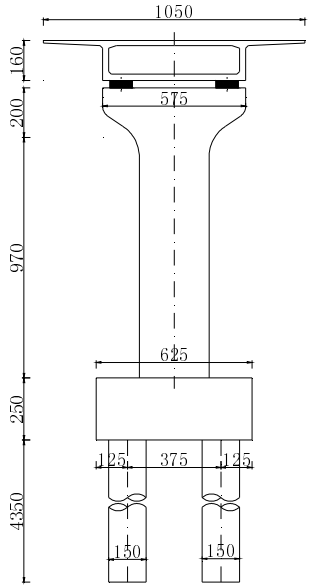


Fig. 2 Cross sectional view of the bridge (unit: cm)

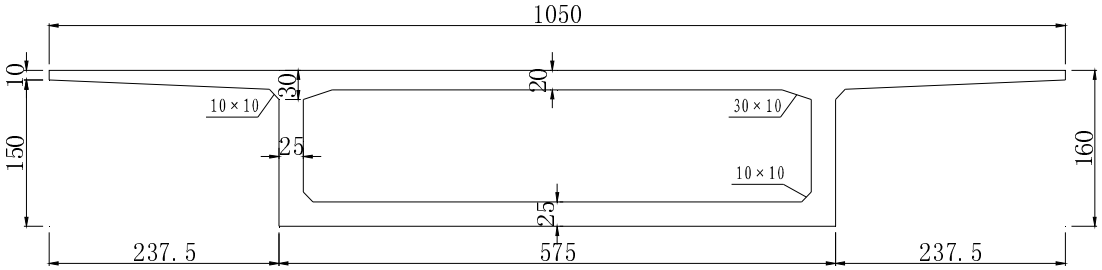


Fig. 3 Sectional view of the main girder (unit: cm)

All the main girders and piers of the bridge are modeled using beam elements. The self-mass is converted by lumped mass. The second phase load is also converted into mass. The rigidity of the pedestals in three rotational directions is set to 0. For the degree of freedom in three translational directions, the large-scale rigidity is set for the constrained degree of freedom, and the sliding degree of freedom is set to be 0.The piers and pile caps are in rigid connection, and the bases are modeled as a six-spring model.

**Target parameter analysis of seismic response**

Introduce straight girder bridges for comparison, set the target parameter as the reciprocal (B/R), and the radius of curvature of the straight bridge here is regarded as $R = \infty$ .Change the target parameters in two cases: (1) keep B constant, and the value of B/R changes with R; (2) keep R

constant, and the value of B/R changes with B. The following is presumed: (1) the benchmark straight girder bridge is regarded as a model free of error, i.e., the response ratio of the result calculated with a regular girder bridge to that calculated using finite elements is taken as the benchmark; (2) The sum of the pier base bending moment along the bridge and across the bridge is taken as the combined bending moment of the pier top.

Table 1 The finite element model parameters list

| | R(m) | B(m) | R/B | B/R | Central angle(°) | Girder length(m) |
|---|---|---|---|---|---|---|
| Model 1 (benchmark) | ∞ | 10.5 | ∞ | 0 | ∞ | 22 |
| Model 2 | 210 | 10.5 | 20 | 0.05 | 6 | 22 |
| Model 3 | 105 | 10.5 | 10 | 0.1 | 12 | 22 |
| Model 4 | 52.5 | 10.5 | 5 | 0.2 | 24 | 22 |
| Model 5 | 26.25 | 10.5 | 2.5 | 0.4 | 48 | 22 |
| Model 6 (benchmark) | ∞ | 5.25 | ∞ | 0 | ∞ | 22 |
| Model 7 | 210 | 5.25 | 40 | 0.025 | 6 | 22 |
| Model 8 | 105 | 5.25 | 20 | 0.05 | 12 | 22 |
| Model 9 | 52.5 | 5.25 | 10 | 0.1 | 24 | 22 |
| Model 10 | 26.25 | 5.25 | 5 | 0.2 | 48 | 22 |
| Model 11 (benchmark) | ∞ | 21 | ∞ | 0 | ∞ | 22 |
| Model 12 | 210 | 21 | 10 | 0.1 | 6 | 22 |
| Model 13 | 105 | 21 | 5 | 0.2 | 12 | 22 |
| Model 14 | 52.5 | 21 | 2.5 | 0.4 | 24 | 22 |
| Model 15 | 26.25 | 21 | 1.25 | 0.8 | 48 | 22 |

(1) The first case: B is kept constant, and the value of B/R changes with R. The deck width of the bridge is set that B = 10.5 m, 5.25 m, 21 m respectively, and the radius of curvature R, is changed to carry out comparative analysis on the seismic response, the corresponding models of which are models 1-5, models 6-10 and models 11-15. Listed are only the seismic responses of each model when B = 10.5 m (The hand calculation values in the table denote the seismic response calculated with the regular girder bridge).

Based on the results, the effects of the changing B/R on the response ratio of the first order vibration mode response period and of the pier base bending moment when B is constant (10.5 m) are illustrated respectively, as in the following figures 4 and figures 5.

Figures 4 and 5 show that, when B is constant, due to the longitudinal and traverse seismic effect, the response ratio of the first order vibration mode period and of the pier base bending moment are both in an increasing trend as B/R increases, and on condition that the deck width of the bridge is constant, the larger the value of B/R is (i.e., the smaller the value of R/B is), the greater the difference between the seismic response of the curved girder bridge and the result calculated with a regular girder bridge is. Specifically, the increases of the response ratio of the first order vibration mode period are smaller, all within 10%, and the increases of the response ratio of the pier base bending moment are greater. Due to the traverse seismic effect, when B/R = 0.5 (R/B = 2.5), the result coming

from finite element model is already 40% larger than that calculated with the regular girder bridge, and the result of longitudinal seismic effect is also 20% larger.

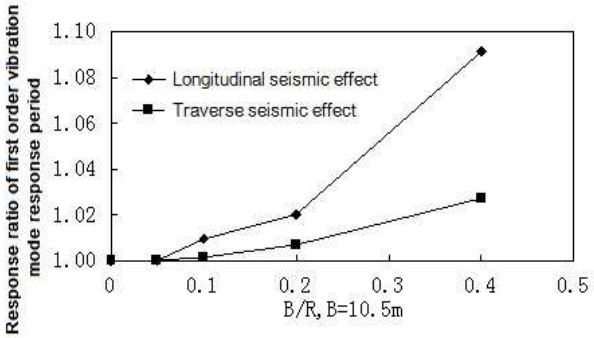


Fig. 4 Changing pattern of the response ratio of first order vibration mode period

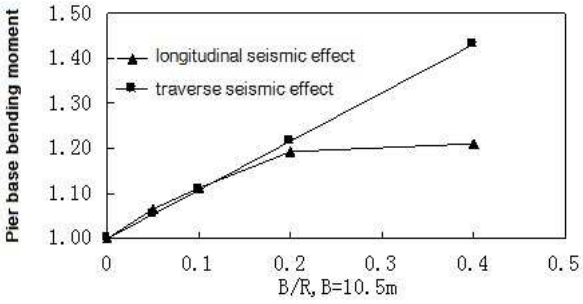


Fig. 5 Changing pattern of the response ratio of the pier base bending moment

As for the case of B = 5.25 m, 21 m, the changing patterns due to the seismic effect are similar to the above case that B = 10.5m. Without showing the detailed data table, only the changing patterns of the corresponding response ratio of the first order vibration mode response period and of the pier base bending moment are illustrated, as shown in figures 6- figures 9.

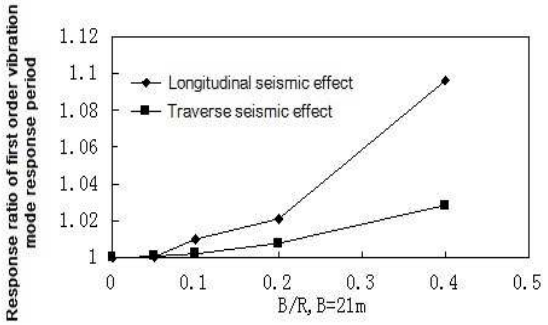


Fig. 6 Changing pattern of the response ratio of first order vibration mode period

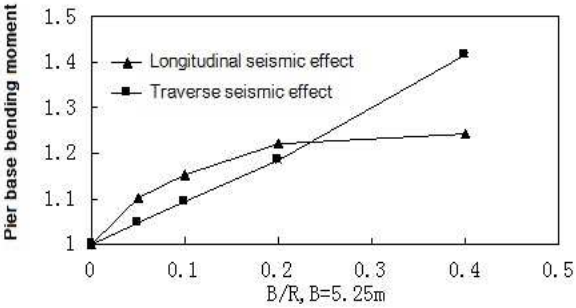


Fig. 7 Changing pattern of the response ratio of the pier base bending moment

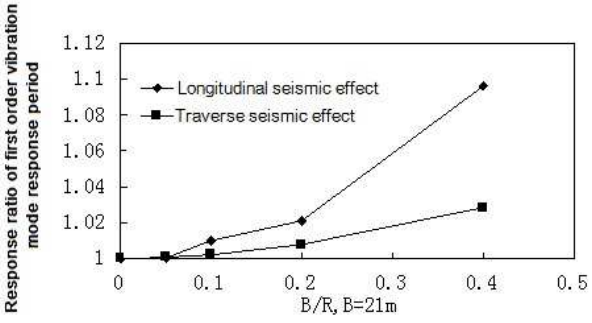


Fig. 8 Changing pattern of the response ratio of first order vibration mode period

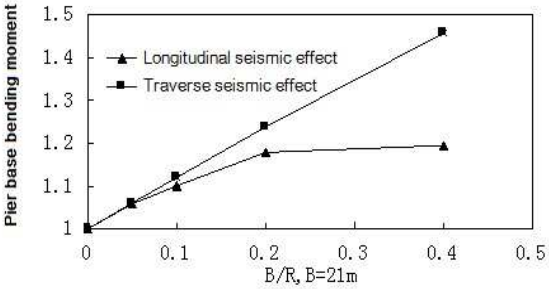


Fig. 9 Changing pattern of the response ratio of the pier base bending moment

As shown in figures 6- figures 9, with respect to different deck widths of the bridge, the changing patterns of the response ratio of first order vibration mode response period and of the pier base bending moment are similar. There is only slight difference in relative rate of rise between longitudinal and traverse seismic effects.

(2) The second case: R is kept constant, and the value of B/R changes with B. The radius of curvature is set that R = 210 m, 105 m, 52.5 m respectively, and the deck width of the bridge B, is changed to carry out comparative analysis on the seismic response, the corresponding models of which are models 7, 2, 12, models 8, 3, 13, and models 9, 4, 14. Listed are only the seismic responses of each model when R = 105 m (The hand calculation values in the table denote the seismic response calculated with the regular girder bridge).

Figures 10- Figures 15 show that, when R is constant, due to the longitudinal and traverse seismic effect, the changes of the response ratio of the first order vibration mode period and of the pier base bending moment are both insignificant, or, on condition that the radius of curvature is constant, the impact of the change of B/R value due to the deck width change of the bridge on the difference between the seismic response of the curved girder bridge and the result calculated with a regular girder bridge is insignificant. Specifically, the changes of the response ratio of the first order vibration mode period are mostly within 1%, and although the changes of the response ratio of the pier base bending moment are slightly greater, they are mostly within 10%.

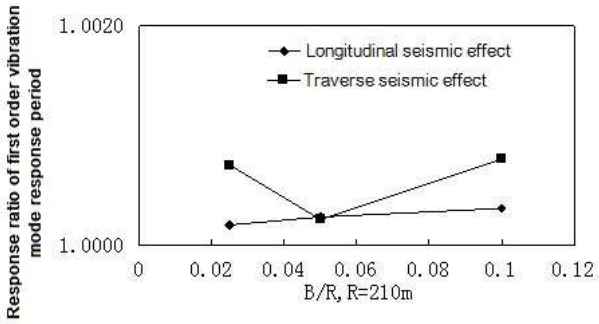


Fig. 10 Changing pattern of the response ratio of first order vibration mode period

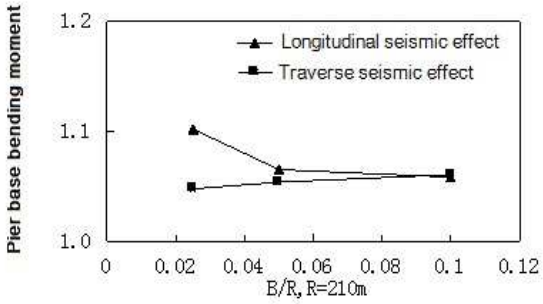


Fig. 11 Changing pattern of the response ratio of the pier base bending moment

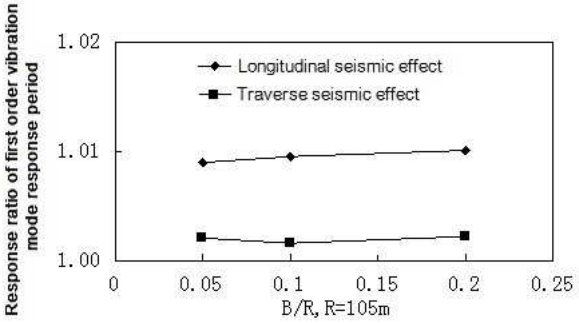


Fig. 12 Changing pattern of the response ratio of first order vibration mode period

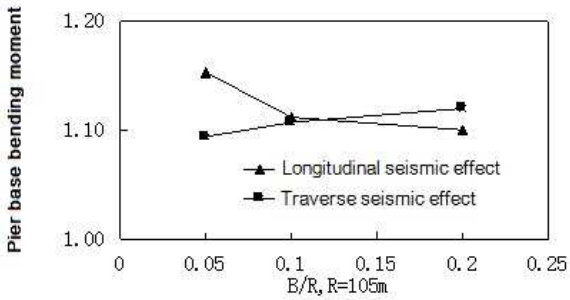


Fig. 13 Changing pattern of the response ratio of the pier base bending moment

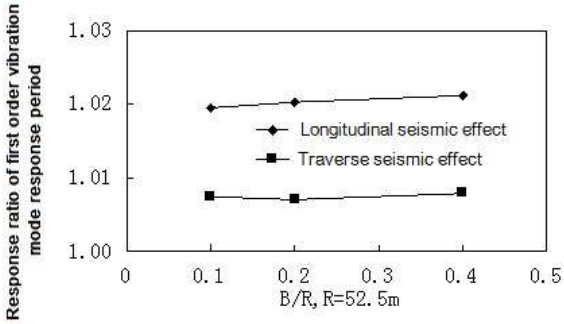


Fig. 14 Changing pattern of the response ratio of first order vibration mode period

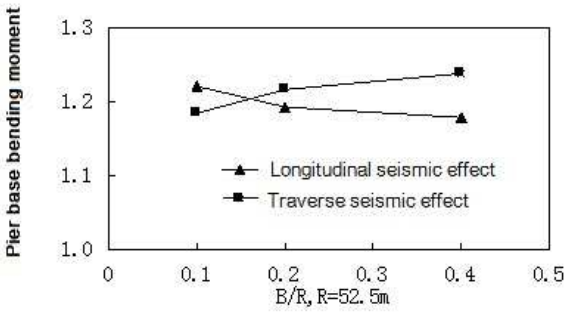


Fig. 15 Changing pattern of the response ratio of the pier base bending moment

## Conclusion

A radius of curvature 20 times greater than the deck width of the bridge (R≥20b) is required as a specification in the regular bridge simplification conditions of the seismic response of curved girder bridges. Selecting benchmark bridges and employing parameter analysis method, this article studies on the effect of R/B value of the curved girder bridge on the response ratio of the seismic response calculated using the finite element model and that using a regular girder bridge. This study shows: (1)

On conditions that the deck width of the bridge is constant, the smaller the radius of curvature and the larger the B/R value (i.e., the smaller the R/B value) of the curved girder bridge are, the greater the difference between the seismic response of the curved girder bridge and the result calculated in a regular girder bridge is, and the difference is more significant under traverse seismic effect than that of longitudinal seismic effect. (2) On conditions that the radius of curvature is constant, the impact of the change of B/R value due to the deck width change of the bridge on the difference between the seismic response of the curved girder bridge and the result calculated in a regular girder bridge is insignificant.

Compared with the deck width of the bridge, the difference between the seismic response of the curved girder bridge and the result calculated with a regular girder bridge is more sensitive to the radius of curvature, so more attention should be paid to the radius of curvature when determining whether a curved girder bridge can be simplified into a regular girder bridge in computation. If the radius of curvature R is too small, simplification into regular bridges in computation lacks reasonableness even for the curved girder bridges satisfying the specification requirement that R≥20B.

**Acknowledgements**

The writers thank the National Natural Science Foundation of China (51208376), the Fundamental Research Funds for the Central Universities （20123103）for the financial support.

**References**

[1] G.H. Li, D Shi, C.P. Heins. Finite Element Method for Seismic Analysis of Curved Bridges [J]. Journal of Tongji University, 1984, 23(1): 1－21

[2] L.C. Fan. Seismic Protection of Bridges [M]. Shanghai: Tongji University Press, 1997

[3] D.S. Zhu, L.S. Yu, S.Z. Liu. Study on Ground Motion Input Directions of Irregular Bridges [J]. Journal of Lanzhou Railway University, 2000, 19(6): 37－40

[4] L.Y. Nie, J.Z. Li. Nonlinear Analysis and Seismic Estimation on Curved Beam Bridge [J]. Journal of Tongji University, 2004, 32(10): 1360－1364

[5] Y. Sun, W.D. Zhuo, Z.Z. Fang. Literature Review of Seismic Study for Curved Girder Highway bridges [J]. 2006

[6] J.Y. Chen. Research on Seismic Response Characteristics of Curved Girder Bridges [D]. Beijing Jiaotong University, 2012

[7] W.M. Yan, X. Li, Y.J. Chen. Review on the Current State of Curved Girder Bridge Seismic Protection Research [J]. 2011 Proceedings III of 2011 International Conference on Technology of Architecture and Structure, Beijing, China.

[8] L. Wang, X.Y. Zhou, W.M. Yan. Simplified Analysis Method for Seismic Response of Curved Bridges [J]. Engineering Mechanics, 2006, 23(6): 77-84

[9] J. B. Chen. Research on Seismic Response Characteristics of Curved Girder Bridges [D]. Beijing Jiaotong University, 2012

*Applied Mechanics and Materials Vols. 580-583 (2014) pp 1729-1733*
*© (2014) Trans Tech Publications, Switzerland*
*doi:10.4028/www.scientific.net/AMM.580-583.1729*

# Study on the Characters of Seismic Response Spectra Based on China Financial Information Mansion

Li Ming[1,3,a], Wang Yuanqing[2,b], Tao Wei[1,c], Wang Bin[1,d],
Yu Qingxian[1,d], Wu Lili[3,e] and Shan Renliang[3,f]

[1] Jangho Group Co., Ltd. , Beijing, 101300 , China;

[2] Tsinghua University, Beijing, 100084, China;

[3] China University of Mining & Technology, Beijing, 100083, China;

[4] Shenyang Jianzhu University, Shenyang, 110168, China.

[a]dingxianxing@126.com, [b] wang-yq@mail.tsinghua.edu.cn, [c] taowei@jangho.com,
[d]wangbin06@jangho.com, [e] wull03@mails.tsinghua.edu.cn,[f]srl@cumtb.edu.cn.

**Keywords:** Response Spectra, Seismic Coefficient, Magnification Factor, Characteristic Period

**Abstract.** Rare study is done on floor response spectrum of super-high rise building, but it is an important condition for the seismic response analysis of floor subsidiary structure. Therefore, based on the early calculation model of China Financial Information Mansion, the floor response spectrum is calculated under different input ground motion. The floor and ground response spectrum is compared with each other from the seismic coefficient, dynamic amplification coefficient, characteristic period and the form of response spectrum. The results shows that: the floor seismic coefficient and the magnification coefficient are greater or smaller than the ground ones, the biggest difference of which is nearly 1 times; all the floor character period are greater than the ground ones, the biggest difference of which is over 60%; there are obvious differences between the floor and ground dynamic magnification factor spectra form under some conditions, of which the second peak of the former one is probably very large, even near to the peak of the first one, while the latter has no such phenomenon. Therefore, during the process of calculating the seismic response of floor subsidiary structure, it is necessary to consider the change of floor seismic coefficient, dynamic magnification factor, characteristic period and spectra form based on the main structure.

## Introduction

China Financial Information Mansion, Z15 Tower and tower in southern district no. 3 of Beijing Olympic are all designed with glass curtain wall at the high position of them. But the seismic influence coefficient curve of *Chinese code for seismic design of building* adopted in calculating the earthquake action of curtain wall is set up based on ground motion, yet the actual motion that inputs into glass curtain wall is the floor motion. So, it becomes one of the focuses of civil engineers on what the difference is between them. The seismic influence coefficient curve is another form of acceleration response spectra, so the research on seismic influence coefficient curve can be changed to study the acceleration response spectra. A great deal of research about the floor acceleration response spectrum is done for nuclear reactor plant [1-4], and less study is done for ordinary civil building, especially there is few study done for super high rise building[5-7]. Therefore, the difference between ground and floor acceleration response will be discussed based on the early calculation model of China Financial Information Mansion.

## Selection of input ground motions

In order to analyze the difference between ground and floor acceleration response spectra, four typical ground acceleration time history curves are selected, which is near to the site classification of Chinese code from "Ⅰ" to "Ⅳ". All the ground motions are adjusted according to the same dimension. The

adjusted peak ground acceleration (*PGA*) is 0.05g, 0.1g, 0.2g and 0.4g separately, which corresponds to the seismic precautionary intensity 6, 7, 8, 9 . The main information of the ground acceleration is listed in table.1, in which $T_p$ is the characteristic period of them.

**Table.1 The main iformation of the selected ground motions**

| name | happen year | component | *PGA* [cm/s$^2$] | Duration [s] | $T_p$ [s] | site category |
|---|---|---|---|---|---|---|
| Qian An | 1976 | North-South | 132.4 | 22.02 | 0.13 | Ⅰ |
| EMC FAIRVI | 1987 | North-South | 130.4 | 28.26 | 0.35 | Ⅱ |
| EL Centro | 1940 | North-South | 341.7 | 30.00 | 0.54 | Ⅲ |
| Tian Jin | 1976 | North-South | 145.8 | 7.64 | 1.03 | Ⅳ |

## Early calculation model of China Financial Information Mansion

Steel and reinforced concrete composite structure is adopted in China Financial Information Mansion. The total height of it is 360m, and the total width of it is 55m. Glass curtain wall is designed nearly at the elevation from 267m to 345m. Several forms of structure are designed during the stage of designing, one of which is adopted in this paper. Because the main object of this study is to analyze the difference between ground and floor acceleration response spectra , there is no effect on the study result even though the models set up based on the early and final design are different. The characteristic periods ($T_p$) of the former 20-order modes of the early calculation model are listed in table 2.

**Table 2 The character periods $T_p$ of the former 20-order modes of the early calculation model**

| mode | $T_p$（s） | mode | $T_p$（s） | mode | $T_p$（s） | mode | $T_p$（s） |
|---|---|---|---|---|---|---|---|
| 1 | 7.14 | 6 | 1.74 | 11 | 0.88 | 16 | 0.43 |
| 2 | 7.11 | 7 | 1.38 | 12 | 0.76 | 17 | 0.42 |
| 3 | 4.25 | 8 | 1.37 | 13 | 0.61 | 18 | 0.40 |
| 4 | 2.47 | 9 | 1.10 | 14 | 0.60 | 19 | 0.38 |
| 5 | 2.46 | 10 | 0.89 | 15 | 0.55 | 20 | 0.38 |

## Analysis of floor response spectra characters

**Analysis Content of Response Spectra.** The design response spectra of China seismic code [8] is provided as the form of seismic influence coefficient ($\alpha$) curve, shown as Eq. 1,

$$\alpha = k\beta = \begin{cases} (0.45+5.5T)\alpha_{\max} & 0 \le T < 0.1 \\ \alpha_{\max} & 0.1 \le T < T_g \\ \left(\dfrac{T_g}{T}\right)^{0.9} \eta_2 \alpha_{\max} & T_g \le T < 5T_g \\ \left[\eta_2 0.2^{\gamma} - \eta_1 (T - 5T_g)\right]\alpha_{\max} & 5T_g \le T < 6.0 \end{cases} \tag{1}$$

where, $k$ is seismic coefficient, $\beta$ is dynamic magnification coefficient, $\alpha_{max}$ is the maximum value of seismic coefficient, $\eta_1$ is adjustment coefficient for adjusting the slope of descent phase, $\gamma$ is attenuation index, $\eta_2$ is damping adjustment coefficient, $T$ is structural natural vibration period, $T_g$ is characteristic period. There are different kinds of calculation methods for calculating $T_g$ and they are compared in reference [9]. Because this study is intended to analyze the difference of $T_g$ between the floor response spectrum and the ground response spectrum, the popular one is adopted, which is expressed as $T_g = 2\pi EPV/EPA$. *EPV* and *EPA* are effective peak velocity and effective peak acceleration separately [9].

Because $\alpha_{max} = k\beta$, the analysis of floor response spectrum can be instead by analyzing the seismic coefficient and dynamic magnification coefficient spectrum, yet the analysis of dynamic magnification coefficient spectrum can be instead by analyzing the maximum value $\beta_{max}$ , $T_g$ and the shape of it. So, in the following, the ground and floor response spectra of China Financial Information Mansion will be compared and analyzed from the above four aspects.

**Analysis of Seismic Coefficient.** The time history response of early calculation model of China Financial Information Mansion is calculated with the select ground motion as input ground motion. The floor acceleration time history is extracted from the results, and by using them as input motion, the seismic coefficient, $\beta_{max}$, $T_g$ and shape of dynamic magnification coefficient ($\beta$) spectrum of different floor, site classification and intensity degree are also obtained, shown as table3, 4, 5 and fig.1. In these tables, 6, 7, 8, 9 is intensity degree.

From table 1, it can be seen that the relationship of floor seismic coefficient and ground seismic coefficient is related with site category and the location of floor: the maximum floor seismic coefficient appears in floor 10, 70, 20 and 60 for site category from Ⅰ to Ⅳ, which has no obvious law for the location of maximum floor seismic coefficient; the seismic coefficient is either greater or less than the ground seismic coefficient, the maximum ratio ($R$) of the maximum floor seismic coefficient to the ground one is 1.63, the minimum one of which is 0.90. This is mainly because the characteristic period of ground motion is different, which will induce the seismic response of the main structure different. So it can be concluded that it's necessary to consider the change of seismic coefficient for calculating the seismic response of attachment structure.

**Table 3 Seismic coefficient of different site category and floor lacation**

| floor No | Site Ⅰ | | | | Site Ⅱ | | | | Site Ⅲ | | | | Site Ⅳ | | | |
|---|---|---|---|---|---|---|---|---|---|---|---|---|---|---|---|---|
| | 6 | 7 | 8 | 9 | 6 | 7 | 8 | 9 | 6 | 7 | 8 | 9 | 6 | 7 | 8 | 9 |
| ground | 0.05 | 0.1 | 0.2 | 0.4 | 0.05 | 0.1 | 0.2 | 0.4 | 0.05 | 0.1 | 0.2 | 0.4 | 0.05 | 0.1 | 0.2 | 0.4 |
| 10 | 0.05 | 0.09 | 0.18 | 0.36 | 0.05 | 0.11 | 0.21 | 0.43 | 0.05 | 0.1 | 0.2 | 0.4 | 0.05 | 0.11 | 0.21 | 0.43 |
| 20 | 0.03 | 0.05 | 0.1 | 0.2 | 0.05 | 0.09 | 0.18 | 0.36 | 0.06 | 0.12 | 0.25 | 0.5 | 0.06 | 0.11 | 0.23 | 0.45 |
| ... | ... | ... | ... | ... | ... | ... | ... | ... | ... | ... | ... | ... | ... | ... | ... | ... |
| 60 | 0.02 | 0.04 | 0.08 | 0.17 | 0.03 | 0.06 | 0.12 | 0.24 | 0.05 | 0.1 | 0.2 | 0.4 | 0.08 | 0.16 | 0.33 | 0.65 |
| 70 | 0.03 | 0.06 | 0.11 | 0.22 | 0.06 | 0.12 | 0.24 | 0.48 | 0.05 | 0.09 | 0.18 | 0.37 | 0.07 | 0.14 | 0.29 | 0.58 |
| 80 | 0.01 | 0.03 | 0.05 | 0.1 | 0.05 | 0.09 | 0.18 | 0.36 | 0.06 | 0.11 | 0.23 | 0.46 | 0.1 | 0.19 | 0.39 | 0.78 |
| $R$ | 0.90 | 0.90 | 0.90 | 0.90 | 1.20 | 1.20 | 1.20 | 1.20 | 1.24 | 1.24 | 1.24 | 1.24 | 1.63 | 1.63 | 1.63 | 1.63 |

**Analysis of $\beta_{max}$.** From table 4, it can be seen: the maximum of $\beta_{max}$ appears in floor 10, 70, 20 and 60 for site category from Ⅰ to Ⅳ, which is not always the same with the location of the maximum seismic coefficient; the floor $\beta_{max}$ is either greater or less than the ground $\beta_{max}$, but the maximum one is always larger than the ground $\beta_{max,}$ and the difference value of them may be very large; the maximum ratio ($R$) of the maximum $\beta_{max}$ to the ground one is 1.98, the minimum one of which is 1.52, which shows that the main structure has amplification effect on the ground acceleration time history. So it can be concluded it's necessary to consider the change of $\beta_{max}$ for calculating the seismic response of attachment structure.

**Analysis of $T_g$.** From table 5, it can be seen: the maximum $T_g$ appears in floor 80, 60, 80 and 80 for site category from Ⅰ to Ⅳ, which has no obvious law but they always appears in high location of the main structure; the floor $T_g$ is always bigger than the ground one, and the difference degree declines for site category from Ⅰ to Ⅳ; the maximum ratio of the floor $T_g$ to the the ground one is 1.66, the minimum one is 1.20. So it can be concluded that the floor $T_g$ is smaller than the ground $T_g$ and it's necessary to consider the change of $T_g$ for calculating the seismic response of attachment structure.

**Table 4 $\beta_{max}$ of different site category and floor location**

| floor No | Site Ⅰ | | | | Site Ⅱ | | | | Site Ⅲ | | | | Site Ⅳ | | | |
|---|---|---|---|---|---|---|---|---|---|---|---|---|---|---|---|---|
| | 6 | 7 | 8 | 9 | 6 | 7 | 8 | 9 | 6 | 7 | 8 | 9 | 6 | 7 | 8 | 9 |
| ground | 3.13 | 3.13 | 3.13 | 3.13 | 3.15 | 3.15 | 3.15 | 3.15 | 3.26 | 3.26 | 3.26 | 3.26 | 3.26 | 3.26 | 3.26 | 3.26 |
| 10 | 2.83 | 2.83 | 2.83 | 2.83 | 3.43 | 3.43 | 3.43 | 3.43 | 3.60 | 3.60 | 3.60 | 3.60 | 3.07 | 3.07 | 3.07 | 3.07 |
| 20 | 4.02 | 4.02 | 4.02 | 4.02 | 4.28 | 4.28 | 4.28 | 4.28 | 2.64 | 2.64 | 2.64 | 2.64 | 2.53 | 2.53 | 2.53 | 2.53 |
| … | 4.75 | 4.75 | 4.75 | 4.75 | 3.54 | 3.54 | 3.54 | 3.54 | 4.52 | 4.52 | 4.52 | 4.52 | 3.07 | 3.07 | 3.07 | 3.07 |
| 60 | … | … | … | … | … | … | … | … | … | … | … | … | … | … | … | … |
| 70 | 3.43 | 3.43 | 3.43 | 3.43 | 6.22 | 6.22 | 6.22 | 6.22 | 5.51 | 5.51 | 5.51 | 5.51 | 4.97 | 4.97 | 4.97 | 4.97 |
| 80 | 3.46 | 3.46 | 3.46 | 3.46 | 4.97 | 4.97 | 4.97 | 4.97 | 3.08 | 3.08 | 3.08 | 3.08 | 3.84 | 3.84 | 3.84 | 3.84 |
| *R* | 1.52 | 1.52 | 1.52 | 1.52 | **1.98** | **1.98** | **1.98** | **1.98** | **1.69** | **1.69** | **1.69** | **1.69** | 1.52 | 1.52 | 1.52 | 1.52 |

**Table 5 Tg of different site category and floor lacation**

| floor No | Site category Ⅰ | | | | Site category Ⅱ | | | | Site category Ⅲ | | | | Site category Ⅳ | | | |
|---|---|---|---|---|---|---|---|---|---|---|---|---|---|---|---|---|
| | 6 | 7 | 8 | 9 | 6 | 7 | 8 | 9 | 6 | 7 | 8 | 9 | 6 | 7 | 8 | 9 |
| ground | 0.13 | 0.13 | 0.13 | 0.13 | 0.35 | 0.35 | 0.35 | 0.35 | 0.54 | 0.54 | 0.54 | 0.54 | 1.03 | 1.03 | 1.03 | 1.03 |
| 10 | 0.18 | 0.18 | 0.18 | 0.18 | 0.35 | 0.35 | 0.35 | 0.35 | 0.62 | 0.62 | 0.62 | 0.62 | 0.96 | 0.96 | 0.96 | 0.96 |
| 20 | 0.18 | 0.18 | 0.18 | 0.18 | 0.41 | 0.41 | 0.41 | 0.41 | 0.67 | 0.67 | 0.67 | 0.67 | 1.14 | 1.14 | 1.14 | 1.14 |
| … | … | … | … | … | … | … | … | … | … | … | … | … | … | … | … | … |
| 60 | 0.24 | 0.24 | 0.24 | 0.24 | 0.59 | 0.59 | 0.59 | 0.59 | 0.91 | 0.91 | 0.91 | 0.91 | 1.41 | 1.41 | 1.41 | 1.41 |
| 70 | 0.21 | 0.21 | 0.21 | 0.21 | 0.32 | 0.32 | 0.32 | 0.32 | 0.50 | 0.50 | 0.50 | 0.50 | 0.61 | 0.61 | 0.61 | 0.61 |
| 80 | 0.37 | 0.37 | 0.37 | 0.37 | 0.58 | 0.58 | 0.58 | 0.58 | 0.96 | 0.96 | 0.96 | 0.96 | 1.58 | 1.58 | 1.58 | 1.58 |
| *R* | 1.66 | 1.66 | 1.66 | 1.66 | 1.54 | 1.54 | 1.54 | 1.54 | 1.40 | 1.40 | 1.40 | 1.40 | 1.20 | 1.20 | 1.20 | 1.20 |

Analysis of the Shapes of β Spectrum. To compare the ground and floor shapes of β spectrum, the β spectrums of ground, 20-floor, 40-floor, 60-floor and 80-floor are extracted. Because the difference of βmax and Tg is analyzed in the above, in the analysis of the shapes of β spectrum, the βmax of each β spectrum is adjusted to 2.5 in proportion, and at the same time, the Tg of each β spectrum is also adjusted to the location of the maximum βmax in proportion. The adjusted β spectrum is shown in Fig.1.

From fig.1, it can be seen for site category Ⅰ, the maximum β first appeared in β spectrum is obviously higher than the second appeared one, such as the maximum β of the 20th-floor is 2.5, the second maximum one is 1.4, the difference between them is 78%, and furthermore the difference of some floors decreases with site category changing from Ⅰ to Ⅳ, such as for site category Ⅱ, the difference of the 60th-floor is 40%, yet for site category Ⅲ and Ⅳ, this difference is less than 4%. It can be concluded that the shapes of floor and ground β spectrum may be different greatly, and there may not only one peak value in β spectrum for the participation of high mode vibration mode. So, large difference may be made during the process of calculating the seismic response of attachment structure, if ground design spectrum is adopted directly.

## Conclusions

It can be concluded from the above results:

The maximum floor $k$ and $\beta$ is either greater or less than the corresponding ground one, and this difference is relevant to the floor location and site category. The floor $T_g$ is always bigger than the ground one, and the difference degree decreases with the site category from Ⅰ to Ⅳ, and on the high floor, this difference may be very large. So it's necessary to consider the changes of $k$, $\beta$ and $T_g$ when calculating the seismic response of attachment structure.

There may be great difference between ground and floor $\beta$ spectrum, the second peak value of which even can almost reach to the first peak value, and this difference is related with site category and floor location. So it's necessary to consider the changes of $\beta$ spectrum when calculating the seismic response of attachment structure.

Because there may be great difference between ground and floor $k$, $\beta$, $T_g$ and shapes of $\beta$ spectrum, time history analysis is necessary for calculating the seismic response of attachment structure.

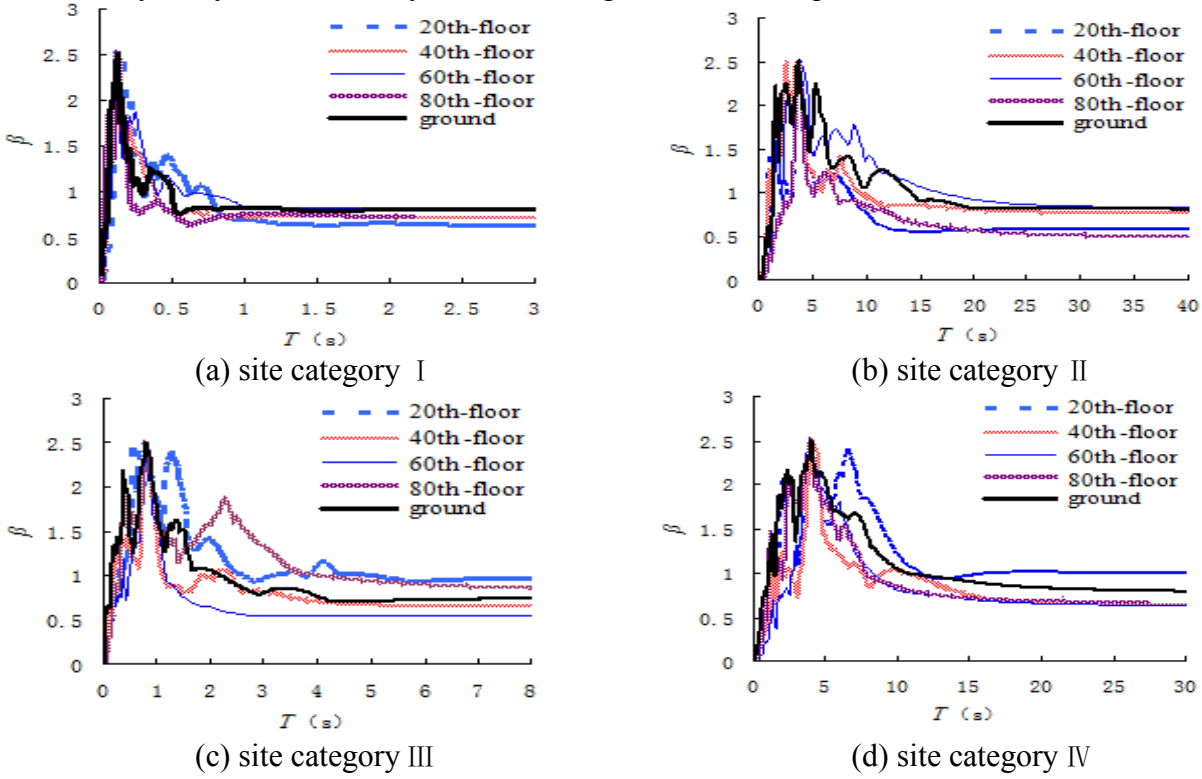


(a) site category Ⅰ (b) site category Ⅱ

(c) site category Ⅲ (d) site category Ⅳ

**Fig.1 Shapes of β spectrum of different site category**

**Acknowledgements**

This work was financially supported by Beijing Postdoctoral Research Foundation and Science and Technology Planning Project of Beijing, China (No.Z131110000213 135).

**References**

[1] X. Y. Zhu, R. Pan and J. B. LI: Nuclear Techniques Vol.36 (2013), p. 50-57.

[2] J. J. Feng, J.B. Li and H. Zhong: Water Resources and Power Vol.28 (2010), p. 67-69.

[3] X. Xiong, C. M. Ying and L. C. Zhang: Engineering Journal of Wuhan University Vol.45 Sup (2012), p. 284-286.

[5] Y. Zhang: Amplification and Earthquake Response Analysis of High-rise Building (Master's Degree Thesis, Institute of Engineering Mechanics, China Earthquake Administration 2011).

[6] Q. Qin and Y. Nie: Journal of Building Structures Vol.22 (2001), p. 15-20.

[7] Q. Qin and Y. LI: Journal of Tsinghua University (Sci & Tech) Vol.37 (1997), p. 84-88

[8] Code for seismic design of buildings (China Architecture & Building Press 2010)

[9] M. Li: Research on the Design of Structure Considering the Effect of Near-fault Horizontal Acceleration. (Master's Degree Thesis, Institute of Engineering Mechanics, China Earthquake Administration 2010)

*Applied Mechanics and Materials Vols. 580-583 (2014) pp 1734-1741*
*© (2014) Trans Tech Publications, Switzerland*
*doi:10.4028/www.scientific.net/AMM.580-583.1734*

# Time-Frequency Analysis of Non-stationary Ground Motions Via Multivariate Empirical Mode Decomposition

Yanwen Su[1, a], *Guoqing Huang[1, b], Liuliu Peng[1, c]

[1]School of Civil Engineering, Southwest Jiaotong University, Chengdu 610031, China

[b]ghuang1001@gmail.com

**Keywords:** Time-frequency analysis; Multivariate Empirical Mode Decomposition; Hilbert transform; Non-stationary ground motions; Correlation.

**Abstract:** In this paper, MEMD-based scalogram and coscalogram, and instantaneous frequency spectral are proposed to characterize the data derived from the multivariate non-stationary process. The scalogram and instantaneous frequency spectral capture spectral evolution of each component while the coscalogram reveals embedded intermittent correlation between two components. Compared with scale-based scalogram and coscalogram, frequency-based instantaneous frequency spectral provides more detailed portrayal for multivariate data. The effectiveness of the proposed MEMD-based time-frequency analysis framework is validated by numerical examples of uniformly and generally modulated ground motions.

## Introduction

In engineering community, the ground motions typically show non-stationary characteristics. Although wavelet transform have good time-frequency resolution, essentially it requires a series of a priori base functions. To circumvent this difficulty, Huang et al. [1, 2] introduced empirical mode decomposition (EMD). However, since mode mixing and mode misalignment exist in EMD approach, EMD is majorly limited to univariate non-stationary processes. Recently, Rehman and Mandic [3, 4] have introduced multivariate empirical mode decomposition (MEMD), which is suitable for analyzing n-variate non-stationary data. The advantage of MEMD is that it can produce the same number of intrinsic mode fuctions (IMFs) for the multiple signals, and align the corresponding IMFs from different channels across the same frequency range. Based on MEMD, it is possible to establish time-frequency description framework for multivariate non-stationary processes, especially, the time-frequency correlation analysis for two non-stationary processes.

In this study, the time-frequency analysis for multivariate non-stationary processes is proposed based on MEMD. MEMD-based scalogram and coscalogram, and instantaneous frequency spectral are developed to capture spectral evolution and intermittent correlation hidden in non-stationary multivariate data. The example of uniformly and generally modulated ground motions are used to evaluate MEMD-based time-frequency analysis framework.

## Theoretical Background

### *Multivariate Empirical Mode Decomposition*

EMD and EEMD perform well for the univariate signal, whereas they often fail in characterizing the multivariate signal. One major reason can be attributed to mode misalignment. Even if the numbers of IMFs for all components of multivariate signal are identical, spectral contents (or scales) for the IMFs on the same level may be significantly dissimilar. With the help of the newly-developed MEMD [3, 4], each component in the multivariate signal can be decomposed simultaneously so that the IMFs are matched both in the number and scale. Hence, mode and scale alignment can be achieved and the characterization of the multivariate signal becomes available.

Suppose a multivariate signal $\{\mathbf{x}(t)\}=\{x_1(t),x_2(t),\cdots x_p(t)\}$ with $p$ components. The $p$-dimensional multiple envelopes can be defined by projecting the signal along multiple directions in $p$-dimensional space and then interpolating their extrema. Subsequently, the local mean shall be determined by averaging these envelopes [4]. Since the estimation of the local mean can be regarded as an approximation of the integration of all the envelopes along multiple directions in a $p$-dimensional space, the accuracy of this treatment is largely dependent on how uniformly the direction vectors are chosen. The low-discrepancy Hammersley sequence (quasi-Monte Carlo sampling) will be used to generate direction vectors in that these vectors will be more uniformly distributed over other schemes, such uniform angular sampling. The direction vectors in $p$-dimensional space can be equivalently represented as points on the corresponding unit ($p$-1) sphere. The IMFs of the non-stationary $p$-variate signal can be obtained by following algorithm.

1, Generate $N$-point Hammersley sequence via sampling on a unit ($p$-1)-sphere;

2, Calculate projections of the input signal $\{\mathbf{x}(t)\}$ along direction vectors $v^{\theta_n}$, for $n=1,2,\cdots N$ (the whole set of direction vectors), where each projection is denoted by $q^{\theta_n}(t)$;

3, Find the time instants $\{t_i^{\theta_n}\}_{n=1}^N$ corresponding to the maxima of the set of projected signals $\{q_i^{\theta_n}(t)\}_{n=1}^N$;

4, Interpolate $[t_i^{\theta_n},\mathbf{x}(t_i^{\theta_n})]$ to obtain multivariate envelope curves $\{\mathbf{e}^{\theta_n}(t)\}_{n=1}^N$ using cubic spline;

5, Determine the mean of envelope curves,

$$\boldsymbol{\mu}(t)=\frac{1}{N}\sum_{n=1}^{N}\mathbf{e}^{\theta_n}(t). \tag{1}$$

6, Extract the "detail" $\mathbf{c}(t)$ using $\mathbf{c}(t)=\mathbf{x}(t)-\boldsymbol{\mu}(t)$. If the 'detail' $\mathbf{c}(t)$ satisfies the stoppage criterion for a multivariate IMF, step (2)-(5) will be carried out to obtain the 2nd, 3rd and higher order IMFs. The stoppage criterion for MEMD is identical to that proposed by Huang et al. (1998) in EMD.

*Hilbert Transform*

For any mono-component signal $y(t)$, complex analytic form $z(t)$ of the signal can be constructed by Hilbert transform (HT), i.e.,

$$z(t)=y(t)+iH[y(t)]=a(t)e^{i\phi(t)}. \tag{2}$$

where $H[y(t)]=(P/\pi)\int_{-\infty}^{\infty}y(s)/(t-s)ds$ is HT, in which $s$ is the variable of integration and $P$ denotes the Cauchy principle value; $i=\sqrt{-1}$; the instantaneous amplitude (IA) and phase are given by

$$a(t)=\sqrt{y(t)^2+(H[y(t)])^2}\ ;\ \phi(t)=\tan^{-1}\{H[y(t)]/y(t)\}. \tag{3}$$

Based on Eq. (2), instantaneous frequency (IF) is defined as the derivative of instantaneous phase.

$$f(t)=\frac{1}{2\pi}\frac{d}{dt}\phi(t). \tag{4}$$

## MEMD-based Time-frequency Analysis

The frequency analysis framework will be presented in followings. Firstly, all components in a $p$-variate signal $\{\mathbf{x}(t)\}$ are decomposed simultaneously into IMFs using MEMD. Then the HT will be adopted to estimate instantaneous frequencies (IFs) and instantaneous amplitudes (IAs) of the IMFs. Thus each component of the multivariate signal $x_j(t)$ can be expanded as

$$x_j(t)=\sum_{m=1}^{M}c_{jm}(t)=\mathrm{Re}[\sum_{m=1}^{M}a_{jm}(t)e^{i\int\omega_{jm}(t)dt}] \tag{5}$$

in which $c_{jm}(t)$ represents the $m$th IMF of component signal $x_j(t)$; Re denotes real part; $a_{jm}(t)$ and $\omega_{jm}(t)$ are the IA and IF of $c_{jm}(t)$, respectively.

According to Eq. (5), MEMD scalogram of $x_j(t)$ can be defined by squared IAs of IMFs, which is expressed as

$$s_{jj}^m(t) = a_{jm}^2(t) \ . \tag{6}$$

Clearly, MEMD scalogram can be plotted on a time-scale plane, which reveals the spectral evolution of the component process. Analogously, if the products of corresponding IAs from two different component processes are also represented on the time-scale plane, MEMD coscalogram can be obtained. The MEMD coscalogram of the two components $x_j(t)$ and $x_k(t)$ is defined as

$$s_{jk}^m(t) = a_{jm}(t)a_{km}(t) \ . \tag{7}$$

This coscalogram uncovers the elusive correlation between two components of multivariate process.

An alternative to represent non-stationarity is directly based on the frequency, which is similar to the well-known Hilbert instantaneous frequency spectral. The definition of IF spectral for $x_j(t)$ based on MEMD is given by

$$S_{jj}^m(t,\omega) = a_{jm}^2(t)\delta[\omega - \omega_{jj}^m(t)] \ . \tag{8}$$

where $\delta(\cdot)$ represents the Dirac delta function and $\omega_{jj}^m(t)$ is IF for *m*th IMF of component $x_j(t)$.

## Applications

In the following, a uniformly modulated (with amplitude non-stationarity) and a fully non-stationary (with both amplitude and frequency non-stationarities) ground motions are considered to illustrate the efficacy of MEMD-based time-frequency framework.

*Uniformly modulated ground motions*

Consider a uniformly modulated multivariate non-stationary processes consisting of ground motions at two locations $\{x(t)\} = \{x_1(t), x_2(t)\}^T$ with 150m distance where $x_1(t) = A_1(t)\overline{x}_1(t)$ ; $x_2(t) = A_2(t)\overline{x}_2(t)$ ; and $A_1(t)$ and $A_2(t)$ are the modulation functions defined as [5]

$$A(t) = \frac{\exp(-ct) - \exp(-dt)}{\max[\exp(-ct) - \exp(-dt)]} \ . \tag{9}$$

with c=0.125 and d=0.25 for $A_1(t)$; and c=0.25 and d=0.5 for $A_2(t)$. It is noted that modulation function $A_1(t)$ changes more slower than $A_2(t)$.

The power spectral of the corresponding stationary processes $\overline{x}_1(t)$ and $\overline{x}_2(t)$ are identical, described as

$$K_0(f) = 4\pi S_0 \frac{f_g^4 + 4\zeta_g^2 f_g^2 f^2}{(f^2 - f_g^2)^2 + 4\zeta_g^2 f_g^2 f^2} \tag{10}$$

in which $S_0$=0.1cm$^2$/s$^3$, $f_g$=15/(2$\pi$)Hz and $\zeta_g$=0.25.

The auto evolutionary power spectral density (EPSD) of $x_1(t)$ and $x_2(t)$ are given as

$$S_{kk}(f,t) = A_k^2(t)K_0(f), \quad (k = 1,2) \ . \tag{11}$$

and the cross EPSD of $x_1(t)$ and $x_2(t)$ are described as

$$S_{12}(f,t) = A_1(t)A_2(t)K_0(f)Coh_{12}^0(f) \ . \tag{12}$$

The coherency function between $x_1(t)$ and $x_2(t)$ is given as [e.g., 5]

$$Coh_{12}^0(f) = \rho(d_{12}, f)\exp\left(-i2\pi f \frac{d_{12}}{v_{12}}\right) \tag{13}$$

$$\rho(d_{12}, f) = \beta\exp\left[-\frac{2d_{12}}{\alpha\theta(f)}(1-\beta-\alpha\beta)\right] + (1-\beta)\exp\left[-\frac{2d_{12}}{\theta(f)}(1-\beta-\alpha\beta)\right] \tag{14}$$

$$\theta(f)=\theta_0\left[1+(\frac{f}{f_0})^b\right]^{-1/2} \tag{15}$$

where $d_{12}$ represents the distance between two locations, and $d_{12}$=150m; $v_{12}$ is the wave propagation velocity, and $v_{12}$=2000m/s; $\alpha$=0.147; $\beta$=0.736; $\theta_0$=5210m/s; $b$=2.78; and $f_0$=1.09Hz.

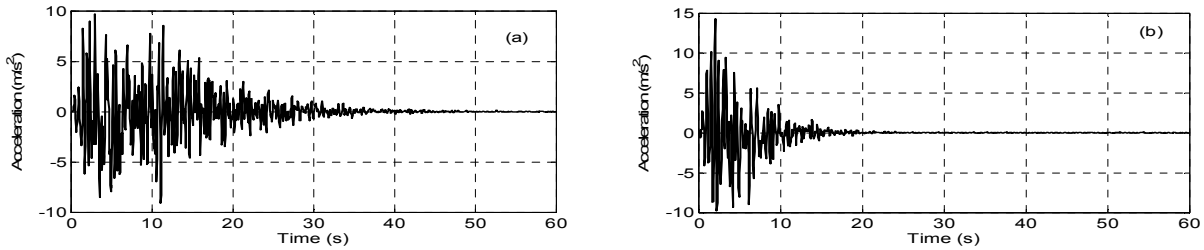


**Fig. 1. Simulated non-stationary ground motions with separable EPSD**

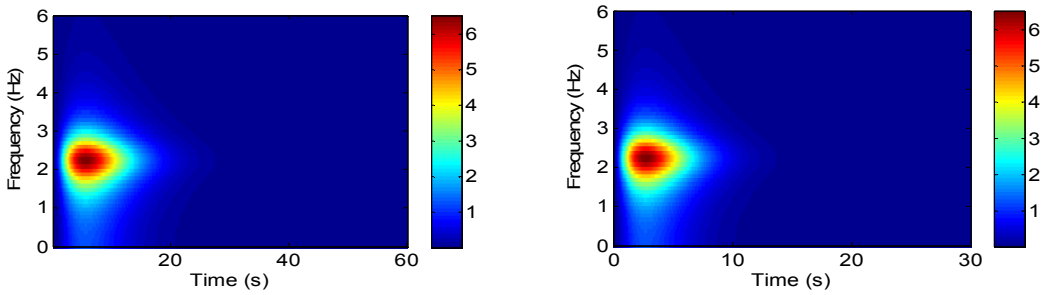


(a) location 1 (b) location 2

**Fig. 2. The target EPSD results**

The ground motions samples of $\{x(t)\}$ are generated by first simulating $\{\overline{x}(t)\}=\{\overline{x}_1(t),\overline{x}_2(t)\}^T$ via the spectral representation method (SRM) [6], and then multiplying the corresponding modulation functions. The simulation results of non-stationary ground motions at the two locations are shown in Fig. 1(a-b), and the target EPSD results are displayed in Fig. 2(a-b). The target spectral of the first and second locations indicate that the frequency vary from 0-6Hz with dominate freqeuncy of 2.5 Hz, and the mainly energy of the first location concentrate in time of 0-20s, while the energy of the second location concentrate in time of 0-10s.

MEMD is carried out for these two simulated samples, respectively. MEMD results are shown in Fig.3 (a-b). Note that 11 IMFs for each ground motion are obtained. Clearly, MEMD generates the same amount of IMFs and has a reliable performance in mode alignment.

The MEMD scalograms and coscalogram of the ground motions at two different locations are presented in Figs. 4(a-c). Note that the bright red and yellow colors represent high intensity energy, while the blue color represents low intensity energy. In scalograms, it is observed that the 1st-3rd IMFs contain large energy, while the 7th-11th IMFs have negligible energy for ground motions at both locations. In time domain, the dominant energy varies in the interval of 0-20s for the first location and 0-10s for the second location, which is consistent with Fig. 2. In Fig. 4(c), the light patches in the coscalogram enable us to detect the intermittent correlation between this two different ground motions. The resulting coscalogram of these two processes shows the distinct correlation of the 2nd and 3rd IMFs. Clearly, these two samples are well correlated in the lower frequency, which may result in large structural responses.

Fig. 5(a-b) give a sharp description of the time-varying frequency contents. It is seen that, the energy and frequency content vanish until the time of 40s for the first location, and of 20s for the second location. IF spectrals give the energy variation with time. Clearly, the time-varying rate of frequency content is slight, which is attributed to the estimate of the frequency from phase information. Overall, frequency content is approximate to time invariable. On the other hand, the

amplitude non-stationarity can be found for both samples. Both observations reflect the time-frequency characteristics of the uniformly modulation ground motions. The frequency-based approach also provides the consistent results with that based on the scale in Fig. 4. Also the dominate frequency can be found to be around 2.5 Hz from Fig. 5, which consists with Fig. 2.

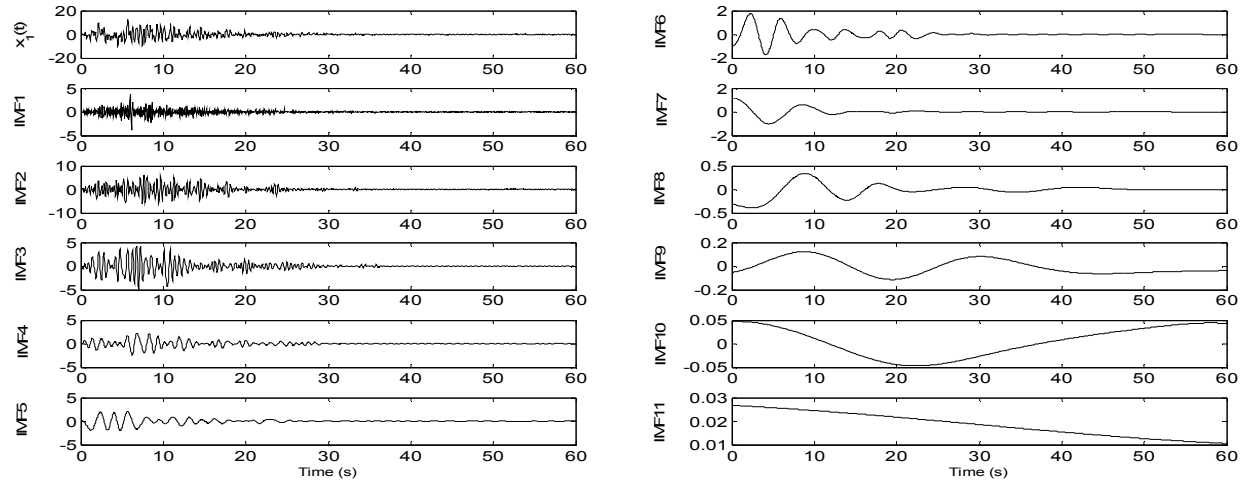


(a) location 1

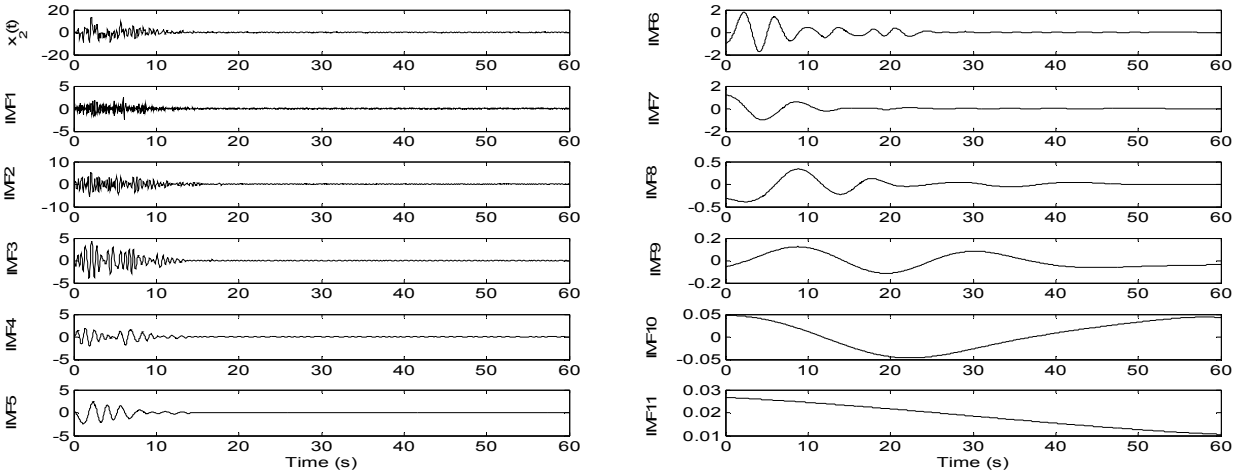


(b) location 2

**Fig. 3. MEMD results**

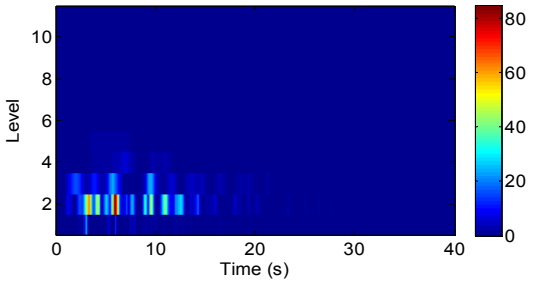


(a) scalogram, location1

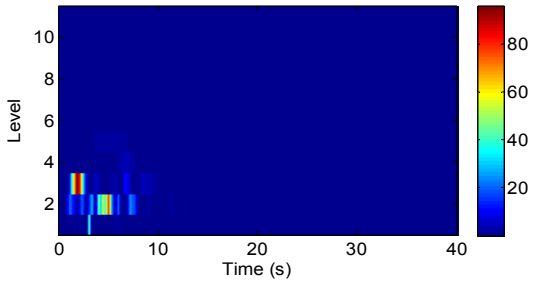


(b) scalogram, location2

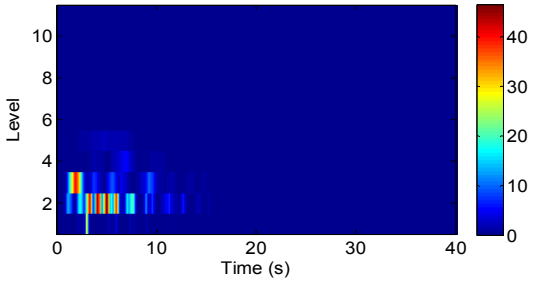


(c) coscalogram

**Fig. 4. MEMD scalograms and coscalogram**

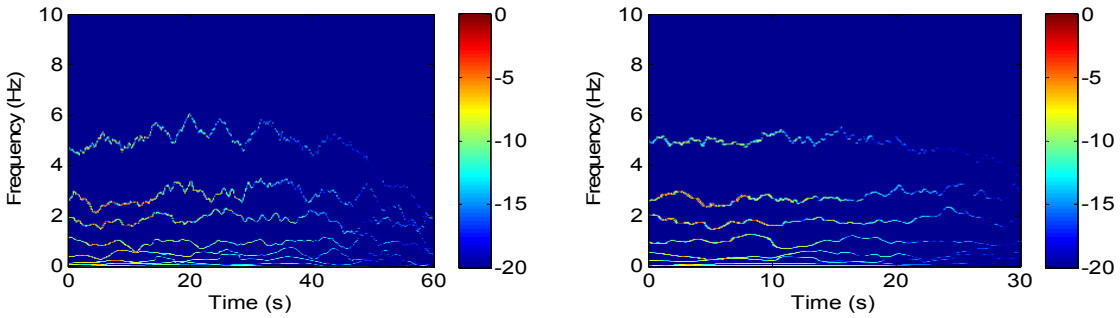


**Fig. 5. IF spectral**

*Generally modulated ground motions*

Consider a more general multivariate non-stationary processes consisting of ground motions at two points $\{x(t)\}=\{x_1(t),x_2(t)\}^T$ with 1200m distance along the direction of wave propagation. The EPSD presented in [7] is used, as shown in following equation

$$S_{kk}(\omega,t)=S(\frac{\omega}{5\pi})^2 e^{-0.15t}t^2 e^{-(\frac{\omega}{5\pi})^2 t},\quad (k=1,2)\,. \tag{16}$$

where $S$ was set to 0.03.

By comparison with Eq. (11) and Eq. (12), Eq. (16) describes a non-separable EPSD because of the variables of time and frequency cannot be decoupled. Hence, this is a fully non-stationary processes with both amplitude and frequency non-stationarities. The coherency function between $x_1(t)$ and $x_2(t)$ have the identical form with Eq. (13-15), but different parameters. Herein, $v_{12}$=2000m/s; $\alpha$=0.0186; $\beta$=0.636; $\theta_0$=31200m/s; $b$=2.95; and $f_0$=1.51Hz.

Nonstationary process simulation can be conducted by improved SRM [8]. The simulated results of non-stationary ground motions are shown in Fig. 6. The target EPSD is displayed in Fig. 7, which the frequency varies from 0-4Hz and the large energy occurs during 0-20s.

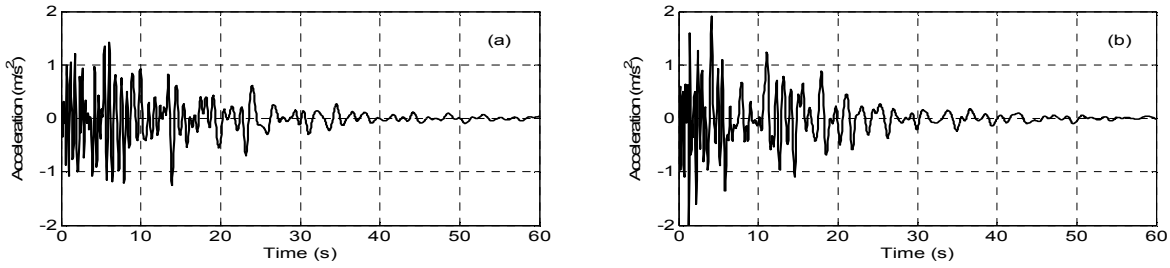


**Fig. 6. Simulated non-stationary ground motions with non-separable EPSD**

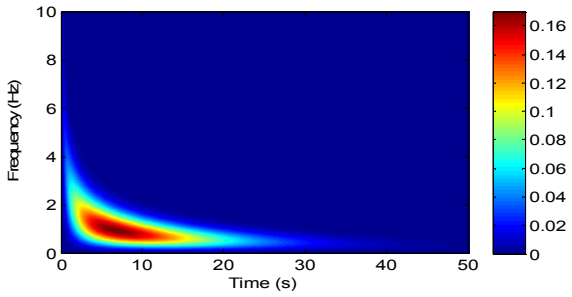


**Fig. 7. The target EPSD result**

MEMD is employed to decompose two simulated samples, respectively and the total of 11 IMFs are acquired. Herein, MEMD results are not shown for brevity. MEMD scalogram and coscalogram are displayed in the following Fig. 8.

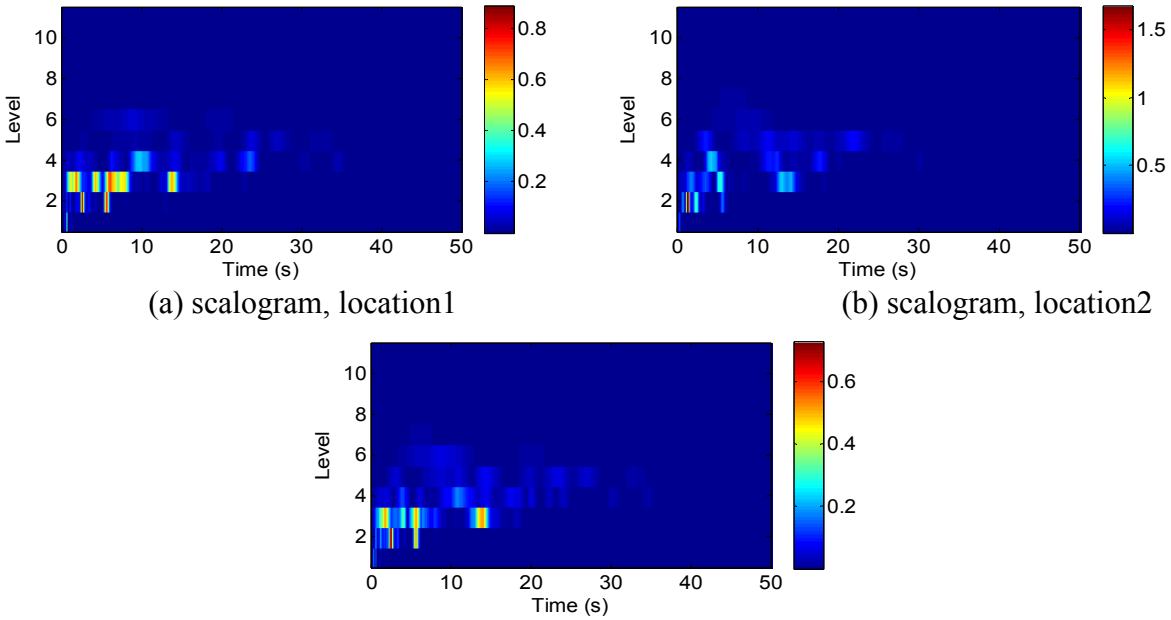


(a) scalogram, location1 (b) scalogram, location2




(c) coscalogram

**Fig. 8. MEMD scalograms and coscalogram**

The scalograms and coscalogram results plotted in Fig. 8 are consistent with those in Fig. 7. In scalograms, the evolution of energy can be observed in various scales. It is also found that the majority of the energy of the ground motion concentrates in the lower frequency region. For the first location, the 2nd-4th IMFs contain large energy. Similarly, the most of energy spread over the 2nd, 3rd and 4th IMF components for the second location. The dominant energy varies in the interval of 0-15s for both locations. Fig. 8(c) reveals the correlation between two ground motions. It is seen that the largest correlation is relevant with the 2nd and 3rd IMF components within time duration of 0-15s.

Fig. 9 illustrate the information regarding the variation of energy intensity and frequency content. It is found that the larger energies are observed around 0-2Hz during the duration of 0-20s. The IF spectral indicates the presence of high frequency energy early in the ground motions, which attenuates with time, that is, a sharp frequency non-stationarity can be detected. It is shown that this non-stationarity in frequency content can have a significant effect on the response of both linear and nonlinear structure [9]. On the other hand, amplitude non-stationarity can also be found. Therefore, for general full non-stationary ground motions, both of frequency non-stationarity and amplitude non-stationarity hiding in the non-stationary process can be discovered.

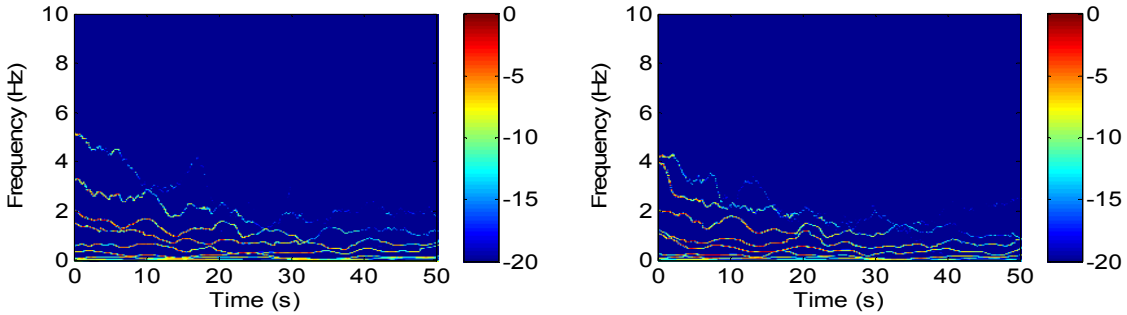


**Fig. 9. IF spectral**

## Conclusions

This study proposed a new adaptive time-frequency analysis framework for multivariate non-stationary processes based on MEMD. In this framework, MEMD was used to decompose multivariate data and subsequently the meaningful IA and IF were estimated by Hilbert transform. Compared with EMD, the superior features of the mode (both of number and scale) alignment and

less mode mixing processed by MEMD provided an opportunity to analyse the non-stationarity embedded in the multivariate process, especially, the elusive intermittent correlation between two components. Furthermore, MEMD-based scalogram and IF spectral were suggested to describe the evolutionary characteristics of non-stationary component process, while coscalogram was developed to reveal the elusive intermittent correlations between two different component processes. The application of the proposed approach to uniformly and generally modulated ground motions had verified the efficacy of MEMD-based time-frequency description framework and thus helped to capture the time-frequency characteristics of the non-stationary processes.

**Acknowledgements**

The supports by "Young Thousand Talents Program (China)", the National Science Foundation of China (Grant No. U1334201) and Ministry of Transport of China (Grant No. 201231835250) are greatly acknowledged.

**References**

[1] N.E. Huang, Z. Shen, S.R. Long, et al. The empirical mode decomposition and the Hilbert spectral for nonlinear and non-stationary time series analysis. Proceedings of the Royal Society of London A, 454, 903-995. (1998)
[2] N.E. Huang, Z. Shen and S.R. Long: submitted to Annual Review of Fluid Mechanics. (1999)
[3] N. Rehman and D.P. Mandic: submitted to IEEE Transactions on Signal Processing. (2010a)
[4] N. Rehman and D.P. Mandic: submitted to Proceedings of the Royal Society. (2010b)
[5] G. Huang and X. Chen: submitted to Engineering Structures. (2009)
[6] G. Deodatis: submitted to Journal of Engineering Mechanics. (1996)
[7] P.D. Spanos and I.A. Kougioumtzoglou: submitted to Probabilistic Engineering Mechanics. (2012)
[8] G. Huang, H. Liao and M. Li: submitted to Probabilistic Engineering Mechanics. (2013)
[9] J.P. Conte. Effects of earthquake frequency nonstationarity on inelastic structural response. Proceedings of the 10th World Conference on Earthquake Engineering, A. A. Balkema: Rotterdam, The Netherlands, 1992.

*Applied Mechanics and Materials Vols. 580-583 (2014) pp 1742-1745*
*© (2014) Trans Tech Publications, Switzerland*
*doi:10.4028/www.scientific.net/AMM.580-583.1742*

# Study of Intake Tower under an Earthquake using the Power Spectral Method based on ANSYS

Xia Hua[1, a], Changquan Yu[1,b], Weihua Zhu[1, c], Kun Zhao, Chunlin Huang

[1]Harbor and Offshore Engineering College, HOHAI University, Nanjing, Jiangsu, 210098, China

[a]511535659@qq.com, [b]512743627@qq.com, [c]weihua_zhu@126.com

**Keywords:** ANSYS, Intake tower, Earthquake, Power spectral density (PSD) analysis

**Abstract.** In this paper, the power spectral density method based on ANSYS is carried out to study the intake tower finite element model under an earthquake. A power spectral density function is obtained and disposed to be smooth. Then it is used to study the intake tower when the seismic wave occurs in the direction of flow and perpendicular to the direction of flow .This study provides theoretical basis for reinforce and transform of the intake tower structure.

## Introduction

Earthquake is a natural disaster which causes enormous losses to human. The anti-seismic capacity of hydraulic structures is becoming more and more important. The spectral density method has risen in the recent 30 years. This method is based on probability theory and mathematical statistics and it is the most scientific method to study a random process[1-4]. This paper uses spectral density method to study the intake tower to calculate the largest displacement, providing theoretical basis for reinforce and transform of the structure. At last, the security of the intake tower is assessed from the viewpoint of probability.

## Calculation of seismic power spectral density curve

In order to represent a random process Y(t) roundly, the interdependence between two random variables at different time needs to be studied. So define correlation function:

$$R_Y(t_1,t_2)=E[Y(t_1)Y(t_2)],\qquad \tau=t_2-t_1$$

Power spectral has the Fourier transform relationship with correlation function:

$$S_Y(\omega)=\frac{1}{2\pi}\int_{-\infty}^{\infty}R_Y(\tau)e^{-i\omega\tau}d\tau$$

Correlation function has the inverse Fourier transform relationship with Power spectral

$$R_Y(\tau)=\int_{-\infty}^{\infty}S_Y(\tau)e^{i\omega\tau}d\tau$$

From the relationship above, the seismic wave within a limited duration can be transformed into the self-correlation function. Then the self-correlation function was transformed into the power spectral density function using FFT method[5-6].

Considering that vertical bearing capacity of the structure is large, the test only applied horizontal seismic load to the structure. The records of a North-South river are neat, so the test used its seismic record curve as load to affect the structure. The peak ground acceleration is$1.5\,m/s^2$ and it is smaller than the earthquake in degree nine. Therefore, all accelerations multiplied by 3.33. The amplified acceleration duration curve is shown in fig.1

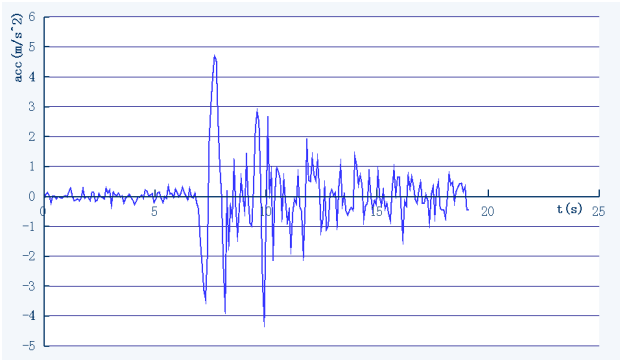


Fig. 1 The amplified north-south river records

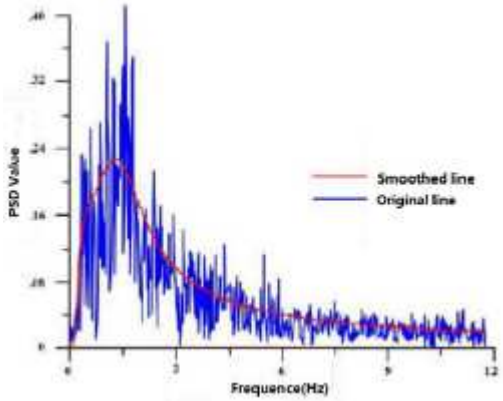


Fig. 2 Diagram of Seismic wave power spectral density calculations

The diagram of Seismic wave power spectral density calculations in fig.2 is obtained from the amplified north-south river records in fig.1. Then the PSD curve was disposed to be smooth.

## Finite element analysis of seismic power spectral density

In this paper, the power spectral method based on ANSYS is taken to calculate the displacement and stress of the structure when seismic wave contented a normal distribution occurs. The diagram of seismic wave power spectral density calculations is shown in fig 2. When the research is carried out, two situations when the seismic wave occurs in the direction of flow and perpendicular to the direction of flow are both considered.

The output from spectral density calculations based on ANSYS is a random variable which contents a normal distribution. The normal distribution of a random variable can be described by mean and variance well in mathematics. The earthquake process is a random process with a mean equaling to 0. Therefore, the output can be described absolutely just by variance. The probability is 68.3% when random variable is within $\pm 1\sigma$, 95.4% within $\pm 2\sigma$, 99.7% within $\pm 3\sigma$.The calculation only extracts the result within $\pm 1\sigma$.

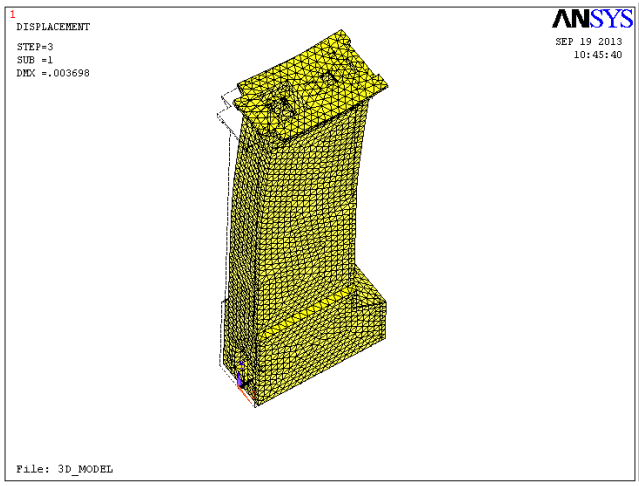


Fig.3 Structure seismic PSD excitation $1\sigma$ results downstream direction

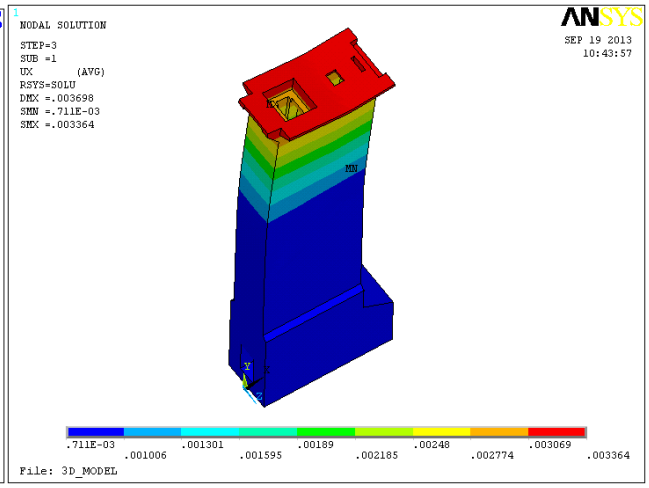


Fig.4 Structure seismic PSD excitation downstream direction $1\sigma$ displacement nephogram

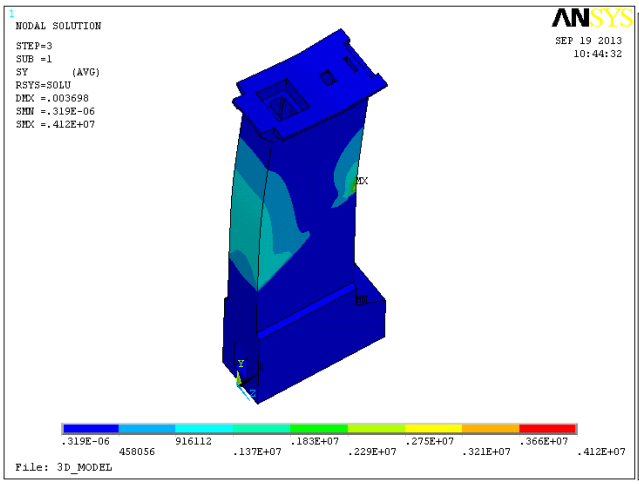


Fig.5 $1\sigma$ First principal stress distribution under the excitation of the of seismic PSD spectrum

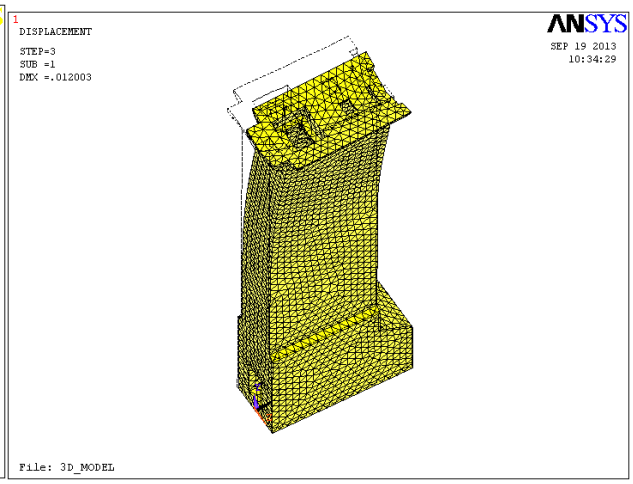


Fig.6 Structure seismic PSD excitation $1\sigma$ results vertical flow direction

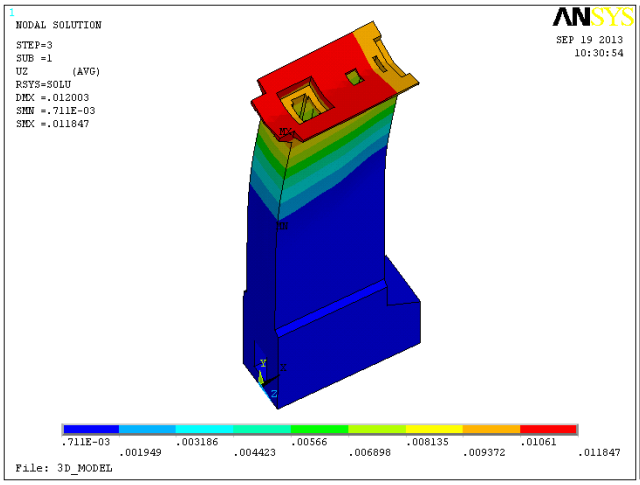


Fig.7 Structure seismic PSD excitation vertical flow direction $1\sigma$ displacement nephogram

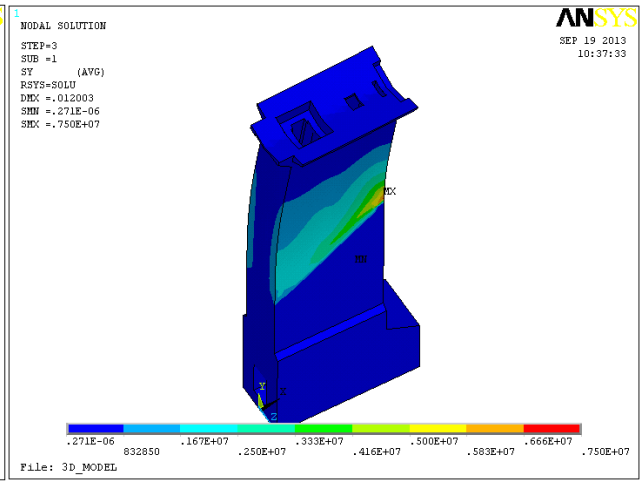


Fig.8 $1\sigma$ First principal stress distribution under the excitation of the of seismic PSD spectrum

From fig.3, fig.4 and fig.5, it is seen that the structure has displacement in the direction of flow when the seismic wave occurs in the direction of flow. The displacement is a random variable which contents a normal distribution.The largest $1\sigma$ displacement is 0.3364 cm, which occurs in the top of the structure. The overall deformation of the structure is accord with its second order vibration mode. The $1\sigma$ first principal stress is 4.12 MPa. It occurs in the constraints because excessive constraints cause oversize reaction. Therefore, this part still needs enough attention and it is better to reinforce it by reinforcements.

From fig.6, fig.7 and fig.8, it is seen that the structure has displacement perpendicular to the direction of flow when the seismic wave occurs perpendicular to the direction of flow. The displacement is a random variable which contents a normal distribution.The largest $1\sigma$ displacement is 1.1847cm, which occurs in the top of the structure. The overall deformation of the structure is accord with its first order vibration mode. The $1\sigma$ first principal stress is 7.5 MPa. It occurs in the constraints because excessive constraints cause oversize reaction. Therefore, this part still needs enough attention and it is better to reinforce it by reinforcements.

## Summary

In this paper, the PSD method based on ANSYS is taken to calculate the displacement and stress of the intake tower when seismic wave contented a normal distribution occurs. The result shows that

the probability of dehiscence is above 68.3% when structure is under an earthquake and the maximal displacement occurs in the top of the structure. It means that it is very likely that the top of the structure rip off under the earthquake in degree nine.Therefore, it is necessary to strengthen the top of the structure by reinforcements or other methods.

**References**

[1]Hangen Ni and Chongpan Jin, Seismic Characteristics of Dam and Aseismic Calculation[M]. 1994.
[2]Yunlong He, Shuyuan Lu and Yahui Duan, Seismic Dynamic Response Analysis of Gravity Dam[J]. 1998(3).
[3]Chongshi Gu and Xuehong Li, Study of the Workability of Multiple-arch Dam[J].China Engineering Science, 2000, 2(10): 30-39.
[4]Maosong Huang, Jiangu Qian and Shiming Wu, Earth Dam Dynamic Strain Localization and the Adaptive Finite Element Analysis of Progressive Failure ,Chinese Journal of Geotechnical Engineering,2000, 2(10): 30-39.
[5]Qingbin Li, Chuhan Zhang and Guanglun Wang, Dynamic Damage Constitutive Model of Concrete under the Uniaxial State[J]. Journal of Hydraulic Engineering,1994, 12: 55-60.
[6]Wujun Liu, Raolong Chen, Zheng Si and Rui Fan,, three-dimensional finite element dynamic analysis of the asphalt concrete core wall dam[J].Journal of Water Resources and Water Engineering, 2009, 20(6): 154-156.

*Applied Mechanics and Materials Vols. 580-583 (2014) pp 1746-1749*
*© (2014) Trans Tech Publications, Switzerland*
*doi:10.4028/www.scientific.net/AMM.580-583.1746*

# STUDIES ON SEISMIC MEASURES TO IMPROVE MASONRY INFILLED WALL

Yao-jun ZHANG [1,a] Xu-sheng DUAN [1,b] Xin-yuan WANG [1,c] cui-ling ZHOU [1] Yong SUN *

[1]Civil Engineering and Water Conservancy College of Shandong Agriculture University , Taian China

[a]email:wugenshui@163.com, [b]email: tumudxs@126.com,[c]email:dianawxy@gmail.com

**Keywords:** masonry infilled wall ; earthquake action ; seismic fortification measures

**Abstract.** brittle nature of masonry infilled wall and the wrong connection with the main structure , resulted in the destruction phenomenon in the earthquake . Based on the destruction phenomenon ,this paper analysis the Earthquake damage of masonry infilled wall , according to code for seismic design of buildings(GB50011—2001) and code for seismic design of masonry structures(GB50003—2011) , some seismic fortification measures were proposed in this paper aimming to improve seismic capability of infilled wall, thereby alleviate loss caused by earthquake.

Masonry material is widely used in china because of its low cost and easy availability. Masonry infilled wall is popular in frame structure and frame-shear wall structure. However, in recent earthquakes happened in china, especially in Wenchuan earthquake and Lushan earthquake, the performance of masonry structure is barely satisfactory. In areas where seismic intensity reached 7 degrees, 8 degrees, and 9 degrees, the main structure of many structures that are well designed were not destructed, however the destruction of infilled wall was very common instead. For example, the new teaching building of Lushan middle school , which was built after the 512 great earthquake in 2008 according to the standard construction of anti eight degree seismic intensity, was damaged in the latter earthquake, especially for the frame filled walls. The large scale cracking of masonry infilled walls in seismic region and the possibility of immediate collapse of some masonry walls caused the structure unserviceable. The buildings were rated as danger in seismic emergency assessment. For buildings that are classified as second seismic precaution criterion, such as medical buildings and buildings in middle school and primary school, the function of the building was interrupted after earthquake, which has great influence to the society. The increased rehabilitation cost led to unnecessary economic loss.

Because of the fast economic development and fast improvement of living standard in China, higher seismic capability for buildings is widely expected. In our existing "three level" seismic precautionary target, it is common sense and urgent need for engineers to improve the seismic capability of non-structural components, prevent or alleviate seismic damage of these walls and to take efficient design method and seismic measures.

## 1.Seismic damage performance of masonry infilled walls

### 1.1 Seismic damage caused by irregular plane and vertical structural assembly of walls.

The main building structure is regular in plane and vertical assembly, but the masonry infilled walls are irregular, which is shown in two aspects: 1. walls are rare in one side, but dense in the other side. This would cause the stiffness eccentricity of actual structure and torsion failure during earthquake; 2. To form large space for ground floor, fewer walls are assembled, while more walls are assembled in upper structure, forming a up-rigid-down-soft structure. During earthquake the structural deformation concentrated in the bottom of the structure, which caused excessive deformation in bottom and severe destruction such as collapse of walls. As indicated in Fig.1

**1.2** Inappropriate connection between masonry infilled wall and the main structure

Masonry infilled wall built between the columns and the michinaga breast wall because of windows on the wall opened to the columns , which forms the actual built-in function for frame column. The column constrained by rigid constraints from the breast which makes the effective length of column

shorter, becomes short column .then the seismic shear force subjected by the column increases ,as a result , shear failure of the column occurrs. oblique cracks appears on the column in the range of window heigh , even brittle failure happens as shown in Fig. 2 . Interior masonry partition which isn't built to the top of the frame beam in frame structure and single-story factory buildings ,or exterior wall which is built partially between the concrete columns,would also cause the frame column becoming into a short column and lead to shear failure.

Fig.1

Fig.2

**1.3 Seismic hazard diversity of masonry infilled wall caused by different types of structural**

The deformation of frame structure is given priority by shear deformation in horizontal earthquake action . As a result, the story drift of the bottom floor is much larger and the destruction of the masonry infilled wall at the bottom floor is the most serious.However the deformation of frame - wall structure in horizontal earthquake action is between the bend and shear deformation. The story drift of the upper structure is larger .Therefore, the upper infilled walls are damaged heavier.

**2.Measures for strengthening seismic capability of masonry infilled wall**

The main reason for the destruction of the masonry infilled wall is: The low shear capacity , The small deformation capacity, The invalid connection between wall and frame. The wall tend to be damaged on shear-failure or scattered in horizontal earthquake action. When the strength and stiffness of masonry infilled wall which is built in the middle of the frame column and beam is bigger, the horizontal earthquake produced by earthquake shocks on the wall will push the frame, which would cause the destruction of the beam-column joints. Some requirements can be found in "code for seismic design of buildings'' (GB50011-2010) in China, which specifies that a seismic adverse effect on frame should be estimated to obviate the destruction of the main structure caused by these unreasonable arrangement of the frame infilled walls and partition walls.

**2.1 The plane and vertical arrangement of Masonry infilled wall should be regular**

Masonry infilled wall is different from the light partition wall, although it is also a nonstructural component. To a large extent masonry infilled wall can change the dynamic characteristics of structure because of its bigger lateral stiffness and influence the seismic performance of the whole structure. So we cannot arrange masonry infilled wall as random . In order to avoid torsional vibration because of eccentricity of structure in earthquake shocks ,the plane arrangement of walls should be uniform and symmetric ,and the vertical arrangemen should be consistent in order to avoid the adverse increase of shear force for frame in floor where the infilled wall is interrupted. If there are functional requirements that masonry infilled wall can't be built in the bottom floor, We need to consider the practical layer stiffness, including the stiffness of the infilled wall. In addition ,some bracing can be designed in the bottom floor to adjust the stiffness ratio between the layers and avoid the formation of the weak floor.

**2.2 Ameliorating connection of masonry infilled wall and column**

The connection of masonry infilled wall and frame or single-story factory affect the dynamic performance and seismic capacity of the whole structure. The influence on frame will be different as the different ways is used in the connection between the two things.

Code for seismic design of buildings specifies that: when the length of the wall is larger than 5m, tie bar should be used between the top of the wall and the beam; when the length of the wall is larger

than 8m or is twice the floor height, reinforced concrete structural columns should be used. When the height of the wall is larger than 4m， horizontal tie beam along the whole length of the wall which is connected to columns should be used in the middle of the wall. In earthquake zone, cracks can be found in walls whether code for seismic design is complied with or not. X-cracks can be found in walls between structural column and frame column, as indicated in Fig3. The author presents that when the length of walls is larger than floor height, it is appropriate to use structural columns and horizontal tie beam. With the coordination of structural column and horizontal tie beam, it is possible to limit the development of cracks and to prevent collapse of walls. As indicated in Fig.4.

Fig.3

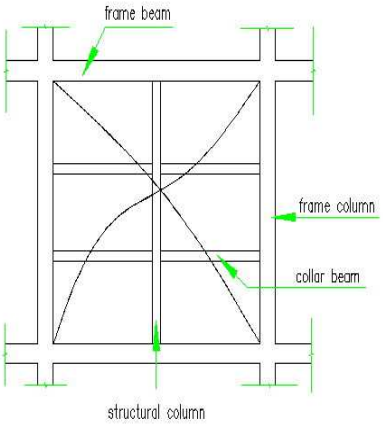


Fig.4

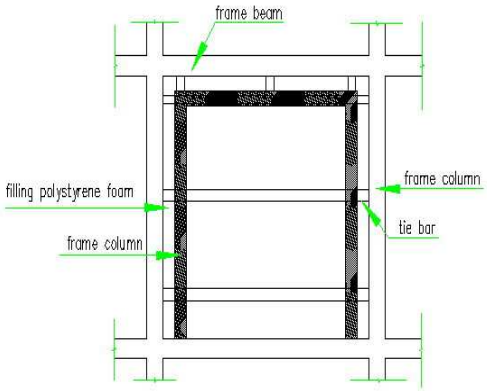


Fig.5

In addition, flexible connection can also be adopted between masonry infilled walls and frame. If using this kind of connection, when calculating frame structure only the weight of the masonry infilled wall should be considered while the influence of its stiffness and strength could be ignored. If intercolumniation of the main structure is small, and the length of the masonry infilled wall is not large, the author presents that the disconnection way of the wall and the main body can be used as shown in Fig. 5. Gaps should be reserved between both ends of the infilled wall and the frame column, so as between the top surface of wall and frame beam. polystyrene foam plastic slat or polyurethane foam material, and silicone rubber or other elastic sealing materia can be used in sealing the gaps between the frame and the wall. The size of the gap can be determined according to the allowed frame structural deformation between layers in the basic and rare earthquakes, which should not be less than 20mm. The structural columns should be set on both ends of the infilled wall (In construction of the structural columns within masonry infilled wall, there is no need to set combed joints). The distance between structural columns should not be too large, the vertical reinforcement in structural columns should be joined with the embedded parts or reserved steel in the frame beam. The reserved tie bars in frame column can be anchored in the structural columns in walls. Every 500mm 2Φ6 tie bars should be set between wall and structural columns. The length of tie bars extended into the wall should be determined according to the requirements of seismic code. In order to ensure out-plane stiffness of the masonry infilled walls, level collar beam or reinforced concrete belt could be added along the height direction of the wall. The disconnection of the infilled wall and frame beam-column is in order to

reduce the beam-column's incremental launching affection and constraints which are produced by the masonry infilled wall in earthquake and to avoid the damage of the frame. Grip iron can also be used in the releasing connection of the masonry infilled wall and frame.

**2.3 improving the shear resistance of masonry infilled wall**

Material strength grade of masonry infilled wall should not be too low,Otherwise, when the frame has a slight change , masonry infilled wall might crack, and easy to be damaged,even causing casualties and property losses in accidental loads or low horizontal earthquake action，Masonry infilled wall consists of block and mortar,In the case of shear-compressive failure and shear-bond failure ,The strength of the block almost doesn't impact on shear strength of masonry .But mortar strength has a direct effect on shear strength of masonry whatever kinds of damage . Especially in shear-compressive failure and shear-bond failure , The increase of mortar strength is more obvious to improve the shear strength of masonry. Therefore, When choosing materials of masonry infilled wall, mortar strength should be appropriate to be improved, so as to improve the shear resistance capacity of the wall.

In concrete-block wall, a core column can also be set. The shear capacity of masonry infilled wall is also influenced by concrete in core column. Due to its own shear strength of concrete in core column and 'hook-action'between core column and masonry wall , the shear strength of masonry infilled wall is improved greatly with the increase of concrete strength in core column.

**2.4 Ensure the construction quality of the wall**

When the masonry infilled wall builded , the full degree of horizontal mortar joint , the thickness of horizontal mortar joint , The moisture content of the brick and masonry bond are related to the construction quality of masonry wall.If the construction quality of the wall is ignored , the seismic resistance of the wall will be reduced.so we can't neglect the construction quality for the wall is designed not to support certain loads.

## 3 Conclusion

Masonry infilled wall can't adapt to the movement and deformation produced by the frame (including frame-wall structures )because of its brittle nature and poor integrity . After a series of earthquakes , a large number of cracks and collapses had been seen.At present , lightweight wallboard is still unable to be used widely in our country ,while the application of masonry infilled wall is common .More attention must be payed to the concept design and details of seismic design of masonry infilled wall,which Can greatly reduce the seismic damage of buildings, reduce the economic loss and the threat to people's life and property caused by the earthquake.

## References

[1] Code for design of masonry structures（GB50003—2001）

[2] Code for seismic design of buildings（GB50011—2010）

[3] Building Structure：Technical communication,2013.5：28—30，in chinese

[4] Chuxian- Shi.masonry structure[M]，China Building Industry Press，2003.7 ,in chinese

[5] Dingguo- Feng， Sheliang- wang,.Aseismic stucture Design[M]，Wuhan Industry Press，2001.9 ,in chinese

[6] Yujun-Yang,Yuzhou- Sima.Masonry Structure[M]，Higher Education Press，2004.11 ,in chinese

[7] Yaojun -Zhang，Jinzhao -Zhuang-.Aseismic stucture Design[M]，China WaterPower Press，2013.2,in chinese.

*Applied Mechanics and Materials Vols. 580-583 (2014) pp 1750-1754*
*© (2014) Trans Tech Publications, Switzerland*
*doi:10.4028/www.scientific.net/AMM.580-583.1750*

# A suggestion to the vertical earthquake action stipulated in seismic design specification

Liu Haiming[1,a] *Tao Xiaxin[2,b] Wang Jinyuan[2]

[1] China Merchants Chongqing Communication Research & Design Institute Co., Ltd, State Key Laboratory of Bridge Engineering Structural Dynamics, Chongqing, 400067, China

[2] School of Civil Engineering, Harbin Institute of Technology, Harbin 150090, China

[a]haiming716@163.com, [b]taoxiaxin@aliyun.com

**Keywords:** Earthquake action; Response spectrum; vertical action; Site coefficient; Characteristic period

**Abstract.** In order to further regulate the vertical earthquake action in seismic design specification, to overcome the unreasonable and inconvenient flaws in certain conditions by using vertical to horizontal spectra ratio function, the feasibility of stipulating vertical design response spectrum with the same way of horizontal one is deal with in this paper.

1513 sets of three component records during 64 earthquakes from NGA-west1 database are selected and grouped by magnitude, distance and site conditions. Average acceleration response spectrum of each group is generalized to get the corresponding mean maximum amplitude and effective peak acceleration EPA. Furthermore, some groups with EPA in an interval are merged into one. Once again, the parameters, such as maximum amplitude and characteristic periods of each final grouping are acquired by the same way. The former is divided by the corresponding horizontal value for site category, to obtain the site coefficient for vertical action. Finally a preliminary suggestion of vertical site coefficient and characteristic period are presented. Comparison of observed data with results from the new suggestion and those from spectral ratio shows that the improvement of this study is obvious.

## Introduction

As well known, vertical ground motion plays an important role on damage of engineering structure during earthquake [1]. However, engineers for seismic design think highly of horizontal earthquake action stipulated in seismic design specification, since there is no lateral support on the upper part of the most engineering structure, and there is always more redundancy in structure capacity to vertical load in general. In checking calculation for seismic design of large scale and/or complex structure, the combine effect of actions at two or three directions should be taken into account. In most of seismic design codes, vertical action is stipulated simply as the half or two third of the horizontal one, i.e. the all amplitudes of design acceleration spectrum are scaled by the same reduction ratio, while the shape of the spectrum keeps the same as the horizontal one[2]. In those specifications that the vertical action is specially stipulated, the design spectrum is scaled by a spectral ratio that provides the reductions in different period ranges, so the shape of vertical spectrum could be different from the horizontal one[3], or by other spectral parameters also could define different spectrum for the vertical action from the horizontal one[4]. The shortcomings of the former are pointed out and a preliminary result of the latter is presented in this paper.

**The necessity to modify the relative provisions in Guidelines for Seismic Design of Highway Bridges (GSDHB)**

GSDHB provides vertical design spectra by vertical to horizontal (V/H) spectral ratio, constant 0.65 for rock site, ratio function for soil site as follows [3].

$$\mathrm{R}=\begin{cases}1.0 & T<0.1\\ 1.0-2.5(T-0.1) & 0.1\le T<0.3\\ 0.5 & T\ge 0.3\end{cases} \tag{1}$$

where T is for period in second. The horizontal spectra is provided as

$$S=\begin{cases}S_{\max}(5.5T+0.45), & T<0.1s\\ S_{\max}, & 0.1s\le T\le T_g\\ S_{\max}(T_g/T), & T>T_g\end{cases} \tag{2}$$

where，$S_{\max}$ is the maximum amplitude of the spectrum; $T_{\mathrm{g}}$ is characteristic period in second. The $S_{\max}$ is defined as

$$S_{\max}=2.25C_iC_sC_dA \tag{3}$$

where A is design basic acceleration of ground motion from seismic zoning map; $C_i$ is the important coefficient, takes value of 1.0 for type A bridge; $C_s$ the site coefficient; $C_d$ the damping adjustment coefficient, 1.0 for damping ratio 0.05. The $C_s$ is a new one to emphasize the effect of local site condition on $S_{\max}$, not only on the character period $C_s$ is not related with vertical action provision directly, but is necessary to provide the action with same way for horizontal one. The same provision is adopted in Specification of seismic design for highway engineering [5].

The idea to do with this way is from the two facts, spectral ratio is much more stable than spectral parameters in statistics, and the number of vertical motion data is just about half of the horizontal one, not enough for statistics to take into account the various A values and site categories. However, for soil site, there should be a slope segment from $T_g$ to 0.3 second on the vertical spectrum curve, and there should be one more decreasing segment from 0.3 second to $T_g$ with rate faster thane $\mathrm{T}^{-1}$ if $T_{\mathrm{g}}$ less than 0.3 second, neither easy nor reasonable in design. This fact shows the necessity to present a new modification in this paper.

**Data base from NGA-west1 and the preliminary grouping**

Data base from NGA (Next Generation Attenuation) program in the United States are adopted in this paper. Totally 1513 recording sets during 64 earthquakes with magnitude 4.2 to 7.9 from 1952 to 2003, are chosen with 4 criterions, PGA no less than 200 gals, recorded at ground or at basement or the first floor in building less than three stories, data on site condition is available, and data of response spectra, earthquake parameters, data of observation stations are also available. Recording data is not adopted if there is no vertical record in a set.

Data grouping is the key step in spectra parameters since the A value depends on $S_{max}$ that varies with magnitude, distance and site condition. The preliminary grouping on site category as I，II and III by Chinese site classification criterion, but category IV can not be taken as a group since the data is too few, just 6 in 1513; on magnitude as [4.5，5.5]，（5.5，6.5]，（6.5，7.5] and（7.5，8.5），in brief M5, M6, M7 and M8 respectively, the number of record sets are 251, 340, 496 and 420; on distance as（0，10]，（10，30]，（30， 50]，（50，100]，（100，200]，the corresponding number of record sets are 53，252，313，339，274 and 276. The numbers of each grouping are listed in table 1.

Table 1 The data set numbers in preliminary groupings

| Site category | Distance | M5 | M6 | M7 | M8 | Total |
|---|---|---|---|---|---|---|
| I | 0-10 | 3 | 5 | 4 | 3 | 15 |
| | 10-30 | 11 | 8 | 23 | 6 | 48 |
| | 30-50 | 9 | 17 | 21 | 8 | 55 |
| | 50-80 | 8 | 12 | 19 | 18 | 57 |
| | 80-120 | 7 | 3 | 22 | 18 | 50 |
| | 120-200 | 2 | 0 | 4 | 21 | 27 |
| II | 0-10 | 4 | 13 | 11 | 4 | 32 |
| | 10-30 | 28 | 77 | 52 | 16 | 173 |
| | 30-50 | 51 | 89 | 48 | 29 | 217 |
| | 50-80 | 55 | 49 | 76 | 54 | 234 |
| | 80-120 | 35 | 16 | 61 | 69 | 181 |
| | 120-200 | 3 | 7 | 96 | 75 | 181 |
| III | 0-10 | 0 | 5 | 1 | 0 | 6 |
| | 10-30 | 4 | 8 | 18 | 1 | 31 |
| | 30-50 | 9 | 8 | 10 | 14 | 41 |
| | 50-80 | 8 | 13 | 13 | 14 | 48 |
| | 80-120 | 9 | 8 | 8 | 18 | 43 |
| | 120-200 | 5 | 2 | 9 | 52 | 68 |

**Acquiring of EPA values and the final grouping**

From each group, a mean acceleration response spectrum is obtained by simple arithmetic average. Then the mean spectra are generalized from eq. (2). An example for site category II, M6 and distance 80-120 km is shown in Fig. 1.

Equivalent peak acceleration EPA is acquired from the maximum amplitude of the generalized spectrum for each group by means of dividing the maximum amplitude by the constant 2.25 in eq. (3). The EPA here for grouping is for horizontal component, since A on seismic zoning map is defined as horizontal one and for site category Ⅱ. Therefore, the final grouping is decided as EPA 0.05, 0.1, 0.15, 0.2, 0.3, and 0.4g with value ranges of no larger than 0.05, 0.05 to 0.13, 0.13 to 0.18, 0.18 to 0.25, 0.25 to 0.35, and no less than 0.35g. The corresponding distance R and magnitude M intervals are R∈（10，200] and M∈ [4.5，5.5]，R∈（50，200] and M∈（5.5，6.5], R∈（80，200] and M∈（6.5，7.5] for EPA 0.05g; R∈（30，50] and M∈（5.5，6.5], R∈（50，80] and M∈（6.5，7.5], for EPA 0.1g; R∈（10，30] and M∈（5.5，6.5], R∈（30，50] and M∈（6.5，7.5], for EPA 0.15g; R∈[0，10] and M∈ [4.5，6.5]， R∈（10，30] and M∈（6.5，7.5] for EPA 0.2g; R∈[10，50] and M∈ [6.5, 8.5) for EPA 0.3g; R∈[0，10] and M∈ [6.5, 8.5) for EPA 0.4g, according the statistical result.

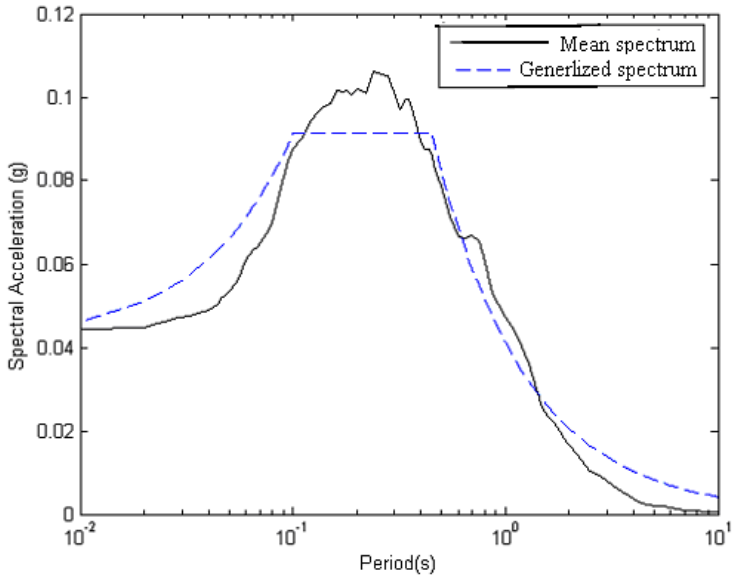


Figure 1 An example of mean spectrum and its generalized one

**A preliminary suggestion of vertical action**

Once again, the $S_{max}$ of each final group are acquired from the same way as mentioned above. This two step procedure is very significant to avoid the mistakes to grouping with PGA or $S_{max}$ of the original records.

The site coefficient values could be obtained from the ratios of vertical $S_{max}$ for site category I, II and III to the corresponding horizontal ones for category II. The suggested values generalized to keep the small increment as 0.05, are listed in table 2. One can see from the table that the average value for site category I is about 0.65, and getting larger as A value increasing for the other two site categories.

Table 2 Vertical site coefficient values suggested by the paper

| A<br>Site category | 0.05g | 0.1g | 0.15g | 0.2g | 0.4g |
|---|---|---|---|---|---|
| I | 0.70 | 0.55 | 0.50 | 0.55 | 0.80 |
| II | 0.60 | 0.60 | 0.70 | 0.75 | 1.00 |
| III | 0.50 | 0.65 | 0.75 | 1.20 | 1.20 |

The characteristic period values could be acquired from the mean generalized spectra for the 6 groups and 3 site types, and the results are listed in table 3. One can see from the table, the characteristic period of vertical component is shorter than that of horizontal component, and not change so much with the site category.

Table 3 The characteristic period values acquired in the paper

| A<br>Site category | 0.05g | 0.1g | 0.15g | 0.2g | 0.4g |
|---|---|---|---|---|---|
| I | 0.18 | 0.25 | 0.21 | 0.18 | 0.28 |
| II | 0.31 | 0.35 | 0.19 | 0.18 | 0.15 |
| III | 0.27 | 0.24 | 0.15 | 0.15 | 0.15 |

## Conclusion

Based on a new data base from NGA-west1, the values of site coefficient and characteristic period for vertical component are acquired statistically by the same way for horizontal one, listed in table 2 and table 3.

It shows that this way is better than the way of spectral ratio, not only the vertical spectra always keep shapes with three segments, but also the deviations of the observed data to spectra suggested in this paper. Of course, the spectral ratio in eq. (1) was obtained from data base with some differences from the one adopted in this paper.

A new data base with much more records was released in 2012 as NGA-west2 by NGA project. The final suggestion should be from the result of the new data, so the suggestion of this paper is just a preliminary one that shows the possibility to stipulate vertical earthquake action in seismic design specification by the same way for horizontal action. The parameters for site category should be inferred further from the limited data and variation trend of the parameter with site category.

## Acknowledgements

This paper is financially supported by the National Nature Science Foundation of China (51178151 and 51178435), International Science & Technology Cooperation Program of China (2011DFA21460), and KJ1343 of Special Scientific Research Fund of IWHR，China.

## References

[1] Qian Peifeng. Building structure, 1979, (03): 1-8

[2] Ministry of housing and urban-rural development of the People's Republic of China, General Administration of Quality Supervision, Inspection and Quarantine of the People's Republic of China. Code for seismic design of buildings (GB50011- 2010). 2010

[3] Ministry of Transport of the People's Republic of China. Guidelines for Seismic Design of Highway Bridges (JTG/T B02-01-2008). 2008

[4] State Standard of the People's Republic of China. Code for seismic design of unclear power plants (GB50267-97). 1997

[5] Ministry of Transport of the People's Republic of China. Specification of seismic design for highway engineering (JTG B02-2013). 2013

[6] Geng Shuwei, Tao Xiaxin. Erathquake engineeringand engineering vibration, 2004, (05):33-38.

*Applied Mechanics and Materials Vols. 580-583 (2014) pp 1755-1758*
*© (2014) Trans Tech Publications, Switzerland*
*doi:10.4028/www.scientific.net/AMM.580-583.1755*

# Seismic Response Analysis for Assembled Precast Concrete Residence

Zhaobo Meng[1,a], Yu Cao[1,b], Guandong Qiao[2,c] and Yongsheng Zhao[1,d]

[1]School of Architecture & Civil Engineering, Liaocheng University, Liaocheng 252059, China

[2]School of Civil Engineering, Xi'an University of Architecture and Technology, Xi'an, 710055, China

[a]mengzhaobo@lcu.edu.cn, [b]caoyusmile@126.com,

[c]qiaoguandonghy@126.com, [d]zhaoyongsheng@lcu.edu.cn,

**Keywords:** Assembled precast concrete residence, Finite element, Seismic response analysis, Interbedded drift angle

**Abstract.** Assembled precast concrete structure is composed of precast element, which needs to be assembled and connected as the main force component. It is propitious to the development of building industrialization, enhancing production efficiency and promoting green building. Seismic response of a 6 storey assembled precast concrete residence was analyzed based on finite element software ANSYS. The results show that stiffness of assembled precast concrete residence is larger, and all of interbedded drift angles comply with stipulations of the standard.

## Introduction

A large number of repetitive work is completed by prefabricated production line in assembled precast concrete, which is high mechanization and automation. Combining with standardization of component, work efficient could be improved greatly and construction period could be shorted[1]. Compared to traditional residence, industrialized residence, represented by assembled precast concrete residence, saves more concrete and steel and promotes the recycling of waste. Assembled precast concrete residence is one of building structure development directions in China.

RL Hutchinson et al.[2] had a research on 9 shell walls connected by post-tensioned method, analyzing failure mechanism and characteristics of node. Sritharan S et al.[3] did a pseudo-dynamic test of 5-storey prefabricated concrete structure. Huiying Wang et al.[4] analyzed mechanical performance, deformation characteristics and internal force distribution characteristics through the loading experiment of composite slab. Weiwei Sun et al.[5] proposed two new unbonded post-tensioned assembled concrete couped short-pier shear wall structures. Seismic response of a 6-storey assembled precast concrete residence in Liaocheng was analyzed based on finite element software ANSYS.

## Project overview

The assembled precast concrete residence (shown in Fig.1) is located in Liaocheng, Shandong Province, with a total construction area of 5595.39m$^2$, 6 stories high, each storey height being 3m. Floor slab is made of PK prefabricated composite slab, and external wall is made of composite thermal insulation wallboard. The node connection pattern is embedded column, concealed coping made of current pouring concrete.

The thickness of wallboard and floor are 160mm and 100mm respectively, with the cross sectional dimension of embedded column and concealed coping being 160mm×300mm. Concrete grade is C30, and steel grade is HRB335.

Fig. 1 The assembled precast concrete residence

**finite element model**

The finite element model was established by the way of integrated model. Wallboard and floor were simulated by Solid65, with rebar simulated by parameter setting. Horizontal and vertical reinforcement ratio were 0.2% and 0.25% respectively. Boundary condition is limiting UX, UY, UZ and rotation of three directions. The finite element model is shown in Fig. 2.

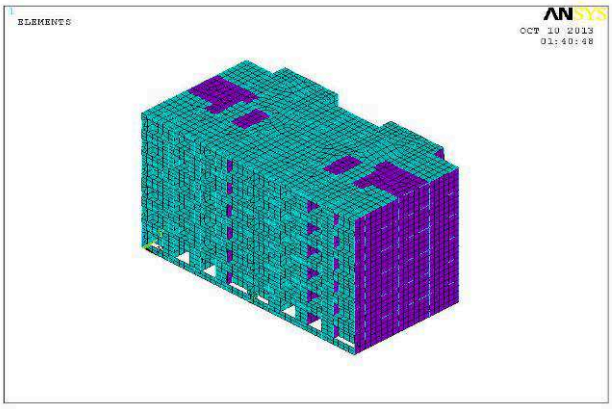


Fig. 2 Finite element model

**Analysis of dynamic characteristics**

Modal analysis to the finite element model was made through Block Lanczos provided by ANSYS, and the 5 order natural vibration period and frequency was got, as shown in Table 1.

Table 1 Natural vibration period and frequency

| order | natural vibration frequency（Hz） | natural vibration period（s） |
|---|---|---|
| 1 | 12.208 | 0.082 |
| 2 | 14.237 | 0.070 |
| 3 | 15.909 | 0.063 |
| 4 | 28.512 | 0.035 |
| 5 | 33.895 | 0.029 |

The first vibration mode of the structure is X-direction horizontal vibration, and the second is Y-direction horizontal vibration, with the third and forth being torsion. The vibration modes are shown in Fig. 3~6.

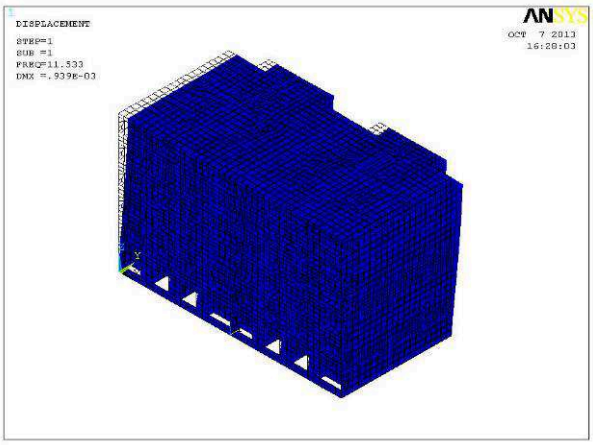


Fig. 3 The first vibration mode(X-direction)

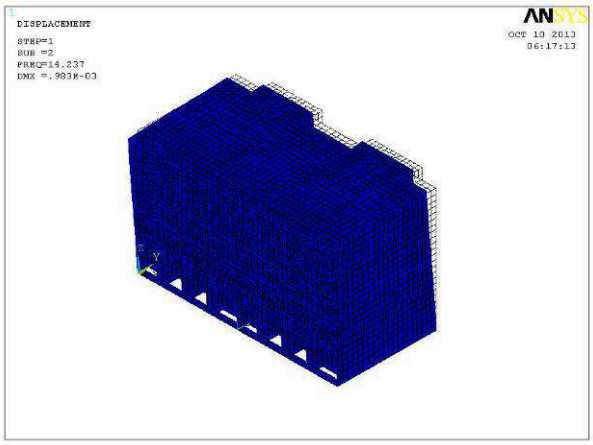


Fig. 4 The second vibration mode(Y-direction)

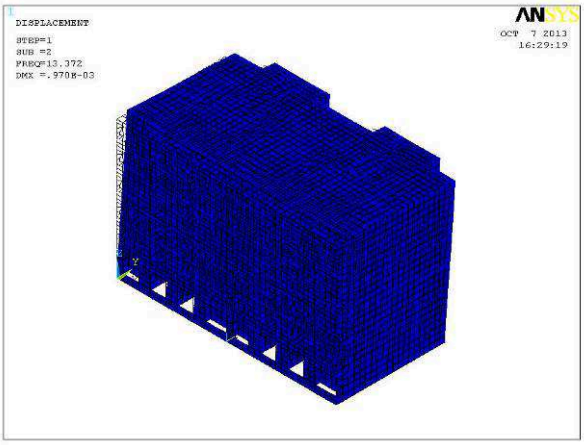


Fig. 5 The third vibration mode(torsion)

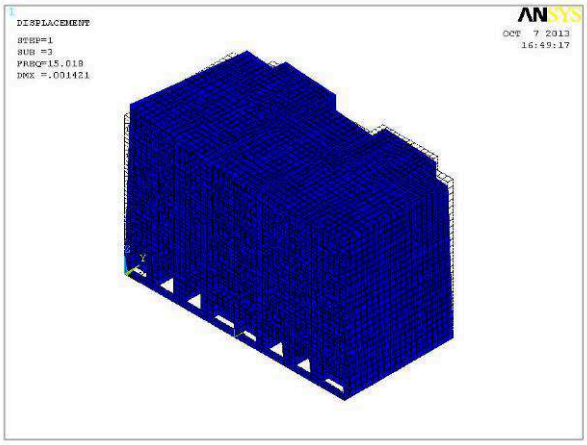


Fig. 6 The forth vibration mode(torsion)

## Seismic response analysis

Seismic response analysis of structure is closely related to peak acceleration, duration of earthquake, and properties of soil. Seismic fortification intensity of Liaocheng is 7, and seismic acceleration is 0.15g, with site category being Ⅲ. According to frequently occurred earthquake, the maximum value of earthquake acceleration used by time-history analysis is 35cm/s$^2$, so Elcentro wave was chosen to analyze. Some of displacement time history curves are shown in Fig. 7~8.

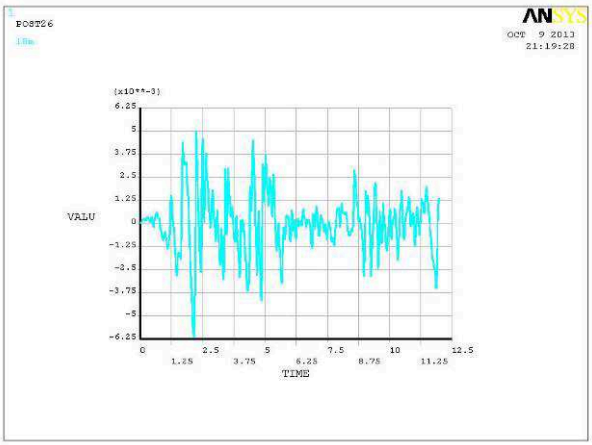


Fig. 7 H=18m (Y-direction)

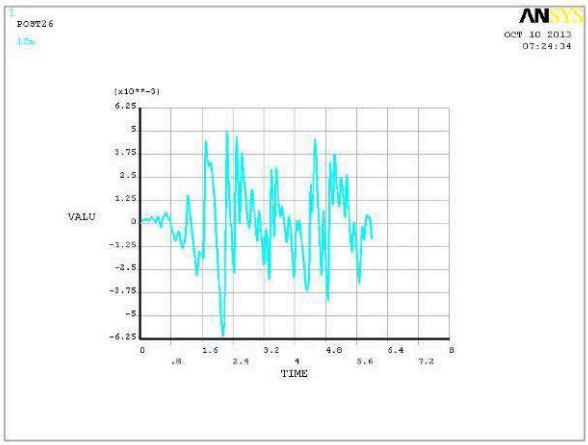


Fig. 8 H=12m (X-direction)

The maximum displacements of each floor were got by analyzing the displacement time history curves, and interbedded drift angles (shown in Table 2) were calculated.

Table 2 Interbedded drift angle

| | Each floor roof | Storey (m) | maximum displacement (mm) | interbedded drift angle | specification limit |
|---|---|---|---|---|---|
| Y-direction | 18 | 3 | 6.25 | 1/3500 | 1/1000 |
| | 15 | 3 | 5.4 | 1/3300 | |
| | 12 | 3 | 4.5 | 1/2500 | |
| | 9 | 3 | 3.28 | 1/3000 | |
| | 6 | 3 | 2.3 | 1/2600 | |
| | 3 | 3 | 1.125 | 1/2666 | |
| X-direction | 18 | 3 | 7.9 | 1/3750 | 1/1000 |
| | 15 | 3 | 7.1 | 1/3529 | |
| | 12 | 3 | 6.25 | 1/2068 | |
| | 9 | 3 | 4.8 | 1/1875 | |
| | 6 | 3 | 3.2 | 1/1875 | |
| | 3 | 3 | 1.6 | 1/1875 | |

By the above calculation, the integral rigidity of the structure is large, with no weak storey existed, and the interbedded drift angles less than the standard value. So the material parameter and geometric parameter of the assembled precast concrete structure all meet the requirements.

## Conclusions

By analyzing seismic response of assembled precast concrete structure, conclusions are shown as follows:

(1) The first vibration mode of the structure is X-direction horizontal vibration, and the second is Y-direction horizontal vibration, with the third being torsion, whose natural vibration frequencies are 12.208Hz, 14.237Hz and 15.909Hz respectively.

(2) In the 7 degree seismic fortification intensity area and Ⅲ site category, making the thickness of wallboard and floor be 160mm and 100mm, concrete grade be C30, and steel grade be HRB335, the integral rigidity of the structure is large, with no weak storey existed, and the interbedded drift angles less than the standard value. So the assembled precast concrete structure meet the requirements.

## References

[1] A.A.Yee. Structural and Economical Benefits of Precast/Pretressed Concrete Construction. PCI JOURNAL,2001,46(4):34—42

[2] RL Hutchinson, SH Rizkalia, M lau, JS Huevel. Horizontal Post-Tensioned Connections for Precast Concrete Load bearing Shear Wall Panels [J]. PCI Journal, 1991(4):67-62

[3] Sritharan S., Igarashi A., Priestley M.J.N., Seible F. Test Design of the PRESSS Five-storey Precast Concrete Building [C]. Proceedings. 68th Annual Convention. Structural Engineers Association of California. Snata Barbara. CA.1999:255-261

[4] Huiying Wang. Research on Industrialized House System of Precast Concrete Structure [D]. Guangzhou University, 2007.(In Chinese)

[5] Weiwei Sun. Study on Seismic Capacity and Design Method of Unbonded Post-pier Wall [D]. Southeast University, 2007.(In Chinese)

*Applied Mechanics and Materials Vols. 580-583 (2014) pp 1759-1762*
*© (2014) Trans Tech Publications, Switzerland*
*doi:10.4028/www.scientific.net/AMM.580-583.1759*

# Study of Ultimate Displacement of Timber Structures in Chinese Ancient Buildings

Minggang Xu[1,2,a], Zhuowei Ding[2,b]

[1] Key Laboratory of Urban and Architectural Heritage Conservation (Southeast University), Ministry of Education, Nanjing, Jiangsu, 210096, China

[2] Nanjing Technical Vocational College, Nanjing, Jiangsu, 210019, China

[a]xuminggang800311@163.com, [b] dingzw1963@126.com

**Keywords:** Seismic Design, Ultimate Displacement, Timber Structures, Tenon-mortise Joints, Chinese Ancient Buildings, axial compression ratio.

**Abstract.** The available methods to determine the ultimate displacement of the building structures have been put forward, and the disadvantages of the methods are analyzed. According to the seismic design theory based on displacement of structures and reinforcement standard of Chinese ancient architecture, which refers to the modern structural engineering requirements, the ultimate displacement of the timber structure on Chinese ancient buildings, which is under the obvious P-Δ second-order effects, has been studied. The ultimate displacement and the drift ratio limit value of different axial compression ratio are determined by the experiments and Theoretical calculation. The results of the study of ultimate displacement can provide the technical support for the rehabilitation of the ancient timber buildings.

## Introduction

Traditional seismic design is a kind of design based on strength, which controls the structural capacity by the ultimate capacity of the buildings[1,4]. With the research and studies of the structural capacity step by step, it is realized that the dissipation of deformation capacity and energy capacity is the key reason for the collapse of timber structure. So, it is reasonable to make the seismic design based on the ultimate displacement. It is most important thing for seismic design to the timber structure of ancient buildings to create the stable criterion with the large earthquake.

## Determination Method of the Ultimate Displacement

**The ultimate displacement of the timber structure on the code.** According to the specification of the strengthening and maintenance to ancient timber buildings, the drift ratio limit value of the timber structure is 1/30 in the deformation checking of seismic design. So, the ultimate deformation of the timber structures of ancient buildings is expressed as follows:

$$\Delta u = [\theta]_p = \frac{1}{30} H \tag{1}$$

In the formula, "H" is equivalent to the height of the column of timber structure, $[\theta]_p$ is equivalent to the elastic-plasticity drift ratio limit value.

**The ultimate displacement based on the residual horizontal capability.** In engineering, the residual horizontal capability is defined as the 85 percent or 75 percent of the biggest horizontal capability, and the corresponding elastic-plasticity displacement is the ultimate displacement. As is shown in fig.1, the biggest horizontal capability of the structure column is as $P_{max}$, the $0.85P_{max}$ is the residual horizontal capability whose corresponding displacement of the $0.75P_{max}$ is $\Delta u2$.

**The anti-overturning of the timber structure of ancient buildings.** As is shown in fig.2 of the reference [5], the anti-overturning ultimate displacement is confirmed that the biggest horizontal inertial force of earthquake $F_E$ is confirmed as follows:

$$F_E = \mu G_w \tag{2}$$

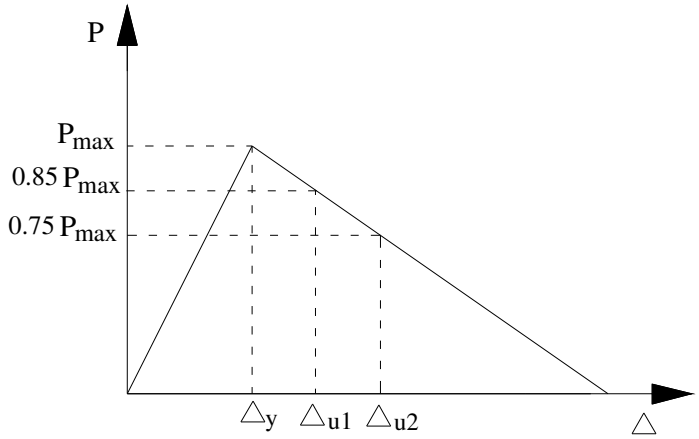


Fig.1 Ultimate displacement based on the residual horizontal capability

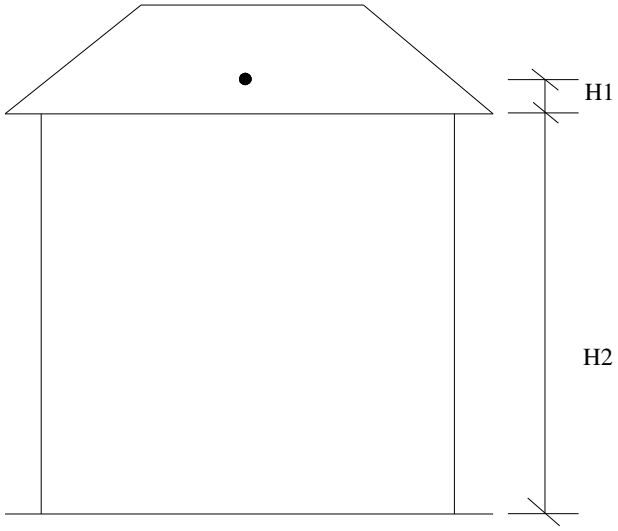


Fig.2 Calculation sketch of ancient timber buildings

The total overturning of earthquake $M_e$ is conformal as follows:

$$M_e=F_E(H_2+H_1/3)=\mu G(H_2+H_1/3) \tag{3}$$

The anti-overturning moment which is proved by the weight of the structure is confirmed as follows:

$$M_R =G[0.5L-\Delta u] \tag{4}$$

$$\Delta u = 0.5L-u(H+h/b) \tag{5}$$

The premise of the ultimate displacement formula creation above the wooden frame to resist overturning is assumed as the upper structure rigidity good rigid block, and only one side of the pivot around the state. In fact, a typical ancient timber structure is composed of a base, column layer and frame layer which are three relatively independent parts.

The connection between the timber components is mortise and tenon joint, which makes the ancient timber structure not be an absolute rigid. The self vibration period of this type of structure is longer. Under horizontal earthquake action, it is easy to produce the column frame swing instead of the whole structure. In addition, the rational control of high aspect ratio is used to prevent the

possibility of overturning the wooden structure in the structure layout of Chinese ancient timber architecture, which is in references [6][7][8].

**Method to determine the ultimate displacement in this paper**

There are a lot of factors which influence the ultimate displacement of the timber structure such as the material strength of the timber, rigidity of the tenon-mortise joints and the axial compression ratio. There is a obvious P-Δ second-order effects in the timber structures whose lateral displacement is big, because of the semi-rigid tenon-mortise joints. So, it is more important for the axial compression ratio to the ultimate displacement of the timber structure. The ultimate displacement and the drift ratio limit value of different axial compression ratio is shown in the table1.

From the table1, we can see that With the increase of axial compression ratio, the ultimate displacement was decreased by using calculation method1 and method2. This paper determined the ultimate displacement under different axial compression ratio, met the limit displacement required maintenance and strengthening of ancient timber buildings technical specification (referred to as the standard value of value) as the standard.

Table1 Ultimate displacement and the drift ratio limit value of different axial compression ratio

| Structure number | | compression ratio | Method1 | | Method2 | | | |
|---|---|---|---|---|---|---|---|---|
| | | | $\triangle_u$ (mm) | $\theta_p$ | $\triangle_{u1}$ (mm) | $\theta_{p1}$ | $\triangle_{u2}$ (mm) | $\theta_{p2}$ |
| Result1 | KJ1 | 0.1 | 50 | 1/30 | 25.21 | 1/60 | 30.17 | 1/50 |
| | KJ2 | 0.1 | 50 | 1/30 | 20.13 | 1/75 | 22.04 | 1/68 |
| | KJ3 | 0.1 | 50 | 1/30 | 19.47 | 1/77 | 22.41 | 1/68 |
| | KJ4 | 0.1 | 50 | 1/30 | 26.33 | 1/56 | 32.26 | 1/46 |
| | Average value | 0.1 | 50 | 1/30 | 22.79 | 1/65 | 26.50 | 1/56 |
| Result2 | Th1 | 0.1 | 50 | 1/30 | 38.10 | 1/40 | 44.64 | 1/34 |
| | Th2 | 0.09 | 50 | 1/30 | 41.69 | 1/36 | 50.20 | 1/30 |
| | Th3 | 0.08 | 50 | 1/30 | 44.10 | 1/34 | 56.27 | 1/26 |
| | Th4 | 0.07 | 50 | 1/30 | 47.91 | 1/32 | 63.66 | 1/23 |
| | Th5 | 0.06 | 50 | 1/30 | 53.44 | 1/28 | 72.91 | 1/21 |
| | Th6 | 0.05 | 50 | 1/30 | 61.06 | 1/25 | 85.37 | 1/18 |

**Conclusion**

From table1, the ultimate displacement in this paper is confirmed as follows:

When the range of the axial compression ratio is $u<0.06$, the ultimate displacement is the 1/30 of the timber column; When the range of the axial compression ratio is $0.06<u<0.09$, the ultimate

displacement is the 1/40 of the timber column; When the range of the axial compression ratio is u>0.09, the ultimate displacement is the 1/50 of the timber column.

**Acknowledgements**

This work was financially supported by Key Laboratory of Urban and Architectural Heritage Conservation (Southeast University), Ministry of Education, China (KLUAHC 1306).

**References**

[1] T.Nakagawa, M.Ohta. simulations of two-story frame models [J]. J Wood Sci，2003

[2] T.Nakagawa, M.Ohta. simplification and quantification of the calculating method [J]. J Wood Sci., 2003

[3] Seo,J.M., Choi, I.K., Lee,J.R. Static and cyclic behavior of wooden frames with tenonjoints under lateral load [J]. J. Struct. Engrg.,ASCE, 1999

[4] William M.Bulleit, L.Bogue Sandberg, Matthew W. Drewek, Tonia L. O'Bryant. Behavior and modeling of wood-pegged timber frames[J].J. Struct. Engrg., ASCE, 1999

[5] Bengtsson Charlotte, Kemmsies Martin, Johansson Carl-Johan. Production control methods for glued-in rods for timber structures. Proceedings, World Conference on Timber Engineering. Whistler Resort British Columbia ,Canada.2000

[6] Kangas Jorma.Design of connection based on V-form glued-in rods. Proceedings, World Conference on Timber Engineering. Whistler Resort BritishColumbia ,Canada. 2000

[7] Andrew H Buchanan, Peter J Moss, P kevis Townsend.Reinforced bars epoxy bonded in Glue Laminated Timber.1990 International Timber Engineering conference, Tokyo，1990

[8] Lawrence a. Loltis robert J.Ross daniel F. Windorski.Fiberglass-reinforced Bolted Wood Connections. Forest Products Journal, 1998

*Applied Mechanics and Materials Vols. 580-583 (2014) pp 1763-1766*
*© (2014) Trans Tech Publications, Switzerland*
*doi:10.4028/www.scientific.net/AMM.580-583.1763*

# Expected Annual Earthquake Loss Analysis Based-on CMR of Structures

Lina Xian[1,2, a], Xiaoying Ou[3,b]

[1]College of Resources and Civil Engineering, Northeastern University, Shenyang, Liaoning 110004, China

[2]College of Applied Technology, Liaoning Technical University, Fuxin, Liaoning 123000, China

[3] Department of Civil Engineering, Dalian University of Technology, Dalian, Liaoning 116024, China

[a]lngdxln@163.com, [b]ou_xiaoying@163.com

**Keywords:** Collapse Margin Ratio, Expected Annual Loss, Survival Probability, Incremental Dynamic Analysis, Probability of Collapse

**Abstract.** Incorporating the probability of seismic hazard, expected annual earthquake loss with different collapse margin ratio (*CMR*) has been studied in this paper. Nonlinear simulation models of reinforced concrete (RC) frames were analyzed using incremental dynamic analysis (IDA) under continuous earthquake intensity. The analytic results from four examples of RC frames show that the expected annual loss has negative correlation with the *CMR* of the concerned structures, and seismic loss basically decreases with increasing *CMR* at given ground motion intensity. The proposed idea herein could be regarded as a promising improvement on the quantification of earthquake loss estimation by utilizing *CMR* of structures.

## Introduction

Structural seismic damage prediction is to calculate cost of repair or reconstruction of structures under earthquake. Pacific Earthquake Engineering Research Center has proposed performance-based earthquake engineering that uses earthquake loss to quantify specific structure seismic performance [1,2,3].

The methodology has four steps including seismic hazard analysis, structural analysis, damage analysis and loss analysis. A total probability triple integral equation incorporating these mentioned steps is proposed. This is done by quantifying the rate of exceedance of a level of ground shaking; inter-relating the level of ground shaking with structural response and quantifying the likelihood of facility closure given a certain level of damage. Dhakal and Mander [4] used four-integral formula to estimate expected annual loss and converted the seismic risk into economic loss. The story-based loss estimation method improved and simplified the PEER method which became efficient and less computationally expensive than previous approaches [5]. Limiting the amount of time and resources spent on the loss estimation process will hopefully facilitate the acceptance of performance-based seismic design methods into the practical engineering community. So the earthquake loss assessment should rise to the building-level. The global damage index has been used to quantify building-level damage as the ratio between repair costs over the total replacement value of the building [6].

However all these methods do not give the seismic capability index of structure before earthquake loss is calculated. A methodology to assess seismic anti-collapse capacity was described in the Applied Technology Council project (ATC-63) [7], and the collapse margin ratio (*CMR*) introduced in ATC-63 is a reasonable index to evaluate total seismic capacity of a structure. Each structure has a *CMR* easily manipulated. Bigger is the *CMR,* larger seismic capacity has the structures [8]. Hence, the objective of this paper is to build a relationship between *CMR* and earthquake loss based on IDA method, which can provide an insight into new earthquake loss assessment method.

## Theoretical direct earthquake loss estimation framework

The used method herein is based on the PEER framework formula, involving four-steps as follow, and considering the collapse safety margin by collapse margin ratio (*CMR*) of structures [1].

$$\lambda(DV) = \iiint G(DV \mid DM) \left| dG(DM \mid EDP) \right| \left| dG(EDP \mid IM) \right| \left| d\lambda(IM) \right| \tag{1}$$

*DV* is quantitative measure used to assess seismic performance. *DS* defines different discrete states of the structure which includes the requirement of tasks specific repair. *EDP* is used to describe the seismic response of the structure such as peak or transient displacements and/or accelerations. *IM* defines the intensity of the earthquake hazard to the structure. The process of loss estimation incorporating *CMR* is shown as follow.

**Seismic hazard analysis**

Seismic hazard model describes the occurrence over time of a given ground motion intensity *IM* (e.g. structural fundamental spectral acceleration is used in this paper). This relation, commonly known in the form of a ground-motion IM and annual rate of exceedance $\lambda(IM)$, is expressed by the following power law equation [9]:

$$\lambda(IM)=k_0\cdot(IM)^{-k} \tag{2}$$

Where, $k$ and $k_0$ are empirical constants. Seismic hazard curves are given in Fig.1 (a) and (b).

**Collapse margin ratio of structure and collapse probability**

On the basis of fragility curve, ATC-63 report [7] gives a definition of *CMR* to quantitatively identify seismic safety margin of structures. *CMR* is the ratio of the median intensity of the collapse level ground motions, $IM_{50\%}$, to the maximum considered earthquake intensity, $IM_{MCE}$. IDA is the default procedure as suggested in ATC-63 report in which a number of strong ground motion are deliberately selected and a series of collapse intensities can be obtained correspondingly at the collapse-critical state of the structure of concern. With the results from IDA, collapse fragility can be defined through a cumulative distribution function which relates the ground motion intensity to the probability of collapse $P(C|IM)$.

$$CMR=IM_{50\%}/IM_{MCE} \tag{3}$$

**Structural response analysis**

Based on IDA method, structural response *EDP* due to differences in ground motions of the same intensity *IM* is obtained. The following equation Eq.4 assumes that *EDP* at given *IM* is lognormally distributed, see [3] for more details.

$$P_{CMR}(EDP>edp\mid IM)=\Phi_{CMR}\left(\frac{\ln edp-\mu_{\ln EDP|IM}}{\sigma_{\ln EDP|IM}}\right) \tag{4}$$

**Loss analysis and build relationship between CMR and loss**

When combining the probability for being within a damage state for a given *EDP* together with the associated loss ratio for each damage state, the loss ratio for that *EDP* is found. The total probable financial loss due to earthquakes of a given probability is the sum of the corresponding values for damage states, this can be written as Eq.5 [5]:

$$E_{CMR}(L_T\mid IM)=\sum_{j=1}^{5}P_{CMR}(DS_j\mid IM)\cdot L_{j,DS_j}\cdot P_{CMR}(NC\mid IM)+P_{CMR}(C\mid IM) \tag{5}$$

Combining directly with the ground motion hazard to get the mean and variance of the loss occurred on a per annum basis, see Eq.6:

$$\lambda_L=\int E_{CMR}(L_T\mid IM)\left|\frac{d\lambda(IM)}{d(IM)}\right|d(IM) \tag{6}$$

Where, $P_{CMR}(DS_j|IM)$ and $L_{j,DSj}$ are the respective probability and loss ratios for the $j^{th}$ damage state of structure with *CMR*.

**Example**

In this section, four reinforced concrete structures with different *CMR* have been used to verify the proposed method. These structural *CMR* curves have no intersection, see in Fig.2. Structural parameters and detailed design of these structures can be found in the reference [6]. The results of IDA are shown in Fig.2 and Fig.3, (horizontal axis of Fig.2 normalized by spectral acceleration of MCE then *CMR* can be obtained in Fig.3). $CMR_1$=2.61, $CMR_2$=2.06, $CMR_3$=1.51, $CMR_4$=1.46, so $CMR_1>CMR_2>CMR_3>CMR_4$.

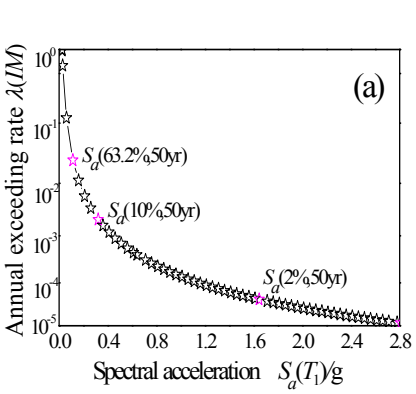


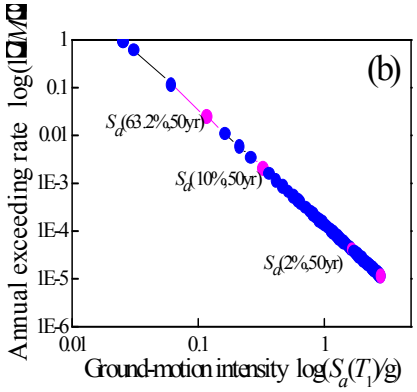


Fig.1 Seismic hazard in (a) linear coordinate (b) log-log coordinate

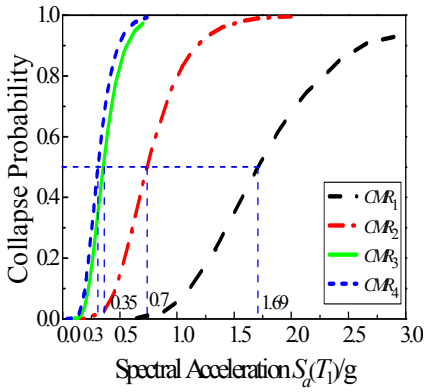


Fig.2 Collapse probability Curves

Fig.4 shows survival probability curves of structure with different *CMR* at a given damage level. It can be seen that a high value of *CMR* denotes a great survival probability at the same ground motion intensity. Consequently increased *CMR* can decrease damage probability of structure before collapse. The expected earthquake loss ratio basically decreases with increasing *CMR* at given ground motion. Each line represents a ground motion $S_a(T_1)$ continuously increasing from bottom to top and filling the whole rectangular space that consist of loss ratio and *CMR*, see in Fig.5. The relationship of loss ratio and *CMR* at five given intensity is shown in Fig.6.

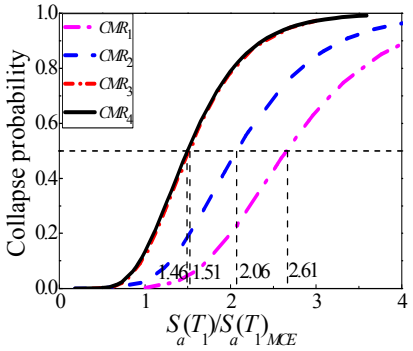


Fig.3 Collapse probability curve $S_a$ normalized by $S_{a,MCE}$

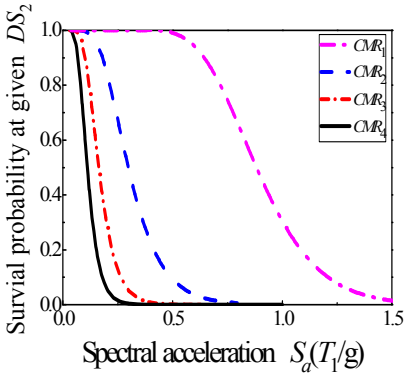


Fig.4 Survival probability at given damage state with different *CMR*

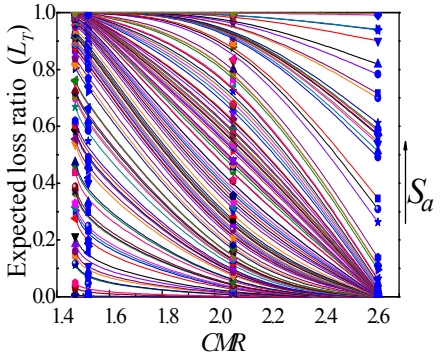


Fig.5 Curves of earthquake losses varying with *CMR* at continuous intensity

As shown in Fig.7, the earthquake loss ratio has negative linear relationship to *CMR* at design basic earthquake and maximum considered earthquake intensity respectively. Expected loss ratio at annual probability of *IM* is given in Fig.8. The loss ratio becomes smaller as the annual exceeding probability becomes bigger. Annual expected loss is the area beneath curve which calculated from Eq. 6, $CMR_1$ is the largest one among these four structures, while structural expected annual loss with $CMR_1$ is the smallest one significantly.

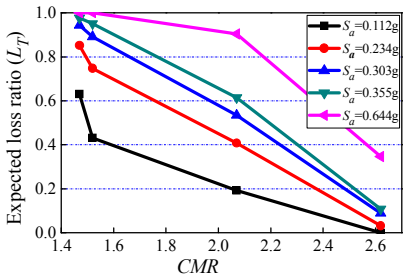


Fig.6 Curves of earthquake losses varying with *CMR* at five given intensity

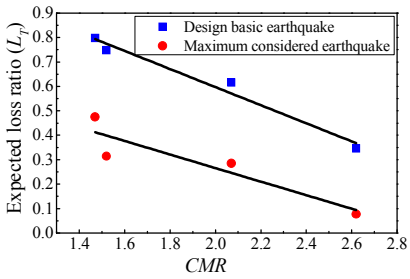


Fig.7 Negative linear relationship between loss and *CMR*

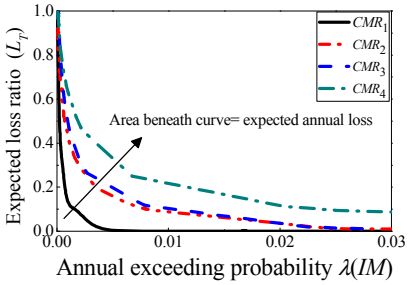


Fig.8 Annual earthquake losses with different *CMR*

## Conclusion

An approach to associate *CMR* with expected annual loss ratio of structure has been established. The results show that seismic expected annual loss decreases with increased *CMR* at a given ground motion intensity, but reduction rate of loss over *CMR* depends on the ground motion intensity. Expected annual loss ratio has negative relationship with *CMR* and can be reduced by improving *CMR* of structure.

## References

[1] P. Fajfar, Krawinkler, Performance-Based Seismic Design Concepts and Implementation. PEER Report 2003/03. University of California, Berkeley, September (2004).

[2] S.K. Kunnath, L. Larson, L. Miranda, Modeling considerations in probabilistic performance-based seismic evaluation: case study of the I-880 viaduct, J. Earthquake Engineering and Structural Dynamics. 35 (2006) 57-75.

[3] E. Miranda, H. Aslani, Probabilistic Response Assessment for Building-Specific Loss Estimation. PEER Report 2003/03. University of California, Berkeley, September (2003).

[4] R.P. Dhakal, J.B. Mander, Financial risk assessment methodology for natural hazards. Bulletin of the New Zealand Society of Earthquake Engineering, 39(2) (2006) 91-105.

[5] C.M. Ramirez, E. Miranda, Building-specific loss estimation methods & tools for simplified performance-based earthquake engineering. Report No.171, Department of Civil and Environmental Engineering, Stanford University, May (2009).

[6] L.N. Xian, Z. He, Engineering Mechanics (in Chinese), Accepted, Paper ID: 2013-0881, (2014)

[7] Applied Technology Council (ATC-63), Quantification of Building Seismic Performance Factors. Washington DC, America: FEMA, (2008).

[8] C.B. Haselton, G.G. Deierlein, Assessing seismic collapse safety of modern reinforced concrete moment-frame buildings. California: Stanford University, (2007).

[9] B.A. Bradley, R.P. Dhakal, J.B. Mander, Tokyo, Japan:10th International Conference on Statistics and Probability in Civil Engineering, 2007:Dj.M. Maric, P.F. Meier and S.K. Estreicher: Mater. Sci. Forum Vol. 83-87 (1992), p.119

*Applied Mechanics and Materials Vols. 580-583 (2014) pp 1767-1770*
*© (2014) Trans Tech Publications, Switzerland*
*doi:10.4028/www.scientific.net/AMM.580-583.1767*

# Earthquake Mitigation Effect Analysis Of Hysteretie DamPers In Steel frame

Chao Xu [1, a], Yongfeng Niu [1,b] and Yongxie Zhao [1,c]

[1]School of Civil Engineering,Jilin Jianzhu University,Changchun,China

[a]tianya880217@126.com, [b] yongxiezhao@163.com, [c]1140416324@qq.com

**Keyword:** Mild steel dampers; Steel Frame; Hysteretic loop; ABAQUS

**Abstract:** This paper analyses the frame without mild steel dampers and the frame installed the new T- type , box –type and S-type mild steel dampers by FEM ABAQUS. The results shows the frame installed the new mild steel dampers have smaller yield displacement and the fuller hysteresis curve at low cyclic load, but the initial stiffness, yield strength , stiffness after yielding are greater. Research shows that the new type mild steel dampers have good energy performance, and have the better effect to seismic framework.

## Introduction

Earthquake disaster since ancient severely threat to human's survival and development. For example the Tangshan earthquake in 1976, and after 32 years later, the Wenchuan earthquake in 2008, even the Yushu earthquake in 2010, has caused serious personal and property losses. With the improvement of science and technology and people's living standard, the ability of prevent earthquake disasters has been improved, the structure of the damping control technology has get more and more researchers' attention both at home and abroad due to its characteristic of economy applicable energy consumption, simple structure, convenient maintenance, and the better damping effect. so the technology has become an effective method to dissipate earthquake energy.

The method of Earthquake energy dissipation and vibration is controlling the structure expected deformation by setting energy dissipation devices, so that the structure of subject does not occur serious damage under the severe earthquake, in which , the mild steel damper as a reasonable energy dissipater because of its low yield point, the higher flexibility and ductility, the better deformation tracking ability, the lesser effect on its performance by environment and the temperature, and it can absorb a lot of energy in the elastic-plastic deformation process, also low steel cost etc., has on the agenda gradually.

## Material selection

The new T- type , box –type and S-type mild steel dampers are showed in Fig. 1.Which are made from steel Q235, material constitutive relation uses ideal elastic-plastic material model , the relevant parameters in Table 1.In the Table 1, $f_y$ is yield stress, $f_b$ is ultimate strength, E is modulus of elasticity, $\varepsilon_y$ is yield strain and $\varepsilon_u$ is ultimate strain.Steel Frame use section steel HW176×204×12×12, steel support are pipes in Outer diameter of 50mm and inside diameter of 30mm.

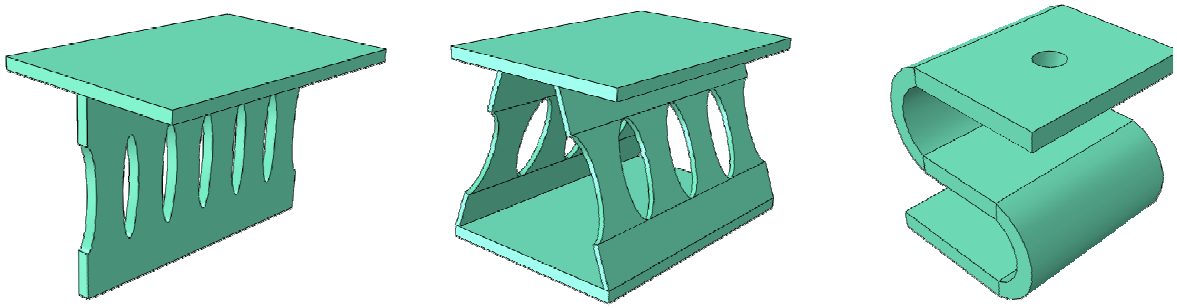

T- mild steel damper box- mild steel damper S- mild steel damper

Fig. 1

Table 1.Relevant performance parameters of Q235 steel

| $f_{y(\mathrm{N/mm^2})}$ | $f_{b(\mathrm{N/mm^2})}$ | $E(\mathrm{N/mm^2})$ | $\varepsilon_y$ | $\varepsilon_u$ |
|---|---|---|---|---|
| $235\times10^6$ | $370\times10^6$ | $210\times10^9$ | $1.119\times10^{-3}$ | $4.669\times10^{-3}$ |

**Loading model**

The model test loading model used displacement control loading method, often controlling load though Yield displacement or a percentage of the maximum the maximum displacement between layers. Displacement control loading method can be divided into three types according to the different Load amplitude: variable amplitude loading , amplitude loading and mixing amplitude loading.This article select variable amplitude displacement loading mode, appling horizontal displacement load on the coupling point. For the Fig.2:

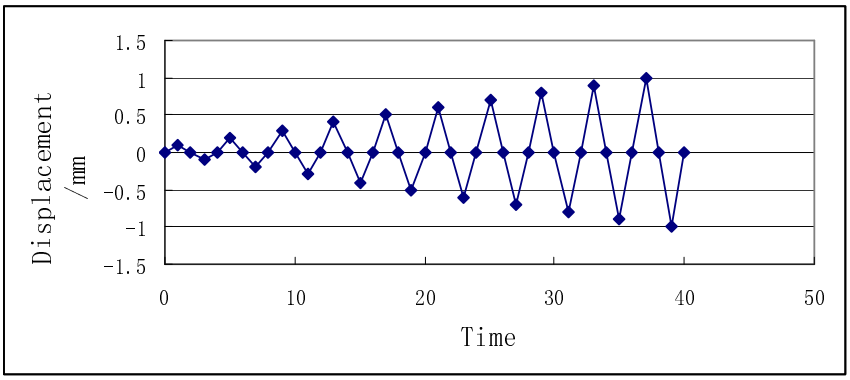


Fig.2 Displacement control loading method

**ABAQUS Simulation**

**4.1 Model building**

This paper modeling selects a layer framework façade,and computational model for a certain simplification,including:

1.It is considered full consolidation , no relative slip between beams, the support plate and the inclined column , dampers and the upper and lower surfaces connected with it;

2,Framework's deformation force only considered within the plane.

3.The connection of bottom of supporting inclined steel column to the beam seen as full consolidation.

### 4.2 Impact of mild steel dampers to the frame structures seismic performance

#### 4.2.1 Study on steel frame seismic performance without mild steel dampers

Fig.3 shows steel frame's Mises stress cloud and force - displacement hysteresis curve without mild steel dampers under cyclic load.

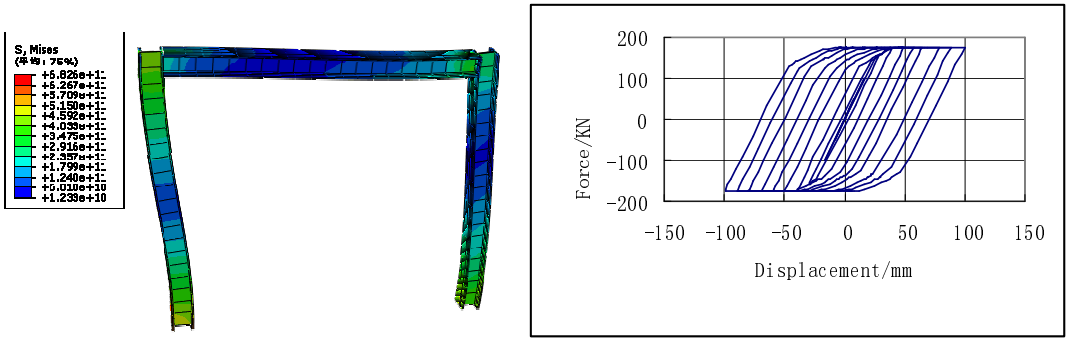


Fig.3 Framework is not installed damper

#### 4.2.2 Study on steel frame seismic performance with new mild steel damper

In Fig. 4-7 shows the Mises stress cloud and force - displacement hysteresis curve which framework with new T- type , box –type and S-type mild steel dampers under low cyclic load.

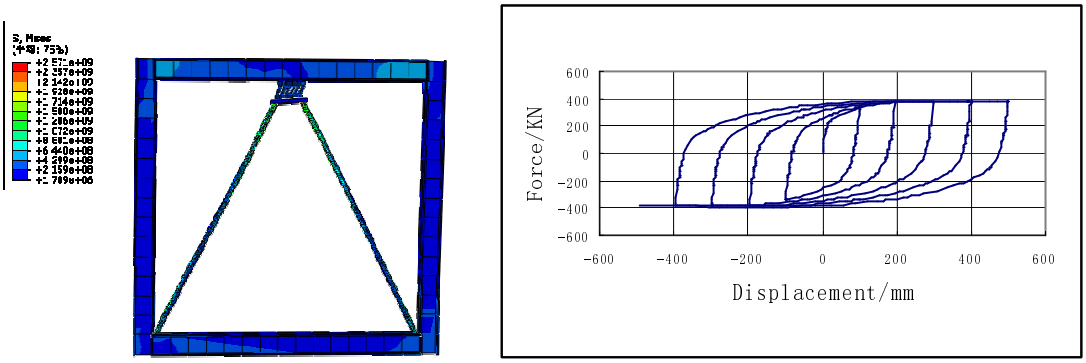


Fig. 4 Framework with new T- type mild steel damper

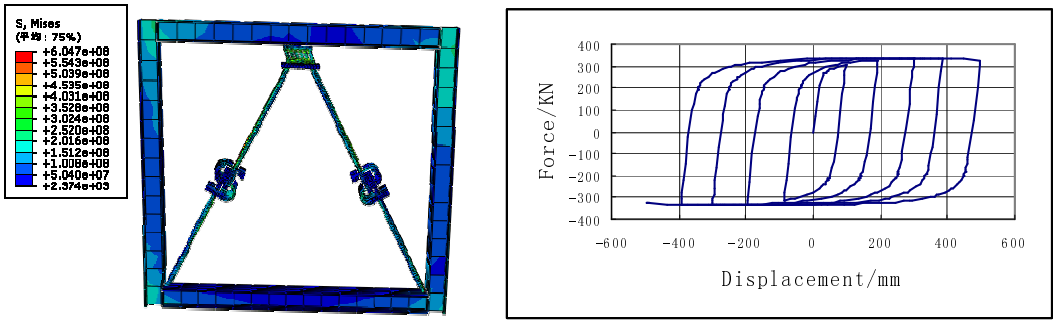


Fig. 5 Framework with new S-T- type mild steel damper

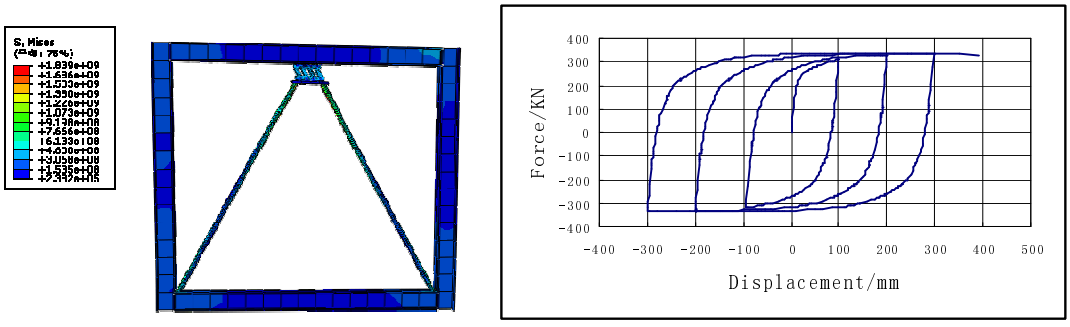


Fig. 6 Framework with new box- type mild steel damper

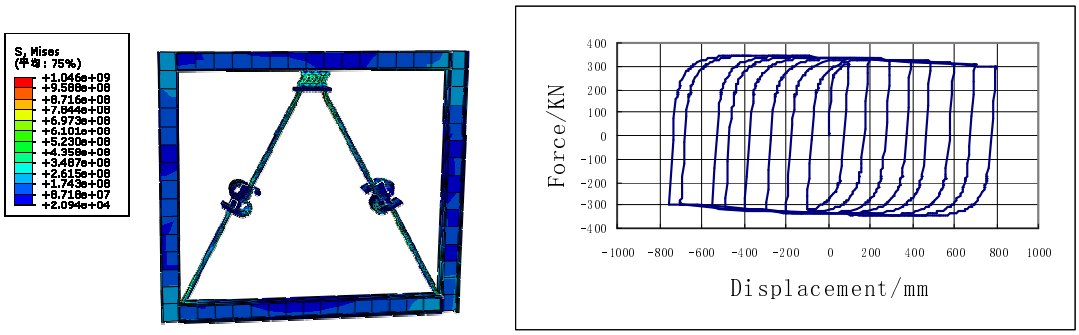


Fig. 7 Framework with new S-box- type mild steel damper

### 4.2.3 The results contrast

The model in Fig. 3-7 is divided into five conditions,they were frame without mild steel dampers, and frame install T, S-T, box, S-box. Calculation results in Table 2

Table 2. Calculation results

| Specimen No. | Not Installed | *T* | *S-T* | *box* | *S-box* |
|---|---|---|---|---|---|
| Yield displacement/mm | 29.51 | 26.78 | 28.75 | 27.26 | 25.13 |
| Yield force/KN | 158.35 | 255.29 | 260.84 | 255.04 | 297.20 |
| Initial stiffness $/10^3$ MP | 5.366 | 9.532 | 9.044 | 9.356 | 11.827 |
| Post-yield stiffness $/10^3$ MP | 0.319 | 5.468 | 3.255 | 6.499 | 0.822 |
| Equivalent damping ratio | 0.64 | 1.02 | 1.147 | 0.98 | 1.23 |

## Conclusion

We can see from the calculation results. Yield displacement of frame installed mild steel dampers are greeter than the not installed ones, but which have the bigger yield force,initial stiffness,post-yield stiffness and equivalent damping ratio, it is that framework in the case of mild steel dampers installed to advance into the plastic state. And frames have full hysteresis curves under low cyclic load. So the structure can absorb seismic energy very well and with good energy performance after installing the mild soft steel dampers.

## References

[1]ZHOU Yun. JINSHU HAONENG JIANZHEN JIEGOU SHEJI[M]WU Han: Wuhan University of Technology Press, 2006: 1(In Chinese).

[2]WANG Shuang. Parametic analysis and seismic performance of new Perforated H-shaped steel damper. Guangzhou university, 2012.5(In Chinese).

[3]LUO Chunfeng, SHI Weixing, GAO Xi.Shock Absorption Analysis of High — rise ReinforcedConcrete Framework with Mild Steel Damper. ournal of Jiamusi University ( Natural Science Edition), 2012.5(In Chinese).

*Applied Mechanics and Materials Vols. 580-583 (2014) pp 1771-1775*
*© (2014) Trans Tech Publications, Switzerland*
*doi:10.4028/www.scientific.net/AMM.580-583.1771*

# Analysis of earthquake damages and seismic reinforcement of bridges

Bingbing Fan[1, a], Canhui Zhao[1,b], Long Zhang[1,c] and Liang Li[1,d]

[1]School of civil engineering of Southwest Jiaotong University, Chengdu,Sichuan province,China

[a]wudifan90_05@163.com, [b]zch2887@home.swjtu.edu.cn, [c]13658087657@163.com, [d]ll19890219@126.com

**Keywords:** earthquake, old bridges, seismic damage of bridges, seismic reinforcement of bridges

**Abstract:** In recent years, with the frequent occurrence of earthquakes, the impact of earthquakes on the bridge has been increasing. Every time the earthquake occurred, bridges there almost got varying degrees of damages, hindering the normal traffic and losing the important role as emergency rescue and disaster relief channels and emergency shelters. Therefore, the seismic loads must be taken fully into account in the bridge design and seismic strengthening of bridge is necessary. Besides, the old bridges already put into normal operation must be reinforced appropriately according to the site condition. This paper described the various types of seismic damage of bridges and summarized several methods of seismic reinforcement of bridges.

## Introduction

As an important part of highway and railway lines, the bridge not only plays a vital role in protecting the traffic, but also promotes the economic development. In recent years, there are frequent earthquakes, such as the Chi -Chi Earthquake in Taiwan (1999), the Sichuan Wen chuan Earthquake (2008) and the East Japan Earthquake (2011). Study on aseismic design of bridges gradually got attention, during which seismic strengthening is essential. It is very important to carry out the seismic capacity evaluation and take appropriate measures to reinforce old bridges in seismic areas for they were short of consideration of earthquake resistance in the initial design.

## Seismic damage on bridges

Forms of bridge earthquake damages could be obtained by consulting earthquakes happened in history. Those earthquakes almost occurred at the junction of tectonic plates, belonging to tectonic earthquake. Because of the mountain terrain the bridges are mainly beam bridges and arch bridges. According to the form damages would be divided into the following categories:

**Simple-supported bridge**

For the main beam, due to the discontinuity, the effect of seismic force will produce large longitudinal displacement, causing the occurrence of girder falling. The lateral displacement of the main girder may cause large displacement of supports or even bearing cavity and supports might be thrown out. Bridge deck pavement may have extrusion uplift, crushing and cracking damage. Failure modes of crushing, against the ear and water stop opening often happen to the expansion joints.

Constraint block restricting the transverse displacement of the main beam show shear failure or directly is bumped to fly. The pier may incline due to falling beams. The entire pier may crush because stirrups in pier are insufficient or unreasonable. Cracks might appear at the top and end of the pier and the coping. Gravity abutment suffer wall crack damage or even collapse while pile column abutment and ribbed slab abutment often appear cracks in the column, rib cracking, ear wall cracking, retaining wall collapse and other forms of damage. Sandy and Light clay loam ground where the underground water level is high will produce the sand liquefaction under earthquake, leading to failure of the foundation.

**Continuous bridge**

In the earthquake the longitudinal displacement of the bridge girder is small because of its continuity. However, for continuous beam frame bridge and continuous beam bridge having part of the piers and beam consolidation, the girder could crack since the piers restrain its longitudinal

displacement. But the small longitudinal displacement of the beam will produce larger displacement outside the curve along the radial direction when the bridge is not straight. Because the main beam is continuous, a cross-falling beam will completely change internal forces of the remaining spans, may resulting in collapse of the whole bridge. Laminated rubber bearing is less prone to roll and curl due to the large plane size and thickness, but the bolts will suffer shear failure and flexural failure. Basin rubber bearing will show damages like the limiting block's destruction, pre buried bolts' being sheared and seat connection failure.

The continuous beam bridge pier is divided into fixed pier and non fixed pier according to the connection between the pier and girder. In general the fixed pier' s damage is severer, especially when the bridge is a curved bridge with sharp radius. Piers may tilt due to earthquakes and lack of stirrups configuration and small section size. The plastic hinge occurs at the top or bottom of the pier. Joins between tie beams and piers could be destroyed. Seismic damages of foundation of continuous bridge are similar to that of simple-supported bridge but that the damages often emerge on the whole beam for its continuous statically indeterminate structure when subjected to secondary geological disasters.

**Arch bridge**

For the arch bridge, lateral stability is weaker than that of longitude. The vault and arch foot are more prone to crack transversely. Besides, transverse cracks may emerge at the main arch in solid arch bridge. Transverse connection between rib arches is likely to break. These damages usually happen to reinforced concrete arches. As for masonry arch, it either crack or crush because of its filler. Solid arch often show damages like cracks at the side wall and joint between side wall and main arch cut with dislocation. In general, cross wall and web arch crack occur at arch bridges with web arches.

Since the main arch is very sensitive to the defection of the arch foot, gravity masonry structure with big rigidity is usually used for pier. So the pier either suffers slight damage or collapse directly. Bridge abutment may have cracking at front wall and side wall. Earthquake damages of foundation have the similar but clearer impact on the arch bridge to that on the beam bridge.

## Seismic reinforcement of bridges

**Guidance**

According to the importance of structure, the bridge structure can be divided into two categories. One is the general structure, the other is the important structure. For the former, low reinforcement level can be performed, while the later needs higher reinforcement level.

Generally the upper structure is designed to be the flexible structure so that stress and displacement are in elastic stage during the earthquake. Dropping beam is mainly induced by large vibration of the lower structure and different vibration of different piers. Thus the lower structure is the key of seismic strengthening and more measures should be taken to ensure its strength and stability.

**Methods**

As is seen, the damage can be divided into more partial and less overall destruction. Common method now for those bridges still can work is taking corresponding repair measures. For bridges not having suffered the earthquake, reinforcement should be carried out on each component or appropriate steps need be taken to improve the overall structure ductility.

1 Measures to prevent the beam dropping:

(1) Use the cable restraint device

Setting the cable constraint is the most common method for simply-supported bridge, being able to reduce the longitudinal displacement of the main girder. Vertical clearance between the beam and the lower pavement should be ensured.

(2) Set the splice plate connecting device

For the steel beam, splice plate can be used to connect the web so that the main beam is continuous in the abutment. It is generally applicable to a straight bridge. But the construction is not very convenient because positions of support, transverse beams, and stiffeners may need to be changed.

(3) Install lever

In the expansion joints and joints between hinges and the upper structure the levers could be installed. In 1971, California adopted this method and gott the best effect for disaster reduction at the minimum cost.

(4) Increase bearing area of the hinge support

Local damages in hinge support, for example, the concrete falling off, mainly due to the smaller actual available size than the original design size. Thus, increasing the bearing area will not only reduce the damages but also avoid falling beam in some way.

(5) Strengthen the cap beam

the cap beam is destroyed mainly by lack of flexural and shear strength. The common measure is adding backing plate in which prestressed reinforcements are set on the cap beam.

(6)The pipe seat extender

If a longer restraint device is hoped to be used, the longitudinal displacement may increase, causing the girder fall. So it is necessary for the longer restraint device to work with a pipe seat extender. The pipe seat extender of a strong pipe will be set in the cored hole or the formed hole. The cored hole may be lifted up in vertical if the elastic rubber pads need to be replaced. If the longitudinal restraint device is shorter than The pipe seat extender, the former will yield first, making the later not work. So, longitudinal restraint device must be compatible with seismic displacement of the hinge node.

(7) Set limitator

When bridges withstand transverse excitation, the relative displacement can be restricted by limitators. Limitators are now in common use in America and Japan. In America, adjacent spans are connected in transverse, longitude and vertical at bearings. While in Japan, limitators are used with many different materials and kinds, such as flexible connectors and steel connectors. Now a novel method is using memory alloy limitator to reinforce simply-supported girder bridges. Memory alloy limitator will still be in the elastic range under large deformation. Its super elasticity will reflect a significant effect when restricting the relative displacement of adjacent spans of the multi-span simply supported bridge.

(8) Add the lateral support

In general, lateral rigidity between the beams is supplied by the lateral support systems or diaphragms, resisting loads of wind, earthquake and so on. Adding support, stiffening rib and diaphragm near the bearing helps to reinforce lateral stiffness at bearings so that lateral displacement will be decreased under the earthquake.

2 Steps to prevent the destruction of bridge pier:

(1) Increase support section of pier appropriately

For masonry pier, pier damages show two extreme kinds like slight damage and collapse because of the limited bearing capacity. Increasing support section of pier is able to add its bearing capacity when materials can not be changed.

(2) Set horizontal and vertical constraints

The weak of bridge pier appears in the plastic hinge position. According to the expected locations(top and bottom of the pier) of plastic hinges the horizontal and vertical external constraints can be set to enhance the flexural ductility and shear strength. What foreigners mostly use is reinforcing steel casing outsourcing and reinforcement technology of FRP composite materials. Compared to other reinforcement materials, FRP composite materials show advantages of easy and rapid construction, high reliability and good durability, will being greatly used in the future.

(3) Set column cage

For reinforced concrete pier, setting the column cage will limit the radial expansion strain at the plastic hinge area in certain circumstances. Experimental results show that if the radial expansion

strain is limited below 0.001, the reinforced connector will kept consolidate and produce full plastic moment capacity of the section. Contrary to limiting radial strain, when provide enough constraints in the plastic hinge region, over 0.001 of radial expansion strain will be allowed so that a hinge may be formed. Using column cage could improve the ductility, the flexural and shear capacity of bridge piers. Nowadays, common column cages are steel column cage, concrete cage, advanced composite material cage and wire wrapped cage. Different material cages have different range of applications.

3 Reinforcement of foundation:

Analysis of many foundations of different types indicates that only increasing the flexural and shear capacity dose not have much of obvious effect, for the increase of the flexural capacity will lead to the increase of earthquake force transmitting from the column to the foundation. So increasing column strength should coordinate with foundation reinforcement.

General methods of foundation reinforcement are adding an overlay to improve the base shear capacity, broadening foundation equably and increasing the contact area . Another approach is to put the foundation anchor into soil or connect the pile with cap via the connecting rod passing through the foundation.

4 Use seismic isolation and special energy dissipation device:

(1) Foundation isolation

Setting the isolation device between the upper structure and foundation to prevent earthquake energy transferring to the upper structure will reduce the seismic response. This technology is not universal for the old bridge because of expensive reinforcement and hard construction. But many new designed and built bridges have adopted this technology.

(2) Isolation bearings

Lead rubber bearing, high damping rubber bearing and the friction pendulum isolation bearing are the commonly used isolation bearings. Lead rubber bearing formulates when a lead is inserted into the middle of laminated rubber bearing. In earthquake lead yields and the stiffness is reduced, prolonging the natural period of vibration. High damping rubber bearing is made of sulfides of high damping rubber materials and steel members, with the shape is similar to natural rubber bearing but has good damping performance. Friction pendulum isolation bearings dissipate energy by friction damping, which can be used to adjust the vibration period of the whole bridge structure system to reduce Seismic response.

(3) Add energy dissipation device

Damper is a common energy dissipation device with many kinds such as the metal yield damper, friction damper, viscoelastic damper and viscous damper. The same principle is taking use of damping to reduce seismic energy and effect of earthquake. Energy dissipation devices have been adopted by many bridges at home and abroad, showing good reduction effect in the earthquake.

## Summary

Seismic reinforcement of the bridge is of great significance for the large impact imposed by the earthquake. This paper has carried out a detailed description of the various forms of destruction of the bridge and made a summary of the current common strengthening methods. Each method has its characteristics and suitable scope. I hope this paper can provide some reference to seismic strengthening of existing bridges. With the advance of science and technology, there will be new thought about seismic design of bridges and new technologies will be used for seismic reinforcement.

## References

[1] Lichu Fan. Bridge Seismic(in Chinese) [M]. ShangHai: Tongji University Press, 1997

[2] Aijun Ye, Zhongguo Guan. Bridge Seismic(in Chinese) [M]. Beijing: China Communications Press, 2011

[3] Jianya Xiao. The analysis of bridge seismic retrofit technology(in Chinese) [J]. Heilongjiang Science and Technology Information, 2010

[4] Sanwei Wang. Selection of bridge seismic retrofit method(in Chinese) [J]. Railway Engineering, 1995

[5] Zhihui Xing & Fuzhen Li. The analysis of bridge seismic retrofit technology(in Chinese) [J]. Highway Communication Science Technology, 2006

[6] Qing fangLv, Hong Zhu & Pu Zhang. New technology of seismic strengthening of buildings in Japan (in Chinese) [J]. Construction Technology, 2008

[7] Hengyang Song. Implications of Wenchuan earthquake damage to bridges for seismic strengthening of existing simply supported beam bridge in mountainous area(in Chinese) [J]. Southwest Highway, 2008

[8] Fuwei Huang, Xiaofeng Xu & Wanshan Zheng. Present situation and development trend of bridge seismic retrofit technology(in Chinese) [J]. Technology of Highway and Transport, 2003

*Applied Mechanics and Materials Vols. 580-583 (2014) pp 1776-1781*
*© (2014) Trans Tech Publications, Switzerland*
*doi:10.4028/www.scientific.net/AMM.580-583.1776*

# Research on Shaking Table Test of Base and Story Isolation Structures

Guochen Zheng [1,2,a] Hangli Xu [3,b]

[1] Earthquake Administration of Fujian Province, Fuzhou 350003,China

[2] College of Civil Engineering, Fuzhou University, Fuzhou 350108, China

[3] Fujian Jiangxia University, Fuzhou 350108, China

[a]44138911@qq.com, [b]346013819@qq.com

**Keywords:** Base isolation; story isolation; shaking table test; natural vibration period; damping ratio; damping effect

**Abstract:** The shaking table tests are conducted on a 5-floor steel frame model with a scale down of 1:6. The traditional anti-seismic structure and isolation structures with isolation layer in different position are adopted. The results indicate that the natural vibration periods of isolation structure are longer than anti-seismic structure, and when the isolation layer is located in a lower position, the period becomes longer and the damping effect is better.

## Introduction

Isolation is a new protective technology of Engineering damping in aseismic engineering field. Isolation technology can effectively solve many problems, and the seismic response of isolation structure is reduced by avoiding the site predominant periods.

Significant progress has been achieved over the past years on the practice and research of base isolation structure, and a lot of projects have adopted, then the design of base isolation structure in our country is received in *code of aseismic design of buildings*. The isolation device is installed between foundation and superstructure in base isolation system, it can significantly reduce the lateral stiffness of the structure, increase the structural nature period in order to avoid the predominant period, efficiently dissipate seismic energy and to reduce seismic response.

Story isolation is a new development of isolation technology, seismic response is controlled by story isolation structure with setting isolation layer between shear walls or top of columns and floor[1]. Isolation layer is an important influencing factor in the damping mechanism of the story isolation structure, within the scope of certain frequency ratio, when the location of isolation layer is approach to the base of the structure, its mechanism is similar to that of base isolation; when the location of isolation layer is approach to the roof of the structure, its mechanism is similar to that of TMD[2].

For comparing and analyzing the damping effect of base and story isolation structures, shaking table tests are performed. Because lager story drift will cause destruction of the structure, and lager absolute accelerations can create intense felt of the earthquake under seism action, story drift and absolute accelerations have a linear relationship with damping effect of structures. So this article discusses the damping effect of story drift and absolute acceleration about base and story isolation structures.

## Structure Model

Because different damping mechanisms of story isolation structures are shown with isolation layers in different position, in this test, isolation layers are located at first-layer column upper end (hereinafter, 1st CUE); second-layer column upper end (hereinafter, 2nd CUE)and fourth-layer column upper end (hereinafter, 4th CUE) respectively.

The shaking table tests are conducted on a 5-floor steel frame model with a scale down of 1:6, which simulate traditional anti-seismic structure (hereinafter, TASS) , base and story isolation structures.

In order to facilitate the replacement of isolation layer, the tests applies analogous theory to design a steel frame model which are composed of two-layer and one-layer models, each model is pulled together with different combinations. Sketch of model frame is shown in Figure 1 and different combinations of model is shown in Figure 2.

After being calculated, one-layer steel frame model weighs 160kg and the top model weighs 48kg. Depending on the outcome of our detailed design, there might need 800kg counter-weights connected to the each layer of model, so total models weigh 6000kg, similarity coefficient of structural model is shown in table 1.

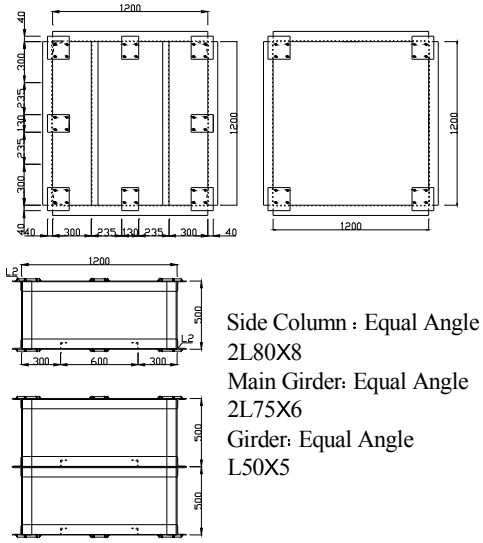


**Fig.1 Sketch of Model**

**Tab.1 Similarity Coefficient of Structural Model**

| physical quantity | symbol | dimension | Similarity Coefficient |
|---|---|---|---|
| length | $S_l$ | L | 1/6 |
| elasticity modulus | $S_E$ | $ML^{-1}T^{-2}$ | 1 |
| stiffness | $S_k$ | $MT^{-2}$ | 1/100 |
| acceleration | $S_a$ | $LT^{-2}$ | 8/3 |
| Time | $S_T$ | T | 1/4 |
| velocity | $S_v$ | $LT^{-1}$ | 2/3 |
| displacement | $S_x$ | L | 1/6 |
| Mass | $S_m$ | M | 1/1600 |

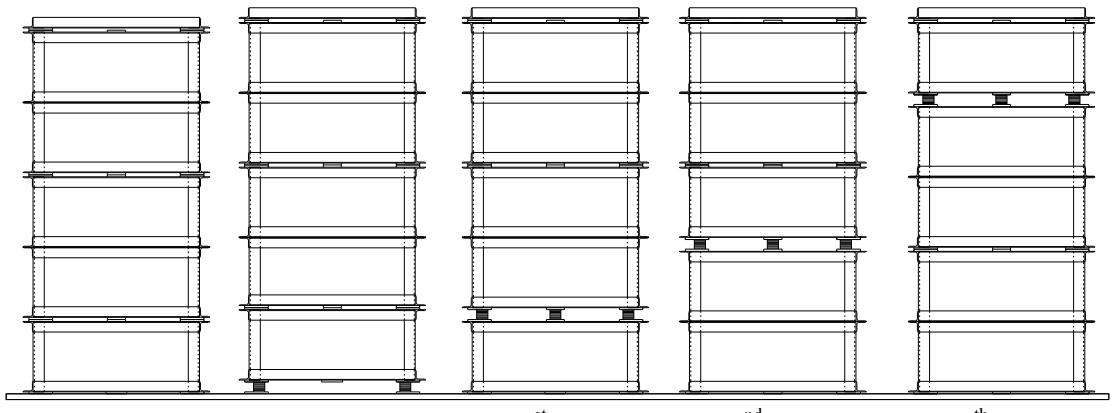


**Fig.2 Isolation Way of Different Combinations**

## Isolation Bearing Model

Non-lead rubber bearings (GZP80) which contain natural rubber are used in this test, the concrete size and mechanical property are shown in Table 2.

**Tab.2 Concrete Size and Mechanical Property of Isolation Bearing**

| Serial Number | Parameters | Parameter Values | Serial Number | Parameters | Parameter Values |
|---|---|---|---|---|---|
| 1 | Outside Diameters (mm) | 90.0 | 10 | Steel Plate Aggregate Thickness(mm) | 19.0 |
| 2 | Inside Diameters(mm) | 80.0 | 11 | Hole Diameter(mm) | 20.5 |
| 3 | Total Height(mm) | 59.0 | 12 | The First Form Factor | 20 |
| 4 | Connection Plate Thickness(mm) | 10.0 | 13 | The Second Form Factor | 4 |
| 5 | Rubber Layer Thickness(mm) | 1.0 | 14 | Pressure Bearing Area($mm^2$) | 4700 |
| 6 | Rubber Storey Number | 20 | 15 | Damping Ratio | 0.07 |
| 7 | Rubber Aggregate Thickness(mm) | 20.0 | 16 | Permissible Lateral Displacement(mm) | 44.0 |
| 8 | Steel Plate Aggregate Thickness(mm) | 1.0 mm | 17 | Lateral Stiffness(kN/mm) | 91.0 |
| 9 | Steel Plate Storey Number | 19 | 18 | Vertical Stiffness(kN/mm) | 70.0 |

## Shaking Table Test

### 4.1 Loading and Collection Device

The shaking table test finished in Key Laboratory of Earthquake Engineering and Structural Retrofit (Beijing University of Technology). The specific technical parameters of seismic shaking table are as follows:

(1)Table size:3m×3m; (2)Table Self-weight:6t; (3)max load:10t; (4)frequency range: 0.1~50Hz; (5)max acceleration of no-load:2.5g; (6)max acceleration of full-load: 1.0g; (7)max displacement:±127mm; (8)max velocity: ±600mm/sec; (9)max torque:30t×m.

The collection devices which include three sensors (ICP, SW-1 and SW-3) and data acquisition system (IMC), ICP is installed in table-board, the middle part of girders and the middle part of floor beams in isolation superstructure, which collect absolute acceleration; SW-3 is installed in each layer to collect story drift; SW-1 is installed in isolation layer to collect displacement of isolation layer specially. Based on the above, seven ICP, five SW-3 and one SW-1 is used in the tests.

### 4.2 Seismic Wave

According to the selection principle of seimic wave, Taft (NS) and Elcentro (NS) are chosen, seismic duration is compressed into a quarter on the basis of simulated law and seismic peak acceleration is adjusted to 0.4g.

### 4.3 Test Conditions

The shaking table tests contain TASS, base isolation structure and story isolation structures with different isolation layers. Four rubber bearings are adopted in isolation layer. Test conditions are shown in Table 3.

**Tab.3 Test Conditions**

| Test Condition | Isolation layer position | Seismic wave |
|---|---|---|
| 1 | $1^{st}$ CUE | Elcentro |
| 2 | | Taft |
| 3 | $2^{nd}$ CUE | Elcentro |
| 4 | | Taft |
| 5 | $4^{th}$ CUE | Elcentro |
| 6 | | Taft |
| 7 | TASS | Elcentro |
| 8 | | Taft |
| 9 | Base Isolation | Elcentro |
| 10 | | Taft |

## Test Results and Analysis

By literature [5], elastic and plastic permissible displacement of model is 1.67mm and 10mm respectively because the story height is 500mm; By literature [6], when absolute acceleration exceed 0.53g, people may feel uncomfortable. With stronger absolute acceleration, we can feel greater discomfort.

For each test, the acceleration input can't completely the same, in order to contrastive analysis on vibration results of model in different test conditions, accelerations are normalized. Assume structure model is in linear elasticity, normalization can be calculated below:

$$\text{Normalized response value} = \frac{\text{Design acceleration amplitude}}{\text{Measured acceleration amplitude}} \times \text{Actual acceleration amplitude}$$

In order to intuitionistic compare the damping effect of base and story isolation, this article introduced a concept of damping ratio. Definition:

$$\text{Damping ratio} = \left(1 - \frac{\text{Peak response of (TASS} - \text{story isolation)}}{\text{Peak response of TASS}}\right) \times 100\%$$

### 5.1 Dynamic Characteristics of Structural Model

Through Analysis, dynamic characteristics of TASS, base isolation, 1st CUE, 2nd CUE and 4th CUE are shown in Table 4.

**Tab.4 Dynamic Characteristics**

| Structural Style | Natural Period (sec) | Equivalent Damping Ratio |
|---|---|---|
| TASS | 0.152 | 0.021 |
| Base Isolation | 0.699 | 0.062 |
| 1st CUE | 0.685 | 0.065 |
| 2nd CUE | 0.606 | 0.063 |
| 4th CUE | 0.334 | 0.061 |

Through Table 4, we can see:

(1) Natural Period of TASS is much lower than other isolation structure, that is close to the Elcentro Period and syntony likely occur. In different isolation structures, natural period of base isolation structure is the longest than others, when the position of isolation layer rise, natural period of story isolation fall.

(2) Equivalent Damping Ratio of TASS is much lower than other isolation structure, and that is in keep with steel structure; equivalent damping ratios of base and story isolation structure approach to the design damping ratio of rubber bearing, so damping ratio of rubber bearing should be adopted in isolation superstructure.

### 5.2 Seismic Analysis of TASS

Through the normalized processing, story drifts and absolute accelerations of TASS are shown in Table 5.

**Tab.5 Seismic Analysis of TASS**

| Floor | Elcentro | | Taft | |
|---|---|---|---|---|
| | Story displacement (mm) | Absolute Acceleration (g) | Story drift (mm) | Absolute Acceleration (g) |
| 1 | 0.99 | 0.733 | 0.88 | 0.549 |
| 2 | 0.76 | 0.925 | 0.71 | 0.814 |
| 3 | 1.14 | 1.129 | 1.31 | 1.100 |
| 4 | 0.39 | 1.227 | 0.40 | 1.238 |
| 5 | 0.28 | 1.453 | 0.31 | 1.360 |

Through Table 5, we can see:

(1) Peak acceleration of model increases with the rising of floor; maximum story dispplacement occur in the third floor, and in others, story drift decreases with the rising of floor.

(2) Whatever seismic wave is used, peak accelerations of all floors are far exceeded 0.53g, and that might be strong felt; story drifts of all floors are lower than elastic permissible displacement, and the structure will not damage in earthquake.

### 5.3 Absolute Accelerations of Base and Story Isolation Structures

Through the normalized processing, Peak acceleration of base isolation structure, 1st CUE, 2nd CUE and 4th CUE are shown in Figure 3.

Through the Figure 3, we can see:

(1) Absolute acceleration damping effect of base isolation is superior to that of story isolation.

(2) Damping effect of absolute acceleration decrease with the rising of isolation layer; when isolation layer is located at first-layer column upper end, damping effect is similar to that of base isolation.

(3) When isolation layers are located at second-layer and fourth-layer column upper end, peak absolute acceleration in the substructure of story isolation is close to or slightly greater than that of TASS.

(4) No matter what kind of isolation structures, peak absolute accelerations in superstructure of story isolation are all below 0.53g, so there is no felt in earthquake.

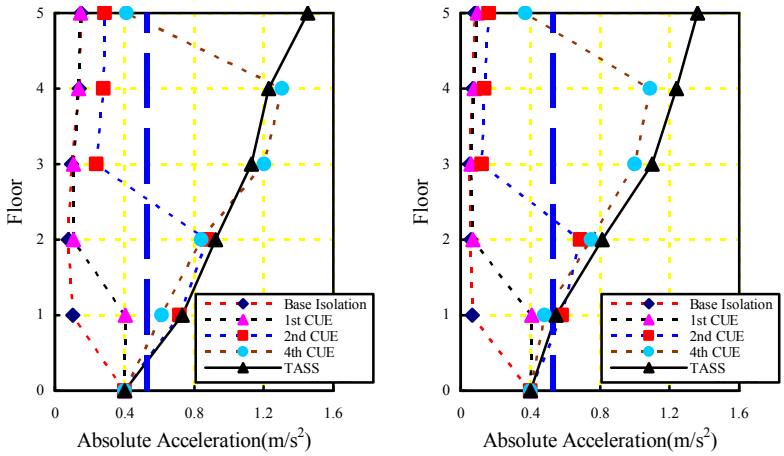


(a)Elcentro (b)Taft

**Fig.3 Peak Absolute Accelerations of Structural Model**

### 5.4 Story Drifts of Base and Story Isolation Structures

Through the normalized processing, Peak story drifts and damping ratios of base isolation structure, 1st CUE, 2nd CUE and 4th CUE are shown in Table 6.

**Tab.6 Peak Story drifts and Damping Raitos of Base and Story Isolation Structures**

| Base Isolation | | | | Story Isolation | | | | | | | | | | | |
|---|---|---|---|---|---|---|---|---|---|---|---|---|---|---|---|
| | | | | 1st CUE | | | | 2nd CUE | | | | 4th CUE | | | |
| Elentro (mm) | Damping Ratio (%) | Taft (mm) | Damping Ratio (%) | Elentro (mm) | Damping Ratio (%) | Taft (mm) | Damping Ratio (%) | Elentro (mm) | Damping Ratio (%) | Taft (mm) | Damping Ratio (%) | Elentro (mm) | Damping Ratio (%) | Taft (mm) | Damping Ratio (%) |
| 0.004 | 99.5 | 0.002 | 99.7 | 0.006 | 99.3 | 0.005 | 98.4 | 0.04 | 95.5 | 0.02 | 93.5 | 0.09 | 89.8 | 0.08 | 74.2 |
| 0.06 | 89.1 | 0.04 | 93.0 | 0.06 | 89.1 | 0.03 | 92.5 | 0.12 | 78.2 | 0.06 | 85.0 | **5.44** | — | **4.24** | — |
| 0.05 | 97.1 | 0.03 | 98.4 | 0.08 | 95.4 | 0.05 | 96.2 | 0.30 | 82.8 | 0.09 | 93.1 | 0.28 | 49.1 | 0.16 | 60.0 |
| 0.13 | 86.2 | 0.08 | 91.6 | 0.12 | 87.2 | 0.06 | 91.5 | **7.32** | — | **8.17** | — | 0.41 | 76.4 | 0.30 | 77.1 |
| 0.14 | 90.4 | 0.09 | 94.3 | **7.94** | — | **3.47** | — | 0.32 | 66.0 | 0.10 | 85.9 | 0.46 | 51.1 | 0.37 | 47.9 |
| **16.14** | — | **11.50** | — | 0.17 | 88.4 | 0.09 | 89.8 | 0.35 | 76.0 | 0.23 | 73.9 | 0.52 | 64.4 | 0.47 | 46.6 |

Through Table 6, we can see:

(1) No matter what kind of isolation structures, peak story drifts is much lower than that of TASS.

(2) When isolation layer is located at first-layer column upper end, damping effect of story drift is significant and similar to that of base isolation.

(3) Damping effect of story drift decrease with the rising of isolation layer.

## Conclusion

After analysis, we can see, as follows :

(1) No matter what kind of isolation structures, Natural period is much longer than that of TASS, and when the position of isolation layer rise, natural period of isolation fall. Base on this, the seismic response of isolation structures is reduced by avoiding the site predominant periods.

(2) equivalent damping ratios of base and story isolation structure are in accordance with design damping ratio of rubber bearing, and when earthquake occours, isolation structures can absorb energy from seismic wave, then rubber bearings dissipate energy in form of damping energy and hysteretic dissipated energy.

(3) Compared with TASS, no matter what kind of isolation structures, absolute accelerations and story drifts can be reduced effectively.

(4) when the location of isolation layer is approach to the base of structure, infrastructure displacement and superstructure acceleration of the isolation layer both significant reduce, its mechanism is similar to that of base isolation; when the location of isolation layer is approach to the roof of structure, not obvious change between infrastructure displacement and superstructure acceleration, its mechanism is similar to that of TMD.

**References**

[1] Ai Qi. State-of-the-art of story isolation system. Earthquake Engineering and Engineering Vibration, 2004(6):114~120. (In Chinese)

[2] Ai Qi, Yunteng Lin, Guochen Zheng. Research on working mechanism of story isolation structure. Earthquake Engineering and Engineering Vibration, 2006(4):114~120. (In Chinese)

[3] Yuhua Zhu, Weixing Shi, Xilin Lv, et.al. Research on Shaking Table Test of Base Isolated Buildings. Journal of Tongji University, 2001(5):505~509. (In Chinese)

[4] Fulin Zhou. Engineering Vibration Control. Beijing: Seismological Press, 1997.

[5] Jiwu Guo. Seismic Design of Buildings. Beijing: China Architecture & Building Press, 2002.

[6] Jian Xu. Handbook on building vibration. Beijing: China Building Press, 2002.

*Applied Mechanics and Materials Vols. 580-583 (2014) pp 1782-1785*
*© (2014) Trans Tech Publications, Switzerland*
*doi:10.4028/www.scientific.net/AMM.580-583.1782*

# Vulnerability analysis of existing buildings under seismos

Xianhong Meng[1,a] , Guozhi Yang[1,b]

School of Civil Engineering, Shenyang Jianzhu University, Shenyang China, 110168

[a] cexhmeng@sjzu.edu.cn, [b] yangctrlx@163.com

**Keyword:**Structural vulnerability, Existing buildings, Nonlinear static method, Risk Assessment

**Abstract.**By studying the structure of vulnerability analysis and abroad , on their respective merits and defects were compared and analyzed to select the best of vulnerability research methods. Combined with the existing building characteristics, the nonlinear static method on both the vulnerability analysis of old buildings also applicable conclusions. Effective solution to the existing buildings under earthquake disaster risk assessment.

## Introduction

In recent years, Earthquakes Disaster occur frequently. According to a domestic data from Domestic Disaster Prevention Committee indicate the extent of the earthquake damage on the existing old buildings is much higher than the implementation of the new specification seismic building measures[1] . Research the damage of existing building structures under the Earthquake, have guiding significance for the improvement of the structure design of the future and post disaster restoration stage.

The research method of vulnerability can be roughly divided into four categories: Experience Class, SEMI computing classes, Experimental study class, Calculation of the class. By analyzing the characteristics of four research methods, concluded the computational analysis class research methods in the study of vulnerability also applies to existing buildings. This paper studies the different buildings and different structure forms of existing buildings.

## Experience class vulnerability research methods

Vulnerability research began in the seventy s of the 20th century. This approach is in considering the uncertain factors on the basis of earthquake, according to the researchers of judgment and set up. It called the experience research methods. It was first proposed by America scholar Whiteman in 1973 [2]. It can be a wide range of estimates and judgments for a variety of types of building structure in a region. It can be a wide range of estimates and judgments [3].

In China, this type of research method appeared in the late 20th century. Yang Yucheng , Li Dahua issued a system PDSMSMB-1 in 1990 . The earthquake test and practical application show, the system is easy to use to predict results that can be achieved expert level [4]. Scholars Shi Lili, Qiao Jianping, have thorough research to the Wenchuan area after the disaster vulnerability zoning [5]. Contribution Weighted Overlay Model what they proposed made the research method more perfect.

The characteristics of experience research method is limited. In the house of the investigation can not be controlled in the number of samples. The factor affects the further development and application of the method.

**SEMI computing class vulnerability research methods at home and abroad**

Scholars Madas P and Elnashai A S have put forward a semi empirical calculation method. Scholar Lv Dagang put forward the structural reliability analysis with empirical formula based on probability [6]. Zhou Yanlong, Zhang Peng proposed the seismic vulnerability analysis is an important research direction of the seismic performance of the structure [7]. The method that Ding Yang used in the paper Seismic Damage Assessment Of Vulnerability Curves Based On Concrete Column was simple and reliable [8]. Scholar Liu Jingbo, Liu Yangbing studied in the steel-concrete composite structure seismic performance and seismic fragility problems [9].

This method also has many deficiencies.Although there are some theoretical basis for sample collection, but not representative.The differece between structures is great, and it is hard to spread.

**Experimental study abroad class of vulnerability research methods**

Scholars Aycardi and AM Reinhorn analyze the structure of vulnerability using vibration table by simulating seismic waves. Wang Dongwei, Zhu Xiaoqing proposed the experimental method based on pushover analysis of seismic vulnerability of building structures and failure correlation [10].Yi Zhiqian, Zhao Zhi pointed out that the peak acceleration vibration parameters refering to the standard promulgated in 2001 [11]. Scholars Zhu Nanhai, Ye Jihong made the theory of vulnerability [12]. Their study is based on experimental studies .

The advantage of this approach is that the structural model can use the historical data to meet the requirements of free choice, but this approach severely limits the number of received , size, laboratory equipment and the conditions of the test sample to a certain extent.

**Calculation analysis class vulnerability research methods at home and abroad**

The fourth kind of method is Calculation analysis class.This method is divided into two kinds：Dynamic analysis,The static elastic analysis.

The static elastic analysis.This kind of method is to choose real or artificial seismic wave using the static elastic analysis method to analysis the capacity spectrum and demand spectrum of the structure, and further get the analysis of structure vulnerability curve. Foreign Madas P proposed nonlinear static structural damage probability method to analyze fragility curves.[13]

The function of structural vulnerability with the method of the static elastic analysis:

$$\mathrm{P}\ (D \geq d_i \mid S = S_k) = \varphi\left[\frac{1}{\beta_d} \ln\left[\frac{S_k}{M_d}\right]\right]$$

Tips: P(D≥di|Sk) means the damage probability of not less than a certain state of Di at a given Sk damage. Md means the median of the damage state of d. βd means the standard deviation of d. φ means the cumulative standard normal distribution function(CDF).

Dynamic analysis. This method uses the artificial or natural seismic wave seismic load, so as to be sure with the control the loading. Scholar Liu Yangbing has carried on the analysis to the seismic capacity probability of reinforced concrete structure, get the fragility curve [14]. Scholar Zhu Jian has conducted the research to the reinforced concrete structure seismic risk analysis and vulnerability analysis, finally gets the relationship between them [15]. Wang Mengfu scholars studied the dynamic increment method in the application of the high-level structure [16].

Compared the four types, it is shown in Table 1.

Table 1

| The types | The main features | Main defects |
|---|---|---|
| Experience study | With general, housing constructions and regional differences with the result of analysis is more obvious | Sample size is not to be controllable, lack of inference to be based on |
| Semi empirical calculation | Combining the probability formula of structural reliability analysis method is simple and easy | Not representative , analyze large differences |
| Experimental study | The test results are convincing, easy to get the fragility curves, but the spectrum of single | Restrict factor is large. Eg: Equipment |
| Simulation analysis | Reflect the general with the random characteristics of nonlinear, meet the requirements. | The process of analysis is complex |

It can be seen from the above table : computational analysis in four categories vulnerability research method is more reasonable and reliable.

**conclusion**

After comparing the analysis methods in the field of structure vulnerability according to the literature from home and abroad, we can conclude that the calculation methods and analysis is reasonable method in this paper. From the table we can see that the existing buildings including masonry, reinforced concrete structure, frame structure, steel structure. It is consistent with the the previous studies.Therefore, we can study the existing building vulnerability by analysis of calculation method.The buildings are divided according to different time and intensity,it provides the seismic safety evaluation, earthquake disaster prevention and provide the basic materials of seismic design method based on reliability.

**Acknowledgments**

This work was financially supported by the Project of National Key Technology R&D Program in the 12th Five Year Plan of China (2012BAJ11B02)

**References**

[1] Gai Chengcheng,Weng Wenguo, Journal of Tsinghua University.(in Chinese), 2011.(51)05:627-631

[2] Whitman R V, Reed J W, et al. Journal of Earthquake Damage Probability Matrices. 1973,12:2531-2540

[3] Abbie Liel,Hesham Tuwair, Journal of Structures Congress. 2010:58-69.

[4] YangYucheng, LiDahua, et al, Journal of Institute of Engineering Mechantes(in Chinese). 1990

[5] Shi Lili, Qiao Jianping, et a, Journal of SiChuan University(in Chinese). 2009.41(5):57-61

[6] Lv Dagang, Li Xiaopeng, et,al, Journal of Natural Disasters(in Chinese). 2006.15(2):107-114

[7] Zhou Yanlong, Zhang Peng, Journal of SiChuan Architecture(in Chinese). 2010.30(3):110-114

[8] Ding Yang, Wu Min, et,al, Journal of Engineering Mechanics(in Chinese). 2012.29(1):81-86

[9] Liu Jingbo, Liu Yangbing, et,al, Journal of China Civil Engineering Journal(in Chinese). 2010.43(2):39-47
[10] Wang Dongwei, Zhu Xiaoqing, et,al, Journal of China World Earthquake Engineering(in Chinese). 2006.22(2):19-23
[11] Yi Zhiqian, Zhao Zhi, et,al, Journal of China Eatrhquake Engineering And Engineering Vibration(in Chinese). 2003.23(4):195-200
[12] Zhu Nanhai, Ye Jihon, Journal of Vibration And Shock(in Chinese). 2011.30(6):248-255
[13] Gai Chengcheng, Wang Wenguo, et,al, Journal of Tsinghua University(in Chinese). 2011.51(5):627-631
[14] Liu Yangbing, Liu Jingbo, et,al, China Civil Engineering Journal(in Chinese). 2010.43(2):39-47
[15] Zhu Jian, Tan Ping, et,al, Journal of Huazhong University(in Chinese). 2010.38(5):109-116
[16] Wang Mengfu, Liu Feifei, in: Research of A Method for Incremental Dynamie Analysis and Its Applieation in tall building struetures. Hunan. HunanUniversity. 2010.

*Applied Mechanics and Materials Vols. 580-583 (2014) pp 1786-1789*
*© (2014) Trans Tech Publications, Switzerland*
*doi:10.4028/www.scientific.net/AMM.580-583.1786*

# Finite Element Analysis of Seismic Responses of a Large-cantilever Stadium Structure

Zeyu Sun [1,a], Qiao Jin [1,b], Lianguang Jia [1,c], Qiang Wang [1,d], Yi Ma [2,e], Chi Xu [2,f]

[1]School of Civil Engineering, Shenyang Jianzhu University, Shenyang, China

[2]Shenyang Construction Engineering Quality Inspection Center, Shenyang, China

[a]sunzeyu900429@163.com, [b]goldenfss@163.com, [c]syjlg@163.com, [d]wangqiangsy@163.com, [e]13998248486@163.com, [f]xuchi88@foxmial.com

**Keywords:** Response spectrum analysis; Large-span and large-cantilever; Complete Quadratic Combination (CQC);Transfinite structure; Midas/gen procedure

**Abstract.** In this paper, based on the Midas/gen platform, a three-dimensional finite element model(FEM) for a transfinite stadium with a large-span and large-cantilever roof , located in Shenyang, was used to study its potential responses to seismic activities. In the numerical analysis, an earthquake spectrum stipulated by the Chinese Seismic Code(GB50011-2010) was adopted to calculate the bidirectional horizontal displacements by the Complete Quadratic Combination(CQC) method on the basis of the response spectrum analysis. The computational results indicate that the maximum displacements in both of the two horizontal directions locate at the top of this structure, i.e. the transfinite part of the roof.

## Introduction

With China's architectural structures to top, large and modern development, more and more buildings in China , or some parts of them, are constructed beyond the limitation of the Chinese Seismic Code[1-2]. According to the relative regulations of the Code, Shaking table model tests and numerical simulations for these structures should be performed in advance.The target stadium presented in this paper is constructed in Shenyang, the capital of Liaoning Province in Northeastern China , the finite element model (FEM) of which is shown in Fig.1. In the figure of the FEM, a transfinite part is emphasized.

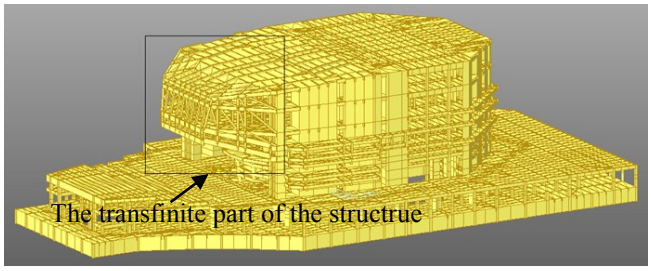


Fig.1 FEM of the target stadium

Because of existence of the transfinite part, it is necessary to numerally simulate the seismic characteristics of the whole structure, especially that of the transfinite part in this stadium. Therefore , a response spectrum analysis was developed in this paper to determine the potential responses to earthquake activities.

## Finite element modelling

With rapid development in computer technology and computational mechanics algorithms, three-dimensional finite element analysis has become a routine design tool of complex structures. Based on the Midas/gen platform, four kinds of elements were employed in establishing the FEM of the objective structure: beam elements, suitable for nonlinear large rotations and strians, were employed to model the columns and beams. Truss elements were used to model the brace. Meanwhile, slab elements and wall elements were used to simulate the mechanical properties of the floors and shear walls in the structure.

**Modal Analysis**

On the basis of the modal-analysis modules in the Midas/gen software, we developed a computational modal analysis for determining the natural frequencies and mode shapes of a structure. The first 10 modes were extracted and the mode shape for each individual mode was depicted, as shown in Table 1. And the former 5 ordered vibration shapes were drawn in Fig.2. From Table 1 and Fig.2, we can see that the stiffness of the transfinite part of the structure is relatively weaker, and hence the transfinite part of the structure is sensitive to earthquakes, as compared with any other parts of the structure.

Table 1 Summary of the former 10-ordered inherent frequencies and mode shapes

| Orders | Circular Frequency (rad/sec) | Natural Frequency (cycle/sec) | Cycle (sec) | vibration direction |
|---|---|---|---|---|
| 1 | 802673 | 1.3158 | 0.7600 | horizontal（swing along the shorter axis） |
| 2 | 13.5757 | 2.1606 | 0.4628 | horizontal（swing along the longer axis） |
| 3 | 16.9179 | 2.6926 | 0.3714 | Vertical (the large cantilever end) |
| 4 | 18.3346 | 2.9180 | 0.3427 | 1st Vertical (the transfinite part of the roof) |
| 5 | 19.6556 | 3.1283 | 0.3197 | 2nd Vertical (the transfinite part of the roof)<br>1st Torsional (the roof) |
| 6 | 20.7467 | 3.3019 | 0.3029 | 1st Torsional (the whole structure) |
| 7 | 20.8804 | 3.3232 | 0.3009 | 2nd Torsional (the whole structure) |
| 8 | 22.7797 | 3.6255 | 0.2758 | 3rd Torsional (the whole structure) |
| 9 | 23.5038 | 3.7407 | 0.2673 | 2nd Torsional (the roof) |
| 10 | 24.1727 | 3.8472 | 0.2599 | 4th Torsional (the whole structure) |

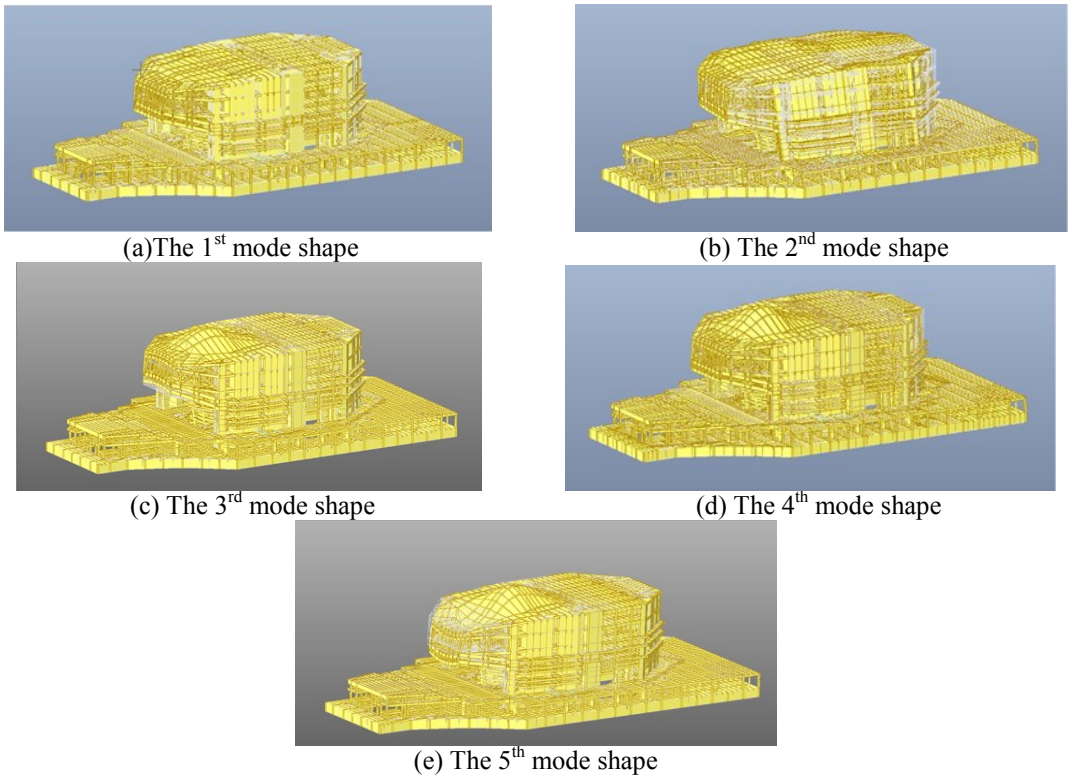

(a)The 1st mode shape (b) The 2nd mode shape

(c) The 3rd mode shape (d) The 4th mode shape

(e) The 5th mode shape

Fig.2 Diagram of the former 5 mode shapes

**Response spectrum analysis of the structure**

For earthquake-resistant designs, a structure should meet performance requirement at two different levels, depending upon the magnitude of earthquake actions[3]. The first level of performance essentially requires structural response in the elastic range without significant structural damage

under a moderate earthquake action, and the second level of performance requires that the structure does not collapse under a severe earthquake event with rare occurrence. The target structure in this paper is located in Shenyang, the capital of Liaoning Province, where there are hard soil deposits with a short predominant period. According to the Seismic Zoning Map in China, the construction site is in a region of 7 degree seismic intensity. A response spectrum has been defined based on the design response spectra stipulated in the Chinese Seismic Code(GB50011-2010), as shown in Fig.3. The first 20 translational-torsional coupling modes were used to calculate the seismic response of the structure by the Complete Quadratic Combination (CQC) method on the basis of the response spectrum analysis[4]. The damping ratio of the structure was assumed to be 5% for all 20 modes. And the seismic responses in the two orthogonal directions were calculated correspondently.

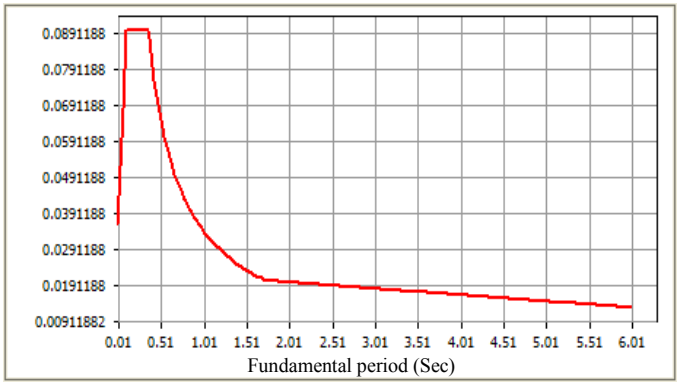


Fig.3 Design response spectrum

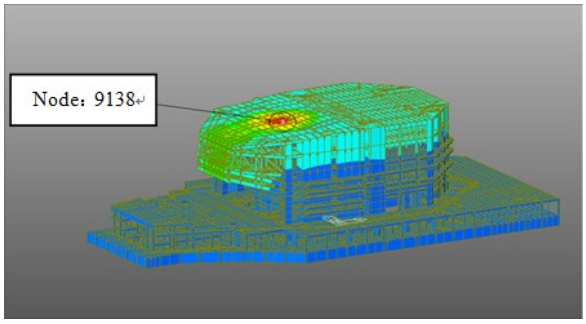


Fig.4 Displacement contour in x direction

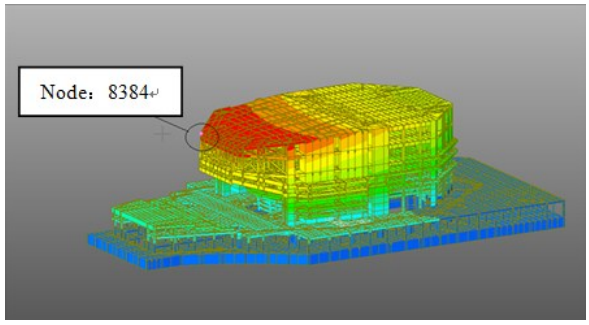


Fig.5 Displacement contour in y direction

Table 2 Maximum displacements of the key nodes of the transfinite part at different elevations

| Elevation（m） | Node | y-direction excitation | |
|---|---|---|---|
| | | $D_{y-direction}$（m） | $D_{x-direction}$（m） |
| 46.896 | 8420 | 0.006858 | 0.001348 |
| 42.9 | 7905 | 0.006014 | 0.001388 |
| 31.937 | 6669 | 0.004267 | 0.001576 |
| 28.337 | 9024 | 0.003939 | 0.001546 |
| Elevation（m） | Node | x-direction excitation | |
| | | $D_{x-direction}$（m） | $D_{y-direction}$（m） |
| 46.896 | 8419 | 0.006656 | 0.001341 |
| 42.9 | 7904 | 0.006014 | 0.001379 |
| 31.937 | 6668 | 0.004265 | 0.001559 |
| 28.337 | 9025 | 0.003939 | 0.001528 |

Through the response spectrum analysis, displacement contours in x direction and y direction subjected to x-direction excitation and y-direction excitation are shown in Fig.4 and Fig.5, respectively. The results of the response spectrum analysis indicate that the maximum displacements

in both directions locate in the region of the transfinite part of the structrue, which means that the transfinite part of the structrue is the most sensitive to earthquakes. Table.2 shows that the maximum displacements of key nodes of the transfinite part of the structure at different elevations. In Table 2, the maximum displacements in the y direction are larger than those in the x direction, which can be attributed to the greater x-directional lateral stiffness of the whole model. The story shear forces of the transfinite part of the structure at different stories are shown in Table 3. At the same story, the y-direction story shear forces under y-direction excitation are larger than their x-direction counterparts.

Table 3 Story shear forces of the transfinite part of the structure

| Story | Elevation（m） | Excitation direction | Story shear force | |
|---|---|---|---|---|
| | | | X-direction (N) | Y-direction (N) |
| 12F | 42.90 | X | 8611.50 | 416.41 |
| 8F | 20.45 | X | 33058.00 | 1423.20 |
| 4F | 12.30 | X | 38604.00 | 1421.20 |
| 1F | 0.00 | X | 39201.00 | 1569.50 |
| 12F | 42.90 | Y | 325.68 | 9806.40 |
| 8F | 20.45 | Y | 1326.00 | 36629.00 |
| 4F | 12.30 | Y | 1466.40 | 39921.00 |
| 1F | 0.00 | Y | 1569.50 | 42663.00 |

## Conclusions

A study on the dynamic characteristics and seismic responses of a large-cantilever stadium structure was presented in this paper. Based on the Midas/gen platform, a 3D finite element model of the structure was established to investigate the seismic performance of the structure by using the response spectrum analysis. The seismic analysis results of the structure indicate that the transfinite part of the structure is the weakest link of the whole structure if it is attacked by earthquakes in future. Therefore, it should be much careful when a structrue, or a part of it, needs to be designed beyond the Code limitation.

## References

[1] JGJ3-2010.Concrete structures in high-rise buildings , 2010.

[2] GB50011-2010, Seismic Design Code of Building, 2010.

[3] Li Jie. Jianhua Li.Multiple support excitation structure of random earthquake response analysis of the response spectrum method [J] ,Earthquake Engineering and Engineering Vibration. 2004 (3).

[4] Jianmei Sun,JiHong Ye.Wennang Cheng,Simplification of the multi-support response spectrum method. Journal of Southeast University(natural science Edition),2003(5).

# CHAPTER 5:

# Hydraulic Engineering, Water Resources and Hydrology

*Applied Mechanics and Materials Vols. 580-583 (2014) pp 1793-1798*
*© (2014) Trans Tech Publications, Switzerland*
*doi:10.4028/www.scientific.net/AMM.580-583.1793*

# A two-dimensional numerical model for shallow water flows over variable topographies

Biao Lv, Shaoxi Li

Key Laboratory of Engineering Sediment, Ministry of Transport, Tianjin Research Institute for Water Transport Engineering, Tianjin, 300456, China slxlvbiao@163.com

**Keywords:** shallow water flows; well-balanced Roe-type scheme; Finite-volume formulation; bed slope source term;

**Abstract.** Based on well-balanced Roe's approximate Riemann solver, a numerical model is developed for the unsteady, two-dimensional, shallow water flow with variable topographies. In this model, an efficient methods are applied to treat the source terms and to satisfy the compatibility condition on unstructured grids. In the method, different components of the bed slope source term are considered separately and the compatible discretization of the components is presented. The newly developed model is verified against analytical solutions and measured date, with good agreement.

## Introduction

The discretization of the shallow water (SW) equations has received considerable attention in the past two decades and many upwind scheme have successfully solved channel flows [1-3]. However, their use in the presence of irregular topographies usually problematic, due to the imbalance between the source terms and the flux gradients [4]. In fact, most shock-capturing finite volume schemes for the SW equations, are obtained by using approximate Riemann solvers which have been originally designed for hyperbolic systems without considering the source terms. Therefore, in the presence of source terms, those schemes may lead to oscillations.

In the stagnant conditions, the water should stay at rest over variable bottom topography without influence from outside. Jin [5] developed the interface method, which preserves the steady-state condition up to second-order accuracy on structured grids, but his approach is not directly usable on unstructured grids. Mohammadian et al. [6] developed a numerical model using the Roe's method which satisfies the *C* Property. However, although their scheme is mass conservative, it is not fully conservative since the gravity terms are not discretized in a conservative manner.

In the paper, a numerical model is developed to solve shallow flows with variable topographies on unstructured grids. The developed model is shown to satisfy the *C* property when combined with Roe's scheme and the surface gradient method for calculating the water depth at the interface. Moreover, the proof of the *C* property is also presented. The model is applied to three numerical tests to show the performance of the scheme over variable topographies.

## Mathematical formulation

The two-dimensional governing equations are obtained by integrating the Navier-Stokes equations over the flow depth. The continuity and momentum equations are written as

$$\frac{\partial U}{\partial t}+\nabla E=S \tag{1}$$

with $E=(F,G)$, in which

$$U=\begin{pmatrix} h \\ hu \\ hv \end{pmatrix},\quad F=\begin{pmatrix} hu \\ hu^2+0.5gh^2 \\ huv \end{pmatrix},\quad G=\begin{pmatrix} hv \\ huv \\ hv^2+0.5gh^2 \end{pmatrix},\quad S=S_0+S_f=\begin{pmatrix} 0 \\ ghS_{0x} \\ ghS_{0y} \end{pmatrix}+\begin{pmatrix} 0 \\ -ghS_{fx} \\ -ghS_{fy} \end{pmatrix} \tag{2}$$

where *u* and *v* are velocity components in the *x* and *y* directions respectively; h is water depth; *g* is gravitational acceleration; $(S_{0x},S_{0y})$ are bed slopes in the *x* and *y* directions, respectively; $(S_{fx},S_{fy})$ are

friction slopes in the $x$ and $y$ directions, respectively. In this study, the friction slopes are estimated by the Manning formula

$$S_{0x}=\frac{\partial z}{\partial x},\quad S_{0y}=\frac{\partial z}{\partial y},\quad S_{fx}=\frac{n^2u\sqrt{u^2+v^2}}{h^{4/3}},\quad S_{fy}=\frac{n^2v\sqrt{u^2+v^2}}{h^{4/3}} \tag{3}$$

where $z$ is the distance between the bed surface and the reference level and $n$ is Manning's roughness coefficient.

## Discretization and algorithm

**Calculation of the fluxes.** A cell center finite volume method will be formulated over a triangular control volume, where the variables stored at the centre of the cells are represented as piecewise constants. From Eq.(1) the conservative equation over the area of the $i$th control volume can be written:

$$\frac{\partial U_i}{\partial t}A_i+\sum_{k=1}^{NS}E_k^*dl_k=\int_{\Omega_i}S\mathrm{d}\Omega \tag{4}$$

where $A_i$ is the area of the control volume $\Omega_i$; $E_k^*$ is the convective fluxes; $dl_k$ is the length of control volume boundary; $NS$ is the number of control volume boundary.

The convective fluxes $E_k^*$ are calculated by a Roe's scheme. Details of the convective fluxs discretization have been described in Ref.[7].

**Calculation of bed slope term in irregular topographies.** As mentioned before, the bed slope term is considered separately in the source term (2). This usually leads to an imbalance between the water surface gradient term ($0.5gh^2$) and the bed slope term, and consequent produces the numerical error. For example, in complicated topographies with the stagnant initial condition, the water will not remain stagnant.

In order to avoid the numerical error, an efficient method is introduced in this paper.

**Method. Considering different components of the bed slope term separately.** By considering different components of the bed slope term separately, the source and the flux gradient terms are inherently balanced.

Here, the bed slope term is written as

$$\begin{aligned}gh\frac{\partial z}{\partial x}&=g\frac{\partial(hz)}{\partial x}-gz\frac{\partial h}{\partial x}=0.5g\frac{\partial(hz)}{\partial x}+0.5g\frac{\partial(hz)}{\partial x}-gz\frac{\partial h}{\partial x}\\&=\underbrace{0.5g\frac{\partial(hz)}{\partial x}}_{B_1}+\underbrace{0.5gh\frac{\partial z}{\partial x}}_{B_2}-\underbrace{0.5gz\frac{\partial h}{\partial x}}_{B_3}\end{aligned} \tag{5}$$

where

$$B_1=\frac{0.5g}{A_i}\left(\frac{h_1^L+h_1^R}{2}z_1\Delta y_1+\frac{h_2^L+h_2^R}{2}z_2\Delta y_2+\frac{h_3^L+h_3^R}{2}z_3\Delta y_3\right) \tag{6}$$

$$B_2=\frac{0.5gh_i}{A_i}\left(z_1\Delta y_1+z_2\Delta y_2+z_3\Delta y_3\right) \tag{7}$$

$$B_3=\frac{0.5gz_i}{A_i}\left(\frac{h_1^L+h_1^R}{2}\Delta y_1+\frac{h_2^L+h_2^R}{2}\Delta y_2+\frac{h_3^L+h_3^R}{2}\Delta y_3\right) \tag{8}$$

**Proposition.** The numerical scheme presented in previous sections, satisfies the C property with (5)-(8).

**Proof.** The stagnant condition leads to

$$(uh)_i^{n+1}A_i=(uh)_i^nA_i-0.5g\Delta t(h_1^2\Delta y_1+h_2^2\Delta y_2+h_3^2\Delta y_3)+\Delta tA_i(B_1+B_2-B_3) \tag{9}$$

$$=(uh)_i^nA_i-0.5g\Delta t(h_1(h_1-z_1)\Delta y_1+h_2(h_2-z_2)\Delta y_2+h_3(h_3-z_3)\Delta y_3)+\Delta tA_i(B_2-B_3) \tag{10}$$

$$=(uh)_i^nA_i-0.5g\eta_0\Delta t(h_1\Delta y_1+h_2\Delta y_2+h_3\Delta y_3)+\Delta tA_i(B_2-B_3) \tag{11}$$

and

$$\begin{aligned}(B_2-B_3)A_i &= 0.5gh_i((h_1-\eta_1)\Delta y_1+(h_2-\eta_2)\Delta y_2+(h_3-\eta_3)\Delta y_3)\\ &\quad -0.5gz_i(h_1\Delta y_1+h_2\Delta y_2+h_3\Delta y_3)\\ &= 0.5g(h_i-z_i)(h_1\Delta y_1+h_2\Delta y_2+h_3\Delta y_3)+0.5g\eta_0 h_i(\Delta y_1+\Delta y_2+\Delta y_3)\\ &= 0.5g\eta_0(h_1\Delta y_1+h_2\Delta y_2+h_3\Delta y_3)\end{aligned} \tag{12}$$

Substituting (12) in (11) we obtain

$$(uh)_i^{n+1}A_i=(uh)_i^n A_i \tag{13}$$

Hence, the *C* property holds.

## Model applications

In order to focus on the performance of the numerical scheme, three examples are proposed herein for variable topographies.

**Propagation of a smooth save over a bump.** The numerical experiment takes place in a square pool 1m×1m. At the centre of the pool a symmetric bump in the bottom is mathematically defined in the form

$$z(x,y)=\max\left[0.0,0.25-5*\left((x-0.5)^2+(y-0.5)^2\right)\right] \tag{14}$$

The ability of the methods to preserve the initial steady state in time is analysed. We start from still water as the initial condition covering partially the bump in a frictionless domain fully closed by vertical wall.

$$H=0.1\,\text{m},\quad u=0\,\text{ms}^{-1},\quad v=0\,\text{ms}^{-1} \tag{15}$$

The domain is discretized by 3122 triangular grids.

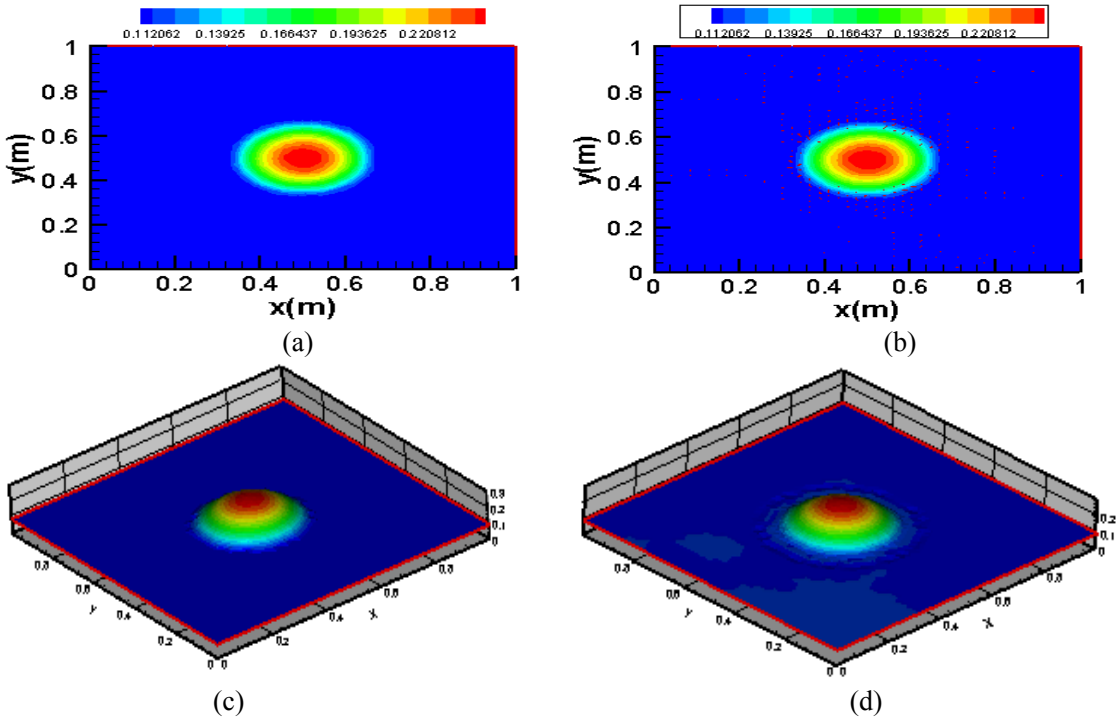


Fig.1 Iso-contour water levels and velocity field (a,b) and free surface (c,d) of steady state in a closed pool using the method (a,c) proposed here and using an upwind method (b,d) in this test case.

The upper plots in Fig.1 show the iso-contour water levels together with the velocity field. Lower figures show the free surface. On the left the results are obtained using the method in this paper while on the right the upwind scheme is used. It can be seen that water easily jumps over the bump in the latter case showing the presented scheme preserve the *C* property, directly related with mass conservation.

**Steady flow over a bump.** The topography is new defined as

$$z(x)=\begin{cases}0.2-0.05(x-10)^2 \; if\; 8<x<12\\ 0 \qquad\qquad otherwise\end{cases} \tag{16}$$

Depending on the initial and boundary conditions, the flow may be subcritical, transcritical (with or without a steady shock), or supercritical. The analytical solution of this problem is given in Reference [10]. The domain is discretized by 2566 triangular grids.

Three different cases are considered below by imposing downstream and upstream boundary conditions for the water depth ($h$) and discharge ($hu$), respectively:

(1) Transcritical flow without shock: $h$=0.66 m only when the flow is subcritical and $hu$=1.53 $m^3$/h.

(2) Transcritical flow with shock: $h$=0.33 m and $hu$=0.18 $m^3$/h.

(3) Subcritical flow: $h$=2 m and $hu$=4.42 $m^3$/h.

The surface profiles are plotted in Fig.2 and Fig.3. They show good agreementd with the analytical solutions. The computed water discharges are also compared in Fig.4-Fig.6 with the analytical ones, which show a very small numerical oscillations.

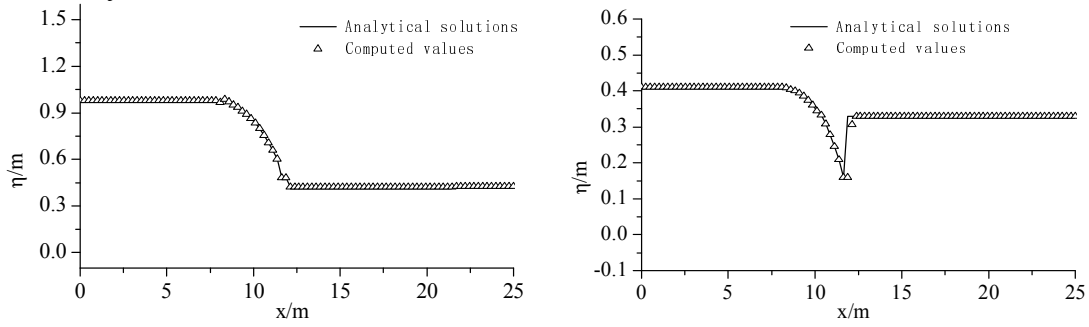


Fig.2 Water surface elevation in steady trans-critical flow without a shock (a) and with a shock (b).

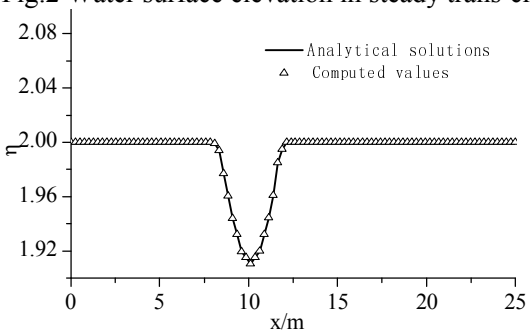


Fig.3 Water surface elevation in steady sub-critical flow

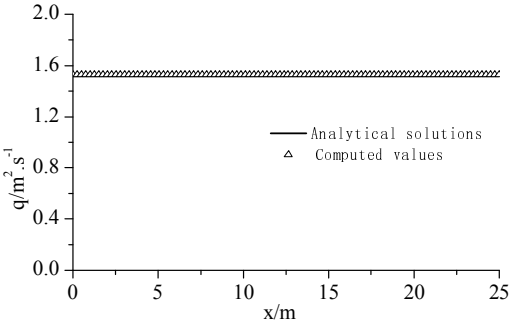


Fig.4 Water discharge in steady transcritical flow without a shock.

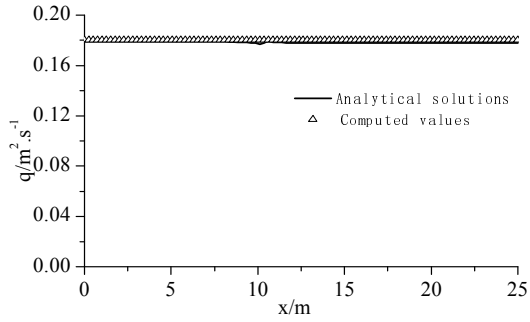


Fig.5 Water discharge in steady transcritical flow.

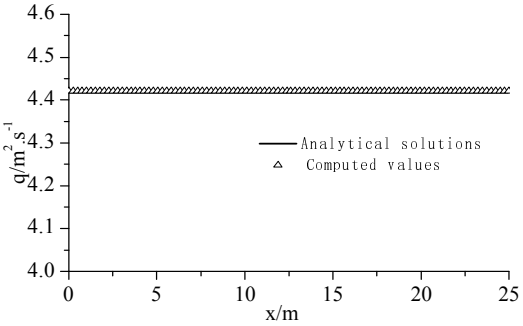


Fig.6 Water discharge in steady subcritical flow with a shock.

**Application to the Bohai sea.** The Bohai Sea is a semi-enclosed sea, which connects with the Huanghai Sea. The tidal wave from the Huanghai Sea propagates through the Bohai Strait into the Bohai Sea. In Bohai Sea the tidal movement is one of the prominent hydrodynamic processes. Fig.7 show the topography of the Bohai Sea and the locations of the gauging points. *AB* is the open boundary. Six conditions have been considered: Bayuquan, Jinzhou port, Jingtang port, Tanggu, Huanghua port and Penglai port, respectively. There are 6973 nodes together which forms 13221 triangular meshes. The time step is 36 s. Fig.8 show the water surface elevation comparisons at six

gauging points in 25h. Tidal current field distribution of Bohai Sea are shown in Fig.9. It can be drawn that the numerical model is reasonable and can be applied to study the tidal currents in Bohai Sea.

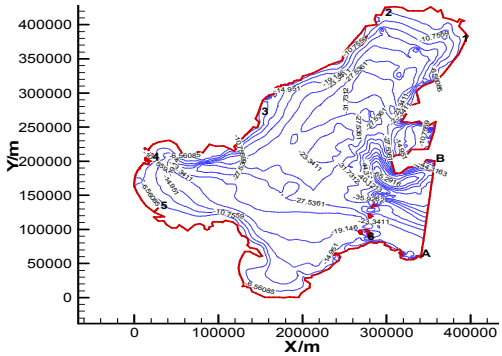


Fig.7 The topography of the Bohai Sea and the locations of the gauging points

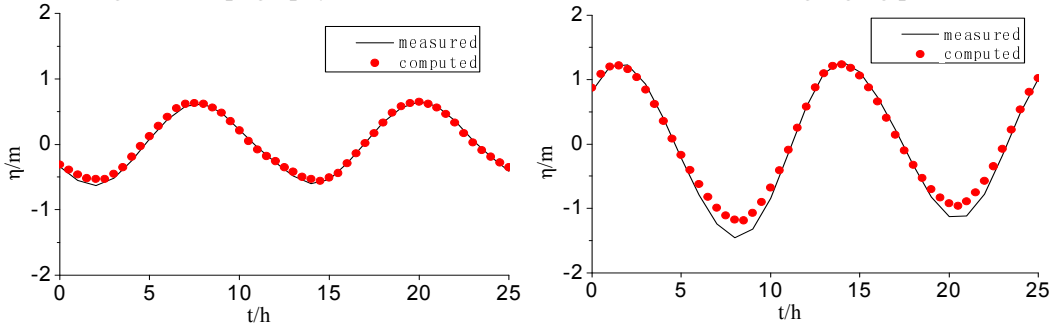


(a) Penglai (b) Huanghua

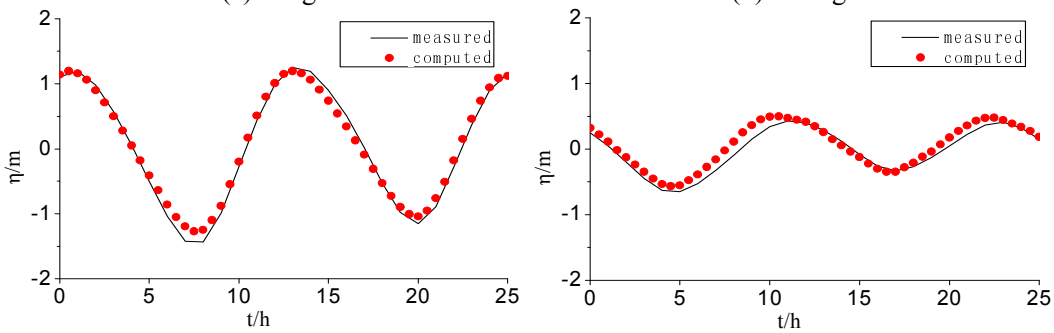


(c) Tanggu (d) Jingtang

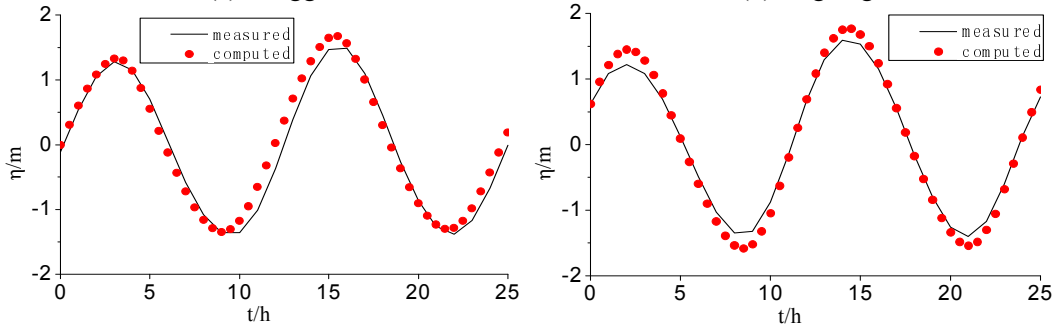


(e) Jinzhou (f) Bayuquan

Fig.8 Comparisons of water surface elevation at gauging points in 25h.

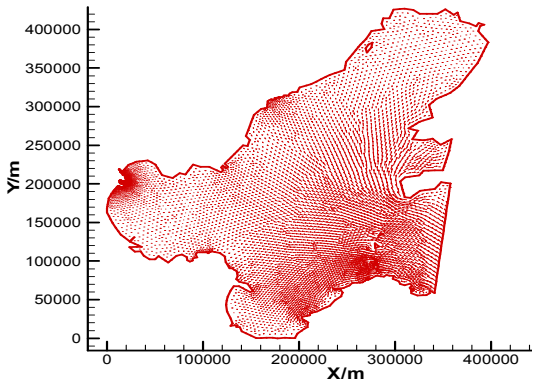


Fig.9 Computed velocity in the surface layer at 25h

## Conclusions

In this paper, an efficient method have been applied to treat the bed source terms and satisfy the compatibility property on unstructured grids. Numerical confirmation of the compatibility property of the two-dimensional shallow water flow model proposed by the authors is presented. Contrary to many available schemes, our approach can be easily implemented on unstructured grids and it takes advantage of being flexible for complicated geometry boundaries with irregular topography. Good agreement between numerical results and experimental data indicates the capability and efficiency of model for the simulation the complex flow phenomenon with irregular topography .

## References

[1] P.Glaister: Journal of Hydraulic Research**,** Vol.26 (1988), P. 293.

[2] D.Zhao, H.W.Shen and G.Q.Tabios: Journal of Hydraulic Engineering**,**Vol.120(1994), P.863.

[3] C.G.Mingham and D.M.Causon: Journal of Hydraulic Engineering**,**Vol.124(1998), P.605.

[4] P.Brufau: Journal of Hydrodynamics, Vol.17(2005), P.306.

[5] S.Jin: Mathematical Modelling and Numerical Analysis**,**Vol.35(2001), P.631.

[6] A.Mohammadian, D.Y.Le and M.Tajrishi: Advances in Water Resources, Vol.28(2005), P.429.

[7] P. Brufan, M. E .Vazquez and P.Garcia: International Journal for Numerical Methods in Fluids, Vol.39(2002), P.247.

[8] J.G.Zhou, D.M.Causon and C.G.Mingham: Journal of Computational Physics, Vol.168(2001), P.1.

[9] R.J.LeVeque: Journal of Computational Physics, Vol.146(1998), P.346.

[10] P.Brufau and P.Garcia: International Journal for Numerical Methods in Fluids, Vol.33(2000), P.35.

*Applied Mechanics and Materials Vols. 580-583 (2014) pp 1799-1802*
*© (2014) Trans Tech Publications, Switzerland*
*doi:10.4028/www.scientific.net/AMM.580-583.1799*

# An Inversion Method of the Material Parameters for Gravity Dams

ZHANG Dongdong[1,a], FENG Xin[1,b], ZHOU Jing[1,c]

[1]Faculty of Infrastructure Engineering, Dalian University of Technology, Dalian 116024,China

[a]zhangdongdong4509@126.com, [b]fengxin@dlut.edu.cn, [c]zhouj@dlut.edu.cn

**Keywords:** inversion; Gravity dam; material parameter; least square; regularization

**Abstract.** A regularization based method of inversely analyzing the material parameters for the gravity dams is presented in this paper. The measured noise of the displacement often leads to the ill-posed solutions of the dam inversion. A least square scheme was adopted for the inverse analysis by using of the displacement measurements, and the L-curve algorithm was proposed to perform the regularization in the inversion computation. The proposed method actually utilizes the sensitivity of the measured displacements with respect to the sub-regional material parameters. Thus a simplified algorithm was developed to calculate the sensitivity coefficients by using the standard finite element procedure. To investigate the effectiveness of the proposed method, the numerical simulations on a concrete gravity dam were carried out. The results demonstrate that the presented method can accurately obtain the material parameters of the dam by using of the inverse analysis, which has the potential for assessing the integrity of the gravity dams.

## Introduction

With the continuous development of monitoring technology, some scholars prefer to use dam safety monitoring data for inversing the dam material parameter, and this method has been approved to be available. Among them, the displacement back analysis based on displacement measurement information became a common method of dam material parameter inversion. There are three main methods which can solve the optimization problem of the inversion process: the traditional non-linear optimization method, the intelligent optimization algorithm and the combination of the former [1,4]. Research on the first kind of optimization method has been started for a long time, it is easy to operate and its solution accuracy is relatively high. Thus, the concrete dam parameter inversion method used in this paper is regularization algorithm. In the progress of solving this problem, the sensitivity coefficient will be used. In this paper, an easy method of calculating sensitivity coefficient was deduced.

## Inversion process and principle of the material parameter

Because of the influence of the Poisson's ratio on the deformation of dam is very small, this paper only consider the elastic modulus as the research object. The expression of objective function [1] is given below,

$$\min(f(\widehat{E}))=\sum_{i=1}^{N}(u_i(\widehat{E})-u_i^0)^2. \quad (1)$$

Here $\widehat{E}$ is a vector which consists of each concrete-dam partition elastic modulus. $u_i(\widehat{E})$ represents the crest displacement. $u_i^0$ is the observation value. $N$ is the number of water level points.

The material parameter inversion progress is to make the objective function reach the minimum. Gauss-Newton algorithm is commonly used for solving unconstrained optimization problems, this method needs a coefficient matrix. This matrix might became an ill-conditioned matrix because of the

effect of the measurement error [2]. The ill-conditioned matrix may make the results deviated from the actual value. In order to solve this problem, Tikhonov proposed a regularization method, this method can improve the ill-condition of the coefficient matrix through introducing a regularization factor. After adding a regularization factor, the original aim function is transformed as follows [3]:

$$\min(f(\widehat{E}))=min\left\{\sum_{i=1}^{N}(u_i(\widehat{E})-u_i^0)^2+\mu^2\sum_{i=1}^{n}(E_i-E_i^0)^2\right\}. \tag{2}$$

Here $\mu^2$ is the regularization factor. $E_i$ is elastic modulus after iteration. $E_i^0$ is the elastic modulus before iteration. The following is the inversion procedure based on Matlab software:

1) Establishing a finite element model of the gravity dam, different material partitions use different material parameters. Set the step size θ to 0. Based on the superposition principle, the global stiff matrix can be assembled by each partition stiff matrix,

$$\{K\}=\{K_1\}+\{K_2\}+\ldots+\{K_n\}. \tag{3}$$

Where $\{K\}$ is the global stiff matrix, $\{K_i\}$ is the partition stiff matrix. Assume the dam concrete and foundation rock is linear elastic, if the elastic modulus value of partition $j$ is $E_j$, $\{K_j\}$ can be written as:

$$\{K_j\}=E_j*\{K_j\}^e. \tag{4}$$

Here $\{K_i\}^e$ is the partition geometric stiff matrix. It can be calculated through making the elastic modulus of partition $i$ to 1, the others($i\neq j$) to 0. Put Eq. 4 into Eq. 3,we can obtain:

$$\{K\}=\sum_{i=1}^{n}E_i*\{K_i\}^e. \tag{5}$$

2) Calculating the global stiff matrix $\{K\}^\theta$ through using Eq. 5. The crest displacement vector can be calculated by:$\{u_\theta\}=inv(\{K\}^\theta)*\{f\}$.Then, compute the aim function value of step $\theta$;

3) Calculating the sensitivity coefficients matrix $A_\theta$ and coefficient matrix $Q_\theta$. The following is the expression of $A_\theta$,

$$A_\theta=\begin{pmatrix}\frac{\partial u_1^\theta}{\partial E_1} & \frac{\partial u_2^\theta}{\partial E_1} & \frac{\partial u_3^\theta}{\partial E_1} & \cdots & \frac{\partial u_N^\theta}{\partial E_1}\\ \frac{\partial u_1^\theta}{\partial E_2} & \frac{\partial u_2^\theta}{\partial E_2} & \frac{\partial u_3^\theta}{\partial E_2} & \cdots & \frac{\partial u_N^\theta}{\partial E_2}\\ \vdots & \vdots & & \ddots & \vdots\\ \frac{\partial u_1^\theta}{\partial E_n} & \frac{\partial u_2^\theta}{\partial E_n} & \frac{\partial u_3^\theta}{\partial E_n} & \cdots & \frac{\partial u_N^\theta}{\partial E_n}\end{pmatrix}. \tag{6}$$

Where $\frac{\partial u_i}{\partial E_j}$ is sensitivity coefficient which can be got through Eq.9. Its solution procedure is given in Part 3. $Q_\theta$ is expressed as $Q_\theta=A_\theta*A_\theta^T$ ;

4) Use the L-curve algorithm to determine the regularization factor $\mu_\theta$;

5) Add the regularization factor to the Gauss-Newton normal equation $(Q_\theta+\mu_\theta^2 I)\,p^\theta=-g_\theta$, $g_\theta=A_\theta*(\{u^t\}-\{u^0\})$. Solve this normal equation, the elastic modulus increment vector $p^\theta$ is got;

6) Compute the new iteration elastic modulus vector by add $p^\theta$ to $\widehat{E}^\theta$, $\widehat{E}^{\theta+1}=\widehat{E}^\theta+p^\theta$. Judge the convergence rule, if $min\{f(\widehat{E}^\theta)\}<fmin$, then stop iteration computing, output $E^\theta$ and $min\{f(\widehat{E}^\theta)\}$, else, $\theta=\theta+1$, go to step 2).

**Solving process of the sensitivity coefficient**

Assume the dam is equivalent linear elastic, according to the physical equation of the finite element method:

$$\{K\}\{u\}=\{f\}. \tag{7}$$

Here, $\{K\}$ is the global stiff matrix of the dam, it is relevant to the geometry and material parameter. Compute the partial derivative of $E_i$ on both side of Eq. 10, then

$$\{K\}\frac{\partial\{u\}}{\partial E_i}+\frac{\partial\{K\}}{\partial E_i}\{u\}=0,$$
$$\frac{\partial\{u\}}{\partial E_i}=-\{K\}^{-1}\frac{\partial\{K\}}{\partial E_i}\{u\}. \tag{8}$$

According to Eq. 5, $\frac{\partial\{K\}}{\partial E_i}=\partial(\sum_{i=1}^{n}E_i*\{K_i\}^e)/\partial E_i$. In this formula, $\{K_i\}^e$ is the partition geometric stiff matrix, so it has nothing to do with $E_i$. The partial derivative is $\frac{\partial\{K\}}{\partial E_i}=\{K_i\}^e$,put it into Eq. 9, the sensitivity coefficient is obtained,

$$\frac{\partial\{u\}}{\partial E_i}=-\{K\}^{-1}\{K_i\}^e\{u\}. \tag{9}$$

**Proof calculation and analysis**

Take the dam cross-section in Fig. 1 as geometric model, establishing a finite element model. Assume the actual elastic modulus value for each partition is *($E_1$=15GPa, $E_2$=20GPa, $E_3$=25GPa, $E_4$=20GPa*), the Poisson's ratio is $\mu_1=\mu_2=\mu_3=0.17$, $\mu_4=0.22$, the density of dam concrete unified take $\rho^c=2350kg/m^3$, the foundation rock density take $\rho^r=2700kg/m^3$. The finite element model is meshed by plane strain element, there is 1916 elements, 3900 degrees of freedom. Compute the crest displacement under water pressure, body-weight, uplift pressure and silt pressure. Take the compute $\{u^r\}$ value plus 1% random error as observation displacement $\{u^0\}$, it can be expressed by $\{u^0\}=\{u^r\}\pm rand[-0.01,0.01]*\{u^r\}$. If the actual modulus can be inversed through the process above, then the algorithm is useful for solving material parameter inversion problem. Tab.1 is the inversion parameter changes table for each step. It can be seen that the aim function was convergent in step 3. The convergence speed is fast. The relative error of the inversed results and actual values is given in Tab.2. It is relatively small. The deformation of relative error is $\Delta_i=[(\widehat{E}_i-E_i^0)/E_i^0]\times100\%$. These results can indicate that this algorithm is practicable. In the inversion progress described above, the water level vector is $\{H_i\}=\{76,77,78,79,80\}$, the initial iteration elastic modulus is $\{\widehat{E}^0\}=$ ($E_1$=10GPa,$E_2$=15GPa,$E_3$=20GPa,$E_4$=15GPa), the convergence rule is $f_{min}<2e\text{-}7$.

Table 1 Changes of the iteration parameters

| θ | μ | $E_1$ | $E_2$ | $E_3$ | $E_4$ | $\frac{\partial\{F(\hat{E})\}}{\partial E_1}$ | $\frac{\partial\{F(\hat{E})\}}{\partial E_2}$ | $\frac{\partial\{F(\hat{E})\}}{\partial E_3}$ | $\frac{\partial\{F(\hat{E})\}}{\partial E_4}$ | $\{F(\hat{E})\}$ |
|---|---|---|---|---|---|---|---|---|---|---|
| | | [Gpa] | | | | [$m^2$/Pa] | | | | [$m^2$] |
| 0 | 6.6E-16 | 10.0 | 15.0 | 20.0 | 15.0 | -6.52E-15 | -1.64E-14 | -1.12E-14 | -2.26E-14 | 2.12E-04 |
| 1 | 4.2E-14 | 13.8 | 19.1 | 22.2 | 19.2 | -7.25E-16 | -2.14E-15 | -1.90E-15 | -2.89E-15 | 9.36E-06 |
| 2 | 2.1E-13 | 14.4 | 20.1 | 23.2 | 20.6 | -4.16E-17 | -1.18E-16 | -1.09E-16 | -1.56E-16 | 5.43E-08 |
| 3 | | 14.5 | 20.3 | 23.8 | 20.7 | -1.82E-18 | -4.14E-18 | -3.58E-18 | -5.12E-18 | 1.79E-08 |

Table 2 Comparison between the inversion results and actual values

| Inversion parameter | $E_1$ | $E_2$ | $E_3$ | $E_4$ |
|---|---|---|---|---|
| Actual value [GPa] | 15.0 | 20.0 | 25.0 | 20.0 |
| Inversion result [GPa] | 14.5 | 20.3 | 23.8 | 20.7 |
| Relative error$\Delta_i$ [%] | 3.3 | 1.5 | 4.8 | 3.5 |

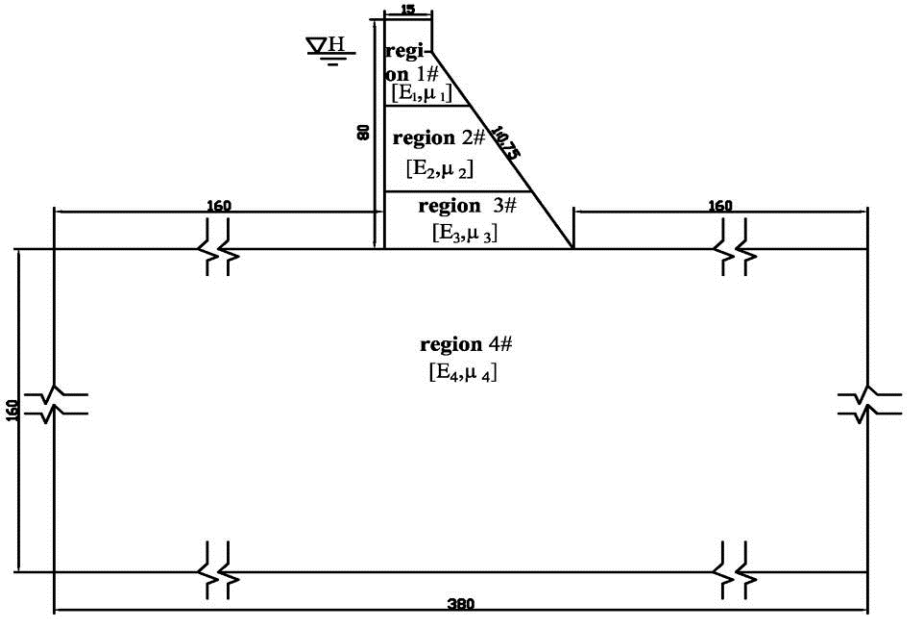


Fig. 1 Material subregions of the dam

## Conclusion

In this paper a method for solving the sensitivity coefficients was presented. This method makes it more fast and accurate to compute the sensitivity coefficients. A program that can fast and effectively inverse the materials parameter of the gravity dam was proposed. The effectiveness of the new method is verified by the numerical simulations. The results show that the proposed method has some advantages such as rapid convergence speed, high convergence accuracy and good stability.

## Acknowledgements

The authors would gratefully thank the financial support by the Sate Key Development Program for Basic Research of China with Grant No. 2013CB035906 and Education Department of Liaoning Province with Grant No. L2012010.

## References

[1] Wu Zhongru: *Safe Monitoring Theory & Its Application of Hydraulic Structures* (Higher Education Press, China 2003).

[2] Liu Yingxi, Li Shouju, Chen Changlin: Journal of Hydraulic Engineering Vol. 30 (1999), p. 38-44

[3] Feng Xin, Zhou Jing, Fan Yingfang: Journal of Hydraulic Engineering Vol. 35 (2004), p. 101-105

[4] Kang Fei, Li Junjie, Xu Qing: Journal of Hydraulic Engineering Vol. 40 (2009), p. 736-742

*Applied Mechanics and Materials Vols. 580-583 (2014) pp 1803-1806*
*© (2014) Trans Tech Publications, Switzerland*
*doi:10.4028/www.scientific.net/AMM.580-583.1803*

# An new approximate formula for contracted depth in Quadratic parabola shaped channels

Fengling Li

Department of architecture and civil engineering , Huizhou University ,

Huizhou, Guangdong, 516007, China

mmlflmm@163.com

**Key word :** irrigation channels; quadratic parabola; contracted depth; approximate solution

**Abstract:** On the basis of summarizing the predecessors' research, based on the contracted depth basic equation mathematical transformation of quadratic parabola shaped sections, the interrelation between dimensionless contracted depth and the dimensionless parameter were analyzed, we obtain the approximate formula for contracted depth in Quadratic parabola shaped channels, it is simpler and accurate, It's maximum relative error are less than 0.12% in the utility range.

## Introduction

At present, many scholars studied on theoretical or iterative formula for contracted depth and normal depth of quadratic parabola shaped section[1-5]. The approximate solution on contracted depth of quadratic parabola form channel has not been well studied. In this paper, through to mathematical transformation for the contracted depth basic equation of quadratic parabola shaped section. Introducing the dimensionless parameters, analyzing the relationship between dimensionless contracted depth and the dimensionless parameters, according to the water and wastewater engineering norms and hydraulic engineering norms, we get calculation formula for contracted depth in quadratic parabola shaped channels

## Quadratic parabola cross-section contracted depth basic equation [4]:

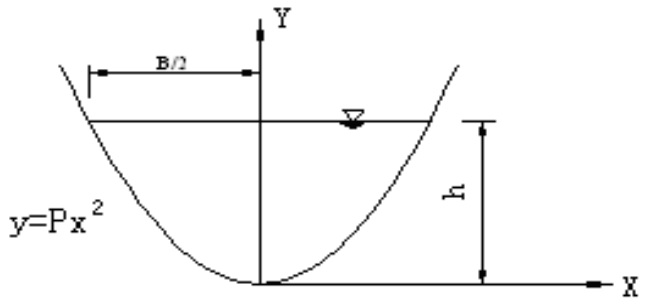


Fig1. Cross-section of quadratic parabola-shape

$$E_0 = h_c + \frac{Q^2}{2g\phi^2 A_c^{\,2}} \tag{1}$$

Where： $E_0$： total head in the contraction section ( $m$ ), $h_c$： contracted depth ( $m$ ), Q - flow, ($m^3/s$), $g$： Acceleration of gravity( $m/s^2$ ), $\phi$ - Velocity coefficient, $A_c$ - water sectional area, ($m^2$).

Where: $A_c = \frac{4}{3} P^{-\frac{1}{2}} h_c^{\frac{3}{2}}$ (2)

In order to study convenient, we are defining dimensionless contracted depth $\alpha$

$$\alpha = \frac{h_c}{E_0} \tag{3}$$

Combine equation (1), equation (2) and equation (3), we get the Simultaneous equation, and then we can obtain a equation for the contracted depth of the quadratic parabola shaped channels.

$$\left( \frac{9Q^2 p}{32g\phi^2 {E_0}^4} \right)^{\frac{1}{3}} = \alpha(1-\alpha)^{\frac{1}{3}} \tag{4}$$

Suppose K is non-dimensional parameter,

$$k = \left( \frac{9Q^2 p}{32g\phi^2 {E_0}^4} \right)^{\frac{1}{3}} \tag{5}$$

The equation can be as follows:

$$k = \alpha(1-\alpha)^{\frac{1}{3}} \tag{6}$$

**An approximate calculation formula of dimensionless contracted depth**

Adopting trial and error method, making a computation program to gradually optimized fitting, we get an approximate calculation formula for dimensionless contracted depth of quadratic parabola shaped cross section:

$$\alpha_1 = k(1.6k^{3.64} + 0.21k + 1)^{1.77} \tag{7}$$

**Formula evaluation**

When setting different dimensionless contracted depth $\alpha \in [0,0.50]$ of quadratic parabola shaped cross section, non-dimensional parameter k can be figured out according to equation(6), dimensionless contracted depth $\alpha_1$ can be figured out according to equation(7)， and then to calculate the relative error $\Delta = \frac{\alpha_1 - \alpha}{\alpha} \times 100$ .On the basis of results listed in Table 1，Maximum relative error is less than 0.12%, The results show that the precision meets the needs of project.

**Table 1 Non-dimensional Parameter Contracted Depth Calculation Error**

| The correct dimensionless depth $\alpha$ | Dimensionless coefficient k | The calculation dimensionless depth $\alpha_1$ | Relative error $\Delta$ (%) |
|---|---|---|---|
| 0 | 0 | 0 | 0 |
| 0.02 | 0.019866 | 0.020013 | 0.064 |
| 0.04 | 0.039460 | 0.040041 | 0.102 |
| 0.06 | 0.058776 | 0.060071 | 0.118 |
| 0.08 | 0.077808 | 0.080092 | 0.115 |
| 0.10 | 0.096549 | 0.100097 | 0.097 |
| 0.12 | 0.114994 | 0.120081 | 0.068 |
| 0.14 | 0.133136 | 0.140045 | 0.032 |
| 0.16 | 0.150966 | 0.159990 | -0.006 |
| 0.18 | 0.168478 | 0.179923 | -0.043 |
| 0.20 | 0.185663 | 0.199849 | -0.075 |
| 0.22 | 0.202514 | 0.219780 | -0.100 |
| 0.24 | 0.219019 | 0.239723 | -0.116 |
| 0.26 | 0.235171 | 0.259688 | -0.120 |
| 0.28 | 0.250959 | 0.279684 | -0.113 |
| 0.30 | 0.266371 | 0.299716 | -0.095 |
| 0.32 | 0.281397 | 0.319788 | -0.066 |
| 0.34 | 0.296024 | 0.339897 | -0.030 |
| 0.36 | 0.310239 | 0.360035 | 0.010 |
| 0.38 | 0.324027 | 0.380188 | 0.050 |
| 0.40 | 0.337373 | 0.400334 | 0.083 |
| 0.42 | 0.350261 | 0.420440 | 0.105 |
| 0.44 | 0.362673 | 0.440463 | 0.105 |
| 0.46 | 0.374590 | 0.460348 | 0.076 |
| 0.48 | 0.385990 | 0.480028 | 0.006 |
| 0.50 | 0.396850 | 0.499417 | -0.117 |

**Calculation contracted depth application example**

It is known that the parameters of Quadratic parabola shaped channels $y = 0.25x^2$ . Where：total head $E_0 = 10.31m$ , velocity coefficient $\phi = 0.95$ , solved the contracted depth $h_c$ when the flow $Q = 220 m^3/s$ .

**Answer:**

Firstly, to calculate dimensionless coefficient K;

Using Formula（5）to calculate $k = \left( \frac{9Q^2 p}{32 g \phi^2 {E_0}^4} \right)^{\frac{1}{3}} = 0.324023$

Using Formula（7）to calculate $\alpha_1 = k(1.6k^{3.64} + 0.21k + 1)^{1.77} = 0.380183$

Using Formula（3）to calculate $h_c = \alpha E_0 = 3.920$ (exact value is 3.918 m) relative error is 0.05%.

**Conclusion**

The approximate calculation formula the absolute maximum relative error of contracted depth was 0.12% respectively in the utility range. It can satisfy the demand of practical engineering.

**Acknowledgements**

This Research was financially supported by the Research Fund of Huizhou University (No. $C_5$10.0211)

**References**

[1] Qin Lu, Zhengzhong Wang, Wugang Ren. A formula for quickly calculating water depth at vena contraction in parabola form channel [J].Agricultural Research in the Arid Areas, 2007，2s (2):134136. (in Chinese)

[2] Yanfeng Zhao, Songbai Song, Qinqian Meng. A direct calculation method for wader depth in parabolic shaped channel with contracted section[J].Water Resources and Hydropower Engineering, 2008，39 (3):36 37. (in Chinese)

[3] Hui Wen, Fengling Li. Analytical solution of water depth in parabolic shaped channel with contracted section [J] Journal of Yangtze River Scientific Research Institute, 2009 26(9):32 一 34. (in Chinese)

[4] Swamee Prabhata K, Rathie Pushpa N. Exact solutions for normal depth problem [J] . Journal of hydraulic Research , 2004 , 42 ( 5 ):541 一 547

[5] Hui Wen, Fengling Li. Explicit formula of hydraulic calculation of semi-cubic parabola-shaped channel [J]. Yellow River, 2010,32(1) :75-76. (in Chinese)

*Applied Mechanics and Materials Vols. 580-583 (2014) pp 1807-1811*
*© (2014) Trans Tech Publications, Switzerland*
*doi:10.4028/www.scientific.net/AMM.580-583.1807*

# Analysis of the Influence of Bottomland change on waterway conditions in Liyushang in middle reaches of the Yangtze River

Yude Zhu [1, a], Jun He[2, b]

[1]Tianjin Water Transport Engineering Science Institute, Ministry of Transport, Tianjin China 300456

[2] Tianjin Port & Channel Engineering Co., Ltd.,

[a]Zhuyude2800@sina.com, [b]22845474@qq.com

**Keywords:** The middle reaches of the Yangtze River, bottomland change, waterway conditions, Influence

**Abstract.** This study Base on the HuangLianzhou heart beaches and Shejiwang tidal flat of years of evolution, revealing the relationship between HuangLianzhou heart beaches and Shejiawan tidal flat erosion and Waterway conditions, and explore affecting factorsof the waterway poor conditions , which have a guiding significance for the solution to the current problem of the river channel.
Since the water storage of the Three Gorges Project, which subject to change on runoff and sediment, the middle reaches of the Yangtze River 'balance is broken, an increase in the length of the water, resulting in a lot of relaxation of the original section of marshland erosion, wide and shallow river to development, has gradually become a more unstable river type. Year of data in a limited variation between the marshland and waterways conditions become blurred, but relative to the increasingly grim situation waterways, water and sediment study islet in the new era of changing characteristics and relationship with the channel changing conditions but is engineering practice urgent need to solve the problem. In this paper, the recent variation of marshland landscape of the Middle Yangtze River LiyushanWaterway study [1,4], based on similar problems existing Liyushan waterway landscape studies, to provide a reference for waterway management.

## Waterway Overview

Liyushan Waterway landscape located at the end of the middle reaches of the Yangtze River, then put on a Gepaiji waterway, until next Wuxue waterways, long 13km (Figure.1). The middle of the river long maintained two narrow width slightly curved shape to relax, Waterway in the middle relaxed Panjiagang to the left bank plate Gonglongwan presence elongated side beach, beach side called Shejiawan, in the heart of partial relaxation of the right bank of the river segment kept bent Beach, namely HuangLianzhou heart Beach. HuangLianzhou section into the dry season will be relaxed about the two branches, bending the right slot, narrow and deep; left slot straight. Wide.

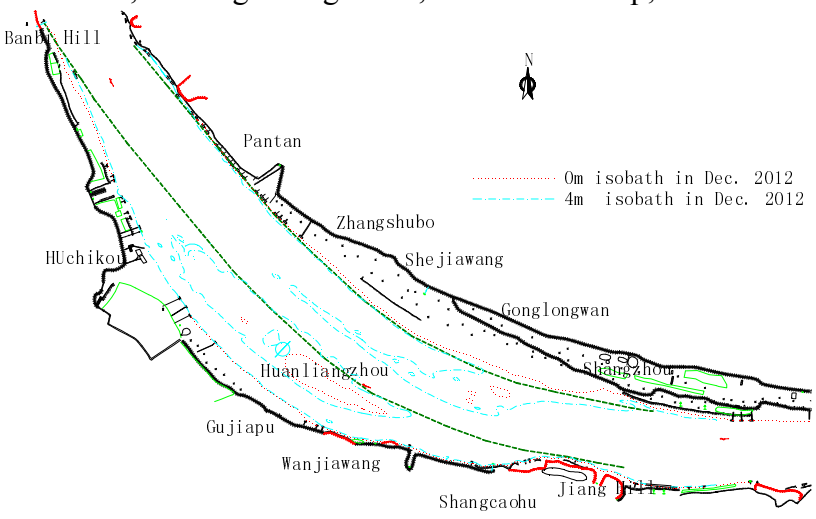


**Figure.1,River Regime Chart of Liyushan waterway**

Prior to 1998 Liyushan Waterway of Huang Lianzhou rely on the right bank of the landscape, in the form of side beaches, more stable, middle river channel, a good channel conditions. 1998 ~ 2008 Beach rushed back to the right and was cut Huang Lianzhou beach gradually developed heart formation, but relatively small-scale, local waterways often not satisfied 4 5m construction standards. Since 2008, Huang Lianzhou beach heart of a certain size, the North line width groove depth at 200m above 4.5m, etc. Overall, the north channel inlet and outlet points exist sandbags shallow water and sediment in adverse conditions

**Changes of erosion and river bottomland**

**Huanglianzhou heart beaches**

Right after the Three Gorges reservoir shore beach with red back, Huanglianzhou heart beaches form, since the heart of North Beach Huanglianzhou groove formed longitudinally little change; But the larger lateral position changes, the maximum amplitude at about 800m .

April 2008 before the beach is relatively small Huanglianzhou heart slowly silting smaller Huanglianzhou the silting process, the rapid development of deep red South Passage, north width shallow channel changing conditions and poor; April 2008 until January 2010, and in the heart Huanglianzhou Beach develop into a certain size, growth slowed South Passage, North Passage of the conditions improved markedly, this process Huanglianzhou despite some erosion, but still much larger than the range 0m line deposition cycle 2005 to 2008; 2010 to a relatively large amount of water, until February 2011, heart Beach siltation occurs, the area increases, the beach top siltation. The past two years, Huanglianzhou heart again in beach erosion state, south trough development, beach area continues to decrease heart of the dry season, in March 2012 the North remains shallow trough export package, the minimum depth of 3.8m; until April 2013, the occurrence of cardiac Beach the trend of erosion, beach body size has been reduced, but the beach crest elevation change little.

**Shejiawan side beach**

Since the mid-century, Shejiawan convex side beach shore beaches as long-standing , Shejiawan side beach 0m line changed little. Gorges reciprocating cyclical trends Shejiawan low beach erosion since Impoundment.

2003-2008 before Shejiawan whole red beach side retreat, head alternating erosion mainly in the red tail scour relatively large, since 2008 silt washed down the beach side. 2008 Beach rushed back to the right before the original period Huang Lianzhou develope into a certain size. In recent years, the two sides on the edge of the shallow beach area sections were washed back ( Figure 2 ) , in October 2007 where beach side development, the shallowest depth of about 0m ( sailing base , the same below ) ; until April 2008 , while beach substantial erosion, the maximum scour depth of about 7m; until September 2009 , while beach erosion reversal of deep grooves , the deepest water depth of about 10m; until November 2012 , the occurrence of large-scale deposition deep grooves , most shallow depth of about to 2.5m; until April 2013 , while beach erosion into the groove again , the maximum scour depth of about 6m. The above changes show that Shejiawan beach side bar high when part of the basic stability, low magnitude larger beach erosion and sediment under certain conditions, while the disc home Harbour and flood sediment silt is easy to fall into the beach , and in the dry season are red Beach into the slot ( Figure.2 ) reciprocating cyclical trends .

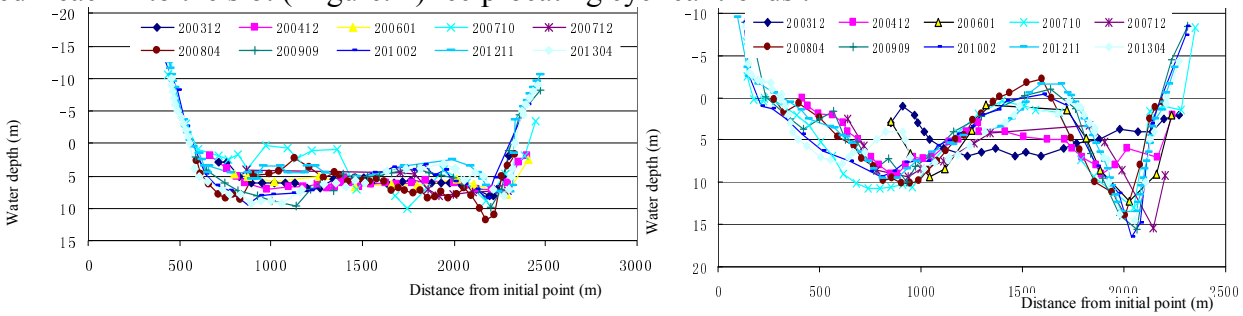


**Figure.2,Huanglianzhou near the characteristic change in erosion**

**Changes of marshland and waterways**

**Huanglianzhou heart beaches and Shejiawan side beach relationship analysis**

Before the Three Gorges Project , when Huanglianzhou beach erosion body atrophy , because power is more mainstream right, Shejiawan beach side beach at the edge of the hydrodynamic necessarily weaker, low beach beach beach side edge will be fully developed . When Huanglianzhou heart beach development , indicating that the water main axis of power left , sediment waters off the beach in the heart Huanglianzhou silt ,Huanglianzhou Chau body Expand , deep grooves abutting a certain degree of deviation from the mainstream Huanglianzhou body power , deep grooves difficult to obtain sufficient erosion, Shejiawan side beach beach erosion edge lower back . Prior to 1998, Shejiawan shore beach side bar and right shift ( Fig. 3) , such as the 1986 Huang Lianzhou side beach is relatively large , compared Shejiawan beach side development, but due to the mainstream of the 1990s, the South side, Huang Lianzhou erosion atrophy, the following paragraph on the right side of beach Shejiawan significantly developed . Therefore, Shejiawan beach and right on the shore side beach there is an obvious shift in the correspondence.

Since the Three Gorges Project , subject to significantly reduce the impact of sand , Shejiawan beach side beach and Huanglianzhou shift in the relationship between heart obvious . For example , from April 2008 to January 2010 ,Huanglianzhou Heart Beach, Shejiawan side beach segments have different levels of erosion, and the lower section of beach side Shejiawan siltation occurs ; January 2010 to February 2011 Huanglianzhou heart Beach, beach segments Shejiawan side siltation in varying degrees , and Shejiawan side beach erosion occurred following paragraph ; February 2011 to February 2012 Huang Lianzhou some beach erosion heart , Shejiawan slight edge segments beach erosion , the following paragraph Shejiawan side beach has siltation ; February 2012 to April 2013 Huanglianzhou heart beach erosion further reduced, Shejiawan side beach segments have siltation, erosion next paragraph , but exports form a shallow trough north ridge(Fig. 4).

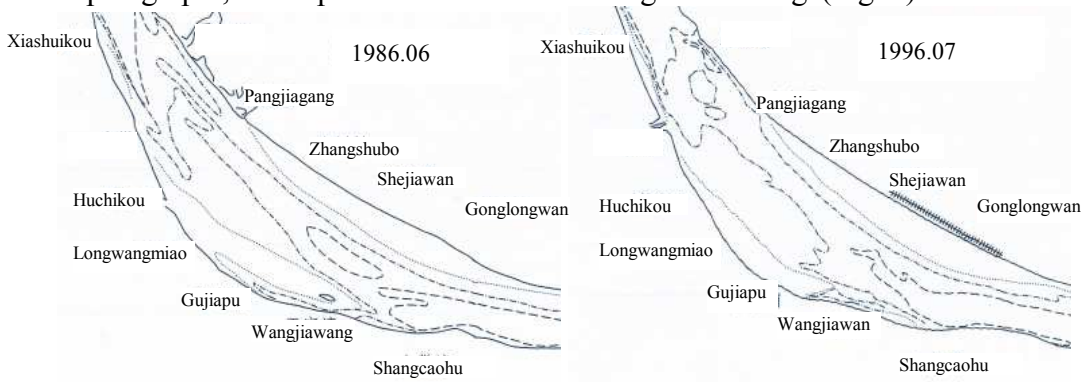


**Figure.3, Before 1998 Shejiawan and the right side beach shore beaches change**

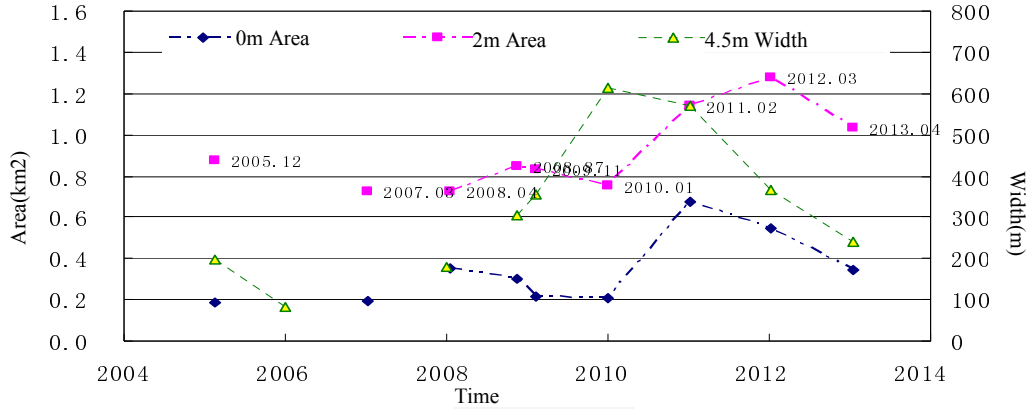


**Figure.4, Huanglianzhou area and 4.5m minimum width change**

**Recent changes in characteristics of marshland and waterways**

Right before the Three Gorges reservoir shore beaches due to be cut , relaxed segments form the dry north-south pattern of two slots , slots in a given period in southern bypass certain conditions, the pros and cons of the North Passage of the condition depends on the fairway on both sides of the boundary conditions change , that is, from the size of the heart and its changes Huanglianzhou beach and beach side Shejiawan common decision. Beach erosion when Huanglianzhou contraction , indicating longer flows through the heart of mainstream left edge of the beach , beach heart downsizing , downsizing heart beach , while the left edge of the beach abuts the heart of the main channel also developed ; same time as the more mainstream power right, SheJiaWan beach side beach at the edge of the hydrodynamic necessarily weaker, low beach -side edge of the development, expansion and development of the right side of beach , which narrowed the North Passage dry river is conducive to the main channel fairways improve conditions.When Huanglianzhou heart beach development,indicating that the water main axis of power left , sediment waters off the beach in the heart Huanglianzhou silt ,Huanglianzhou body scale , deep grooves abutting a certain degree of deviation from the main stream Huanglianzhou body power , deep grooves difficult to obtain sufficient erosion ; while Shejiawan side beach beach erosion edge lower back, dry river width increases, the channel condition is becoming worse. Therefore,can not be isolated from Huanglianzhou Island to correlate changes in body size or bad channel conditions, from both sides of the fairway boundary change considerations. After the Three Gorges reservoir , if there is enough sediment sources ,Huanglianzhou will vary with changes in dynamic conditions and or increase or decrease when increasing the channel conditions may be poor , otherwise good ; key is that when Huanglianzhou appears to promote its increasing when hydrodynamic conditions , if Huanglianzhou Chau body is small, and not enough sand source development of its size , its channel conditions than the larger continents body worse , because the smaller body means the North Passage Island more Shejiawan side beach beach flood low- margin growth in the dry river is great , this dynamic conditions , the adverse effects of water withdrawal cyclical process of erosion on the north passage down the fairway will be highlighted. Meanwhile if there is cause Huanglianzhou downsizing beach beach body hydrodynamic conditions, when the larger beach Huanglianzhou ,compared to the current channel conditions with better hydrodynamic conditions.

**Conclusions**

Before the impoundment of the Three Gorges Huanglianzhoure and Shejiawan beach body stable, and there is correspondence between the shift; after previous smaller Huanglianzhou Three Gorges reservoir silting process in South trough scour depth development rapid, shallow north width, changing channel conditions and poor in2008. Beach after Huanglianzhou develops into a certain size, growth slowed South Passage, North Passage of the conditions improved markedly in 2008

Due to the right shore beach Three Gorges reservoir is cut, which formed the dry northern and southern sections and relaxed groove pattern, a period of time in the South Passage shunt certain conditions, and the pros and cons of the North Passage of the condition depends on the both sides of the fairway boundary conditions and sediment volume changes, from the size of the heart and its changes Huanglianzhou beach and beach side Shejiawan joint decision cannot be isolated from the body size variation Huanglianzhou continents to associate good or bad channel conditions.

Affected by the great flood of 1998 imports of river scour depth development of the right side of the mainstream right-swing, the right shore beach cut; combined with water and sediment interception affected by the Three Gorges Project, North and South were scouring trough occurred while broadening the river, Huanglianzhou development, gradually formed the dry river-slot pattern, the Three Gorges reservoir destroy the correspondence between bottomland and waterway conditions.

**Acknowledgements**

This work was supported by Jingjiang waterway engineering science and technology projects in the YangtzeRiver,the National HighTechnology Research and Development Program(2012AA112508)

**References**

[1] Yude Zhu,Research on Physical Model Fixed Bed Experiment for Channel Regulation Works of Liyushan Reach in the Middle Reach of the Yangtze River Tianjin Water Transport Engineering Science Institute, In China, 2013

[2]Lin Jiang Feasibility Study Report on Channel Regulation Works of Liyushang Reach in the Middle Reach of the Yangtze River, The Yangtze River Channel Design Research Institute, In China, 2013.

[3] WS LI,. Some thoughts about technical problem on regulation of waterway in the middle and lower reach of the Yangze river Journal of Waterway and Harbor, 5(2006) 223-226, In China.

[4] YD ZHU. Discussion on waterway regulation ideas for XinZhou~JiuJiang reach in middle Yangtze River. Journal of Waterway and Harbor,2(2012) 130-134, In China.

*Applied Mechanics and Materials Vols. 580-583 (2014) pp 1812-1815*
*© (2014) Trans Tech Publications, Switzerland*
*doi:10.4028/www.scientific.net/AMM.580-583.1812*

# Analysis on Hydrodynamic Load that Induces High Dam Body Vibration

Chuntao Wang[1,a], Hongxia Ding[1,b], Hui Lv[2,c]

[1] college of science and technology, Nanchang University, 339 Beijing road, Nanchang,330000，Jiangxi, China

[2] Jiangxi Vocational College of Economic Management, 269 Wolong road, Nanchang,330088，Jiangxi, China

[a]lwct@sina.com, [b]83110281@qq.com, [c]154245788@qq.com

**Keywords:** arc dam, vibration, hydrodynamic load

**Abstract.** It is difficult to get a theoretic answer to the water flow load features of high dam flood discharge. Through direct measurement of water flow load features by arranging a surface pressure cell, the complicated point-surface conversion was avoided, and the shock load and surge load features were obtained. For the dam body outlet wall pressure, isolated the fluctuating load applied to the plunge pool floor and the downstream dam surface, the impact of the fluctuating load to the arch dam dynamic response at the flood discharge flow outlet was obtained, and then the equivalent fluctuating load on each discharge flow outlet was obtained by using flow-induced vibration back analysis. The test shows that the energy of the shock load and the surge load mainly centers in a frequency range between 0~1Hz, the shock load is about 2.5-6 times that of the surge load, and the surge load is about 4 times that of the outlet wall pressure.

## Introduction

The flood discharge mode of an arch dam can be divided into two modes: dam body flood discharge and bank side flood discharge. The dam body flood discharge refers to flood discharge by setting surface, mid-level (bottom) outlets as drainage galleries for flood discharge, while bank side flood discharge refers to flood discharge by the bank side spillway or flood discharge tunnel. Dam body outlet flood discharge can simplify the pivot arrangement and reduce engineering cost for flood discharge. In particular, with the development of underground opening technology and the use of modern construction method, the problem of the two major structures (flood discharge buildings and power station) occupying the riverbed position has been solved satisfactorily. For this reason, the mode of dam body outlet flood discharge has been used in many large arch dam pivotal projects in China, such as Ertan, Xiaowan, Xiluodu, Jinping, Goupitan and Laxiwa, etc.

The large power of high dam flood discharge leads to a very large flood discharge current load. Whether this flood discharge load will generate or not, through the foundation and the bank bedrock, a dynamic excitation to a high dam, resulting in the dam body and the dam abutment generating a flow-induced vibration that exceeds the allowable range, is a significant issue that relates to the engineering safety of a high arch dam.

The flood discharge load applied to a dam body includes the shock load and surge load in the downstream riverbed, the dam body outlet fluctuating wall pressure and the storm wave load. The magnitude of the storm wave load can be calculated according to some measured data, such as the wind speed, the wave height and etc. However, the determination of the flood discharge current load, including the shock load, the surge load and the dam body outlet fluctuating wall pressure, is more difficult. In particular, though a lot of work has been done in respect of the shock load [1-4], little is known about the amplitude and the frequency of the flood discharge current fluctuating load and the point-surface conversion, therefore, it is relatively a reliable method of obtain the flood discharge current load by model test.

**Test Establishment**

Xiaowan high arch dam was selected for the model test, the model scope includes the whole dam body (including the surface outlet, mid-level outlet and bottom outlet), and the downstream river stilling basin. The model scale was 1:150.

$P_D'$ represents the dynamic load generated by the submerged impinging jet striking the downstream riverbed; $P_L'$ represents the dynamic load directly applied to the dam body by the discharge flow-induced surge in the plunge pool; $P_K'$ represents the dynamic load generated by the discharge flow to the outlet wall. These fluctuating loads are continuously distributed random loads, and the fluctuating pressure at each point changes with the spatial position and the time. To avoid the complex point-surface conversion, a pressure cell was used in the test to measure various current loads.

To test the surface fluctuating load, a $32\times15\,cm^2$ surface pressure cell was arranged on the plunge pool floor. When the surface outlet discharged flood separately, the pressure cell was installed on the floor chainage 0+165 $m$. When the mid-level outlet discharged separately, the pressure cell was installed on the floor chainage 0+290 $m$. When they discharged jointly, the installation chainage was 0+210 $m$. A $32\times15\,cm^2$ surface pressure cell was also arranged on the arch dam downstream dam to measure the surface fluctuating pressure of the surge in the plunge pool to the downstream dam. As the mode of action and position of the fluctuating load acting on the outlet was very complex and hard to measure directly, a test method was used to isolate the fluctuating load acting on the plunge pool floor and the arch dam downstream dam (the method was to draw away the falling overflow so that it would not strike the plunge pool), to obtain the impact of the fluctuating load on the discharge flow outlet to the arch dam dynamic response, and the flow-induced vibration back-analysis[5] was used to solve the “equivalent” fluctuating load on each discharge flow outlet, and to establish a correlativity between the flood discharge flow head and the “equivalent" fluctuating load.

**Results and Discussions**

The testing results of $P_D'$ and $P_L'$ for various discharge flow working conditions of Xiaowan arch dam are shown in Table 1:

Table 1 Overall fluctuating load of Xiaowan high arch dam (root mean square value) [KPa]

| Working condition | Check flood level joint flood discharge | | Design flood level joint flood discharge | | Normal pool level surface outlet separate flood discharge | |
|---|---|---|---|---|---|---|
| | Shock | Surge | Shock | Surge | Shock | Surge |
| Root mean square value of the load | 22.0 | 4.90 | 19.6 | 4.80 | 18.2 | 3.70 |

Generally speaking, the shock fluctuating load to the plunge pool floor increases monotonically with the decrease of the downstream depth of water; and the overall surge fluctuating load to the dam body downstream surface shows little change with the downstream water level, and it generally increases slightly with the downstream depth of water; both the fluctuating loads generally increase with the rise of the upper level. With different combinations of the upstream and downstream water level, the root mean square value of the shock overall fluctuating load on the floor is usually 2.5~6 times that of the surge overall fluctuating load on the dam body downstream surface, and the specific value of the two decreases with the increase of the downstream water depth. The surface fluctuating pressure to the plunge pool floor generated by the flood discharge is the greatest at the joint flood discharge, mid-level outlet separate flood discharge is lightly higher than the surface outlet flood discharge while the hydrodynamic shock pressure measured with a piezometric tube shows that the surface outlet flood discharge is higher than the mid-level flood discharge. The analysis indicates that rolling magnitude in the plunge pool generated by the mid-level outlet discharge is larger than that of the surface outlet, and the synchronous action scope of the fluctuating pressure is great, therefore, the

amplitude reflected on the surface fluctuating pressure is that the mid-level outlet discharge is slightly higher than the surface outlet discharge. The typical time history pressure is shown in Fig. 1.

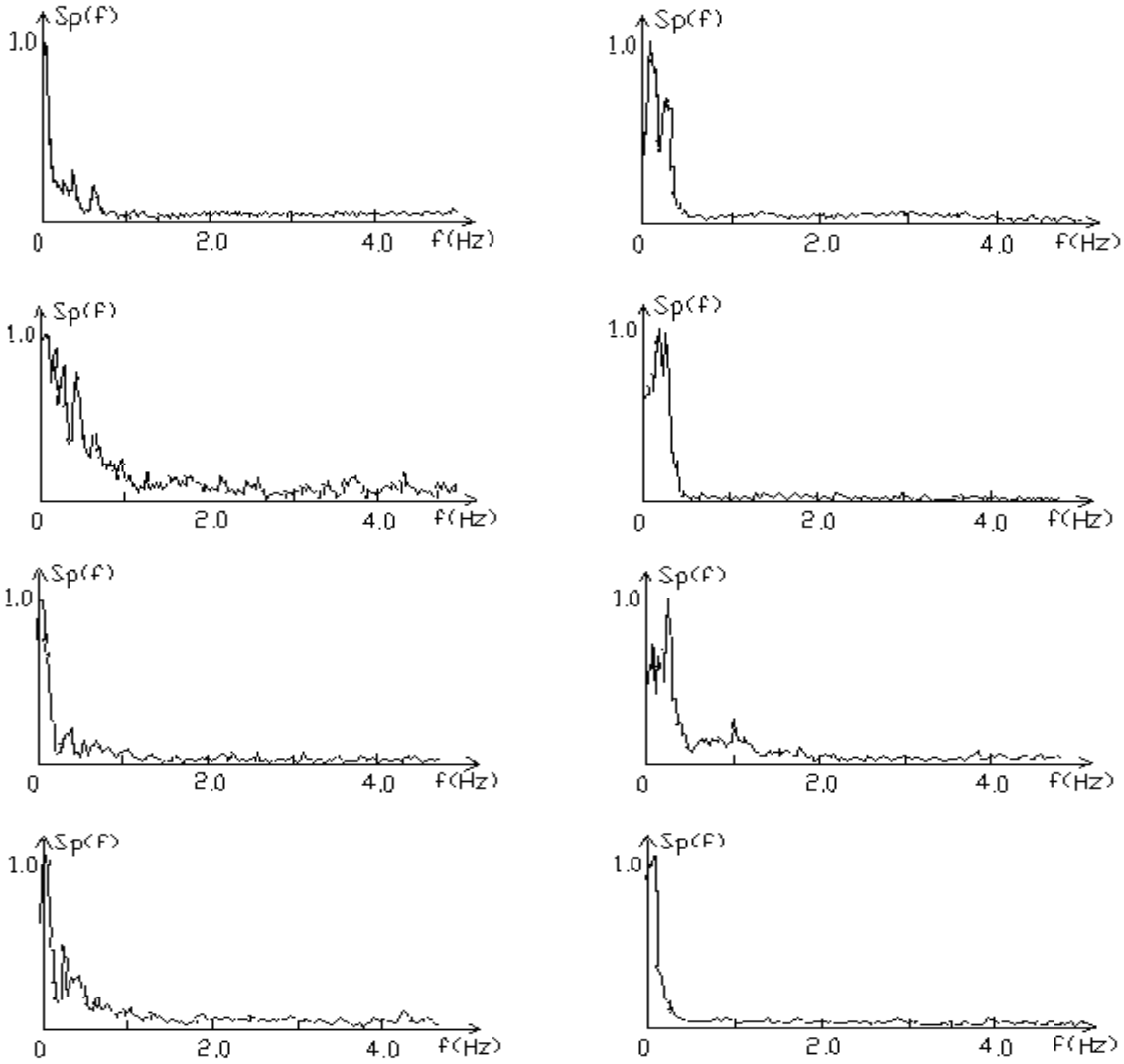


Shock fluctuating load spectrograph Surge fluctuating load spectrograph

Fig. 1 Typical surface fluctuating load spectrograph

The energy of the overall fluctuating load is distributed in a frequency scope of 0~5Hz, and mainly concentrates in a frequency scope of less than 1Hz , which belongs to a low frequency fluctuation. The frequency spectrum of the overall (surface) fluctuating load is shown in Fig. 2.

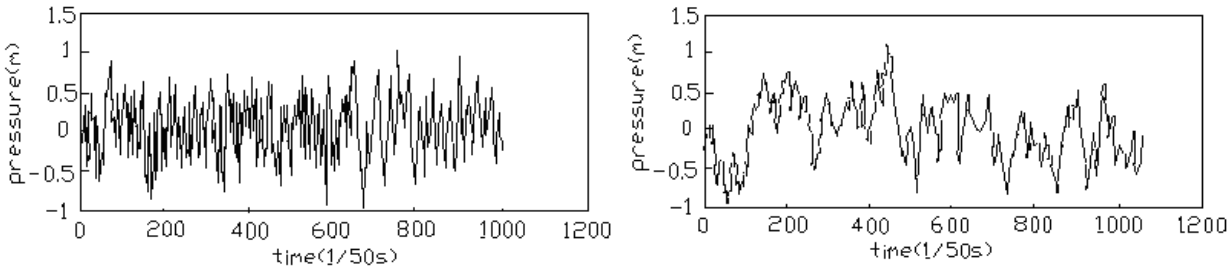


Shock fluctuating load hydrograph Surge fluctuating load hydrograph

Fig. 2 Typical surface fluctuating load hydrograph

The fluctuating pressure $P'$ acting on the discharge outlet side wall can be regarded as having a relation with the kinetic head $U^2/2g$ as follow:

$$P' = \alpha U^2/2g . \quad (1)$$

α should change with the flow regime, and the overall fluctuating load on the outlet can be regarded as being in direct proportion to the fluctuating pressure $P_K^{'}$ and the action area $A^{'}$. Let the action area and the discharge area have: $A^{'}$=βA, then the overall fluctuating load on the outlet has:

$$P_K^{'} = \alpha \frac{U^2}{2g} \beta A = C_f Q \sqrt{H} \tag{2}$$

Where $Q$ is the discharge quantity, calculated in $m^3/s$, and $H$ is the acting head in the outlet, calculated in $m$. The dynamic response under the fluctuating load on the discharge flow outlet is measured through isolating the plunge pool shock and surge fluctuating load, then the "equivalent" fluctuating load is analyzed from the feedback, the mid-level outlet overall fluctuating load $C_f$ can be obtained, which may be taken as $9\times10^{-3}$, and the surface outlet overall fluctuating load $C_f$ can be taken as $7\times10^{-3}$.The outlet overall fluctuating load of the outlet can be estimated in line with the above formula. Normally, 1/4 of the downstream surge can be taken as the outlet overall fluctuating load.

## Conclusion

The floor block would not be acted upon by an uplift force if the plunge pool floor joints are in a good condition, but would bear a significantly large shock load. In this paper, the surge load applied to the dam face downstream and the shock load applied to the plunge pool floor are measured through a model test, the load root mean square value under a specific upstream and downstream water level is given, the relation of magnitude between the two is studied and the respective frequency spectrum is provided.

As it is impossible to measure directly the outlet fluctuating wall pressure of the dam body, the method of isolating other flood discharge flow load is applied, so that the response is generated entirely from the outlet wall pressure, and then the outlet wall pressure load can be obtained by back-analysis on this response. Finally, 1/4 of the downstream surge can be used as the outlet overall fluctuating load for approximate analysis.

## References

[1] Lin Jiyong, Lian Jijian, Calculation of Amplitude of Point-Surface Fluctuating Wall Pressure under Binary Jet Action, Journal of Hydraulic Engineering, December 1988, P34~40. In Chinese.

[2] Huang Zhongwei, Chen Jin, Experimental Study on Dynamic Water Pressure of High Arch Dam Flood Discharge and Plunge Pool Floor, Journal of Hydraulic Engineering, November 1992, P50~56. In Chinese.

[3] Xu Duoming, Yu Changzhao, Impact Pressure of Plane Jet on River Channel Bottom and Its Fluctuating Features, Journal of Hydraulic Engineering, May 1983, P52~58. In Chinese.

[4] Cui Guangtao, Chen Rongguang, Lin Jiyong, Dynamic Water Pressure of Submerged Impinging Jet on Riverbed and Issue of Bedrock Protection, Journal of Tianjin University, February. 1982. In Chinese.

[5] Lian Jijian, Cui Guangtao et al, Back-analysis on Flow-induced Vibration Response of Hydraulic Structure, Water Resources and Hydraulic Engineering, August 1998, 51~54. In Chinese.

*Applied Mechanics and Materials Vols. 580-583 (2014) pp 1816-1822*
*© (2014) Trans Tech Publications, Switzerland*
*doi:10.4028/www.scientific.net/AMM.580-583.1816*

# Analysis on seepage effects of plastic concrete cut-off wall in construction and operation period of hydropower station tail channel

Yan Guoxin[1, 2,a], Wu Wei[1,2,b]

[1]Yellow River Conservancy Technical Institute, Kaifeng, China 475004

[2]Engineering Technology Research Center of Small Watershed Conservancy University of Henan Province, Kaifeng, China 475004

[a]hhsyygx@163.com, [b]hhswww@163.com

**Keywords:** plastic concrete; numerical simulation; seepage field; cut-off wall

**Abstract.** By numerical calculation, it analyzed the seepage effects of plastic concrete cut-off wall in in construction period. On construction period, the seepage flow from inside of channel to outside at unit length is 0.753m$^3$/h. The seepage flow from under plastic concrete cut-off wall is 0.646m$^3$/h which is 85.79% of total seepage flow. Under certain condition on operation period, the seepage flow from inside of channel to outside at unit length is 0.394m$^3$/h. The seepage flow from under plastic concrete cut-off wall is 0.358m$^3$/h which is 90.86% of total seepage flow. Under another condition on operation period, the seepage flow from inside of channel to outside at unit length is 0.249m$^3$/h. The seepage flow from under plastic concrete cut-off wall is 0.236m$^3$/h which is 94.78% of total seepage flow. In It showed the plastic concrete cut-off wall has obvious effect.

## Introduction

In hydraulic projects, the seepage problems of main structures is an important practical problems which must be solved in the process of design and construction[1].The ordinary treating measures are concrete cut-off wall. It uses special machines to make grooves and holes on the permeable foundation of covering layer and to pump mud into them. The mud fixes the walls of grooves and holes. And then, it uses conduit to pour concrete into grooves and holes which replaces mud. The continuous concrete wall is constructed to cut off seepage flow.

Plastic concrete cut-off wall develops to solve problems of rigid concrete cut-off wall. It uses mixed materials of clay and bentonite to replace some cement in ordinary concrete. It is a soft wall[2].

It established mathematical model of geotechnical seepage by numerical analysis[3]. Under different operating conditions in construction and operation periods, it concretely analyzed the effect of plastic concrete cut-off wall in tailing water channel of hydropower station which can give references to solve similar problems.

## Calculating conditions

According to problems concerned in design and construction, it chose classic cross sections to simulate which referred to seepage field, seepage stability and seepage flow discharge in construction period, and forecasted seepage field in operation period. Table 1 shows the calculating conditions.

Table 1 Calculating conditions

| No. | condition | Elevation of water level outside channel（m） | Elevation of water level inside channel（m） |
|---|---|---|---|
| 1 | construction period | 420.00 | 398.00 |
| 2 | no hydropower unit operating | 419.00 | 411.00 |
| 3 | one hydropower unit operating | 410.00 | 403.50 |

**Numerical calculation of FEM for effect of plastic concrete cut-off wall in construction period**

In construction period, in numerical simulated zone, the elevation of bottom is 360m and the elevation of top is 420.5m. The horizontal distance is from center line to 156m left far away. Meshing the computation zone, there are 4259 elements and 2372 jets. The FEM model is shown in Fig 1.

According to simulation calculation of seepage field in construction period, the results are got. The overflow of saturation line is under drift sand and gravel filling layer. The elevation of overflow is 402.50m. In unit length, the seepage flow discharge from outside of channel to inside of channel is $2.0905\times10^{-4}m^3/s$. The seepage flow discharge under plastic concrete cut-off wall is $1.7942\times10^{-4}m^3/s$. That means, in unit length, the seepage flow discharge from outside to inside of channel is $0.753m^3/h$ and the seepage flow discharge under plastic concrete cut-off wall is $0.646m^3/h$.

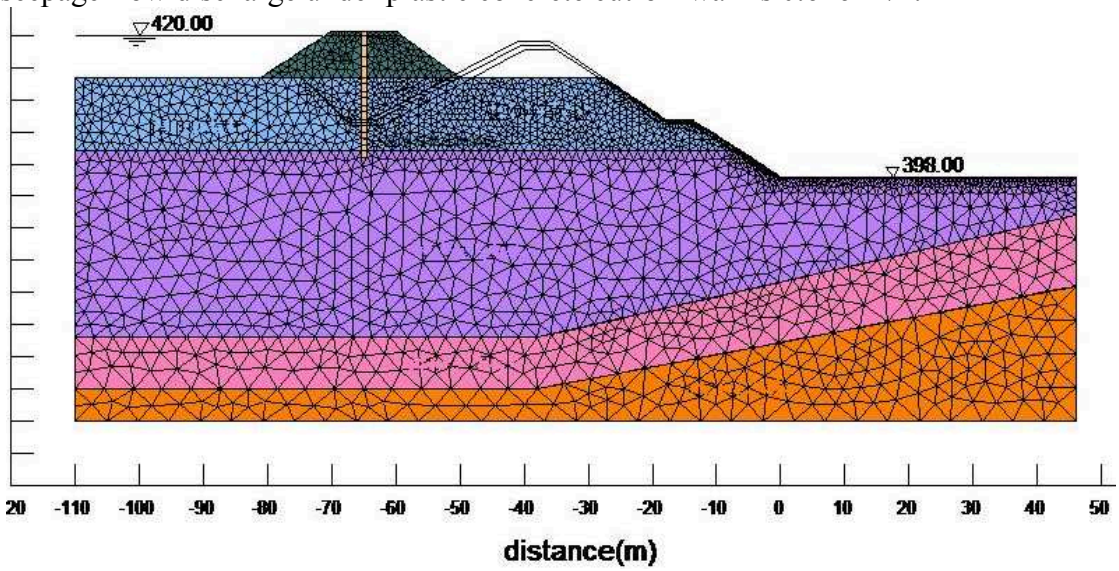


Fig 1 Grids meshing of FEM in computation zone in operating condition of No.1

It shows that there is 85.79% of total seepage flow discharge from outside to inside of tailing water channel through cut-off wall. Cut-off wall has good effect. The seepage flow discharge of $0.753m^3/h$ from outside to inside of tailing water channel is allowed in construction process.

In Table 2, the hydraulic slope in cut-off wall is 3.76～7.90 which is less than allowable hydraulic slope and makes seepage stable.

Table 2 Hydraulic gradients in front of and behind cut-off wall

| Y value of cut-off wall | Hydraulic slope of in front of cut-off wall | Hydraulic slope of behind cut-off wall |
|---|---|---|
| 4.01E+02 | 4.31E+00 | 3.76E+00 |
| 4.02E+02 | 7.02E+00 | 5.76E+00 |
| 4.03E+02 | 6.24E+00 | 6.24E+00 |
| 4.04E+02 | 6.27E+00 | 6.27E+00 |
| 4.05E+02 | 6.30E+00 | 5.25E+00 |
| 4.06E+02 | 6.31E+00 | 6.31E+00 |
| 4.07E+02 | 7.90E+00 | 7.90E+00 |
| 4.07E+02 | 6.33E+00 | 5.28E+00 |
| 4.08E+02 | 6.32E+00 | 6.34E+00 |
| 4.09E+02 | 6.25E+00 | 6.29E+00 |
| 4.10E+02 | 6.18E+00 | 6.24E+00 |
| 4.11E+02 | 6.13E+00 | 6.19E+00 |
| 4.12E+02 | 6.09E+00 | 6.16E+00 |
| 4.14E+02 | 5.09E+00 | 5.13E+00 |
| 4.15E+02 | 6.11E+00 | 6.14E+00 |

| | | |
|---|---|---|
| 4.17E+02 | 6.10E+00 | 5.12E+00 |
| 4.18E+02 | 6.10E+00 | 6.13E+00 |
| 4.20E+02 | 5.08E+00 | 4.39E+00 |
| 4.21E+02 | 7.62E+00 | 7.64E+00 |

In Table 3, it is shown that the pore water pressure head changes from 17.7m in front of cut-off wall to 5.30m behind cut-off wall. Cut-off wall has an obvious influence on decreasing pressure head. The decreasing of pressure head of pore water is very good for stability of channel seepage. Table 3 shows cut-off wall plays an important role.

Table 3 Pressure head at elevation of 402m under operation condition of No.1

| jet | X value | Pressure head （m） | | jet | X value | Pressure head （m） |
|---|---|---|---|---|---|---|
| 1 | -1.10E+02 | 1.80E+01 | | 38 | -5.37E+01 | 4.87E+00 |
| 2 | -1.08E+02 | 1.80E+01 | | 39 | -5.23E+01 | 4.80E+00 |
| 3 | -1.07E+02 | 1.80E+01 | | 40 | -5.10E+01 | 4.74E+00 |
| 4 | -1.05E+02 | 1.80E+01 | | 41 | -4.96E+01 | 4.67E+00 |
| 5 | -1.04E+02 | 1.80E+01 | | 42 | -4.82E+01 | 4.59E+00 |
| 6 | -1.02E+02 | 1.80E+01 | | 43 | -4.69E+01 | 4.52E+00 |
| 7 | -1.00E+02 | 1.80E+01 | | 44 | -4.55E+01 | 4.44E+00 |
| 8 | -9.89E+01 | 1.80E+01 | | 45 | -4.41E+01 | 4.36E+00 |
| 9 | -9.73E+01 | 1.80E+01 | | 46 | -4.28E+01 | 4.28E+00 |
| 10 | -9.57E+01 | 1.80E+01 | | 47 | -4.14E+01 | 4.20E+00 |
| 11 | -9.41E+01 | 1.80E+01 | | 48 | -4.00E+01 | 4.11E+00 |
| 12 | -9.25E+01 | 1.80E+01 | | 49 | -3.87E+01 | 4.02E+00 |
| 13 | -9.09E+01 | 1.80E+01 | | 50 | -3.73E+01 | 3.93E+00 |
| 14 | -8.93E+01 | 1.80E+01 | | 51 | -3.60E+01 | 3.84E+00 |
| 15 | -8.77E+01 | 1.79E+01 | | 52 | -3.46E+01 | 3.75E+00 |
| 16 | -8.61E+01 | 1.79E+01 | | 53 | -3.32E+01 | 3.65E+00 |
| 17 | -8.45E+01 | 1.79E+01 | | 54 | -3.19E+01 | 3.55E+00 |
| 18 | -8.29E+01 | 1.79E+01 | | 55 | -3.05E+01 | 3.45E+00 |
| 19 | -8.13E+01 | 1.79E+01 | | 56 | -2.91E+01 | 3.34E+00 |
| 20 | -7.97E+01 | 1.79E+01 | | 57 | -2.78E+01 | 3.23E+00 |
| 21 | -7.81E+01 | 1.79E+01 | | 58 | -2.64E+01 | 3.12E+00 |
| 22 | -7.66E+01 | 1.79E+01 | | 59 | -2.50E+01 | 3.00E+00 |
| 23 | -7.50E+01 | 1.79E+01 | | 60 | -2.37E+01 | 2.88E+00 |
| 24 | -7.34E+01 | 1.78E+01 | | 61 | -2.23E+01 | 2.76E+00 |
| 25 | -7.18E+01 | 1.78E+01 | | 62 | -2.09E+01 | 2.62E+00 |
| 26 | -7.02E+01 | 1.78E+01 | | 63 | -1.96E+01 | 2.49E+00 |
| 27 | -6.86E+01 | 1.77E+01 | | 64 | -1.82E+01 | 2.34E+00 |
| 28 | -6.70E+01 | 1.77E+01 | | 65 | -1.69E+01 | 2.19E+00 |
| **29** | **-6.54E+01** | **1.77E+01** | **In front of cut-off wall** | 66 | -1.55E+01 | 2.03E+00 |
| **30** | **-6.46E+01** | **5.30E+00** | **Behind cut-off wall** | 67 | -1.41E+01 | 1.86E+00 |
| 31 | -6.32E+01 | 5.26E+00 | | 68 | -1.28E+01 | 1.68E+00 |
| 32 | -6.19E+01 | 5.21E+00 | | 69 | -1.14E+01 | 1.47E+00 |
| 33 | -6.05E+01 | 5.16E+00 | | 70 | -1.00E+01 | 1.24E+00 |
| 34 | -5.91E+01 | 5.11E+00 | | 71 | -8.66E+00 | 9.75E-01 |

| | | | | | |
|---|---|---|---|---|---|
| 35 | -5.78E+01 | 5.05E+00 | 72 | -7.30E+00 | 5.98E-01 |
| 36 | -5.64E+01 | 4.99E+00 | 73 | -6.60E+00 | 2.52E-01 |
| 37 | -5.51E+01 | 4.93E+00 | 74 | -6.20E+00 | 0.00E+00 |

**Numerical calculation of FEM for effect of plastic concrete cut-off wall under operating condition in operation period**

There are two operating conditions in operation period of hydropower station. They are operation condition of No.2 and operation condition of No.3 For the two operation conditions, the grids meshing of FEM are same. In the numerical simulation zone, the elevation of bottom is 360m and the elevation of top is 419m. The horizontal distance is from center line of tailing water channel to 156m left far away. Meshing the computation zone, there are 4259 elements and 2372 jets. The FEM model is shown in Fig 2.

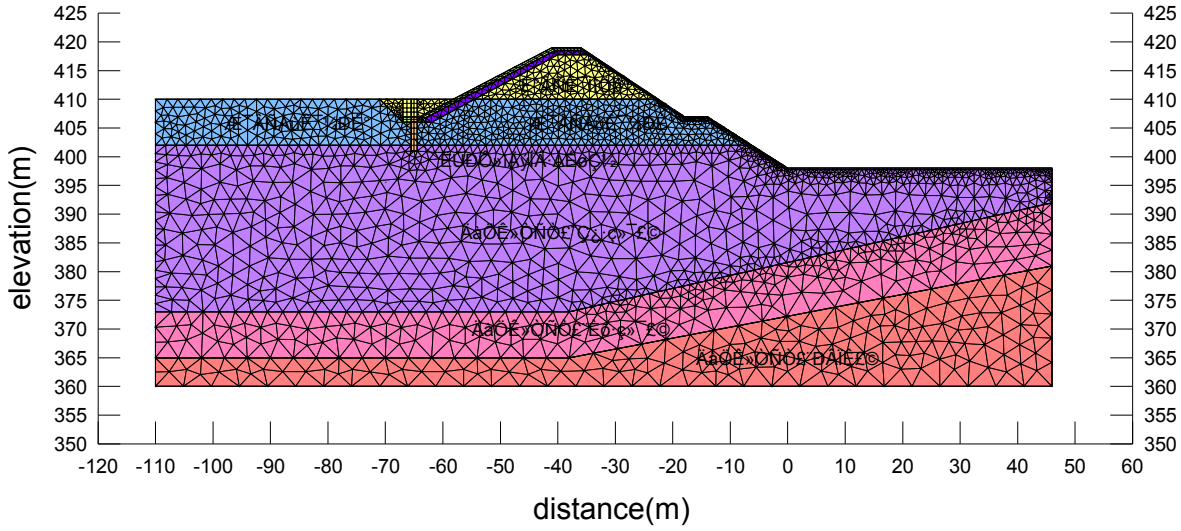


Fig 2 Grids meshing of FEM in computation zone in operating condition of No.2 and No.3

### 3.1 Numerical calculation of FEM for effect of plastic concrete cut-off wall under operating condition of No.2

According to calculation results , the factors of seepage field in calculation zone are got. In unit length, the seepage flow discharge from outside of channel to inside of channel is $1.0948\times10^{-4}m^3/h$. The seepage flow discharge under plastic concrete cut-off wall is $9.9583\times10^{-5}m^3/h$. It means that 90.86% total seepage flow discharge goes under plastic concrete cut-off wall. The plastic concrete cut-off wall has a good effect.

In Table 4, because of plastic concrete cut-off wall occurring, the pressure head changes from 16.9m in front of cut-off wall to 9.54m behind of cut-off wall.

Table 4 Pressure head at elevation of 402m under operation condition of No.2

| jet | X value | Pressure head | | jet | X value | Pressure head |
|---|---|---|---|---|---|---|
| 1 | -1.10E+02 | 1.70E+01 | | 36 | -5.38E+01 | 9.39E+00 |
| 2 | -1.08E+02 | 1.70E+01 | | 37 | -5.25E+01 | 9.38E+00 |
| 3 | -1.06E+02 | 1.70E+01 | | 38 | -5.12E+01 | 9.36E+00 |
| 4 | -1.05E+02 | 1.70E+01 | | 39 | -4.99E+01 | 9.35E+00 |
| 5 | -1.03E+02 | 1.70E+01 | | 40 | -4.85E+01 | 9.33E+00 |
| 6 | -1.01E+02 | 1.70E+01 | | 41 | -4.72E+01 | 9.32E+00 |
| 7 | -9.93E+01 | 1.70E+01 | | 42 | -4.59E+01 | 9.30E+00 |
| 8 | -9.75E+01 | 1.70E+01 | | 43 | -4.45E+01 | 9.29E+00 |
| 9 | -9.58E+01 | 1.70E+01 | | 44 | -4.32E+01 | 9.27E+00 |
| 10 | -9.40E+01 | 1.70E+01 | | 45 | -4.19E+01 | 9.26E+00 |
| 11 | -9.22E+01 | 1.70E+01 | | 46 | -4.05E+01 | 9.24E+00 |
| 12 | -9.04E+01 | 1.70E+01 | | 47 | -3.92E+01 | 9.23E+00 |
| 13 | -8.86E+01 | 1.70E+01 | | 48 | -3.79E+01 | 9.21E+00 |
| 14 | -8.69E+01 | 1.70E+01 | | 49 | -3.65E+01 | 9.19E+00 |
| 15 | -8.51E+01 | 1.70E+01 | | 50 | -3.52E+01 | 9.18E+00 |
| 16 | -8.33E+01 | 1.70E+01 | | 51 | -3.39E+01 | 9.16E+00 |
| 17 | -8.15E+01 | 1.70E+01 | | 52 | -3.25E+01 | 9.15E+00 |
| 18 | -7.97E+01 | 1.70E+01 | | 53 | -3.12E+01 | 9.13E+00 |
| 19 | -7.80E+01 | 1.70E+01 | | 54 | -2.99E+01 | 9.11E+00 |
| 20 | -7.62E+01 | 1.70E+01 | | 55 | -2.86E+01 | 9.10E+00 |
| 21 | -7.44E+01 | 1.70E+01 | | 56 | -2.72E+01 | 9.08E+00 |
| 22 | -7.26E+01 | 1.69E+01 | | 57 | -2.59E+01 | 9.07E+00 |
| 23 | -7.08E+01 | 1.69E+01 | | 58 | -2.46E+01 | 9.06E+00 |
| 24 | -6.91E+01 | 1.69E+01 | | 59 | -2.32E+01 | 9.04E+00 |
| 25 | -6.73E+01 | 1.69E+01 | | 60 | -2.19E+01 | 9.03E+00 |
| **26** | **-6.55E+01** | **1.69E+01** | **In front of cut-off wall** | 61 | -2.06E+01 | 9.03E+00 |
| **27** | **-6.50E+01** | **1.32E+01** | **In cut-off wall** | 62 | -1.92E+01 | 9.02E+00 |
| **28** | **-6.45E+01** | **9.54E+00** | **Behind of cut-off wall** | 63 | -1.79E+01 | 9.01E+00 |
| 29 | -6.32E+01 | 9.52E+00 | | 64 | -1.66E+01 | 9.01E+00 |
| 30 | -6.18E+01 | 9.50E+00 | | 65 | -1.52E+01 | 9.01E+00 |
| 31 | -6.05E+01 | 9.48E+00 | | 66 | -1.39E+01 | 9.00E+00 |
| 32 | -5.92E+01 | 9.46E+00 | | 67 | -1.26E+01 | 9.00E+00 |
| 33 | -5.78E+01 | 9.44E+00 | | 68 | -1.12E+01 | 9.00E+00 |
| 34 | -5.65E+01 | 9.43E+00 | | 69 | -9.91E+00 | 9.00E+00 |
| 35 | -5.52E+01 | 9.41E+00 | | 70 | -8.58E+00 | 9.00E+00 |

### 3.2 Numerical calculation of FEM for effect of plastic concrete cut-off wall under operating condition of No.3

According to calculation results , the factors of seepage field in calculation zone are got. In unit length, the seepage flow discharge from outside of channel to inside of channel is $6.9140\times10^{-5}m^3/h$. The seepage flow discharge under plastic concrete cut-off wall is $6.5565\times10^{-5}m^3/h$. It means that 94.78% total seepage flow discharge goes under plastic concrete cut-off wall. The plastic concrete cut-off wall has a good effect.

In Table 5, it is shown that the pressure head at left of cut-off wall is 7.92m, in the middle of cut-off wall 5.57m and behind cut-off wall 3.23m. The pressure head decreasing through cut-off wall is 4.69m. After cut-off wall, the pressure head decreasing through drift gravel and sand layer is 1.69m.

Table 5 Pressure head at elevation of 402m under operation condition of No.3.

| jet | X value | Pressure head (m) | | jet | X value | Pressure head (m) |
|---|---|---|---|---|---|---|
| 1 | -1.10E+02 | 8.00E+00 | | 36 | -5.38E+01 | 3.05E+00 |
| 2 | -1.08E+02 | 7.99E+00 | | 37 | -5.25E+01 | 3.02E+00 |
| 3 | -1.06E+02 | 7.99E+00 | | 38 | -5.12E+01 | 2.99E+00 |
| 4 | -1.05E+02 | 7.99E+00 | | 39 | -4.99E+01 | 2.96E+00 |
| 5 | -1.03E+02 | 7.99E+00 | | 40 | -4.85E+01 | 2.93E+00 |
| 6 | -1.01E+02 | 7.99E+00 | | 41 | -4.72E+01 | 2.90E+00 |
| 7 | -9.93E+01 | 7.99E+00 | | 42 | -4.59E+01 | 2.87E+00 |
| 8 | -9.75E+01 | 7.99E+00 | | 43 | -4.45E+01 | 2.83E+00 |
| 9 | -9.58E+01 | 7.99E+00 | | 44 | -4.32E+01 | 2.80E+00 |
| 10 | -9.40E+01 | 7.99E+00 | | 45 | -4.19E+01 | 2.76E+00 |
| 11 | -9.22E+01 | 7.99E+00 | | 46 | -4.05E+01 | 2.73E+00 |
| 12 | -9.04E+01 | 7.99E+00 | | 47 | -3.92E+01 | 2.69E+00 |
| 13 | -8.86E+01 | 7.99E+00 | | 48 | -3.79E+01 | 2.66E+00 |
| 14 | -8.69E+01 | 7.99E+00 | | 49 | -3.65E+01 | 2.62E+00 |
| 15 | -8.51E+01 | 7.99E+00 | | 50 | -3.52E+01 | 2.58E+00 |
| 16 | -8.33E+01 | 7.99E+00 | | 51 | -3.39E+01 | 2.54E+00 |
| 17 | -8.15E+01 | 7.98E+00 | | 52 | -3.25E+01 | 2.50E+00 |
| 18 | -7.97E+01 | 7.98E+00 | | 53 | -3.12E+01 | 2.46E+00 |
| 19 | -7.80E+01 | 7.98E+00 | | 54 | -2.99E+01 | 2.41E+00 |
| 20 | -7.62E+01 | 7.98E+00 | | 55 | -2.86E+01 | 2.37E+00 |
| 21 | -7.44E+01 | 7.97E+00 | | 56 | -2.72E+01 | 2.33E+00 |
| 22 | -7.26E+01 | 7.97E+00 | | 57 | -2.59E+01 | 2.28E+00 |
| 23 | -7.08E+01 | 7.96E+00 | | 58 | -2.46E+01 | 2.23E+00 |
| 24 | -6.91E+01 | 7.95E+00 | | 59 | -2.32E+01 | 2.19E+00 |
| 25 | -6.73E+01 | 7.93E+00 | | 60 | -2.19E+01 | 2.14E+00 |
| **26** | **-6.55E+01** | **7.92E+00** | **In front of cut-off wall** | 61 | -2.06E+01 | 2.09E+00 |
| **27** | **-6.50E+01** | **5.57E+00** | **In cut-off wall** | 62 | -1.92E+01 | 2.03E+00 |
| **28** | **-6.45E+01** | **3.23E+00** | **Behind of cut-off wall** | 63 | -1.79E+01 | 1.98E+00 |
| 29 | -6.32E+01 | 3.22E+00 | | 64 | -1.66E+01 | 1.92E+00 |
| 30 | -6.18E+01 | 3.20E+00 | | 65 | -1.52E+01 | 1.87E+00 |
| 31 | -6.05E+01 | 3.18E+00 | | 66 | -1.39E+01 | 1.81E+00 |
| 32 | -5.92E+01 | 3.15E+00 | | 67 | -1.26E+01 | 1.74E+00 |
| 33 | -5.78E+01 | 3.13E+00 | | 68 | -1.12E+01 | 1.68E+00 |
| 34 | -5.65E+01 | 3.11E+00 | | 69 | -9.91E+00 | 1.61E+00 |
| 35 | -5.52E+01 | 3.08E+00 | | 70 | -8.58E+00 | 1.54E+00 |

## Conclusions

(1) According to simulation calculation of seepage field in construction period, in unit length, the seepage flow discharge from outside to inside of channel is0.753 $m^3/h$ and the seepage flow discharge under plastic concrete cut-off wall is 0.646 $m^3/h$. There is 85.79% of total seepage flow discharge from outside to inside of tailing water channel through cut-off wall.

(2) According to simulation calculation of seepage field under operating condition of No.2, the seepage flow from inside of channel to outside at unit length is 0.394m3/h. The seepage flow from under plastic concrete cut-off wall is 0.358m3/h which is 90.86％ of total seepage flow. The decreased hydraulic head through plastic concrete cut-off wall is 7.36m which is 90% of total decreased hydraulic head.

(3) According to simulation calculation of seepage field under operating condition of No.3, the seepage flow from inside of channel to outside at unit length is 0.249 m3/h . The seepage flow from under plastic concrete cut-off wall is 0.236m3/h which is 94.78％ of total seepage flow. The decreased hydraulic head through plastic concrete cut-off wall is 4.67m which is 72% of total decreased hydraulic head.

**References**

[1] Huang Yanhong. Simulation analysis of FEM on seepage flow and its influence on stability of slopes of dam and bank[D].Wuhan: Huazhong University of Science and Technology, 2006.

[2] Su Yuan. The Effect Analysis of Plastic Concrete Cut-off Wall for Earth-rock Dam Stability [D]. Jinan: Shandong University, 2013.

[3] WU Yanqing, ZHANG Zhuoyuan.Rock Mass Hydraulics[M].Chengdu: sejtu press,1995:93～113.

*Applied Mechanics and Materials Vols. 580-583 (2014) pp 1823-1827*
*© (2014) Trans Tech Publications, Switzerland*
*doi:10.4028/www.scientific.net/AMM.580-583.1823*

# Application of MIKESHE model in water environmental management for Guishui River Basin

Z., Zheng [1, a], J., Zhang [1,b], H.L.Gong [1,c], J.W, Huang [2,d],

[1] State Key Laboratory Incubation Base of Urban Environmental Processes and Digital Simulation, Capital Normal University,

[2] Beijing A.C.H.F Civil Engineering & Technology Corporation

[a]zzme110@126.com, [b] maggie2008zj@yahoo.com(corresponding author),

[c]gonghl@263.net, [d] hjw2003@sina.com

**Keywords:** MIKESHE, hydrologic cycle, hydrologic response, water environmental management

**Abstract.** In order to comprehensively analyse hydrological environment system of watershed, it is particularly important to couple the surface water and groundwater for better underding the entire hydrologic cycle. Guishui river basin, located in Beijing, was selected as the research area to build a MIKE SHE hydrological integrated model to simulate the surface runoff. The hydrologic response in the Guishui river basin was explored. This study will enrich the experience of the domestic application about MIKESHE model and provided scientific basis for regional water resources planning and management. In the paper, the development process and present research situation of integrated hydrological models were overviewed, concluding the principle of model structure. Considering the water environment issues in the study area (such as water pollution, water resource utilization, watershed underlying surface, climate change, etc.), the integrated hydrological model was setup based on MIKESHE for the simulation year of 2005 to 2010. The preliminary results showed that it is feasibile to apply the MIKESHE model in the study area for water environmental management. Furthermore, some valued suggestions and perspectives about the water environmental problems in the study for the future were provided.

## Introduction

With the social economy developing, the population increasing and urbanization since the 21st century, the human living environment has suffered different levels of pollution and destruction, so the water environment becomes a top priority. Recently in a series of domestic water pollution which has threaten the survival of Human being and sounded the alarm to strengthen water environment management. Because the groundwater has a close relationship with surface water in the hydrologic cycle, so the coupling research of surface water and groundwater is particularly important for comprehensive watershed hydrological simulation environment system analysis.

The hydrological cycle system is an open process containing a highly complex multi-factor interaction. Distributed hydrological model based on physical basis is the important means to describe the hydrologic cycle. MIKESHE model is a typical representative of distributed hydrological model, which covers the main process of the hydrological cycle, including evapotranspiration, infiltration, surface runoff, saturated flow, unsaturated flow, and open channel flow.

## Model Description

**MIKESHE integrated hydrological model overview.** In 1969 Freeze and Harlan proposed a distributed water model framework based on water dynamic partial differential equations of physics[1]. In 1982, in the European Union fund, the British Institute of hydrology, France SOGREAH consulting company and the Danish Hydraulic Institute jointly developed the earliest SHE model which was most representative[2]. Model requires hydrological parameters with strong physical meaning which can be determined by watershed characteristics and hydrological experiment

. At the aspect of the hydrological model large numbers of research is made in foreign but there is a few works in our national. For example, In 2008, Liu Chenfeng applied the distributed hydrological model MIKE SHE to simulate the artificial forest ecosystem hydrological process of poplar (P. - eur americanacv.) [3]. In the 1992 , J.C.BATHURST had carried on the analysis to the SHE distributed hydrological model from the structure, which was applicable to the prediction of land use change an d climate change impacts on hydrological cycle. [4].In 2002 R. F. V á zquez, J. Feyen J. Berlamont et al. simulated drainage in the basin in Belgium (586 km ²) through the dynamic application code of MIKE SHE hydrological model. [5].

**Characteristics and Application of MIKE SHE Model.** It is the basic characteristics of MIKESHE distributed that the model uses the conservation of energy， mass and momentum. Compared to the empirical hydrological models , MIKESHE can calculate a point or a surface hydrological response process based on the spatial structure and the parameters. The model fully consider the the influence by rainfall, climate change, land use and watershed underlying surface changes on river basin for water generation and concentration. Coupling between groundwater and surface water has great advantages which can simulate the interactive process of river flow, water quality， water level, and underground runoff. The development of GIS spatial data analysis and processing platform also provides technical support [6] for this type of distributed surface and groundwater model.

MIKE SHE hydrological model has been widely used in the world to manage water resources and ecological environment between surface water and groundwater, mainly items as follows in table1:

Table1 Application of MIKESHE model [7]

| | |
|---|---|
| Ecological evaluations | • Groundwater management |
| Water quality remediation | • Environmental impact assessments |
| Impact of land use and climate change | • Aquifer vulnerability mapping |
| Contamination from waste disposal | •Impact of agriculture |
| Soil and water management | • River basin management and planning |
| Wetland management and restoration | • Floodplain studies |

The model uses two-dimensional layered structure. Vertical dimension of watershed hydrological processes and parameters,from top to bottom, includes canopy interception layer, snowmelt runoff layer, soil infiltration, unsaturated layer, and underground runoff saturated runoff layer.Basin is divided into small grids of different scale in the horizontal dimension.The main hydrological process of the model can be expressed by the mass, momentum and energy conservation finite-difference PDE.It can be also expressed by empirical equations.The figure(Fig.1) is shown below.

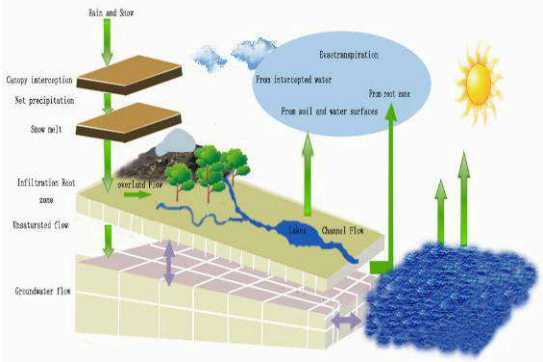


Fig.1 Hydrologic processes simulated by MIKE SHE

The model uses the modular structure, with different hydrological processes, forming a unified model of hydrological cycle system. Basic modules : 1 water movement module (WM); 2 water quality module (WQ) [1]

## Methodol

**Data Preparation.**Yanqing County belongs to the continental monsoon climate. Located in the transition zone of semi-arid and sub-humid, Yanqing County has a mild climate, cool in summer and warm in winter. The long-term average precipitation is 429 mm. The basin area is 632.5 square kilometers, and the average annual rainfall is 429mm.The prepared data include DEM, land use distribution, basin river network, meteorological data, soil, groundwater conductivity and other parameters. Watershed position is shown in Figure 2.

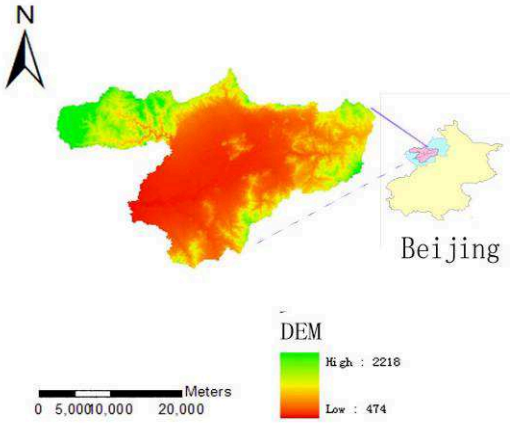


Fig. 2 Guishui river basin of Yanqing

**Simulation.** MIKE SHE model processes the data of hydrologic cycle and input prepared data to the model. Simple process is shown in figure3.

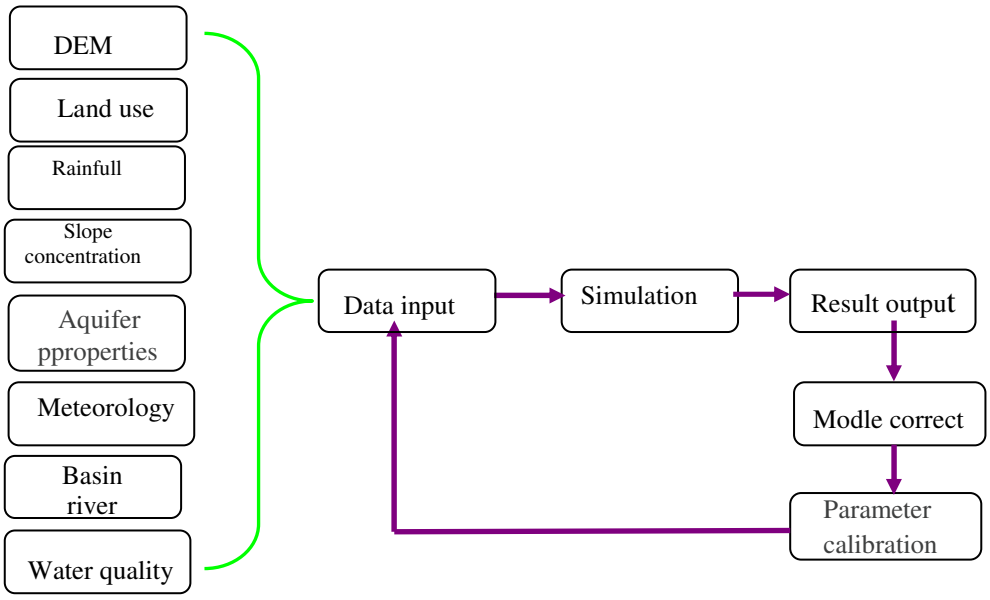


Fig.3 . Process of Simulation

This study inputs the GIS data, the hydrological parameters of the DEM data etc. into the MIKE SHE model in Guishui River Basin. The research area is divided into cell based on X, Y direction, NX=100, NY=100, and mesh size is 500m. Preprocessed data conclude actual evapotranspiration data in 2005-2010(fig4), land use maps in1980 (fig5) and 2005(fig6) etc.

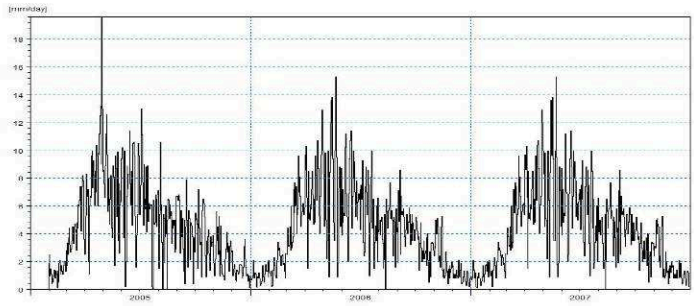

Fig. 4 Evapotranspiration of the year of 2005-2010

The model divides the basin using the Tyson polygon method and adopts rainfall data of 6 stations in the year of 2005 -2010. These six rainfall stations represent the division of the basin, as shown in the Fig 5.

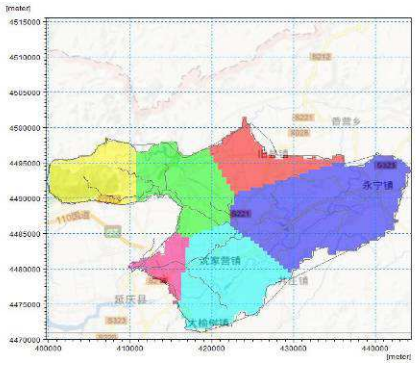

Fig.5 Tyson polygon

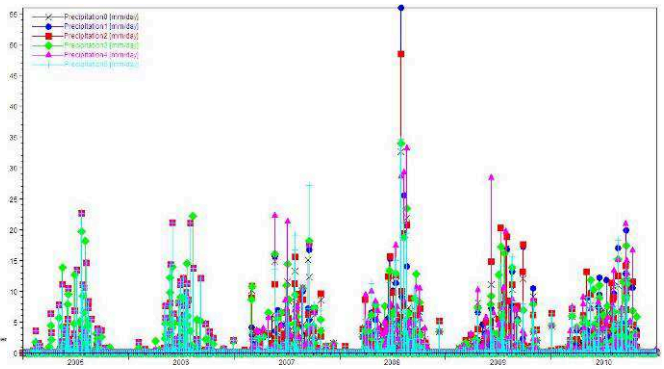

Fig.6. Rainfall of 6 stations in the year of 2005 -2010

MIKE11 one-dimensional water quality model is coupled to the MIKE SHE. The water exchanges between channel and subsurface saturated zone. The river recharge groundwater when the river water level higher than water table, it is opposite instead. Water exchange between saturated zone and river basin is shown in figure --. Surface water environment pollution will cause the cross contamination with groundwater, Process of water quality change in the unsaturated zone, the zone of saturation, river, and overland flow is simulated by using model Different spatial levels detailed data and information provide the important basis for the management of water environment.

## Conclusion and Implication

The integrated hydrological model was setup based on MIKESHE for the simulation year of 2005 to 2010. The preliminary results showed that it is feasibile to apply the MIKESHE model in the study area for water environment management. Furthermore, some valued suggestions and perspectives about the water environmental problems in the study for the future were provided.

(1)How to get physical characteristics of basin conveniently, economically and accurately, such as elevation, land use, soil, vegetation and other attributes.

(2)To build reasonable coupling between MIKESHE model and other related models solve the specific problem of water environment,, such as seawater oil pollution, groundwater pollution control and local river engineering analysis and so on.

(3)Considering apply model and hydrological information system into wider range of aspects, such as the prediction in river channel water level of traffic flow, agricultural irrigation and check of conservancy facilities, etc.

## Acknowledgment

Project 41271004 supported by NSFC; Beijing Municipal Science & Technology New Star Project Funds (2010B046) and Supported by Beijing Natural Science Foundation (8123041).

**References**

[1] X.Z.Xue etc., Hydrological Models, Sciencep, beijing，2009 (In Chinese).

[2] Sangjun Im, Hyeonjun Kim, Chulgyum Kimm, et al. Assessing the impacts of land use changes on watershed hydrology using MIKE SHE[J]. Environmental Geology 2009, 57(1): 231-239.

[3] Chenfeng Liu，Zhiqiang Zhang etc., Modeling the Hydrological Processes of A Poplar Plantation Ecosystem by MIKE SHE,2008 (In Chinese).

[4] J.C.Bathurst, Future of Disstuibuted Modeling: The Systeme Hydrologique Europeen. Hydrological Processes, VOL.6,265-277 .

[5] R. F. Vázquez, J. Feyen, J. Berlamont, Preliminary results from an uncertainty analysis by using the MIKE SHE code, ERB and Northern European FRIEND Project 5 Conference, Demänovská dolina, Slovakia,2002

[6] W. Rui，W.Z.Geng，X.Jun, Advances in the Integrated Surface Water and Groundwater Model, PROGRESS IN GEOGRAPHY. Commun. 27(2008) 37-41 (In Chinese).

[7] DHI:MIKE SHE User Guide(2011)

*Applied Mechanics and Materials Vols. 580-583 (2014) pp 1828-1841*
*© (2014) Trans Tech Publications, Switzerland*
*doi:10.4028/www.scientific.net/AMM.580-583.1828*

# Design of a Pressurized Trapezoidal Shaped Conduit Using the Rough Model Method (Part 2)

Bachir ACHOUR[1,a*], Ali BEDJAOUI[2,b]

[1,2]Research Laboratory in Subterranean and Surface Hydraulics (LARHYSS)

University of Biskra, PO Box 145, RP 07000, Biskra, Algeria

[a]bachir.achour@larhyss.net , [b]ali_bedjaoui@yahoo.com

**Keywords:** Rough Model Method, Pressurized conduit, Trapezoidal shaped conduit, Turbulent flow, Discharge, Energy slope.

**Abstract.** Through the Rough Model Method (RMM) an explicit calculation is proposed to solve the complex problem of the design of a pressurized trapezoidal shaped conduit characterized by three linear dimensions. Firstly, the method is applied to a rough model of the same shape in order to establish the equations governing its geometric and hydraulic characteristics. These equations are then secondly used to easily deduce the required linear dimensions of the current conduit by introducing a non-dimensional correction factor. The application of the obtained relationships requires only a strict minimum of data. All relationships provided in this article are applicable to the entire domain of the turbulent flow. Practical examples are taken to enable the hydraulic engineer to better understanding the advocated method and to observe the facility with which design of such a geometric profile can be performed.

## Introduction

In the field of hydraulics, three main problems may arise in the practice of hydraulic engineer. The first problem concerns the computation of the discharge in order to determine the discharge capacity of a channel or conduit. Generally, this problem can be solved explicitly by combining the Darcy-Weisbach and Colebrook-White relationships, expressing the energy slope and the friction factor respectively. The second problem concerns the computation of the energy slope in order to adjust it if necessary. Determining the energy slope is an implicit problem since the Darcy-Weisbach relationship uses the friction factor whose expression is itself implied. For this reason, some authors have proposed approximate relationships for friction factor, especially for pipes [1, 2, 3]. The third problem is related to the design of the channel in order to determine its linear dimensions. For most geometric profiles of channels or conduits, the design is often a complex problem [4] and its basic relationships are implicit. To solve the problem of the design, the hydraulic engineer uses very laborious graphical methods or iterative procedures [5, 6, 7]. The three main problems that we have just cited involve the combination of three basic relations, namely Darcy-Weisbach, Colebrook-White and Reynolds number relationships [1, 2, 3]. Reynolds number is a dimensionless number that expresses the ratio of inertial forces to viscous forces and quantifies then the relative importance of these two forces under a given flow conditions. Despite the fact that these three basic relations are complete and that they contain all the parameters governing the turbulent flow, however they do not allow to express the linear dimensions of the channel in an explicit form. For every geometric profile of known channels, it is often necessary to find approximate relationships to solve the problem of design. Regarding the pressurized trapezoidal shaped conduit, the literature does not disclose any study related to the three main problems of the turbulent flow. This type of profile is nevertheless widely used in practice as water supply lines, sanitary sewers, culverts and storm drains or penstocks as well. For this reason, the main objective of this paper is to contribute to enrich the literature by studying this conduit under pressurized condition of the flow. Our focus will be especially on its design, contributing significantly to this problem. Three linear dimensions characterize this channel and will be determined by clear, reliable and particularly explicit methods. The problem of the design will be solved by a new theoretical approach known as the Rough Model

Method (RMM) [1]. The three basic equations of turbulent flow are applied to a rough conduit model characterized by an arbitrarily assigned relative roughness value. This is a referential rough model from which the required linear dimensions are directly deduced. Resulting RMM equations are not only explicit but also cover the entire domain of Moody diagram [8], corresponding to Reynolds number $R \geq 2300$ and relative roughness varying in the wide range [0; 0.05]. Note that the RMM has been recently successfully applied to the design of a pressurized vaulted rectangular conduit [9].

**Basic equations**

The relationships on which the study is based are simple well known hydraulic equations namely, Darcy-Weisbach equation, Colebrook-White equation and Reynolds number formula.
The energy slope of a conduit or channel is given by the Darcy-Weisbach relationship as:

$$J = \frac{f}{D_h}\frac{Q^2}{2gA^2} \tag{1}$$

where $Q$ is the discharge, $g$ is the acceleration due to gravity, $A$ is the wetted area, $D_h$ is the hydraulic diameter and $f$ is the friction factor given by the well known Colebrook-White formula as:

$$\frac{1}{\sqrt{f}} = -2\log\left(\frac{\varepsilon / D_h}{3.7} + \frac{2.51}{R\sqrt{f}}\right) \tag{2}$$

where $\varepsilon$ is the absolute roughness and $R$ is the Reynolds number which can be expressed as :

$$R = \frac{4Q}{P\nu} \tag{3}$$

where $\nu$ is the kinematic viscosity and $P$ is the wetted perimeter.

**Referential trapezoidal rough model**

The application of the rough model method (RMM) is based, for the sake of calculation, on a referential rough model shown in Fig.1b.

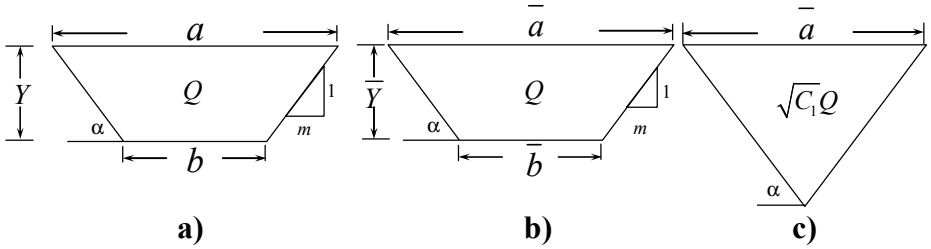


Fig. 1: Geometric elements of the studied conduits.
a) Pressurized trapezoidal conduit, b) Trapezoidal rough model, c) Triangular rough model

The pressurized trapezoidal shaped conduit subject of this study is shown in Figure 1a. It is characterized by three linear dimensions, namely the horizontal dimensions "$a$" and "$b$" and the minimum height "$Y$". The linear dimensions of the rough model shown in Figure 1b are distinguished by the symbol "$\bar{}$". The section is characterized by a side slope $m$ horizontal to 1 vertical. The rough model we consider is a pressurized trapezoidal conduit characterized by $\bar{\varepsilon} / \bar{D_h} = 0.037$ as the arbitrarily assigned relative roughness value. The chosen relative roughness value is so large that the prevailed flow regime is fully rough. Thus, the friction factor is $\bar{f} = 1/16$ according to Eq. 2 for $R = \bar{R}$ tending to infinitely large value. Applying Eq. 1 to the rough model leads to:

$$\bar{J} = \frac{\bar{f}}{\bar{D_h}}\frac{\bar{Q}^2}{2g\bar{A}^2} \tag{4}$$

Bearing in mind that $\overline{D_h} = 4\overline{A}/\overline{P}$ and $\overline{f} = 1/16$, Eq. 4 can be rewritten as:

$$\overline{J} = \frac{1}{128g}\frac{\overline{P}}{\overline{A}^3}\overline{Q}^2 \tag{5}$$

The wetted perimeter $\overline{P}$ and the water area $\overline{A}$ are expressed in different forms, depending on the chosen linear dimension.

If one selected the linear dimension "*a*", then $\overline{P}$ and $\overline{A}$ are respectively:

$$\overline{P} = \overline{a}\left[C_1 - (C_1 - 2)\overline{\beta}\right] \tag{6}$$

$$\overline{A} = \overline{a}^2\frac{(1-\overline{\beta}^2)}{4m} \tag{7}$$

where $C_1 = \sqrt{1+m^{-2}} + 1$, $\overline{\beta} = \overline{b}/\overline{a}$.

If the chosen linear dimension is "*b*", then $\overline{P}$ and $\overline{A}$ can be written respectively as:

$$\overline{P} = 2\overline{b}\left(1 + C_1\overline{Y}^*\right) \tag{8}$$

$$\overline{A} = \frac{\overline{b}^2}{m}\overline{Y}^*\left(1 + \overline{Y}^*\right) \tag{9}$$

where $\overline{Y}^* = \frac{m\overline{Y}}{\overline{b}}$.

Finally, when the chosen linear dimension is "*Y*", $\overline{P}$ and $\overline{A}$ are then given respectively by the following relationships:

$$\overline{P} = 2m\overline{Y}\left(C_1 + \overline{Y}^{*-1}\right) \tag{10}$$

$$\overline{A} = m\overline{Y}^2\left(1 + \overline{Y}^{*-1}\right) \tag{11}$$

**Computation of the linear dimension "*b*"**

**Fundamental equations**

To determine the linear dimension "*b*" by the RMM, it is necessary to establish the equation of the flow in the trapezoidal rough model shown in Fig.1b. In addition, the following data must constitute the data of the problem: the discharge *Q*, the energy slope *J*, the side slope *m* or the angle $\alpha$ (Fig.1), the linear dimension "*a*", the absolute roughness $\varepsilon$ and the kinematic viscosity $\nu$.

Assume $\overline{J} = J$ and $\overline{Q} = Q$. Applying Eq. 5 to the trapezoidal rough model, along with Eq. 6 and Eq.7, one can obtain the following relationship:

$$Q^* = \frac{\sqrt{2}\left(1-\overline{\beta}^2\right)^{3/2}}{\left[C_1 - (C_1-2)\overline{\beta}\right]^{1/2}} \tag{12}$$

where $Q^*$ is the relative conductivity expressed as:

$$Q^* = \frac{m^{1.5}Q}{\sqrt{g\overline{J}a^5}} \tag{13}$$

Eq. 12 can be easily rewritten under the following form:

$$Q^{*\,2/3} = \left(\frac{2}{C_1}\right)^{1/3}\frac{1-\overline{\beta}^2}{\left(1-\frac{C_1-2}{C_1}\overline{\beta}\right)^{1/3}} \tag{14}$$

Calculation showed that, for all values of $m$ and $\overline{\beta}$, one can write:

$$\frac{C_1 - 2}{C_1}\overline{\beta} < 1 \tag{15}$$

The inequality (15) allows to observe that the function

$$\left(1 - \frac{C_1 - 2}{C_1}\overline{\beta}\right)^{1/3}$$

may be subject to a limited development. For a limited development of second order, one can write:

$$\left(1 - \frac{C_1 - 2}{C_1}\overline{\beta}\right)^{1/3} \approx 1 - C^*\overline{\beta} - \left(C^*\overline{\beta}\right)^2 \tag{16}$$

where :

$$C^* = \frac{C_1 - 2}{3C_1} \tag{17}$$

Inserting Eq. 16 into Eq. 14, leads to:

$$Q^{*\,2/3} = \left(\frac{2}{C_1}\right)^{1/3} \frac{1 - \overline{\beta}^{\,2}}{1 - C^*\overline{\beta} - C^{*2}\overline{\beta}^{\,2}} \tag{18}$$

Eq. 18 can be reduced to:

$$Q^* = \sqrt{\frac{2}{C_1}}\left[\frac{1 - \overline{\beta}^{\,2}}{1 - C^*\overline{\beta}(1 + C^*\overline{\beta})}\right]^{3/2} \tag{19}$$

Eq. 19 is in fact a second order equation in $\overline{\beta}$ which can be written as:

$$\overline{\beta}^{\,2} - \frac{C^* q^{\,2/3}}{1 - C^{*2} q^{\,2/3}}\overline{\beta} + \frac{q^{\,2/3} - 1}{1 - C^{*2} q^{\,2/3}} = 0 \tag{20}$$

where:

$$q = Q^*\sqrt{\frac{C_1}{2}} \tag{21}$$

One can easily show that the real root of Eq. 20 is as:

$$\overline{\beta} = \frac{C^* q^{2/3} + \sqrt{(C^* q^{2/3})^2 - 4(q^{2/3} - 1)(1 - C^{*2} q^{2/3})}}{2(1 - C^{*2} q^{2/3})} \tag{22}$$

Note that in Eq. 22 only $\overline{\beta}$ is unknown, since $C^*$ and $q$ are the known parameters.

An intense program of calculation showed that the Eq. 22 is an excellent approximate relationship applicable for a wide range of trapezoidal rough models, provided $\overline{\beta} < 1$, $\alpha \le 75°$.

When the discharge in the rough triangular model, corresponding to $\overline{\beta} = 0$, is equal to $\sqrt{C_1}Q$, the linear dimension $\overline{a}$ is the same in the triangular and trapezoidal rough models (Fig.1). For the discharge $\sqrt{C_1}Q$, the relative conductivity given by Eq. 13 becomes:

$$Q^* = \frac{m^{1.5}\sqrt{C_1}Q}{\sqrt{gJ\overline{a}^{\,5}}} \tag{23}$$

For $\overline{\beta} = 0$, Eq. 19 along with Eq. 23 leads to:

$$\frac{m^{1.5}\sqrt{C_1}Q}{\sqrt{gJ\overline{a}^{5}}} = \sqrt{\frac{2}{C_1}} \tag{24}$$

Thus, one can deduce the following equations:

$$Q^* = \frac{m^{1.5} Q}{\sqrt{gJ\bar{a}^{-5}}} = \frac{\sqrt{2}}{C_1} \tag{25}$$

$$q = Q^* \sqrt{\frac{C_1}{2}} = \frac{1}{\sqrt{C_1}} \tag{26}$$

$$\bar{a} = \left( \frac{m^3 Q^2 C_1^{\,2}}{2gJ} \right)^{1/5} \tag{27}$$

Eq. 27 expresses the linear dimension $\bar{a}$ of the trapezoidal rough model when the discharge is $\sqrt{C_1}Q$. This relation is of particular interest, since it allows to explicitly calculating the linear dimension $\bar{a}$ of the trapezoidal rough model for the known values of the parameters *m*, *Q*, *g* and *J*.

**Non-dimensional correction factor of linear dimension**

The RMM states that any linear dimension "*L*" of a conduit and the linear dimension "$\bar{L}$" of its rough model are related by the following equation, applicable to the whole domain of the turbulent flow:

$$L = \psi \bar{L} \tag{28}$$

where $\psi$ is a non-dimensional correction factor of linear dimension, less than unity, which is governed by the following relationship [10] :

$$\psi \cong 1.35 \left[ -\log \left( \frac{\varepsilon / \overline{D_h}}{4.75} + \frac{8.5}{\bar{R}} \right) \right]^{-2/5} \tag{29}$$

where $\bar{R}$ is the Reynolds number in the rough model given by :

$$\bar{R} = \frac{4Q}{\bar{P}\nu} \tag{30}$$

**Computation steps of the linear dimension "*b*"**

For the given following data *Q*, *J*, *m* (or $\alpha$), *a*, $\varepsilon$ and $\nu$, the steps below are recommended to compute the required dimension linear "*b*" of the pressurized trapezoidal conduit shown in Fig.1a.

1. Compute $C_1 = \sqrt{1 + m^{-2}} + 1$, $C^*$ using Eq. 17 and *q* by the use of Eq. 26.
2. Applying Eq. 22, the parameter $\bar{\beta}$ is then worked out. Note that at this step of calculation, the computed value of $\bar{\beta}$ corresponds to a discharge equal to $\sqrt{C_1}Q$.
3. Compute the corresponding linear dimension $\bar{a}$, according to Eq. 27.
4. Apply Eq. 6, Eq. 7 and Eq. 30 to determine the wetted perimeter $\bar{P}$, the water area $\bar{A}$ and the Reynolds number $\bar{R}$, respectively. The hydraulic diameter $\overline{D_h} = 4\bar{A}/\bar{P}$ is then worked out.
5. Knowing $\overline{D_h}$ and $\bar{R}$, compute the non-dimensional factor of linear dimension $\psi$ by the use of Eq. 29.
6. Assign to the trapezoidal rough model the linear dimension $\bar{a} = a/\psi$. This change in dimension corresponds to the discharge *Q* and the relative conductivity $Q^* = m^{1.5} Q / \sqrt{gJ(a/\psi)^5}$ according to Eq. 13. It mainly results in the equality $\bar{\beta} = \beta$ given by Eq. 22. The parameters $C^*$ and *q* must be calculated by applying Eq. 17 and Eq. 21 respectively.
7. Once $\beta$ is calculated, the required value of the linear dimension "*b*" is finally $b = a\beta$.

**Example 1**

Compute the linear dimension "*b*" of the pressurized trapezoidal conduit shown in Fig.1a, for the following data:

$Q = 0.399\,m^3/s$, $J = 10^{-3}$, $\alpha = 45°(m = 1)$, $a = 1.6\,m$, $\varepsilon = 10^{-4}\,m$, $\nu = 10^{-6}\,m^2/s$

1. The parameter $C_1$ is : $C_1 = \sqrt{1+m^{-2}} + 1 = \sqrt{1+1^{-2}} + 1 = \sqrt{2} + 1 = 2.41421356$

   According to Eq. 17 and Eq. 26, $C^*$ and $q$ are respectively:

   $$C^* = \frac{C_1 - 2}{3C_1} = \frac{\sqrt{2}+1-2}{3\times(\sqrt{2}+1)} = \frac{\sqrt{2}-1}{3\times(\sqrt{2}+1)} = 0.05719096$$

   $$q = \frac{1}{\sqrt{C_1}} = \frac{1}{\sqrt{2.41421356}} = 0.64359425$$

2. Using Eq. 22, the parameter $\overline{\beta}$ is:

   $$\overline{\beta} = \frac{C^* q^{2/3} + \sqrt{(C^* q^{2/3})^2 - 4(q^{2/3}-1)(1-C^{*2}q^{2/3})}}{2(1-C^{*2}q^{2/3})} = 0.526983224$$

3. According to Eq. 27, the linear dimension $\overline{a}$ of the triangular rough model flowing a discharge $\sqrt{C_1}Q$ is:

   $$\overline{a} = \left(\frac{m^3 Q^2 C_1^2}{2gJ}\right)^{1/5} = \left(\frac{1^3 \times 0.399^2 \times 2.41421356^2}{2\times 9.81\times 10^{-3}}\right)^{1/5} = 2.162517506\,m$$

   This value of $\overline{a}$ is also that of the trapezoidal rough model shown in Fig.1b, flowing the discharge *Q*.

4. Applying Eq. 6, Eq. 7 and Eq. 30, the wetted perimeter $\overline{P}$, the water area $\overline{A}$ and the Reynolds number $\overline{R}$ are respectively:

   $$\overline{P} = \overline{a}\left[C_1 - (C_1 - 2)\overline{\beta}\right] = 2.162517506\times\left[2.41421356 - (2.41421356-2)\times 0.526983224\right] = 4.748736989\,m$$

   $$\overline{A} = \overline{a}^2\,\frac{(1-\overline{\beta}^2)}{4m} = 2.162517506^2 \times \frac{(1-0.526983224^2)}{4\times 1} = 0.844442498\,m^2$$

   $$\overline{R} = \frac{4Q}{\overline{P}\nu} = \frac{4\times 0.399}{4.748736989\times 10^{-6}} = 336089.3652$$

   Thus, the hydraulic diameter $\overline{D_h} = 4\overline{A}/\overline{P}$ is then:

   $$\overline{D_h} = 4\overline{A}/\overline{P} = \frac{4\times 0.844442498}{4.748736989} = 0.7112986\,m$$

5. According to Eq. 29, the non-dimensional correction factor of linear dimension is:

   $$\psi = 1.35\left[-\log\left(\frac{\varepsilon/\overline{D_h}}{4.75} + \frac{8.5}{\overline{R}}\right)\right]^{-2/5} = 1.35\times\left[-\log\left(\frac{10^{-4}/0.7112986}{4.75} + \frac{8.5}{336089.3652}\right)\right]^{-2/5} = 0.75604689$$

6. Assign to the trapezoidal rough model the following linear dimension according to Eq. 28:

   $$\overline{a} = \frac{a}{\psi} = \frac{1.6}{0.75604689} = 2.116270849\,m$$

   The new value of the relative conductivity is then:

   $$Q^* = \frac{m^{1.5}Q}{\sqrt{gJ(a/\psi)^5}} = \frac{1^{1.5}\times 0.399}{\sqrt{9.81\times 10^{-3}\times 2.116270849^5}} = 0.61831569$$

   Applying Eq. 21 results in:

   $$q = Q^*\sqrt{\frac{C_1}{2}} = 0.61831569\times\sqrt{\frac{2.41421356}{2}} = 0.67933363$$

7. Inserting the computed values of $C^*$ and $q$ into Eq. 22, one may obtain:
   $\overline{\beta} = \beta = 0.499948303 \approx 0.5$
8. Finally, the required value of the linear dimension "$b$" is then:
   $b = a\beta = 1.6 \times 0.5 = 0.8\ m$
9. One can continue the calculation by writing that the minimum height $Y$ of the pressurized trapezoidal conduit is:
   $$Y = a\frac{1-\beta}{2m} = 1.6 \times \frac{1-0.5}{2 \times 1} = 0.4\ m$$

**Computation of the linear dimension "*a*"**

**Fundamental equations**

In order to compute the linear dimension "*a*", it is necessary to establish the equation of the flow in the trapezoidal rough model. Furthermore, the linear dimension "*a*" is dependent upon the following data, namely the discharge $Q$, the energy slope $J$, the side slope $m$ or the angle $\alpha$ (Fig.1), the linear dimension "*b*", the absolute roughness $\varepsilon$ and the kinematic viscosity $\nu$.

Since "*b*" is the chosen linear dimension, the wetted perimeter $\overline{P}$ and the water area $\overline{A}$ of the trapezoidal rough model is then given by Eq. 8 and Eq. 9 respectively. For $\overline{J} = J$ and $\overline{Q} = Q$, applying Eq. 5 to the trapezoidal rough model results finally in:

$$Q^* = 8\frac{\left[\overline{Y}^*\left(1+\overline{Y}^*\right)\right]^{3/2}}{\left(1+C_1\overline{Y}^*\right)^{1/2}} \tag{31}$$

where the relative conductivity $Q^*$ and the relative height $\overline{Y}^*$ are expressed respectively as:

$$Q^* = \frac{m^{1.5}Q}{\sqrt{g\overline{J}\overline{b}^5}} \tag{32}$$

$$\overline{Y}^* = \frac{m\overline{Y}}{\overline{b}} \tag{33}$$

As we can see, Eq. 31 is implicit towards the relative height $\overline{Y}^*$. We will expose in what follows two methods for its analytical resolution. Note that Eq. 31 can be easily rewritten as:

$$Q^{*2/3} = 4\frac{\overline{Y}^*\left(1+\overline{Y}^*\right)}{\left(1+C_1\overline{Y}^*\right)^{1/3}} \tag{34}$$

Let us assume:

$$z = \left(\overline{Y}^* + \frac{1}{2}\right)^2 \tag{35}$$

Thus, Eq. 34 becomes:

$$Q^{*2/3} = 4\frac{(\sqrt{z}-1/2)(\sqrt{z}+1/2)}{\left[1+C_1(\sqrt{z}-1/2)\right]^{1/3}} \tag{36}$$

or :

$$Q^{*2/3} = 4\frac{z-1/4}{\left[1+C_1(\sqrt{z}-1/2)\right]^{1/3}} \tag{37}$$

Developing Eq. 37 results in:

$$z=\frac{1}{4}+\left(\frac{Q^*}{8}\right)^{2/3}\left[1+C_1(\sqrt{z}-1/2)\right]^{1/3} \tag{38}$$

Eq. 38 is in the following form:

$$z=a_0+\theta\phi(z) \tag{39}$$

where:

$a_0=1/4;\ \theta=(Q^*/8)^{2/3};\ \phi(z)=\left[1+C_1(\sqrt{z}-1/2)\right]^{1/3}$

According to Lagrange's theorem [11], the function $f(z)$ is given in terms of an infinite series, corresponding to:

$$f(z)=f(a_0)+\sum_{i=1}^{\infty}\frac{\theta^i}{\Gamma(i+1)}\left\{\frac{d^{i-1}}{dx^{i-1}}[f'(x)\phi^i(x)\right\}_{x=a_0} \tag{40}$$

In our case, one can write:

$f(z)=\sqrt{z}-1/2=\overline{Y}^*,\ f'(x)=\frac{1}{2\sqrt{x}}$ and $f(a_0)=\sqrt{a_0}-1/2=0$

Thus, according to Eq. 40, the relative height $\overline{Y}^*$ can be expressed as:

$$\overline{Y}^*=\sum_{i=1}^{\infty}\frac{(Q^*/8)^{2i/3}}{\Gamma(i+1)}\left\{\frac{d^{i-1}}{dx^{i-1}}\left(\frac{\left[1+C_1(\sqrt{x}-1/2)\right]^{i/3}}{2\sqrt{x}}\right)\right\}_{x=1/4} \tag{41}$$

The function $\Gamma$ is defined as $\Gamma(i+1)=i!$

Eq. 41 gives the exact value of the relative height $\overline{Y}^*$. However, the exact solution is obtained at infinity and one should truncated the series at an $i$ order such that the difference between $\overline{Y_{i+1}}^*$ and $\overline{Y_i}^*$ is the smallest as possible.

We can also provide, for solving Eq. 31, a numerical process which consists in approaching successively the solution. For this, observe that $z$ is greater than 1/4 according to Eq. 35 for $\overline{Y}^*>0$. Consider then, as the first value of $z$, $z_0=1/4$. According to Eq. 38, compute the next values of $z$ i.e.:

$$z_1=\frac{1}{4}+\left(Q^*/8\right)^{2/3}\left[1+C_1(\sqrt{z_0}-1/2)\right]^{1/3},$$

$$z_2=\frac{1}{4}+\left(Q^*/8\right)^{2/3}\left[1+C_1(\sqrt{z_1}-1/2)\right]^{1/3}$$ …and so on.

The process stops when $z_i$ and $z_{i+1}$ are sufficiently close. This is the numerical procedure that we will apply in the calculation of the linear dimension "*b*" of the pressurized trapezoidal conduit, through a practical example.

**Computation steps of the linear dimension "*a*"**

The calculation of the linear dimension "*a*" requires the following data: $Q$, $J$, $m$ (or $\alpha$), $b$, $\varepsilon$ and $\nu$. For these, the following steps are useful for calculating the linear dimension "*a*".

1. Compute $C_1=\sqrt{1+m^{-2}}+1$
2. Assume $\overline{b}=b$ and determine the relative conductivity $Q^*$ according to Eq. 32.
3. For $z_0=1/4$ and using Eq. 38, compute:

$$z_1=\frac{1}{4}+\left(Q^*/8\right)^{2/3}\left[1+C_1(\sqrt{z_0}-1/2)\right]^{1/3}$$

Once $z_1$ calculated, determine :

$$z_2 = \frac{1}{4} + \left(Q^* / 8\right)^{2/3} \left[1 + C_1(\sqrt{z_1} - 1/2)\right]^{1/3}$$

.....

$$z_{i+1} = \frac{1}{4} + \left(Q^* / 8\right)^{2/3} \left[1 + C_1(\sqrt{z_i} - 1/2)\right]^{1/3}$$

Stop the calculation procedure when $z_{i+1} \approx z_i$ .

4. For $z_i$ , compute the relative height $\overline{Y}^*$ by the use of Eq. 35 which leads to $\overline{Y}^* = \sqrt{z_i} - 1/2$ .
5. With the known values of the parameters $C_1$ , $b$ and $\overline{Y}^*$ , determine the wetted perimeter $\overline{P}$ and the water area $\overline{A}$ according to Eq. 8 and Eq. 9 respectively. Deduce then the hydraulic diameter $\overline{D_h} = 4\overline{A} / \overline{P}$ and the Reynolds number $\overline{R}$ by the use of Eq. 30.
6. Knowing $\overline{D_h}$ and $\overline{R}$ , use Eq. 29 for the calculation of the non-dimensional correction factor of linear dimension $\psi$ .
7. Assign to the trapezoidal rough model the following dimension linear $\overline{b} = b / \psi$ according to Eq. 28. This change in dimension results in the equality $\overline{Y}^* = Y^*$ .
8. Compute the new value of the relative conductivity $Q^* = m^{1.5} Q / \sqrt{gJ(b/\psi)^5}$
9. With $C_1$ and the new value of $Q^*$ , compute the values of $z$ following the same steps described in 3.
10. Once the final value of $z$ determined, use Eq. 35 to compute $Y^*$ which can be expressed as:

$$\overline{Y}^* = Y^* = \frac{mY}{b} = \sqrt{z} - 1/2$$

leading to :

$$Y = \frac{b}{m}(\sqrt{z} - 1/2)$$

11. Finally, the required value of the linear dimension "$a$" is obtained applying the following equation given by geometrical considerations on Fig.1a:

$$a = b + 2mY \tag{42}$$

**Example 2**

Compute the linear dimension "$a$" of the pressurized trapezoidal shaped conduit shown in Fig.1a, for the following data using the numerical process described in 5.2:

$Q = 2.78 m^3 / s$ , $J = 10^{-3}$ , $\alpha = 60° (m = 0.577350269)$ , $b = 1m$ , $\varepsilon = 10^{-3} m$ , $\nu = 10^{-6} m^2 / s$

1. The parameter $C_1$ is:

$$C_1 = \sqrt{1 + m^{-2}} + 1 == \sqrt{1 + 0.577350269^{-2}} + 1 = 3$$

2. According to Eq. 32 for $\overline{b} = b$ , the relative conductivity $Q^*$ is:

$$Q^* = \frac{m^{1.5} Q}{\sqrt{gJb^5}} = \frac{0.577350269^{1,5} \times 2.78}{\sqrt{9.81 \times 10^{-3} \times 1^5}} = 12.3122999$$

3. With the values of $C_1$ , $Q^*$ and $z_0 = 1/4$ , the numerical process described in 5.2 converges at the eighth step of calculation. The final result is : $z_8 \approx z_7 = 2.39006687$
4. According to Eq. 35, the relative height $\overline{Y}^*$ is:

$$\overline{Y}^* = \sqrt{z_8} - 1/2 = \sqrt{2.39006687} - 1/2 = 1.04598411$$

5. Applying Eq. 8 and Eq. 9 for $\overline{b} = b$ results respectively in:

$$\overline{P} = 2\overline{b}\left(1 + C_1 \overline{Y}^*\right) = 2\times 1\times\left(1 + 3\times 1.04598411\right) = 8.27590466\ m$$

$$\overline{A} = \frac{\overline{b}^2}{m}\overline{Y}^*\left(1 + \overline{Y}^*\right) = \frac{1^2}{0.577350269}\times 1.04598411\left(1 + 1.04598411\right) = 3.70670454\ m^2$$

Thus:

$$\overline{D_h} = 4\overline{A}/\overline{P} = 4\times 3.70670454 / 8.27590466 = 1.79156464$$

$$\overline{R} = \frac{4Q}{\overline{P}\nu} = \frac{4\times 2.78}{8.27590466\times 10^{-6}} = 1343659.75$$

6. The non-dimensional correction factor of linear dimension $\psi$ is then:

$$\psi = 1.35\left[-\log\left(\frac{\varepsilon/\overline{D_h}}{4.75} + \frac{8.5}{\overline{R}}\right)\right]^{-2/5} = 1.35\times\left[-\log\left(\frac{10^{-3}/1.79156464}{4.75} + \frac{8.5}{1343659.75}\right)\right]^{-2/5} = 0,78268959$$

7. Assign to the trapezoidal rough model the following linear dimension according to Eq. 28:

$$\frac{b}{\psi} = \frac{1}{0.78268959} = 1.27764571\ m$$

8. The new value of the relative conductivity is then:

$$Q^* = \frac{m^{1.5}Q}{\sqrt{gJ(b/\psi)^5}} = \frac{0.577350269^{1.5}\times 2.78}{\sqrt{9.81\times 10^{-3}\times 1.27764571^5}} = 6.67333997$$

9. Using the computed values of $C_1$ and $Q^*$, we have determined the value of $z$ according to the numerical process described in step 5.2, for $z_0 = 1/4$. We found that the process converges at the eighth step of calculation corresponding to: $z_8 \approx z_7 = 1.56260904$.

10. According to Eq. 35, the relative height $Y^*$ is then:

$$\overline{Y}^* = Y^* = \frac{mY}{b} = \sqrt{z_8} - 1/2$$

$$\text{or : } Y = \frac{b}{m}(\sqrt{z_8} - 1/2) = \frac{1}{0.577350269}(\sqrt{1.56260904} - 1/2) = 1.29911365\,m \approx 1.3\,m$$

11. According to Eq. 42, the required value of the linear dimension "*a*" is finally:

$$a = b + 2mY = 1 + 2\times 0.577350269\times 1\,3 \approx 2.5\,m$$

**Computation of the linear dimensions "*a*" and "*b*" for "*Y*" imposed**

**Fundamental equations**

The last problem that we must solve is the determination of the linear dimensions "*a*" and "*b*" when the height of the conduit is a given data. Thus, the data of the problem are namely the discharge *Q*, the energy slope *J*, the side slope *m* or the angle $\alpha$ (Fig.1), the height of the conduit "*Y*", the absolute roughness $\varepsilon$ and the kinematic viscosity $\nu$. For these, the RMM can establish the equation of the flow by applying Eq. 5 to the pressurized trapezoidal rough model shown in Fig.1b, according to the theoretical development that follows. Remember that since the height *Y* is imposed, the wetted perimeter $\overline{P}$ and the water area $\overline{A}$ are governed by Eq. 10 and Eq. 11 respectively. In this section, assume once again $\overline{J} = J$ and $\overline{Q} = Q$. Inserting Eq. 10 and Eq. 11 into Eq. 5, one can write:

$$J = \frac{1}{64g}\frac{\left(C_1 + \overline{Y}^{*-1}\right)}{m^2\overline{Y}^5\left(1 + \overline{Y}^{*-1}\right)^3}Q^2 \tag{43}$$

where $\overline{Y}^*$ is governed by Eq. 33. Note that since $C_1 = \sqrt{1 + m^{-2}} + 1$, then:

$$m^{-2} = C_1(C_1 - 2) \tag{44}$$

Using Eq. 44, Eq. 43 can be rewritten as:

$$Q^{*2} = 64\frac{\left(1+\overline{Y}^{*\,-1}\right)^3}{C_1(C_1-2)\left(C_1+\overline{Y}^{*\,-1}\right)} \tag{45}$$

where the relative conductivity $Q^*$ is expressed as :

$$Q^* = \frac{Q}{\sqrt{gJ\overline{Y}^5}} \tag{46}$$

Let us assume:

$$z = 1+\overline{Y}^{*\,-1} \tag{47}$$

Inserting Eq. 47 into Eq. 45 and rearranging, results in:

$$z^3 - \frac{C_1(C_1-2)Q^{*2}}{64}z - \frac{C_1(C_1-2)(C_1-1)Q^{*2}}{64} = 0 \tag{48}$$

We thus obtain a cubic equation in $z$ without second-order term. Its discriminant is:

$$\Delta = \left[\frac{\sqrt{C_1(C_1-2)(C_1-1)}\,Q^*}{8\sqrt{2}}\right]^4 \times \left(1-\frac{\sqrt{C_1(C_1-2)}}{12\sqrt{3}(C_1-1\ )}Q^*\right)\left(1+\frac{\sqrt{C_1(C_1-2)}}{12\sqrt{3}(C_1-1)}Q^*\right) \tag{49}$$

Eq. 49 shows that two cases arise:

1. $Q^* \le \frac{12\sqrt{3}(C_1-1)}{\sqrt{C_1(C_1-2)}}$, then $\Delta \ge 0$. The real root of Eq. 48 is:

$$z = \frac{Q^*\sqrt{C_1(C_1-2)}}{4\sqrt{3}}ch(\gamma/3) \tag{50}$$

where the angle $\gamma$ is governed by :

$$ch(\gamma) = \frac{12\sqrt{3}(C_1-1)}{Q^*\sqrt{C_1(C_1-2)}} \tag{51}$$

Taking into account Eq. 47, the relative height $\overline{Y}^*$ is such that:

$$\overline{Y}^{*-1} = \frac{Q^*\sqrt{C_1(C_1-2)}}{4\sqrt{3}}ch(\gamma/3) - 1 \tag{52}$$

2. $Q^* \ge \frac{12\sqrt{3}(C_1-1)}{\sqrt{C_1(C_1-2)}}$, then $\Delta \le 0$. The real root of Eq. 48 is:

$$z = \frac{Q^*\sqrt{C_1(C_1-2)}}{4\sqrt{3}}\cos(\gamma/3) \tag{53}$$

The angle $\gamma$ is given by:

$$\cos(\gamma) = \frac{12\sqrt{3}(C_1-1)}{Q^*\sqrt{C_1(C_1-2)}} \tag{54}$$

According to Eq. 47, the relative height $\overline{Y}^*$ is:

$$\overline{Y}^{*-1} = \frac{Q^*\sqrt{C_1(C_1-2)}}{4\sqrt{3}}\cos(\gamma/3) - 1 \tag{55}$$

Eq. 52 and Eq. 55 give the exact value of the relative height $\overline{Y}^*$.

**Computation steps of the linear dimensions "*a*" and "*b*" for "*Y*" imposed**

In this section, the known parameters of the problem are the discharge *Q*, the energy slope *J*, the side slope *m* or the angle $\alpha$ (Fig.1), the height of the conduit "*Y*", the absolute roughness $\varepsilon$ and the kinematic viscosity $\nu$. To compute the linear dimensions "*a*" and "*b*", simply follow the calculation steps below.

1. Compute $C_1 = \sqrt{1+m^{-2}} + 1$, $C^*$ using Eq. 17 and $q$ by the use of Eq. 26.
2. Applying Eq. 22, the parameter $\overline{\beta}$ is then worked out.
3. Compute the corresponding linear dimension $\overline{a}$, according to Eq. 27.
4. Apply Eq. 6, Eq. 7 and Eq.30 to determine the wetted perimeter $\overline{P}$, the water area $\overline{A}$ and the Reynolds number $\overline{R}$, respectively. The hydraulic diameter $\overline{D_h} = 4\overline{A}/\overline{P}$ is then deduced.
5. Knowing $\overline{D_h}$ and $\overline{R}$, compute the non-dimensional factor of linear dimension $\psi$ by the use of Eq. 29.
6. Assign to the trapezoidal rough model the linear dimension $\overline{Y} = Y/\psi$ according to Eq. 28. This change in dimension corresponds to the discharge $Q$ and the relative conductivity $Q^* = m^{1.5}Q/\sqrt{gJ(Y/\psi)^5}$. It mainly results in the equality $\overline{Y}^* = Y^*$ given by Eq. 52 or Eq. 55, in accordance with the sign of the discriminant $\Delta$.
7. Compute then $\overline{Y}^{*-1} = Y^{*-1}$ using Eq. 52 or Eq. 55.
8. Bearing in mind that $\overline{Y}^{*-1} = \dfrac{\overline{b}}{m\overline{Y}} = Y^{*-1} = \dfrac{b}{mY}$, the required linear dimension "*b*" is then:

$$b = mY\overline{Y}^{*-1} \tag{56}$$

9. From geometrical considerations carried out on Fig.1a, the needed linear dimension "*a*" is such that:

$$a = b + 2mY \tag{57}$$

**Example 3**

Compute the linear dimensions "*b*" and "*a*" of the pressurized trapezoidal shaped conduit shown in Fig.1a, for the following data:

$Q = 1.7\,m^3/s$, $J = 2\times10^{-4}$, $Y = 1.3\,m$, $\varepsilon = 10^{-3}\,m$, $\alpha = 60°(m = 0.577350269)$, $\nu = 10^{-6}\,m^2/s$.

1. The parameter $C_1$ is:

   $$C_1 = \sqrt{1+m^{-2}} + 1 = \sqrt{1+0.577350269^{-2}} + 1 = 3$$

   According to Eq. 17 and Eq. 26, $C^*$ and $q$ are respectively:

   $$C^* = \frac{C_1 - 2}{3C_1} = \frac{3-2}{3\times3} = \frac{1}{9}$$

   $$q = \frac{1}{\sqrt{C_1}} = \frac{1}{\sqrt{3}}$$

2. Using Eq. 22, the parameter $\overline{\beta}$ is:

   $$\overline{\beta} = \frac{C^*q^{2/3} + \sqrt{(C^*q^{2/3})^2 - 4(q^{2/3}-1)(1-C^{*2}q^{2/3})}}{2(1-C^{*2}q^{2/3})} = 0.596343232$$

3. According to Eq. 27, the linear dimension $\overline{a}$ of the triangular rough model flowing a discharge $\sqrt{C_1}Q$ is:

   $$\overline{a} = \left(\frac{m^3Q^2C_1^2}{2gJ}\right)^{1/5} = \left(\frac{0.577350269^3\times1.79^2\times3^2}{2\times9.81\times2\times10^{-4}}\right)^{1/5} = 4.179707537\,m$$

   This computed value of $\overline{a}$ corresponds also to the value of the same linear dimension of the trapezoidal rough model.

4. Applying Eq. 6, Eq. 7 and Eq. 30, the wetted perimeter $\overline{P}$, the water area $\overline{A}$ and the Reynolds number $\overline{R}$ are respectively:

$$\overline{P} = \overline{a}\left[C_1 - (C_1 - 2)\overline{\beta}\right] = 4.179707537 \times \left[3 - (3-2) \times 0.596343232\right] = 10.04658231\ m$$

$$\overline{A} = \overline{a}^2 \frac{(1-\overline{\beta}^2)}{4m} = 4.179707537^{\ 2} \times \frac{(1 - 0.596343232^2)}{4 \times 0.577350269} = 4.874509694\ m^2$$

$$\overline{R} = \frac{4Q}{\overline{P}\nu} = \frac{4 \times 1.7}{10.04658231 \times 10^{-6}} = 676847.09$$

Thus, the hydraulic diameter $\overline{D_h} = 4\overline{A} / \overline{P}$ is:

$$\overline{D_h} = 4\overline{A} / \overline{P} = \frac{4 \times 4.874509694}{10.04658231} = 1.94076335\ m$$

5. The non-dimensional correction factor of linear dimension $\psi$ is then:

$$\psi = 1.35\left[-\log\left(\frac{\varepsilon / \overline{D_h}}{4.75} + \frac{8.5}{\overline{R}}\right)\right]^{-2/5} = 1.35 \times \left[-\log\left(\frac{10^{-3} / 1.94076335}{4.75} + \frac{8.5}{676847.09}\right)\right]^{-2/5} = 0.78189471$$

6. Assign to the trapezoidal rough model the following linear dimension according to Eq. 28:

$$\overline{Y} = \frac{Y}{\psi} = \frac{1.3}{0.78189471} = 1.66262795\ m$$

The new value of the relative conductivity is then:

$$Q^* = \frac{m^{1.5} Q}{\sqrt{gJ(Y/\psi)^5}} = \frac{0.577350269^{1.5} \times 1.7}{\sqrt{9.81 \times 2 \times 10^{-4} \times 1.66262795^5}} = 10.7674218$$

7. Calculation shows that:

$$Q^* \le \frac{12\sqrt{3}(C_1 - 1)}{\sqrt{C_1(C_1 - 2)}} = 24$$

We can thus conclude that the relative height $\overline{Y}^*$ is governed by Eq. 52 in which the angle $\gamma$ is given by Eq. 51 as:

$$ch(\gamma) = \frac{12\sqrt{3}(C_1 - 1)}{Q^*\sqrt{C_1(C_1 - 2)}} = \frac{12 \times \sqrt{3} \times (3-1)}{10.7674218 \times \sqrt{3 \times (3-2)}} = 2.22894584$$

leading to $\gamma = 1.4400673$ *radians*

Applying Eq. 52 results in:

$$\overline{Y}^{*-1} = \frac{Q^*\sqrt{C_1(C_1 - 2)}}{4\sqrt{3}} ch(\gamma / 3) - 1 = \frac{10.7674218 \times \sqrt{3 \times (3-2)}}{4 \times \sqrt{3}} ch(1.4400673 / 3) - 1 = 2.00798717$$

Finally, according to Eq. 56 and Eq. 57, the required linear dimensions "*b*" and "*a*" are respectively:

$$b = mY\overline{Y}^{*-1} = 0.577350269 \times 1.3 \times 2.00798717 = 1.50710551 m \approx 1.50\ m$$

$$a = b + 2mY = 1.5 + 2 \times 0.577350269 \times 1.3 \approx 3\ m$$

## Conclusions

The main purpose of the study was to design a pressurized trapezoidal shaped conduit by the use of a new method known as the Rough Model Method or RMM. The design consisted in calculating the three linear dimensions that characterize the conduit, considering the strict minimum of data. The principle of the RMM has consisted in judiciously applying the three basic equations of turbulent flow to a referential rough trapezoidal shaped model for which the equations of the flow has been established. These equations were subsequently used to derive explicitly the searched linear dimensions by the use of a non-dimensional correction factor of linear dimension whose major role has been highlighted. The calculation made use of mathematical considerations, such as limited development, successive solution approach, or third-degree equations that have been effectively resolved by trigonometric and hyperbolic functions. The explicit steps of calculation were clearly

presented and one can observe the degree of their simplicity. Practical examples have been taken to better explain the calculation procedure.

**References**

[1] B. Achour, A. Bedjaoui, Turbulent Pipe-Flow Computation Using the Rough Model Method, J. Civil Engineering and Science, 1(1) (2012) 36-41.

[2] P.K. Swamee, A.K. Jain, Explicit equations for Pipe-flow Problems, J. Hyd. Engineering, ASCE, 102(5) (1976) 657-664.

[3] B. Achour, A. Bedjaoui, Computation of Friction Factor in Pipe, Larhyss Journal, 5 (2006) 197-200.

[4] P.K. Swamee, N. Swamee, Design of noncircular sections, J. Hyd. Res., 46(2) (2008) 277-281.

[5] R.O. Sinniger, W.H. Hager, Constructions Hydrauliques, 1ère Ed., Ed. Lausanne, Suisse: Presses Polytechniques Romandes, 1989.

[6] V.T. Chow, Open channel hydraulics, McGraw Hill, New York, 1973.

[7] R.H. French, Open Channel Hydraulics, McGraw Hill, New York, 1986.

[8] L.F. Moody, Friction factors for pipe-flow, Transactions ASME (1944).

[9] B. Achour, Design of Pressurized Vaulted Rectangular Conduits Using the Rough Model Method, Advanced Materials Research, 779-480 (2013) 414-419.

[10] B. Achour, A. Bedjaoui, Discussion of Explicit Solutions for Normal Depth Problem, by P.K. Swamee, P. N. Rathie, J. Hyd. Res., 44(5) (2006) 715-717.

[11] E.T. Whittaker, G.N. Watson, A Course of Modern Analysis, Cambridge University Press, Cambridge, UK, 1965.

*Applied Mechanics and Materials Vols. 580-583 (2014) pp 1842-1845*
*© (2014) Trans Tech Publications, Switzerland*
*doi:10.4028/www.scientific.net/AMM.580-583.1842*

# Evaluation of the Effects of Channel Regulation Engineering Works in Typical Braided Reach

Jianqiao Han[1, a], Liqin Li[2,b]

[1]State Key Laboratory of Water Resources and Hydropower Engineering Science，

Wuhan University, Wuhan 430072, China

[2]China Institute of Water Resources and Hydropower Research, Beijing 100044, China

[a]hjq13@163.com, [b]371004907@qq.com

**Keywords:** navigation conditions; engineering effects; braided reach

**Abstract.** The evaluation of the effects of regulation engineering in Jiayu-Yanziwo reach is presented through the process of: (a) the introduction of study area and regulation works; (b) the establishment of a two-dimensional flow and sediment numerical model; (c) the evaluation of regulation works effects. According to the phenomenon of river process, a series of engineering to prevent the sand bar from erosion are designed. The effects of prevent works is simulated by 2D numerical model verified with measured data. After impound of the prevent engineering, the min navigation width while depth is 3.7m is greater than 150m, the good navigation conditions will maintained in next decade.

## Introduction

In the middle Yangtze River, exist in a large number of a branching channel. Sand bar and channel changes frequently with different water and sediment conditions, which often cause great deterioration in waterway conditions [1]. In generally, navigational will become worse if sandbar erosion and channel sedimentation. This problem appeared on many reach, such as Shashi, Wuguizhou, Jiepai reach. Since Jiepai waterway regulation project implemented in 1994, waterway regulation engineering has become the most effective way to solve navigation problem. In the process of engineering design, accurately performance evaluation is the most important part [2].Due to complex constrained factors, effects of evaluation work is quite difficult. After decades of development, three evaluation methods, including measured data analysis, physical model, mathematical model, has been formed. The mathematical model method is increasingly popular in the study of engineering effect evaluation with its feature of efficiency, flexible and small cost, which also shows high availability in simulating results[3,4]. This paper take Jiayu-Yanziwo reach as an example , the cause and solution of navigation engineering was identified, then the waterway conditions after the project carried out in ten years were simulated by a 2D flow-sediment mathematical model ,which was established and verified by recently measured data..

## Study Area and Background

**Study Area.** Jiayu-Yanziwo reach located in Hubei province, was key navigation obstruction reach of the middle Yangtze River(Fig.1). Recently, the minimum channel maintenance measure is 3.5m×80m×750m, assurance rate of 98%. At 2020, this criterion will be raised to 3.7m×150m×1000m. In Jiayu reach, water flow be divided into three branches by Huxian Island and Fuxing Island, the left branch is the main navigation way because its water depth deep enough. In Yanziwo reach, exports is controlled by Yinjiazhou node, the right bank Fuliang Island exists, water flow is divided into two channel by Yanziwo beach. The main branch periodically in the swing around branches, navigation channel is not stable.

**Plan of Regulation Engineering Works.** The main problem of Jiayu reach is erosion at the left edge of Huxian Island, the head beach of Fuxing Island, split ratio increases in the middle channel. In Yanziwo reach, the right branch erosion and split ratio increases, the import of left branch bandwidth,

flow is hard to focus wash navigation channel. To solve above problems, pavement works to protect bench from erosion are proposed. The final scheme is shown in Fig.1, one fishbone-bench protection belt is applications in head of Fuxing Island at Jiayu reach, and in Yanziwo reach, one fishbone-bench protection belt is carried out in head of Yanziwo bench, two bed protection belt in tail.:

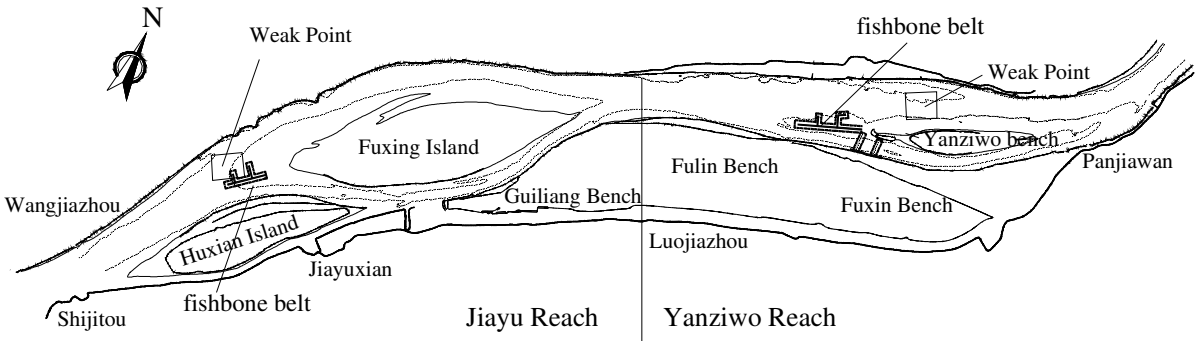


**Fig.1 Sketch of Jiayu-Yanziwo reach**

## Method

In this paper, a 2D flow-sediment mathematical model is adopted to evaluate the effects of regulation engineering on navigation condition.

**Model Theory.** Control equations of the model are as follows:

(1) Flow continuity equation

$$\frac{\partial H}{\partial t}+\frac{1}{C_\xi C_\eta}\frac{\partial}{\partial \xi}\left(huC_\eta\right)+\frac{1}{C_\xi C_\eta}\frac{\partial}{\partial \eta}\left(hvC_\xi\right)=0 \tag{1}$$

(2) Flow momentum equation

$\xi$ direction:

$$\frac{\partial u}{\partial t}+\frac{1}{C_\xi C_\eta}\left[\frac{\partial}{\partial \xi}\left(C_\eta u^2\right)+\frac{\partial}{\partial \eta}\left(C_\xi vu\right)+vu\frac{\partial C_\eta}{\partial \eta}-v^2\frac{\partial C_\eta}{\partial \xi}\right]=-g\frac{1}{C_\xi}\frac{\partial H}{\partial \xi}$$
$$-\frac{u\sqrt{u^2+v^2}n^2g}{h^{4/3}}+\frac{1}{C_\xi C_\eta}\left[\frac{\partial}{\partial \xi}\left(C_\eta\sigma_{\xi\xi}\right)+\frac{\partial}{\partial \eta}\left(C_\xi\sigma_{\eta\xi}\right)+\sigma_{\xi\eta}\frac{\partial C_\xi}{\partial \eta}-\sigma_{\eta\eta}\frac{\partial C_\eta}{\partial \xi}\right] \tag{2}$$

$\eta$ direction:

$$\frac{\partial v}{\partial t}+\frac{1}{C_\xi C_\eta}\left[\frac{\partial}{\partial \xi}\left(C_\eta vu\right)+\frac{\partial}{\partial \eta}\left(C_\xi v^2\right)+uv\frac{\partial C_\eta}{\partial \xi}-u^2\frac{\partial C_\xi}{\partial \eta}\right]=-g\frac{1}{C_\eta}\frac{\partial H}{\partial \eta}$$
$$-\frac{v\sqrt{u^2+v^2}n^2g}{h^{4/3}}+\frac{1}{C_\xi C_\eta}\left[\frac{\partial}{\partial \xi}\left(C_\eta\sigma_{\xi\eta}\right)+\frac{\partial}{\partial \eta}\left(C_\xi\sigma_{\eta\eta}\right)+\sigma_{\eta\xi}\frac{\partial C_\eta}{\partial \xi}-\sigma_{\xi\xi}\frac{\partial C_\xi}{\partial \eta}\right] \tag{3}$$

(3) 2D non-equilibrium suspended sediment transport equation

$$\frac{\partial hS_L}{\partial t}+\frac{1}{C_\xi C_\eta}\left[\frac{\partial}{\partial \xi}\left(C_\eta huS_L\right)+\frac{\partial}{\partial \eta}\left(C_\xi hvS_L\right)\right]=$$
$$\frac{1}{C_\xi C_\eta}\left[\frac{\partial}{\partial \xi}\left(\frac{\varepsilon_\xi}{\sigma_s}\frac{C_\eta}{C_\xi}\frac{\partial hS_L}{\partial \xi}\right)+\frac{\partial}{\partial \eta}\left(\frac{\varepsilon_\eta}{\sigma_s}\frac{C_\xi}{C_\eta}\frac{\partial hS_L}{\partial \eta}\right)\right]+\alpha_L\omega_L\left(S_L^*-S_L\right) \tag{4}$$

(4) Riverbed deformation equation

$$\gamma_s \frac{\partial Z_L}{\partial t} = \alpha_L \omega_L (S_L - S_L^*) \quad \text{L=n1…n2} \qquad (5)$$

The discrete format of equations was finite volume method. Numerical method, boundary conditions and other solution on key problems as movable boundary technique could be found in the reference [5, 6].

**Model Calibration and Validation**. There are 300*100grid points in Shijitou to Panjiawan 35km long, model parameters were determined by the data measured in 2012, The roughness in beach was in the range of 0.025 to 0.032, and in channel was about 0.014 to 0.026. Fig.2 shows the velocity distribution, the verification of Erosion and deposition distribution was shown in Fig.3.The above comparison between calculated and measured values proved that, this model could simulated the characteristics of water and sediment transport in this reach accurately, and be used to carry out the work of trend forecasting and evaluation of programs.

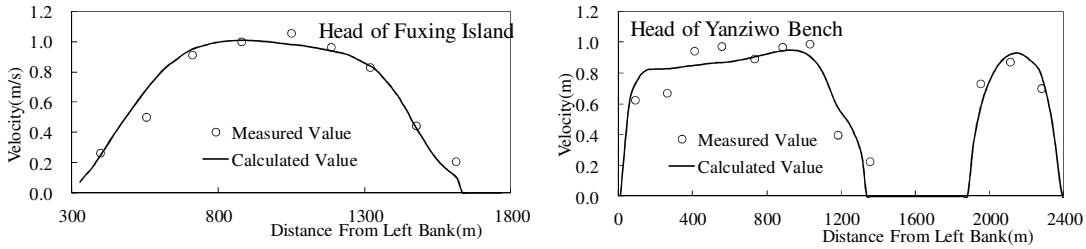


**Fig.2 Verification of velocity distribution (Q=11400m$^3$/s)**

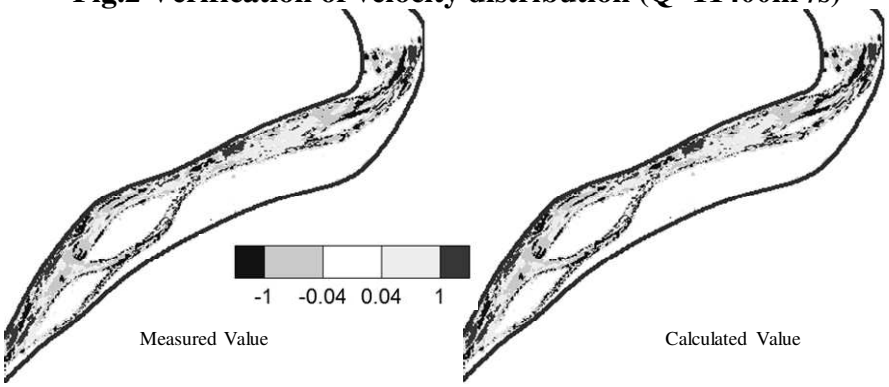


**Fig.3 Comparison between calculated and measured values of erosion distributions from 2011-2012.**

**Numerical simulation condition**. Flow and sediment process of 2006-2010+1998+2006-2009 were employed in the calculation of the navigation results after the regulation projects. The initial terrain was November 2011's.

## Results

**Navigation Condition**. The morphology of Fuxing Island and Yanziwo Bench which periodically scouring and silting has been maintained after impound of engineering. Fig.4 shows the min premise navigation width while navigation depth is 3.7m in inlet of left branch at Jiayu and Yanziwo reach. The result shows that, compared the non-engineering, navigation width is increased largely, such as 2016, the width in Jiayu reach is 180m than non-engineering, hinders navigation problem is resolved. In 2014, 2016, 2018, 2020, 2022, the width of Jiayu reach are 360m, 350m, 190m, 300m ,350m, Yanziwo reach are 270m, 320m, 380m, 330m, 290m. No matter when, width of channel are great than 150m, the min required width. Thus, the good navigation condition is maintained after the project.

**Adverse effects**. Artificial engineering construction will cause adverse effects, causing adjustment of river regime or increase the flood pressure, so small adverse effects was the premise of projects construction. The simulation result of water dynamics in conditions of no-engineering and later

engineering shows that, the max change value of near-bank velocity is 0.01m/s, water level is 0.007m, diversion ratio of right branch is 0.21%. The impoundment of the projects cannot cause significant changes of flow conditions.

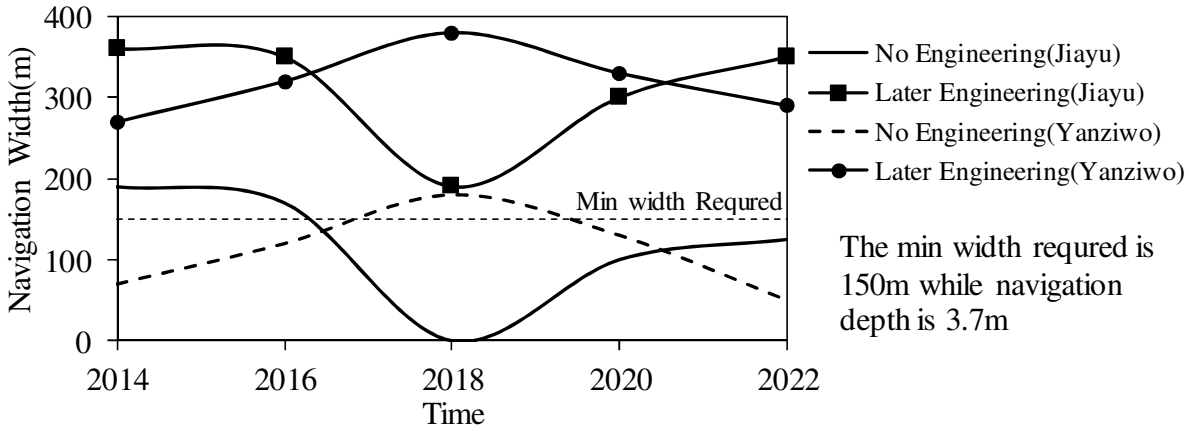


**Fig.4 The min navigation width in the future decade**

## Conclusions

(1) One 2D flow-sediment mathematical model established in this paper could simulated the characteristics of water and sediment transport in Jiayu-Yanziwo reach accurately, and be used to carry out the work of trend forecasting and evaluation of programs.

(2) The effects of navigation engineering simulated show that, good navigation condition is maintained in next decade.

## References

[1] Jinyou Lu: Fluvial Processes and Regulation of Yangtze River (China Water Power Press, China 2005).

[2] Jianshi Zhao, Zhongjing Wang and DaoxiWang: Water Resour Manage. Vol. 23(2009), p.1387

[3] Conaway, J. S., E. H. Moran: Geological Survey. 1225(2004), p. 22

[4] Christine L. May, Bonnie Pryor, Thomas E. Lisle, and Margaret Lang. Water Resources Research. Vol. 45(2009),p1

[5] Yongjun Lu, Zhaoyin Wang, Liqin Zuo: International Journal of Sediment Research Volume 20, Issue 4 (2005), p. 333.

[6] Weiming Wu, Yitian Li: One and two-dimensional nesting mathematical model for river flow and sedimentation, The Fifth International Symposium on River sedimentation Vol. 1 (1992), p. 547

*Applied Mechanics and Materials Vols. 580-583 (2014) pp 1846-1851*
*© (2014) Trans Tech Publications, Switzerland*
*doi:10.4028/www.scientific.net/AMM.580-583.1846*

# Experimental Study on Engineering Properties Of Cemented Sand and Gravel

Hua Fu[1, 2,3,a],Jiangang Feng[4 b], Huaqiang Han[1, 2, 3,c], Hua Ling[1, 2, 3,d]

[1]Nanjing Hydraulic Research Institute, Nanjing 210029, China

[2] Key Laboratory of Earth-Rock Dam Failure Mechanism And Safety Control Techniques, Ministry of Water Resource,Nanjing 210029, China.

[3] Skate Key Laboratory Of Hydraulic—Water Resources And Hydraulic Engineering, Nanjing 210029, China

[4]Hohai University, Nanjing 210029, China

[a]hfu@nhri.cn， [b] jgfeng@hhu.edu.cn，[c] hqhan@nhri.cn， [c]hling@nhri.cn

**Key words:** Cemented sand and gravel, static and dynamic properties

**Abstract**: The static and dynamic triaxial shear tests and deformation tests on CSG (cemented sand and gravel) are conducted with different amount of added cementing materials. The mechanical indexes and parameters have obvious increments with mixing of cementing material and accumulation of curing days. However the increments will become mild with further adding of cementing material. The deformation curve of CSG test sample is similar to the curve of sand-gravel sample without mixing with any cementing material, and they both follow the trend of semi-logarithmic decrement law. The dynamic permanent deformation of CSG increases with the increments of confining pressure, consolidation stress and dynamic stress. Thus this deformation still can be calculated using the constitutive model of dynamic residual deformation proposed by Zhujiang Shen Academician.

## Introduction

CSG (Cemented Sand and Gravel) is a new type of material for dam construction works and it is produced by adding cement, coal ash and water to rock based material such as riverbed gravel or excavation muck which can be easily found near dam sites, and mixing them with simple device. The physical properties of CSG change from granular material into concrete material with this mixing of cementing material [1]. The cement sand and gravel (CSG) dam owes the advantages both of the concrete faced rock-fill dam (CRFD) and roller compacted concrete (RCC) gravity dam. Engineering experience compared with RCC dam demonstrated that it has low requirement of foundation, rapid speed in construction and low cost. Compared with CFRD dam that nearly a half of material can be saved, it also can reduce the influence on the nature environment. It is clear that CSG dam will find wide application in the future [2-3]. Because of these advantages of CSG dam, it has attracted much attention of experts abroad [4-10]. The physical property of CSG is not fully understood yet. At present, researches on physic-mechanical property of CSG material are based on the concrete theory and usually the uniaxial compression test is adopted to study the CSG physical properties.few experimental studies on dynamic property of CSG can be found in the literature. In our research herein, both static and dynamic properties in mechanics and deformation of different CSG are investigated using triaxial tests, and the influences of different mixed cementing material on CSG are also discussed.

## Test Method

Natural sand and gravel was used as the aggregate for tests and its gradation is shown in Table 1. The mass density of aggregate was controlled as 2.29g /cm$^3$. Static tests were classified into four groups: without any cementing material, with 60kg/m$^3$, 80kg/m$^3$, 90kg/m$^3$ of cementing materials. The cementing material was cement and coal ash. The cement was P.O.42.5R and coal ash was

secondary ash, and their mixed ratio was 6:4 in weight. The water cement ratio was set to 0.8 and the curing days was 28. One more compared test for CSG with 80 kg/m$^3$ of cementing material was also conducted with a curing days of 90. The dynamic triaxial tests were classified into two groups: without any cementing material and with a cementing material of 40 kg/m$^3$ P.O.42.5R cement. The water cement ratio was 0.8 and the curing days was 28.

Table 1 The aggregate gradation

| Name | Percent of particle size range（%） | | | | | |
|---|---|---|---|---|---|---|
| | 60~40 mm | 40~20 mm | 20~10 mm | 10~5 mm | 5~1 mm | 1~0 mm |
| Sand and gravel | 25.8 | 24.8 | 16.5 | 11.4 | 9.0 | 12.5 |

## Test Results and Discussion

**Static triaxial test results.**The test samples were prepared artificially with the same dimension of $\Phi 300\times 700$ mm, different amounts of cement, coal ash and water were added into different test samples. The confining pressure were set to 4 levels, 300 kPa, 600 kPa, 1000 kPa and 1500 kPa, during the test procedure and the test results are shown in Figrue 2.

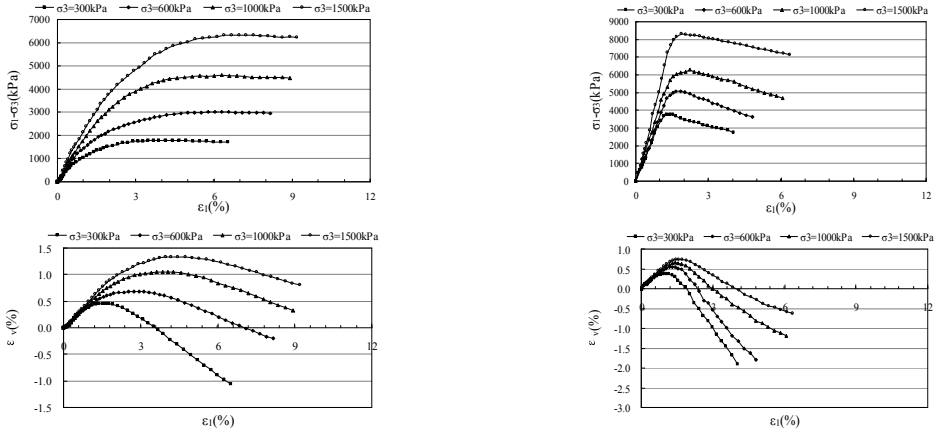


No cementing material 60 kg/m$^3$ cementing material (curing for 28 days)

Figure 2 Results of static triaxial tests

the elastic nonlinear Duncan model is adopted to process the experimental data and the calculated experimental parameters are listed in Table 2.

Table 2 Parameters of Duncan model in triaxial shear test

| Sample | Cementing (kg/m$^3$) | Curing days | $c$ (kPa) | $\varphi$ (degree) | $K$ | $n$ | $R_f$ | $G$ | $F$ | $D$ |
|---|---|---|---|---|---|---|---|---|---|---|
| Sand- gravel | 0 | e/ | 163.2 | 40.9 | 1220.2 | 0.32 | 0.64 | 0.39 | 0.12 | 7.25 |
| CSG | 60 | 28 | 617.8 | 40.6 | 2641.7 | 0.28 | 0.14 | 0.37 | 0.08 | 13.25 |
| | 80 | 28 | 766.9 | 40.2 | 3369.5 | 0.24 | 0.13 | 0.38 | 0.09 | 13.20 |
| | | 90 | 842.1 | 40.5 | 3644.2 | 0.26 | 0.10 | 0.40 | 0.10 | 15.00 |
| | 90 | 28 | 842.3 | 39.9 | 3742.5 | 0.23 | 0.11 | 0.38 | 0.09 | 13.95 |

The results indicate that:

The peak value of damage increases with the increment of adding cementing material after consolidation grouting. However the $\varphi$ value, which is an indication of linear intensity, decreases a bit, while the c value has an apparent increasing. Fine grained sand and rough gravels will cement to each other after adding the cementing material, which makes the bite force be strong, thus increase the intensity of the sand and gravel material. The increased intensity of material leads to a low sensitivity to its confining pressure. The relationship between peak values of damage $(\sigma_1-\sigma_3)_f$ under their respective levels of confining pressure and intensity index $\varphi$ is listed in Table 3. Under the confining pressure of 300 kPa, the peak value of damage increases by 1969 kPa to 3153 kPa. With an increment of confining pressure to 1500 kPa, the peak value of damage only increases a bit with an increased value of 1988 kPa- 3035 kPa. The damage peak value is not

sensitive to confining pressure since the increased values under high and low confining pressure are almost the same. Therefore, a decreased $\varphi$ value and an increased c value can be observed from our results.

The peak value of damage increases by 31.4%-109.7%, and the model parameter K increases by 116.5 % with the increment of added cementing material from 0 kg/m$^3$ to 60 kg/m$^3$. The peak value of damage increases by 6.9%-19.1%, while the model parameter K increases by 27.6 %, if the added cementing material is increased from 60 kg/m$^3$ to 80 kg/m$^3$. In the end, with the added cementing material be increased from 80kg/m$^3$ to 90kg/m$^3$, the peak value of damage increases by 2.3%-5.3%, and the model parameter K increases by 11.1 %. The results of different amount of added cementing materials indicate that the mechanical properties of CSG become stronger (larger) with more added cementing material, while this increment in intensity will be mild essentially.

Different curing days test was conducted for the same amount of added cementing material of 80kg/m$^3$ and the results show that, the peak value of damage increases by 3.0%-8.2%, and the model parameter K increases by 8.2%-13.5% with the increment of curing days from 28 to 90. In other words, the intensity of CSG has already reached 92.5%-95.8% of its fracture strength within 28 curing days.

Table 3 Damage peak values and intensity indexes

| Sample | Cementing material (kg/m$^3$) | Curing days | Peak value of damage (kPa) | | | |
|---|---|---|---|---|---|---|
| | | | Confining pressure 300kPa | Confining pressure 600kPa | Confining pressure 1000kPa | Confining pressure 1500kPa |
| Sand-gravel | 0 | 0 | 1794 | 3011 | 4587 | 6331 |
| CSG | 60 | 28 | 3763 | 5067 | 6276 | 8319 |
| | 80 | 28 | 4483 | 5538 | 6690 | 8892 |
| | | 90 | 4768 | 5962 | 7233 | 9275 |
| | 90 | 28 | 4723 | 5883 | 6881 | 9095 |

**Dynamic triaxial test results.**The CSG test samples were installed on the dynamic triaxial machine after curing. Dynamic modulus and dynamic residual deformation were investigated.

The relationship between modulus of dynamic shear $G_{d\max}$ and averaged principal stress $\sigma_m$ are shown below:

$$G_{d\max} = kP_a\left(\frac{\sigma_m}{P_a}\right)^n \tag{1}$$

The dynamic parameters *K* and *n* are listed in Table 4.

Table 4 Test results of dynamic modulus

| Sample | Cementing material (kg/m$^3$) | Curing days | *K* | *n* |
|---|---|---|---|---|
| Sand-gravel | 0 | 0 | 2312 | 0.36 |
| CSG | 40 | 28 | 3771 | 0.24 |

The Figure 4 shows the dynamic properties of CSG increases a lot after adding a 40 kg/m$^3$ cementing material, and the parameter K of modulus of dynamic shear increases by 1.63 times. The dynamic shear modulus is not that sensitive to the averaged principal stress $\sigma_m$ due to the increment of itself intensity, thus make the dynamic shear modulus coefficient *n* be small.

For the tests of dynamic residual deformation, The final axial dynamic strains and dynamic volumetric deformations under different confining pressure, consolidation ratios and dynamic stresses are plotted in Table 5.

Table 5 Maximum axial dynamic strains and dynamic permanent volumetric deformations of CSG with 40kg/m3 cementing material

| Consolidation ratio $k_c$ | 1.5 | | | 2.0 | | |
|---|---|---|---|---|---|---|
| Confining pressure $\sigma_3$/kPa | Dynamic stress ratio $\tau_d / \sigma_3$ | Max. axial dynamic strain $\varepsilon_a$/% | Max. dynamic volumetric strain $\varepsilon_v$/% | Dynamic stress ratio $\tau_d / \sigma_3$ | Max. axial dynamic strain $\varepsilon_a$/% | Max. dynamic volumetric strain $\varepsilon_v$/% |
| 300 | 0.4 | 0.05 | 0.10 | 0.5 | 0.11 | 0.09 |
| | 0.8 | 0.10 | 0.19 | 1.0 | 0.16 | 0.17 |
| 600 | 0.4 | 0.11 | 0.14 | 0.5 | 0.18 | 0.12 |
| | 0.8 | 0.21 | 0.27 | 1.0 | 0.28 | 0.23 |
| 1000 | 0.4 | 0.15 | 0.19 | 0.5 | 0.26 | 0.19 |
| | 0.8 | 0.33 | 0.34 | 1.0 | 0.48 | 0.31 |
| 1500 | 0.4 | 0.22 | 0.22 | 0.5 | 0.36 | 0.22 |
| | 0.8 | 0.50 | 0.39 | 1.0 | 0.66 | 0.36 |

As can be seen from Figure 4 and Table 5, the dynamic permanent deformation of CSG with an added 40kg/m$^3$ cementing material increases a lot with the respective increment in confining pressure, consolidation stress and dynamic stress. When there is an increase in confining pressure, the increments of axial dynamic strain, amplitude of dynamic strain and dynamic permanent volumetric strain are also observed. When there is an increase in consolidation stress, an increment of dynamic permanent shear deformation and a reduction of amplitude of dynamic strain can be found. If the test sample is under the same confining pressure and consolidation stress, the axial dynamic strain, amplitude of dynamic shear strain and dynamic permanent volumetric deformation increase with the increment of dynamic stress applied on that CSG sample.

The residual deformation curves before and after consolidation grouting are shown in Figure 5. The deformation curve of CSG test sample with an added 40kg/m$^3$ cementing material has a similar trend as the curve of sand-gravel sample without adding any cementing material. They both follow the semi-logarithmic decrement law. Thus the experimental parameters can be analyzed according to the constitutive model of dynamic residual deformation [19] given by Zhujiang-Shen Academician. The increment of dynamic residual volumetric strain $\Delta\varepsilon_v$ and the increment of residual shear strain $\Delta\gamma_s$ can be calculated through equations below:

$$\Delta\varepsilon_v = c_1(\gamma_d)^{c_2} \exp(-c_3 S_1)\frac{\Delta N_L}{1+N_L} \tag{2}$$

$$\Delta\gamma_s = c_4(\gamma_d)^{c_5} S_1 \frac{\Delta N_L}{1+N_L} \tag{3}$$

among equations, $\Delta N_l$ and $N_l$ are the increment and accumulation of equivalent vibration times. $c_1$, $c_2$, $c_3$, $c_4$, $c_5$ are the five parameters of dynamic residual deformation. Those parameters are listed as Table 6.

Table 6 Comparisons of dynamic residual deformation model parameters

| Sample | Cementing material (kg/m$^3$) | Curing days | $c_1$ (%) | $c_2$ | $c_3$ | $c_4$ (%) | $c_5$ |
|---|---|---|---|---|---|---|---|
| Sand-gravel | 0 | 0 | 0.41 | 0.72 | 0 | 5.23 | 0.81 |
| CSG | 40 | 28 | 0.21 | 0.60 | 0 | 3.14 | 0.50 |

The CSG dynamic residual deformation characteristics have been improved a lot with adding of the 40kg/m$^3$ cementing materials. The figures 4 shows there are obvious reductions of both residual axial deformation and residual volumetric deformation under the same stress conditions. The model parameter of dynamic residual axial strain has decreased by 48.8% and the parameter of dynamic residual volumetric strain has reduced by 40.0%.

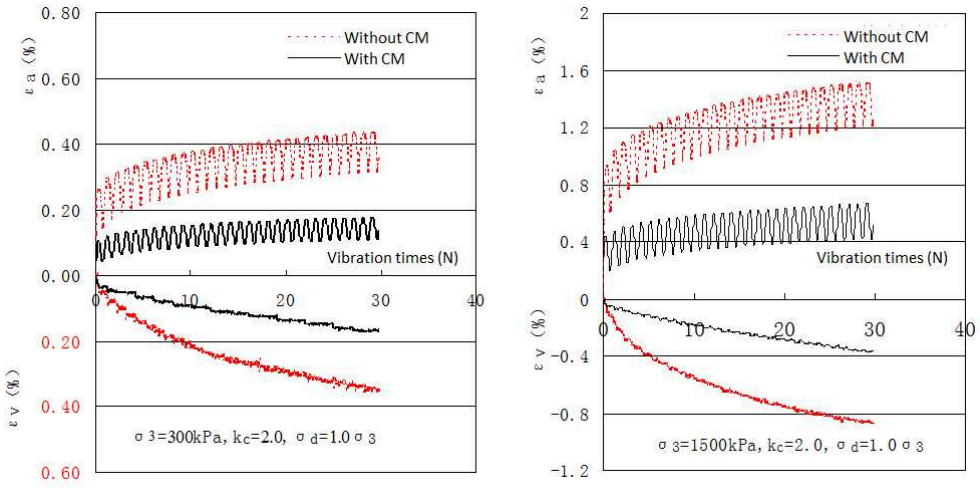


Figure 4 Comparsions of dynamic residual deformations with and without CM (cementing material)

## Conclusion

From the studies of mechanics and deformation of CSG material using both static and dynamic triaxial test methods, the following conclusions can be drawn:

The peak value of damage for CSG material increases obviously with the increment of added cementing material. However, the linear intensity index $\varphi$ may have a decrement, while the index c will have an obvious increment with the adding of cementing material. In general, the mechanical indexes increase with the adding of cementing material and this increment will become mild in the end. The peak value of damage and model parameter K of CSG increase with the increment in curing days from 28 days to 90 days,

The sand-gravel material show a reduction of damage ratio from 0.64 to 0.11 with the increased amount of cementing material. The strain-stress curve of CSG material can change from nonlinear type into the linear elastic type. To summarize, the CSG changes from elastic-plastic material into linear elastic material with the increment of added cementing material.

The deformation curve of CSG with an adding of cementing material has a similar trend as the curve of sand-gravel sample without adding any cementing material, and they are matching with the semi-logarithmic decrement law. The confining pressure, consolidation ratio and dynamic stress have significant influences on the CSG dynamic permanent deformation. The enlargement of pressure or stress will increase the permanent deformation of CSG.

## Reference:

[1] Raphael .J .M. The Optimum Gravity Dam, Rapid Construction of Concrete Dams[C]. ASCE,New York, 1970.

[2] Londe P, Lino M. Hardfill Dam, The Faced Symmetrical Hardfill Dam: a New Concept for RCC[J]. International Water Power & Dam Construction. 1992,44(2):19-24.

[3] Shuyuan Lu,Xinjun Tang.A brief introduction to a novel dam type-Face cenment rockfill dam[J].Journal of Yangtze River Scieitific Research Institute. 1998,15(02):54-56.

[4] Shihua Yang.Lin Yishan selected papers of water treatment [M], 1981,562-575.

[5] D.G.Coumoulos and T.P.Koryalos, Lean RCC dams—laboratory testing methods and quality control procedure during construction[C]. Madrid: Proceedings 4th international Symposiumon Roller Compacted Concrete Dams, 2003 :233-238.

[6] S.Batmaz, Clidere dam-107m high roller compacted dam(RCHD) in Thrkey[C]. Madrid: Proceedings 4th international Symposium on Roller Compacted Concrete Dams,2003:121-126.

[7] A.F.Gurdil, and S.Batmaz, Structural design of Cindere Dam[C]. Madrid: Proceedings 4th international Symposium on Roller Compacted Concrete Dams, 2003:439-446.

[8] Y.Hattori, et al, Construction of a sediment trap Dam using CSG conctete[J]. Dam Technology, 1993,150(3):50-58.

[9] Nagayama, et al, Development of the CSG construction method for sediment trap dams[J].Civil Engineering Journal, 1999,41(7):6-17.

[10] Zhongming Teng, Trapezoid CSG dam and material properties[J], International Hydropower, 2005,(3):39-42.

*Applied Mechanics and Materials Vols. 580-583 (2014) pp 1852-1855*
*© (2014) Trans Tech Publications, Switzerland*
*doi:10.4028/www.scientific.net/AMM.580-583.1852*

# Finite element analysis of stress deformation of earth-rock dam on narrow valley

Fu-yong Chu[1, a]

[1]School of Civil Engineering, Lishui University, Lishui, Zhejiang 323000, China

[a]cfy1976@hhu.edu.cn

**Keywords:** core rockfill dam; finite elements; stress deformation; narrow velley.

**Abstract:** The three-dimentional finite element analysis is adopted to simulate and cauculate the stresses and deformations of a certain core rockfill dam on narrow velley, with Duncan-Chang E-ν model during its completion and operation periods by incremental loading. The results show that the stresses and deformations of core rockfill dam on narrow velley are allowble and the design proposal is reasonable, which provides the theoretical basis for similar engineering.

## Introduce

With the development of dam construction technique, height of domestic earth-rock dam has reached the 300m[1]. As a important dam type, earth-rock dam play an important role. If a certain dam will be constructed on some bad geological condition such as thick overburden layer, earth-rock dam often has competition and even is the unique choice.

During the past few decades, A Large number of research on sress deformation of earth-rcok dam has been carried out by many scholars abroad, and have obtained certain achievements[2-7]. However, research on sresses deformations of earth-rcok dam on narrow valley is relative less. On the other hand, with the development of computer simulation technology, three-dimensional finite element(FEM) technique is often used to analyze the stress and deformation of rock-fill dam, which provides a theoretical basis for the preliminary design of the dam.

Therefore, the FEM stress and deformation of rock-fill dam on narrow valley in completion and test-operation period are analyzed by the Duncan Chan model in this dissertation. The resuts of research provide the theoretical basis for similar engineering.

## FEM Model

The maximum height of a certain rock-fill dam on narrow velley is 136m and the maximum height of the bedrock is about 92.5m. The major materials of the rock-fill dam are as shown in figure 1. When unit grids are divided, the majority elements such earth rock material and concrete etc are usually divided into eight nodes hexahedron element, and the minority elements are divided into six nodes pentahedron or divided into four nodes tetrahedron. The graph of 3D FEM mesh, is as shown in figure 2.

During the calculation of 3D FEM, the process of construction stage and operation stage of dam body is considered. The rock-fill material of dam body is using Duncan Chan model[8]. The model parameters of calculation are as shown in table 1. In order to simulate the discontinuity

appearing on the contact place between the concrete and earth-rock, Goodman joint element of zero thickness is set.

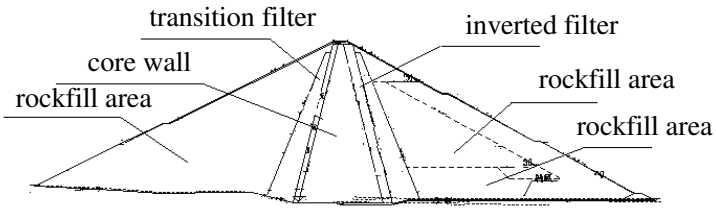


Figure 1 Typical sections and materials district

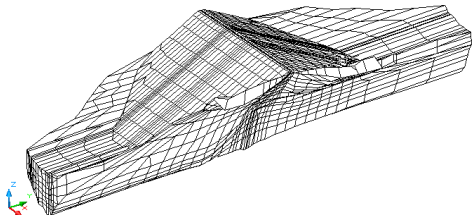

Figure 2 3D FEM mesh

Table 1 Model parameters of Duncan Chang E-ν model

| name | $\rho$ (g/cm$^3$) | $\Phi$ (°) | $R_f$ | $K$ | $n$ | $G$ | $F$ | $D$ | $K_{ur}$ | $\Delta\Phi$ (°) | $C$ (kPa) |
|---|---|---|---|---|---|---|---|---|---|---|---|
| gravel material of core wall | 2.30 | 36.50 | 0.62 | 560 | 0.420 | 0.32 | 0.140 | 3.00 | 840 | 0.00 | 55 |
| clay | 1.73 | 19.00 | 0.70 | 155 | 0.430 | 0.40 | 0.070 | 2.00 | 233 | 0.00 | 10 |
| material of inverted filter | 2.05 | 47.20 | 0.74 | 750 | 0.400 | 0.45 | 0.003 | 3.50 | 1125 | 8.80 | 0 |
| material of transition filter | 2.15 | 50.80 | 0.76 | 860 | 0.480 | 0.40 | 0.003 | 4.00 | 1290 | 8.60 | 0 |
| rockfill | 2.25 | 53.60 | 0.74 | 1000 | 0.500 | 0.35 | 0.004 | 3.00 | 1500 | 9.40 | 0 |
| material of overburden | 1.35 | 42.00 | 0.52 | 1100 | 0.420 | 0.35 | 0.010 | 1.50 | 1650 | 0.00 | 0 |

## Analysis of calculation results

The rock-fill dam on narrow velley is analyzed by using 3D FEM under Duncan Chang E-ν model, whose maximum deformation and related stress are listed in the table 2. Table 2 show that there are some differences between in completion and in test operation period on the stress and deformation characteristics. Now stress and deformation of dam body and cutoff wall will be analyzed specially.

Table 2 Three dimensional FEM schems and values of stress and deformation

| working condition | maximum of dam body settlement (cm) | maximum of horizontal displacement to upstream (cm) | maximum of horizontal displacement to downstream (cm) | maximum of top of cutoff wall settlement (cm) | maximum horizontal displacement of top of cutoff upstream (cm) | $\frac{\sigma_z}{\gamma h}$ |
|---|---|---|---|---|---|---|
| completion | 126.43 | -28.62 | 34.70 | -8.53 | 1.12 | 0.601 |
| Test operation period | 121.49 | -19.09 | 38.66 | -8.06 | 21.58 | 0.595 |

Note: $\sigma_z/\gamma h$ is the average ratio between vertical stress of each unit of core in valley and gravity stress valley in the range of 1/3～2/3 height of dam.

## Deformation characteristics of dam body

Contour of longitudinal Settlement and Contour of longitudinal horizontal displacement of core wall in operation and test operation period are given in figure 3. It is shown that the deformation distribution law during compelition and in test operation period are almost same.

Fig 3(a) and s fig 3(b) show that the maximum settlement of the dam body in completion and test operation are both on nearby the place of 1/3 height of dam. The maximum settlement of the dam

body in completion is 126.43cm, which account for the 0.93percent of height of dam and the maximum settlement of the dam body during test operation is 121.49cm, which account for the 0.89 percent of height of dam. From the data of the maximum settlement of the dam body in completion and test operation we can see that the data in test operation is slightly smaller, which mainly because of the buoyancy of water.

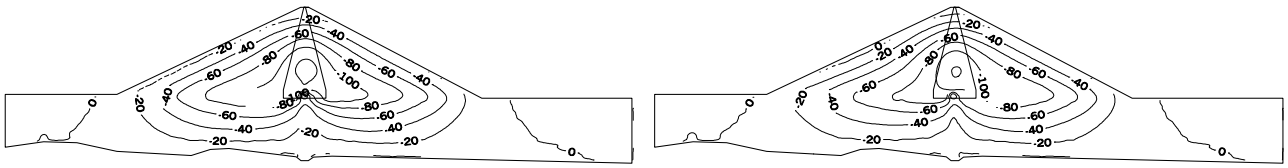

(a) completion (b) test-operation period

Figure 3 Contour of longitudinal Settlement of core wall (unit: cm)

Contour of longitudinal horizontal displacement of dam body along the river during compeliton and test operation period are given in figure 4. It is shown that the deformation distribution law of dam body along the river during compelition and in test operation period are almost same.

Figure 4(a) and figuire 4(b) show that the horizontal displacement along the river during completion and test operation period both show that the law to the downstream because of effect of water load. And the displacement of dam body along river to the downstream during completion is 34.7cm, which is descreased by 11.4% than the result during test operation period ..

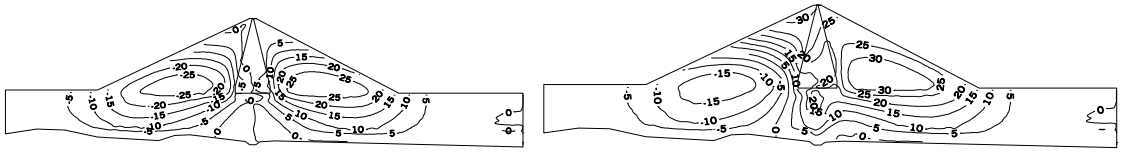

(a) completion (b) test-operation period

Figure 4 Contour of longitudinal horizontal displacement riveralong(unit: cm)

**Stress characteristics of dam boy**

Contour of longitudinal major principal stress and contour of longitudinal minor displacement of dam body during completion and test operation period are given in fig 5～fig 6. Fig 5(a) and figuire 5(b) show that the major stress distribution law of dam body during completion and during test operation period are almost same, that is, which uniformly reduce along the altitude. Among them, the maximum of the major stress under during test operation period is 1.97MPa, which is increased by 3.14% than that during complition. On the other hand, the value of $\sigma_z/\gamma h$ during compliton is more bigger than that during test operation period which shows that arc effect of core during complication is more obvious.

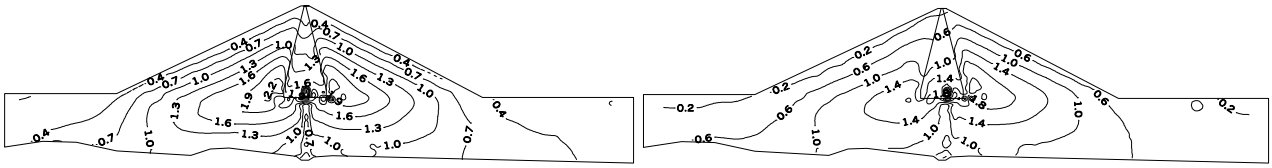

(a) completion (b) test-operation period

Figure 5 Contour of longitudinal major principal stress (unit: $MP_a$)

Fig 6(a) and figuire 6 (b) show that the minor stress of dam body appears phenomenon of stress centralization at nearby the place of 1/3 height of the bottom of dam body, and the distribution law

of minor stress distribution law of dam body during completion and during test operation period are almost same. It is worth mentioning, there is no appear tensile stress at the range of dam body. Among them, the minor stress of dam body during complition is 0.03MPa and that of dam body during test operation period is 0.04MPa.

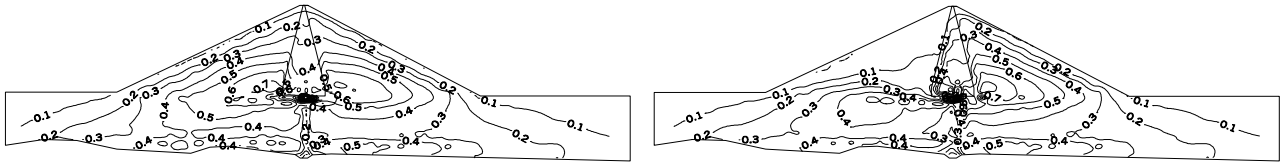

(a) completion (b) test-operation period

Figure 6 Contour of longitudinal minor principal stress (unit: $MP_a$)

**Summary**

Through comparative FEM analysis of earth rockfill dam on narrow valley during complition and during test operation period, the differences of stress and deformation between during complition and during test operation period are analyzed especially and some conclusions are obtained as following:

(Ⅰ) The maximum settlement of the dam body during test operation period is more bigger than that during complition, and they are both less than one percent which shows that stresses of dam body are all in the reasonable range.

(Ⅱ) The Result shows that arc effect of core during complication is more obvious than that during test operation period. Therefore, some reasonable measures must be adopted during compliton.

(Ⅲ) For the earth-rock dam on narrow valley, the rheology of rockfill and humidification characteristics are both needed to be concered, which has great influence for the stess and deformation. Related research remains to further expansion.

**References**

[1] ZHU Bai-li, SHEN Zhu-jiang. Calculation soil mechanics[M]. Shanghai: Shanghai science and technology press, 1990: 46-60.

[2] QIAN Jia-huan, YIN Zong-zhe. Geotechnical theory and calculation[M]. Beijing: Chinese water resource and hydropower press, 2003: 54-60.

[3] WILLIANM L, BODTMAN. Design and preformance of Shiroro rock fill dam[J]. CFRDS-Design Construction and Performance Sympoism on CFRD[C]. ASCE Detroit, Oct, 1985: 231-251..

[4] LU Wen-bo. Study on stress and deformation of core dam in thick overburden[D]. Xi'an: Xi'an university of technology, 2007.

[5] Zhu S, Gu G C. CFRD Built on the Alluvial Deposit [A]. Proceedings international symposium on high earthrock fill dams[C]. Sponsored by ICOLD ,CSHEE.Beijing ,Oct ,1993 :184～195.

[6] Choi H S. Design considerations for the 205m high Bakun dam in Sarawak, Malaysia [A] . Transactions of the 19th ICOLD [C], Q73 R8: 103 ~ 121.

[7] N.L. DE S. PINTO. Foz do Areia and Segredo CFRDS212Years Evolution [A] . Proceedings International symposium on high earth2rock fill dams[C]. Sponsored by ICOLD, CSHEE. Beijing ,Oct ,1993 :373～380.

[8] DUNCAN J M, ZHANG C Y. Nonlinear analysis of stress and strain in soils[J]. Journal of Soil Mechanics and Foundation Division, 1970, 96 (SM5): 1 629－1 653.

*Applied Mechanics and Materials Vols. 580-583 (2014) pp 1856-1859*
*© (2014) Trans Tech Publications, Switzerland*
*doi:10.4028/www.scientific.net/AMM.580-583.1856*

# Philosophical Reflections on Chinese Water Resource Management

Yingfei Liu [1, a], Benqing Ruan [1,b] and Congcong Xie [1,c]

[1]China Institute of Water Resources and Hydropower Research,China,100038

[a]yfliu@iwhr.com, [b]ruanbq@iwhr.com, [c]cc_xie1990@163.com

**Keywords:** Chinese water resource management, Governing by nature, Philosophical Reflections, Lao Tzu's philosophy.

**Abstract.** Water is crucial to production, and is the foundation of ecology. Building a reasonable management system for water resources is necessary and important, and it's an inevitable requirement of our strategy of sustainable development. In the management of behavior, philosophical base determines the behavior trends. With the development of socio-economic development, the strategy of water resources management has changed a lot in China. In this paper, the problems caused by improper water resources management modes and by overly governing by people are discussed and a series of water management reform proposals are developed on the bases of the ancient Chinese management philosophy. The paper then gets the conclusion that the water resource management reform is actually following the management path from "governing by people" to "governing by nature".

## Introduction

Water is crucial to production, and is the foundation of ecology. Building a reasonable management system for water resources is necessary and important, and it's an inevitable requirement of our strategy of sustainable development. In the understanding of the relationship between man and water, people generally experienced from the "Unconstrained water use" when the amount of water supply was greater than the demand, to the "Unregulated exploitation of water resources" when the amount of water supply and demand was balanced, to "water crisis" now. Awareness and management mode of water resource is developing with the rapid growth of economic and social development and is gradually perfecting. However, as any scientific management, we should explore the general principles and philosophy of water resources management. In the management of behavior, philosophical base determines the behavior trends. "The central committee of the communist party of the state council on accelerating the development of water conservancy reform decision" [1]claims that the strict management of water resources is a way to accelerate the transformation of economic development strategic initiatives. How to carry out strict management of water resources? What is the future development of Chinese water resources management model? What kind of philosophical path water management should follow? These are major theoretical problems the water conservancy decision makers are facing.

## The conditions of water resources management development

Water management is mainly about the social water cycle management which attaches on the natural water cycle[2]. Before the late 70s, when China's economic development was relatively backward, the water resources was far more than the demand, therefore, there was no need for regional co-ordination of government management. Household's water intake modes and the manners were determined by themselves. In the 80s, with the rapid development of economy and city construction, industry water consumption was increasing. A lot of constructions were carried out in waterhead areas, which led to the local water supply contradictions. However, in this period, the contradiction with water is not so prominent between the sectors. After the 80 s, the obvious contradiction between supply and demand of water resources is showed with the rapid economic development and the sharply increasing population. In order to get a reasonable water resources development, State is required to exercise on

behalf of the ownership of water resources management for unified planning and scheduling to satisfy various departments and industry needs.

## Current water management problems

**Decentralized management.** The state-owned institutions manage water resources respectively according to the division of duties. In some areas, water resources management is even delegated directly to local governments. For example, water conservancy administrative departments are responsible for the management of large rivers, while municipal departments are responsible for the management of urban water supply and drainage, while environmental protection departments are responsible for the conservation and management of water environment, and so on. Since water resources management content is dispersed into different sectors (such as water conservancy department, urban construction department, environmental protection department, etc.), it is difficult to achieve the goal of unified planning and the intelligent use of water resource. Since the public sectors are only responsible for their own management activities, it is difficult to implement effective water management measures. In addition, the lack of communication between those departments causes the contradictions and conflicts occur frequently. All these factors lead to the low efficiency of utilization and allocation of water resources.

**Low Water resources management level.** Water management is mainly focus on water supply management, namely water conservancy project management, with the purpose only to maximize meet the demand of production and domestic water. This management mode is a kind of extensive management mode, which is not only intensified the contradiction between supply and demand of water resources, but also brings a series of ecological problems. In addition, the unconstrained concept of water use and the utilization of water resource mode of identifying the needs by supply, led to the increasing water demand.

**Lack of proper water management regulations.**With the economic and social development and water conditions change, the relevant legal provisions have been unable to meet the actual needs. The existing water management regulations have been difficult to regulate water management activities. Imperfect management system results in particularly serious water pollution and waste. Relevant policies and regulations liability provisions are too rigid and difficult to operate. The government crackdown on illegal behavior is not enough, and the water administrative enforcement is lax. In addition, the lack of incentive mechanism of the comprehensive utilization of water resources and protection, has restrained the high efficient and sustainable water resources utilization in technological innovation and scientific and technological progress.

## Philosophy of “governing by nature”

The eternal topic of ancient Chinese philosophy is the pursuit of the harmonious relationship between human and nature. Chinese philosophy pays more attention to the concept of harmony and order, which may provide an answer for the dilemma in the current water resources management. " Lao tze " is a famous political science book, which emphasizes the nature as the core value, and with “governing by nature” as the achievement of the method. The book put metaphysics, dialectics and the “governing by nature” to an organic whole[3], and its management ideas such as“powers as cook fresh" and so on are regarded highly by managers at home and abroad. "Doing nothing" is the core of a Lao tze thought idea, and it is a necessary measure and the way of Lao tze to achieve natural world. Lao tze’s "doing nothing" is not inaction, but the meaning of "governing by nature", namely " As long as you follow the way of nature, everything can be done well." Do things complying with the requirements of the nature is "governing by nature", while against the nature is called " governing by people ".Lao tze, whose thought is generally regarded as metaphysics, is not easy to be understood and is rarely adopted by modern scientific management. But getting rid of the limitations of the ancient philosophy, Lao tze’s thought has an important significance for water resources management in the modern China. Review of China's water resources management process, the government have

changed mode of water resources management, from decentralized management to centralized management, from decentralisation to centralized power, from governing by people to governing by the regime. It is a kind of proof of the philosophy idea of "conforming to the nature of all things without artificial interference." "Governing by people" and "governing by nature", seems to be incompatible, but as methods, they are both the means to achieve the ultimate goal of "governance". The "good governance" in the modern management should strengthen the government public administrative functions and expand the market-oriented reform of urban management.

## The philosophy path of the development of China's water management

At present, the water resources management system in most developed countries is relatively mature, however, the system constructions of water management in developing countries are lacking. In the developing country, the organization form of water resources protection, legal system, administrative system, non-governmental organizations and the technology of protection of water resources have gradually become the study hotspot. In general, the water resources management in China changes from 70 s "doing nothing" to "can do" in recent 20 years, and will present the philosophy of "governing by nature- governing by people- governing by nature" path to the future development,. We think the future of China's water resources management will present the following trend:

**Unified management.** The basic contents of "governing by nature" is integrity, that is to say, the nature and human beings are inseparable as a whole. Since the existence and the change of the universe is an integral system, we should keep the universe as a whole orderly and harmonious. Science and time will prove that the holistic concept is correct. If the harmonious is destroyed by people, it will cause the change of the whole world. The harmony idea has a guiding significance to the sustainable development of economy and society. Since water resources is in the natural hydrological cycle of precipitation - runoff - evaporation, the natural property of water requires it is treated as a complete system for unified management, rather than artificial division management which is separately governed by urban and rural areas, by surface water and groundwater. Therefore, the use of water resources should form a "headwater – water supple - water use- drainage - sewage treatment" circulatory system. Besides, new public management reforms that include of change of government function, government authorization, the enterprise management mode, competition mechanism, etc, should be reference to the water resources management system reforms in order to improve the operational efficiency of the water administration department.

**Comprehensive management.** Water management is a broad concept, which should include the aim, object, method, content and the laws and regulations that ensure the normal order of the management of water resources, as well as the social foundation that ensure water management[4]. The development and utilization of water resources should be in the whole environment, such as social and economic environment. Water resources management is a comprehensive management, such as surface water, groundwater, wastewater, and should be organically combined with the economic structure, ecological system and social development, etc. Water resource forms a natural system according to the river basin, so only the unified management by river basin can provide a rational allocation. In healthy social water cycle process[5], drainage water quality does not destroy the natural water cycle, which relate to environment and ecology. Water management should focus on improving the utilization ratio of water and water repeating utilization efficiency, and reduce the water consumption and water consumption per unit of GDP, so as to realize the social water cycle in harmony with the natural hydrological cycle.

**Governing by both the government and the market.** Water resources management will absorb the market mechanism. The government's management of water economy has reference to the planned economy management mode, but too many "promising and rule" make the market does not play its due role. The government should take the market as a guidance, formulate reasonable water price and pollutant emission standards, in order to implement cost recovery. Besides, the government should establish the reasonable water price system, according to the demand supply ability and

dynamic adjustment of water level of science and technology, and also establish perfect water price accounting to the supervision and management system. The particularity of water resource market determines the water resources allocation can't be completely mediated by the market, therefore, the future water resources management model will change to the model of combination of government and the market.

**Establishing integrated river basin management system.** The legislations and practices of world's developed countries and regions, have reflected the development trend of integrated river basin management, that is, from the traditional watershed management to ecosystem-based integrated watershed management changes, and achieved good results. China should establish integrated river basin management system in order to put economic development, social welfare and environmental sustainability integration, to fit our water resources development, utilization, protection and management needs. In addition, with the establishment of water markets, water disputes will be increasing, so deal with water disputes water resources management will become an important work. Currently there is urgent need for a unified and complete clear responsibilities, rigid, operable water laws and regulations.

**Establishing mechanism of public participation.** In the Lao Tzu's philosophy, system alone will not solve all problems if people's inner state isn't improved, and water management also abides by this principle. Only people improve the inner realm, can they consciously carry out conservation of water resources activities. Only people with the idea of protection of water resources, the harmony of man and nature can be achieved. Through publicity activities to enhance the community's concern for water resources, so that everyone enhanced awareness of water conservation, with "saving" way to build a resource-saving and environment-friendly green living.

## Conclusion

Nature is the way the universe works, and it is a unified and spontaneous action. Everything in the world and every change has its inevitability and has to run through cooperation. History has proved that the development of science and technology often need to pay a heavy price. However, rational human beings should learn from ancient philosophy, instead of killing the goose that lays the golden eggs, that is, beyond the limit load of resources and environment. The ultimate goal of water resources management is to make the limited water resources to create the greatest social and economic benefits as well as the best ecological environment, or, with a minimum investment to meet the demand of the social and economic development of water resources. In order to make the limited water resources can give full play to support and guarantee the development of economy and society, we must philosophize on water resources management, and seek the solution of the "bottleneck" of water management. By complying with the natural law, can we realize the "no exception" target by "governing by nature", and promote the optimal allocation of water resource conservation, utilization and effective protection.

## References

[1] The central committee of the communist party of China under the state council on accelerating the development of water conservancy reform decision. China Water Resources.Vol.4(2011) ,p.1

[2] Wuqun Cheng, Yanhong Zhang: *Water Resources Crisis Emerge and Management*( China Water Power Press, Beijing 2010).

[3] Xiaogan Liu: Social Sciences in China. Vol.6(1996) ,p.1

[4] Ruiju Liang: The unified management of water resources (China Water Power Press, Beijing 2003).

[5] ZHANG Jie, XIONG Biyong:*The Principle and Applicat ion of Water Health Circulation*. (China Architecture & Building Press, Beijing 2006).

*Applied Mechanics and Materials Vols. 580-583 (2014) pp 1860-1863*
*© (2014) Trans Tech Publications, Switzerland*
*doi:10.4028/www.scientific.net/AMM.580-583.1860*

# Research and Discussion of Impervious Wall Construction Based On Continuous Vertical Slotting Technology

Lixin Zhang[1,a *], Yong Li[2,b], Zhao Zhang[3,c], Jingtao Niu[4], Haiyang Yu[5]

[1,2,3,4,5]Water Resources Research Institute of Shandong Province, Ji'nan, Shandong, 250013, China

[a]517597761@qq.com

[b]360136481@qq.com

[c]allenzhangzhao@live.cn

**Key words:** vertical, slotting, impervious wall, gasbag.

**Abstract:** Continuous vertical slotting technology is used in underground excavation, where the underground slots are separated into several sections taking advantage of the elasticity and flexibility of gasbags to construct flexible and rigid underground continuous impervious walls with different materials.

## Introduction

Tension over water resources has arisen, especially in the northern area, with the development of China's economy. Water storage architectures and river engineering projects such as reservoirs and barrages are constantly constructed to alleviate the problem.

In order to solve the seepage problem of newly built reservoir, river foundation and levee body, we have gone further and more extensive in researches on imperviousness technology, proposing and developing technologies of various forms. The research and application of these technologies, among which vertical plastic spreading imperviousness technology is a more functional one, have solved practical problems in engineering to a large extent.

In the massive practical engineering applications of vertical plastic spreading imperviousness technology over the years, quite a few problems have been detected. Therefore, we've come up with an idea of impervious wall construction based on continuous vertical slotting technology and started relevant research on the development and expansion of the technology.

## Two key links in vertical plastic spreading imperviousness technology

Research on vertical plastic spreading imperviousness technology is a scientific research task raised in 1987 by Water Resources Research Institute of Shandong Province. The technology was first brought up as a functional imperviousness technology aiming at the seepage and deformation problems existed in plain reservoir dams and river embankments, is now widely used in areas such as tailings dams and landfill pollution prevention.

Vertical imperviousness of levees, according to the ultimate goal of general design, is to build a vertical impervious curtain in corresponding position. Vertical plastic spreading imperviousness technology is realized following such steps: dedicated slotting machines dig continuous slots of certain width and depth vertically in reservoir dams, river embankments and other soils wanting imperviousness, and then lay geomembrane inside the slots, forming impervious curtains with geomembrane as the main body.

There are two key links within this technology: slotting and geomembrane laying.

(1) Slotting

Slotting is to dig continuous slots of certain width and depth in soil layers with dedicated slotting machines for geomembrane laying.

Depth and length of the slots are determined by the designer according to the geological and other specific conditions on site, while the former depth is generally controlled within 16 meters due to the performance limit of slotting machine.

Width of the slots, usually at around 0.3m, is subjected to the geomembrane laying process requirements; this could meet the demand for geomembrane laying and backfill amount in most engineering projects.

(2) Geomembrane Laying

Geomembrane laying is the main purpose of the technology; among the many laying methods, membrane rod method and direct laying method are more common.

In membrane rod method, a bundle of geomembranes, with width slightly larger than the depth of slots, is rolled up on a membrane rod and set vertically in a slot; with its free end fixed, it could be moved forward along with the slotting machine by a certain traction on the rod the geomembranes on the rod could thus be laid in the slot; a new bundle will be connected to the exhausting one to continue the procedure. Geomembranes are laid vertically in the slots in this way to form a curtain. This method is intuitive, easy to operate and reliable.

Direct laying method is where geomembranes are directly sunk into the slots excessive geomembrane length in each sinking is inadvisable; the depth shall consist with that of the slots, usually at 5-8m. Overlapping length of the follow-up geomembranes with the previous is required to guarantee their continuity; weight is commonly applied to their bottom when sinking. This method shall be chosen after prudent consideration when slots are at a fast accumulation speed.

**Problems**

Years of vertical plastic spreading imperviousness technology spreading and applying has seen various problems, including slot accumulation, animal and plant penetration, engineering adaptability etc.

The problem of slot accumulation is ubiquitous within the engineering application process; there are differences between its speed, quantity and size, though. Some soil has higher particle content; it accumulates faster and thicker, adding up the difficulty and even effecting the quality of geomembrane laying procedure-the laying could be lacking in depth and facilities might be buried.

Burrows are often found in levee slopes during engineering, with termite nests being the most common ones; these do much damage to geomembrane impervious bodies, making them more seepaging-prone. On the other hand, plants are widely distributed on most levees; those with developed roots have a strong penetration of geomembranes. The plants die and wither, but the numerous holes remain on the impervious bodies, leaving risks of seepage.

Researches found that geomembrane has a general aging resistance of at least 50 years, which could hardly qualify some projects. This is another defect of the technology.

Despite the fact that impervious curtains containing mainly geomembranes are low at costs and faster in construction, the above problems have restricted the development of the technology to some extent. Replacing impervious materials using current slotting technology could be an assumption to solve the problems, only if the following key technology problems are tackled. First, the now available slots are continuous; theoretically their width and depth are fixed while the length could be prolonged. Long slots shall be separated into several sections if concrete or other impervious materials are applied; fast separation speed is required as slotting shall not be ceased during construction to reduce the siltation volume-many as the techniques, none of them could adapt the high speed of current slotting machines. Second, it is crucial to develop one or more impervious materials for the slotting technology. Third, multifunction cars could be developed to simplify the wall grouting and slot separating procedure during construction for higher efficiency.

**Discussion on several key technologies**

We have, based on the above assumptions, discussed and started relevant research work.

(1) High-speed slot separation technology

Low-head continuous diaphragm wall is widely used now in hydraulic engineering; sequenced and slotted grouting or coupling adding is used in construction, complexing its procedures, slowing its speed, disabling its continuity, and risking its quality. The wall separating and joining methods have shown under-development; they could hardly meet the needs of current project in cost, speed, quality and other aspects.

Gasbag technology has an extensive application in ocean engineering hoisting, transportation, collision preventing and other areas; the new gasbag is characterized by strong stress resistance, good abrasion resistance, high intensity and fine reusability. A heterotype of gasbag could be developed based on these advantages for slot separation to better solve the above mentioned problems.

So far we have completed the process design work on heterotype gasbag separation body and some of the achievements have been applied for patents.

(2) Impervious material

The main currently used continuous diaphragm wall materials are concrete, cement mortar, and self-solidifying mortar. But considering from the costs and slot adaptation aspects, reinforced self-solidifying mortar applied better to the technology.

Given the ubiquity of slot accumulation, research shall orientate toward the full utilization of soil aggregate from the accumulation-reinforced self-solidifying mortar could be formed by adding a certain proportion of cement, bentonite, other common wall materials and extra to-be-studied additives to it. Relevant work is in progress, aiming at lower costs, and full utilization of local materials, good imperviousness, and good adaption to deformation capacity.

(3) Multifunction Car

The placement and recovery of slot separation bodies, together with wall grouting are two important links during construction; combining the two could add up convenience to construction and improve production efficiency. The process design of multifunction car is in progress, and part of the achievements has been applied for patents.

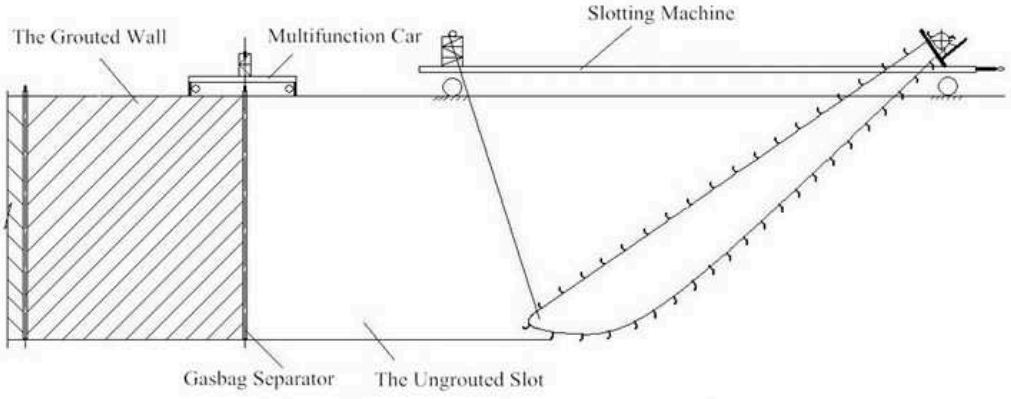


*Diagram of Slotting Technology and Impervious Wall Construction*

Illustrated above is a diagram of current slotting technology and impervious wall construction. The construction process can be included as follows: the currently well-developed slotting machine could dig continuous slots during construction; multifunction car could be used to place gasbags for separation on slotting-slot collapse could be reduced to maximum extent; grouting system from the multifunction car is then used to grout the slots, followed by removing the gasbag separation bodies from the slots with its lifting & recovery system; this whole process of impervious wall construction is finished as the holes are refilled with the same wall material.

## Conclusion

Years of vertical plastic spreading imperviousness technology application has seen good economic and social benefits, making it one of the main technologies in fundamental imperviousness area. Meanwhile, its limitations have been gradually recognized; its core technology of slotting, nevertheless, has great advantages and promising prospects. The simple process and low costs of the slotting technology is the foundation of this research.

The research makes a combination of slotting process, slot separation technology and special wall materials, while taking full advantage of the grout within slotting process and other material characteristics for impervious wall construction. It fills some gaps of vertical plastic spreading technology, and acts as a new imperviousness technology of high practicability.

## References

[1] The Design and Application of Continuous Diaphragm Wall, Aisen Cong. China WaterPower Press, Oct, (2000).

[2] Geosynthetics Engineering Application Manual Compilation Committee, Geosynthetics Engineering Application Manual [M]. Beijing: China Architecture & Building Press, (2006).

[3] Analysis of Several Problems in Vertical Plastic Spreading Impervious Technology Construction, Lixin Zhang etc. Shandong Water Conservancy, total volume 115.

*Applied Mechanics and Materials Vols. 580-583 (2014) pp 1864-1869*
*© (2014) Trans Tech Publications, Switzerland*
*doi:10.4028/www.scientific.net/AMM.580-583.1864*

# Research of Eco-compensation among Basin Cascade Hydropower Station Development and management

Xinmin Zhou[1, a], Meng Zhao[2,b]

[1]Hanzhong Huanghe Medium-Sized Hydropower Development Co．Ltd．Xi'an 710061,China.

[2]State Key Laboratory Base of Eco-Hydraulic Engineering in Arid Area （Xi'an University of Technology),710048, China.

[a]526451716@qq.com, [b]myles.910129@gmail.com

**Keywords:** Eco-compensation, cascade hydropower stations, environmental impact.

**Abstract.** Eco-compensation was involved in many subject area, and the concept and connotation of Eco-compensation were discussed from the multi-disciplinary perspective by the scholars of different research areas. Hydropower, as one kind of green energy,is an important component of the China's energy development. Owing to the delay of the cumulative effect on ecological environment caused by hydropower development, the unbalanced distribution of interests between the cascade hydropower stations, and the mass of industry and departments involved in cascade hydropower development, Eco-compensation system of the cascade hydropower development is becoming more complicated.For this reason, it is significant to analyze the environmental impact during cascade hydropower development, and to establish a full Eco-compensation mechanism for the cascade hydropower development. In this paper, the basic framework of the Eco-compensation system includes five parts: the subject, the object of compensation, compensation standards and methods of determining compensation, forms of compensation, process control of compensation, then the content of these five aspects was detailed. On this basis , the problems which should be solved urgently in the cascade development of Eco-compensation mechanisms have been advised,these discussion and analysis will provide some reference for the further research and practice.

## Introduction

The development(CHSD) of these basin cascade hydropower stations,which include Lancang river, Jinsha river, Huanghe, Dadu river, Wujiang and Hongshui river,speed up the process of hydropower development(Yun-long, 2006),concurrently the development of hydropower resources produces the negative influence to ecological environment. The distribution of ecological and related economic benefit is unfair between the protectors and beneficiaries, destroyers and victims for the ecological environment.The beneficiaries have the ecological benefits freely,the protectors cannot get the economic incentives,the destroyers failed to take responsibility and cost of the environment destroyed, and the victims cannot obtain economic compensation.The distortion of the relationship between ecological protection and economic interests is not merely facing great difficulties in ecological protection and water conservancy construction but also affecting the balance between the different regions and other ecological protection and construction.In order to ensure the river basin water resources and ecological protection as well as economic development, the performance of environmental protection responsibility of hydropower developers should be promoted,we should establish the Eco-compensation system of cascade hydropower stations development and bring the system into the environmental impact assessment which has important significance(H. WANG, 2008).

The Cascade hydropower stations is different from the independent hydropower stations in the aspect of the water use, operation scheduling, production management and external contact etc.Concurrently the cumulative effect from the Cascade hydropower stations development on the ecological environment has delayed,the distribution imbalance of interests is between the different cascade hydropower stations, the Cascade hydropower stations is involved in many departments and industries which make the Eco-compensation system of cascade hydropower stations development

more complicated.At present,there are a lot of researches on hydropower development including Eco-compensation theory,ecological value theory and environmental impact prediction in China(RUAN, XU, & ZHANG, 2008).However, these focus on the single hydropower stations,the Cascade hydropower stations research is less.This paper tries to design an integrate framework for the Eco-compensation system of cascade hydropower stations development to introduce briefly some concept such as the subject of Eco-compensation,the object of Eco-compensation,the standard of Eco-compensation and the method of standard determination, the form of Eco-compensation,the action or process control of Eco-compensation in this system and to give some reference and enlightenment for the further research.

**the Connotation of the Eco-compensation System in CHSD.**

Due to the Eco-compensation involved with many fields of study,different scholars in the field of study discuss the concept and connotation of the Eco-compensation from the different views of subject.Hydropower development of Eco-compensation can be defined the series of activities in the compensation, recovery, comprehensive treatment etc. on the ecological system, natural resource and pollution of the environment which have destroyed by hydropower development and related industry(Lv, 2003).

The scale and characteristic of the CHSD determine the important impact on the environment.Reasonable Eco-compensation system should be fully considered its environmental effect,social effect and ecological effect and make these effects convert to economic information feedback to the planning and management of the national economy,in this way the theory and method can be offered for feasible scheme of solving environmental problems (C. Wang, 1994).According to the current market economy system and the environmental protection laws and regulations, the CHSD Eco-compensation should follow some basic principles:(1) valley ecology and system theory principle,(2) environmental resources and pay for the use of the principles of sustainable development, (3) the ecological threshold value and internalization principle of the external cost .

**the CHSD Eco-compensation System**.

The CHSD Eco-compensation system should include the following five aspects of content:(1) the Eco-compensation subject,(2) the Eco-compensation object,(3) the Eco-compensation standard and ESTABLISH standard approach,(4) the Eco-compensation forms,(5) the Eco-compensation action and process controller, here are emphasis on fifth point because in the current conditions active and conscious the compensation rarely appears.

**2.1Eco-compensation Subject**.

Hydro developers is an important subject of Eco-compensation.The CHSD Eco-compensation is involved in water conservancy, shipping, power, irrigation, flood control, ecological, environmental protection, tourism and so on, there is a single department not running normally.At present in China,only the government can represent the organization of whole basin in the public interests and can play a role in the CHSD Eco-compensation,and it can properly solve the contradiction between the basin ecological construction and the economic development ,and it has the ability to resolve the environmental problems which cannot be solved spontaneously by market with regard to making laws and system, the macroeconomic regulation and control, policy and financial support,and it will become a leading role in the CHSD Eco-compensation(WU & CHEN, 2007).

**2.2Eco-compensation Object.**

First of all, the basin CHSD changed the utilization of the original water and soil resources .For example the reservoir discharged lower water temperature have an influence on agricultural and fishery production efficiency and output,and the reservoir may increase the underground water level in the future to cause the salinization of cultivated land around(FU, CHEN, & XIE, 2009), therefore the Eco-compensation subject must make up to the local governments, units and individuals whose interests are affected to make corresponding compensation.Secondly, the compensation of the ecological environment and the public environment is important and difficult. Because the environmental influence by CHSD is delaying,a lot of ecological problems appear after the accumulation of a long time , once the ecological balance is destroyed ,it will make a great of loss and the local residents need to spend a lot of manpower and finance to protect the environment and

establish a new ecological balance. These loss including biodiversity, soil erosion, water pollution as well as geological disasters, cannot be directly measured and compensated in economic way,and need long-term environmental monitoring and protection to prevent the happening of the adverse consequences in the future.All of these forms of compensation for the ecological environment and public environment, in essence, are repair and protection to ecological environment(CAO & LIU, 2010).Finally the ecological environmental protectors and residents in the reservoir area pay for the protection of the basin ecological environment, which profoundly impact their economic benefit and ecological benefit, and the local government need to compensate for them.

**2.3the Eco-compensation Standard and Establish Standard Approach**

Eco-compensation standard is the core of Eco-compensation in the CHSD and it is related to the effects of Eco-compensation and the bearable ability of the Eco-compensation object. Only when the government make a scientific and reasonable evaluation for ecological loss can we construct Eco-compensation mechanism successfully.

**2.3.1the Basis of Compensation Standard**

The calculation basis of CHSD Eco-compensation standard can be considered generally from the following six aspects:

(1) Ecological cost estimation. We must have to evaluate the impact, which will be caused by the CHSD. But most of the environmental impact is not directly measured by market value and is hardly expressed in money. In this condition we will need to use the substitute market method, by estimating the cost of the same amount and quality of ecological services and product,to infer the costs of the impact in CHSD.

(2) To calculate the profit of ecological environmental beneficiaries.Ecological beneficiaries did not pay for own products and services enjoyed,which makes ecological environmental protectors not get right reward ,and the beneficiaries need to pay these reward for them. Therefore, the Eco-compensation standard can be calculated by the market trading price of the product or service and the quantity of trading .

(3) To calculate the cost of ecological environmental recovery. The CHSD will cause the destruction of vegetation, water and soil loss, water resource wastage and biodiversity reduction in some areas, then these will directly affect ecosystem services function of water conservation, water and soil conservation, landscaping, climatic regulation and biological feed in these areas. Therefore, according to the principle of whoever damage recovery, we need to calculate the cost of environmental improvement and ecological environmental recovery as a reference for the Eco-compensation standard.

(4) To calculate the value of ecosystem services. The standards in the index and estimates of the value still lack an unified standard and has a larger gap between the compensation ability of ecosystem service function and realistic compensatory ability. Therefore, generally in accordance with the ecosystem services function to calculate the compensation standards is only as a reference and theoretical limit of compensation(Chen, 2010).

(5) The willingness to pay of Eco-compensation subject.Willingness to pay is the developer and beneficiaries of the CHSD who are willing to pay the amount of economic compensation money for the CHSD.

(6) Payment capacity. Local fiscal capacity and CHSD payment capacity is an important aspect and must be considered in the process of CHSD Eco-compensation.

**2.3.2the Establishment of Standard Approach**

According to the research at home and abroad, for the Eco-compensation, using ecological service function value assessment is difficult directly as compensation and is operable with the loss of opportunity cost accounting.The establishment of Eco-compensation standard is usually measured from two aspects:on the one hand, how much is the cost of ecological environment which will be protected and which will be constructed by the Eco-compensation subject in the CHSD area;on the other hand, how much is the value of ecological resources themselves and the other ecological value which has destroyed by the CHSD.At present,establishing standard approach basically has the following five methods:

(1) Cost-effect method. This method is based on ecological resources provided by environment effect to calculate the effect of quantitative values.

(2) Income loss method. This method is mainly evaluating the benefits of ecological resources from the point of the loss of ecological resources.

(3) Travel cost method.This method is established on the Recreation demand patterns and mainly applied to evaluate the specific tourist area. It is the most widely used in developed countries as an indirect evaluation method(Qiu-cheng, 2009).

(4) Market valuation method.Ecological change will lead to the change of productivity and the cost of production. Therefore,this kind of change can be calculated the value of ecosystem products and services.

(5) Survey evaluation method.In order to obtain the individual value of ecological products and services, we must obtain the money maximum amount of willingness to pay for ecological products and services(F. Wang, 2006).

**2.4the Eco-compensation Forms**

The government compensation and market compensation are consist of the Eco-compensation forms.Government compensation can be interpreted the compensatory way of government's fiscal transfer payment and policy support to implement compensation mechanism.The compensatory way can be divided into money, objects, policy, economic cooperation and technical support,which is shown in Fig.1 below.

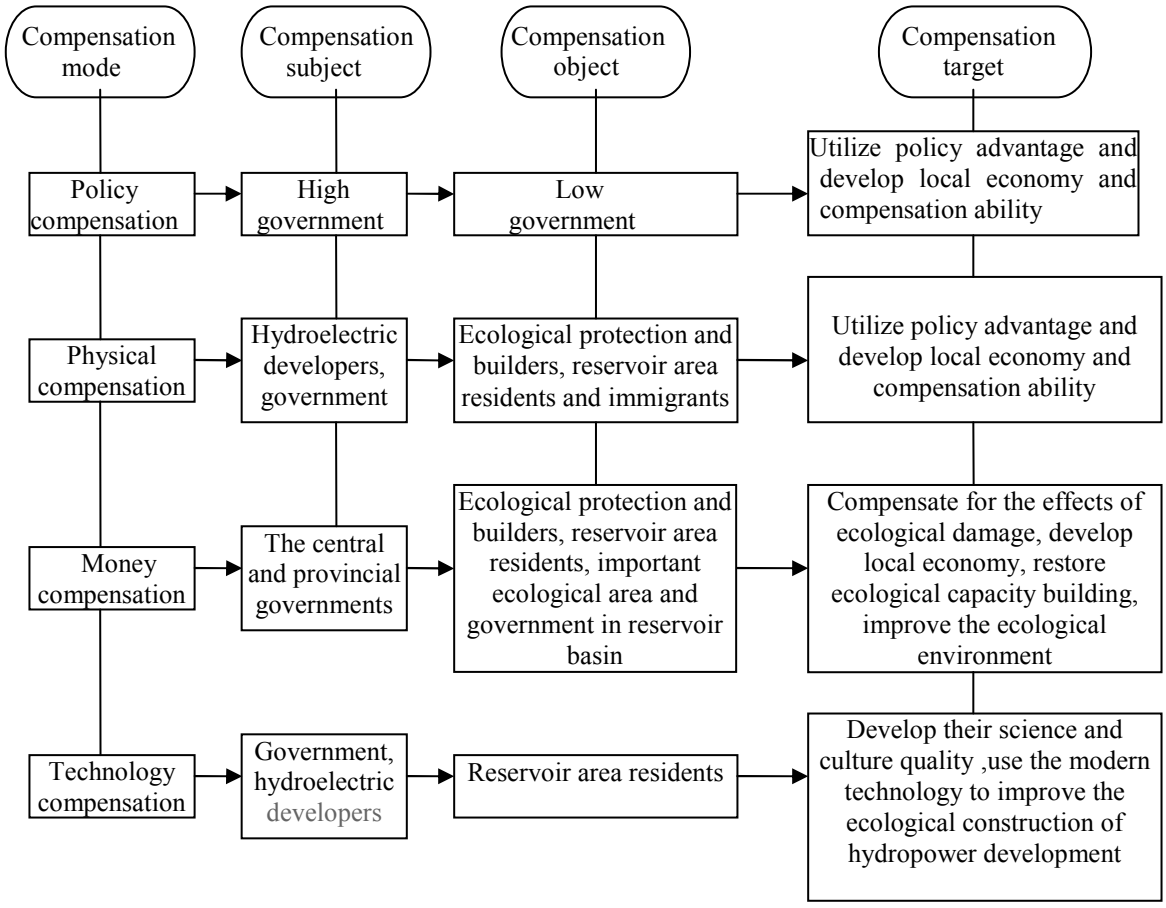


**Fig.1 Schematic Diagram of Compensation**

Market compensation is the voluntary negotiation between the Eco-compensation subject and object in the river basin upstream and downstream under the guidance of the government implement.The main way of market compensation can be used from two aspects:on the one hand,to adopt the model of basin water agreement implements rewards and punishments or compensation according to the standard. On the other hand, the water right transfer and emissions trading mechanisms is carried out(Jun, Huiyuan, & Jinnan, 2005).

**2.5the Eco-compensation Action and Process Controller**

In order to rationally develop and utilize the hydroelectric resource and reliably protect the ecological environment,under the current circumstances, our nation and local government need to summarize practical experience of the Eco-compensation and more strengthen law enforcement of the environmental protection and carry out the necessary and compulsory administrative intervention. We must involve the hydroelectric resource Eco-compensation into standardized and legalized track.

**the Problems Existing in the CHSD Eco-compensation**

Because the current cumulative effect research of ecological environment of river basin CHSD is not very deep and the CHSD joint operation technology is complexity and its benefit compensation mechanism is pluralism.There exist the following problems in the CHSD Eco-compensation mechanism, which will be established(Mao, 2009):

(1) The cumulative effect of ecological environment impact on Eco-compensation.The cumulative effect is the superposition and expanding of human activity space-time distribution impact on ecological environment(ZHONG, LIU, & GENG, 2007).

(2) The compensation benefits between the hydropower stations have some impacts on the Eco -compensation.The hydropower stations joint development and operation can save investment, shorten the construction period, increase the capacity, improve the management level and has obvious advantages. But the benefits of the investment subject between the hydropower stations would be changed,this part of the change is the watershed of compensation benefits. How to define and apportion these benefits is a problem to be solved in utilization of river basin water.

(3) Strengthen and increase the consciousness of public participation in Eco-compensation.The CHSD Eco-compensation, as a kind of economic means, is the redistribution of economic interests involving many Eco-compensation subjects and benefit adjustment. Therefore, this will need all social classes and the public active participation in the process of determining the CHSD Eco-compensation and especially pay close attention to opinion of the disadvantaged(Li, 2009).

**Acknowledgments**

The study is supported by the Ministry of Science and Technology of China (2012CB723201).

**References**

[1] CAO, L.& LIU, C. (2010). Discussion on Eco-compensation method for hydropower development. Water Resources and Hydropower Engineering, 7, 003.

[2] Chen, X. (2010). The Mechanism Research for Including of Ecological Compensation in Environment Impact Assessment. (Master), Southwest Jiaotong University.

[3] FU, P.CHEN, K. & XIE, Y. (2009). Method for environment impact assessment of hydropower development considering social factors [J]. Journal of Hydraulic Engineering, 8(2), 1012-1017.

[4] Jun, W. Huiyuan, Z, & Jinnan, W. (2005). Policy evaluation and framework discussion of ecological compensation mechanism in China. Research of Environment Sciences, 18(2), 1-8.

[5] Li, J. (2009). Research of Benefits Compensation Mechanism Among Basin Cascade Hydropower Plants. (Master), Huazhong University of Science and Technology.

[6] Lv, Z. (2003). Beyond and conservatism of environmental law under vision of sustainable development innovation (Vol. 01).

[7] Mao, T. (2009). Legal Thinking about Watershed Ecological Compensation System in China. (Master), Southwest University of Political Science and Law.

[8] McNally, A. Magee, D. & Wolf, A. T. (2009). Hydropower and sustainability: Resilience and vulnerability in China's powersheds. Journal of Environmental Management, 90, S286-S293.

[9] Qiu-cheng, T. (2009). Eco-compensation Standard and Mechanism [J]. China Population Resources and Environment, 6, 003.

[10] RUAN, B.-q, XU, F.-r. & ZHANG, C.-l. (2008). Review of research and practice of river basin ecological compensation [J]. Journal of Hydraulic Engineering, 10, 009.

[11] Wang, C. (1994). Water conservancy construction project environmental impact economic profit and loss analysis. JOURNAL OF ECONOMICS OF WATER RESOURCES.

[12] Wang, F. (2006). Hydropower development and ecological environment management.

[13] WANG, H. (2008). The Mechanism Research for Including of Ecological Compensation in Environment Impact Assessment. (Doctor), China University of Geosciences (Beijing).

[14] WU, D.-y.& CHEN, X.-l. (2007). Study on ecological compensation mechanism in water power development [J]. Water Resources & Hydropower of Northeast China, 5, 025.

[15] Yun-long, C. (2006). Study on Regulating Benefit Compensation Mechanism for Cascade Hydropower Stations' Joint Operation [J]. Electric Power Technologic Economics, 6, 014.

[16] ZHONG, H.-p, LIU, H. & GENG, L.-h. (2007). Cumulative effects of Lancang River basin cascade hydropower development on ecology and environment. Journal of Hydraulic Engineering, S1.

*Applied Mechanics and Materials Vols. 580-583 (2014) pp 1870-1873*
*© (2014) Trans Tech Publications, Switzerland*
*doi:10.4028/www.scientific.net/AMM.580-583.1870*

# Research on Channel Regulation Parameters of Daijiazhou Reach in Middle Yangtze River

Wanli LIU [1, a]

[1] Key Laboratory of Engineering Sediment of Ministry of Communications, Tianjin Research Institute for Water Transport Engineering, Tianjin 300456, China

[a]tjtgliuwanli@163.com

**Keywords:** regulation water level; regulation width; channel regulation parameters

**Abstract.** Channel regulation parameters include two important indicators, the regulation water level and regulation width. Through shoal-full water level method, bed-forming discharge method and experience method, the regulation water level was presented. At the same time, through calculation method and experience methods used in sufficient depth channel, the channel regulation width was put forward. The relevance between the regulation water level and regulation width was established. The specific regulation parameters were adopted in Daijiazhou reach.

## Introduction

Determining reasonable regulation parameters is the most important technical work in channel regulation [1-2]. Channel regulation parameters include two important indicators, the regulation water level and regulation width, and the two indicators are relevant. In the past, the correlation analysis of channel regulation parameters had not been studied through theoretical research and quantitative analysis. Therefore, on the basis of previous researches, it is necessary to study on regulation parameters relevance, in order to promote the development of channel regulation subject.

## Basic situation about projected river reaches

Daijiazhou reach located in in the middle Reach of the Yangtze River. It connects with Shazhou channel upward and Huangshi channel downwards. The total length is about 34 km (as shown in Fig.1), which includes Bahe channel and Daijiazhou channel. From the Ganyinge to Bahekou is the Bahe channel, length is about 14 km, the plane morphological is straight to relax. From the Bahekou to Huifengji is the Daijiazhou channel, length is about 20 km, the plane morphological is the micro bend branch, Daijiazhou channel is one of shallow channel in the middle Yangtze River.

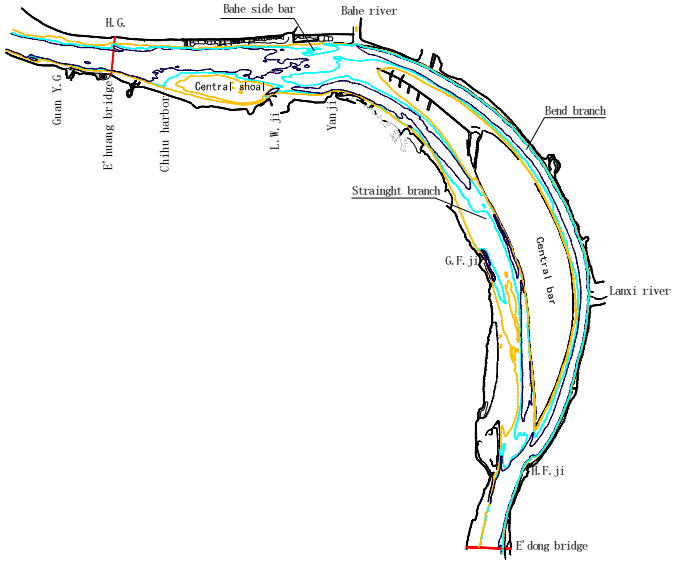


Fig.1 River regime of Daijiazhou reach in middle Yangtze river

The channel regulation target is 4.5 m ×200 m×1050 m; the navigation guaranteed rate is 98%. In order to achieve the channel regulation target, channel regulation engineering needs to be carries. Choosing the reasonable channel regulation parameters is the basic to determine the channel regulation project [3].

**Regulation water level**

In order to determine the regulation water level, this paper uses the bank full water level method, bed forming discharge method and experience method.

**The shoal-full water level method.**

This paper uses the average elevation of the side shoal as the regulation water level. Channel verification show that, when the new island beach full, tall and outstanding, the straight channel conditions was significantly improved. Since 1984, when the channel condition is good in the straight channel, by statistics the bank full water level of the low beach, calculate the side shoal every year average based on the navigation 0.8 m~1.6 m.

**The bed-forming discharge method.**

The river bed formation is concerned with the size of the flow, frequency and gradient, to determine the approximate regulation water level, this paper uses the $Q\sim Q^2JP$ curve (as shown in Fig.2).

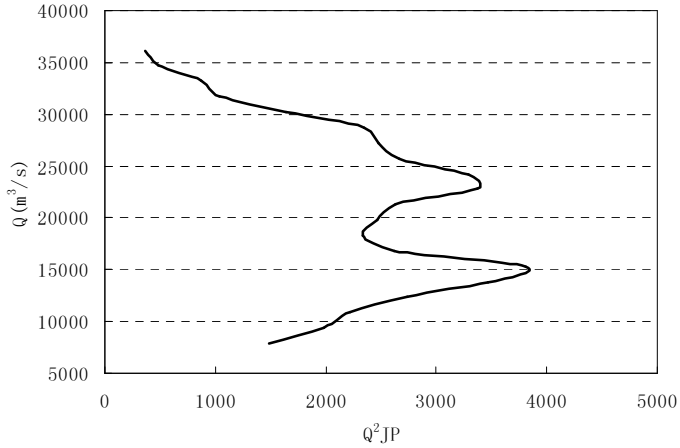


Fig.2 The relationship between Q and $Q^2$ P

It can be seen that the two river bed forming peak discharge is obvious, and regulation water level can be intended to be the second level bed flow corresponding. In the $Q\sim Q^2JP$ Curve, corresponding to the second bed building discharge (flow discharge is 15324 $m^3/s$), the corresponding water level is 11.64 m, higher than the design water level above 3.8 m.

**The Experience method.**

According to Riverbed revolution and channel regulation [1], the Riverbed Evolution and Renovation", regulation water level is higher than the general design water level above 0.7 m ~ 1.5 m.

According to the existing engineering experience data and other shoal regulation research results in the Yangtze River[3-5], it has a reference to determine the regulation water level (as shown in Table 1). By the statistics, as a general rule, the regulation level generally is higher than the design water level 2.5 m ~3 m. Considering the regulation water level deriving primarily based on the data before storage, using these experiences to after storage may have certain deviation. Considering the Three Gorges after 175 m impoundment, at present, the river dry season water function has been given to full play, the channel conditions has improved, the construction elevation should be lower than implementation project before storage, and as the reservoir impoundment, if the river bed undercutting, at the same mass flow dry water level will decreased, while the elevation relatively short project will relatively increase with dry water level decreasing, thus win the good channel dimension security, which is equivalent to through a spur dike engineering to form the good and favorable high beach.

Table1 The existing research results of water level in the middle and lower Yangtze river

| channel | Jiepai | Luxikou | Luohuizhou | Wuxue | Zhangjizhou south | Dongliu |
|---|---|---|---|---|---|---|
| Above the design water level（m） | 3.0 | 3.0 | 3.0 | 2.5 | 3.0 | 3.0 |

**Regulation width**

Through calculation method and good experience method, the channel regulation width is put forward.

**The calculation method.**

According to Waterway regulation Engineering technical standards, the regulation width calculation formula as follow:

$$B_2 = KB_1\left(\frac{H_1}{\eta H_2}\right)^y$$

Where $B_1$=water surface width when the regulation water level before renovation; $B_2$=regulation width (m); $H_1$=section average water depth under the regulation water level before renovation; $H_2$=channel design section average water depth under the regulation water level; K=1.0, η =1.0, y=4/3.

The calculation parameter into the formula getting the Bahe channel regulation width is 1193m, the straight channel regulation width is 911m (as shown in Table 2).

Table2 The regulation width calculation value

| Channel/ branch | $B_1$（m） | $H_1$（m） | $H_2$（m） | $B_2$（m） |
|---|---|---|---|---|
| Bahe channel | 1700 | 4.6 | 6 | 1193 |
| Bend channel | 630 | 4.3 | 5 | 515 |
| Straight channel | 1150 | 4.2 | 5 | 911 |

**The experience method in sufficient depth channel.**

When Daijiazhou Reach channel condition is good and the beach type is relatively good, the excellent river cross-section transition section has choose as the simulation object, establish the correlation between the river width under the regulation water level and the minimum water depth within the provision navigation width under the design water level (as shown in Fig.3). From the figure, Bahe channel average river width of is about 1200 m, straight channel average river width is about 900 m.

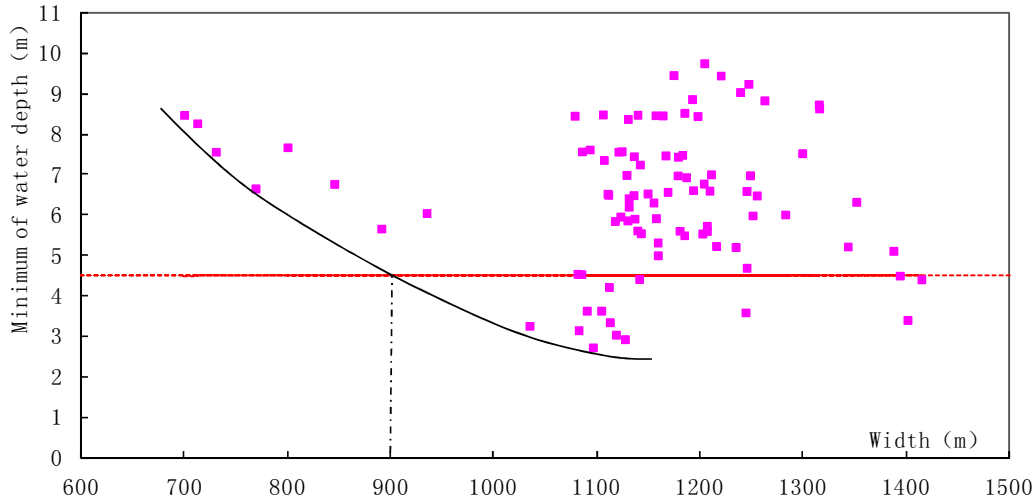


Fig.3 The relationship between the river width and the minimum water depth

**Determine the regulation parameters**

According to the conservation principle, this paper derived the regulation parameters relational expressions:

$$(B_0 - B_2)\frac{1}{n}(H_1 - H_2)^{5/3} J^{1/2} = (B_1 - B_2)\frac{1}{n} H_1^{5/3} J^{1/2}$$

Where $B_0$=low water river width; $B_1$=straight channel regulation width I (900 m); $B_2$=straight channel regulation width II; $H_1$=corresponding depth under regulation level I (8.84 m); $H_2$=corresponding depth under regulation level II. The $B_0$, $B_1$, $H_1$ into the formula, when the straight channel regulation width ($B_2$) is 850 m; the straight channel regulation width narrow 50 m, which compared to $B_1$, $H_2$ is about one meter lower than $H_1$.

At the same time, by physical model and mathematical model [6-7], the engineering effect for different height, different length were tested and calculated. When the regulation water level is 7.84 m, the regulation width is 850 m; when the regulation water level is 8.84 m, the regulation width is 900 m, the two values all are considered to be appropriate.

**Conclusions**

The channel regulation parameters were studied by using several methods. The results showed that the two channel regulation parameters are relevant, and the correlation expression was proposed. Based on the physical model and mathematical model of Daijiazhou reach in middle Yangtze river, the engineering effect for different structure height and length were tested and calculated. It turned out that when the regulation water level is 7.84 m, the regulation width should be 850 m, meanwhile, when the regulation water level is 8.84 m, the regulation width should be 900 m. The both sets of figures are considered to be appropriate, and it can be well applied to engineering implementation.

**Acknowledgements**

This work was financially supported by National Natural Science Foundation of China (51209112), National High Technology Research and Development Program 863 (2012AA112508), National Technology Research Project (2013DFA81540), and Basic research funding of national commonweal research institutions (TKS120102, TKS120201, TKS130202).

**References**

[1] J. H. Xie, et al, *Riverbed revolution and channel regulation*. Wuhan: Wuhan University of Hydraulic and Electric Engineering, (1990) (in Chinese).
[2] Q. X. Pan, et al, *Sediment problem research of the Three Gorges Project*. Beijing: Chinese water conservation and electricity publishing house, (1999), p.71-105, (in Chinese).
[3] W. L. Liu, et al, *Channel regulation technology of long reach in Yangtze river*. Tianjin: Tianjin institute for water transport engineering, (1999) (in Chinese).
[4] W. S. Li, Journal of Waterway and Harbor, 28(6), (2007), p.418-424 (in Chinese).
[5] W. L. Liu, Journal of Waterway and Harbor, (2009), P. 31-36, (in Chinese).
[6] W. L. Liu, et al, *Research Report on Physical Model of Daijiazhou reach in Middle Yangtze River*, Tianjin: Water Transport Engineering Science Institute, Ministry of Transport, (2009) (in Chinese).
[7] W. L. Liu, Journal of Waterway and Harbor, (2011), P.259-263 (in Chinese).

*Applied Mechanics and Materials Vols. 580-583 (2014) pp 1874-1877*
*© (2014) Trans Tech Publications, Switzerland*
*doi:10.4028/www.scientific.net/AMM.580-583.1874*

# Research on the Feasibility of Water Diversion Project

Lihua Zhang[1,a] , Guanghui Wang[2,b] and Xiaohui Hao[3,c]

Water Resources Research Institute of Shandong Province, Ji'nan,Shandong,250013, China

[a]lily9804@126.com, [b] 691388339@qq.com, [c] 541077436@ qq.com

**Key words:** Water Resources Shortage; River and Reservoir Networking; Regulating Reservoir (Diversion and Storage Reservoir); Water Pumping Station; Long Distance and High Lift Water Delivery

**Abstract:** The research on the feasibility of Feicheng Water Diversion from Dawen River Project is based on a thorough investigation in the actual condition of water resources in Feicheng city. It is found that on the one hand this city has been suffering from water shortage, while on the other hand it has allowed most of the water flowing away in vain from Dawen River, which runs through this area. To resolve this contradiction, this research demonstrates the feasibility of networking of Dawen River and Shangzhuanglu Reservoir through engineering measures to realize the optimal allocation of water resources

## Project Introduction

Located in the west of Mount Taishan, Feicheng city is one among the basic economic competitiveness top 100 in national country-level, among the most regional power top 100 for national small and medium-sized cities and among provincial ecological economy top 10. However, its multi-year average total water resources is 260,000,000$m^3$ , and per capita water resources is 271$m^3$ , taking up only 12% of that of the country,84% of that of the province and 76.3% of that of the Taian city. With the rapid development of the construction of small towns and local industries at present, water consumption will grow gradually, and the shortage of water resources has become the bottleneck restricting local economic development.

Runing through the south of Feicheng, with a length of 36.42km within this city, Dawen River is one of the main guest water resources in Feicheng city. The water from Dawen River runs through with a great amount, but with a very low utilization rate. In order to overall use these surface water resources, some project measures are presented after field reconnaissance, relevant information reference and consultations with the local authorities. These measures will be used to divert the remaining water from Ansun Trunk Canal to Shangzhuanglu reservoir for regulation on the condition of meeting the needs of Ansun Irrigation area, which will make the preliminary target of realizing the water supply to urban and Bianyuan industrial park, and maximizing the utilization of the guest water resources from Dawen River.

## The Necessity of Project Construction

2.1The project construction can solve the increasingly prominent contradiction between supply and demand of water resources

With a multi-year average precipitation of 658.8mm, Feicheng city is seriously poor in water. Its rainfall has a large interannual variation and is distributed uneven temporally and spatially, which are easy to cause alternating droughts and floods or continuous draughts. It is estimated that the

water shortage of the whole city is 106,000,000 $m^3$ at the 75% guaranteed rate in current year. At the same time, the excessive exploitation of underground water due to large water consumption has caused an overdraft area of 256$km^2$ underground [1]. This increasing prominent contradiction between water supply and demand makes it very necessary to implement the water diversion project to maximize the surface water availability to meet the requirements for industrial and agricultural development.

2.2 Project construction is necessary for agricultural irrigation

There are 5 small (I) and 13 small (II) reservoirs with total utilizable capacity of 10,099,000 $m^3$ in the Shangzhuanglu reservoir controlling basin, which makes the inflow water relatively inadequate. According to the operation situation of reservoirs in many years, their perennial inflow water is about 3,000,000 $m^3$, which is much lower than the utilizable capacity of 10,140,000$m^3$ and is not able to meet the requirements of irrigation for 21,000 acres of area. The implementation of this water diversion project will enlarge the effective irrigation area in Shanzhuanglu and improve the guaranteed rate of irrigation.

2.3 Project construction can meet the needs of water supply for ecological purpose in urban area

Longshan River runs across Feicheng city from west to east. It twists and turns like a long jade belt, making a belt shape of park in the south of the city. However, its natural look and the surrounding landscape are diluted due to the upstream shortage and serious siltation. This water diversion project will divert the water from Shangzhuanglu reservoir to Longshan River through pipes to meet the need of ecological water use in urban area.

**The feasibility of project construction**

3.1The water resources can meet the needs of diversion project

The inflow water of Dawen River comes from the series of data measured from 1956 to 1999 and the deducted calculation of data from 2000 to 2007 in Linwen hydrological station, which is located in the upstream 3km from Zhuanshe dam. It is analyzed from above data that the inflow water are 780,000,000$m^3$ , 370,000,000$m^3$ and 120,000,000$m^3$ respectively under the guaranteed rate of 50%, 75% and 90%.

Water balance calculation result shows, in the condition of inflow guaranteed rate of 90% and full load operation of Water Diversion Project, the first-stage project can divert 34,670,000 $m^3$ of water from Sun Trunk canal per year to ensure water supply of both 5,000,000$m^3$ per year for industrial and urban purpose respectively and 16,150,000 $m^3$ for agricultural purpose along its way and for ecological purpose in Xiaohui River, the second-stage project can divert 34,670,000 $m^3$ of water from Sun Trunk canal per year to ensure water supply of both 10,000,000$m^3$ per year for industrial and urban purpose respectively and 6,160,000 $m^3$ for agricultural purpose along its way and for ecological purpose in Xiaohui River

Therefore, the water resources can meet the needs of water diversion project.

3.2 It is technologically feasible for water diversion project

Shangzhuanglu reservoir is medium-sized. Its flood control and water storage capacity were improved greatly with its utilizable capacity reaching 10,140,000 $m^3$ after 2010, when it fulfilled its enforcement task. The water diversion project can fully use its larger utilizable capacity to divert the water to meet the needs of water supply for industrial purpose in dry seasons.

Three pipelines will be set for the water diversion project. There are no obvious block buildings along the lines, and the pumping stations and pipelines have a good geological and topographical condition, which makes an easy construction possible. Therefore, the project is technologically feasible.

The Zhanghou reservoir under construction has both regulation and wetland purification function. The inflow water from Ansun Trunk canal will be purified preliminarily after running through Zhanghou Reservoir.

3.3The water diversion project is economically feasible

According to the preliminary financing draft, the project from intake gate to Shangluzhuang reservoir will be invested by government, the fund of the middle part from Shangzhuanglu reservoir to urban section will come from government investment half, while the other half comes from bank loan, the fund of the other part of the project from Shangzhuanglu reservoir to Bianyuan industrial park will come from bank loan totally. In normal flow year, with full load operation, the cost of water diversion for industrial purpose will be ￥1.01/ $m^3$ for the first stage and ￥0.80/ $m^3$ for the second stage of the project, the cost of urban water diversion will be ￥1.24/$m^3$ for the first stage and ￥0.97/$m^3$ for the second stage. Therefore, it is economically rational to implement this water diversion project.

## General programming

4.1Project scale

The designed water flow is 2$m^3$/s. The industrial and urban water supply is both 5,000,000$m^3$ per year for the first stage and is both10, 000,000$m^3$ per year for the second stage. According to the above specifications, this project is belonged to medium-sized water diversion project, and is rated as grade III. The main constructions like water transmit project, pumping station, and sluice are graded as level 3.

4.2 Overall deployment

The project of water diversion from Dawen River consists of water intake project, water transmitting project and pumping stations, etc. Its overall deployment is as follows:

Set an intake sluice in the eastern side of Zhanghou Hollow dam of Ansun Trunk canal and transmit water to Zhanghou reservoir, and there in the pumping station the water will be pressurized and then transmitted into Shangzhuagnlu reservoir through the pipelines set along the Xiaohui river, waiting for regulation. After being pressurized in the down stream of reservoir, the water will be diverted to Bianyuan industrial park through pipelines. At the same time, set Moshan pumping station in the upstream of Shangzhuanglu reservoir, where the water will be pressurized and then diverted to Feicheng city through the set pipelines

## Main construction

5.1 Water intake project

Intake sluice and regulating sluice will be set in the eastern side of Zhanghou hollow dam of Ansun trunk canal. Both sluices have two holes, each 2.0m wide. The sluices have steel doors with a height of 2.5m and piers and plates with reinforced concrete structure.

The channel of Xiaohui River, located in the upstream of Zhanghou hollow dam, has formed into a rather large area of wetland due to its low-lying location. In this project, the wetland will be built into a small (II)-sized reservoir with capacity of 300,000 $m^3$ by dredging and down digging, and renovating on both sides of its embankment.

In order to facilitate the operation management of water diversion project, the top of dam will be designed to be 6m wide and be paved with asphalt according to traffic requirements, and the altitude will be determined by the flood control plan of Xiaohui River channel

5.2 Water transmitting project

The water pipeline is divided into three sections. The first one, with two RPMs of diameter 1000mm, is 9km long from Zhanghou Pumping station to Shangzhuanglu reservoir. The second one is 12km long from Shangzhuanglu reservoir to industrial park. It has also two RPMs with diameter of 600mm, of which one will be set in the first stage and the other will be set in the second stage. The third line is 18km long from Moshan Pumping station to Feicheng city. One RPM with diameter of 800mm and one RPM with Diameter of 600mm will be set in the first stage and second stage respectively.

5.3 Pumping station

There Pumping stations will be constructed, including Zhanghou pumping station, Shanghzhuanglu Pumping station and Moshan pumping station. Zhanghou Pumping station will be located in the north of Zhanghou reservoir, Shangzhuanglu Pumping station will be in the downstream of its reservoir and Moshan pumping station will be in the original address where Moshan pumping station was located.

The designed water flow of Zhanghou Pumping station will be $2m^3/s$ and the designed lift height will be 50m, according to which, three single stage double suction centrifugal pumps will be applied for the first stage, and five will be applied for the second stage, among which one is used for emergency.

The designed water flow of Shangluzhuang Pumping station will be $0.25m^3/s$ for the first stage and $0.50m^3/s$ for the second stage with a designed lift height of 30m. Two single stage double suction centrifugal pumps will be applied for the first stage, and three will be applied for the second stage, among which one is used for emergency.

The designed water flow of Moshan Pumping station will be $0.5m^3/s$ for the first stage and $0.7m^3/s$ for the second stage with a designed lift height of 70m. Four single stage double suction centrifugal pumps will be applied for the first stage, and five for the second stage, among which one is used for emergency.

## Conclusion

The water diversion project from Dawen River is a multi-purpose project mainly used for industrial purpose, and also for agricultural and urban ecological purpose. On completion of the project, the annual water flow will reach 34,960,000 $m^3$ and the annual water supply scale will reach 10,000,000 $m^3$, which can meet the needs of Bianyuan industrial park, and can also meet the needs of urban area for ecological purpose to improve the local ecological environment to become a new economic growth point locally. Therefore, this project is technically and economically feasible, and will bring notable benefits in economy, society and environment.

## Reference

[1] Liu Dongmei, Diyan, Yang Jifang: The first exploration of Feicheng employing the most strict water resources management system (Shandong Water Conservancy, 2011.1)

*Applied Mechanics and Materials Vols. 580-583 (2014) pp 1878-1882*
*© (2014) Trans Tech Publications, Switzerland*
*doi:10.4028/www.scientific.net/AMM.580-583.1878*

# Simulation Method of Particle Size Scale for Fine Sand Model

Wanli LIU[1, a] , Xiaofei LIU[1], Peijiu YUE[1]

[1] Key Laboratory of Engineering Sediment of Ministry of Communications, Tianjin Research Institute for Water Transport Engineering, Tianjin 300456, China

[a]tjtgliuwanli@163.com

**Keywords:** movable-bed model; gravity similarity; resistance similarity; particle size scale

**Abstract.** In sediment movable bed model, the basic similar conditions include the flow movement similar and the sediment movement similar. In water flow movement similar conditions, the velocity scale of the Freund's similarity and resistance similarity is inconsistency, and the flow resistance is the function of bed material grain size and flow intensity. In sediment movement similar, the particle size scale forms are not consistent too, and they are also related to the flow conditions, so the sediment partial size scale is difficult to determine. According to the research, the similar conditions can be focused on primary and secondary one, and put the primary one as the design basis. In view of the waterway regulation, the regulation flow discharge should be the design basis, others allowed a certain deviation; In the straight reach, resistance similarity should be the design basis, Freund's similarity allowed a certain deviation; In the bend reach, the Freund's similarity and resistance similarity should be simultaneously satisfied; For the bed load model, the incipient motion should meet similarity condition; The suspended sediment model should meet the sediment suspension similarity; For the non-uniform sediment, median particle size should be the design basis. According to the above principles, the sediment particle size scale can be determined.

## Introduction

Plain rivers are generally the fine sand river bed. In the model design, the basic similar conditions include the water flow movement similar and the sediment movement similar conditions. In addition to Freund's similarity, other similar conditions all include particle size scale. So the particle size scale is the key scale in the movable bed model design (as shown in Fig.1). Because the similar conditions of theoretical foundation are different, so the particle size scale is inconsistent, and they are related to the flow conditions. Due to the flow conditions of the two scales are also inconsistent, the contradictions are intricate too. How to correctly and reasonably determine the particle size scale is a major problem in the movable bed model design. So far, researches on this problem are still insufficient [1-5]. So it is necessary to carry on the further research and put forward the design method about the particle size scale.

Fig.1 The fine sand simulation of movable-bed model

**Basic similar conditions**

**Flow movement similar conditions.**

The flow movement similar conditions are as follows:

Gravity similarity:

$$\lambda_U = \lambda_h^{1/2} \tag{1}$$

Resistance similarity:

$$\lambda_U = \lambda_h^{2/3} / \lambda_n e^{1/2} \tag{2}$$

**Sediment movement similar conditions.**

The sediment movement similar conditions are as follows:

Sediment starting similarity:

$$\lambda_{U_0} = \lambda_U \tag{3}$$

Sediment suspension similarity:

$$\lambda_\omega = \lambda_U / e^m \tag{4}$$

Where $\lambda_U$ =average velocity scale; $\lambda_h$ =average flow scale; $\lambda_n$ =roughness scale; e=model variable rate, that is the reciprocal of slope scale; $\lambda_{U_0}$ =incipient motion velocity scale; $\lambda_\omega$ =sediment deposition velocity scale; m=prototype sediment suspension index function, the change interval from 0.5 to 0.75, the average value is 0.63.

**Determine the incipient motion velocity**

**Incipient motion velocity of prototype sediment.**

At present, most of sediment incipient motion velocity formula lack the natural river measured data, in principle, which cannot be used to estimate the prototype natural rivers. If the measured bed load sediment transport rate and velocity curves exist, which can be conveniently extended to sediment transport rate close to 0, this velocity is approximated the incipient motion velocity; if there is no field data, the following equation is suggested [4], that is:

$$U_0 = 0.512\sqrt{\frac{r_s - r}{r}}[D^{3/4} + 2.5(0.7 - \varepsilon)^4 / D]^{1/2} h^{0.2} \tag{5}$$

Where $U_0$ =prototype incipient motion velocity(m/s); $\gamma_s$ =sediment bulk density; $\gamma$ =water bulk density; D=sediment grain size; $\varepsilon$ =sediment porosity, general the value is 0.4.

It should be pointed out, natural river water, sediment and bed sand sizes are varied, so no matter what prototype incipient motion velocity determining methods are approximate.

**Incipient motion velocity of model sediment.**

The following equation is suggested for cohesive model sediment, that is:

$$U_0 = 1.14\sqrt{\frac{\gamma_s - \gamma}{\gamma} gD}\left(\frac{h}{D}\right)^{1/6} \tag{6}$$

Cohesive model sediment can still use formula (5), model sediment incipient motion velocity is not only related with $\gamma_s$ and D, but also related with the physical and chemical properties of materials, formula (5) and formula (6) can only be used to estimate, finally need to be confirmed by flume experiment.

**Determine the roughness**

**Prototype roughness.**

Manning formula is uniform flow resistance equation, where n is the solid circles along the average roughness, for movable bed, the bed roughness is constituted by surface (sand) and form (sand wave) resistance. Natural river is general non-uniform flow, still use the Manning formula, the river is processed as the quasi uniform flow, so its roughness meaning will be widen, not only including the original intention, but also including the partial loss, which caused by plane form and morphology

changes along the River, N is an average comprehensive roughness, which is reversed by the measured water surface curve. Natural rivers at all flow levels, the riverbed composition and the bed form are inconsistent, plane form and morphology are also inconsistent, comprehensive roughness change, all flow levels roughness should be calculated obtained, at least in the flood, medium and dry flow.

**Model roughness.**

To determine the model roughness is a difficult problem, usually measured by flume experiment. As mentioned above, the compound roughness including local resistance, only in the geometric similarity normal model may be similar. With rectangular tank measurement roughness as model roughness is only a kind of approximate, the greater changes of prototype plane modality and section morphology, the deviation is greater.

In the uniform flow high flow state district (movable plane bed), Manning coefficient of the sediment bed can be estimated by the Zhang Youling formula, that is:

$$n_m = 0.0166 D_m^{1/6} \tag{7}$$

## Bed load model test design

**Basic field data.**

(1) The bed sediment grading curve, $D_{50}$, $D_{95}$, $D_5$ etc;

(2) All levels of flow water depth, flow velocity and Manning coefficient;

(3) The relation curves of measured bed load sediment transport rate and flow velocity.

**Similar conditions choice principles.**

Bed load model should satisfy formula (1) to (3). The combined solution formula (1) and (2), available:

$$n_m = n_p e^{1/2} \Big/ \lambda_h^{1/6} \tag{8}$$

The combined solution formula (1) and (3), available:

$$U_{om} = U_{op} \Big/ \lambda_h^{1/2} \tag{9}$$

The combined solution formula (2) and (3), available:

$$\lambda_{U_0} = \lambda_U = \lambda_h^{2/3} \Big/ \lambda_n e^{1/2} \tag{10}$$

or, $$U_{om} = U_{op} e^{1/2} n_p \Big/ n_m \lambda_h^{2/3} \tag{11}$$

In the formula (8) to (11), $n_p$, $n_m$ and $U_{op}$ are the flow condition function, at all flow levels, to meet the similar requirement is very difficult. Therefore, according to the nature of research problem, the principle of emphasize and choice as follow:

(1) Straight or micro bend, braided reach, resistance similarity is the main, should be meet. The gravity similarity can be appropriate deviation, the deviation degree as follow:

$$\Delta F_r = \left(1 - \lambda_U / \lambda_h^{1/2}\right) \times 100\% = \left(1 - \lambda_h^{1/6} / \lambda_n e^{1/2}\right) \times 100\% \tag{12}$$

According to the experience, straight reach deviation degree should not exceed 50%; the micro bend and braided reach deviation degree should not exceed 30%.

(2) In the curved reach, the gravity and resistance similarity is very important, should also be meet, at least in the key flow levels should be meet, meet the formula (8), in other flow levels, resistance similarity can be appropriate deviation. Resistance similarity deviation degree without practical experience, Xie Jianheng puts forward, as far as possible, the hydraulic elements from caused by the resistance deviation from locate in observation accuracy range, generally not more than 5% [3].

Because the resistance similarity deviation, the actual occurrence depth scale is $\lambda_h'$, velocity scale becomes $\lambda_U'$, because flow scale invariant, there is:

$$\lambda_Q = \lambda_L \lambda_h^{3/2} = \lambda_L \lambda_h' \lambda_u' = \lambda_l \lambda_h'^{5/3} / \lambda_n e^{1/2} \tag{13}$$

$$\lambda_h' = \lambda_n^{3/5} e^{3/10} \lambda_h^{9/10} \tag{14}$$

$$\lambda_U' = \lambda_h^{3/5} / \lambda_n^{3/5} e^{3/10} \quad (15)$$

Hydraulic elements deviation degree as follow:

$$\Delta\lambda_h = \frac{\lambda_h - \lambda_h'}{\lambda_h} = \left(1 - \lambda_n^{3/5} e^{3/10} \Big/ \lambda_h^{1/10}\right) \times 100\% \quad (16)$$

$$\Delta\lambda_U = \frac{\lambda_h^{1/2} - \lambda_U'}{\lambda_h^{1/2}} = \left(1 - \lambda_h^{1/10} \Big/ \lambda_n^{3/5} e^{3/10}\right) \times 100\% \quad (17)$$

Because the discharge per unit width unchanged, flow velocity increased, water depth decrease, in formula (16) and formula (17), the symbol is opposite.

(3) Both the straight reach or curved reach, in the key flow levels, the starting similar conditions should meet, which are the formula (11), in other flow levels, the movable requirements should meet, i.e.:

$$U_m > U_{om} \quad (18)$$

## Suspended load model test design

**Basic field data.**

In addition to the 5.1, prototype suspended load grading curve is needed.

**Similar conditions choice principles.**

Suspended load model should satisfy formula (1) to (4). According to Zhang Ruijin settling velocity formula, the particle size scale can be calculated by equation (4):

$$\lambda_d = 0.0179 \frac{d_p \omega_p}{\nu \lambda_\omega} \{[1 + 121.6 \frac{\gamma_{sm} - \gamma}{\gamma} g \nu (\frac{\lambda_\omega}{\omega_p})^3]^{1/2} - 1\} \quad (19)$$

There is one more restriction condition in Suspended load model, at all flow levels, at the same time, to meet the basic similar conditions, the difficulty greatly increased, therefore need to emphasize and choice.

(1) The primary and secondary selection of water flow movement similar conditions is same as the bed load.

(2) The suspended similar firstly meet the formula (4). The suspended load exercise intensity is biggest in flood period during the river bed deformation, and the suspended load is in an absolutely dominant position, so $\lambda_U$ should be designed according to flood discharge. The incipient motion similar should be a secondary importance, but in order to meet the low water channel deformation similarly, the regulation discharge should meet the incipient motion similar, and other flow discharges meet the condition of the formula (18).

## Conclusions

The movable bed model sediment particle size scale involves many complex factors, so the similarity is difficult to be fully satisfied. Even if some minor conditions and influence factors deviation are allowed, and makes some simplify, the programs are still very tedious and complicated. On the other hand, the model sediment, the model materials and the geometry scale are more restricted, which result in the design being very difficult. Based on theoretical research, the design principles of particle size scale for model sand were put forward. Base on the principles, the design methods of the particle size scale were put forward.

## Acknowledgements

This work was financially supported by National Natural Science Foundation of China (51209112), National High Technology Research and Development Program 863 (2012AA112508), National Technology Research Project (2013DFA81540), and Basic research funding of national commonweal research institutions (TKS120102, TKS120201, TKS130202).

**References**

[1] P. J. Yue, Journal of Waterway and Harbor, 30(1), (2009)，p.31-36 (in Chinese).

[2] Professional Committee of Chinese Hydraulic Engineering Society Sediment. *Sediment Manual.* Beijing: China Environmental Science Press, (1992), (in Chinese).

[3] J. H. Xie, et al, *River simulation*. Wuhan: Wuhan University of Hydraulic and Electric Engineering, (1993) (in Chinese).

[4] C. H. Li, *River engineering model test*. Beijing: People communication Press, (1981), (in Chinese).

[5] R. J. Zhang, *River dynamics.* Wuhan: Wuhan University of Hydraulic and Electric Engineering, (1988) (in Chinese).

*Applied Mechanics and Materials Vols. 580-583 (2014) pp 1883-1887*
*© (2014) Trans Tech Publications, Switzerland*
*doi:10.4028/www.scientific.net/AMM.580-583.1883*

# Study On Navigation Technology Of Waterway At Hub Downstream And Bridge Area Overlapping

Xin Liu[1,2,a]

[1] Key Laboratory of Engineering Sediment of Ministry of Communications; Tianjin Research Institute of Water Transport Engineering, Tianjin 300456, China

[2] School of Civil Engineering, Tianjin Key Laboratory of Port and Ocean Engineering, Tianjin University, Tianjin 300072, China

[a]liuxin806@163.com

**Keywords:** Hydro-junction；Hub downstream；Bridge area；Overlapping area；Regulation scheme；Navigation security.

**Abstract.** The article has used the technical route of data analysis, physical model test and ship model tests combining, studied the navigation technology of waterway in area below QianWei hydro-junction and bridge sections overlapping in Minjiang River, then proposed the regulation scheme, which effectively improved navigation conditions in the region, finally summarized and put forward the navigable protection technologies and measures in area below hub and bridge area.

## Forward

In the inland waterways, the shiplock entrance area and connecting section, or bridge area channel are all regions of high requirements to navigable flow conditions, but also need to focus on navigation security. The study involved the channel in entrance area and connecting section below Qianwei hub in MingJiang River, also involved QianWei bridge area channel, in particular, need to point out which also involves overlapping segments between connecting section and the bridge area waterways, navigable environment is extremely complex. Therefore, specialized research on navigation security technology is necessary, which to guarantee the safety of navigation. The approaches of analysis, physical model and ship model tests combined are adopted to study the regulation scheme in district below hub and bridge area, it ensure that the relevant requirements of navigable flow conditions. Meanwhile, combined inland shipping information technology and inland channel navigable technology, put forward new generation of navigation protection technology at complex district to assure navigation security in specialized conditions, which guarantees the safety of navigation.

## General situation of the reach

Qianwei navigation power junction located is faintly-curved reach, and about 18.km upstream of dam axis is Min Dong bridge building，where the right bank has lenient ZhenJiangBa and ChaYuBa pebbles sandbars, and the two total length 4650m, right of which is deputy branch.

Affected by the downstream HuNiBa pebble sandbar jacking at the left side, the mainstream gradually began toward to right and crossing the river since the LeYi freeway MingDong bridge downstream approximately 1km, and about 300m upstream of dam axis mainstream flow straightly

along the right bar, the left of which HuNiBa pebble sandbar about 1800m, at its widest point approximately 500m, on the left is deputy branch, beginning to flow when the discharge reaches about 4000$m^3$/s .

The river width of HuNiBa reach is about 200 ~ 250m in the dry season, while bankfull in flood season the maximum width up to about 1100m，then HuNiBa pebble sandbar in approximately 1.2km downstream of the dam axis flooded basiclly, under riverbed gradually become relatively narrow, Minjiang River Qianwei bridge has been built is located, away from the axis of the Qianwei hub upstream about 1.45km, and dists HuNiBa shoal tail about 300m. Qianwei bridge main navigation spans 240m, its left and right side of the vice-hole span of 60m, the main hole basically across the river bridge area flood, in various periods of low water navigable waters.

**Hub Overall Layout**

The main hydraulic structures of qianwei project layout from right to left as follows: right bank gravity dam, lock (and the right of the lock section reserved for second-tier shiplock position), 28-hole flood (flushing) gates, right bank emergency gate storage slot dam section, powerhouse and installation section, left bank gravity dam（including fish passage section.

**Below dam and bridge area channel regulation research**

The reach of studied area is more complex, hub located is Zhongzhou sandbar, where less than 300m downstream is Qianwei Bridge, which main navigable hole towards to sandbar tail. while the hub constructed, its downstream approach entrance area from the bridge is only about 730m, the river on behalf of the ship using 1 +2 × 1000t pushing fleets, entrance zone length is 2.5 times the master of 400m. While according to standard regulations, the bridge district range of bridge upstream 4 times captain to downstream 2 times of representative ship, namely upstream 640m to downstream 320m, so the ship get out about 90m of entrance have also entered the bridge area waterways, overlapping range of about 310m, both the entrance aream, connecting section or bridge area waterway are different from the general area of natural waterways, require more to the navigable flow and waterway conditions.

**4.1 Navigable flow conditions research of approach entrance area and the connecting section in shiplock downstream**

The results showed that when the discharge Q≥ 4000$m^3$ / s, the entire current from the upstream left side power-station tailrace rushed straight to the dry main channel at the end of downstream approach entrance area, where biol, swirling water coexist, and formed a wide range of circulation zone on the right of approach entrance area, so the transverse velocity and circulating flow in approach entrance area all can not meet the "standard" requirement under various discharge.

**4.2 Navigation flow condition analysis in bridge area**

According to the experimental research purposes, determined surface velocity observed that range of bridge upstream 600m to downstream 300m waterway. According to the experimental observation: under various discharges, there existed a wide range of large transverse velocity in bridge area upstream.

Thus, the navigable flow conditions in approach entrance area and bridge area under present shiplock designs are poor, far beyond the standard specifications, in urgent need to carry out regulation research.

### 4.3 Regulation measures of Navigation flow conditions in below dam, bridge area

Based on Qianwei hub layout characteristics, riverbed terrain below dam, combined the observational data analysis of velocity, modifications mainly by adjusting the excavation region of the riverbed downstream the dam, controlling flood (flushing) gates opening sequence and opening height in order to achieve smooth transfer of discharged flow, so the velocity distribution uniformity and minimize or eliminate the flow regime. The main improvement measures include:

（1）Enlarge the excavation scope of riverbed at power station tailrace downstream left side

Appropriately shift the levees of power station downstream to left bank, and enlarge the excavation scope of riverbed in dam downstream left side, to guide the power station tail water and main stream discharged from the dam offseting to left appropriately, change the unfavorable situation of mainstream rushing to approach entrance area. Remediation excavation elevation remains 315m, while attention to the protection of Qianwei bridge pier that has been built.

（2）Appropriate retaining original riverbed terrain along the left side of shiplock

Retain original riverbed terrain along the shiplock and under approach entrance area, in order to achieve the purpose of sepatating or weakening the discharged mainstream expanding to entrance area.

（3）Reasonable adjust the opening way of flood (flushing) gates

While the upstream discharge over the station full-load flow, first properly open the floodgates closed to shiolock, and then turn the control to open the flushing gates and closed floodgates from left to right, in order to achieve the perpose of smoothing transfer of discharged water flow and improving the harmful regime in approach entrance area.

After the regulation implementated, by expanding the excavation scope of riverbed at power station tailrace downstream left side, appropriate retaining original riverbed terrain along the left side of shiplock, adjusting the opening way of flood (flushing) gates and other measures，effectively smooth the the flow downstream of the dam, the phenomenon of flow discharged straight into the under entrance area tail disappeared, and biol, swirling water and return current regimen has disappeared (or maximum compressed), velocity peak decreases, the velocity distribution tends to be uniform, navigation flow conditions have greatly improved in entrance area, bridge area(including overlapping section) at various discharges.

## Complex navigation security technologies

The study involves entrance area below Qianwei dam, connecting section，but also involves Qianwei Bridge waterway area, in particular, need to point out that also involves overlapping channel of connecting section and the bridge area, navigable environment is extremely complex. Therefore, need for specialized navigable security technologies to protect the safety of navigation.

### 5.1 Navigation protection technology and the implementation in hub downstream and bridge area

（1）Implementation of navigable flow conditions sensing measurement technology in real time at waterway site

By arranging multiple water level, velocity, visibility, wind conditions automated collection and transmission system along the range of entrance area to Qianwei Bridge downstream 2km, transer the data be collected in real time to waterway navigable command center;

（2）Real-time numerical simulation forecasting and security decision-making platform development research

Conduct real-time numerical simulation forecasting and security decision-making platform development in hub downstream to Qianwei Bridge channel. Use the waterway natural data returned in real time from sensing at site to calculate in real-time, given the scale and navigable waterway conditions, and relying on GIS gives live three-dimensional image, achieving the navigation conditions display of above special district in real time, providing support for navigation decision-making.

（3）Ship security monitoring and management system under all-weather and complicated navigation conditions

By integrating the safe distance control technology of ship sailing, intelligent beacon navigation technology of BeiDou system integrated with AIS, construction nearby or crossing the river warning systems, protecting ship sailing safety in night of an integrated technology formed from night ship collision avoidance equipments etc, establish the ship security monitoring and management system and set of technologies under all-weather and complicated navigation conditions, to protect the safety of ships at night navigation.

（4）Equip new water ship/person emergency alarm and rescuing, accident traceing system in complicated navigacable district

The reach that navigable flow conditions complex, ship traffic heavy, especially night navigation achieved, put forward higher requirements to the maritime search and rescue. The locating and rescuing system aimed to personnel falling into the water and vessel inland including: ① all-weather inland ship and staff in distress positions tracking and rescuing system in real time; ②personnel intelligent lifesaving facilities with function of automatic positioning; ③AIS Class B portable search and rescue system suitable for small ship safety supervision; ④Intellisense and automatic alarm shipborne equipment based on the sailing state of ship in distress;⑤shipborne AIS navigational information facilities applied to ship accident traceing.

**5.2 Complex navigation security assurance measures**

After the completion of shiplock of Qianwei hub, the ship will sail through the mouth area and the connecting section directly into the bridge area waterways, navigation conditions subject to various restrictions, inevitably affect the safety of navigation. If not on-site management and security protection to the water area, once the accident, will bring significant economic losses and adverse social impact. Therefore must be taken and established measures to protect the ship pass the region safely, improving the navigation environment and maintaining good navigation order, and ensuring the safety of bridge and ship.

（1）Synthesize navigable conditions and ship model testing of Qianwei hub shiplock upstream and downstream waterway, it is recommended $Q = 11000m^3 / s$ is the highest navigable discharge, $Q = 12000m^3 / s$ to limit navigable discharge.

（2）Suggest to establish a reasonable way to open the gates of the hub, take certain restrictive navigable measures, maneuver carefully, in order to ensure safe navigation of ships.

（3）In order to protect the safety of navigation in bridge area, it should improve water safety supervision mechanism, equip necessary security infrastructure and take long-term security maintenance, bridge area waterway equip completely of navigation mark, bridge opening mark and other facilities, and water safety supervision facilities, etc.

（4）When the ship either upstream or downstream through the waterway in bridge area, should be familiar with navigable situation of waterways in advance, particularly pay attention to grasp the bridge clearance height, maximum height of the own ship, draught, height of tide and time of tide in bridge district, etc. Meanwhile, should consciously abide bridge navigation regulations, aviod the situation of overtaking, sailing tied with others boats.

（5）Strengthen the implementation and application of above navigation security protection technology, and coordinate closely with the patrol boats at site.

（6）Strengthen the training of the crew, increase the navigation rules and navigation environment propaganda.

## Conclutions

（1）The study involves entrance area below Qianwei dam, connecting section，but also involves Qianwei Bridge waterway area, in particular, need to point out that also involves overlapping channel of connecting section and the bridge area, navigable environment is extremely complex. The approaches of analysis and physical model combined are adopted to study the navigation flow conditions in reach below hub and bridge area, determined the waterway regulation scheme.

（2）Put forward the navigable protection technology in hub downstream reach which under complex conditions ( dam downstream and bridge area connecting), establish related measures to protect the ship pass the region safely, improving the navigation environment and maintaining good navigation order, ensuring the safety of bridge and ship.

## Reference

[1] XuYue Hu,Biao Li,LiJun Xu. A Review of Research on Navigation Flow Condtion of Hydro-junction. WatewrayEngineering,2005(11):59-64

[2] YiBing Li,etc. On Standard of Flow Conditions for Navigation in Transitional Reach Outside Entrance[J].TianJin: Journel Of Waterway And Harbour,2004,(4)

[3] YiBing Li. Ship Model Test Research Of Upstream And Downstream Approach Entrance Area And Connecting Section Of ZhuZhou Navigation-Power Junction Shiplock. Tianjin Research Institute of Water Transport Engineering M.O.T .2001

[4] U.S.Army Corps of Engineers. Hydraulic Design of Navigation Locks，1975

*Applied Mechanics and Materials Vols. 580-583 (2014) pp 1888-1892*
*© (2014) Trans Tech Publications, Switzerland*
*doi:10.4028/www.scientific.net/AMM.580-583.1888*

# Study on Sandy Pebble Reach Riverbed Erosion and Deposition Basic Law after the Three Gorges Reservoir

Xiaofei LIU [1, a] , Mei-li Zhang [2] , Zhiwei YE [3]

[1]Key Laboratory of Engineering Sediment of Ministry of Communications, Tianjin Research Institute for Water Transport Engineering, Tianjin, China

[a]liuxiaofei2348@163.com;

[2]China International Water & Electric Corp, Beijing, China

[3]Changjiang Waterway Bureau, Wuhan, China

**Keywords:** sandy pebble Reach, riverbed erosion and deposition, basic law

**Abstract.** After the Three Gorges Reservoir, sandy pebble Reach incoming water and sediment conditions has change, the changes of incoming water and sediment conditions might make sandy pebble reach riverbed scouring-erosion variation. This paper study on sandy pebble reach riverbed erosion and deposition basic law after the Three Gorges Reservoir, and provide the decision basis for large-scale system renovation in the middle Yangtze River.

## Channel Overview

In the middle Yangtze River, sandy pebble Reach from Yichang to Dabujie, total length is about 116.4 kilometers. Sandy pebble reach is divided into two sections, the upper and lower sections. The upper section from Yichang to Zhicheng is called Yizhi reach, plane modality mostly is the straight micro bend, Yizhi reach mainly contains Yichang and Yidou channel. The lower sections from Zhicheng to Dabujie, plane modality mostly is the bending braided, mainly contains Lujiahe and Zhijiang~Jiangkou channel.

## The median and flood riverbed erosion and deposition basic law

(1)After the Three Gorges reservoir, sandy pebbles reach riverbed overall performance consistency erosion.

After the Three Gorges reservoir, in addition to 2008, sandy pebbles reach median and flood riverbed appear a little deposit, the rest of the year median and flood riverbed show erosion. Because of the inter-annual incoming water and sediment conditions changes, the inter-annuals erosion intensity is different, but there is a basic feature, which is the big waters, the erosion intensity is big, the small water, the erosion intensity is small. Such as: in 2006, the inflow is small, so the erosion intensity was only about 0.2 $m^3$ / km, in 2005, the inflow is big, the erosion intensity is 38.0 $m^3$ / km.

(2) After the Three Gorges reservoir, sandy pebble reach median and flood riverbed erosion intensity is bigger before 175 m than after 175 m.

Before 175m water storage, sandy pebbles reach median and flood riverbed erosion intensity was about 171.7 $m^3$ / km, accounting for 71.2% of the total erosion intensity, after 175 m water storage, median and flood riverbed erosion intensity gradually weakened.

(3) After the Three Gorges reservoir, before the 175 m water storage, sandy pebbles reach median and flood riverbed erosion intensity shows inter-annuals sample size; after the 175 m water storage, median and flood riverbed erosion intensity gradually weakened.

Before 175 m water storage, the erosion intensity alternate size between inter-annuals, that is last year lager erosion intensity, next year small erosion intensity; after 175 m water storage, the erosion intensity showed a trend of continuous weakening.

After the Three Gorges reservoir, from analysis the changes of sandy pebbles reach incoming water and sediment conditions, we can see, sandy pebbles reach median and flood erosion intensity change rule along time was adapted to the incoming water and sediment condition changes. After the Three Gorges reservoir, Yichang hydrological station small runoff, the low flow rate increases year by year, sediment discharge and sediment concentration greatly reduced, suspended sediment median diameter taper, a large number of coarse grain sediment was blocked in the library district, reservoir discharge's "clear water sand" is considered unsaturated sediment, therefore sandy pebble reach overall performance consistency erosion. Incoming water and sediment conditions inter-annual changes cause the erosion intensity inter-annuals changes, such as in 2005 years, the inflow is big, the riverbed erosion intensity is strong; in 2006, the inflow is small, the riverbed erosion intensity is weak, inter-annuals median and flood riverbed erosion intensity are not of uniform size, with the further development of scour, sand pebble riverbed sediment showed a certain degree of coarsening, the riverbed formed on the surface coarsening layer and prevent further erosion, before 175 m water storage, the riverbed erosion intensity is big, after 175 m water storage, the erosion intensity is small.

Table 1 Median and flood riverbed erosion intensity statistics

| Start-stop | length (km) | year | Dry riverbed | shoal | Median and flood riverbed |
|---|---|---|---|---|---|
| Yichang~Zhicheng | 60.8 | 2003 | -47.9 | -14.0 | -61.9 |
| | | 2004 | -27.0 | -6.8 | -33.8 |
| | | 2005 | -35.7 | -2.3 | -38.0 |
| | | 2006 | -0.7 | 0.5 | -0.2 |
| | | 2007 | -36.2 | -1.6 | -37.8 |
| | | 2008 | -3.6 | 4.8 | +1.2 |
| | | 2009 | -20.8 | -4.4 | -25.2 |
| | | 2010 | -18.3 | 1.2 | -17.1 |
| | | 2011 | -12.9 | -0.4 | -13.3 |
| | | 2012 | | | -13.3 |
| | | 2003~2012 | | | -239.4 |

Remark: " +" deposit, "-" erosion.

(4) After the Three Gorges reservoir, from Yichang to Dabujie, sandy pebbles reach follow the general rules, in hub downstream erosion intensity gradually weakened from top to bottom, sandy pebbles reach plane modality and riverbed composition uneven changes along the way, so that the riverbed erosion along the way were also unevenly distributed.

Early in the Three Gorges reservoir, sandy pebbles reach riverbed erosion intensity gradually weakened, near the dam, the total erosion intensity in Yizhi Reach should be slightly larger than in Lujiahe Reach.

However the movable bed composition makes it possible to scour. Riverbed composition changes along the way, so that the riverbed erosion intensity along the way was unevenly distributed. The riverbed composition strong impact, the erosion amount and erosion intensity were small; the

riverbed composition weaker impact, the erosion amount and erosion intensity were big. In the three sandy pebbles reach, Yichang reach erosion amount was smaller, Yidou and Lujiahe reach erosion amount represent over 90%, so from 2002 to 2012, sandy pebbles riverbed erosion mainly located in Yidou and Lujiahe reach.

(5) After the Three Gorges reservoir, sandy pebbles reach rebuilding balance process is a gradually top-down development.

Yizhi reach is mainly composed of Yichang and Yidou channel, after the Three Gorges reservoir, in 2003, Yichang channel riverbed erosion intensity show the biggest, in subsequent years riverbed erosion intensity decreases, the riverbed erosion intensity shows inter-annuals alternate size; from 2003 to 2009, Yidu channel riverbed erosion intensity reach maximum, to 2010, riverbed erosion intensity began to abate, but still outweigh the Yichang channel.

Lujiahe reach is mainly composed of Guanzhou and Lujiahe channel, after 2009, Lujiahe reach appeared substantial erosion. after the Three Gorges reservoir, Guanzhou channel overall performance consistency erosion, 2009 years ago, Guanzhou channel was adjusted by narrow erosion and deposition, after 2009 GuanZhou channel riverbed erosion intensity become bigger, especially after entering the trial impoundment, GuanZhou channel riverbed erosion intensity rapidly increases, from 2010 to 2012, GuanZhou channel riverbed erosion intensity totaled 1.85 million $m^3$ / km, accounting for 64% of the total erosion intensity. 2006 years ago, Lujiahe channel riverbed show deposition; from 2006 to 2009 , median and flood riverbed showed just as small cumulative erosion; after 2009 Lujiahe channel occurred significant erosion, from 2008 to 2012 Lujiahe channel riverbed erosion intensity is 98.6 $m^3$/ km, accounting for nearly 70% of total erosion intensity.

Before 2006, ZhiJiang ~ jiang channel riverbed erosion has no significant response to the incoming water and sediment conditions changes, riverbed erosion and deposition shows inter-annual alternate size; from 2006 to 2009, median and flood riverbed erosion intensity increased, with the exception of 2006 ~ 2010 waterway regulation engineering implementation, riverbed slightly deposition, 2010 years later, median and flood riverbed erosion intensity significantly increased.

Therefore, with the development of the three gorges reservoir, sandy pebbles reach rebuilding balance process is a gradually top-down development, the maximum erosion intensity section already move to Lujiahe channel.

**The dry riverbed erosion and deposition basic law**

(1) Dry riverbed erosion and deposition basic law are basically the same with median and flood riverbed erosion and deposition.

Table 1 shows: sandy pebbles reach dry riverbed and riverbed erosion and deposition variation along time is basically consistent.

(2) Dry riverbed deformation is the main part of riverbed deformation.

After the Three Gorges reservoir, limited by the boundary conditions, sandy pebbles reach dry riverbed deformation is the main part of riverbed deformation, the erosion mainly concentrated in the dry riverbed. With the Three Gorges water level higher, dry riverbed erosion amount proportion is constantly increasing.

For example, in Yizhi reach, from October 2002 to October 2011, dry riverbed erosion intensity is 203.1 $m^3$ / km, the median and flood riverbed erosion intensity is 226.1 $m^3$/ km, dry riverbed erosion intensity accounts for 90%, shoal erosion intensity is 230.2 $m^3$ / km, accounts for only 10%. Dry riverbed erosion intensity is greater than shoal erosion intensity; the erosion body locates in the

low flow channel. Yizhi reach in the Three Gorges first two years operation, dry riverbed erosion intensity accounted for less than 80%, to 2009, the riverbed scouring almost entirely from the low flow channel.

(3) Sandy pebbles reach thalweg performance for the cut.

After the Three Gorges reservoir, Yichang channel is mainly composed of longitudinal incised. From October 2002 to October 2011, Yichang channel thalweg longitudinal section cut an average of 1.7 meters, and the maximum scour depth is 5.4 meters.

After the three gorges reservoir, Yidu channel relative to Yichang channel, erosion intensity is bigger, from October 2002 to October 2011, Yidu channel thalweg longitudinal section cut an average of 5.3 meters, and the maximum scour depth is 18.0 meters.

Guanzhou channel right branch thalweg are relatively stable, the import section thalweg is high and convex, between 2010 and 2012 imports section thalweg accretion, thalweg show substantially. And for the left branch, the left branch import section is relatively stable, the middle and lower section thawleg substantial cut, from 2009 years ago the uneven variety is generally below the 10 meters.

Lujiahe channel, due to the sand and stone deep grooves layer can be washed limited, after the three gorges reservoir, the sand and stone thalweg elevation stable, in addition to 2005 to 2006, the sand thalweg elevation significantly changed, from 2006 to now, thalweg elevation basically stable, sand and stone thalweg have bigger difference.

After the Three Gorges reservoir, ZhiJiang ~ jiangkou channel thalweg also showed some degree cut. ZhiJiang ~ Jiangkou channel are also scouring and deposition, but overall performance scouring, its characteristic is: above ZhiJiang erosion intensity is less than under ZhiJiang, the deep groove erosion intensity is greater than the high convex shoals.

**Shoals erosion and deposition basic law**

(1)Sandy pebbles reach shoal also overall performance erosion, but the shoals erosion intensity compared with the dry riverbed erosion intensity is small.

After the Three Gorges reservoir, sandy pebbles reach shoal also overall performance erosion, erosion intensity compared with the dry riverbed erosion intensity is small. Such as: in 2003, dry riverbed annual average erosion intensity is 479000 $m^3$ / km, and shoal annual average erosion intensity was only about 140000 $m^3$ / km; in 2005, dry riverbed average annual erosion intensity is 357000 $m^3$ / km, and the shoal annual average erosion intensity was only about 23000 $m^3$ / km; in 2007, dry riverbed average annual erosion intensity is 362000 $m^3$ / km, and the shoal annual average erosion intensity was only about 16000 $m^3$ / km.

(2) Sandy pebbles reach high beach erosion intensity slightly larger than low beach erosion intensity.

Sandy pebbles reach, from October 2002 to October 2011, high beach annual average erosion intensity is 133000 $m^3$ / km; the low beach annual average erosion is 98000 $m^3$ / km, high beach erosion intensity slightly bigger than the low beach erosion intensity.

**Conclusions**

Through field research, data compilation and analysis, this paper study on the basic law of the sandy pebble Reach riverbed erosion and deposition after the Three Gorges Reservoir, the main conclusions can be summarized as the following aspects:

(1) After the Three Gorges reservoir, sandy pebbles reach riverbed overall performance consistency erosion;

(2) After the Three Gorges reservoir, sandy pebble reach median and flood riverbed erosion intensity is bigger before 175 m than after 175 m;

(3) After the Three Gorges reservoir, before the 175 m water storage, sandy pebbles reach median and flood riverbed erosion intensity shows inter-annuals sample size; after the 175 m water storage, median and flood riverbed erosion intensity gradually weakened;

(4) After the Three Gorges reservoir, from Yichang to Dabujie, sandy pebbles reach follow the general rules, in hub downstream erosion intensity gradually weakened from top to bottom, sandy pebbles reach plane modality and riverbed composition uneven changes along the way, so that the riverbed erosion along the way were also unevenly distributed;

(5) After the Three Gorges reservoir, sandy pebbles reach rebuilding balance process is a gradually top-down development;

(6) Dry riverbed erosion and deposition basic law are basically the same with median and flood riverbed erosion and deposition; dry riverbed deformation is the main part of riverbed deformation; Sandy pebbles reach thalweg performance for the cut;

(7) Sandy pebbles reach shoal also overall performance erosion, but the shoals erosion intensity compared with the dry riverbed erosion intensity is small; sandy pebbles reach high beach erosion intensity slightly larger than low beach erosion intensity.

**Acknowledgements**

This work was financially supported by National Natural Science Foundation of China (51209112), National High Technology Research and Development Program 863 (2012AA112508), Western Region Communications Construction Project (201132822430, 20113282241760), and Basic research funding of national commonweal research institutions (TKS120102, TKS120201, TKS130202).

**References**

[1] Guanlun Zhou, et al, *Manual of Navigation Engineering*. Beijing: People Communication Press, (2004) (in Chinese)

[2] Guanlun Zhou, et al, *Watercourse Regulation in Chuanjiang River*. Beijing: People Communication Press, (1998) (in Chinese)

[3] Songren Wu., *Simulation Test of Port and Waterway Engineering*. Beijing: People Communication Press, (1998) (in Chinese)

[4] Lihe Chai., Exploration On similarity theory from new viewpoint. Natural, Vol.22 (3), 1992, p.168-170(in Chinese)

[5] Research on Key Technology for Stability of shoal protection band in waterway in middle and lower reaches of Yangtze River., Yangtze River Waterway Planning and Design Institute. (2006) (in Chinese)

*Applied Mechanics and Materials Vols. 580-583 (2014) pp 1893-1896*
*© (2014) Trans Tech Publications, Switzerland*
*doi:10.4028/www.scientific.net/AMM.580-583.1893*

# Study on the Horizontal Velocity Distribution in Natural Rivers

Hua Ge[1, a], Lingling Zhu[1, b] and Xibing Zhang[1, c]

[1] Changjiang River Scientific Research Institute, Wuhan 430010, China

[2] Hydrology Bureau, Yangtze River Water Resources Commission, Wuhan 430010, China

[a] gh-102@126.com, [b] zhulingling1012@163.com, [c] jss9871@vip.163.com

**Keywords:** horizontal velocity distribution; sediment numerical model; allocation of the erosion and deposition area

**Abstract.** In this article, the horizontal flow velocity in natural rivers was studied, and its formula was established based on the theoretical analysis. Then some key parameters in the formula were determined by regression analysis based on large amount of measured data in the middle reaches of the Yangtze River. This formula can be widely applied in the allocation of the erosion and deposition area in 1D sediment numerical models.

## Introduction

The formula of the horizontal velocity distribution in natural rivers has a wide application in the hydraulic engineering and the river training. Especially in the 1D sediment mathematical models, it is important to allocate the erosion and deposition area along the section direction, since the 1D model gives only the total erosion and deposition area. At present, plenty of the studies have been carried out to solve this problem based on theoretical analysis and experiment researches [1-11]. The achievements of these studies usually have some difficulties in the actual applications since the clear division of the beach and groove is required in natural rivers, while the shapes of the sections in natural rivers are usually ever-changing, and it is hard to get a clear division of the beach and groove. As a result, it is an effective way to solve the specific problems through the basically analysis and the regression analysis based on measured data. In this article, the horizontal flow velocity in natural rivers was studied, and its formula was established based on the theoretical analysis. Then some key parameters in the formula were determined by regression analysis based on large amount of measured data in the middle reaches of the Yangtze River. This formula can be widely applied in the allocation of the erosion and deposition area in 1D sediment numerical models.

## Theoretical Analysis

For the straight rivers, application of the Chezy Formula can be applied to the points of the sections, extended from the situation of the average of the section. For the situation of the total section, the average velocity can be written as:

$$U = C\sqrt{RJ} \tag{1}$$

In Eq.1, $U$ is section average velocity, $C$ is the Chezy parameter, $R$ is the hydraulic radius, and $J$ is water surface slope. $C$ can be determined based on the Manning formula:

$$C = R^{1/6}/n \tag{2}$$

In Eq.2, $n$ is the integrated roughness coefficient of the cross section. By Substituting Eq. 2 into Eq. 1, the cross section velocity can be written as:

$$U = \frac{\sqrt{J}}{n} R^{2/3} = KR^{2/3} \tag{3}$$

In Eq. 3, $K$ is defined as:

$$K = \frac{\sqrt{J}}{n} \tag{4}$$

By assuming that the parameter $K$ remains the same along the section, the velocity of the specific points in the section can be written as:

$$U_i = KR_i^{2/3} \tag{5}$$

At present, Eq .5 is widely used in most of the applications to allocate the erosion and deposition area in 1D sediment numerical models. From the derivation process in the up text we can see that the parameter $K$ is closely related to the resistance of the river bed surface, and relatively large errors will be caused because of the simple assuming that the parameter $K$ remains the same along the section.

In China, most of the alluvial rivers have the compound cross sections consisted of beaches and grooves, such as the lower reaches of the Yangtze River and the Yellow river, main stream of the Huaihe River and Songhuajiang River. For most cases, the shapes of the cross sections in natural rivers are ever-changing, and it is hard to give a clear division of the beaches and grooves. As a result, it is usually difficult to apply the formula, which is based on the clear division of the beach and groove, to resolve the actual problems. According to the up analysis, by assuming that K is non-uniform along the cross section, the relationship of the point velocity $U_i$ and the average velocity $U$ can be written as:

$$\frac{U_i}{U} = \frac{\sqrt{J_i}}{\sqrt{J}} \frac{n}{n_i} \frac{R_i^{2/3}}{R^{2/3}} \tag{6}$$

It can be seen from Eq. 6 that the relationship between $U_i$ and $U$ is closely related to those of the water depth, roughness and water surface slope. Assuming that the water surface slope is the same in each area of the cross section, Eq. 6 can be simplified as:

$$\frac{U_i}{U} = \frac{n}{n_i} \frac{R_i^{2/3}}{R^{2/3}} \tag{7}$$

In Eq. 7, $n/n_i$ closely is related to the distribution of the resistance along the cross section. The parameter, relative bank width was introduced to solve the transverse distribution of the flow resistance [12, 13]:

$$n_i = \frac{n}{f(\eta)} \left( \frac{J_i}{J} \right)^{1/2} \tag{8}$$

In Eq. 8, $\eta=y/B$ is relative bank width, $y$ is the distance from initial point, $B$ is the river bank width. By plotting the data measured in Laijiapu, Tiaoguan, Tiepu and Dongshi reaches of Yangtze River and Yellow River, the expression is obtained as:

$$f(\eta) = A\eta^2 + B\eta + C \tag{9}$$

Before the actual usage of Eq. 9, the location of the cross section in the bend river needs to be firstly confirmed, and this brings some difficulties to the application in 1D river hydraulic mathematical model. Actually, in natural rivers, the water level is always in the changing process, the amplitude of the $\eta$ variation is fairly large for different water levels. As a result, the application the relative bank width brings some extra difficulties. In 1D model, the relative flow depth, $H/H_i$ can be easily to be derived, so it is taken instead of the relative bank width in this article. Then by the simple assuming that the water surface slope is the same in each area of the cross section, the relative flow velocity can be written as:

$$\frac{U_i}{U} = f(\lambda) \tag{10}$$

In Eq. 10, $\lambda=H_i/H$ is the relative flow depth.

**Regression Analysis**

A good deal of measured data of the velocity transverse distribution was collected to define the key parameters in the function $f(\lambda)$. The total number of the measured sections is 118, which were measured in Yichang, Yidu, Lujiahe and Shashi reaches downstream from Three Gorges reservoir,

ranging from March, 2003 to February, 2009. The information of the measured data was showed in Table 1.

**Table 1** Information of the measured data

| Reach name | Date of measurement | Number of the sections |
|---|---|---|
| Yichang | March, 2003 | 5 |
| Yidu | March, 2003 | 4 |
| | October, 2004 | 4 |
| | April, 2005 | 4 |
| Lujiahe | March, 2003 | 11 |
| | February, 2004 | 17 |
| | March, 2005 | 5 |
| | March, 2006 | 5 |
| | January, 2007 | 5 |
| Shashi | November, 2004 | 17 |
| | November, 2005 | 6 |
| | September, 2006 | 10 |
| | March, 2007 | 4 |
| | May, 2007 | 6 |
| | February, 2009 | 15 |

It can be seen from Eq. 6 that $U_i/U$ is partially proportional to $(R_i/R)^{2/3}$. Since $H_i/H$ is basically equal to $R_i/R$ in natural rivers, $(H_i/H)^{2/3}$ can be taken as one of the parameters in $f(\lambda)$. In the physical concept, the greater the pressure is, the greater the resistance would be. In the river flow, the bigger the water depth is, the greater the pressure would be. As a result, the bigger the water depth is, the greater the resistance would be. Combining the investigation of Eq. 9, the simple assumption can be given as:

$$n/n_i = A\left(H_i/H\right)^2 + B\left(H_i/H\right) + C \tag{11}$$

By substituting Eq. 11 into Eq. 7, the $f(\lambda)$ can be expressed as:

$$f\left(\lambda\right) = A\lambda^{8/3} + B\lambda^{5/3} + C^{2/3} + D \tag{12}$$

Results of the regression analysis base on the measured data showed in Table 1 are as follows:

$$A = -0.011873 \quad B = -0.13063 \quad C = 1.18042 \quad D = -0.066352 \tag{13}$$

Fig. 1 gives the contrast of measured values and calculated values carried out by using Eq.12 with parameter value in Eq. 13.

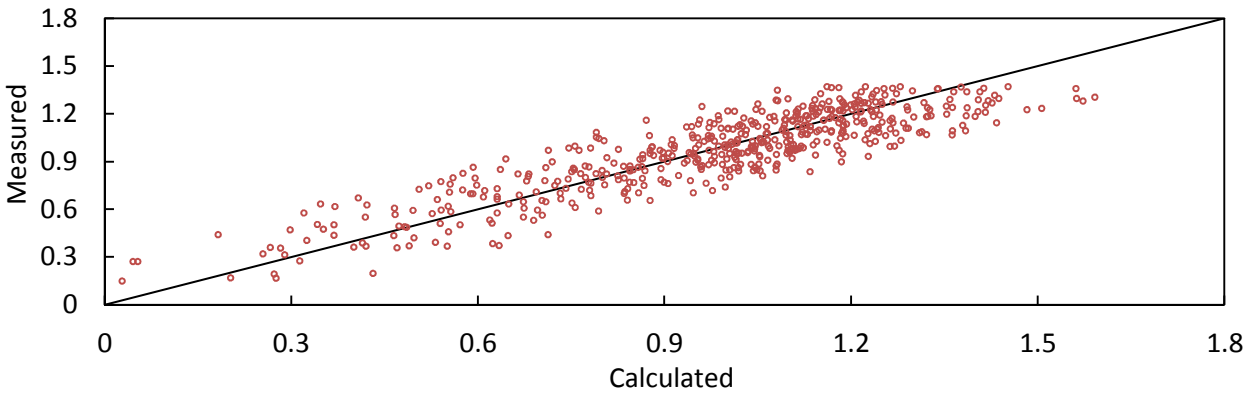


**Figure 1** Contrast of measured and calculated values

**Summary**

In this article, the horizontal flow velocity in natural rivers was studied, and its formula was established based on the theoretical analysis. Then the key parameters in the formula were determined by regression analysis based on large amount of measured data in the middle reaches of the Yangtze River. This formula can be widely applied in the allocation of the erosion and deposition area in 1D sediment numerical models.

**Acknowledgements**

This work was financially supported by the National Natural Science Foundation of China (51209013).

**References**

[1] WANG Wei, CAI Jinde. Computation of discharge distribution for overbank flow. Journal of Chengdu University of science and technology. 6(1990): 69-76

[2] ZHOU Yilin, CHEN Li, WANG Mingfu. Study on transverse distribution of velocity in overbank sediment carrying flows. Journal of sediment research. 3(1996): 56-63

[3] WANG Shuangming, SUN Xihuan, PAN Guangzai. The numerical simulation of flow and sediment in channel with composite section. Journal of Taiyuan University of technology. 1(2000): 60-63

[4] LI Weixin. Calculation of overbank flow in compound channel. Journal of Sichuan University (engineering science edition). 4(2001): 6-8

[5] XU Weilin. Study on computational method of overbank flow in channels with compound cross section. Shuili Xuebao. 6(2002): 21-31

[6] LI Biao, HU Xuyue, XU Lijun. Review of research work of overbank distribution of flow velocity in compound channel. Journal of waterway and harbor. 4(2005): 228-231

[7] LUO Tianfeng, LV Hongxing. Discussion of velocity profile in open channel with U-shaped cross section. Journal of irrigation and drainage. 2(2006): 12-14

[8] ZHANG Tuqiao, MA Jian, SUN Dongpo. LI Guoqing. Flow pattern of compound section river bend. Journal of Zhejiang University (engineering science). 6(2007): 990-994

[9] HUAI Wenxin, LIANG Aiguo. YANG Zhonghua, SHEN Jie. Experimental and numerical study on behavior of flow in an unsymmetrical compound channel. J . Huazhong Univ. of Sci. & Tech. (Nature Science Edition). 12(2007): 95-98

[10] LIU Chen, PING Kejun. Roughness transverse distribution of plane 2-D flow numerical simulation in river. Journal of waterway and harbor. 2(2008): 113-118

[11] WU Teng, ZHANG Hongwu, ZHANG Hao. Transverse distribution of flow velocity in compound channel and its effects on floodplains levees. Shuili Xuebao. 5(2009): 535-541

[12] LI Yitian, XIE Jianheng. Mathematical modeling of two dimensional flow in alluvial rivers. Shuili Xuebao. 11(1986): 11-15

[13] YAO Wei, LI Yitian. Study on flow resistance transverse distribution in braided river. Journal of Sichuan University (engineering science edition). 1(2007): 38-43

*Applied Mechanics and Materials Vols. 580-583 (2014) pp 1897-1900*
*© (2014) Trans Tech Publications, Switzerland*
*doi:10.4028/www.scientific.net/AMM.580-583.1897*

# Study on the Uplift Force of Plunge Pool Slab

Chuntao Wang[1,a], Banghua Xie[1,b], Wenhui Zeng[1,c]

[1] college of science and technology, Nanchang University, 339 Beijing road, Nanchang,330000，Jiangxi, China

[a]lwct@sina.com, [b]39131325@qq.com, [c]18017100@qq.com

**Keywords:** Plunge pool slab, Uplift force. Power spectrum

**Abstract.** The impact of the flood discharge water flow from a high dam is rather great on the slab of a plunge pool, and may cause damages to the plunge pool and consequently endangers the dam body safety. Therefore, a reverse arch slab model was established on the base of a study on and a simulation of the rational scale of gaps between the plates of the plunge pool slab. The model was an arch ring containing 7 slabs. The uplift force time history of each slab was measured, and the uplift force power spectrum and probability density were analyzed. The test result shows that the uplift energy mainly centers in 0-15Hz frequency bandwidth, and mostly within 1Hz. It belongs to a low frequency and big amplitude vibration.

## Introduction

As the flood discharge power of a high dam is rather great, the impact of the flood discharge water flow is tremendous on the slab of a plunge pool, and may cause damages to the plunge pool and consequently endangers the dam body safety. Therefore, it is significant to the dam safety to understand the failure mechanism of the plunge pool.

The failure of the plunge pool is caused by the uplift force. As there are construction joints between the building blocks of the plunge pool slab, the high speed impact jet flow not only acts on the top surface of the slab, but also transmits to the bottom surface of the slab through the joints when the waterstop between the joints is damaged. There is a phase difference between the top surface and the bottom surface of the slab, which leads to the bottom surface pressure greater than the top surface pressure of the slab at a certain moment, and forms an uplift force. At present, there are various opinions about the propagation law of hydrodynamic pressure in the joints.

GRehbinder [1] put forward a seepage flow model. Zhao Yaonan et al [2] came up with a water body oscillation model. V. Fiorotto et al [3] first introduced a transient flow model, and analyzed the propagation features of the pulsating pressure in the joints, seeing the water body in the joints as a pulsating pressure propagation media. Liu Peiqing et al [4,5] analyzed the propagation features of the pulsating pressure in the joints and they thought that the pulsating uplift force acting on the slab block is caused by the different propagation speed of the pulsating pressure wave on the top and bottom surface of the block rather than simply an issue of the phase difference. And they provided a prediction formula for a maximum possible uplift force. The above research results are generally divided into three models: the seepage flow model, the water body oscillation model and the transient flow modal. Both the seepage model and the water body oscillation model regard the water body in the joints as doing some movement, therefore the transfer of pressure depends on the propagation of the moving water body. In fact, as the size of the joints is very small, these two models cannot satisfactorily explain the features of the rapidly changing pulsating pressure in the joints. The transient flow model believes that the pressure in the joints propagates in the form of a wave, and the water body in the joints as the propagation media of the pressure wave, may better conform to the actual situation.

At present, studies in various aspects have been made on the time average and pulsating hydrodynamic pressure and the magnitude and spectral characteristics of the uplift force, etc. and have achieved important results, but so far no recognized conclusions have been drawn. Due to

limited existing prototype projects and difficulties in prototype observation, and also because of the complicated water flow pattern in a plunge pool, it is difficult to have an accurate theoretical analysis on it, and therefore the study on the load characteristics of the plunge pool still largely dependants on model experiments.

## Test Principle

Slab analogue simulation must meet the similarity of the hydraulic conditions and that of structural dynamic conditions. This needs to be guaranteed from two aspects: an elastic material that meets the hydraulic conditions and the structural dynamic similarity; correctly simulate the size of the joints of the pulsating pressure propagation between the blocks.

A hydro elastic model that uses added weight rubber as the test material can simultaneously meet the hydro condition and structural dynamic condition [6], therefore, the first aspect is easy to meet.

The width of the joints must also be taken into consideration so that the joints are similar to those of the prototype. Perspectives are inconsistent theoretically and practically as the joint water flow is rather complicated. We preliminarily think that this joint flow belongs to the scope of laminar flow where the Froude number no longer applies. Therefore, it is incorrect to reduce the joint width according to the model length scale $\lambda_L$. According to document [7], if the geometric scale is 100, the joint width scale will be 3.16. That is, the size of the joints in the prototype is actually at the same order of magnitude with that of the model joints. Therefore, when the similarity of the joint flow field for the model and for that of the prototype is met, the pressure pulsation is also met. In principle, the joint size between the blocks should not be controlled by geometric similarity. This judgment provides a realistic basis for the model test.

## Test Establishment

When studying the slab block uplift force in the model, assuming there was no friction between each block, therefore, the anti-floating stability calculation method for an individual block was the same regardless of a flat slab or a reverse arch slab. See Fig. 1 for the uplift testing device.

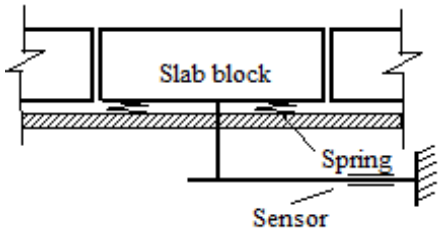


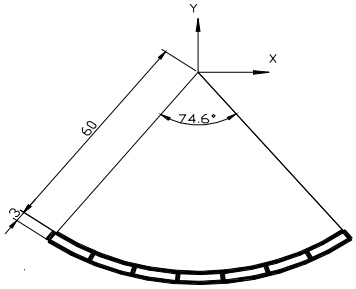


**Fig. 1 Diagram of the uplift testing device of the model** **Fig.2 Geometric features of a reverse arch slab**

Each block was supported on the model slab by 4 springs, and the slab was linked to the sensor by a metal rod. When setting the instrument to zero in static water, the measured value in the model was the uplift force applied to the block. This method of directly measuring the uplift force on the whole block not only avoided the trouble of requiring a point-area conversion when measuring a single point pressure previously, but also had an advantage of an intuitive and definite physical significance.

We conducted an uplift force analogue simulation on a plunge pool slab in accordance with the above simulation principle and test method. This reverse arch slab central angle was 74.6°. the transverse jointing for every 10m formed an arch ring, with the width of the arch ring of 10m. The longitudinal jointing divided uniformly the arch ring into 7 blocks, with the block thickness of 3m. The geometric features are show in Fig. 2

Material features of the slab:

Slab: Submerged weight $\gamma$=14,500 $N/m^3$; elastic modulus E＝25 $GPa$; Poisson ratio $\mu = 0.17$.

Bed rock: Unit weight: $\gamma$=25,000 $N/m^3$; elastic modulus E＝22 $GPa$; Poisson ratio $\mu = 0.22$.

Anchor bar: Unit weight $\gamma$=78,000 $N/m^3$; elastic modulus E＝200 $GPa$.

The model was designed according to gravity criteria, and the geometric scale was 1:100. See Table 1 for each parameters of the model.

**Table 1. Uplift test model scale on reverse arch slab**

| Physical quantity | Quantity of flow | Flow rate | Time | Acceleration | Force | Intensity of pressure |
|---|---|---|---|---|---|---|
| Scale | 100000 | 10 | 10 | 1 | 1000000 | 100 |

## Results and Discussions

The test recorded 4,096 groups of uplift synchronous data, and the statistic features of the test results are shown in Table 2.

**Table 2. Uplift synchronous test statistic results on reverse arch slab [Pa]**

| Load | Block 1 | Block 2 | Block 3 | Block 4 | Block 5 | Block 6 | Block 7 |
|---|---|---|---|---|---|---|---|
| Maximum | 79991 | 152520 | 83780 | 51010 | 83780 | 94396 | 53353 |
| Average | 21661 | 29830 | -6159 | -48960 | -6159 | 24406 | 14413 |
| $\sigma$ | 15010 | 27670 | 25030 | 20070 | 25030 | 11240 | 8390 |
| Maximum of 3σ assurance | 66600 | 112800 | 68800 | 11100 | 68800 | 58100 | 39600 |

See Fig. 3 for the uplift force time history:

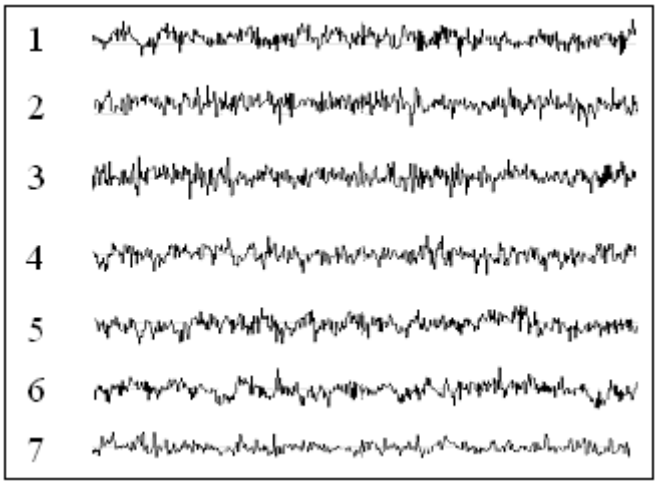


**Fig. 3 Measured load hydrograph of the model reverse arch slab block**

It can be seen from the Table 2 that block 2 has the maximum uplift force, and block 1 is in a moderate position of 7 blocks in terms of the uplift force applied to it. Below is an analysis on the power spectral density and probability distribution of block 1 and block 2, respectively in order to find out the magnitude –frequency characteristic of the uplift force. The uplift force power spectrum features of each block are show in Fig. 4, and the probability density and probability distribution are shown in Fig. 5.

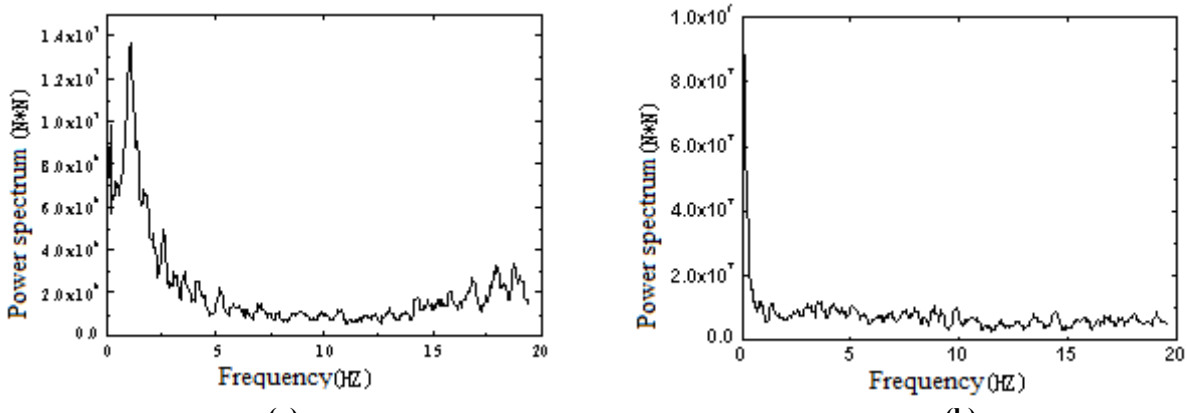


**(a)** **(b)**

**Fig. 4 The uplift force power spectrum. (a) block 1. (b) block 2.**

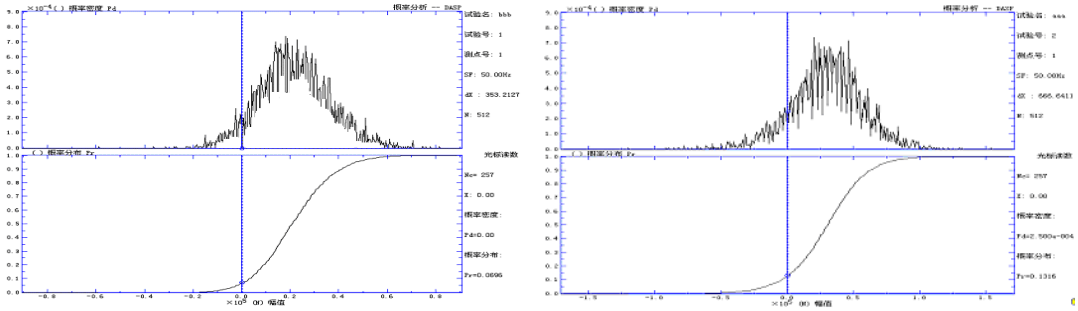

(a) (b)

**Fig. 5 The uplift force probability density and probability function. (a) block 1. (b) block 2.**

Due to the measurement error in the model test, and due to the difference between the model water flow pattern and the prototype, the difference of the uplift force magnitude between each block is great, but the spectrum is basically the same. It is believed that they are all subject to normal distribution. The above figure indicates that the energy mainly centers in 0-15Hz frequency bandwidth, and mostly within 1Hz. It belongs to a low frequency and big amplitude vibration. The oscillation of other blocks also has the similar features.

## Conclusion

The slab block is acted on by an uplift force when the plunge pool slab joints are damaged. A reverse arch plunge pool slab block test is designed according to the scale 1:100 in this paper, which indicates that the uplift force on each block of the reverse arch slab has some differences but they belong to the same order of magnitude. The oscillation energy mainly concentrates within 11Hz. It belongs to a low frequency and big amplitude vibration.

## Acknowledgements

This work was financially supported by the Jiangxi science and technology support program (2009ZDG07600).

## References

[1] G.Rehbinder, Slot Cutting in Rock with a High Speed A Water Jet, Int. J.Rock Mech. Min. Sic., Vol.14, 1977, PP 229-234.

[2] Zhao Yaonan, Liang Xingrong. Investigaion on fluctuating pressure transmission along joints. Journal of Tianjin University, March 1988, P55-65. In Chinese.

[3] V. Fiorotto and A. Rinaldo. Turbulent pressure fluctuations under hydraulic jumps, J. Hydro. Res., IAHR, VOL.30, NO.4, 1992

[4] Liu Peiqing, Dong Junrui, Yu Changzhao, Mechanism of the fluctuating Pressure transmission in cracks of bed rock. Journal of Hydraulic Engineering, December 1994, 31~36. In Chinese.

[5] Liu Peiqing, Li Zhongyi, Dong Junrui, On the mechanism of the fluctuating Pressure transmission in cracks of bed rock. Journal of Hydraulic Engineering[J], April 1996, 27~32. In Chinese.

[6] Cui Guangtao, et al. Hydro-elastic modal experimental study on the Ertan arch dam vibration by discharge flow. Journal of Tianjin University[J]. January 1991. In Chinese.

[7] Yang Min, Peng Xinmin et al. Study on experiment simulation of slabs in Plunge Pool. March 2002. P41. In Chinese.

*Applied Mechanics and Materials Vols. 580-583 (2014) pp 1901-1905*
*© (2014) Trans Tech Publications, Switzerland*
*doi:10.4028/www.scientific.net/AMM.580-583.1901*

# The direct solution on normal depth of an egg-shaped section tunnel

Hui Wen

Department of architecture and civil engineering , Huizhou University

Huizhou, Guangdong, 516007, China

wenhui-hzu@163.com

**Key words:** hydraulics; egg-shaped section; normal depth; direct method

**Abstract:** An egg-shaped is consisted of four parts: One arc bottom, two side circular arc arch and one circular arc roof umbrella arch. It is complex shape. Aiming at traditional methods there are complicated and the defects of inaccurate. on the basis of summarizing the predecessors' research, Based on the normal water depth basic equation mathematical transformation of egg-shaped sections, the interrelation between dimensionless water depth and the dimensionless parameter were analyzed, We use the power function as the formula form, with minimum residual standard deviation as the goal, the coefficients of the formula can be calculated based on the theory of optimization and regression. Then, we get calculation formula for normal water depth. This formula is not a piecewise function, and need not to choose the suitable formula according to the dividing flow. The results can be directly calculated. Results of the example calculation and error analysis showed that the maximum relative error of normal water depth was 0.675% respectively in the utility range (The ratio of water depth divided by height of tunnel is from 0.05 to 0.85). Using this algorithm, above 92 % of the computation error on normal water depth was less than 0.25%. The average error of the formulas was not more than 0.118% .The hydraulic calculation formula will be widely used in engineering design and project management due to its high accuracy and simple form.

## Introduction

At present, many scholars studied on calculation formula for normal water depth of circle, and city-opening section, solve practical problems in engineering[1-2]. An egg-shaped has the following characteristics[3]:1. Through the same flow its section width which is smaller, more conducive to the layout of the underground pipeline; 2. because of section height is greater than the width, Its vertical bearing capacity is greater than the other forms; 3. Through the same flow, its section height greater than the other forms, this would provide facilitating for manual dredging and maintenance; 4. It is suitable for rapid changes of flow, particularly during small flow through large diameter. It has the advantages of high velocity, high ability of anti sedimentation. So it is most commonly used in Foreign city sewage, rainwater pipeline engineering. Now, The direct solution on normal water depth of egg-shaped section tunnel has not been well studied. In this paper, through to mathematical transformation for the uniform flow equation of egg-shaped section, introducing the dimensionless parameters ,analyzing the relationship between dimensionless depth and the dimensionless parameters, according to the water and wastewater engineering norms and hydraulic engineering norms, we get calculation formula for normal water depth.

**Water cross-section of egg-shaped**

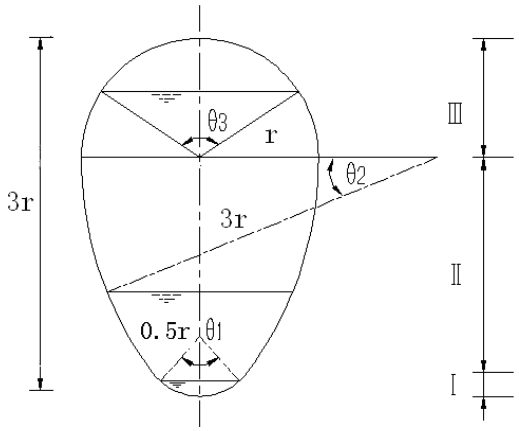


Fig.1 Zonal plan for calculating normal depth of an egg shaped cross-section.

**Hydraulic parameters of egg-shaped cross-section**

X- dimensionless normal water depth. $X = h/3r$ (1)

Three situations can be divided according to the dissimilarity of dimensionless depth X:

Table 1 Hydraulic parameters

| The range of dimensionless depth | The formula |
|---|---|
| I region<br>$0 < X \le \frac{1}{15}$ or $0 < \theta_1 \le 1.85459$ | $A = 0.125\,\mathrm{r}^2(\theta_1 - \sin\theta_1)$<br>$\chi = 0.5\,\mathrm{r}\theta_1$<br>$\theta_1 = 2\arccos(1-6X)$ |
| II region<br>$\frac{1}{15} < X \le \frac{2}{3}$ or $0 \le \theta_2 < 0.64350$ | $A = \mathrm{r}^2[3.02333 - 9\theta_2 - (3\cos\theta_2 - 2)(3\sin\theta_2 - 2\tan\theta_2) + 4\tan\theta_2]$<br>$\chi = \mathrm{r}(4.78830 - 6\theta_2)$<br>$\theta_2 = \arcsin(\frac{2}{3} - X)$ |
| III region<br>$\frac{2}{3} < X \le 1$ or $0 < \theta_3 \le \pi$ | $A = \mathrm{r}^2[4.59413 - 0.5(\theta_3 - \sin\theta_3)]$<br>$\chi = \mathrm{r}(7.92990 - \theta_3)$<br>$\theta_3 = 2\arccos(3X-2)$ |

**Uniform flow basic equation**

$$Q = \sqrt{i}A^{5/3}n^{-1}\chi^{-2/3} \quad (2)$$

Where: Q - discharge, $m^3/s$, i - channel bottom slope, $A$ - water sectional area, $m^2$, n – rough coefficient, $\chi$ - wetted perimeter, m.

**Ascertaining the suitable range of the dimensionless depth**

Literature shows that the free space above the water level require not less than 15 % of the whole cross-sectional area of the tunnel. exceeding this range is meaningless[4].

$$\frac{A}{A_0} = 0.85 \tag{3}$$

Where: $A_0$ - the area of egg-shaped cross-section

$$\frac{\left[4.59413 - 0.5\left(\theta_3 - \sin\theta_3\right)\right]r^2}{4.59413\, r^2} = 0.85 \tag{4}$$

This equation is the triangle transcendental equation, trying calculating solution are $\theta_3 = 2.19163$, $X = 0.81911$。Consider the appropriate extension, the upper limit value is 0.85, According to the actual most engineering application situation, the Lower limit value is 0.05.

**Implicit function expression of normal water depth of egg shaped cross section**

$$\frac{nQ}{\sqrt{i}\,r^{\frac{8}{3}}} = \begin{cases} \dfrac{\left[0.125\left(2\arccos(1-6X) - \sin\left(2\arccos(1-6X)\right)\right)\right]^{\frac{5}{3}}}{\left[\arccos(1-6X)\right]^{\frac{2}{3}}}, & 0 < X \le \dfrac{1}{15} \\ \dfrac{\left[3.02333 - 9\arcsin(\frac{2}{3}-X) - \left(3\cos(\arcsin(\frac{2}{3}-X)) - 2\right)\left(3\sin(\arcsin(\frac{2}{3}-X)) - 2\tan(\arcsin(\frac{2}{3}-X))\right) + 4\tan(\arcsin(\frac{2}{3}-X))\right]^{\frac{5}{3}}}{\left[4.78830 - 6\arcsin(\frac{2}{3}-X)\right]^{\frac{2}{3}}} & \dfrac{1}{15} < X \le \dfrac{2}{3} \\ \dfrac{\left[4.59413 - 0.5\left(2\arccos(3X-2) - \sin\left(2\arccos(3X-2)\right)\right)\right]^{\frac{5}{3}}}{\left[7.92990 - 2\arccos(3X-2)\right]^{\frac{2}{3}}} & \dfrac{2}{3} < X \le 1 \end{cases} \tag{5}$$

**A direct calculation formula for dimensionless normal water depth**

$$M = \frac{nQ}{\sqrt{i}\,r^{\frac{8}{3}}} \tag{6}$$

In order to study convenient, assume

By the optimization method of fitting, the direct calculation formula for dimensionless normal water depth of egg shaped cross section was obtained:

$$X = 0.420M^{0.523} + 0.002M^{3.164} + 0.003 \qquad M \in [0.015151, 3.152211] \tag{7}$$

**Formula evaluation**

Table 2. Distribution of relative error

| The correct dimensionless depth $X^*$ | Dimensionless coefficient $M$ | The calculation dimensionless depth $X$ | Relative error $\Delta$ (%) |
|---|---|---|---|
| 0.050 | 0.015151 | 0.049948 | -0.104 |
| 0.100 | 0.061020 | 0.100287 | 0.287 |
| 0.200 | 0.234791 | 0.199861 | -0.069 |
| 0.300 | 0.514979 | 0.300080 | 0.027 |
| 0.400 | 0.891784 | 0.399973 | -0.007 |
| 0.500 | 1.348380 | 0.499217 | -0.157 |
| 0.600 | 1.862754 | 0.598803 | -0.199 |
| 0.700 | 2.408678 | 0.700433 | 0.062 |
| 0.800 | 2.932281 | 0.800376 | 0.047 |
| 0.850 | 3.152211 | 0.844263 | -0.675 |

We investigation 10000 data within the common project , The results show that largest relative error is less than 0.675% . The average error is only 0.118%, which is less than 0.25% accounted for 92%.

**Calculation normal water depth application example**

It is known that the parameters of egg shaped cross section. The top arch radius $r = 2.5m$ , bottom slope $i = 1/1000$ , rough coefficient $n = 0.014$ , solved the normal water depth h when the flow $Q = 78\, m^3/s$ .

Answer:

Firstly, to calculate dimensionless coefficient M;

$$M = \frac{nQ}{\sqrt{i}\, r^{\frac{8}{3}}} = 2.9995$$

Using Formula（6）to calculate

Using Formula（7）to calculate $X = 0.420M^{0.523} + 0.002M^{3.164} + 0.003 = 0.8136$

Using Formula（1）to calculate $h = 3rX = 6.102$ (exact value is 6.107 m) relative error is 0.085%.

**Conclusion**

The simple approximate formula has high accuracy, Within the suitable range of the engineering, the absolute maximum relative error is 0.675%. It can satisfy the demand of practical engineering.

**Acknowledgements**

This Research was financially supported by the Research Fund of Huizhou University (No. $C_5$10.0211)

**References**

[1] Hui Wen, Fengling Li. Further study on explicit formula for normal water depth of uniform flows in circular pipes[J]. Advances in Science and Technology of Water Resources, 2012, 32(6): 15－17. (in Chinese with English abstract).

[2] Hui Wen, Fengling Li. Discussion again of the approximate calculation for the normal water depth of the city-opening Section Tunnel[J]. Water and Wastewater Engineering, 2008, 34(11): 42－43. (in Chinese with English abstract)

[3] Ye Tao, Yue Jia . hydraulic calculation and hydraulic element analysis for the non pressure pipe line in egg shaped cross section [J]Water and Wastewater Engineering, 2009, 35(S1): 428－430. (in Chinese with English abstract )

[4] Hydroelectric Investigation and Design Institute of SPC DL/T5195-2004 Specification for design of hydraulic tunnel[S]. Beijing: China electric power press, 2004.

*Applied Mechanics and Materials Vols. 580-583 (2014) pp 1906-1909*
*© (2014) Trans Tech Publications, Switzerland*
*doi:10.4028/www.scientific.net/AMM.580-583.1906*

# The Study of Available Water Resources in Northern Shaanxi

Xi-jun Wu[1,2]

[1]Department of Construction Engineering, Yulin College, Yulin, China

[2]State Key Laboratory Base of Eco-hydraulic in Arid Area (Xi'an University of Technology), Xi'an, China

Wxj0826@163.com

**Keyword:** Northern Shaanxi; water resources; available water resources; surface water; groudwater

**Abstract:** In order to alleviate the contradictions about water resources shortage and socio-economic development in Northern Shaanxi, the water resources and their availability were studied. Through use the method of surface water resources deducte river ecological basic flow and flood discharge, calculated the surface available water resources and total available water resources of Northern Shaanxi, summarized their distribution characteristics. Study result showed that the available water resources of Northern Shaanxi is low, only 1.6 billion $m^3$, available rate is 40%, water resources and their availability principally distribute in Yulin.

## Introduction

Under the influence of global climate change, large-scale economic development and other multiple factors, China's water resources situation is undergoing new changes, so need to analyze and estimate available water resources [1]. Available water resources is both the conditions of comprehensive plan saving, configuration, development, utilization and treatment measures of regional water resources, and the basis of analysis water resources carrying capacity [2]. Northern Shaanxi is China's major energy and chemical industry base, water resources shortage, the contradiction between supply and demand of water resources increasingly sharp in recent years [3].

## Study Area and Research Methods

**Study Area**. North Shaanxi include Yulin and Yan'an two city of Shaanxi province, has abundant coal, oil and natural gas resources, is the rare resource-rich region of China. The region area is 80,300 km2, altitude 900-1500 m, in the central part of the Loess Plateau, drought and less rainfall, severe shortage of water resources. North Shaanxi average annual rainfall is 454.3 mm, 65% concentrated in July, Aug and Sep, rainfall showed a decreasing trend from south to north. Runoff variation regularity and characteristics is basically same with rainfall, this leading to uneven distribution in spatial and temporal of water resources. Fig 1 is the river system diagram of North Shaanxi.

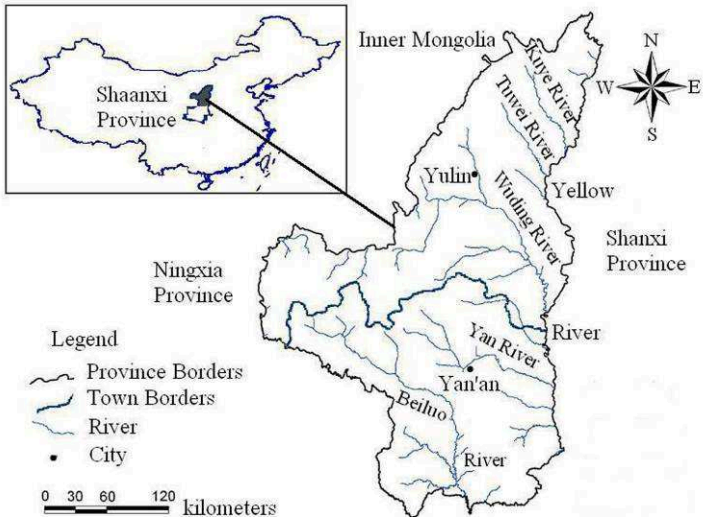


Fig. 1 The river system diagram of Northern Shaanxi

**Research Methods and Data Sources**. According the mastered data and materials, make the average annual surface water resources deduct the river ecological basic flow and flood discharge, take available surface water resources [4], the product of groundwater recharge and mineable coefficient is available groundwater resources, then calculate the available water resources of different regions and rivers, summarizes its characteristics and law. The data comes from "Shaanxi Water Conservancy Statistical Yearbook" [5] and" Shaanxi Water Resources Integrated Planning" [6], also references the "Shaanxi Water Function Regionalization "and other materials. As data source is not consistent, so the data may have some deviation.

## The Available Water Resources in North Shaanxi

**Calculation Methods**. Available water resources, it refer that in the foreseeable period, based on consideration of life, production and ecological environment water, the one-time maximum water can be used in total water resources[7]. Available water resources including available surface water and available groundwater, it was the addition of both then deducted repeat amount. The repeat amount was the ditch seepage of plain shallow groundwater and the exploitation of field infiltration recharge. The following is estimated formula [8]:

$$W_a=W_{s,a}+W_{g,a}-W_r \quad (1)$$

Wa is available water resources; Ws,a is available surface water; Wg,a is available groundwater; Wr is the repeat between both.

The surface water resources including the water can't be used and impossible used. The water can't be used must satisfied river ecological basic flow, and avoid the ecological environmental degradation and destruction. The impossible used water was unable to use and limited by various factors and conditions, it is the flood that beyond project largest storage capacity and supply capacity [9]. Surface water resources deduct the river ecological basic flow and the flood discharge, get available surface water resources. With formula (2) expression [10]:

$$W_{s,a}=W_s-W_e-W_f \quad (2)$$

Ws is surface water resources; We is river ecological basic flow; Wf is impossible used flood discharge.

The simple methods calculate river ecological basic flow is certain proportion of surface water resources. Flood water resources deducted reservoir stored water resources and water consumption in flood period is the flood discharge.

**Calculation Steps.** Based on the collected data, according to the above method calculate the available water resources in North Shaanxi. Calculation steps as follows, results as Table 1.

1) Confirm the river ecological basic flow: according to the domestic and foreign research results and the author's Weihe ecological base flow research [11], the river ecological basic flow of North Shaanxi was considered as 20% average annual runoff.

2) Flood water resources: according to the statistics of runoff in North Shaanxi, July to October is flood period, and the water resources of 4 months flood period is about 60% of the annual runoff.

3) Surface water consumption in flood period: because water consumption is average, and flood period is 4 months, so the surface water consumption in flood period is one-third of annual surface water consumption.

4) Flood discharge water: flood water resources deducted reservoir stored water resources and surface water consumption in flood period, the reservoir stored water resources and water consumption in flood period select maximum statistical data of each year, this paper is the 2010's data.

$$W_f=W_{f,s}-W_{r,s}-W_{u,s} \quad (3)$$

Wf,s is flood water resources; Wr,s is reservoir stored water resources; Wu,s is surface water consumption in flood period.

5) According to the formula (2), make the annual average surface water resources deduct river ecological basic flow and the flood discharge, get available surface water resources.

$W_{s,a}=W_s-W_e-W_f$

$=W_s-0.20W_s-(0.60W_s-W_{r,s}-W_{u,s})$

$=0.80W_s-(0.60W_s-W_{r,s}-W_{u,s})$

If: $0.60W_s-W_{r,s}-W_{u,s}\leq 0$, $W_{s,a}=0.80W_s$

If: $0.60W_s-W_{r,s}-W_{u,s}>0$, $W_{s,a}=0.20W_s+W_{r,s}+W_{u,s}$

Table. 1 The available surface water resources of North Shaanxi unit:100 million $m^3$

| District | ecological basic flow | flood discharge | reservoir stored water | water consumption of flood period | available surface water |
|---|---|---|---|---|---|
| Yulin | 3.69 | 3.37 | 4.42 | 1.37 | 9.48 |
| Yan'an | 2.58 | 4.90 | 1.16 | 0.50 | 4.24 |
| North Shaanxi | 6.27 | 8.27 | 5.58 | 1.87 | 13.72 |

From Table 1 we can know, North Shaanxi surface water available rate is low, the main reason is the flood discharge too much, about 827 million m3, the principal pathway increase available surface water is to reduce flood discharge in future, this can be achieved by constructing lots reservoirs and micro water storage engineering. Even in Northern Shaanxi unable to use temporarily, if can staggered with Yellow River mainstream flood peak, the flood discharge of North Shaanxi can also become Yellow River available water resources. [12].

**Available Groundwater Resources.** The Shallow available groundwater resources refers to the maximum amount of water allowed to be taken out from underground aquifer that in the condition of economic reasonable, technology feasible, water quality deteriorative, won't cause underground water level continued decline, land subsidence and other environmental geological problems. Although regional hydrogeology condition analysis, according to the total groundwater recharge, underground water level observation, actual yield, and other material, carries on simulation and calculation, confirm the mineable coefficient, and then calculate available groundwater resources of region.

$$W_{g,a}=\rho W_{g,r} \quad (4)$$

$W_{g,a}$ is available groundwater; $\rho$ is groundwater mineable coefficient; Wg,r is groundwater recharge;

According to relevant materials and calculation [6], the North Shaanxi annual average groundwater recharge is 1.04 billion m3, average mineable coefficient is 0.55, so the available groundwater resources in North Shaanxi is 571 million m3, including 458 million m3 of Yulin.

**Available Water Resources.** Through the above result, according to formula (1), we can get the total available water resources in North Shaanxi, Table 2.

Table. 2 Available water resources in North Shaanxi unit:100 million $m^3$

| District | Surface water | Groundwater | Repeat | Total | Rate |
|---|---|---|---|---|---|
| Yulin | 9.48 | 4.58 | 2.76 | 11.3 | 0.42 |
| Yan'an | 4.24 | 1.12 | 0.57 | 4.79 | 0.35 |
| North Shaanxi | 13.72 | 5.71 | 3.33 | 16.09 | 0.40 |

It can be get from Table 2, Northern Shaanxi available surface water, available groundwater and available total water respectively is 1.372 billion m3, 571 million m3 and 1.609 billion m3, now can satisfied the water demands, but due to uneven distribution, some area available water resources is still very shortage. It is predicted that in 2015 the water demand in North Shaanxi will be 1.5 billion m3, 2.4 billion m3 in 2020, at that time, only through the Yellow River water diversion to meet the demand. In North Shaanxi the available water resources spatial distribution law is same with water resources, water available rate is 40%, far less than 60% of GuanZhong region, it also have the potential of increasing available water resources by engineering measures. Table 3 is the water resources and availability of primary rivers in Northern Shaanxi.

Table. 3 The available water resources of primary rivers in Northern Shaanxi unit:100 million m3

| River | Water resources | Availble water resources | Rate |
|---|---|---|---|
| Wuding River | 13.08 | 5.63 | 0.43 |
| Yan River | 2.82 | 0.80 | 0.28 |
| Beiluo River | 9.50 | 4.26 | 0.45 |
| Kuye River | 6.30 | 0.95 | 0.15 |
| Tuwei River | 3.50 | 1.40 | 0.40 |
| Total | 35.20 | 13.04 | 0.37 |

## Conclusions

To sum up, in North Shaanxi the water resource is lacking, distribution is uneven, groundwater accounts for big ratio, and ecological environment is fragile, after 1980's surface runoff decrease obviously. It can be get through the calculation and analysis of available water resources, North Shaanxi available water resources is few, only 1.6 billion m3, and the available rate is 40%, but also have the increasing potential, as water resources, available water resources mainly distribute in Yulin; Future in North Shaanxi, the main way increased available water resources is the engineering measures to reduce flood discharge and divert water from Yellow River, and non-engineering measures to save water resources.

## Acknowledgements

This work was financially supported by the State Key Laboratory Base of Eco-Hydraulic Engineering in Arid Area Open Research Fund (No. 2013KFKT-3); the Natural Science Basic Research Plan in Shaanxi Province of China (No. 2011JM5004); the Education Department Scientific Research Plan in Shaanxi Province of China (No. 12JK0489)

## References

[1] National Integrated Water Resources Planning Leading Group Office, The National Integrated Water Resources Planning File. (2003). (in Chinese)
[2] H G Zhang, X Zhang, S Y Lv, etc,Yangtze River, vol. 39 (17) , ( 2008) , p.18, (in Chinese)
[3] Yulin Water Supplies Bureau, *Yulin Water Conservancy "Twelve Five-Years" Development Planning*. (2011**)**. (in Chinese)
[4] Y J Fu, J S He, D P Mu, etc, Journal of Arid Land Resources and Environment, vol. 25 (1), ( 2011) , p.107, (in Chinese)
[5] Department of Water Resources of Shaanxi Province, *Shaanxi Water Conservancy Statistical Yearbook(2001-2010)*. (2011). (in Chinese)
[6] Department of Water Resources of Shaanxi Province, *Shaanxi Water Resources Integrated Planning*, (2009**).** (in Chinese)
[7] Institute of Water Power Planning and Design, Ministry of Water Resources, *The Estimate Methods of Available Water Resources (trial implementation).* (2009). (in Chinese)
[8] Qu W, "*Study on Available Water Resoucres in Arid Inland Regoin of Northwest"*, HoHai University. (2005). p.12 (in Chinese)
[9] C H Hu, Z N Wu, J S Gao, *etc*, ARID LAND GEOGRAPH, vol. 33 (3), ( 2010). p.404**.** (in Chinese)
[10] X S Du, Z Q Xia, vol. 23 (1) ( 2003). p.14**.** (in Chinese)
[11] X J Wu, H E Li, Y Dong, Transactions of the CSAE, vol. 27 (11), ( 2011). p.154**.** (in Chinese)
[12] X J Wang, J J Lian, Zone Research, vol. 25 (3), ( 2008). p.342**.** (in Chinese)

*Applied Mechanics and Materials Vols. 580-583 (2014) pp 1910-1917*
*© (2014) Trans Tech Publications, Switzerland*
*doi:10.4028/www.scientific.net/AMM.580-583.1910*

# Mechanical Characteristics Analysis on Flexible Mattress in Downstream Sinking Based on Lumped Mass Method

Zhihua Sun[1, a], Manling Cheng[2,b]

[1]School of Mechanics and Architecture Jianghan University, Wuhan China, 430056

School of Transportation Wuhan University of Technology, Wuhan China, 430063

[2] WuHan Business University，WuHan，China, 430056

[a]email: cmlssh@qq.com, [b]email: 751681130@qq.com

**Key words:** Lumped Mass Method, Flexible Mattress, Downstream Sinking, Mechanical Characteristic

**Abstract:** Downstream sinking technology of flexible mattress has wide application in erosion protection, berth firm and bank protection. During sinking of flexible mattress, the distance get gradually between the landing position of the mattress and the laying mattress ship, then the suspense length and mattress's self-weight are also increase because of the ship's move. Therefore the tension in mattress is also change continuously, so the calculation of the tension becomes difficult. By using lumped mass method, the mattress can be separated into several lumped mass which are connected using non-mass springs, with the laying distance increase, the length and self-weight of the mattress can be increase gradually, and according to forces equilibrium equation, the tension and profile of the mattress can be obtained.

## Introduction

Stability of a dam depends on steadity of the dam's protective bottom in waterway regulation engineering. As a new type protective bottom structure, flexible mattress with concrete ballast which is made from geotextiles and concrete ballasts has wide application in erosion protection, berth firm and bank protection because of its antifilferability, isolation, erosion protection, wholeness and applicability.[1]

When a flexible mattress is sank, general a downstream sinking way is used, because it can suit better the erosion deformation of riverbed after engineering. But during downstream sinking, the distance is bigger between the landing position of mattress and laying ship because of the ship's movement, so the mattress length and its self-weight are increase continuously, then the tension's calculation becomes difficult because of the various length and its self-weight. For security, a calculation method of the tension is needed.

Lumped mass method[2] is that, the continuous mattress is separated into several element, the mass of every elements are located even to element's ends, and every elements are connected by non-mass springs, considering the weight of mattress, buoyance, tension of laying ship to mattress, and apply force of hydrodynamic, establishing the force equilibrium equation of element. Solve for the tension of element mattress and using the relation of tension's change and mattress geometry change which is caused by it, and iterating gradually. Then the tension and profile of mattress with various length and self-weight can be just obtained.

**Calculation Modal**

A flexible mattress consists of a mat and fasten ballasts to it, the mat consists of geotextile and a longitudinal stiffening rib, the rib sews on the mat along the length direction, its length is same as the mat's length, the ends of the rib are made up into rings easy to connect of mattress body, sets of two fasten strip sewed on between the rib and mat cloth along transverse are used to tie ballasts. Longitudinal stiffening rib with a certain width is made from polyacrylic, it sewed on mat cloth at intervals of distance. The ballast is a concrete block, it has a certain dimension (length×width×thickness), between each block has a certain distance, and disposed even on the mat.

For a flexible mattress with concrete ballasts, the mass of concrete block is too much more than the mass of geotextile, stiffening rib and tie strip, so the mass of mat cloth, stiffening rib and tie strip can be ignored. Let the concrete block treat as a lumped mass, then the flexible mattress is just treated as a mattress modal which consists of many lumped mass and non-mass mat.

Let mattress is separated into n elements along the longitudinal, the two ends of every element are lumped mass (concrete ballast), the middle is mat (mat cloth and stiffening rib), their centers are taken as the centers of every element. The below end of first element is landing point of mattress on the riverbed, the upper end of nth element connected the roll of laying ship. As shown as Fig.1, the mass of every element are distributed to the ends of a element, that is, the mass of every element is sum of the half mass in two ends, and applied on the center of the element, hydrodynamic acting force applied also on the center, as shown as Fig.2.

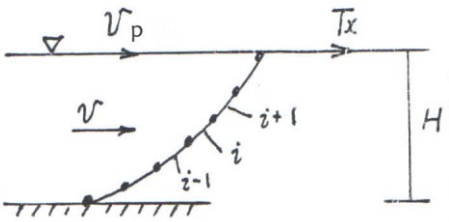


Fig.1 Model of mattress

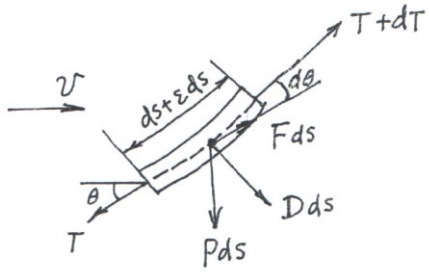


Fig.2 Forces acting on element

Where,

$P_i$ — sum of the half weight under water in two ends of $i$ th element

$D_i$ — normal component of hydrodynamic acting force of $i$ th element

$F_i$ — tangential component of hydrodynamic acting force of $i$ th element

$T_{x_i}$ ——horizontal component of tension in $i$ th element

$T_{y_i}$ ——vertical component of tension in $i$ th element

- Geometry of micro segment of mattress body

Take any micro segment on mattress body, then

$$dx = (1+\varepsilon)ds \cdot \cos\theta \quad (1)$$

$$dy = (1+\varepsilon)ds \cdot \sin\theta \quad (2)$$

where, $\varepsilon = \frac{\Delta S}{S} = \frac{T}{EA}$ (3)

$\varepsilon$ ——expansion of unit length of mattress body $T$ ——tension in mattress body

$E$ ——elastic module of mattress body $A$ ——section area of mattress body

- Mechanic analysis of micro segment of mattress body

What apply to any micro segment of mattress body are: tensions $T$ and $T+dT$ in the ends of the micro segment of mattress body ( $dT$ is the change of the tension), the weight P under water of the ballasts in ends, and the normal component D and tangential component F of the hydrodynamic acting force to the segment.

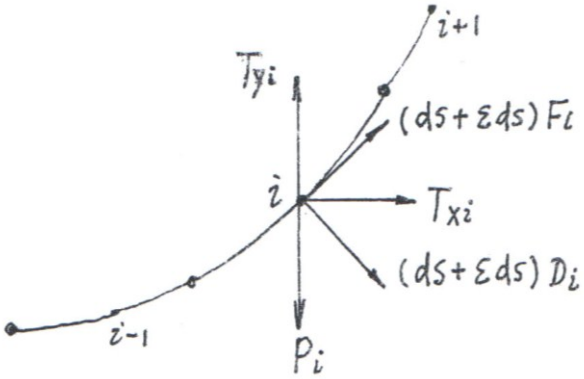


Fig.3 Forces acting on micro segment of mattress body

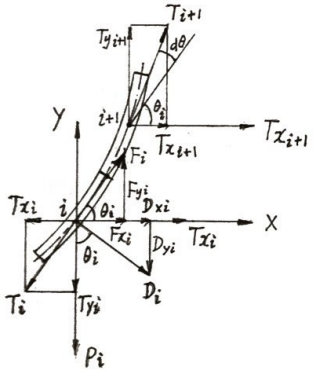


Fig.4 Forces acting on element

From Fig.3, the force equilibrium equation of the micro segment can be established

$$(T+dT)\cos d\theta - T - Pds\cdot\sin\theta + F(1+\varepsilon)ds = 0 \quad (4)$$

$$(T+dT)\sin d\theta - Pds\cos\theta - D(1+\varepsilon)ds = 0 \quad (5)$$

Where,

$dT$ —— the change of tension $d\theta$ —— the change of angle

$ds$ —— the length of micro segment

P—— sum of the half weight under water in two ends of micro segment

Formula (4) is divided by $ds$, then $\frac{T+dT}{ds}\cos d\theta - \frac{T}{ds} - P\sin\theta + F(1+\varepsilon) = 0$

When $d\theta \to 0$, $\cos d\theta \to 1$, then above can be written as

$$\frac{T+dT}{ds} - \frac{T}{ds} - P\sin\theta + F(1+\varepsilon) = 0$$

That is $\frac{dT}{ds} = P\sin\theta - F(1+\varepsilon)$ (6)

As same as above, formula (5) is divided by $ds$, then

$$\frac{T+dT}{ds}\sin d\theta - \frac{Pds}{ds}\cos\theta - \frac{D(1+\varepsilon)ds}{ds} = 0$$

When $d\theta \to 0$, $\sin d\theta \to d\theta$, then above formula can be written as

$$(T+dT)\frac{d\theta}{ds} - P\cos\theta - D(1+\varepsilon) = 0$$

That is $T\frac{d\theta}{ds} + \frac{dT\cdot d\theta}{ds} - P\cos\theta - D(1+\varepsilon) = 0$

$dT\cdot d\theta$ is ignored, then $\frac{d\theta}{ds} = \frac{1}{T}\left[P\cos\theta + D(1+\varepsilon)\right]$ (7)

- Mechanical analysis of element

For any element $i$, its one end's tension is $T_i$, in the other end has tension $T_{i+1}$ of the neighboring element $i+1$, besides, has also the sum $P_i$ of the half weight under water of ballasts in the ends, and the normal component $D_i$ and tangential component $F_i$ of hydro-dynamic acting force. As shown as Fig.4.

Then the force equilibrium equation of element $i$ can be obtained.

$$T_{x_{i+1}} = T_{x_i} - F_i \cos\theta_i (ds + \varepsilon ds) - D_i \sin\theta_i (ds + \varepsilon ds) \quad (8)$$

$$T_{y_{i+1}} = T_{y_i} - F_i \sin\theta_i (ds + \varepsilon ds) + D_i \cos\theta_i (ds + \varepsilon ds) + P_i \quad (9)$$

$$T_{i+1} = \sqrt{T_{x_{i+1}}^2 + T_{y_{i+1}}^2}, \quad (10)$$

where

$T_{x_i}, T_{x_{i+1}}$ — component in X direction of the tension in element $i$ and $i+1$, respectively

$T_{y_i}, T_{y_{i+1}}$ — component in Y direction of the tension in element $i$ and $i+1$, respectively

$D_i, F_i$ — normal and tangential component of hydrodynamic acting force to element $i$, respectively

Hydrodynamic acting force to an element is[3]

$$\sum F = \rho Q \beta V = \rho (VA) \beta V = \rho A \beta V^2$$

Its normal component $D = \rho A \beta V^2 \sin^2\theta$ (11)

Its tangential component $F = \rho A \beta V^2 \cos^2\theta$ (12)

where

$\rho$ ——density of water $(1000 kg/m^3)$ $Q$ ——flow of river

$A$ ——passage section area of an element

$\beta$ ——momentum calibration coefficient, $\beta = 1.02 \sim 1.05$

$V$ ——average velocity of flow at passage section, here we take index number formula about velocity of flow and $n = \frac{1}{7}$, then the relation between the velocity of flow at various height to riverbed and that of water plane can be obtained:

$$V = V\mathrm{p}(\frac{y}{H})^{\frac{1}{7}} \quad (13)$$

Where,

$V$ ——velocity of flow at height $y$ to riverbed

$V_p$ ——velocity of flow at water plane

$y$ ——height to riverbed $H$ ——depth of river

So the normal and tangential component of hydrodynamic acting force of $i$ th element can be written as, respectively

$$D_i = \rho A_i \beta \left[ V_P \cdot (\frac{y_i}{H})^{\frac{1}{7}} \right]^2 \sin^2\theta \quad (14)$$

$$F_i = \rho A_i \beta \left[ V_P \cdot (\frac{y_i}{H})^{\frac{1}{7}} \right]^2 \cos^2\theta \quad (15)$$

where

$\mathrm{A_i}$ ——passage section area of $i$ th element, is equal to $(y_{i+1} - y_i) \times$ width of mat cloth.

$y_i$ ——height of the center of $i$ th element to riverbed

Because the number and direction of two tensions in neighboring element $i$, $i+1$ are all changed, that leads to the center positions and the angles to horizontal direction of elements $i$, $i+1$ are also changed, as shown as Fig.5, and

$$x_{i+1} = x_i + (ds + \varepsilon ds)\cos\theta_{i+1} \quad (16)$$

$$y_{i+1} = y_i + (ds + \varepsilon ds)\sin\theta_{i+1} \quad (17)$$

$$\theta_{i+1} = \theta_i + d\theta_i \quad (18)$$

From formula (6), ( 7)

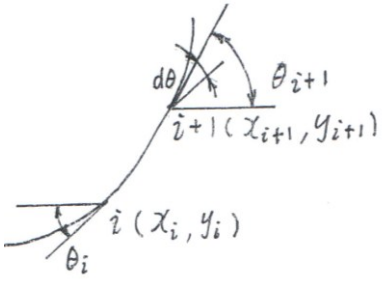


Fig.5 Geometry of neighboring element

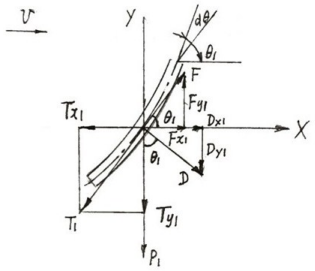


Fig.6 Forces acting on the first element

$$ds_i = \frac{dT_i}{P_i \sin\theta_i - F_i(1+\varepsilon)} = \frac{T_i d\theta_i}{P_i \cos\theta_i + D_i(1+\varepsilon)}$$

Then $$d\theta_i = \frac{dT_i}{T_i} \cdot \frac{P_i \cos\theta_i + D_i(1+\varepsilon)}{P_i \sin\theta_i - F_i(1+\varepsilon)} \quad (19)$$

Where $$dT_i = \sqrt{(dT_{x_i})^2 + (dT_{y_i})^2} \quad (20)$$

$$dT_{x_i} = T_{x_{i+1}} - T_{x_i} \quad (21)$$

$$dT_{y_i} = T_{y_{i+1}} - T_{y_i} \quad (22)$$

From formula (16) ~ (18), if every length $ds$ of laying mattress are know, then the central position and azimuth of next element $i+1$ are depended on the change $d\theta_i$ of angle to horizontal direction of the preceding element $i$, and from formula (19), $d\theta_i$ is depended on the tension $T_i$ and its change $dT_i$ of the element, hydrodynamic acting force and the weight $P_i$ under water of the ballast.

But in the first element of mattress, has only the weight under water of ballast and hydrodynamic, as shown as Fig.6, so the force equilibrium equation of the first element is

$$F_{x_1} + D_{x_1} - T_{x_1} = 0 \quad (23)$$

$$F_{y_1} - D_{y_1} - T_{y_1} - P_1 = 0 \quad (24)$$

From (23), ( 24)，we obtained the tension of the first element

$$T_{x_1} = F_{x_1} + D_{x_1} \quad (25)$$

$$T_{y_1} = F_{y_1} - D_{y_1} - P_1 \quad (26)$$

And $$T_1 = \sqrt{T_{x_1}^2 + T_{y_1}^2}$$

According to above, the calculation flow chart of profile and tension of mattress can be obtained, as show as Fig.7.

According to the result of calculation, connecting the coordinates ( $x_i$, $y_i$, $i = 1 \cdots n$) of whole elements, we can obtain the profile of mattress, also according to tensions of every element ($i = 1 \cdots n$), the tensions diagram can be obtained.

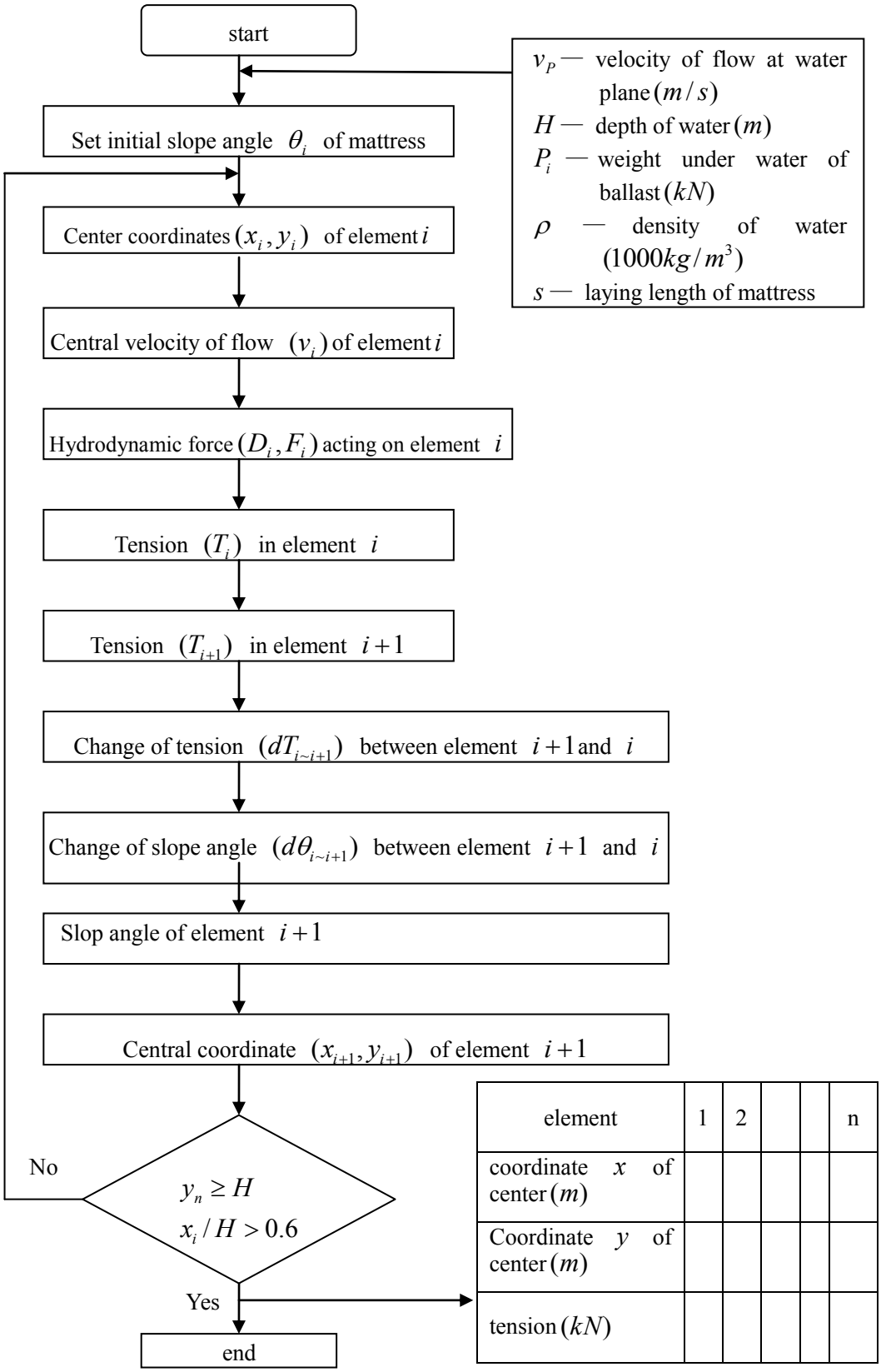


Fig. 7 Calculation flow chart

**Example**

A downstream sinking technology applied on a waterway. The depth of water is 8.5m, the velocity of flow at water plane is 0.89m/s. Suppose the relative movement displacement $\Delta x$ is taken as 0.6H, width of the mattress is 22m, the width of stiffening rib is 7cm and set one at interval of 25cm along the width direction, the ballast is made from concrete block with $40cm \times 26cm \times 12cm$, the mass of mattress under water of unit area is $W_1 = 64.12kg/m^2$. Solve for the tension and profile of mattress in downstream sinking.

- Suppose conditions:
  (1) Calculate the tension and profile of mattress with unit width (1m)
  (2) Divided elements along the longitudinal direction, the length of every element is $S = 1m$
  (3) Taking $\beta = 1.05$
  (4) No consider the elastic deformation of mat (cloth and rib), that is $\varepsilon = 0$
- Result
  (1) The profile and tension of the mattress are shown as Fig.8.

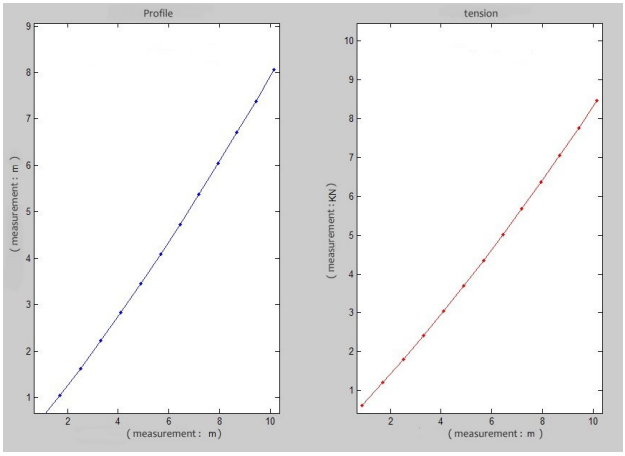


Fig.8 Profile and tension of mattress in $H = 8.5m$, $v_P = 0.89m/s$

(2) The coordinates X, Y of every element's center, raters of slop of tangent and tension are show as table 1.

| Element | 1 | 2 | 3 | 4 | 5 | 6 | 7 |
|---|---|---|---|---|---|---|---|
| Coordinate $x$ of center $(m)$ | 0.866 | 1.701 | 2.518 | 3.322 | 4.114 | 4.897 | 5.670 |
| Coordinate $y$ of center $(m)$ | 0.5 | 1.050 | 1.627 | 2.222 | 2.832 | 3.455 | 4.088 |
| Rate of slope of tangent | 0.577 | 0.659 | 0.706 | 0.741 | 0.770 | 0.796 | 0.818 |
| Tension $(kN)$ | 0.616 | 1.197 | 1.802 | 2.421 | 3.052 | 3.694 | 4.346 |
| Element | 8 | 9 | 10 | 11 | 12 | 13 | 14 |
| Coordinate $x$ of center $(m)$ | 6.436 | 7.195 | 7.946 | 8.691 | 9.430 | 10.162 | 9.403 |
| Coordinate $y$ of center $(m)$ | 4.73 | 5.383 | 6.043 | 6.710 | 7.384 | 8.065 | 10.215 |
| Rate of slope of tangent | 0.840 | 0.860 | 0.878 | 0.896 | 0.913 | 0.929 | 1.469 |
| Tension $(kN)$ | 5.008 | 5.679 | 6.361 | 7.052 | 7.753 | 8．463 | 11.583 |

## Conclusion

By using lumped mass method, the profile and tension of mattress in downstream sinking can be obtained. The advantages of the method are:

(1) Physical meaning of the mathematical equation is clear.
(2) High calculation efficiency.
(3) Being suited to the analysis of non-linear, non-uniform mattress.

## REFERENCES

[1] Cao Mian, Application of Flexible Mattress in Waterway Regulation Engineering of the Yangtze River, Port & Waterway Engineering, Total 368 No.9, Sep. 2004 (in Chinese)

[2] Tang You-gang, etc, Analysis of snap Tension of Deep Water Mooring with Lumped Mass Method, Journal of Tianjin University, vol 42, No.9, Aug. 2009 (in Chinese)

[3] Zhao-zhenxing, He-jianjing, Mechanics of Hydropower, Qinghua University Press, 2005 (in Chinese)

*Applied Mechanics and Materials Vols. 580-583 (2014) pp 1918-1922*
*© (2014) Trans Tech Publications, Switzerland*
*doi:10.4028/www.scientific.net/AMM.580-583.1918*

# Research on navigable ship model test in curved waterway

Changhong Wang [1,a]，Xiaobing Cheng [1,b]

[1]. Tianjin Research Institute for Water Transport Engineering,Tianjin 300456,China;

[a]45221707@qq.com [b]29012886@qq.com

**Keywords:** bend reach; navigation obstruction；ship model; necessary width

**Abstract**：The flow of bend reach is complicated, which is difficulty for intersection of shi p,and is accident prone. According to the lower reaches of the Hanjiang River MaKou reac h of ship model test results, the relationship between channel width and flow are summarized when ship navigation sail in bend reach, which indicated that at approximately the same spee d, navigation width of sailing through the bend upward are much smaller than down. As velo city or flow angle increases, the ship track width is broader, and channel width is also broader . the ship control and peer safety management points are forwarded in the lower reaches of Hanjiang river bend, which can provide reference for similar engineering design and researc h of waterway.

## Navigable river bend ship safety awareness

The river bend channel, not only bending but also narrow, which limited the ship curved scale and increase the difficulty of ship maneuvering. For channel improvement project of the river bend, not only width and depth of the navigation problem, but also flow velocity, flow pattern and width of ship in corners ship attitude and track are considered. The distribution of flow velocity is not uniform, so that the ship motion situation is more complex[1]. The results are not very well in study of curved route and route in advanced channel bends River, Therefore, in study of channel regulation, it is necessary for high grade waterway regulation scheme optimization and navigation safety guarantee to conduct ship model test, studying the problem in running posture, through the elbow river when the track width, curvature radius of large tonnage ships, At present, only straight navigation single line and double line width calculation formula is given in the "waterway regulation engineering technical specifications (JTJ312-2003)" on the general channel , for the bending section of the channel width about how to determine and calculate is not clear. The 3static calculation of track width, the distance between the ship and the ship away from the shore Line width for navigation calculation formula is only considered, the dynamic factors caused by water flow and induced yaw pitch etc is not considered."Standard inland navigable inland waterways in 2004" pointed out that the bending section width should be widened at base line segments on the channel width, widening value can be determined by calculation or experimental study [2].

For curved channel, channel conditions have great effect on navigation safety. Curved cha nnel must have a certain width and depth conditions for navigation [3-4], at the same time, the radius of curvature of the channel should not be too small. The ship through the windingchan nel, smaller bending radius of curvature , bigger fleet scale, urgent flow , ship angle, drift ang le and yaw angle are larger, which leading addition channel width and track width increase,

and navigation is difficulty [5]. The route planning and line layout of bend channel is different l ine channel, the general layout principle:entrance slightly expanded (gradient),bendingtop sectio n widest,export of curve become narrow. In general , widening the channel bends is in the co rners of the inside, but also in the medial and lateral curve equivalent widening. Afterwidening , straight channel smooth connection enable the smooth water flow.

**General situation of typical shoal**

MaKou beach located in the lower reaches of the Hanjiang River, it is from Yang Chi Kou down to the ZhuJiahe, full-length is10.9km. MaKou beach is typical bend river with narrow width. Both sides have dikes, and the dikes are all with embankment. Because the constraint of dikes and revetment , wing of mainstream is limited, which belongs to typical two river one embankment. Last century, Makou experienced development process of forming –development -natural cut offs. in the face of the flood in 1983 , tin bend ended the evolution of natural cut off, forming a new bend, which shortened 5.9km than old .When in middle and low water b ending radius is only 400m with poor conditions. By influence of cross-strait dike, curve evol ution is restricted and curvature radius is invariable. The navigation obstruction of Makou bea ch is mainly of small radius of curvature and ship crossing difficult, at the same time, ben d obstacle is the concave deep grooves exist or development also influence for bend widthfor navigation.

**Ship model test under different flow conditions**

The ship navigation situation of curving bend is in downstream over the bay, side to side. The ship speed is large, and speed reducing is slow, control ability is poor after stopping. Ship speed of countercurrent is slow and easy to control. Because of the bigger velocity andlow angle when ship is sailing in the stream bend, ship to the low potential side drift faster [6].Makou beach belongs to the typical curved channel, bending angle is140 degree, navigation obstruction of Makou reach is mainly of small radius of curvature and ship crossing difficult,planning channel scale is 2.4m * 90m * 500m(depth x double width * bending radius), but in the curved section of ship safety rendezvous navigation width needs to be widened, specific width need to be determined through test.

**Conditions of bend flow and width test of the ship curved fairway.** Multiple groups of ship model under different flow conditions of Makou beach are tested [7]. The width of channel of bend inlet, bend top and outlet section is studied. Flow velocity, flow direction andwidth of relationship between statistics on two-way navigable under different flow conditions are shown in Table 1~ Table 3, in the sheet flow rules of pointing to convex bank is "-". The transition section in the upper inlet bend or changeover portion, the maximum velocity profile is often biased point. After entering the curve, the mainstream gradually shifted to the side of concave bank, at the top of the bend part of partial on the concave bank, transversegradient enhanced water, with curved, gradually recover in the flow momentum side ofconcave bank concentration, transverse gradient to has turn away. This kind of change of the bend flow have an effects on the maneuvering ship, the adjustment is along with the water change.

The inlet of curve (Table1): the channel width of ship increases with increase of lateral velocity. when the direction of flow point to concave bank, which much influence the width down. Ship is easy to drift to the concave bank as extrusion of ship model by oblique flow, which lead to stern to starboard deviated from midline ion; When the water toward the con vex bank, operation is difficult upward and width is slightly larger; The problem is mainly t he width beyond the route down in inlet section, ship model convert the upstream navigatio n width.

Table.1 The relationship between flow conditions and the ship curved fairway width in entrance section of bend

| flow($m^3$/s) | velocity(m/s) | Flow direction(°) | Track width (down)m | Track width (upward)m | Necessary width m |
|---|---|---|---|---|---|
| 447 | 1.38 | -4 | 54 | 28 | 125 |
| 1500 | 1.41 | 7 | 60 | 25 | 131 |
| 2500 | 1.43 | -4 | 62 | 40 | 135 |
| 5000 | 1.85 | 3 | 54 | 26 | 128 |
| 447 | 1.25 | 8 | 42 | 25 | 93 |
| 447 | 1.21 | 3 | 27 | 32 | 85 |
| 5000 | 1.89 | -5 | 58 | 38 | 140 |

The top bending section (Table2): the velocity is smaller than flow velocity of inlet ben d , but the necessary width is large. The flow turn to the concave, and the angle is large. Witht he increase of flow rate, width is also larger. Track width is widest in the top bend , which as great impact on the ship model ship model down. It needs manipulate large rudder angle t o adjusting motions and avoiding ship starboard meeting concave bank .Track width is 55~95 m down ;navigation width of ship model was affected by upward flow direction, track width d own is wider, so upstream ship is close to the convex bank , though flow velocity is very s mall , Upward navigation width increases as corresponding angle increase .

Table.2 The relationship between flow conditions and the ship curved fairway width in urved roof of bend

| flow($m^3$/s) | velocity(m/s) | Flow direction(°) | Track width (down)m | Track width (upward)m | Necessary width m |
|---|---|---|---|---|---|
| 1500 | 0.98 | 10 | 63 | 30 | 161 |
| 2500 | 1.08 | 13 | 70 | 34 | 150 |
| 5000 | 1.56 | 15 | 86 | 36 | 185 |
| 447 | 0.65 | 16 | 55 | 36 | 130 |
| 4000 | 1.72 | 16 | 85 | 40 | 182 |
| 5000 | 1.84 | 16 | 90 | 45 | 185 |
| 9000 | 2.05 | 25 | 93 | 55 | 215 |

Outlet section of bend (Table 3):The flow is relatively smooth in outlet section, the ship width increases with the velocity of flow. Velocity is small without cross flow, but because tra ck zone width is larger in the curved top,it needs some time to adjust state in top bend.Wi dth of outlet section is still exceed the prescribed navigation width of straight section.
Ship upward in outlet section is relatively easy to secure, upward track zone width is influe nced small by the variation of the flow velocity ,basically in the range of 25~40m. The shi p curved width is smaller than bending width in the top section under the same flowcondition s .

Table.3 The relationship between flow conditions and the ship curved fairway width in outlet section of bend

| flow($m^3$/s) | velocity(m/s) | Flow direction(°) | Track width (down)m | Track width (upward)m | Necessary width m |
|---|---|---|---|---|---|
| 447 | 0.94 | 0 | 49 | 26 | 102 |
| 2500 | 1.43 | 2 | 68 | 30 | 132 |
| 447 | 0.85 | 4 | 60 | 30 | 110 |
| 815 | 1.08 | 0 | 58 | 30 | 114 |
| 447 | 0.90 | 0 | 45 | 25 | 131 |
| 5000 | 1.95 | 6 | 72 | 35 | 168 |
| 9000 | 2.42 | 7 | 81 | 40 | 195 |

**Summary.** The test showed: the ship sail through bending, in order to turn and overcome the influence of bend flow,it need to produce significant drift and additional width for navigation , and with the increase of channel flow velocity, the route of the ship also produce a certainl ateral drift. navigation width of sailing through the bend upward are much smaller than down. The same fleet at approximately the same speed, sailing through the same bend, the width upw ard is smaller than down. That is to say, the same fleet line can through bend upward, but it is not sure downward .As velocity increasing down, track width is greater, and change is obv ious.

## Conclusion

For ship navigable conditions of curved river , factors affecting the safety of ships through t he main curve include radius of the curve, flow velocity , mainstream and flow channel angle designed of bend .Any factors changed will change the ship curved lines and curved width [8].A nalysis of the width of track cornering test on multi ship with running posture,rudder angle, forak ou beach, velocity and direction are bent on ship (especially downward curved) have great infl uence on the track width. For the improvement of channel condition, optimized space of the curvature radius is small. For the flow velocity and direction, it has optimization space, espec ially in the design route, as far as possible according with the current mainstream bend flow path, design ship curved route. At the same time, with the addition of some renovation proje ct to adjust and optimize the flow curve, which make it fitting design route, security will great ly enhanced.

In order to improve the safety of navigation in channel, channel management department need to complete set safety warning device, strengthen training, improve the driver safety technology . From the influence of ship integrated analysis of curved factors, ship turning operation needs to pay attention to the following points: (1) navigators should accurately grasp channel hydrological data. Drivers need to make detailed analysis and Research on bending leg before sailing. (2) The ship sailing in the corners should slow down properly. Because the ship by the bend flow produced by the action of drift, and ship drift with the increase of speed and increase. Properly reduce speed to reduce the transverse drift. (3) With a small rudderangle operation to correct heading drift. The ship from the bend down, because flow dynamic axis near the convex bank, can be appropriate to concave small rudder angle corrected heading drift; the ship from the bend upward with the opposite. The curve is concave convex surface river flow from flow, flow is the opposite, but the overall effect of lower surface flow by cross flow, so the ship should be close to the point of some. The ship to the concave side by rudder should be carefully, and suitable for small rudder angle. (4) Shipshould navigate near bend channel flow dynamic axis to avoiding occurrence of loxodrom.(5) Ship should be accompaniedby sound signals to remind other boat to striving for collision avoidance.

**References**

[1] Zhiyun Li,Guoping Guo, research and countermeasure about the effects of channel bends to the ship's navigation, China Shipping,2007(3):8-10.

[2]JB50139—2004 standards of inland navigation.Beijing: Publishing House of Chinese plan 2004.

[3] Renjie Tang,Xuyue Hu,DAI Y T, Study on the situation of water flow in bend reach, Journal of Waterway and Harbor,2009(4):108-111.

[4] Yong Li. The ship control . Beijing: China Communications Press, 1999110~150

[5] Yuting Dai The Characteristics of Bend2flow. Hunan Communication Science and Technology , 2008 (1) :127 - 130.

[6] Jie Li, Analysis of ship motion in river bend,Journal of ship design,1994(9):30-33.

[7] Changhong Wang, Xiaobing Cheng , remediation measures of typical beach of the lower reaches of the Hanjiang River . Tianjin: Research Institute for Water Transport Engineering, 2013

[8] Wanzheng Ai, Jiahong Wang, Reliability analysis of navigable channel bends, China Water Transport , 2010,10(12):9-10.

*Applied Mechanics and Materials Vols. 580-583 (2014) pp 1923-1927*
*© (2014) Trans Tech Publications, Switzerland*
*doi:10.4028/www.scientific.net/AMM.580-583.1923*

# Data Assimilation of River Networks Using Extended Kalman Filter

Yifan Chen[1, a], Jinglin Qian[1, b]

[1]Zhejiang Institute of Hydraulic & Estuary, Hangzhou 310020, China

[a]zjucoolboy@163.com, [b]qjlhz@163.com

**Keywords:** river network; data assimilation; extended kalman filter

**Abstract.** In order to improve the accuracy of river network hydraulic model, extended kalman filter was used for real-time updating model states. In a simulation example of a river network composed of 14 channels, it systematically analyzed the effects of process and measurement noises on state correction. The results show that the extended kalman filter is able to effectively carry out data assimilation of non-linear river network system, and big process noise in combination with relatively small measurement noise is recommended for state correction.

## Introduction

Research on real-time correction technology, which is to improve flood simulation and forecast of river network hydraulic model, is an important subject. Fread[1,2] applied kalman filter in the FLDWAV model developed by USA National Weather Service. Shiiba [3] used reduced rank square root method coupling kalman filter to deal with colored noise. Ge Shouxi [4] took observable variables, roughness coefficients and both as state variables, respectively, combining with kalman filter. Zhou quan [5] proposed an alternate correction method which alternates stage and discharge as state variables. Romanowicz [6] used kalman filter combined with adaptive prediction technology for Severn River stage correction, according to the real-time data received form sensors. Madsen [7] and Wu Xiaoling [8, 9] introduced spatial information based on gain matrix into optimizing process noise matrix.

Advantages of kalman filter include hige-speed computing, small required compute memory and ease of error analysis, which are useful for real-time updating system states. Up to now, the standard kalman filter for linear system and extended kalman filter for non-linear system have been developed. On the basis of nonlinearity of river network hydraulic model, extended kalman filter is adopted for real-time state correction in the present paper.

## Mathematical model

In general, river network hydraulic equations can be expressed as:

$$\boldsymbol{F}(\boldsymbol{X},t)=0 \tag{1}$$

Where $\boldsymbol{F}$ represents a group composed of the hydraulic equations, and the Saint-Venant equations are used to describe one-dimensional flow motion in the present paper. $\boldsymbol{X}$ is the state variable vector, and $t$ denotes the time.

After discretizing hydraulic equations along the space and the time coordinates with consideration of process white noise (refer to the reference [10]), Eq. (1) is finally rewritten as:

$$\boldsymbol{X}_k=\boldsymbol{\Phi}_k(\boldsymbol{X}_{k-1},k-1)+\boldsymbol{\Gamma}_k(\boldsymbol{X}_{k-1},k-1)\boldsymbol{W}_k \tag{2}$$

Where $\boldsymbol{\Phi}_k$ denotes the non-linear state equations at time step $k$-1, $\boldsymbol{\Gamma}_k$ is the noise weighting matrix, $\boldsymbol{W}_k$ is the process noise vector with average equal to zero.

If measurement instruments are distributed in river network, measurement equations with consideration of measurement white noise can be defined as:

$$\boldsymbol{Y}_k=\boldsymbol{H}_k(\boldsymbol{X}_k,k)+\boldsymbol{V}_k \tag{3}$$

Where $\boldsymbol{Y}_k$ is the measurement variable vector, $\boldsymbol{H}_k$ denotes the measurement equations at time step $k$, $\boldsymbol{V}_k$ is measurement noise vector with average equal to zero.

Combining Eqs. (2) and (3), non-linear dynamic system of river network can be expressed as:

$$\begin{cases} \boldsymbol{X}_k = \boldsymbol{\Phi}_k(\boldsymbol{X}_{k-1}, k-1) + \boldsymbol{\Gamma}_k(\boldsymbol{X}_{k-1}, k-1)\boldsymbol{W}_k \\ \boldsymbol{Y}_k = \boldsymbol{H}_k(\boldsymbol{X}_k, k) + \boldsymbol{V}_k \end{cases} \tag{4}$$

The non-linear system of above equations needs a linearization. With the assumption that corrected state variable vector $\hat{\boldsymbol{X}}_{k-1}$ have been got at time step *k*-1, Eq. (4) can be linearized as, using Taylor one-order expansion:

$$\begin{cases} \boldsymbol{X}_k = \dfrac{\partial \boldsymbol{\Phi}_k}{\partial \hat{\boldsymbol{X}}_{k-1}} \boldsymbol{X}_{k-1} + [\boldsymbol{\Phi}_k(\hat{\boldsymbol{X}}_{k-1}, k-1) - \dfrac{\partial \boldsymbol{\Phi}_k}{\partial \hat{\boldsymbol{X}}_{k-1}} \hat{\boldsymbol{X}}_{k-1}] + \boldsymbol{\Gamma}_k(\hat{\boldsymbol{X}}_{k-1}, k-1)\boldsymbol{W}_k \\ \boldsymbol{Y}_k = \dfrac{\partial \boldsymbol{H}_k}{\partial \hat{\boldsymbol{X}}_{k/k-1}} \boldsymbol{X}_k + [\boldsymbol{H}_k(\hat{\boldsymbol{X}}_{k/k-1}, k) - \dfrac{\partial \boldsymbol{H}_k}{\partial \hat{\boldsymbol{X}}_{k/k-1}} \hat{\boldsymbol{X}}_{k/k-1}] + \boldsymbol{V}_k \end{cases} \tag{5}$$

Where $\dfrac{\partial \boldsymbol{\Phi}_k}{\partial \hat{\boldsymbol{X}}_{k-1}}$ is linear state operator, $\dfrac{\partial \boldsymbol{H}_k}{\partial \hat{\boldsymbol{X}}_{k/k-1}}$ is linear measurement operator.

Referring to the reference [11], the extended kalman filtering algorithm with its calculation procedure shown in Fig.1 is expressed as:

1. State prediction

$$\hat{\boldsymbol{X}}_{k/k-1} = \boldsymbol{\Phi}_k(\hat{\boldsymbol{X}}_{k-1}, k-1) \tag{6}$$

2. Error variance prediction

$$\boldsymbol{P}_{k/k-1} = \frac{\partial \boldsymbol{\Phi}_k}{\partial \hat{\boldsymbol{X}}_{k-1}} \boldsymbol{P}_{k-1} \left[ \frac{\partial \boldsymbol{\Phi}_k}{\partial \hat{\boldsymbol{X}}_{k-1}} \right]^T + \boldsymbol{\Gamma}_k(\hat{\boldsymbol{X}}_{k-1}, k-1)\boldsymbol{Q}_k \boldsymbol{\Gamma}_k(\hat{\boldsymbol{X}}_{k-1}, k-1)^T \tag{7}$$

3. Gain matrix

$$\boldsymbol{K}_k = \boldsymbol{P}_{k/k-1} \left(\frac{\partial \boldsymbol{H}_k}{\partial \hat{\boldsymbol{X}}_{k/k-1}}\right)^T \left[\left(\frac{\partial \boldsymbol{H}_k}{\partial \hat{\boldsymbol{X}}_{k/k-1}}\right) \boldsymbol{P}_{k/k-1} \left(\frac{\partial \boldsymbol{H}_k}{\partial \hat{\boldsymbol{X}}_{k/k-1}}\right)^T + \boldsymbol{R}_k\right]^{-1} \tag{8}$$

Where $\boldsymbol{R}_k$ is observational error covariance.

4. State correction

$$\hat{\boldsymbol{X}}_k = \hat{\boldsymbol{X}}_{k/k-1} + \boldsymbol{K}_k[\boldsymbol{Y}_k - \boldsymbol{H}_k(\hat{\boldsymbol{X}}_{k/k-1}, k)] \tag{9}$$

5. Error variance correction

$$\boldsymbol{P}_k = (\boldsymbol{I} - \boldsymbol{K}_k \frac{\partial \boldsymbol{H}_k}{\partial \hat{\boldsymbol{X}}_{k/k-1}}) \boldsymbol{P}_{k/k-1} \tag{10}$$

**Case study**

The layout of a hybrid river network is shown in Fig.2, and its section data and boundary conditions can be found in the reference [12] in details.

Tests regarding the impact of different process noise and measurement noise on data assimilation are carried out. Node stage variables are taken as state variables, and three cascaded solving method [10] is adopted for solving Eq. (2). In the tests, it assumes that two gauge stations are set at the 9th node denoted as station 1 and the 13th node denoted as station 2. Stage process noises $W_k$=0.005, 0.01, 0.02m are tested in combination with three different measurement noises $V_k$=0.005, 0.01, 0.02m, respectively, as shown in table 1.

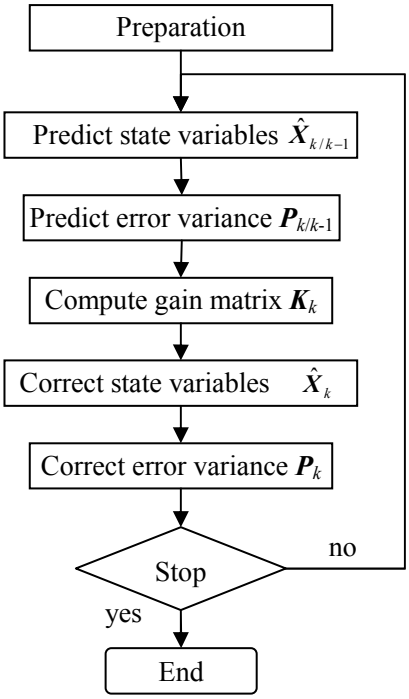


Fig.1 Flowchart of extended kalman filter

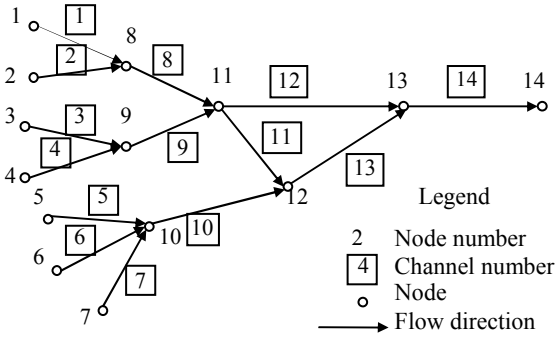


Fig.2 The schematic diagram of a river network

Table 1 Set of tests (√: succeed, ×: fail)

| $W_k$/m | $V_k$/m | | |
|---|---|---|---|
| | 0.005 | 0.01 | 0.02 |
| 0.005 | √ | √ | √ |
| 0.01 | √ | √ | √ |
| 0.02 | √ | √ | √ |

Figs.4 and 5 show the effects of process noise $W_k$ and measurement noise $V_k$ on real-time correction of state variables at gauge station 1 and 2, respectively. Compared to Fig.3, it is noticeable that state variables corrected using extend kalman filter are much more accurate than that without correction, i.e. , extended kalman filter presented in this paper is useful for updating hydraulic model states of non-linear river network system. After some time steps of correction, the errors are close to zero. We can also find that the smaller the measurement noise $V_k$ is, the smaller is the error. However, the smaller the process noise $W_k$ is, the bigger is the error.

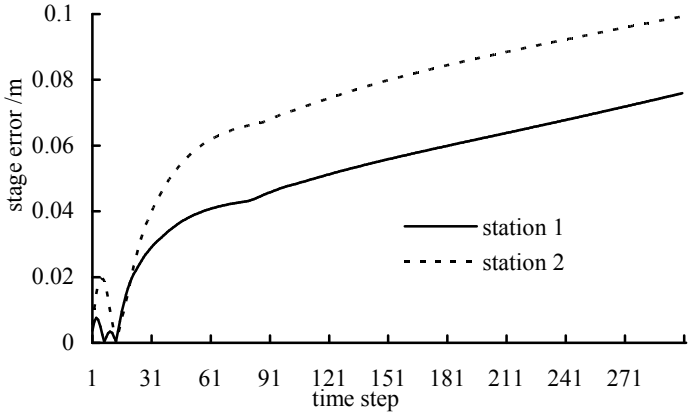


Fig.3 Hydrograph of errors between simulated and observed stage at stations 1, 2 without correction

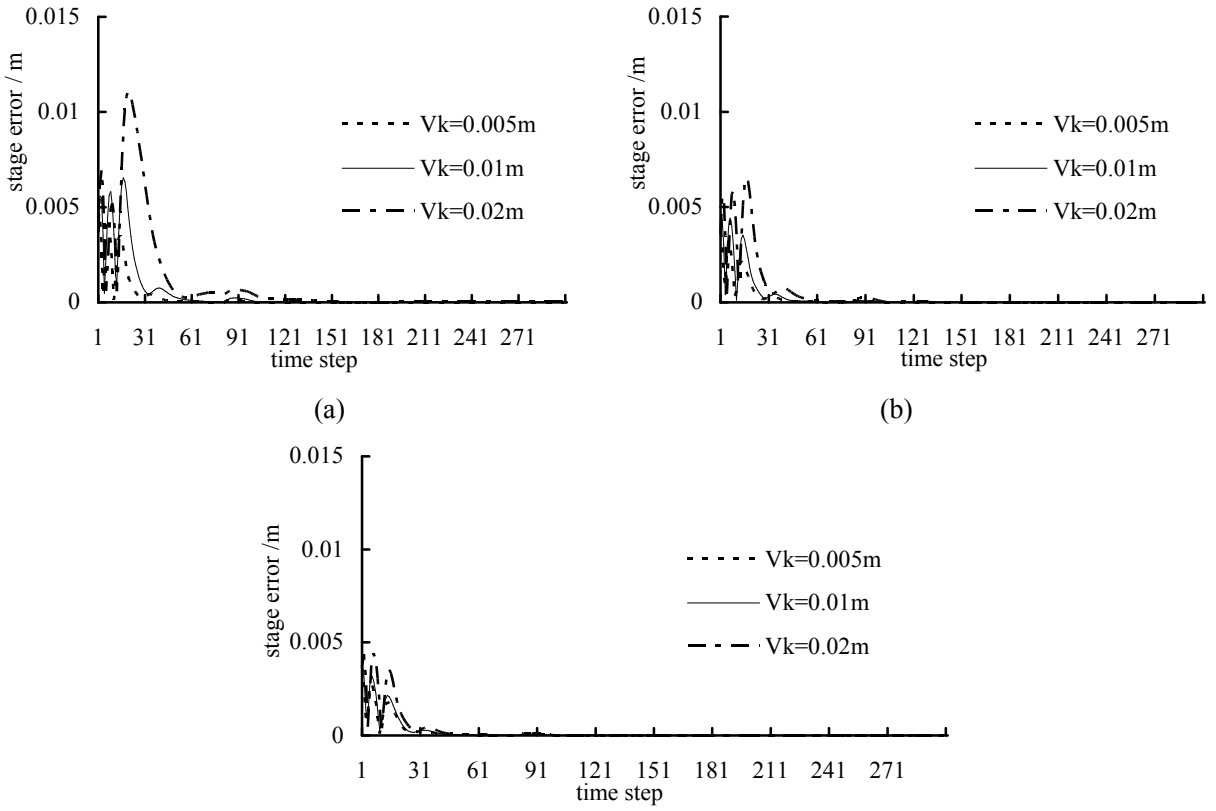


Fig.4 Hydrograph of errors between corrected and observed stage at station 1
(a) $W_k$=0.005m; (b) $W_k$=0.01m; (c) $W_k$=0.02m

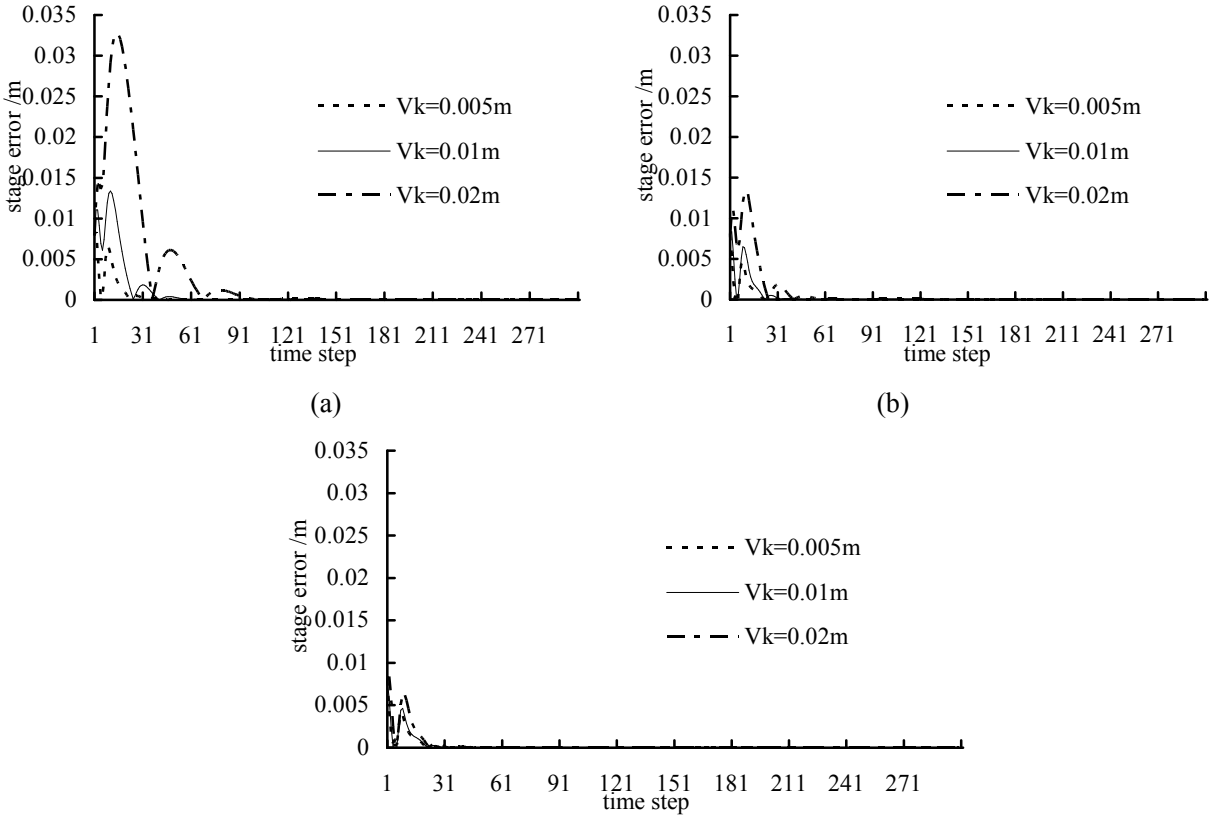


Fig.5 Hydrograph of errors between corrected and observed stage at station 2
(a) Wk=0.005m; (b) Wk=0.01m; (c) Wk=0.02m

## Conclusion

A robust model for real-time state correction for non-linear river network system combining with extended kalman filter is developed in the present paper. Tests taking account of both process noise and measurement noise are carried out to examine their effects on dada assimilation. The numerical results show that extended kalman filter can effectively improve the accuracy of river network hydraulic model. Furthermore, correction with big process noise, small measurement noise yields better results than that with small process noise, big measurement noise.

## Acknowledgements

The authors of the present paper greatly appreciate the support of Innovation Team Program of Zhejiang Science and Technology (2010R50035).

## References

[1] Fread D L, Jin M: submitted to ASCE International Symposium on Engineering Hydrology (1993).

[2] Jin M, Fread D L: submitted to Local Organizing Committee of The XXV Congress (1993).

[3] Shiiba M, Laurenson X, Tachikawa Y: submitted to Hydrological Processes (2000).

[4] Shouxi Ge, Haiyun Chen, Yurong Li: submitted to Journal of Hydraulic Engineering (In Chinese, 2005).

[5] Quan Zhou: *Research on the real-time correction method in flood forecasting* (In Chinese, Hohai University, China 2005).

[6] Romanowicz R J, Young P C, Beven K J: submitted to Water Resources Research (2006).

[7] Madsen H, Skotner C: submitted to Journal of Hydrology (2005).

[8] Xiaoling Wu, Chuanhai Wang, Xiaohua Xiang: submitted to Journal of Hohai University (In Chinese, 2008).

[9] Xiaoling Wu, Xiaohua Xiang, Chuanhai Wang, et al: submitted to Chinese Journal of Hydrodynamics (In Chinese, 2010).

[10] Xiaoming Xu, Jianjing He, Deguan Wang: submitted to Journal of Hydrodynamics (In Chinese, 2001).

[11] Hongliang Zhao: *Study on space-time variability of geo-mechanical parameters with ensemble Kalman filter data assimilation Method* (In Chinese, Institute of Rock & Soil Mechanics, Chinese Academy of Sciences, China, 2006).

[12] Islam A, Raghuwanshi N S, Singh R, et al: submitted to Journal of Irrigation and Drainage Engineering (2005).

*Applied Mechanics and Materials Vols. 580-583 (2014) pp 1928-1931*
*© (2014) Trans Tech Publications, Switzerland*
*doi:10.4028/www.scientific.net/AMM.580-583.1928*

# Numerical Analysis of the Influences of Water Level on Seepage Stability of Tailing Dam

Fangding He[1,a,*], Xuefeng Cao[2,b], Xia Yang[1] and Zhidong Zhou[3,c]

[1]Hydraulic Research Institute of Shandong Province, Jinan,250014,China

[2]Jinan Hydrology and Water Resources Investigation Bureau, Jinan,250014,China

[3]School of Civil Engineering, Shandong University,Jinan,250061,China

[a]6974554@126.com, [b]6974470@126.com, [c]zhouzhidongdzd@163.com

[*]corresponding author

**Keywords:** hydraulic engineering; tailing dam; seepage stability; saturation line; numerical analysis.

**Abstract.** Understanding the influences of water level on seepage stability of tailing bay is an important topics in hydraulic engineering design. The seepage stability of tailing bay under different water level was calculated with the numerical simulation software FLAC3D and the change laws of water pore pressure and saturation line in the dam was analyzed. The results show that the saturation line in the dam is a parabolic curve and the pore pressure changes in layers. With the increasing of water level, the saturation line in the heaping dam ups rather obviously while it is not obvious in the initial dam. The maximum pore pressure in the bottom of the dam increases with the relationship of water level up, the shallow of the saturation line is in the heaping dam heel.

## Introduction

As it can be seen from some accident cases of tailing dam, almost all of the tailing dam accident are associated with water, it is because of the tailing dam is both the storage of tailing and water, and the presence of water makes the geotechnical problems of tailing dam engineering become more complicated[1-3].

Except for the specification of the characteristics of initial dam and the slope ratio of the tailing dam from the initial engineering design, in the operation period, other factors are all of dynamic changes with the interaction of water. Water is the key influence factor of the deformation and stability of dam. Saturation line is the lifeline of tailing dam, its location is one of the most important parameters in the analysis of stability, and it is also an important characteristic of distinguish tailing dam safety or not. So it is very meaningful to study the water seepage behavior in the tailing dam.

The saturation line of the tailing dam is different from common earth-rock dam. The influence factors on saturation line include: the water table, the drainage of initial dam and rainfall, etc. In general, some measures are helpful to control the saturation line, however, when it comes to rainstorm and flood, the seepage stability of the dam is not guaranteed[4-5].

In this paper, the seepage stability of tailing dam under different water level was analyzed with the numerical simulation software FLAC3D, the water lever is 15 meters, 20 meters and 25 meters, respectively, the results can provide certain references for the similar hydraulic engineering.

## Numerical computational model

In this paper, finite difference program FLAC3D based on the Fast Lagrangian Method was used to calculate and analyze influences of water level on seepage stability of tailing bay. The numerical computational model was shown in Fig. 1, in which the heaping dam size was based on the initial engineering design. Horizontal displacement constraints and vertical displacement constraints were set in the right and bottom of the numerical computational model, respectively. The grid meshing was shown in the Fig.2.

According the functions of FLAC3D, the saturation table was just the interface between up zero and down zero of water pore pressure, so in this paper pore water pressure nephogram were used for not only showing the location of the saturation line, but also showing the distribution law of pore pressure in the dam.

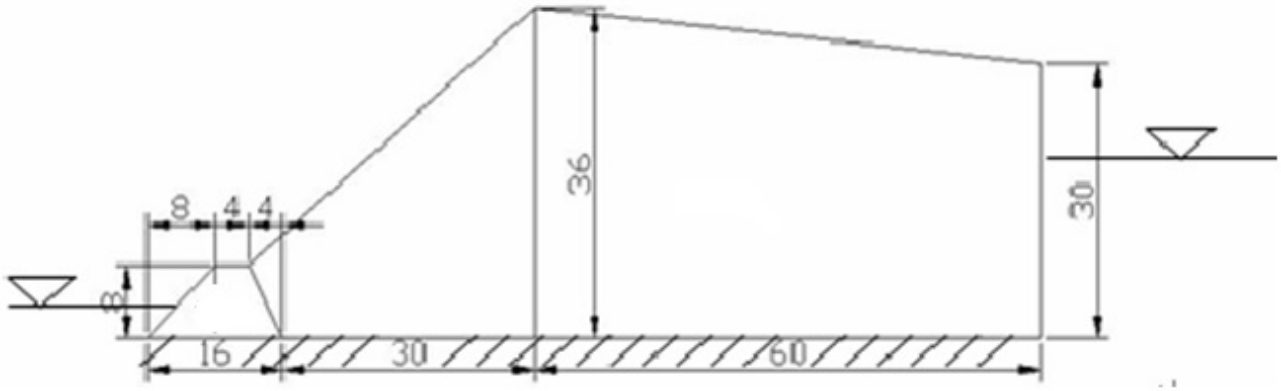


Fig.1 Numerical computational model and boundary conditions

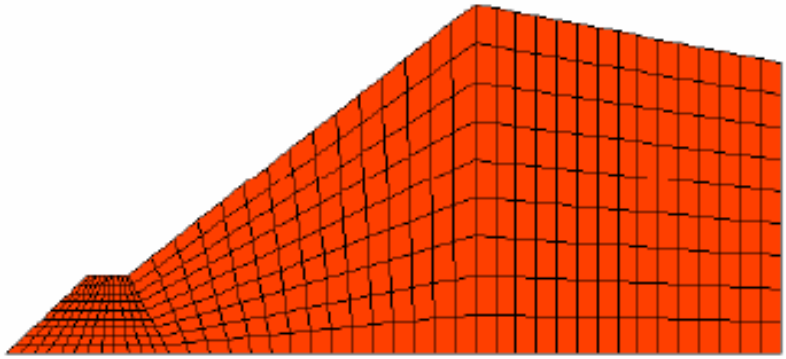

Fig.2 Grid meshing

**Material Properties**

During the numerical analysis, the Mohr-Coulomb model was adopted to simulate the soil behavior of elastic-plastic deformation. Based on the data of engineering geologic examination, the soil was divided into four layers(light mild clay mild, mild clay mild, mild clay mild and sandstone from the top down) and the initial dam. The bottom of the dam was sandstone, which was treated as impervious layer. The physical and mechanical properties of foundation soil was illustrated in Tab.1. According to Equation (1) and (2), the bulk modulus and shear modulus can be converted from elasticity modulus.

Bulk Modulus: $$K=\frac{E}{3(1-2\upsilon)} \quad (1)$$

Shear Modulus: $$G=\frac{E}{2(1+\upsilon)} \quad (2)$$

Tab.1 The physical and mechanical properties of soil layers

| soil class | ω（%） | $e$ | $\rho$（kg/m$^3$） | $E_s$（MPa） | $K_{20}$（cm/s） | $c$（kPa） | $\varphi$（°） |
|---|---|---|---|---|---|---|---|
| initial dam | - | - | 2100 | - | $20\times10^{2}$ | 0 | 40 |
| light mild clay mild | 23.1 | 0.83 | 1970 | 12.3 | $2.0\times10^{-5}$ | 13.4 | 24.0 |
| mild clay mild | 17.6 | 0.74 | 2000 | 10.65 | $3.4\times10^{-4}$ | 16.8 | 24.6 |
| mild clay mild | 16.5 | 0.68 | 2020 | 3.92 | $3.2\times10^{-4}$ | 20.1 | 25.0 |
| sandstone | - | - | 2110 | 4.62 | - | - | - |

**Results**

In order to analysis the influences of water level on the seepage stability, three cases of water lever had been put forward in this paper, the water lever is 15 meters, 20 meters and 25 meters, respectively. The numerical analysis results were shown in Fig.3~Fig.5. In Fig.6, the saturation lines were drawn under different water levels.

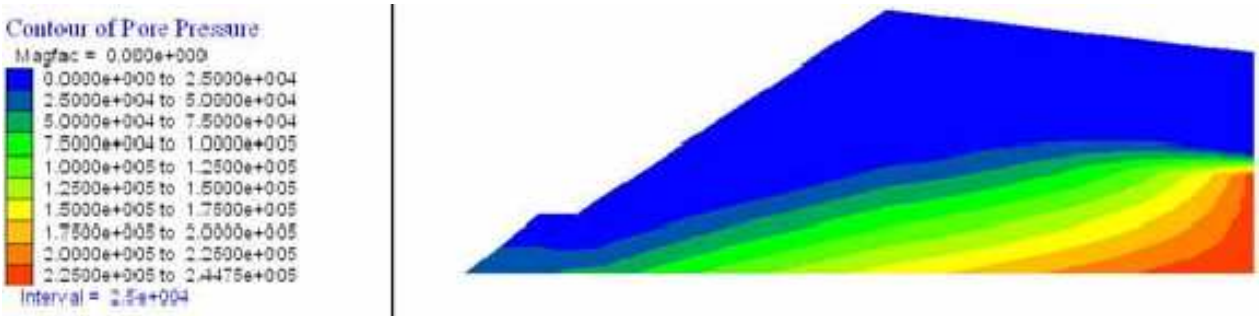


Fig.3 The saturation line when the water level is 15 meters

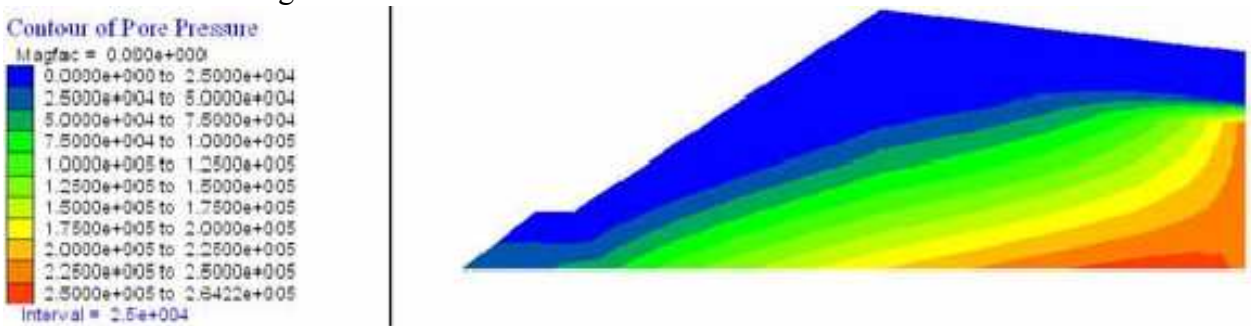


Fig.4 The saturation line when the water level is 20 meters

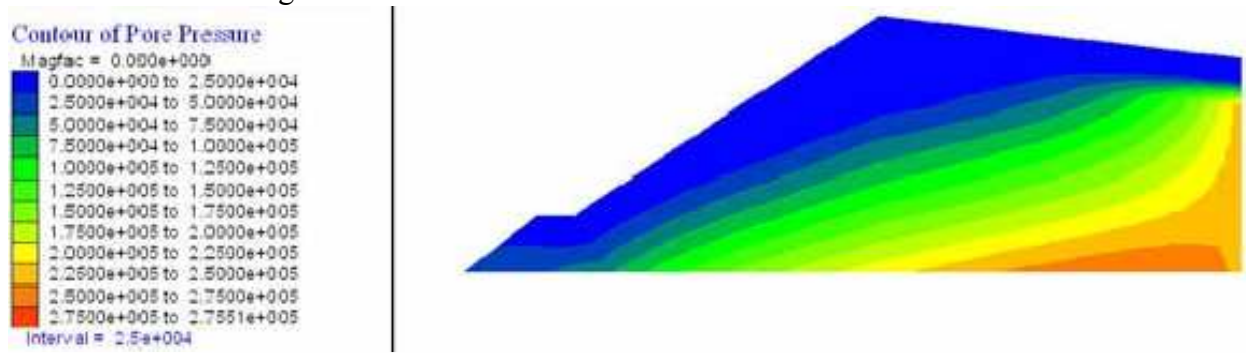


Fig.5 The saturation line when the water level is 25 meters

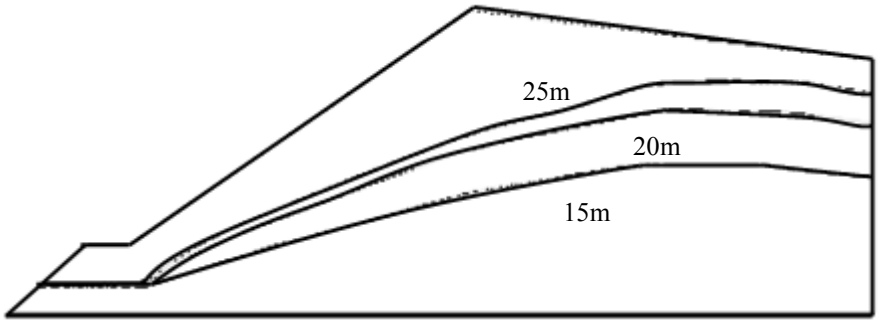


Fig.6 The saturation lines with different water levels

As we can see from Fig.3 to Fig.6, the saturation line in the dam is a parabolic curve and the pore pressure changes in layers. With the increasing of water level, the saturation line in the heaping dam ups rather obviously while it is not obvious in the initial dam. The maximum pore pressure in the bottom of the dam increases with the relationship of water level up, As the water level increases from 15 meters to 25 meters, the maximum pore pressure in the tailing dam increases from 244kPa to 275kPa, the shallow of the saturation line is in the heaping dam heel.

**Some suggestions for strengthening tailing dam**

Improve the stability of the tailing dam is mainly through change the seepage conditions, drop the height of saturation line, short the ratio of tail dam slope and speed up the consolidation of tailing dam.

(1)Drop the height of saturation line is mainly through improving the dam drainage, draining away water from the dam, finally improving the shear strength and slope stability of tailing dam.

(2)Reverse compaction in the downstream of slope toe of the tailing dam to improve the slope stability and enhance the antiskating force of tailing dam, and setting inverted filter to accelerate draining away water from the tail dam, speed up the consolidation of tailing dam and improve the slope stability.

(3)Shorten the ratio of slope to improve the slope stability of tailing dam, however, it is a contradiction with the capacity of reservoir and should coordinate the various interests between the capacity of reservoir and the slope stability of tailing dam.

(4)Strengthening the dam and speeding up the consolidation of tailing dam, such as setting anti-slide piles, setting the row the system and grouting technique, etc.

**Conclusions**

Based on the data of engineering geologic examination, the paper mainly conducts numerical analysis towards influences of water level on seepage stability of tailing bay, accordingly the following conclusions can be made: that the saturation line in the dam is a parabolic curve and the pore pressure changes in layers. With the increasing of water level, the saturation line in the heaping dam ups rather obviously while it is not obvious in the initial dam. The maximum pore pressure in the bottom of the dam increases with the relationship of water level up, the shallow of the saturation line is in the heaping dam heel. In addition, some reasonable suggestions were given to improve the stability of the tailing dam, can provide some references for practical engineering.

**Acknowledgements**

This work was financially supported by Binhai comprehensive utilization of water resources and the most strict water resources management and demonstration (201201116).

**References**

[1]MA Chixiang, QIN Huali, XU Shufang, LU Dongling. Study on the Seepage Field of Tailinging Dam Based on Water-Soil Interaction[J]. Metal Mine, 2009,39(05): 168-171.

[2]XING Yue. Analysis of the Influence of Water-Soil Coupling Interaction on the Stability of Tailinging Dam[D]. Shenyang: Northeastern University, 2009.

[3]WEI, Zuoan; YIN, Guangzhi; WANG, J. G, etc. Design, Construction and Management of Tailingings Storage Facilities for Surface Disposal in China: Case Studies of Failures[J]. Waste Managerment and Research,2013, 31(1):106-112.

[4]SONG Chuanwang, CAO Shanzhong, YU Guangming. Influence Analysis of Optimal Arrangement of Aub-Dams on Stability of Tailingings Dam[J]. Journal of Qingdao Technological University,2012, 33(5):18-22.

[5]OZER A T, BROMWELL L G. Stability Assessment of an Earth Dam on Silt/Clay Tailingings Foundation: A Case Study [J]. Engineering Geology,2012, 151:89-99.

*Applied Mechanics and Materials Vols. 580-583 (2014) pp 1932-1939*
*© (2014) Trans Tech Publications, Switzerland*
*doi:10.4028/www.scientific.net/AMM.580-583.1932*

# Experimental study on the air-cooling of concrete aggregate

ZENG Miao[1], GUO Chaohong[1], KANG Zhiming[2], GUAN Wei[2], LU Fei[2],

WANG Gang[1], TANG Dawei[1]

([1.] Institute of Engineering Thermophysics, Chinese Academy of Sciences, Beijing 100190;

[2.] PowerChina Xibei Engineering Corporation Ltd, Xi'an 71000 )

**Keyword:** Concrete aggregate; air cooling; temperature distribution; flow resistance; porosity

**Abstract:** The temperature distribution and the flow resistance of air-cooled concrete aggregate are investigated in order to provide engineering guidance for the energy economization and design optimization. First, an aggregate bin is down-scaled and installed on an indoor experiment table, then tests are performed for different aggregate sizes and different inlet air velocity, with or without upper air duct. The results show that with the decrease of aggregate size, the temperature distribution turns more uniform, but the flow resistance increases; with the increase of wind velocity, the cooling rate is enhanced, but meanwhile the flow resistance is increased. So for different size of aggregates, an optimal wind velocity exists. Having an upper air duct not only enhances the cooling rate but also increases the cooling uniformity.

## Background

Concrete construction in hydro-structure, cement hydration heat leads to a sharp rise of temperature in the concrete. Natural cooling of mass concrete is insufficient, and inside and outside temperature variation generates thermal stress. To prevent the concrete cracks due to thermal stress, the highest temperature inside the concrete must be strictly limited[1,3]. One of the most effective ways is to pre-cool one or more materials of the concrete to reduce the concrete outlet temperature. Air-cooling is the most widely applied measures of pre-cooling. Concrete aggregate is cooled in a semi-closed bin by the cold air flowing through the lower side air intake, after exchanging heat with the aggregate from the top of the bin, heated cold air returns through the upper back air return vent to circulate. However, due to air flow leakage, fan selection does not match well with the aggregate and bin structure is unreasonable, pre-cooling efficiency is only 20-25% in actual engineering applications, which causes great waste of cooling capacity[2,6].

In this paper, the influence of aggregate size, inlet flow rate and the presence of upper air duct on the temperature change and flow resistance of aggregate is analyzed in to acquire necessary data for establishing a highly accurate simulation model to lay the foundation for developing a specialized software, and to improve the efficiency of pre-cooling in engineering applications.

## The similarity principle and the experimental set-up

### 2.1 The similarity principle

Experimental conditions are selected on the basis of real project and similarity principle. Only with the same form of differential equations, the phenomenon is to be able to involve a similar problem. The similar physical phenomenon must have the equal criterion. The similar heat transfer

phenomenon must have the same Nusselt number $Nu$. $Nu = \alpha d/\lambda$, λ is the thermal conductivity of aggregate, d is the diameter of aggregate, the convective heat transfer coefficient α is the function of Reynolds number $Re$ and Prandtl number $Pr$, $Pr$ is the physical parameter of air. It's considered that if the air of experiment and actual situation have the same $Re$, they have the similar heat exchange. When the two fluids have the similar movement, which must have the equal $Re$. $Re = ul/\upsilon$, $\upsilon$ is the air physical parameter, $l$ is the distance of adjacent aggregates, $u$ is the velocity, and therefore the air flow rate in experiment must equal to the real project[4,5,7]. In other words, if the air flow rate of experiment is identical with the actual, which can be considered to have the similar movement and heat exchange.

2.2 Experimental system

The real project: (1) cool aggregate bin size (length × width × height): 5m x 5m x11.5m, inlet \ outlet height difference: 4.6m;

(2) inlet \ outlet Size: 0.8m x 0.8m;

(3) air inlet louvre size (L × H): 4.8mx 0 1m; number: 16;

(4) inlet velocity: 25m / s;

(5) particle packing density: 1600 kg/m3 (true density: 2500 kg/m3).

Experiment: (1) cool aggregate bin size (L × W × H): 1m × 1m ×2m, inlet \ outlet height difference: 1m; inlet \ outlet size: 0.16mx 0.16m (reduced scale 5:1);

(2) piercing blinds duct size: 0.9m×0.01m; quantity: 16;

(3) inlet velocity: 21 ~ 35m / s, the porosity: 0.4 ~ 0.5;

(4) inlet air temperature is lower than the aggregate temperature of about 10 ℃;

(5) the kinds of aggregate of experiment are small(5 ~ 20mm), middle (20 ~ 40 mm), large(40 ~ 80 mm).

According to the air volume balance:

$$Q_{GC} = A_{HJM}.u_{HJM} = A_{JFK}.u_{JFK} \quad (1)$$

$$= 5 \times 5 \times v_{HJM} = 0.8 \times 0.8 \times 25$$

Wherein, $Q_{GC}$ is the total air, $A_{HJM}$ is the cross-sectional area, $u_{HJM}$ is the average cross-sectional speed, $u_{JFK}$ the inlet speed.

By the formula (1) can be obtained average cross-sectional speed,: $u_{HJM} = 0.64\text{m/s}$

The aggregate gap flow rate:$u_{KX} = \frac{u_{HJM}}{\varepsilon} = \frac{u_{HJM}}{0.3\sim0.5} = 2.13\sim1.28\ \text{m/s}$ (2)

Where, ε is the porosity of the aggregate (concrete aggregate porosity in the range of 0.4 to 0.5).

Experimental principle is to keep the aggregate gap flow rate constant, the total air of experiment: $Q_{SY} = A_{HJM}.u_{HJM} = 1 \times 1 \times 0.64 = 0.64\text{m}^3/\text{s} = 2304\text{m}^3/\text{h}$

Blower selection parameters: Flow rate $Q_{SY} = 0.64\text{m}^3/\text{s} = 2304\text{m}^3/\text{h}$

In actual engineering the blower pressure head is about 1000Pa ~ 2500Pa, flow path of cold air is 5m; flow path of cold air in experiment is about 1m, so pressure head in experiment is less than 500Pa.

The final choice of fan model and parameters:

Model: Cy-3.2A; inlet air flow can be adjusted; rated flow 2996$\text{m}^3/\text{h}$; pressure head 1300Pa; power 2.2KW.

At the Aggregate bin inlet and outlet pressure sensors are respectively arranged for measuring the flow resistance of the material layer; anemometer is installed at the inlet to monitor the cold air flow. The real experimental system is shown in Figure 1.

The three aggregate sizes, with or without up-duct and speed are combined to form the 12 kinds of experimental conditions as shown in Table 1. Figure 2 shows the arrangement of the temperature measuring point in the bin, most experimental conditions are chosen for the measurement section 1 to 5, 1,7 two conditions selected measurement section 0-4 layers, 11 selected section -1 to 3 layers.

Experimental procedures:

(1) charge and record the aggregate weight and volume, and then calculate the aggregate porosity;

(2) Check the sealing of the bin, adjust the valve of blower to control air flow;

(3) Start the blower, record the measuring point temperature, import/output pressure, speed real-time;

(4) Run for at least one hour, then stop the blower, and save the measurement data;

(5) discharge aggregate, replace the type of aggregate in the order of large, middle, and small, and add or cancel the upper-duct, and repeat the previous four steps.

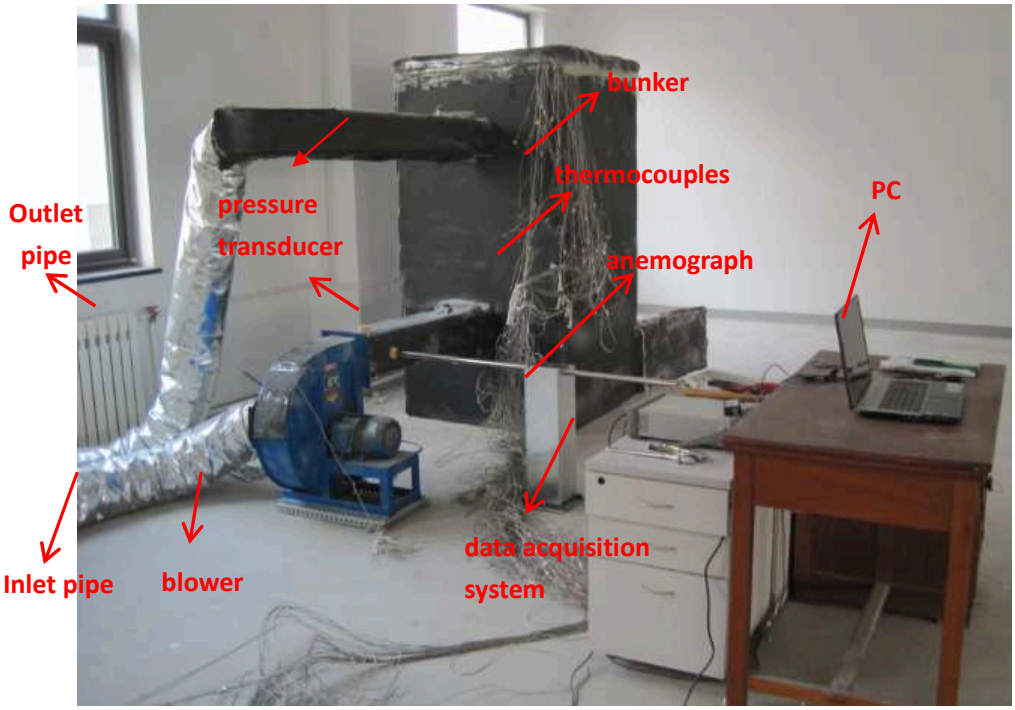


Fig.1 Air-cooling system

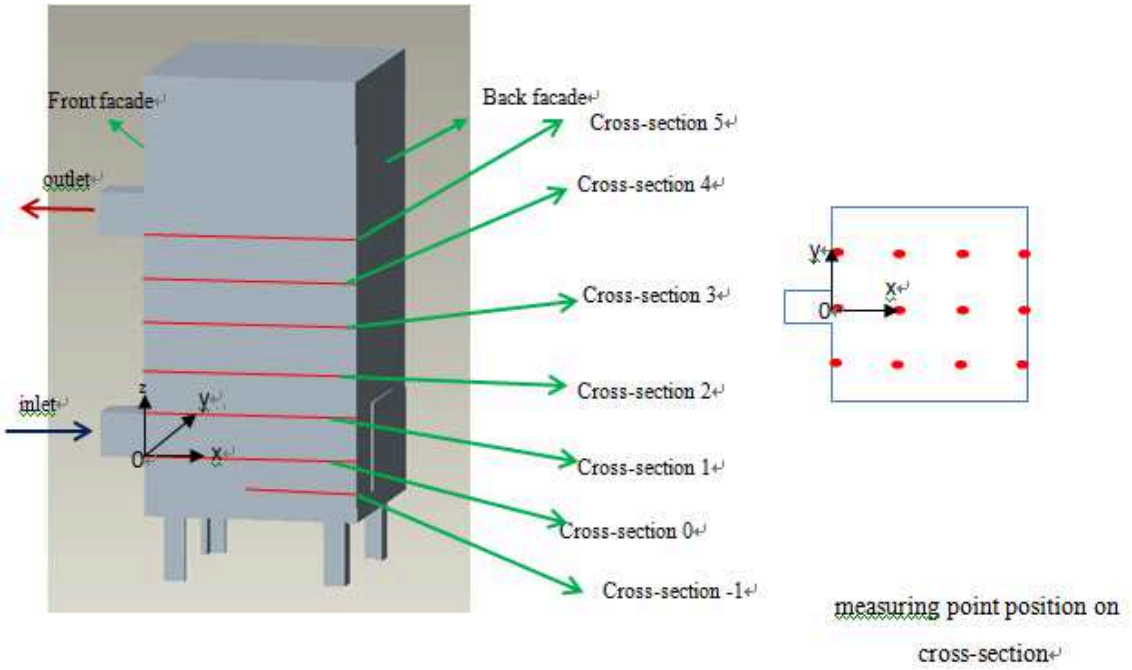


Fig2. Arrangement of temperature measuring points in the air-cooling experiment

Table1. 12 combinations of experimental conditions

| Case No. | Aggrega-te size, mm | With or without upper-duct | velocity m/s | Packing density kg/m$^3$ | porosity | Aggregate initial temperature ℃ | Inlet average temperature℃ |
|---|---|---|---|---|---|---|---|
| 1 | 40-80 | without | 16.9 | 1578.183 | 0.41764 | 21.0505 | 7.8 |
| 2 | 40-80 | without | 19.762 | 1569.085 | 0.42100 | 20.297 | 14.425 |
| 3 | 40-80 | with | 18.974 | 1518.013 | 0.43985 | 24.114 | 8.034 |
| 4 | 40-80 | with | 27.55 | 1542.15 | 0.43094 | 23.027 | 13.52 |
| 5 | 20-40 | without | 13.86 | 1534.818 | 0.43365 | 23.425 | 12.77 |
| 6 | 20-40 | without | 22.477 | 1534.818 | 0.43365 | 22.763 | 8.465 |
| 7 | 20-40 | with | 11.32 | 1510.007 | 0.44280 | 21.085 | 13.816 |
| 8 | 20-40 | with | 15.353 | 1485.225 | 0.45195 | 23.137 | 14.032 |
| 9 | 5-20 | without | 14.44 | 1460.94 | 0.46091 | 24.452 | 9.04 |
| 10 | 5-20 | without | 17.944 | 1460.94 | 0.46091 | 22.231 | 14.689 |
| 11 | 5-20 | with | 13.78 | 1476.539 | 0.45515 | 20.606 | 10.332 |
| 12 | 5-20 | with | 18.23 | 1461.771 | 0.46060 | 23.372 | 15.74 |

## Discussion of experimental results

### 3.1 Aggregate temperature variation

Initially, the aggregate's temperature is average close to room temperature. Centerline temperature on section 0 is low, because section 0 is under the inlet duct, which connected with the outdoor directly through the blower, and the outdoor temperature is about 5 ℃, so the temperature at the center line of the section 0 is low. For all conditions, from the section at the inlet to the section at the outlet, the temperature is gradually increased. Therefore, all the conditions of cooling trend is the same: the section close to the inlet duct cooled first, farther from the inlet duct cooled later. For all operating conditions, the cooling trend on each section is the same: the aggregate temperature on the back facade is the fastest, on the front facade is the slowest; as time goes on, the aggregate temperature on section gradually tends to balance to the inlet air temperature. This is

because the cold air flow resistance in inlet duct is small, the air could flow directly through the duct and change flow direction to the both sides of the duct until after encountering the back façade. So, the inlet duct and the back façade's intersection region will produce cold accumulation, aggregate cool fastest. The law of aggregate cooling is: in the center of the inlet duct, the vertical aggregates have the same cooling trend. As shown in figure 3, in the center of the inlet duct, the upper and lower temperature fields are substantially symmetrical. In other words, the aggregates are not simply cooled in the region from inlet to outlet, below the inlet duct, the aggregate will obviously be cooled.

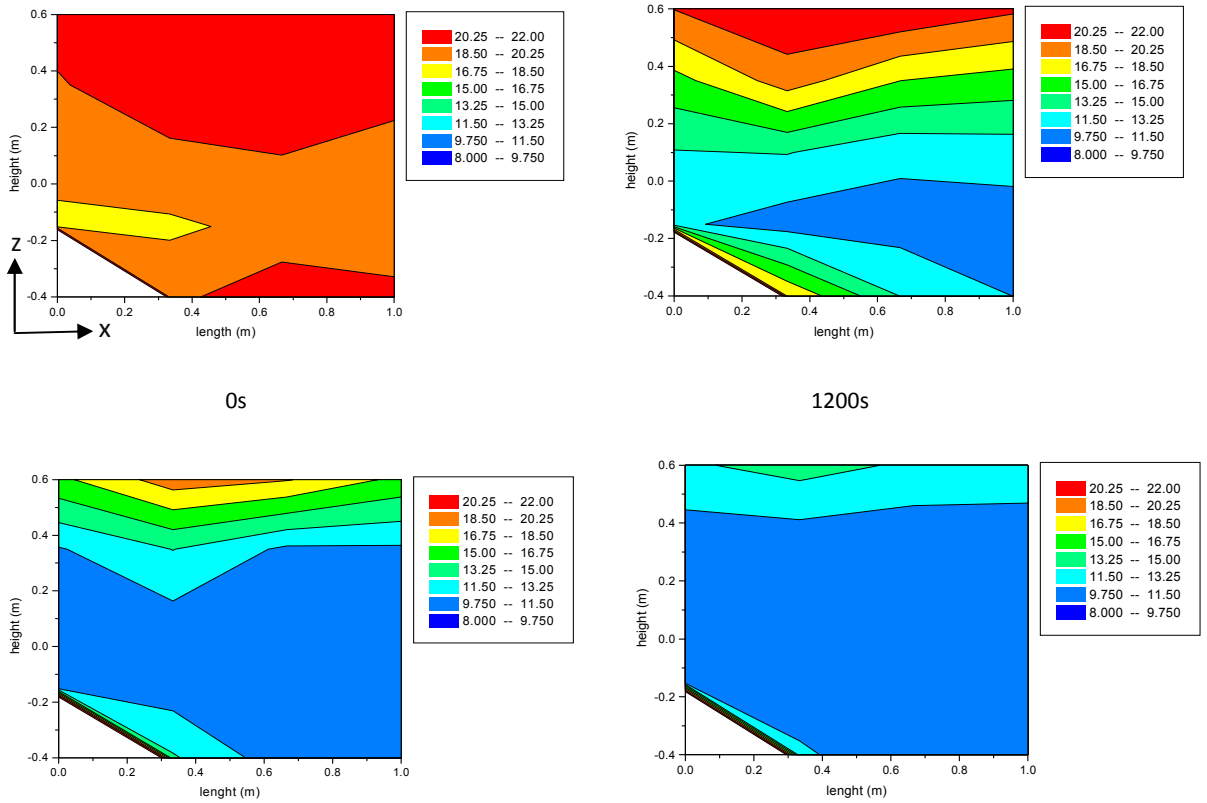


0s 1200s

2400s 3600s

Fig3. Temperature field of the centre section (Case No.11)

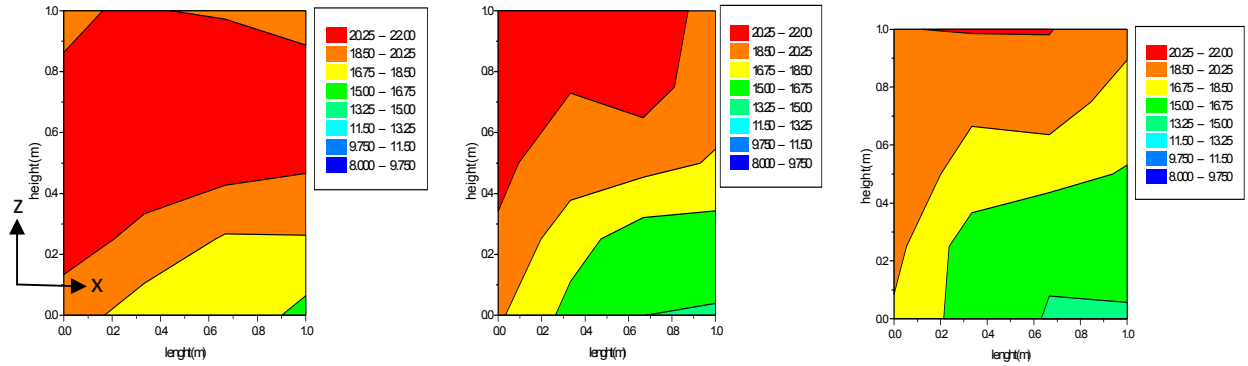


1200S 2400S 3600S

Case No.2 Temperute field in the center section without upper-duct

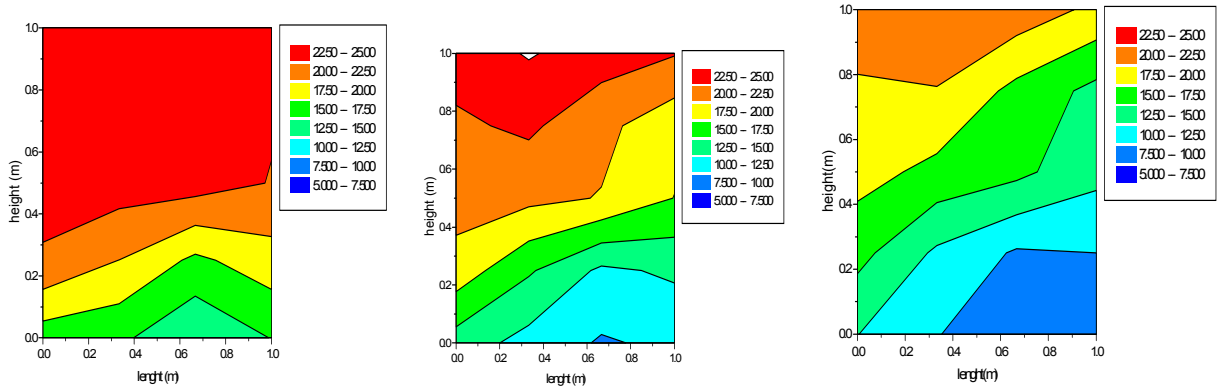


1200S 2400S 3600S

Case No.3 Temperature field in the center section with upper-duct

Fig4. Temperature field of large aggregate with and without upper-duct

Figure 4 shows the comparison of large aggregate temperature between the situation with and without upper-duct. Because the inlet air temperature is different, so do not compare the temperature gradient only compare isotherms distribution. As can be seen from the figure, at the front facade aggregate cool more easily and the temperature field has better uniformity in the case with upper-duct. Figure 5 shows the comparison of average temperature change of a middle aggregate with and without upper-duct. Only under the conditions of similar speed are the initial temperature and inlet air temperature comparable. From the figure, the situation with upper-duct whose average temperature cooling rate of the aggregate is slightly faster.

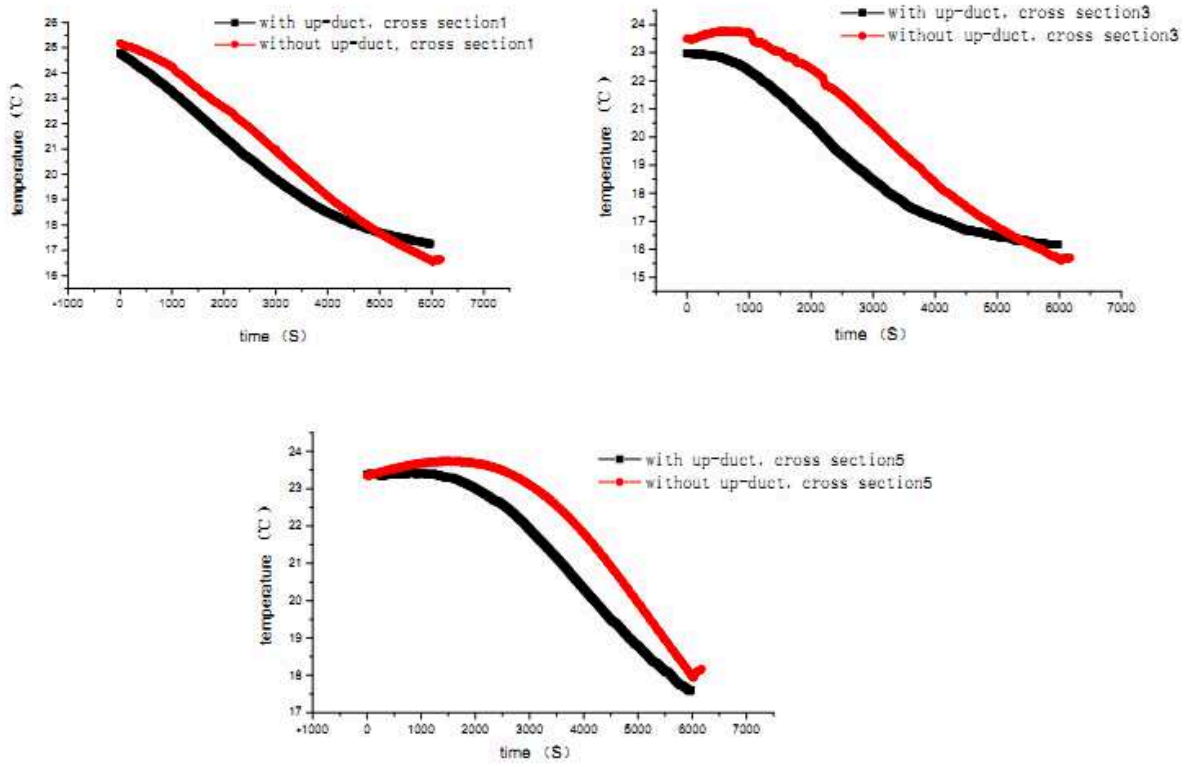


Fig.5 Average temperature of middle aggregate in three cross sections with and without upper-duct(No. 5, 8)

The greater porosity or smaller aggregates average diameter, the more uniform temperature distribution in the cross section. From figure 6, the small aggregate has the most uniform temperature distribution on center section, second is middle aggregate, the most uneven is large aggregate. The main reason is that the porosity of large is 0.417-0.439, middle is 0.434-0.451, small is 0.455-0.461, the small aggregate has the greatest porosity. And because the small aggregate has the greater void density, the air flow and temperature field distribute more uniformly.

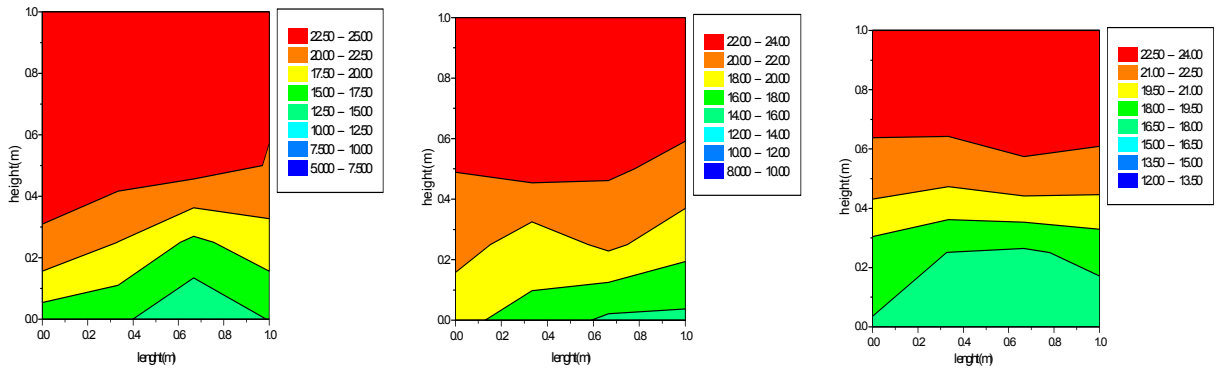


large middle small

Fig.6Centre section temperature of large, middle, small aggregate with upper-duct at 1200s

3.2 Aggregate drag variation

Figure 7 is a graph of relationship between air speed and pressure. From the figure, as the intake air flow rate increases, the drag in the bin increases. When the air quantities are close, for example the air flow rate of 17.94 ~ 19.13m/s, the aggregate diameter is smaller, the pressure grows more obviously. This is because the smaller the diameter of the aggregate, the smaller the gap, the greater the flow resistance of air flow in it. Comparison with and without the upper-duct conditions data is showed in the situation of without up-duct, in which the pressure is large and increasing trend is evident, while in the situation of with upper-duct, the pressure is obviously lower than without the upper-duct.

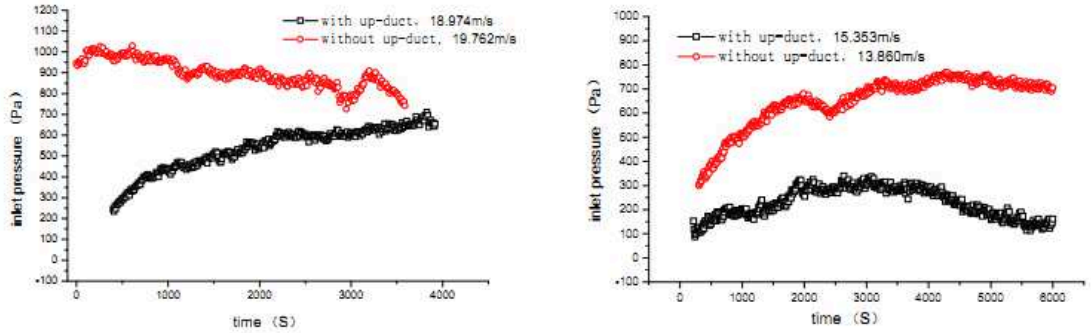


large middle

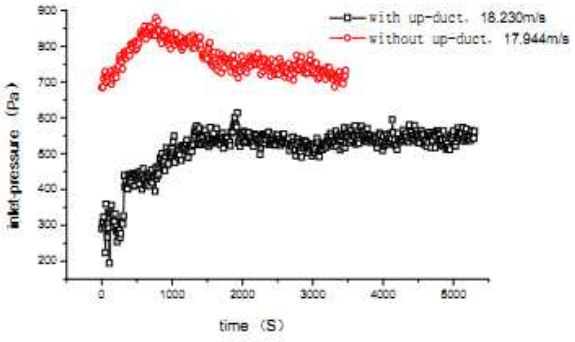


Fig7. Pressure distribution with and without upper-duct

## Conclusion

Experimental results of this work show that, the upper and lower temperature fields are substantially symmetrical with respect to the center of the inlet duct. The temperature in the section closest to the inlet duct is the lowest, and the back facade is cooled faster than the front facade, so the inlet duct should not be too close to the discharge port.

With the increase of the intake air flow rate, the aggregate cooling is enhanced, but meanwhile the air flow resistance increases; with the decrease of aggregate diameter, the temperature distribution turns more uniform, but the pressure drop grows more obviously. So there is an optimum value of the air velocity for the cooling of different diameter aggregates.

It is also found that at the situation of without upper-duct, the pressure drop is large and the increasing trend is clearly, pressure drop increases at a power function of the gap speed; at the situation with upper-duct, the pressure drop is small and increases to approach a certain value, the cooling rate of aggregate average temperature is slightly smaller, and the temperature field is more uniform. Thus, considering both the temperature uniformity and the flow resistance, the situation with upper-duct has evident advantage.

## References

[1] ZHU Bofang, WANG Tongsheng, DING Baoying, GUO Zhizhang. Hydraulic concrete structure temperature stress and temperature control. Water Power Press.

[2] WENG Dingbo, YE Shuiquan. Aggregate airflow resistance performance test. Water Power Construction Machinery, 1991（2）:1-5.

[3] ZHU Bofang. Present and Future of temperature control and prevent the concrete dam cracks. Journal of Hydraulic Engineering 2006（Vol.37, No.12）.

[4] YANG Shiming, TAO Wenquan. HEAT TRANSFER. Higher Education Press.

[5] Chunxiang Qian, Guibo Gao. Reduction of Interior Temperature of Mass Concrete Using Suspension of Phase Change Materials as Cooling Fluid, Construction and Building Materials, 2012(26): 527-531

[6] MA Chao, LIU Yanfeng, GUAN Wei. Turbulence research of air-cooled aggregate material layer, Water Resources and Power, 2011,29（11）:117-118.

[7] Zeng S Q, Hunt A, Greif R. Geometric Structure and Thermal Conductivity of Porous Medium Silica Aerogel, ASME Journal of Heat Transfer,1995,117(4):1055-1058

*Applied Mechanics and Materials Vols. 580-583 (2014) pp 1940-1945*
*© (2014) Trans Tech Publications, Switzerland*
*doi:10.4028/www.scientific.net/AMM.580-583.1940*

# Sensitivity Analysis of Concrete Face Rock-fill Dam Parametric Based on the Intelligent Algorithm

Qiao Yan [1, a], Zhanhong Gao [2, b] and Zhicheng Song [2, c]

[1]National Dam Safety Research Center, Wuhan, 430072, China

[2] College of Hydraulic and Environmental Engineering, China Three Gorges University, Yichang 443002, China

[a]yanqiao666@163.com, [b]gao_zhanhong@126.com, [c]464820805@qq.com

**Keywords:** Rock-fill dam; Duncan E-B model; particle swarm optimization neural network; orthogonal test method; sensitivity analysis.

**Abstract.** Sensitivity analysis of model parameters is a rock fill parametric inversion analysis method to determine the unknown parameters. Traditional sensitivity analysis is basically a lot of trial or the method of single factor analysis based on a large amount of calculation, but, unable to reflect the real situation. The method of particle swarm optimization based on neural network based nonlinear mapping relationship between model parameters and displacement to finite element simulation of dam deformation. Basing on the orthogonal design, the methods of range analysis and variance analysis method were used for sensitivity analysis of the parameters of Duncan E-B model and the impact of various parameters on the dam displacement, and then it can be as the parameters of rock fill dam provide basis for determining the unknown parameters inversion.

## Introduction

In the process of formulating the layout and measures of rock-fill dam (CFRD), the accuracy of structural deformation to a large extent depends on the accuracy of chosen mechanics parameters in the mechanical calculation [1]. As one of the common models used in the mechanical calculation and parameter inversion of concrete face rock-fill dam (CFRD) [2], Duncan E-B model is used to determine the mechanical parameters of CFRD in the displacement back analysis. Because of too many model parameters in the constitutive model, there are still problems in solving the model parameters through limited field information. Discrete degree is a major characteristic in Rock mechanical test, as well as high cost of experiment but a small amount of test. Then get the mechanical parameters with large errors and poor representation. The reliability will be smaller if the above parameters are used in the deformation calculation. Sensitivity analysis method should be used to effectively evaluate the parameter perturbation's effect on results of stability analysis and determine the major and minor mechanical parameters and optimize the arrangement of rock mechanics test scheme [3].

Sensitivity Analysis determines the sensitivity degree through the analysis on the attributes of model parameters. According to the theoretical analysis and engineering experience, some parameters which has the smaller influence on the output variables are get rid of, and the strong sensitivity of parameters are considered in the practical research to reduce the complexity of the research process of model parameters. Not only is the accuracy of results improved in the very great degree, but also the corresponding problem can be solved using the ranking results of sensitivity factors [4]. In this paper, basing on the PSO-NN (particle swarm optimization optimizing neural network) and orthogonal combination method, a network model of intelligent algorithm was built to analysis the sensitivity of parameters of Duncan E-B model combining with range analysis and variance analysis method, not only can the interaction between various parameters be considered, but the amount of calculation can be reduce and make the method simple and accurate.

**The Theoretical Basis and Concrete Steps of the Analysis of Rock-fill Parametric Sensitivity**

Particle swarm algorithm is simple, fast convergence and high robustness, strong global search capability, fast search speed, high efficiency, can be massively parallel computing to speed up the calculation, and do not need to use the feature information of the problem itself, can make up for the local minimum problem of BP neural network. BP neural network uses a local search method to compensate the problem of particle swarm accuracy. The key of particle swarm optimization neural network is to establish a mapping between particle swarm particle dimensions of space and connection weights neural networks and to make neural networks mean square error as a function of particle swarm adaptation [5].

Accordingly, the particle swarm optimization and artificial neural network algorithms are combined to create particle swarm optimization neural network model to simulate the t finite element analysis and do the displacement calculation. Nerve grid structure input and output layer nodes are 8, hidden layer is set to 11, the use of particle swarm optimization BP neural network weights and thresholds, the population size of the algorithm is N = 50, the largest of the algorithm execution iterations is $T_{max}$ = 300, cognitive learning factor is $c_1$ = 1.5, social learning coefficient is $c_2$ = 1.5, the flight speed of control sub is $V_{max} = 0.1X_{max}$, inertia weight ω with the increase in the number of iterations is reduced from 0.9 linear as 0.4, L-M error indicator algorithm is 0.0001, using MATLAB toolbox written PSO BP neural network program, the learning process shown in Figure 1.

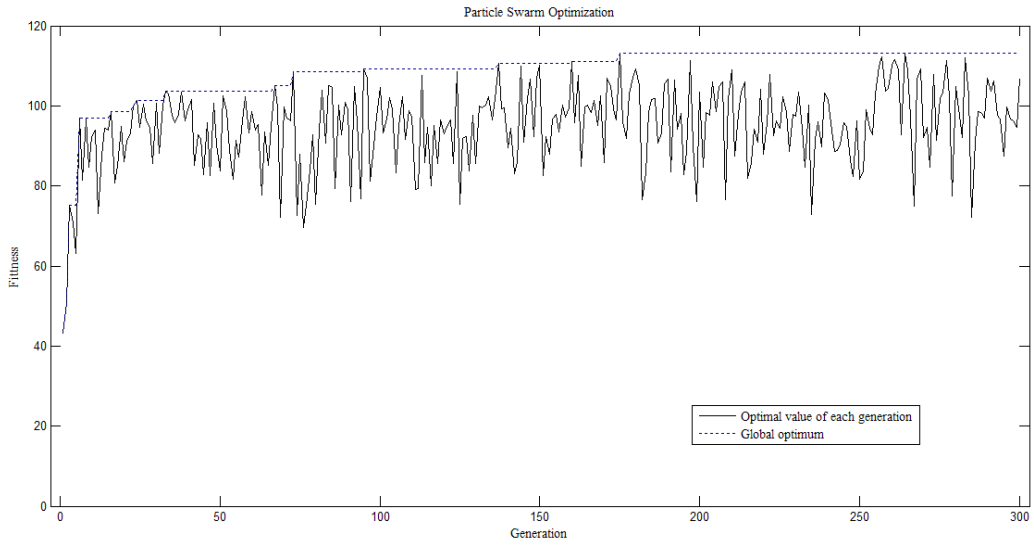


Fig. 1 The learning process of particle swarm optimization BP neural network

By learning and training process, particle swarm optimization neural network already contains inherent nonlinear relationship between parameters and displacement to determine the right input and output layer weights and thresholds. Orthogonal design [6] is one of the multivariate sensitivity analysis methods commonly used, which is based on orthogonal table, high efficiency, quick and economical method of experimental design is mainly based on orthogonally the selection of representative points, has two basic characteristics in the selection of representative points: neat comparability and balanced dispersion. This test method is designed to pick out from a comprehensive test of the sample points with orthogonal nature of the sample points as a test basis, these sample points possess representative, and the orthogonal design just with fewer numbers of experiments can identify each model factors affecting the degree of influence. In this paper, on the basis of this method, range and variance analysis method is used to analysis variance for Duncan E-B model parameter sensitivity analysis.

**Sensitivity analysis of the model parameter**

**The program of orthogonal experimental design.** Duncan E-B model has eight parameters, as shown in table 1.According to the suggested values of roller compaction test results of the scene of the Shuibuya and the calculating parameters of Duncan E-B model, the material calculation parameter values in the form can be determined. According to the principle of orthogonal test[7], select the program of orthogonal test for $L_{18}(2^1\times3^7)$, that is in the constitutive model, of which one parameter bit level has two, the rest seven parameter bit levels have three, because it is relatively simple to determine the dry density of rock-fill, and the dry density of the material shown in the table are the smallest difference, so choose the bit level of the dry density is 2, the rests are 3 bit levels, factors of bit level as shown in table 2, the chosen orthogonal table as shown in table 3.

**Tab.1 Material calculation parameters**

| **Material** | $\rho_d$ /(g·cm$^{-3}$) | K | m | $K_b$ | n | $\varphi_0$ /(°) | $\Delta\varphi$ /(°) | $R_f$ |
|---|---|---|---|---|---|---|---|---|
| maximum | 2.10 | 800 | 0.05 | 400 | 0.25 | 50 | 8.4 | 0.78 |
| minimum | 2.25 | 1200 | 0.20 | 800 | 0.45 | 56 | 10.5 | 0.85 |

In the table above, $\rho_d$ is density; K is cardinal of tangential modulus; n is index of tangential modulus; $R_f$ is damage ratio; $K_b$ is bulk
modulus; m is modulus index.

**Tab.2 Factor Levels**

| Level | $\rho_d$ /(g·cm$^{-3}$) | K | m | $K_b$ | n | $\varphi_0$ /(°) | $\Delta\varphi$ /(°) | $R_f$ |
|---|---|---|---|---|---|---|---|---|
| 1 | 2.10 | 800 | 0.03 | 400 | 0.20 | 49 | 8.0 | 0.76 |
| 2 | 2.25 | 1000 | 0.13 | 600 | 0.35 | 53 | 9.5 | 0.81 |
| 3 | | 1200 | 0.23 | 800 | 0.50 | 57 | 11.0 | 0.86 |

**Tab.3 Orthogonal design**

| Num. | $\rho_d$ | K | m | $K_b$ | n | $\varphi_0$ | $\Delta\varphi$ | $R_f$ |
|---|---|---|---|---|---|---|---|---|
| 1 | 2.1 | 800 | 0.03 | 400 | 0.2 | 49 | 8 | 0.76 |
| 2 | 2.1 | 800 | 0.13 | 600 | 0.35 | 53 | 9.5 | 0.81 |
| 3 | 2.1 | 800 | 0.23 | 800 | 0.5 | 57 | 11 | 0.86 |
| 4 | 2.1 | 1000 | 0.03 | 400 | 0.35 | 57 | 11 | 0.86 |
| 5 | 2.1 | 1000 | 0.13 | 600 | 0.5 | 49 | 8 | 0.76 |
| 6 | 2.1 | 1000 | 0.23 | 800 | 0.2 | 53 | 9.5 | 0.81 |
| 7 | 2.1 | 1200 | 0.03 | 600 | 0.2 | 53 | 9.5 | 0.86 |
| 8 | 2.1 | 1200 | 0.13 | 800 | 0.35 | 57 | 11 | 0.76 |
| 9 | 2.1 | 1200 | 0.23 | 400 | 0.5 | 49 | 8 | 0.81 |
| 10 | 2.25 | 800 | 0.03 | 800 | 0.5 | 53 | 9.5 | 0.76 |
| 11 | 2.25 | 800 | 0.13 | 400 | 0.2 | 57 | 11 | 0.81 |
| 12 | 2.25 | 800 | 0.23 | 600 | 0.35 | 49 | 8 | 0.86 |
| 13 | 2.25 | 1000 | 0.03 | 600 | 0.5 | 49 | 11 | 0.81 |
| 14 | 2.25 | 1000 | 0.13 | 800 | 0.2 | 53 | 8 | 0.86 |
| 15 | 2.25 | 1000 | 0.23 | 400 | 0.35 | 57 | 9.5 | 0.76 |
| 16 | 2.25 | 1200 | 0.03 | 800 | 0.35 | 57 | 8 | 0.81 |
| 17 | 2.25 | 1200 | 0.13 | 400 | 0.5 | 49 | 9.5 | 0.86 |
| 18 | 2.25 | 1200 | 0.23 | 600 | 0.2 | 53 | 11 | 0.76 |

Based on the PSO-BP network model which is used for simulating the finite element to get the replacement, and according to the Orthogonal test table which was shown in table 3, the result table shows in table 4.

**Tab.4 The results of orthogonal design**

| Num. | Sample 1 | | Sample 2 | |
|---|---|---|---|---|
| | vertical displacement | horizontal displacement | vertical displacement | horizontal displacement |
| 1 | -1.28799 | -0.207883 | -1.45405 | 0.092518 |
| 2 | -0.796263 | -0.148198 | -1.043461 | 0.147399 |
| 3 | -0.543421 | -0.11652 | -0.832149 | 0.166891 |
| 4 | -1.105448 | -0.102238 | -1.308297 | 0.017362 |
| 5 | -0.73055 | -0.192305 | -0.997545 | 0.196219 |
| 6 | -0.615777 | -0.19246 | -0.890471 | 0.210923 |
| 7 | -0.848539 | -0.132613 | -1.070734 | 0.094449 |
| 8 | -0.567461 | -0.085614 | -0.839391 | 0.119754 |
| 9 | -0.984618 | -0.095689 | -1.251296 | 0.057871 |
| 10 | -0.672652 | -0.106289 | -0.952966 | 0.146007 |
| 11 | -0.730143 | -0.222162 | -1.329307 | 0.26085 |
| 12 | -0.799222 | -0.188341 | -1.087011 | 0.208669 |
| 13 | -0.846963 | -0.109596 | -1.110058 | 0.095373 |
| 14 | -0.703185 | -0.197123 | -0.976966 | 0.204216 |
| 15 | -1.049632 | -0.104605 | -1.313964 | 0.050181 |
| 16 | -0.644747 | -0.087483 | -0.91936 | 0.109451 |
| 17 | -1.121987 | -0.11047 | -1.374067 | 0.047393 |
| 18 | -0.785961 | -0.136635 | -1.071345 | 0.13803 |

**Variance components method of the parameter sensitivity analysis.** To evaluate the degree of sensitivity of each parameter by the size of the rank difference belongs to intuitive analysis, but the size of the rank difference does not have a comparatively objective evaluation standard. In order to solve this problem, in this paper, we re-analyzed the data variance, analysis of variance is resolved by the sum of squared residuals, constructing F statistic, test the significance of factor effect and interaction effect. Based on the theoretical calculation method of analysis of variance, write computing program, using SAS software, calculated the sum of squared residuals of each factors, due to the output of the software to take up the space is larger, in order to save space, to adjust the format of the results, omit a level of average output data, results as shown in table 5.

**Tab.5 Results of Variance Analysis**

| | **parameters** | **SS** | **$d_f$** | **MS** | **F** | **P** | **Rank** |
|---|---|---|---|---|---|---|---|
| **S1-V** | $\rho_d$ | 0.000195 | 1 | 0.000195 | 0.001209 | 0.975423 | 6 |
| | K | 0.00206 | 2 | 0.00103 | 0.006395 | 0.993645 | 7 |
| | m | 0.027315 | 2 | 0.013657 | 0.084801 | 0.921828 | 3 |
| | $K_b$ | 0.269606 | 2 | 0.134803 | 0.837003 | 0.544365 | 1 |
| | n | 0.000253 | 2 | 0.000126 | 0.000784 | 0.999216 | 4 |
| | $\varphi_0$ | 0.087372 | 2 | 0.043686 | 0.27125 | 0.786628 | 2 |
| | $\Delta\varphi$ | 0.016781 | 2 | 0.00839 | 0.052097 | 0.950483 | 8 |
| | $R_f$ | 0.013344 | 2 | 0.006672 | 0.041427 | 0.960221 | 5 |
| | Sum | 0.739033 | 17 | 0.043473 | | | |
| | Error | 0.322108 | 2 | 0.161054 | | | |
| **S1-H** | $\rho_d$ | 1.44E-06 | 1 | 1.44E-06 | 0.000161 | 0.991025 | 7 |
| | K | 0.005192 | 2 | 0.002596 | 0.28962 | 0.775422 | 2 |
| | m | 0.001849 | 2 | 0.000925 | 0.103144 | 0.9065 | 4 |
| | $K_b$ | 0.000623 | 2 | 0.000311 | 0.034746 | 0.96642 | 6 |
| | n | 0.007418 | 2 | 0.003709 | 0.413807 | 0.70731 | 1 |
| | $\varphi_0$ | 0.001452 | 2 | 0.000726 | 0.080995 | 0.925074 | 5 |
| | $\Delta\varphi$ | 0.001924 | 2 | 0.000962 | 0.107318 | 0.903083 | 3 |
| | $R_f$ | 2.11E-05 | 2 | 1.05E-05 | 0.001176 | 0.998825 | 8 |

| | | | | | | | |
|---|---|---|---|---|---|---|---|
| | Sum | 0.036407 | 17 | 0.002142 | 0 | 0 | 0 |
| | Error | 0.017927 | 2 | 0.008963 | 0 | 0 | 0 |
| **S2-V** | $\rho_d$ | 0.002474 | 1 | 0.002474 | 0.019219 | 0.90244 | 3 |
| | K | 0.001256 | 2 | 0.000628 | 0.00488 | 0.995144 | 2 |
| | m | 0.005954 | 2 | 0.002977 | 0.023125 | 0.977398 | 4 |
| | $K_b$ | 0.292406 | 2 | 0.146203 | 1.135769 | 0.468215 | 1 |
| | n | 0.004298 | 2 | 0.002149 | 0.016695 | 0.983579 | 5 |
| | $\varphi_0$ | 0.06753 | 2 | 0.033765 | 0.262301 | 0.792204 | 7 |
| | $\Delta\varphi$ | 0.001778 | 2 | 0.000889 | 0.006905 | 0.993142 | 6 |
| | $R_f$ | 0.000521 | 2 | 0.000261 | 0.002024 | 0.99798 | 8 |
| | Sum | 0.633669 | 17 | 0.037275 | 0 | 0 | 0 |
| | Error | 0.257452 | 2 | 0.128726 | 0 | 0 | 0 |
| **S2-H** | $\rho_d$ | 0.000303 | 1 | 0.000303 | 0.013929 | 0.916834 | 5 |
| | K | 0.008664 | 2 | 0.004332 | 0.198833 | 0.834144 | 2 |
| | m | 0.007623 | 2 | 0.003812 | 0.174958 | 0.851094 | 3 |
| | $K_b$ | 0.008807 | 2 | 0.004404 | 0.202123 | 0.831862 | 1 |
| | n | 0.005813 | 2 | 0.002907 | 0.133417 | 0.882288 | 4 |
| | $\varphi_0$ | 4.15E-05 | 2 | 2.07E-05 | 0.000952 | 0.999049 | 8 |
| | $\Delta\varphi$ | 0.001255 | 2 | 0.000627 | 0.028796 | 0.97201 | 6 |
| | $R_f$ | 0.001105 | 2 | 0.000553 | 0.02537 | 0.975258 | 7 |
| | Sum | 0.077186 | 17 | 0.00454 | 0 | 0 | 0 |
| | Error | 0.043573 | 2 | 0.021786 | 0 | 0 | 0 |

In table 5, the S1-V is Vertical displacement of sample 1; the S1-V is horizontal displacement; so is the S2-V and S2-H. The value of F is statistical quantity value, the greater the value of P, the lower the sensitivity degree of the parameters. From the results of table 5, the size of the sensitivity degree of the 8 parameters is shown below:

In Sample 1, the parameters' sensitivity priority in subsidence displacement is $Kb>\varphi_0>m>n>R_f>\rho_d>K>\Delta\varphi$; the parameters' sensitivity in horizontal displacement is $n>K>\Delta\varphi>m>\varphi_0>K_b>\rho_d>R_f$;

In Sample 2, the parameters' sensitivity priority in subsidence displacement is $K_b>K>\rho_d>m>n>\Delta\varphi>\varphi_0>R_f$; the parameters' sensitivity in horizontal displacement is $K>K_b>m>n>\rho_d>\Delta\varphi>\varphi_0>R_f$.

And, when $P<0.05$, the factors have a significant effect on the test results, or that the factors are the main factors that influence the experimental index. However, the results show that the value of eight parameters factor P more than 0.05, therefore it need further analysis, obtains a new analysis of variance table. For settlement displacement and horizontal displacement gradually eliminate the least significant factor, using the same program to calculate every step of variance table, if finally get a factor of $P<0.05$, indicating that the factor is a very significant factor, on the contrary, if the element has not a value of $P<0.05$, indicating that none of these factors significantly affect the results.

The settlement displacement and horizontal displacement of the sample 1,2, have made the most insensitive factors, the results show that the settlement displacement weed out the three parameters, the remaining elements of the $P<0.05$;horizontal displacement weed out the most sensitive factors remaining 7 factors, P value is still>0.05. The result indicates that Duncan E-B model has little effect on the horizontal displacement, and has a great effect on the settlement displacement. Therefore, the parameters inversion analysis of stone of rock-fill dam, mainly anti-settlement displacement analysis, the results are reliable. Comparing the analysis with analysis of variance, the difference between the two is not great, indicating the results are reliable.

## Conclusions

This paper uses the method of particle swarm optimization algorithm of neural network combined with orthogonal design method to achieve a sensitivity analysis of Duncan E-B model, using analysis of variance, combined with SAS software to calculate the effect of the settlement and horizontal displacement, the results can be used as parameters to be inversed parameters inversion process determine the concrete face rock-fill dam reference. Using orthogonal experiment design Samples, greatly reducing the number of tests and calculations, but using this design method can reflect the inherent law in essence, but also improve work efficiency.

The sensitivity analysis of Duncan E-B model showed that, the influence of K, Kb, n, m on the settlement of displacement are more significant, but the impact of the model parameters horizontal displacement is not very significant, therefore, in the process of rock-fill dam inversion analysis, suggestions focusing on the point of vertical settlement of rock-fill dam displacement observation values of Duncan E-B model parameters of inversion analysis.

## Acknowledgements

This work was financially supported by Fund of National Dam Safety Research Center (The project No. is NDSKFJJ1202).

## References

[1] Zhongli Huang, Guangke Zhang: Jilin Water Conservancy, 2009 (02),p.1. (In Chinese)

[2] Yanlong Li, Shouyi Li and Zhanfeng Ding: Journal of Hydraulic Engineering, 2013(07), p.873. (In Chinese)

[3] Guang Zhang, Weishen Zhu: Rock and Soil Mechanics, 1993(01), p.51. (In Chinese)

[4] Yi Cai, Yan Xing, Dan Hu: Beijing Normal University (Natural Science), 2008(01), p.9. (In Chinese)

[5]Liu Kun, Tan Ying,He Xingui: Peking University (Natural Science),2011(02), p.238. (In Chinese)

[6] Ruijiang Liu, Yewang Zhang and Chongwei Wen: Experimental Technology and Management, 2010(09), p.52-55. (In Chinese)

[7] Liu Wenqing: Experimental design. Beijing: Tsinghua University Press, 2005, 64. (In Chinese)

*Applied Mechanics and Materials Vols. 580-583 (2014) pp 1946-1952*
*© (2014) Trans Tech Publications, Switzerland*
*doi:10.4028/www.scientific.net/AMM.580-583.1946*

# Study on the present situation and development of groundwater monitoring technology

Qinghua Guan[1, a], Fulin Li[1,b],Xuequn Chen[1,c]

Yufeng Zhang[2, d], Chanjuan Tian [2, e]

[1]Water Resources Research Institute of Shandong Province, Key Laboratory of Water Resources and Environment of Shandong, JInan250000, China

[2]School of Resources and Environment, University of Jinan, JInan250000, China

[a]qhguan0120@163.com, [b]fulinli@126.com,[c]cxq1115@126.com

[d]1050207345@qq.com ,[e]954466488@qq.com

**Keywords:** Groundwater monitoring technology, Aquifer, Multilevel monitoring technology

**Abstract.** In order to investigate the groundwater level and quality, and study the groundwater contaminant in vertical and the dynamics relation in different aquifers, the place of sampling and monitoring need to be installed in the relevant position of the aquifers to differentiate groundwater from different aquifers. In recent years, groundwater monitoring and sampling system has made great progress, this paper focuses on the current study and development of groundwater monitoring well technology, and analyses the development and the applied direction of monitoring well technology from single-well monitoring to multi-level monitoring, which would provide scientific references for domestic related and groundwater contaminant.

## Single-well monitoring

In the groundwater monitoring, the way of monitoring is a single well or a group wells that are different depth single wells in China from 70s to 90s. The single well often is complete well (Fig.1), that is a well with drilling multiple aquifers, and drilling holes in the well pipe with the aquifers. So the groundwater in the well is mixed level and mixed water quality; A group wells is in the same area drilling different depth single wells, and every well only monitors one aquifer, other aquifers must be sealed, a group wells can achieve monitor the goal of aquifer water level and quality[1], group wells need to make sure the numbers and the depth of the monitoring wells depending on the drilling data (Fig. 2).

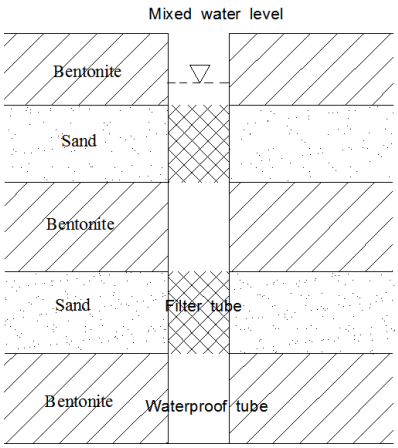


Fig.1 Single well monitoring mixed water

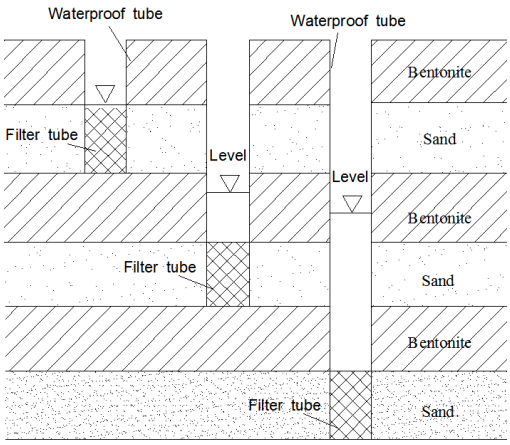


Fig.2 Group wells monitoring different aquifers

Single-well technique carrys on construction according to the requirement of the hydrogeological drilling procedures, site hydrogeological drillings on the basis of hydrogeological mapping and geophysical prospecting and chooses an appropriate drilling method according to mechanical and physical properties of rocks, drilling, as well as pore size, depth, and construction conditions. Construction procedures include drilling, changing pulp, lowering pipe, filling gravel material, sealing water, washing well and so on. Drilling hole wall, the size and depth of the pore should be checked and the drilling as well as the bottom of the hole should be cleaned up before lowering pipe. First, approximately 0.2m thick clean sand or gravel is placed in the bottom of the hole, and then pipes of monitoring well are installed vertically in the center of the hole and filter pipes are installed in the monitoring aquifer. After the well pipes installation is complete, filter material is filled around the filter pipes. The filter material should be extended about 0.5m above the top of the filter pipe during reclamation. Being sealed water on the top of the filter pipes through filling clay ball, the thickness of sealing water should be more than 5m. The annular gap between the borehole and well pipe should be backfilled with clay after sealing water.

Single-well punches each aquifer in the vertical and without sealing water by stratification, groundwater in the single-well mixed monitoring wells is mixed up the entire groundwater within monitoring length. Groundwater contamination plume is usually thin and highly stratified, and the table, quality and temperature of water in single-well monitoring wells all come from the mixed aquifer, the real pollutant concentration and pollutant distribution of groundwater are concealed[2]. Therefore, the data collected does not accurately reflect the characteristics of specific groundwater. Group-well monitoring wells can monitor the water table and water quality in different aquifers. Although its advantages are simple and easy to construct, the disadvantages is the large number of drills, the large area covering, expensive, the longer period and the inconvenience of monitoring and management in single monitoring well. The pipe material of monitoring wells use steel or cast iron pipe during this period. However, this material is easy to corrode and is difficult to maintain and its life is also very short. With the development of the technology of groundwater monitoring, the accuracy of groundwater monitoring is increasingly high demand. The technology of groundwater monitoring is developing towards the technology of single span multi-level monitoring.

## The monitoring technology of multi-pipe in a well

The monitoring technology of multi-pipe in a drill that is also called nested monitoring well[3] is respectively to choose different length of pipe under the monitoring to the selected monitoring layer, then backfilling gravel in aquifer and backfilling clay in impermeable layer, to realize different aquifers monitoring and sampling in a well. Monitoring pipe material is PVC pipe, just as Fig.3 which is the structure of 3 pipes in a well. ① pipe monitors unconfined aquifer, ② pipe monitors the first confined aquifer and ③ pipe is the second confined aquifer, all of which coarses sand respectively are

backfilled in the aquifer. Backfilling clay in impermeable layer can achieve artificial sealing in monitoring well, which will monitor different aquifers of groundwater.

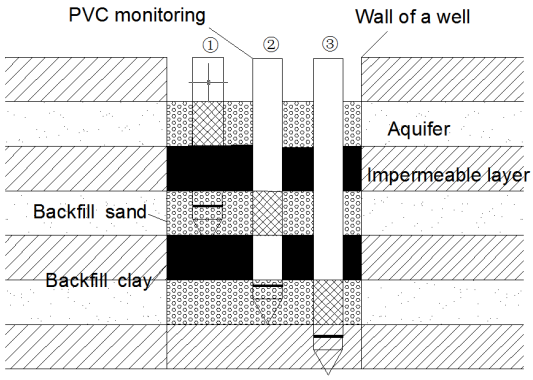


Fig.3 The structure of 3 pipes in a well

The national project of "The groundwater monitoring of multi-pipe in a well" which organized and implemented by Henan Academy of Geological Environment Monitoring in 90s, which conducted the multi-pipe monitor installation. The project team implemented groundwater monitoring wells demonstration project of "The naked drill four times as well" by using PVC-U plastic pipe in the west of Zhengzhou city. The single well can monitor depth up to 350m, that is a well with a hole monitoring four aquifers, which groundwater aquifers monitoring depth is 70~82m, 172~190m, 250~268m, 316~328m. Drilling structure of "The naked drill four times as well" project was designed as 0~200m, which depth aperture is 600mm, depth is 200~350m,aperture is 450mm.In the drilling process of drilling without the metal pipe protecting wall, and in the absence of pipe without wall protecting, the technology of four pipes in a drill, it has four times working procedures with step by step into the well from down to up program( downing pipe - casting gravel - sealing ) just as Fig.4, then washing well and pumping test by air compressor and drill pipe which the diameter is 50mm, was conducted respectively in a well.

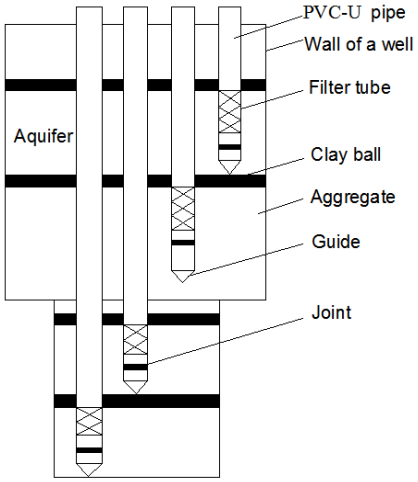


Fig.4 The process of "The naked drill four times as well"

The multi-pipe technology is able to achieve monitoring more than one aquifer of water in a well, and solve the aging problem of groundwater monitoring, that is a technology with settling some technical problems such as the quantity of monitoring hole into the hole, large area, investment, the inconvenience of monitoring and management and so on[4]. Furthermore, it has the advantage by using PVC-U plastic pipe of light quality, low cost, no corrosion, no scaling etc.But this technology has some technical issues in the process of promoting the use. When the well depth is 350m, monitoring aquifers is 4, it need to construct four times with four monitoring pipes which install into the well more than 1000m. It should be sealed up surrounding many monitoring pipes (monitoring pipe number is consistent with the monitoring layers). It is very difficult to seal in different aquifers, which must make sure seamless among the pipes, or it will cause the string between the aquifers.

Besides, the more monitoring aquifers, the more monitor pipes, the bigger diameter is required about the well, it also has certain requirements about rigs and drill. For our current drilling technology, it does not suitable to layer for deep and multi-layered groundwater and will cause a big waste of materials with the increase in monitoring horizon and technical difficulty of layered plugging wells.

At present, the groundwater monitoring wells in China are mostly mixed wells. With the increasing amount of groundwater exploitation and deepening study of environmental problems caused by groundwater overdraft, level of refinement, it requires that the groundwater should be stratified sampling, monitoring and analysis to know the hydraulic connection between each aquifer and convective changes of groundwater contamination. So monitoring technology should be changed from single monitoring well to a multi-pipe monitoring well, just as nested monitoring wells construction technology in spite that it has some problems such as the big diameter of wells and the number of monitoring pipes, and in order to solve the problem, it gradually developed continuous multi-channel monitoring technology internationally.

**The continuous multi-channel monitoring technology**

In order to improve the investigation and monitoring level of groundwater pollution, research and development of multi-channel monitoring system is an important direction of groundwater monitoring technology development. The developed countries such as Europe, America, Canada and Japan are the leader in groundwater monitoring which has formed continuous multi-channel monitoring technology. It can obtain water levels and samples for every aquifer accurately in a well, which is a important technology with improving PVC pipe, which is designed multiple channels in a pipe, and each channel can be monitored for a target aquifer. The process of PVC monitoring pipe design is shown in Fig.5, Fig.5-a is continuous three-channel monitoring pipe, which can monitor three-aquifer and Fig.5-b seven-channel can monitor seven .This monitoring pipe must be installed in accordance with the aquifer characteristics of drilling, dividing the target aquifer position, the corresponding block in position of monitoring of drilling pipe, so as to achieve the requirement of target aquifer. Besides, installing this pipe can use the conventional drilling techniques, thereby arrive the multi-level with sealing in impermeable layer.

The continuous multi-channel technology is currently more advanced in monitoring groundwater contaminant which is also called CTM system in Canada. This pipe can make 3 or 7 channels from high-density polyethylene (HDPE) pipe [5], which 3 channels diameter of pipe is 28mm with the channel diameter 9.5mm, and the 7channels-pipe is 43mm with channel diameter 10mm and 9.5mm, and the standard length is 30m, 60m, 90m.With the developed technology of drilling well, installing pipe and sealing impermeable layer, the depth can arrive to 150m.

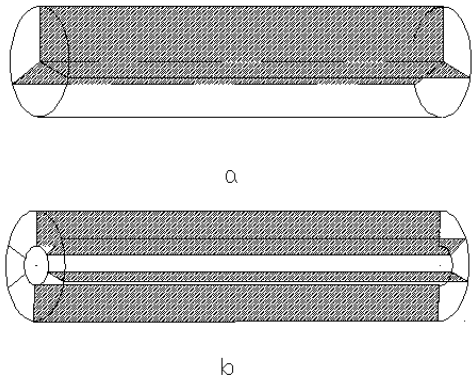


Fig.5 a and b are respectively 3 and 7 channel PVC monitoring pipe

Compared with other monitoring wells, it can arrive to monitor seven different aquifer in a well, without large diameter of drill, the advantages are: samples less be polluted, inexpensive, saving a lot of PVC pipes, installing easy, and it is only one pipe that sealing more easier than the multi-pipe, and can avoid stringing between aquifers, sealing easy and reliable around one pipe. High-resolution data can improve the accuracy of the information underground contamination, making it easier to control precisely dynamic changes in groundwater level water quality and improve the efficiency of

monitoring wells. So far, application of this technology in foreign countries is given priority to monitor shallow groundwater pollution, which monitoring depth is between 20~50m; in the application of monitoring Jinan springs, monitoring depth is up to 150m, which can achieve monitoring the water level and water quality simultaneously to analysis the hydraulic connection between each aquifer and further analysis the origin of spring. But as the depth increases, the requirements of corresponding installation, stratified sealing technology are much higher.

The continuous multi-channel technology is more advanced groundwater monitoring system in the world, with modular processing of monitoring pipe and simple construction, and it is only one pipe which reduces the installed times than multi-pipe. But the channel diameter is small, for example, the channel diameter of 3-channel pipe is 9.5mm invented by Solinst Company in Canada, the middle one of the 7-channel is 9.5mm, others are10mm. As a result, the measurement and collection of groundwater level should be matched with dedicated micro-level gauge and sampler.

**Waterloo Multilevel Groundwater Monitoring Technology**

The Waterloo System is used to obtain groundwater samples, hydraulic head measurements and permeability measurements from many discretely isolated zones in a single borehole[6].The system uses modular components which form a sealed casing string of various casing lengths, packers, ports, a base plug and a surface manifold. This allows accurate placement of ports at precise monitoring zones,such as fig.6. Monitoring pipes attached to the stem of each port indicidually connect that monitoring zone to the surface. The standard system is built on 2"Sch. 80PVC TO fit 3"-4" boreholes and uses 3 ft long packers. Stainless steel components .

An important consideration in planning an investigation involving the installation of deep multilevel wells with Waterloo Systems is the “planned” location for each well[7], such as the precise location, monitoring port and the sealing location. Water Resources Research Institute of Shandong Province designs and installs the system in Jinan to monitor the groundwater, the process is:Constructions the well and records the lithology and aquifer; designs the monitoring location according to the drilling; Once the multilevel wells were constructed, engineers installs the Waterloo Groundwater Monitoring Systems on surface; It can be put them into the wells as soon as the modular components are assembled; at last, the impermeable layer must be sealed. According to the project schedule, the depth of well is 250m in Jinan, 6 aquifers, The lithology of aquifers is Quaternary, Teriary, Diorite Intrusion, Carboniferous-Permian, the Ordovician Limestone. It took 40 days to construct the drill and 3 days to instill the Waterloo System. Although installation of the Waterloo systems was a time consuming prcess, the pay-off was in the ease of groundwater sampling. Because the system are permanently installed, the time in the field for decontaminating sampling equipment is eliminated. Purge valumes are also small, thereby minimizing purging time and water disposal costs.

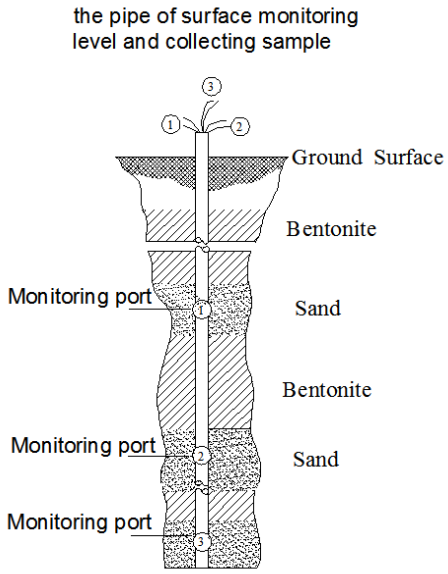


Fig.6 The waterloo multilevel system

Compared with traditional monitoring wells,the advantages of the multilevel are: Obtaining detailed 3D date of floe and concentrations;Geting date integrity; Reducing project costs; Purging and sampling times reduced; Fewer drilled hole; Reducing site disturbance; Variety of monitoring options.But the system is complex, we must accurately grasp the stratigraphic information, the port location and the monitoring location , and so on. So, the engineer must be trained professionally, and the work must be careful, accurate.

## Conclusion

This article introduces the situation and development of the groundwater monitoring in China and other countries, it has realized the three-dimensional groundwater monitoring from single well to many pipes in a well that every pipe monitoring an aquifer, to multilevel monitoring. It can be known well the different aquifers water level and water quality in a single well, especially it provides site assessors with a better understanding of three-dimensional groundwater flow and the distribution of contaminants in the subsurface. Remediation strategies can then be targeted more precisely, focusing efforts in the most effective manner. Multilevel monitoring is important for the research the contamination of groundwater, the hydraulic connection of different aquifers and the origin of spring, and it provides advanced technical support and construction experience for the next step of groundwater monitoring.

## Acknowledgements

This work was financially supported by thethe Ministry of Water Respirces of the People,s Republic of China 948 Project (201103), State Oceanic Administration People's Republic of China Project (201105020) and International science and technology cooperation projects(2012DFG22140).

**References**

[1] Jitian Zheng, Jianzeng Wang. Review of foreign groundwater pollution investigation[J]. Reconnaissance Science and Technology.6：20~23.( 2005,in Chinese )

[2] Deize Dias Lopes, Sandra M.C.P. Silva,et al.Geophysical technique and groundwater monitoring to detect leachate contamination in the surrounding area of a landfill e Londrina (PR e Brazil)[J].Journal of Environmental Management .113:481~487.（2012）

[3] Chengming Ye,Xiaojie Li,et al.Foreign groundwater pollution investigation techniques of monitoring wells[J]. Exploration Engineering.57~60.( 2007,in Chinese )

[4] John Weatherill，Stefan Krause，et al.Nested monitoring approaches to delineate groundwater trichloroethene discharge to a UK lowland stream at multiple spatial scales [J].Journal of Contaminant Hydrology.158:38~54.（2014）

[5] Byoung-Young Choi ,Seong-Taek Yun,et al.Hydrogeochemical interpretation of South Korean groundwater monitoring data using Self-Organizing Maps [J].Journal of Geochemical Exploration .137:73~84.（2014）

[6] Chengming Ye, Weiguo Xing,Zhiren Feng.The new groundwater monitoring wells - Full multi-level monitoring wells.China Geological Survey Bureau.Proceedings of groundwater survey in serious water shortage.Geological Publishing.( 2004,in Chinese )

[7] Linda M. McGlochIin, Desingn considerations for multilevel monitoring wells. R.G. EARTH TECH Colton, CA 92324.

*Applied Mechanics and Materials Vols. 580-583 (2014) pp 1953-1960*
*© (2014) Trans Tech Publications, Switzerland*
*doi:10.4028/www.scientific.net/AMM.580-583.1953*

# Impact of the Cascaded Reservoirs and the Tributaries Confluence on the Eco-hydrology of the Reserve in the Upper Reaches of Yangtze River

ZHAO Li [1, a*], PENG Qidong [1,b], CHEN Quchang [1,c], LI Chong [2,d] and YIN Zhengjie [3,e]

[1] China Institute of Water Resources and Hydropower Research, Beijing 100038, China

[2] China Three Gorges Corporation, Beijing 100038, China

[3] Yangtze River Scientific Research Institute, Wuhan 430010, China

[a]zhao-li985@163.com , [b]pengqd@iwhr.com , [c]chenqc@iwhr.com , [d]lichong@iwhr.com, [e]yinzj@mail.crsric.cn

**Keywords:** cascaded reservoirs, eco-hydrology, mitigation of the tributaries confluence,

**Abstract.** For studying the impacts of the tributaries confluence on the hydrological processes in the downstream reaches of the four cascaded reservoirs in the downstream of Jinshajiang River, this paper simulated the daily discharge at the outlet of the cascaded reservoirs and along the reserve mainstream in typical years with the operation programming of the reserve and MIKE11 hydrodynamic model, and eco-hydrology indicators were selected and calculated by IHA to quantify the hydrology process. The result showed that at Xiangjiaba Gauge Station discharge on April and May increased by about 100%, the discharge in low flow year decreased by 50% and the timing of annual 1-day minimum discharge has significantly alteration. The confluence of Minjiang River could effectively mitigate the impacts of the cascaded reservoirs on eco-hydrology of the downstream of the confluence, but the mitigation of others three tributaries were not significant. Moreover the pre-flood high flow in the downstream of the Minjiang River confluence increased by 50%, and other indicators alteration were not significant.

## Introduction

As the primary driving force of river ecosystems, the natural flow regime plays a critical role in sustaining native biodiversity and ecosystem integrity[1-2]. River management for the main purpose of social and economic benefits, such as power generation, irrigation, navigation, has greatly changed the natural flow regime. The alteration of the flow regime can lead to significant changes in the physical, chemical, geomorphic and biological processes of aquatic ecosystem, which in turn may result in negative consequences on ecosystem product and serves[3-5].

The downstream reach of Jinshajiang River is one of the cases with enormous hydropower resources. There are four cascaded reservoirs construction or planning, respectively Xiangjiaba(XJB), Xiluodu(XLD), Baihetan(BHT) and Wudongde (WDD)(Fig.1), are mainly used for power generation, meanwhile taking flood control, irrigation and navigation into consideration as well. The total regulated storage capacity of the four reservoirs is $2.0\times10^{10}$ $m^3$, and the storage coefficient during the reservoirs operation is up to 13.4%. There is a national reserve for the Rare and Endemic Fishes located in the downstream of the reservoirs, where the intensive spawning grounds, feeding grounds, and wintering grounds for all kinds of the rare and endemic fish can be found. The cascaded reservoirs operation will have impact on eco-hydrological process in the downstream of the reserve, and then effect the fish growth and reproduction in the reserve.

The tributaries carrying water, sediment and nutriment can give rise to the change of hydrology, geomorphology and biological distribution in the mainstream, then mitigate the impact of reservoir operation on downstream [6-8]。 Many domestic existing studies about the influence of these cascaded reservoirs are primarily focus on control cross-section in the downstream of reservoirs [9-11], however, it is unclear about the eco-hydrology alteration in the downstream of these tributaries entry point. If

the tributaries confluence within the reserve could mitigate the impact of the cascaded reservoirs, it has great significance for the protection for the rare and endemic fishes of the reserve.

This paper simulated the hydrological process along the reserve reaches before and after operation in typical year, to evaluate the combined impact of the cascaded reservoirs and the tributaries confluence on the ecological alterations along the mainstream in the reserve.

## Methods

**Study area.** For the maintenance of the unique natural habitat and abundant aquatic biodiversity in the upper Yangtze River, the National Nature Reserve for the Rare and Endemic Fishes in the Upper Reaches of the Yangtze River (NNRARSF) was established. The range of the reserve is from 1.8 km below XJB reservoir to Songgai Town in Chongqing in the mainstream of Yangtze River and partly tributaries reaches (Fig.1). The major protected species are for the Chinese paddlefish, Dabry's sturgeon, and Chinese sucker, along with another 67 endemic species of the Upper Yangtze.

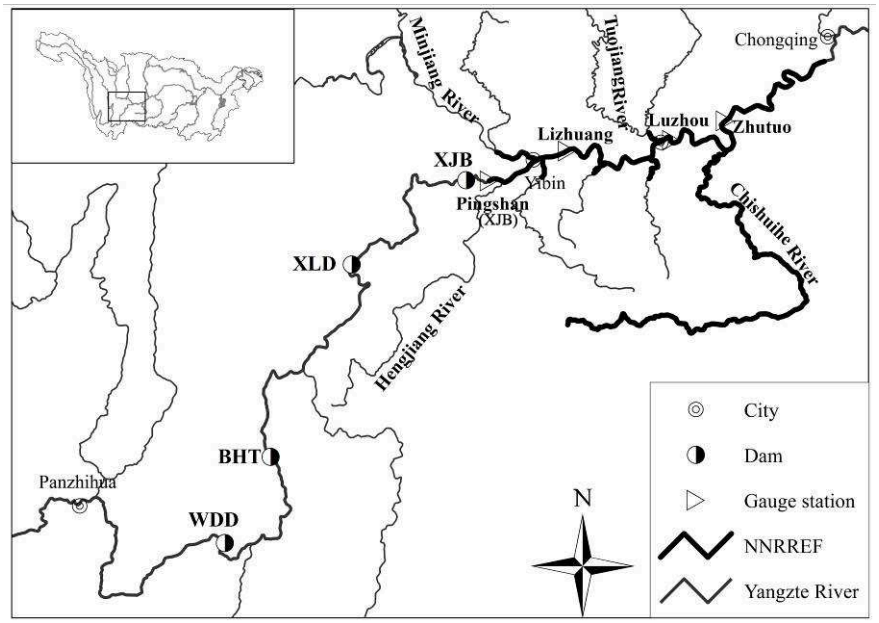


**Figure 1 Location of the cascaded reservoirs and the Gauge Station**

**Gauge Station.** Pingshan Gauge Station was located in the upstream of the reserve, and XJB Gauge Station was instead of Pingshan when the XJB reservoir was built. Therefore, the flow at Pingshan and XJB Gauge Station represent inflow of the reserve before and after regulated respectively. The daily discharge of Lizhuang, Luzhou, Zhutuo Gauge Station represent the hydrological process below confluence of Minjiang River, Tuojiang River and Chishuihe River. The daily discharge at the stations above-mentioned could reflect the hydrological process along the reserve mainstream.

**Indicators of Hydrologic Alteration.** There are many quantitative index of hydrological process, and Olden think that the Indicators of Hydrologic Alteration can reflect a wealth of information represented by these index through the redundancy and choice of 171 hydrological indicators [12]. The Indicators of Hydrologic Alteration (IHA version 7.1) is a statistical package that computes 33 parameters or indices from historic flow or stage records. These parameters can be placed in five groups that are relevant to ecological conditions: (1) magnitude of monthly water conditions, (2) magnitude and duration of annual extreme conditions, (3) timing of annual extreme conditions, (4) frequency and duration of high and low pluses, and (5) rate and frequency of condition changes (Richter et al. 1996). These parameters provide information on ecologically significant features of surface and ground water regimes influencing aquatic, wetland, and riparian ecosystems. For example, the timing of annual extreme discharge conditions would affect the life cycles of organisms that are

adapted to the natural flood cycle [13-14]. Due to discrete time series data and research objectives, this paper chose those indicators except for frequency and duration of high and low pluses.

**Reservoirs combined operation model.** Based on the measured discharge from 1965-1999 at Pingshan Gauge Station, 1974, 1979 and 1972 was choose to stand for the high flow year, the normal flow year and the low flow year, and every hydrological year is from June 1 to May 31 next year. Using reservoir operation scheduling, the four reservoirs combined operation model was established for the purpose of the maximum generated energy, considering the minimum relese discharge of XJB resevoir 1200 $m^3/s$, and developed the POA algorithm for solving optimization model. Fig 2 showed the daily discharge at Pingshan Gauge Station before regulatin and XJB Gauge Station after regulation in different typical year.

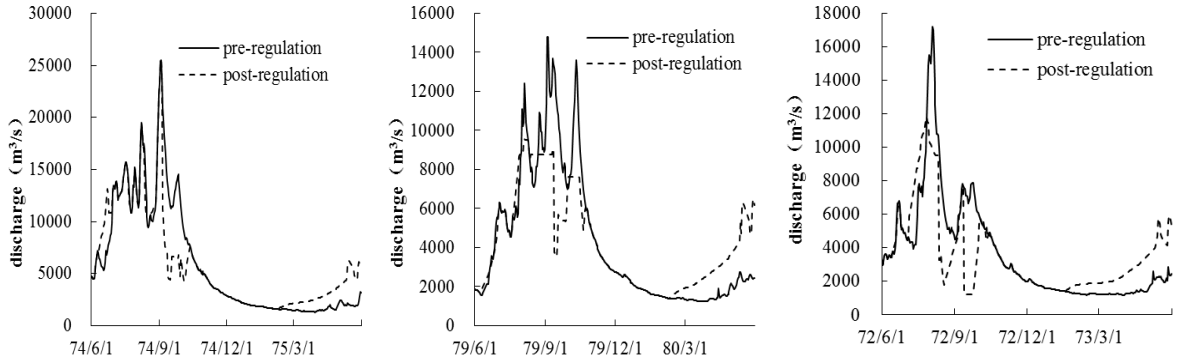


（a）high flow year （b）normal flow year （c）low flow year

**Fig.2 Comparisons between the measured flow at Pingshan Gauge Station for unregulated condition and the simulated flow at Xiangjiaba Gauge Station for regulated condition**

**Hydrodynamic model.** MIKE11 was used to simulate the flow and water level from Pingshan Gauge Station to Zhutuo Gauge Station. The flow at Pingshan and XJB Gauge Station as upper boundary was input, and the water level at Zhutuo Station as lower boundary, the discharge of Hengjiang, Minjiang, Tuojiang and Chishuihe as boundary. The dischage in 2001 for calibration model parameter, the discharge in the normal year for testing the model, the measured and simulated daily table at Luzhou Gauge Station was shown as Fig.3.

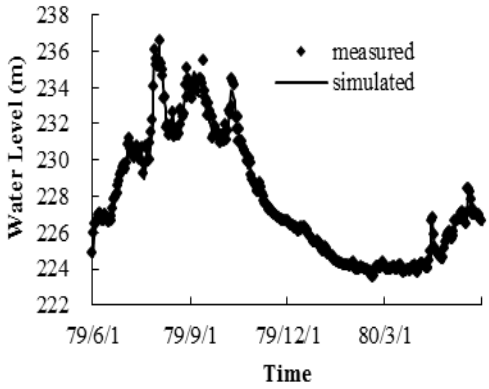


**Figure 3 Comparison of the measured and simulated water level at Luzhou Gauge Station**

## Result

**Variation in the ecohydrological indicators.** Table 1 and Table 2 show the variation in the eco-hydrological indicators at XJB and Zhutuo Station. The indicators at XJB would be changed significantly after the reservoirs regulation. The monthly discharge from March to May increased by more than 50% in different typical year, up to 131% on May in high flow year. The timing of the 1-day minimum discharge was significantly changed, especially retardation time in low flow year up to 165 days, when the reservoir was in storage period. If the eco-hydrological process in the reserve changed

as significantly as XJB Station, the growth and reproduction of the fishes would be influenced negatively.

The change of most indicators at Zhutuo Station was smaller than at XJB Station. The change rate of the monthly dischage from March to May in differently typical year was from 32% to 57%, and the timing of 1-day minimum discharge was ahead of 36, 8, 67 days in respectively high, nomal, low flow year. It indicated that the tributaries confluence could effectively mitigate the impacts of the cascaded reservoirs on eco-hydrology in the downstream.

**Tab.1 The change rate of the eco-hydrological indicators at Xiangjiaba and Zhutuo Gauge Station**

| | XJB Gauge Station | | | Zhutuo Station | | |
|---|---|---|---|---|---|---|
| | high flow year | normal flow year | low flow year | high flow year | normal flow year | low flow year |
| January | 0% | 0% | 10% | 0% | 0% | 4% |
| February | 18% | 15% | 49% | 9% | 7% | 27% |
| March | 66% | 73% | 67% | 32% | 37% | 39% |
| April | 93% | 102% | 114% | 48% | 51% | 57% |
| May | 131% | 118% | 116% | 55% | 53% | 49% |
| June | 29% | 0% | 0% | 18% | 0% | 0% |
| July | 0% | 6% | 19% | 0% | 3% | 10% |
| August | 0% | -3% | -39% | 0% | -1% | -28% |
| September | -42% | -39% | -51% | -26% | -22% | -34% |
| October | -17% | -19% | 0% | -12% | -11% | -1% |
| November | 0% | 0% | 0% | 0% | 0% | 0% |
| December | 0% | 0% | 0% | 0% | 0% | 0% |
| 1-day min | 21% | 12% | 2% | 2% | 9% | 21% |
| 3-day min | 21% | 13% | 2% | 0% | 9% | 21% |
| 7-day min | 20% | 14% | 0% | 0% | 7% | 21% |
| 30-day min | 24% | 18% | 24% | 4% | 5% | 24% |
| 90-day min | 29% | 29% | 36% | 15% | 17% | 21% |
| 1-day max | 0% | -36% | -31% | 0% | 0% | 0% |
| 3-day max | 0% | -34% | -30% | -2% | -2% | -2% |
| 7-day max | -2% | -27% | -29% | -4% | -2% | -2% |
| 30-day max | -6% | -20% | -10% | -2% | -6% | -1% |
| 90-day max | -7% | -20% | -17% | -6% | -10% | -7% |
| Rise rate | -34% | -57% | -41% | -7% | -10% | -5% |
| Fall rate | 37% | -30% | 51% | 12% | -1% | 19% |
| Number of reversals | -29% | -35% | -40% | 30% | 5% | 0% |

**Tal.2 The change of the timing of annual 1-day maximum and minimum discharge**

| Typical yerar | Timing of 1-day min | | Timing of 1-day max | |
|---|---|---|---|---|
| | XJB | Zhutuo | XJB | Zhutuo |
| high | -53 | -36 | 0 | -27 |
| nomal | -42 | -8 | -30 | -4 |
| low | 165 | -67 | -7 | 0 |

“-”:ahead , “+”: delay

**The change in indicators along the mainstream.** As shown in the Table 1, the indicator alteration between XJB and Zhutuo Station is not completely equal. For example, the change rete of 1-day, 3-day and 7-day minimum discharge at Zhutuo Station is larger than at XJB Station, and other indcators is smaller . The ecological hydrology indexes are divided into four categories, respectively long-term discharge, short-term discharge, timing of extreme discharge and rate and frequency of change. The long-term discharge includes monthly discharge, 30-day mean discharge and 90-day mean discharge, and the short-term discharge includes 1-day, 3-day, 7-day mean discharge.

The long-term discharge indicators. Taking the discharge on May for an example, it was analyzed of the variation in the long-term indicators along the river. As shown in Fig.4a, the variation rate of the discharge on May at Lizhuang Station decreased by more than 50% in different typical year, while the difference among Lizhuang, Luzhou and Zhuotuo is less than 10%. For long-term discharge indicators, the tributaries confluence did not change the difference along mainstream between pre-regulation and post-regulation, but the discharge increasing due to the tributaries confluence caused the change rate decrease. The discharge on May at XJB increased by more than doubled after regulation while increasing by about 50% at Zhutuo, but the variable amplitude was 2800$m^3$/s both at XJB and Zhutuo Station.

The indicators of short-term discharge. Taking 1-day minimum discharge for an example, the variation tendency in short-term discharge may be differnt in high, normal and low flow year (Fig.4b). In low flow year, 1-day minimum discharge at XJB was 1180 $m^3$/s before regulation, emerged in low flow period; while after regulatin it wasesigned minimum release discharge 1200$m^3$/s and emerged in storage period, basically the same as pre-regulation. 1-day minimum discharge at Lizhuang, Luzhou and Zhutuo emerged in low flow period both pre-regulation an post-regulation, and the reservior regulation caused the minimum discharge increase by about 400$m^3$/s， therefore, the change rate was larger than XJB. In normal and high flow year, the minimum discharge at XJB after regulation still emerged in low flow period. The variation of the minimum discharge at the four stations was essentially the same in normal flow year, while in high flow year the variation at Lizhuang, Luzhou and Zhutuo was smaller than at XJB. For the short-term indicators, the tributaries confluence may lead to the variation in the timing with distance, so the change rate along the mainstream was different.

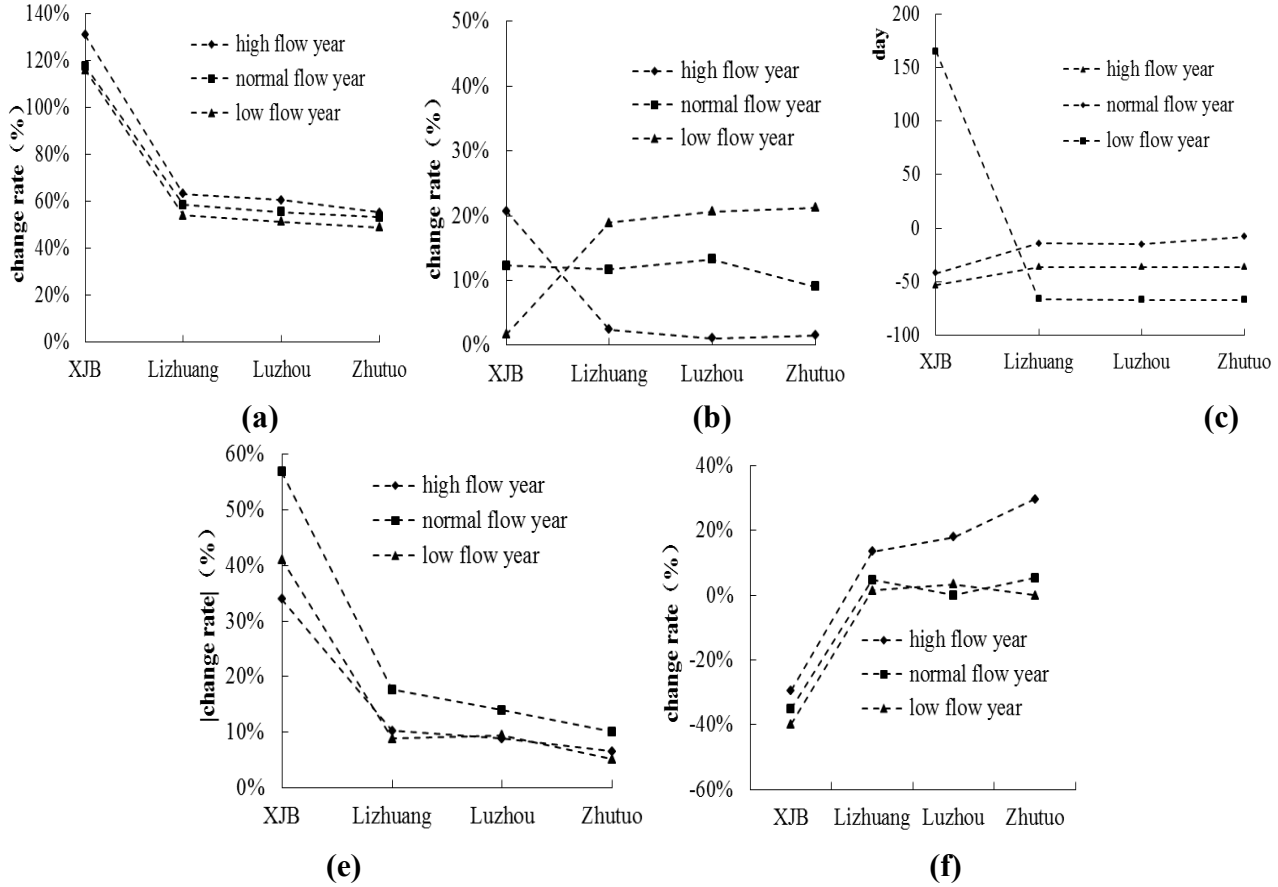


**Fig.4 The variation along river in (a) the discharge on May, (b) the 1-day minimum discharge, (c) the timing of minimum discharge, (d) the rise rate and (f) the number of reversals**

The indicators of timing. Fig.4c showed the variation in the timing of minimum discharge along the mainstream before and after regulation. Due to the regulation of the cascaded reservoirs, the timing of minimum discharge at XJB in low flow year was in storage period (not in low flow period). The minimum discharge at Lizhuang, Luzhou and Zhutuo was in advance about two month, but still in low flow period. The minimum discharge at all stations in normal and high flow year emerged in the low flow period, and the variation with distance was not significant.

The rate and frequency of change. The variation tendency in rise and fall rate with distance was same, taking the rise rate as an example. The absolute value of variation in rise rate decreased with distance in different typical year as shown in Fig.4e. The number of reversals at XJB decreased by 30% after regulation, and the variation at Lizhuang, Luzhou and Zhutuo almost was equal to 0 in low and normal year, but increased in high flow year (Fig.4f).

## Discussion

**Impact of the tributaries confluence.** It was conclued by above anlysis that the eco-hydrological characteristic at Lizhuang, Luzhou and Zhutuo was almost identical. The runoff of the Minjiang accounts for 60% of the runoff of Pingshan Station, and Hejiang, Tuojiang and Chishuihe accounts respectively for 6%, 11% and 7%. The confluence of Minjiang could effectively mitigate the impacts on eco-hydrology in the downstream of the confluence, and the mitigation of others three tributaries were not significant. It was the reason why the eco-hydrological process in the downstream of the Minjiang River confluence did not change significantly with distance.

The typical year chose is before 1980 when there was not large constructed reservoir. Since 20th century, there are several reservoir built in the Yalongjiang and Minjiang，including Ertan reservoir impounding in 1999 and Pubugou reservoir impounding in 2010, the regulated storage capacity respectively $33.7\times10^8 m^3$ and $38.8\times10^8 m^3$. The reservoir in tributaries has influenced on hydrology at Zhutuo Station, and the Fig.5 shows the variation in discharge on January since 1991. The increase after 2000 and the maximum discharge in 2011 are related with the reservoir operation. In addition, the total regulated storage capacity all planning reservoir in the Daduhe River ( a tributary of Minjing) is up to $105.5\times10^8 m^3$, and the effect of the reservoir operation in the tributary may weaken the mitigation effect of tributaries confluence.

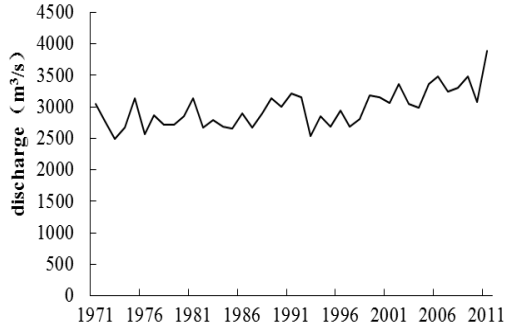


**Fig.5 The temporal variation in the discharge on January at Zhutuo station**

**Ecological impact of the eco-hydrology alteration.** The reaches in the downstream of the Minjiang River confluence play an important role in maintaining the natural habit integrity. The increase (<20%) in the minimum discharge caused by reservoir operation could result in increasing in water depth, perhaps in favor of the fish wintering. The increase in the pre-flood high flow may impact the fish spawning and migration. Because the spawning in autumn is not the main behavior in the reserve [15], the decrease in the discharge during the storage period would not have significant impact on the fish reproduction.

**Impact of the cascaded reservoirs on the other habitat factors.** The cascaded reservoir operation would also cause changes in water temperature, dissolved oxygen and sediment and other

processes, accompanied by changes in the hydrological regime. While the four cascaded reservoirs combined operated, the 34 species of fish with reproduction record in the reserve will be affected by water temperature variation [16]. From the existing monitoring results, the dissolving oxygen in the reserve has not been influenced significantly by current reservoir operation since the XJB and XLD reservoir impounded. But the clean water may destroy the balance of sediment transport in the reserve, which would have a greater impact on fish habitat and nutrients.

**Impact of reservoir regulation.** According to the current flood control scheduling, the cascaded reservoirs need to lower water level to flood water level in pre-flood high flow period, which will produce higher flow than natural conditions. The effects of high flow and flood pulse on sediment erosion will impact adversely on the fish within the reserve, so the maximum flow should be confined considering the ecological demands [15]. The flood diversion areas in the middle reaches of Yangtze River could substitute perhaps for flood control by cascade reservoirs at Jinsha River downstream as flood risk management alternative [17]. In addition, if the joint optimal operation with in both tributaries and mainstream was carried out, the influence on the reserve ecosystem would be reduced.

## Summary

The cascaded reservoirs have great impacts on eco-hydorlogy at XJB station, and the import of the Minjiang could mitigate the influence on the eco-hydrology in the downstream of the entry point of Mingjiang. The pre-flood high flow increaced by about 50% in the downstream of the Minjiang confluence, and other eco-hydrological indicators changed slightly, which may have less impact on the fish.Taking the impacts of the tributaries reservoirs on confluence discharge into consideration, the mitigation effect of tributaries confluence may weaken. The effect of variation in other habitat factors on the fish may be greater than the variation in eco-hyrology due to cascaded reservoirs operation. The further research on the impact on other environmental factors needs to be carried out, to provide theoretical basis and technical support for the ecological operation of cascade reservoirs and the reserve management.

## Acknowledgements

The study is supported by the 12th Five-Year National Science and Technology Support Projects (2012BAC06B01) and China Three Gorges Corporation (07011033).

## References

[1] Poff N L, Allan J D, Bain M B, et al. The natural flow regime-a paradigm for river conservation and restoration [J], Bioscience, 1997, 47:1163-1174.

[2] Wang Junna, Dong Zheren, Liao Wengen, et al. An environmental flow assessment method based on the relationships between flow and ecological response: A case study of the Three Gorges Reservoir and its downstream reach. Sci China Tech Sci, 2013, 56(6):1471-1484.

[3] Richter B D, Mathews R, David L, et al. Ecologically sustainable water management: managing river flows for ecological integrity [J]. Ecological Applications, 2003, 13(1): 206-224.

[4] Poff N L, Julie K H, Zimmerman. Ecological responses to altered flow regimes: a literature review to inform the science and management of environmental flows [J]. Freshwater Biology, 2010, 55(1):194-205.

[5] Murchie K J, Hair K P E, Pullen C E, et al. Fish response to modified flow regimes in regulated rivers: research methods, effects and opportunities [J]. River research and applications, 2008, 24(2):197-217.

[6] Rice S P, Greenwood M T. Tributaries, sediment sources and the longitudinal organization of macroinvertebrate fauna along river systems [J]. Canada Journal of Fish Aquatic Science, 2001, 58：824-840.

[8] Preece R M, Jones H A. The effect of Keepit Dam on the temperature regime of the Namoi River, Australia. River Research and Applications, 2002, 18:397-414.

[9] Wang Bo, Huang Wei, Yin Zhengjie. Impact on river ecological flow of large cascade reservoirs—for example cascade reservoirs in downstream reaches of Jinshajiang River [J]. Resources and Environment in the Yangtze Basin, 2009,18(9):860-864.

[10] Wang Junna, Li Chong, Liao Wengen. Impacts of the regulation of Three Gorges-Gezhouba cascaded reservoirs on downstream eco-hydrology [J]. Journal of Hydroelectric Engineering, 2011, 30(2):84-90.

[11] Guo Wenxian, Wang Hongxiang, Xu Jianxin, et al. Effects of Three Gorges reservoir on the downstream eco-hydrological regimes during the spawning of important fishes [J]. Journal of Hydroelectric Engineering, 2011, 30(3):22-26.

[12] Olden J D, Poff N L. Redundancy and the choice of hydrologic indices for characterizing streamflow regimes [J] River Research and Applications, 2003, 19(2):101-121.

[13] Richter B D, Baumgartner J V, Powell J, et al. A method for assessing hydrologic alteration within ecosystems [J]. Conservation Biology, 1996, (10): 1163-1174.

[14] Richter B D, Baumgartner J V, David P, et al. A spatial assessment of hydrologic alteration within a river network [J]. Regulated Rivers: Research and Management, 1998(14), 329-340).

[15] TNC. The final report on the workshop for the ecological flow in the downstream of Jinshajing [R], 2009.

[16] Luo Huihuang, Li Qian, Li Chong. The impact of water temperature during the fish reproduction in the upper Yangtze River due to the cascade development in the lower Jinsha River [J]. Journal of China Institute of Water Resources and Hydropower Research, 2012, 10(4):256-259.

[17] TNC. The feasibility study on ecological compensation funding mechanism for sustainable hydropower in Yangtze River [R], 2010.

*Applied Mechanics and Materials Vols. 580-583 (2014) pp 1961-1965*
*© (2014) Trans Tech Publications, Switzerland*
*doi:10.4028/www.scientific.net/AMM.580-583.1961*

# Shape Optimization for Arch Dam with Sequential Quadratic Programming Method

Yin Duan[1, a], Wei Yuan[2, b], Huibo Liu[1, c]

[1]Changjiang Institute of Survey, Planning, Design and Research, Wuhan 430010, China

[2]State Key Laboratory of Water Resource and Hydropower Engineering Science, Wuhan University, Wuhan 430072, China

[a]duanyin_0224@126.com, [b]yw_0201@126.com, [c]liuhuibo@cjwsjy.com.cn

**Keywords:** Arch dam, Optimization design, FEM, Sequential Quadratic Programming method

**Abstract:** The sequential quadratic programming method is introduced in arch dam shape optimization design. In the optimization computation, the arch dam volume is taken as objective function, and the calculation is realized by automatically considering loading process, equivalent stress computation and simulation of shape optimization for arch dam based on FEM. A parabola arch dam is used as a numerical example. The result shows that the optimized figure is much safer and more practical, which indicates that the SQP method is an effective way for optimization design of arch dam shape.

## Introduction

The geometric shape of arch dam is a main factor to influence its safety and stability. And it will also affect the project cost. Accordingly, considering the safety and economy, it is very important to optimize the geometric shape of arch dam [1].

Optimization design of arch dam Shape, which belongs to constrained nonlinear programming problem, is to find out the optimal shape of dam at the given boundary conditions and constraints by means of mathematical programming method.

There are many optimization methods in recent years, such as complex method [2-3], generalized multiplier method, general reduced gradient method, and sequential quadratic programming method (SQP method) [4-5].

The SQP method, which combines the advantages of the steepest descent algorithm, quasi-Newton method, POWELL conjugate gradient algorithm and BFGS variable metric algorithm, has high computational efficiency and is recognized as the best algorithm for solving smooth nonlinear programming problem. In this paper, the SQP method will be introduced in optimization design of arch dam shape.

## Definition of the problem

Model of arch dam configuration optimization is expressed as seeking for optimization variable $X=[X_1, X_2, ..., X_n]^T$ to make the objective function to minimum, and meeting the constraint conditions on geometry and structural responses such as stress, displacements and natural frequencies, etc.

*(1) The description of the geometric model of arch dam*

Geometric model of arch dam is used to describe the geometry, size and location of arch dam. Usually, the successive type geometric model is adopted on the shape design of arch dam. Upstream face curve, downstream face curve, middle face curve, and thickness of arch ring all can be used to describe the geometric model of arch dam. In this paper, a parabola arch dam is used as an example. Based on that, the middle face curve and thickness of arch ring are used to give the description of the geometric model of arch dam.

Fig.1 shows us the arch crown cantilever, which is the highest beam in arch dam. The section of arch crown cantilever can be defined as long as the curve *Yc(z)* of middle face and the thickness *Tc(z)* of arch crown cantilever has been defined.

Fig.2 shows us the horizontal arch ring of arch dam. The geometric model of horizontal arch ring can be described by the arch axis function *Yi* and the thickness of arch ring *Ti*.

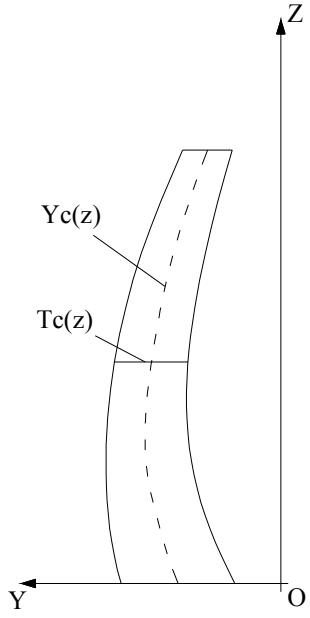


Fig.1 Arch crown cantilever

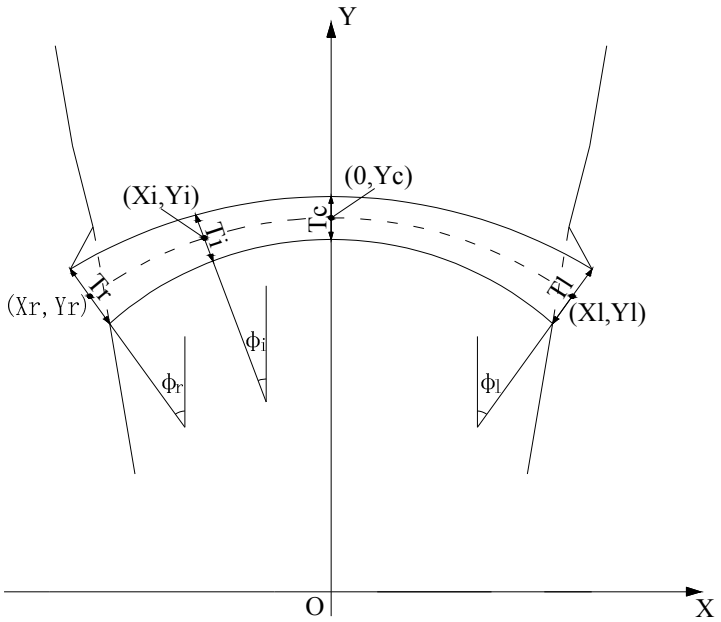


Fig.2 Horizontal arch ring

According to the parabolic equation, every point on center line of arch can be written as:

$$Yi = \begin{cases} Yc - Xi^2/(2\times Rcr) & (Xr \le Xi \le 0) \\ Yc - Xi^2/(2\times Rcl) & (0 < Xi \le Xl) \end{cases} \tag{1}$$

Thickness *Ti* of arch ring can be expressed as:

$$Ti = \begin{cases} Tc + (Tr - Tc)\times(1-\cos\phi i)/(1-\cos\phi r) & \phi r \le \phi i \le 0 \\ Tc + (Tl - Tc)\times(1-\cos\phi i)/(1-\cos\phi l) & 0 < \phi i \le \phi \end{cases} \tag{2}$$

Where: *Yc* is *Y* coordinate of centre of crest circle. *Xl(Xr)* is *X* coordinate of left(right) arch abutment. *Rcl(Rcr)* is arch centerline's curvature radius of crest cantilever of left(right) semi-arch. *Rcr(Rcl)* can also be written with *Yl(Yr)* which is *Y* coordinate of left(right) arch abutment, $Rcl = Xl^2/2\times(Yc-Yl)$, $Rcr = Xr^2/2\times(Yc-Yr)$. *Tc* is thickness of arch crown cantilever, *Tl(Tr)* is thickness of left(right) arch abutment.

*(2) Optimization variables*

Optimization variables of arch dam shape optimization are used to describe the arch dam's configuration. By changing them, the configuration of arch dam can be adjusted neatly to ensure the feasibility of seeking for the optimum configuration. For a parabola arch dam, the configuration of arch dam can be described by above 8 variables(in Eq.1~2), each of which can be written as following thrice function of z coordinate axis:

$$F = a + b\times\frac{Z}{H} + c\times(\frac{Z}{H})^2 + d\times(\frac{Z}{H})^3 \tag{3}$$

*(3) Objective function*

Usually, the lowest cost or dam concrete earthwork is used as objective function in arch dam configuration optimization.

$$V = \int_{zbot}^{ztop} A(z)dz \tag{4}$$

Where: *zbot* and *ztop* separately represent dam base elevation and crest elevation，*A(z)* is Area of Horizontal arch ring.

*(4) Constraint conditions*

Constraint conditions are parameters designed to ensure safety and convenience. For arch dam, the main constraint conditions include geometry constraint conditions, stress constraint conditions, and so on.

1) Constraint of the minimum of dam top thickness: $t_{\min} - \overline{t_1} \geq 0$

2) Constraint of maximum overhanging angle of upstream and downstream faces: $m_1 - \overline{m}_1 \leq 0$

3) Constraint of maximum center angle at control elevation: $\varphi_{\max} \leq [\varphi]$

4) Stress constraint conditions can be expressed as follows: $|\sigma_t|_{\max} \leq [\sigma_t]$; $|\sigma_c|_{\max} \leq [\sigma_c]$

Where: $\overline{t_1}$ is allowable thickness. $\overline{m_1}$ is allowable overhanging degree. $[\varphi]$ is allowable center angle. $[\sigma_t]$ and $[\sigma_c]$ separately denote the allowable tensile stress and compression stress.

**Math model**

The mathematical model of optimization of arch dam shape can generally expressive as follows.

Objective function: min *f(x),* and Constraint function: s.t. *c(x)=0 i=1,2,...,m* (5)

Where: design variable $\{x\}=[x_1,x_2,...,x_n]^T \in R_n$, objective function *f(x)* and constraint function *c(x)* are functions defined in $R_n$.

The problem above can be written as following unconstrained problem by applying Lagrange function.

$$\min L(x,\lambda) = f(x) + \lambda^T c(x) \tag{6}$$

Where $\lambda = (\lambda_1, \lambda_2, \cdots, \lambda_m)$ is Lagrange Multiplier.

The extreme value condition of unconstrained optimization problem (K-T condition) is:

$$\nabla L(x,\lambda) = \nabla f(x) + \nabla c(x)\lambda = 0 \quad \text{and} \quad c(x) = 0 \tag{7}$$

Where, $\nabla c(x) = [\nabla c_1(x), \nabla c_2(x), \cdots, \nabla c_m(x)]$, $\nabla c_j(x) = [\frac{\partial \nabla c_j}{\partial x_1}, \frac{\partial \nabla c_j}{\partial x_2}, \cdots, \frac{\partial \nabla c_j}{\partial x_n}]^T$, $j = 1,2,\cdots,m$

Obviously, the solution of Eq.(7) is optimal solution of unconstrained problem(6). We can solve the Eq.(6) by applying Newton method, and the iterative formula can be written as:

$$x^{(k+1)} = x^{(k)} - G_{(k)}^{-1}\nabla L(x^{(k)}, \lambda^{(k)}) = x^{(k)} - G_{(k)}^{-1}(\nabla f(x^{(k)}) + \nabla c(x^{(k)}))\lambda^{(k)} \quad \text{and}$$

$$x^{(k+1)} = x^{(k)} - \nabla c(x^{(k)})^{-1} c(x^{(k)}) \tag{8}$$

Where, $G_{(k)}^{-1}$ is the Hesse inverse matrix of Function $L(x,\lambda)$ at point $x^{(k)}$. Avoiding Hesse Matrix inversion，a variable matrix $H_{(k)}$ is introduced to approximate Hesse Matrix during the iterative process(Approximation method will be introduced later).

Therefore Eq.(8) can be modified as:

$$\begin{bmatrix} H & \nabla c(x) \\ \nabla c(x) & 0 \end{bmatrix} \begin{bmatrix} d \\ \lambda \end{bmatrix} = -\begin{bmatrix} \nabla f(x) \\ \nabla c(x) \end{bmatrix} \tag{9}$$

Where, $d = x^{(k+1)} - x^{(k)}$, $x = x^{(k)}$, $\lambda = \lambda^{(k)}$, $H = H^{(k)}$.

Eq.(9) is just iterative equation of K-T condition(7) by applying Newton method. It's easy to prove that iterative formula (9) is also the K-T condition of the following QP problem:

$$min \quad \frac{1}{2}d^T Hd + \nabla f(x)^T d \qquad \text{and} \qquad s.t. \ \ \nabla c(x)^T d + c(x) = 0 \tag{10}$$

Because the Lagrange function of the QP problem is:

$$L(d,\lambda) = \frac{1}{2}d^T Hd + \nabla f(x)^T d + \lambda^T [\nabla c(x)^T d + c(x)] \tag{11}$$

Thus, the *K-T* condition of local minima can be written as:

$$\nabla_d L(d,\lambda) = Hd + \nabla f(x) + \nabla c(x)\lambda = 0 \quad \text{and} \quad \nabla_\lambda L(d,\lambda) = \nabla c(x)^T d + c(x) = 0 \tag{12}$$

From the discussion above, we master the mainly basic steps of the SQP method. Firstly, we gain the solution of QP problem (10) by applying Newton method on *K-T* conditions(7) of question(5). Then by solving QP problems (10), we get a new iteration point $(x^{(k+1)}, \lambda^{(k+1)})$, and start a new iteration. And after that, we repeat the steps above until we get approximate optimal solution.

**Numerical examples**

In this section, a parabola arch dam is used as an example. The main parameter of the dam can be described concisely as follows:

*(1) Calculation parameter*

The height of dam is 92m. The silt saturation is 18.5KN/m$^3$. The silt internal friction angle is 14°. Material parameters of the dam concrete are: volume weight of $\gamma_c$ = 24KN/m$^3$, poisson ratio of $\mu_c$ =0.1667, linear expansion coefficient of $\alpha=0.7\times10^{-5}$/℃, elastic module of $E_c$=25.5GPa. internal friction angle of dam f=14°.

Material parameters of the foundation rock are: elastic module of 14.2GPa, Poisson ratio of 0.25, linear expansion coefficient of $1.0\times10^{-5}$/℃ and bulk density of 27KN/m$^3$.

Dam base elevation is assumed to be 0. Temperature load is shown in Table 1. In this calculation we only consider the condition of fixing the location of arch abutment during the optimization. Then the objective is to find the smallest arch dam volume by mainly adjusting following four variables in the calculation: the thickness of crown cantilever, the thickness of left arch abutment, the thickness of right arch abutment, and arch centerline's curvature radius of crest cantilever. And all the other parameters can be described by these variables.

Table 1 Temperature load

| Elevation (m) | 0 | 20 | 40 | 60 | 80 | 92 |
|---|---|---|---|---|---|---|
| Tm(℃) | 2.71 | 0.66 | -0.25 | 0.02 | 1.39 | 5.84 |
| Td(℃) | 14.37 | 12.46 | 13.19 | 11.36 | 6.80 | 0 |

*(2) Constraint conditions*

The main constraint conditions in this calculation are as follows. Allowable overhanging degree is 0.3. Allowable center angle is 110°. Allowable tensile stress is 1.5MPa. Allowable compression stress is 5.0MPa.

*(3) Calculation result and analyzing*

The stress computation adopts 3D linear elastic FEM. The optimizing mesh mainly adopts Eight-node hexahedron element, supplemented by tetrahedron and prism for the transition of boundary and rock structure. Comparison of characteristic parameters before and after optimization is shown in Table 2. Considering the figures above, the calculation will converge in about 7~8 iterative operations, which shows that SQP method has high computational efficiency.

What's more, comparing the shape after optimization to the shape before optimization, the bottom thickness has been obviously reduced, while both maximum overhanging degree and maximum center angle increase, making the whole body turns to be more convex to upstream. The dam volume of parabola configuration decreases from primary $17.7\times10^4m^3$ to $14.7\times10^4m^3$ by 17%. After optimization the maximum principle tensile stress of dam body is 1.48MPa and the maximum principle compression stress is 4.96MPa. The indexes can meet the stress control standards basically.

Therefore, the configuration after optimization is obviously better than the before one. And SQP method is proved to be an effective method for optimization design of arch dam shape.

Table 2 Comparison of characteristic parameters before and after optimization

| | before optimization | after optimization | Allowable value |
|---|---|---|---|
| Dam volume ($10^4m^3$) | 17.7 | 14.7 | ------ |
| Max overhang degree at upstream | 0.152 | 0.198 | 0.3 |
| Max overhang degree at downstream | 0.223 | 0.266 | 0.3 |
| Max center angle | 86.22° | 86.60° | 110° |
| Max tensile stress（MPa） | 0.95 | 1.48 | 1.5 |
| Max compression stress（MPa） | 3.933 | 4.96 | 5.0 |

## Conclusions

The sequential quadratic programming method is introduced in optimization design of arch dam shape in this article. A sample computation is done by using the program developed by the author. The results indicate that after optimization, the shape of arch dam is thinner, and the geometrical curvature is increased in some degree, the volume is decrease in nearly 17%, the tensile and pressure stress almost reach the constrain boundary, means the shape reaches the best shape in theory. Convergence is reached after 7~8 iterations, indicating the program is efficient and stably.

## References

[1] More.J.J, Wright.S.J. Optimization Software Guide [M]. SIAM, Philadelphia, 1993.

[2] Li Shou-yi, Ding Lu-jun, Zhao Li-juan, et al. Optimization design of arch dam shape with modified complex method[J]. Advances in Engineering Software, 2009, 40(9): 804-808.

[3] Zhang Xiao-fei, Li Shou-yi, Chen Yao-long. Optimization of geometric shape of Xiamen arch dam [J]. Advances in engineering software, 2009, 40(2): 105-109.

[4] Zhou Wei, Zhou Chang-bin, Chang Xiao-lin. A contact model based on the SQP algorithm and engineering application [J]. Applied Mathematics and Computation, 2008, 198(2): 916-924.

[5] Zhu Bo fang. Optimum design of arch dams [J]. Dam Engineering, 1990, 1(2):131-145(in chinese).

*Applied Mechanics and Materials Vols. 580-583 (2014) pp 1966-1970*
*© (2014) Trans Tech Publications, Switzerland*
*doi:10.4028/www.scientific.net/AMM.580-583.1966*

# Unsteady Flow Impact on Downstream Waterways and Control Measures Research Of PingBan hub In Nanpanjiangjiang River of GuiZhou

Xin Liu[1,2,a]

[1] Key Laboratory of Engineering Sediment of Ministry of Communications; Tianjin Research Institute of Water Transport Engineering, Tianjin 300456, China

[2] School of Civil Engineering, Tianjin Key Laboratory of Port and Ocean Engineering, Tianjin University, Tianjin 300072, China

[a]liuxin806@163.com

**Keywords:** unsteady flow; spread regularity; rapid characteristic analysis; channel improvement

**Abstract:** After the completion of the hub on river, its scheduling unsteady flow generated an adverse impact on the downstream navigation. In this paper, according to the unsteady flow data of PingBan hub in Nanpanjiangjiang River in Guizhou province, researched unsteady flow spread characteristics and rule in hub downstream channel. Studies have shown that: unlike general water level changes in hub downstream, the waterlevel amplitude attenuation along is not obvious in researched reach; Clear the concept of unsteady flow additional velocity, additional slope，through this theory reveals the ship ascending rapids mechanism difficultly under unsteady flow condition. On this basis, proposed channel regulation methods and measures in hub downstream, which provided support for the hub downstream channel regulation.

Nanpanjiangjiang and Beipanjiang river all originate MaXiong mountain in ZhanYi County of YunNan Province, the two river joins at the vicinity of ZheXiang in Wangmo County of Guizhou Province and named HongShui River, belongs to ZhuJiang river system, is the main tributaries of upper main stream Xijiang River，which is an important channel to the sea in southwest region, and also is high-grade channel that Ministry of Transport planned. Longtan hydro-power station in HongShui River located in Tian'e County of GuangXi Province, which is currently under construction only next to the Three Gorges hydropower project, backwater to BaiDi shoal tail of Nanpanjiangjiangjiang River. From fluctuating backwater zone tail of BaiDi shoal upstream to upper PingBan hub is water level not linking-up reach, 28km long, which has many rapids at this range, together with the effects of unsteady flow by power station scheduling, made the navigation conditions very complex in hub downstream, increase the difficulty at water level not linking-up reach. For channel regulation, we must first analyze rapids, currently it is a technical problem in unsteady flow condition, this paper carried out research on the above theory, provides assistance to the channel regulation below the dam.

## General situation of the reach

Nanpanjiang River originate in south of MaXiong Mountain in ZhanYi County of YunNan Province, where to the confluence full-length 914km, drop 1873.7m, average slope of 2.05 ‰; The length of HuangNi river mouth to confluence in Guizhou Province is 266km, drop 428m, average slope 1.6 ‰.

Nanpanjiang River located in hilly areas. Pingban hub as a reverse regulation hub of TianShengQiaoⅡ Hydropower Station, has a certain role to cut daily regulation of which impact on downstream water level fluctuation amplitude; According to analysis, the water level ranged up to 3m ~ 4m daily in Pingban hub downstream, hours ranged up to 1.3m ~ 1.8m, still can not meet the security requirements of navigation.

Effected by water and sediment regulation of station upstream, the overall riverbed deformation and sediment problems in Nanpanjiang river are not serious, riverbed material mainly composed of bedrock, gravel, partly pebbles and coarse sand. Large slope, fast-flowing, poor flow regime, severe navigation flow conditions, and daily regulation further exacerbated the regime. Now Pingban hub to confluence 114.2km reach the standard of Ⅳ waterway, waterway scale of 1.6m×50m×330m(width × depth × bend radius), using 95% guaranteed rate of navigable which can sail 500t self-propelled motor vessels.

## Hub Overview

### 2.1 Longtan Hydropower Station

Longtan Hydropower Station is located in Guangxi province Red River upstream from the Tian'e county 15km, the fourth in cascade on the Hongshui River, involving the reservoir area in Guangxi and Guizhou provinces (regions). Recent years have the ability to regulate, privileged to electric power generation, incorporating with flood protection, navigation improvement overall efficiency, the station has gone to oprate on December 7, 2009.

### 2.2 Pingban Hydropower Station

Pingban Hydropower Station is Nanpanjiang river comprehensive development and utilization of the third cascade, linking up with TianShengQiao station(Ⅱ) upstream and Longtan station downstream. Hydropower station located in Longlin County of Guangxi province, on the Nanpanjiang river of Xinzhou river mouth upstream 200m, is a boundary river station crossing Guangxi and Guizhou provinces. Station normal pool level 440m, dead water level 432m, total reservoir capacity 310 million $m^3$, regulating capacity 101 million $m^3$, of daily regulation reservoir. By august 2005, all generator units put into operation.

## Unsteady flow rule, spread characteristics and effects on navigation conditions research

In order to develop water resources better in the river, TianShengQiao station(Ⅰ), (Ⅱ), Pingban as well as downstream Longtan hydropower station on river efftcted by flood control scheduling and electric power dispatching, which that unsteady flow of station discharged will have a significant impact on waterways navigation.

### 3.1 Spread laws and features of unsteady flow that daily regulation station generated in hub downstream

According natural waterway observation data analysis under unsteady flow conditions of Nanpanjiang river daily regulation station, sorting out the unsteady flow characteristics as follows:

3.1.1 Daily flow changes frequently

One of the features of unsteady flow, the discharge varies greatly, and the water level fluctuated wildly, changes frequently.

Under natural conditions, the average daily discharge and water level of reach are relatively stable in the dry season, and level amplitude is small, only change greatly in flood season due to the mountain rivers. After Pingban plant operated, the process of discharge changed obviously and discharge distribution was uneven, it may sudden change to several thousand from several hundred, and flow changes without regularity，which is extremely unfavorable for shipping.

3.1.2 The water level changes greatly and amplitude attenuation unconspicuous along the flow in hub downstream

Due to friction, channel storage, irregular cross-section and other factors, unsteady flow process to occur attenuation in spreading，velocity decreases, wave height becomes smaller, unsteady flow effects weaken and gradually stabilize stream.

According to data analysis of water level changes in Pingban plant downstream, daily water level fluctuation amplitude up to 3m ~ 4m, hour level luffing also reach 1.3m ~ 1.8m, level luffing great. Banba wharf located 2km downstream of Pingban hub, Baidi shoal located downstream of the Banba 67.4km, where the lowest end of Longtan hub fluctuating backwater zone in Nanpanjiang river. Seen from the figure, the hub discharged unsteady flow caused great level amplitude in Banba wharf which near the hub，and while the unsteady flow spreading from Banba wharf to downstream, wave crests became smooth along, and wave height attenuated somewhat but slower in rate of decay, the biggst wave height attenuation generally below 0.5m despite spreading more than 60 kilometers, the unsteady flow waveform changed little and peak valley is still evident, the flow showed significant unsteady flow characteristics, different from the general hub downstream unsteady flow propagation characteristics.Generally as the hub discharge spreading distance increases, wave crest tend to flat and wave trough raise, wave height reduce significantly, and after the longer distance it shows certain steady flow characteristics.

3.1.3 Wave crest flow decreasing with the wave trough flow ascending along the river

In the processs of hub discharged unsteady flow spreading along the river, because of the impact of channel storage capacity(natural river has the function of remaining surplus and supplying deficiency, storage more for reserve), peak vally overlap each other and gradually decay along the flow . Maximum flow of Pingban station is 888$m^3$ / s, the minimum is 82$m^3$ / s, when the unsteady flow spread to downstream the maximum flow decreases and minimum flow increases gradually.When it comes to Baidi shoal tail, the maximum flow and minimum flow become 798$m^3$/s, 106$m^3$/s，wave crest spread to Baidi shoal from Pingban hub takes about 9 hour.

Seen from the above, the amplitude of variation of wave crest flow and wave trough flow are further small to general in the process of unsteady flow spreading, similar to reasons of water level changes, tmainly due to the channel storage and resistance becoming smaller along the river.

3.1.4 Wave crest and trough velocity decreasing along the flow

Due to the impact of riverbed slope (riverbed slopes gradually slow down from upstream to downstream), the velocity of Wave crest and trough spreading slowly diminished.

### 3.2 The daily regulation unsteady flow in Pingban hub downstream effect on navigation conditions

The daily regulation unsteady flow in Pingban hub downstream effect on navigation conditions mainly in water depth, velocity and slope changes at stations downstream，due to the long distance of studied reach and rapids too much, take Yanzishi shoal ( away from Pingban 11.4km)as an example. Yanzishi shoal located at water lever not linking-up reach between Longtan hub and Pingban hub, whcih is "bottleneck" reach of Nanpanjiang river transportation, play a role in controlling both the grade of waterway and capacity of Nanpanjiang river. Power station scheduling cause water level of discharge fluctuated greatly and exacerbated the rapids obstructing navigation, the impact on the channel as follows by unsteady flow calculation:

①Water depth

The design flow of the river is 275$m^3$/s, corresponding design depth of 1.6m, counted the instantaneous flow process in January 1～4, 2008 of Pingban station: it is 38 hours that the flow less than design flow in total of 85 hours of discharge process, when the discharge wave spread to Yanzishi shoal it's only 35 hours, which can not meet the requirements of navigation guaranteed rate.

②Velocity

Because the discharge of unstead flow changes along with the time, and thus its hydraulic indicators such as water level, velocity and others change the same time, compared unsteady flow with the steady flow there will be an additional velocity. What's called additional velocity refers to the velocity of unsteady flow at different time points in a period of time, and the difference between the velocity of steady flow disgcharge that equal to average disgcharge of unstead flow during the same period generated is additional velocity, that $\Delta V= V-\overline{V}$, mainly to describe the impact of unsteady flow changes on vessel navigation.

Counted the instantaneous discharge of Pingban in January 1～4 ,2008 total 85 hours: the average discharge was 412 $m^3$/s during that period, research shows that: the instantaneous velocity at wave crest is bigger than velocity in average flow, and at wave trough time most of the instantaneous velocity are less than or equal to the velocity under average flow; At wave crest time (2008-1-2 2008-1-2 12:00 ~ 23:00) the additional velocity is maximum which reached to 3.15m/s at represent section when discharge of 412$m^3$ / s, and the same time which the maximum instantaneous velocity of 3.84m/s, additional velocity of 0.69m/s. The Yanzishi shoal flow torrential in natural conditions, it will further increase the velocity if coupled with the unsteady flow, which is not conducive to

③Additional slope

Additional slope refers to the slope of unsteady flow at different time points and distances in a period of time, which the difference between the slope of steady flow disgcharge that equal to average disgcharge of unstead flow during the same period generated is additional slope, that $\Delta J= J-\overline{J}$, mainly to describe the impact of unsteady flow changes on vessel navigation.

The rapids slope at wave crest is bigger than slope under average flow, at wave trough time most of the instantaneous rapids slope are also bigger than slope under average flow, only a small part period which is smaller than rapids slope under average flow. At wave crest time (2008-1-2 11:00) the additional slope is maximum which reached to 2.20‰ when discharge of 412$m^3$/s, and the same time the instantaneous slope of 2.79‰，additional slope of 0.59‰. From the results we can see: it

will form additional slope in waterway when the water level rise abruptly, which have certain adverse effects on ship sailing conditions.

## Channel improvements and regulation measures in daily regulation station downstream

### 4.1 Channel regulation in in daily regulation station downstream

The water level and discharge amplitude of daily regulation station are large, and water depth not enough in dry season that the consistency of navigation was damaged; water level rise and drop precipitous which affect the waterway stability, so it requires channel regulation in daily regulation station downstream by needed.

(1)Regulation principles

Take the Nanpanjiang river bedrock reach, based on the causes of rapids, adopted the measures of reef explosion, cuting mouth and regulating structures, etc., eliminated or reduced adverse flow regime, slowed down the velocity, facilitates navigation of the ship safely.

(2) Regulation methods

Dominated riverbank protection, strengthening revetment, removal the part of cusp, smooth shoreline，stabilize the current and reduce the mainstream swing. Regulating structures should adopt the low dam, because the Low dam safety and stability is better resistant to water level rise and drop precipitous.

### 4.2 Channel stabilization measures in daily regulation station downstream

Daily regulation station impact on downstream channel: first the water level and discharge amplitude of daily regulation station are large, and water depth not enough in dry season that the consistency of navigation was damaged; water level rise and drop precipitous which affect the waterway stability. Need to take appropriate measures, including: ①stabilize base flow and limit the minimum discharge flow; ②egalization of optimizing dispatch management

## Conclutions

The paper accorded to the unsteady flow data of PingBan hub in Nanpanjiang River in Guizhou province, carried out the research and conclusions are as follows:

(1)The unsteady flow propagation characteristics and rule in hub downstream channel research indicated that: unlike general water level changes in hub downstream, the water level amplitude attenuation along the river is not obvious.

(2)Put forward the concept of additional velocity and additional slope, revealed the ship ascending rapids difficultly mechanism under unsteady flow condition.

(3) Proposed channel regulation methods and measures in hub downstream, which provided support for the channel regulation in hub downstream.

## Reference

[1] JinXiang Yan, etc. LongTan in Hongshui River Channel Regulation Model Test Research. Tianjin Research Institute of Water Transport Engineering, 1992, 12.

[2] Mountain waterway regulation, China Communications Press, 1975, 7.

[3]XuYue Hu, Biao Li, LiJun Xu. A Review of Research on Navigation Flow Condtion of Hydro-junction. WatewrayEngineering, 2005(11):59-64.

[4]ShouRen Zhen, etc. Study on the Navigation and Power Station for Hump Modulation of Three Gorges and Gezhouba Project[J].International Journal Hydroelectric Energy. 20（2）,2002 : 7 - 12.

[5]XiaoLi Wu, etc. Effects of peak regulation at Three Gorges Power Station on navigation[J]. Advances in Science and Technology of Water Resources, 23（6）,2003：7-9.

*Applied Mechanics and Materials Vols. 580-583 (2014) pp 1971-1974*
*© (2014) Trans Tech Publications, Switzerland*
*doi:10.4028/www.scientific.net/AMM.580-583.1971*

# 3D Dynamic Numerical Simulation of Water Flow in Stilling Basin with Flaring Gate Pier

Chun Qiu, Chenglan Liu

Sichuan College of Architecture Technology, Deyang, 618000, China

Email: qiu3216@163.com

**Keywords:** Dynamic numerical simulation; VOF method; X Shaped flaring gate pier; Stilling basin

**Abstract.** 3D numerical simulation is carried out for the water flow in stilling basin with X shaped flaring gate pier when the radial gate uses four different opening velocities. The space-time change law of hydraulic characteristics is obtained. The water level in the stilling basin is relatively higher while using lower opening velocities during the processes. The negative pressure exists on weir surface while the relative opening degree is less than 0.55; the maximal pressure on the slab of ogee section and stilling basin increases and moves to downstream with the gate opening. The results can provide important basis for shape optimization of practical engineering.

## Introduction

Flaring gate pier and stilling basin is used widely as an important energy dissipater. Many numerical and experimental researches on it have been carried out recently. Y.L.Li, P.Gao[1,2] studied the velocity field in a stilling basin by numerical simulations. T.Zhang[3] simulated the water flow of FGP and the steps. H.G.Ni[4] gave a simplified hydraulic calculation method for flaring gate pier and stilling basin.

Z.X.Liang[5] studied the style designing of X shaped flaring gate piers. C.Qiu[6,7] studied the dynamic property of the water flow in stilling basin with Y shaped flaring gate pier. In this study, 3D numerical simulation on water-air two-phase flow in stilling basin with X shaped flaring gate pier is carried out by using RNG $k-\varepsilon$ model while the radial gate uses four different opening velocities, i.e., $\omega_1 = 0.2697 rad/s$ , $\omega_2 = 0.0539 rad/s$ , $\omega_3 = 0.0269 rad/s$ , $\omega_4 = 0.0135 rad/s$ corresponding to four opening times: $t_1 = 3s$ , $t_2 = 15s$ , $t_3 = 30s$ , $t_4 = 60s$ .

## Numerical model and running conditions

The fundamental equations are as follows

Continuity equation $$\frac{\partial \rho}{\partial t} + \frac{\partial \rho u_i}{\partial x_i} = 0 \tag{1}$$

Momentum equation

$$\frac{\partial \rho u_i}{\partial t} + \frac{\partial}{\partial x_j}\left(\rho u_i u_j\right) = -\frac{\partial p}{\partial x_i} + \frac{\partial}{\partial x_i}\left[\left(\mu + \mu_t\right)\left(\frac{\partial u_i}{\partial x_j} + \frac{\partial u_j}{\partial x_i}\right)\right] \tag{2}$$

$k$ equation

$$\frac{\partial(\rho k)}{\partial t} + \frac{\partial(\rho u_i k)}{\partial x_i} = \frac{\partial}{\partial x_i}\left[\left(\mu + \frac{\mu_t}{\sigma_k}\right)\frac{\partial k}{\partial x_i}\right] + G_k - \rho\varepsilon \tag{3}$$

$\varepsilon$ equation

$$\frac{\partial(\rho\varepsilon)}{\partial t} + \frac{\partial(\rho u_i \varepsilon)}{\partial x_i} = \frac{\partial}{\partial x_j}\left[\left(\mu + \frac{\mu_t}{\sigma_\varepsilon}\right)\frac{\partial \varepsilon}{\partial x_i}\right] + \frac{C_{1\varepsilon}\rho\varepsilon}{k}G_k - C_{2\varepsilon}\rho\frac{\varepsilon^2}{k} \tag{4}$$

Where $\rho$ and $\mu$ are the density of the averaged volume fraction and molecule viscosity, $p$ is modified pressure; $\mu_t$ is turbulent viscosity coefficient related to turbulent kinetic energy $k$ and turbulent viscosity dispassion ratio $\varepsilon$, which can be expressed by the equation as $\mu_t = \rho C_\mu \frac{k^2}{\varepsilon}$; $C_\mu$ is an empirical constant. The constants in the equations include, $C_{1\varepsilon}$=1.42, $C_{2\varepsilon}$=1.68, $C_\mu$=0.085, $\sigma_k$=0.7179, $\sigma_\varepsilon$=0.7179.

The length and the width of the whole computational region are 6.10m and 0.30m, respectively. The origin of coordinate system is set at the intersection of the crest of overflow dam and the centerline of the floor of the stilling basin, where the axes of X, Y and Z can be seen from Fig.1. a). Fig.1. b).show the map of grids of radial gate and X shaped flaring gate pier.

The inlet of the head water reservoir is divided into two parts; the upper and lower are both pressure inlet. The pressure function relation is used to control constant water level of reservoir. Pressure inlet is also applied on top of reservoir, spillway and stilling basin. The outlet is pressure outlet; others are solid boundary conditions.

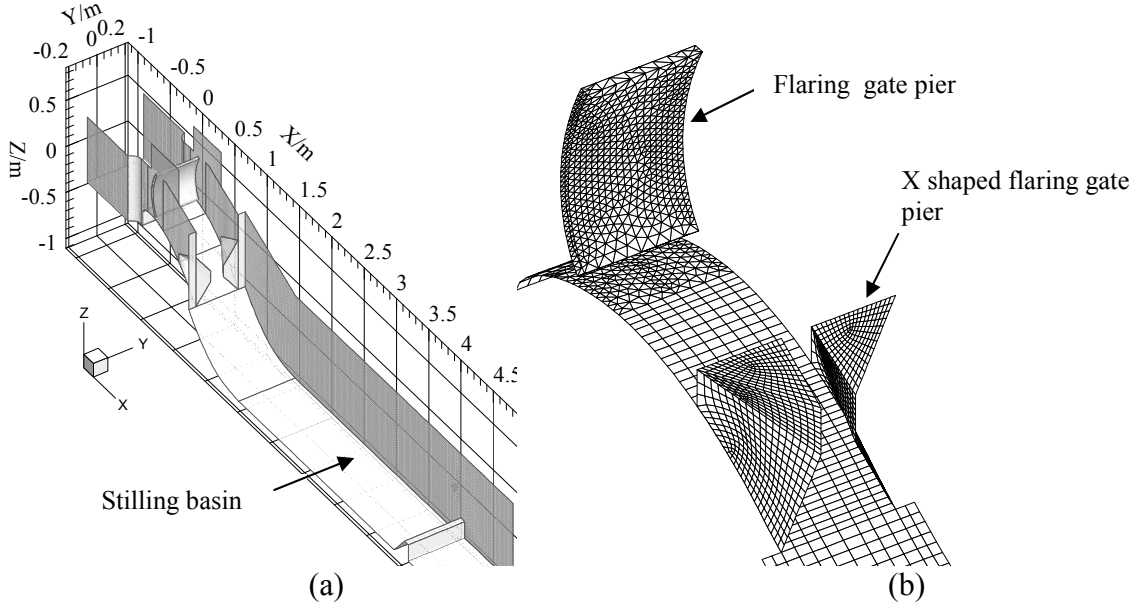


Fig.1 a) Numerical simulation region b) Map of grids of particular region

**Water Surface Profile**

From Fig.2 we can see that the depth of the mainstream becomes larger and larger with the increase of the relative opening degree (e). For the three different long opening times, water crown is formed at e=0.5 because of the deflection of side walls of the flaring gate piers, but the water crown appears until e=0.7 while using $t_1$. The height of the water crow corresponding to the lower opening velocity is always larger than that corresponding to the higher one during the whole process, and the difference is especially obvious while e>0.4; the impact caused by the water jet is also relatively larger because of the lower water level. This is the problem that the attention should be given.

During the process, water level before radial gate drops seriously at e=0.7, which is the transition period of sluice flow and weir flow. The phenomenon is also observed in model experiment.

Fig.3 shows the distribution of the velocity in the middle section of the spillway while using $t_4 = 60s$. The maximal velocity located at ogee section appears at e=0.3; the peak value is 4.4m/s and nearly invariant after than. The velocity of water flow in the stilling basin is relatively small because the water is strongly aerated and turbulent.

Velocity field of x=0.7m (the outlet of the X shaped flaring gate pier) at four different opening degrees is shown in Fig.4. The water profile near the side walls is higher than that in the middle

section part while e=0.7 because of the rapid flow shock wave caused by the side walls of flaring gate pier. The phenomenon will disappear if e<0.6. The velocity of the section increases according to time before e=0.3 and nearly unchanged after then. The maximal value is 3.9m/s.

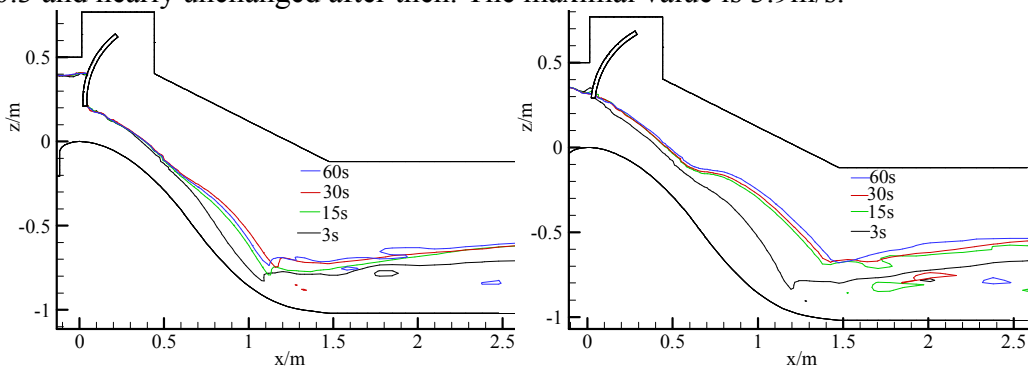


e=0.5 e=0.7

Fig.2 Comparison of the water surface profile along the middle section of overflow weir under the four different opening times

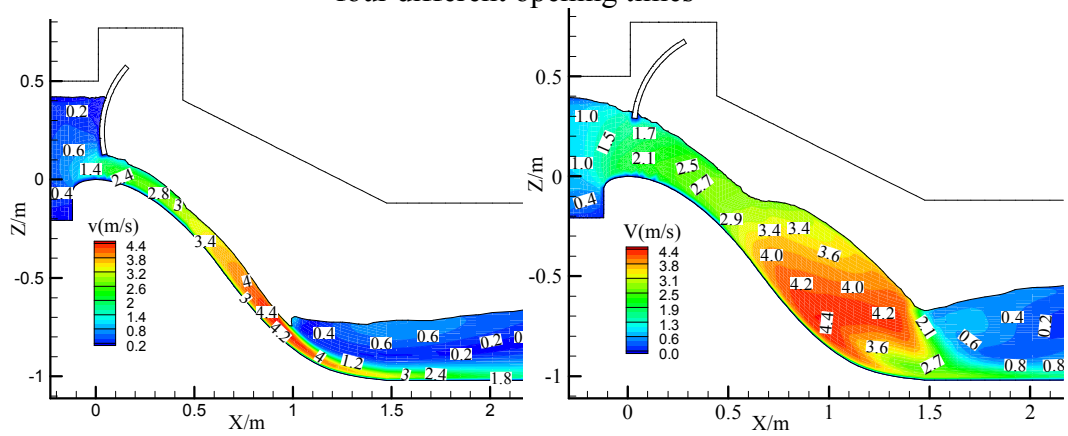


e=0.3 e=0.7

Fig.3 Velocity fields of the section y=0m while using $t_4 = 60s$

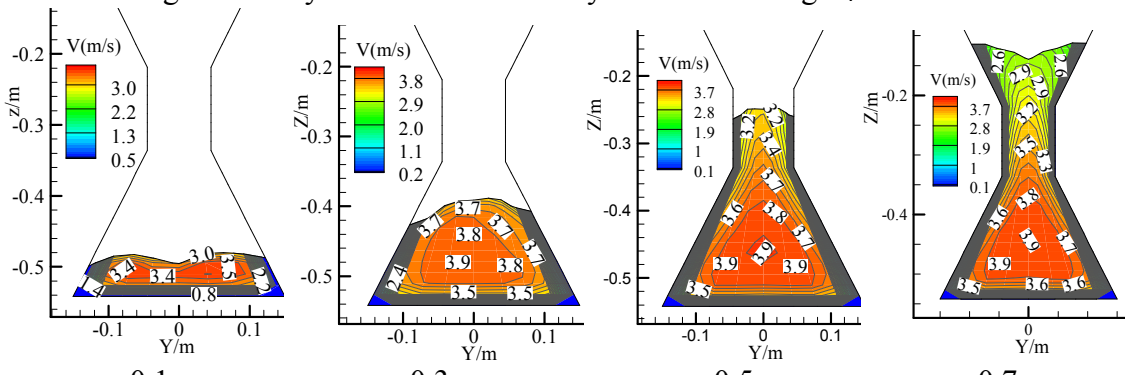


e=0.1 e=0.3 e=0.5 e=0.7

Fig.4 Velocity distribution of the cross section x=0.7m at different openings by using $t_3 = 30s$

**Pressure characteristics**

The pressure characteristics on the slab of stilling basin according to the opening degrees are shown in Fig.5. The maximal pressure on the floor is located at the rear part of stilling basin while e<0.7, which is mainly because the water jet is situated at the anti-arc region. With the water jet becomes longer, the impact region reaches the foreside of the stilling basin at e=0.7, and the value of the pressure is 6200Pa. During the whole opening process, negative pressure is always observed on the surface of X shaped flaring gate pier, which is the condition must be considered during the primary design.

The pressure distribution along the centerline of overflow dam and the stilling basin is shown in Fig.6. It can be seen that pressure of spillway before x=0.1 decreases with the opening, because the pressure is mainly static pressure produced by the water body in the reservoir. The water level of reservoir decreases according to the opening, so the pressure accordingly decreases.

The maximal pressure on the floor of stilling basin is rising and the location of maximal value shifting to downstream with the time for the water jet becomes longer, and the maximal pressure is 6109Pa while e=0.75. Negative pressure emerging at lower part of weir crest(x=0.6) sustains about 19s and disappears after e=0.5; the peak value is 193.5Pa, which is the basis for shape optimization. .

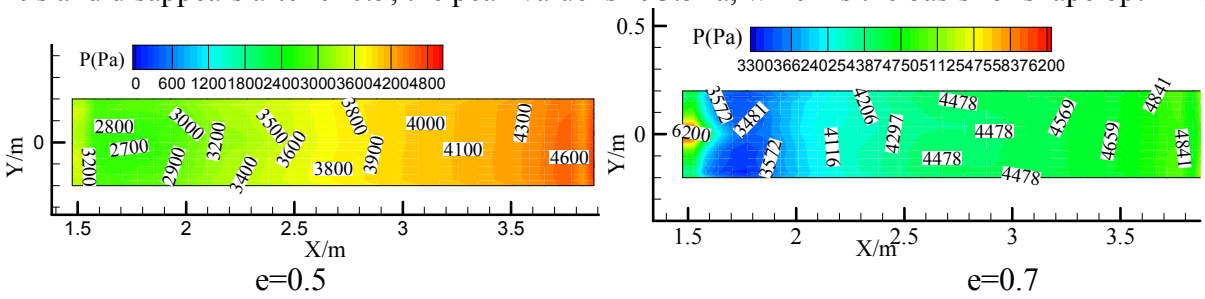


Fig.5 Distribution of the pressure on the floor of stilling basin while using $t_4 = 60s$

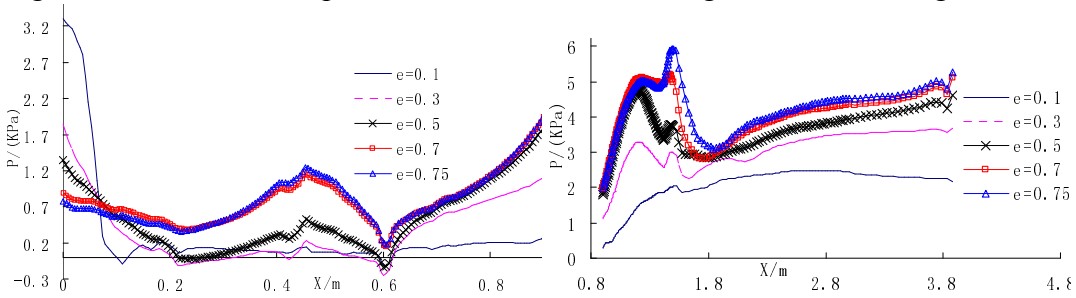


Fig.6 Variation of pressure distribution on the middle section of the spillway surface and the slab of stilling basin at $t_3 = 30s$

## Conclusions

3D dynamical numerical simulation is carried out for the unsteady flow of X shaped flaring gate pier and stilling basin by using RNG $k-\varepsilon$ model and dynamic mesh technology. The water surface profile corresponding to the four different opening velocities is analyzed. Velocity distribution is reflected in detail; the pressure distribution on the floor of weir surface and stilling basin are also pointed out. The results can provide important reference for run mode of finished hydraulic engineering.

## References

[1] Y.L. Li, G.C. Hua and J.M. Zhang et al: Journal of Hydrodynamics.Vol. 21(2006), p.26 (In Chinese)
[2] P. Gao, Y.Q.Yang and J.Deng et al: Journal of Sichuan University (Engineer Science edition). Vol.38 (2006), P.70 (In Chinese)
[3] T.Zhang, C.Wu, H.S.Liao and Y.H.Hu: Journal of Hydrodynamics,Ser.B. Vol.17(2005), p.338
[4] H.G.Ni: Journal of Hydraulic Engineering. (1998), P.19 (In Chinese)
[5] Z.X.Liang, J.B.Yin and Z. Zheng: Journal of Northwest A&F University(Nat. Sci. Ed.). Vol.36(2008),p.206(In Chinese)
[6] C.Qiu, M.J.Diao and L.L.Xu: Applied Mechanics and Materials. Vols.170-173(2012), P.3687
[7] C.Qiu, M.J.Diao and L.L.Xu: Journal of Sichuan University(Engineer Science edition). Vol.44(2012),p.19(In Chinese)

*Applied Mechanics and Materials Vols. 580-583 (2014) pp 1975-1980*
*© (2014) Trans Tech Publications, Switzerland*
*doi:10.4028/www.scientific.net/AMM.580-583.1975*

# Finite Element Analysis of Seismic Response of Exposed Steel Penstock in Hydropower Station

Yuan Liu[1, a], Changzheng Shi[1, b] and Hegao Wu[1, c]

[1]State Key Laboratory of Water Resources and Hydropower Engineering Science, Wuhan University, Wuhan, Hubei, 430072,China

[a]lyuan@whu.edu.cn, [b]scz4@163.com, [c]wbf1988@vip.sina.com)

**Keywords:** Exposed penstock, Earthquake, Sliding support, Finite element method, Dynamic time-history analysis

**Abstract:** Using finite element method, the seismic responses of an exposed steel penstock in a hydropower station were analyzed. The results show that the penstock is constrained weakly due to the expansion joint and sliding supports, so the penstock can adapt to the deformation during the earthquake well, and the stress caused by the earthquake is small which will be benefit for the strength and safety of the penstock. However large acceleration and displacement in transverse direction may be induced under strong earthquake, in addition, the penstock will be likely to jump apart from supports in vertical direction. So it is better to equip caging device to limit transverse sliding and vertical jumping in an appropriate range in order to ensure the safety and stability of the whole structure.

## Introduction

Possessing the advantages of definite mechanical feature, convenient maintenance and inspection, simple structure and excellent anti-seepage ability, the exposed steel penstock has been widely used in small and medium scaled hydropower stations and water diversion projects [1]. But horizontal displacement and temperature stress may be induced by installation deviation or temperature change [2]. In order to reduce the influence of aforementioned factors, expansion joint is usually set between two adjacent anchorage blocks, and meanwhile sliding supports are adopted to make the steel pipe deform relatively freely in horizontal direction. However, relative motion may occur between the pipe and support piers under earthquake due to the small stiffness of the structure, and the pipe may even fall from the supports, leading to serious destruction.

So far a few studies have been done on the dynamic behaviors of exposed steel penstock by prototype test and finite element method. The prototype vibration test of exposed steel penstock with large diameter in Baishan hydropower station showed that the probability of substantial vibration of inclined section in transverse and vertical direction was large [3]. The dynamical finite element analysis of exposed steel penstock for inverted siphon indicated that the sliding supports were the weak connecting component during earthquake [4]. In practical engineering, due to the contribution of vertical caging device, the probability that penstock separated from supports and jumped upward entirely was small. So far, there is no seismic damage cases of exposed steel penstock, but analogous cases existed in bridge structures. According to the introduction in the article [5], support piers displaced in Wenchuan earthquake, furthermore, the decrease of the contact force between support and bridge span led to the decrease of friction force between bridge and pier, so it was more likely to cause seismic damage such as girder falling, and it also brought out the pounding between support piers and above structure, such as the support impacting damage of

Nielsen Bridge in Kobe earthquake in Japan of 1995 [6]. So in this paper, the dynamic analysis of an exposed steel penstock in a hydropower station with high head was conducted by finite element method using software ANSYS in order to discuss the movement characteristics of the penstock during the earthquake.

**Finite element analysis**

**Model details**

One inclined segment of exposed steel penstock between two anchor blocks in a hydropower station was studied in this paper, of which the overall length was 73.33 m. The penstock with an inner diameter of 2.5 m and a shell thickness of 38 mm bore the internal water pressure ranging from 4.62MPa to 5.00MPa. 9 sliding supports were arranged along pipeline numbered consecutively 1#~9# from upstream to downstream, and the distance between adjacent supports was 7.5 m. One expansion joint was set between the upstream anchor block and support 1# (see Fig.1).

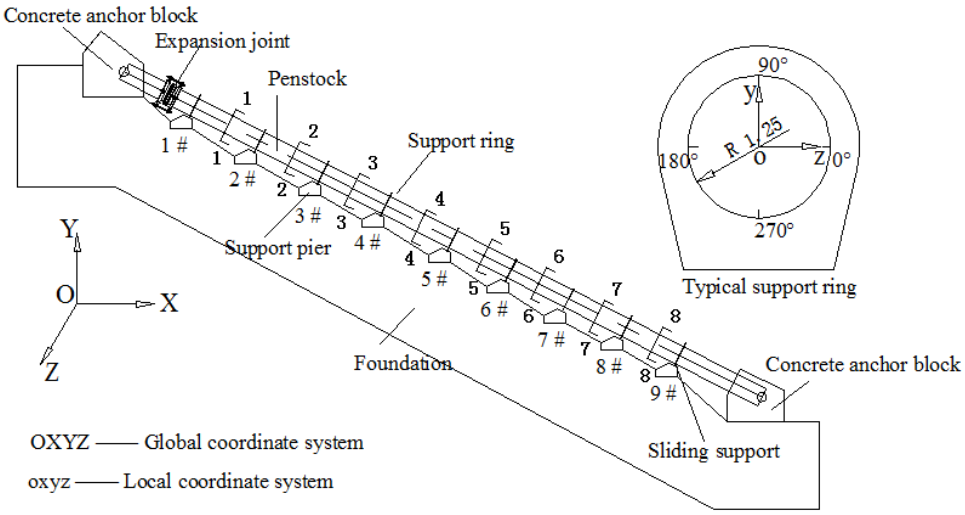


Fig.1 Layout of the exposed steel penstock

According to dimensions of the structure, a finite element model was established, including steel penstock, support rings, sliding supports, concrete anchor blocks and support piers, expansion joint and foundation. The concrete structure and rock were simulated by solid element, while the steel structures simulated by shell element, the expansion joint was simulated by beam element whose axial stiffness equalled to the stiffness of expansion joint. In order to simulate the contact and sliding behaviors between the two sliding surfaces of the support, contact and target elements were set of which the interaction followed the coulomb's friction law, and the friction coefficient was 0.1. The finite element model was shown in Fig.2. The material mechanical parameters were list in Table.1.

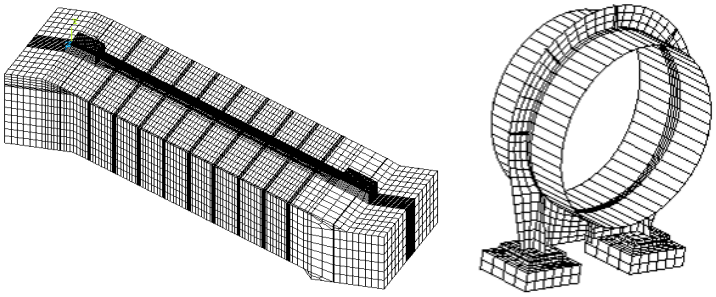

(a) (b)

Fig.2: (a) FE model (b) Meshes of support

Table.1 Material mechanical parameters

| Material | Elastic Modulus(GPa) | Poisson Ratio | Bulk Density(kN·m$^{-3}$) |
|---|---|---|---|
| Steel | 206 | 0.3 | 78.5 |
| Concrete | 25.5 | 0.167 | 25.0 |
| Bedrock | 5 | 0.2 | 26.0 |

**Calculation conditions**

The earthquake wave shown in Fig.3 with the peak ground acceleration 2.76 m·s$^{-2}$ was chosen in the dynamic analysis. Time-history analysis method was adopted in the analysis with the time step of 0.02 s [7,8]. The earthquake wave was input from X, Y, Z three directions simultaneously, however the peak acceleration in the horizontal direction was 2.76 m·s$^{-2}$, and 1.84 m·s$^{-2}$ in the vertical direction. The foundation was regarded as massless base and only the elasticity was taken into account.

During the calculation, static analysis was executed first to gain the displacement and stress status of the structure subjected to internal water pressure and dead loads which was used for the basic state of seismic analysis. To simplify the calculation, the dynamic interaction between water and pipe was ignored, but the inertial effect of water quality was considered through the mass element attached to the pipe wall along the pipeline [9]. The upstream and downstream surfaces of the bedrock were constrained in normal direction, and the bottom surface was constrained completely, and others were regarded as free boundary.

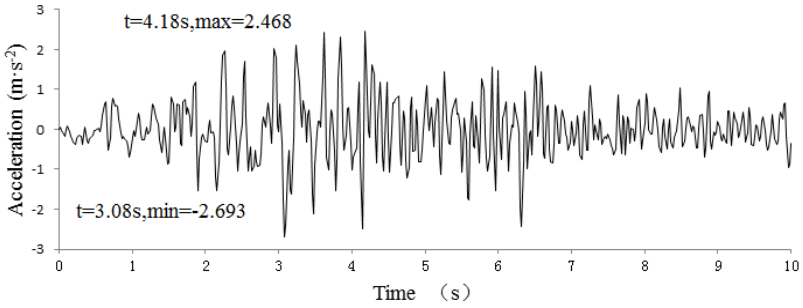


Fig.3 Acceleration time-history in horizontal direction

**Result and analysis**

Two anchor blocks are set at two ends of the penstock, which fix the penstock on the slope, so the responses of anchor blocks and pipes buried in anchor blocks are small under the earthquake, while the responses of other pipe sections are relatively obvious. In order to analyze the dynamic response distribution law along the pipeline, the mid-span section between adjacent support piers numbered section 1～8 consecutively (shown in Fig.1) are analyzed carefully. Later analyses mainly focus on the section 4 located at the middle span of the pipeline to make description of the dynamic response in each direction.

**Acceleration response.** The time-history curves of acceleration of waist point (0°) on section 4 under each direction are shown in Fig.4, and the acceleration responses of most parts of the structure are similar to this point. As shown in Fig.4, the acceleration of specific point reaches the peak acceleration during the period of 3 to 5 s in each direction, which is slightly later than the input wave.

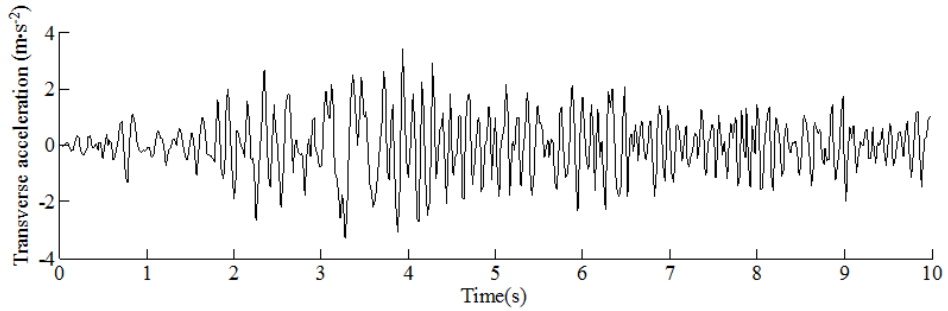


(a) transverse acceleration

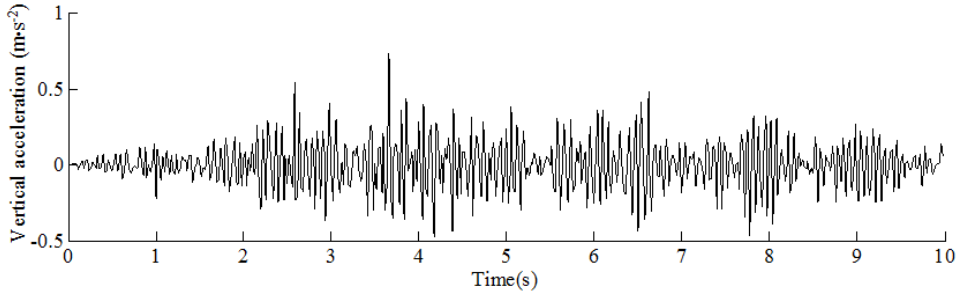


(b) vertical acceleration

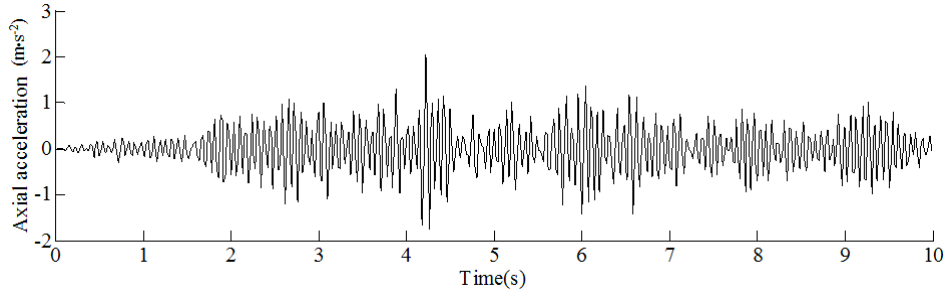


(c) axial acceleration

Fig.4 Time-history of the acceleration of waist point on section 4-4 in each direction

The peak acceleration of all specific sections in each direction is shown in Table.2. The largest peak acceleration in axial and vertical direction both appear at the middle section of pipe under the earthquake, and transverse peak acceleration is nearly symmetrical about center point of the pipeline. The peak acceleration reaches 2.58 $m \cdot s^{-2}$, 1.15 $m \cdot s^{-2}$ and 3.43 $m \cdot s^{-2}$ in axial, vertical and transverse direction respectively, and the acceleration in transverse direction is obviously larger than the other two.

Table.2 Peak acceleration of specific section in each direction

**($m \cdot s^{-2}$)**

| Direction | Section | | | | | | | |
|---|---|---|---|---|---|---|---|---|
| | 1 | 2 | 3 | 4 | 5 | 6 | 7 | 8 |
| axial | 1.54 | 2.09 | 2.43 | 2.58 | 2.54 | 2.30 | 1.87 | 1.30 |
| vertical | 1.23 | 1.21 | 1.15 | 1.15 | 1.14 | 1.15 | 1.21 | 1.21 |
| transverse | 2.71 | 3.47 | 2.03 | 3.43 | 3.39 | 2.17 | 3.38 | 2.89 |

**Dynamic displacement response analysis of exposed steel penstock.** During the earthquake, the movement of steel penstock represents the characteristics of reciprocating motion on the support piers in horizontal direction and jumping up and down in vertical direction. However the influences of earthquake on the movements in three directions are distinct. Though the pipe could jump up

from the piers during the earthquake, the height of jump doesn't exceed 1.0 mm due to the action of gravity of pipe and water. Because the stiffness of the pipe in transverse direction is much smaller than the stiffness in axial direction, the movement in transverse direction is more obvious. For long-distance and large-span exposed steel penstock with expansion joint and sliding supports, transverse stiffness is usually not enough, so that the penstock swings from side to side and the transverse displacement relative to the support piers is large as shown in Fig.5. Fig.6 illustrates the peak relative displacement of each section in three directions along the pipeline. The maximum transverse displacement occurs at middle part of the pipe, and the value reaches 10.8 mm. Large sliding in transverse direction between pipe and supports will destroy supports easily and make the penstock drop down from support piers, which is not benefit for the safety and stability, so it should be restricted in an appropriate range in practical project.

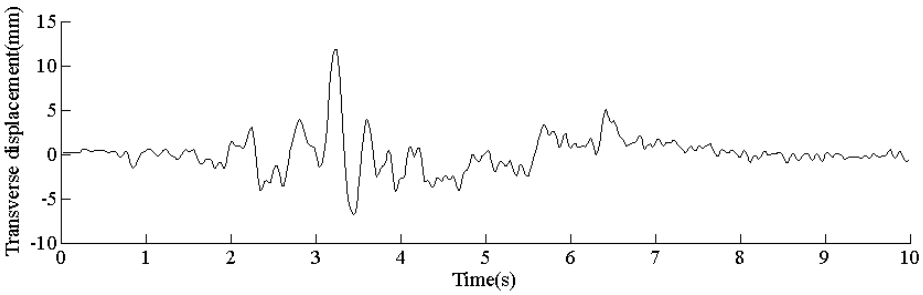


Fig.5 The time-history of transverse displacement of section 4 relative to support 5

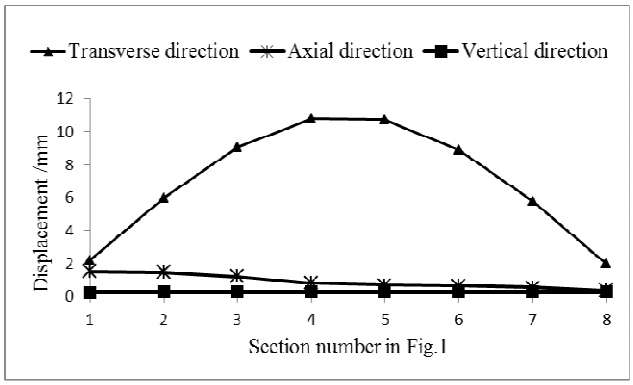


Fig.6 Peak displacement relative to support piers of each section caused by earthquake

**Stress analysis.** Fig.7 describes the Mises stress envelope diagram of pipe segment between support 4 and 5 under static loads and earthquake. Under the static loads of which the chief load is internal water pressure the steel pipe mainly subjects to tensile force in circumferential direction, and the stress is uniform along axis except the parts adjacent to support ring. Under the earthquake the regularities of stress distribution are similar to the state under static loads, but the stress value increases by 20~30 MPa. It illustrates that under the earthquake the stress is still controlled by internal water pressure mainly, and the effect of earthquake load on stress is slight because of the ability of the penstock to move freely in horizontal direction. The results show that the penstock can adapt to the deformation induced by the earthquake well attributing to the sliding supports and expansion joint, so the stress and deformation caused by the earthquake is small, which will be advantageous to ensure the strength and safety.

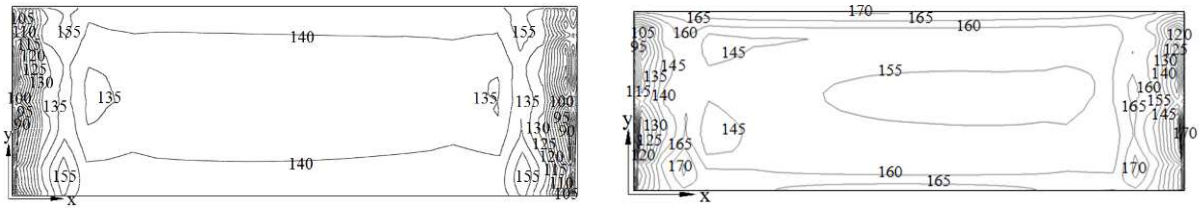

(a) under static loads (b) under earthquake

Fig.7 Mises stress envelope diagram of pipe segment between support 4 and 5 (MPa)

## Conclusion

The penstock can adapt to the deformation during the earthquake well attributing to the sliding supports and expansion joint, and the stress caused by earthquake changes slightly compared to the stress caused by static loads. So the strength of penstock will not be threatened by earthquake obviously. However the earthquake will induce transverse acceleration and displacement, and large relative transverse sliding between penstock and supports may occur due to the weak constraint of expansion joint and sliding supports under strong earthquake, especially at the middle part of the penstock which is away from the constraint of anchor blocks both at upstream and downstream ends. Aforementioned phenomenon is disadvantageous to ensure the strength and safety, so it is better to equip relevant caging device to limit the relative displacement in an appropriate range.

## Acknowledgements

This work was financially supported by the Chinese Post-doctoral Science Foundation (2013M542058).

## References

[1] Y.Li and G.P.Ma: Design research and engineering application on large inverted siphon penstocks. (China Power Press, Beijing 2010). ( In Chinese)

[2] Z.Y.Yang: Displacement analysis and reinforcement measures of exposed steel penstock of Yanghu hydropower station. (China Water & Power Press, Beijing 2006). ( In Chinese)

[3] T.Huang, S.J.Jiang and J.Wang: J. Dam Observation and Geotechnical Tests 1995;19(1)：p. 16-19．( In Chinese)

[4] C.Z.Shi, H.G.Wu, Y.Li, et al. J. Journal of Hydroelectric Engineering 2012; 31(2) : p. 198-205．( In Chinese)

[5] R.Xu: Research on multiple poundings of bridges under vertical earthquakes. (Nanjing University Press, Nanjing 2011). ( In Chinese)

[6] TanimuraS, SatoT, UrnedaT, et al. J. International Journal of Impact Engineering 2002;(27): p. 153-160.

[7] H.Q.Yan and Q.F.Luo: J. Recent Developments in World Seismology 2012;(6):p. 157-157. ( In Chinese)

[8] L.T.Wang, H.F.Ma, H.Q.Chen, et al. J. Water Resources and Power 2012;30(1)：p. 66-69. ( In Chinese)

[9] M.L.Lou: J. Water Resources and Hydropower Engineering 1994; (9)：p. 8-11. ( In Chinese)

*Applied Mechanics and Materials Vols. 580-583 (2014) pp 1981-1984*
*© (2014) Trans Tech Publications, Switzerland*
*doi:10.4028/www.scientific.net/AMM.580-583.1981*

# Joint Regulation and Storage of Surface Water and Groundwater in Rushan River Basin

Minghui Niu[1, a], Zhenghe Xu[1,b] and Xi Wang[2,c]

[1]School of Resources and Environment, University of Jinan, Jinan, China, 250022

[2]School of Soil and Water Conservation, Beijing Forestry University, Beijing, China, 100083

[a]niumh_2012@163.com, [b]xu4045@126.com, [c]shwx512@163.com

**Keywords:** Joint regulation and storage; surface water; groundwater

**Abstract.** Based on the regulating principles, the modes of joint regulation and storage of surface water and groundwater in Rushan River Basin are simulated using multi-objective programming method. The study suggests two modes as "two dry years and one normal year" and "four dry years and one wet year". The results indicate the guarantee rates of water supply are improved, with increasing the exploitation quantity in dry years and the recharge in wet years. The study provides a strong guarantee for water resources regulation and promotes the sustainable development of regional water resources.

## Introduction

The coastal area of Shandong Province lacking water resources is one of the serious water shortage areas. With the development of social economy, the phenomenon that water demand is greater than supply has become more and more prominent. The imbalance of that has gradually started to hinder the local economic sustainable development [1-2]. Increasing the scale of transferring water is hardly to solve the problems of local water resources fundamentally. The concept of " Resources Water " should be taken as the guiding ideology [3], and the problems during the development and utilization of water resources in the area are needed to realize adequately. Based on this, sustainable development and utilization of surface water and groundwater could be obtained with reason and effect.

In order to further promote the water supply and demand balance for Rushan River Basin, the joint regulation of surface water and groundwater is studied with the liquidity, systematicness, regulatory and recoverability of water resources. It can improve the utilization of water and alleviate the harm to ecological environment due to groundwater over exploitation [4]. There is great application value for optimal allocation and improving the management of water resources.

## Basic situation of study area

Rushan River Basin located in RuShanShi Midwest of Shandong Province, belongs to the low mountains and hills in Jiaodong Area. The alternating distribution of mountains, hills and plains are presented with a total area of 1015.80 $km^2$. The basin is a typical warm temperate maritime monsoon climate with four seasons. Winter is not severe cold, and summer is not very heat. There are such characteristics as warm climate, small temperature difference, long sunshine time and abundant rain. The water resources are surface runoff and underground latent water with the mean annual rainfall of about $5.77\times10^8m^3$. Surface water accounts for $4.3\times10^8m^3$ and groundwater accounts for$1.47\times10^8m^3$. The per capita consumption is much lower than the national average because of serious water shortage. So the rational utilization and effective protection of water resources are very urgent.

## Situation of exploitation and utilization of water

The total catchment area is about 232.7$km^2$ with an active storage of $2.254\times10^7m^3$. There are 54 small reservoirs, and they are annual regulation. The water supply capacity depends on the size of

active storage and the volume of incoming water. The projects of surface water storage are shown in Table 1.

Tab.1 Water storage projects of surface water in Rushan River Basin

| Projects | Amount | Catchment area ($km^2$) | Total storage (million $m^3$) | Active storage (million $m^3$) | Major function (water supply) |
|---|---|---|---|---|---|
| Longjiaoshan Reservoir | 1 | 277 | 107.89 | 59.16 | Domestic, industrial, agricultural |
| Taiyi Reservoir | 1 | 28 | 18.96 | 12.50 | Industrial and agricultural |
| Yuanli Reservoir | 1 | 15 | 10.98 | 7.00 | Agricultural |
| Small Reservoir | 54 | 92.6 | 20.60 | 11.65 | Agricultural |
| Ponds | 297 | 140.1 | 16.33 | 10.89 | Agricultural |

Special hydrogeological structure and economic development strategy of Rushan River Basin determine the overall layout of groundwater development and utilization. Water for urban and rural residents depends on the exploitation of shallow groundwater, and there are 1134 electromechanical wells.

## Joint regulation and storage

Groundwater over-exploitation will cause the water lowering and the ground subsidence [5]. A joint regulation should be reasonable arrangement and efficient utilization of surface water and groundwater resources. The principles in the study are full use of precipitation, regulating use of surface water, protective exploitation of groundwater. In case of consecutive dry years, the premise is to avoid destroying the environment. It can be properly depleted aquifer space to increase the amount of groundwater supply sparing capacity. Then increasing the quantity of groundwater recharge is carried out to recover the water level during wet years. This method can improve the guarantee rate of water supply [6].

Water resources in Rushan River Basin are precipitation, surface water and groundwater. And utilizations of water are domestic, industrial and agricultural irrigation water. Surface water can transform into groundwater using recharge measures through Rushan River. The groundwater reservoir located in downstream is used to adjust surface water and groundwater in time.

**The classifications of water.** When the water supply is less than demand, a high level of water supply should be ensured and low-level be reduced. Based on the use of water in the area, the first and second and third grade water use sectors are domestic, industrial production and agricultural irrigation water, respectively. The reservoirs with low adjustment ability are priority to supply water, then reservoirs with high ability are used to supply water. The order is medium-sized reservoirs and ponds, Longjiaoshan Reservoir, groundwater reservoir, respectively.

**The objective function.** The objective is the minimum of water deficiency as

$$\min f(x) = \sum_{w=1}^{W} \sum_{u=1}^{U(W)} \left[ F_u^W - \sum_{s=1}^{S(u)} x_{su}^w \right]. \tag{1}$$

Where $f(x)$ is water deficit; $W$ expresses the amount of region; $F^w{}_a$ represents the water demand of $w$ region $u$ user; $U(w)$ is the amount of user in $w$ region; $S(u)$ is the amount of headwater with single direction in $w$ region; $x^w{}_{su}$ is the water supply quantity of $s$ headwater to $w$ region $u$ user.

**The constraint conditions.** Water constraints consist of water demand and supply constraints. Water demand constraint represents to ensure the water quantity for different users. Water supply constraint refers to the supply for users must not exceed the ability of the headwater provided [7].

1) The available water is expressed by

$$\sum_{w=1}^{W} \sum_{u=1}^{U(w)} x_{au}^w \le R_a, \sum_{w=1}^{W} \sum_{u=1}^{U(w)} x_{su}^w \le R_s^w. \tag{2}$$

Where $x^w{}_{au}$ is the water supply quantity of $a$ headwater to $w$ region $u$ user; $R_a$ is the available water of $a$ headwater; $R^w{}_s$ is the available water of $s$ headwater; other symbols are same with equation (1).

2) The carrying capacity of water is presented by

$$x_{au}^{w} \le Q_{a\max}^{w}, x_{su}^{w} \le Q_{s\max}^{w}. \tag{3}$$

Where $Q^{w}_{amax}$ is the maximum carrying capacity of $a$ headwater to $w$ region; $Q^{w}_{smax}$ is the maximum carrying capacity of $s$ headwater to $w$ region; others are same with equation (2).

3) The water demand is expressed by

$$G_{u\min}^{w} \le \sum_{s=1}^{S(w)} x_{su}^{w} + \sum_{a=1}^{A} x_{au}^{w} \le G_{u\max}^{w}. \tag{4}$$

Where $G^{w}_{umin}$ is the minimum water demand of $w$ region $u$ user; $G^{w}_{uman}$ is the minimum.

4) The water balance of Longjiaoshan Reservoir is expressed by

$$\begin{cases} U_{i+1} = U_i + W_{come} - \sum W_{use} - W_{loss} (i = 1,2,...,108;1,2,...,180) \\ 750.00 \le U_i \le ActiveStorage, U_{108} \ge 750.00, U_{180} \ge 750.00 \end{cases}. \tag{5}$$

Where $U_{i+1}$, $U_i$ are the storage capacities of reservoir at the beginning and ending of $i$ period; $W_{come}$ is the inflow; $W_{use}$ is the use; $W_{loss}$ is the total of evaporation and leakage and surplus water.

5) The water balance of groundwater reservoir is expressed by

$$\begin{cases} V_i = V_{i+1} + Rp_i + Rs_i + Rb_i + Ar_i - Dp_i - E_i (i = 1,2,...,108;1,2,...,180) \\ 0 \le V_i \le 1618.40, U_{108} \ge 809.2, U_{180} \ge 809.2 \end{cases}. \tag{6}$$

Where $V$ is storage capacity, and $V_0$ is the one second of the maximum; $R_p$ is precipitation infiltration recharge; $R_s$ is surface water infiltration recharge; $R_b$ is lateral recharge; $A_r$ is artificial recharge; $D_p$ is the exploitation; $E_i$ is the evaporation.

## Results and Discussion

The calculation of adjusting Longjiaoshan Reservoir and groundwater reservoir shows that the uneven rainfall is presented with water depletion in dry season and water residual in flood season. According to the precipitation data from 1961 to 2010 hydrological year, Rushan River Basin continuously appears four dry seasons from 1980 to 1984, however, from 1986 to 1988 and from 1991 to 1993 are the two dry years. From the supply perspective, the modes of "four dry years and one wet year" and "two dry years and one normal year" are selected as modes of regulation and storage to improve the probability of water supply.

**The "two dry years and one normal year".** Based on the principle of joint regulation, the mode of "two dry years and one normal year" is simulated after calculating the actual water demand and reservoirs pondage, as shown in Table 2.

Tab.2 The mode of "two dry years and one normal year" before and after regulation.

| Hydrological year | Domestic water (million $m^3$) | | | | Agricultural water (million $m^3$) | | | |
|---|---|---|---|---|---|---|---|---|
| | Before | | After | | Before | | After | |
| | Supply | Deficiency | Supply | Deficiency | Supply | Deficiency | Supply | Deficiency |
| 90% | 10.95 | 12.775 | 23.725 | 0.00 | 15.1287 | 53.3522 | 10.4776 | 58.0034 |
| 75% | 10.95 | 0.00 | 10.95 | 0.00 | 8.7645 | 20.3803 | 27.396 | 1.7488 |
| 50% | 10.95 | 0.00 | 10.95 | 0.00 | 3.9132 | 0.00 | 3.9132 | 0.00 |

In 90% hydrological year with water shortage, the domestic water should be ensured preferentially. The simulation increases groundwater of $1.2775\times10^{7}m^3$ for domestic water and decreases groundwater of $4.65\times10^{6}m^3$ for irrigation, then the total increasing exploitation of groundwater is $8.1239\times10^{6}m^3$. In 75% hydrological year with adequate water for production and livelihood, the simulation increases groundwater exploitation of $1.86315\times10^{7}m^3$ for agricultural irrigation. And in the flood season it increases the recharge of $1.85916\times10^{7}m^3$. In 50% hydrological year, it increases the recharge of $8.1638\times10^{7}m^3$. At last, the water table can be restored. Compared to the results of before and after joint regulation of surface water and groundwater, the effect is presented better,

**The "four dry years and one wet year".** In 75% hydrological year, the simulation ensures that there is no deficiency of domestic water. Increasing agricultural water of $1.8923\times10^7m^3$ and the recharge of $1.24465\times10^7m^3$ in flood season is taken. In 25%, the recharge of $7.2041\times10^6m^3$ is increased in flood season, as shown in Table 3.

Tab.3 The mode of "four dry years and one wet year" before and after regulation.

| Hydrological year | Agricultural water (million $m^3$) | | | |
|---|---|---|---|---|
| | Before | | After | |
| | Supply | Deficiency | Supply | Deficiency |
| 75% | 8.7645 | 20.3803 | 27.6875 | 1.4573 |
| 75% | 8.7645 | 20.3803 | 27.6875 | 1.4573 |
| 75% | 8.7645 | 20.3803 | 27.6875 | 1.4573 |
| 75% | 8.7645 | 20.3803 | 27.6875 | 1.4573 |
| 25% | 0.00 | 0.00 | 0.00 | 0.00 |

By simulating the scheme of joint and storage, it not only eases the shortage of water resources in Rushanhe Reservoir Basin, but also avoids the threat of a potential flood in dry years. It improves the utilization of water resources and promotes the sustainable development of regional water resources.

## Summary

According to the imbalance of supply and demand water in Rushan River Basin, the joint and storage of surface water and groundwater is simulated during the 25%, 50%, 75% and 90% hydrological years. The study proposes two modes as "two dry years and one normal year" and "four dry years and one wet year". The first one suggests to increase groundwater of $1.2775\times10^7m^3$ for domestic water and decrease $4.65\times10^6m^3$ for irrigation in 90%. In 75%, the agricultural water of $1.86315\times10^7m^3$ and the recharge of $1.85916\times10^7m^3$ are increased. And in 50%, the increasing recharge of $8.1638\times10^7m^3$ is obtained. The second mode shows the increasing agricultural water of $1.8923\times10^7m^3$ and the increasing recharge of $1.24465\times10^7m^3$ in 50%. And in 25%, the recharge of $7.2041\times10^6m^3$ is increased in flood season.

## Acknowledgments

This research was financially supported by Project of Major Water Conservancy Scientific Research and Technology Promotion in Shandong Province (SDSLKY201229), the Special Scientific Research of Hydraulic Public Welfare Profession of MWR (201201115), the Special Scientific Research of Hydraulic Public Welfare Profession of MWR (201201116) and Shandong Province Water Conservancy Research and Technology Promotion Projects (SDSLKY201306).

## References

[1] Divakar L, Babel M S, Perret S R, et al. in: Journal of Hydrology. Sci. Vol. 401 (2003) p. 22-35.
[2] Abolpour B, Javan M, Karamouz M. in: Applied soft computing. Vol. 7 (2007) p. 265-285.
[3] Read L, Madani K, Inanloo B. in: Journal of environmental management. Vol. 133 (2014) p. 343-354.
[4] Chang F J, Wang K W. in: Journal of Hydrology. Sci. Vol. 507 (2013) p. 124-133.
[5] Guangjie Yu. In: Gansu Water Conservancy and Hydropower Technology. Vol. 46 (2010) p. 6-10.
[6] Xinghui Qu, Xiuying Gu. In: Hydrology. Vol. 25(2005) p. 23-25.
[7] Shoujian Du. In: Xi'an University of Technology, 2009.

*Applied Mechanics and Materials Vols. 580-583 (2014) pp 1985-1988*
*© (2014) Trans Tech Publications, Switzerland*
*doi:10.4028/www.scientific.net/AMM.580-583.1985*

# Comprehensive Evaluation for Utilization Efficiency of Rain-flood Resources in Rushan River

Sifang Zhou[1, a], Zhenghe Xu[1, b], Shanshan Yang[1, c], Ke Kong[1, d] and Yuan Xiu[1,e]

School of Resources and Environment, University of Jinan, Jinan, China, 250022

[a]zhssff@126.com, [b]xu4045@126.com, [c]yangshsan@163.com, [d]koker@sohu.com, xiuyuan1990@sina.com

**Keywords:** Fuzzy Matter-element Method, Comprehensive Evaluation, Rain-flood Resources, Utilization Efficiency, Rushan River

**Abstract.** Using fuzzy mater-element method, the comprehensive utilization efficiency of rain-flood resources in Rushan River is assessed. The uncertainty of the comprehensive utilization efficiency is processed by the fuzzy principle. Then the representative indexes are selected, and the standard values of indexes are indicated. After normalization, the close degree and weight coefficient are calculated. On basis of that, the rating membership of the comprehensive utilization efficiency is for grade II, equal "good". So the paper concludes that the utilization of rain-flood resources in Rushan River Basin is feasible and effective. It provides follow-up support for the research of the utilization of rain-flood resources.

## Introduction

Comprehensive assessments for utilization efficiency of rain-flood resources include quantitative evaluation of economic and ecological effects and qualitative evaluation of social effects. It is a multiple attribute decision making process, including incompatible problems of single index evaluation results [1]. In addition, the demarcation of rain-flood resource utilization effects is fuzzy. Fuzzy element analysis method gives huge advantage in dealing with fuzzy incompatible information [2]. As a consequence, the vague principle is a logical and effective method to deal with this problem. In order to provide a new reference method for the evaluation of rain-flood resources, comprehensive utilization efficiency is assessed by using fuzzy element method based on entropy [3] in Rushan River.

## Basic situation of study area

Located in Jiaodong Peninsula, Rushan River Basin belongs to typical warm temperate maritime monsoon climate. The median annual rainfall is 747.7 mm. The interannual variation of rainfall is obvious, with minimum annual rainfall of 338.4 mm (1999), while the maximum is 1358.9 mm (1964). In addition, precipitation is distributed unevenly across per year. The rainfall in flood season accounted for 75.2% of the annual total, and most of it is concentrated in July and August[4]. Perfect storage projects for rainwater collection are available in the basin. Surface water storage space is sufficient as having one large reservoir, two medium reservoirs, 354 small reservoirs. There are 13 regulating dams with the ability of impound flood are distributed on Rushan River. Meanwhile, Rushan River Underground Reservoir is at the downstream of Rushan River, which a natural rich water zone.

## Fuzzy element evaluation of comprehensive utilization efficiency

It is a complex, multi-level comprehensive evaluation process to evaluate the comprehensive efficiency of rain flood resources utilization, because of not only numerous evaluation indexes, but also the fuzziness and uncertainty existing in effects and relative relationship. The effect evaluation standard, evaluation index and its characteristic values are considered as matter elements by using

matter-element analysis theory, and then the measured data and evaluation level are normalized to obtain the grade limit values (classical domain and joint domain), close degree and weight coefficient [5]. Fuzzy matter-element model is established for comprehensive efficient evaluation of rain-flood resources in Rushan River Basin.

$$R = \begin{bmatrix} M & C_1 & x_1 \\ & C_2 & x_2 \\ & \vdots & \vdots \\ & C_n & x_n \end{bmatrix}$$

**Normalization of evaluation index system.** Comprehensive evaluation indexes are selected to reflect the development and utilization status of rain-flood resources in the basin. There are seven comprehensive evaluation indexes, and $C_1$ is effective irrigated area (10000 acres); $C_2$ is vegetation coverage ratio (%); $C_3$ is recharge volume of groundwater (106 $m^3$); $C_4$ is water consumption per capita ($m^3$); $C_5$ is standard waterlogged area ratio (%); $C_6$ is flood utilization ratio in flood reason (%); $C_7$ is dirt to diameter ratio (%). Table 1 shows the true values of the seven indicators for comprehensive evaluation of rain-flood resources utilization. And five standard parameter values are given in Table 2. The five grade levels ranging from I to V list as excellent, good, fair, acceptable and poor, respectively.

Table 1 True values of comprehensive evaluation indexes

| Index | $C_1$ | $C_2$ | $C_3$ | $C_4$ | $C_5$ | $C_6$ | $C_7$ |
|---|---|---|---|---|---|---|---|
| Value | 30.5 | 45.4 | 30 | 26.54 | 75 | 28 | 8.3 |

Table 2 Standard parameter values of comprehensive evaluation indexes

| Grade | $C_1$ | $C_2$ | $C_3$ | $C_4$ | $C_5$ | $C_6$ | $C_7$ |
|---|---|---|---|---|---|---|---|
| I | 35 | 65 | 45 | 40 | 90 | 50 | 5 |
| II | 30 | 50 | 30 | 30 | 75 | 30 | 7 |
| III | 25 | 30 | 20 | 25 | 60 | 25 | 9 |
| IV | 20 | 20 | 15 | 20 | 50 | 15 | 12 |
| V | 10 | 10 | 5 | 10 | 30 | 10 | 15 |

Comprehensive effect index for the rain-flood resources utilization are normalized. For positive related indicators, such as the effective irrigated area, vegetation coverage ratio, etc., are normalized according to the equation (1). While the negative related indicator (dirt to diameter ratio, for instance) is standardized according to the equation (2). True valves and standard parameter values of comprehensive evaluation indexes after normalization are shown in Table 3 and 4, respectively.

$$d_i = 1 - (x_i - x_5)/x_i \quad d_i = 1 - (x_i - x_5)/x_i \tag{1}$$

$$d_i = x_i / x_5 \tag{2}$$

Table 3 True values after normalization

| Index | $C_1$ | $C_2$ | $C_3$ | $C_4$ | $C_5$ | $C_6$ | $C_7$ |
|---|---|---|---|---|---|---|---|
| Value | 0.328 | 0.220 | 0.167 | 0.377 | 0.400 | 0.357 | 0.553 |

Table 4 Standard parameter values after normalization

| Grade | $C_1$ | $C_2$ | $C_3$ | $C_4$ | $C_5$ | $C_6$ | $C_7$ |
|---|---|---|---|---|---|---|---|
| I | 0.286 | 0.154 | 0.111 | 0.250 | 0.333 | 0.200 | 0.333 |
| II | 0.333 | 0.200 | 0.167 | 0.333 | 0.400 | 0.333 | 0.467 |
| III | 0.400 | 0.333 | 0.250 | 0.400 | 0.500 | 0.400 | 0.600 |
| IV | 0.500 | 0.500 | 0.333 | 0.500 | 0.600 | 0.667 | 0.800 |
| V | 1.000 | 1.000 | 1.000 | 1.000 | 1.000 | 1.000 | 1.000 |

**Fuzzy matter element model for comprehensive evaluation.** After normalization, we determined the class domain ($R_I$-$R_V$) and joint domain ($R_B$) of the standard fuzzy elements. And then, fuzzy matter element model M was obtained for comprehensive efficiency evaluations in Rushan River .

$$R_{\mathrm{I}}=\begin{bmatrix} B_{\mathrm{I}} & C_1 & (0,0.286) \\ & C_2 & (0,0.154) \\ & C_3 & (0,0.111) \\ & C_4 & (0,0.250) \\ & C_5 & (0,0.333) \\ & C_6 & (0,0.200) \\ & C_7 & (0,0.333) \end{bmatrix} \quad R_{\mathrm{II}}=\begin{bmatrix} B_{\mathrm{II}} & C_1 & (0.286,0.333) \\ & C_2 & (0.154,0.200) \\ & C_3 & (0.111,0.167) \\ & C_4 & (0.250,0.333) \\ & C_5 & (0.333,0.400) \\ & C_6 & (0.200,0.333) \\ & C_7 & (0.333,0.467) \end{bmatrix} \quad R_{\mathrm{III}}=\begin{bmatrix} B_{\mathrm{III}} & C_1 & (0.333,0.400) \\ & C_2 & (0.200,0.333) \\ & C_3 & (0.167,0.250) \\ & C_4 & (0.333,0.400) \\ & C_5 & (0.400,0.500) \\ & C_6 & (0.333,0.400) \\ & C_7 & (0.467,0.600) \end{bmatrix}$$

$$R_{\mathrm{IV}}=\begin{bmatrix} B_{\mathrm{IV}} & C_1 & (0.400,0.500) \\ & C_2 & (0.333,0.500) \\ & C_3 & (0.250,0.333) \\ & C_4 & (0.400,0.500) \\ & C_5 & (0.500,0.600) \\ & C_6 & (0.400,0.667) \\ & C_7 & (0.600,0.800) \end{bmatrix} \quad R_{\mathrm{V}}=\begin{bmatrix} B_{\mathrm{V}} & C_1 & (0.500,1.000) \\ & C_2 & (0.500,1.000) \\ & C_3 & (0.333,1.000) \\ & C_4 & (0.500,1.000) \\ & C_5 & (0.600,1.000) \\ & C_6 & (0.667,1.000) \\ & C_7 & (0.800,1.000) \end{bmatrix} \quad R_{\mathrm{B}}=\begin{bmatrix} B & C_1 & (0,1.000) \\ & C_2 & (0,1.000) \\ & C_3 & (0,1.000) \\ & C_4 & (0,1.000) \\ & C_5 & (0,1.000) \\ & C_6 & (0,1.000) \\ & C_7 & (0,1.000) \end{bmatrix} \quad R_{\mathrm{M}}=\begin{bmatrix} M & C_1 & 0.328 \\ & C_2 & 0.220 \\ & C_3 & 0.167 \\ & C_4 & 0.377 \\ & C_5 & 0.400 \\ & C_6 & 0.357 \\ & C_7 & 0.553 \end{bmatrix}$$

**Weight coefficient and close degree.** Correlation function values of individual eigenvalue are calculated according to the following equations:

$$\omega\ (x_i, X_{ij}) = \left| x_i - \frac{1}{2}(a_{ij}+b_{ij}) \right| - \frac{1}{2}(b_{ij}-a_{ij}) \qquad i=1,2,...n \tag{3}$$

$$\omega\ (x_i, X_{iB}) = \left| x_i - \frac{1}{2}(a_{iB}+b_{iB}) \right| - \frac{1}{2}(b_{iB}-a_{iB}) \qquad i=1,2,...n \tag{4}$$

$$K_j(x_i) = \frac{\omega\ (x_i, X_{ij})}{\omega\ (x_i, X_{iB}) - \omega\ (x_i, X_{ij})} \tag{5}$$

Where, $\omega$ is the distance between eigenvalue and standard values; K(x) is the correlation function values of the individual eigenvalue.

The weight coefficients of eigenvalues were determined, and membership degree was calculated. Calculate the membership degree before close degree. The greater close degree, the closer distance from evaluated sample to standard level. Therefore, categories can be divided based on close degree. When $K_j = \max K_j$ (M), then assess thing M belongs to grade j. The equations to calculate weight coefficient and membership degree are following.

$$\alpha_{ij} = b_{ij} / \sum_{i=1}^{n} b_{ij} \quad i=1,2,...n \quad j=1,2,...,m \tag{6}$$

$$K_j(M) = \sum_{i=1}^{n} \alpha_{ij} K_j(x_i) \tag{7}$$

Where, $\alpha_{ij}$ is weight coefficient; K(M) is membership degree.

Table 5 Close degree

| $K_{ij}$ | $K_{i1}$ | $K_{i2}$ | $K_{i3}$ | $K_{i4}$ | $K_{i5}$ | $K_{i6}$ | $K_{i7}$ |
|---|---|---|---|---|---|---|---|
| $K_{1j}$ | 0.148 | 0.432 | 0.500 | 0.507 | 0.200 | 0.786 | 0.971 |
| $K_{2j}$ | 1.105 | -4.704 | 0.000 | 0.486 | 1.000 | 6.500 | 1.233 |
| $K_{3j}$ | 0.017 | -0.084 | 0.000 | -0.058 | 0.000 | -0.062 | -0.095 |
| $K_{4j}$ | 0.282 | 1.055 | 1.000 | 0.066 | 0.333 | 0.136 | 0.117 |
| $K_{5j}$ | -0.016 | 0.101 | 0.000 | 0.130 | 0.000 | 0.071 | 0.241 |

Calculate close degree and weight coefficient by using equations (3) - (7), and the results are presented in Table 5 and Table 6, respectively

Table 6 Weight coefficient

| $\alpha_{ij}$ | $\alpha_{i1}$ | $\alpha_{i2}$ | $\alpha_{i3}$ | $\alpha_{i4}$ | $\alpha_{i5}$ | $\alpha_{i6}$ | $\alpha_{i7}$ |
|---|---|---|---|---|---|---|---|
| $\alpha_{1j}$ | 0.171 | 0.092 | 0.067 | 0.150 | 0.200 | 0.120 | 0.200 |
| $\alpha_{2j}$ | 0.149 | 0.090 | 0.075 | 0.149 | 0.179 | 0.149 | 0.209 |
| $\alpha_{3j}$ | 0.139 | 0.116 | 0.087 | 0.139 | 0.173 | 0.139 | 0.208 |
| $\alpha_{4j}$ | 0.128 | 0.128 | 0.085 | 0.128 | 0.154 | 0.171 | 0.205 |
| $\alpha_{5j}$ | 0.143 | 0.143 | 0.143 | 0.143 | 0.143 | 0.143 | 0.143 |

**Results and comparison**

Comprehensive correlation values of each element about different grades I-V can be calculated according to Tables 5 and 6 and the equations (1) - (2).

$K_{\mathrm{I}}(M)=0.5028$; $K_{\mathrm{II}}(M)=0.803$; $K_{\mathrm{III}}(M)=-0.044$; $K_{\mathrm{IV}}(M)=0.3638$; $K_{\mathrm{V}}(M)=0.087$

It can be seen that $K(M)=\max K_{\mathrm{j}}(M)=K_{\mathrm{II}}(M)$ from the above results, so the evaluation result is grade II, meaning good.

**Conclusions**

A comprehensive evaluation for utilization efficiency of rain-flood resources was conducted by using the fuzzy matter-element evaluation method in Rushan River. It considered economic, social, ecological factors fully, which could avoid one sidedness of evaluation causing by the single factor. Evaluation results provide a reliable basis for the development of Rushan River Basin. The comprehensive evaluation grade for utilization efficiency of rain-flood resources is grade II, which meaning good. It indicated that under the precondition of continuing original social, economic and ecological state, the comprehensive effects tend to be good after utilization program of rain-flood resource implemented. As a consequence, the coordinated development degree of the basin should have been further improved.

**Acknowledgements**

This research was financially supported by the Public Special Ministry of Water Resources (201201116), the Public Sector Ministry of Water Resources (201201115), Water Conservancy Research and Technology Promotion Projects in Shandong Province (SDSLKY201229) and Shandong Province Water Conservancy research and technology promotion projects (SDSLKY201306).

**References**

[1] Yi Wang,Weifeng Yang: International Journal of Rock Mechanics & Mining Sciences. Vol.52 (2012) p.50-55.
[2] Zhiyong Zhou, Xiaoju Zhang: Procedia Environmental Sciences. Vol.18(2013)p.227–235.
[3] Nurnadiah Zamri, Lazim Abdullah: Procedia Computer Science. Vol.24(2013)p.42–53.
[4] Li Yang, Jin Zhao,Yuxia Hou: Shandong Water Conservation. Vol.12(2011)p.19-20. (In Chinese)
[5] Dongjun Liu, Zhihong Zou: Journal of Environmental Sciences. Vol. 24(2012)p.1210–1216.

*Applied Mechanics and Materials Vols. 580-583 (2014) pp 1989-1992*
*© (2014) Trans Tech Publications, Switzerland*
*doi:10.4028/www.scientific.net/AMM.580-583.1989*

# Study on Tidal Current and Sediment for Dredging Project in Yamen Channel

Jie He[1,2,a] , Lipeng Shi[3,b] , Yingjun Sun[4,c]

[1]Nanjing Hydraulic Research Institute, Nanjing, China

[2]State Key Laboratory of Hydrology-Water Resource and Hydraulic Engineering, Nanjing, China

[3] North China University of Water Resources and Electric Power, China, Zhengzhou, China

[4]Hydrology bureau of Zhejiang Province, Hangzhou, China

[a]jhe@nhri.cn, [b]shilp2004@163.com, [c]yingjun373@163.com

**Keywords:** Huangmaohai bay, Tidal current, Sediment, Mathematical model.

**Abstract.** Yamen channel is the important sea-route from Yinzhou Lake to Gaolan harbor in Zhuhai city through Huangmaohai Sea. Based on the recent hydrologic data and the seabed change, the numerical model is validated, and some advanced dredging plan for Yamen channel is simulated in the movement of tidal current and sediment, and the number of the sediment silting in channel is calculated. The result shows that there are some preponderance for the east channel in the tidal current and sediment, and the sediment is filling up in the mouth bars mostly. Moreover, the east channel has the potential to improve the channel standard, which can be developed firstly in the common condition.

## Introduction

Yamen channel is an important sea-route through Huangmaohai Sea, which total distance is about 38.0km from the Yamen entrance to the Hebao Island and Gaolan Island. Yamen entrance is upward to Hutiaomen Channel, downward to Huangmaohai Sea. Hutiaomen Channel is straight to the stream Xijiang. Now, the ship with 5000-ton can pass Yamen channle by regulated. The length of Yinzhou Lake inside Yamen entrance is about 30.0km, with the width of 1.5km to 2.0km, and the depth is between 8.0m to 15.0m. The berths with 10,000 tons can be build on both sides of Yunzhou Lake. Gaolan Port in Zhuhai city under construction on the east side of Huangmaohai Sea will compose harbor group with other ports within Yinzhou Lake(Chen Huizhen, 2000). It can be seen that there is great practical significance to construct the Yamen navigable channel and enhance its shipping ability.

Chinese scholars have done a lot of exploration and research in the selection of the east route and the west route as to advance the Yamen channel navigable standards since the first groove excavation was tested in the ford of Huangmaohai Sea in April 1994. Wu-Jiang Lu (1995) has concluded the deposition rate in the mouth bar is small and it's location is moving to the sea gradually, using fixed-bed thick water-sediment model test to calculate and analyse the mouth bar on the eastern route of Yamen Channel. According to the measured data and numerical results, Rui-Jie Li(2005) confirmed the main parameters in chamfer siltation formula, and estimated siltation intensity and volume of different channel dredging options, and thought the whole channel siltation was not serious, and the channel and the sea was in the balance of micro-silt basically status. By estimating siltation in intensity and volume at the extreme hydrological conditions of different options about Yamen channel, Jian Ding (2005) thought there was a greater siltation in Yamen channel and the water area during the typhoon, tide, large flood at the same time, and siltation under the flight path of the west Channel at the role of big storms is much larger than that of the east channel. Huanmaohai Sea was suspended sediment transporting, and the silting deposition of Yamen channel after excavation was also caused by the suspended sediment mainly. However, the hydrological data used in prophase studies are measured in 1992, and the data of landform scour-and-silt was surveyed in 1990. Now the

excavation works of Yamen channel available for the 5000-ton ship is completed in November 2006. So it is necessary to adopt the recent hydrological observation, landform scour-and-silt data to analyze and evaluate the Yamen Channel.

## Channel Scour and Silt

Three topographic surveys under water in channel have been carried out in the June, August and October of 2007 since Yamen channel was completed in November 2006. According to above 4th sea-route surveyed data of Yamen channel, the scour-and-silt intensity of channel is calculated and its temporal and spatial distribution is analyzed, combined with the water and sediment environment in Huanmaohai Sea. The results show that Huanmaohai Sea is belonged to a typical tidal estuary, and the Yamen channel with 5000-ton has the character "South High, North low and the central prominent". And the seasonal changes is present that it's silting in flood season and scouring in dry season. Annual siltation was about 1.8 million m3 in the main excavation part of Yamen channel, and the number of main groove siltation was 1,650,000 $m^3$(more than 90%). There is scoured sometimes or silted sometimes on the east and west slope with the seasons, and its deposition is rarely, so the total deposition of both slope is only hundreds of thousands m3. The main siltation is located in the mouth bar, and the number of siltation in the channel is about 920,000 m3, of which 710,000 m3 in groove channel, and east and west slope respectively 90,000 and 120,000 m3. The impact of slope stability of the sea route on the groove should merit our attention. The character of siltation in Yamen channel can be summarized as that siltation intensity is high in southern and low in northern, and the mouth bar much higher, and the siltation is significant in floods seasons and weak in dry seasons, the slope scouring or silting sometimes, impacting the adjustment of groove. Four group topographic surveyed data of groove channel above can provide strong support for the validation of numerical model in this paper.

## Dredging Project

Through several analysis of channel topographic survey data after Yamen channel dredging completed, the mouth bar of east channel (KP9-KP17) is still the main siltation segment, and the average siltation intensity is about 1.0 meters annually. 5000-ton ship can pass normally through the maintenance dredging. The west channel keeping the natural water depth can meet 3000-ton ships to run. To enhance the navigation capacity of the Yamen channel, the designed department puts forward the west channel upgraded to 5000 tons (7.7m water deep) and the east channel to 30,000 tons (-11.5m) of the two designed options. By using the tidal current and sediment mathematical model, the tidal current and sediment movement are simulated and the channel sediment siltation is calculated, and some conclusion would be avaluable for the designing the Yamen channel’s shipping standard.

## Tidal Current and Sediment Movement

From the Huanmaohai Sea falling current pattern in Fig.1, the tide current inside bay is mostly reversing current restricted by the shore boundary. The current in Huanmaohai Sea is divided into east, central and west three-ply by Dajin island, Hebao island, Damang island and other islands. The middle entrance (from Dajin island to Hebao island) is the main water way for the tidal current in Huanmaohai Sea. As the water depth in east entrance larger, the tidal current flow is larger than that in the western. The falling tidal current is divided into three part through three entrances inside the bay, and the three-ply current is gathered together and upward to the top of bay. There is near 10 degree angle between the direction of west channel and falling tidal current, and the direction of east channel is basically consistent with tidal current. Compressed by Damang island and Sanjiaoshan island near KP8, the velocity of flood tide and ebb tide is bigger than other channel segments. The channel dredging will be not produced significantly impact on Huangmao bay at the hydrodynamic

environment, and the current flow is adjusted along groove only in the water near channel, the depth of excavation larger, the phenomenon more significant.

The distribution of sediment concentration is showed in fig.2, which is simulated under the ebb tide in Huanmaohai Sea. The distribution of sediment concentration is present that large inside bay and small outside, large in deep groove and small in side shoal, big during ebb tide and small during flood tide. The maximum sediment concentration is in the deep waters of the central bay during ebb-tide, for the bed load on bay waist arising due to tidal current. The sediment concentration along the west channel is more than 0.40kg/m$^3$, and the sediment concentration along the east channel is smaller relatively, however the sediment concentration is still around 0.30kg/m3 in the mouth bar. So it can be seen that water and sediment environment near the east channel is more superior than that of west channel.

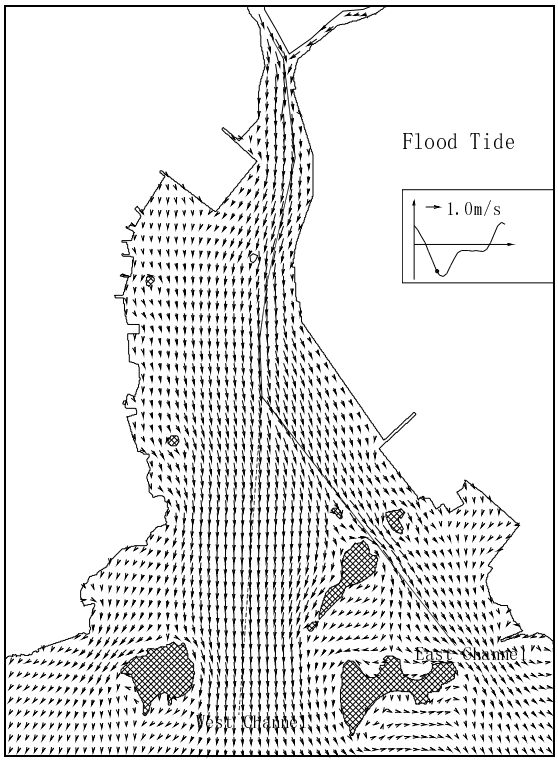


Fig.1 Falling Current Pattern

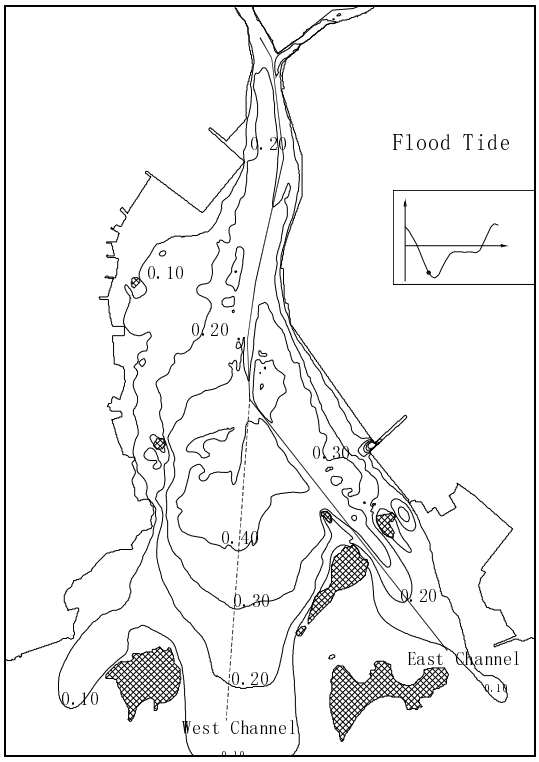


Fig.2 Sediment Distribution in Falling Current

**Siltation along Channel**

The siltation in groove along the west channel of 5,000 ton and the east channel of 30,000 ton are calculated by the model combined with validated parameters, and the distribution of the silting intensity along the west channel and east channel are seen Fig.3 and Fig.4 respectively. The siltation along the west channel is relatively mild, and the average siltation intensity is 0.38m annual. When the water depth of the west channel dredging to 7.7m (fitted to 5,000 tons), the siltation intensity is increased widely, expressed the increase gradually from south to north, but the southern section of the channel is near that of natural status, and the siltation intensity in northern section is the largest, which largest siltation thickness is 1.76m annual. The average siltation intensity is 1.13m annual after the west channel dredging completed, added 0.75m annual than before. Siltation along the east channel is showed saddle-shaped distribution which is highest on the north section, slightly higher on the southern section and slightly lower in middle. Constrainted by terrain, the flow cross-section of channel near KP8 is narrowed down and velocity is increased, and the siltation near this groove is smallest. When the depth of east channel dredged to 11.5m, the siltation intensity along channel is increased in general, and the increase of siltation intensity is small in southern section (KP0-KP8) and slightly larger in northern section, so it is present increasing 0.33m annual than before as a whole. It can be seen that the sediment accretion amount of east channel is less than that of west channel, and the east channel has further potential to improve the shipping standard under the same circumstance.

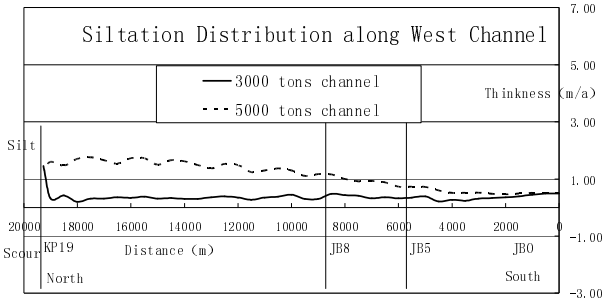


Fig.3 Siltation Distribution along West Channel

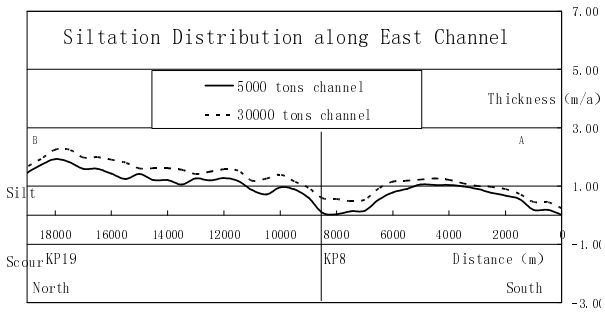


Fig.4 Siltation Distribution along Eest Channel

## Conclusion

The hydrological data in 2006 and change of terrain in the east channel are adopted as validation information in this model. Through simulating and calculating the project of the west channel with 5,000 tons and the east channel with 30,000 tons, the results show that there is an angle changes between the direction of the west channel and the flow direction of tidal current, and the siltation in groove is serious high where the sediment concentration is higher, which is consistent with the results of previous studies. The environment of water and sediment are relatively better in the east channel, and the sediment siltation is mainly located on the mouth bar. The siltation along channel does not increase much under 30,000 tons standard through maintenance dredging normally. Therefore, the east channel has further potential to enhance the shipping standards, and it can be preferential chose to develop under the same conditions.

## References

[1] Chen H.Z. *Yamen channel renovation research*[J]. China Water,2000, NO.12:pp.35-36.

[2] Lu W.J. *Fixed bed and turbid water model test of Yamen east channel chamfer*[J]. The ocean engneer, 1995,VOL.13, No.2:pp. 37-45.

[3] Li R.J., Wang Ch.J., *Accretion analysis of Yamen channel in the mouth of the Pearl River* [J]. China Harbor Construction, 2005,Vol.135, No.4:pp.5-7.

[4] Ding J., Tao A.F., *Sudden silt analysis of Yamen channel in the mouth of the Pearl River* [C]. Progress in Water Resources and Hydropower Technology, 2005, Vol.25, No.6:pp.41-45.

[5] Xin W.J., He J., *The analysis of scour and silt change of Yamen channel* [R]. Nanjing Hydraulic Research Institute, 2008.8.

[6] Xin W.J., *Numerical model of 2-D estuarial suspended sediment motion under the interaction of tidal flow and waces* [J]. The ocean engineering, 1997,No.2:pp.30-47.

[7] Xin W.J., He J., *The analysis of tidal current and sediment Mathematical Model of Yamen channel* [R]. Nanjing Hydraulic Research Institute, 2008.8.

*Applied Mechanics and Materials Vols. 580-583 (2014) pp 1993-1999*
*© (2014) Trans Tech Publications, Switzerland*
*doi:10.4028/www.scientific.net/AMM.580-583.1993*

# Analysis of Monitoring and Settlement Prediction of Wenzhou Shoal Seawall

Haiyun Wei[1,a], Guoqian Liang[2,b], Chaojie Zhang[1,c]

[1]Zhejiang Institute of Hydraulics & Estuary, Hangzhou, 310020, China

[2]Zhejiang Tongji vocational college of science and Technology, Hangzhou, 311231, China

[a]weihy07@126.com, [b]lianggq@msn.com, [c]zcjie2004@126.com

**Key words:** Seawall; Monitoring; Layered settlement; Vane shear strength; Settlement prediction

**Abstract:** The foundation of Wenzhou shoal project is soft and deep. The stability control issue of building seawalls on the deep soft foundation was solved by using a composite foundation treatment of plastic drainage plates and geotextile, combining with the in-situ monitoring. The in-situ monitoring data of Wenzhou shoal project was analyzed and the settlement prediction analysis was conducted. Basing on the conventional exponential curve fitting method, the settlement prediction model is presented for the classified construction on soft foundation. Considering the non-linear of deformation and soil consolidation with load changes, the model used the settlement deformation characteristics under the last load to predict the settlement development under the next load.

## Introduction

Wenzhou shoal located outside the Oujiang Estuary, between Lingkun island (belong to Ouhai district of Wenzhou City) and Niyu island (belong to Dongtou county of Wenzhou City), was a development relatively complete and largest tidal resources within the Oujiang estuary area. Wenzhou shoal Lingni seawall full length 14.5 kilometers was currently the longest sea-crossing dike in China. Dike elevation was 5.8m~6.3m, by 50 years tide control standard design, crest road width 10.5m with double lane. The original foundation ground elevation was -3.0m~-1.0m. The surface soil was composed of newly sedimentary mud flow or mud, with thickness of 0.5m~1.0m. The foundation soils within 40 m depth were composed of high water content, high compressibility, high dexterousity, low strength muck and mucky soils [1,2]. The physical and mechanical indexes of soil foundation were shown in Table 1. The soft foundation was treated with Prefabricated Vertical Drain (PVD) + geotextile + overburden layer, where spacing and depth of the PVD were 1.4m ~1.5m and 20m ~22m respectively. The typical cross-section schematic was shown in Fig. 1.

In order to ensure the smooth progress of seawall construction, to grasp the foundation consolidation and intensity changes, must carry on the comprehensive safety monitoring in the seawall during filling, to ensure security and stability of the seawall. In this paper, the ground surface settlement, pore water pressure, horizontal displacement and layered settlement of Wenzhou shoal Lingni seawall during construction were systematically analyzed. Basing on the measured settlement data analysis, the empirical formula was presented for the calculation settlement during construction.

## In-situ monitoring program

In order to ensure the stability of seawall foundation in filling process, to master deformation law of foundation soil in preloading period, as well as the choice of the reasonable construction schedule, in-situ monitoring instruments were buried in Lingni seawall during construction, to monitor ground settlement, layered settlement, horizontal displacement, vane-shear strength and pore water pressure. In-situ monitoring instrument layout schematic diagram of Section K11+050 was shown in Fig. 2.

**Table 1** Physical and Mechanical Indexes of soil foundation

| Soil layer | Water content (%) | Wet density (g/cm$^3$) | Void ratio | $C_q$ (kPa) | $\Phi_q$ (°) | $C_{cq}$ (kPa) | $\Phi_{cq}$ (°) |
|---|---|---|---|---|---|---|---|
| clay silt | 36.0 | 1.84 | 1.00 | 4.7 | 15.5 | / | / |
| muck | 70.3 | 1.62 | 1.78 | 2.7 | 1.6 | 4.7 | 13.5 |
| Ⅲ$_1$ muck and silt interbedded | 55.0 | 1.70 | 1.38 | 6.0 | 4.2 | 5.4 | 14.7 |
| silty-fine sand | 34.2 | 1.82 | 0.90 | 0.0 | 31.0 | 0.0 | 31.0 |
| Ⅲ$_2$ muck | 61.3 | 1.63 | 1.71 | 7.5 | 2.8 | 7.9 | 13.0 |
| Ⅲ$_3$ muck | 60.1 | 1.63 | 1.69 | 10.3 | 2.4 | 11.1 | 11.7 |
| mucky clay | 51.4 | 1.69 | 1.43 | 12.5 | 4.3 | 15.5 | 13.4 |

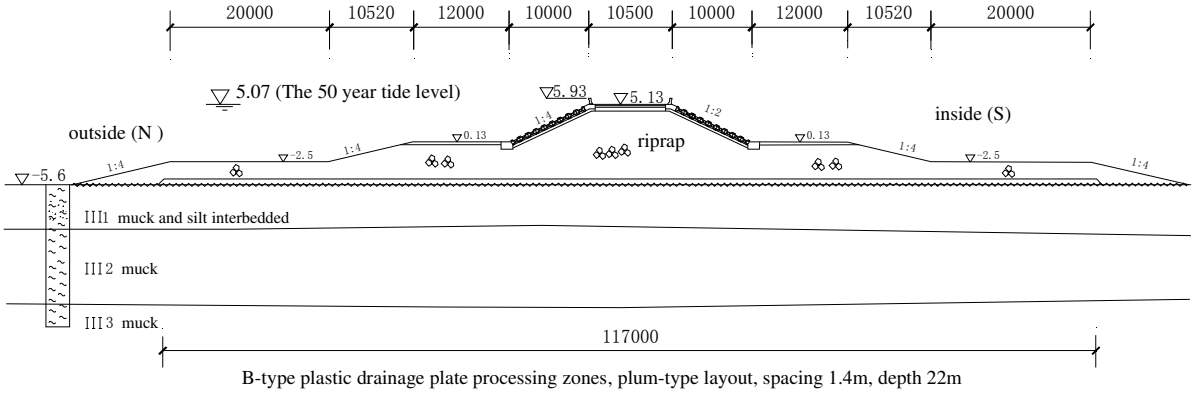


B-type plastic drainage plate processing zones, plum-type layout, spacing 1.4m, depth 22m

Unit:length in millimeter, elevation in meter

**Fig. 1.** The typical cross-section schematic of Lingni seawall

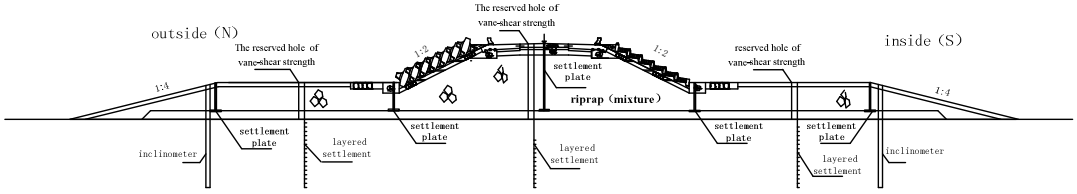


(a) The schematic diagram of in-situ monitoring instrument layout

The work amount of section N1 1+450

| items | legend | symbol | unit | number | note |
|---|---|---|---|---|---|
| settlement plate | ⊥ | D8-1~5 | entries | 5 | |
| layered settlement | △ | FS1~FS3 | hole count | 3 | deep 36 m |
| inclinometer | ◆ | F1~F2 | hole count | 2 | deep 41 m |
| reserved hole of vane-shear strength | ⊕ | SZ4~9 | hole count | 6 | |

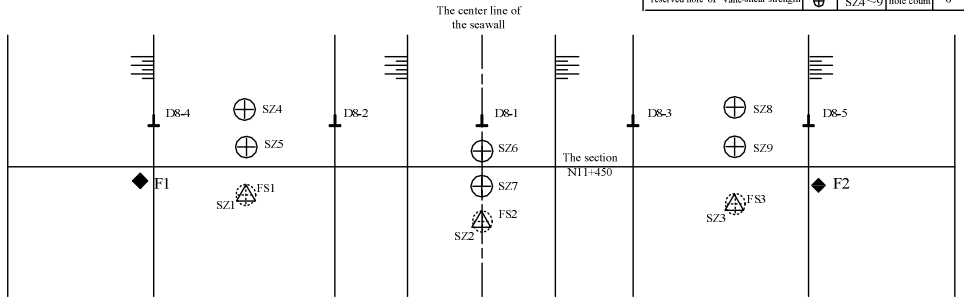


(b) The layout diagram of in-situ monitoring instruments

**Fig. 2.** In-situ monitoring instrument layout schematic diagram of Section K11+050

## Analysis of in-situ monitoring results

### 3.1 Ground surface settlement

As applying the first level load, the sedimentation rates were initial generally greater than the 30mm/d, even more than 100mm/d, but they decayed very quickly. On the third day the sedimentation rates usually less than 30mm/d, after 5 days ~10 days less than 10mm/d, after 3 months the sedimentation rate gradually reduced to 1mm/d ~2mm/d, and has kept near the rate. When applying the first level to the fifth level loads, immediate settlement is obvious, especially the first level load. The sedimentation rate was significantly associated with the load (or filling thickness). To apply over-load not only made sedimentation rate abnormally increase and the attenuation of sedimentation rate was relatively slow. Before applied the second level load，the settlement rate of D9-1 measuring point (which located on the axis of Section K10 + 850) was 3 mm/d. When apply the second level load(i.e. filling thickness 2.52m which was greater than the design filling thickness 2.0 m), although the seawall foundation did not appear instability phenomenon, but the maximum sedimentation rate is as high as 87 mm/d, after nearly 12 days the sedimentation rate was down to 10 mm/d. Therefore, the construction technology which applied multi-stage loading and reduced each level load could significantly reduce the immediate settlement. According to statistics, the immediate settlement accounted for 25%~30% of the total settlement during the construction.

Further studies showed that over-loading could result in a range of foundation where shear stress of soil reached the critical value and elastic deformation developed into plastic deformation, even may occur the whole damage of foundation [3,4,5]. Even if the foundation did not appear obvious instability phenomenon, excessive shear deformation could cause destruction of the foundation soil structure, which would be very unfavorable for post-construction settlement control.

### 3.2 Layered settlement

The soft soil foundation of this project was composed of soft clay layers with different properties. This project applied layered settlement monitoring to find out the compression of each soil layer, to determine consolidation degree of different depths. Fig. 3 shows the observation results of layered settlement located on the axis of Section K11 + 050.

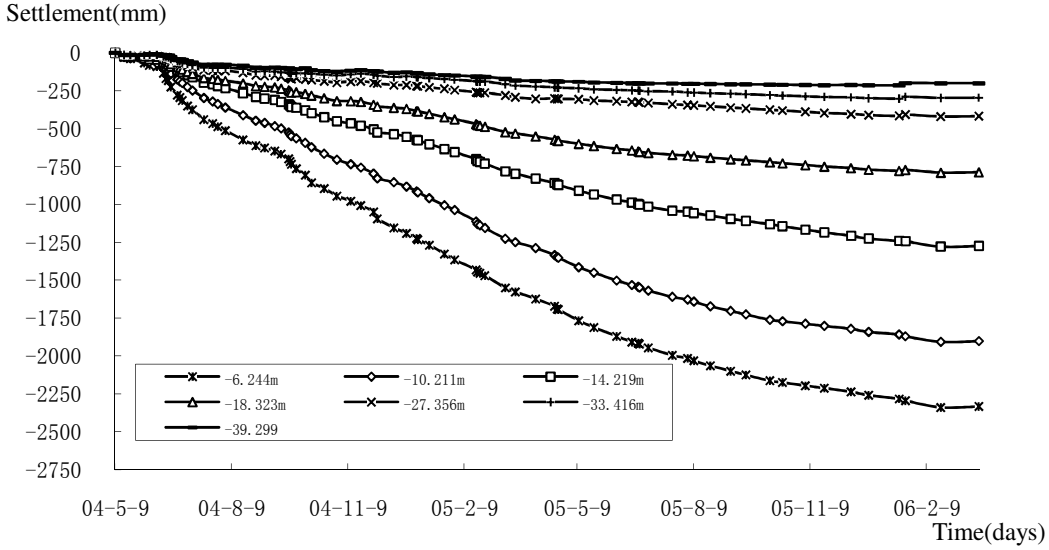


**Fig. 3.** The curves of layered settlement on the axis of Section K11 + 050

The observation results showed that when the project completed, the settlement occurred mainly in the board area, and accounted for approximately 72% of the settlement amount. It indicated that the role of the drainage board to accelerate consolidation settlement is significant. The settlement of underlying deep soft soil layers accounted for about 20% of the total settlement. The underlying deep soft soil layers mainly experienced vertical drainage and its consolidation time was long,

which would cause the sustainable development of large post-construction settlement [3]. Design should take measures to make the most settlement of foundation complete in construction period, effectively reduce the post-construction settlement and a series of problems which post-construction settlement could bring to the subsequent structure engineering.

### 3.3 Horizontal displacement

Fig. 4 shows variations of horizontal displacement with depth at south side of repression layer of Section k11 + 050. The observation results showed that in the initial stage of loading, the horizontal displacement of foundation soil mainly occurred in the board area; the largest displacement was located at -10 m elevation. With the increase of load, especially after applied the third and the fourth level loads, the horizontal displacement developed toward the deep.

After filling repression layer up to its design elevation, only filling soil in the center of seawall, the increasing trend of horizontal displacement decreased. It indicated that repression layer played a good back pressure effect.

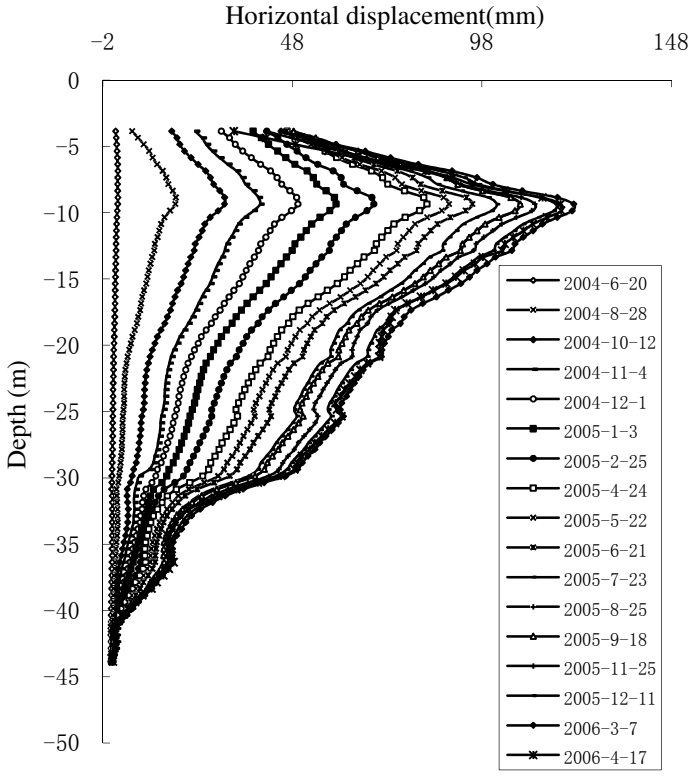


**Fig. 4.** Variations of horizontal displacement with depth at south side of repression layer of Section K11 + 050

### 3.4 Pore water pressure

Fig. 5 shows variations of excess pore-water pressure with time on the axis of Section K11 + 050. The observation results showed that excess pore-water pressure dissipated significantly in the board area. It indicated that the role of the drainage board to accelerate the consolidation of seawall foundation was very significant. When the project completed, the average degree of consolidation of foundation was more than 80%, and the pore pressure in underlying deep layers slowly dissipated. During loading, the pore-water pressure coefficient B is generally 0.3 ~ 0.5 (below -12.5 m elevation), which was in the normal range. The B value is the excess pore-pressure divided by the total load. The pore-pressure monitoring data showed that the pore-pressure increased in the underlying deep layers of foundation during load interval. It was due to viscous effect of soil skeleton, the upper thick layer of clay delayed the dissipation of pore-water pressure in deep layers. Due to the stress relaxation effects of the soil skeleton, the increase of pore-pressure which the deep

layers produced in unit time exceeded its dissipation, so resulting in the pore-water pressure increase [6,7].

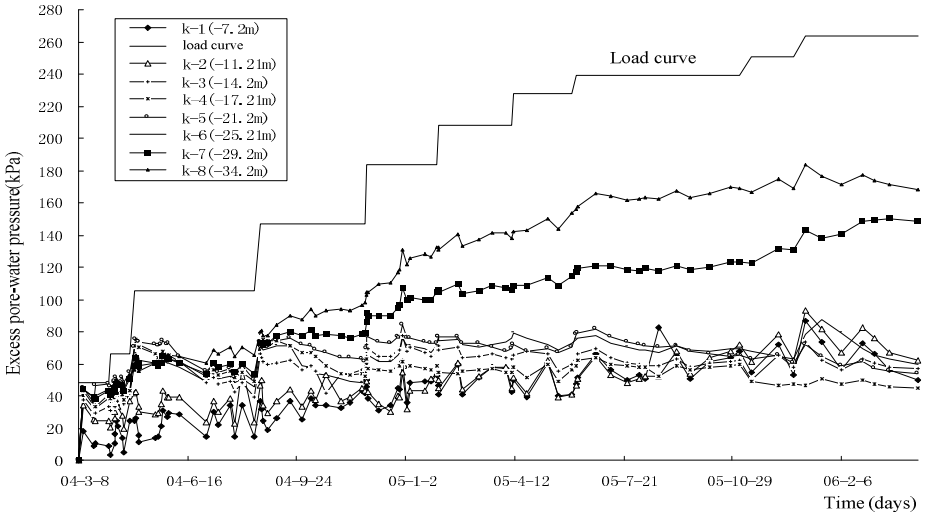


**Fig. 5.** Variations of excess pore-water pressure with time on the axis of Section K11 + 050

### 3.5 Vane shear strength

In order to evaluate the effect of foundation treatment, two groups of vane strength tests were carried out at Section K11 + 050, in which a group in early stage of loading, another group in later stage of loading. Contrast of two groups of vane strength test results was shown in Table 2.

The test results showed that the soil strength in the board area of dike foundation and repression layer has significantly increased, where the soil strength of dike foundation grew more pronounced. In drainage plate processing area, the soil strength increase of muck and sand interbedded layer (Ⅲ 1) was most pronounced. Comparing with the drainage plate processing zone, the strength of the underlying soil layers increased but not significantly. It indicated that the role of the drainage board to accelerate consolidation of seawall foundation was very significant.

**Table 2** Contrast of two groups of vane strength test results

| Layer Code | Soil layer | Depth range (m) | Vane strength increase of repression layer (kPa) | Vane strength increase of dike foundation (kPa) |
|---|---|---|---|---|
| $Ⅲ_1$ | muck and silt interbedded | 0～6 | 27～32 | 36～40 |
| $Ⅲ_2$ | muck | 6～21 | 8～26 | 10～30 |
| $Ⅲ_3$ | muck | 21～30 | 3～5 | 3～6 |

### Settlement prediction

Due to lack of detailed geotechnical parameters of foundation soils, it was difficult to accurately calculate the reserved settlement of seawall. At present, the settlement curve fitting which basing on the field measured settlement was an accepted more reasonable settlement prediction method. Basing on the traditional exponential curve fitting method, a new model of settlement prediction was presented for the classified construction on soft foundation. Considering the non-linear nature of deformation and the soil consolidation nature with load changes and combining with the characteristics of grading construction, the model used the settlement deformation characteristics under the last load to predict the settlement development under the next load.

Based on the hypothesis that settlement development was in line with the exponential curve, the settlement fitting equation under the No. i level load could be expressed as Eq. 1:

$$S_{ti} = S_{0i} + (S_{li} - S_{0i})[1 - \alpha_i e^{-\beta_i (t - t_{0i})}] \quad (1)$$

where: $t_{0i}$ is initial time of settlement curve fitting under the No. i level load; $S_{0i}$ is the settlement corresponding to time $t_{0i}$ under the No. i load; $S_{li}$ is final settlement under the No. i level load; $\alpha_i$, $\beta_i$ are undetermined parameters under the No. i level load.

If the No. i level loading period was longer, $S_{li}$, $\alpha_i$ and $\beta_i$ parameters of the above equation could be determined by the exponential curve fitting, basing on the measured settlement. By studying variation rule of $\alpha_i$ and $\beta_i$ under all level loads, the settlement under the No. i+1 level load could be predicted. Contrast of measured settlement and predicted settlement according to this method was shown in Fig. 6.

Further studies showed that the predicted settlement which considering soil consolidation nature with load changes, can better predict the settlement in construction period under various level loads and the post-construction settlement within a certain period of time.

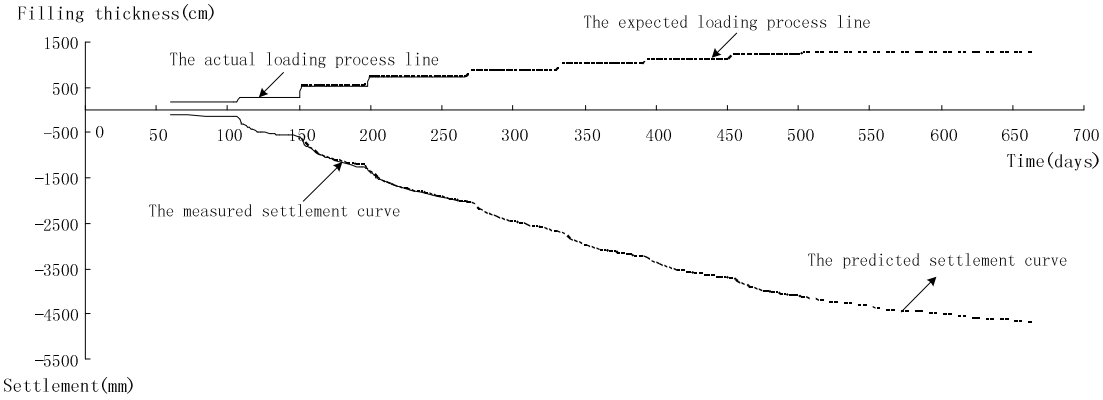


**Fig. 6.** Contrast of measured settlement and predicted settlement on the axis of Section K 8 + 850

## Conclusions

(1) During Wenzhou shoal seawall construction, by in-situ monitoring, engineer may at any time to master the foundation deformation and drainage consolidation, determine the loading time, loading rate control, dynamic guide the engineering construction.

(2) For stack and preloading drainage in deep soft soil foundation, the loading rate must be strictly control. Over-loading could result in a range of foundation where shear stress of soil reached the critical value and elastic deformation developed into plastic deformation, even may occur the whole damage of foundation. Even if the foundation did not appear obvious instability phenomenon, excessive shear deformation could cause destruction of the foundation soil structure, which would be very unfavorable for post-construction settlement control.

(3) Prefabricated vertical drain was suitable for the soft foundation treatment, which effectively shortened drainage distance of foundation soil, accelerated consolidation of foundation soil, increase strength of foundation, reduced the grated load interval, and speeded up the construction progress.

(4) The settlement of underlying deep soft soil layer accounted for 20% of the total settlement. The underlying deep soft soil layers mainly experienced vertical drainage and its consolidation time was long, which would cause the sustainable development of large post-construction settlement. Design should take measures to make the most settlement of foundation complete in construction period, effectively reduce the post-construction settlement and a series of problems which post-construction settlement could bring to the subsequent structure engineering.

## Acknowledgements

This work was supported by Zhejiang Province Key Science and Technology Innovation Team (2010R50035), Public Welfare Industry Scientific Research Special Funds of Ministry of Water

Resources (201201043), Zhejiang Province Natural Science Fund project (LY3E090002) and Zhejiang Provincial Laboratory of Hydraulic Disaster Prevention and Mitigation.

## References

[1] Zhejiang Guangchuan Engineering Consulting Co., Ltd. In-situ monitoring report of Wenzhou shoal Lingni seawall (the bid 1 section of the first-stage project) [R]. 2006. (in Chinese).

[2] Zhujiang Shen. Engineering properties of soft soil and soft soil foundation design [J]. Chinese Journal of Geotechnical Engineering, 1998, 20(1): 100 ~111. (in Chinese) .

[3] Mesri G, Choi Y K. Settlement analysis of embackment on soft clays. ASCE Journal of Geotechnical Engineering, 1985, 111: 441~464.

[4] Berre T, Poskitt T J. The consolidation of peat [J]. Geotechnique, 1972, 22(1): 27 ~52.

[5] Tanvenas F, Leroueil S. The behavior of embankment on clay foundations. Canadian Geotechnical Journal, 1980, 17: 236~260.

[6] Yan Lou. Technique of vacuum drainage preloading[M]. Beijing: China Communications Press, 2002. (in Chinese) .

[7] Jiancai Zhu, Xiaogui Wen, Xiaonan Gong. Dissipation of pore water pressure in soft foundation reinforced by vacuum drainage preloading [J]. Journal of Hydraulic Engineering, Shuli Xuebao, 2004 (8): 123 ~128. (in Chinese) .

*Applied Mechanics and Materials Vols. 580-583 (2014) pp 2000-2006*
*© (2014) Trans Tech Publications, Switzerland*
*doi:10.4028/www.scientific.net/AMM.580-583.2000*

# Comparative study on design of exposed penstock laid on ground using Chinese and American specifications

Lei Hu [1, a], Hegao Wu [1, b], Changzheng SHi [1, c], Yinghan Xie [2, d]

[1]State Key Laboratory of Water Resources and Hydropower Engineering Science, Wuhan University, Wuhan 430072, China

[2]Changjiang institute of survey, planning, designing and research, Wuhan 430010, China

[a]leih1209@gmail.com, [b]wbf1988@vip.sina.com, [c]scz4@163.com, [d]yhxie01@hotmail.com

**Keywords:** hydropower station, exposed penstock laid on ground, DL/T 5141-2001, ASCE No.79, allowable stress, load combination.

**Abstract.** In this paper, differences by using selected three typical specifications—DL/T 5141-2001 (Chinese), ASCE No.79 in the version of 1993(American) and ASCE No.79 in the version of 2012 (American)—in structural design of exposed steel penstock were explored. A practical example about exposed penstock laid on ground applied in hydropower station was also used to analyze specifications clearly. The result shows that the main differences between Chinese and American specifications are allowable stress and load combination. The former is direct factor of calculating exposed penstock shell thickness. Therefore, ASCE No.79 (2012) designs the minimum wall thickness, followed by DL/T 5141-2001 and the last is ASCE No.79 (1993), which is correspondingly contrary to sort by allowable stress. Basically, ASCE No.79 (2012) defines lower safety coefficient for exposed penstock, which is identical with authoritative rules of pressure vessels in the U.S.A and EU. The safety of DL/T 5141-2001 has been proved via rich engineering experience and this specification is recommended for Chinese projects. Besides, ASCE No.79 (2012) is recommended.

## Introduction

The specification for design of steel penstocks for hydroelectric stations (DL/T 5141-2001) was formulated and promulgated by China renewable energy engineering institute (CREEI) in May 2002. It plays significant role in design of Chinese steel penstocks. Besides, there are some other kinds of widely used specifications for steel penstocks or pressure vessels in the world, such as "Unfired pressure vessel" issued by European Committee for Standardization (EN 13445-2002), ASCE Manuals and Reports on Engineering Practice No.79"Steel Penstocks" promulgated by American Society of Civil Engineers (ASCE No.79), "ASME Boiler & Pressure Vessel Code" enacted by American Society of Mechanical Engineers (ASME BPVC). The design principles, methods and load combinations are different among each other. Xu et al. [1] raised the concept of equivalent safety coefficient based on yield strength and tensile strength respectively, which was used to evaluate safety level of several representative penstocks codes of hydropower stations and pressure vessels standards in China and other countries (e.g. U.S.A, Japan). It emphasized safety level of each specification but did not involve specific design method of one type of steel penstocks. The actual mechanical behavior of steel penstocks was not used to compare design results.

The exposed penstock laid on ground is supported by a series of buttresses. An anchor block at the turning is set up to fix penstock. There is an expansion joint between two anchor blocks to adapt to relative deformation [2]. This paper aims at analyzing exposed penstock laid on ground using DL/T 5141-2001 [3] and ASCE No.79 (the version of both 1993 and 2012) [4,5]. If unspecified type is after ASCE No.79 in this paper, something in common is discussed. In view of one practical project, depending on actual mechanical behavior, the design results also reflect the differences analyzed.

**Comparison on design methods between two standards**

**Design principles.** DL/T 5141-2001 adopts limit-state design method based on theory of probability, the design equation is characterized by partial factors. ASCE No.79 adopts allowable stress method. The basic principle of stress classification is introduced into both of them.

After all, stress of each calculation point should meet strength requirement. According to above two standards, the fourth strength theory is recommended as

$$\sigma=\sqrt{\sigma_\theta^{\,2}+\sigma_x^{\,2}+\sigma_r^{\,2}-\sigma_\theta\sigma_x-\sigma_\theta\sigma_r-\sigma_x\sigma_r+3(\tau_{\theta x}^{\,2}+\tau_{\theta r}^{\,2}+\tau_{xr}^{\,2})}\le[\sigma] \quad (1)$$

where $\sigma$ is the equivalent stress, also known as von Mises stress; $[\sigma]$ is allowable stress of steel; $\sigma_x$ is axial normal stress, $\sigma_\theta$ is circumferential normal stress, $\sigma_r$ is radial normal stress, all are positive as tensile stress, $\tau_{\theta x}$ , $\tau_{\theta r}$ and $\tau_{xr}$ are shear stress.

**Allowable stress.**The basic principle of stress classification is introduced into both. DL/T 5141-2001 differentiates stress into general primary membrane stress, local primary membrane stress and local primary membrane stress plus primary bending stress. ASCE No.79 differentiates stress into primary stress and secondary stress, where primary stress is divided into general primary membrane stress, local primary membrane stress and primary bending stress.

In DL/T 5141-2001, the allowable stress is calculated by

$$[\sigma]=\frac{1}{\gamma_0\varphi\gamma_d}f \quad (2)$$

where $\gamma_0$ is coefficient for importance of structure depending on security level, $\varphi$ is coefficient for design condition, $\gamma_d$ is structure coefficient depending on type of stress and working condition, $f$ is design value of steel strength.

In ASCE No.79, the allowable stress is defined as

$$[\sigma]=K\times S \quad (3)$$

where $K$ is coefficient for increasement of stress according to type of stress and working condition, $S$ is basic allowable stress intensity. ASCE No.79 in version of 1993 formulates that, the basic allowable stress intensity should be the lesser of one-third of the minimum specified tensile strength or two-thirds of the minimum specified yield strength. The version of 2012 formulates that the basic allowable stress intensity is the smaller of tensile strength/2.4 or yield strength/1.5. Table 1 gives allowable stress of two kinds of rolled steel.

**Table 1 Allowable stress in DL/T 5141-2001 and ASCE No.79 under normal condition[Mpa]**

| Type of steel | Standards | General primary membrane stress | Local primary membrane stress | local primary membrane stress +primary bending stress | local primary membrane stress +primary bending stress+secondary stress |
|---|---|---|---|---|---|
| Steel with high tensile strengt | DL/T 5141-2001 （16-50mm） | 231 | 285 | 337 | — |
| | ASCE No.79 (1993) | 203 | 305 | 305 | 610 |
| | ASCE No.79 (2012) | 254 | 381 | 381 | 610 |
| Q345R | DL/T 5141-2001 （≤36mm） | 181 | 223 | 264 | — |
| | ASCE No.79 (1993) | 157 | 235 | 235 | 470 |
| | ASCE No.79 (2012) | 196 | 294 | 294 | 470 |

**Service conditions and load combinations.** DL/T 5141-2001 differentiates service conditions into lasting condition, intermittent condition, occasional condition and contains six types of load

combinations. By contrast, there are normal condition, intermittent condition, emergency condition, exceptional condition, construction condition and hydro-test condition in ASCE No.79. Each service condition has its own load combination. Relatively speaking, load combinations in ASCE No.79 are more comprehensive. Considering length, normal condition (lasting condition) is the only one to be used in comparison on design of exposed penstock. It is governing factor as well.

As previously mentioned design principle of DL/T 5141-2001 that the design equation is characterized by partial factors, all loads including dead loads and live loads have corresponding partial factors. However, ASCE No.79 assign a value of 1.0 to all load factors. As for exposed penstock, partial factors of hydrostatic pressure are all equal to 1.0 in DL/T 5141-2001 and ASCE No.79.

Analytic equations for calculation of the equivalent stress of steel are simplified. The finite element method, by contrast, is more visual and accurate and easily accepted by engineers. Therefore, finite element software ANSYS is used to help designing a practical exposed penstock in above three specifications in this paper.

## Application

**FEM model.**An anchor block amounts to a fixed end and penstock between two anchor blocks is independent. Based on a practical project, a length of exposed penstock between two anchor blocks was designed using both DL/T 5141-2001 and ASCE No.79. The diameter is 2.5m with internal water pressure of 5.86 to 6.35Mpa (Hydrostatic pressure and water hammer pressure are all contained). Finite element model, shown as Fig.1, consists of steel penstock, expansion joint, supporting ring, sliding support, anchor block and rock foundation with 17 meters in width and 10 meters in depth. Steel penstock and supporting ring are modeled by shell element. Solid element is used to model concrete anchor block and rock foundation.Supporting ring is set above support at intervals of 8m, in which face to face contact elements are used to simulate sliding effect with friction coefficient 0.1, shown as Fig.2. Bellow expansion joint is modeled by truss element and equivalent stiffness is 5.8MN/m. Foundation is normally restrained at surrounding and bottom side. The thickness of penstock shell is confirmed in normal condition and load combinations based on DL/T 5141-2001 and ASCE No.79 are the same. Self-weight including steel, concrete and water, internal water pressure and temperature load are combined into the model. The preliminary wall thickness is calculated by

$$t = \frac{Pr}{[\sigma]} \qquad (4)$$

where t =penstock shell thickness required to resist the design pressure P (mm);

P=internal pressure (at centerline of pipe) (MPa);

r=inside penstock radius (mm);

$[\sigma]$=allowable stress of steel.

The penstock shell thickness applying allowable stress of steel with high tensile strength in DL/T 5141-2001 and ASCE No.79 (1993 and 2012) respectively are 36mm, 32mm and 40mm, which do not contain thickness that used to resist rusting, abrasion or errors in manufacturing (2mm in general).

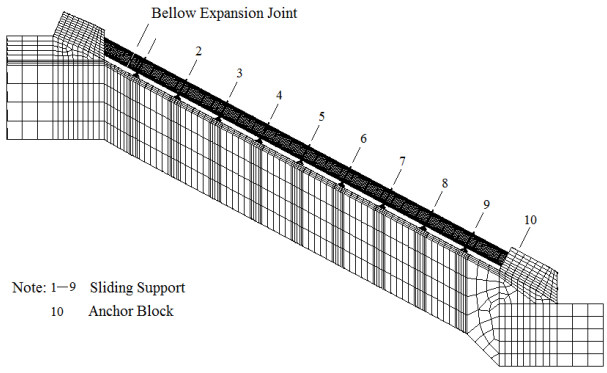


**Fig. 1 FEM model**

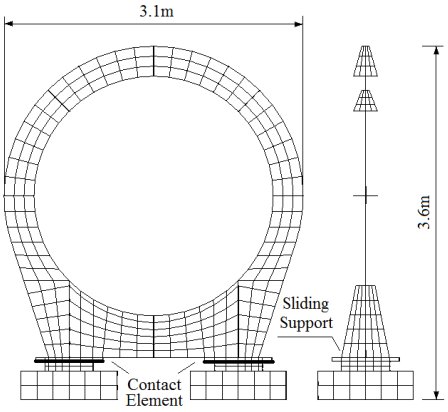


**Fig. 2 Supporting ring**

**Result.**The exposed steel penstock can be separated into three basic regions for mechanical behavior: (1) Shell outside stiffener or discontinuity ( Middle layer of shell is general primary membrane stress and surface layer is local primary membrane stress plus primary bending stress ); (2) Shell at stiffener or discontinuity ( Middle layer is local primary membrane stress and surface layer is local primary membrane stress plus secondary stress); (3) Stiffener itself is treated as general primary membrane stress at middle layer. These aforesaid regions are numbered as 1, 2 and 3 respectively. The chief design purpose is to meet requirement in Table 1 in whichever region.

Figure 3~4 reflect mechanical behavior of exposed steel penstock using DL/T 5141-2001. The equivalent stress of steel is mainly caused by hoop stress. Shell at stiffener has less stress because that hoop deformation is restricted by supporting ring. The local primary membrane stress, local primary membrane stress plus bending stress and local primary membrane plus secondary stress are all much less than allowable stress. Penstock shell thickness is controlled by general primary membrane stress, which belongs to region 1. 36mm (calculated thickness) is what given to penstock shell, also is the supporting ring. Generally speaking, it is a principle that supporting ring has about same thickness with adjacent penstock shell, which is out of welding. Figure 3 shows that general primary membrane stress across region 1 do not exceed 231 MPa, the exactly numerical value of allowable stress for steel with high tensile strength. When it comes to ASCE No.79, the above mentioned value changes but other method and mechanical behavior are uniform. That is to say, general primary membrane stress is still the key point for penstock shell thickness.

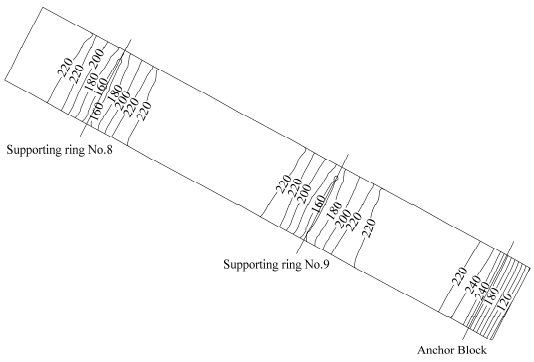


**Fig. 3 Contours of von Mises stress at middle layer of penstock**

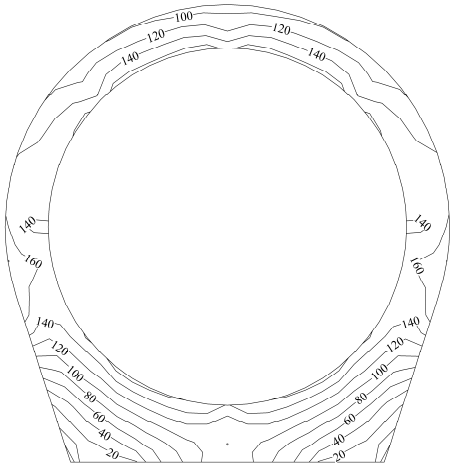

**Fig. 4 Contours of von Mises stress at middle layer of supporting ring**

## Disscusion

**Direct reason.**Generally, the diversion system of hydropower station includes several continuous segments of exposed penstock between two anchor blocks. Each should be designed separately with

previously introduced method. Internal water pressure gradually increases from upstream to downstream which are numbered consecutively 1~11, as shown in Table 2. For this project, the ultimately defined penstock shell thickness is shown in Table 2

The numerical value of allowable stress for steel used to welding into penstock shell, is direct factor to determine the wall thickness in whichever specification. ASCE No.79 (2012) defines the maximum allowable stress, followed by DL/T 5141-2001 and ASCE No.79 (1993). Sort by thickness of penstock shell proves to be correspondingly contrary.

**Table 2 Design Results**

| Pipe segment | DL/T 5141-2001 | | ASCE No.79 (1993) | | ASCE No.79 (2012) | |
|---|---|---|---|---|---|---|
| | Penstock shell thickness (mm) | Type of rolled steel | Penstock shell thickness (mm) | Type of rolled steel | Penstock shell thickness (mm) | Type of rolled steel |
| 1 | 14 | A | 16 | A | 14 | A |
| 2 | 20 | A | 22 | A | 20 | A |
| 3 | 24 | A | 26 | A | 22 | A |
| 4 | 28 | A | 30 | A | 26 | A |
| 5 | 22 | B | 26 | B | 20 | B |
| 6 | 26 | B | 30 | B | 24 | B |
| 7 | 30 | B | 34 | B | 28 | B |
| 8 | 34 | B | 36 | B | 30 | B |
| 9 | 36 | B | 40 | B | 34 | B |
| 10 | 38 | B | 42 | B | 34 | B |
| 11 | 40 | B | 46 | B | 38 | B |

Note: For rolled steel, 'A' represents Q345R; 'B' represents steel with high tensile strength up to 600MPa.

**Fundamental reason.** By using DL/T 5141-2001, the conventionally so-called safety coefficient of allowable stress is resolved into several partial factors like Eq. 2. While ASCE No.79 sets it directly shown as Eq. 6. For comparative purpose, this study adopts the concept of equivalent safety coefficient from reference [1]. It is a coefficient synthesizing partial factors for loads and material properties. For exposed penstock, only considering hydrostatic pressure and water hammer pressure, it is defined as

$$K = \frac{\gamma_0 \varphi \gamma_d \gamma_s (\gamma_{Q1} + \gamma_{Q2} \rho_h)}{1 + \rho_h} \tag{5}$$

$$[\sigma] = \frac{f}{K} \tag{6}$$

where $\gamma_0$, $\varphi$, $[\sigma]$ and $\gamma_d$ are same meaning as that in Eq. 2; $\gamma_{Q1}$ is partial factor of hydrostatic pressure and $\gamma_{Q2}$ is partial factor of water hammer factor; $\gamma_s$ is partial factor of steel yield strength or tensile strength; $\rho_h$ is ratio of water hammer pressure to hydrostatic pressure; $f$ is yield strength or tensile strength of steel. Values of factors above are shown in Table 3. The safety coefficients or equivalent safety coefficients, both are called safety coefficient for short, of above-mentioned three specifications are listed in Table 4, where $K_y$ is safety coefficient of yield strength and $K_t$ is that of tensile strength. Besides, some American and European authoritative rules for construction of pressure vessels such as EN 13445-2002, "ASME Boiler & Pressure Vessel Code, Section 8 Division 2, Alternative Rules, Rules for Construction of Pressure Vessels" (ASME BPVC-VIII-2) with two versions of 2004 and 2007 are also contained to contrast and learn.

Frequently-used steel types for penstock in hydropower station are listed in Table 1. As to other types used, both yield strength and tensile strength changes a little. Ratios of the former to the latter all

exceed 0.67 for two types, so $K_t$ is used to determine allowable stress in ASCE No.79. Apparently, these three specifications compared mainly in this paper have different safety coefficients. ASCE No.79 (2012) defines the minimum safety coefficient, followed by DL/T 5141-2001and ASCE No.79 (1993), same sort as design thickness and adverse sort with allowable stress. That is, ASCE No.79 (2012) has relatively lower safety level for exposed penstock. Renewed specifications have all boosted allowable stress based on tensile strength of steel with yield ratio more than 0.625. Some authoritative rules of pressure vessels in the U.S.A or European Union (EU) evaluate alike level in their latest version. The progress of rolled steel and welding technology contribute a great share in the revolution. Considering acceptability of engineers participating in whichever work of design, supervision, construction or investment, ASCE No.79 (2012) is recommended. Attentively, China has implimented DL/T 5141-2001 and rich engineering experience (e.g. sky lake and south motain hydropower station using exposed penstock) proves it safe. So DL/T 5141-2001 is still appropriate for Chinese projects.

**Table 3 Common values of partial factors in DL/T 5141-2001 (Exposed penstock, Q345R)**

| $\gamma_0$ | $\varphi$ | $\gamma_d$ | $\gamma_{Q1}$ | $\gamma_{Q2}$ | $\gamma_s$ | $\rho_h$ |
|---|---|---|---|---|---|---|
| 1.1(Class I), 1.0(Class II) | 1.0(Lasting condition), 0.90(intermittent condition), 0.85(occasional condition) | 1.6 | 1.0 | 1.1 | 1.08(yield strength) 1.63(tensile strength) | 0.1~0.4 |

**Table 4 Values of K according to several specification (Exposed penstock, Q345R)**

| Country or region | Type of specification | Name or code | $K_y$ | $K_t$ |
|---|---|---|---|---|
| CHINA | Steel penstock | DL/T 5141-2001 | 2.0 | 2.9 |
| U.S.A | Steel penstock | ASCE No.79 (1993) | 1.5 | 3.0 |
| U.S.A | Steel penstock | ASCE No.79 (2012) | 1.5 | 2.4 |
| U.S.A | Pressure vessel | ASME BPVC- VIII -2 -2004[6] | 1.5 | 3.0 |
| U.S.A | Pressure vessel | ASME BPVC- VIII -2-2007[7] | 1.5 | 2.4 |
| EU | Pressure vessel | EN 13445-2002[8] | 1.5 | 2.4 |

Note: Values for DL/T 5141-2001 are suitable for steel penstock of class I in lasting condition and $\rho_h$ values 0.3.

## Conclusions

From comparison of designing exposed penstock using DL/T 5141-2001(Chinese) and ASCE No.79(American), it comes to several conclusions as follows.

(1) Differences of rules: DL/T 5141-2001 adopts limit-state design method based on theory of probability, the design equation is characterized by partial factors. ASCE No.79 adopts allowable stress method. The basic principle of stress classification is introduced into both of them. Calculation of allowable stress is main difference. ASCE No.79 (2012) defines the maximum allowable stress, followed by DL/T 5141-2001 and the last is ASCE No.79 (1993).

(2) Differences of design results: For general, exposed penstock shell thickness is confirmed by general primary membrane stress. Allowable stress is direct factor when calculating wall thickness. Consequently, Sort by wall thickness leads to just inverse order compared with that by allowable stress.

(3) Differences of safety level: The basic reason for differences of design results is safety level of each specification. Though ASCE No.79 (2012) has relatively lower level among the three, it is same as renewed version of rules for pressure vessels in the U.S.A and EU which are authoritative. It is related to higher quality of rolled steel and welding. So, ASCE No.79 (2012) is recommended for international projects because it may be convenient to pass though examination and save investment. Attentively, DL/T 5141-2001 is safe according to accumulated engineering experience and it is suitable for Chinese projects for same reason.

**Refrences:**

[1] Bin Xu, Jianguo Hou, Xuwen An, et al. Journal of Hydraulic Engineering, 2012, 43(8): 957-966. (in Chinese)
[2] Shanding Ma, Ruze Wang. Hydropower station [M]. Beijing: China Water Power Press, 1996. (in Chinese)
[3] DL/T 5141-2001, specifications for design of steel penstocks of hydroelectric stations [S]. Beijing: China Electric Power Press, 2001. (in Chinese)
[4] ASCE 79-1993: ASCE Manuals and Reports on Engineering Practice No.79"Steel Penstocks"[S]. American Society of Civil Engineers，New York，1993 .
[5] ASCE 79-2012: ASCE Manuals and Reports on Engineering Practice No.79"Steel Penstocks" (Second Edition）[S]. American Society of Civil Engineers，New York，2012 .
[6] ASME BPVC-VIII-2-2004 "ASME Boiler & Pressure Vessel Code, Section 8 Division 2, Alternative Rules, Rules for Construction of Pressure Vessels" [S]. American Society of Mechanical Engineers, 2004.
[7] ASME BPVC-VIII-2-2007 "ASME Boiler & Pressure Vessel Code, Section 8 Division 2, Alternative Rules, Rules for Construction of Pressure Vessels" [S]. American Society of Mechanical Engineers, 2007.
[8] EN 13445-2002 "Unfired pressure vessel" [S]. European Committee for Standardization, 2002.

*Applied Mechanics and Materials Vols. 580-583 (2014) pp 2007-2010*
*© (2014) Trans Tech Publications, Switzerland*
*doi:10.4028/www.scientific.net/AMM.580-583.2007*

# Current Situation and Development of SHPF Project in China

Chun Man Guan

General Institute of Water Rescources and Hydropower Design and Planning, Beijing 100120, China

1070282544@qq.com

**Keywords:** small hydropower; substitutive fuel; ecology; construction; development

**Abstract.** The project of substituting small hydropower for fuel (SHPF project in short) in China has been implemented for ten years and has achieved significant economic, social and ecological benefits. The construction, completion situations, results and major experience of the SHPF project are summarized. The existing problems are analyzed. Some suggestions are given for the construction and management of similar projects in future.

## Basic situations

### (1) Planning of SHPF Project

The rural residents in China have used firewood and straws as their domestic fuel for a long time. The excessive deforestation has caused vegetation deterioration in some regions, leading to ecological deteriorations such as severe soil erosion and air pollution. In order to fundamentally solve the rural fuel problem in mountainous regions and to consolidate the achievements of Grain to Green Programme (GTGP) and Natural Forest Conservation Program (NFCP), the Chinese government has decided to implement the SHPF project.

In 2003, the Ministry of Water Resources (MWR) of P. R. China carried out the pilot work of the SHPF project in 26 counties in Sichuan, Yunnan, Guizhou, Guangxi and Shanxi Provinces (Autonomous Region), the installed capacity has an increase of 58 000 kW, and it has benefited 0.22 million populations.

In 2006, MWR expanded the SHPF project to 81 pilot items, the installed capacity has an increases of 0.150 million kW and the annual generating capacity is 210 million kWh, and it has benefited 0.633 million populations.

Since 2008, MWR has fully implemented the SHPF project and aimed at 1022 items by the year of 2015, with an increase of installed capacity of 1.7056 million kW and the annual generating capacity of 2.438 billion kWh, which will benefit 6.7771 million populations.

### (2)Progress of SHPF Project

By the end of 2012, MWR had arranged 163 items of the SHPF project, among which 26 were implemented in 2003 and 81 in 2006. Besides, MWR had planned to implement 56 items from 2009 to 2015. Up till now, 139 items have been completed and are continuing to bring the benefits.

## Implementation Effect of SHPF Project

The SHPF project is an important measure to develop low-carbon economy, circle economy and to establish resource-conserving and environment-friendly society. It manifests the concept of "Human-oriented" and the striving for building a beautiful China. It is also a people-benefit project, and it will lighten the burden on farmers, adjust the energy structure in rural areas and realize ecological, social and economic benefits.

### (1)Realization of considerable ecological benefits

The statistics show that the 139 completed projects have brought the installed capacity of hydropower station of 393 640 kW, and 266 684 kW of which is brought by the small hydropower stations. The installed capacity has electrified 258 511 households, i.e., 973 535 populations. The SHPF project has a total investment of 3.07171 billion RMB Yuan. The calculated results indicate that the project has an

annual reduction of firewood consumption of about 0.242 million t and provides the electricity of 242.26 million kWh per year, with a direct reduction of $CO_2$ emission of 0.223 million t. Accordingly, the forest area of 310 000 $hm^2$ will be preserved, bringing carbon sequestration 630 000 t and oxygen release of 560 000 t to the air. Furthermore, the soils of 474 000 t per year will be conserved, and nitrogen of 796 t, phosphorus of 263 t and potassium of 7897 t can be avoided.

**(2)Great improvements in rural living conditions**

Using the clean energy, the farmers minimize the harm of polluted gas produces by the firewood and coal consumption. Their hard physical labor and accidents for firewood in the hills may be avoided, and it may help them to change the outmoded customs and enjoy the healthy and convenient modern life. All these will improve the farmers' overall qualities and thus facilitate the construction of rural material progress and the development of a harmonious society in the pilot area.

**(3)Increase of farmers' income, reduction of their living cost and improvement of long-term wealth creation**

In the pilot areas, a large number of labor forces are free from some strenuous manual work like cutting firewood. The SHPF project helps an average household to spare the workload that may otherwise have to be done by one laborer for fifty days. The farmers utilize this extra-time to go out as migrant workers or engage in all kinds of sidelines, by which each household can receive an increase in their income from hundreds to thousands RMB Yuan. After the implementation of the SHPF project, each household can reduce its electricity bill, ranging from 100 to 200 RMB Yuan.

**(4)Stimulating development of other industries and new rural construction**

Along with the concept of "Human-oriented", the local governments in most pilot areas take the SHPF project as a golden opportunity to integrate resources. By combining the new rural construction, they make the overall plans to utilize the fund for rural health, road building and other supportive means so as to give full play to farmers' initiative in road building and improvement of water, kitchens, pens and latrines, which will comprehensively promote the environment renovation in the rural areas of China.

**Major experiences**

**(1) Formulation of policies and determination of responsibility**

During the construction process of the SHPF project, all provinces (autonomous regions) have formulated different management methods to guide their construction, management and fund use of the SHPF project according to their own situations.

**(2)Integration of multi-channel investment and cooperation of various departments**

The counties (districts and towns) of most pilot items can organize various departments of water resources, forestry and communications to integrate multi-channel investment of seismic rehabilitation, poverty alleviation, mountainous resettlement, domestic water safety and village roads. They can also combine the small hydropower stations with rural electrification construction to improve the pilot areas by full use of the policies of returning farmland to forests and farmer-benefiting.

**(3)Extensive propaganda and active participation of inhabitants**

The SHPF project is a systematic engineering and directly relates to the inhabitants' benefits, change of rural backward production and living styles and promotion of farmers' living quality. The governments at various levels hold mobilization and group meetings to extensively delivery the policy, character and significance of the SHPF project. The inhabitants understand their responsibilities, rights and duties and actively support and participate in the project construction so as to build a satisfactory situation for the smooth implementation of the SHPF project.

**(4) Normal operation and management for sustainable efficiency of SHPF project**

All the provinces (autonomous regions) have formulated the three-right separation management system of ownership right, operation right and utilization right of the SHPF project, defined the responsibilities and duties of the management agencies at various levels, specified the power supply

and utilization order and signed an agreement with the SHPF project consumers to not cut trees and to protect ecological environment. They have also prepared the relevant management institutions and methods for the consumers' responsibilities and duties for the power supply and utilization and eco-environmental protection. Accordingly, the management mechanism for the long-term satisfactory operation of the SHPF project has been established.

## Major problems

**(1)Need for optimization of overall project layout**

At present, the SHPF project is distributed across most provinces in both northern and southern areas of China. Due to cold winter, water endowments, abundant coal and convenient transportation, the mountainous regions in northern areas of China are not suitable places for the SHPF project. Meanwhile, the project cannot be implemented in some counties or cities in need owing to the exclusion in the prescribed scope in China.

**(2)Improvement for selection of pilot areas**

The economic conditions in some pilot areas are satisfactory. Hardly any difference in "substituting fuel wood with SHPF electricity" can be seen between those areas and the surrounding non-project areas. The discounted electricity price does not stimulate the replacement for fuel, and the local government and public are not active in participation.

In addition, there are still many non-project mountainous regions with poor economic conditions. The farmers use a large sum of firewood instead of electricity as domestic fuel, which is a threat to the local environment. It is urgent for us to implement the SHPF project to arouse the farmer's initiative to use electricity and their awareness to protect and improve the ecological environment.

**(3)Innovation of construction modes**

Most provinces don't have ideal conditions for developing and constructing power supply points. The investment is relatively high. Several provinces have already halted the development of small hydropower stations as well as the next stage of the project plan. If we insist on giving priority to building new stations and supplying electricity nearby, it will be more difficult for us to carry out the project. Hence, the construction modes need innovation.

## Suggestions

**(1)Optimization of overall project layout**

The people in the northern areas of China mainly use coal and straws for heating. It's advisable to reduce the SHPF project in the north areas and expand it to the southern areas of China, such as the southwest areas and the middle and lower reaches of Yangtze River. The local government in the northern areas of China should take other measures to solve the farmers' heating problem. For those places where the SHPF project is necessary, the pilot programs should be continued if reasonable.

**(2)Cautious selection of pilot areas**

Besides the consideration of the areas of GTGP and NFCP as well as the key management regions of soil erosion, it is preferable that the selection conditions should include the farmers' poverty, climate and environmental sensitivity. The limited fund should mainly be used to help the regions with low income and heavy burden on environmental protection. Only in this way can the effect of the project be better. Moreover, it will help regulate the psychological imbalance of the farmers in the surrounding non-project areas.

It is suggested that the planning of the SHPF project both at national and provincial levels should be amended. By regarding the county as the unit, the government should implement the project gradually and programmatically based on the demand.

**(3)Establishment of encouragement and withdrawal mechanism**

We should implement a progressive pricing for the electricity produced by the small hydropower. Within the specified electricity range, the smaller the hydro-electricity is consumed, the lower the electricity price is. That is, the "encouragement" for farmers to use electricity instead of firewood or

straws. Furthermore, the withdrawal mechanism for the small hydro-electricity should be established. The agreements of small hydro-electricity supply should clarify the length of its discount service. Once the per capita net income (PCNI) reaches a certain level (better off), the small hydro-electricity should withdraw from the area. Another region will be chosen as the pilot area so as to consolidate and expand the sustainable benefits of small hydropower stations.

**(4)Extension of construction modes**

In addition to building new power stations, each province can adopt different modes based on its own situation. Either reconstructing old power stations or purchasing the existing small hydropower stations is advisable. We'd better shorten the construction period and bring the benefits of project as soon as possible. The national policies of mandatory scraping should be implemented gradually in order to force the aged, inefficient and nonrenewable hydropower stations to withdraw from the market, which in turn it will create more opportunities for the more rational development of the water resources as well as their provision for the public welfare.

## Summary

The SHPF project is a livelihood and moral engineering to alleviate farmers' burden and to adjust rural energy structure and to realize ecological, economic and social benefits. The SHPF project directly serves the rural areas and farmers, protects and improves the ecological environment, promotes the production and living conditions in the rural areas, and raises the farmers' income. It is necessary and significant for the realization of sustainable development of rural economy and society and the establishment of well-off society. The pilot items provide some experience for the extensive implementation of the SHPF project and promote its full construction and implementation in China.

Therefore, in order to raise the government's decision-making level and the investment benefits, the following procedures are adopted: (1) the experience and lessons from the construction and management of the SHPF project are summarized; (2) the efficiency and the existing problems are scientifically evaluated; (3) the construction and management of the SHPF project is further improved; (4) the guidelines, principles, object, layout, investment direction and countermeasures of the SHPF project are rationally determined.

## References

[1] Law of the People's Republic of China on Regenerable Energy resources (2005). (in Chinese)

[2] Management methods for post-evaluation of water resources construction projects (trial) (Ministry of Water Resources [2010] No. 51) (in Chinese)

[3] Bureau of Rural Hydropower and Electrification Development of Ministry of Water Resources. Construction and Management of Small Hydropower Station for Fuel. China Water Power Press, 2010.9.

[4]Guidelines of calculating ecological benefits on the project of small hydropower substituting for fuel(SL593-2013). (in Chinese)

[5] Standard of Substituting Small Hydropower for Fuel (SL468-2009). (in Chinese)

[6] MWR Planning of ecological protection for small hydropower stations in China (2003), Planning of ecological protection for small hydropower stations in China from 2006 to 2008 (2006), Planning of small hydropower stations in China from 2009 to 2015 (2008). (in Chinese)

[7] Dong Zhe-ren, Sun Ya-dong. Principles and Technologies of Eco-Hydraulic Engineering. China Water Power Press, 2007. (in Chinese)

[8]Liu Hai-feng. Ecological problems in modern water conservancy projects and eco-water conservancy projects[J]. Urban Construction Theory Research, 2011. (in Chinese)

*Applied Mechanics and Materials Vols. 580-583 (2014) pp 2011-2014*
*© (2014) Trans Tech Publications, Switzerland*
*doi:10.4028/www.scientific.net/AMM.580-583.2011*

# Geo-stress Direction Evaluation Method based on Numerical Simulation

SC.Xu[1,2,a], CY.Jin[3,b]

[1]School of architecture and Civil Engineering, Shenyang University, Shenyang, Liaoning 110044, China

[2]Key Laboratory of Liaoning Province for environmental geotechnical engineering, Shenyang, Liaoning 110044, China

[3]Research Center for Safe Deep Mining, Northeastern University, Shenyang, Liaoning 110044, China

[a]xusuchao@163.coml, [b]jcy@163.com

**Keywords:** tunnel engineering, excavation procedure, numerical simulation, FLAC[3D].

**Abstract:** The phenomenon of spalling at Baihetan Hydropower Station is influenced by such factors as the stress redistribution in surrounding rock, the local stress concentration and also poor properties of disturbed belt. In this paper, a series of numerical simulation were carried out and some beneficial conclusions were gained as follows: 1) the ratio of maximum shear stress and uniaxial compressive strength is more rational in the prediction of spalling and can give confident explanation for "V" shape pits; 2) the in-situ geo-stress direction is in accordance with NNE and NE.

## Introduction

Baihetan Hydropower Station is located in the lower reaches of the Jinsha River. In-situ investigation shows that different intense spalling occurs in surrounding rock after excavation with 0.5-3m depth "V" shape pits. In this paper, a series of numerical simulation work were carried out in order to explain the spalling phenomenon. Finally, by analyzing the simulation results, we give some beneficial conclusions which could provide scientific reference and important technical support for spalling prediction in the constructing process of the rock engineering deeply mined in hard brittle rock mass.

## Computation Model

According to the testing tunnel position, a simulation model was established as Fig 1 which are PD62-1, PD62-2 and PD62-3. For the purpose to explain the principal stress affection for rib spalling, four groups of stresses were structured which were 23MPa (maximum horizontal principal stress), 16MPa (minimum horizontal principal stress), 8MPa (vertical stress) with the direction of NNW(N20° W), NNE(N20° E), NE( N45° E) and NEE( N65° E).

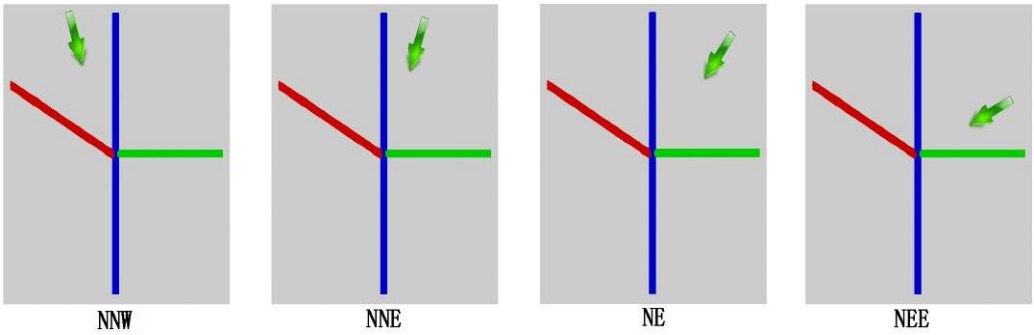


Fig. 1 Different Principle directions

## Results

For the reason that high geo-stress condition and different mechanical properties of aphanitic basalt, rock mass deterioration model which is proved reasonable for the evaluation of brittle rock under high stress was adopted[1-3]. The results of maximum principal stress and energy release rate were gained as follows by fig 2.

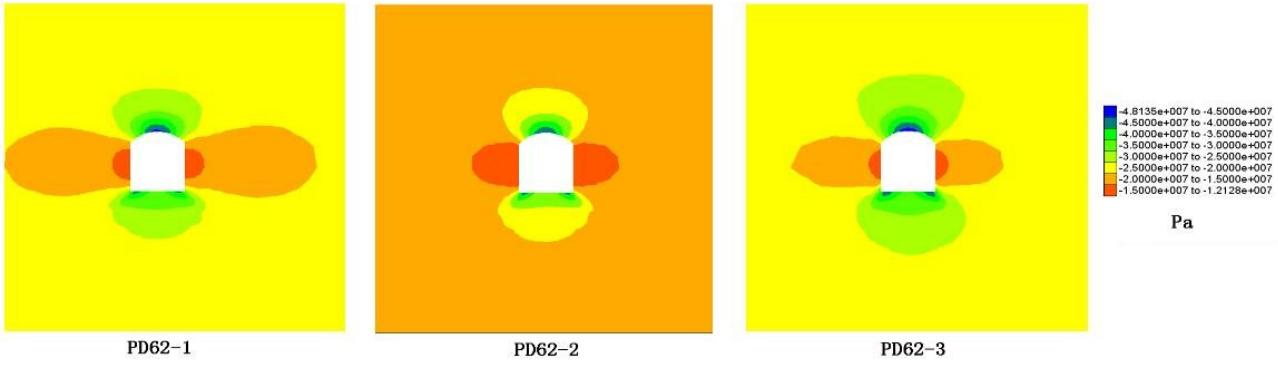


(a). maximum principal stress of NNW geo-stress

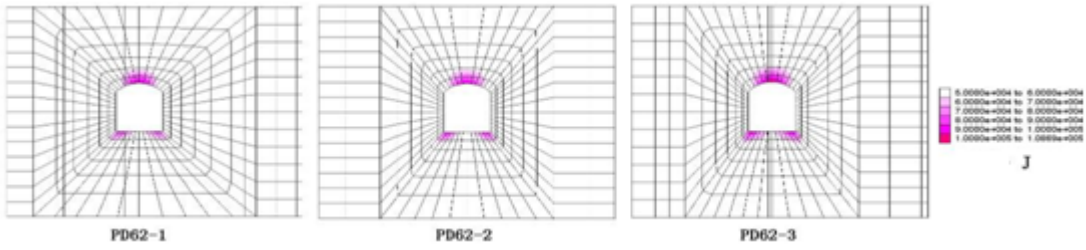


(b). energy release rate of NNW geo-stress

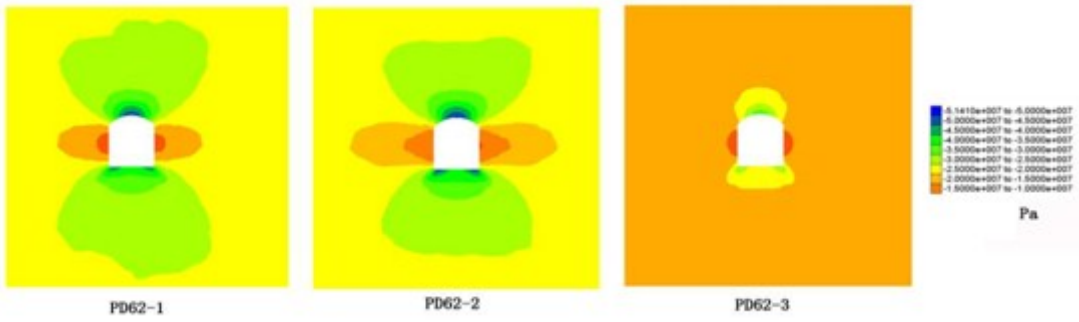


(c). maximum principal stress of NNE geo-stress

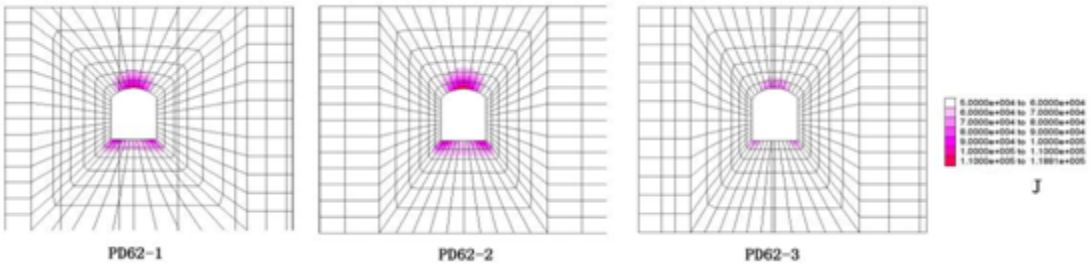


(d). energy release rate of NNE geo-stress

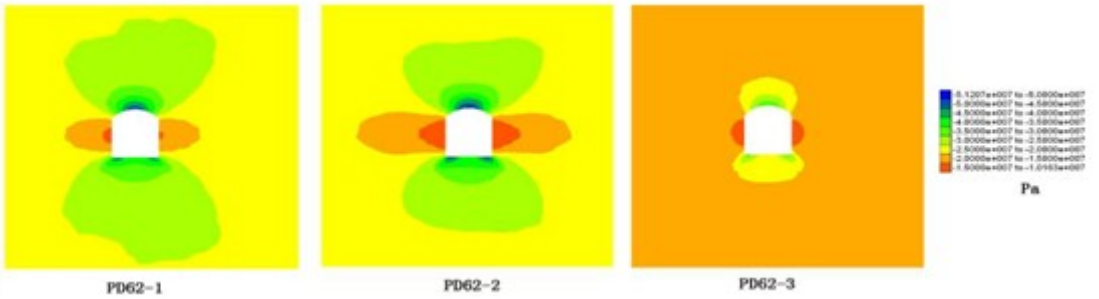


(e). maximum principal stress of NE geo-stress

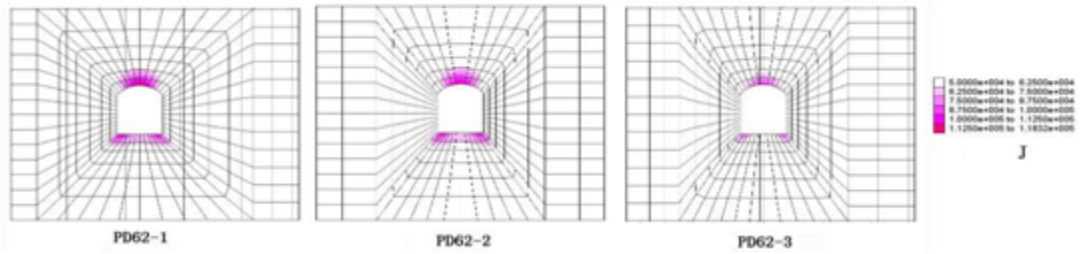


(f). energy release rate NE geo-stress

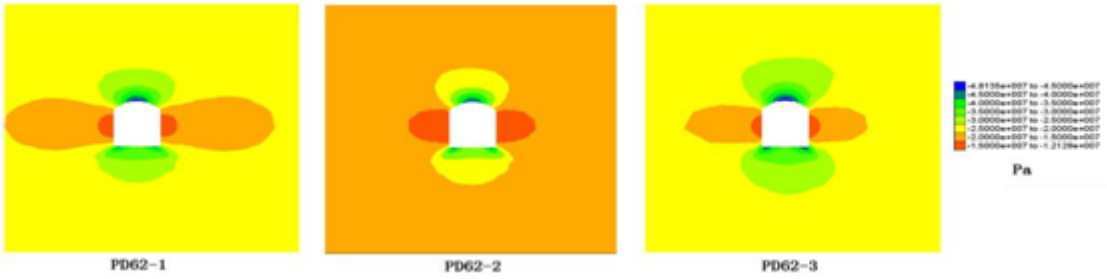


(g). maximum principal stress of NEE geo-stress

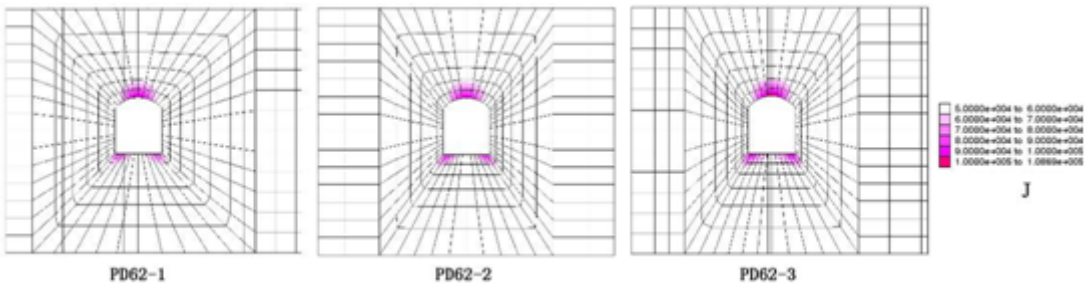


(h). energy release rate of NEE geo-stress

Fig 2.Results under different geo-stress directions

**Analysis and Conclusions**

Generally speaking, stress redistribution usually occurs after excavation of tunnel and caverns and rib spalling can be considered as a kind of brittle failure for hard rock induced by local stress concentration[4-5]. As a non-ejection brittle failure, rib spalling is the result of stress redistribution in surrounding rock. So, 《Standard for classification of engineering rock masses》gives a definition by the ratio of uniaxial compressive strength and maximum initial vertical hole axis stress ( $R_c / \sigma_{\max}$ ) as an rule for brittle rock burst. In this definition, stripping and off block occurs with more new fractures when $R_c / \sigma_{\max}$ is 4-7. Secondary stress field in surrounding rock is of obvious difference due to different cavern shape. Furthermore, the brittle failure extent is also of great difference due to different shear stress. So, Russene provides another index which is $\sigma_\theta / \sigma_c$ ( $\sigma$ is maximum shear stress , $\sigma$ is uniaxial compressive strength ) and gives that low-amplitude brittle failure (rib spalling) occurs when $\sigma_\theta / \sigma_c$ is 0.2-0.3. By the results of simulation and in-situ testing at the top of the tunnel, the value of $\sigma_\theta / \sigma_c$ is 0.32 and rib spalling occurs and this is in accordance with in-situ condition. So we can safely come to the conclusion that rib spalling probably occurs at the top of testing tunnel which is the reason of "V" failure that proved by numerical simulation. Meanwhile, by statistical results of spalling intensites, we can know that the in-situ geo-stress direction is in accordance with NNE and NE.

**Reference:**

[1]. TAN Chen-xuan, WANG Rui-jiang, SUN Ye. Numerical modelling estimation of the 'tectonic stress plane' (TSP) beneath topography with quasi-U-shaped valleys[J]. International Journal of Rock Mechanics and Mining Sciences, 2004, 41: 303－310.

[2]. Xu-Suchao，FENG-Xiating，CHEN-Bingrui. Experimental study of skarn under uniaxial cyclic loading and unloading tests and acoustic emission characteristics [J]. Rock and Soil Mechanics, 2009, 30(10): 2929-2934.

[3]. FAIRHURST C. Stress estimation in rock: A brief history and review[J]. International Journal of Rock Mechanics and Mining Sciences, 2003, 40: 957－973

[4]. Xu-Suchao, CHEN-Bingrui, Jin-Changyu. Study on the Prediction Method for Brittle Failure of Hard Rock Based on Acoustic Emission Test [J]. Advanced Materials Research. Volumes 594 – 597.

[5]. SHENG Qian, HUANG Zheng-jia, WU Ai-qing. Reasonable selection of underground house axis based on the stability of determinde blocks in the Three Gerges project[J]. Chinese Journal of Rock Mechanics and Engineering, 2002, 21(Supp. 1): 1958－1961

*Applied Mechanics and Materials Vols. 580-583 (2014) pp 2015-2018*
*© (2014) Trans Tech Publications, Switzerland*
*doi:10.4028/www.scientific.net/AMM.580-583.2015*

# Influence of the bridge on the flood controlling in the river

Xinzhou Zhang[1, a], Xiping Dou[1, b], Zengxiang Jiao[1, c] and Yinyan Song[2, d]

[1]Nanjing Hydraulic Research Institute, Key Lab of Port, Waterway and Sedimentation Engineering of the Ministry of Transport, Nanjing, 210029, China

[2]Jiangsu Province Hydrology and Water Resources Investigation Sub-Bureau of Xuzhou, Xuzhou, 221006, China

[a]xinzhouzhang@126.com, [b]xpdou@nhri.cn, [c]zxjiao@nhri.cn, [d]yysong@126.com

**Keywords:** Bridge; Flood Controlling; Water Level; Flow Velocity

**Abstract.** It was convenient to go through the river after the building of bridge, but the flow water around the bridge can be influenced seriously. The level of water will become high and the velocity will reduce because of the influencing of resistance water by the bridge pier, and the level and the velocity of downstream water decreased. Between the bridge piers the velocity will increase where the water was extruded. All of these will have an effect to the safety of bridge and river flood controlling. In this paper, a 2D numerical model is established to simulate the variation of the level and velocity after the bridge was built, and to learn the effecting of the bridge on the flood controlling.

## Introduction

While the economic of the coastal and along the river had developed greatly, the human beings built a large number of bridges on river and made the traffic much more convenient. But, all of them could threat the safety of flood controlling, and also bridge scour pit endanger their safety. Therefore, before the bridge would be built, it need to analysis the variation of flow water and the level of water, velocity and calculate the depth of local scour around the bridge by all kind of construction. And so it provided technical for the construction of bridge. A 2D numerical model **i**s established to study the effecting of bridge construction to the flow of river and the research will provide reference for similar projects.

## Numerical Mode

The river which is 20km long and 250m wide is influenced by tides significantly called tidal river, the vertical average slope is 0.2‰. The cross-section is compound, the bottom of river is -1.0m, on both sides of the elevation of the volume is 5m. Both of sides are plain and low-lying terrain and the river is influenced by the tide jacking. While the flood flow is more than 2000$m^3$/s, it will be overflowing. So the river is two-way and alluvial river. A once-in-a-century flow is about 5000 $m^3$/s,and the average level of high tide is 4.2m off the coast. The bridge will be treated as solid boundary because of so many bridges and docks along the river. Others are computed by increasing roughness.

The continuity equation, momentum equation of tidal current and sediment transport equation in numerical model are discretized using FVM (Finite Volume Method):

$$\frac{\partial \varsigma}{\partial t}+\frac{\partial Hu}{\partial x}+\frac{\partial Hv}{\partial y}=0 \tag{1}$$

$$\frac{\partial Hu}{\partial t}+\frac{\partial Huu}{\partial x}+\frac{\partial Huv}{\partial y}=-gH\frac{\partial \varsigma}{\partial x}-\frac{\partial H\overline{u'u'}}{\partial x}-\frac{\partial H\overline{u'v'}}{\partial y}+\frac{\tau_{sx}-\tau_{bx}}{\rho}+fHv \tag{2}$$

$$\frac{\partial Hv}{\partial t}+\frac{\partial Huv}{\partial x}+\frac{\partial Hvv}{\partial y}=-gH\frac{\partial \varsigma}{\partial y}-\frac{\partial H\overline{v'u'}}{\partial x}-\frac{\partial H\overline{v'v'}}{\partial y}+\frac{\tau_{sy}-\tau_{by}}{\rho}-fHu \tag{3}$$

Where u and v are the flow velocity components on the direction of x-y, $\varsigma$ is water lever, $H$ is total water depth, $\rho$ is water density, $f$ is Coriolis affect coefficient, $\tau_{sy}$ and $\tau_{by}$ is shearing force acting on water surface and riverbed respectively.

According to the contents of research, tasks and project area terrain conditions and to be similar with the water flow movement ,the numerical model calculate the range of bridge for upstream and downstream of 2.5km.It is established with the latest measurement bed topography to calculate the verification and engineering. The grid of the model is equidistant in order to reflect the scale, make the mesh density around the bridge. The local terrain and the grids about upstream and downstream are shown in Fig.1. Validation process of tide and flood calculation shows that the coefficient of roughness is 0.018 when the tide influence, and it is 0.028~0.030 effected by the flooding. The time step is 0.5s while the simulation is run off.

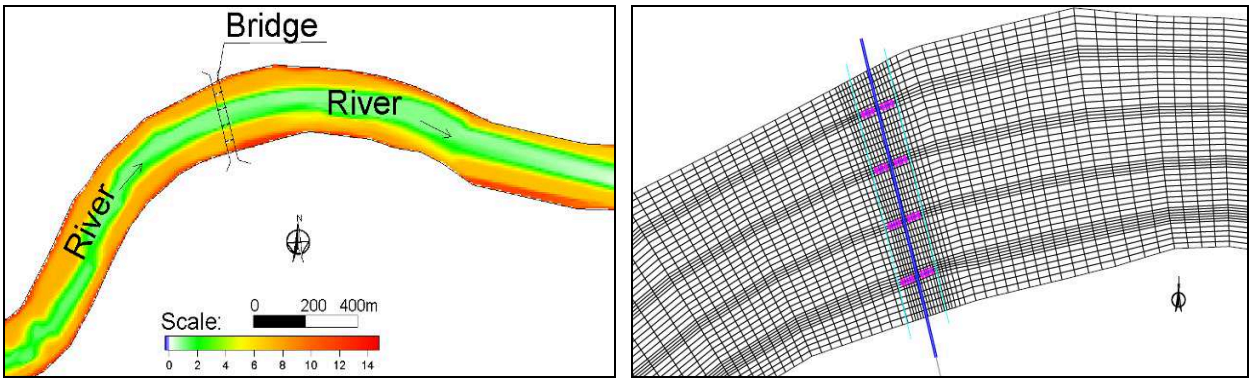


Fig.1 The local terrain and the grid

## Influence of bridge on flood controlling

**Influence on the water level.** The bridge will have an impact on the level of water after it will be built. The upstream increase and the downstream reduced. Fig.2 is the distribution of water level after the project, from the calculation results, the height of the maximum backwater is 20.9cm, the height of maximum backwater is 4.5cm near shore. The level of upstream which 25m away form the pier axis increase 6-8cm.

**Influence on the flow velocity.** Fig.3 is the variation of velocity after the project. Form the result of diagram and calculation, it shows that water flow around the bridge pier and the velocity decreases in the areas of both upstream and downstream. But the velocity of near shore and the intermediate of piers are increase .It can increase by 0.7m/s in front of piers and decrease by 2m/s behind, the maximum of velocity can increase by 0.2m/s in the intermediate of piers. In the upstream, 25m far away form the axis of bridge ,the velocity of water reduced by 0.1m/s. Fig.4 is the distribution about the variation of velocity about the 100m and 300m in the upstream ,the front and behind of bridge ,the 100m and 300m in the downstream. It concludes six sections (CS1-CS6). From the distribution of velocity, obviously, it increased between the bridges (CS3-CS4). Affected by the bridge pier, the velocity increased in the downstream about 100m away, and it reduced in the area of rear cover. The project could not influence the areas of 300m far away, and the flow rate is less than 0.06m/s.

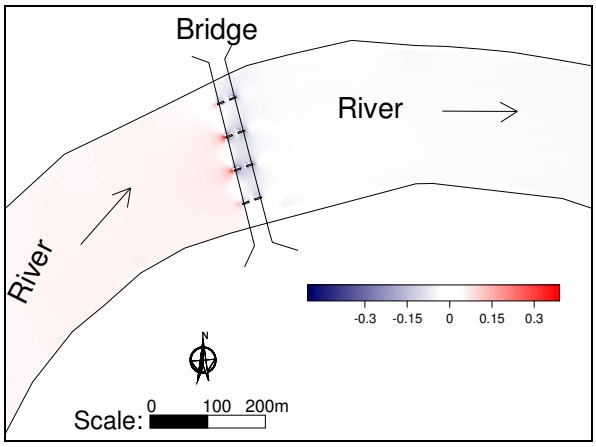


Fig. 2 The distribution of level

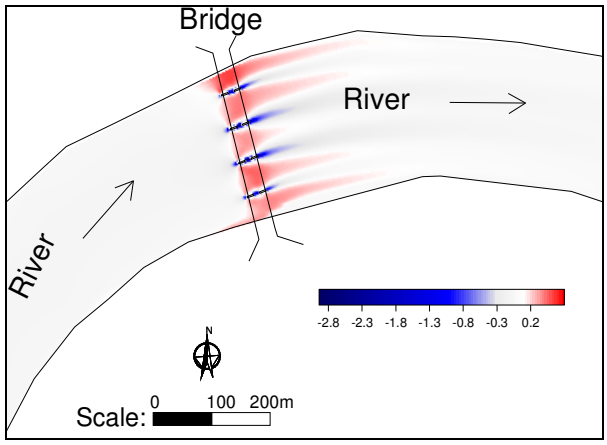


Fig.3 The distribution of local velocity

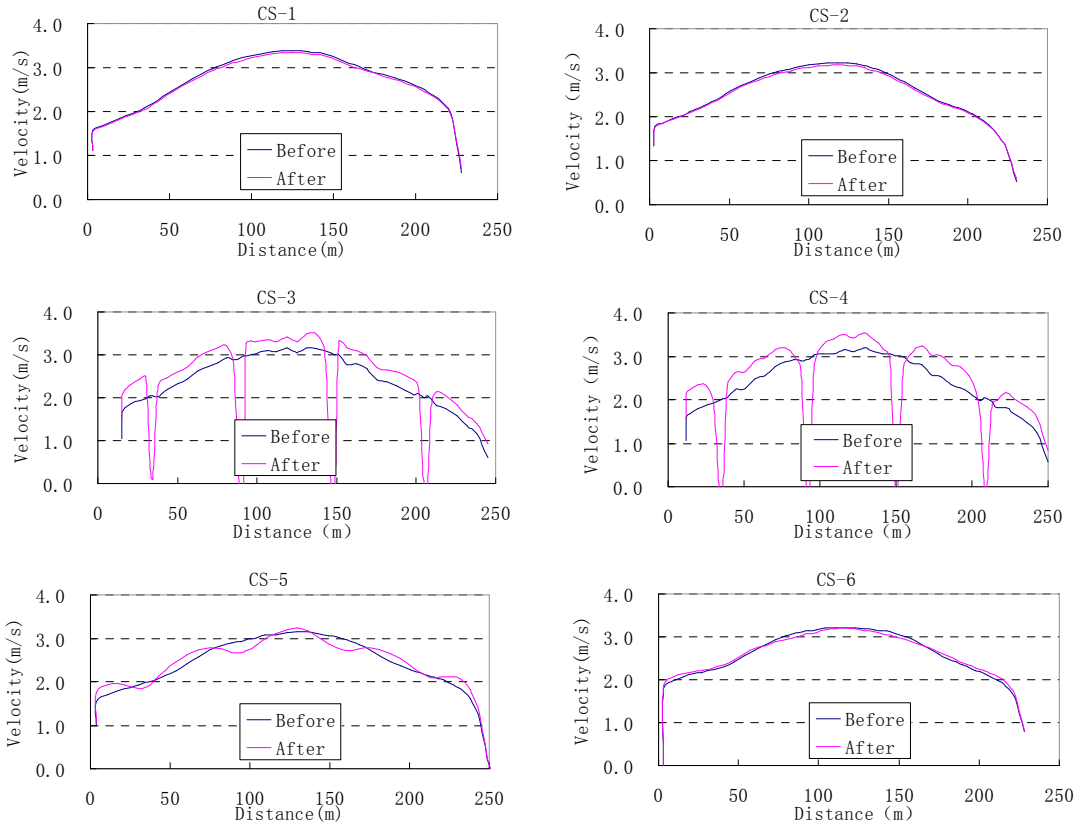


Fig.4 The distribution of velocity about different sections

## Local scour

By the block of flow to the pier, the flow regime changes dramatically, the streamline bend sharply, and it forms vortex near the bed surface so it scour the sediment around the piers to form a local scour pit. According to *The specification of survey and design to highway and bridge* (Chinese industry standard JTJ062-91), the formula can be used to calculated the local scour of bridge pier about the cohesive soil river.

$$H_b = K_\xi B^{0.6} I_L^{1.25} V \qquad (4)$$

Where $H_b$ is the depth of local scour about the piers , $K_\xi$ is the coefficient of type pier, $B$ is the width of piers, $I_L$ is the liquidity index of cohesive soil, $V$ is the flow velocity .

According to the geological condition around the bridge, the form of bridge and once-in-a-century, when the $K_{\xi}$ is 1.0, $B$ is 4.8m, $I_L$ is 0.5, $V$ is 3.15m/s, though the formula of local scour can calculate the depth of scour.

$$H_b = 4.8^{0.6} \times 0.5^{1.25} \times 3.15 = 3.39(m) \quad (5)$$

The result which estimated by the empirical formula showed that the depth of local scour is about 3.39m and less than the depth of piers ,so it impact little on the safety of the bridge.

## Conclusions

A 2D Numerical Model is established to calculate the variation of the level and velocity of water according to the latest terrain, before and after the bridge was built, calculate the depth of local scour by using the method of empirical formula and movable bed model. Basically got the following conclusions:

(1)The influence of the piers to the level of water: After the bridge construction, the backwater can reach by 20.9cm in front of the pier. It is about 1.5km in the upstream and downstream while the backwater can influence along the bridge axis, and the generally indicate high is 5.0-7.0cm upstream along the axis of bridge.

(2)The influence of piers to the velocity of water: When the bridge is completed, the areas of 1km in the upstream and downstream, the velocity can be changed in 1 cm/s.100m-300m away in front of the bridge, the velocity of both sides is not change obviously and the deep groove of the central river reduced. The velocity of bridge between increased, so does the shore.

(3)Because there are so many old bridge along the river and the deck of bridges are low enough so that while the large flood it is easily jam the span and make the level of water to raise, so it should consider this situation in the design of the bridge.

## Acknowledgments

The project is financially supported by Ministry of Transport major special science and technology projects of China (Grant No. 201132874640) and Ministry of Water Resource's Nonprofit Special Funds for Science Research of China (Grant No. 201201070).

## References

[1]Patankar S V: A Calculation Procedure for Two Dimensional Elliptic Situations, Numerical Heat Transfer, (1981), P.409-425

*Applied Mechanics and Materials Vols. 580-583 (2014) pp 2019-2022*
*© (2014) Trans Tech Publications, Switzerland*
*doi:10.4028/www.scientific.net/AMM.580-583.2019*

# Monthly rainfall Analysis in west part of Chongqing

Lin qin[1, a], Junying Jin [1*],Qian Zhang[1] and Dake Wang[1]

[1]College of Resources and Environment, Southwest University, Chongqing, 400715, China

[a]swuqinlinaa@163.com, *Corresponding author:junyingjin@126.com

**Keywords:** Monthly Rainfall, Rainfall Distribution, Normal Distribution Analysis.

**Abstract.** Rainfall information is critical in understanding the hydrologic balance on a global scale and the complex interactions among the small-and large-scale components within the hydrologic cycle[1]. In this study, the monthly rainfall data from 1976 to 2006 at the stations of Rongchang, Dazu, Tongliang and Yongchuan were used to analyze the statistical characteristics and trends of rainfall changes in the west of Chongqing. The average monthly rainfall at Rongchang, Dazu, Tongliang and Yongchuan were 89.4mm, 83.5mm, 88.3mm and 84.8mm in thirty years. The probability distribution of rainfall is a normal distribution. Moreover, the histogram of frequencies showed a clear tendency toward a obvious seasonality of the rainfall distribution [2].

## Introduction

One of the most important aspects of climate variable that requires thorough investigation is the time distribution of monthly rainfall and its historical changes. Rainfall is the most important climatic change since it gives rise to opposite phenomena such as drought and floods. In order to develop an effective management strategy, it is paramount to understand and assess the impact of the rainfall resource on the ecosystem[3]. A mass of studies on rainfall variability have been undertaken all over the world using various statistical procedures. A significant reduce in the number of rainy days and a significant increase in the rainfall intensity values have been identified in many places in the world, such as America and China.

Chongqing is located in the junction of the Yangtze River and the Jialing River in a humid subtropical monsoon climate. With an area of approximately 82402.95km$^2$.The average elevation is 400m and the average precipitation is 1200mm/y. The mainly terrain type are mountainous and hilly. We chose four stations rainfall data in the west of Chongqing to analyze the rainfall distribution characteristic. The average value for the four regions at Rongchang, Dazu, Tongliang and Yongchuan is considered the most representative for Chongqing[4].

In this study, the distribution of monthly rainfall in the west of Chongqing were analyzed at four stations using data from 1976 to 2006; then the questions were discussed as follows:(1) Are there any trends in the monthly rainfall for different parts of Chongqing? (2) Is there any obvious normal distribution in the monthly rainfall for different parts? (3) Are the monthly rainfall patterns stable or variable? In this study, mathematical statistics methods and ensemble canonical correlation were used to study the rainfall features.

## Methodology

The statistical methods such as the Linear trend analysis and Mathematical statistical methods were used in order to obtain the monthly rainfall characteristics parameter such as the average value, the minimum value, the maximum value, the coefficient of variation and etc. Using the linear correlation methods to establish the linear regression equation. By means of T test method tests whether hydrological sequence significant trend [5].

The formulas of statistical characteristic are as follows:

$$t = \frac{x - \bar{x}}{s_x} \tag{1}$$

Where. $\bar{x}$ :averagae value of series x ,$s^x$ :standerd deviation of series x

$$p = \frac{m - 0.375}{n + 0.25} \tag{2}$$

$$x_{cal} = \bar{x} + t * s_x \tag{3}$$

$$y_{cal} = \bar{y} + t * s_y \tag{4}$$

Where.m :rank n: amount of total data series.

A characteristic of a normal distribution is that data represented by this distribution on probability paper plot a straight line. The horizontal axis of this paper expresses probability of exceedence, p, or non-exceedence, q, on a non-linear scale and the vertical axis the values analyzed. In order to plot the distribution in a spreadsheet the scale of the horizontal axis has to be linear. A linear scale is obtained in terms of the normalized value t, derived from a normal distribution which is related to the probability of exceedence (or non-exceedence).

## Results and Analysis

### Monthly rainfall distribution

Based on the 31years monthly rainfall data on four rainfall stations, that is Rongchang station, Dazu station, Tongliang station and Yongchuan station, monthly rainfall distribution of Chongqing are shown in figure 1.

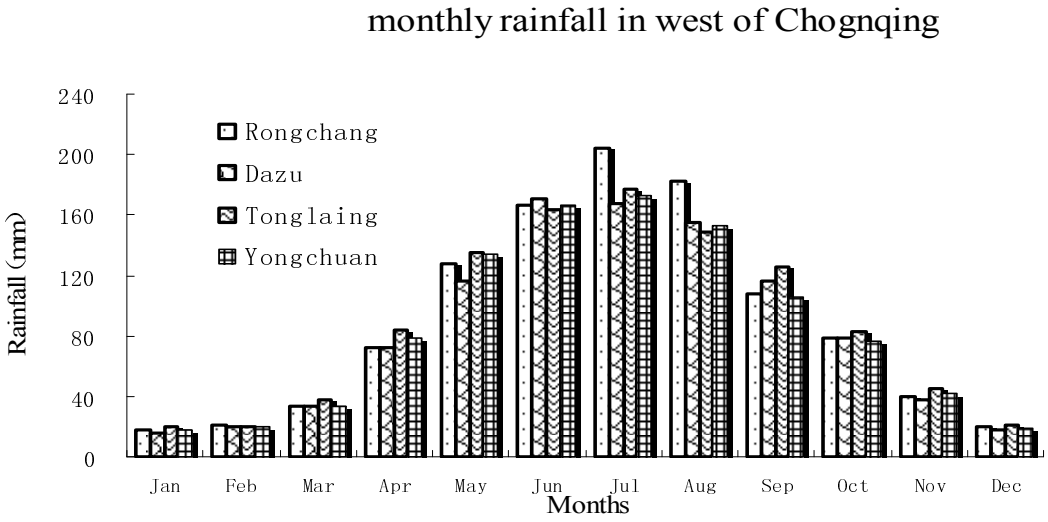


Fig. 1 Average monthly rainfall in the west of Chongqing

Fig.1 showed that the rainfall was uneven distributed all over the year, the rainfall mainly focused on June, July and August, the total rainfall amount of these three month were almost 48.75% of total annual rainfall. It is very clear to know these lots of rainfall may lead to serious flood which can bring disaster to west of Chongqing.

In contrast, the rainfall in Dec, Jan and Feb was very low, the rainfall amount of these three month were only 6% of total amount of annual rainfall, and these three month were low flow seasons in Chongqing, and droughts might occur frequently, which led to serious problems to the whole areas, for example, water shortage will make agriculture yield reduction, also have bad effects on industries, domestic etc.

Also, the figure 1 showed that average monthly rainfall data range from a minimum of 3.7mm in January at Dazu to a maximum of 596.6mm in July at Rongchang and denote a seasonality of the distribution.

For the seasonal rainfall distribution, the percentage of rainfall in spring(Mar-May.), summer(Jun-Aug.), autumn(Sep-Nov.), winter(Dec-Feb.) were 22%, 52%, 20%, and 6% respectively.

The average monthly rainfall at Rongchang, Dazu, Tongliang and Yongchuan were 89.4mm, 83.5mm, 88.3mm and 84.8mm in 30-year.

**Annual rainfall distribution**

The average of annual rainfall distribution is showed in figure 2 based on four rainfall stations.

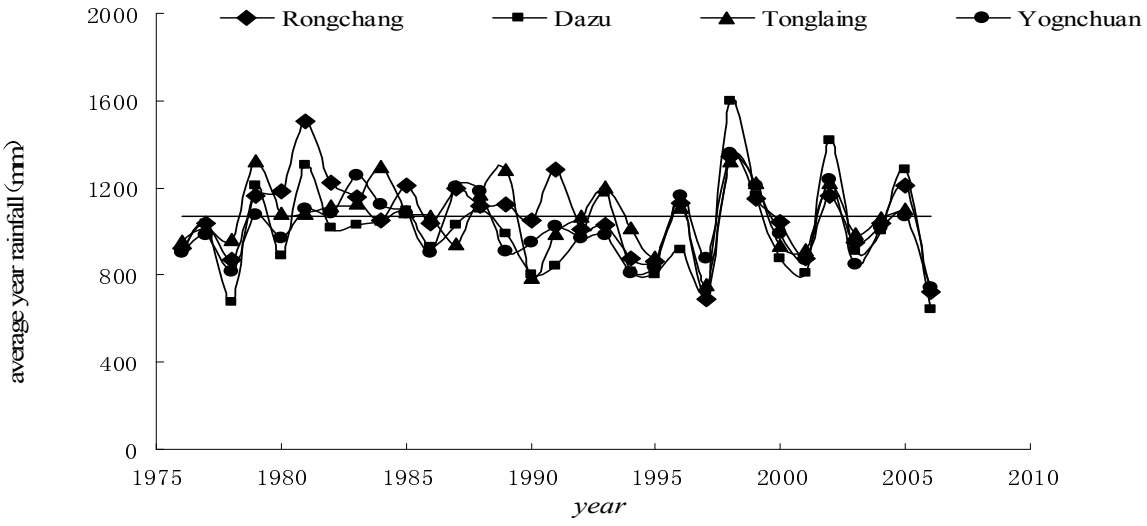


Fig. 2 The average annual rainfall in the west of Chongqing

Fig.2 showed that the average of annual rainfall over the west of Chongqing is quite variable and irregular. The highest annual rainfall was 1601.3mm in 1998, and based on the survey, a serious flood happened around China in 1998. The lowest average annual rainfall just was 639.7mm in 2006. Before 1998 there is no significant trend in the rainfall patter. During 1998 to 2006 there is fluctuation cycle about 5~6 years.

Compared with the average annual precipitation, there are 12-year high flow years, and 19-year dry years. A higher rainfall concentration, represented by greater percentages of the yearly total precipitation in a few very rainy days, has the potential to cause floods and also droughts phenomena. As a consequences, it will increase economic and life losses.

**Normal distribution analysis**

The normal distribution and lognormal distribution of monthly rainfall was analyzed based on the rainfall data of January for four rainfall stations, the results were showed in figure 3.

From the figure 3, we can noticed that the frequency distribution of monthly rainfall values is skewed and the one with the logarithm of the monthly rainfall values is not. The frequency distribution of ln(x) looks more like a normal distribution.

The frequency distribution of ln(x) is more like a normal distribution. And the frequency distribution of monthly rainfall values is not so that confirm to the distribution of normal.

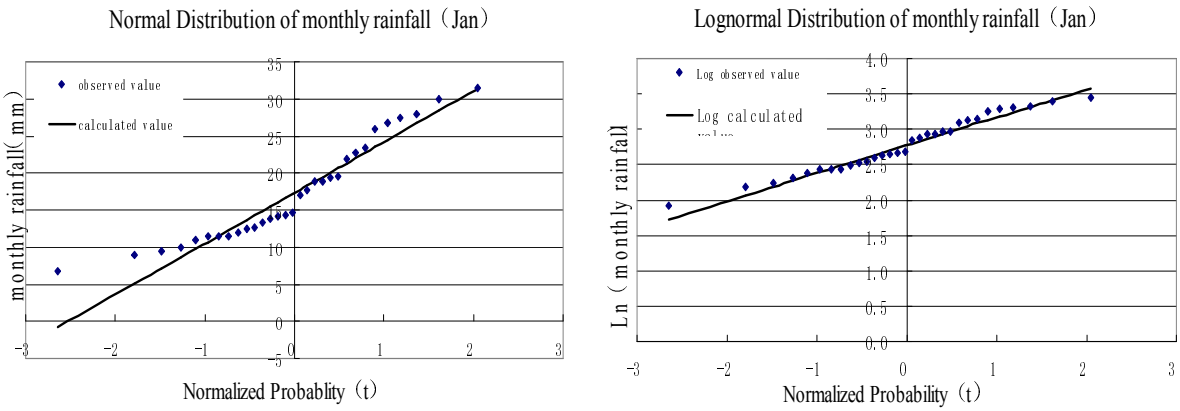


Fig. 3 Normal and Lognormal distribution of monthly rainfall

## Summary

The analysis of monthly rainfall distribution throughout the year is extremely important because of its high impact on environmental phenomena like floods, droughts, soil erosion and slope stability, but also on water management.

The paper took the west of Chongqing as an example, analyzed the variation characteristics and variation trend estimation and accumulation departure, and revealed the complex structure of monthly rainfall in the west of Chongqing in multiple time scale. The results showed that the monthly rainfall in the west of Chongqing is relatively stable. The rainfall variation was different in the four seasons, and the rainfall increased in summer and autumn， and decreased in spring and winter, moreover, it showed the period and mutation point of rainfall sequence in different time scale, and identified the main cycle[6].

## Acknowledgements

The research was financially supported by the National Major Science and Technology Projects for Water Pollution Control and Management (2012ZX07104-003) and the “Guangjiong”Research Fund of College of Resources and Environment, Southwest University (20130208), and the support was gratefully acknowledged.

## References

[1] F.Adler.Robert, J.Huffman, George,Chang,Alfred. The Version-2 Global Precipitation Climatology Project (GPCP) Monthly Precipitation Analysis(1979-Present). American Meteorological Society, 11(2003), p.1147-1166.

[2] R.Coscarelli, T.Caloiero. Analysis of Daily and Monthly Rainfall Concentration in Southern Italy (Calabria region). Journal of Hydrology, 416-417 (2012), p.145-15.

[3] Analysis of a 27-year Rainfall Data(1977-2003) in the Sultanate of Oman. International Journal of Climatology, 29(2009), p.605-617.

[4] Zhong chen, Xuemei ren, Xinqin zhou,etc. Temporal-Spatial Distribution of Precipitation in Chongqing. Journal of Sichuan Teachers College (natural science), 24(2003),p.171-176.

[5] Chunlin zhang, Yannian ma, Zhihong yang. Analysis on Precipitation Change Trend in Yaohe Basin. Gansu Water Conservancy and Hydropower Technology, 48(2011), p.8-10.

[6] Wen liu，Mignming cao，Jinxi song. Spatia-temporal Distribution and Temporal Periodicity Annual Precipitation in Shanxi Province. Arid Land Geography, 36(2012), p.865-874.

*Applied Mechanics and Materials Vols. 580-583 (2014) pp 2023-2028*
*© (2014) Trans Tech Publications, Switzerland*
*doi:10.4028/www.scientific.net/AMM.580-583.2023*

# Optimization Study on Drainage System for Canal of Middle Route Project of SNWT in Expansive Soil Area with High Groundwater Level

Hao dong CUI [1,3,a], Jia fa ZHANG [1,3], Guo sheng ZHU [1,3], De xu WU [2,3], Wei ZHANG [1,3] and Jin long WANG [1,3]

[1].Yangtze River Scientific Research Institute, Wuhan 430010, China

[2].Changjiang Institute of Survey, Planning, Design and Research. Wuhan 430010, China

[3] National Research Center for Dam Safety Engineering Technology, Wuhan 430010, China

[a]seep3d@qq.com

**Keywords:** Middle Route Project of SNWT; excavated channels; drainage cushion; water pressure head; seepage field regulations; numerical simulation.

**Abstract.** The seepage field regulation is important for the stability canal liner plate and slope for along the Middle Route of the South-to-North Water Transfer Project, especially for stretches excavated in expensive soil area with groundwater level. In order to analyzing the rationality and efficiency of seepage regulation measures comprehensively, a typical section was modeled, and the seepage field was simulated with the 3D finite element technology. The distribution of seepage field was analyzed and the seepage control measures were compared. The results show that water pressure on the underside of canal pavement would be reduced significantly by the measures, such as the measure of drainage cushion with drainage holes which open just when ground water level is higher than the canal water level, the measure with drainage cushion replaced by the drainage board. The differences among the two kinds of measure were compared. Their application conditions were discussed and proposed.

## Introduction

The Middle Route of the South-to-North Water Transfer Project is an oversize inter-basin water transfer project. The main canal will be operated under complex conditions of climate and groundwater, the channel water level will also change with water scheduling, and the maintenance conditions will be experienced during the period of water supply, so the effective seepage control measures is key to the engineering safety and effective operation [1]. The seepage control goal is the stability of drainage slopes and channel lining board in areas of high groundwater drainage excavation section. The dewatering sand cushion and the geomembranes and drainage holes are set below the channel bottom as the seepage control measures during in preliminary design of excavation section, some drainage holes are as seepage control measures for canal slope and the expansive soils is be replaced by cement soils along the canal expansive soil slope. The design idea is applicable and effective under most conditions[2], but sand cushion of drainage slopes is a higher cost and the cushion thickness is difficult to strictly control in the excavation channel, the construction progress takes more time and effort, there are many other negative factors during construction.

## A brief introduction to the FEM of three dimensional seepage

The seepage calculation of excavated channel involves precise simulation methods of solving seepage free surface, drain holes, summarized as follows.

### 2.1 Procedure of Nodal Virtual Flux for Unconfined Seepage Filed

In unconfined seepage problem, the free surface of seepage is nonlinear boundary. The location of the free surface, the line of exit points and the real domain of seepage are unknown first, which need iteration to obtain the solution to the unconfined seepage problem. The procedure of nodal virtual flux

that is progressively developed and perfected in the references [3~6] can solve this problem conveniently without mesh modification and the relevant iteration formula is as follows.

$$Kh = Q - Q_2 + \Delta Q \quad (1)$$

Where K, h and Q are the conductive matrix, the vectors of hydraulic head and the nodal equivalent flux related to the total calculation domain of $\Omega=\Omega_1+\Omega_2$, respectively; $\mathbf{Q}_2$ represents the vector of virtual nodal equivalent fluxes; $\Delta Q = K_2 h$ denotes the vector of the nodal fluxes which are contributed by virtual elements and transient elements in the virtual domain $\Omega_2$; $\Omega_1$ denotes the real domain of seepage below free surface of seepage and $\Omega_2$ denotes the virtual domain of seepage located above the free surface.

**2.2 Simulation of Seepage Behaviors of Drainage hole**

There are many drainage measures including a lot of drainage holes which play a role of water discharge and pressure relief in the seepage filed in the channel or dam foundation, if the location of free surfaces at the holes is higher than the top surfaces, the holes are fully filled with seepage water, otherwise there is no water overflowing out from the holes in bottom or slope of channel. The holes action is required on both the theory and algorithms rigorous simulation techniques to solve the drainage holes of its impact on seepage field; The procedure of simulation of holes is progressively developed and perfected in the references [4] can solve this problem conveniently without mesh modification and the drainage hole relevant iteration formula is the "equivalent nodal flow method" [7] in each hole, its mathematical formulation is as follows Eq. 2:

$$Q(x_i) = -\sum\sum K_{ji}^{e} (h^{it})^{e} \quad (2)$$

Where in each symbol, drainage holes and validation of solving specific references [4]. This overhaul of the channel flow calculations, channel slope holes handle that uses the method.

## Effect Analysis of Seepage Control of Canal

### 3.1 Project overview

A three-dimensional section of a typical canal seepage model was modeled in the Middle Route of the South-to-North Water Transfer Project in Xi chuan County, Henan Province, there are holes and geomembranes in seepage control of the South-to-North Water Transfer Project in areas of high groundwater drainage excavation section in the preliminary design. the typical cross-section shown in Figure 1. The measure of drainage cushion is replaced by the drainage board in this article (optimization case). Calculation parameters are shown in Table 1.

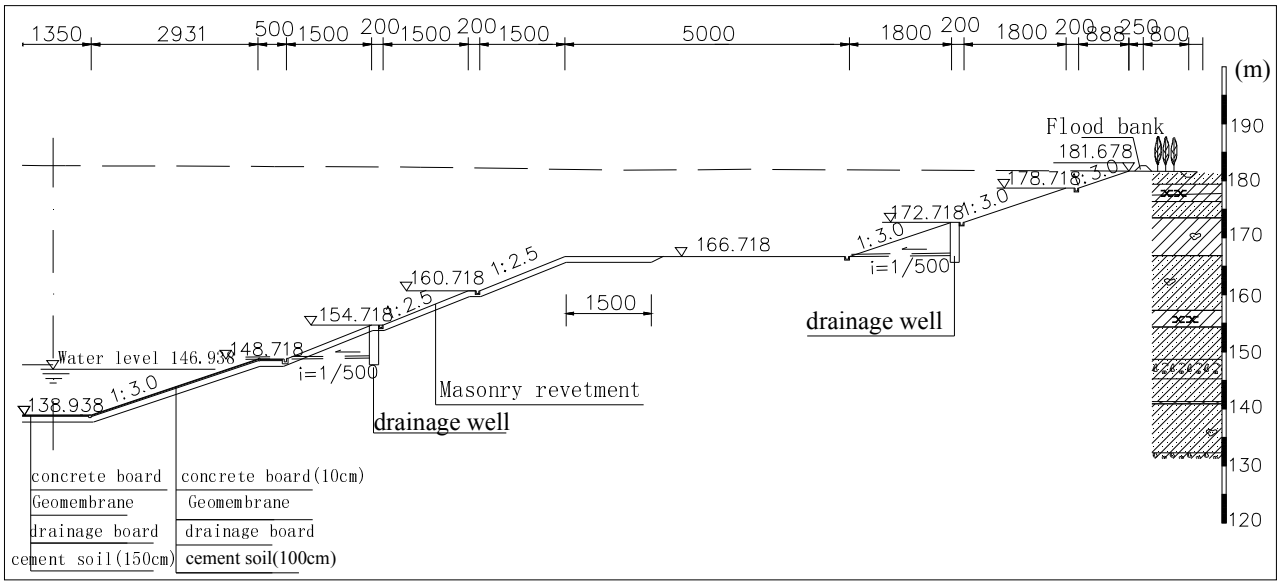


**Fig.1 The section of typical canal**

**Table 1 The permeability coefficient of the typical canal**

| number | formation | Permeability coefficient |
|---|---|---|
| 1 | Silty clay (0~3m) | $1.0\times10^{-4}$ |
| 2 | silty clay (3~7m) | $5.0\times10^{-5}$ |
| 3 | silty clay (under 7m) | $5.0\times10^{-6}$ |
| 4 | silty clay | $1.2\times10^{-6}$ |
| 5 | clay | $8.0\times10^{-7}$ |
| 6 | sand cushion | $1.0\times10^{-3}$ |
| 7 | backfill | $1.0\times10^{-5}$ |
| 8 | concrete underlay board | $1.0\times10^{-11}$ |
| 9 | drainage board | $1.0\times10^{-1}$ |

### 3.2 Research Programs and Model

The dewatering sand cushion（thickness 25cm） and the geomembranes and three ranks drainage holes（the spacing of two holes is 10m, the layout of holes is along channel center and slope feet longitudinal）are set below the channel bottom as the seepage control measures during in preliminary design of excavation section. The expansive soils is be replaced by cement soils along the canal expansive soil slope(the cement soils thickness is 150cm under the first level stairs and 100cm under second stairs). The canal drainage wells are layout at altitude of slope is 154.7m and 172.7m, the well diameter is 1.5m and the spacing is 20m between the two wells.

The one of optimization measures is that the sand cushion is replaced by the drainage board grid in channel slope and channel bottom (Figure 2). There are four calculation cases, including cases of operation period and maintenance period, the detailed introduction of cases is the table 2.

**Table 2 The calculation cases**

| number | Programs description | Notes |
|---|---|---|
| F1 | Channel water level 146.938m;holes spacing is 10m; sand cushion(thickness 25cm,Permeability coefficient $1.0\times10^{-3}$cm/s), drainage wells; other parameters in table 1. | preliminary design case; operation period |
| F2 | Channel water level 138.938m, other same F1. | maintenance period |
| F3 | drainage board grid (coefficient $1.0\times10^{-1}$cm/s,4×4m);other same F1.. | optimization case; operation period |
| F4 | Channel water level 138.938m in bottom; other same F3. | optimization case; maintenance period |

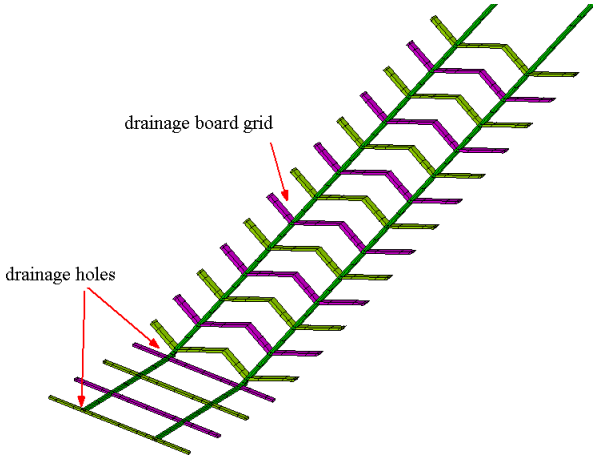


**Fig.2 Drainage board grid models**

The model is one side of the channel center, the calculation results is affected by the range of the upper boundary references [9], the distance is 600m between upper boundary and sloping top, upstream water level is 181.6m, Downstream water level is 146.938m, downstream water level is 138.938m in maintenance period; the level of the bottom of model is 90m.The model bottom and the

boundary of symmetry are impervious boundary, the channel slope is drainage boundary; the holes and the wells are treated with the theory in referece[4]. The model element is 6 sided 8-node element, the drain hole is modeling with real element, the node number of F1 model is 77 126 and the element number is 70 817. F1 grid is shown in Figure 3.

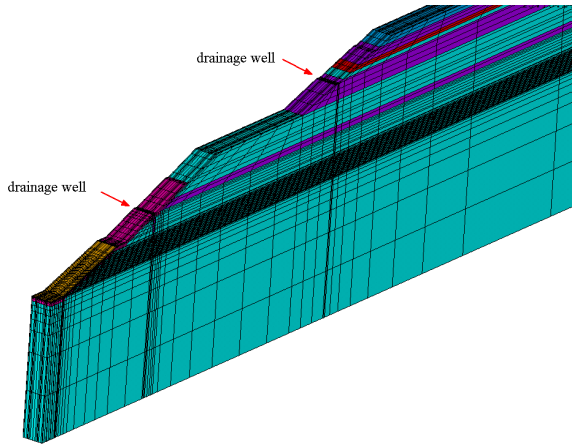


**Fig.3 3-D FEM meshes of the channel**

### 3.3 Analysis and comparison of calculation results

In this paper, the effect of seepage control is analyzed with the characteristics of seepage field and the maximum pressure head in bottom lining plate in operation period and maintenance period. The water pressure head difference is the value between the statistical point and drainage water depth.

#### 3.3.1 Effect of seepage control of F1

Results indicate that effect of seepage control is clear and the seepage control measures is reasonable, the water head pressure correctly reflects the effects of boundary conditions and control measures of the cases from Figure 4~5.

The case F1 is the preliminary design case, the seepage field distribution is slight impacted by the well of first level stairs, seepage free surface is near the foot of the channel platform, the water head pressure is low under bottom of lining board(Figure 4), the water head difference is 0.10m in the channel lining board(Table 3), which is enable to the lining board stability. The case F2 is the maintenance period case of preliminary design, The figure 5 results show that the exit points of seepage flow is at foot of the continental slope, the two ranks wells are below the seepage free surface in the channel slope. The water head difference of F2 is 0.15m, which is higher than the result of F1 in the channel lining board, but it is also to meet the requirements of stability of channel lining board[1]. In conclusion, the seepage control measures are reasonable for this channel section in preliminary design case.

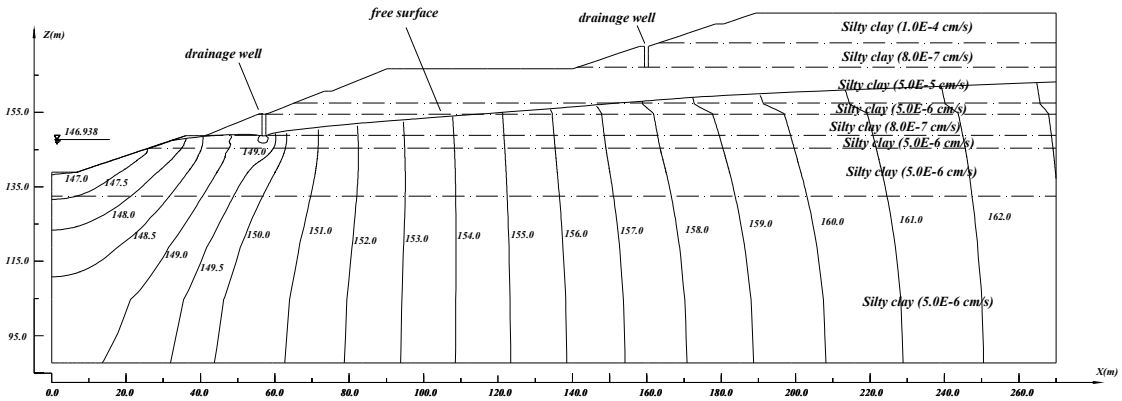


**Fig.4 The water head contour of case 1 (unit: m)**

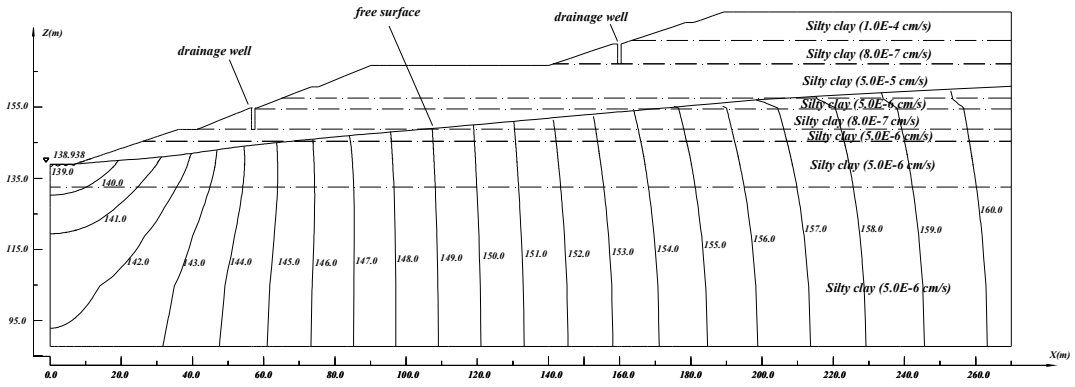


**Fig.5 The water head contour of case 2 (unit: m)**

### 3.3.2 Effect of optimization case

The measure of drainage cushion is replaced by the drainage board in F3, the water pressure distribution is sparse in the bottom and slope of channel(Fig 6), the water head difference is 0.05m in the channel lining board. The seepage field distribution is impacted by the well of first level stairs slightly, water pressure distribution is similar to F1 near the wells.

The case F4 and F2 are same to maintenance period, but permeability coefficient of drainage cushion is difference of 100 times between the two cases, the water head contours of distribution are more similar, drainage wells are above at the free surface in drainage slope (Figure 6, Figure 7). The maximum water pressure head difference is 0.11m in the channel lining board in case F4. So, the drainage cushion is replaced by the drainage board is also effective, and the measures are relatively more economical and easy construction.

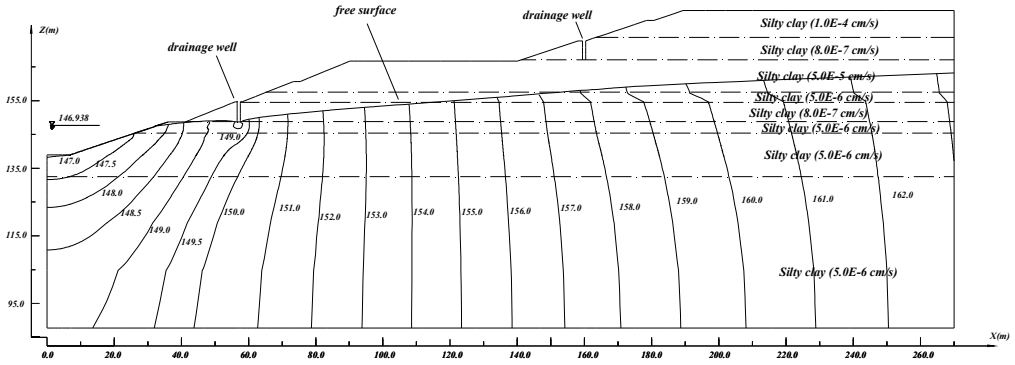


**Fig.6 The water head contour of case 3 (unit: m)**

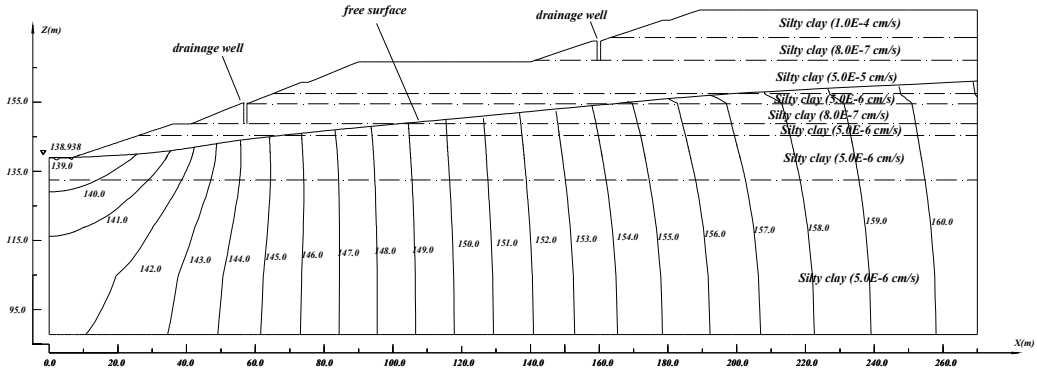


**Fig.7 The water head contour of case 4 (unit: m)**

### 3.3.2 Control measure's effect comparison

Former section research suggests that the water pressure of operation period is higher than the water pressure in maintenance period, so the lining board stability is controllable in maintenance period, the maximum water pressure head difference is 0.15m in the channel lining board in preliminary design case. But the water pressure head difference is 0.11m in the case F4, at same time, the drainage cushion is instead of the drainage board grid (coefficient $1.0\times10^{-1}$cm/s). These results

Indicate that affection of seepage control of drainage board grid is obviously, its biggest advantage is low cost and easy construction.

**Table 3 The maximum water pressure heads of cases**

| case | F1 | F2 | F3 | F4 |
|---|---|---|---|---|
| maximum water head difference / m | 0.10 | 0.15 | 0.05 | 0.11 |

## Conclusion

(1).The measures of preliminary design and optimization of seepage control measure has a significant effect, which can be able to guarantee the stability of channel lining board. Through the drainage holes which open just when ground water level is higher than the canal water level, gravity drainage and seepage field of self-regulation can be realized.

(2). The measures with drainage cushion replaced by the drainage board, not only can reduce costs, facilitate construction and reduce the difficulty of quality control, and even improve the seepage control effect. However, the permeability of the drainage board material is necessary to strictly control the quality of the indicators, and in the long run to avoid leakage.

## Acknowledgements

This work was financially supported by the Natural Science Foundation of China (51279016), The National Key Technology R&D Program (2011BAB10B04) and The Special Fund of Chinese Central Government for Basic Scientific Research Operations in Commonweal Research Institutes (CKSF2012023/YT; CKSF2014058/YT).

## References

[1] ZHANG Jia-fa,LIN Shui-sheng,WU De-xu, LI Shao-long. Seepage Field Regulation for Rockfill Coferdam and Foundation Pit[J]. Journal of Yangtze River Scientific Research Institut,2013,30(2):20-26.

[2] CUI Hao-dong, ZHANG Jia-fa, ZHANG Wei, ZHU Guo-sheng. Numerical analysis of seepage field for typical canal stretch on confined aquifer of Middle Route Project of South-to-North Water Transfer[J]. Rock and Soil Mechanics,2010,31(suppl 2): 447－451

[3] Zhu Yueming, Wang Ruyun, Xu Hongbo.: Some techniques for solution to free surface seepage flow through arch dam abutments. In Proceedings of the Intern. Symposium on Arch Dams, Nanjing, China, Oct. 1992..

[4] CUI Hao-dong, ZHU Yue-ming, WU Shi-yong. Numerical simulation for densely-distributed drainage holes in seepage field with free surface[J]. Chinese Journal of Geotechnical Engineering, 2008, 30(3): 440-445.

[5] CUI Haodong, ZHU Yueming, ZHANG Jia-fa, ZHU Guosheng. Analysis on Seepage Field and Preliminary Evaluation on Seepage Control Effect of Rock mass around Deep Buried Caverns[J]. Journal of Yangtze River Scientific Research Institute.2009,26(10): 71-75.

[6] ZHU Yue-ming, CHEN Jian-yu, GONG Dao-yong, et al. Refined solution to seepage in arch dam foundation with FEM[J]. Chinese Journal of Geotechnical Engineering, 2003, 25(3): 326-330.

[7] ZHU Yue-ming. Darcy seepage discharge calculation with node method[J]. Journal of Hohai University, 1997, (4): 105-108.

[8] CHENG Zhan-lin,LI Qing-yun,GUO Xi-ling,GONG Bi-wei. Study on the Stability of Expansive Soil Slope[J]. Journal of Yangtze River Scientific Research Institut. 2011,28(10):102-111.

*Applied Mechanics and Materials Vols. 580-583 (2014) pp 2029-2032*
*© (2014) Trans Tech Publications, Switzerland*
*doi:10.4028/www.scientific.net/AMM.580-583.2029*

# Precipitation Characteristics and Trend in the Hsiao-Ching River Basin of Jinan City during the Past 50 Years

Lin Lin[1, a], Jian Liu[1, b], Jiwen Huang[1, c], Xuequn Chen[1, d], Qinghua Guan[1, e] and Yi Tang[1, f]

[1]Shandong Provincial Key Laboratory of Water Resources and Water Environment, Water Research Institute of Shandong Province, Jinan, Shandong, 250014, China

[a]llin_mail@126.com, [b]water_liujian@163.com, [c]sdskyhjw@126.com, [d]cxq1115@126.com, [e]qhguan0120@163.com, [f]tangyi1023@hotmail.com

**Keywords:** Hsiao-Ching River Basin, Jinan City, Precipitation, Trend Analysis, 1956-2007.

**Abstract.** Monthly precipitation data from Huangtai Bridge Station were used to study seasonal and annual precipitation characteristics and trend. The covered time-period is from 1956 to 2007. Different methods including linear regression, 5-year moving average, anomalies in decadal scale and the Mann-Kendall test were applied in the study. Nearly two-thirds of the total rainfall amount is concentrated in summer, with autumn and spring months to follow, and only about 3% in winter. An increasing trend in spring months is found. It starts in 1978, becomes significant after 2002, and probably continues into the future. A decreasing trend is recorded in winter and begins in 1980. No significant trend is found in summer, autumn and yearly precipitation. The same fluctuations are observed between summer and annual precipitation indicating the dominant influence of the summer season.

## Introduction

Hsiao-Ching River has played an important role in flood control, drainage and irrigation in Shandong Province. It is the only river of the province having navigable inland waterways and sea shipping and its navigation history has extended nearly 900 years. The river has a total length of 237 km and a catchment area of 10336 $km^2$, which originates from Jinan springs and flows into Bohai Sea from west to east through Jinan, Zibo, Binzhou, Dongying and Weifang [1,2]. Hsiao-Ching River in Jinan City has a total length of 70.5 km and a catchment area of 2792 $km^2$. The catchment contains 18 tributaries whose drainage areas cover more than 30 km2. Major tributaries are seasonal and begin in hills, which are located in the south bank of the main river [3,4]. Hsiao-Ching River is the most important river of Jinan city and has become ecological corridor, economic and cultural corridor historically. The river is the city's only river draining off the floodwater, the frequent occurance of floods has caused loss of the facilities and human lives in history, including the most recent extreme rainstorm and flash flood event happened on 18th July 2007 [5,6]. Good understanding of rainfall changes is therefore crucial to urban flood security and sustainable development [7,8]. The purpose of this study is evaluating rainfall characteristics and trends during past 50 years in Hsiao-Ching River catchment of the city.

## Materials and Methods

Huangtai Bridge hydrological station is located in the east of Jinan city and is one of the key national stations, which was built in 1916. It is the boundary between the upper and middle reaches of the Hsiao-Ching River. The continuous precipitation data of the station are a representative example of the catchment in the city. Monthly precipitation data from Huangtai Bridge Station are used to study seasonal and annual precipitation characteristics and trend. The covered time-period is from 1956 to 2007. Different methods including linear regression, 5-year moving average, anomalies in decadal scale and the Mann-Kendall test are applied in the study.

## Results and Discussion

**Precipitation characteristics.** The seasonal and annual characteristics of precipitation in the Hsiao-Ching River basin of Jinan city from 1956-2007 are shown in Table 1. The basin has an average annual precipitation of 682.8mm, a maximum of 1140.7mm in 1962 and a minimum of 297.5mm in 1968. Small wet-dry change of annual precipitation is observed by the relative lower max/min value (3.85) and Cv value (0.31). In seasonal scale, summer precipitation indicates the highest percentage (66.4%) of the year, autumn and spring follow up with 16.8% and 13.5% respectively, and the winter only accounts for 3.3%. Cv values in all seasons are significantly higher than in the whole year. The highest value of 0.65 is found in winter and its max/min value reaches up to 283.0, reflecting an apparent wet-dry change. Cv and max/min values in other seasons range from 0.40 to 0.53 and from 6.8 to 15.0, which showed a smaller wet-dry change.

Table 1 Precipitation characteristics from 1956 to 2007

| | Average | | Cv | Maximum | | Minimum | | Max/Min |
|---|---|---|---|---|---|---|---|---|
| | value(mm) | percent | | value(mm) | year | value(mm) | year | |
| Spring | 92.3 | 13.5% | 0.49 | 209.4 | 1980 | 30.8 | 1981 | 6.8 |
| Summer | 453.5 | 66.4% | 0.40 | 870.1 | 1962 | 78.3 | 1968 | 11.1 |
| Autumn | 114.5 | 16.8% | 0.53 | 293.2 | 1961 | 19.5 | 1981 | 15.0 |
| Winter | 22.6 | 3.3% | 0.65 | 56.6 | 1989 | 0.2 | 1995 | 283.0 |
| Annual | 682.8 | 100% | 0.31 | 1144.7 | 1962 | 297.5 | 1968 | 3.85 |

**Trends for seasonal precipitation.** A positive trend is noticed in spring season by linear regression and 5-year moving average analysis (see Fig.1a). Spring precipitation anomalies in decadal scale indicate that the late 1950s, 1970s and 1980s has been dry years over past 50 years and the precipitation tends to rise since the 1970s (see Table 2). Fig. 1b illustrates the normal and the retrograding curve (UF and UB curve) of the Mann-Kendall test at the 95% significance level. An increasing trend is recorded after 1978, which becomes sharp after 2002.

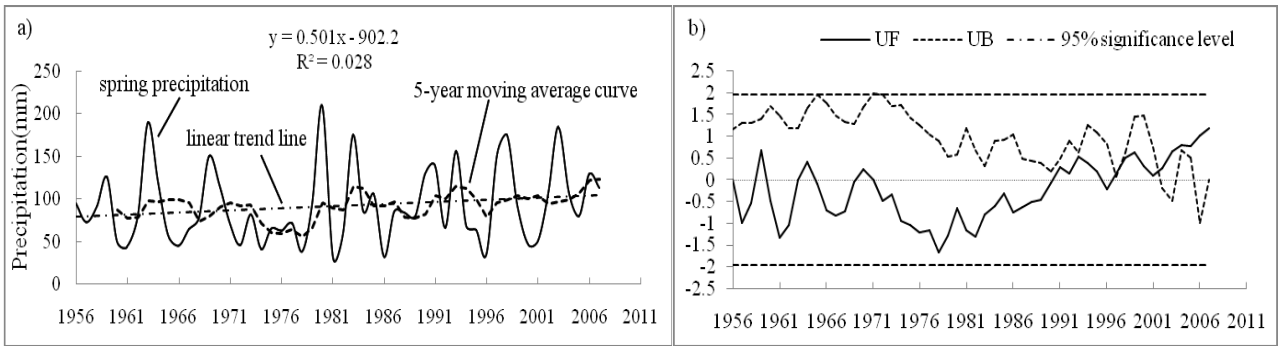


Fig. 1 Trend analysis of spring precipitation

Table 2 Precipitation anomalies in decadal scale from 1956 to 2007

| | 1956-1960 | 1961-1970 | 1971-1980 | 1981-1990 | 1991-2000 | 2001-2007 |
|---|---|---|---|---|---|---|
| Spring | -5.71% | 2.40% | -15.31% | -5.99% | 7.96% | 19.70% |
| Summer | -4.98% | 1.53% | 10.01% | -12.17% | 2.15% | 1.39% |
| Autumn | -27.70% | 12.85% | 4.37% | -15.42% | 8.75% | 4.71% |
| Winter | 16.57% | 2.46% | 20.91% | -9.69% | -8.36% | -22.67% |
| Annual | -8.19% | 3.46% | 6.03% | -11.62% | 3.06% | 4.52% |

No significant trend is recorded in the results of linear test of summer and autumn precipitation. 5-year moving average analysis reflects similar wet-dry fluctuations in summer and autumn (see Fig.2a and Fig.3a). Also the results of precipitation anomalies in decadal scale in summer are in good

agreement with the results in autumn. Dry years are found in the late 1950s and 1980s, and wet years are found in the 1960s, 1970s, 1990s, and afterwards until the end of the examined period (see Table 2). MK trend test shows that summer precipitation began to fluctuate since the late 1950s, and the abrupt change is occurred in 1961 and1965 (see Fig.2b). In autumn, the application of MK test cannot identify an observable trend and the abrupt change is found in different decades (see Fig.3b).

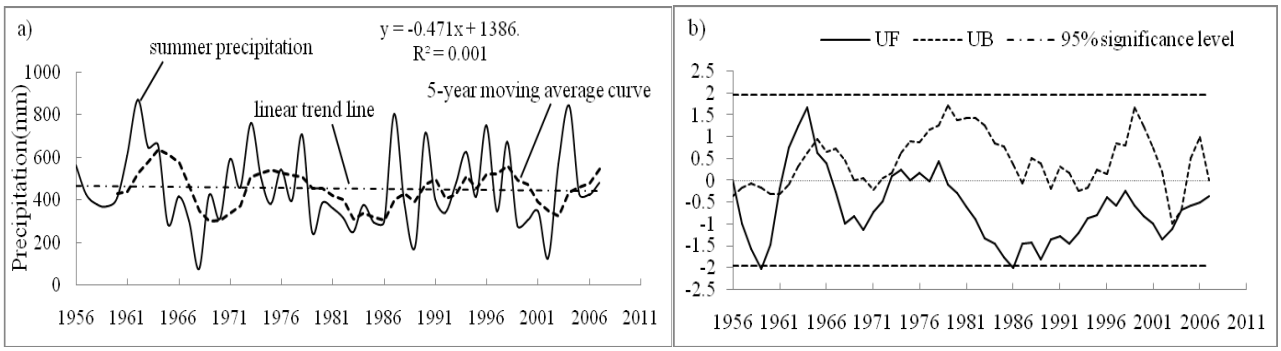


Fig. 2 Trend analysis of summer precipitation

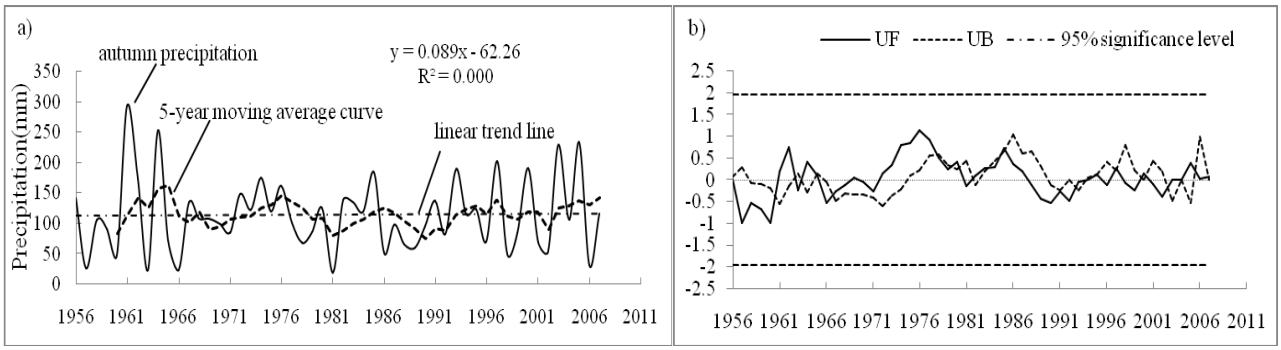


Fig. 3 Trend analysis of autumn precipitation

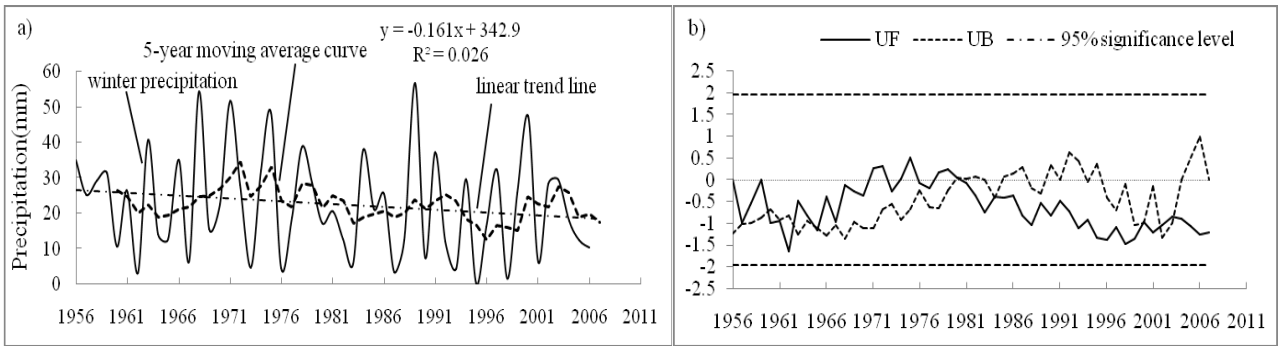


Fig. 4 Trend analysis of winter precipitation

The precipitation trend in winter is decreasing over time (see Fig.4a). Wet years are recorded since the 1980s and dry years afterwards (see Table 2). The MK test indicates twice abrupt changes in 1963 and 1980 (see Fig.4b).

**Trends for annual precipitation.** As shown in Fig. 5a, no significant linear trend is found in annual precipitation. The 5-year moving average curve has the same fluctuations with summer months. The change of anomalies in decadal scale (see Table 2) and UF curve of the MK test (see Fig.5b) are also consistent with the trend in summer. Abrupt changes are mainly recorded in the 1960s and after 2000. These results show the dominant contribution of summer rainfall to the whole year, and the positive trend in spring and the negative in winter have little impact on it.

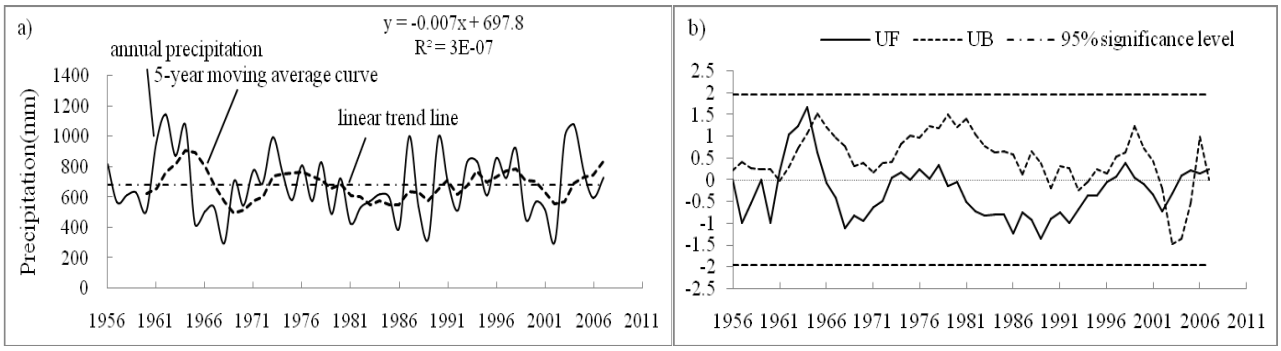


Fig. 5 Trend analysis of annual precipitation

## Conclusions

The Hsiao-Ching River basin in Jinan city has an average annual precipitation of 682.8mm and it is very unevenly distributed. The percentage during summer reaches 66.4% of the year, the autumn and spring follow up and the winter only accounts for 3.3%. The wet period in spring season is recorded in the 1990s and afterwards. An increasing trend in spring precipitation starts in 1978 and becomes sharp after 2002, reflecting the possibility of a continuously positive trend in the future. The decreasing trend is found in winter season and begins in 1980. Then the dry period occurs after the 1980s. As for summer and autumn, no significant trend is found and the wet and dry period almost occurs alternately. The abrupt change in summer precipitation is recorded in 1961 and 1965, and in autumn is found in different decades.Abrupt changes of yearly precipitation are recorded in the 1960s and after 2000. The same trend and fluctuations are observed between summer and annual precipitation, recognizing the main influence of the summer season.

## Acknowledgements

This work was financially supported by the International Science & Technology Cooperation Program of China (2012DFG22140) and the Governmental Public Industry Research Special Funds Project (201201113).

## References

[1] Y.J. Lu: *Hsiao-Ching River* (China Meteorological Press, Beijing 2007). (In Chinese)

[2] L. Lin, F.L. Li, X.Q. Chen, J.W. Huang, Q.W. Bu and S.D. Fu: Yellow River Vol. 35 (2013), p. 77 (In Chinese with English abstract)

[3] L.G. Wang, H. Li, Y.C. Wang and J.J. Qiu: Journal of Agro-Environment Science Vol. 30 (2011), p. 986 (In Chinese with English abstract)

[4] Information on http:// news.iqilu.com/other/20110930/1011189.shtml (In Chinese)

[5] Information on http://news.xinhuanet.com/society/2011-09/28/c_122100078.htm (In Chinese)

[6] S. Dou: *Research on flood and rainstorm characteristics in Xiaoqing River of Jinan city and its channel elevation design* (Shandong University, Jinan 2008). (In Chinese with English abstract)

[7] M.S.Y.C. Ngah, I. Reid and M. Hashim: Middle-East Journal of Scientific Research Vol. 11 (2012), p. 668

[8] A. Karagiannidis, T. Karacostas, P. Maheras and T. Makrogiannis: Adv. Geosci Vol. 20 (2009), p. 39

*Applied Mechanics and Materials Vols. 580-583 (2014) pp 2033-2036*
*© (2014) Trans Tech Publications, Switzerland*
*doi:10.4028/www.scientific.net/AMM.580-583.2033*

# Research on Structure Design of U type canal of seepage-proofing

Jinglu Sun[1, a], Bing Zhang[1, b],Shoujie Zhang[1,c]

[1] Heilongjiang Province Key Laboratory of Engineering in seasonal frozen soil area, Heilongjiang Academy of water conservancy, 150080, China

[a]sunjinglu74@163.com

**Keywords:** Structure design, U-type canal, Seepage-proofing.

**Abstract.** New U (moment) implements the optimum water section of rectangular slot structure, besides all advantages of the traditional U and T-shaped slot in the canal seepage, also has advantages of reducing covers area of higher performance and price ratio. The kind of canal seepage control structure is upgrading products of the traditional U and T-shaped slot. In this paper, through design research on new U (moment) slot structure, giving U (moment) slot structure size, it can provide technical support for the product development of new type U (moment).

## Introduction

"U" shaped groove structure widely has been used in water conservancy project, especially in the small and medium-sized sluice dam, culverts, and aqueduct, and this structure form was used usually for import and export connection segment [1].U-shaped channel slot is the best form having integrated hydraulic, engineering economy, covers an area and so on[2]."U" shaped section is close to the best water hydraulic cross section of concrete channel. Wetted perimeter is shortest, and mechanical performance is good. Good anti-seepage effect, simple construction, quick progress, integrity is strong [3-8].The kind of structure can reduce the loss and the dosage of concrete in construction process, shorten the construction period, and reduce the project cost. It can alleviate the traffic inconvenience, such as better seepage prevention effect, improve the utilization of water resources, and achieve the goal of the water-saving irrigation [9].

According to statistics of the ministry of water resources of rural water conservancy department, at present, in our country defense system of floods integrated is not perfect enough, for a long time, our country irrigation district ageing, disrepair, functional decline phenomenon such as common, especially the field channel is not perfect, benefit of water conservancy facilities is difficult to play. Most of the irrigation and water conservancy facilities in our country were planned in the sixties and seventies of the last century, farmland irrigation and drainage system, inefficient irrigation and drainage channels. With the development of the new rural construction, energy saving, environmental protection, improve productivity have become the urgent need, a large number of promotion in farmland channel system concrete u-shape canal engineering can effectively exert the benefit of irrigation and water conservancy facilities. Concrete u-shape slot is used in concrete masonry materials of plain concrete or reinforced concrete channels. Because cast-in-situ construction of U slot is difficult, the current use prefabricated more. Usually length is 50-100cm, cross-sectional size is 30-100cm, with wide groove depth of 25-100cm, wall thickness of 3 ~ 5cm. there was a kind of the homemade steel model, with a small vibrator inserting vibrating. But concrete needs certain curing period, so it is not economic to adopt a lot of steel model in period of construction. Also having the method of vibration precast and rolled plate way such as prefabricated concrete u-shaped slot, but quality of the u-shaped was poor[10-11].

As development of comprehensive agricultural and increase of basic farmland water conservancy project investment, u-shaped channel has been more and more widely used. So the design and related technology of the u-shaped channel is very important [12]. In 2011 the Central Committee issued 1 document, holding the highest specifications of water conservancy work conference, starting in 2012 four provinces in the northeast "save and increase food operation". But under the lateral canal to the field "last one kilometer" is the most weak link, irrigation and water conservancy is low standard,

poor matching, aged disrepair and benefit attenuation, "the last kilometer" problem of farmland irrigation and drainage is increasingly prominent.

## Research on new U (moment) tank structure design

**Formulate concrete technology parameters of new type U (matrix).**The compressive strength of concrete is C50, frost resistance coefficient is F300.

**Structure size design of new U-shaped (moment) slot.** New U (moment) slot structure diagram is shown in Fig.1 and Fig.2. New u-shaped groove parameters (matrix) are shown in Table 1.

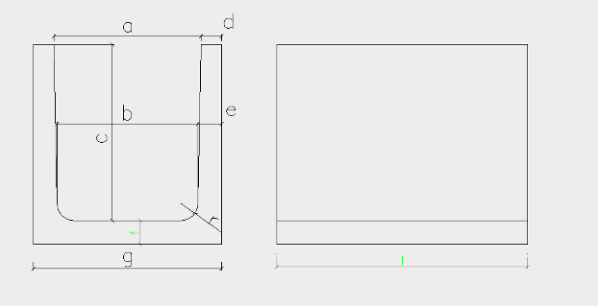


Fig.1. New type U (moment) diagram

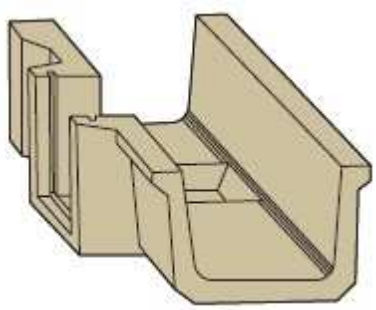

Fig.2. Intake schematic

Table1. New u-shaped groove parameters (matrix)

| Specifications | Section size (mm) | | | | | | | | | quality (kg) |
|---|---|---|---|---|---|---|---|---|---|---|
| | a | b | c | d | e | f | g | r | l | |
| 300*400 | 300 | 270 | 400 | 40 | 55 | 55 | 380 | 40 | 2000 | 295 |
| 400*500 | 400 | 360 | 500 | 40 | 60 | 60 | 480 | 60 | 2000 | 394 |
| 500*600 | 500 | 460 | 600 | 70 | 90 | 80 | 640 | 80 | 2000 | 720 |
| 600*700 | 600 | 550 | 700 | 70 | 95 | 95 | 740 | 80 | 2000 | 929 |
| 1000*1000 | 1000 | 920 | 1000 | 80 | 120 | 120 | 1160 | 100 | 2000 | 1696 |

**Stability calculation of new type U (moment).** According to reference literature [13], stability analysis and calculation of design strength grade of concrete is C30, strength of concrete tensile is $R = 17.5kg/cm^2$, the safety factor is $k = 2.5$, plastic influence coefficient of the tension zone of the concrete $r = 1.55$ and wet density of soil $\gamma = 1.8t/m^3$, internal friction Angle $\Phi = 26^0$, the bending moment of the concrete can satisfy the demands of earth negative bending moment. The concrete is C50 and is adopted for copper coated fiber in this article, so its tensile strength is higher.

## Construction technology of new type U (moment)

**Construction machinery and equipment.** Farm transporter can be adopted that is suitable for agricultural transportation in the field. According to the engineering actual situation, a certain type of excavator was adopted. New bucket shape is triangle width not less than 2200 mm.

**Construction process of new type U (moment).** construction process of new type U (moment) irrigation canal seepage is including of construction preparation, earthwork excavation and filling to check slot, canal bottom sand cushion layer , transportation, bonding expansion water sealing strip, reviewing elevation - lifting new type U (torque) , backfill components ,testing, inspection and completion of acceptance. The Construction process was shown in Fig.3.

(a) (b)

(c) (d)

(e) (f)

Fig.3. Construction process

**Technology advantage of New type U (moment) construction**

Length of new U (moment) slot is 2000 mm, is four times for a traditional u-shaped channel seepage of trapezoidal channel of the length of 500 mm. water inlet, complete equipments and supporting components are easily installed, simple, more convenient and quick construction speed. Construction mechanization degree of new U (matrix) slot is high and easy to control quality.

**Conclusions**

Prevention effect of prefabricated u-shaped slot is good as a kind of channel lining material. Because it can focus on production, technology is simple, easy to guarantee quality. Because of the continuous manufacture of u-shaped slot, the thinner of thickness determines the characteristics of its low cost. Because its contact area is large with the ground, so the foundation of strong adaptability, poor geological place still can be use.

It is suitable for small and medium-sized water channel, and U-shaped slot is not affected by the influence of underground water, soil, topography, climate, such as irrigation channels. It is very convenient for demolition if the line will be reformed, so the kind of structure has very good adaptability and flexibility.

New type U (moment) product truly achieve the best filling cross-section. Besides having the advantages of traditional u-shaped slot in the canal seepage, but also having high mechanical properties, excellent durability, good environmental performance, assembly quality and high cost performance. The structure is a kind of upgrading products of the traditional U-shaped slot. It can solve "the last kilometer" problem of the farmland irrigation channels. Through the research on the new type U (moment) construction technology, the technology can for provide the reference for product application of the new type U.

**Acknowledgements**

The paper was supported by the Ministry of water resources "948" project (No. 201316).

**References**

[1]W.H.Shao,F.L.Liu : submitted to Journal of Water conservancy of Jilin(2004). (In Chinese)

[2]S.Q.Qian: submitted to Journal of hydraulic engineering (1993). (In Chinese)

[3]D.C.Zhang: submitted to Journal of Agriculture in Gansu(2012). (In Chinese)

[4]H.X.Wang: submitted to Journal of Water conservancy and hydropower construction. (In Chinese)

[5]Z.G.Huang, S.Z.Liu and G.H.Bai: submitted to Journal of Modern agricultural science and technology (2010). (In Chinese)

[6]R.G.Zheng and D.S.Xu: submitted to Journal of Water conservancy of Jilin(2007). (In Chinese)

[7]C.Q.Yin: submitted to Journal of Gansu water conservancy and hydropower technology (2011). (In Chinese)

[8]R.C.Li: submitted to Journal of Sichuan building materials (2007). (In Chinese)

[9]R.R.Zhou: submitted to Journal of Hunan water conservancy and hydropower technology (2011). (In Chinese)

[10]G.Ma and S.B.Cai: submitted to Journal of Irrigation water conservancy (2009). (In Chinese)

[11]A.W.He and: submitted to Journal of The Huaihe River (2007). (In Chinese)

[12]H.P.Zheng,H.H.Zheng and H.M.Jian: submitted to Journal of Henan water conservancy and the south to north water diversion project (2009). (In Chinese)

[13]B.S.Bai: submitted to Journal of Zhejiang water conservancy science and technology (1988). (In Chinese)

*Applied Mechanics and Materials Vols. 580-583 (2014) pp 2037-2040*
*© (2014) Trans Tech Publications, Switzerland*
*doi:10.4028/www.scientific.net/AMM.580-583.2037*

# Simulation Study on Deposition Downstream Floodgates in Estuarine

Xinzhou Zhang[1, a], Yinyan Song[2, b] and Shaoming Chen[1, c]

[1]Nanjing Hydraulic Research Institute, Key Lab of Port, Waterway and Sedimentation Engineering of the Ministry of Transport, Nanjing, 210029, China

[2]Jiangsu Province Hydrology and Water Resources Investigation Sub-Bureau of Xuzhou, Xuzhou, 221006, China

[a]xinzhouzhang@126.com,[b]yysong@126.com,[c]smchen@nhri.cn

**Keywords:** Estuary with Sluice；Numerical Model；Sediment Transport；Siltation Characteristics

**Abstract.** Siltation in the rivers downstream of floodgates is serious in China, making the discharge capacity of rivers decrease obviously and threatening the flood control in upper rivers. Tidal wave deformation is one conclusive dynamic factor leading to siltation downstream of floodgates in estuaries. A 2-D numerical model of tide and sediment transport is established to simulate the distribution of sediment siltation downstream of the floodgate, and several conclusions are obtained in this paper which can provide some theoretical basis for the prediction and analysis of the siltation characteristics in lower reach caused by floodgates in estuaries.

## Introduction

In order to defend against tides for the development of agricultural production, lots of sluices have been built in coastal areas of China since 1950s, with the number of about 300 now. Siltation in the rivers downstream of floodgates is very serious in China and according to statistics, among the 58 sluices with the drainage flow of over 100$m^3$/s in Jiangsu province, 5 almost are silted up, 15 are in severe siltation and the other 38 are relatively less silted. Besides, in the 35 estuaries with sluice constructed in Haihe River basin, there are 22 in serious siltation, where the upper and lower reaches are universally silted, causing the river drainage capacity reduced by 60%. Siltation in the rivers downstream of floodgates makes the discharge capacity of rivers decrease obviously and threatening the flood control in upper rivers, and influencing the agricultural production. Therefore, it is vital to do research about siltation downstream of floodgates.

Study on siltation downstream of floodgates in China began with research on Sheyang estuary by G.R. Dou (1963), showing that tidal wave deformation was main factors leading to sedimentation downstream sluice. Tidal wave deformation and reflection usually occur under the influence of river morphologic resistance when it comes into the estuary, which will be more evident in the estuaries where floodgates have been built. Tidal wave will be reflected fully by floodgate, and tidal wave properties change from progressive wave to standing wave, there being a significant phase difference between hydrographs of flow velocity and tide level. Besides, high tide level rises while low tide level goes down, duration of flood tide is shortened and mean depth of flood tide decreases while those of ebb tide go opposite. Therefore, flow velocity of flood tide increases and that of ebb tide decreases, respectively. Sediment transport capacity of flood tide is enhanced relative to ebb tide due to the change of hydrodynamic characteristics, so that the sediment which is carried into the river by flood tide cannot be taken back to estuary by ebb tide, and then deposited in the lower reach downstream the floodgate.

## Numerical Model and the Calculation Schemes

To study the sediment characteristics in lower reach caused by floodgates in estuaries, a 2D numerical model of the tidal currents and sediment transport is built based on the prototype of the floodgate in the estuary of the Sheyang River. The actual morphology of the estuary of the Sheyang River is simplified and applied as the open sea condition of the model. The open boundary of the model is about 12 km from the estuary, near the -15m contour. In addition, the area covered by the model between its South and North boundaries is about 21km wide (Fig.1). In the model, the approach channel was simplified into a 10km-long and 660m-wide compound channel. The bottom of the inner passage of the approach channel is about 220m wide, with its elevation at -9.0m. Side slope of the passage is 1:8, and the bottom elevation of the point bar is at about 0.0m.

The hydrodynamic boundary condition of the model is designed on the basis of the actual condition in the estuary of the Sheyang River. The high tide level is at 3.75m and the low tide level is 0.75m (Fig.2). The hydrodynamic condition of the open sea remains unchanged in the study. Fig.3 is the calculation topography and grid of the numerical model, the calculation grid number is 125×101=12625. The grids in lower reach of floodgates are refined, and the minimum feature size is 15m, the maximum feature size 400m in coast outside.

Fig.1 Domain of model boundary

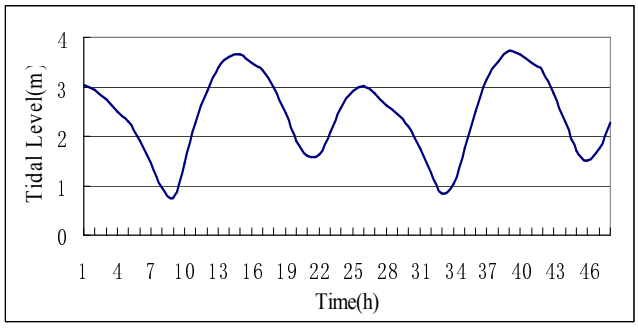


Fig.2 Design curve of tide on outer boundary

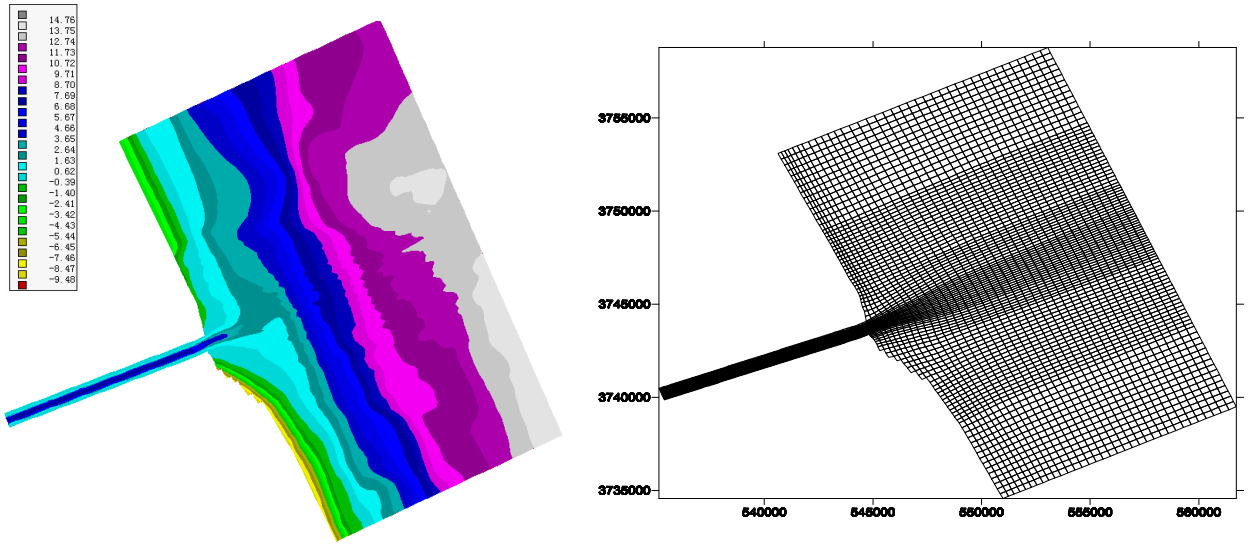


Fig.3 The calculation topography and grid of the numerical model

The continuity equation, momentum equation of tidal current and sediment transport equation in numerical model are discretized using FVM (Finite Volume Method):

$$\frac{\partial \varsigma}{\partial t}+\frac{\partial Hu}{\partial x}+\frac{\partial Hv}{\partial y}=0 \tag{1}$$

$$\frac{\partial Hu}{\partial t}+\frac{\partial Huu}{\partial x}+\frac{\partial Huv}{\partial y}=-gH\frac{\partial \varsigma}{\partial x}-\frac{\partial H\overline{u'u'}}{\partial x}-\frac{\partial H\overline{u'v'}}{\partial y}+\frac{\tau_{sx}-\tau_{bx}}{\rho}+fHv \tag{2}$$

$$\frac{\partial Hv}{\partial t}+\frac{\partial Huv}{\partial x}+\frac{\partial Hvv}{\partial y}=-gH\frac{\partial \varsigma}{\partial y}-\frac{\partial H\overline{v'u'}}{\partial x}-\frac{\partial H\overline{v'v'}}{\partial y}+\frac{\tau_{sy}-\tau_{by}}{\rho}-fHu \tag{3}$$

$$\frac{\partial HS}{\partial t}+\frac{\partial HuS}{\partial x}+\frac{\partial HvS}{\partial y}=\frac{\partial}{\partial x}(H\varepsilon_x\frac{\partial S}{\partial x})+\frac{\partial}{\partial y}(H\varepsilon_y\frac{\partial S}{\partial y})+\alpha\omega(S_*-S) \tag{4}$$

River bed evolution can be calculated by next formula:

$$\gamma_0\frac{\partial \eta_s}{\partial t}=\alpha\omega(S-S_*) \tag{5}$$

Incipient motion estimate formula of cohesive sediment and sediment transport capacity of tidal currents and waves are key parameters in numerical model of tide and sediment transport. Dou (1999) analyses the group characteristics and the movement characteristics of cohesive sediment, and deduced a calculation formula for starting velocity including bulk density effect, according to the effect of cohesive force between fine particles, water depth and bulk density etc.

$$u_c=k'\left(\ln 11\frac{h}{\Delta}\right)\left(\frac{\Delta}{\Delta_*}\right)^{1/6}\sqrt{3.6\frac{\rho_S-\rho}{\rho}gd+(\frac{\gamma_0}{\gamma_0^*})^{2.5}\frac{\varepsilon_0+gh\delta(\delta/d)^{1/2}}{d}} \tag{6}$$

Where $k'$ is coefficient ($k'$=0.26 for impending motion, $k'$=0.32 for little motion, $k'$=0.41 for general motion), $\Delta$ is the roughness height of bed surface ($\Delta$=1mm for d$\leqslant$0.5mm, $\Delta$=2d for d>0.5mm), $\Delta_*$=20mm, $\rho_S$ and $\rho$ are the density of sediment particles and that of water respectively, $\gamma_0$ and $\gamma_0^*$ are the dry volume weight and the stable dry volume weight of the sediment on the bed surface. $\varepsilon_0$ is synthetic parameter of cohesive force whose value is related to the physcical and chemical properties of the particle materials, and also to the origanic content and siltation environment for cohesive soil, $\varepsilon_0$=1.75cm$^3$/s$^2$ for natural sediment. $\delta$ is the parameter of water film thickness, and $\delta=2.31\times10^{-5}$cm.

Luo (1997) deduced a calculation formula for sediment transport and carrying capacity for different wet densities of fluid mud, an overall verification of the calculation formula is made, and satisfactory results are obtained, showing that the calculation formula can be used as practical formula for the study of engineering-related sediment problems.

$$S^*=0.296\gamma_s\left(\frac{\gamma}{\gamma_w}\right)^{12.8}\frac{V^2}{gD} \tag{7}$$

Where $\gamma_w$ is wet densities of fluid mud，$\gamma$ is densities of water, $\gamma_s$ is densities of sediment, $V$ is water velocity under the common action of tidal currents and waves, $D$ is water depth.

**The Siltation Characteristics in Lower Reach Caused by Floodgates**

The change curve of tidal level, current velocity and sediment concentration where is 4km length downstream floodgates are shown in Fig.4. It shows that hydrodynamic characteristics changed after building sluices include the duration and mean water depth of flood tide decreases, the averaged velocity of flood tide increases while those of ebb tide change in the opposite direction, and the high tide level is heightened while the low one goes lower. Flow velocity of flood tide increases and that of ebb tide decreases, respectively. Sediment concentration of flood tide is enhanced relative to ebb tide due to the change of hydrodynamic characteristics, so that the sediment which is carried into the river by flood tide cannot be taken back to estuary by ebb tide, and then deposited in the lower reach downstream the floodgate.

Fig.5 shows the distribution of sediment siltation downstream the floodgate which simulated by numerical model. It can be found that deposition thickness near the floodgate is larger than siltation thickness in estuarine, there is a slope from floodgate to estuary. The distribution characteristics of sediment siltation downstream the floodgate keeps consistent with the measured data.

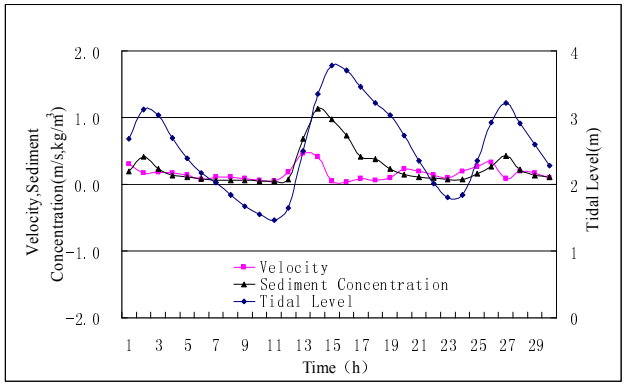


Fig.4 The change curve of tidal level, current velocity and sediment concentration

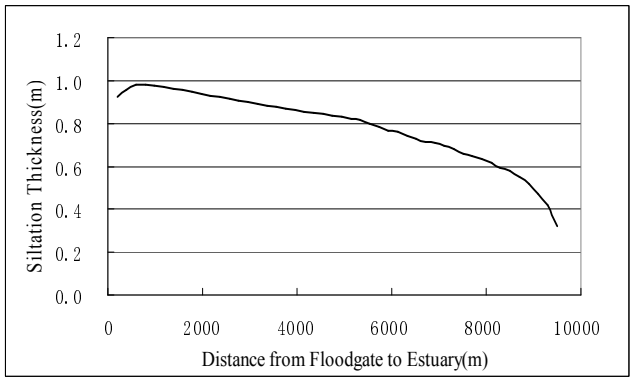


Fig.5 The distribution of sediment siltation downstream the floodgate (one year)

## Conclusions

The simulation results of tide current and sediment transport numerical model show that tidal wave deformation after building sluices makes the ratio increases of flood tide velocity and ebb tide velocity, and the sediment which is carried into the river by flood tide is larger than by ebb tide. Because coastal bottomland can provide enough sediment resource in the period of flood tide, while sediment deposited in lower reach of floodgates can't be eroded by bb tide. The simulation results can reflect the processes of siltation downstream the floodgate in estuaries.

## Acknowledgments

The project is financially supported by Ministry of Transport major special science and technology projects of China (Grant No. 201132874640) and Ministry of Water Resource's Nonprofit Special Funds for Science Research of China (Grant No. 201201070).

## References

[1] Dou Guoren, Analysis of Silting Problems under Sheyang River Floodgate. Collected Paper of Dou Guoren, Beijing: China Water Power Press (2003)

[2] Xu Xuesong: Study on Siltation Characteristics in the Estuary with Sluices Constructed. Master Degree Dissertation, Hohai University (2012)

[3] Luo Zhaosen: Study on Fluid Mud-Carrying Capacity, Sediment Transport and their Application, Journal of Sediment Research, Vol. 4, (1997), p.42-46

[4] Dou Guoren: Incipient Motion of Sediment under Currents, China Ocean Engineering, Vol.14, (2000), p.391-416

*Applied Mechanics and Materials Vols. 580-583 (2014) pp 2041-2044*
*© (2014) Trans Tech Publications, Switzerland*
*doi:10.4028/www.scientific.net/AMM.580-583.2041*

# Study on Time Effect of Rock Fill Dam Seepage Line

Xiuyu Tao[1, a,*], Dong Xiang [1,b],Wei Sun[1,c], Yong Li[1]

[1]Hydraulic Research Institute of Shandong Province,Jinan,250014,China

[a]6974554@126.com, [b]6974470@126.com, [c]zhouzhidongdzd@163.com

[*]corresponding author

**Keywords:** hydraulic engineering; earth dam; saturation line; time effect.

**Abstract:** In dam seepage line monitoring process, dam saturation line "inverted siphon" phenomenon appeared. In order to study the time effect, indoor model test were done. The dam seepage line rules and conditions were determined. The results show that when the reservoir water level dips, the dam seepage line with the decreasing of the water level will drop. But the changing has lagged far behind. Hysteresis and permeability dam, seepage path length, the upstream water level and other factors related to the rate of decline.

## Introduction

The dam and homogeneous clay core dam are mostly good clay impervious core wall. Earth dam project management, invasive lines are important means of monitoring and analysis of dam safety. According to some dam monitoring data , the dam seepage line had "inverted siphon" phenomenon contrary to the traditional theory. To further verify and explain these phenomena, it was necessary to theoretical research the dam seepage and infiltration line performance[1]. Model test was designed to study the phenomena.

Based on the experimental data and the theoretical analysis, this paper studied the time effect of rock fill dam seepage line. The dam seepage line rules and conditions were determined. Its particularity and universality was studied and a universal theory was found. Traditional theory of seepage line was fixed. Water levels fall in the front of the dam and dam body seepage line within will be reduced with the decreasing of water level before dam. Analysis and interpretation of the causes of the phenomenon and the factors were useful to guide project management and ensure the safety of the dam.

## Model test

### Similarity scale

The most intuitive way to research dam seepage problems was sand tank model tests. In order to re-play the natural state of water, the model must be based on a certain scale than similar criteria.

Its initial state was bound to be established on the downstream water level when unsteady seepage caused by water level falling was considered[2]. A certain moment, the steady flow field, the time scale is the same as the stable seepage[3]. Generally take prototype model materials natural material, so that make the model and the prototype of the hydraulic gradient and the permeability strength were completely equal, in order to maximize the prototype situation.

### Model dimension

Homogeneous earth dam of cohesive soil was used in model. The length of the general hydraulic structure model scale was 20 ~ 120 . According to reservoir dam section size, typical model was 1.0 m high and 0.2 m wide. Dam bottom width was 2.5 m[4]. Along the dam axis length was 1 m. In order to protect the dam slope stability, dam upstream and downstream dam surface used geotextile and sandy pebble slope, model section as shown in Fig.1.

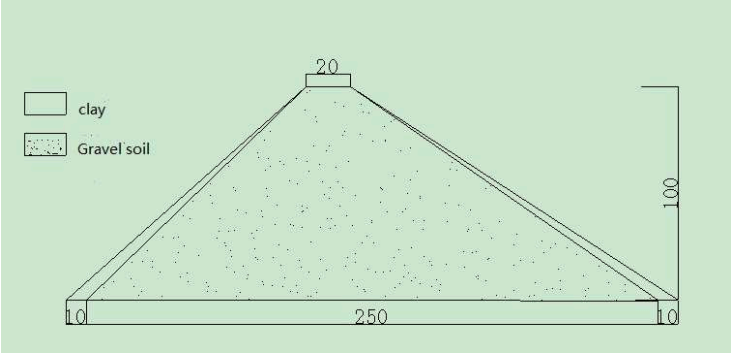


Fig.1 Cross-sectional dimension of model(unit: cm)

According to the similarity criterion, the 1/40 scale model was designed and placed in the tank model.Using 10 mm thick steel plate as the model of tank, the main stress components at the same time to facilitate the observation experiment phenomenon[5].For easy observation of the change of water level, piezometric tube arranged at the side of the glass. Piezometric tube arrangement was shown in Fig.2.

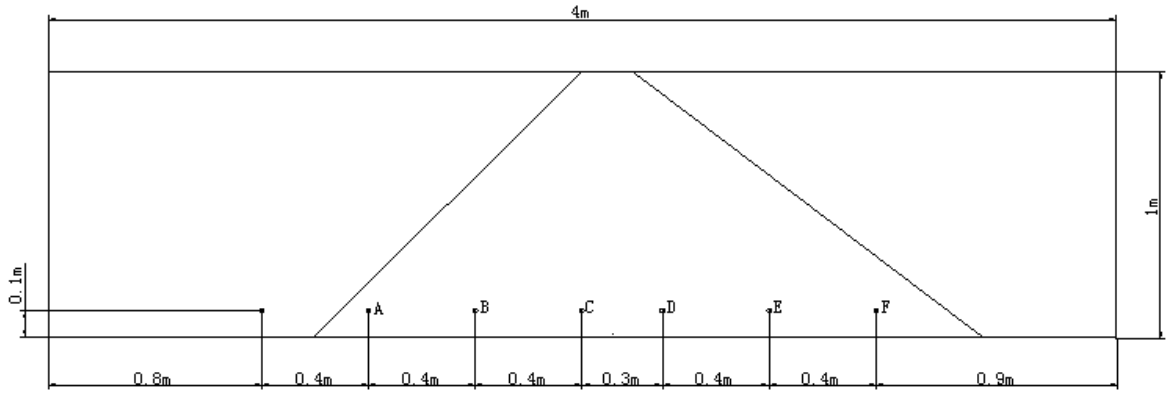


Fig.2 Piezometric tube arrangement

Toughened glass was used on both sides . The strength of toughened glass was big and had high transparency.This could ensure the safety in the process of observation.The casing cofferdam contacted surface with model to prevent steel corrosionand the relative slip crack leakage, etc. In order to prevent the dam and model slot interface around the seepage phenomenon, rubber strips were prepared in the tub. Detailed design was shown in Fig.3.

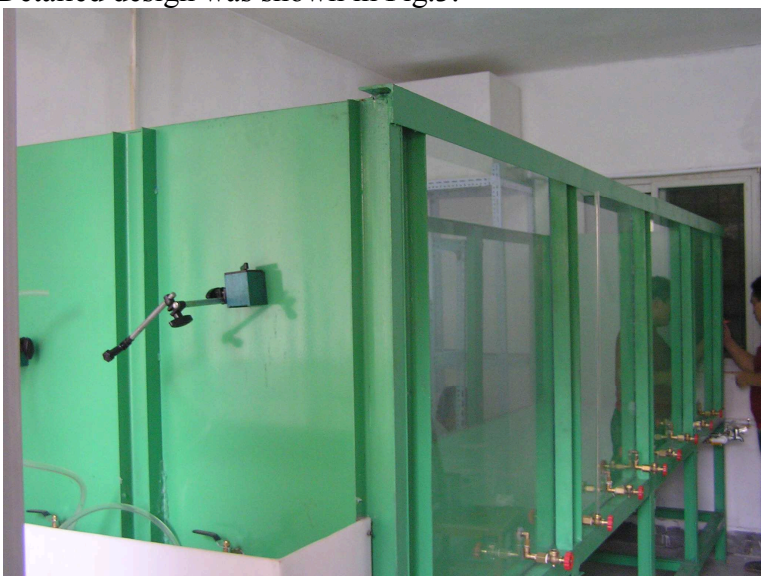

Fig.3 Sand tank model experimental device

## Result Analysis

### Hysteresis

Three groups of model test results showed that when the water level upstream of the dam became lower, the saturation line will decreased with the decreasing of the water level. But changes in the dam seepage line laged behind the dam water level. Fig.4 was the result of second model.

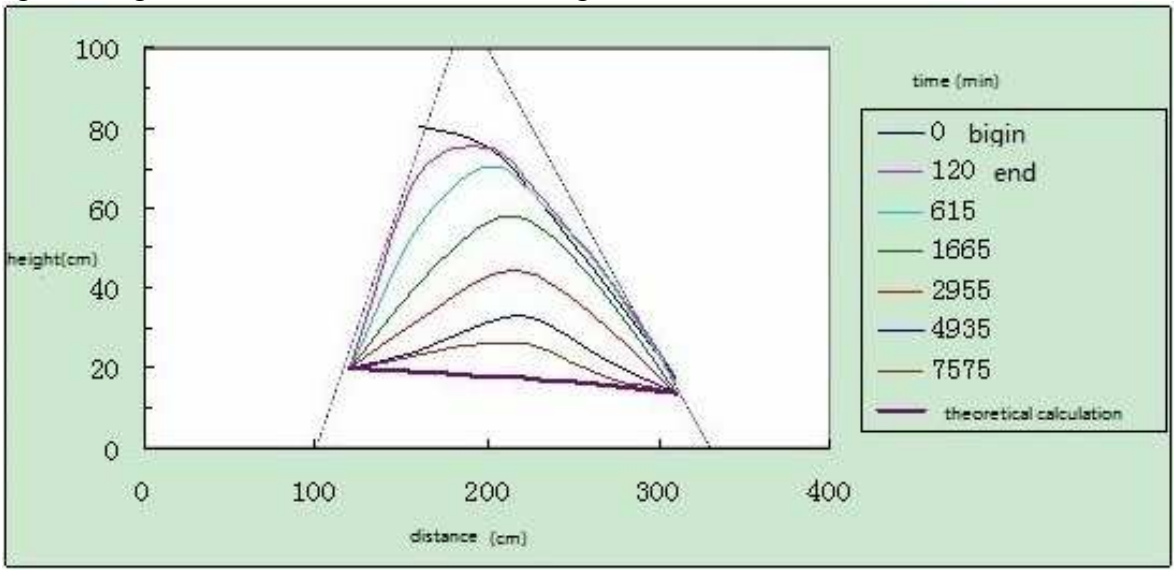


Fig.4 The result of second model.

The time to start was made zero moment. As can be seen from the Fig.4, the dm seepage line had obvious hysteresis, saturation line shaped like a parabola opening down. When the saturation line stability, its shape was still a certain degree of anti-arc. The highest point of the dam seepage line growth in the horizontal position changing over time, beginning with the passage of the downstream direction, after a period of time and gradually moved back upstream.

### Lag time

Analysis the difference of the testing process of each piezometric water level and the actual measured value between the final stable value over time change process, the length of the lag time would be ensured. Fig.5 was the second set of model test measured pressure tube dam water level and the actual measured value difference between the final stable value over time diagram, take time to turn on the water started at time 0.

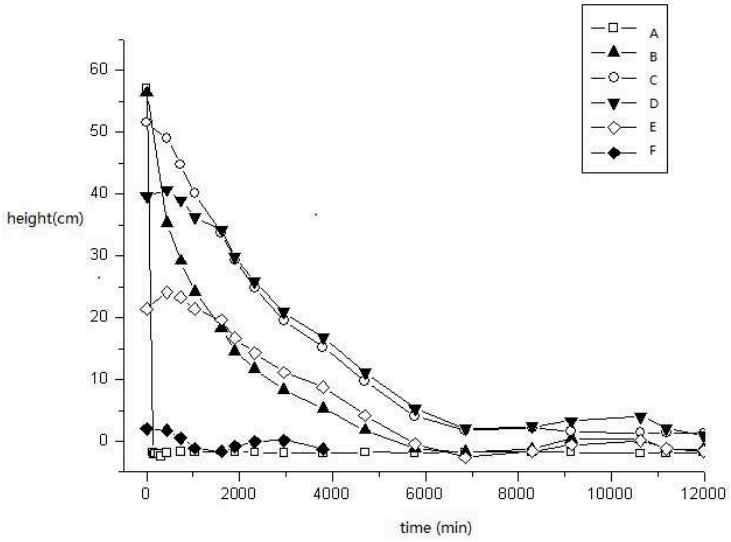


Fig.5 The stability of piezometer

As can be seen from the Fig.5, the decline in the water level of the dam, different piezometer location, the water level changed at different rates, piezometric level changed in the middle of the dam slow, steady time was needed.

## Conclusions

Water levels fall in the front of the dam and dam body seepage line within will be reduced with the decreasing of water level before dam. It lags the changing of water level in the front of the dam.

By comparing the experimental model, the dam and the dam seepage line lag time was related to filling density (permeability) . The more loose, the bigger the permeability coefficient, the shorter the saturation line lag time; The larger dam filling density, the smaller the coefficient of permeability.

Time to turn on the water level drops the total time of 2/3, the effects of lag on the upstream slope of the dam seepage stability and strength and stability of the dam saturation line the largest reservoir in the actual operation of the process, the time should be strengthened and dam seepage stability monitoring.

## Acknowledgements

This work was financially supported by Binhai comprehensive utilization of water resources and the most strict water resources management and demonstration (201201116).

## References

[1] Weiqiao Wang, Qingsen Shang, chuan Wang, Weidong Cao: The plasticity of the Yellow River alluvial silt and compaction control standard analysis[J]. Journal of Shandong University (Engineering Science), 2003(5): 589-592.

[2] Aiqin Shen, Xiangwen Li. Sand and low liquid limit hit-solid filling roadbed compaction mechanism and construction technology research[J]. China Journal of Highway and Transport, 2000, 13 (4): 12-15.

[3] Haibo Liu. Saturated silt and cohesive plastic soil construction technology of subgrade reclamation[J]. Journal of East China Jiaotong University, 2003, 20(5): 23-25.

[4] Congcong Liu, Gusheng Zhang. Experimental study of wet lime improved soil[J]. Construction in Shanxi, 2006, 32 (19): 145-146.

[5] Fei Wen. Excessively wet soil treatment technology research[D]. Xi'an: Chang 'an University, 2004.

*Applied Mechanics and Materials Vols. 580-583 (2014) pp 2045-2049*
*© (2014) Trans Tech Publications, Switzerland*
*doi:10.4028/www.scientific.net/AMM.580-583.2045*

# Temperature rebound influenced by environment temperature analysis of the irrigated area of a high arch concrete dam under constrcution

Xunhui Chen[1, a *],Yaoying Huang[1,b] and Bailin Xu[1,c],Dandan Liu[2],Xiaobin Wei[1]

[1]College of Hydraulic & Environmental Engineering,China Three Gorges University,Yichang 443002,China

[2]College of Science and Technology, China Three Gorges University,Yichang 443002,China

[a]xunhuichen@sina.com, [b]huangyaoying@sohu.com, [c]xubailin106@163.com

**Keywords:**Environment temperature, Irrigated area, Temperature rebound, Thermal conductivity, Simulation analysis, Heat preservation benzene board

**Abstract.**For a temperature rebound in the irrigated high arch dam during the construction period, using finite element method to research the influence of environment temperature to temperature rebound of the irrigated high concrete arch dam. Assuming that the initial temperature of the dam concrete is the joint grouting temperature. This paper presents a simulation of the temperature rebound of the high arch dam which is caused by the monthly average environment temperature, and performs sensitivity analysis to research the influence of thermal conductivity and surface heat preservation on the temperature rebound. According to the analysis,when the high arch dam sealing temperature is lower than the dam site annual average temperature, the dam site temperature inevitably would flow backward,slowly,to the irrigation area.The larger the thermal conductivity is,the quicker the temperature rebound speed will be. And benzene board insulation can reduce concrete temperature rebound rate, if the heat preservation benzene board is thicker,the temperature rebound rate is smaller.

## Introduction

When the age of concrete of high arch dam reaches more than 120 days, and the temperature of concrete reaches the sealing temperature, then begin to conduct joint grouting. Sealing temperature is the reference temperature of temperature load in arch dam, it directly influences the arch dam rising temperature load and dropping temperature load. If the sealing temperature is low, it will be beneficial to reduce the tensile stress in the dam, currently we usually conduct joint grouting at annual average temperature or slightly below the annual average temperature. Take Ertan dam, Xiaowan, Xiluodu and Jinping high arch dams for example, the annual average temperature at dam site are 19.8 ˚C, 19.1 ˚C, 19.7 ˚C and 17.2 ˚C respectively, and Sealing temperature are 12.0 ~ 16.0˚C, 12.0 ~ 17.5˚C, 12.0˚C~ 16.0˚C and 13.0˚C~ 15.0˚C respectively. And it will take several years to construct mass concrete before water storage. In recent years, high concrete arch dam temperature monitoring shows that there is a great temperature rise in joint grouting area (already irrigated area) after the end of the second-phase water circulation , even some irrigated area has 3 ~ 4˚C temperature rebound after 180days~360days. The great temperature rebound and the lasting time are considered by construction units. High arch dams generally use high content fly ash concrete, for example, the mixing quantity of fly ash is 30% in Xiaowan and Ertan ,it is 35% in Xiluodu and Jinping. Since the hydration of fly ash concrete depends on the CaO,which is the secondary product of cement hydration, therefore the heat release speed is slow, Zhang Guoxin etc.[1] consider that late heat release of high content fly ash concrete is the main reason of temperature rebound of irrigated area, during the middle cooling circulation, the age of concrete is long enough, although majority of the cement hydration heat release has been complete, the high content fly ash concrete will continue to release heat slowly for a long time. For the joint grouting temperature is below the dam site annual average temperature, Huang Yaoying etc.[2] analysis the temperature rebound based on the theory of natural cooling circulation or temperature rebound , in his opinion , he maintains that the main reason of temperature rebound is the environment temperature flowing backward slowly to the irrigated

area. That the physical causes of a temperature rebound whether is mainly caused by high content fly ash late heat release or by environment temperature flowing backward is still controversial. So this paper analyzes the influence of environment temperature to internal temperature of high concrete arch dam with temperature field simulation program. Due to the heat preservation effect of upstream and downstream of benzene board has a great influence on calculation results, we perform sensitivity analysis with the equivalent heat transfer coefficient on it.

**Quasi Stable Temperature Field Calculation Principle**

Mass concrete temperature heat conduction equation is as follows[3]

$$\frac{\partial T}{\partial \tau} = a\left(\frac{\partial^2 T}{\partial x^2} + \frac{\partial^2 T}{\partial y^2} + \frac{\partial^2 T}{\partial z^2}\right) + \frac{\partial \theta}{\partial \tau} \tag{1}$$

Where $a$ is thermal diffusivity , it can be expressed as $a = \frac{\lambda}{c\rho}$, and $a, \lambda, \rho$ is thermal conductivity, specific heat and density respectively.

To the irrigated high concrete arch dam, because the age of concrete has reached more than 120 days, most of the cement hydration heat release has been complete.Currently we are lack of adequate analytical data on high content fly ash late heat release, this paper mainly studies the influence of environment temperature to temperature rebound of the irrigated area.Assuming irrigated concrete $\frac{\partial T}{\partial \tau} \neq 0$, $\frac{\partial \theta}{\partial \tau} = 0$. so Eq.(1) can be simplified as quasi stable temperature heat conduction equation

$$\frac{\partial T}{\partial \tau} = a\left(\frac{\partial^2 T}{\partial x^2} + \frac{\partial^2 T}{\partial y^2} + \frac{\partial^2 T}{\partial z^2}\right) \tag{2}$$

During construction period, because both upstream and downstream are cofferdam, dam has not yet been filling , so the irrigated area is belong to the third temperature boundary condition

$$-\lambda \frac{\partial T}{\partial n} = \beta(T - T_a) \tag{3}$$

Where $\beta$ is concrete surface heat transfer coefficient, $T_a$ is environment temperature, $n$ is the normal-to-wall direction, $\lambda$ is thermal conductivity.

Through dispersing dam concrete, we can get finite element control equation of quasi stable temperature field , it is as follows

$$\left(\boldsymbol{H} + \frac{1}{\Delta \tau_n}\boldsymbol{R}\right)\boldsymbol{T}_{n+1} - \frac{1}{\Delta \tau_n}\boldsymbol{R}\boldsymbol{T}_n + \boldsymbol{F}_{n+1} = 0 \tag{4}$$

where $\Delta\tau_n$ is calculation step; $\boldsymbol{H}$ , $\boldsymbol{R}$ is heat conduction matrix and heat capacity matrix respectively; $\boldsymbol{T}$ is node temperature array; $\boldsymbol{F}$ is boundary temperature load array; $\boldsymbol{n}$ is the number of time intervals .

**Projects**

Take a high concrete arch dam which is under construction in southwest as an example, in order to reduce the dam concrete temperature to sealing temperature , the process of cooling circulation can be

divided into three stages:the first cooling circulation, the second cooling circulation and the third cooling circulation .

**Three-dimensional Finite Element Model.** Finite element model. In order to research the influence of environment temperature to temperature rebound of the irrigated area, This paper selects two riverbed dam sections and their corresponding foundations to establish three-dimensional finite element model with the eight-node hexahedral isoparametric elements, 7092 units ,among the units there are 5652 units in the dam, three-dimensional finite element model is shown in Fig. 1.

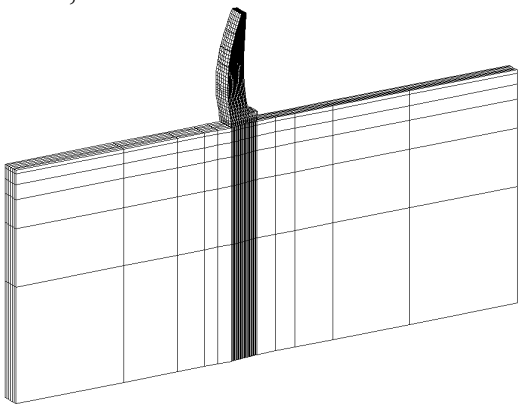

**Fig. 1** Three-dimensional FEM model

**Calculating Parameters.** Assuming the concrete surface is bare, the exothermic coefficient is $1005\,\mathrm{kJ/(m^2\cdot d\cdot ℃)}$; assuming concrete surface is covered with 3cm insulation benzene board, the exothermic coefficient is $95.52\,\mathrm{kJ/(m^2\cdot d\cdot ℃)}$; assuming concrete surface is covered with 5 cm insulation benzene board, the exothermic coefficient is $58.56\,\mathrm{kJ/(m^2\cdot d\cdot ℃)}$;beside, coefficient of concrete conduction is $184.9\,\mathrm{kJ/(m^2\cdot d\cdot ℃)}$; concrete density is $2663\,kg/m^3$; concrete specific heat capacity is $860\,\mathrm{kJ/(m^2\cdot d\cdot ℃)}$; bedrock thermal conductivity is $184.9\,\mathrm{kJ/(m^2\cdot d\cdot ℃)}$; bedrock density is $2663\,kg/m^3$; bedrock specific heat capacity is $860\,\mathrm{J/(kg\cdot ℃)}$.

**Initial Conditions**.The initial dam temperature is 13˚C.

**Boundary conditions.**This model takes all sides of bedrock and transverse joints as insulated boundary, takes rock bottom as ground temperature boundary(it is 20˚C), the rest of the boundary is the third boundary condition.The expression of annual average temperature is $T_a = 19.79 + 8.04\cos(2\pi(t+153)/365)$ ,taking the effect of solar radiation into consideration, environment temperature is annual average temperature plus 3˚C.

**Calculated Cases.** Case 1: thermal conductivity is equal to 0.8 times the given design value without taking any measures; Case 2: thermal conductivity is equal to the given design value with 3cm benzene board ; Case 3: thermal conductivity is equal to the given design value with 5cm benzene board ; Case 4: thermal conductivity is equal to 0.8 times the given design value with 3cm benzene board; Case 5: thermal conductivity is equal to 1.2 times the given design value with 5cm benzene board ;

## Calculation Results Analysis

Temperature field simulation calculation results are shown in Fig. 2 and Fig. 3 and Table 1.This paper selects three different heights—34.5m( the thickness along the river is 58m) , 130.5m ( the thickness along the river is 48m) , 235.5m ( the thickness along the river is 30m)， all of which are using foundation surface as a standard.And average temperature rebound in table 1 refers to the average temperature rebound of all the nodes at 130.5m height at a particular time .

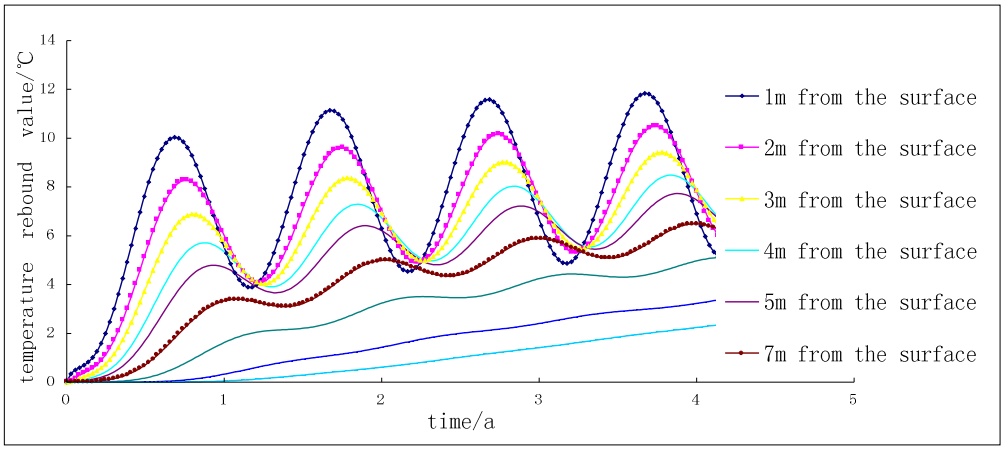


**Figure. 2** Temperature rebound process line of the section of 130.5m high above foundation surface of case 2

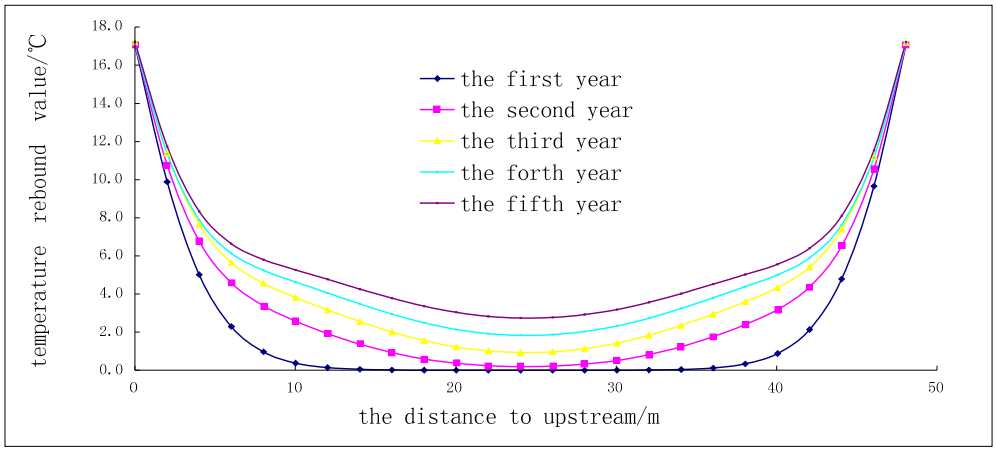


**Figure.3** Temperature rebound distribution along the river direction of section 130.5m high above foundation surface at the highest temperature moment of case 2

**Table.1** Average temperature rebound of the section of 130.5m high above foundation surface

| Time | 1year | 2years | 3years | 4years | 5years |
|---|---|---|---|---|---|
| Case1 | 2.27 | 3.31 | 4.18 | 4.81 | 5.35 |
| Case2 | 1.88 | 2.90 | 3.73 | 4.38 | 4.94 |
| Case3 | 1.63 | 2.60 | 3.40 | 4.04 | 4.60 |
| Case4 | 1.72 | 2.64 | 3.39 | 3.98 | 4.48 |
| Case5 | 1.72 | 2.78 | 3.63 | 4.33 | 4.92 |

## Conclusions

(1)During construction period, upstream dam has not yet been filling, because there exist differences between joint grouting temperature and environment temperature in irrigated area, so environment temperature would cause the temperature of irrigated area increasing slowly.The closer to the concrete surface , the bigger the temperature rebound will be and the more dramatic the environment temperature fluctuations will be, what's more ,temperature rebound of the irrigated concrete Shows a upward trend of cycle fluctuation when environment temperature changes.As is shown in figure. 2, when the distance is 1m far away from the concrete surface, temperature fluctuation reaches up to

6.69˚C,when the distance is 4m far away from the concrete surface, temperature fluctuation is only 1.31˚C.

(2)It can be learned from several selected sections that the smaller the thermal conductivity is, the slower the temperature rebound speed will be, on the contrary, the quicker the temperature rebound speed will be.Taking the cross section of 130.5m as an example, with 3cm benzene board covered in concrete surface , and thermal conductivity is respectively equal to given design value and 0.8 times given design value, when the joint irrigation is done for 5 years, average temperature rebound is respectively equal to 4.28˚C and 3.84˚C;while with 5cm benzene board covered in concrete surface, and thermal conductivity is respectively equal to given design value and 1.2 times given design value, when the joint irrigation is done for 5 years, average temperature rebound is respectively equal to 3.99˚C and 4.32˚C.

(3)Due to environment temperature would cause the temperature of irrigated area increasing slowly., benzene board insulation can reduce concrete temperature recovery rate , besides, the heat preservation effect of 5 cm benzene board is better than the heat preservation effect of 3 cm benzene board .Just as figure. 1 shows, when concrete surface is respectively covered with no benzene board insulation, 3 cm benzene board insulation and 5cm benzene board insulation, the average temperature rebound is respectively equal to 5.35˚C, 4.94˚C and 4.60˚C after joint grouting for 5 years.

## Acknowledgement

The research is supported by National National Science Foundation of China(No. 51209124)

## References

[1] Guoxin Zhang, Yi Liu,Ming Jie, Hydration heat combined function model of high fly-ash concrete and its application in engineering [J] Journal of Hydroelectric Engineering, 2012, 31(4):201-205. In Chinese

[2] Yaoying Huang, Yihong Zhou, Shaowu Zhou. Temperature rebound influenced by environment temperature analysis of the irrigated area of a high arch concrete dam under constrcution [J] Journal of Mechanics and Practice, 2013,35(4):36-39. In Chinese

[3] Bofang Zhu. Thermal stresses and temperature control of mass concrete [M] Beijing: China Electric Power Press 1999. In Chinese

*Applied Mechanics and Materials Vols. 580-583 (2014) pp 2050-2054*
*© (2014) Trans Tech Publications, Switzerland*
*doi:10.4028/www.scientific.net/AMM.580-583.2050*

# The numerical simulation of the flow field in the micro-pressure inner loop reactor

LIU Jiang-chuan[1, a], YIN Zhi-gang[1,b] and JI Wei[1,c]

[1]School of Water Resources and Environmental Engineering, Changchun Institute of Technology, Changchun 130012, China

[a]Liujiangchuan@yeah.net, [b]Yinzhigang1972@163.com, [c]Jiwei2012gc@163.com

**Keywords:** the micro-pressure inner loop reactor, numerical simulation, mixture model

**Abstract.** The treatment of the urban sewage and the Organic industrial wastewater has been transformed from removing of the organics to the Removal of organic matter and nitrogen, phosphorus. According to the deficiency of the Traditional wastewater treatment process，the micro-pressure inner loop reactor is put forward to solve the Anaerobic, anoxic and aerobic environmental issues in this paper. Aiming at the newly development of the micro-pressure inner loop reactor, based on the methods of Computational Fluid Dynamics, using the methods of computational fluid dynamics, By analyzing the velocity distribution field, flow lines, the gas volume fraction and other factors, the result shows that the reactor Meets the actual needs of the project, and provides a theoretical basis for practical engineering equipment.

## Introduction

The Urban sewage discharge and the Wastewater in industrial production has become a major pollution source of the urban water[1][2]. So, in the current and future, the treatment of the urban sewage has been the most important thing of the Urban Water Conservation and Urban water environmental protection. At present, the batch reactor and continuous reactor have been mainly used in The Treatment process of the Municipal sewage and industrial wastewater. By separating the three reactors of Anaerobic, anoxic and aerobic, the Continuous reactor solves the Oxygen environment issues; by separating the three stages of Anaerobic, anoxic and aerobic, the Batch reactor solves the Oxygen environment issues[3][4]. Some achievements have been achieved by the two types of reactors in the Sewage treatment. But, in the 21st century, due to the change of sewage water quality and the treatment of the urban sewage and the Organic industrial wastewater has been transformed from removing of the organics to the Removal of organic matter and nitrogen, phosphorus. The Traditional processors will face a serious shortage[5][6]. For example, the Continuous reactor makes the Microbial flora of various function not conduct fully biochemical reactions in the whole environment, to solve the problem of carbon source, by using the method of reflux can also cause reflux power consumption. Batch reactor also has the issue which the Microbial flora of various function cannot conduct all biochemical reaction[7].

Aiming at the new problems, which are encountered in the treatment of city sewage and industrial wastewater, the micro-pressure inner loop reactor has been put forward and built in this paper. By using the method of Computational fluid dynamics[8], Micro pressure of inner loop reactor flow field velocity field, pressure field and phase change are simulated by using the multiphase flow model, And Provides a reference basis for The further optimization and industrial equipment.

## The Micro-pressure Inner Loop Reactor

Micro pressure internal circulation reactor is proposed based on the traditional reactor, the top of the reactor is almost closed and the reactor internal is at a micro pressure. Under the effect of the aeration, The Mixed liquid of wastewater with microorganisms (activated sludge)stay mixed circulating inside the reactor, the concentration of dissolved oxygen is gradually increased from the

reactor center outward, respectively forming the area of hypoxia, anaerobic and aerobic. In the hydrodynamic action, the concentration of activated sludge is gradually decreasing from the center of the reactor outward, realizing all the reaction of the three kinds of functional bacteria.(See Fig.1 and Fig.2)

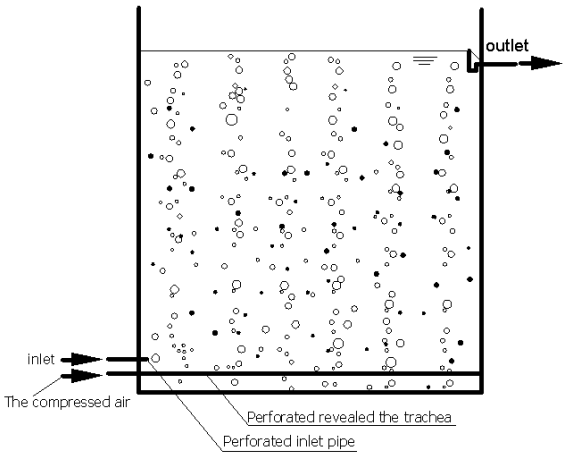


Fig.1 Traditional reactor

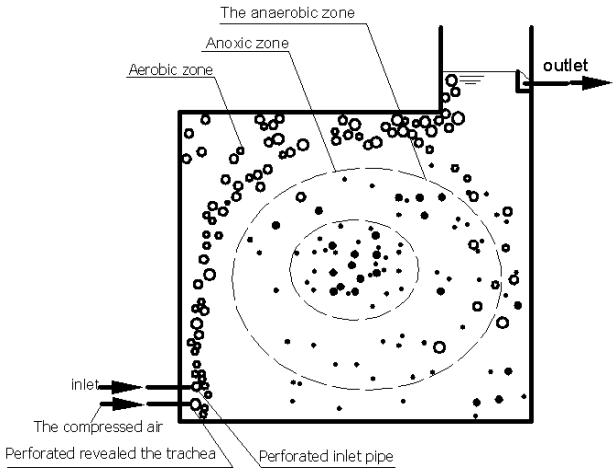


Fig.2 Micro pressure internal circulation reactor

**The control equation**

The Fluid flow of the micro-pressure inner loop reactor is a little more complex, it belongs to the multiphase turbulent flow. The basic equation for hybrid model mainly includes the following.

The continuity equation: $\frac{\partial}{\partial t}(\rho_m)+\nabla\cdot(\rho_m\vec{v}_m)=\dot{m}$

The Momentum equation is got though the summation of all respective phase momentum equation, it can be represented as the following:

$$\frac{\partial}{\partial t}(\rho_m\vec{v}_m)+\nabla\cdot(\rho_m\vec{v}_m\vec{v}_m)=-\nabla p+\nabla\cdot\left[\mu_m\left(\nabla\vec{v}_m+\vec{v}_m^T\right)\right]+\rho_m\vec{g}+\vec{F}+\nabla\cdot\left(\sum_{k=1}^{n}\alpha_k\rho_k\vec{v}_{dr,k}\vec{v}_{dr,k}\right)$$

The relative speed is defined as the second phase: $\vec{v}_{qp}=\vec{v}_p-\vec{v}_q$

The relationship between the relative speeds and the drift velocity can be represented by the following formula:

$$\vec{v}_{dr,p}=\vec{v}_{qp}-\sum_{k=1}^{n}\frac{\alpha_k\rho_k}{\rho_m}\vec{v}_{qk}$$

The equation of volume fraction:

$$\frac{\partial}{\partial t}(\alpha_p\rho_p)+\nabla\cdot(\alpha_p\rho_p\vec{v}_m)=\nabla\cdot(\alpha_p\rho_p\vec{v}_{dr,p})$$

**Numerical Simulation**

The micro-pressure inner loop reactor which is used in this model is shown as the figure 3, The length of the container is 80 cm, The height of the container is 60 cm, The width which is located at the top of the right side of the tube is 8 cm, and the height is 30 cm, it is connected with the atmosphere. The G pipe is a Burst pipe; the Value of gas detonation in the calculation is 1.4m3/h, the Specific size of the G pipe is shown in Figure 2. The quadrilateral non-uniform structured grid is used in the whole area, It generates 5253 nodes, and The number of the grid unit is 5075, to improve the accuracy, encrypting the grid around the Burst pipe. The meshing is shown in the figure 4.

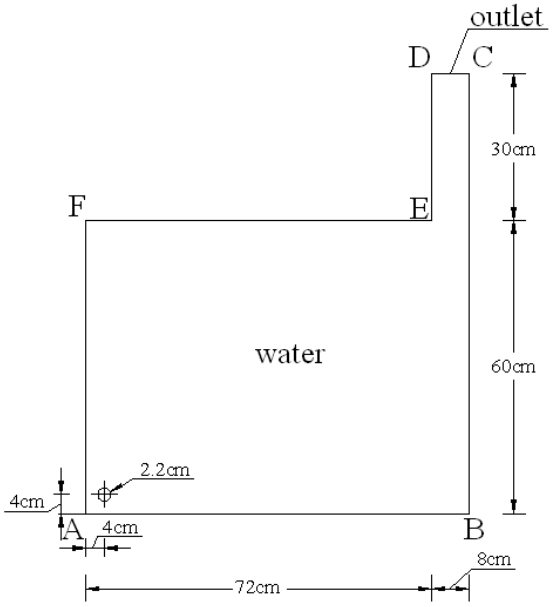


Fig.3 The model size of reactor

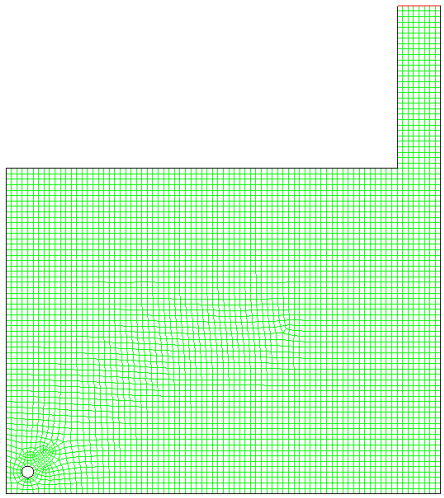

Fig.4 The mesh diagram of reactor

**Boundary conditions**

There mainly are three kinds of boundary conditions in this model, including the Inlet boundary, the Outlet boundary and the solid wall boundary. The conditions of Speed import are calculated by the turbulent kinetic energy (k) and the turbulent dissipation rate(ε).

The intensity of turbulence (I) is $I = \frac{u'}{u} = 0.16\left(\mathrm{Re}_D\right)^{-\frac{1}{8}}$

The turbulent kinetic energy (k) is $\kappa = 1.5\left(\bar{u}I\right)^2$

Turbulent energy dissipation rate( $\varepsilon$ ) is $\varepsilon = C_\mu^{3/4}\frac{\kappa^{3/2}}{l}$

The outlet is set as the turbulent full development of free export pressure; the pressure of the outlet is the atmospheric pressure. The solid wall boundary is set as the solid wall boundary.

**The Simulation Results and Discussion**

By calculating, we can get the velocity distribution field; trace the whole calculation domain and the volume fraction of air, the calculation results are shown in the figure 4 to figure 7. (1)The figure 4 is a velocity vector diagram of the hybrid model, the boundary of the contact with the atmospheric outlets meets the reality, because the gas which is squeezed out constantly can cause the velocity of gas-liquid mixing, and the velocity vector is Sometimes positive, sometimes the reverse. The enlarge figure circular pipe is shown in the figure 5. (2) The calculation of the whole flow field of the region is shown in the figure 6, due to the shot of the gas, the stillness of the water in the whole area is affected and begins to flow, at the same time because of the influence of gravity flow, making the streamline approximate an oval, that conform to the actual situation. (3) When the gas shouts into the water from the pipe, because of the smaller gas density, and the pipe is close to the left wall, the gas in the water will soon get close to the left wall and move up along the wall; The volume fraction of the gas will continue to increase due to the gas gathering on the wall, this is consistent with actual situation.

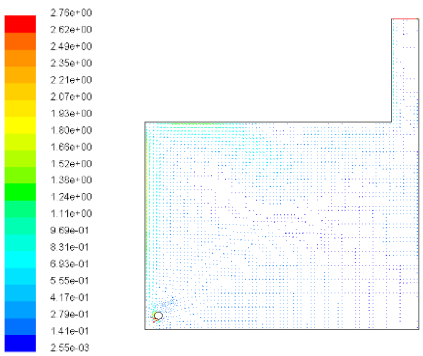

Fig.4 Velocity profile(m/s)

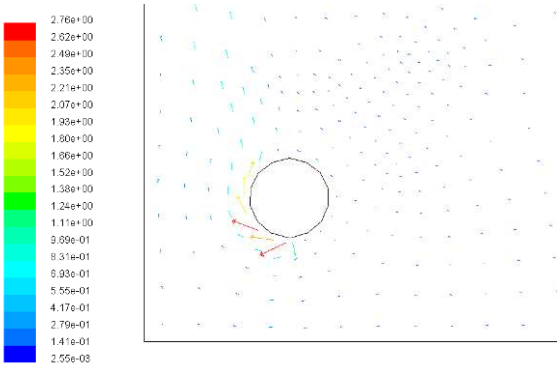

Fig.5 Enlarged drawing on outlet

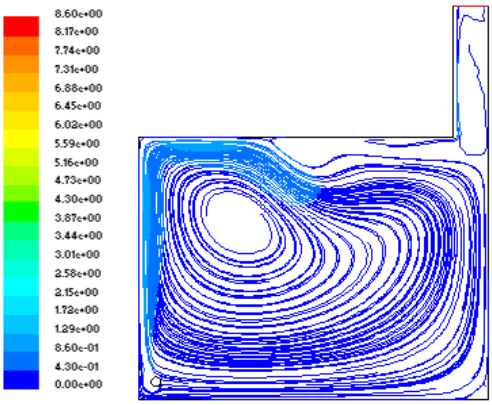

Fig.6 Path lines colored by velocity magnitude (m/s)

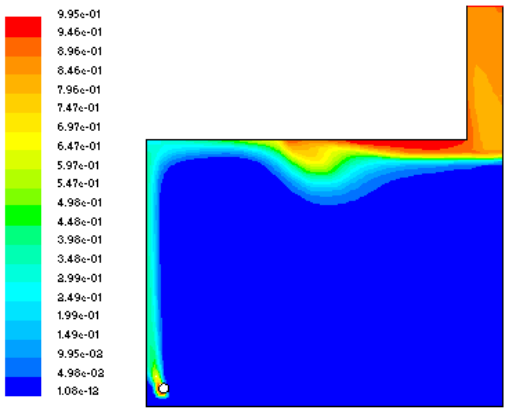

Fig.7 Contours of volume fraction of air

## The Conclusion

Aiming at the new questions that the treatment of the urban sewage and industrial wastewater, the micro-pressure inner loop reactor is put forward and built in this paper, under the action of aeration, the interior of the reactor is at the state of mixing cycle, that can form anaerobic, anoxic and aerobic zone respectively. The aeration problems of the micro-pressure inner loop reactor are simulated by the methods of the hybrid model of multiphase flow, which is based on computational fluid dynamics. The gas volume fraction, the velocity vector distribution and flow field which are acquired from the whole area, we can see that, the calculation result is in conformity with the actual situation. The numerical experiments show that, the micro-pressure inner loop reactor meet the water treatment requirements and it provides a theoretical basis for practical engineering equipment production.

## Acknowledgements

This work was financially supported by the National Natural Science Foundation of China (Grant No.51179011 ).

## References

[1] HU Lin-lin, WANG Jian-long, WEN Xiang-hua, etal, Improvements on Biological Nitrogen Removal Under Low Dissolved Oxygen Concentration, China Journal of Applied and Environmental Biology, 9(4). 444-447(2003)(In Chinese)

[2] WANG Jian-long, WANG Shu-ying, PENG Yong-zhen, etal, Simultaneous Nitrogen and Phosphorous Removal Under Low DO in a Hybrid Biological Reactor, Environmental Science, 29(3). 655-659(2008) (In Chinese)

[3] WANG Dong-bo, LI Xiao-ming, ZENG Guang-ming, etal, Simultaneous Nitrogen and Phosphorous Removal in the Reactor of Inner Loop SBR without Anaerobic Phase, Environmental Science, 28(3). 534-539(2007) (In Chinese)

[4] BIAN De-jun, REN Qing-kai, WAN Li-guo, Effects of Aeration Volume on Velocity Distribution of Fluid in Multi-Flora Biological Wastewater Treatment Reactor, Advanced Materials Research, 255.2740-2744(2011) (In Chinese)

[5] LIU Miao, CHEN Rui-yang, LI Guang-zhu, etal, Simulataneous Nitrogen Removal in the Micro-Pressurized Fluidized Hybrid Biological Reactor, Journal of Jilin University(Earth Science Edition), 42(3). 832-836(2012) (In Chinese)

[6] REN Qing-kai, LI Cheng-bing, LIU Jiang-chuan, etal, The CFD Numerical Simulation and Experimental Study on Micro-Pressure Internal Circulation Reactor, J. Changchun Inst. Tech. (Nat. Sci. Edi.), 14(4). 11-14(2013) (In Chinese)

[7] XU W, YU G, XUE C H, etal, Biochemical Changes Associated with Fast Fermentation of Squid Processing By-Products for Low Salt Fish Sauce, Food Chemistry, 107(4).1597-1604(2008) (In Chinese)

[8] XIAO Hao-fei, ZHOU Mei-hua, CFD Simulation of Gas-Liquid Flow in Aeration Tank, Journal of Anhui Agri. Sci. 38(4).1955-1958(2010) (In Chinese)

*Applied Mechanics and Materials Vols. 580-583 (2014) pp 2055-2062*
*© (2014) Trans Tech Publications, Switzerland*
*doi:10.4028/www.scientific.net/AMM.580-583.2055*

# Vibration Analysis and Human Comfort Evaluation of Underground Hydropower House

Dan Fu [1, a], Hegao Wu [1, b]

[1]State Key Laboratory of Water Resources and Hydropower Engineering Science, Wuhan University, Wuhan 430072, China

[a]303960788@qq.com, [b]wbf1988@vip.sina.com

**Keywords:** Hydraulic structure; main powerhouse; vibration; human comfort; pressure fluctuation; finite element method

**Abstract:** Human comfort is of great importance to main powerhouse and vibration level should be controlled below the human comfort limit. Comparison of ISO2631/1-1985 and ISO2631/1-1997 was performed firstly in this study. It points out that weighted root-mean-square acceleration is basic variable for vibration evaluation. The reduced comfort boundary of 2 hours (0.260m/s$^2$) in 1985 version is very close to the comfort threshold (0.315m/s$^2$) in 1997 version. Above two values were selected as human comfort standard in this paper. After that, 3D dynamic finite element model of HongPing pumped storage station was established and vibration analysis under pressure fluctuations was conducted using time history method. The calculation results indicated that vibration of generator floor was mainly caused by the multiples of runner blade number frequency. Vibration level of generator floor would not lead to human discomfort.

## Introduction

As a place to transform hydraulic energy to electric energy, structural vibration in hydropower house is unavoidable. Harmful results due to structural vibration can be summarized into three aspects: (a) Long-term severe vibration may lead to damage and fatigue in powerhouse's components which affects the normal usability and durability of structures. (b) Vibration is disadvantageous to the performance of electric equipments and instruments. (c) Operating personnel would feel uncomfortable in strong vibration condition which is also harmful to their health if accumulated working time is too long. In addition, if vibration leads to obvious human discomfort, vibration level may be considered as unacceptable even though it has no essential effect to structure and electronic equipment. Currently, insufficient importance has been attached to human comfort in vibration analysis and evaluation for hydropower house. Research on vibration evaluation method and standard has been unfortunately lagged behind. In fact, the work to study human ride comfort with literature [1-3] in public transport is very active.

In this paper, the new standard (ISO2631-1997) and the old version (ISO2631-1985) for human exposure to whole-body vibration were compared firstly. Vibration evaluation method applied to main powerhouse was proposed through above comparison. Based on the dynamic FE model of powerhouse structure of HongPing pumped storage station, vibration analysis under fluctuation pressure using dynamic time history method was performed. At last, vibration evaluation of main powerhouse was conducted using the stated evaluation method.

**ISO2631/1-1985 standard**

Vehicle, mechanical equipment and industrial activity can all make human body be exposed to vibration environment that affects human comfort and normal activity, even health and safety. Therefore, it is of great importance to scientifically evaluate the negative effects from whole-body vibration.

Based on sufficient research achievements about human whole-body vibration, ISO formulated the earliest vibration evaluation standard (ISO2631/1-1985). Now related evaluation literature for hydropower house in China are all put forward by referencing it [4-6]. This standard provides three kinds of vibration exposure boundaries: health and safety boundary, reduced work efficiency boundary and reduced comfort boundary. Evaluation methods include frequency spectrum method and frequency-weighed acceleration method which is stricter than the former in most cases. Only if the whole vibration energy focus on one octave, two methods are equivalent. When frequency spectrum method is taken, this standard provides a specific value of reduced comfort boundary corresponding to a certain vibration frequency *f* and period *T*. Health and safety boundary and reduced work efficiency boundary can be determined by multiplying the comfort value by 6.30 and 3.15 respectively. For the other method, ISO2631/1-1985 provides frequency weighting curves in three directions that are applicable to all evaluation contents and body postures. Weighted root-mean-square acceleration $a_{\mathrm{w}}$ can be calculated according to equation (1) or (2). Then $a_{\mathrm{w}}$ should be compared to the minimum value of reduced comfort boundary for the purpose of human body's comfort evaluation. The evaluation of health and safety or reduced work efficiency can be performed in the same way.

$$a_{\mathrm{w}} = [\frac{1}{\mathrm{T}}\int_0^{\mathrm{T}} a_{\mathrm{w}}^2(\mathrm{t})\mathrm{dt}]^{\frac{1}{2}} \tag{1}$$

$$a_w = [\sum(W_i a_i)^2]^{\frac{1}{2}} \tag{2}$$

Equation (1) is the form in time domain and $a_{\mathrm{w}}(\mathrm{t})$ is weighed acceleration as a function of time *t*. Equation (2) is the form in frequency domain and $\mathrm{W_i}$ and $a_{\mathrm{i}}$ are weighted factor and root-mean-square acceleration in the ith one-third octave respectively. ISO2631/1-1985 points out that if vibration amplitude in two or three directions are close, vector sum $a_{\mathrm{v}}$ of them should be calculated according to equation (3). Then the vector sum $a_{\mathrm{v}}$ should be compared to the minimum value of three kinds of boundaries in Z direction.

$$a_{\mathrm{v}} = \sqrt{\mathrm{k_x^2}a_{\mathrm{wx}}^2 + \mathrm{k_y^2}a_{\mathrm{wy}}^2 + \mathrm{k_z^2}a_{\mathrm{wz}}^2} \tag{3}$$

In equation (3), $k_x$, $k_y$ and $k_z$ are the directional factor. The evaluation standards according to IS2631/1-1985 are listed in Table 1 in which the numbers in bracket are vibration period. Considering that the possibility of accumulated vibration time of operating personnel surpassing 8 hours in main powerhouse is very low, so the reduced comfort standards corresponding to 2 hours are also presented in Table 1. The values of 8 hours are more suitable for central control room where operating personnel stays relatively long.

Table 1 ISO2631/1-1985 evaluation standard

| Boundary | Variable | Evaluation standard/(m/s$^2$) | |
|---|---|---|---|
| | | Vertical（Z） | Horizontal（X, Y） |
| Health and safety | $a_{\mathrm{wx}}, a_{wy}, a_{wz}$ | 0.63(8h), 1.07(4h) | 0.44(8h), 0.69(4h) |
| | $a_v$ | 0.63(8h), 1.07(4h) | |
| Reduced work efficiency | $a_{\mathrm{wx}}, a_{wy}, a_{wz}$ | 0.32(8h), 0.54(4h) | 0.22(8h), 0.35(4h) |
| | $a_v$ | 0.32(8h), 0.54(4h) | |
| Reduced comfort | $a_{\mathrm{wx}}, a_{wy}, a_{wz}$ | 0.10(8h), 0.26(2h) | 0.07(8h), 0.18(2h) |
| | $a_v$ | 0.10(8h), 0.26(2h) | |

**ISO2631/1-1997 standard**

ISO2631/1-1997 aims to evaluation of human exposure to whole-body vibration for four aspects: health, comfort, perception and motion sickness. Compared to 1985 version, the concept of reduced work efficiency due to vibration has been deleted. For evaluation method, weighted R.M.S acceleration $a_{\mathrm{w}}$ is specified as the basic variable with condition that crest factor is less than 9 and the frequency spectrum method has also been eliminated in 1997 version. If crest factor is greater than 9, additional evaluation methods including running R.M.S method or fourth power vibration dose method should be adopted. ISO2631/1-1997 provides six frequency weighting curves for different evaluation contents and body postures. The curves in three directions corresponding to original version have also been modified slightly. The biggest difference between two versions is that the concept of exposure period has been eliminated in 1997 version for human comfort evaluation. ISO2631/1-1997 suggests that there is no consequent relation between subjective comfort with vibration period. What's more, no exact reduced comfort boundary is presented because same vibration level may leads to different results for different persons. The actual feeling depends on many other factors (individual condition, activity type, etc.). New standard gives approximate indications of likely reactions to various magnitudes of overall vibration values in public transport. There are six sections with various feelings and Table 2 lists two of them. For hydropower house, it's basically reasonable to reference the vibration standards in 1997 version with the reason that in powerhouse and in public transport people can both tolerate some degree vibration. No reading and resting activities exist in powerhouse, so acceptable vibration level may be higher than that in public transport.

For human health evaluation, 1997 version points out the maximum of weighted R.M.S accelerations in three directions should be used as the evaluation variable. Vector sum $a_{\mathrm{v}}$ of directional weighted R.M.S accelerations should also be calculated as the evaluation variable if vibration magnitudes in different directions are close. In Table 2 eVDV is estimated vibration dose value which is used be the auxiliary variable. Similar to 1985 version, evaluation variable for human comfort is vector sum $a_{\mathrm{v}}$ of directional weighted R.M.S accelerations. The evaluation variable for perception is the maximum of weighted R.M.S accelerations (Max $\{a_{\mathrm{wx}}, a_{wy}, a_{wz}\}$) in three directions. Additional evaluation method is recommended if the condition of basic method is not met, but the standard does not give detailed information for additional method. Details summarized from ISO2631/1-1997 are given in Table 2.

Table 2 ISO2631/1-1997 evaluation standard

| Content | Variable | Standard/(m/s$^2$) | Period |
|---|---|---|---|
| Health | $a_v$ | 0.45～0.80 | 8 hours |
| | eVDV | 8.5～17/(m/s$^{1.75}$) | 8 hours |
| Comfort | $a_v$ | Less than 0.315 | not comfortable |
| | | 0.315～0.63 | a little uncomfortable |
| Perception | Max$\{a_{\mathrm{wx}}, a_{wy}, a_{wz}\}$ | 0.01～0.02 | 0.015 is median value |

For main powerhouse, making an attempt to limit structural vibration to be below perception level is not necessary and unpractical. Considering the low possibility of accumulated vibration time surpassing 8 hours in main powerhouse, recommended health limits listed in Table 1 and Table 2 can be amplified properly. In engineering practice, vibration level is likely assessed be unacceptable while it leads to human discomfort, thus the definition of human comfort is significant. However, there is no specific comfort standard for hydropower house in China. The practical experiences from pumped storage projects indicated that if vibration level can meet the reduced comfort boundary in ISO2631/1-1985, other else requirements can all be met for main powerhouse. However, related literature did not demonstrate the vibration period corresponding to above mentioned comfort boundary. Considering that 1985 version has been applied for a long time in China, this paper still takes it as a major reference. As stated before, vibration period *T* is an essential variable in 1985 version. The reduced comfort boundaries for 2 hours and 8 hours are respectively 0.26m/s$^2$ and 0.10m/s$^2$ in Table 1. For main powerhouse, adopting the value of 2 hours is more reasonable than that of 8 hours while the former is very close to the human comfort threshold 0.315 m/s$^2$ in 1997 version.

## Engineering project

### Calculation condition

Four reversible hydroelectric generating sets with 300MW unit capacity are installed in HongPing pumped storage station. Rated speed is500r/min and number of runner blades is 9. The form of one joint for one unit is taken in this station. This study established a 3D dynamic FE model for 2# main powerhouse and rock range the FE model contained equaled three times of the span of main powerhouse. Sketch map of 3D dynamic FE model is shown in Fig.1 and model of powerhouse is shown in Fig.2. Main powerhouse was concreted attaching to the excavation surface and joint bars were set between rock and structure, therefore in FE model elements of rock and structure shared the same nodes on boundary B. Viscous-elastic artificial boundary was set on boundary C to simulate the dynamic stiffness of infinite rock. Concrete grade of powerhouse is C25. Material of spiral case, stay ring and liner of draft tube and generator pit is steel. Material parameters adopted in this paper are listed in Table 3. In the global coordinate system of the model, Z-axis is vertical with the positive direction moving upward and Y-axis is horizontal with the positive direction along water direction, X-axis is horizontal, specifically perpendicular to Y-axis.

Table 3 Material parameters

| Material | Density/(kN/m$^3$) | Young's modulus/GPa | Poisson's ratio |
|---|---|---|---|
| Concrete(C25) | 25.0 | 28.0 | 0.167 |
| Steel | 78.5 | 210 | 0.30 |
| Rock | 27.0 | 10.0 | 0.23 |

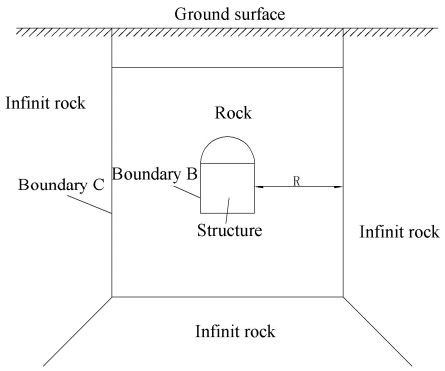


Fig.1 Dynamic model of underground powerhouse

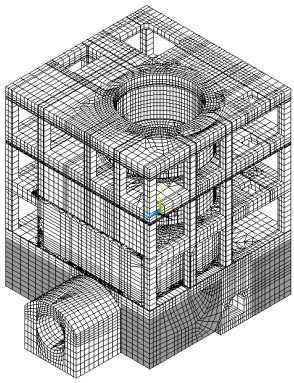

Fig.2 Finite element meshes for powerhouse structure

Model tests of hydraulic turbine were accomplished by turbine manufacturers. Pressure fluctuation tests under eleven different kinds of output conditions at maximum head 565m, rated head 540m and minimum head 520m were performed. For the measurements of the pressure fluctuations, dynamic pressure transducers were installed at the following locations: spiral case inlet, vaneless space, between head cover and runner crown, between bottom ring and runner band, draft tube cone and draft tube elbow. Sampling frequency is 4800Hz and sampling time is 10s.

In this paper, rated power at rated head was selected for vibration analysis of main powerhouse. Pressure fluctuation signals of model were transposed to prototype conditions by referencing literature [5]. Spectral characteristic of vaneless space point and draft tube cone point in prototype condition are shown in Fig.1 and Fig.2. As seen in two figures, dominant frequencies in vaneless space are runner blade number frequency and multiple frequencies of it. Dominant frequencies of draft tube cone are 66Hz and the rated rotation frequency 8.33Hz. Characteristic amplitude of pressure fluctuation in draft tube is significantly less than that in vaneless space.

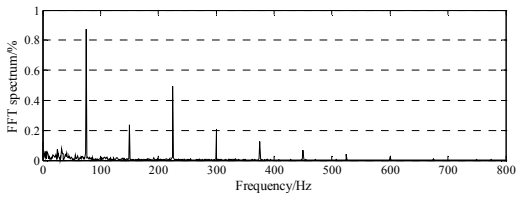


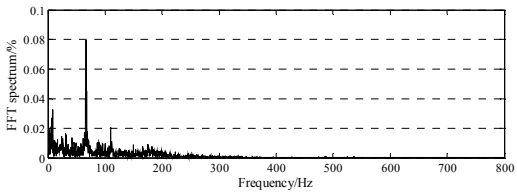


Fig.3 Pressure fluctuation FFT spectrum in vaneless space Fig.4 Pressure fluctuation FFT spectrum in draft tube cone

**Vibration analysis and evaluation of generator floor**

Root-mean-square of vertical acceleration (RMSVA) of generator floor is shown in Fig.5. Vector sum of root-mean-square of accelerations (VSRMS) in three directions is shown in Fig.6. The difference between two figures occurs at stair hole where RMSVA is 0.1m/s$^2$ and VSRMS is 0.3m/s$^2$. It indicates that at stair hole horizontal acceleration is relatively big. RMSVA and VSRMS

are almost at the same level in the rest region of generator floor, it demonstrates vertical acceleration is the major component. The maximum value of VSRMS locates at bottom right corner and the value of this point is 0.825m/s$^2$. This point is selected as the vibration feature point of generator floor.

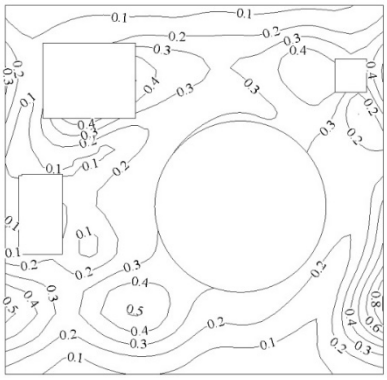

Fig.5 R.M.S of vertical acceleration of generator floor（m/s$^2$）

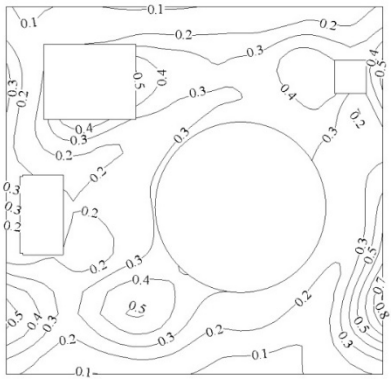

Fig.6 Vector sum of R.M.S of accelerations（m/s$^2$）

Feature point's vibration time history signal and FFT spectrum in three directions are shown in Fig.7~Fig.12. The initial 1s or 1.5s of time history signal is captured out for showing. From these figures we know, peak acceleration in X direction is below 0.2m/s$^2$ and the dominant frequencies includes 75Hz, 150Hz and 225Hz corresponding to runner blade number frequency, double and triple of it. Peak acceleration in Y direction is below 0.3m/s$^2$ and dominant frequencies are similar to that of X direction, but FFT spectrum of 150Hz and 225Hz in Y direction is bigger than that in X direction. Peak acceleration in Z direction is 1.588m/s$^2$ and the dominant frequency is 75Hz while the pressure fluctuation of 66Hz in draft tube has a little contribution to feature point's vibration response. Above statements indicate that vibration of generator floor is mainly caused by pressure fluctuation in vaneless space, dangerous frequencies for generator floor are multiples of runner blade number frequency.

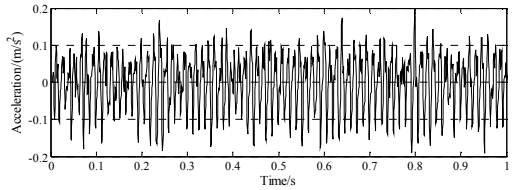


Fig.7 Acceleration time history in X direction

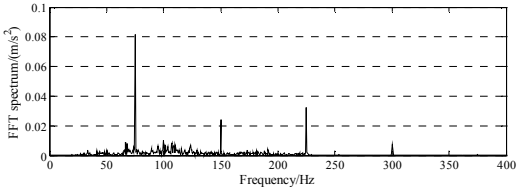


Fig.8 Acceleration FFT spectrum in X direction

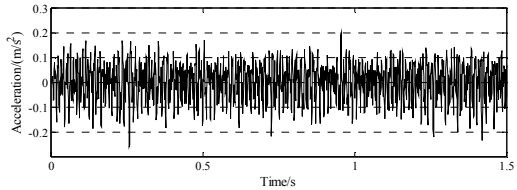


Fig.9 Acceleration time history in Y direction

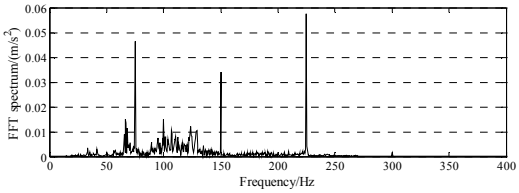


Fig.10 Acceleration FFT spectrum in Y direction

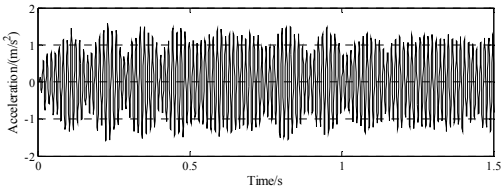


Fig.11 Acceleration time history in Z direction

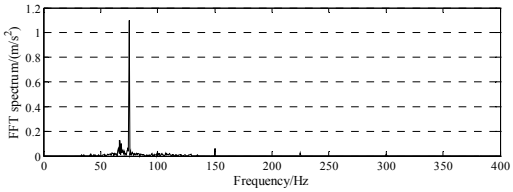


Fig.12 Acceleration FFT spectrum in Z direction

Table 4 Feature Point's vibration evaluation parameters

| Evaluation variable | Direction | | | Vector sum |
|---|---|---|---|---|
| | X | Y | Z | |
| Root-mean-square of acceleration /(m/s$^2$) | 0.0731 | 0.0738 | 0.8195 | 0.8260 |
| Weighted root-mean-square of acceleration /(m/s$^2$) | 0.0016 | 0.0012 | 0.1226 | 0.1226 |
| Crest factor | 2.73 | 3.56 | 1.94 | |

Feature point's root-mean-square of acceleration and weighted root-mean-square of acceleration in three directions are listed in Table 4. In addition, crest factors in three directions are also listed. Frequency curves used in calculation are from ISO2631-1997 and the calculation is performed by MATLAB. Power spectrum of acceleration signal is calculated in the first step, then weighted root-mean-square value is carried out according to equation (4) which is equivalent to equation (2). In equation (4), $P_i$ is power spectrum density of the ith octave.

$$a_{\mathrm{w}} = [\sum w_i^2 P_i \Delta f]^{\frac{1}{2}} \quad (4)$$

As listed in Table 4, feature point's crest factors in three directions are all less than 4, so basic evaluation method in ISO2631-1997 is feasible. Taking no account of frequency weighting, vector sum of root-mean-square of three directional accelerations (VSRMS) is 0.8260m/s$^2$ which exceeds reduced comfort boundary of 2 hours (0.260m/s$^2$) in ISO2631-1985 and comfort threshold (0.315m/s$^2$) in ISO2631-1997. It even exceeds health evaluation standard of 8 hours in both standards. But if frequency weighting is considered, vector sum of weighted root-mean-square accelerations in three directions is 0.1226m/s$^2$ which exceeds perception threshold (0.01m/s$^2$~ 0.02m/s$^2$) but is less than reduced comfort boundary of 2 hours in ISO2631-1985 and comfort threshold in ISO2631-1997. It indicates that under rated power at rated head, human would feel obvious vibration but vibration level would not lead to human discomfort. Vibration of generator floor is acceptable in the view of human body comfort.

**Summary**

Weighted root-mean-square acceleration should be used as basic evaluation variable. Additional evaluation method should be taken if crest factor of vibration acceleration signal exceeds nine. For main powerhouse, vibration level should be controlled under the human comfort limit. ISO2631/1-1985 contains vibration period concept and the comfort boundary of 8 hours is some stricter for main powerhouse. In fact, the comfort boundary of 2 hours (0.260 m/s$^2$) is close to the comfort threshold (0.315m/s$^2$) in ISO2631/1-1997. Above two values are selected as human comfort standard in this paper.

Vibration analysis of HongPing main powerhouse indicated that vibration of generator floor is mainly caused by the multiples of runner blade number frequency. Evaluation results showed that vibration level of generator floor would not lead to human discomfort. At last, we must realize that it is necessary to formulate a specialized standard for human exposure in hydropower station because of main powerhouse's particularity.

**References：**

[1] International Standard Organization. ISO 2631-1-1985 Evaluation of human exposure to whole-body vibration, Part1: General requirements[S]. ISO, 1985.

[2] International Standard Organization. ISO 2631-1-1997 Mechanical vibration and shock evaluation of human exposure to whole-body vibration, Part 1: General requirements[S]. ISO, 1997.

[3] British Standards Institution. BS 6841-1987 British standard guide to measurement and evaluation of human exposure to whole-body mechanical vibration and repeated shock[S]. BSI, 1987.

[4] SONG Zhiqiang, MA Zhenyue, CHEN Jing, et al. Dynamic analysis on powerhouse of Longtousi Hydropower Station [J]. Journal of Hydraulic Engineering, 2008, 39(8):916-921.

[5] XING Xianglin, CHENJiankang, LIAO Chenggang, et al. Vibration response of large underground powerhouse [J]. Journal of Vibration and Shock, 2013, 32(9):21-27.

[6] CHENJing, MA Zhenyue, LIU Zhiming, et al. Dynamic analysis of Three Gorges hydropower house [J]. Journal of Hydroelectric Engineering, 2004, 23(5): 36-39, 21.

*Applied Mechanics and Materials Vols. 580-583 (2014) pp 2063-2070*
*© (2014) Trans Tech Publications, Switzerland*
*doi:10.4028/www.scientific.net/AMM.580-583.2063*

# Working Performance of Anti-Arch Segments on the Left Bank Slope of Xiangjiaba Gravity Dam

ZHOU Qiujing[1, a], GAO Peng[2, b], GONG Zhaoguang[2, c] AND Li Haifeng[1, d]

[1]Department of Structures and Materials, China Institute of Water Resources and Hydropower Research, Beijing 100038, China

[2] Xiangjiaba Project Construction Department, China Three Gorges Corporation, Sichuan Yibin 644625, China

[a]zhouqj@iwhr.com, [b]10177559@qq.com, [c] 158164518@qq.com, [d] lihfdlut@126.com

**Keywords:** Gravity dam, Anti-arch dam segment, Working performance, Deformation, Stress.

**Abstract.** The working performance of a gravity dam with an anti-arch shape differs from that of conventional gravity dams. To understand the working performance of the anti-arch segments on the bank slope of Xiangjiaba dam, linear and non-linear finite element methods were used to analyze the deformation, stress, the state of transverse joints, and cracks during operation. The anti-sliding stability coefficient of each dam segment and the safety degree of the dam were also calculated. Results show that under non-grouting of transverse joints and well grouting of cracks, deformation rules are consistent in all investigated segments and are in accord with those of conventional gravity dams. The dam heel and dam toe are subjected to compressive stress. During cold seasons, a tensile stress region is observed on top of the dam body, wherein tensile stress is smaller than tensile strength. Transverse joints are opened, whereas cracks are generally stable and closed under compression. The anti-sliding stability coefficient and safety degree of each dam segment are above 3.0, which satisfies the design code.

## Introduction

A gravity dam, which is one of the most important dam types, typically has a linear layout. Such dam maintains stability and satisfies the strength requirement through its dead weight. In some special cases wherein topographical or geological constraints are salient, a broken-line or curved-line layout is observed. For example, Danjiangkou Dam [1] and Xiangjiaba Gravity Dam [2] have a counter-arched shape in several segments. Force distribution varies with the specific layout of a dam, thus further influencing the working performance of a dam [3]. Based on monitoring data and research results [4], the following situations may occur when Danjiangkou Dam has no transverse joint or has an extremely narrow transverse joint. 1) Deformation. The counter-arched segments tend to deform downstream during summer and upstream during winter. The displacement of the dam top exhibits a contrary annual variation trend compared with a linear-type dam segment. The deformation value is closely related to the joint configuration. 2) Stress. The water level is generally high during summer. Moreover, the dam body exhibits a downstream deformation under high temperature. The superposition of these two effects tends to aggravate dam heel stress. When the water level is low during winter and the dam body exhibits an upstream deformation, dam toe stress deteriorates. Hence, the kerf concept is adopted during later stages. 3) Transverse joint. The state of the transverse joint varies with joint width, grouting elevation, and bedrock, thereby influencing the deformation and stress of the dam; 4) Stability. The anti-sliding stability of a counter-arched dam segment also differs from that of a conventional gravity dam. Under the same hydraulic thrust, large dam body results in high anti-sliding coefficient. Based on these situations, the working performance of the counter-arched segment obviously differs from that of a conventional gravity dam. Information on various aspects of gravity dams with a linear layout is abundant. However, counter-arched gravity dams have not been intensively studied. Existing literature has focused on the qualitative analysis of monitoring data and on the partial stress analysis of dam heels, which affects judgment of the overall safety of the project.

The Xiangjiaba Hydraulic Power Station is located between Yibin County in Sichuan Province and Shuifu County in Yunnan Province. This gravity dam has a maximum height of 162 m. The slope dam segments on the left bank, which consist of 12 pieces, have a total length of 199.92 m. The highest section of the dam is 122 m. The six dam segments from left segment 7 to 12 along the riverbed are arranged in an arch shape on the plane view, with the sum of the central arc angle being 54°. The six dam segments from left segment 13 to 18 along the slope are arranged in a linear pattern. Figure 1 shows the layout of the slope dam segments, and Figure 2 shows the cross-sectional view of a typical dam. The left segments exhibit the following features. 1) The slope dam segments on the left bank are counter-arched, thus making them significantly different from conventional gravity dams. 2) The base elevation and height of different segments differ significantly, which influences dam working performance. 3) The dam heel is close to the free face of the foundation, which is not completely stable. 4) Several cracks appear on the dam during construction. These cracks may affect structural integrity to certain extent. Based on these features, conducting an in-depth analysis on the left segments of Xiangjiaba Dam is necessary to further understand the working performance of the dam, including deformation, stress, anti-sliding stability and safety degree. This work provides technical support for dam operation and subsequent engineering designs.

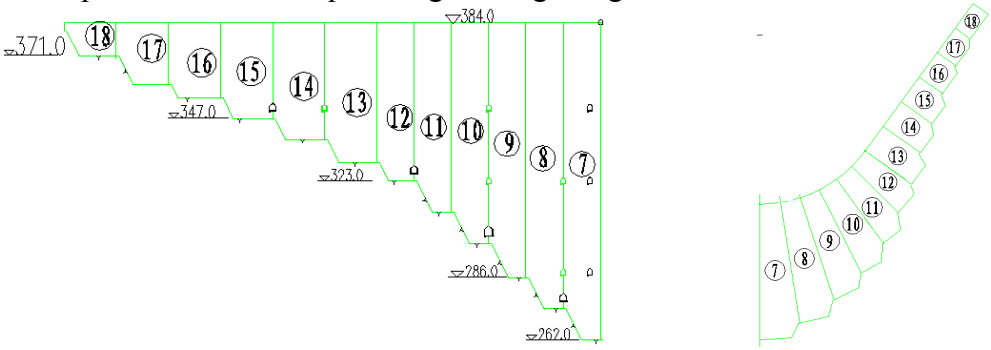


Fig. 1 Layout of the left segments on the slope of Xiangjiaba Dam

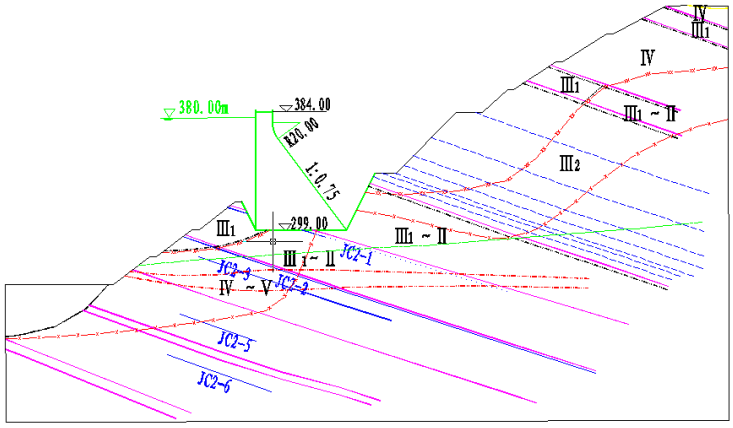


Fig. 2 Cross-sectional view of the dam

## Analysis method and model

**2.1 Analysis method.** Normal working performance is calculated via linear elastic finite element analysis [5]. The dead weight of the dam body, hydrostatic pressure, silt pressure and temperature load are considered. Temperature load is calculated with the following method [6]. The mean temperature of the dam site over the years is taken as the initial temperature of the dam body and the bedrock. The monthly mean air temperature over the years is taken as the boundary condition to calculate the temperature fields of the dam body and the foundation in the future years. The temperature field in October which is close to the annual mean temperature is used as the initial temperature field. The quasi-steady temperature fields of the dam body and the bedrock after several years of impoundment

are obtained by considering boundary conditions such as air temperature and reservoir water temperature. The differences in the temperature field during winter (January) and summer (July) relative to the temperature field in October are considered as temperature drop and temperature rise loads, respectively.

Anti-sliding stability is calculated by using the material mechanics analysis method specified in the design code [7]. The safety degree of the dam body is obtained through non-linear finite element analysis [8]. The Durcker-Prager yield criterion is adopted for the bedrock, whereas the Mohr-Coulomb yield criterion is adopted for the dam concrete and the weak intercalated layer. The model is assumed as an ideal elastic-plastic model.

Transverse joints and cracks are simulated as contact elements. Three states are involved in the calculation, namely, opened, in contact and bonded (the state after grouting). There is no transmission of force when a joint or crack is opened. The contact state enables a transmission of compressive and shears forces with certain values. The bonded state allows withstanding tensile, compressive and shears forces. Once the bonding element yields under tension, the stress acting on the element is adjusted. Then, tensile stress shifts to adjacent elements. Under the compressive-shear state, an element yields and softens when the shear stress exceeds shear strength. Cohesive force also disappears. The element can only withstand friction. The excess part of stress shifts to the adjacent element. After adjusting the stress on the element, the yield criterion for the element under stress is rejudged until the judgment is completed for all contact elements. All finite element analyses are performed by Saptis software for multi-field simulation and non-linear analysis. This software was developed by the Department of Structure and Materials, China Institute of Water Resources and Hydropower Research [9, 10].

**2.2 The model.** According to topographical and geological conditions, dam body structure and material zoning, a calculation model that can objectively and accurately simulate the dam structures and geological structures is established. The model involves the concrete and bedrock zones, weak intercalated layer of dam foundation, dominant joints, compressive rupture zones, transverse joints, cracks, and main corridors. The model has 364,283 nodes and 413,343 elements, as shown in Figure 3.

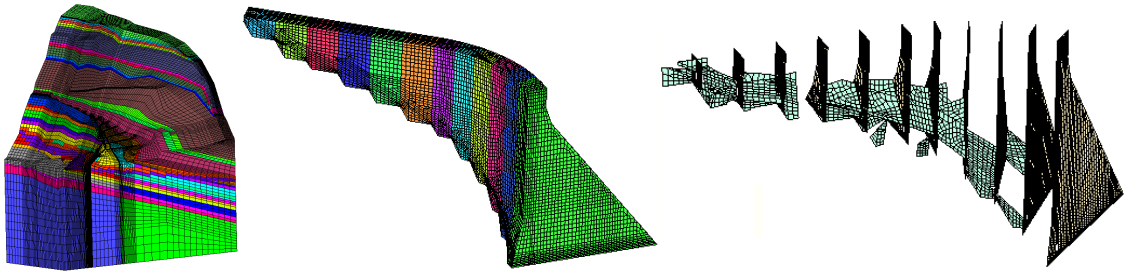

a. Foundation b. Dam c. Transverse joints and cracks

Fig. 3 The model

## Working performance

**3.1 Temperature.** After impoundment, the dam gradually achieves the quasi-steady temperature field under the joint actions of earth temperature, air temperature and water temperature. After 30 years of impoundment, the temperature field of the structure under the normal water level is shown in Figure 4. Meanwhile, Figure 5 shows the temperature variation curves at different elevation points. Based on these figures, the temperatures of the underground portion of the upstream face and the interior of the dam remain basically unchanged. Meanwhile, the temperature of the downstream face and the top section change periodically with air temperature. The lowest and highest temperatures are 7℃ and 26.5℃, respectively.

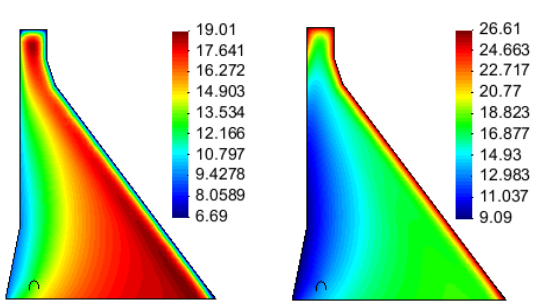


Winter Summer

Fig. 4 Temperature field of the dam

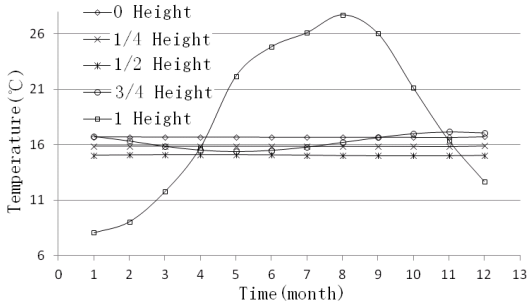


Fig. 6 Temperature curve of different heights

**3.2Deformation.**In calculation, the cracks are considered well grouted and its strength is equal to the test result, while the transverse joints are not grouted. The radial and tangential displacements of the midpoints of the upstream face at the top of dam segments for typical water levels at different seasons are obtained, as shown in Table 1. The radial deformations of all dam segments point downstream, while the tangential deformation points toward the middle of the riverbed. Therefore, the structure generally exhibits deformations downstream and toward the middle of the riverbed. Temperature change has a significant effect on dam deformation. The temperature of the upstream face is constant under the influence of the water temperature of the reservoir. By contrast, the downstream face has a fluctuating temperature because of the influence of air temperature. Therefore, the downstream face contracts during winter. Moreover, the dam basically exhibits downstream deformation. During summer, the downstream face expands and the dam exhibits upstream deformation. The non-grouting of transverse joints illustrates that the deformation of the dam segments is similar to that of conventional dams, and that no adverse effect is posed on the dam.

Table 1 Radial and tangential deformations of the dam under different working conditions (mm)

| Deformation | Working conditions | Left 7# | Left 8# | Left 9# | Left 10# | Left 11# | Left 12# |
|---|---|---|---|---|---|---|---|
| Radial | Normal water level + winter | 25.97 | 25.73 | 24.29 | 21.72 | 14.53 | 12.34 |
| | Normal water level + summer | 20.95 | 20.55 | 19.15 | 16.77 | 9.59 | 7.56 |
| | Dead water level + winter | 17.9 | 17.28 | 16.08 | 14.29 | 8.49 | 6.56 |
| Tangential | Normal water level + winter | 13.02 | 12.31 | 11.26 | 9.87 | 9.71 | 8.64 |
| | Normal water level + summer | 10.86 | 10.45 | 9.69 | 8.6 | 6.31 | 5.13 |
| | Dead water level + winter | 10.41 | 9.59 | 8.62 | 7.45 | 5.62 | 4.09 |

**3.3 Stress.** The vertical stress of the dam heel and dam toe on each dam segment according to the results of the finite element analysis is shown in Table 2. Under the action of dead weight, hydraulic pressure, silt pressure, slag pressure at the back and temperature, the dam heel and the dam toe are in a compressive state. The magnitude of the compressive stress on the dam heel and the dam toe is related to the height of the dam segment, upstream water level and temperature. The stress generally increases with increasing dam height. At high water level and low air temperature, the compressive stress of dam heel decreases. At low water level and high air temperature, the compressive stress of the dam toe decreases.

Figure 6 shows the stress nephograms of the upstream and downstream faces of the dam at different seasons and water levels. The dark color indicates the tensile stress region. When temperature is low during winter, a tensile stress region is observed above the water level of the upstream face and downstream face. Tensile stress is smaller (typically less than 0.3 MPa) at low water levels. In some sites, tensile stress is 0.3MPa - 0.6 MPa, which falls within the allowable range of concrete tensile strength. When temperature is high during summer, nearly no tensile stress is observed to affect the overall safety of the structure.

Table 2 Vertical stress on the dam heel and the dam toe (MPa, negative is compressive)

| Dam segment | Dam heel | | | Dam toe | | |
|---|---|---|---|---|---|---|
| | Normal water level + winter | Normal water level + summer | Dead water level + winter | Normal water level + winter | Normal water level + summer | Dead water level + winter |
| 12# | -0.58 | -0.96 | -1.38 | -1.75 | -2.13 | -1.3 |
| 11# | -1.36 | -1.69 | -2.1 | -1.09 | -1.82 | -0.83 |
| 10# | -0.61 | -0.84 | -1.29 | -1.26 | -2.13 | -0.92 |
| 9# | -1.47 | -1.64 | -2.08 | -1.9 | -2.61 | -1.46 |
| 8# | -1.54 | -1.73 | -2.31 | -2.03 | -2.82 | -1.64 |
| 7# | -2.35 | -2.4 | -2.69 | -2.14 | -2.67 | -1.86 |

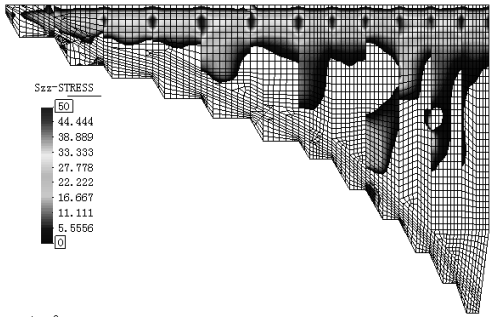


Normal water level + winter upstream

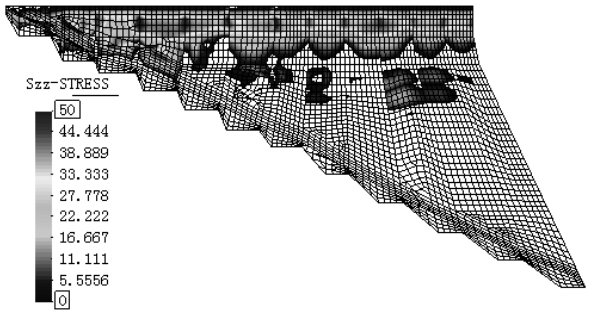


Normal water level + winter downstream

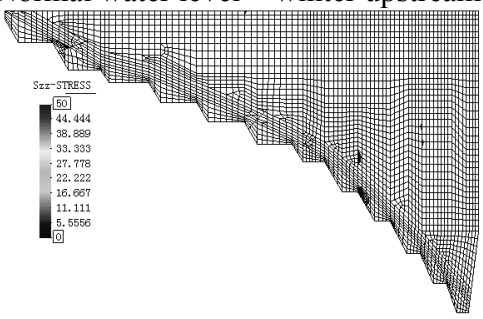


Normal water level + summer upstream

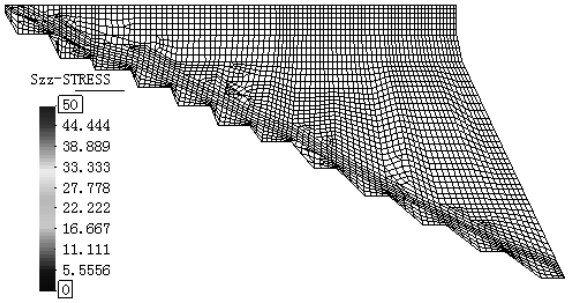


Normal water level + summer downstream

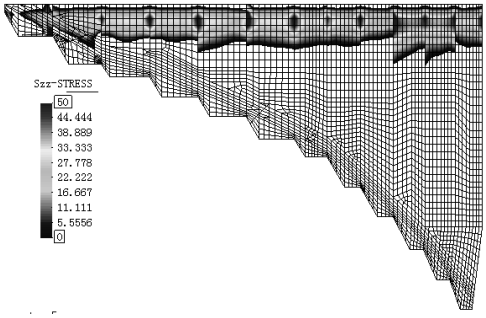


Dead water level + winter upstream

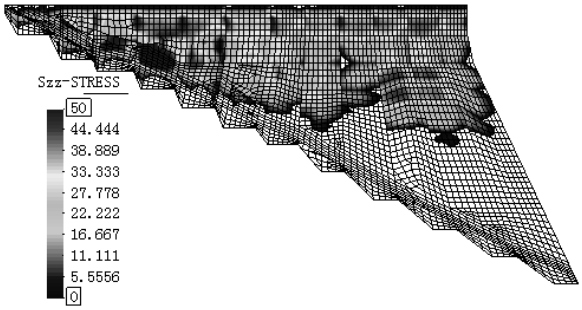


Dead water level + winter downstream

Fig. 6 Stress nephograms at different seasons and water levels (0.01MPa)

**3.4 State of transverse joints and cracks.** After impoundment, upstream hydrostatic pressure radially acts on the upstream face of the dam segment. Segments left 7 to 12 are arranged in a counter-arched shape. Thus, there is the trend of disintegration and deformation. Transverse joints are generally opened without contact. Each dam segment withstands load independently, which is consistent with the deformation rule of conventional dams.

The cracks of the dam are mainly distributed in the upstream curtain grouting corridor, as well as scattered in the transverse joint corridor and several drainage galleries. Most cracks run parallel to the dam axis or form a small angle with the dam axis. Therefore, the cracks are subjected to compressive stress under normal water loads and a tensile region does not exist. The magnitude of normal stress varies regularly. Compressive stress gradually decreases from left to right and from low to high elevation. The distribution pattern of shear stress resembles that of normal stress. Shear stress gradually decreases from right to left and from low to high elevation. The magnitude of shear stress also decreases from the downstream to the upstream face. Compressive stress is generally below 2.0 MPa, or above 4.0 MPa in some positions. Shear stress is mostly smaller than 0.7 MPa in cracks on the upstream face, whereas the maximum shear stress of the downstream face is below 1.8MPa. Shear stress of the cracks on the corridor is less than 1.4 MPa. In Calculating strength after grouting, the friction coefficient of 0.75 and the cohesive force of 0.60 MPa are used for analysis. Cracks are generally in a bonded state after grouting. Except for some elements that yield at the cracks on the corridors of left segments 9, 10 and 18 corridors, as well as those on the upstream face of left segment 12 and 13, all other elements are in a bonded state. Thus, cracks are generally stable.

## Safety analyses

**4.1 Anti-sliding stability.** Checking calculation is performed via the using material mechanics method for each left segment. Table 3 shows the anti-shear and anti-sliding stability coefficients at the foundation plane of each dam segment. Under the existing load and other parameters, the anti-sliding stability coefficients of the foundation plane of each left non-overflowing segment are above 3.0. Load increases and stability coefficient decreases with increasing dam height. The counter-arched segments from left segment 7 to 11 have anti-sliding stability coefficients larger than 3.0. The stability coefficients of the dam segments beyond left segment 12 are large and satisfy the design code requirements.

Table 3 Anti-sliding stability coefficients

| No. of dam segment | Bottom elevation | Anti-sliding stability coefficient | No. of dam segment | Bottom elevation | Anti-sliding stability coefficient |
|---|---|---|---|---|---|
| 7# | 262m | 3.44 | 13# | 330m | 4.53 |
| 8# | 274m | 3.06 | 14# | 339m | 5.62 |
| 9# | 286m | 3.1 | 15# | 347m | 8.4 |
| 10# | 299m | 3.14 | 16# | 355m | 9.12 |
| 11# | 311m | 3.53 | 17# | 360m | 11.64 |
| 12# | 323m | 4.06 | 18# | 371m | 48.23 |

**4.2 Safety degree.** Safety degree analysis is performed via the overloading method. Therefore, the upstream water level is regarded as the normal water level. Then the unit weight of water is constantly increased for non-linear calculations. According to the overload coefficient $\lambda$, the ratio of the calculated unit weight of water to the actual unit weight is used to evaluate the overall safety of the arch dam. The non-convergence of calculation is considered as final safety degree [11]. Two models are used for the calculation: the single dam segment model and the overall model. In the former, only one dam segment is considered, and its interaction with other dam segments is ignored. Therefore, the overload capacity varies from one dam segment to another. In the latter, contact with other dam

segments at the site of transverse joints is observed. Such contacts lead to interactions. If calculation is impeded by the low overload capacity of a particular dam segment, then calculation cannot be done for other dam segments either.

Figure 7 shows the deformation curves of each dam segment in the single dam segment and overall model. Figure 8 shows the yielding process of a typical dam segment. It is obvious that the deformation of the dam and the yielding degree increase with increasing overload. Deformation at the early stage increases linearly, and the overall structure is in an elastic state. Deformation mutation occurs at later stage. This phenomenon happens earlier at higher sections of the dam segments than at lower sections. The deformation increases rapidly, and so does the yielding degree. The overall structure is in the plastic stage. The deformation increases rapidly at constant load or increasing load. The structure is on the verge of total failure. The calculation results from single dam segment model and overall model are inconsistent. The result varies for each dam segment in the single dam segment model. However, the result from the overall model depends on the dam segment with the lowest safety degree. In addition, the interaction between the dam bodies also influences the calculation result, and not to the extent of affecting the final safety evaluation. The safety degree calculated by the overall model is 3.8. The lowest safety degrees (3.4) are obtained for the left segment 7 and 8 in the single dam segment model. The safety degrees from left segment 9 to 15 are in the range of 3.8 to 7.8. The safety degrees of left segment 16 to 18 exceed 8.0, which are the highest among all dam segments.

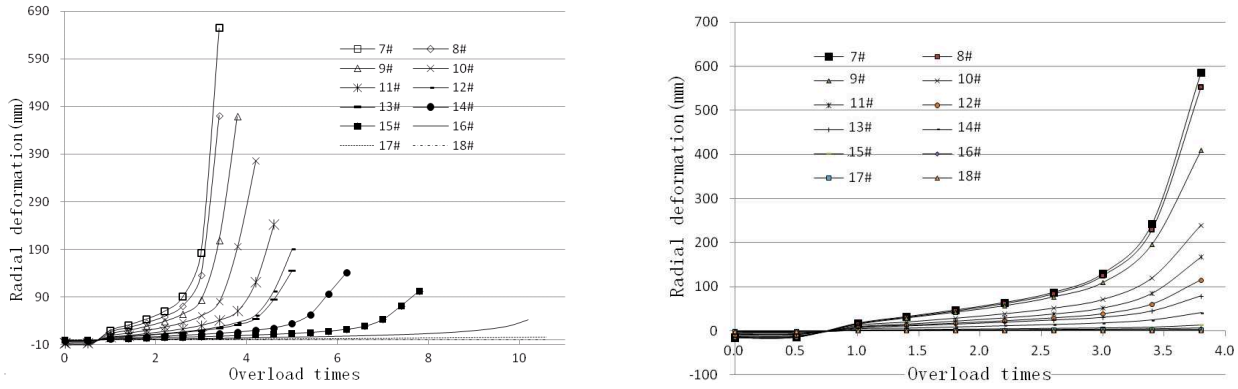


Fig. 7 Maximum deformation curves of each dam segment under different overload times

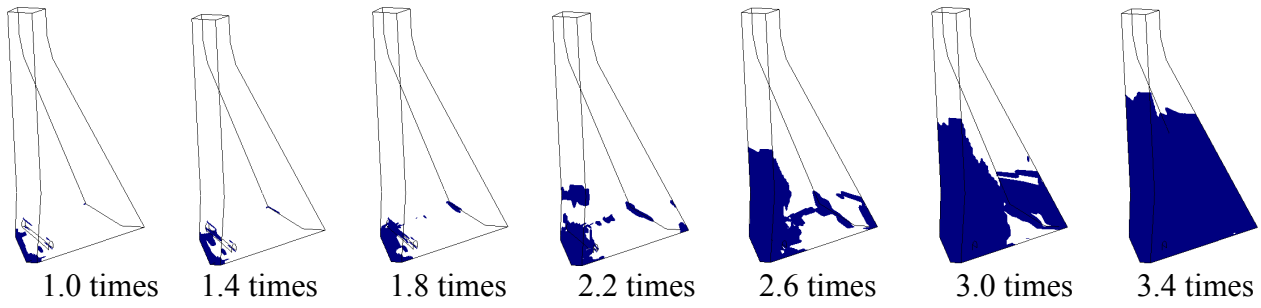


Fig.10 Yielding process of typical dam segments under different overload times (dark color: yielding)

## Conclusion

The left segments (7 to 12) on the slope of Xiangjiaba Gravity Dam with a counter-arched shape were analyzed in detail to assess the working performance of the dam. The results include dam temperature, deformation, stress, state of transverse joints, cracks, coefficient of anti-sliding stability, and safety degree. The results show,

With proper arrangement, the transverse joints of counter-arched dam segments are all opened after normal impoundment. Moreover, these joints are basically dependent on each other. Deformation, stress distribution and change rule are consistent with those for conventional gravity

dams, and no adverse effect is produced. The dam heel and the dam toe are subjected to compressive stress in each left segment. During cold seasons, a tensile region is observed on top of the dam. However, tensile stress is generally below 0.3MPa. The maximum tensile stress is approximately 0.6MPa, which is smaller than the tensile strength of concrete.

Grouting of the cracks in the dam is performed. Base on the analysis at 0.75 friction coefficient and 0.6MPa cohesive force, the cracks are generally in a compressive state. Except for local yielding at the base of cracks in several dam segments, cracks are mostly stable.

The anti-sliding stability coefficients and safety degrees of each dam segment are above 3.0, which satisfy the design code requirements.

**References**

[1] Maixing, L. D. J. Construction Technology of Heightening Project of Danjiangkou Dam for the South-to-north Water Transfer Project. Water Power, Vol.3 (2008), p.20.

[2] Feng Shurong. General layout of Xiangjiaba Hydropower Project.Water Power, Vol, 2 (1998), p, 13.

[3] Zhou Qiujing,Yang Bo,Lian Chengzhi,etl. Influence of transverse joint grouting on working performance of xiangjiaba slope anti-arch dam blocks. Water Resources and Power, Vol, 2(2012), p, 89.

[4] Cui Jianhua,Gong Yaqi,Xiao Hanjiang. The Effect of Joint-Cutting on Turning Dam Section at the Right Bank of Danjiangkou Dam. JOURNAL of Yangtze River Scientific Research Institute,Vol,4(2011),p,49.

[5] Bofang, Zhu: *Principle and application of finite-element method*(Press of Water Conservancy and Hydropower, China 1998).

[6] Bofang, Zhu: *Temperature Stress and Temperature Control of Mass Concrete*(China Electric Power Press, China 1999).

[7] Chinese Design Code :*Design specification for concrete gravity dams*(Press of Water Conservancy and Hydropower, China 2005).

[8] Zhang Guoxin,Liu Yi,Zhou Qiujing.Study on real working performance and overload safty of high arch dam.Science in China Series E-Technological Sciences,Vol,51(2008),p,48.

[9] Zhang, G. Development and application of SAPTIS-a software of multi-field simulation and nonlinear analysis of complex structures (Part I). Water Resources and Hydropower Engineering, Vol.1(2013),p,31.

[10] Zhou Qiujing,Zhang Guoxin.Development and application of SAPTIS-software of multi-field simulation and nonlinear analysis of complex structures(Part II). Water Resources and Hydropower Engineering, Vol.9 (2013), p, 39.

[11] Bofang, Zhu., Chaoran, Zhang:*Research on the Structural Safety of High Concrete Arch Dams*(China Water Power Press, 2010).

*Applied Mechanics and Materials Vols. 580-583 (2014) pp 2071-2073*
*© (2014) Trans Tech Publications, Switzerland*
*doi:10.4028/www.scientific.net/AMM.580-583.2071*

# Main engineering geological problems and evaluation on the reservoir engineering of Yellow River water diversion and irrigation area

Zhiquan HUANG [1,a], Tailin CHEN [2,b], Anming WANG [1,c]

[1]North China University of Water Conservancy and Electric Power, Zhengzhou 450011,China

[2]Henan Vocational College of Water Conservancy and Environment, Zhengzhou 450011, China

[a]huangzhiquan@ncwu.edu.cn, [b]talent29@163.com, [c]463077840@qq.com

**Key words:** leakage of reservoir area; bank stability; Yellow River water diversion and irrigation; saline; seismic liquefaction

**Abstract:** Engineering geology survey was carried out on the reservoir engineering of Yellow River water diversion and irrigation area, main engineering geology problem including leakage problem of reservoir area, shore stable and siltation problem around the reservoir, siltation problem of storehouse district, connected the river course and the pilot, water leakage river course, earthquake liquefication and immerse and salinification were analyzed and appraised, the corresponding project measure was proposed against the infiltrates of the storehouse district.

## Engineering Survey

A Yinhuang irrigation reservoir engineering is 6.15km from East to West, and 1.10km from north to south. The planning area is 3.20 $km^2$, which is divided into east reservoir and west reservoir. The reservoir is the plain reservoir formed by artificial excavation. The ground elevation is 51.50 ~ 51.80m. The planning water area is 3.51 $km^2$, lead, with water channel surface area of 0.26 $km^2$. The normal water level of the reservoir is 51.00m; the maximum water depth is 6.00m. Reservoir strata structure is the type of adhering sand multilayer structure. There is the horizontal leakage problem after impoundment of reservoir. This paper makes analysis and evaluation of the main engineering geological problems for the irrigation reservoir project area.

## Geological Survey

The site is located in the North China Plain. The geomorphic units belong to Yellow River alluvial plain, with flat terrain. The west is slightly higher than the east, with local residual sand dune. Reservoir formation is mainly composed of Quaternary Holocene (Q4) and the upper Pleistocene (Q3) alluvial sandy loam, silty sand clamp, heavy silt loam and silt clay strata. The reservoir distribution features are as follows. The upper strata is composed by the first layer of sandy loam, the second layer of silt loam silty sand, and the third layer of silty sand and sandy loam, which is excavation layer for reservoir formation. The thickness of the first layer of sandy loam is 3.7 ~ 7.5m, with uneven soil. The thickness of the second layer is 0.3 ~ 4.2m. The third layer of silt sand and silt loam: the thickness of silt sand is 7.2 ~ 9.0m, the sandy loam is 0.5 ~ 5.6m, with large variation of thickness and uneven soil. The middle stratum is composed by the 4th layer of silty clay and the fifth layer of fine sand, which is the reservoir foundation and substratum. The thickness of the fourth silty clay layer is of 1.3 ~ 7.2m; the distribution is not continuous, which belongs to the micro-low permeability, can be used as a relatively impermeable layer. The thickness of the fifth layer of fine sand is 5.5 ~ 18.0m, with high thickness and sandy inequality. The thickness of the sixth layer of heavy silt loam is 4.3 ~ 13.3m, with sandy loam, light silty loam and fine sand lens; the layer is of micro - low permeability, can be used as a relatively impermeable layer.

**The main engineering geological problems in reservoir area and the evaluation**

**3.1. Leakage problem of the reservoir**

The average digging depth is about 6.0m. The dike is 5 ~ 7.5m higher than the reservoir bottom. Reservoir strata structure is adhesive multilayer structure types; the lithology is in sandy soil, clip with heavy silt loam and silty clay layer. The first layer of sandy loam soil is of medium permeability; the second layer of silt loam is of low permeability in general; local parts are general permeable; the third layer of silt is in the medium permeability; the third layer of silty clay is with micro - low permeability. It has the horizontal leakage problem after impoundment of reservoir.

The reservoir bottom is composed of the layer of silt loam, the third layer of silty sand, sandy loam, the fourth layer of silty clay, the fifth layer of fine sand and the sixth layer of heavy silt loam and the seventh layer of fine sand. Sandy loam soil is with medium permeability generally; powder and fine sand is with moderate to high permeability; silty clay and silty loam is with micro - low permeability. The fourth layer of silty clay is with low permeability, which can be used as relative water- resisting layer. But the space distribution is not continuous, some or most of the section is lack of the layer. The third layer of silty sand and sandy loam and bottom fifth layer of silty sand are moderately permeable, which is directly connected with the stratum, thus forming the leakage path. It has the vertical leakage problem after impoundment of reservoir.

**3.2 Bank stability and deposition problems of the reservoir**

Reservoir's excavation depth is 6 ~ 7m. The surrounding ground height is of about 1m, the bank slope height is about 7 ~ 8m. According to the above analysis of soil layer, the first layer of sandy loam soil has medium dense, with moderate permeability, low strength, and poor anti erosion ability; the second layer of silt loam has loose structure, with weak permeability, local parts with medium permeability; the stability is poor; the third layer of sandy loam and silty sand is in a little dense shape, with moderate permeability, low strength, poor anti erosion ability. The reservoir stratum, under the reservoir conditions, is prone to reservoir bank collapse. To sum up, the surrounding bank slope's stability is poor. It should take appropriate protection measures. The surrounding bank slope rate can be set to 1:2.5 to 1:4.0.

**3.3 siltation problems of reservoir, connecting channel and river water diversion channel**

The lithology of the upper strata of field was mainly sandy soil, storage water was carried out in the reservoir, connecting channel and river water diversion channel, because the sandy loam and silty sand have the characteristic of medium permeability, low shear strength and poor anti-erosion ability, under the water erosion and scour effect, sandy soil slope collapse and reservoir sedimentation were easily happened. According to the design data, Silt content of reservoir can reach 1~2kg/m3, which can also make the reservoir and river sedimentation, so the sedimentation of reservoir and river should be taken corresponding measures.

**3.4 Earthquake liquefaction problem**

Seismic basic intensity of field was VII, seismic peak acceleration was 0.15G. Site 20m soil layer under the ground is the fourth recent (Q4) formation. In addition to the first layer of silty clay and clay content was greater than 17%, the rest of the layer clay content is less than 17%,

Through calculating the shear wave velocity, combining the measured average hear wave velocity, according to engineering geological survey specification of water hydropower (GB50487-2008)， soil liquefaction was preliminary judged, The fourth layer of silty clay was a non liquefied soil, The first layer of sandy loam, the second layer of silt, the third layer of silt and the fifth layer of fine sand soil were probably liquefied soil, so soil liquefaction should be judged again. Which should be done according to building seismic design specification (GB50011-2010), standard penetration blow number method was adopted. Liquefaction of saturated sand soil under 20m range was existed, with a serious liquefaction rank, so the corresponding measures should be taken.

### 3.5 Immersion and salinization problem

According to the codes on water conservancy and hydropower engineering geological survey (GB50487-2008) and appendix D, submerged groundwater threshold values were calculated. Three dimensional seepage calculation analysis indicated that, without seepage measures, The water table around the reservoir within 100m groundwater level was 50~51m, groundwater deep was 0.3~1.5m, which was smaller less than critical value of immersion groundwater, so immersion and salinization problem were existed, thereby which led to foundation conditions deteriorated near village, the substation, and new community. so the corresponding anti-seepage measures should taken.

### 3.6 anti-seepage measures

The fourth layer of silty clay has low permeability, which can be used as relative water-resisting layer, But the space distribution is continuous in the western region, only part of the section is lack of the layer. which has certain sedimentary thickness and can be used as the impervious curtain lower. But the east reservoir layer distribution was not continuous, sedimentary thickness varied greatly, which could not be used as relative water- resisting layer, The thickness of the sixth layer of heavy silt loam was large, stable distribution was continuous, only sandy soil skylight was existed in local area. the layer was of micro-low permeability, can be used as a relatively impermeable layer deposition. so the reservoir anti-seepage curtain or wall should be bound to the surface, and the lower limit should be 0.5 ~ 1.0m in the sixth layer of heavy silt loam.

## Summary

Through the investigation of Yinhuang irrigation reservoir engineering, it was finded that the reservoir seepage problems, reservoir bank stability and sedimentation, river water diversion, connection and siltation problems, seismic liquefaction, immersion and salinization and other engineering geological problems were existed in the reservoir, especially the of reservoir leakage problem was the most prominent, this paper gave the treatment measures of reservoir leakage problem.

## References

[1]The national standard of the people's Republic of China. Code for water resources and hydropower engineering geological investigation (GB50487-2008)[S]. Beijing: Chinese Planning Press, 2009

[2]The national standard of the people's Republic of China. Code for seismic design of buildings (GB50011-2010) [S]. Beijing: China Architecture Industry Press, 2010

[3]Zhang Guihua, Zhang YiBing, Tian Yongjun, Hu Shihui. 3D finite element seepage calculation and analysis of Yellow River irrigation reservoir, Henan water conservancy and the south to North Water Diversion Project, 2012, (16):72-73

*Applied Mechanics and Materials Vols. 580-583 (2014) pp 2074-2077*
*© (2014) Trans Tech Publications, Switzerland*
*doi:10.4028/www.scientific.net/AMM.580-583.2074*

# Research on the Calculation Method of Earth Pressure on the Back Side of Large Cylinders

HE Jialong[1, a]

[1] Hohai University, College of Water Conservancy and Hydropower Engineering, Nanjing, China

[a]815356713@qq.com

**Keywords:** Large cylinders,earth pressure,arch effect,calculation method.

**Abstract.** The study on calculation method of earth pressure around the circle of large cylinders will be deduced in this paper. The arch effect of soil is introduced into study. Considering the soil arch effect, different stress sections appear in the soil between two cylinders due to the change of stress state. Equations are established respectively in these sections and the analytic solutions to the equations are obtained.

Large cylindrical structure are brought in China in recent decades, and it began to promote as a new type of port [1]. This paper focuses on the distribution of large cylindrical structure plane earth pressure on the back side of large cylinders.

Currently earth pressure on the back side of large cylinders widely used formula is Levacheve formula [2], and the premise of the formula is put forward as there is no interaction between adjacent cylinder. But it works in practice and experimental studies [3] were found, after filling the cylinder will form soil vaulted arch [4]. In this paper, the different extents are proposed in the research process calculation formula of soil pressure: limit state sector, the pressure arch sections and loose state sector, as shown in Figure 1.

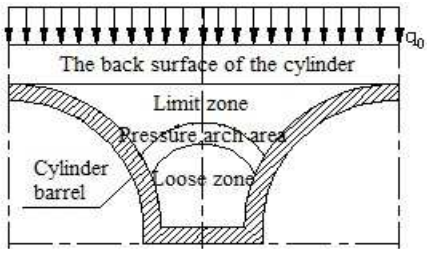


Fig.1 Three Stress Sections Distribution

## Earth pressure of limit state sector

This paper avoid pressure arch arch axis characterization studies directly, and a situation made some assumptions based on the state of the soil in the limit to derive formulas limit state soil earth pressure.

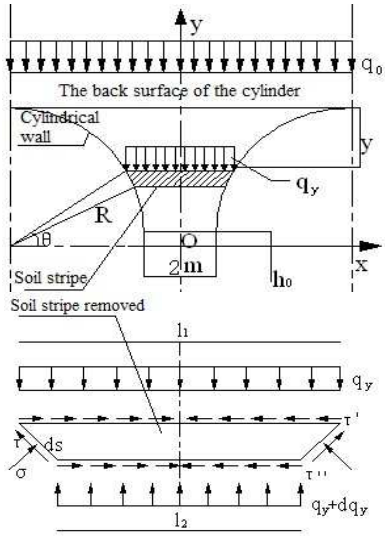


Fig.2 Earth Pressure Calculation Model

As is shown in figure 2 . There are $\sum Y_i = 0$ , mean that: $q_y l_1 - (q_y + dq_y) l_2 - 2\sigma \sin\theta ds - 2\tau \cos\theta ds = 0$

$\sigma$ - radial cylindrical shell reaction force, $\tau$ - reaction force to cut the shell column, $r$ - cylinder diameter, $m$ - cylinder interface slot width, $\theta$ - central angle.

So: $a = 1 + m/r$ , there are: $dq_y = \dfrac{q_y \sin\theta - \sigma \sin\theta - \tau \cos\theta}{a - \cos\theta} d\theta$ .

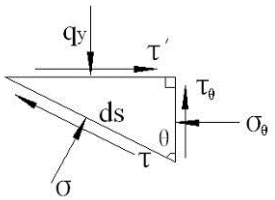


Fig.3 Differential Element

Remove an adjacent differential unit cell shown in Figure 3. There are:

$\sum X_i = 0$, mean that

$$\sigma \cos\theta + \tau' \sin\theta = \tau \sin\theta + \sigma_\theta \cos\theta \tag{1}$$

$\sum Y_i = 0$, mean that

$$q_y \sin\theta = \tau_\theta \cos\theta + \tau \cos\theta + \sigma \sin\theta \tag{2}$$

So: $$\sigma_\theta = K_i q_y \tag{3}$$

$K_i$ - soil lateral pressure coefficient;When $\dfrac{\pi}{2} - \delta \le \theta \le \dfrac{\pi}{2}$ ,i=1; When $0 < \theta < \dfrac{\pi}{2} - \delta$ ,i=2;

The value is not the same $\theta$ , the friction contact surface of the cylindrical wall are different.

At that time $\dfrac{\pi}{2} - \delta \le \theta \le \dfrac{\pi}{2}$ ($\delta$ of external friction angle of the soil), the soil on the slope triangular element is self-steady state, the friction can not reach the limit, it can be assumed:

$$\tau = \sigma c \tan\theta \tag{4}$$

Consolidated (1) (2) (3) (4), the solution of basic differential equations can be obtained as follows:

$$q_y = C_0[a - 1 + (a+1)\tan^2\frac{\theta}{2}]^{\frac{-K_1 a^2}{a^2-1}} \times (\tan\frac{\theta}{2})^{\frac{K_1}{a-1}} \times (1 + \tan^2\frac{\theta}{2})^{K_1} \quad , \quad \frac{\pi}{2} - \delta \le \theta \le \frac{\pi}{2} \tag{5}$$

$C_0 = q_0 (2a)^{\frac{K_1 a^2}{a^2-1}} (2)^{-K_1}$ .

At the time $0 < \theta < \dfrac{\pi}{2} - \delta$ , assuming the friction reach the limit, mean that:

$$\tau = f\sigma \tag{6}$$

$f$ - the soil and the friction coefficient of the tube wall, $f = \tan\delta$.

The (6) into (1) (2) finishing available $\sigma = \varphi(\theta) q_y$ ,

$$\varphi(\theta) = \frac{K_2 \cos^2\theta - \sin^2\theta}{\cos 2\theta - f \sin 2\theta} \tag{7}$$

$$K_2 = \tan^2(\frac{\pi}{4} - \frac{\delta}{2}) \tag{8}$$

Comprehensive (7) (8) we can get the solution: $q_y = (a - \cos\theta) \cdot e^{-d \cdot \varphi_1(\theta)} \cdot e^{-fd \cdot \varphi_2(\theta)}$

$d = \dfrac{\cos\delta}{\sin\delta + 1}$; $\varphi_1(\theta) = \int \dfrac{\sin(b+\theta)\sin\theta}{\cos(b-\theta)(a-\cos\theta)} d\theta$; $\varphi_2(\theta) = \int \dfrac{\sin(b+\theta)\cos\theta}{\cos(b-\theta)(a-\cos\theta)} d\theta$ .

**Earth pressure pressure arch section**

The load decreasing trend makes a zone between the soil to form a single barrel characterization arch axis alone bear the remaining external loads is possible.

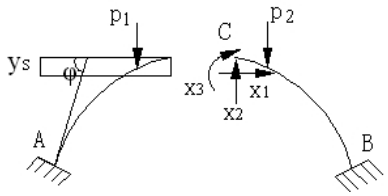


Fig.4 Pressure Arch Model

As is shown in Figure 4, we have a matrix expression:

$$\begin{Bmatrix} M \\ Q \\ N \end{Bmatrix} = \begin{bmatrix} 1 & -x & y-y_s \\ 0 & \cos\varphi & -\sin\varphi \\ 0 & -\sin\varphi & -\cos\varphi \end{bmatrix} \begin{Bmatrix} X_1 \\ X_2 \\ X_3 \end{Bmatrix} + \begin{Bmatrix} M_P \\ Q_P \\ N_P \end{Bmatrix} \tag{9}$$

Surface of the internal forces of any length of arch: $M_P = \frac{-q}{2}x^2$ , $Q_P = qx\cos\varphi$ , $N_P = -qx\sin\varphi$ .

$$\begin{bmatrix} \delta_{11} & 0 & \delta_{13} \\ 0 & \delta_{22} & 0 \\ \delta_{31} & 0 & \delta_{33} \end{bmatrix} \begin{Bmatrix} X_1 \\ X_2 \\ X_3 \end{Bmatrix} + \begin{Bmatrix} \Delta_{1p} \\ \Delta_{2p} \\ \Delta_{3p} \end{Bmatrix} = \{0\} \tag{10}$$

To enable $\delta_{13} = \delta_{31} = 0$, move some extra binding action point C along the $y$ axis distance $y_s$ , making integration $\int_s \frac{\overline{M}_1 \overline{M}_3}{EI} ds = 0$ . Simplification can be obtained by: $y_s = \int_s \frac{yds}{EI} \Big/ \int_s \frac{ds'}{EI}$.

Equation (10) simplifies to: $\begin{bmatrix} \delta_{11} & 0 & 0 \\ 0 & \delta_{22} & 0 \\ 0 & 0 & \delta_{33} \end{bmatrix} \begin{Bmatrix} X_1 \\ X_2 \\ X_3 \end{Bmatrix} + \begin{Bmatrix} \Delta_{1P} \\ \Delta_{2P} \\ \Delta_{3P} \end{Bmatrix} = \{0\}$

So: $[X_1 \quad X_2 \quad X_3]^T = -\begin{bmatrix} \frac{\Delta_{1P}}{\delta_{11}} & \frac{\Delta_{2P}}{\delta_{22}} & \frac{\Delta_{3P}}{\delta_{33}} \end{bmatrix}^T$; $\delta_{11} = \int_s \frac{ds}{EI} = \frac{-2a}{EI}\left[-\frac{1}{8a^2}\ln(2al - 2aB) + \frac{l}{2}B\right]$

$B = \sqrt{l^2 + \frac{1}{4a^2}}$ ; $\delta_{22} = 0$ ; $\delta_{33} = \int_s \frac{(y-y_s)^2 ds}{EI} + \int_s \lambda \frac{\sin^2\varphi ds}{GA} + \int_s \frac{\cos^2\varphi ds}{EA}$ ; $\int_s \frac{\cos^2\varphi ds}{EA} = \frac{-2a}{EA}\left[\frac{-1}{8a^2}\ln 2a(l-B) + \frac{Bl}{2}\right]$

$\int_s \frac{(y-y_s)^2 ds}{EI} = \frac{a^2}{EI}\int_{-l}^{0} x^4\sqrt{1+4a^2x^2}\,dx + \frac{4a^2(y_s - c)}{EI}\int_{-l}^{0} x^2\sqrt{\frac{1}{4a^2} + x^2}\,dx - \frac{2a\left(c^2 - 2y_s c + y_s\right)}{EI}\int_{-l}^{0}\sqrt{\frac{1}{4a^2} + x^2}\,dx$ ;

$\int_s \lambda \frac{\sin^2\varphi ds}{GA} = \frac{2a\lambda}{GA}\left[\ln 2a(l-B) + \frac{l}{B}\right]$ ;

Free term is: $\Delta_{1P} = \int_s \frac{M_p ds}{EI} = \frac{qa}{EI}\left[\frac{1}{128a^4}\ln 2a(-B+l) + \frac{l}{8}KB\right]$

$K = 2l^2 + \frac{1}{4a^2}$ ; $\Delta_{3P} = \int_s \frac{(y-y_s)M_p ds}{EI} - \int_s \frac{\sin\varphi Q_p ds}{GA} - \int_s \frac{\cos\varphi N_p ds}{EA}$ ; $\int_s \frac{\sin\varphi Q_p ds}{GA} = \frac{2a\lambda}{GA}\int_{-l}^{0} \frac{qx^2 dx}{\sqrt{1+4a^2x^2}}$ .

$\int_s \frac{(y-y_s)M_p ds}{EI} = \frac{-qa}{2EI}\int_{-l}^{0} x^4\sqrt{1+4a^2x^2}\,dx - \frac{q(c-y_s)}{2EI}\int_{-l}^{0} x^2\sqrt{1+4a^2}\,dx$ ;. $\int_s \frac{\cos\varphi N_p ds}{EA} = \frac{q}{EA}\int_{-l}^{0} \frac{x^2}{\sqrt{\frac{1}{4a^2} + x^2}}dx$

**Loose soil pressure status section**

Silo pressure formula can be used to calculate the earth pressure value of the section.

As is shown in Figure 5, which acts on: sheet body weight $\gamma Fdy$ ; sheet body facing the top of the vertical pressure $q_y$ ; pressure of the bottom surface upward $q_y + dq_y$ ; periphery of the sheet body frictional resistance $\mu dyq_y Kf$ . Then: $\gamma Fdy + Fq_y - F(q_y + dq_y) - \mu dyq_y Kf = 0$ ; $dy = \frac{dq_y}{\gamma - fK\frac{\mu}{F}q_y}$

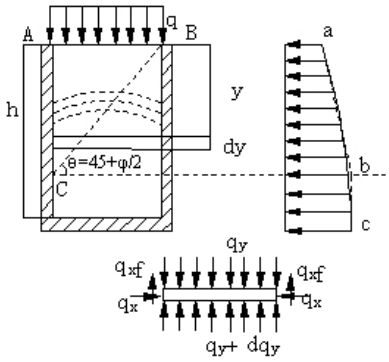


Fig.5 Inner Earth Pressure Calculation Model

So: $q_y = \frac{\gamma F}{fK\mu}(1-\exp\left(-\frac{fK\mu y}{F}\right)) + q\exp(-\frac{fK\mu y}{F})$; $q_y$ - silo filler surface from a depth of packing pressure on the $y$ section; $\gamma$—Severe filler; $q$—Uniform load on the filler surface; $F$—Cross-sectional area of the silo; $\mu$—Circumference of the inner wall of the silo.

Applied to the horizontal position of the side wall of pressure: $q_x = q_y K$.

**Discussion and Levacheve earth pressure formula**

Given the role Levacheve radial force on the cylinder wall and tangential force formula is:

When $\frac{\pi}{2}-\delta<\theta<\frac{\pi}{2}, \sigma = q_y \sin^2\theta$ ; $\tau = 0.5q_y \sin 2\theta$ ;When $\theta<\frac{\pi}{2}-\delta, \sigma = q_y \frac{\sin\theta\cos\delta}{\sin(\theta+\delta)}$ ; $\tau = q_y \frac{\sin\theta\sin\delta}{\sin(\delta+\theta)}$.

If $\frac{\pi}{2}-\delta \le \theta \le \frac{\pi}{2}$ so $K_1 = 0$, mean that lateral pressure $\sigma_\theta = K_1 \cdot q_y = 0$ . The lateral pressure into the basic differential equations (5), we have: $q_y = q_0$ $(\frac{\pi}{2}-\delta \le \theta \le \frac{\pi}{2})$

The $\sigma_\theta$ into (1) (2), we have: $\sigma = q_0 \sin^2\theta, \tau = 0.5q_0 \sin 2\theta$.

So, the expressions Levacheve recommended formula obtained above is consistent.

Similarly, when $0<\theta<\frac{\pi}{2}-\delta$ , taking $\tau' = 0$, then: $\sigma = q_0 \frac{\sin\theta\cos\delta}{\sin(\theta+\delta)}; \tau = q_o \frac{\sin\theta\sin\delta}{\sin(\theta+\delta)}; q_y = q_0$.

The actual effect of external loads due inward squeeze, the influence of the cylinder adjacent soil arching effect will appear. Thus, this article assumes done more in line with inter-tube real stress state of the soil, it seems more reasonable in theory, but also from a more general applications.

**Summary**

This paper introduce soil arching barrel earth pressure calculation of large cylindrical structures, depending on the stress state of the soil behind the cylinder body, the partition segments earth pressure calculation.

**References**

[1] CCCC Third Harbor Consultants. New Structures of Terminal. Beijing: China Communications Press, 1998

[2] Levacheve C.H. Application of Thin Shell in Hydraulic Structures.translated by Zhao Y, Xiang K X, Wang D L. Beijing: China Communications Press, 1982

[3] Liu J Q. Deformation of Large-diameter Cylindrical Buried Structures. Chinese Journal of Geotechnical Engineering, 1994, 16(2):64-72

[4] Wu Z S,Zhang L M,Hu D.Studies on the Mechanism of Arching Action in Loess.Journal of ChengDu University of Science and Technology, 1995;(2):15-19

*Applied Mechanics and Materials Vols. 580-583 (2014) pp 2078-2081*
*© (2014) Trans Tech Publications, Switzerland*
*doi:10.4028/www.scientific.net/AMM.580-583.2078*

# Utilizing GIS in the development of water quality river modeling for Penchala River, Malaysia

Faridah Othman[1,a], Alaa-Eldin Mohamed Elamin[2,b], Siti Azireen Hezza Azahar[3,c] and Siti Asiah Muhammad[4,d]

[1,2,3,4]Civil Engineering Department, Faculty of Engineering, University of Malaya, Kuala Lumpur, Malaysia

[a]faridahothman@um.edu.my, [b]alaa_elnoor@yahoo.com, [c]azireen21@yahoo.com.my, [d]hmct_90@yahoo.com

**Keywords:** Penchala River, water quality modelling, GIS.

**Abstract.** The quality of river water has been an important issue, due to its significant important function to the human being. In Asia, Malaysia is considered as one of the most speedily urbanizing countries and it's facing huge environmental challenges. An increased pressure on urban areas has been generated by rapid manufacturing especially in the Penchala River Basin. Penchala River originates from Kiara Hill and passes through several important townships as it flows through residential and industrial areas before meeting with Klang River. Although the river is relatively short, with an approximately 12 km in length with a catchment area of 28 kilometer square, this catchment is noted to be under environmental stress emanating from storm water pollution, solid waste, sedimentation and micro-pollutant. To study the water pollution issue, it is always best if it is tied up with the geographic information system. The objective of this study is to use the GIS for preparing and organizing the geometric data to satisfy the water quality model requirements. As a result of this study, a digital map for Penchala River has been created.

## Introduction

Water is considered as an important element in the keep up of all forms of life, most living organisms can only survive for short periods without water. Therefore, any change in the distribution quality of the natural and water has an environmental effects that can be devastating [1, 2]

The water quality management has been an important issue for decades nevertheless the current situation of the water quality management in the world is quite far from satisfactory [3-5]. This is due to the increasing of the population as well as the economic development [6-11].

In term of water resources management, the water quality modeling was often employed as a supporting tool for the aquatic environment assessment, and the calculated results provided valuable information for improvement water quality management [12]. Although the mathematical models have been used by the scientists to assess river water quality, however, the application of these models in risk assessment and environmental management is quite limited due to the difficulty in preparing the input data and explaining the model output. Previous studies have shown that the water quality modeling can be coupled with geographical information system (GIS) to determine the strategy for the water resources management [13, 14]. GIS are a strong tool for understanding, modeling, and managing complex stream water problems [15]. GIS are increasingly used to process spatial data representing pollution factors and to study how vulnerable a particular area is to the pollution of groundwater or the potential risk of contamination of surface waters [16-18].

## Study Area and Methodology

**Study Area.** Malaysia, one of the most rapidly urbanizing countries in Asia, faces major environmental challenges. Penchala River which flows through the south-western parts of Petaling Jaya in Selangor, Malaysia, is one of the most polluted river in the Klang valley. The Penchala River catchment covers an area of about 28 $km^2$ passing through the urban areas. The main river

length is about 12 km. Industrial & residential areas are the major land use in the river basin, and almost 70% of river length has been concrete-lined when it passes through residential and industrial area [19].

As Penchala River runs through the city, its water quality is greatly affected by the land use and activities of the area. Urbanization has been linked to the degradation of the urban waterways, which has produced an adverse effect on the quantity and quality of the water resources. In view of the urgency to minimize and control the water quality degradation, the state government has chosen Penchala River in "One State One River" program in keeping the river clean [20]. The "One State One River" program has been launched in 2002 by the Department of Irrigation and Drainage Malaysia (DID), with the objective to restore the selected rivers in each state to a minimum water quality class of II by the year 2015. The idea of this program is to involve everyone into the managing of a selected river in each state and collect all the resources to rehabilitate and protect that river [21].

**Topographic map and DEM.** Fig. 1 shows the topographic map of Penchala River basin with a scale of 1:250,000. The map has been processed using the techniques of the GIS to produce the digitized river network. Thus, the length of each reach can be measured using the GIS techniques to satisfy the river model.

The Digital Elevation Model (DEM) for the study area has been obtained and from this model the elevations and slopes can be calculated to fulfill the river model requirements.

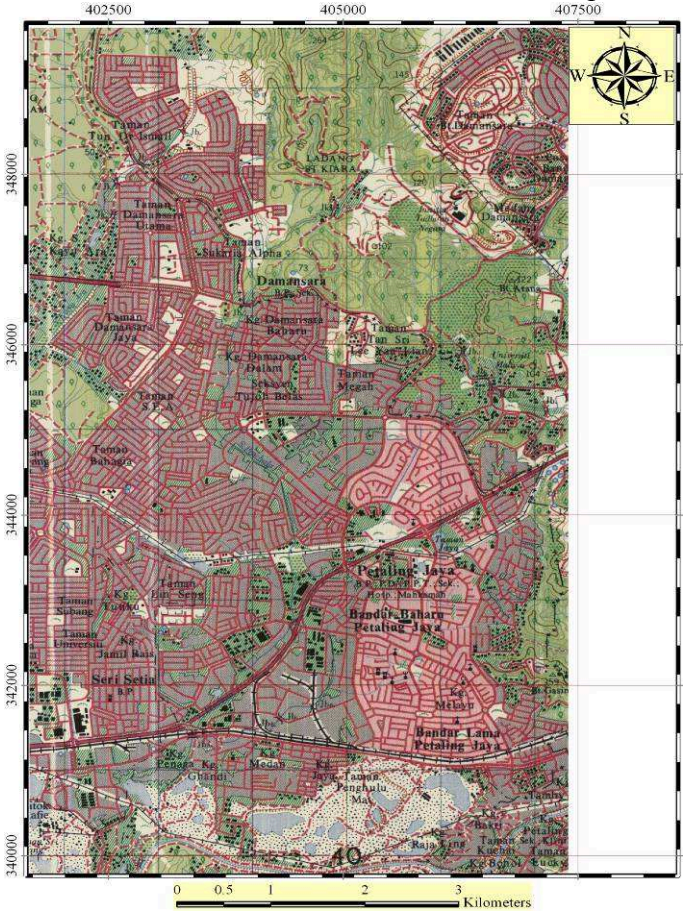


Fig. 1: The topographic map of Penchala River basin

**Monitoring, sampling stations and sources of pollution.** Beside the geometric data, the hydrological, hydraulic and water quality data are also required to satisfy the water quality model requirements. Thus, water quality monitoring and sampling stations along the river are also needed to satisfy the water quality model. Eight water quality monitoring stations have been set up along Penchala main river and its tributaries.

In addition, the spatial location of the pollution sources along the Penchala River basin has been collected in a digital shape file format. These are essential to identify the locations and loadings of the effluent form the point sources that are discharging into the river.

## Results

All the shape files have been imported into the GIS environment. As a result, the digital map for Penchala River basin has been created to assess the running of the river water quality model. As shown in Fig. 2, the generated digital map represented in the GIS environment in three feature types; points, lines and polygons. For instance, the main river and its tributaries represented as line features, while the sampling stations represented as point features. The created map is a physical map which means that it can be edited and modified any time according to the phenomenon changes along the river basin. It can be clearly seen that most of the point sources are concentrated at the downstream of Penchala River.

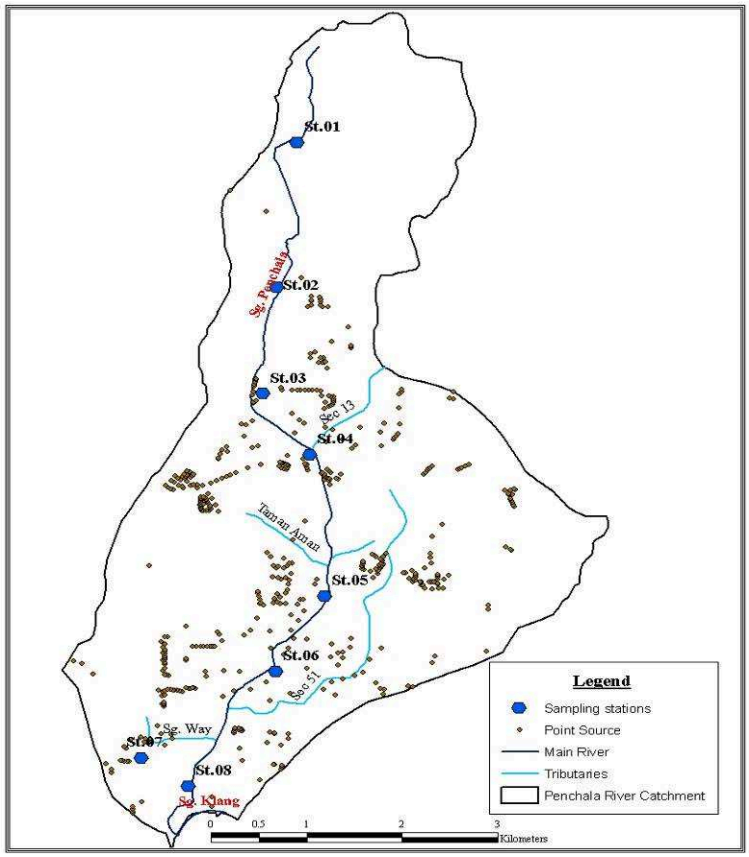


Fig. 2: The digital map for Penchala River basin showing the sampling stations and point sources

## Conclussions

The current study represents the spatial data of Penchala River basin that can be used to assess the monitoring and assessment of the river water quality. The GIS tools and techniques were applied to acheive the objectives. The study shows the importance of GIS applications in the managements of the river water quality.

## Acknowledgements

The authors highly appreciate the finanicial support by LRGS (203/PKT/6720004) and (RG244-12AFR) for the study. The authors are greatly indebted to the Department of Environment Malaysia, Department of Irrigation and Drainage Malaysia for their support on this study. We are most grateful and would like to thank the reviewers for their valuable suggestion, which led to a substantial improvement of the article.

**References**

[1] E.D.S. George Tchobanoglous. Addison-Wesley. Vol. 1. 1987, Canada: Addison-Wesley.

[2] C. Pringle, Hydrological Processes, 2003. 17(13): p. pp. 2685–2689.

[3] A.K. Biswas, Water International, 1991. 16(4): p. 219-224.

[4] A. Elshorbagy and L. Ormsbee, Environmental Modelling & Software, 2006. 21(5): p. 689-698.

[5] M. Falkenmark, Hydrological Sciences Journal, 1997. 42(4): p. 451-466.

[6] Y.Y. Haimes, Systems, Man and Cybernetics, IEEE Transactions on, 1992. 22(3): p. 413-417.

[7] Z.W. Kundzewicz, Hydrological Sciences Journal, 1997. 42(4): p. 467-480.

[8] D.P. Loucks, Hydrological Sciences Journal, 1997. 42(4): p. 513-530.

[9] E.J. Plate, Water International, 1993. 18(2): p. 84-94.

[10] S.I. Simonovic, Water International, 1996. 21(4): p. 223-232.

[11] J. Xia and K. Takeuchi, Hydrological Science Journal, 1999. 44: p. 462–474.

[12] C. Fan, W.-S. Wang, and M.-C. Liao. in *Environmental Informatics Archives*. 2007. International Society for Environmental Information Sciences (ISEIS).

[13] M.A. Lenzi and M. Di Luzio, European Journal of Agronomy, 1997. 6(1–2): p. 1-14.

[14] S.T.Y. Tong and W. Chen, Journal of Environmental Management, 2002. 66(4): p. 377-393.

[15] J.J. Fletcher, S. Qingyun, and M.P. Strager. in *Info-tech and Info-net, 2001. Proceedings. ICII 2001 - Beijing. 2001 International Conferences on*. 2001.

[16] S. Dunn, et al., in *Diffuse pollution conference*. 2003: Dublin, Ireland. p. 59– 65.

[17] C. Giupponi and I. Vladimirova, Science of the Total Environment, 2006. 359(1–3): p. 57-75.

[18] D.Q. Kellogg, et al., in *Rhode Island water quality programme*. 1999: University of Rhode Island, USA.

[19] R. River Basin Initiative. Wetland Management & Conservation 2006 2013; Available from: http://www.riverbasin.org/index.cfm?&menuid=73&parentid=65.

[20] DID. 2010, Department of irrigation and drainage: Malaysia.

[21] DID. 2009 17 July 2009 [cited 2013 26-March]; Available from: http://www.water.gov.my/index.php?option=com_content&task=view&id=380&Itemid=395.

*Applied Mechanics and Materials Vols. 580-583 (2014) pp 2082-2087*
*© (2014) Trans Tech Publications, Switzerland*
*doi:10.4028/www.scientific.net/AMM.580-583.2082*

# Data Mining Model in Regional Target Decomposition of Water Resources Utilization Efficiency

Huawei Chen [1,2, a], Jiwen Huang [1,2,b], Bing Li [1,2,c]
Shidong Fu [1,2,d], and Xin Zhang [1,2,e]

[1] Water Research Institute of Shandong Province, Jinan 250014, China

[2] Shandong Province Key Laboratory of Water Resources and Environment, Jinan 250014, China

[a]chenhuawei8036@163.com, [b]sdskyhjw@126.com, [c]icefuture@163.com

[d]xuri1986@foxmail.com, [e]lszhangx@163.com

**Keywords:** the K-means clustering, ARIMA model, water utilization efficiency, target decomposition, Shandong province

**Abstract.** Data mining model is the most important technical basis of the control target decomposition for the most stringent water resources management of Shandong province. K-means clustering model is adopted to analysis the water withdrawal of industrial added value per ten thousand yuan in 2010. Based on the yearly industrial water consumption trend from 1995 to 2010 of 17 municipal-level cities in Shandong province, the ARIMA (p, d, q) model is established through a lot of fitting and optimization and then the regional industrial water demand and water utilization efficiency in 2015 were forecasted. According to the proposed principal and technical route of target decomposition, the industrial water utilization efficiency target in 2015 of the whole province and 17 municipal-level cities are defined respectively.

## Introduction

To promote the most stringent water resources management system and ensure to realize the main goal of development, utilization, saving and protection of water resources, the General Office of the State Council issued "the most stringent water resources management assessment method" (the General Office of the State Council, [2013] Reference No. 2), requires the provinces, autonomous regions, and municipalities directly under the central government assess the implementation of the most stringent water resources management. The water utilization efficiency control target is stipulated in the assessment method, and the water withdrawal of industrial added value per ten thousand yuan in 2015 should be 25% lower than in 2010.

## Statistical Analysis of Data Mining Model[1]

Data mining model is widely used in statistical analysis techniques such as correlation analysis, regression analysis, variance analysis, cluster analysis, discriminant analysis, time series analysis method, etc. In all of the data mining technology, the statistical model of data mining tools is one of the most mature technology in the data mining, and has been widely used. Clustering analysis and variance analysis can be used in the classification of different business behavior and characteristics in water resources management, thus the different business groups can be determined and the government can implement distinguish management mode. Correlation analysis can be used in finding the relationship between various influencing factors in the complex water resources system. Regression analysis and time series analysis can be used to predict the regional water resources in the future, also can be used in short-term, mid-term and long-term water consumption forecasting. K-means clustering and Autoregressive Moving Average Time Series Model (ARIMA) are mainly used in this article for data statistical analysis, forecasting.

**K-means clustering [2]-[3].** The term k-means was first used by James MacQueen in 1967 and the method has been successfully used in various topics, ranging from market segmentation, computer vision and geostatistics. K-means algorithm process is as follows:

Step 1: Given a set of observations $(x_1, x_2, x_3, \cdots, x_n)$, where each observation is a d-dimensional real vector， set $I$=1 and initialize the center of the $k$ clusters $Z_j(I), j = 1, 2, \cdots, k$;

Step 2: Calculate the distance of each data object and the centroid.

$$D(x_i, Z_j(I)), i = 1, 2, \cdots, n, j = 1, 2, \cdots, k \tag{1}$$

If $D(x_i, Z_k(I)) = \min\left\{D(x_i, Z_j(I))\right\}, j = 1, 2, \cdots, k$, then $x_i \in C_k$;

Step 3: Set $I = I + 1$, calculate the new means to be the centroids of the observations in the new clusters.

$$Z_j(I+1) = \frac{1}{n}\sum_{i=1}^{n_j} x_i^{(j)}, j = 1, 2, \cdots, k \tag{2}$$

And also calculate the Sum of Squares Estimator (SSE).

$$E(I+1) = \sum_{j=1}^{k}\sum_{p \in C_k}^{k} \left\| p - Z_j(i) \right\|^2 \tag{3}$$

Step 4: Discriminant: if $\left\|E(I+1) - E(I)\right\| \geq \varepsilon$, then $I = I + 1$ and return to step(2), else the algorithm is ended.

**Autoregressive integrated moving average (ARIMA) Model [4]-[5].** In statistics and econometrics, and in particular in time series analysis, an autoregressive integrated moving average (ARIMA) model proposed by Box and Jenkins is a generalization of an autoregressive moving average (ARMA) model. ARIMA model can be generally expressed as follows.

$$x_t = \varphi_1 x_{t-1} + \varphi_2 x_{t-2} + \cdots + \varphi_p x_{t-p} + \varepsilon_t - \theta_1 \varepsilon_{t-1} - \theta_2 \varepsilon_{t-2} - \cdots - \theta_q \varepsilon_{t-q} \tag{4}$$

Where $\varphi_1$， $\varphi_2$,…， $\varphi_p$ are autoregressive coefficients, p is the order of regression, $\theta_1$， $\theta_2$,…， $\theta_q$ are the average moving coefficients, $p$ is the moving average order; $\{\varepsilon_i\}$ is a white noise series. If $d$ is the representation of difference order, then the model can be abbreviated as ARIMA ($p,d,q$).

## Process of Regional Target Decomposition of Water Resources Utilization Efficiency

**Principles and technical route.** According to the provincial status of water utilization efficiency in 2010 and the control target which the nation decomposed to Shandong Province; considering the regional water resources characteristics, economic and social conditions as well as the industrial water development in the future; adhere to the principles such as promoting the improvement of water utilization efficiency and benefit, promoting the change of water utilization pattern and economic development pattern, and promoting the monitoring and management of water utilization. The technical route of the target decomposition for water withdrawal of industrial added value per ten thousand yuan is shown in the Fig. 1.

**K-means clustering analysis.** Using the variable “water withdrawal of industrial added value per ten thousand yuan” the 17cities of Shandong province can be divided into six categories. The clustering result is shown in Table 1. Table 1 shows that Qingdao, Weihai city, Yantai city are relatively high in industrial water utilization efficiency; Yantai city is the highest, and Laiwu city is the lowest. Table 2 shows that the probability P corresponding to statistics F is 0.000, and there is significant difference in the six categories for the mean of variable “water withdrawal of industrial added value per ten thousand yuan”. Based on the clustering result and the whole target of the province that the water withdrawal of industrial added value per ten thousand yuan in 2015 should be 25% lower than in 2010, the target decomposition (the declining ratio of water withdrawal of industrial added value per ten thousand yuan) program of 17 cities in 2015 can be preliminarily proposed in six categories which is shown in Table 3.

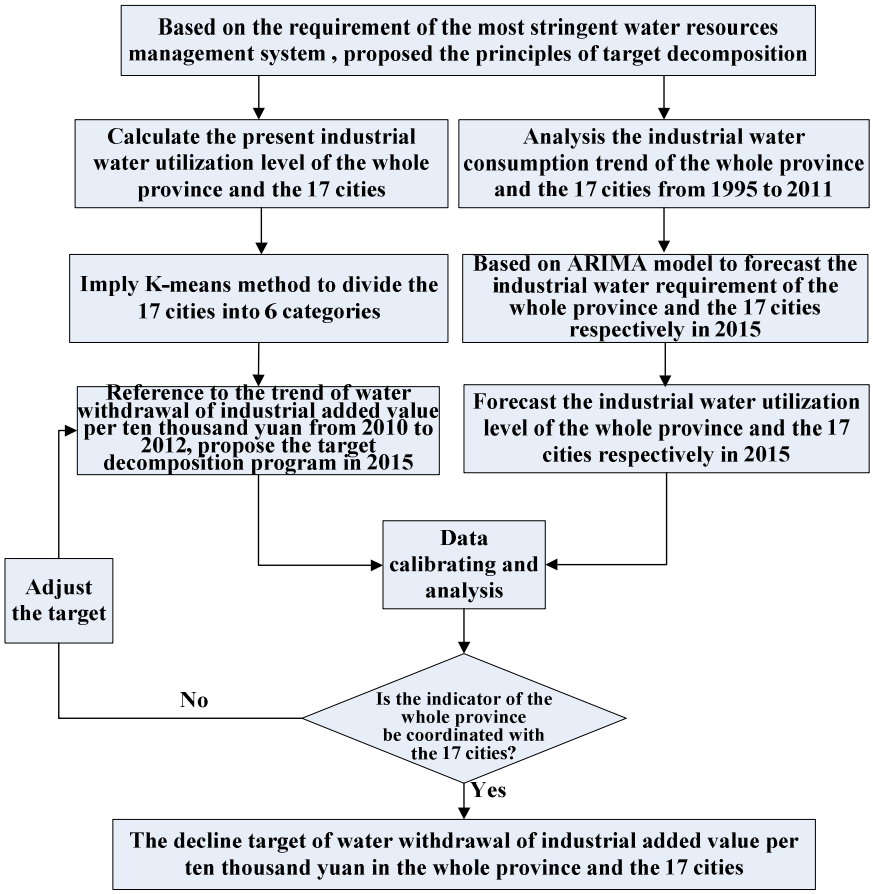


Fig. 1 Technical route of the target decomposition for water withdrawal of industrial added value per ten thousand yuan

Table 1 The clustering result

| category | administrative region | water withdrawal of industrial added value per ten thousand yuan ($m^3$) | the final superior cluster center |
|---|---|---|---|
| 1 | Qingdao City | 7.07 | 6.2 |
| | Yantai City | 5.01 | |
| | Weihai City | 6.53 | |
| 2 | Dongying City | 9.62 | 9.62 |
| 3 | Jinan City | 18.71 | 18.27 |
| | Zaozhuang City | 16.41 | |
| | Weifang City | 16.96 | |
| | Jining City | 17.68 | |
| | Rizhao City | 19.35 | |
| | Linyi City | 18.56 | |
| | Dezhou City | 18.71 | |
| | Liaocheng City | 19.74 | |
| 4 | Zibo City | 14.98 | 14.14 |
| | Taian City | 14.53 | |
| | Binzhou City | 12.81 | |
| 5 | Heze City | 22.85 | 22.85 |
| 6 | Laiwu City | 37.61 | 37.61 |

Table 2 Calculation result of the clustering statistics

| | clustering | | deviation | | F | Sig. |
|---|---|---|---|---|---|---|
| | mean squared deviation | df | mean squared deviation | df | | |
| water withdrawal of industrial added value per ten thousand yuan（$m^3$） | 179.367 | 5 | 1.19 | 12 | 151.16 | 0 |

Table 3 The preliminarily proposed target decomposition program in 2015

| category | administrative region | water withdrawal of industrial added value per ten thousand yuan（$m^3$） | declining ratio (2010-2015) |
|---|---|---|---|
| 1 | Qingdao City | 7.07 | 10% |
| | Yantai City | 5.01 | |
| | Weihai City | 6.53 | |
| 2 | Dongying City | 9.62 | 18% |
| 3 | Jinan City | 18.71 | 25% |
| | Zaozhuang City | 16.41 | |
| | Weifang City | 16.96 | |
| | Jining City | 17.68 | |
| | Rizhao City | 19.35 | |
| | Linyi City | 18.56 | |
| | Dezhou City | 18.71 | |
| | Liaocheng City | 19.74 | |
| 4 | Zibo City | 14.98 | 20% |
| | Taian City | 14.53 | |
| | Binzhou City | 12.81 | |
| 5 | Heze City | 22.85 | 30% |
| 6 | Laiwu City | 37.61 | 35% |

**Based on ARIMA model to forecast the industrial water requirement.** Implying the exponential smoothing method, ARIMA model and artificial neural network method to analysis the industrial water consumption trend of the 17 cities from 1995 to 2011, the results show that the data series are not smooth change data series, and the catastrophe point occurred around 2004. Therefore, ARIMA model is adopted to simulate the nonstationary sequence difference processing and respectively forecast the industrial water demand of 17 cities in 2015, then get the industrial water utilization efficiency of 17 cities in 2015. The forecast result is shown in table 4.

Table 4 The forecast result of industrial water demand and utilization efficiency in 2015

| administrative region | ARIMA *(p,d,q)* | industrial water demand in 2015 (ten thousand $m^3$) | industrial added value in 2015(forecasted by the rate of increase method)( one hundred million Yuan) | water withdrawal of industrial added value per ten thousand yuan in 2015 ($m^3$) |
|---|---|---|---|---|
| Jinan City | (3,2,0) | 30608 | 2129 | 14.38 |
| Qingdao City | (3,2,0) | 23005 | 3606 | 6.38 |
| Zibo City | (3,1,0) | 30408 | 2480 | 12.26 |
| Zaozhuang City | (3,1,1) | 13111 | 1164 | 11.27 |
| Dongying City | (3,0,1) | 20293 | 2480 | 8.18 |
| Yantai City | (3,0,1) | 15104 | 3407 | 4.43 |
| Weifang City | (3,2,1) | 32205 | 2390 | 13.48 |
| Jining City | (3,0,1) | 24085 | 1818 | 13.25 |
| Taian City | (3,2,1) | 17759 | 1396 | 12.72 |
| Weihai City | (3,2,0) | 9314 | 1520 | 6.13 |
| Rizhao City | (3,0,1) | 10548 | 727 | 14.5 |
| Laiwu City | (2,2,1) | 10845 | 458 | 23.69 |
| Linyi City | (3,0,1) | 22370 | 1553 | 14.4 |
| Dezhou City | (3,0,1) | 18205 | 1217 | 14.96 |
| Liaocheng City | (3,2,1) | 17549 | 1331 | 13.19 |
| Binzhou City | (3,0,1) | 14316 | 1127 | 12.7 |
| Heze City | (3,2,1) | 14186 | 822 | 17.25 |
| Shandong Province | | 323910 | 29625 | 10.93 |

Table 4 shows that the provincial industrial water demand will reach 3.2391 billion m³ by 2015. Combined with the prediction of industrial added value, the derived water withdrawal of industrial added value per ten thousand yuan was 10.93 m³ in 2015, slightly more than 10.67 m³ (the industrial water utilization efficiency goals in 2015, decline 25% compared with 2010). Therefore, the goal that the whole provincial water withdrawal of industrial added value per ten thousand yuan shoud be 25% lower than in 2010 will be realized with the province promoting of water-saving society construction, by adjusting the product structure and improving the production process.

**Data calibrating and target decomposition program adjusting .** According to the forecasted result of industrial added value and the preliminarily proposed target decomposition program in 2015, the industrial water demand of 17 cities can be derived respectively and thus the whole provincial industrial water demand which is the sum of the 17 cities' is about 3.16238 billion m³. But based on the forecasted result of industrial added value and the industrial water utilization efficiency goals in 2015 (10.67 cubic meter per ten thousand yuan ) the whole provincial industrial water demand will be 3.16099 billion m³. The two results of the provincial industrial water demand have slight difference. Therefore the preliminarily proposed target decomposition program in 2015 should be adjusted. The adjusted target decomposition program in 2015 is shown in Table 5. After calibrating again the whole provincial industrial water demand is coordinated with the 17 cities', that is the indicator of the whole province is coordinated with the 17 cities'.

Table5 The adjusted proposed target decomposition program in 2015

| administrative region | the adjustde decline ratio of water withdrawal of industrial added value per ten thousand yuan (2010-2015)(%) | water withdrawal of industrial added value per ten thousand yuan ($m^3$) |
|---|---|---|
| Jinan City | 25 | 14.03 |
| Qingdao City | 17 | 5.87 |
| Zibo City | 19 | 12.13 |
| Zaozhuang City | 39 | 10.01 |
| Dongying City | 23 | 7.41 |
| Yantai City | 10 | 4.51 |
| Weifang City | 23 | 13.06 |
| Jining City | 23 | 13.61 |
| Taian City | 17 | 12.06 |
| Weihai City | 10 | 5.88 |
| Rizhao City | 15 | 16.45 |
| Laiwu City | 29 | 26.7 |
| Linyi City | 22 | 14.48 |
| Dezhou City | 30 | 13.1 |
| Liaocheng City | 25 | 14.81 |
| Binzhou City | 17 | 10.63 |
| Heze City | 30 | 16 |
| Shandong Province | 25 | 10.67 |

## Conclusions and suggestions

Implying the data mining model in regional target decomposition of industrial water resources utilization efficiency can provide scientific and effective technical support to the most strict water resources management in Shandong province. Therefore according to the data characteristic of water resources management and information needs, using a efficient statistical model algorithms, extracting useful information and knowledge from plenty of water resources data can provide a new analysis method and scientific decision support to solve the problems in the field of water resources management.

**Acknowledgements**

This work was financially supported by the Ministry of Water Resources' Special Funds for Scientific Research on Public Welfare (201201113), Sub-project of National Science and Technology Major Project on Water Pollution Control and Treatment (2012ZX07404-003).

**References**

[1] X.J. Zhang: China Institute of Water Resources and Hydropower Research, 2007, p.11

[2] J. Cheng: Liaoning Normal University, 2008, p.15

[3] X.X. Wang, Y.D. Wang: Journal of Computer Research and Development, vol. 40(2003) , p.869

[4] X.Z. Liu, J.H. Shao: Journal of Mathematics in Practice and Theory, vol. 36(2006) , p.8

[5] H.R. Wang, J. Kang, X. Lin: Systems Engineering-Theory & Practice, vol. 10(2008) , p.167

[6] J.L. Jin, K.Y. Wu and Y.M. Wei: SHUILI XUEBAO, vol. 39(2008), p.401

[7] J.Z. Sun, S.Q. Chen: Systems Engineering, vol. 22(2004), p. 35

*Applied Mechanics and Materials Vols. 580-583 (2014) pp 2088-2091*
*© (2014) Trans Tech Publications, Switzerland*
*doi:10.4028/www.scientific.net/AMM.580-583.2088*

# The RCC Arch Dam Analysis During Overload

Yu Xia [1, a], Ying-ye Yu[2, b], Xiao-lian Zhao [3,c] and Zhong-qing Zhang [4,d]

[1]Civil Engineering and Architecture College of Guangxi University of Science and Technology, Liuzhou, China

[2] Logistic Service Management Centre of Guangxi University of Science and Technology, Liuzhou, China

[3].College of Resources and Environment, Guangxi University, Nanning China

[4] College of Civil and Architecture Engineering, Guangxi University, Nanning, China

[a]summ-rain@163.com, [b]4288921@qq.com [c]xiaolianbsh@126.com, [d]zhangzq@gxu.edu.cn

**Keyword:** overload analysis arch dam RCC.

**Abstract.** It does numerical analysis on the overload of RCC arch dam named wanjiakouzi, through the analysis, we try to find the damage process of the dam. It does elastic-plastic analysis by FEM. Result shows that the horizontal cracks are usually a very important clue, it means the dam will reach its ultimate capacity.

## Introduction

Due to the high safety and less cost of arch dam, it is built all over the world [1], Arch dam is one kind of important dam type, because of material strength's full display, large load bearing capacity, small body, convenient flood discharge arrangement, potential high safety, perfect earthquake resistance performance and so on; it receives domestic and foreign engineers' favor. Because arch dam has a strong overload capacity, auto-regulation characteristic and low project construction cost, over one half of the world dams, which are above 200m high, are arch dam [2]. The largest number of arch dam has been built in China [3]. It can be quickly and simply constructed, uses less concrete per unit, and generates less heat, so engineers pay much attention to it. Arch dam's height will be much higher in the future, safety analysis becomes a key problem. Safety analysis research of arch dam has achieved much by scientific research institute and university, but there are still many questions for further study. The paper does researches on the overload analysis of the highest RCC dam of the world named wanjiakouzi.

## Basic Theory

The yield criterion of materials is the Drucker-Prager criterion - the yield cone surface is through outside vertices of yield hexagon in the following calculations. Plastic flow rule is the orthogonal flow rule. The yield function of Drucker-Prager model is

$$F = \alpha I_1 + \sqrt{J_2} - k = 0 \tag{1}$$

Where $\alpha$, $k$ = parameter of material, $I_1$ = the first stress tensor invariant, $J_2$ = the second stress tensor invariant. They can be got from the following equation.

$$I_1 = \sigma_x + \sigma_y + \sigma_z \tag{2}$$

$$J_2 = \frac{1}{6}\left[(\sigma_x - \sigma_y)^2 + (\sigma_y - \sigma_z)^2 + (\sigma_z - \sigma_x)^2\right] + \tau_{xy}^{\ 2} + \tau_{yz}^{\ 2} + \tau_{zx}^{\ 2} \tag{3}$$

$$\alpha = \frac{2\sin\phi}{\sqrt{3}(3 - \sin\phi)} \tag{4}$$

$$k = \frac{6c^{'}\cos\phi}{\sqrt{3}(3 - \sin\phi)} \tag{5}$$

Where $\sigma_x^{\ 2}, \sigma_y^{\ 2}, \sigma_z^{\ 2}, \tau_{xy}^{\ 2}, \tau_{yz}^{\ 2}, \tau_{zx}^{\ 2}$ = stress component $\phi = tg^{-1}f^{'}$.

Stress-strain relationship of concrete is linear before the failure in the tensile, the matrix which describes it is list below.

$$[D_c^{ck}] = \frac{E}{(1+v)(1-2v)} \begin{bmatrix} (1-v) & v & v & 0 & 0 & 0 \\ v & (1-v) & v & 0 & 0 & 0 \\ v & v & (1-v) & 0 & 0 & 0 \\ 0 & 0 & 0 & \frac{(1-2v)}{2} & 0 & 0 \\ 0 & 0 & 0 & 0 & \frac{(1-2v)}{2} & 0 \\ 0 & 0 & 0 & 0 & 0 & \frac{(1-2v)}{2} \end{bmatrix} \quad (6)$$

Where: E = young's modulus for concrete ν = poisson's ratio for concrete

**Modeling of a crack**

The presence of a crack at an integration point is represented through modification of the stress-strain relations by introducing a plane of weakness in a direction normal to the crack face. Also, a shear transfer coefficient βt is introduced which represents a shear strength reduction factor for those subsequent loads which induce sliding (shear) across the crack face. The stress-strain relations for a material that has cracked in one direction only become:

$$[D_c^{ck}] = \frac{E}{1+v} \begin{bmatrix} \frac{R^t(1-v)}{E} & 0 & 0 & 0 & 0 & 0 \\ 0 & \frac{1}{(1-v)} & \frac{v}{(1-v)} & 0 & 0 & 0 \\ 0 & \frac{v}{(1-v)} & \frac{1}{(1-v)} & 0 & 0 & 0 \\ 0 & 0 & 0 & \frac{\beta_t}{2} & 0 & 0 \\ 0 & 0 & 0 & 0 & \frac{1}{2} & 0 \\ 0 & 0 & 0 & 0 & 0 & \frac{\beta_t}{2} \end{bmatrix} \quad (7)$$

If the crack closes, then all compressive stresses normal to the crack plane are transmitted across the crack and only a shear transfer coefficient βc for a closed crack is introduced. Then the matrix can be expressed as

$$[D_c^{ck}] = \frac{E}{(1+v)(1-2v)} \begin{bmatrix} (1-v) & v & v & 0 & 0 & 0 \\ v & (1-v) & v & 0 & 0 & 0 \\ v & v & (1-v) & 0 & 0 & 0 \\ 0 & 0 & 0 & \beta_c \frac{(1-2v)}{2} & 0 & 0 \\ 0 & 0 & 0 & 0 & \frac{(1-2v)}{2} & 0 \\ 0 & 0 & 0 & 0 & 0 & \beta_c \frac{(1-2v)}{2} \end{bmatrix} \quad (8)$$

The stress-strain relations for concrete that has cracked in two directions are:

$$[D_c^{ck}] = E \begin{bmatrix} \frac{R^t}{E} & 0 & 0 & 0 & 0 & 0 \\ 0 & \frac{R^t}{E} & 0 & 0 & 0 & 0 \\ 0 & 0 & 1 & 0 & 0 & 0 \\ 0 & 0 & 0 & \frac{\beta_t}{2(1+v)} & 0 & 0 \\ 0 & 0 & 0 & 0 & \frac{\beta_t}{2(1+v)} & 0 \\ 0 & 0 & 0 & 0 & 0 & \frac{\beta_t}{2(1+v)} \end{bmatrix} \quad (9)$$

If both directions reclose,

$$[D_c^{ck}] = \frac{E}{(1+v)(1-2v)} \begin{bmatrix} (1-v) & v & v & 0 & 0 & 0 \\ v & (1-v) & v & 0 & 0 & 0 \\ v & v & (1-v) & 0 & 0 & 0 \\ 0 & 0 & 0 & \beta_c \frac{(1-2v)}{2} & 0 & 0 \\ 0 & 0 & 0 & 0 & \beta_c \frac{(1-2v)}{2} & 0 \\ 0 & 0 & 0 & 0 & 0 & \beta_c \frac{(1-2v)}{2} \end{bmatrix} \quad (10)$$

The stress-strain relations for concrete that has cracked in all three directions are:

$$[D_c^{ck}] = E\begin{bmatrix} \frac{R^t}{E} & 0 & 0 & 0 & 0 & 0 \\ 0 & \frac{R^t}{E} & 0 & 0 & 0 & 0 \\ 0 & 0 & \frac{R^t}{E} & 0 & 0 & 0 \\ 0 & 0 & 0 & \frac{\beta_t}{2(1+\nu)} & 0 & 0 \\ 0 & 0 & 0 & 0 & \frac{\beta_t}{2(1+\nu)} & 0 \\ 0 & 0 & 0 & 0 & 0 & \frac{\beta_t}{2(1+\nu)} \end{bmatrix} \tag{11}$$

The open or closed status of integration point cracking is based on a strain value $\varepsilon_{ck}^{ck}$ called the crack strain. For the case of a possible crack in the x direction, this strain is evaluated as

$$\varepsilon_{ck}^{ck} = \begin{cases} \varepsilon_x^{ck} + \dfrac{\nu}{1-\nu}\varepsilon_y^{ck} + \varepsilon_z^{ck} & \text{if no cracking has occurred direction} \\ \varepsilon_x^{ck} + \nu\varepsilon_y^{ck} & \text{if y direction has cracked} \\ \varepsilon_x^{ck} & \text{if y and z direction has cracked} \end{cases} \tag{12}$$

Where: $\varepsilon_x^{ck}$, $\varepsilon_y^{ck}$, $\varepsilon_z^{ck}$ =three normal component strains in crack orientation. The vector $\{\varepsilon'\}$ is computed by: $\{\varepsilon^{ck}\} = [T^{ck}]\{\varepsilon'\}$ where: {ε'} = modified total strain (in element coordinates), {ε'}, in turn, is defined as: $\{\varepsilon'\} = \{\varepsilon_{n-1}^{el}\} + \{\Delta\varepsilon_n\} - \{\Delta\varepsilon_n^{th}\} - \{\Delta\varepsilon_n^{pl}\}$, where: n = substep number $\{\varepsilon_{n-1}^{el}\}$ =elastic strain from previous substep, $\{\Delta\varepsilon_n\}$ =total strain increment, $\{\Delta\varepsilon_n^{th}\}$ ,=thermal strain increment, $\{\Delta\varepsilon_n^{pl}\}$ =plastic strain increment. If $\varepsilon_{ck}^{ck}$ is less than zero, the associated crack is assumed to be closed. If $\varepsilon_{ck}^{ck}$ is greater than or equal to zero, the associated crack is assumed to be open. When cracking first occurs at an integration point, the crack is assumed to be open for the next iteration.

Finite element model is 230 meters wide, 270 meters long, 360 meters high, it is shown in Fig. 1, Parameters are listed in Table 1.

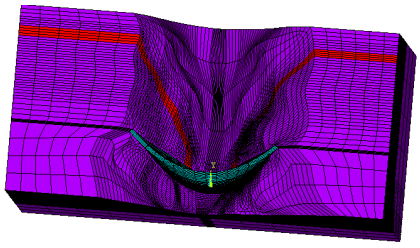

Fig. 1 Finite element model

Table. 1 Material parameters

| Location | Young's modulus (Gpa) | Density ($KN/m^3$) | Poisson's ratio | Cohesive force(Mpa) | Friction angles (°) | Coefficient of thermal expansion($10^{-6}$) |
|---|---|---|---|---|---|---|
| Dam | 18 | 2350 | 0.167 | 2 | 56 | 4.87 |
| Abutment | 14 | 2730 | 0.25 | 0.9 | 45 | |
| Base | 11 | 2700 | 0.27 | 0.7 | 42 | |
| Unconformity | 3 | 2660 | 0.3 | 0.35 | 35 | |

Abutment force is got by integral of node stress of arch dam. The force direction of abutment and coordinate system is coincident. Moment direction complies with right-hand rule.

## Conclusions

The numerical simulation results (Fig. 2) show that the initial cracks appear at the bottom of the dam, where are strongly constrained. The cracks are usually vertical. They are developing from bottom to the up of the dam along the foundation surface. When the dam nearly reaches its ultimate capacity of overload, the horizontal cracks appear on the top arch ring, which begin from two sides of arch ring to the middle. It is calculated by strength reverse method. It means that when the material strength reduces, the top arch ring and the base face will be damaged first. The result is a little different from that by water specific gravity overcharge method and water-level overcharge method. The main reason it that the loads are different. The load of strength reverse method is much the same with a arch dam in operation. The material strength reduces after a long work period. The numerical calculation by this method may be much the same with the real case.

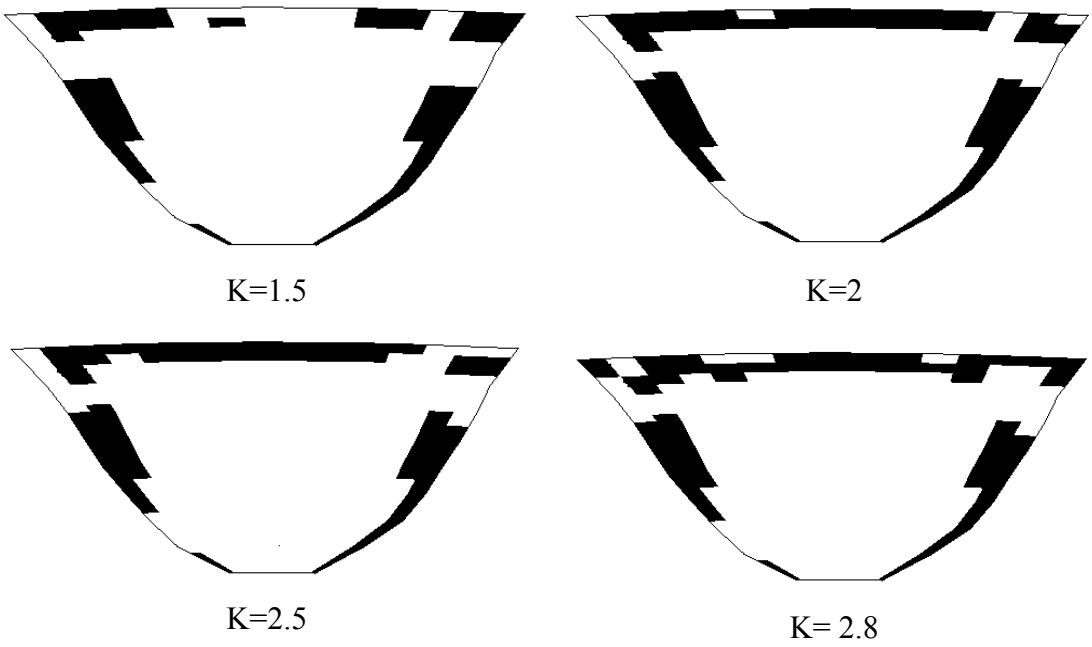


Fig. 2 Overload calculation by strength reverse method ( k=overload factor )

## Acknowledgement

This study is supported by the Guangxi Natural Science Foundation (2013GXNSFBA019247). Science Plan Projects of Guangxi Education Department (Grant No: 201203YB130), the Doctor Foundation of Guangxi University of Science and Technology (11Z02).

## References

[1] Nai-hua Ru, Zhong-sheng Jiang: *The Accident and Safety of Arch Dam* (China waterpower stress, Peking 1995).

[2] Guo-hua Liu, Shu-yu Wang: study on thrust angles of high arch dam abutment during overloading. Vol 33(1999) , p.40-46.

[3] Zan Li, Fei Chen, Jian-bo Zheng. *Super high arch dam junction analysis and key problem study* (China power stress, Peking 2004)

*Applied Mechanics and Materials Vols. 580-583 (2014) pp 2092-2095*
*© (2014) Trans Tech Publications, Switzerland*
*doi:10.4028/www.scientific.net/AMM.580-583.2092*

# Study on damage of concrete dam subjected to combined action of earthquake and slide surge

Li Jing[1], Xu Qiang[2],Chen Jian-yun[3, a], Lu Guo-shuai[4]

[1, 2, 3, 4] Faculty of Infrastructure Engineering, Dalian University of Technology, Dalian 116023, China

[a]eerd001@dlut.edu.cn,

**Keywords:** gravity dam, damage evaluation, extreme disaster, earthquake, slide surge

**Abstract.** It is possible for hydraulic engineering located in high intensity earthquake area under the action of extreme disaster induced by earthquake and secondary slide surge. Several impact action models of slide surge were introduced and the damage evolution of concrete gravity dam subjected to combined action of different sequences of earthquake and secondary slide surge were studied based on nonlinear numerical analysis. The effects of different time sequences of combined earthquake and slide surge were compared and the safety performance analysis was performed. The results show that the combined form has great effects on the damage evolution law of concrete gravity dam.

## Introduction

Generally speaking, seismic safety of water retaining structure and reservoir slope stability are the most critical problems of hydraulic engineering located in high intensity earthquake area. However, the potential reservoir landslide will be in an alternate state of wetting and drying for a long time under the influence of water level fluctuation caused by reservoir operation, which can decrease the anti-sliding stability of potential landslides. At the same time, the ground motion is random and unpredictable, the reservoir slope reinforcement measures will show aging and performance degradation under the action of earthquake, heavy rain and other environmental conditions, so there is a real possibility that landslides slid into the reservoir and cause huge landslide surge when reservoir slopes lose its stability in the process of earthquake, under the influence of aftershocks after the strong shock or heavy rain. It seriously threaten the security of the people's lives and wealth near the landslides area and downstream area if a high dam subjected to extreme combined action of high head surge pressure and ground motion increase its crash risk. There is no lack of some tragic accidents that large-scale landslides surge lead to devastating disasters to the security of the people's lives and wealth near downstream area: 1972 Shimabara, Japan; 1934 Tafjord, Norway and 1963 Vaiont Italy, all of them caused different degrees of personnel casualties.

At present, the study of landslides surge disasters at abroad and China mainly focus on surge height and its influence on the reservoir bank, the major research approach are model test, empirical formula and statistical regression analysis, which basic idea is that some important factors selected firstly, then combined with model test and analyzed by the statistical regression method, and finally the empirical equation is concluded [1]. However, there have been a few studies with the impact height and pressure of surge to the dam of finite height, especially there have been almost no researches on the dam damage situation under the action of different times combination of earthquake and landslides surge, which include different distance from the landslides to the dam and landslides occurs at different times during or after the process of ground motion. In consequence, it is of great significance to carry out researches on this field for exploring the seismic safety and bearing capacity of concrete gravity dam located in high intensity earthquake area under extreme conditions and providing references on the risk management and emergency measures for the hydraulic complex.

## The impact model of surge

The impact model of surge is the most important among a large number of studies on landslide surge. There are very few data on the impact model of surge against the dam at this stage, so usually

many researchers refer to the static model of wind-wave pressure on the straight wall water retaining structure mentioned in the《Specifications for load design of hydraulic Structures》 or 《Code of Hydrology for Sea Harbour》[2]. However, landslide surge and wind-wave have different mechanism, so they shall have different corresponding impact model of pressure.

In fact, reservoir water subjected to the combined action of high-speed impact and squeezing at the same time while the large reservoir landslide slid into reservoir at high speed, which makes the invasion depth water subjected to shock pressure and the combined action throughout the whole reservoir water from top to bottom and then the surge occurs , when the surge is blocked by the dam in the process of propagation, it will have dynamic impact pressure on the dam in the range of reservoir water depth. This idea is confirmed in the model test[3] , it showed that the dynamic model of surge impact pressure on the upright surface of dam is vertical distribution under the static water level with the amplitude of impact pressure head is about 1.77～1.89 times the height of surge, which is very different from the model of wind-wave pressure. So in this paper, we take the amplitude of impact pressure head under the static water level 1.9 times the height of surge, while consider that the amplitude of impact pressure in the range of 1.9 times surge height along the dam above the static water level is applicable to hydrostatic pressure distribution form. Sometimes any water mass can overflow the dam crest after the surge impact the dam under the combination of different reservoir water level and surge height, therefore, the distribution model of surge pressure can be divided into no overflow and overflow accordingly, as shown in Figure 1: H as the reservoir water depth, h as the height of surge and η as the height of surge climb along the dam is 1.9 times the height of surge.

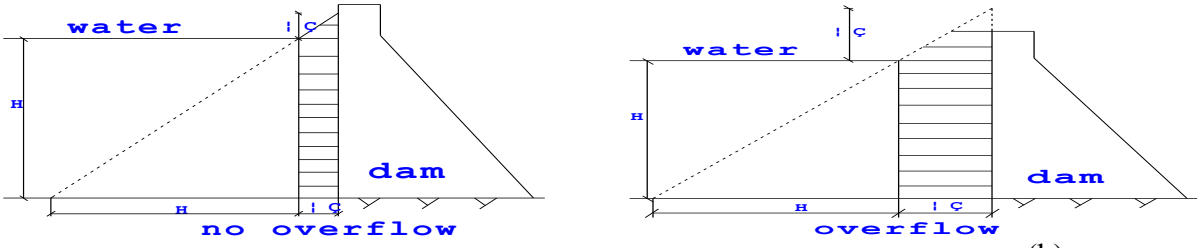


(a) (b)

Fig.1 The distribution model of surge pressure: (a) no overflow (b) overflow

On the other hand, the impact pressure of surge is a kind of dynamic and short-lived load, we can conclude that an impulse period of surge is 0.6s-1.5s according to the model test of landslide surge[4], in one period, the process of the impact pressure is similar to a half sine-wave. In this paper, we take the impact period of surge for T as 1s and the amplitude process of impact pressure as a half sine-wave. The emergence of surge is due to the exchange of reservoir landslide and water mass on kinetic energy and its process of propagation is first a sharp attenuation, then a slow attenuation. once the process of landslide is completed, there will no more new kinetic energy exchange to the reservoir water so that it will be unable to provide a steady stream of power for surge to impact the dam with a consistent high pressure head for a long time, so we can only discuss the impact of a period of initial surge height against the dam.

## The effects of earthquake and surge on the dam

In this paper, the model of Koyna dam is selected as a calculation object, its geometry as shown in Figure 2. We take the Koyna seismic wave as the ground acceleration and set its peak acceleration as 0.4g. The dam material use the elastic-plastic damage model of concrete[5,6] and take the elastic modulus as 31GPa, density as 2643Kg/m³, Poisson's ratio as 0.2, dilation angle as 36.3, initial compressive strength as 13MPa, ultimate strength as 24.1MPa and tensile strength as 2.9MPa. The finite element mesh of dam choose the structured quadrilateral mesh and the geometry of elements are no more than 2m as shown in Figure 3, the bottom border of dam is fixed.

In March 1961, the scale of Tangyanguang landslide occurred in Hunan Zhexi reservoir is 1.65×106m³, it caused 21m high surge; in June 1985, the scale of Hubei Three gorges Xintan

landslide is 3×107m³ and the height of surge it caused was as high as 40m. The height of surge will have attenuation in the process of propagation to the upstream and downstream area, so this paper takes the height of surge in front of the dam as 10m, and analyses the effects of surge and earthquake combined under different times on the dam. Simulation analysis and calculation are performed on 5 working conditions as shown in Table 1.

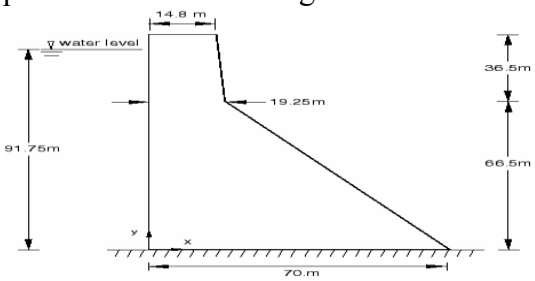


Fig.2 The geometry of Koyna dam

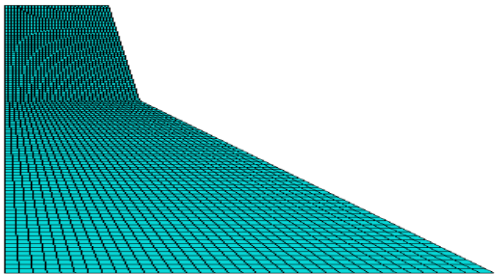

Fig.3 The dam element mesh

Table.1 Combination of surge and earthquake under different times

| Condition 1 | Condition 2 | Condition 3 | Condition 4 | Condition 5 |
|---|---|---|---|---|
| Static+ seismic | Static+ seismic+ surge | Static+ seismic (surge peak acts at 2.81s) | Static+ seismic (surge peak acts at 3.24s) | Static+ seismic (surge peak acts at 4.18s) |

Static load includes the hydrostatic pressure and gravity of the dam, it works in all steps, the surge step is 1s and the earthquake step is 10s. For condition 2 is just a surge step more than condition 1 at the end of earthquake step, so the calculation results of condition 1 included in condition 2, the relative displacement of dam crest and the plasticity and damage dissipation energy of dam body under condition 2 as shown in Figure 4 and Figure 5.

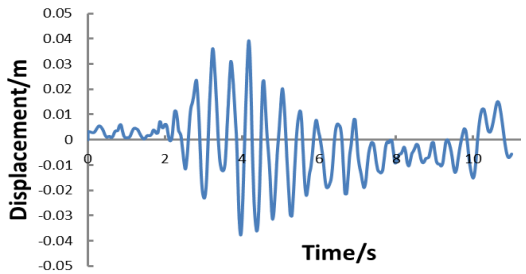


Fig.4 Displacement of dam crest

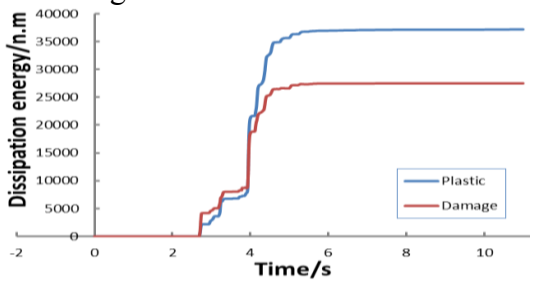


Fig.5 Dissipation energy

We can consider that superpose the surge peak time to the times when the plastic damage of upstream surface increase sharply due to the surge have an adverse effect on the upstream surface, and then explore the effects of the most unfavorable combinations on the dam. It can be seen that these moments at which the dam's dissipation increase sharply corresponding to the amplitude positive relative displacement of dam crest are 2.81s, 3.24s, 4.18s from Figure 4 and Figure 5. If we select these three moments for the surge peak work at, the combination of surge and earthquake will have more effects on the dam. Taking working conditions under these moments as condition3,4 and 5, the relative displacement of dam crest under working condition1,3,4 and 5 as shown in Figure 6.

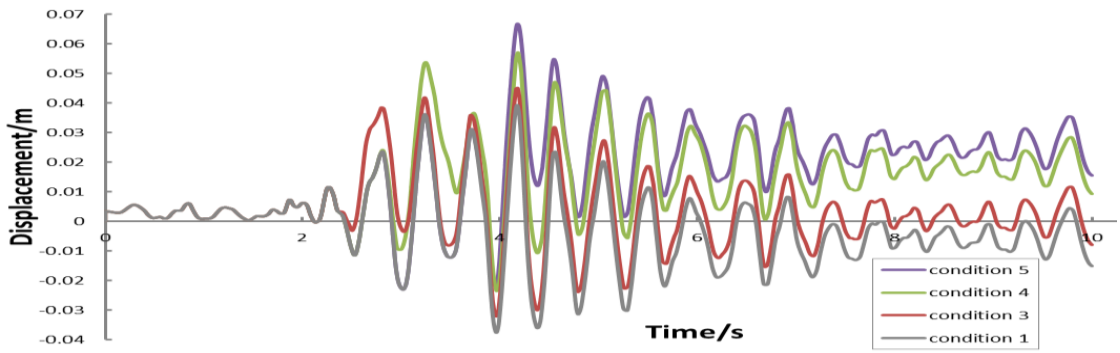


Fig.6 Relative displacement of dam crest under 4 conditions

It can be seen from Figure 6 that the positive relative displacement of dam crest under working condition3, 4 and 5 are all increase sharply at each moment of surge peak than condition1 and reach the peak value in each process of earthquake, while these displacement are all less than condition1.

This paper hold the idea that surge has good effects on the positive relative displacement of dam crest, which makes the upstream surface more likely to be damaged. The positive peak inertia force of ground motion combine with the surge peak at different moments have different effects on the upstream surface, the more seriously the upstream surface damaged, the greater decrease in the strength of dam anti-positive motion and the larger positive relative displacement of dam crest in the subsequent ground motion. The upstream surface damage increase sharply provides a larger space for dam releasing stress in the subsequent motion, and reduces the stress concentration area of the downstream surface which makes the dam still have a large strength of anti-negative motion, so the negative relative displacement of dam crest decreases in the subsequent motion.

## Conclusions

This paper selects a reasonable model of surge pressure and explores the effects of combined action of surge and earthquake on the dam. Surge can occurs at any moments in the process of earthquake (some of unfavorable conditions are analyzed) and concludes that combined action of surge and earthquake at some moments has much more effects on the dam.

## Acknowledgements

This study was supported by the State Key Development Program for Basic Research of China (No. 2013CB035905) and the National Natural Science Foundation of China (Grant No. 51109029 ).

## References

[1] WANG Yang. YIN Kun-long, Analysis of Movement Process of Landslide in Reservoir and Calculation of Its Initial Surge Height [J], Earth Science –Journal of China University of Geosciences, Vol. 28(5):579-582 (2003)

[2] JIA Chao, WANG Zhipeng, GAO Feng, REN Qingwen, High-dam risk analysis considering secondary disaster of earthquake [J], JOURNAL OF HYDROELECTRIC ENGINEERING. Vol. 30(6):34-39 (2011)

[3] Huang Jin-lin, Study on the Surge of Reservoir Bank Landslide and It's Effect on Dam Body [D], Tianjin: Tianjin University (2011)

[4] Xu Bo, The research on landslide waves generated by landslide and its propagation process [D], Changsha: Changsha University of Science and Technology (2000).

[5] Sherong Zhang, Gaohui Wang, Wenqi Sa, Damage evaluation of concrete gravity dams under mainshock -aftershock seismic sequences [J]. Soil Dynamics and Earthquake Engineering, 50:16-27 (2013)

[6] Lee J, Fenves G.L, A plastic-damage concrete damage model for earthquake analysis of dams [J].Earthquake Engineering and Structural Dynamics, Vol. 27(9):937-956 (1998)

*Applied Mechanics and Materials Vols. 580-583 (2014) pp 2096-2102*
*© (2014) Trans Tech Publications, Switzerland*
*doi:10.4028/www.scientific.net/AMM.580-583.2096*

# Research on the Dam Foundation Stability and Reinforcement Measures of the 12th sluice section of XiangJiaba Hydropower Station

Wang Xian-jun[1,2,a] Zhao Xiao-xi[1,b]

[1]College of Civil Engineering and Architecture, China Three Gorges University, Yichang 443002, China

[2]Rock Mechanics in Hydraulic Structural Engineering, Ministry of Education,Wuhan 430072, China

[a]153675771@qq.com,[b]215923600@qq.com

**Key words:** anti-sliding stability; strength reserve coefficient method; rigid equilibrium limit method; reinforce; concrete cogging; XiangJiaba Hydropower Station

**Abstract:** By two-dimensional nonlinear finite element strength reserve coefficient method and the rigid body limit equilibrium method respectively, a comprehensive study of the stability of the 12th sluice section of XiangJiaba hydropower station is made and some conclusions of the instability mode and the lack of safety are reached. The reinforcement measures, which set up concrete cogging at the dam heel and put up additional drainage holes at the stilling basin,are proposed and calculated by the strength reserve coefficient method and the rigid body limit equilibrium method respectively again,Results show that the dam foundation safety meets the code's standards if the . reinforcement measures are adopted.

## Introduction

XiangJiaba Hydropower station is the last one of the step electric stations on Jinsha River. It is one of the key power points among China's West-East Electricity Transmission Projects. The total capacity is 6000MW. The foundation bedrock mainly consists of Trias marshes of the XuJiahe formation of fluvial facies sandstone, mudstone and coal-bearing stratum. The lithology and lithofacies vary, and the cross bedding develops. The quality of rock masses is mainly II and III, there are local III2 or IV kinds. A 2km length of geniculate bend coal serves as the skeleton which has obliquely penetrated at the dam site. The core of the dam obliquely crosses between the sluice section and the dam axis, and dips steeply to the downstream. As a result, it forms a steep fracture zone which is narrow in the upstream and wide in the downstream. 11 local small faults distributes in the dam foundation of the river bed. The angle of the joints and fissures are mostly in a steep and medium dip. Low angle joints develop in strata fracture zones of a steep dip to a certain extent. The combination of these negative factors has formed the geological background of XiangJiaba Dam's deep slide.

Anti-sliding stability of gravity dams is one of the key techniques in dam designing. To confirm the dams' safety and put forward related reinforcement measures in relation to demand are important parts in gravity dams designing, especially for significant dams and complex dam foundations. According to the actual geological conditions and the designers' suggestions, this paper took the 12th sluice section of XiangJiaba as a typical example to make a comprehensive analysis on the stability of the dam foundation and put forward structure reinforcement schemes. The nonlinear finite element strength reserve coefficient method and the rigid body limit equilibrium method were used in this paper.

**Nonlinear finite element analysis**

**Characteristics of the dam and distributions of the structural surface of the dam foundation.**The 12th sluice section of XiangJiaba Hydropower Station has a height of 154m. Dam crest has a width of 50m, and bottom width of 166m. The $T_3^{2-3}$ and $T_3^{2-5}$ rock formations with soft lithology are distributed in the bedrock. The top and bottom surface of the bedrock are fracture zones with a width of 0.2m, and they have better continuity (as the Pn layer shown in Figure 1. Moreover, there are intercalary strata from JC2-5 to JC2-8, with a specific distribution shown in Figure1.

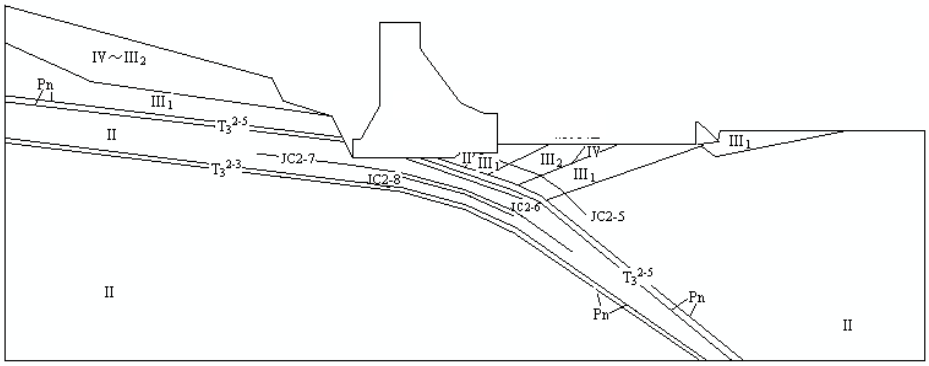


Fig.1 Surface distributions of the rock mass structure of the 12th sluice section

**Ranges and conditions of the calculation.**The calculation range of the two-dimensional finite element model extends from the dam heel 398m to the upstream, about 2 times longer more than the dam's height, and extends from the dam site 490m to the downstream, about 3 times longer more than the dam's height. Foundation depth extends below 231m from the building surface, about 1.5 times higher of the dam's height. Normal restraints are adopted for the upstream and downstream boundary of the dam foundation. The normal impounded level in the upstream is 380m, and 265.8m is the tailwater level in the downstream. The calculation loads included water pressure in up and down stream, silt pressure, uplift pressure, seepage pressure and dead weight. The casting work of the gravity dam is divided into 12 steps. Ideal elastic-plastic model was adopted in the material constitutive relation. Mohr-Coulomb criterion which is in conformity with the related flowing rule was used in yield criterion.

**Structure surfaces simulation.**Intercalary strata JC2-5 to JC2-8, $T_3^{2-3}$ layer, $T_3^{2-5}$ Pn layer and the bearing surface are thin, and they have obvious anisotropy. So these layers were simulated by jointed material model with anisotropy. General isotropic unit elements were adopted in the other parts. Parameters of the material calculation are shown in Table1.

Table 1 Material parameters

| | density [KN/m$^3$] | Elastic modulus [GPa] | Poisson's ratio | Friction coefficient | cohesion [MPa] |
|---|---|---|---|---|---|
| concrete | 24 | 25.5 | 0.167 | | |
| Ⅱ | 26.0 | 20.0 | 0.22 | 1.2 | 1.4 |
| Ⅲ1 | 26.0 | 11.75 | 0.25 | 0.99 | 1.0 |
| Ⅲ2 | 26.0 | 9.25 | 0.28 | 0.865 | 0.8 |
| Ⅳ | 26.0 | 4 | 0.30 | 0.65 | 0.45 |
| T32-3 | 26.0 | 1.28 | 0.28 | 0.45 | 0.175 |
| T32-5 | 26.0 | 1.28 | 0.30 | 0.45 | 0.175 |
| Pn | 26.0 | 1.28 | 0.40 | 0.35 | 0.1 |
| Intercalary strata JC | 23.0 | 0.72 | 0.40 | 0.42 | 0.14 |

**Analysis of the unstable models and the stability of the dam foundation.**Based on the nonlinear finite element strength reserve coefficient method, the analysis of the dam foundation stability was carried out by reducing the structure surfaces or the strength parameters progressively in possible sliding channels. Then we could obtain the progressive failure process, as well as the whole safety degree of the foundation stability. Therefore this paper intends to confirm the unstable modes and the whole safety degrees by studying the development processes of the yield zones.

As is shown in Fig.2, when the strength reserve coefficient reached 1.0, the crack rock at the dam heel came to yield, communicated with the interlayer JC2-7. Soft rock $T_3^{2-3}$ and $T_3^{2-5}$ appeared yield regions in a certain range. When the strength reserve coefficient reached 1.9, the crack rock at the dam heel penetrated through the interlayer JC2-7 and communicated with the soft rock $T_3^{2-3}$. Soft rock $T_3^{2-3}$ and $T_3^{2-5}$ were almost yield entirely. Each JC interlayer also appeared faster and various degrees' development. A small amount of compression zones appeared at the resistance body of the tail rock. When the strength reserve coefficient reached 2.4, the layer JC2-7 of shallow low-angle dip fully penetrated through the site. JC2-5 and JC2-6 layers almost penetrated through the site. The tail rock resistance block had formed yield zones of compression and shear force with an angle of 23°~27°, and it had connected with the upper yield zone of soft rock $T_3^{2-5}$, forming a sliding channel which leaded to instability of the dam.

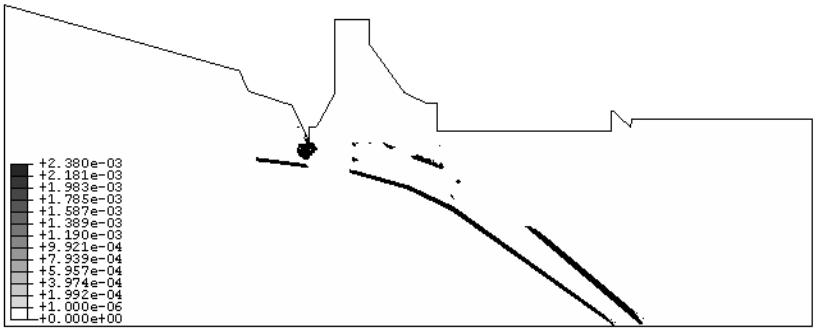


Fig.a The distribution of the yield zones when the strength reserve coefficient is 1.0

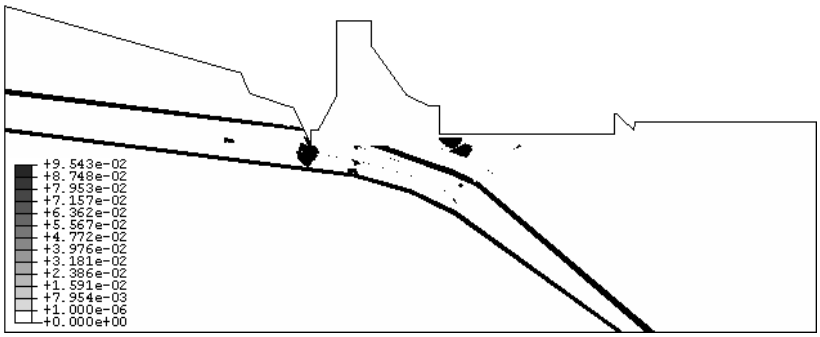


Fig.b The distribution of the yield zones when the strength reserve coefficient is 1.9

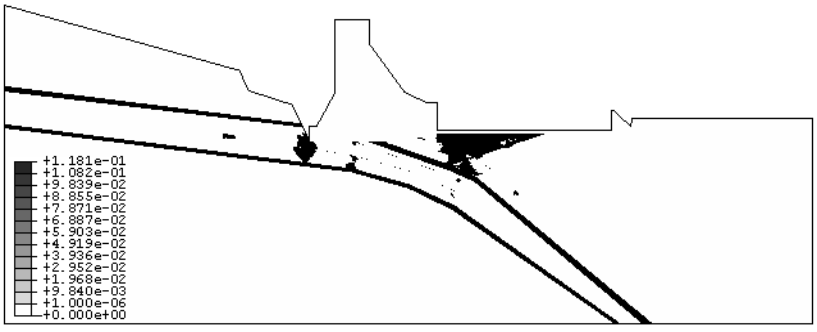


Fig.c The distribution of the yield zones when the strength reserve coefficient is 2.4

Fig.2 Development of the yield zones of dam foundation

The research on the development of the dam foundation yield zones indicated that, with the increase of the strength reserve coefficient, the strength parameters of the dam structure surface and tail rock resistance block reduced. The dam and its bedrock slid along the layer JC2-7 or the soft rock $T_3^{2-3}$ and the Pn mudded interlayer on top and bottom. When the strength reserve coefficient reached 2.4, the tail rock resistance block would lead to instability of the dam foundation because of the lack of resistance. Therefore the strength reserve coefficient of the dam safety degree should be 2.4.

The nonlinear finite element method has considered the deformation of the rock mass properties such as sliding and yield, compared with the rigid body limit equilibrium method which takes the sliding rock mass as a rigid body, so it would weaken the strength of the rock material. What's more, supposing the common boundary of the two sliding bodies as a vertical line in the calculation of the safety factors of the double sliding plane by the rigid body limit equilibrium formula is ill grounded. It will get a much higher safety factor, leading to a unsafe results. Above all, the factors mentioned above would all lead to a smaller strength reserve coefficient calculated by the nonlinear finite element method than the one of the rigid body limit equilibrium method. So the strength reserve coefficient that meets the safety requirements should be less than the standard 3.0 by the nonlinear finite element method. But there is no safety evaluation standard so far. It is still difficult to judge whether the dam is stable. We should double-check the dam's safety by the rigid body limit equilibrium method.

**Analyses of the rigid body limit equilibrium method**

When analyzing the dam foundation stability of the 12th sluice section of XiangJiaba by the rigid body limit equilibrium method according to the nonlinear finite element analyses and the geological conditions of the dam foundation, we can generalize the instability models of the dam foundation as the double sliding surface and formulate the slipping boundary and calculation conditions as follows:

The major sliding plane: From the perspective of the structural plane distributions, the interlayer JC2-6,JC2-7,JC2-8 and soft rock $T_3^{2-3}$ , $T_3^{2-5}$ and Pn layer on top and bottom all can serve as the potential sliding surfaces. But the major sliding plane searched by the nonlinear finite element analyses turned out to be the interlayer JC2-7 or soft rock $T_3^{2-3}$ and Pn mudded intercalation on top and bottom. The results illustrated that these three factors are more dangerous than any other potential major sliding planes. Therefore we can assume interlayer JC2-7 and soft rock $T_3^{2-3}$ Pn layer (Because of the soft rock $T_3^{2-3}$ and Pn mudded intercalation on top and bottom distributes in a narrow band region continuously. It is safe to simplify the two layers as Pn mudded intercalation.) as the potential major sliding planes to carry out the rigid body limit equilibrium analyses. The connectivity rate of the crushing Pn silt layer is 100%. The comprehensive shear strength parameters of the interlayer were defined with area weighting factor method.

The profile of the sliding shear: $III_1$,$III_2$,IV kinds' rock mass had developed surfaces resisting the slide after yield to pressure and shear. The angle of the surface is 23°~27°according to the finite element analysis. This paper adopts 23°as the angle of the sliding surface. The comprehensive shear strength parameter would be adopted according to the categories of the rock mass in relation to rocks' quality division graph.

Direction of resistance block: The direction of resistance block has a large effect on the safety factor. It should be demonstrated before putting into use as the standard required. The second failure surface had passed through part of $II_1$,$II_2$ layers and soft rock $T_3^{2-3}$ ,so the sliding friction coefficient of the second failure surface reached 0.93 in weighted calculation and the K reached 3.5. The angle

of the resistance block direction is 15°according to the empirical formula. What's more, the angle between the principal stress of resistance block and horizontal plane was about 20°on the basis of finite element analyses. The angle of the resistance block direction should be 15°for caution's sake.

The rigid body limit equilibrium method was adopted to carry out the analysis of the stability of the 12th sluice section on the basis of the sliding boundary and calculation conditions. The calculation results are shown in Table2.

Table 2 Deep sliding stability analysis of the 12th sluice section

| Major sliding plane | Comprehensive shear strength parameter of the major sliding plane | | Comprehensive shear strength parameter of the profile of the sliding shear | | Safety factor |
|---|---|---|---|---|---|
| | *f'* | *c'/MPa* | *f'* | *c'/MPa* | |
| JC2-7 | 0.43 | 0.15 | 0.87 | 0.82 | 2.65 |
| $T_3^{2-3}$Pn layer | 0.35 | 0.1 | | | 3.01 |

Table 2 shows that The safety factor in relation to the sliding mode which put layer JC2-7 as the major sliding plane was 2.65. Layer JC2-7 and layer $T_3^{2-3}$ Pn are more dangerous than any other potential sliding planes, so we can confirm that the safety factors of other potential major sliding planes are larger than the standards required 3.0 except the one of layer JC2-7. The safety factor that represents the whole safety degree of gravity dam is 2.65. The figure doesn't meet the standard requirements. Measures should be taken to the reinforcement.

**Research & Assessment of reinforcement measures**

The control conditions of dam foundation stability should be confirmed before designing reinforcement measures. The calculation results of the strength reserve coefficient method and the rigid body limit equilibrium method show that, the dam and part of the bedrock were sliding along layer JC2-7, extruding the tail rock resistance block near the dam toe. The tail rock resistance block lost its balance for lack of enough resisting force. Therefore, increasing the anti-sliding ability or the tail rock resisting force could be the methods to enhance the stability of the dam foundation. Otherwise, reducing the uplift pressure of the building surface also benefits the foundation stability.

As is shown in Fig.1, the major sliding surface JC2-7 shallow buried at the dam heel. The deep cutoff trench can be set up at dam heel in the case of not affecting the project's time limit. It can not only increase the anti-sliding ability of layer JC2-7 but also work as a diaphragm wall. Moreover, the work of setting up cutoff trench would link up with curtain grouting, and the work's excavation volume is small. For the above-mentioned considerations, this paper intends to adopt some measures to reinforce the foundation. Setting up concrete trench to cut off the layer JC2-7 and putting up additional drain holes at the stilling basin are useful measures. The design of the cogging reinforcement scheme is shown in Fig.3.

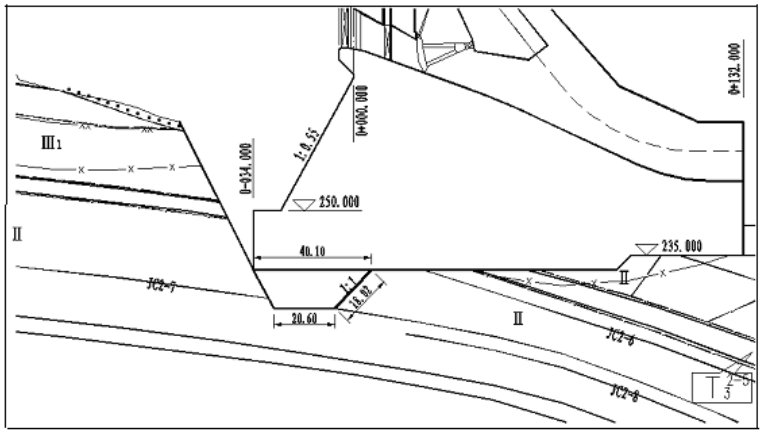


Fig.3 The deepened profile of the cogging at dam heel of the 12th sluice section

In view of the reinforcement schemes suggested, the strength reserve coefficient reached 2.8 which was calculated by the strength reserve coefficient method, and the safety factor reached 3.01 which was calculated by the rigid body limit equilibrium method. The results meet the standard requirements.

## Conclusions

[1] In order to find out the failure mechanism and the safety degree of the 12th sluice section of XiangJiaba hydropower station, this paper has carried out the analysis of the stability by the two-dimensional nonlinear finite element strength reserve coefficient method and the rigid body limit equilibrium method separately. The nonlinear finite element analyses indicated the instability mode. The dam and its bedrock slid along the layer JC2-7 or the soft rock $T_3^{2-3}$ and the Pn mudded intercalation interlayer on top and bottom, extruding the tail rock resistance block and leading to instability of the dam foundation. The strength reserve coefficient 2.4 characterizes the safety degree of dam foundation. The minimum of the safety factor turns out to be 2.65 by the rigid body limit equilibrium method. The corresponding major sliding plane is layer JC2-7. All the factors mentioned above are smaller than the standard required 3.0. So it is necessary to adopt reinforcement measures.

[2] This paper has put forward reinforcement schemes according to the instability mode of dam foundation. To set up concrete trench to cut off the layer JC2-7 and put up additional drain holes at the stilling basin. The calculation results of the two methods indicated that the stability of dam foundation increased after the reinforcement to a certain degree. The strength reserve coefficient has increased from 2.4 to 2.8, and the safety factor has increased from 2.65 to 3.01. Consequently, the results meet the standard requirements.

## Acknowledgements

This work was financially supported by Rock Mechanics in Hydraulic Structural Engineering of Ministry of Education Opening Foundation (RMHSE1203).

**References**

[1] SL319-2005.Design specification for concrete gravity dams[S].
[2] Wang Zhiliang.The anti-sliding stability of a dam via the three inclined planes method[J]. Journal of hydraulics Engineering,1982, (05):31-37.
[3] Lai Guo-wei,Wang Hong-shuo,Lu Shu-yuan.Stability analysis of dam foundations with weak layer[J].Journal of the Wuhan Institute of Hydraulic and Electric Engineering,1987,20(4):1～10.
[4] Ge Xiu-run, Ren Jian-xi, Li Chun-guan, Zheng Hong.3D-FEM analysis of deep sliding stability of 3# dam foundation of left power house of the Three Gorges Project[J]. Chinese Journal of Geotechnical Engineering,2003,25(4): 389～394.
[5] Liu Jin-long, Luan Mao-tian, Zhao Shao-fei, Yuan Fan-fan, Wang Ji-li.Discussion on criteria for evaluating stability of slope in elastoplatic FEM based on shear strength reduction technique[J].Rock and Soil Mechanics,2005,26(8): 1345～1348.

*Applied Mechanics and Materials Vols. 580-583 (2014) pp 2103-2107*
*© (2014) Trans Tech Publications, Switzerland*
*doi:10.4028/www.scientific.net/AMM.580-583.2103*

# Experimental Investigation on the Segregation of Landslide Dam Materials

Ming Zhang[1, a], Fei Wang[1,b], Gujie Mouse[1,c], Weitao Luo[1,d], Hongwu Zhang[1,e] and Yaoru Liu[1,f]

[1] State Key Laboratory of Hydroscience and Engineering, Department of Hydraulic Engineering, Tsinghua University, Beijing 100084, P.R. China

[a]mzhang@tsinghua.edu.cn, [b]wangfei07@163.com, [c]msgj_833@126.com, [d]luowt08@gmail.com, [e]zhhw@tsinghua.edu.cn, [f]liuyaoru@tsinghua.edu.cn

**Keywords:** experimental investigation, grain size distribution, landslide dam, particle segregation.

**Abstract:** Large landslides usually dam lakes that may easily fail and then result in catastrophic flood threatening the population downstream. The grain size composition within landslide dams is considered as a vital factor that impacts the timing of failure and the resulting magnitude of flood. Therefore, experiments were conducted to investigate the features of size distribution in accumulation bodies. The results indicate that the grain size distribution varies in different parts of the deposits. The inverse grading phenomenon can be observed. Grains in the front of the deposit are coarser, while grains in the rear are finer. For the front of the deposit, the grains in the middle are finer than the other two sides. The grain size segregation is believed to be the governing mechanism that contributes to this special distribution. The speculations of the grain size distribution inside the landslide dam are presented.

## Introduction

Landslide lakes occur once landslides block natural river flows and form landslide dams. Usually, the structure of landslide dams is weak and unstable, especially when water level rises high. It will easily fail due to piping or overtopping. Its breach may lead to catastrophic flood threatening the lives and properties of people living downstream. On May 12, 2008, an earthquake of magnitude 8.0 took place at Wenchuan, Sichuan Province, China. According to the preliminary investigation, 257 earthquake induced landslide lakes formed, 32 of which may cause flood disaster [1]. Tangjiashan Landslide Lake was the most dangerous one at that time, with maximum water storage of 320 million $m^3$. The landslide dam was approximately 124 m and 90 m high on the left and right sides, respectively and its volume is about $2.437\times10^7 m^3$. The potential breach posed a severe threat to 1.2 million people as the lake site was just 5km upstream from Beichuan County Seat [2].

In the sample of documented landslide dam failures, overtopping and piping are respectively the first and second common causes of dam failures [3]. As one of the most important characteristics of landslide dams, the grain size composition plays a key role in deciding the erodibility, permeability of the dam materials, thereby impacting the timing of failure and the resulting magnitude of flood in both failure modes. Because of this, some dam failure models, e.g., Breach, a widely used model for earthen dam failure [4], require grain sizes as crucial parameters of computation.

The grain size distribution of landslide dam materials may have special features. According to the researches of granular materials, the movement of granular materials will lead to particle size segregation, that is, larger particles tend to move upward to the top layer of the granular flow [5-7]. The dry landslide debris slips down the mountain at a high speed before forming a landslide dam. During this process, materials of the landslide dam may segregates, which probably contributes to special size distribution. Moreover, field investigations reveal that there indeed exist some typical features of grain size distribution of rock avalanche deposits and landslide dams [8-11]. However, since most of landslide dams will breach within a short period of time, for example, 60% of the landslide dams induced by Wenchuan Earthquake failed within a month [12], there are only a few opportunities to make field investigations on landslide dams, which is far from enough. Therefore, experimental investigation needs to be conducted to study the forming process of landslide dams, which contribute to a better understanding of its grain size distribution.

## Methodology

We use a steel slope shown in Fig.1 to study the mechanism of the accumulation and segregation of landslide debris. The slope is 5.40m long, 3.24m high and 2.50m wide, with 5cm high walls on both left and right sides of the slope. The surface of the slope is a plane, without any special treatment to make the slope smoother or rougher, that is, the coefficient of friction of the slope is the same as normal steel. The slope is set on horizontal ground, with enough space in front of the slope allowing the experimental material to accumulate. A bulldozer is used to carry and pour the experimental material from the top of the slope, shown in Fig.2. The experiment material should be poured continuously in an appropriate speed.

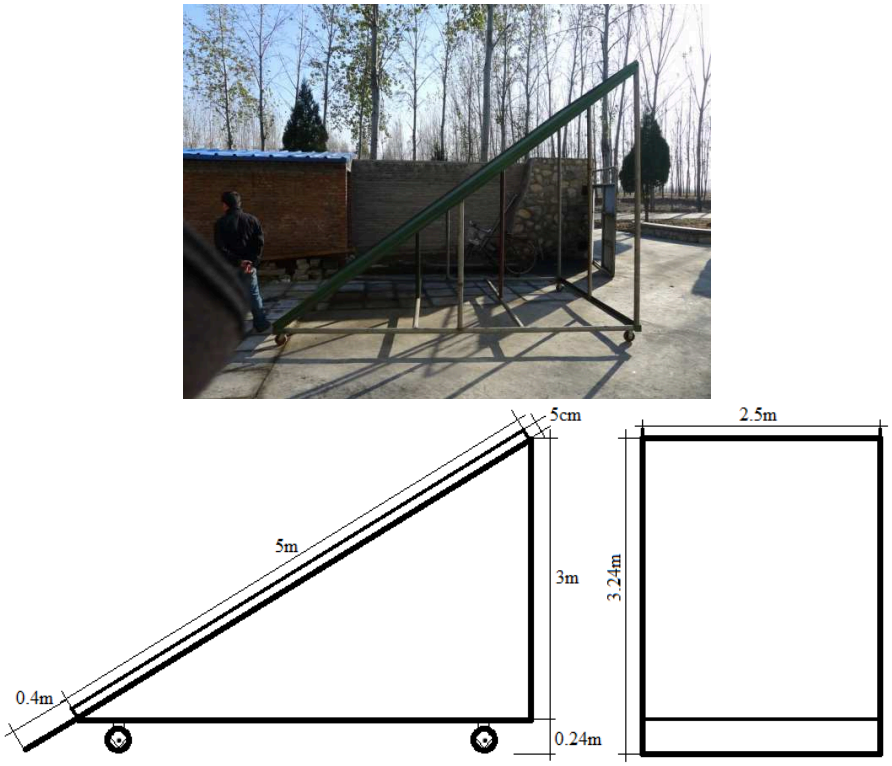


Figure 1 Photo and dimensions of the steel slope.

The experimental material is a homogeneous dry mixture of a certain amount of pebbles, coarse sands and fine sands, as shown in Fig.3. About 0.45m$^3$ experimental material is used in each experiment. Before experiment, about 1 kg material will be taken as an initial sample. After material being poured down the slope, another 11 samples will be taken from different positions of the deposit, as shown in Fig.4. Then all of the 12 samples are analyzed using standard gradation test. A series of geotechnical sieves is utilized, with the diameters of sieve pores being, respectively, 10mm, 6mm, 4mm, 3mm, 2mm, 1mm, 0.8mm and 0.6mm.

Figure 2 Bulldozer carrying experimental material.

Figure 3 Experimental material.

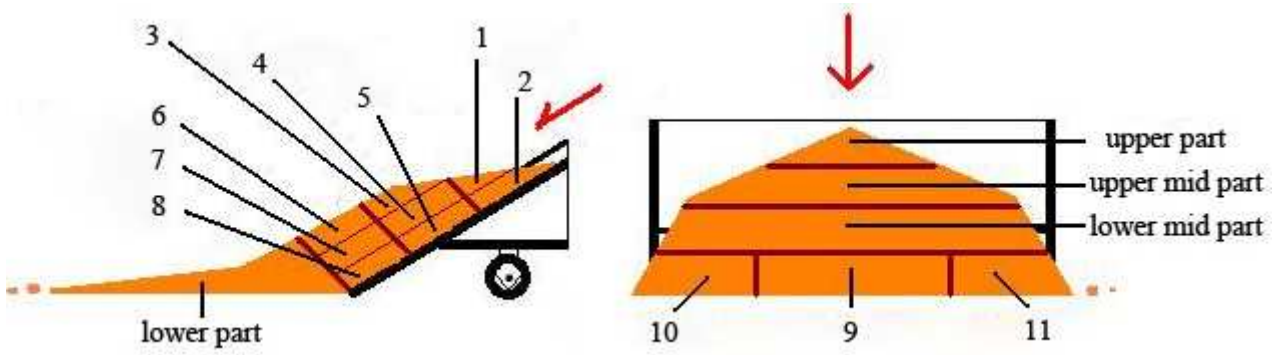


Figure 4 Sampling locations: 1) top layer of upper part, 2) bottom layer of upper part, 3) top layer of upper middle part, 4) middle layer of upper middle part, 5) bottom layer of upper middle part, 6) top layer of lower middle part, 7) middle layer of lower middle part, 8) bottom layer of lower middle part, 9) middle foot part, 10) right foot part, 11) left foot part.

## Results

Five experiments were conducted. In each experiment the initial grain size distribution of experimental material and the initial speed are slightly different.

The shape of the deposit is close to a triangle cone, as shown in Fig.5a. From the detailed view given in Fig.5b, inverse grading, which is an evidence of particle size segregation, can be observed.

We analyzed 60 samples from the 11 selected locations in the 5 experiments by sieving method. The results are shown in Fig.6.

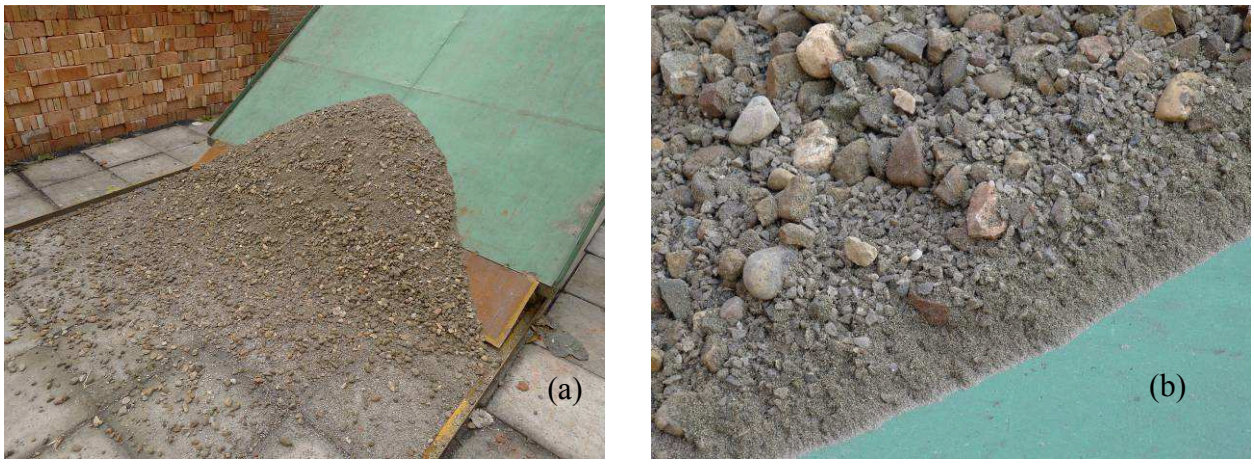


Figure 5 Shape and detailed view of the deposit.

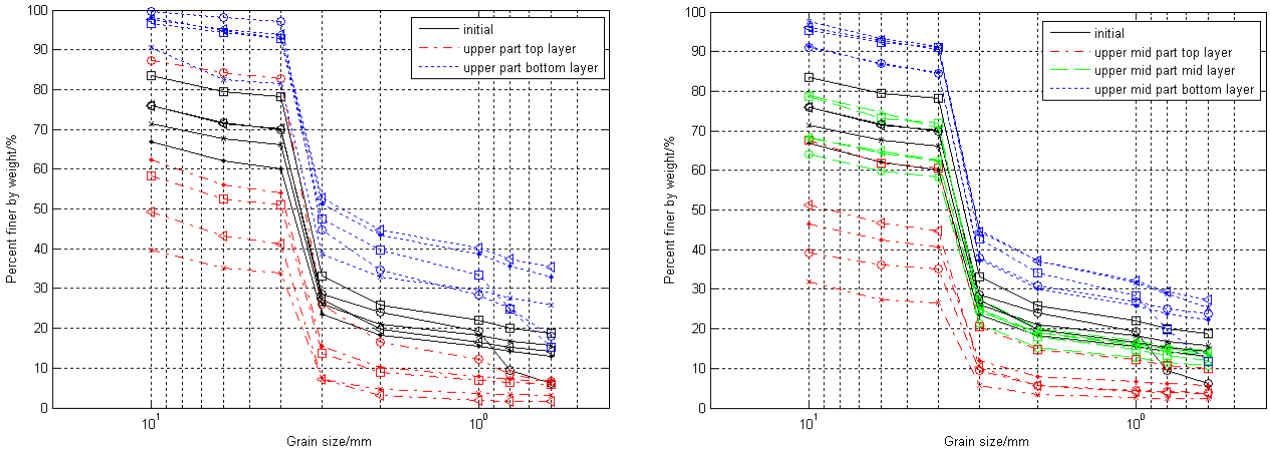


(a) upper part (b) upper middle part

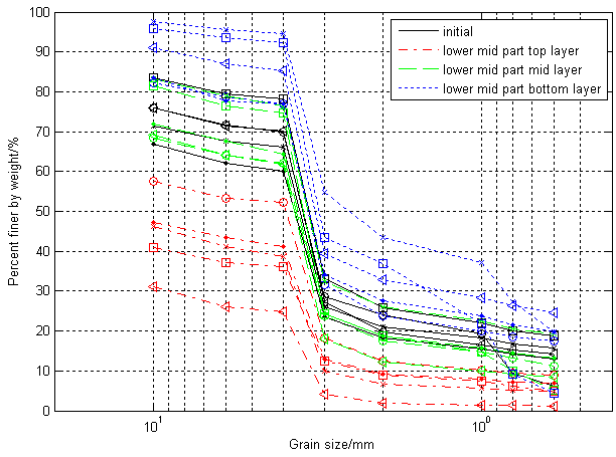


(c) lower middle part

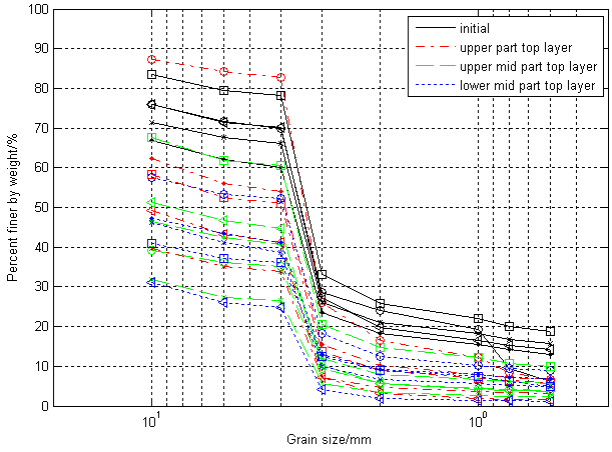


(d) top layers in different parts

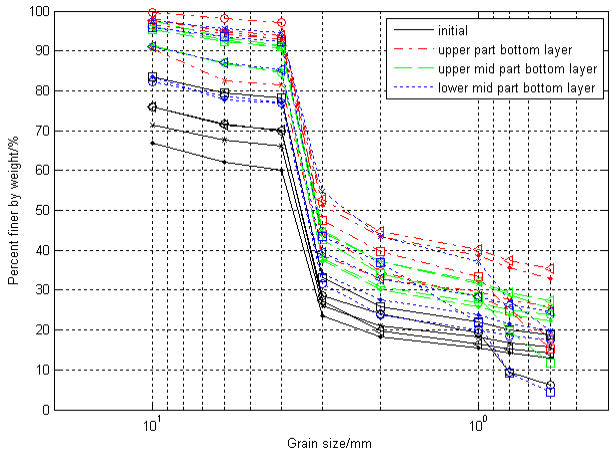


(e) bottom layers in different parts

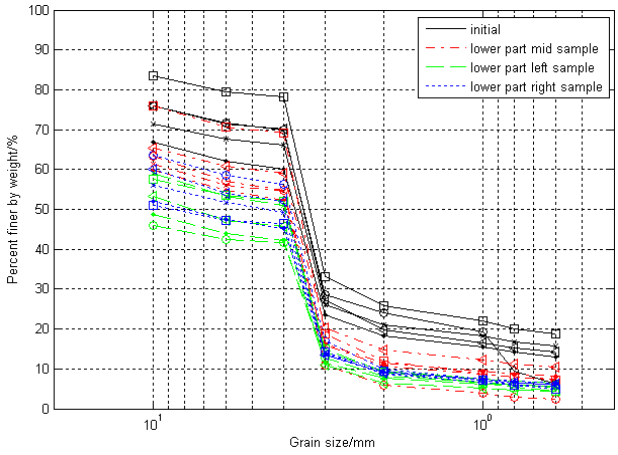


(f) lower part

Figure 6 Grain size accumulation curves of selected locations of the deposit.

Fig.6a to Fig.6c show the difference between different layers. It is shown in Fig.6 that the grain size of bottom layer is much coarser than those in top layer and initial sample. In most samples of top layer of upper part, 40% of the material is larger than 10 mm, and there are almost no grains $<2$mm. In contrast, about 95% of the material in bottom layer consists of grains $<4$mm. The same feature can also be seen in upper middle part and lower middle part, as shown respectively in Fig.6b and Fig.6c. Besides, the grain size of middle layer is between the sizes of top layer and bottom layer and is close to the size of initial sample. These are all the features of inverse grading.

Fig.6d and Fig.6e show the variation of grain size distribution in different parts, i.e., the upper part, the upper mid part and the lower mid part. Comparing the distributions with each other, no remarkable regularity can be obtained. The results in different experiments are diverse. However, for the grain size of top layers, in most of the experiments, the grain in upper part is finer than in both upper middle part and in lower middle part, while there is no relation noticed between distributions of upper middle part and lower middle part. And for the grain size of bottom layers, although the size distributions of different parts are close to each other, the grain size of upper part tends to be finer than other two parts.

Fig.6f shows the grain size distribution of lower part. Lower part is thinner and quite different from other parts. It is obvious that grain size in lower part is coarser than initial sample. Moreover, we can notice that grain size in the middle is finer than in the left and right.

## Conclusions

Experiments were conducted to investigate the grain size distribution within landslide dams. The results indicate that the grain size distribution varies in different parts of deposits. To be more specific, the phenomenon of inverse grading is obvious. Grains in the front of the deposit are coarser, while grains in the rear are finer. For the front of the deposit, grains in the middle are finer than the other two sides. Particle size segregation is convinced to be the governing mechanism that contributes to this special distribution. Meanwhile, according to the experimental results, we speculate the grain size distribution within land slide dams. The speculations are partly consistent with field investigations. Moreover, limitation of our experiments is discussed and suggestions for further study are proposed.

## Acknowledgements

This work was financially supported by the general program and key program of National Natural Science Foundation of China (11172147, 51039003) and the State Key Laboratory of Hydroscience and Engineering (2013-KY-2).

## References

[1] P. Cui, Y.Y. Zhu, Y.S. Han, et al.: Landslides, Vol.6, No.3 (2009), pp.209-223.

[2] N. Liu, Z.Y. Chen, J.X. Zhang, et al.: Journal of Hydraulic Engineering, Vol.136, No.11 (2010), pp.914-923.

[3] J.E Costa, R.L. Schuster: Geological Society of America Bulletin, Vol.100, No.7 (1988), pp.1054-1068.

[4] D.L. Fread: Hydrologic Research Laboratory, National Weather Service, NOAA (1988), pp.311-335.

[5] S.B. Savage, C.K.K. Lun: Journal of Fluid Mechanics, Vol.189 (1988), pp.311-335.

[6] J.M. Ottino, D.V. Khakhar: Annual Reviews of Fluid Mechanics, Vol.32 (2000), pp.55-91.

[7] A.R. Thornton, J.M.N.T. Gray, A.J. Hogg: Journal of Fluid Mechanics, Vol.550 (2006), pp.1-25.

[8] N. Casagli, L. Ermini, G. Rosati: Engineering Geology, Vol.69, No.1-2 (2003), pp.83-97.

[9] G.B. Crosta, P. Frattini, N. Fusi: Journal of Geophysical Research: Earth Surface, Vol. 112, No.F1 (2007), pp.F01006.

[10] S.G. Evans, R.L. Hermanns, A. Strom, et al.: Lecture Notes in Earth Sciences, Vol.133, Springer Berlin Heidelberg (2011), pp.479-498.

[11] G.H. Wang, R.Q. Huang, T. Kamai, et al.: Engineering Geology, Vol.156 (2013), pp.28-36.

[12] X.M. Fan, van C.J. Westen, Q. Xu, et al.: Journal of Asian Earth Sciences, Vol.57 (2012), pp.25-37.

*Applied Mechanics and Materials Vols. 580-583 (2014) pp 2108-2111*
*© (2014) Trans Tech Publications, Switzerland*
*doi:10.4028/www.scientific.net/AMM.580-583.2108*

# Relaxation Analysis of the Arch Dam Foundation Rock masses of Jinping Ⅰ Hydropower Project

Bi Xiao[1, a], Dongni Zhou[2,b] and Zhenghui Min[3,c]

[1]Changjiang Institute of Survey, Planning, Design and Research, Wuhan, 430010, China

[a]xiaobi@cjwsjy.com.cn, [b]bonnie_zhou1111@yahoo.com.cn, [c]minzhenghui@cjwsjy.com.cn

**Keywords:** Finite element method, Relaxation, Limit tensile strain, Jinping Ⅰ hydropower station

**Abstract.** The arch dam of Jinping Ⅰ hydropower station is on obvious high ground area, and the foundation rock masses may relaxed while excavating. Limit tensile strain is put forward to be relaxation criterion. By three-dimensional elastic-plastic finite element method analyzing, and imitating the dam excavating steps, the maximum principle strain of the dam foundation rocks is obtained. The research indicates that the maximum principal strain of upstream side is greater than that of downstream side commonly, and some area would relaxed, with 41m maximal relaxed depth. By engineer analogical research with Xiaowan arch dam foundation rock mass, which have relaxed while excavating, the calculate method and criterion of this paper are reliable, and they can provide reference for engineer design.

## Introduction

In high ground stress area, due to unloading relaxation effect, rock masses rebound deformation orientation the free face, with the ground stress reduce in superficial and concentration in a larger extend in deeper place of the slope. In the stress adjustment process, relaxation crack produced or original crack expand, which cause rock masses relaxation and weaken the rock masses [1, 2, 3]. For the important function of rock masses in arch dam foundation plane, it possess important value in theory and engineering practical to bring forward reasonable unloading relaxation criterion and analyzing the unloading relaxation scope.

Jinping Ⅰ hydropower station is locates on Sichuan province, which is an important cascade hydropower station. The installed capacity is 3600MW, and the dam type is concrete double curvature arch dam, with 1885m crest elevation and 305m dam height, which is the highest arch dam in the world. The dam site is a typical V shaped canyon, with strongly geology structure action. The bed rocks are mainly metamorphic rock, in addition, there is a small amount of lamprophyre vein(X), and some unfavorable geological structures exist, mainly are f2, f5, f8, f13 and f14. The rock masses are mainly weaken weathered. The ground stress measured on site indicates that first principal stress of more than 70% positions exceed 20MPa, with a few exceed 40MPa, which is of obvious high ground stress area. The geology structure of both banks slope is complex. Affected by stress releasing, gravity and other factors, the slope obviously rebound toward the free face.

## The finite element model and computation condition

The finite element model is constructed according to the geological condition and excavation steps. Along and transverse the stream are X and Y direction respectively, while Z direction is vertical upward. The calculation scope is 800m along the stream, 500m transverse the stream of both banks, and the elevation of the model bottom is 1300m. The model before excavation is shown in Fig.1, and the model after excavation is shown in Fig.2. There are 132686 nodes and 294057 elements, in which 63681 elements would be excavated. Developmental faults such as f2, f5, f8. f13, f14, lamprophyre vein(X) and superficial strong and weak unloading area are constructed in the model.

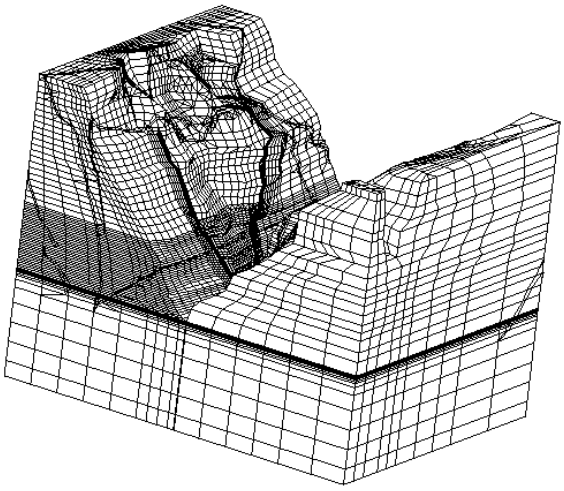

Fig.1 The FEM model before excavation

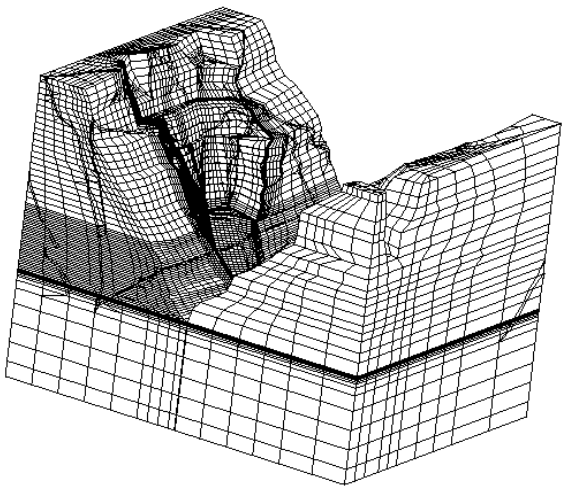

Fig.2 The FEM model after excavation

On the basis of the geological exploration on site and designers' suggestions, material parameters are as Table 1.

Table 1 Material parameters

| Material classification | Deformation modulus (GPa) | Poisson ratio | Unit weight ($MN/m^3$) | Cohesion strength (MPa) | Angle of internal friction ($^o$) |
|---|---|---|---|---|---|
| II | 26 | 0.22 | 0.0280 | 2.0 | 53.5 |
| III1 | 12 | 0.25 | 0.0278 | 1.5 | 46.9 |
| III2 | 8 | 0.27 | 0.0274 | 0.9 | 45.6 |
| IV1 | 3 | 0.30 | 0.0270 | 0.6 | 35.0 |
| IV2 | 2 | 0.30 | 0.0265 | 0.4 | 31.0 |
| V | 0.4 | 0.35 | 0.0265 | 0.02 | 16.7 |
| faults | 0.4 | 0.35 | 0.0265 | 0.02 | 16.7 |

The initial ground stress field is obtained by regression analysis based on measured stress on site. The load is mainly dead weight. Because the natural underground water level is low and the rocks are porous, the seepage field is not taken into consideration. The computation software is self-making FEM [4, 5, 6], which is based on elastic-plastic theory and bolted jointed rock masses model. The software had been successfully used in many major hydropower engineering.

According to the designed construction order of the arch dam foundation rock masses, 27 excavation steps are divided to simulate the excavation process. The yield criterion is D-P equivalent circle criteria, whose degree of safety is between the inscribed circle and the circumscribed circle.

Currently, there is no maturity unloading relaxation criterion for arch dam foundation rock masses. The physical quantities those used are mainly displacement, stress, point safety degree, strain, and so on. While excavating, the rock masses with larger displacement, massive stress reduce, minor point safety degree probably be relaxed. But these are just relative qualities. We consider the reason why the rock masses relaxed is strain exceed the limit tensile strain of the material in some direction, thus lamellar fractures appeared perpendicular to the direction. The limit tensile strain can be obtained by testing. So limit tensile strain is adopted to judge rock masses relaxation. By consulting the designers, the limit tensile strain of foundation rock masses( except exposure faults and their influence areas) of Jinping Ⅰ hydropower station is 0.0002. It should pay attention that the strain here is not strain increment while excavating, but total strain, which contains both initial strain caused by initial ground stress and strain increment while excavating.

**Relaxation analysis**

The maximum principal strain contour map is shown in Fig. 3, and the maximum principal strain contour map of typical cross section of the foundation, which is along the arch dam axis, is shown in Fig. 4.

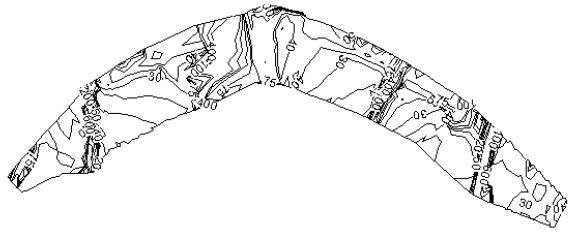

Fig.3 The maximum principal strain contour map

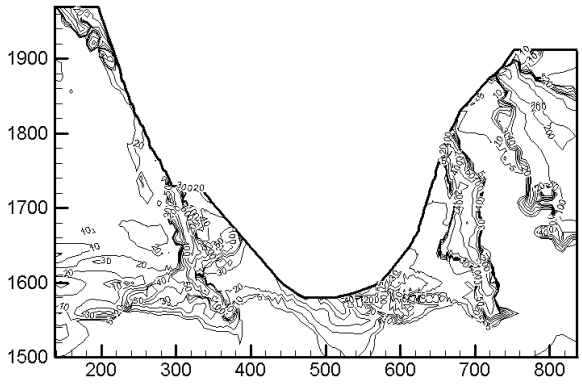


Fig.4 The maximum principal strain contour map of typical cross section

It can be seen from the figure that: (1) the maximum principal strain of upstream side is greater than that of downstream side commonly; (2) while 0.0002 is adopted as the limit tensile strain of the foundation rocks, the areas that would relaxed are shown by thick lines in Fig. 5; (3) if the limit tensile being lager than 0.0004 is adopted as criterion for strongly relaxation, the areas would be strongly relaxed are shown by thick lines in Fig.6; (4) the relaxation depth of the left bank is 22.5m in the elevation of 1610m, 17.5m in the elevation of 1590m, and 26.5m in the elevation of 1580m; the relaxation depth of the middle riverbed is 41m in the elevation of 1580m, and rock masses in the elevation of 1670m of the right bank would not relaxed. Being affected by locational faults or fracture zone, relaxation depth of rock masses in these places cannot be analyzed.

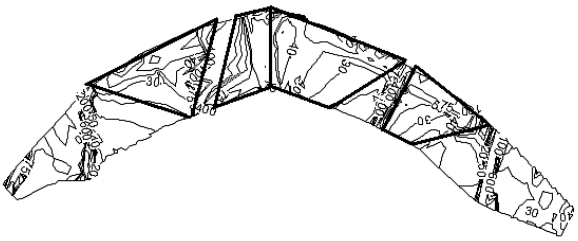

Fig.5 Foundation areas that would relax

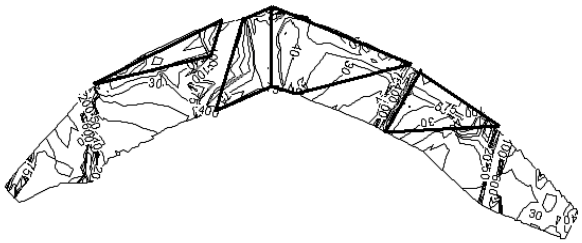

Fig.6 Foundation areas that would strongly relax

**Engineering analogical research**

Considering that there is no enough proven on relaxation criterion of arch dam foundation rock masses, Xiaowan arch dam, which is similarly high arch dam in high ground stress area, is adopt as example of analogy engineering and engineering analogy analysis is carried out. Lower foundation rocks of Xiaowan dam are mainly weak weathered or fresh granite gneiss, with no exposed large fault. By consulting the designers, the limit tensile strain of the rock masses is 0.00015.

After calculate on Xiaowan project by the same computation method and relaxation criterion, we can conclude that (1) the foundation rock masses under the elevation of 990m on the left bank and 975m on the right bank would relaxed; (2) the relaxation depth of the left bank is 8.5m in the elevation of 990m, 8.5m in the elevation of 975m, and 8.0m in the elevation of 953m; the relaxation depth of the right bank is 8.5m in the elevation of 953m, 2.0m in the elevation of 975m; the relaxation depth of the middle riverbed is 9.0m in the elevation of 953m.

The foundation rock masses of Xiaowan arch dam relaxed while excavating. Compared with the actual foundation rock masses relaxation while excavating Xiaowan arch dam foundation, the calculated relaxation scope and depth are consistent. So, it indicates that the above calculate method and relaxation criterion are reliable. According to the analogical research results, the foundation rock masses of arch dam of Jinping Ⅰ hydropower station would probably relaxed after excavation.

## Conclusions

Rock masses excavating in high ground stress areas would relaxed. Limit tensile strain is put forward to be relaxation criterion in this paper. Three-dimensional finite element model of dam site of Jinping Ⅰ hydropower station is constructed. By elastic-plastic finite element method and imitating the excavating process, the maximum principle strain is obtained. The analyses indicate that the maximum principal strain of upstream side is greater than that of downstream side commonly. After compared with limit tensile strain of the rock masses, which obtained by consulting the designers, the maximum principal strain of rock masses in some area is larger than the limit tensile strain of it. So the rock masses in some area may relax. By analyzing the typical section, the maximum relax depth is about 41m. Xiaowan arch dam was adopt as example of analogy engineering and engineering analogy analysis was carried out. It indicates that the calculate method and excavation criterion are reliable. According to the analogical research results, the foundation rock mass of arch dam of Jinping Ⅰ hydropower station would probably relaxed.

The research of this paper is preliminary, and the theory of rock masses unloading relaxation is complex. There are following shortages remain which need further researching: (1) rock masses is usually bolted while excavation and unloading relaxation is varied with time, which are not taken in consideration in this paper; (2) the unloading relaxation criterion of limit tensile strain have not applied commonly, which need to be proven in more engineering practices.

## References

[1] Xu Dong-jun GENG Nai-guang. The various stress paths causing deformation and failure in rocks[J]. Rocks and Soil Mechanics, 1986, 7(2):17-25. (in Chinese)

[2] WU Gang. Comparison of failure effects of rock mass under loading and unloading conditions[J]. Rocks and Soil Mechanics, 1997, 18(2):13-16. (in Chinese)

[3] HA Qiu-ling. Rock slope engineering and unloading nonlinear rock mass mechanics[J]. Chinese Journal of Rock Mechanics and Engineering, 1997, 16(4): 386-391. (in Chinese)

[4] CHEN Sheng-hong, QIANG Sheng, CHEN Shang-fa, Study on the three-dimensional composite element model of bolted rock masses [J]. Chinese Journal of Rock Mechanics and Engineering, 2003, 22(1): 1-8. (in Chinese)

[5] QIANG Sheng, CHEN Sheng-hong. Three dimensional elasto-viscoplastic composite element model for discontinuous rock masses [J]. Chinese Journal of Rock Mechanics and Engineering, 2004, 23(20): 3390-3396. (in Chinese)

[6] CHEN Sheng-hong, PETER Egger, XIONG Wen-lin. Rheological model and three dimensional elasto viscoplastic finite element method of jointed rock masses reinforced by bolts[J]. Journal of Hydraulic Engineering. 1998, (9):23-29. (in Chinese)

# CHAPTER 6:

# Coastal Engineering

*Applied Mechanics and Materials Vols. 580-583 (2014) pp 2115-2119*
*© (2014) Trans Tech Publications, Switzerland*
*doi:10.4028/www.scientific.net/AMM.580-583.2115*

# Research on the Influence of Diking in Shallow Sea of Tangdao Bay on Marine Environment

Yun Hai Xu[1, a], Xiao Hui Hao , Xin Mei Dong

[1]Li Shan Road 125, JiNan China

[a] xuyunhai1963@163.com

**Keywords:** TangDao Bay, Marine Environment, Flow Filed, Numerical Simulation

**Abstract.** In the process of comprehensive treatment for the Tangdao Bay in Qingdao,the dikes need to be constructed firstly and then the construction for treatment can be started,in this paper,the author uses the two-dimensional mathematical model to analyze the change of the flow field in the water area of Tangdao Bay before,during and after the diking construction in simulation and analyze the influence on the marine environment after diking.By use of the diking method of throwing sand in jute bags,the new secondary pollution caused in the diking construction process can be prevented effectively and nice economic and social benefits can be obtained.

## Introduction

Tangdao Bay extends from the northeast to southwest with the depth of 4.5 km and width of 2.5 km,The bay is in narrow long pocket shape with the area of 17km$^2$ and coastal line of about 23.9 km.Niu Dao is located in the middle of the bay with the area of 0.2km$^2$.In the low tide,it can be connected to the continent. In recent years,the sludge accumulation is very serious in the water area of the bay,which affects the sailing line and environment of water body.Recently,the comprehensive treatment project for the Tang Dao Bay includes sludge clearance,wharf,port pool and sailing line construction,etc.,of which the area of sludge clearance section is 2.602 million m$^2$and the total volume of sludge excavation is 7.132 million m$^3$.However,there are thousands of acres of mariculture farm in the open sea area of NiuDao and the farm is connected to the sludge clearance area.If no engineering measures are taken in the construction,a lot of sludge, sand and contaminated water will surge into the open sea from the south side and north side as the tide rises and falls,causing the whole TangDao Bay and even the open sea become muddy.Consequently, not only the farm is severely affected,but also the natural ecological resources of the sea are damaged. According to the natural conditions and construction requirements, to protect the farm in the open sea from being affected,maintain the natural ecological resources of the sea, the treatment area needs to be isolated from the open sea to prevent causing new secondary pollution in the diking construction process and provide good environment for the treatment engineering. After technical and economic comparison,the scheme of diking in the shallow sea is used.In this paper, the author analyzes the influence of diking on marine environment by the numerical simulating calculation to the flow field in the bay before and after dike is built.

## Calculation and Analysis for Change in the Flow Field before and after Diking

2.1 Features of TangDao Bay Area

The water is shallow in the Tang Dao Bay. According to the topographic map for the interior part of TangDao Bay, the relation between the water level and water area, water storage volume inside the bay is as shown in the table 1.

Table 1 Relation between the Water Level and Water Area, Water Storage Volume inside the Bay

| Water Level (m) | -2.42 | -1.48 | -1.08 | -0.3 | 0.5 | 1.08 | 2.08 |
|---|---|---|---|---|---|---|---|
| Water Area (Ten thousand m$^2$ ) | 35 | 70 | 240 | 550 | 630 | 680 | 690 |
| Water Volume (Ten thousand m$^3$ ) | 80 | 130 | 192 | 500 | 972 | 1352 | 2037 |

### 2.2 Overview for Diking Engineering

The dikes newly built are located in the south side and north side of NiuDao and divided into the south dike and north dike with the length of 809.1 and 605m respectively,the maximum height of 11.7 m； The width at the top of the dikes is 5 m and the backpressure platform of 5～15 m is set at the either side.The material used for building the dikes is the jute bags filled with sand.Before the erection and water blocking in the engineering, the sea water freely accesses into the bay area for treatment; According to the construction organization and design,a posterior built section of diversion gap is set at the trench of the south dike with the length of 150～200 m and the filling elevation 0.5～1.0 m lower than other dike sections.The flow rate and flow regime of sea water at the reserved gap and entrance are uniform and also easy to be observed and controlled.When the whole dikes are built above the designed high water level,the horizontal closure and erection are performed and the diking task is completed.

### 2.3 Hydrological Computation Data

#### 2.3.1 Designed Wave Height

Because NiuDao is located at the northwest～southeast direction of NiuDao, only the designing wave factors at different recurrence interval for the section of NiuDao～ancient pier in the high tide need to be calculated. According to the forecasting method regulated in the *Technical Code for Port Engineering* , it is calculated the designed wave height of one occurrence in ten years for the section of Niu Dao is 1.40 m.

#### 2.3.2 Tide and Tidal Current

Results of statistics and harmonic analysis indicate the main amplitude rate between the solar and lunar semidiurnal constituent for Tang Dao Bay is 0.25,The tidal current of TangDao Bay belongs to the semidiurnal constituent, and the movement form of tidal current is reciprocating flow pattern.

According to one-month tide data and the synchronous data of big port, it is calculated that the mean duration for tide rising in the bay is 5h 45min, the mean duration for tide falling is 6h 39min, the mean monthly maximum tide water level is 1.08 m, the mean monthly minimum tide water level is -1.48m and the mean monthly seal level is -0.19m.

The possible maximum flow rate of tidal current and the possible maximum movement distance of water particles in the bay are about 1.1m/s and 11.3km respectively.

### 2.4 Numerical Simulation Calculation

2.4.1 Establishment of Numerical Model

Because the water is shallow in TangDao Bay, the two-dimensional mathematical model is used for simulation. The equation set for the mean shallow water with the two-dimensional depth is:

$$\frac{\partial \zeta}{\partial t} + \frac{\partial (Hu)}{\partial x} + \frac{\partial (Hv)}{\partial y} = 0 \tag{1}$$

$$\frac{\partial u}{\partial t} + u\frac{\partial u}{\partial x} + v\frac{\partial u}{\partial y} - fv + \frac{\tau_{bx} - \tau_{ax}}{H} + g\frac{\partial \zeta}{\partial x} = 0 \tag{2}$$

$$\frac{\partial v}{\partial t} + u\frac{\partial v}{\partial x} + v\frac{\partial v}{\partial y} + fu + \frac{\tau_{by} - \tau_{ay}}{H} + g\frac{\partial \zeta}{\partial y} = 0 \tag{3}$$

$$H = h + \zeta \tag{4}$$

In the equation set: t is time; ζ is the water level; H is the overall water depth; h is the depth of undisturbed water depth; μ and ν are components of flow rate of sea water along x, y directions respectively; f is Coriolis coefficient; g is accelerated speed of gravity; τhx, τhy are components of frictional force along x, y directions respectively; τax, τay are components of wind-stress along x, y directions respectively.

Calculating the boundary conditions:

The normal flow rate at the closed boundary is 0 and the tide equation at the open boundary is:

$$\xi = \sum_{i=1}^{N} f_i H_i \cos[\sigma_i t + (V_{ot} + V_i) - G_i] \tag{5}$$

In the equation, N is the number of constituent, fi, σi, (Voi+Vi) are intersection point factor, angular frequency and initial phase of tidal constituent no. i respectively; Hi, Gi are amplitude as well as late angle adjusting and constant of tidal constituent no. i respectively.

The influence of overland runoff increased by the rainfall is not taken into account.

The initial condition is set as 0, namely: μ=ν=ζ=0

The ADI method is used for the array of difference. The gridding distance in x direction is set as 75 m and the gridding distance at y direction is set as 92 m.

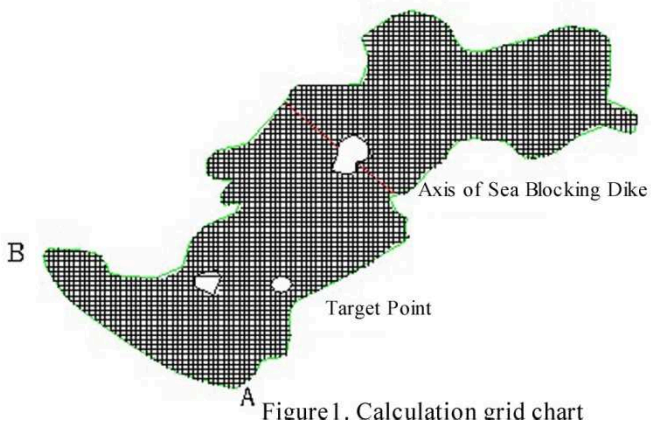


Figure 1. Calculation grid chart

The step length of calculation is set as 6 seconds.

Calculation grid chart is shown in Figure 1.

2.4.2 Change of Flow Rate, Water Level before and after Diking

The section A-B is selected to predict the change of the tide surging volume. The calculation indicates the tide surging volume is $2.99\times10^7 m^3$ before diking and the tide surging volume is $2.73\times10^7 m^3$ after diking, reducing by $3.6\times10^6 m^3$ compared with the one before diking. Figure 2 is the calculation result of the change of flow rate at the representation point in the target sea area. From the figure 2, it can be seen that the change of flow rate before and after the diking is within ±0.22m/s, increasing or decreasing by 25% compared to the original one; it indicates the diking has certain influence on the tide field of the bay.

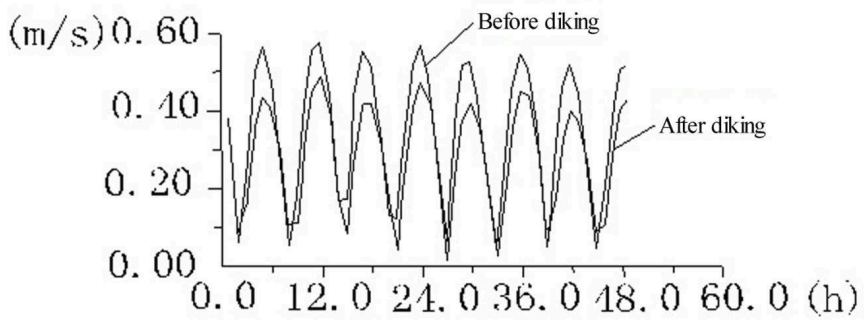


Figure 2 Change of Flow Rate as Time at Some Representation Point before and after Diking

In the process of dikes construction, the calculation and analysis for the change of water flow is: In the process of erection in the construction of dikes, the change of water level and flow rate at the closure gap is large; thus, the hydraulic power is calculated according to the following formula:

$$Q = \sum b_i \varepsilon m \sqrt{2g}\,(H_{\text{outer}} - H_{\substack{\text{elevation of the bottom} \\ \text{of sluice and entrance}}})^{3/2}\,\sigma$$

In the formula, Q is the flow passing through the closure gap; ∑bi is the overcurrent width; H is the water depth; σ is the submerging coefficient.

Figure 3 and figure 4 are the change of water level as the time when the overcurrent width is 100m and 50 m respectively. According to the water level, the maximum flow rate is calculated to be 2.8m/s.

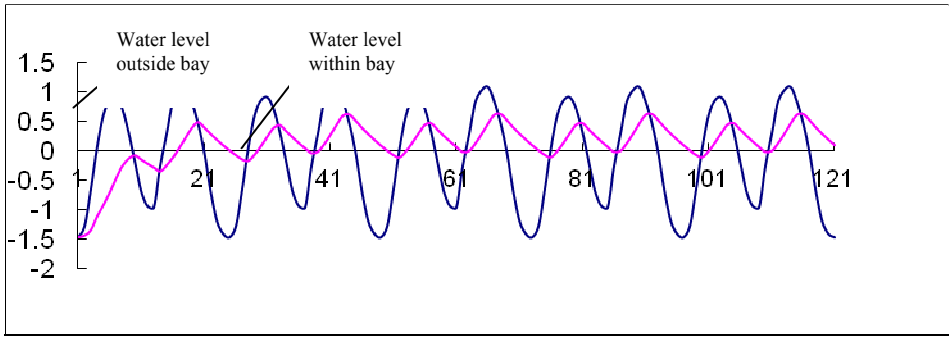


Figure 3 Change Process of Water Level When the Overcurrent width is 100 m

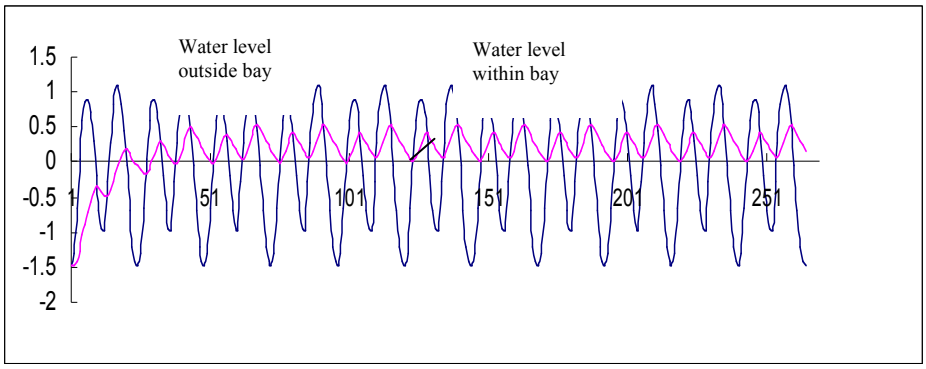


Figure 4 Change Process of Water Level When the Overcurrent width is 50 m

### 2.5 Analysis for Change of Flow Field and Engineering Measure

From the calculation results, it can be seen that change occurs at the flow field of the bay in comparison before diking and after diking. Generally, the flow rate is reduced somewhat and water exchange weakens, however, it doesn't cause great influence on the water environment in the bay; In the diking process, the flow cross-section at the erection opening, the flow rate is nearly increased by two times and the movement distance of water particles is nearly increased by tow times accordingly, so it is liable to cause pollution to the open sea and affect the engineering effect if no measures are taken.

In the erection for diking, the engineering measures to be taken include replacing the diking by the jute bags filled with sand with diking by throwing sand in jute bags, and the sand is pure medium sand; controlling the clay content within 1.5%. Because the measures above are taken,no new secondary pollution is caused in the construction, achieving the expected objective.

## Summary

From the calculation results, it can be seen that change occurs at the flow field of the bay in comparison before diking and after diking；Generally, the flow rate is reduced somewhat and water exchange weakens. By use of the diking method of throwing sand in jute bags, the new secondary pollution caused in the diking construction process can be prevented effectively and good economic and social benefits can be obtained.

## References

[1] *Sea Reclamation Works of China*, China Water Power Press, Oct. 2000.

*Applied Mechanics and Materials Vols. 580-583 (2014) pp 2120-2123*
*© (2014) Trans Tech Publications, Switzerland*
*doi:10.4028/www.scientific.net/AMM.580-583.2120*

# System Analysis of Construction Quality Control Measures of Coastal Levee

Xinquan Wang[1,a], Hong Li [2,b], Shangyu Han [3,c]

[1] Zhejiang University, City College ,Hangzhou, China

[2] Nanchang University, College of Science and Technology, Nanchang, China

[3] Nanchang Hangkong University, College of Engineering and Architecture, Nanchang China

[a]547369461@qq.com, [b]492517673@qq.com,[c] hanshangyu1979@163.com

**Keywords:** Coastal Levee Construction; Quality Accident; Monitoring System; Quality Inspections; Early Warning System.

**Abstract:** The phenomenon of the actual situation leave the design index is very common during the civil project construction especially in the coastal levee construction. As the way to reduce the probability of diseases occurrence, from the aspect of quality accident analysis, construction quality monitoring moisture, quality inspection and accident early warning system, the paper studied the levee construction quality control monitoring system deeply and advanced some useful conclusion.

## Introduction

Recent years, the design theory and quality control theory has made great progress in coastal moisture levee construction, but still some shortcoming, mainly reflected in the comprehensive knowledge of many quality affecting factors, quality control systems are imperfect, and so on, resulting in frequent quality accidents during the project construction especially in the coastal levee construction.

In response, some scholars have conducted targeted research. Liu Ying-xin[1] think we can do project quality comprehensive evaluation and control from the physical quality of proposed projects, quality assurance data, design quality, environmental factors and other aspects. Li Xu-hui[2] emphasized the emphasis of quality control is the "cause" control. Li Hua-ming[3] proposes using the Gray Markov model to predict the quality and optimal cost. Liu Hui-ming[4] proposed the standardized criteria of seawall proof. Wang Ke-qin[5] studied height elevation of land formation, embankment and wave retaining wall by analysis the design principles, moisture-proof system division, moisture standards.

## Coastal Levee Quality Accident Analysis

A．Levee stability

Landslide is the disease phenomenon when the levee slope instability. The Cracks began to appear at the top of the levee or the levee slope, with the development of cracks the landslide formed. For the prevention and treatment of stability problems, the participation unit of the project should strengthen the genesis of key sections of the site inspection and monitoring, forecasting the danger timely. And focusing on the levee analysis and cracks monitoring, clarify the cause of the cracks.

B．Levee seepage

Water or other fluids flow in the rock medium such as pores or fissures, referred to as seepage. Moisture seepage control is very important to ensure the security and stability of the levee, if the seepage problem cannot be resolved, will lead to an immeasurable loss. The levee seepage damage mainly includes piping, seepage loopholes, pit (or nest, collapse pits) and so on.

C．Crack

Crack is the common danger in the levee construction and operation; sometimes it may be a harbinger of other dangers. From the aspect of parts appear, the cracks can be divided into surface

cracks and internal cracks; from the causes of the cracks it can be divided into uneven subsidence cracks, landslides and cracks, shrinkage cracks and vibration cracks.

D. Storms scour

Moisture levee embankment will be storms during its construction, if the phenomena cannot be controlled timely, along with the development of scour, it will endanger the safety of the levee.

## Quality Accident Relationship

The relationship of the upper quality accident is very complex, from a macro aspect, it can be predigest as Fig.1.

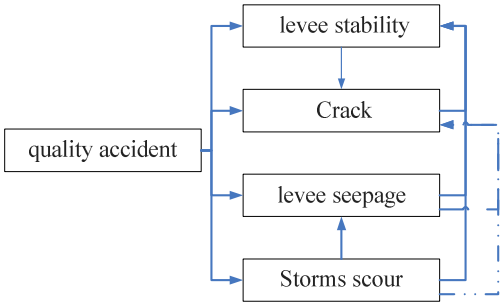


Fig.1 The relationship of the quality accident

## Quality Monitoring System of Coastal Ievee

Controlled by a large number of uncontrollable factors, the actual construction process of the quality indicators often deviation from the expected case. The purpose of monitoring in the process of the project construction is done by setting a series of on-site monitoring program, with the help of modern means of monitoring to identify the actual state of the construction quality.

## Monitoring Items Analysis

Current levee monitoring items always including labor inspection, surface subsidence monitoring, deep horizontal displacement monitoring, pore water pressure monitoring, slope horizontal displacement monitoring, crack monitoring, soil pressure monitoring. The results of surface subsidence monitoring can be used for the evaluation of the levee settlement. The deep horizontal displacement, crack monitoring, pore water pressure monitoring primarily reflects the steady state. The earth pressure monitoring is used to reflect the stress state of the earth structures, levee soil pressure inside the levee.

A. Monitoring Systems Design

Based on the actual situation of one levee construction project, the monitoring system can be designed as Fig.2.

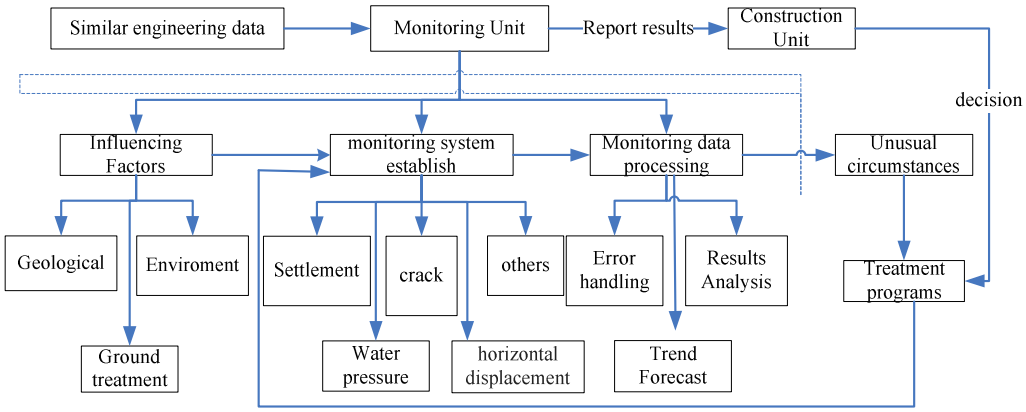


Fig.2 Monitoring system of levee construction project

## Coastal Levee Construction Quality Inspections

As the way to ensure the quality of levee construction, some projects often need to inspect the engineering quality based on the actual situation of the project and related specifications testing.

A. Slope engineering inspection

Content slope engineering testing including: concrete revetment thickness, strength of concrete, concrete samples described, cushion thickness and particle analysis and so on.

B. Revetment engineering inspection

The main content of revetment engineering inspection is to detect the underwater riprap section line.

C. Building quality inspection

The content of building quality inspection includes: Detection the variety of raw materials, mainly test the physical and mechanical properties of materials; Concrete testing, take the on-site sample to do some laboratory test.

D. Seepage engineering quality inspection

The content of seepage engineering quality inspection include: the on-site detection of various materials' (including cement, admixtures, sand, stone, etc.) physical and mechanical properties on-site detection; cutoff wall quality testing, including the wall material quality testing and integrality detection of wall .

## Establishment of Accident Early Warning System

System for the quality control of levee construction not only according to the specification and design requirements for the engineering quality control, also according to the field monitoring, detection data, factor analysis, risk assessment, which can be helpful to make an accurate analysis of the accident trend and accident state.

A. Function analysis of early warning system

The function of levee engineering quality early warning system mainly manifests into three aspects, namely the alarm function, emergency function and recovery function.

(1) Alarm function

Alarm function includes the monitoring, feature recognition, diagnosis and alarm of the construction management and disease status. It does this by setting the boundaries of various diseases, and forecasting the behavior of some possible diseases or phenomena that may arise to the imbalance state, which can be useful to standardize the construction process.

(2) Emergency function.

Emergency function is according to the alarm information and risk trend, take preventive measures in advance to prevent the occurrence of diseases and ensure project quality.

(3) Recovery function.

The recovery function refers to the alarm control failure, engineering accident occurs, a passive remedial action taken. It is in accordance with the project monitoring data and information related to the accident, decision analysis, to determine the appropriate remedial measures which can helpful to ensure the engineering loss at a minimum.

B. Warning implementation process

According to the security early warning theory, combined with field monitoring data and test results, the levee project early warning process consists of identifying alert, looking for the alert source, analyzing the warning signs, warning and alarm response decision-making. The useful early warning process is shown in Fig.3:

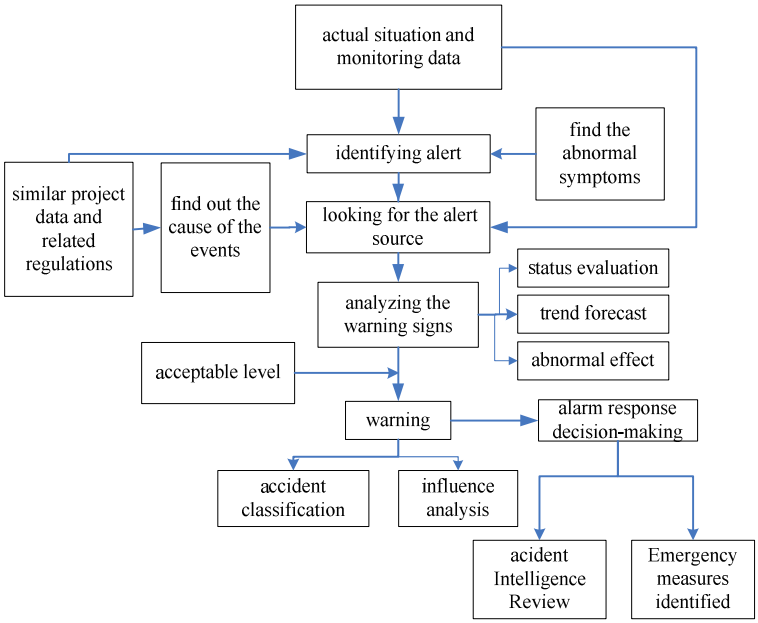


Fig.3 Early warning process sketch of levee project

## Summary

Combined with the actual situation and the researches of levee construction, the paper studied the levee construction quality control monitoring system from the aspect of quality accident analysis, construction quality monitoring moisture, quality inspection and accident early warning system, get the following conclusions:

A. In order to improve the quality of the project, the construction unit should pay more attention on the possible accident and establish reliable monitoring and inspection system during the construction process.

B. Reasonable set of project monitoring and detection systems are very helpful to improve the construction quality and reduce the probability of occurrence of disease.

C. Timely and accurate warning for variety possible exceptions is most important measure to reduce the occurrence of disease during the levee construction.

## References

[1] Liu Ying-xin, Li Qing-li. 1998. An Evaluating Method of Building Quality[J]. JOURANAL OF NROTHERN JIAOTONG UNIVERSITY, 22(1):92-95

[2] Li Xu-hui. 2006. Study on Owner Project Management System[J].Construction Management Modemization, 89(4):23-26.

[3] Li Hua-ming.2009. System analysis and optimization control of the construction quality cost [D]. Xi'an University of Architecture and Technology

[4] Liu Huiming, Li Weitao. 2008. Study of seawall Standard. [J]. China water resources. (16) :29-33.

[5] Wang Ke-qin, Dong Cheng-zan. ,2009. Discussion on Tide-break & Flood-control Standards and Elevation Design for the Phase I Project of Reclaiming Fields from the Sea in Tianjin Lingang Industrial Park[J]. Port Engineering Technology,186(46):16-19.

*Applied Mechanics and Materials Vols. 580-583 (2014) pp 2124-2128*
*© (2014) Trans Tech Publications, Switzerland*
*doi:10.4028/www.scientific.net/AMM.580-583.2124*

# Experimental Study on Mooring Manner and Safety Operation for 450,000DWT Supertanker

Bing Jiang[1,2,a], Xuanjun Huang[3,4,b], Yingxue Lv[3,4,c],Xianbo Zhang[3,4,d]

[1]National Marine Data and Information Service, Tianjin, 300171, China

[2]The Key Laboratory of Digital Oceanic Science and Technology, SOA, Tianjin, 300171, China

[3]CCCC Tianjian Port Engineering Institute Co. Ltd., Tianjin, 300222, China

[4]CCCC-key Hydrodynamic Laboratory for Coastal Engineering, Tianjin, 300222, China

[a]jiangbing@mail.nmdis.gov.cn, [b]huangxuanjun@tpei.com.cn, [c]lvyingxue@tpei.com.cn, [d]zxianbo@163.com

**Keywords:** Supertanker, Steel line, Cable force, Mooring manner, Experiment Research

**Abstract.** At present, many oil tank wharfs of 300,000DWT which taken the maximum of 450,000DWT supertanker into account had been built in our country. In this paper, through the physical model test on 450,000DWT supertanker, the mooring line tension with different mooring arrangements, cable diameters and cable materials were studied and the wave condition for the supertanker safety operation was given. The results showed that: on the same wave condition, to increase the steel cable's diameter could reduce the ship's movements, which could enhance the ability to operation. In addition, using the combination cable on the same diameter instead of the steel cable could reduce the tension of mooring line and increase the working ability effectively. The research results can provide reference and guidance for the future of supertankers mooring operation.

## Introduction

With the rapid development of the international petroleum sea transportation, the scale and the capacity of the oil tanker were increased quickly. Now the main large oil tanker in active service is 300,000DWT[1]. Since 2002, South Korea's Daewoo heavy industries build four 450,000DWT supertankers with double hull, then the capacity of the oil tanker was developed to 450,000DWT supertanker gradually. For this purpose, many domestic wharf structure of 300,000DWT oil tanker was designed for the 450,000DWT supertanker. Such as 300,000DWT crude oil wharf of Qingdao port, 300,000DWT crude oil terminal of Caofeidian port, 300,000DWT fuel oil wharf of Ningbo, 300,000DWT crude oil wharf of Quanzhou and so on. Based on the experiment of mooring manner and the safety operation condition for 450,000DWT supertanker carried out by the combined action of wind, wave and current, it can be shown that the different cable diameter and cable material had the influence of the ship movements and line tensions, and the wave condition for the supertanker safety operation was given. The research results can provide reference and guidance for the future of supertankers mooring operation, which has the great realistic significance and research value.

## Experimental Condition

**Vessel Parameters.** The vessel size information and the dynamic parameters of the 450,000DWT supertanker were shown in table1.

**Design Layout Plan of Terminal.** The terminal is composed of one working platform, two fender dolphins and six mooring dolphins with the butterfly layout. The berth length is 455m. Every fender dolphin installed two C3000H standard rubber fender with a drum a board, the designed reaction force is 4400kN.

**Arrangement and Parameters of Mooring Lines.** There were three kinds of cable specifications:

The steel cable of the diameter 44mm, which break force was 1070kN.

The steel cable of the diameter 52mm, which break force was 1470kN.

The combination cable of the diameter 52mm, which break force was 1470kN. The combination cable mainly for the steel cable and the hook joint with 15m long nylon cable of the diameter 100mm.

The arrangements of steel cable of the diameter 44mm and 52mm were 3-4-4-3, the arrangements of combination cable of the diameter 52mm was 4-3-3-2, the different arrangements were showed in Fig.1a and Fig.1b.

Table 1 450,000DWT supertanker parameters

| Vessel Scale | | | | | |
|---|---|---|---|---|---|
| Length overall (m) | | Breadth (m) | | Depth (m) | |
| 380 | | 68 | | 34 | |
| dynamic parameters | | | | | |
| Loadage | Displacement(t) | Draft(m) | Gravity Center High(m) | Buoyant Center High(m) | Rolling Period(s) |
| Full Load | 555527 | 24.5 | 23.03 | 13.45 | 16.31 |
| Ballast | 176145 | 10.74 | 20.71 | 6.62 | 9.36 |

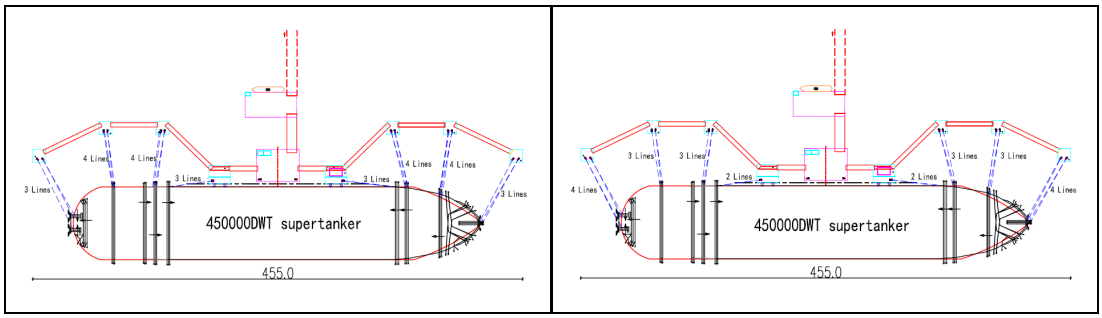


Fig.1a Mooring lines arrangements (3-4-4-3) Fig.1b Mooring lines arrangements (4-3-3-2)

**The standards of vessel safety operation.** According to the guidelines of OCMIF and the experience of past tanker mooring test[2,3], the standards of the large tankers ship operation are shown that the surging ≤±2.0m, the swaying ≤±2.0m, the heaving ≤±0.5m, the rolling ≤±2°, the maximum line tension did not exceed 50% of the line break force, the maximum impact force on fenders did not exceed the designed reaction force.

## Experimental Method

**Equipment and Measuring Instrument.** The testing was carried out in the wave basin of 60m in length, 40m in width, and 1m in depth. The measuring instrument include data acquisition system, wave height transducer, six degree freedom meters, fenders and cable force instrument, and ADV.

**Model Scale.** Following the gravitational similarity and the Wave Model Test Regulation (JTJ/T234-2001)[4], the geometric scale of the model is 1:60.

**Model of Vessel.** The vessel model (seeing Fig2a) and prototype were satisfied with similarity conditions as Geometric similarity, Gravitational similarity and Dynamic similarity.

**Fender simulation.** The simulation for fender should make sure the reaction force-deflection curve and absorbed energy curve were similar to the prototype (seeing Fig2b).

**Mooring Line simulation.** To make sure that the length and elasticity of mooring line in test was similar to prototype (seeing Fig.2c). The line force ~ elongation curve was according to the formula in Wave Model Test Regulation.

**Wave simulation.** The wave was calibrated at the berth with the JONSWAP spectrum.

Fig.2a Model of vessel

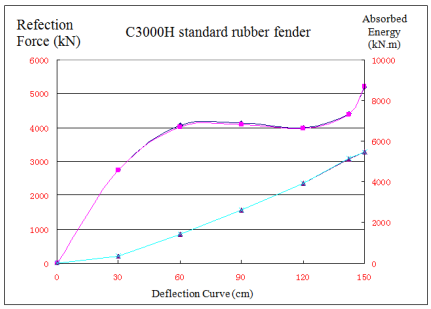


Fig.2b Fender simulation

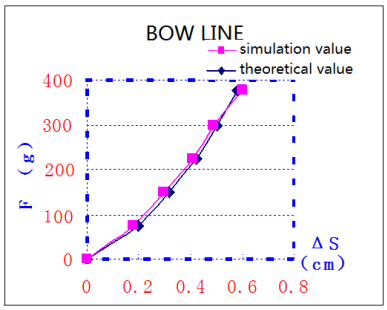


Fig.2c Mooring Line simulation

## Test Results

In the general ship mooring test, the influence on the mooring ship on the beam sea was greater than the following and quartering seas by the same wave condition. The combination of the ship's loadage with water level, the full load with low water level and the ballast with high water level were the most adverse condition in ship mooring test. According to the relevant regulations of "Design Code of General Layout for Sea Port" in our country, the permitted wave height，wave period and wind for large oil tanker safety working were $H_{4\%}$≤1.5m, T≤8s and wind speed was less than 6 grades. So the experiment used the condition of the beam sea and beam wind, which the wave height was $H_{4\%}$=1.2m, 1.5m and the wave period was T=7s, 8s. The test conditions and schematic diagram were shown in table 2 and Fig.3 respectively.

Based on the above test conditions, the swaying and the rolling of six degree freedom, the maximum line tension and the maximum impact force on fenders were discussed in the paper.

Table 2 Mooring test condition of 450,000DWT supertanker

| Loadage | Water level | Wave | Wind and Current |
|---|---|---|---|
| Full load | DLWL 0.68m | Beam sea $H_{4\%}$=1.2, 1.5m，T=7, 8s | Offshore wind with13.8m/s Flood current with 0.85 m/s |
| | | | Onshore wind with13.8m/s Ebb current with 1.0 m/s |
| Ballast | DHWL 7.06m | Beam sea $H_{4\%}$=1.5m，T=7, 8s | Offshore wind with13.8m/s Flood current with 0.85 m/s |
| | | | Onshore wind with13.8m/s Ebb current with 1.0 m/s |

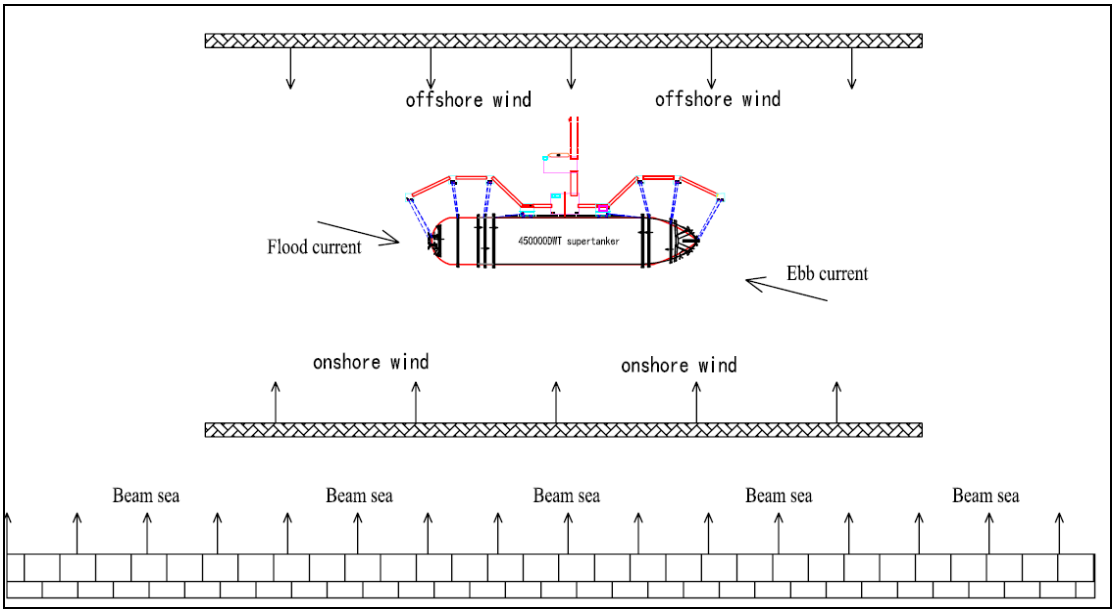


Fig.3 Test working schematic diagram

The test results of steel cable with 44mm and 52mm were shown in table 3 and table 4, the test result of combination cable with 52mm was shown in table 5.

Table 3 Test results of steel cable with 44mm（mooring lines arrangements with 3-4-4-3）

| test conditions | Wind and Current | Wave condition | swaying（m） | rolling（°） | maximum line tension（kN） | maximum impact force on fenders（kN） |
|---|---|---|---|---|---|---|
| the full load with low water level | Offshore wind and Flood current | $H_{4\%}$=1.5m T=7s | 0.84 | 0.29 | **652** | 3016 |
| | | $H_{4\%}$=1.2m T=7s | 0.65 | 0.29 | **566** | 1249 |
| | | $H_{4\%}$=1.5m T=6s | 0.53 | 0.16 | 425 | 971 |
| the ballast with high water level | Offshore wind and Flood current | $H_{4\%}$=1.5m T=7s | 0.95 | 1.59 | **694** | 3008 |
| | | $H_{4\%}$=1.2m T=7s | 0.73 | 0.79 | **590** | 1251 |
| | | $H_{4\%}$=1.5m T=6s | 0.68 | 0.65 | 529 | 1114 |

Table 4 Test results of steel cable with 52mm（mooring lines arrangements with 3-4-4-3）

| test conditions | Wind and Current | Wave condition | swaying（m） | rolling（°） | maximum line tension（kN） | maximum impact force on fenders（kN） |
|---|---|---|---|---|---|---|
| the full load with low water level | Offshore wind and Flood current | $H_{4\%}$=1.5m T=8s | 0.76 | 0.39 | 729 | 3852 |
| | Onshore wind and Ebb current | $H_{4\%}$=1.5m T=8s | 0.56 | 0.33 | 653 | **4507** |
| | | $H_{4\%}$=1.5m T=7s | 0.36 | 0.26 | 369 | 4318 |
| the ballast with high water level | Offshore wind and Flood current | $H_{4\%}$=1.5m T=8s | 0.82 | 1.56 | **1018** | 3889 |
| | | $H_{4\%}$=1.5m T=7s | 0.74 | 1.38 | 725 | 3408 |
| | Onshore wind and Ebb current | $H_{4\%}$=1.5m T=8s | 0.64 | 1.33 | 687 | **4459** |
| | | $H_{4\%}$=1.5m T=7s | 0.55 | 1.08 | 502 | 3376 |

Table 5 Test results of combination cable with 52mm（mooring lines arrangements with 4-3-2-2）

| test conditions | Wind and Current | Wave condition | swaying（m） | rolling（°） | maximum line tension（kN） | maximum impact force on fenders（kN） |
|---|---|---|---|---|---|---|
| the full load with low water level | Offshore wind and Flood current | $H_{4\%}$=1.5m T=8s | 1.04 | 0.24 | 547 | 2955 |
| | Onshore wind and | $H_{4\%}$=1.5m T=8s | 0.63 | 0.38 | 336 | **4507** |

| | | | | | | |
|---|---|---|---|---|---|---|
| | Ebb current | $H_{4\%}$=1.5m T=7s | 0.54 | 0.25 | 328 | 4327 |
| the ballast with high water level | Offshore wind and Flood current | $H_{4\%}$=1.5m T=8s | 1.09 | 2.00 | 777 | 3536 |
| | Onshore wind and Ebb current | $H_{4\%}$=1.5m T=8s | 0.61 | 1.72 | 306 | 4364 |

**Remarks:** The bold data in the table above was exceeding the ship safety operation conditions.

According to the test results, on the ballast condition when mooring line arrangements was 3-4-4-3, and under the combined action of the wave ($H_{4\%}$=1.5m, T=7s), offshore wind and flood current, the maximum swaying and line tension of the steel cable with 44mm were 0.95m and 694kN which was exceeded 50% of the line breaking force. When increased cable diameter to 52mm, the maximum swaying was 0.74m and the maximum line tension was 725kN. Although the line tension was bigger, the value was not exceeding the 50% of the line breaking force. So to increase the steel cable's diameter could enhance the vessel's ability to operation.

In addition, on the ballast condition and under the combined action of the wave ($H_{4\%}$=1.5m, T=7s), offshore wind and flood current, the maximum swaying, rolling and line tension of steel cable with 52mm were 0.82m, 1.56°, and 1018kN. When using the combination of cable with the line arrangements of 4-3-3-2, the maximum swaying, rolling and line tension were 1.09m, 2.0°, and 777kN. The reason was that the elastic deformation of combination cable was large, so the ship's swaying was increased, but the cable's number and the tension was reduced, which enhanced the vessel's operation ability relatively.

## Conclusions

It can be seen from the mooring test results of the 450,000DWT supertanker that on the combined action of wind, wave, current of different water level and loadage. The safety operation wave condition by using steel cable with 44mm was $H_{4\%}\leq$1.5m, T≤6s under the mooring lines arrangements of 3-4-4-3. The safety operation wave condition by using steel cable with 52mm was $H_{4\%}\leq$1.5m, T≤7s under the mooring lines arrangements of 3-4-4-3. And the safety operation wave condition by using combination cable with 52mm was $H_{4\%}\leq$1.5m, T≤7s under the mooring lines arrangements of 4-3-3-2.

Furthermore, by increasing the steel cable's diameter did not reduce the line tension, but could reduce the ship's movements, enlarge the line breaking force and enhance the ship operation ability. Compared with the pure steel cable, the vessel's movements increase with the increment of elastic deformation of composite cable. However the cable's number and the line tension was reduced with the improvement of vessel's operation ability relatively.

## Reference

[1] Tingliu Xu, Keqiang Zhu, Jianghua Zhou, Zhouhong Jiang: Port Engineering Technology Vol.49, NO.1 (2012), p.4

[2] Rixiang Zhang, Zhongbo Liu, Ningchuan Zhang: China Offshore Platform Vol.18, NO.1 (2003), p.28

[3] Changli Wei, Yue Sui, Hua Xu: China Harbour Engineering. No.6 (2012), p.26

[4] *Wave Model Test Regulation*（JTJ/T 234-2001）Ministry of Transport of the People's Republic of China.

*Applied Mechanics and Materials Vols. 580-583 (2014) pp 2129-2133*
*© (2014) Trans Tech Publications, Switzerland*
*doi:10.4028/www.scientific.net/AMM.580-583.2129*

# Experimental Study on the Offshore Positioning and Installing of Large Caisson

Xuanjun Huang [1,2,a], Wenzhong Zhang [1,2,b], Bing Jiang [3,4,c], Yingxue Lv [1,2,d]

[1]CCCC Tianjian Port Engineering Institute Co. Ltd., Tianjin, 300222, China

[2]CCCC-key Hydrodynamic Laboratory for Coastal Engineering, Tianjin, 300222, China

[3]National Marine Data and Information Service, Tianjin, 300171, China

[4]The Key Laboratory of Digital Oceanic Science and Technology, SOA, Tianjin, 300171, China

[a]huangxuanjun@tpei.com.cn, [b]zhangwenzhong@tpei.com.cn, [c]jiangbing@mail.nmdis.gov.cn, [d]lvyingxue@tpei.com.cn,

**Keywords:** large caisson, positioning, movement, cable force, experiment and research.

**Abstract.** The traditional method of the offshore caisson positioning and installing is using the barge or floating crane, but for the large caisson with 26,000 tons, the method is unable to achieve apparently. In this paper, the offshore location and installation of the large caisson with mooring line system and anchor cable system are studied. The research gets the wave and flow conditions results as well as the related and advertent items, which provide the reference for large caisson positioning and installation as well as the similar engineering construction technology.

## Introduction

At present, the caisson was widely used in the port engineering construction in our country, such as the harbor wall, piers, breakwaters, and lighthouses, etc. The caisson weight was development from hundreds of tones to tens of thousands of tones with the development of port construction to deepwater. For example, the large caisson with 26,000 tons was used in the main cable tower foundation of the Bridge of Dalian South Binhai Avenue engineering [1]. The caisson's size, weight and area was far more than the traditional scale, which was the first in china. As to the construction technology for the large caisson, It was concreted on the shore or in dock, then was floated to the engineering sea area for positioning and sink to the rubble-mound foundation smoothly by filling water.

In the whole process of the construction, the stage of positioning and sinking at sea was the most difficult and critical. The traditional construction method was using the barge, but for the capacity of large caisson, this method was difficult and high risk. On this study, two positioning method was adopted. One was using cable system to position, which was similar to the vessel docking on port, on this method, two small caissons was set in advance in the engineering area, the large caisson was docking on the small caisson, through adjusting the cable to marine positioning and sinking,( seeing in Fig. 1). Another method was using anchor system to position, on this method, six anchors were set up in advance in engineering area, the large caisson was moored on the anchor, through adjusting the tightness of the anchor cable to marine positioning and sinking, (seeing in Fig. 2).

## Physical Model Test

**Caisson Model.** The large caisson with 26,000 tons was tested in the study[2], which basic size was shown in table1.

**Cable Simulation.** The nylon rope with the diameter of 80mm was used in the positioning with cable system, which breaking force was 900 kN.

The steel line with diameter of 44mm and length of 240m was used in the positioning with anchor system, which breaking force was 1070 kN.

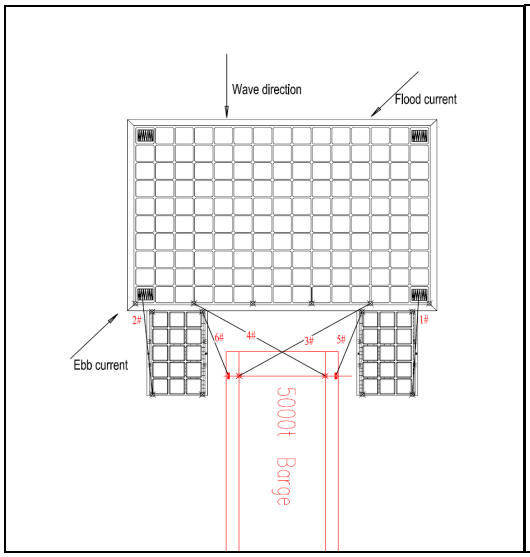


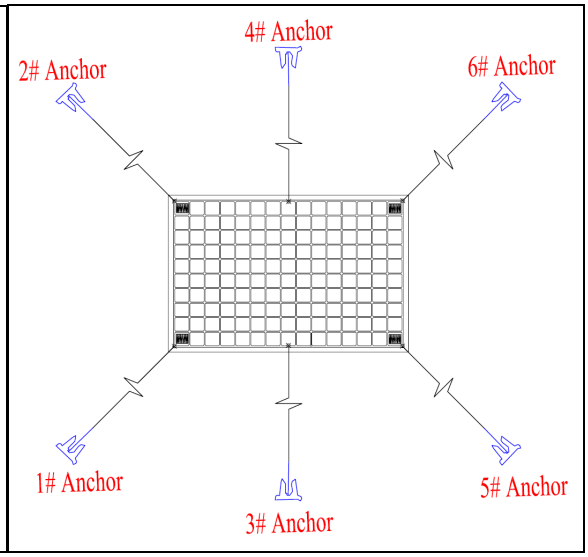


Fig.1 Positioning with cable system Fig.2 Positioning with anchor system

Table1 The basic size of the caisson (Scale:1:40)

| basic size | length（m） | width（m） | height（m） | draft（m） | displacement（t） |
|---|---|---|---|---|---|
| Prototype value | 69.0 | 44.0 | 17.0 | 8.29 | 26000 |
| Model Values | 1.725 | 1.10 | 0.425 | 0.207 | 0.406 |

**Wave Condition.** The nature water depth of the offshore area was 18m and the water depth of the foundation bed was 15m. The wave condition was shown in table2.

Table2 Wave condition

| | |
|---|---|
| Wave condition | Wave direction was positive for caisson long axis (seeing figure 1 and figure 2). |
| Wave spectrum | Code for seaport hydrology spectrum of China |
| Positioning with cable system | $H_{13\%}$=1.0m， T=5.0s, 6.0s |
| Positioning with anchor system | $H_{13\%}$=0.8m~1.2m， T=6.0s~8.0s |

## Test Results for Positioning with Cable System

**Test Program.** The installation process of cable system to position was that: firstly, two small caissons were set in advance in the engineering area, a 5,000 tons barge was stop behind the small caissons[3], the front two rope of barge were moored on the small caissons and the back two rope of barge were anchored in the sea. There were four ropes on the large caisson to make it docked on the small caisson, two were moored on the small caissons and two were moored on the barge. Through adjust the cable to make the large caisson marine positioning and sinking.

**Test Content.** The movements and the cable force under the different draft (d=8.29m,14.5m) and the conditions of wave ($H_{13\%}$=1.0m, T=5s, 6s) and current (V=0.5m/s, 0.2m/s) were given[1] (seeing figure 1). The movement was given the swaying and rolling of the large caisson, and the cable force was given the maximum value of the cables. The test photos were shown in figure 3 and the test results were shown in table 3.

Fig.3 Testing photos for Positioning with cable system

**Test Analysis.** It can be seen from the test that:

(1) Under the wave action, the bigger the caisson draft, the smaller the swaying and rolling, each cable force was relatively uniform, the largest cable force did not exceed 200kN.

(2) Under the combination of spring tide and waves, the large caisson was docked on the small caisson and had drift on the length wise direction, due to which the cable forces on large caisson were not uniform as well as the large impact force on the small caisson.

(3) Under the combination of ebb tide and waves, the large caisson was left from the small caisson and the impact force on the small caisson was 0kN. Each cable force was relatively uniform; the largest cable force did not exceed 200kN when the flow velocity did not exceed 0.2m/s.

(4) According to the large caisson positioning by cable system, the impact force on small caisson was very large on the condition of spring tide, so we should select the better wave condition with slack current or the ebb tide of less velocity for positioning. The wave and flow conditions on positioning were the $H_{13\%}$ less than 1.0m, T less than 6s and the ebb velocity less than 0.20m/s. If the velocity was bigger, it was sensible to enhance the strength of cable or increase the number of cable, but the velocity of ebb should not be more than 0.50 m/s.

Table3 The test results of the large caisson positioning with cable system

| Draft | Wave | Current | Swaying (m) | Rolling (°) | Impact force on small caisson (kN) | The maximum cable force (kN) |
|---|---|---|---|---|---|---|
| 8.29m | $H_{13\%}$=1.0m T=6s | none | -1.04~0.26 | -1.48~1.82 | 8073 | 194 |
| | | Flood with 0.50m/s | -0.99~0.31 | -0.90~1.09 | 10000 | 427 |
| | | Ebb with 0.50m/s | -0.55~0.84 | -1.09~1.25 | 0 | 215 |
| | | Flood with 0.20m/s | -0.65~0.12 | -0.98~1.06 | 8301 | 129 |
| | | Ebb with 0.20m/s | -1.03~0.24 | -0.92~1.18 | 0 | 195 |
| 14.5m | $H_{13\%}$=1.0m T=6s | none | -0.80~0.31 | -0.27~0.18 | 7942 | 99 |
| | | Flood with 0.50m/s | -0.59~0.04 | -0.32~0.42 | 9025 | 562 |
| | | Ebb with 0.50m/s | -0.42~0.36 | -0.23~0.20 | 0 | 286 |
| | | Flood with 0.20m/s | -0.54~0.05 | -0.21~0.39 | 8213 | 182 |
| | | Ebb with 0.20m/s | -0.86~0.38 | -0.35~0.36 | 0 | 190 |

Remarks: swaying is positive in the wave direction, negative in inverse wave direction

## Test Results for Positioning with Anchor System

**Test Content.** The Schematic plot of Caisson positioning with anchor system was shown in Fig. 2. The caisson's swaying, rolling and the maximum value of cable tension were given in the test results. The test photos were shown in Fig. 4 and the test results with different waves ($H_{13\%}$=0.8m~1.0m, T=6s~8s) and drafts (d = 8.29 m, 10.5 m, 13.0 m, 14.0 m, 15.0 m) were shown in Fig. 5.

Fig.4 Test photos of positioning with anchor system

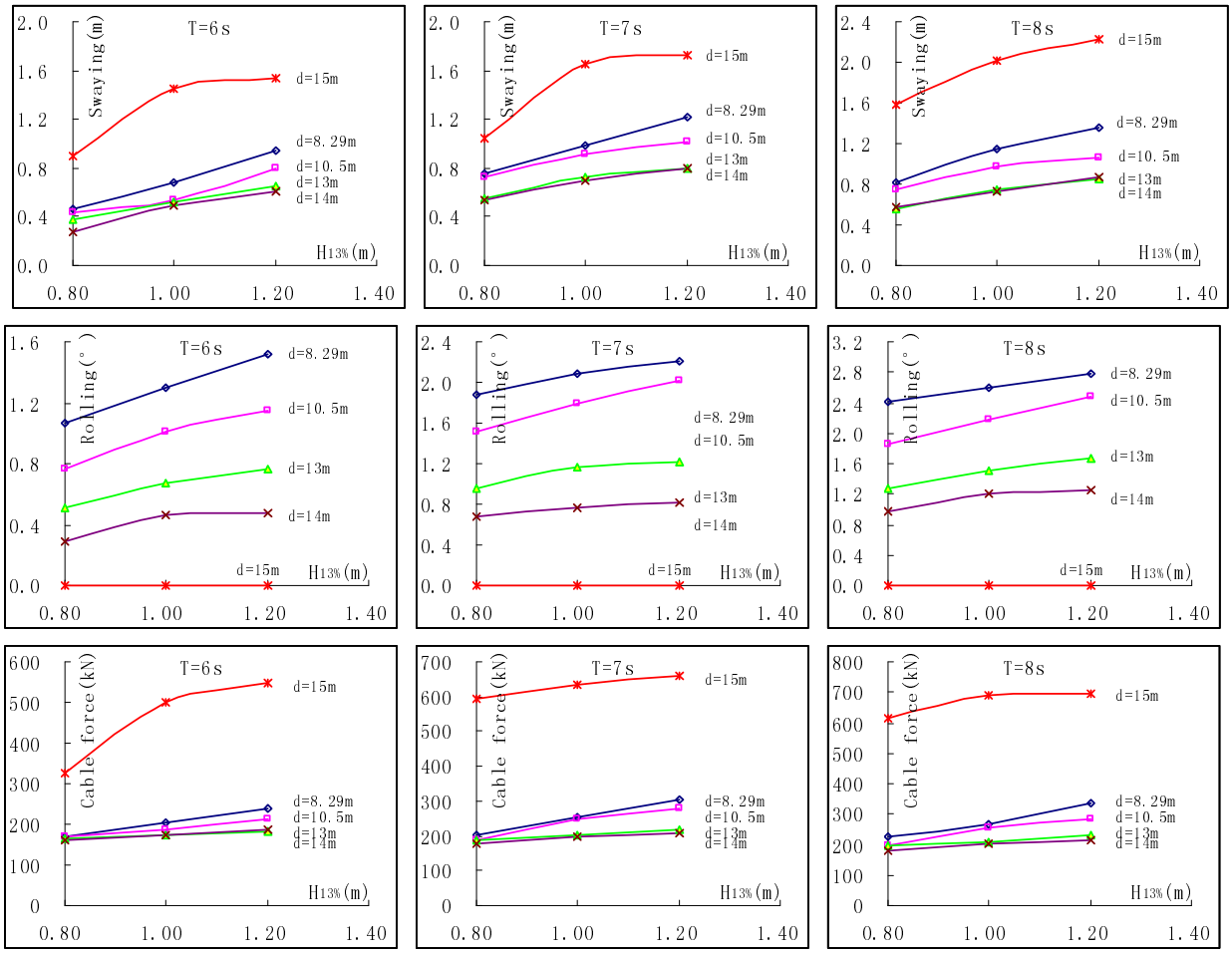


Fig.5 Testing results for positioning with anchor system

**Test Analysis.** It can be seen from the test that:

(1) The large caisson moved back and forth following the wave before it was located on the foundation. The swaying, rolling and anchor cable forces were increased with wave height and period, but were decreased with drafts. Along with the rising of the drafts, the stability of the caisson was better.

(2) When the caisson was just located on the foundation (d = 15.0m), the swaying and anchor cable forces under the wave action were much bigger than other drafts. Mainly because there was still the displacement under the wave action, however due to the friction on the bottom of the foundation bed,

this displacement was no longer the back and forth movement, which swaying was increased gradually, and the cable forces on the sea side were gradually increasing. Eventually the anchor system was built up a new balance.

(3) According to the test results, it's better to increase the caisson draft appropriately when the large caisson was positioned with anchor system. The most dangerous stage was the caisson near or just located on the foundation bed, it was necessary to take some corresponding measures to prevent the caisson moving on the foundation bed, for example assisted by tug, at the same time increased the caisson's gravity as soon as possible, or using barge lifting the enough weight on the caisson, to ensure the stability of caisson.

## Conclusions

In this paper, two methods of the large caisson offshore positioning were introduced, and the movements and the cable tension under wave action were given by the physical model test. According to the research results, when the large caisson was positioned by cable system, it should choose the better wave condition when the ebb current velocity was little or slack. If the flow was large to enhance the strength of cable or increase the number of cable. When the large caisson was positioned by anchor system, it's better to increase the caisson draft appropriately. To ensure the stability of caisson, it should take some corresponding measures to prevent the caisson moving on the foundation bed when the caisson near or just located on the foundation bed.

## References

[1] Qian Wang, Yong Gang Tan: Advanced Materials Research Vol. 368-373, (2012), p.1491

[2] Wave Model Test Regulation（JTJ/T 234-2001）Ministry of Transport of the People's Republic of China.

[3] Kang Song-tao, Hong Ling-yun: China Harbour Engineering No.4 (2013), p.53

*Applied Mechanics and Materials Vols. 580-583 (2014) pp 2134-2140*
*© (2014) Trans Tech Publications, Switzerland*
*doi:10.4028/www.scientific.net/AMM.580-583.2134*

# TWO-DIMENSIONAL FINITE ELEMENT ANALYSIS OF LABORATORY SEAWALL MODEL

Zhang Jian[1,a], Zhai Jian-feng[2,b],Wang Xian-Mei[3,c],Chen Jie[4,d]

[1,2,3,4] Jiangsu Provincial Communications Planning and Design Institute Co., Ltd., Nanjing 210005, China

[1,2,3,4] Aquatic Transportation Center, Nanjing 211100, China

[a.]beifangnanhai19@163.com;[b.]zhaijianfeng@jsjty.com.cn;[c.]wxm@jsjty.com;

[d.] chenjie@jsjty.com

**Keywords:** Two-Dimensional finite element, seawall, numerical analysis, constitutive models

**Abstract:**Two-Dimensional finite element analysis was used to investigate the performance of seawall construction over weak subgrade soil using artificial base layer material consisted of cemented sand cushion comprising geosynthetics materials. Two types of base layer materials pure sand and cemented sand comprising husk rich ash and two types of geosynthetics materials geogrid and geotextile were used. Constitutive models were used to represent different materials in numerical analysis. The competence of two-dimensional numerical analysis was compared with experimental results. Numerical results showed a superior harmony with the experimental results. Finite element analysis model proved to be a great tool to determine the parameters that are difficult to measure in laboratory experiments. In addition, finite element analysis has the benefit of cost and time saving when compared to experimental investigation work. Numerical results showed strain induced in geosynthetics eliminated beyond a distance approximately equal six times of footing width.

## INTRODUCTION

Numerical analysis based on a method of finite element is a powerful tool for studying the performance and characteristics of different earth work applications. Applying finite element analysis can determine the complicated parameters that would be difficult to measure in experimental work. In addition, finite element analysis is used as a good alternative process for laboratory investigation studies especially in case of large physical models, which leads to saving the time and costs associated with construction of physical models. Several investigators, including Duowen and Hargrove (2006), Chandra and Khaled (2005), Mauricio (1998), Rodrigues (1998), Hashem et.al (2000), Ahmed (2004), Hassona et.al (2005) and Love et.al (1987) investigated the performance of reinforced soil system using numerical analysis based on finite element analysis method. Finite element code called DSC-SST-2D was used to predict the field behavior of reinforced soil based on advanced constitutive models (Chandra and Khaled, 2005).

The main objective of this study is develop a methodology to predict the performance of pavement structure underneath the contact area of wheel over weak subgrade seawall layer using artificial cemented sand layer comprising husk rice ash reinforced with geosynthetics materials using numerical analysis based on finite element method in two dimensional analysis. A comparison between numerical and experimental results is presented. The parameters investigated in this research include the thickness of the base layer sand or artificial cemented sand, type of geosynthetics, position of geosynthetics within base layer thickness and type of base layer materials. The comparison is also verified using previous experimental studies related to this study area as a comparison between numerical and experimental to evaluate the validity of numerical analysis.

## NUMERICAL PARAMETERS

As mentioned above the main four different materials used in the experiment are soft clay, sand, artificial cemented sand and geosynthetics. Modified cam model, hyperbolic model, linear elastic model and slip surface model were used to represent soft clay soil, layer of sand or artificial cemented materials, geosynthetics and the interface between different materials surfaces respectively. These parameters are presented in Table 1.

To obtain a complete set of non-linear elastic-plastic, that called hyperbolic, model parameters, unconsolidated drained Traixial compression tests were conducted on representative sand and cemented sand samples. Two modules are used in this method, the initial modules Ei and the tangential modules, Et are calculated as per the following.

Table 1. Numerical parameters of modified cam clay model

| Property | Value | Property | Value |
|---|---|---|---|
| Over-consolidation ratio (OCR) | 1.00 | Nu (ν), (Specific volume) | 1.94 |
| Lambda (λ) | 0.21 | Kappa (κ) | 0.04 |
| Gamma (Γ) | 0.80 | Mu (M) | 0.28 |
| Pre-consolidation pressure (Pc) | 0.31 | Unit weight, ( γ ) | 17.9 kN/m2 |

$$E_i = K_L P_a \left( \sigma_3 / P_a \right)^n \tag{1}$$

$$E_t = \left[ 1 - \left\{ R_f (\sigma_1 - \sigma_3)(1 - \sin\phi) \right\} / \left\{ 2C(\cos\phi) + 2\sigma_3 \sin\phi \right\} \right]^n \times E_i \tag{2}$$

Where, Ei= initial insitu modules as a function of confining pressure (σ3) and atmospheric pressure (Pa), KL= loading modules number, Pa= atmospheric pressure (used as a normalizing parameter),

σ3= confining pressure, n= exponent for loading behaviour, Et= Tangent modules, ϕ= Friction angle of soil, RF= ratio between the asymptote to the hyperbolic curve and the maximum shear strength, σ1= major principal stress and σ3 = minor principal stress.

The parameters describing the young's modules based on a hyperbolic fit to the stress-strain curve are K, n, C, ϕ and Rf. The different numerical parameters of hyperbolic model for different features of sand cushion layer used in this research to represent in finite element analysis are presented in Table 2.

Table 2. Numerical parameters of hyperbolic model for different sand features

| Property | Value | |
|---|---|---|
| | sand | Cemented sand |
| Friction angle, $\phi$ | 34.00° | 38° 15' |
| Cohesion, C kN/c2 | 0.00 | 13.00 |
| Failure ratio, Rf | 0.73 | 0.72 |
| Modulus exponent, n | 0.06 | 0.33 |
| Modulus number | 380 | 487 |

The interaction characteristics between the soil mass and any different material type can be modeled by introducing interface elements models that called slip surface model as mentioned above. The different values of shear stiffness are tabulated in Table 3.

Table 3. Shear stiffness values for different interface composite materials

| Interface Surface | K shear (N/mm) | Interface Surface | K shear (N/mm) |
|---|---|---|---|
| Clay-sand | 12.00 | Sand-geotextile | 88.00 |
| Clay-cemented sand | 13.00 | Sand-geogrid | 112 |
| Clay-geotextile | 6.00 | Cemented sand-geotextile | 46.00 |
| Clay-geogrid | 5.10 | Cemented sand - geogrid | 53.50 |

Numerical model analysis configuration

Two-dimensional plain strain finite element analysis was used to simulate a width of footing that is representing the contact stress area of wheel vehicle in the field over seawall construction underlying weak subgrade soil layer. Only half of the physical model is considered in numerical analysis due to an axisymmetric at the center of the footing. The configuration alignments of finite element mesh in y-vertical and x-horizontal directions is shown in Figure 1. For mesh installation, different elements types are used 8-nodes quadrilateral element to signify modified cam clay and hyperbolic models, 4-nodes quadrilateral element to signify linear elastic and slip surface models, and 6-nodes triangular element to signify transition process in different area sizes of elements.

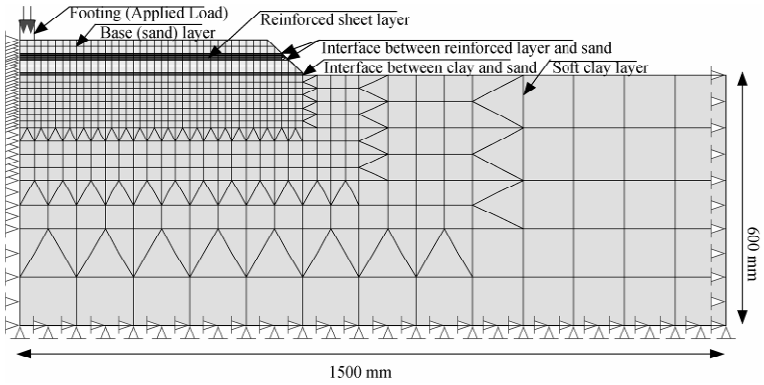


Figure 1. Configuration alignments of finite element mesh in two-dimensional

## RESULTS AND ANALYSIS

Stress pattern mechanism

Parameters investigated herein include the thickness of base layer, type of base material, geosynthetics type and position of geosynthetics sheet within base layer thickness. Stress distribution mechanism is a very important output of finite element analysis in case of earthwork construction analysis because it has used as a judge for the performance of seawall construction over weak subgrade layer in case of introducing stabilization techniques. Vertical stress contour lines in case of base layer thickness H = B, H is the base layer thickness and B is the width of footing, for different types of base layer materials of sand and artificial cemented sand over soft clay soil are shown in Figure 2. From these figures, it is clear that when cemented sand material introduced to the system the depth of stress bulb shifted up comparing with case of sand material alone. Therefore, existing cemented sand cushion in the system has a good resistance for stresses and the stress bulbs have a little extension within soft clay soil, which lead to increasing the bearing capacity of subgrade soil to sustain more loads comparing with case of sand cushion only.

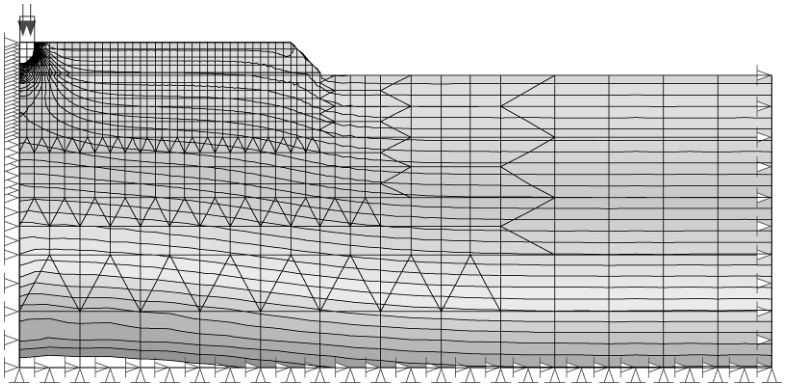

Figure 2. Vertical stress distributions contour lines in case of sand alone without additives for base layer thickness H=B

Figure 3 show the stress distribution contour lines in case of samples comprising one layer of geosynthetics located above clay directly and another layer within the mid of sand layer respectively for case of sand thickness H=B . From these figures, it is noticed that when

geosynthetics materials are applied, the stress bulbs squeeze and seems flatter in longitudinal direction before reaching the subgrade layer. Therefore, seawall stabilization, for two cases of base layer materials is increased when geosynthetics materials introduced to the system. This can be explained on the light of the following reasons: Firstly, most of stresses are cutting before to reach the subgrade layer. The second reason, the stress distributed over a large area that followed by decreasing in the stress values reaching to the subgrade layer. The third, when vertical stress applied to geosynthetics sheet, the stress adsorbed by geosynthetics and shifted to horizontal stress resisted by these materials, so the stability of seawall is increased and the resistance against applied loads is also increased.

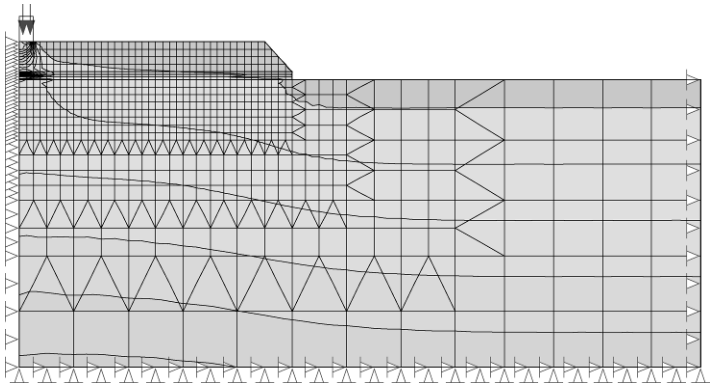

Figure 3. Stress distribution contour lines in case of sample H=B comprising one sheet of geogrid above clay layer

Displacement pattern mechanism

Deformations distribution pattern mechanism one of the important numerical analysis outputs to study the performance of seawall stabilization with different base layer materials. Deformed mesh is representing the deformation and corrugation happened within seawall mass after completing the process of loading. Figure 4 show the deformations in the mesh for sand and cemented sand layers. These figures indicate that the deformation pattern in case of sand layer is higher than the deformation in case cemented sand layer. These results confirm that the performance of seawall when cemented sand layer introduced is much pronounced than pure sand layer.

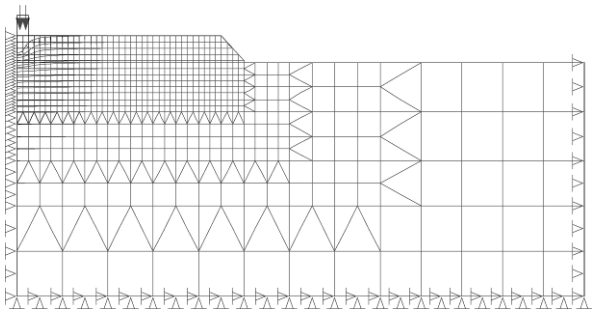

Figure 4. Mesh deformation in case of using sand for base layer thickness, H=B

Variation in Y-strain against horizontal distance along geogrid sheet at different positions for geosynthetics, the first position above clay layer directly and the second position in the mid of base layer are shown in Figure5.

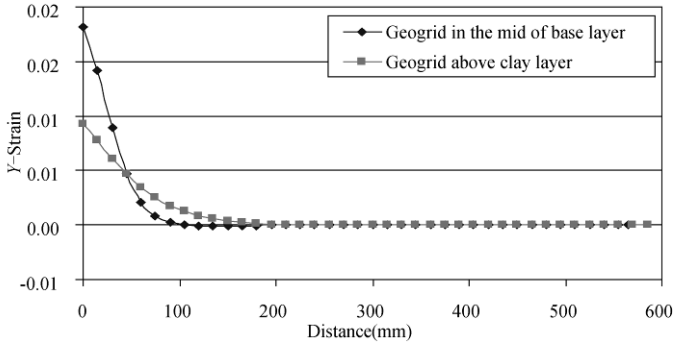


Figure 5. Variation in Y-strain against horizontal distance induced on geogrid sheet within base layer thickness in case of base layer thickness H=B

Deformations appear clearly beneath the footing and is gradually reduce until a distance that is approximately three times the width of the footing, it means six times of footing width because the problem solved as axisymmetric. It can be explained this results, when geogrid placed near to the footing affected early with stress comparing with geogrid placed at a deep distance from the footing. So when geogrid sheet placed near to the footing a high performance is obtained because the stress cutting early before to reach the weak clay layer and this result agree with experimental results for stress-settlement relationships.

## CONCLUSIONS

Based on above results the following conclusions can be drawn:

Two-dimensional finite element analysis is a good powerful too to study the performance of reinforced earth works.

Numerical results showed that artificial cemented sand is a good technique in seawall stabilization especially when geosynthetics introduced to the system comparing with identical sample having sand material. Increasing the thickness of base layer for both materials used enhancing the performance of stabilization.

Performance of geosynthetics in both of sand and cemented materials is a good while geogrid is much pronounced than geotextile. Numerical results indicated the best performance for geosynthetics is obtained when reinforced sheets are located nearest to the footing.

Vertical strain induced in geogrid is less than induced in geotextile and the effect of strain within geosynthetics mass eliminated after a distance equal six times of footing width.

Finite element analysis method gave good satisfactory results comparing with experimental results. In addition, a good agreement between these results and previous study results investigated the same way of parameters.

## ACKNOWLEDGEMENTS

The authors are grateful for the financial support from the Natural Science Foundation of Jiangsu Province (BK2012086). We would also like to thank the anonymous reviewers for their assistance.

**REFERENCE**

[1] Abdel-Khalek H. M. (1994). Geotechnical behaviour of soil reinforced with geogrid, M.Sc. Thesis, Civil Eng. Dept., Cairo University, Egypt.

[2] Ahmed A. (2004). Utilization of shredded waste tires in the strengthening of unpaved roads over soft clay. Ph.D. Thesis, Civil Eng. Dept., Faculty of Engineering, El-Mina University, El-Minia, Egypt.

[3] Chandra S. Desai and Khaled E. El-Hoseiny. (2005). Prediction of field behavior of reinforced soil wall using advanced constitutive model Journal of Geotechnical and Geoenvironmental Engineering, ASCE, 131 (6): 729-739.

[4] Duncan J.M., Chang C.Y. (1970). Nonlinear analysis of stress and strain in soils. Journal of Soil Mechanics and Foundations Divisions, ASCE, 96 (SM5): 1629-1654.

[5] Duowen Ding and S. Keith Hargrove. (2006). Non linear stress-strain relationship of soil reinforced with flexible geofibers. Journal of Geotechnical and Geoenviromental Engineering, ASCE, 132 (6): 791-794.

[6] Hassona F.A. Hassan M.A. Hashem M.D. Marei N.A. and Aly A.A., (2005). Numerical analysis of laboratory model footing. Bulletin of the Faculty of Engineering, Faculty of Al-Azhar Engineering, Cairo, Egypt, 119 (1).

[7] Hashem M. D., Abdel-Megeed M. and Youness A. H. (2000). Elastic-plastic finite element analysis of pullout resistance of geosynthetics in sandy Soil. Bulletin of the Faculty of Engineering, Assiut University, 29 (1): 127-134.

[8] Love J.P., Burd H.J., Milligan G.W.E. and Houlsby G.T. (1987). Analytical and model studies of reinforcement of a Granular layer on a soft clay subgrade. Can. Ceitechincal Journal, 24: 611-622.

[9] Mauricio A. (1998). Numerical analysis of pavement base reinforced with geogrid, Proc. 6th. Int. Conf. on Geosynthetics, Atlanta, Georgia USA, 891 – 894.

[10] Marei E.A., (1998). Enhancing the performance of foundations resting on very soft clay using cemented and composite sand cushions. Ph. D. Thesis, Civil Eng. Dept., Faculty of Eng., Cairo University, Egypt.

[11] Rodrigues R. M. (1998). Performance predication model for asphalt overlays with geotextile interlayer on cracked pavement, Sixth international conference on geosynthetics, Atlanta, Georgia, USA, (2): 973-976.

[12] Saleh, N. S. (1996). Study of strip footings on geosynthetics-reinforced sand underlain by weak clay. Ph.D. Thesis, Civil Eng. Dept., Cairo University, Cairo, Egypt.

[13] SIGMA/W Users Guide, Version 5. (2001). Software computer program for finite element in stress-deformation analysis. Geo-Slope International Ltd., Calgary, Alberta, Canada.

*Applied Mechanics and Materials Vols. 580-583 (2014) pp 2141-2145*
*© (2014) Trans Tech Publications, Switzerland*
*doi:10.4028/www.scientific.net/AMM.580-583.2141*

# Accuracy Comparison for the Ocean Tide Models in EstuarineTidal Prediction, the Pearl River Estuary

Lei Zhu[1, a], Xiaoling Yin[1,b] and Liao Jiang[1,c]

[1]School of Civil Engineering and Transportation, South China University of Technology, Guangzhou, China

[a]juneyylei@gmail.com, [b]arxlyin@scut.edu.cn, [c]jiang18986015121@163.com

**Keywords:** ocean tide model, tidal prediction, RMS misfits, Pearl River Estuary

**Abstract.** Ocean tide models with satellite altimetry can simulate global ocean tides conveniently and accurately. However, it was not sure for them to have a same good performance in estuaries and coastal zones. To assess their accuracy in the Pearl River estuaries, tidal elevations were computed respectively by three models NAO.99b, OTPS and WWT, and compared with the hourly observed data. RMS misfits were calculated and the results suggest that the models are competent to demonstrate the basic time features of tides and the accuracy is not lower than that of traditional methods in some certain periods and areas. The models behave better in the mouth zones, especially in the open area outside, but in the upstreams have differences between dry season and flood season. At the entrances, compared with the river-dominated estuary, the models indicate more accurate estimations for the tide-dominated estuaries. WWT is recommended among these three models.

## Introduction

Ocean tides primarily influence ocean surface variation. Ocean tidal prediction is of critical importance for industrial and agricultural production, water conservancy, transportation and ecological environment. Furthermore, numerical simulation relative to estuarine hydrodynamic process usually needs ocean tides as boundary conditions [1]. The traditional methods of tidal prediction can be classified into two categories: regression analysis and harmonic analysis [2], though some other methods have also been proposed by the scholars [3,4]. The predictive error of these traditional methods is usually 20-30cm and it is difficult to use them properly in the areas lack of observational data [5]. Although hydrodynamic models can have more advantages, the computation is complex and strenuous [6].

A finite element method derived from hydrodynamic equations can estimate ocean tides [7] and has developed into a global ocean tide model in 1990s. Thanks to satellite altimetry, nowadays ocean tide models can have an accuracy of 2-3cm RMS (root-mean-square) error in deep ocean [8,9]. However, their uncertainties usually inflate significantly in estuaries, coastal zones and shallow seas [10,11]. Nevertheless, some researches indicated that the model accuracies in both China Sea and northwest Pacific Ocean are comparable to that in deep ocean [12-14]. As they are developing increasingly and become a convenient and available method for tidal prediction, we need to know how accurate they are for a particular estuary.

Pearl River Delta has a complicated river net system and three main estuaries: Lingdingyang Bay, Modaomen Estuary and Huangmaohai Sea. To assess the accuracy of ocean tide models in these estuaries, NAO99b, OTPS and WWT are used to predict the hourly tides at the points where the tide gauges have been set up, and the RMS misfits to the observed data are calculated and compared according to different locations, seasons and estuary types.

## Ocean tide models

Satellite altimetry is an active remote sensing technique introduced in 1970s, which makes it available to observe global ocean surface height [15]. In recent years, global or regional ocean tide models,

which are derived either by assimilating altimetry data only or in combination with tide gauge data into hydrodynamic models, have a variety of application in scientific researches and engineering.

In this article, the following three models are involved:

(1) NAO.99b

NAO.99b [16] is developed by assimilating about 5 years of T/P altimeter data, representing major 16 constituents with a spatial resolution of 0.5°. Compared with measured data of 200 tide gauges distributing along China Sea coast, the prediction of NAO.99b shows a better agreement than many other models, such as GOT4.7, FES2004, EOT10a and TPXO7.2 [8,17].

(2) OTPS

OTPS has a spatial resolution of 1/30° owing to combining altimeter data of T/P and Topex Tandem and being validated by 61 coastal and shallow tide gauges' data. Nine principle tidal constituents (M2, S2, N2, K2, K1, O1, P1, Q1 and M4) can be predicted, which is based on global and/or regional barotropic inverse tidal solutions obtained with OTIS [18].

(3) WWT

Tidal elevations and hydrograph in given period and location can be obtained easily on the official website of WWT (http://worldwidetide.com/). WWT's prediction is also based on OTIS, but has some improvement on computation [19].

## Comparison and analysis of prediction accuracy

We applied the three models in the places of tide gauge installation in the Pearl River estuary. But we noticed that the models had their playing scopes, i.e. S6 in Fig.1 was beyond. Thus the locations of these places concerned are shown in Fig. 1. The hourly tides obtained from the models were then compared with the measured values via the gauges.

To assess the modeling accuracy, the RMS misfit of tidal elevations are calculated, which is defined as:

$$\mathrm{RMS} = \left[\frac{1}{n}\sum_{i=1}^{n}\left(L_p^i - L_m^i\right)^2\right]^{1/2} \tag{1}$$

where $L_p^i$ and $L_m^i$ are tide levels at time *i* of ocean tide model and tide gauge data respectively, and *n* is the total number of times.

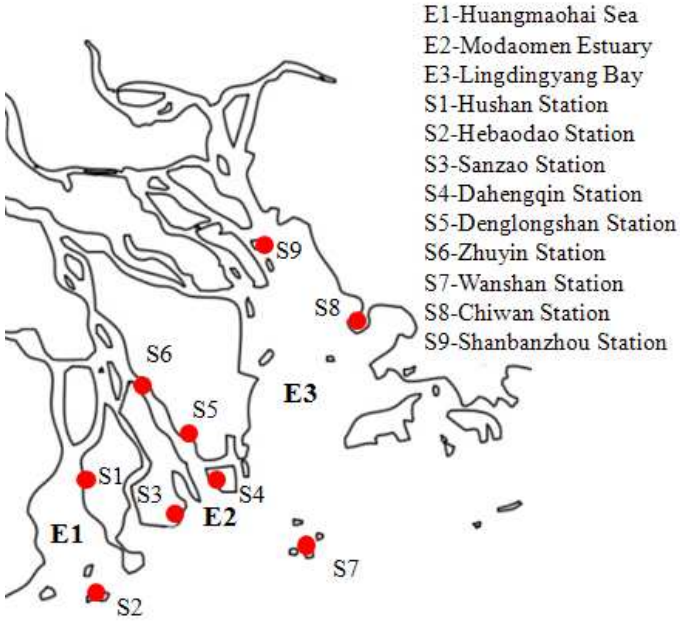


Fig. 1. Location of the tide gauges in Pearl River Estuary

**Comparison of time features of the tides.** The predicted tides compared with measured data during Feb. 2001 at Sanzao Station are shown in Fig. 2. The tidal curves of each model are generally in accordance with measured data except for a few individual moments with about one-hour errors, which suggests that the models are competent to the basic time characteristics of the tides.

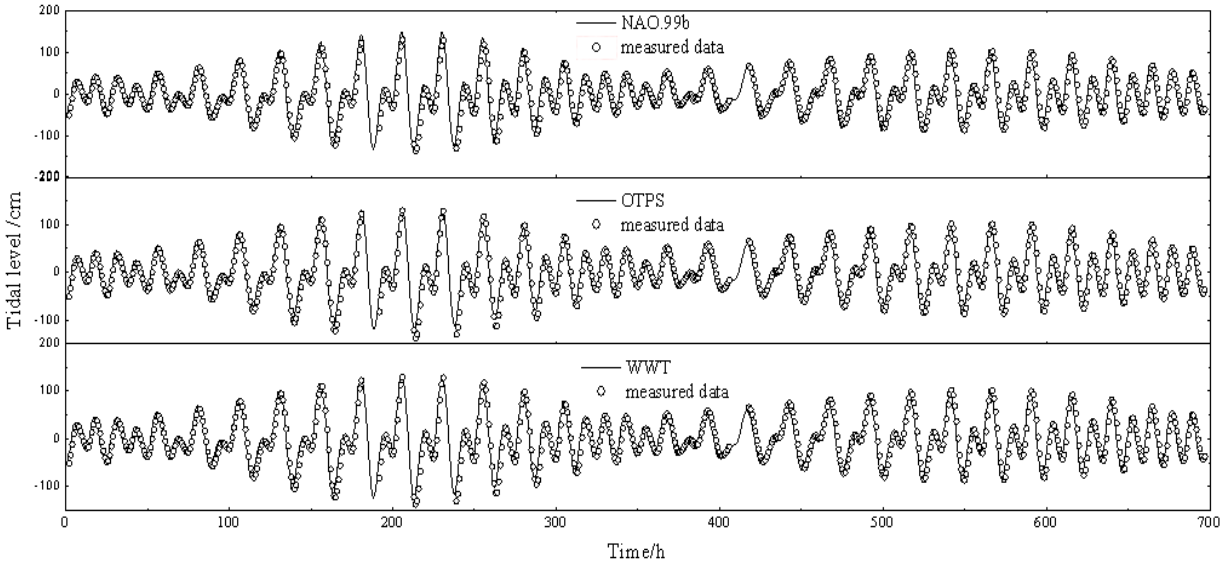


Fig. 2. The tidal curves of each model and measured data during Feb. 2001 at Sanzao Station

**Accuracy comparison at different locations in the same estuary.** The tides were predicted at Denglongshan, Dahengqin and Sanzao Station in or near Modaomen Estuary during Jan. 2006 and 2007. The result of RMS misfits is shown in Tab 1.

Tab 1. The RMS misfits at different stations in Modaomen Estuary. Note that "/" indicates the location is beyond model's coverage and italic letters represent the least RMS in a row. [cm]

| Tide gauge | Period | RMS misfit | | | |
|---|---|---|---|---|---|
| | | NAO.99b | OTPS | WWT | Average value |
| Sanzao | 2006.01 | 10.80 | 9.94 | *9.24* | 9.99 |
| | 2007.01 | 14.84 | 14.23 | *13.45* | 14.17 |
| Dahengqin | 2006.01 | 14.42 | 11.43 | *11.07* | 12.31 |
| | 2007.01 | 14.89 | 12.26 | *11.92* | 13.02 |
| Denglongshan | 2006.01 | 25.11 | / | *19.59* | 22.35 |
| | 2007.01 | 24.54 | / | *19.68* | 22.11 |

In Tab 1, at Sanzao and Dahengqin which are near the entrance, the RMS misfits of the three models are less than 15cm and the average is about 12cm, but at Denglongshan in the upstream the values are about 22cm. It can be seen that the RMS misfits increase gradually as the location moves from estuarine entrance to upstream in a specified estuary. Even so, the accuracy at estuarine entrance is higher than traditional methods'. Accordingly it can be assumed that a better accuracy can be gained in the area far outside from estuary.

**Accuracy comparison during flood and dry seasons.** Upstream runoff which is different during dry and flood seasons has an impact on tidal propagation in estuary. To evaluate the influence of runoff on model accuracy, the tidal levels at Sanzao, Dahengqin, Denglongshan and Shanbanzhou Station during both flood and dry seasons were predicted by the three models, with Tab. 2 showing the result.

From Tab 2, the average RMS misfits of the three models during flood and dry seasons are both 8.45cm at Sanzao Station. In contrast, compared with dry seasons, the RMS misfits during flood seasons are much larger at Dahengqin, Denglongshan and Shanbanzhou Station. Besides, the average RMS misfits at Shanbanzhou Station are larger than 30cm regardless of the season. As shown in Fig. 1, Sanzao Station lies in the open area outside Modaomen Estuary, suffering from little influence of runoff. By contrast, Dahengqin and Denglongshan Station are located inside Modaomen Estuary which has a substantial runoff during flood season. Shanbanzhou Station is in the upstream area of

Lingdingyang Bay, influenced by the runoff of Humen and Jiaomen Gate. As a result, the RMS misfits are immense and the difference between flood and dry season is obvious. Hence it is recommended that the predicted position had better deviate from the direction of runoff especially during flood season.

Tab 2. The RMS misfits during flood and dry seasons. Note that "/" indicates the location is beyond model's coverage and italic letters represent the least RMS in a row. [cm]

| Tide gauge | Period | | RMS misfit | | | |
|---|---|---|---|---|---|---|
| | | | NAO.99b | OTPS | WWT | Average value |
| Sanzao | dry | 2004.01 | *8.63* | 9.80 | 8.75 | 8.45 |
| | | 2001.02 | 7.25 | 7.70 | *6.39* | |
| | | 2007.02 | 8.73 | 10.39 | *8.41* | |
| | flood | 1998.07 | 7.91 | 7.82 | *6.84* | 8.45 |
| | | 2006.09 | 10.56 | 10.99 | *9.59* | |
| | | 2001.10 | 7.86 | 7.68 | *6.77* | |
| Dahengqin | flood | 2004.07 | 22.03 | 19.82 | *18.96* | 20.27 |
| Denglongshan | flood | 2004.07 | 38.20 | / | *33.70* | 35.95 |
| Shanbanzhou | dry | 1979.03 | / | 44.93 | *26.96* | 35.94 |
| | flood | 1978.07 | / | 50.86 | *34.01* | 42.44 |

**Accuracy comparison of different estuaries.** Pearl River Estuary is known for its different kinds of sub-estuaries. Huangmaohai Sea and Lingdingyang Bay belong to tide-dominated estuaries while Modaomen Estuary is a river-dominated estuary [20]. The accuracy comparison of different estuarine areas is shown in Tab 3.

Tab 3. The RMS misfits in different estuaries. Note that "/" indicates the location is beyond model's coverage and italic letters represent the least RMS in a row. [cm]

| Estuary | Period | Tide gauge | RMS misfit | | | |
|---|---|---|---|---|---|---|
| | | | NAO.99b | OTPS | WWT | Average value |
| Modaomen | 2006.01 | Dahengqin | 14.42 | 11.43 | *11.07* | 12.31 |
| | | Delongshan | 25.11 | / | *19.59* | 22.35 |
| Huangmaohai | 2001.01 | Hebaodao | 10.44 | 9.72 | *9.29* | 9.81 |
| | | Hushan | 30.63 | *25.18* | 26.11 | 27.31 |
| Lingdingyang | 2001.01 | Wanshan | 8.07 | *8.00* | 11.02 | 9.03 |
| | | Chiwan | *27.19* | 40.75 | 43.05 | 37.00 |

According to the RMS misfits in Tab 3, the average value of Danghengqin Station (12.31cm) is larger than that of Hebaodao and Wanshan Station (<10cm). At the entrances, hence, the models indicate more accurate estimations for tide-dominated estuaries. However, the RMS misfits at Denglongshan Station inside Modaomen Estuary are less than that of the stations inside Huangmaohao Sea and Lingdingyang Bay. So it is not appropriate to compare the accuracies of an estuary as a whole. The accuracy at a specified location inside an estuary is influenced by many factors such as the distance from entrance, local bathymetry, and hydrodynamic processes besides estuarine type.

Compared with the other two models, WWT has a higher accuracy in overall, especially in the entrance area, and a larger applying coverage.

## Conclusions

As the predictive accuracy of ocean tide models is considered unsure sometimes in coastal zones, to assess their performances in Pearl River Estuary, the RMS misfits of tidal levels generated from three ocean tide models (NAO99b, OTPS and WWT) against measured data were calculated. The comparison and analysis suggest that (1)ocean tide models are competent to demonstrate the basic time features of tides, and the accuracy of tidal levels is not lower than traditional methods' in some

certain periods and areas. (2)The models behavior better in the mouth zones, especially in the open area outside.(3)The accuracies in upstream have a certain difference between dry season and flood season. (4)At the entrances, compared with the river-dominated estuary, the models indicate more accurate estimations for tide-dominated estuaries. There is no clear conclusion inside the estuary because of more influencing factors. (5)WWT is recommended among these three models.

Ocean tide model is a convenient and available tool for tidal prediction in estuarine area. To obtain a better accuracy, it is recommended that the predicted position had better deviate from the direction of runoff and keep away from upstream as much as possible especially during flood season.

**Acknowledgements**

The authors greatly appreciate for Research Centre for Coastal Ocean Science and Technology of Sun Yat-Sen University providing some of software packages and original data.

**References**

[1] Jing Peng ,Qidong Peng. Water Resources and Hydropower Engineering, 10:78-82 (2005). (In Chinese)
[2] Shangwei Chen,Zhaosen Jin. Journal of Hydraulic Engineering, 6:41-47 (1989). (In Chinese)
[3] Liju He ,Qihua Li, Marine Forecasts, 8:29-37(2009). (In Chinese)
[4] Yanchu Li, Dewei Xu,Hailin Ruan. Acta Oceanologica Sinica, 8:29-37 (2009). (In Chinese)
[5] Ling Yu,Guohong Fang. Advances in Marine Science, 4:133-141(2010). (In Chinese)
[6] Biao Wang, Jianrong Zhu . Journal of Tropical Oceanography, 4:17-27 (2012) (In Chinese)
[7] Le Provost, C.; Vincent, P. Journal of Computational Physics, 8:273-291 (1986).
[8] Le Provost, C.; Bennett, A.F.; Cartwright, D.E. Science, 2:639-642 (1995).
[9] Dawei Li,Jiancheng Li,Taoyong Jin ,and Minzhang Hu. Journal of Geodesy and Geodynamics, 8:106-110(2012). (In Chinese)
[10] A.J.E. Smith, O.B. Andersen. Progress in Oceanography, v40,1-4:325-336 (1997).
[11] Brian K. Arbic, Chris Garrett. Continental Shelf Research, 4:564-574 (2010).
[12] Xinxuan Sun, Jun Xu , Jingyang Bao. Bulletin of Surveying and Mapping, 7:16-18 (2006). (In Chinese)
[13] Jing Hu,Rui Chen..Periodical of Ocean University of China, 7:224-230 (2007). (In Chinese)
[14] Jingyang Bao , Dingbo Chao, Jian cheng Li. ACTA GEODAETICA ET CARTOGRAPHIC SINICA, 2:17-23 (2000) (In Chinese)
[15] Guojun Zhai, Motao Huang, Yongzhong Ouyang, et al. Hydrographic Surveying and Charting, 01:57-62 (2002). (In Chinese)
[16] K. Matsumoto et al.. Journal of Oceanography, v56:567-581 (2000)
[17] H. S. Fok, H. Baki Iz, C. K. Shum, et al. Evaluation of Ocean Tide Models Used for Jason-2 Altimetry Corrections. Marine Geodesy, Vol. 33, Iss. sup1 (2010).
[18] Paul J. Martin et al. Use of the Oregon State University Tidal Inversion Software (OTIS) to Generate Improved Tidal Prediction in the East-Asian Seas[R]. Ocean Dynamics and Prediction Branch Oceanography Division, 4 (2009).
[19] Gary D. Egbert, Svetlana Y. Erofeeva. Journal of Atmospheric and Oceanic Technology, 2:183-204 (2002).
[20] Chun Chu Li et al. Processes and evolution law of China Southern estuarine[M ]. BeiJing:Science Press: 8-11 (2004) (In Chinese)

*Applied Mechanics and Materials Vols. 580-583 (2014) pp 2146-2149*
*© (2014) Trans Tech Publications, Switzerland*
*doi:10.4028/www.scientific.net/AMM.580-583.2146*

# Numerical Model on Hydrodynamic Impact from HZM Bridge

Jie He[1,2,a] , Yingjun Sun[3,b] , Xinsheng Zhao[4,c]

[1]Nanjing Hydraulic Research Institute, Nanjing, China

[2]State Key Laboratory of Hydrology-Water Resource and Hydraulic Engineering, Nanjing, China

[3]Hydrology bureau of Zhejiang Province, Hangzhou, China

[4]Hydrology Bureau of Yellow River Conservancy Commission, Zhengzhou, China

[a]jhe@nhri.cn, [b]yingjun373@163.com, [c]zhaoxinsheng@126.com

**Keywords:** Numerical Model, Finite Volume Method, Hydrodynamic Impact, HZM Bridge.

**Abstract.** In this paper, a 2D model for the simulation of shallow water flow by convection and diffusion over variable bottom is presented, which is based on the FVM (finite volume method) over triangular unstructured grids. The format of Reo's approximate Riemann is adopted to solve the flux terms. And the bed slope source term is treated by split in the form of the flux eigenvector. For the diffusion terms, the divergence theorem is employed to obtain the derivatives of a scalar variable on each triangular cell. The numerical model is adopted to simulate the hydrodynamic impact from HZM (Hongkong-Zhuhai-Macao) bridge on Pearl River estuary. The simulated results show that the HZM bridge has little influence on the distribution of hydrodynamic environment in the Pearl River estuary.

## Introduction

The shallow water equation has been experienced in FDM (Finite Difference Method), FEM (Finite Element Method) and FVM (Finite Volume Method) usually In the numerical discretization method,. The Finite Volume Method is an improved Finite Difference Method with a combination of Finite Element Method, and it can be strictly satisfied to physical quantity conservation through integral of each control volume[1]. Simulated by Finite Volume Method based on unstructured mesh, the numerical solution research of shallow water equations has gone from one-dimensional, two-dimensional to three-dimensional, where the boundary flux calculation between cells became the emphasis in solving shallow water equations. However, in shallow water, the diffusion motion is mostly not taken into account about the impact of shallow water equations. As the diffusion motion is an indispensable item of equations, and it's an important factor in the stability of numerical solution of shallow water equations in simulating actual flow movement [2]. Therefore it's necessary to conduct special studies of the numerical solution of shallow water equations combining with FVM based on unstructured grids.

The calculation of numerical flux is a very important part of solving shallow water equations with Finite Volume Method based on unstructured mesh. There are a lot of solutions to the numerical flux, such as Roe's approximate Riemann solver [3], HLL, as well as arithmetic average schemes and so on. The source terms treatment is also critical in shallow water equations, the simple treatment may lead to still water flowing over variable topography. The usual method is splitting source terms according to the decomposed form of eigenvectors of convective terms feature matrix [4]. The diffusion motion contains partial differential quadratic term, and the surface integral is translated into line integral after integrated over the calculating element, but there is still a differential term, which is one of the main reasons that diffusion motion isn't easy to deal with in solving shallow water equations [5]. In this paper, the diffusive flux in the interface is calculated by average of element interface, and it's treated similar to the Finite Element Method for the differential terms, so it can achieve numerical solution of shallow water equations with diffusion motion. Then the flow pattern around a pillar in tank are simulated, the result is present the model could be applied to simulate the complicated current structure in the water area around the hydraulic construction.

**Governing Equation**

When the size of plane is much larger then the vertical, two-dimensional shallow water equations can be used to describe the flow motion of calculated water area. Taking turbulence into account, flow governing equation can be expressed as formula (1).

$$\frac{\partial U}{\partial t}+\nabla E=S+\nabla E^{d} \tag{1}$$

with $U=(d,du,dv)^{T}$, $d$ is the total water depth, $d=h+\eta$ ($h$ is the water depth under horizontal plane, $\eta$ is the surface fluctuation, figure 1), $E=(F,G)$, and

$$F=\begin{pmatrix} du \\ du^{2}+gh^{2}/2 \\ duv \end{pmatrix},\quad G=\begin{pmatrix} dv \\ duv \\ dv^{2}+gh^{2}/2 \end{pmatrix} \tag{2}$$

where u and v are the velocity along the x and y coordinates, respectively.

The turbulent diffusion of equation is expressed as: $E^{d}=(F^{d},G^{d})$, where

$$F^{d}=\begin{pmatrix} 0 \\ \varepsilon_{x}d\partial u/\partial x \\ \varepsilon_{x}d\partial v/\partial x \end{pmatrix},\quad G^{d}=\begin{pmatrix} 0 \\ \varepsilon_{y}d\partial u/\partial y \\ \varepsilon_{y}d\partial v/\partial y \end{pmatrix} \tag{3}$$

and $\varepsilon_{x}$、$\varepsilon_{y}$ are the kinematic edd viscosity coefficients along the x and y coordinates, respectively, here isotropy is taken, then $\varepsilon_{x}=\varepsilon_{y}=\varepsilon$, $\varepsilon$ can be expressed as $\varepsilon=kdU_{*}$, where $U_{*}$ is the shear velocity, and it can be expressed as $U_{*}=\dfrac{n\sqrt{g(u^{2}+v^{2})}}{d^{1/6}}$.

The source term $S$ is written as formula(4).

$$S=S_{0}+S_{f}=\begin{pmatrix} 0 \\ gd(S_{0x}+S_{fx})+fv \\ gd(S_{0y}+S_{fy})-fu \end{pmatrix} \tag{4}$$

where $S_{ox}$ and $S_{oy}$ are bed slopes along the $x$ and $y$ coordinates, respectively, $S_{0x}=-\partial z_{b}/x$, $S_{0y}=-\partial z_{b}/y$, $z_{b}$ is the bottom level, and $S_{fx}$, $S_{fy}$ are the friction losses in terms of the Manning's roughness coefficient $n$:

$$S_{fx}=-\frac{n^{2}u\sqrt{u^{2}+v^{2}}}{d^{4/3}},\quad S_{fy}=-\frac{n^{2}v\sqrt{u^{2}+v^{2}}}{d^{4/3}} \tag{5}$$

The superscript $f$ is Coriolis force, $f=2\omega\sin\phi$, $\omega$ is the Earth's rotation speed, $\phi$ is the geographical latitude.

**Numerical Solution**

To be convenient for calculating, the computational domain is discrete using triangular grids, the variables are located herein at the geometric centers of the cells, and each grid cell represents a control volume. The formula (1) is integrated over computational domain, Gauss's theorem applied to integral given as follow formula (6).

$$\frac{\partial}{\partial t}\int_{\Omega}U d\Omega+\oint_{\partial\Omega}(E\cdot n)dl=\int_{\Omega}S d\Omega+\oint_{\partial\Omega}(E^{d}\cdot n)dl \tag{6}$$

the integral of each unit can be written as formula(7)

$$\frac{\partial U_i}{\partial t} A_i + \oint_{\partial \Omega_i} (E \cdot n - E^d \cdot n) dl = \int_{\Omega_i} S d\Omega_i \tag{7}$$

Where $Ai$ is the area of the cell $\Omega_i$ , $l$ is the boundary of triangle, the boundary integral of each cell is approximated by a summation over the triangle edges.

$$\oint_{\partial \Omega_i} (E \cdot n - E^d \cdot n) dl = \sum_{k=1}^{3} (E_k \cdot n_k - E^d{}_k \cdot n_k) l_k \tag{8}$$

The format of Reo's approximate Riemann is adopted to solve the convective numerical fluxes through one edge of triangle (such as the edge $l$ between adjacent cells $i$ and $j$ , $R$ and $L$ are the both sides of $l$ , respectively), the calculated type is as follow formula (9).

$$E \cdot n = \frac{1}{2}[(E \cdot n)_R + (E \cdot n)_L - \Delta E^*] \tag{9}$$

where $(E \cdot n)_R$ and $(E \cdot n)_L$ are numerical fluxes on both sides of interface, $\Delta E^*$ is the corrected value of flux on both sides and it's written as formula (10).

$$\Delta E^* = \sum_{k=1}^{3} \alpha_k |\lambda_k| e_k \tag{10}$$

where $\lambda_k$ and $e_k$ (k=1,2,3) are the eigenvalues and eigenvectors of convective characteristic matrix $A$ , it satisfies $\Delta E = A \Delta U$ , matrix form as follow formula (11).

$$A = \frac{\partial (E \cdot n)}{\partial U} = \begin{bmatrix} 0 & n_x & n_y \\ \left(\bar{c}^2 - \bar{u}^2\right) n_x - \bar{u}\bar{v} n_y & 2\bar{u} n_x + \bar{v} n_y & \bar{u} n_y \\ -\bar{u}\bar{v} n_x + \left(\bar{c}^2 - \bar{u}^2\right) n_y & \bar{v} n_x & \bar{u} n_x + 2\bar{v} n_y \end{bmatrix} \tag{11}$$

The $\bar{u}$ , $\bar{v}$ and $\bar{c}$ in matrix are calculated by mass-weighted average, they are expressed as follow formula (12).

$$\bar{u} = \frac{u_R \sqrt{d_R} + u_L \sqrt{d_L}}{\sqrt{d_R} + \sqrt{d_L}}, \quad \bar{v} = \frac{v_R \sqrt{d_R} + v_L \sqrt{d_L}}{\sqrt{d_R} + \sqrt{d_L}}, \quad \bar{c} = \sqrt{\frac{g(d_R + d_L)}{2}} \tag{12}$$

The eigenvalues of $A$ are present as formula (13).

$$\lambda_1 = \bar{u} n_x + \bar{v} n_y + \bar{c}, \quad \lambda_2 = \bar{u} n_x + \bar{v} n_y, \quad \lambda_3 = \bar{u} n_x + \bar{v} n_y - \bar{c} \tag{13}$$

The corresponding eigenvectors are shown as (14).

$$e_1 = \left(1, \bar{u} + \bar{c} n_x, \bar{v} + \bar{c} n_y\right)^T, \quad e_2 = \left(0, -\bar{c} n_y, \bar{c} n_x\right)^T, \quad e_3 = \left(1, \bar{u} - \bar{c} n_x, \bar{v} - \bar{c} n_y\right)^T \tag{14}$$

The corresponding coefficients of each term are respectively formula (15) and (16).

$$\alpha_{1,3} = \frac{\Delta d}{2} \pm \frac{1}{2\bar{c}} \left[\Delta(du) n_x + \Delta(dv) n_y - (\bar{u} n_x + \bar{v} n_y) \Delta d\right] \tag{15}$$

$$\alpha_2 = \frac{1}{\bar{c}} \left(\left[\Delta(dv) - \bar{v} \Delta d\right] n_x - \left[\Delta(du) - \bar{u} \Delta d\right] n_y\right) \tag{16}$$

where $\Delta(\bullet) = (\bullet)_R - (\bullet)_L$ .

**Hydrodynamic Impact from HZM Bridge**

The HZM(Hongkong-Zhuhai-Macao) bridge connects Hongkong, Zhuhai and Macao district, and it strctchs across the Pearl River estuary. A lot of piers and three large artifical islands would have some impact on the hydrodynamic environment in the Pear River estuary.

The isoline of velocity variation in water area nearby the bridge before and after engineering is showed in Figure 1. From the amplitude and range of the velocity variation in engineering waters in the process of flood and ebb tide we can see the east and west artificial islands in main navigable area and the man-made islands on Macao port are still main area of velocity variation, and the velocity of waters on upstream and downstream face is decreased after the brige constructed. Because the island and piers narrowed overcurrent section, the velocity of the main navigable waters between the eastern and western islands and the water area between the pier is increased when the bridge finished. If taking 0.02m/s as discriminant criteria of velocity variation, the coverage impacted by the artificial islands is within 5.0km upstream and downstream the bridge location, and the coverage of none-navigation area is within 1.0km water area up and down the bridge axis.

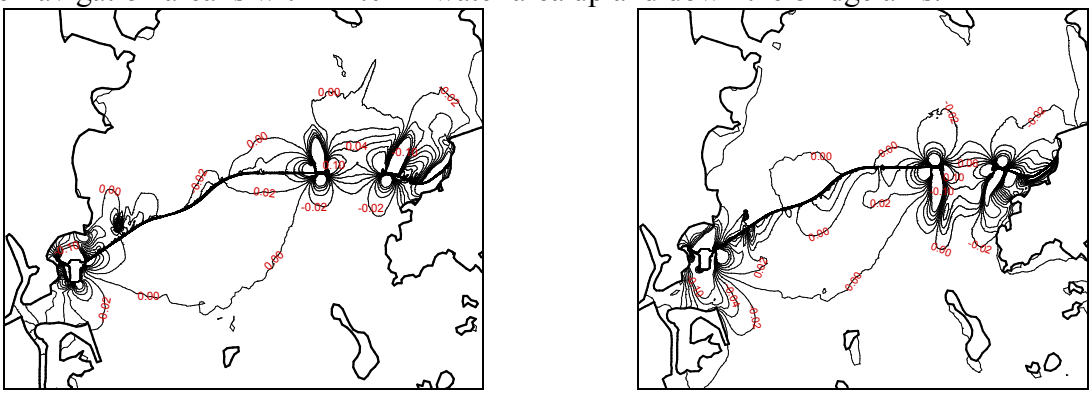

Flood tide Ebb tide

Fig1. Flow velocity change before and after HZMB in Lingding sea

## Conclusions

The numerical model of the shallow water flow is introduced to simulate the hydrodynamic impact from HZM (Hongkong-Zhuhai-Macao) bridge on Pearl River estuary. The shallow water equation is based on the FVM (finite volume method) over triangular unstructured grids. The format of Reo's approximate Riemann is adopted to solve the flux terms. And the bed slope source term is treated by split in the form of the flux eigenvector. For the diffusion terms, the divergence theorem is employed to obtain the derivatives of a scalar variable on each triangular cell. The computed results show that the HZM bridge has little influence on the distribution of hydrodynamic environment in the Pearl River estuary.

## References

[1] P.L.Roe. *Approximate Riemann solvers, parameter vectors, and difference schemes*[J]. Journal of Computational Physics, 1997, 135, p.250-258.

[2] A.Harten, P.D. Lax, B. van Leer. *On upstream differencing and Godunov-type schemes for hyperbolic conservation laws*[J]. SIAM Rev. 1983, 25, p.35-61.

[3] P.Brufau. *Zero mass error using unsteady wetting–drying conditions in shallow flows over dry irregular topography*[J]. Int. J. Numer. Meth. Fluids 2004, 45, p.1047-1082.

[4] Benedict D.Rogers. *Mathematical balancing of flux gradient and source terms prior to using Roe's approximate Riemann solver*[J]. Journal of Computational Physics, 2003, 192, p.422-451.

[5] P.Brufau. *Two-dimensional dam break flow simulation*[J]. International Journal for Numerical Methods in Fluids, 2000, 33, p.35-57.

*Applied Mechanics and Materials Vols. 580-583 (2014) pp 2150-2153*
*© (2014) Trans Tech Publications, Switzerland*
*doi:10.4028/www.scientific.net/AMM.580-583.2150*

# The Research of Flow Resistance Property in the Tugging and Mooring of Tube Segment

Qiu Zhengzhong [1, a *] and Min Dong [2,b]

[1] CCCC Second Harbor Engineering Co., Ltd, Wu Han, Hu Bei, 430040

CCCC Water Transportation Consultants Co., Ltd, 100007

[a]bqiuzhengzhong@126.com, [b]117043742@qq.com

**Keywords:** fluent; tugging; mooring; resistance coefficient; numerical simulation

**Abstract.** The tube tugging and mooring is the key step in the process of the immersed tunnel, and the most important theoretical is the calculation of water flow force. According to the numerical simulation and physical model of the tube in the Pearl River, the difference value of the flow resistance coefficient can be calculated. The fluent software is used to simulate the process of the tube tugging and mooring. On the basis of the empirical data of the tube experiment in the Pearl River, the flow resistance coefficient is obtained in the process of the tube tugging.

## Introduction

By now, more than 100 immersed tunnels have been built at home and abroad and the construction technology has been maturing. In the process of immersed tunnel, the most important theoretical is the calculation of water flow force. By the related data analysis, the water flow force consists of frictional resistance, wave-marketing resistance and viscous pressure resistance. The frictional resistance is due to the effect of water viscosity, which makes the hull surface friction force. For the wave-marketing resistance, when the vessel motions in the static water, there will be a pressure area at the ship bow and a suction area at the stem. That will prevent the vessel due to the pressure difference in the motion direction of the vessel. The viscous pressure resistance is due to the viscous effect of water caused by the pressure resistance of the pressure difference front and back of the vessel. The water resistance coefficient in the process of the tube floating is studied in the paper[1-3].

## Numerical calculation of the flow resistance coefficient in the Pearl River

**parameter specification.** Calculate the difference value of the flow resistance coefficient between the numerical simulation and physical model of the tube in the Pearl River at the same boundary conditions. According to the book “design and construction of immersed tunnel”, the boundary conditions are introduced as follows.

The immersed tube length 2m, width 0.674m, height 0.156m, draft 0.136m

The numerical mesh: 200m×6m×0.17m

Sea-water density: 1.0×103kg/m³, viscosity: 1.003×10-3pa*s

When horizontal anchor, the velocity is 0.15m/s; when Longitudinal floating, the velocity is 0.302m/s

**The numerical simulation model.** The fine calculation model 1:1 is set up to describe the change of the flow field around the tube accurately and reduce the calculation errors. The tetrahedral mesh is adopted to the three-dimensional flow field in the channel and foundation trench.

Define origin of coordinates on the free surface, just center of poor upper surface. The water flows along the x-axis. As the distance between the bottom of the tube and the bed is relatively short, the flow velocity will be rapidly magnified when the tube incident flows. To obtain better calculation accuracy, the mesh spacing of the tube underside is 0.01, growth factor 1.1 and the maximum interval 0.05. In the end the total number of units is 1874740, with 389228 nodes. The model is shown as follows.

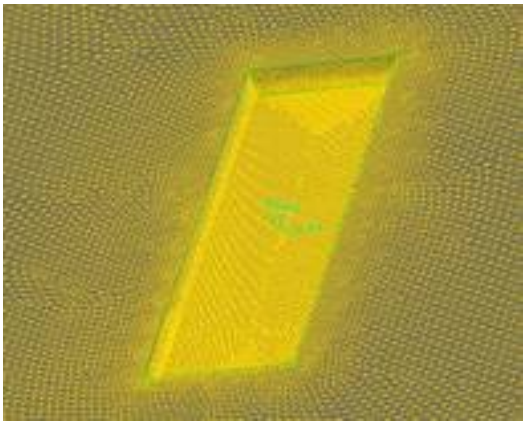

Figure1 Sketch map of tube mesh encryption

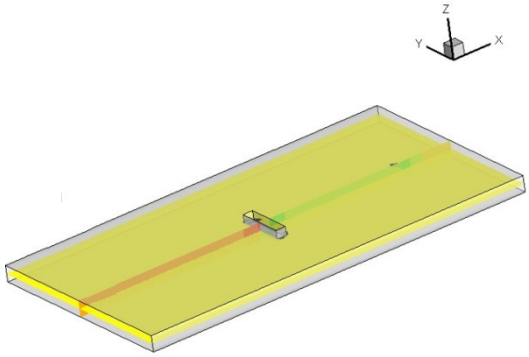


Figure 2 Sketch map of model section

**The calculation value of numerical simulation and physical model.** Comparing to physical model, the calculation value of the numerical simulation is increased by about 18% at the same operating condition seen from table 1. The reason of that are pretreatment processes, boundary layer setting and limits of the grid computing capacity of the fluent software.

Table1 Calculated Value of Numerical Simulation and Physical Model of the Tube in the Pearl River

| NO. | Tube Condition | Flow Velocity | Depth Draft Ratio | Resistance Coefficient | Amplification |
|---|---|---|---|---|---|
| 1 | horizontal anchor | Physical Model Value | 1.06m/s | 1.25 | 18.6% |
| | | Numerical Simulation Value | 1.06m/s | 1.25 | |
| 2 | Longitudinal floating | Physical Model Value | 2.135 m/s | 1.25 | 18% |
| | | Numerical Simulation Value | 2.135 m/s | 1.25 | |

## Analysis of computing result on the flow resistance coefficient of certain project tube

**Calculate purpose.** According to the data of the immersed tube tunnel, the calculation of the most unfavorable conditions that the least depth draft ratio of 180m standard tube sections is chosen. When the tube in the foundation trench wanting for sinking, the depth draft ratio of 180m standard tube sections is among 1.55~3.71 of the minimum design level -1.63m. The least depth draft ratio of 180m standard tube sections is chosen as the maximum resistance coefficient tube and the maximum capacity of the software fluent6.3 is chosen to calculate the resistance coefficient[4].

**Parameter specification.** Calculate the flow resistance coefficient of the numerical simulation at the preset boundary conditions. The boundary conditions are introduced as follows.

When horizontal anchor

The channel, width 200m, depth 13m

The numerical mesh: 1000m×200m×13m

The flow velocity is 1.5 m/s perpendicular to the face of tube incident flow.

When Longitudinal floating

The immersed tube length 180m, width 38m, height 11.4m, draft 11.4m

The numerical mesh: 1000m×760m×18m

The flow velocity is 1.5 m/s perpendicular to the face of tube incident flow.

**Result of calculation model.** The fine calculation model 1:1 is set up to describe the change of the flow field around the tube accurately and reduce the calculation errors. The tetrahedral mesh is adopted to the three-dimensional flow field in the channel and foundation trench.

Define origin of coordinates on the free surface, just center of poor upper surface. The water flows along the x-axis. The mesh spacing of the tube underside is 1.0, growth factor 1.2 and the maximum interval 3. The mesh spacing of the tube side is 2, growth factor 1.2 and the maximum interval 3. In the end the total number of units is 2095773, with 448338 nodes.

From figure 3-4, more than one vortex in the horizontal direction comes into being in the two sides of tube that incident flow and tail end. Seen from figure 4, because of groovy, the flow section is larger and the flow velocity is smaller. There is no vortex in the vertical direction of tube tail end.

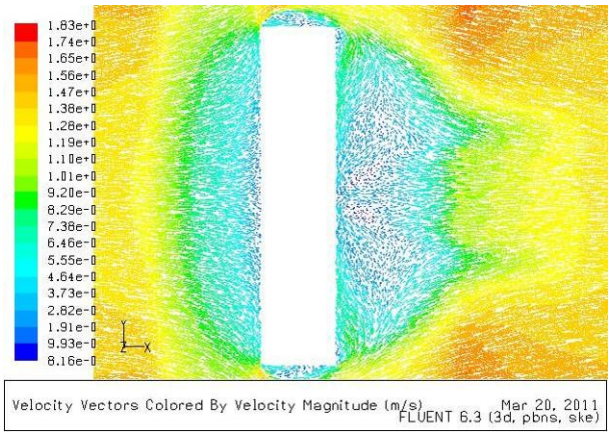


Figure 3 Flow field velocity vector of cross section

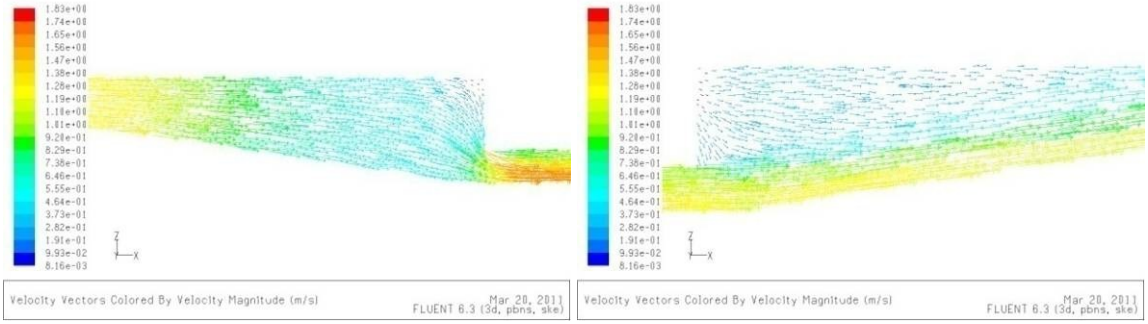


Figure 4 Flow field velocity vector (front end and tail endlongitudinal section)

**The calculation value of numerical simulation.** The flow velocity changes as the flow section changes. There is no vortex in the vertical direction in the tail end and very large flow separation in the horizontal direction[5].

The drag coefficient also has some relationship to the discharge capacity in the bottom of the tube. This also means depth draft ratio has some influence on the resistance coefficient

Table2 The calculated value of three-dimensional numerical simulation of the tube

| Tube Condition | Flow Velocity | Tube size | Depth Draft Ratio | Resistance Coefficient | remark |
|---|---|---|---|---|---|
| horizontal anchor | 1.5m/s | 180×38×11.4m | 1.55 | 2.31 | Turbulent flow |
| Longitudinal floating | 1.5m/s | 180×38×11.4m | 1.14 | 1.45 | Turbulent flow |

## Conclusions

By means of the comparison of calculated value between the numerical simulation and physical model of the tube in the Pearl River, the value of numerical simulation is larger by about 18% than the value of physical model under both horizontal anchor condition and longitudinal floating condition, which indicates that the software fluent is reliable.

According to the reliability of software fluent, the resistance coefficient of certain project when tube mooring is 1.96, as the value of numerical simulation is 18% larger than the value of physical model. In a similar way, when tube floating, the resistance coefficient of certain project is 1.23.

**References**

[1] Jan Saveur, Walter C. G-rantz. Structural design of immersed tunnels. Tunneling and Underground Technology. 1993. 8(2). 123-133

[2] Zhou Yu, et al. Experimental investigation on element immersing process of immersed tube tunnel. China Ocean Engineering. 15(4). 531-540

[3] Pan Yongren, Ding Mei. Techniques for sinking and jointing tube sections of a large immersed tube tunnel. Modern Tunneling Technology. 41(5). 1-11

[4] Cai Rongquan et al. A numerical investigation of free surface viscous flow around the ship by combination of rankine source method with rinsfs. Journal of Ship Mechanics. 2000. 4(3). 1-14

[5] Yang Xianghui, et al. Time domain research on wave making of moving submerged body. Journal of Ship Mechanics. 2007. 11(6). 848-858

*Applied Mechanics and Materials Vols. 580-583 (2014) pp 2154-2165*
*© (2014) Trans Tech Publications, Switzerland*
*doi:10.4028/www.scientific.net/AMM.580-583.2154*

# Tieshan Port Development Plan: Evaluation of the Long Wave Induced Resonance Using a Numerical Mild-slope Model

Zhao Hongjun[1, a *], Yang Jie[1,b] and Chen Guoping[1,c]

[1] Key Laboratory of Coastal Disasters and Defence (Ministry of Education), Hohai University, Nanjing 210098, China

[a]loyhg@hhu.edu.cn, [b]Jie_yang@hhu.edu.cn, [c]gpchen1965@163.com

**Keywords:** Numerical simulation, Mild-slope model, Long wave, harbor resonance

**Abstract.** The general development plan of Tieshan port is designed to be long and narrow, for which the long wave induced resonance may be problematic. Within the present work, a numerical study on the effects of this kind of resonance is conducted. The simulations are performed with the use of the mild-slope model developed in Ref. [1], which was further validated in the present work to be able to predict reasonable results for the harbor resonance. To evaluate the wave resonance for the plan of Tieshan port, 71 offshore wave conditions with the period ranging from 50*s* to 400*s* have been calculated. The rationalities of the numerical solutions are analyzed through comparisons with the theoretical ones, and the general agreement is seen to be reasonable. Some preliminary results for the harbor resonant modes, the resonant periods and the corresponding amplification factors for the plan of Tieshan port have been presented.

## Introduction

Tieshan port is situated in Tieshan Bay, as seen in Fig. 1 (a), a southeast bay which is located in the northeast of Beibu Gulf, South China Sea, This port is being planed. Fig. 1 (b) shows the general development plan of Tieshan port, from which we see that the configuration of this plan consists of four rectangular harbors, with Harbor 1 (2840*m*×1000*m*) facing to the south-southeast, and with Harbor 2 (2100*m*×1000*m*), Harbor 3 (2700*m*×1000*m*) and Harbor 4 (7700*m*×1000*m*) connecting at the mouth, facing to the south-southwest. Within this general development plan, the long wave induced resonance might be problematic. This will be investigated numerically in the present work by using the mild-slope model developed in Ref. [1].

Harbor oscillations have been regularly observed in specific sea around the world, for example, the Longkou Harbor, China [2], the Hualien Harbor, Taiwan [3], the Port of Long Beach, USA [4], and etc. A harbor has certain resonant frequencies, or periods, depending on its size, geometry and water depth. If the period of the incident wave coincides with the harbor's resonant period, then this wave will be seized and amplified in the harbor. Sometimes, the amplification factor of the maximum wave height within the harbor relative to the wave height outside the harbor was so large that it would endanger the cargo loading and unloading activities, hamper the ship accommodations and damage the mooring facilities. Therefore, during the design stage, to avoid any undesirable resonant mode which may be close to the resonant periods of the ship-mooring system, it is important for the designers and planners to know the characteristics of the harbor oscillations, including the resonant mode, the resonant period and the amplication factor.

In previous, analytical, numerical and physical models are typical means used to determine the resonant characteristics of a harbor [5-7]. Nowadays, with the development of computer resources and numerical techaniques, numerical models, such as the mild-slope models [3, 8-9] and the Boussinesq models [10-11], have been more and more applied to this problem. Although the Boussinesq model can describe the nonlinear wave transformation behaviors, the higher order derivatives containing in the governing equations make the model's application to relative large areas very time-consuming. Therefore, in the present work the mild-slope model was chosen as a means to study the wave resonant characteristics of the plan of Tieshan Port.

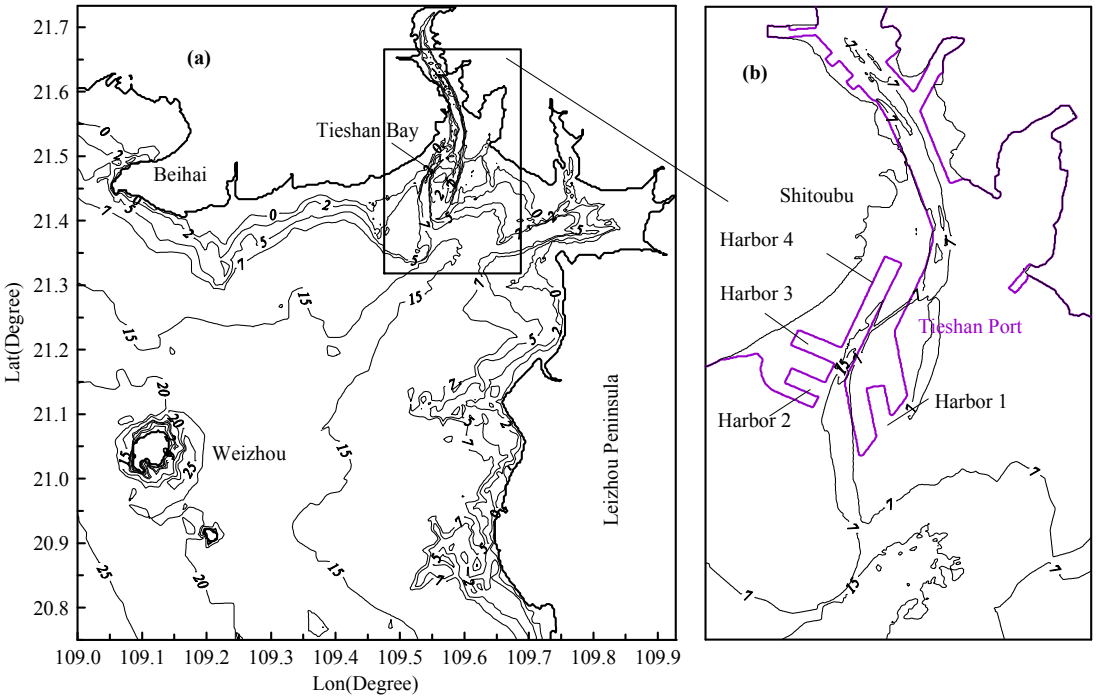


Fig. 1 The general development plan of Tieshan Port.

**Mathematical Foundations of the Mild-slope Model**

The numerical model used in this work is the mild-slope model that was developed in Ref. [1]. Some different numerical techniques for the wave generation and absorption have been introduced to this model. These will be briefly described in this section.

The governing equation of the mild-slope model is the time-dependent mild-slope equation that accounts for the energy dissipation and the internal wave generation, written as:

$$\frac{\partial^2 \zeta}{\partial t^2} + \sigma f_s \left(\frac{k}{k_c}\right)^2 \frac{\partial \zeta}{\partial t} - \left(\frac{\sigma}{k_c}\right)^2 \nabla^2 \zeta = S^*, \tag{1}$$

where $\zeta$ is the effective wave displacement; $\sigma$ is the wave frequency; $f_s$ is the wave energy dissipation coefficient; $k$ is the wave number, and it can be related to the wave frequency $\sigma$ by the linear wave dispersion relation; $k_c$ is the effective wave number, and it can be expressed as:

$$k_c{}^2 = k^2 - \nabla^2 \left(\sqrt{cc_g}\right) \Big/ \sqrt{cc_g}\,, \tag{2}$$

where $h$ is the local water depth; $C$ and $C_g$ are the wave velocity and the wave group velocity, respectively.

$f_s$ is the dissipation term that describes the wave energy dissipation in a sponge layer. According to Lee and Yoon [12], this term can be expressed as:

$$f_s = \begin{cases} 0, & x > x_s \\ \dfrac{\sigma^2}{k^2 cc_g}\left(\dfrac{e^{d/s}-1}{e-1}\right), & x < x_s \end{cases} \tag{3}$$

where $d$ is the distance from the point to the begining of the spone layer; $s$ is the width of the sponge layer; and $x_s$ is the begining location of the sponge layer.

$S^*$ is the source term that describes wave generation, and it can be expressed as:

$$S^* = \left(\frac{\sigma}{k_c}\right)^2 \frac{S}{g\sqrt{cc_g}}, \tag{4}$$

where $S$ is the internal wave generation funtion. According to Kim, *et al.* [13], $S$ can be expressed as:

$$S(x,y,t) = 2gc_g \delta(x - x_s)\cos(\theta)\eta_i, \tag{5}$$

where $\delta(x-x_s)$ is the Direclet function; $\theta$ is the angle of the incident wave direction relative to the generation line; $\eta_i$ is the incident wave free surface. According to the linear wave theory, $\eta_i$ can be expressed as:

$$\eta_i = \frac{H_i}{2}\cos\left(k_x x + k_y y - \sigma t\right), \tag{6}$$

where $k_x$ and $k_y$ are the wave number respectively in $x$ and $y$ direction; $H_i$ is in the incident wave height.

Eq. (1) is a time-dependent partial differential equation, which can be solved by a finite difference scheme developed in Ref. [1]. Setting the physical variables ($\zeta$, $k_c$, $C$, $C_g$ , $f_s$ and $S^*$) at the grid nodes, the finite difference scheme for Eq. (1) with constant space step $\Delta x$ , $\Delta y$ and time step $\Delta t$ can be described as:

$$\begin{aligned}&\frac{\zeta_{i,j}^{n+1}-2\zeta_{i,j}^{n}+\zeta_{i,j}^{n-1}}{\Delta t^2}+\sigma f_s\left(\frac{k}{k_c}\right)^2\frac{\zeta_{i,j}^{n+1}-\zeta_{i,j}^{n-1}}{2\Delta t}\\&=\left(\frac{\sigma}{k_c}\right)^2\left(\frac{\zeta_{i+1,j}^{n}-2\zeta_{i,j}^{n}+\zeta_{i-1,j}^{n}}{\Delta x^2}+\frac{\zeta_{i,j+1}^{n}-2\zeta_{i,j}^{n}+\zeta_{i,j-1}^{n}}{\Delta y^2}\right)+S^{*n}\end{aligned} \tag{7}$$

Re-arranging Eq. (7), we can obtain

$$\zeta_{i,j}^{n+1} = a_0\zeta_{i,j}^{n-1} + a_1\zeta_{i,j}^{n} + a_2\left(\zeta_{i+1,j}^{n}+\zeta_{i-1,j}^{n}\right) + a_3\left(\zeta_{i,j+1}^{n}+\zeta_{i,j-1}^{n}\right) + \frac{\Delta t^2}{a}S^{*n} \tag{8}$$

where $a_0 = -\left(1-\sigma f_s\left(k/k_c\right)^2\Delta t/2\right)/a$, $a_1 = 2\left(\frac{1}{a}-a_2-a_3\right)$, $a_2 = \left(\sigma\Delta t/\left(k_c\Delta x\right)\right)^2/a$, $a_3 = \left(\sigma\Delta t/\left(k_c\Delta y\right)\right)^2/a$, and $a = 1+\sigma f_s\left(k/k_c\right)^2\Delta t/2$. For the detailed calculation process of Eq. (8), one can see Ref. [1].

**Validation of the Mild-slope Model**

The above Mild-slope model has been validated in Ref. [1] through three benchmarks, including (1) the combined refraction and diffraction over a submerged elliptic shoal on a slope, (2) the resonant Bragg reflection of monochromatic waves from a sinusoidal ripple patch, and (3) the wave transformation near a shore parallel breakwater.

In this work, in order to validate the model's capacity to simulate the harbor resonance phenomenon, the wave transformation in a fully rectangular basin with a constant depth connected to the open-sea was numerically computed.This is a classical case of harbor resonance that has been widely studied by many researchers [3, 6, 8-9]. Analytically speaking, such a case is relatively simple to handle, but numerically it is complicated to simulate, because the numerical results are somewhat sensitive to the extent of the infinite ocean in the simulation. Fig. 2 shows the computational domain for this case. Here, the infinite ocean was approximated by a finite rectangular region $400m\times150m$. The geometry of the rectangular basin is $6m\times31m$, and the water depth is $25.73m$. The up side, the right side and the left side of the outer domain were all treated as the passing through boundaries, and these were attrived by arranging the sponge layer with width of $2.5L$ ($L$ is the wave length) along each of them. While for the inner basin's boundary and its perimeter, the total reflection boundary conditions were specfied. In order to capture the respond curve of the harbor, 23 different incident wave conditions with period ranging from $5.0s$ to $14.0s$ were numerically simulated. These waves were generated internally at $y_s$=$181m$, and the generated wave height $H_i$ was $0.1m$. The space grid is set as $\Delta x = \Delta y = 1.0m$ , and the time space is $\Delta t = 0.04s$ . The model runs until the waves in the computational domain reach the steady state.

Referring to Fig. 3 and Fig. 4, where the computed time series of the normalized free surface displacement ($\eta/H_i$) at the harbor mouth (position A) and at the harbor end (Position O) for $T$=$11.3s$ and $T$=$5.5s$ are presented, we can find that the numerical results are stable. The relative wave height

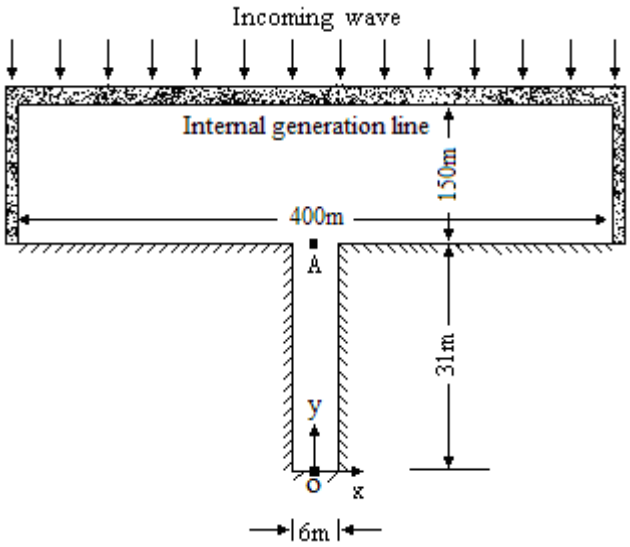


Fig.2 Computational domain for a fully-open rectangular harbor

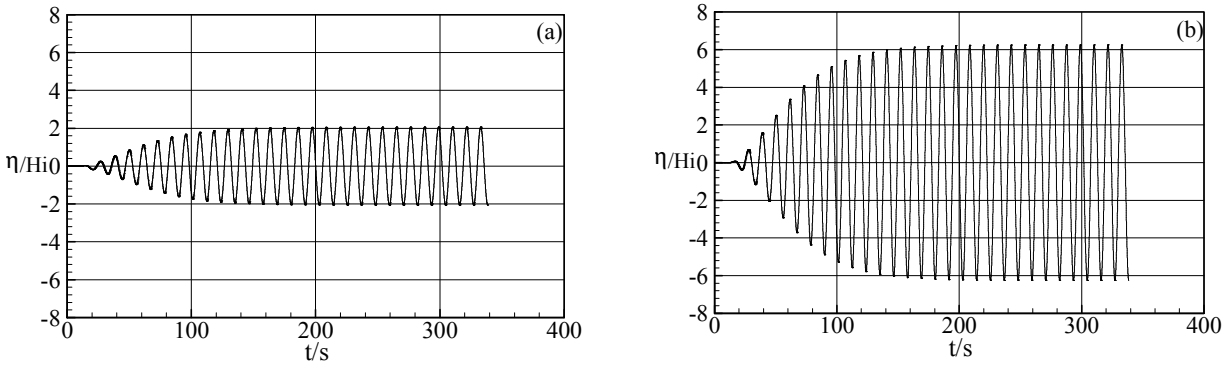


Fig. 3 Time series of the surface displacement for the case of $T$=11.3$s$. (a) surface displacement at Point A, and (b) surface displacement at Point O

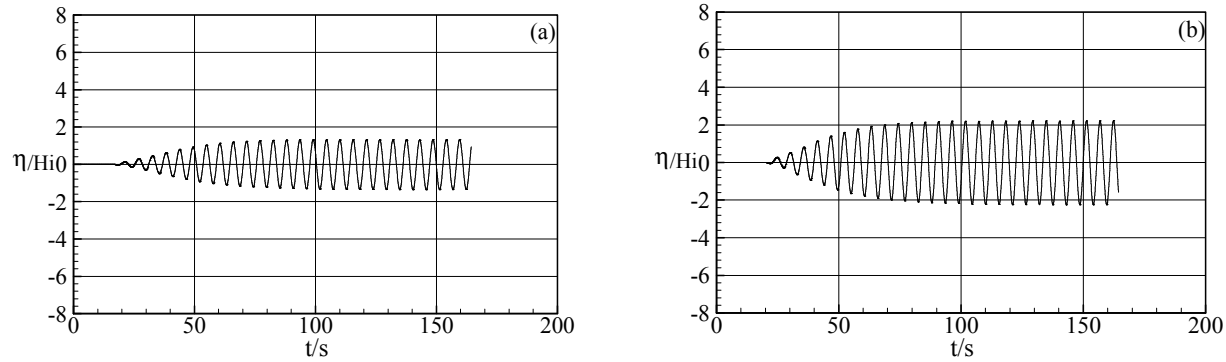


Fig. 4 Time series of the surface displacement for the case of $T$=5.5$s$. (a) surface displacement at Point A, and (b) surface displacement at Point O

dirtributions inside and outside the rectangular harbor for $T$=11.3$s$ and $T$=5.5$s$ are, respectively, ploted in Fig. 5 (a) and (b), showing that for the case of $T$=*11.3s*, the value of the relative wave height increases from 4.1 at $y$=31.0$m$ to 12.6 at $y$=0.0$m$, while for the case of $T$=5.5$s$, the relative wave height in the harbor has a peak value of about 4.6 at approximately $y$=0.0$m$ and $y$=24.0$m$, the relative wave height reachs the minimum of about 0.16, at about $y$=12.0$m$. As for the nearly semi-circular patterns of the wave height contours near the mouth shown in Fig. 5, we should refer this to the scatter waves propagated outward from the harbor entrance.

The computed response curve of the rectangular harbor is presented in Fig. 6, where the abscissa is the normalized harbor length $kl$ ($k$ is the incident wave number, and $l$ is the length of the harbor), and

the ordinate is the normalized wave height at the harbor end ($H_O/2H_i$). If the rectangular harbor does not exist, the wave height would be doubled due to the specified total reflection boundary condition.

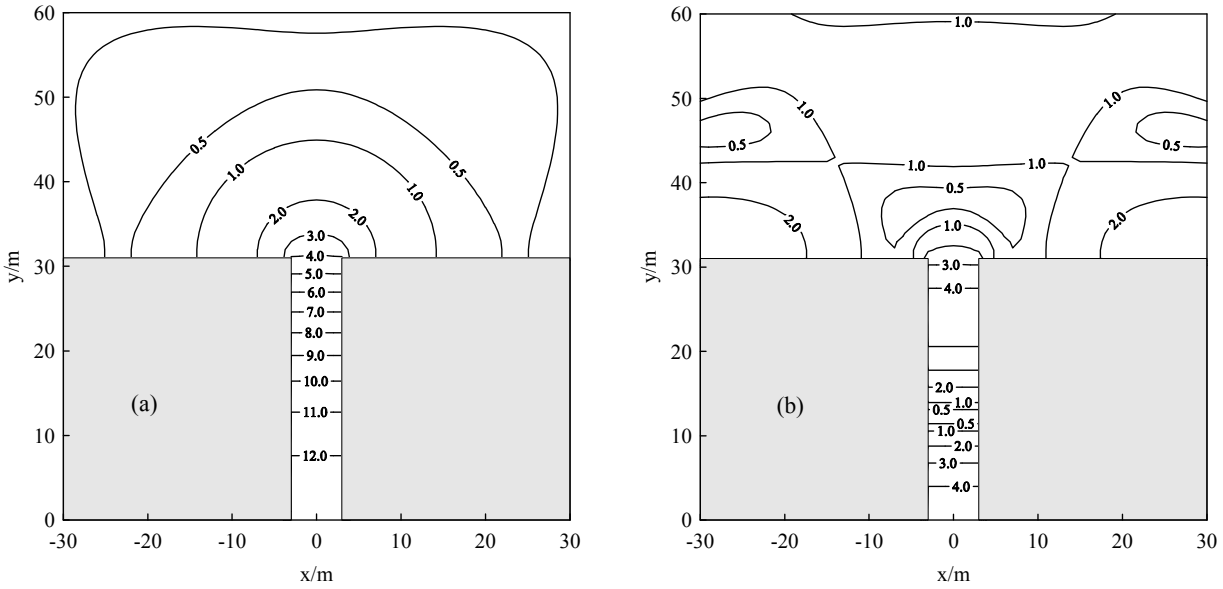


Fig. 5 Computed relative wave height ($H/H_i$) distributions inside and outside the harbor. (a) the relative wave height contour for $T$=11.3$s$, and (b) the relative wave height contour for $T$=5.5$s$

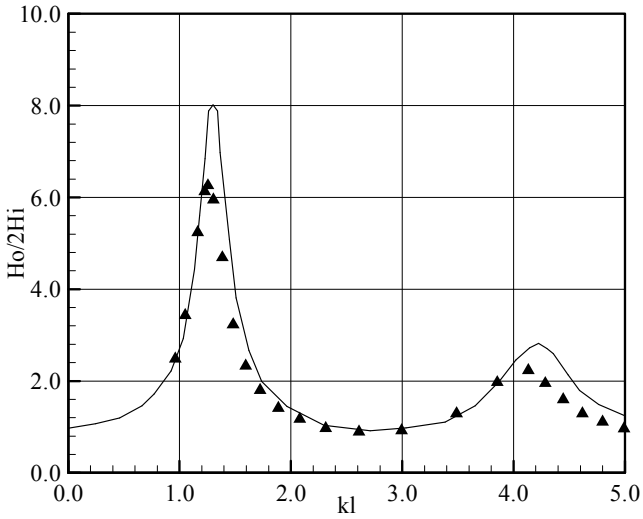


Fig. 6 Comparisons for the normalized wave height between the numerical results (▲▲▲) and the analytical ones (——) at the harbor end (Position O).

Therefore, the doubled wave height $2H_i$ is used to normalize the calculated wave height. From this fiture, we can see that the wave height relative to the standing wave at the harbor end is very large, as high as 6.3, when the period is about 11.3$s$. This is the first mode of the harbor resonance. We can also detact the second resonant mode at about $T$=5.5$s$, and the relative wave height for this mode is about 2.3. The analytical response curve of this harbor given by Lee [6] was also ploted in Fig. 6 for comparison conveniences, from which we can see the numerical results are in agreement with the theoretical ones, indicating that the mild-slope model can be applied to the simulation of the harbor resonant phenomenon.

**Evaluation of the Long-wave Induced Resonance for the Plan of Tieshan Port**

In order to study the resonant responses of Tieshan Port, nearly 71 offshore wave conditions in the SSW direction with period ranging from 50$s$ to 400$s$ were calculated. These waves were generated internally in the computational domain, and the generated wave height $H_i$ is 0.1$m$. Since the resonant

periods of a harbor depends mainly on its size, geometry and depth, therefore we donot consider the depth variation outside the port, and the outside depth was set the same as the inside of the port. Considering the numerical results might be affected by the size of the computational domain, we choose a large area of 45*km*×24 *km* (see Fig. 7) to conduct the numerical computations. The grid size of 25*m*×25*m* is selected for the computational domain. On the one hand, the 25-*m* grid resolution can accurately describe the harbor geometry. On the other hand, this resolution can also garantee to accuratly simulate the wave fiel even for the case of the minimum wave length. The time step is set as 1.0*s*. This time step is small enough to garantee the stability of the numerical calculations even for the case of the longest wave length. The shoreline boundaries and the four computational domain boundaries were all set as the open boundary conditions, and to further minimize the effects of the pseudo-reflected waves, the sponge layers with width of 0.5*L* were also used with the combination of the open boundary conditions. As for the inner and outer harbor boundaries, the total reflection conditions were specified. This is because, even for the slope structures, the structure dimension of O(100*m*) is relatively small compared to the wave length dimension of O(1000*m*) in the present study.

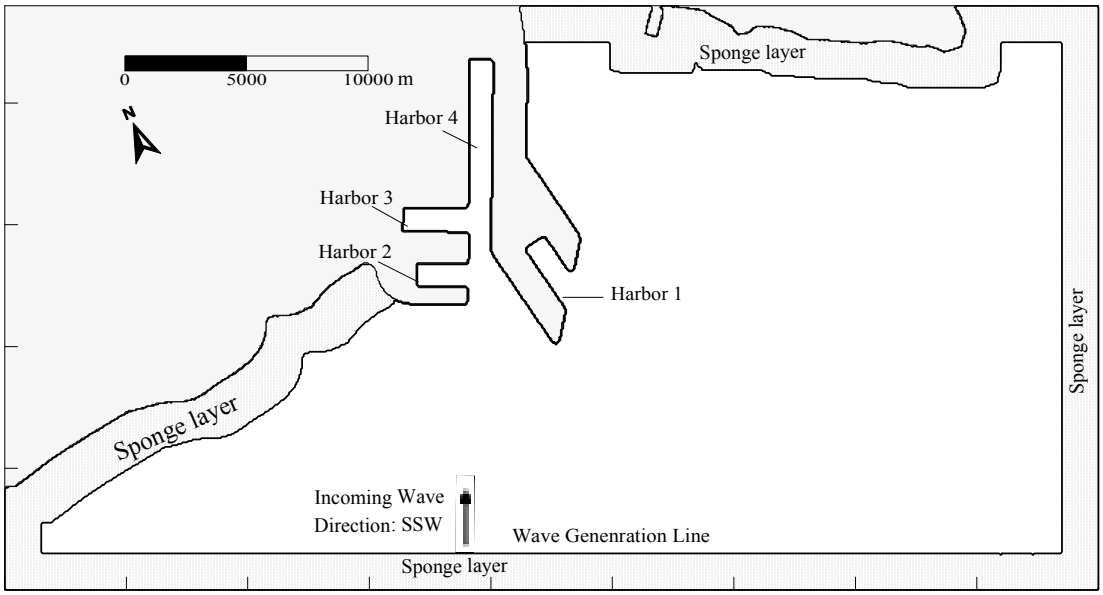


Fig. 7 Computational domain for calculating the long-wave induced resonance in Tieshan port

Fig. 8 (a) to (h) respectively shows the distributions of the computed relative wave height ($H/H_i$) for different wave periods inside and outside Tieshan port. From these figures, we can see that the wave height distributions inside the port for the periods smaller than 150*s* all exhibit two dimensional characteristics, with apparent node and anti-node regions generating alternatively inside the four harbors. While for the periods larger than 150*s*, the wave height distributions inside the four harbors all behave to be one dimensional, with the node and anti-node line nearly parallel to the harbor's transverse axis. Besides that, we can also see some high energy regions along the east perimeter of the port, which should be attributed to the oblique wave reflection. The number of these high energy regions decreases with the increase of the incident period, and their strength increases with waves penetrating into the inside of the port.

When the wave resonance occurs, the node and anti-node regions like standing waves would be formed in the harbor, and the locations of these node and anti-node regions would be different for different incident wave periods. Hence, instead of wave height at the harbor's backwall, we choose the maximum relative wave height and the mean relative wave height of each harbor to study their resonant responses. Fig. 9 (a) to (c) respectively shows the respond curves of the mean relative wave height and the maximum relative wave height for Harbor 2, Harbor 3 and Harbor 4. From these fitures, we can see that the responce of the mean relative wave height behaves the same as that of the maximum relative wave height, and they both fluctuate with the incident wave period. For some

certain periods, there exist the extreme values, indicating that harbor resonance might occurs when these periods are achieved. As for the problem of a long rectangular harbor connecting to an infinite open sea, Mei [14] used to give the following analytical solution to predicate the harbor resoance:

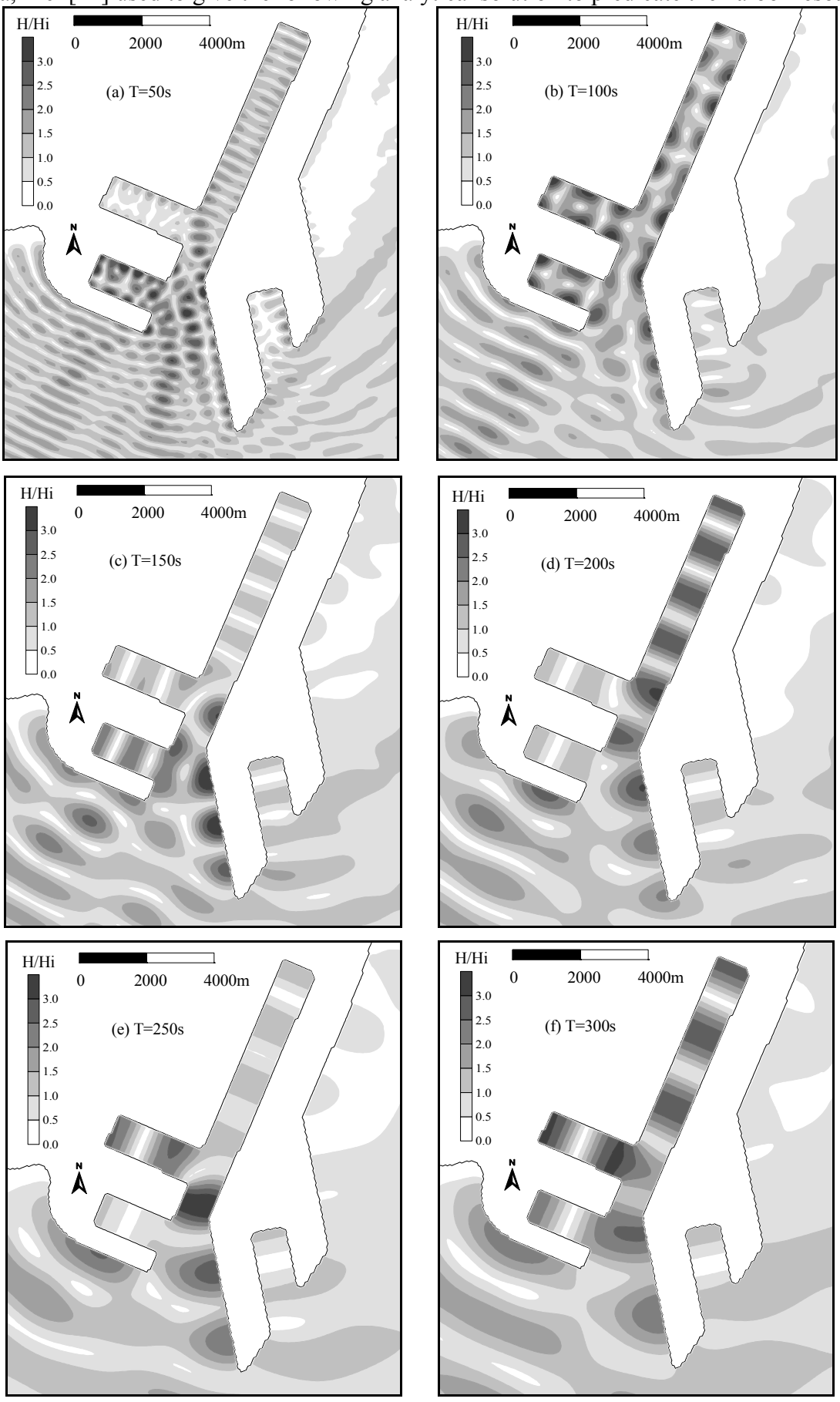

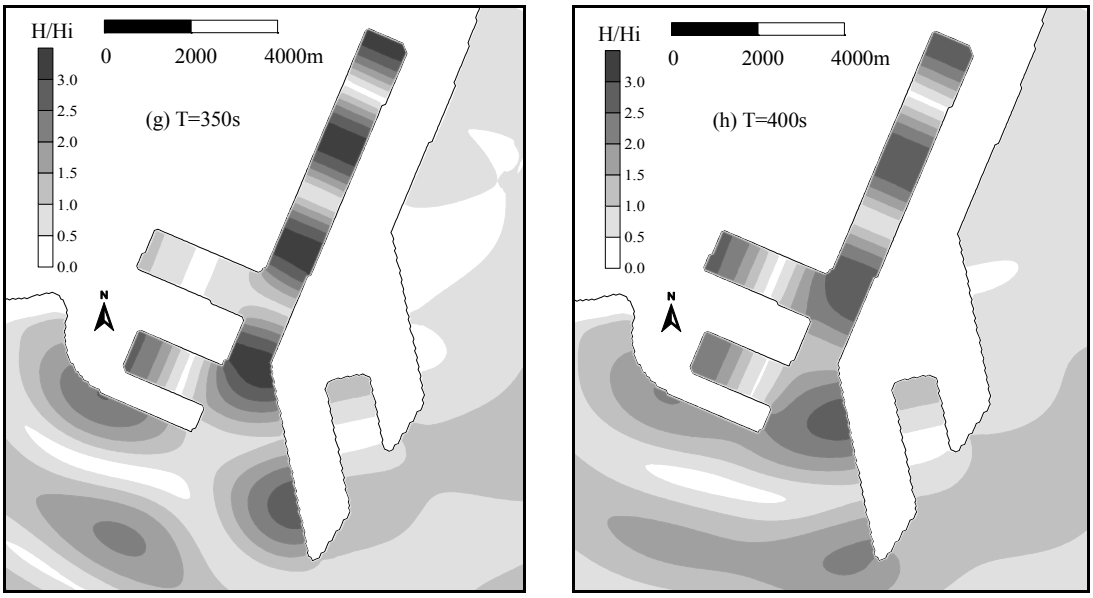


Fig.8 Distribution of the computed relative wave height $H/H_i$ for different incident wave period

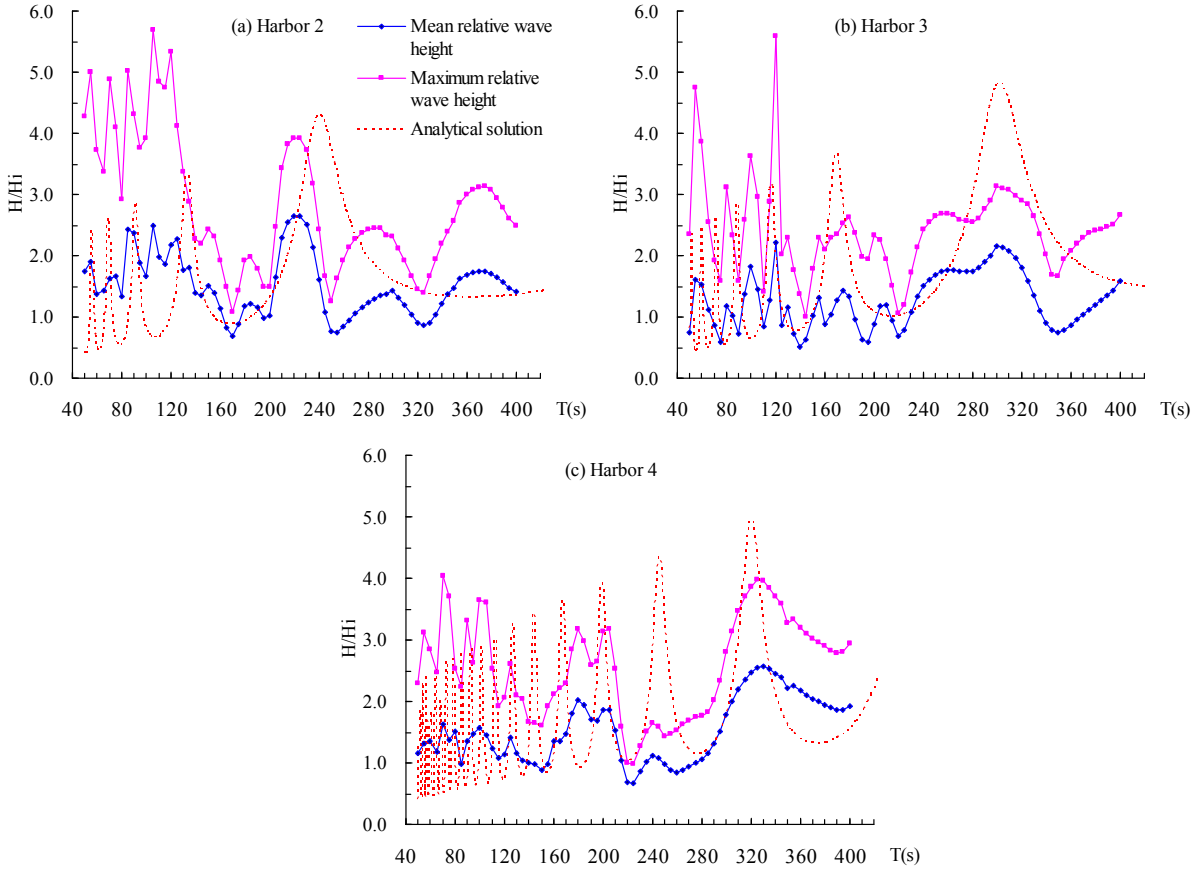


Fig.9 Response curves of the mean relative wave height and the maximum relative wave height for Harbor 2 (a), Harbor 3 (b), and Harbor 4 (c)

$$\vartheta = \left[ \cos kl + \frac{2ka}{\pi} \sin kL \ln \frac{2\gamma ka}{\pi e} - ika \sin kl \right]^{-1} \tag{9}$$

where $\vartheta$ is the amplification factor relative to the standing wave height; $l$ and $a$ are respectively the length and half width of the harbor; and $\ln \gamma = 0.5772157$ is the Euler constant.

Here, Eq. (9) was used to estimate the resonant periods and the corresponding amplification factor for Harbor 2, Harbor 3 and Harbor 4. For conveniences of comparisons, these analytical results were also ploted in Fig. 9 as the dashed lines. Comparing the numerical results with the analytical ones, we

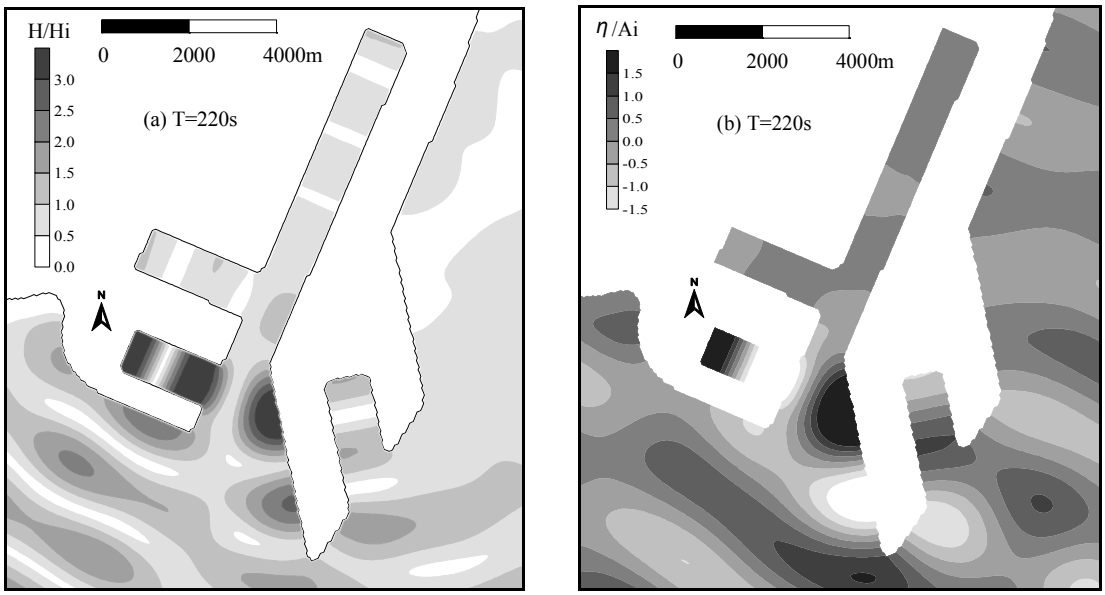


Fig.10 Distribution of the relative wave height $H/H_i$ (a), and the relative free surface $\eta/A_i$ (b), when the wave period is $T$=220$s$. Note that the resonance of the second mode occurs in Harbor 2.

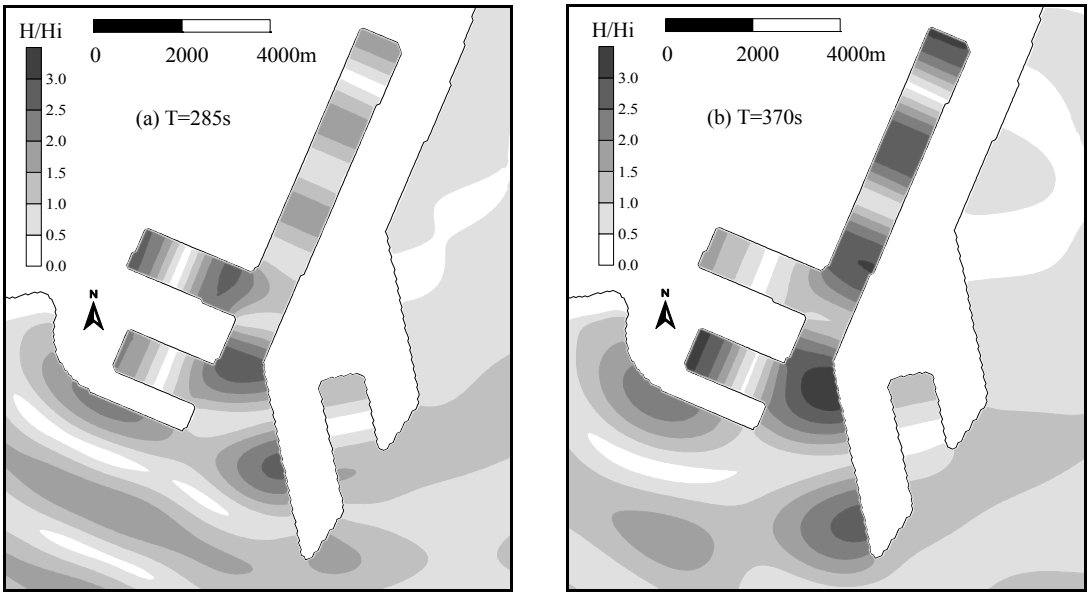


Fig.11 Distribution of the computed relative wave height $H/H_i$ for $T$=285$s$ (a) and $T$=370$s$ (b). Note that for the two periods the resonance of the second mode occurs in Harbor 2.

can see that most of the resonant periods for the three harbors predicated by Eq. (9) have been captured by the numerical models, and the predicated resonant periods by the analytical and numerical models agrees fairly well. As for the amplication factor, when the higher resonant modes occur, i.e., the resonant periods smaller than 150$s$, the numerically predicated amplication factors appear obviously to be higher than the analytical ones. This should be attributed to the fact that the higher resonant modes occuring in the harbor mainly behave to be two dimenssional: the longitudinal resonance and the tranverse resonance are both intrigered in the harbor (see Fig. 8a and 8b). These phenomena cannot be predicated by the analytical theory. While for the lower resonant modes, i.e., the resonant periods larger than 150$s$, the numerically predicated amplication factors agree with the analytical ones. This is because for the lower resonant mode, the wave height patterns in the harbor mainly behaves to be one dimensional (see Fig. 8c to 8h), i.e., the longitudinal resoncance is seen to be the main exhibitions. Further analyzing the numerical and analytical results, the following characteristics for the resonances of the plan of Tieshan port can be obtained.

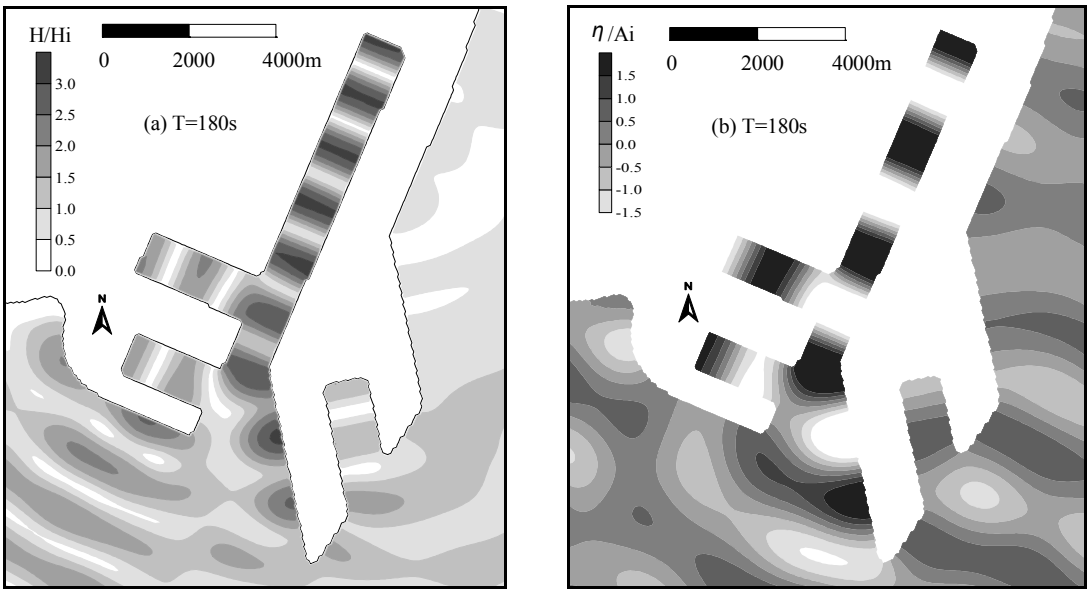


Fig.12 Distribution of the relative wave height $H/H_i$ (a), and the relative free surface $\eta/A_i$ (b), when the wave period $T$=180$s$. Note that while the resonance of the third mode occurs in Harbor 3, the resonance of the seventh mode also occurs in Harbor 4.

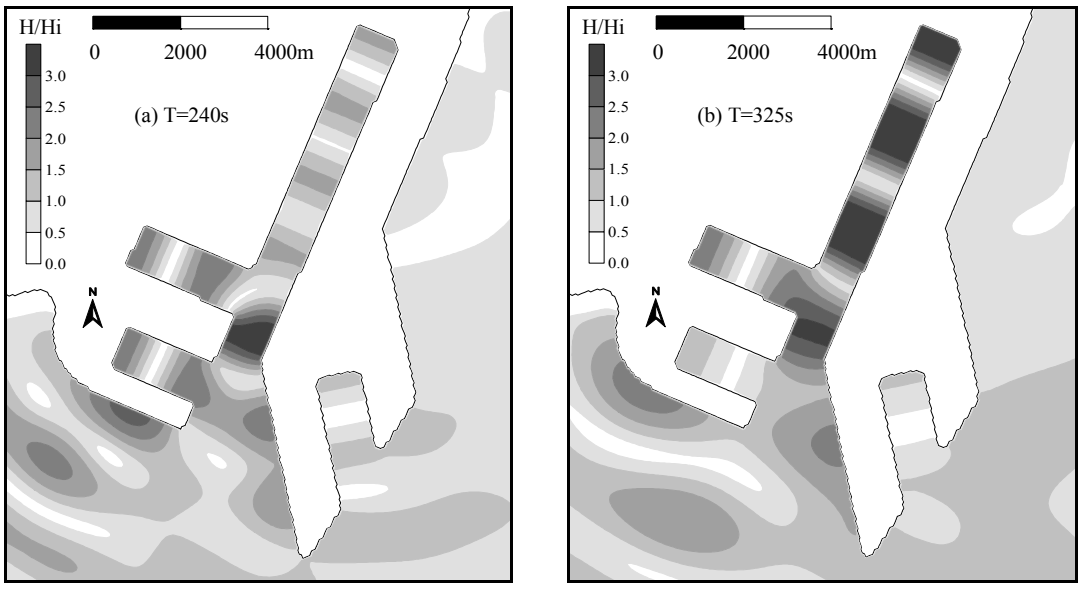


Fig.13 Distribution of the computed relative wave height $H/H_i$ for $T$=240$s$ (a) and $T$=325$s$ (b). Note that for the two periods, the resonance of the fifth mode and the fourth mode, respectively, occurs in Harbor 4.

(1) The numerical results of Fig. 9 (a) shows that one of the main resonant period for Harbor 2 is $T$=220$s$, and the corresponding maximum relative wave height inside this harbor is about 4.0. As for this case, Fig. 10 (a) to (b) respectively shows the relative wave height and the relative free surface distributions inside and outside the port. Examining the patterns of the wave height and the free surface distributions in Harbor 2, we can see that the resonance occurring at this period exhibits to be one dimensional, and there obvously exist the scatter waves radiated out of the harbor mouth. The two node regions and the three anti-node regions existing in Harbor 2 mean that the resonance occurring at this period is of the second mode. The numerically predicated resonant period $T$=220$s$ agrees well to the analytical one $T$=240$s$. In addition, the numerical results of Fig. 9 (a) also shows another two resonant periods $T$=285$s$ and $T$=370$s$ that donot captured by the analytical ones. As for the relative wave height distributions for these two periods, one can see Fig. 11 (a) to (b). Examining the wave

height distributions shown by Fig. 11, we see that the wave climates in Harbor 2 are obviously influenced by the scatter waves propagated out of Harbor 4. Further counting the numbers of the node and anti-node regions, we know that the resonances of these two periods are both of the second resonant mode, which should be caused by the scatter waves that propagate out of Harbor 4.

(2) From the numerical results shown in Fig. 9 (b), we see that the 180-*s* and 300-*s* periods are the two resonant periods of Harbor 3, and the corresponding maximum relative wave height for these two resonances are respectively 2.6 and 3.2. Referring to the distributions of the relative wave height and the relative free surface for $T$=180*s*, one can see Fig. 12 (a) to (b). While for the relative wave height distributions for $T$=300*s*, one can see Fig. 8 (f). Counting the number of the node and anti-node regions, we know that the resonances occurring at these two periods are respectively of the third resonant mode, and of the second resonant mode. Furthermore, the numerically predicated resonant periods (170*s* and 300*s*) agrees fairly well with the analytical ones (180*s* and 302*s*). Comparing the numerically predicated amplification factor of the second mode of Harbor 2 with that of Harbor 3, we can see that even the length of Harbor 2 is smaller than that of Harbor 3, the amplification factor of the former is a bit larger than that of the latter. This should be attributed to the fact that Harbor 3 is sheltered a bit more than Harbor 2. In addition, when the third resonant mode occurs in Harbor 3, the seventh resonant mode was also excited in Harbor 4.

(3) From the numerical results of Fig. 9 (c), we know that when the incident wave period occur at 180*s*, 200*s*, 240*s* and 325*s*, the resonances will be excited in Harbor 4, and the corresponding resonant modes are respectively of the seventh mode, the sixth mode, the fifth mode and the fourth mode. These numerical resonant periods agrees well with the analytical ones (167*s*, 200*s*, 250*s* and 320*s*). Further comparing the strength of the four resonances in Harbor 4, one can see that the fourth resonant mode is the largest. For the relative wave height distributions of the seventh mode and the sixth mode of Harbor 4, one can see Fig. 12 (a) and Fig. 8 (d), respectively. While for the fifth mode and the fourth mode occurring in Harbor 4, one can see Fig. 13 (a) to (b), respectively. All of these figures show that when the resonances occur in Harbor 4, the scatter waves radiated out of this harbor will eventually influence the wave height climates both in Harbor 2 and in Harbor 3. An obvious case is that the 285-*s* and 370-*s* resonant periods of Harbor 2 should be excited by the scatter waves that propagate out of the mouth of Harbor 4.

## Summary

In this paper, a numerical study on the long wave induced resonance has been conducted for the plan of Tieshan port. The simulations were performed with the use of the mild-slope model which was developed in Ref. [1], and further validated through a classical benchmark to examine its ability to predict the wave resonance phenomenon in a harbor. To evaluate the resonance period and the corresponding amplification factor for the plan of Tieshan port, 71 offshore wave conditions with the period ranging from 50*s* to 400*s* have been calculated. The rationalities of the numerical results were examined through comparisons with the theoretical ones. It is shown that the resonances induced by the waves with period larger than 150*s* are quite different from those induced by the waves with period smaller than 150*s*. The resonance occurring at the period larger than 150*s* is seen to be nearly one dimensional, mainly behaving to be longitudinal. While the resonance occurring at the period smaller than 150*s* is seen to be two dimensional, both the longitudinal and transverse resonances existing in the port. After carefully examining the numerical results, the resonant period, the amplification factor and the corresponding resonant mode for each harbor of the plan of Tieshan port have been given.

## Acknowledgements

This work was financially supported by the Jiangsu Province Natural Science Foundation for the Young Scholar (BK20130827), and the National West Traffic Construction Science and Technology Item (20113288081540).

**References**

[1] H.J. Zhao, Z.Y. Song, F.M. Xu and R.J. Li, An extended time-dependent numerical model of the mild-slope equation with weakly nonlinear amplitude dispersion, Acta Oceanol. Sin. 29, 2 (2010) 5-13.
[2] X. Wang, K. Li, Z. Yu and J. Wu, Statistical characteristics of seiches in Longkou Harbour, J. Phys. Oceanogr. 17 (1987) 1063-1065.
[3] J.P.Y. Maa, C.H. Tsai, W.J. Juang and H.M. Tseng, A preliminary study on typhoon Tim induced resonance at Hualien Harbor, Taiwan, Ocean Dyn. 61 (2011) 411-423.
[4] J.B. Michael, D. David and B. Thomas, Modeling of harbor resonance in port of long beach, Civil Engineering in the Oceans VI (2006) 479-493.
[5] A.T. Ippen and Y. Goda, Wave-induced oscillations in harbors: the solution for a rectangular harbor connected to the open-sea, Hydrodynamics Lab., M.I.T. Technical Repport. 59 (1963).
[6] J. Lee, Wave-induced oscillations in harbours of arbitrary geometry, J. Fluid Mech. 45 (1971) 375-394.
[7] H.S. Chen and C.C. Mei, Oscillations and wave forces in a man-made harbor in the open sea, Proc. 10th Symp. Naval Hydrodyn., Office of Naval Research, 1974, pp. 573-594.
[8] G.J.M. Copeland, A practical alternative to the mild-slope wave equation, Coastal Eng. 9 (1985) 125-149.
[9] B. Li, An evolution equation for water waves, Coastal Eng. 23 (1994) 227-242.
[10] T.G. LePelletier and F. Raichlen, Nonlinear oscillations in rectangular tanks, J. Eng. Mech. 114 (1988) 1-23.
[11] G.H. Dong, G. Wang, X.Z. Ma and Y.X. Ma, Numerical study of transient nonlinear harbor resonance, Sci. China Tech. Sci. 53 (2010) 558-565.
[12] C. Lee and S.B. Yoon, Internal generation of waves on an arc in a rectangular grid system, Coastal Eng. 54 (2007) 357-368.
[13] G. Kim, C. Lee and K.D. Suh, Internal generation of waves: Delta source function method and source term addition method, Ocean Eng. 34 (2007) 2051-2264.
[14] C.C. Mei, The applied dynamics of ocean surface waves, World Scientific Press, New York, 1989.

*Applied Mechanics and Materials Vols. 580-583 (2014) pp 2166-2169*
*© (2014) Trans Tech Publications, Switzerland*
*doi:10.4028/www.scientific.net/AMM.580-583.2166*

# Wave Kinematics and Pressure Field of Third-Order Theory for Bichromatic Bi-Directional Waves in Water of Finite Depth

Hu Huang[1, a *], Guoliang Liu[1,b]

Shanghai Institute of Applied Mathematics and Mechanics, Shanghai Key Laboratory of Mechanics in Energy Engineering, Shanghai University, Shanghai 200072, China

[a]hhuang@shu.edu.cn, [b]776824721@qq.com

**Keywords:** Wave Kinematics and Pressure fields, Bichromatic Bi-Directional Waves, Third-Order Theory, Nonlinear Dispersion Relation, Ambient Currents, Finite Water Depth

**Abstract.** Based on the third-order theory for bichromatic bi-directional waves in water of finite depth, a set of explicit formulas for the state-of-the art quantities of wave kinematics for horizontal and vertical particle displacements, velocities and accelerations, and wave pressure field is developed, and would be much more accurate and realistic in the design of harbor, coastal and offshore structures and their structural members.

## Introduction

Strictly speaking, the ocean surface waves are never monochromatic and monodirectional, they are nothing but multi-chromatic and multi-directional. The latter is, however, much less theoretically studied [1-4] because of its dramatic increased complexity, let alone its wide range of applications in engineering. In fact, the former is most dominant in existing wave models, such as famous Stokes theory [5],short-crested waves [6,7] and mild-slope equations [7,8], thus leading to all kinds of applications [9,10] which have inevitably gives rises to a variety of marine problems concerned with how to compute loads on harbor, coastal and offshore structures and how the structures respond to these loads.

The solutions given in [2,4] for bichromatic bi-directional water waves propagating over a horizontal bottom provide the basis for applications to a variety of problems of engineering interest. In particular, the water particle kinematics and the pressure field within the wave are directly related to the calculation of forces on bodies. For the purposes of this study, this paper is devoted to a third-order explicit solution with the phase functions, $\theta_n = \omega_n t - \boldsymbol{k_n}\cdot\boldsymbol{x}$, for the water particle displacements, $(\zeta_x,\zeta_y,\zeta_z)\equiv(\boldsymbol{\zeta_x},\zeta_z)$, velocities, $(u,v,w)\equiv(\boldsymbol{u},w)$, accelerations, $(a_x,a_y,a_z)\equiv(\boldsymbol{a_x},a_z)$,and the pressure field $p$.

## Particle Displacements

$$\begin{aligned}\zeta_x = \int \boldsymbol{u}(\boldsymbol{x},z,t)\,dt = \boldsymbol{U}t - \varepsilon[\sum_{r=1}^{2}\frac{\boldsymbol{\kappa}_r F_r}{\omega_{1r}+\boldsymbol{U}\cdot\boldsymbol{\kappa}_r}\cosh\kappa_r(z+h)(a_r\sin\theta_r - b_r\cos\theta_r)]\\ -\varepsilon^2[\frac{(\boldsymbol{\kappa_n}\pm\boldsymbol{\kappa_m})F_{n\pm m}}{(\omega_{1n}+\boldsymbol{U}\cdot\boldsymbol{\kappa_n})\pm(\omega_{1m}+\boldsymbol{U}\cdot\boldsymbol{\kappa_m})}\cosh\kappa_{n\pm m}(z+h)(A_{n\pm m}\sin\theta_{n\pm m} - B_{n\pm m}\cos\theta_{n\pm m})\\ +\sum_{r=1}^{2}\frac{\boldsymbol{\kappa}_r F_{2r}}{\omega_{1r}+\boldsymbol{U}\cdot\boldsymbol{\kappa}_r}\cosh\kappa_{2r}(z+h)(A_{2r}\sin 2\theta_r - B_{2r}\cos 2\theta_r)]\\ -\varepsilon^3[\frac{(\boldsymbol{\kappa_n}\pm 2\boldsymbol{\kappa_m})F_{n\pm 2m}}{(\omega_{1n}+\boldsymbol{U}\cdot\boldsymbol{\kappa_n})\pm 2(\omega_{1m}+\boldsymbol{U}\cdot\boldsymbol{\kappa_m})}\cosh\kappa_{n\pm 2m}(z+h)(A_{n\pm 2m}\sin\theta_{n\pm 2m} - B_{n\pm 2m}\cos\theta_{n\pm 2m})\\ +\frac{(\boldsymbol{\kappa_m}\pm 2\boldsymbol{\kappa_n})F_{m\pm 2n}}{(\omega_{1m}+\boldsymbol{U}\cdot\boldsymbol{\kappa_m})\pm 2(\omega_{1n}+\boldsymbol{U}\cdot\boldsymbol{\kappa_n})}\cosh\kappa_{m\pm 2n}(z+h)(A_{m\pm 2n}\sin\theta_{m\pm 2n} - B_{m\pm 2n}\cos\theta_{m\pm 2n})\end{aligned}$$

$$+\sum_{r=1}^{2}\frac{\boldsymbol{\kappa}_r F_{3r}}{\omega_{1r}+\boldsymbol{U}\cdot\boldsymbol{\kappa}_r}\cosh\kappa_{3r}(z+h)(A_{3r}\sin 3\theta_r - B_{3r}\cos 3\theta_r)$$
$$+\sum_{r=1}^{2}\frac{(\omega_{1r}+\boldsymbol{U}\cdot\boldsymbol{\kappa}_r)F_{13r}-\omega_{1r}\omega_{3r}F_r}{(\omega_{1r}+\boldsymbol{U}\cdot\boldsymbol{\kappa}_r)^2}\boldsymbol{\kappa}_r\cosh\kappa_r(z+h)(a_r\sin\theta_r - b_r\cos\theta_r)], \quad (1)$$

$$\zeta_z=\int w(\boldsymbol{x},z,t)\,dt=-\varepsilon[\sum_{r=1}^{2}\frac{\kappa_r F_r}{\omega_{1r}+\boldsymbol{U}\cdot\boldsymbol{\kappa}_r}\sinh\kappa_r(z+h)(a_r\cos\theta_r+b_r\sin\theta_r)]$$
$$-\varepsilon^2[\frac{(\kappa_n\pm\kappa_m)F_{n\pm m}}{(\omega_{1n}+\boldsymbol{U}\cdot\boldsymbol{\kappa_n})\pm(\omega_{1m}+\boldsymbol{U}\cdot\boldsymbol{\kappa_m})}\sinh\kappa_{n\pm m}(z+h)(A_{n\pm m}\cos\theta_{n\pm m}+B_{n\pm m}\sin\theta_{n\pm m})$$
$$+\sum_{r=1}^{2}\frac{\kappa_r F_{2r}}{\omega_{1r}+\boldsymbol{U}\cdot\boldsymbol{\kappa}_r}\sinh\kappa_{2r}(z+h)(A_{2r}\cos 2\theta_r+B_{2r}\sin 2\theta_r)]$$
$$-\varepsilon^3[\frac{(\kappa_n\pm 2\kappa_m)F_{n\pm 2m}}{(\omega_{1n}+\boldsymbol{U}\cdot\boldsymbol{\kappa_n})\pm 2(\omega_{1m}+\boldsymbol{U}\cdot\boldsymbol{\kappa_m})}\sinh\kappa_{n\pm 2m}(z+h)(A_{n\pm 2m}\cos\theta_{n\pm 2m}+B_{n\pm 2m}\sin\theta_{n\pm 2m})$$
$$+\frac{(\kappa_m\pm 2\kappa_n)F_{m\pm 2n}}{(\omega_{1m}+\boldsymbol{U}\cdot\boldsymbol{\kappa_m})\pm 2(\omega_{1n}+\boldsymbol{U}\cdot\boldsymbol{\kappa_n})}\sinh\kappa_{m\pm 2n}(z+h)(A_{m\pm 2n}\cos\theta_{m\pm 2n}+B_{m\pm 2n}\sin\theta_{m\pm 2n})$$
$$+\sum_{r=1}^{2}\frac{\kappa_r F_{3r}}{\omega_{1r}+\boldsymbol{U}\cdot\boldsymbol{\kappa}_r}\sinh\kappa_{3r}(z+h)(A_{3r}\cos 3\theta_r+B_{3r}\sin 3\theta_r)$$
$$+\sum_{r=1}^{2}\frac{(\omega_{1r}+\boldsymbol{U}\cdot\boldsymbol{\kappa}_r)F_{13r}-\omega_{1r}\omega_{3r}F_r}{(\omega_{1r}+\boldsymbol{U}\cdot\boldsymbol{\kappa}_r)^2}\kappa_r\sinh\kappa_r(z+h)(a_r\cos\theta_r+b_r\sin\theta_r)]. \quad (2)$$

## Particle Velocities

$$\boldsymbol{u}=\boldsymbol{U}-\varepsilon[\sum_{r=1}^{2}\boldsymbol{\kappa}_r F_r\cosh\kappa_r(z+h)(a_r\cos\theta_r+b_r\sin\theta_r)]$$
$$-\varepsilon^2[(\boldsymbol{\kappa_n}\pm\boldsymbol{\kappa_m})F_{n\pm m}\cosh\kappa_{n\pm m}(z+h)(A_{n\pm m}\cos\theta_{n\pm m}+B_{n\pm m}\sin\theta_{n\pm m})$$
$$+\sum_{r=1}^{2}2\boldsymbol{\kappa_n}F_{2n}\cosh\kappa_{2n}(z+h)(A_{2n}\cos\theta_{2n}+B_{2n}\sin\theta_{2n})]$$
$$-\varepsilon^3[(\boldsymbol{\kappa_n}\pm 2\boldsymbol{\kappa_m})F_{n\pm 2m}\cosh\kappa_{n\pm 2m}(z+h)(A_{n\pm 2m}\cos\theta_{n\pm 2m}+B_{n\pm 2m}\sin\theta_{n\pm 2m})$$
$$+(\boldsymbol{\kappa_m}\pm 2\boldsymbol{\kappa_n})F_{m\pm 2n}\cosh\kappa_{m\pm 2n}(z+h)(A_{m\pm 2n}\cos\theta_{m\pm 2n}+B_{m\pm 2n}\sin\theta_{m\pm 2n})$$
$$+\sum_{r=1}^{2}\boldsymbol{\kappa_r}F_{13r}\cosh\kappa_r(z+h)(a_r\cos\theta_r+b_r\sin\theta_r)$$
$$+\sum_{r=1}^{2}3\boldsymbol{\kappa_r}F_{3r}\cosh\kappa_{3r}(z+h)(A_{3r}\cos\theta_{3r}+B_{3r}\sin\theta_{3r})], \quad (3)$$

$$w=\varepsilon[\sum_{r=1}^{2}\kappa_r F_r\sinh\kappa_r(z+h)(a_r\sin\theta_r-b_r\cos\theta_r)]$$
$$+\varepsilon^2[\kappa_{n\pm m}F_{n\pm m}\sinh\kappa_{n\pm m}(z+h)(A_{n\pm m}\sin\theta_{n\pm m}-B_{n\pm m}\cos\theta_{n\pm m})$$
$$+\sum_{r=1}^{2}2\kappa_r F_{2r}\sinh\kappa_{2r}(z+h)(A_{2r}\sin\theta_{2r}-B_{2r}\cos\theta_{2r})]$$
$$+\varepsilon^3[\kappa_{n\pm 2m}F_{n\pm 2m}\sinh\kappa_{n\pm 2m}(z+h)(A_{n\pm 2m}\sin\theta_{n\pm 2m}-B_{n\pm 2m}\cos\theta_{n\pm 2m})$$
$$+\kappa_{m\pm 2n}F_{m\pm 2n}\sinh\kappa_{m\pm 2n}(z+h)(A_{m\pm 2n}\sin\theta_{m\pm 2n}-B_{m\pm 2n}\cos\theta_{m\pm 2n})$$
$$+\sum_{r=1}^{2}3\kappa_r F_{3r}\sinh\kappa_{3r}(z+h)(A_{3r}\sin\theta_{3r}-B_{3r}\cos\theta_{3r})$$
$$+\sum_{r=1}^{2}\kappa_r F_{13r}\sinh\kappa_r(z+h)(a_r\sin\theta_r-b_r\cos\theta_r)]. \quad (4)$$

**Particle Accelerations**

$$
\begin{aligned}
a_x = {} & \varepsilon[\sum_{r=1}^{2}(\omega_{1r}+\boldsymbol{U}\cdot\boldsymbol{\kappa}_r)\kappa_r F_r \cosh\kappa_r(z+h)(a_r\sin\theta_r - b_r\cos\theta_r)] \\
& + \varepsilon^2\{[(\omega_{1n}+\boldsymbol{U}\cdot\boldsymbol{\kappa}_n)\pm(\omega_{1m}+\boldsymbol{U}\cdot\boldsymbol{\kappa}_m)](\boldsymbol{\kappa}_n\pm\boldsymbol{\kappa}_m)F_{n\pm m}\cosh\kappa_{n\pm m}(z+h)(A_{n\pm m}\sin\theta_{n\pm m} - B_{n\pm m}\cos\theta_{n\pm m}) \\
& \quad + \sum_{r=1}^{2}4(\omega_{1r}+\boldsymbol{U}\cdot\boldsymbol{\kappa}_r)\kappa_r F_{2r}\cosh\kappa_{2r}(z+h)(A_{2r}\sin\theta_{2r} - B_{2r}\cos\theta_{2r})\} \\
& + \varepsilon^3\{[(\omega_{1n}+\boldsymbol{U}\cdot\boldsymbol{\kappa}_n)\pm 2(\omega_{1m}+\boldsymbol{U}\cdot\boldsymbol{\kappa}_m)](\boldsymbol{\kappa}_n\pm 2\boldsymbol{\kappa}_m)F_{n\pm 2m}\cosh\kappa_{n\pm 2m}(z+h)(A_{n\pm 2m}\sin\theta_{n\pm 2m} - B_{n\pm 2m}\cos\theta_{n\pm 2m}) \\
& \quad + [(\omega_{1m}+\boldsymbol{U}\cdot\boldsymbol{\kappa}_m)\pm 2(\omega_{1n}+\boldsymbol{U}\cdot\boldsymbol{\kappa}_n)](\boldsymbol{\kappa}_m\pm 2\boldsymbol{\kappa}_n)F_{m\pm 2n}\cosh\kappa_{m\pm 2n}(z+h)(A_{m\pm 2n}\sin\theta_{m\pm 2n} - B_{m\pm 2n}\cos\theta_{m\pm 2n}) \\
& \quad + \sum_{r=1}^{2}9(\omega_{1r}+\boldsymbol{U}\cdot\boldsymbol{\kappa}_r)\kappa_r F_{3r}\cosh\kappa_{3r}(z+h)(A_{3r}\sin\theta_{3r} - B_{3r}\cos\theta_{3r}) \\
& + \sum_{r=1}^{2}[(\omega_{1r}+\boldsymbol{U}\cdot\boldsymbol{\kappa}_r)F_{13r} + \omega_{1r}\omega_{3r}F_r]\kappa_r\cosh\kappa_r(z+h)(a_r\sin\theta_r - b_r\cos\theta_r)\}, \qquad (5)
\end{aligned}
$$

$$
\begin{aligned}
a_z = {} & \varepsilon[\sum_{r=1}^{2}(\omega_{1r}+\boldsymbol{U}\cdot\boldsymbol{\kappa}_r)\kappa_r F_r \sinh\kappa_r(z+h)(a_r\cos\theta_r + b_r\sin\theta_r)] \\
& + \varepsilon^2\{[(\omega_{1n}+\boldsymbol{U}\cdot\boldsymbol{\kappa}_n)\pm(\omega_{1m}+\boldsymbol{U}\cdot\boldsymbol{\kappa}_m)]\kappa_{n\pm m}F_{n\pm m}\sinh\kappa_{n\pm m}(z+h)(A_{n\pm m}\cos\theta_{n\pm m} + B_{n\pm m}\sin\theta_{n\pm m}) \\
& \quad + \sum_{r=1}^{2}4(\omega_{1r}+\boldsymbol{U}\cdot\boldsymbol{\kappa}_r)\kappa_r F_{2r}\sinh\kappa_{2r}(z+h)(A_{2r}\cos\theta_{2r} + B_{2r}\sin\theta_{2r})\} \\
& + \varepsilon^3\{[(\omega_{1n}+\boldsymbol{U}\cdot\boldsymbol{\kappa}_n)\pm 2(\omega_{1m}+\boldsymbol{U}\cdot\boldsymbol{\kappa}_m)]\kappa_{n\pm 2m}F_{n\pm 2m}\sinh\kappa_{n\pm 2m}(z+h)(A_{n\pm 2m}\cos\theta_{n\pm 2m} + B_{n\pm 2m}\sin\theta_{n\pm 2m}) \\
& \quad + [(\omega_{1m}+\boldsymbol{U}\cdot\boldsymbol{\kappa}_m)\pm 2(\omega_{1n}+\boldsymbol{U}\cdot\boldsymbol{\kappa}_n)]\kappa_{m\pm 2n}F_{m\pm 2n}\sinh\kappa_{m\pm 2n}(z+h)(A_{m\pm 2n}\cos\theta_{m\pm 2n} + B_{m\pm 2n}\sin\theta_{m\pm 2n}) \\
& \quad + \sum_{r=1}^{2}9(\omega_{1r}+\boldsymbol{U}\cdot\boldsymbol{\kappa}_r)\kappa_r F_{3r}\sinh\kappa_{3r}(z+h)(A_{3r}\cos\theta_{3r} + B_{3r}\sin\theta_{3r}) \\
& \quad + \sum_{r=1}^{2}[(\omega_{1r}+\boldsymbol{U}\cdot\boldsymbol{\kappa}_r)F_{13r} + \omega_{1r}\omega_{3r}F_r]\kappa_r\sinh\kappa_r(z+h)(a_r\cos\theta_r + b_r\sin\theta_r)\}. \qquad (6)
\end{aligned}
$$

**Pressure Field**

$$
\begin{aligned}
\frac{p}{\rho g} = {} & -z - \frac{1}{g}\frac{\partial\Phi}{\partial t} - \frac{1}{2g}\left|(\nabla+\frac{\partial}{\partial z})\Phi\right|^2 = (-z-\frac{\boldsymbol{U}^2}{2g}) - \frac{\varepsilon}{g}[\sum_{r=1}^{2}\omega_{1r}F_r\cosh\kappa_r(z+h)(a_r\cos\theta_r + b_r\sin\theta_r)] \\
& - \frac{\varepsilon^2}{2g}\left(c_n{}^2 + c_m{}^2\right) - \frac{\varepsilon^2}{g}\{\{[(\omega_{1n}\pm\omega_{1m})F_{n\pm m} + \frac{h}{4}(\boldsymbol{\kappa}_n\cdot\boldsymbol{\kappa}_m - \kappa_n\kappa_m)F_nF_m]\cosh\kappa_{n\pm m}(z+h) \\
& \qquad + \frac{h}{4}(\boldsymbol{\kappa}_n\cdot\boldsymbol{\kappa}_m + \kappa_n\kappa_m)F_nF_m\cosh\kappa_{n\mp m}(z+h)\}(A_{n\pm m}\cos\theta_{n\pm m} + B_{n\pm m}\sin\theta_{n\pm m}) \\
& \qquad + \sum_{r=1}^{2}[2\omega_{1r}F_{2r}\cosh\kappa_{2r}(z+h) + \frac{h}{2}\kappa_r{}^2F_r{}^2](A_{2r}\cos\theta_{2r} + B_{2r}\sin\theta_{2r})\} \\
& - \frac{\varepsilon^3}{g}\{\{[(\omega_{1n}\pm 2\omega_{1m})F_{n\pm 2m} + \frac{h}{2}(\boldsymbol{\kappa}_n\cdot\boldsymbol{\kappa}_m - \kappa_n\kappa_m)F_nF_{2m} \\
& \quad + \frac{h}{2}(\boldsymbol{\kappa}_n\cdot\boldsymbol{\kappa}_m \pm \kappa_m{}^2 \mp \kappa_m\kappa_{n\pm m})F_mF_{n\pm m}]\cosh\kappa_{n\pm 2m}(z+h) \\
& \quad + \frac{h}{2}(\boldsymbol{\kappa}_n\cdot\boldsymbol{\kappa}_m + \kappa_n\kappa_m)F_nF_{2m}\cosh\kappa_{n\mp 2m}(z+h) \\
& \quad + \frac{h}{2}(\boldsymbol{\kappa}_n\cdot\boldsymbol{\kappa}_m \pm \kappa_m{}^2 \mp \kappa_m\kappa_{n\pm m})F_mF_{n\pm m}\cosh\kappa_n(z+h)\}(A_{n\pm 2m}\cos\theta_{n\pm 2m} + B_{n\pm 2m}\sin\theta_{n\pm 2m}) \\
& + \{[(\omega_{1m}\pm 2\omega_{1n})F_{m\pm 2n} + \frac{h}{2}(\boldsymbol{\kappa}_n\cdot\boldsymbol{\kappa}_m - \kappa_n\kappa_m)F_mF_{2n} + \frac{h}{2}(\kappa_n{}^2 \pm \boldsymbol{\kappa}_n\cdot\boldsymbol{\kappa}_m + \kappa_n\kappa_{n\pm m})F_nF_{n\pm m}]\cosh\kappa_{m\pm 2n}(z+h) \\
& \quad + \frac{h}{2}(\boldsymbol{\kappa}_n\cdot\boldsymbol{\kappa}_m + \kappa_n\kappa_m)F_mF_{2n}\cosh\kappa_{m\mp 2n}(z+h)
\end{aligned}
$$

$$+\frac{h}{2}(\kappa_n^{\,2}\pm\boldsymbol{\kappa_n}\cdot\boldsymbol{\kappa_m}+\kappa_n\kappa_{n\pm m})F_mF_{n\pm m}\cosh\kappa_m(z+h)\}(A_{m\pm 2n}\cos\theta_{m\pm 2n}+B_{m\pm 2n}\sin\theta_{m\pm 2n})$$

$$+\sum_{r=1}^{2}[\omega_{1r}F_{3r}\cosh\kappa_{3r}(z+h)+h\kappa_r^{\,2}F_rF_{2r}\cosh\kappa_r(z+h)](A_{3r}\cos\theta_{3r}+B_{3r}\sin\theta_{3r})$$

$$+\{(\omega_{1n}\omega_{3n}F_n+\omega_{1n}F_{13n})\cosh\kappa_n(z+h)+\frac{c_n^{\,2}\kappa_n^{\,2}}{2h}F_nF_{2n}\cosh\kappa_{3n}(z+h)$$

$$+\frac{c_m^{\,2}}{4h}[(\boldsymbol{\kappa_n}\cdot\boldsymbol{\kappa_m}\pm\boldsymbol{\kappa_m}^{\,2}+\kappa_{n\pm m}\kappa_m)F_mF_{n\pm m}\cosh\kappa_{n\pm 2m}(z+h)$$

$$+(\boldsymbol{\kappa_n}\cdot\boldsymbol{\kappa_m}+\boldsymbol{\kappa_m}^{\,2}-\kappa_{n+m}\kappa_m)F_mF_{n+m}\cosh\kappa_n(z+h)$$

$$+(\boldsymbol{\kappa_n}\cdot\boldsymbol{\kappa_m}-\boldsymbol{\kappa_m}^{\,2}-\kappa_{n-m}\kappa_m)F_mF_{n-m}\cosh\kappa_n(z+h)]\}(a_n\cos\theta_n+b_n\sin\theta_n)\}$$

$$+\{(\omega_{1m}\omega_{3m}F_m+\omega_{1m}F_{13m})\cosh\kappa_m(z+h)+\frac{c_m^{\,2}\kappa_m^{\,2}}{2h}F_mF_{2m}\cosh\kappa_{3m}(z+h)$$

$$+\frac{c_n^{\,2}}{4h}[(\boldsymbol{\kappa_n}\cdot\boldsymbol{\kappa_m}\pm\boldsymbol{\kappa_n}^{\,2}+\kappa_{n\pm m}\kappa_n)F_nF_{n\pm m}\cosh\kappa_{m\pm 2n}(z+h)$$

$$+(\boldsymbol{\kappa_n}\cdot\boldsymbol{\kappa_m}+\boldsymbol{\kappa_n}^{\,2}-\kappa_{n+m}\kappa_n)F_nF_{n+m}\cosh\kappa_m(z+h)$$

$$+(\boldsymbol{\kappa_n}\cdot\boldsymbol{\kappa_m}-\boldsymbol{\kappa_n}^{\,2}-\kappa_{n-m}\kappa_n)F_nF_{n-m}\cosh\kappa_m(z+h)]\}(a_m\cos\theta_m+b_m\sin\theta_m)\}\,. \qquad (7)$$

**Summary**

Including the nonlinear third-order dispersion relation and the effects of an ambient current, this paper obtains a series of perturbation formulas for bichromatic bi-directional wave kinematics and pressure field in water of finite depth. The formulas are both an extension of the common Stokes waves [5, 7-10] from monochromatic monodirectional to bichromatic bi-directional waves and an extension of [6,7] from monochromatic to bichromatic short-crested waves, thus probably providing the state-of-the art in harbor, coastal and offshore engineering [9,10].

**Acknowledgements**

This work was financially supported by the Natural Science Foundation of China (11172157), Shanghai Pujiang Program (12PJD001) and Shanghai Program for Innovative Research Team in Universities.

**References**

[1] H.A. Schaffer, C.M. Steenberg, Ocean Engng. 30 (2003) 1203-1231.
[2] P.A. Madsen, D.R. Fuhrman, J. Fluid Mech. 557 (2006) 369-397.
[3] H. Huang, Y.B. Xia, Acta Physica Sinica, 60 (2011) 044702. (in Chinese)
[4] P.A. Madsen, D.R. Fuhrman, J. Fluid Mech. 698 (2012) 304-334.
[5] G.G. Stokes, Trans. Cambridge Philos. Soc. 8 (1847) 441-455.
[6] J.R.C. Hsu, Y. Tsuchiya, R. Silvester, J. Fluid Mech. 90 (1979) 179-196.
[7] H. Huang, Dynamics of Surface Waves in Coastal Waters, Higher Education Press-Springer, Beijing-Berlin, 2009.
[8] M.W. Dingemans, Water Wave Propagation over Uneven Bottoms, World Scientific, Singapore, 1997.
[9] S.K. Chakrabarti, Handbook of Offshore Engineering, Elsevier Ltd, Amsterdam, 2005.
[10] C.C. Mei, M. Stiassnie, D. K.-P. Yue, Theory and Applications of Ocean Surface Waves, World Scientific, Singapore, 2005.

*Applied Mechanics and Materials Vols. 580-583 (2014) pp 2170-2176*
*© (2014) Trans Tech Publications, Switzerland*
*doi:10.4028/www.scientific.net/AMM.580-583.2170*

# A kind of floating breakwater sheltering deep water aquaculture

Xiaofei Cheng[1,2, a]

[1] Marine Science and Technology School, Zhejiang Ocean University, Zhoushan 316000, China

[2] Fujian Research Institute of Communications Science and Technology, Fuzhou 350004, China

[a]xiaofeichengg@163.com

**Keywords:** Floating breakwater; catamaran raft; wave-attenuating and oscillation-inhibiting device

**Abstract.** This paper briefly introduces the design, construction and wave attenuation effect test of a kind of floating breakwater sheltering deep water aquaculture. This novel floating breakwater structure is composed of 28 standard modules and corresponding anchoring systems, and each standard module comprises a catamaran raft and a wave-attenuating and oscillation-inhibiting device, with a length of 30 m, a width of 7 m, a depth of 2 m and a draft of 1.1 m. Each catamaran raft employs a box-shaped multi-ribbed beam-and-slab structure, and was constructed using high-performance concrete and ferrocement materials and internally filled with polystyrene foam plastics. Each wave-attenuating and oscillation-inhibiting device uses a detachable split box-shaped structure and was pre-fabricated using high-performance concrete, with a length of 2 m, a width of 1.638 m and a height of 2 m. Each standard module is anchored using 6 anchor chains, each of which has an on-floor length of about 25 m. After construction, this floating breakwater system was tested for wave attenuation effect, and the data analysis results show that the floating breakwater system has a wave attenuation effect of up to 50 %.

## Introduction

As a major marine aquaculture province in China, Fujian Province is currently dominated by offshore shallow water aquaculture, but the offshore shallow water aquaculture threatens the safe operation and oceanic water environment of existing ports. Therefore, there is a movement to transfer marine aquaculture from offshore areas to open sea areas, to promote the development of the oceanic economy, to drive good circulation of ecosystems, to ensure quality and safety of aquatic products and to push ocean exploitation from shallow sea areas to deep sea areas. However, large waves in the open seas threaten the deep water aquaculture in the marine aquaculture industry, and good shelter facilities [1] need to be established so as to provide shelter for the deep water aquaculture.

This paper introduces a kind of novel floating breakwater, which is composed of 28 standard modules and corresponding anchoring systems. Each standard module comprises a catamaran raft and a wave-attenuating and oscillation-inhibiting device. Through model and pilot testing in 2011–2013, this floating breakwater system was constructed in the sea area to the east of Fujian Province, preliminarily forming an artificially sheltered water area with a given range, to provide a relatively safe production site for deep water aquaculture with a good ecological environment. After the construction was completed, the wave attenuation effect of the floating breakwater system was tested using acoustic wave and current (AWAC) acoustic Doppler current profilers (1 MHz, AWAC) imported from Norway, and the test results indicate that the wave attenuation effect is good, reaching 50 %. This paper briefly describes the design, construction and wave attenuation effect test of this floating breakwater system.

**Design overview.**

**Main body structure.** This floating breakwater system is composed of 28 standard modules and corresponding anchoring systems, as shown in Figure 1. The standard modules constitute the main structure of the floating breakwater system, and each standard module comprises a catamaran raft [2] and a wave-attenuating and oscillation-inhibiting device, as shown in Figures 2 and 3. The figures show that there are a total of 6 tether piles provided at both ends and in the middle of the main deck, corresponding to which anchor chain pipes are set up between the main deck and the bottom plate. There is an inspection hole provided in the main deck of each anti-sinking compartment, which is closed in normal times to prevent sea water from entering the compartment.

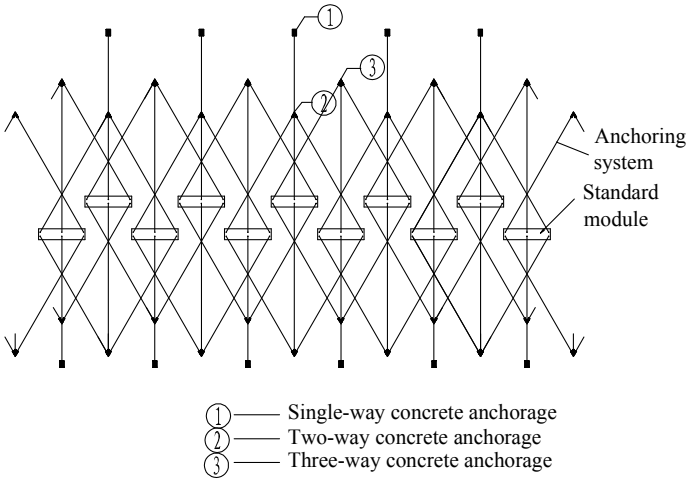


Fig. 1 Floating breakwater layout diagram

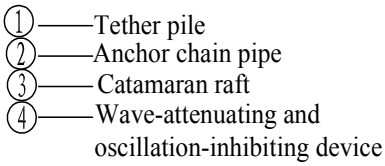


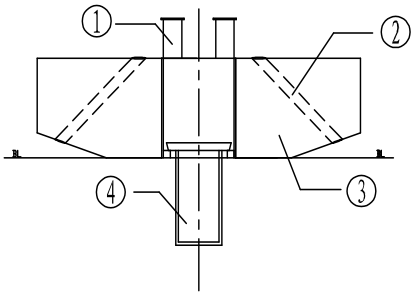


Fig. 2 Cross-sectional view of standard module

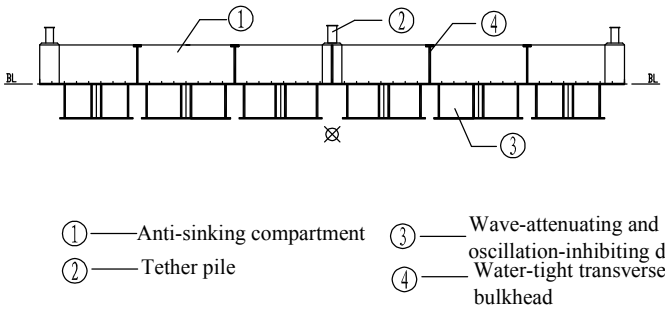


Fig. 3 Side view of standard module

A catamaran raft is one body formed of two fully-enclosed units connected with head and tail closing plates, a middle baffle plate, a web beam and a bottom traverse. Each unit has an overall length of 30.00 m, a molded breadth of 2.50 m and a molded depth of 2.00 m, the unit spacing is 2.00 m, and the design draft is 1.1 m. Each unit is provided with 6 anti-sinking compartments under the main deck, so one catamaran raft has a total of 12 anti-sinking compartments, to meet the requirement that if any two compartments are damaged with water entering, the catamaran raft will not sink. According to need, waste foam plastics in the aquaculture zone and floating materials on the water surface can be filled into each anti-sinking compartment to effectively reduce the quantity of water entering the compartments after the anti-sinking compartment is damaged, and thus to improve the anti-sinking performance; onsite polymer foaming technology can also be used to fully fill the internal space of each anti-sinking compartment so that the raft becomes an all-weather anti-sinking floating body, to ensure the unsinkability of the main body structure in any damage case. Under the main deck of each unit of a raft, there are 6 anti-sinking compartments divided by 5 water-tight transverse bulkheads; each unit has a box-shaped

multi-ribbed beam-and-slab structure to fully exert the mechanical properties of different structural materials, and to increase the strength and rigidity of the main body structure under the effect of waves. The internal rib frame and longitudinal members in each unit are ferrocement thin-wall members, to decrease the deadweight of the structure and the consumption of main materials; the side plates and head and tail closing plates are shaped vertically using high-frequency grouting of composite material ferrocement, as they are the places easiest to corrode under the direct wave impact and wave-splashing alternating dry-wet effect. The deck and bottom plate facilitate good construction operating conditions and a convenient module disassembly operation, and they are formed with high-performance ship-making concrete. In addition to paint coating, sufficient corrosion allowance is reserved for the steel members of the catamaran raft, which are in direct contact with sea water, so that their useful life is as consistent as possible with that of the main body structure.

The wave-attenuating and oscillation-inhibiting device is located below the baseline of the catamaran raft, to increase the dipping depth, underwater side projection area and water-carrying mass moment of inertia of the main body structure, and thus to improve the wave-attenuating and oscillation-inhibiting effect. This device has a detachable split box-shaped structure, and is prefabricated using high-performance concrete, with a length of 2 m, a width of 1.638 m and a height of 2 m. Bevel faces are provided on both sides of the top, which are connected with an elastic supporting device for the longitudinal bottom and fixed via embedded stainless steel bolts and clamp plates. Each catamaran raft and corresponding wave-attenuating and oscillation-inhibiting device can move synchronously under the effect of waves, with some micro-displacement allowed. According to need, there is a piece of fixed ballast added above each wave-attenuating and oscillation-inhibiting device, to adjust the height of the center of gravity and swing period of the standard module.

Each standard module is located by two vertical chains and four inverse cross chains; ends of each anchor chain are connected to an anchorage and a tether pile, respectively, and the on-floor length of each anchor chain is about 25 m. The tether piles are set up at both ends and in the middle of the catamaran raft. The tether piles in the middle are used as fixing devices for two vertical chains, while the tether piles at both ends are used as fixing devices for the four inverse cross chains. The anchor chain pipes corresponding to tether piles are set up between the deck and the bottom plate of two units of each raft, and the areas around each anchor chain pipe, under the deck and above the bottom plate, are locally reinforced using reinforced concrete. Each anchor chain passes through a corresponding anchor chain pipe and enters the water from the bottom of the raft. The size and species of anchor chain, and the form, dimensions and functions of anchorage, are determined through analysis and calculation according to the design operating conditions and considering relevant model test results and sea-floor geological conditions [3,4].

**Model test.** The model test was carried out in a wind wave current tank of No. 708 Research Institute China State Shipbuilding Corporation, and the movement of the standard module, the anchor chain force, and the wave parameters of the water zone sheltered by the wave-attenuating system were determined under specified wind, wave and current effects, to provide a basis for design and use of floating breakwaters. Figure 4 is schematic diagram of the layout in the model test.

The test tank was 9 m wide and 28 m long, with a maximum water depth of 2 m (adjustable using a false bottom), and the overall flow rate in the tank was a maximum of 0.3 m/s. The floating breakwater model was formed by alternately arranging 5 standard modules. The test water depth was 1.0 m, the flow rate was 0.2 m/s with a flow direction identical to the wave direction, and the test wind velocity was 6.0 m/s and 10.4 m/s with the wind direction identical to the wave direction; wind machines were used to simulate wind field and wind velocity. In the regular wave test, about 10 different wavelengths were used, and regular waves with a height of about 0.05 m were created. The irregular wave spectra used were ITTC double-parameter spectra [5]; and the spectrum equation is as follows:

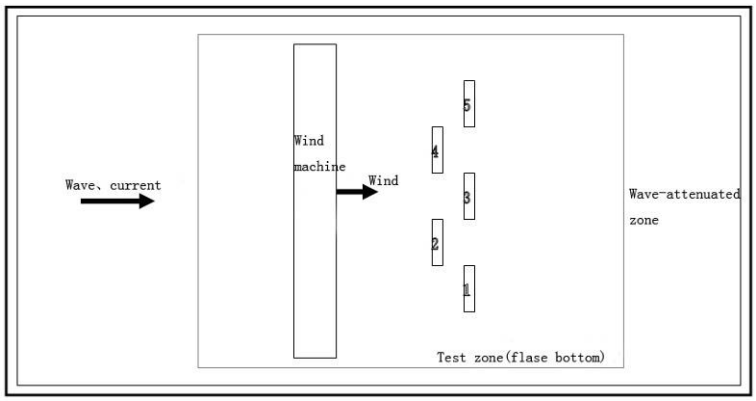


Fig. 4 Schematic diagram of layout in model test

$$S(\omega)=\frac{173H_S^2}{T_1^4\omega^5}\exp\{-\frac{691}{T_1^4\omega^4}\}. \quad (1)$$

where $\omega$ is the circular frequency of the waves, $H_s$ is the effective wave height, and $T_1$ is the spectral centroid period of the waves. The relationship between $T_1$ and spectrum peak period $T_p$ is $T_1=0.772T_p$. For this test, the irregular waves were taken as: effective wave height $H_s$=14cm, spectral centroid period $T_1$=1.24s; and effective wave height $H_s$=18cm, spectral centroid period $T_1$=1.54s. Irregular waves equivalent to actual 120 minutes (24 minutes in the model test) were created in the tank. Both regular and irregular waves were transverse waves.

Figure 5 shows pictures of the model test. The model test results indicate that the floating breakwater with this structure has a relatively good wave attenuation effect on short waves with a period of less than 4 s and long waves with a period of more than 12 s; with the wave period in the operation sea area as a reference, the standard module can be appropriately broadened to achieve the wave attenuation effect on relatively long waves. Under the wind and wave effects, the wave attenuation effect of the floating breakwater can reach 50 % without mutual collision between all standard modules. For the detailed model test results, see the Model Test Report of Floating Wave Attenuating System in Mariculture Area [6].

Fig. 5 Pictures of model test

**Construction overview.** Through uniform planning and arrangement, two floating breakwaters, one oriented from south to north and the other oriented from east to west, were set up in a sea area, about 3 km from the coast, to the east of Dinghai Village, Xiaocheng Town, Lianjiang County, Fujian Province, using natural sheltering conditions of Taiyu Island, to constitute a wave-attenuating facility with an overall length of 2.32 km, forming a sheltered water zone for deep water aquaculture with an overall area of about 1.3 $km^2$. The overall layout diagram of the constructed floating breakwaters is shown in Figure 6.

Fig. 6 Schematic diagram of overall layout of constructed floating breakwaters

Based on actual situations in the construction sea area, different arrangement and combination methods were used for the standard modules of the floating breakwater system. The floating breakwater on the east side in a strong wave direction is double-rowed, and that on the south side in a secondarily-strong wave direction is single-rowed. The floating breakwater on the east side is composed of 18 standard modules, with longitudinal spacing of 60 m and transverse spacing of 30 m, and which, together with Taiyu Island, have an overall length of 1,350 m. The floating breakwater on the south side is composed of 10 standard modules, longitudinally arranged in a single row, with spacing of 60 m, which, together with Taiyu Island, have an overall length of 974 m.

At present, the fabrication and anchor locating of the floating breakwaters have been completed, and Figure 7 shows the double-row floating breakwater on the east side in the strong wave direction.

Fig. 7 Pictures of floating breakwater on the sea

**Wave attenuation effect test.** After the floating breakwaters were constructed, two AWAC acoustic Doppler current profilers (1 MHz, AWAC) were arranged in front and behind the floating breakwater on the east side in the strong wave direction, to monitor the wave height at those positions in real time. The AWAC acoustic Doppler current profilers were arranged in front and behind the middle module of the floating breakwater, at 9 m from each corresponding edge of the standard module; Figure 8 shows the arrangement orientation. The onsite installation and layout of

the AWAC acoustic Doppler current profilers are shown in Figure 9. Synchronous monitoring during the typhoon season was conducted from August 8, 2013 to October 20, 2013, when 9 major typhoons, including Utor, Trami, Kong-rey, Usagi and Fitow, occurred, and the test results indicate that the main body structure of this floating breakwater was not damaged during the typhoon season with wind speeds up to level 12, and that the wave attenuation effect can reach 50 %. The specific test results will be published in later papers.

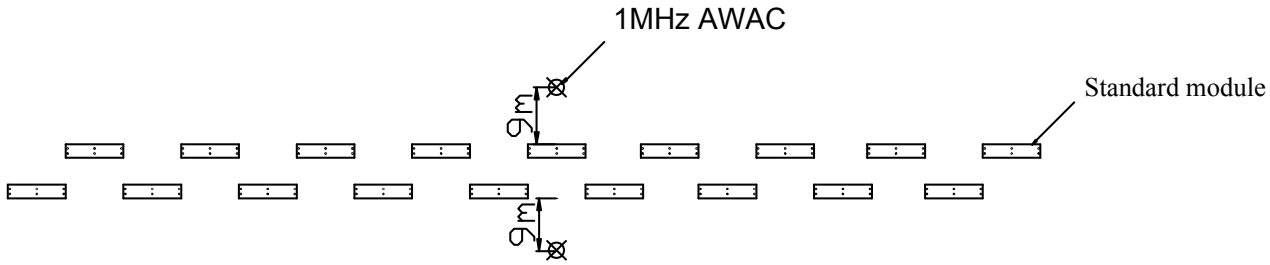


Fig. 8 Arrangement orientation diagram of AWAC acoustic Doppler current profilers

Fig. 9 Installation and layout of AWAC acoustic Doppler current profilers

**Conclusions.** This paper briefly introduces the design, construction and wave attenuation effect test of a kind of floating breakwater sheltering deep water aquaculture. This novel floating breakwater structure is composed of 28 standard modules and corresponding anchoring systems, and each standard module comprises a catamaran raft and a wave-attenuating and oscillation-inhibiting device, with a length of 30 m, a width of 7 m, a depth of 2 m and a draft of 1.1 m. Each catamaran raft employs a box-shaped multi-ribbed beam-and-slab structure, and was constructed using high-performance concrete and ferrocement materials and internally filled with polystyrene foam plastics. Each wave-attenuating and oscillation-inhibiting device used a detachable split box-shaped structure and was pre-fabricated using high-performance concrete, with a length of 2 m, a width of 1.638 m and a height of 2 m. Each standard module was anchored using 6 anchor chains, each having an on-floor length of about 25 m.

The wave attenuation effect test was conducted for the floating breakwater system during typhoon season, and the test results from data analysis indicate that this floating breakwater system can survive level 12 wind speeds, and that its wave attenuation effect can reach 50 %.

This project is a model project for marine aquaculture development for offshore areas to deep sea areas, and this technology also provides technical support for construction of deep water wharves in open sea areas.

**Acknowledgements**

The author would like to extend his sincere appreciation to the Key Agricultural Technology Project of Fujian Province [2011N0007] for technical and funding support, and to Professor Zhu for participating in the study.

**References**

[1] Huang, G. F., The application of the HDPE floating breakwater for healthy aquiculture, Journal of Fujian Fisheries, 4(2006), pp.32-35.

[2] Shunichi I., Kazumi T., Yasuhiro S., Study on the performance of a floating breakwater with two boxes, Proceedings of The Twelfth International Offshore and Polar Engineering Conference, 2002, pp. 773-778.

[3] Vazquez-Hernandez AO, Ellwanger GB, Sagrilo LVS, Reliability-based comparative study for mooring lines design criteria, Appl. Ocean Res., 28 (6) , 2006, pp.398-406.

[4] Roberto Montes-Iturrizaga, Ernesto Heredia-Zavoni, Francisco Silva-Gonzalez, On the estimation of mooring line characteristic resistance for reliability analysis, Appl. Ocean Res., 29(2007), pp.239-241.

[5] Xu Jingbo, Bian Xin-qian, Fu Ming-yu, Simulation and spectral analysis of random sea wave, Computer Engineering and Applications, 46(36), 2010, pp. 226-229.

[6] Yu Zihong, Model test report of floating wave attenuating system in mariculture area, China StateShipbuilding Corporation Seventh Eight Based Research Institute, 2010.

*Applied Mechanics and Materials Vols. 580-583 (2014) pp 2177-2180*
*© (2014) Trans Tech Publications, Switzerland*
*doi:10.4028/www.scientific.net/AMM.580-583.2177*

# Analysis of Gravity Foundation for Offshore structure under Cyclic Loads

GAO Rui [1,a] , YANG Ling Qiang [1.b], and Wang Yan[1,c]

[1]School of Civil engineer and architecture, University of Jinan, Jinan, Shandong province, China

[a]cea_gaor@ujn.edu.cn,[b]cea_yanglq@ujn.edu.cn, [c]cea_wangyan@ujn.edu.cn

**Keywords:** Offshore structure ; Cyclic Loads; Uncertainty analysis.

**Abstract.** Cyclic characteristic of offshore environmental load may cause the accumulation of foundation settlement and excess pore pressure in the subsoil. This may lead to conditions that jeopardize the structural stability and operability of the wind turbine. This paper discusses the analysis steps of the responses of non-cohesive subsoil under cyclic loads for a gravity base foundation system.

## Introduction

Two of the main design criteria for an offshore wind turbine foundation are the structural stability and operability during its designated service life. These include the stability of subsoil and the settlement of the foundation. A critical[1] factor for the operability of the wind turbine is the tilting of the structure, which can be caused by uneven settlement of the foundation.

In the common design practice for civil structures, the structural stability is proven for several preselected singular static loads[2]. This approach is in general accepted for structures which only experience monotonic loading condition. However, it is still questionable whether this approach is applicable for structures which constantly experience dynamically changing loading condition. In reality, the loading history and sequence play a significant role in the subsoil response and the overall structural stability, particularly due to the influence of pore fluid and permeability of the subsoil.

## Eqivalent Load

Direct analysis of irregular cyclic load in geotechnical field, where the subsoil properties actually changes due to the loading itself will require an advanced constitutive model. The challenge will be even greater when the analysis is required for a high number of cycles. One way out from this problem will be to replace the irregular loads with equivalent uniform cyclic loads. The soil behavior under uniform cyclic load can be described in a simpler way. The high cyclic accumulation model[3] (Niemunis, 2000) for example is developed for uniform cyclic loads.

Equivalent load can be understood as the uniform cyclic load with a certain number of cycles, which gives the same effects as the irregular cyclic loads. From geotechnical point of view, these effects are the cyclic settlement and development of the excess pore pressure. However, it is actually unlikely to find the equivalent load concerning the subsoil response. Every different load level transferred through the foundation footing also possesses a different range of affected subsoil area. It is only possible to determine the cyclic load which gives the closest possible approximation to the actual subsoil response. Furthermore, equivalent load is only appropriate to represent regularly recurring loads. For analysis of extreme load level, it is better to use the real load sequence. Loads acting on gravity base foundations for offshore wind turbines are the superposition

of wave, current, wind and machinery forces. The result is irregular cyclic load sequences (cf. Fig. 1). This irregular load sequence can be simplified by decomposing the loads into predefined groups of cyclic loads. Each group of cyclic load is represented by a certain average level and amplitude. The number of occurrence corresponding to each group can be determined using the rainflow counting method (Clormann, 2001)[4]. The information about the chronological load sequence is however lost in the process.

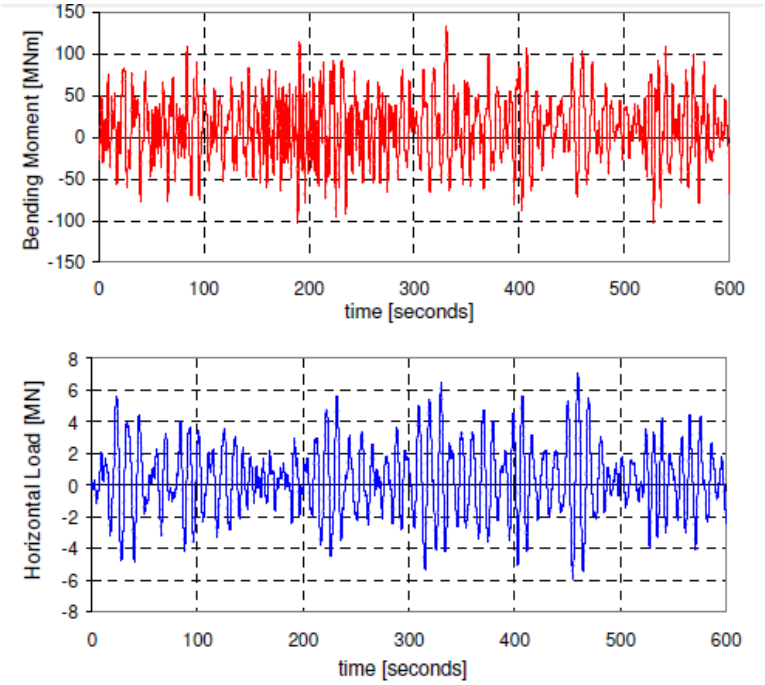


Fig. 1 Typical load sequence acting on foundation for offshore structure

**Case study**

an analysis of the subsoil response under a gravity foundation during a peak wave of a storm is presented. The effect of the preloading is however not considered. The purpose of this calculation is to analyze the pore pressure development and its effect to the overall stability of the foundation under an extreme load. The analysis is carried out in a three dimensional finite element calculation with the finite element program *Tochnog Professional* and the Hypoplastic material model. To consider the effect of the pore fluid, the pore pressure is coupled with the stress of the soil skeleton in element.

The gravity foundation is a cross shaped box girder made of prestressed reinforced concrete with four separated plates at the ends of the boxes and an effective dead weight of approximately 80 MN. The concrete structure is modeled as a linear elastic material. In order to simplify the analysis, the skirt under the plates is not included. The whole model has about 61000 elements and 66000 nodes (see Fig.2 ).

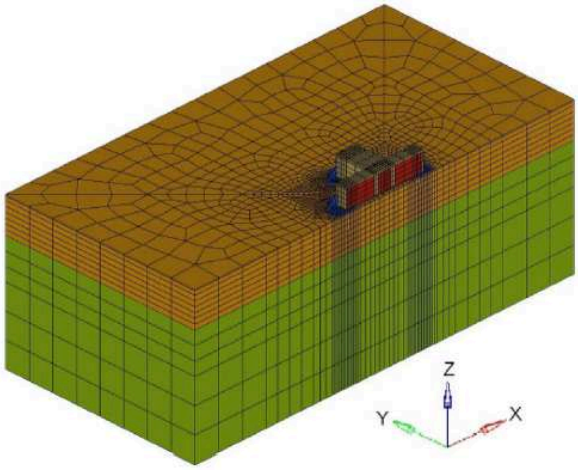


Fig. 2 Finite element mesh of the gravity base foundation and subsoil

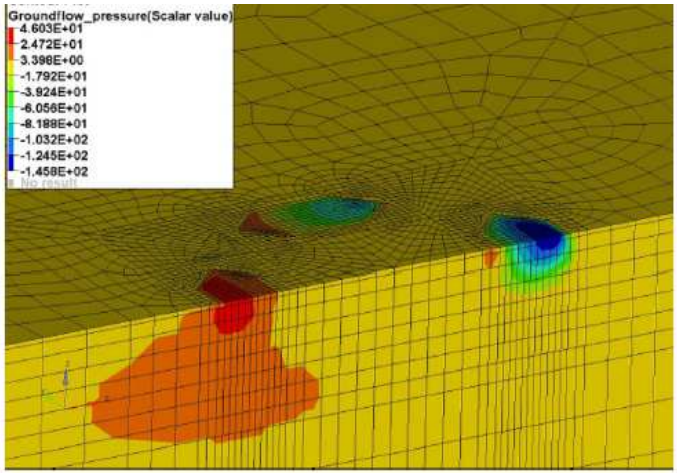


Fig. 3 Excess pore pressure at the moment of the maximum load (t = 37.75 seconds)

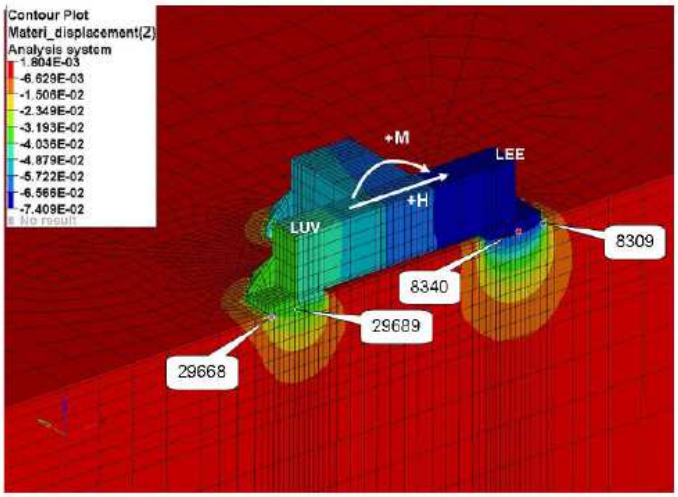


Fig.4 Contour plot of the vertical deformation

The excess pore pressure during the maximum load (t = 37.75 seconds) is shown in Fig.3. Excess of pore pressures occur under the plate at LEE side (away from direction of load) and a negative excess pore pressure at the LUV side (facing the direction of load).The settlement are shown in Fig. 13 (t = 37.75 seconds) and Fig.4. The average vertical displacement at the end of the load sequence is about 11 cm. For a wind turbine structure the tilting is crucial in the foundation design. The maximal tilting reaches about 0.055° to the Left side during the maximal load level at t = 37.75

seconds. The remaining tilting at the end of the load sequence is however only about 0.01° to the Right side. The allowable differential settlement is usually specified by the wind turbine manufacturer. A typical design requirement for an offshore wind turbine given by DNV-OS-J101 as an example is that the permanent accumulated tilt should not exceed 0.25°at seabed.

## Conclusions

A practical method to determine the equivalent load for application in a more complex numerical analysis is presented in this paper. An analysis concept for the foundation of an offshore wind turbine which experiences a high number of cyclic loads has also been proposed. This concept will be proven through back analysis of load simulation which is currently performed on a full-scale gravity base foundation.

## Acknowledgements

This work was financially supported by Natural Science Foundation of Shandong province(No : ZR2012EEL24 and ZR2012EEM025).

## References

[1] Acker, P. and Ulm, F.-J. (2001) Creep and shrinkage of concrete: physical origins and practical measurements. Nuclear Eng. Des. 203, 143–158.
[2] Bazant, Z. P. and Panula, L. (1978) Practical prediction of time-dependent deformations of concrete – Part II: basic creep. Mater. Struct. (RILEM, Paris) 11, 307–316
[3] Farinha, M. L. B. (2000) Strains and stresses measured in concrete dams. MSc thesis. Instituto Superior Te´cnico, Universidade Te´cnica de Lisboa, Lisbon.
[4] Bazant, Z. P. (2001) Prediction of concrete creep and shrinkage: past, present and future. Nuclear Eng. Des. 203, 27–38.

*Applied Mechanics and Materials Vols. 580-583 (2014) pp 2181-2184*
*© (2014) Trans Tech Publications, Switzerland*
*doi:10.4028/www.scientific.net/AMM.580-583.2181*

# Application status and development trend research of ecological revetment in Jiangsu inland waterway

Zhang Jian[1,2],Zhai Jian-feng[1,2],Wang xian-mei[1,2],Chen Jie[1,2]

[1.] Jiangsu Provincial Communications Planning and Design Institute Co., Ltd., Nanjing 210005，China

[2.]Aquatic transportation center, Nanjing 211100, China

**Keywords:** inland waterway; ecological revetment; structural style; technique feature

**Abstract:** With the development of social economy and acceleration of constructions of inland waterway transportations, the adverse impacts on ecological environment are gradually known by people. Under the circumstance of protecting the environment we live, the generalization of technology of ecological bank revetment will be an irresistible trend of the development of inland waterway. Combining the examples of constructions of ecological bank revetments in inland waterways in Jiangsu Province, this thesis presents us the discussion on the structural style, technique features, as well as the application principles of ecological bank revetments, meanwhile puts forward the prospects of technology of ecological bank revetment.

## Introduction

Hard revetments were adopt in most of ttraditional inland waterway, which excessive emphasis on the function of transporting, less considering the ecological effect and environmental effect.Hard revetment cut off the matter and energy between river and bank, reduced the purification of the river. With the development of social economy and inland waterway transporting, people not only to require the safe of waterway, but also integrate the factors of natural landscape and ecological environment protection. In order to meet the need of new situation, the inland waterway should not only satisfy the requirements of strength, stability, durability and safety, also give full consideration to coordinated development between people and nature. Then, inland waterway revetment technology also turn from pure engineering technology to the ecological engineering technology development, and the ecological revetment technology increasingly widespread attention

## The main types and technology characteristics of ecological revetment in Jiangsu province

The ecological revetment is new types of bank revetment which use plants with combination of civil engineering. The ecological revetment set of landscape function, ecological function and self-purification functions into an organic whole, which on behalf of the development direction of bank protection. The main types and technical characteristics of ecological in Jiangsu province are introduced in this paper, which provided the basis for widely used of ecological revetment.

(1) Ecological bag revetment

Fig.1 Ecological bags

Ecological bags have filter function, which not only prevent loss of filler, but also realize normal moisture communication in the soil. Ecological bag can provides plenty of moisture and let the plant through bag body. The roots pass into soil of the engineering foundation, like countless of anchors which stable bag bodies. Further achieve the goal of building permanent stability slope and greatly reduces the maintenance cost.

(2) Gabion revetment

Fig.2 Gabion revetment

This kind of revetment structure can be well fusion with local natural environment, and voids between filler can provides good channels for moisture and nutrient, which provide growing space for aquatic life. This kind of structure have a strong ability of anti-washout and a high strength of flood fighting, which could be applied to fast velocity river. In addition to this, this kind of structure have a low cost such as slurry masonry structure.

(3) Precast block revetment

Fig.3 Precast block revetment

Precast block revetment have a high adaptability to small deformation and strong ability of anti-washout. This kind of revetment have a better effect of planting grass because of high porosity and good permeability, which improve ecological environmental by forming a natural revetment and reinforce the slope by the roots.

(4) Box-type revetment

Fig.4 Box-type revetment

The advantage of box-type structure lies in saving loss of concrete material, and the cavity reserved along length direction can be filled with non-fine concrete, stone etc. This kind of revetment have an effective treatment to waste soil, and a low project cost. In additional to this, structure of box-type revetment is simple and stress condition is good, and resistance to overturning moment is improved because of force of friction between concrete and wall.

(5) Self-embedded revetment

Fig.5 Self-embeded revetment

Blocks between lumps of self-embedded revetment without mortar and other consolidation measures, which have characteristics of good stability, fast construction, low cost and adaption to soft ground etc. With the optimizing of self-embedded structure, self-embedded greening revetment is generated. This kind of structure consist of embedded block, plastic stick, filter and soil, which wall surface and body could be planted. When applied in water environment, underwater structure could be planted aquatic plants and provided survival space for fish, given a better interpretation to ecological revetment.

**Application principles of inland waterway revetment in Jiangsu Province**

Although ecological revetment has widely used in inland waterway construction and achieved a good results, but suitability of the type of revetment still not have a clear guidance. Construction of ecological revetment should choose suitable structure according to the characteristics of engineering, some principles of application are introduced in following.

(1) The principle of adjust measures to local conditions

Construction of ecological revetment are affected by town planning, site condition, geological condition etc. Therefore, the selection of ecological revetment should be fully researched the prominent factors and considered other factors.

(2) Principles of Hydrodynamic

Restricted channel should consider alternate arrangement of revetment type because of section coefficient is small and the influence of ship wave is bigger. In section of which coefficient is smaller and hydrodynamic is stronger, the hard revetment can be used. And in section of straight which coefficient is bigger, ecological revetment can be widely used.

(3) Principles of construction and easy maintenance

Because of revetment engineering is not converged on a point, but along the layout. Reducing maintenance work and ensuring operation will be of great important in operation period, so it should consider life-cycle cost in selection process.

## Conclusions

(1) Ecological revetment sets of landscape functions, ecology functions and self-purification functions into an organic whole, which is development trend and requirements of construction in present and future. The structure of ecological revetment is varied, which should be considered according to the characteristics of waterway. Ecology notion also should be integrated into design, promoting ecological construction of inland waterway.

(2) Application of ecological revetment should well considered surrounding environment and hydrodynamic characteristics, and pay attention to joint use of ecological revetment and hand revetment.

(3) Concept of life cycling and resource saving should be integrated into design and construct of ecological revetment. We should using ecological method to solve the ecological problems and carrying out ecological concept of sustainable development. The inland waterway in the future will not only being a main transport passage, but also a green and environmental ecological corridor.

## Acknowledgements

The authors are grateful for the financial support from the Natural Science Foundation of Jiangsu Province (BK2012086). We would also like to thank the anonymous reviewers for their assistance.

## Reference

[1] Kristina M Hufford，Susan J Mazer. (2003).Plant ecotypes：genetic differentiation in the age of ecological restoration[J]. Trends in Ecology and Evolution,18(3):147-155.

[2] Hession W C，Johnson T E，Charles D F，et al. (2000).Ecological benefits of riparian restoration in urban watersheds study design and preliminary results[J]. Environmental Monitoring and Assessment, 63:211-222.

[3] Xie San-tao,Zhu Qing. (2009).Review on Ecological Restoration on Flinty Riparian by Urban Rivers[J] Environmental Science & Technology, 5(32):83-87.(in chinese)

[4] Xia Ji-hong，Yan Zhong-min. (2004)Advances in research of ecological riparian zones and its trend of development[J]. Journal of Hohai University（Natural Sciences）,32(3):252-255.(in Chinese)

[5] He Heng，Chen De-chun，Wei Wen-bai. (2005).Ecological bank and its application in regulation of urban rivers [J].Water Resource Protection,21(6):56-58.(in Chinese)

[6] Wang Xin-jun，Luo Ji-run. (2006).A preliminary study of ecological embankment construction for urban river restoration [J].Journal of Fudan University（Natural Science）,45(1):120-127.(in Chinese)

[7] Chen Min-xi, Chen Fang-qing. (2007).Application of landscape ecology principle in river levee construction[J]. China Rural Water and Hydropower,49(1): 84-87.(in Chinese)

*Applied Mechanics and Materials Vols. 580-583 (2014) pp 2185-2188*
*© (2014) Trans Tech Publications, Switzerland*
*doi:10.4028/www.scientific.net/AMM.580-583.2185*

# Computation and Analysis of Buttressed Quay's Floor

Qingchen Ning[1, a *], Xu Yang[1, b], Yan Shi[1, c] and Lun Li[2, d]

[1]College of Harbour, Coastal and Offshore Engineering, Hohai University, Nanjing, Jiangsu, 210098, China

[2]Hunan Provincial Communications Planning Survey & Design Institute, Changsha, Hunan, 410008, China

[a]ningqingchen@126.com, [b]yangxu0916@163.com, [c]shi88yan@163.com, [d]leerain624246070@163.com

**Keywords:** Buttressed Quay, Floor, Internal Force, Finite Element Method (FEM).

**Abstract.** In the design and construction code for gravity quay, the inner floor of multi-ribbed buttressed quays generally is divided into two parts to calculate. The part within 1.5 times the rib spacing is as a three fixed edges and one simply-supported slab. The restriction effect of the three fixed edges is the same. However, because of the difference in thickness between vertical plate and rib with the change in the vertical direction of the flow, the effect of them is not the same. It will lead to the result deviating. Sometimes, there will be a phenomenon that the maximum bending moment of inner floor is smaller than the mid-span moment. Finite element software ANSYS was used to make a 3D numerical simulation on a buttressed quay in this paper. Shortcomings in the current code are addressed by comparing the calculation results. This can provide references for engineering design.

## Introduction

Buttressed quay is a reinforced concrete structure which consists of vertical plate, floor and rib. It has advantages of simple structure, rapid construction, mature technology and low cost compared with other gravity quays [1]. Currently, in the design and construction code for gravity quay, the calculation of floor's internal force by following provision: on the floor of multi-ribbed buttressed quay, divide the inner floor into inner and outer part in the location of 1.5 times the rib spacing. The inner part is as a slab whose three edges are fixed and one simply-supported, while the outer part is as continuous [2]. When using this method assumes that the restriction effect of vertical plate and rib on the floor is the same. However, because of the difference in thickness between the vertical plate and rib with the change in the vertical direction of the flow, the effect of them is not the same. It will lead to the result deviating. Besides, when the force on the floor becomes more complex, there will be a phenomenon that the maximum bending moment of inner floor is smaller than the mid-span moment. This paper took another simplified method to calculate the internal force of the floor. In order to make the buttressed quay structure design more reasonable, the finite element software ANSYS was used to calculate the floor's internal force as well. Making an analysis of the calculation results of three methods and provide guiding suggestions on the practical project design.

## Engineering example

The quay of the example is a multi-ribbed buttressed structure, as show in Fig.1. The length of each structural segment is 13m, thicknesses of the ribs are all 0.6m, the spacing of the rib is 3.6m and the length of the cantilever is 1.1m.

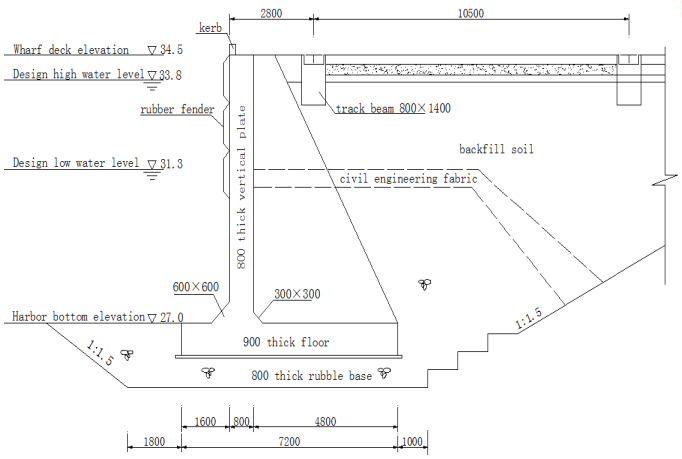


Fig.1 Cross-section of the buttressed quay

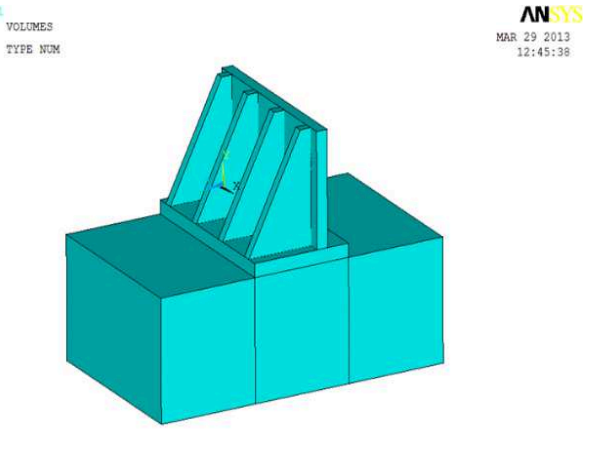


Fig.2 Finite element model of buttressed quay

## Calculation of the floor's internal force

**Design loads and load combination.** Active earth pressure caused by self-weight of backfill soil calculated with the Rankine formula [3]; foundation reaction force calculated with the formula of eccentric compression. Research on the floor of buttressed quay during the completion period, then the remaining water pressure, uplift pressure, ship impact force and surface load can be ignored. So load combination is structural weight + earth pressure.

**The common calculation method.** On the inner floor of multi-ribbed buttressed quay, the inner part is as a slab whose three edges are fixed and one simply-supported, while the outer part is as continuous. The front toe of floor is as a cantilever structure [2].

When use three fixed edges and one simply-supported slab to calculate the internal force of floor, the force acting on the floor can be decomposed into uniform load and triangular load, middle floor moment (Mx, Mz), the maximum moment (Mxmax, Mzmax), bearing moment (Mx0, Mz0) with the action of uniform load and triangular load can be calculated by using the static structural calculation handbook. Then the two calculation results can be superimposed (hereinafter referred to as the method 1) [4]. When the force on the floor becomes more complex, sometimes in order to simplify the calculation, the triangle load can be taken the mean value as a uniform load to calculate the floor's internal force (method 2) [5]. The calculation results according to the above two methods are shown in Table 1.

Table 1 Floor moment calculation results (kN·m)

| moment | Mx | Mxmax | Mz | Mzmax | Mz0 | Front toe |
|---|---|---|---|---|---|---|
| FEM | 23.2 | 26.65 | 23.81 | 24.78 | -24.6 | 280.7 |
| method 1 | 3.61 | 0.8 | 9.98 | 9.78 | -20.9 | 296.5 |
| method 2 | 4.16 | 4.88 | 8.84 | 9.06 | -19 | 296.5 |

**Finite element model.** In order to accurately reflect the internal force of floor, three-dimensional numerical model has been established by finite element software ANSYS 10.0. The finite element model of buttressed quay and foundation soil were created with soild-45 unit (the eight-node element), as show in Fig.2. This paper mainly studies the structure as a whole buttressed its floor's internal force distribution. Therefore, for the active earth pressure of backfill soil, the paper used Rankine earth pressure formula simplified earth pressure as the horizontal static force acting on the vertical plate. The vertical earth pressure on the floor directly took soil weight on the floor surface.

**Inner floor calculation result.** Extracting the bending moment of inner floor in FEM calculation results, and compared with the simplified calculation. The results are shown in Table 1.

As can be seen from Table 1, both positive and negative results are consistent, and the trend is also consistent. However, FEM results significantly larger than simplified calculation results, main reasons:

(1) Foundation reaction force distribution is different in the FEM and simplified calculation method.

(2) There are some problems to the simplified calculation method. In this paper, the thickness of the vertical plate and rib is different, so the restriction effect of both of them on the floor is different. Besides, the size of rib along the vertical direction of flow is changing. This allows the restriction effect of rib on the floor is also changing. However, the restriction of three fixed edges is the same in the static structural calculation handbook.

(3) FEM considering the deformation and stress of buttressed plate as a whole; simplified calculation method only considering the load in the region of inner floor, and then calculate the internal force of floor with the static structural calculation handbook. This also lead to a large deviation between two calculation results.

In addition, it can be seen in Table 1, Mx, Mz larger than Mxmax, Mzmax in the method 1 calculation results. The reason is that the external forces acting on the floor are broken down to a downward uniform load and an upward triangle load in the calculation process, then separately calculate the internal force of the floor under the action of them, and superimpose the two results. However, the maximum bending moment of inner floor in a downward uniform load is positive; the maximum bending moment in an upward triangle load is negative. And generally they do not appear at the same point, directly overlay them allows the maximum reduced. Thus causes this problem.

**The influence of rib spacing on the floor's internal force.** Change the rib spacing, respectively for L=3.2, 4.0, 4.4m, to observe the change of foundation reaction force and internal force of floor.

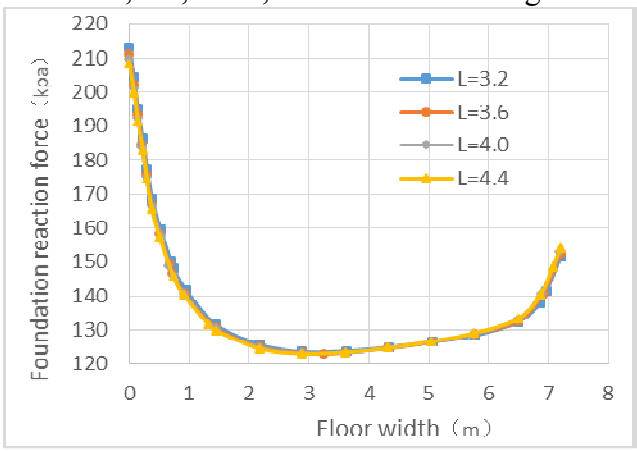


Fig.3 With the foundation reaction force change in different rib spacing

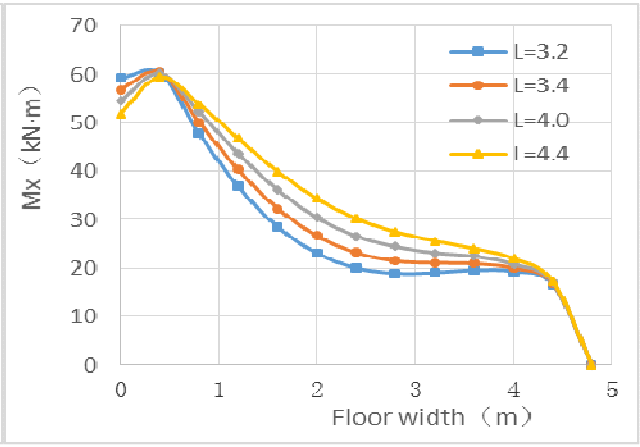


Fig.4 The floor moment Mx

As can be seen from Fig.3, foundation reaction force distribution is almost no change with the increase of rib spacing. Extracting the floor moments: Mx, Mz, Mz0. Observing the bending moment changes with the rib spacing:

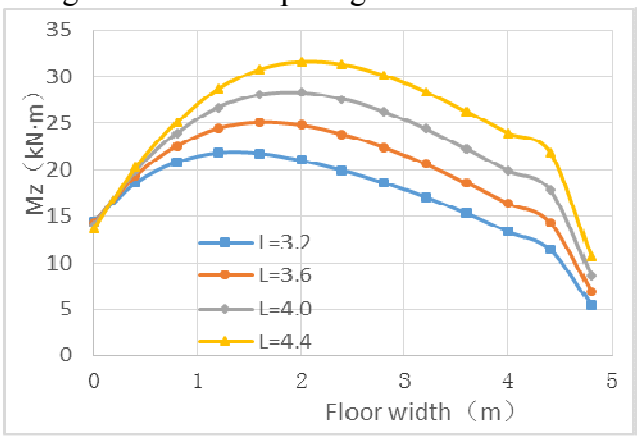


Fig.5 The floor moment in the middle ribs Mz

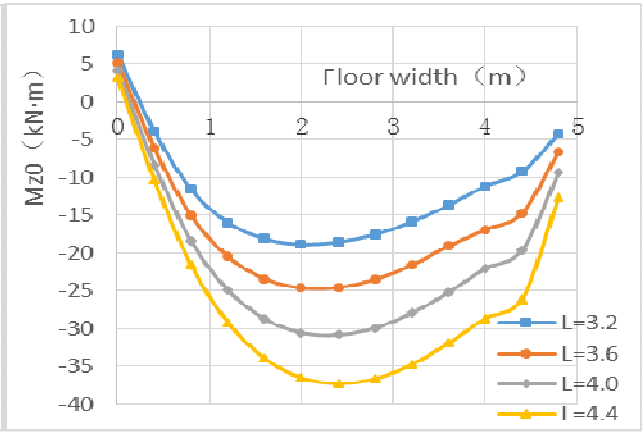


Fig.6 The floor moment in the floor junction with ribs Mz0

Fig.4, Fig.5 and Fig.6 reflects the bending moment changes with the distance of ribs. It is shown that foundation reaction force is basically unchanged with the increase of rib spacing. The bending moment increased with the increase of rib spacing, and the moment changes more and more obvious. Meanwhile, the internal force of floor was calculated with two simplified calculation methods. Get the floor's internal force in different rib spacing as shown in Table 2.

Table 2 Calculation results of floor's internal force in different rib spacing (kN·m)

| rib spacing | 3.2m | | | 3.6m | | | 4m | | | 4.4m | | |
|---|---|---|---|---|---|---|---|---|---|---|---|---|
| | FEM | Method 1 | Method 2 | FEM | Method 1 | Method 2 | FEM | Method 1 | Method 2 | FEM | Method 1 | Method 2 |
| Mx | 20.06 | 2.33 | 2.84 | 23.2 | 3.61 | 4.16 | 26.62 | 5.3 | 5.71 | 30.23 | 8.13 | 7.67 |
| Mxmax | 23.07 | -0.65 | 3.61 | 26.65 | 0.8 | 4.88 | 30.41 | 3.03 | 6.33 | 34.34 | 5.65 | 7.96 |
| Mz | 19.93 | 8.26 | 7.52 | 23.82 | 9.98 | 8.84 | 27.62 | 11.58 | 9.95 | 31.32 | 13.23 | 10.88 |
| Mzmax | 21 | 7.47 | 7.71 | 24.78 | 9.78 | 9.06 | 28.31 | 11.72 | 10.17 | 31.61 | 13.51 | 11.11 |
| Mz0 | -18.6 | -16.9 | -15.8 | -24.6 | -20.9 | -19 | -30.8 | -24.7 | -22 | -37.3 | -28.2 | -24.7 |

Comparative analysis of the calculation results in Table 2. The calculation results of method 1 and 2 are less than FEM, and Mx, Mz larger than Mxmax, Mzmax in the method 1 calculation results. This shows that when superimpose on the maximum bending moment calculated by the uniform load and triangular load in the opposite direction, because of the maximum bending moment do not appear at the same point, and therefore it cannot be directly superimposed. So it is partial to the danger if they are forced to overlay in engineering design. While the calculation results of method 2 which simplify triangle load as a uniform load are very close to method 1, and can reflect the maximum bending moment of inner floor. It can provide a reference for engineering design.

## Conclusions

(1) Through the comparative analysis of results with three kinds of methods including two simplified calculation methods and one FEM, using the FEM for spatial simulation is feasible.

(2) Because of the difference in thickness between the vertical plate and rib with the change in the vertical direction of the flow, the restriction effect of three fixed edges is not the same. All reasons lead to the calculation results tending to smaller, so the calculation result of two simplified methods should be amended appropriately for the safety of the engineering.

(3) When the force on the floor becomes more complex, and the direction is opposite after simplified to uniform load and triangular load. There will be a phenomenon that the maximum bending moment of inner floor (Mxmax, Mzmax) is smaller than mid-span moment (Mx, Mz) in method 1. At this point the triangle load can be taken the mean value and simplified as a uniform load which is method 2 in this paper. Whichever is greater as the design value in the calculation results of two simplified methods.

## References

[1] Rendi Guan, Lun Li, Lei Sun. Computation and Analysis of Buttress Quay's stress [J]. Science Technology and Engineering, 2012, 12(23):5936-5941.(In Chinese)

[2] Design and Construction Code for Gravity Quay (JTS167-2-2009) [M]. (In Chinese)

[3] Tinghao Lu. Soil Mechanics (Ⅱ). Nanjing: Hohai University Press, 2002:198-200. (In Chinese)

[4] Jian Yao, Gang Gan, Shufu Chen, et al. Building structure static calculation Practical Handbook [M].China Architecture & Building Press, 2009:151-178. (In Chinese)

[5] Changguo Xu. Discussion on the buttresses designed gravity quay structure [J]. Port & Waterway Engineering, 1990,2:14-17. (In Chinese)

*Applied Mechanics and Materials Vols. 580-583 (2014) pp 2189-2193*
*© (2014) Trans Tech Publications, Switzerland*
*doi:10.4028/www.scientific.net/AMM.580-583.2189*

# Research of sediment transport trend and erosion-deposition characteristic of Yangma Island sea area

YingWang[1, a], WeiYe[2,b] , and Mingchang Li[3,c]

Tianjin Research Institute for Water Transport Engineering, M.O.T,Tianjin, China

ruozhu1106@163.com

**Keywords:** Yangma Island; sediment transport; erosion-deposition; numerical simulation.

**Abstract.** The article adopts the methods of long shore sediment transport calculation, historic chart comparison and numerical simulation of ECOMSED and analyses erosion-deposition characteristic of the Yangma Island sea area. Research shows that the deposition-dominating areas are located at the southwest of study area, while the beach between Xin'an River and Yuniao River shows slightly erosion trend.

## Introduction

Yangma Island is located in the northern part of Shandong Peninsula and 9 km away from Muping District, Yantai City [1]. Its geographical position is shown in Fig1. It is the third largest island in Jiaodong Peninsula.

The tidal condition of Yangma Island sea area is under the control of north yellow sea tidal wave system. Its tide type belongs to regular semidiurnal tide. By the harmonic analysis of survey data on March 19 and 20, 2009, the current is mostly in the rectilinear current movement. The tidal current type is composed of regular semi-diurnal tide and irregular semidiurnal tide. According to the statistical data，often wave direction for the whole year are N, NNW and NW and the strong wave direction is N. The max wave height is 4.7m.

## Analysis of sediment transport trend

### 2.1 sediment characteristics

The coastal type of Yangma Island is the bedrock coast. Coarse sand , silty sand and silver sand are the main bottom sediment types. The sediment characteristic and distribution range are shown in Fig2.

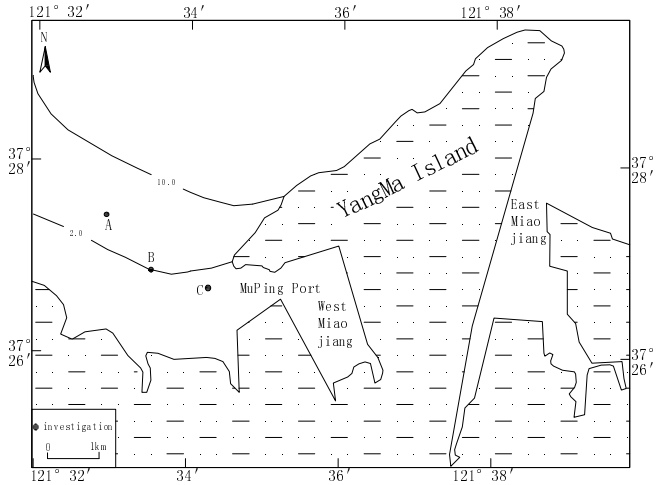


Fig.1 The position of Yangma Island

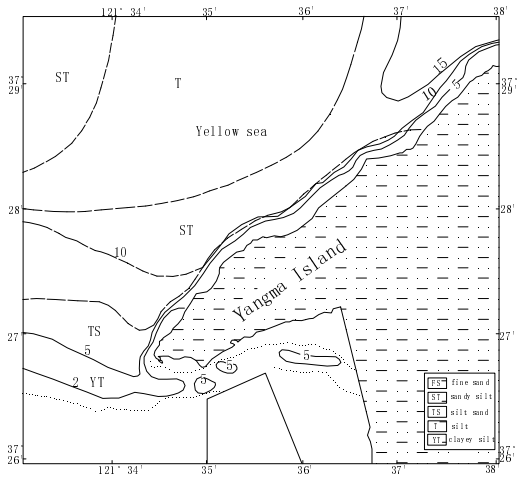


Fig.2 Sediment distribution of study area

### 2.2 sediment source

The main sediment sources are from river sediment and longshore sediment transport.

**River sediment transport**

There is no big river flowing into the study sea area, only two seasonal rivers which are Xin'an River and Yuniao River. Yuniao River is 14.5 km long, there is a reservoir upstream. Xin'an River with annual sediment discharge $2\times10^5$ t is 40 km long, which river runoff and sediment runoff are increasingly reducing .

**Longshore sediment transport**

1. The active depth of sand

The paper adopts experience formula[2] to calculate the active depth of sand.

The coastal types is sandy coast in southeastern Mou Ping port. Due to the influence of the topography, specially impact of NW, NNW, NNE, N, NE, ENE and E wave, 90% of sands are actived in the zone of wave breaking. According to the calculation results of formula[4],we know the active depth of sand is 0.62m-2.14m under general wave conditions. While the $H_{1/3}$ wave height (4.9m) appears in heavy sea, the active depth can reach 2.14 m. The calculation results are shown in table1.

Table 1 The active depth in action of wave

| wind direction | significant wave height（m） | period (s) | active depth (m) |
|---|---|---|---|
| NW | 1.76 | 4.4 | 0.86 |
| WNW | 1.92 | 4.6 | 0.94 |
| NNW | 2.4 | 5.0 | 1.15 |
| NNE | 2.4 | 5.1 | 1.17 |
| N | 4.9 | 4.9 | 2.14 |
| NE | 1.92 | 4.7 | 0.93 |
| ENE | 1.6 | 4.1 | 0.77 |
| E | 1.3 | 3.6 | 0.62 |

Seabottom slope: tanβ=0.01

2. The motion depth of sand

Jiaju Liu[3] considered that the motion depth of sand is less than 4 m in the zone of wave breaking. Due to the impact of offshore wind and waves, the sand was active easily under wave action and then transport following tidal current movement. The coarse particle was active hardly when the depth reached 4m. The paper applies Komar's and Miller's formula [4] to calculate the active depth of sand. The calculation results are shown in table2.

Table 2 The initiate depth in action of wave

| significant wave height（m） | the motion depth (m) | | | | |
|---|---|---|---|---|---|
| 1.76 | 1.32 | 1.98 | 3.30 | 3.30 | 3.30 |
| 1.92 | 1.56 | 2.34 | 3.90 | 3.90 | 3.90 |
| 2.4 | 1.62 | 2.43 | 4.06 | 4.06 | 4.06 |
| 4.9 | 1.38 | 2.07 | 3.45 | 3.45 | 3.45 |
| 1.92 | 1.32 | 1.98 | 3.30 | 3.30 | 3.30 |
| 1.6 | 1.56 | 2.34 | 3.90 | 3.90 | 3.90 |
| 1.3 | 1.62 | 2.43 | 4.06 | 4.06 | 4.06 |
| grain size(φ) | 1 | 2 | 3 | 4 | 5 |

3. Longshore sediment transport

On sandy coast longshore sediment transport occurred in the zone of wave breaking [5]. There are the close relation to morphological evolution and longshore sediment transport on Yangma Island coast.

Now Yangma Island has become a peninsula. Longshore sediment transport from west of Muping Port and northwestern coast of the island is important to balance to erosion-deposition of study sea

area. Coastal type of northwestern island belongs to bedrock coast, which grain size is coarser and sediment discharge along wave coast is very small. So the western coast of Muping Port's longshore sediment transport calculation is very important to the whole sea area.

The paper uses the wave data of ocean station of Zhifu Island for longshore sediment transport calculation. The America CERC formula [6] is applied in the calculation. Result shows that direction of sand transport is from west to east in western Muping Port and amount of sediment transport is $4.2\times10^5 m^3/a$. The calculation results are shown in table3.

Table 3 The results of longshore sediment transport（unit：$\times10^5 m^3/a$）

| Wave direction | N | NNW | NW | WNW | Sed discharge |
|---|---|---|---|---|---|
| Sed discharge | +1.81 | +1.62 | +0.872 | −0.06 | +4.25 |

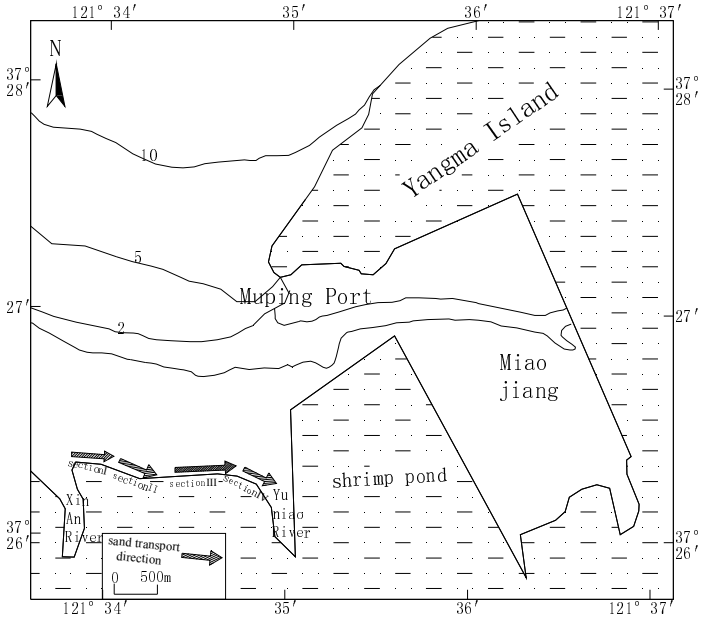


Fig.3 The direction of longshore sediment transport

**sed transport trend**

The sediment supply of the study area is mainly from river and longshore sediment transport. Amount of sediment transport is $4.2\times10^5 m^3/a$. Due to the barriers of Yangma Island and sea wall, the fastest sed deposition amount is located near the channel of Muping Port. However, because this part is in the wave shadow zone of island, the deposition trend will continue to exist.

## Numerical simulation

### 3.1 research method

The method of ECOMSED [7] numerical simulation is applied to obtain the seafloor evolution situation of the Yangma Island sea area.

### 3.2brief introduction

The sediment scouring and deposition model equation.

$$\frac{\partial C_k}{\partial t}+u\frac{\partial UC_k}{\partial x}+v\frac{\partial VC_k}{\partial y}+\frac{\partial (W-W_{s,k})C_k}{\partial z}$$

$$=\frac{\partial}{\partial x}\left(A_H\frac{\partial C_k}{\partial x}\right)+\frac{\partial}{\partial y}\left(A_H\frac{\partial C_k}{\partial y}\right)+\frac{\partial}{\partial z}\left(K_H\frac{\partial C_k}{\partial z}\right)$$

Where: $C_K$ is the concentration of $k$ sediment suspension, in which $k$ = 1, 2, respectively representing the sticky and non-sticky deposits; $A_H$ is the horizontal diffusion coefficient; $K_H$ is the vertical eddy viscosity coefficient; $E_k$ and $D_k$ are the scouring and deposit functions of $k$ sediment

suspension; $\eta$ is the sea surface fluctuations; H is water depth; $W_s$ is the settling velocity of suspended sediment.

### 3.3 numerical simulation

**Analysis of numerical simulation of erosion-deposition**

Under normal weather, the erosion-deposition characteristic of seabed around Yangma Island is shown in Fig4. It can be seen from the Figure that the whole study area show the laws that coastal area of Yangma Island slightly eroded and offshore area deposited entirely. The maximum deposition thickness is within 15cm/a and maximum erosion thickness is 1cm/a. The southwestern coastal area of Yangma Island has always been slight deposition. The deposition thickness is within 1cm/a. The southwest sea area of Yangma Island has been deposition and its deposition thickness is between 0.5cm/a to 5cm/a. The place which has fastest deposition amount is located near the channel of Muping Port. The beach between Xin'an River and Yuniao River shows slightly erosion trend and its erosion thickness is within 1cm/a.

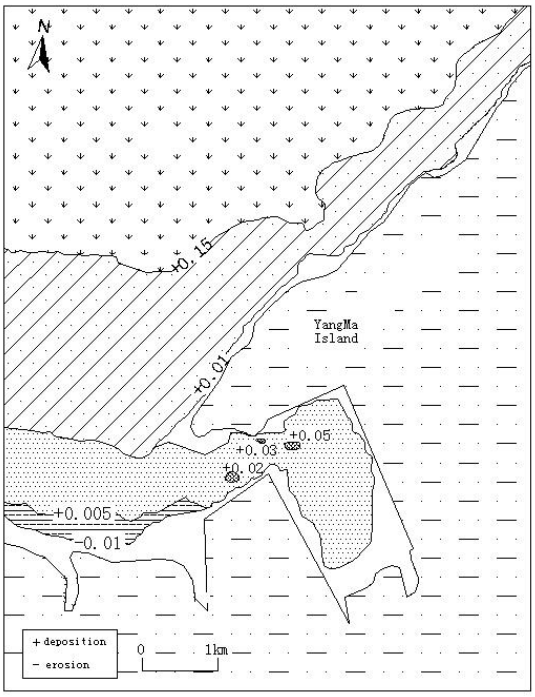


Fig.4 Annual erosion and silting height under normal climate（unit：m）

**Model validation**

For the accurate results of numerical simulation, the application of software of AutoCAD and Suffer, language of Visual basic and historic chart comparison(form 1976 to 2009) are adopted. Results are shown as follows.

In the northwestern coastal area of Yangma Island the coast type is bedrock coast, between the area of 2m depth contour shows slightly deposition trend.The depth contour moves less than 20m and its deposition thickness is within 1cm/a.

The depth contour between Xin'an River and Yuniao River moves slightly to land and its erosion trend is not obvious. There are two major aspects for the erosion. Reducing the coast sediment source leads to erosion directly. The other is related to the tidal current. During flood tide, the sediments on the northeastern side and southwestern side of Yangma Island are transported to its southern sea are with the flood tide. Current velocity declines caused sediments deposition in this area. During ebb tide, the sediments in strong current area of on southwestern entrance of Yangma Island is transported to the adjacent sea area outside the entrance. The flow velocity declines rapidly and the sediments then caused obvious deposition.

In southeastern sea area of coastal area of Yangma Island, the 2m depth contour and 5m depth contour moves outside obviously. That is to say: deposition occur in the area. The main deposition

changes were located near channel of Muping Port. However, because this part is in the wave shadow zone of island, the deposition trend will continue to exist. But annual deposition amount is extremely small. In addition the increase of land reclamation and weakened tide dynamic are the main reasons of fine grained sediment deposition here.

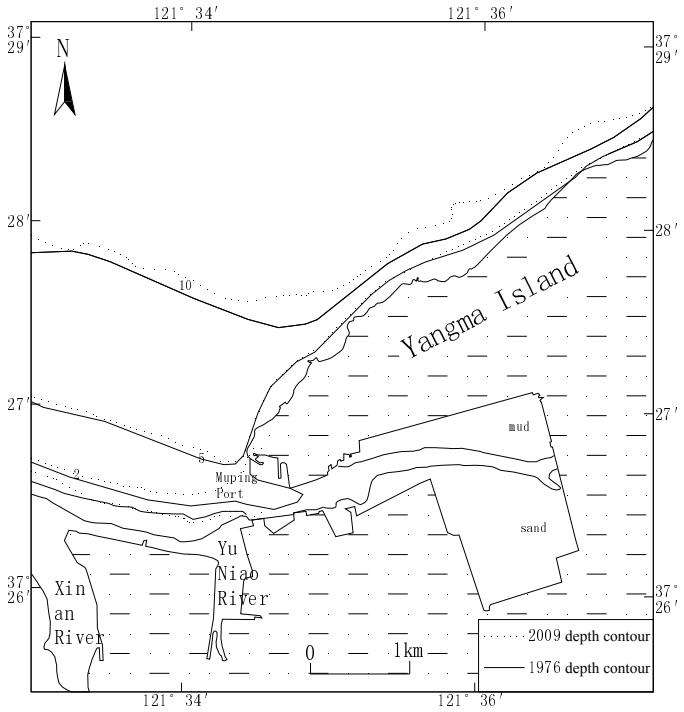


Fig.5 Comparison chart of fathom line form 1976 to 2009

## Conclusion

1.The river and longshore sediment transport are the main sediment source in sea area of coastal area of Yangma Island ;

2.The southwest coastal area of Yangma Island has always been slight deposition and its deposition thickness is between 0.5cm/a to 5cm/a ;

3.Historic chart comparison(form 1976 to 2009) shows the simulation of ECOMSED can precisely reflect the erosion-deposition characteristics in area of Yangma Island.

## References

[1] Chinese bay, Shandong science and technology Press.1995,p. 226

[2]Ruifang Chang: Coastal engineering environment.1997,p. 132-133

[3]Jiaju Liu, research on sediment Incipient motion under wave condition.1966,p. 10-13

[4] Huapeng Qin,Jinren Ni and Yitian Li:Journal of Sediment Research. vol.(10)2002,p.92

[5]Guosheng Li,Hailong Wang:Journal of Geographical Science.vol.60 (2005), p.707

[6]Blumberg A F,in:A estuarine and coastal ocean version of POM, chapter,3, 1996

[7]Van Rijn:Journal of Hydrodynamic Engineering. vol.110(1984) ,pp.1613

*Applied Mechanics and Materials Vols. 580-583 (2014) pp 2194-2197*
*© (2014) Trans Tech Publications, Switzerland*
*doi:10.4028/www.scientific.net/AMM.580-583.2194*

# Study on the evolution of artificial beach in Xiamen

Guanglu Wang [1, a]

[1] Tianjin Research Institute for Water Transport Engineering, Tianjin 300456,China;

[a]wglas4@163.com

**Keywords:** beach restoration, beach evolution, monitoring.

**Abstract.** Taking Xiamen Xiangshan-changweijiao beach project as an example, study the technology of beach restoration. Xiangshan-changweijiao beach locates at the SE of Xiamen Island, which has already been eroded out. The restoration project was finished by the first step and the beach showed better performance than history after one year evolution. By analyzing the environment of shore, designing beach factors, technology of beach fill placement, study the beach restoration and evolution of artificial beach, inquiry the theory of beach nourishment in China.

## The natural conditions of artificial coast

Xiangshan - Changweijiao artificial beach project is located in the eastern coast of Xiamen Island, with a total length of 1.5km, is currently the largest artificial beach. Kinmen Island and many small islands are around the east and south sea area, and the Shoreline towards NNE. Out side waves are difficult to spread in the area, which is possible to bring the longest wind and wave field around the project. The underwater topography of the project sea area is more complex. In the mean sea level contour to 5m deep seabed topography is irregular, distribution alternates with tidal channel and shallows. Both sides of the coast north and south are respectively protected by the Xiangshan and Changweijiao rock headland, the coastline is north-south asymmetry concave arc. According to the site survey and the existing information, geomorphic units of restoration area includes laterite plateau coast, bedrock headland coast, artificial embankment, intertidal beaches, underwater shoal, deep grooves and so on.

## Artificial beach restoration

The coastal function is clear that the east coast of Xiamen is an important tourist area. in order to reduce the impact on the other part of coast ,the restoration shoreline was designed base on Dynamic equilibrium, and the shoreline was arranged as possible to perpendicular to ordinary wave direction. So the shoreline was designed into two arcs towards northeast.

The fill may be placed well above the shoreline as dune nourishment, on the dry beach and near the waterline, across an extended portion of the profile that stretches from the dry beach to well offshore, or completely offshore as a sand bar. The fill with medium-coarse sand of 0.5mm median diameter, was placed on the dry beach and near the waterline in this project. Once sand is placed on the beach, waves and currents redistribute the material offshore and alongshore until a stable configuration is achieved. Depending on local conditions, a nourished beach may take several months or years to reach the equilibrium condition. [1].

## Beach stability analysis

Grain size grading of the ‘native’ and ‘borrow’ material is necessary for assessing the feasibility of a beach nourishment project. The application of the beach fill model involves calculation of two factors, an overfill factor RA and a renourishment factor RJ, where: RA = the estimated number of cubic meters of fill (nourishment) material required to produce 1 cubic meter of beach material when the beach is in a condition compatible with the native material. It is used to estimate the initial quantities of nourishment required; RJ = the ratio of the rate which borrow material will erode to the

rate at which the native beach material is eroding. It is used to estimate how often renourishment may be required [2, 3]. The values of RA and RJ are determined graphically based on the knowledge of the mean grain size and sorting characteristics of the native and borrow materials. Figure 7 shows isolines of the overfill factor RA and renourishment factor RJ, where: $M_\Phi$= the mean diameter of the grain size distribution in phi units; $\sigma_\Phi$= the standard deviation of the grain size distribution in phi units (a measure of sorting); subscript b refers to borrow material; subscript n refers to native material

The survey of Chinese bay [4] and the report of Xiamen Xiangshan-Changweijiao beach restoration project, showed that $M_\Phi n$=1.22, $M\Phi b$=1.44, $\sigma_\Phi n$=0.78,$\sigma_\Phi b$=0.55. Based on the data as shown in Figure 1, the sands, generally, are not too fine or too well sorted, which would result in the nourishment between unstable and stable.

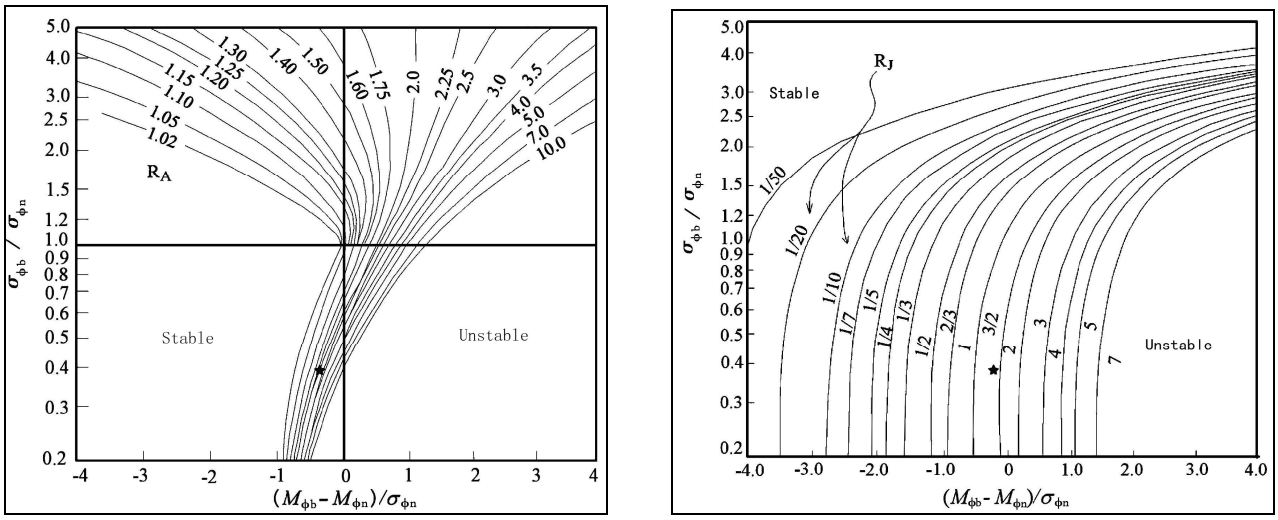


Fig.1 (a) Isolines of the adjusted overfill factor, RA, for values of Phi mean difference and Phi sorting ratio (b) Isolines of the renourishment factor, RJ, for values of Phi mean difference and Phi sorting ratio

**Evolution of artificial beach**

After fill placement, the beach still needs evolution for several years. According to Dean, base on many artificial beach of America, it needs nourishment every 5~7 years, the half period beach is Negative Correlation with the near shore effective wave and coast line corrosion rate, but positive Correlation with the length of beach [4 - 15 ] . According to Combe and Soileau, there is erosional"Hot Spots" that corrosion rate are quicker than beside part. Erosional"Hot Spots" is helpful for estimating the period of beach [16 - 17]. It's convenient for monitoring and renourishment to make clear character in different period of beach, so the study gives an ideal evolution of artificial beach, which is no renourishment and guarding, shown in table 1.

Tab.1 The evolution stages of artificial beach

| types / stages | pocket beach and beach adjacent to Inlets) | long straight beach and seawall beach |
|---|---|---|
| Primary period (less than 1 year) | Shoreline is same as the fill placement; beach face is narrow and steep, with thick sediment and coarse grain, a banding distribution. | Shoreline shape is same as the fill placement, mostly along the coast. |
| shaping period (1-2 years) | Shoreline shape change continuously ,beach face becomes wide ,with erosional"Hot Spots", beach berm becomes narrow, and beach sediment is fine. | Offshore sediment transports obviously, the beach sands spread to Downstream, with erosional"Hot Spots". |

| | | |
|---|---|---|
| maturity period (2-6 years) | Shoreline shape has a suitable arc, with special Landforms, beach face very Broad and gentle, and sediments become fine from land to sea. | none |
| Decline period (more than 6 years) | Shoreline is back off greatly, beach face become steep, sediments are coarser, beach volume reduces. | Shoreline turn to the status before fill placement, coarse grains remnant. |

**Post-project monitoring**

After the fill placement, the beach shape was as shown in figure 2.the monitoring was followed immediately.

(Before) (After)

Fig.2 Satellite photos before and after the beach project

Well-planned performance monitoring allows for verification and future improvement to project design and modeling, as well as justification of project necessity and renourishment intervals. Sufficient project monitoring is a necessity, particularly in chronically eroding locations that pose a challenge to coastal engineering practitioners.

The wind waves are most toward NE～E in winter of Xiamen. After one winter's monitoring, it's shown that beach profiles became gentle from north to south, and beach face became wide. In the middle part of beach, there was a islets which turned into a erosional"Hot Spots". The south part of beach with no shelter and open, eroded most. Tidal zone sediments became fine, especially in middle zone. From the above characters, it's sure that the beach was during shaping period.

**Conclusions**

Artificial beach in Xiamen discussed in the papers, was filled with medium-coarse sand of 0.5mm median diameter, base on the theory it's just between stable and unstable. By the profile, the sediment and the planform, the evolution of artificial beach can be divided into four stages. According to monitoring, it is clear that plan form adjustment began immediately after nourishment and that the relatively high-energy wave events following both the initial and repair nourishments resulted in profile equilibration. Both profile and plan form adjustment can occur rapidly given the appropriate site conditions and energy levels. The beach discussed has come into shaping period just one year.

**References**

[1]Department of Boating and Waterways and State Coastal Conservancy. California Beach Restoration Study[R]. California, 2002.

[2]U.S. Army Corps of Engineers. Shore Protection Manual [M].Washington: Washington. D C , 1984. 5-6 , 6-25.

[3] Compilation Committee of bays Chinese. Chinese bay (eighth part)[M].Beijing： China Ocean Press, 2007.

[4] Beachler K E. The Positive Impacts to Neighboring Beaches from the Delray Beach Nourishment Program [A]. Proceedings, Sixth National Conference on Beach Preservation Technology: The State of the Art of Beach Nourishment[C]. 1993, 223-238.

[5]Bodge K R, E J Olsen . Aragonite Beach Fill at Fisher Island, FL[J]. Shore and Beach, 1992, 60(1): 3 - 8.

[6]Combe A J, C W Soileau. Behavior of Man-Made Beach and Dune [J]. Grand Isle, Louisiana, Proceedings, Coastal Sediments '87, ASCE, New Orleans, LA, 1987, 1232-1242.

[7]Davis R A, Wang P, Silverman B. Comparison of the Performance of Three Adjacent and Differently Nourished Beaches on the Gulf Peninsula of Florida." Journal of Coastal Research[J], 2000, 16:396-407.

[8]Dean R G. Realistic Economic Benefits from Beach Nourishment [A]. Twenty-first International Conference on Coastal Engineering, ASCE[C]. 1988. 1558-1572.

[9]Dean R G, C H Yoo. Beach Nourishment in the Presence of Seawall [J]. Journal of Waterway, Port, Coastal and Ocean Engineering, 1994, 120( 3): 302-317.

[10]Dean R G, R A Dalrymple. Coastal Processes with Engineering Applications [M]. Cambridge University Press, 2002, 475.

[11]Erickson, K.M. (1995) "Town of Palm Beach Project Design Memorandum, " Report Submitted to the Town of Palm Beach, FL, Applied Technology and Management, Inc, Gainesville, FL.

[12]Ernest R G, E Martin, B Howard, A M Black. The Effect of Beach Nourishment on Sea Turtle Nesting: A Case Study on Hutchinson Island, Florida [A]. Proceedings, 11th Beach Preservation Technology Conference[C], Compiled by L. S. Tait, Florida Shore and Beach Preservation Association, Tallahassee, FL, 1998. 93 - 108.

[13]Fletemeyer J R. 1999 Delray Beach Sea Turtle Monitoring Report[R]. Report Submitted to Delray Beach, FL.1999.

[14]Shows E W. Florida's Coastal Setback Line - An Effort to Regulate Beachfront Development [J]. Coastal Management Journal, 1978, 4(1-2): 151-164.

[15]Trindell R, D Arnold, K Moody, B Morford. Post-Construction Marine Turtle Nesting Monitoring on Nourished Beaches [A]. Proceedings, 11th Beach Preservation Technology Conference[C]. Compiled by L. S. Tait, Florida Shore and Beach Preservation Association, Tallahassee, FL.1998. 77 – 92.

[16]Dean R G, R Liotta, G Simon. Erosional Hot Spots[R]. UFL/COEL-99/021, Coastal and Oceanographic Engineering Department, University of Florida, Gainesville, FL. 1999.

[17]Kraus N C, F A Gagliano. Beach Erosional Hot Spots: Types, Causes and Solutions [A]. Proceedings, 14th Beach Preservation Technology Conference, Compiled by Linda Tait, Florida Shore and Beach Preservation Association, Tallahassee, FL. 2001. 64 - 80.

*Applied Mechanics and Materials Vols. 580-583 (2014) pp 2198-2201*
*© (2014) Trans Tech Publications, Switzerland*
*doi:10.4028/www.scientific.net/AMM.580-583.2198*

# Three Dimensional Physical Model Study on Penang Fishing Port Project

Ciheng Zhang[1, a], Baolei Geng [1, b]

[1] Key Laboratory of Engineering Sediment of Ministry Communications, Tianjin Research Institute for Water Transportation Engineering; No.2618, Xingang Erhao Road, Tianjin, 300456, China

[a]zchfirestrom@126.com, [b]gbl@tiwte.ac.cn

**Keywords:** Three Dimensional, Physical Model Test, Fishing Port Project, Wave.

**Abstract.** A three-dimensional physical model was used to study the wave distribution around breakwater in Malaysia Penang. Model tests were carried out by using the L-type action absorption directional wave generator in a 45m×40m wave basin at TIWTE in Tianjin China. The incident wave conditions were checked first in the laboratory and a series steps were introduced to construct the bathymetry and breakwater structure. By comparing the test results, the improved top elevation of breakwater is +4.5m, and the recommendation length of northern part of breakwater is 65m.

## Introduction

A three-dimensional physical model study was carried out, on the proposed design for the breakwater system. The objectives of this study is to ascertain the sheltering effect of the breakwater on the berthing and mooring area, and to achieve optimization of the design. The project site is located at the north-eastern coast of Peninsular Malaysia. A location plan is shown in Fig. 1. For implementation of the project, two training walls, two outer breakwater and one navigation channel will be constructed, the layout plan is shown in Fig. 2.

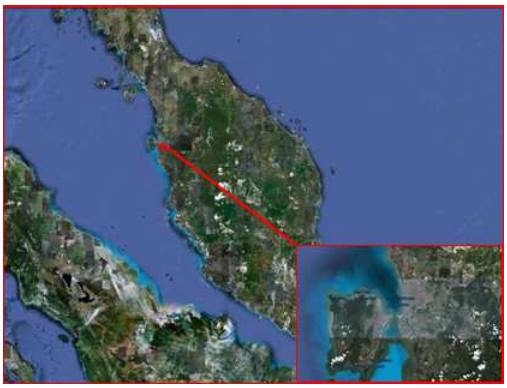

Fig. 1 Location plan of project site

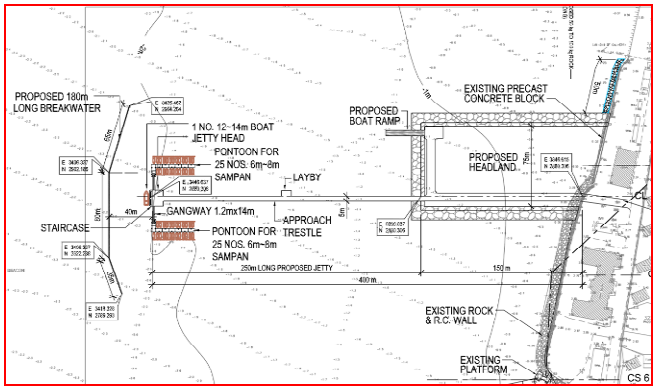


Fig. 2 The layout plan

## Test Conditions

**Wave and Water Level Conditions** The tests were carried out for three offshore wave direction which namely 240ºN, 270ºN and 300ºN at offshore; Three water levels which namely Design water level for model test (DWL) at +3.315m CD, Mean high water spring (MHWS) at +2.69m CD and Mean lowest low water spring (MLWS) at +0.72m CD; 100 years return periods is considered in this paper.

The position of the wave gauges for model is shown in Fig 3. In calibration test, wave gauges $S_4$ to $S_6$ are located at -3m isobaths, as the $P_1$ to $P_3$ in provided condition. The wave height distributions of DWL are shown in Fig. 4.

**Breakwater Structure** The length of breakwater is 180m, northern part is 65m, middle part is 80m, southern part is 35m. The top elevation of piled breakwater is +3.6m. The structure of piled breakwater is shown in Fig. 5.

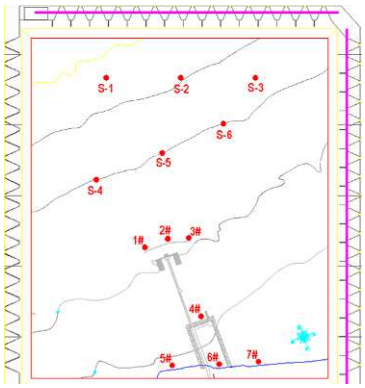


Fig. 3 Positions of wave gauges in model

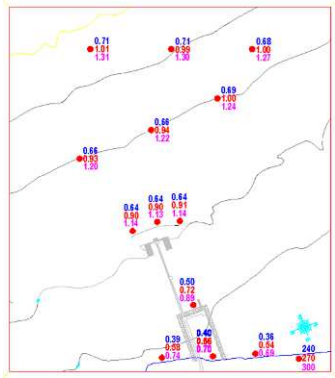

Fig. 4 Wave height result of 100yrs wave under DWL

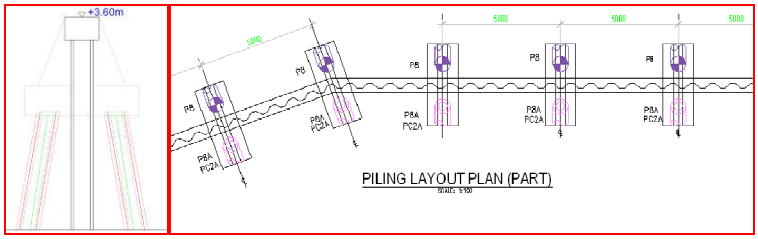


Fig. 5 Structure of Piled Breakwater

## Model Scale

The model is constructed to a linear length scale of 1:30 undistorted. As gravity and inertia forces are the dominant forces in the present model, the Froude similarity law is applied for conversion of the model measurements to prototype values. The following scales apply accordingly:

Length scale: $1:\lambda = 1:30$

Time scale: $1:\sqrt{\lambda} = 1:5.48$

Velocity scale: $1:\sqrt{\lambda} = 1:5.48$

Force scale: $1:\lambda^3 = 1:27000$

Mass scale: $1:\lambda^3 = 1:27000$

## Model Construction

The model study is performed in another wave basin which is 38m length and 34m width. Fig. 6 illustrates the model bathymetry construction process.

Fig. 6 Construction of Model Bathymetry

The bathymetries of the piled breakwater models are constructed to a linear length scale of 1:30, as a fixed bed in accordance with the bathymetry charts provided by project consultants. The model breakwater construction process is illustrated in Fig. 7.

Fig. 7 Construction of Model Breakwater

**Test Equipment** The waves of 3D model are generated by an L-type action absorption directional wave generator, which is an advanced wave generator by international standards. The wave basin is 45m length, 40m width and 1.0m height. The longer side of L-type wave generator is 38m long with 77 wave generating elements. The shorter side of L-type wave generator is 33m long with 67 wave generating elements. The model wave conditions are simulated by the irregular wave generator system. The maximum wave generating capability is 40cm and the maximum wave period is 5.0s.

The wave height is measured by the Hydrodynamic Data Collection System SG2008, using capacitance-type wave gauges, which can automatically collect and analyze the wave heights and wave periods, fitted with built-in temperature compensation. The wave gauges have a wave height measurement range of 0.1~40cm, an accuracy of ±0.5% of the measured value, and sampling rate (output) of 1~200Hz.

## Test Results for Original Design

Wave gauge layout for piled breakwater is shown in Fig. 8. Based on the wave distribution result, the wave height at most extraction point at mooring area are less than 0.3m, but the wave height at 6 points are more than 0.3m, the maximum wave height is 0.41m. The wave distribution results after construction of model are shown in Fig. 9. The test photography is shown in Fig.10.

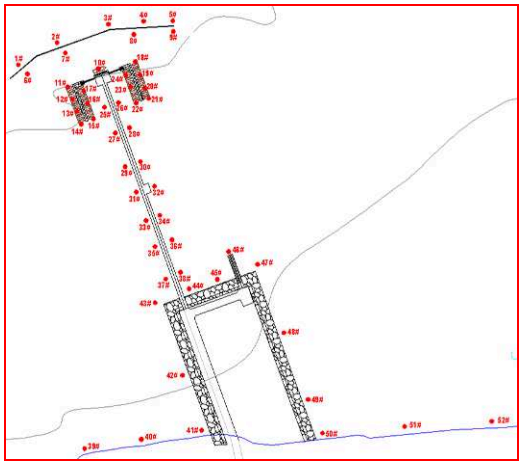

Fig.8 Wave gauge layout

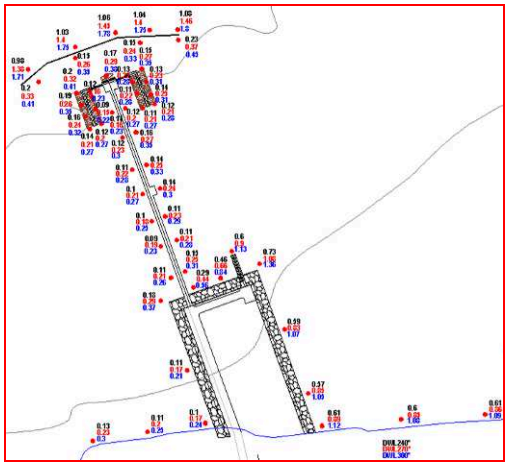

Fig.9 Wave distribution results for 100yrs

Fig.10 Test Photography of Original Design (DWL, 300ºN, 100yrs)

## Test Results for Optimization Design

Based on test result of original design, the most important influence elements of wave height at mooring area are overtopping and diffraction wave. Increasing the top elevation of breakwater can decrease the overtopping, and extend the length of breakwater can decrease the diffraction wave. The improved top elevation is +4.0m, +4.2m and +4.5m, and the improved length of northern part breakwater is 70m, 75m, 80m and 85m.

For top elevation increasing, when the breakwater length is 180m, the wave height result is adopted, and for breakwater length extend, when the top elevation is +4.5m, the wave height result is adopted. For different top elevation, under 100yrs (DWL, 300ºN) wave action, the amount of overtopping wave is shown in follow: +3.6m: 23%; +4.0m: 15%; +4.2m: 10%; +4.5m: 4% wave splashing.

And based on the comparison result of different top elevation, the wave height at mooring area is decreased with the top elevation increasing, about 10% decrease from +3.6m to +4.5m. But for the comparison result of different breakwater length, the wave height at mooring area is decreased with the length extend, but not obvious.

Above all result, the improved top elevation of breakwater is +4.5m, and the recommendation length of northern part of breakwater is 65m. It can be considered as recommendation design.

## References

[1] Sg Terengganu River Improvement Project, Malaysia—3D Stability Study of Breakwater. Preliminary report for Inai Kiara Sdn Bhd, Selabgor Darul Ehsan, Malaysia by DHI Water & Environment (2008).

[2] 3D Stability Test Study for Yantai Eastern Port. Tianjin Research Institute for water transport Engineering, (2007), in Chinese.

[3] B.L. Geng, C.H. Zhang, Y.F. Cao, A Laboratory Study on the Wave Distribution around Breakwater. Applied Mechanics and Materials Vols. 170-173 (2012), p. 2312-2315.

[4] C.H. Zhang, A.L. Ziauddin, H.B. Chen, Y.F. Cao: Research on armor units stability in 3D and 2D physical model. Proceedings of the $6^{th}$ international conference on Asian and Pacific coasts (APAC2011), Hongkong, China. (2011), p.442

*Applied Mechanics and Materials Vols. 580-583 (2014) pp 2202-2205*
*© (2014) Trans Tech Publications, Switzerland*
*doi:10.4028/www.scientific.net/AMM.580-583.2202*

# Study on the Panel of the High-pile Wharf Near Estuary Based on the Finite Element Method

Xu Yang [1, a *], Qingchen Ning [1, b], Yan Shi [1, c] and Gaoxiang Xia [2, d]

[1] College of Harbour, Coastal and Offshore Engineering, Hohai University, Nanjing, 210098, China

[2] Anhui Transport Consulting & Design Institute Co.,Ltd, Hefei, 230000, China

[a]yangxu0916@163.com, [b]ningqingchen@126.com, [c]shi88yan@163.com [d]zhousan0528@163.com

**Keywords:** Panel, Estuary, High-pile Wharf, Wave Force.

**Abstract.** The high-pile wharf near estuary under wave subjects to great wave force. The wave force can cause destruction of the wharf superstructure. Current research focuses on the case where the forward direction of the wave is perpendicular to or inclined to the wharf front line and mostly applied physics modelling experiments. This paper is to study the case where the wave is parallel to the front line of the high-pile wharf. Take a high-pile wharf near estuary as a model and use the finite element software Ansys to establish the space model. Analysis of internal forces and the destruction of high-pile wharf are made. Meanwhile, the preliminary solution depending on the destruction are proposed, providing references for projects.

## Introduction

The wave force must be considered in high-pile wharf structural design as an important external load, especially to the wharf without the cover. It is closely related to the safety of wharf structures, such as beams, slabs & pile foundations, but its running and working mechanism is very complex [1]. Current research focuses on the case where the forward direction of the wave is perpendicular to or inclined to the wharf front line, and mostly applied physical modelling experiments [2]. This paper mainly studies the case where the wave's forward direction is parallel to the wharf front line. Taking a high-pile wharf near estuary engineering [3].as an example, use finite element software Ansys to build its space model [4] and take its internal forces& deformation for the analysis to investigate the effect of wave force to high-pile wharf structures.

## Engineering example

**Dimension parameters.** This project structure belongs to the high-pile wharf with beams and slabs. Its platform's length is 213m and width is 20m. Each structure segment consists of eight lateral bents and the length is 53.2m. The lateral bent's length is 7m. The wharf top elevation is 4.35m, while pile bottom elevation is -48.30m and mud surface elevation is -5.85m. The pile length is 50m.

**Wind regime.** The wind speed in different return periods is determined by the frequency analysis to the annual maximum series measured by weather station nearby. Specific measurement values are shown in Table 1.

Table 1 Wind speed(m/s)

| return period (year) | wind group | | | | | | | |
|---|---|---|---|---|---|---|---|---|
| | N-NNE | NE-ENE | E-ESE | SE-SSE | S-SSW | SW-WSW | W-WNW | NW-NNW |
| 100 | 25.7 | 35.5 | 40.5 | 27.3 | 23.6 | 21.2 | 46.6 | 33.7 |
| 50 | 23.6 | 33.3 | 37.5 | 25.1 | 22.0 | 20.1 | 41.1 | 31.1 |
| 20 | 20.7 | 30.4 | 33.3 | 22.3 | 19.8 | 18.5 | 34.0 | 27.6 |

**Wave paremeters.** The project is in the southeast coast of Zhejiang monsoon region. In this region, Northerly winds prevailing in winter and southerly winds prevailing in summer, the spring and autumn are in the alternate period. Through observation, winter waves mainly northerly, the

frequency of occurrence in the north-northeast is approximately 53% -59% and the east-southeastern is 35% -38%. Summer waves mainly east-southeasterly, the frequency is approximately 69% -72%. Spring waves also mainly east-southeasterly, the frequency is approximately 55% -67%. September waves is like the Summer,while October&November is like the winter. Under the influence of Ao River, wind and wave has almost equal frequency. Wave paremeters are shown in Table 2.

Table 2 Wave paremeters

| Wave direction | Water level | $H_{1\%}$(m) | $H_{4\%}$(m) | $H_{5\%}$(m) | $H_s$(m) | $\overline{H}$(m) | $\overline{T}$(s) | L(m) |
|---|---|---|---|---|---|---|---|---|
| E | 4.97 | 3.69 | 3.20 | 3.11 | 2.66 | 1.76 | 15.5 | 141.8 |
| ESE | 4.97 | 3.51 | 3.04 | 2.95 | 2.52 | 1.66 | 15.5 | 132.1 |
| SE | 4.97 | 3.39 | 2.92 | 2.84 | 2.42 | 1.59 | 15.5 | 132.1 |

**Model building.**This paper made the model in the following order: upper structure of the wharf; pile foundation; contact with pile and soil. Using the Spring simulates the interaction of soil and pile and the Spring's stiffness is calculated by "m" method. Using coupling connects the upper structure and pile foundation. The finite element model of high-pile wharf are shown in Figure 1.

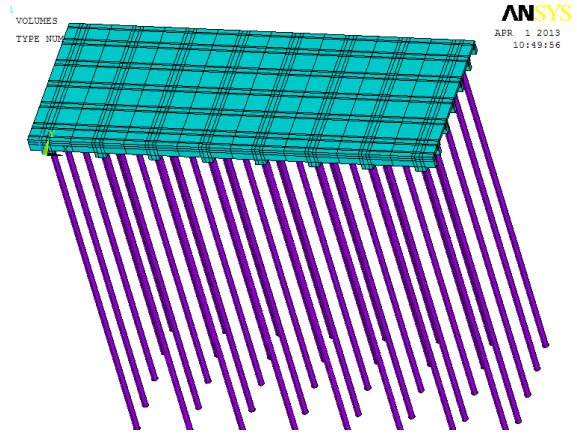


Figure 1 The finite element model of high-pile wharf

**Load.** Loads acting on the wharf include structural weight, ship mooring force, ship impact force, current force. By comparison, using Guoda's formula [5] calculates the wave uplift force and using Shenzuyin's formula [6] calculates the wave horizontal force. When design high water level is 3.85m, uplift force calculation results on the high-pile wharf panel are shown in Table 3 and horizontal force calculation results are shown in Table 4.

Table 3 Uplift force calculation results on the high-pile wharf panel

| return period | direction | $K_1$ | $K_2$ | n | α | π | η | γ | H | L | d | P(Pa) |
|---|---|---|---|---|---|---|---|---|---|---|---|---|
| 100years | E | 4.2 | 1.4 | 2.5 | 0.2 | 3.1 | 5.8 | 9.8 | 3.4 | 133.0 | 8.0 | 214.8 |
| | ESE | 4.2 | 1.4 | 2.5 | 0.2 | 3.1 | 5.1 | 9.8 | 3.3 | 124.1 | 8.0 | 188.3 |
| | SE | 4.2 | 1.4 | 2.5 | 0.2 | 3.1 | 4.9 | 9.8 | 3.2 | 124.1 | 8.0 | 180.9 |

Table 4 Horizontal force calculation results on the high-pile wharf panel

| return period | direction | water level | D (m) | H (m) | L (m) | T(s) | eflectional coefficient Kr | reflected wave height Hr(m) | ho (m) | wharf apron average pressure p(kN/m$^2$) |
|---|---|---|---|---|---|---|---|---|---|---|
| 100 years | E | 5.0 | 10.8 | 3.7 | 141.8 | 14.5 | 1.5 | 5.5 | 0.4 | 5.8 |
| | ESE | 5.0 | 10.8 | 3.5 | 132.1 | 14.5 | 1.5 | 5.3 | 0.3 | 5.2 |
| | SE | 5.0 | 10.8 | 3.4 | 132.1 | 14.5 | 1.5 | 5.1 | 0.3 | 4.9 |

**Results and analysis.** Displacement and the first main stress of the high-pile wharf in two conditions are analyzed. In condition one, the wave cresh is just completely into the bottom of high-pile wharf. In condition two, wave cresh acts in the middle.

**Displacement analysis.** The displacement results are shown in figure 2~figure 4. From them it can be knew that because the panels and stringers formed a mutual restrain, the maximum displacement

of panel in the z direction is basically occurred in the middle position of the width direction and Z-direction displacement of the panel has a local mutation in the variation process of the width direction. This is in line with reality. Meanwhile, as the crest moving, the uplift forces on the panel also moved and the deformation in the z direction basically coincides with the position of the crest, usually the maximum displacement occurring at the center of the peak. Comparing the results in different varying directions, Changes of panel z-direction displacement in the longitudinal direction are smoother than that in the width direction.

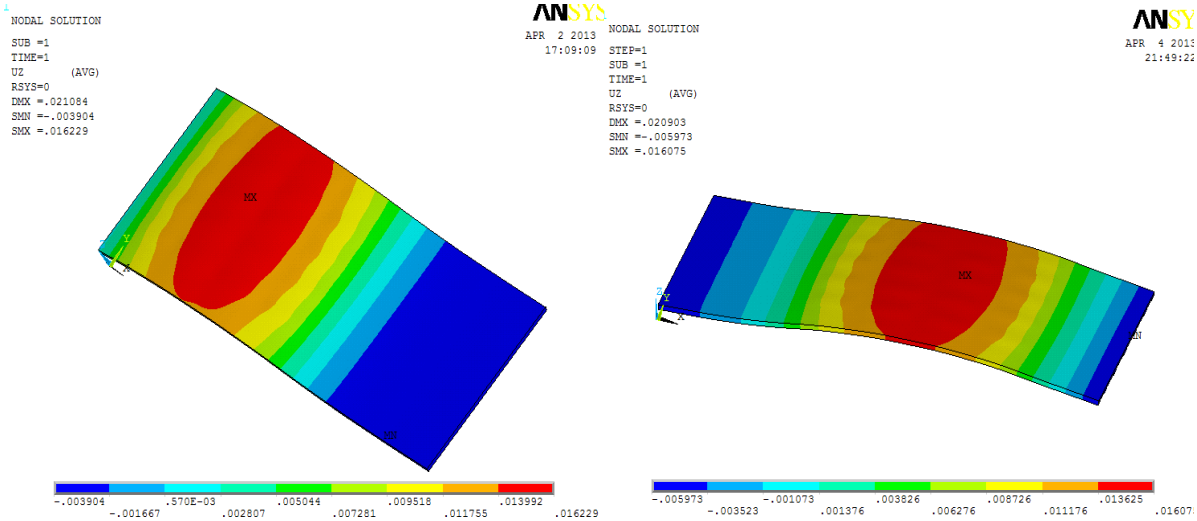


(a) condition one (b) condition two

Figure 2 The displacement in the z direction of the panel

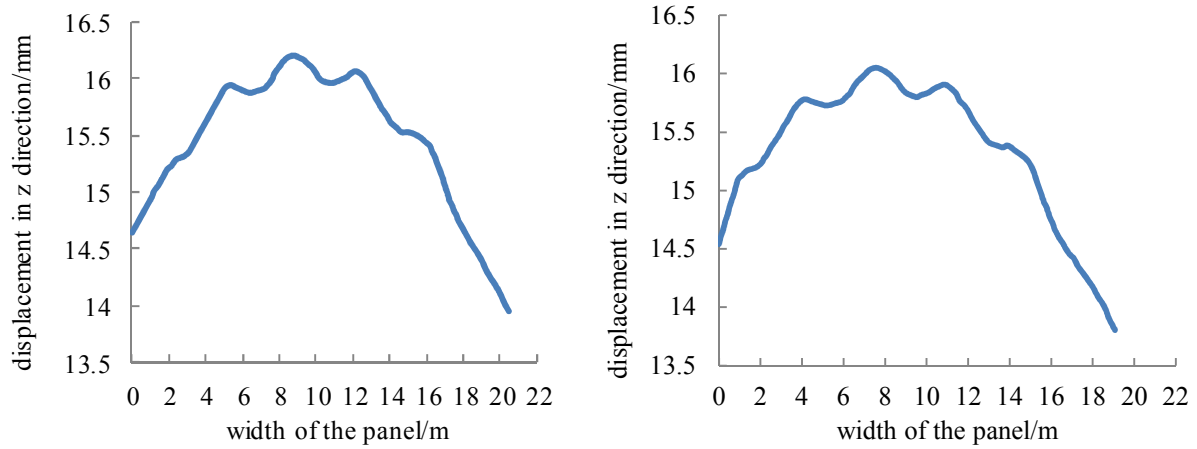


(a) condition one (b) condition two

Figure 3 The displacement in the z direction varying with the width of the panel

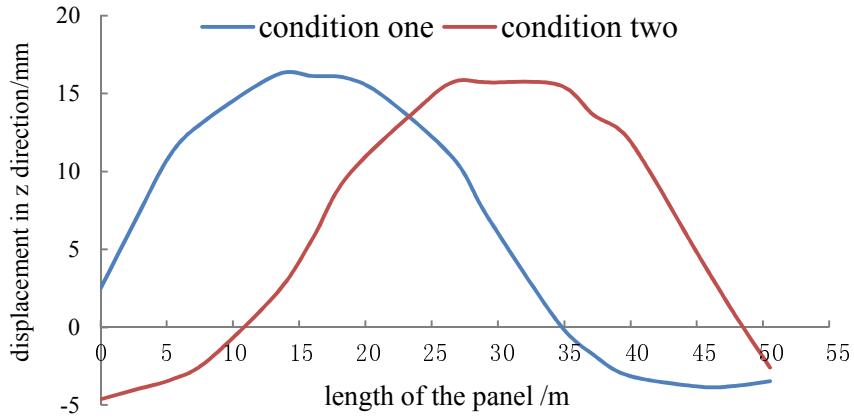


Figure 4 The displacement in z direction varying with the length of the panel

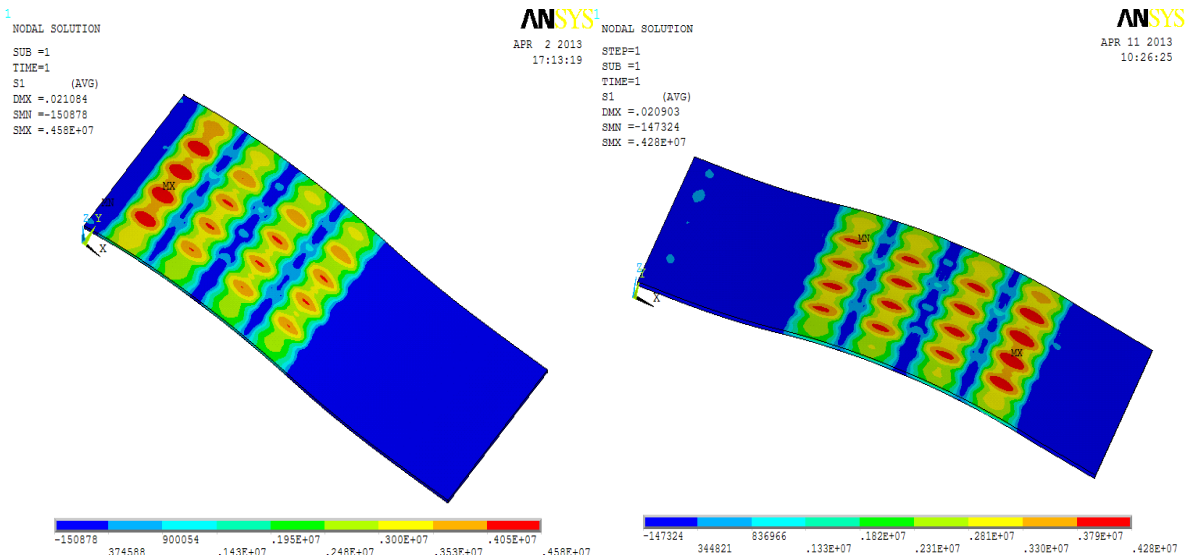


(a) condition one (b) condition two

Figure 5 The Ansys analysis results of the first main stress on the panel

**Stress analysis.** As can be seen from the figure 5, the maximum stress in condition one is 4.58 MPa, the maximum stress in condition two is 4.28 MPa and these stresses belong to the tensile stress. When the wave acts on the wharf, the local stress of panel is large and concentrated in the center. Meanwhile, the tensile stress of panel concentrates at the panel surface, while the compressive stress occurs at the bottom. In most cases, the tensile stress is much greater than the compressive stress, so the crack may appear on the panel, then local failure will occur. Sometimes the panel may be thrown by the waves or cause a large-scale destruction, so there will be great hidden for the security of this condition. Therefore, if there is a greater wave acting on the wharf. a wave dissipation facilities or wharf partially perforated panels must be considered to reduce the impact of waves on the role of the panel to prevent its damage.

## Conclusions

Under the action of the wave, the large displacement and tensile stress of the panel occurred which may cause local failure, even severely destroy to the wharf superstructure, leaving a great hidden for the security of the wharf, especially in the peak position. Therefore, if there is a greater wave acting on the wharf, a wave dissipation facilities or wharf partially perforated panels should be considered to reduce the impact of waves on the role of the panel to prevent its damage.

## References

[1] S.Y. Yan, Calculation on uplift superstructure of high-piled wharf[J]. Technology Wind, 2011 (7): 175-176.

[2] Y.R. Zhou, G.P. Chen, H.L. Huang, et al, Experimental study on uplift forces of waves on a horizontal plate of an open-wharf[J], The ocean engineering, 2004, 22(4):43~50.

[3] R.D. Guan, G.X. Xia, H.X. Liu, Finite Element Analysis of the High-pile Wharf Foundation Pile under Current Forces[J]. Science Technology and Engineering, 2012, 20(21):5206-5212.

[4] J. Huang, X.C. Yu, Z.Y. Chen. Finite element analysis of the impact of wave forces on high-pile wharf structures[J]. Traffic engineering and technology for national defence, 2010, 8(3):40~45.

[5] D. Guo, B.H. Cai. Calculation on uplift forces of waves on an open-wharf [J], Journal of East China Technical University of Water Resources Engineering, 1980(1):14~33.

[6] Z.Y. Sheng, D. Guo. On evaluation of wave force acting on open pier supported on piles in deep water[J]. Journal of East China Technical University of Water Resources Engineering, 1984, (2):54~65.

*Applied Mechanics and Materials Vols. 580-583 (2014) pp 2206-2209*
*© (2014) Trans Tech Publications, Switzerland*
*doi:10.4028/www.scientific.net/AMM.580-583.2206*

# Appropriate Jackup Selection in Disturbed Wellsite by Pile Inserting and Pulling in Offshore Oilfield

Yongning An[1,a,*], Qingfeng Song[2] and Jing Li[1]

[1]Tianjin Research Institute for Water Transport Engineering, M.O.C, Tanggu, Tianjin, China

[2]Zhejiang Engineering Prospecting Institute, Ningbo, Zhejiang, China

[a]17106241@qq.com

**Keywords:** Offshore Oilfield. Pile inserting and pulling. Wellsite. Jackup. Pile ultimate bearing capacity. Punch-through analysis.

**Abstract.** Pile inserting and pulling activities may occur for many times in some wellsite in Offshore Oilfield, that resulted in serious stratum disturbance and complex strength change, it's difficult to select appropriate jack-up drilling platform in the workover process latterly. By applying American Petroleum Institute <API RP 2A-WSD> norms, calculating the pile bearing capacity of two typical jackup, combing with the actual data of jackup emplaced, this paper analyzes and compares the suitability of various type of jackup in place in seriously disturbed wellsite by pile inserting and pulling, and then offers a proposal on how to select the appropriate jackup in such wellsite as a reference.

## Introduction

Marine engineering geophysical survey revealed that pile inserting and pulling activities may occur for many times in some wellsite in Offshore Oilfield, that resulted in serious stratum disturbance and complex strength change, it's difficult to select appropriate jack-up drilling platform in the workover process latterly. This paper used an offshore oil wellsite as a typical example to investigate how to select an appropriate jackup in disturbed wellsite by pile inserting and pulling.

## Typical Wellsite Overview

There had been many times pile inserting and pulling activities of Jack-up drilling platform in some offshore oil wellsite and the activities would lead to serious stratum disturbance and complex strength change which had impact on inserting piles activities of workover jackup[1-2]. According to explanation of high resolution shallow seismic profile , pile inserting and pulling disturbance is divided into three categories,single pile inserting and pulling disturbance, location overlapping multiple pile insertion and pollout disturbance,location adjacent multiple pile inserting and pulling disturbance(fig.1).

As can be seen in fig.1, pile inserting and pulling disturbance's influence depth is 7m around.The pile pits formed in site after pile inserting and pulling and the amplitude of the reflected wave is weak which reflected the difference between its internal components and surround because of pile pits destroyed the original formation structure and new sedmiment was filled into pile pits. The plane infuence scope of single pile inserting and pulling disturbance is about 8~10m(fig.1a) larger than common pile pits. The plane infuence scope of location overlapping multiple pile insertion and pollout disturbance is about 20m(fig.1b) which were formed in pre-pile pits. The plane infuence scope of location adjacent multiple pile inserting and pulling disturbance is about 40~70m(fig.1c), which were formed in adjacent location in the same period and the short distance between each pile pits leaded to original stratum collapse so joined together.

As can be seen in fig.1, pile inserting and pulling disturbance's influence depth is 7m around.The pile pits formed in site after pile inserting and pulling and the amplitude of the reflected wave is weak which reflected the difference between its internal components and surround because of pile pits

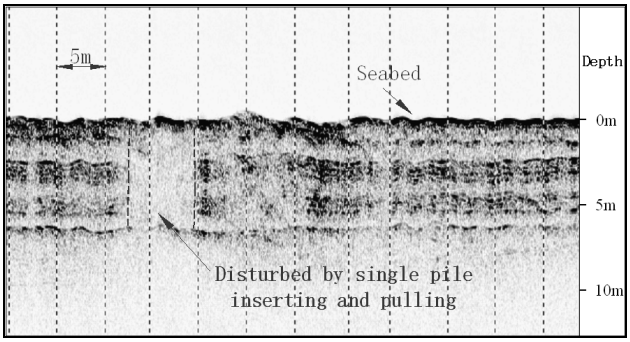


(a) disturbed by single pile inserting and pulling

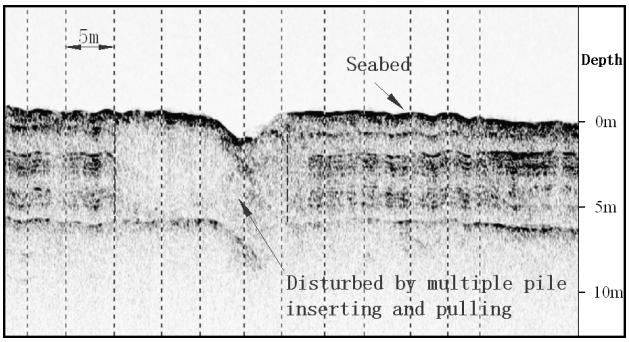


(b) disturbed by overlapping multiple pile inserting and polling

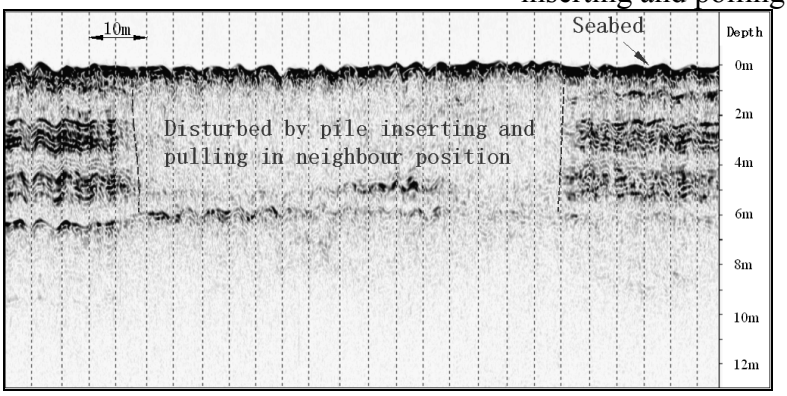


(c) disturbed by location adjacent multiple pile inserting and pulling

Fig.1 Seismic profile of inserting and pulling disturbance in typical wellsite

destroyed the original formation structure and new sedmiment was filled into pile pits. The plane infuence scope of single pile inserting and pulling disturbance is about 8~10m(fig.1a) larger than common pile pits. The plane infuence scope of location overlapping multiple pile inserting and polling disturbance is about 20m(fig.1b) which were formed in pre-pile pits. The plane infuence scope of location adjacent multiple pile inserting and pulling disturbance is about 40~70m(fig.1c), which were formed in adjacent location in the same period and the short distance between each pile pits leaded to original stratum collapse so joined together.

In terms of topography on sea level, single pile inserting and pulling and location adjacent multiple pile inserting and pulling's seabed surface were gently because of long time filling by hydrodynamic scouring action.And the filling substance consolidation degree was high. There was big pile pits in the seabed where occurred location adjacent multiple pile inserting and pulling disturbance that reflect the occurrence of shorter pile inserting and pulling and the pile pits was not filled. Reflection amplitude is different in the stratum below the pile pits demonstrating the components or materials strength different and the carrying capacity is the most complex.

Drilling data reveals the pile hole inside and outside layer composition and strength as follows.

The original stratum outside of the pile pits: (1) Silt, brown, medium dense, layer bottom depth of 4.2m. (2) Mucky silty clay, gray and black, soft plastic, layer bottom depth of 5.8m. (3) Silty clay, gray and black, plastic, layer bottom depth of 7.1m. (4) Silt, gray and black, medium density, layer bottom depth of 9.0m. (5) Silt, light gray, dense, layer bottom depth 10.2m. (6) Silt, brown, dense, maximum depth of 16.0m.

Disturbed stratum inside of the pile pits: (1) Silt, brown, dense ,layer bottom depth of 3.2m. (2) Silty clay, taupe, hard plastic, layer bottom depth of 5.8m .(3) Silt, brown, dense, maximum depth of 10.0m.

**Working Jackup Emplacement and Process Analysis**

The wellsite experienced two twice inserting and pulling emplacement. The diameter of Jackup No.1 pile shoe is 5.7m, single pile ultimate bearing capacity is 17920kN, did not insert to a predetermined depth when emplacement. The diameter of Jackup No.2 pile shoe is 8.5m, single pile ultimate bearing capacity is 23415 kN.

The two stern piles of Jackup No.1 inserted to a predetermined depth 7.1m and bow pile inserted to 4.0m. After analysis that may be encountered in stratum disturbed by the early pile inserting and pulling. Engineering geophysical results indicated that a number of pile pits widely distributed in wellsite, specifically around the bow pile. When the formation strength inside the pile pits is higher than outside, inserting depth will be less than that calculated based on the original formation.

Table 1 Pile strength parameters inside and outside pile pits in typical wellsite

| stratum outside of the pile pits | | | | | stratum inside of the pile pits | | | | |
|---|---|---|---|---|---|---|---|---|---|
| Layer No. | layer bottom depth (m) | undrained shear strength $C_u$(kPa) | pile-soil friction angle δ(°) | ultimate bearing capacity factor $N_q$ | layer No. | layer bottom depth (m) | undrained shear strength $C_u$(kPa) | pile-soil friction angle δ(°) | ultimate bearing capacity factor $N_q$ |
| 1 | 4.2 | / | 20 | 12 | 1 | 3.2 | / | 23 | 16 |
| 2 | 5.8 | 18 | / | / | 2 | 5.8 | 80 | / | / |
| 3 | 7.1 | 28 | / | / | 3 | 10.0 | / | 30 | 40 |
| 4 | 9.0 | / | 23 | 16 | | | | | |
| 5 | 10.2 | / | 29 | 37 | | | | | |
| 6 | 16.0 | / | 27 | 27 | | | | | |

At the same time, considering the stratum inconsistency inside or outside of pile pits, recalculated the single pile ultimate bearing capacity of Jackup No.1 and Jackup No.2 and to evaluate the suitability of the pile emplacement and safety of piercing damage (fig.2).

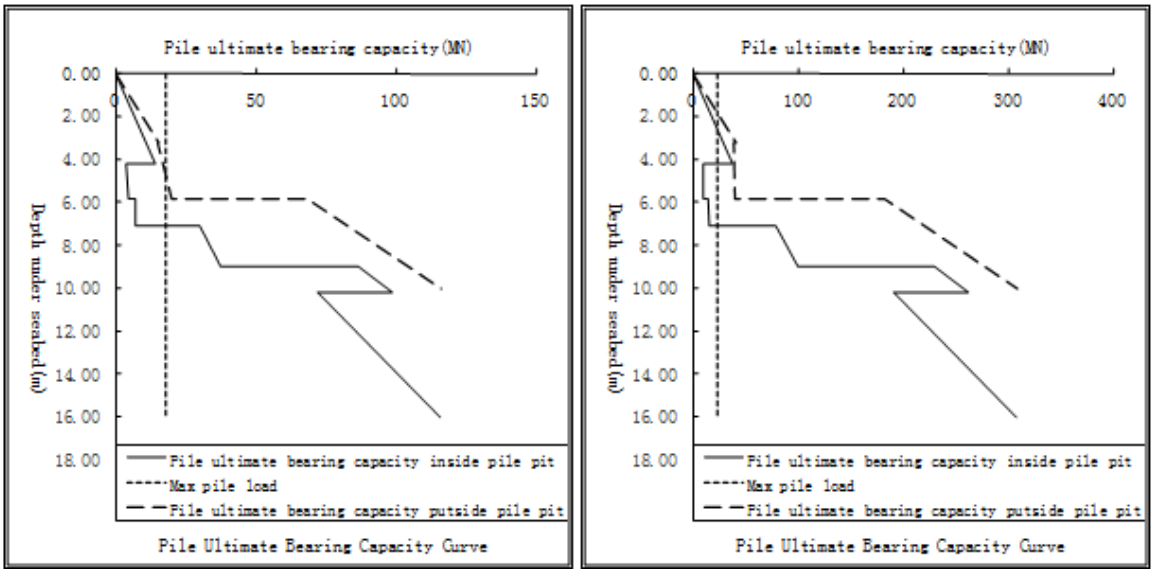


(a) Calculated result of Jackup No.1 (b) Calculated result of Jackup No.2

Fig.2 Pile Ultimate Bearing Capacity Curve

When Jackup No.1 re sitting, its theory insert depth is not unified because of inhomogeneity of bearing stratum. The theoretical insert depth of the two stern piles of jackup which was outside of pile pit was same to predicted 7.1m. The theoretical insert depth of the bow pile of jackup which was inside of pile pit was 4.8m shallower than predicted .

The theoretical inserting depth of jackup No.2 was 1.9m inside of pile pits. The soft stratum would occurred piercing damage when the inserting depth was 2.3m outside of pile pits though the ultimate bearing capacity could meet the requirements. It is safe when the inserting depth is7.1m.

In the case of the surface covered by a thick silt, the stratum strength is higher than original stratum after long time later of the pile pits forming. In a decade or even more time, waves, currents, storm surges, cold, earthquakes and other geological forces had been continuously or intermittently to play the role, so that silt filled inside the pile pits drainage consolidation [3-6], thereby becoming dense. However, the pile pits formed by insertion of jackup No.1 was only less than 2 months without the full action of geological forces.. Only pile toe was compacted by pile shoe and the pile side solid collapsed after pulling should be deemed remolded and the stratum strength was lower than original stratum. Therefore, in calculating two stern piles of Jackup No.1, depth7.1m above could be calculated according to reshape, the following parts could be calculated according to reshape original stratum.

After analysis, although plug-in depth of each leg of jackup No.2 was inconsistent, but had been inserted to stabilize bearing stratum, the difference insertion can be used in re sitting. In this case, it should be noted self-stable of jackup [7].

## Conclusion

(1) In general, stratigraphic strength inside pile pits after pile inserting and pulling is larger than that in original stratum. For example, when the seabed is covered with thick silt, a long time later after the pile inserting and pulling, the strength inside the pile pits would be larger. However, after a relatively short time, the strength inside the pile pits would be smaller.

(2) When the jackup is emplaced, it is difficult to prejudge the pile is inserted inside or outside the pile pits. If it is planned to insert to a dense stratum inside the pile pits but actually insert to outside, the pile will go on insert to deeper, it's unsafe if the inserting depth is larger than allowed. If it is planned to insert to stratum outside the pile pits but actually not, the pile will be inserted to a shallower depth and the inclining of jackup increased.

(3) If the surface layer is thick and dense silt, there's always a little change occurred inside the pile pits after pile inserting and pulling. It's suitable to emplace a jackup with big pile shoe that will not insert too deep, a piercing damage check should be done previously.

(4) When it's seriously and unevenly disturbed in the upper stratum, it's NOT appropriate to emplace a jackup with small pile shoe. For each leg is more easily to insert to different strength stratum, that will lead to inconsistent inserting depth, thus increasing the risk of self-stability of jackup. In addition, the actual strength in disturbed stratum is difficult to investigate accurately, it also increases the risk of jackup emplacement.

## References

[1] Li Jing, Design for integral jackup of production and repair in Chengdao Oilfield, *Petroleum Planning & Engineering,* vol. 5, pp. 18-19, 2002.

[2] ZHANG Min-sheng, LIU Hong-jun, et al, Study of liquefaction of silty soil and mechanism of development of hard layerunder wave actions at Yellow River Estuary, *Rock and Soil Mechanics*, vol. 30, pp. 3347-3356, 2009.

[3] FENG Xiu-li, et al, Geomorphological evolution and geological disastersanalysis in Chengdao sea area of the Yellow River Delta, *Rock and Soil Mechanics*, vol. 25(Supp), pp. 17-20, 2004.

[4] Song Qing-feng, Wu Jian-zheng, et al, Study on disturbance and renewal of shallow soil in the Yellow River Subaqueous Delta Area due to pile inserting and pulling, *coastal engineering*, vol. 22, pp. 11-18, 2007.

[5] American Petroleum Institute, *Recommended practice for planning, designing and constructing fixed offshore platforms—working stress design( API RP 2A-WSD)*, Dec 2000.

[6] WU Qiu-yun, ZHOU Yang-rui, et al, Applying of the punch-through analysis method of rig-drilling ship Bohai Open up Oilfields, *coastal engineering*, vol. 18, pp. 16-21, 1999.

[7] Ji Chunqun, Sun Dongchang, Analysis of stability against overturning and foundation bear force for jack-up rig, *Journal of Shanghai Jiaotong University*, vol. 30, pp. 79-85, 1996.

# CHAPTER 7:

# Construction Technology

*Applied Mechanics and Materials Vols. 580-583 (2014) pp 2213-2219*
*© (2014) Trans Tech Publications, Switzerland*
*doi:10.4028/www.scientific.net/AMM.580-583.2213*

# Complementary Use of Inductive Test and BendingTest for the Characterization ofSFRC

LIAO Lin[1, a*], CAVALARO Sergio[2, b], de la FUENTE Albert[3, c], AGUADO Antonio[4,d]

[1, 3, 4] Universitat Politècnica de Catalunya, Jordi Girona 1-3, Building C1. 08034 Barcelona. Spain

[2]Universitat Politècnica de Catalunya, Jordi Girona 1-3, Building B1. 08034 Barcelona. Spain

[a]lin.liao@upc.edu,[b]sergio.pialarissi@upc.edu

[c]albert.de.la.fuente@upc.edu, [d]antonio.aguado@upc.edu

**Keywords:**CSFRC, SFRSCC, Bending test, Inductive test, Fibre orientation, Fibre distribution

**Abstract:**Many researches have been conducted in past decades for promoting the application of steel fibre reinforced concrete (SFRC), either conventional or self-compacting. However, the differences of post-crack behaviour and the properties of these two types of concrete remains unclear. The objective of this paper is to analyse such differences in terms of flexural behaviour, fibre orientation and contribution as well as the fibre content. For that, an extensive experimental campaign was carried out. In total 3 mixes of self-compacting and 3 mixes with traditional concrete were produced with the nominal fibre contents of 30kg/m$^3$, 45kg/m$^3$ and 60kg/m$^3$. In each series, specimens were produces and characterized bythree point bending test (code EN 14651) and inductive test. The results illustrate how fibre orientation and distribution justify the differences in the mechanical behaviour of the materials and the scatter of the bending test results.

## Introduction

Many studies were performed in past decades to promote the application of steel fibre reinforced concrete (SFRC)[1,2,3].The introduction of steel fibres in the concrete matrixproduces several advantages, such as increase inthe energy absorption capacity and in the post-cracking flexural tensile strength of the material. Moreover, fibres could behave as alternative of conventional reinforcement so that the passive reinforcementcould be removed total or partially from concrete.

With the reduction of skilled construction workers, it is more and more difficult to build good quality structural elements. In order to mitigate this thorny issue, self-compacting concrete (SCC) appeared in 1988 [4]. Since then, a lot of studies were devoted to the development of the material, leading to reduction of manpower or time required for construction, as well as safety improvements and noise reduction.

By introducing steel fibres in SCC on may combine the advantages from both types of concrete. In this matter, research about steel fibre reinforced self-compacting concrete (SFRSCC) has been highlighted since it was first put into use in real structural elements [5,6].

In order to ensure the quality of SFRC, it is important to characterize the post-cracking behaviour and to evaluate the fibre content. On one hand, the characterization of post-cracking residual tensile strength is usually performed through three point or four point bending test. On the other hand, the fibre content is estimated according to the procedure established in [7]. For that, specimens must be either crushed or fresh concrete should be washed in order to separate the fibres that are then weighed. These tests not only demand a lot of time of execution but also are expensive and environmentally unfriendly. In addition to that, limited number of tests that may be performed per day compromise both the statistical representativeness of the results and the effectiveness of the quality control system.

The objective of this paper is to propose an alternative to the traditional quality control system used for SFRC. First, study on conventional steel fibre reinforced concrete (CSFRC) and SFRSCC by conducting three point bending test to characterize e their post-cracking behaviour will be presented. Then a non-destructive test “inductive test” would be carried out on cubic specimens and

extracted samples to estimate the fibre content and fibre orientation and distribution within the specimens. Finally, further analysis of post-cracking behaviour according to bending and inductive test will give an objective evaluation of the material tested.

## Materials

The compositions of the mixtures used in the experimental programme are presented in the Table 1. It is necessary to point out that GLENIUM TC1425 is a water-reducing admixture based on the high activity behaviour of polycarboxylate, and X-SEED is a suspension of CSH nanoparticles, which acts as crystallization nucleus to activate the cement hydration, thus increasing the resistance of concrete at the initial stage.

The low carbon hooked end steel fibre used in the experimental campaign was the MasterFiber 502, supplied by BASF Chemical Company. The main characteristics of the fibre are shown in Table 2.

Tab.1: Mix composition of CSFRC and SFRSCC [in kg/m$^3$]

| Mixtures | CSFRC | SFRSCC |
|---|---|---|
| Sand 0/5 | 817 | 1200 |
| Fine aggregate 5/15 | 404 | 500 |
| Coarse aggregate 12/20 | 810 | 200 |
| Water | 156 | 165 |
| CEM I 52.5 R UNILAND | 312 | 380 |
| Glenium TC 1425 | 2.19 | 4.56 |
| XSEED | 6.24 | 7.6 |
| MasterFibre 502 | 30, 45 and 60 | 30, 45 and 60 |

Tab.2: Characteristics of MasterFiber 502

| | |
|---|---|
| Tensile strength | Min. 1000 N/mm$^2$ |
| Length | 50±1 mm |
| Diameter | 1.0 mm±0.1 mm |
| Aspect ratio | 50 |
| Number of fibres per kg | 3000 |

## Experimental study

### 3.1. Specimens

Three batches of concrete with the fibre content of 30 kg/m$^3$, 45 kg/ m$^3$ and 60 kg/ m$^3$ were produced in concrete plant both for CSFRC (numbered as CSFRC-30, CSFRC-45, CSFRC-60) and SFRSCC (numbered as SFRSCC-30, SFRSCC-45, SFRSCC-60). For each batch of concrete, the fresh state properties were tested.All of them met the requirements of [8,9,10,11].

### 3.2. Tests

In order to evaluate the mechanical properties SFRC at hardened state, compression test and 3 point bending test were carried out in accordance with thestandards [12,13].Additionally, inductive test was carried out to estimate the amount and distribution of fibres within the specimen.Table 3 shows the detail information respect to different tests for each dosage.

Tab.3: Concrete tests performed at hardened state

| Test type | Regulation | Variable | Nº of specimen | Dimension (mm) |
|---|---|---|---|---|
| Compression Test | UNE-EN 12390-3 | fc | 9 | ϕ150×300 |
| 3 Point Bending Test | UNE-EN 14651 | $f_L$ $f_{R,1}$ $f_{R,2}$ $f_{R,3}$ $f_{R,4}$ | 3 | 150 x150 x 600 |
| Inductive Test | | Fibre content and orientation | 8+6 | 150 x 150 x 150 |

Taking into account that, the amount and the orientation of fibres in the SFRC are directly related to its mechanical behaviour. The inductive test proposed by Torrents et al [14] and improved

by Cavalaro et al [15]is used to quantify the amount and the distribution of fibres in SFRC specimens. It presents a high accuracy, robustness and allows assessing a big volumes of material in a short time.

The inductive test is composed by a coil and a LCR impedance analyser. The coil receives an electric current and generates a magnetic field in its interior. Variations of the field due to the modification of the magnetic permeability inside the coil are measured. These modifications are induced by the introduction into the environment of elements with different permeability than the air, as is the case of SFRC. The introduction of a SFRC specimen into the system generates an inductance change which can be measured [14].

In this experimental programme, two types of cubic specimens with 150 mm of side were characterized to evaluate the differences that might exist depending on the nature of the sample. The first type consisted of specimens cast in moulds whereas the second type were cubes extracted from the beams once the bending test was completed. Figure 1a depicts the zones of the extractions of the cores. The first cut was performed respecting a 75 mm distance from the extremities of the beams, with the intent of reducing the influence wall-effect that exist close to the moulds. In total, 8 moulded cubes and 6 extracted cores were obtained per mix.

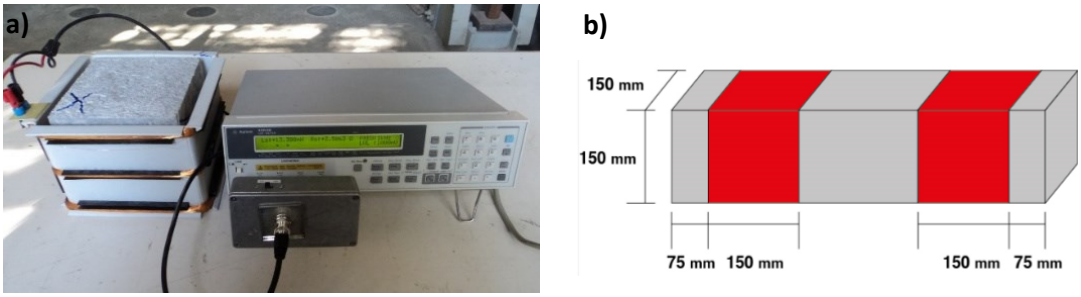


Fig. 1: a) Inductive test set-up and b) Extracted cubic sample

The summed inductance value measured in each specimen for the axes X, Y and Z is related with the fibre content, while the proportion between measurements provide information about the fibre orientation. For that, however, the values of inductance should be calibrated. Therefore, four specimens from different series were crushed after inductive test. This was done by first compressing the specimens to complete failure. Then the chunks were fed into a grinding machine. Once the specimens were reduced to rubble, the fibres were retrieved by a magnet and weighed by a scale with the accuracy of 0.0001kg. A linear regression was applied to correlate the summed inductance change and the fibre content ($C_f$), as shown in Fig. 2. As observed in previous works [14,15], a linear relation exists between both parameters.

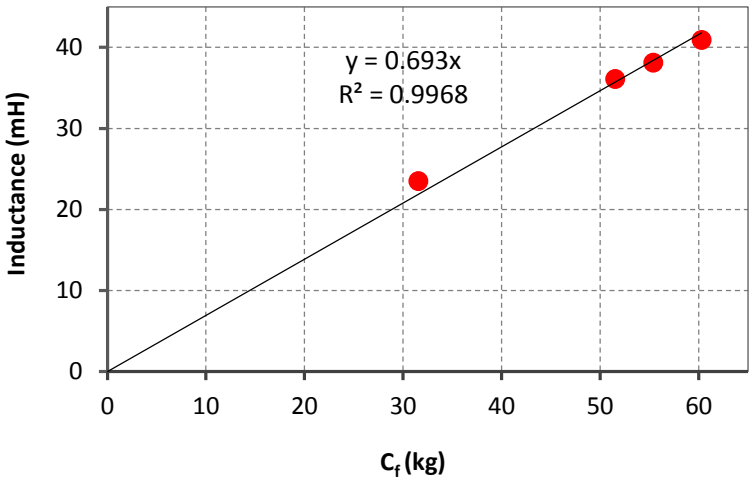


Fig. 2: Inductance-$C_f$ relationship based on inductive test

## Results and analysis

### 4.1 Compression test

The results obtained are shown in Table 4, together with its average strength and CV (coefficient of variation). For CSFRC, the average compressive strength at 28 days is 64.7 MPa, whereas the SFRSCC is 67.5 MPa, slightly higher than CSFRC.

Tab.4: Compressive strength [in kN/mm$^2$] and C.V

| Series | Day 1 | | Day 7 | | Day 28 | |
|---|---|---|---|---|---|---|
| | Mean | C.V (%) | Mean | C.V (%) | Mean | C.V (%) |
| CSFRC-30 | 20.2 | 1.2 | 54.4 | 1.8 | 65.1 | 0.3 |
| CSFRC-45 | 19.7 | 2.4 | 54.6 | 0.8 | 63.9 | 1.5 |
| CSFRC-60 | 21.5 | 1.5 | 54.8 | 0.2 | 64.9 | 1.9 |
| SFRSCC-30 | 25.4 | 2.1 | 56.1 | 2.9 | 70.5 | 1.2 |
| SFRSCC-45 | 18.3 | 0.8 | 55.2 | 1.8 | 66.3 | 1.3 |
| SFRSCC-60 | 17.1 | 1.5 | 53.4 | 1.3 | 66.7 | 4.2 |

As may be seen in Table 4, the increase in the fibre dosage did not lead to a significant difference in the compressive strength. This is consistent with the studyfrom [16]. Likewise, the fibre dose does not affect the scatter in the compressive strength, which at 28 days at 1.13MPa for the CSFRC and 2.65MPa for SFRSCC.

### 4.2 Three point bending test

Figure 3 shows the Load - CMOD curves obtained from three point bending test as the average value recorded for each series.

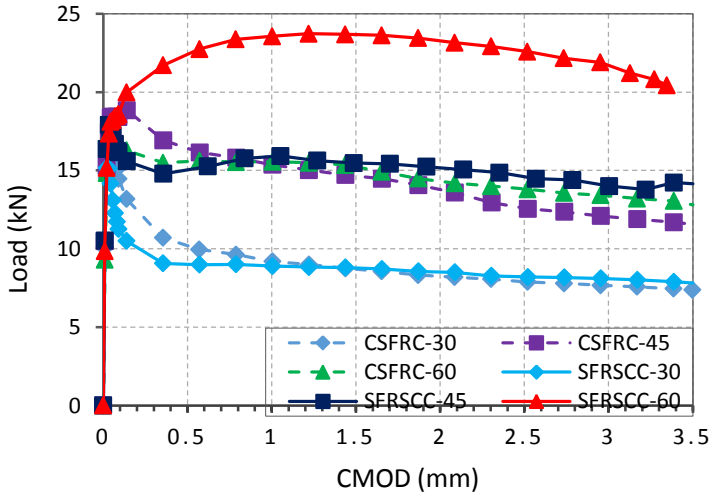


Fig. 3: Load - CMOD relationship curves obtained from three point bending test

A similar tendency is observed in all curves. Initially, the concrete shows a linear behaviour until the first-crack appears. Then a sudden drop due to stiffness decrease of specimen occurs. After a certain crack opening, the fibres bridging the crack become active and provide a residual resistant capacity. According with Figure 3, the SFRSCC shows a better post-crack behaviour than the CSFRC. This is especially evident in the series with 60 kg/m$^3$. In this case, the mix with SFRSCC shows a hardening behaviour while the mix with SFRC presents softening behaviour.

Table 4 shows the average limit of proportionality (LOP) and residual flexural tensile strength ($f_{R,i}$) of different series of beams.

All mixes show similar values of LOP, except for the ones with 30 kg/m$^3$ that present the smallest values. On the other hand, the $f_{R,i}$ increases with the fibre dosage for both types of concrete. As expected, the use of a higher dosage leads to an increase in the number of fibres that bridge the crack and contribute to the residual strength.

Tab.5: Three point bending test results [in kN/mm$^2$] and C.V

| Series | LOP | | $f_{R,1}$ | | $f_{R,2}$ | | $f_{R,3}$ | | $f_{R,4}$ | |
|---|---|---|---|---|---|---|---|---|---|---|
| | Mean | C.V (%) | Mean | C.V (%) | Mean | C.V (%) | Mean | C.V (%) | Mean | C.V (%) |
| CSFRC-30 | 5.17 | 1.1 | 3.15 | 8.4 | 2.7 | 2.5 | 2.44 | 1.8 | 2.22 | 6.4 |
| CSFRC-45 | 5.76 | 3.82 | 5.06 | 20.28 | 4.54 | 22.02 | 3.89 | 22.18 | 3.6 | 22.7 |
| CSFRC-60 | 5.49 | 12.4 | 4.81 | 19.25 | 4.71 | 21.89 | 4.26 | 22.12 | 4 | 22.63 |
| SFRSCC-30 | 4.99 | 9.94 | 2.85 | 28.37 | 2.79 | 32.11 | 2.61 | 32.67 | 2.47 | 34.96 |
| SFRSCC-45 | 5.8 | 8.48 | 4.72 | 1.91 | 4.86 | 3.66 | 4.67 | 5.84 | 4.33 | 5.79 |
| SFRSCC-60 | 5.89 | 2.66 | 7.13 | 17.23 | 7.54 | 16.64 | 7.12 | 11.56 | 6.41 | 11.76 |

The results show again that, for the same fibre dosage, the mixes SFRSCC presents a higher residual strength ($f_{R,2}$, $f_{R,3}$ and $f_{R,4}$) than the equivalent mixes with CSFRC. Such trend becomes more evident as the fibre content increases. The improved behaviour of SFRSCC might be attributed to a more favourable orientation of fibre regarding the cracking plane. The high flowability achieved in this type concrete provides more freedom of movement to the fibres. In this context, fibres tend to align perpendicular to the casting direction that coincides with the cracking plane. On the contrary, the lower consistency of CSFRC restrict the movement of fibres, which assume an orientation not as favourable. Notice that this trend is not observed for $f_{R,1.}$ The main reason for that may lay in the influence of the concrete matrix failure for small crack openings. In other words, the more favourable orientation of the fibres in the case of SFRSCC is not perceived since for small crack openings some of the fibres are not activated and the response of the concrete matrix might affect the results.

As shown in Figure 3, a general similar tendency could be observed in all curves, it mainly consists of three stages. Initially, the concrete shows a linear behaviour until the first-crack appears; then there is a sudden drop due to stiffness decrease of concrete, in this phase, the plain concrete lost workability and the steel fibres haven't started to make contribution to the concrete matrix. After a short adjustment, the fibres bridge in the crack work as the reinforced bars to bare the flexural tensile strength, and makes the concrete maintain substantial load until reaching final failure.

To study the post-crack behaviour of the concrete comprehensively, it can be seen from the Figure 3, systematically, the SFRSCC shows a better post-crack behaviour than the CSFRC, especially in the series which has 60 kg/m$^3$. Moreover, there is no significant difference in terms of the load for the first-crack either in CSFRC or SFRSCC. This reveals that by adopting the 3 point bending test, on the condition of with same dosage of fibres, the type of concrete makes slight influence on the limit of proportionality (LOP).

It is worth to point out that, for both type of concrete with 60 kg/m$^3$ steel fibres show a slight different behaviour after the first-crack appears. This phenomenon called concrete bending hardening, which refers to the situation where the post-crack flexureal tensile strength is higher than the first-crack flexural tensile strength. It usually occurs at the concrete with fibre dosage above 50 kg/m$^3$ with relative high aspect ratio [16].

### 4.3 Inductive test

Figure 4 shows the contribution of the fibres in the 3 axes calculated according with the formulations by Cavalaro et al. [15] with the results from the inductive test for moulded (a and c) and extracted (b and d) specimens.

It is known that the addition of steel fibres could reduce the workability of the concrete matrix. However, it is still not ascertained if the fibre orientation and distribution will be affected by the increment of fibre content. Therefore, it is of interest to evaluate the influence of fibre content on the fibre orientation and distribution within the concrete.

As shown in Figure 4, the contribution of fibres in the X and Y axes are always bigger than in Z axis. Precisely, no matter how much the amount of steel fibre is, the orientation number and the contribution of steel fibres in each axis keep a similar ratio. Consequently, based on the results obtained, the fibre dosage does not affect the orientation inside the concrete.

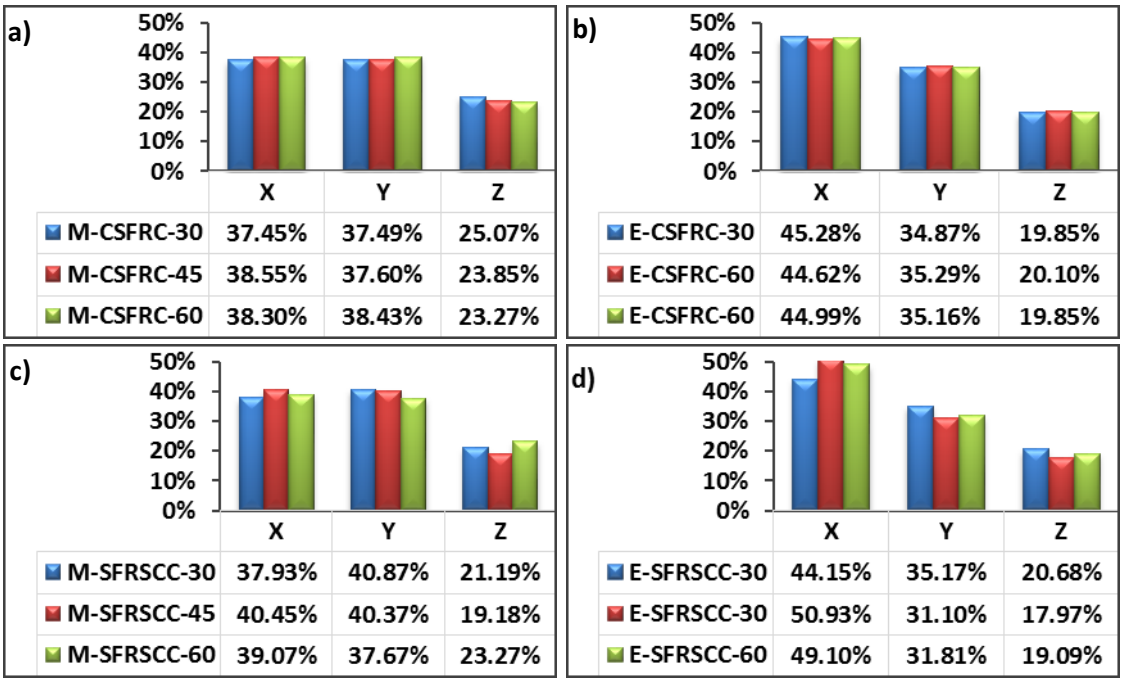


Fig. 4: Contribution of fibres in different axes obtained from inductive test

Additionally, the proportion of the contribution of steel fibres in X, Y and Z approximates 4:4:2 for moulded specimens. On the other hand, this proportion changes to 4.5:3.5:2 approximately in the case of extracted specimens as a result of the influence of the concrete flow.

Moreover, the Figure 4 indicates that the contribution of fibres percentage in X axis in extracted samples are bigger than in the moulded specimens, whereas in Y axis the opposite conclusion was obtained. This observation illustrates that, for both type of concrete, steel fibres are more likely to align parallel to the longitudinal direction of the prismatic beams.

Moreover, the mixes of SFRSCC with 45 kg/m$^3$ and 60 kg/m$^3$ show higher proportion of fibres aligned with the X axis than the equivalent mixes of CSFRC. This is consistent with the better performance in terms of residual strength of SFRSCC and the explanation provided in the previous section.

## Conclusions

The following conclusion can be drawn from this research programme:

- The residual flexural tensile strength$f_{R,i}$is proportional to the fibre dosagefor both type of concrete.
- The SFRSCC shows a better post-crack behaviour than CSFRC in the premise of the same fibre dosage.
- Combining the analysis results of 3 point bending test and inductive test results, it is feasible to evaluate the post-crack behaviour of SFRC with a high reliability.
- The inductive test presents a high accuracy and robustness to predict the fibre orientation and distribution within the concrete, as well as to detect differences in the fibre content.

## Acknowledgements

This paper has been accomplished under the framework of the project “FIBHAC:Self-compacting Fibres and Concrete. Development of a new concept of precast segments fortunnels”, project subscribed to the programme INNPACTO 2011(IPT-2011-1613-420000).In this sense, the authors want to thank the Ministry of Science and Innovation of Spain for theeconomic support provided for its execution. The first author would like to acknowledge thescholarship received from China Scholarship Council.

**References**

[1] J. I. Daniel, S. H. Ahmad: State-of-the-Art Report on Fibre Reinforced Concrete Reported by ACI Committee 544 vol. 96, no. Reapproved, (2002)

[2] F. de Larrard, T. Sedran: Mixture-proportioning of high-performance concrete. Cement and Concrete Research, vol. 32, no. 11, pp. 1699–1704, Nov. (2002)

[3] Blanco, A: Characterization and modelling of SFRC elements. PhD Thesis, UPC, Barcelona, Spain. (2013)

[4] H. Okamura and M. Ouchi: Self-Compacting Concrete. Journal of Advanced Concrete Technology, vol. 1, no. 1, pp. 5–15, 2003.

[5] L. Ferrara, Y.-D. Park: A method for mix-design of fibre-reinforced self-compacting concrete. Cement and Concrete Research, vol. 37, no. 6, pp. 957– 971, Jun. (2007)

[6] B. Akcay and M. A. Tasdemir, "Mechanical behaviour and fibre dispersion of hybrid steel fibre reinforced self-compacting concrete," Construction and Building Materials, vol. 28, no. 1, pp. 287–293, Mar. (2012)

[7] UNE-EN 14721: Test method for metallic fibre concrete - Measuring the fibre content in fresh and hardened concrete. (2006)

[8] UNE 83313: Concrete tests. Determination of the consistency of fresh concrete. Slump method. (1990)

[9] UNE 83361: Self-compacting concrete. Characterization of the flowability. Slump-flow test. (2007)

[10] UNE 83317: Concrete tests. Fresh concrete. Determination of the density. (1991)

[11]UNE 83315CONCRETE TESTS. DETERMINATION OF AIR CONTENT OF FRESHLY MIXED CONCRETE. METHODS PRESSURES. (1996)

[12] UNE-EN 12390-3: Testing hardened concrete - Part 3: Compressive strength of test specimens. (2011)

[13] UNE-EN 14651: Test method for metallic fibered concrete - Measuring the flexural tensile strength (limit of proportionality (LOP), residual). (2007)

[14] Torrents JM, Blanco A: Inductive method for assessing the amount and orientation of steel fibres in concrete. Mater Struct. 45(10):1577-92. (2012)

[15] Cavalaro, S. H. P, Lo´pez R: Improved assessment of Fibre Content and 1 Orientation with Inductive Method in SFRC. Mater Struct. 45(10):1577-92. (2012)

[16] ERMCO: Guidance to fibre concrete (Properties, Specification and Practice in Europe). (2012)

*Applied Mechanics and Materials Vols. 580-583 (2014) pp 2220-2223*
*© (2014) Trans Tech Publications, Switzerland*
*doi:10.4028/www.scientific.net/AMM.580-583.2220*

# Research on New Type Quantitative Nondestructive Pre-stress FRP Sheet Tension Fixture

Guangshan Zhu[1,2, a], Longsheng Bao[2,b] and Chao Guo[2,c]

[1] Northeasten University, Shenyang,Liaoning,110819,China.

[2] School of Civil Engineering, Shenyang Jianzhu University, Shenyang, Liaoning, 110168, China

[a]jiandazgs@126.com, [b]yulingsy@163.com, [c]guochaoglovel@126.com

**Keywords:** Tension Fixture, Pre-stress FRP Sheet, Non-destruction, Quantify Tension.

**Abstract.** Traditional pre-stress FRP sheet tension fixture must have the beam of the bridge slotted to reduce the cross-section of the beam. Besides, stress on the FRP sheet is irregular with local stress concentration. Its indirect load pre-stress, as well as quantitative criterion of pre-stress born by FRP sheet is not accurate. To solve the above problems, a newly-developed self-balanced type pre-stress FRP sheet tension fixture has been introduced. Such a tension fixture consists of welded steel frame, a mechanical jackscrew, a dynamometer and a strain gauge. It is able to give specified stress onto the FRP sheet accurately while not damaging the beam cross-section. At the same time, with the combination of ANASYS Workbench and UG8.0 Software, also states the simulation analysis of the new type tension fixture, including its stress under practical work and deformation state, which initially proves the scientific and economic usefulness of such tension fixtures.

## Introduction

At present, the main method of reinforcing the concrete of the beam is to tension the pre-stressed FPR sheets, that is to say, through slotting on the beam of the bridge and changing the position of the fixture in the slot, the pre-stress is able to be controlled, as shown in Fig.1 [1-3]. Such a method is easy with simple technology. However it has the following problems:

Reducing the cross-section of the existing beam: To make the installation of fixture convenient and simple, the slot is always chosen in the middle of the beam, while such position has the largest bending moment. Slotting in this position will definitely reduce the cross-section of the beam, which unquestionably worsens the stress state of the beam [4, 5].

Damaging the protective layer of the existing beam: Beams reinforced with pre-stressed FPR sheets need follow-up reinforcing because of their old age and insufficiency in carrying capacity. Slotting on the beam will damage the concrete protective layer. Thus the working environment of existing steel bars goes worse and worse.

Uncertainty of stress determined by FRP sheet: As shown in Fig.2, FRP stress is controlled indirectly through the changing of fixture position in the slot. The pre-stress is influenced by the displacement of the fixture as well as the friction between the concrete and FRP sheets. Local stress concentration will easily occur and FRP sheet is easily to be destroyed. Standard pre-stress determined by FRP sheet cannot be measured and guaranteed [6-7].

Aiming at solving the above problems, a newly-developed pre-stressed FRP sheet tension fixture is introduced in this paper. The new type fixture tensions the FRP sheets without hurting the existing cross-section of the girder. Besides, it makes the measurement of pre-stress determined by FRP sheet more accurate and precise. Thus, it possesses broad application prospects and practical value in the field of pre-stressed FRP sheet reinforcing the beam.

## Design of the new-type pre-stressed FRP sheet tension fixture

The new-type tension fixture takes self-balancing system. To improve the rigidity of the fixture under tension stress and reduce loss of pre-stress caused by the deformation of the fixture, the

tension fixture is designed to consist of an overall welded steel framework. To satisfy the quantitative control requirement of pre-stress determined by FRP sheet, the friction between FRP sheets and the fixture will be reduced by pulley blocks and trolley system. At the same time, the tension of FRP sheet is controlled by the mechanical jackscrew; the strain gauge is installed at the bottom left of the fixture while the dynamometer is at the right side with one end fixed.

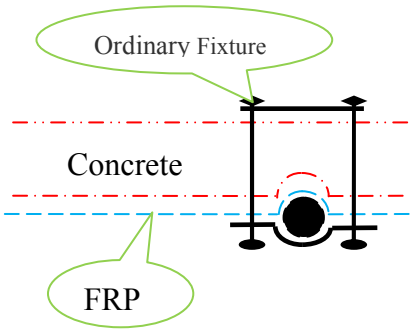


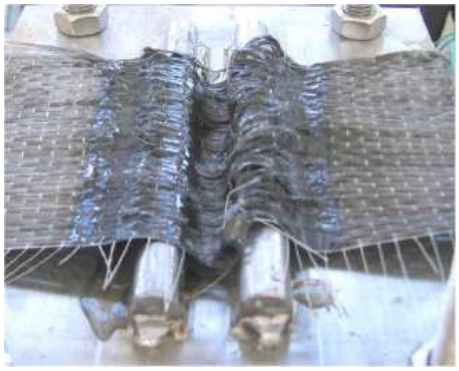

Fig.1 Ordinary Pre-stress FRP Fixture Fig.2 Ordinary Pre-stress FRP destroy

During the operation, put the pre-stressed FRP sheet onto the top of the tension fixture; the two ends of the FRP sheet, along the trolley, shall be fixed on both sides of the fixture. Turn on the jackscrew; the steel wire ropes are pushed by the jackscrew and the pulley will drive the left-side fixture to tension the FRP sheet. When the dynamometer on the right side reaches certain value, the strain gauge shall be reset. Then go uploading until there is a correspondence relation between the tension and deformation. Pay attention to the value shown on the dynamometer and make sure the accurate and precise of the pre-stress. The 3D model of the integrated design and the main design size indexes are shown in Fig.3. Length of the main girder: 2450(mm); width350 (mm); height 600(mm). The main beam is made up of 8#cjannel steel and is constructed through welding; the thickness of the soldering block is 15mm; the material of the welding assembly is 20# steel. The secondary beams and supports are connected with the main beam by M8 high-strength bolts. The supports on both sides of the fixtures are 45mm processed thick steel plates which are connected by bolts and truckles to make sure the maneuverability of the fixtures.

## Analysis on the deformation of the new-type tension fixture

The new-type fixture belongs to 3-dimensional high-order statically indeterminate tensioning system; to verify the feasibility of such fixtures in actual work, its finite element model has been developed with the help of ANASYS Workbench and UG 8.0 Software to analyze its stress state and deformation degree under design load. Deformation analysis on the fixture is achieved by finite element method:

Finite element analysis progress: First, by applying UG 8.0 Software, transform 2D design plan made with CAD to 3D design data archived in IGS files, then by the ANASYS Workbench Geometry model reads design data in up IGS files，and achieves the calculate by ANASYS Mechanical model.

Finite element analysis parameters: Element Type：8 nodes Solid 183; Typical Element Size: 200mm; Boundary conditions：Four groups of fixed fixture (the fixture applies self-balancing system; uploading can be carried out after fixing the fixtures on the ground under the beam). Load conditions: upload 100 KN stress symmetrically both in horizontal and vertical (maximum designed tension) on trolleys of both sides. The stress is assumed to be the reactive force by the FRP sheet which is most unfavorable to the fixtures.

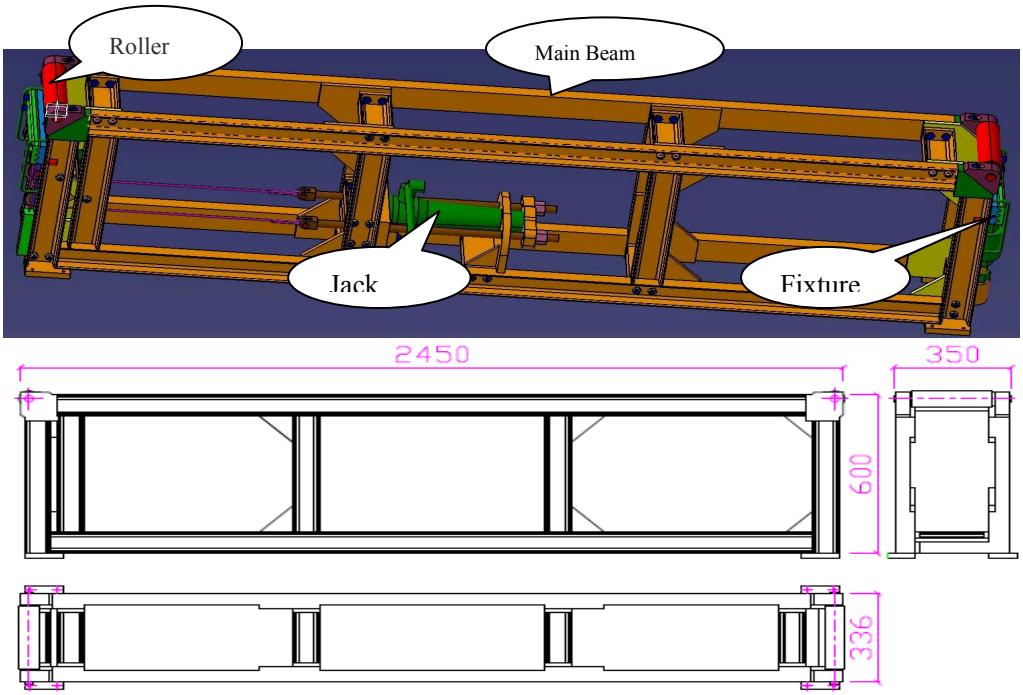


Fig.3 New Type Fixture Design Pictures Unit (mm)

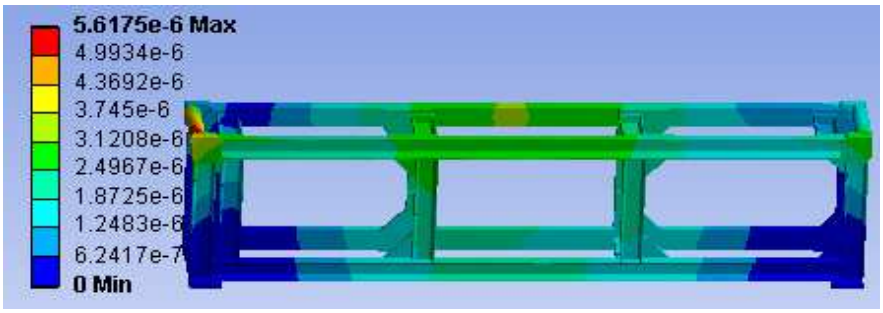


Fig.4 New Type Fixture Total Deformation

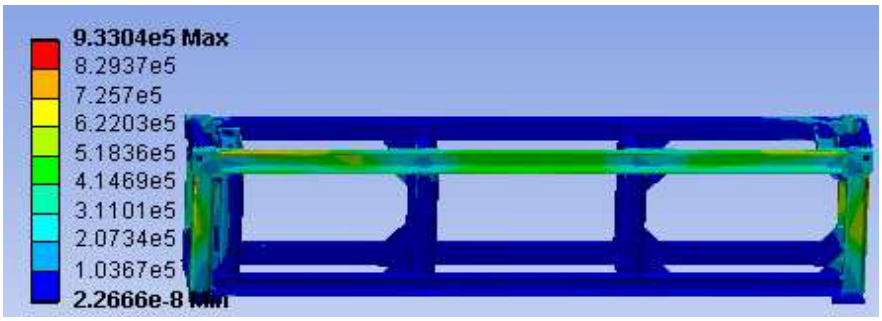


Fig.5 New Type Fixture Equivalent Stress

Finite element analysis results: The fixture total deformation is on the Fig.4, and the equivalent stress on the Fig.5. From Fig.4 we can see that deformation mainly occurs around trolleys of the fixtures, the total deformation is 0.5mm, the max strain is 5E-6; from Fig.5 we can infer that and the max stress is 0.83Mpa. The above data shows that under the design load, the new type tension fixture is in flexible working conditions. Loss of pre-stress caused by the deformation of the fixtures can be ignored in the whole tension system.

## Conclusion

Through statements and analysis in the thesis, the following conclusion can be drawn:

The new-type tension fixture is self-balancing so it can operate without counter-force facilities and more adaptable in practical work. At the same time, it possesses advantages such as easy handling and high adaptability. It also can be recycled to lower the cost of the engineering.

Through the dynamometer on the fixture, the value of pre-stress determined by FRP sheet can be accurately achieved, which provides technical guarantee for pre-stressed FRP sheet reinforcing the beam.

By reading the strain gauge at the end of the fixture, deformation degree of the fixture under various pre-stress can be achieved precisely.

By using the new-type tension fixture, there's no need to slot on the girder, so there will be no damage to the girder. Meanwhile, the pre-stress determined by the FRP will be regular and even without local stress concentration.

## References：

[1] Xiaoying Chen,Mingzheng Chen,Tangning Li.Shanxi Architecture, 2009, 35(8): p.62(In Chinese)

[2] Xiuli Du,Jianwei Zhang,Zongca Deng. Engineering Mechanics, 2007, 24(II): 62-74 (In Chinese)

[3] Shouping Shang,Hui Peng,Hua Tong,Donghui Wei,Linghong Zeng.Journal of Building Structures, 2003, 24(5): 24-30 (In Chinese)

[4] Shawulieti Baikaiyi,Lieping Ye,Yong-xin Yang,Jiangbo Zhang. Construction Technology, 2004, 33 (6): 23-24 (In Chinese)

[5] Jing Zhuo,Tangning Li,Shijian Xing,Mi Zhou. CHINA Civil Engineering journal, 2007, 40(1): 15-20 (In Chinese)

[6] Jing Zhuo,Tangning Li,Qingxue Zhang,Mi Zhou.Building Structure, 2006, 36(3): 22-24 (In Chinese)

[7] Xiaoying Chen,Tangning Li,Mingzheng Chen,Yin Huang.Engineering Mechanics, 2009, 26(6): 186-192 (In Chinese)

*Applied Mechanics and Materials Vols. 580-583 (2014) pp 2224-2227*
*© (2014) Trans Tech Publications, Switzerland*
*doi:10.4028/www.scientific.net/AMM.580-583.2224*

# Analysis on Impact of the Node Connection Pattern for Fastener-style Steel Pipe Formwork Support

li Liu[1, a] ,Bo Wang[2,b] , Juchao Wang [3,c] and Yanan Liu [4,d]

[1]School of Civil Engineering Shenyang Jianzhu University, Shenyang, China

[2]School of Civil Engineering Shenyang Jianzhu University, Shenyang, China

[3]School of Civil Engineering Shenyang Jianzhu University, Shenyang, China

[4] School of Civil Engineering Shenyang Jianzhu University, Shenyang, China

[a]liuli1219@sina.com, [b]miwbmang@163.com, [c]jiejiaowang123@163.com,[d]theral@163.com

**Keywords:** formwork support, node connection, ANSYS, semi-rigid joint

**Abstract.** Fastener-style steel pipe formwork support is currently the most widely used form of template support during the domestic construction. At present, there are many models for the node connection pattern. This paper used ANSYS to build different connection pattern models of formwork support and draws the conclusion that the connection pattern of semi-rigid nodes is the most conform to the actual working conditions. This provide the basis for the theoretical research on fastener-style steel pipe formwork support.

## Introduction

Since fastener-style steel pipe formwork support belongs to the time-varying structure and is often recycled. However, academe has biggish difference between rigid joint [1] and hinged join for right-angle fastener node. There is a large difference between the calculation results of two ways.

A series of finite element model on perfectly rigid hinged and semi-rigid joint were established apart to analysis on impact of the node connection pattern of formwork support to its stable bearing capacity [2-5]. By comparing the results of the stable bearing capacity under different conditions with those known on the actual working conditions, node connections pattern that best meet the actual working conditions are obtained. Thus, reference points are provided for the theoretical research on fastener-style steel pipe formwork support.

## Calculation Model

Referring to the test, five groups of calculation model were set up. Steel pipe's outer diameter was 0.048 m, wall thickness was 0.003 m, elastic modulus was 2.06 e11, Poisson's ratio is 0.25. The models were shown in table 1. Test 1 set a bracing. Test 2 set two bracing. The others didn't set bracing.

**Table1** Model parameter

| parameter / Number | longitudinal spacing (mm) | departure spacing (mm) | drawing pace (mm) |
|---|---|---|---|
| 1 | 1200 | 1200 | 1800 |
| 2 | 1200 | 1200 | 1800 |
| 3 | 1200 | 1200 | 1800 |
| 4 | 1200 | 1200 | 900 |
| 5 | 900 | 900 | 900 |

## Establishing Finite Element Model

ANSYS was used to build the calculating model. Beam4 unit was choose for vertical tube and horizontal tube[6]. Link8 element was used to simulate the vertical bracing and horizontal bracing [7]. Combin14 element was choosen to simulate joint [8]. The finite element models were shown in fig 1.

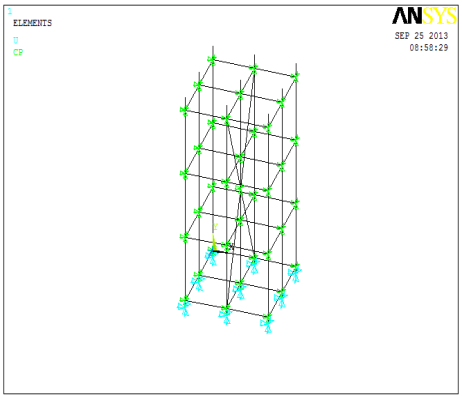


Test 1 Finite element model

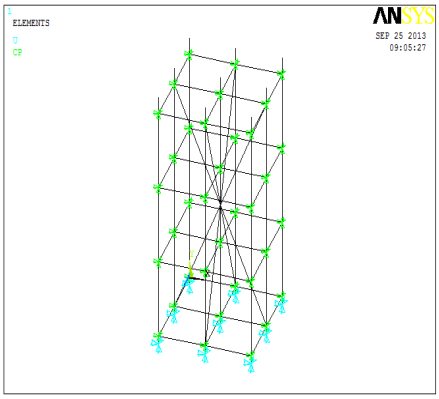


Test 2 Finite element model

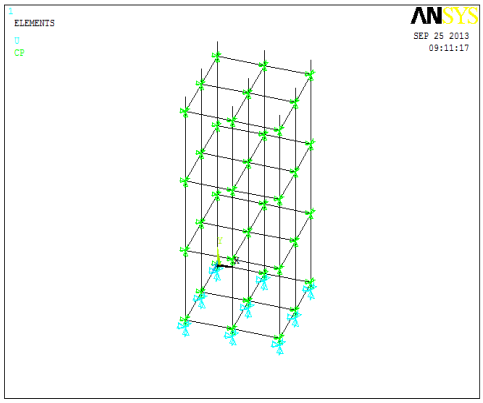


Test 3 Finite element model

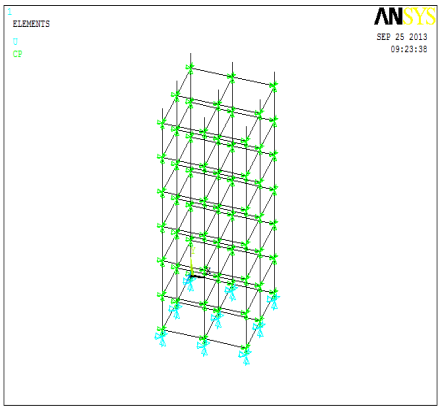


Test 4 Finite element model

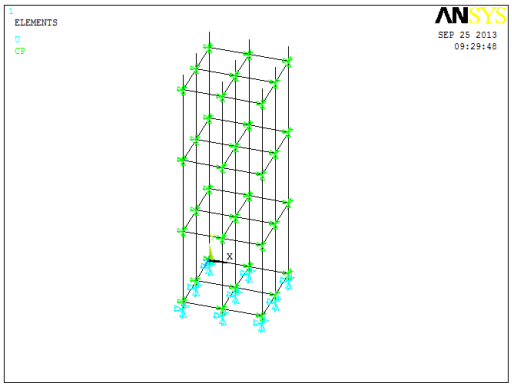


Test 5 Finite element model

**Fig. 1** The finite element models

## Finite Element Analysis

With the resort on ANSYS we have performed the eigenvalue buckling analysis, compare ultimate bearing capacity under the condition of various model types with the experimental values of stability bearing capacity. Those types are the models considering perfectly rigid and hinged joint, semi-rigid joint that initial stiffness is10000, 20000, 50000, 80000and1000000. Analyse the various factors that affect the stability of formwork support and find the regularity.

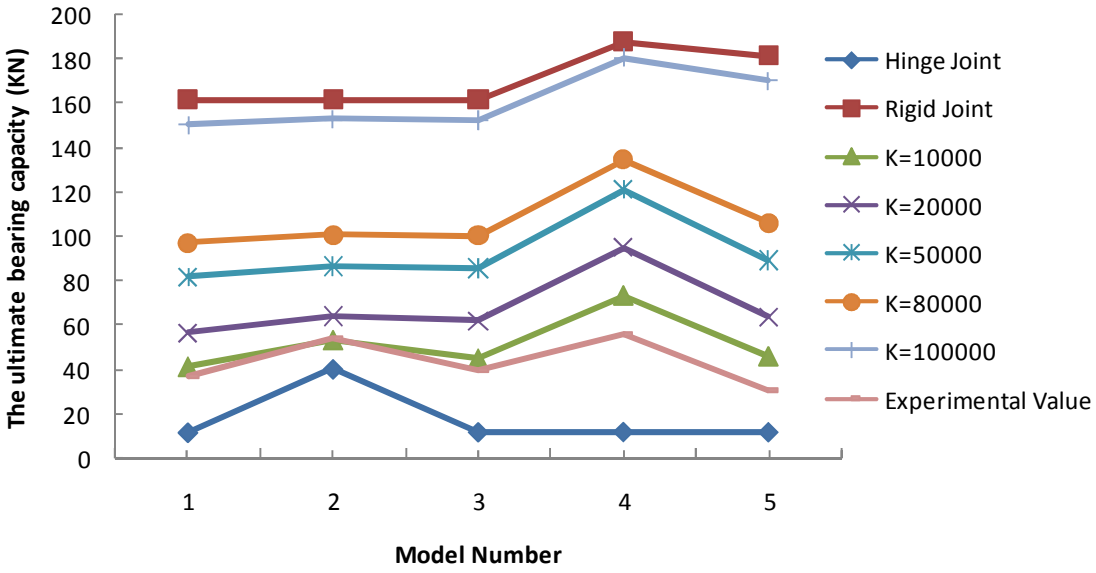


**Fig. 2** The ultimate capacity of formwork support in all simulation conditions

It can be seen from fig 2 that the bearing capacity of the vertical tube do not reach the theoretical calculation value of material strength in all tests. The destruction form of vertical tube is buckling failure.

The experimental values of stability bearing capacity are simply located quite far away from the ultimate bearing capacity of perfectly rigid and hinged model. But, the experimental values have accordance well with the ultimate bearing capacity of the model. Initial stiffness is 10000 in the model. This shows that the node at the intersection of horizontal tube and the vertical tube is close to the semi-rigid join that transfers part of the bending moment.

With the increase of initial stiffness, ultimate bearing capacity of the model is gradually increasing. The size of the initial stiffness has an impact on ultimate bearing capacity with the semi-rigid nodes in mind. The bigger the initial stiffness is, the greater ultimate bearing capacity is. Fastener tightening moment is the direct influencing factor for initial stiffness. Therefore, in theory, the greater fastener tightening moment is, the better whole stable bearing capacity is and the greater the ultimate bearing capacity is. This shows that the tightening extent of fastener has a big influence on whole stable bearing capacity.

## Conclusions

By simulating the model under three kinds of situations, perfectly rigid, hinged and semi-rigid joint, it can be concluded that the results of model under the semi-rigid join have accordance well with the experimental results.

The tightening extent of fastener has a big influence on whole stable bearing capacity for formwork support. With the increase of fastener initial stiffness, ultimate bearing capacity of the model is dramatically increasing. To ensure fastener torque value is the key to guarantee the structure stiffness of formwork support. Therefore, the fastener tightening moment should be strictly inspected to ensure the safety of the formwork support during the construction.

**References**

[1] Jianmin Liu, Huimin Li: Construction Technology, 2005, 34(3).

[2] Kaishan Hu: *Study·on Mechanical Capability of Modular Tubular Falsework Joined by Couplers in Chinese* [D], Zhejiang University, 2007.

[3] Junjie Yang, et al: Architecture Technology, 2006, 37(8): 613-615.

[4] Huazhen Zhang: *Semi-rigid Joint and Global Stability Capacity Research of High-formwork-supports with Couplers in Chinese*, [D], Xi'an University of Architecture and Technology,2009.

[5] Xin Nie, et al: Industrial Construction, 2007, 37(11): 99-103.

[6] Nan Xie, et al: Engineering Mechanics, 2012, 29: 164-169.

[7] Caixia Chen, et al: Journal of Hunan Institute of Engineering (Natural Science Edition), 2006, 3: 024.

[8] Zhihua Chen, et al: Engineering Mechanics, 2010, 11: 017.

*Applied Mechanics and Materials Vols. 580-583 (2014) pp 2228-2231*
*© (2014) Trans Tech Publications, Switzerland*
*doi:10.4028/www.scientific.net/AMM.580-583.2228*

# Analysis on Lateral Deformation of High-formwork in Different Column's Spacing of Bridging

li Liu[1, a] , Bo Wang[2,b] , Yanan Liu[3,c] and Juchao Wang[4,d]

[1]School of Civil Engineering Shenyang Jianzhu University, Shenyang, China

[2]School of Civil Engineering Shenyang Jianzhu University, Shenyang, China

[3]School of Civil Engineering Shenyang Jianzhu University, Shenyang, China

[4] School of Civil Engineering Shenyang Jianzhu University, Shenyang, China

[a]liuli1219@sina.com, [b]miwbmang@163.com, [c]theral@163.com,[d]jiejiaowang123@163.com

**Keywords:** ABAQUS, high-formwork, bridging, deformation

**Abstract.** Setting bracing is conducive to stabilize formwork support in high-formwork system. ABAQUS was used to build the calculating model of high-formwork system to simulate and analyse lateral deformation of high-formwork in different column's spacing of bridging. The results show, increasing column's spacing of bridging can add the whole lateral displacement of high-formwork, but, it is not obvious. Increasing appropriately column's spacing can save material during construction.

## Introduction

Along with the improving requirement of high and tall across the space on the industrial and civil building, the high-formwork is used more and more frequent, the usage requirements are also more and more high during construction[1].Since high-form belongs to the time-varying structure[2-4], it is easy to cause global or local buckling, it may cause the collapse of the whole high-formwork system when the situation becomes serious, and thus many accidents happen[5-6]. Therefore, whole stability of the high-formwork system plays an important role in construction safety.

It is urgently needed that researching on high-formwork to provide favorable data of calculation theory of high-formwork system, facing hidden danger easily caused by high-formwork design and control during construction.

In this paper, ABAQUS was used to build the model of high-formwork system to simulate lateral deformation of high-formwork in different column's spacing of bridging. Based on the analysis of column's spacing of the formwork support erected by continuous vertical bridging mentioned in the code[7],and this provide the theoretical basis for the design of construction scheme and the revision of the Safety Technical Code for Building Construction Template JGJ162—2008.

## Calculation Model

According to the code requirements, high-formwork calculation models were designed: Spacing of vertical tube was 1.2m, the pace was1.8m, the distance between the bottom transom and the ground was 0.2m, the length of the top horizontal tube extending from top was 100mm, the height of the formwork support was 14.4m, the area of it was 24m×24m. Continuous vertical bridging were used around the formwork support and horizontal bridging were set at the top, middle and bottom of the formwork support. Analyze separately the whole lateral displacement of high-formwork in the case that column's spacing of bridging was 8m,10m,12m,14m. The type of tube was Q235, its specification was Φ48×3.5mm. The specific parameters were shown in table 1 and 2.

**Table1** Pipe section properties

| d[mm] | t[mm] | A[$cm^2$] | I[$cm^4$] | W[$cm^3$] | i[cm] |
|---|---|---|---|---|---|
| 48 | 3.5 | 4.89 | 12.19 | 5.08 | 1.58 |

**Table2** Pipe material parameters

| EX[pa] | μ | f[pa] |
|---|---|---|
| $2.06\times10^{11}$ | 0.3 | $2.05\times10^{8}$ |

## The Finite Element Model

ABAQUS was used to build the calculating model of high-formwork system. The calculating element was linear beam element [8-9]. The node at the intersection of horizontal tube and the vertical tube was processed to rigid connection [10]. The high-formwork finite element model was shown in fig 1.

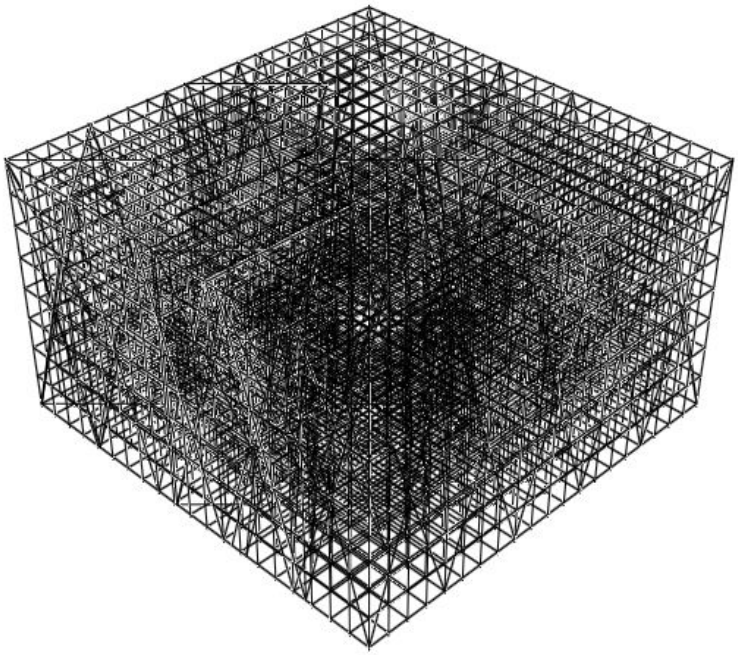

**Fig.1** The finite element model of high-formwork system

Applying concentrated force at the node of the upper of the formwork support by the creat load command in the load module and adding the boundary condition at the bottom of the formwork support by the creat boundary condition command to make that U1,U2,U3,UR1,UR2andUR3 were equal to zero, namely, the bottom was consolidated.

## Finite Element Analysis

This paper got deformation nephogram of the model, using post processing of ABAQUS. The column's spacing of bridging was 10m in the model. The deformation nephogram was shown in fig 2. The variation of the column's spacing of bridging and the whole displacement of high-formwork system was shown in fig 3.

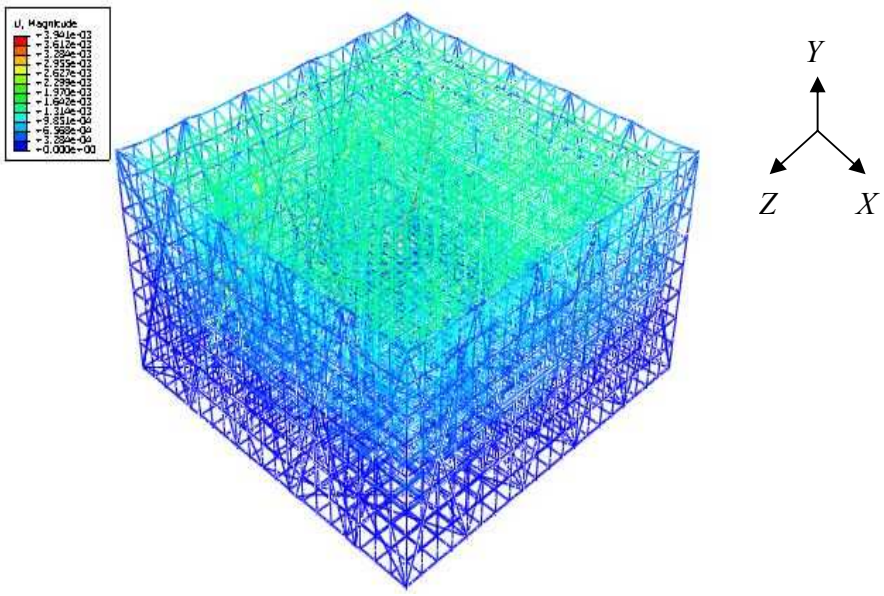


**Fig.2** Deformation nephogram of 10m model

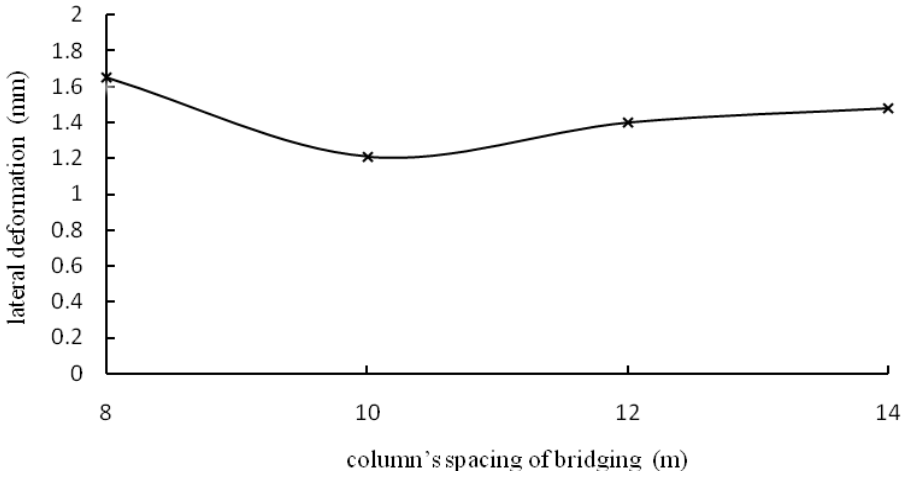


**Fig.3** Variation of the lateral deformation t with the change of column's spacing of bracing

It can be seen from fig 2 that the upper lateral displacement of high formwork system is larger than the lower lateral displacement under symmetrical loading. Lateral displacement near the bottom of the fixed end is minimum.

As can be seen from fig 3, the values of lateral displacement of high formwork system is 1.21mm when the column's spacing of bridging is 10m, which is required for the code. With the increase of the column's spacing of bridging, the lateral displacement of frame body is gradually increasing. When the distance increased from 10m to 14m is increased by 25%, the lateral displacement is increased from 1.21mm to 1.48mm. It is increased by 22%.

The difference between the two lateral displacement is very small. The one is 10m required for the code, the other one results from appropriate increase of the column's spacing of bridging. Therefore, column's spacing of bridging can be properly relaxed.

In addition, the change of the internal force of horizontal bracing is regularity. The internal force of horizontal bracing at the top is maximum. The internal force of horizontal bracing is gradually reduced with the height of high-formwork system decreasing. The internal force at the bottom is minimum. This is because mechanical behavior of vertical tube at the top are bigger, internal force of vertical tube is partly shared by horizontal tube, horizontal bridging has restraining effect on it, when the high-formwork system forces.

## Conclusions

The upper lateral displacement of high formwork system is larger than the lower lateral displacement under symmetrical loading.

Increasing the column's spacing of bridging have little impact on lateral displacement of high-formwork system. Based on the practice, column's spacing of bridging can be properly relaxed so as to save material during construction.

## References

[1] Jianping Qiu: *Research and Application of Fasener-type Steel Tubular high Formwork Support in Chinese,*[D], Chongqing University(2008).

[2] Changming Hu: *Studies on Experiment and Theory of Steel Construction Connected with Fasteners in Chinese,* [D],Xi'an University of Architecture and Technology(2008)

[3] Buyin She, Zhengxing Guo: Industrial Construction 2011, 41(1): 1-5.

[4] Wei Du,Yugang Qi: Yangtze River, 2009 (12): 8-8.

[5] Yong Du: Accident *Analysis and Safety Countermeasures on Tall Formwork Support in Chinese,* [D], Inner Mongolia University of Science and Technology(2012).

[6] Rui Qiu, Li Qiu, Yanzeng Wu: Architecture and equipment 2013, 7(1): 58-60.

[7] JGJ162-2008 Technical code for safety of forms in construction, [S].

[8] Jinchang Wang, Yekai Chen: *Application of ABAQUS in Civil Engineering,* [M], Zhengjiang University Pass, 2006.

[9] Guilian Yi, Yunkang Sui and Jiazheng: Neural artificial neural networks,2004(4) 264-276.

[10] Yuan Mei,Changming Hu,Zhengyong Zhou: Journal of Xi'an University Of Architecture And Technology, 2009,40(2):42-46.

*Applied Mechanics and Materials Vols. 580-583 (2014) pp 2232-2234*
*© (2014) Trans Tech Publications, Switzerland*
*doi:10.4028/www.scientific.net/AMM.580-583.2232*

# Influence of Bridging Arrangement Location on the Mechanical Characteristics of the High-formwork Support System

Li Liu[1, a]; Yanan Liu[2,b] , Bo Wang[3,c] and Juchao Wang[4,d]

[1]School of Civil Engineering Shenyang Jianzhu University, Shenyang, China

[2]School of Civil Engineering Shenyang Jianzhu University, Shenyang, China

[3]School of Civil Engineering Shenyang Jianzhu University, Shenyang, China

[4] School of Civil Engineering Shenyang Jianzhu University, Shenyang, China

[a]liuli1219@sina.com, [b]theral@163.com, [c]miwbmang@163.com, [d]jiejiaowang123@163.com

**Key words**: high-formwork, bridging, lateral migration, arrangement location

**Abstrac**t. Bridging play a important role in guarantee the stability of the high-formwork support system as a whole, its arrangement location will affect the force of the frame body. This paper used the finite element analysis method to compare the bridging arrangement location under the beam with the bridging under the board which was arranged according to certain modules. the results show, the arrangement spacing of the bridging under the beam is greater than the bridging under the board, but its frame body lateral migration is smaller, sharing part of the axial force of beam bottom rod at the same time, that means the bridging under the beam is more beneficial for the stability of high-formwork support system.

## Introduction

With the increasing demand of industrial and civil construction on height-span space, tall template support system requirements are increasingly high. Tall template system is different from the common template support system, during the construction process, the frame body is more prone to total or partial structural instability ,even cause the collapse of the entire template system when the situation becomes serious, form a vicious accident loss. Thus, the overall stability of the tall template becomes an important factor related to construction safety. In recent years, domestic and foreign scholars [1-3] studied the template support system, but there are many factors affecting the overall stability of tall template, the stress and deformation of the support frame body is influenced by many factors during the process of construction, it is comparatively complicated process. this article we compared the bridging arrangement under the beam with the bridging under the board which was arranged according to certain modules by the finite element analysis method, the results show, the bridging arrangement spacing under the beam is greater than the board, but its frame body lateral migration is smaller, The conclusion provides theoretical basis for the current specification revision and the construction scheme design.

## Calculation Model

According to the actual conditions, design calculation model of high-formwork body, thickness of the plating was 120mm, space between upright tubes was 1.2m, horizontal bar spacing step length was 1.8m, the template erection height was 16.2m,erection area was 19.9m×4.4m,the size of each beam were: 1 # 1.0m×1.8m; 2 # 0.6m×1.2m; 3 # 0.24m×0.72m, the distance between the bottom horizontal tube and the ground was 200mm, the height of the top horizontal tube extending to the pole tip was 100mm.Model of Planar graphs were shown in Figure 1.

Based on the calculation model, established two different bridging arrangement model, respectively: (1)At the bottom of each 1#,2#,3#beam arranged a vertical bridging;(2)Along the direction of the frame body parallel to the beam arranged a vertical bridging under the board every

3.6m. Continuous vertical bridging were arranged around the formwork support according to the requirement of standard.

High-formwork support system model was built by ABAQUS[4-7] finite element analysis software, the calculating unit of the calculation model select linear beam element, the scale of the beam element was greater in a certain direction significantly than the scale of the other direction, And choose the bearing longitudinal based structure for simulation. Selection of beam unit based on the following assumptions: structural deformation can be determined by all along the beam length direction position function ,when define a beam element, the different between the solid element and shell element is that the solid element should firstly establish cross-sectional size and geometry shape, define the beam section characteristics and material parameters. The node at the intersection of horizontal tube and the vertical tube was processed to ideal rigid connection [8].

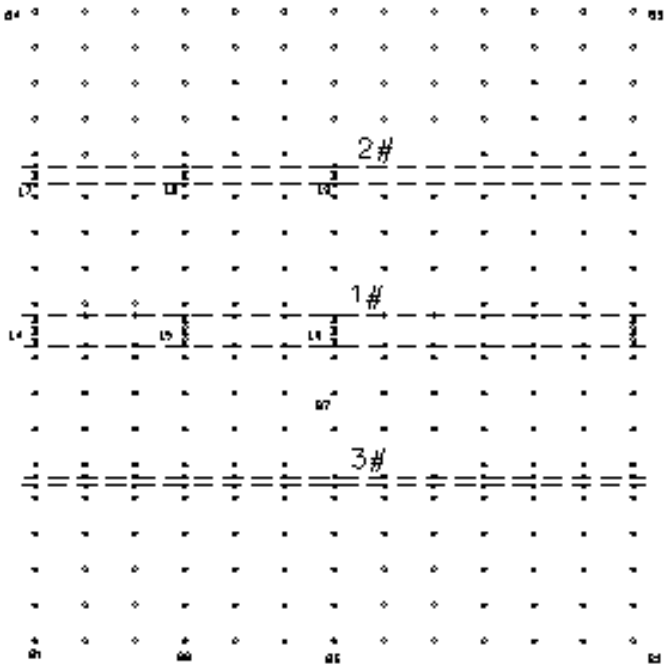


**Fig.1** The plan of the model

**Finite Element Analysis**

**The analysis of bridging arrangement location on the lateral migration of high-formwork support system**. By applying the same symmetry load on the two different arranged bridging position of high-formwork support system, the results indicate: when the vertical continuous bridging were arranged under the beam, the maximum displacement of high formwork support system is 1.01mm,the overall lateral migration of the frame decreases in turn from top to bottom, near the bottom of the fixed end displacement is minimum, its value is almost zero. Its lateral migration value from top to bottom followed by 1.01mm, 0.93mm, 0.82mm, 0.71mm, 0.62mm, 0.57mm, 0.44mm, 0.36mm, 0.19mm, 0.09mm ; when the bridging are arranged under the board, the maximum overall displacement of high formwork support system was 1.27mm,with reducing of the height of the bracket ,its lateral migration value were 1.87mm,1.52mm,1.38mm,1.24mm,0.97mm, 0.81mm,0.74mm,0.67mm,0.49mm,0.31mm,0.23mm,0.17mm.

The bridging arrangement spacing under the board was smaller than the beam, but the frame body lateral migration of beam is 0.86mm shorter than the bridging arrangement under the board, indicating that the bridging under the beam is more beneficial for the stability of high-formwork support system. The bridging spacing under the beam was 4.4m, it's spacing was smaller than the

bridging spacing under the board, but its lateral migration of the frame body is still smaller than the board, the whole stability is good.

**The analysis of bridging arrangement location on the beam bottom rod internal forces.** Discuss separately the influence of the two bringing arrangement location on the axial force of 1#-3# the beam, axial force of beam under different bridging arrangement location are shown in table 1

**Table 1** Axial force of beam under different bridging location

| Pole-axis force [KN] / location | 1# | 2# | 3# |
|---|---|---|---|
| Under the beam | 6.21 | 1.36 | 0.87 |
| Under the board | 8.42 | 3.03 | 2.49 |

Thus, the axial force of the beam decreased when the bridging under the beam. Take 1 # beam for example, the axial force of the beam is 2.21kN smaller than the bridging under the board . It is due to axial force of the opposite pole of bridging under the beam plays a role of constraints, sharing part of the axial force of the pole, and the beam bottom belong to high risk section of the high-formwork supports system at the same time, therefore the bridging under the beam is beneficial to relieving dangerous cross section.

## Conclusions

To sum up, Bridging arrangement location have a considerable influence on the frame body force, the arrangement spacing of the bridging under the beam is greater than the bridging under the board, but its frame body lateral migration is smaller, while sharing part of the axial force of beam bottom rod, the bridging arrangement under the beam is conducive to the overall stability of high-formwork support system, is advantageous to the construction safety, and can save materials, has a good economic characteristics.

## References

[1] Weibin, Li, Tong Liu, Zhengxing Guo:*Research on the safety of Tube-and-coupler Formwork Support and Construction Suggestions,*[J].Beijing: architectural technology, 2004.

[2] Yongtian Cai:*Scaffolding and Formwork Support Frame Collapse Accident Analysis,*[M].Beijing: China's new technology and new products, 2010:1-3.

[3] Chan,S.L,Zhou,Z,Chen,W.F,Peng,J.L,and. Pan,A.D,*Stability Analysis of Semirigid Steel Scaffolding, Engineering Structures*, 17(8),568-574

[4] Jingchang Wang, Yekai Chen: *Application of ABAQUS in Civil Engineering*, Zhengjiang University Pass, 2006.

[5] Guilian Yi,Yunkang Sui and Jiazheng Du;*Application of Python-based ABAQUS Preprocess and Post Process Technique in Analysis of Gearbox Vibration and Noise Reduction,*[J]. Neural artificial neural networks, 2004(4) 264-276.

[6] Na Wang:*Numerical Analysis and Construction Monitoring Technology Research of Concrete Structure High Formwork Supporting System,*[D]. Anhui: Anhui Jianzhu University, 2013:7-8.

[7] Yiping Shi,Yurong Zhou:*The ABAQUS Inite Element Analysis Examples,*[M]. Beijing: mechanical industry press, 2006.

[8] Yuan Mei,Changming Hu,Zhengyong Zhou:*Statistical Analysis of Loads of Supporting Structure for Tall and Large Falsework During Construction,*[J].Journal of Xi'an University of Architecture and Technology,2009,40(2):42-46.

*Applied Mechanics and Materials Vols. 580-583 (2014) pp 2235-2238*
*© (2014) Trans Tech Publications, Switzerland*
*doi:10.4028/www.scientific.net/AMM.580-583.2235*

# Research on Influence of Concrete Pouring Sequence on Stability of High-Formwork Support System

li Liu[1, a] , Juchao Wang[2,b], Bo Wang[3,c] , and Yanan Liu[4,d]

[1]School of Civil Engineering Shenyang Jianzhu University, Shenyang, China

[2]School of Civil Engineering Shenyang Jianzhu University, Shenyang, China

[3]School of Civil Engineering Shenyang Jianzhu University, Shenyang, China

[4] School of Civil Engineering Shenyang Jianzhu University, Shenyang, China

[a]liuli1219@sina.com, [b]jieqiaowang123@163.com, [c]miwbmang@163.com, [d]theral@163.com

**Keywords:** High-formwork, finite element analysis, concrete pouring sequence, stability

**Abstract.** ANSYS finite element analysis software is used to simulate the changes of maximum lateral displacement of the high-formwork support system in different sequences of pouring concrete. In the condition of loading which was applied from one side to the other side, the maximum lateral displacement of the frame had a sudden increase in each loading process. In the condition of loading which was applied symmetrically, the maximum lateral displacement of the high-formwork steadily rising nearly straight with the load applied. So the symmetrical pouring concrete ways is better for the whole stability of the high-formwork.

## Introduction

With the development of modern cities, there appeared more and more large engineering, high formwork support system was applied more widely. In recent years, high formwork collapse accidents had occurred, some of them had led to serious consequences and caused irreparable damage to the country and people's life and property [1-3]. Therefore, the overall stability of formwork support is one of important factors which must be considered in the construction. There are many factors that affect the stability of formwork support. The study found that the sequence of concrete pouring was usually ignored in the process of construction. In order to make the operation convenient, they often poured concrete from one side to the other side and caused serious accidents in the concrete pouring stage [4]. This paper got a conclusion after studied the concrete pouring sequence through the finite element analysis. It is that pouring sequence of concrete can't be ignored and pouring symmetrical can make high-formwork more stability. The conclusion provide a reliable basis for the revision of high-formwork support system design and the current code, provide the reference for the construction plan, reduce incidence of collapse accident, to ensure high-formwork support system use safely.

## Calculation Model

The height of high-formwork erection was 16.2m, the area was 19.9 x 14.4 m, the spacing of vertical pole was 1.2m, the pace of horizontal pole was 1.8m. The section area of the middle beam was 1.0m× 1.8m.The remaining two beam in the left and right sides were 0.6m × 1.2m and 0.24m × 0.72m. The type of the steel pipe was Q235, its specification was Φ48×3.5mm.

The high-formwork was arranged around the continuous vertical bridging and the bottom of beam was also set vertical bridging. The sweeping rod, the top rod was arranged horizontal bridging, The middle part of the high-formwork were respectively arranged two bridging. Regardless of wind load, seismic load and the dynamic load in the process of calculation.

## High-Formwork Finite Element Simulation

**Element Selection and Node Processing.** In this paper, ANSYS was used to simulate the model of high-formwork system. BEAM4 was used to simulate the vertical pole and horizontal pole. The BEAM4 was uniaxial stress element which could bear pulling, pressing, bending moment, torque. The element had six degrees of freedom for each node: X, Y, Z linear displacement in three directions and angular displacement rotate around the X, Y, Z three axis. And it could be used to calculate the stress hardening and large deformation. The Link8 was used to simulate the vertical bridging, horizontal bridging. To simulate "semi-rigid" connection through combin14, it was spring damper element and can be applied to simulate one-dimensional, two-dimensional or three-dimensional elastic damping effect in longitudinal or torsional.BEAM4 was used to simulate the the vertical pole and horizontal pole. BEAM8 and combin14 were used to simulate bridging and the connection of the fastener node [5-7]. Establishing "semi-rigid" model whose initial stiffness was K=50000N · m/rad to compare.

The external diameter of the steel pipe was 48mm, the wall thickness was 3.0mm, the sectional area was 4.24cm$^2$,the Elastic Modulus was $2.06\times10^{11}$pa, the Poisson's ratio was 0.25, the yield strength was $2.05 \times 10^8$pa.The finite element model of high-formwork was shown in fig 1.

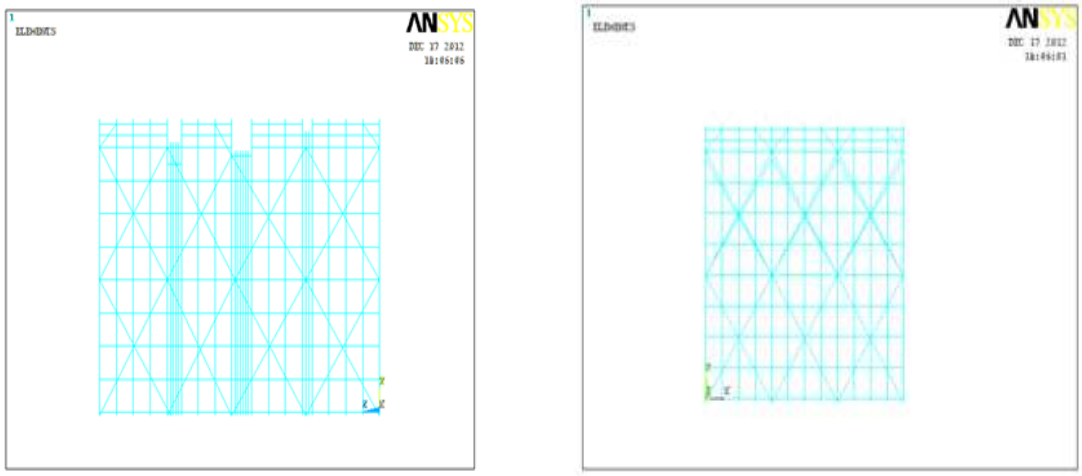

The Y-Z elevation drawing The X-Y elevation drawing

Fig. 1 The finite element model of high-formwork

**Loading Scheme.** In the calculation model, beam loaded seven times and plate loaded three times, to calculate the load value of each beam and plate in each loading process, to assign the load value to each vertical pole. To simulate concrete pouring through different loading sequence, the load was applied on the vertical pole which under beam and plate. There were two loading sequence in each loading process, loading from one side to the other side and from middle to both sides,comparing the stability of High-formwork Support System in different loading sequence.

**Influence of Concrete Pouring Sequence on the Stability of the Frame.** Lateral changes in symmetrical loading process were shown in fig 2. Lateral changes in asymmetrically loading process were shown in fig 3.

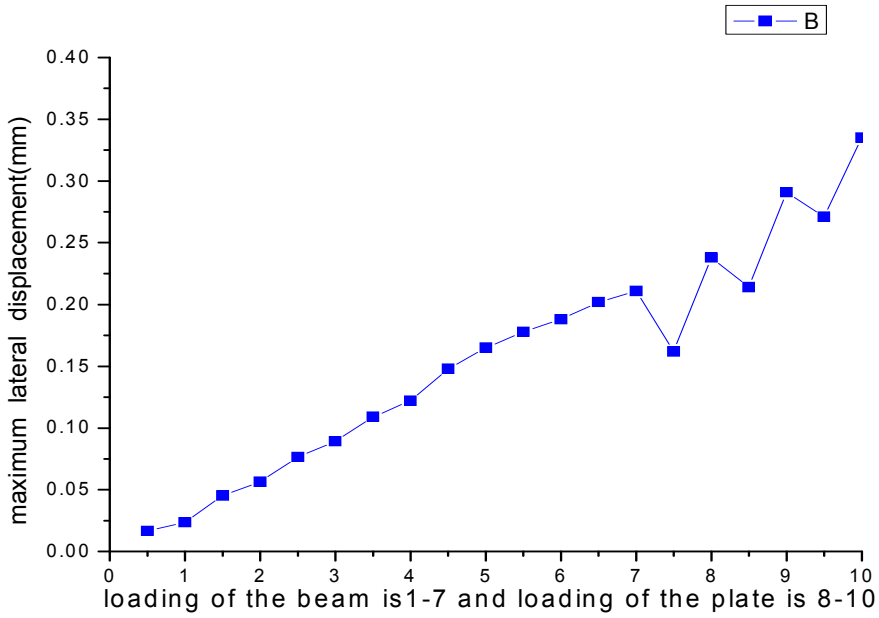


Fig.2 Middle to both sides maximum lateral changes in loading process

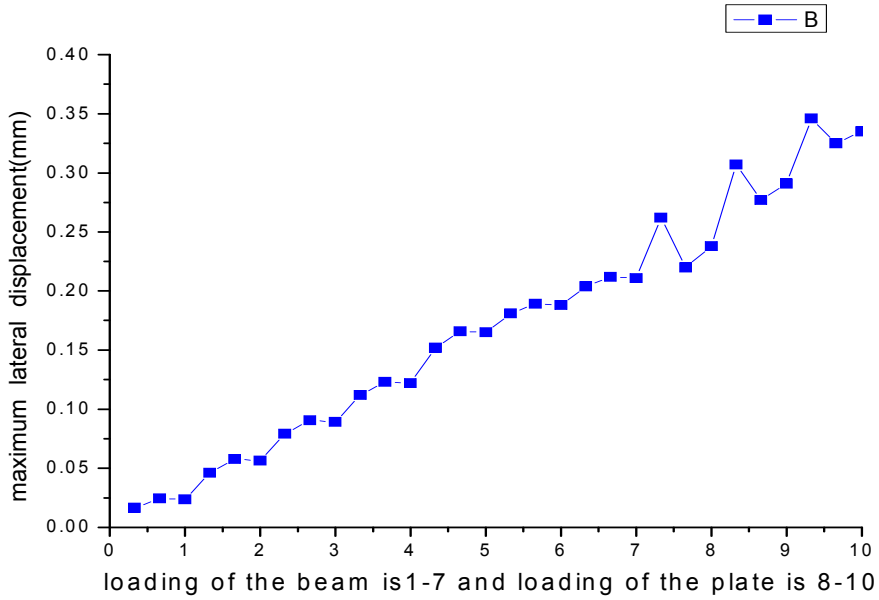


Fig. 3 One side to the other maximum lateral changes in loading process

It can be seen from fig 2and fig3, the maximum lateral displacement of the high-formwork steadily rising nearly straight with the load applied from the middle to both sides. when loaded on plate, the maximum lateral displacement had a sudden increase in the loading process, the reason is that the lateral displacement was produced by the load which applied on the plate offset some of the lateral displacement was produced by the load which applied on the beam. In the condition of loading which was applied from one side to the other side, the maximum lateral displacement of the high-formwork had a sudden increase in each loading process when applied on the beam. This was due to more force was distributed on one side of the beam,lead to the lateral displacement was too large. Loading on plate, due to the force also tilted to one side, the maximum lateral displacement increased. The sequence of pouring concrete from the middle to the sides should be adopted, so that we can avoid the lateral deformation of high-formwork is too large in the concrete pouring stage.

## Conclusions

To sum up, in the process of High-formwork Support System construction, if the way of pouring concrete from one side to the other side of the beam was adopted, the lateral displacement of the high-formwork would have a sudden increase in the concrete pouring stage, Thus the overall stability of high-formwork would be impacted and the probability of malignant accident would be increase. However, if the way of symmetrical pouring concrete was adopted, lateral displacement would rise more smoothly, the overall structure would more stable. Therefore, In order to reduce templates collapse accident, it is appropriate to use the way of symmetrical pouring concrete.

## References

[1] Jian Zhang, Liang Cai, Jianwei Miao: Prototype Experimental Research of Global Stability of High-Formwork-Support System in Chinese, Journal of Shenyang Jianzhu University(Social Science), 2011: 35-38.

[2] Zhihua Chen, Zhengran Lu, Xiaodun Wang, Qun Liu: Research on the Bearing Capacity of Steel Tubular Formwork Support with Coupler Without X-bracing Based on The Partially-Sway Single Post Stability Theory in Chinese [J], Engineering Mechanics 2010,27(11):99-105.

[3] Jian Zhang, Jianwei Miao, Simulation Research of Stability of High-Formwork Support System in Chinese [D], Engineering Mechanics, 2012: 66-70.

[4] Junjie Yang: Relation Between Concrete Placing Route and Formwork Supporting System Response in Chinese [J]. Construction Technology, 2006(7): 205-212

[5] Jianguo Tan: Using ANSYS6.0 for Finite Element Analysis in Chinese [M] , Peking University Press, 2002: 211-213

[6] Haifeng Xhao, Di Jiang, Using ANSYS8.0 for Analysis of Engineering Structure Instance in Chinese [M], China Railway Publishing House, 2004: 90-93.

[7] Xinmin Wang, Numerical Analysis of Engineering Structure Based on ANSYS [M], china communication press,2007: 21-25.

*Applied Mechanics and Materials Vols. 580-583 (2014) pp 2239-2243*
*© (2014) Trans Tech Publications, Switzerland*
*doi:10.4028/www.scientific.net/AMM.580-583.2239*

# The Integration of New Technology Research on Composite Inorganic Fiber Acoustic Insulation Spray in Engineering Construction

Junyi Shao [1, a], Dong Wang [2, b]

[1]Qingdao Technological University, China

[2]Qingdao Technological University, China

[a]qdlgdx@163.com, [b]15589808134@163.com

**Keywords:** Composite inorganic fibers; Hybrid nozzle; Sector coverage; Multiple mixed nozzle; High-strength interfacial agent;

**Abstract.** Composite inorganic fiber spray technology was based on high-strength interfacial agent, then sprayed an appropriate mixed proportion of ultrafine diameter (D <4μm) composite inorganic fibers, adhesives, cement and other raw materials through a dedicated spray equipment on the building roof (ceiling)or flank, which formed a homogeneous, porous, durable and eco-friendly cover layer. The key technology is combined composite inorganic fiber sprays' adhesive, mixing, porous, insulation and acoustic fireproof mechanism with three key technology working principles " high-strength interfacial agent sector coverage ", " composite inorganic fibers + adhesive multiple mixed spray " and " continuous overall seamless fireproof insulating layer ", to achieve integrate engineering effects of insulation, fastness, energy-efficient, sound-absorbing and homogeneous coverage. The new technology solves acoustic insulation problems of public buildings with fireproof requirements as: underground garage ceiling, elevator shafts and fire passage, etc.

## Introduction

Composite inorganic fiber insulation, fireproof and sound absorption spray is a new construction technology. Raw materials utilized ultrafine glass wool or rock wool(D <4μm) and sprayed into building roof (ceiling) or sidewalls with adhesives and cements through a dedicated spray equipment, which could achieve integrate effect of fireproof, insulation , sound absorption and waterproof. Currently, composite inorganic fiber spray can be applied to various types of buildings and public buildings sound-absorbing, acoustic ceiling and curtain wall insulation works, especially for the underground garage ceiling, elevator shafts, fire passage [1]. But there existed some problems in the construction process:

1) The selection of spray gun is unreasonable and the spraying is too concentrated. The situation will lead to non-uniform spray interface and waste fiber materials in the construction process.

2) All kinds of raw materials are not fully mixed through the spray gun. The condition leads to spray on the surface of uneven thickness, which affects the use function.

3) Interfacial agent adhesive is ineffective and spraying method is unreasonable. This condition causes the phenomenon of inorganic fiber shedding.

## Features of composite inorganic fiber

1) High-quality: the ultrafine and low-density of composite inorganic fiber mixed with spray by one-step modeling. The layer quality is uniform and has good thermal insulation, noise-absorption properties [2].

2) Security: the mixture of composite inorganic fibers and adhesive sprayed into grassroots interfacial agent through gun muzzle, forming a whole seamless insulation, anti-crack and fireproof layer, which quality is reliable and stable.

3) Eco-friendly: interfacial agent with good adhesion, mixed spraying with low loss, fiber composite inorganic is pollution-free and dust-free with a lifetime as long as the building itself and has good environmental protection function.

4) Economy: raw materials are mass production in the domestic, and construction process is simple and easy to operate with low construction costs and high construction efficiency.

**Composite inorganic fiber spray integrate new technical principle**

1) High adhesion principle

Using specially formulated high-strength interfacial agent forms a highly viscous boundary layer, which provides good conditions for inorganic fiber insulation layer construction; Detail in Fig1.

2) Uniform coverage principle

The high-strength interfacial agent sprays by dual-port, cross-forms sector cover with uniform coverage, high efficiency and materials-saving; Detail in Fig2.

3) Homogeneous and equal thickness principle

The multiple mixed spray technology of composite inorganic fibers and adhesive allows ultrafine inorganic fiber mixes with uniform, sprays with high-quality, loss with low, easily control with spray thickness;

4) A lifetime as long as the building principle

Composite inorganic fibers coordinated with cement, water and high-strength interfacial agent, formulate scientific and rational, bond solid and reliable, form fireproof insulating layer together with ceiling or wall, which can be a lifetime as long as buildings in an indoor environment.

**Fig.1:** Hybrid nozzle

**Fig.2:** High-strength interfacial agent sector coverage

**Composite inorganic fiber spray operation technical points**

**Construction Process**

Composite inorganic fiber acoustic insulation spray construction process includes: construction preparation; base surface treatment; measuring(positioning , screeding);high-strength interfacial agent spray; (steel reinforcement); composite inorganic fiber multi-mix spraying; surface rolling smooth integration; protective layer spraying; checking (repairing); site clean-up ;acceptance.

**Operating technical points**

**Construction preparation**

1) Checking with the drawing to determine spray portion and non-spray portion;

2) Evacuating compressed cotton fibers, continuously filling spray cotton into the sprayer and keeping adequate fiber material inside;

3) The person was responsible for diluting adhesive liquid with water under the ratio in the ingredients jar equipped with high-speed blender;

**Base surface treatment**

1) Using compressed air or water fully sprays base dust and dirt;

2) Checking hanging pieces and embedded parts solidity, loose parts should be fastened;

3) Checking base surface quality, if the primordial surface has been damaged or have serious cracks, it should be repaired and meet regulatory requirements.

**Pre-spray primer at the base surface**

After the base surface cleaning, using well high-strength interfacial agent spray adhesive aqueous which acts as pre-spray interfacial agent treatment for base surface, the dose should be appropriate and uniform, not expose at the end, not flow. Detail in Fig3.

**Fig.3:** Hybrid nozzle construction work

**Composite inorganic fiber spray**

1) Spraying equipment commission

In strictly accordance with the equipment instructions test spraying host pressure, plastic pump pressure and feeding device, through template test spray, measurement of glue flow and the amount of cotton, gradually adjust air pressure range and feed mixing speed, until the fiber spraying status is stable, glue and cotton meet process requirements.

2) Placing thickness control points partition

Each5m$^2$area set up a standard aerated concrete block (15mm × 15mm × spray thickness).

3) Spray insulation layer construction

Adjusting working pressure and feeding device to ensure fiber feed uniform, stirring speed of 30 ~ 45r/min; regulating the ratio of water and glue, stirring together evenly, along with the spray to the base surface. Spray gun away from the base surface is preferably 400mm ~ 600mm, spray cotton content appropriate for the 0.8kg/min ~ 1.25kg/min each spray thickness of 30mm or less, which should ensure continuous evenly sprayed on the grassroots, cannot reveal at the end.

4) If the spray thickness less than standard, fill spray should be carried out in a timely manner, forms homogeneous spray insulation.

**Spray layer surface shaping**

After half an hour later for spray insulation layer dry on the surface, using a dedicated tool for surface processing according to the different requirements of insulation or sound absorption engineering. In general, dedicated platen should be pressed down 5mm; corners should be dealt with smooth, keeping right angles to form a continuous insulating seamless layer.

**Spraying protective layer**

Leveling directly through spraying hydrophobic agent or insulation mortar to form a protective layer at the surface of shaped product; spraying waterproof coating, waterproofing agent to the insulating layer, forming a waterproof protective surface layer.

**Enhanced a3nchorage**

When the ceiling (roof) spray thickness>60mm or sidewalls spray thickness>80mm, alkali-resistant fiberglass mesh or galvanized steel mesh should be used to lay reinforced. After leveling with mortar in spray layer, using expansion bolts fixed insulation layer together with steel mesh reinforcing layer on the substrate surface.

**Construction site cleanup**

Construction site should be cleaned after spraying, clearing the rebound material and removing protective enclosure, scaffolding.

**Spray product protection and precautions**

1) Avoid drilling, chiseling in the base after the completion of spraying, installing various pipelines, ducts and other equipment hanging pieces in advance;

2) Avoid mechanical impact or water erosion in the early dry-cured;

3) For susceptible to mechanical impacts parts，sticking fiberglass cloth or other protective material to protect fiber layer surface ;

4) Avoid dusty polluting surface layer, keep spray area cleaning environment;

**Applications and examples**

Composite inorganic fiber acoustic insulation spray technology successfully applied in several projects in Qingdao Economic and Technological Development Zone. First used in the underground garage ceiling acoustic insulation projects, the area of composite inorganic fiber spraying approximately 15,210 $m^2$. Engineering Practice has proved that the technology achieves the performance targets as follows:

1) High-strength interfacial agent water -screen sector coverage technology owns good uniformity, low loss (≤ 5%), high shear bond strength (≥ 0.5MPa);

2) Composite inorganic fiber + adhesive multi-mixing gun spraying technique owns smaller mixing ratio error (≤ 1%), a uniform thickness control (≤ 1mm);

3) Continuous whole seamless fireproof insulating layer technology owns lower thermal conductivity≤ 0.040W / m • k, good compactness, pit depth ≤ 2mm, no cracks, no peeling.

**Economic benefit analysis**

From the perspective of current market material price, the operator costs, construction ancillary costs and other costs, compared the unit square project cost with composite inorganic fiber spraying in the process, the technology has a larger profit margin which pre-tax profit reach around 15%.

**Social benefit analysis**

Inorganic fiber composite spray insulation, fireproof, sound-absorb is a new technology, compliance with national industrial policy "energy savings ", which is insulation engineering and fire proof engineering technology.

## Conclusions

The integration of new technology research on composite inorganic fiber acoustic insulation spray set in engineering practice, repeatedly demonstrated the difficulties and key construction process in the construction process. Through a combination of theoretical analysis and engineering experience, integrate fireproof, sound-absorbing, insulation with energy-saving, firmness. Practice has proved that the paper proposes three key technology " high-strength interfacial agent sector coverage ", " composite inorganic fibers + adhesive multiple hybrid spray " and " continuous overall seamless fire insulating layer combination form", achieve the optimization of building fireproof insulation, energy-saving and durable. The new technique can be widely used in the construction of basement and underground garage. The resistance of acoustic insulation to ensure class A fireproof quality; bonding firm and no cracking, eliminates the security risks which reduces labor costs and achieve a high-quality, economical and environmentally friendly construction goals.

## References

[1]Donjon Tan, Ying Wang, Penki Wang, Japing Zhao Applications and problems of non-combustible exterior mineral insulation materials [J], New Building Materials, 2011 (11):35-37.

[2]Ying Shi. A new generation of wall insulation technology -Inorganic fiber spraying [J], Liaoning Building.2012 (8):83-84.

*Applied Mechanics and Materials Vols. 580-583 (2014) pp 2244-2248*
*© (2014) Trans Tech Publications, Switzerland*
*doi:10.4028/www.scientific.net/AMM.580-583.2244*

# The Technology Innovation of Green Soft Ground Handling Based on Squeezing and Consolidation Composited

Junyi Shao [1, a], Xiao Zhang[2, b]

[1]Qingdao Technological University, China

[2]Qingdao Technological University, China

[a]qdlgdx@163.com, [b]402159264@qq.com

**Keywords:** Life-cycle environmental load evaluation techniques, cement mixing pile, spiral pump pressure CFG pile, squeezing and consolidation composited technology;

**Abstract.** In this paper, we sorted soft foundation treatment technology by quantifying based on evaluation technique of life cycle environmental load and choose cement mixing pile which life-cycle environmental load is small and spiral pump pressure CFG pile which carrying capacity is high to integrate. It not only improved soil compaction effects, but also solved the problems of other technologies in the foundation process, such as low carrying capacity, reduced diameter, broken pile, virtual pile and so on. Besides, it has reduced the cost of the project and the application prospects are broad.

## Introduction

At the present stage, the schemes of soft foundation treatment technology are numerous. For the same project, there may be many technologies meeting its safety indicators such as carrying capacity, settlement and so on. Under the constraints of energy conservation and environmental protection how to choose a foundation treatment technology which both ensures the construction period and is affordable is one of the hot in the field of architecture and foundation engineering.

## Process principle of innovative technologies

Based on life-cycle environmental load evaluation techniques, first we implanted the factors of technology, economy, environment and period, and then we sorted soft foundation treatment technology by quantifying, as shown in Fig.1. Such sorting results are more in line with the principles of green construction.

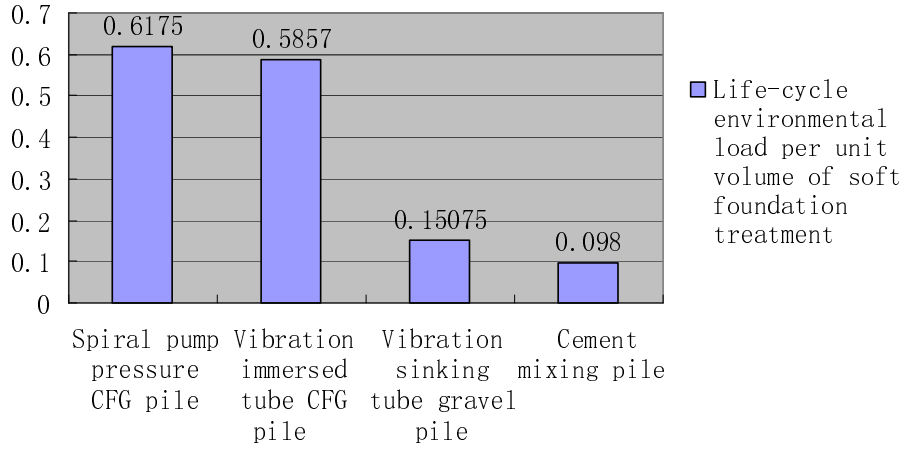


Fig.1: Life-cycle environmental load per unit volume of soft foundation treatment technology

Cement mixing pile is inexpensive and its construction is simple, but the foundation bearing capacity is limited; Environmental load of gravel pile is small, while soil compaction pressure is big and easily breaks pile; spiral pump pressure CFG pile can form high strength composite foundation by squeezing soil between the piles, while life-cycle environmental load is large.

Using the above two methods to integrate, first fix soil between piles by cement mixing pile , then squeezing soil between piles by spiral pump pressure CFG pile. It enhances the effect of compaction and improves the bearing capacity, at the same time; it reduces the cost and environmental impact of the project and provides a complementary and optimized combination for foundation treatment.

**Process flow**

Squeezing and consolidation composited technology of spiral pump pressure CFG pile and cement mixing pile, construction process as shown in Fig.2:

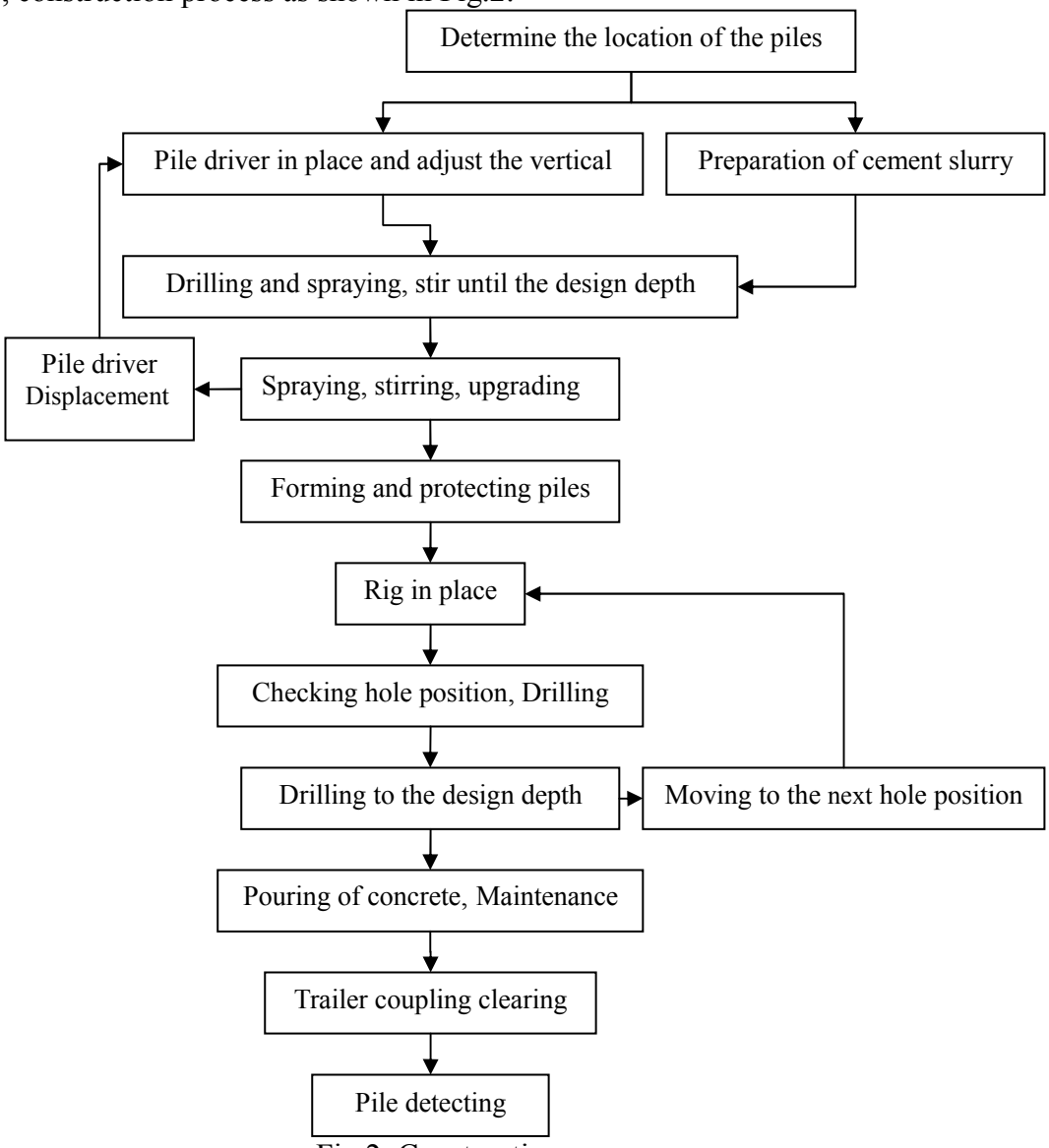


Fig.2: Construction process

**Scope of application**

Squeezing and consolidation composited technology of spiral pump pressure CFG pile and cement mixing pile has the features with large carrying capacity and small ground deformation. It is suitable for soft clay, silt, sand and other ground handling. Besides, it is also suitable for high requirements of noise and mud pollution.

**Application Example**

Qingdao, a regional transformation and resettlement housing, Building E 3, 4, 5, 9, 10, construction area is 120000 $m^2$, 1 basement and ground floor is 30. Make Foundation bearing capacity not less than 300KPa by foundation treatment.

**Carrying capacity calculation** if all use cements mixing piles, the calculation results are as follows:

Pile diameter: $d = 550mm = 0.55m$ $A_P = \pi \cdot (\frac{d}{2})^2 = 0.237m^2$ single pile bearing:

$$R_a = \eta \cdot f_{cu} \cdot A_P = 0.3 \times 3000 \times 0.237 = 213.3KN \quad (1)$$

Area displacement ratio:

$$m = \frac{f_{spk} - \beta \cdot f_{sk}}{\frac{R_a}{A_p} - \beta \cdot f_{sk}} = \frac{300 - 0.3 \times 120}{\frac{213.3}{0.237} - 0.3 \times 120} \times 100\% = 30.6\% > 30\% \quad (2)$$

It is unreasonable, so it should not use cement mixing pile single.

In the formula, $\eta$ --------Pile strength reduction factor,

$f_{cu}$ [2]-----Cube compressive strength of the average at 90d age of interior reinforced soil test block which is at the same ratio of cement-soil of cement mixing pile body,

$f_{spk}$ [2]----Capacity eigenvalues of composite foundation (KPa),

$f_{sk}$ [2]-----Carrying capacity eigenvalues of soil between piles (KPa),

$\beta$ --------Carrying capacity reduction factor of soil between piles (KPa).

If all use spiral pump pressure CFG piles, the calculation results are as follows:

Pile centric axial compressive loading ultimate strength:

$$q_c = \mu \cdot q_{cu} = 0.64 \times 10000 = 6400KN \quad (3)$$

Ultimate bearing capacity of single pile:

$$p_{pf} = q_c \cdot A_P = 6400 \times 0.237 = 1516.8KN \quad (4)$$

Allowable bearing capacity of single pile:

$$p_{pc} = p_{pf} / K = 1516.8 / 2 = 758.4KN \quad (5)$$

Area displacement ratio:

$$m = \frac{f_{spk} - \beta \cdot f_{sk}}{\frac{R_a}{A_p} - \beta \cdot f_{sk}} = \frac{300 - 0.3 \times 120}{\frac{758.4}{0.237} - 0.3 \times 120} \times 100\% = 8.3\% < 30\% \quad (6)$$

It meets the requirements of the replacement rate.

While, due to the high life-cycle environmental load of spiral pump pressure CFG pile, as shown as Fig.1, we should minimize the spiral pump number of CFG pile during the construction process. In this example, we select the cement mixing pile and spiral pump pressure CFG pile to use compositely.

Cement mixing pile and spiral pump pressure CFG pile composite foundation:

Calculate according to the number ratio of 7:3 of cement mixing piles and spiral pump pressure CFG piles:

Allowable carrying capacity of single pile:

$$R_a = 0.7 \times 213.3 + 0.3 \times 758.4 = 376.83KN \quad (7)$$

The composite area replacement rate:

$$m = \frac{f_{spk} - \beta \cdot f_{sk}}{\frac{R_a}{A_p} - \beta \cdot f_{sk}} = \frac{300 - 0.3 \times 150}{\frac{376.83}{0.237} - 0.3 \times 150} \times 100\% = 16.5\% < 30\% \quad (8)$$

It meets the design requirements.

The test verified, cement mixing pile and spiral pump pressure CFG pile combined used in accordance with the ratio of 7:3 can meet the requirement of final foundation carrying capacity.

Pile spacing calculation:

The total area of piles: $16.5\% \times 850 = 140.25 m^2$ the number of piles: $140.25 \div 0.237 = 593$ (Excluding stockades), arranged by type of quincunx as shown as Fig.3, excluding stockades, assuming pile spacing was x, y, then:

$$(\frac{35.15}{x}+1)\times(\frac{23.25}{x}+1)+\frac{35.15}{x}\times\frac{23.25}{x}=593 \tag{9}$$

Namely, $x = 1.7117m$ $y = \frac{\sqrt{2}}{2} \times 1.7117 = 1.2104m$

During construction in accordance with integrated technology, we shall be in accordance with the "first the peripheral later center" construction sequence for construction, piles detailing of the site layout as shown as Fig.3 (excluding stockades).

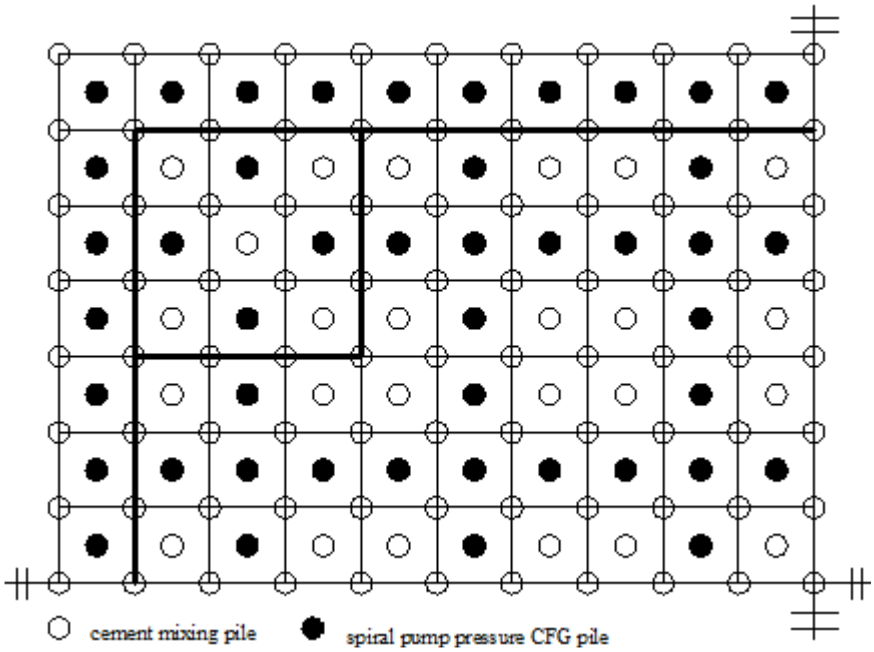


Fig.3: General arrangement drawings of integrated technology

After sampling inspection of a wide range, single pile bearing meets the requirements.

**Cost calculation.** If all use cement mixing piles, the calculation of direct costs as follows:

$$n_1 = \frac{m \cdot A}{A_P} + 50(\text{stockades}) = \frac{0.306 \times 850}{0.237} + 50 \approx 1148 \tag{10}$$

Project amount: $V_1 = 1148 \times 8 \times 0.237 = 2176.608 m^3$

According to 2011 construction price list of Shandong Province, the base price is 1388.4 *Yuan* per $10\,m^2$, so the cost of cement mixing piles: $2176.608 \div 10 \times 1388.4 = 302200.25$ *Yuan*.

If all use spiral pump pressure CFG piles, the calculation of direct costs as follows:

$$n_2 = \frac{m \cdot A}{A_P} + 50(\text{stockades}) = \frac{0.083 \times 850}{0.237} + 50 \approx 348 \tag{11}$$

Project amount: $V_2 = 348 \times 0.237 \times 8 = 659.808 m^3$

According to 2011 construction price list of Shandong Province, the base price is 2011.21 *Yuan* per 10 $m^2$, so the cost of spiral pumps pressure CFG pile: $659.808 \div 10 \times 2011.21 = 132701.24$ *Yuan*.

Cement mixing pile and spiral pump pressure CFG pile composite foundation:

Cost calculation of composite foundation:

The number of cement mixing pile:

$$n_3 = \frac{m \cdot A}{A_p} + 50(\text{stockades}) = \frac{0.7 \times 0.165 \times 850}{0.237} + 50 \approx 465 \tag{12}$$

The number of spiral pumps pressure CFG pile:

$$n_4 = \frac{m \cdot A}{A_p} = \frac{0.3 \times 0.165 \times 850}{0.237} \approx 178 \tag{13}$$

The pile length: $l = 8m$

Project amount of cement mixing pile: $V_3 = n_3 \cdot A_P \cdot l = 465 \times 0.237 \times 8 = 881.64m^3$

Project amount of spiral pump pressure CFG pile:

$$V_4 = n_4 \cdot A_P \cdot l = 178 \times 0.237 \times 8 = 337.49m^3 \tag{14}$$

According to 2011 construction price list of Shandong Province, the total cost of composite foundation:

$$881.64 \div 10 \times 1388.4 + 337.49 \div 10 \times 2011.21 = 190283.22 \ \textit{Yuan} \tag{15}$$

**Economic benefit analysis**

To meet the request of the foundation bearing capacity, the cement mixing piles and spiral pump pressure CFG piles construct with the ratio of 7:3 in the project example, its cost is 190283.22 *Yuan*. If we use a single foundation treatment method to construct, the cost of cement mixing pile is 302200.25 *Yuan*; the construction cost is too high. While, the cost of spiral pump pressure CFG pile is 132701.24 *Yuan*, but the environmental load is too high, so we use cement mixing pile and spiral pump pressure CFG pile to integrate for construction, it not only solve the problem of foundation carrying capacity, but also control costs and reduce the environmental load effectively and provide reference basis for the foundation treatment scheme selection and integration.

Compared with cement mixing pile, only a building foundation (approximately 995m$^2$) can save 111917.03 *Yuan*.

**Conclusion**

This is the first use of environmental load evaluation techniques for soft foundation treatment plan to sort comprehensively by quantifying. It provides a more scientific basis for technology scheme comparison. Used cement mixing pile and spiral pump pressure CFG pile to integrate, first fixed soil between piles by cement mixing pile, then squeezed soil between piles by spiral pump pressure CFG pile, it not only improves soil compaction effects, but also solves the problems of other technologies in the foundation process, such as low carrying capacity, reduced diameter, broken pile, virtual pile and so on. It can eliminate liquefaction, unconfined stiffness of composite foundation defects. It satisfies the requirement of the large tower structure complicated foundation treatment and used for soft sticky, sandy, silty ground. The subsidence and deformation meet the specification requirements.

**References**

[1] Shandong consumption quota of construction project, Construction department of Shandong province, China Building Industry Press, 2011.

[2] Xiaonan Gong. Ground Handling Manual, Beijing: China Building Industry Press, 2008.

[3] Minghua Zhao. Soil Mechanics and Foundation Engineering, Wuhan: Wuhan University of Technology Press, 2010.

[4] Qianmiao Yang. Full life-cycle environmental impact of quantitative evaluation of building products, Tianjin, Tianjin University, 2009

*Applied Mechanics and Materials Vols. 580-583 (2014) pp 2249-2252*
*© (2014) Trans Tech Publications, Switzerland*
*doi:10.4028/www.scientific.net/AMM.580-583.2249*

# Causes and Solutions for the Common Problems in Rotary Drilling Cast-in-place Pile Construction

Zhaoyin Zhou[1,a], Changyou Zhang[1,b]

[1]School of Civil Engineering and Architecture, Chongqing University of Science and Technology, Chongqing, 401331, China

[a]zzy2485@126.com, [b]zcy56@126.com

**Keywords:** Rotary Drilling Cast-In-Place Pile, Construction Craft, Quality Control, Measures

**Abstract.** Quality control in the rotary drilling cast-in-place pile construction is of great difficulty. Once a quality problem occurs, it would have an impact on the quality of the whole project. The text mainly analyzes the causes for the common problems in rotary drilling cast-in-place pile construction and gives some corresponding measures to solve them combined with engineering cases.

## Introduction

Rotary drilling cast-in-place piles to adopt a rotary drilling rig to pierce and form a pile. According to the methods of piercing, it could be divided into rotary drilling cast-in-place pile in dry operation, rotary drilling cast-in-place pile in damp operation, all steel casing and protective wall of rotary drilling cast-in-place pile. In recent years, rotary drilling cast-in-place pile construction has been a new-type construction method for pile foundation, which is employed in bridge and building engineering projects and has a broad application prospect.

Take Chongqing area as an example, manual cast-in-place pile construction has been eliminated due to the lack of operational safety assurance for workers and the low efficiency during the process. Given the rock high fill mountainous geological conditions of Chongqing area, rotary drilling cast-in-place pile is the first choice for pile foundation. But in the application process, many quality problems occur, such as hole pull collapse, bottom sediment, reinforcing cage float, and localized necking in the pile hole. They have caused a profound influence on the quality of the rotary drilling cast-in-place pile. If the problem could not be solved in time, it would have detrimental effects on the quality of the entire project. Therefore it requires engineering staffs' high attention during the construction.

## The common problems in rotary drilling cast-in-place pile construction and cause analysis

**1.1 Water emitting of steel casing.** The outer wall of the steel casing emits water. The more serious cases will induce foundation subsidence, incline and displacement of the steel casing, which will cause pile hole deviation. Even it is hard to go on the construction. The main reason is that the earth around it is not dense enough when it is embedded, or the water level in the steel casing varies largely, or the bit hits it when it rises and falls.

**1.2 Slow drilling or no drilling footage.** Drilling is slow in hard plastic clay layers. Generally, it takes 8 to 10 hours, which accounts for 60% to 70% of the penetration time for on pile. It is mainly for the reason that the type of bit is incorrect, setting angle for the alloy cutter is improper, the depth of earth cut by a cutter is too shallow, the bit counterweighs, and the bit is thoroughly coated with clay.

**1.3 Collapse of the wall of pile hole.** After and during the piercing, the wall collapses in varying degree. Bubbles appear constantly in the emitted mud. Sometimes the water level decreases suddenly. All of them are the harbingers of collapse. The main reasons are that the earth is lax, the mud protective wall is not good enough; the embedding of the steel casing is bad, the inner water level is not high; the speed of the bit is too fast or its idling time is too long are causes for the bottom collapse. Or waiting and perfusion time after piercing is too long.

**1.4 Localized necking in the pile hole.** Localized necking means that localized hole size is smaller than the designed size. Poor performance and large water loss of mud causes water swelling of plastic layer or form lax honeycomb thick mud cake; improper distance between neighboring pile constructions, the stresses in the layers of soil has not been diffused, soft clay creeps in new holes, or the bit size wears excessively are the main causes.

**1.5 Displacement and incline of pile hole.** Great vertical deviation or bends appear after piercing. The main causes are that the installation of the drilling rig is not flat or the virtual earth under the platform causes uneven sinking; pile holder is unstable, drill pipe guide inclines, underground barriers like old foundation or big rocks, heterogeneous foundations or bedrock inclines.

**1.6 Too much sediment in the bottom.** Silting in the bottom; extremely thick residual mud sandy or the collapsed walls drop into the bottom. It mainly due to the fact that the hole is not completely cleaned, the percentage of mud is low or it is replaced by clean water in the cleaning process; the hanging position of steel reinforcement cage is not directed at the center; the earth scrubbed drops into the bottom; concrete pouring is not in time after cleaning the hole which causes the mud sediment and there is no unify bottom elevation which measures the thickness of sediments.

**1.7 Steel reinforcement cage floats.** Steel reinforcement cage floats, apart from the obvious reason that catheter raises the hook, the main reason is that the surface of concrete is right to the bottom of steel reinforcement cage, the bottom of catheter is 2 to 3m below the bottom of steel reinforcement cage, the speed of concrete pouring is fast so that the dropped concrete strokes upward, its buoyancy is more than the gravity of steel reinforcement cage.

## Control measures for common problems occurred in rotary drilling cast-in-place pile construction

**2.1 Guarantee embedding quality of steel casing.** Choose and tamp clay which has the optimal water content when embedding the bottom and walls of steel casing; dig a hole in the proper height in the steel casing so as to retain 1-1.5m water head height within it; prevent the bit from hitting the steel casing in rise and fall; fill and tamp the steel casing with clay when it emits water for the first time. If it falls or displaces seriously, it should be reworked and embedded again.

**2.2 Change bit in time according to the soil condition.** Change or improve the bit, rearrange the setting angle, shape, and orientation of the cutter, increase weights, reinforce sediments emission, reduce mud percentage or use drilling method, adopt reverse circulation drilling method.

**2.3 Adjust the percentage of mud in time, and careful manipulation to prevent the collapse of hole.** Deeply embed steel casing in lax soil layer, tamp the soil, use high grade mud, increase the percentage and viscosity of mud, raise the steel casing, add mud after well completion, keep the required water head height, guarantee the manufacturing quality of steel reinforcement cage, prevent transformation; align with the hole in hoisting, hang direct and guide, sink slowly, prevent hitting the wall; after the piercing, pouring concrete in time, the interval is no more than 3 hours and quicken the speed and reduce the time as much as possible; before placing the steel reinforcement cage in the hole, backfill the cement mortar, clay composite to the place which is 1-2m below the collapsed hole depth, or backfill and tamp the whole hole and then clean the bottom of the hole with the original bit and high grade mud. In the case that a slight collapse caused the steel reinforcement cage, use the bit, of which the size is shorter than that of steel reinforcement cage and high-grade mud or catheter to clean the hole.

**2.4 By adjusting the percentage of mud and adopting excavation method to assure that no contractive necking occurs.** When you have predicted or the necking has happened, you should use high-grade mud, control the share and viscosity of mud and reduce water loss. When the designed distance between two piles is less than 4D, you should construct in every two or three piles; the construction of a new pile should be started 36 hours after the piling of its neighboring pile; choose a double guide gauge protection cage bit; use mud and full-scale bit to clean the hole and finish concrete-filled steel tube after cleaning the hole as soon as possible.

**2.5 Ensure that the drilling rig has been installed to the right position, check and adjust in time during the construction.** The installation should be upright, flat, stable, three points: front edge tangent point, swing center and steel casing center should be in the same surface and same line; steel casing does not incline, drill pipe is not bend, drive rod keeps upright; add guide frame, control and hang the swivel; adopt collar to pressurize where is possible; clean underground barrier; except the adaptation of light reduction and slow shift technique parameters in soft and hard layers, from the soft plastic clay layers, especially when enter the hard plastic clay layer from flowing plastic clay layers and sand layer or from soft soil layer to bedrock, the taper guide bit in the bottom should be changed into flat guide bit or bit without a guide; adopt open caisson or pile hole digging to clean underground barriers; when the inclination occurs in the hard plastic clay layers, use the mixture of sand and soil to backfill the area 1-2m higher than the targeted area, when it becomes dense enough, use flat alloy bit to have a light reduction and slow shift on the inclination; when the bedrock inclines, throw rubbles, of which the size is from 20-40mm, to the area which is a little bit higher than the inclination area, when it is dense enough, use flat alloy bit, rolling bit or flat calyx bit to correct it.

**2.6 Assure the quality of hole cleaning.** Raise the bit by 10-20 cm from the bottom after piercing, keeps slow steering and more than 30 minutes'' cycle time; use high-grade mud in cleaning hole, control the share and viscidity of mud and do no replace mud with clean water directly, steel reinforcement cage should be put on the bottom slowly and horizontally; the thickness of sediment is accounted from the bottom surface of the hole; raise the impact of concrete on the bottom of the hole in the first pouring, the distance between the bottom of catheter and the bottom of the hole should be controlled within 30 to 40cm.The amount of concrete in the first pouring should satisfy the requirement that the end of the catheter could be embedded more than 1.0m in the concrete, use interval blocking and concrete to clean the residual sediment.

**2.7 Slow down the concrete pouring speed and reduce the floating of steel reinforcement cage.** To prevent the floating of steel reinforcement cage, you need to slow down the concrete pouring speed when the end of the catheter is lower than the bottom of the steel reinforcement cage by 2 to 3m and the surface of the concrete is within 1m higher or lower than the bottom of steel reinforcement cage. The fastest speed permitted by the drilling rig is related to the size of the pile. When the concrete surface has been higher than the bottom of the frame by 4m, raise the catheter to the height, which is 2m higher than the bottom of the frame, and then get back in a normal pouring speed. Except for the above-mentioned method, steel reinforcement cage itself should be accounted for. The common method is to weld and fix the frame on the steel casing, or to reduce the amount of stirrup below the steel reinforcement cage to a proper amount (within 2m below it); or to extend the four main reinforcement in the frame to the bottom of the hole; or to install one or two stiffening reinforcement, of which the size is no less than that of the main reinforcement, and weld proper traction reinforcement on the bottom of the steel reinforcement cage. When the floating of steel reinforcement cage occurs, the pile driver stops pouring concrete immediately, control the steel reinforcement cage with the help of some equipment like steel casing and drilling rig. When the floating is little, slow down the pouring speed when it has been controlled; when the floating height is large, the pile could not satisfy the requirement of design, you need to draw the steel reinforcement cage, clean the hole and re-pour concrete.

## Conclusions

Rotary drilling cast-in-place pile is a new type of building foundation pile construction craft, which can be applied to all kinds of complicated geological conditions like flowing mud, soft soil, gravel and quicksand in the rotary drilling pile construction. Because of fast speed of drilling bit, high degree of automation, accurate locating, less labor cost, good environmental performance, high working efficiency and low construction cost in the construction process, its value attracts more and more attention. However, in real rotary drilling construction, there are still many above-mentioned problems. In order to have better control over the pile quality constructed through the rotary drilling

cast-in-place pile method, the following several points should be attached importance to in the construction:

3.1 Get prepared before drilling. Such as, understand the geological condition, placement of the field, and mud preparation.

3.2 Keep record and analysis in time during the drilling process, ready to know the geological condition, check indexes like inclination of the hole, percentage of mud frequently, find out problems and adjust immediately.

3.3 When the depth and size of the hole has reached the requirement of design, clean the hole and hang the steel reinforcement cage in time. When the steel reinforcement cage is in position, recheck the thickness of sediment in the bottom and clean the hole for the second time.

3.4 Take proactive measures to prevent the floating of steel reinforcement cage, and adjust the percentage of concrete to guarantee the quality of concrete.

With rotary drilling cast-in-place pile construction craft becoming more mature, all areas make their local standards. Its construction craft and method get more application. During the construction process, professional technicians' strict control and master of technology key points are needed, constant experience accumulation, further absorption of advanced technology and craft, guarantee construction quality, and ensure the process of a project and its economic profit.

## References

[1] Kong Fanlin, Li Chengfang, Yuan Youxin. Analysis and Countermeasures of Rotary Drilling Pile Construction Quality in Chongqing[J].Chongqing Architecture,2013,12(3):21-22.

[2] DBJ50-156-2012.Technical Specification for Rotary Drilling Cast-in-place Pile[S].Chongqing, Chongqing Urban Construction Committee,2013.

[3] Xiong Qidong, Li Chengfang, Kong Fanlin. Discussion on Construction Quality Control over Rotary Drilling Cast-in-place Pile[J].Chongqing Architecture,2013,12(1):41-43.

[4] Luo Luanfeng. Construction Technology for Rotary Drilled and Bored Pile Applied to Pile Foundation Engineering in Nanchang West Railway Station[J].Building Construction,2011,33(12):1071-1071.

[5] Qiu Hualin. Application of Rotary Drilling Piles in Deep Foundation Pit Supporting Projects of Shenzhen[J].Guangdong Architecture Civil Engineering,2011,12:7-9.

[6] Yu Zhengbing, Xu Jianhua, Li Xiaocheng. Analysis on Construction Technology of Dry Hole Rotating Drill Pile[J].Chongqing Architecture, 2012,11(8):25-27.

[7] Zhang Xiu-hua.In Support of Rotary Drilling Pile in Soft Soil Area of Deep Excavation Technology [J].Construction Quality,2012,30(2):53-55.

*Applied Mechanics and Materials Vols. 580-583 (2014) pp 2253-2256*
*© (2014) Trans Tech Publications, Switzerland*
*doi:10.4028/www.scientific.net/AMM.580-583.2253*

# Determining the degree of mobility of building systems

Oleinik Pavel Pavlovich[1], Grigorieva Larisa Stanislavovna[2]
and Brodsky Viktor Isaevich [3,]

[1] Doctor of Technical Sciences, The Department of Technology and building organization of production, Moscow State University of Civil Engineering (MGSU), 26 Yaroslavskoe shosse, Moscow, 129337, Russian Federation
[2] Doctor of Chemical Sciences, The Department of Composite Materials Technology and Applied Chemistry, Moscow State University of Civil Engineering (MGSU), 26 Yaroslavskoe shosse, Moscow, 129337, Russian Federation
[3] Ph.D, The Department of Technology and building organization of production, Moscow State University of Civil Engineering (MGSU), 26 Yaroslavskoe shosse, Moscow, 129337, Russian Federation
pehel@yandex.ru

**Keywords:** Construction of buildings, mobility, system, labour force, material and technical resources, stages, organisations, buildings, moved, permanent constructions, intensity.

**Abstract.** The present article examines the principles and aspects of building degree of mobility systems, the parameters defining the mobility. The dependences of determining the degree of mobility for different periods of construction.

Mobility is a key feature of the building system that characterizes the industry's ability to carry out a rapid concentration of manpower and material resources in the area of construction (reconstruction) in order to implement the planned commissioning of facilities and production capacity.

This property is connected to the constant mobility of labor resources, relocation from one object to the construction of machines and mechanisms, delivery structures and materials, the use of mobile buildings. Each object contains erected mobile elements that provide the necessary production and social conditions for workers, and for every construction organization has an extensive range of items such as sets of machines and mechanisms, mobile sets of buildings and structures, etc [1].

In remote and underdeveloped regions, except the above mobile elements, to create a mobile base of construction, industrial and technological base configuration, shift and basic residential settlements, as well as necessary engineering infrastructure for the sustenance of the mobile units.

Thus, the degree of mobility in the construction industry is the straight line, depending on the development of the areas and places of permanent deployment of construction organizations. So for most regions of Siberia, the Far East, rural , mountain and desert and semidesert areas, where the decisive factors are difficult climatic conditions and lack of database construction industry, the mobility of the construction industry is significantly increased through the creation of autonomous functioning industrial, social and engineering spheres.

Should distinguish between two aspects of the building system for mobility: moving the elements of production in the area of construction and their concentration to the desired level [2].

The first aspect characterizes the parameters of a mobile construction organization - range of mobile elements, their number in the kit, duration of delivery, the costs of dismantling, transportation, etc.

These elements are formed separately for a period of pioneering development of the territory, and for the preparatory and main periods of construction replaced or supplemented by new ones (Table 1).

In this part of the resources of a construction company belonging to the category of stationary (permanent buildings and structures, machinery equipment, etc.) are not eligible for relocation to new areas.

Table 1
Distribution of mobile elements by period of construction

| Types of elements | Periods of construction | | |
|---|---|---|---|
| | pioneering | preparation | principal |
| Labor resources | H | H | H |
| Machinery and equipment | H, P | H, P | H |
| Motor transport | H, P | H, P | H |
| Mobile buildings and constructions | P | P | H |
| The power tool | H, P | H, P | H |
| Mounting accessories | H, P | H, P | H |
| Inventory means scaffolding | H, P | H, P | H |

The table H - elements that are not migrating to other periods of construction, P - the elements going over different periods of construction. Consequently, the mobility of the construction company can be determined by the ratio of items moved to the construction site to the total number of elements on the balance of the construction company:

$$\hat{E}_{\tilde{n}} = \frac{\sum_{i=1}^{7} \cdot \sum_{j=1}^{n} \cdot R_{iJ}^{M}}{\sum_{i=1}^{7} \cdot \sum_{j=1}^{n} \cdot R_{ij} + \sum_{k=1}^{m} \cdot R_{k}^{P}}$$

where $R_{iJ}^{M}$ -number of displaced j-th of mobile elements i-th group in the new construction area;

$R_{iJ}$ - number of j-th of mobile elements i-th group in the construction of the organization;

$R_{k}^{P}$ - the number of fixed elements of a construction company.

The second aspect of the concept of mobility building system reflects the values of mobility in the construction of the object (the length of deployment capacity, compliance with these capacities calculated volumes of work, etc.). These parameters characterize the intensity of the construction works. Here we have in mind the intensity of the manufacturing processes of work, creating a building product and intensity of providing for their respective industrial and social conditions - building industry, industrial and technological base configuration, power plants, boilers, cooling towers, etc. In this context, the degree of mobility in the construction of the object is recommended to set the ratio of intensity of work and services, requiring the construction of mobile elements to the intensity of work on the project as a whole:

$$K_{c} = \frac{\sum_{l=1}^{L} J_{l}^{M} + \sum_{p=1}^{P} J_{p}^{EM}}{J_{0}}$$

where $J_{l}^{M}$ - the intensity of the *l*-th construction and assembly work requiring of mobile elements;

$J_{p}^{EM}$ - the intensity of the *p*-services;

$J_o$- construction of intensity.

$$J_0 = \frac{V}{T}$$

where $V$ - volume of construction works;

$T$ - duration of construction.

The above expression determining the degree of mobility in the construction of the object is integral. For certain periods of construction degree of mobility is set by the corresponding parameters of the period:

pioneer period:

$$\hat{E}_{o}^{H} = \frac{\sum_{l=1}^{L_1} J_l^M + \sum_{p=1}^{P_1} J_p^{EM}}{J_H}$$

where $J_н$- the intensity of the pioneer period of construction work;

$L_1$ - number of species of pioneer work period;

$P_1$ - number of types of services in the pioneer period;

preparatory period:

$$K_{o}^{P} = \frac{\sum_{l=L_1+1}^{L_2} J_l^M + \sum_{p=P_1+1}^{P_2} J_p^{EM}}{J_P}$$

where $J_n$ - the intensity of the construction work of the preparatory period;

$L_2$ - the number of species of the preparatory period;

$P_2$ - is the number of types of services during the preparatory period;

basic period:

$$K_{o}^{o} = \frac{\sum_{l=L_2+1}^{L} J_l^M + \sum_{p=P_2+1}^{P} J_p^{EM}}{J_3}$$

where $J_3$ - the intensity of the construction works of the main period;

$L$ - number of basic types of work period;

$P$ - number of types of services during the main period.

Compliance with degree of mobility in the construction of the object and the degree of mobility of the building organization characterizes the organizational and technical level of the building system and its commitment to achieving this goal.

Calculations show that the minimum degree of mobility of a construction company can not be less than 0.2. Such organizations are working on a very limited area, such as in large cities, maneuvering mainly labor and technical resources. The beginning of a zone of high mobility should be considered as the mobility of the order of 0.8.This area is typical for construction companies, usually leading work on a rotational form of labor organization and possessing besides labor and technical resources appropriate mobile manufacturing bases, shift camps and engineering units.

Graphical interpretation of the relationship exponents mobility construction industry is shown in Fig. 1. It should be borne in mind that the relationship between the degree of mobility is given one object and one building organization without loss of productivity in the facility and related costs. In the case of the construction of the object by several organizations in the index of mobility $K_0$ allocated respective shares for each building organization.

Promotion of mobility of the construction industry, which is closely connected with the need to reduce labor costs for construction sites, has several lines. Key areas for reducing labor costs, especially important for the development of new areas not only provide the highest possible degree of prefabrication construction products, but also increase labor intensity, the formation of rational composition of workers and improve working conditions. A special place in mobile construction takes industrialization as the basic foundation of the industry.

The first direction contains mainly technical and technological factors reducing the complexity. The second direction is basically provides maximum utilization of labor resources in time and skill. In addition, this area includes measures to maximize the use of mechanization, quality of work, the elimination of various losses, strengthen labor discipline, etc. The third and fourth directions, being content mainly organizational, solved, usually on pre-production phase and implemented over a long period of time.

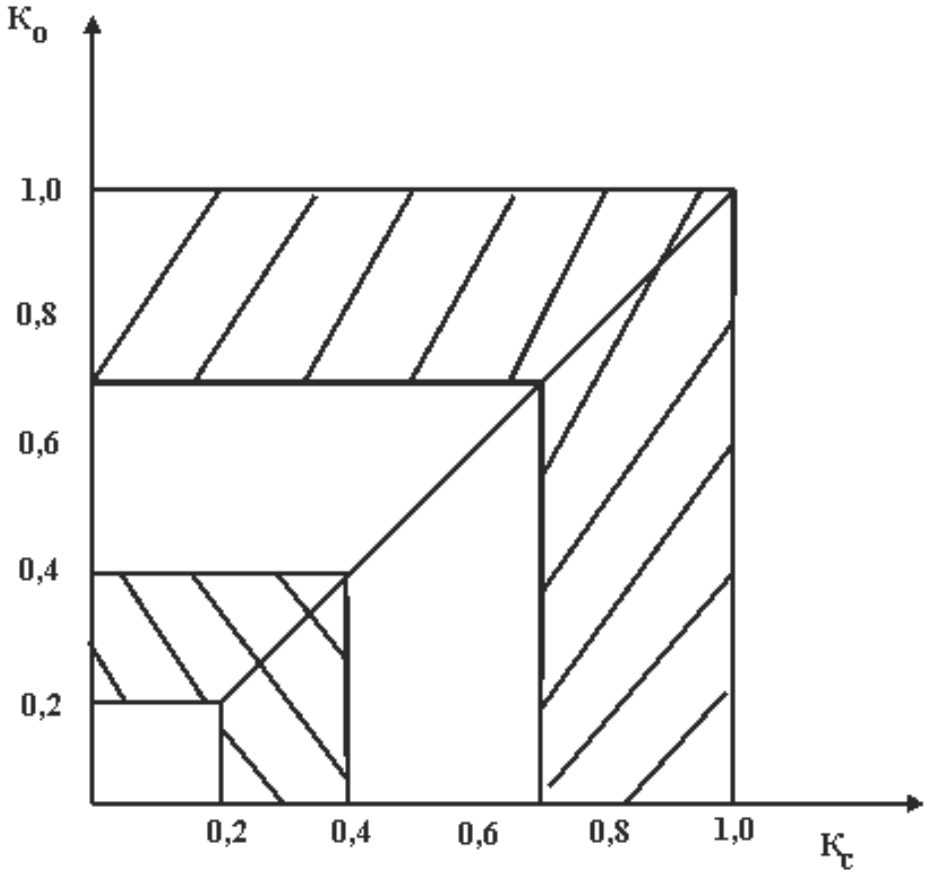


Fig.1.Relationship between mobility exponents Kc and Ko.

Thus one of the basic principles of construction of mobile systems as a result of consideration of the relationship is to achieve the integrity of the mobile building system in relation to the adequacy of the degree of mobility of construction companies and the degree of mobility in the construction of facilities. Besides providing the necessary mobility of building production can be carried out by grouping elements and forming the basis of this work, industrial, commercial, and engineering fields.

## References

[1]. P.P. Oleinik, V.I. Brodsky, Methods for Determining the Duration of Construction of Objects: submitted to Journal of Industrial and Civil Construction (2012).

[2]. P.P. Oleinik, B.F. Shirshikov, Organizing the building site featuring construction shacks . Moscow, MGSU, 2008, 428 p.

*Applied Mechanics and Materials Vols. 580-583 (2014) pp 2257-2261*
*© (2014) Trans Tech Publications, Switzerland*
*doi:10.4028/www.scientific.net/AMM.580-583.2257*

# Engineering application of precast assembly integral shear wall structure on housing industrialization

Yong Wang[1],Yanni Zhang[2,a],Feng Yang[2,b] and Xiaoxi Xia[2]

[1] College of communication and art, University of Shanghai for Science and Technology, Shanghai, 200093,China.

[2] School of Environment and Architecture, University of Shanghai for Science and Technology, Shanghai ,200093,China;

[a] yanninizi@163.com, [b] 591083426@qq.com.

**Keywords:** Residential industrialization, Assembly integral shear wall structure, prefabricated components, prefabricated composite wall, grouting sleeve connection technology, exterior walls

**Abstract.**With the implement of policies which are to accelerate the transformation of economic development mode and go to a new road of industrialization, the industrialization of residential construction has entered a new stage of development. This paper lists the structure engineering example which is Beijing holidays landscape D1, D8#floor and discusses the key technologies of engineering examples and application status of precast assembly integral shear wall structure in the residential industrial engineerings, then propose some difficulties and challenges in the process of the housing industrialization .

## Introduction

With the development of national macro economy and science, the construction of residential industrialization of our country has already entered a new stage of development, and has shown good momentum of development. In the residential industrialization process, the core technology is the selection of structure system. it is difficult to realize the residential industrialization, not to study and solve the main structure technology. Any kind of industrialization of residential design and structure of the system are limited by the technical, economic and certain conditions corresponding to a certain level of industrialization. Industrialized housing system should use the most common structure. At present, the main structure system of our country industrialized housing is frame structure, shear wall structure and frame shear wall structure[1]. But the frame structure is not suitable for industrialized residential requirements due to existing standard constraints and highly restricted , so the shear wall structure system is currently used in industrialized residential structure. Harbin town Rock 18 layers of precast concrete shear wall structure and the Beijing holiday scenery D1, D8# floor assembly integral shear wall structure are two important pilot of residential industrialization in our country, as shown in Fig.1 and Fig.2.

Figure.1 Harbin Rock town 18 layer structure of prefabricated concrete shear wall

Figure.2 Beijing holiday scenery D1, D8# floor assembly integral shear wall structure

Some domestic leading enterprises developed some own features of industrialized housing system by constantly exploring and innovating based on the reference and the introduction of foreign advanced technology in the industrialization of residential roads. As the focus of the assembly integral shear wall structure system, the part or all of concrete structure adopt the load-bearing precast wall panels, form reliable transmission mechanisms by connecting joints, and meet the bearing capacity and the deformation ability, the shear wall structure is called as the assembly type shear wall structure[2]. Assembly integral shear wall structure with precast concrete shear wall panel component and cast-in-situ concrete shear wall is vertical and horizontal structure of the lateral force resisting members, form a connected by integral of a reinforced concrete shear wall structure, the structure of the system so that the structure has good overall rigidity and bearing capacity. More and more popularization, structure system widely used in domestic residential industrialization pilot in the current.

Assembly integral shear wall structure can be divided into precast concrete shear wall structure and some precast shear wall structure. Because the more prefabricated components, the requirements of production and construction requirements will be higher. We can not reach the level that all the members are pre production in the current industrialization level and the level of construction technology , so the current industrialization pilot project mainly uses the precast wall, staircase, balcony, wall cast-in-situ or inner wall prefabricated part of cast-in-situ structure system. In recent years, various provinces and cities nationwide have started the industrialization of residential pilot and promotion work, and have built a batch of pilot project. Assembly integral shear wall structure system is introduced from abroad with the domestic situation is improved and has been gradually recognized and applicated in the process of industrialization. Application status of D1, D8# building in Beijing holiday scenery as an example of assembly integral shear wall structure in the housing industrialization in this paper.

## Introduction of the engineering situation

The project is located in Beijing Fengtai District Village No. 108. D1# floor,the building area is 11396.5 square meters. There are 4 units, of which 1 underground floors, the ground layer 15; the height of the building is 44.25 meters; D8# floor, the building area is 21141 square meters. There are 7 units, of which 2 underground floors, the ground layer 15; the height of the building is 44.25 meters.

## The project system assembly integral shear wall structure system

This project is the first industrialized residential pilot project in beijing. The main structure system of this project is the assembly type shear wall structure, where in the inner wall is the wall of cast-in-place reinforced concrete shear wall, exterior walls for assembly. Each unit has 31

components, including: external wall plate 6 blocks, window 6 blocks, fireproof board 1 block, balcony wall 1 block, balcony decoration 1 board, laminated floor 12 blocks, balcony block 2 boards, stairs block 2 boards. Prefabricated rate is about 25%. See Fig.3 ,there are a prefabricated wallboard and prefabricated stair boards in the project. Thermal insulation materials and structural materials (steel reinforced concrete) of the external wall and the bay window on the north and South outside wall are combined into a whole. These components are produced in the factory, and then installed in the field, more than three layers begin assembling construction.

Fig. 3 Prefabricated wallboard and prefab stair boards

**The connection technology of assembly integral shear wall structure**

Along with the advance of the housing industrialization in China and the continuous improvement of assembly integral shear wall structure system, the grouting sleeve connection technique ,as one methed of the concrete prefabricated ,is naturely paid more and more attention. Grouting sleeve connection is a new type of steel structure due to the needs and technology development and engineering practice, the connection mode has been used to make up the deficiency of the traditional steel structure connection (including welding and bolt connecting). Principle of grouting sleeve is that steel connected through the hollow sleeve casting from the two opening into the sleeve, it doesn't need to overlap or welding, steel sleeve and filled with high strength micro expansive structural mortar to complete the connection between the steel bar[3].It strengthens the positive interaction between it and the sleeve mainly by means of mortar by sleeve confining effect, plus itself has the property of micro expansion. The reinforcement can transfer the stress of steel bar bar with the positive force and the friction of surface roughness. This method is much researched and applicated because of its simple operation.New cement grouting sleeve developed by Beijing Jianmao group and China Metallurgical Construction Research Group are used in Beijing holiday scenery D1, D8# building project based on this technology ,it has optimized the reinforcement structure of wall panel, and reduced the difficulty of steel binding.So this technology has become a breakthrough technology in the process of housing industrialization. Fig.4 shows the cement grouting reinforcement sleeves in this project.

Fig. 4 Cement grouting reinforcement sleeves in this project

Cement grouting reinforcement joint used in this project is composed of reinforced one end of the threaded ,sleeve ,the other one with ribbed steel bar and non-shrinkage cement mortar. The diameter is between with 14- 20. Before in use, the first, one end of a steel bar will be made into straight thread, then connect with the sleeve threaded end, and prefabricate in precast concrete components. In construction site, another prefabricated would be inserted adapter sleeve of the member, the gap between the cement mortar and steel sleeve fill up with the cement mortar to harden, The two bars are connected together. This new type of cement grouting reinforced joint grouting has many advantages.For example,it is easier, the structure of filling cavity and threaded hole is more advanced, high machining precision, ensure the joint performance, especially for accurate positioning of steel sleeve in the production of precast reinforced, and the concentricity of the steel bar is more accurate than the joint of two ends with filling in cement mortar.

**Construction technology of wall panels**

With the speeding up of "building industrialization, housing industrialization", the external wall panels have come true integrate production at the factory with Bearing, insulation, decoration, etc at the same time[4,5]. The precast facade of this engineering is the sandwich type, as illustrated in Fig. 5: its inner is structure layer stress, the thickness is 200mm according to the structure stress calculation ;It is the insulation layer in the middle, the material is glass fiber connector with heat resistance to ensure that the insulating layer and the structure have the same life, and to avoid thermal bridge and improve the effect of heat preservation.The outermost layer is protective layer with 50mm thick, but also the decoration layer with the clear water concrete, giving person with plain and natural the appearance of the lasting appeal.

Fig. 5 The prefabricated composite wall in Beijing holiday scenery D1, D8# building

Although the external wall thermal insulation technology has been used in the pilot project of residential industrialization, the problem of external wall thermal insulation life still is a problem need to solve in the process of housing industrialization. Generally,the life of subject structure require fifty years or more, how to realize the prefabricated insulation wallboard and main structure with the same life is still in research and discussion.

**Waterproof technology of wall panels**

In the assembly structure, there are inevitably level or vertical cracks between the precast wall panels with the main structure and the precast wall panels in the assembly process,the waterproof problem of wallboard and these cracks has not been properly resolved.That is the fundamental reason restricting the development of China's housing industrialization in a certain extent. Therefore, the seepage prevention system of the project is more advanced, more reliable. There are four heavy protection system: First, the vertical joint adopts the structure self waterproofing, using

cast-in-place concrete in joints of two block wall, which make All blend into one harmonious whole.; Second, horizontal seam adopts structure waterproof, there are prefabricated groove on the top and bottom panels to prevent water into the room. Third, waterproof materials(modified silicone rubber) are used in the joints of exterior wall. Fourth, it has formated decompression cavity at the seams inside and set the exhaust pipe every three layers to the exclusion of water vapor.

**Fire prevention technology and its advantages of the wall panels**

Precast wall panels have many advantages: Firstly, the production, processing and storage of Insulation materials are all completed in the factory, it can minimize the probability of fire occurrence as long as the management and production is scientific .Secondly, To take some measures in the production process to improve the overall fire performance of precast wall panels. Such as the weatherability sealant, fireproof sealing strip (not burning ) are used to prevent fires in the horizontal joints and vertical joints in this project, it is more effective to set the fire separation zone.Finally, the precast wall panels as a whole to be installed and the whole process does not contact the insulating layer, ensured the safety of construction.

**Conclusions**

The Residential industrialization of our country has entered a new stage of development from a relatively extensive stage,although we have achieved good results in the aspect of connecting technology , there are many problems to be solved in practice. In this project, such as D1# D8# floor, only North and south wall is prefabricated, east-west gable is still cast-in-place because of unresolving the issues of buried pipelines and just avoiding the pipeline integration problems by adjusting the electrical position. Therefore, only part of the room floors are precast, the others including corridor, kitchen, bathroom all are cast-in-place,the advantages of laminated floor are limitted. So the pipeline integration problems will be inevitable in the process of industrialized residential; Because the bay window is overweight, up to 5 tons, the wall can not be precasted ,resulting in prefabricated composite wall are not continuous, so it is impportant to reduce the weight and the depth of bay window.

**Acknowledgement**
The financial support of Shanghai graduate student innovation fund is gratefully acknowledged.

**References**

[1] Jianhua zhu,linfeng yu,yongming zhu: Study on the construction and strategy of current our country industrialized housing[J]. China concrete and cement products, 2013,3:62-65.( In Chinese)
[2] Zesen fan: Innovation create assembly water - COFCO Vanke holiday town of D1, D8 residential building prefabricated new technology [J]. Architectural journal, 2012,4:63-64. ( In Chinese)
[3] Ziliang wu: Steel sleeve grouting connection technology of [J]. The housing industry, 2011,6:25-32. ( In Chinese)
[4] Lei tang,zhengxing guo,niancai dong,yungang chen: Exterior wall precast concrete shear wall structure heat preservation technology research [J]. Construction technology, 2011,40 (342): 13-15. ( In Chinese)
[5] Tong chen,huiqin guo,tao ma,heng qin: Application of assembly integral shear wall structure in the pilot project of housing industrialization[J]. Building structure, 2011,41(2): 27-30. ( In Chinese)

*Applied Mechanics and Materials Vols. 580-583 (2014) pp 2262-2265*
*© (2014) Trans Tech Publications, Switzerland*
*doi:10.4028/www.scientific.net/AMM.580-583.2262*

# Features and Construction of Prefabricated Buildings

Yuhong Zhao [1, a]

[1] Sichuan College of Architectural Technology, Department of Civil Engineering, Deyang, Sichuan, China 618000

[a]540895565@qq.com

**Keywords:** Prefabricated, Features, Production and Transportation, Lifting, Connections

**Abstract.** Prefabricated buildings have the advantages of convenient construction, low cost, energy saving and environmental protection, etc., it is suitable for industrial production of buildings, lifting and connections of prefabricated components are key to construct the prefabricated buildings.

## Introduction

Prefabricated construction refers to the method that transport the main components and accessories manufactured by factories, such as girders , boards, pillars, walls and stairs, balconies and others to the construction site with the use of industrial production, use crane to lift the components and accessories to the designed location, then connect the components and accessories as well as nodes together by using the ways of reserving poles for planting reinforcing bars, pressure grouting, concreting after the production of keyways or post concreting.

1.1 Features of Prefabricated Buildings

1.1.1 Industrial Production and Easy Installation

Prefabricated building is a kind of environmental building with functions of energy-saving, land-saving, water-saving and materials-saving, steel components, building claddings and wallboards have achieved industrial production with quick and easy on-site installation. Components can be constructed in an assembly line with high industrialization. Prefabricated wallboards can satisfy the individual needs of designers and building developers to create styles of Chinese, Continental, American, Japan, Korea and others. Wallboards and finishes can be completed simultaneously and succeed one time, as shown in Figure 1 and Figure 2.

Fig 1. Exterior Wallboards with Windows and Exterior Wall Paint

Fig2. Exterior Wallboards with Exterior Wall Tiles

1.1.2 Reduction in Costs and Convenient Construction

Steel consumption of prefabricated buildings is only 30-40kg/m2, saving 30% -40 % of construction steel. Prefabricated components are on-site assembled after processed in the factory, reducing the turnover materials and tools as well as their leasing expense, the construction speed of part of the buildings has increased by 4-6 times, the economic benefits gained due to the shortening of construction period is considerable.

1.2.3 High Degree of Mechanization and Reduction in Equipments of on-site Construction Staff

Prefabricated buildings use a lot of finished and semi-finished components for installation and construction, the labor intensity is greatly reduced, the number of on-site construction staff has fallen more than 30%, which also leads to a corresponding decrease in the number of on-site construction management staff, thereby reducing labor costs.

1.2.4 Features of Thermal Insulation and Superior Performance

Prefabricated buildings can organize walls with different thicknesses and structures according to climate and temperature in different regions. Its energy-saving effect can achieve the current national energy-saving requirements. Data show that when the prefabrication rate of residence reaches to 37%, it can save water by 36%, electricity by 31%, reducing construction waste by 83%, simultaneously, achieving 60% reduction in material consumption and 50% in energy consumption.

1.2.5 Environmental Protection and Good Economy

Prefabricated buildings are prefabricated and semi-prefabricated, which greatly reduces the on-site wet construction, the great reduction in construction of mould boards and cast-in-site concrete helps to reduce the impact of construction on the surrounding environment, dust and noise pollutions have been effectively controlled. Prefabricated components have flat surfaces, good appearance and accurate size, they can integrate the functions of decoration, heat preservation, thermal insulation, layout of water pipeline and wires, thus to bring sound technical and economic benefits.

1.2.6 High Quality Assurance Rate

The construction of prefabricated buildings can achieve fully automated production and modernized control. The component size is highly precise and is manufactured according to a very rigorous testing standard, which brings a high quality assurance rate and an enhancement in seismic resistance. After the "5.12" Wenchuan earthquake, the factory buildings of Dong Qi in Han Wang, which locates in a strong earthquake area, whose brick walls had already collapsed, but the external prefabricated wallboards are still hanging in the pillars( see in figure 3 ).

Fig 3. Factory Buildings of Dongfang Turbine Co. Ltd. in Hanwang after the Earthquake

## Factory Production and Transportation of Prefabricated Components

2.1 Casting & Compacting and Maintenance of Concrete

Before casting the prefabricated concrete components, the mold, release agent brushing, reinforcement cage quality, control measures of protective layers, reservation for pores, accessories and other items should first be hidden and then checked and accepted, only if they satisfy all of the requirements, concrete casting and compacting are permitted; the height of concrete feeding should be less than 500mm and evenly laid; after the forming of concrete, it requires to use plug-in vibrator for jolt ramming, the jolt ramming should be conducted tightly row by row, vibrator should not contact with reinforcement cage, tiles and embedded parts: concreting should be carried out continuously, and simultaneously observe the mold, door frames, embedded parts to avoid deformation and displacement. Anything unusual requires for timely reinforcement and corrective measures.

When casting and compacting of prefabricated concrete components are completed, they need timely maintenance. Steam curing is adopted to ensure the quality of prefabricated components.

2.2 Stack of Prefabricated Components

Stacking methods are divided into horizontal stack and vertical stack, in principle, wallboard adopts vertical stack, floor boards, roof boards and pillar components adopt both of the two methods, girder components adopt horizontal stack. Ground laying should be compacted or concreted, pads are necessary when the grounds are stacked one on top of the other.

2.3 Transportation of Prefabricated Components

In order to prevent the occurrence of cracks, damages and deformations etc. in components, the appropriate transport vehicles and transport bench should be selected, be careful when loading and unloading, the cushioning materials need to be placed between the transport bench and carriages. During the transportation, it requires to use steel wires or fixture to sufficiently fix the components, make sure safe driving and prevent the phenomenon of over speed driving or sudden braking.

## On- site Construction of Prefabricated Components

3.1 Lifting of Prefabricated Components

The lifting of prefabricated components is a very important aspect of the construction of prefabricated buildings, it is mainly divided into dry system and wet system, the difference between the two system is that the lifting time and connect ways of prefabricated exterior wallboards are different.

Wet System: The lifting of wallboards is conducted before the floor grouting. The lifting process of wet system is: lofting → lifting of the prefabricated pillars → lifting of the big prefabricated girders → lifting of the small prefabricated girders → floor lifting → exterior wall lifting → balcony board lifting → stairs lifting → cast-in-site structural engineering and electromechanical piping → floor grouting.

The installation of a wet wall system is: reserve the anchoring bars on the upper wall, then insert them into the folded cast-in-site layer. When casting the floor, the upper wallboards and structure are cast together with cast-in-site concrete technique, the lower wallboards are connected with iron parts, there is a certain space to slide, which makes it easy to shake following the earthquakes (including wind).

Dry System: Wallboard lifting is carried out when the whole structure is completed. There is no need to reserve anchoring bars in the folded layer of wallboard; the top part and bottom part of wallboard are connected by 4 iron parts for bearing and adjustment. Its lifting process is: lofting → lifting of prefabricated pillars → lifting of the big prefabricated girders → lifting of the small prefabricated girders → floor lifting →balcony board lifting → stairs lifting → cast-in-site structural engineering and electromechanical piping → floor grouting → complete the structure → exterior wall lifting.

3.2 Connection of Prefabricated Components

Connection of prefabricated components is another important aspect of the construction of prefabricated buildings. The joint's quality directly determines the integrity and seismic resistance of prefabricated buildings.

3.2.1 Welding Connection

Connection of steel plates, connection of steel plate and reinforcing bars as well as connection of reinforcing bars are completed by welding. Welding should reasonably select welding method, conditions, order and preheating and other measures, try to minimize welding stress and welding distortion.

3.2.1 Mechanical Connection

The prefabricated pillars are connected by sleeve connector, cast with high-strength non-shrink cement mortar. Reinforcing bars connected by mortar from sleeve connector, whose yield strength

should not exceed 500 MPa and tensile strength should not exceed 630 Mpa. Strength of high-strength non-shrink cement mortar should reach more than 80 MPa (Figure 4).

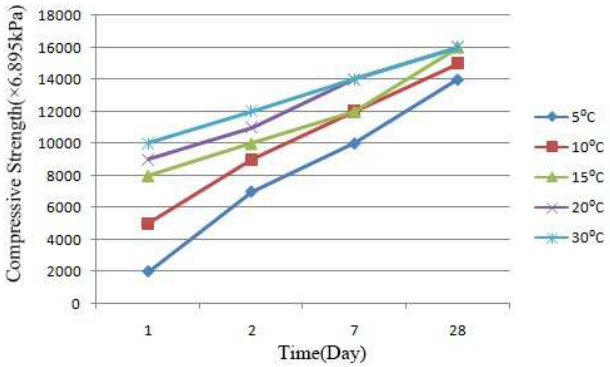


Fig 4. Statistics of Changes in Compressive Strength of Non-shrink Cement Mortar

3.2.2 Connection of Cast-in-site Concrete

Relatively narrow joints such as joint of prefabricated girder and prefabricated pillar, vertical joints of shear walls are connected by the using of cast-in-site concrete technique. In order to prevent the cement grouting from surface of prefabricated component and connection surface of mould board, the mould board should be tight and secure.

3.2.3 Connection of Mortar

Seams, component joints of wallboard or floor board, fillings or facings of metal accessories for connection as well as parts needed to guarantee the durability and fire resistance are mainly connected by mortar. First, clean the surface of the components, and then wet it with water. When constructing with mortar, it is necessary to ensure the laying width of mortar is the same with that of components, and mud trowel is needed for shaping mortar, make sure the laying height of mortar is 1.5 times of that of construction seam ( adjust the height of the material in horizontal direction).

**Summary**

Prefabricated building is applied in several projects in Nanjing, it is obviously fast, simple, energy-saving and good, which makes it the development direction of China's industrialization of construction, in accordance with the green building concept; it is particularly applicable to residential buildings with wide range and large amount.

**References**

[1]Weijian Zhao: Ultra-high Strength Materials and Precast Concrete Structures *The 21st Academic Conference of China Structure Engineering*

[2]Jian Sun, Shengming Wang, Xingming Du: Application of Prefabricated Concrete Structure in High-rise Housing *Construction Technology* 2011.11

[3]Qinjian Jiang: Summary on Development of Assembled Concrete Building both Home and Abroad *Architecture Technology* 2010.12

[4]Chao Han, Jinhua Wu: On Key Technique for Prefabricated Concrete Structures Of Architectural Industrialization *Shanxi Architecture* 2013.7

[5]Yonggen Wu, Jianwei Bai: Construction Quality Assessment of Prefabricated Building Structure Components *Building Construction* 2013.35(2)

[6]Jiehua Chen: Study on Construction Technology for Prefabricated Residence *Building Construction* 2013.35(6)

[7]Dunjun Wu, Jie Wang, Ning Li: Application Research of Prefabricated Technology in High *Building Construction & Design for Project* 2012.7

*Applied Mechanics and Materials Vols. 580-583 (2014) pp 2266-2271*
*© (2014) Trans Tech Publications, Switzerland*
*doi:10.4028/www.scientific.net/AMM.580-583.2266*

# Connecting Passage Construction for the Foundation Pit under Existing Optical Fiber Cable

Hanqing Cao[1, a], Nan Lou[1,a] and Weijiu Cui [1,2,b]

[1] Shanghai Construction CO.,LTD, Shanghai, China

[2] School of Civil Engineering, Tongji University, Shanghai , China

[a]hanki0901@163.com, [b]897835249 @qq.com

**Keywords:** Connecting passage, optical fiber cable, construction technology, finite element modeling.

**Abstract.** Puli center project protects the original soil with pipe roof technology through combining the field analysis and finite element modeling while constructing the connecting passage of foundation pit under the existing optical fiber cable, so as to avoid the optical fiber cable from producing too big settlement to cause the adverse effect, and then constructs the connecting passage of foundation pit. After field monitoring, the maximum settlement of pipeline conforms to the deformation control standard of optical fiber cable, and this technology has certain innovation, which can provide reference for the similar project.

## Introduction

With the urbanization process and increasing tension of construction land, our underground urban complex, air defense project and metro are emerged constantly; and the development and utilization of underground urban space have been entered into rapid development period [1]. The construction of connecting passage seems especially important to build the underground communication network, so that the various underground spaces form convenient traffic.

Ranging from underground tunnel to pipeline channel, the connecting passage has wide application range. The early construction technology of connecting passage is mostly derived from the municipal engineering, and the underground municipal pipeline excavates the pipe trench with open cut technology, and then paves the pipeline. But the open cut will have impact on the above-ground building use and road traffic, therefore, in recent years, the dark cutting technology is used widely, such as pipe-jacking operation technology, etc. [2,3].

In this article, the common channel in the underground connecting passage and municipal engineering is different, and this channel is used for passing the optical fiber cable of communication being used at the top, the deformation control standard [5] of optical fiber cable is high, and the conventional construction technology is difficult to guarantee the requirement of deformation control, therefore, it should perform the careful demonstration and study. One the one hand, the subject study can solve the design and construction difficulties of connecting passage, and on the other hand, can enrich the building technology of connecting passage, so as to provide the reference for the similar project.

## Project Profile

**Overview of connecting passage.** This channel is the channel between the subcellar for eastern skirt building and subcellar of western main building of Jinan Greenland Center, the two north-south optical fiber cables is passed on the channel, the ground elevation is 32.35m-32.58m, the elevation of optical fiber cable is 31.47m-31.52m, and the buried depth of optical fiber cable is 0.83m-1.09m. The section of channel is rectangular and its width is 9.0m; and the roof elevation is -5.80m, and the elevation of bottom plate is -11.0m. The main building and skirt building of this project are excavated respectively, the eastern foundation pit is supported with bond angle of cast-in place pile, the high

grouting pile is applied among the pile and is lapped with the supporting pile to form curtain for cutting of water; and the western foundation pit is supported with the underground diaphragm wall and concurrently used as curtain for cutting of water.

**Geological conditions.** Within the range of exploration depth, the site stratum consists of quaternary artificial layer filling, quaternary Holocene to upper Pleistocene diluvium, quaternary eluvium and cretaceous diorite weathering zone. The main soil layer is: miscellaneous fill, silt, silty clay, clay, residual soil, rubble and weathering diorite.

During exploration, the depth of groundwater of site measured is 3.45-5.04m, and the elevation is 27.20-28.57m. The western river to the groundwater level of site (which is mainly quaternary upper pore water has small influence to rangeability. But in case of flooding the rainy season, the river water can surge over the river, so it has certain influence to construct the west of site, and especially foundation pit of main building. The groundwater exposed by site is quaternary upper pore and bedrock weathering fissure water, which have slight bearing pressure.

## Deformation Analysis and Control Measure of Optical Fiber Cable

**Distribution of optical fiber cable.** This project mainly protects the cable, and the strike of two cables is shown the Figure 1. The protection cable area is also equipped with inspection well, wherein the bottom elevation of inspection well is +29.75m to +30.36m. Before the formal construction, the detecting instrument will be used for further confirmation, to guarantee the safety.

**Deformation analysis of optical fiber cable.** The optical fiber cable is paved in ---times of the last century, and its outer side is protected with precast concrete block and the joint is not subjected to any treatment, so in case of not producing the differential settlement, it will produce big shear force, cause the break of optical fiber cable easily, and bring the huge loss. In the construction process of foundation pit project, the main reason causing the deformation of optical fiber cable is as follows:

- Land subsidence caused by soil loss produced in the construction process of pipe-jacking and retaining pile.
- Land uplift caused by the large-scale jet grouting pile construction and untimely stress release.
- Land subsidence caused by reducing the groundwater substantially for a long time.
- Retaining body deformation and land subsidence around caused by unbalanced force produced while the excavation of foundation pit, big deformation produced by soil and water and soil loss outside the pit.

**Deformation control measure of optical fiber cable.** After the expert argumentation, the settlement deformation of optical fiber cable is set at 20mm temporarily according to the spefication. The following measures are taken to reduce the pipeline deformation:

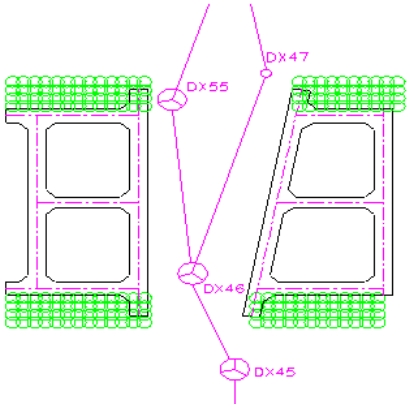


Fig. 1 Distribution figure of optical fiber cable

- Verify the strike of pipeline before construction.
- Take the reasonable construction measure, and finally determine the pipe-jacking construction.
- Perform the information construction according to the monitoring data.

## Finite Element Modeling

**Analysis method.** The software Plaxis of professional large geotechnical engineering finite element analysis is use for performing the simulation analysis to the pipe-jacking construction according to the finite element method of plane strain continuous medium. This project uses the Hardening-Soil model to simulate the constitutive relation of soil, and this model is an improved model of simulating the rock-soil behavior. HS model has 11 parameters totally, part of which is parameter of model itself, part of which can be obtained from the geotechnical engineering exploration report, and another part of which is obtained by inverse analysis through the monitoring data of many similar projects.

**Calculation and analysis.** This project takes the north-south profile for analysis, and the pipeline is pipeline DX45-DX5 nearest to the steel pipe and is considered according to the flexible pipeline. The steel pipe is dragged back after the steel pipe is hole-formed, the influence for drilling diameter of pipeline is relatively small during the construction, and the hole position far away from the pipeline has little influence to it, so this considers the influence of five steel pipes hole-forming respectively to central pipeline while calculation.

Model calculation area: Take 30m in the vertical range and 50m in the horizontal range.

Structure parameter: The elasticity modulus of steel is 2.1×104MPa, the Poisson's ratio is 0.31, and the severity is 25kN/m3. The specific parameter is shown in the Table 1.

Totally, divide into 6 working conditions through the “Element Birth and Death” technology simulation, wherein the specific working condition is as follows:

- Working condition I: Generate initial ground stress field.
- Working condition II: Construct the first hole, including the slurry retaining wall.
- Working condition III: Drag the steel pipe back after the first hole is constructed completely; and lead hole for the second hole, and perform the slurry retaining wall.
- Working condition IV: Drag the steel pipe back after the second hole is constructed completely; and lead hole for the third hole, and perform the slurry retaining wall.
- Working condition V: Drag the steel pipe back after the third hole is constructed completely; and lead hole for the fourth hole, and perform the slurry retaining wall.
- Working condition VI: Drag the steel pipe back after the fifth hole is constructed completely.

The maximum vertical displacement after forming hole through simulation is 9.84mm, the maximum horizontal displacement is 2mm, and the maximum vertical deformation is steel pipe is 5mm, shown in the Figure 2, Figure 3 and Figure 4.

The maximum shaft force of steel pipe is 29KN/m, its maximum shear force is 10.6KN/m, and its maximum bending moment is 1KNm/m, shown in the Figure 5.

After simulation, it can reach the corresponding requirement through protecting optical fiber cable with pipe-jacking operation.

Table 1 Table for analytical element type and constitutive model

| Object | Element Type | Number of nodes | Constitutive Model |
|---|---|---|---|
| Soil | Triangle | 15 | HS model |
| Pipeline | Beam element | 3 | Linear elasticity |
| Steel pipe | Beam element | 3 | Linear elasticity |
| Contact surface of pile and soil | Contact surface element | 15 | Coulomb criterion |

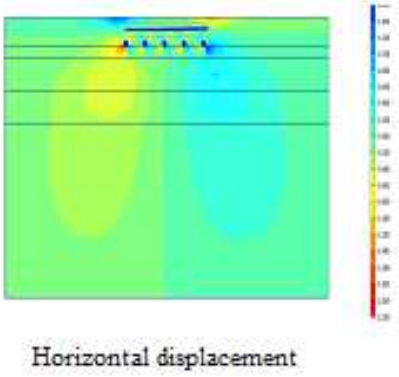


Fig.2 Overall horizontal displacement fringe after hole-forming

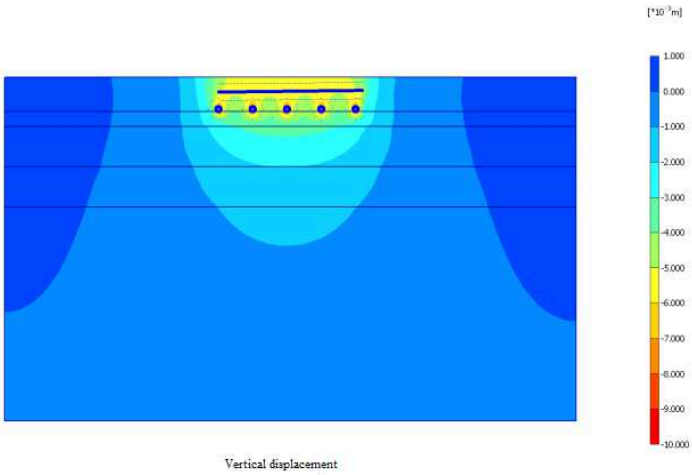


Fig.3 Overall vertical displacement fringe after hole-forming

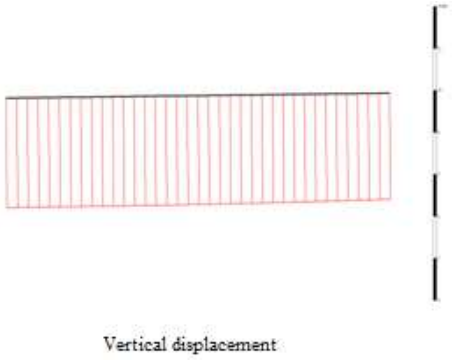


Fig.4 Overall vertical displacement fringe of pipeline after hole-forming

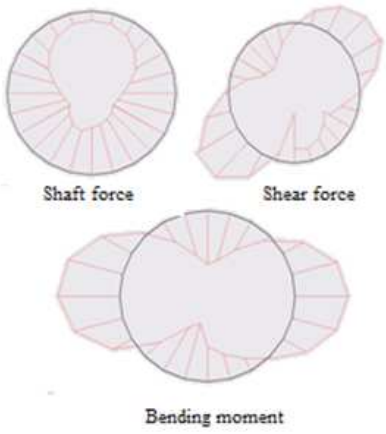


Fig.5 Internal force diagram of steel pipe

## Key Technology of Connecting Passage Construction

**Construction technology process of connecting passage.** The construction technology process of connecting passage is shown in Fig.6.

**Innovation measure in construction .**The pipe-jacking operation uses Φ426 steel pipe, of which the length is measured according to the drawing; and the relation of pipe roof and pipeline is shown in the Figure 7.

The engineering technicians put heads together and take many innovation measures of project technology, to overcome the difficulties in the construction process of connecting passage.

- Take the measure of hitting one every three to reduce the disturbance of drilling to soil and influence of adjacent hole passage, namely, the construction sequence of hole-forming is “1, 4, 7”, and “2, 5, 8”; and cycle the operation until the hole-forming is complete.
- Perform many hole-forming to the drill with different diameters, and change the jacking into pulling back. Since the construction of underground structure at two sides of channel is completed and the remaining space cannot meet the requirement of jacking of steel pipe once, this project constructs with the form of dragging back the steel pipe after leading hole. In order to reduce the disturbance of construction to soil, the drill of which the diameter is 100mm is used for drilling in the hole-forming operation process, drill of which the diameter is 200mm

is used for drilling, drill of which the diameter is 300mm is used for drilling, and then drill of which the diameter is 400mm is used for drilling, so as to complete the construction.

- Adjust the angle of drill rod, and guarantee hole-forming quality. If the length of drill rod is too long, its deflection will have impact on the hole-forming quality. Adjust the angle of drill rod, and finally determine the drilling angle of drill rod through testing continuously, to guarantee the hole-forming at two sides is on the same line.
- Arrange the slurry pouring jacket. Due to forming hole horizontally while forming hole, the slurry is easy for losing. Considering that part of slurry at the pipe roof hole-leading stage and back enlarge stage is lost, which may cause the formation of hole wall, the slurry pouring jacket is arranged, to guarantee that the slurry level in the hole is always located above the hole location, and the hole wall is stable.

Main structure of pouring jacket: arrange 1000×600 steel cover box, of which the wall thickness of pouring jacket is 10mm; arrange U-shaped groove at the drill rod position, of which the groove width is 100mm; and arrange rubber seal plate of which the thickness is 10mm and rubber pressing plate outside the pouring jacket. The pouring jacket is shown in the Figure 8.

The pouring jacket plays big role of guaranteeing the slurry level and guaranteeing the efficiency and quality of forming groove.

**Construction effect.** The monitoring items are arranged according to the specification [4], to guarantee the safety in the construction process. The final monitoring result shows that: the maximum vertical displacement of soil is 12mm, which is close to simulated data, stating that the construction technology effect is relatively good, and can guarantee the project safety.

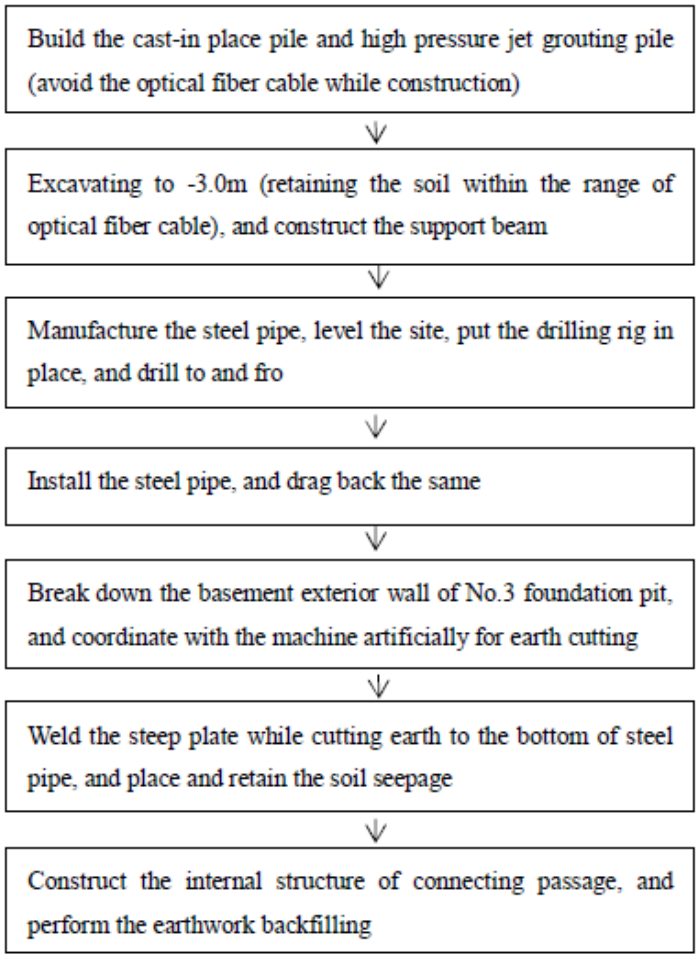


Fig. 6 Construction technology process diagram

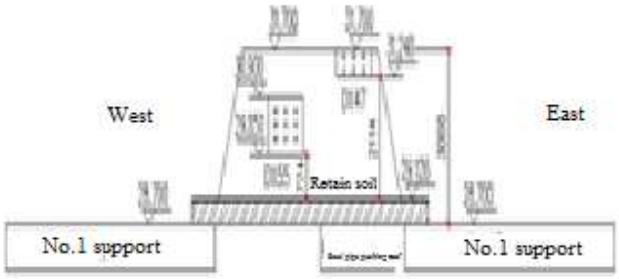


Fig.7 Relational graph of northern pipeline and steel pipe of foundation pit

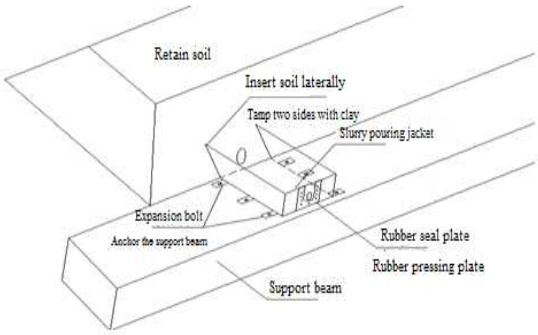


Fig.8 Aerial view of pouring jacket

## Conclusion

In this construction technology, the final land settlement monitoring is 12mm, which plays the role of protecting the optical fiber cable, and has innovation, being worthy of popularization and application.

The angle of drill rod can guarantee the hole-forming level while drilling in from one side and out from the other side, to avoid the error influence of hole-forming due to deflection of drill rod.

The pouring jacket has positive effect for guaranteeing the slurry level, to guarantee the hole-forming quality and efficiency, and be convenient for manufacture and installment, and therefore, it can be used as the auxiliary equipment of slurry level of horizontal hole-forming.

## References

[1] Qain Qihu. Current situation evaluation and prospect forecast for development and utilization of underground space of Chinese city [M]. Academic papers of Shanghai underground space integrated management. (In Chinese)

[2] Huo Changjun, etc. Development of tunnel construction technology with sallow buried-tunnelling method [J]. Municipal Technology. 2009,27(03),274-279. (In Chinese)

[3] Feng Haining. Influence and countermeasure for environmental effect of pipe jacking [J]. Hangzhou: Zhejiang University, 2003. (In Chinese)

[4] Ministry of Housing and Urban-Rural Development of the People's Republic of China. Technical Code for Monitoring of Building Foundation Pit Engineering GB50497-2009[M]. Beijing: China Planning Press, 2009. (In Chinese)

*Applied Mechanics and Materials Vols. 580-583 (2014) pp 2272-2276*
*© (2014) Trans Tech Publications, Switzerland*
*doi:10.4028/www.scientific.net/AMM.580-583.2272*

# Experimental Study of Effects of Operation Parameters on Efficiency of Vibratory Pile Driving

Huiping ZHENG [1, a], Lin CHEN [1,b], Wei WANG [2,c], Liqiang Peng[1,d], Jiayu ZHANG [1,e]

[1]School of Mechanical Engineering, Hebei University of Science and Technology, Shijiazhuang Heibei, 050018, china

[2]Nanjing Chenguang Group Co. Ltd, Nanjing Jiangsu 210006, China

[a]hpzheng@126.com, [b]1033740300@qq.com, [c]568258429@qq.com

[d]pq200600@163.com, [e]zhangjyv@163.com

**Keywords:** vibratory pile driving; soil sample; efficiency of vibratory pile driving; experimental research

**Abstract.** Vibratory pile driving is a common application method of piles foundation construction. A test bed was designed and built according to the principle of vibratory pile driving. The test bed is composed of excitation system, machinery parts and signal acquisition system. At first soil samples with different relative compactness and different saturation were made. Then tests of vibratory pile driving have been done by using the soil samples and the test bed. For each soil sample, time of pile sinking to the bottom of the container was recorded respectively under the condition of the exciting force with same amplitude. The time represents efficiency of vibratory pile driving. The former is shorter and the latter is higher. Relationships between efficiency of vibratory pile driving and exciting frequency, relative compactness of soil, saturation of soil were researched respectively by single factor method. The experimental results have guide meaning to vibratory pile driving construction.

## Introduction

Pile foundation is the part of a structure used to carry and transfer load of the structure to soil or rock with strong hardness and small compressibility, which located at some depth below ground. Pile foundations possess of many properties, including its high bearing capacity, good stability, small and uniform settlement, low sedimentation rate and fast convergence speed [1]. In addition, pile foundation is constructed easily by machinery. Its construction method also has a variety of ways: hammer piling, static pressure pile driving, and vibratory pile driving, etc [2]. Hammer piling is to press the pile into the soil with the force provided by pile head under the impact of the pile hammer. The disadvantage of this method is that a lot of noise will be produced at the moment when pile hammer impacts pile and pile tip is easy to damage. Static pressure pile driving is to press the pile into the soil by strong static pressure. In this construction method a little noise is produced and the pile head is protected from damage. At the same time, being equipped with more weight, heavy work will be finished in assembling and transportation when static pressure pile driver transfers workplace. Therefore it is not only a long construction period and high costs but also high bearing capacity requirement of the construction site [3]. In process of vibratory pile driving, the pile generates a longitudinal vibration of a certain frequency under the action of periodic excitation force generated by vibration pile hammer. Meanwhile the soil around the pile moves in a forced vibration state. Then the side friction resistance of the pile from the soil will be greatly reduced. Under the action of gravity of pile and hammer pile, and exciting force of pile hammer, the pile sinks into the soil after overcoming the soil resistance [4]. This kind of construction method has a lot of outstanding advantages such as strong penetration force, high efficiency of pile driving, good quality, less damage to pile head in the process of pile driving, low noise, simple operation etc [5,6].

**Design of a test bed for vibratory pile driving**

A test bed for vibratory pile driving is composed of excitation system, machinery part and signal acquisition system. Its composition diagram is shown in figure 1. The test bed built for vibratory pile driving as shown in figure 2.

Excitation system provides an excitation force for the pile, which frequency and magnitude can be adjust. It consists of a signal generator, a power amplifier and an electric vibrator. In experiment of pile driving, the signal generator generates a sine signal and the power amplifier magnifies power of the sine signal. Then the amplified sine signal is input to the electric vibrator. Finally, the vibrator outputs excitation force varied by sine curve which can realize the function of vibratory pile hammer.

Vibration pile hammer and pile move in vertical direction. The pile sinks straight down into the soil. Machinery part is used to implement the relative motion of the pile and soil, namely, pile driving movement. The signal acquisition system is used to collect the magnitude of the vibration force from the vibrator.

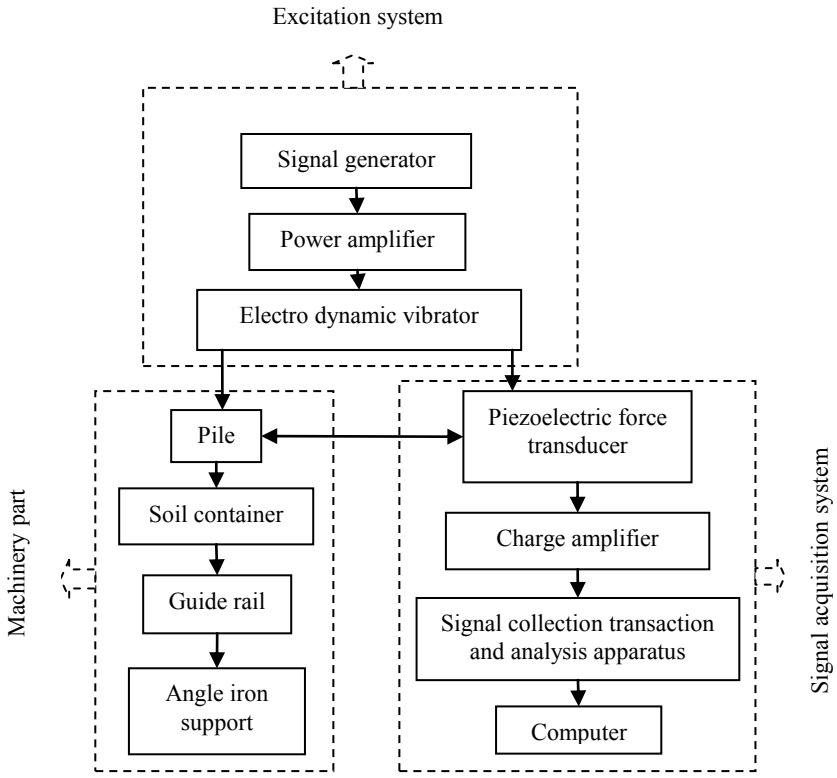


Fig.1 Sketch map of a test bed for vibratory pile driving

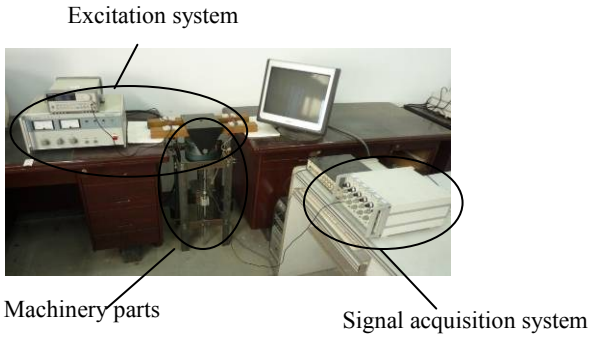


Fig.2 A set up for vibratory pile driving

### Making of soil sample

In following experiment, sandy soil is used to make sample of soil. The minimum dry density $\rho_{dmin}$ and maximum dry density $\rho_{dmax}$ of the sandy soil are 1.27 g/cm$^3$ and 1.66 g/cm$^3$ respectively, which are obtained via measurement of relative density of sandy soil [7]. In process of making sample of soil, at first ratio of water and the dry sandy soil were determined via match calculation. Then we put right amount of water and the sandy soil in a container and mixed them up until smooth. Finally soil sample was compressed to the designed volume by an electric stripper.

In order to study the impacts of different relative compactness of soil on the process of vibration pile driving, two kinds of relative compactness ($D_r$) of the soil sample were prepared for the follow experiment. Their relative compactness ($D_r$) of the soil sample were 40% and 60% respectively.

In order to study the impacts of different saturation of soil on the process of vibration pile driving, two kinds of saturation ($S_r$) of the soil sample were prepared for the follow experiment. Their relative saturation ($S_r$) of the soil sample were 20% and 40% respectively.

### Test contents of the process of vibratory pile driving

More detailed research on the process of vibratory pile driving was conducted for different physical properties of soil samples in the test bed shown in figure 2. Excitation frequency can be divided into three bands: low-frequency stage (15Hz, 20Hz), middle-frequency stage (40Hz, 50Hz) and high-frequency stage (60Hz, 80Hz). Test contents are as follows:

- Research the relationship between soil saturation and efficiency of vibratory pile driving under the same condition of excitation force, excitation frequency and the relative compactness.
- Research the relationship between relative compactness and efficiency of vibratory pile driving under the same condition of excitation force, excitation frequency and soil saturation.
- Research the relationship between excitation frequency and efficiency of vibratory pile driving about different physical properties of soil.

### Results and analysis of the test

In the test, in order to ensure that the amplitude of excitation force output from vibrator is same in each test, settings of the signal generator and power amplifier are as follows. Rapidly increase the amplitude of sine voltage signal from 0.000Vpp to 3.000Vpp by adjusting knob of signal generator. Put power amplifier in "high impedance" working mode and adjust the scale line of potentiometer knob always located in the intermediate position of the scale line of the “gain”. For a soil sample, time of pile sinking to the bottom of the container is recorded in given excitation frequency. It represents efficiency of vibratory pile driving. The former is shorter and the latter is higher.

**Relationship between soil saturation and efficiency of vibratory pile driving.** Two groups of soil sample are prepared and each one has two kinds of soil samples which have same relative compactness and different saturation.

For one group of soil sample, their relative compactness ($D_r$) is 40%, and saturation ($S_r$) is 20% and 40% respectively. The time of pile sinking to the bottom of the container is recorded in different excitation frequency and same amplitude of excitation force and the result is shown in figure 3a. It shows that at the same excitation frequency the pile need more time to sink to the bottom of the container when saturation ($S_r$) is 20% than it does when saturation ($S_r$) is 40%.

For another group of soil sample, their relative compactness ($D_r$) is 60%, and saturation ($S_r$) is 20% and 40% respectively. Settings of signal generator and power amplifier remain unchanged and record the time of pile sinking to the bottom of the container, the result is shown in figure 3b. It shows that at the same excitation frequency the pile need more time to sink to the bottom of the container when saturation ($S_r$) is 20% than it does when saturation ($S_r$) is 40%.

As a result, under the condition of exciting force and exciting frequency, the higher the degree of soil saturation, the higher efficiency of vibratory pile driving for soil sample with same relative

compactness. Therefore, vibratory pile driving method is suitable for construction of the soil with high saturation.

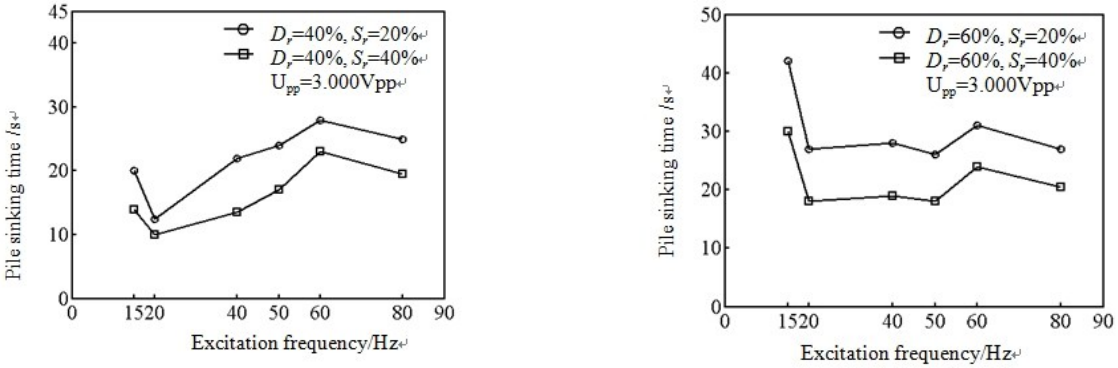


a) $Dr$ = 40% b) $Dr$ = 60%

Fig.3 Relationship between saturation of soil and pile sinking time

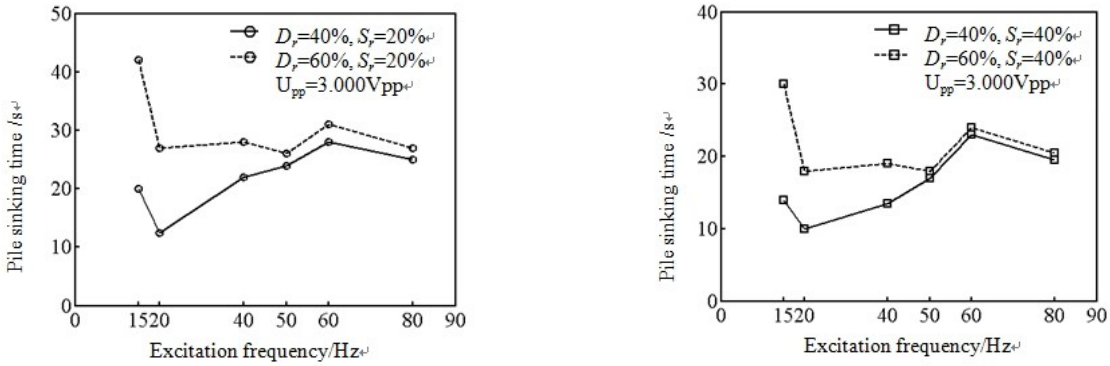


a) Sr = 20% b) Sr = 40%

Fig.4 Relationship between relative compactness of soil and pile sinking time

**Relationship between relative compactness of soil and efficiency of vibratory pile driving.** In the same manner test result of relationship between relative compactness and efficiency of vibratory pile driving is shown in figure 4a and figure 4b. It indicates that the pile need more time to sink to the bottom of the container when compactness ($D_r$) is 20% than it does when compactness ($D_r$) is 40% at the same amplitude and frequency of excitation force for two group of soil sample which saturation is 20% and 40% respectively. As a results, under the condition of same exciting force and exciting frequency, the lower degree of soil compactness, the higher efficiency of vibratory pile driving for soil sample with same saturation. Therefore, vibratory pile driving method is suitable for construction of the soil with low degree of compactness.

**Relationship between excitation frequency and efficiency of vibratory pile driving.** Make soil samples with required saturation and relative compactness and then conduct the test of vibratory pile driving at the exciting force with same amplitude and different frequency. Time of pile sinking to the bottom of the container is shown in table 1. It shows that when exciting frequency in low frequency band the efficiency of the vibratory pile driving is the highest for soil sample with low relatively compactness. While exciting frequency is in middle frequency band the efficiency of the vibratory pile driving is the highest for soil sample with high relatively compactness.

By comparing figure 3a and 3b, we find that the distance between two lines is large in middle and high band. It indicates that time of vibratory pile driving changes bigger when the saturation of soil sample changes in this frequency band. While comparing figure 4a and 4b, we find that the distance between two lines is little in middle and high frequency band. It means that time of vibratory pile driving changes smaller when the relatively compactness of soil sample changes in this frequency band. Thus it can be seen that the relative compactness of soil has less effect on the efficiency of vibratory pile driving and the change of saturation of soil has more impact on the efficiency of

vibratory pile driving when the vibration frequency of the vibratory pile driving in middle and high frequency band.

Table 1 Corresponding exciting frequency of the highest efficiency of vibratory pile driving

| Physical properties of soil sample | Amplitude of sine vibration signal($V_{PP}$) | Excitation frequency (Hz) | Shortest time of pile driving（s） |
|---|---|---|---|
| $D_r = 40\%$，$S_r = 20\%$ | 3.0 | 20 | 12.5 |
| $D_r = 40\%$，$S_r = 40\%$ | 3.0 | 20 | 10 |
| $D_r = 60\%$，$S_r = 20\%$ | 3.0 | 50 | 26 |
| $D_r = 60\%$，$S_r = 40\%$ | 3.0 | 50 | 18 |

## Conclusions

Experimental research on the process of vibratory pile driving has done on the test bed made by own. Some conclusions are as follows:

- Under the condition of the same vibration force, vibration frequency and relative compactness of soil, the higher the degree of saturation of soil, the higher the efficiency of vibratory pile driving. Under the condition of the same vibration force, vibration frequency and the saturation of the soil, the lower the relative compactness of soil, the higher the efficiency of vibratory pile driving. Therefore, vibratory pile driving method is suitable for the construction of soil with high saturation, low relative compactness.
- When the vibration frequency of the vibratory pile driving in middle and high frequency band, the relative compactness has less effect on the efficiency of vibratory pile driving, but saturation has more impact on the efficiency of vibratory pile driving.
- For soil with lower relatively compactness, efficiency of vibratory pile driving is highest when exciting frequency of the vibratory pile driving in low frequency band. For soil with higher relatively compactness, it is highest when exciting frequency of the vibratory pile driving in middle frequency band.

## References

[1] Liu Xiyuan: *Foundation Engineering* (China Building Materials Press, Beijing 2009) (In Chinese)

[2] Fei Yuyuan and Sun Zhen: *Civil Engineering Construction* (China Machine Press, Beijing 2006) (In Chinese)

[3] College of Civil Engineering and Architecture, Xi'an University of Architecture and Technology: *Concrete Machinery and Pile Driving Machinery* (China Construction Industry Press, Beijing1982) (In Chinese)

[4] Nogami T, Ren Fenzhi and Chen JenwhaVertical: Journal of Geotechnical and Geoenvironmental Engineering. Vol.5(1997), P. 422-429

[5] Zhang Zhonghai: Construction Machinery. Vol. 3(2001), P. 39-41 (In Chinese)

[6] Shen Baohan: Construction Technology. Vol. 30(11) (2001), P. 44-45 (In Chinese)

[7] Ministry of Water Resources: *GB/T 50123-1999 Standard for Soil Test Method of the People's Republic of China* (China Planning Press, Beijing1999) (In Chinese)

*Applied Mechanics and Materials Vols. 580-583 (2014) pp 2277-2280*
*© (2014) Trans Tech Publications, Switzerland*
*doi:10.4028/www.scientific.net/AMM.580-583.2277*

# The study about anti-seismic structures stirrup construction blanking length theory calculation

Huiling Li[1,a*],Xuxiang Cui[1,b],Yuhan Zhao[1,c]

[1.]Management Institute, Shenyang Jianzhu university, Shenyang, China

[a]Lihuiling092@163.com, [b]cuixroll0418@live.cn, [c]376299780@qq.com

**Keywords**: stirrup; construction; blanking length; new norm;empirical calculation method

**Abstract:** According to the new norm's requirements and regulations for stirrup and related construction , deducing the theoretical calculation formula of stirrup blanking length of anti-seismic component in different levels. And analyzing it and the three empirical calculation methods comparatively, to find out the application conditions and scope of the empirical calculation method.

## Introduction

With the rapid development of China's high-rise buildings, the demand for steel is growing incessantly, and occupying a large proportion in engineering materials.Currently, there is no uniform standards and calculation rules between beams stirrup length calculation methods and blanking budgets length calculation methods when calculating the steel engineering quantities.The empirical calculation methods are often used[1]. But some methods will bring lots of construction issues on stirrup blanking length and thickness of concrete cover, which affected the safety and anti-seismic performance of components and structure.The problem about finding a method which is both accurate and fast will be discussed in this paper,combined with the new《Design of Concrete Structures(GB 50010-2010)》and《Earthquake Resistant Design Code(GB 50011-2010)》(hereinafter referred to as the new norms) in theory.

## Theoretical calculation of stirrup blanking length[2]

Stirrup blanking length should be calculated with the size of the center line of the bending stirrup. The thickness of concrete cover is defined according to the new norm.As shown in Fig.1.

Stirrup blanking length=Outsourcing size- Measure the difference+ The added value of hook

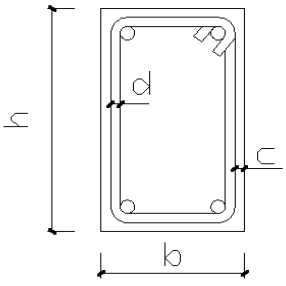


Fig.1 Stirrup theoretical calculation of blanking length

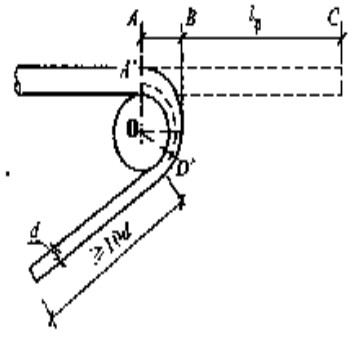


Fig.2 Stirrup bend 135 $^{o}$ hook growth calculation diagram

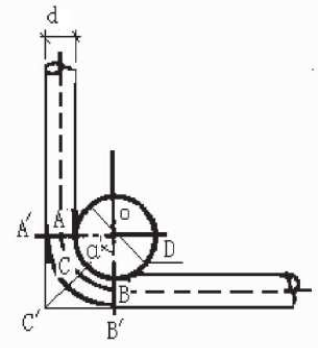


Fig.3 A measure of the central stirrup bending 90° difference calculation diagram

**The stirrup outsourcing Size.**Outsourcing size is the outer contour size indicated in construction drawing, and it also refers to the size of steel skin fold line. According to Fig.1, the stirrup outsourcing size can be calculated as follows:

$$\text{Outsourcing size} = 2*(b+h)-8c \quad (1)$$

**The added value of stirrup end of 135° bend hook.**The calculation diagram Fig.2 shows:

The added value of 135 ° hook = $A'D'$-AB+$l_p$=$135^0$ /$360^0$* $\pi$ *(D+d)-(D/2+d) +$l_p$

$$=0.678D + 0.178d+l_p \quad (2)$$

D in the equation refers to diameter of the curve center, the value shown in Table 3;d refers to diameter of stirrup;$l_p$ refers to the straight length of stirrup hook;In the anti-seismic design, the value of the straight length is max(10d, 75).

Substituting D =2.5d(level I) and D =5d(level II) into the equation above, the added values of stirrup end of 135° bend hook of this two levels are 1.87d +$l_p$ and 3.75d +$l_p$.

**Measure the difference of 90° stirrup bend hook.** The result of different intensity level of steel is listed in Table 1.

Measure the Difference of 90° =$A'C'$+$B'C'$ -arc ABC= 2（D/2+d）- $\pi$ （D+d）$90^0$/$360^0$ (3)

Table 1 Stirrup $90^0$ measurement difference table

| Intensity levels of stirrup | Angle of Bend | Curved inside diameter D | Measure the difference |
|---|---|---|---|
| HPB235 | $90^O$ | D=2.5d | 1.75d |
| HRB335 | $90^O$ | D=5d | 2.29d |

**Theoretical calculations of stirrup blanking length of anti-seismic structure**

Theoretical calculated value of stirrup blanking length L= outsourcing size -3*measure the difference of 90° +2*the added value of 135° stirrup hook (4)

Substituting the results of equation(1), (2), (3) into equation(4), and the new calculation results are shown in Table 2.

Table 2 Stirrup theoretical calculation of blanking length value table

| Stirrup types | Curved inside diameter D | Stirrup diameter | L |
|---|---|---|---|
| HPB235 | D=2.5d | ≥8 | 2*(b+h)-8c+18.5d |
| | | 6 | 2*(b+h)-8c+1.87d*2+150-1.75d*3 |
| HRB335 and above | D=5d | ≥8 | 2*(b+h)-8c+20.6d |
| | | 6 | 2*(b+h)-8c+3.57d*2-2.29d*3+150 |

2*(b+h) -8c means the outsourcing perimeter. When the diameter of stirrup is larger than 8, the theoretical calculation of stirrup blanking length equation can be simplified as follow:

Outsourcing perimeter +21d (5)

According to the new norm,concrete protective layer thickness value fo beams, pillar stirrup is 20mm. After calculating the blanking length of different diameter of anti-seismic stirrup, the results are listed in the Table 3.

Table 3 Stirrup anti-seismic structure simplified calculation of blanking length table (mm)

| Steel level | Curved inside Diameter D | Diameter of stirrup | | | | |
|---|---|---|---|---|---|---|
| | | 6 | 8 | 10 | 12 | 14 |
| Level Ⅰ | D=2.5d | 2(b+h)-20 | 2(b+h)-15 | 2(b+h)+25 | 2(b+h)+65 | 2(b+h)+100 |
| Level Ⅱ and above | D=5d | 2(b+h)-10 | 2(b+h) | 2(b+h)+50 | 2(b+h)+90 | 2(b+h)+130 |

2(b+h) is the section perimeter. According to Table 3, blanking length of different diameter stirrup can be got only by knowing its section perimeter.

**The analysis of calculation of stirrup blanking length in new norm**

The thickness of the concrete protective layer in new norm is the distance from the outermost layer of steel to the surface of concrete. But in the old, the thickness of the concrete protective layer is the distance from the outer edges of stress longitudinal steel to the surface of concrete. Therefore, the outsourcing size of stirrup in the old norm can be expressed as:

$$\text{Outsourcing size} = 2(b+h) - 8c + 8d \tag{6}$$

Compared with equation.1, the thickness of the concrete protective layer in new norm increase a little, but the blanking length decrease. Table 4 shows the results comparatively.

Table 4 Anti-seismic structure under the old and the new norm stirrup blanking length calculation (mm)

| Steel levels | Equation in new norm(anti-seismic) | Equation in old norm (anti-seismic) |
|---|---|---|
| HPB235（Level Ⅰ） | 2(b+h)-8c+18.5d | 2(b+h)-8c+26.5d |
| HRB335 （Level Ⅱ） | 2(b+h)-8c+20.6d | 2(b+h)-8c+28.9d |
| Protective layer | c=20 | Beam c=25, Pillar c=30 |

**Comparative analysis between the theoretical calculation of stirrup blanking length and the empirical ones**

**The commonly used empirical calculation of stirrup blanking length.** The first empirical method: Budget stirrup length =section perimeter of component =2(b+h)[3]; the second empirical method: Stirrup blanking length =perimeter of stirrup +adjusted value of stirrup =2(b+h) -8c+ adjusted value of stirrup[4](To simplify the stirrup blanking length, the adjusted value of stirrup is got by merging the added value of stirrup hook and measure the difference. And the adjusted value is listed in Table 5).

Table 5 Stirrup adjustment value table(mm)

| Stirrup measuring methods | Diameter of stirrup | | |
|---|---|---|---|
| | 6 | 8 | 10～12 |
| Outsourcing size | 50 | 60 | 70 |
| Insourcing size | 100 | 120 | 150～170 |

The last one: Budget stirrup length =outsourcing perimeter +the added value of hook =2(b+h) -8c+the added value of hook[5]

b, h, c represents the width, height and the thickness of the protective layer of beams and pillar.

**Example of calculation conditions.** The beam section of anti-seismic frame 300mm*600mm. Intensity level of concrete is C30. Environment level of concrete is first grade. diameter of stirrup is 6, 8,10,12. Thickness of protective layer is 20mm. Stress longitudinal steel using four 22mm diameter of HRB335 ordinary steel. Double stirrup, solve the blanking length L of single stirrup.

Table 6 is got by substituting the diameters in the example into Table 3 and three empirical methods.

Table 6 Three types of stirrups blanking length calculation method of analysis and calculation comparison table

| length / method / diameter | Theoretical calculation mm | First empirical method mm | Second empirical method mm | Third empirical method mm |
|---|---|---|---|---|
| 6 | 1790 | 1800 | 1690 | 1804 |
| 8 | 1800 | 1800 | 1700 | 1858 |
| 10 | 1850 | 1800 | 1710 | 1912 |
| 12 | 1890 | 1800 | 1710 | 1967 |

It can be known from Table 6. When stirrup diameter is 6 or 8, the first empirical method can be used to calculate the stirrup blanking length for its small error rate; When stirrup diameter is 10 or 12, the results of this method is less than theoretical calculation. So it's not applicable. For he second method is deduced from non-seismic stirrup hook, the blanking length it calculated are all negative deviation and not meet the conditions. The results of the third method is larger than the theoretical calculation, error rate is less than 5%. So it is more suitable for calculating the quantity of construction stirrup budget.

## Conclusion

It is simple and fast to get the stirrup blanking length by looking up Table 3,and the calculation of stirrup blanking length in old norm can be continue used. Compared with theoretical calculation, when stirrup diameter is no less than 8, the first empirical method can be used to calculate the stirrup blanking length. The second empirical method is only applicable for non-seismic design. The last one has an reasonable rate of deviation and can be used as the stirrup budget length.

## References

[1]Wang Jian. The general theoretical methods about the length of the anti-seismic structural elements' stirrups [J]. Journal Of Taiyuan University，2003,4(3). In Chinese

[2]Li Huiling. Civil Engineering Construction[M].Dalian: Dalian University of Technology Press,2009.In Chinese

[3]Qi Baoku. Project appraisal. [M].Da Lian: Dalian university of technology press，2009. In Chinese

[4]The construction manual(4th edition) .Beijing.：China building industry press,2003.In Chinese

[5]Mu Jingbo. Civil Engineering Construction[M].Beijing.：China building industry press，2009.In Chinese

*Applied Mechanics and Materials Vols. 580-583 (2014) pp 2281-2284*
*© (2014) Trans Tech Publications, Switzerland*
*doi:10.4028/www.scientific.net/AMM.580-583.2281*

# Components and guidance for constructional rearrangement of buildings and structures within reorganization cycles

Volkov Andrey, prof., DSc.[1,a], Chulkov Vitaliy, prof., DSc., [2,b], Kazaryan Ruben, prof., DSc.[3,c], Fachratov Muhammed, prof., DSc.[4,d], Kyzina Olga, PhD.[5,e], Gazaryan Robert, Ph.D.[6,f],

[1,2,3,4,5,6] Moscow state university of civil engineering, 129337, Russia, Moscow, Yaroslavskoye shosse, 26

[a]volkov@mgsu.ru, [b]vitolch@gmail.com, [c]r.kazarian@mail.ru, [d] fahratov@mail.ru, [e]kuzinaolnik2009@yandex.ru, [f]gazaryan.robert@gmail.com

**Keywords:** visual (infographic) modeling; assignment and documenting of models; technologization, organization, computerization and intellectualization of activity and control over it, integrated documenting.

**Abstract:** constructional rearrangement is a special case of «Rearrangement» phase in reorganization cycle. It is a set of measures, works and solutions implemented to improve operating characteristics of a construction facility. The main goal of CR objects is to bring them to the condition meeting the needs of users or requirements of regulatory documentation using the methods of architectural, planning and functional transformation.

The need in CR is related to many factors (need to increase the affordability of housing, improvement of housing stock operating quality, refinement of urban-planning, architectural and environmental approaches to forming living environment, implementation of energy-conserving systems, etc.) [1].

CR is an aggregate of nomenclature, structure and interrelations of constructional rearrangement characteristics which are never implemented simultaneously.

Guidance for CR include: visual (infographic) modeling [2,3]; assignment and documenting of models; technologization, organization, computerization and intellectualization of activity and control over it.

Activity co-organization processes and technologies include: integrated documenting, infographics, screening, scoping, diagnostics, monitoring, outsourcing, facility management, outstaffing, logistics, coaching, engineering, consulting and a series of other well-known and innovative activity technologies.

CR components:

- working processes organization principles;
- constructional rearrangement processes;
- types of works performed;
- construction materials and structures;
- employed mechanical and transportation means;
- principles, technologies and parameters for assessing quality and comfort of human habitation within rearranged HME system.

CR types:

- well-known, time-proved and publicly recognized (repair, re-construction, restoration);
- emerged in our practice during «perestroika» variants of CR of facilities and areas (as well as innovative terms defining these variants: renovation, recomposition, reversal, etc.), which are at their «development», «careful study» and «approval» stages in construction, directive and regulatory documentation and there-fore requiring certain explanation.

In the course of CR of urban infrastructure facilities the difficulties occur related to referring certain types of rearrangement works to the corresponding CR type in order to qualify the functional activities of construction organizations and complexes correctly.

For instance, capital repairs will not increase the cost of construction facility, but its reconstruction will. The costs for repairing property assets can be recognized when calculating the profits tax immediately after the works have been completed. But reconstruction will increase the book value of property and will be written-off via depreciation allowance. It is more favorable for an organization to formalize CR as repairs, but it's often difficult to distinguish capital repair from reconstruction.

An accountant not familiar with construction cannot do this in most cases, if the term «reconstruction» is not expressly specified in the contract. However, reconstruction is mentioned in the contracts very rarely. Usually, a simple term «repair works» is used. The term «reconstruction» is specified only when CR works are of great significance. Therefore many firms, without going into particulars, charge the costs under such contracts to the prime cost at once. However, what is written in the contract may have little importance, and during the review the tax officers will be mainly examining the nature of works performed but not the contract itself. Upon identifying a violation they will additionally impose profits tax and property tax.

Therefore, slowly but surely, CR specialists come to the following conclusion: to increase the efficiency of implementation of CR plans and programs for buildings and structures, it is reasonable to single out innovative types of CR from the general «crusty» boundaries of reconstruction and repair.

When rationalizing the need: single out a local component of a known CR type and assign it with a status of a new separate CR type; form a directive and administrational documentation support for an new CR type; make this CR type a multiversion business object; form the variety of its organizational and technological subtypes; rate activity processes, indicators and performance levels of such new CR type. For example, execution of alteration works which, according to the current regulations are referred to reconstruction, can be transformed to a separate innovative CR type called «recomposition».

Lots of modern innovative CR subtypes are open, it means that as reasonable interests and various types of demands emerge, new innovative CR subtypes can be created.

Presently, the group of innovative subtypes includes the following:

Renovation - forced vacation of territory (demolition of buildings and structures, retrieval of utilities from underground, etc.) to provide a possibility for new construction depending on the extent of preservation of the structures located in such territory (term by Vedeneyev N.S. and Maklakova T.G. was applied to CR by Resin V.I. in directive documents by Moscow Government).

Recombination (recomposition, restructurization) arrangement of com-ponents in a new order with the elements of innovation and increase of habi-tation comfort on a new technical basis (term by Schreiber K.A. was applied to CR by Ginsburg A.V. and Kuznetsov S.V.);

Reversation - alteration of designated purpose, legal status and owner-ship pattern of a facility being rearranged (term by Chulkov V.O. was applied to CR by Golubeva N.N.).

Retrivation (from retrieve - restore, find) - bringing a facility being rear-ranged into a good repair by way of annexing to the old functional system of the building a new system providing for local or entire repla-cement of elements of such new system (using assembly/disassembly principle) and ensuring elimination of obsolescence of the building and normal operation of the facility (term by Kuzina O.N. was applied to CR by Chulkov V.O. and Kuzina O.N.). The old functional system is the main bearing structure of the building, the new system - add-on systems of buildings, structures and internal premises finishing.

The structure of «Retrivation» CR is given on fig.1.

Technical rehabilitation (sanitation) - complex of measures aimed at restoration of operating prope-rties and refurbishment of buildings and structures which bring them to a new condition, maximally complying with the cur-rent requirements. Such measures can also be taken to increase energy-conserving properties of the structures and in case of impossibility of demolition and

eviction. An integrated reha-bilitation means an overall refurbishment of the building, including utilities, however, without alterations. It is larger than capital repairs but smaller than reconstruction.

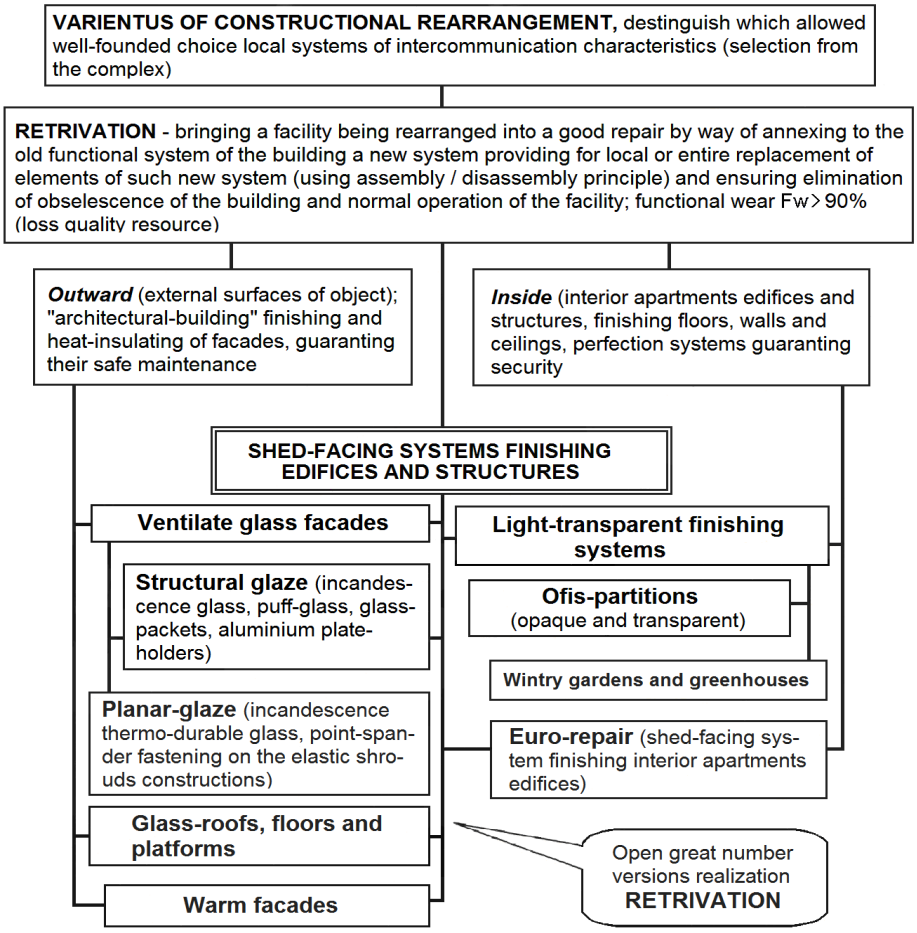


Figure 1. Structure of «Retrivation» CR

When further construction or CR of a facility is impossible or unfavorable, but the improvements of market conditions or company's financial situation are expected in future, such facility under construction undergoes a preservation process. Upon the expiry of preservation the measures on depreservation of facility under construction can be performed, it means the working processes can be resumed. Preservation is used in cases when a facility needs to be «frozen» for a period over 6 months.

The set of measures to preserve a facility:

- preparation of a plan including all organizational and legal measures and construction works on preservation of the facility;
- elaboration of method statement for the works required to preserve the facility under construction;
- management of organization and execution of all construction works related to presservation of the facility.

The preservation of a facility consists of the following stages:

- inventory of construction facilities;
- check of availability and accuracy of all technical documentation (drawings, cost estimates, construction journals and other documents);
- examinations and inspection measurements.

The following types of works should be carried out:

- works protecting the building structures and equipment of the facility against aggressive environmental exposure;
- fire protection of the facility;
- enclosure of excavation pits and through holes in slabs);

- reinforcement of the walls;
- fixation of all moving elements of building structures.

Research and design of system «man - technology - environment, MTE» predetermined the integ-ration of technics and sciences about man and his working activity, led to emergence of a new psycho-physiological terms of reference.

These tasks are related:

first, to description of characteristics of a human and his activities within the management systems;

second, to development of new resources for activities, mainly concerned with provision of inte-raction between human and machines in certain environmental conditions and with requirement of quantitative assessment, measurement and monitoring of the human comfort level at performance of certain activities;

third, to allocation of functions between operator and machine, to arrangement of cooperation thereof.

Currently, there is a long-felt need and finally became possible in principle comprehensively to study labor activity basing on all sciences, which scope of research is human being as the subject of labor, knowledge and communication.

It is easy to see that failure of labor activity currently includes not only a distortion of human physiological functions, but also failure of any of his functions such as labor, knowledge (informative function) and the function of communication. At intersection of psychology, physiology and engineering, has appeared a new science about principles of labor process - it is ergonomics. Ergonomic analysis of normal and pathological state is a fascinating and faintly studied problem of modern psychology, biology, medicine, and antropotechnics.

The living conditions of modern humans became significantly different from those in which happened a formation of human being and human society. Large number of new factors arising from scientific, technological and social progress impact humans. Ionizing radiation, all kinds of toxic substances, noise, vibration, excessive mental stress, intensification of work are becoming the hallmarks of civilization.

Furthermore, the human body is widely influenced by consumption of food products, undergone various types of processing, as well as mass taking of antibiotics, sulfanilamides, hormonal, and other highly active pharmaceuticals.

In this regard, study of issue of human adaptive capacity is of particular importance because morphological and physiological characteristics of man, formed over a long period of evolution during millions of years, may not change with the same speed as technological processes and environment chan-ging. That particular comprehensive approach to the issue will afford to over-come the common perception of the standard permanence. Only such a synthetic approach may ensure an adequate knowledge of normal human development, otherwise there will always arise paradoxical points of view about childhood as «immature», «abnormal» adultness and about relativity of standard definition.

**References**

[1] Chulcov V.O. Re-arrangement. Organizational, human and technical reliability of construction/ Series “Infographicfl basis of functional systems”/ Edited by V.O.Chulcov.- M.: SvR-ARGUS, 2005.

[2] Chulcov V.O., Kyzina O.N. Retrieving - innovative direction in a functional system of construction renjvation.- Garold of VSCU.- 2011.- №8.

[3] Sudakov K.V., Chulcov V.O., Kazaryan R.R., Glazachev O.S., Dmitrieva N.V., Komarov N.M. Antropotechnics: Norm in every living thing and artificial beings / Edited by professor V.O.Chulcov.- M.: SvR-ARGUS, 2013.- 320s, ill.

*Applied Mechanics and Materials Vols. 580-583 (2014) pp 2285-2288*
*© (2014) Trans Tech Publications, Switzerland*
*doi:10.4028/www.scientific.net/AMM.580-583.2285*

# Mold-unloading-lifting and Lifting-transportation's Construction Checking of Composite Wallboard in Industrial Production

Chunyi Xu[1, a], Lei Yan[2,b], Chunlei Xu[3,c] and Shikai Jiang[1,d]

[1]School of Civil Engineering, Shenyang Jianzhu University, Shenyang 110168, China

[2]Shenyang City Construction Engineering Quality Supervision Station, Shenyang 110002, China

[3]Tieling municipal commission of housing and urban-rural development, Tieling 112000, China

[a]xuchunyiyi@163.com, [b]yl_9800@163.com, [c]117132079@qq.com, [d]jskpk@hotmail.com

**Keywords:** Precast fabricated structure, Composite wallboard, Mold-unloading-lifting; Construction checking.

**Abstract.** Take composite wallboard of residential parts as object of study, use investigation and theoretical calculation to check unfavorable conditions of Mold-unloading-lifting and lifting-transportation in industrial production. mold-unloading coefficient and dynamic coefficient value are researched according to summarize domestic and foreign standard, and give out suggested dynamic coefficient values of construction checking of lifting-transportation for composite wallboard. It can provide reference of production and development of residential parts.

## Introduction

Modernization of housing industry has been gradually put on the agenda with the emerge of reform of the wall, building energy efficiency project and other relevant policies. Fabricated structure residential has been more popular and taking increasingly proportion among individuals for its advantages such as on-site assembly, green environmental protection, and convenient for industrial and standardizing production.

But industrialized construction technology research and applications is still in its infancy, production technology is not well developed and with low level of industrialization, industrialized building system occupies low shares in construction market of our country. There are still many issues must be resolved such as the construction checking of mold-unloading-lifting and lifting-transportation of residential parts. The paper take composite wallboard of residential parts as object of study, use investigation and theoretical calculation to check unfavorable conditions of mold-unloading-lifting and lifting-transportation in industrial production. It can provide reference of production and development of residential parts.

## Embedded hanging pieces

Through the investigation of prefabricated member manufacturers found that the common hanging pieces have rings and dedicated embedded hanging pieces.

The rings is to embed HPB300 reinforced in the specified location in composite panels (welding together with main reinforcement). Besides, it cannot be cold treatment. Because the load of the ring is normally dynamic load. If the flexibility is inadequate, the ring will occur brittle fracture easily, yet the ductility and toughness of the reinforced will decreased after cold treatment. It shown in Fig. 1.

The form of special embedded hanging pieces has embedded nuts, embedded boom and reserved lifting holes, and using the combined dedicated spreader to achieve lifting. The buried nuts are the most common. It is with the use of high-strength bolts. When it is being used, embedded nuts into the specified location in composite panels. When lifting, screw the bolts and nuts together, and hang on the lug bolt with hook. And then, it can be lift. It shown in Fig. 2.

Fig. 1 Composite panels embedded rings

Fig. 2 Composite wallboard embedded nut and bolts

In practical engineering applications, because of low design strength and anchorage length, the rings made by hot rolled round steel bars may consume more and having bad economy. Meanwhile, when the Installation is complete, the exposed parts of the rings must be cut off. Otherwise the appearance quality and durability of precast member will be influence. So there are many component factories begin to use dedicated embedded hanging pieces, embedded nuts are the most common. No matter what component is chosen, it must meet the requirement of being lifting safely under the effect of self weight. (Steel rings are calculated in reference of GB50010-2010[1]).

## Construction checking of mold-unloading-lifting

To consider the influence of the adsorption force, we can introduce mold-unloading adsorption coefficient to recheck when composite wallboard receive adsorption force from mold on the surface of concrete structures during mold-unloading-lifting.

The component values are multiplied by the weight of the standard mold-unloading adsorption coefficient as equivalent load standard value. Mold-unloading adsorption coefficient is related to components and mold surfaces' condition and it can be determined by testing.

Table 1 is some commonly used prefabricated mold-unloading coefficient specified by PCI Design Handbook[2] of the USA.

Table 1 Mold-unloading coefficient in PCI design handbook

| type of component | mold surface conditions | |
|---|---|---|
| | exposed aggregate, mold release agent coating | smooth surface, oiled |
| Flat without active side mold and slot, slot edge | 1.2 | 1.3 |
| Flat with active side mold and slot, slot edge | 1.3 | 1.4 |
| Flat with Chute(Such As T-Shaped Plate, Double-T Board) | 1.4 | 1.6 |
| Flat with Carved Face | 1.5 | 1.7 |

In our country, the construction standard mold-unloading adsorption coefficient takes 1.5 based on domestic practical engineering experience.

**Examples of checking:**

A composite wall, plate length b = 3600mm, plate height a = 2850mm, thickness t = 330mm, using level lifting on 4 points, to make positive moment between lifting points and negative moment at lifting point roughly equal, referring to the United States' PCI design Handbook[2] and determine the position of lifting points, shown in Fig. 3. Before mold-unloading, the compressive strength has been measured with the concrete conditions of test cubes conservation and the value is 18.5Mpa, now checking whether mold-unloading-lifting is satisfied.

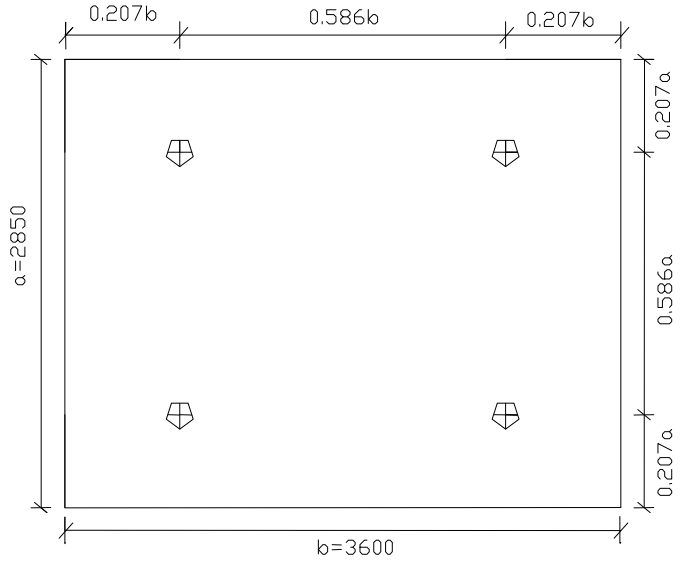


Fig. 3 Lifting point diagram

Solution: Known $f_{cu}$ = 18.5Mpa, $f_{tk}$ =1.46Mpa(according to standard GB50010-2010[1]);

Reinforced concrete density takes $25\times10^{-6}$ N /mm$^3$;

mold-unloading adsorption coefficient takes 1.5;

the equivalent uniform load q= $330\times25\times10^{-6}\times1.5 = 12.4\times10^{-3}$ N/mm$^2$;

owing to 0.5a =0.5×2850=1425mm ＜15t = 15×330 =4950mm, the calculate width takes 0.5a;

Then the biggest moment of maximum: $M^{+}_{\max} = M^{-}_{\max} = \frac{1}{2}\times\frac{1}{2}a\times q\times(0.207b)^2$, maximum tensile stress: $\delta_{\max} = \frac{M_{\max}}{at^2/12} = 0.19Mpa$.

There $\delta_{\max} < f_{tk}$, it is requirement and can be lift.

**Construction checking of lifting-transportation**

Lifting-transportation means is lifting and placing the prefabricated components into specified site, including lifting, transportation and field erection. When checking, field personnel should consider the impact of the dynamic load and the wallop generated in the process of lifting. Generally by pull-in dynamic coefficient to consider the dynamic load, the weight standard value of component multiplied by dynamic coefficient as the equivalent standard value. Table 2 is the current domestic and foreign standards for dynamic coefficient value[3-5].

The complexity and importance of the lifting process should be taken into consideration, and the lifting checking dynamic coefficient is suggested that taks1.5 as possible; when there are any reliable experiences, power coefficient can be adjusted according to actual stress situation.

Table 2 The dynamic coefficient in domestic and international current standards

| standards | dynamic coefficient |
|---|---|
| 《Code for design of concrete structure》GB50010-2010 | 1.5 |
| 《Assemble large residential building design and construction code》JGJ1-91 | 1.5 |
| 《Technical standard for reinforced concrete lift slab structure》GBJ130-90 | 1.2 |
| 《Code for design of concrete structures of railway bridge and culvert reinforced and prestressed》 | 1.2 |
| U.S.A《PCI Design Manual》 | 1.2 |
| Hongkong《Standard for construction of precast concrete》 | 1.2 |

## Conclusions

This paper describes the types of embedded hanging pieces (rings and embedded nut). By an example using mold-unloading coefficient check calculating unfavorable conditions of mold-unloading-lifting of composite wallboard in industrial production. And summarize domestic and foreign standard, give suggested dynamic coefficient values of check lifting-transportation.

## Acknowledgements

This work was financially supported by the Project in Science Research of Department of Education of Liaoning Province(L2013231); Key Projects in the National Science & Technology Pillar Program during the 12th Five-Year Plan Period of China(2012BAJ16B05); The scientific research foundation of Shenyang Jianzhu University(2013127)

## References

[1] GB50010-2010, Code for design of concrete structures.2010. (in Chinese)

[2] Precast and Prestressed Concrete Institute. PCI design handbook(7th Edition).PCI,Chicago, Illinois,2010.

[3] J11791-2011, Liaoning provincial standard for production and acceptance of precast concrete. 2011. (in Chinese)

[4] Zhang xiaoyong. *The production technology of component factory in prefabricated assembly type frame structure.* Building and construction. Forum Vol. 34 (2012), p. 206-207.(in Chinese)

[5] Gong zhihong: *The construction technology of prefabricated component in assembly house.* Science and technology information. Forum Vol. 22 (2010), p. 81-82.(in Chinese)

*Applied Mechanics and Materials Vols. 580-583 (2014) pp 2289-2293*
*© (2014) Trans Tech Publications, Switzerland*
*doi:10.4028/www.scientific.net/AMM.580-583.2289*

# Discussions on Foundation Pit Construction Scheme of Large Building in Mountain Area

Mengjie LIN[1,a]

[1]Hunan Communication Polytechnic, Hunan Changsha 410004, China

[a]Email: lindalux@qq.com

**Key words:** Large building; Foundation pit; Groundwater control; Slope stability

**Abstract:** Based on the analysis of the engineering geology and the hydrology data of a large construction project along the river in Hunan province, according to the engineering design requirements and the local construction conditions, the paper analyzed in-depth on deep excavation, groundwater control and high slope treatment schemes. The results can provide a reference for similar engineering problems.

## Introduction

With the rapid development of the city and utilization of underground space, the theories and research on pit projects have also become increasingly sophisticated. Because various factors often cause some technical problems in the process of pit excavation, leading to numerous damages to the surrounding environment and the building structure. Therefore, the construction program must be technologically advanced, safe and reasonable to ensure the stability and safety of the building itself and the surroundings roads and underground facilities. So the foundation pit engineering has strong regional characteristics, and the past experiences have important reference value.

The pit supporting structure should be designed be by the limit state method expressed by partial coefficients. Meanwhile, the design should consider the horizontal deformation of the structure, and identify the limit deformation of the supporting structure according to the surrounding environment. In addition, the methods for controlling pit groundwater can be divided into dewatering, collection, recharge, cutoff and so on. When the dewatering scheme may affect the stability and security of the pit and its surroundings, the recharge method should be applied. As to the cutoff scheme, the dewatering method should be adopted when the pit water amount or the water pressure is great [1].

## Project overviews

A large building along the river locating in the mountainous area with high slope areas, takes the way of large excavation, according to one of the principles of engineering design requirement to minimize the demolition of houses and farmland occupation to the greatest extent. The pit is 121.7m along the flow direction, 76.3m wide and the bottom elevation is about -9.10m. The geological environment, and the climatic and hydrological conditions of the area are complex. According to the project arrangements, the storm season and the seepage may affect the slope stability and cause uneven subsidence during the excavation construction of the foundation pit.

The geological conditions of pit areas are shown in Table 1. The excavation mainly involves 10 different geological sub-layers with 2~4m thick silt clay. The layers of ③-3、④-1 and ②-5 are the main aquifer, with the vertical and horizontal permeability $K=A\times10^{-5}\sim A\times10^{-4}$cm/s, belonging to weak aquifer. The cohesive soil layers of ⑤ and ③-2 with groundwater horizontal motion has

good horizontal bedding, whose K (vertical) =A×$10^{-7}$cm/s, K (level) = B×$10^{-5}$cm/s. The peat layer is between ②-2 and ②-3, with high compressibility, soft, low intensity. Under the effect of groundwater flow, ④-1 and ③-3 composed of light sandy loam layer may produce quicksand.

**Table 1 Geological parameters of foundation pit**

| Layer | Soil bottom elevation / m | Natural Moisture | Consolidation | | Permeability coefficient （20°C）/(cm/s) | Allowable Bearing |
|---|---|---|---|---|---|---|
| | | | c/kPa | φ/(°) | | |
| ①-1 | 2.0～4.4 | — | 16/8 | 31/30 | 4.1×$10^{-6}$（6.0×$10^{-5}$）(Vertical) | |
| ②-2 | 0.3～1.8 | 36.7 | 13/10 | 23/20 | 3.2×$10^{-6}$（9.5×$10^{-6}$）(Vertical) | 84 |
| ②-3 | 0.1～-4.7 | 48.9 | 15/11 | 17/15 | 8.5×$10^{-6}$（2.7×$10^{-5}$）(Vertical) | 63 |
| ②-5 | -5.0～-5.2 | 35.3 | 11 | — | 3.0×$10^{-5}$（2.8×$10^{-5}$）(Vertical) | 119 |
| ③-1 | -2.4～-3.1 | 26.9 | 40/28 | 21/19 | 1.1×$10^{-7}$（3.6×$10^{-7}$）(Vertical) | 361 |
| ③-2 | -3.3～-8.5 | 30.2 | 31/21 | 22/20 | 4.2×$10^{-7}$（9.2×$10^{-7}$）(Vertical) | 149 |
| ③-3 | -6.8～-8.6 | 32.2 | 5/5 | 37/34 | 1.4×$10^{-4}$（1.9×$10^{-4}$）(Level) | 118 |
| ④-1 | -9.0～-11.6 | 33.1 | — | — | 6.6×$10^{-4}$(Vertical) | 123 |
| ⑤ | -3.2～-15.1 | 34.9 | 17/13 | 18/16 | 4.1×$10^{-7}$（1.6×$10^{-4}$） | 110 |
| ⑤` | -4.9～-15.8 | 35.6 | 12/5 | 29/26 | 1.3×$10^{-6}$（2.5×$10^{-6}$） | 112 |
| ⑥ | -17.6～-20.1 | 23.3 | 56/46 | 24/21 | 1.7×$10^{-7}$（6.2×$10^{-6}$） | 298 |

**Note：①The former in the permeability coefficient value column is the arithmetic average of the values, and in parentheses are the average large-value；②In the "Consolidation fast shear" column, the left of the slash is the arithmetic average and the right is the small value average.**

**Comparison of excavation schemes**

(1)To reduce the damage caused by the river-side seepage to the pit, the 24cm-thick 130m-long 19.2m-deep underground continuous diaphragm wall was set, relatively embedded in about 0.4 ~ 0.6m depth of the impervious bed.

(2) Preliminarily design 1m and 2m-wide bridleway respectively at 3.7m and 2.5m height, where the inlet and drainage pipes and the intercepting ditch were arranged in the 3.7m-wide bridleway. Based on the slope stability calculation, the upper limit of the excavated slope elevation is 3.7m corresponding to the slope 1:1.5, and at 2.5~3.7m elevator is 1:2.5, at-2.5m is in 1:2.5. Thus the total excavation is 198,000$m^3$.

The dewatering and drainage plan and slope cut program are the two key issues of high slope areas along the river.

① There were three slope grading scheme. The design found two possible sliding planes, namely layer ⑤ and layer ②-3, and the latter one is in the middle of the slope.

Table 2 shows the three design conditions, working conditions, results and proposals.

**Table 2 Comparison of excavation schemes**

| Program code | A | B | C |
|---|---|---|---|
| **Engineering Level** | Temporary buildings 4 | | 10-year return flood control requirements |
| **Side slope safety factor** | K≥1.05 | K≥1.15: Well point dewatering effective. | K≥1.2 |

| | | | |
|---|---|---|---|
| **requirements** | | K≥1.05:Well point dewatering failure | |
| **Shear strength index** | Direct fast shear minimum average | K≥1.15: Consolidation fast shear minimum average. K≥1.05: Direct fast shear mean | According to geological conditions, sum up the design value |
| **Drainage** | Normal groundwater levels : -2.1m; 10m from slope top to the bottom: linear change | Well point dewatering | Light well in 3.5m height; Injection well in -1.0m height. |
| **Calculation Method** | Swedish Arc Method, self compiled program. | Slope stability analysis computer program | Arc sliding method |
| **Results** | Three platforms:5m+5m+5m. Slope 1:2.5. $K_{up}$=1.453, $K_{down}$=1.082 | Slope 1:1.5, K=1.292 Slope 1:2.5, K=1.06 | Slope 1:1.5, 1:2.5; 1:2.0, K=1.26 |
| **Proposal** | Set 5m wide bridleways at 3.90m, 0.00m, -4.10m elevation; slope 1:2.5 | Above ②-3: Slope 1:3; Blow ②-3: Slope 1:2. | Set 3 m bridleways at 3.60 m elevation and 2 m bridleway. at -1.20 m elevation; slope 1:1.5, 1:2.5, 1:2.0. |

② Use ditches and diving pool to collect rainwater and groundwater into catchment.

The key point of the dewatering and drainage program is groundwater pumping, where the water level should be lowered below the pit base, in order to ensure the smoothly concrete pouring and foundation pit excavation.

The pumping geological experiments on the confined aquifer at 3.31m~3.52m elevator showed that this layer has a moderate permeability, and the permeability coefficient is K = 2.25 × 10-4cm / s. When the groundwater was lowered down to 3.4 ~ 3.7m elevator, the radius of influence is 35m. To make the gushing at 240 ~ 360$m^3$ / day, the groundwater level should be controlled at -9.1m.

Set the deep test wells at the northeast corner of the pit, diameter φ800mm, bottom elevation 17.0m, depth 25m and make ensure the pressure water head at -9.1m after the dewatering. Finally, the multilayered-ring light well point dewatering gained acceptance.

(3) Above all, the excavation program was determined as follows:

① There are two most unfavorable circular sliding planes: the deep arc sliding above the hard soil layer along the -12.6m elevation⑥ and the sliding plane above the top local hard soil with the elevation-0.2m ③-1, where the former one was taken for slope design.

② According to the relevant specifications, the slope stability coefficient is taken as1.20. And according to the design specifications in Shenjiang, the slope stability safety factor is 1.44. Take the arithmetic mean of the consolidation fast shear peak as the standard value of the soil shear strength at the sliding plane. And the excavation depth exceeds 10m, belonging to the first level pit [2].

Comprehensively considering the above three programs, due to reserve sufficient width of soil to ensure the stability of the continuous wall, the paper proposed an annular arrangement of four wells and three-point grading scheme bridleways, and chose different sliding stability indicators for slope calculation. In Table 3, According to the circular slip calculations, it can meet the specification requirement K = 1.20. when the slope is 1:2.5 with three bridleways, $K_{min}$ = 1.47. According to the Shenjiang specifications, $K_{min}$ = 1.85(＞1.44). However, the total failure of dewatering wells should be considered to make sure the grading scheme appropriate, not conservative.

**Table 3 Results of slope stability calculation (slope 1:2.5)**

| Well point / Type of safety coefficient | Completely valid | | Failure | |
|---|---|---|---|---|
| | $K_{up}$ | $K_{down}$ | $K_{up}$ | $K_{down}$ |
| Mean of small values of consolidation fast shear | 1.46 | 1.92 | 1.22 | 1.06 |
| Arithmetic mean of fast shear consolidation | 1.88 | 2.18 | 1.53 | 1.4 |

**Key points of excavation process**

During the excavation process, there was about $20\times10^4m^3$ soil taken out from the foundation. In the actual implementation process, considering the protection of the pit bottom and the construction of the deep cement mixing pile, the excavation was divided into two phases.

After the first phase of the excavation, the bottom elevation was about-6.3m or so; and at the second phase the bottom elevation was excavated to -9.1m through miniature backhoe digging machines and manual excavation. Furthermore, the protection measures have adopted as follows:

① After the light well point played the role controlling water, the excavation of the stage can start and should strictly follow the principle of "dewatering first, excavation later".

② Drainage ditches should be set at the top of the slope and each platform, and then collect water drained by pumps in order to ensure a good drainage system on the construction site.

③ To strengthen the slope protection, the geotextile should be prepared for the soil slope protection in rainy season except plasterring plain concrete on the lowest layer.

④ To guide the construction, the professional staff should be entrusted to monitor changes in groundwater level, settlement, inclinometer and other aspects during excavation..

⑤ Prohibit the upright excavation deeper than 2m, and strengthen the management and control of the construction site.

⑥ Solutions to emergency:

a. When the excavation was close to the design base elevation, local wing walls appeared the phenomenon of fine sand stream. Then the technicist increased the drainage and speeded up local construction, thus completing the bottom sealing as soon as possible.

b. The tilt and the deformation of an observation point in the northwest slope exceeded the specification in one day's time. So the local construction was suspended for four days and did not take any measures until the slope regain stability [3].

**Conclusions**

(1) The terrain-geological and hydrology-weather conditions should be accurately grasped to make appropriate countermeasures for groundwater control and slope treatment. Furthermore, make contingency plans for unexpected problems is needed.

(2) Because of the significant shear indicator of the slope, the most unfavorable results should be introduced to calculate, and the slope design should consider the impact of precipitation.

(3) Close attention should be paid to the deformation and stability of the main pit structure and the surrounding buildings, and strengthening the monitoring and measurement and performing informationization construction are important guarantee for safe and effective excavation.

**References**

[1] Zeng Yuan, Zhigao Li, Yibin Wang. Excavation impact on nearby subway station factors [J] Underground Space and Engineering, 2008 (4): 642-645

[2] Kanghe Xie, Chongmin Liu. Layered soil excavation induced precipitation [J] Journal of Zhejiang University: 2002, 36 (3): 239-242

[3] Xiaohui Luo. Deep excavation coupled seepage and stress analysis [J] Engineering Survey, 1996

*Applied Mechanics and Materials Vols. 580-583 (2014) pp 2294-2298*
*© (2014) Trans Tech Publications, Switzerland*
*doi:10.4028/www.scientific.net/AMM.580-583.2294*

# Outstripping engineering preparation of construction sites

Oleinik Pavel Pavlovich[1],
Grigorieva Larisa Stanislavovna[2] and Brodsky Viktor Isaevich [3]

[1] Doctor of Technical Sciences, The Department of Technology and building organization of production, Moscow State University of Civil Engineering (MGSU), 26 Yaroslavskoe shosse, Moscow, 129337, Russian Federation

[2] Doctor of Chemical Sciences, The Department of Composite Materials Technology and Applied Chemistry, Moscow State University of Civil Engineering (MGSU), 26 Yaroslavskoe shosse, Moscow, 129337, Russian Federation

[3] PhD, The Department of Technology and building organization of production, Moscow State University of Civil Engineering (MGSU), 26 Yaroslavskoe shosse, Moscow, 129337, Russian Federation

pehel@yandex.ru

**Keywords:** construction site, a combination of milestones, the intensity of work

**Abstract.** The basic scheme of intensive implementation preparatory work, the general form of the formulas for determining the structure and amount of preparatory work performed prior to the start of construction.

A prerequisite for the planned deployment of construction works is the performance of preparatory work in the volume providing an implementation of the construction of the specified rate [1, 2]. In this context, the main task of choosing effective solutions organization of the preparatory period is to determine:

structure and the amount of work necessary and sufficient for the timely opening of the front work on the construction of buildings and structures ;

structure and the amount of work performed in accordance with the basic construction and installation works .

Currently available theoretical positions to implement the Preparatory works are inconclusive solve the above problem. Moreover, in the construction industry organization theory there is no clear methodology for the development of preparatory work in time and space, taking into account the totality of the factors influencing a variety of techniques and building facilities [3, 4].

Basic provisions on the organization of engineering site preparation should include:

advancing the construction of permanent utilities and facilities for the construction of water, heat , steam, compressed air and electricity ;

Ahead of off-site and intra- device roads for use in the construction process;

anticipatory lining of engineering networks for transport communication, , assembly and storage areas ;

lining combined with the construction of engineering networks of underground hour children of buildings and structures ;

combined gasket different kinds of utilities outside the zones and under construction projects mounting and storage areas ;

organization of production and living conditions on construction sites for the erection of mobile systems from the inventory of buildings, construction in the preparatory period and the use of permanent buildings for the needs of the construction of the existing buildings .

These provisions are implemented adequately provided subdivision construction site on homogeneous sites on functional characteristics of the work. Such homogeneous sites organized into ten groups (tab. 1).

Table 1 Systematization of homogeneous regions by functional signs

| Group number | Functional features |
|---|---|
| I | Land, land construction site, to be clearing with the demolition of buildings |
| II | Land, land construction site, to be planning ensuring runoff |
| III | Land construction site intended for organize mobile (inventory) of buildings and their complexes |
| IV | Land with communications, providing needs construction site in energy resources (water, heating, electricity, etc.) |
| V | Areas with transport routes (roads, railways) used in the construction process, and areas of communications, traceable under them |
| VI | Land with communications within storage sites, assembly and consolidation of structures and equipment |
| VII | Land with communications within the mounting zones construction of buildings and structures |
| VIII | Land for advancing the construction of buildings and structures, used for construction needs |
| IX | Land with utilities and foundations of buildings and structures combined with earthy grooves |
| X | Land with communications is mounting zones construction of buildings |

It is necessary to consider the following:

- Work in groups I - VIII (denoted by the volume of these works $V_{\text{П}}^{'}$) is - are crucial for the opening of the front main construction and installation of the works and should be fully executed prior to the construction of the object ;

- Work on group IX ($V_{\text{П}}^{''}$) must be carried out simultaneously with the device of foundations (underground parts) buildings and structures;

- Work on the group X ($V_{\text{П}}^{'''}$) does not hinder the opening of the front main construction works.

Thus, the amount of preparatory work for each direct object under consideration can be represented as :

$$V_n = V_{\text{П}}^{'} + V_{\text{П}}^{''} + V_{\text{П}}^{'''}, \quad (1)$$

where $V_n$ - amount of preparatory work (thousand RUB; man-days).

Number of homogeneous sections and the amount of work on them depend on the density of the object settings for synthesizing the entire set of influencing factors : the size and area of the territory ; availability of production , transport and engineering communications; cooperation of the main and auxiliary facilities; composition commissioning of new systems and queues. Meanwhile housing density change significantly even within the same industry. For example, enterprises of mining and chemical industry are building density 28% and the production of synthetic fibers - 50%. For light industrial building density is 21-61% , vehicle construction - 13-65 %, etc.

We introduce a factor as the ratio of the density of buildings:

$$p = \frac{F}{S}, \quad (2)$$

where: $F$ - building area;

$S$ - area of the enterprise within the enclosure.

Then the expression (1) can be determined as a function of density for the settings :

$$V_n(p) = V_{\text{П}}^{'}(p) + V_{\text{П}}^{''}(p) + V_{\text{П}}^{'''}(p) \quad (3)$$

But, on the other hand, the amount of preparatory work can be expressed through and the amount of work performed prior to the construction of the object $V_{\Pi}^{C}(p)$ :

$$V_{\Pi}(p)=V_{\Pi}^{D}(p)+V_{\Pi}^{C}(p) \tag{4}$$

As noted earlier, prior to the construction of the object in full compliance with the scope of work - $V_{\Pi}^{'}(p)$, and in combination with the basic construction and assembly pa - bots - the amount of work $V_{\Pi}^{''}(p)$. As for the scope of work $V_{\Pi}^{'''}(p)$, then the density of the development company , which tends to zero $p \to 0$ , the number of sites is mounting zones construction of buildings occupies a significant part of the territory of the construction site, and the amount of work in these areas tends to $V_{\Pi}^{'''}(p)$. At the same time, with increasing housing density $p \to 1$, the number of such sites and theoretically reduced their volume is equal to zero when $p = 1$. Therefore, when the development density coefficient from *0 to 1* is " transfusion " volumes $V_{\Pi}^{'''}$, in $V_{\Pi}^{'}$ and volume $V_{\Pi}^{''}$ . And as the site-specific portion of the volume all the preparatory works are permanent $V_{\Pi}^{'}, V_{\Pi}^{''}, V_{\Pi}^{'''} \to const$, then the pattern changes in the structure and scope of the preparatory period under review is presented as a function of the density of buildings :

$$V_{\Pi}^{'''}(p)=V_{\Pi}^{''',D}(p)+V_{\Pi}^{''',C}(p), \tag{5}$$

where: $V_{\Pi}^{''',D}(p)$- amount of preparatory work for the groups X, executed before the main construction works;

$V_{\Pi}^{''',C}(p)$ - amount of preparatory work for the group X, performed in combination with the main building and construction and installation works (CIW).

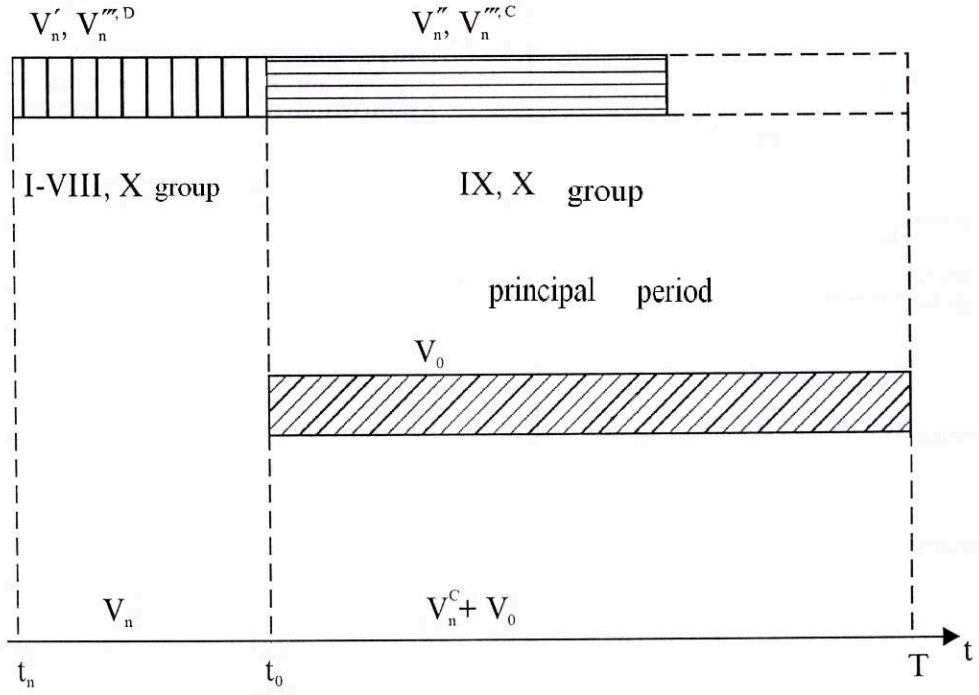


Fig.1. Schematic diagram of the intensive implementation spadework

This provision is essential and allows all the variety of options for the implementation of organizational solutions preparatory work reduced to a single diagram (Fig. 1).

Thus, the calculations necessary to use the general form of the formulas for determining the structure and volume of preparatory work performed prior to the construction of the object:

$$V_{\Pi}^{D}(p) = V_{\Pi}^{'} + V_{\Pi}^{'''',D}(p) \tag{6}$$

in combination with CIW:

$$V_{\Pi}^{C}(p) = V_{\Pi}^{''} + V_{\Pi}^{'''',C}(p) \tag{7}$$

Analysis of statistical data and the calculations showed that the subject:

$p \le p_0$ - Are as preparatory work performed prior to elevated of the object, and the preparatory work carried out in combination with the main building and construction works;

$p \succ p_0$ there are only preparatory work performed prior to elevated of object, ie $V_{\Pi}^{III,C}(p) = 0$

The simulation of the workload, it was found that $p_0$ = 0.71 (Fig. 2). Calculation formulas $V_{\Pi}^{D}(p)$ and are $V_{\Pi}^{C}(p)$summarized in Table 2 .

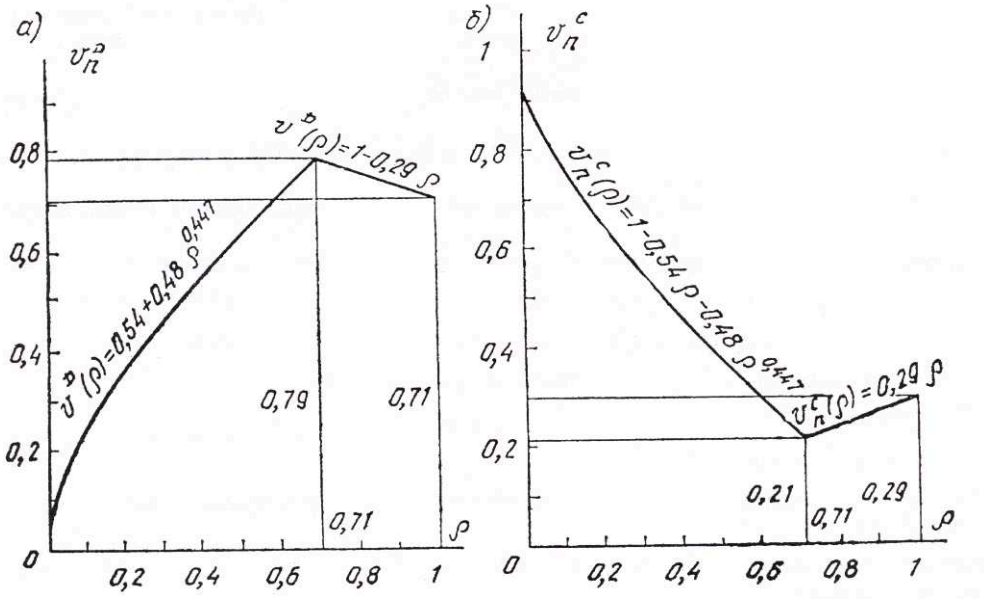


Fig. 2. Dependence volume distribution preparatory work performed:
prior to the construction of the object; b) in combination with the basic CIW

Table 2. Summary table of the estimated volume of rationing schemes preparer

| Design scheme | density ratio building | Volume of preparatory work performed: | |
|---|---|---|---|
| | | prior to construction object: $v_{\Pi}^{D}(p)$ | in combination main CIW, $v_{\Pi}^{C}(p)$ |
| 1 | $p \le 0,71$ | $(0,54p - 0,48p^{0,447})V_{\Pi}$ | $(1- 0,54p - 0,48p^{0,447})V_{\Pi}$ |
| 2 | $p > 0,71$ | $(1 - 0,29)V_{\Pi}$ | $0,29p\ V_{\Pi}$ |

Scheme 1 includes changes to the curvilinear law on the interval [0; 0.71] = 0 to 0.79.

Scheme 2 seems to be linear law of variation $v_{\Pi}^{D}(p)$ in the interval ( 0.71, 1.0 ) from $v_{\Pi}^{D}(p \succ 0,71) \prec 0,79$ to $v_{\Pi}^{D}(1,0) = 0,71$.

For the case of the distribution volume of preparatory work carried out in combination with the basic construction and installation works, there is a specular reflection function $v_{\Pi}^{D}(p)$ followed by the amount of shift $\Delta$ = +1.

Values of the functions $v_{П}^{'}$, $v_{П}^{''}$, $v_{П}^{'''}$, $v_{П}^{''',D}$, $v_{П}^{''',C}$, $v_{П}^{D}$, $v_{П}^{C}$ depending on changes in housing density $p$ increments $\Delta p = 0{,}05$ are given in Table 3 and represent the corresponding fraction of the volume of preparatory work. In this

$$V_{П} + V_{П}^{II} + V_{П}^{III} = 1$$

Table 3. Distribution function of the volume of preparatory work

| $p$ | $v_{П}^{'}(p)$ | $v_{П}^{''}(p)$ | $v_{П}^{'''}(p)$ | $v_{П}^{''',D}(p)$ | $v_{П}^{''',C}(p)$ | $v_{П}^{D}(p)$ | $v_{П}^{C}(p)$ |
|---|---|---|---|---|---|---|---|
| 1 | 2 | 3 | 4 | 5 | 6 | 7 | 8 |
| 0,05 | 0,19 | 0,02 | 0,79 | -0,03 | 0,82 | 0,16 | 0,84 |
| 0,10 | 0,26 | 0,03 | 0,71 | -0,02 | 0,73 | 0,23 | 0,77 |
| 0,15 | 0,31 | 0,04 | 0,65 | -0,02 | 0,67 | 0,29 | 0,71 |
| 0,20 | 0,35 | 0,06 | 0,59 | 0,00 | 0,59 | 0,35 | 0,65 |
| 0,25 | 0,38 | 0,07 | 0,55 | 0,02 | 0,53 | 0,40 | 0,60 |
| 0,30 | 0,41 | 0,09 | 0,50 | 0,03 | 0,47 | 0,44 | 0,56 |
| 0,35 | 0,45 | 0,10 | 0,45 | 0,04 | 0,41 | 0,49 | 0,51 |
| 0,40 | 0,47 | 0,12 | 0,41 | 0,07 | 0,34 | 0,54 | 0,46 |
| 0,45 | 0,50 | 0,13 | 0,37 | 0,08 | 0,29 | 0,58 | 0,42 |
| 0,50 | 0,52 | 0,15 | 0,33 | 0,10 | 0,23 | 0,62 | 0,38 |
| 0,55 | 0,55 | 0,16 | 0,29 | 0,12 | 0,17 | 0,67 | 0,33 |
| 0,60 | 0,57 | 0,17 | 0,26 | 0,14 | 0,12 | 0,70 | 0,30 |
| 0,65 | 0,58 | 0,19 | 0,23 | 0,16 | 0,07 | 0,74 | 0,26 |
| 0,70 | 0,60 | 0,20 | 0,20 | 0,18 | 0,02 | 0,79 | 0,21 |
| 0,75 | 0,63 | 0,22 | 0,15 | 0,15 | 0,00 | 0,78 | 0,22 |
| 0,80 | 0,65 | 0,23 | 0,12 | 0,12 | 0,00 | 0,77 | 0,23 |
| 0,85 | 0,66 | 0,25 | 0,08 | 0,09 | 0,00 | 0,75 | 0,25 |
| 0,90 | 0,68 | 0,26 | 0,06 | 0,06 | 0,00 | 0,74 | 0,26 |
| 0,95 | 0,70 | 0,28 | 0,02 | 0,02 | 0,00 | 0,72 | 0,28 |
| 1,00 | 0,71 | 0,29 | 0,00 | 0,00 | 0,00 | 0,71 | 0,29 |

**References**

[1] P.P. Oleinik, Building organization. Conceptual bases. Models and methods. Information-systems engineering. M.: Profizdat 2001.

[2] P.P. Oleinik, V.I. Brodsky Technique regulation of rates implementation the preparatory work: : submitted to Journal of Technology and organization of construction industry (2013)/

[3] I.G. Shepelyov, Mathematical methods and models of management in construction. M.: Graduate School, 1980.

[4] V.A. Kharitonov, Underground buildings and structures on the industrial and civil values. M.: ASV, 2008.

*Applied Mechanics and Materials Vols. 580-583 (2014) pp 2299-2302*
*© (2014) Trans Tech Publications, Switzerland*
*doi:10.4028/www.scientific.net/AMM.580-583.2299*

# Research on the problems and Countermeasures for steam curing of assembled composite wallboard

Chunyi Xu[1, a], Lei Yan[2,b],Chen Li[1,c] and Zhiwei Cao[1,d]

[1]School of Civil Engineering, Shenyang Jianzhu University, Shenyang 110168, China

[2]Shenyang City Construction Engineering Quality Supervision Station, Shenyang 110002, China

[a]xuchunyiyi@163.com, [b]yl_98@163.com, [c]331245963@qq.com, [d]eve.soul@163.com

**Keywords:** Prefabricated construction; Assembled composite wallboard; Industrialized production; Steam curing

**Abstract.** For researching principle and production line state of steam curing of composite wallboard, the art have been conducted through actual investigation and field test. Based on the influence of steam curing on the strength of high performance concrete, durability and volume stability, put forward suggestions of steam curing system; Several problems have been raised for steam curing in the actual production, then some correlative improve measurements are given. Provide the reference for the production and development of the residential part in our country.

## Foreword

With the implementation of the policy on wall innovation and energy saving, housing industry modernization is on the agenda gradually. Prefabricated housing structure has becoming increasingly popular for its advantage of environment protecting, convenient for factory production and standardization production, field assembly. Use ratio has become higher and higher[1]. As one of the most rapid development materials[2], composite wall panel has the advantage of light weight, high strength, heat preservation and sound insulation, especially the same lifespan of insulating layer as the structure comparing to the ordinary wall materials. At present, the prefabricated housing system is still in its infancy, whose the technology is not perfect enough, especially the research of industrial production is very rare, techniques of production is laggard, industrialization level is low.

The found from the actual investigation are that curing time and curing conditions are not uniform is the main factors that restrict the assembled composite wallboard production efficiency and increase the cost. With the precast production change rapidly, research on the steam curing technology in China still remained in the last century. Backward technology, maintenance and monitoring is only determined by experience, no innovation, no improvement. When the production number is large, appear that steam curing can not keep up with the other processes of the rhythm, leading to low efficiency, increase the cost. So it is urgent need to improve the steam curing plan.

## Steam curing equipment for the industrialized production of composite wall panel

Steam curing is a kind of ordinary pressure and wet and heated curing, which a curing technique that could accelerate the hardening of concrete when the medium temperature does not exceed 100, and the RH is above 90%. Steam curing can be divided into four period, procuring, heating period, constant temperature period, cooling period. Currently there are three kinds of common steam curing equipment, curing cover, vertical curing kiln, horizontal tunnel curing kiln[3].

**Curing cover:** It is apply to fixed horizontal curing kiln, which the steam pipe lays under the pedestal in advance. Canvas puts on the components directly ,and open the steam pipe valve to start steam curing. Curing cover is poorly equipped, and poor heat preservation effect. The operation is a waste of time and energy. It shown in Fig. 1.

**Vertical curing kiln:** It is apply to assembly line production mode. There are two lines in kiln ,up and down. The product raises layer by layer on one side of the kiln, and move to the other side by the

small flat car, then descend layer by layer, Kiln has been divided into three rising phase, stabilization phase, decreasing phase by the theory that high temperature steam up ,the low temperature air flow down. Vertical curing kiln has the advantage of saving the workshop area, easily continuous operation, less consumption of steam. But the investment is large ,and the equipment is hard to repair. It shown in Fig. 2.

**Horizontal tunnel curing kiln:** It is apply to assembly line production mode. The products go through the kiln from one end, pass by the rising phase, stabilization phase, and decreasing phase and go out from the other end of the kiln. The advantage is continuous flow process, but it is hard to divide the three phases, the temperature and humidity are hard to control, In addition, steam will leak because the kiln is hard to close. It shown in Fig. 3.

Fig. 1. The Curing cover

Fig. 2 The vertical curing kiln

Fig. 3. Horizontal tunnel curing kiln

## The determination of steam curing system

It is known that parameter such as rest period, heating/cooling rate, constant temperature time could not be increased or decreased separately. For example, although extend the rest period could enhance the strength of concrete, durability and volume stability, but too long rest period could affect the production efficiency, so strength, durability, volume stability, and the demand of production cycle must be considered when selecting parameters[1~5].

By the contrast analysis of “Code for production construction and quality acceptance of concrete member in assembly integrated precast building” in Shanghai, “The design and construction technical guide for framed concrete structure”provided by Kajima Corporation in Japan, “Production and acceptance procedures of precast concrete component” in Liaoning province, and consider the problems in the actual production process, this paper has given the steam-system, which the rest period should be less than 2 hours, 3 hours is suggested to ensure the performance of the component development without affecting the production efficiency(the rest period is determined by environment temperature, which is concluded by the experimental results of influence of stop time on

concrete performance under different environment temperatures),method such as covering membrane, humidification should be taken to keep the components humid, the temperature in plant should not be less than 5℃, heating rate should be between 10℃~20℃/h, the maximum curing temperature should be no more than 55 ℃.The maximum temperature should be reduced appropriately, considering the water loss too fast would cause the cracking on concrete surface and XPS deformation by heat .Constant temperature time should be no less than 4 hours, which is vary depending on the plant maintenance equipment and local temperatures, etc. As shown in Figure 3.1 is the proposed steam curing system by this paper.

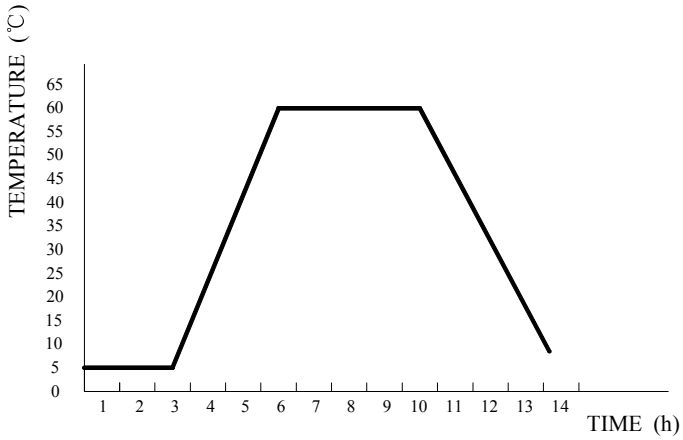


Fig. 3.1 Steam curing system

**The current situation and problems for the industrialized steam curing of composite wall panel**

Four problems have been summarized by reviewing the related literatures [1~5]and field survey of several prefabricated concrete factories in Shenyang:

(1) When the production is low, assembly line production mode is a waste time and energy, production efficiency is low, at this time, fixed horizontal curing kiln should be used, then the kiln in assembly line has been leaved unused.

(2) When the production is high, steam curing procedure is too slow comparing to other procedures, reduce the production efficiency.

(3) The technical study for the steam curing of composite wall panel is. few .The research in our country still stay at the end of last century. The research of pros and cons is not enough, curing monitor can be only determined only by experience.

(4) Some domestic manufacturers have just introduced dynamic model production lines, but automation level has been reduced because the research is so few. Cost has been increased for the long time of curing.

**Proposed scheme of Improved steam curing**

Considering the problems above, some suggestions for improving steam curing have been provided:

(1) Shorten the rest period to improve production efficiency: the rest time could be optimized by demoulding strength and strength and volume stability of 28 days curing after steam curing. the high the temperature is ,the shorter time the rest period is ,but there would always have a shortest rest period in different environment temperatures. Shenyang Yuhui factory uses the secondary curing to shorten the rest period, the products have been put into curing kiln in rest period time, which could help the products get the early strength in advance. And consequently shorten the rest period, practice has proved that time could be shorten by half.

(2)Adopting temperature-gradient method or variable speed temperature rise: most of the steam curing use one time heating up method, one time heating up method is a common method of steam curing .But the curing time is too long. Temperature-gradient method could make the concrete

strength increase gradually at low temperature ,until it could resist the damage caused by second phase fast heating-up, then temperature rise to constant temperature rapidly. This method could reduce the damage caused by heating up. It could also reduce the rest period, and curing time as well.

(3) Fixed horizontal curing kiln is the traditional production mode, which is discouraged by its resource utilization, huge waste of energy and resources. But since the fabricated structure of our country is in its initial stage. Component demand is not so much, the factory production is not stable, so this method has become safer mode of production. The curing equipments like vertical curing kiln and horizontal tunnel curing kiln have been put on hold even though they could save lots of time and energy. So it is necessary and meaningful develop a flexible production line which could not only make the most of curing equipment but also ignore the limit of the production.

## Conclusions

Based on the influence of steam curing on the strength of high performance concrete, durability and volume stability, put forward suggestions of steam curing system; Several problems have been raised for steam curing in the actual production, then some correlative improve measurements are given. The research of this article is to promote the industrialization of modern construction progress, which not only meet the demand of the national development strategy, but also is an inevitable choice for modern building industrial upgrading. Provide the theory support for the enterprise and the reference for national standards. And improve the quality of the fabricated composite wall panel, large-scale industrial production and labor productivity.

## Acknowledgements

Key Projects in the National Science & Technology Pillar Program during the 12th Five-Year Plan Period of China(2012BAJ16B05).

## References

[1] Baoju Liu．Study on efficiency of fly ash and its application in steam curing concrete. Central South University, (2007).(in Chinese)

[2] Zhou Jialing. The influence on mechanical properties of reactive powder concrete curing. Central South University, (2003).(in Chinese)

[3] Peng Bo. Influence of Steam-Curing System on Performance of High Strength Concrete. Wuhan university of technology, (2007).(in Chinese)

[4] Liu Baoju, Xie Youjun, Zhou Shiqiong, etal．*Some factors affecting early compressive strength of steam-curing concrete with ultrafine fly ash*. Cement and Concrete Research, Vol. 31 (2001), p. 1455-1485.(in Chinese)

[5] He Zhihai，Liu Baoju．*Hydration characteristics of steam curing cement-fly ash composite binder*.CONCRETE, Vol. 12 (2005), p. 67-70.(in Chinese)

*Applied Mechanics and Materials Vols. 580-583 (2014) pp 2303-2307*
*© (2014) Trans Tech Publications, Switzerland*
*doi:10.4028/www.scientific.net/AMM.580-583.2303*

# Temperature cracks of concrete engineering analysis and treatment measures

GENG ZHANG

Department of civil engineering , Xinjiang Construction Vocational Technology Institute ,Urumqi 830026 ,China.

260021488@qq.com

**Keywords:** concrete temperature cracking temperature stress treatment measures.

**Abstract.** In the building construction project occupies an important position in the concrete , cracks appeared in the concrete work is more common , the cause of cracks in the concrete temperature control and crack prevention measures such as on-site concrete temperature were analyzed .

## Introduction

Concrete works , the temperature stress and temperature control is important. This is mainly due to two reasons . Concrete temperature cracks often appear in the construction , affect the integrity and durability of the structure . During operation , the temperature change has a significant impact on the stress can not be ignored state structure . We encountered mainly construction temperature cracks , this article on the causes and treatment measures in construction of concrete cracks were analyzed.

## Organization of the Text

### 1 Cause crack

There are several reasons for the concrete cracks , that the changes in temperature and humidity during hardening of the concrete release large cement hydration heat , the internal temperature rising to the surface due to tensile stress . Late in the cooling process , or due to constraints based on the old coagulation , will appear in the tensile stress in the concrete . Reduce the temperature of the concrete surface will cause a lot of tension stress . When these tensile stresses exceed the capacity of the concrete cracking , cracks will appear . Many internal concrete humidity changes or changes little slower , but larger changes or surface moisture may change dramatically . Such as conservation ill , when dry wet surface deformation constrained internal shrinkage of concrete, often leads to cracks. Concrete is a brittle material , the compressive strength of tensile strength 1/10 , ultimate tensile strain just short loading time (0.6 ~ 1.0) × 104, when the limit position of the long-term loading deformation extends only ( 1.2 ~ 2.0) × 104. Since the raw material is uneven, unstable water-cement ratio , and transportation and pouring during segregation , in the same piece of concrete tensile strength is uneven , there are many low tensile strength , easy cracks weak site. In concrete , the tensile stress is mainly borne by the reinforced concrete to withstand compressive stress only . In the plain concrete or reinforced concrete on the edge of the site if there is a tensile stress within the structure , the concrete shall rely on their own commitments. General design requirements in both the tensile stress does not occur or occurs only to a small tensile stress . But in the construction of the concrete by the maximum temperature is cooled to a stable temperature during operation , often causing considerable tensile stress in the concrete . Temperature stress can sometimes exceed other stresses caused by external loads , and therefore grasp the temperature variation of the stress is extremely important for the structural design and construction reasonable .

### 2 Analysis of temperature stress

According formation temperature stress can be divided into the following three phases:

( 1 ) Early : pouring concrete from the beginning to the end of basic heat cement , usually about 30 days . Two features of this stage , first emit a lot of heat of hydration of cement , the second is the

dramatic changes in coagulation and elastic modulus . Since the change in the elastic modulus , residual stress formed during this period in the concrete .

( 2 ) Interim: from basic cement exothermic effect until the end of the concrete when cooled to a stable temperature only, this time , the temperature stress is mainly due to cooling and external temperature changes caused by concrete , the stress and the early formation of residual stress superposition , little changed in the meantime on the elastic modulus of coagulation .

( 3 ) Late : Concrete completely cooled after operation period. Temperature stress is mainly caused by external temperature changes , these stresses and residual stress of the first two phases of superposition .

Depending on the cause of stress caused by temperature can be divided into two categories:

( 1 ) Stress of the : without any constraints or boundary structure completely still , if the internal temperature distribution is non-linear due to the structure itself bound to each other appears and temperature stress. For example , a bridge pier , the structure size is relatively large, while the concrete cooling surface temperature is low, the internal temperature is high, the surface tensile stress , compressive stress occurs in the middle.

( 2 ) stress constraints : all or part of the boundary of structures is outside the constraints are not free of stress caused by the deformation . As concrete box girder roof and concrete fence .

Both temperature and shrinkage of concrete stress is often caused by stress joint action .

**3 Measures to crack Temperature control and prevention**

To prevent cracks , reduce temperature stress can proceed from the constraints of controlling the temperature and improve two aspects .

Measures to control the temperature as follows:

( 1) Heavy unreinforced concrete or less muscle mass , the total does not exceed 20% admixture of large stones , reduce the amount of concrete in order to reduce the heat of hydration of cement and conservation purposes .

( 2 ) improving reinforcement . In order to ensure that the upper and lower layers are each pouring temperature tendons , the proposed design will be distributed tendons make the appropriate adjustments . Temperature distribution should be fine ribs , usually with ϕ 8 steel , bi- reinforcement , spacing 15 cm. Such temperatures can enhance the ability to resist stress .

( 3) The aggregate gradation improvement in mass concrete is generally used in grit or coarse sand , fineness modulus is generally about 2.3 to 3.0. Gravel particle size generally require the use of a continuous gradation of coarse aggregate to the preparation of concrete , should try to use a larger diameter well-graded gravel . With dry concrete , mixed mixes, plus air-entraining agent or plasticizing agent in concrete measures to reduce the amount of cement ; reduce the heat of hydration of cement and deformation , or use low heat of hydration heat of hydration of cement in concrete preparation such as slag cement , pozzolana Portland cement, fly ash cement , composite cement , etc.

( 4 ) when mixed with a certain amount of mixing fly ash concrete admixtures can replace part of the cement , concrete and can improve viscoplastic . Improve pumpability , reduced heat of hydration of concrete , improve late strength ; adding water or gravel with water cooling to reduce the temperature of the concrete pouring ;Decrease when pouring concrete

( 5 ) days of pouring hot thickness , the use of heat pouring level ;

( 6 ) pipes buried in concrete , pass into the cold water to cool ;

( 7 ) the conservation of mass concrete and the internal temperature is monitored to measure the surface temperature and the internal temperature of the concrete after pouring through technical measures for the temperature control requirements within the scope of the design , when the design is no specific requirement when temperature should not exceed 25 ℃. Set reasonable removal time , when temperatures plunged surface insulation , concrete surface in order to avoid the occurrence of sharp temperature gradient ;

( 8 ) the construction and long-term exposure to pouring concrete block surface or thin-walled structures , insulation measures taken during the cold season ;

Improvements constraints are:
( 1 ) reasonably parting block ;
( 2 ) to avoid excessive fluctuations basis ;
( 3 ) reasonable arrangements for the construction process , to avoid excessive height and lateral long-term exposure ;

In addition, to improve the performance of concrete , improving crack resistance and strengthen conservation , prevent surface shrinkage , particularly to ensure the quality of concrete is very important to prevent fractures , special attention should be avoided through the cracks appeared to be restored after its structural integrity it is very difficult , so the construction should be to prevent the occurrence of cracks penetrating dominated .

( 1 ) improve the constraints , reducing temperature stress . Stratified block or pouring concrete, a reasonable set of horizontal or vertical construction joints , or in the appropriate location set construction pouring belt to relax the constraints extent , reduce the length of the heat storage capacity of each pouring to prevent the accumulation of heat of hydration reduce temperature stress . Between massive concrete foundation and concrete cushion Heavy sliding layer settings , such as the use of flat- poured asphalt or paved membrane. In the vertical plane , keyway site set up buffer layer , such as the laying of asphalt after 30 ~ 50 mm polystyrene foam board or wood wool to remove embedded solid role in the release of restraint stress .

( 2 ) improve the ultimate tensile strength of concrete . Following the coarse aggregate with a good choice , and strictly control the clay content , strengthen vibrated concrete, concrete density and tensile strength , reduced shrinkage deformation , to ensure construction quality. Take the second feeding method , the second vibration method , and remove surface water after pouring , enhance early conservation , improve early age or the corresponding tensile strength and modulus of elasticity of concrete . The temperature setting is necessary on the basis of mass concrete reinforcement inside , the turning point in the cross section deformation and , at the end, the turning point of the roof and walls , holes and around the corner to increase the diagonal structure reinforcement to improve the stress concentration to prevent cracks .

In concrete construction , in order to increase turnover template , often require new cast concrete form removal as soon as possible . When the temperature is higher than the temperature of the concrete should give due consideration to the removal time , so as not to cause cracks in the concrete surface early . New cast early form removal , surface caused great tensile stress, a " thermal shock " phenomenon. In the early concrete pouring , because distributing heat of hydration , causing considerable surface tensile stress , when the surface temperature of the high temperature compared , then removal of the template , the surface temperature dips, would inevitably lead to a temperature gradient , resulting in an additional surface tensile stress , thermal stress superposition hydration plus concrete shrinkage , tensile stress surface a large value , there is a risk of cracks , but if the insulation material is promptly covered with a light at the surface after removal of the template , such as foam sponge , the concrete surface to prevent excessive tensile stress has a significant effect.

Reinforced stress has little effect on the temperature of mass concrete , because the rate of muscle mass concrete containing very low . Just reinforced concrete impact on the general . At a temperature below the yield stress is not too high and the limit conditions , the performance of steel is stable regardless of the state of stress , time and temperature. Linear expansion coefficient of linear expansion coefficient of steel and concrete difference is small, the internal stress between the two occur only small changes in temperature . Since the elastic modulus of the steel is 7 to 15 times the modulus of elasticity of concrete , when the stress reaches the tensile strength of the concrete cracking , steel stress will not exceed 100 ~ 200kg/cm2 ..... So , you want to use in concrete reinforced to prevent small cracks very difficult. But the cracks in the reinforced structure generally becomes more than the number of small spacing, width and depth of the smaller . And if the bar diameter thin and dense spacing , good crack resistance of concrete to enhance the effect . Surface of the concrete and reinforced concrete structures are often thin and shallow cracks occur , most are shrinkage cracks .

Although such cracks are generally shallow , but the strength and durability of its structure is still some impact.

To ensure the quality of concrete work to prevent cracking and improve the durability of concrete , proper use of admixtures is also one of the measures to reduce cracking . Use water-reducing agent, such as crack , practice, summed up its main role is to :

( 1 ) the presence of a large number of pores in the concrete road, the capillary force generated in the capillary after the evaporation of water , drying shrinkage of the concrete . Increasing the diameter of the pores can be reduced capillary surface tension , but will reduce the strength of concrete .

( 2 ) water-cement ratio is an important factor affecting concrete shrinkage , the use of water-reducing agents can crack the concrete to reduce water consumption by 25%.

Important factors

( 3 ) the amount of cement concrete shrinkage also doped water subtraction concrete cracking agent under conditions to maintain the strength of concrete can be reduced by 15 percent the amount of cement , aggregate usage by increasing its volume to add.

( 4 ) water-reducing agents can improve the cracking grout consistency and reduce bleeding of concrete , reduce shrinkage deformation sink .

( 5 ) improve adhesion grout and aggregate to improve the crack resistance of concrete .

( 6 ) to be bound by concrete shrinkage during tensile stress, the tensile stress when the crack is generated is greater than the tensile strength of concrete . Water-reducing agent can effectively improve the cracking of the concrete tensile strength, a substantial increase in crack resistance of concrete.

( 7 ) allows the mixing of concrete admixtures dense , and can effectively improve the anti-carbonation of concrete, reducing carbonation shrinkage .

(8 ) mixed with water reducing agent for concrete crack retarding the appropriate time in the effective prevention on the basis of cement hydration heat quickly , avoid plastic shrinkage due to cement long-term non-condensable brought increased.

( 9 ) mixed with good workability of concrete admixtures , easy to touch the flat surface , the formation of micro- film to reduce water evaporation , reduce drying shrinkage .

Many retarding admixtures have increased workability, improve the function of plasticity in engineering practice should be more research into the experimental comparison and , simply by improving external conditions , may be more simple than the economy.

## 4 Early concrete curing

Practice has proved that the common concrete cracks , most of surface cracks at different depths , mainly due to the temperature gradient caused by the sudden drop in temperature in cold areas also easy to form cracks. So, to say the insulation on the concrete surface to prevent early cracks especially important.

From the viewpoint of temperature stress , thermal insulation should meet the following requirements:

( 1 ) prevent the temperature difference between the inside and outside of concrete and concrete surface gradient , to prevent surface cracks.

( 2 ) prevent the concrete super cold , should try to try to make the construction period of not less than the minimum temperature of the concrete using a stable temperature of the concrete .

( 3 ) to prevent the old concrete too cold to reduce the constraints between old and new concrete .

Early curing of concrete , the main purpose is to maintain proper temperature and humidity conditions in order to achieve the effect of two aspects, one of the concrete from adverse temperature and humidity deformation of the invasion, prevent harmful shrinkage and shrinkage . On the one hand the cement hydration smoothly to achieve strength and crack resistance design.

Optimum temperature and humidity conditions are interrelated . Coagulation on insulation measures often have the effect of moisture .

Theoretically, the water contained in the newly poured concrete fully meet the requirements of more than cement hydration . However, due to evaporation and other factors often cause water loss ,

delay or interfere with cement hydration , the easiest and the concrete surface directly affected by such adverse effects . So the first few days after concrete pouring conservation is a critical period in the construction must pay attention to . You can take specific measures to deal with :

( 1 ) According to the plan layout , check the temperature before pouring the concrete situation and prevent damage to the point of laying pouring the facility , and to establish an initial value measurement points . Before the initial setting of concrete , the implementation of secondary bleeding treatment , overcoming early due to cracks caused by dehydration , and the amount of water covering film , the insulation measures and implement .

( 2 ) According to Shi group requirements, strict measures to check the insulation of concrete implementation . Concrete pouring process and the conservation period, the concrete should be closely monitored during temperature changes . Since when pouring from 1 ~ 7 d, measured every 1 h time ; Section 8 ~ 14 d, measured every 4 h. Control temperature difference of concrete, when the temperature difference exceeds 25 ℃ should supervise the construction side to further strengthen the implementation of insulation measures

( 3 ) large volume concrete is generally less than 7 d, the strength of concrete block and concrete conservation center of the plate according to the same conditions of temperature change and determine the curing cycle. Curing Concrete should heat, moisture and technical measures to cool slowly , usually when pouring in thickness greater than 3 m, requires consideration of measures to cool the cooling water circulation inside the concrete, set the cooling water , and through the concrete temperature measurement and control center the temperature inside the concrete surface or the cooling water temperature is controlled within 25 ℃.

## 5 Conclusion

The above construction of the relationship between the temperature of the concrete and the cracks were on the theory and practice of preliminary study , although the causes of academia and calculation methods for concrete cracks have different theories , but for specific advice for prevention and improvement measures is relatively uniform , while applying the effect in practice is relatively good , concrete construction is up to us seeing much comparative , multi- analysis problems, and more summary , combined with a variety of preventive treatment measures, concrete cracks are completely avoidable.

## References

[1] GB50204-2011. Concrete Construction Quality Acceptance [S].

[2] JGJ52-2006. Ordinary concrete sand stone quality standards and test methods [S].

[3] Construction Manual Writing Group . Construction Manual [M] Beijing : China Building Industry Press, 2003 :

[4] Tian Shan Lou, Huang Xiong . Prevention of concrete projects of common quality problems [J]. Construction Management Modernization , 2004:51-53

[5] Tie Meng Wang. Crack Control of buildings [M] Shanghai : Shanghai Science and Technology Press , 1997.

[6] Bo Fang Zhu . Mass concrete temperature stress and temperature control [M] Beijing : China Electric Power Press , 1999

*Applied Mechanics and Materials Vols. 580-583 (2014) pp 2308-2315*
*© (2014) Trans Tech Publications, Switzerland*
*doi:10.4028/www.scientific.net/AMM.580-583.2308*

# The double-layernonstationaryheat conduction. Measures to prevent the formation ice-damson the roof.

PetrichenkoMikhail Romanovich[1, a], NemovaDarya Viktorovna[2, b], TarasovaDarya Sergeevna [3, c], StaritcynaAnastasiiaAndreevna[4, d].

[1]Saint-Petersburg State Polytechnical University, Russian Federation

[2]Saint-Petersburg State Polytechnical University, Russian Federation

[3]Saint-Petersburg State Polytechnical University, Russian Federation

[4]Saint-Petersburg State Polytechnical University, Russian Federation

[a]gidravlika@cef.spbstu.ru, [b]darya.nemova@gmail.com,

[c]tarasovads@gmail.com, [d]a.staritsyna@mail.ru

**Key words:**energy efficiency, heat balance equation, cold attic, roof covering, icicle, ice-dam.

The following article deals with the problem of icicles formation on the roofs and the elimination methods. The attic roofs with pitched roofing are highly susceptible to this negative phenomenon.

In work warming of garret overlappings as a method of prevention of formationice-dams on roofs of buildings in the operation, being characterized is in detail considered by the lowest temperatures of external air.

## Introduction

The last winters were remembered not only with mass snowfalls butwithnumerous victims of icicles. Every wintermany people suffer from the icicles falling from roofs. According to Agency of medico-social information on February 26-28, 2010 in St. Petersburg 56 people suffered from iciclesin only three days. Thus it is limited not onlyto physical injuries. People get to hospitals, remain disabled people, lethal outcomeoccur. Besides, falling of icicles does also material harm. The icicles fall commonly enough on the cars parked near buildings. Moreoverformation of icicles causesdestruction of eaves and drainpipes. Ice in the frozen drain blocks outflow of thawed snow, thawed snow can leak on walls, under a roof and in rooms, yielding more considerable damages [1].

Most often icicles are formed on acting sites of a facade of the building on eaves, balcony peaks, roof edges. At necessary for process of formation of an icicle conditions, in one days its weight can considerably will increase. The weight of some icicles can reach 300 kg, and length more than a meter. Icicles can be broken off and fall down, damaging everything that meets to them on a way.For obvious reasons, the problem of the formation of ice dams is relevant.

If the gravity operating on an icicle, as a result of growth of its weight exceeds strength of ice in a point of the beginning of growth, the icicle will collapse. At the termination of intake of thawed snow growth of an icicle stops, and at a temperature over zero there is a reduction of the sizes and mass of an icicle due to thawing.

At a roof with a small bias it is rather difficult to avoid formation of frost on it at various options of external conditions.

## The overview

Petrichenko M.R. in works proposed procedure that makes it possible to assign the rate of drop in water level in the upper pool, which eliminates failure of earthen structures [20-21]. Petrichenko M.R in works [22-23] offered to replace the traditional Dupuis formula by the condition of the minimum of the functional reflecting the average quadratic norm of the departure of the curvilinear profile of the free surface from a straight line.

Petrichenko M.R. revealed that successful plotting of the depression curve for the plane problem of filtration in homogeneous soils can solve many engineering problems of hydrotechnical construction while organizing surface drawdown, or maintaining a difference in the levels of a filtering embankment. In solving this problem, it is important to have a representation of the actual position of the depression surface to evaluate the stability of soil masses subject to filtration action. Determination of the position of the depression curve is based on use of Dupee's hypothesis for average filtration rate, and integral formulas for the flow rate through a homogeneous soil mass. It is readily demonstrated that the equation of nonuniform motion is a required condition of the minimum for F(h) (in uniform motion, F(h) = 0). Dupee's depression curve has minimum length and maximum free-surface gradient [24-25].

Petrichenko M.R. derived an energy-balance equation for an integral flow with a variable flow rate over a particular length. The equation was applied to the confluence of flows [27-28]. Unsteady heat and mass transfer in combustion chambers of internal combustion (primarily Diesel) engines are analyzed and experimental data are reviewed. A stable correlation is found to exist between the instantaneous local heat transfer coefficients and the thermal resistance of the pseudolaminar boundary layer on the chamber wall. Other governing factors are also analyzed [29]. Petrichenko M.R presented [30-31] an algorithm for the problem of flame propagation rate in combustion of a homogeneous fuel-air mixture in the cylinder of an internal combustion engine. It is assumed that the mixture is not 'overturbulized' and that the flame front is spherical. The model used for the phenomenon is based on a turbulent transport mechanism. In the near-wall region the combustion mechanism follows a fine-scale mechanism, but in the core, a large-scale mechanism. Experiments permitted determination of the character and numerical value of coefficients which consider the effect of turbulence on flame front propagation in the combustion chamber of a ZMZ-4021 engine. The principles presented can be used as the basis of an algorithm for heat liberation rate in an internal combustion engine with external mixture formation.

Possibilities of utilizing quasi-stationary techniques in calculating flows through exhaust ducts of internal combustion engines have been discussed in some studies [32] with two major assumptions entertained: gas parameters obey laws and relations prevailing in fully stationary flow, in circumstances of quasi-stationary flow, and pressure remains the same throughout the entire volume of the internal combustion engine system at any fixed instant of time. An approximation analysis is conducted.

The paper [33] discusses problems concerning the formation of an oil film in the clearance between a piston ring and the internal combustion engine cylinder liner. An expression is derived for the lift force of the piston ring. The variation of the lift force with piston speed and the speed of the radial movement of the ring is shown. The results of calculation of oil film thickness under the sealing piston ring in 1ChN16/17 type diesel engines are presented.

The purpose of work [34] is to obtain a description of the fluctuation for component of the induced difference of the scalar potential in transducers of correlation flowmeters and to refine the limits of the inductionless approximation and possibilities of meeting the requirements imposed on transducers.

Gorshkov A.S., Vatin N.I.,Urustimov A.I. and Rymkevich P.P. in the scientific work consider the reason of formation of icicles on roofs of buildings.Insufficient thermal insulation and lack of appropriate ventilation of a garret cause heating of a roofing covering to above-zero temperature and snow fusion above a dam while temperature on a roofing plumb remains lower than zero [38].

New experimental data are presented [35] on nonstationary and transient operating conditions of closed liquid metal loops with MHD pumps. The investigations were made by utilizing the automated system of experiment staging, ″control system - experiment″. It is shown that the type of the transient process as well as the type of external characteristics of pumps are determined by the magnitude of the system drag coefficient. Characteristic ranges of flowrate and pressure pulsations, both as regards the amplitude and frequency of transient processes as well as the nonlinear effects connected with the startup of high-capacity pumps in a liquid metal loop, are noted.

The measurement of volumetric flow rate of a liquid-metal heat transfer agent in heat transfer loops is a serious technical problem, which may be solved by applying correlation methods of measurement. The object of the present study is to derive an equation describing the change in the space-time correlation functions of the velocity fluctuation components on increasing the spatial separation and to solve this equation for a well-developed turbulent flow of a conducting liquid with axisymmetric mean velocity profile [36-37].

**Method of controlling ice dams on the roof**

The most widespread way of fight against icicles in the Russian Federation is a manual mechanical removal of frost by means of shovels [1], that is industrial climbers come and start forcing down icicles from a roof simply. Naturally, all this creates certain problems for people: sidewalks and that people weren't run over by cars are blocked, bypassing the blocked foot zones, isblocked also part of the road. One more minus of such way of fight against icicles: the high cost of services of industrial climbers - municipal services try to save on them.

Recently try to force down icicles and by means of the pneumatic weapon. But this way doesn't look very reliable.

One more method of fight is a removal of icicles by ultrasound. This method is based on formation in the special device of a powerful ultrasonic impulse which influences the formed icicles and bringing to destruction and the subsequent controlled falling of icicles on a sidewalk surface. At the described method there is a lot of shortcomings. Most important - the big initial cost of system on 1 running meter of the protected eaves, reaching 200 Euros.

The method of cable heating is based on protection of a surface of a roof and a drain, by heating, by means of a special heatallocating (heating) electrocable. Necessary parts of a roof and drain are warmed - where the congestion of snow, formation of ice and icicles is possible. The positive side at such decision doesn't raise doubts: on a roof and a drain icicles and noticeable quantities of ice that protects both a roof, and a drain from any damages aren't formed and guarantees long service of modern roofs.

The main lack of such anti-freezing system, the realizing method of cable heating is the considerable cost of a heating cable and control units and big consumed electric power that demands noticeable costs of payment of the electric power [3].

Having carried out the short review of existing ways of fight against icicles, it is possible to draw a conclusion that the problem needs be not to solved, and to warn [4-7, 16-18].

**The formation of ice dams**

It is widely known that ice is formed of water at a temperature less than zero degrees Celsius. Snow on roofs thaws even in the coldest weather because of heat getting from an attic and from solar radiation. Water flows down to the roof edge where, contacting to the cold surface blown by air, freezes [2]. All snow which has thawed on a roof at the subzero temperature of external air turns into ice on eaves and gutters as on these sites of a roof heat from the house doesn't arrive. On formation of ice on a roof, icicles, such factors, as the steepness of a slope and her roughness influence. If the slope corner (depending on a roughness) more than 40 - 60 degrees, at snowfall snow cover on a roof isn't formed [11,14].

The thermal stream arriving through a roof at the expense of heat conductivity and an infiltration, is spent for heating of snow cover. In certain cases it is enough this thermal stream for melting (thawing) of snow on a surface of a roof and formation of water. At ambient temperature fall the part of a liquid phase hardens and ice is formed. Receipt of warmth from a surface of a roof leads to that the two-phase system the water ice divided by a contact surface is formed.

Process stylization the such. Let the axis x>0be directed from the roof having temperature of $T_h$, surpassing temperature of melting ($T_h$>273K). The area x>0consists of two parts divided by the contact x0 plane. In area x<x0 environment temperatureT is more than temperature of phase transition $T_0$ ($T>T_0$), is more right than the contact plane, in area $x>x_0$, temperature of the

environment is lower than temperature of phase transition. In other words, there is a hot phase (water)more to the left of the contact plane, there is a cold phase (ice)more to the right of the contact plane. Phases are divided by the contact plane. On the plane of contact there is a spasmodic change of phases,water turns into ice on an interval of zero length. Actually, of course, transformation of phases happens on some set of the values x filling the eutectic niche; otherwise, there is a vicinity of a point of $x_0$, ($x_0$-δ, $x_0$+δ)in which both phases, liquid and firm, water and ice, are in a condition of thermodynamic balance.

Let:

1. Temperature in section x>0 is equal to $T_h$ and remains not less $T_0$ in between $0<x<x_0$, i.e. $T=T_h>T_0$
2. Heat diffusivity coefficient on an interval $0<x<x_0$ is equal to $a_h$,on an interval $x> x_0$ is equal to $a_c$.
3. For water (approximately): $a_h=5*10\text{-}7m^2/s$; for ice (approximately): $ac=10\text{-}7m^2/s$. In any case $a_h>a_c$.

Then:

1. Temperature distribution in the space occupied by mix of water and ice has an appearance:

$$T = T_h erfc\left(\frac{x}{2\sqrt{a_h t}}\right), 0 < x < x_0;$$

$$T_0 = T_h erfc\left(\frac{x_0}{2\sqrt{a_h t}}\right); \quad (1)$$

$$T = T_0 erfc\left(\frac{x - x_0}{2\sqrt{a_c t}}\right), x_0 < x < \infty;$$

2. Length of the eutectic niche is:

$$2\delta = \frac{x_0}{2}\left(\frac{1}{\sqrt{a_c t}} - \frac{1}{\sqrt{a_h t}}\right) \underset{t\to\infty}{\to} 0 \quad (2)$$

3. Speed of movement of the contact $x=x_0$ plane dividing water and ice is equal:

$$c := \frac{dx_0}{dt} = \frac{x_0}{2t} \quad (3)$$

4. Then the instant provision of a contact surface is equal:

$$x_0 = x_0^{'} \ln\sqrt{\frac{t}{t_0^{'}}} \quad (4)$$

$x_0^{'}$ – initial values of coordinate

$t_0^{'}$ – initial values of time

5. The stop of a contact surface occurs when the thermal stream extending from a surface of a roof in area x>0, is insufficient for ice melting. Otherwise, the thermal stream going from water, on a surface of contact has to surpass a thermal stream in ice.
   Density of a thermal stream is more left than the contact plane is:

$$\dot{q_h}(x_0 - 0, t) = T_h\sqrt{\frac{\lambda_h \rho_h C_h t}{\pi}} \exp\left(-\frac{x_0^2}{4a_c t}\right) \quad (5)$$

λ, ρ, c -heat conductivity coefficient, density and a water thermal capacity.

Density of a thermal stream is more right than a contact surface is:

$$\dot{q}_c(x_0+0,t)=T_0\sqrt{\frac{\lambda_c\rho_c C_c t}{\pi}} \tag{6}$$

If thermal streams on both sides of contact coincide, movement of a contact surface stops. Otherwise, approximately:

$$\frac{T_h}{T_0}=\sqrt{\frac{\lambda_c\rho_c C_c}{\lambda_h\rho_h C_h}}>1 \tag{7}$$

Also, one of the defining factors influencing education in the winter of icicles on roofs and eaves are parameters of heattechnical properties of a roof (warming), and also ventilation of subroofing space [7].

This method of fight against frost on roofs was taken as a basis by specialists of the St. Petersburg polytechnical university, City Service and PAROC Group management company. The warming of garret overlappings which is conducted by means of new technology - inflatable cotton wool (Figure 1) was offered. Inflatable cotton wool, first of all, is specially intended for thermal insulation of overlappings and hard-to-reach spots. Use of inflatable cotton wool is the alternative solution of isolation of subroofing space. Installation of this material requires the special equipment - the vozudokhoduvny car. Of carrying out such works is result seamless, Thermotechnical a uniform layer of a heater of the subroofing space, providing preservation of a necessary difference of temperatures no more than 2 degrees between temperatures in and outside of an attic. Both the frost, and icicles for lack of temperature differences aren't formed [12].

Fig. 1. Inflatable cotton wool.

The necessary component of the described constructive decision is a wind-shelter design which isolates connection between an external wall and a ceiling beam from external air and provides ventilation in garret space.

It turns out that the roof is better warmed, the smaller thermal stream resembles through it, therefore, snow on it thaws in smaller quantity. Thus the thick snow cover on a roof is some kind of heater. The thermal insulation of a roof is better made and the snow layer is thinner, the at smaller subzero temperature thawing of snow [13] will stop.

Such improvement of warming of a roof not only saves heat and energy resources, but also reduces quantity of being formed ice on eaves and drains of a roof [15]. The organization of ventilation of subroofing space external air gives more considerable effect. The ventilation is better, the it is more effect. In this case, the roofing carpet is cooled with cold external air, and snow thawing on a roof doesn't happen.

The cost of processing of garret overlapping on this technology will cost 820 rubles for 1 sq.m.

Now works on renovation of subroofing spaces on four buildings are carried already out, all is up to the end planned to warm garret overlappings of six more houses of old construction. The total area of the warmed subroofing space will make eight thousand square meters. During the whole heating period for an independent expert assessment of a heater of PAROC complex monitoring

will be carried out. It includes visual research of a condition of garrets, determination of the actual heat conductivity of a heater, measurement of temperature and humidity of air in rooms, an assessment of technical condition of a roof, rafter system and garret overlappings, and also photofixing and thermovision inspection [12].

**References**

[1] Rekonstrukcijakrysh Sankt-Peterburg anaosnovelegkih stal'nyh tonkostennyh konstrukcij iantiobledenitel'nojsistemy / N. I. Vatin [i dr. ] // Inzhenerno-stroitel'nyjzhurnal. 2010. №2. S. 59-64.

[2] Palej A.A. Obustrojstvokryshbeznalediisosulek. // Federal'noe gosudarstvennoe uchrezhdenie «Gosudarstvennyj okeanograficheskijinstitutimeniN.N.Zubova». URL: http://oceanography.ru/content/blogcategory/0/66/ (data obrashhenija: 11.10.2012)

[3] Metodybor'by s sosul'kaminakryshah // Termoplaza.ruKabel'nyesistemyobogreva. URL: http://termoplaza.ru/index.php?x=roof2 (data obrashhenija 11.10.2012)

[4] Nazmeeva T.V. Obespechenieprostranstvennojzhestkostipokrytija v zdanijahiz LSTK // Inzhenerno-stroitel'nyjzhurnal. 2009. №6. S. 12-15

[5] Gusev N.I., Kubasov E.A. Konstruktivnye reshenija po predotvrashheniju obrazovanija naledejnakryshah // Regional'najaarhitekturaistroitel'stvo. 2011. № 1. S. 100-107

[6] Gusev N.I., Kubasov E.A., Kochetkova M.V. Sredstvadljaudalenijanaledej s krysh // Regional'naja arhitekturaistroitel'stvo. 2011. № 2. S. 104-108.

[7] Puzikov A.N., Biksaleev R.V. Sistemaventiljaciiskatnojkryshi // patent naizobretenie RU 2250970 25.11.2002

[8] Skopylatov I.A., Mahaneva N.V., Alekseev G.V. Vodostochnyjzhelobdljakryshi // patent naizobretenie RU 2161680 20.01.1999

[9] Ustrojstvokryshizdanijaisooruzhenija / Zhmur V.V., Komchatov V.F., Lapshin V.B., Palej A.A., JablokovM.Ju. // patent naizobretenie RU 2244790 05.03.2003

[10] Il'in V.B., Beljaev B.V. Ustrojstvo dlja predotvrashhenija obledenenijakromokkryshiiobrazovanijasosulek // patent naizobretenie RU 2237220 18.11.2002

[11] Bugaev A.S., Lapshin V.B., Palej A.A. Vodoochistka. Pochemuvozniklaproblemasosulek? // Vodopodgotovka. Vodosnabzhenie. 2010. № 3. S. 14-25.

[12] Vasin A.P. Teplovizionnoeobsledovaniezdanijianalizprichinobrazovanijanaledej // Vestnikgrazhdanskihinzhenerov. 2011. № 2. S. 92-98.

[13] Raschetnyj metod obosnovani jatehnologicheskih meroprijatijapo predotvrash henijuobrazovanijaledjanyhdambnakryshahzdanij so skatnojkrovlej / Gorshkov A.S., Vatin N.I., Urustimov A.I., Rymkevich P.P. // Inzhenerno-stroitel'nyjzhurnal. 2012. T. 29. № 3. S. 69-73.

[14] Akimov V.A., Durnev R.A., SokolovJu.I. Opasnye gidrometeorologicheskie javlenijanaterritoriiRossii // Nauchno-populjarnoeizdanie FGU VNII GOChS (FC). Moskva. 2009.

[15] Aver'janova O.V. Jekonomicheskajajeffektivnost' jenergosberegajushhihmeroprijatij // Inzhenerno-stroitel'nyjzhurnal. 2011. № 5. S. 53-59.

[16] Ivanov A.N., Trembickij M.A. Penobeton zadannoj srednej plotnostidljauteplenijacherdachnyhperekrytij // Inzhenerno-stroitel'nyjzhurnal. 2011. № 8. S. 19-24.

[17] Kornienko S.V. Ocen kavlijanija zonograzh dajushhihkonstrukcijnateplozashhituijenergo jeffektivnost' zdanij // Inzhenerno-stroitel'nyjzhurnal. 2011. № 8. S. 5-12.

[18] Rekonstrukcija krysh Sankt-Peterburga na osnove legkih stal'nyh tonkostennyh konstrukcijiantiobledenitel'nojsistemy / Petrov K.V., Zolotareva E.A., Volodin V.V., Vatin N.I., Zhmarin E.N. // Inzhenerno-stroitel'nyjzhurnal. 2010. № 2. S. 59-64.

[19] Nemova D.V. Jenergojeffektivnyetehnologii v ograzhdajushhihkon strukcijah // Stroitel'stvounikal'nyhzdanijisooruzhenij. 2012. № 3. S. 77-82.

[20] Petrichenko, M.R. (2012). Nonsteady filtration in a uniform soil mass // Power Technology and Engineering. №46 (3). C. 198-200.

[21] Bukhartsev, V.N., Petrichenko, M.R. (2012). Nonsteady filtration in a uniform soil mass // Power Technology and Engineering. №46 (3). C. 1-3.

[22] Bukhartsev, V.N., Petrichenko, M.R. (2012). Problem of filtration in a uniform rectangular soil mass is solved by variational principles // Power Technology and Engineering. №46 (3). C. 185-189.

[23] Bukhartsev, V.N., Petrichenko, M.R. (2012). Problem of filtration in a uniform rectangular soil mass is solved by variational principles // Power Technology and Engineering. №46 (3). C. 1-5.

[24] Bukhartsev, V.N., Petrichenko, M.R. (2011). Approximation of the depression curve of the inflow to an ideal trench // Power Technology and Engineering. №44 (5). C. 374-377.

[25] Bukhartsev, V.N., Petrichenko, M.R. (2011). Approximation of the depression curve of the inflow to an ideal trench // Power Technology and Engineering. №44 (5). C. 1-4.

[26] Petrichenko, M.R., Khar'kov, N.S.(2009). Experimental study of the pumping action of helical flow // Technical Physics. №54 (7). C. 1063-1065.

[27] Bukhartsev, V.N., Petrichenko, M.R. (2001). Condition of mechanical-energy balance of an integral flow with a variable rate // Power Technology and Engineering. №35 (4). C. 189-194.

[28] Bukhartsev, V.N., Petrichenko, M.R. (2001). Condition of mechanical-energy balance of an integral flow with a variable rate // Hydrotechnical Construction. №35 (4). C. 189-194.

[29] Bukhartsev, V.N., Petrichenko, M.R. (2001). Conditions of mechanical-energy balance of an integral flow with a variable rate // Hydrotechnical Construction. №35 (4). C. 189-194.

[30] Petrichenko, M.R. (1991). Convective heat and mass transfer in combustion chambers of piston engines. Basic results // Heat transfer. Soviet research. №23 (5). C. 703-715.

[31] Petrichenko, R.M., Kanishchev, A.B., Zakharov, L.A., Kandakzhi, B. (1990). Some principles of combustion of homogeneous fuel-air mixtures in the cylinder of an internal combustion engine // Journal of Engineering Physics. №59(6). C. 1539-1544.

[32] Petrichenko, R.M., Kanishchev, A.B., Zakharov, L.A., Kandakzhi, B. (1991). Some principles of combustion of homogeneous fuel-air mixtures in the cylinder of an internal combustion engine // Journal of Engineering Physics. №59(6). C. 1539-1544.

[33] Petrichenko, R.M., Mezheritskii, A.D. (1989). Options in the quasi-stationary method of designing impulse turbines for supercharging internal combustion engine systems // Soviet energy technology. №5. C. 13-17.

[34] Petrichenko, R.M., Shabanov, A.Yu. (1985). Gidrodinamikamaslyanogosloya pod porshnevy mikol'tsamidvigateleivnutrennegosgoraniya. | [Hydrodynamics of Oil Film Under Internal Combustion Engine Piston Rings.] // Trudy LPI. №411. C. 38-42.

[35] Vatin, N.I. (1985). Weight vector of a conduction transducer of a correlation flowmeter // Magnetohydrodynamics New York, N.Y. №21 (3) C. 316-320

[36] Bocheninskii, V.P., Vatin, N.I., Shmarov, V.S. (1981). Rezul'taty issledovaniya perekhodnykh protsessov v zhidkometallicheskikhkonturakh s mgd-nasosami

[37] Vatin, N.I., Mikhailova, T.N. (1986). Computation of cross correlation function of induced potential for developed turbulent flow with axisymmetric mean velocity profile // Magnetohydrodynamics New York, N.Y.

[38] Gorshkov A.S., Vatin N.I., Urustimov A.I. and RymkevichP.P.. Raschetnyiy metod obosnovaniya tehnologicheskih meropriyatiy po predotvrascheniyu obrazovaniya ledyanyih dambnakryishahzdaniy so skatnoykrovley. // Inzhenerno-stroitel'nyjzhurnal. 2012. №3. S. 69-71.

*Applied Mechanics and Materials Vols. 580-583 (2014) pp 2316-2319*
*© (2014) Trans Tech Publications, Switzerland*
*doi:10.4028/www.scientific.net/AMM.580-583.2316*

# Construction Technology of High-rise Building Structure

Peng Cheng [1, a], Xinfu Chen[2,b], Lang Wu[3,c]

[1]Jiangxi College of Applied Technology, Ganzhou,Jiangxi 341000, China
[2]Jiangxi Institute of Economic Administrators, Nanchang,Jiangxi 330088, China
[3]College of Civil Engineering, Nanchang Institute of Technology, Nanchang,Jiangxi 330044, China

[a]158482992@qq.com, [b]42872576@qq.com, [c]wulang19812005@126.com

**Key words:** high-rise buildings; construction technology; safety management

**Abstract.** The construction of high-rise building has a lot of features such as large capital investments, narrow operation face and long construction period. This puts forward higher requirements for technology. Characteristics of high-rise building construction, the construction quality controlling and construction safety managements were analyzed in this paper.

With the rapid development of high-rise buildings, the construction engineering structure becomes a variety, increasing scale and gradually towards the direction of building exterior complication and difficulty in construction of large comprehensive development. Aiming at these phenomena in this paper, the related high-rise building construction technology was analyzed and explored.

## High-rise Building Construction Characteristics

(1) High-rise building construction period is long, layer number of buildings, the work high above the more, the construction difficulty is high, the big workload and complicated technology. As a result, the vertical transport, high safety, fire prevention, communications, water, and the processing of construction waste problems become one of the characteristics of the high-rise building construction [1].

(2) In order to ensure the overall stability of high-rise building construction, needs to be buried deep under the ground 5 m, a layer or two layers of building construction, in improving the reliability of the foundation at the same time can be auxiliary equipment layer and the garage, etc.

(3) High-rise building construction period is generally long, the huge manpower, material consumption, seasonal span construction is inevitable, the staff and the engineering quality put forward higher requirements.

(4) High-rise building construction land tensions, surrounding environment is complex, in order to ensure the normal conduct of engineering equipment, the proper use of the material, need to arrange the site temporary facility engineering, as far as possible reduce the storage in the high-rise building construction materials, equipment, make full use of the goods and prefabricated components and semi-finished materials.

## High-rise Building Construction Quality Control

(1) To control the construction scheme in the high-rise building. If the construction scheme is not appropriate, will be prone to the safety of the foundation pit collapse accident. Once foundation pit depth more than 5 m, it must please have rich experience and professional knowledge of the expert group to carry on the deep foundation pit project demonstration, only through expert argumentation support plan to continue to organize the construction[2].

(2) The quality of the high-rise building need accurate measurement and elaborates construction. The measurement is the most crucial parts of the high-rise building is the building axis, elevation, verticality control, and the accuracy of the measurement data will directly affect the quality of the whole building construction, must go through strict measurement for many times.

(3) High-rise buildings appear cracks in construction process; the corresponding control measures must be taken. Construction in the high-rise building concrete amount is larger, the intensity is high, the concrete crack needs to prevent in advance. For new pouring concrete, it is necessary to control the component moisture curing, avoid surface moisture to evaporate quickly, make the internal force is too large, lead to cracking. For water after concrete internal temperature difference to control within the 20 ℃, avoid the ambassador from the internal cracking of concrete temperature difference.

## High-rise Building Construction Technology

### 3.1 Deep foundation construction technology

Deep foundation construction technology is the building structure, one of one of the most important technology in the construction, and the construction technology is more complex, easy to cause the construction of key parts of the accident. So in the construction should be very specific, ensure construction safety.

**(1)** In details for the whole process of foundation construction engineering should limit detection and analysis, and puts forward some corresponding solutions. To vigorously promote the information construction, a lot of specific construction example can prove that, for the construction quality and safety is a very effective and necessary protection methods and means is to analysis the whole process of deep foundation construction and monitoring.

**(2)** About how to solve the problem of groundwater, to take reasonable method. According to the different situations, such as: the state of groundwater, depth, and soil of different take different approaches. More commonly used the method of lowering groundwater has deep well, Ming set face, adopt the method of single stage and multistage or injection well point, so that it can effectively prevent groundwater impact on infrastructure construction and the foundation pit. Also need to be aware of is that when the groundwater is abundant, precipitation impeded relatively difficult time should adopt the corresponding cutoff appropriate measures to form a water curtain.

**(3)** For foundation pit supporting structure, should according to the natural conditions and the conditions of the equipment management. Such as environment, geology, hydrology, takes a different approach. Inverse arch wall, soil nail wall, such as the underground continuous wall, pile, etc., at the time of application should be combined with the basement of the relevant situation, try to reduce the cost of investment. For the soil body around, want to further on the soil of the foundation pit, should take deep mixing method, grouting, compaction, so that you can prevent the soil slope instability caused by the collapse accident.

### 3.2 The transformation layer construction technology

Engineering structure construction when need to make some decorate, contrary to common building stiffness is used in upper class need larger shear wall, and the lower stiffness to switch to smaller frame column. Want to realize such the structure of the way, you need in the arrangement of the transformation layer structure floors.

**(1)** Template support system construction. The main purpose of the high-rise building conversion layers is used to convert the fluctuation of the load of high-rise building and balance. Its construction is very complex and difficult. In order to ensure the construction of high-rise building structure. Need to choose a suitable template support system, it can be a supporting system for the

load transfer method or one-time molding supporting system, can also be combined with casting method supporting system, etc. Specific support system to choose or according to the scene of the construction environment and construction characteristic to the appropriate configuration. In the template configuration and support system design. First of all have to draw a diagram. To the construction of relevant personnel of detailed interpretation of the template construction process, support, disassembling and arrangement method, etc. In counting parts and template site, it is forbidden to use inferior and does not conform to the provisions of the fittings and template, fundamentally guarantee the mould and the quality of the material[3].

**(2)** Transformation layer of steel construction. In order to ensure the transformation layer construction quality, in the construction of the transformation layer reinforced materials to make a turn, accurate, this request must be careful about design idea, documents and relevant regulations. Also, accurate arranged reinforcement in place the order. Transformation layer reinforced joint is generally arranged in taper thread connections or cold pressing sleeve and flash butt welding, and to solve the problem of the rotation of the elbow reinforcement, generally adopt the method of nipple. Because transformation layer for the construction of the need to install a large amount of reinforcement and big diameter, beam-column node. Steel bar colligation and in place of the difficulty is bigger, so under the reinforced material must be conducted in strict accordance with the order of the row of reinforcement, thus reduced the difficulty of the steel binding and in place, and guarantee the construction quality of steel. In the reserve reinforced positioning control to ensure that in the transformation layer section is greater than the reserve of steel reserve the accuracy of the reinforcement. Ensure floor pay-off shear wall in the positioning line and control line, girder projection line and control line are released. Ensure that all reserved inserted reinforcement layout construction has carried out in strict accordance with the design standards. After final review on measuring accurate, will provide fixed on the original steel reinforcement.

### 3.3 Concrete construction technology

**(1)** High-rise building construction concrete consumption is big, should try to use ready-mixed concrete and pump concrete.

**(2)** Rainfall distribution on 10-12 in areas such as the high strength concrete is suitable for high-rise building bottom column, but unfavorable use should be paid attention to in the construction of high strength concrete, lest cause shrinkage.

**(3)** After concrete pouring should be timely maintenance, especially pay attention to not ignore the concrete wall, column and other body parts vertical concrete. To choose water should be developed according to the season and the engineering characteristics, steam, composite heat storage, electric heating, curing methods, such as film and cover and other insulation materials.

**(4)** Standard layer of floor slab concrete structures of tall building, the strength level of the beam are generally consistent, and the strength level of the plate and beam intensity lower than that in column, and bottom-up gradually reduced, thus node intensity difference exists, is not conducive to the construction operation, so effective measures should be taken to ensure the construction quality.

**(5)** Post-cast strip shall be proposed by the design unit of pouring time and location, and consult with the contractor; The early appropriate chooses of post-cast strip, compensating shrinkage concrete pouring. Before pouring concrete, clean up the surface of post-cast strip, after casting also covers maintenance should be carried out on the surface.

### High-rise Building Construction Safety Management

Too much attention to the construction enterprises improve product quality, improve the economic benefit, often ignored the security problems in site construction, for enterprise's quality department should give full play to its functions, Ann is content with professional safety knowledge, with administrative reward, laws and regulations as the means, comprehensively enhance the safety awareness of construction personnel, constantly improve the self safety of construction personnel.

Must not blindly pursue the progress of the construction process, construction speed should be safe as guarantee, construction before and want to do a good job of supervision and management in the construction process, and to find potential safety hazard in time and exclusion, establish the safe production responsibility system, perfect the security system.

## Conclusion

High-rise building with the constant development of the socialist modernization has become the important symbol of urbanization today, the structure of the high-rise building and high-rise building construction process of an important component of the construction process, to people's production and the work has a very important influence, so the construction technology of high-rise building engineering construction structure becomes very meaningful.

## Reference

[1] Zhang Aiqing. High-rise building construction technology[J]. Engineering construction and design, 2009.

[2] Liu Jianxin. Introduction to the high-rise building structure construction [J]. Small and medium-sized enterprise management and technology, 2009.

[3] Tian Chunming. Problems that should be paid attention to during construction of high-rise building structure [J]. Science and technology of China,2010.

*Applied Mechanics and Materials Vols. 580-583 (2014) pp 2320-2323*
*© (2014) Trans Tech Publications, Switzerland*
*doi:10.4028/www.scientific.net/AMM.580-583.2320*

# Research on the characteristics and status of recycled concrete filled steel tube

Bing Wang [1, a], Xiao Liu[1, b], Xiao Yu[1,c]

[1]School of Architectural and Civil Engineering, Shenyang University, Shenyang, 110044, China

[a]liuxiao19740701@sina.com, [b]489298344@qq.com , [c]283292935@qq.com

**Keywords:** Concrete filled steel tube, Recycled concrete, High temperature resistant.

**Abstract.** Utilization of waste concrete has a great significance for environmental protection; concrete filled steel tube is a way of utilization of waste concrete. At the same time, the recycled concrete on the center tube has a "hoop" function, can compensate for the deviation of mechanical properties of recycled aggregate concrete. This paper introduces the characteristics of steel recycled concrete, and introduces the research status of domestic experts and scholars on it, based on the above; the future application of the recycled concrete in steel pipe is presented.

## The characteristics of steel tube filled with recycled concrete

The mechanical properties of recycled concrete compared with ordinary concrete fell and variability increased mostly are used for non-structural system of road. In order to make better use of recycled concrete, some scholars from the view of combined structure the recycled concrete is poured into the steel tube concrete formed steel tube filled with recycled concrete, the use of the function of ferrule(constraint) of steel tube for the core of recycled concrete so that the core of recycled concrete in the state of pressured from three direction to improve recycled concrete compressive strength and resistance to deformation, and the core concrete can enhance the stability of steel tube so that the mechanical properties of recycled concrete are improved, and the mechanical advantage of steel and concrete to play their respective, provides an important way for the resource utilization of waste concrete. The steel tube recycled concrete as a new type of structural members, the present research about this aspect is still in the immature stage.

The steel tube recycled concrete is a composite material which be formed by filling recycled concrete into the pipe, it can give full play to the existing advantages of steel tube filled with concrete, and give a solution to the enormous pressure that waste concrete to ecological environment, also, for the material of recycled concrete , because it has very good high temperature performance, its mechanical properties are rarely influenced by temperature, the increase of temperature did not significantly decrease the mechanical properties, the properties that make up the shortcomings of low resistance to fire performance of steel, which makes the high temperature for steel recycled concrete applied to concrete filled steel tubular structure, and for the application of recycled concrete provided broad prospects in structural engineering. Therefore, research on steel pipe concrete attached importance by more and more countries（As show Figure1.

(a)Expressway of Yaan to Lugu

(b)Construction site

(c)Industrial production

(d)Site installation

Fig.1 The engineering examples of steel tube filled with recycled concrete

**High temperature resistant performance of steel tube filled with recycled concrete**

In the disasters that people faced, fire is the one which has highest frequency of occurrence and the largest span of time and space. In all sorts of disaster, fire is the most often and common one of the main disasters threatening public safety and social development. Fire damage to buildings is very large, steel reinforced concrete structure at the time of the fire, because the concrete protective layer thickness is small, resulting in a fire occurs, the high temperature will through concrete protective layer to affect the internal reinforced steel. Experiments show that, when the temperature exceeds 300 ℃, steel will lost the ability to load. At the same time, concrete under certain temperature will decompose into lime and carbon dioxide which not have adhesive force, causing the floors collapsed, the building suffered catastrophic destruction. According to the statistics, since twenty-first Century, the building fire accounted for about 80% of the total number of fire. For example: the evening of 9 February 2009 21 am, in the construction of the CCTV new site park and cultural center catastrophic fires, building fire, smoke over an area 21,333 square meters, of which 8,490 square meters burned area, causing direct economic losses of 16383 million (Figure 2a);At 14:00 on November 15, 2010, a high-rise apartment Shanghai Jiaozhou Road, Yuyao Road caught fire, the fire led to 58 people were killed (Figure 2b).

(a)

(b)

Fig.2 Building fires occur

With the development of modern architecture, people's requirement of function structure form are increasing, the ground structure to the large span, tall and complex forms of development, to the development of multilayer three-dimensional underground structure. When the column at a higher axial pressure, if adopt to ordinary concrete column, the column cross-sectional dimension must be designed bigger. And with the increase of column section size, will not only take up the use of the

building space, but also the formation of small shear span ratio of the short column, easy to cause the brittle failure, it is not allowed to exist in the design; If use the steel structure, cross section area of the column member although diminished, but the member under pressure, the member's overall buckling and local buckling often precede the section strength and failure, and fire resistance performance is poor. For example, the 911 terrorist attacks on the United States is due to the steel used, resulting in a fire when the temperature exceeds the fire resistance of steel, resulting in huge economic losses and casualties.

Steel tube concrete structure due to the absorption of recycled concrete has strong ability, at high temperatures, the ductility and strength decreased, but due to buckling, internal core concrete filled steel tube can effectively delay the steel under high temperature. Therefore, steel tube concrete structure at the time of the fire is better compared with the fire resistant performance of ordinary reinforced concrete structure and the fine steel structure.

**Research Status of steel tube filled with recycled concrete**

The sit-ting room is the family activity center with large area, and suitable for placing big plant in the corner or the sofa, generally in large foliage plants, and beside the window, we can place four season flowers, or hang the small plants on the wall as the decoration. But place too many plants, otherwise it will appear to be too vulgar to be endured.

Hallways and other room area is lesser, and is suitable to place some small plant, or hang plants in the space for decoration. We should take the plants of general room concentrated in a corner or the place in our sight. If we feel a bit monotonous, we can consider that divide them into one or two groups to decorate.

In addition, in the current structure of the bedroom, it inevitably exists concave and convex, so that, we'd better use plant green decorative to remedy or have a balance. If we plant ivy on the surface of the column, we can get poetic sentiment.

**Considering the position of the view line**

From the beginning of the last century, the world gradually began working on steel tube filled with recycled concrete after high temperature regeneration; China also began to study the relevant aspects of strength. Domestic and foreign researchers have mechanical properties of recycled concrete and recycled concrete members conducted in-depth research, but also began to reinforced concrete structures or components manufactured from recycled concrete research, but because of the performance limitations of waste concrete itself, is currently recycled concrete in the actual project is also largely confined backfill and other non-structural forces or by the use of a smaller force, the application of recycled concrete is on relatively low levels. In order to make concrete waste be more reasonable used, in recent years, our country scholars at home and abroad research and application is still in the model of initial stages of combined the concrete filled steel tube structure and the utilization of recycled concrete. The study has the following several aspects:

He Dong, Qiu Cichang, Wang Qingyuan [1]analyzed the whole process of load-deformation curve of steel tube filled with recycled concrete on the different substitution ratio when it under axial compression, and done the experimental study, got the load of steel tube concrete under axial compression deformation curve and the load changing trend, the numerical results are in good agreement with the experimental results.

Ye Xin, Yang Youfu [2]studied on the steel tube concrete flexural members, and studied the 4 square steel tube concrete member and the 4 steel tubes for pure bending test of recycled concrete member, observe and analyze the failure modes and mechanical properties, take the calculation method of fiber model to verify the test results, the results show that: steel tube filled with recycled concrete bending members with similar mechanical properties of common concrete filled steel tube, steel tube filled with recycled concrete pure bending stiffness and flexural capacity decrease with recycled concrete replacement rate increase.

Li Weining, Xu Jinjun, Chen Zongping [3]studied the interface bond slip performance of steel tube filled with recycled concrete, designed 10 square steel tube concrete specimens, by changing the three parameters of testing rate, concrete strength grade and buried depth of substituted recycled concrete, got the load slip curves between recycled concrete filled square steel core and interface, and analyzes the ultimate bond strength and bond strength of sliding effects parameters, results show that: load slip curve is divided into non slip stage, stress rising stage, mutation and decline phases four stages, the bond strength by the substitution rate of the minimum, the embedded length of time is least, the influence of concrete strength is maximum.

Hou Rui[4] has studied the constant high temperature steel mechanical properties of recycled concrete columns of the shaft , test design 40 different temperature, different sizes of aggregate replacement ratio, different cross sections specimens, and analysis of the constant high temperature steel recycled concrete axial compressive failure mode, the interaction between the section and working mechanism the stress distribution and the core concrete and the steel tube with ABAQUS, studied the factors influencing coefficient of compressive strength and elastic modulus of the influence factors, and put forward the constant high temperature steel simplified recycled concrete axial compression bearing capacity and modulus of elasticity formula.

## The prospect of steel tube filled with recycled concrete

Existing research results show that steel tube filled with recycled concrete has similar mechanical properties with steel pipe concrete, which not only has the common advantages with concrete filled steel tube, but also has some unique advantages: the fire resistance performance of recycled concrete is better than ordinary concrete, which helps to improve the recycled concrete as the core concrete of concrete filled steel tubular members durability. Steel tube concrete member having good ductility and the later bearing capacity, good mechanical properties, is a kind of structure form which is more promising. The steel tube recycled concrete can achieve waste resources' reuse, save natural resources, conducive to the Protect environment, its ecological significance is important.

## Acknowledgement

It is a project supported by National Science Foundation (51308347).

It is a project supported by colleges and universities in Liaoning Province Outstanding Young Scholar growth plans (21503040399).

## References

[1] Dong He,Cichang Qiu,Qingyuan Wang.Steel tube concrete axial compression load - deformation of theoretical study and experimental analysis [J]. Journal of Sichuan University, 2010, 42 (2): 49-53.

[2] Xin Ye, Youfu Yang. Steel tube concrete subjected to bending properties of [J].Earthquake engineering and engineering vibration, 2005 (03).

[3] Weining Li,Jinjun Xu,Zongping Chen.The regeneration of square steel tube concrete experimental study on the bond slip properties of [J]. Guangxi University, 2012, 37 (1): 68-74.

[4] Yixiang Liu,Xiaoxiong Zha. Steel tube concrete column bearing capacity and progress of study on the fire resistance performance of [J]. Steel building structures, 2012,14 (3): 48-52.

*Applied Mechanics and Materials Vols. 580-583 (2014) pp 2324-2327*
*© (2014) Trans Tech Publications, Switzerland*
*doi:10.4028/www.scientific.net/AMM.580-583.2324*

# The Countermeasures on Temperature and Shrinkage Crack of Mass Concrete

Xianchun Zheng [1, a], Pengfei Li [1,b], Sizhong Sun [1,c]

[1] Hebei Institute of Architecture and Civil Engineering,

Zhangjiakou，Hebei，075000，China

[a]zjkjyzxc@163.com, [b]doomood@163.com, [c]sun8905508@163.com

**Keywords:**Mass concrete,Temperature crack,Shrinkage crack,Countermeasures

**Abstract.** Combined with practical engineering，this paper analyzes the mechanism of mass concrete temperature and shrinkage cracks, from raw material selection, structure design, construction, monitoring and management five aspects,the author respectively gives the countermeasures on temperature and shrinkage crack of mass concrete, reference for engineers.

## Introduction

As built object shape is increasing, the corresponding structural scantlings is bound to increase.For concrete structure, when the volume of a component or larger area to produce larger temperature stress in the reinforced concrete structure and components, such as not to take special measures to reduce the temperature stress is bound to lead to concrete cracking.The cracking of the temperature is not simple construction method, also involves structural design, structural design, material selection, material composition, constraint condition and the construction environment, and many other factors. The current industry standard JGJ55-2000" the mix proportion design of ordinary concrete regulation"is defined as:" concrete structure entity minimal size is equal to or greater than 1 m, or is expected to be caused by cement hydration heat of concrete internal and external temperature difference is too large and cause of concrete crack."

## The Causes of Cracks

The section size of large mass concrete structure, the possibility of cracks caused by external load is small, but in the hydration reaction of cement hydration heat release a large amount, due to the large volume, not easy to heat, causing significant temperature rise, leading to increased volume.When the deformation is not constrained, won't produce stress of concrete structure.But in fact the deformation would be constrained, there are two kinds of constraints.One is external constraint, and the other is the internal constraints.Concrete pouring on rocks or on old concrete, its volume change will be bound by external rocks and old concrete, due to cement early hydration heat up sharply, volume expansion, under pressure, but because of the concrete elastic modulus is low, the compressive stress is very small;Heat coming from the later period of cement hydration heat is reduced, greater than the hydration heat, the temperature is reduced, the volume contraction, are in bondage to the rock and concrete by into tensile state of stress, so the concrete elastic modulus increased large tensile stress is produced.Internal constraints are caused by the heat of hydration of cement produced inside the concrete is not easy to send out, the surface is easy to send out, so the surface temperature is lower than the interior., in contrast, the expansion of the internal volume by surface constraints in compression state, the surface of the volume contraction (especially the temperature drop or water) by the internal constraints, tensile stress is produced.Because concrete is a brittle material, low tensile strength, ultimate tensile strain is small (less than $1 \times 10^{-4}$).When the deformation temperature, deformation is restrained its internal cause tensile stress is very easy to exceed the ultimate tensile strength and cracks.

**The Countermeasures on Crack of Mass Concrete**

**Material selection**

**Using low heat of hydration of cement.**Because of the different size of mineral composition and admixture of cement hydration heat differences.Tricalcium aluminate and silicate high calcium content, high hydration heat;Admixture of cement hydration heat is low.So choose low hydration heat or in the concrete hydration heat of cement varieties, such as slag Portland cement, fly ash cement, composite cement, etc.Unfavorable use early strength cement.

**Reduce the dosage of cement and the amount of water.**Cement hydration heat temperature changes of mass concrete is the primary sources of lead to volume change.Wet and chemical change will cause the volume change, but are usually far less than the volume change produced by the hydration heat of cement.Except by hydration heat low thermal cement, therefore, to reduce the temperature deformation, there should be one thousand to reduce the dosage of cement, reduce the dosage of the water.According to the test every 10 kg of cement, reduce the hydration heat will make the temperature of the concrete corresponding lift 1 ℃.This requires:

- On the premise of meet the structural safety, try to reduce the strength of the design requirements.
- Mixed with fly ash.The heat of hydration of the fly ash is much less than the cement, 7 days is about 1/3 of the cement, 28 days is about half of the cement.Reduce the dosage of cement mixed with fly ash can effectively reduce the hydration heat.The strength of the mass concrete usually require lower, allowed to take part in more fly ash.In addition, small water demand of high quality fly ash, water reducing effect, can reduce the unit water use of concrete and cement dosage;Can also reduce the volume shrinkage of concrete, some still a slight expansion, is beneficial to crack.Mixing fly ash can restrain alkali - aggregate reaction and prevent the resulting cracks.
- The mixed water reducing agent.Mixing water reducing agent can effectively reduce the unit water use of concrete, thus reducing the cement dosage.Retarded type water reducing agent and inhibitory effect of cement hydration, can reduce the hydration temperature rise, is beneficial to crack.Adding of mass concrete is mainly calcium lignosulphonate water reducing agent, which has obvious dispersion effect of cement particles, can effectively increase the liquidity of concrete mixture, and can make the cement hydration is fully, improve the strength of the concrete.If the concrete strength unchanged, can save 10% of cement, which can reduce the hydration heat, can obviously delay the hydration heat release rate at the same time, heat peak also corresponding delay.

**Using micro expansive cement.**Using micro expansive concrete, the purpose of expansion is when the temperature and shrinkage of concrete, shrinkage compensation, to prevent the cracks.But currently using micro expansive cement, most early, the concrete expand on heating and cooling has been expanding when finished, also started to shrink, can only make up of compressive stress increases slightly, the effect of shrinkage compensation.So you should use the expansion of the late

**The linear expansion coefficient of the aggregate.**Concrete is composed of cement paste and aggregate, the linear expansion coefficient of linear expansion coefficient for cement paste and aggregate of the weighted average (volume) of the concrete.The coefficient of cement slurry is 11 ~ 16 x $10^{-6}$ / □;The linear expansion coefficient of aggregate depending on the type of parent rock.The linear expansion coefficient of different rocks difference is very big.Aggregate volume accounted for more than 75% in mass concrete, the linear expansion coefficient of aggregate on the reduction of concrete linear expansion coefficient, and the function of decreasing temperature deformation is very significant.

**Strengthen the structure design**

To prevent the mass concrete temperature crack, in improving the boundary constraint and structural design, also can take some technical measures.Such as reasonable poured subsection, setting sliding layer, the reasonable configuration of reinforced, buffer layer, avoid stress concentration, etc.

**The measures to eliminate external constraint**

- Rock can spread a thin layer of sand gravel;
- On the old concrete paving asphalt linoleum, usually with a blanket a oil practice;

- Side of rock or the old concrete, can be separated with asphalt felt.

**Reasonable configuration of reinforced.**Set up necessary temperature reinforcement in the concrete, the variable cross-section and the turning point, such as turning point and the hole bottom, the roof and wall corner, etc., add diagonal structure reinforcement, in order to improve stress concentration.

**Adopting reasonable construction method**

**In low temperature season, at low temperature of casting.**In addition to the cement hydration temperature rise, the temperature of the concrete itself is the cause of volume change.Conditional should try to avoid casting in the summer.If they can't do that, you should avoid in high temperature at noon pouring.

**Reduce the concrete temperature.**When mixing concrete mixing water can be added in ice (can reduce 3 ~ 4 ℃) and cooling aggregate (can reduce more than 10 ℃).Within the structure of buried pipes, through the low temperature water cooling, cooling of high efficiency, small cold energy loss.Casting piece not too thick, can be used on the surface of water cooling, also has a good effect.

**Surface heat insulation protection.**Crack of mass concrete, especially the surface crack, mainly due to the large temperature difference between inside and outside.After casting, the cement hydration temperature rise of concrete, the surface easy to cooling temperature is low, internal cooling temperature is higher, not easily relatively surface shrinkage internal expansion, surface shrinkage is governed by internal tensile stress is produced.But the tensile stress is small, usually not more than concrete tensile strength and cracks.Only encounter cold air attacks at the same time, or excessive ventilation, cooling or water cooling the surface when the fracture occurs (5 ~ 20 days after casting) most likely to happen.Surface heat insulation protection to prevent surface cooling is too large, reduce the temperature difference between inside and outside, is the effective measures to crack.

**Control the concrete into the mold temperature.**In order to reduce the total mass concrete temperature rise, reduce the temperature difference between inside and outside structure, coagulation of mould temperature control measures is very important.People die temperature, closely related to the temperature of the machine, also with the number of transport, the distance, transport, construction of climate related.About the concrete into the mold temperature control, all countries have clear rules.Our country should be no more than 25 ℃, the United States ACI construction manual regulation is less than 32 ℃, Japanese architectural society reinforced concrete construction regulations in mud is not more than 35 ℃.According to the experience of the engineering practice in our country, it is recommended that the coagulation on the highest one mould temperature should be controlled below 32 ℃.

**Slow cooling rate of concrete.**After mass concrete casting, enhance its surface heat preservation, moisture curing, plays an important role in prevent concrete cracks.The effect of heat preservation and maintenance has three: first reduce the coagulation on the temperature difference between inside and outside, to prevent surface crack;The second is to prevent the concrete surface is too cold, avoid to produce cracks, the third is the slow cooling rate on the coagulation, to cut new and old concrete on the lower level constraints.Moisture curing can reduce the drying shrinkage on the coagulation, makes a concrete cement hydration smoothly, to improve the ultimate tensile strength on the coagulation, has positive effect to control cracks.Insulation materials commonly used wood pattern, sack, sawdust, dry sand, etc.After the final set of concrete, adopts the water storage curing is a very good method, not only has the effect of heat preservation and heat insulation, but also can delay the coagulation and the cooling rate, reduce the center and surface of the concrete temperature difference value.

**After setting up reasonable pouring belt**

Using the method of "latter pouring belt", the concrete structure is divided into several segments, concrete pouring concrete of the reoccupy after 30 ~ 40 d closed. "Latter pouring belt" is the construction design, during the period of temporary temperature and shrinkage deformation cracks, it can effectively reduce the temperature stress and shrinkage stress on the coagulation.Under normal construction conditions, space between "latter pouring belt" is generally 20 ~ 30 m, width is about 0.5

~ 1.0 m.In structure stress concentration areas, appropriate and anti-crack reinforcement to make local enhancement processing, in must be horizontal construction joint position of the section construction, increasing the number of dark beam to prevent crack propagation.

**To strengthen the construction monitoring work**

The mass concrete temperature monitoring is an important technical measures, it helps to grasp the situation, timely and accurate provide scientific basis for handling measures.Monitor the temperature inside the concrete, concrete temperature measurement is commonly used in data recorder, it attached to printing system, each measuring point temperature can be printed on the record paper, can also direct reading.According to the temperature of each measuring point. Can be timely to map the concrete internal temperature change curve, control concrete theoretical calculation value, analysis of existing problems, and targeted to the corresponding technical measures are taken.

**An engineering example**

A three layers of the earth, the underground engineering, construction area of 17968.26 m2, foundation slab length 84.5 m, 53.4 m wide, 1.8 m thick, C30 concrete strength grade, permeability grade for the S8, mass concrete.In the engineering construction in the central floor, setting post-cast strip width 1 m, concrete grade, C35 mixed UEA expansive admixture, wet curing 20 days before casting.The structure of post-cast strip as shown in figure 1.

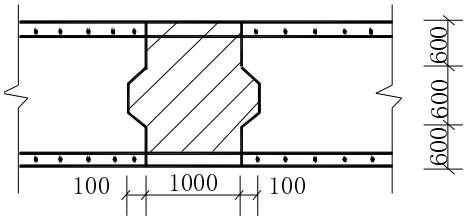


Fig.1 The Structure diagram of latter pouring belt

In order to ensure the concrete strength and integrity to meet the design requirements, try to reduce the dosage of cement, reduce caused by cement hydration heat of concrete temperature difference between inside and outside.Reduce secrete water in the process of concrete pouring and curing shrinkage, reduce the external restraint degree to prevent cracks, determine the strength grade 52.5 Portland cement, adding fly ash ( Ⅱ type) and micro expansive agent UEA double mixing of concrete technology.Adopted in construction are described in this article the method of strengthening temperature monitoring, not present any floor cracks and leakage.

## Conclusions

Above all, to prevent the cracks of mass concrete, one of the key: use the cement of low hydration heat, reduce the dosage of cement, as far as possible choose small linear expansion coefficient of aggregate, adopting reasonable construction method, good cooling and surface heat insulation protection, eliminate or reduce the external constraints, improve the concrete tensile ability.

## References

[1] Fenglan Lan. The construction of mass concrete crack control technology is analysed. Real estate Tribune ,2013(14) (In Chinese)

[2] Zaizhi Sun.The formation and prevention of mass concrete cracks. Urban construction theory research, 2012(33) (In Chinese)

[3] Zuowen Sun. High-rise building basement floor control points during the construction of large volume concrete cracks is studied. Urban construction theory research, 2013(02) (In Chinese)

[4] Sufang Han. Reinforced concrete structure crack control guidelines.Chemical industry press,2005(In Chinese)

*Applied Mechanics and Materials Vols. 580-583 (2014) pp 2328-2331*
*© (2014) Trans Tech Publications, Switzerland*
*doi:10.4028/www.scientific.net/AMM.580-583.2328*

# Reinforcement Method Choice of Deep Soft Soil Foundation

Chunmei Zhang[1, a], Lijuan Liang [2, b] Chao Huang[3, c]

[1]Architecture and Civil Engineering School, Inner Mongolia University of Science and Technology, Baotou, 014010, P.R. China

[2]Shanghai jianke Engineering Consulting Co., Ltd. Shanghai, 200032, P.R. China

[3]Architecture and Civil Engineering School, Inner Mongolia University of Science and Technology, Baotou, 014010, P.R. China

[a]jpxt@163.com, [b]lianglijuan@jkec.com.cn,[c]15058101880@163.com

**Key words:** foundation reinforcement, soft soil, composite foundation

**Abstract.** Soft soil's properties including low bearing capacity and large deformation leads to the necessity of reinforcement of foundation when it is made of soft soil. This article illustrates the features and applications of different methods, through the comparison of them.

## Project Profile

Soft soil foundation has remarkable structural, rheological, properties as well as high compressibility, low shear strength, low permeability and low bearing capacity. It also has a very long duration before the completely consolidation under the self-weight of soil layer or external load. It is unqualified to bear large building load without any extra processing, or there will be a risk of local shearing and whole sliding and even possible large building settlement or differential settlement. For the long time consumed before the stabilization of settlement—several years or even tens of years on thick soft soil, the deformation and stabilization requirements cannot be satisfied, so the reinforcement processing is indispensable. We choose different programs depending on the difference of the conditions of engineering, geological conditions of foundation or composition of soil. Generally, perfect foundation processing method does not exist. We have to act appropriately to the situation to ensure the realization of the processing. [1]

## Methods

## Compacting

**CFG pile method.** CFG piles and cement-flyash-stone piles, through hydrated reaction of cement and pozzolanic reaction of fly ash, or can help gravel pile to replace and reinforce the foundation by compacting, so that the consolidation is achieved. The pozzolanic reaction mechanism is like the following. [2]

$$XCa(OH)_2 + SiO_2 mH_2O = xCaOSiO_2 nH_2O$$

In the chemical equation, x is the kind of composite material and lime, the proportion of active silicon oxide, environment temperature and the duration of reaction. The settled gravel pile reinforcement is a good drainage channel, which also bears the loads together with the soil, forming a composite foundation.

CFG pile composite foundation improves the bearing capacity of composite foundation by the combined action of CFG piles and adjacent soil. Its strength and compression modulus are relatively even, which is beneficial to the superstructure considering stress and structure seismic. Flexible cushions can also be put between CFG piles and foundation, which artificially meets the condition for piles to penetrate into the cushions from the top, and the cushions can to a certain degree compensate the differential settlement of foundation. In this way, the problem of relative deformation can be adjusted or even solved so that effective contact stress of adjacent soil is increased and the shear strength and bearing capacity of piles are improved.

**Sand-gravel pile compacting.** This method reinforces the foundation in two ways: compacting and replacement. Compacting is to place sand-gravel piles into the foundation so the foundation soil is compacted during the formation of the piles, and the adjacent soil and piles form a composite foundation. Replacement is to replace foundation soil by the same volume of large-diameter, compacted sand-gravel piles, so that the piles and adjacent soil form a composite foundation, and then bear the upper load together, increasing the bearing capacity and stability of soil. It also helps the drainage and its consolidation works well, so it is widely applied.

## Preloading

It can be achieved by surcharge loading or vacuum preloading. Surcharge preloading is to stack the raw materials on the foundation in the purpose of preloading consolidation, in which the strength of foundation is improved. It properly suits the area with convenient transportation and abundant raw materials. Surcharge preloading leads to positive pore stress. The preloading effect goes better when the soil permeability coefficient in the reinforcement region is larger. The processing details are as followings. Pave a $50cm$-thick sand cushion on the surface of foundation to be reinforced. The cushion will act as horizontal drains. Then let sand wicks or plastic drainage boards squeeze into soil body to be vertical drains. Pave airproof thin films on the cushion above the soft soil to be reinforced. Keep the edges of the films buried into the soil. Get the soil under the film exhausted to vacuum with the help of the pipelines buried in the cushion. The vacuum soil is extended downward through plastic drainage boards so the plastic drainage reaches a level of vacuum, which spreads through sand pores so that a vacuum gradient occurs. Then the pore water goes out through sand well and plastic boards, which leads to consolidation. The decreasing of $u$ will increase $\sigma'$ to achieve the consolidation.

$$\sigma' = \sigma - u$$

where $\sigma'$ — the effective stress of soil particles, （$kPa$）

$\sigma$ — the total stress of soil , （$kPa$）

$u$ — the pore water pressure （$kPa$）.

During reinforcing the soft foundation of expressway, surcharge and vacuum preloading can be combined, which is called surcharge-vacuum combined preloading. We can shorten the construction duration by using roadbed filled soil as load. Then we can take the advantage of both and solve the problems of earth filling speed caused by the surcharge method and ultimate load caused by vacuum method.

## Chemical Reinforcement

**Deep stirring.** Its mechanic is to stir the mixture of cement and saturated soft soil, which caused the hydrolysis and hydration reactions of cement, and then a stable structural integrity occurs. The hydrolysis and hydration reactions strengthen the cement soil. The local stirring and mixing of solidified agent and origin foundation soil utilize the origin soil to the maximum. The side extrusion force upon adjacent soil and soil outside the piles is low during stirring, so there is hardly any effect toward the buildings around. Meanwhile, there is no vibration, noise and pollution, so execution downtown or in an area of high building density is acceptable. Other advantages are like the flexibility of design and low cost.

**Vibroflotation.** It is economical but time consuming, so not appropriate for time-limited projects. We can either wet or dry vibroflotation. The wet one is to pound the soil by water pressure, leading to the rearrangement of soil particles so the number of pores reduces and the compacting is realized. At this point, fill crushed stones into the pounded holes to form a composite foundation, which improves the bearing capacity. The dry one is not feasible downtown because a large amount of slurry comes out during the execution of vibroflotation, which will pollute the environment. So it does not suits projects downtown.

**High pressure jet grouting.** This method is suitable for soft soil layer, such as the alluvial layer and eluvium layer of Quaternary Period. It widely suits different kind of conditions and is easy to execute. We can also control the shape of consolidation. Both vertical and oblique jetting are available. It asks for simple equipment, easy management and low cost but supplies high durability so is a good choice of permanent projects. We drill injection pile, which has a jet, into a predetermined depth of the soil layer with the help of drilling machine. Then spray the mud or water out of the jet with a pressure of $20-40kPa$, producing a squirt flow to destruct the soil layer. A proportion of tiny particles emit out to the ground with the mud, while other soil particles mix with the mud and rearrange, forming a composite foundation. This method is applied in sandy soil, cohesive soil, loess and mucky soil.

**Dynamic compaction.** The properties are simple equipment requirement, easy processing, favorable strengthening effect, wide application, low operation stuff request, fast execution, low cost and no consumption of cement or steel. The foundation bearing capacity will take a 1-5 times increase and the reinforced depth is generally $5-10$ meter. The shortages are drastic vibration, noise so it's hard to be used in the high-building-density area downtown. Dynamic compaction asks for strictly control of some construction parameters such as cushion thickness, tamping potential energy. It also has a high demand for the geological conditions of the area to be reinforced, which determines the depth. And this method works well for floury soil and sandy soil.

Dynamic compaction replacement can be used to process deep thick soft soil foundations, which is a new foundation replacement method developed from dynamic compaction reinforcement in the recent years. Both pile replacement and integral replacement are available. We fill in crushed stones and dynamic compact simultaneously so we get crushed stone piers in the foundation, which, together with soil and crushed stone cushion, forms a composite foundation and bears the upper load so the foundation settlement is reduced and the bearing capacity is increased. The mechanic is like follows. When the soft soil is compacted, the space for organic matter decomposition in the soil is compressed and gas goes outward, causing instantaneous deformation of soil and pore water pressure increase. Under the repetitive impact force, local liquidations take place in the foundation and the soil structure is destroyed when the pore water pressure approaches the adjacent soil overburden pressure. At the same time, the compacting-caused shock wave spreads in the soil and rearranges the stress in the soil. When the tensile pressure at a point in the soil surpassed the tensile strength, there will be a crack as well as a change of the permeability of soil. Afterward the pore water overflows and the soil consolidates continually. As the consolidation going, pore water pressure decreases and thixotropic phenomenon is under control.

## Conclusions

**The combination of reinforcement methods.** We have plenty of methods, but none is omnipotent and everyone has its own application scope and limitations. We should combine some of them when necessary, in order to get the expected result.

In the reinforcement project of the podium foundation of Shanghai Yang Guang Ming Di, six columns along the same vertical axis between the 2nd and the 6th layer of the podium were removed for the request of utilization, resulting in shortage of pile foundation bearing capacity. What's more, the foundation soil mainly consisted of cohesive soil, silt soil and sandy soil so it was difficult to deal with the underground water. A method of grouted bolts and static pressing steel pipe piles, combining the theories of grouting and pile foundation, was applied. In detail, there were three solid-drawn steel pipe piles under each column, and after pressing the piles, injection pipes are inserted for grouting. A combined bond between solidified body and piles, foundation and baseboard was constructed. It worked well and saved money and time. [3] A seven-floor brick-concrete residential building in Qinhuangdao, whose ground floor was 0.15 meters above outdoor floor due to the high underground water level, consumes much money because the precast pile must be into peddle bed 1.2-1.5 meters. The situation was not ideal even after reinforcing the saturated silt soil by dynamic compacting: there was not an enough increase in bearing capacity

after the processing, the compacting effective depth was small and the foundation soil showed obvious discreteness. Vibroflotation of gravel piles was also suitable on account of long duration, difficulties in pollution discharging and high cost. Then the solution became dynamic compacting of gravel piles, which overcame the shortages of dynamic compacting and the high cost and long duration of grouting pile and vibroflotaion pile. Eventually, the bearing capacity of composite foundation significantly went up.

**Applications of new materials.** Based on the origin method, we can also change the construction equipment or use new materials. The engineering geological condition of the run way of an airport is like follows. The upper part was sandy silt with good permeability and high strength, while the substratum was mucky soil which was waterproof and had low strength. The constructors used plastic drainage board surcharge preloading method, setting deep drainage board to remarkably improve the drainage condition of the substratum. It was able to meet the designed consolidate requirement timely so the settlement problems of the run way was thoroughly solved. [4] Though it spent more money and time than dynamic compacting, the implement was simpler, easier more widely available. The demand of geological condition of area to be reinforced was loose as well. The plastic drainage board surcharge preloading method worked well in reinforcing, especially for the soft layer in substratum, in which the residual settlement after processing was effectively controlled. So the execution was well-off with a satisfying result.

## References

[1] Ming-hua Zhao, Xue-yan Xu. Foundation Engineering, Higher Education Press [M], (2004). (in Chinese).

[2] Da-gen Su. Civil Engineering Materials, South China University of Technology Press[M], (2003). (in Chinese).

[3] Xiao-qing Ma, Practice of The New Technology of Grouted Bolt Static Pressing Steel Tube Pile in Foundation Reinforcement Engineering, [J].Building Construction, (2001). (in Chinese).

[4] Wei-dong He, Analysis and Comparison of Dynamic Compacting and Plastic Drainage Board Surcharge Preloading Methods, [J].Building Construction, (2011). (in Chinese).

*Applied Mechanics and Materials Vols. 580-583 (2014) pp 2332-2335*
*© (2014) Trans Tech Publications, Switzerland*
*doi:10.4028/www.scientific.net/AMM.580-583.2332*

# Bending Resistance of a Slender Plate Girder With Longitudinal Stiffener

Stefan I. Gutiu[1, a*], Catalin Moga[2,b]

[1,2] Faculty of Civil Engineering, Technical University of Cluj-Napoca, 400020, Romania

[a]stefan.gutiu@infra.utcluj.ro, [b]catalin.moga@dst.utcluj.ro

**Keywords:** slender plate girder, stiffener rigidity, bending resistance, Eurocode 3

**Abstract.** This paper presents an analysis regarding the bending resistance of a slender plate girder having a longitudinal stiffener in the compression zone of the web.The influence of the longitudinal stiffener rigidity on the bending resistance of a slender girder of Class 4 section is analyzed, starting from the hypothesis that the transversal stiffeners are infinitely rigid.

## Introduction

Steel plate girders having the webs made by thin plates which are of Class 4 sections are frequently utilized in steel structures because they are economically efficient.

Because some part of the web is buckled when the limit stresses are reached, this zone becomes ineffective but it remains important with regard to the girder rigidity. By disposing one or more longitudinal stiffeners the girder web will be divided in sub panels of a lower section class so that the ineffective zones can be diminished or eliminated.

In this paper we carry out a comparative analysis regarding the bending resistance of a Class 4 steel plate girder: of a girder without longitudinal stiffener versus the same girder with a longitudinal stiffener of different compression stiffness. A simplified method to evaluate the girder bending resistance, useful in pre-design is proposed.

## Theoretical Basis. Simplified Method to Evaluate Bending Resistance of a Stiffened Girder

According to [1] and [2] the resistance to pure bending of a steel plate girder is determined as: $M_{c.Rd} = (W_{eff.min} f_y)/\gamma_{M0}$ (for class 4 cross sections) or $M_{c.Rd} = (W_{el.min}\sigma_{lim})/\gamma_{M0}$ (for stress limits). Stress $\sigma_{lim}$ is the limiting stress of the weakest part of the cross section in compression.

In case of a stiffened web with one longitudinal stiffener located in the compression zone, Figure 1, this stiffener is considered a strut supported on an elastic foundation.

For the calculation of $A_{s\ell}$ and $I_{s\ell}$ the gross cross section of the column should be taken as the gross area of the stiffener and adjacent parts of the plate. For the stress distribution, as shown in Figure 1.b, the "column" cross section is given in Figure 1.c.

The elastic critical buckling plate of the stiffener can be calculated as follows:

$$\sigma_{cr.s\ell} = \begin{cases} \dfrac{1.05\ E}{A_{s\ell}} \dfrac{\sqrt{I_{s\ell}\ t^3\ b}}{b_1\ b_2} & -\text{if } a \geq a_c = 4.33\ \sqrt[4]{\dfrac{I_{s\ell}\ b_1^2\ b_2^2}{t^3\ b}} \\ \dfrac{\pi^2 E\ I_{s\ell}}{A_{s\ell}\ a^2} + \dfrac{E\ t^3 b\ a^2}{4\pi^2\left(1-\upsilon^2\right)A_{s\ell}\ b_1^2\ b_2^2} & -\text{if } a < a_c = 4.33\ \sqrt[4]{\dfrac{I_{s\ell}\ b_1^2\ b_2^2}{t^3\ b}} \end{cases} \quad (1)$$

The elastic critical force of the longitudinal stiffener is:

$$N_{cr} = \sigma_{cr.s\ell} \cdot A_{s\ell} \quad (2)$$

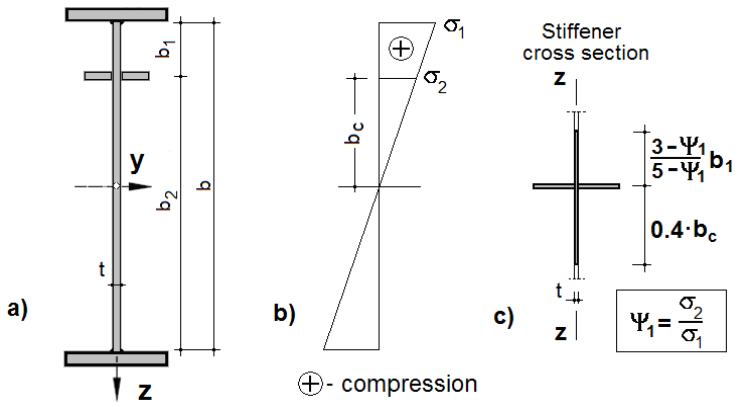


Figure 1. Girder with longitudinal stiffener

An accurate calculation regarding the bending resistance of the stiffened girder should be made as specified in [3], §4.5 and Annex A, by taking into account the interaction between plate and column buckling to evaluate the stress limit. For the girder pre-design a simplified design method is proposed as follows:

1. Knowing the critical force $N_{cr}$, the compression buckling resistance of the longitudinal stiffener can be determined:

$$N_{c.Rd} = \chi \cdot \frac{A_{s\ell.eff} \cdot f_y}{\gamma_{M1}}, \quad \text{where}: \ \chi = \chi\left(\bar{\lambda}_c = \sqrt{\frac{A_{s\ell.eff} \cdot f_y}{N_{cr.s\ell}}}\right) \tag{3}$$

2. The bending resistance of the girder can be approximately evaluated with the following relations:
   Upper subpanel Class 1 or Class 2:

$$M^r_{c.Rd} = \chi \cdot M_{c.Rd} \tag{4.a}$$

   Upper subpanel Class 3 or Class 4:

$$M^r_{c.Rd} = \begin{cases} M_{c.Rd} & -\text{if}: \Psi_1 \le \chi \\ K \cdot M_{c.Rd} & -\text{if}: \Psi_1 > \chi \end{cases} \tag{4.b}$$

where: - $M_{c.Rd}$ is the bending girder resistance considering that the stiffener is perfectly rigid;

- K is a reduction coefficient determined in such a way that the stresses $\chi \cdot f_y$ (Figure 2) should not be exceeded in the stiffener area: $K = f_y^{/} / f_y = \chi / \Psi_1$.

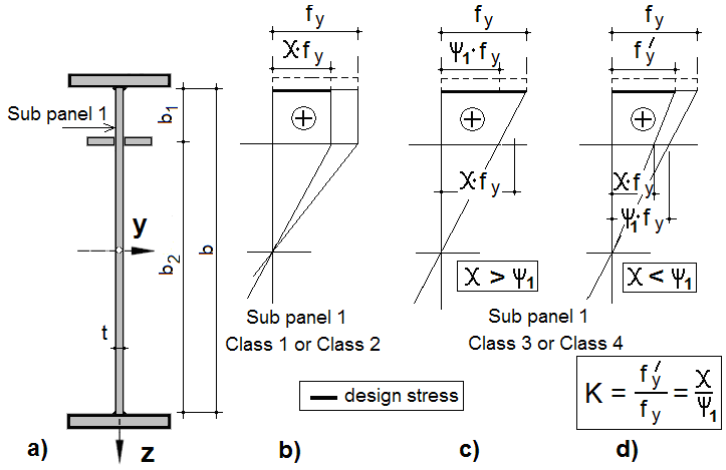


Figure 2. The reduction factor K

**Analysis example**

A comparative analysis regarding the pure bending resistance of a plate girder with a longitudinal stiffener located in the compression zone of the web is performed in this worked example. The following cases are subject to analysis: Case 1 - Girder without stiffener; Case 2 - Girder with a very rigid longitudinal stiffener in the compression zone; Case 3 - Girder with a flexible longitudinal stiffener; the stiffener is not considered as active part of the girder cross section; Case 4 - Girder with a flexible longitudinal stiffener; the stiffener is considered as active part of the girder cross section; Case 5 - Girder is working in the elasto – plastic domain.

**Design data:** Girder cross-section: web 2600x12 mm, flanges 650x30 mm; the girder stiffeners are at the distance of 2500 mm and have sufficient stiffness to create nodal lines for the buckled web; steel S355 for all girder elements.

The synthesis of the comparative analysis is presented in Table 1 & Table 2.

Table 1. Case 1 & Case 2 – Effective Cross Sections and Girder Bending Resistance

| **Case 1**. Girder without stiffener | **Case 2**: Girder with a very rigid longitudinal stiffener in the compression zone |
|---|---|
| 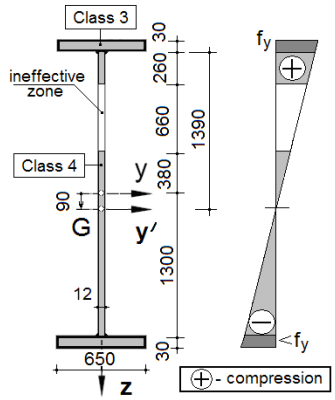 | 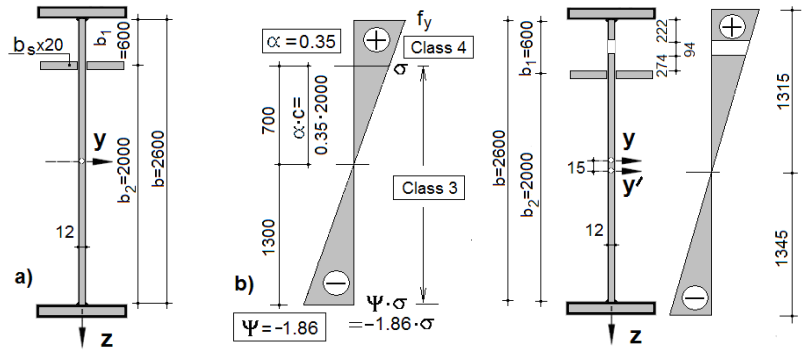 |
| $M_{c.Rd} = 20\,054$ kNm | $M_{c.Rd} = 22\,090$ kN · m |

Table 2. Case 3 & Case 4 – Effective Cross Sections and Girder Bending Resistance

| **Case 3**: Girder with a flexible longitudinal stiffener; the stiffener is not considered an active part of the girder cross section | **Case 4**: Girder with a flexible longitudinal stiffener; the stiffener is considered an active part of the girder cross section |
|---|---|
| 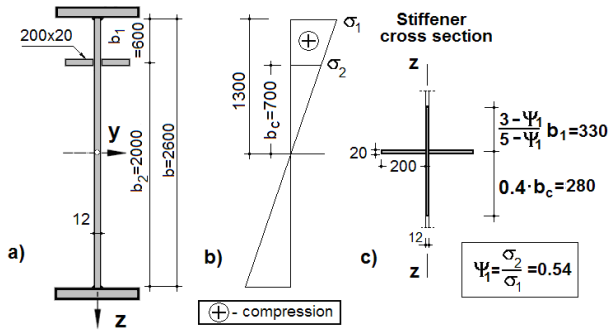 | 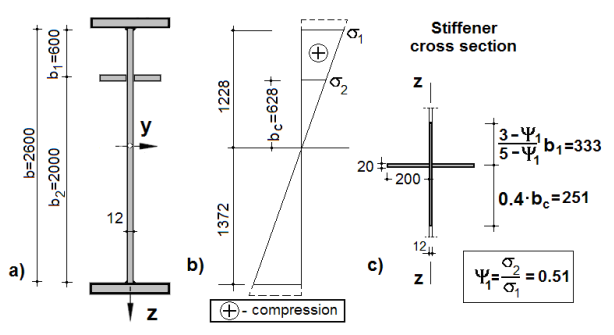 |
| $M_{c.Rd} = 22\,090$ kN · m | $M_{c.Rd} = 22\,386$ kN · m |

**Case 5**: Girder is working in the elasto – plastic domain

If two or more longitudinal stiffeners will be used, the girder cross section will be of Class 2 or of Class 1 and the girder bending resistance is:

$$M_{c.Rd} = (W_{pl} \cdot f_y) / \gamma_{M0} = 25\,404 \text{ kN} \cdot \text{m}$$

## Conclusions and Final Remarks

Steel plate girders having the webs made by thin plates which are of Class 4 sections are frequently utilized in steel structures because they are economically efficient.

Because some part of the web is buckled when the limit stresses are reached, this zone is ineffective but it is still important in what concerns the girder rigidity.

By disposing a longitudinal stiffener, the girder web is divided in two sub panels and thus the ineffective zones can be diminished or eliminated.

The increase of the girder bending resistance is more significant if the longitudinal stiffener is considered as an active part of the girder cross section.

In Table 3 the analysis results are centralized.

Table 3. Analysis results

| Case | Girder Type | Bending Resistance $M_{c.Rd}$ [kN · m] | Efficiency Factor $C = \frac{M_{c.Rd}}{M_{c.Rd}^{gr.w.stiffener}}$ |
|---|---|---|---|
| **1** | Girder without stiffener | 20 054 | 1.00 |
| **2** | Girder with a very rigid longitudinal stiffener in the compression zone | 22 090 | 1.10 |
| **3** | Girder with a flexible longitudinal stiffener; the stiffener is not considered an active part of the girder cross section | 22 090 | 1.10 |
| **4** | Girder with a flexible longitudinal stiffener; the stiffener is considered an active part of the girder cross section | 22 386 | 1.12 |
| **5** | Girder is working in the elasto – plastic domain | 25 404 | 1.27 |

## References


[1] EN1993-1. EUROCODE 3. *Design of steel structures,* (2003)

[2] EN1993-2. EUROCODE 3. *Design of steel structures.Part 2: Steel bridges*, (2005)

[3] EN1993-1-5. EUROCODE 3. *Design of steel structures. Part 1.5: Plated structural elements*, (2006)

[4] B. Åkesson: *Plate Buckling in Bridges and other Structures*, Taylor & Francis. London, (2007).

[5] B. Johansson, R. Maquoi, G. Sedlacek, C. Müller, D. Beg: *Commentary and worked examples to EN 1993-1-5 „Plated structural elements"* (programme of CEN/TC 250, 2007)

[6] St. I. Gutiu, C.Moga: *Influence of longitudinal stiffener rigidity on bending resistance of a slender plate girder.* Proceedings of the international conference DEDUCON, Sustainable Development in Civil Engineering, Iasi, Romania, (2011)

[7] P. Moga, St. I. Gutiu, C. Moga: *Proiectarea elementelor din otel.* UTPRESS Cluj-Napoca, Romania, (2012)

*Applied Mechanics and Materials Vols. 580-583 (2014) pp 2336-2340*
*© (2014) Trans Tech Publications, Switzerland*
*doi:10.4028/www.scientific.net/AMM.580-583.2336*

# Processing status and utilization of construction waste in China and the West

Fengjun Liu[1, a], Feifei Suo[1,b]

[1] School of Civil Engineering, Henan University of Science&Technology, 471023, Henan Luoyang, P.R.China

[a]lfjhaust@163.com , [b]prettysophie@sina.com

**Keywords**: Construction waste, Resource utilization, Processing status

**Abstract.** With the rapid development of economy and urbanization, more and more construction waste is produced. The construction waste consumes lots of space and pollutes the environment. Therefore，how to deal with it well is attracted more and more attention and research. The legal system and the treatment processes for construction waste resource utilization between china and the west are compared. Furthermore, considering the fact that a few deficiencies appear in construction waste resource utilization in china, some pertinent suggestions are put forward.

## Introduction

With the rapid development of economy and urbanization, construction waste is hard to avoid. According to their generation source, construction waste can be divided into building and demolition construction waste. As its name implies, building waste, is solid waste produced in building, rebuilding or expansion projects. Demolition waste generates thanks to demolished buildings, or met irresistible factors (such as volcanic eruptions, earthquakes, floods, war, etc.). Construction waste, a misplaced resource, not only takes up a lot of spaces but also pollutes the environment. The construction waste resource utilization is a method to solve this thorny problem which must be taken into account. Although there are several differences between China and the West, the purpose of the construction waste resource utilization is the same.

## Technology and Legal System in China and Abroad

The construction waste recycling starts earlier in the United States and forms a set of system in aspects of related policies and practical applications. In 1980, the *Superfund Law* was made. It stipulated: “Any company producing industrial waste must properly handle it by themselves, and is not allowed to freely dump industrial waste” [1]. In 1965, the *Solid Waste Disposal Act* was enacted. Information disclosure, reporting, resource recycling, regeneration demonstrations, technology development, recycling standards, economic stimulus and the use of priority, occupational protection, civil litigation and other solid waste recycling policies were included in this act. After several revisions, the laws and regulations related to construction waste in the United States have been gradually improved.

Germany is the first country in the world to carry out the circular economic legislation. Germany has developed several laws and regulations such as the *Waste Disposal Law, the circular economy and waste disposal law* and so on, to deal with construction waste since 1978. [1]. Compared with other countries, the legislation is rigorous in Germany, which is conformity with its reality.

After the Second World War, due to the support of the United States and other western countries, Japan's economy developed rapidly. But Japan, as an island country, saw the contradiction between economic development and land resources had been becoming increasingly prominent. As a result, the construction waste management started in the late 1960s. The corresponding laws, regulations, policies and measures to promote the transformation and utilization of construction waste were formulated, which included *Recycled Aggregate and Recycled Concrete Norms*, *Recycling Law*, *Building Recycling Law*, *Construction Materials Recycling Law*, *Green Purchasing Law* [1].

In China, the construction waste management is based on the *Urban Construction Waste Management Regulations* promulgated by the Ministry of Construction. The regulation came into effect in June 1, 2005, which required any individual or organization was not allowed to dump and bury building waste at random.

At present, the domestic legislation system is not perfect in China. Experiences about the related laws, regulations and management could be learned from the western countries, which results in fewer detours. Moreover, a large amount of construction waste would be avoided, and negative effects on the environment would be reduced.

## Construction Waste Treatment Technology in China and Abroad

**Foreign Technology in Construction Waste Management.** American construction waste utilization can be divided into three levels [1] [2]. Low-level utilization, for example, on-site sorting using and general backfilling, accounts for 50% ~ 60% of construction waste. Intermediate utilization is accounting for about 40% of construction waste. For example, base materials of buildings and roads, which is processed into aggregates by treatment plants, and then made into a variety of building bricks and so on. High-level utilization is little, a typical example of which is construction waste could be reduced into cement and asphalt.

Germany is the first country in the world to implement environmental labeling. Each region has a large comprehensive construction waste reprocessing plant. In Berlin there are more than 20 plants [2]. The technique of using construction waste to reforge recycled aggregate is leading the way in the world. The comprehensive and advanced production technology is formed due to long-term practice, continuous improvement and support of the corresponding mechanical equipments.

Fig.1 shows that the construction waste treatment process is widely used in developed countries [3].

Japan has already built a number of construction waste processing plants. Construction waste recycled products are eventually accepted by the market, which ascribes to a long period of production operations, continuous improvement of production processes and equipment. Currently, the basic ideas of construction waste in Japan are the same with Germany. However, the unique features in the treatment of construction waste are that its each step has a higher degree of refinement, and the device is more advanced. Its process equipments include the conventional separation equipment, electromagnetic separation equipment, fuel rotary separation equipment, incombustibles sorting equipment and other advanced equipment [1].

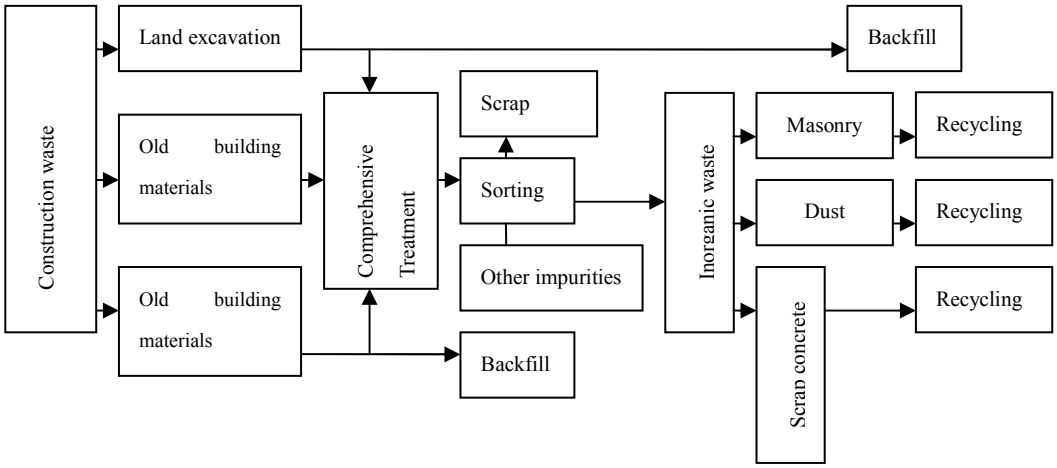


**Fig.1 Construction waste treatment process widely used in developed countries**

**Construction Waste Treatment Technology in China.** Waste building concrete and bricks could be made into new coarse and fine aggregate, which could be used to produce such products of the corresponding strength grade as concrete, mortar or wall panels, floor tiles and other building materials products [4]. When some curing agents added, the reforged aggregate could be used as road pavement base as well.

Waste residue could be applied to road construction, fillers, foundation, etc. It could be used directly without crush because of its relatively small particle. Therefore, construction waste treatment costs relatively little, and the use of waste residue is more convenient.

Waste timbers without apparent damage could be used to reconstruct the building, while badly damaged wooden components could be used as renewable raw materials of paper, mosquito coils, composite sheet, energy, home improvements and so on.

Scrap steel and other metal scrap materials could be directly reused or reforged. In general, the recovered steel is returned to steelworks, where it is remade, its impurities removed, and then it is made into various types of steel products before flowing into the market again [4].

Fig.2 shows that the construction waste treatment process is used in China [3].

As is shown in Figure 1, the circulation operation mode is used in the construction waste treatment process in advanced countries such as America, Germany and Japan. Construction waste can be recycled and applied to building spaces as renewable resources. Figure 2, operated by the linear model, shows that single treatment process is widely used in China. However, if analysis is made on construction waste treatment process of China and the West, disparities are presented evidently.

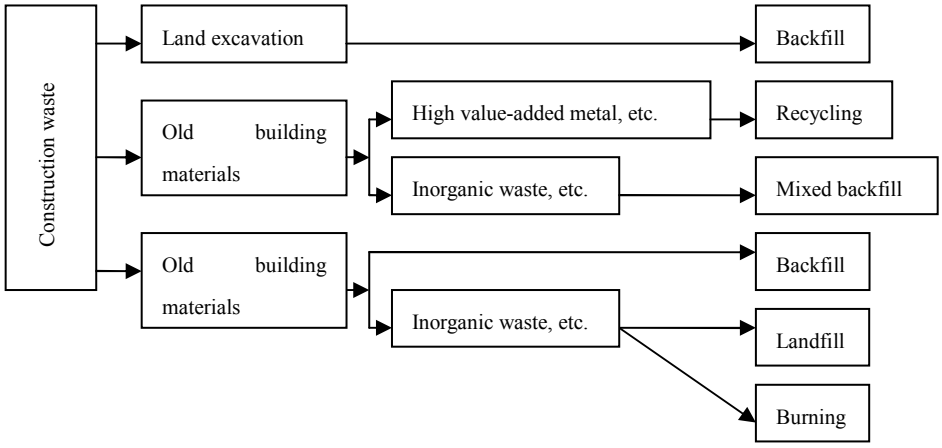


**Fig.2 Construction waste disposal process used in china**

## Countermeasures for China's Construction Waste Resource Utilization

**Several Problems about China's Urban Construction Waste Treatment** [5]**.** The level of construction waste classified collection is low. Most construction waste could only be collected as a mix.

The rate of construction waste recycling utilization is low.

The technology of construction waste treatment and resource utilization in China is backward. Construction waste in urban always is dumped into some landfills directly, which not only occupies a lot of land spaces, but also pollutes the environment.

Little investment is spent in urban construction waste treatment, policy measures are still not perfect, and the construction worker's environmental awareness is quite weak.

The enforcement of relevant policies, laws and regulations are not strong enough, and the standardization degree of construction waste treatment is low.

**Construction Waste Resource Utilization Should be Started with the Following Aspects.** Adopt the full life cycle management mode. Take the building cycle management model into the whole process, break the traditional linear model of the "building materials - building - building rubbish", and form the circular economic model of the "building materials - building - construction waste - recycled materials"[2].

Strengthen the legislation work for construction waste recycling. In the recycling of construction waste, the relevant government department should formulate special laws and regulations to prohibit landfilling available construction waste. What's more, the rules for construction waste sorted collection and storage should be stipulated. And, apply economic levers to regulate the disposal of construction waste [2] [6].

Carry out scientific research on construction waste recycling.

Strengthen education on construction waste resource utilization. Widely publicize the construction waste is a kind of available resources, improve environmental consciousness of construction workers, and introduce the latest technology and methods of construction waste utilization to the related units and individuals.

## Conclusion

Compared with China, construction waste resource utilization is at a higher level in many developed countries. It starts late in China, and there is a large gap behind of the advanced

international level. In order to realize the utilization of construction waste, China's national conditions should be taken into consideration. It should be started with such aspects as legal, management, technology and others, to promote the process of construction waste comprehensive utilization. Only in this way, can China effectively solve the problem of construction waste, develop the recycling economy, build a conservation-minded society and promote the sustainable development.

**References**

[1] Faguang Leng and Gengxin He, ect.: *Environmental Sanitation Engineering* Vol.17 (1) (2009),p33 (In Chinese)

[2] Ting Du and Yong Chang, ect.: *Journal of HuNan Urban Construction College* Vol.11(2) (2002),p35 (In Chinese)

[3] Hanming Chen: The Advice of Improving the Level of Recycling Construction Garbage in China. *Sixth National Civil Engineering Graduate Academic Forum,* 2008. (In Chinese)

[4] Luochun Wang and Xinxue Li, ect,: *Environmental Sanitation Engineering* Vol.16 (3) (2008),p26 (In Chinese)

[5] Zijiang Yang: *Recycling Research* (3) (2003),p26 (In Chinese)

[6] Jun Zhao and Shiyun Zhong, ect.: *Coal Ash China* Vol.13(2) (2001),p3 (In Chinese)

# CHAPTER 8:

# Water Supply and Drainage Engineering

*Applied Mechanics and Materials Vols. 580-583 (2014) pp 2343-2345*
*© (2014) Trans Tech Publications, Switzerland*
*doi:10.4028/www.scientific.net/AMM.580-583.2343*

# Effects of Different Irrigation Amount on Yield and Quality of Greenhouse Tomatoes

Chen Zhuang[1,a], Mohmed Abdallah Mohmed Abdalhi[2,b]

[1,2]School of Hydraulic,Power and Energy Engineering, Yangzhou University

No.131 Jiangyang Middle Road,Yangzhou,225009,China

[a]chenzhuangyzu@gmail.com, [b]434611753@qq.com

**Keywords:** tomato;irrgation amount;yield;quality

**Abstract.** In order to determine the proper irrigation amount of summer tomatoes,taking drip irrigation in green house,5 irrigation volume including 990 $m^3/hm^2$, 1485 $m^3/hm^2$, 1980 $m^3/hm^2$(CK), 2475 $m^3/hm^2$, 2970 $m^3/hm^2$ were set,and the effects of different irrigation amount on the yield and quality of tomato in greenhouse were studied. The results showed that with the increase of irrigation amount,the soluble solid content,titratable acid content,Vc content and irrigation water use efficiency of tomato decreased. In treatment T1, T4, T5 ,yield decreased by 26.3%, 6.5%, 15.8%. In treatment T2 , the yield decreased by 1.9%,while the irrigation water use efficiency increased by 20.8%,and the soluble solids content,titratable acid content and Vc content increased.It was concluded that the optimum irrigation amount was1485 $m^3/hm^2$.

## Preface

Tomato is one crops of the common important vegetable,in recent years, scholars have done a lot research in the irrigation amount.Many scholars discussed effects of different irrigation amount in different growth stage on yield and quality of greenhouse tomatoes.Irrigation amount and effect on yield and quality of the relationship showed the same changes [1-5] , Guo Haitao [6] believed in tomato fruit flowering period, reducing the amount of irrigation will increase yield,but there was less irrigation amount research on tomato from planting to harvest.The experiment considered 5 different irrigation amount,try to find the yield and fruit quality difference between 5 treatment,aiming to provide a reference for water management of tomato.

## Materials and Methods

1.1Experiment material

Tomato variety:Oudun.

1.2 Experiment methods

Experiment was conducted in the greenhouse from March to July,the greenhouse was located in experiment field of school of Horticulture and Plant Protection,Yangzhou University. The size of greenhouse is 30m×6m,15 plots whose size is 6m×1m were set,in each plot there were two lines of tomatoes,arrangement is shown in Figure 1. Tomatoes was planted in March 8th,the distance between lines is 60cm, while the distance between plants is 30cm.Irrigation started from March 11th, five irrigation volume including 990 $m^3/hm^2$, 1485 $m^3/hm^2$, 1980 $m^3/hm^2$(CK), 2475 $m^3/hm^2$, 2970 $m^3/hm^2$ were set, each treatment is repeated three times.The water was irrigated by drip under membrane.

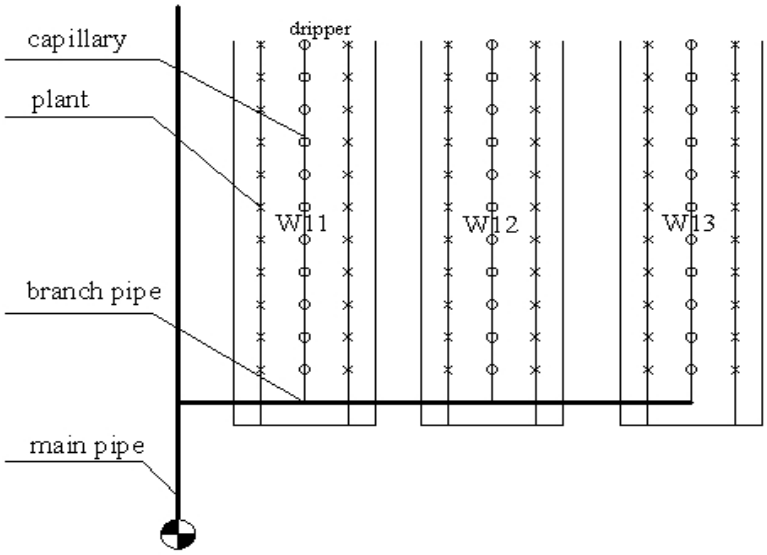


Figure1 Schematic Diagram of Tomatoes

1.2 Experiment methods

Experiment was conducted in the greenhouse from March to July 2013 ,the greenhouse was located in experiment field of school of Horticulture and Plant Protection,Yangzhou University. The size of greenhouse is 30m×6m,15 plots whose size is 6m×1m were set,in each plot there were two lines of tomatoes,arrangement is shown in Figure 1.

Tomatoes was planted in March 8th,the distance between lines is 60cm, while the distance between plants is 30cm.Irrigation started from March 11th, 5 irrigation volume including 990 $m^3/hm^2$, 1485 $m^3/hm^2$, 1980 $m^3/hm^2$(CK), 2475 $m^3/hm^2$, 2970 $m^3/hm^2$ were set, each treatment was repeated three times.The water was irrigated by drip under membrane.

1.3 Measurement items and methods

Quality of tomatoes: Measure quality of fruits in the flourishing period.

Soluble solids content (RHBO-90) was measured by a handheld refractometer,titratable acid content was measured by acid-base titration,Vc content was measured by spectrophotometry.

Yield:Pick fruits when they are mature and calculate the production.

## Results and analysis

2.1 Effects of different irrigation amount on quality of tomatoes

2. 1. 1 Effect on soluble solids content

With the increase of the irrigation amount, soluble solids content of tomatoes decreased,difference between 5 treatments is not significant(Table 1).The results showed that with the increase of irrigation amount，the soluble solid content decreased,which is consistent with former scholars' conclusion [7].

Table 1 Effects of different irrigation amount on fruit quality of tomato

| Treatment | soluble solids content （%） | titratable acid content （%） | Vc content （mg/kg） |
|---|---|---|---|
| T1 | 4.71 a | 0.46aA | 12.87Aa |
| T2 | 4.75 a | 0.41bB | 12.10Aa |
| T3 | 4.65 a | 0.41bB | 10.60bB |
| T4 | 4.46 a | 0.35bB | 9.46BC |
| T5 | 4.40 a | 0.34aA | 8.26Bc |

2. 1. 2 Effect on titratable acid content

With the increase of the irrigation amount, titratable acid content of tomatoes decreased. Treatment T2 and T4 had no significant difference with CK,but all the significance <treatment T1 and T5.The results showed that with the increase of irrigation amount,titratable acid content decreased,which is consistent with former scholars' conclusion [8].

2. 1. 3 Effect on Vc content

With the increase of the irrigation amount,Vc content of tomatoes decreased. Treatment T4 and T5 had no significant difference with CK,but all the significance <treatment T1 and T2. The results showed that with the increase of irrigation amount, Vc content decreased.It is concluded that decrease of irrigation amount will increase the quality of tomatoes.

2.2 Effect of different irrigation amount on yield and irrigation water using efficiency

With the decrease of the irrigation amount,yield of tomatoes decreased.Treatment T2 reduced by 1.9% compared with CK,while treatment T1 and T5 reduced by 26.3% and 15.8%, the differences have reached a significant level(Table 2). The results showed that irrigation amount has significant impact on yield, but less impact on T2 and T4.So it is concluded that the proper irrigation amount is treatment T2.

Table 2 Effects of different irrigation amount on yield and irrigation water use efficiency

| Treatment | irrigation amount （m3） | Yield （kg） | water use efficiency （kg/ m3） | Compared to CK （%） | |
|---|---|---|---|---|---|
| | | | | yield | water use efficiency |
| T1 | 1.095 | 49.566 bB | 45.27 | -26.3 | 68.8 |
| T2 | 1.8808 | 65.927aA | 35.05 | -1.9 | 20.8 |
| T3(CK) | 2.5062 | 67.216 aA | 26.82 | - | - |
| T4 | 3.0567 | 62.843 aA | 20.56 | -6.5 | -23.3 |
| T5 | 4.9147 | 56.615cb | 11.52 | -15.8 | -57.0 |

## Conclusion

The research show that with the increase of irrigation amount, the soluble solid content,titratable acid content,Vc content and irrigation water use efficiency of tomato decreased.Compared to CK,either increase or decrease the amount of irrigation,the yields declined [7] . In the treatment T2,although the yield slightly declined, but soluble solid content，titratable acid content,Vc content increased,besides water use efficiency significantly improved.Therefore it is considered that appropriate irrigation amount of tomatoes in the spring and summer is 1485 $m^3/hm^2$.

## References

[1] Zushi K,Matsuzoe N. Effect of soil water deficit on VitaminC,sugar,organic acid,amino acid and cartene contents of large-fruited tomatoes[J].Japan Soc Hort Sci,1998,67 ( 6) : 927－933.

[2] Liu Mingchi,Chen Diankui.Effects of deficit irrigation on yield formation and quality of cherry tomato fruit[J].Chinese Vegetable,2002,( 6) : 4－6.

[3] Liu Mingchi,Liu XiangLI. Effects of deficit irrigation on quality and yield of tomato fruit[J].Chinese Vegetable,2005 ( Supplement) : 46－48.

[4] Yin Shaomei,Hu Xiaotao, Kang Shaozhong,Cai Huanjie,Liang Baolei. Response of greenhouse tomato yield and quality to the results of deficit irrigation[J].Journal of Irrigation and Drainage,2011,30 ( 3) : 39 －42.

[5] Stevens M A,Kadera A. Potential for increasing tomato flavorvia increasing sugar and acid content[J]. Amer Soc HortSci，1979，104: 40 － 42.

[6] Guo Haitao,Zou Zhirong,Yang Xingjuan，Zhou Hefang . Effects of Regulated deficit irrigation on physiological indexes, yield, quality and water production efficiency of tomatoes[J].Agricultural Research in the Arid Areas,2007,25 ( 3) : 133 －137.

[7] Wang Feng,Du Taisheng,Qiu Rangjian.Deficit irrigation system of Greenhouse tomatoes based on principal componential analysis [J].Journal of Agricultural Engineering,2011,27 (1) : 75 － 79.36.

[8] Gao Fangsheng.Effect of soil moisture on tomato growth and some physiological characteristics[D]. Shandong Agricultural University,2006

*Applied Mechanics and Materials Vols. 580-583 (2014) pp 2346-2349*
*© (2014) Trans Tech Publications, Switzerland*
*doi:10.4028/www.scientific.net/AMM.580-583.2346*

# Emergency Supply of Drinking Water

Marek Teichmann [1, a], František Kuda [2, b], Zbyněk Proske [3, c]

[1, 2, 3] VŠB – Technical University of Ostrava, Faculty of Civil Engineering, Department of Urban Engineering, Ludvíka Podéště 1875/17, 708 33 Ostrava – Poruba, Czech Republic

[a] marek.teichmann.st@vsb.cz, [b] frantisek.kuda@vsb.cz, [c] zbynek.proske@vsb.cz

**Key words:** emergencies, emergency situation, crisis situation, contingency plan, emergency preparedness plan, replacement, emergency water supply.

**Abstract.** The article deals with the ways of dealing with the concept of drinking water supply in the event of emergencies and crisis situations. The contribution defines concepts related to crisis planning, describes preventive measures to ensure a prompt resolution of a situation, solution to minimize the damage caused by the incident and, last but not least, the possible ways of ensuring the supply of drinking water in emergency situations.

## Introduction

Occurrence of emergency situation in the production and distribution of drinking water can never be excluded. The probability of their occurrence increases with the increasing influences of the civilization. The cause of an emergency situation can often be the action of natural phenomena, whose intensity and frequency is induced by a number of natural laws, and in some cases even the humans. The most significant natural influencing phenomena manifesting in water management are floods. The influences of civilization then include, for example, various types of industrial accidents. Since that incident can not be ruled out, it is necessary to eliminate the negative consequences to an acceptable level. To eliminate the effects of such emergencies, the government creates its own security system. [1]

Timely and adequate readiness of the state and the stakeholders for a potential incident is then the decisive factor in managing emergencies at the optimal time and with minimal consequences. In the water sector, which is part of the critical infrastructure of the state, contingency planning is a necessity, especially because of its complete linkage to civil life and operation of public infrastructure.

## Emergencies and crises

Emergencies may represent natural effects, negative effects caused by human activity, accident threatening human health, property, goods and, ultimately, the environment.

An emergency situation arises, when the sovereignty and territorial integrity of a country is directly threatened, hence the operation of the economy, trade and industry, state and local governments, international commitments, lives and health of the population, property, goods, environment, etc., and such a threat can not be prevented by normal activities of administrative bodies, local government bodies, armed forces, rescue squads, emergency and other services, as well as the consequences of these situations can not be eliminated by common practice of these bodies and institutions.

A crisis situation can be understood as a form of emergency which is induced by a violation of one of the segments of critical infrastructure. In this case, a state of crisis is usually declared, i.e. a state of emergency, state of danger or a state of national emergency. [2,3,4]

## Contingency planning in water management

Contingency planning is a form of preventive measure in case of emergency and crisis situations to ensure minimized damage caused by the crisis and especially a plan that helps to quickly deal with the situation. These especially include the situations arising mainly by natural influences,

while their timing and duration can not be accurately determined. Similar are some situations caused by human activities, which can not be assumed. A typical representative of an emergency caused by natural phenomena are floods, which can have a very negative impact on water management. Likewise, an event of emergency can be induced by industrial accidents, which are a typical representative of emergency caused by human activity. It should be noted that the emergence of such situations in water management can not be ruled out and therefore it is necessary to be able to face these situations and minimize negative impacts to an acceptable level. Such situations are addressed today by contingency planning, as only a high-quality and timely readiness of stakeholders for any incident can provide a fast and efficient mastery in minimal time and with minimal consequences. Part of these preventive measures are incorporated in the contingency plan itself for the relevant territory or local government unit and plan of emergency preparedness of the institutions and bodies involved. [1,5,6]

The contingency plan is a set of documents containing a description and analysis of threats, summary of emergency procedures and measures in case of a situation of crisis. This plan is prepared by the competent authority, such as municipality, county, or state as one of the preventive measures in case of a crisis situation. It consists of two parts, namely basic part containing mainly the subject of potential sources of risk and threat analyses, a list of organizations and entities providing measures given by the contingency plan and characteristics of those organizations and entities of crisis management. The second part of the contingency plan is the annex part incorporating in particular the list of critical resources and measures for different types of crises, plans of the necessary supplies, connections, medical support, material and technological support and the like. The annex part of the contingency plan includes agility plan containing the response of the processor of the contingency plan for the declaration of the state of emergency and its readiness to fulfil the tasks set by contingency plan, such as the location of the planned or emergency sites of crisis staffs, including an overview of their equipment, list of people who will be working the crisis staff, the manner of convening the crisis staff and also the protection itself in case of threat to the crisis staff. [1,2,3,7]

Upon the actual processing of the crisis plan, the processor includes various cooperating agencies and organizations, such as the competent authority included in the contingency plan of emergency supplies of drinking water in the event of a crisis using services of an organization operating water supply systems. In this case, the organization is obliged to participate in addressing the crisis situations. The competent authority therefore concludes a contract with such organization, such as a contract on securing emergency water supplies and technical assistance under a crisis situation and the organization must provide a plan of emergency preparedness. Emergency preparedness plan itself serves the purpose of the organization involved in the crisis plan and comprises especially the very functioning of the organization in crisis situations and ways of securing and performing of the tasks outlined by the contingency plan. [1,3]

**Replacement and emergency water supply**

Replacement water supply is an activity whose purpose is to ensure the drinking water supply of the required quantity and quality for all users in the event of an outage of drinking water supply from the public water supply main due to emergencies or possible repairs. This is followed-up by emergency water supply, which is the way in which, in case of emergencies, replacement securing of the necessary amount of drinking water of the required quality is addressed, if the current drinking water supply system is partially or completely non-functional.

In the case of outage of a water source, non-compliance with the required values for drinking water quality at the outlet of the water treatment plant or an emergency in on drinking water feeder for the points of consumption or a fault on the distribution network it is sometimes necessary to cut off the entire system of public water supply in the consumption site. In this case, there is need for replacement and emergency drinking water supplies, which normally greatly complicates the living conditions in the given area and usually does not solve the water supply for the operations of the technical and technological operational units where there is a permanent supply of the required

quantity of water and often at the necessary pressure required to run the entire operation. At the same time the failure of the supply of drinking water also completely eliminates fire water supply from public water mains throughout the territory. It is therefore necessary that stakeholders are prepared for such incidents and be able to handle the situation at optimal time and with minimal consequences. [1]

For such situations, the operator of public water supply shall ensure replacement drinking water supply, which is performed according to his plan of emergency preparedness and this supply is ensured in reachable distance and in the extent for necessary personal use. The method of securing replacement water supply stems mainly from the technical possibilities and conditions under which it is possible to use several methods to provide for the supply of drinking water. The easiest way to provide a replacement of drinking water supply is the trucking of drinking water in truck tanks or stable tanks that are refilled as needed. Another source may be the functionally fixed aboveground or underground hydrant in reachable distance, which is equipped with a hydrant extension for the withdrawal of drinking water. [4]

*Fig. 1 Discharge stand for emergency water supply* [8]

Alternatively, functional and accessible aboveground or underground hydrants can also be used for direct connection to the internal water system of the given facility. Other ways to ensure the supply include the cut-off of the section which is the subject of failure and then replace it with the temporary ground pipeline, possibly connecting the site to an alternative source of water supply.

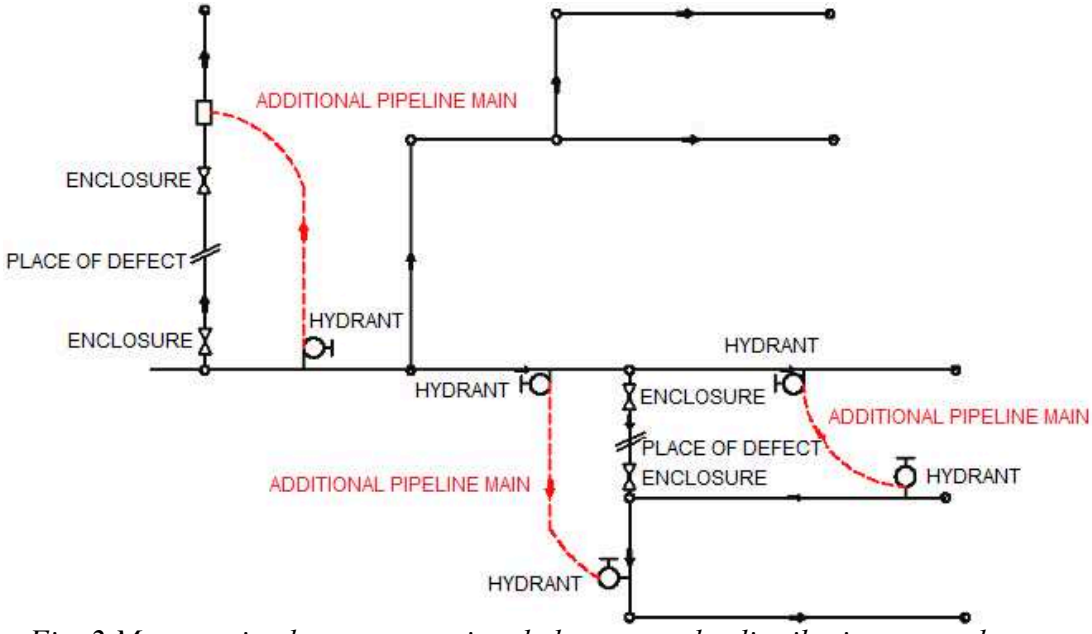


*Fig. 2 Means to implement operational changes to the distribution network structure*

It may thus be for example a connection to another functional water supply pressure zone, provided that the supply of drinking water will be either of higher or lower pressure condition, a temporary water supply connection for example led along the road surface at the distant functional above-ground or underground hydrant or a connection to another alternative source of raw water,

such as public well, in which case it is necessary to equip the temporary water supply with mobile water treatment plant facility.

Complications in these methods may occur in the event of adverse weather conditions when temperatures can fall below freezing point and there is a risk of water freezing. In these cases the preferred method is the distribution of drinking water with tank trucks or stable tanks located in heated areas. [4]

## Summary

Due to the ever increasing global population going against the gradual reduction of drinking water, we can also expect greater problems in the field of water management and the inherently related emergencies. The crisis situations arise naturally, therefore not only due to human activities, and therefore it is important to be prepared for such a contingencies, since the lack of water carries a particular risk to the health and life of the population and therefore can be fatal, especially in large populated areas. [1]

It is therefore important that especially the state authorities, water authorities and organizations are prepared in the long term for such facts, since being able to handle such a crisis requires advance preventive measures set in advance, such as contingency plans, including not only the relevant legislative requirements, but also the overall evaluation of all sources of water, including the allocation of strategic reserves, preparation of technical equipment for an emergency, training of rescue teams, as well as technical means of communication between the entities affected by the crisis and, last but not least the preparation of the plan of fire protection of urban areas in crisis caused by the situation of water scarcity. If we adopt the above measures and take possibly some further actions, we get a real chance to handle emergency situations and thereby reduce the potential damage caused by the same.

## Acknowledgements

This work were supported from the funds of the Student Grant Competition of the VŠB – Technical University of Ostrava. Project registration number is SP2014/140.

## References:

[1] KROČOVÁ, Š.: Havárie a řízení vodního hospodářství, SPBI Spektrum, Ostrava 2006, ISBN: 80-248-1246-0

[2] PROCHÁZKOVÁ, D.: Bezpečnost a krizové řízení, POLICE HISTORY, Praha 2006, ISBN: 80-86477-35-5

[3] KOŽÍŠEK, F.: Nouzové zásobování pitnou vodou - Metodické doporučení SZÚ – Národního referenčního centra pro pitnou vodu, ÚNMZ Praha 2007

[4] Davidson, A., Howard, G., Stevens, M., Allan, P., Kirby, L., Deere, D., Bartram, J.: Water Safety Plans. WHO/SDE/WSH/05.06. Revise Draft, WHO 2005

[5] KROČOVÁ, Š.: Strategie dodávek pitné vody, SPBI Spektrum, Ostrava 2009, ISBN: 978-80-7385-072-2

[6] ŠENOVSKÝ, M., ADAMEC, V., ŠENOVSKÝ, P.: Ochrana kritické infrastruktury, SPBI Spektrum, Ostrava 2007, ISBN: 978-80-7385-025-8

[7] ČSN EN 15975-1 Zabezpečení dodávky pitné vody – Pravidla pro rizikový a krizový management – Část 1: Krizový management

[8] Information on http://www.vodomer.cz

*Applied Mechanics and Materials Vols. 580-583 (2014) pp 2350-2353*
*© (2014) Trans Tech Publications, Switzerland*
*doi:10.4028/www.scientific.net/AMM.580-583.2350*

# Integrated Fuzzy Evaluation of Raw Water Eutrophication based on GIS

LIU Jun-ping[1, a *], SHAO Jia-wei[1,b], DONG Fei-long[1,c] and Ma Xiao-yan[1,d]

[1]College of Civil Engineering and Architecture, Zhejiang University of Technology, Hangzhou 310014, China

[a]LJP23@163.com, [b]rain542380809@live.com, [c]dongfeilong86@126.com, [d]mayaner@163.com

**Keywords:** raw water; eutrophication; evaluation; GIS; entropy weight method.

**Abstract.** To do a research about raw water eutrophication of water plants in Hangzhou, samples of raw water in Jiuxi, Xiangfu, Nanxing, Qingtai Plant were collected and analyzed to get more than 10 water quality indexes. Turbidity, DO, COD, TN, $NH_3$-N and CHL-a serving as example. supported by GIS, integrated fuzzy evaluations of raw water eutrophication in July and December were completed applying entropy weight method. The result shows that in terms of the nutrient degree, Xiangfu is the most qualified while the least one is Qingtai. Overall, raw water in December is of higher quality than July.

## Introduction

Although China's economy is rapidly developing, environment and health problems, however, are becoming increasingly serious. How to guarantee water quality in urban and rural areas becomes a major problem. The latest hygienic standard for drinking water came out in July, 2012. The range of water quality inspection expanded a lot. There were only 35 indexes of water quality testing before the standard came out, which fell far behind the developed countries. Then the new standard's indexes increased to 106, which almost reached the international advanced level and could guarantee the tap water to be drunk without extra process. With the new standard, water quality was improved a lot. The water plants in cities supply residents with safe tap water, and undertake the task to purify raw water of rivers. When the ability to process raw water and the processing water yield is certain, the raw water quality will exert a significant impact on water treatment technology, equipment, operating efficiency and so on.

## Review of Study

**General situation of Study Area.** Hangzhou Water Industry Group administers 5 water plants, Qingtai, Xiangfu, Nanxing, Jiuxi and Chishanfu (the first four plants are studied), whose scope of water supply covers main urban area of Hangzhou, part of Yuhang and Xiasha. And the turbidity of processed water is under 0.2NTU. The designed water supply capacity can come to 1700,000 m3.

**Data Collection.** Samples of raw water were collected from water inlet of Jiuxi, Nanxing, Xiangfu and Qingtai in July and December, 2012. After the collection, the samples were taken to laboratory immediately to be analyzed. The analyzation covered more than 10 indexes, and Turbidity, DO, COD, TN, NH3-N and CHL-a were chosen to be studied.

**Research Method.**

**Geographic Information System.** GIS collects, saves, calculates and illustrates the data with computer technology based on the geographic data of earth surface [1]. The water quality evaluation used to process data manually or apply certain software, the results of evaluation only come out in the form of chart. However, these traditional methods hardly reflect the spatial distribution, and are not able to express the information vividly[2]. Then GIS offers some relevant methods. The ability of spatial analysis is the most pivotal and strongest function of GIS, also the difference between GIS and other computer aided software; spatial analysis makes quantitative description of spatial matters, making consequences more objective and accurate[1]. Based on the electronic map whose accuracy is 2 km, the map was input into ArcMap, in which the positions of these four water plants were marked

as points, the water front of the West Lake and Qiantang River was marked as lines, the water supply area of each water plant, the West Lake, and Qiantang River were marked as polygons. And the geographic information of each element was input into the attribute table. Necessary annotation was added on the picture as well. After editing, a manipulable GIS digital map came out.

**Entropy Weight Method**. Entropy is suitable for the measurement of amount of valid information and systematic level of disorder that known data contains and determining the weight at the same time. Entropy weight method determines the weight of each index according to the difference between each monitoring index, and is widely applied in water quality fuzzy evaluation as an objective method of determining weights[3]. The theory of entropy weight method is to quantify and assess comprehensively the information of every unit to be evaluated. Determining weight of each factor with entropy weight method could simplify the assessment process and enhance the accuracy of integrated fuzzy evaluation of raw water eutrophication. When certain index value of every object varies a lot from one to another, the entropy is small, indicating that the amount of information it provides is big, and its weight ought to be big; on the contrary, when certain index value of every object varies a little from one to another, the entropy is is big, indicating that the amount of information it provides is small, and its weight ought to be small; when certain index value of every object is exactly equal, it means that the index's information is useless and could be removed from the evaluation system[4].

## Integrated Fuzzy Evaluation of Eutrophication

### Step of Entropy Weight Method.

**Normalize the Matrix of Original Data.** Define the original matrix that consists of $m$ evaluation indexes and $n$ evaluation objects as $A=(a_{ij})_{m\times n}$. $a_{ij}$ is the $j$th original data of object $i$[3]. Apply different normalization formula to index that is better when it is bigger and index that is better when it is smaller. The normalized matrix is $R=(r_{ij})_{m\times n}$.

To index that is better when it is bigger such as DO, the normalization formula is

$$r_{ij}=\frac{a_{ij}-\min\limits_{j}\{a_{ij}\}}{\max\limits_{j}\{a_{ij}\}-\min\limits_{j}\{a_{ij}\}}. \tag{1}$$

To index that is better when it is smaller such as TN, the normalization formula is

$$r_{ij}=\frac{\max\limits_{j}\{a_{ij}\}-a_{ij}}{\max\limits_{j}\{a_{ij}\}-\min\limits_{j}\{a_{ij}\}}. \tag{2}$$

**Define the Entropy.**

$$h_i=-k\sum_{j=1}^{n} f_{ij}\ln f_{ij},\quad f_{ij}=\frac{r_{ij}}{\sum\limits_{j=1}^{n} r_{ij}},\quad k=\frac{1}{\ln(n)},\ \text{when } r_{ij}=0,\ f_{ij}=0. \tag{3}$$

**Define the entropy weight.**

$$w_i=\frac{1-h_i}{m-\sum\limits_{j=1}^{m} h_i},\ (0\le w_{ij}\le 1,\ \sum_{1}^{m} w_i=1). \tag{4}$$

**Figure out integrated weighted nutrition state index $m_{ij}$.**

$$m_{ij}=\sum_{i=1}^{n}(a_{ij}\times w_i). \tag{5}$$

**Integrated Fuzzy Evaluation in July.** Four water plants and six indexes consist the original matrix of water quality evaluation. The four water plants are Jiuxi, Xiangfu, Nanxing and Qingtai. Six evaluation factors are Turbidity, DO, COD, TN, NH3-N and CHL-a.

$$A=\begin{bmatrix} 22.60 & 5.30 & 77.30 & 60.20 \\ 5.26 & 4.70 & 3.64 & 5.46 \\ 1.65 & 3.41 & 1.77 & 1.76 \\ 0.74 & 1.32 & 1.60 & 1.38 \\ 2.26 & 2.87 & 2.70 & 2.17 \\ 0.0006 & 0.0006 & 0.0018 & 0.0029 \end{bmatrix}, \text{ then } R=\begin{bmatrix} 0 & 0 & 0 & 0 \\ 0.233 & 0.887 & 0.047 & 0.091 \\ 0.927 & 0.357 & 0.977 & 0.971 \\ 0.967 & 0.751 & 0.979 & 0.977 \\ 0.900 & 0.459 & 0.965 & 0.964 \\ 1 & 1 & 1 & 1 \end{bmatrix}.$$

$$H=\{h_i\}=[0 \quad 0.628 \quad 0.955 \quad 0.995 \quad 0.973 \quad 1]$$
$$W=\{w_i\}=[0.690 \quad 0.257 \quad 0.031 \quad 0.003 \quad 0.019 \quad 0]$$
$$M=\{m_j\}=[17.04 \quad 5.03 \quad 54.38 \quad 43.04]$$

$m$ is the integrated embodiment of the six indexes. The smaller $m$ is, the better is water quality.

**Integrated Fuzzy Evaluation in December.**

$$A=\begin{bmatrix} 16.00 & 9.00 & 42.00 & 16.00 \\ 7.43 & 8.01 & 6.76 & 6.57 \\ 3.04 & 2.29 & 3.24 & 3.16 \\ 0.20 & 0.02 & 0.28 & 0.72 \\ 3.83 & 3.91 & 4.61 & 4.26 \\ 0.0037 & 0.0003 & 0.0067 & 0.0038 \end{bmatrix}, \text{ then } R=\begin{bmatrix} 0 & 0 & 0 & 0 \\ 0.464 & 0.890 & 0.161 & 0.410 \\ 0.810 & 0.746 & 0.923 & 0.803 \\ 0.988 & 0.998 & 0.993 & 0.955 \\ 0.761 & 0.566 & 0.890 & 0.734 \\ 1 & 1 & 1 & 1 \end{bmatrix}.$$

$$H=\{h_i\}=[0 \quad 0.892 \quad 0.740 \quad 1 \quad 0.991 \quad 1].$$
$$W=\{w_i\}=[0.731 \quad 0.079 \quad 0.190 \quad 0 \quad 0.007 \quad 0].$$
$$M=\{m_j\}=[12.89 \quad 7.67 \quad 31.88 \quad 12.84].$$

**Evaluation of Raw Water Eutrophication Based on GIS.** Spatial analysis function was applied to analyze the integrated value of raw water nutrient degree in the water supply area in order to find the demarcation point. Then raw water nutrient degree was divided into 4 levels: medium-nutrient, light-eutrophic, meso-eutrophic and hyper-eutrophic, as shown in Fig. 1.

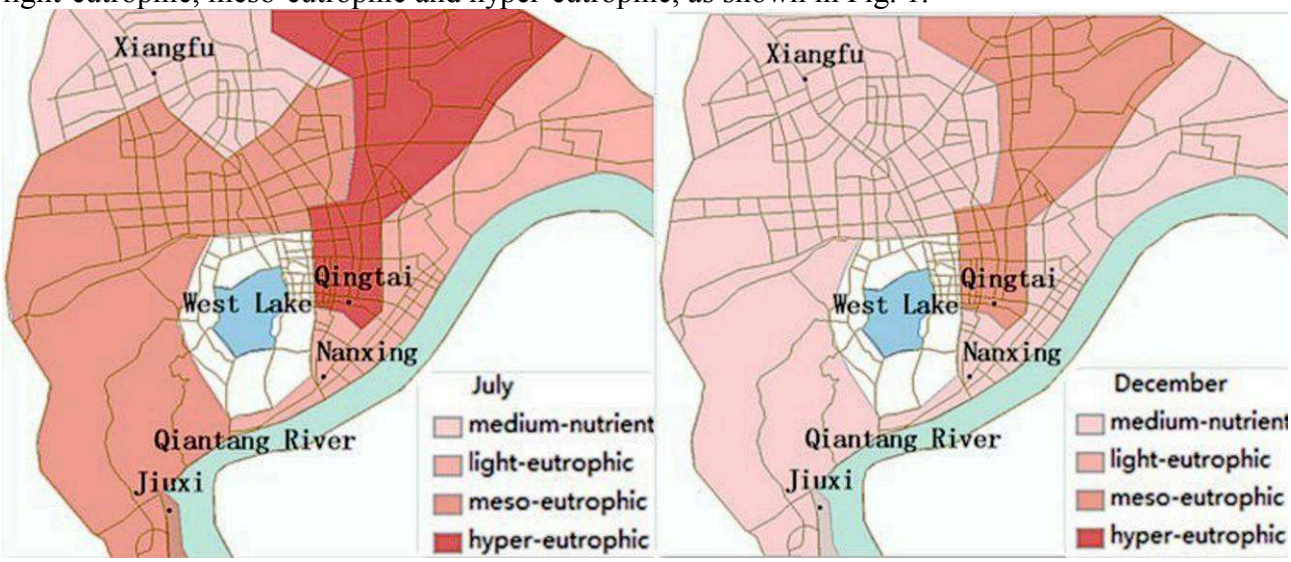


Fig. 1 Distribution Map of Nutrient Degree

As is shown in Fig. 1, in July, raw water nutrient degree in Xiangfu is the lowest, graded as medium-nutrient; raw water nutrient degree in Nanxing is graded as light-eutrophic; raw water nutrient degree in Jiuxi is graded as meso-eutrophic; raw water nutrient degree in Qingtai is the highest, graded as hyper-eutrophic. While in December, except that raw water nutrient degree in

Xiangfu remains to be medium-nutrient, raw water nutrient degree in other three water plants all drops. Raw water nutrient degree in Nanxing drops from light-eutrophic to medium-nutrient; raw water nutrient degree in Jiuxi drops from meso-eutrophic to medium-nutrient; raw water nutrient degree in Qingtai drops from hyper-eutrophic to meso-eutrophic.

**Analysis of Research.** Raw water nutrient degree in December drops to some extent compared with that in July. One of the factors is DO, whose content is in close relation to oxygen partial pressure of atmosphere and water temperature. Under the natural condition, oxygen content of atmosphere hardly changes, so water temperature is the main factor. The lower water temperature is, the higher DO is. Another factor is that raw water that water plant gets is usually deep water. Algae blooms in summer, shades and isolates the air, thus destroys the balance of oxygen exchange between oxygen in water and air. Photosynthesis of plants under water is limited as well. In the meantime, oxygen is consumed greatly by respiration, reducing the content of DO in deep water substantially.

Due to the fact that Xiangfu gets raw water from Dongtiao River, its raw water nutrient degree is lower than the other three water plants, which reflects the fact that Qianjiang River's water quality is not good. Because China is the largest exporter of textiles, and Zhejiang's capacity could account for 50 percent. There are many textile printing and dyeing enterprises in industrial parks in Xiaoshan and Shaoxing, which discharge sewage that is not up to standard into Qiantang River.

## Summary

Supported by raw water data, raw water quality was analyzed and evaluated in the eutrophication reaearch based on GIS. In July, raw water nutrient degree in Xiangfu is the lowest, followed by Nanxing, Jiuxi and Qingrai, ranging from low to high. In December, raw water nutrient degree in Jiuxi, Nanxing and Qingtai all drops. On the whole, raw water nutrient degree in Xiangfu is the lowest and water quality is the best; raw water nutrient degree in Qingtai is the highest and water quality is the worst. According to the raw water quality in Jiuxi, Nanxing and Qingtai, there is eutrophication in water body of Qiantang River and the water quality is not good.

## Acknowledgements

This work was financially supported by the Key Scientific and Technological Innovations Teamwork Project(2012R10035-11), National Natural Science Foundation of China (51208468) and Natural Science Foundation of Zhejiang Province (51208468).

## References

[1] TANG Guo-an, Yang Xin, ArcGIS Geographic information system spatial analysis experiment tutorial, first ed., Science Press, Beijing, 2006.

[2] CAO Fang-ping, ZOU Zheng-rong, The design and realization of river water quality evaluation system based on GIS, J. Science of Surveying and Mapping. 34 (2009) 192-193.

[3] ZOU Zhi-hong, SUN Jing-nan, REN Guang-ping, Study and application on the entropy method for determination of weight of evaluating indicators in fuzzy synthetic evaluation for water quality assessment, J. Acta Scientiae Circumstantiae. 25 (2005) 552-556.

[4] QIU Wan-hua, Management decision making and application of entropy, first ed., China Machine Press, Beijing, 2002.

*Applied Mechanics and Materials Vols. 580-583 (2014) pp 2354-2357*
*© (2014) Trans Tech Publications, Switzerland*
*doi:10.4028/www.scientific.net/AMM.580-583.2354*

# Research of Hydrodynamics of Biofilter with Surface Feed.

E.S. Gogina[1,a], O.V. Yantsen[2,b], O.A. Ruzhitskaya[3,c]

[1] Professor of the Department Wastewater and water ecology, Federal State Educational Institution of High Professional Education 'Moscow State University of Civil Engineering' (MGSU), 129337, Russia, Moscow, Yaroslavskoe shosse, 26

[2] Specialist in the field of water supply and wastewater of the Department Wastewater and water ecology, Federal State Educational Institution of High Professional Education 'Moscow State University of Civil Engineering' (MGSU), 129337, Russia, Moscow, Yaroslavskoe shosse, 26

[3] Associate Professor of the Department Wastewater and water ecology, Federal State Educational Institution of High Professional Education 'Moscow State University of Civil Engineering' (MGSU), 129337, Russia, Moscow, Yaroslavskoe shosse, 26

[a]GoginaES@mgsu.ru, [b] YantsenOV@mgsu.ru, [c]RuzhitskayaOA@mgsu.ru

**Keywords:** Biological treatment, biofilter, feed, contact time, waste water, reconstruction, treatment plants, integrated waste water treatment.

**Abstract.** The paper deals with the calculation of the contact time of waste water in the body of feed in the biofilter to determine the optimum settings.

## Introduction

There are a lot of biofilration treatment plants nowadays that work with overloading capacity and pollution values, so the issues of modernization of such plant are of the top priority.

Biofilters are widely used for the waste water treatment plants of a small capacity, in Moscow region it means about 70% of overall biofilter use. A Majority of them demands reconstruction and intensification of treatment processes, because most of them can provide only insufficient biological waste water treatment with discharge is BOD -30 mg/l. [1]

## Research of hydrodynamics of biofilter

Reconstruction allows avoiding solid capital costs comparing with new construction and meanwhile can show significant improvement in treatment quality.

Definition of optimal flow, hydraulic load and choice of efficient feed is important for a biofilter maintenance, and this can be done by means of reconstruction.

Feed of biofilters can be of volumetrical and surface type. The last one is of the big interest due to its lower weight and significant porosity. When designing new types of feed it is strongly needed to make it durable, rigid, chemically, biologically and frost-resistant, with a developed surface, low volume weight and high porosity. [2]

The research was made to define contact time of wastewater with surface feed in biofilter body because of the fact that this parameter has a significant influence at biochemical oxidation e.g. intensity and efficiency of biochemical treatment depends among other on length of the path, that drops of waste water pass on surface of feed.

The experiment was decided to be carried out using surface rigid feed. Polymer samples can suit for these purposes especially light weight that is another advantage. There were crimped cuts of polyethylene pipes chosen (fig.1) for this research. Mass of one element – 1.51 g, unit weight – 191 g per cubic meter.

Fig. 1. The surface feed

There is a solutuion of non-oxidized dye (red, E124, 1.5 g diluted in 200 ml of distilled water) to pass through cylindrical laboratory model of biofilter (that consists of a 60 liter cistern with a pump to supply waste water to the upper part of the biofilter , a distribution system for steady waste water supply and the model of biofilter made of perspex ,circular in plan, 2 meters high, 0, 1 in diameter, feed is 1,9 metres high) with fixing of color change in the discharge water by means of photocolorimetry.

There are three modes of flow set – 58 l/day, 108 l/day, 173 l/day. Dye solution (25 ml) was put instantly together with inlet water. Samples of discharge water were taken within fixed time intervals from dye input and until entire vanishing of colour.

Afterwards these samples were investigated for transparency by means of photocolorimetry. The investigation resulted in diagrams that show the dependence of colour intensity to the sample collection time. This diagram is compared with the curve drawn according to the optical density of a dye with various concentrations.

The experiment #1 on the method above was made with a flow 57,89 l/sec.

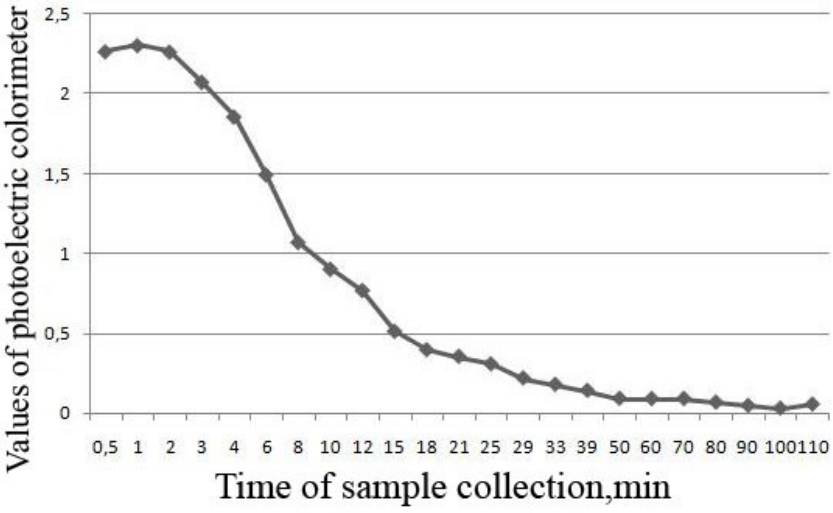


Fig.2. The diagram showed the dependence of colour intensity to the sample collection time (flow 57,89 l/sec.)

The experiment #2 was made with a flow 172,8 l/sec, afterwards a curve was drawn.

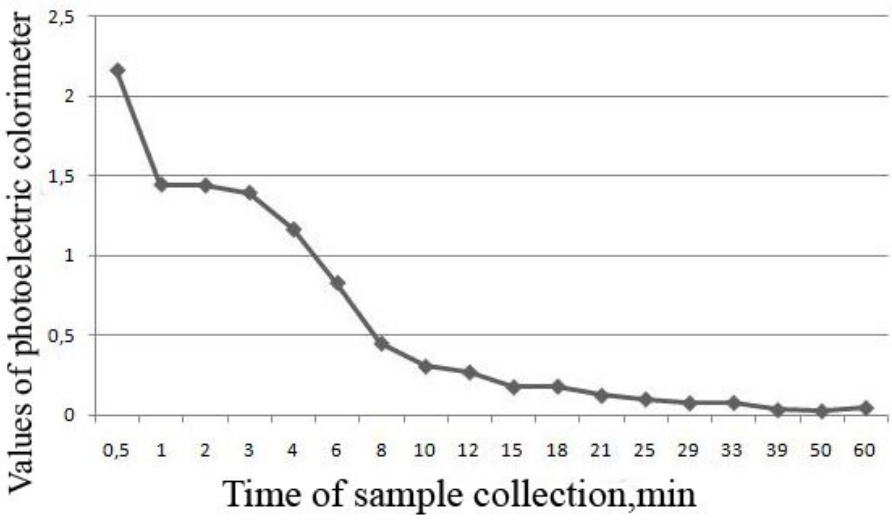


Fig.3. The diagram showed the dependence of colour intensity to the sample collection time (flow 172,8 l/sec.)

The experiment #3 was made with a flow 108 l/sec, afterwards a curve was drawn.

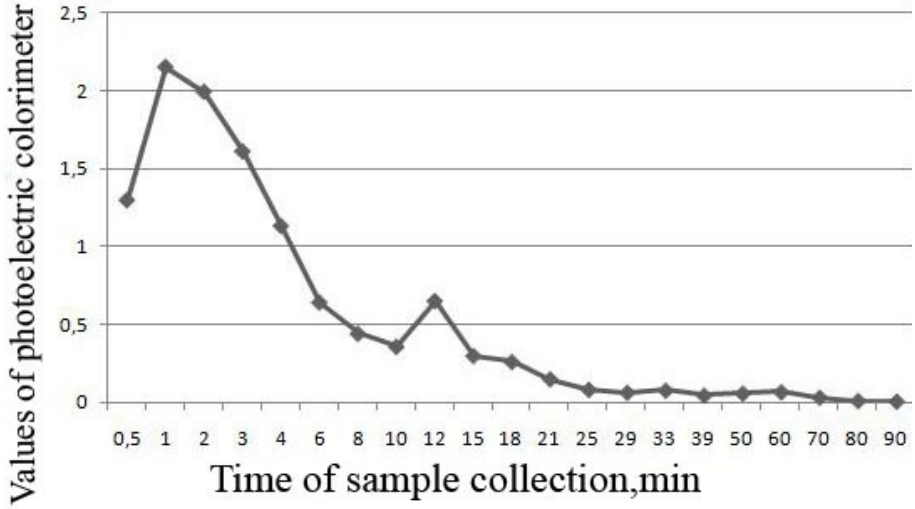


Fig.4. The diagram showed the dependence of colour intensity to the sample collection time (flow 108 l/sec.)

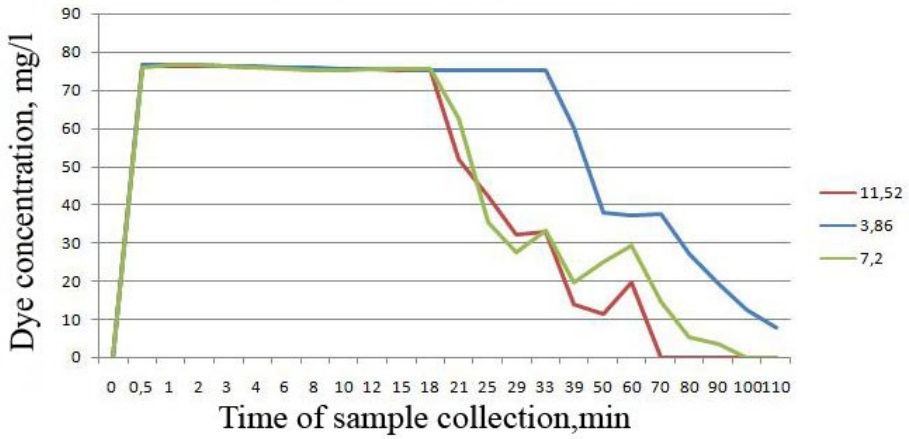


Fig.5. Diagram of dye concentration change depending on treatment time in biofilter body with various hydraulic loads

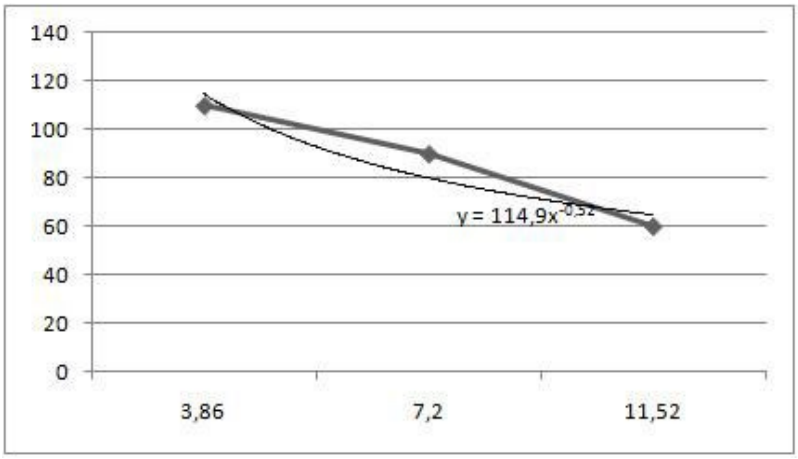


Fig.6 The diagram was made based on fig.5.

Average time of the water stay in the biofilter can be expressed as follows

$$t = \frac{C \times H}{q^n}$$

H –height of the feed,
Q – hydraulic load,
C and n – constants, that are depended on the surface of biofilm in a uint of feed volume, on viscosity of liquid and construction of a feed.

When H is 1.9 m the equation is

$$t = 114{,}9 \times 1{,}9 \times q^{-0{,}52}$$

After putting values of hydraulic load we get 108.2, 78.2 and 61.25 correspondingly.

**Conclusions:**

Overall experiment showed that this type of feed has features needed for the optimal work of biofilter for all tested flows and suits for WWTP reconstruction including integrated treatment.

**References**

[1] E.S. Gogina, V.P. Salomeev, O.A. Ruzhitskaya, Yu.P. Pobegaylo: *Methodology of wastewater treatment plant renovation.* Water Supply and Sanitary Technique. (2013). 6. pp. 33-37.

[2] Makisha N, Gogina E. *Floating feed in ammonium removal*. Applied Mechanics and Materials. 2013. T. 361-363. C. 632-635.

*Applied Mechanics and Materials Vols. 580-583 (2014) pp 2358-2362*
*© (2014) Trans Tech Publications, Switzerland*
*doi:10.4028/www.scientific.net/AMM.580-583.2358*

# Research On UV/$TiO_2$ Photocatalytic Oxidation of Organic Matter In Drinking Water and Its Influencing Factors

Jinhui Zhao

(College of Environmental, Nanjing University of Technology, Nanjing, P R China)

zjh-huaxian@163.com

**Keywords-** drinking water; photocatalysis; organic matter; removal efficiency

**Abstract—**UV/$TiO_2$ photocatalytic of filtrated water are conducted in S waterworks which take Yangtze River as its source water in Nanjing. Self-made glass supported nano-$TiO_2$ film and photocatalytic reactor are used for the experiment. Results show that TOC removal efficiency can reached 45% -63% within 2h-3h, Organic matter removal efficiency is positively related with the • OH generated in photocatalytic process. The influence factors on TOC removal efficiency follows the sequence: light intensity, dissloved oxygen, reaction time and pH. Changes of UV absorption characteristics in photocatalytic process indicate that the saturation of organic matter increase significantly, this is conductive to control the risk taken by disinfection by-products. Results proved that UV/$TiO_2$ photocatalytic is a promising technology for the removal of organic pollutants in drinking water, it can improved the chemical safety of drinking water.

## Introduction

In recent years, the chemical safety of drinking water caused by organic pollutants in water has become one of the main problems. Sanitary Standards for Drinking Water (GB5749-2006) set higher quality standard for drinking water. Facing the deteriorating source water quality, conventional water treatment process can't fully meet the new standards [1]. Domestic and foreign research and practice indicate that the conventional coagulation, sedimentation and filtration processe can only remove 20% -30% organic matters from water. How to strengthen the traditional treatment process and develop new drinking water treatment process to control organic pollutants has become an urgent problem.

UV/$TiO_2$ photocatalytic advanced oxidation technology is receiving more and more attention in drinking water treatment. In 1972, Fujishima and Honda reported that the radiation of $TiO_2$ can induce sustainable oxidation reduction reaction of water in the photocell and generate hydrogen[2]. Since then, scholars have conducted much researches on the removal effect of photocatalysis on priority pollutants [3], humus [4, 5] and algal toxins [6] in water. Moreover, some scholars further studied the photocatalytic oxidation kinetics of organic matter [7]. However, there still lack systemic research on the removal efficiency and influencing factors of UV/$TiO_2$ on the organic substance in drinking water.

## Equipments and Methods

### Experimental equipments

A self-made photocatalysis reactor are made with glass-supported $TiO_2$ film adhered inside (Fig.1), A 18w ultraviolet germicidal lamp in a 6cm-diameter quartz socket tube are used in the reactor as UV light source, the major wavelength of the lamp is 253.7nm.

XRD analysis shows that the $TiO_2$ film crystal morphology is anatase. The surface morphology of the film is studied by a Veeco Autoprobe CP–R model atomic force microscopy, AFM image shows that the average particle size is 13.2 nm. The average film thickness is 14.88 nm and the relative surface roughness is 15.5% (Fig. 2).

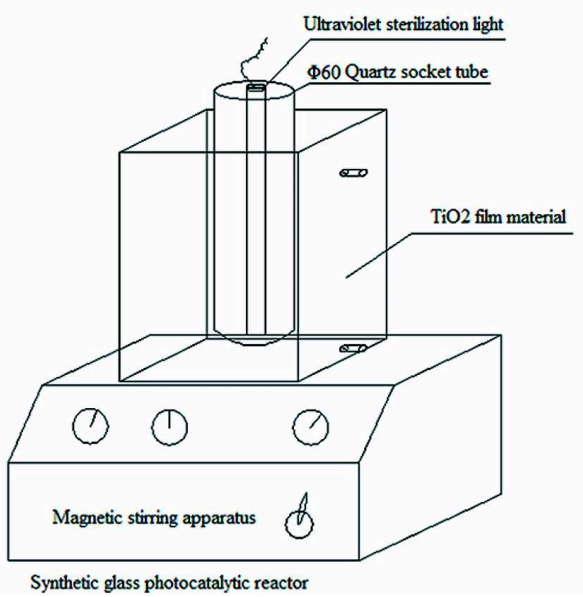


Fig.1 Experimental equipment of photocatalytic

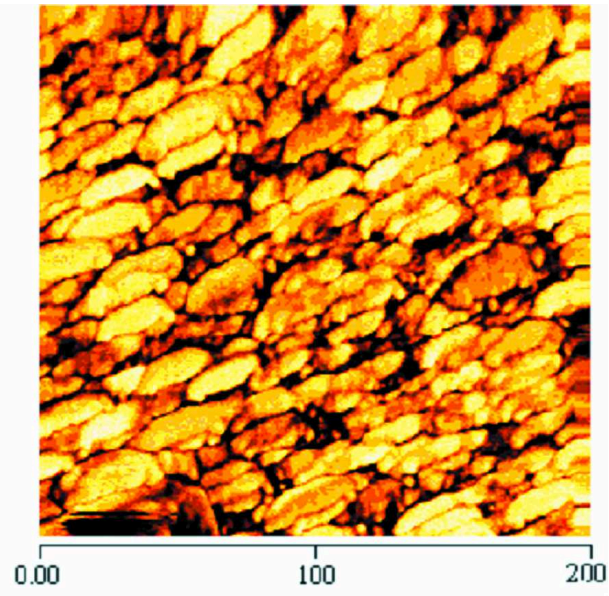


Fig.2 AFM image of $TiO_2$ film

## Experimental Methods

Take TOC as a characteristic index for organic matters, removal efficiency of UV/$TiO_2$ photocatalysis on trace organic matters in filtered water are studied, relationship between TOC removal efficiency and the amount of •OH generated are studied by correlation analysis. In addition, the influence of UV light intensity, reaction time, pH, dissolved oxygen are analyzed through $L_9$ ($_3^4$) orthogonal experiments.

Photocatalytic experiments of filtered water are conducted under the optimal conditions determined by the above orthogonal experiments, transformation of organic matter in photocatalytic process are studied by comparing spectral scanning characteristics and changes of SUVA value of water sample before and after photocatalysis.

The determination methods of conventional water quality indexs listed in Table 1 all adopt the national standard method [8]; UV intensity is determined by a UV-B dual-channel ultraviolet irradiation made by Beijing Normal University; TOC is determined by analytikjena AG Multi N/C2100 TOC analyzer; DO is determined by a Shanghai Leici JPB-607 type magnetic dissolved oxygen meter; absorption spectrum scanning characteristics are analysied by a general T6 new century UV/Vis spectrophoto meter.

• OH is determined by the photometry method which use salicylic acid as molecular probes [9]. Specific methods are: prepare 150mg/L salicylic acid, place it in the photocatalytic reaction system, determine the amount of hydroxylation-2, 3-dihydroxy benzoic acid produced by the absorbance under 510nm.

## Results and Discussion

### Removal efficiency of UV/$TiO_2$ photocatalysis of organic matter in water

The content of organic matter in raw water of S waterworks is relatively low, most of the organic matters are dissolved organic matters. The DOC content in source water is 2.86mg/L and accounting for 82.52% of TOC. After coagulation, sedimentation, and filtration, DOC content can be reduced to 2.14mg/L and the corresponding removal rate is 25%, it is proved that the removal effect of organic matter by conventional process is limited.

Under the UV intensity of 0.25mw/$cm^2$, static photocatalytic experiments are conducted in the self-made photocatalytic reactor, the variation of TOC and • OH during photocatalysis are shown in Fig. 3.

Results shows that the TOC content in filtered water decreased from 2.284mg/L to 1.255mg/L within 180min, the corresponding removal efficiency is 45.05%. The content of 2, 3- dihydroxy benzoic acid generated is 0.647mmol/L. Supposing that a • OH attacks a salicylic acid molecule forms a 2, 3 -dihydroxy benzoic acid molecule, thus, the captured • OH is 0.647mmol/L. The removal efficiency of photocatalysis on organic matter in filtered water is significantly proportionate to the amount of • OH generated, results indicate that • OH is the main active substance leading to the mineralization of organic matter, thus, optimizing the reaction condition to maximum the generation of • OH is the key to improve removal efficiency.

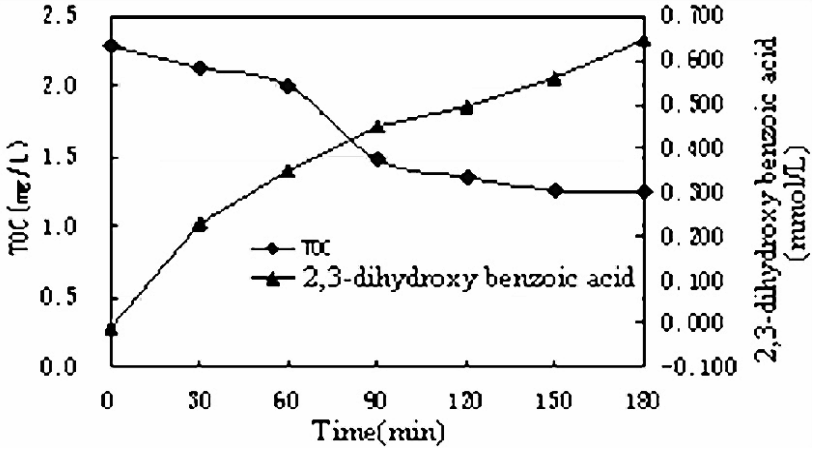


（T=22℃，DO=5.34，pH=6.85）

Fig.3 Removal effeciency of TOC by static photocatalysis

**Research on influencing factors of UV/$TiO_2$ photocatalysis of organic matter**

**Orthogonal experiment results of UV/$TiO_2$ photocatalytic**

UV light intensity, dissloved oxygen, reaction time, and pH value are selected as four main influencing factors according to our former reaserch. The dissolved oxygen content in filtered water is 3.55mg/L under the experimental conditions, the stable value of dissolved oxygen in the reactor are 5.58 mg/L, 7.21 mg/L when the aeration amount are 50L/h and 150L/h respectively.

Results of the orthogonal experiment are shown in table 1.

The values of R in table 1 show the importance of several factors, the importance of the four factors follows the sequence: light intensity, dissloved oxygen, reaction time and pH. Light intensity and dissolved oxygen are main factors that affect removal efficiency of UV/$TiO_2$ photocatalytic on organic matter in filtered water.

It can be seen from the orthogonal test results that the group-6 test (light intensity = 3.3 mw/$cm^2$, DO = 7.21 mg/L, time = 60min, pH = 5.0) reaches the highest TOC removal rate-53.2%. Because pH is not the important influencing factors, in addition, pH of filtered water is about 7 and it is unlikely to regulate pH of drinking water in production practice. Therefore, additional experiments are conducted by improving the level of light intensity, DO and reaction time. light intensity is increased to 4.2 mw/$cm^2$, dissolved oxygen reaches to 7.48 mg/L under the aeration amount of 200L/h, reaction time is extended to 3h. Results show that TOC has declined from 1.826 mg/L to 0.665mg/L and the corrsponding removal efficiency is 63.58%. Therefore, increase light intensity, DO, reaction time in a certain range can improve oxidation effect, but further increase of the level of influencing factors can only increase removal efficiency slightly. Studies have shown that under lower radiation flux condition, the reaction rate(r) is linearly dependent to the radiation flux ($\Phi$); under moderate radiation flux condition, r is linearly dependent to $\Phi^{1/2}$; under high radiation flux condition, r is irrelevant with $\Phi$[10]. As the surface of the $TiO_2$ thin film is limited, high light intensity will lead to lower efficiency of photons, which is not economic; higher levels of dissolved oxygen will increase energy consumption; long reaction time will increase the volume of treatment facitilty and increase the project costs. Therefore, the level of influencing factors should

be reasonably controlled from the point of cost, it is suggested that the reasonable light intensity should be controlled in 2-3 mw/cm$^2$, while suitable reaction time is 2-3h.

Table 1 $L_9$（$3^4$）orthogonal experimental results of UV/ $TiO_2$ photocatalytic

| Experimental arrangements | UV Light intensity(mw/cm$^2$) | dissloved oxygen (mg/L) | reaction time (min) | pH | TOC removal ratio（%） |
|---|---|---|---|---|---|
| 1 | 1.3 | 3.55 | 30 | 5.0 | 18.1 |
| 2 | 1.3 | 5.58 | 60 | 7.0 | 28.9 |
| 3 | 1.3 | 7.21 | 120 | 9.0 | 38.3 |
| 4 | 2.5 | 3.55 | 60 | 9.0 | 38.1 |
| 5 | 2.5 | 5.58 | 120 | 5.0 | 42.1 |
| 6 | 2.5 | 7.21 | 30 | 7.0 | 48.5 |
| 7 | 3.3 | 3.55 | 120 | 7.0 | 41.3 |
| 8 | 3.3 | 5.58 | 30 | 9.0 | 42.2 |
| 9 | 3.3 | 7.21 | 60 | 5.0 | 53.2 |
| M1 | 28.433 | 33.500 | 36.267 | 37.800 | |
| M2 | 42.900 | 37.733 | 40.067 | 39.567 | |
| M3 | 45.567 | 46.667 | 40.567 | 39.533 | |
| R | 17.134 | 14.167 | 4.300 | 1.767 | |

**Transformation of organic matter in the process of UV/$TiO_2$ photocatalysis**

Light intensity in the reactor are controlled to be 2.5mw/cm$^2$ during photocatalytic treatment of filtered water, take water samples at the react time of 1 min, 60 min, 90 min, 120min respectively. Measure spectral scan characters of the water sample between wavelengths from 190 to 450nm.The results are shown in Fig. 4.

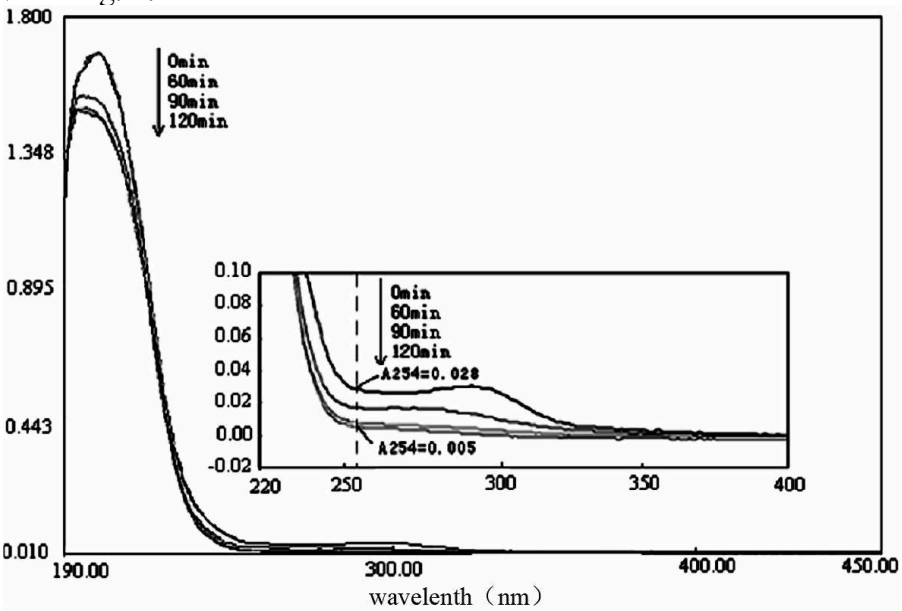


Fig. 4 Spectral scanning curve of filtered water by photocatalytic process

It can be seen that filtered water show an apparent absorption characteristics within the range of 190-240nm, this indicate that double-bond olefin compounds exists in water. In addition, there is an obvious absorption characteristics within the range of 250-320nm, this indicate that conjugated system organic exists in water. Experiment shows that the absorbance within the two intervals decreases significantly, which indicates that the photocatalytic process has a good removal effect on those types of organic matters, for example, $UV_{254}$ decrease 82.14% within 2h. Such kinds of substances in water are mainly human substances as well as organic matters with unsaturated

structure, these substances usually have high chlorine reactivity and also regarded as the main precursors of disinfection by-products—THMs. So, it can be deduced that photocatalysis has a sound removal effect on disinfection by-products precursors and improve chemical safety of drinking water.

## Conclusions

Following conclusions can be get by the research on UV/$TiO_2$ photocatalysis of filtered water:

(1) The glass supported nano-TiO2 photocatalysis has a good removal effect on trace organic pollutants in drinking water; it can greatly improve the chemical safety of drinking water. Organic matter removal efficiency is positively correlated to the amount of • OH generated in the process.

(2) Orthogonal tests on influencing factors show that the importance sequence of influencing factors are as follows: light intensity, DO, reaction time, pH. DO act as electron acceptor and have an obvious impact on photocatalytic effect. Enhancing the level of each factors is conductive to improving TOC removal efficiency, however, under the comprehensive consideration of TOC removal efficiency and cost, it is suggested that light intensity should be controlled in 2-3 mw/$cm^2$, and the reaction time should be controlled within 2-3h.

(3) UV/$TiO_2$ photocatalysis has a good removal effect on double-bond olefin compounds and the organic compound with conjugated system. Its removal efficiency on $UV_{254}$ is higher than the removal efficiency of TOC; this is conductive to control the risk of disinfection by-products and improve drinking water safety.

## References

[1] Shun-Lin Yue. Urban water quality issues [J]. China water supply and drainage, 1997, 13: 35-38. (In Chinese)

[2] A.Fujishima and K. Honda. Electrochemical proteolysis of water at a semiconductor electrode[J]. Nature, 1972,238(5358): 37-38.

[3] Tian Li & Zhengfu Chen. The deep clean-up effect of photocatalytic oxidation for urban water[J]. Environmental Science, 1998, 18 (2) :167-171.

[4] Wang Fuping, Sun Dezhi & Junhui Wang et al. Use the fiber Ti02 as a photocatalyst degradation to degrade humic substances in drinking water [J]. High Technology Letters, 1998,8 (12): 21-24.

[5] Tian Li & Chaopeng Chen. Study on activated carbon adsorption-- - photocatalytic deep water purification process [J]. Shanghai Environmental Science, 2002,21 (6) :342-343. (In Chinese)

[6] J.Rapala, K.Lahti L. A.Rasanen, A. L.Esala, S. I.Niemela& K.Sivonen. Endotoxins associated with cyano bacteria and their removal during drinking-water treatment [J]: Water research, 2002, 36 (10): 2627-2635.

[7] R. W.Mattews. Photo Oxidation of organic material in aqueous suspensions of titaniμm dioxide [J]. Water Res., 1990,24(5):653

[8] State Environmental Protection Administration editorial board of "Monitoring Analysis Method of Water and Wastewater ". Monitoring Analysis Method of Water and Wastewater[M] Fourth Edition, Beijing: China Environmental Science Press, 2002. (In Chinese)

[9] Xuechang Ren, Zaifeng Shi& Lingren Kong. The determination of the probe method of salicylic acid molecular of hydroxyl radical in the photocatalytic system of $TiO_2$thin film[J] Environmental Science, 2008,28 (4): 705-709.

[10]D. F.Ollis, E.Pellizzetti& N Serpone. Destruction of water contaminants[J] Environ. Sci. Technol., 1991 92(25): 1523-1528.

*Applied Mechanics and Materials Vols. 580-583 (2014) pp 2363-2366*
*© (2014) Trans Tech Publications, Switzerland*
*doi:10.4028/www.scientific.net/AMM.580-583.2363*

# The Development of Prestressed Concrete Cylinder Pipe in China

Zhang Hongyu[a], Peng Hua[b], Chen Xiang[c]

College of Civil Engineering, Wuhan University, Wuhan 430072, P.R.China

[a]ptlemoon@163.com, [b]huapeng904@163.com, [c]119345020@qq.com

**Keywords:** Prestressed Concrete Cylinder Pipe; Development Survey; Water Supply; Pipeline Manufacturing

**Abstract.** *Prestressed Concrete Cylinder Pipe* (PCCP) consists of a steel cylinder lined with concrete, then helically wrapped with a wire and coated with a dense mortar. PCCP has excellent structural properties, so it is widely used in various water-transportation projects around world. This paper presents a review of development of PCCP in China, which was summarized as three stages: *the period of exploratory development*, *the period of cooperative development*, and *the period of independent development*. The development process of design and production technique, the application in China, the construction and development prospect of PCCP were made a detailed discussion in each stage.

## Introduction

Prestressed concrete cylinder pipe, PCCP for short, is a kind large-diameter composite pipe of high pressure resistance, corrosion resistance and good anti-seepage performance. PCCP combines the tensile properties of high-strength steel wire, compressive strength of concrete and impermeability of steel cylinder, gives full play to the physical and mechanical properties of various materials. So it was widely used in large amount of water projects around the world[1, 2].

The first PCCP pipeline was produced in 1939 in Paris, France. The engineer Bonna designed a 1800mm-diameter PCCP based on prestressing technique and prestressed concrete pipe, and installed in Clombes water pipe network of Paris. The pipe was design within the water pressure 0.35MPa, and with full-length of 1500m. During the same period, the United States Company LookJoint had also developed a similar PCCP, after which PCCP had entered a rapid development period[3-10]. After 70 years of development PCCP has been widely used in various large-scale water projects of the world, such as: Libya's *Great Man-Made River Water Project* is the world's largest PCCP project, which has a total length of over 5000 km, and is hailed as "the eighth wonder of the world." PCCP was introduced into China in the eighties of the last century. After 30 years of development, it has formatted a certain application and production scale. There were detailed descriptions of PCCP's development history in China from the beginning of PCCP entering China in this paper. It could be figered out that the development of PCCP in China fell into three stages: the period of exploratory development, the period of cooperative development, and the period of independent development. The PCCP development process in China could also be the technological advances and improvements of PCCP in the process. By this paper, the researchers were able to clearly understand the technology development process of PCCP, to carry out more further research to accelerate the development and application of PCCP in China.

## Period of exploratory development (1980s)

In the eighties of last century, after the reform and opening up, some of Chinese research institutes and enterprises had begun to introduce, digest and absorb the advanced technologies of American PCCP pipeline. In 1984, Suzhou Research Institute of concrete and cement products cooperated with the pipe plant of Yingkou water company, using simple methods developed and produced a diameter of 600mm lined prestressed concrete cylinder pipe (PCCPL), which was used in water projects. In the same time, in 1985, cement pipe plant in Nanjing cooperated with the Beijing Research Institute of

Municipal Engineering, produced PCCPL of 600mm and 1200mm diameter using self-stressing concrete, which was installed in Jianyang Hydropower Project, Fujian and Nanjing water supply pipelines. It could be figered out that most of research institutes and enterprises in china would rather find their own way in PCCP production technology research in this period. It could be calles exploratory development phase, in which PCCP had a simple method of manufacturing, a relatively small diameter, and less production.

**Period of cooperative development (1990s)**

With the in-depth reform and opening up, and under the guidance of reform and opening up policy, some foreign advanced technology and information of PCCP through various channels accessed to the Chinese market, so that Chinese enterprises could introduce, digest and absorb foreign advanced technology and critical equipment. Thus the development of PCCP producing and applying was accelerated in China.

Shandong Electric Power pipeline Engineering Company (SEPPEC) introduced some key technology and equipment from the U.S. PCCP company Ameron in July 1986, such as: welding machine for spirally rolled steel cylinder, socket production equipment, pipe mold of 2600mm diameter, connectors and spreader. Basis on these equipments, it produced the first batch of PCCPE with 2600mm diameter as the plant circulating water pipe in June 1990. That filled the blank of PCCP producing and applying in China. Meanwhile, Hangzhou Research Institute of Mechanical Design (HRIMD) in the supporting of the national electricity company, researched and designed the vertical differential reeling machine and the vertical roller spray machine, and produced the welding machine for spirally rolled steel cylinder with 1600mm diameter mandrel on the basis of mapping Ameron's mandrel. So that a well-equipped , advanced technology and large-diameter PCCP production line was built, and produced PCCPE of1600mm diameter for Yellow River Diversion Project Zibo section. In 1998, SEPPEC introduced a welding machine to produce PCCP with 1200mm diameter below, thus it can produce PCCP with a variety diameter below 2600mm, and became a PCCP pipeline manufacturing company with relatively sound equipments in China.

Wuxi Huayi Pipeline Co. prepared to establish PCCP production plant from 1990. Then Huayi Pipeline Co. introduced a welding machine and socket production equipment from Ameron Company of the United States, and improved the vertical differential reeling machine and the vertical roller spray machine and spreaders by HRIMD. So that the company built a well-equipped production lines and put into operation in April 1995, and produced a number of PCCPE with 1400mm diameter, followed by producing 15km PCCP with 1200mm diameter for Suzhou Singapore Park. Shenzhen sun pipeline Company was founded in 1992, and introduced a complete set of production equipment from Price Brothers Company of the U. S. in the same year. its production line can produce a diameter of 900 ~ 2600mm of PCCP. In 1999 a vertical differential reeling machine which can produce PCCP with 3000mm diameter was provided by HRIMD and Heda Mechanical Engineering Co. Ltd.

By the turn of the century, the first three companies which had introduced PCCP production line produced a total of over 700 km, from 600 to 3000mm diameter PCCP pipeline, which was applied in more than 80 projects. During this period, Chinese companies assisted by foreign (mainly U.S.) PCCP advanced production technology, meet the needs of domestic projects through the introduction of foreign mature PCCP production lines and self-developed key production equipment simultaneously. It was a critical stage in which China PCCP industry started to take off.

**Period of independent development (the 21$^{st}$ century)**

In the 21st century, with the rapid launch of China's infrastructure construction, the Chinese PCCP industry experienced a wave of PCCP manufacturing plant construction boom to adapt to market demand off. In addition to the initial three PCCP production enterprises, there had been more than a dozen PCCP production plants emerged After 2000, such as Sichuan Jinwei, Xinjiang Guotong, Zibo Longquan, Jilin Electric Power, Beijing Heshan, Hohhot Wanlian Jiangsu Zhongyi, etc. According to

incomplete statistics, there have been more than 40 PCCP manufacturing enterprises, and more than 50 PCCP production lines up to now. It is showing a thriving scene. Among these plants, someof them are new constructions, others are converted by factories producing prestressed concrete pipe (PCP). Some PCCP production lines' products are already being used in the practical project. According to the statistics in 2010, the annual PCCP designed production capacity of China had reached more than 1000 km, the pipe's diameter ranged from 400mm ~ 4800mm, and the applicable operating pressure ranged from 0.2 to 2.0MPa, and the maximum covering soil reached deep of 10m above.

In order to promote the construction and development of China's water engineering technology, Hangzhou Reacher Institute of Mechanical Design digested and absorbed of Ameron's PCCP manufacturing technology, and developed PCCP production equipment and production technology for the Chinese conditions. Its subsidiary Heda concrete mechanical Engineering Co. Ltd is an excellence enterprise developed by itself, which can provide a full set of PCCP manufacturing equipment and technology. Heda can produce key equipment of PCCP manufacturing, such as: welding machine, reeling machine and spray machine, which can produce pipe with diameter range from 500mm to 4000mm. Now, many Chinese enterprises have chosen PCCP manufacturing equipments which were produced by Heda Company, so that not only the cost is saved, but also the construction speed is speeded up. Thereby the competitiveness of Chinese companise is increased, while the development of Chinese PCCP industry is also beneficial.

More and more PCCP plants were built in China, and most of them had choosen domestic production facilities indicated that China's PCCP production and manufacturing had been completely free from dependence on foreign technology. It can rely on the country's own forces, rather than rely on imported equipment. All indications are that PCCP industry development in China has entered a brand new phase. There are a number of PCCP production line are still preparing to build or already under construction, which shows that PCCP production and application in China is in a good momentum of vigorous development. However, how to ensure that these manufacturers can produce qualified PCCP, and guarantee the quality of PCCP in the practical projects, is the key to the healthy development of China PCCP production. That is definitely a very important task.

## Application of PCCP in China

Currently, PCCP has been widely used in various fields in China, such as: water conservancy, electricity, municipal, water supply and drainage, and also successfully used in the Guangdong Ling'ao Nuclear Power Station. In particular, PCCP has an unique advantage in the long-distance and high-volume water diversion projects, such as: the connection project of Yellow River Diversion Projec in Wanjiazhai of Shanxi Province is about 138.6km long, of which from Fen River reservoirs to Taiyuan Huyan water plant was in the use of PCCP with the diameter of 3000mm, length of 43.2km, working pressure of 0.6 ~ 1.0MPa, and deep of 2m ~ 8m covering soil. The Huiningzhuang - Daning section pipeline, which is a section of Middle Route Project of South-North water diversion from Beijing to Shijiazhuang emergency project, has a length of 56.4km,and use double pipes of large diameter PCCP. The maximum diameter is 4000mm, working pressure is from 0.6 to 1.0MPa, and the maximum covering soil reached deep of 10.5m. In addition, there are some other projects, such as: Xinjiang Irtysh River Diversion Projec lead the water from Irtysh river to Urumqi. The 2800mm diameter PCCP was used in three large inverted siphon project, which were in a total length of 10km. The pipeline with double parallel arrangement had a working pressure of 1.6MPa, a deep of 4m covering soil, and a single length of 7.25km. The project was completed in 2006, but because of the project's specific location, complex ground conditions, bad weather and construction conditions, it can be regarded as the most difficult of PCCP project in China comprehensively. Yangling water Supply Project is located in Shanxi Province. The pipeline with double diameter of 1200mm PCCPE has a length of 17.86km, the maximum working pressure of 1.4MPa, the maximum deep of 16m covering soil. Due to the Guanzhong economic zone and Guanzhong urban belt ,where the project

located, Yangling water Supply Project has to cross with rails, roads, rivers, and channels. It makes the project even more difficult in construction.

PCCP also has extensive applications in the electric power system. Such as: The PCCP produced by Shandong Electric Power pipeline company was used for water supplemental system, water recycling system and water delivery system. The effect turned out to be great. After nearly 30 years of development, PCCP is widely used in the circulating water system of various power plants for its outstanding ability to resist internal pressure. In the area of municipal water supply and drainage, PCCP is more widely used. The largest PCCP application was Shanghai Sewage treatment Project, which embedded 3.91km PCCP with 3600mm diameter in coastal soft foundation. It created a typical case of minimal disturbance to the environment and fast construction speed.

## Summary

The development and application of PCCP have been more than 70 years of history. Although China started relatively late, but the starting point is quickly established on the basis of introducing and absorbing foreign latest technology, and thus it‘s a relatively high starting point. The application of the technology was closed with the foreign advanced degrees. PCCP has many advantages of its own feature, therefore increasingly being used in a variety of projects. According to incomplete statistics, it has been installed more than 700 km PCCP and operated through the implementation in China. With the rapid development of China's industry and the continuous improvement of people's living standards, the demand for water is in the fast-growing, and so as the demand for large diameter pipe. Therefore it requires more specialized manufacturing equipment, transportation and installation equipment to meet the requirements. In consideration of this, we need to accelerate research and development process, and promote the development and application of PCCP in China.

## References

[1] ANSI/AWWA C304-2007 AWWA Standard for Design of Prestressed Concrete Pressure Pipe[S]. Denver, CO: American Water Works Association, 2007.
[2] ANSI/AWWA C301-2007 AWWA Standard for Prestressed Concrete Pressure Pipe, Steel-Cylinder Type[S]. Denver, CO: American Water Works Association, 2007.
[3] Alavinasab A, Padewski E, Higgins M. Effects of the Location of Broken Prestressing Wire Wraps in Structural Integrity of a Damaged PCCP[A]. Pipelines 2013@ sPipelines and Trenchless Construction and Renewals—A Global Perspective[C], Fort Worth, Texas, 2013. ASCE:767-774.
[4] Ge S, Sinha S K. The Effect of Negative Pressure on a Failed 54-Inch PCCP with a Malfunctioning Valve in the Pipeline-A Case Study[A]. Pipelines 2013@ sPipelines and Trenchless Construction and Renewals—A Global Perspective[C], 2013. ASCE:693-704.
[5] Weare R E. PCCP sewerage force main structural condition assessment and asset management approach[A]. Pipelines 2007: Advances and Experiences with Trenchless Pipeline Projects[C], Boston, Massachusetts, 2007. ASCE:1-11.
[6] Zarghamee M S. Hydrostatic Pressure Testing of Prestressed Concrete Cylinder Pipe with Broken Wires[A]. Pipelines 2003:New Pipeline Technologies, Security, and Safety[C], Baltimore, Maryland, 2003. ASCE:294-303.
[7] Zarghamee M S, Fok K. Analysis of prestressed concrete pipe under combined loads[J]. Journal of Structural Engineering, 1990,116(7):2022-2039.
[8] Zarghamee M S, Fok K, Sikiotis E S. Limit-states design of prestressed concrete pipe. II: Procedure[J]. Journal of Structural Engineering, 1990,116(8):2105-2126.
[9] Zarghamee M S, Heger F J, Dana W R. Experimental Evaluation of Design Methods for Prestressed Concrete Plpe[J]. Journal of transportation engineering, 1988,114(6):635-655.
[10] Zarghamee M S, Ojdrovic R P, Dana W R. Coating delamination by radial tension in prestressed concrete pipe. I: Experiments[J]. Journal of Structural Engineering, 1993,119(9):2701-2719.

*Applied Mechanics and Materials Vols. 580-583 (2014) pp 2367-2369*
*© (2014) Trans Tech Publications, Switzerland*
*doi:10.4028/www.scientific.net/AMM.580-583.2367*

# The single-sludge denitri-nitrification system in reconstruction of wastewater treatment plants in the Russian Federation

E.S. Gogina[1,a], I.A. Gulshin[2,b]

[1] Professor of the Department Wastewater and water ecology, Federal State Educational Institution of High Professional Education 'Moscow State University of Civil Engineering' (MGSU), 129337, Russia, Moscow, Yaroslavskoe shosse, 26

[2] Employee of the Department Wastewater and water ecology, Federal State Educational Institution of High Professional Education 'Moscow State University of Civil Engineering' (MGSU), 129337, Russia, Moscow, Yaroslavskoe shosse, 26

[a]GoginaES@mgsu.ru, [b] Gulshin-dii@yandex.ru

**Keywords:** Wastewater, ecology, treatment plants reconstruction, deep biological wastewater treatment, nitrification, denitrification.

**Abstract.** The paper investigates the optimal parameters of the single-sludge denitri-nitrification system and their compliance with the existing wastewater treatment plants in Russia

Ecological status of water resources is causing great concerns of the population of the Russian Federation. The pollution of fresh water – rivers and lakes – is a result of the dumping of wastewater. In Russia the standards for wastewater discharge have increased in the nineties of the twentieth century. So the main question was the removal of nutrients (nitrogen and phosphorus compounds). In recent years there have been many studies of developing new methods of wastewater treatment, and of transferring Western technologies to Russian treatment plants. But the main problem now is that most of the stations in Russia were built more than thirty years ago. And now they are in need of renovation. It takes a lot of financial resources, but the possibilities are limited. Therefore it is necessary to carry out the reconstruction with minimal monetary costs, maximum usage of existing tanks and equipment, and satisfactory quality of wastewater treatment to the standards [1].

In Moscow State University of Civil Engineering there are extensive researches in the field of biological wastewater treatment, including the removal of nutrients. The results of the researches were used for constructions and reconstructions of treatment plants in Russia.

Technological Scheme "Deep biological ammonium-nitrogen removal activated sludge system", which was developed and patented in MGSU, treats wastewater biologically in the aeration tank, which is divided into a sequence of alternating anoxic and aerobic zones. Reconstruction of biological treatment under this Scheme is possible with minimal cost, and quality of treatment satisfies the modern standards (table 1).

**Table 1**. Parameters of the biological wastewater treating systems.

| Parameters of wastewater treatment | Different technologies of wastewater treatment | The basic technology of wastewater treatment, developed in MGSU |
|---|---|---|
| BOD in effluent, mg/l | 10 - 15 | 4 - 6 |
| Ammonium NH4 – N in effluent, mg/l | 0,6 - 1,5 | Less than 0,39 |
| Phosphate PO4 – P in effluent, mg/l | 0,8 - 1,5 | 0,4 - 0,6 |

Nowadays in the Russian Federation there are about sixty two percent of the plants with aeration tanks, thirty three percent of biofiltration plants, and five percent of the plants with only mechanical treatment. The main objective of the present study was to investigate the possibility of applying the single-sludge denitri-nitrification system in reconstruction of wastewater treatment plants in the Russian Federation. Only plants with aeration tanks were studied, because only they can be reconstructed with the Scheme.

The study included fifty three treatment plants of various Russian cities. According to the questionnaires has been received data for each treatment plant about the influents and the effluents, the features of the construction and the operation of structures at the station and data about the cost of aeration in the aeration tanks and so on. The location of the studied treatment plants is on the map (figure 1).

**Fig. 1.** The location of the studied wastewater treatment plants.

From the initial data were calculated the basic parameters of the aeration tanks, including the amount of air required for denitrification and nitrification. The calculation of the required amount of air has been produced by the method developed in MGSU. This method includes both normative calculations and practical experience of operating the aeration tanks (working with the single-sludge denitri-nitrification scheme) [2]. The results of the calculations were compiled for further analysis (table 2).

**Table 2**. Some of the data resulting from research.

| Technological parameters | Minimal value | Average value | Maximal value |
|---|---|---|---|
| Food to Microorganisms ratio mgBOD/day | 60 | 256 | 725 |
| Flow rate, m3/day | 144 | 162876 | 500000 |
| Treatment time, hour | 8 | 8,2 | 14 |
| Volume of the aeration tank, m3 | 46 | 26782 | 164900 |
| Q of air without the reserve, m3/hour | 48 | 15916 | 95900 |
| Q of air with reserve, m3/hour | 72 | 28874 | 143855 |
| Q of air in fact, m3/hour | 35 | 27557 | 167000 |

According to the analysis, sixty five percent of the studied wastewater treatment plants may be reconstructed according to the single-sludge denitri-nitrification scheme. It will greatly enhance the quality of wastewater treatment.

It is important that the calculations were made on the basis of the amount of air that is produced by the existing station`s blowers. Therefore reconstructions don`t require replacements of blowers and can be done in stages.

## References

[1] E.S. Gogina, V.P. Salomeev, N.A. Makisha. *Addressing nutrient removal from wastewater.* Water supply and sewerage. (2011). 3. pp. 44-53.

[2] E.S. Gogina, N.A. Makisha. *Development of technology for the modernization of artificial biological wastewater treatment*. Vestnik MGSU. 2012. 11. pp. 204-209.

*Applied Mechanics and Materials Vols. 580-583 (2014) pp 2370-2373*
*© (2014) Trans Tech Publications, Switzerland*
*doi:10.4028/www.scientific.net/AMM.580-583.2370*

# Study on the Treatment of Compound Micro-polluted Groundwater by Contact Oxidation Process under Different Filtration Rates

Yuhua ZHAO[1, a], Jie CHENG[1,b] , Xu YAN[2,c] , Di WANG[3]

[1]School of Municipal and Environment Engineering, Shenyang Jianzhu University, Shenyang China

[2] Inner Mongolia Academy of Urban Planning and Design, Hohhot China

[3] Liaoning Design Institute of Urban and Rural Construction and Planning, Shenyang China.

[a]zyh088@sina.com, [b]826786939@qq.com, [c]839550148@qq.com

**Keywords:** Compound micro-polluted groundwater, contact oxidation filtration, iron, manganese

**Abstract.** The compound micro-polluted groundwater was treated by three-stage contact oxidation filters with total 1.5m ceramic layer. The filtration rates, in accordance with the time sequence, were respectively 1m/h, 1.5m/h, 2m/h, 3m/h and 4m/h. The result indicated that, in the condition of sufficient dissolved oxygen, the effluent concentration of iron, manganese, ammonia nitrogen and $COD_{Mn}$ can met the National Drinking Water Standards. Under the range of filtration rates the average effluent concentration was respectively that 0.073 mg/L, 0.278 mg/L, 0.229 mg/L, 0.172 mg/L and 0.199mg/L for iron; 0.150 mg/L, 0.180 mg/L, 0.110 mg/L, 0.150 mg/L and 0.359 mg/L for ammonia nitrogen. The average concentration of manganese was 1.828mg/L with dropping aeration only, compare with that 0.323mg/L with strengthening aeration under filtration rate 1m/h. And the manganese concentration was 0.061mg/L, 0.062 mg/L, 0.084 mg/L and 0.071 mg/L, respectively under the range of filtration rates of 1.5-4m/h by strengthening aeration. Because of the biological system in filter layer no perfect, humic acid and low temperature, the average removal rate of $COD_{Mn}$ was only 16.10% under the 1m/h filtration rate. Then when the rates were up to 1.5m/h-3m/h, effect of $COD_{Mn}$ removal increased and the water treated met the Standard with the maturity of filter layer. But under the rate 4m/h $COD_{Mn}$ concentration of effluent was exceed the Standard. Meanwhile, in the range of 1m/h-3m/h, consumption of dissolved oxygen respectively were 19.26mg/L, 14.73mg/L, 13.99mg/L and 13.99mg/L.

## Introduction

For geological reasons, the concentration of iron and manganese in groundwater exceeds the national Drinking Water Standards in some areas. In recent years, the groundwater is contaminated due to the infiltration of surface water pollution into the underground. The polluted groundwater is called compound micro-polluted groundwater (CMPG, for short). It is worth attention that the ammonia nitrogen and organic pollutants in the groundwater, make the water treatment harder[1,2]. Bio-contact oxidation filter has the advantage that can remove iron and manganese in the same filter layer at the same time[3]. In some condition, bio-contact oxidation filter can remove the iron, manganese, ammonia nitrogen and organic pollutants in the CMPG[3,4]. The bio-filter layers not only contains autotrophic bacteria (including Iron Bacteria, Manganese Bacteria, Nitrobacteria), but also has heterotrophic bacteria, which are trained by the CMPG[4]. The competition for dissolved oxygen (DO) among the microorganisms is one of the important factors to removing effect. Three-stage aeration bio-contact oxidation filter is used to treat CMPG for drinking water.

## Experimental Method

**Experiment Apparatus.** The experiment apparatus is composed of same three pice of plexiglass columns filled with ceramsite as filter layer. The inner diameter of the column is 47 mm, 700 mm in height, and the layer height is 50 mm, supporting layer for 50 mm. The overflow port is set for 50 mm above the filter layer. H\The ceramsite size are from 1.25 to 1.25 mm. As shown in figure 1.

The experiment time was 270 days in total. Specific plan was as shown in table 2. Water dropping into columns above the inlet 50 cm is for aeration. In 95th day one aeration device is set in the second column above the filter layer for strengthening aeration.

**Water Used.** Experimental water is comprised of groundwater, humic acid, urea, starch, $NH_4Cl$, $MnSO_4 \cdot 5H_2O$ and $FeSO_4 \cdot 7H_2O$. Table 1 is for water quality.

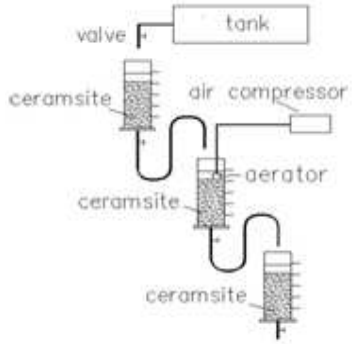


Fig.1 Schematic of apparatus

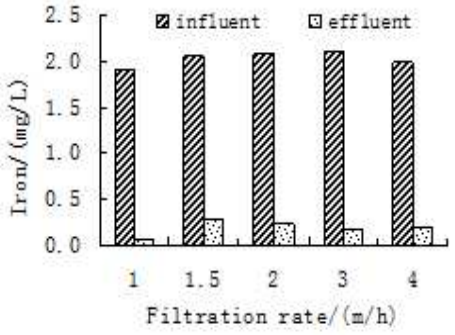


Fig.2 The iron removal effect

**Tab.1 Water quality**

| Item | Fe | Mn | $NH_3$-N | $COD_{Mn}$ |
|---|---|---|---|---|
| Range(mg/L) | 1.0-3.0 | 1.6-3.2 | 2.2-4.0 | 2.3-5.1 |

**Tab.2 Range of filtration rates**

| Time(d) | 1-164 | 165-195 | 196-208 | 209 -246 | 247-270 | 95-270 |
|---|---|---|---|---|---|---|
| Rate(m/h) | 1 | 1.5 | 2 | 3 | 4 | Increasing aeration |

**Analysis Indexes and Methods of Water Quality.** Analysis indexes and methods of water quality are detailed in table 3.

**Tab.3 Analysis Indexes and Methods**

| Item | Method | Instrument | Item | Method | Instrument |
|---|---|---|---|---|---|
| Fe | Phenanthroline spectrophotometry | spectrophotometry | $COD_{Mn}$ | Acidic potassium permanganate titration | |
| Mn | Formaldoxime spectrophotometry | spectrophotometry | DO | | HQ30d portable DO instrument |
| $NH_3$-N | Nessler's reagent spectrophotometry | spectrophotometry | | | |

## Results and Discussions

The range of filtration rates was shown in tab.3. Under 1m/h, include drop aeration stage and increasing aeration stage, namely 1-fist and 1-second.

**Iron Removal Effect.** The result is shown in fig.2. With 1m/h, 1.5m/h, 2m/h, 3m/h and 4m/h, the average concentrations of effluent were respectively 0.073mg/L, 0.278mg/L, 0.229mg/L, 0.172mg/L and 0.199mg/L. Because ferrous ion is easily oxidized, the lower the filtration rates are, the better the removal efficiency is. When the rate was up to 1.5m/h, the results were worse. The reason may be that filter layer was saturated. After backwashing, the filtration rate up to be 1.5m/h, microorganism needs certain time to adapt to the new environment. When the filtration rate is 2-3 m/h, microorganism would have been adapted to the new environment. When the filtration rate up to be 4m/h, and after running four days, it need backwashing. After that, the removal effect of iron ion is stable. Thus proved that biological membrane is mature, can effectively remove the iron ion in the MPCG.

**Manganese Removal Effect.** The result is shown in fig.3. the effluent concentrations of manganese were 1.828mg/L, 0.323mg/L, 0.061mg/L, 0.062mg/L, 0.084mg/L and 0.071mg/L respectively under 1m/h-first, 1m/h-second, 1.5m/h, 2m/h, 3m/h, 4m/h. A number of studies have demonstrated that temperature and DO are a key factor for biological filter to remove manganese. Because of the stronger absorption, during the early stage of device operating, the treatment effect is also better. Due to the higher concentration of ferrous ion, in oxidation sequence of manganese lags behind the $NH_3^-$-N, and all bacterium are aerobic bacteria. Therefore, only when DO condition is adequate, the treatment effect can reach the Standard. At the 95th day aeration device was set in the second filter inlet. DO concentration changes are shown in table 4. The effluent concentration of manganese was 1.83mg/L(under 1m/h by drop aeration only), as contrast, the effluent concentration is 0.32mg/L(increasing aeration device) and still have a downward trend, and finally will reach the

Standard. Compared with before, the concentration of DO increased 3.10mg/L, and the consumption in the filter was 14.13mg/L. Obviously, the average removal rate raised by 57.78%. In fact, the growth of bacteria in filter layer is a decisive factor on removing manganese. Iron ion in the MPCG stimulated oxidation activity of manganese removal bacteria. For the entire device, the three-stage filter provides plenty of places for microorganisms to reproduce, so the filter had higher biomass, and logically has the very good removal effect on manganese. Continue to improve the filtration rate to 1.5-4m/h, effluent concentration of manganese was low. In the filtration rate up to be 1.5m/h and 4m/h respectively, device was backwashed. When finish backwashing, the data in the figure can be seen that no matter how to change the filtration rates, the treatment effect was not affected.

**Tab.4 The DO average concentration** (mg/L)

| Time | First filter | | Second filter | | Third filter | |
|---|---|---|---|---|---|---|
| | Inflow | effluent | Inflow | effluent | Inflow | effluent |
| 1-94d | 9.05 | | 5.00 | | 5.80 | |
| 95-270d | 7.85 | 0.82 | 8.10 | 1.90 | 5.97 | 5.07 |

**Ammonia Nitrogen Removal Effect.** As shown in fig.4, when filtration rate range is 1m/h-4m/h, the removal effeciency of NH4+-N is obvious. The initial average concentration of ammonia nitrogen in MPCG was 3.5mg/L, the average effluent concentration of it was 0.15mg/L. Nitrifying bacteria through nitrification to remove ammonia nitrogen, because nitrifying bacteria is aerobic bacteria, enough content of DO is key role for ideal treatment effect.

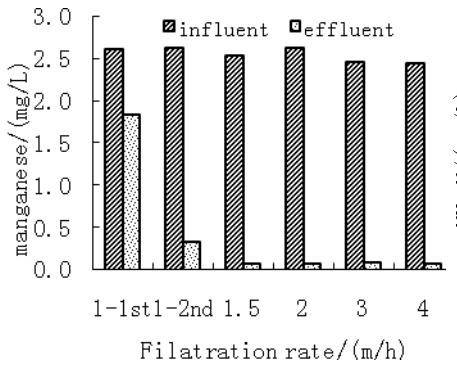


**Fig.3 The manganese removal effect**

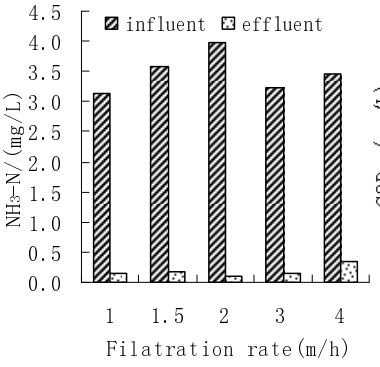


**Fig.4 The $NH_3$-N removal effect**

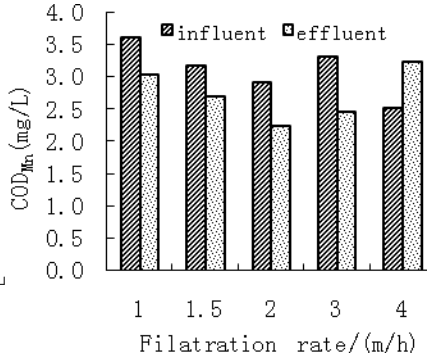


**Fig.5 The $COD_{Mn}$ removal effect**

The reason why it is suitable for the growth of nitrifying bacteria which need long time generating is due to non-uniform granular, that will lead to the inner surface and the concave part of ceramsite produced relatively thick and stable biofilm formation, and also less affected by hydraulic conditions. After succeeding at biofilm formation, denitrifying bacteria can thrive in low organism environment, then multiply much faster than heterotrophic bacteria, nearly be superiority strains. Since the 95th day, it added the aerating device to ensure adequate dissolved oxygen. Nitrification is much better than before, ammonia nitrogen removal efficiency obviously. Under the scale of filter speeds was 1-4m/h, removal rate of it respectively was 95.22%, 94.97%, 97.24%, 95.38%, 89.64%. Although the removal rate was the lowest under 4m/h, but still can meet the Standard. Therefore, the filtration rate changes do not affect stability biofilm to remove ammonia nitrogen with filtration rate no more than 4 m/h.

**$COD_{Mn}$ Removal Effect.** As shown in figure 5, the $COD_{Mn}$ average concentrations of CMPG were 2.39-3.60mg/L. Under the range between 1m/h to 4m/h, the average concentrations of effluent respectively were 3.02mg/L, 2.69mg/L, 2.23mg/L, 2.46mg/L and 3.2 mg/L and the removal rate respectively were 16.10%, 14.99%, 23.15%, 25.88% and 28.49%. The concentrations of effluent were under 3 mg/L than is the limited concentration of the Standard with the filtration rates of 1.5m/h-3 m/h. Generally the removal rate is low. It is because of the test device short running time, low room temperature(under 12˚C) in early time, then the biological systems in the filter layer is not yet perfect. The most important is because of the humic acid in MPCG and the competition between all kinds of microorganisms in the filter layer. Humic acid is macromolecular organics. Microorganisms can't capture it, and also wouldn't be able to degrade it. Therefore, it only was

removed by microorganisms' extracellular enzyme and biological membrane flocculation and adsorption. In addition, humic acid is easy to chelate iron and manganese, and then generate clathrate which is difficult to dissolve in water. The result indicated that among iron, manganese, ammonia nitrogen and $COD_{Mn}$ in MPCG, $COD_{Mn}$ is difficult to remove by contact oxidation filter. But with the extension of the running time and temperature (18˚C-22˚C） increase, the removal rate increased. And the $COD_{Mn}$ concentration met the Standard. From 247th to 270th days, the filtering rate was 4 m/h with temperature of 18˚C-14˚C, and in this period was 5m/h for three days. The filtration rate increases too fast in a short time and the temperature dropping, so that made the treatment effect of abnormal. In addition the large amount of organism accumulated before, even to the extent that the effluent concentration higher than influent. Humic acid is decomposed by microorganisms into simple organic compounds that are more easily to detect by potassium permanganate, this also is one of the important reasons for the poor treatment effect. So this method for MPCG to remove organic pollutants, needs to be further in-depth study. further

**Dissolved Oxygen Consumption.** The result is shown in table 5. With increasing aeration and the filtration rate of 1 m/h, the removal rate of iron, manganese, $COD_{Mn}$ is in higher levels(compared with drop aeration only). In particular, the average removal rate of manganese increased by 57.78%. And when filtration rate was 1-3m/h, DO consumption and filtration rate are inversely proportional. This is consistent with a rule, that the lower filtration rate, the more consumption of DO. Because of increasing filtration rate, MPCG will stay in the filter for a shorter time, and then the biological membrane contact oxidation time is shortened too, so the consumption of DO will be less. But the biofilm has been mature in the filter, no matter how to change filtration rates, the results (including iron, manganese and ammonia nitrogen) do not change. With filtration rates within 4m/h, the removal effect is obvious and stable for iron, manganese and ammonia nitrogen.

**Tab.5 DO consumption and average removal rate of each index**

| Filtraton rate (m/h) | DO consumption (mg/L) | Average removal rate | | | |
|---|---|---|---|---|---|
| | | Fe | Mn | $NH_3$-N | $COD_{Mn}$ |
| 1(Drop aeration only) | — | 96.86% | 29.89% | 88.27% | -3.09% |
| 1 (Increasing aeration) | 19.26 | 95.17% | 87.67% | 94.52% | 9.25% |
| 1.5 | 14.73 | 86.37% | 97.59% | 94.97% | 14.99% |
| 2 | 13.99 | 88.96% | 97.63% | 97.24% | 23.15% |
| 3 | 13.99 | 91.80% | 96.57% | 95.38% | 25.88% |
| 4 | — | 90.24% | 97.19% | 89.16% | -10.31% |

## Conclusions

(1) For the iron, manganese and ammonia nitrogen，the treated water can meet the national Drinking Water Standards by three-stage under the filtration rates as 1 m/h, 1.5 m/h, 2 m/h, 3 m/h and 4 m/h. And the effect is also stable. For $COD_{Mn}$ the filtration rate should not exceed 3m/h.

(2) Sufficient dissolved oxygen is necessary for effective treatment of MPCG. With the increase of filtration rate, consumption of dissolved oxygen decreased slightly.

## References

[1] Yuhua Zhao，Yan Li．Journal of Shenyang Jianzhu University in Chinese. Vol.27(2012), p.746

[2] A. G.. Tekerlekopoulou, D. V. Vayenas. Biological Engineering Journal. Vol. 39(2008), p.215

[3] Chunna Zhang. Antagonism of Iron and Manganese in Groundwater to Micro Contaminants in Aeration-Contact Oxidation Filtration Process, School of Municipal and Environmental Engineering, Shenyang Jianzhu University in Chinese (2012)

[4] Yan Li. Research on Treatment Regularity of Iron and Manganese as well as Contaminants from Underwater with Biological Filter, School of Municipal and Environmental Engineering, Shenyang Jianzhu University in Chinese ( 2011)

*Applied Mechanics and Materials Vols. 580-583 (2014) pp 2374-2379*
*© (2014) Trans Tech Publications, Switzerland*
*doi:10.4028/www.scientific.net/AMM.580-583.2374*

# ultra-high-rise-building water

# supply and drainage system design

Yanan Si[1, a],Ming Zhou[2,b]，Yuhang Liu[3]，Ling Deng[4]

[1]Kunming university of science and engineering institute of municipal engineering level 2011 graduate students，650500，China

[2]The dean of Kunming university of science and engineering institute of municipal engineering，650500，China

[3]Shenzhen deep water Consulting Ltd.，518000，China

[4]Shenzhen huayang international engineering design company，518038，China

[a]1018838375@qq.com.,[b]591731298@qq.com.

**Key words:** ultra-high-rise-building，water supply and drainage system，fire fighting system，middle water tank

**Abstract:** With the rapid development of chinese economy,to speed up the modernation of the society more and more ultra-high-rise-building rise abruptly.This article as Liuhe square project in Shengzhen city an example,elaborated the water supply system, drainage system,and fire fighting system design in water supply and drainage system design.

## Introduction

High-rise building of the international conference in 1972 the high-rise building has been divided into four classes, including a fourth category that building height of more than 100m high-rise building construction is called ultra-high-rise-building. In recent years , the level of economic and social development by leaps and bounds , with the process of urbanization, building height of 100m above the high-rise building continued to increase , particularly in compensation for the use of land , urban centers of the scarcity of land , building height is constantly increased. Rapid economic development in China has brought the rise of raising building and construction technology , construction is moving in the direction of ultra develop . This will not only be able to solve the congestion caused by the urban population living and working environment , but also to ease the current tension in urban land pressure , therefore , the development of high-rise buildings is the future trend of building development. High-rise and ultra-high-rise-building designed with the general theoretical and computational methods and low-rise multi-storey building designs, but because of the multi-layered architecture , multi-functional, structural complexity and difficulty of the depth of its design are relatively increased. Many difficulties with increasing height , building water supply and drainage design to bring , unlike high-rise building high-rise building , the presence of multiple water supply system partition , fire systems requirements, pipe drainage system , the interface has strict requirements and other issues. This article as Liuhe square project in Shengzhen city an example,describes the design of super high-rise building water content.

**Project Summary**

Liuhe commercial plaza located in Shenzhen Plateau montainous area , located in the hinterland of Pegasus Plaza (Plateau montainous Square ) which the core point of Plateau montainous, Liuhe commercial plaza is the only real estate development projects, but also first change change old project of Plateau montainous ,was designated by the government in Plateau montainous district urban renewal of demonstration projects. The project covers an area of 39084m2, with a total construction area of 214750 m2. This project has nine of 26-42 layer business-living buliding near the ground, there are seven high-rise residential , a ultra-high-rise multiple-use building, one super high-rise residential , underground 2 floors. Among them the seven high-rise residential each of 12 layer, ultra-high-rise multiple-use building have 36 layer, building altitude is 139.8 m, ultra-high-rise residential 39 layer, building altitude is 151.8 m, underground 2 floor is garage and equipment room, garage for the underground layer 2 local at ordinary times, for civil air defense in wartime.

**Lifing Water Supply System Design**

This water supply water source project chooses urban tap wate, from this plot of land on the east and west on both sides of the municipal water feeding respectively introduced a DN200 feed pipe for the project life, fire water, and outside a circular pipe network, water supply pressure is 0.2 Mpa.

**Daily water consumption**

The project of residential living water rationing takes 300L / person • day, business of 5 L/m2 • d, the maximum daily life of the project water consumption is 1699m3; unforeseen maximum daily water consumption of water by 10 percent, the total water consumption to 18689 m3.

**Feedwater system partition**

In order to ensure water security , combined with architectural features, water district the project are as follows :

Ⅰ Area : Underground 2 floors - 4 floors , directly from the municipal water supply pipe network .

Ⅱ Area: Middle Ⅰ area in 5-14 layer, due to the low zone 2 floors underground life water pump room variable frequency pumps by the pressure reducing valve for water supply after decompression.

Ⅲ Area: Middle Ⅱ area in 15-24 layer, from underground 2 layer life water pump room of the central frequency conversion pumps by the pressure reducing valve for water supply after decompression.

Ⅳ Area : High Ⅰ area in 25-29 layer, water pump room by 2 floors underground life high area of variable frequency pumps by the pressure reducing valve for water supply after decompression.

Ⅴ Area : High Ⅱ area in 30-39 layer, high water pump room by 2 floors underground life zone of variable frequency pump up to the roof water tank and then directly by the water tank water supply, namely adopt the combination of water pump, water tank.

**Life water pump and water tank**

According to the use of functional division and convenient management in the future, the project of commercial and residential in the use of water meter set separately, separate measurement, and set up the independent life pool and pressurized equipment, frequency conversion for water pump

group. According to the working principle of water pump, the smaller the difference between the peak flow and low flow, water pumps in high efficient area of the running time is longer, the more conducive to energy conservation. The project more than 8 layers for high-end residential traffic, tend to be more uniform, so choose frequency conversion water supply way.
The project life and fire the pool set apart, near J negative on the second floor of the basement, which pools the effective volume of residential life is 250 cubic meters, two lattice; Business is 100 cubic meters.

**Sewer System Design**

Sewer system uses rain and sewage seprate system . Indoor uses sewage , waste diversion system, set up specific vent stack, namely three vertical pipe drainage system.

**Sewage System**

The highest daily displacement of this engineering is 1529 m3. After centralized sewage produced food grease trap grease into the basement finished by supporting the sewage lifting unit extraction outdoor sewage pipe network ; ground floor small shops catering waste requires users to set up before being discharged to the sewer network outdoor grease trap treatment; the remaining wastewater is discharged to the outdoor gravity sewer network , and then discharged into the septic tank treatment municipal sewage pipe network. Flush water through underground garage submersible sewage pump sewage pipe network upgrade to outdoor access municipal sewer .

**Rainwater System**

Adopt an organized drainage, roof rainwater collection and outdoor rain after confluence , the nearest into the municipal storm sewer system . Shenzhen storm rainfall intensity calculated using the formula, the formula is:

$$q = 9.194 \times (1 + 0.460 \lg P)^{0.555} /(t + 6.840) l / s \cdot ha$$

Among them the recurrence interval : five-year senior roofing , outdoor venue by two years , according to the entrance ramp to the underground garage for 50 years .
Duration of rainfall : roofing by 5min, outdoor venues by 10min.

**Condensed Water System**

Air conditioning condensation water in the bottom of the indirect drainage works at the podium roof can be discharged to the nearest water bucket or drain and ensure the outlet from the ground 150mm, pipe layer nearest the door to the outside row gullies .

**Fire Fighting System Design**

**Fire fighting water consumption**
According to “the code for fire protection design of tall buildings” in this project indoor fire hydrant water consumption of 40 L/s, outdoor to 30 L/s, fire duration for 3 h. According to " code of design for sprinkler systems " by the underground garage and commercial grade Ⅱ dangerous level design , design of water taken 30L/s, fire duration is 1h. According to the "fixed artillery fire extinguishing system design specifications," water cannon system to take water 40L / s, fire duration takes 1h. Water hydrant , automatic sprinkler water and fire water cannons water of this project as shown in **Table 1**.

**Table 1 Fire water consumption**

| Fire range | Fire fighting system | Design of water/（L/s) | Fire life/h | A fire water consumption /m3 |
|---|---|---|---|---|
| Indoor | Fire hydrant | 40 | 3 | 432 |
| | Automatic sprinkler | 30 | 1 | 108 |
| | Fire monitor | 40 | 1 | 144 |
| Outdoor | Fire fighting | 30 | 3 | 324 |

**Refuge floors and roof fire water tank**

The project is set up on the roof 18 m3 of water tank and pressurization voltage regulation equipment, reserve fire early fire consumption of 10 min. Among them,the 13 and 29 layer of the ultra-high-rise multiple-use and residential buliding, while also offering the device layer ..

**Hydrant system**

According to “the code for fire protection design of tall buildings” in this project indoor fire hydrant water consumption of 40L / s, Outdoor is 30 L / s, fire duration of 3h; calculated the project 's fire water hydrant system volume 650m3, two grid , where fire hydrant water is 432m3, fire pond water from the municipal water supply .

Indoor hydrant system uses a temporary high-voltage systems, indoor is equipped with special fire hydrant pipes.System is divided into three zones for the low zone underground 2 floors – 3 layer , District 4 layer to 30 layers, high zone 31 layer to 39 layer. The lower zone system and underground pump room fire hydrant 2 layer after decompression supply pressure pump by a roof high water tank through the valve regulator ; high zone system from the ground layer 2 double outlet hydrant pressure pump supply by roof Fire high water tank be regulated ; fire hydrant at the mouth of the water pressure is more than 0.5Mpa using vacuum regulator hydrant . Fire standpipe arrangement to ensure the same level of two adjacent hydrants gun enrich the water column can be protected at the same time to reach any part of the range . Fire hydrant enrich the water column is not less than 13m, in addition to the hydrant Fire elevator room , the rest are equipped with Fire hydrant reel . In addition to A, B, C, D, E, F, G ( four or more ) , the other at the ground hydrant boxes need to configure a fire hose reel , hose length of 25m. Are located outside the high , medium and low zones hydrant pump adapter 3 sets of water to the interior of each system .

**Automatic sprinkler system**

The project is set in the ground three 540m3 reinforced concrete fire water pressure pump and automatic sprinkler , sprinkler water storage room 108m3, indoor fire water 432 m3, two fire water grid ; roof set 18 m3 of reinforced concrete Fire a water tank .

( 1 ) Set the location and device . The layers of super high-rise projects , among asylum , both commercial and underground garages with automatic sprinkler systems.

( 2 ) The automatic sprinkler system works vertically divided into two zones , the system uses a temporary high repression. Low Zone : 3 -storey underground to 28 layers , 29 layers to 39 layers of underground high zone . Low area consists of 3 floors underground pump room supply pressurized sprinkler pump pressure , high roof by fire water tank through the valve regulator ; high zone

system consists of three levels of underground sprinkler pump room supply pressure pump by roof high water tank and regulator device regulation.

( 3 ) nozzle level requirements . The super high-rise residential projects of public walkways decorated with concealed sprinklers ; garage , equipment room using orthostatic nozzle ; Business section in addition to commercial atrium , lobby , function rooms and theaters using spray nozzle type lower ceiling , the rest are used in commercial establishments upright sprinklers K = 80. Underground garage, water density mall is 8L/min.m2, active area 160 m2; spray strength in other parts of the floor area is 8L/min.m2, active area 160 m2. Using closed nozzle 93 ℃ glass ball on commercial catering kitchen stove , using the rest of the glass ball 68 ℃ closed nozzle .

( 4 ) sprinklers installed. Nozzle diameter were taken over DN15mm, in contact with the water distribution pipe diameter DN25mm. Sidewall sprinklers takeover diameter DN20mm, in contact with the water distribution pipe diameter DN32mm, while the upper sidewall sprinklers located Poly hot plate .

( 5 ) has a pump room in the basement and ultra- high-rise residential roofing wet automatic alarm valve , each alarm valve pressure does not exceed 1.2Mpa, the number of nozzles is generally not responsible for more than 800 .

( 6 ) are located outside the high and low zone automatic sprinkler system pump adapter to the indoor water systems , including high zone 2 sets of pump adapter , the lower zone 4 sets pump adapter .

**Fixed artillery fire extinguishing system**

According to the specification requirements in clear height of more than 12m commercial atrium to set a fixed artillery fire extinguishing equipment , the project in the ultra- high-rise 15-storey complex building has an atrium , in this layer set two fixed fire water cannons . This system uses automatic scanning ZDMSO.8/20SYA shoot water at high altitude water cannons , each muzzle diameter of DN65mm, working pressure is 0.8Mpa, single shot flow 20L / s, protection radius 50m. Fixed fire artillery temporary water supply system for the high-pressure system , negative two fire pump room located on the ground floor fixed fire artillery fire pumps , fire water tank with a high roof to ensure the system is connected through the valve to maintain the most negative point pressure water cannon .

**Extinguishers provided**

Residential : A ~ G are light hazard class A class configuration 2 2Kg ammonium phosphate fire extinguisher in each fire box office . H, J Building is a serious risk of grade A class configuration 2 5Kg ammonium phosphate fire extinguisher at each hydrant , and to ensure maximum protection from the location of fire extinguishers does not exceed 15m, the distance over protection should be added two 5Kg ammonium phosphate fire extinguisher . Commercial : Commercial belongs to the class A dangerous level , configuration 2 4 Kg ammonium phosphate fire extinguisher at each hydrant , and to ensure maximum protection from the location of fire extinguishers does not exceed 20m, the distance over protection should be added two 4Kg ammonium phosphate fire extinguisher .

Underground Garage: underground garage by dangerous Class B Class design , set 2 4 Kg ammonium phosphate fire extinguisher at each hydrant fire hydrant in the middle position and the adjacent , and to ensure maximum protection from the fire extinguisher does not exceed 12m, more than protection from the position should be added two 4Kg ammonium phosphate fire extinguisher.

## Conclusion

In recent years, the rapid development of high-rise buildings , high-rise buildings of the design of the drainage system requirements also put forward higher requirements. In building water supply , drainage , etc., to be developed , the problem is still a lot of innovation and research . As a building drainage design staff, should be based on technical , security, economic principles , in practice, to innovation , to find the best drainage design programs to meet the new requirements of architectural design development to meet the continuous improvement of people's material cultural requirements, is to embark on the basis of sustainable development and protection.

## Reference

[1] Hongyi Deng. The construction of the building facilities of water supply and drainage design [J]. Science and technology innovation herald,2008,31(21)
[2] Yang Ling. Overrun the characteristics of the high-rise building water supply and drainage system design [J]. Water supply and drainage,2010,36(01)
[3]GB50015-2003, Code for design of building water supply and drainage Bei Jing[S]: China plans to press
[4]GB50016-2006, Code of Design on Building Fire protection and prevention Bei Jing[S]: China plans to press
[5]GB50140-2005, Code for design of extinguisher distribution in buildings Bei Jing[S]: China plans to press
[6]GB50045-95(2005), Code for fire protection design of tall buildings Bei Jing[S]: China plans to press
[7]GB50084-2001(2005), Code of design for sprinkler systems Bei Jing[S]: China plans to press
[8]GB500338-2003，Code of design for fixed fire monitor extinguishing systems Bei Jing[S]: China plans to press
[9]GB50352-2005, Code for design of civil buildings Bei Jing[S]:China plans to press

*Applied Mechanics and Materials Vols. 580-583 (2014) pp 2380-2383*
*© (2014) Trans Tech Publications, Switzerland*
*doi:10.4028/www.scientific.net/AMM.580-583.2380*

# Treatment of raw water in Yangtze Chenhang Reservoir by Diatomaceous Earth Precoat Filtration

Wenqi Zhou[1, a], Dong Zhang [1], Hui Ye[1], Zheng Wang[1], Zheng Yang [2], Chunlin Zhang[2]

[1] National Engineering Research Center of Urban Water Resources, Shanghai 200082, China;

[2]Shanghai Safbon water service Co. Ltd., Shanghai 201716, China;

[a]email: zwqbati@163.com

**Keywords:** diatomaceous earth; precoat filtration; turbidity; drinking water treatment

**Abstract.** Taking the raw water of Yangtze Chenhang Reservoir as the research object, the characterization of diatomaceous earth, and the removal efficiency of $COD_{Mn}$, turbidity by precoat filtration process were investigated by pilot experiment in this paper. The results showed that diatomaceous earth patterns having porous structure and the pure silica peak at 2θ angles 21.980, 36.080, 31.460 and 28.430 in XRD analysis. Precoat filtration has a good stability to remove solid suspended particle, effluent turbidity was remained about 0.05NTU. Precoat filtration had no effect on removing $COD_{Mn}$. The pressure of 50KPa could be defined as a critical point in this experiment. Beyond the critical point, the devices should be stop and backwash, to resume operation pressure. Overall, precoat filtration can be defined as a filtration technique for relatively low turbidity raw waters.

## Introduction

During World War II, the US Army needed a portable, efficient filter to remove Entamoeba histolytica, a protozoan parasite prevalent in the Pacific war zone, from drinking water. The army developed precoat filtration, which successfully removed the cysts. Since 1949, precoat filtration has been used in the filtration of sugar syrups, fruit juices, wine, beer, and water. Now, precoat filtration is a US Environmental Protection Agency (US EPA) accepted filtration technique for potable water treatment [1]. More than 170 potable water treatment plants using precoat filtration have been constructed. As a new water treatment technology, diatomaceous earth precoat filtration could remove suspended particles without adding chemicals [2]. The main objectives of this study were to evaluate the feasibility of the application of precoat filtration enhance the turbidity removal in Yangtze Chenhang Reservoir raw water.

## Material and method

**Raw water.** The main feature parameters of experimental raw water were shown in Table 1.

Table 1 Water Quality of Raw water

| parameter | $COD_{Mn}$ mg/L | Turbidity NTU | $UV_{254}$ $cm^{-1}$ | Conductivity μS/cm | Fe mg/L | Mn mg/L |
|---|---|---|---|---|---|---|
| value | 1.4-2.7 | 5-45 | 0.027-0.103 | 280-860 | 0.33-1.04 | 0.002-0.58 |

**Pilot process parameters.** Pilot-scale was $6m^3/h$. Coagulant used PAC (alumina content 10%) and the dosage was about 20mg/L. After coagulation and sedimentation, raw water were flowing into sand filtration ($3m^3/h$) and precoat filtration ($3m^3/h$). The filter area was $1.5m^2$. The dosage of precoat was 0.9kg, turn on the precoat pump to bring the diatomaceous earth to the filter. When all the filter media is on the filters, change the valving to bring raw water and body-feed to the filter. Dosage of body-feed was 4.32mg/L.

**Materials and Physical characterizations.** The diatomaceous earth sample was provided by Lin Jiang Imerys Diatomite Co, Ltd. A Rigaku D/Max 2500 powder diffractometer (Cu *Kα* radiation) was used to obtain powder XRD patterns. The surface textures of the samples were observed using scanning electron microscopy (SEM) with a JEOL JSM-6700F (JEOL Co., Japan) apparatus.

## Results and discussion

**Characterization of diatomaceous earth.** SEM micrographs of diatomaceous earth (DE) are shown in Fig.1 [3,4]. The porous structure of DE can be clearly seen in Fig.1 (b). The filtering medium used in precoat filtration is composed of fossil-like skeletons of microscopic water plans called diatoms, which range in size form under 5 to more than 100 micrometers. These algae have the capability of extracting silica form water to produce their skeletal structure. We could see in Fig.2, that the XRD patterns having the pure silica peak at 2θ angles $21.98^0$, $36.08^0$, $31.46^0$ and $28.43^0$. These peaks are consistent with the report in literature. Diatomaceous earth is distinguished not only by the Diatom species, but also by its purity of $SiO_2$. Most of the constituents of diatomaceous earth are practically inert. The soluble portion of diatomite is very low(less than 1%). The chemically inert characteristics mean that diatomaceous earth could safely be used for filtration of water, beverage, or other liquids for human consumption.

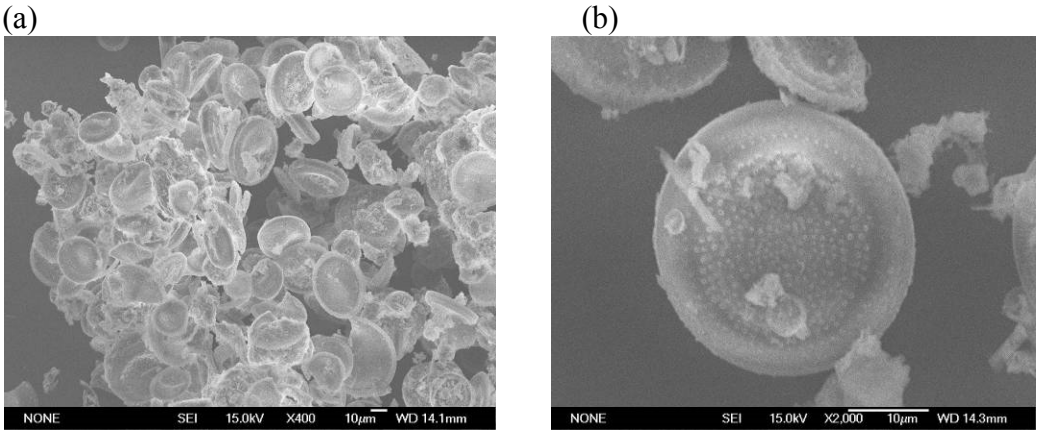


Fig.1 SEM photographs (×400 and ×2000) of diatomaceous earth

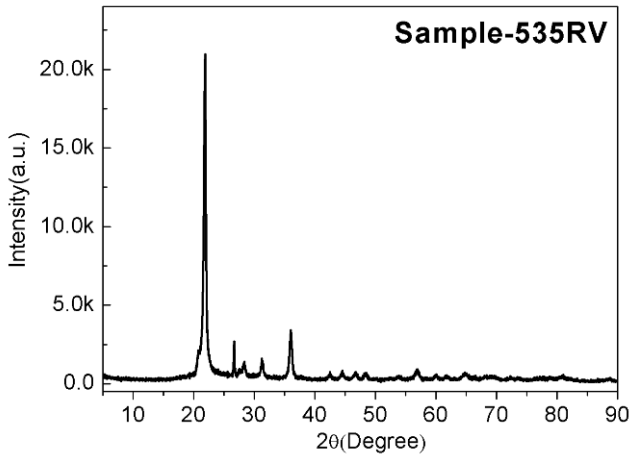


Fig.2 XRD patterns of the diatomaceous earth sample(535RV)

**Turbidity removal.** The turbidity of different process was shown in Fig.3, within 32 hours of running time, effluent turbidity of precoat filtration was remained about 0.05NTU, the removal rate of turbidity was more than 90%. Compared with the precoat filtration process, the effluent turbidity of sand filtration was affected by the filtration rate, sedimentation tank sludge period, and other factors.

The effluent turbidity of sand filtration was changed form 0.05NTU to 0.25NTU, even though the removal rate of turbidity in sand filtration was more than 88%, which indicate that precoat filtration has a good stability to remove solid suspended particles. Diatomaceous earth (DE or diatomite) filtration can be defined as a filtration technique for relatively low turbidity waters, generally below 10 turbidity units (NTU). A survey of direct filtration practice, including precoat filtration plants, indicated that 80 percent of the plants had an average source water turbidity of 5 NTU or less. The maximum turbidity at 80 percent of the plants was 40 NTU or less[2].

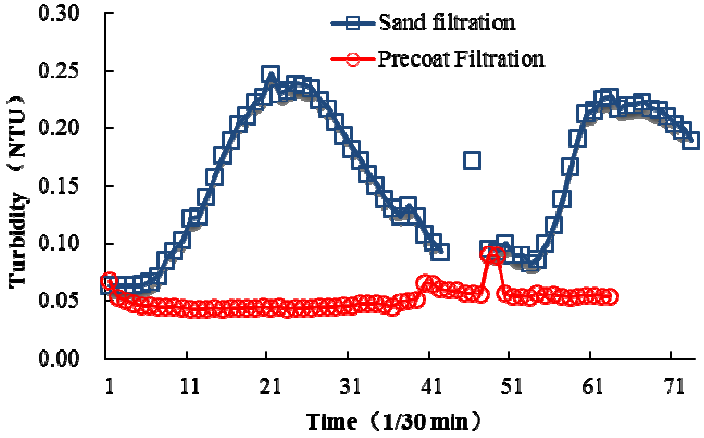


Fig.3 The effluent turbidity of sand filtration and precoat filtration

**$COD_{Mn}$ removal.** As shown in Fig 4, under different operation conditions, the effluent $COD_{Mn}$ of precoat filtration was 1.38 mg/L, which was closer to the effluent of sedimentation (1.36 mg/L) and sand filtration (1.32 mg/L). It was showed that precoat filtration had no effect on removing $COD_{Mn}$. The removal of organics combined process mainly depends on the process of coagulation and sedimentation. Therefore, in order to make the effluent quality meet the national drinking water standard (GB5749-2006, less than 3 mg/L), the production units should use coagulation and sedimentation, or other pre-oxidation process to ensure the effective removal of organic matter in raw water.

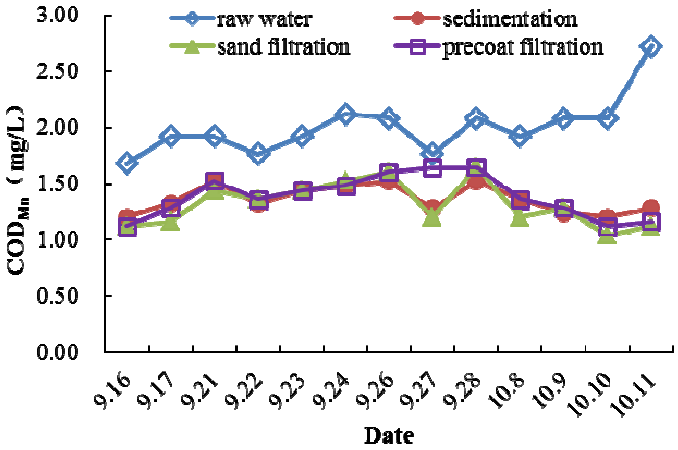


Fig.4 The effluent $COD_{Mn}$ of different process

**Hydraulics.** The hydraulics of precoat filtration process was investigated in Fig.5. By analyzing flow and pressure data during the operation, the hydraulics of the device was changed. It was showed that when the pressure up to 50KPa, the effluent flow dropped from the $3m^3/h$ to $2.9m^3/h$. For the devices used in this experiment that the actual operating pressure must not exceed 50KPa, otherwise it will

lead to decline in effluent flow. Thus, the pressure of 50KPa could be defined as a critical point. Beyond the critical point, the devices should be stop and backwash, to resume operation pressure.

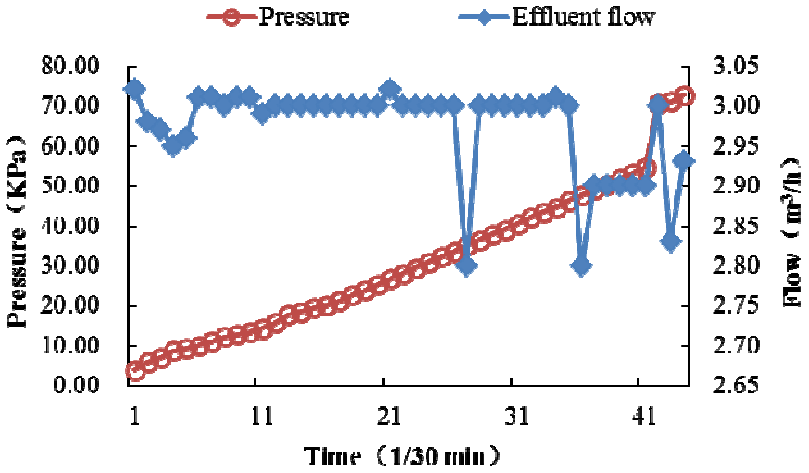


Fig.5 The hydraulics of precoat filtration process

## Conclusions

Diatomaceous earth patterns having porous structure and the pure silica peak at 2θ angles 21.980, 36.080, 31.460 and 28.430. Precoat filtration has a good stability to remove solid suspended particle, effluent turbidity was remained about 0.05NTU. Precoat filtration had no effect on removing $COD_{Mn}$. The pressure of 50KPa could be defined as a critical point in this experiment. Beyond the critical point, the devices should be stop and backwash, to resume operation pressure. Precoat filtration can be defined as a filtration technique for relatively low turbidity raw waters.

## Acknowledgements

This work was financially supported by the Shanghai Natural Science Foundation (12ZR1410000), National science and technology major project of water pollution control and treatment (2012ZX07403-002).

## References

[1] George P. Fulton. Diatomaceous Earth Filtration for Safe Drinking Water, Reston, Virginia: American Society of Civil Engineers (2000).

[2] American Water Works Association (AWWA). *Precoat Filtration* Manual M30, 2nd edition. Denver, Colorado: American Water Works Association (1995).

[3] Angela F. Danil de Namor, Abdelaziz El Gamouz, Sofia Frangie, et al. Turning the volume down on heavy metals using tuned diatomite. A review of diatomite and modified diatomite for the extraction of heavy metals from water diatomite and modified diatomite for the extraction of heavy metals from water, Journal of Hazardous Materials, Vol. 241 (2012), 14-31.

[4] Wen-Tien Tsai , Chi-Wei Lai, Kuo-Jong Hsien. Characterization and adsorption properties of diatomaceous earth modified by hydrofluoric acid etching, Journal of Colloid and Interface Science, Vol. 297 (2006) 749-754.

*Applied Mechanics and Materials Vols. 580-583 (2014) pp 2384-2388*
*© (2014) Trans Tech Publications, Switzerland*
*doi:10.4028/www.scientific.net/AMM.580-583.2384*

# Choosing an optimal trenchless renovation method for pressure and non-pressure pipes

Vladimir Orlov[1, a], Ilya Averkeev[1, b]

[1]Moscow State University of Civil Engineering, Department of Water Supply, Yaroslavskoye sh. 26, 129337, Moscow, Russia

[a]orlov950@yandex.ru, [b]ilji4.msk@gmail.com

**Keywords**: trenchless renovation, pressure pipes, non-pressure pipes, pipelines network

**Abstract.** The paper presents the innovative decision of the problem of choosing the most effective pipe renovation method among the wide range of them. To solve this problem a computer program called "Repair 2012" was developed. The factors influencing the selection process of optimal renovation method for pressure and non-pressure pipes and the theoretical base for creating a computer program are described. The program algorithm based on weighted analysis of these factors. Weighting coefficients for each factor are calculated using arithmetical mean for all concerning trenchless methods. The income and outcome user information, the sequence of the process of working with the program are represented in the article. The process and results on determining an optimal renovation method are shown as an example.

## Introduction

The use of trenchless technologies for infrastructure network rehabilitation makes it possible to accelerate the repairing processes with an opportunity to reach high ecological and economical factors, which are the most important ones for effective operation of urban area.

Trenchless technologies used for pipelines network renovation have to provide energy, resources and costs savings and to prevent (reduce sharply) leakages into the environment as well. A variety of trenchless methods for pipe network rehabilitation exist in the modern market, therefore municipal services got confused with question of using the most effective renovation method in certain cases. This fact makes scientists, designers and constructors decide to use a wide range of techniques or strategies for the selection of optimal renovation method. Most modern studies are devoted to choosing the optimal techniques for pipe laying [1-5], in a less degree – to rehabilitation woks [6-8]. Different researches use available software (ExpertChoice [5]) or computer-based information system (DSS [4]) as well as self-developed programs [1, 3]. The municipal service in large cities such as Moscow and Sankt-Petersburg need an efficient tool to create strategy of pipe network renovation.

## Theory

The selection of renovation methods starts with assessment of some critical factors. The primary importance have: costs (marked as C), technological duration of the process (D), mean lifetime (T), technical (B) and hydraulic (H) factors. In order to take into account all these factors it is necessary to reveal an average one, which may become the main criteria for choosing an optimal renovation method. For this purpose lots of information needs to be processed. In this case it is more convenient to process all this information in the computer program using weighted factors calculation.

Cost factor (C) means building and repairing works cost for one meter of a pipe for a specified trenchless method and diameter (Eq. 1). Weighted cost factor is:

$$K_C = \frac{C}{C_W}, \qquad [1]$$

where $C_w$ is an arithmetical mean value of costs of all concerning trenchless methods.

Technological factor (T) means the duration of the entire working cycle (in days) on a section of 100 m in length for specified trenchless method and diameter (Eq. 2). Weighted value is:

$$K_D = \frac{D}{D_W}, \quad [2]$$

where $D_w$ is an arithmetical mean value of duration of all working cycles for specified trenchless method.

Lifetime factor (T) means the frequency of carrying out rehabilitation process (times/year) for specified trenchless method rehabilitation – it is the inverse value of renovated pipe lifetime (Eq. 3). Weighted lifetime factor is:

$$K_T = \frac{T}{T_W}, \quad [3]$$

where $T_w$ is an arithmetic time mean of frequency of carrying out the rehabilitation process of all concerning trenchless methods.

Technical factor (B) means diameter loss (in percents) after carrying out the specified trenchless rehabilitation method (Eq. 4). Weighted technical factor is:

$$K_B = \frac{B}{B_W}, \quad [4]$$

where $B_w$ is an arithmetical mean value of diameter loss for all concerning trenchless methods.

Hydraulic factor (H) is the inverse value of the main criteria of waste water pipelines – Chezy coefficient (for gravity-flow pipelines) or ratio of hydraulic friction λ (pressure pipes).

Total weighted factor for certain trenchless method is the sum of all factors (Eq. 5):

$$\sum(K_C + K_T + K_D + K_B + K_H). \quad [5]$$

The minimal total weighted factor means the priority of given method among the others. An algorithm for computer program was based on theoretical considerations mentioned above.

The algorithm contains the income and outcome forms, which includes the following data:

- information about the repair section with particular data about the specific water flow (pressure or gravity), diameter and material, damage level and failure characteristics;
- information about methods for trenchless rehabilitation according to the pipe type.

Boundary conditions (cycles) are installed in the algorithm of calculating optimal parameters:

- the external cycle, which serves to extract those trenchless methods, which are used with an optimal diameters that differ from the repairing one;
- the first internal cycle, which divides trenchless methods according to their materials (metal/nonmetal);
- the second internal cycle, which divides trenchless methods according to defect characteristic;
- the third internal cycle which deals with minimal total weighted ratio of 5 optimization factors.

**Results and discussion**

As one of results the developed program called “Repair 2012” gives us the printouts of outlet information and designs a graph to illustrate weighted factors of optimal trenchless method for pipe renovation. The program is worked out as a database of all trenchless technologies, which can be used for water supply and sewer networks. The program includes four inserts to illustrate passport data and other information, such as: water flow behavior, pipe diameter, material and failures (Fig. 1 and 2).

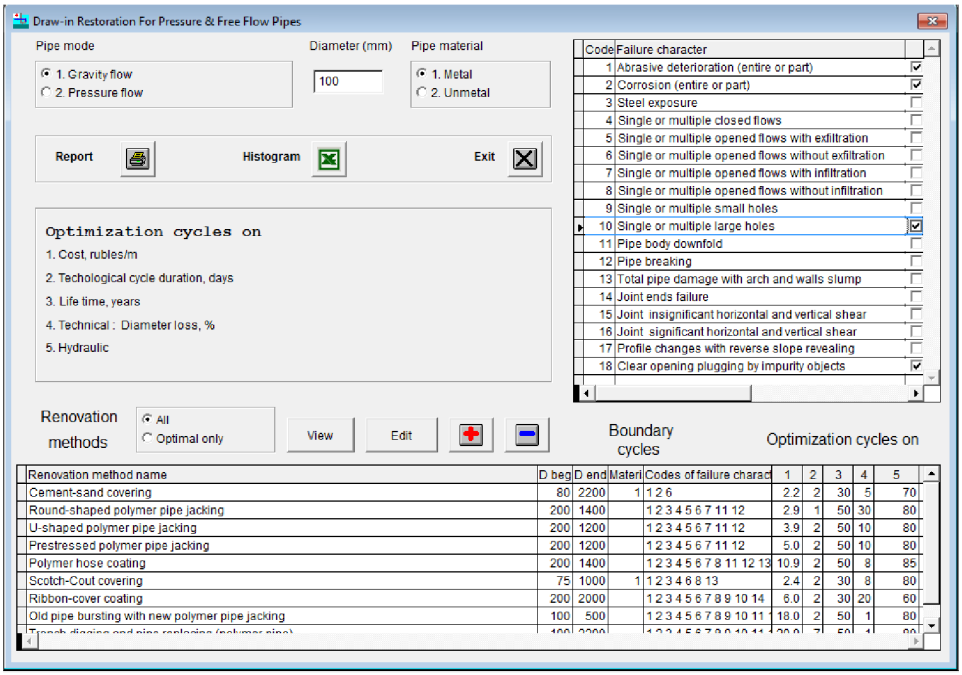


Fig. 1. The example of the first dialog box for non-pressure pipe.

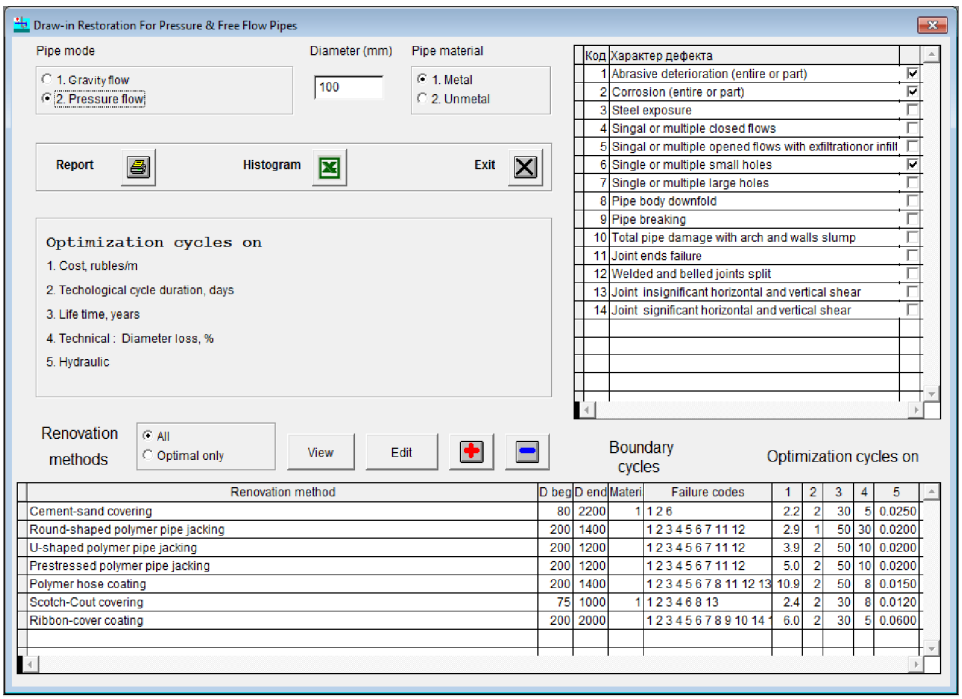


Fig. 2. The example of the first dialog box for pressure pipe.

Optimization cycles are placed hear to divide 5 positions according to criteria factors: C (1), D (2), T (3), B (4), H (5).

The information given in the lower part of the box includes the list of all trenchless methods with boundary parameters used for each method (diameter range, material codes and the type of defects, which can be removed by certain method), including the data on optimization factors (1-5).

There are “Show”, “All methods” and “Only acceptable”, “Change”, “+” and “–“ buttons above the methods data. These buttons make it possible to enter the particular method, change its parameters or delete lines in the box. The typical defect lists for pressure and non-pressure pipes are represented in dialog boxes (Fig. 1 and 2).

The operation process during the work with the given program is represented below.

At first user should input the following data: flow mode of pipe network (pressure or gravity), diameter of the existing pipeline, pipe material (metal/nonmetal) and pipe defects (as a code).

After data input the program automatically generate some changes:

- the 5th line in the "Optimization cycles on:" shows Chezy coefficient, $m^{1/2}/s$ (for non-pressure pipes), or hydraulic friction ratio λ (nondimensional quantity);
- the method titles with all the input data in lines as they also depend on flow dynamics;
- the defects list according to the chosen flow type.

It is also possible to make manual changes for the failure nature (quality factor) as well as their quantity (quantity factor).

The program also allows to user to input changes and additions in renovation methods list. Prior to operating changes and additions, it is necessary to push the buttons "All" and "Show". In order to change information in particular method line or to add a new method (database changing mode) it is necessary to use "Correct" button. Thereafter user checks the exact method to get the possibility to verify new information. In order to confirm changes user should press the button "Apply". Filling the data in cells "Boundary cycles" and "Optimization cycles on" provided by entering the start and final diameters, code of pipe material, which can be renovated by specific method (1 – metal, 2 – nonmetal, 0 – the others), failures codes, data concerning described above five factors.

In order to add a new method into the database, the "+" button should be pressed to get a new line called "New method"; the "–" button is used to delete any method in line.

The work with the program ends using buttons "All" and "Output form".

In you want to display only valued methods for this particular case study, user may press the button "Only valued" and then again "Output form".

Table 1
Final results on automated analyze and choosing an optimal renovation method

| **D = 600 mm** | | | | | | | | | | | |
|---|---|---|---|---|---|---|---|---|---|---|---|
| **Renovation method** | **Factors** | | | | | | | | | | |
| | Cost C [rubles/m] | Weighted cost $K_C=C/C_W$ | Technological, cycle duration D [days] | Weighted technological $K_D=D/D_W$ | Time (opposite the life time) T [1/year] | Weighted time $K_T=T/T_W$ | Technical (diameter looses) B [%] | Weighted technical $K_B=B/B_W$ | Hydraulic ratio H | Weighted hydraulic $K_H=H/H_W$ | Total |
| 1. Cement-sand covering | 3.2 | 0.3988 | 2 | 0.7619 | 0.0333 | 1.4286 | 5 | 0.5479 | 0.0250 | 1.2739 | 4.4111 |
| 2. Round polymer pipe jacking | 4.0 | 0,4984 | 1 | 0.3810 | 0.0200 | 0.8571 | 30 | 3.2877 | 0.0200 | 1.0191 | 6.0433 |
| 3. U-shaped pipe jacking | 4.5 | 0.5607 | 2 | 0.7619 | 0.0200 | 0.8571 | 10 | 1.0959 | 0.0200 | 1.0191 | 4.2948 |
| 4. Prestressed pipe jacking | 5.0 | 0.6231 | 2 | 0.7619 | 0.0200 | 0.8571 | 10 | 1.0959 | 0.0200 | 1.0191 | 4.3571 |
| 5. Cured in place pipe | 2.5 | 0.3115 | 2 | 0.7619 | 0.0200 | 0.8571 | 8 | 0.8767 | 0.0150 | 0.7643 | 3.5716 |
| 6. Scotchkote covering | 5.0 | 0.6231 | 2 | 0.7619 | 0.0333 | 1.4286 | 8 | 0.8767 | 0.0120 | 0.6115 | 4.3017 |
| 7. Trench excavation and pipe replacing (polyethylene pipes) | 20.0 | 2.4922 | 5 | 1.9048 | 0.0200 | 0.8571 | 1 | 0.1096 | 0.0200 | 1.0191 | 6.3828 |
| 8. Trench excavation and pipe replacing (ceramics and cast iron pipes) | 20.0 | 2.4922 | 5 | 1.9048 | 0.0200 | 0.8571 | 1 | 0.1096 | 0.0250 | 1.2739 | 6.6376 |

It is also possible to print out a histogram, which reveals the dynamics of optimization process.

Table 1 represents an example of such a printout on choosing an optimal renovation method for a section of non-pressure pipeline. Fig. 3 represents a histogram for this case. Such histograms help users and designers to estimate and compare optimization parameters in order to determine an optimal method.

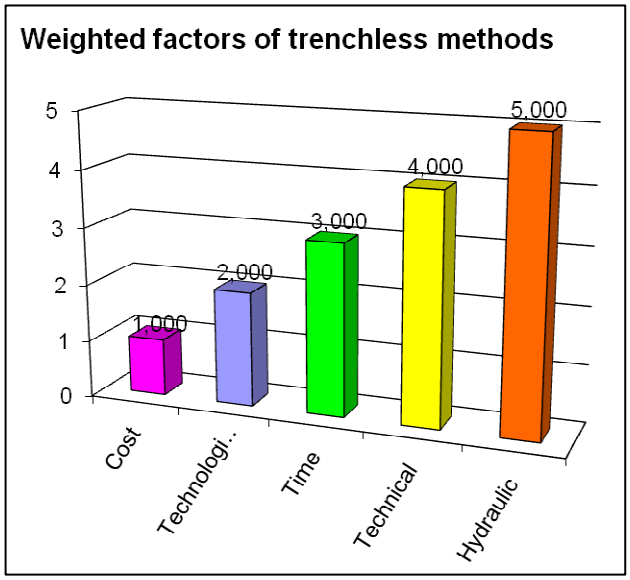


Fig. 3. The example of the histogram for optimal method for non-pressure sewer network.

## Conclusions

1. A computer program for selection an optimal renovation method for trenchless rehabilitation of pressure and gravity water supplying and water disposal pipelines is developed for specialists and engineers from the design and operating organizations.
2. As a result the program displaying a histogram for each particular case study, which reveals proportions of operating costs, technological duration of renovation works, lifetime, technical and hydraulic factors of optimal renovation trenchless method, which has the minimal weighted factor.

## References

[1] A. Zwierzchowska, The optimum choice of trenchless pipe laying technologies, Tunnelling and Underground Space Tech. 21, Is. 6 (2006) 696-699.
[2] M. Ueki, C.T. Haas and J. Seo, Decision tool for microtunneling method selection, ASCE Journal of Construction Engineering and Management 1252 (1999) 123-131.
[3] Abraham, D. M., H. Baik, and S. B. Gokhale. Development of a Decision Support System for Selection of Trenchless Technologies to Minimize Impact of Utility Construction on Roadways. Publication FHWA/ IN/JTRP-2002/07. Joint Transportation Research Program, Indiana Department of Transportation and Purdue University, West Lafayette, Indiana, 2007.
[4] S. Gokhale, M. Hastak, Decision aids for the selection of installation technology for underground municipal infrastructure systems, Tunnelling and Underground Space Tech. 15 (2000) 1-11.
[5] P. Adamovic, C. Dunovic and M.M. Nahod, Expert choice model for choosing appropriate trenchless method for pipe laying, http://bib.irb.hr/datoteka/348146.Adamovic_Dunovic_Nahod_Prag_09_2007.pdf [April 2014].
[6] E. Waligorski, The challenge of selecting the right sewer rehabilitation method, International No-Dig 2013 - 31st International Conference and Exhibition, Sydney, Australia, 1-4 September 2013. Paper 2.11.
[7] L. Scholten et al., Strategic rehabilitation planning of piped water networks using multi-criteria decision analysis, Water Research 49 (2014) 124-143.
[8] A. Sargaonkar, S. Kamble and R. Rao, Model study for rehabilitation planning of water supply network, Computers, Environment and Urban Systems 39 (2013) 172-181.

*Applied Mechanics and Materials Vols. 580-583 (2014) pp 2389-2393*
*© (2014) Trans Tech Publications, Switzerland*
*doi:10.4028/www.scientific.net/AMM.580-583.2389*

# Design and development of the urban water supply pipe network information system based on GIS

Xiaohong Wang[1, a*], Yajing Liu[1,b] ,Zheng Wang[1, c,] Wei Zhang[1,d]

Hebei United University, Hebei Tangshan 063009, China; Hebei Key Laboratory of Mining Development and Security Technology, Hebei Tangshan 063009, China

[a]glwxiaohong@163.com, [b]lyj2206@163.com, [c]wangzheng@heuu.edu.cn, [d]heuu_zhangwei@126.com

**Keywords:** GIS, water supply network, System development, maintenance

**Abstract.** Urban water supply systems are the primary guarantee for life and enterprises to work orderly, according to the requirements of water resource department and the technical feasibility for the management system, the water supply pipe-network information system was designed and developed. The system was developed in C # language and SuperMap Objects as secondary development components. The applicability and weaknesses of the system was analyzed in order to provide better service for the water conservancy work digitally.

## Introduction

Urban water supply pipe network systems composed of a series of structures and distribution pipe network are critical infrastructure for urban economic development and that are the primary guarantee for life and enterprises to work orderly[1]. With the development of production, the city gradually expanded and the city's water supply network continuously updated. Water supply network becomes a lifeline of the city and it is closely related to the normal life of the city residents. Urban water supply systems were built underground with the hidden, large-scale, huge dada and complex characteristics. The traditional management methods by drawings and diagrams were difficult to manage and utilized a large number of constantly updated urban water supply pipe network information effectively. GIS is a computer assisted system for the capture，organization，storage，retrieval，query，update，analysis and display of spatial data[2]. GIS with the specific function of Visualization and spatial analysis can meet the requirements mentioned above, as an advanced technology used in the field of urban water supply. GIS has a positive effect on urban water supply planning, information inquiry, quick repairs, accurate positioning, optimal allocation of staff, etc [3-6]. This system was developed for a city in North China by C # language and SuperMap Objects as secondary development components, in order to provide better technical services for the city's water management and transport.

## Requirement analysis

The system designed based on customer demand analysis and the water management department as the service object, it should have the functions as following:

To display the information of all kinds of water supply network in the city, providing information query and search quickly for the user, that conducive to management and scheduling range.

Basic on the information of the water supply pipe network, user can position the damage valves exact location timely in order to determine which valves need closed and how to channelize.

Basic on the existing layout of the city's water supply network, the system provided basis for the new water supply network pipeline.

## General design of the system

**Design of the system main flow.** The user can user this water supply network geographic information system after login. When user enter the main interface of the system， they can monitor and manage the information of the urban water supply network, including editing, query, maintenance analysis, displaying of water delivery mode, calling the Symbol Selector and various kinds data entering. In addition, the system also provides other assist functions such as particular location marked of the water pipeline, different levels of valves marked and map production output. The flowchart of the system main flow was shown in Fig.1.

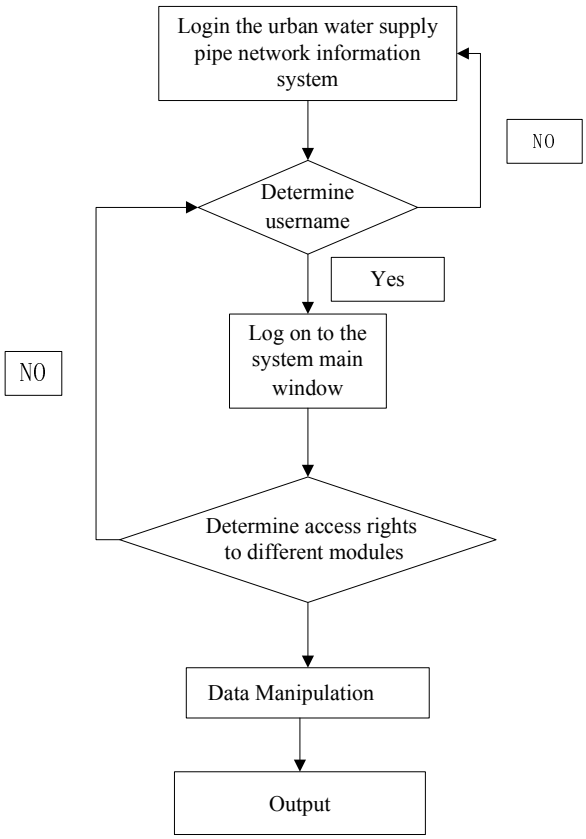


**Fig.1** The flowchart of the system main flow

**Data Storage.** Development of urban water supply network geographic information system needed the strong support of database system. And given urban water supply network information was different from other relevant spatial geographic information, there were two kinds of database those were attributes database and spatial database for storage and management of data. The system design mainly uses SQL Server and the SDB data engine of SuperMap Objects for data processing.

**Design of the system main function modules.** Combined with the actual situation of the city, the main function modules of the management system can be divided into data editing of the pipeline, the water supply network information query and map making. Each main function module has different sub-modules of function shown in Fig.2.

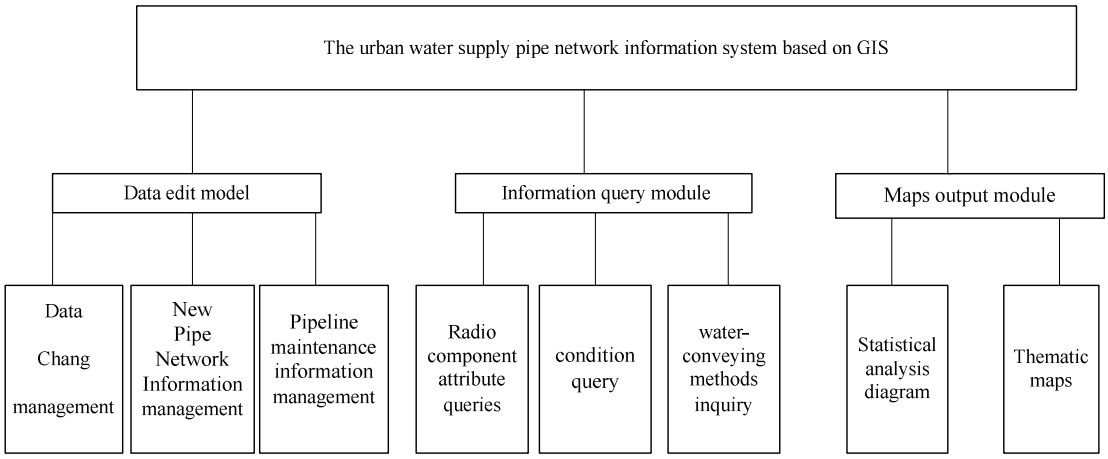


**Fig.2** The flowchart of the system main flow

## Detailed design of the system

**The water supply pipe network information editing module.** That was mainly to adapt to the development of water supply network or create constantly changing in the city, the relevant data can be update on the map in real time via the system. The main pipeline data editing module fulfils three main functions those were data change management, new pipe network information management, management of pipeline maintenance information and decision analysis based on the above information. The function module diagram was shown in Figure 3.

**The water supply pipe network information query module.** That mainly in order to facilitate user to query information of the city water supply pipeline. Its features include a radio component attribute queries, condition query (such as location, water supply) and water-conveying methods inquiry. The function module diagram was shown in Figure 4.

**Maps output module.** User can make some Statistical analysis diagram and specific module maps by map making model，including a compass, scale, coordinate grid, diagram generation for water supply, etc.

## System implementation

**Main interface.** The main interface provided a window for user interact with the information system, it reflects the overall layout of the system, can directly express the most function of the system. It reflected the overall layout of the system and expressed the most function of the system directly. An operating interface of the system with intuitive, concise, friendly characteristics can greatly improve the operation efficiency. The system minimized redundancy controls on interface and number and distribution of child windows were designed reasonable to maximize the efficiency for user.

**The menu bar and toolbar.** Accurate classification for the system menu made user stick out a mile to the program function and improved operation efficiency. The system menu bar includes the following functions:

File: open, create, add data, load CAD, save as, and exit.

Editor: copy parallel, split, rotate, extend, trim, fillet, add bookmarks, labeling features, etc.

View: zoom, pan, full size, clear screen and the layout view and map view.

System toolbar includes some commonly tools, such as open, save, zoom, etc, to facilitate users.

**Right-click menu function.** Attribute table of right click menu showed the attributes data in an elected layer and displayed in another window, recorded the total number of attribute data. Right click menu is convenient for user to add data, opening and closing layer, select elements and map view in the map window.

**Map Global Display.** Global map display is primarily a thumbnail map and user can change its area in the view by changing the position of thumbnail map border.

**Comprehensive query and analysis.** The system provides four queries by SoDatasetVector.QueryEx of SuperMap Objects that can help users to accurately retrieve the information they need.

Service area queries: The main function is to query service area, numbers of population of the water supply pipeline and water station through the buffer analysis in different conditions.

Water station query: That was a kind of map query, it convenient for the user to capture the spatial and attribute data those they need about water station and positioned the location.

Water pipeline component query: User can query target position of water supply pipeline and valve according to different conditions.

Water-conveying methods query: User can find out the water-conveying methods was branched, cyclic or others through this function to scheduling and emergency better.

On the basis of the information above mentioned the system design analysis capabilities that can provide decision support for users.

**Maintenance analysis.** User can analyze and optimize the water maintenance of water supply network through the system; it was the effective method to troubleshooting when the valve trouble happened. There were two kind of maintenance analysis i.e. valve maintenance analysis and pipeline maintenance analysis.

Valve maintenance analysis: The position of valve damaged can be to determine the position of valves which should be closed and which spare valve should be opened. Steps of valve maintenance analysis as following: Maintenance analysis - valve maintenance analysis - select the type of valve damaged and its properties - analysis and get conclusion.

Analysis of Water supply pipeline maintenance: The location of damaged pipeline and area which was serviced can be found by this system to adjust water supply scheduling timely. Steps of v Analysis of Water supply pipeline maintenance as following: Maintenance analysis - analysis of Water supply pipeline maintenance - select the type of pipeline damaged and its properties - analysis and get conclusion.

**Map production.** User switch to Layout view then in the layout view adding a command button, compass, grid, scale, coordinate grid network, then you can map production output.

## Conclusions

The water supply geographic information systems of a city in north China was designed and development basic on the analysis of existing distribution information of the city. The system implements the functions included comprehensive query and analysis, maintenance analysis, map production and some basic functions such as the menu bar and toolbar, right-click menu function, etc. The system has friendly interface, simple operation, good compatibility, strong function, can provide fast and efficient service for water management. The system relied on the mathematics, graphics, computer science and other disciplines, so there was better practicability and comprehensive.

**Acknowledgments**

The authors gratefully acknowledge the fund provided by Tangshan Science and Technology Bureau Project (No.12140208A-4) and Hebei United University Youth Fund Project (Z201221) for the work presented in this paper.

**References**

[1] Xushi Yan, Jinchu Fan. *Water Supply Engineering* (4th Edition), Chinese Building Industry Press(1999), p.45-46. (In Chinese).

[2] Kang-tsung Chang. *Introduction to Geographic Information Systems* (5th Edition), McGraw-Hill Education(Asia)(2010).

[3] Yuwei Kang, MinzhenZhai, Minju Zhang. *Water Tchnology*, 2(2008),35-38.

[4] Xinlong Song, Lei Ma. *Science of surveying and Maping*, vol.33(2)(2009),p.140-141. (In Chinese).

[5] Xuan Liu, Yuzhu Liu, Jianqing Lu. *Geomatics & Spatial Information Technology,* vol.34 (5)(2011), p.141-147. (In Chinese).

[6] Xiao Meng, Cheng Lei, Yinhe Luo.*Water Conservancy Science and Technology and Economy*, vol.16(3)(2010), p.340-342. (In Chinese).

*Applied Mechanics and Materials Vols. 580-583 (2014) pp 2394-2397*
*© (2014) Trans Tech Publications, Switzerland*
*doi:10.4028/www.scientific.net/AMM.580-583.2394*

# Model Precision Assessment of Water Distribution System Based on Uncertainty Analysis

Shihu Shu [1], Xiaoming Zheng [2], Jiuli Ruan[2]
[1] No.230 XuChang Road, YangPu District, Shanghai Chian 200082, ssh314@126.com
[2] No.455 YuXiu Road, FengXian District, Shanghai Chian 201400

**Keywords:** Water Distribution System; Hydraulic Model; Uncertainty Analysis; Random Sampling

**Abstract.** This research analyzed the operation characteristics of the urban water supply network, the space and time change rule of water consumption and the micro modeling process. Using typical simulation software and the corresponding computer environment, the authors took a simple network, e.g., the pipe network model parameters, and under the conditions of variables uncertainty. and created a new Hydraulic Model. Corresponding uncertainty quantitative techniques of water supply network computer model technology were put forward, and new integration software was developed on that basis.

## Introduction

Computer simulation is the foundation of the planning, design and operation of the pipeline network of a water supply network system. A lot of engineering of mathematical model describe the system behavior with the certain method. However, all real-life problems in some way are accompanied by uncertainty. In the process of network modeling, uncertainty may come from parameter measurement, parameter estimation process, mathematical certainty and uncertainty. These contradictions will seriously affect the reliability of the simulation and optimization results[1].

Since the beginning of the 1970s, when the idea of uncertainty of the model was proposed, study in this area has created extensive interest of different background researchers, thus pushing the discussion and fusion of the process identification theory, filtering theory, time series analysis and sensitivity analysis method in the applications of the environment system, and created the feasible tools of uncertainty analysis[2].

If each input parameter in the model of probability distribution is independent of each other, then the probability distribution of the output parameters can also seek but, in most cases, the function relation of input and output parameters can't be expressed using an analytical equation, and therefore other methods have to be used, such as sensitivity analysis (SA), Monte Carlo simulation method (MCS) and Latin super cubic sampling method (LHS), fuzzy sets method and random sampling simulation method, etc. Random sampling method is a favorable method to study the random variables using a digital computer, and it is a kind of uncertainty analysis method [3].

This paper using random sampling preliminary quantified the uncertainty interval of the model result caused by the uncertainty of the model parameters, puts forward the new proposals evaluation model accuracy, technical route of model uncertainty analysis.

**Setting of parameters interval.** Take pipe C value as an example, the original each tube C value is fixed, before simulation the value of C needed to be input, such as a new line of cast iron pipe (without inner liner) C a value for 130, but the actual condition is probably 125 or 135, so set an uncertainty interval [125, 135], also can be set to a [120, 140], the lower interval can be set by yourself according to the actual situation, every time when all the pipe from the simulation of C value interval randomly an integer modeling.

**Interval setting of state variable.** Take water demand at the nodes (nodal demand) as an example, the original water demand every moment of each node is fixed value, such as 10 l/s, basic water demand and demand pattern must be input in the dynamic model, basic demand model of water each time multiplied by the amount of water coefficient is the water each time, need before simulation prior input, because users maters are read every two months or one month, it is hard to know exactly water

use volume of each node a certain time, so it needs to set a numerical interval, such as [5, 15], the lower interval according to the actual situation of their input, every time when simulation from all the interval randomly a numerical modeling.

**Control of interval numerical precision.** Pipeline roughness coefficient C value generally is integral, Take [120, 140] interval as an example, the interval of integer 21, respectively for 120,121... 139,140, each time to take a random integer for simulation; The amount of water needed to node precision interval define your own, as a decimal or two decimal places, with the [5, 15] interval as an example, if take a decimal numerical precision, the interval but random numerical including 5.0, 5.1, 5.2,..... 14.9, 15.0; If take two decimal places of numerical precision, the interval but random numerical including 5.00, 5.01, 5.02,..... 14.99, 15.00.

**Stability control of the results.** Each a sampling simulation, get a simulation results, two sample after the simulated results of simulation to get the lower interval, after a sampling each simulation, the modification of the corresponding the lower interval. As the first sample simulation results node pressure for 1 is 20 m, and the second sampling simulation node pressure for 1 is 21 m, the node output interval for 1 [20, 21], if the third sampling simulation of pressure for nodes 1 is 22 m, the modification of the output of node 1 interval for [20, 22], the fourth sampling simulation node pressure for 1 is 19 m, the modification of the 1 output node interval for [19, 22], the more sampling simulation, the more stable interval can be get. Different scale of the network simulation test sample, and concludes that the simulation results interval to the basic stability simulation times, as the basis of simulation times set, so as to different scale, the different sections of the numerical precision sampling simulation Settings reasonable termination conditions.

## Case Study

Put this simple system for double headwater system, node 1 and 7 for water source node, the flow from 1 to the pipeline network is10 l/s, from 7 to the pipeline network is 20 l/s, the node flow for 3, 4, 5, 8 is 7 l/s, 5 l/s, 5 l/s, 13 l/s, node 2 and 6 for transmission node, node flow is zero. The pressure of node 1 is known, the head is 20 m, and the specific properties, see table 1. According to above pipe and node data hydraulic adjustment with, that all the pipe flow and node pressure, seen in table 2.

Table 1. Pipeline and Nodes Properties of Network Deterministic Model

| Pipe | Length (m) | Diameter (mm) | C-value | Node | Demand (*l*/s) |
|---|---|---|---|---|---|
| 6-4 | 1000 | 300 | 170 | 1 | -10.00 |
| 4-2 | 650 | 300 | 50 | 2 | 0 |
| 2-3 | 110 | 150 | 60 | 3 | 7.00 |
| 2-1 | 400 | 200 | 145 | 4 | 5.00 |
| 4-5 | 500 | 200 | 100 | 5 | 5.00 |
| 6-8 | 400 | 250 | 100 | 6 | 0 |
| 6-7 | 1000 | 300 | 170 | 7 | -20.00 |
| 3-8 | 500 | 200 | 100 | 8 | 13.00 |

Table 2. Calculation Results of Network Deterministic Model

| Node | Pressure [m] | Pipe | Flow [*l*/s] |
|---|---|---|---|
| 1 | 20.00 | 6-4 | 5.32 |
| 2 | 19.79 | 4-2 | -4.68 |
| 3 | 19.41 | 2-3 | 5.32 |
| 4 | 19.70 | 2-1 | -10.00 |
| 5 | 19.56 | 4-5 | 5.00 |
| 6 | 19.72 | 6-8 | 14.68 |
| 7 | 19.92 | 6-7 | -20.00 |
| 8 | 19.43 | 3-8 | -1.68 |

Hypothesis model parameters in table 3 ， the uncertainty in the interval is normal distribution, random sampling among those the middle value can get great probability, take out medium on both sides of the small probability. 100 times the random sampling results of simulation see table 4. Finally, using the method of probability and statistics, statistical results of interval probability density distribution (table 4 of 4-5 pipe flow simulation results of interval for [3.5, 6.5].

Table 3. Node Properties of Network Uncertainty Model

| Node | Demand [l/s] | Pressure [m] |
|---|---|---|
| 1 | [-10.2, -9.8] | [19.5, 20.5] |
| 2 | 0 | |
| 3 | [4.9, 9.1] | |
| 4 | [3.5, 6.5] | |
| 5 | [3.5, 6.5] | |
| 6 | 0 | |
| 7 | [-20.4, -19.6] | |
| 8 | [9.1, 16.9] | |

Table 4. Calculation Results of Network Uncertainty Model

| Pipe | Flow [l/s] | Node | Pressure[m] |
|---|---|---|---|
| 6-4 | [2.64, 8.12] | 1 | [19.5, 20.5] |
| 4-2 | [-5.57, -3.69] | 2 | [19.28, 20.30] |
| 2-3 | [4.47, 6.23] | 3 | [18.76, 20.00]] |
| 2-1 | [-10.20, -9.80] | 4 | [19.16, 20.24] |
| 4-5 | [3.50, 6.50] | 5 | [18.92, 20.16] |
| 6-8 | [11.71, 17.59] | 6 | [19.19, 20.25] |
| 6-7 | [-20.40, -19.60] | 7 | [19.39, 20.45] |
| 3-8 | [-3.85, 0.71] | 8 | [18.80, 20.04] |

**New Suggestions For Accuracy Evaluation**

Considering the uncertainty of the model parameter, uncertainty interval of the simulation results can be preliminary quantified by random sampling simulation, node pressure and the simulation results of the pipe flow has some uncertainty, therefore, model checking is no longer the simulation results and the measured curve scatterplot comparison, but look at the proportion of the field observation point fall in the interval of the simulation results (seen in Fig.1).

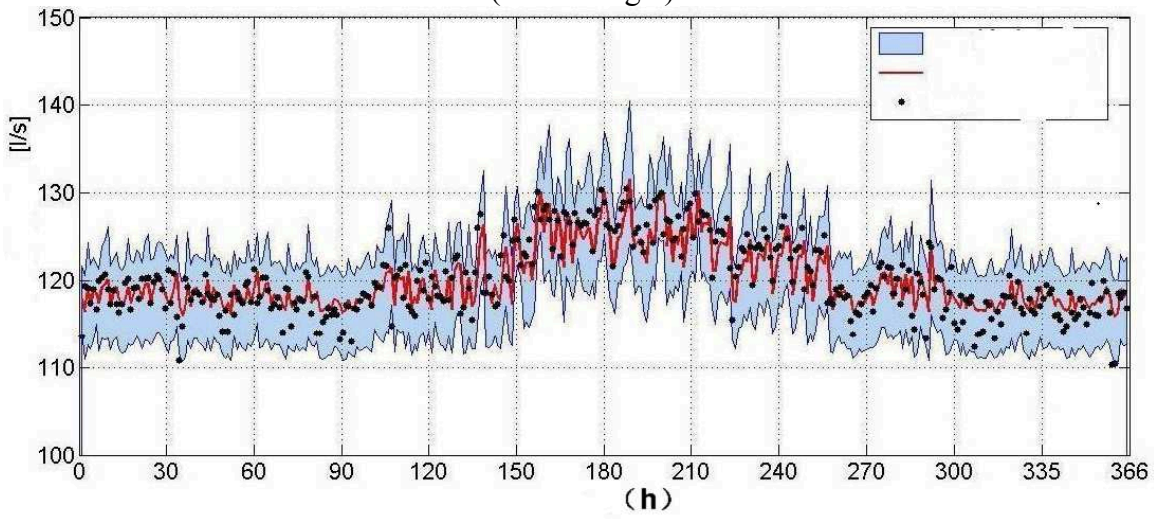


Fig.1 The checking result of the model

The author used to make a comprehensive comparison of the pipe net certainty model accuracy of every international research institutions, and put forward the pipe network model accuracy suitable for China's national conditions[4]. However, with the deepening of the uncertainty research, the simulation results not only, but in certain interval. Through the example analysis of the pipe network model parameters and state variables from the uncertainty of the simulated results of uncertainty, and the simulation method based on random sampling of preliminary quantify the simulation results of the uncertainty of the interval, is put forward based on the analysis of the uncertainty model checking precision analysis new method, the Suggestions model has 90% scattered point fall in the simulation results in the interval for precision of the model.

Water supply network model checking standard belong to the technical requirements and methods of the engineering construction acceptance, with the lack of unity still technical requirements. Because the model checking standard depends on the purpose of the modeling, different uses of the model with a different precision, so a lot of practice can unified technical requirements to the pipe network model checking.

## Conclusions

Water supply network model accuracy evaluation has been no unified technical specifications or standard, the simulation results of the node pressure, for example, proposed 100% pressure monitoring stations measured and simulation value of no more than 2 m or error 3 meters, which is based on static model. For dynamic model, no boundary for all the time to meet the above requirements and average value meet the demands, because most of the time there will be no more than two meters or 3 meters error, but there are a few time beyond this range. In this paper based on the analysis of uncertainty evaluation model has new ideas overcome the defects, and can be used as a reference, but also needs a large number of modeling practice.

## Acknowledgements

Part of this work was supported by National science and technology major project of water pollution control and treatment (2012ZX07403-002) and Shanghai Rising-Star Program (12QB1400900).

## References

[1] Shu, S. H. (2011). Analysis and progress of water supply pipe network system indeterminacy theory [J]. China Water and Wastewater. 27(16):30-33

[2] Shu, S. H. (2011). Water Distribution System Modeling and Simulation with Monte Carlo Method [C]. Proceedings of 2011 International Conference on Economic, Education and Management (ICEEM2011) , Macao, China, March 5-6

[3] Shu, S. H. (2011). Uncertainty analysis of water supply network system based on the random sampling [M]. Postdoctoral report of Tongji university. Shanghai

[4] Shu S. H, et al. (2008). Discussing of model checking standard of water hydraulic and water quality [J]. China Water and Wastewater. 24(18):104-106

*Applied Mechanics and Materials Vols. 580-583 (2014) pp 2398-2402*
*© (2014) Trans Tech Publications, Switzerland*
*doi:10.4028/www.scientific.net/AMM.580-583.2398*

# The selection of priority pipe sections for sewer network renovation

Vladimir Orlov[1, a *], Alexey Andrianov[1, b]

[1]Moscow State University of Civil Engineering, Department of Water Supply, Yaroslavskoye sh. 26, 129337, Moscow, Russia

[a]orlov950@yandex.ru, [b]alexei-waterlab@yandex.ru

**Keywords**: computer program, renovation, trenchless technologies, non-pressure pipes, sewer network

**Abstract.** Operative and planned rehabilitation of old pipe networks, including water disposal systems, is a relevant objective of modern city. It is especially difficult to make pipeline reconstruction works in large cities with high construction area density, transport moving intensity, also full of multifunctional both underground and above-ground infrastructure. All these factors set a lot of restrictions for open excavation methods of pipelines repair and reconstruction. That is the reason why trenchless technologies are becoming more popular among the engineers. A wide range of trenchless techniques provides people with convenient method of fast and effective reconstruction processes in comparison with durable and inconvenient open excavation. This fact leads to a necessity of creating a strategic planning of pipeline rehabilitation. This article presents how to operate the first step of such strategic planning – choosing the priority pipe section for sewer network renovation. The most convenient way for choosing one specific section from a great range is to use a program package based on mathematical algorithm that takes into account a quantity of different factors. This paper presents such a program created by authors and describes its interface, date input and processing.

## Introduction

The process of sewerage renovation includes three interrelated problems: choosing the priority pipe section for reconstruction; finding out an optimal renovation method (trenchless methods take great advantages under the common open excavation methods); providing hydraulic compatibility of existent pipes and new sections in regard with the whole system [1]. Successive and careful systematization and analysis of pipe defects are needed to solve the first problem. For this purpose inventory and television diagnostic research are used in order to determine the main external influence factors. The use of special computer programs allows us to make the process of carrying out all these investigations easier.

The deep investigations concerning this problem including international experience resulted in facing the fact that there is still no finished strategy of choosing the priority object for renovation [2-5]. There are some complicated approaches using artificial neural networks to estimate pipeline network conditions but they are difficult to implement in practice [6, 7]. The process of solving this problem, regarded with the similar conditions but with the use of different techniques, comes to the results, which significantly differ from each other. It happens because of subjective factors prevalence and ways of thinking and making decisions in each strategy are various. Some cities still don't have any strategy of wide-scale failures removing. The regional operating organizations of such cities use so-called «fire-brigade» and «patching the holes» methods. There are some megalopolises where pipe renovation strategy is still under development [7].

## Application example

The developed by authors program automates the process of determining the priority object for renovation with taking into a consideration all factors, which destabilize the pipe network. This program will allow specialists from other countries to carry out the complex analysis of pipe

network condition. In other words, this innovative project makes a great contribution to advancement of trenchless technologies worldwide.

Moreover, without a system of selection the priority renovation objects the increasing of accident condition of the whole pipeline network can't be excluded. The absence of rehabilitation work planning leads to accident frequency increase which in turn results in carrying out immediate off-schedule undesirable rehabilitation work resulting in substantial operational costs. Moreover all these reconstruction and repair operations have a great influence on ecology and social costs. The use of proposed program gives an opportunity to significantly reduce this influence.

It's important to stress, that this project is economically advantageous, because the use of this program doesn't need additional financial investments.

The imaginary town is taken as a basic example (Fig 1a) to show how the program works. Sewer system of this town has been being under operation for 20 years.

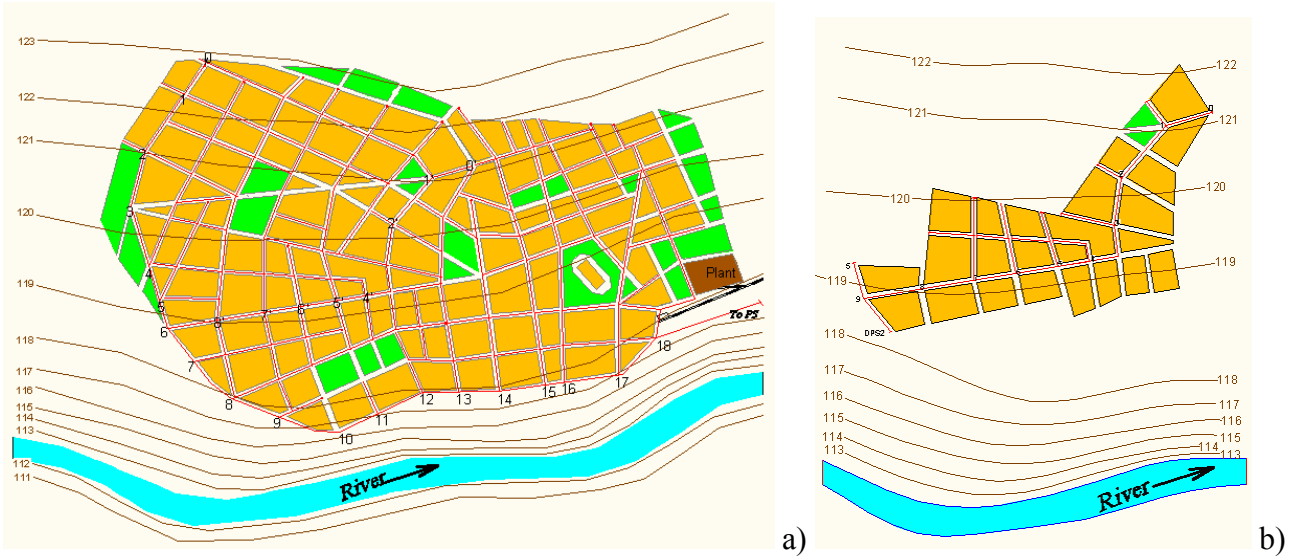


a) b)

Fig. 1. City plan with sewer network (a) and selected fragment (b)

According to the relief of this area, the sewerage scheme was designed as crossed one with one sewerage basin. The pipeline system serves 112 blocks, that is why it is difficult to represent the whole information about it. In order to minimize the number of network sections to examine, a specific fragment was selected (Fig. 1b).

This fragment includes 12 blocks, which are served by the part of the whole sewer network, coming across the center of the town. For the whole system, including the researching fragment, pipe diameters and materials are known. The prevalent pipe material is ceramics.

In given example a complex estimation work was carried out for determining the technical condition of sewerage network. This work was based on taking to a consideration the number of external factors, which have a greatest influence on pipe condition and accident-free work efficiency. All this factors are evaluated on point scale. According to developed algorithm the most worthless condition has the section, which has gained maximum amount of points.

The key factors, which considered to be the most destructive for pipeline systems, include: pipe diameters and materials, water quality, hydraulic characteristics, the setting year and the laying depth of pipes, soil condition, ground water presence and character [1, 8]. These and others factors are represented in rating passports of different sections.

Fig. 2 illustrates the example of such passports. According to the sewer chambers, each pipe section has its own number.

In order to fill in all the positions in this passport, one should use the information from hydro-geological map of the area (Fig. 3), geological map (Fig. 4), the map of transport moving intensity (Fig. 5), including design data and teleinspection results with all pipe failures.

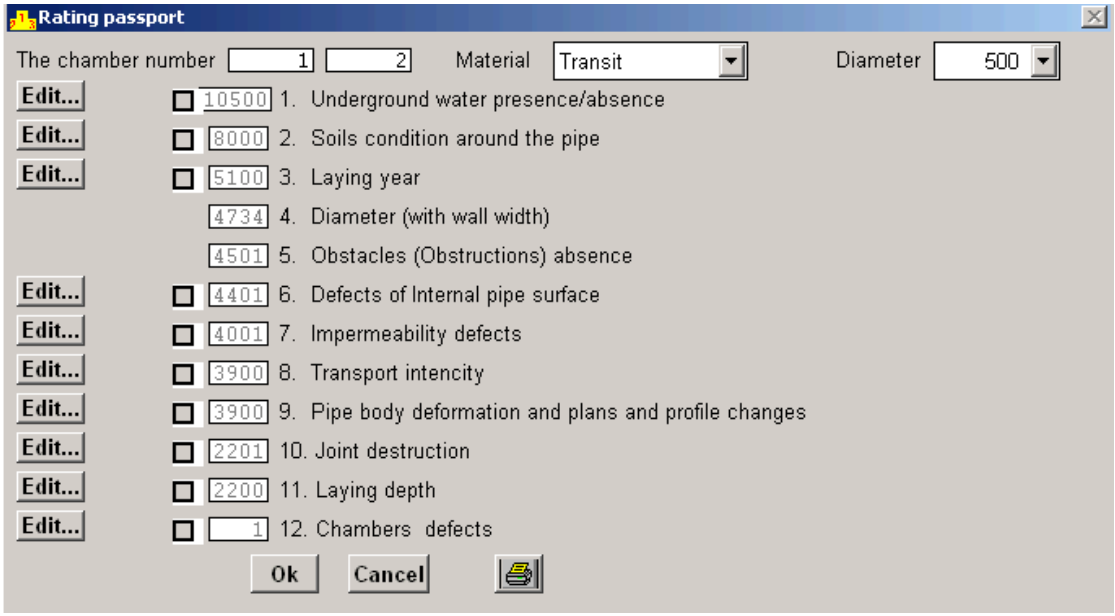


Fig. 2. The example of rating passport for section number 1-2.

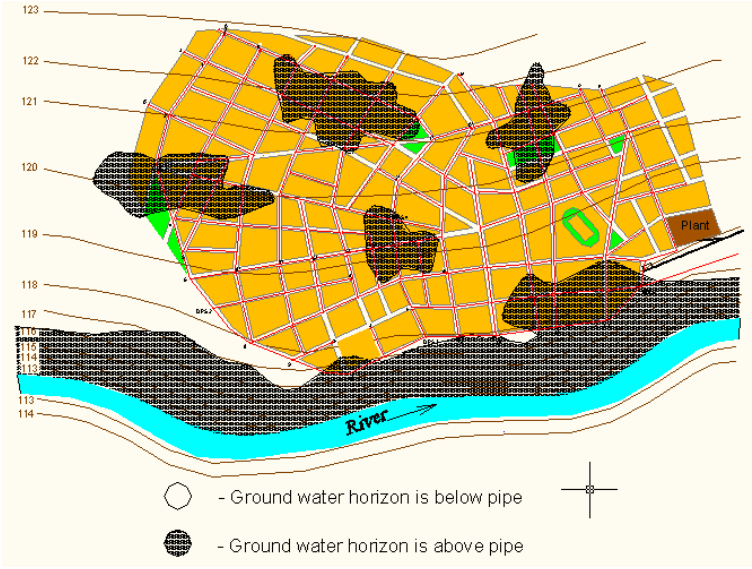


Fig. 3. Hydro-geological map

Fig. 4. Geological map

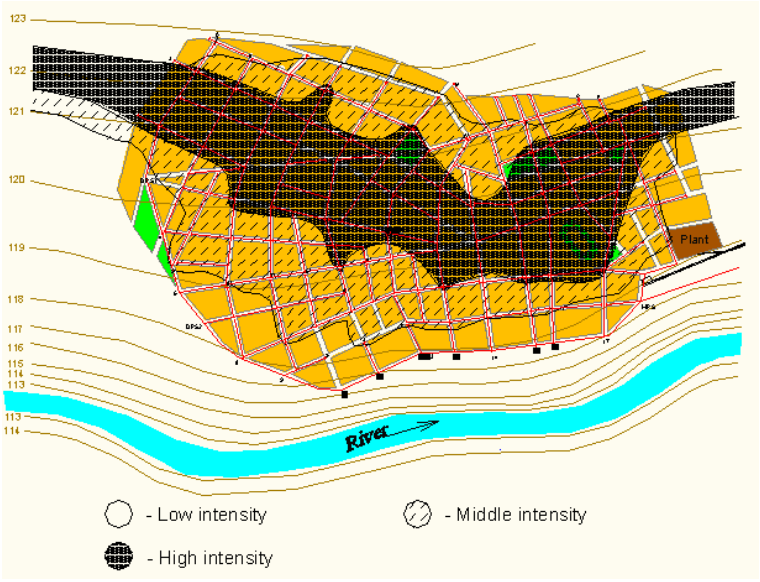


Fig. 5. The map of transport moving intensity

The work of this computer program results in assignment a certain amount of points to each section of the system. According to these points, all sections of concerned fragment can be divided into 2 parts: the priority renovation sections and sections for perspective renovation.

Table 1
The final results of pressure-free sewerage pipes rating

| Chambers | Points | Diameters, mm | Material |
|---|---|---|---|
| 4-5 | 52824 | 400 | C |
| 3-4 | 52574 | 300 | C |
| 2-3 | 52227 | 250 | C |
| 7-8 | 48066 | 600 | A |
| 1-2 | 47866 | 200 | C |
| 0-1 | 47859 | 200 | C |
| 6-7 | 47675 | 500 | A |
| 8-9 | 46574 | 600 | A |
| 5-6 | 47403 | 500 | A |

Material: C (ceramics), I (iron), A (asbestos-cement), P (polyethylene)

The final results (Table 1) represent the rating of studied sections. Having analyzed this table, we can make a conclusion, that the section, limited with the chambers number 4 and 5 (400 mm in diameter, ceramics), which is situated at the top of the table, has the maximum amount of points, so that is why it should be recommended for priority renovation. The section number 5-6 has the minimum amount of points. According to the data obtained, the diagram renovation priority has been made, where each section is represented with its own priority points (Fig. 6).

The diagram also illustrates two possible periods of renovation: the priority renovation area (sections number 4-5, 3-4, 2-3) and the area of perspective renovation (sections number 7-8, 1-2, 6-7, 8-9, 5-6).

## Conclusions

Operative and planned rehabilitation of old pipe networks is a relevant objective of modern city. The computer program was developed to help engineer with planning of renovation priority of sewer networks. The renovation priority based on complex estimation of pipe technical condition compared with all other ones.

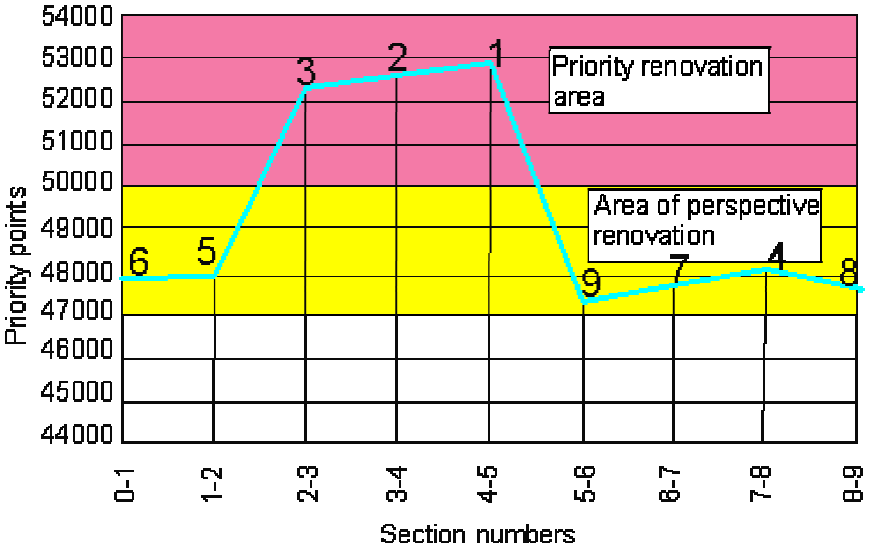


Fig. 6. Diagram of renovation priority

In conclusion it is important to stress, that the data obtained in this program, can't give the final decision about the object which should be renovated first. The printouts serve as the basic materials for specialists (engineers), who ought to make the final decision on renovation of any particular object. In other words, human factor has preferences, while computer program make it possible to carry out the detail complex analysis of pipeline network condition.

**References**

[1] S.V. Khramenkov, The strategy of modernization of water supply networks, Stroyizdat, Moscow, 2005.
[2] R.A. Fenner, Approaches to sewer maintenance: a review, Urban Water 2, Is. 4 (2000) 343-356.
[3] E. Waligorski, The challenge of selecting the right sewer rehabilitation method, International No-Dig 2013 - 31st International Conference and Exhibition, Sydney, Australia, 1-4 September 2013. Paper 2.11.
[4] S.T. Ariaratnam and J. Matthews, Research roadmap for main breaks, International No-Dig 2013 - 31st International Conference and Exhibition, Sydney, Australia, 1-4 September 2013. Paper 2.7.
[5] S.V. Khramenkov, V.A. Orlov and V.A. Harkin, The process of water disposal system's rehabilitation optimization, Stroyizdat, Moscow, 2002.
[6] V. Sousa, J.P. Matos and N. Matias, Evaluation of artificial intelligence tool performance and uncertainty for predicting sewer structural condition, Automation in Construction 44 (2014) 84-91.
[7] R. Jafara, I. Shahroura, I. Juranb, Application of Artificial Neural Networks (ANN) to model the failure of urban water mains, Math. and Comp. Modelling 51, Is. 9-10 (2010) 1170-1180.
[8] V.A. Orlov, Engineering infrastructure construction and rehabilitation, Academy, Moscow, 2010.

*Applied Mechanics and Materials Vols. 580-583 (2014) pp 2403-2407*
*© (2014) Trans Tech Publications, Switzerland*
*doi:10.4028/www.scientific.net/AMM.580-583.2403*

# Hydraulicsoflooping

Julia Zolotova[1, a *]

[1]Polytechnicheskaya str.,29, Saint-Petersburg, Russia

[a]yszolotova@gmail.com,

**Key words:** looping, pressure loss, hydraulic resistance, the actual distribution of expenses, energy efficiency

**Abstract:**This article describes the urgency of studying the reduction of hydraulic loss in terms of energy efficiency.

*Looping* is a section of the pipeline, which is laid in parallel with the main pipeline. Distribution of expenses on Looping`s branches in the valid movement minimizes dissipation in the flow and, consequently, reduces the energy losses in the piping network.

Literature describes the calculation of a system of parallel lines through quite cumbersome calculations. The purpose of this work is to create a method of simple and quick calculation of looping.

The article describes the simplest case of the connection: every branch does not contain any nodes, neither a source nor wastewater. Testing calculation of looping is represented in three conditions: looping`s resistance coefficient shown, partial expenses` calculation is transformed to rotating circulants and looping`s statics equations coincide with necessary condition of a minimum.

## Introduction

Nowdays energy efficiency is the main strategic objective of the energy policy of all countries and Russia as well. Of course it entails the development of the legal framework that is proved by emergence of Federal law of November 23, 2009 N 261-FZ «On energy saving and increasing energy efficiency and about modification of separate acts of the Russian Federation»and of standard GOST R 50001 «Energy management systems. Requirements and guidelines». As a result, the market of energy-saving materials and technologies is rapidly developing. However, there are not enough solutions for reducing energy losses in the piping network, caused byviscous friction, so-called pressure losses.

Considering that the operation of pumps and fans spends up to 80 % of electricity in life-support systems of building, reduction of hydraulic losses will reduce the power inputs of the buildings.

This article is dedicated to a construction, which can be regarded as part of a package of energy efficiency measures – looping. It is a parallel joint of downstream conduit, widely used in hydraulic networks for division and connection of streams of hot and cold water or air. The flow of transported product in the main pipeline is reduced in the area oflooping. That reduces the total loss of pressure at overcoming the hydraulic resistance. Therefore, capacity ininvariable pressure pipeline increases the more significant the more cross-sectional area of looping is.

Settlement scheme of looping is shown on picture 1. Flow separation is in point 1 (site - source) and connection of flows occurs in point 2 (site - runoff).

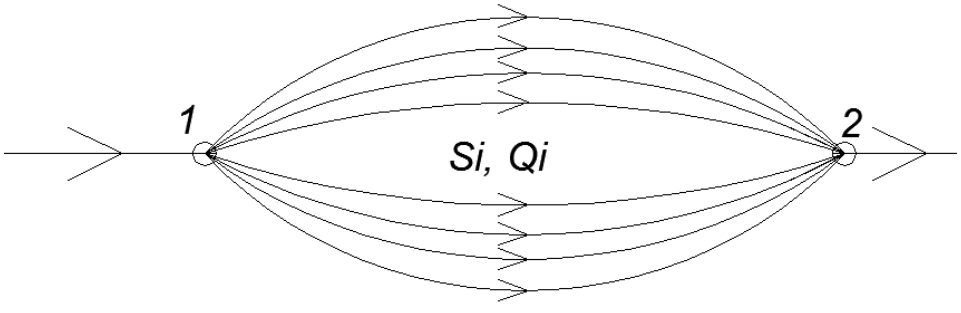


Pic. 1 Scheme of looping

In the elementary case, which is considered in the article, it is supposed that every branch ($S_i$, $Q_i$) doesn`t contain joints, sources, nor runoffs.

**Literature review and research objective:**Today great attention is paid tothe question of reducing of pressure losses [1-26].

However, a review of material related specifically to the application looping showed almost no sources.

The purpose of this work is to test a simple method of calculation of systems of parallel lines (looping).

According to that authors were faced by the following tasks:

1. Transformation of partial expenses` calculation to rotating circulants
2. Development of simple algorithm of variation in any order

**Research description:** Pressure loss [26-27] in every branch is calculated by the formula

$$h_r = S_i Q_i^2, \tag{1}$$

where $Q_i$ –partial expense in i-th branch, $S_i$ - resistance coefficient in i-th branch, which is defined by this formula

$$S_i = \left(\frac{\lambda_i}{D_i} \cdot l_i + S_i\right) \cdot \frac{1}{2g \cdot A_i^2}, \tag{2}$$

where $\lambda_i$ - coefficient of hydraulic friction, $D_i$ - diameter of cross-section, $l_i$ –length of the branch, $A_i$ - area of cross-section.

For hydraulically long pipeline

$$S_i = \frac{l_i}{K_i^2}, \tag{3}$$

where $K_i$ - resistance module.

Then method of calculation of looping can be represented by the following 3 theorems:

1. Looping`s resistance coefficient will be:

$$S = \frac{1}{\left(\sum_{i=1}^{n} \frac{1}{\sqrt{S_i}}\right)^2} \leq \min(S_i)_i^n = 1. \tag{4}$$

Actually, if

$$h_r = S_i \cdot Q^2, \tag{5}$$

and

$$Q = \sum_{i=1}^{n} Q_i, \tag{6}$$

then

$$\sqrt{\frac{h_r}{S}} = \sum_{i=1}^{n} \sqrt{\frac{h_r}{S_i}}. \tag{7}$$

The inequality is obviously a consequence of an inequality of Cauchy. Looping`s coefficient of resistance doesn't surpass resistance of the branch with the maximum throughput (with the minimum resistance).

2. Partial flow [28] is :

$$q_i = \frac{Q_i}{Q} = \frac{\sqrt{S_{\alpha i} \cdot S_{\alpha i+1} \ldots S_{\alpha n-1}}}{\sum_{j=1}^{n} \prod_{j=1}^{n-1} \sqrt{S_{\alpha j} \cdot S_{\alpha j+1} \ldots S_{\alpha j+n-1}}}, \tag{8}$$

where $\alpha_{i,\ldots}$ , $\alpha_{n-1} \neq i$, $n \geq 2$.

For example, for looping that consists of 4 branches :

$$q_1 = \frac{\sqrt{S_2 S_3 S_4}}{\sqrt{S_1 S_2 S_3}+\sqrt{S_2 S_3 S_4}+\sqrt{S_3 S_4 S_1}+\sqrt{S_4 S_1 S_2}}, \quad (9)$$

$$q_2 = \frac{\sqrt{S_3 S_4 S_1}}{\text{denom}}, \quad (10)$$

$$q_3 = \frac{\sqrt{S_4 S_1 S_2}}{\text{denom}}, \quad (11)$$

$$q_4 = \frac{\sqrt{S_1 S_2 S_3}}{\text{denom}}, \quad (12)$$

where$\text{denom} := \sqrt{S_1 S_2 S_3} + \sqrt{S_2 S_3 S_4} + \sqrt{S_3 S_4 S_1} + \sqrt{S_4 S_1 S_2}$.

It easy to notice, that there is a cycle of combinations of n by n-1 numbersin the denominator and a cycle of combinations of n-1 – numbers (that do not contain an index i) in numerator.

3. In the actual motion we can use Kelvin`s principle of minimum dissipation [29-32], that is described by the formula:

$$\sum_{i=1}^{n} S_i q_i^3 \rightarrow \min, \sum_{i=1}^{n} q_i = 1, \quad (13)$$

Formula of Lagrange satisfies that condition (13):

$$L_\lambda(\vec{q}) = \sum_{i=1}^{n} S_i q_i^3 + \lambda \cdot \sum_{i=1}^{n} q_i, \quad (14)$$

On achievable partial expenses works such equality for all i ϵ 1(1)n:

$$S_i q^2 + \frac{\lambda}{3} = 0, \quad (15)$$

It means, that all $S_i q^2$ are equal andthis leads to the 1st and 2ndtheorems . So the actual distribution of expenses along the branches of looping brings to the smallest value of dissipation in the flow, that crosses looping.

This 3rd theorem is used by K.I. Strahovich for calculation of pipeline systems [34].

**Conclusion:**

Thus much easier and less labor-consuming calculation looping has been tested. Itsalgorithmcanbedividedinto 3 conditions:

1. Looping`s coefficient of resistance doesn't surpass resistance of the branch with the minimum resistance.
2. Calculation of partial flow is reduced to calculating fractions.
3. Looping`s statics equations coincide with necessary condition of a minimum.

**References:**

[1] Girgidov A.D., Prokof'ev V.A. Numeric modeling of the interaction of a turbulent flow and a granular medium // Water Resources. 1992. T. 18. № 2. P. 128-134.

[2] Tseytin D. N., Nemova D. V., Kurasova E. V. Autonomous power installation with complex power effective electroproviding // Construction of Unique Buildings and Structures. 2013. №5 (10). P.1-11 (rus)

[3] M. Saberia, H. Arabzadehb, A. Keshavarzc. Numerical Analysis of Buried Pipelines with Right Angle Elbow under Wave Propagation // Procedia Engineering. Volume 14. 2011. P. 3260–326.

[4] Girgidov A.A., Girgidov A.D., Fedorov M.P. Use of dispersing springboards to reduce near-bottom velocity in a toe basin // Power Technology and Engineering. 2012. T. 46. № 2. P. 113-115.

[5] Bukhartsev V.N., Petrichenko M.R. Approximation of the depression curve of the inflow to an ideal trench // Power Technology and Engineering. 2011. T. 44. № 5. P. 374-377.

[6] Girgidov A.D. Self-aeration of open channel flow // Power Technology and Engineering. 2012. T. 45. № 5. P. 351-355.

[7] Girgidov A.D. Calculating the liquid flow from a hole in a pressurized pipeline // Power Technology and Engineering. 2001. T. 35. № 7. P. 348-352.

[8] Hsu-HaoYanga, Yen-Liang Chen. Finding K shortest looping paths with waiting time in a time–window network // Applied Mathematical Modelling. Volume 30. Issue 5. May 2006. P. 458–465.

[9] Girgidov A.D. Evaluation of water-hammer reduction in a pipe containing a deformable body // Power Technology and Engineering. 2010. T. 44. № 1. P. 10-14

[10] Altshul A.D. Gidravlicheskiyesoprotivleniya [Hydraulic resistance]. M.:Nedra, 1970. 216 p. (rus)

[11] Bukhartsev V.N., Petrichenko M.R. Condition of mechanical-energy balance of an integral flow with a variable rate // Power Technology and Engineering. 2001. T. 35. № 4. P. 189-194.

[12] Petrichenko M.R., Khar'kov N.S. Experimental study of the pumping action of helical flow // Technical Physics. The Russian Journal of Applied Physics. 2009. T. 54. № 7. P. 1063-1065.

[13] Bukhartsev V.N., Petrichenko M.R. Nonsteady filtration in a uniform soil mass // Power Technology and Engineering. 2012. T. 46. № 3. P. 198-200.

[14] Bukhartsev V.N., Petrichenko M.R. Problem of filtration in a uniform rectangular soil mass is solved by variational principles // Power Technology and Engineering. 2012. T. 46. № 3. P. 185-189.

[15] Bukhartsev V.N., Petrichenko M.R. Nonsteady filtration in a uniform soil mass // Power Technology and Engineering. 2012. P. 1-3.

[16] Bukhartsev V.N., Petrichenko M.R. Problem of filtration in a uniform rectangular soil mass is solved by variational principles // Power Technology and Engineering. 2012. P. 1-5.

[17] Andriyashev M.M. Gidravlicheskiyeraschetyvodoprovodov i vodoprovodnykhsetey [Hydraulic calculations of water pipelines and water mains]. 109 p. (rus)

[18] Petrichenko M.R. Spravochnikkonstruktora [Designer`s compendium]. SPb. Politekhnik. 2006. P. 419-445. (rus)

[19] Molodtsov N.I., Petrichenko M.R. Opredeleniyeintensivnostiteplootdachi v sistemezhidkostnogookhlazhdeniyavtulkitsilindra [Determination of the intensity of heat transfer in liquid cooling system of cylinder liner]. // Dvigatelestroyeniye. №10. 1982. P. 27-29. (rus)

[20] Petrichenko M.R. Konkretnyyezadachigidravlikiperemennogoraskhoda [The specific tasks of hydraulics variable rate]// Lectures and reports of the 12-th international school on hydrodynamics. M.: RAN. 1999. P.131-133. (rus)

[21] Petrichenko M.R., Van Yuyyan. Gidravlicheskiyezadachiraschetasistemokhlazhdeniya // Dvigatelestroyeniye (K 100-letiyu N.Kh. Dyachenko) [Hydraulic calculation tasks cooling systems] // Propulsion engineering.SPb.SPbGU. 2004. P. 105-114. (rus)

[22] Bukhartsev V.N., Petrichenko M.R. Gidravlicheskaya forma usloviyaekstremumadissipatsiimoshchnostidlyabeznapornykhpotokov v prizmaticheskikhruslakh [Hydraulic shape extremum conditions dissipation power for gravity flows in rectangular channels]// Magazine of Civil Engineering. 2008. №2. P. 5-7. (rus)

[23] Babenko A. P., Strelez I. V. Hydraulic size, as the main characteristic in calculating sump // Construction of Unique Buildings and Structures, 2013, №6 (11). P.34-42.(rus)

[24] Chunxia Long, Jianyu Guan. A method for determining valve coefficient and resistance coefficient for predicting gas flowrate // Experimental Thermal and Fluid Science. Volume 35. Issue 6. September 2011. P. 1162–1168.

[25] Y. Peet , P. Sagaut, Y. Charron. Pressure loss reduction in hydrogen pipelines by surface restructuring // International Journal of Hydrogen Energy. Volume 34. Issue 21.November 2009. P. 8964–8973.

[26] GáborFekete, LászlóVarga. The effect of the width to length ratios of corrosion defects on the burst pressures of transmission pipelines // Engineering Failure Analysis. Volume 21. April 2012 . P. 21–30.

[27] Young-Do Jo, Daniel A. Crowl. Individual risk analysis of high-pressure natural gas pipelines // Volume 21. Issue 6. November 2008. P. 589–595.

[28] I.G. Baoku , B.I. Olajuwon , A.O. Mustapha. Heat and mass transfer on a MHD third grade fluid with partial slip flow past an infinite vertical insulated porous plate in a porous medium // International Journal of Heat and Fluid Flow. Volume 40. April 2013. P. 81–88.

[29] Petrichenko M.R. Extrem characteristics, available surface and «the principle of minimum dissipation» for gravity flows [Ekstremali, kharakteristiki, svobodnyyepoverkhnosti i «printsipminimumadissipatsii» dlyabeznapornykhpotokov] // Scientific-technical compendium of SPbSPU. 2013. №166. P.179-182. (rus)

[30] ShpakovskiyR.Yu. Printsipminimumadissipatsii i identifikatsiya temperatury poverkhnosti ispareniya [The principle of minimum dissipation and identification of surface temperature evaporation] // News of higher education institutions. Problems of energy. 2012. №7-8. P.34-45. (rus)

[31] Giorgio Sonnino, JarahEvslin. The minimum rate of dissipation principle // Physics Letters A. Volume 365. Issues 5–6. 11 June 2007. P. 364–369.

[32] H. Kozlu, B.B. Mikic, A.T. Patera Minimum-dissipation heat removal by scale-matched flow destabilization // International Journal of Heat and Mass Transfer. Volume 31. Issue 10. October 1988. P. 2023–2032.

[33] Tao Sun, Paul Meakin, Torstein Jøssang A minimum energy dissipation model for drainage basins that explicitly differentiates between channel networks and hillslopes // Physica A: Statistical Mechanics and its Applications. Volume 210. Issues 1–2. 15 September 1994.P. 24–47.

[34] StrakhovichK.I..Prikladnayagazodinamika [Applied gas dynamics] L-M.:ONTI,1937. 113 p. (rus)

*Applied Mechanics and Materials Vols. 580-583 (2014) pp 2408-2411*
*© (2014) Trans Tech Publications, Switzerland*
*doi:10.4028/www.scientific.net/AMM.580-583.2408*

# The Water Usage Method and Spatial Structure Type of Spring Village in Northern China

Yawei Kong[1, a]

[1]College of Architecture and Urban Planning, Shandong Jianzhu University,

Jinan, P. R. China, 250101

[a]kywnd@163.com

**Keywords:** Spring village, water usage, spatial structure, type, conservation

**Abstract.** Spring village is a widely existing type of human settlement in northern China, the spring water usage with natural environment is the main factor of the heterogeneous spatial structure in spring village. By the analysis for hierarchically usage of multi-kind values, this paper introduces the spatial structure and feature of typical villages under the views of living, manufacture, ecology and landscape. Meanwhile, based on the combination of modern function requirement and spring water usage, the settlement-spatial conservation, which relies on natural environment, is seen as the essential way for the sustainable development of spring settlement.

## Introduction

As the living area by adapting and utilizing nature, human settlement not only provides various spaces for living and relaxing etc., but is the place for manufacture. [1] In the development period, local nature environment decides the eternal form and internal space of settlement. Especially the area with spring water became the first choice for ancient people to living. Through the activities of living, manufacture and social communication, spring settlement has been one of typical settlement for combining spring water with topography.

In northern China, for the widely existing karst groundwater system, most villages in which people live and produce with spring water are built for the wisdom of utilizing nature resources. Through the integrated research of the water usage and spatial structure in spring village, the conservation strategies which ensure the optimizing use of spring water and sustainable development of spring village, are provided to satisfy the multiple requirement of living, manufacture and landscape.

## Basic Principle

In northern China, the emerging areas of spring water are always in mountains or on the plains near mountains, the distribution of spring villages thereby is determined, [2] the emerging amount of spring water is determined by the water-collection area of supplying and the pressure. While at the top of mountain slope, for the less area and pressure, the limit spring water only satisfies living of small village. Near the valley or beach, to avoid the latent danger of fluid or humid, the villages are built on the high spaces and wells are excavated for water supply, the areas near spring are utilized for farm or cultivation. The best situation is the spring water emerges on the foot of mountain, in the alley and on the plain close to mountain, different kinds of spring villages are appeared for the various combinations between spring-emerging forms and local environments.

The emerging forms of spring water are decided as punctiform well, linear stream and regional pond for the form of water, also as the static collecting water area and the dynamic overflowing stream. In reality, the layouts and forms of villages are determined by the different emerging ways and various drawing methods. In Fig. 1, with static well or less-overflowing pond, the spring water always becomes the center of villages, as well as be utilized only for living, meanwhile the larger ponds appear the effects of regulating the micro-climate and beautifying the environment. If the spring emerging amount reaches certain scale, shown in Fig. 2, various dynamic spring water forms,

such as pond with overflowing water and stream, come into being, the structure of villages always becomes linear form by the overflowing water, the spring water is utilized not only for living, but for irrigation, cultivation, production and other manufacture ways, as well regulating climate, beatifying environment and other ecological and landscaping requirement.

Fig. 1 Spring as the center of village
——Xichexiang Village,Jinan City

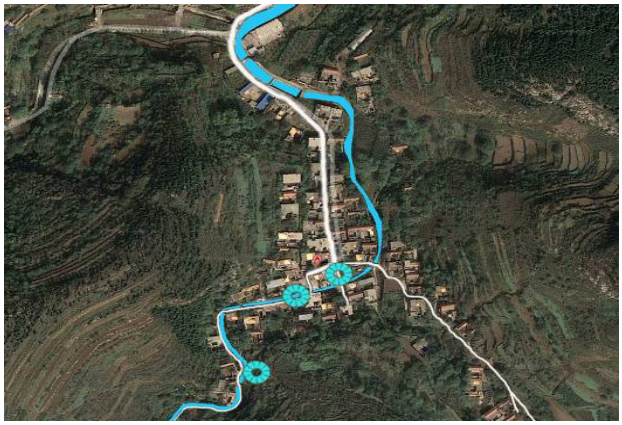

Fig. 2 Village space along the river
——Yuhequan Village,Jinan City

## Water Usage and Space Structure

**Living.** The space structure of villages, in which the living value of spring water appears, is determined by the emerging form of spring water. As Fig. 3 shown, the emerging forms of spring water that influence the space structure of this kind villages rely on present three kinds as static water without overflowing, static water with overflowing and dynamic stream with overflowing. Towards the static water, two situations are presented as out of village and in village. Therefore, dynamic stream with overflowing is always combined with village tightly, and treated as the main influent fact for the space structure of village.

| Spring Form | Location | Usage Method | Space Structure | Typical Case | Diagram |
|---|---|---|---|---|---|
| Well (Static water) Without overflowing water | In village | Directly drinking and washing, in modern, using piper and pump for water. | Spring as the center of village, public place around spring water. | Xichexaing Village (Zhangqiu Town, Jinan City) | |
| | Out of village | Taking water by hand or piper, terrace farmland along the lane. | The main road along the lane of taking water, buildings around the road. | Heilongyu Village (Licheng Town, Jinan City) | |
| Well or Pond (Static water) With overflowing water | In village | Emerging water for drinking, overflowing water for washing. | Static water as the center, the main part of village along overflowing water. | Yuhequan Village (Licheng Town, Jinan City) | |
| | Out of village | Hidden piper for taking water by height difference or pump, overflowing water for landscape. | Linear space structure along overflowing water. | Xilihu Village (Zhangqiu Town, Jinan City) | |
| Stream (dynamic water) With overflowing | In village | Dynamic water utilized besides living. | Village along the stream or overflowing water. | Nanduo Village (Zhangqiu Town, Jinan City) | |
| Legend | village farmland pond road water piper spring | | | | |

Fig. 3 The space structure of villages in which the spring water is utilizing for living

**Manufacture.** The manufacture-value of spring water is influenced mostly by the emerging amount, after living usage; the rest spring water is taken mainly for farm or cultivation, otherwise for producing or industry. In Fig. 4, because of the higher requirement of land in manufacture, the producing area is parallel arranged with village, the emerging point of spring water becomes the major factor to influence the space structure of village. Meanwhile, the space of village is influenced by dynamic water which appears in the village.

| Usage | Location | Usage Method | Space Structure | Typical Case | Diagram |
|---|---|---|---|---|---|
| Farm | In village | Overflowing water passing farmland with additional living and landscape value. | Spring and overflowing water in the middle of village and farmland. | Touquan Village (Jingxing Town, Shijiazhuang City) | 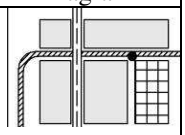 |
| | Out of village | Overflowing water passing farmland directly, pumping station for water. | Spring along the village, part of the village along overflowing water. | Zhongtao Village (Dongping Town, Taian City) | 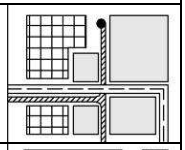 |
| | | Spring water taken by piper or pump for farming, landscape value appearing. | The emerging point of spring water as the center of village and farmland. | Xincheng Village (Taian District, Taian City) | 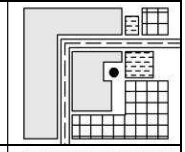 |
| Culti-vation | In village | Cultivation along the overflowing water with additional landscape value. | Less influence of spring water for the space of village, the space around overflowing appearing flexible. | Shangquan Village (Daiyue District, Taian City) | 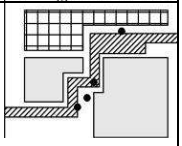 |
| | Out of village | Taking spring water to pond by channel, for cultivation as planting lotus or feeding pig and fish. | Spring water separated from village. The space structure of village appearing Checkerboard form. | Zhifang Village (Daiyue District, Taian City) | 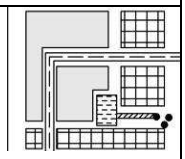 |
| | | Huge emerging amount of spring water for large area fishing pond. | The road connecting spring water and village influencing the space structure of village. | Potou Village (Jingxing Town, Shijiazhuang City) | 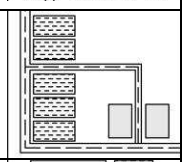 |
| Produce | In village | Canning drinking wate. | Spring emerging point as the center of village and static water. | Longquan Village (Yicheng District, Zhumadian City) | 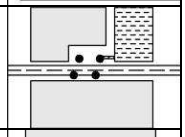 |
| | Out of village | Better quality for spring water. | Spring water besides village with less influence. | Jiunvquan Village (Dongping Town, Taian City) | 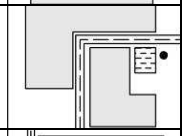 |
| Industry | In village | Gold industry poplar in history, and influencing village space and custom. | Spring water as the center of village and farmland. | Tongjing Village (Yinan Town, Linyi City) | 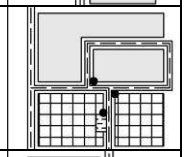 |
| | Out of village | Abundant spring water for pottery industry. | Spring water influencing lowly the space structure of village. | Hongshan Village (Jiexiu Town, JiInzhong City) | 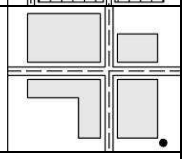 |
| Legend | village farmland pond road water piper spring | | | | |

Fig. 4 The space structure of villages in which the spring water is utilizing for manufacture

**Landscape**. Emerging forms, which include punctiform well, linear stream and regional pond, are the first influent factor for the ecological and landscaping values of spring water. In Fig. 5, Temples and trees are always arranged in the social area of punctiform well which is the main source of

water, but the ecological value is not outstanding. While near the dynamic overflowing stream or static gathering pond, on the one hand constant-temperature spring water appears important ecological value of regulating temperature, eliminating dust and protecting species diversity, on the other hand the landscape environment of spring character appears in the practice of utilizing the synthetical values of spring water.

| Emerging Form | Spring Form | Usage Method | Space Structure | Typical Case | Diagram |
|---|---|---|---|---|---|
| Punctiform well | Wells part of which connecting overflowing water | Spring as the public area and core of landscape, with less ecological value | Spring as the center of village, coexisting springs as the muiti-center of same village | Xiaosi Village (Zhangqiu Town, Jian City) | 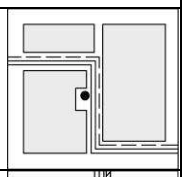 |
| Linear stream | With overflowing water or several springs | Higher ecological and landscaping values, important effects for living and manufacture | Space structure along the overflowing water, part of village around the water | Yuhequan Village (Changqin Town, Jian City) | 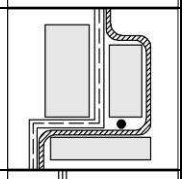 |
| Regional pond | Large area pond with overflowing | Higher ecological and landscaping values for farm and cultivation | Gathering water as the center of village and land, spring as the core of public place | Nanmi Village (Linzhou Town, Anyang City) | 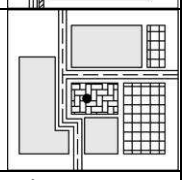 |
| Legend | village farmland pond road water piper ● spring | | | | |

Fig. 5 The space structure of villages in which the spring water is utilizing for landscape

Especially in typical villages, such as Niangziguang Village in Yangquan City and Huangsi Village in Xingtai City, more than two emerging kinds of spring water exist, meanwhile the living, producing, ecological and landscaping values appear, the space structure presents typical features of spring village. [3]

## Conclusion

"Dwelling by spring water" is the wisdom of ancient people to living with nature, while special natural environments induce abundant space structures of spring villages. [4] As special case of utilizing nature, the practices of utilizing synthetical values of spring water, create different special structures of spring villages; reflect the ecological wisdom of living with nature, and present higher values of history and culture. Under the pressure of modern life, the values of spring water are ignored; the style and features of most spring villages disappear in modern construction. For ecological civilizing construction becomes one of the basic national strategies, it is urgent to protect spring villages with ecological wisdom, the essential way for the sustainable development, presents as the conservation of space structures and features by not only combining modern requirement with values of spring water, but utilizing spring water according of natural environment.

## Acknowledgements

This work was financially supported by National Natural Science Foundation of China (project No.:51178256).

## References

[1] Information on http://baike.baidu.com/view/355562.htm

[2] Y.P. Liang, W.T.Wang: submitted to Acta Geoscientica Sinica (2010).

[3] F. Gu: submitted to New Architecture (2010).

[4] J.H. Zhang, L.N. Wang: submitted to Architectural Journal (2007).

# CHAPTER 9:

# Heating, Gas Supply, Ventilation, Air Conditioning Works and Daylighting Design

*Applied Mechanics and Materials Vols. 580-583 (2014) pp 2415-2420*
*© (2014) Trans Tech Publications, Switzerland*
*doi:10.4028/www.scientific.net/AMM.580-583.2415*

# Simulation and analysis of thermal performance of internal recycle double skin facades

Cun Hui[1,2,a], Yuanqing Wang[2,b], Bin Wang[1,c], Wei Tao[1,d] and Shenglin Zheng[1,e]

[1]Jangho Group Company Limited, Beijing, 101300, China

[2]Department of Civil Engineering, Tsinghua University, Beijing, 100084, China

[a]huicun@jangho.com, [b]wang-yq@mail.tsinghua.edu.cn, [c]wangbin06@jangho.com, [d]taowei@jangho.com, [e]Ericzheng@jangho.com @jangho.com

**Keywords:** Double Skin Facades, Thermal Performance, CFD, Comprehensive Heat Transfer Coefficient, Thermal Channel

**Abstract.** Simulation and analysis of heat transfer process in internal recycle double skin facades(DSF) of the established standard model were carried out by computational fluid dynamics(CFD). Comprehensive heat transfer coefficient under the condition of different ventilation rate of DSF with and without blinds was studied. The results show: the increase of the ventilation rate can not only improve the comprehensive heat transfer coefficient, but also improve the temperature of inner surface of the inner curtain wall. Double skin facades can improve the comfort level of the indoor environment, reduce the energy loss of the palisade structure and reduce energy consumption.

## Introduction

The glass curtain wall is used more and more widely in high-rise building in recent years. Its thermal performance is a important indicator about the energy saving effect of the whole building. Double skin facades can stabilize the temperature and illumination of the indoor environment and strengthen the function of ventilation and air change on the one hand; and can improve the thermal insulation ability, reduce the noise outside and save energy on the other hand. So the DSF will become one of the new development direction of environmental protection and energy saving. Technology.

Most DSF studies now are based on CFD simulation. Many researchers (Stec 2003, Howell 2001, Safer 2005, Manz 2004, Tanaka 2009, Gratia 2004, 2007) have studied the ventilation and the thermal performance of the DSF. The DSF has good engineering application value and good market prospect. As the more and more using of the DSF, accurate analysis on the performance of the DSF and determination of its economic performance and energy saving effect have become the urgent need of social development.

Simulation and analysis of DSF of the established standard model were carried out by using the software Fluent. The performance of the DSF under the condition of different ventilation rate was studied.

## Analysis model

**Structure and parameters.** The standard model of the paper is internal recycle DSF, the schematic diagram of it is shown in Fig. 1. The Fig. 1 (a) shows the detalis of the cross section about DSF with blinds and the dividing of the cross section which can be imported to the Gambit as areas to be mapped. The Fig. 1 (b) shows the detalis of the cross section about DSF without blinds and the dividing of the cross section which can be imported to the Gambit as areas to be mapped.

**Dimension details.** Plate size is 1500mm×3000mm. The width of the thermal channel is 300mm. The cross sectional dimension of outlet, which is in the middle position at the top of the DSF, is 100mm×100mm.

**Physical model.** The outer glass wall is insulating glass, the inner of which is air. The thickness of the outer glass wall is 6mm+12mm+6mm. The inner glass wall is 6mm thickness full tempered glass. The aluminum blind is 3mm thickness.

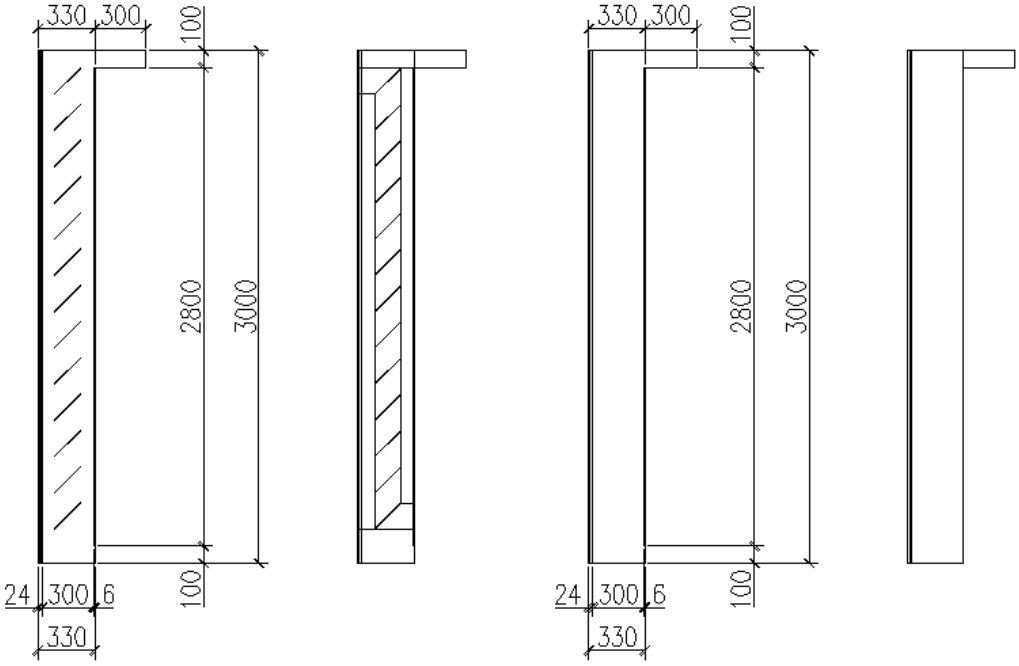


(a) (b)

Fig. 1 Standard model of the internal recycle DSF

**Boundary conditions.** The temperature of indoor and outdoor air are 20°C and -20°C respectively. The convective heat transfer coefficient of indoor and outdoor air are 3.6W/($m^2$•°C) and 16W/($m^2$•°C) respectively. The wind speed of outlet is 1.35m/s.

**Steps of analysis.**

(1) The standard model is established by AutoCAD as Fig. 1 (a). The model is seperated as quadrangles and the quadrangles are transformed to surface units, which are shown in Fig. 1 (b). Then the standard is exported and saved as *.sat file.

(2) Through software Gambit, the*.sat file is imported and all the surface units are meshed as structured grids which are extruded to 1500mm form a standard volumn.

(3) The cell zone conditions and boundary conditions are defined through software Gambit, and the *.mesh file is exported.

(4) The *.mesh file is imported in Fluent and the relevant parameters are defined. Then the calculation of the standard model is carried out and the post processing is made.

## Results and analysis

**Flowing of air layer.** The flowing of the air layer in the DSF is an important characteristic about the DSF and is the key indicator about the thermal performance, ventilation and energy saving. The velocity distribution of the middle section of the internal recycle DSF with blinds and without blinds are shown in Fig. 2 and Fig. 3, respectively.

It can be seen that: (1) the air flows out throuth the fan under the action of airflow, and in order to keep balance, it need the air flows in the air layer. This process can discharge the indoor heat, reduce the indoor temperature and improve the indoor comfortableness. (2) The air speed near the top of air inlet of inner and outer glass wall is faster than other space. (3) Because of the existence of blinds, there is reverse flow between the blinds. (4) The velocity of the DSF with blinds (4.65 m/s) is larger than the DSF without blinds (3.18 m/s). (5) The velocity distribution of the DSF without blinds is much more regular than the DSF without blinds.

From the above, the air flow in the air layer can bring the indoor heat into the air layer of the DSF, which can stabilize the temperature in a certain range. So the double skin facades have great thermal performance and can improve the comfortableness of the indoor environment.

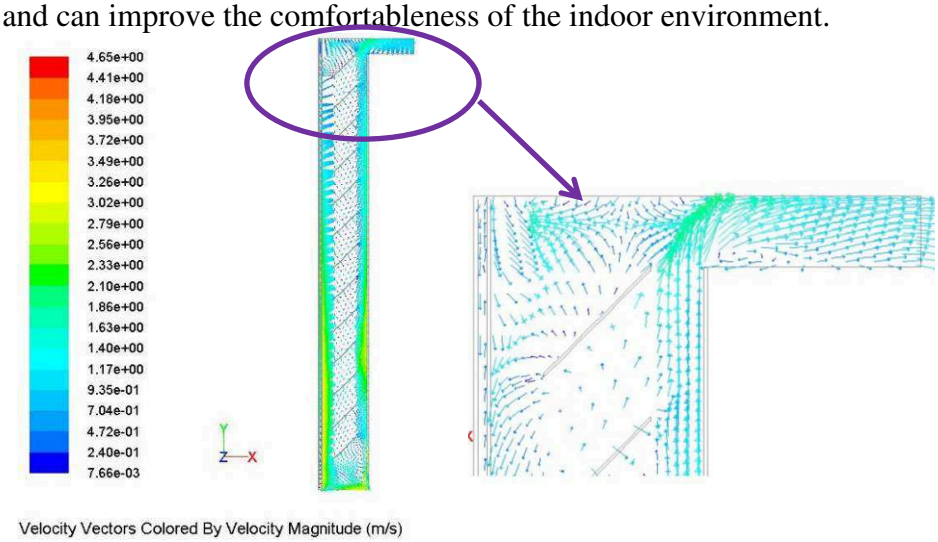


Fig. 2 The velocity distribution of the DSF with blinds

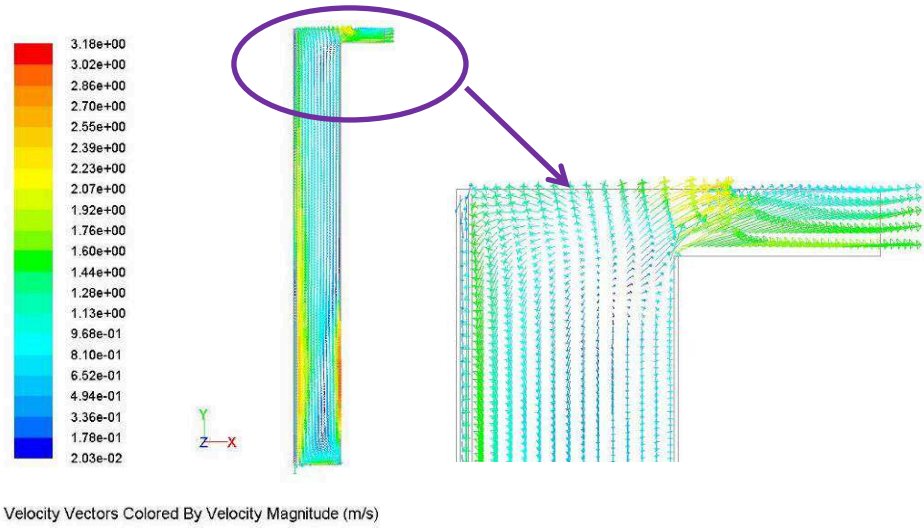


Fig. 3 The velocity distribution of the DSF without blinds

**Temperature field.** The temperature distribution of the middle section of the internal recycle DSF with blinds and without blinds are shown in Fig. 4 and Fig. 5, respectively. The temperature distribution can more intuitive reflect the ventilation and thermal properties of the DSF. The temperature of internal surface of inner glass wall is an important parameter of the indoor environment comfortableness and building energy consumption. The temperature of internal surface of inner glass wall is higher, and the temperature difference between it and indoor air is smaller in winter, the energy loss through the envelop enclosure is litter and the thermal radiation from glass surface to indoor air is much more.

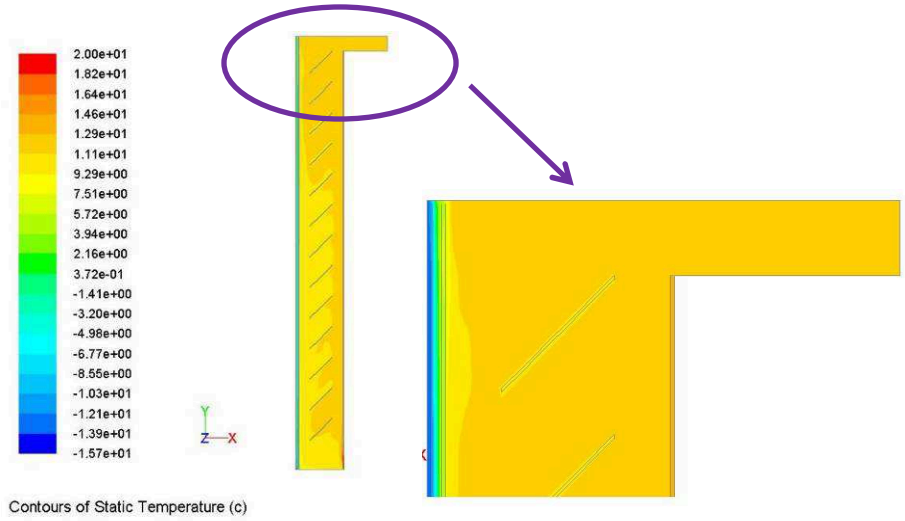


Fig. 4 The temperature distribution of the DSF with blinds

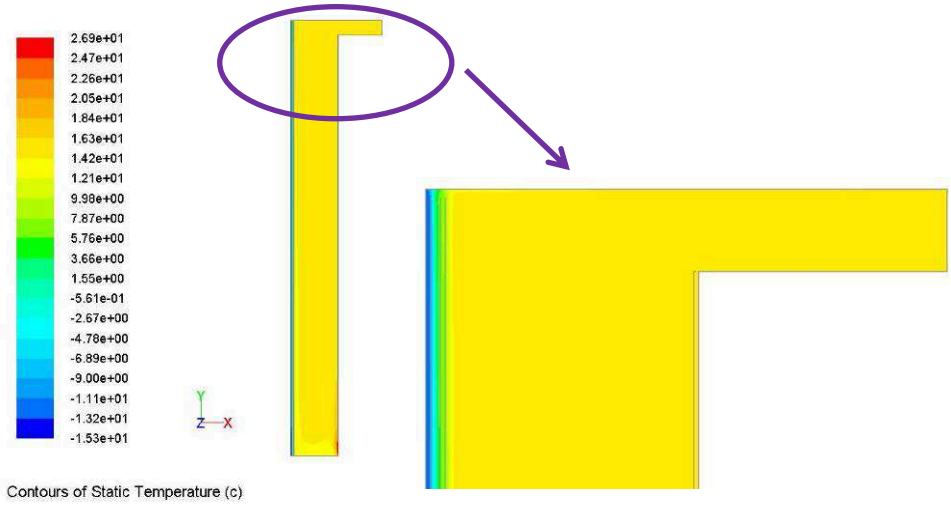


Fig. 5 The temperature distribution of the DSF without blinds

**The influence of ventilation rate of the DSF.** The direct influencing factor of the ventilation rate of the DSF is air speed of the outlet.

$$Q=V\times A \tag{1}$$

In eq. (1), Q is the ventilation rate, V is the air speed of the outlet and A is the sectional area of the outlet.

The temperature of internal surface of inner glass wall, the comprehensive heat transfer coefficient and comprehensive heat transfer resisitance of the different analysis model with blind and without blinds of different air speed of outlet are shown in Table 1 and Table 2, respectively.

Table 1 The results of different analysis model with different air speed of outlet (with blinds)

| Air speed of outlet (m/s) | Internal surface temperature (°C) | Comprehensive heat transfer coefficient (W/(m$^2$•°C)) | Comprehensive heat transfer resisitance ((m$^2$•°C)/W) |
|---|---|---|---|
| 0.5 | 11.93 | 1.012 | 0.988 |
| 1.0 | 13.42 | 0.817 | 1.224 |
| 1.35 | 13.59 | 0.797 | 1.255 |
| 1.5 | 13.66 | 0.788 | 1.269 |
| 2.0 | 13.84 | 0.766 | 1.305 |

From Table 1, it can be seen that: (1) as the increasing of air speed of outlet, the temperature of internal surface of inner glass wall increases, the comprehensive heat transfer coefficient decreases and comprehensive heat transfer resisitance increases. (2) The thermal properties of the DSF improve significantly when the air speed of outlet increases to 1.0 m/s from 0.5 m/s. (3) When the air speed of outlet increases from 1.0 m/s to 2.0 m/s, the thermal properties does not improve obviously.

Table 2 The results of different analysis model with different air speed of outlet (without blinds)

| Air speed of outlet (m/s) | Internal surface temperature (°C) | Comprehensive heat transfer coefficient (W/(m$^2$•°C)) | Comprehensive heat transfer resisitance ((m$^2$•°C)/W) |
|---|---|---|---|
| 0.5 | 14.75 | 0.656 | 1.524 |
| 1.0 | 15.33 | 0.585 | 1.709 |
| 1.35 | 15.85 | 0.521 | 1.919 |
| 1.5 | 16.37 | 0.458 | 2.183 |
| 2.0 | 17.43 | 0.327 | 3.058 |

There are almost the same regularitide in Table 2 as in Table 1. When the air speed of outlet of DSF with blinds is the same as the DSF without blinds, the internal surface temperature and comprehensive heat transfer resisitance of DSF with blinds are less than these of DSF without blinds. This is because the material of blinds is aluminum alloy and the heat transfer coefficient of the blinds is much large than the air's.

## Conclusions

Through the simulation and analysis of the DSF using CFD method, the conclusions can be get as follows:

(1) Relatively stable continuous flow field can be obtained through DSF. The air flow in the air layer can bring the indoor heat into the air layer of the DSF, which can improve the comfortableness of the indoor environment and reduce energy consumption.

(2) As the increasing of air speed of outlet, the temperature of internal surface of inner glass wall increases, the comprehensive heat transfer coefficient decreases and comprehensive heat transfer resisitance increases.

(3) The ability of energy saving of double skin façade is much better than single glass curtain wall. The results of standard model in this work can be applied to other environmental types.

(4) The DSF, which is a form of energy conservation and ecological envelop enclosure, has a broad prospect of engineering application.

## Acknowledgements

The author would like to thank his collaborators from and support of Jangho Group Company Limited.

## References

[1] Stec, Wojtek, and A. H. C. Van Paassen. "Defining the performance of the double skin facade with the use of the simulation model." Proceedings of Building Simulation. Vol. 3. 2003.

[2] Howell, S. A., and I. Potts. "On the natural displacement ventilation flow through a full scale enclosure, driven by a source of buoyancy at floor level." Seventh International IBPSA Conference. 2001.

[3] Safer, Nassim, Monika Woloszyn, and Jean Jacques Roux. "Three-dimensional simulation with a CFD tool of the airflow phenomena in single floor double-skin facade equipped with a venetian blind." Solar Energy 79.2 (2005): 193-203.

[4] Manz, H., A. Schaelin, and H. Simmler. "Airflow patterns and thermal behavior of mechanically ventilated glass double façades." Building and Environment 39.9 (2004): 1023-1033.

[5] Tanaka, H., Okumiya, M., Tanaka, H., Young Yoon, G., & Watanabe, K. "Thermal characteristics of a double-glazed external wall system with roll screen in cooling season." Building and Environment 44.7 (2009): 1509-1516.

[6] Gratia, Elisabeth, and Andre De Herde. "The most efficient position of shading devices in a double-skin facade." Energy and Buildings 39.3 (2007): 364-373.

[7] Gratia, Elisabeth, and Andre De Herde. "Natural cooling strategies efficiency in an office building with a double-skin façade." Energy and buildings 36.11 (2004): 1139-1152.

[8] JGJ/T 151-2008 Calculation specification for thermal performance of windows, doors and glass curtain-walls. ( in Chinese )

*Applied Mechanics and Materials Vols. 580-583 (2014) pp 2421-2427*
*© (2014) Trans Tech Publications, Switzerland*
*doi:10.4028/www.scientific.net/AMM.580-583.2421*

# Analysis and Evaluation for the Economic Performance of Ground Source Heat Pump System with Waste Heat Recover

Zhongchao Zhao[1, a], Weixian Feng[1, b*], Haojun Mi[1] and Yong Xue[2]

[1]School of Energy and Power Engineering, Jiangsu University of Science and Technology, Zhenjiang, Jiangsu, 212003, China

[2]Jiangsu Josun Air Conditioner Co., Ltd, Taixing, Jiangsu, 255441, China

[a]zhongchaozhao@just.edu.cn, [b]673599299@qq.com

**Keywords:** Ground source heat pump, Heat recovery, Annual cost, Whole life cycle, Economic analysis.

**Abstract.** Economic performance of investment capital, operational costs and supplying costs of domestic hot water for different scenarios of ground source heat pump system (GSHPS), which designed for a hotel located in the hot summer and warm winter area, have been analyzed using the dynamic annual cost method. The results show that the investment capital decreased while the operational costs increased first and then decreased with the ratio of waste heat recovery of GSHPS increased. The comprehensive benefit of GSHPS with waste heat recovery is distinct compared with conventional GSHPS. When the ratio of waste heat recovery is 50%, the dynamic annual costs of GSHPS are minimum and achieve the optimization of energy-saving effect.

## Introduction

Energy is an important basic material for human survival and development. With the booming of the economy, energy consumption has increased sharply. In the future, the world's energy supply must become more sustainable. In China's energy consumption structure, the proportion of building energy consumption reached to 32% of total amount, while the energy of HVAC has reached about 60% of building energy consumption [1], which is the dominated. Therefore, it becomes essential necessary to take measures to reduce the energy consumption of HVAC.

Currently, to explore energy-efficient air-conditioning system has already become the industry's research focus. The ground source heat pump is one of promising means of reducing the consumption of fossil energy resources, and hopefully reducing the cost of delivered energy for residential heating [2]. The ground temperature is relatively stable in the whole year, which is higher than ambient temperature in winter and lower than ambient temperature in summer. The characteristic makes its energy efficiency is much more than the traditional system. With little premium energy (electric energy) input, ground source heat pump transfers low temperature thermal energy into high temperature thermal. That is to say, getting the heat from ground supply heating to indoor space in winter, and the recycles are revised in summer.

In the hot summer and warm winter area, cooling period is generally longer for 1 to 2 months, than that of the heating period, and the cooling load intensity in summer greater than that of the heating load intensity in winter. Therefore, the amounts of heat extracted from and injected to the ground are not balanced. This unbalance requires either extra ground loop heat exchanger or some mechanisms for assisting the system by rejecting excess heat. The cost of installing the extra ground heat exchangers (GHE) may be excessive, and the operational efficiency of heat pump will be declined due to the soil temperature increment [3]. How to avoid heat pump's operating efficiency drop caused by the amount unbalance of heat between extracted from and injected to the ground, and utilizing the waste heat of condenser has become the focus of engineering applications. Combining with a commercial hotel located in Zhenjiang, Jiangsu Province, which provides 24 hours hot water, this study puts forward the ground source heat pump system to meet the building heating/cooling demand, the gas boiler or the heat-recovery of condensation provides four kinds of design scenarios to make

domestic hot water. Economic performance of capital cost, operational cost and supplying cost of domestic hot water for different scenarios of GSHPS have been analyzed using the dynamic annual cost method.

## Description of the Project and the Design Scenarios

**Description of the Project.** To evaluate the performance of GSHPS, the system was installed in a commercial hotel located in Zhenjiang, Jiangsu Province. The hotel has a living area of 32630m$^2$, air-conditioning area of 24470m$^2$, 340 standard rooms, with an average occupancy rate of 70%, namely 476 people living in. The hotel's air conditioning system is designed for cooling in the summer and heating in the winter, 24h domestic hot water supply throughout the year. According to state regulations [4], the heat load of 65℃ domestic hot water for star hotel is about 1565kW, average hourly heat consumption of 813kW, the amount of hot water consumption is 95 tons per day (T/day). The total design cooling and heating load for the building is 4160kW and 1792 kW, respectively, calculated by the Dest software [5]. Consequently, to recover the heat from condenser can meet the needs of energy to heat the domestic hot water. In the present study, an economic analysis was performed to determine the performance of ground heat pumps.

**Description of the Design Scenarios.** The conventional ground source heat pump injects condensation heat into the ground in summer, which will lead to heat accumulation, and waste a great quantity high-grade energy. To give a brief definition, heat recovery technology is the heat pump recovers and recycles the waste heat when the system is operating by some ways. Recovery of waste heat by heat pump system could decrease the discharge of urban waste heat, protect environmental and save energy. Figure 1 shows the principle of heat recovery system.

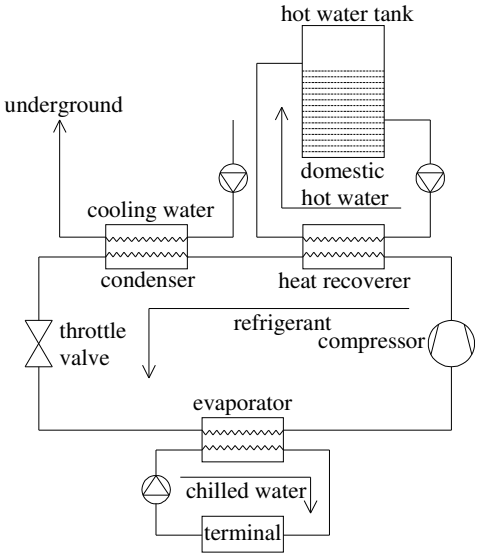


Fig. 1 The principle of heat recovery system

This study selected four kinds of economic and effective solution to analysis on account of the hotel's demand.

1) Scenario 1: ground source heat pump system in combination with gas boiler

The air conditioning is made up of three water source heat pump units. The cooling capacity and cooling power is 1308kW and 215kW, respectively. The heating capacity and heating power is 1420kW and 315kW, respectively. The hot water is supply by a gas boiler with hot water load of 800kW.

2) Scenario 2-4: ground source heat pump system with waste heat recovery system

The air conditioning of the scenario is consisted of three water source heat pump units. The cooling capacity and cooling power is 1416kW and 257kW, respectively. The heating capacity and heating

power is 1526kW and 347kW, respectively. The GSHPS is used for hot water supply. In summer, the systems of scenario 2-4 recover 813kW (the ratio of waste heat recovery is 20%), 1248kW (the ratio of waste heat recovery is 30%) and 2080kW (the ratio of waste heat recovery is 50%), respectively. Other seasons, heat pump units are set to the mode of making hot water in order to provide the required domestic water.

## Calculations of Buried Pipe Length

The performance of GSHPS depends on the design of GHE. Furthermore, the main fee of ground source heat pump project is drilling costs and buried pipe fee, accordingly the calculation of buried pipe length is extremely important.

The length of buried pipe was calculated base on geological conditions and pipe thermal performance from the references [6-10]. The design principles for buried pipes met the standards issued by the International Ground Source Heat Pump Association (GSHPA) [11].

In summer, the length of GHE was calculated based on the cooling load and hot water load, i.e.

$$L_c = \frac{1000Q_c\left(R_P + R_S \cdot F_c\right)}{\left(T_{\max} - T_\infty\right)} \frac{COP_c + 1}{COP_c}. \quad (1)$$

In winter, the length of GHE was determined by the heating load and hot water, i.e.

$$L_h = \frac{1000Q_h\left(R_P + R_S \cdot F_h\right)}{\left(T_\infty - T_{\min}\right)} \frac{COP_h - 1}{COP_h}. \quad (2)$$

Specific symbol in the above equations listed in reference [12]. The calculated results of the pipe's length are shown in table 1.

## Economic Analyses of the Design Scenarios

To obtain profound insight into the project investment capital and operational costs, in this work, the investment capital is calculated by multiplying prices of the apparatus with their installations costs, and the operational costs are assessed based on the investigated thermal loads of the borehole heat exchangers.

**Investment Capital Analysis.** The investment capital of the GHE is assessed by the amount of money invested for accomplishing the project. Prices of the components such as U-tube and hot water devices are the main difference of the systems.

The length of GHE can be formulated as (1)-(2). It is obvious that the main parts of the GHE costs for installation of the GSHP system are the drillings and grouting material, which is about 100 RMB/m. The investment capital of hot water mainly include hot water tank, heat water pump, gas boiler and the difference cost between the heat recovery unit and the conventional unit. The investment capital of the scenarios is listed in Table1.

Table 1 The investment capital of the scenarios

| Scenarios | GSHPS with gas boiler | GSHPS with waste heat recovery | | |
|---|---|---|---|---|
| | Scenario 1 | Scenario 2 | Scenario 3 | Scenario 4 |
| Costs of hot water devices [RMB] | 181440 | 60400 | 74600 | 80650 |
| Length of GHE [m] | 98810.0 | 80150.3 | 72956.5 | 58612.9 |
| Costs of GHE [RMB] | 9881000 | 8015030 | 7295650 | 5861290 |
| Total costs [RMB] | 10062440 | 8075430 | 7370250 | 5941940 |
| Per area costs [RMB/m$^2$] | 308.4 | 247.5 | 225.9 | 182.1 |
| The fraction [%] | — | 19.7 | 26.8 | 40.9 |

As can be seen from the table, the investment capital of GSHPS with waste heat recovery is less than the conventional GSHPS with gas boiler. The results show that the investment capital of hot water system increased and the GHE costs decreased with the ratio of waste heat recovery of GSHPS increased. The total costs depend on the hot water system and the length of GHE. Because the drillings investment of this research is high, the investment capital of the project decreased with the ratio increased of GSHPS' waste heat recovery. Compared with scenario 1, the investment capital of scenario 4 decreased by 126.3 RMB/$m^2$, and the fraction is 40.9%.

**Operational Costs.** The operational costs in air conditioning mode and in hot water mode are the main operational costs components.

1, the system operates in air conditioning mode

In summer, the energy consumption of compressor and the load of building inject to the underground, which is the cooling load of the GHE. In winter, the heat transform between GHE and ground is equal to the load of building subtracts the compressor's energy consumption.

When the ground source heat pump operated individually, the COP of system and the load of GHE in summer is 2.8 and 5656.57kW, respectively. In winter, the COP of system and the load of GHE is 4.19 and 1364.32kW, respectively. When the ratio of waste heat recovery is 20% (832kW), the load of BHE decreased to 4824.57kW, the COP in summer increased to 3.44. Due to the length reduction of buried pipe, the COP in winter decreased to 4.10. The power of hot water pump is 10.8kW. When the ratio of waste heat recovery is 30% (1248kW), the load of GHE decreased to 4408.57kW, and the COP in summer increased to 3.5. Due to the reduction of buried pipe length, the COP in winter decreased to3.96. The power of hot water pump is 16.2kW. When the ratio of waste heat recovery is 50% (2080kW), the load of GHE decreased, the COP in summer, the COP in winter and the power of hot water pump is 3576.5kW, 3.66, 3.7 and 24.3kW, respectively. This study has analyzed the annual energy consumption of the different scenarios, which is listed in table 2-4. Table 2 and 3 shows the operational costs of air conditioning and hot water, respectively. The total costs are shown in table 4.

Table 2 The operational costs of air conditioning

| Scenarios | GSHPS with gas boiler | GSHPS with waste heat recovery | | |
|---|---|---|---|---|
| | Scenario 1 | Scenario 2 | Scenario 3 | Scenario 4 |
| Operational time in summer [h] | 3312 | 3312 | 3312 | 3312 |
| Energy consumption in summer [kWh] | 4920685.7 | 4005209.3 | 3936548.6 | 3764459.0 |
| Operational costs in summer [RMB] | 4428617.1 | 3604688.4 | 3542893.7 | 3388013.1 |
| Operational time in winter [h] | 2520 | 2520 | 2520 | 2520 |
| Energy consumption in winter [kWh] | 1077766.1 | 1101424.4 | 1140363.6 | 1220497.3 |
| Operational costs in winter [RMB] | 969989.5 | 991282.0 | 1026327.3 | 1098447.6 |
| Total operational costs [RMB] | 5398606.6 | 4595970.3 | 4569221.0 | 4486460.7 |
| Per area operational costs [RMB/$m^2$] | 165.4 | 140.9 | 140.0 | 137.5 |
| The fraction [%] | — | 14.9 | 15.4 | 16.9 |

In terms of operational costs, only the operational costs of air conditioning were accounted. While the labor, equipment maintenance, management costs and other expense were not took into account. In summer, the efficiency of system increased and the operational costs increased, meanwhile, the operational costs of auxiliary equipments such as water pumps increased because of the heat recovery. In winter, the efficiency of system decreased and the operational costs increased with the length of

GHE decreased. It can be seen from table 2, the operational costs of air conditioning decreased with the ratio of waste heat recovery of GSHPS increased. Compared with scenario 1, the air conditioning operational costs of scenario 4 decreased by 27.9 RMB/$m^2$. The fraction is 16.9%.

2, The operational costs of hot water

This project is a hotel building, which has hot water demand annually.

Table 3 shows the hot water operational costs of heat recovery are less than gas boiler. The operational costs increased with the ratio of heat water increased. This finding indicates that the smaller the ratio is, the less the cost is. Compared with scenario 1, the hot water operational costs of scenario 4 decreased by 37.6 RMB/$m^2$. The fraction is 58.4%.

Table 3 The operational costs of hot water

| Scenarios | GSHPS with gas boiler | GSHPS with waste heat recovery | | |
|---|---|---|---|---|
| | Scenario 1 | Scenario 2 | Scenario 3 | Scenario 4 |
| Operational time in summer [h] | 2880 | 2880 | 2880 | 2880 |
| Energy consumption in summer [kWh] | — | 31104.0 | 46656.0 | 69984.0 |
| Operational costs in summer [RMB] | — | 27993.6 | 41990.4 | 62985.6 |
| Operational time in other seasons [h] | 5580 | 5580 | 5580 | 5580 |
| Energy consumption in other seasons [kWh] | — | 812956.1 | 841697.0 | 900843.2 |
| Operational costs in other seasons [RMB] | — | 731660.5 | 757527.3 | 810758.9 |
| Total operational costs [RMB] | 2102237.3 | 759654.1 | 799517.7 | 873744.5 |
| Per area operational costs [RMB/$m^2$] | 64.4 | 23.3 | 24.5 | 26.8 |
| The fraction [%] | — | 63.9 | 62 | 58.4 |

Table 4 The total operational costs

| Scenarios | GSHPS with gas boiler | GSHPS with waste heat recovery | | |
|---|---|---|---|---|
| | Scenario 1 | Scenario 2 | Scenario 3 | Scenario 4 |
| Total operational costs [RMB] | 7500844.0 | 5355624.4 | 5368738.7 | 5360205.2 |
| Per area operational costs [RMB/$m^2$] | 229.9 | 164.1 | 164.5 | 164.3 |
| The fraction [%] | — | 28.6 | 28.4 | 28.5 |

It is obvious that the total operational costs of GSHPS with waste heat recovery are less than GSHPS with gas boiler. The results show that the operational costs increased first and then decreased with the ratio of waste heat recovery of GSHPS increased. And the fraction is 28.5%.

**Economic Analysis.** The investment capital and the operational costs are different economic indicators, which only reflect one aspect of economy. While the comprehensive benefit of GSHP requires a comprehensive economic indicators. The dynamic annual cost method is a powerful tool, particularly when it is used in the analysis and design of experiments. Economic performance of investment capital and operational costs for different scenarios has been analyzed using the dynamic annual cost method [13]. Thus, the annual cost (AC) is calculated by

$$AC = \frac{i(1+i)^n}{(1+i)^n - 1} \times C_0 + C \,. \tag{3}$$

Where, $i$ is the interest rate, 10%, $n$ is the service life, in this study, the life of GSHPS and boiler is assumed to be 50 and 10 years, respectively, $C_0$ is the investment capital, RMB, $C$ is the annually operational costs, RMB. Table 5 shows the economic analysis for each scenario.

Table 5 The economic analysis for each scenario

| Scenarios | GSHPS with gas boiler | GSHPS with waste heat recovery | | |
|---|---|---|---|---|
| | Scenario 1 | Scenario 2 | Scenario 3 | Scenario 4 |
| Investment capital [RMB/m$^2$] | 330.6 | 247.5 | 225.9 | 182.1 |
| Annually operational costs [RMB/m$^2$] | 229.9 | 164.1 | 164.5 | 164.3 |
| AC [RMB/m$^2$] | 262.9 | 188.9 | 187.1 | 182.5 |

Dynamic annual cost method, when used in the initial planning phase of a project, can identify such situations and save the project money and embarrassment. It is obvious that GSHPS with waste heat recovery is more economic than GSHPS with gas boiler. As can be seen in table 5, tiny difference is between the dynamic annual costs of scenario 2 and 3. The costs of scenario 4 are minimum. Therefore, scenario 4 is the most effective system with regards to energy and economics.

## Conclusions

Economic performance of investment capital, operational costs and supplying costs of domestic hot water for different scenarios of GSHPS, which is designed for a hotel located in the hot summer and warm winter area, have been analyzed using the dynamic annual cost method. From the analysis of the results, the following conclusions can be drawn:

1) In the area with hot summer and warm winter, the combination of heat pumps and hot water system, as in system scenario 3 and 4, with the heat pump to produce domestic hot water is effective. The production of hot water can reduce the over-reliance on the boiler, electric heaters and other energy-consuming heating equipment. Meanwhile, with the heat recovery of condensation, the condensing temperature decrease, and the heat pump system becomes more efficient and the investment capital is less because the system consumes less power.

2) According to the investment capital and the annually operational costs, ground source heat pump system with suitable heat recovery ratio is more economical than the conventional ground source heat pump system with gas boilers. In addition, the investment capital decreased while the total operational costs increased by a small margin with the ratio of waste heat recovery increased.

3) Considered on the total costs, which including the investment capital and the operational costs after $n$ years operated, the comprehensive benefit of GSHPS with waste heat recovery is distinct compared with conventional GSHPS. When the ratio of waste heat recovery is 50%, the dynamic annual costs of GSHPS are minimum and achieve the optimization of energy-saving effect.

**Acknowledgements**

The authors would like to acknowledge the joint innovation and research funding of Jiangsu Province (BY2013066-09) for their supports in this research.

## References

[1] Z.M. Ni and X.K: Construction Economy Vol. 10 (2012), p.101

[2] J. Cheng, B. Hao, S. Liu and Y.N. Liu: Construction Economy Vol. 8 (2013), p.97

[3] H.Q. Ma and W.D. Long: HV&AC Vol. 39(2009), p.102

[4] GB50015—2003(2009), Code for design of building water supply and drainage.
[5] Y. Jiang. *Building energy efficiency technology and application—Dest* (China Architecture & Building Press, Beijing 2006).
[6] Y. Gu and D.L. Oneal: ASHRAE Transaction Vol. 104(1998), p. 34
[7] M. Ramamoorthy and H. Jin: ASHRAE Transaction Vol. 107(2001), p. 26
[8] R.Y. Xie. *Design of ground source heat pump system* (China Architecture & Building Press, Beijing 2001).
[9] GB 50366-2005, Technical code for ground-source heat pump system.
[10] Air-conditioning heating & refrigeration institute (AHRI). *Ground-source heat pump engineering manual* (W. Xu, Trans) (China Architecture & Building Press, Beijing 2001).
[11] R.L.D. Cane, P. Eng and D.A. Forgas: ASHRAE Transaction Vol. 97(1991), p. 909
[12] M.F. Li, G.F. Zhou and B. Fan: Chinese Journal of Refrigeration Technology Vol. 38(2009), p. 61
[13] B.J. Zheng, Y. Zou and S.Z: Building Energy Efficiency Vol. 40(2012), p. 75

*Applied Mechanics and Materials Vols. 580-583 (2014) pp 2428-2431*
*© (2014) Trans Tech Publications, Switzerland*
*doi:10.4028/www.scientific.net/AMM.580-583.2428*

# Experimental investigations on effect of particles removal in cleanroom with non-unidirectional airflow

Wang Yu[1,2 a]

[1] State Key Laboratory of Building Safety and Built Environment, Beijing, China

[2] School of Energy and Safety Engineering, Tianjin Chengjian University, Tianjin, China

[a]wy41523@126.com

**Keywords:** cleanroom, non-unidirectional airflow, particles removal

**Abstract.** Efficient airflow delivery is key to achieve effective contamination control for a high-performance cleanroom. The influence of airflow organization on effect of particles removal in cleanroom with non-unidirectional airflow was investigated in this paper. A series of experiments were conducted on a cleanroom experimental platform with different airflow organization modes and supply air volume variation by frequency converter ( 40 to 50 Hz, 5Hz interval) on air-supply fan unit. The results showed that higher cleanliness could be gained at local area in cleanroom with radial airflow organization. Moreover, the outcomes from these experiments indicated that particle concentration at measuring points appeared more orderly when the cleanroom operated with radial airflow organization. The conclusion can be drawn that radial airflow can benefit contamination control at local area for cleanroom operation with non-unidirectional airflow when compared with ceiling-supply and wall-return airflow organization.

## Introduction

Effective contamination control attributes to efficient airflow in high-performance cleanroom. An efficient airflow system may not only reduce initial costs, but also help cleanrooms achieve operation reliability.[1,2]

Air-recirculation system with ceiling supply and wall-return airflow is traditionally used in non-unidirectional airflow cleanroom. While in the traditional airflow cleanroom, locations and layouts of the production lines affect much on particle diffusion.[3] with the demond for better contamination control in engineering applications to achieve higher cleanliness, it is important to optimize airflow design to meet cleanliness requirements and to achieve effective particle removal.

Airflow organization and air-supply volume are major factors determining particle removal effect in cleanroom, then a series of experimental investigations need be conducted to better understand particle distribution in non-unidirectional airflow cleanroom affected by airflow organization mode.

## Experimental methods

The experimental investigations were conducted in cleanroom2 of a multi-zone experimental platform. Fig.1 shows the schematic diagrams of the platform, in which cleanroom1 is designed as ISO5 cleanliness, cleanroom2 is designed as ISO6 cleanliness class with two airflow organization modes can be chosen, one is Radial airflow pattern with top-aside-radiation supply and down-aside wall-return airflow path (Valve2 open and Valve1 closed), the other is traditional airflow pattern with ceiling-supply and wall-return airflow path (Valve1 open and Valve2 closed).

Electronic frequency converter is configured in air-supply fan unit. During the experiments, the comparison of particle removal effect between radial airflow pattern and traditional airflow pattern in cleanroom2 with different send air volume can be investigated.

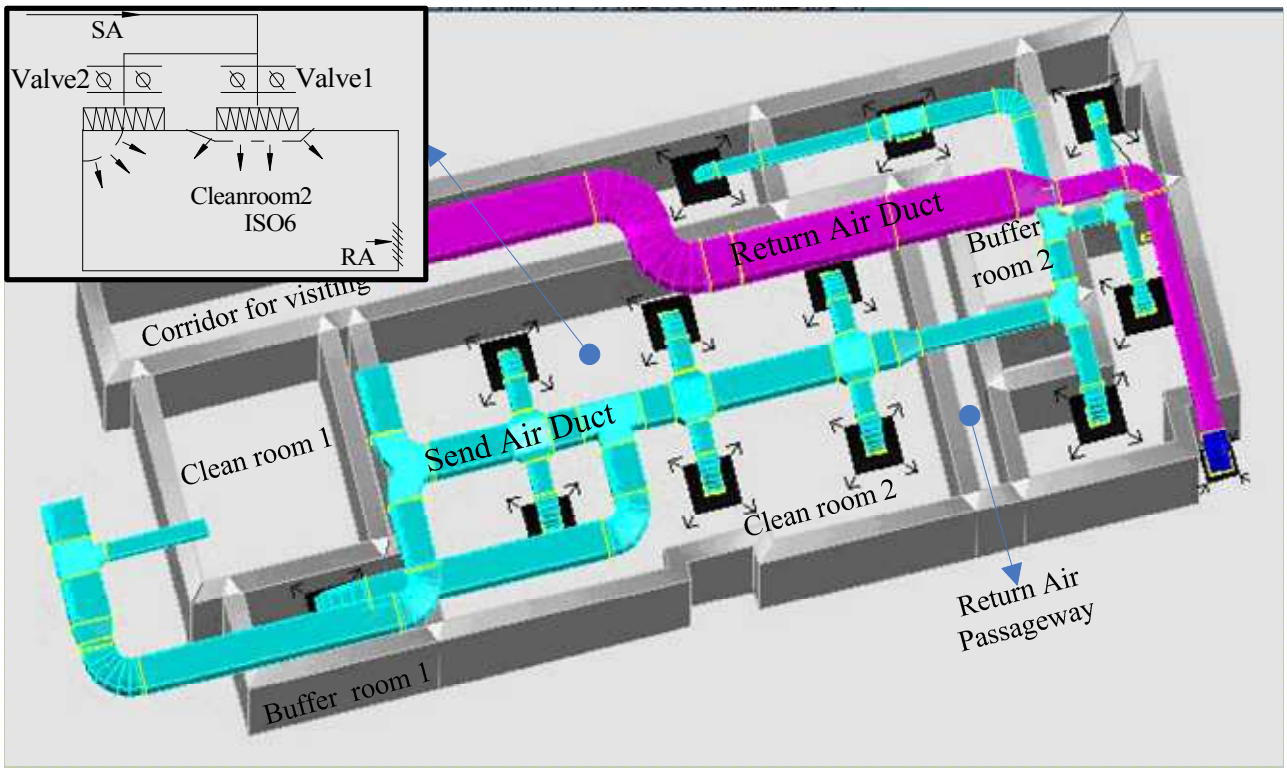


Fig.1 Schematic of airflow path in the cleanroom experimental platform

Judging by design code for clean room and acceptance code for ventilation works[4,5], the measuring points is arranged in cleanroom2, as shown in Fig.2. Laser particle counter is employed to measure particle concentration level in the investigated zone.

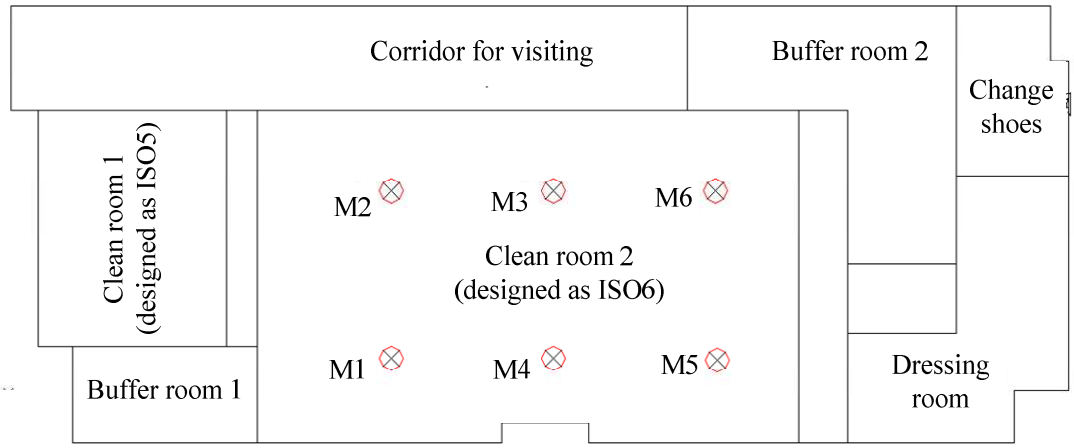


Fig.2 Schematic of measuring points in the investigated zone

## Results and discussions

Particle distributions in cleanroom2 measured during experiments are shown in Fig.3 and Fig.4. The characterization of minienvironment in cleanroom2 appeared to be effective in maintaining particle-concentration levels well below what was designated (ISO6-cleanliness-class).

Fig.3 reveals concentrations of particles at points M1-M6 decrease consistently with the increase of air-supply (frequency converter varied from 40Hz to 50Hz) when cleanroom2 operated with radial airflow, and particle-concentration levels at points M1-M5 in cleanroom2 with radial airflow well below what appeared in cleanroom2 with traditional airflow, while concentrations of particles at points1-6 trend to uniformity till air-supply fan working at 50Hz. It indicates that local cleanliness are effectively controlled under radial airflow during cleanroom operation.

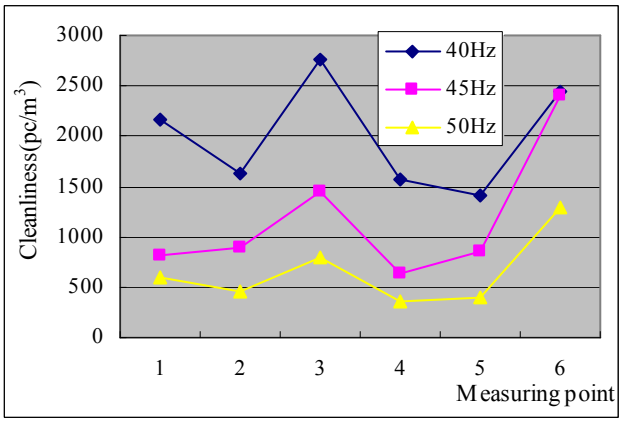


(a) Operation with radial airflow

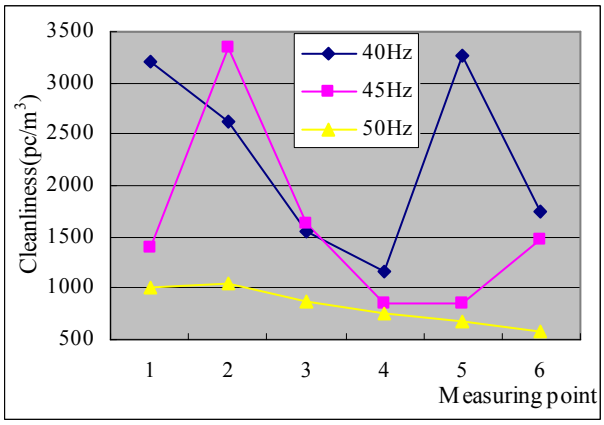


(b) Operation with traditional airflow

Fig.3 Comparison of particle distribution between two airflow patterns

Fig.4 reflects that particle removal comparison between two airflow patterns under different air-supply conditions. It is shown in Fig.4(a) that particle distributions appear irregular in cleanroom2 with either radial airflow or traditional airflow when air-supply fan working at 40Hz. It can be seen from Fig.4(b) and Fig4(c) that particle concentrations near air inlet such as M1 and M2 when air-supply fan working at 45Hz are almost at the same level as what in cleanroom2 with air-supply fan working at50Hz. Then the conclusion can be drawn that radial airflow not only benefit particle removal but also achieve energy-saving for air-supply system when sufficient air are delivered into cleaning zone for maintaining cleanliness requirement.

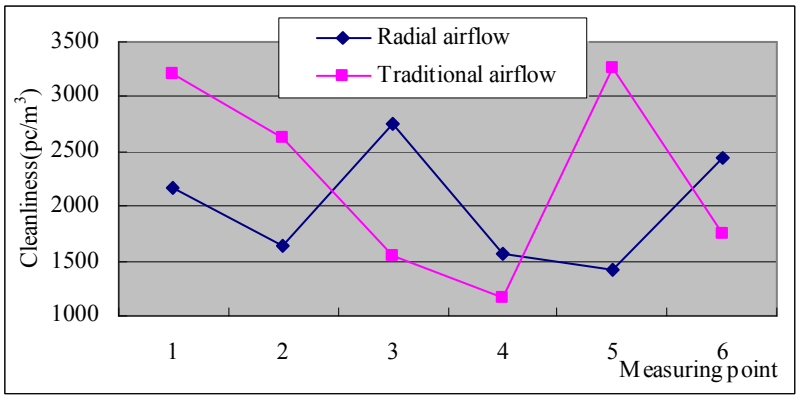


(a) air-supply fan working at 40Hz

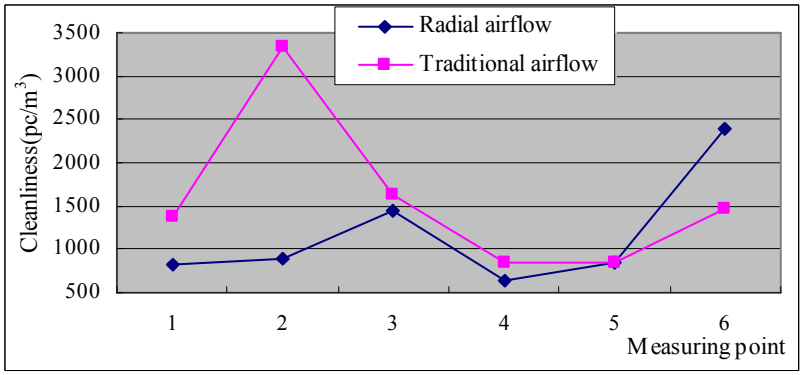


(b) air-supply fan working at 45Hz

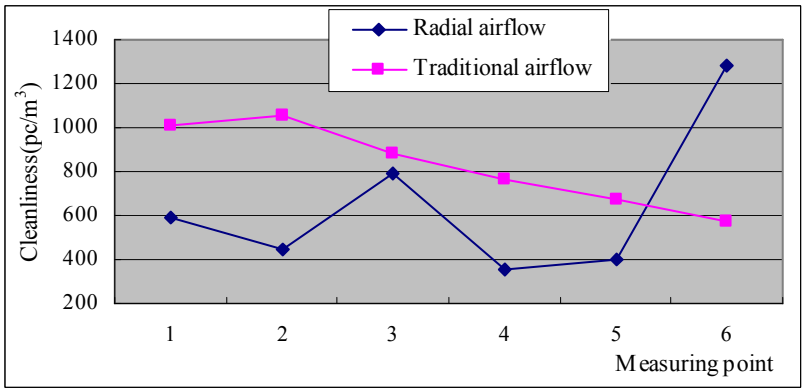


(c) air-supply fan working at 50Hz

Fig.4 The influence of air-supply fan operational state on particle distribution

## Conclusions and recommendations

Based upon measurements and comparisons of particle distribution in the non-unidirectional airflow cleanroom with different airflow organizations, the following conclusions are drawn:

·Cleanliness measurements in the cleanroom with radial airflow operation appeared to be more effective in particle removal than what was appeared in the cleanroom with traditional airflow operation.

· Particle distribution appears similar with air-supply variation when radial airflow is employed in the non-unidirectional airflow cleanroom, which is suitable for reasonable layouts of production lines and tool equipment in cleanroom operation and benefit operational energy-saving.

The experimental investigations provide quantitative data to characterize particle removal effect in non-unidirectional airflow cleanroom that were in operation at as-built state. Additional investigations would be need for further evaluating acceptable air-supply volume and air-change rates in cleanroom with radial airflow organization.

## Acknowledgements

This work was supported by the Opening Funds of State Key Laboratory of Building Safety and Built Environment.

## References

[1] Tengfang Xu. Considerations for efficient air flow design in cleanrooms. Journal of the IEST 2004 edition, 24-28.

[2] Tengfang Xu. Characterization of minienvironments in a cleanroom: assessing energy performance and its implications. Building and Environment. 2008(43), 1545-1552.

[3] Ti Lin, Yun-Chun Tung, Shih-Cheng Hu, Chen-Yen Lin. Effects of the removal of 0.1μm particles in industrial cleanroom with fan dry coil unit return system. Aerosol and air quality research. 2010(10), 571-580.

[4] Code for design of clean room (in Chinese), GB 50073-2001,35-40.

[5] Code of acceptance for construction quality of ventilation and air conditioning works (in Chinese), GB 50243-2002,94-97.

*Applied Mechanics and Materials Vols. 580-583 (2014) pp 2432-2437*
*© (2014) Trans Tech Publications, Switzerland*
*doi:10.4028/www.scientific.net/AMM.580-583.2432*

# Calculation and analysis of gravity head coefficient in hot water heating system

Wenwen Xie[a], Yongzheng Fu[b]

College of Urban Construction, Wuhan University of Science and Technology,

No. 199 Xiongchu Avenue, Wuhan, P.R.China 430070

[a]472614272@qq.com, [b] fuyongzheng@163.com

**Keywords:** mathematical expectation; gravity head coefficient; operation regulation; design supply and return water temperature

**Abstract:** This paper presented a method of mathematical expectation to calculate gravity head coefficient, and this method was applied to calculate the value of gravity head coefficient of some selected cities in China in different operation regulation mode and different design supply and return water temperature. The results show that gravity head coefficient calculated by this method reflects the average value during the whole heating period. It has more representative significance. When the temperature of design supply and return water in heating system is reduced, the gravity head coefficients change very little. In different operation regulation modes, the gravity head coefficients change larger. The gravity head coefficients have a certain difference in different areas.

## Introduction

In the two-pipe hot water heating system, although gravity head was a limited proportion in the total cycle power, it is one of the important reasons to produce vertical imbalance. It must be considered in designing hydraulic calculation of the system. The gravity head cannot be selected by 100% of the value of design conditions. The reason is that operation regulation will be conducted according to the outdoor temperature change in the actual operation. That is, in different stages of heating, the temperature of supply and return water varies. Thus the gravity head will be reduced at the beginning and end of the heating season. Therefore, when calculating the gravity head, a relatively eclectic coefficient (the ratio of calculated gravity head to designed gravity head) will be selected to ensure that the change of indoor temperature does not affect human comfort.

Ref. [1] describes that gravity head under the outdoor temperature corresponding to the gravity head coefficient should be selected. The outdoor temperature can represent a long duration of the heating period. According to this theory, there are currently two methods to calculate gravity head coefficient. One is that the design value of gravity head coefficient is the ratio of the outdoor mean air temperature during heating period $t_p$ corresponding to gravity head and designed gravity head. The reason is that, all over the country, duration hours of less than or equal to $t_p$ accounts for almost 50% of total hours during heating period. This method is called the $t_p$ algorithm. Another is that a certain outdoor temperature interval is selected, which can represent a longer duration hours during heating period. Then an average value of the outdoor temperature corresponding to the gravity head coefficient in the temperature interval can be calculated. For example, in the Ref. [2], the relative heat load ratio is 0.8 ~ 0.5 during more than 70% of the whole heating period. Then the relative heat load ratio for heating within the range of 0.8 to 0.5 corresponding to the gravity head coefficient can be calculated. Then the average value is calculated. The average value is the design value of gravity head coefficient.

From the perspective of probability, mathematical expectation method is adopted to calculate the gravity head coefficient. And this method is applied to calculate the value of gravity head coefficient of some cities in China in different operation regulation modes and different temperatures of design supply and return water.

**Definition and calculation of the expectation of gravity head coefficient**

Gravity head coefficient is the ratio of calculated gravity head to designed gravity head. Its expression is:

$$B=\frac{\Delta P}{\Delta P'} \quad (1)$$

In formula, $B$ is the gravity head coefficient; $\Delta P$ is calculated gravity head, Pa; $\Delta P'$ is designed gravity head, Pa.

Without considering water pressure generated by water cooling in the circulation line, gravity head in radiator heating system is the result of joint action of the density difference between supply and return water of system and the vertical height difference between radiator cooling center and heating center. Its expression is:

$$\Delta P = gh(\rho_h - \rho_g) \quad (2)$$

In formula, g is the acceleration of gravity, 9.81 m/s$^2$; h is the vertical height difference between radiator cooling center and heating center, m; $\rho_g$ and $\rho_h$ are the supply and return water density of system, kg/m$^3$.

When the system is determined, the variables are $\rho_g$ and $\rho_h$ in Eq. (2). Because of incompressible water, $\rho_g$ and $\rho_h$ are related to $t_g$ and $t_h$, which are the supply and return water temperature of the system. The supply and return water temperature of heating system changes with the outdoor temperature $t_w$ change. Its variation is related to the mode of heating operation regulation. From Eq. (1) and Eq. (2), B is a function of $t_w$. It is set to $B(t_w)$.

The outdoor temperature interval $t_{w,i-1} < t_w \le t_{w,i}$ at heating period corresponding to the average duration hours can be got by the table of the average duration hours of outdoor temperature $t_w \le t_{w,i}$ in some cities[3]. The outdoor temperature interval $t_{w,i-1} < t_w \le t_{w,i}$ at heating period can be taken as a uniform distribution. The more duration hours of the interval are, the greater the corresponding probability $P(t_{w,i-1} < t_w \le t_{w,i})$ is. Probability density $f(t_w)$ of an interval $(t_{w,i-1} < t_w \le t_{w,i})$ can be obtained.

$$f(t_w) = \frac{P(t_{w,i-1} < t_w \le t_{w,i})}{t_{w,i} - t_{w,i-1}} \quad , \quad t_{w,i-1} < t_w \le t_{w,i} \quad (3)$$

The function expression of mathematical expectation is that:

$$E[B] = \int_a^b B(t_w)\, f(t_w) dt_w \quad (4)$$

In formula, $E[B]$ is the mathematical expectation of gravity head coefficient during whole heating period; $a$ represents outdoor design temperature for heating $t_w'$, ℃; $b$ is the outdoor temperature at the beginning and end of the heating season, typically 5℃; $B(t_w)$ represents the gravity head coefficient B when the outdoor temperature is $t_w$; $f(t_w)dt_w$ represents the probability when the outside temperature is $t_w$.

Integral expression of gravity head coefficient expectations is too complex. When $\Delta t_w$ is very small (take $\Delta t_w$= 1℃here), Eq. (4) can be simplified as:

$$E[B] = \sum_{j=a}^{b} B(j) f(j) \times 1 = \sum_{j=a}^{b} B(j) f(j) \quad (5)$$

In formula, j is the outdoor temperature $t_w$ at heating period, ℃; $B(j)$ represents the gravity head coefficient B when the outdoor temperature is j; $f(j)$ represents the value of probability density when the outside temperature is j. When j is discontinuity point of $f(j)$, $f(j) = \frac{f(j^+)+f(j^-)}{2}$.

**Calculation of practical examples**

Take Tianjin as an example to calculate the expectation of its gravity head coefficient using the method above.The average duration hours of outdoor temperature $t_w \le t_{w,i}$ at Tianjin is shown in Table 1.

Table 1 The average duration hours of outdoor temperature $t_w \leq t_{w,i}$ at Tianjin

| $t_w$ | -10 | -8 | -6 | -4 | -2 | 0 | 3 | 5 |
|---|---|---|---|---|---|---|---|---|
| hours | 69 | 127 | 330 | 700 | 1235 | 1833 | 2465 | 2928 |

When +3℃<$t_w$≤+5℃, the average duration hours is 2928-2465=463h. P(+3℃<$t_w$≤+5℃) =463/2928=15.81%. According to probability density function of uniform distribution, f($t_w$)=15.81%/2=7.9%, +3℃<$t_w$≤+5℃. Similarly, the probability density values of other interval can be obtained, the results are shown in Figure 1.

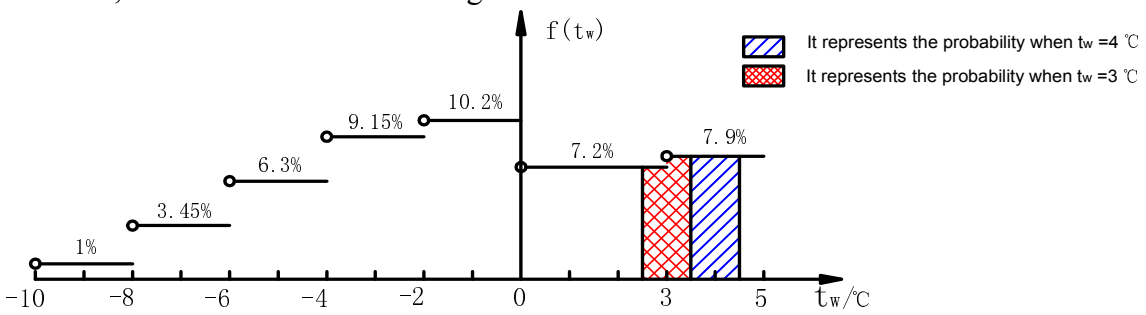


Figure 1 The distribution of f($t_w$) at Tianjin

From the Figure 1, f(+5℃)=(7.9%+0)/2=3.95%, f(+4℃)=7.9%, f(+3℃)=(7.9%+7.2%)/2= 7.55%.And so on,different outdoor temperatures for heating corresponding to the probability density values f(j) of Tianjin can be calculated. If the operation regulation mode for heating system is quality regulation and design supply and return water temperature for heating system is 75/50℃, different outdoor temperatures for heating corresponding to gravity head coefficients B(j) can be calculated. f(j) and B(j) are shown in Table 2.

Table 2 The different outdoor temperatures for heating corresponding to f(j) and B(j) at Tianjin

| $t_w$ | 5 | 4 | 3 | 2 | 1 | 0 | -1 | -2 | -3 | -4 | -5 | -6 | -7 | -8 | -9 |
|---|---|---|---|---|---|---|---|---|---|---|---|---|---|---|---|
| f(j) | 3.95 | 7.90 | 7.55 | 7.20 | 7.20 | 8.70 | 10.20 | 9.68 | 9.15 | 7.73 | 6.30 | 4.88 | 3.45 | 2.23 | 1.00 |
| B (j) | 0.40 | 0.41 | 0.48 | 0.52 | 0.56 | 0.61 | 0.64 | 0.68 | 0.73 | 0.77 | 0.81 | 0.84 | 0.90 | 0.95 | 1.00 |

E[B] can be calculated from the Table 2, $E[B] = \sum_{j=a}^{b} B(j)f(j) = 0.628$. The expectation of gravity head coefficient at Tianjin is 0.628. Under the same conditions, in other words, when design supply and return water temperature for heating systems is 75/50℃ and the operation regulation mode for heating system is quality adjustment, the gravity head coefficient calculated by $t_p$ algorithm is 0.64. From the results of two methods, it can be seen that gravity head coefficients between the two methods have little difference.

Duration hours curves of the same outdoor average daily temperature of some cities in China is relatively flat, no obvious peak. Duration hours curves of the same outdoor average daily temperature in Russia has obvious peak interval. When design supply and return water temperature for heating systems is 95/70℃ and the operation regulation mode for heating system is quality regulation, the gravity head coefficient calculated by $t_p$ algorithm is 0.36. But the gravity head coefficient calculated by the algorithm of this article is 0.43.

The above analysis show that when duration hours of the same outdoor average daily temperature have smaller change, the result of the algorithm of this article is relatively close to the result of $t_p$ algorithm. However, when duration hours of the same outdoor average daily temperature have larger change, the result has a slight deviation. The result of the algorithm of this article is closer to the true value of 0.4. The reason is that the result of $t_p$ algorithm is a reflection of 50% time of heating period, but the expectation reflects the average during the whole heating period, which has more representative significance.

**The values of E[B] in some cities**

**The basic formula of operation regulation for heating system.** Operation regulation modes of centralized heat-supply in hot water heating system include quality regulation, flow regulation, quality regulation with flow varied by steeps, quality - flow optimization regulation and intermittent regulation. Since the major consideration of this paper is that supply and return water temperature for heating system changes with the outdoor temperature change. Three operating regulation modes will be discussed. They are quality regulation, quality regulation with flow varied by steeps and quality - flow optimization regulation respectively.

The formula of quality regulation is:

$$t_g = t_n + 0.5\left(t_g' + t_h' - 2t_n\right)\overline{Q}^{1/(1+b)} + 0.5(t_g' - t_h')\overline{Q} \quad (6)$$

$$t_h = t_n + 0.5\left(t_g' + t_h' - 2t_n\right)\overline{Q}^{1/(1+b)} - 0.5(t_g' - t_h')\overline{Q} \quad (7)$$

In formula, $t_g$ is supply water temperature of heating installation,℃; $t_h$ is return water temperature of heating installation,℃; $t_n$ is indoor design temperature for heating, taking 20℃ here; $t_g'$ is design supply water temperature for heating, ℃; $t_h'$ is design return water temperature for heating, ℃; b is the radiator cooling index, available from manuals and samples, typically 0.3; $\overline{Q}$ is relative heat load ratio for heating, $\overline{Q} = \frac{t_n - t_w}{t_n - t_w'}$ .

The formula of quality regulation with flow varied by steps is:

$$t_g = t_n + 0.5\left(t_g' + t_h' - 2t_n\right)\overline{Q}^{1/(1+b)} + 0.5\frac{(t_g' - t_h')}{\varphi}\overline{Q} \quad (8)$$

$$t_h = t_n + 0.5\left(t_g' + t_h' - 2t_n\right)\overline{Q}^{1/(1+b)} - 0.5\frac{(t_g' - t_h')}{\varphi}\overline{Q} \quad (9)$$

In formula, $\varphi$ is the flow ratio, 0.75 here. The remaining symbols and the symbols of quality regulation formula are the same.

The formula of quality - flow optimization regulation is[2]:

$$t_g = t_n + 0.5\left(t_g' + t_h' - 2t_n\right)\overline{Q}^{1/(1+b)} + 0.5(t_g' - t_h')\overline{Q}^{1-m} \quad (10)$$

$$t_h = t_n + 0.5\left(t_g' + t_h' - 2t_n\right)\overline{Q}^{1/(1+b)} - 0.5(t_g' - t_h')\overline{Q}^{1-m} \quad (11)$$

In formula, *m* is flow optimization regulation coefficient. Its physical meaning is the percentage that flow regulation accounted for heating regulation in optimization regulation of system under the premise of ensuring the normal operation of system. *m* is taken 1/3 in two-pipe heating system. The remaining symbols and the symbols of quality regulation formula are the same.

**The formula of B .**From Eq. (1) and Eq. (2), it can be obtained that:

$$B = \frac{\Delta P}{\Delta P'} = \frac{\rho_h - \rho_g}{\rho_h' - \rho_g'} \quad (12)$$

$t_g$ and $t_h$ under a certain outdoor temperature can be calculated from Eq. (6) and Eq. (7). Then check the table of the relationship between the density and temperature of water[3]. $\rho_g$ and $\rho_h$ can be obtained. Thereby B can be calculated in different operation regulation modes and different design supply and return water temperature. The method of quality regulation with flow varied by steps and quality-flow optimization regulation are the same.

**The values of E[B] in some cities and their analysis.** The design supply and return water temperature for heating system is set for 95/70 ℃, 85/60 ℃ and 75/50 ℃. Calculation results are tabulated in Table 3.

From the table, it can be seen that. When design supply and return water temperature for heating system is reduced, the gravity head coefficients change very little. The reason is that when design supply and return water temperature for heating system are 95/70 ℃, 85/60 ℃ and 75/50 ℃ respectively. The density differences are 15.89 kg/m$^3$, 14.59 kg/m$^3$ and 13.185 kg/m$^3$ respectively.

From the formula of operation regulation, different design supply and return water temperature corresponding to supply and return water temperature with outdoor temperature change is different. Consequently the density difference between supply and return water is different. Thus B varies from Eq. (12). Why do they change little? Ref. [1] describes, for the low-temperature water heating system, when the pressure was constant, the density difference between supply and return water and the temperature difference between supply and return water has a linear relationship whose slope is 0.64. In other words, $\frac{\rho_h-\rho_g}{t_g-t_h}=0.64$. Bringing the value into Eq.(12). $B=\frac{t_g-t_h}{t_g'-t_h'}$ can be got. Bring operation regulation formula into this formula. Since the temperature difference between design supply and return water is constant, B is relevant to $\overline{Q}$ and it has nothing to do with design supply and return water temperature. Due to the linear relationship of the density difference between supply and return water and the temperature difference between supply and return water is fitted and is not exact, B changes little in different design supply and return water temperature.

Table 3 The E[B] values of some cities in China

| city | Quality regulation | | | quality regulation with flow varied by steps | | | quality - flow optimization regulation | | |
|---|---|---|---|---|---|---|---|---|---|
| | 95/70 | 85/60 | 75/50 | 95/70 | 85/60 | 75/50 | 95/70 | 85/60 | 75/50 |
| Beijing | 0.63 | 0.64 | 0.63 | 0.74 | 0.74 | 0.73 | 0.70 | 0.70 | 0.69 |
| Tianjin | 0.63 | 0.64 | 0.63 | 0.75 | 0.75 | 0.74 | 0.70 | 0.70 | 0.69 |
| Harbin | 0.56 | 0.57 | 0.55 | 0.62 | 0.63 | 0.60 | 0.64 | 0.64 | 0.62 |
| Changchun | 0.56 | 0.57 | 0.55 | 0.63 | 0.64 | 0.61 | 0.64 | 0.64 | 0.62 |
| Urumqi | 0.59 | 0.59 | 0.58 | 0.66 | 0.66 | 0.64 | 0.66 | 0.66 | 0.64 |
| Shenyang | 0.57 | 0.57 | 0.56 | 0.65 | 0.65 | 0.63 | 0.64 | 0.65 | 0.63 |
| Hohhot | 0.57 | 0.57 | 0.56 | 0.65 | 0.65 | 0.63 | 0.65 | 0.65 | 0.63 |
| Yinchuan | 0.58 | 0.59 | 0.58 | 0.68 | 0.68 | 0.67 | 0.66 | 0.66 | 0.64 |
| Xining | 0.62 | 0.62 | 0.61 | 0.71 | 0.72 | 0.70 | 0.69 | 0.69 | 0.68 |
| Taiyuan | 0.62 | 0.63 | 0.62 | 0.72 | 0.72 | 0.70 | 0.69 | 0.70 | 0.69 |
| Lanzhou | 0.65 | 0.65 | 0.65 | 0.75 | 0.75 | 0.74 | 0.72 | 0.72 | 0.71 |
| Shijiazhuang | 0.66 | 0.66 | 0.66 | 0.77 | 0.77 | 0.76 | 0.73 | 0.73 | 0.72 |
| Xi'an | 0.69 | 0.69 | 0.69 | 0.84 | 0.83 | 0.83 | 0.75 | 0.76 | 0.75 |
| Zhengzhou | 0.67 | 0.67 | 0.67 | 0.82 | 0.82 | 0.81 | 0.74 | 0.74 | 0.74 |
| Jinan | 0.65 | 0.65 | 0.64 | 0.78 | 0.78 | 0.77 | 0.71 | 0.72 | 0.71 |

The gravity head coefficients change greatly in different operation regulation modes. The B ranges from 0.55 to 0.69 in quality regulation. The B ranges from 0.62 to 0.84 in quality regulation with flow varied by steps. The B ranges from 0.62 to 0.76 in quality-flow optimization regulation. The reason is that circulating flow- rate is constant in quality regulation at the whole heating period. The smaller flow-rate is remained at the stage of higher outdoor temperature in quality regulation with flow varied by steps. The flow-rate is 75% of design circulating flow- rate. There are quality regulation and flow regulation in quality - flow optimization regulation at the whole heating period. Quality regulation accounts for 67% of the share and flow regulation accounts for 33% of the share. Therefore, the modes of operation regulation for heating system are different, the range of B values are different.

The gravity head coefficients have a certain difference in different area. The reason is that $\bar{Q}$ and f(j) are the two factors that affect gravity head coefficient. When $t_w'$ is same and different outdoor temperature corresponding to the values of probability density f(j) are similar, the calculated gravity head coefficient is same. For example, $t_w'$ are both -9℃ at Beijing and Tianjin. Their f(j) are similar. The calculated gravity head coefficient is same. When $t_w'$ is same and different outdoor temperature corresponding to the values of probability density f(j) are not similar, the calculated gravity head coefficient is not same. For example, $t_w'$ are both -9℃ at Xi'an and Zhengzhou. Their f(j) are not similar. The calculated gravity head coefficient is not same.

## Conclusion

A method using mathematical expectation to calculate gravity head coefficient was presented. The calculated results reflect the average value during the whole heating period. When duration hours of the same outdoor average daily temperature have larger change, this method is still applicable.

When design supply and return water temperature for heating system is reduced, the gravity head coefficients change very little. In different operation regulation modes, the gravity head coefficients change greatly. The gravity head coefficients have a certain difference in different areas.

## References

[1]PinghuaZou, Xiaoxia Wang and Xiumu Fang: HVAC, Vol. 33 No. 1 (2003), p. 58-61[In Chinese] [2]Xiaoting Wu: Master Dissertation Of Tianjin University (2002) [In Chinese]

[3] Yaoqing Lu: *Practical design handbook of heating and air conditioning (Second edition)* (China Architecture & Building Press, Beijing, 2012) [In Chinese]

[4] Yuzhuo Tian: *Heating Engineering (First edition)* (Machinery Industry Press, Beijing, 2008) [In Chinese]

[5]Deying Li, Jiang Chen, Lianyou Li. *The method of optimal regulation of quality -flow in hot water heating system.* National HVAC refrigeration Symposium 2000, (2000) p.75-78 [In Chinese]

[6]Guangbei Tu: *Heat metering technique (first edition)* (China Architecture & Building Press, Beijing, 2003) p.75-78 and 137-140 [In Chinese]

# CHAPTER 9:

# Heating, Gas Supply, Ventilation, Air Conditioning Works and Daylighting Design

*Applied Mechanics and Materials Vols. 580-583 (2014) pp 2441-2446*
*© (2014) Trans Tech Publications, Switzerland*
*doi:10.4028/www.scientific.net/AMM.580-583.2441*

# Study on the Current Situation of Economic Analysis of Ice Storage Air-conditioning System

Li Yuna, Wang Sifu, Lv Tuzhai, Lang Shaofei

Zhengzhou Electric Power College, Zhengzhou, 450004, China

yah0133@163.com

**Key words:** Ice Storage Air-conditioning System; Economic Analysis; Evaluating Methods

**Abstract:** Ice storage air-conditioning system has incomparable advantages than a lot of of conventional air -conditioning system example for "peak shifting and valley filling". The ice storage air-conditioning systems on the research states of the economic analysis are summed up from the building of economic analysis model,the introduction of the special systems , as well as the impact of economic factors in this paper. This paper outlines several main methods about economic evaluation of the ice storage air-conditioning systems,points out some issumes in the course of the study and some places needing to improve.

## Introduction

With China's rapid economic development, the improvement of people's living, air-conditioning system spreads rapidly, so the electricity consumption of air-conditioning increases day by day, the electricity consumption of air-conditioning in Shanghai has reached the total building electricity with more than 40% , Jiangsu, Shanghai city didn't allowed air-conditioning entering the family on account of the lack of electric power . At present, the ice storage air-conditioning system can realize the merits of "peak shifting and valley filling" ,which caused by the attention of electric power department. Ice storage air conditioning system has more advantages , but the initial investment is more than conventional air-conditioning , so economic research of the ice storage air-conditioning is the premise of popularization and application of ice storage air-conditioning technology. In this paper, the author summarizes the recent economic analysis of ice storage air-conditioning system , on the basis of existing research points out some problems and areas for improvement about the ice storage cold economic , meanwhile hopes that it can promote application and popularization of the ice storage air-conditioning system in China.

## Research Situation of Economy on Ice Storage Air-conditioning

Generally Ice storage system includes the charging cycle and cooling cycle, it can be divided into cold storage, ice storage, eutectic salt storage and gas hydrate cold storage four ways according to the storage medium. Because the cold storage capacity of ice storage system is large, the volume of ice storage tank is greatly reduced, and easy to realize the standardization and seriation of cold storage equipment; at the same time, ice storage tank also can be produced on site, its request is not high, that can save a lot of money . Economy is the foundation of the survival of ice storage air-conditioning , there are many evaluation of the ice storage system about its economy by domestic researchers and engineers from many aspects , summarized as follows:

### 1.1 the Establishment of Economic Analysis Model for Economic Analysis

Establishment of ice storage economy analysis model for economic analysis is a very effective method. Some researchers at home and abroad establish the economic analysis model of ice cold storage system from the different angle, and come to a conclusion by combined with example.

The literature [1]John Wiley et al. give the typical lexamples through establishing analysis,model of the exergy and comparing with the traditional energy analysis model, finally state that the exergy analysis model have great practical significance in the economical evaluation of ice storage air-conditioning system. The literature [2] establishes economic model through the annual,cost index respectively during the life period, the initial investment and the annual operating cost , and analyse the economic for example with a construction area of Harbin of ice storage air-conditioning system, that explain it had unmatchable advantages. The literature [3] establishes economic model respectively from initial investment, operating cost and peak power consumption, but also come to two economic indicators taking an ice storage air-conditioning system for example, by compared with the conventional air conditioning , one is the reduction of peak power of air-conditioning ; two is recovery period of the increase investment of use . The literature[4] establishes model about saving year electricity , obtain five indicators about a comprehensive evaluation of the ice storage air-conditioning system of economic and social benefits, such as recovery period of the increase investment, the transfer coefficient of performance, rate of peak power, the reducing rate of performance,rate of refrigerator, capacity ratio of refrigerator and cool storage rate of air-conditioning's load.

### 1.2 Economic Analysis on Special Forms of Ice Storage System

With the development of the ice storage technology, pure ice storage system has been unable to meet the economic demand of user , so a special ice storage system arises.

The research on these aspects has a lot: ice storage system combined with low temperature air supply system is introduced respectively from the initial investment and running costs in the literature [5],results show that this system can greatly reduce the size of the wind pipe, pump power, so to reduce initial investment and running costs, at the same time to save space, and improve this system competitiveness. the literature [6] has operation cost as the indicator by aiming at three conditions (refrigeration, heating,ice) heat pump unit, and compile analysis software, then concludes energy consumption of heat pump unit and cold storage device under different load conditions by simulating cooling load of a air-conditioning period and operation of heat-pump,takes the effects of initial investment into account, finally calculates the cost in different cold storage operation scheme.

### 1.3 Using Engineering Examples for Economic Analysis

At present, many domestic scholars analyse its economy respectively from two aspects of initial investment and operation cost through the typical engineering examples, and explain that ice storage air-conditioning system is better than conventional air-conditioning system [7] [8]. On the basis of the coupling relationship among building function, price and other factors, The author analyses its economy aiming at the typical functional building in Shanghai are, and put forward a set of ice storage air conditioning system scheme in the literature [1].

### 1.4 Economic Influencing Factors of Ice Storage Cooling System

#### 1.4.1 Price of Electricity

Ice storage system is the product of the national electricity policy, therefore, the structure of price of electricity becomes the direct factors that affect the economy of the ice storage cold from the social benefits.

#### 1.4.2 Operating Mode and Operating Strategy

For the ice storage system, its economy mainly depends on the initial investment cost and operation cost. However, the selection of its running mode is the precondition of the selection of cold storage equipment capacity, because the rational system mode can determine the appropriate storage device's size, thus saving the initial investment cost; and saving operating costs as far as possible from the aspects of perfecting the operation strategy of the ice storage system.

#### 1.4.3 Ice Packing Factor

In the ice storage air-conditioning system, ice packing factor of ice storage tank is the direct factors influencing the economical performance of ice storage air-conditioning system. Ice packing factor refers to the ratio of ice's quality in the ice water mixture. It marks the volume unit of storage in the cold ice storage tank, its size has no ground for blame role in initial investment, operating cost and life cycle cost .

The literature [9] points out the suitable range of changes in the proportion of cold storage rate; the literature [10] points out the best selected range of storage rate ; the literature [11] put forward different view to definition and optimization of cool storage proportion; the literature[12] illustrates the relationship between rate of ice storage and ice storage air-conditioning factors of economy from different angles; the literature [13] introduces the calculating method for optimizing the storage rate; the literature [14] combines with a typical project, analyzes the effect of cold storage system on the economic, obtains curve relationship between the storage rate and among initial investment, annual operating cost , investment recovery period, on the basis of economy analysis method of the traditional storage cooling system.

### Economic Evaluation Method of Ice Storage Cold Air-conditioning System

There are many methods for the economic evaluation of the ice cold storage,at present simple static economic evaluation method and dynamic economic evaluation method are the most commonly used[15-17].

### 2.1 Single Static Economic Evaluation Method

The evaluation index of this method is investment recovery period. Investment recovery period of ice storage cold air-conditioning is that its increased investment divides by its operating costs of annual savings . After the recovery period of investment, operating cost of annual savings is economic benefit that the users net .

i. Calculation of initial investment cost increasing of ice storage air conditioning system

$$\Delta I = I_s - I_c \quad (1)$$

In the type: $I_s$ stands for initial investment of ice storage air-conditioning system (yuan); $I_c$ stands for initial investment of conventional air-conditioning system (yuan); $\Delta I$ stands for initial investment of increasing of the ice storage air-conditioning system (yuan).

ii. Calculation of saving operating cost throughout the year of ice storage air conditioning system

$$\Delta P = P_s - P_c \tag{2}$$

In the type: $P_s$ stands for total electricity running throughout the year of ice storage air conditioning system (yuan)； $P_c$ stands for total electricity running throughout the year of conventional air-conditioning system (yuan); $\Delta P$ stands for the amount of the annual power consumption saving of ice storage air-conditioning system (yuan).

iii. Calculation of investment recovery period

$$n = \Delta I / \Delta P \tag{3}$$

In the type: $n$ stands for investment recovery period (years).

Simple static economic evaluation method is the most simple and intuitive when using. But this method is generally believed that if the investment recovery period is less than 5 years that the system is economically feasible. When the investment recovery period is longer, we should adopt the dynamic economic evaluation method, so as to make the evaluation more practical.

### 2.2 The Dynamic Economic Evaluation Method

The dynamic economic evaluation is more perfect and precision than the single static economic evaluation method . It can be divided into dynamic payback period analysis and life cycle investment analysis method.

#### 2.2.1 Analysis Method of Dynamic Investment Recovery Period

i. If only considering the effect of the time value of money , computational formula of dynamic investment recovery period is as follows:

$$\sum_{n=0}^{N} \frac{E_n}{(1+R_0)^n} = \sum_{n=0}^{k} \frac{I_n}{(1+R_0)^n} \tag{4}$$

In the type: N stands for dynamic investment recovery period (years)； $R_0$ stands for the standard discount rate；k stands for the ending year of investment； $E_n$ stands for the net earnings of N years； $I_n$ stands for the investment of N years.

ii. In addition to consider the time value of money, but also consider factors such as energy prices are affected by inflation, then computational formula of the dynamic investment recovery period is as follows:

$$N = \frac{\log\{1-(i-c-e)\frac{I_s - I_c}{P_c - P_s}}{\log\{\frac{1+e}{1+i-c}\}} \quad (5)$$

In the type: N， $I_s$， $I_c$， $P_s$， $P_c$ with the above； $i$ stands for interest； $c$ stands for the rate of prices rising； $e$ stands for the rate of energy costs rising.

### 2.2.2 Analysis Method of Life Cycle Investment

This method is also called the net present value method. It analyzes economy coming from the using life cycle of the whole equipment .Life cycle investment includs all life cycle cost, energy consumption cost of the building, equipment purchase, installation, maintenance, replacement cost, and other expenses related to the investment.

When all the money is transformed into the net amount, it has to consider the past and the future funding of equivalence

$$NPV = \sum_{N=1}^{L}\{\frac{E_n}{(1+R)^n}\} - I_c \quad (6)$$

In the type: NPV stands for the net present value； $E_n$ stands for the net income of N years；R stands for the discount rate； $I_c$ stands for a one-time investment；L stands for economic life.

When the net present value (NPV)> 0, it means the project scheme is feasible.When using the net present value to evaluate several schemes, if the service life of the scheme is the same, the optimal net present value is the highest scheme. So,the economic life and the discount rate must be carefully selected. Economic life of equipment is the length of time that the equipment can continuously use.For cold storage equipment, although cool storage tank may last longer, but the biggest economic life is thought to be 20 years. The discount rate represents the return on investment that the people would expect.

## The Existing Problem and Needs to be Improved of Ice Storage Air-conditioning System in the Process of Economic Evaluation

The economic evaluation of ice storage air-conditioning system is for a system's engineering, needs to make concrete analysis to specific ngineering, comes to the reasonable conclusion. In evaluating the ice storage system and establishing the model, we need to pay attention to the built model can fully reflect the initial investment and operating cost of this system, so that economic evaluation is more objective and fair. Most of the literature when narrating economy influence of ice storage rate of the ice storage air-conditioning system, just give roughly best cool storage rate scope, and there is no specific instructions, which remains to be further research. Economical analysis of ice storage air-conditioning system is more complex, some people design the relevant software of economic analysis, but whether software itself really evaluate the economy of ice storage system, we still should do further research, so as to make it perfect.

## Conclusions

This paper summarizes the research status of economic analysis of ice storage air-conditioning system from four aspects, and shows economy analysis of research work has made some progress in the ice storage air conditioning system in our country. Also it pointes out that the model of the ice storage air-conditioning system, the optimal cool storage rate and efficiency analysis software of ice storage and so on need further in-depth study, so as to promote the development of ice storage air-conditioning system in our country.

## References：

[1] John Wiley & Sons, Ltd. Thermal energy storage systems as a key technology in energy conservation[J]. International Journal of Energy Research, 2002, 26(7): 567 – 588.
[2] li Xiaoyan. economic analysis and comparison of Ice storage air-conditioning system [J]. Journal of Harbin University of Commerce, 2004,20(2):223-226.
[3] Fang Guiyin ,Chen Zeshao. Economic Analysis and Comparison of Storage Air-conditioning System [J]. Energy Research and Information,2000,16(4):23-27.
[4] Zhang Hua,Wang Yiyi. Evaluation Method of Ice Storage Air-conditioning System. [J]. Energy Conservation Technology,1997,(4): 44-47.
[5] Chen Yeqing and so on. Technology and Economic Analysis for the System of Cold Air Distribution with Ice Storage [J]. Refrigeration and Air Conditioning,2004,4(4): 80-84.
[6] Zhang Jinyang and so on. Economic Analysis Method of Air-conditioning System Using Three-operating Condtion Heat-pump Unit and Ice-thermal Storage Technique Three Conditions of Heat Pump Units Use Cold Storage Technology of Ice [J]. Refrigeration Air Conditioning and Power Machinery,2004,25(6): 57-59.
[7] Meng Gongqiao,Hu Hong. Design and Economic Analysis of Ice-thermal Storage System on Zhejiang Huating Street Concentrated Air Conditioning [J]. Refrigeration Air Conditioning and Power Machinery,2004,25(4): 69-71.
[8] Cai Lude and so on. Ice Storage System of Ramada Plaza Tianlu Hotel in Wuhan[J]. HV&AC,2002,32(1): 70-73.
[9] Lu Shengli. Effects of Cool Storage Proportion on Expenditure of Equipment and Operation[J]. HV&AC,1998,28(3): 57-59.
[10] Yang Shuming. Determination of the Optimal Ice Storage Rate[J]. HV&AC,1999，29(3):73.
[11] Yin Pin. Query about the Concept of the “Storage Rate”[J]. HV&AC，1999, 29(3): 23-24.
[12] Hua Mingruo and so on. Relationship between the Ice Thermal Storage Proportion and Economic Factors of Ice Thermal Storage Air Conditioning[J].J.University of Shanghai for Science and Technology，2002, 24(2):113-118.
[13] Zhang Lijun,Zhang Pin. Impact of Ice Storage Rate on the System Economic Effects and Determination of Its Optimum[J]. HV&AC, 1997, 27(5): 2-5.
[14] Du Yanxia and so on. Study on Storage Rate and Economical Performance of Ice-stotage Air-conditioning System[J]. Journal of Refrigeration,2004, (2):46-49.
[15] Fang Guiyin. The New Technology of Cool Storage Air-conditioning Engineering [M].Beijing：People's Posts and Telecommunications Press.2000:255-256.
[16] Ma Yuchi. The Economic Analysis of Ice Storage Air-conditioning System [D]. Xi'an University Of Architecture And Technology, 2005.
[17] Jiang Fuwei. The Technical and Economic Study of Ice-storage Air-conditioning System [D]. Dalian：Dalian Maritime University, 2003.

*Applied Mechanics and Materials Vols. 580-583 (2014) pp 2447-2451*
*© (2014) Trans Tech Publications, Switzerland*
*doi:10.4028/www.scientific.net/AMM.580-583.2447*

# A CFD Simulation of Indoor Natural Ventilation of a Residential District In Zhuzhou

Zhiyong Wang[1,a], Shunfu Yang[1,b*], Changrong Liu[1], Tianyu Zhang[1], Na Cui[1]

[1]School of Civil Engineering, Hunan University of Technology, Zhuzhou, Hunan, China, 412007

[a]zywang668@126.com, [b]ford_young@163.com

**Keywords:** natural ventilation; CFD; numerical simulation; residential district

**Abstract.** With the promotion of building energy conservation, many residential areas are closely link with energy saving in design phase, and natural ventilation becomes the key to reduce building energy consumption. Thus, house design and building distribution of residential district is particularly important. Computational fluid dynamics (CFD) get rapid development in recent 20 years, especially in architectural design. This text established a model of part of a residential district in Zhuzhou based upon ANSYS FLUENT CFD software, and used numerical simulation method to simulate the condition of indoor natural ventilation under typical summer climate when the doors and windows of buildings were opened. The distribution regularities of indoor velocity field and pressure field and etc have been gotten. These data provide a theoretical basis to evaluate the building distribution of residential area.

## Introduction

Nowadays residential energy consumption accounts for more proportion of building energy consumption in China. Compared with mechanical ventilation and air conditioning, natural ventilation show the remarkable advantages of energy saving and environmental protection on the premise to meet the requirements. The main purpose of applying natural ventilation is to make full use of natural wind to take away the indoor quantity of heat and reduce the service time of air conditioning when the outdoor temperature is benefit to room draught in transition season. It is possible to achieve the goal of energy saving by this way. But there are some limitations on layout in a few constructions. The indoor comfort of some rooms in these constructions is greatly influenced by the poor effect of natural ventilation. Therefore, studying the law of indoor natural ventilation becomes the most important premise of indoor environment design.

## Architectural overview and meteorological conditions

The plane sketch of simulating region in this residential district is shown in Fig. 1. Building A to E has the same house type. They have a total of 30 floors and there are 4 households in each storey. The floor height of building A to E is 3.3 meters. The structure of each house type is shown in Fig. 2. Building F to J are single-family villas, they all have the same house type. These villas have three floors which height could arrive at 3.3 meters. Our research mainly focused on the third floor, the structure is also shown in Fig. 2. This residential district is in Zhuzhou city where is located in the subtropical monsoon climate zone which mainly prevail south wind and northwest wind in summer. We operated this simulation on the condition that the outdoor temperature was at 27℃ and chose 2.2m/s as the south air velocity.

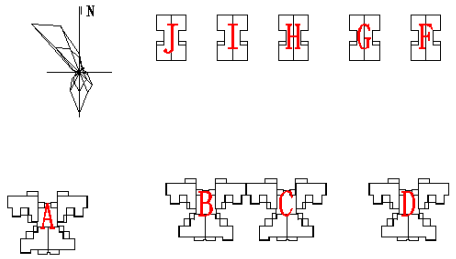


**Fig. 1. The plan sketch of simulated building in the residential district**

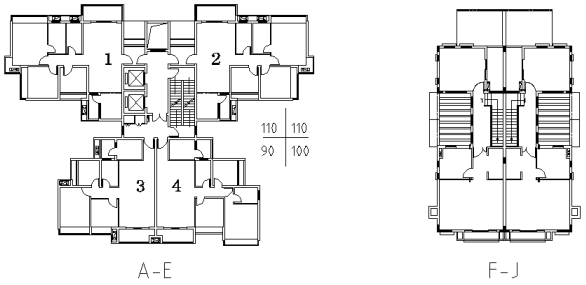


**Fig. 2. The standard floor layout of each building**

## Mathematical and physical model

At present, most commercial CFD software select finite volume method to solve the calculation. We calculated the indoor natural ventilation by regarded it as the stationary flow of incompressible turbulent flow. Chose RNG $k$-$\varepsilon$ model as the turbulence models, and assumed that the airflow meet the continuity equation; momentum conservation law and the law of conservation of energy.

In the RNG $k$-$\varepsilon$ model, the effect of small-scale was reflected by large-scale movement and the revised viscosity item. Thus, the small-scale movement could be systematically removed from the control equation. After some changed, the $k$ equation and epsilon equation we got as follow was very similar to the standard $k$-$\varepsilon$ model.

$$\frac{\partial(\rho k)}{\partial t}+\frac{\partial\left(\rho k u_i\right)}{\partial x_i}=\frac{\partial}{\partial x_j}\left[\alpha_k \mu_{eff}\frac{\partial k}{\partial x_j}\right]+G_k+\rho\varepsilon \tag{1}$$

$$\frac{\partial(\rho\varepsilon)}{\partial t}+\frac{\partial(\rho\varepsilon u_i)}{\partial x_i}=\frac{\partial}{\partial x_j}\left[\alpha_\varepsilon \mu_{eff}\frac{\partial \varepsilon}{\partial x_j}\right]+\frac{C_{1\varepsilon}\varepsilon}{k}G_k-C_{2\varepsilon}\rho\frac{\varepsilon^2}{k} \tag{2}$$

Where $\alpha_k = \alpha_\varepsilon = 1.39$; $\mu_{eff}$ is the sum of turbulent viscosity coefficient and kinetic viscosity coefficient; $C_{1\varepsilon}$ and $C_{2\varepsilon}$ is the empirical constant; $G_k$ is a item of $k$ which represent turbulent kinetic energy caused by average velocity gradient.

The continuity equation is expressed as:

$$\frac{\partial\rho}{\partial t}+\nabla(\rho\boldsymbol{u})=0 \tag{3}$$

Where $\rho$ is the density; $t$ is the time; $\boldsymbol{u}$ is the velocity vector of fluid.

The momentum conservation equation is defined as:

$$\frac{\partial(\rho u)}{\partial t}+\nabla(\rho u\boldsymbol{u})=\nabla(\mu\,\mathrm{grad}\,u)-\frac{\partial p}{\partial x}+S_u \tag{4}$$

Where $u$ is a component of the velocity vector $\boldsymbol{u}$ in the x direction; $p$ is the pressure on the infinitesimal body of fluid; $S_u$ is the generalized source term of momentum conservation equation.

The energy conservation equation can be written as:

$$\frac{\partial\rho T}{\partial t}+\nabla(\rho\boldsymbol{u}T)=\nabla\left(\frac{k}{c_p}\mathrm{grad}\,T\right)+S_T \tag{5}$$

Where $c_p$ is the specific heat; $T$ is the temperature; $k$ is the heat transfer coefficient of fluid; $S_T$ is the viscous dissipation term.

**Model building and meshing**

The simulation was on the condition that it was natural ventilation when all the doors and windows indoor were opened. Considering the computer's memory and operating speed, we simplified the actual buildings into two-dimensional model and simulated the natural ventilation in people main activity area of third floor and tenth floor. The area is 1.5 meters high from the local ground. In order to accurately simulate the air moving in and out of the room, researchers selected a region which is 300 meters in length and 200 meters in width as the simulation area. The buildings to be simulated were put in the middle of the area. We chose unstructured grids for computational domain and defined the indoor grid size as 400 millimeters for the purpose to obtain a more accurate calculation results. Due to few influence on indoor simulation, the external grid was gradually increasing from indoor to outdoor with an amplification factor of 1.12.

**Set of boundary conditions**

Inlet boundary conditions: There is a gradient wind in the vertical direction because of the friction caused by the ground. Gradient wind is distributed on the basis of the law of boundary layer. The computational formula is shown below:

$$\frac{v}{v_s}=(\frac{z}{z_s})^{\alpha} \tag{6}$$

Where $v$ and $z$ represent average air velocity and height respectively; $v_s$ and $z_s$ represent average air velocity and height at standard height respectively (most countries often take 10 meters); $\alpha$ is the ground roughness coefficient, it is generally take 0.3 for downtown area which have dense and higher buildings. Chose velocity inlet as the inlet boundary conditions, the wind speed at different heights were calculated by Eq. 6.

Outlet boundary conditions: outflow boundary.

On both sides of the fluid domain: moving wall boundary.

Building envelope: no slip wall boundary.

**The results and analysis of numerical simulation**

**The simulated results and analysis in people main activity area of third floor**

Fig. 3 to Fig.6 shows that the rooms on the windward side of building A to E got excellent indoor ventilation effect; the air velocity can reach to 1 to 2.5 m/s. People in the room can feel the wind flow. Meanwhile, the wind can take away the quantity of heat in the room and reduce the energy consumption of air conditioning.

As to the rooms on the leeward side, the ventilation effect varies from building to building. The air velocity in house type 1 of building A and B is maintained below 1 m/s, it's indoor temperature is higher than other rooms, the ventilation effect is poor and the age of air is greater than 100 seconds. The reason is that the incoming flow blocked by the house type 3 and it formed a separation zone in which the incoming flow bypass house type 1 and moving backwards. These rooms should rely on air conditioning to assist the interchange of air inside the room in summer.

As a result of blocked by elevator shaft, the ventilation effect is also less obvious in house type 2 of building E. There is almost no air circulation in most rooms except sitting room which has an air velocity about 2 m/s at the entrance. The age of air in these rooms is greater than 120 seconds and the temperature is relatively high. Thus, they also need air conditioning to assist the interchange of air in the summer.

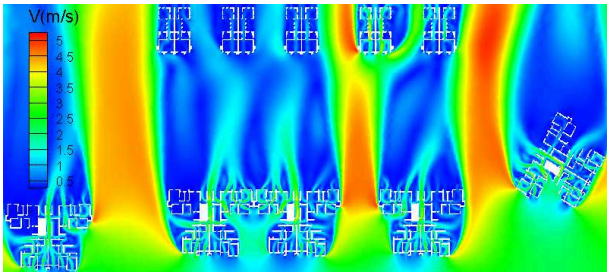


**Fig. 3. Contours of the velocity**

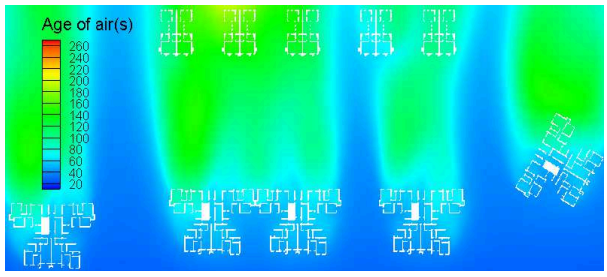


**Fig. 4. Contours of the age of air**

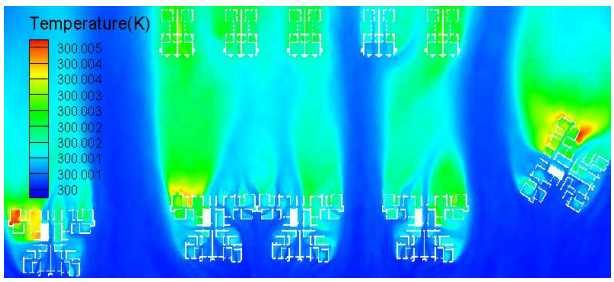


**Fig. 5. Contours of the temperature**

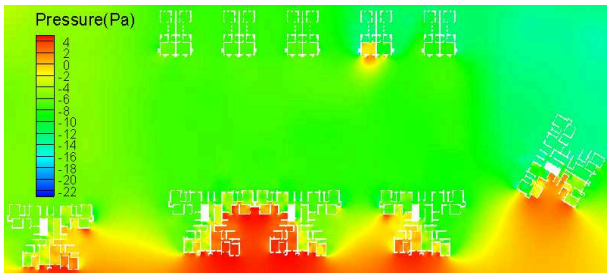


**Fig. 6. Contours of the pressure**

Incoming flow suddenly blocked between building B and C for the small spacing of two buildings and formed a strong wind pressure in this region. The pressure contribute to the natural ventilation in house type 2 of building B and house type 1 of building C. Maximum air velocity of indoor can reach up to 3.5 m/s, it gives people a sense with the breeze caress the cheeks.

For the height of building A to E is nearly 100 meters, it form a cavity area on there backfaces. The wind velocity in this area is rather small. Then, a wake zone which extend to a distance at several times of the building height is formed because the kinetic energy loss of airflow. Building H to J just located in the wake zone of building B to D. Though the wind is weak and the wind direction is not stable in this area, building F to J has an unobstructed indoor structure which can help to generate cross ventilation in the north and south direction. So, there are two obvious air channel appear in building H to J, the air velocity in channel can reach to 1.5 to 2 m/s.

Building G is out of the wake zone. The incoming flow get through between two tall buildings, this increase the air pressure and air velocity and form a wind tunnel at last. It ensures building G a perfect ventilation effect; the maximum indoor air velocity can reach up to 4 m/s, and the age of air is also maintained a level below 100 seconds. Building G is able to keep a good indoor thermal comfort completely by natural ventilation.

**The simulated results and analysis in people main activity area of tenth floor**

Fig. 7 to Fig. 10 shows that the speed of incoming flow on tenth floor was faster than third floor, it is because of the gradient wind. These improve the natural ventilation of several rooms. For example, house type 1 of building B get a maximum air velocity at 2 m/s along with the strengthening of natural ventilation, and the age of air is kept below 70 seconds. The quantity of heat in rooms is taken away by natural ventilation.

There is a slightest change on ventilation in house type 1 of building A and house type 2 of building E, the indoor air velocity is still at a slow level, the temperature is relatively high, these rooms still need the help of air conditioning to meet the indoor air quality.

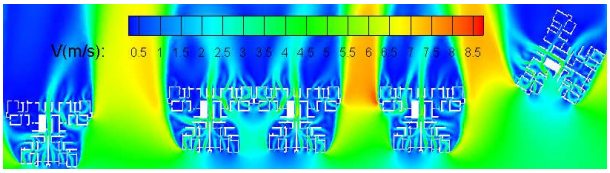


Fig. 7. Contours of the velocity

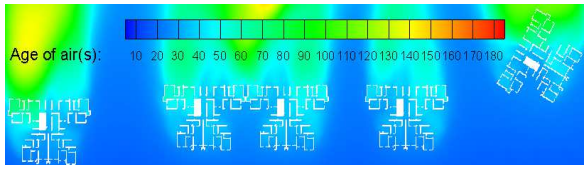


Fig. 8. Contours of the age of air

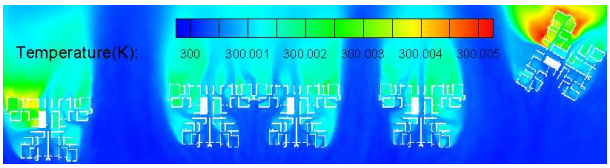


Fig. 9. Contours of the temperature

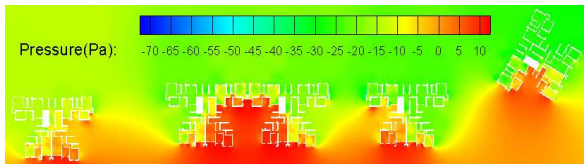


Fig. 10. Contours of the pressure

## Conclusions

The study shows that using CFD software to simulate indoor ventilation has an important value of engineering application, for it can reduce the research and development (R&D) cost and guarantee the feasibility and reliability of design. Many detail data and graphics have been gotten from this numerical simulation, such as air velocity, air age, temperature and pressure of architecture. It can be found from these results that it is reasonable of most architectural design except a small part need to be improved. A majority of rooms can make the most of natural ventilation to eliminate indoor quantity of heat and satisfy the requirement of comfort and energy saving.

## Acknowledgements

This work was financially supported by the Scientific Research Fund of Hunan Provincial Education Department (13A001), Hunan Provincial Natural Science Foundation of China (12JJ4042, 13JJ6065), the National Key Technology R&D Program of China (2011BAJ03B07), the Program of Science and Technology of Hunan Province (2012WK3040) and Natural Science research Program of Hunan University of Technology (2011HZX20, 2012HZX19).

## References

[1] Hanqing Wang. The fluid flow numerical calculation method and application of HVAC. Science Press, Beijing, 2013. (in Chinese)

[2] Weiding Long, Yong Wu. Building energy-saving technology. China Building Industry Press, Beijing, 2009. (in Chinese)

[3] Fengying Yan, Xinhua Wang and Youcong Wu. A simulation of indoor natural ventilation and thermal comfort based on CFD. Journal of Tianjin University, 42(2009): 407−412. (in Chinese)

[4] Zengji Cai, Tianyu Long. Fluid mechanics pump and fan (Fourth edition). China Building Industry Press, Beijing, 1999. (in Chinese)

[5] Zheng Wen, Liangchen Shi and Yiru Ren. Application course of FLUENT fluid calculation. Tsinghua University Press, Beijing, 2009. (in Chinese)

[6] Fujun Wang. Analysis of computational fluid dynamics—Principle and application of CFD software. Tsinghua University Press, Beijing, 2004. (in Chinese)

[7] Zhanzhong Han, Jing Wang and Xiaoping Lan. FLUENT—Examples and application of fluid engineering simulating calculation (Second edition). Beijing Institute of Technology Press, Beijing, 2010. (in Chinese)

*Applied Mechanics and Materials Vols. 580-583 (2014) pp 2452-2456*
*© (2014) Trans Tech Publications, Switzerland*
*doi:10.4028/www.scientific.net/AMM.580-583.2452*

# Analysis of influence factors on the Internal-melt Ice-on-tube while Melting

Yi Liu[1,a]

[1]School of Energy and Civil Engineering, Harbin University of Commerce, Harbin Song Bei Xue-hai Street ,District No.1, Harbin, 150028, China

[a]liuyiyuanhongyan1975@126.com

**Keywords:** ice storage system, internal-melt ice-on-tube, numerical simulation, enthalpy method.

**Abstract.** The numerical simulation is widely used in study of the ice storage system. The model about melting is established and solved by using enthalpy method. Natural convection of the melted water in the course of melting is studied. Effects on the performance of heat-exchange, caused by variation of velocity of the refrigerant, inner diameter of the tube, initial temperature of the external water and inlet temperature of the refrigerant, are simulated and analyzed.

1. As the increase of cryogen inlet temperature, the influence of natural convention is more and more in the process of melting heat transfer.
2. Under the conditions of the different cryogen velocity, the different diameter of tube and the different initial temperature of ice layer, the effect of natural convention also is different in the process of melting heat transfer.

## Introduction

The ice storage system is widely used because of its simple design and obviously economy. The overseas study of the ice storage system starts in 1930s and now the technique is already mature [1,2,3]. The domestic study of the ice storage system starts in1990s and is still in underway stage. The studies focus on the melting and icing models [4,5], and the experiments of the ice storage system [6,7].

It is more complicated to analyze the heat transfer process when melting because it always goes with phase change. So the academic studies of melting always neglect the natural convection. But in fact the influence of natural convection is very great and can not be neglected. In the paper, the melting process of the ice storage tube is calculated by using enthalpy method, Natural convection is considered. The effects of some initial parameters on natural convection have been simulated and analyzed.

## Physical Model

When setting up the melting model which chooses the glycol as cryogen under considering natural convection, make the following assumptions to simplify the problem:

1) Because the length of the tube is much more than its diameter, so neglect the radial heat transfer and polar heat transfer of the cryogen.
2) The initial temperature of the ice in the groove is uniform and is a constant temperature , $T_{ice} \prec 0^{\circ}C$;
3) During the whole process of the heat transfer, properties of glycol, ice and water always keep the same; however, when dealt with volume stress in the momentum equation, water density was considered as variance, other ones was still considered as constant;
4) The thickness of the ice storage tube wall is very thin, and thermal conductivity is great. Therefore, the thermal resistance can be neglected;
5) The thermal insulation capability of groove wall is strong. Therefore, the heat loss to the surroundings can be neglected;

6) Viscous dissipation of water is neglected;
7) Volume change caused by phase change is neglected.

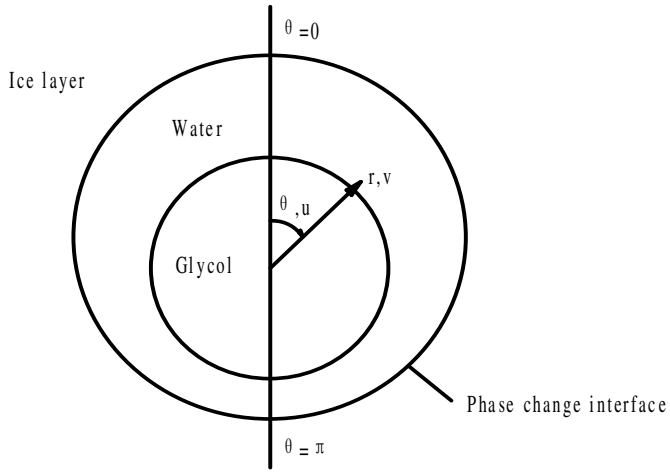


Figure.1 Physical model and coordinate system

## Mathematicl Model and Solution Method

Fig 1 shows the physical model of the section which is vertical to the axis in the ice melting process under natural convention and the polar coordinate system. According to the physical model, mathematical model can be conducted as follows:

**Continuity equation**

$$\frac{1}{r}\frac{\partial}{\partial r}(rv)+\frac{1}{r}\frac{\partial u}{\partial r}=0 \tag{1}$$

**Momentum equation**

Radial direction *r*

$$\rho\frac{\partial v}{\partial \tau}+\frac{\partial}{\partial r}(\rho vv)+\frac{1}{r}\frac{\partial}{\partial \theta}(\rho uv)-\frac{\rho u^2}{r} = \rho g\beta(t-t_{\mathrm{ph}})\cos\theta-\frac{\partial p}{\partial r}+\frac{1}{r}\frac{\partial}{\partial r}(r\mu\frac{\partial v}{\partial r})+\frac{\mu}{r^2}\frac{\partial^2 v}{\partial \theta^2}-\frac{2\mu}{r^2}\frac{\partial u}{\partial \theta}-\frac{v}{r^2} \tag{2}$$

Polar angle direction $\theta$

$$\rho\frac{\partial u}{\partial \tau}+\frac{\partial}{\partial r}(\rho vu)+\frac{1}{r}\frac{\partial}{\partial \theta}(\rho uu)-\frac{\rho uv}{r} = -\rho g\beta(T-T_{\mathrm{ph}})\sin\theta-\frac{1}{r}\frac{\partial p}{\partial \theta}+\frac{1}{r}\frac{\partial}{\partial r}(r\mu\frac{\partial u}{\partial r})+\frac{\mu}{r^2}\frac{\partial^2 u}{\partial \theta^2}+\frac{2\mu}{r^2}\frac{\partial v}{\partial \theta}-\frac{u}{r^2} \tag{3}$$

**Energy equation**

$$\rho c_{\mathrm{p}}[\frac{\partial T}{\partial \tau}+\frac{\partial}{\partial r}(vT)+\frac{1}{r}\frac{\partial}{\partial \theta}(uT)] = \frac{1}{r}\frac{\partial}{\partial r}(rk\frac{\partial T}{\partial r})+\frac{1}{r}\frac{\partial}{\partial \theta}(\frac{1}{r}k\frac{\partial T}{\partial \theta})+\frac{\partial}{\partial z}(k\frac{\partial T}{\partial z}) \tag{4}$$

**Energy equation of enthalpy method**

Using enthalpy method, energy equation (4) can be converted as follows:

$$\frac{\rho}{c_{\mathrm{p}}}\frac{\partial h}{\partial \tau}+\frac{\partial}{\partial r}(\rho vT)+\frac{1}{r}\frac{\partial}{\partial \theta}(\rho uT) = \frac{1}{r}\frac{\partial}{\partial r}(r\frac{k}{c_{\mathrm{p}}}\frac{\partial T}{\partial r})+\frac{1}{r}\frac{\partial}{\partial \theta}(\frac{1}{r}\frac{k}{c_{\mathrm{p}}}\frac{\partial T}{\partial \theta})+\frac{\partial}{\partial z}(\frac{k}{c_{\mathrm{p}}}\frac{\partial T}{\partial z}) \tag{5}$$

Where:

$$t - t_{ph} = \begin{cases} (h - h_s^*)/c_s & h < h_s^* \\ 0 & h_s^* \le h \le h_l^* \\ (h - h_l^*)/c_l & h > h_l^* \end{cases} \quad (6)$$

$$\rho = \begin{cases} \rho_s & h < h_s^* \\ \rho_l & h > h_l^* \end{cases} \qquad k = \begin{cases} k_s & h < h_s^* \\ k_l & h > h_l^* \end{cases} \quad (7)$$

Meanings of the above symbols:

| | | | | | |
|---|---|---|---|---|---|
| $\theta$ | polar coordinate | $(m)$ | $r$ | radial coordinate | $(m)$ |
| $z$ | axial coordinate | $(m)$ | $v$ | radial velocity | $(m/s)$ |
| $u$ | peripheral velocity | $(m/s)$ | $\rho$ | density | $(m^3/kg)$ |
| $\mu$ | kinetic viscosity | $(Pa \cdot s)$ | $\tau$ | time | $(s)$ |
| $g$ | acceleration of gravity | $(m/s^2)$ | $\beta$ | volume expansion coefficient | (1/℃) |
| $k$ | heat conductivity coefficient | $(w/[m \cdot °C])$ | $c_p$ | specific heat | $(kJ/(kg \cdot K))$ |
| $T$ | temperature | $(K)$ | $ph$ | phase change point | |
| $h$ | normal specific enthalpy | $(kJ/kg)$ | $h_s^*$ | ice specific enthalpy | $(kJ/kg)$ |
| $h_l^*$ | water specific enthalpy | $(kJ/kg)$ | $c_s$ | ice specific heat | $(kJ/(kg \cdot K))$ |
| $c_l$ | water specific heat | $(kJ/(kg \cdot K))$ | | | |

**Solution of The Governing Equation**

\In this paper, the solution domain is dispersed by using inside-node method. Governing equations are integrally dispersed using the control volume method and the staggered grid technology. The discrete equations are solved using SIMPLE algorithm. Because of the nonlinear coupling relationship of each variable, during the process of applying SIMPLE algorithm, sub-relaxation iteration method is used to accelerate converging of the nonlinear problem [8].

**Simulation Result and Analysis**

The shape of the ice storage box is considered as columniation, basic parameters for calculation are given in Table 1.

Table 1 Basic parameters for calculation

| | | | |
|---|---|---|---|
| Fluid specific heat | 3.85 kJ/(kg·℃) | Ice heat conductivity | 2.215 W/(m·℃) |
| Fluid density | 1030 kg/m$^3$ | Ice density | 916 kg/m$^3$ |
| Fluid heat conductivity | 0.5 W/(m·℃) | Ice specific heat | 2090 J/(kg·℃) |
| Fluid kinetic viscosity | 1.77 mPa·s | Water heat conductivity | 0.551 W/(m·℃) |
| Fluid velocity | 0.5 m/s | Water density | 1000kg/m$^3$ |
| Fluid inlet temperature | 20 ℃ | Water specific heat | 4187 J/(kg·℃) |
| Inside diameter of tube | 17 mm | Ice-water phase change temperature | 0 ℃ |
| Outside diameter of tube | 20 mm | Ice-water phase change Latent heat | 335kJ/kg |
| Inside diameter of box | 0.4m | Initial temperature of ice | -0.5℃ |
| Outside diameter of box | 1m | | |

In order to analyze the influence of different initial parameters to natural convection, we define $r_{in\text{-}out}$ as follow:

$$r_{in-out} = \frac{r_{in-top} + r_{out-top}}{2} \quad (6)$$

$r_{in-top}$ top melting radius of the intake (m)

$r_{out-top}$ bottom melting radius of the exit (m)

Simulation result and analysis as follows:

Figure.2 shows the influence of different intake temperature to natural convection. At the initial of melting, natural convection is very weak because there is little water, so the influence is little. But along with the quantity of water increasing, natural convection become more and more strong, and the influence will become strong gradually. The higher temperature and the stronger natural convection, this is because that the increase of the liquid intake temperature causes the increase of the difference in temperature, and then the increase of the difference in temperature causes the increase of natural convection.

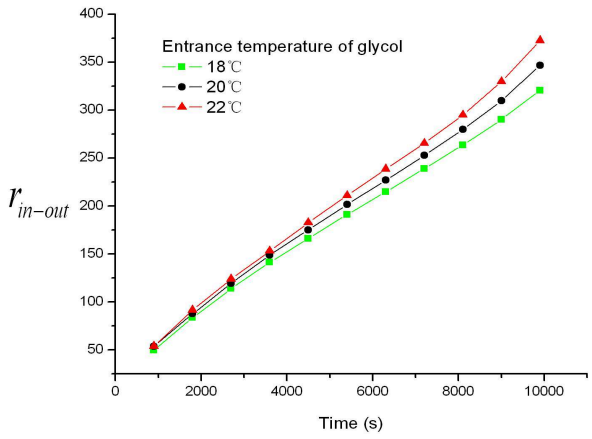


Figure.2 Influence of glycol entrance temperature on $r_{in-out}$

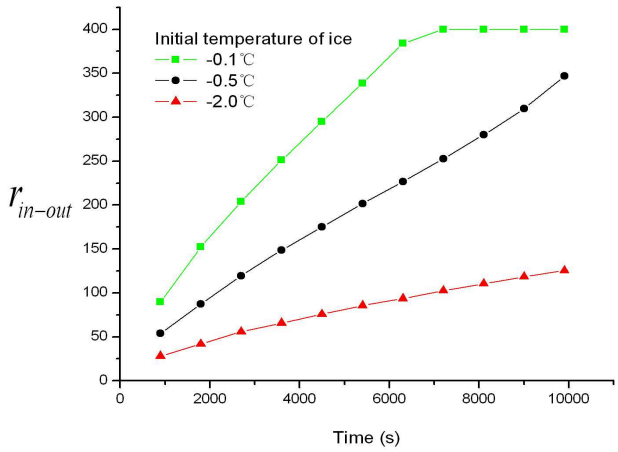


Figure.3 Influence of initial temperature of ice on $r_{in-out}$

Figure.3 shows the influence of different ice initial temperature on natural convection. From the above chart we can find that the intake temperature of ice influence natural convection very greatly. The lower ice temperature and the weaker intensity of natural convection, this is because that the ice needs more quantity of heat if the ice temperature becomes lower, and accordingly natural convection will occur even later. At one time we also find that the influence of the ice temperature will become stronger along with time going. This is because that if the ice temperature is higher, the quantity of the melted water is more, accordingly the intensity of natural convection will be stronger at the same time.

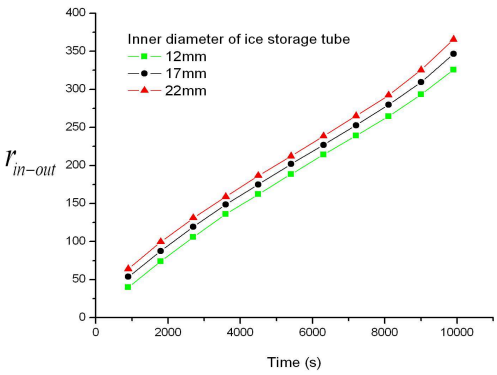


Figure.4 Influence of inner diameter of ice storage tube on $r_{in-out}$

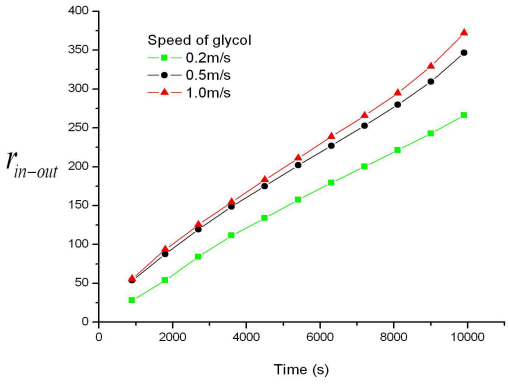


Figure.5 Influence of velocity of glycol on $r_{in-out}$

Figure.4 shows the influence of different tube inner diameter to natural convection. From the above chart we can find that the influence of the inner diameter is almost linear. This is because that the change of the inner diameter mainly influences the quantity of the cryogen which drills through the tube, but the influence to the temperature field is smaller, so the influence of the inner diameter is almost linear.

Figure.5 shows the influence of different cryogen velocity to natural convection. From the above chart we can find that the influence of cryogen velocity will gradually become stronger along with time. This is because that the heat exchange between cryogen and water will increase along with the increase of the cryogen's velocity, so the temperature grade of water will increase and natural convection will increase. At the same time, we can find that the grade of natural convection intensity will descend along with the increase of the cryogen velocity. This is because that grade of the heat exchange between cryogen and water will descend along the cryogen velocity.

## Summary

1. The influence of the inner diameter of the storage tube is almost linear.
2. The influence of the cryogen initial temperature, the cryogen velocity and the ice initial temperature on natural convection will increase along with time.

## References

[1] D. Arnold. Dynamic Simulation of Encapsulated Ice Stores-Part1: Model Development and Validation. ASHRAE Transfer. 1990，96：566~571.
[2] Akio Saito. Recent Advances in Research on Cold Thermal Energy Storage. (2002)
[3] Akbari H, Mertol A. Thermal Energy Storage for Cooling of Commercial Buiding. Kilkis S. Energy Storage Systems. 1989：315~347.
[4] Zhong Yi，Huang Hu，Zhong Xiao-song. Icing progress outside the tube of the ice storage. Journal of Harbin Institute of Technology. 2004，(10)：1310~1313.
[5] Zhong Xian-bing，Li Fang-qing. Numerical simulation of the ice ball heat transfer. Building Energy & Environment. 2002，(3)：26~29.
[6] Yan Gang. Experiment of Concretionary of ice storage ball. Refeigeration & Air-Condition. 2002，(4)：22~24.
[7] Du Nen-jie. Icing experiment of conchoidal pipy ice storage box. Fluid Machinery. 2004，(10)：42~45.
[8] Tao Wen-quan, Numerical Heater Transfer. Xi'an Jiaotong University Press.(2001)

*Applied Mechanics and Materials Vols. 580-583 (2014) pp 2457-2460*
*© (2014) Trans Tech Publications, Switzerland*
*doi:10.4028/www.scientific.net/AMM.580-583.2457*

# Effect of the circulation flow velocity in ground heat exchangers on system operation

Zishu Qi [1, 2, 3, a],Qing Gao [1, 3, *b],Yan Liu[1, 3],Zhenhai Gao [1] and Li Bai[2]

[1]State Key Laboratory of Automotive Simulation and Control, Jilin University, Changchun 130025, PR China

[2] Key Laboratory of Songliao Aquatic Environment of Ministry of Education, Jilin Jianzhu University, Changchun 130118, PR China

[3] Department of Thermal Energy Engineering, Jilin University, Changchun 130025, PR China

[a]senior00685@163.com, [b] gaoqing@jlu.ed.cn

**Keywords:** ground source heat pump; flow velocity; system operation; power consumption

**Abstract.** The heat pump system by using earth energy is increasing very rapidly. In this paper, by studying the underground heat exchanger heat transfer mode, the computing platform for ground source heat pump system was established. Through a engineering case, the influence character of the circulation flow velocity in ground heat exchangers on the fluid temperature, the heat pump power consumption, and the length of system were analyzed, which provide an approach for system engineering design and operation prediction, and for the thermodynamic analysis of performance of system year by year and prospective study to guide the engineering practice.

## Introduction

Despite the certain development of ground source heat pump（GSHP）and related underground storage technology, some work still should be strengthened, such as the influence law of the circulation flow velocity in ground heat exchangers, which is one important problem for system operation. In fact, in unbalance load area, the longer application of the large scale GSHP engineering has caused underground energy decay and system efficiency decline, and become bottleneck and obstacle to the sustainable application, so complex science and technical question in large-scale heat pump system by using earth energy need to be researched, to provide the reference and analysis method for improving the operation reliability in different regions and the evaluation analysis of long-term operation efficiency on system, which can be used to guide engineering applications, to ensure the progress of science and technology and healthy development in earth energy utilization technology[1].

In the paper, through a engineering case, the influence character of the circulation flow velocity in ground heat exchangers on the fluid temperature, the heat pump power consumption and the length of system were analyzed, which provide an approach for system engineering design and operation prediction.

## The ground heat exchange model

In the paper [2] [3]**,** it systematically explored the establishment of modules, module scarf and coupling call based on Matlab/Simulink calculation control platform, established the basic analysis method of heat pump system. The calculation diagram is shown in Fig.1. Eskilson developed an approach to determine the temperature distribution around a borehole based on a hybrid model combining analytical and numerical solution techniques called G function[4] [5]. The theory of G

function of ground heat exchanger is used to compute the borehole temperature and the thermal resistance of borehole by entering relevant parameter of ground heat exchanger and thermophysical property date of ground, and output of the fluid temperature at the outlet of ground heat exchanger, the heat pump power consumption and the length of system.

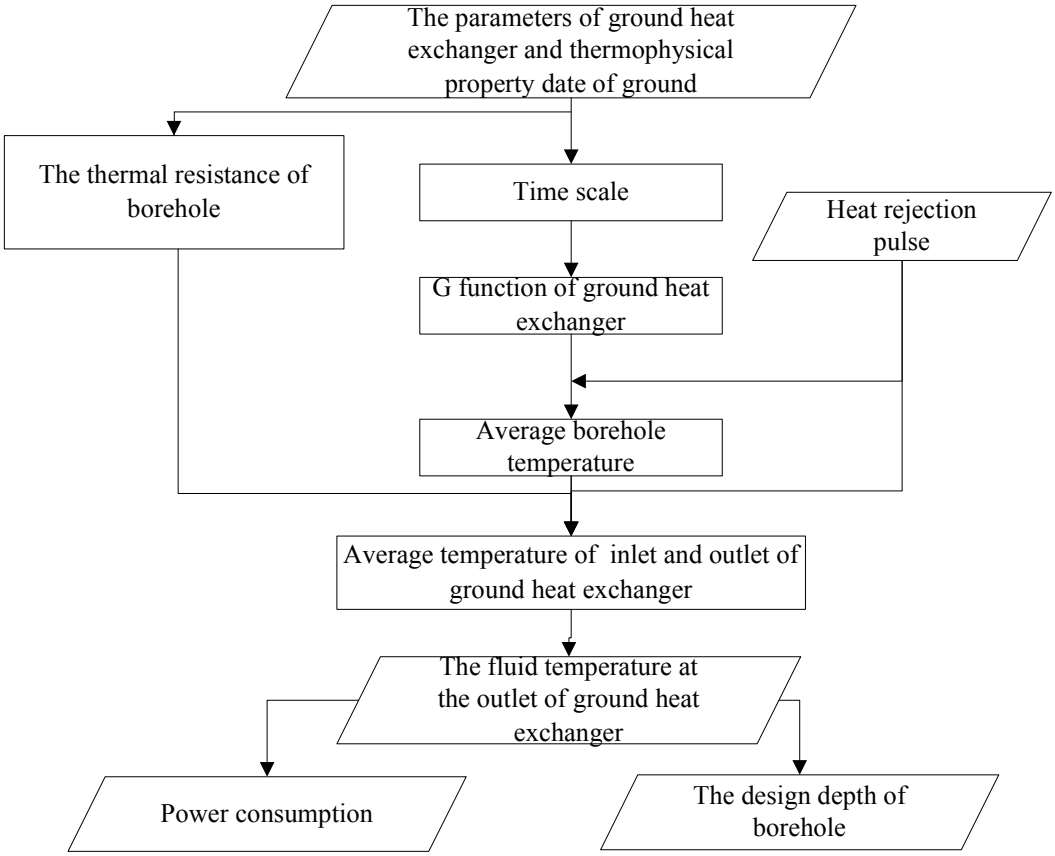


Fig. 1 The calculation diagram

This provided hourly data for the space heating loads or cooling loads for the building in Changchun, China, a summary of the loads are shown in Fig.2. The purpose of this case is to research the influence character of the circulation flow velocity in ground heat exchangers on the fluid temperature, the heat pump power consumption and the length of system for the space heating loads or cooling loads for 20 years. It is very important for proper flow velocity in ground heat exchangers. The research on the influence law of the circulation flow velocity ($v_1$=0.13m/s, $v_2$=0.26m/s, $v_3$=0.52m/s, $v_4$=0.78m/s) in ground heat exchangers on system operation.

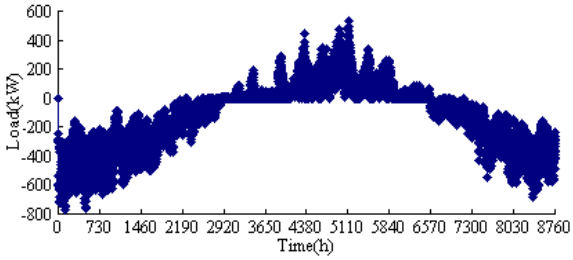


Fig. 2 Building loads

**Results and discussion.**

**The outlet fluid temperature of GHE (ground heat exchanger).** As can be seen from the Fig.2, in Changchun, the heat load significantly greater than cooling load annual and the average fluid temperature of GHE declines year by year. In 20 years operation time, the outlet fluid temperature of GHE can be calculated in Fig.3. As the same loads, the higher outlet fluid temperature of GHE in summer and the lower temperature in winter when the higher circulation flow velocity and quantity,

because of the smaller difference temperature between cycle fluid and the underground. The outlet fluid temperature of GHE change is significant when flow rate increase from $v_1$=0.13m/s to $v_2$=0.26m/s, but little difference when flow rate increase from $v_1$=0.52m/s to $v_2$=0.78m/s.

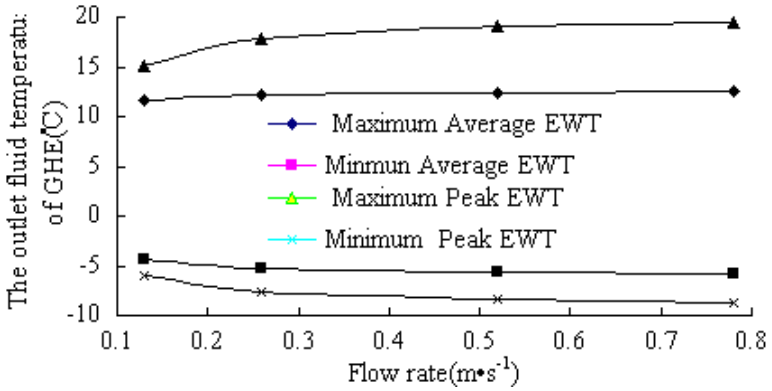


Fig. 3 The fluid temperature of GHE

**Power consumption.** The power consumption for heat pump can be calculated in four situations in Fig.4. In Changchun, the power consumption for heat pump is increase due to the fluid temperature is decrease year by year. With higher circulation flow velocity, the energy consumption is apparent increase. The power consumption increase 48912.16kWh when flow rate increase from $v_1$=0.13m/s to $v_4$=0.78m/s, in 20 years. When flow rate is 0.78m/s, because of the imbalance of heating and cooling load, the average fluid temperature of GHE decreases year by year, power consumption for heat pump rises 6.18% for 20 years.

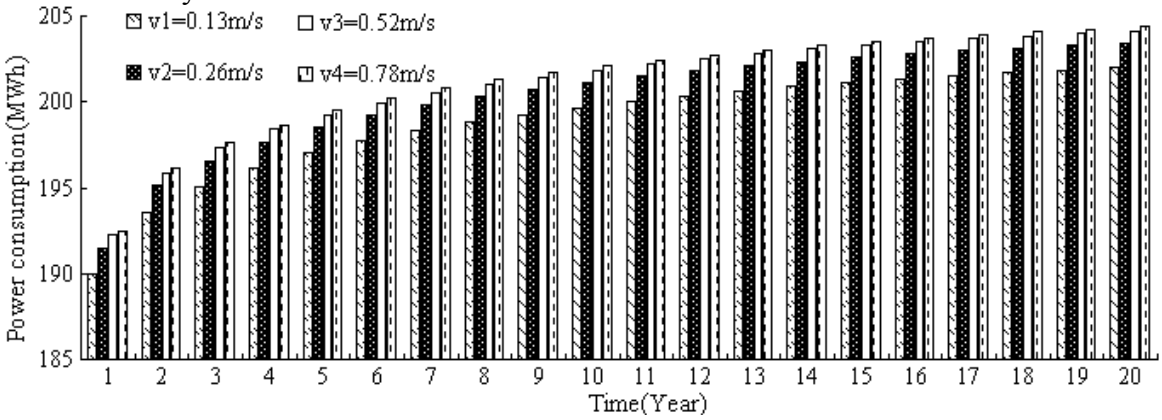


Fig. 4 Power consumption

**The design depth of borehole.** The design depth of borehole is limited to the minimum fluid temperature at the outlet of ground heat exchangers, and it decides initial cost and the life of project directly. In this case, we select the minimum fluid temperature at the outlet of ground heat exchangers is -6℃. The deepest depth of borehole and biggest initial cost are caused by the increment of the flow velocity in the ground heat exchangers. In the Fig.5, a relationship diagram for the depth of borehole and flow rate in the ground heat exchangers. Under this design conditions, we have to redesign the system for optimal solution for the flow velocity. The design depth of borehole rises 20.01% from 100.28m to 120.35 when flow rate increase from $v_1$=0.13m/s to $v_4$=0.78m/s.

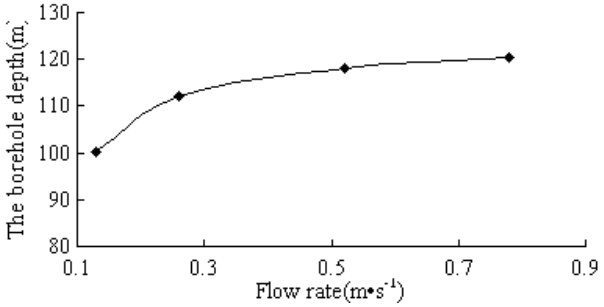


Fig. 5 The depth of borehole

## Conclusion

In the paper, it is to study of underground heat exchanger heat transfer mode and calculate fluid temperature at the outlet of ground heat exchangers. Through a engineering case, the influence character of the circulation flow velocity in ground heat exchangers on the fluid temperature, the heat pump power consumption and the length of system were analyzed, which provide an approach for system engineering design and operation prediction.

## Acknowledgements

The authors gratefully acknowledge the financial support from the NSFC (National Natural Science Foundation of China) under the grant No. 51376080, 51076059, 41072198, Key Laboratory of Songliao Aquatic Environment of Ministry of Education, Department of Education of Jilin Province under the grant No.237(2014), Ministry of Housing and Urban-Rural Development of the People's Republic of China, Doctor Scientific Research Staring Foundation of Jilin Jianzhu University.

## References

[1] Zishu Qi. Diversity and Efficiency on Energy Mechanism of Heat Pump System by Using Earth Energy, Doctoral Dissertation. Jilin University, China, 2012.

[2] Zi shu Qi, Qing Gao, Yan Liu, Y.Y. Yan, Jeffrey D. Spitler. The performance improvements of a ground-coupled heat pump system for both building heating and cooling modes. Advanced Materials Research, Vol. 354-355 (2012)，P807-810.

[3] Zi shu Qi, Qing Gao, Yan Liu, Y.Y. Yan, Jeffrey D. Spitler. Analysis and research on the performance of the ground source heat pump system in different areas of China. Applied Mechanics and Materials，Vol. 148-149 (2012)，P1137-1140.

[4]Xiaowei Xu. Simulation and optimal control of hybrid ground source heat pump systems, PhD Dissertation. Oklahoma State University, Oklahoma, USA, 2007.

[5] Spitler, J.D. 2000. GLHEPRO -- A Design Tool For Commercial Building Ground Loop Heat Exchangers. Proceedings of the Fourth International Heat Pumps in Cold Climates Conference, Aylmer, Québec. August 17-18, 2000.

*Applied Mechanics and Materials Vols. 580-583 (2014) pp 2461-2465*
*© (2014) Trans Tech Publications, Switzerland*
*doi:10.4028/www.scientific.net/AMM.580-583.2461*

# Energy saving design of a training center in Dongguan

LAI Xue -jiang[1,a],DU Zhi-heng[2,b], ZHANG Zhen-qin[2,c]

[1]School of Engineering, Guangdong Ocean University, Zhanjiang, China

[2]Architectural design research Institute of SCUT, China

[a]Laixuejiang1@21cn.com, [b]dzh1981@126.com, [c]443575560@qq.com

**Keywords:** Building energy-saving design; Air conditioning system energy-saving design; Lighting system energy-saving design;

**Abstract.** A training center design as an example, the impact of building energy-saving design on building energy consumption are showed. Energy-saving design options of air conditioning system and refrigerator are given. Lighting power density of the lighting system energy-saving design and the project of energy-saving design are provided.

## Introduction

Building energy consumption refers to energy consumption of residential buildings and public buildings in using process. Heating, air conditioning, ventilation, lighting, hot water supply, cooking, all kinds of electrical appliances, elevators and other aspects of energy consumption are comprised. At present, for the annual energy consumption of public buildings, heating and air conditioning system is accounted for 40%~50%, lighting energy consumption is accounted for 30%~40% and other energy consuming equipment is 10%~20%. In the heating and air conditioning energy consumption, the energy consumption causing by the high heat transfer coefficient of building's exterior-protected structure is accounted for 20%~50%[1]. Therefore, to meet energy-saving demands, mainly at design time three ways should be implemented: Improvement of thermal performance of building's exterior-protected structure; Improving the energy efficiency of heating and air conditioning equipment; Limiting the lighting power density.

## Building summary

The training center is located in Dongguan city, the total construction area is 19828 $m^2$. Built-up area is 9810$m^2$, the building layer is 3 layer aboveground and 1 layer underground. Building height is 21 m, the conditioning area is 5510 m². The building construction heads for South. Garage, chiller rooms are in underground layer. Auditorium, service rooms, reception rooms and awards gallery are at the first floor. Service rooms and discussion rooms are at the second floor. Discussion rooms, training classrooms and seminar rooms are at the third floor. Architectural drawing are presented in Fig. 1~ Fig. 4.

1.1 Reinforced concrete buildings parameters

External wall thermal parameters are shown at table 1.

Tables1: External wall thermal parameters

| position | Name of the main materials of the wall's construction | Thickness（mm） | λ(W/m.k） | Total area（$m^2$） | K（W/$m^2$.k） | Dm |
|---|---|---|---|---|---|---|
| Packed wall | cement mortar | 25 | 0.93 | | | |
| | air-entraining concrete | 200 | 0.22 | | | |
| | lime mortar | 25 | 0.81 | | | |
| beam | cement mortar | 25 | 0.93 | 6811.51 | 1.68 | 3.47 |
| | reinforced beam | 200 | 1.74 | | | |
| | lime mortar | 25 | 0.81 | | | |
| column | cement mortar | 25 | 0.93 | | | |
| | reinforced column | 550 | 1.74 | | | |
| | lime mortar | 25 | 0.81 | | | |

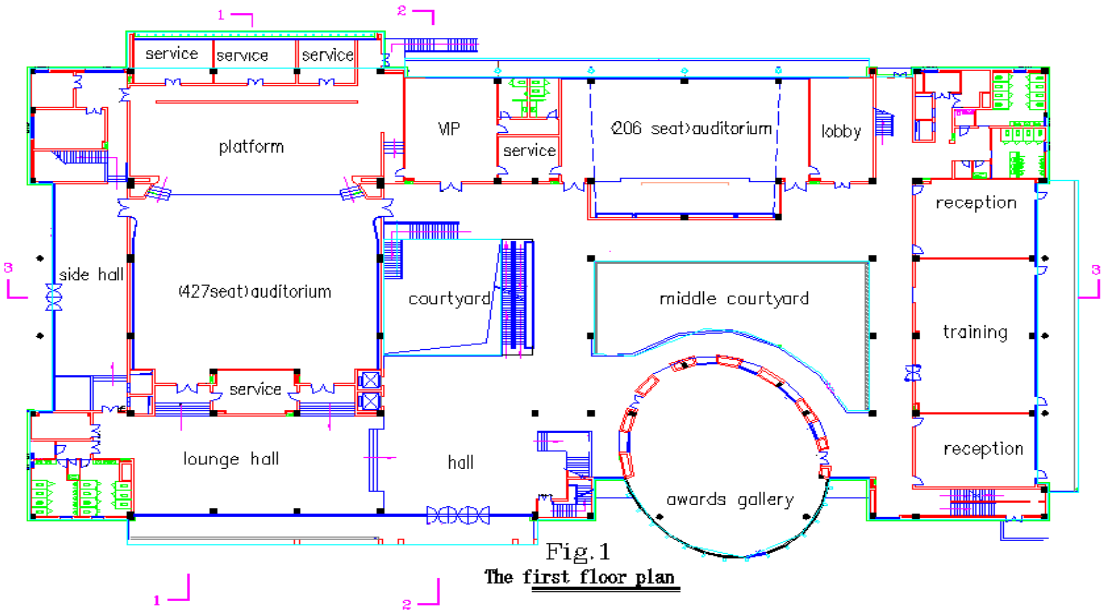


Fig.1
The first floor plan

1.2 Roof covering thermal parameters, shown at table 2.

1.3 Glass curtain wall , outside window:

LOW-E double glazing(6 lower photopermeability+12 air +6 transparent), K=1.8 W/（$m^2$·K), sun-shading coefficient Sc=0.38, visible light transmission =0.48.

1.4 Floor: ①K=1.266 W/（$m^2$·K）；②K=1.339 W/（$m^2$·K）；③K=1.349 W/（$m^2$·K）；

## Building energy-saving design

2.1 Building natural ventilation

Table 2: Roof covering thermal parameters

| position | Name of the main materials of the wall's construction | thickness （mm） | λ (W/m.k) | Total area （$m^2$） | K (W/$m^2$.k) | Dm |
|---|---|---|---|---|---|---|
| roof covering | cement mortar | 30 | 0.93 | 3890.2 | 0.67 | 3.21 |
| | fine sand concrete (bidirectional) | 40 | 1.74 | | | |
| | lime mortar | 35 | 0.93 | | | |
| | expanded polystyrene granule thermal insulation mortar | 20 | 0.06 | | | |
| | extruded polystyrene Board | 30 | 0.037 | | | |
| | reinforced concrete | 120 | 1.74 | | | |
| | cement mortar | 30 | 0.93 | | | |

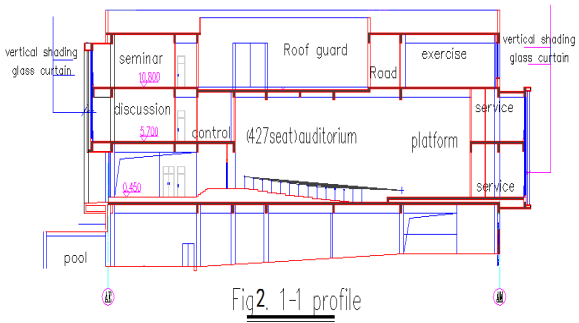


Fig2. 1-1 profile

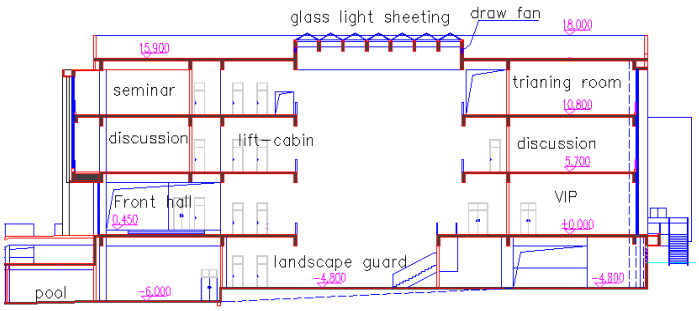


Fig3. 2-2 profile

The construction head facing south's building is advantage to natural ventilation in architecture. Building entrances are designed in staggered arrangement which is advantage to air flow. There is the middle courtyard which has not proof, which is advantage to hot air discharge up.

2.2 Buildings' insulated sun-shading design

Buildings' insulated sun-shading has the roles which are to prevent the heat and to cool down the air and to prevent glare and UV. There are sun-shading elements, roof gardens ,glass light sheeting, aluminum grille in the building.

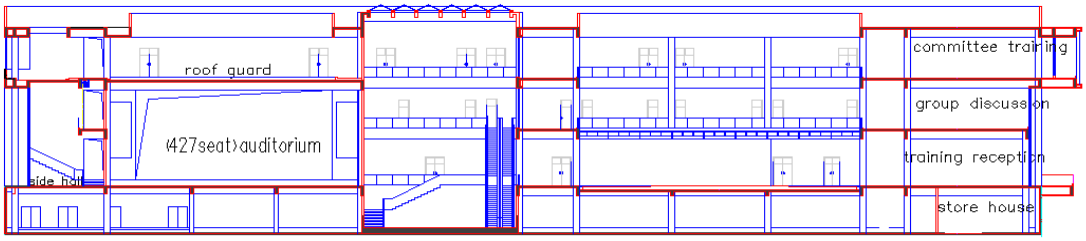


Fig4. 3-3 profile

The 427-seat auditorium located in the northwest corner of the building is the maximum heat load of this building. The service rooms at the first and second floor have the radiant gain heat's exterior-protected structure from fig.2 and fig.1. The north exterior-protected structure of the service rooms is glass curtain wall which has K=1.8W/m$^2$.K heat transfer coefficient and has vertical sun-shading, so the north exterior-protected structure radiant gain heat is reduced largely. The 427-seat auditorium's roof is roof garden. From JGJ-75-2003 *《Design standard for energy efficiency of residential buildings in hot summer and warm winter zone》* , as calculating the total thermal resistance of the roof, the equivalent thermal resistance value of planting roof is 0.5m$^2$.K/W, the auditorium roof heat transfer coefficient calculation process is as follows:

Total thermal resistance of the planting roof shall be determined by the following formula:

$$R_0 = R_i + R + R_e + R_h \quad (1)$$

formula: $R_0$—— Total thermal resistance of the planting roof.

$R_i$—— Inner face heat transfer resistance, $(m^2 \cdot K/W)$;$R_i = 0.11$.

$R_e$——Outer face heat transfer resistance, $(m^2 \cdot K/W)$; $R_i = 0.06$.

$R_h$——The equivalent thermal resistance value of planting roof, $(m^2 \cdot K/W)$;$R_h = 0.5$

R---Roof structures resistance of the heat transfer; $(m^2 \cdot K/W)$

$$R = \sum_{i=1}^{n} R_i \quad (2)$$

$$R_i = \frac{\delta_i}{\lambda_i} \quad (3)$$

Table 2 parameters are substituted (1) to (3), calculate $R_0 = 2.01(m^2 \cdot K/W)$.

The heat transfer coefficient of the planting roof is $K = 1/R_0 = 0.498(W/m^2 \cdot K)$;

After increasing the planting guard on the roof ,heat transmission coefficient has fallen down (0.67-0.498)/0.67=25.7%,so the planting roof's radiant gain heat is reduced largely. The side hall is at the west side of the auditorium, there is no direct radiation of heat, so the radiant heat gain of the auditorium's exterior-protected structure is less, air conditioning energy consumption is significantly reduced.

From fig.1 it can be seen that the south face of awards gallery increasing the vertical metal plate at outer of the glass curtain wall which effects the vertical sun-shading roles. Increasing vertical shading, overall sun-shading coefficient is reduced from 0.38 to 0.238. so the glass curtain wall 's radiant gain heat is reduced largely. Light colored blinds at the upper of the glass curtain wall and at the bottom of the glass curtain wall also help ventilation.

**Air conditioning system energy saving design**

3.1 Design parameters of air-conditioning system

The energy-saving building is a training center which collecting office and training. Air-conditioned rooms' interior design parameters are different that varying with different rooms' function. The air-conditioned rooms' interior design parameters are shown in Table 3.

Table 3 Air-conditioned rooms' interior design parameters

| room | summer temperature(℃) | summer relative humidity (%) | fresh air($m^3$/h.P) |
|---|---|---|---|
| The first floor auditorium | 26 | 40~60 | 20 |
| The rest room | 26 | 40~60 | 30 |

3.2 Summer air conditioning loads, refrigerating system

The air conditioning load per unit area (KW/$m^2$) is smaller than the design estimates unit area air conditioning cooling load (KW/$m^2$) from Table 4 shows, energy-saving design works.

3.3 Programmer narrative for air conditioning system energy saving design

Due to the rooms' different functions, used time is not the same, so refrigerating systems are adopted the following methods:

Table 4 .Summer air conditioning loads, refrigerating system and lighting power density values

| location | air conditioning area（$m^2$） | air conditioning loads（KW) | unit area air conditioning cooling load （W/$m^2$） | design estimates unit area cooling load （W/$m^2$） | refrigerating systems | lighting power density value （W/$m^2$） |
|---|---|---|---|---|---|---|
| small auditorium and service | 560 | 90 | 160 | 269 | VRF | 15 ( auditorium) 9(service） |
| training reception | 420 | 64 | 152 | 191 | VRF | 15 |
| group discussion | 1410 | 246 | 174 | 235 | VRF | 9 |
| awards gallery | 370 | 70 | 189 | 200 | VRF | 9 |
| seminar rooms | 460 | 75 | 163 | 235 | VRF | 9 |
| large exercise and training room | 875 | 164 | 187 | 200 | VRF | 9 |
| training room and front hall | 485 | 75 | 155 | 191 | VRF | 9 |
| large auditorium and service | 1670 | 380 | 228 | 269 | Air cooled scroll chiller | 15(auditorium) 9(service） |

VRF= VRF air conditioner

（1）Large auditorium and auxiliary rooms are sent cooling-air by the full-air low speed blower way. Cabinet type air conditioners are set in the air conditioning machine room that send cooling-air through the duct to indoor. The air conditioning ducts are located in floor ceiling. The splitters sends the air downward . Return air through the air ducts hided in ceiling from the air conditioning machine room with negative pressure to door hinge air ports backs to the rooms. Other service rooms are mounted the fan-coil system. Hided horizontal fan coils are mounted ceilings of the rooms, which air flow line is upward sending and upward return way, sending air mode adopts side sending air mode. Refrigerating system is the air cooled scroll chillers, the air cooled scroll chillers and cold circulating pump are mounted on the roof floor. Choose typical air-cooled scroll chillers: cooling capacity 212KW, power consumption 71KW, COP 3.0. Meet COP≧ 2.6 (scroll type) specifications.

(2) Other conditioning rooms: Each floor is divided into two to four units, each unit has a set of commercial VRF air conditioning machines (cold), selection of frequency conversion adjustment, or digital scroll air conditioning unit. Outdoor units are mounted in roof floor. Four-sides block-top indoor units send the cooling air by the upward sending and upward return way. Select the typical VRF air conditioner: cooling capacity 123.5KW, power consumption 38KW, COP 3.0. Meet COP≧ 2.3 (According to the joint dust selection) specifications.

(3) Air conditioning water systems' transportation energy efficiency ratio: transportation energy efficiency ratio ER=0.002342H/(ΔT.η) ,designing water pump head H=25m，difference in temperature of the feed pipe and return pipe ΔT=5℃, Pump efficiency in designη=75%，so ER=0.0156, Meet ER≤0.0241 specifications.

(4) The high efficiency and low power consumption air conditioning and ventilation products are used in designing, room temperature control designing is used.

（5）A grid line foil laminated glass wool felt is used in the air conditioning system duct insulation, The thickness of the grid line foil laminated glass wool felt is 30mm, the density is 40Kg/$m^3$, the transmission coefficient is $\lambda \leq 0.033$W/m.K , the thermal resistance value is R=0.857 $m^2$.K/W, Meeting the specification which is the minimum thermal resistance of the duct's thermal insulation materials $\geqq$ 0.74 $m^2$.K/W.

**Energy-saving design of lighting system**

The International Commission on illumination lighting principles:

(1)According to room's function designing illumination;
(2)With meeting the illumination requirements, energy-saving lighting design is used;
(3)Meeting the color demonstrating requirements, using efficient lighting units;
(4)Low glare and efficient lamps are used;
(5)Highly reflective materials are used in indoor designing;
(6)Designing the effective circuit loop;
(7)Setting the energy management device;
(8)Using artificial lighting and natural lighting;
(9)Regular cleaning and maintenance of lighting apparatus are needed.

There are the side light, the top light, the middle courtyard light of the natural lighting form of the building. According the building's own characteristics, proceeding from the practical operability, the lighting power density values of each rooms are shown in table 4. Energy-saving design of lighting system are used as follow:

(1) For general lighting the small diameter straight tube fluorescent lamps are used. Low wattage ceramic metal halide lamps are used in importance lighting area

(2)Lighting is controlled by sound and light control unit in public area, so the unnecessary lighting is reduced.

(3)Selection rational line path, line length is shorten as far as possible ,so line loss is cut down.

(4)Installing human body movement sensors in the bathroom and lounge, the lighting is automatically turned off when there are no people in these areas. The outdoor road lighting adopts photoelectric control and controls by band reduced light at different periods. Adopting sound and light control for the lighting at indoor passages and other parts of the public areas, minimum illumination requirement is met and the energy-saving effect is achieved.

**Summarize**

For the public buildings, energy consumption is more. If energy-saving design is considered ,building energy consumption is reduced surely. Therefore, design of construction energy-saving should be designed as part of the design of architecture.

**References**

[1] Information on http://www.chinagb.net/weixin/20140103/103301.shtml.
[2] Jointly announcing by China Academy of building research and Building energy efficiency Committee of China construction industry association: *GB50189- 2005, Design standard for energy efficiency of public buildings. [S]*. China architecture and building press, China 2005.
[3] Jointly announcing by Ministry of Housing and Urban-Rural Development of the People's Republic of China and General administration of quality supervision, inspection and quarantine of the People's Republic of China: *GB 50019- 2003, Code for design of heating ventilation and air conditioning[S]*. China planning press, China 2004.
[4] Ministry of Housing and Urban-Rural Development of the People's Republic of China: *GB 50176-93 Thermal design code for civil building [S]*. China planning press, China 1993.
[5]Jointly announcing by Ministry of Housing and Urban-Rural Development of the People's Republic of China and General administration of quality supervision, inspection and quarantine of the People's Republic of China: *GB50034-2013 Standard for lighting design of buildings[S]*. China architecture and building press, China 2013.

*Applied Mechanics and Materials Vols. 580-583 (2014) pp 2466-2470*
*© (2014) Trans Tech Publications, Switzerland*
*doi:10.4028/www.scientific.net/AMM.580-583.2466*

# Calculation of the maximum length of the directly buried cooling pipes applied in the district cooling system(DCS)

Chaoyi Tan[1,2, a], Haihua Hu[1,2] ,Mengmeng Wang[1,2],Zhenzhen Pan[1] ,
Hanqing Wang[1,2,b]

[1]School of Civil Engineering, Hunan University of Technology,
Zhuzhou, Hunan Province, China, 412007

[2] Collaborative of Innovation Center, Hunan University of Technology,
Zhuzhou, Hunan Province, China, 412007

[a] tanchaoyi123@126.com, [b]Corresponding author: hqwang@126.com

**Keywords:** Energy efficiency,DCS, Direct burial cooling pipe, Maximum length

**Abstract.** Formula of the maximum length of direct burial cooling pipes used in the district cooling system(DCS)was derived, by means of establishing the mathematical relationship between the maximum temperature rise of the pipe, under which the energy efficiency of the refrigeration unit would not decrease, and the thermal equilibrium of the pipe. And an engineering application with DCS in Zhuzhou was analyzed. The results showed that the insulation measures should be applied to the directly buried cooling pipes in engineering applications, appropriately with a thermal insulation layer of 0.04m.

## Introduction

The district cooling system is characteristic of energy conservation, environmental protection, easy operation and management and so on. However, if the system is not appropriately designed, these advantages cannot be fully exhibited. It has been reported by Hui Rongna[1] that the economical effects of the DCS in Beijing Zhongguancun Village are far from satisfaction due to the bad match during the design. In addition, the economical effects of the DCS in Guangzhou University City is not satisfactory as a result of the excess cooling load of the system. In order to make full use of the advantages of the DCS, key parameters of the system have to be determined during the design, in terms of the characteristics of cooling technology of the DCS. Among these parameters, the length of direct cooling pipe is directly related to the temperature rise of chilled water, which further affects the energy efficiency of refrigeration unit and the pipe transportation.

A series of regulations concerning the energy efficiency of refrigeration unit and the transportation energy efficiency ratio of the cooling pipes have been put forward in the Design standard for energy efficiency of public buildings [2]. As a result, the length of pipes must meet the national energy-saving requirement. Applying the principle of minimum overall energy consumption, conclusion was obtained that the best cooling area is determined by the characteristic of thermal power unit, as well as heating parameters, structure and functions of the buildings and the local meteorological conditions[3]. In addition, conclusion was obtained by Zhujijun and Liujin that the energy efficiency ratio during a whole year could reach a higher grade with a small investment and high reliability, if the cooling radius is not greater than 1000m[4]. However, a length of 650m was considered to be the ideal cooling radius for energy conservation purpose by other researchers, such as Zhangsi Zhu and Yangjun. Moreover, they concluded that the maximum cooling radius of the DCS in engineering applications should not exceed 960m[5].

Although there have been a lot of researches on the design of the DCS, however, studies on the calculations of the maximum length of direct burial cooling pipes of the DCS are rare at present, and the theories to guide the design of the DCS are actually in short. In this work, a method is introduced to determine the maximum length of direct burial cooling pipes of DCS.

**Determining the maximum length of direct burial cooling pipes with the insurance of the non-decreasing of the energy efficiency grade of the refrigeration unit**

Fundamental of this method is explained as follows. Assuming the refrigeration unit has a certain energy efficiency grade before incorporating into the pipelines, the grade will decrease after connecting to the pipelines, due to the requirement of the lower temperature of the chilled water(as a result of heat loss, there is an increase of the chilled water), to ensure the power of the terminals.

The maximum temperature difference resulting in the decrease of the energy efficiency grade of the refrigeration unit, is the maximum allowed temperature rise of the chilled water, which is caused by power loss of the pump and the heat loss of the pipe. Based on the analysis above, the maximum length of direct burial cooling pipes of DCS can be determined by establishing the heat balance equations.

*Allowed temperature rise of the chilled water*

Energy efficiency grade coefficient of refrigeration unit can be defined with Eq.1 according to the Lorenz Cycle's Circulation principle,

$$COP_i = k_i \times \frac{T_0 + 2\Delta t_{ij}}{T_k - \left(T_0 + 2\Delta t_{ij}\right)} \quad j \geq i, i = 1,2,3; j = 1,2,3 \tag{1}$$

where $COP_i$ is the energy efficiency's grade coefficient of the refrigeration unit. $T_0$ and $T_k$ indicate the cold source temperature and hot source temperature in Kelvin, respectively. As to the value of $T_k$, 313K is an appropriate choice if the Freon refrigeration unit is adopted in the system. $k_i$ is the comprehensive correction coefficient, considering the effects of internal structure of *i*-grade energy efficiency of the refrigeration unit on heat transfer and the effects of cooling pipes on the performance of refrigeration units due to heat loss.$\Delta t_{ij}$ is temperature rise in Kelvin of the chilled water of the one-way cooling pipes of refrigeration unit when energy efficiency in *i* grade drops to *j*. Therefore$\Delta t_{ii}=0$. Finally, $2\Delta t_{ij}$ denotes the temperature rise of the chilled water of double-way cooling pipes of refrigeration unit when energy efficiency in *i* grade falls to *j*.

If $T_0$ in Eq.1 is replaced by the outlet temperature of the refrigeration unit, $t_m$, Eq.1 can be expressed as Eq.2.

$$COP_i = k_i \times \frac{\left(t_m + 2\Delta t_{ij}\right) + 273}{T_k - \left[\left(t_m + 2\Delta t_{ij}\right) + 273\right]} \tag{2}$$

Provided that the allowed maximum temperature rise of the chilled water is$\Delta t_{ij}$ when the energy efficiency grade decreases by one grade, the value of$\Delta t_{ij}$ can be derived by substituting the energy efficiency grade coefficient of the i+1grade into Eq.2.

$$t_{ij} = \frac{k_i\left(t_m + 273\right) - COP_{i+1}\left(T_k - t_m - 273\right)}{-2\left(COP_{i+1} + k_i\right)} \tag{3}$$

If the result is less than 0, the chilled water(outlet water temperature of the unit) has to be reduced.The energy efficiency grade coefficient of refrigeration units varies with the type and the cooling capacity. For a refrigeration unit with a cooling capacity greater than 1163kw, the value of $k_1$ and $k_2$ approximate 0.72 and 0.66, respectively. Substituting these values into Eq.3, the result turn out to be $\Delta t_{12}$=-1.31℃, $\Delta t_{23}$=-1.43℃, $\Delta t_{13}$=-2.84℃.

*Heat loss of the chilled water of DCS and the thermal balance*

There are mainly two reasons for the temperature rise of the chilled water in water pipelines of DCS. One is the heat loss caused by the heat exchange between chilled water and the surrounding environment outside the pipe; the other is that heat loss caused by the friction heat of the chilled water pumps.

*a) Reason one*

Generally speaking, outdoor pipelines of the DCS are directly buried. Therefore, heat loss due to the heat transfer between the chilled water in the pipe and the environment outside the pipe can be obtained according to Eq.4,

$$\Phi = \frac{\pi l\left(t_w - t_g\right)}{\frac{1}{d_1\alpha_n} + \frac{1}{2\lambda_1}\ln\left(\frac{d_2}{d_1}\right) + \frac{1}{2\lambda_2}\ln\left(\frac{d_3}{d_2}\right) + \frac{1}{d_3\alpha_w}} \tag{4}$$

where $\Phi$ is the heat loss of direct buried pipe in *W*. And *l* means the length of the pipes in *m*. $t_w$ is the ambient temperature outside pipe insulation, and its value is often thought to be 24℃. $t_g$ is chilled water temperature in Celsius inside the pipe. $d_1$ and $d_2$ are the inner and outer diameter of the pipes. And $d_3$ is the total outer diameter of the pipe including the thermal insulation layer. Namely $d_3=d_2+2\delta$, where $\delta$ is the thickness of the insulation layer. $\lambda_1$ and $\lambda_2$ are the thermal conductivity coefficient of the pipe and thermal insulation material, respectively. $\alpha_n$ is the convective heat transfer coefficient of the chilled water inside the pipe, usually with a value of 6000W/($m^2$.K). And $\alpha_w$ means the convective heat transfer coefficient outside the pipe. Moreover, the value of $1/(d_3\alpha_w)$ is usually be neglected if the pipe is buried directly.

*b) Reason two*

According to related studies, the heat loss caused by friction heat of the pump accounts for 80% of the total power consumption of the distribution networks[6]. The result can be obtained according to Eq.5 as below.

$$Q_b = 0.8\frac{\gamma GH}{\eta} \tag{5}$$

In Eq.5, $Q_b$ is the heat loss caused by the friction heat generated by the pumps. And $\gamma$ is the density of the chilled water. *G* is the volume flow rate of chilled water, and $G=\pi d_1^2 v/4$ where *v* is the velocity of chilled water. *H* denotes the lift head (in *m*) of the pumps, and $H=1.1(2\times 1.4R_0l/\gamma)$ where $R_0$ is specific frictional resistance of pipe(in Pa/m). $\eta$ means the efficiency of chilled water pumps.

*c) Deduction of the thermal balance equation*

The Temperature rise of the chilled water per unit time in the pipe is equal to the heat transferred to the pipe and the increased internal energy caused by the friction heat caused by the water pumps. According to the analysis above, the thermal balance equation can be expressed as below,

$$C\rho G\left|\Delta t_{ij}\right| = \Phi + Q_b \tag{6}$$

where C is the specific heat capacity of chilled water and ρ is the density of chilled water.

*Calculation of the allowed maximum length of the directly buried cooling pipes*

Substituting Eq.4 and Eq.5 into Eq.6, meanwhile replacing *l* with $l_{1ij}$, the formula can be obtained as Eq.7.

$$l_{1ij} \prec \frac{\left\{\frac{1}{d_1\alpha_n} + \frac{1}{2\lambda_1}\ln\left(\frac{d_2}{d_1}\right) + \frac{1}{2\lambda_2}\ln\left[\frac{\left(d_2+2\delta\right)}{d_2}\right]\right\}\cdot\eta\rho C v d_1^{\,2}\left|\Delta t_{ij}\right|}{4\eta\left(t_w - t_g\right) + 2.464R_0 v d_1^{\,2}\cdot\left\{\frac{1}{d_1\alpha_n} + \frac{1}{2\lambda_1}\ln\left(\frac{d_2}{d_1}\right) + \frac{1}{2\lambda_2}\ln\left[\frac{\left(d_2+2\delta\right)}{d_2}\right]\right\}} \quad j \geq i, i = 1,2,3;\ j = 1,2,3 \tag{7}$$

In Eq.7, $l_{1ij}$ corresponds with$\Delta t_{ij}$, namely the allowed maximum length of directly buried cooling pipes in refrigeration unit, under which the energy efficiency grade of the unit will not decrease.

## Analysis on an engineering application

*Initial parameters and the calculation of the allowed maximum length of the directly buried pipes*

Initial parameters of the DCS in Shennong town in Zhuzhou are listed in table 1.

Tab.1 Initial parameters

| Parameter | Description | value |
|---|---|---|
| Rated power | Centrifugal chiller | 1614 KW |
| $\eta$ | Efficiency of the Chilled water pump | 0.7 |
| $t_w$ | Soil temperature in summer | 24℃ |
| $\lambda_1$ | Thermal conductivity of the pipe wall | 45W/(m.K) |
| $\lambda_2$ | Thermal conductivity of the insulation layer | 0.033W/(m.K) |
| $d_1$ | Inner diameter of the pipe | 350mm |
| $v$ | Velocity of the water flowing in the pipe | 1.66m/s |
| $\delta$ | Thickness of the insulation layer | 70mm |
| $t_g$ | *T*emperature of the chiller water | 7℃ |
| $R_0$ | specific frictional resistance of the pipe | 85.69Pa/m |
| $\alpha_n$ | Convectional heat transfer coefficient inside the pipe | 6000W/(m$^2$.K) |

Substituting $\Delta t_{12}$=-1.31℃, $\Delta t_{23}$=-1.43℃ and $\Delta t13$=-2.84℃ into Eq.7, the results turn out to be $l_{112}$=14870m, $l_{123}$=16233m and $l_{113}$=32238m.

*Analysis on the maximum length of the directly buried pipe*

Defining all the parameters in Eq.7 as fixed values, except $\delta$, and regarding the maximum length of the pipe as a function of the thickness of the insulation layer, $l_{1ij}=f(\delta)$,the variation of the maximum length with the thickness of the insulation layer can be obtained, which are illustrated in Fig.1 and Fig.2.

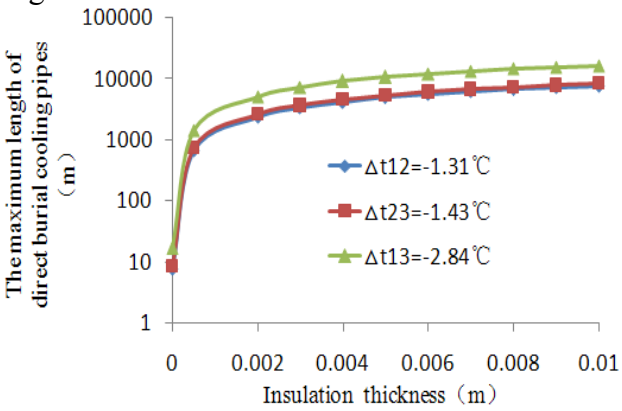


Fig.1 Relationships between the maximum length of directly buried cooling pipes and the thickness of the insulation layer

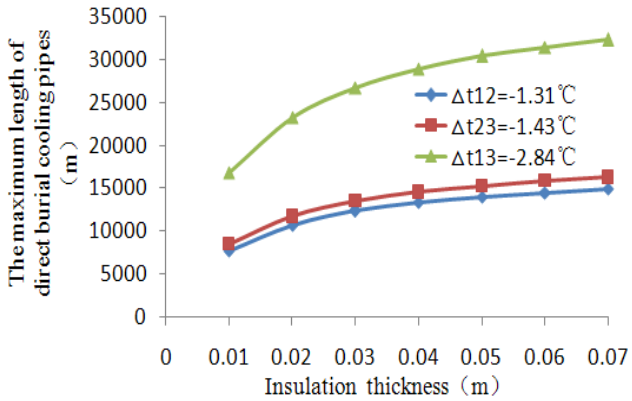


Fig.2 Relationships between the maximum length of directly buried cooling pipes and the thickness of the insulation layer

As is shown in Fig.1, on condition that the energy efficiency grade does not decrease, when the thickness of the insulation layer is less than 0.0005m, the allowed maximum length decreases rapidly. And when $\delta$=0, the maximum length can just reach tens of meters. Even when $\delta$=0.0005m, the allowed maximum length is only hundreds of meters. However, the maximum length can reach 2000 meters when $\delta$=0.002m, which suggests that thermal insulation measures should be taken in the directly buried pipe in DCS.

In addition, as indicated in Fig.2, the maximum length of the pipes increases with the thickness of the insulation layer. The maximum length can reach up to 13300 meters when a 0.04-m insulation layer is applied. However, the increment of the pipe maximum length changes insignificantly thereafter. Therefore, thermal insulation layer with a thickness of 0.04m is usually regarded to be appropriate in engineering applications.

## Conclusions

The calculation of the maximum length of directly buried cooling pipes adopted in DCS is of great significance. In this work, formula of the maximum length of directly buried cooling pipes used in the district cooling system was derived. And an analysis on the engineering application in Shennongcheng town project was conducted. The results showed that thermal insulation layer with a thickness of 0.04m is appropriate in engineering applications.

## Acknowledgements

This work was financially supported by the "12th five-year" National Key Technology R&D Program (2011BAJ03B07).

## References

[1] R.N.Hui,Q.Xui,D.Y.Lin and W.F.Xu: Building Energy Efficiency Vol.35(2007),p.47. (in Chinese)
[2] MC.PRC,AQSIQ.PRC:Design standard for energy efficiency of public buildings GB50189-2005 . (2005). (in Chinese)
[3] J.S.Du,L.Fu and Y.Jiang:HV&AC Vol.33(2003),p.111. (in Chinese)
[4] J.J.Zhu,J.Liu:Refrigeration Vol.23(2004),p.69. (in Chinese)
[5] S.Z.Zhang,J.Yang and W.D.Long:HV&AC Vol.38(2008),p.116. (in Chinese)
[6] Y.H.Peng,Z.W.Lin and H.M.Fu: Journal of Donghua University(Natural Science Edition) Vol.37 (2011) ,p.109. (in Chinese)

*Applied Mechanics and Materials Vols. 580-583 (2014) pp 2471-2474*
*© (2014) Trans Tech Publications, Switzerland*
*doi:10.4028/www.scientific.net/AMM.580-583.2471*

# Discussion on Ventilation Requirement for Meeting Indoor Air Quality

Mengjie LIN[1,a], Qinqin LIU[1] and Zimao PENG[1]

[1]Hunan Communication Polytechnic, Hunan Changsha 410004, China

[a]Email: lindalux@qq.com

**Keywords:** Indoor air quality; Pollutant concentration; Ventilation

**Abstract:** Based on the calculation method and the analysis method of the ventilation requirement, the paper discussed the necessary ventilation referring to the standard of the allowed indoor $CO_2$ concentration, the necessary ventilation with oxygen as the standard and the calculation method and correction method of the full amount of required ventilation to remove the waste heat or wet. According to the pros and cons of the methods described above, the paper proposed the corresponding countermeasures to meet the indoor air quality and the fresh air needed by indoor personnel.

## Introduction

The indoor air quality is a complex issue involving multi-disciplinary. There are a variety of pollutants affecting air quality which can be summarized as toxic and harmful gases, tobacco smoke, dust production and fungi and other microbial contamination. In industrial ventilation and dust design, the common method is to use the appropriate equipment and technology to control the concentration of pollutants and indicators of pollution within the allowable range. The pollutants in the residential buildings and office building are different to that of industrial buildings, such as the sources of indoor pollutants contained the personnel exhaled carbon dioxide, the building decoration materials, the cleaning agents volatiles, the furniture, the smoking fumes and so on, while the main pollutants in the office buildings are the carbon dioxide and the odoriferous of the devices (Table 1). For a long time, because people lack of knowledge on the health effect of low concentration of indoor air pollution, especially the impact of the unnoticeable indoor air pollution, leading to a long time involving in low concentration pollutant and pythium odor, people's physical and mental health have been affected severely.

**Table1 Source of indoor air pollutants and its influencing factors [1]**

| Pollutant sources | Specific factors |
|---|---|
| Indoor environment | Pattern of life, building renovation, personnel density, etc. |
| Outdoor environment | Surrounding environment, community planning, architectural |
| Air conditioning and ventilation systems | New wind, air, pipeline, operation and management, etc. |

In order to solve the above problem of indoor air pollution, people often use the ventilation method to achieve the acceptable indoor air quality, or use the introduction of new air dilution method, which not only can control the concentration of pollutants in the air below the harmful concentration limit determined by the norms, but also can make the indoor air quality accepted by most people and effectively avoid the adverse effects on health [2]. But in the current ventilation process, the ventilation volume is always short of in-depth consideration, based on which this paper analyzed the calculation method of the required indoor ventilation.

**Methods of ventilation**

Based on the purpose of eliminating waste heat or wet and diluting the harmful substances, the conventional ventilation calculation method can respectively calculate the amount of needed ventilation, and takes the maximum as the design ventilation. The research methods of ventilation are as follows:

**1）The calculation method of provisions**

Because the pollution associated with personnel and buildings is superimposed considering the effect on the human feelings, the required ventilation is the sum of the corresponding amount of ventilation for the two parts. The calculation equation is as follow [3]:

$$G = R_P P_D D + R_b A_b \tag{1}$$

Where: $G$—design needed fresh air, L/s or $m^3/h$; $R_P$—personal minimum fresh air, $m^3$; $P_D$—number of persons in the room; $D$—variation coefficient; $R_b$—minimum fresh air required per unit area, $L/m^2$; $A_b$—indoor building area, $m^2$.

Consider the following two different situations: when the indoor pollutants have not mutually influence，the individual new ventilation can be respectively calculated to achieve the required standards of fresh air, and then take the maximum as the ventilation requirement, which has been used for the current fresh air standard; when the certain indoor pollutants may have mutually influence, the maximum method can't be applied to calculate the necessary fresh air, while the reasonable method should be summed up to obtain the desired indoor fresh air. To ensure the number of ventilators, the personal total air volume should not be less than 7.5L/s [2].

**2）Analysis and calculation method**

Not only because of the need to eliminate the indoor thermal and wet load of the indoor ventilation, but also to ensure the indoor air quality, for the high indoor pollution or the strong contamination existing in construction, the indoor air quality can be calculated with the mass balance method, such as equation (2) [3]:

$$Q = \frac{N}{(C_y - C_j)E_y} \tag{2}$$

Where: $Q$—amount of ventilation required to ensure indoor air quality, L/s or $m^3/h$; $N$—indoor pollutants generated within unit time, $\mu_g$ /h; $C_y$—allowable indoor pollutant concentration, $\mu_g$ / $m^3$ ; $C_j$—pollutant concentration of entering the building, $\mu_g$/ $m^3$; $E_y$—ventilation efficiency.

The method of calculating fresh air need to consider the type and the nature of pollutants, the dissemination speed, the allowable concentration values and other factors, and conducts the calculation comprehensively. The two methods for calculating the ventilation are based on multiple indicators, and the algorithm is more accurate, while in some office buildings and civil buildings, the ventilation calculation often considers only one or a few main pollutants, such as the necessary ventilation to the standard of the allowable indoor $CO_2$ concentration and the allowable necessary ventilation of total volatile organic compound (TVOC) concentration and so on.

**Necessary ventilation of allowable indoor $CO_2$ concentration**

Because human body can exhale a large amount of $CO_2$ in the metabolic process, and the concentration of $CO_2$ is associated with other air pollutant caused by human metabolism, so the indoor $CO_2$ concentration is often used as an important indicator for indoor air quality [4]. The $CO_2$

generation of human body is concerned with the energy metabolism and body surface area. The amount of $CO_2$ and necessary fresh air under different activity intensity is shown in Table 2.

**Table2 Product of $CO_2$ and necessary fresh air [4]**

| Activity intensity | Amount of $CO_2$ occurs [$m^3$/(h· person)] | Necessary fresh air to be different $CO_2$ allowable concentration [$m^3$/(h· person)] | | |
|---|---|---|---|---|
| | | 0.1% | 0.15% | 0.2% |
| Sit still | 0.0144 | 20.6 | 12 | 8.5 |
| Very light | 0.0173 | 24.7 | 14.4 | 10.2 |
| Light | 0.023 | 32.9 | 19.2 | 13.5 |
| Medium | 0.041 | 58.6 | 34.2 | 24.1 |
| Heavy | 0.0748 | 106.9 | 62.3 | 44 |

Some experiments and research on controlling the concentration of carbon dioxide as an indicator of ventilation systems show that the calculation method can not only ensure the indoor air quality, but also save energy. In recent years, studies have shown that the indoor pollutants include carbon dioxide in addition to other pollutants, such as the above-mentioned pollutants generated by the interior decoration, furniture and building materials, pollutants generated by the conditioning system itself. The high concentration of these pollutants can make people feel uncomfortable, and some pollutants can have direct harm on people's health, so the indoor pollutants generated by nonhuman factors has been put forward to quantitatively describe the problem, which is because the ventilation system of simple indicators to control the carbon dioxide is difficult to eliminate their influence on the indoor air quality. Therefore, the method is applicable to teaching architecture, building of high-density populations, or other environment with the carbon dioxide as the main indoor pollutants. Meanwhile, solving the ventilation can only depend on the concentration of carbon dioxide as an indicator without causing large ventilation errors.

**The required ventilation to eliminate heat or wet** [3]

The required ventilation to eliminate the waste heat or wet can be calculated with equation (3):

$$G = \frac{Q}{c(t_n - t_w)} kg/s \tag{3}$$

Where: $G$—full ventilation, kg/s; $Q$—indoor waste heat, kg/s; $C$—specific heat of air quality, 1.01KJ/(kg•℃); $t_n$—exhaust-air temperature, ℃; $t_w$—entering-air temperature, ℃.

The required ventilation to eliminate the remaining wet can be calculated by equation (4):

$$G = \frac{W}{d_n - d_w} kg/s \tag{4}$$

Where: $W$—indoor remaining wet content, g/s; $d_n$, $d_w$—respectively the moisture content of the exhaust air and the entering air, g / kg.

The fresh air of air-conditioning system should not be less than 10% and not less than the greater of the following two values: (1) the local exhaust volume to supplement the room and the fresh air needed to keep the interior pressure; (2) ensure personal fresh air per hour required to meet the health requirements.

**Necessary ventilation of the required oxygen**

The fresh air should be able to provide enough oxygen to meet the breathing of indoor personnel in order to maintain the normal physiological activities. The oxygen demand for human body depends

on the levels of energy metabolism. According to the theoretical analysis[4], it can be obtained that the oxygen required in very light activities is approximately 0.0187 $m^3$ / (h • person), which shows that the required fresh air of breathing oxygen is not great, and could be satisfied under normal ventilation condition.

**Ventilation correction**

The calculated result of the fresh air and ventilation needs to be corrected combining with the actual situation. If the building facilities increase or decrease, or the use of building has changes, the required ventilation may changes accordingly, so it needs for building contamination correction. If the person in the room changes and the number of working hours is changed, and the room is part of the load state, the fresh air should be changed accordingly and need for dynamic process correction. If there are people who do not accept the indoor air quality, it is needed to carry out unacceptable correction by increasing the fresh air on the basis of the original population.

Based on the above-mentioned calculation method, the total wind can be obtained for the buildings. However, the deficiency is that the formulas can not identify how much amount of fresh air of indoor personnel is needed in the total amount of wind and how much is necessary for the sewage and breathing. Moreover, people often neglect the improvement significance of the indoor air quality by increasing the new wind. Some field tests and research show that simple increase in airflow can't completely solve the problem of indoor air quality [5], so which means that it is necessary to study the effective indoor fresh air of ventilation effectiveness.

The ventilation effectiveness consists of two parts: one is to ensure the adequate fresh air; another is the fresh air which can directly delivery into the breathing zone and rapidly discharge the indoor air pollutants through some organizational forms of airflow. The ventilation effectiveness should be comprehensively studied based on the calculation method combined with the law of human metabolism.

**Conclusions**

(1) When the indoor pollutants have not mutually influence on each other，each individual ventilation can be calculated to achieve the required standards of fresh air, and then take the maximum value as the indoor required ventilation; When certain indoor pollutants may have mutually influence, the fresh air needed to exhaust various pollutants should be summed to obtain the desired indoor required ventilation.

(2) It is needed to modify the calculated results of the fresh air and the ventilation considering with the actual situation.

(3) The simple increase in airflow can't completely solve the problem of indoor air quality, the comprehensive analysis of the ventilation effectiveness should be conducted according to the calculation method mentioned above and combined with the law of human metabolism.

**References**

[1] Hao Cheng. Research on measures of demand control ventilation based on personnel adaptability [D]. Chongqing: Chongqing University, 2012: 9-11.(In Chinese)

[2] Ping Dai. Analysis and evaluation of building indoor air quality [D]. Daqing: Daqing Petroleum Institute. 2003: 24-26. (In Chinese)

[3] Ministry of Housing and Urban-rural Development. Civil Building Heating Ventilation and Air Conditioning Design Specifications [S]. GB50736-2012.

[4] Yingxin Zhu. Build Environmentology [M]. Beijing: China Building Industry Press, 2009: 154-155. (In Chinese)

[5] Shibin Geng, Baojia Yang. Research on IAQ based demand controlled ventilation [J]. Building Energy Ventilation and Air Conditioning, 2003: 2-3. (In Chinese)

*Applied Mechanics and Materials Vols. 580-583 (2014) pp 2475-2479*
*© (2014) Trans Tech Publications, Switzerland*
*doi:10.4028/www.scientific.net/AMM.580-583.2475*

# Simulation Study on Characteristics of Ultra-low Temperature Heat Pump Air Conditioning System for Pure Electric Vehicles

Haijun LI[1,a], Guang-Hui ZHOU[2,b], An-Gui LI[3,c], Xu-Ge LI[4,d], Jie CHEN[5,e] Tong CHEN[6,f]

[1,3] School of Environmental & Municipal Engineering, Xi'an University of Architecture and Technology, Xi'an 710055, Shanxi,China;

[1,2,4,5,6] School of Energy & Environment, Zhongyuan University of Technology, Zhengzhou 450007, Henan,China

[a]haijun_li007@126.com, [b]zghzut@126.com, [c]visitli@sina.com, [d]357034845@qq.com, [e]739121120@qq.com, [f]137742087@qq.com

**Keywords:** pure electric vehicles, ultra-low temperature, heat pump, simulation

**Abstract:** In view of high discharge temperature of compressor, the heating performance attenuated seriously, even unable to work properly and other issues of normal heat pump air conditioning system for electric vehicles under low temperature conditions, a gas-mixing heat pump air conditioning system for pure electric vehicles is designed. Based on the first law of thermodynamics and coupling properties among all components, the mathematical model of this system is established. The analog computation of main performance parameters of this system is carried out by this model, having a better match in comparison with experimental results. By simulation, the results show that the system can effectively solve the problems of high exhaust temperature from compressor and heating performance attenuation seriously of non-gas-mixing heat pump air conditioning system for pure electric vehicles under low temperature condition.

## Introduction

Oil-fueled automotive heat pump air conditioning system (HPACS) used the waste heat of the engine as the heat source in winter, while electric vehicles heat can only rely on PTC heating electric heating and other ways, due to the heat source is limited, which would further increase the consumption of battery power and reduce the car battery's capacity. In order to solve this problem, HPACS as well as solar assisted and other different forms[1] was put forward by related scholars. For the electric vehicles, the heating efficiency of the heat pump system is far greater than other heating methods. when outside ambient temperature below 10˚C, the heating capacity of normal system which used medium temperature refrigerant R134a attenuate seriously, compressor discharge temperature is too high due to the compressor suction pressure is too low and the heat pump system cannot work normally. Related scholars concerned with $CO_2$ as the refrigerant in the heat pump system, the system performance is better than R134a heat pump system, $CO_2$ has a very good thermal performance especially in the low temperature, and $CO_2$ is more environmentally than R134a as a natural refrigerant [2]. But the pressure of $CO_2$ heat pump system is too high and go against the reliability and security of the system, automotive air conditioning parts need to be redesigned and the cost is too high. For this series of problems, combined with the characteristics of low temperature heat-pump technology and automobile air conditioning system, a gas-mixed heat pump system for pure electric vehicle with R134a as refrigerant is designed by our research group.

The article is based on previous research, establish mathematical model for every part of the system according to the coupling characteristics among the components, each component model will be connected to form a mathematical model which can predict the performance of the system, and the performance of the system is simulated under variable condition.

**Mathematical model of gas-mixing heat pump system for pure electric vehicle**

The flowchart of gas-mixing heat pump system for pure electric vehicle is shown in Fig 1, the system model primarily focused on the thermodynamic cycle of the whole system, as well as coupling calculation among the each component model. Mathematical model of the system mainly includes: mathematical models of low pressure injection scroll compressor, internal and external heat exchanger, gas-mixing heat exchanger, electronic expansion valves and thermal physical parameters of refrigerant R134a.

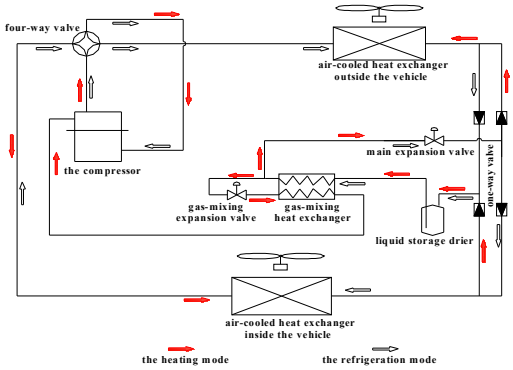


Fig 1 Schematic of gas-mixing heat pump system for pure electric vehicle

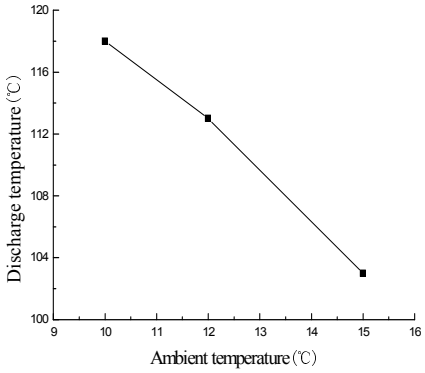


Fig 2 Compressor discharge temperature variation with respect to Outside ambient temperature

**2.1. Mathematical model of system components**

Thermo physical parameter of refrigerant R134a in this system adopts Cleland thermodynamic property models, the model is simple and practical and the amount of calculation is smaller[3]. Compressor in this system is low pressure gas-injection type scroll compressor, its mathematical model is mainly divided into two parts when set up, first, refrigerant mixture model in suction chamber is established, and then mathematical model of compressor compression process is established, in order to calculate refrigerant flow and compressor power and other parameters that affect the system's performance.

As the system simulation requires a certain precision, and stability and running speed, the internal and external heat exchanger model using separated-phase lumped-parameter dynamic models. According to the different state of refrigerant, condenser divides into superheat region, two-phase region, and supercool region[4]. The cell division of superheat region and supercool region is based on temperature drop of refrigerant, two-phase region according to enthalpy of refrigerant. Similarly, the evaporator can be divided into two-phase region and superheat region, the cell division of two-phase region in accordance with the enthalpy value, and superheat region according to the temperature drop. Parallel flow heat exchanger used by the system is a micro channel heat exchanger, according to the structural characteristics of the air side finned tube; the air side heat transfer coefficient adopts the experimental correlations of WangC.C et al.[5]. Condenser and evaporator refrigerant side of the single-phase region heat transfer coefficient adopts the heat transfer correlation of Gnielinski[6]. The heat transfer coefficient of condenser refrigerant two-phase region adopts correlations of Akers[7]. The heat transfer coefficient of evaporator two-phase region adopts the experiment correlation which is presented by Kandlikar and suitable for micro-channel boiling heat transfer[8]. For the main refrigerant cycle gas-mixing, heat exchangers corresponds to condensers, in which refrigerant supercool further, the cell division in accordance with the temperature drop; for the auxiliary cycle, gas-mixing heat exchanger is equal to the evaporator, the cell division of two-phase region is based on the enthalpy value, and superheat region is based on temperature drop. Electronic expansion valve through the stepper motor to make the valve core has the continuous displacement, changing the refrigerant flow area, and then the mathematical model is established according to the momentum equation and energy conservation. The known parameters of the heat exchanger model

calculation process are heat exchanger structure parameters, the refrigerant and air inlet parameters, according to the known parameter calculate the heat transfer performance of heat exchanger.

### 2.2. System mathematical model

The mathematical model of gas-mixing heat pump system for pure electric vehicles is established based on various parts of the system model and the thermo physical parameters model of refrigerant R134a. The model connects internal and external heat exchanger, electronic expansion valve, and mixed-air heat exchanger into an organic whole. Under variable conditions, dynamic performance parameters were simulation when the system is stable, the heating capacity and the energy efficiency ratio (EER) of system can be obtained by calculating.

### Simulation analysis

According to the model of gas-mixing heat pump system for pure electric vehicles established above, When the air side temperature of internal condenser remained 20˚C, with the air side temperature of external evaporator are 10˚C, 5˚C, 0˚C, -5˚C, -10˚C, -15˚C, assuming that the condensing temperature is 45˚C, 50˚C and evaporator outlet temperature is the outside air temperature, calculate the main performance parameters of the system.

### 3.1. Simulation error analysis

In order to verify the reliability of the system model, table 1 is comparison between simulation value and experiment test value result when ambient temperature is 10 ˚C, 5 ˚C, 0 ˚C, - 5 ˚C, -10 ˚C, -15 ˚Cand the condensation temperature is 45 ˚C. It can be seen from the table, the error of the simulation results and the experimental results within 10%, it shows that the system model can be used to analyze performance of the system[9]. Main causes of the error: the heat transfer coefficient used in the simulation calculation is empirical formulas fitted by experimental results, although it has been amended, still has some limitations for different operating conditions. In the calculation process of the compressor model, the compression process is based on the ideal isentropic compression, ignoring the irreversible loss of the clearance volume and other aspect, so will cause errors.

Table 1 Comparison between simulation model and experimental result ($T_k$=45 ˚C)

| Performance ($T_k$=45˚C) | Discharge temperature（˚C） | | | Heat capacity（W） | | | EER | | |
|---|---|---|---|---|---|---|---|---|---|
| Ambient temperature（˚C） | Simulation | Experiment | Error（%） | Simulation | Experiment | Error（%） | Simulation | Experiment | Error（%） |
| 10 | 72.6 | 75.4 | 3.7 | 5383 | 4962 | 8.5 | 3.38 | 3.10 | 9.2 |
| 5 | 70.7 | 74.3 | 4.8 | 4622 | 4336 | 6.6 | 3.01 | 2.81 | 7.7 |
| 0 | 69.1 | 73.1 | 5.6 | 4051 | 3779 | 7.2 | 2.71 | 2.48 | 8.5 |
| -5 | 68.7 | 72.2 | 4.9 | 3426 | 3220 | 6.5 | 2.41 | 2.19 | 9.3 |
| -10 | 66 | 69.3 | 4.3 | 2762 | 2674 | 3.3 | 2.01 | 1.90 | 6.1 |
| -15 | 57.3 | 61.4 | 6.7 | 2620 | 2505 | 4.6 | 1.85 | 1.69 | 9.4 |

*$T_k$: Condensing temperature

### 3.2. Results analysis

The experimental test performance of the non-gas-mixing heat pump system under low temperature condition are shown in Fig 2, Fig 3. It can be seen from Fig 2, the compressor discharge temperature rise from 103˚C to 118˚C as the ambient temperature decreases from 15˚C to 10˚C. When the ambient temperature continues to drop, the compressor discharge temperature will exceed the allowed maximum discharge temperature 120˚C, the system cannot continue to run. It can be seen from Fig 3, the heating capacity decreased rapidly with the ambient temperature reduced, This is due to suction

pressure of system reduced with the ambient decreased, and the specific volume of refrigerant R134a increased gradually while the suction vortex of scroll compressor was invariant, causing the refrigerant mass flow of the system reduced, so the heating capacity decreased gradually. It can be seen from the above data, when the ambient temperature was below 10˚C, the compressor discharge temperature will exceed the allowed 120˚C in normal heat pump circulation system for pure electric vehicle, so the system cannot run normally.

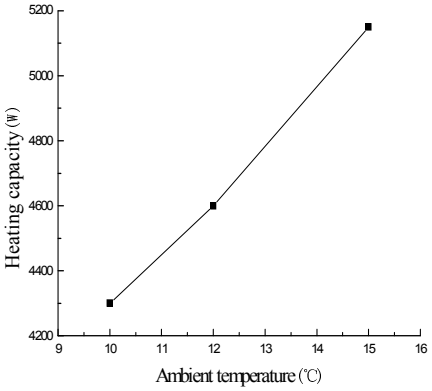


Fig 3 Heating capacity variation with respect to Outside ambient temperature

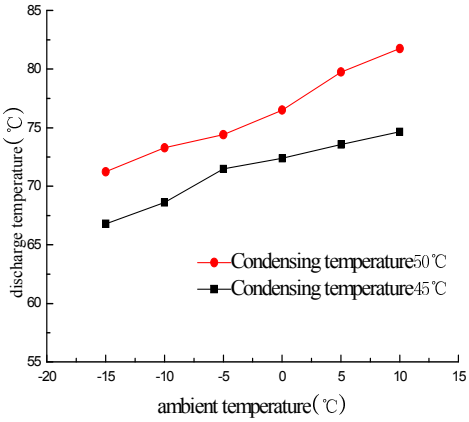


Fig 4 Compressor discharge temperature variation with respect to Outside ambient temperature

Under different condensing temperatures, the compressor discharge temperature in gas-mixing HPACS for pure electric vehicle varies with the outside ambient temperature is shown in Figure 4. It can be seen from the figure, the compressor discharge temperature lower with the reduction of the outside temperature under different condensing temperatures. Because refrigerant of the auxiliary cycle pass gas-mixing heat exchanger, then enter the mixing chamber of the compressor to mix adiabatically with refrigerants in the main cycle, the degree of superheat of refrigerant absorbed by compressor is reduced, the discharge temperature decrease after isentropic compression of compressor. The compressor discharge temperature is 71˚C at -15˚C, much less than the allowed maximum discharge temperature 120˚C, the system can operate normally.

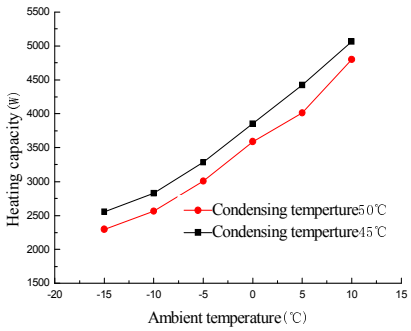


Fig 5 Heating capacity variation with respect to Outside ambient temperature

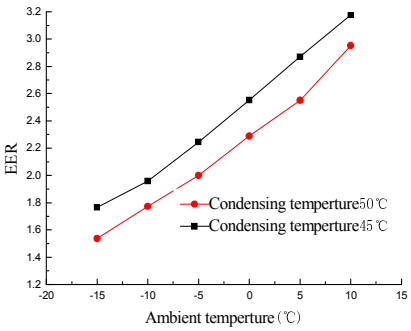


Fig 6 EER variation with respect to Outside ambient temperature

As shown in Fig 5, the heating capacity of the gas-mixing HPACS for pure electric vehicle reduced gradually with the decrease of outside ambient temperature. The system can run normally and the heating capacity improved greatly with respect to the non-gas-mixing HPACS for pure electric vehicle. When the ambient temperature is 10˚C, the heating capacity of the gas-mixing HPAC is 5383W, while the normal HPAC is 4200W, the heat capacity increases about 28%. Because after adopting gas-mixing HPACS, refrigerants from the auxiliary cycle mixed with refrigerants from the main cycle in compressor suction chamber reduce the degree of superheat of compressor suction, the specific volume of working fluid decreases and the mass flow increase, the heating capacity of the

gas-mixing HPACS will be greatly improved respect to normal HPACS. The evaporation pressure of external heat exchanger decreases with the reduction of ambient temperature, so it cause a reduction of the compressor suction pressure, the refrigerants specific volume increase. when the outside ambient temperature decreased from 10˚C to -15˚C, the heating capacity of the gas-mixing HPACS is reduced by 50%. the heating capacity slightly down with the rise of the condensing temperature, as the rise of condensing temperatures causes evaporating temperature of outside heat exchanger rising, the refrigerants specific volume increase, refrigerant mass flow lower. When the outside ambient temperature is 10˚C, the heating capacity reduces from 2620W to 2296W with the condensing temperature increases from 45˚C to 50˚C.

As shown in Fig 6, the heating efficiency of the system is about 1.7 when the ambient temperature is -15˚C, which is still greater than the efficiency of PTC heating methods used by electric vehicle normal HPACS when the outside ambient temperature is below 10 ˚C.

## Conclusions

This paper establish the model of gas-mixing HPACS for pure electric vehicle, and simulation the discharge temperature, the heating capacity and EER of the system under different condensing temperatures and outside ambient temperatures. The results show that after the use of mixed gas, the compressor discharge temperature of heat pump system is decreased about 40.5%, the heating capacity of the system increases by about 28% under low temperature; the system EER increases by more than 70% compared with normal HPACS for electric vehicle; solving some problems that the discharge temperature is too high , and attenuation of heating performance of non-gas-mixing HPAC under low temperature condition, it has a positive role in promoting the application of the heat pump technology in the pure electric vehicles.

## Acknowledements

This work was supported by the Research Funds of Key Laboratory of Heating and Air Conditioning, The Education Department of Henan Province(No. 2013HAC203), and the Ministry of Science and Technology of Henan Province (No. 112102210515, No. 122102210056).

## References

[1] Ma Guoyuan, Shi Baoxin, Chen Guansheng, etc. Journal of solar energy. 2 (2001). 176-180. in chinese

[2] Xie Zhuo, Chen Jiangping, Chen Zhijiu. Journal of automobile engineering. 8 (2006) .763-765. in chinese

[3] Ding Guoliang etc. New working substance of refrigeration and air conditioning. The calculation method of thermal physical properties and practical chart. 2003. in chinese

[4] Ding Guoliang, Zhang Chunlu. Simulation and optimization of refrigeration and air conditioning equipments. 2001. in chinese

[5] Wang C C, Lee C J, Chang C T, et al. International Journal of Heat and Mass Transfer. 11 (1998). 1945-1956.

[6] Gnielinsk. International Chemical Engineering. 16 (1976). 359-368.

[7] Akers W W, Deans H A, Iccrosser O. Chemical Engineering Progress Symposium Series.29 (1959) .71-176.

[8] Kandlikar S G, Steinke M E. 2003.

[9] Zhao Pengcheng, Ding Guoliang, Zhang Chunlu, etc. Journal of solar energy. 3 (2004) .383-387. in chinese

*Applied Mechanics and Materials Vols. 580-583 (2014) pp 2480-2483*
*© (2014) Trans Tech Publications, Switzerland*
*doi:10.4028/www.scientific.net/AMM.580-583.2480*

# The effectiveness of implementing automated ventilation system in premises intended for public using

[1,a]Shilkina Svetlana, Ph.D, associate professor., [2,b]Trusov Artur

[1]Associate professor of Moscow state university of civil engineering (National research university, MSUCE), Moscow, 129337, Yaroslavskoye shosse, 26

[2]Post-graduate student of Moscow state university of civil engineering (National research university, MSUCE), Moscow, 129337, Yaroslavskoye shosse, 26

[a]shilkina@bk.ru, [b]trusov.artur@gmail.com

**Keywords:** automated ventilation system, ventilation in public catering, recovery ventilation, recuperation, variable frequency drive

One of the most important topic of 21th century is energy savings, and many countries create enterprises which develop standards and codes for construction, repairs and building renovations, including a realistic, cost-effective recommendation aimed at making city buildings become cleaner and more energy efficient. For example, one of these enterprises is C 40 Cities Climate Leadership Group.

This group is a network of the world megacities taking action to reduce greenhouse gas emissions, to increase energy efficiency of municipal services and to adapt to climate change.

In this regard, we consider the application of engineering systems of the building automation aimed at energy savings. So, substantial part of the energy consumption in the building intended for public use is heating ventilation and air-conditioning (HVAC) systems.

In this article HVAC systems in public catering will be considered, since many factors should be taken into account while designing. For example, the imbalance between the dining room and the kitchen ventilation systems can prevent kitchens smells getting to dining room area.

For air quality to remain at the highest level, HVAC systems should include several supply and exhaust systems, and to achieve greater economic and energy efficiency recuperation and recirculation systems should be applied and variable-frequency drive (VFD) should also be used.

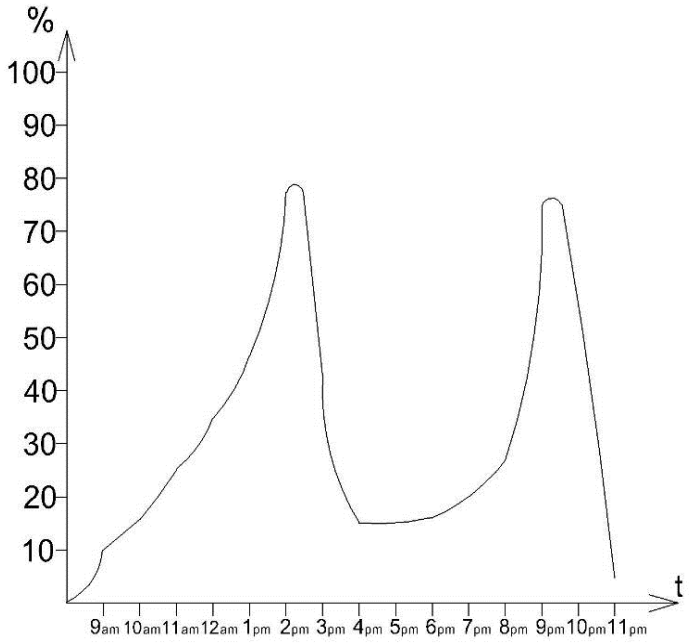


Fig.1 Graph of the volume of visitors on the time

The recirculation system is applied to mix high quality air, which is processed by supply ventilation, with the outdoor air. Air quality is monitored by carbon dioxide sensor, which is located in the exhaust air duct.

A carbon dioxide sensor or CO2 sensor is an instrument for the measurement of carbon dioxide gas. The most common principles for carbon dioxide sensors are infrared gas sensors (NDIR) and chemical gas sensors. Measuring carbon dioxide is important in monitoring indoor air quality and many industrial processes.

This system is particularly effective when there is a large temperature difference between the outdoor and indoor air, because less energy is consumed for heating or cooling.

Figure 1 shows the number of visitors on the time. This graph shows that recirculation will be working from 9am to 1pm and from $3^{30}$pm to $8^{30}$pm, when number of the visitors is less than 60%.

However the recirculation has some restrictions on sanitary and hygienic standards. Smell from the kitchen could spread to dining room, therefore the use of this system in public catering is undesirable.

In this case recuperative heat exchangers are widely used. Heat recovery ventilation, also known as HRV, is an energy recovery ventilation system using equipment known as a heat exchanger which employs a counter-flow heat exchanger (countercurrent heat exchange) between the inbound and outbound air flow.

Recovery ventilation efficiency reaches up to 70%, and it generally saves heating energy during winter period. It also depends on several factors. A thermal wheel is the most effect. A thermal wheel, also known as a rotary heat exchanger, or rotary air-to-air enthalpy wheel, or heat recovery wheel, is a type of energy recovery heat exchanger positioned within the supply and exhaust air streams of an air handling system, or in the exhaust gases of an industrial process, in order to recover the heat energy. But for public catering recuperator, or cross plate heat exchanger, is more suitable, because thermal wheel can bring unwanted odors.

A recuperator is a special purpose counter-flow energy recovery heat exchanger positioned within the supply and exhaust air streams of an air handling system, in order to recover the waste heat.

In HVAC, recuperators are commonly used to re-use waste heat from exhaust air normally expelled to atmosphere. Devices typically comprise a series of parallel plates of aluminium, plastic, stainless steel, or synthetic fibre, alternate pairs of which are enclosed on two sides to form twin sets of ducts at right angles to each other, and which contain the supply and extract air streams. In this manner heat from the exhaust air stream is transferred through the separating plates, and into the supply air stream.

The recuperator's drawback is that condensation can become frozen in the cold periods. In order to control the icing, the differential pressure switches (DPS) are used, and apply a bypass of supply duct. DPS - is a form of switch that closes an electrical contact when a certain set pressure has been reached on its input. The switch may be designed to make contact either on pressure rise or on pressure fall.

So, principle of operation is that when the icing reaches a maximum level, DPS sends a signal to the controller. Then controller sends a signal to the damper actuator and opens the bypass, and exhaust air heats the recuperator and condensate is drained into a special hole. Also, it is recommended to use a heat exchanger at a temperature not lower than -30$^{o}$ C. in this case, the supply air passes through the bypass.

According to my research, with the use of recuperator in public catering efficiency reaches 54% in winter, and 46% in summer. The recuperator is located in supply and exhaust system of the dining room. Net dining room area is 112 square meters.

Through economic analysis, we conclude the following:

$Q = 0.278 \bullet \mathrm{Ca} \bullet \mathrm{Ga} \bullet (t_K - t_H)$ – amount of heat calculation to air heating, watt (1)

$$\mathrm{Gw} = \frac{(3.6 \bullet Q)}{\mathrm{Cw} \bullet (\mathrm{t1} - \mathrm{t2})}$$ – consumption of a heat-transfer agent kg/h, (2)

provided that the temperature indoors is 16 $^{o}$C, according RCC 2.08.02–89, and mean air temperature -1,8$^{o}$C, according RCC 23-01-99*. In my variant the city is St. Petersburg. RCC– is Russian Construction Code (SNIP).

All data obtained from diploma paper.

Gw = 997.40 kg/h - this is a consumption of a heat-transfer agent, before applying of recuperator, after applying the consumption is 435,856 kg.

Sh.w. = Ah.w. $\bullet$ Ph.w . – expenditures for hot water, RUB/year, (3)

where Ah.w.– is annual hot water consumption ton/year, Ph.w. – price ton of water RUB/t, according as heating season is 220 days.

Sh.w.= 256,199.2 RUB/year – this are expenses for hot water before applying recuperator, and after its applying the expenses reduce to 112, 727. 65 RUB/year.

Also one of the very important device to energy saving is variable-frequency drive (VFD). VFD (also termed adjustable-frequency drive, variable-speed drive, AC drive, micro drive or inverter drive) is a type of adjustable-speed drive used in electro-mechanical drive systems to control AC motor speed and torque by varying motor input frequency and voltage.

VFDs are used in applications ranging from small appliances to the largest of mine mill drives and compressors. However, about a third of the world's electrical energy is consumed by electric motors in fixed-speed centrifugal pump, fan and compressor applications and VFDs' global market penetration for all applications is still relatively small. This highlights especially significant energy efficiency improvement opportunities for retrofitted and new VFD installations.

Over the last four decades, power electronics technology has reduced VFD cost and size and improved performance through advances in semiconductor switching devices, drive topologies, simulation and control techniques, and control hardware and software.

Use them necessary almost on all fans in ventilation systems, to change motor speed. If not applied VFD, fans will working in full power, and hence is not energy efficient. Depending on time of day number of customer is different, this means that air exchange should change. Figure 1 proves it, the graph shows VFD's working.

Trough economic analysis we conclude the following:

$$Sel.en. = \Sigma Ni \bullet Tyear \bullet Pel.en. \bullet Ce \text{ – electricity costs,} \quad (4)$$

where ΣNi – total power of used electromotors (kW). Tyear - operating time per year. Pel.en. - price of electricity 1kW*hour. Ce – coefficient of ancillary costs to electricity.

In my diploma paper 2 supply and 4 exhaust ventilation systems were applied. VFD was used with all fans. Total power of used electromotors is 12.8 kW.

$$Sel.en = 12{,}8 \bullet 5040 \bullet 3{,}6 \bullet 1 = 232{,}243.2 \text{ RUB\year}$$

Used graph which located in Fig.1, I calculated total power of fans, with applying of VFD, and total power decrease about 2,5 times.

$$Sel.en = 4.77 \bullet 5040 \bullet 3{,}6 \bullet 1{,}15 = 99{,}528.91 \text{ RUB\year}$$

Therefore, applying VFD decreased power consumption more than two times.

As already mentioned the fan speed depends on carbon dioxide content in the room. This rule will be used with all rooms except kitchen, there will be extract hoods over hotplates and in washing place will be applies. Also fan speed control cannot be used with the light detector and temperature sensor, because regulation cannot be exact, and optimal conditions will not be achieved if misregulated.

In my diploma paper I tried to keep optimal conditions. I controlled the fan speed which is located in the kitchen's exhaust system by amount of activated burners, located in the cooker. That means relay was installed on each control knob for burners, and relay contact closes when burners turn on, after that relay signal is send to the controller. Then analog signal the logic of controller is send to the VFD, and depending on the number of activated burners, the fan speed will be changed.

For example, if one burner is activated the fan will be working by 20%, if two burners are activated the fan will be working by 40 %, and if all the burners activated the fan will be working full power. Fan schedule is almost similar to Fig. 1.

Although kitchen's exhaust system is not controlled by carbon dioxide sensor, the system has to be related with other systems. In order to do it, it is necessary to install a set point in controller, whereby the imbalance between dining room and kitchen would be observed.

Thus, applying recuperation system, variable frequency drive, and most importantly the right automated approach, we make comfortable conditions for visitors and staff, also we save heat and energy recourses, which in turn can save the money.

**References**


[1] *Volkov A.* Building Intelligence Quotient mathematical description // Applied Mechanics and Materials (Trans Tech Publications, Switzerland). – Vols. 409–410 (2013). – pp. 392–395.

[2] *Sedov A., Volkov A., Chelyshkov P.* Usage of building information modeling for evaluation of energy efficiency // Applied Mechanics and Materials (Trans Tech Publications, Switzerland). – Vols. 409–410 (2013). – pp. 630–633.

[3] *Volkov A., Vodnev N.* System engineering numerical representation of the quality parameters living and working environment. Recursive procedure dive into levels detailization of objects: basic mathematics and logic // Promishlennoye i grazhdanskoye stroitelstvo. – 2013. – №9. – pp. 6–8.

[4] *Volkov A.* General Information Models of Intelligent Building Control Systems: Basic concepts, determination and the reasoning.// Advanced Materials Research (Trans Tech Publications,Switzerland).–Vols.838-841(2014).–pp.2969-2972.

[5] *Volkov A.,* General Information Models of Intelligent Building Control Systems: Basic concepts, determination and the reasoning // Advanced Materials Research (Trans Tech Publications, Switzerland). –Vols. 838-841 (2014) pp. 2973-2976

[6] *Ginzburg A.V.* The automation of the organizational technological construction reliability designing. M.: SEP RIA. (1999)

[7] *Ginzburg A.V., Kagan P.B.* CAD of construction organization. The journal "CAD and graphics", № 9, 32-34. (1999).

[8] *Kagan P., Kulikov V.* Information modeling of urban planning development.// Applied Mechanics and Materials (Trans Tech Publications,Switzerland).– Vols. 409-410 (2013) pp 951-954

[9] *Chelyshkov P., Volkov A., Sedov A.* Application of computer simulation to ensure comprehensive security of buildings // Applied Mechanics and Materials (Trans Tech Publications, Switzerland). – Vols. 409–410 (2013). – pp. 1620–1623.

[10] *Volkov A.A., Muminova S.R.,* Devaluation modelling for residantial buildings // Advanced Materials Research (Trans Tech Publications, Switzerland). –Vols. 860-863 (2014) pp. 2864-2867

[11] *Volkov A.A., Yarulin R.N.* Avtomatizatsiya proektirovaniya proizvodstva remontnykh rabot zdaniy i inzhenernoy infrastruktury [Computer–Aided Design of Repairs of Buildings and the Engineering Infrastructure]. // Vestnik MGSU [Proceedings of Moscow State University of Civil Engineering]. 2012. – no. 9. – P. 234-240.

[12] *Volkov A.A.* Homeostatic control of buildings // Housing construction. 2003. № 4. pp. 9-10.

[13] *Volkov A.A., Chelyshkov P.D.* Algorithm of scenario verification of buildings and complexes engineering decisions in cad-systems. Vestnik MGSU [Proceedings of Moscow State University of Civil Engineering]. 2011, no. 5, pp. 344—347.

[14] *Volkov A.A., Chelyshkov P.D., Sedov A.V.* Abstraktnaya kharakteristika nadezhnosti (dolgovechnosti) pri vybore optimalnoy struktury sistemy avtomaticheskogo upravleniya v SAPR [Abstract Characteristic of Reliability (Durability) in Selection of the Optimal Structure of an Automatic Control System in CAD]. Vestnik MGSU [Proceedings of Moscow State University of Civil Engineering]. 2013, no. 1, pp. 218—224.

*Applied Mechanics and Materials Vols. 580-583 (2014) pp 2484-2487*
*© (2014) Trans Tech Publications, Switzerland*
*doi:10.4028/www.scientific.net/AMM.580-583.2484*

# "Breathing House"—New Air System for Healthy Residential Buildings

Dong Tiexin[1, a] , Yan Zhenyu [2, b]

[1]Inner Mongolia University of Science and Technology, Baotou, Inner Mongolia,China

[2]University of Applied Arts Vienna, Vienna, Austria

[a]dtxjack1982@163.com,[b]architect_yanzhenyu@hotmail.com

**Keywords:** new air system, healthy housing

**Abstract:**
As the continual improvement of human living standards, healthy housing became a hot topic and was attached more and more emphasis whatever from the profession or the public. Professionally, better ventilation is one of the most important facets of the healthy housing. Compared with the traditional ventilation system, this paper illustrates the new air system that makes a full use of natural resources, directly and simply changes the normal traditional housing to the healthy housing, through the concept, philosophy, typology and property of the new air system. Additionally, it takes the "*Dong Ya Shi Ji Cheng*" in Batou as typical example of healthy housing, in order to demonstrates the advantages of the new air system more clearly.

## The background

A myriad of previous research indicate that the air pollution level of indoor is 5-20 times higher than the outdoor one, and people stay indoor much longer than outdoor. On the other hand, more respiratory diseases resulted from the indoor air pollution, for instance the air pollution caused by the interior decoration, and people inhales the floating bacterial particles due to the closed transom prevents the natural ventilation. Especially as the emergence of SARS and avian influenza, the quality of indoor air condition became a inescapable issue of healthy housing.

Modern society promotes healthy housing which maximize the people's better physical and psychological experience. Therefore, the quality of indoor air condition is undoubtedly an important indicator of the comfortable living condition. In general, the traditional ventilation methods could be summarized as follows:

(1) Traditional window: it could exchange the air quickly, but causes several problems particularly for the high-rise buildings. When the widow open, the sand dust and cold air will come inside of the room. It often caused air floating particle, air turbulence and noise problems as well.

(2) Ventilator: the exhaust volume is huge, but the noise problem will increase while the longer you use it. It is only positive for the shortly and partly exhaust without rational organized flowing path. In fact, its effect is negative which could not be considered as the real air exchange.

(3) Large central air condition system has the New air systems. However, this system is very complex and has poor operability. The traditional design of positive pressure ventilation has the disadvantage to exclude the polluted air. The air hose is the place easily accumulate with dust and bacterial, the most corner is breeding ground for the infecting organisms.

(4) small domestic central air condition system : it has the ventilation hole, but it can't completely exchange the air from outside. The fresh air can't be sent into the room without the exhaust system, and the bad smell can't go out either. It is impossible to fundamentally change the inside air quality.

In north Europe, the VMC has been invented fifty years ago. Spanish have already equipped their new houses with VMC in the 1970s. French introduced new regulation on ventilation in 1958, and the VMC were used widespread in 1969. In 1989, American ASHRAE drew up “Indoor air quality ventilation specifications”. In Germany, residential ventilation systems have become an indispensable part of their lives. In 2000, EU unified the standards on residential ventilation. With the improving of building air tightness, it caused “new house disease” and other diseases accompanied with the chemicals, polluted air and inadequate ventilation. So Japan put Mechanical Ventilation Facility into “Basic Architecture” as enforcement. In accordance with these regulations, every building has to ventilate all day, and the ventilation should reach 0.5 times per hour. However, VMC as a new ventilation system in China has been stepping into our lives.

**The concept and philosophy of the new air system**

The new air system is constituted of four parts: fans, inlet, vents and various pipes. A series of pipes connects the fans and vents. The fans installed in the ceiling could exhaust the polluted air through vents, created the air pressure difference. Therefore, the fresh air could come into the room through inlet which guarantees the air circulation. In reality, a series of rational organized air flow and continual low wind energy design (100 $m^2$ housing only use a kilowatt hour per three days) promise the inside fresh air condition.

We take the second phase of "*Dong Ya Shi Ji Cheng*" in Baotou as an example. It uses a new air system of Panasonic which is a diversified ventilation system based on three principles of mechanical ventilation system and natural ventilation system. The fans is installed in the ceiling, the inlet is on the window frame. Most of the exhaust pipes are installed in the ceilings of aisle and toilet, while the inlet doesn’t need pipeline to occupy the space in the ceiling. The room where people stay for more than three hours should provide 30 $m^3$fresh air per hour, the master bedroom is 50 $m^3$ per hour and the other bedrooms are 30 $m^3$ per hour, while the places don’t stay can be laid aside to provide fresh air, such as the kitchen, the bathroom and the equipment room. Based on the principles above, this system determines the area to supply fresh air, the air volume and the duration to ventilate in the different rooms. This system divides the house into two areas, one is positive pressure area and the other is negative pressure area. The positive one includes bedrooms and the living rooms. while the negative one includes kitchens, bathrooms and aisles. The fresh air is brought in from the clean area and force the polluted air going out from the filthy area, which makes sure that the inhabitant can enjoy the fresh air all day.

This system named as Thermal Comfort Ventilation which could keep the fresh air inside and exchange the polluted air to the outside. It can increase the body’s heat dissipation to prevent the sick caused by the moist skin. This kind of ventilation is also named as the cooling-house ventilation, because it can cool the building when the temperature is higher than the outside.

Furthermore, "*Dong Ya Shi Ji Cheng*" is known as “the breathing house”. It has these advantages as follows:

(1) the house could breathe the fresh air.

(2) It’s benefit for human's mental and physical health, and has moisture proof and disinfection effect.

(3) The guarantee of the power engine is five to eight years, and it saves energy. The motor power is 38W, 90 $m^2$ room only need 1 kWh electricity per day.

(4)National standards for noise defined that the day time is 40 db, the night 30 db. The fresh air system is less than 30 db low-noise system.

(5)Through adjust the controller, it could control the temperature according to the weather. Therefore, the air exchange might not change the inside temperature.

**The property and Types of Fresh Air System**

The fresh air system is divided into three types based on the property :

(1)Single-pass Fresh Air System

It uses the natural air supply and mechanic exhaust system. The rationale is when the system is running, the organized air flow will continuously exhausted the stagnant air to the outside from the most polluted areas, and then the outside fresh air can be led into the room through the air inlet from the most active place into the room, maintaining indoor air fresh. The route of airflow is that the fresh air enters from the living room and then exhaust from the bathroom and kitchen.

The advantage of Single-pass Fresh Air System is that the preliminary investment is low and the indoor pipelines are relatively less. Because the fresh-air-supply of Single-pass Fresh Air System is through pressure difference between the room and outside. Hence it is heavily impacted by the quality of atmospheric air, and is not able to filter or disinfect the incoming air. It will take indoor heat and cold away during the exhausting procedure, which wastes the energy.

(2)Two-way Fresh Air System

The Two-way Fresh Air System is a supplement to the Single-pass Fresh Air System in certain aspects. It is composed of two sets of systems. One is mechanic exhaust system, the other is mechanic air supply system. Compared to natural supply, the difference between mechanic air exhaust system and Single-pass Fresh Air System is that the fresh air gets into the room through the pipes of supply system. The arrangement of pipes is the airflow paths, which is better to the airflow organization. Meanwhile, the fresh air can be improved, such as dehumidification, humidification, disinfecting and heating, according to the requirements. It is suitable for the rooms with special requirements of the air quality. It is able to make the room being in a state of micro-pressure, which can effectively isolate invalid air from entering through the gap of doors.

Two-way Fresh Air System uses the mechanical ventilation, so the fresh air can be filtered and disinfected effectively. But the cold or heat will be discharged outdoors during the procedure of supplying and exhausting, which will cause the energy waste. Furthermore, it needs much more pipes and the preliminary investment is higher.

(3)All-air Heat Recovery Exchanger Ventilation System

The advantage is it has a heat exchange module which combines the supplying and exhausting. The structural components consist of fresh air host, inlet, outlet, pipe network and speed switch etc. The host is usually set in the balcony, kitchen, bathroom, ceiling or storage rooms. It has the same operational principle with Single-pass Fresh Air System. When it works, the indoor polluted air and particulates are discharged outside by the exhaust pipe. Meanwhile, fresh air is coming in through the ventilator. But the difference is the heat recycle ventilation system which is improved from the Single-pass Fresh Air System, could absorb and supply heat. In the heat exchange module, the heat of exhaust air will be exchanged with the supplying fresh air. Therefore, it can achieve the goals of recycling cold in summer and heat in winter, which can save energy and improve the indoor air quality.

All-air Heat Recovery Exchanger Ventilation System uses the mechanical ventilation, so the fresh air can be filtered and disinfected effectively. In the process of supply and exhaust, it is able to recycle the energy of exhaust air, saves energy. But it needs more pipes and the priliminary investment is quite higher.

**The Limitation of The New Air System**

(1) Limitation of installation. For instance, the new air system should be installed in the ceiling with other pipeline.

(2) Regional Limitation. Anti-frost wind measures should be considered in Cold regions to use the new system

(3) Limitation of Energy saving. The new wind load will reach 30% of heating in the cold areas.

(4) Requirements of Multifunction. For instance, the room requires air purification, humidification, dehumidification, sterilization.

(5) Requirements of Technical and economic. It needs comprehensive consider the Run-time investment costs, use effect systems, maintenance fees to control costs.

**The Advantages of The New Air System**

(1) Ventilation. People could not only enjoy the natural fresh air, but also filter indoor air, cleared the long-term harmful gases caused by interior decoration, and conducive to human health without opening the window.

(2) Avoiding "Air-condition disease".

(3) Large electricity distribution capacity can no longer be considered; Partly exhaust equipment in kitchen, bathroom can be cancelled; Window screen is not necessary; Only the bottom of the door in kitchen and bathroom needs screen; Main engine could put in the ceiling of kitchen or bathroom; the exhaust port is flexible, and the area of the pipe shafts are reduced.

**Conclusion**

Currently, China's building energy saving should based on the sustainable development of the energy value promoting model. For instance, the solar air system as the auxiliary heating system in winter is a new fresh air system combined the solar energy and technology of changing thermal storage. The solar energy could heat the fresh air, while the additional solar energy could be stored in the thermal storage device, used for bad weather. In this case, it maximizes the use of solar energy, and guarantees the long time work of the new air system.

Only the low energy consumption of heath building could create the sustainable living environment. The new air system is just on the way towards to the promising. Healthy housing, energy conservation and other development concepts have laid a solid foundation for the widely application of new ventilation system in the residential buildings and other public buildings.

**References**

[1]Liao Chunbo, New Air System In Residential Buildings (2006), Residential Technology Press

[2]Hou Xianhong, New Ventilation System In Residential Buildings (2011), Urban Housing Press

*Applied Mechanics and Materials Vols. 580-583 (2014) pp 2488-2491*
*© (2014) Trans Tech Publications, Switzerland*
*doi:10.4028/www.scientific.net/AMM.580-583.2488*

# Research on the construction technology of radial underground heat exchanger and its heat exchange performance

Ronghui Wang, Qinghua Wang, Ye Feng

(Construction engineering college of Jilin University, Changchun, Jilin Province, 130061)

**Key words**: Radial heat exchange wells; Buried tube heat exchanger；Heat exchange performance

**Abstract**：5 radial heat exchange wells were designed, and the different angle drilling, drilling pipe, and grouting backfill construction technology was studied. In addition, the heat transfer performance of the buried radial heat exchange wells was tested. The results show that, design of pipe equipment is feasible, construction is convenient, and the ratio of backfill material is reasonable; the heat transfer performance of 90 °buried tube is the best. The smaller the angle with the ground heat exchanger, the greater the heat exchange performance is affected by the surface temperature.

## Outline

Ground source heat pump engineering both domestic and abroad, a single U or dual U type vertical tube HDPE is usually used as underground heat exchangers. But when the ground-source heat pump technology developed rapidly in the city and buried pipe region adjacent to the road, bridge or other buildings, land constraints make heat well spacing decreases, the low efficiency of heat exchange, or the heat transfer well depth increase project cost. Therefore, by inclined way to alleviate or solve this problem, the road or green slope to the building foundation and the surrounding has been paved, neither destroy the building or bridge structure, and can save a lot of buried pipe construction land.The buried heat exchanger can be composed of HDPE tube of multiple sets of double U or single U, heat exchange wells according to different direction and angle are arranged radial. Radial heat exchange wells covers an small area, saves the land resources, high heat exchange efficiency, is a new type of ground source heat pump system of outdoor heat exchanger.

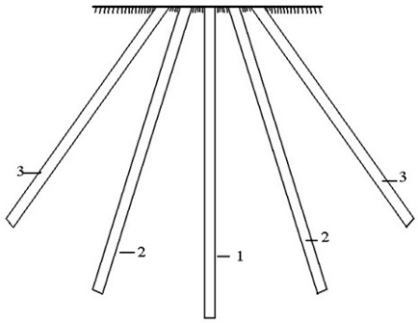


Figure 1 Radial heat exchange wells

Based on the problems, this paper designs 5 radial heat exchange wells and research the heat transfer performance and construction technology. Shown in figure 1, 5 wells are symmetrically arranged, angle with the ground are 90 °, 60 ° and 30 °, length is 100m. HDPE tube of single U is placed in hole, which diameter is 32mm.

**Construction of radial heat exchange wells**

Use the hydraulic pressure driving head of JDZ-5 ground coring drilling rig developed by Jilin University. Drill the radial wells, drilling diameter is180mm.

After the construction of radiation wells, began the decentralization of underground pipe. Because the inclined of the borehole, the commonly pipe decentralization method can not be used, therefore, a special down tube apparatus had been designed, the apparatus comprising a fixed hollow hammer with tip head, the end of pipe placed in the empty weight core, then poured into the hollow core of the concrete, after the concrete was hardened ,underground pipe can be fixed with the hammer ,as shown in Figure 2. The hammer can play a protective role of underground during placing down the pipe tube , also can increase the weight of the pipe, and made the decentralization of underground pipe more smoothly into the borehole. After the decentralization of the tube, filled with backfill material, and connected the underground pipe to the interior through horizontal pipe.

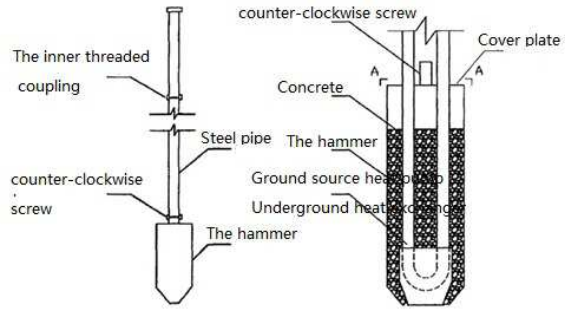


Figure 2 Schematic diagram of tube laying device the structure of heat exchanger buried underground

The heat transfer performance of buried tube strongly depends on the quality of backfill process. Some projects often use mixture of 80%-95% bentonite and 5%-20% cement. In this paper, through the indoor test of the heat transfer performance of the backfill material, several more ideal backfill material are obtained, which are shown in table 1.

Table 1 The backfill material

| Serial number | The backfill material proportion | | |
|---|---|---|---|
| | Sand | Cement | Bentonite |
| 1 | 0 | 20% | 80% |
| 2 | 20% | 0 | 80% |
| 3 | 10% | 20% | 70% |
| 4 | 20% | 0 | 80% |

The plunger mud pump is used to backfill. To prevent backfill material solidification, the process of grouting interval time should not be too long. If considering it is in winter, the temperature is low, it can increase the grouting pump alternating grouting.

**Heat transfer performance testing of radial heat exchange wells**

A portable ground thermal response test instrument, developed by Jilin university, is suffered an underground irrigation thermal test, used to simulate the heat pump units in summer cooling exchanger and heat transfer situation of formation. Test has three stages that include the cycle of reactive power, constant heat flux test and constant temperature. Five radial heat wells of thermal are tested in July 2011. Test time is shown in table 2, and test related conditions are shown in table 3. Among them, the number of buried tube heat exchanger respectively are: 1 # is 90°, 2 # and 3 # is

60°, 4 # and 5 # is 30°. On the basis of test, on the basis of linear source model[1], combining with the parameter estimation method[2], using matlab programming fitting to calculate the coefficient of thermal conductivity of 1 # well to 5 # well and other thermal physical property parameters, and the calculate according to test data per linear meter for heat and so on are shown in table 4.

Table 2 Test time of hot filling

| No. | No power cycle time | The stage of constant heat flux | The stage of constant temperature | Total time on test |
|---|---|---|---|---|
| 1# | 4h6min | 51h50min | 37h22min | 93h19min |
| 2# | 1h15min | 55h16min | 37h50min | 93h7min |
| 3# | 1h21min | 50h58min | 45h55min | 98h26min |
| 4# | 2h57min | 57h55min | 33h11min | 91h6min |
| 5# | 1h1min | 49h | 50h6min | 98h6min |

Table 3 Test conditions

| No. | Initial temperature˚C | The stage of constant heat flux | | The stage of constant temperature | |
|---|---|---|---|---|---|
| | | Set Temperature difference ˚C | Flow m³/h | Set into the well temperature ˚C | Flow m³/h |
| 1# | 8.74 | 2.63 | 1.382 | 34.84 | 1.459 |
| 2# | 8.67 | 2.63 | 1.431 | 34.86 | 1.443 |
| 3# | 8.63 | 2.6 | 1.422 | 34.82 | 1.43 |
| 4# | 8.53 | 2.8 | 1.335 | 34.87 | 1.35 |
| 5# | 8.46 | 2.78 | 1.34 | 34.89 | 1.366 |

Table 4 The test results

| No. | The stage of constant heat flux | The stage of constant temperature | | Thermal parameters | | |
|---|---|---|---|---|---|---|
| | Per meter for Quantity of heat W/m | Import well circulating water temperature ˚C | per meter for Quantity of heat W/m | The heat conduction coefficient λ W/(m·K) | Drill hole thermal resistance Rb （mK/W） | Thermal diffusion coefficient α 10-6m2/s |
| 1# | 43.51 | 5.41 | 90.51 | 2.8358 | 0.3037 | 0.7405 |
| 2# | 43.98 | 5.08 | 85.52 | 2.8166 | 0.3783 | 0.7456 |
| 3# | 43.16 | 4.08 | 67.04 | 2.9141 | 0.5015 | 0.7206 |
| 4# | 43.64 | 5.68 | 89.44 | 2.9246 | 0.2702 | 0.7180 |
| 5# | 43.56 | 5.21 | 83.06 | 2.2859 | 0.3636 | 0.9187 |

As can be seen from table 2 to table 4:

The initial ground temperature of 4 #, 5 # (30 °) heat exchange wells has difference of only 0.07 ˚C, are basically the same; During the test, the flow keep stable. Compared with the set value, deviation does not exceed 0.005m ³ / h; temperature difference compared with the set value does not exceed 0.02˚C; get results of heat exchange per meter from calculation of flow and temperature difference, in constant flux phase were 43.64W/m, 43.56 W/m, with difference of only 0.08W/m, In the constant temperature stage into the wells were 89.44W/m, 83.06 W/m, with difference of only 6.38W/m, we can take the average of # 4 and # 5 as heat exchange under the conditions.

The initial ground temperature of 2 #, 3 # (60 °) heat exchange wells has difference of only 0.04 ˚C, are basically the same; During the test, the flow keep stable. Compared with the set value, deviation does not exceed 0.009m ³ / h; temperature difference compared with the set value does not

exceed 0.03 ˚C; get results of heat exchange per meter from calculation of flow and temperature difference, in constant flux phase were 43.98W/m, 43.16 W/m, with difference of only 0.82W/m, In the constant temperature stage temperature difference were 5.08˚C, 4.08˚C, with difference of only 1˚C.The calculated heat exchange per meter were 85.52W/m, 67.04 W/m, with difference of 18.48W/m. The heat exchange of 3 # is less, because the temperature difference of recycled water is less.

The initial ground temperature of 1 # (90 °) heat well and other well temperature has difference of 0.3 ˚C, are basically the same; at the stage of constant temperature difference of 0.3 ˚C, are basically the same; at the stage of constant temperature testing, its heat exchange performance is higher than other heat well，so vertical buried tube heat transfer performance is the best.

## Conclusion

Through the heat injection test of underground heat radiating exchanger, the following conclusions can be drawn:

(1) Pipe device of radial tube heat exchanger design is feasible, construction is Convenient; the ratio of backfill material is reasonable.

(2) The heat transfer performance of 90 ° buried tube system (Take cold capacity) is the best, can be 90.51 W/m. The taking cold capacity of 60°and 30° buried pipe is closed, Respectively are 85.52W/m, 86.25 W/m. Buried pipe heat exchanger performance will be affected by the surface temperature in a certain extent.

(3) The difference of circulating water temperature directly affects the size of per meter of heat exchange. The greater the temperature difference is, the greater the heat will be.

## References

[1]Wang Qinghua,<Simulation of heat transfer and development of rock and soil thermophysical properties of in situ testing instrument>, April 2009

[2] Zhang Lei,<Ground heat transfer model and numerical underground rock thermal conductivity measurement>, Jinan: Shandong Architecture University Master Thesis; April 2011

# CHAPTER 10:

# Oil, Gas and Mineral Exploration

*Applied Mechanics and Materials Vols. 580-583 (2014) pp 2495-2501*
*© (2014) Trans Tech Publications, Switzerland*
*doi:10.4028/www.scientific.net/AMM.580-583.2495*

# Optimization of acid fracturing design in Yubei fractured reservoir

Liyang Song[1], Xiaoru He[2],Jicheng Zhang[2]

[1]China University of Petroleum in Beijing, 100000, China

[2]Northest Petroleum University, Daqing, 163318, China

**Key words:** acid fracturing; fracture parameter; construction parameter

**Abstract:** This paper recommends the application of acidic fracturing technology for horizontal wells in Yubei region basing on its fractured reservoir's characteristics, and the numerical simulation method is used to optimize the parameters of acidic fracturing. According to the results of optimization, the proper acid system is selected, and the construction parameters of acidic fracturing are optimized. According to the results of numerical simulation, we recommend the fracture half-length to be 120m, the fracture conductivity to be 30D.cm, and the fracture number to be 5. According to the properties of reservoir in Yubei region and the optimization results of fracture half-length and fracture conductivity, the alternative injection of crosslinked acid and ordinary gelled acid is recommend. The injection rate of crosslinked acid is $5m^3$/min, with volume $300m^3$. The injection rate of ordinary gelled acid is $6m^3$/min, with volume $300m^3$.

## Introduction

The Yubei oilfield of Tarim develops natural fractures, and the reservoir heterogeneity is strong, so that it is suitable to use acidic fracturing technology on the horizontal wells in this area. Usually, the multi-stage fracturing is needed because the horizontal wells are long, and the fracture parameters should be optimized in this process. Since the temperature of the reservoir is high, and fractures are developed, and the reaction rate of the acid and the rock during the acidic fracturing is high, the acid filtration during the acidic fracturing construction is serious, which negatively affects the acidic fracturing effect. In this regard, the acid system should be carefully chosen, and measures should be taken to reduce the acid filtration. This requires the optimization of the construction parameters of acidic fracturing. The oil production and the construction efficiency will be significantly improved by optimizing the fracture parameters and the construction parameters during the acidic fracturing.

This paper investigates the geological characteristics in Yubei region, so that the proper acidic fracturing technology can be determined. The Eclipse software was used to simulate the fracturing process, and the orthogonal analysis method was applied on the studying of effects of different fracture parameters on the productivity, so that the half-length, the conductivity and the numbers of the fractures were optimized in this process. Then, according to the half-length and the conductivity that were optimized, the FRACTPROPT software was used to optimize the injection rate and the volume of the acid system during the construction process, so that the best construction method can be obtained.

**The optimization of fracture parameters**

In this paper, the Yubei 1-3 horizontal well was the target well. The Eclipse software is used to optimize the fracture parameters. The basic geological parameters are as follows:

Table 1 Basic geological parameters

| Depth of the top face (m) | Avera-ge poro-sity | Average vertical permea-bility (mD) | Average horizontal permea-bility (mD) | Surface oil density (g/cm3) | Surface water density (g/cm3) | Volume factor of crude oil | Oil viscosity (mpa.s) | Water saturation |
|---|---|---|---|---|---|---|---|---|
| 5770 | 1.5% | 0.37 | 3.58 | 0.93 | 1.07 | 1.105 | 8.35 | 0.2 |

Table 2 Compressibility factor of crude oil

| Pressure （MPa） | Compressibility factor(1/MPa) |
|---|---|
| 54.03~50 | $8.49\times10^{-4}$ |
| 50~40 | $9.76\times10^{-4}$ |
| 40~30 | $10.28\times10^{-4}$ |
| 30~20 | $11.31\times10^{-4}$ |
| 20~10 | $12.30\times10^{-4}$ |

Input the parameters of reservoirs and wells into the Eclipse software, and the dual-porosity medium model was used.

**The optimization of fracture half-length.**Select the fracture half-length as 20m, 35m, 50m, 65m, 80m, 95m, 110m, 125m, 140m, the Eclipse software was used to calculate the corresponding cumulative oil production under different fracture half-length. Put the nine cumulative oil production curves together to compare and analyze, graphics are as follows:

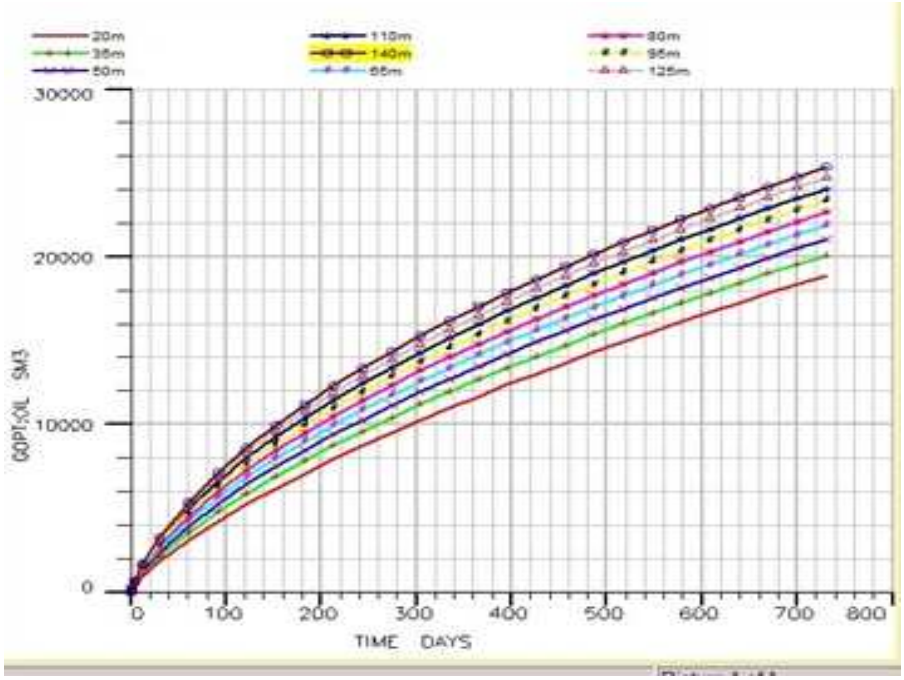


Figure 1 Cumulative oil production under different fracture half-length

As can be seen from the figure, with the increasing of the fracture half-length, the cumulative oil production is increasing, when the fracture half-length increases to about 120m, with the increasing of fracture half-length, the increasing rate of cumulative oil production is small. Considering economic factors, it is not economical to continue to increase the fracture half-length, so we take 120m as the optimal fracture half-length.

**The optimization of fracture conductivity.**Select the fracture half-length as 120m, and then select the fracture conductivity as 10D.cm，20D.cm，30D.cm，40D.cm，50D.cm. After running the program, the cumulative oil production under different fracture conductivity is obtained. Put the 5 curves together and analyze, the results are as follows:

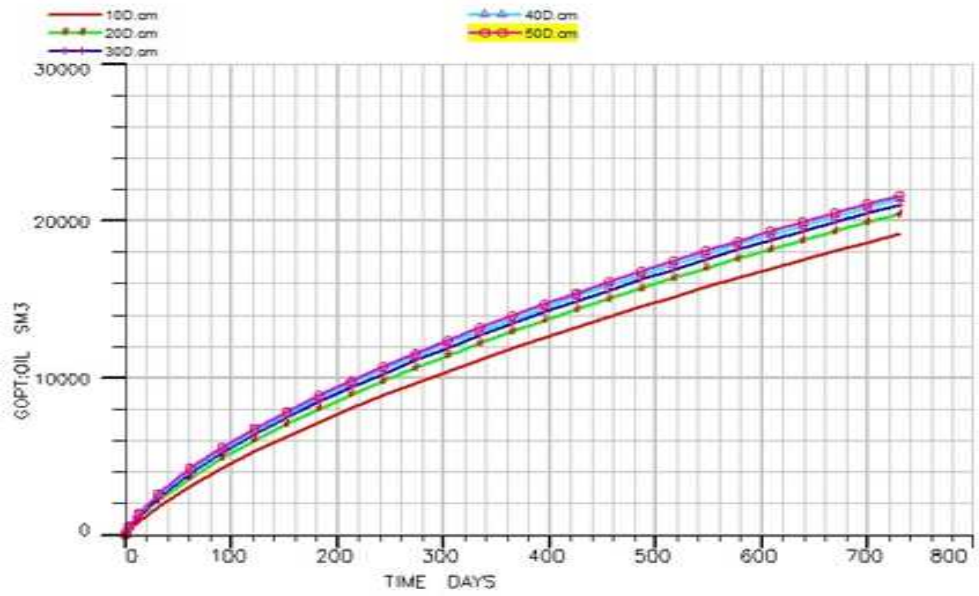


Figure 2 The cumulative oil production under different fracture conductivities.

As can be seen from the figure, with the increasing of fracture conductivity, the cumulative oil production is increasing. When the fracture conductivity increases to 30D.cm, the effect of fracture conductivity on the cumulative oil production is small (almost equals to zero). Considering economic factors, the optimal fracture conductivity is 30D.cm.

**The optimization of fracture number .**Select the fracture half-length as 120m, and the fracture conductivity as 30D.cm, and found 5 models with the same parameters except for the fracture number. Select the fracture number as 2, 3, 4, 5, 6. After running the program, the cumulative oil production under different fracture numbers is obtained. Put the 5 curves together and analyze, the results are as follows:

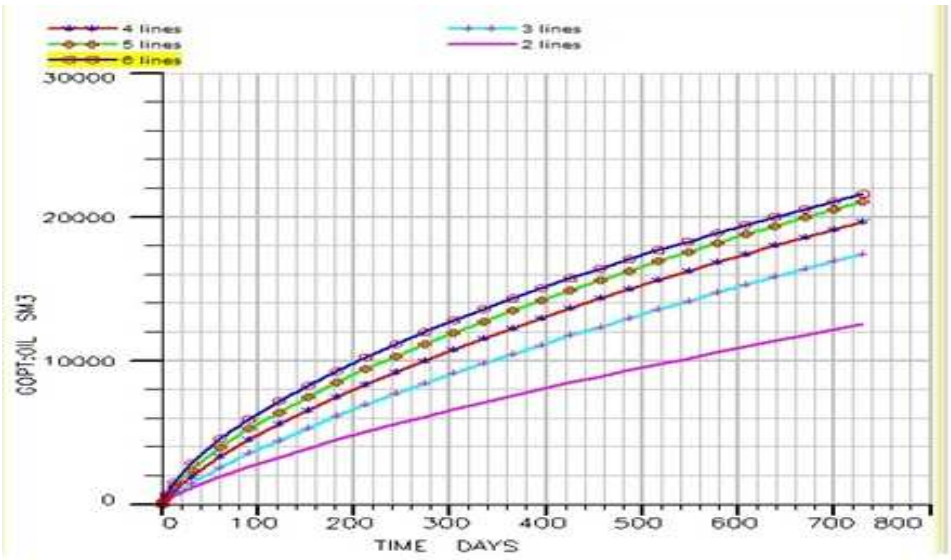


Figure 3 Cumulative oil productions under different fracture numbers

As can be seen from the figure, with the increasing of the fracture number, the cumulative oil production is increasing. When the fracture number increases to 5, the effect of fracture number on the cumulative oil production is small. Considering economic factors, the optimal fracture number is 5.

**The selection of acid system**

The selection of the acid system is based on the reservoir temperature, rock type, rock composition, the optimization result of fracture parameters, and the impacts of acid viscosity on the height of the fracture. Since the reservoir temperature of Yubei1-3 horizontal well is high, and consists a large proportion of carbonate, the calcite content is very high, and there is plenty of limestone and dolomite, it can be designed to alternatively inject the crosslinked acid and the gelled acid. According to the optimization results of the fracture parameters, the fracture conductivity is 30D.cm. Though field tests, the corresponding fracture heights under different acid viscosities are shown as follows:

Table 3 Fracture heights under different acid viscosities.

| Acid viscosity mPa·s | Inject rate $m^3$/min | Volume $m^3$ | Fracture height m |
|---|---|---|---|
| 51.2 | 5 | 700 | 46.59 |
| 107 | 5 | 700 | 53.71 |
| 159.5 | 5 | 700 | 57.95 |
| 195 | 5 | 700 | 60.48 |
| 238.7 | 5 | 700 | 63.34 |
| 317 | 5 | 700 | 69.13 |
| 358.9 | 5 | 700 | 70.05 |
| 380 | 5 | 700 | 71.13 |

Considering all the factors, the crosslinked acid is selected as the main acid type, hydrochloric acid is used to make crosslinked acid, the concentration of hydrochloric acid should be at around 20%.When the acid system is determined, we can begin to simulate the acid fracturing construction by using FRACTPROPT software, and optimize the construction parameters.

**The optimization of construction parameters**

**The optimization of injection rate.**The acid etched fracture length is affected by the acid filtration and the acid-rock reaction. The acid filtration is affected by the characteristics of the reservoir and the acid system. The injecting rate determines the flooding rate of acid in the fracture. Lower flooding rate means more acid filtration near the wellbore, so that the active acid seepage distance can be increased by increasing the injection rate. Considering the need to increase the active acid seepage distance, the high injection rate should be selected. However, the injection rate is limited by the friction, the device performance, and the network pressure. This paper mainly studies the acid injection rate.

Select the fracturing fluid viscosity as 200mpa.s. The viscosity of the crosslinked acid is selected as 205mPa.s. The viscosity of the gelled acid is 40mpa.s. Respectively input the injection rate $3m^3$/min，$5m^3$/min，$7m^3$/min，$9m^3$/min into the FRACTPROPT software and run the program. Observe the change in fracture length, fracture conductivity under different injection rates. The simulation results are as follows.

Table 4 Fracture length under different injection rates

| Injection rate (m3/min) | 3 | 5 | 7 | 9 |
|---|---|---|---|---|
| Dynamic fracture length(m) | 92.6 | 138.7 | 133.2 | 130.4 |
| Acidic erosion fracture length(m) | 83.4 | 129.41 | 126.60 | 121.71 |

Comparing the tables and figures above, when the injection rate is $5m^3$/min, the fracture conductivity decline is smooth. When the fracture half-length reaches to 120m, the fracture still possesses conductivity to some degree. In this view, the optimal injection rate is $5m^3$/min.

**The optimization of acid volume.**The acid unevenly etches the fracture surface, so that the fracture will possess conductivity. The acid volume determines the fracture conductivity and effective length. Because of the acid filtration and the high speed of the acid-rock reaction, the effective half-length of the fracture will not increase in proportion to the increase of the acid volume. In order to obtain the optimal 120m fracture, different acid volumes are used to realize to optimization of acid volume.

The injection rate has been determined as $5m^3$/min, and the main acid is crosslinked acid with viscosity 204mPa.s, input the acid volume $300m^3$, $500m^3$, $700m^3$ into the FRACTPROPT software. Then, run the program, so that we can obtain the fracture length and fracture conductivity under different acid volumes. The simulation results are as follows.

Table 5 Fracture length under different acid volume

| Acid volume (m3) | 300 | 500 | 700 |
|---|---|---|---|
| Dynamic fracture length (m) | 92.4 | 142.8 | 185.0 |
| Acidic etched fracture length(m) | 85.01 | 129.4 | 161.5 |

According to the tables and figures above, when the acid volume is $300m^3$, the fracture conductivity is too small. When the acid volume is $700m^3$, the fracture conductivity curve becomes steep. When the acid volume is $500m^3$, the fracture still possesses conductivity to some degree when the fracture length reaches to 120m. Considering all the factors, the optimal acid volume is $500m^3$.

**Pump injection program.**Alternatively inject the gelled acid and the crosslinked acid into the reservoir. The injection rate of crosslinked acid is $5m^3$/min, and the volume of crosslinked acid is $300m^3$. The injection rate of gelled acid is $6m^3$/min, and the volume of gelled acid is $300m^3$. According to the simulation, the dynamic fracture length is 163.3m, the acid etched fracture length is 148.7m. The fracture configuration is as follows:

Then, we can compare the fracture conductivity after alternative injecting and only using crosslinked acid, the results are as follows:

According to the tables and figures above, alternatively injecting 300m3 crosslinked acid and 300m3 gelled acid has better effect than injecting 500m3 crosslinked acid only. Therefore, the optimal crosslinked method is alternative injection method.

## Conclusions

1. The acidic fracturing technology can be applied in Yubei region.
2. The optimal fracture half-length is 120m, the optimal fracture conductivity is 30D.cm, and the optimal fracture number is 5.
3. The optimal injection method is alternatively injecting crosslinked acid (with volume $300m^3$ and injection rate $5m^3$/min) and gelled acid (with volume $300m^3$ and injection rate $6m^3$/min).

**References**

[1] Nolte K G. Determination of fracture parameters from fracture pressure decline[J]. SPE Journal, 2000.

[2] Rick Gdanski. A Fundamentally New Model ofAcid Worm-holing in Carbonates[J]. SPE Journal, 1999.

[3] Romero,J,Gulrajani,S.N. Three-Dimensional Transport in Acid Fracturing Treatments: Theoretical Development and Consequences for Hydrocarbon Production[J]. SPE39956, 2001.

[4] Ke Hu, Qiwei Wang, Ping Guo et al. Comprehensive Evaluation of High Temperature Foaming Agent and New Product Developing. Journal of Qinghai University of Science and Technology (Natural Science Edition)[J]. 2010. 31(3): 274-278.

[5] Minfeng Chen, Zhaoxin Lang, Hanqiao Jiang. Study on thermal-surfactant combined flooding for the development of heavy crude reservoir[J]. 2008. Journal of Xi an Shiyou University (Natural Science) 20(2):46-51.

*Applied Mechanics and Materials Vols. 580-583 (2014) pp 2502-2507*
*© (2014) Trans Tech Publications, Switzerland*
*doi:10.4028/www.scientific.net/AMM.580-583.2502*

# Optimization of black oil model-CO2 flooding

# In low permeability reservoir

Liyang Song[1], Jiancheng Wei[2], Xiangmin Xu[1],Ting Gao[1]

[1]China University of Petroleum in Beijing, 100000, China

[2]Northeast Petroleum University, Daqing, 163318, China

**Keywords:** pressure gradient; permeability; $CO_2$ flooding; pressure gradient

**Abstract:** This paper mainly studied the influence of starting pressure gradient in $CO_2$ flooding. The capillary pressure of low permeability reservoir is much larger than the ordinary reservoir, so that the influence of starting pressure gradient can not be ignored. Since $CO_2$ flooding will be widely used in the development of low permeability reservoirs, it is necessary to study the influence of starting pressure gradient. This paper mainly used Runge Kutta Fehlberg Method and Adams Fourth-order Predictor-Corrector to solve the black oil model, which was founded to study the process of $CO_2$ flooding. These two methods considered the starting pressure gradient during the $CO_2$ flooding, and the influence of reservoir permeability and crude oil density were studied by founding black oil model and use these two methods to solve the model. We have compared the production rate with staring pressure gradient and without starting pressure gradient.

## Introduction

In China, water flooding is widely used in almost all the oil field. However, in low permeability reservoir, the effect of water flooding is bad. Because of the low permeability, it is hard for water to flow in the reservoir. In this case, $CO_2$ flooding technology in low permeability reservoir is developing rapidly. The numerical simulation of $CO_2$ flooding technology is playing an important role in the application of $CO_2$ flooding in the real oil field. Normally, the Eclipse software is used to simulate the process of $CO_2$ flooding, and black oil model or compositional model were founded to study characteristics of oil production with this technology. Unfortunately, the starting pressure gradient can not be considered in the Eclipse software, which is one of the main short-comings of Eclipse software. We will be too positive when we estimate the oil production rate without considering the starting pressure gradient. This may be dangerous when we decide some project plans according to such estimation, so that it is necessary to consider the starting pressure gradient when we simulate the process of $CO_2$ flooding in low permeability reservoirs.

## Theoretical model

**Black oil models.**In this project, black oil model was founded to simulate the process of $CO_2$ flooding in low permeability reservoirs. The seepage flow mathematical model and computer software for black oil is called black oil model. In traditional definition, black oil is non-volatile compared with light volatile oil, and it is heavy and dark. Now, the definition of black oil model is much wider, which are models with there features stated below:

(1) Contain three phases: oil phase, water phase, gas phase.
(2) Oil phase contains two components: oil component and gas component.

**Numerical method.**Runge-Kutta Method of Order Four can be described as:

$$w_0 = \alpha$$

$$k_1 = hf(t_i, w_i)$$

$$k_2 = hf(t_i + \frac{h}{2}, w_i + \frac{1}{2}k_1)$$

$$k_3 = hf(t_i + \frac{h}{2}, w_i + \frac{1}{2}k_2)$$

$$k_4 = hf(t_{i+1}, w_i + k_3)$$

$$w_{i+1} = w_i + \frac{1}{6}(k_1 + 2k_2 + 2k_3 + k_4)$$

## Basic geological information

Table 1 Geological data

| Rock compressibility ($MPa^{-1}$) | Surface crude oil density ($g/cm^3$) | Volume factor of crude oil | Minimum miscible pressure (MPa) | Original gas-oil ratio ($m^3/t$) | Average permeability ($\mu m^2$) | Average porosity | Formation saturation pressure (MPa) | Oil viscosity (Mpa/s) |
|---|---|---|---|---|---|---|---|---|
| $12*10^{-5}$ | 0.8 | 1.04 | 29 | 20 | $1.26*10^{-3}$ | 0.11 | 4.75 | 6.5 |

Table 2 Relationship between injected $CO_2$ volume and oil formation physical parameters

| pressure（MPa） | $CO_2$ content（%） | Gas oil ratio（$m^3/t$） | Volume factor | Expansion coefficient | Oil viscosity（mPa·s） | Oil density（$g/cm^3$） |
|---|---|---|---|---|---|---|
| 5.26 | 0 | 1.116 | 1 | 24.34 | 2.8 | 0.7729 |
| 7.83 | 5.47 | 1.141 | 1.022 | 42.06 | 2.16 | 0.7679 |
| 10.33 | 9.18 | 1.187 | 1.064 | 64.43 | 1.888 | 0.7525 |
| 13.39 | 14.62 | 1.228 | 1.100 | 87.57 | 1.723 | 0.7423 |
| 16.05 | 19.77 | 1.378 | 1.235 | 124.14 | 1.483 | 0.702 |
| 18.95 | 25.86 | 1.418 | 1.271 | 159.93 | 1.402 | 0.6853 |
| 22.4 | 33.68 | 1.427 | 1.279 | 191.83 | 1.316 | 0.6784 |
| 26.74 | 40.46 | 1.638 | 1.468 | 314.74 | 1.155 | 0.6588 |
| 33.57 | 58.6 | 1.97 | 1.765 | 379.92 | 1.051 | 0.5708 |

Table 3 Reservoir fluid characteristic parameters

| composition | Critical Pressure（bar） | Critical temperature（℃） | Critical volume | Eccentric factor | Molecular weight（g/mol） | Equation Coefficient（Ωa） | Equation Coefficient（Ωb） |
|---|---|---|---|---|---|---|---|
| $N_2$ | 33.944 | -146.95 | 0.09 | 0.04 | 28.013 | 0.45724 | 0.07796 |
| $CO_2$ | 73.866 | 31.55 | 0.094 | 0.225 | 44.01 | 0.45724 | 0.07796 |
| $C_1$ | 46.042 | -82.55 | 0.098 | 0.013 | 16.043 | 0.45724 | 0.07796 |
| $C_{2+}$ | 44.666 | 74.703 | 0.18513 | 0.13438 | 39.839 | 0.45724 | 0.07796 |
| $C_{5+}$ | 32.974 | 202.26 | 0.31886 | 0.25517 | 74.707 | 0.45724 | 0.07796 |
| $C_{7+}$ | 28.797 | 301.85 | 0.433 | 0.312 | 107 | 0.45724 | 0.07796 |
| $C_{9+}$ | 23.521 | 360.93 | 0.55437 | 0.39725 | 138.88 | 0.45724 | 0.07796 |
| $C_{12+}$ | 19.11 | 423.8 | 0.70897 | 0.50215 | 183.54 | 0.45724 | 0.07796 |
| $C_{17+}$ | 15.459 | 491.3 | 0.90724 | 0.6337 | 247.92 | 0.45724 | 0.07796 |
| $C_{22+}$ | 12.704 | 560.54 | 1.1551 | 0.80108 | 336.4 | 0.45724 | 0.07796 |

## Result from Eclipse

**Reservoir permeability's influence on oil production.**We has chosen different reservoir permeability. After running the program, we obtained different oil production rates. Then, the relationship between reservoir permeability and oil production rate can be expressed as the curve below:

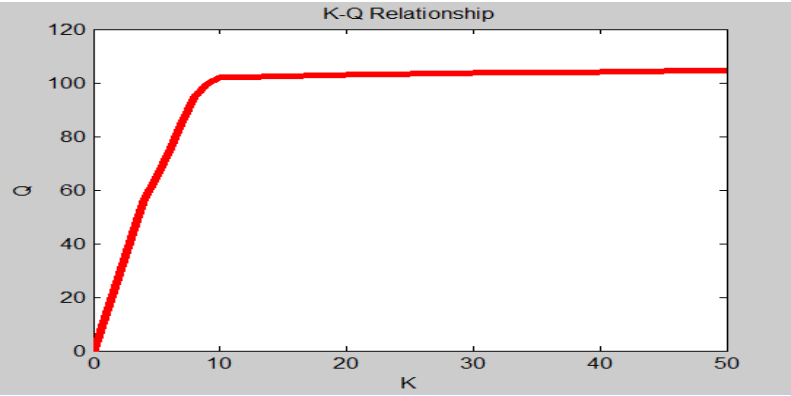


Figure 1 Relationship between permeability and oil production rate

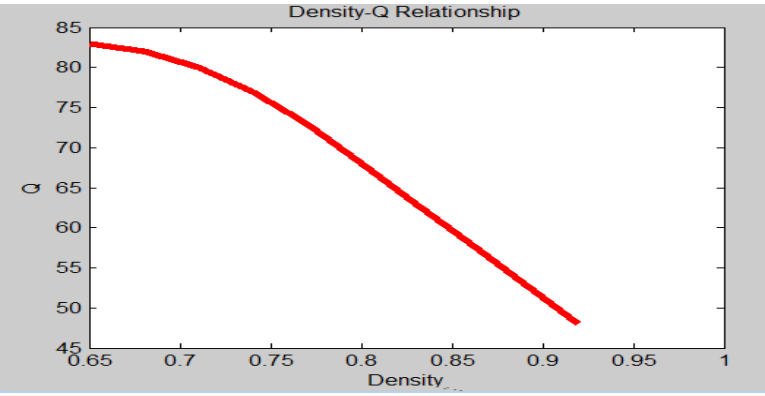


Figure 2 Relationship between oil density and oil production rate

**Results from numerical analysis methods**

A significant short-coming of Eclipse software is that the starting pressure gradient can not be considered when founding a black oil model. In this case, we will positively estimate a much higher production rate than the real one. In low permeability reservoirs, because of the low porosity and low permeability, the capillary pressure in these reservoirs are much higher than other ordinary reservoirs, and the interfacial tension in the capillary also causes significant resistance to the fluid flow. Obviously, it is necessary to consider the starting pressure gradient when simulating the $CO_2$ flooding in the low permeability reservoir. In this paper, Runge Kutta Fehlberg Method and Adams Fourth-order Predictor-Corrector were used to found the $CO_2$ flooding black oil model. Both methods have three main steps: match the reservoir permeability –oil production curve and the crude oil density-oil production curve obtained from Eclipse; consider the starting pressure gradient and modify the codes, so that we can get the modified reservoir permeability-oil production curve and crude oil density-oil production curve; compare the two curves, and analyze the influence of starting pressure gradient.

**Match the curves from Eclipse**

**Runge Kutta Fehlberg Method.**First, we use Runge Kutta Fehlberg method to found the numerical model of the low permeability reservoir. Program 1, program 2 and program 3 was created in this process to match the relationship between the permeability and oil production rate and the relationship between the crude oil density and the oil production rate with the results from the Eclipse.

Change the permeability in program 1, the corresponding production rate will be obtained.Table 4 shows the relationship between reservoir permeability and oil production rate according to the results from program 1.

Table 4 Relationship between reservoir permeability and oil production rate

| i | K(md) | Q(m3/s) |
|---|---|---|
| 0 | 0 | 0 |
| 1 | 1 | 9.519283 |
| 2 | 2 | 20.88549 |
| 3 | 3 | 29.88468 |
| 4 | 4 | 39.7442 |
| 5 | 5 | 53.31579 |
| 6 | 6 | 60.26761 |
| 7 | 7 | 67.30559 |
| 8 | 8 | 81.99021 |
| 9 | 9 | 99.1983 |
| 10 | 10 | 1.03E+02 |
| 11 | 20 | 103.5 |
| 12 | 30 | 104 |
| 13 | 40 | 104.7 |
| 14 | 50 | 105 |

Then, according to the data in Table 4, program 2 was created to do interpolation. After running program 2, we got figure 3, which reflects the relationship between the reservoir permeability and the oil production rate. We can compare figure 3 with figure 1.

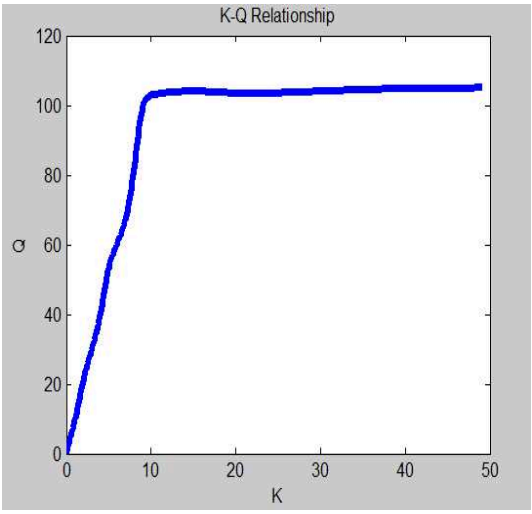


Figure 3 Results from Matlab

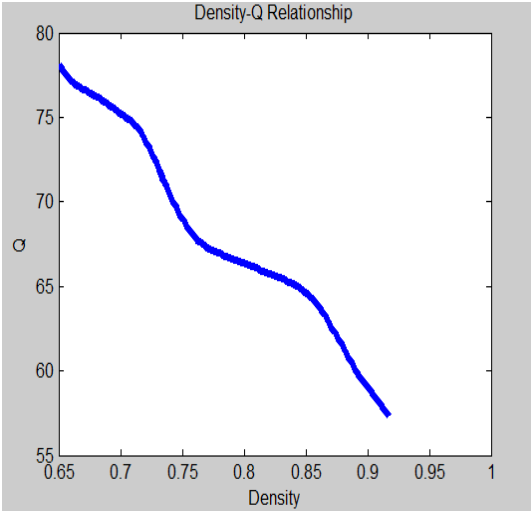


Figure 4 Results from Matlab

By comparing the results from the Matlab and the results from Eclipse, we can see the maximum relative error of the calculated permeability-oil production rate by using Runge Kutta Fehlberg method is about 16.7 %.( we assume the results from Eclipse is accurate in this case).

Then, let the reservoir permeability remain the same, and change the oil density in program 1. After running the program 1, we will get the corresponding oil production.

After running program 3, we got figure 4, which reflects the relationship between the oil density and the oil production rate. We can compare figure 4 with figure.

By comparing the results from the Matlab and the results from Eclipse, we can see the maximum relative error of the calculated oil density-oil production rate by using Runge Kutta Fehlberg method is about 8.2%.(We assume the results from Eclipse is accurate in this case).

## Conclusions

1. It is practical to use numerical analysis method to improve black oil model when solving the problems in petroleum engineering, such as considering the starting pressure gradient in the numerical simulation of injecting $CO_2$ to develop low permeability reservoirs.

2. Runge Kutta Fehlberg Method can effectively simulate the black oil model, but the oil production rate will diverge when we use Adams Fourth-order Predictor-Corrector to solve the same equation. Obviously, it is better to use Runge Kutta Fehlberg Method to solve the similar problems in petroleum engineering.

3. In low permeability oil reservoirs, the influence of starting pressure gradient is significant, while in high permeability oil reservoirs, the influence of starting pressure gradient is weak.

4. With the increasing of oil density, the influence of starting pressure gradient on oil production rate will decrease. However, in low permeability reservoirs, the effect of starting pressure gradient will still remain in a high value even if the oil density is high. The effect of starting pressure gradient can never be ignored in low permeability reservoirs.

5. From the result of Eclipse, we can conclude that the oil production rate will increase with the increase of reservoir permeability, and the oil production rate will decrease with the increase of oil density.

**References**

[1] Zhang Ji-Cheng, Song Kao-Ping. Considerable potential remains after Daqing polymer flood [J]. Oil & Gas Journal, Sept. 15, 2008, 106(35):61-66.

[2] Cooker Jr C E. Method of Determining Fluid Saturations in Reserviors [P]. U.S. Patent 35909273,1971.

[3] G. S. Wylie et al. Coring Technology for point Mclntyre wells, SPE 26353 1993.

[4] Hui Li, Infant Sun, Junping Shi. Research and Application on CO2 and Dissolver Assisted Horizontal Well Steam-injection to Develop Super Heavy Oil. Paper SPE 131061 presented at the CPS/SPE international Oil & Gas Conference and Exhibition[J]. 2010. Beijing, China,8-10 June.

[5] Class, H. Ebigbo, A. Helming, R.,Dahle,H,K. and J.M. Nordbotten. 2009. Abenchmark study on problems related to CO2 storage in geologic formations. Comp. geosci.13: 409-434.

[6] Yih-BorChang, CoatsBK, NolenJS. A compositional model for $CO_2$ flood including $CO_2$ Solubility in water [J]. SPEREE, 1998:155~160.

*Applied Mechanics and Materials Vols. 580-583 (2014) pp 2508-2512*
*© (2014) Trans Tech Publications, Switzerland*
*doi:10.4028/www.scientific.net/AMM.580-583.2508*

# Experimental study of self-suction spraying with pressure gas and water

Zhongfei Ma[1,2,a] Guangrong Lin [1,b] Zhen Zhang [1] Hongling xie[1]

([1].School of environment and safety engineering, Jiangsu University, Zhen Jiang 212013,China;

[2].State Key Laboratory of Coal Resources and Safe Mining, China University of Mining &Technology, Xu Zhou 221008,China)

[a]zfma@163.com,[b]murphy00@foxmail.com

**Keywords:** pressure gas and water; spray; effective range ; droplet size; parameters

**Abstract.** In order to find out the factors influencing self-suction spraying with pressure gas and water performance, the working principle of the spray was analyzed, orthogonal experiments were conducted, in which influenced of different air flow, bronchia- nozzle distance, nozzle diameter as well as the diffusion angle on the effective rang and spray particle size were tested, the optimal matching of parameters was obtained. The results showed that, the optimal configuration parameters could be obtained by orthogonal test of self-suction spraying with pressure gas and water, to provide data support for the design of efficient spraying device.

## Introduction

Industrial dust exists in many industries and fields, such as mining industry, metallurgy industry, manufacturing industry, which has been a serious threat to the safety production and staff occupational health. As an effective measure of water spraying dust control technology, it is widely used. However, the conventional spray has deficiency (lower dust removal efficiency and higher water consumption), to solve the problems effectively, the self-suction spraying with pressure gas and water technology was put forward, and related experimental study was made.

## Principle of self-suction spraying with pressure gas and water structure

Self-suction spraying with pressure gas and water is characterized by the mixture of high pressure on gas water as the jet medium and the suction power, seen as the combination of compressed air water spray and suction spray.

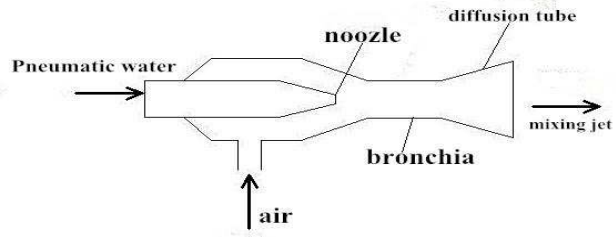


**Figure 1** Structure of self-suction spraying with pressure gas and water

Self-suction spraying with pressure gas and water is what shown in figure 1 .With the mixture of low pressure water and high pressure air flow through the nozzle jet at a high speed, external effect of air makes the water jet airflow disordered and broken, big diameter droplets are developed. High-speed jet momentum transformation with air at the same time makes part of kinetic energy into the jet pipe pressure, leading to the decreases of pipe pressure, and thus forms certain pressure

difference between inside and outside, sucking the air outside in [1].Mixing jet goes into the bronchia in a high speed, as a result of the bronchia diameter becoming smaller. The jet flow is certain and will be at a higher speed through the bronchia, leading to a continuous fluid breaking into droplets. Droplets with particle size larger will be further broken into smaller droplets under the action of air flow. When mixing jet runs into diffusion section, the interaction of gas and droplets will form a small bubble, which has the very high speed due to the effect of air flow, breaking as the surrounding pressure decreasing at the same time, the droplets are further broken.

The suction spray can reduce the spray droplets size effectively and improve the atomization effect. It also has characteristics of self-priming spray, the high-speed mixed gas water jet as the suction power, which can further improve the atomization effect. Due to the use of high pressure air as power of the spray, low water supply pressure can meet the needs of the spray and that reduces the demand on water pressure, to a certain extent, saves the water resource.

**The test system and the solution**

The main devices were shown in figure2. Experimental water was tapwater from municipal network water supply, aspirated into water supply line by high pressure water pump and controlled by the valve.

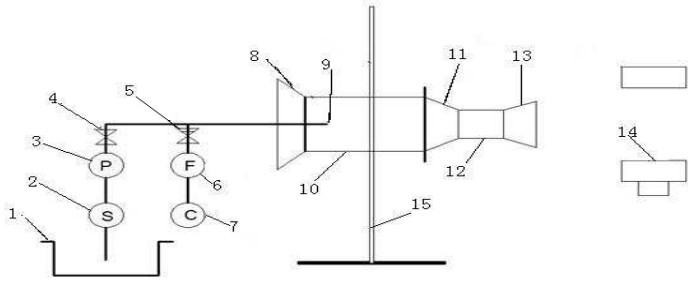


1 - water tank; 2 - high pressure water pump; 3 - pressure gauge; 4,5- the one-way check valve; 6 - flowmeter;7 - air compressor; 8 – wind collector 9 - nozzle;10 - suction chamber; 11 - reducer; 12 - bronchia; 13 - diffusion tube; 14 - particle size measuring instrument; 15 stents

**Figure2** Self-suction spraying with pressure gas and water system

The main parameters of structure of the sprayer were as follows: wind collector inlet diameter of 140 mm, the wind collector length of 30 mm; suction chamber diameter of 80 mm, length of 115 mm; reducer contraction half Angle of 18 °; bronchia diameter of 70 mm, length of 5 mm; diffusion tube angle alpha took 30 °, 45 ° and 60 ° respectively; bronchia- nozzle distance could be adjusted to 50 mm and 67 mm, 84 mm; the nozzle diameters were 2 mm, 3 mm, 4 mm respectively.

The spray particle size SMD (Sautur Mean Diameter) value and the effective range (L) [2] were chosen as spray performance index, spray particle size was tested by Winner318 laser particle size analyzer, the range was measured directly with metric scale [3].

The experiment used the orthogonal design method [4]. Test factors and levels were shown in table 1, four levels were randomized.

**Table1** Factors and levels

| level | A compressed air flow ） | B (nozzle aperture ) | C (diffusion angle ) | D （bronchia-nozzle distance） |
|---|---|---|---|---|
| 1 | 15 $m^3$/h | 2 mm | 30° | 50 mm |
| 2 | 20 $m^3$/h | 3 mm | 45° | 67 mm |
| 3 | 25 $m^3$/h | 4 mm | 60° | 84 mm |

Testing scheme with $L_9$ ($3^4$) orthogonal table arrangement, the test results were shown in table 2. Just nine times experiment was carried out to understand the corresponding factors which affected the performance of spray.

**Table 2** Experimental plan table and results

| NO. | A compressed air flow | B nozzle aperture | C diffusion Angle | D bronchia-nozzle distance | performance index | |
|---|---|---|---|---|---|---|
| | | | | | range (m) | SMD (μm) |
| 1 | 1 | 1 | 1 | 1 | 1.50 | 71.1 |
| 2 | 1 | 2 | 2 | 2 | 2.0 | 53.9 |
| 3 | 1 | 3 | 3 | 3 | 1.85 | 66.4 |
| 4 | 2 | 1 | 2 | 3 | 2.00 | 68.2 |
| 5 | 2 | 2 | 3 | 1 | 1.86 | 39.9 |
| 6 | 2 | 3 | 1 | 2 | 2.40 | 63.0 |
| 7 | 3 | 1 | 3 | 2 | 2.35 | 73.0 |
| 8 | 3 | 2 | 1 | 3 | 2.44 | 44.7 |
| 9 | 3 | 3 | 2 | 1 | 2.32 | 58.3 |

**Test result and analysis**

The test data in table 3 was analyzed, the average level of various factors $K_{ij}$ was obtained, corresponding to different factors of poor $R_i$ (see table 3). Poor reflects the influence of various factors on the target size. As shown in table 3, in terms of effective range, $R_A > R_D > R_B > R_C$ ;in respect of the spray particle size (SMD), $R_B > R_D > R_A > R_C$. So the order of the four factors impact on the effective range was: compressed air flow > bronchia-nozzle distance > nozzle aperture > diffusion angle; The order of the influence on the spray particle size was: nozzle aperture > bronchia-nozzle distance > compressed air flow > diffusion angle.

**Table 3** Data analysis

| Program | | A | B | C | D |
|---|---|---|---|---|---|
| range (m) | $K_{Ij}$ | 5.35 | 5.85 | 6.34 | 5.68 |
| | $K_{2j}$ | 6.26 | 6.30 | 6.32 | 6.75 |
| | $K_{3j}$ | 7.11 | 6.57 | 6.06 | 6.29 |
| | $\overline{K_{1j}}$ | 1.78 | 1.95 | 2.11 | 1.89 |
| | $\overline{K_{2j}}$ | 2.09 | 2.10 | 2.10 | 2.25 |
| | $\overline{K_{3j}}$ | 2.37 | 2.19 | 2.02 | 2.10 |
| | Rj | 0.59 | 0.24 | 0.09 | 0.36 |
| SMD (μm) | $K_{Ij}$ | 191.40 | 212.30 | 178.80 | 169.30 |
| | $K_{2j}$ | 171.10 | 138.50 | 180.40 | 189.90 |
| | $K_{3j}$ | 176.00 | 187.70 | 179.30 | 179.30 |
| | $\overline{K_{1j}}$ | 63.80 | 70.77 | 59.60 | 56.43 |
| | $\overline{K_{2j}}$ | 57.03 | 46.17 | 60.13 | 63.30 |
| | $\overline{K_{3j}}$ | 58.67 | 62.57 | 59.77 | 59.77 |
| | $R_j$ | 6.77 | 24.60 | 0.53 | 6.87 |
| | $K_{Ij}$ | 86064 | 82615 | 113778 | 107508 |

| | | | | | |
|---|---|---|---|---|---|
| Complex (L/SMD) | $K_{2j}$ | 114038 | 138309 | 106226 | 107393 |
| | $K_{3j}$ | 126572 | 105750 | 106670 | 773 |
| | $\overline{K_{1j}}$ | 28688 | 27538 | 37926 | 35836 |
| | $\overline{K_{2j}}$ | 38013 | 46103 | 35409 | 35798 |
| | $\overline{K_{3j}}$ | 42191 | 35250 | 35557 | 37258 |
| | $R_j$ | 13503 | 18565 | 2517 | 1460 |

Levels mean reflected the level of the various factors affect index . The level of the four factors average size in the effective range of sorting, respectively: $\overline{K_{3A}} > \overline{K_{2A}} > \overline{K_{1A}}$ , $\overline{K_{3B}} > \overline{K_{2B}} > \overline{K_{1B}}$ , $\overline{K_{1C}} > \overline{K_{2C}} > \overline{K_{3C}}$ , $\overline{K_{2D}} > \overline{K_{3D}} > \overline{K_{1D}}$; In the aspect of the spray particle size sorting, respectively : $\overline{K_{1A}} > \overline{K_{3A}} > \overline{K_{2A}}$ , $\overline{K_{1B}} > \overline{K_{3B}} > \overline{K_{2B}}$ , $\overline{K_{2C}} > \overline{K_{3C}} > \overline{K_{1C}}$ , $\overline{K_{2D}} > \overline{K_{3D}} > \overline{K_{1D}}$.

Can be concluded from this, in terms of effective range, when the air flow rate, nozzle aperture, diffusion angle and bronchia nozzle distance of 25 $m^3$ / h respectively, 4 mm, 30 ° and 67 mm, spraying worked as the best effective range; In terms of the spray particle size SMD, when the air flow rate, nozzle aperture, the diffusion Angle and bronchia nozzle distance of 20 $m^3$ / h respectively, 3 mm, 30 °, and 50 mm, spray particle size SMD was minimal.

Since the greater the effective range, the better, and the spray particle size as small as possible (the reciprocal of the spray particle size the more the better). So the ratio of two indicators (L/SMD) was a comprehensive index to select the optimal model. Still can use intuitive analysis it was concluded that the mean level of various factors ($K_{ij}$) and their corresponding poor $R_i$ (see table 3) : $R_B > R_A > R_C > R_D$, $\overline{K_{3A}} > \overline{K_{2A}} > \overline{K_{1A}}$ , $\overline{K_{2B}} > \overline{K_{3B}} > \overline{K_{1B}}$ , $\overline{K_{1C}} > \overline{K_{3C}} > \overline{K_{2C}}$ , $\overline{K_{3D}} > \overline{K_{1D}} > \overline{K_{2D}}$.Can be concluded that the four factors influencing the comprehensive efficiency from big to small order: B>A>C>D,and the optimal combination model for $A_3B_2C_1D_3$, so eventually want to choose the optimal combination model was compressed air flow for 25 $m^3$ / h, nozzle aperture of 3 mm, the diffusion Angle of 30 ° and bronchia-nozzle distance was 84 mm.

## Discussion

From the above analysis, in the effective range and the SMD of best combination factors C and D levels in the critical level[5], in order to understand the critical level of the index, the influence of the factors to the level of the mean as the ordinate, analysis of four factors index (see table 2).

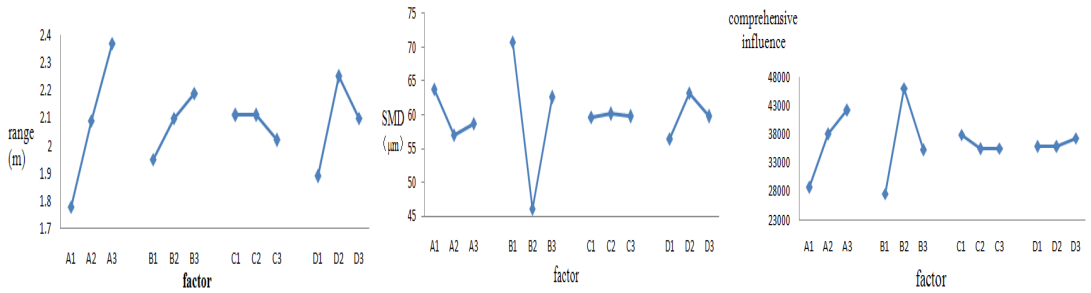


**Figure 3**. Factors and index analysis

(1) Compressed air flow When the value changed from 15 to 20 $m^3$/h, the effective range and the comprehensive factors significantly increased, and the spray particle size decreased obviously; Flow from 20 $m^3$/h to 25 $m^3$/h, increased significantly, while the spray particle size increase, the effective range of the comprehensive factors. Suggesting that take factors A between at 20 ~ 25

$m^3/h$, spray particle size of optimal value, the factors of A greater than 25 $m^3/h$ level had increased the effective range and the comprehensive factors would also help.

(2)Nozzle aperture When the size changed from 2 mm to 3 mm, the effective range and comprehensive factors increased rapidly, while the spray particle size decreased significantly; but from 3 mm to 4 mm effective range and the spray particle size increases the comprehensive factors which showed that B near the 3 mm was better.

(3) Diffusion angle When angle changed from 30 to 45 degrees, the spray particle size increased, the effective range was almost the same as significant reduction in the comprehensive factors; but from 45 degrees to 60 degrees spray particle size was reduced, effective range fell while the comprehensive factors raised slowly which suggests that the good was less than 30 degrees.

(4) Bronchia- nozzle distance Which can be found from the factor index analysis diagram, bronchia nozzle distance from 50 mm to 67 mm.The effective range and the spray particle size were both rising, and comprehensive factor index falling. When the bronchia nozzle distance from 67 mm to 84 mm ranges and the spray. Particle size was decreased effectively, comprehensive factor index would be on the rise. This showed that take factors D greater than 67mm can make comprehensive factors larger increase.

This conclusion was under the condition of this experiment, the results of other conditions remain to be further studied.

## Conclusion

In this paper, the self-suction spraying with pressure gas and water technology related technology was researched, and through the orthogonal experiment preliminarily determining the compressed air flow, the structure of the nozzle aperture and spray on the range of a self-suction spraying with pressure gas and water and spray particle size effects. Study showed that the four factors influence on the effective range of the order was: compressed air flow from>nozzle aperture>diffusion angle> bronchia-nozzle distance, and the order of the influence on the spray particle size was: nozzle aperture> bronchia nozzle distance> air flow diffusion Angle, to the order of the comprehensive factors were: nozzle aperture>compressed air flow>diffusion angle > bronchia-nozzle distance.

## Acknowledgments

The thesis was subsidized by the Open Research Fund (12KF09) of State Key Laboratory of Coal Resources and Safe Mining, China University of Mining and Technology.

## References:

[1] Cunqiang Chen, Test on technology of dust catcher with compressed water at Orifice, Science and Technology Innovation Herald, 8(2012)93-95.

[2] Zhongfei Ma, Industrial ventilation and dust control, Chemical Industry Press, Bei Jing, 2007

[3] Zhen Zhang, Experimental study of dust suppression by self-suction spraying of pressure gas and water, Master Thesis, Jiangsu university , 2013

[4] Rongxin Wang, Mathematical statistics, Xi Xn Jiao Tong University Press, Xi An, 1986

[5] Zhongfei Ma, Qiang Yan, Huapeng Cao, Study on parameters affecting performance of hydrosphere swirling jet dust catchers, Mining&Processing Equipment, 39 (2011)19-22

*Applied Mechanics and Materials Vols. 580-583 (2014) pp 2513-2517*
*© (2014) Trans Tech Publications, Switzerland*
*doi:10.4028/www.scientific.net/AMM.580-583.2513*

# Study on surface deformation law of western chengchao iron induced by underground mining

Yichao Zhou[1, a]*, Congxin Chen[1,b] , Xiumin Liu[1,c] , Kaizong Xia[1,d]

[1]State Key Laboratory of Geomechanics and Geotechnical Engineering, Institute of Rock and Soil Mechanics, Chinese Academy of Sciences, Wuhan 430071, China

[a]zhouyichao1@126.com, [b]cxchen@whrsm.ac.cn, [c]28926531@qq.com, [d]Xiakaizong1988@sina.com

**Keywords:** surface deformation; tectonic-stress-type mining; FLAC3D; shift line

**Abstract.** Analysis of the surface deformation law in mines can provide a significant guide to safety operation of important structures around. For mental mine, field monitoring and simulation are the major methods to study its surface deformation. Chengchao iron mine is a typical mental ore. Taking it as background engineering, the Flac3D is used to simulate its engineering geology condition and mining technology, and study its surface deformation law. It turns out that the simulation results are very close to the field monitoring data. With the mining on, important structures such as ore dressing workshop and new auxiliary shaft will go into the shift line range. It is necessary to adjust the mining program for the safety of the important structures.

## Introduction

Metal mining is very different from coal mine in strata structure, morphology of ore body, occurrence conditions and mining methods. In mental mine, surface deformation from underground mining can be considerably complicate for varied facts. The forecast of shift angle and sink angle is always inaccurate, which makes the mine's construction planning often improper and land acquisition and residents relocation scope too small. Sever economic lost has been caused and serious threat has been made to the safe operation of mine [1, 2]. So, it is a significant issue to do research on the surface deformation law from underground mining in mental mine.

Chengchao iron is of tectonic stress type and has complicate engineering geology conditions. The underground mining has made the surface deform severely and collapse time after time [3, 4]. This paper aims at studying the surface deformation law of western area of Chengchao iron, by employing FLAC3D to simulate its engineering geology and mining technology. Finally, the change of shift line in the process of mining and the deformation of ore dressing workshop and new auxiliary shaft are known.

## Engineering background

Geology situation

Chengchao iron [5, 6] is located in Ezhou city Hubei province, which belongs to hilly area. The major strata include granite, sandy shale, marble and diorite.

The preferred tectonic tracks in mine are faults and joints. The most important fault is Chengchaobei fault whose dip direction is 190° and dip angle ranges from 47 degree to 80 degree. The hanging wall is marble and the downthrown block is granite. The preferred joints include two groups, whose strike directions are 330 degree and 30 degree respectively, and dip angles are both 70 degree.

Before mineralization, Chengchao iron had experienced intense tectonic movement repeatedly, in which the tectonic stress is considerable complicate. According to the field stress tests, the present orientation of major principal stress is parallel to the ore body strike. In granite, the principle compressive stress is 18.63 Mpa, azimuthal angle is N87°W which is close to the east-west direction. The ratio of horizontal stress to the vertical one is 1.4.

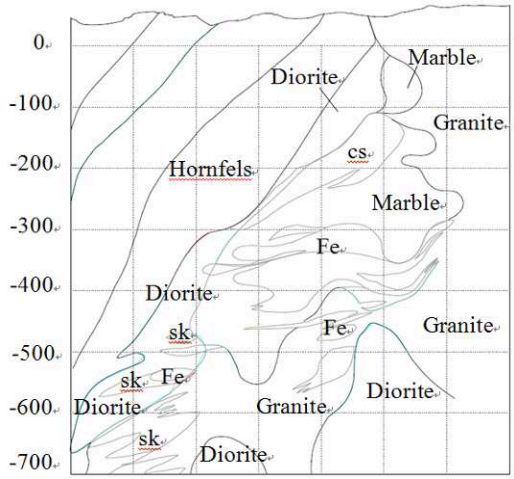


Fig.1 Geological profile of section No.35

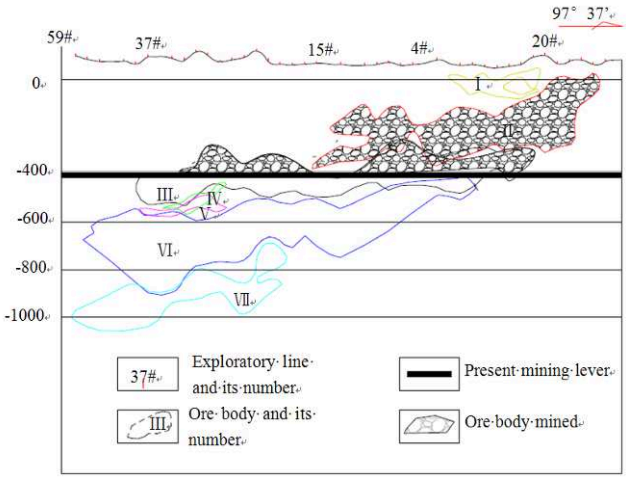


Fig.2 Geological section showing longitudinal map projection of ore bodies

Brief introduction of mining

The ore deposit is divided into two parts east and west by the 15th exploratory line. The western mine has four ore bodies, namely Ⅲ, Ⅳ, Ⅴ, Ⅵ, Ⅶ. Now, Ⅲ ore is being mined. For Ⅲ ore, the east-west length is 850m, the south-north length ranges from 120m to 450m.

In Chengchao iron, the ore is always mined with sublevel caving method and no sill pillar. The finished levels in Ⅲ ore include -290m, -307.5m, -325.5m, -342.5m, -358m and -375.5m. Both of -395m and -410.5m are now being mined. The golf perimeter of the finished level is shown in fig.3.

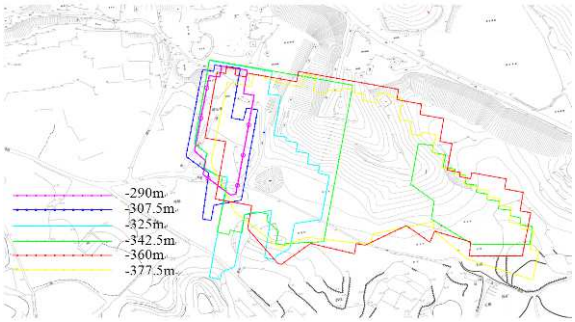


Fig. 3 Golf perimeter

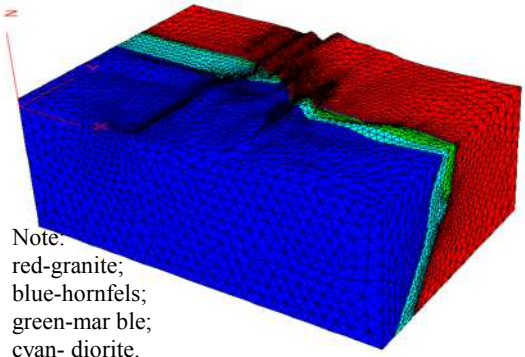

Note:
red-granite;
blue-hornfels;
green-mar ble;
cyan- diorite.

Fig.4 Model meshing

**Numerical simulation with Finite difference method**

With finite difference method FLAC3D, study the surface deformation law of western area of Chengchao iron, by simulating its engineering geology conditions and mining technology. Determine the change of shift line in the process of mining and the deformation of ore dressing workshop and new auxiliary shaft.

Description of computing model

The scope of model should be set larger than the estimate range of influence. Besides, considering the occurrence of ore body, the model scope was determined. Take the ore body as geometry center, set the vertical direction from surface to underground -1000m level, east-west length 3000m, south-north length 2000m. The mesh model is shown in fig. 3.

The lithology and geological structure simulated in model have been simplified. The granite and granite porphyry are grouped the same category and the scatter altered skarn, dioritic porphyrite and chloritization diorite. Choose their average parameter as the calculated one. For geology structure, only Chengchaobei fault and the preferred joint whose occurrence is 238° ∠60° are taken into account.

Boundary conditions

The side faces of model, including front, back, left and right faces, are applied slide constraints restraining their normal displacement. And the bottom is fixed without displace in all direction. The horizontal tectonic stress is applied, which makes the $\sigma_{xx}$ is 1.28 times of $\sigma_{zz}$, $\sigma_{yy}$ is 0.48 time of $\sigma_{zz}$.

Parameters for calculating

The rock constitution is of ubiquitous-joint type and the mechanical parameters of rock and joint are shown in table 1 and table 2 respectively.

Table 1 Rock mechanical parameters

| Lithology | γ kN/m$^3$ | E GPa | μ | φ Deg | c MPa | $\sigma_t$ MPa |
|---|---|---|---|---|---|---|
| Hornfels | 22.3 | 3.0 | 0.23 | 31.8 | 1.84 | 0.7 |
| Iron ore | 43.3 | 5.3 | 0.31 | 38.1 | 2.48 | 0.25 |
| Anhydrite | 28.3 | 2.1 | 0.26 | 23.9 | 1.24 | 0.12 |
| Marble | 26.7 | 2.6 | 0.28 | 30.2 | 1.70 | 0.17 |
| Granite | 24.7 | 2.0 | 0.27 | 29.6 | 1.61 | 0.16 |
| Diorite | 26.3 | 1.9 | 0.27 | 31 | 0.8 | 0.16 |
| Fault | 25.9 | 1.3 | 0.35 | 27 | 0.55 | 0.1 |

Table 2 Joint mechanical parameters

| Lithology | Kn GPa | Ks GPa | φ deg | c MPa | $\sigma_t$ MPa |
|---|---|---|---|---|---|
| Hornfels | 7.0 | 5.5 | 27 | 0.74 | 0.18 |
| Iron ore | 9.0 | 7.0 | 35 | 2.0 | 0.20 |
| Anhydrite | 5.0 | 4.5 | 22 | 1.2 | 0.12 |
| Marble | 6.5 | 5.0 | 19 | 0.26 | 0.03 |
| Granite | 6.0 | 4.3 | 25 | 0.48 | 0.05 |
| Diorite | 7.0 | 5.5 | 21 | 0.2 | 0.02 |

Set of calculating conditions

From -270m to -412.5m, the mining method simulated is sublevel caving method without sill pillar while below -412.5m, it was changed to be sublevel caving method with sill pillar. In the process, the mining time, mining location and mining method are all simulated in system.

According to the mining record, the mining activity is simulated for each 17.5m. From -290m to -500m, there are 13 sections. The detailed sets are shown in table 3.

Table 3 Mining conditions

| Number | Level | Thickness/m |
|---|---|---|
| 1 | 270～290 | 20 |
| 2 | 290～307.5 | 17.5 |
| 3 | 307.5～325 | 17.5 |
| 4 | 325～342.5 | 17.5 |
| 5 | 342.5～360 | 17.5 |
| 6 | 360～375.5 | 17.5 |
| 7 | 375.5～395 | 17.5 |
| 8 | 395～412.5 | 17.5 |
| 9 | 412.5～430 | 17.5 |
| 10 | 430～447.5 | 17.5 |
| 11 | 447.5～465 | 17.5 |
| 12 | 465～482.5 | 17.5 |
| 13 | 482.5～500 | 17.5 |

## Analysis of calculation

When the calculation finished, the results were compared with the field monitoring data. The major information will be shown as follows.

(1) The simulation before -395m lever is very close to the monitoring data in the whole deformation law and trend, except that there are a few differences in value. And the two history collapses around 2006 can be found corresponding phenomena in the simulation. It proves that the simulation is effective and the results are of guidance significance to the next mining.

(2) From the settlement contour map of 2cm shown in fig. 4(a) and total displacement contour map of 4cm fig. 4(b), the shape of critical deformation extension line in footwall mining area is like a saddle with the middle point between the new auxiliary shaft and skip shaft no northern displacement. The phenomenon can also be found in monitoring contour, which proved the validity of the simulation.

(3) The center of surface deformation moved with the shift of underground mining. When mining from -342.5m to -360m level, the center of surface deformation moved 140m eastward. When mining from -377.5m to -395m level, the center of surface deformation moved 140m in NEE. When mining from -412.5m to -430m level, the center of surface deformation moved eastward 50m again.

(4) With mining developing deep and goaf area extending, the important structures will be influenced gradually. In -342.5-360 mining stage, surface deformation extended fastest, with 290m east-west-ward and 120m south-north-ward. The new auxiliary shaft, measures shaft, ore dressing workshop and other important structures except skip shaft all go into surface deformation of 2cm. In -360-377.5 mining stage, surface deformation extended the most slowly, with 40m east-west-ward and 30m south-north-ward. In the next stage, the major direction of surface deformation is east-west. And the extending velocity is 88m per level. The shape of critical deformation range will change from ellipse to saddle.

(5) From the simulation results, the surface deformation of the place where important structures such as new auxiliary shaft locate will increase with mining developing deep. It is necessary to adjust the mining program for the safety of the important structures.

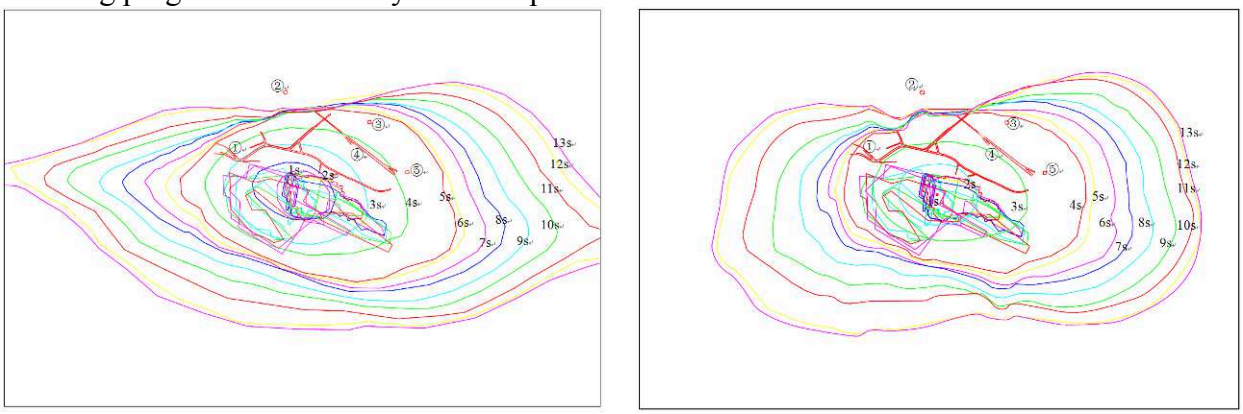


a. Distribution map of 2cm settlement boundary line for all levels

b. Distribution map of 4cm total displacement boundary line for all levels

Note:

① Ore dressing workshop
② Skip shaft
③ New auxiliary shaft
④ Transporting tunnel
⑤ measures shaft

1s -270~-290 level
2s -290~-307.5 level
3s -307.5~-325 level
4s -325~-342.5 level
5s -342.5~-360 level
6s -360~-377.5 level
8s -395~-412.5 level
9s -412.5~-430 level
10s -430~-447.5 level
11s -447.5~-465 level
12s -465~-482.5 level

Fig. 4 Distribution map

## Conclusions

The finite difference method FLAC3D has been used to study surface deformation law of western Chengchao iron by simulating the engineering geology condition and mining technology. Comprehensive analysis has been done to the calculation results, and some important conclusions have been got.

(1) The simulation results are very close to the monitoring data in the whole deformation law and trend, except that there are a few difference in value. It proves that the simulation is effective and the results is of guidance significance to the next mining.

(2) With mining developing deep and goaf area extending, the important structures will be influenced gradually.

(3) Surface deformation of place where important structures such as new auxiliary shaft locate will increase with mining developing deep. It is necessary to adjust the mining program for the safety of the important structures.

**Acknowledgements**

This work was financially supported by the National Natural Science Foundation of china (No. 51274188)

**References**

[1] HUANG Pinglu, CHEN Congxin, XIAO Guofeng, et al. Study of rock movement caused by underground mining in mines with complicated geological conditions [J]. Rock and Soil Mechanics, 2009, 30(10): 3020 – 3024. (In Chinese)

[2] CAO Yang, YAN Ronggui, HE Yueguang, et al. Macroscopic destroy of tectonic stress type surface movement [J]. Mining and Metallurgical Engineering, 2002, 22(2): 31 – 33. (In Chinese)

[3] CHEN Congxin, XEAO Guofeng, XIA Kaizong, et al. Surrounding surface deformation monitoring and forecasting in Chengchao Iron subsidence [R]. Wuhan: Institute of Rock and Soil Mechanics, Chinese Academy of Sciences, 2013. (In Chinese)

[4] CHEN Congxin, XIAO Guofeng, XIA Kaizong, et al. Surface deformation monitoring and forecasting in eastern area of Chengchao Iron due to underground mining [R]. Wuhan: Institute of Rock and Soil Mechanics, Chinese Academy of Sciences, 2012. (In Chinese)

[5] XIA Kaizong, LIU Xiumin, CHEN Congxin, et al. Study on surface deformation caused by underground mining in western area of Chenchao iron mine[J]. Chinese Journal of Rock Mechanics and Engineering, Have been included. (In Chinese)

[6] XIA Kaizong, CHEN Congxin, FU Hua, et al. analysis of influence of discontinuities on surface deformation in eastern area of Chengchao iron mine. (In Chinese)

*Applied Mechanics and Materials Vols. 580-583 (2014) pp 2518-2523*
*© (2014) Trans Tech Publications, Switzerland*
*doi:10.4028/www.scientific.net/AMM.580-583.2518*

# Adsorption Research of Polymer on Oil Sands in Qidongyi Block of Xinjiang Conglomerate Reservoir

NIE Xiaobin[1,2] GUO Ying[3,a] LOU Qingxiang[1,2] LIU Weidong[4,b]
SUN Linghui[4] and LI Jiye[5]

[1] Experimental detection research institute of Xinjiang Oilfield, Karamay Xinjiang 834000, China;

[2] Xinjiang Uygur Autonomous Region key laboratory of conglomerate reservoir, Karamay Xinjiang, 834000, China;

[3] Institute of Porous flow & Fluid Mechanics, University of Chinese Academy of Sciences ,Langfang, Hebei, 065007 China;

[4] Langfang Branch of PetroChina Research Institute of Petroleum Exploration & Development, Langfang, Hebei, 065007,China.

[5] Oil Testing and Perforating Company, Daqing Oilfield Company, PetroChina,Daqing 163412, China

[a]guo82y@163.com; [b] lwd69@petrochina.com.cn.

**Keywords:** Conglomerate reservoir; polymer;; static adsorption; dynamic retention.

**Abstract.** In the process of polymer flooding in porous media, polymer was detained due to interactions between surface adsorption and polymer molecules， and this could lead to negative effects on oil displacement. For polymer adsorption in Xinjiang conglomerate reservoir, HPLC analysis was adopted to study the static and dynamic laws. Results have showed that the adsorption process could be divided into 3 stages: rapid growth, slow growth and stable state. With the loss of polymer molecular weight, equilibrium adsorption quantity reduces gradually. The adsorption amount is different for the same polymer on four types of oil sands. For equilibrium adsorption, the maximum value is argillaceous sandstone, followed by conglomeratic sandstone.The third is argillaceous gravel, and the minimum is sand gravel. For polymer flooding in conglomerate cores, the dynamic retention amount of seriate conglomerate is much greater than that of fine particle conglomerate. These data have provided reference for project design of polymer flooding in conglomerate reservoir.

## Introduction

During the course of polymer flooding in porous media, polymer solution would be diluted by formation water, and it was stranded due to surface adsorption, mechanical capture, hydrodynamic trap and the interactions between polymer molecules[1]. It is certain that this retention could lead to negative effect on oil displacement.

For the polymer on surface of core particles, adsorption amount are affected by many factors, which are the types of polymer, molecular weight, degree of hydrolysis, salinity, rock composition, surface properties of particles, environmental temperature and so on. Compared with small molecules for solid-liquid adsorption, macromolecule polymer solution has many traits[2]. Nowadays, there are a lot of research on application of polymer flooding in sandstone reservoir. For polymer in sandstone, adsorption is in keeping with the Langmuir isotherm adsorption law. Rarely research has focused on polymer adsorption in conglomerate reservoir. No comparison study has been published currently about sandstone and glutenite.

## Experimental conditions and methods

**Experimental material** These adsorption experments are correlated with four types of polymer, whose molecular weight is 10 million, 15 million, 20 million and 25 million respectively. Xinjiang oilfield has provided the products of polymer. The hydrolyzing degree is 25%, and the solid content is 91.2%. Formation water and injected water were simulated by medicals, and the specific ion content were shown in table 1. In these experments, oil sand particles could be divided into four types, which are argillaceous sandstone ,conglomeratic sandstone, argillaceous gravel and sand gravel. All oil sands and core samples had came from Qidongyi block in Xinjiang oilfield.

**Table. 1 Salinity of formation water and injected water for Qidongyi Block in Xinjiang oilfield**

| Category | $HCO_3^-$ | $Cl^-$ | $SO_4^{2-}$ | $Ca^{2+}$ | $Mg^{2+}$ | $K^+$ and $Na^+$ | Salinity |
|---|---|---|---|---|---|---|---|
| Injected water(mg/L) | 146.7 | 103.0 | 33.8 | 58.0 | 8.4 | 55.3 | 405.2 |
| Formation water(mg/L) | 3407.0 | 5168.0 | 68.0 | 94.0 | 17.0 | 4525.0 | 13279.0 |

## Experimental procedure

**Static adsorption** Firstly, a series of polymer solution were conducted with the known concentration to get criterion concentration curves,, then it is need to determine the relationship of concentration with optical density by high performance liquid chromatography (HPLC) analysis[3]. Oil sand particles were mixed with polymer solution which were deployed with different concentration. The weight of oil sand is 2.0 gram for each test sample, and solid to liquid ratio is 1：9. The mixture was put in water-bathing constant temperature vibrator for 24 hours at 34.3℃[4]. The mixture was separated by high-speed centrifuge after oscillation to get solid and liquid respectively. Concentration can be got by using HPLC after adsorption of oil sands in polymer solution. According to optical density of test samples, their polymer concentration can be computed by standard curves[5]. Adsorption was calculated by fomula (1).

$$\Gamma = \frac{(C_0 - C_1) \times V}{1000G} \tag{1}$$

Where，$\Gamma$ is static adsorption capacity,mg/g；$G$ is quality of oil sands, g；$C_0$ and $C_1$ are polymer concentration before and after adsorption respectively, mg/L，$V$ is the volume of solution, mL.

**Dynamic retention** After selection of cores, it is also need to get the quality of each core. These cores were put in a vacuum for 8 hours, then they were saturated by formation water. Parameters such as porosity and permeability are available by relevant experimental instruments. Polymer solution was injected into cores after being kept in thermostat for 1 hours at 34.3℃. Collected at export of displacement device, polymer solution was analysed by HPLC to get the specific cconcentration[6]. When the concentration of injected polymer is equal to that of effluent, it is time to stop injecting polymer and to end this experiment. Dynamic retention was computed by equation (2).

$$A_r = \frac{C_0 V_f - \int_0^{V_t} C dV}{1000W} \tag{2}$$

Where, $A_r$ is the retention capacity of polymer,mg/g；$C_0$ is the concentratin of injected polymer, mg/L；$V_f$ is the volume of injected polymer,mL；$C$, $V$ are the concentration and volume of polymer

of effluent samples separately,mL; $V_t$ is the total volume of injected polymer and water,mL; $W$ is the weight of core, g.

## Experimental results and analysis

**Static adsorption** Four kinds of oil sands were employed in these experiments, and they were argillaceous sandstone , conglomeratic sandstone, argillaceous gravel and sand gravel. Argillaceous sandstone and conglomeratic sandstone contain a certain amount of clay and gravel respectively. Argillaceous gravel and glutenite refer to the conglomerate having a small quantity of mud and sand separately.

The results of polymer static adsorption experiment were showed in figure 1. With the increase of polymer concentration, the adsorption quantity also enhanced gradually for one unit quality of oil sands. As surface coverage fraction (solute on the surface of the oil sand particles) increasing, the adsorption of particles gradually reached equilibrium status when the polymer concentration is about 700 mg/L. The whole adsorption process can be divided into three stages:

Stage I: With the increase of polymer concentration, individual molecule accelerates to the surface of adsorbent, and the number of polymer molecules increases quickly on surface of oil sands. It also shows that the thread size of a single polymer molecule is small in the dilute solution, so the activated adsorption bits occupied by individual molecule are relatively less.

Stage II: Adsorption quantity increases slowly. When the adsorption of polymer on the adsorbent has reached a certain degree, a few of adsorption bits exists on the surface. Adsorption volume changes slowly with the increase of polymer concentration, and monolayer adsorption is basically saturated.

Stage III: State of dynamic stable equilibrium. Saturated by monolayer adsorption, parts of surface have adsorbed two or more layers of molecules. On the surface of adsorbent, polymer in the solution would act on molecules which had been adsorbed by particles, so polymer may be associated together. When the concentration reaches critical associating point, a structure of dynamic physical crosslinking network was formed by polymer's mutual combination. In the solution, individual polymer molecule was impacted by both of adsorbed molecules and association aggregation. Adsorption of particle surface is in the state of dynamic stable equilibrium.

Because of interactions of ions and molecules in the solution, rates of adsorption and desorption are differrent. The adsorption on surface of various particles is different for the same polymer at adsorption equilibrium. For equilibrium adsorption, the maximum value is from argillaceous sandstone, followed by conglomeratic sandstone.The third is argillaceous gravel, and the minimum is sand gravel.

Under the condition of same quality of oil sands, larger surface area is beneficial to the adsorption of polymer at active point. Take 25 million molecular weight for example, both the surface area of argillaceous sandstone and the adsorption activity point are the maximum, and the adsorption quantity is 5.6 mg/g for argillaceous sandstone. For conglomeratic sandstone, argillaceous conglomerate and sand gravel, the adsorption are 3.2 mg/g, 3.0 mg/g, and 2.8 mg/g respectively.

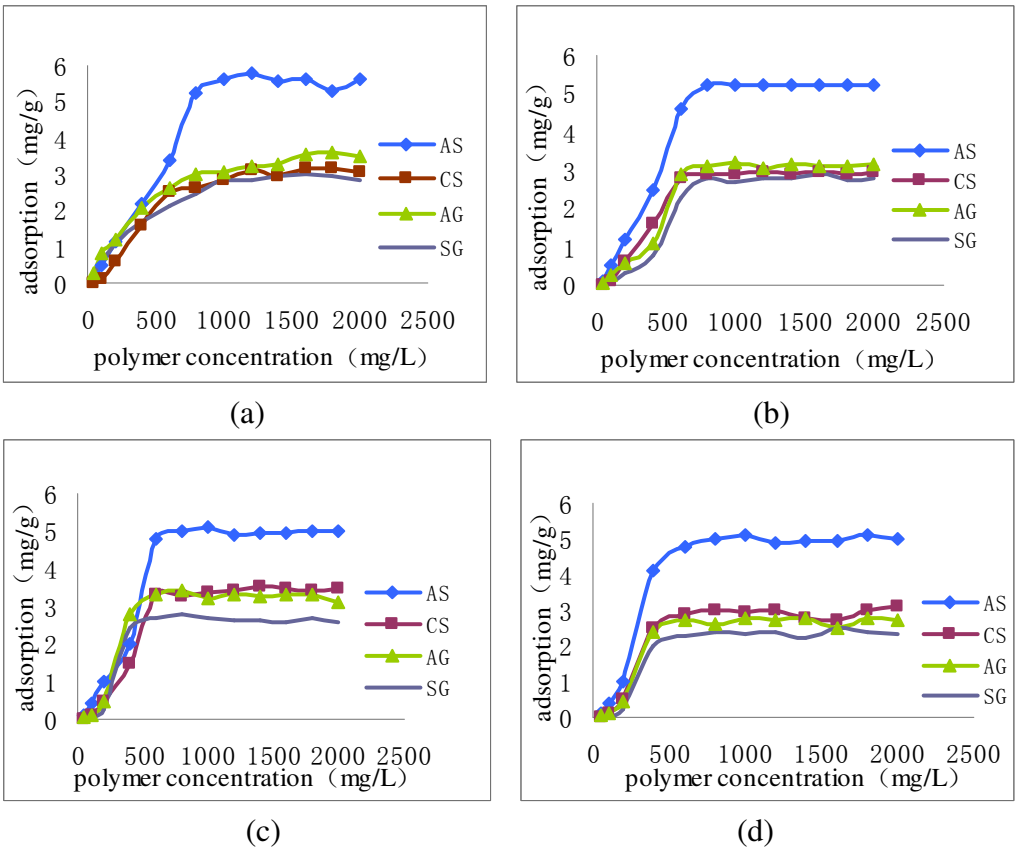


**Fig. 1 Static adsorption of polymer on oil sands**

(a, b, c, d are the polymer of molecule weight 25 million, 20 million, 15 million and 10 million respectively, these abbreviations of AS, CS, AG and SG are argillaceous sandstone, conglomeratic sandstone, argillaceous gravel and sand gravel separately)

These curves of adsorption isotherm presented "L" type. The polymer adsorption is in keeping with the Langmuir isotherm law. Under the same polymer concentration, due to the extension of molecular chains, small molecular weight of polymer has more freedom. It is easy to contact with adsorption activity bits for smaller molecule. At the same time, smaller molecular weight polymer is more likely to deviate from the sands' surface for less chance of association and more freedom, so the adsorption for small molecule is much more than that of high molecule.

**Dynamic retention** When polymer flows in porous media of reservoir, hydrodynamic trapping and mechanical capture would occur on the rock surface due to its pore structure and permeability heterogeneity[7]. It is generally considered that four mechanisms have caused the polymer retention, and they are surface absorption, mechanical capture, capture of fluid dynamics and interactions between polymer molecules[8]. Dynamic retention experiments have simulated the retention phenomenon when polymer flows through the conglomerate reservoir. These cores can be divided into two categories, fine particle and seriate conglomerate. These experiments involved gravel particles whose diameter is between 0 and 4 mm. The fine particle conglomerate's diameter is in uniform distribution of 0 to 1 mm, while the seriate conglomerate' particle diameter is in uneven distribution between 0 and 4mm.

**Table.2 Dynamic retention capacity of polymer in different cores**

| Core numbers | Category | Water permeability(mD) | Molecule weight (million) | Concentration (mg/L) | Retention capacity(mg/g) |
|---|---|---|---|---|---|
| 1 | Fine particle conglomerate | 12.1 | 1500 | 1200 | 0.66 |
| 2 | Fine particle conglomerate | 43.2 | 1500 | 1200 | 0.61 |
| 3 | Fine particle conglomerate | 145.2 | 2500 | 1200 | 0.67 |
| 4 | Seriate conglomerate | 413.0 | 2500 | 1500 | 0.75 |

For core numbers of 1,2,and 3, dynamic retention of fine particle were 0.66 mg/g, 0.61 mg/g and 0.67 mg/g separately. The difference of quantity is very small in polymer dynamic retention. The dynamic retention for core number 4 is 0.75 mg/g, which is significantly greater than that of fine particle conglomerate in table 2.

In seriate conglomerate cores, more adsorption activity points, pore throat structure and particle surface are beneficial to the adsorption retention. In the process of core flowing, polymer solution does not go along with the wall of hole. It is difficult to spread to areas with small permeability for polymer solution in the cores, so value of dynamic retention is much smaller than that of static adsorption.

## Conclusions

1. The static adsorption process could be divided into 3 stages: rapid growth, slow growth and stable state. Due to differences from composition of sand particle, surface areas and adsorption activity points, the maximum value of equilibrium adsorption is from argillaceous sandstone, followed by conglomeratic sandstone. Argillaceous gravel is less than conglomeratic sandstone, and the minimum is from sand gravel.
2. Multilayer adsorption and intermolecular association would occurred on the surface of oil sands. Polymer adsorption for 25 million molecular weight is the largest, followed by 20 million molecular weight. The third is 15 million molecular weight, and the minimal adsorption is 10 million molecular weight. Determining the allocation of pore throats, particle size distribution has a significant impact on polymer retention. The dynamic retention for seriate conglomerate is significantly greater than that of fine particle conglomerate.

## Acknowledgements

The authors wish to thank the experimental detection research institute of Xinjiang Oilfield, Xinjiang Uygur Autonomous Region key laboratory of conglomerate reservoir, and Langfang Branch of PetroChina Research Institute of Petroleum Exploration & Development, under which the present work was possible.

## Reference

[1] Chengzhi Yang. The chemical flooding enhancing oil recovery. Beijing: Petroleum industry press (1999), p.70-75.

[2] Shiyu Ma. Polymer and practical method of reservoir engineering. Beijing: Petroleum industry press (1995), p.120-152.

[3] Yefei Wang, Dingyong Zhang, Xiaoming Le. Journal of the University of Petroleum, Vol. 26 (2002), p.59-61.

[4] Zhongqiang Tian, Chunyan Sui, Guozhuang Wang. Oilfield Chemistry, Vol.19 (2002), p.169-172,.

[5] Daoshan Li, Jirui Hou, Ruijuan Xu. Oilfield chemistry, Vol. 12(2001), p.358-361.

[6] Jinbang HU, Xuejun Li, Chenglin Han. Oilfield Chemistry, Vol. 8(1991), p.320-324.

[7] Puhua Yang, Chengzhi Yang. Chemical flooding enhancing oil recovery. Beijing: Petroleum industry press, (1998).

[8] Rui Weng. Oil and gas recovery technology, Vol. 5 (1998), p.51-56.

*Applied Mechanics and Materials Vols. 580-583 (2014) pp 2524-2527*
*© (2014) Trans Tech Publications, Switzerland*
*doi:10.4028/www.scientific.net/AMM.580-583.2524*

# Analysis on Permeability of High Permeability Layer-penetration Oil Influencing Factors

FANG Yu [1, a]

[1] Anhui expressway holding group Co., LTD, Hefei, China 230088

[a]506155526@qq.com

**Keywords:** permeability condition, penetrating agent, emulsifier, permeation resistance, high permeability permeate layer emulsification asphalt

**Abstract:** This article from the permeability condition, half-rigid base type, material requirements, penetrating agent and emulsifier choice, permeation resistance, etc., through the analysis of the factors affecting the permeability of permeable layer of emulsified asphalt, and guided by the factors above, we developed and prepared a new high permeability permeate layer emulsification asphalt, the tests showed that it has good permeability.

## Introduction

According to Technical specification for construction of highway asphalt pavement (JTG F40-2004): All kinds of asphalt pavement's base have to splash layer-penetration and it can't be omitted when lower seal coat is installed above the base. But in the practice of engineering, permeable layer of emulsified asphalt penetration results is unsatisfactory to meet regulatory requirements[1]. Factors affecting the permeability of the permeable layer of emulsified asphalt in this article did a more detailed analysis, and based on the principles identified in the analysis, research and development of new high-permeability emulsified asphalt.

## Penetration of the layer-penetration oil condition

**Wetting function.** Therefore, after the semi-rigid regimen, grass surface must be cleaned not leave dust, mud, debris, etc., and be napping treatment. In order to increase the contact area with the primary emulsion surface, the grass-roots aggregate surface should be exposed to reach better wetting.

**Permeation.** Since the semi-rigid base is a porous structure, emulsified asphalt through the first primary surface under gravity and slowly penetrate the grassroots interior. Wetting effection and penetration are closely related. Emulsified asphalt first wetting base material and then penetrate to the base material , the smaller the wetting angle on the material surface to form, the emulsion is more easily extended in the base material and penetrate to the grass roots. The greater difference between surface tension of the emulsion and grassroots and the smaller the wetting angle emulsion formation, the smaller the penetration resistance, so the more easy to penetrate.

**The role of penetrating agent.** In the infiltration process, emulsified asphalt surface tension is relatively large, so adding penetrant is a feasible and applicable method so that it can reduce the surface tension, enhance the role of grassroots infiltration and can diffuse into the grass.

Typically, there are two ways of penetrant incorporation, one is adding quantitative emulsifier firstly, and then melt the asphalt and join the colloid; another one is added quantitative penetration to the already produced emulsified asphalt. Experience has indicated that the first way better dispersion, the property is more uniform, because penetrant with asphalt and emulsifier in sufficient shear and grind in colloid.

In the process of study, a mixed mode is used, namely the osmotic agent is added to hot asphalt, and then join the colloid mill with emulsifier solution through the preparation of oil layer. The test proved that this approach can promote the asphalt emulsion to obtain a better stability of emulsified asphalt compared to other ways, suitable for the preparation of high permeable transparent layer oil.

Gasoline, kerosene, diesel and other permeable material is often used to dilute bitumen, now kerosene is generally incorporated in the high penetration emulsified asphalt as penetrative solvent. In this study, a novel penetrant is used to improve the performance of asphalt and to promote asphalt emulsion, this penetrant non-volatile, substantially non-polluting to the environment.

## Characteristics of semi-rigid base

**Semi-rigid base type.** According to the literature[3], semi-rigid base material classified by type of structure can be divided into suspension dense structure, the skeleton structure and the skeleton dense pore structure, as shown in Figure 1 to Figure 3

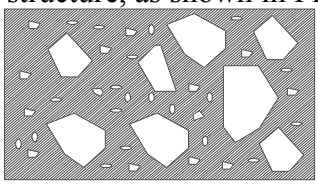

Figure1 Suspended solid structure

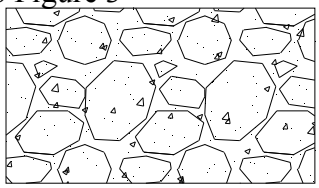

Figure 2 Framework-dense structure

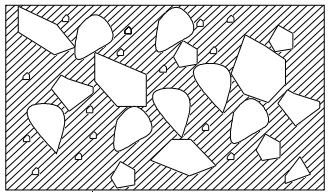

Figure 3 Framework-pore structure

In order to ensure adequate strength of the material and infiltration capacity,of transparent layer of oil and have some anti-erosion properties and crack resistance, semi-rigid material skeleton dense structure mix is more desirable transparent layer of oil on the material has a certain ability to penetrate

**Half-rigid base course surface aggregates.** Ease of emulsified asphalt into semi-rigid base is directly related to not only the bitumen droplets own intrinsic viscosity, but also the primary material composition the fine powder materials. the greater penetration resistance, the harder penetration.

Porosity, roughness and humidity and other factors of Aggregate surface also directly affect the material to absorb water in emulsion, thus affecting the emulsion breaking speed. When the surface of porous aggregates rough or loose surfaces, the water emulsion will soon be absorbed by the aggregate, to speed up the demulsification of emulsion; But on the other hand, large pore and number for emulsion infiltration.

## Analysis of factors affecting the penetration resistance

**Base surface and interface tension.** Tension between the liquid and gas phase interface is called surface tension. Tension between liquids and liquids, liquids and solids is collectively referred to as the interfacial tension. While layer-penetration material of surface tension and half rigid base material of surface tension poor value more hours, two species material between of interface tension more big, layer-penetration oil more not easily to base penetration; that base material and layer-penetration material contact area is small, and base surface voids smaller, formed of interface will tension very big , led to asphalt particles cannot in gravity role through into grass-roots. Emulsified asphalt in the penetration resistance of a half-rigid surface is mainly from the interfacial tension.

**Layer-penetration of viscosity of emulsified asphalt.** Viscosity is a major indicator reflects the quality of emulsified asphalt, construction primary control targets, directly affects the size of the viscosity of emulsified asphalt emulsion liquid. Asphalt emulsion evaporation residue content is the main factors affecting the viscosity of emulsified asphalt, evaporation residue content, the higher the greater the viscosity of emulsified asphalt; lower evaporation residue content, viscosity of emulsified asphalt will be smaller. Asphalt emulsion evaporation residue on penetration of a direct relationship between speed and depth, lower evaporation residue content, then penetrate better. Therefore, in order to ensure the osmotic effect, lower viscosity requirements are met as far as possible on the basis of modified asphalt emulsion evaporation residue content.

To explore the evaporation residue content on priming effect of emulsified bitumen viscosity and penetration, anion-crack slow emulsifier used in the study, add the appropriate amount of highly adhesive and penetrant agent, different priming emulsion evaporation residue content on half-rigid asphalt Distributor, observes its penetrant effect, as shown in table 1.

Evaporation residue levels on priming effect of layer-penetration of viscosity of emulsified asphalt Table 1

| Evaporation residue content/% | 40.5% | 42.7% | 44.5% | 45.1% | 46.8% | 47.9% | 49.2% |
|---|---|---|---|---|---|---|---|
| Viscosity of EngueraE25 | 1.68 | 1.81 | 2.0 | 2.10 | 2.21 | 2.27 | 2.41 |
| Storage stability | Good | Good | Good | Good | Good | Good | Good |
| Penetration depth /mm | 10 | 8 | 7 | 6 | 5 | 3 | 1 |

Table 1 reveals that with the increase in evaporation residue content, viscosity increases, penetration depth decreases; when the evaporation residue content of 40%,, stability is still very good, mainly due to the high viscosity of the join, better make the bitumen particles suspended in the aqueous solution, when evaporation residue content of about 40~45%, and layer-penetration oil work well

**Demulsification of layer-penetration emulsified asphalt speed.** At the time of construction, it played its bonding capabilities of emulsified asphalt, tar particles from separating aqueous, asphalt emulsion dispersion of particles gathered in knots, in aggregate or combined form a continuous cover film on the road. The developing process is shown in Figure 2-6. From a permeable layer of emulsified asphalt infiltration perspective, its emulsion speed should not be too fast.

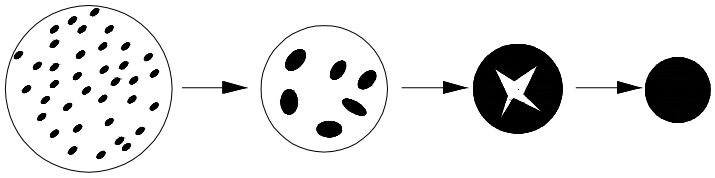

Figure 2-6 General process of decomposition of emulsion

Demulsification mechanism of cationic and anionic is a difference [4], this difference is mainly caused by Yang and anionic emulsifiers are different in nature.

Cationic emulsified asphalt emulsion through hydrophilic emulsifier molecules-amino good affinity with the aggregate surface, adsorption, forming bridges, asphalt-microspheres by emulsifier molecule this bridge reach the aggregate surface, and film formation and aggregate exposure. At the moment of filming, film of asphalt and aggregates produce larger extrusion force, moisture squeezed out of aggregate surface, making it volatile quickly. Therefore, cationic emulsified asphalt emulsion, condenses, forming quickly.

Anionic emulsified asphalt emulsion is by adhesion between asphalt and aggregate wrap aggregates. Emulsifier molecules themselves and aggregate surface compatibility, poor absorption and therefore did not play a bridge role, filming cannot occur when you squeeze the moisture out, and uniform distributions bituminous membrane surface moisture through the asphalt and aggregate bead gaps between the increasingly volatile. At the same time, due to the hydrophilic emulsifier molecules with more atoms of oxygen hydrogen-bonding association formed a solid combination of water, water evaporation is slow, time required is longer, after the moisture completely volatile, asphalt films to fully wrap aggregates. Therefore, anion emulsified asphalt emulsion, condenses, forming a long time.

**High permeability type layer-penetration oil material requirements**

For asphalt materials must be made of high quality asphalt, such as Donghai 90# asphalt. Emulsifier, demulsification and slower due to priming requirements, to make emulsion better penetration, plus decided demulsification mechanism of cationic emulsion speed too fast, this article recommends the use of slow-crack slow clotting anionic emulsifiers. Additives, in order to guarantee the new layer of asphalt emulsion to have certain character must be added with a certain volume of high viscosity to

ensure grass-roots good bonding with the surface to ensure its structural stability. In order to make emulsions with high penetration ability must be added with a certain volume of penetrating agent. This paper in order to overcome the traditional penetrating agent (such as kerosene, diesel) defects will pollute the environment, uses a new type of non-volatile, its molecular weight close to the penetration of the kerosene solvent in order to set this new layer of emulsified asphalt used as part of protecting the environment.

Based on the analysis above, select several emulsifier which emulsion slow, Donghai 90# asphalt, emulsified asphalt water-oil ratio of 45:55, not high viscosity, adding a certain amount of penetrating agent. Half-rigid specimen, judging permeability of emulsified asphalt, to filter criteria for emulsifiers, test results are shown in table 2.

Influence of emulsifier on permeability of emulsified asphalt Table 2

| Emulsifying agent type | Cationic | | Anionic |
|---|---|---|---|
| | A | C | B |
| The emulsifying process | Smooth | Smooth | Smooth |
| Emulsion speed | Mild-breaking | Slow-breaking | Slow-breaking |
| Viscosity of EngueraE25 | 2.01 | 1.98 | 1.86 |
| Amount of emulsifier /% | 1.5 | 1.4 | 1.5 |
| Evaporation residue content /% | 42.3 | 41.5 | 42.8 |
| Storage stability | Good | Good | Good |
| Penetration depth /mm | 0 | 1 | 5 |

As can be seen in Table 2, emulsified asphalt which is produced by cationic emulsifier B and anionic emulsifier C has certain permeability in the semi-rigid member, but the penetration effect of the anionic emulsifier cationic emulsifiers C is significantly better than the cationic emulsifier B. Previous engineering experience also shows that in the cement, lime, fly ash semi-rigid, since the material is highly alkaline, cationic emulsified asphalt is difficult to penetrate, the anionic emulsified asphalt material should be adopted as a transparent layer.

## Conclusions

In this paper, the layer of emulsified asphalt material, penetrating agent, emulsifier choice and requirements, semi-rigid type of aggregate penetration factors were analyzed, and then the selection of requirements is pointed out ; According to the analysis result, permeability test shows that penetration effect of high infiltration emulsified asphalt in this paper is good.

## References

[1] Gaopeng Wang, Song Yang, Yang Li. Application of high permeability emulsified asphalt in high-grade Highway. 2006, 5(4):11-13.

[2] Seed H B, Chen C K and Lee C E. Resilience characteristics of sub-grade soil and their relation to fatigue failures in asphalt pavement. Proceeding of Internal Conference on the Structural Design of Asphalt Pavement. University of Michigan. 1968:611-636

[3] Aimin Sha. Semi-rigid base material properties [j]. China Journal of Highway and Transport. 2008, 21(1): 1-5

[4] Jian Xu, Chupeng Li, Lin Xu, Yonglin Qin. Foreign contrast and revelation of cationic emulsified asphalt technical requirements [J]. Chinese and foreign road, 2004, 24 (2) : 67-70

*Applied Mechanics and Materials Vols. 580-583 (2014) pp 2528-2532*
*© (2014) Trans Tech Publications, Switzerland*
*doi:10.4028/www.scientific.net/AMM.580-583.2528*

# Industry clusters innovation action model based on the CAS theory —Shanxi magnesium industry

Fuzhou Luo [1,a], Shuling Liu [2,b]

[1]school of management, Xi'an University of Architecture & Technology, Xi'an 710055, China

[2] school of management, Xi'an University of Architecture & Technology, Xi'an 710055, China

[a]363840573@qq.com,[b]372603553@qq.com

**Key Word:** CAS theory; Cluster; Complex adaptive; Knowledge Innovation; emerge

**Abstract:** Based on complex adaptive systems (CAS) theory, using the method of case studies to explore the Shaanxi Province magnesium industry cluster knowledge innovation behavior. Based on the complexity stimulus—response rules, build the knowledge innovation system of metallic magnesium industry cluster main body behavior patterns; Based on complex adaptive - learning, building the overall behavior pattern of magnesium metal industry cluster knowledge innovation system; and based on the complex level—emerge theory, build the magnesium industry cluster evolution behavior pattern of knowledge innovation system. Use CAS theory to solve the problem of knowledge innovation in industrial cluster, which offers a basis for realize the sustainable and health development of industry cluster better.

## Introduction

The important driving force of human society's development is the innovation of industry, including technological innovation and knowledge innovation. Potter [1] believes that industry cluster is a group of geographically close and interconnected companies and associated institutions, they are in the same specific industry areas. Due to the commonality and complementary, they have the industry links and affect each other. Ji-ci Wang believes that industrial cluster is a group of businesses and organizations that are geographically adjacent and interconnected, they have industry contacts and influence each other[2]. We can consider industrial cluster is industry agglomeration in geographic economic geography phenomenon because of the need for economic development in a certain region [3]. The knowledge innovation system of industrial cluster is a complex nonlinear system, there are a lot of feedback and emergence of the problem that reductionism cannot be used to explain and study. When the university of Michigan's professor Holland[4] put forward Complex Adaptive System (Complex Adaptive System, hereinafter referred to as CAS) theory, let a person find everything new and fresh. Also aroused the home and foreign scholars' study enthusiasm, they use CAS theory in their field of study. Foreign theorists have begun to use CAS theory of enterprise technology innovation cluster study the issue and began to focus on the phenomenon of innovation clusters. But overall is still in its beginning and exploring stage, the study of knowledge innovation clusters are relatively small.

## Research methods

This study uses case study method, tries to take a comprehensive view of industry cluster in Shaanxi Province, and metal magnesium based on the actual situation, in-depth study of the

knowledge innovation behavior of industrial cluster based on CAS theory. On the other hand, knowledge innovation of industrial clusters should consider industry characteristics and regional characteristics and different development phases. Based on CAS theory, the research on knowledge innovation of magnesium and other non-ferrous metal industrial cluster has not appeared basically. And the foreign and domestic research achievements can't be directly applied to the knowledge innovation of nonferrous metal industry cluster. The case study is particularly applicable to the field of new or existing insufficient research field, it is suitable for the explanatory and exploratory research[5].

**Based on the complexity stimulus—response of operation mechanism of knowledge innovation main body behavior patterns of industrial cluster**

According to the theory of Holland, stimulus - response model is used to describe the different performance of adaptive principal way of unification, it illustrates the main body ability to respond to the environment in different times. This model mainly includes three parts: detector set, IF/THEN rule set, and effecter set. Using industry cluster of magnesium which in Shanxi as an example for discuss.

Based on the analysis of the factors of the complex adaptive features of knowledge innovation of industrial cluster and influence, establishes the knowledge innovation of industrial cluster stimulus -- response model. As shown in Figure 1. The model intended to describes the shanxi magnesium industry cluster behavior and reflect the main body of knowledge innovation from the micro level behavior, and reveals the essence characteristic and the behavior mechanism of knowledge innovation .

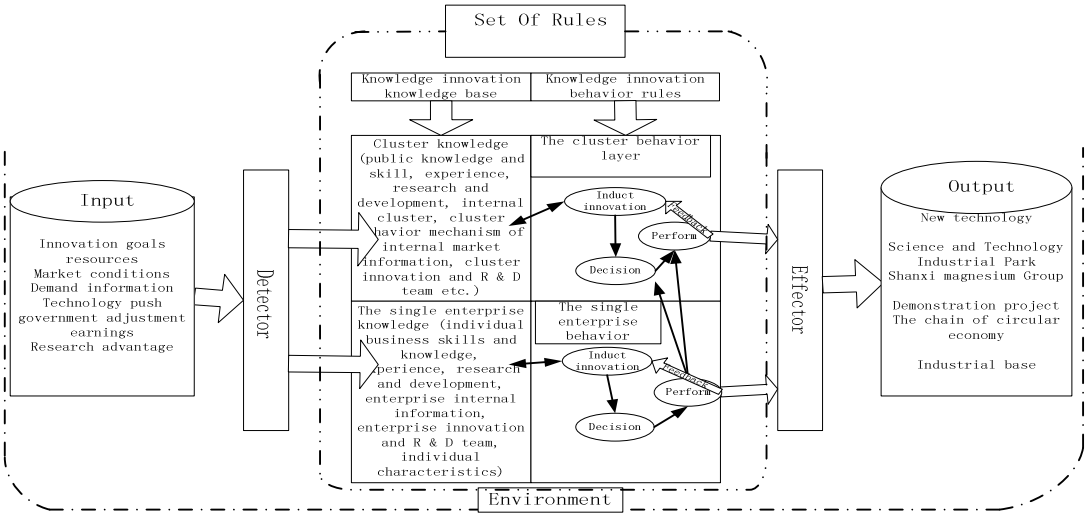


Figure 1 Shanxi metal magnesium industry clusters innovation stimulus-response model

Industrial cluster knowledge innovation influenced by four factors ,which are the front of the market pull, technology driven, enterprise internal uncertainty, government macro support. Innovation environment including enterprise innovation goals, within the cluster resource condition, metal magnesium at home and abroad market conditions, market demand, technology, the government macroeconomic regulation and control, enterprise or the entire industry profitability, development advantage. These factors of any changes will stimulate the knowledge innovation of industrial cluster, the whole environment and knowledge innovation is inseparable relationship. IF environment changes, THEN subject will through their own rules of conduct or behavior mechanism for knowledge innovation. Can be seen in the figure1, the target detector transmitted

goals to the cluster knowledge innovation subject, subject try to innovation based on existing knowledge. Since the knowledge innovation clusters are geographically close, and many companies which together form the industrial advantages, so in the process of knowledge innovation clusters will appear subject knowledge innovation and individual enterprises. Knowledge innovation of individual enterprises can't be ignored, it will serve the cluster of knowledge innovation. As a complex adaptive features of identification, flow, building block. In single enterprise cluster has its own characteristics, advantages and disadvantages, while the single enterprise knowledge innovation, information will be passed to the industry cluster, new technology and new knowledge new achievements of multiple enterprise gathers together can promote the overall development of the industry cluster, strengthen the competitiveness of the whole industry. Every achievement will feedback to the knowledge base, so as to accumulate experience for knowledge innovation in the next.

**Operation mechanism of knowledge innovation of industrial cluster overall behavior patterns based on Adaptive - learning**

Shanxi metal magnesium industry cluster as a whole is the highest level of main body of knowledge innovation system, remove the technology reform, technology research and development, self organizing group, subsystem level such as the main body to gather effect, more important is the overall model of behavior reflected Shanxi magnesium industry cluster innovation network in the industry or economic system or the international and domestic the higher level. To maintain Shanxi unique industrial clusters of metal magnesium, it is necessary to adaptive learning continuous and ongoing process of adaptive learning and knowledge innovation behavior of industrial clusters. CAS theory, the main body of adaptive learning is knowledge innovation cluster system to external changes in the environment of reaction. The reaction is subject cluster knowledge innovation system with the accumulation of experience, by changing their behavior rules, thus improving its ability to fit for the environment. Cluster body rule knowledge innovation system transformation is through the rules of local search and global search and the new rules of the discovery process [6].CAS theory attaches great importance to the active adaptation of the individual, the system still isolated individuals is almost meaningless, Only through individual and individual, individual and environment, mutual influence, interaction between system to active and appear new features, thus increasing the diversity and complexity of the whole, to provide a steady stream of power for the continuous improvement of the overall. And cluster complex adaptive learning ability of whole namely cluster behavior main body of knowledge innovation. The key for Knowledge innovation system to adapt to the dynamic changes of external environment, to achieve continuous innovation is cluster complex adaptive learning subject of knowledge innovation. So, must improve its complex adaptive learning ability in order to improve the cluster knowledge innovation ability. Based on the analysis above, the adaptive -learning mode operation of Shanxi magnesium industry cluster mechanism of knowledge innovation system which shown in figure 2.

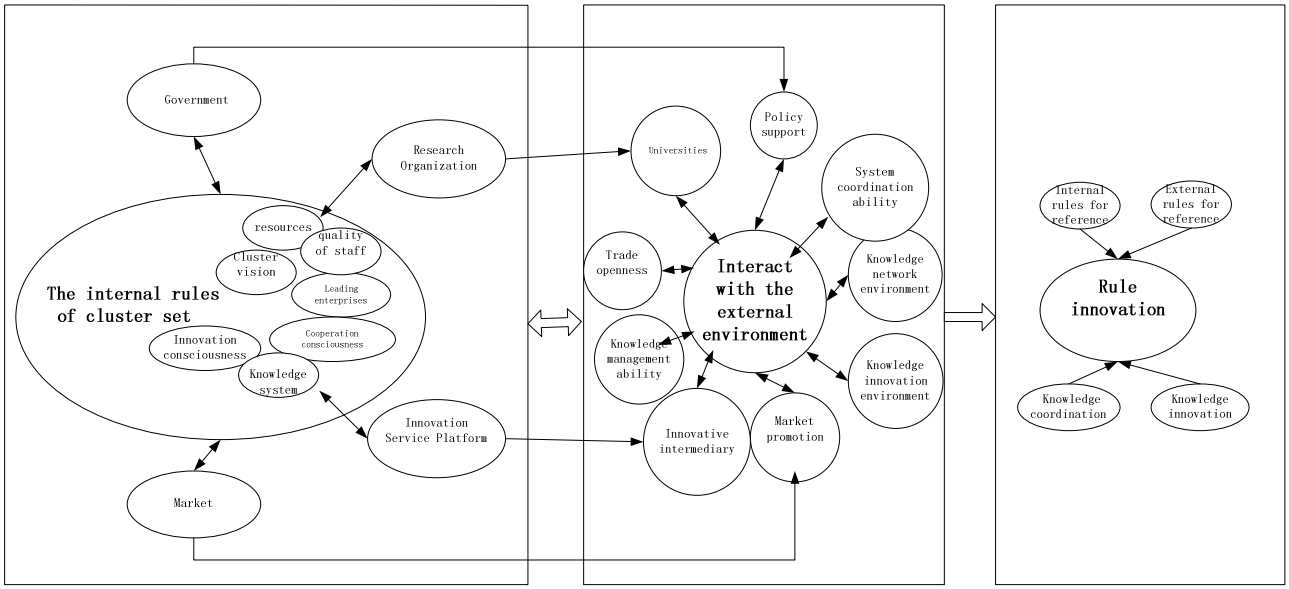


Figure 2 The adaptive – learning mechanism in Shaanxi Province metal magnesium industry clusters innovation overall pattern of behavior

**The operation mechanism of evolution patterns of behavior level- emerging knowledge innovation system based on Industrial Clusters**

The CAS theory, complex adaptive-learning of metal magnesium industry clusters innovation system will produce feedback. Positive feedback can strengthen the industrial cluster learning function, while the negative feedback is eliminated. On the one Hand, low level subject to survive within the cluster, must timely adjust, change the mode of thinking and behavior of enterprise development business and positively associated with high levels of body communicate and work together to achieve the goal. Industry cluster in the system, on the other hand, collaborative mechanism between the main body, make each level subject mutual influence, interaction, mutual constraints, have the same or similar to adapt to the learning activity (i.e., imitation). When a certain level of emergent phenomena, levels of emergent phenomena and the same will also produce, which are called "synergistic effect". With interaction and mutual influence between different level sunder the impetus of the nonlinear characteristic, produce the phenomenon of the emergence of a higher level. So, knowledge of industrial cluster innovation system with the steps of the emergent properties to evolve.

The magnesium metal industry cluster knowledge innovation system will produce three levels of emergence according to the search and selection of Shanxi Province magnesium industry cluster knowledge innovation system evolution in the scope of the rules and the way. Self-development : As you can see in the adaptation-learning model ,the first step in the search of industry cluster rule is the rules of Local Search, and start from the internal Shanxi magnesium metal industrial cluster, and make copies of itself if the rules are effective , while eliminate the rules which are invalid. This can lead to failure if search effective rules is unsuccessful. Or successfully find the effective rules but we did not create a successful application, it can also lead to the failure . Dynamic mock: After local rules' Searching and copying successfully then will form emergence, by the rules of globally search , when found the successful rules , then following the the dynamic imitation rules and eliminate weak imitation dynamic rules. If the dynamic imitation is not successful, it will lead to an unsuccessful knowledge innovation. Innovation emergence: when find the effective rules in the course of generally searching rules, we not only imitating and learning but also using it as base to reorganize rules. With the emergence of level growth in Shanxi magnesium industry cluster

knowledge innovation system , the adaptability and level complexity of Shanxi magnesium industry cluster knowledge innovation system appear to be on the rise. Based on the above analysis, we can construct the hierarchical emergence model of Shaanxi Province magnesium industry cluster knowledge innovation system evolution and show it in Figure 3.

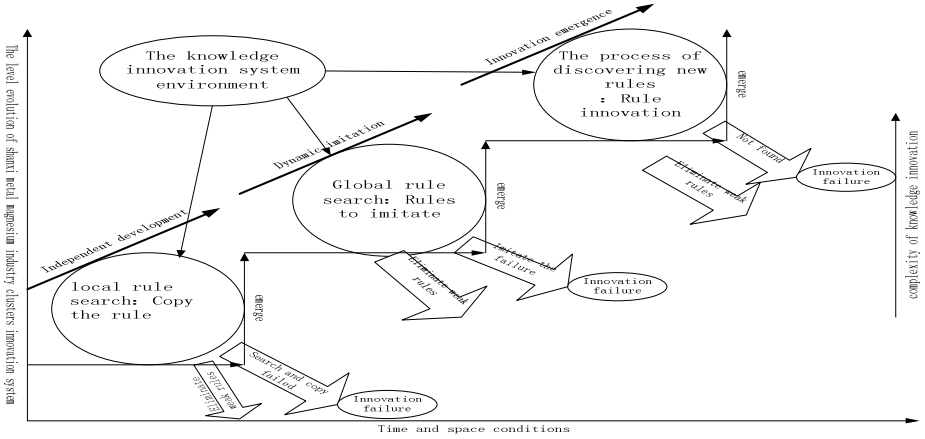


Figure 3 Shaanxi metal magnesium industry clusters innovation system level emerging patterns

## Conclusion

Knowledge innovation is a dynamic process. Knowledge innovation often appears to be uncertainty and emergent properties. The study of knowledge innovation and complex adaptive will be filled with new content with the transformation of time and space. Knowledge innovation theory and complex adaptive will constantly improved in the development.

The use of CAS theory on the research of magnesium industry clusters innovation behavior mode is a new perspective. In order to analysis and solve the problem of shanxi magnesium industry cluster's knowledge innovation, first is the innovation of individual subject behavior, then the whole. Most critical is level –emerging.

Using CAS theory to solve the problem of knowledge innovation in industrial cluster, which offers a basis for realize the sustainable and health development of industry cluster better.

## References

[1] Porter:Cluster and the new competition．Harvard Business Review:77-90．［M］

[2] Jici-Wang: Beyond the cluster- To explore the Chinese industrial cluster theory. [M]. Science Press, in Chinese, 2011.

[3] Holland: Hidden order. Translator: Xiaomu Zhou, Hui Han. [M]. Education Press of Shanghai science and technology, in Chinese, 2000

[4] Enhua Hu, Hong Liu: Research on innovation behavior of industrial clusters based on complex adaptive system. [J]. Chinese Technology Forum.2007.01

[5] Jin Chen, Yinjuan Yang, The synergy theory basis and connotation of innovation. [J]. Science research.2012.02

[6] Ting Chen: Study on eco city system model based on CAS theory. [D].Chongqing: Chongqing University, in Chinese,2011, 06

*Applied Mechanics and Materials Vols. 580-583 (2014) pp 2533-2538*
*© (2014) Trans Tech Publications, Switzerland*
*doi:10.4028/www.scientific.net/AMM.580-583.2533*

# Research on Construction Technology of The High Permeability Type Layer-penetration Oil Production

HU Gang[1, a]

[1] Anhui expressway holding group Co., LTD, Hefei, China 230088

[a] 975267082@qq.com

**Keywords:** high permeability layer-penetration oil Penetration depth

**Abstract:** Current specification, does not specify the full construction process. In practice, the majority of construction units according to their own experience, hard to get reliable assurance of construction quality. In the early development of new and the high permeability type layer-penetration oil on the basis of construction of the test section of this article relies on permeable layer, oil on high permeable layer construction process, quality testing, and control indicators complete process was studied, test construction and achieved good results.

## Introduction

Asphalt concrete pavement and cement stabilized crushed stone and lime-fly ash bound macadam semi-rigid base course for interlaminar bond quality, is one of the most important factors affecting the service life of the asphalt concrete pavement, if integration between the two is not good, opening under load and rain, prone over asphalt pavement early damage. Now widely recognized, the layer-penetration oil seep into the grass-roots level in some depth, can improve the basic ability to resist water erosion, reducing water damage to the grass-roots, are important factors in reducing asphalt pavement over [1]. Thus, the layer-penetration as an important bonding of asphalt concrete pavement with semi-rigid base layer is essential and permeable layer surface of semi-rigid base materials can penetrate a certain depth, enhanced integrity of the grass-roots bonding interface and form the most important [2].

Is not stated in the specification as the existing asphalt pavement construction of concrete construction procedure and requirements, most of the construction company didn't have the experience of successful construction of the layer-penetration, so it is necessary to combine a number of successful construction projects, construction steps and points to the layer-penetration in a systematic study. Main problems of current construction of the layer-penetration as the following [3]: ① spraying oil hard penetration with base deep enough (around 5mm); ② normal solids content less concentration of 30%~35%, a spray of more than 1.2kg/m2 easily flowing surfaces along the cross slope or gradient at the grassroots level. If two spraying, the asphalt penetrate into the base level at the second time. ③ semi-rigid cleaned is not clean; ④ spread unevenly; ⑤ when the air temperature is low, due to the duration and other reasons, cannot be completely breaking; ⑥ permeable layer of construction equipment and vehicles damaged. Therefore, during the construction process should be avoided and overcome these problems in the construction of oil. Construction technique of transparent layer of oil block diagram shown in Figure 1.

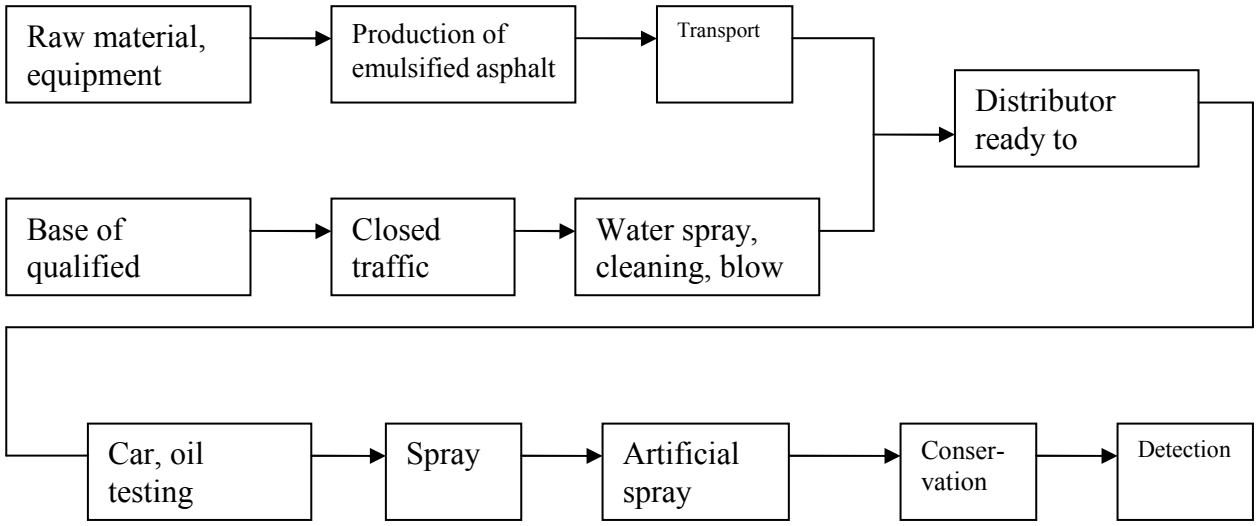


Figure 1 The high permeability type layer-penetration oil spray technology

**Preparation for construction**

**Pavement Base to prepare.** (1) Prior to construction, be obtained from the construction section "Pavement Base acceptance from".

(2) After the primary health 3~5d, brushes, dehairing machines for surface or grass-roots local "mirror" site, as far as possible so that top surface of cement stabilized crushed parts of coarse aggregate exposure and then spreading through the layer of oil.

(3) Air compressor base surface clean, cannot remain airborne particles.

(4) Before the spreading oil, must block the curbs and artificial structures, to avoid contamination.

**Select the appropriate job segment length.** As far as oil production capacity, taking into account the tanker transport distance, selecting the suitable for spreading of the day length.

**Combinations of equipment and construction personnel.** Each construction work surface should be equipped with the appropriate amount of air compressors, water truck, bituminous distributor, before the Spraying oil, should be preheated and fix the nozzle, ensuring uniformity of penetration oil spray, insulation oil tankers and command vehicle (traffic control, test) and configured with 2 sets of temperature, the amount of spray test equipment, total construction staff of about 20 people per class.

**Test sections of the construction**

Used oil contains no kerosene, test section of the 200m spreading to achieve the following objectives:

(1) To qualify for construction layer-penetration oil spray volume and blending ratios;

(2) To determine the spreading speed of the vehicle;

(3) Examination of the depth of oil penetration (≥ 5mm) and a reasonable spread of time;

(4) Determine the appropriate length of each work surface;

(5) To determine the standard construction method of priming.

Use of raw materials, construction machinery, construction method and test section of test projects are in line with the provisions of,confirmation by the supervision inspection qualified, Experimental Section Construction Summary can be written as above, reviewed by Director approval and after the company approved, starting the construction of 1km standard. 1km standard escalation summary report at the end, as declared officially started based on a large area.

**Spray time**

Penetration depth and layer-penetration oil spray time had a close relationship. Tests and practice has proved that the pervious layer of oil in semi-rigid base has not yet hardened when spraying, the penetration depth of the largest, growth and strength increases with age, oil is increasingly difficult to penetrate. Semi-rigid base after the semi-rigid materials have not been due to consolidation, base close to graded, priming oil easily penetrate half rigid base, but with the increased strength of semi-rigid materials, its internal structure will be more and more dense, and oil penetration will become increasingly difficult. Therefore, layer-penetration oil spray at the base should be laminated after forming as soon as possible.

States to the layer-penetration oil spray time rules are basically the same [4], for example, the United Kingdom specification states that for base course of cement stabilized, turbine oil should be laminated after forming an hour later at the base level as soon as possible; United States highway construction norm of base course of cement stabilized, the layer-penetration oil should be carried out immediately after the final pressure; Technical code for construction of Highway asphalt pavement provides, for permeable layer of half-rigid base oils should be immediately rolled back slightly at the base level to dry up, but have not been spraying case hardening.

However, spray priming prematurely, likely to affect the strength of the surface layer of half-rigid base, so spreading on permeable layer of half-rigid base oil, preferably after the paving of semi-rigid 3~5d sprays, which can guarantee the layer-penetration oil penetration depth, while also ensuring the strength of the surface layer of half-rigid base.

**Spraying dosage**

The layer-penetration oil spray shall be adopted according to the degree of semi-rigid surface rough trying to sprinkle OK. Distributor shall travel at a constant speed 30km/h speed, start time as short as possible, get to spread rate, running at the same time must be straight and stable. For ensuring a permeable layer asphalt distributor fully and evenly, achieves the proper penetration effect, spray to spraying dosage the back does not form an apparent runoff for the standard, the spreading quantity control in 0.8~1.2kg/m2, large engineering practice should be taken into account. Requires closed the distributor circuit on time when spraying end, so as to avoid residual oil film formed.

Distributor after the job is complete, timely organization assisted jobs, clear spray excessive amount of spilled oil runoff or uneven parts, parts of the film occurs promptly clean up to remove, when artificial spray sprayer.

**Spreading measures**

Layer-penetration oil asphalt distributor truck spraying should be used, speed and select the appropriate nozzle, spray and spray, and remained stable. After layer-penetration oil methods and measures for standard data identified, the asphalt layer can be made sprinkle, but distributor for actual construction was sprinkle, due to the large amount, it must be according to the paving area, standard content and per unit area of bitumen emulsion, calculated with reasonable accuracy synthesis of emulsion, and calculates spray distributor of road speed; a sprinkler success, does not fill as far as possible. When emulsion sprinkling, taking the following a series of measures to ensure the quality of the spray.

(1) To clean the surface of the base. First use broom to clean it twice, and then rinse with water gun, make pit slot dips dust discharge with the current roadbed.

(2) To ensure that the surface of the emulsion at the grass-roots moist (but not the water) state sprinkles in order to increase the amount oil seepage. Primary flushing of water has dried on the surface, to be carried out before the sprinkler.

(3) Strict control emulsion breaking time and the interval time of paving on the surface. Ensure that layer-penetration oil in front of the emulsion asphalt infiltration 70% complete, asphalt firmly

embedded within the grassroots, pending demulsification infiltration process, after the water evaporates, paving layer. Paving layer at the earliest time after waiting for 24h, but also not easy clearance is too long, with no more than 3d advisable.

**The layer-penetration conservation**

Layer-penetration up to seal (if any) shall be closed before the end of construction traffic; after the end of the conservation, cannot cut off the transport case, appointed commanding vehicles slow (less than 20km/h).

After spreading, generally require closed 24h traffic; if you need timely sealing job, requires demulsification and 8h may be carried out. Spray priming oil after strict traffic controls, traffic is strictly prohibited until the priming oil full penetration.

**The Penetration depth**

Technical Code For Construction of Highway Asphalt Pavement (JTG F40-2004) explicitly requested through the depth of the layer-penetration oil penetration should be no less than 5mm. If you are not into grass-roots just spilled on the surface to form an oil film, it does not play the consolidation, stability, adhesion and waterproof functions. Because the bonding layer is too thin to pavement process, the oil film is easy with grass-roots off, or is punctured by coarse aggregate for structural layers below.

**Testing method of construction quality and controlling index**

**Inspection methods**. (1) Spraying dosage detection: aluminum trays placed on the primary receiving oil, electronic weighing scales, according to pallet back-calculate the size of each square of the spray volume.

(2) Detection of penetration effect: After spreading 48h to conduct penetration testing, the drill core samples measure the penetration height shall prevail.

(3) Detection of adhesion between layers: Bonding between layers of permeable layer should include two requirements: one is layer-penetration oil and grass-roots bonded well formed turbine oil demulsification of spreading a thick layer of asphalt film, requires this layer bituminous membrane, even in the absence of shed-skin cloth and chip cases, vehicle passage would bring bitumen membrane, making a round of the India. Second, asphalt concrete layer after completion of construction, the following also to excellent adhesion between the layer and the grass-roots level and requested that the following layer and the grass-roots level drill-core samples to be joined together into a whole.

**Control indexes.** Layer-penetration with the high permeability type layer-penetration oil, major technical indicators are shown in table 1.

High permeability type oil technical requirements Table 1

| Test items (unit) | | Unit | Technical requirements | Test method |
|---|---|---|---|---|
| Demulsification velocity | | | Slow crack | T 0658 |
| Particle charge | | | - | T 0653 |
| Sieve residue on sieve (1.18 mm) | | % | ≥0.1 | T 0652 |
| Viscosity | Viscosity of Enguera E25 | | 1~4 | T 0621 |
| Evaporated residue | Residue content | % | ≤40 | T 0651 |
| | Needle penetration | 0.1mm | 100~300 | T 0604 |
| | solubility | % | ≤97.5 | T 0607 |
| Room temperature storage stability | 1d | % | ≥1 | T 0655 |
| | 5d | % | ≥5 | |

During the construction of oil, shall be as provided in table 2 and table 3, inspection of turbine oil.

Frequency of detection of oil raw material quality Table 2

| Project | Inspection frequency | Detection method |
|---|---|---|
| Viscosity | After the first approach of determining material sources, abnormal, a full set of tests, the construction of each class testing viscosity, evaporation residue 1 time | |
| Evaporated residue | | |
| Water content | | |

Construction process quality inspection requirements Table 3

| Project | Quality or allowable deviation | Inspection frequency | Detection method |
|---|---|---|---|
| Spraying dosage （kg/m2） | 0.8~1.2 | 1/paragraph per job | With cardboard weigh |
| Distributing uniformity | Uniformity | At any moment | Visual inspection |
| From the next operation the construction interval (h) | ≥24 | 1/paragraph per job | With the watch |
| Depth of penetration （mm） | ≥5 | 1/paragraph per job | Core, feet |
| Demulsification and base surface adhesion | Thicker bitumen film, not wheels belt, leaving only the round print | Spraying 48h | Visual inspection |
| Interlayer bonding | Base and below layer bonded to a whole | After paving layer below | Linger-sometimes constantly sampling |

**Construction equipment and testing instruments**

**Main machine in construction of prime coats**

Machinery equipment parts table Table 4

| Serial number | Device name | Number | Notes |
|---|---|---|---|
| 1 | Intelligent emulsifying asphalt distributor | 1 | Spray quantity does not change with speed |
| 2 | Small milling machines or dehairing machines | 2 | To meet construction requirements |
| 3 | Powerful sweeper | 1 | |
| 4 | Road sweeper | 1 | |
| 5 | Air compressor | 4 | |
| 6 | 8tWater truck | 2 | |

**Construction quality testing equipment for layer-penetration**

Layer-penetration quality testing devices Table 5

| Serial number | Instruments and equipment name | Quantity |
|---|---|---|
| 1 | Ruler or measuring tape | 1 |
| 2 | core drilling machine | 1 |

**Environmental protection measures**

(1) The layer-penetration material production, the self-system should be set up in the factory's waste disposal and sewerage facilities, in order to avoid water pollution.

(2) Prior to spraying oil, such as curbs, bridge and culvert structures must be covered, to avoid contamination.

(3) The layer-penetration oil spray volume should meet the requirements, does not cause the massive flow of slopes, farm, and pollution.

(4) Spray oil section must carry out a traffic control to avoid crosstalk with other processes in order to stop construction and transportation pollution.

**Points for attention in layer-penetration construction**

(1) Oil preferably at asphalt distributor truck spraying evenly, before the spray oil, should be preheated and dredge nozzle, nozzles should be used according to the priming oil viscosity select and ensure uniform spray, uneven asphalt distributor truck spraying times switched to hand-sprayed asphalt Distributor. A graying omission should be artificial to sprinkle, sub-skin cloth and immediately spray excessive amount of suction of dust or sand, if necessary, properly compacted.

(2) Spray layer-penetration oil to clean the road, shielding protective curbs and artificial structures to avoid contamination.

(3) The layer-penetration oil spray process should ensure that penetration oil spray volume spraying personnel shall not adjust or change.

(4) Keeping time after layer-penetration oil spray priming variety and climatic conditions is determined by testing, ensure that volatile thinners put in liquid asphalt, infiltration and evaporation of emulsified asphalt and paving asphalt surface as soon as possible to prevent vehicle damage.

(5) Temperature is below 10℃ or in case of strong wind or rain penetration shall not be sprayed.

**References**

[1]Zhaobin Xia, Bo Ma. Development of emulsified asphalt at home and abroad and its application [J]. Oil and Natural Gas Chemical Industry, 2000, 29 (2): 89-91

[2]Yuli Zhao, Libin Zhang, Zhanqing Mao. Cationic emulsified asphalt layer construction summary [J]. Heilongjiang Traffic Science and Technology, 2002 (2): 10 to 13

[3] Jian Xu, Chupeng Li, Lin Sun, Yongchun Qin. Foreign contrast and revelation of cationic emulsified asphalt technical requirements [J]. Chinese and Foreign Road, 2004, 24 (2): 67-70

*Applied Mechanics and Materials Vols. 580-583 (2014) pp 2539-2544*
*© (2014) Trans Tech Publications, Switzerland*
*doi:10.4028/www.scientific.net/AMM.580-583.2539*

# Research on High Permeability Layer-penetration oil production

GUAN QIN[1]

[1] Anhui expressway holding group Co., LTD, Hefei, China 230088

[a]809251326@qq.com

**Keywords:** High permeability layer-penetration oil emulsifying machine oil-water ratio

**Abstract:** Domestic and foreign road construction for many years of practical experience shows that pavement early damage and between the base and the surface layer of oil related to the quality of construction, the quality of life of the future road surface layer has a major influence[1]. In order for the preparation of high-permeable dialysis oils heavy investment in production, combined with permeable layer of oil in the production of enterprises, taking into account the conditions and existing equipment of enterprises, the paper layer on oil production, put forward the requirements for equipment, processing parameters, control indicators.

## High permeability type layer-penetration oil material requirements

High permeability layer-penetration oil using the Donghai 90# asphalt and removing acidic residue salts, kerosene is not included, and added a new type of infiltration solvent and high viscosity. Based on actual laboratory tests combined with mass production needs, presented highly permeable strata oil production scale of the main components, as shown in table 1. Suppliers can be combined with the actual situation in this range adjustment to good production stability of layer-penetration oil.

Table 1 Production scale of Various materials in the high permeability type layer-penetration oil

| Main ingredients | Scale | Notes |
|---|---|---|
| High adhesive | 0.3%~0.4% | Growth over time, the binding effect is getting better and better |
| Penetrating agent | 8%~10% | Non-kerosene diluent, non-volatile, pollution-free, on the grass-roots level without damage |
| Emulsifier | 1.4%~1.6% | Anionic emulsifier |
| Water | 52%~56% | Tap water or ground water |
| The Donghai 90# asphalt | 28%~32% | Various performance indicators than other asphalt emulsion |
| Salt-removed acid slag | 4%~5% | Recycling of asphalt modification, improve the performance of emulsified asphalt |

## The production process and control conditions

### 1.1 The choice of production equipment

Higher production in the high permeability type layer-penetration oil emulsifier is the most crucial equipment. Mechanical emulsion effects mainly on the size and evenness of the asphalt emulsion particles[2]. The ideal emulsifying machine should make the asphalt emulsion particles small, uniform, in order to enhance the stability of the emulsion. Emulsification machine is complete asphalt liquid scattered broken device. Its performance quality has important influence on the quality of the emulsion. Commonly used mulser have agitator emulsifying machine, the homogenizer mulser, colloid mill several forms of the emulsifying machine adopt more is colloid mill type emulsifying machine. Can be correctly chosen emulsifying machine equipment, will directly affect the quality of the emulsified asphalt. All kinds of emulsifying machine principle and characteristics are shown in Table 2.

Table 2 Principle and characteristics of various kinds of the emulsifying machine

| Emulsifying equipment | Principle | Characteristic | Disadvantages |
|---|---|---|---|
| Stirrer machine | Through the high speed rotating blades, cut mixing, great cut effect on melting asphalt, bitumen particles dispersed into many small, evenly dispersed throughout the emulsion to form dark brown asphalt suspension | simple and practicable | Poor uniformity of bitumen particles |
| Homogenizer class | Motor drive gear pump with high speed rotation, the input of liquid asphalt and emulsion by gear pump and reciprocating cycle of injection dispersion. Chemical injection mouth diameter is small, from gear pump to piping under a lot of pressure, from the head of a small note the asphalt emulsion and liquid mouth spewed a lot of cutting force, making it a mixture of fog. Iterative multiple times, by mechanical and hydrodynamic effects make the asphalt of asphalt into very fine particles, and are evenly dispersed in the emulsion, forming a stable asphalt emulsion | Homogenization head part is no rotating parts manufacturing processes more easily. Emulsification effect is better than that of agitator emulsification | Easy to jam, use the first requirement of asphalt and emulsifier aqueous solution carefully filtering |
| Colloid mill class | Rotation in the stator, rotor, the mixture from imported into, in under the action of centrifugal force, through the gaps between the rotor and stator, liquid asphalt in the gap by the effects of the centrifugal force and friction force of rotor, is ground into very fine particles, flow from exports | Emulsion is a high degree of refinement, good storage stability, emulsification effect is better than that of homogenizer emulsifying machine | |

As can be seen in the table: category colloid mill emulsion machine for emulsified asphalt emulsion advantage a lot, and be able to make the bitumen particles evenly, storage stability,the high permeability type layer-penetration oil production more favourable. Therefore, recommended enterprises using high permeability emulsified colloid mill class machines-oil production.

### 1.2 The oil-water ratio control

Asphalt emulsion oil and water than typically 60:40 or 50:50. For the high permeability type layer-penetration oil production, oil-water ratio control in 45:55, solid content can be as low as necessary to 40%. Enterprise on-site monitoring of oil production than the main methods: one is the observation with the naked eye, according to the worker's experience, General color is Brown, takes the form of a fluid, liquid; the second is to field test it, determination to adjust oil evaporation residue ratio, its oil-water ratio error not exceeding ± 5%.

Oil and water temperature is one of the important indicators of emulsified asphalt production. Emulsion temperature control between 55 ° c ~70 ° c, temperature control of asphalt between 120° c~135° c. Production, the temperature of the asphalt and liquid soap, according to the weather control with flexible production times. In principle the difference between oil and water temperature below 85 ° c, and less than 200 ° c oil temperature of. Prevent aging of asphalt on the asphalt temperature is too high, preventing excessive water temperature causes evaporation, water vapor and temperature too high possible cause and expansion tank.

### 1.3 Preparation of emulsifying agent solution and its temperature control

Preparation of emulsifying agent solution is directly related to high osmotic priming oil quality is good or bad. Through laboratory tests found that the emulsifier amount control in 1.2%~1.6% are relatively modest, when preparation of emulsions generally is added emulsifier in a fixed container, plus the amount of water, then adding quantitative high viscosity, the container is best installed mixer, emulsifier and high-viscosity fully soluble in water, emulsifying agent solution mix.

Preparation of high permeable dialysis due to oil emulsifier, sensitivity to the temperature of the water is relatively high, therefore, need to be adjusted according to the ambient temperature, summer high temperatures at around 50 ℃ temperature control of emulsion, spring and emulsion temperature at 60 ℃, winter temperature, latex at about 70 ℃ for temperature control. Note: when the water temperature is low (especially in winter), you should add the water temperature to 30 ℃ then add emulsifiers, for faster dissolution of the emulsifier, increase its solubility, making it fully dissolved.

### 1.4 The mix asphalt proportions and temperature control

Preparation of the high permeability type layer-penetration oil chose to remove acid residues of salt and the Donghai 90# asphalt mixing, removes the acidic residue of salt mixed into the Donghai 90# asphalt bituminous mix, through laboratory studies, the Donghai 90# removal of acidic residues of salt mixed asphalt and quality control between 7:1~6:1.

To the Donghai 90# asphalt heated to 100, desalt acidic slag when heated to a molten state mixed into the Donghai 90# asphalt, and through the blender mixing, mixing heating temperature control at about 125.

### The penetrating agent added

The laboratory test found that penetrating agent added in the mixed asphalt effect is better. Penetrating agent is a kind of thick liquid, can be directly added to the asphalt mixture, under normal temperature. If there is a phenomenon of solidification in winter, it can be heated slightly and add to the asphalt mixture, and a mixing device in the mixture in container and heating device, the mixing, and heated to the temperature of the emulsified asphalt in asphalt need, is about 125 ℃, penetrating agent adding quantity control at 8% ~ 10%.

### 1.5 The production process

Before the high permeability type layer-penetration oil production, check all valves and pipes, and the temperature of diesel preheat to 80 ℃ or so, start the diesel pump, preheat emulsification ball mill, and relevant asphalt heating pipes, after being emulsified surface hot mill and pipe heat stop heating. Control valves, joined the high adhesive with good emulsifier solution, heating the mixture of asphalt and penetrating agent to the specified temperature, start the mulser, restart the asphalt pump, adjust the oil-water ratio, can be emulsified asphalt production. In the process of emulsification, still need to be careful observation, according to the test of oil content to fine-tune.

### Adjustments and improvement of the production equipment

The high permeability type layer-penetration oil production has four links: First is the configuration of emulsifier aqueous solution; scond is through the emulsified oil production through layer; three is highly adhesive to add; Fourth, through oil product storage and use.

In this paper, the research and development of the high permeability type layer-penetration oil of asphalt materials adopted two kinds of asphalt mixture, joined the desalt acid slag, so the preparation technology with conventional through layers of oil product is different. According to this topic based on a projection of the specific conditions of the production equipment, put forward in the production

of high permeability type layer-penetration oil need to make the following improvements in the production equipment: (1)Add a small heating function, storage containers, storage need to add the material of waste tire pyrolysis tar; (2)Add a small storage container, to store the added penetrating agent; (3)Conventional asphalt containers to increase mixing features, make it mix evenly. Due to the high permeability type layer-penetration oil raw materials for Donghai 90# waste tire pyrolysis of asphalt mixture of asphalt and asphalt materials, and removes the acidic slag and penetration of salt spray into the asphalt container and stir to make it mix; (4)Emulsion between emulsion flow meter and emulsifying machine install the check valve in the pipeline. To prevent thermal pressure is greater than the emulsion asphalt, and rushed to dilute liquid jar; (5)Liquid tank installed on the device, easy mixing emulsifier solution and solution; (6)Due to good emulsified asphalt production also need to add a certain amount of high adhesive, and make its mixing, therefore, the transparent layer of oil product storage tanks to increase the mixing function.

## The production processes and its condition control

### 4.1Production precautions

(1) Before asphalt, aqueous solution entering the mulser must use fine mesh filter, lest production block; (2)Before the emulsification machine starting, must be conducted with hot diesel cleaning after use; (3)The emulsion storage containers must be sealed, in order to avoid clutter and into rain. Produce a good product should be stored in sealed container, minimize the finished product is exposed to air, to avoid the surface crust or demulsification floe; (4)Before emulsification machine and asphalt pump start-up, should first dial the pulley and shaft coupling with the hand, less because of the presence of asphalt solidification in the machine and all of a sudden start motor to burn out; (5)When you start the emulsification and there must be "water supply, oil supply after" stop the emulsion must be "just closed after oil and water".

### 4.2 The preparation works before production

(1)Transparent layer of oil production equipment in accordance with the requirements of emulsified asphalt production equipment to be checked. To ensure operated of the equipment normally, the timely processing of all kinds of problems and ensure smooth production; (2)To confirm the number required for the production of transparent layers of oil, various quantities of raw materials to ensure adequate; (3)Heating the raw material to the specified temperature: ①Advance according to the proportion of water added to the production equipment emulsifier blending tank and adds an emulsifier to the provisions of the mark, after the incorporation of the quantitative high viscosity, heated to a predetermined temperature and stir well; ②Asphalt is heated to around 100℃ in storage tanks, waste tire antipyretic asphalt is heated to around 100℃, remove the acid residue of salt and osmotic agent joined Donghai 90# asphalt container in proportion, and stir well and heat it to about 125℃.

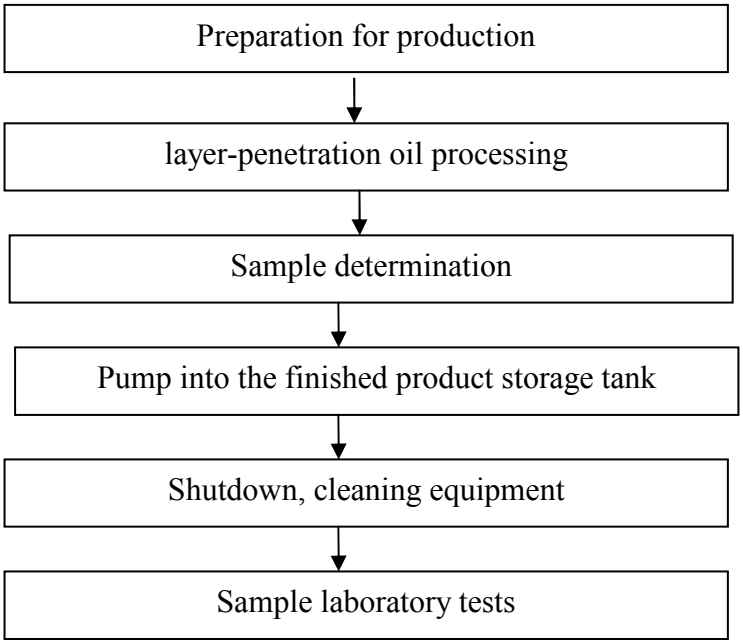


Fig.1 The high permeability type layer-penetration oil production

After the temperature of various raw materials up to standard, to begin production: (1)Asphalt outlet valve open, opens a blending of emulsifying agent tank outlet valve; (2)Start the emulsification machine, simultaneously closes emulsifying machine heat conducting oil heating system; (3)Start the emulsion pump, adjust speed, until the emulsion stability outflow; (4)Start the asphalt pumps, adjust the speed; (5)According to experience, adjust and asphalt emulsion pumping speed; (6)Probably to reach a suitable proportion, sampling determination of content, and adjust the machine according to the results of the determination; (7)Start finished taking the pump, the emulsion production pump into the finished product storage tank.

### 4.4 Production completed requirements

(1) After the outage, order in contrast to boot. Asphalt pump close, shedding all emulsifier emulsion solution, emulsion pump stopped, finally closed colloid mill; (2)Emulsified asphalt production after the cleaning equipment; (3)Sample laboratory tests; (4)Long time no longer produced, closed heat-conducting oil heating system.

### 4.5 The high permeability type layer-penetration oil storage

After the high permeability type layer-penetration oil produced should be stored in a closed container to minimize exposure to air and emulsified asphalt to avoid breaking the surface of the crust caused by or occur flocculation; emulsion to prevent separation of the mixing device may be provided in the container , but not involved in the air.

## Conclusion

This requirements for permeable layer of emulsified asphalt production equipment, production processes, process control, product storage, and so did the study, has been highly permeable strata oil production process. According to the results of this research, and successfully applied in engineering practice, making road construction quality has been improved.

## References

[1] Gaopeng wang, Song Yang, Yang Li. High penetration emulsified asphalt penetration layer application in high-grade highway [J]. Journal of Guangdong Transportation Vocational Technical College. 2006, 5 (4) : 11-13.

[2] Sousa J B, Taylor R and Tanco A J. Analysis of some laboratory testing systems for asphalt aggregate mixtures. Presented at the 70th Annual Meeting of the Transportation Research Board, ioashington D. C, 1991:1035-1046.

*Applied Mechanics and Materials Vols. 580-583 (2014) pp 2545-2549*
*© (2014) Trans Tech Publications, Switzerland*
*doi:10.4028/www.scientific.net/AMM.580-583.2545*

# The Influences and the Mechanism of Action of Grinding Aid Agent During Micro Fine Particle of Lean Hematite Ore of Grinding Operation

Liang Bing[1,2 a *] Zhang Jinrui[1,2] Han Miaomiao[1,2] Zhao Libing[1,2]

[1]College of Mining Engineering, Hebei United University, Tangshan 063009,Hebei,China;

[2]Mining Development and Safety Technology Key Lab of Hebei Province, Tangshan 63009, Hebei, China;

[a]tsliangbing@126.com

**Key word:** hematite, griding aids, griding efficiency, mechanism of action

**Abstract:** In this paper, the effect of citric acid on the hematite was studied and the mechanism was analyzed. The results indicated that under the condition of the optimal grinding medium, compared with the result without citric acid added, with citric acid added at the mass of 0.10% of the hematite, the content of -0.074mm of grinding production was increased by 7.11%; physical adsorption and chemical adsorption which were on the surface of hematite produced by citric acid can reduce viscosity of grinding pulp, change surface potential of the hematite, and reduce the hardness on the surface of the hematite. Therefore citric acid can improve the grinding efficiency of the hematite.

Our country can use in industry of the iron ore types, including hematite ore accounted for 18%, mainly occurs in the sedimentary type, weathering leaching type and metamorphosed sedimentary type, and the volcano intrusive activities related to iron ore deposits, which belongs to the refractory mineral, mainly distributed in Liaoning, Hebei, Hubei, Hunan, Sichuan and Inner Mongolia province (area). The characteristics of China's hematite ore is: large reserves, low grade, fine particle size distribution, complex composition, mineral processing technology economics etc.

Because of the ore of fine-grained dissemination, in the -0.01mm grade, hematite accounted for 36%, -0.02mm accounted for 54.6%, and the gangue minerals quartz, biotite and clay minerals is more, grinding process prone to mud, therefore, plays an important role in grinding process.

This article with citric acid as the grinding agent, with reserves of 2.3 billion a hematite in Hebei province as an example to carry out the fine grain of lean hematite grinding efficiency, combined with grinding pulp viscosity, hematite surface potential index and the characteristics of adsorption mechanism of grinding aid are studied.

## Test materials and test methods

### 1.1 Preparation and properties of the sample

Hematite ore sample used in the test taken from Hebei LuanXian Sijiaying iron ore plant. Broken to below 2 mm, the sample after smashing blending division, a per 1kg, for subsequent grinding test and study.

#### 1.1.1 Multi-elementanalysis of ore

Table 1 Ore multi-element analysis (%)

| Element | TFe | FeO | $SiO_2$ | CaO | $Al_2O_3$ | MgO |
|---|---|---|---|---|---|---|
| Content(%) | 29.14 | 4.04 | 46.63 | 0.89 | 2.12 | 1.46 |
| Element | S | P | $K_2O$ | $Na_2O$ | MnO | $TiO_2$ |
| Content(%) | 0.083 | 0.053 | 0.41 | 0.086 | 0.090 | 0.073 |

According to the analysis results, the iron grade of 29.14%, the main impurity in the ore is $SiO_2$ and $Al_2O_3$, followed by MgO and CaO, S and P content is relatively low. $(CaO+MgO)/(SiO_2+Al_2O_3)=0.048 < 0.5$ for the acid ore.

**1.1.2 Phase analysis of iron ore**

Table2 Ore iron phase analysis results(%)

| Mineral name | Fe of magnetic minerals | Fe of Hematite, limonite iron minerals | Fe of iron carbonate minerals | Fe of iron silicate minerals | Fe of iron sulfide minerals | Total Fe |
|---|---|---|---|---|---|---|
| Content（%） | 6.34 | 22.09 | 0.35 | 0.05 | 0.12 | 29.14 |
| Iron distribution rate（%） | 21.32 | 75.66 | 1.20 | 0.15 | 0.45 | 100.00 |

The analysis result shows that full iron phase the sample average is 29.14%, compared with normal selected ore grade is high, but the deviation is small. Useful iron mineral in ore are mainly hematite and limonite iron minerals, the iron distribution rate was 75.66%, followed by the distribution of the magnetic iron accounted for 21.32%, the sum of hematite, limonite iron and magnetic accounts for about 96.98% of the iron, the ratio of other iron minerals is smaller, the content of iron carbonate accounted for 1.2% and also contains a small amount of iron sulfide and iron silicate.

**Effect of citric acid on the grinding efficiency**

Mill test specifications for XMQ-67 type 240×90cone ball mill, the effective volume of 6.65L.

Experimental grinding agent is anhydrous citric acid, also known as folic acid. The molecular formula is $C_6H_8O_7$. At room temperature, citric acid is a colorless transparent crystal or white granules or white crystalline powder, odorless, slightly deliquescent in wet air.

A lot of experiments and Optimization testing in the early, to determine the best ratio of steel ball medium in the grinding process is Φ31mm: Φ26mm: Φ19mm=12.18%: 26.00%: 62.98%, material ball ratio is 1.20, the grinding time is 3min. Each test selection of testing sample is 1kg.

**2.1 Reagent dosage and concentration test**

Experiments were carried out in citric acid grinding concentration each difference of 10%, get a reagent dosage and the grinding efficiency, the specific relationship as shown in figure 1.

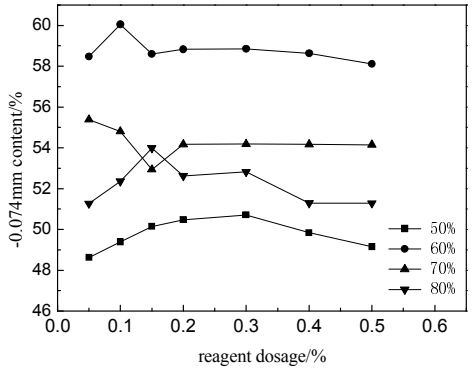


Fig. 1 The relation of amount of citric acid and -0.074mm content of products

We can see from Figure 2, under different concentration, amount of citric acid corresponding to -0.074mm content of products is different. At the concentration of 50%, the grinding efficiency as been gradually increases and increases to a maximum at0.05%~0.3%, but the grinding efficiency is 2.22% lower than no dosing, therefore low concentration is not suitable for grinding. At the

concentration of 60%, the amount of reagent concentration of 0.1% reached the maximum grinding efficiency, grinding mineral content increased in -0.074mm 7.11% higher than when no dosing, reagent rate between 0.1% ~ 0.15% when its production rate of 0.074 mm trend is flat and slightly lower. At the concentration of 70%. When the grinding concentration is 80%, adding agent has no grinding effect, but inhibited slightly. According to the test results, the final determination of citric acid optimum amount is 0.10%, the concentration of 60%.

## Mechanism analysis

### 3.1 Citrate adsorption characteristics of hematite surface

Add citric acid and not add citric acid grinding infrared spectrum diagram as shown in figure 2.

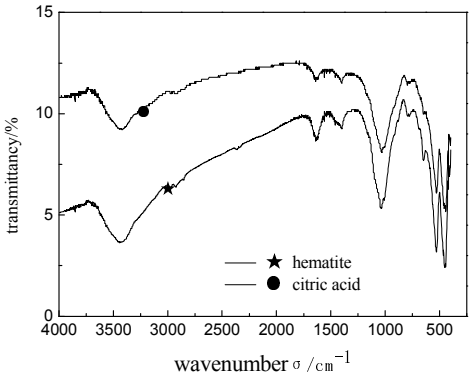


Figure 2 IR spectra of hematite and hematite in presence of citric acid

Solid star infrared spectral curves of hematite, solid round infrared spectrum curve for adding grinding agent hematite. As you can see from Figure 3, the role of micro-fine hematite and citric acid, -OH stretching vibration absorption peak moved from 3431.80cm-1 to 3423.50cm-1, while the peak surface width significantly, indicating the possible formation of hydrogen bonds, the chemical adsorption, adsorption layer is formed on the mineral surface, increases the space repulsion. The characteristic peak of 2975.58cm-1 move to 2967.28cm-1, the characteristic peak of 1635.94cm-1 move to 1631.80cm-1, the characteristic peak of 1403.69cm-1 move to 1399.54cm-1 and the characteristic peak of 1034.56cm-1 move to 1026.27cm-1, this shows the effect of hematite and citric acid, the surface has a physical adsorption or chemical adsorption, reaction with the metal cation generated hydrophilic group, enhanced the dispersion of suspended particles in the pulp, and then to reduce the effects of pulp viscosity.

### 3.2 Effect of citric acid on the viscosity of the slurry

The amount of citric acid is not at the same time, the change of pulp viscosity as shown in figure 3.

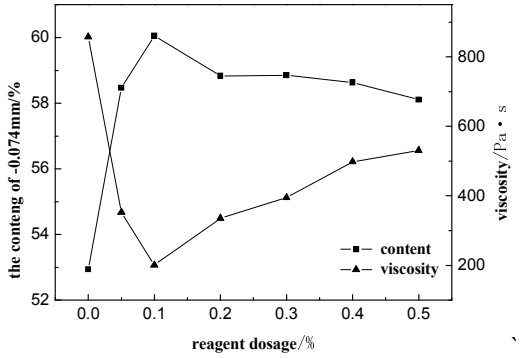


Fig.3 The influence of the citric acid on the viscosity and the -0.074mm content

As can be seen from the figure 4, the changing rule of the slurry viscosity is inversely proportional to the rate of mineral grinding. The viscosity of the slurry itself is 857.5 Pa·s. When the citric acid 0.05%, pulp viscosity decreased rapidly; When increase the amount of citric acid to 0.1%, the viscosity of pulp reached a minimum limit of 201.7 Pa·s; Then continue to increase the amount of citric acid, slurry viscosity is rising trend but not growth. Also can be seen, the addition of citric acid increased from 0.2% to 0.5%, the slurry viscosity change a little. Through the comparison of the two map, can determine the viscosity of the slurry and the grinding efficiency is a certain link under certain conditions, reduce the slurry viscosity is beneficial to improve the grinding efficiency of mill at high concentration.

**3.3 Effect of citric acid on pulp potential**

Hematite and joined citric acid hematite surface potential changing with the solution pH value as shown in figure 4.

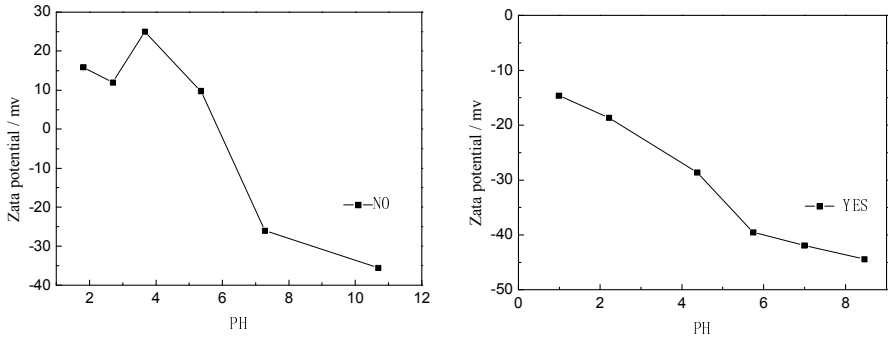


Fig.4 Relationship between before and after adding citric acid surface potential of hematite and the pH value of the solution.

As you can see from Figure 5, naturally the microgranular hematite pH value is 6.9. When adding agen, the matite electric potential from -26mV decreased to -73mV, negative ζ zeta potential of mineral surface is higher, particle electric potential absolute value is larger, strengthened the mutual repulsion between particles, enhanced the dispersion of suspended particles in the pulp, prevented re-condensation of the particles after crushing and mineral adhesive to barrel wall and so on. This is consistent with the previous slurry viscosity experiment, the dispersion strengthening, its relative pulp viscosity decreases, the flow becomes strong, reduce the grinding effects between particles.

**Conclusion**

Due to the Hebei area have more Anshan type hematite ore, its main characteristic is the dissemination size is fine, dissociation is difficult, so the grinding aid is one of the effective measures to improve the grinding efficiency and reduce the energy consumption of grinding.

In the process of hematite grinding using citric acid. In the optimal experimental conditions, add the equivalent of hematite mass fraction 0.10% citric acid compared with no added, can make the content of 0.074mm in grinding increased by 7.11%.

Citric acid form hydrogen bond on surface of hematite, the physical adsorption and chemical adsorption, reducing the grinding pulp viscosity, changed the potential on the surface of the hematite, reducing the hardness on the surface of the hematite. Through the above factors work together, to improve the grinding efficiency of hematite.

This research is funded associated research and development on key technology of Highly Efficient Recovery of Micro-fine low hematite（2012DFr70320）

Supported by the scientific research fund project of Hebei United University. (serial number: Z201301)

Supported by Hebei Province Natural Science Fund project. (serial number: E2013209308)

**References**

[1] Gao Tai, Guo Xiaofei, Yuan Zhitao, etc. Application and Development Tendency of Beneficiation Technology of Hematite in China[J]. Metal Mine, 2010 (8): 97-101.

[2] Liu Jie, Zhou Mingshun, Zhai Liwei, etc. Present status of China's complex refractory iron ore studyJ]. China Mining, 2011(5): 63-67.

[3] Zhu Yiming, Han Yuexin, Wang zehong, etc. Selective Grinding of Low Grade Bauxite in Ball Mill Grinding [J]. Metal Mine, 2009(6): 60-64.

[4] Wang Zehong, Xu Chang, Li Guofeng. Study on Increasing the Grinding Efficiency of the Oolitic Hematite from Western Hubei Province with Sodium Hexametaphosphate[J]. Metal Mine, 2013(5): 71-74.

[5] Li Maolin, Wang Bin, Zhu Yong, etc. Influence of grinding aids on grinding of the high phosphorus oolitic hematite from western Hubei Province [J]. Journal of Wuhan University of Science and Technology, 2011(2): 93-96.

*Applied Mechanics and Materials Vols. 580-583 (2014) pp 2550-2553*
*© (2014) Trans Tech Publications, Switzerland*
*doi:10.4028/www.scientific.net/AMM.580-583.2550*

# Rapid Excavation Technical Research of Blasting Mining Face in Liangzhuang Mine

Zhengbin Yan[1, a], Xiao Xu[1, b], Taotao Li[1, c], Shang Wu[1], Shiyan Ma[1]

[1]School of mechanics & civil engineering, China University of Mining and Technology (Beijing), Beijing, 100083, China

[a]xuehuajun7792@163.com, [b]xuxiaobull@163.com, [c]561295407@qq.com,

**Keywords:** Blasting face, Drive speed, Blasting parameters, Air column interval charging structure

**Abstract:** The paper studied the driving blasting mechanism and blasting parameters in working face, in order to improve the advance rate of blasting mining face in Liangzhuang mine. The research results show that taking the air column interval charging structure can reduce the peak pressure on the borehole wall, change the distribution ratio of explosion energy, decrease the smash district radius and increase the effect of secondary stress wave. To improve the energy utilization efficiency was improved in this structure, the consumption was reduced by 35.3%, the cyclical footage from 0.8m to 1.2m and crushing effect is obvious.

## Introduction

In mining engineering, almost all ore are cutting and crushing with blasting method and blasting operations account for almost 1/4 ~ 1/3 of the whole production operation cycle. In mine exploiting, the basic tunneling method is utilizing blasting excavation [1-2]. In order to speed up the advance rate of coal rock roadway, deep hole blasting method was adopted in coal seam roadway. Choosing a good cut blasting parameters, determining the loose circle, improving the utilization rate of perforation and decreasing unit consumption are became increasingly important [3]. In this paper, the scope of the demolition loose zone was determined and explosive energy was used efficiently through researching the blasting theory and blasting parameter, obtaining a good blasting effect in field industrial test.

## Engineering situation

The test coal seam was located in Liangzhuang Mine 11310 working face of Xinwen mining area, occurrence condition of the thirteenth layer coal is relatively complex, immediate roof of roadway is four gray, basic roof are four ash and sandstone, direct floor is fine sandstone and the coal bed is silty sand rock. The coal seam entrained the unequal thickness coal gangue and some places also mingled with relatively hard pebbles, physical and mechanical parameters of coal and coal gangue are shown in Table 1.

Due to the impact of these factors, in Liangzhuang Mine, production difficulty of the thirteen coal layer mining faces is large; Hole utilization rate is low, the arrangement is unreasonable, the unit explosive consumption is high and circulating footage is small. It also increase the workers' labor intensity and reduce the output of coal. According to the basic conclusion of theory analysis and laboratory model test, this paper puts forward a set of effective feasible blasting parameters, which is on the basis of a large number exploratory industrial test from the hole diameter and hole arrangement. It is also in view of the complex coal seam with coal gangue. By adopted the parameters, it is improved the production process, the construction speed and quality, achieving the high yield and efficiency goal of thin coal seam.

Table 1 Physical and mechanical parameters of coal and coal gangue

| | Bulk density $\rho$(kg/m$^3$) | Compressivestrength $\sigma_t$(MPa) | Tensile strength $\sigma_t$(MPa) | Elastic modulus E(MPa) | Poisson ratio $\mu$ | Internal friction angle(°) | Cohesion c(MPa) | P wave propagation (m/s) |
|---|---|---|---|---|---|---|---|---|
| Coal | 1470 | 11.3 | 2 | 2800 | 0.30 | 17 | 1.6 | 1380 |
| Gangue | 2600 | 63.7 | 5 | 12000 | 0.25 | 32 | 12 | 2150 |

Note: in order to describe the convenient, original blasting scheme called "plan 1", the improved blasting scheme called "plan 2".

## Experimental method

The field experiment is using coal blasting method, known as blasting mining, which is a common coal drop method in coal mine. It can be applied to all kinds of complicated geological changing conditions. The manufacturing process of coal blasting method includes drilling, charging, plugging and shooting. In order to ensure the safety in production, improve the effect of coal drop, cut down the consumption of materials and get the appropriate blasting fragmentation, it should make coal drop to transport as much as possible and improve the loading rate of blasting, trying to increase the number of each blasthole to save time. At the same time, decorating blasthole and charge weight reasonably and reducing the consumption of explosives and detonator, which are also important.

## The original blasting technical scheme

**Blasthole arrangement.** Blast hole arranged three blossom cup. The layout diagram of blast hole in working face is shown in Fig. 1. The blast hole parameters as shown in Table 2.

Table 2 Blast hole feature table

| Names | Hole-space(m) | Location | | Angle | | Hole depth (m) | Charge weight (kg) |
|---|---|---|---|---|---|---|---|
| | | From the bottom (m) | From the top(m) | Elevation, depression (°) | Level(°) | | |
| Up hole | 0.8 | 1.2 | 0.3 | 10~15 | 85 | 1.3 | 0.6 |
| Down hole | 0.8 | 0.3 | 1.2 | 10~15 | 85 | 1.3 | 1.1 |

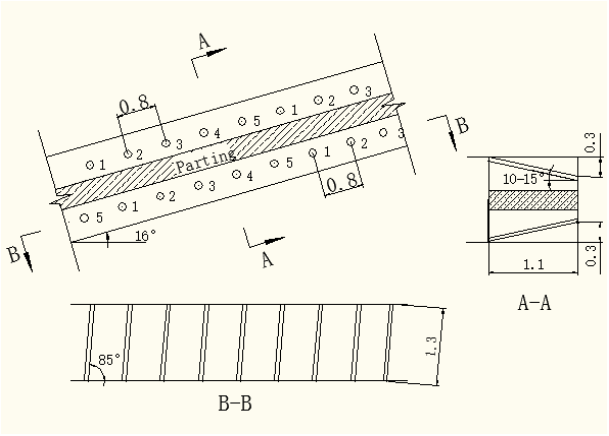


Fig. 1 Original hole layout Unit: m

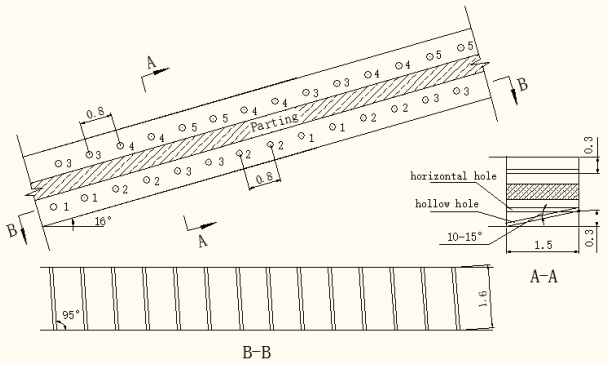


Fig. 2 Optimizing perforation plan Unit: m

**Blasting method.** Using SMZ - 1.2 portable electric drill to drill and choosing wet drilling type, diameter of the hole is φ42, the depth is 1.3m and row spacing is 0.8m. Using φ36 cartridge emulsion explosive and 1~5 millisecond delay electric detonator blasting, taking the positive charge structure series shooting. Set the explosive used water mud blast and mud blast, each charge is 25 explosives and each charging needs one-time initiating.

**Calculation of specific charge.** With each 10.0m is a unit of length calculation, hole for counting formula is N=0.5L/a. Computing available: a total of the up and down two rows is 25 blasthole, which under each row has 12.5 holes on average. The table 2 shows that each hole charge of the up row is 0.6kg, each hole charge of the bottom row is 1.1kg, a total of 21.25kg. Within the unit length blasting volume is 16.5m$^3$. Consumption calculation formula of the blasting is q=M/V, type: q-optimal charge quantity, kg/m$^3$, M-total drug consumption, kg, V-the original rock blasting volume, m$^3$. The practical unit consumption of blasting scheme is 1.288 kg/m$^3$.

The specific charge of underground caved ore related to many factors, such as ore property, explosive performance, mining amplitude width, blast hole diameter and blast hole depth. In general, the narrower the amplitude width is, the deeper the blast hole is, and the larger the specific charge is. The physical and mechanical parameters of the thirteenth coal and coal gangue as shown in Table 1. It can be seen that the universal applicable coefficient f are less than 8, so this plan remains to be improved.

**Blasting effect.** Based on field monitoring, the average circulation blasting footage is around 0.8m, the rate of residual eye is up to 39% after the blasting, and explosives consumption is relatively high (1.288kg/m$^3$) and the rate of prop wrecking is 36%, coal toward the direction of the gob throw excessive, thus increasing the labor intensity, material costs, labor-consuming, and time-consuming, not to mention efficient production.

## Test on Optimization of Blasting Parameters

**Problems.** Through field condition and the observation and analysis of blasting effects, in order to increase production and efficiency, to achieve the purpose of high-yield in thin seam, the major problems working face need to be resolved include: improve circulation footage; control throwing volume; reduce consumption of explosives.

If the top and the bottom eye explosion at the same time, the charge weight is proportional to the displacement of conveyor and the number of Collapse down pillars, in order to improve circulation footage and control the amount of coal drop, The general practices to achieve the goal are increasing the free surface, reducing consumption and improving explosives utilization ; using loose blasting, full use of explosives energy and prolong explosive stress wave and duration of action of coal will play a good role. The program intends to optimize the axial direction of linear charge, blast hole space, initiation sequence, the air column interval and so on.

**Test Scheme.** On the basis of exploratory tests, through comparative analysis, we began a formal test after obtaining obvious results. Through theoretical analysis and lots of experiment groping, summed up the blasting parameters suitable for thirteenth layer coal of Liangzhuang mine, as shown in Table 3.

Table 3 Blast hole feature table

| Names | | Hole space(m) | Location(m) | | Angle(°) | | Hole depth (m) | Charge weight | |
|---|---|---|---|---|---|---|---|---|---|
| | | | From the bottom | From the top | Elevation, depression | Level | | Vol | Kg |
| Up hole | 3#,5# | 0.8 | 1.2 | 0.3 | 0 | 95 | 1.6 | 3.0 | 0.6 |
| | 4# | 0.8 | 1.2 | 0.3 | 0 | 95 | 1.6 | 2.5 | 0.5 |
| Down hole | horizontal | 0.8 | 0.3 | 1.2 | 0 | 95 | 1.6 | 4.5 | 0.9 |
| | hollow hole | 0.8 | 0.3 | 1.2 | 10~15 | 95 | 1.6 | 5.0 | 1.0 |

In order to fully utilize the energy blast, at the bottom and top of blast hole, respectively, plus set an "empty pipe" to achieve the air column spacing, the length according to the nature of the coal seams, according to the nature of the coal mine, take the air column length of 0.1 ~ 0.15m. Use emulsion explosives Φ36 drug volume produced by Xinwen Mining Bureau and use of 1 to 5ms extension segment given electric detonators guns blasting, Dan arrangement is shown in Fig. 2. Fig. 2 shows that it is a positive charge, shooting series.

**Explosives consumption calculation.** Referring 4.3 formula to calculate the length of 10.0m as a unit, there were two rows up and down the borehole 25, both the up hole and the down hole has 12.5.Within 10m range of total drug 18.75kg. Within 10m range blasting volume of 22.5m$^3$, blasting consumption is 0.833kg/m$^3$. Explosives consumption value within the allowable range.

**Test results.** After a number of experiments, by improving existing technology and blasting parameters, and gradually expand the scope of the experiment, and achieved remarkable results, explosives consumption to reduce 0.455kg/m$^3$, and is within the allowable range. Circulating footage reached 1.2m, a 12% reduction in the collapse of the pillars, coal toward the direction of the gob reducing the amount of 80%, well shaped Muck pile, no tentacles, no nose, no residual eye, made a good technical and economic benefits.

## Conclusion

Experimental results show that the scheme two is very suitable for this coal seam.

Blasting effect is obvious by using air column interval charging structure. Coal gangue crushing significantly and achieve better crushing effect, reducing the damage to the roof and reducing vibration.

Muck pile has been effectively controlled within the design range. Reducing the workload of shovel coal, reduce labor intensity. Muck pile in tests showed ideal parabolic shape, the whole muck pile move forward, the coal toward the gob decreased by 80%.

Reducing the consumption of explosives. Since changing the charging structure, so that the energy can be effective and rational used, making consumption reduced by 35.3%.

Improved utilization of the embrasure by changing the parameters of the original blasting technology and to improve the utilization of the embrasure, making cycling footage from the original 0.8m up to 1.2m.

## References:

[1] Min Gong, Yalun Yu, Jingwei Tong. Study on the Methods of Analysis for Transient Isochromatio and Isopachic Fringes [J].Explosion and Shock Waves1997, 17(3): 255-261.

[2] Jun Dai, Qi Yong. Researches on Blasting Parameters of Triangle Burn Cut [J]. Explosion and Shock Waves. 2000, 20(4): 364-368.

[3] Yongqi Xu. Coal Mining [M].Xuzhou: China University of Mining and Technology Press, 1991.

*Applied Mechanics and Materials Vols. 580-583 (2014) pp 2554-2557*
*© (2014) Trans Tech Publications, Switzerland*
*doi:10.4028/www.scientific.net/AMM.580-583.2554*

# Numerical simulation study on setting stopping line of working face in Shuguang mine

Huajun Xue[1,a], Jun Chen[1,b], Bo Liu[2,c], Jie Kong[1], Zhijun Hao[1]

[1]School of mechanics & civil engineering, China University of Mining and Technology (Beijing), Beijing, 100083, China;

[2]Beijing Urban Construction Engineering Co. Ltd, Beijing, 100083, China

[a]296504206@qq.com, [b]84157203@qq.com, [c]693170148@qq.com

**Keywords:** Stopping line; Numerical simulation; Security coal pillar; Stability of surrounding rock

**Abstract.** The surrounding rock deformation of pedestrian roadway was serious under the influence of the working face. And it has affected the safety and normal use of roadway. To ensure the long-term stability of the pedestrian roadway surrounding rock and increase the coal recovery rate of working face, the paper studied the position of stopping line of 1203 working face by numerical simulation. The results show that setting 115m wide of security coal pillar between 1203 working face and pedestrian roadway that the area of stress concentration near the working face has less effect on the pedestrian roadway could better control the surrounding rock stability of the pedestrian roadway and meet the need of the long-term normal production use. It narrows the width of security coal pillar, increase the coal resources recovery rate and achieve the better economic benefits.

## Engineering Situation

The length of pedestrian roadway in Shuguang mine which is development roadway of mining area is 1500m and service life is long. And the section shape of roadway is vertical wall-round arch. Since the pedestrian roadway excavation, the surrounding rock has a certain deformation under the influence of the working face. And it has threatened the life safety of workers and affected the normal use of roadway. On the premise of ensure the stability of roadway, the paper studied the position of stopping line of 1203 working face by numerical simulation for lengthening the distance of stopping line of working face, increasing the coal resources recovery rate to achieve better economic benefit.

## Setting Initial Model

**Establish Basic Model.** The selection of FLAC3D model range is directly related to the correctness of the calculation results.Model range is too big, computer energy spent in vain,Otherwise the calculation results will be distorted and cannot give guidance for practical engineering , so it is crucial to choose a reasonable range of the model [1]. According to rock mechanics principle, influence range of stress after roadway driving is about 3 to 5 times the width of the roadway, Considering the size of the roadway, The shape of the pedestrian roadway cross-section is straight wall semicircle, and roadway height 3.5m, width 3.8m, so The length, width and height of the model is 258.2m×10m×86.6m respectively. Once you determine the size of the calculation model,a corresponding number of calculation grid is determined, In the program in order to reduce the error caused by meshing, length-width ratio of grid should not greater than 5, For the key research,the grid can be more intense.To sum up, in order to as far as possible consistent with the the geological condition at the same time, considering the modeling is convenient and reasonable. Model is shown in Fig. 1. And the x-direction is divided into up to 134 mesh, y direction is divided into up to 5 mesh, z direction is divided into 53 grids,A total of 22,320 units. The entire model from top to bottom in turn for sandy mudstone, fine sandstone, mudstone, coarse sandstone, mudstone, siltstone and fine sandstone, siltstone, sandstone, mudstone, fine sandstone, sandy mudstone, fine sandstone, sandy mudstone, fine-grained sandstone, mudstone, 1# coal, silty mudstone, fine sandstone, mudstone,

sandy mudstone, sandstone, 2# coal, siltstone, silty mudstone, 3# coal, shale, siltstone, sandstone, fine sandstone and sandy mudstone, pedestrian roadway located in the 2# coal and sandstone layers.

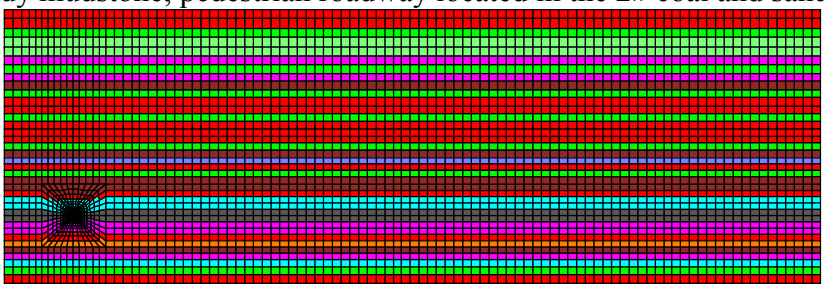

Fig. 1. Initial model

**Select the Constitutive Model.** Constitutive relation of rock and soil is defined by a number of experiments to test small amount of rock, soil elastic-plastic stress - strain curves, and then through the soil plasticity theory and the assumption with certain necessary supplementary conditions, and then promote the results of experiment to the complex stress and composite state to calculate the stress and strain of universal relations; The stress-strain relationship expressed in mathematical expressions, which is called constitutive relation of rock and soil. According to the analysis of rock mechanics, combined with information obtained from the field test, this numerical analysis use Morh-Coulomb constitutive relation

**Generation of Initial Stress.** There is no real force boundary conditions in FLAC3D, stress in the model can only balance stress with gravity stress through stress redistribution. The initial stress field is gravity stress field, and that accord with actual situation of shallow underground projects initial stress field. Main pedestrian roadway of Shuguang Mine and 1203 working face are at depth of -500m. They belong to general underground roadway engineering. The ground stress law is almost same to that of general underground engineering, mainly because horizontal stress is smaller than vertical stress. The initial ground stress field of this kind of project is generated by rock and soil gravity, $\sigma_{zz} = \rho g z$ , $\sigma_{xx} = \sigma_{yy} = \frac{\sigma_{zz} v}{1 \quad v}$. Besides, due to elastic solution, when the system reached equilibrium, yield area does no generate in the rock and soil mass [2-3].

Initial stress of model in this way is shown in Fig. 2. Fig. 2 shows that the vertical stress is about 14.67MPa, and horizontal stress is about 8.56MPa. The result meets with theoretical analysis and field test.

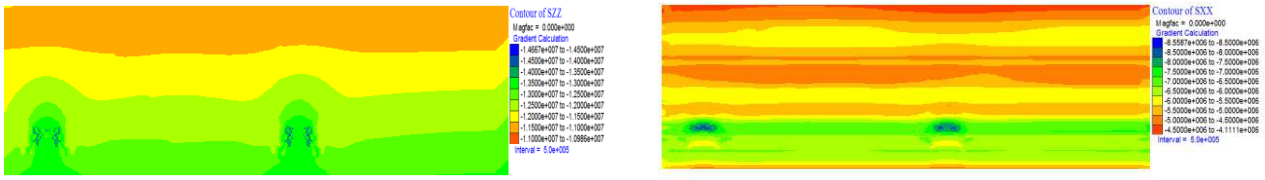


a Vertical stress b Horizontal stress

Fig. 2. Initial stress of model

## Stability Analysis of Main Pedestrian Roadway

Considering the actual geological conditions, the stopping line of 1203# face is differentially set 35, 40, 45, 50, 55, 60, 65, 70, 75, 80, 85, 90, 95, 100, 105, 110, 115, 120, 125, 130, 135, 140m from the main pedestrian roadway in the numerical simulation, so as to confirm best position that feasible for technology and reasonable for economic.

The rock vertical deformation nephogram when the coal pillar set at 115m is shown in Fig. 3. Different color present different deformation and deformation decreased from blue to red. Fig. 3 shows that the roof almost collapses, and maximum roof subsidence of working faces is about 4.2m. The rock deformation section of pedestrian roadway when the coal pillar set at 115m is shown in Fig. 4. After mining stop of 1203#, the surface deformation damage of main pedestrian roadway increased,

the stress concentration area transfers to deep area, especially right side destruction area and degree of damage increase than ever before. Fig. 4 shows that maximum movement of left side is 74.65mm, maximum movement of right side 94.65mm, maximum roof deflection 36.81mm, which is compared to that before stoping, surfaces deformation increase, left side -6.78mm, right side 12.54mm, roof -8.38mm. It shows that working face stoping has greatest influence to right side of main pedestrian roadway.

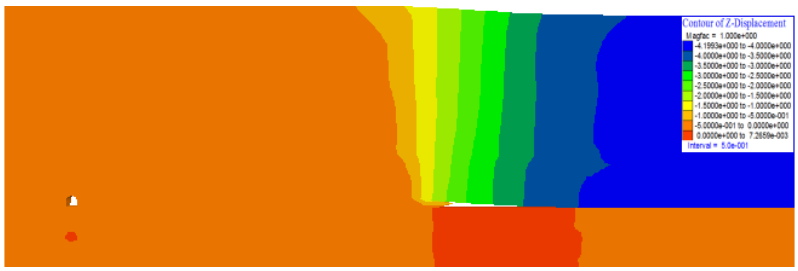


Fig. 3. Rock vertical deformation nephogram when the coal pillar set at 115m

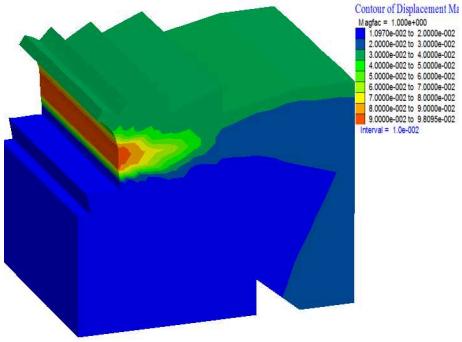


Fig. 4. Rock deformation section of pedestrian roadway when the coal pillar set at 115m

The rock vertical stress nephogram when the coal pillar set at 115m is shown in Fig. 5. Different color present different stress and deformation decreased from blue to red. Fig. 5 shows that the area of stress concentration was formed near goaf due to roof subsidence of 1203 working face. But it has less effect on the pedestrian roadway. The area of stress concentration was in the deep of surrounding rock of roadway sides because the ground stressare mainly vertical stress.

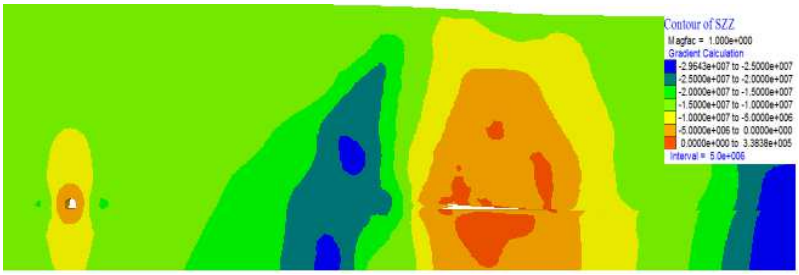


Fig. 5. Rock vertical stress nephogram when the coal pillar set at 115m

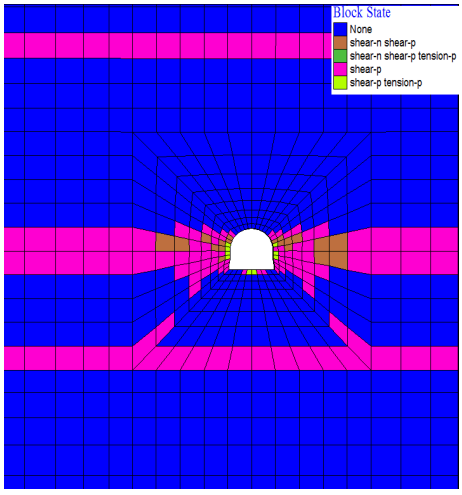


Fig. 6. Rock plastic zone distribution maps when the coal pillar set at 115m

The rock plastic zone distribution maps when the coal pillar set at 115m is shown in Fig. 6. Fig. 6 shows that the surrounding rock stress state in the two sides of roadway is obvious poor to the roof and floor of roadway. The surrounding rock surface of roadway has different degree of tensile failure, including two sides, roof and floor of roadway. The shallow surrounding rock plastic tensile fracture scope increased obvious. And the thickness of tensile plastic zone is about 0.42m. The shear failure area is in the deep of surrounding rock. And the thickness of plastic zone in the floor is 0.42m. The scope of plastic zone is throughout between the sides of roadway and security coal pillar of 1203 working face.

The increase rate of deformation of pedestrian roadway to 1203 working face no stopping when setting different width of security coal pillar after stopping mining of 1203 working face in Shuguang mine is shown in Fig. 7. Fig.7 shows that the pedestrian roadway surrounding rock surface deformation is increased obviously under the influence of 1203 working face mining when the security coal pillar width is less than 75m. And the deformation is reduced in the left side and roof, is

increased in the right side when the security coal pillar width is more than 75m. The deformation in the right side is changed less and the deformation of pedestrian roadway could meet the requirements of production safety. The position of stopping line of 1203 working face could be considered to set at the distance to pedestrian roadway 115m.

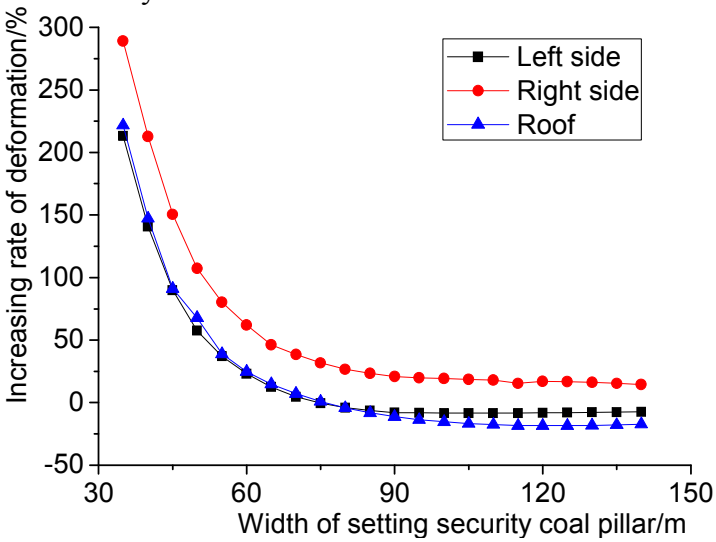


Fig. 7. Increase rate of deformation of pedestrian roadway to 1203 working face no stopping when setting different width of security coal pillar

## Conclusions

Through studying the position of stopping line of 1203 working face by numerical simulation, it shows that setting 115m wide of security coal pillar between 1203 working face and pedestrian roadway that the area of stress concentration near the working face has less effect on the pedestrian roadway could better control the surrounding rock stability of the pedestrian roadway and meet the need of the long-term normal production use. It narrows the width of security coal pillar, increase the coal resources recovery rate and achieve the better economic benefits.

## Author

**The First Author.** Huajun Xue, male, born in 1989, doctor, mainly engaged in Rock and Soil Mechanics scientific research.

**The Second Author.** Jun Chen, male, born in 1990, doctor, mainly engaged in Rock and Soil Mechanics scientific research.

## References

[1] Bo Liu, Yanhui Han. FLAC Principle, Instance and Application Guide [M]. Beijing: China Communications Press, 2005.

[2] Xuebin Li, Huajun Xue, Renshu Yang etc. Design of support parameters of broken and soft rock roadway in deep mine [J]. China Mining Magazine, 2013, Vol.22, No.12: 79-83.

[3] Shuwei Sun, Hang Lin, Lianwei Ren. Application of FLAC3D in Geotechnical Engineering [M]. Beijing: China Waterpower Press, 2011.

*Applied Mechanics and Materials Vols. 580-583 (2014) pp 2558-2563*
*© (2014) Trans Tech Publications, Switzerland*
*doi:10.4028/www.scientific.net/AMM.580-583.2558*

# The research of gas drainage technology in Daning coal mine

Zhongming Zhao[1, a], Gang Wang[1,b]

[1] Shool of Energy Science and Engineering, Henan Polytechnic University, Jiaozuo454000, China

[a]zzm@hpu.edu.cn, [b]774195307@qq.com

**Keywords:** Outburst; Drilling field; Borehole; Gas prsssure; Drainage rate

**Abstract.** 3# coal seam of Daning coal mine is outburst， thus severely restricting the safe production. Based on the analysis of gas emission sources and the logical drainage parameters, firstly, Daning coal mine arranged some drilling fields, then utilized the VLD-1000-type rig to drill boreholes, achieving the integrated gas drainage of the coal seam and goaf. Finally, there is a test on the drainage result. The results showed that, through this kind of integrated gas drainage technology, the highest value of gas pressure in the coal seam reduced to 0.63MPa from 1.95MPa after twelve months' drainage, and the gas drainage rate of the whole mine reached 77.6%, achieving efficient use of gas clean energy.

## Introduction

Every year, gas disasters cause huge casualties and property losses, and it is a long way for the prevention and management of gas disasters. In recent years, the technology of gas drainage has become a major measure for gas control [1-3]. In the mining process of Daning coal mine, the gas emission is up to 25.94 $m^3$/t, which is a typical outburst mine. In order to solve the problem of gas outburst, according to gas condition and development system of the mine system of the mine ,Daning coalmine make a choice that it adopts a integrated gas drainage method used in the coal seam and grob. Based on the rational choice of gas drainage parameters, it uses the world-leading VLD-1000-type drilling machine that can drill a directional one-thousand meters deep drilling to drain the gas of the coal seam and goaf , reducing the amount of gas emission in the mining process , achieving safety and efficient production.

## Mine overview

Daning coalmine belongs to the management of Yangcheng County, Jincheng City, Shanxi Province, located in the region of high gas distribution in the Qinshui coalfield. Consequently, it belongs to the high gas coalmine. At the same time , it is designed to possess the production capacity of 4 million t/a. In the whole coalfield, there are two stable coalseams, 3 # seam of Shanxi group and 13 # seam of Taiyuan group. But, for Daning coalmine, currently it is approved of mining 3 # coalseam. In addition, the average thickness of 3 # coalseam is 4.5m, and for the coalseam roof, it is constituded of siltstone mudstone or sandstone, and for the bottom, it is constituded of shale or siltstone.

The whole mine are divided into five mining districts, and they are under the order of first district, third district, second mining district, fourth and fifth districts. For the mining technology, it adopts fully-mechanized mining and tunneling. Currently, the first mining district is largely finished, and the second mining district is mainly mining object, and the third mining district is under the preparation. When first mining district was mined, the maximum of gas emission reached 25.94 $m^3$/ t, bringing a serious threat to mine safety.

**The performance and applications of VLD 1000 meters rig**

The platform of LID-1000 rig uses a design of crawler-piece, and at the same time it is equipped with AMT, MWD, DGS, MECCA guidance system (MWD directional guidance system). Be based on design requirements of gas drainage, it can achieve a directional drilling with the specified target.

Daning mine uses LID-1000 rig mainly for three applications: (a)the pre-pumping of next coalface, mainly by arranging borehole along coal seam in the ventilation roadway of earlier coalface; (b) the gas drainage of the caving zone above goaf, mainly in the ventilation of the coalface, by arranging face-up borehole to reach the gas gathering zone above goaf; (c) the gas drainage through crossing boreholes arranged in the roof or floor.

**The research of gas drainage methods**

According the analysis of the composition of gas emission in Daning coal mine, the amount of gas emission in the coal seam and goaf is larger than that in the excavation face, and the proportion of adjacent layers is the smallest. As a result, Daning mine chooses a way of integrated gas drainage method that is applied in the coal seam and goaf. The methods of gas drainage in the coal seam are following, including gas drainage of the longwall mining coalface , gas drainage of excavation face, and rock roadway drainage. The methods of gas drainage include semi-enclosed gas drainage of goaf and fully enclosed gas drainage of goaf [4].

**Methods of gas drainage in the coal seam.**For the long-wall coalface, there are two types of gas drainage methods that one is draining gas with no-relief( pre-pumping ) and the other is draining gas while mining. Within the range of underground mining, regarding mine development and mining districts, some drilling fields in the tailentry of $3^{\#}$ coalseam should be arranged to vertically fix up directional drilling boreholes into next coalface and developing roadway , and this kind of pre-pumping should be finished before next coalface is mined. At last ,there is a test on the result of pre-pumping. When the result meets the demend, the coalface can be mined. Drainage is continuously carried on while the mining is doing, thus increasing the rate of gas drainage , reducing the amount of gas emission, forming the gas drainage plan of coalface. The arrangement of drainage is shown in Figure 1.

Boreholes along the tailentry of earlier mingning face are arranged to conduct pre-pumping of development roadway in next mining face. At last ,there is a test on the result of pre-pumping, then when the result meets the demend, the roadway can be excavated. It is shown in Figure 1

When there is a rock roadway above or below the seam , drilling field are arranged in the rock roadway, then make use of one-thousand meters rig to carry out gas drainage of coal seam by crossing boreholes. This method is shown in Figure 2.

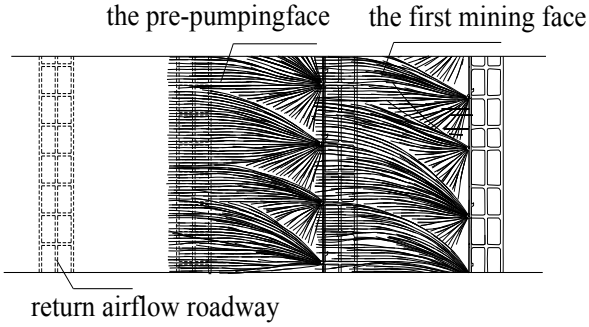


Fig. 1 The gas drainage of the coal seam

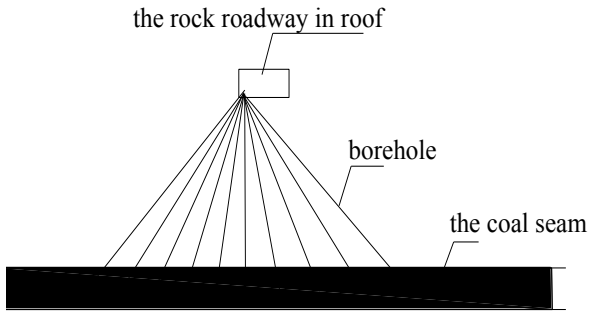


Fig. 2 The gas drainage by rock roadway

**Methods of gas drainage of goaf.** According to the condition of goaf, methods of gas drainage vary, and mainly can be divided into gas drainage of semi-closed goaf and gas drainage of closed goaf.

semi-closed goaf is that it is behind the mining face and continuously exsits with the advance of mingning face. In addition, with the continuous mining, the range of semi-closed goaf is increasing. Since this kind of semi-closed goaf is connected to the ventilating network, with the difference of

ventilation pressure, gas originating from all aspects is flowing into the goaf, then is exhausted through return air. When the amount of gas emission from goaf is larger, the state of gas of coalface up-corner and return air is under overrun level. Especially, when the roof caving causes that the amount of gas is suddenly increasing, it brings a big threat to the safe production.

Therefore, according to the roadway arrangement, there are mainly two methods of gas drainage of semi-closed goaf that one is drilling high-position boreholes above caving zone, and the other is burying drainage pipes. In the term of arranging high-position crossing boreholes above roof, this method is that drilling field are firstly arranged in the ventilation roadway of mining face, then crossing boreholes in drilling field are carried out to capture gas of destroyed zone. In addition, it is also used to drain accumulated gas of goaf [5-6]. This method is shown Figure 3. In the term of burying horizontal excavation pipes in advance, this method is that drainage pipes are embedded before roof cave or conducted in the goaf to drain gas. In order to obtain a better drainage effect, pipes embedded should be designed to have some small holes in the front of the pipes ,and at the same time, these pipes should be located in the zone of higher gas concentration that is above coal seam. This kind of drainage result is not as effective as that of high-position borehole drainage, but the low cost and simple construction. It is shown in Figure 4

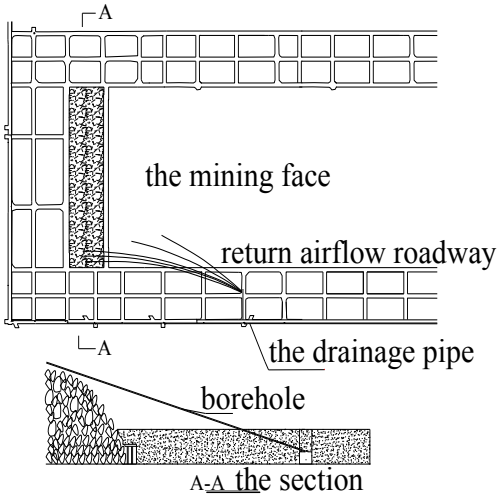


Fig. 3 Arranging crossing boreholes

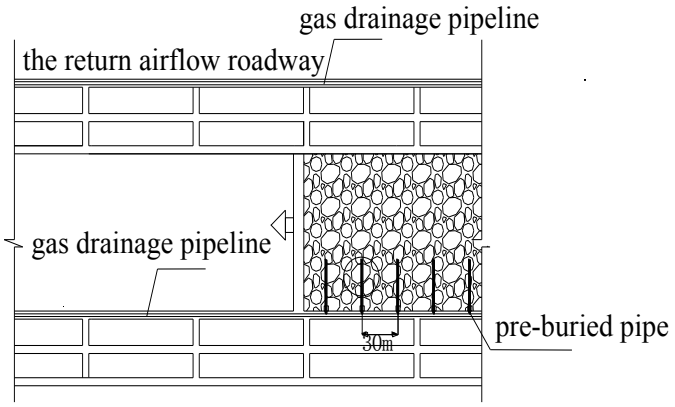


Fig.4 Burying horizontal drainage pipes in advance

closed goaf is that face (or mining area, mine) has completed been mined and is totally closed, also known as the old goaf. Although it is isolated from the ventilation network of whole mine, it is often filled with a lot of high density gas. Gas is still possible to escape out through the crack of isolated coal pillar, thus increasing the burden and unsafe factors to the mining. Daning mine designed a method of making roadway closed to draina gas of goaf. This method is that a hermetic wall is constructed in the roadway to drain gas, with pipes inserting the wall. It is shown in Figure 5.

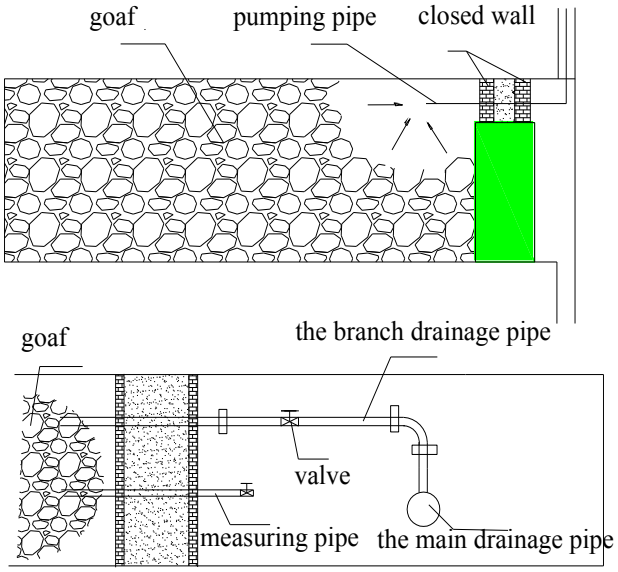


Fig.5 The closed goaf gas drainage

**Determination of drillin field and borehole parameters.** Drilling field should avoid the minging effect and geological tectonic. Meanwhile, it is easily constructed and maintained [7]. And, it should make best use of existing development roadway, preparation roadway, and gateway so that it is easily arranged. For example, drilling fields are arranged in the gateway, and the distance of between them is 120m. Its supporting adopts bolting with wire mesh and cross-section is rectangular with width 5.5m, height 3.8m, and depth 5.5m, as shown in Figure 6.

The main borehole parameters are made of diameter, length, and spacing.

Daning mine applys five sets of VLD-1000-type directional rigs into the use of gas drainage. Drilling method of rig is rotary, and final hole diameter is φ100mm.

Daning Mine utilizes the VLD-1000-type directional rig to obtain boreholes , a longer length. Based on the number of mingning face covered by a borehole, the length of pre-pumping borehole is determined. When the borehole covers a mining face, its length is the sum of mining face length, ventilation roadway width, and transportation roadway width, generally 330-390m. When covering two mining face, the length is generally 650-710m [8-9]. When the roadway in the coal seam is being excavated and the boreholes are arranged along the direction of the roadway, the borehole length is determined by the time of reserved gas drainage. When the roof rock roadway is existed, the length of floor crossing borehole is generally 30-60m, and the end of borehole pass through the floor of coal seam with 0.5m.

The beginning distance of between two boreholes along coal seam is generally 0.4-0.6m, and the terminal distance is 5-8m. The beginning distance of between two roof crossing boreholes or floor crossing boreholes is 0.3-0.5m, and the terminal distance is 3-5m.

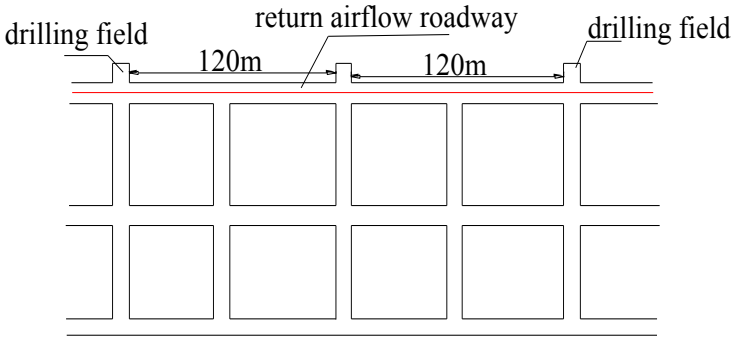


Fig. 6 The drilling field arrangement

## Effect of gsa drainage

**The effect of the coal seam drainage.** In order to analyze the effect of gas drainage, we take 301 full-mechanized mining face as a example. Firstly, some drilling fields in the ventilation roadway of 303 full-mechanized mining face were constructed. Then, boreholes are carried out in the drilling field to drain gas of 301 mining face. Finally, there are a result that after a year's drainage time, gas content of 301 coalface reduces to 7.01$m^3$/t from 17.5$m^3$/t, and gas pressure reduces to 0.63MPa from 1.95MPa. Meanwhile, drainage efficiency of the coal seam is up to 60%. With the changes in drainage time, gas drainage efficiency and gas pressure in the coal seam are shown in Figure 7.

As can be seen from Figure 7, with the extension of drainage time, gas drainage efficiency is progressively increasing, but the growth rate is slower. When the the drainage time reach a year, the drainage rate is up to 60%, and simultaneously the residual gas pressure reduces to 0.63 MPa below outburst value.

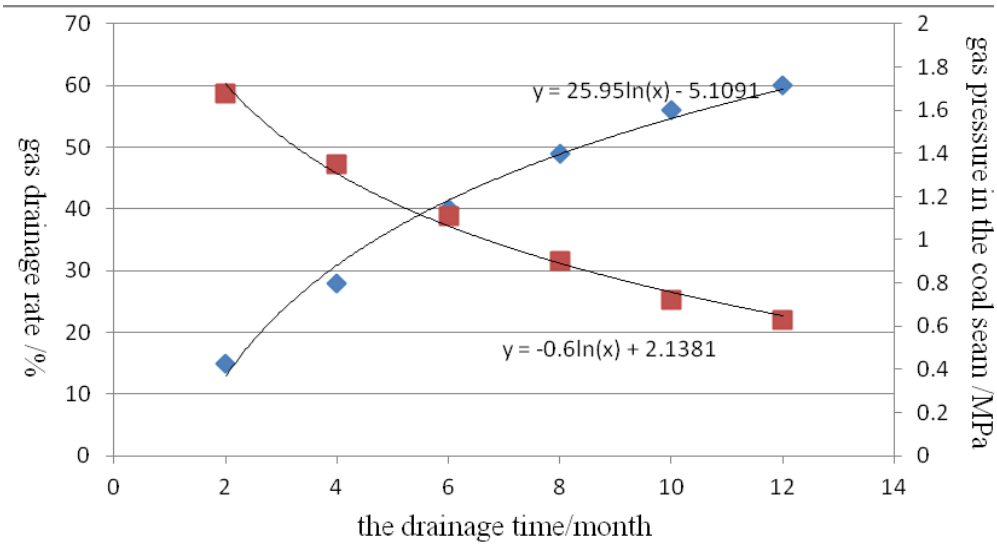


Fig. 7 Gas drainage rate and gas pressure in the coal seam with different drainage time

**The effect of goaf gas drainage.** When the coal face is being mined, large amount of gas will flow out. In this case, Daning mine consider the semi-closed goaf as a critical region where a lot of gas generate. In order to drain semi-closed goaf gas, Daning mine employs two kinds of measures that one is crossing boreholes above roof and the other is burying horizontal drainage pipes in advance. Finally, by monitoring related drainage data, there is a conclusion that the drainage rate in semi-closed goaf is up to 30%. In production, it will produce a lot of closed goaf. If any measure is not taken, safety production will be impossible. As a result, Daning mine determined to construct a closed wall to drainage gas coming from closed goaf. At last, by monitoring drainage data, the drainage rate is up to 25%.

**The effect of the whole mine gas draina.** According to the ventilation report table, by calculating the drainage rate, there is a conclusion that the whole mine drainage rate is up to 77.6%.

The drainage rate formula is,

$\eta=100\%A/(A+B)$

where the value of A is 212.99 and the value of A is 61.31.

## Conclusion

by utilizing the VLD-1000 directional rig to drill boreholes to conduct gas drainage of 301 full-mechanized mining face, after a year's gas drainage, there is a significant effect that the gas drainage efficiency of 301 mining face is 60%, and the coal seam pressure reduced to 0.63MPa, achieving the demand of safe mining. In the semi-closed goaf, by carrying out high-position boreholes above caving zone and burying horizontal excavation pipes, the gas drainage efficiency is 30%. In the

closed goaf, by employing the technology of closed wall, the drainage efficiency is 25%. Obviously, the gas drainage effect is significantly outstanding. By adopting gas drainage of the coal sea and gas drainage of goaf, the drainage efficiency of the whole mine is 77.6%, achieving efficient utilization of gas resources, protecting the natural environment.

**Acknowledgements**

The author would like to thank Prof. Longzhou Fu of Energy Science and Engineering of Henan Polytechnic University for his generous support.

**References**

[1] Tiegang Zhang. Gas control technology for coal mine [ M] . Beijing: Coal Industry Press, 2001. (in Chinese)

[2] C.J. Bibler, J.S.Marshall, R.C.Pilcher. Status of worldwide coal mine methane emissions and use [J]. International Journal of Coal Geology, 1998 , 35: 283-310.

[3] M.L.Ogilvie.Gas in Australian underground coal mines [J]. Mining Engineering,1995,47(1):50-52.

[4] Liang Yuan. The technique of coal mining and gas drainage by roadway retaining and borehole drilling [J]. Journal of China Coal Society, 2008, 33( 8) : 898－902. (in Chinese)

[5] Liang Yuan , Hua Guo, Baotang Shen. Circular overlying zone at longwall panel for efficient methane capture of muctiple coal seams with low permeability [J]. Journal of China Coal Society, 2011, 36. (in Chinese)

[6] Huatai Wu. Study and practice on technology of three-zone linkage 3D coal bed methane drainage in coal mining area [J]. Journal of China Coal Society, 2011, 36( 8): 1312-1316. (in Chinese)

[7] Zhaofeng Wang, Tian Fuchao Tian, Zhao Bin Zhao,et al. The testing of gasdrainage efficiency about feather-veined 1 000 m length-drill hole [J]. Journal of China Coal Society, 2010, 35( 1) : 76-79. (in Chinese)

[8] Minggao Qian, Xiexing Miao, Jialin Xu, et al. Key strata theory in ground control[M]. Xuzhou: China University of Mining and Technology Press, 2003. (in Chinese)

[9] Baiquan Lin, Qingzhao Li, Wei Yang, Haijin Wu, Zhiyong Hao. Gas control technology and applications for the three-soft coal seam based on VLD-1000 drilling systems [J]. Journal of China Coal Society, 2011, 36( 12): 1968-1973.(in Chinese)

# CHAPTER 11:

# Disaster Prevention and Mitigation

*Applied Mechanics and Materials Vols. 580-583 (2014) pp 2567-2571*
*© (2014) Trans Tech Publications, Switzerland*
*doi:10.4028/www.scientific.net/AMM.580-583.2567*

# Analysis on Wind-induced Vibration of Tall Buildings in Hilly Terrain

Yi Sun[1, a], *Nuan Deng[1,b] and Zhengliang Li[2,c]

[1] School of Civil Engineering and Architecture, Chongqing University of Science and Technology, Chongqing, China

[2] School of Civil Engineering, Chongqing University, Chongqing,China

[a]sunyi_cqust@163.com, [b]dengnuan@163.com, [c]lizhengl@hotmail.com

**Keywords:** Hilly terrain, Tall buildings, Wind-induce vibration, Wind tunnel test, Wind speed.

**Abstract.** The responses of tall buildings under wind loads in hilly terrain are remarkably different from that in flat terrain. Wind load codes can't work efficiently or directly to calculate the wind-induced vibration of tall buildings in hilly terrain. Utilizing some wind tunnel test results of wind field in hilly terrain and pressures on tall buildings, the access to response of tall buildings on hilly terrain were provided. Some effects from hill characteristics to building responses were discussed.

## Introduction

As the development of metropolis in hilly terrain, wind-induced vibration of tall buildings in hilly terrain is becoming notable by structural engineering. In most design code, wind load of tall building was derived from vertical profile of mean and fluctuating wind in atmospheric boundary layer, which cannot be applied to hilly terrain directly. Many codes specify hilly terrain correction factors, but only mean wind was concerned while fluctuating wind was ignored.

In order to get wind-induced response of tall buildings, the characteristics of wind filed in hilly terrain must be get first. From 1970s, Jackson [1], Taylor [2], Weng [3], and so on carried out some wind tunnel tests and computational simulations to study mean wind velocity in hilly terrain. In these studies, some formulae to calculate wind velocity in hilly terrain were acquired. Some wind tunnel test researches about tall buildings in hilly terrain were finished. In these researches, mean and fluctuating wind velocity model and wind load spectrum model of tall buildings in hilly terrain were obtained.

In this paper, based on researches of wind tunnel test [4-5], wind-induced responses in along-wind and across-wind direction of tall buildings were calculated in frequency-domain calculation. Some relationship between hill parameters and wind-induced response were discussed.

## Wind tunnel tests

*Tests on wind filed in hilly terrain* [4]

A series of hill models, including different slope and height, were made to get wind field in hilly terrain. In each model, wind velocity in different location and height were get and analyzed. The characteristics of wind field in hilly terrain were discussed, which provide basic conditions to get wind load on tall buildings

The tests were carried out in wind tunnel F-11 in China Aerodynamics Research & Development Center. The size of cross section is 1.4m×1.4m. A pressure measurement system was utilized to probe fluctuating wind velocity in hilly terrain. The cosine model was take to make the hill outline. The scale ratio was 1:1000. Totally, 10 models, with height from 50 m to 200m, were made. Fig. 1 shows a case of test.

After these tests, wind field characteristics in hilly terrain were get. Furthermore, computing method of mean and root-mean-square velocity of fluctuating wind were raised, which becomes the foundation of wind load calculation of tall buildings in hilly terrain.

***Tests on wind load on tall buildings***

A series of wind tunnel test were carried out on wind pressure on tall buildings. Mean and fluctuating wind load of tall buildings on each direction was obtained. In this approach, wind load of any tall building in hilly terrain could be got.

Totally 9 models of tall building were made, including different cross section, height-to-width ratio and width-to-thickness ratio. The scale ratio was 1:500. Mean and fluctuating wind load in every layer of tall buildings can be calculated by integration of wind pressure from 220 pressure holes in surface of models. Fig. 2 shows a tall building model in wind tunnel.

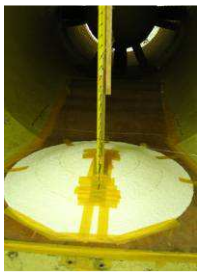

**Fig. 1 Wind tunnel tests on wind field in hilly terrain.**

**Fig. 2 Wind tunnel tests on pressure on tall buildings.**

## Basic assumptions and algorithm in frequency-domain

***Basic assumptions***

(1) No coupling existed in 3 modes of vibration.

(2) Only first mode of vibration was taken into concern in caclulation. Ye Feng 6 made discussion on influence from number of modes of vibration to background and resonant responses. The results showed that calculations only from the first mode could make the results accurate enough.

(3) The first mode of vibration in each direction was linear. Vickery 7 believed that although the actual mode may far away from linear, the error from mode was usually limited to 1%~3%. By this reason, affection from nonlinear mode might be ignored.

(4) Assumptions of coherence function of wind loads in every direction. Coherence function of fluctuating wind velocity was taken to be coherence function of wind load in along-wind direction. Coherence function of vortex shedding was taken to be coherence function of wind load in cross-wind and torsional direction 8. The coherence functions is given by

Along-wind direction:

$$\mathrm{coh}(z_1, z_2, f) = \exp\left(-7f\frac{|z_1 - z_2|}{U}\right) \tag{1}$$

Cross-wind and torsional direction:

$$\mathrm{coh}(z_1, z_2, f) = \exp\left(-f\frac{|z_1 - z_2|}{HL_w}\right) \tag{2}$$

where $z_1$ and $z_2$ are height of two layers, and f is frequency, and U is the mean value of mean wind velocity of 2 layers, and H is height of a building, and Lw is the ratio of size related to vortex shedding to typical width of structures, which could be 1 usually.

***Calculation steps of wind-induced fluctuating response of tall buildings in hilly terrain***

(1) To determine the mean and fluctuating wind speed profile of the building location in hilly terrain.

(2) To determine wind load of each layer.

(3) To calculate the generalized power spectrum density of wind load, by

$$S^*_{P\alpha}(\omega) = \frac{1}{H^2}\sum_{i=1}^{m}\sum_{i'=1}^{m} S_{P\alpha}(z_i;\omega)S_{P\alpha}(z_{i'};\omega)\mathrm{coh}(z_i, z_{i'};\omega)z_i z_{i'} \tag{3}$$

(4) To calculate the fluctuating wind-induced response, by

$$\sigma_\alpha(z) = \sqrt{\int_0^\infty \frac{z^2|H_{\alpha 1}(i\omega)|^2 S^*_{P\alpha}(\omega)}{H^2 M^{*2}_{\alpha 1}}d\omega} \tag{4}$$

**Wind-induced responses of tall buildings in hilly terrain**

In this calculation, class of ground roughness was D in Chinese wind load code. The turbulent density profile in height in given by

$$I(z) = 0.1\left(\frac{z}{H_g}\right)^{-\alpha-0.05} \tag{5}$$

Ten different locations were numbered in the Fig. 3.

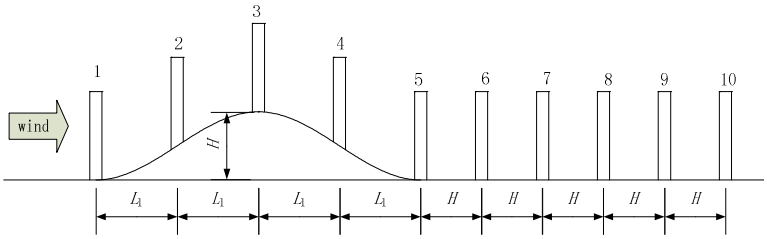


**Fig. 3 Schematic diagram of numbering of location in hills.**

Some other parameters were set as: the building section was square, with 300m high, 60m width and 5s period. The damp ratio of first vibration mode was 0.01 and the reduced density was 190Kg/m$^3$. The wind speed in 10m high was 30m/s, and air density was 1.25 Kg/m$^3$.

***Effect from different slope of hills***

Ten hill models with same height and different slopes were made. The geometry was shown in Tab. 1, where $H$ shows the height and $L_1$ shows the diameter in half height.

**Tab. 1 Geometry of hills of different slopes.**

| | $H$(m) | $L_1$(m) | $H/L_1$ |
|---|---|---|---|
| 1 | 150 | 150 | 1.00 |
| 2 | 150 | 200 | 0.75 |
| 3 | 150 | 250 | 0.60 |
| 4 | 150 | 300 | 0.50 |
| 5 | 150 | 350 | 0.43 |
| 6 | 150 | 400 | 0.38 |
| 7 | 150 | 450 | 0.33 |
| 8 | 150 | 500 | 0.30 |
| 9 | 150 | 550 | 0.27 |
| 10 | 150 | 600 | 0.25 |

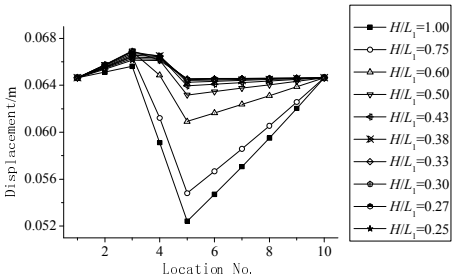


**Fig. 4 Effect of slope of hills on along-wind static response of displacement.**

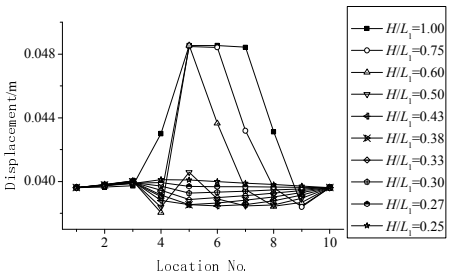


**Fig. 5 Effect of slope of hills on along-wind RMS fluctuating response of displacement.**

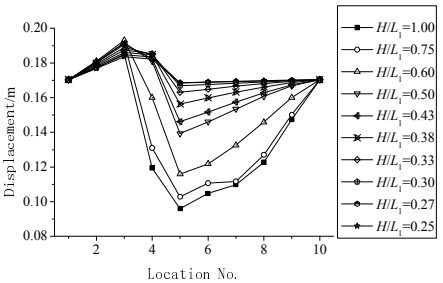


**Fig. 6 Effect of slope of hills on across-wind RMS fluctuating response of displacement.**

Fig. 4 shows the along-wind static response of displacement in the top of tall buildings in different location of different hills. Along direction of wind, the response increases from the hill foot (location 1) in windward side, and reaches to the maximum value at hilltop (location 3). After hilltop, the response becomes to decrease, and get to the minimum value at hill foot in leeside (location 5). After that, the response begins to increase, and recover to be the same with in flat ground (location 1) in location 10.

The speed-up effect is most remarkable in the top, but the maximum speed-up ratio is generated in the height near the ground. With height increases, speed-up ratio decreases rapidly with power law. As a result, speed-up effect doesn't contribute a lot to mean response of displacement.

Fig. 5 shows the along-wind RMS fluctuating response of displacement in the top of tall buildings in different location of different hills.

At the hill top, the fluctuating wind keeps almost the same with in flat ground, while increasing of mean wind contribute little to the generalized wind load and fluctuating response. At the hill foot on leeside, mean wind decreases and fluctuating wind increases. As a result, fluctuating response increases in larger slope hills and decreases in less slope hills.

Fig. 6 shows the across-wind RMS fluctuating response of displacement in the top of tall buildings in different location of different hills. A notable situation is that, the across-wind fluctuating responses are larger than along-wind fluctuating responses.

***Effect from different height of hills***

Four hill models with same slope and different height were made. The geometry was shown in Tab. 2.

**Tab. 2 Geometry of hills of different slopes.**

| | $H$(m) | $L_1$(m) | $H/L_1$ |
|---|---|---|---|
| 1 | 50 | 100 | 0.50 |
| 2 | 100 | 200 | 0.50 |
| 3 | 150 | 300 | 0.50 |
| 4 | 200 | 400 | 0.50 |

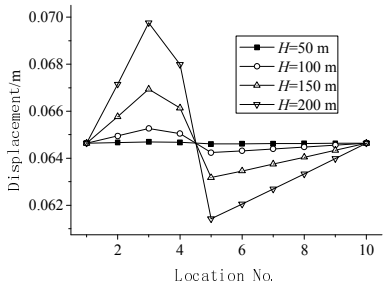


**Fig. 7 Effect of height of hills on along-wind static response of displacement.**

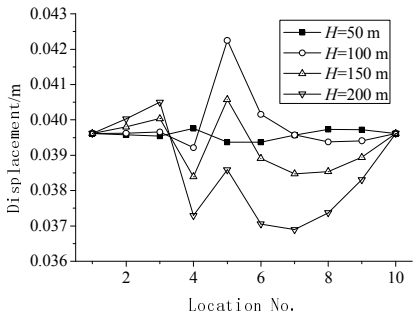


**Fig. 8 Effect of height of hills on along-wind RMS fluctuating response of displacement.**

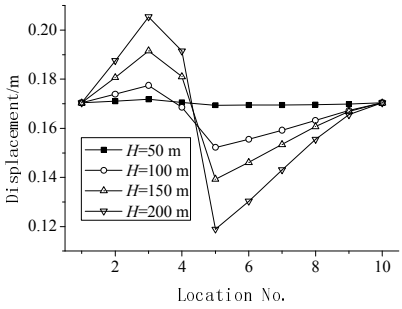


**Fig. 9 Effect of height of hills on across-wind RMS fluctuating response of displacement**.

Fig. 7 and Fig. 8 show the effect of height on along-wind static and fluctuating response of displacement. In hill with low height of 50 m, along-wind displacement of each location keeps almost the same with that in flat terrain. In hill foot of lee side, large fluctuating wind induced to large fluctuating displacement. Fig. 9 shows the across-wind RMS fluctuating displacement, which has the similar shape with the along-wind static displacement.

## Conclusions

(1) Mean and fluctuating wind speed model, wind load model of tall buildings, the Davenport coherence function in along-wind direction and the vortex-shedding coherence function in across-wind and torsional direction could be utilized to get the generalized load spectrum, response spectrum, mean and RMS response of tall buildings in hilly terrain.

(2) In the hill top, small changes of response happen in different slope. In the hill foot of leeside, static response on along-wind direction and fluctuating response on across-wind direction

dramatically reduce with the enlargement of slope, while the fluctuating responses on along-wind increase with the enlargement of slope.

(3) With the height of hill increase, static responses on along-wind direction and fluctuating responses on across-wind direction increase in hilltop and decrease in hill foot of leeside. Fluctuating response on along-wind direction increases notably in hill foot of leeside.

**References**

[1] Jackson,P.S., Hunt, J. C. R.. Turbulent wind flow over a low hill[J]. Quarterly Journal of the Royal Meteorological Society, 101 (1975):929-955.

[2] Taylor, P. A., Lee, R. J.. Simple guidelines for estimating wind speed variations due to small scale topographic features[J]. Climatol. Bull, 18(2) (1984):3-22.

[3] Weng,W., Taylor,P. A., Walmsley, J. L.. Guidelines for airflow over complex terrain: model developments[J]. Journal of Wind Engineering and Industrial Aerodynamics, 86(2-3) (2000):169-186.

[4] Yi, S., Zhengliang, L., Hanjie, H., etc.. Experimental research on mean and fluctuating wind velocity in hilly terrain wind field[J]. Acta Aerodynamica Sinica, 29(5) (2011): 593-599. In Chinese.

[5] Hong, F., Zhengzhi, X., Zhengliang, L., etc.. Experimental study and mathemetical model on wind load spectrum of rectangular super tall buildings[J]. Journal of applied foundation and engineering science, 21(3) (2013): 569-580. In Chinese.

[6] Feng, Y.. Research on wind induced response and static equivalent wind load on along-wind, across-wind and torsional direction of tall buildings[D]. PHD thesis of Tongji University, (2004) Shanghai. In Chinese.

[7] Vickery, B. J.. On the reliability of gust loading factors[C]. Proceeding of a Technical Meeting Concerning Wind Loads on Buildings and Structures. (1970). Building Science Series 30, National Bureau of Standards, Washington, D. C.

[8] Solari, G.. Mathmatical model to Predict 3-D Wind Loading on Buildings[J]. Journal of Engineering Mechanics, 111(2) (1985):254-276.

*Applied Mechanics and Materials Vols. 580-583 (2014) pp 2572-2578*
*© (2014) Trans Tech Publications, Switzerland*
*doi:10.4028/www.scientific.net/AMM.580-583.2572*

# Energy absorption numerical analysis of mine impingement thin-walled components with different configurations

Zhi Tang[1, a], Yishan Pan[2,b], Xiaojing Zhu[3,c]

[1] School of Mechanics and Engineering ,Liaoning Technical University,Fuxin 123000,Liaoning,China
[2] School of Mechanics and Engineering ,Liaoning Technical University,Fuxin 123000,Liaoning,China
[3] School of Mechanics and Engineering ,Liaoning Technical University,Fuxin 123000,Liaoning,China

[a]tangzhi0127@163.com, [b]panyishan_cn@sina.com, [c]zhuxiaojing0608@163.com

**Keywords:** impingement component; bumps; numerical analysis; different configurations; energy absorption characteristics

**Abstract.** For the effective prevention and control of mine bumps, or to a certain extent, to reduce the loss the losses caused by impact ground pressure accident,thin-walled components are proposed to be applied as a scaffold components in roadway supporting. Components impingement is reflected in the component crushed process ,in which the impacting energy absorption and crushing space provide certain amount of energy to free up space. The energy absorption characteristics of different configuration thin-walled components has been simulated with ABAQUS finite element, such as the conventional square,regular hexagon, round and origami square, regular hexagon etc,.and the results showed that: (1) The problem of conventional components is larger load fluctuation coefficient. Origami component is a kind of perfect impingement components ,as it can reduce peak loads and the load fluctuation coefficient effectively. (2) Under different ratios width-to-thickness, components can have different deformation modes, but the relationship of peak load and wall thickness is near linear and has nothing to do with the deformation modes. (3) The component can have a relatively lower crushing peak load and load fluctuation coefficient and relatively higher specific energy absorption,if given a suitable diamond concave angle. impingement components using combined with existing supports can make the existing supports to become top beam impingement support , mudsill impingement support ,two sides impingement support and impingement hydraumatic support and so on.

## Introduction

Our country is rich in coal resources, but most of the coal reserves in deep, the coal resource under the depth of 1000m made up 53% of the total coal resources. With the increase of mining depth, the rock burst occurs more and more frequently[1-2], causing great threat to people's life and property[3]. The occurrence of rock burst has the characteristics of instantaneousness， abruptness and destructiveness, a lot of energy release at the same time , the impact energy can reach up to 103MJ[4-5] . The impact energy plays a major role in the two parts, one part acts on the coal causing the coal and rock broken causing the breakage of coal and rock while another part acts on the roadway support structure. The huge impact can cause the destruction of coal and rock roadway and its support structures. At present, the main methods of the anti-chock support mainly include bolt, U steel, shotcrete support, shed-cable cooperative support. The roadway system satisfied the safety requirements under the static mine pressure, but there is the problem that the ability resisting the impact load is poor.

In today's world, the number of vehicles is increasing, and the speed is more and more fast, collision accidents often occur, which causes serious loss of life and property every year. Therefore, many countries gave high attention on car collision in more than half a century, scientists and engineers was encourage to improve energy absorption device performance[6-8] and the crashworthiness of cars, ships, aircraft and other vehicle[9]. The main evaluation index of the structure crashworthiness is the absorption and dissipation of the impact kinetic energy, a well-designed crashworthiness structure must absorb energy in a controlled manner[10]. With its excellent energy

absorption effect[11-13], the metal thin-walled structure as the energy absorption device has been widely used in aircraft, cars, ships, aerospace, machinery, bridges and other fields[14-18], but the application in the mining areas has not been reported.

If the metal thin-walled structure as supporting components was used in the roadway support structure to absorb impact energy, whether the rock burst can be prevented effectively, or to a certain extent to protect the roadway and the supporting structure? Because the anti-shock components used in mine need large crushing force, there is a need to simulate the bearing capacity and energy absorption properties of the conventional thin-walled components with circular cross -sections, square cross-sections, hexagonal cross-sections and the thin-walled components with folds of square and hexagonal cross-sections.

## Mine Impingement Thin-walled Components Design

**Essential Characteristic of Mine Impingement Thin-walled Components.** The anti-component need to meet the strength that the hydraulic support or supporting structure is not crushed under the normal working state on one hand, while the strength also can't be too big, or it has on effect of energy absorption and anti-shock. On the other hand, the components need to absorb energy as large as possible in the process of deformation and crushing, the space crushing occupied should be as small as possible, in other words, the effective distance of components should be as large as possible under the same height. The effective compression distance is defined as the distance that from the start of compression to the peak crushing load, which shows that components should have the following basic characteristics: The crushing peak load should be higher than a threshold and lower than another threshold; the deformation mode is regular and repeatable, which has high energy absorption, low cost and is easy to install.

The component preventing rockburst is mainly manifested in the following two aspects: the component itself can absorb some of impact energy in the process of crushing; the energy releasing space was provided after the components are crushing, which is equal to the components absorbing some of impact energy once again. This will greatly reduce the impact force effects on the support, which can protect the supporting system better.

Component generally installed on the upper surface of support beam, the bottom surface of the set sill, the top of the hydraulic prop, The bottom of the hydraulic prop or the top beam and the bottom beam, etc. the upper surface of support beam and the bottom surface of the set sill can be installed with a plurality of components, which can make the existing support to be the anti-shock top beam support, the anti-shock set sill support, the anti-shock two sides support and the anti-shock hydraulic prop.

**Impingement Components Geometry Structure Design.** According to the basic characteristics and the main mounting position of impingement components, the length and width of components are designed as 120 ~ 200mm, and the height around 350mm is better. So a thin-walled steel plate with an area of 720mm × 360mm is chosen to make the following five types of components: (1)The circular thin-walled components with radius of 114mm, height of 360mm. (2)The square thin-walled components with side length of 180mm, height of 360mm.(3)The regular hexagon thin-walled components with side length of 120mm, height of 360mm. (4)The square origami thin-walled components with side length of 180mm, height of 352mm.(5)The regular hexagon origami thin-walled components with side length of 120mm, height of 354, 356, 357, 358, 359 mm.

The square origami thin-walled component consists of two modules, which are "stacking" in the axial direction. Each corner region of a individual module has a diamond shape concave angle, which can form preformed crease lines. The surface of a individual module consists of eight congruent triangular faces and eight congruent trapezoidal faces. The module can be developed into a plane, when cut along the middle of the side, which is shown in Fig.1.The composed of origami thin-walled component is shown in Fig.3, in which the dotted line stands for concave angle.

The regular hexagon origami thin-walled component consists of two modules, which are "stacking" in the axial direction. The six corner regions of a individual module all have a diamond shape concave angle, which can form preformed crease lines.The surface of a individual module

consists of twelve congruent triangular faces and twelve congruent trapezoidal faces. The module can be developed into a plane, when cut along the middle of the side, which is shown in Fig.2. The composed of origami thin-walled component is shown in Fig.4, in which the dotted line stands for concave angle.

Both of the square and regular hexagon origami thin-walled components can define the individual modules with three independent geometric parameters: Module width a, module length L and module concave angle width b.Diamond concave angle 2θ is determined by b and L,satisfying the equation,where N is the number of edges.

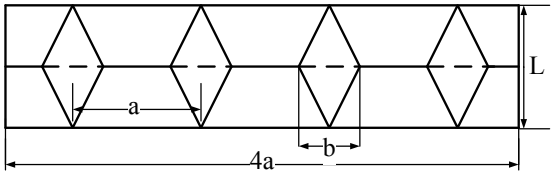


Fig .1 A quadrilateral module unfolds into a plane

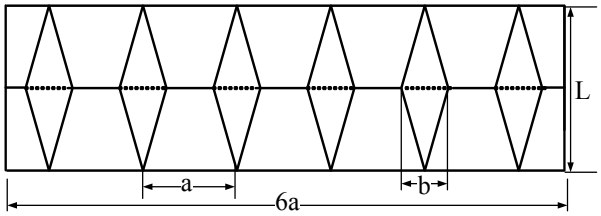


Fig .2 A hexagonal module unfolds into a plane

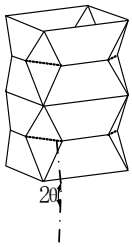


Fig. 3 The square origami thin-walled component

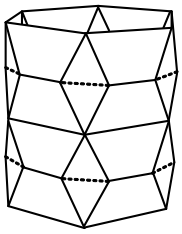

Fig .4 The regular hexagon origami thin-walled component

**Numerical Simulation of the Mine Impingement Thin-walled Components**

**Energy Absorption Performance Evaluation of Impingement Components.** The crushing peak load F max,load fluctuation coefficient Δ,specific energy absorption SEA and compression efficiency SE are used to evaluate the performance of impingement components.

The crushing peak load F max reflects the situation of overload or maximum overload. And F max can be received through the crushing force - distance curve of thin-walled components.

Load fluctuation coefficient Δ can make a effective evaluation for the stationarity of loads in the cushing process of thin-walled components. it is clear that the load fluctuation coefficient should be as small as possible for thin-walled components, which is defined as formula (1).

$$\Delta = \frac{F_{\max}}{\frac{1}{\delta}\int_0^{\delta} F(s)ds} \quad (1)$$

Where F (s) denotes the force , when the compressed distance of thin-walled components is s; δ denotes the compressed effective distance of thin-walled components .

The specific energy absorption SEA is the energy absorbed by unit mass in the effective crushing distance of components, which is defined as formula (2).

$$SEA = \frac{\int_0^{\delta} F(s)ds}{m} \quad (2)$$

Where m denotes the quality of thin-walled components.

The compression efficiency SE is used to measure the deformability of compression efficiency energy absorption structures, which is defined as formula (3).

$$SE = \frac{D}{H}100\% \cdot \tag{3}$$

Where D denotes the effective distance of the compression; H is the height of components.

**Geometry Size Selection of Impingement Components.** Components with different configurations, different thicknesses and widths of module concave angle selected, according to impingement components geometry structure design, as shown in Table 1.

Table 1 The geometry size and the energy absorption characteristics of thin-walled components

| Number | a [mm] | b [ mm] | L [ mm] | 2 θ [°] | Thickness [ mm] | $F_{max}$ [kN] | $F_{mean}$ [kN] | Δ | E [kJ] | SE [%] | SEA [kJ.kg$^{-1}$] | H [mm] |
|---|---|---|---|---|---|---|---|---|---|---|---|---|
| 1 | 120 | 45 | 180 | 172 | 8 | 4402 | 2138 | 2.06 | 620 | 81 | 38.09 | 359 |
| 2 | 120 | 60 | 180 | 169 | 8 | 4305 | 2390 | 1.80 | 707 | 82 | 43.46 | 359 |
| 3 | 120 | 75 | 180 | 167 | 8 | 3962 | 2421 | 1.64 | 663 | 77 | 40.76 | 358 |
| 4 | 120 | 90 | 180 | 165 | 8 | 3608 | 2643 | 1.37 | 703 | 75 | 43.20 | 357 |
| 5 | 120 | 105 | 180 | 162 | 8 | 3513 | 2171 | 1.62 | 601 | 78 | 36.94 | 356 |
| 6 | 120 | 120 | 180 | 159 | 8 | 3250 | 2209 | 1.47 | 641 | 82 | 39.36 | 354 |
| 7 | 120 | 120 | 180 | 159 | 5 | 1702 | 1011 | 1.68 | 282 | 79 | 27.94 | 354 |
| 8 | 120 | 120 | 180 | 159 | 6 | 2270 | 1356 | 1.67 | 377 | 79 | 30.87 | 354 |
| 9 | 120 | 120 | 180 | 159 | 7 | 2653 | 1827 | 1.45 | 530 | 82 | 37.19 | 354 |
| 10 | 120 | 120 | 180 | 159 | 9 | 3775 | 2721 | 1.39 | 778 | 81 | 42.49 | 354 |
| 11 | 180 | 90 | 180 | 156 | 5 | 1441 | 1008 | 1.43 | 249 | 70 | 24.48 | 352 |
| 12 | Square with side length of 180mm | | | | 5 | 2920 | 942 | 3.10 | 283 | 83 | 27.77 | 360 |
| 13 | Regular hexagon with side length of 20mm | | | | 5 | 2867 | 1141 | 2.51 | 342 | 83 | 33.65 | 360 |
| 14 | Round with radius of 114mm | | | | 5 | 2952 | 1111 | 2.66 | 336 | 84 | 32.99 | 360 |

**The Finite Element Model Impingement Components.** The paper adopts the algorithm of dynamic display, chooses S4R element, takes 5 integration points along the thickness direction of the shell, and uses the default value of the software itself to hourglass and bulk viscosity control of the material to set up finite element mode with the finite element software ABAQUS. Besides, in the moding, the primarily elements of the thin-walled component are quadrilateral elements, and only a few triangular elements it has. Thin-walled structures crushing process uses two rigid plates to conduct, namely using a rigid plate to support the bottom of the component and another rigid plate to load on the top of the component. The contact between rigid plates and thin-walled components is defined as the surface -surface contact between components, and the inside and outside surface of components is set as self-contact during deformation. Both of the friction coefficients of two contacts are 0.25. Mechanical Parameters adopt steel T700L parameter model with the density of 7850kg/m3, the elastic modulus of 210GPa, Poisson's ratio of 0.3, the yield strength of 720MPa, ultimate strength of 780MPa. In addition, the test of the mesh density and analysis time is conducted, from which we obtained a satisfactory result with the mesh size of 5 mm, the compression distance of 300mm and the analysis time of 0.03s .

## Numerical Simulation Results Analysis

The axial compressive-deformations of components with different configurations are shown in Fig.5, and the crushing force-distance curves are shown in Fig.6. The axial compressive-deformations of components with different thicknesses are shown in Fig.7, and the crushing force - distance curves are shown in Fig.8. The crushing force - distance curves of components with different angular widths are shown in Fig.9.The simulation results of components are shown in Table1.

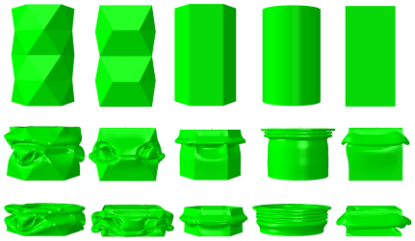

Fig.5 The axial deformation of components with different configurations

Fig.7 The axial deformation of components with different thicknesses

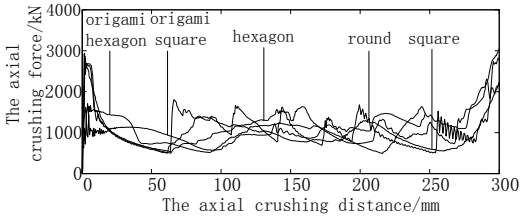


Fig.6 The crushing force - distance curve of components with different configurations

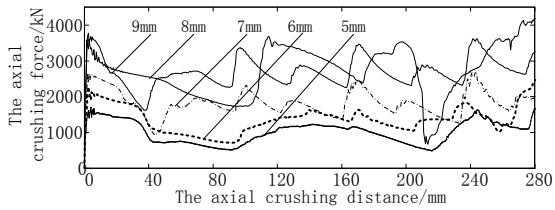


Fig. 8 The crushing force - distance curve of components with different thicknesses

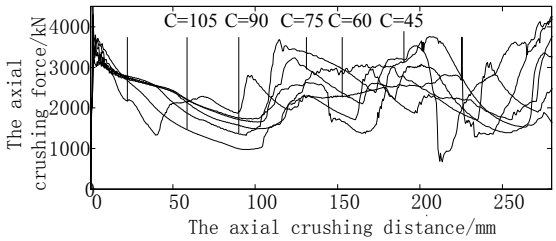


Fig.9 The crushing force - distance curve of components with different angular widths

**Comparison of Components With Different Configurations.** As can be seen from Fig.6: When applyed axial compression loads to components with different configurations, The axial crushing force increased with the deformation rapidly and reached a peak, then decreased to a stable platform for the regular waves of area, finally stepped into the stage of compaction structure and the crushing force increasing rapidly. The regular waves of load is formed by folding components continuously in the stable buckling stage, and each wave represents a partial folding process.

From Table 1,the performance indicators of conventional square, regular hexagon and round thin-walled components with same material (No. 12, 13, 14) is similar to each other ,and the regular hexagon is the best relatively and square relative worst. Compared with conventional components, the origami square and regular hexagon have a lower peak load and load fluctuation coefficient.

**Performance Analysis of Origami Components with Different Thicknesses.** The effect of wall thickness on the energy absorption of components is analyzed, keeping the module width a, module concave angle width b, module length and component height consistent (No. 6-10 components).

As can be drawn from Table 1: The crushing peak loads of wall thicknesses of 6, 7, 8, 9mm are increased by 33%,56%,91%,122% respectively than wall thinckness of 5mm; specific energy absorptions are increased by 10 %, 33%, 41%, 51%; load fluctuation coefficients are reduced by 0.6%, 13.7%, 12.5%, 17.3%; and compression efficiencys are increased by 0%, 3.8%, 2.5%, 2.5%. The relationship between crushing peak load and wall thickness is nearly linear, and a few other

indicators in the case of wall thickness greater than 7mm and less than 7 mm have changed greatly. As can be seen from Fig. 7,it is mainly because the deformation patterns of the wall thickness 7mm have changed, the failure mode of wall thickness less than 7mm is diamond failure mode, and wall thickness greater than 7mm is axisymmetric failure mode.

**Performance Analysis of Origami Components with Different Angular Widths.** Under the conditions of keeping the module's thickness, width a,length L coincident, The effect of module concave angle width b (diamond concave angle) on the energy absorption of components is analyzed (No. 1-6 components).

As can be drawn from Table 2 and Fig. 9 : the crushing peak load is reduced with the module width increasing or concave angle decreasing, but the specific energy absorption , the load fluctuation coefficient and the compression efficiency don't simply increase or decrease. It shows that module concave angular width (diamond concave corner) selection is particularly important for the performance of components. there is a relatively low crushing peak load and load fluctuation coefficient and a relatively high specific energy absorption, when the module concave angular width is 90mm(No. 4 components).

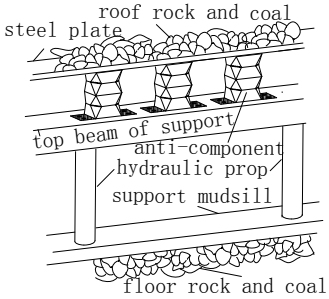


(a) The top beam support of impingement

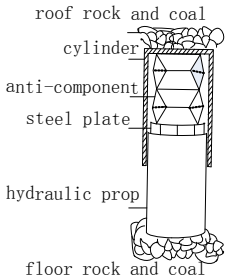


(b) The hydraulic prop of impingement

Fig .10 The component combined with the support diagram

## Conclusions

For the effective prevention and control of mine bumps, or to a certain extent, to reduce the loss the losses caused by impact ground pressure accident, thin-walled components are proposed to be applied as a scaffold components in roadway supporting. Partial function of components using combined with stents is shown in Fig. 10.

The energy absorption characteristics of different configuration thin-walled components has been simulated with ABAQUS finite element, such as the conventional square, regular hexagon, round and origami square, hexagonal etc, and the results showed that:

(1) The performance indicators of conventional square, regular hexagon, round thin-walled components are similar to each other, and a same problem of them is larger load fluctuation coefficient. Origami components can reduce peak loads and the load fluctuation coefficient effectively.

(2) Under different ratios width-to-thickness, the deformation modes of components will change, but the relationship of peak load and wall thickness is near linear and has nothing to do with the deformation modes.

(3) The module concave angular width selection (diamond concave corner) is particularly important for the performance of components. The component can have a relatively lower crushing peak load and load fluctuation coefficient and relatively higher specific energy absorption, if given a suitable diamond concave angle.

If supporting 100 brackets in the impact pressure roadway and installing 5 impingement components (No. 5) on the top beem of each support, the device can absorb 320MJ energy when the impact ground pressure happens and prevent and control coal mine bumps effectively, or to a certain extent, to reduce the losses caused by impact ground pressure accident.

**Reference**

[1] Yangsheng Zhao, ZengchaoFeng, Zhijun Wan. Least energy principle of dynamical fracture of rock mass[J].Chinese Journal of Rock Mechanics and Engineering, 2003,22(11): 1781–1783. ( in Chinese)

[2] B. H. G, E. T. Rock mechanics for underground mining[M]. Beijing: China Coal Industry Publishing House, 1990. ( in Chinese)

[3] Yishan Pan,Zhonghua Li,Mengtao Zhang.Distribution,type,mechanism and prevention of rockbrust in China.Chinese[J]. Journal of Rock Mechanics and Engineering,2003,22(11): 1844-1851. ( in Chinese)

[4] Hao Qin, Xianbiao Mao. Numerical simulation of stress wave induced rock burst [J]. Journal of Mining and Safety Engineering, 2008, 25(2): 127–131. ( in Chinese)

[5] Anye Cao,Jun Fan, Zonglong Mu, et al. Burst failure effect of mining-induced tremor on roadway surrounding rock[J].Journal of China Coal Society, 2010, 35(12): 2006 –2010. ( in Chinese)

[6] Najafi A,Rais-Rohani M. Mechanics of axial plastic collapse in multi-cell,multi-corner crush tubes[J]. Thin-Walled Structures,2011,49: 1-12.

[7] Paik J K, Kim B J, Park D K, etal. On quasi-static crushing of thin-walled steel structures in cold temperature: Experimental and numerical studies. International Journal of Impact Engineering，2011, 38(1):13-28

[8] Jang W Y, Kyriakides S. On the crushing of aluminum open-cell foams: Part I Experiments. International Journal of Solids and Structures, 2009, 46(3-4):617-634.

[9] Chang Qi, Fangliang Dong,Shu Yang，et al.Energy-absorbing characteristics of a tapered multi-cell thin-walled tube under oblique impact [J].JOURNAL OF VIBRATION AND SHOCK,2012,31（24）:102-107. ( in Chinese)

[10] Tai Y S, Huang M Y, Hu H T. Axial compression and energy absorption characteristics of high-strength thin-walled cylinders under impact load.Theoretical and Applied Fracture Mechanics,2010, 53(1): 1-8 ( in Chinese)

[11] Haiyang Song．Simulation of mechanical properties of single-Walled carbon nanotubes by molecular dynamics[J]．Xi'an University of Post and Telecommunications Press,2008.13(1): 149-152. ( in Chinese)

[12] McKinney J, Taylor T. Use of LS-DYNA to Simulate the Airbag Landing Impact Attenuation of the Kistler K1 Reusable Launch Vehicle, In: Proc of 5th International LS-DYNA User's Conference. Southfield,1998,21-30.

[13] Jang W Y,Kyriakides S. On the crushing of aluminum open-cell foams: Part II analysis. International Journal of Solids and Structures, 2009, 46(3-4): 635-650.

[14] Qiyong Wei,Libo Cao,Chongzhen Cui,et al.The optimization of crashworthiness for energy absorbing step-by-step thin-walled structure[C]// The 5th Int Forum of Automotive Traffic Safety (INFATS) . Changsha,2007. ( in Chinese) )

[15] ROSSI A, FAWAZ Z,BEHDINAN K. Numerical simulation of the axial collapse of thin-walled polygonal section tubes [J].Thin-Walled Structures,2005,43(10):1646-1661.

[16] Zhihua Zhong,Weigang Zhang,Libo Cao,et al.Automotive crash safety technology[M]. Beijing: China Machine Press, 2003. ( in Chinese) )

[17] Tehrani P H,Pirmohammad S.Collapse study of thin-walled polygonal section columns subjected to oblique loads[J].Proc.I Mech E Part D: J Automobile Eng,2007,221: 801-810．

[18] Liu R Q,Luo C J, Deng Z Q, et al. Design and selection of aluminum foam for impact damper of legged lunar Lander. In; Proc of The 2nd International Symposium on Systems and Control in Aeronautics and Astronautics. Shenzhen,China, 2008,1-6.

*Applied Mechanics and Materials Vols. 580-583 (2014) pp 2579-2582*
*© (2014) Trans Tech Publications, Switzerland*
*doi:10.4028/www.scientific.net/AMM.580-583.2579*

# Freezing Damage Analysis of Jintaizi Fishing Floor Engineering in Fuyu

Lijun Dou[1, a], Wei Wang[1,b] and Mingyu Xu[1,c]

[1]Changchun Institute of Technology, Changchun

[a]ljdou63@163.com, [b]545543425@qq.com, [c]823330204@qq.com

**Keywords:** Freezing damage, Frame structure, Ice pressure, Structure design

**Abstract.** Frame structure building is widely used for its advantages of flexible space, light weight, saving material, building plan can be flexibly arranged and so on. However, researches on frame structure built in the water in cold areas, under horizontal ice pressure, are very few, and there is also no ice pressure calculation method for this structure form. Combining with the damage phenomenon of Jintaizi fishing floor engineering, analyzed the causes of freezing damage from ice pressure, temperature joint, structure form, and put forward a concept of ice pressure influence width for frame structure under the effect of ice. This article provides a reference for ice pressure calculation and the design of frame structure buildings which built in the water.

## Introduction

Jintaizi fishing floor is located in Shibei reservoir, in Fuyu, Jilin province, which was founded in 2012. It was a single-story building, built in the water, and its form is frame structure. Area of the building is 1600 $m^2$, and this building can be used either for fishing, but also can be used as landscape architecture. According to local meteorological bureau of statistics analysis, the average annual temperature in this region is 4.5°C , and the monthly average temperature difference is 42.1°C. Water in reservoir began to freeze in late October or early November. In winter, the average thickness of the ice is 0.95m. Reservoir ice begins to melt between in late March and early April.

The structural diagram of fishing floor is shown as Fig.1. The plane shape of the building looks like a semicircle, which was designed according to the idea of a bow. The span of the bowstring is 142.8m, and perpendicular to bowstring the span is 69m. This engineering adopted prefabricated pile foundation with reinforced concrete, and the pile bearing capacity is 210kN. Frame columns' section dimension is 400×400mm. The height of columns is 3550mm, and the thickness of slab is 120mm. Frame columns' concrete strength grade is C30, the same to frame beams and floor. The part of bowstring arch close and parallel to the shore; bow arm towards the middle of lake.

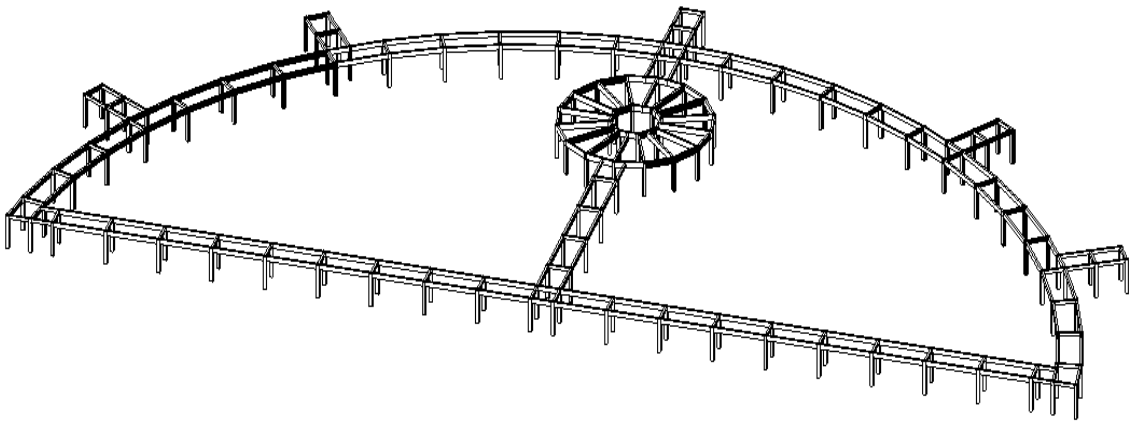

Fig.1.Structural diagram of fishing floor

When ice began to melt, we found that the structure of the overall leaned to the shore suddenly in 2013. More seriously than that, cracks appeared at the position of beam-column joints, especially at

the ends of the bowstring. The inclination of frame columns which near the shore side is more obvious. Phenomena of structural damage are shown as Fig.2.

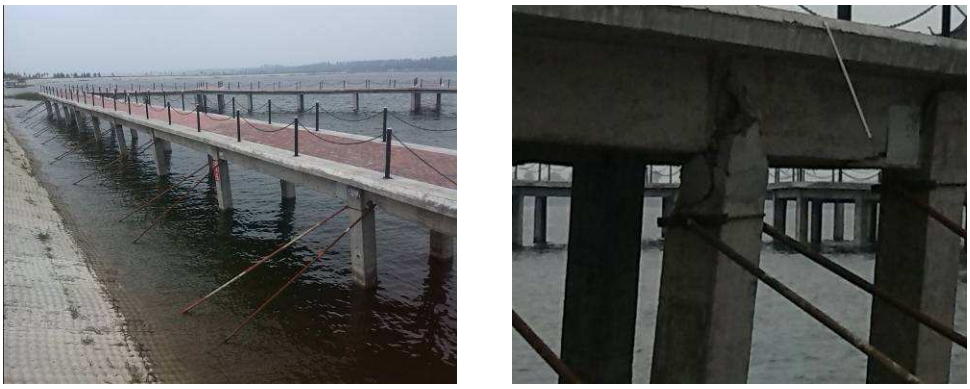

Fig.2. Phenomena of structural damage

**Reasons of Freezing Damage**

Through field measurement of fishing floor and finite element analysis, it is concluded that the main reason made the building leaned to the shore is horizontal ice pressure. Additionally, the floor of the building did not set up temperature joints and the structure form was unreasonable. Under horizontal ice pressure, it increased damage degree of the building, and it is also a significant factor that made the joints badly broken.

**No Consideration of Horizontal Ice Pressure in Structure Design**

Static ice pressure refers to the pressure that ice imposes on static buildings, which can be divided into swelling pressure, ice thrust under the influence of wind and flowing water, and thermal expansion pressure[1]. Thermal expansion pressure is one kind of static ice pressure generated by a 9% volume expansion from water to ice under the building's restraint . However, swelling pressure's impact on buildings is quite minimal and shall not be taken into account. Ice thrust under the influence of wind and flowing water also imposes no notable impact. On the contrast, thermal expansion pressure can do great damage to buildings under varying temperatures as the heated-and-then -expanded ice layer can generate huge thrust, which is the so called ice pressure.

Weak lateral stiffness is one of the disadvantages of frame structure. As a result, the building can not resist the effect of horizontal ice pressure and damages happened. Static ice pressure is influenced by environment, and there is no calculation methods for frame structure buildings which built in the water. Therefore, horizontal ice pressure was ignored in the process of the structure design. There are several different formulas to calculate ice pressure, *Code for Design of Hydraulic Structures against Ice and Freezing Action* provides a simple method by making a comprehensive analysis of them. This method needs to know the thickness of the ice, and the way to get the value is shown as Table 1.

Table 1. Value of Ice Pressure

| Thickness of Ice （m） | 0.4 | 0.6 | 0.8 | 1 | 1.2 |
|---|---|---|---|---|---|
| Ice Pressure （kN/m） | 85 | 180 | 215 | 245 | 280 |

The thickness of ice in Table 1. should be choose from average maximum for previous years , and the value can be interpolated for different thickness of ice[2]. The average ice thickness for previous years in this region is 0.95m, then the value of ice pressure is 237.5kN/m according to Table 1. The width of frame columns is 0.4m, so the ice pressure load on each frame column is 95kN. However, through the analysis of finite element software, the destroy degree of structure was lower under ice pressure. The maximum normal stress on frame columns is 5.6N/mm$^2$, less than compressive strength of C30 concrete, whose design of value is 143N/mm$^2$. Meanwhile this ice pressure cannot cause cracks on the building. Therefore, the ice pressure value calculated by *Code for Design of Hydraulic*

*Structures against Ice and Freezing Action* is small, and this calculation method do not apply to frame structure which in the water.

Ice is continuum. It can cover the frame columns and form a block. Therefore, the ice pressure on frame columns not only includes the impact of ice that has contact area with the frame columns but also that of the ice covering both sides of the frame columns.While calculating the horizontal ice pressure, static ice pressure should multiply a wider distance, ice pressure impact width, which is related to and shall stand between the width of frame column and the span of frame columns. After many trial tests based on the frame structure, it is concluded that the reasonable width shall range from 2m to 4m.

Additionally, according to the statistics of Bureau of Metrology of Jilin Province, 2012 witnessed extreme cold weather, featuring by an unprecedented lowest temperature of -39.8°C. Accompanied by severe weather are thicker ice layer, more remarkable temperature fluctuations and ice volume expansion which leaded to greater static ice pressure. The extremely cold weather, as one of the factors impacting static ice pressure, increased the damage to fishing floor.

**No temperature Joints**

The temperature joints, also called expansion joints, are set in case of the possible fissure on the building under the temperature variations. Surrounded by the lake, this floor experienced remarkable temperature changes more than 70 °C from summer to winter. No temperature joints are set in the building which is slim in shape. This may lead to expansion and contraction of the building under temperature variations and temperature stress of the floor. With the restrain of frame columns, frame columns are imposed impact while the concrete are easy to breach. The coefficient of thermal expansion is 0.00001. The span of bowstring is 142.8m and the length of the bow's back is 219m. Thus, the maximal expansion amounts of bowstring and bow's back are as following.

$$\Delta l_1 = l_1 \times \alpha \times \Delta t = 142480 \times 0.00001 \times 70 = 99.74\text{mm}. \quad (1)$$

$$\Delta l_2 = l_2 \times \alpha \times \Delta t = 219480 \times 0.00001 \times 70 = 153.3\text{mm}. \quad (2)$$

As can be seen from the calculation, bowstring and back of bow have greater expansions and exert significant impact on the building. While the temperature rises, it moves toward the ends of bowstring and back of bow, bringing both horizontal and vertical temperature stress to the frame columns at the sides of bowstring which then slide in both directions. This is consistent with the fact. The width of expansion joint usually stands between 20mm to 30mm and the largest span of the expansion joint in cast-in-place reinforced concrete is 35m[3].Standard temperature joints should have been set in the floor. No temperature joints also contribute to the damage of the building.

**Unreasonable Structure Form**

At first, as can been seen from Fig. 1, the plane graph of the fishing floor can be simplified as an arch structure featuring of generating horizontal impact on the arch toes, under the impact of vertical loads. Horizontal ice pressure can be simplified as the even loads distributed equally in the vertical direction of arch axis. The frame columns have to undertake the impact of the horizontal impact as there are no supports at the arch toes, which leads to movement of the columns via the horizontal direction to the lake. Meanwhile, the joints under the impact of the ice pressure, temperature stress and arch thrust, the ultimate strength of the joints is surpassed and then it does great damage to them. Taking consideration of the comprehensive impact of the ice pressure, the part of joints should be strengthened while section size of beams and columns should be expanded.

Secondly, the fishing floor is a one-span frame structure which shall not be applied in design while the horizontal impact exists. One-span frame structure is difficult in transmitting force and bending moment under horizontal impact， and it is easy to make beam-column joints destroyed. In terms of degrees of freedom, one-span structure is redundant structure with less redundancies and may be damaged totally once one joint is damaged. If double-span or multi-span were applied in design, the

degree of statical indeterminacy will increase and once several constraints out of work will do less damage to the overall structure.

Thirdly, the size of cross section is small which leads to small lateral stiffness and slide of structure under impact of horizontal ice pressure.

## Conclusion

Less lateral stiffness and direct ice pressure are the main reasons that lead to the freezing damage to the fishing floor. Temperature joints shall not be overlooked in cold areas. Neither shall we apply a one-span structure under the influence of horizontal impact. Moreover, the calculating method of ice pressure cited from *Code for Design of Hydraulic Structures against Ice and Freezing Action* is not applicable, and the concept of ice pressure influence width shall be taken into consideration. More researches and discussions need to be taken to find out specific evaluation method. To sum up, ice pressure, larger section size, reasonable temperature joints and two-span or multi-span structure shall be taken into account in designing frame structure in water in cold areas. At present, the fishing floor is out of service and shall be consolidated.

## References

[1] Wang Chuan: Observation of Ice Layer Deformation and Calculation of Static Ice Pressure in Hongqipao Reservoir (2011), In Chinese.

[2] Code for design of hydraulic structures against ice and freezing action (GB/T 50662-2011 ), China Planning Press, (2011), In Chinese.

[3] Code for design of concrete structures ( GB 50010-2010), China Architecture & Building Press, (2010), In Chinese.

*Applied Mechanics and Materials Vols. 580-583 (2014) pp 2583-2588*
*© (2014) Trans Tech Publications, Switzerland*
*doi:10.4028/www.scientific.net/AMM.580-583.2583*

# Mechanical Properties and Calculation Method for Monolayer Cable Net Glass Curtain Wall under Fire Conditions

Gong Lingfeng[1,a], Bai Yin[1,b], Li Siqi[1,c]

[1]School of Transportation Science and Engineering, Beihang University, Beijing 100191, China

[a]smileglfsmile@163.com, [b]baibowenbai@buaa.edu.cn

**Keywords:** steel structure; monolayer cable net; glass curtain wall; fire disaster; mechanical properties; critical temperature.

**Abstract:** The developing trend of large scale curtain wall structure system is monolayer cable net glass curtain wall, so it's important and necessary to study the corresponding calculation method and mechanical properties under fire conditions. The changing rule of the displacement and the maximum cable force with the temperature was analyzed by making series of numerical calculations, and the principle for determining critical temperature was deeply discussed upon the basis of the numerical simulation results. The critical temperature table considering different spans, grid dimensions and cable diameters is given, and the influence on critical temperature has also been studied when initial prestressed force of vertical cable is relatively small. Some suggestions are proposed finally.

## Introduction

The prestressed cable system used high strength steel in monolayer cable net glass curtain wall has a small structural section can avoid the shortcoming of point-supported glass curtain wall, such as could not satisfy the architectural design requirements of large-scale curtain wall structure for use the rigid structural system like steel frame and truss. The monolayer cable net glass curtain wall represent the trends of large scale curtain wall structure [1] can achieve the elegant appearance, simple structure and convenient construction requirements for large space structures.

In recent years, the monolayer cable net glass curtain wall has quickly spread in our country. However, the elastic modulus and yield strength of high strength cables will significantly reduce under high fire temperature. Even that have an obviously influence on the structural mechanical properties. It is difficult to take fire prevention measures on cables and there is glass blowout dangerous. Thus, the mechanical properties and fire resistance calculation methods [2] for monolayer cable net glass curtain wall under fire condition are urgently need.

## Mechanical properties for high strength cables

It should to make clear that the high strength cables material mechanical property parameters changing situation with the temperature rise under fire condition for research the monolayer cable net glass curtain wall mechanical properties under high fire temperature. The high strength cables have many differences with common steel in material properties for the different processing technology [3].

The elastic modulus of structural cables is in range of 147～170 kN/mm$^2$ and the linear expansion coefficient is $3.9\times10^{-6}$ / ℃ [4] at room temperature. Based upon the commonly used cables, normal elastic modulus E take 150kN/mm$^2$, breaking strength fu take 1570MPa and linear expansion coefficient take $3.9\times10^{-6}$ /℃.

There is no domestic and foreign scholars do system research on material properties under high fire condition for various types of cables. The elastic modulus reduction coefficients [5] of cables under high temperature are shown in Tab.1.

**Tab.1 The elastic modulus reduction coefficients of high-strength cables under high temperatures**

| Temperature（℃） | 20 | 100 | 200 | 300 | 400 | 500 | 600 | 700 | 800 | 900 | 1000 | 1100 | 1200 |
|---|---|---|---|---|---|---|---|---|---|---|---|---|---|
| $E_T/E$ | 1.00 | 1.00 | 0.87 | 0.72 | 0.56 | 0.40 | 0.24 | 0.08 | 0.06 | 0.05 | 0.03 | 0.02 | 0.00 |

In the following research, the high strength cables will be taken as the linear elastic material for theirs high yield strength and the little strength reserve after yield, and only consider the elastic modulus with temperature changes. The cables are considered failure when the cable stress higher than the yield strength under the temperature at that time.

## Finite element method analysis

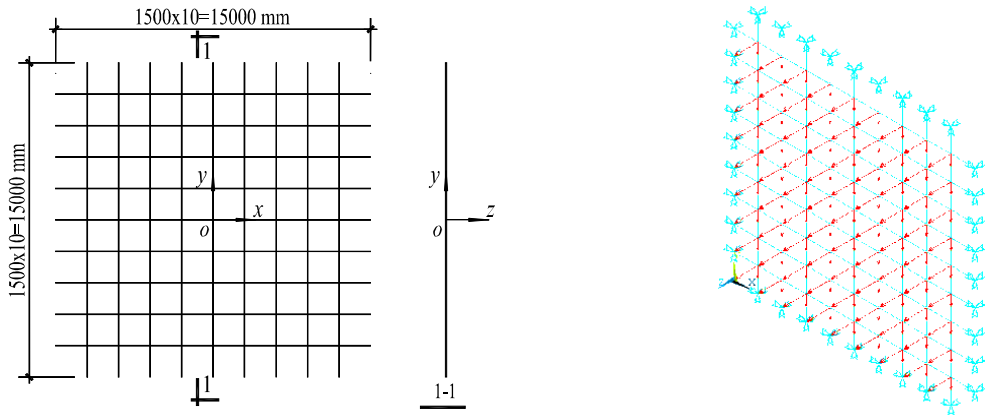


**a)** Geometric model b) Finite element model

**Fig.1 Calculation model of monolayer cable net structure**

The synergism of the glass and cable net has a certain influence on the mechanical properties of the monolayer cable net glass curtain wall at room temperature [6]. But even at the room temperature, it is not easy to determine the connection stiffness of the glass and the cable net nodes. The mechanical of no matter claw or glass cement will be some changes in node connection parts under fire condition, so it is harder to ensure the simulation method. This paper will first conservatively research the structural mechanical performance under fire condition when do not consider the contribution from the glass stiffness, but put the weight of the glass and fittings on the cable net.

The monolayer cable net structure analysis model is established shown in Fig.1a. The size of cable net is 15 m×15 m, the grid size of glass compartment is 1.5 m×1.5 m, the horizontal and vertical cables are adopt φ16 steel strand, and the section area A is 151 $mm^2$. To simplify the calculation, the bearings take fixed end and do not consider the effect of its stiffness on the structure system. The dead weight of the curtain wall fittings takes 0.2 $kN/m^2$, and the horizontal load is 1.0 $kN/m^2$ uniform load which is perpendicular to the glass panel.

The calculation models were established by ANSYS to conduct non-linear analysis on cable net structure under fire condition. LINK10 element was used to simulate cables. Only take the structural maximum deformation and cable force of the calculation results for the space limitation.

The temperature distribution in large space structure is not uniform under fire condition. The monolayer cable net glass curtain wall often can not be applied fire retardant paint for the small cables section, and the intersections of each cable are connected by metal fixture so that the temperature in cables soon able to reach thermal equilibrium and uniform distribution. This consideration is emphasis on safe, so this paper will calculate according to scheme of cables even temperature-increasing.

The initial temperature of cable net is 20 ℃, then uniformly heat to 600 ℃. The horizontal and perpendicular cables are all applied the same initial prestress in the same calculation model. The initial prestress P is range from 40 kN to 140 kN for its value is about 30％of cable breakage stress in engineering practice.

The calculation result changing situation of the monolayer cable net structural maximum displacement and cable force in temperature heating process is shown in Fig.2. The structural maximum displacement of all calculation models are increasing with the temperature rise and the change curves are approximately parallel under different initial prestress. While, as the temperature increases the cable prestress are all obvious relaxation. When cable temperature is lower than 100 ℃

the prestress relaxation speed is slower, but when it higher than 100 ℃ the prestress relaxation speed is obviously faster and the larger initial prestress the faster relax speed.

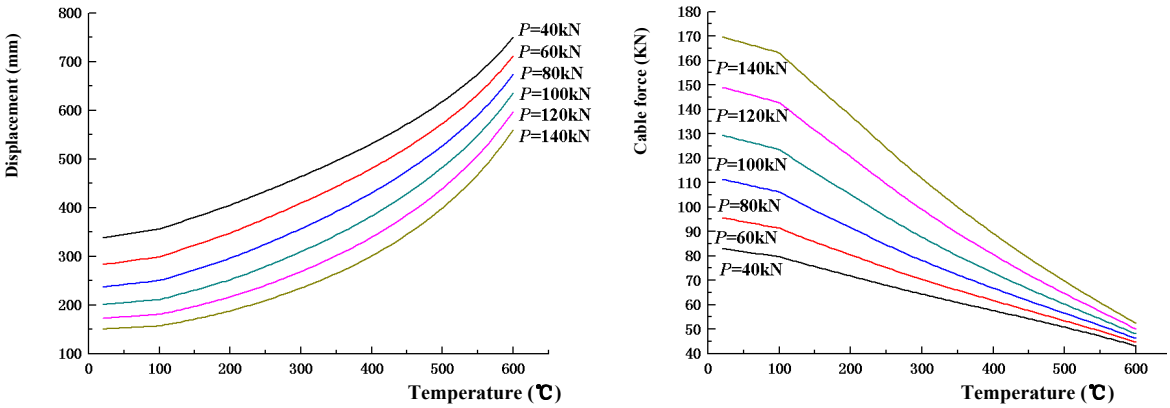


a) The maximum displacement curve b) The maximum cable force curve

**Fig.2 The monolayer cable net maximum displacement and cable force curve varies with temperature**

## Calculation method of critical temperature

According to Point Supported Glass Curtain Wall Engineering Discipline[7], the relative deflection of point supported glass curtain wall supporting structure is can not more than l/300 (l is span of supporting structure ) under composite action, such as wind load. The flexible supporting structures like monolayer cable net have a big different from normal rigid supporting structures, so if use the existing norms to control deflection have distinct irrationality.

Sun Fen, Tsinghua university, discuss the deflection limits of monolayer bi-directional flexible cable glass curtain wall structure based on Beijing New Poly Plaza [8]. The research shows that if the large flexible glass curtain wall structures meet the limit condition of relative deflection is not greater than l/300 need to apply a great prestress on the cable net. It will lead to the additional inner force on the main structure even more than the influence of external load, thus make the members section coarser and the main structure unbearable. Based on the consideration of the ability to adapt to deformation, permeability and economic of point supported glass curtain wall, the vertical deformation of the curtain wall control in l/50 under the effect of the most unfavorable load

Through the previous calculations are not hard to find that the cable net deformation will increase with the temperature rising, but excessive deformation will cause glass twist or broken for too much squeeze. However, it is difficult to simulate the glass collapse in finite element numerical simulation. Based on the engineering practice, we think the deformation of general monolayer cable net glass curtain wall can not over l/50 under the worst combination of loads condition, otherwise easy to cause the glass broken and structural damage [9] finally. This paper determines the monolayer cable net glass curtain wall displacement limit can not more than l/50.

The difference between monolayer cable net glass curtain wall and other large space steel structures is that glass will burst and lead to the destroy of the curtain wall under high temperature condition. The research of glass burst under high temperature is very few in domestic, so this paper adapts the research results of scholars like Hassani [10]. The results are that the burst temperature of 6mm thickness glass is 450 ℃ and should not more than 450 ℃ in order to ensure the integrity of the glass curtain wall.

In addition, cables will have a degree of relaxation for thermal expansion and decrease of the elastic modulus. The cables relax speed under the vertical load combination without consider wind load condition will faster than wind load condition. If the cable tension decreases to zero, it will also cause the structure damage. However, by finite element analysis found that when apply the same prestress on both horizontal and vertical cables in the range of 450℃, the cable tension would never decrease to zero even if the cable stress has a great decrease.

Above all, the monolayer cable net glass curtain wall, applied the same prestress on both horizontal and vertical cables, will take the smaller value between 450℃ and the temperature makes

the maximum displacement reach to l/50 as its critical temperature, and take it as the judgment basis of fire resistant design.

## Calculation for critical temperature of fire-resistant

The monolayer cable net glass curtain wall practical critical temperature table for fire resistant design can be obtained by calculating a large number of numerical models, as shown in Tab.2. This critical temperature table including a more comprehensive range of monolayer cable net glass curtain wall in engineering practice, such as the cable span between 10m and 50m, the aspect ratio is 1.0～2.0, the grid size is 1.0 m～2.5 m, the cable diameter is 12 mm～36 mm, the glass weight is mainly considered based on the commonly used (12 mm+12 mm) insulating glass curtain wall, and the weight of the curtain wall fittings take 0.2 kN/m$^2$.

Based on the usual practice, the cable initial prestress uniformly take the 30％of the breakage stress and the horizontal loads take 1 kN/m$^2$, this will be more safe than a majority cases. The critical temperature table given in this paper can be help structural designers to estimate the fire resistant capacity of monolayer cable net glass curtain wall and quickly to get the highest allowable temperature in fire disaster. This has a good practical significance.

**Table 2 Critical temperatures for monolayer cable net glass curtain wall under fire conditions (℃)**

| Curtain wall geometry size | Grid size | Cable diameter (mm) | | | | | |
|---|---|---|---|---|---|---|---|
| | | 12 | 16 | 22 | 26 | 30 | 36 |
| 10m×10m | 1.0m×1.0m | 329 | 450 | 450 | 450 | 450 | 450 |
| 10m×20m | 1.0m×1.0m | 204 | 373 | 450 | 450 | 450 | 450 |
| 15m×15m | 1.5m×1.5m | -- | 197 | 385 | 450 | 450 | 450 |
| 20m×20m | 1.0m×1.0m | -- | 227 | 405 | 450 | 450 | 450 |
| 20m×20m | 2.0m×2.0m | -- | -- | 201 | 308 | 360 | 450 |
| 20m×40m | 1.0m×1.0m | -- | 195 | 354 | 432 | 450 | 450 |
| 20m×40m | 2.0m×2.0m | -- | -- | 201 | 244 | 303 | 407 |
| 30m×30m | 1.5m×1.5m | -- | -- | -- | 263 | 321 | 425 |
| 30m×45m | 1.5m×1.5m | -- | -- | -- | 202 | 265 | 377 |
| 40m×40m | 2.0m×2.0m | -- | -- | -- | -- | 115 | 206 |
| 50m×50m | 2.5m×2.5m | -- | -- | -- | -- | -- | 76 |

However, vertical cables are mainly bear the glass and fittings weight in engineering practice, so put a low prestress on the vertical cables and only meet the situation that not appear relaxation under room temperature and the most unfavorable load combination condition. Thus , the following will put a low prestress on the vertical cables and calculate the critical temperature under fire condition, and make a compare with Fig.2.

The size of the calculation model is 15m×15m, the grid size is 1.5m×1.5m, the cable diameter is 16mm, and the initial prestress of the horizontal cable is 80KN. The vertical cable prestress is 10%～50% of the horizontal cable, the glass weight is mainly considered based on the commonly used (12 mm+12 mm) insulating glass curtain wall, the weight of the curtain wall fittings also take 0.2 kN/m$^2$, and the calculation results are shown in Tab.3. At this time, take the lowest temperature among the cable temperature when the structure displacement is over l/50 under the load combination with consider wind load condition, the cable temperature when a cable prestress decreases to zero under the load combination without consider wind load condition and 450℃.

Through the comparative analysis, it can be known that when the vertical cable prestress is lower the structure bearing capacity will reduce and lead to the decrease of the structural critical temperature. In general, the displacement transfinite is faster than cable relaxation.

Above all, the low vertical cable prestress has a significant influence on the critical temperature, so can not use the critical temperature table shown in Tab.2. This paper has not give the corresponding fire resistance critical temperature calculating table for the space limitation, but the same calculation method can be used to get the different critical values when the horizontal and vertical cables have a different prestress ratio.

**Table 3 Critical temperatures when lower prestresse in vertical cables (℃)**

| | Prestress ratio of horizontal and vertical cables | | | | | |
|---|---|---|---|---|---|---|
| | 10% | 20% | 30% | 40% | 50% | 100% |
| Displacement transfinite | -- | 24 | 69 | 107 | 128 | 228 |
| Cable relaxation | 112 | 217 | 315 | 420 | 518 | -- |
| Critical temperature | -- | 24 | 69 | 107 | 128 | 228 |

## Summary

1) The structure maximum displacement will increase with the temperature rising of monolayer cable net glass curtain wall, and the relaxation speed of the large initial prestress cable will greater than the lower one.
2) When the horizontal and vertical cables applied the same initial prestress, take the smaller value between 450℃ and the temperature makes the maximum displacement reach to l/50 as the structure critical temperature. When the vertical cable prestress is low, take the lowest temperature among the cable temperature when the structure displacement is over l/50 under the load combination with consider wind load condition, the cable temperature when a cable prestress decreases to zero under the load combination without consider wind load condition and 450℃as the structure critical temperature.
3) Based on a plenty of numerical analysis, the critical temperature table which can be applied to different span, grid size, and cable diameter has been obtained and including a more comprehensive range of monolayer cable net glass curtain wall in engineering practice.

## Acknowledgements

This work was financially supported by the National Natural Science Foundation of China (51208019).

## References

[1] Wu Peng, Zhang Liangping, Dong Shilin, Wang Zhe. The application and research of flexible support systems for glass architectures[J]. Spatial structures, 2002, 8(2): 31-37. (in Chinese)

[2] Shi Yon-jiu, Bai Yin, Wang Yuanqing. Study on Performance-based Fire-resisting Design and Key Technique thereof for Large Space Steel Structures[A]. Cui Jinghao, Proceedings of the fifteenth national conference on structural engineering[C], The fifteenth national conference on structural engineering, Jiaozuo, 2006, Beijing: Engineering Mechanics Journal Press, 2006: 119-126. (in Chinese)

[3] Zhang Haoyu, Zheng Wenzhong. Mechanical property of steel strand at high temperature [J]. Journal of Harbin Institute of technology, 2007, 39(6). (in Chinese)

[4] Zhang Qilin. Cable and membrane structure [M]. Shanghai: Tongji University Press, 2002: 32-37. (in Chinese)

[5] Bai Yin, Shi Yongjiu, Wang Yuanqing. Theoretical Analysis and Numerical Simulation on Mechanical Properties of Large Space Cable-Supported Structures under Fire Conditions [J]. Science in China: Series E, 2009, (8):2340-2349.

[6] Feng Ruoqiang, Wu Yue, Shen Shizhao. Static performance of single-layer plane cable net glass curtain in consideration of glass panel [J]. Journal of Building Structures. 2005, 26(4). (in Chinese)

[7] China Association for Engineering Construction Standardization. CECS 127-2001. Technical Specification for Point Supported Glass Curtain Wall [S]. Beijing, 2001.

[8] Wang Yuanqing, SUN Fen, SHI Yong-jiu, Luo Yi, Xu Yue. The Deflection Performance Analysis of Single-layer Cable Net for Point2supporting Glass Curtain Under Horizontal Load[J]. Building Science, 2006, 22(2): 23-26. (in Chinese)

[9] Feng Ruoqiang, Wu Yue, Shen Shizhao. Static performance of single2layer plane cable net glass curtain in consideration of glass panel. Journal of Building Structures, 2005,26(4):99-105. (in Chinese)

[10] Hassani, S. K., Shields, T. J., and Silcock, G. W., An Experimental Investigation into the Behaviour of Glazing in Enclosure Fire[J]. Applied Fire Science, 1994, 4(5): 303-323.

*Applied Mechanics and Materials Vols. 580-583 (2014) pp 2589-2599*
*© (2014) Trans Tech Publications, Switzerland*
*doi:10.4028/www.scientific.net/AMM.580-583.2589*

# Pregnant Mechanism and Mechanical Model of Rock Landslides in Chair-Shaped Cataclinal Bank Slopes

Xianchun Ma[1,2,a], Xichang Chen[3,b] and Youjun Feng[4,c *]

[1]State Key Laboratory of Hydraulics and Mountain River Engineering, College of Water Resource & Hydropower, Sichuan University, Chengdu, Sichuan, 610065, China

[2]Southwest Research Institute CO.,Ltd. of CREC, Chengdu, Sichuan, 611731, China

[3]Chengdu Research Center of Hydrogeology and Engineering Geology, Chengdu, Sichuan, 610081, China

[4]Department of Information Technology, Sichuan Tourism University, Chengdu, Sichuan, 610100, China

[a]maxianchun1980@163.com, [b]cxc1939@sina.com, [c]fengli522@163.com

**Keywords:** Chair-Shaped Cataclinal Bank Slopes, Rock Landslides, Pregnant and Sliding Mechanism, Mechanical Model, Groundwater Pressure, Prevention Measures.

**Abstract.** The pregnant and sliding mechanism was firstly compared between Vajont and Qianjiangping large rock landslides, which happened in the chair-shaped cataclinal bank slopes. And then the essence of the landslides occurred was deduced. The pregnant and sliding process of the landslides was showed two stages. First, after the first impoundment of the reservoir, the soil and shallow rock at the front of the landslides were slipped and then caused posterior margin of the deep latent sliding surface cracks. So the groundwater supply condition was significantly changed. Second, with the rapidly increase of the groundwater recharge, its pressure on the front of the landslides was also rapidly rise to the critical value which the landslides occurred. Afterwards, the stability mechanical model of the chair-shaped cataclinal bank slopes and critical value formula of the groundwater pressure were established on the basis of the stability mechanical model of general chair-shaped cataclinal slopes, added reservoir water level which was a dynamic load. While working procedures to determine the groundwater pressure was put forward. Last, the theory was certified validity take Liangshuijing rock landslide of the Three Gorges Project area as an example and the monitoring methods and control measures for the landslide were proposed.

## Introduction

In the world, there were two large catastrophic rock landslides caused by reservoir make engineering, rock mechanics and engineering geology academic community shock and concern. The one was Vajont reservoir rock landslide occurred on Oct.9, 1963 in Italy, the other was Qianjiangping rock landslide occurred on Jul.13, 2003 in China's Three Gorges Project reservoir bank.

Since Vajont reservoir rock landslide occurred, many scholars all over the world studied on the landslide and published numerous thesis for decades. After Qianjiangping rock landslide occurred, the case was also. But so far, there is no consensus to germination and sliding mechanism of the large rock landslides [1-7], especially no one put forward the quantify criterion of the landslides prediction. Therefore, a little tentative work was done in this thesis or it could play a valuable role to further understanding these large landslides.

Both Vajont and Qianjiangping rock landslides happened in the chair-shaped cataclinal slope. This cataclinal slope is a kind of easily slipping structure. Chair-shaped cataclinal slope is such cataclinal slope [8], that upper slope angle less than penetrative discontinuities angle, meanwhile penetrative discontinuities angle greater than dip angle causing slide, under slope angle great than penetrative discontinuities angle, meanwhile penetrative discontinuities angle less than dip angle causing slide. Rock stratum angle of upper slope is steep, so the rock declining power will undoubtedly increase. Rock stratum angle of under slope is gentle, so the slip resistance increase, but it avail penetrative

discontinuities leading edge form an effective freeing surface. In view of this, the overall stability of the chair-shaped cataclinal slope depends on the hydrogeological structure and syntagmatic relations of length, height, and angle change of the upper and under slope. It were published by Xichang Chen(2009) that mechanical model of common chair-shaped cataclinal slope and fundamental calculation formula of the rock landslide hydraulic start critical value [9]. On this basis, the special mechanical model of chair-shaped cataclinal reservoir bank slope stability will be established, and forecasting and early warning criteria of the large rock landslides will be put forward in this thesis.

**Vajont Reservoir Rock Landslide**

On 22:39 (GMT) October 9, 1963, The Vajont reservoir rock landslide with a volume of more than $2.4\times10^8 m^3$ rock and gravel occurred in Italian, at the maximum speed of 30m/s. As a result, The Vajont reservoir was scrapped and nearly 3,000 people were killed. It was the worst landslide accident of hydraulic architectural history in Italy [2].

Vajont reservoir was built in Vajont valley, which in the Alps mountains in northern Italian. Vajont valley was formed by deep canyons and two-stage U-shaped glacial valleys. Near the Vajont reservoir dam it was a asymmetric syncline, which the south wing (left bank) steep and the north wing slowed down. The dam built on the upper Jurassic limestone stratum in the raise ends of the syncline. The limestone stratum were gently and a tendency to the upper reaches. So the engineering geological conditions of the dam was quite satisfactory. But near the dam, both sides of the reservoir bank were chair-shaped cataclinal bank slope, and formation of two-stage flat mesa on the slope through the glacial and river erosion. The flat mesa were covered with glacial outwash soils, alluvial soils and ancient slumping mass, etc. The underlying bedrock dip angle of the chair-shaped cataclinal slope was about 40° at upper and middle limestone stratum, and it was nearly horizontal at the bottom of the river valley (Fig. 1).

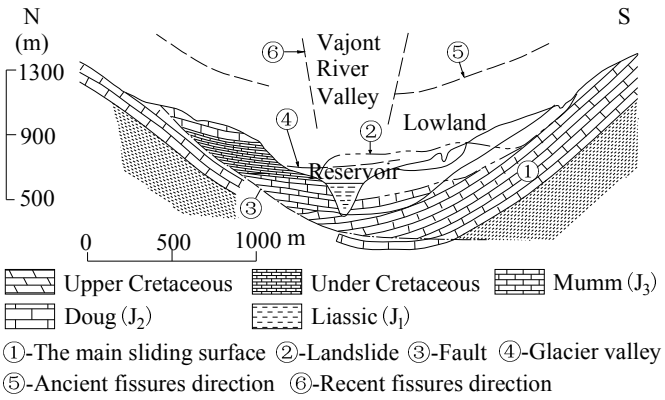


Fig. 1 Geological profile of Vajont valley in Italy (According to Kiersch,1964)

On October 1960, when the initial water level of the Vajont reservoir reached to 642m, close to the below flat mesa on the slope, the rear of the above flat mesa appeared tensile fractures and extended to the eastward. When the water level reached to 652m, the front of the above flat mesa happened collapses and landslides. Obviously, this was due to the uplift pressure of the reservoir water reduced the rock and soil anti-slide force of the front slip resistance section of the above flat mesa. In December 1960 to October 1961, the water level of the Vajont reservoir dropped below 600m, and the displacement rate of rock and soil quickly dropped below 0.3cm/d, and remained stable. But in November 1961, the reservoir water level began to rise again to more than 600m, and with the water level rose, the displacement rate of rock and soil was gradually increased. On November, 1962, when the water level rose to 700m, the displacement rate of rock and soil exceeded 1cm/d. On December 1962 to March 1963, the water level was dropped to 650m, the displacement rate also declined. During this period, the displacement of rock and soil may be partial elastic deformation and show the changes of water pressure intensity. The real landslide (including creep) did not happen during this

period. While After April 1963, the water level began to rise again, and rose to 700m or more in June. At this point, the displacement rate increased progressively, it was to no avail even if the water level was adjusted. And the large rock landslide shocked the world finally happened.

So, what were the key factors that the landslide occurred? The following analysis was divided into three phases to the germination and sliding process of the landslide.

Before reservoir impoundment (Fig. 2). The bank slope was chair-shaped cataclinal slope, which was controlled by the slope structural form, and formation of two-stage flat mesa through the glacial erosion effect. There piled moraine and alluvial on the two-stage flat mesa. On the above flat mesa, moraine was dominated, and there was geomorphological conditions that surface water come together. Because of moraine on the above flat mesa was impermeable, surface water can not infiltrate, so the fissure water internal the slope was relatively poor due to lack of supply. In addition, lay and fissure located front of the slope were easily blocked in the leaching process. Therefore the underground water level near the river bank of the large rock landslide can only remain in place near the river level. So the bank slope was long-term relatively stable.

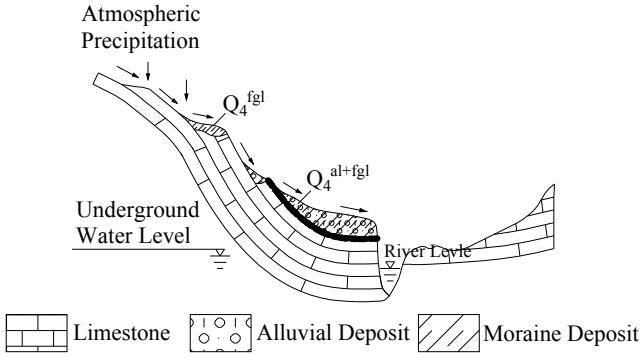


Fig. 2 Geological profile of the Vajont reservoir bank slope before impoundment

Initial stage of reservoir impoundment (Fig. 3a, Fig. 3b). When the water level of the reservoir to 642m ~ 652m, soil and rock at the front of the slope was submerged and shallow soil-rock aggregate landslides were occurred by the reservoir water pressure and uplift force. In the affect of drag and unloading of shallow landslides, it was destroyed that the closed condition, which the top of latent sliding surface of the Vajont reservoir bank landslide. So the tension crack was appeared on the above flat mesa and the groundwater supplementary amount was showered, as well as the groundwater dynamic variety range. Although the slope loads and normal stress imposed on the latent sliding surface was rose with the rise of the reservoir water level, but it was also raised that the drainage datum of the shallow phreatic water and uplift force and dynamic water pressure imposed on the shallow soil and rock. Soil and rock at the front of the slope submerged, that not only induced shallow soil-rock aggregate landslides, but also formed the large easily slipping hydrogeological structure in the rocky slope. Although both rainfall capacity and the reservoir water level was reached higher values, but because of its short duration, so the underground water level (hydrostatic pressure imposed on the front section of the latent sliding surface) in the rocky slope not yet reached the critical value which caused The Vajont reservoir rock landslide. The large rock landslide had not slid. Thus, comply with Pascal principle and hydrostatic pressure formula, it was showed in Fig.3b that groundwater pressure which imposed on the latent sliding surface.

Sliding of the large rock landslide (Fig. 4a, Fig. 4b). After June 1963, due to abundant rainfall, not only the water level of the reservoir continued to rise, it was also rapidly increased that the groundwater level on the latent sliding surface, which infiltration conditions of surface water had been significantly altered. And the rising speed of groundwater level was faster than the speed of the reservoir water level because of large supplementary amount and small hydraulic conductivity and storage space. The rainy season rainfall in 1963 was too large, especially the continuous heavy rain during September 28 ~ October 9. The continuous heavy rain caused the groundwater level on the latent sliding surface continued to rise further. And Finally, groundwater pressure on the latent sliding

surface leading edge reached the critical value that caused the rock landslide slid. So the large catastrophic rock landslide, called Vajont reservoir rock landslide, was occurred. It was a testament to the first slide of the front section stratum of the landslide that the stratum was not crushed and tiled in the Vajont reservoir.

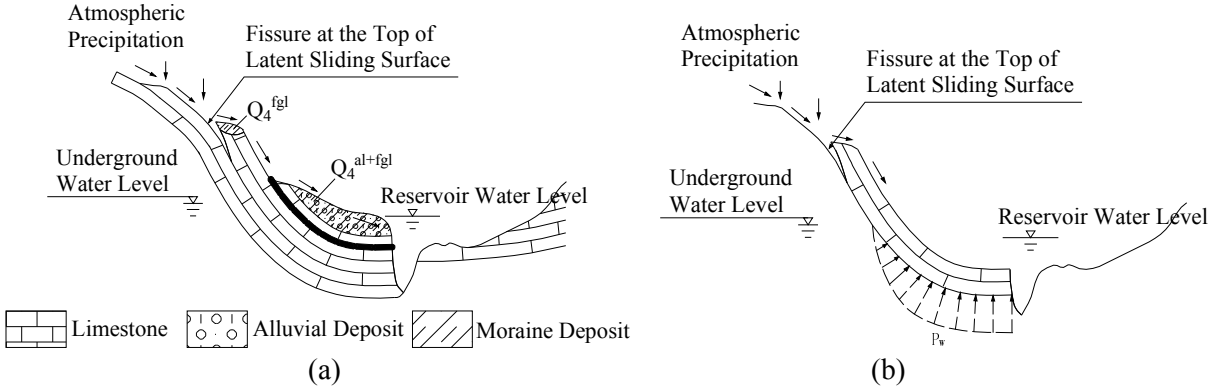


Fig. 3 (a) Geological profile of the Vajont reservoir bank slope in the initial stage of reservoir impoundment and (b) the groundwater pressure distribution

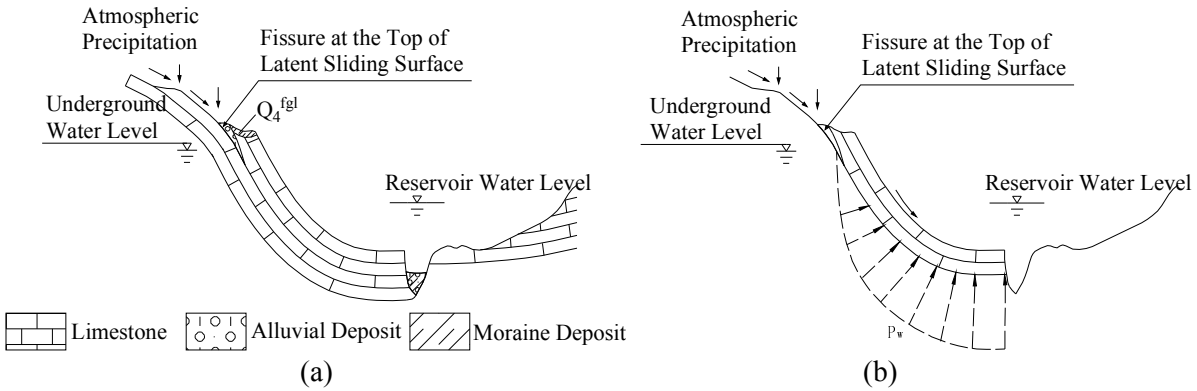


Fig. 4 (a) Geological profile of the Vajont reservoir bank slope and (b) the groundwater pressure distribution of the latent sliding surface at the landslide slid

From the above three phases discussion, it can be seen that germination and sliding process of Vajont reservoir rock landslide was a staged chain reaction. Because of the shallow landslide caused by initial impoundment of the reservoir changed the hydrogeological structure of the chair-shaped cataclinal rocky bank slope, the supply conditions of the latent sliding surface groundwater was improved. So the groundwater pressure that applied to the front part of the rocky bank slope reached to the critical value that the landslide occurred. However, the soil slippage at the front part of the Qianjiangping rock landslide, in the following illustration, may be mainly happened under the water.

**Qianjiangping Rock Landslide**

At 0:20 on July 13, 2003, a landslide with a volume of more than $1500\times10^4 m^3$ occurred on the left bank of the Qinggan River, Shazhenxi Town, Zigui County, Hubei Province, China. This was called Qianjiangping rock landslide. This landslide caused houses collapse, plant destroyed, traffic stop, rivers clogged, 28 people died, 22 fishing boats overturned, 14 fishermen killed. In addition, this landslide also caused 10 people missing and 19 people injured, 1200 people homeless. After the disaster, domestic authorities were extremely concerned about this landslide. One after another experts and scholars were sent to the landslide scene to participate in the disaster relief. And the landslide was carried out detailed investigation and research, and numerous research papers were published on the causes of the landslide. Here the genetic mechanism of the landslide was be analyzed based on existing data and site survey to the landslide.

**Regional Geological Environment and Slope Structure of the Qianjingping Landslide Region.** The Qianjingping landslide was just located in the reverse composite position of the NE-trending Zigui syncline, Xinhua fracture and NW-trending Liuleiguan anticline. Zigui syncline and Xinhua fracture are both component of Huaiyang tectonic system, and mainly finalized in the indosinian period. While Liuleiguan anticline is belong to the Sichuan-Hubei fold belt in the new cathaysian, which finalized in the Yanshanian period. The overall direction of the Sichuan-Hubei fold belt is the NNE to NE, but the Liuleiguan anticline located in the northeast terminal is be turned to NW because of the obstruct of Huaiyang tectonic system. In addition, Xinhua fracture is deep fracture, cutting through before sinian system strata, and has significantly activity in the recent period. The southern extension direction of Xinhua fracture is envisaging Qinggan river, where the front of the landslide take a sharp turn. So, the southern extension direction of Xinhua fracture is likely to pass along the bottom of the landslide failure surface and extend along Luogutong river. This tectonic position and its geological history also formed geologic environment and the structure type of the slope in the area of Qianjingping landslide region. There were many landslides in the Xinhua fracture and its south extension line, such as Liuleiguan landslide ($2600\times10^4m^3$), Shuitianba slump group (160 ~ $1250\times10^4m^3$) and Majiaba landslide ($2882\times10^4m^3$). Therefore, correct understanding of regional geological structure is of great significance for discovering easily slipping structure of the slope in time.

Qianjiangping landslide locate in plunging wing of the Liuleiguan anticline. The strata is amaranthine mudstone and shale interbedded with feldspar quartz sandstone of Niejiashan groups in Jurassic systerm ($J_{1\text{-}2n}$). The strata tendencies is the same as the slope. The strata dip angle is 25°~ 40° above the elevation 180m (upper section), it is 15°~ 20° below the elevation 180m, it is 10°~ 13° at the front of the slope [3-5] (Fig. 5). Obviously Qianjiangping landslide is a rock landslide happened in the chair-shaped cataclinal bank slope, the gully (whether for branch fault in dispute) and fault as its east and west boundaries. The Triassic strata mainly locate in the area of the landslide up to the ridge, as well as the Liuleiguan anticlinal axis. The geomorphic conditions is conducive to pooling the atmospheric precipitation, and converge to the upper of the landslide.

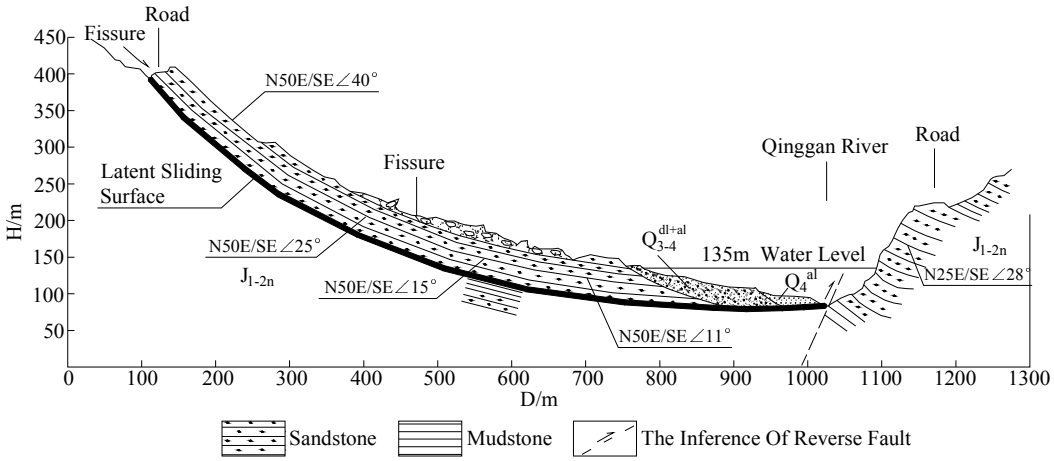


Fig. 5 Diagrammatic section of Qianjiangping landslide on the sliding threshold

**Sliding Process of the Qianjiangping Landslide.** The Qianjiangping landslide located in the left bank of the Qinggan river which is a primary tributary of the Yangtze river, less than 2 km away from the estuary and about 50 km away from the Three Gorges Project dam site. The landslide slid at the 33 days after the 135 m elevation water storage of the Three Gorges reservoir. The Qinggan river elevation was 95 m and the riverbed elevation was 92 m before the Three Gorges reservoir impound. On June 13, 2003, three days after the Three Gorges reservoir impoundment to 135m, intermittent tension cracks began to appear at the position of 400 m elevation. On June 21 to July 11, 2003, the heavy rainfall occurred in the landslide area, with a total rainfall of 162.7mm. Since July 1, 2003, fine cracks were appeared on the silicon factory road about 200m elevation. On July 12, the cracks were

arced and penetrative, open about 2m. On July 12 at 11 PM, there were many obvious cracks on the bank slope and sharply open. About 1:00 the next day, the landslide occured at high sliding speed of approximately 17.6 m/s for 1 minute, then small-scale landslides occurred at the upper edge and sides, five minutes after, the landslide stopped. The shear outlet of the landslide was 100m ~ 110m.

**Pregnant and Sliding Mechanism of the Qianjiangping Landslide.** Modern, there was no obvious indication of deformation and damage in the Qianjiangping landslide area, and there was no history of landslide disasters. However, the landslide incident, as well as the Vajont reservoir rock landslide, showed that can't use pure rock and soil mechanics point of view to treat with bank slope stability problems, which has complex evolution history and environmental conditions, especially not analyze pregnant and sliding mechanism of the landslides just from the mechanical properties of rocks or sliding surfaces. Now pregnant and sliding mechanism of the Qianjiangping landslide was revealed by analyzed the corresponding relationship of the slope structure, dynamic change of the landslide main inducing factors and each part deformation and failure of the slope on the sliding threshold.

First, although the rock slope of the Qianjiangping landslide area was chair-shaped cataclinal bank slope, with free face at the front of penetrative discontinuities, but belonged to the alluvial coast in the rising district during the recent period. Therefore before the Three Gorges reservoir impounded, it was growing and heavier that the soil on the front of sliding resistance segment, with gently dip angle, although the soil also suffered heavy rain, groundwater and flooding erosion, but its overall stability was to a better direction.

On June 1 ~ 10, 2003, the water level of the Three Gorges reservoir reached 135 m elevation, only three days later, intermittent tension cracks began to appear at the position of 400 m elevation. At the moment, the mechanical properties of latent sliding surface itself of the Qianjiangping landslide is unlikely to have a big change. Because the latent sliding surface in the river incised period had experienced 135m ~ 100m elevation change, and also suffered heavy rain, groundwater and flooding erosion, and sliding resistance segment, with gently dip angle, was certainly shorter and thinner than the time of the landslide slid, that through shear strength of the latent sliding surface was more difficult to maintain stable in that time. With the river incision, there had been surface sliding in the free face of slope and accumulated to the front edge, causing the river to the other side and the sliding resistance segment growth. However, these alluvium and colluvium at the gentle slope mesa and the foot of the slope were the modern (from a geological time) to add, so they were easily sliding part or all by flooded and submerged of the Three Gorges reservoir water while the water level rise again to 135 m elevation. Uplift pressure was stressed on the submerged rock at the front of the slope (especially shallow sandstone above river bed mudstone layer) by the reservoir water, so that normal stress on the latent sliding surface was decreased and unloading and drag effect by the sliding of rock and soil landslides was also stressed on the submerged rock. Both of these make the sliding resistance of the front section of the slope further reduce, and lead to the upper steep dip rock adjustable sliding downward with intermittent cracks on the road located in the rear of the landslide. So groundwater recharge conditions above the latent sliding surface was larger changed.

Another effect that the Three Gorges reservoir water level rise was raised groundwater drainage plane, Even under the condition of supplementary amount invariable, the underground water level was also increase correspondingly and easily caused shallow rock and soil slid. However, whether the landslide slid mainly depend on the underground water supply conditions of the deep latent sliding surface.

But very unfortunately, June 21 ~ July 11, 2003, heavy rainfall occurred in the landslide area. At this stage, the tension cracks on the back steep wall of the landslide had been more conducive to the land surface water infiltration and groundwater levels raise rapidly, thus greater groundwater pressure stressed sliding resistance segment of the landslide which resistance forces reduced. However, due to the dynamic changes of the groundwater (especially deep latent sliding surface groundwater) lag behind in rainfall and surface water, two days after the end of the continuous heavy rain, that July 12 ~ 13, 2003, the groundwater level and its pressure on the sliding resistance segment was increased to

the critical value of the landslide slid. When July 12, 2003, the cracks in the back steep wall of the landslide were arced and penetrative, July 12 at 11 PM, there were many obvious cracks on the slope and sharply open, about 1:00 the next day, the rock landslide overall finally slid downward rapidly.

**Revelation of Contrast Analysis and Study between the Vajont Reservoir Rock Landslide and Qianjiangping Rock Landslide**

Pregnant and sliding process of the large rock landslides, such as Vajont reservoir rock landslide and Qianjiangping rock landslide, showed two stages. First, under the influence of initially impoundment of the reservoir, the soil and shallow rock at the front of the slope was slid downward, caused unloading and drag effect, this effect caused posterior margin of the deep latent sliding surface cracks, and then surface water was easy to infiltration to supplying the groundwater. Second, with the rapidly increase of groundwater recharge, its pressure was also rapidly rise to the critical value which caused the landslides. The interval of these two stages, generally may be a few days or a few years, depended on the structure elements of the latent sliding surface, the change degree of the groundwater supply conditions and the recharge growth rate of the groundwater. Tangyanguang landslide occurred in Tuoxi reservoir in 1961, in Hunan province. The slope which the Tangyanguang landslide occurred in was also chair-shaped cataclinal slope. Due to the dip angle of the upper steep sand slate was reached 45°, and the loose layers at the front of the slope was thick, the two stage was just 12 hours apart.

Through analysis the pregnant and sliding process of Vajont reservoir rock landslide, an important understanding can be concluded that with the reservoir water level rise the normal stress on the latent sliding surface was increased and the groundwater supply conditions of the latent sliding surface was changed by the unloading and drag effect, which caused by the submerged soil and shallow rock at the front of the slope slid downward. Often the latter effect was revealed more prominently in the second stage. That was, after hydrogeological structure of the slope changed, inducing factors dynamically had only the possibility of starting the landslides, groundwater pressure would become main mechanical mark which caused the rock landslides. Also known as that the groundwater pressure on the front section of the latent sliding surface reached the critical value, the rock landslides occurs. In addition, it was easy to see that the emergency measures to reduce the water level of the Vajont reservoir adopted by the staff was incorrect, because at that time it was urgently needed to reduce the groundwater level rather than the reservoir water level. Seepage rate of the underground water is far lower than the flow velocity of the reservoir water, so they are impossible to synchronize decline. Through the reservoir level lower rapidly, the pressure difference between reservoir water and groundwater was widen and normal stress and friction on the latent sliding surface was reduced, thereby the landslides sliding was accelerated. Meanwhile, because of rapidly drainage, the flow condition of the reservoir water was complex, even partial vacuum and negative pressure was formatted in the latent sliding surface. As a result, to reduce the water level of the Vajont reservoir was actually added fuel to the fire, accelerated the Vajont reservoir rock landslide slid.

Therefore, detailed investigation and study to the typical landslides case was basis and premise that understand pregnant and sliding mechanism of the reservoir bank landslides, established mechanics model of the reservoir bank slope stability and the critical value formula of the landslide sliding, determined the quantitative marks of prediction and forecasting landslide. Simple rainfall or rise and fall of the reservoir water cannot become iconic factor of the landslides slid, while it was to find the real cause of the rock landslides slid that only to understand the dynamic change of groundwater (especially the groundwater pressure change) before the landslides slid. However, in the three years monitoring of Vajont reservoir rock landslide, it was precisely lack of the dynamic monitoring of groundwater, and therefore it was fail to succeed for lack of a final effort. The incident also exposed many problems of the previous monitoring methods and equipments.

Qianjiangping rock landslide, as well as Vajont reservoir rock landslide, had easily slipping structure of chair-shaped cataclinal slope. Both of the two landslides were occurred under the force of

the successive coupling that the landslide weight force, the reservoir water uplift pressure, unloading stress and drag force by the sliding of front rock and soil landslides and groundwater pressure. When it was the groundwater pressure that final breakthrough stability limit and causing landslides. Although the magnitude of the forces on the slope was different at each place, but specifically for each bank slope section, these forces were measured and can be calculated. Therefore the mechanical model of chair-shaped cataclinal slope stability was established, and the value of hydraulic induced the landslide was calculated. So that correctly regulate or engineering measures adopted in order to improve the stress state of the latent landslide, to achieve the purpose of disaster prevention.

## Stability Mechanical Model of Chair-Shaped Cataclinal Bank Slope and Critical Value of the Rock Landslide Sliding

**Mechanical Model and Critical Value Formula of the Rock Landslide Sliding.** For easy to comparison and understanding, the mechanical model of general chair-shaped cataclinal slope stability in reference [9] (Fig. 6a) was also attached.

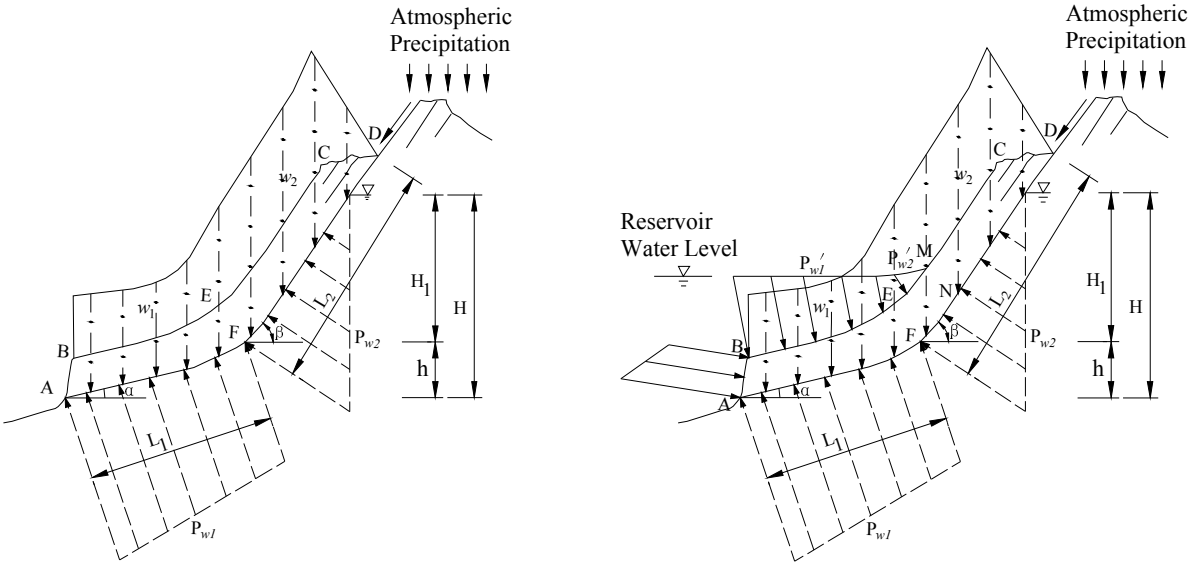


Fig. 6 The pressure diagrammatic section of the unit width of (a) the general chair-shaped cataclinal slope and (b) the chair-shaped cataclinal bank slope (In accordance with the Vajont reservoir bank slope)

In the Fig. 6, – · → gravity vector of the latent sliding body, — — ► interstitial hydraulic pressure vector of the latent sliding surface, ⟶ reservoir water pressure vector of the surface of latent sliding body, $w_1$ —— the per unit area gravity of ABEF section latent sliding body at the gravity center position, $w_2$ —— the per unit area gravity of ECDF section latent sliding body at the gravity center position, $p_{w1}$ —— the per unit area interstitial hydraulic pressure of ABEF section latent sliding body at the pressure center position, $p_{w2}$ —— the per unit area interstitial hydraulic pressure of ECDF section latent sliding body at the pressure center position, $p_{w1}'$ —— the per unit area reservoir water pressure of ABEF section latent sliding body at the pressure center position, $p_{w2}'$ —— the per unit area reservoir water pressure of EMNF section latent sliding body at the pressure center position, $L_1$ —— the length of ABEF section latent sliding surface, $L_2$ —— the length of ECDF section latent sliding surface, $H$ —— elevation difference of the underground water level to A point, $H_1$ —— elevation difference of the underground water level to F point, $h$ —— elevation difference of A point to F point.

After the reservoir water level rise to flat mesa of the slope lower section, water pressure is actually exist perpendicularly to the front free face of the slope, as shown in fig. 6b. But in view of the reservoir water easy mobility and hydraulic connection with the bank slope groundwater, so it is

difficult to resist the slide of the bank slope. For this reason, the reservoir water pressure on the front free face of the slope was not considering in the mechanical model of chair-shaped cataclinal bank slope stability and critical value of the rock landslide sliding. And when the reservoir water level continues to rise to more than the slope turning point of the steep section to flat section, because of the surface covering layer is scattered and thin, even if fall, the unloading and drag effect is often very small, so it can be also ignored. Longitudinal pressure of the reservoir water is perpendicular to the slope surface, it can rough as a normal stress on the latent sliding surface only the dip angle of the slope surface very small differ to the latent sliding surface, otherwise it need to conversion. Although the load of the reservoir water pressure, dynamic variation between the level of dead water and normal high water, had been added to the mechanical model of chair-shaped cataclinal bank slope stability, but its variation range and way is also limited for each specific reservoir bank slope.

From fig.6 it is not hard to see that the slope front section of the penetrative discontinuities smooth (ABEF section) is sliding resistance. The applied forces on the ABEF section have rock mass gravity, interstitial hydraulic pressure, reservoir water pressure, also have total surplus sliding force (*Pr*) of upper dipping section (ECDF section) of the slope. So the hydraulic starting critical value of the landslide is the start value of the total latent sliding body. In order to make calculation formula not too multifarious, the amount of forces had been expressed, their corresponding symbols also use capital letters. So, the mechanical model of chair-shaped cataclinal bank slope stability had been established on the basis of the mechanical model of general chair-shaped cataclinal slope stability. Its computation formula was as follow,

$$K = \frac{(W_1 \cos\alpha + P_{W1}^{'} - P_{W1} t_{w1}) tg\varphi_c}{W_1 \sin\alpha + P_r \cos(\beta - \alpha)} \tag{1}$$

While $K$=1, the critical value of groundwater pressure on the landslide sliding threshold was educed as follow,

$$H_{critical} = \frac{\sqrt{b^2 - 4ac} - b}{2a} + h \,. \tag{2}$$

$$a = \frac{\gamma_w t_{w2} tg\varphi_c \cos(\beta - \alpha)}{2\sin\beta} \,. \tag{2-1}$$

$$b = \gamma_w L_1 t_{w1} tg\varphi_c \,. \tag{2-2}$$

$$\begin{aligned} c = {} & W_1(\sin\alpha - \cos\alpha tg\varphi_c) + W_2 \cos(\beta - \alpha)(\sin\beta - \cos\beta tg\varphi_c) + \gamma_w L_1 h t_{w1} tg\varphi_c / 2 - \gamma_w h_1 l_1 tg\varphi_c / 2 \\ & - \gamma_w h_2 \left[ 2l_1 + l_2 \cos(\beta - \alpha) \right] tg\varphi_c / 2 \end{aligned} \,. \tag{2-3}$$

In the above formula, $\varphi_c$ —— comprehensive internal friction angle of the penetrative discontinuities (latent sliding surface) in the absence of water pressure effect, $t_{w1}$ —— water seepage rate of ABEF section of the penetrative discontinuities (latent sliding surface), $t_{w2}$ —— water seepage rate of ECDF section of the penetrative discontinuities (latent sliding surface), $\gamma_w$ —— unit weight of water, $l_1$ —— distance of B point to E point, $l_2$ ——distance of M point to E point, $h_1$ —— elevation difference of B point to E point, $h_2$ —— elevation difference of M point to E point. The determination method of the $\varphi_c$ and $t_w$ had been introduced in reference [9], it can be constantly improved and supplement in practice in the future.

**Procedures and Methods Determination of Critical Value of The Bank Rock Landslide Sliding.** First of all, according to field investigation data, it was determined that whether there was easily slipping hydrogeological structure. The so-called easily slipping hydrogeological structure, simply speaking, should have at least the following three conditions. The first, the steep section of the chair-shaped cataclinal rock bank slope is close to or even longer than the flat section, and the upper

of the steep section has geographic and geomorphic conditions for surface water collection or has possible leakage drainage engineering. The second, it has aquifer in the slope with good water-resisting top and bottom. The third, the front and side ditch of aquifer may be blocked or covered, so it go against groundwater discharge, and is conducive to groundwater accumulation and its level rise. This stage work is the premise and foundation of later work, it need more geological basic theoretical knowledge and experience of field to identification, and should pay attention to the basic requirement of the engineering geological survey. It must not "do a rough work with outstanding method" (Albert Einstein).

According to the upper rock outcrop of the rock bank slope and the highest crack pulled by shallow rock and soil sliding, the possible highest level of groundwater could be to determine. And the critical value of groundwater pressure on the landslide sliding in low reservoir water level could be to calculated using the Eq. 2. Comparison the two value of number above, to determine whether the rock bank landslide slides. If possible, the landslide stability will be calculated step by step according to the coupling effect of different reservoir water level and groundwater level using the Eq. 1.

Both of the reservoir water level and groundwater level are variable, and it has transformation process from the reservoir water gravity to normal stress and sliding pressure on the latent sliding surface, which is Influenced by the geometry of the surface. Computational process of the critical value of groundwater pressure on the landslide sliding is very complicated, so it can use the matrix method for numerical simulation, and it can calculate under the coupling effect of different reservoir water level and groundwater level with the aid of computer. As a result, the critical value of the landslide most easily slides will be determined. This value is the quantitative mark of landslide prediction and forecasting and reliability evaluation of landslide control measures.

The critical value of groundwater pressure on the landslide sliding threshold was layered calculated with multilayer aquifers of easily slipping hydrogeological structure of the chair-shaped cataclinal bank slope.

**Instance Analysis**

Liangshuijing landslide was formerly known as the Biaoganshang in the reference [8] attached fig.1. The landslide located in Guling town, Yunyang country, on the right bank of the Yangtze river, which was 38 km away from the Yunyang county. When the Three Gorges reservoir water level rise to 172m, the landslide began to appear deformed since the November 2008. According to the monitoring data of geological environmental monitoring station in the Yunyang country, the landslide was increasing deformation at a speed of 1 cm every day, since March 10, 2009. To April 1, the penetrative tension cracks were appeared in the back scarp of the landslide, about 150 m length and 10 cm ~ 25 cm width. The elevation was 105 m at the front of the landslide and 289 m at the back cracks. The landslide was 250 m to 370 m length, 200 m ~ 370 m width, about 35 m of average thickness, with about $360\times10^4 m^3$ total volume. The back scarp of the landslide had been dropped 45 cm ~ 60cm, with 45cm plane displacement.

Liangshuijing landslide was also occurred in the the chair-shaped cataclinal rock bank slope and its stability had been successfully predicted prior to the Yangtze river Three Gorges Project construction. When the reservoir level rise to 172 m, the shallow sliding was occurred at the front of the slope and caused the Yangtze river closure of navigation. It is monitoring that whether or not the landslide occurs through the deep penetrative discontinuities. The monitoring methods of the landslide are mainly displacement monitoring using tiltmeter, but lack of quantitative marker. So, the quantitative evaluation method of whether or not the landslide slides is advised, which adopt the critical value formula of the rock landslide sliding put forward in this paper. And the monitoring of groundwater pressure is strengthen, especially the front section of the landslide. At the same time, to seal of cracks of the landslide back scarp and find out whether other penetrative discontinuities was pulled in order to handle in time. Both of the methods can prevent the landslide slides caused by the groundwater pressure, one is truncation of surface water supplement, the other is drainage decompression to the

deep latent sliding surface at the strata dip angle turn. Meanwhile, the drainage holes and the connecting beams at the top of drainage hole can also prevent shallow rock and soil landslides. Under the condition of the appropriate location and structure, the drainage holes can also be used to monitoring the stability of reservoir rock bank. The monitoring result can also be graded warning according to the mechanical model of chair-shaped cataclinal bank slope stability and critical value of the rock landslide sliding in this paper added the necessary safety.

## Conclusions

Based on study between the Vajont reservoir rock landslide and Qianjiangping rock landslide, it was obtained that the fundamental laws and generality of structural conditions, inducing factors, deformation and failure characteristics of the landslides which occurred in the chair-shaped cataclinal rock bank slope. And it was preliminarily revealed that the pregnant and sliding mechanism of the landslides which showed two stages. The groundwater supply condition of the latent sliding surface was changed by the shallow rock and soil landslide in initial period of the reservoir impoundment. This also created the structure premise that the groundwater pressure on the latent sliding surface rise to the critical value of the rock landslides slid.

Based on the mechanical model of general chair-shaped cataclinal slope stability, it was established that mechanical model of chair-shaped cataclinal bank slope stability and computational formula and work procedures and methods of the rock landslides caused by the groundwater pressure on the latent sliding surface. This provides quantitative criteria of monitoring and early warning for rock landslides and provide design basis of landslides control measures.

After the groundwater levels reached the critical value, the sudden conversion of the hydrodynamic pressure and hydrostatic pressure caused the landslides. So the key to the landslides prevention is timely to intercept groundwater supply and drain the groundwater of latent sliding surface. Meanwhile, it is a more accurate and reliable method that monitoring and warning using of the dynamic changes of the groundwater pressure.

In view of the complexity of this problem, the author would like to see more colleagues took a different understanding to participate in discussion of this issue.

## References

[1] J.G.C. Anderson and C.F. Trigg: *Case-Histories in Engineering Geology* (Geological Publishing House, China 1986). (in Chinese)

[2] L.S. Wang: Chinese Journal of Geological Hazard and Control Vol.18 (2007), p. 145 (in Chinese)

[3] S.R. Xiao, D.F. Liu, F.X. Jiang and X.L. Jiang: Chinese Journal of Rock Mechanics and Engineering Vol.29 (2010), p. 1023 (in Chinese)

[4] B.P. Wen, J. Shen and J.M. Tan: Hydrogeology and Engineering Geology Vol.35 (2008), p. 12 (in Chinese)

[5] S.D. Li, X. Li, Y.H. Liu and X.S. Sun: Hydrogeology and Engineering Geology Vol.35 (2008), p. 18 (in Chinese)

[6] F.C. Dai, J.H. Deng, L.G. Tham, K.T. Law and C.F. Lee: Can. Geotech. J. Vol.41 (2004), p. 1233

[7] F.W. Wang, Y.M. Zhang, Z.T. Huo, Tatsunori Matsumoto and B.L. Huang: Landslides Vol.1 (2004), p. 157

[8] X.C. Chen, et al: *Type and Stability of the Reservoir Banks of the Three Project in Yangtze River* (Sichuan Technology and Science Press, China 1993) (in Chinese)

[9] X.C. Chen, M.C. Gu, S.W. Shi and X.C. Ma: Journal of Engineering Geology Vol.17 (2009), p. 752 (in Chinese)

*Applied Mechanics and Materials Vols. 580-583 (2014) pp 2600-2606*
*© (2014) Trans Tech Publications, Switzerland*
*doi:10.4028/www.scientific.net/AMM.580-583.2600*

# Research on method for the weight definition of evaluation indicator in dump landslides based on rough set

Tingting Luan[1, a *], Zhenhua Xie[2,b] and Shasha Liang[1,c]

[1]Civil and Environment Engineering School, University of Science and Technology Beijing, Beijing 100083, China

[2]Department of Safety Engineering, China Institute of Industrial Relations, Beijing 100048, China

[a]ustb_ltt@163.com, [b]xie0015@sina.com, [c]775728690@qq.com

**Keywords:** rough set; expert scoring; dump landslide; weight calculation

**Abstract.** To combine expert scoring and rough set two kinds of subjective and objective methods, avoiding the indicator weight value is zero, making the expert scoring more efficient, objective. Using the expert scoring method based on rough sets in determining evaluation indicator weights of open-pit dump landslide. Slope density, cohesion, internal friction angle, slope angle, slope height, pore pressure ratio were selected for evaluation indicators of dump landslide. First of all, according to the landslide data collected, to calculate the importance sort of evaluation indicators of the dump landslide based on rough set theory. Then, scores of each indicator corresponds to a certain interval, five relevant experts were selected for scoring. Finally, the weight of each indicator was determined based on the average score. We can know from results, slope angle has the biggest influence on the dump landslide, followed by pore pressure ratio .Slope height and slope density have the minimal impact, which is coincidence with the actual situation of the dump, it shows that the method is more rational and effective .

## Introduction

Currently, the method for determination of the indicator weight includes subjective and objective weighting method. Subjective weighting method is simple, but it requires higher personnel evaluation experience which is influenced by their knowledge and experience; Objective weighting method can effectively convey the data information and differences of the evaluation. The evaluation results are objective and scientific, but sometimes weighting coefficient is unreasonable. In the process of determining the weights, if we can consider both objective and subjective factors, the indicator weight will be more in line with the actual situation, and the assessment accuracy will be improved.

Rough set theory was proposed by the academician Pawlak fron Warsaw University of Technology, in the early 1980s, the theory is about data analysis and reasoning [1-3]. In the process of introducing the rough set theory to China, professor Liu Qing [4], professor Zeng Huanglin and other scholars have made a relatively large contribution.. As the rough set theory can fully reflect the objectivity of the data, without providing any prior knowledge other than the data information, many scholars have studied the weight determination method based on rough set theory. In recent years, the method has been applied in many fields. "Investigation of method for determining factors weights in evaluating slope stability based on rough set theory" is published by Guangyue Wang, Haili Cui and Qian Li in 2009[5]. *"Index weight determination of construction enterprises' social responsibility estimation based on rough set"* is published by Yongshi Pang, Ying Wang in 2012[6]. *"Impact factor weighting analysis of volcanic debris flow of Changbai mountain based on rough set theory"*is published by Yumeng Wang, Chunhong Zou, Han Lv in 2013[7]. However, there is a problem in the indicator weights based on rough set theory: the weight value may be zero, which is not consistent with the actual situation, and the accuracy of the evaluation results is also influential. This paper presents an expert scoring method based on rough set theory. The method combines two methods, which not only can play the advantages, but also avoid the deficiencies, and the weights are more realistic.

## Overview of Rough Set Theory

**Concept of Rough Set.** Definition 1: Command $X \subseteq U$ , when $X$ can be exactly described by attributes subset $B$ (That is the union of attributes subset $B$ of and identified set $U$) $X$ is definable to $B$ , otherwise $X$ is not definable to $B$. Definable set $B$ also called accurate set $B$. Cannot be defined set $B$ is also known as imprecise set $B$ or $B$ Rough (without confusion, it is referred to as $B$ Rough Set) [4].Definition 2: For each concepts $X$, the biggest definable sets that no clear relationship $B$ is contained by $X$ or the smallest definable sets that contain $X$, are able to be determined in accordance with $B$. The former called lower approximation of $B$ (denoted by $B_(X)$), the latter called upper approximation of $X$ (denoted by $\bar{B}(X)$) [4].Definition 3: Set $BN_B(X) = \bar{B}(X) \setminus B_(X)$ is called $B$ boundary of $X$; $POS_B(X) = B_(X)$ is called $B$ positive region of $X$; $NEG_B(X) = U \setminus B_(X)$ is called $B$ negative region of $X$ [4].

**Indiscernible Relationship.**Set theory domain for $U$, $P$ for a subset of condition attributes $C$ , the indiscernibility relation $IND(P)$ determined by $P$ is: $IND(P) = \{(x, y) \in U \times U / \forall a \in P, f(x,a) = f(y,a)\}$ Where: $f(x,a)$ represents the values of theory domain element $x \in U$ about attribute of a; The indiscernibility relation $IND(P)$ constitutes a category of $U$ , denoted by $U / IND(P)$ [5].

**Knowledge Reduction.** Knowledge reduction is the core of rough set theory. As we all known, the knowledge of knowledge base (property) are not equally important, or even some of them are redundant. The so-called knowledge reduction is to keep the classification ability of the knowledge base same, and to delete irrelevant or unimportant knowledge. $R$ is an equivalence relation, $r \in R$, if $IND(R) = IND(R - \{r\})$, r is called the knowledge can be deleted in R ; if $P(R - \{r\})$ is independent, $P$ is a reduction of $R$ [5].

**Attribute Importance.** Order $P$ and $Q$ are a subset of condition attributes $C$ and decision attributes $D$ respectively. Then, the formula $K = \gamma_p(Q) = \frac{|POS_p(Q)|}{|U|}$ indicates that the knowledge $Q$ depends on the knowledge $P$ of degree $K$, denoted by $P \Rightarrow_K Q$ . Wherein: $|U|$ represents a base of $U$ , that is the number of elements in $U$ ; Similarly , $|POS_p(Q)|$ represents the number of elements in $POS_p(D)$ .The importance of subset of attributes $C_i \subseteq C$ about D is defined as $\sigma_D(C_i) = \gamma_c(D) - \gamma_{c-c_i}(D)$ , The larger the value of $\sigma_D(C_i)$ , the greater the importance of the corresponding attribute indicates ; Conversely , the smaller the importance is[5].

## Expert Scoring Method to Determine the Weight Based on Rough Sets

**Expert Scoring Method and its Characteristic.** Expert scoring method refers to consult experts by anonymous methods, then deal with expert opinions, synthesize most experts experience and subjective judgment objectively, and make a reasonable estimate for a large number of factors that is difficult to quantitative analysis, after several rounds of consultation, feedback and adjust, obtaining the final result. Its advantages are simple, intuitive and strong, simple calculation and larger choices, it can consider all evaluation items whether can be quantitative evaluation or not. Its shortage is that the weight is cannot be calculate likely, if experts opinions cannot achieve unity, after consulting experts opinions in multiple rounds. Alone expert scoring method is prone to inconsistent feedback,even after many adjustment, it is difficult to achieve unity, moreover expert scoring method based on rough set can analyze data information objectively by means of rough set theory， and have a objective sort for the importance of weights of evaluation indicators,experts give subjective experience scores based on this objective sort, it can well avoid the situation that experts opinions is difficult to achieve unity[8].

**Steps of Expert Scoring Method to Determine the Weight Based on Rough Sets.**The method to determine the weighting based on rough set theory is entirely according to the objective data, making data mining for the original data, on the basis of the discrete data, and translating weight problems into the problem of attribute importance in rough set; the expert scoring method is entirely according to experts' subjective knowledge and experience, then several rounds of scoring and finally determine the indicator weight; the expert scoring method based on rough set theory is to combine both methods well, mutually to make up their deficiencies, giving full play to the advantage of the subjective and objective methods. Steps of expert scoring method to determine the weight based on rough sets are as follows.

First of all, the rough set method needs to make continuous attribute discrete, namely the continuous attribute domain is divided into a number of interval, different codes for different intervals.

Second, the discrete attribute values form a two-dimensional table, each line describes an object, each column to describe a condition attribute of an object, the last one or two is decision attribute.

Then, to have knowledge reduction, to delete the object with same attribute values, namely repetitive data lines, to make equivalence partitioning for discourse domain according to the condition attributes and decision attributes, after getting rid of some properties, if the change of relevant classification is bigger, it indicated that the properties importance is higher; On the other hand, it shows that the properties importance is lower.

Finally, according to the importance ranking of condition attributes, each condition attribute have each score interval, select a number of experts to give the score for condition attribute, scoring is conform to the prior division score range, then calculating the average value, and normalization, and getting the final weight value.

## Case Study

The open-pit mine dump, a place as acceptance waste rock of open pit mine, is a permanent engineering construction which is indispensable to the open-pit [9]. As our country dump has serious phenomenon such as large capacity, high pile height, insufficient attention to the foundation, disorderly dig the foot of the slope mining brings risks to the stability of the dump, leading to the dump landslide disasters have become increasingly prominent. Dump landslide is the most common occurrence and the highest frequency in dump disaster, however, there are many factors to affect the stability of dump slope, on the basis of both research results and data information from references, to select slope unit weight, cohesion, internal friction angle, slope angle, slope height, Pore pressure ratio as landslide evaluation indicators of opencast mine dump.

There are 25 sets of circular landslide collected in table 1 [10], in this information table, the discourse domain is $\{1, 2, 3,... 25\}$, the condition attribute set is $\{C_1, C_2, C_3, C_4, C_5, C_6\}$, the decision attribute set is $\{D_1, D_2\}$, including: $C_1$ as slope unit weight, $C_2$ as cohesion, $C_3$ as internal friction angle, $C_4$ for slope angle, $C_5$ for slope height, $C_6$ for pore pressure ratio; $D_1$ for stability coefficient, $D_2$ for slope condition. To calculate the attribute importance of indicators in above procedure, the discrete data processing, the selection of discrete values refer to reference 5, the discrete data table is shown in table 2; then the simplified data table is shown in table 3.

**Table 1 Circular landslide data of dump**

| NO. | slope density $\gamma(kN/m^3)$ | cohesion $c(kPa)$ | internal friction angle $\varphi(°)$ | slope angle $\alpha(°)$ | slope height $H(m)$ | pore pressure ratio $\gamma_w$ | stability coefficient | slope condition |
|---|---|---|---|---|---|---|---|---|
| 1 | 20.41 | 24.9 | 13 | 22 | 10.67 | 0.35 | 1.4 | stable |
| 2 | 19.63 | 11.97 | 20 | 22 | 12.19 | 0.405 | 1.35 | unstable |
| 3 | 21.83 | 8.62 | 32 | 28 | 12.8 | 0.49 | 1.03 | unstable |
| 4 | 20.41 | 33.52 | 11 | 16 | 45.72 | 0.2 | 1.28 | unstable |

| | | | | | | | | |
|---|---|---|---|---|---|---|---|---|
| 5 | 18.84 | 15.32 | 30 | 25 | 10.67 | 0.38 | 1.63 | stable |
| 6 | 18.84 | 0 | 20 | 20 | 7.62 | 0.45 | 1.05 | unstable |
| 7 | 21.43 | 0 | 20 | 20 | 61 | 0.5 | 1.03 | unstable |
| 8 | 19.06 | 11.7 | 28 | 35 | 21 | 0.11 | 1.09 | unstable |
| 9 | 22.4 | 10 | 35 | 45 | 10 | 0.4 | 0.9 | unstable |
| 10 | 20 | 20 | 36 | 45 | 50 | 0.5 | 0.83 | unstable |
| 11 | 20 | 0 | 36 | 45 | 50 | 0.25 | 0.79 | unstable |
| 12 | 22 | 0 | 40 | 33 | 8 | 0.35 | 1.45 | stable |
| 13 | 24 | 0 | 40 | 33 | 8 | 0.3 | 1.58 | stable |
| 14 | 20 | 20 | 36 | 45 | 50 | 0.25 | 0.96 | unstable |
| 15 | 20 | 0 | 25 | 20 | 8 | 0.35 | 1.37 | stable |
| 16 | 18 | 5 | 30 | 20 | 8 | 0.3 | 2.05 | stable |
| 17 | 27 | 40 | 35 | 43 | 420 | 0.25 | 1.15 | unstable |
| 18 | 27 | 50 | 40 | 42 | 407 | 0.25 | 1.44 | stable |
| 19 | 27 | 35 | 35 | 42 | 359 | 0.25 | 1.27 | stable |
| 20 | 27 | 32 | 33 | 43 | 301 | 0.25 | 1.16 | unstable |
| 21 | 27 | 32 | 33 | 43 | 289 | 0.25 | 1.3 | stable |
| 22 | 27.3 | 14 | 31 | 41 | 110 | 0.25 | 1.249 | stable |
| 23 | 27.3 | 31.5 | 30 | 41 | 135 | 0.25 | 1.245 | stable |
| 24 | 25 | 55 | 36 | 45.5 | 299 | 0.25 | 1.52 | stable |
| 25 | 31.3 | 68 | 37 | 47 | 213 | 0.25 | 1.2 | unstable |

**Table 2 Discrete decision table**

| NO. | slope density $\gamma(kN/m^3)$ | cohesion $c(kPa)$ | internal friction angle $\varphi(°)$ | slope angle $\alpha(°)$ | slope height $H(m)$ | pore pressure ratio $\gamma_w$ | stability coefficient | slope condition |
|---|---|---|---|---|---|---|---|---|
| Discrete values for 0 | <23 | <21 | <36 | <45 | <60 | <0.26 | <1 | unstable |
| Discrete values for 1 | $\geq 23$ | $\geq 21$ | $\geq 36$ | $\geq 45$ | $\geq 60$ | $\geq 0.26$ | $\geq 1$ | stable |
| 1 | 0 | 1 | 0 | 0 | 0 | 1 | 1 | 1 |
| 2 | 0 | 0 | 0 | 0 | 0 | 1 | 1 | 0 |
| 3 | 0 | 0 | 0 | 0 | 0 | 1 | 1 | 0 |
| 4 | 0 | 1 | 0 | 0 | 0 | 0 | 1 | 0 |
| 5 | 0 | 0 | 0 | 0 | 0 | 1 | 1 | 1 |
| 6 | 0 | 0 | 0 | 0 | 0 | 1 | 1 | 0 |
| 7 | 0 | 0 | 0 | 0 | 1 | 1 | 1 | 0 |
| 8 | 0 | 0 | 0 | 0 | 0 | 0 | 1 | 0 |
| 9 | 0 | 0 | 0 | 1 | 0 | 1 | 0 | 0 |
| 10 | 0 | 0 | 1 | 1 | 0 | 1 | 0 | 0 |
| 11 | 0 | 0 | 1 | 1 | 0 | 0 | 0 | 0 |
| 12 | 0 | 0 | 1 | 0 | 0 | 1 | 1 | 1 |
| 13 | 1 | 0 | 1 | 0 | 0 | 1 | 1 | 1 |
| 14 | 0 | 0 | 1 | 1 | 0 | 0 | 0 | 0 |
| 15 | 0 | 0 | 0 | 0 | 0 | 1 | 1 | 1 |
| 16 | 0 | 0 | 0 | 0 | 0 | 1 | 1 | 1 |
| 17 | 1 | 1 | 0 | 0 | 1 | 0 | 1 | 0 |
| 18 | 1 | 1 | 1 | 0 | 1 | 0 | 1 | 1 |
| 19 | 1 | 1 | 0 | 0 | 1 | 0 | 1 | 1 |
| 20 | 1 | 1 | 0 | 0 | 1 | 0 | 1 | 0 |
| 21 | 1 | 1 | 0 | 0 | 1 | 0 | 1 | 1 |
| 22 | 1 | 0 | 0 | 0 | 1 | 0 | 1 | 1 |
| 23 | 1 | 1 | 0 | 0 | 1 | 0 | 1 | 1 |
| 24 | 1 | 1 | 1 | 1 | 1 | 0 | 1 | 1 |
| 25 | 1 | 1 | 1 | 1 | 1 | 0 | 1 | 0 |

**Table 3 Decision table of knowledge reduction**

| NO. | slope density $\gamma(kN/m^3)$ | cohesion $c(kPa)$ | internal friction angle $\varphi(°)$ | slope angle $\alpha(°)$ | slope height $H(m)$ | pore pressure ratio $\gamma_w$ | stability coefficient | slope condition |
|---|---|---|---|---|---|---|---|---|
| 1 | 0 | 1 | 0 | 0 | 0 | 1 | 1 | 1 |
| 2 | 0 | 0 | 0 | 0 | 0 | 1 | 1 | 0 |
| 3 | 0 | 1 | 0 | 0 | 0 | 0 | 1 | 0 |
| 4 | 0 | 0 | 0 | 0 | 0 | 1 | 1 | 1 |
| 5 | 0 | 0 | 0 | 0 | 1 | 1 | 1 | 0 |
| 6 | 0 | 0 | 0 | 0 | 0 | 0 | 1 | 0 |
| 7 | 0 | 0 | 0 | 1 | 0 | 1 | 0 | 0 |
| 8 | 0 | 0 | 1 | 1 | 0 | 1 | 0 | 0 |
| 9 | 0 | 0 | 1 | 1 | 0 | 0 | 0 | 0 |
| 10 | 0 | 0 | 1 | 0 | 0 | 1 | 1 | 1 |
| 11 | 1 | 0 | 1 | 0 | 0 | 1 | 1 | 1 |
| 12 | 1 | 1 | 0 | 0 | 1 | 0 | 1 | 0 |
| 13 | 1 | 1 | 1 | 0 | 1 | 0 | 1 | 1 |
| 14 | 1 | 1 | 0 | 0 | 1 | 0 | 1 | 1 |
| 15 | 1 | 0 | 0 | 0 | 1 | 0 | 1 | 1 |
| 16 | 1 | 1 | 1 | 1 | 1 | 0 | 1 | 1 |
| 17 | 1 | 1 | 1 | 1 | 1 | 0 | 1 | 0 |

The data table of knowledge reduction, according to the condition attributes and the decision attributes table, is classified as follows:

$U/IND(C)=\{\{1\},\{2,4\},\{3\},\{5\},\{6\},\{7\},\{8\},\{9\},\{10\},\{11\},\{12,14\},\{13\},\{15\},\{16,17\}\}$

$U/IND(D)=\{\{1,4,10,11,13,14,15,16\},\{2,3,5,6,12,17\},\{7,8,9\}\}$

The knowledge classification which have been remove a condition attribute respectively is as follows:

$U/IND(C-C_1)=\{\{1\},\{2,4\},\{3\},\{5\},\{6\},\{7\},\{8\},\{9\},\{10,11\},\{12,14\},\{13\},\{15\},\{16,17\}\}$

$U/IND(C-C_2)=\{\{1,2,4\},\{3,6\},\{5\},\{7\},\{8\},\{9\},\{10\},\{11\},\{12,14\},\{13\},\{15\},\{16,17\}\}$

$U/IND(C-C_3)=\{\{1\},\{2,4\},\{3\},\{5\},\{6\},\{7,8\},\{9\},\{10\},\{11\},\{12,13,14\},\{15\},\{16,17\}\}$

$U/IND(C-C_4)=\{\{1\},\{2,4\},\{3\},\{5\},\{6\},\{7\},\{8,10,11\},\{9\},\{12,14\},\{13,16,17\},\{15\}\}$

$U/IND(C-C_5)=\{\{1\},\{2,4,5\},\{3\},\{6\},\{7\},\{8\},\{9\},\{10\},\{11\},\{12,14\},\{13\},\{15\},\{16,17\}\}$

$U/IND(C-C_6)=\{\{1,3\},\{2,4,6\},\{5\},\{7\},\{8,9\},\{10\},\{11\},\{12,14\},\{13\},\{15\},\{16,17\}\}$

The importance analysis of each condition attribute for decision attribute is as follows:

$POS_{C_1}(D)=\{1,3,5,6,7,8,9,10,11,13,15\}$

$POS_{C-C_1}(D)=\{1,3,5,6,7,8,9,10,11,13,15\}$

$POS_{C-C_2}(D)=\{3,6,5,7,8,9,10,11,13,15\}$

$POS_{C-C_3}(D)=\{1,3,5,6,7,8,9,10,11,15\}$

$POS_{C-C_4}(D)=\{1,3,5,6,7,9,15\}$

$POS_{C-C_5}(D)=\{1,3,6,7,8,9,10,11,13,15\}$

$POS_{C-C_6}(D)=\{5,7,8,9,10,11,13,15\}$

$$\gamma_C(D)=\frac{|POS_C(D)|}{|U|}=\frac{11}{17}$$

$$\sigma_D(C_1)=\gamma_C(D)-\gamma_{C-C_1}(D)=\frac{|POS_C(D)|}{|U|}-\frac{|POS_{C-C_1}(D)|}{|U|}=\frac{11}{17}-\frac{11}{17}=0$$

$$\sigma_D(C_2)=\gamma_C(D)-\gamma_{C-C_2}(D)=\frac{|POS_C(D)|}{|U|}-\frac{|POS_{C_2}(D)|}{|U|}=\frac{11}{17}-\frac{10}{17}=\frac{1}{17}$$

$$\sigma_D(C_3)=\gamma_C(D)-\gamma_{C-C_3}(D)=\frac{|POS_C(D)|}{|U|}-\frac{|POS_{C_3}(D)|}{|U|}=\frac{11}{17}-\frac{10}{17}=\frac{1}{17}$$

$$\sigma_D(C_4)=\gamma_C(D)-\gamma_{C-C_4}(D)=\frac{|POS_C(D)|}{|U|}-\frac{|POS_{C_4}(D)|}{|U|}=\frac{11}{17}-\frac{7}{17}=\frac{4}{17}$$

$$\sigma_D(C_5)=\gamma_C(D)-\gamma_{C-C_5}(D)=\frac{|POS_C(D)|}{|U|}-\frac{|POS_{C_5}(D)|}{|U|}=\frac{11}{17}-\frac{10}{17}=\frac{1}{17}$$

$$\sigma_D(C_6)=\gamma_C(D)-\gamma_{C-C_6}(D)=\frac{|POS_C(D)|}{|U|}-\frac{|POS_{C_6}(D)|}{|U|}=\frac{11}{17}-\frac{8}{17}=\frac{3}{17}$$

Therefore, the importance sorting of indicators attribute is $C_4 > C_6 > C_2 = C_3 > C_1 = C_5$:

Namely: slope angle> pore pressure ratio> cohesion = internal friction angle> slope density= slope height

We select five experts which are related to the slope field, they give the indicators score based on sort of attribute importance, each indicator corresponds to a score range, results of experts scoring are shown in Table 4.

**Table 4 Experts scoring table of landslide indicators**

| indicators | score range | experts scoring | | | | | |
|---|---|---|---|---|---|---|---|
| | | expert 1 | expert 2 | expert 3 | expert 4 | expert 5 | average score |
| $C_4$ | 75-100 | 90 | 85 | 80 | 85 | 80 | 84 |
| $C_6$ | 50-75 | 75 | 70 | 65 | 60 | 70 | 68 |
| $C_2$ | 25-50 | 50 | 45 | 35 | 45 | 30 | 41 |
| $C_3$ | 25-50 | 45 | 40 | 30 | 25 | 35 | 35 |
| $C_1$ | 0-25 | 25 | 25 | 20 | 15 | 20 | 21 |
| $C_5$ | 0-25 | 20 | 15 | 10 | 15 | 20 | 16 |

According to expert scoring conditions, the weight value of slope angle C4 is: 84 / (84 +68 +41 +35 +21 +16) = 84/256 = 0.317

Similarly, the weight values of slope unit weight, cohesion, internal friction angle, slope angle, slope height and pore pressure ratio are respectively: 0.079, 0.155, 0.132, 0.317, 0.06, 0.257.

As can be seen in the impact indicators of open pit mine landslide, the largest influence is slope angle; the second is pore pressure ratio; cohesion force and the friction angle is relatively small, the influence of slope density and slope height is minimal. In terms of slope protection, we should focus on the impact of the major factors.

## Conclusion

1) Rough set theory is completely depart from the objective data, without any subjective impact, the weight value may be zero by the calculation of rough set theory, which is not consistent with the actual situation; and expert scoring method is entirely based on the subjective experience; and is short of objective theoretical guidance, the weights not only need several rounds of feedback and scoring to get, but also difficult to achieve unity. Expert scoring method based on rough set theory could well avoid defects of two methods, and play the advantages of subjective and objective weighting method.

2) The method is used in the weight determination of landslide indicators in open-pit dump; we select five indicators from the dump landslide factors. We finally get indicator weights of open-pit dump landslide by calculating 25 group of objective data, thus to provide a certain basis to protection and governance of the dump, which is more conducive to the safety management of mine enterprises.

3) Since the calculation of rough sets attribute importance is more complicated, a large number of data samples are not suitable for hand calculations, in order to improve the efficiency and accuracy of the computational in future studies, we should consider the rough set software to calculate.

**Acknowledgments**

The research is supported by the national "Twelve- Five" Science and technology support program project of China (project No. 2012BAK09B05).

**References**

[1] Pawlak Z. vol. 11(3), International Journal of Computer and Information Sciences, 1982, pp.341-356.

[2] Pawlak Z. Rough sets: theoretical aspects of reasoning about data. Dordrecht: Kluwer Academic Publisher, 1991.

[3] Kryszkiewicz M. vol. 112(1), Information Sciences, 1998, pp: 39-49.

[4] Qing Liu. *Rough set and Rough reasoning*. Beijing: science press, 2001.

[5] Guangyue Wang, Haili Cui, Qian Li. vol. 30(8), Rock and Soil Mechanics, 2009, pp. 2418-2422.

[6] Yumeng Wang, Chunhong Zou, Han Lv. Journal of disaster prevention and reduction, vol. 29(2), 2013, pp.28-32.

[7] Yongshi Pang, Ying Wang. vol. 26(3), Journal of Engineering Management, 2012, pp.109-113.

[8] Liezhen Chang, Xinmou Ma. Mechanical Management and Development, 2007, pp.4-6

[9] WANG Yun-ming, XIANG Hong-hai. *Stability of dump and its disaster prevention and control*. Beijing: Metallurgical Industry Press, 2011.

[10] Sah N K, Sheorey P R, Upadhyaya L N.vol.31(1), Int. J. Rock Mech. Sci. & Geomech. Abs., 1994, pp. 47-50.

*Applied Mechanics and Materials Vols. 580-583 (2014) pp 2607-2611*
*© (2014) Trans Tech Publications, Switzerland*
*doi:10.4028/www.scientific.net/AMM.580-583.2607*

# Study on Ignition Time of Radiation Cargo in Irradiation Room under Stuck Radioactive Sources

Xiaolin Yao[1,2, a]

[1]Luzhou Vocational and Technical College, Luzhou, Sichuan, 646005, China

[2]Faculty of Geosciences and Environmental Engineering, Southwest Jiaotong University, Chengdu, Sichuan, 610031, China

[a]firesafety@qq.com

**Keywords:** Irradiation room, Radioactive sources, Stuck radioactive sources, Time to ignition.

**Abstract.** Ignition temperatures of common radiation cargo in irradiation room were measured through the experiments, minimum ignition temperature is 210 ℃. In order to discuss the temperature variation and temperature field under stuck radioactive sources, the fire scenario was presented and simulated by FDS. The results show that temperatures rise rapidly when stuck radioactive source broke out within an hour. As the growth of the time, temperatures in irradiation room are rising, but the rising rate is slowing. The temperature field in the irradiation room tends to be the same after three hours. The stuck radioactive source occurred after 2.4 days later, local temperatures can reach 210 ℃, and radiation cargo may be ignited.

## Introduction

With the development of the economic and the society, the irradiation facilities are widely used in irradiation processing, food preservation and sterilization [1]. According to incomplete statistics, there are more than 200 irradiation facilities in our country, of which about 20 are more than one million Ci [2]. If a radiation accident occurs, it will cause significant economic and social impact.

Stuck radioactive sources means that the radioactive sources are stuck in the process of back to source well, not able to reach the design position. Cargo in irradiation room are irradiated for a long time, temperatures constant rising, it may cause a fire, and than lead to a radiation accident. So we must care about the when cargo to be ignited under stuck radioactive sources. Combined with the domestic and foreign research present situation, FAN brought forward some safety measure [3]. QIAO analyzed the reason for the radioactivity fire, and some suggestions for the treatment were presented [4]. XIAO introduced two incidents of stuck radioactive sources. The lessons learned from these events are summarized [5].

Researchers in related fields have only made a rough analysis and research on radioactivity fire. Until recently, there is some lack of sophisticated quantitative analysis about ignition time under stuck radioactive sources. In this paper, typical 60Co irradiation room of hanging chain conveyor has been taken as a research subject. The ignition temperatures of common radiation cargo in irradiation room were measured by the DW-02 ignition point detector. Considering the most disadvantage condition of the irradiation room, the fire scenario was simulated to research the fire risk assessment by FDS under stuck radioactive sources. Ignition time for irradiation room of hanging chain conveyor under stuck radioactive sources was studied by numerical simulation and experiments.

## Model of Irradiation Room

**Irradiation Room Description.** This paper is aimed to research the fire risk assessment on typical $^{60}$Co irradiation room which is located on the ground floor. The room is 15 m long, 7 m wide, 4.6 m high as shown in Fig.1. The thickness of the concrete wall is 2 m. Irradiation room transports cargo through the hanging chain conveyor. There are three doors, one for slings in, one for slings out, and the other one for personal access, with the window closed. The room is equipped with mechanical

ventilation system under normal operating conditions. Radioactive sources are arranged on the shelf uniformly which is about 5 m long, 2 m high, 0.1 m thick, and 1 mm thick aluminum plate wrap around the shelf.

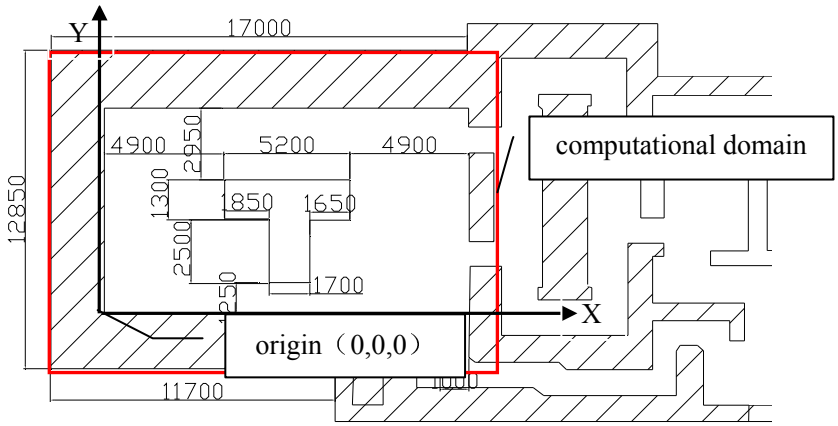


Fig.1 The plans of the irradiation room

**Fire Model of Irradiation Room.**

(1) Analysis of fire risk.

Through the analysis, irradiation room has two major fire risks. One is lead to a fire because the cargo in irradiation room is irradiated for a long time, temperatures constant rising. And the other is destruction of structural member due to high temperature in the room. Through referring to literature at home and abroad, concrete strength is not changed obviously while temperatures are below 300 ℃. Concrete strength decreases and its external surface have cracks when temperature varies between 600-700 ℃. The spalling of concrete might occur and its strength is close to zero when temperature varies between 800-900 ℃ [6]. Ignition temperatures of common radiation cargo are much lower than concrete failures temperature. Therefore ignition temperatures of common radiation cargo are taken as the criterion of fire risk.

In order to analyze fire risk clearly under stuck radioactive sources, ignition temperatures of common radiation cargo should be determined exactly. Regularity of a change in temperature is obtained under typical fire scenarios through the theoretical analysis and the numerical stimulation calculation, and sums up the ignition time, that is, the less time it will take to troubleshoot stuck radioactive sources.

(2) Fire model.

In order to analyze fire risk clearly under the most disadvantage condition, this paper makes the following assumptions:1) $^{60}$Co source releasing heat continuously is equal to the ignition source under stuck radioactive sources. 2) The ventilation system can not work properly. 3) The irradiation room becomes an enclosed space while the exits and entrances are quickly capped by cargo.

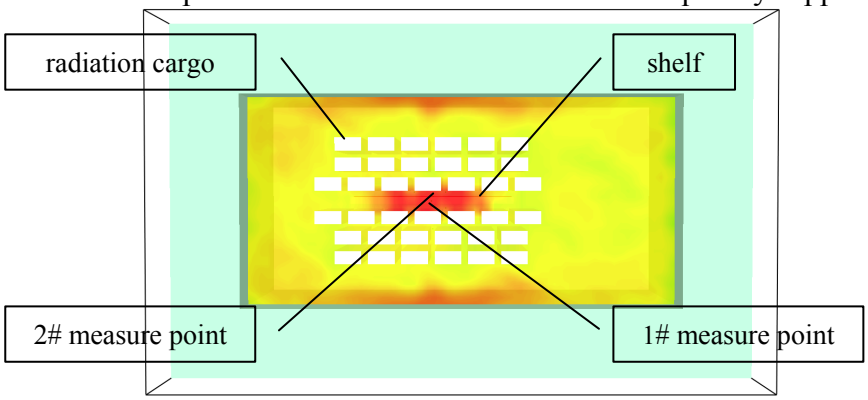


Fig.2 Model of FDS

Fire simulation software FDS widely adopted at home and abroad is used to simulation calculation. Thermal conductivity of concrete wall is 0.72w/m•k. Simulation time is set to six hours because of a long time computation. Model of FDS was built as shown in Fig.2.

Table 1 List of fire scenario

| activity of $^{60}$Co source (Ci) | heat power (kW) | coordinates of 1# measure point | coordinates of 2# measure point |
|---|---|---|---|
| three million | 46.2 | (7.5, 5.3, 2.0) | (7.5, 5.2, 3.5) |

(3) Fire scenarios.

Activity of $^{60}$Co irradiation facilities above one million Ci is not uncommon. According to relationship between activity of 60Co source and heat power, 1000Ci is roughly equivalent to 15.4w. The activity of 60Co source is three million Ci and coordinates of measure points are set up as shown in Table 1.

According to results of linear fitting between 1h and 6h, we can determine whether the temperatures could be ignition point and when to ignition based on the numerical simulation results. This method can calculate accurately and conservatively.

**Experiment of Ignition Temperatures**. The ignition temperatures of common radiation cargo in irradiation room were measured by the DW-02 ignition point detector according to national standards GB4610-84<Test for flammability of plastics temperature test >, as shown in Table 2.

Table 2 Experimental results of ignition temperatures

| **radiation cargo** | **selected reasons** | **ignition temperatures (℃)** |
|---|---|---|
| chili powder | ignited in the radioactivity fire in Qi county of Henan province, typical food | 210 |
| corrugated paper | typical packing materials, lower ignition temperature | 230 |
| toilet paper | typical commodity | 240 |
| gauze | typical medical supplies | 290 |

## Analysis of Simulation Results

**Simulation Results of Temperature Curve**. Three million Ci is equivalent to 46.2kW in the fire scenario. Simulation time is set to six hours as well because of a long time computation. The temperature variety curve in irradiation room is drawn as shown in Fig.3.

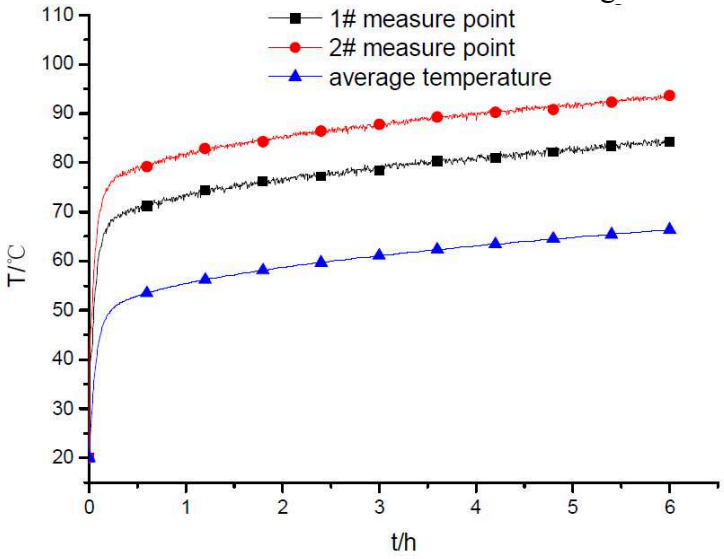


Fig.3 Temperature variety curve of every measure point

The temperatures of computational domain increase to 80℃ rapidly from 0 to 1h. The fire risk of 2#measure point is the largest one on account of the highest temperatures. The liner fitting formula of

temperature for 2#measure point is T=2.2358t+80.6610 as shown in Fig.9. The ignition point of chili powder is 210℃ through experiment. By analysing the simulated result of the liner fitting formula, the time to reach ignition point is about 2.4 days. The radiation cargo in irradiation room may be ignited to cause a radioactivity fire.

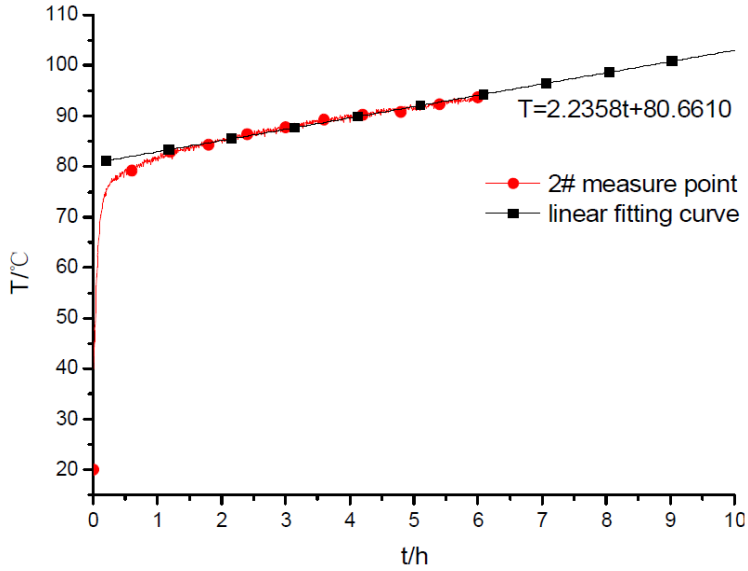


Fig.4 Liner fitting curve of temperature for 2#measure point

**Simulation Results of Temperature Field.** The distribution of temperature field at the height of 3.6 m is presented at different times as shown in Fig.5 Fig.6 and Fig.7. The local space formed by stacking radiation cargo is a relatively closed environment. The increase of temperatures near by the shelf is faster than somewhere else in irradiation room when stuck radioactive source broke out within three hours. The temperature field in the irradiation room tends to be the same after three hours.

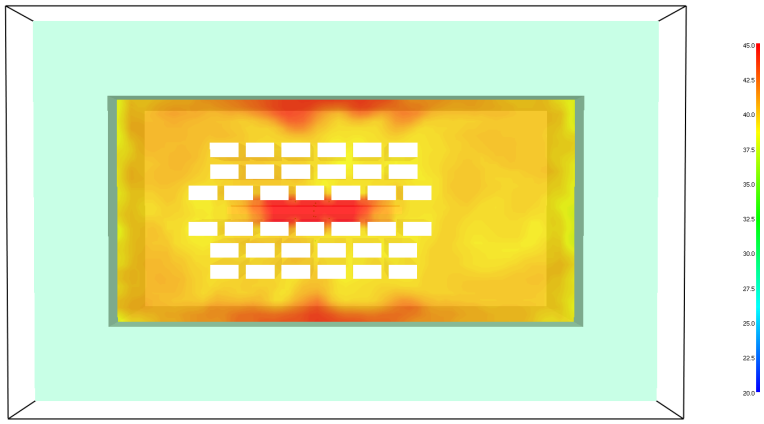

Fig.5 The distribution of temperature field at 2h

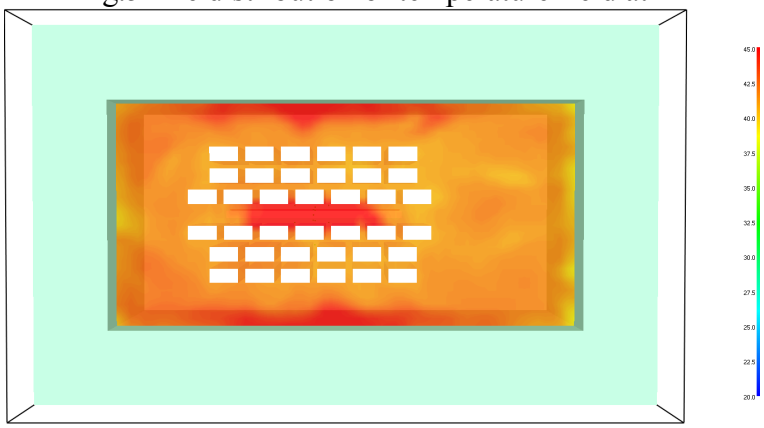

Fig.6The distribution of temperature field at 4h

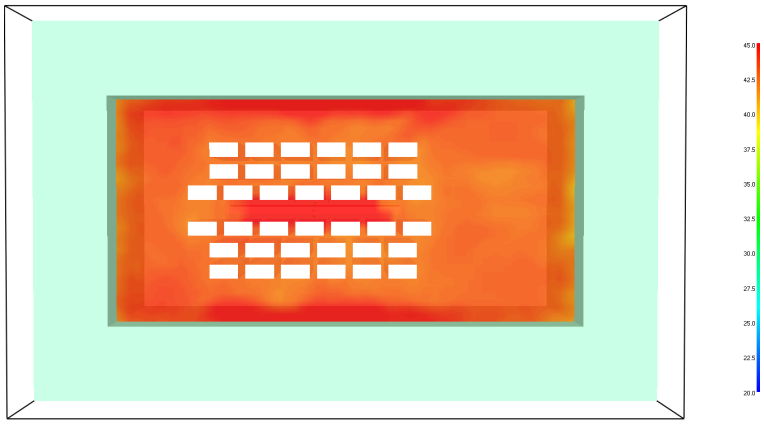

Fig.7 The distribution of temperature field at 6h

## Conclusions

In this paper, typical $^{60}$Co irradiation room has been taken as a research subject. Considering the most disadvantage condition of the irradiation room, the methods combining qualitative and quantitative analysis are used to research the radioactivity fire by numerical simulation and experiments. This paper draws the following conclusions:

(1) The radiation cargo in irradiation room has a low ignition point. The ignition temperatures of chili powder, corrugated paper, toilet paper and gauze are 210 ℃, 230 ℃, 240 ℃ and 290℃ measured by the experiment.

(2) The temperatures of computational domain increase rapidly from 0 to 1h. With time growing, slower growth of temperatures is presented gradually from 1h to 6h. The fire risk of 2#measure point is the largest one on account of the highest temperatures. The liner fitting formulas of temperature for 2#measure point can be obtained in the fire scenario. The irradiation room may be caused a radioactivity fire after 2.4 days under stuck radioactive sources.

The possibility of the radioactivity fire caused by stuck radioactive source is not zero although it is small. The combustibles should be taken away from the irradiation room as soon as possible once the incidents of stuck radioactive sources occur. In order to decrease the temperature of irradiation room, the ventilation system must function correctly to avoid the radioactivity fire.

## References

[1] Meiyang Zheng, Guohua Jin, Genfang Shen: Nuclear Electronics & Detection Technology Vol. 30 (2010), p. 1224.

[2] Rongsheng Yu: Chinese Journal of Radiological Health Vol. 10 (2001), p. 133.

[3] Shengeng Fan, Yongxian Zhang, Changheng Xu: Atomic Energy Science and Technology Vol. 23 (1989), p. 88.

[4] Haitao Qiao, Hang Li: Annual Report For China Institute of Atomic Energy Vol. 12 (2011), p.252.

[5] Xuefu Xiao: Radiation Protection Bulletin Vol. 31 (2011), p. 24.

[6] Junhai Zhao, Maohong Yu, Yunhe Liu, et al: Journal of Northwestern Institute of Architectural Engineering Vol. 12 (1988), p. 1.

*Applied Mechanics and Materials Vols. 580-583 (2014) pp 2612-2615*
*© (2014) Trans Tech Publications, Switzerland*
*doi:10.4028/www.scientific.net/AMM.580-583.2612*

# The Coupling Interaction in the Rankine Method for Concrete Filled Steel Tube Columns under High Temperatures

Yao Yao[1, a], Xin Xin Hu[2,b]

[1] Professor, School of Mechanics, Civil Engineering and Architecture, Northwestern Polytechnical University, ShaanXi 710072, China

[2] Master student, School of Mechanics, Civil Engineering and Architecture, Northwestern Polytechnical University, ShaanXi 710072, China

[a]yaoy@nwpu.edu.cn, [b]xinxinhu90@gmail.com

**Keywords:** CFS column; fire resistance; Rankine approach; shear bond; high temperature.

## ABSTRACT

The Rankine approach has been extended to predict fire resistance of steel, reinforced concrete and concrete filled steel tube (CFS) columns. The conventional Rankine method ignores the coupling interaction and leads to a lower bound prediction compared with actual failure loads, especially for CFS columns. This paper develops a rational and straightforward approach to predict the fire resistance of CFS columns considering the shear bond effect. The method hinges on concept of modified buckling coefficient, and applicable to both axially and eccentrically loaded columns. It shows that the proposed approach predicts the failure load more accurately compared with the traditional Rankine approach. Four case studies comprised of 118 CFS columns from different labs are analyzed to verify the proposed approach. Material deterioration at elevated temperature with regard to the strength and stability of columns is also quantified.

## Introduction

Several of simplified approaches to predict fire resistance of steel, RC and CFS columns have been developed by different researchers. However, most of the approaches are based on the finite element method (FEM) and empirical formulas. The conventional Rankine approach can be expressed as [1]:

$$\frac{1}{P_R} = \frac{1}{P_p} + \frac{1}{P_e} \tag{1}$$

where $P_p$, $P_e$, $P_R$ represent the plastic collapse load, elastic critical load and Rankine load, respectively.

The Rankine formula based interaction approach has been applied to predict the fire resistance of steel columns and frames first by Tang et al. [2]. Their approach divides a column into two hypothetical sub-columns, assuming the two sub-columns act independently of each other and ignore the coupling interaction. In reality, the two sub-columns are deformed together and mutually restricted. The coupling interaction is termed “shear bond”, which increases the ultimate capacity of the column. Yao et al. [3] suggest that the modified approach can predict failure load of RC columns under fire condition more accurately by incorporating the coupling interaction effect into the Rankine formula.

In current work, a modified Rankine approach is proposed to predict the fire resistance of CFS columns by combining the shear bond effect. The coupling interaction effect and the physical meaning are discussed. The effect of shear bond is adapted to predict fire resistance of 118 CFS columns from four laboratories with different column slenderness ratios, concrete covers, cross-sectional areas and fire exposure times. The results show that the developed approach can predict the failure load of CFS columns more accurately compared with conventional Rankine approach.

## Theoretical Model

In order to extend the Rankine approach to predict fire resistance of CFS columns, the authors adopt Eq. 2. For columns subjected to axial load, $P_p$ can be expressed as [4]:

$$P_p = 0.85\beta_c(t)f_c'(20°C)A_c + \beta_{yr}(t)f_{yr}(20°C)A_{sr} + k_y^{tube}(t)f_y(20°C)A_s \quad (2)$$

where $f_c'(20°C)$, $f_{yr}(20°C)$, $f_y(20°C)$ are the cylindrical compressive strength of concrete, yield stress of steel reinforcement and yield stress of steel tube at ambient temperature, respectively; $A_c$, $A_{sr}$, $A_s$ stand for the area of concrete section, steel reinforcement and steel tube; $\beta_c(t)$, $\beta_{yr}(t)$, $k_y^{tube}(t)$ represent the strength reduction of concrete, steel reinforcement and steel tube at elevated temperature.

The elastic critical load $P_e$ can be determined by Eq. 3 [4]:

$$P_e = \frac{\pi^2[0.2E_c(20°C)I_c + E_{sr}I_{sr}]}{(kl)^2} \quad (3)$$

where $k = 1, 0.7, \text{and } 0.5$ for pinned-pinned, pinned-fixed and fixed-fixed end, respectively. $E_c(20°C)$ and $E_{sr}$ are the elastic modulus of concrete and steel reinforcement. $I_c$ and $I_{sr}$ are the second moment of concrete and steel reinforcement area.

To predict fire resistance of CFS column, the original Rankine formula is modified to consider the effect of shear bond:

$$\frac{1}{P_c} = \frac{1}{P_p} + \frac{1}{P_e} - \frac{1}{P_s} = \frac{1}{P_R} - \frac{1}{P_s} \quad (4)$$

where $P_s$ is the effect of the shear bond.

The difference $\Delta_p$ between the Rankine failure load $P_R$ and the actual failure load $P_c$ can be calculated by:

$$\Delta_p = P_c - P_R = \frac{P_R^2}{P_s - P_R} \quad (5)$$

In order to define a general failure curve, the following formula is proposed instead of the original linear interaction equation [3]:

$$\frac{1}{P_c^n} = \frac{1}{P_p^n} + \frac{1}{P_e^n} \quad (6)$$

Eq. 6 represents a modified Rankine approach which incorporates the shear bond effect into the failure interaction. The modified formulas for axially loaded PCFS and RCFS under fire condition can be expressed as:

$$P_c = \frac{P_p P_e}{\sqrt[n]{P_p^n + P_e^n}} \quad (7)$$

The modified formulas for eccentrically loaded RCFS under fire condition can be expressed as:

$$P_c = \frac{[u_{pr}^{core}P_p^{core}(t) + u_{pr}^{tube}P_p^{tube}(t)]P_e}{\sqrt[n]{[u_{pr}^{core}P_p^{core}(t) + u_{pr}^{tube}P_p^{tube}(t)]^n + P_e^n}} \quad (8)$$

## Physical Meaning of the Modified Rankine Approach

Accuracy of the Rankine approach varies with column slenderness ratios, defined by the ratio of the effective length of a column to the least radius of gyration of its cross-section, and the fire exposure time. For CFS columns under fire conditions, the reduction of $P_e(t)$ is much more rapid than $P_p(t)$ due to greater deterioration of $E_cI_c$ and $E_{sr}I_{sr}$ compared with $f_c'$ and $f_{yr}$. For stocky and slender CFS columns, the cross-sectional area of the hypothetical columns is relatively small,

and the effect of shear bond is small. However, for intermediate columns, the values of $P_p(t)$ and $P_s(t)$ are close to each other, and the shear bond effect is large and the prediction of Rankine approach tends to be conservative.

On the other hand, the conventional Rankine approach assumes that two hypothetical sub-columns act independently and ignores the coupling interaction effect. However, there is always some difference between the two failure modes in practice. In reality, the failure modes of two hypothetical sub-columns are deformed together and mutually restricted as the result of shear bond. Thus, the interaction always exists and the conventional Rankine approach tends to be conservative. The accuracy of the Rankine approach depends on the compatibility between the two failure modes of sub-columns. With greater incompatibility between the two failure modes, stronger shear bond will be generated. For this case, the authors propose modified Rankine approach and employ different n values to consider the incompatibility effect between the two failure modes for CFS columns.

## Case study

In current study, a group of 118 CFS columns from four laboratories (Canadian National Research Council Tests, French UTI/CTICM, French CSTB, and UK Borehamwood) [5,6] with different slenderness ratios, tube thickness, concrete covers, cross-sectional areas and fire exposure times are compared with proposed approach and finite element analysis. The object of the case study is to benchmark the accuracy of the modified Rankine approach and investigate the influence of different engineering design factors to fire resistance of CFS columns.

Based on the case studies and the physical meaning of shear bond, the *n* values for columns with different slenderness ratios and fire exposure times are recommended in Table 1. One-hundred and eighteen CFS column tests including both PCFS and RCFS from four different laboratories were used for comparison, the results are shown in Fig. 1. It shows that the modified Rankine approach gives more accurate predictions compared with the original one.

**Table 1: The Recommended *n* Values**

| | $\lambda \geq 44.5$ | $37 \leq \lambda < 44.5$ | $26 \leq \lambda < 37$ | $\lambda < 26$ |
|---|---|---|---|---|
| $t \leq 36$min | | 1.3 | 2.2 | |
| $36 < t \leq 68$min | | 2.2 | 1.3 | |
| $t > 68$min | | 3 | 3 | |
| $t \leq 48$min | 3 | | | 1 |
| $48 < t \leq 86$min | 1 | | | 3 |
| $t > 86$min | 1 | | | 1 |

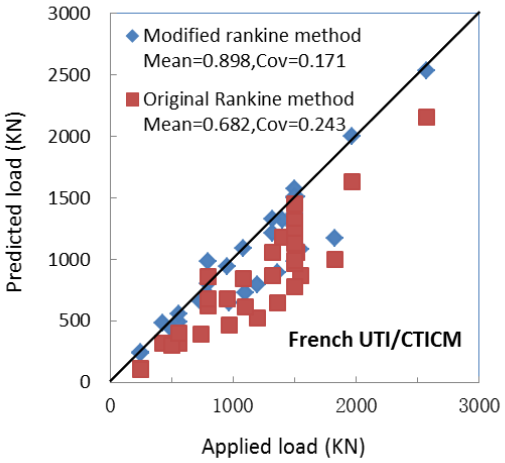


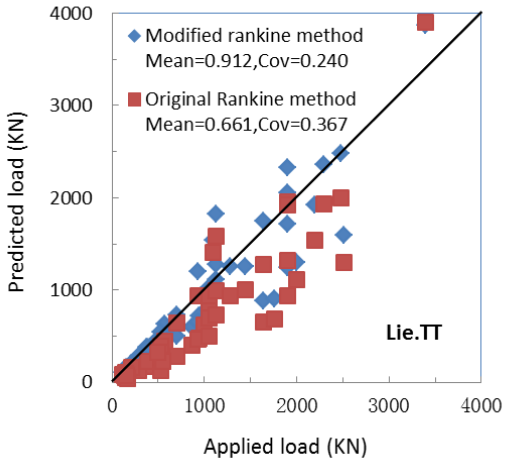

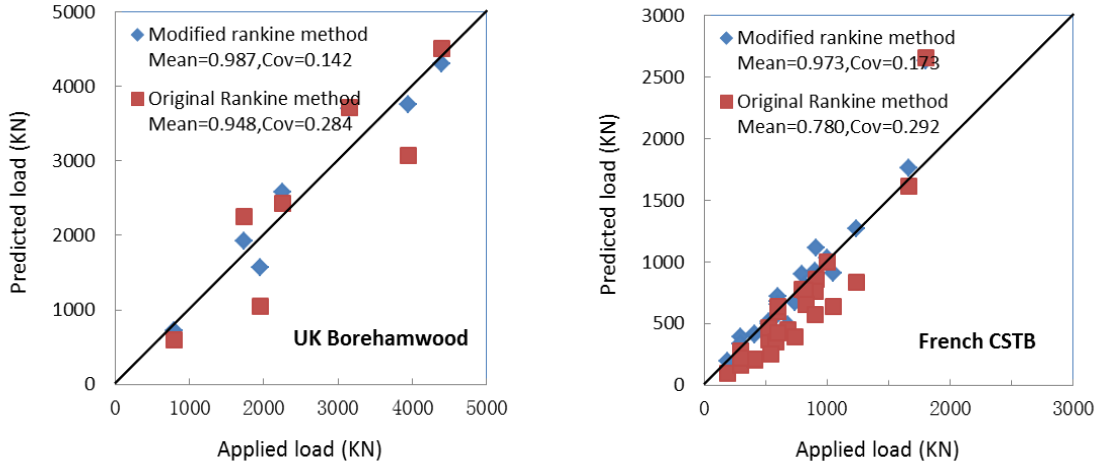


**Fig. 1 The load capacity predicted by modified Rankine approach for four case studies**

## Conclusion

A modified Rankine approach is developed to predict fire resistance of CFS columns under ISO-834 fire conditions, the effect of shear bond is considered in the developed approach. Theoretical basis and the physical meaning of shear bond are discussed. For columns with different slenderness ratios and fire exposure times, the limitations of the original Rankine approach are investigated. Four case studies comprised of 118 CFS columns from different labs are analyzed to verify the proposed approach. It is found that the modified Rankine approach can predict the fire resistance of CFS columns more accurately compared with the original one. In general, the modified Rankine approach is a simplified and straight forward approach to predict fire resistance of CFS columns.

## References

[1] Eurocode 3. Design of steel structures. Part 1.1: General rules and rules for buildings, DD ENV 1993-1-1. London: British Standard Institution; 1992.
[2] C.Y. Tang, K.H. Tan, S.K. Ting. J Struct Eng ASCE Vol. 127(10) (2001), p. 1214.
[3] Y. Yao, K.H. Tan, C.Y. Tang. Eng Struct Vol. 30 (2008), p. 3595.
[4] A.H. Nilson, G. Winter. Design of concrete structures. 11th ed. McGraw-Hill, New York, USA; (1991).
[5] G. Grandjean, J.P. Grimault, L. Petit. Determination de la dure´e au feu des profils creux remplis de be´ton. Rapport Final. Commission des Communaute´s Europe´ennes, Recherche Technique acier, Luxembourg; (1981).
[6] T.T. Lie, M. Chabot. Experimental studies on the fire resistance of hollow steel columns filled with plain concrete. NRC-CNRC internal report no.611. Ottawa, Canada; (1992).

*Applied Mechanics and Materials Vols. 580-583 (2014) pp 2616-2621*
*© (2014) Trans Tech Publications, Switzerland*
*doi:10.4028/www.scientific.net/AMM.580-583.2616*

# The design of unascertained fire risk evaluation system for high-rise civil building based on VB

Li-ning ZHANG[1,a], Jing AN[2,b], Qi ZHANG[3,c]

[1] Mechanical-Electrical Engineering College, Beijing Institute of Technology, Beijing 100081, China

[2] Electronic and Information Engineering College, North China Institute of Science and Technology, Beijing 065201, China

[3] State Key Laboratory of Explosion Science and Technology, Beijing Institute of Technology, Beijing 100081, China

[a]zlining666@163.com, [b]anjing0521@ncist.edu.cn, [c]Qzhang@bit.edu.cn

**Keywords:** High-rise civil buildings; Fire risk evaluation tree; The unascertained evaluation system design; The visual basic(VB) technology.

**Abstract:** The study purpose is to design a comprehensive and visual fire risk evaluation system for high-rise civil buildings. Firstly, according to the characteristics of high-rise civil buildings, based on the hazards identification, combined with the international building fire codes, by using the typical accident causation analysis and other methods, the various uncertain factors affecting high-rise civil building fire are analyzed, and a fire risk evaluation tree for high-rise civil buildings was built. Then the unascertained theory is introduced, and a new visual fire risk evaluation system is designed for high-rise civil buildings based on the unascertained C-clustering model and the visual basic(VB) technology. At last, take the fire survey data of China 8 typical high-rise civil building as example, to make an empirical analysis. The research results can provide a reliable decision support system for the high-rise civil building fire risk management.

## Introduction

High-rise buildings are the inevitable product of the city development, but their fire safety issues are always a difficult problem in the world. At present, take China as example, the fire ladders can reach the height of generally not more than 100 meters, so once fire, the high-rise building often suffered heavy losses(Adam C. et al., 2013). So make scientific evaluation on the high-rise building fire risk, to accurately determine their fire risk level, have very important and practical significance to minimize the high-rise building fire accident occurrence.

The international study on building fire safety evaluation began in 1970s, the main methods and models are the U.S. building fire evaluation method(BF-SEM), the Australia risk assessment model (RAM), the Japanese integrated building fire safety design method, Canada FIRECAM method, and so on. In practical application, those evaluation methods each exhibit some advantages, but there are also some problems(Hao C. and George V. H., 2011).

The building fire safety research started late in China, the representative research results such as WeiCheng Fan discussed the theoretical framework of building fire integrated simulation evaluation. Lixin Yi, etc. established the risk assessment model by using fault tree analysis method and the Markov models model of random process. Hongbing Du, etc. used the fuzzy evaluation method to evaluate the building fire risk. Min Xu, etc. introduced the artificial neural network into the building fire risk assessment, et al. (RING Z.X. et al., 2011; HU B.Q et al., 2004 ).

The above research has made some achievements, but in the study of high-rise building fire risk assessment theory and method, there are still some obvious deficiencies. For example, the high-rise building fire risk evaluation index system differences, some are too complex, some are too simple, have brought many difficulties to the fire risk assessment. The risk evaluation index system targeted not strong, there is no explanation for what kind of high-rise buildings. And the lack of a visual

evaluation system results in the index calculation is more complicated and subjective defect, and so on.

So in this study, according to the characteristics of the high-rise civil building fire, a more scientific risk evaluation tree is built, and also a visual fire risk evaluation system is designed for the high-rise civil buildings based on the unascertained C-clustering algorithm and the visual basic technology.

## The comprehensive and visual evaluation system design

### 2.1 The construction of fire risk evaluation tree for high-rise civil building

Based on the three types hazard identification, combine with the related literatures(Hao C. and George V. H., 2011; RING Z.X., 2011; George V.H. and Noureddine B., 1999; China State Bureau of technical supervision and China Ministry of construction, 2005), use the accident causation analysis and other methods, this study builds the fire risk evaluation tree for high-rise civil buildings(shown in table1).

Table1 The fire risk evaluation tree of high-rise civil buildings

| first level index | second level index | third level index | $x_1$ | $x_2$ | $x_3$ | $x_4$ | $x_5$ | $x_6$ | $x_7$ | $x_8$ |
|---|---|---|---|---|---|---|---|---|---|---|
| the fire protection ability U1 | the building general layout U11 | the fireproof distance U111 | 94 | 72 | — | 94 | 95 | 67 | 68 | 91 |
| | | the surrounding environment U112 | 98 | 64 | 70 | 95 | 92 | 57 | 64 | 90 |
| | the fire resistance rating of buildings U12 | the fire resistance rating of building structure U121 | 83 | 72 | 78 | 83 | 90 | 80 | 83 | 88 |
| | | the fire resistance and smoky of decoration materials U122 | — | 76 | 44 | 84 | 84 | 71 | 80 | 83 |
| | the electrical fire U13 | the electrical equipment reliability U131 | 90 | 80 | 46 | 63 | 81 | 71 | 70 | 84 |
| | | the safety facilities status of power distribution equipment U132 | 90 | 84 | 60 | 69 | 80 | 71 | 71 | 83 |
| | | the wire/cable fire resistance U133 | 70 | 80 | 46 | 67 | 82 | 74 | 69 | 81 |
| | the fire load U14 | the fire load density U141 | 74 | 80 | 84 | 85 | 75 | 49 | 77 | 62 |
| | the fire partition U15 | the horizontal fireproof partition U151 | 83 | 88 | 78 | 70 | 80 | 59 | 69 | 74 |
| | | the vertical fireproof partition U152 | 69 | 88 | 78 | 70 | 80 | 59 | 69 | 74 |
| | the smoke control ability U16 | the smoke control facilities in good condition U161 | 87 | 80 | 62 | 57 | 80 | 64 | 61 | 78 |
| | | the smoke control system design is reasonable U162 | 87 | 80 | 62 | 57 | 79 | 64 | 61 | 79 |
| the fire extinguis-hing ability U2 | the building self extinguishing ability U21 | the automatic fire alarm system U211 | 87 | 84 | 74 | 0 | 90 | 60 | 0 | 88 |
| | | the automatic sprinkler system U212 | 89 | — | 54 | 0 | 90 | 55 | 0 | 85 |
| | | the fire hydrant system U213 | 84 | 80 | 76 | 70 | 89 | 71 | 77 | 87 |
| | | the other fire extinguishing system U214 | 84 | 72 | 54 | 0 | 56 | 50 | 70 | 66 |
| | | the fire water U215 | — | 76 | 68 | 80 | 80 | 86 | 77 | 84 |
| | the fire fighting team capacity U22 | the fire road U221 | 89 | 76 | 68 | 94 | 96 | 68 | 44 | 86 |
| | | the fire elevator U222 | 70 | 76 | 68 | 0 | 50 | 33 | 36 | 83 |
| | | the number and business level of the fire fighting team U223 | 90 | 80 | — | 64 | 64 | 64 | 64 | 64 |
| the fire safety evacuati-on ability U3 | the escape route U31 | the safety evacuation route U311 | 90 | — | 56 | 81 | 53 | 32 | 75 | 79 |
| | | the safety evacuation distance U312 | 90 | 84 | 56 | 84 | 69 | 35 | 78 | 79 |
| | | the number of emergency exits U313 | 86 | 88 | 56 | 30 | 78 | 27 | 52 | 63 |
| | | the safety evacuation width U314 | 90 | 88 | 56 | 31 | 86 | 42 | 58 | 71 |
| | the completeness of safety evacuation and guiding facility U32 | the evacuation signs U315 | 85 | 92 | 42 | 65 | 80 | 53 | 78 | 84 |
| | | the evacuation stairs U321 | 89 | 80 | 56 | 30 | 84 | 54 | 78 | 79 |
| | | the emergency lighting U322 | 85 | 84 | 84 | 41 | 85 | 55 | 73 | 83 |
| | | the fire radio guidance system U323 | 89 | 88 | — | 22 | 28 | 80 | 0 | 77 |
| | | the asylum and rescue shelter U324 | 89 | 76 | 74 | 0 | 0 | 0 | 0 | 64 |
| | | other evacuation facilities U325 | 89 | 0 | 0 | 0 | 0 | 0 | 0 | 51 |

| | | | | | | | | | | |
|---|---|---|---|---|---|---|---|---|---|---|
| the fire safety manage-ment ability U4 | the establishment and implementation of fire safety system U41 | the fire safety system integrity U411 | 95 | 76 | 56 | 76 | 84 | 52 | 63 | 76 |
| | | the fire facilities maintenance check U412 | 86 | 64 | 70 | 71 | 75 | 61 | 68 | 79 |
| | the contingency plans perfection U42 | are there emergency plan U421 | 95 | 80 | 62 | 57 | 67 | 59 | 62 | 77 |
| | | the effectiveness of the emergency plan U422 | 80 | 80 | 62 | 57 | 67 | 53 | 57 | 73 |
| | the people fire prevention education U43 | the fire safety awareness U431 | 80 | 76 | 62 | 71 | 83 | 54 | 69 | 81 |
| | | the fire facilities proficiency U432 | — | 72 | 86 | 64 | 80 | 51 | 68 | 74 |
| | | the public fire prevention education U433 | 70 | 80 | 82 | 75 | 86 | 44 | 67 | 80 |

### 2.2 The unascertained evaluation system design

Due to the uncertainty of the high-rise civil buildings fire occurrence, so through the unascertained modeling to evaluate the fire risk condition of high-rise civil buildings is feasible. The basic ideal of the unascertained C-clustering can refer to literature (LIU K.D et al., 2004; ZHAO C.M. et al., 2004). The modle implementation steps:

(1)Set the sort number K, the system error $\varepsilon$, and the counter $t=0$;

(2)Apply initial classification to $n$ samples, and determine the cluster center vector $m_k^{(0)}(k=1\sim K)$ of each sort;

(3)Calculate the unascertained measure $\mu_{ik}(t)(i=1\sim n,k=1\sim K)$ that sample $x_i$ belongs to the $k$-sort;

(4)Compute $m_k(t+1)=\sum_{i=1}^{n}\mu_{ik}\cdot x_i \Big/ \sum_{i=1}^{n}\mu_{ik}$ ; $k=1$, 2,…,K; get the sort center after the first iteration: $m_1^{(1)},m_2^{(1)},\cdots,m_C^{(1)}$;

(5)Compute $err=\sum_{k=1}^{K}\left\|m_k(t+1)-m_k(t)\right\|$ , if $err\le\varepsilon$ , count the unascertained measure $\mu_{ik}(t+1)(i=1\sim n,k=1\sim K)$ that sample $x_i$ belongs to the $k$-sort, stop iteration and switch to (6); otherwise, set $t=t+1$, and switch to (3);

(6)Output the class Center $m_k^{(t+1)}(k=1\sim K)$ of $K$ , the unascertained measure $\mu_{ik}(t+1)(i=1\sim n,k=1\sim K)$, and apply classification:

Set the reliability as $\lambda$, if $k_0=\min_k\left[(\sum_{l=1}^{k}\mu_{il})\ge\lambda,k=1,2,\ldots,K\right]$

That means $x_i$ belongs to $k_0$.

Based on the fire risk evaluation tree and the unascertained C-clustering model, through Matlab programming, and by using the VB technology, a visual fire risk evaluation system is designed for high-rise civil building in the study, shown in Fig.1.

### Example

In order to verify the feasibility and effectiveness of the fire risk evaluation system established in this study, take the fire survey data of China 8 typical high-rise civil buildings as example, to make an empirical analysis. The 8 typical high-rise civil building are the Shan-xi information building($x_1$)， A high-rise civil building in Jiang-xi province($x_2$), the Vittoria Hotel in Xin-xiang city ($x_3$), the 2# teaching building of NCIST($x_4$), the teaching-laboratory building of NCIST($x_5$), the Yan-jiao cultural plaza($x_6$), the 11# building of Dongmao international residential community($x_7$) and the Yanda international hospital($x_8$).

The survey data is shorwn inTable1, the first three sample data($x_1$ ,$x_2$ ,$x_3$) are direct consulting or indirect conversion data from the literatures(GAO Y., 2010; CAO Y., 2008), the other five sample data ($x_4$, $x_5$, $x_6$, $x_7$, $x_8$) are 5 experts scoring and averaged results.

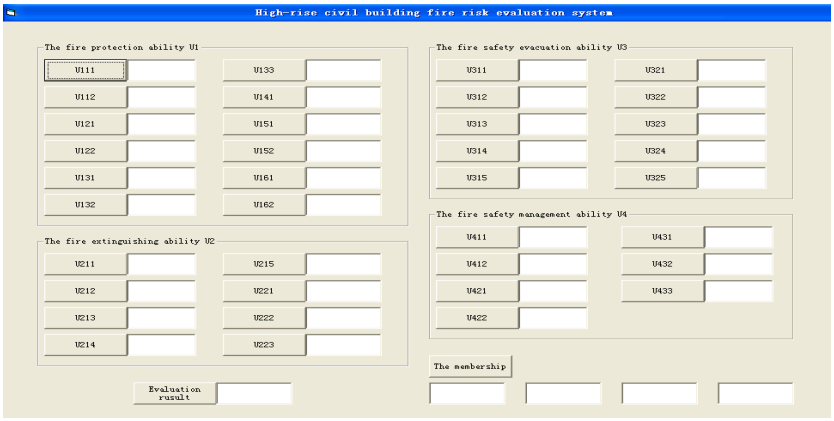


Fig.1 The evaluation system interface

(1) Data complete

For the missing attribute values, the study adopts the mean completer algorithm to filled, for example, for the fireproof distance attribute of sample $x_3$ (the Victoria Hotel), the mean results of other 7 samples in the fireproof distance attribute score is 83, so use "83" to supplement the omission attribute value of sample x3. Similarly, the other missing attribute value can be completed with the same method.

(2) Fire risk evaluation

Firstly, standardized the data in table1, the process omitted. Then input the the normalized data into the evaluation system to classify, let $\lambda$ =0.7, $\alpha_i = 1, \delta = 0.001, \varepsilon = 0.01$, divide the fire risk situation of the 8 samples into four types, that is very dangerous, danger, general and safety. Take sample2 as example, after 34 iterations, the final classification results as shown in Fig.2, the classification error 0.0009761. Similarly, the classification results of all samples seen in Table2.

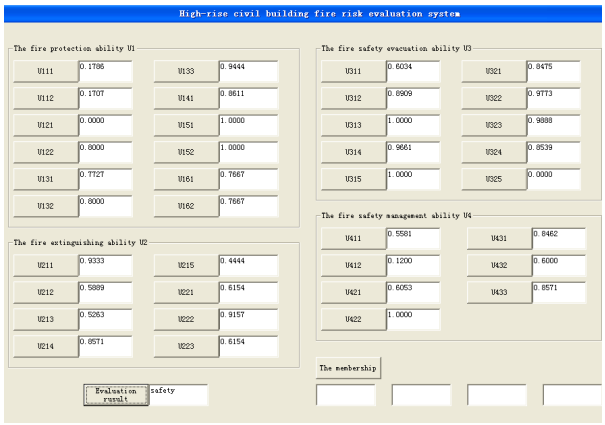


Fig.2 The classification result of sample 2

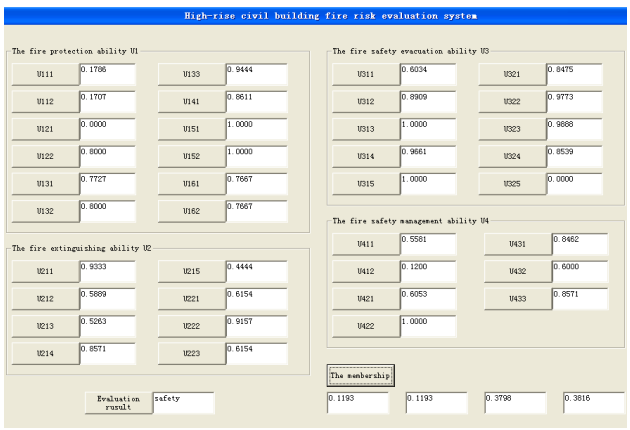


Fig.3 The membership sample 2

Table2 The classification results of all samples

| sample | 1 | 2 | 3 | 4 | 5 | 6 | 7 | 8 |
|---|---|---|---|---|---|---|---|---|
| classification results | safety | safety | general | danger | safety | danger | danger | safety |

The classification results showed that the fire risk level of the sample $x_4$, $x_6$, $x_7$ are danger, the the fire risk level of the sample $x_3$ is general, and the fire risk level of the sample $x_1$, $x_2$, $x_5$, $x_8$ are safety. The classification results of sample $x_1$, $x_2$, $x_3$ are consistent with the literature research results, but the

evaluation process in this study is greatly simplified, the classification results of sample $x_4$, $x_5$, $x_6$, $x_7$, $x_8$ in line with the actual situation.

At the same time, the evaluation system can not only achieve the evaluation results, but also the membership of the sample belongs to each category. For example, the membership sample 2 belongs to various classifications shown in Fig.3, similarly, the membership each sample belongs to various classifications seen in Table3.

Table3 The membership each sample belongs to various classifications

| sample<br>risk level | 1 | 2 | 3 | 4 | 5 | 6 | 7 | 8 |
|---|---|---|---|---|---|---|---|---|
| very dangerous | 0.1296 | 0.1193 | 0.3406 | 0.3569 | 0.1201 | 0.3661 | 0.3783 | 0.0765 |
| danger | 0.1296 | 0.1193 | 0.3406 | 0.3568 | 0.1201 | 0.3661 | 0.3782 | 0.0765 |
| general | 0.3692 | 0.3798 | 0.1598 | 0.1434 | 0.3790 | 0.1342 | 0.1221 | 0.4211 |
| safety | 0.3716 | 0.3816 | 0.1590 | 0.1429 | 0.3807 | 0.1336 | 0.1215 | 0.4259 |

## Conclusions

Through the empirical analysis of the 8 typical high-rise civil building fire statistic data, the results showed that, the visual fire risk evaluation system for high-rise civil buildings based on the fire risk evaluation tree and the unascertained C-clustering method, relative to the literature studies often assessment with the second-grade indexes, the system evaluate with the third-grade indexes, the evaluation result is more objective, and the evaluation process greatly simplified, so the system is more practical. Also the system can not only give accurate evaluation results, but also give the membership of the sample belongs to each category, the research results can provide a reliable decision support system for the high-rise building fire risk process management.

## Acknowledgments

The research presented in this paper was supported by the China National Science Foundation (11072035) and the China university scientific research fund (3142014043).

## References

[1]Adam C., Adam B., Cecilia A.E., Jose T.. Fire safety design for tall buildings. Procedia Engineering, Vol.62(2013), p.169-181

[2]Hao C., George V. H.. Dynamic modeling of fire spread in building. Fire Safety Journal, Vol.46(2011), p.211-224

[3]RING Z.X., ZHAO X.F., SONG H., GAO W.L.. Applied Research of Performance-based Fire Protection Design in a Lame Building. Procedia Engineering, Vol.11(2011), p.566-574

[4]HU B.Q, LIU M., LU Z.M.,2004. Fuzzy evaluation of fire safety in high-rise buildings. Journal of Wuhan University Vol.37(2004), p.67-72(In Chinese)

[5]George V.H., Noureddine B.. Performance criteria used in fire safety design. Automation in Construction, Vol.8(1999), p.489-501

[6]China State Bureau of technical supervision, China Ministry of construction. Code for fire protection design of high-rise civil buildings. Chinese Planning Press, China(2005) (In Chinese)

[7]LIU K.D, CAO Q.K, PANG Y.J.. A method of fault diagnosis based on Unascertained Set. Journal of automation, Vol.30(2004), p.747-756(In Chinese)

[8]C.M.Zhao, S.M. LO, J.A. Lu, Z. Fang. A simulation approach for ranking of fire safety attributes of existing buildings. Firc Safety Journal, Vol. 39(2004), p.557-579

[9]GAO Y.. Analysis on High-building Fire External-fire Factors and Study on Its Safety Evaluation System. Master's degree thesis of Xi'an University Of Architecture And Technology (2010), p.42-45(In Chinese)

[10]CAO Y.. The fuzzy comprehensive evaluation method of high rise building fire risk based on Catastrophe Theory. Master thesis of Central South University (2008), p.28-39(In Chinese)

*Applied Mechanics and Materials Vols. 580-583 (2014) pp 2622-2627*
*© (2014) Trans Tech Publications, Switzerland*
*doi:10.4028/www.scientific.net/AMM.580-583.2622*

# A study of storm surge risk index system

Qiang Liu[1, a], Zhenzhen Yuan[1, b]

[1]School of Engineering, Ocean University of China, Qingdao, Shandong, 266100, China

[a]liuqiang@ouc.edu.cn, [b]yuanzhenzhen6@126.com

**Keywords:** Storm surge, Risk evaluation index, Risk mitigation

**Abstract.** Natural disasters refer to casualties, property damage and social instability. Coastal urban areas with a high population density coupled with the construction of man-made structures are particularly subjected to storm surge hazards, which have become an increasingly urgent problem. In this paper, we try to set up a risk index system, including risk indicator, vulnerability indicator and prevention and mitigation capability index. Each of the risk components has large number of variables and quantities. Through displaying losses and characteristics of the four natural disasters, we put forward suggestions for better disaster mitigation. So that a better understanding of storm surges risk profile and early disaster warning measurement could be achieved.

## Introduction

Storm surge is an abnormal rise of water generated by a storm, over and above the predicted astronomical tide. Storm surge is caused primarily by the strong winds in a hurricane or tropical storm. [1]According to the weather system characteristics induced storm surge, it is usually divided into a typhoon (hurricane) storm surge and extratropical storm surge. [2, 3]Densely populated coastal areas are particularly vulnerable to natural hazards as increasing coastal development has positioned large numbers of people and infrastructure in close proximity to the coast. The tsunami of 26 December 2004 killed more than 220,000 people in 13 countries around the Indian Ocean, and the 11 March 2011 tsunami devastated a whole region in Japan. In 2005, Hurricane Katrina left the United States with a bill of some US$ 125bn (Fig. 1). In Europe, Winter Storms Kyrill (January 2007) and Xynthia (February 2010) cost US$ 10bn and US$ 6.1bn, respectively, the latter claiming 41 lives due to storm surge. Europe reached highest storm surge death toll since 1962, when more than 300 people were killed in Hamburg. Bangladesh (2007) and Myanmar (2008) were hit by tropical cyclones that left thousands dead and vast areas destroyed by wind and flood. Australia's east coast was beleaguered by four consecutive storms, in June 2007 that brought wind, rain, snow and high waves, and drove one large vessel onshore. Only in the case of Africa does one have to go back a few more years to the last major coastal disaster, with the exception of the 2004 Indian Ocean tsunami mentioned above (which killed about 300 people in Somalia, Kenya, Tanzania, Seychelles and Madagascar): namely to 2000 and 2001, when large parts of countries in the south-east of the continent were hit by a number of cyclones. [4]In China, Hainan province has also suffered from storm surge in recently years (Fig.2). Hurricane Sandy occurred in 2011 which affected many areas (Fig.3). In 2013, Typhoon Haiyan attacked Taiwan and many other cities (Fig.4). Here are four pictures about the disaster.

Fig. 1

Fig. 2

Fig. 3

Fig. 4

Fig. 1 Casino in Biloxi, Mississippi, USA after Hurricane Katrina in 2005 (Munich Re)
Fig.2 Haikou city, Hainan province suffered from storm surge in 2010
Fig.3 Hurricane Sandy attacked USA in 2011
Fig.4 Taiwan affected by Typhoon Haiyan in 2013

## The Current Storm Surge Risk Research

### 2.1 The research status abroad

Early natural disaster risk assessment is mainly used in the project; put more emphasis on the possibility of the occurrence of natural disasters. In recent years, with the rise of interdisciplinary, analysis and assessment of natural disasters not only focus on their own research, but also combine with the social and economic characteristics. Human factors are playing an enormous role. Good results have also been achieved. Tun Lin Moe [5] proposed a set of effective natural disaster risk management framework and approach through the study of public facilities. Vassilis Tsoumas [6] suggested the natural disaster risk management should move towards automation direction. Michael K. Lindell [7] put forward the continuity model about the impact of natural disasters and the consequences. Charles Kelly [8] preliminary evaluated the impact of natural disasters on the environment. Gary W. Barrett [9] explored post-emergency response to natural disasters assessment work.

### 2.2 The research status in China

Lihua Feng [10] proposed quantitative indicators of the degree of disaster according to casualties and property losses caused by the storm surge. Qiwang Xu [11] et al. conducted a preliminary study based on direct economic losses and two indicators. Wen Ye [12] used the perception algorithm to discriminate the disaster level, using data of storm surge from Zhanjiang and Guangdong Province.

## Risk Evaluation Index

Based on the understanding of disaster risk, some theoretical frameworks for risk assessment were established. For example, ISDR (International Strategy for Disaster Reduction) (2005) considered the history of the disaster, disaster risk analysis, hazard vulnerability analysis, and risk evaluation consisted of disaster risk evaluation system. IRGC(International Risk Governance Council)

suggested disaster risk assessment, including hazard identification, hazard assessment, disaster bearing system diagram, vulnerability assessment, as well as demographic and economic loss risk assessment and other aspects (ITC, 2009). Zhane Yin (2009) proposed to include risk identification, risk analysis and risk assessment only. Based on the results of previous studies of storm surge disaster risk evaluation, a risk evaluation index could be figured out with risk indicators, vulnerability indicators, disaster prevention and mitigation capability indicators.

### 3.1 Risk indicators

The size of the risk caused by storm surge is a direct factor in the disaster, mainly refers to the intensity of the storm surge disasters, including storm surge own activity intensity and frequency. Therefore, identification of the storm surge hazard index for predicting storm surge disasters and mitigation is important.

(1) The strength of storm surge is the degree of storm surge intensity .The higher intensity can cause stronger waves and a larger increase in the water surface level. In this case, the risk of disasters will cause severe effects.

(2) Maximum surge, tide and waves are direct characterizations of the sea change when the storm surge coming .The greater of its value indicates that the greater variation and thus the greater the risk of disaster bring by storm surge .These changes threaten to exacerbate storm surge risk by increasing the sea penetration, which could lead to coastal flooding and inundation.

(3) Central pressure, wind speed and wind radii, are the direct factors causing variation in sea water. The higher pressure, the greater wind speeds, the larger the radius and the higher wave height will result in higher risk.

(4) Landing sites related to the disaster areas are affected by the storm surge. If it lands in a developed economy with dense population and infrastructure region, it bounds to lead to larger losses and the greater risk as well.

### 3.2 Vulnerability indicators

Vulnerability of hazard is the susceptibility of both biophysical and social systems to a hazard. The length of the coastline, the coastal topography and geographic location and the average altitude terrain, potentially affected areas directly relates to the size of the disaster caused by storm surge. The stretches of coastline, flat terrain, near to the coast, under the average altitude of the regions are more vulnerable to the impact of storm surges. Therefore, the regions possess a higher degree of vulnerability.

Population density, per capita GDP and urban population proportion is also related to the storm surge. The population density is the number of units of square kilometers of the population, per capita GDP represents the degree of economic development in the region. If the proportion of urban residents in the area accounts for a large part, it will have a larger population density and a more developed economy. Then storm surge will cause losses of life and property.

Low proportion of housing, which means the number of potentially affected areas is another factor. Because compared to buildings, cottage is subjected to storm surge. So if the ratio is large, then the extent of the damage to the area housing is higher.

Primary/secondary industry GDP ratio or the ratio of the second industry and the total GDP of the area of primary industry is also the cause. Its value indicates the contribution of agriculture and industrial economy of the area. When storm surge hits the area from time to time, it will cause serious economic losses and bring risk of vulnerability as well.

### 3.3 Disaster prevention and mitigation capability index

Capacity building is the ability of people to deal with storm surge characteristics and features of hazard bearing body outside, including storm surge early warning of disasters, disaster recovery and reconstruction. Its specific indicators are as follows:

Coastal observation stations, dam project number and the average heights of the dam are the direct manifestation of the potential disaster area forecasting ability, the ability of disaster prevention. The

fact that people are living in areas endangered by storm surge is ignored, or eventually forgotten. If we grasp the sufficient data about coastal storm data, the risk of disaster can reduce largely.

Disaster emergency management capabilities include the number of storm surge disaster emergency shelters, relief materials reserve and the number of emergency rescue personnel.

The education of Storm surge risk knowledge is also critical. If everyone can realize the potential risk and the government do the relevant training work, the losses can be reduced to a large extent.

## Improvement Suggestions for Disaster Mitigation

### 4.1 Analysis and Comparison

Indicators about the storm surge in last 10 years are shown in Table 1. Accordingly, we include that some measures should be done in aspect of disaster prevention and mitigation.

| Indicators | | Hurricane Katrina | Typhoon Morakot | Hurricane Sandy | Typhoon Haiyan |
|---|---|---|---|---|---|
| | | 2005 | 2009 | 2011 | 2013 |
| Risk indicators | Affected area | USA, Bahamas, Cuba | Philippines, Japan, China, Taiwan Province of China, South Korea, North Korea | USA, Haiti, Cuba, Bahamas, Dominica, Canada, Jamaica | Marshall Islands, Guam, Philippines, Vietnam, Laos, China, Taiwan Province of China, Hong Kong |
| | Average wind speed (km/h) | 280 | 150 | 185 | 315 |
| | The lowest pressure(hpa) | 898 | 945 | 940 | 890 |
| Vulnerably indicators | The property loss (billion) | 108 | 6.2 | 65.5 | 0.83 |
| | The loss of life | >=1833 | 734 | 268 | >=7986 |

### 4.2 Suggestions for better disaster mitigation

Early warnings and preventions can reduce losses. Preparedness and Planning is the most important procedure. First of all, it should be in the form of land-use regulations for a given coastal area that has a high potential storm surge risk, keeping in mind particularly those areas that are known to have sustained damage in the past. Storm surge hazard perception should be introduced to the people of a coastal area for mitigating loss of life and damage to property. Hazard perception by the public is based on a technical understanding of the phenomenon. The next step could be to learn from historical experience and identification of vulnerable areas with reference to risk of potential loss of life, damage to property and related infrastructure. Prepare a vulnerability atlas that will show areas vulnerable to disaster and determinations of run-up level, which will help in coastal zone plan. The local government should formulate a policy of strategy to manage the disaster and enforce modern construction practice and planning in coastal settlements.

Finally, local residents should get more education for natural disaster prevention to a large extent. They should have knowledge of the mitigation and evacuation procedures when a warning is issued. Above all, people should be educated not to panic after the disaster and wait patiently until the issued warning is waved off or wait for the rescue teams to arrive.

## Discussion

Storm surge disaster risks have dynamic characteristics which reflect storm surge tide conditions (storm surge, astronomical tide and wave surge superimposed) in the intensity and frequency of different design scenarios. The extent of exposure (including disaster prevention engineering measure and non-structural measures) spatial and temporal variation also influences the extent of the storm surge. In recent years, it has been proved that sea level rise will likely increase risk in many coastal areas and will potentially create risk where it was not before. Climate change has also the potential to increase the risk of storm surge hazard due to the enhanced greenhouse effect. We should focus on dynamic assessment of storm surge disaster risk when setting up risk evaluation index system.

## Conclusions

We analyze and summarize the evaluation index system of storm surge risk. The main risk indicators include risk indicators, vulnerability indicators and mitigation of vulnerability index. The government agency can better analyze the impact of storm surge factors and make homologous measures. But with the rapid urban development, the coastal city gathered more people and property. How should we grasp the risk characteristics of the new stage, how to improve disaster mitigation and how to expand multidisciplinary field of urban disaster management will be the subject of future research.

## Acknowledgments

This research is partially supported by the National Natural Science Foundation (No.41371496) and National "Twelfth Five-Year" Plan for Science & Technology Support (No. 2013BAK05B04).

## References

[1] Information on: http://www.nhc.noaa.gov/surge/surge_intro.pdf

[2] Lin Ye, Fujiang Yu: prediction of long-term change and ocean storm surge disaster forecast, 2002, 19 (1): 89-96. (In Chinese)

[3] Qingliang Zhao, Shiyuan Xu, Jun Wang: A Review of Risk Assessment of Storm Surge on Coastal Cities 2007, 5; 32-40. (In Chinese)

[4] Kron W. Coasts: the high-risk areas of the world. Natural hazards, 2013, 66(3): 1363-1382.

[5] Moe T L, Pathranarakul P. An integrated approach to natural disaster management: public project management and its critical success factors. Disaster Prevention and Management, 2006, 15(3): 396-413.

[6] Vassilis Tsoumas Tsoumas, Theodore Tryfonas, (2004) from risk analysis to effective security management: towards an automated approach, Information Management & Computer Security, Vol. 12 (1):91-101

[7] Michael K. Lindell, Mand Prater, C. (2003). “Assessing community impacts of natural disasters”. Nat. Hazards Rev.4 (4), 176-185.

[8] Charles Kelly "Assessing environmental impacts during natural disaster". The development of a rapid environmental assessment methodology. Journal of Environmental Assessment Policy and Management, 2002, Vol.4 (4):475-492.

[9] Gary W.Barrett: quick response to natural disasters, Bioscience, 2005, Vol55 (12).

[10] Lihua Feng: quantitative levels and storm surge disaster notation, Marine science, 2002, 26(1), 40-42. (In Chinese)

[11] Qiwang Xu, Shudong Tan. Study storm surge disaster assessment on economic losses. Marine Science Bulletin .1998, 17(1), 1-12. (In Chinese)

[12] Wen Ye, Meinan Liu, xiaohong Chen. Perceptron algorithm in the storm surge disaster rating of Sun Yat-sen University (Natural Science Edition), 2004, 43(2), 117-120. (In Chinese)

[13] Q Liu, Yuhong Zhang: risk assessment on Storm Surge and coastal Zoning Management, Marine Geology Frontiers Vol .28, No 9. (In Chinese)

[14] Nat Hazards (2012) Tsunami vulnerability assessment in urban areas using numerical model and GIS by Tune Usha .M.V.Ramana Murthy .N.T.Reddy .Pravakar Mishra

[15] V. Sathish Kumar, V. Ramesh Babu, M. T. Babu, G. Dhinakaran, and G. V. Rajamanickam (2008) Assessment of Storm Surge Disaster Potential for the Andaman Islands. Journal of Coastal Research: Volume 24, Issue 2A: pp. 171-177.

[16] Shepard C C, Agostini V N, and Gilmer B, et al. Assessing future risk: quantifying the effects of sea level rise on storm surge risk for the southern shores of Long Island, New York. Natural hazards, 2012, 60(2): 727-745.

*Applied Mechanics and Materials Vols. 580-583 (2014) pp 2628-2634*
*© (2014) Trans Tech Publications, Switzerland*
*doi:10.4028/www.scientific.net/AMM.580-583.2628*

# Review of Different Methodologies and Risk Assessment Models in Storm Surge Disaster Management

Qiang Liu[1, a], Shuo Yang[1, b]

[1] Engineering College, Ocean University of China, Qingdao, Shandong, 266100, China

[a]liuqiang@ouc.edu.cn, [b]iamsure89@126.com

**Keywords:** Storm surge, natural hazard, risk assessment, modeling

**Abstract.** Storm surge causes severe casualties and commercial losses to the habitant living within the range of it frequently, and has been one of the most harmful and prevailing hazards that attacks coastal areas. This paper is dedicated to reviewing and analyzing the methodologies and models that are generally used to assess the storm surge risk. Firstly, by means of analyzing the existing models of hazard risk assessment, indicating the purpose, process and methodologies. Secondly based on the analysis a comparison of the basic profile has taken into practice, and the advantages and limitations of the models are discussed. Finally, associating with the impacts of storm surges that affect China, we bring up a research direction that leads to further studies.

## Introduction

### 1.1 Recent storm surges and the losses

Storm surge is an abnormal rise of water generated by a storm, over and above the predicted astronomical tide. The storm surge is primarily caused by the strong winds of a hurricane or tropical storm. [1] The inundation that brought to coastal areas is the main negative affection coming from storm surges. The destructive power, the regional orientation and the predictability are the main characteristics of storm surges.

Storm surges lead to more casualties and economical losses when comparing to other natural disasters (e.g. volcano eruption, earthquakes, floods or droughts). Table 1 shows the cases that cause considerable losses in the last 10 years.

Table 1 Summary of global cases that cause considerable losses in the last 10 years

| Time | Name | Affected Area | Loss of life(missing people included) | Economic Losses (billion dollars) |
|---|---|---|---|---|
| 2005 | Hurricane Katrina | USA, Bahamas, Cuba | >=1833 | 108 |
| 2009 | Typhoon Morakot | Philippines, Japan, China, Taiwan Province of China, etc. | 734 | 6.2 |
| 2011 | Hurricane Sandy | USA, Haiti, Cuba, Bahamas, Dominica, Canada, Jamaica | 268 | 65.5 |
| 2013 | Typhoon Haiyan | Philippines, Vietnam, Laos, China, Taiwan Province of China, etc. | >=7986 | >=0.83 |

The countries and regions affected are mainly distributed in the west and south of Pacific Rim, and in Caribbean Region.

Since the storm surge is primarily caused by the strong winds of a hurricane or tropical storm, and the disasters can be observed through meteorological satellite, the model of the storm surge can be simulated. Furthermore, after the assessment of the topographical and geographical condition of the coastal area, regions of higher risk and higher vulnerability with respect to storm surge can be found out. We may believe that the hazard of storm surge possesses a characteristic of predictability.

1.2 Storm surge is one of the dominant natural hazards in China

China possesses a coastline as long as more than 32 thousands kilometers (18-thousand-kilometer-long mainland coastline and 14-thousand-kilometer-long island coastline respectively). [2] As located near by the Western Pacific Ocean, China suffered from the frequently occurred typhoons and tropical storms, mainly in the coastal areas in the southeast. Therefore storm surge has become one of the most dominant natural hazards in the coastal areas in China.

In 2012, it is storm surge that causes the most severe economic losses among all sorts of marine hazards and a relatively high percentage of loss of life. (Table 2)

Table 2 Losses of marine hazard of different categories in 2012 [3]

| Category of marine hazard | Loss of life (missing people included) | Percentage of loss of life | Direct economic losses (billion) | Percentage of direct economic losses |
|---|---|---|---|---|
| Storm surge | 9 | 13.24% | 126.29 | 81.35% |
| Wave | 59 | 86.76% | 6.96 | 4.48% |
| Sea ice | 0 | 0 | 1.55 | 1.00% |
| Tsunami | 0 | 0 | 0 | 0 |
| Red tide | 0 | 0 | 20.15 | 12.98% |
| Green tide | 0 | 0 | 0.30 | 0.19% |
| Fluctuation of sea level | 0 | 0 | -- | -- |
| Coastal erosion | 0 | 0 | -- | -- |
| Intrusion of tidal saltwater | 0 | 0 | -- | -- |
| Total | 68 | 100% | 155.25 | 100% |

1.3 Current statement of the risk assessment of storm surge

More and more frequent and severe casualties and commercial losses have been caused by storm surge to the countries and/or regions affected in recent years. Policy makers start to figure out the significance of the research on storm surge. Risk assessment of storm surge provides the basis for risk mitigation and related decision making.

However, there has been few generally adopted approach, let alone well-developed common methodology or guideline to assess storm surge risk. The approaches of storm surge risk assessment models available are divided into three categories according to the analytical level, i.e. qualitative, semi-quantitative, and quantitative approaches. As the precondition of the decision making of risk mitigation, risk assessment model plays an important role during the process of risk management. Nowadays, countries and/or regions affected by storm surge dedicate to establishing their exclusive risk assessment model respectively. But the models do not have connections and are lack of consistency in space and time (e.g. Hurricane Sunday causes enormous losses in US especially New York in 2011, only two years later after a comprehensive assessment on storm surge in New York).

The main purpose of this paper is to compare and analyze different risk assessment models, in order to figure out the proper application to different models. In the following section typical paradigms of different kinds of risk assessment models and brief introduction of the methodologies and the process applied is brought out. Analyses of models are summarized in a table which shows the characteristics of the models mentioned. The advantages and limitations of each model are discussed. And the methodologies applied and a general process of storm surge risk assessment is reviewed according to the studies. Last but not least, vista of future work in assessment, management and mitigation of storm surge risk is discussed.

**Risk Assessment Models**

Storm surge risk assessment is a relatively new and growing discipline that is coming from general approaches, which are usually applied to the general field of risk assessment (e.g. industrial risk and other natural risk such as floods, tsunamis or earthquakes). [4, 5] As an interdisciplinary research, the study on storm has greater complexity and difficulty. Comparison and analysis is carried out to the existing risk assessment models as follows.

2.1 Introduction and comparison of the common used models

**1) Data-based risk assessment models**

Among different kinds of assessment models, some simulation results are based on historical data of specific regions. Apparently, this kind of model tents to be quantitative.

Sufficient historical data with respect to storm surge is a prerequisite to establish data-based risk assessment model. There is only relatively short history that people record the hydrologic information in coastal areas. So it is the reason why few researchers are keen on carrying on risk assessment in a historical data-based way. In order to introduce the data-based method, a paradigm is brought, which is used for risk assessment of tsunamis.

An international project was carried out to assess the risk of tsunamis on the shorelines of Australia and its island territories. [6] The historical record from 1788 to 1995 is applied to the approach of quantitative and qualitative definition of the hazard and the vulnerability, and then these elements are integrated into a comprehensive risk assessment. Risk is considered as the product of hazard multiplies vulnerability. Where hazard is a comprehensive concept relative to historical tsunami data, potential tsunamigenic sources, relevant parameter determinations, probabilistic estimates and tsunami travel time charts. And vulnerability delineates the buildings and natural environments and possible effects thereon from tsunami and the human element. [6]

There are four steps in this model, i.e. 1) hazard assessment, 2) vulnerability assessment, 3) risk assessment and 4) policy making for tsunami warning. In the first step, the study involved the collection, collation and analyses of instrumental data (e.g. tide-gauge records), anecdotal information and published scientific papers and reports. By means of quantification of "Tsunami Hazard Zones" (which differs the hazard level into high, medium and low zones), a tsunami hazard map is established for Australia and its territories. And 4 classes of potential tsunamigenic sources have been identified, i.e. earthquake, submarine volcanoes, submarine landslides and extra-terrestrial impacts. The second step is vulnerability assessment which is defined in quantitative terms as the integration of the existing state of and the uncertainty of the future development in the coastal areas and the islands. According to the occurrence of generic elements such as built environment (e.g. major ports, harbors, fishing industry, etc) and natural environment (e.g. significant coastal geography, tourist areas, etc), vulnerability levels (divided into high, medium and low) are given to the coastal areas and the islands. In the third step, the potential risk levels as Zones A to E which is determined by a comprehensive analysis are presented in a tsunami risk assessment zoning map for the study areas. The final step is a governmental behavior, related to tsunami warning and response system, and is beyond the range of this paper.

It is inevitable that differences between tsunami and storm surge risk assessment model are exist. The differences mainly focus on: 1) source identification; 2) propagation of the wave; 3) forecast and warning. But the process of the assessment such as hazard assessment and vulnerability assessment are pretty similar. So this paradigm can be a reference in storm surge risk assessment.

Because of the shortage of specific data in the study field around the world, it is a great challenge to implement the data-based approaches.

**2) Model -based risk assessment**

Data-based risk assessment models need sufficient historical data when they are put into effect. But few countries or regions possess sufficient scale of successive historical data about storm surge. So risk assessment applies model-based approach can be widely used.

Qualitative risk assessment models e.g. scenario-based ones, and statistical risk assessment model are mainstream approaches to realize risk assessment.

A scenario-based tsunami risk approach is implemented by Nadim and Glade in the West coast of Thailand whose geographical position is familiar with China. [7] This approach considers a series of plausible extreme scenarios causing by a tsunami-generating earthquakes, and involves the following steps:

1. Definition of scenarios for tsunami-generating earthquakes,
2. Computing the tsunami inundation levels,
3. Estimation of tsunami risk for the different scenarios, and
4. Comparison of the estimated risk with tolerable or acceptable risk levels.

The risk is considered as the expected value of loss (human life, economic loss, reputation loss, and so on), and is calculated using the following general expression. (Eq.1)

$$E[loss] = \sum_{S} \sum_{\underline{C}} \underline{C} \times P[\underline{C}|S] \times P[S] \tag{1}$$

Where E[loss] stands for the expected value of loss e.g. of human life, economic loss, reputation loss, etc; C is the particular set of losses; S is the particular scenario; P[S] is the probability of occurrence of scenario; P[C|S] is the conditional probability of losses set C given that scenario S has occurred.

This approach mainly focuses on the loss of human life. The affected population could be divided into three groups according to the probability of the occurrence. Other researchers applied scenario-based model as well, such as Tinti et al. carried out a scenario-based approach for both small and large tsunamis, [8] Pruttipong Apivatanagul et al. applied an optimization probabilistic scenario method to estimate the long-term regional hurricane wind and storm surge hazard. [9]

N. Lin et al. carried out a statistical/deterministic storm surge risk assessment associated with the hydrodynamic model SLOSH (sea, lake, and overland surges from hurricanes) and ADCIRC (advanced circulation model) for New York City. [10] This methodology makes it possible to assess the storm surge risk for data-scarce regions. Implementation steps are as follow:

1. The hurricane model and the SLOSH model (with a relatively coarse grid) are coupled to generate a large number of synthetic surge events around a site of interest.
2. Statistical analysis can then be carried out to estimate the probability density function (PDF) of storm surge heights for the site.
3. Combining the PDF of storm surge heights and the annual storm frequency, which may be estimated from the hurricane model, mean return periods of surge heights can be predicted.
4. Using the ADCIRC model (with a high-resolution grid), an evaluation has been carried out to the “most dangerous storms” of the SLOSH simulations to ensure the accuracy of SLOSH model.

Also statistical analysis of the simulation results was carried out in a large scale. They concluded that storm surge may be well correlated with the wind speed parameters at the site of interest. And the characteristics of the highest storm surges are described as follow: high intensity (i.e. high maximum wind speeds, large pressure deficits, and relatively compact structure) when passing by the site; Slow moving velocity, etc. It is different from some assessment models that the results of the model focus on the annual storm frequency and the mean return period of the storm surge heights. They mentioned that it is meaningful to combine the estimated storm surge caused by hurricanes with other components of coastal flood level in risk assessment for further studies.

Similar paradigms applying statistical approaches are widely used: Jarvinen et al. evaluated storm surges by means of SLOSH simulation model; [11] the work of Pickands et al. is useful for estimating the probabilities of future extremely large observations (including storm surges). [12]

## 2.2 Model Comparison

After reviewing the risk assessment models, we can find some general facts. The calculation of the risk is usually carried out in a statistic or a deterministic (i.e. scenario-based or synthetic) approach depending on the availability of historical data. The consequences of the negative incidents refer to

the elements at risk and the vulnerability of them. The vulnerability assessment mainly focuses on the loss of population and property. However the description of the concept of risk has not been unified, more and more researchers acknowledge it as the product of hazard and vulnerability. And the understanding of hazard and vulnerability differs from each other.

The model types are roughly divided into two groups, i.e. data-based models and model-based ones. The application scope comes into national or regional scale. Although process of every model differs from each other, a general process can be summarized, which will be introduced later on. The output of the models is expressed in various methodologies. (Table 3)

All these commonly applied models possess distinct characteristics of advantages and limitations.

Data-based models possess advantages of convincing evident, the persuasion and a larger research area. However, because of the shortage of the source of historical data, research area can not cover all lately developed regions.

Scenario-based models solved the problem when assessing storm surge risk in data-shortage areas. And a relatively precise simulation can be carried out in research region. The limitations of these models are the effectiveness depends on the consistency of the simulated events and the real ones, and the research area usually very limited.

Statistical models solved the data-shortage problem too. Researchers can obtain specific characteristics of the simulated storm surge. And the model is in favor of a detailed risk mitigation plan. But the accuracy is in proportion to the calculation.

Table 3 Summary of the risk assessment models

| Source | Model type | Application scope | Analysis process | Output |
|---|---|---|---|---|
| Jack Rynn & Jim Davison | Data-based | National | 1) Hazard assessment,<br>2) Vulnerability assessment,<br>3) Risk assessment, and<br>4) Policy making for tsunami warning. | Tsunami hazard map, tsunami risk zonation map |
| Nadim & Glade | Model-based | Regional | 1) Definition of scenarios for tsunami-generating earthquakes,<br>2) Computing the tsunami inundation levels,<br>3) Estimation of tsunami risk for the different scenarios, and<br>4) Comparison of the estimated risk. | Expected value of loss |
| N. Lin et al. | Model-based | Regional | 1) Generate a large number of synthetic surge events,<br>2) Statistical analysis to estimate the probability density function (PDF) of storm surge heights,<br>3) Risk assessment by means of combining the PDF of storm surge heights and the annual storm frequency, and<br>4) Ensure the accuracy of SLOSH model through an ADCIRC evaluation. | Mean return period of the storm surge heights |

Therefore when people choose the risk assessment model, they need to suit to the specific conditions they study.

## Methodologies

The methods applied in the risk assessment models are divided into 2 groups according to the quantitative level. In quantitative approaches, contour lines, thematic risk maps and F-N curves play important roles in quantifying the distribution of storm surge risk in space and time. And statistical analysis and event simulation (e.g. ADCIRC and SLOSH) functioned well in statistical approaching risk assessment model. Otherwise risk matrix (which can be further translated into a thematic risk map in a GIS environment) or empirical approaches such as scoring by experts can be used.

Similarities are found in the general steps of risk assessment. This can be explained by the generic origin of natural risk assessment approaches. The general framework deriving from the reviewed models can be summarized as follow:

1. Definition of the issue. Define the characteristic of the problem and confirm the purpose of the analysis including the research area, level of details, and the quantitative level.

2. Hazard analysis. Define the severity and frequency of the storm surge. The output may involve in this step: probability distribution of the occurrence of a storm surge of various return period, hazard map, risk zoning map, etc.

3. Vulnerability analysis (or consequence analysis). It includes the identification of the elements at risk with respect to the potential storm surge, and the vulnerability of the effected elements. The output may involve in this step: distribution maps of specific elements at risk (population, property, infrastructures etc.); thematic maps of the societal, physical or environmental vulnerability.

4. Risk estimation. Integrate the outcomes from hazard and vulnerability analysis in a quantitative way or a qualitative way or a semi-quantitative way depending on the historical data sufficiency of the research area.

5. Risk evaluation. Compare with the available risk criteria, and determine the acceptability of the risk. If necessary, risk mitigation will be put into effect.

6. Early warning system and emergency plans as well as reconstruction and sustainable disaster management.

## Discussion

Storm surge is one of the most devastating coastal disasters which caused about 80% of marine damages in China. Due to the long history of recording natural disasters in coastal areas, which can dated back to Han Dynasty in 48 BC, [13] historical data-based approaches can be used to assess the risk of storm surge. However, the vulnerability has increased dramatically along with the fast urban development. There is an urgent need to assess the risk. [8] Further research on risk assessment in China can associate model-based models with data-based models to form a complementary effect.

Under the influence of global climate change, temperature may be increasing and sea level may be rising, the occurrence of extreme events turns to be more frequent. On one hand, increasing temperature causes more storm surges nowadays; On the other hand, rising of the global sea level leads to a higher occurrence possibility of storm surge and more severe at the same time. [14] Therefore, hazard, as a potential loss, which is a determining factor when assessing disaster risk, has been more complicated. Storm surge risk mitigation faces a more complicated situation around the world.

Vulnerability is another important part of risk assessment. It is easier and easier to have extreme events happen during 1990 to 2009 based on calculation and estimation to the vulnerability of 11 coastal located provinces or metropolises. And it relates to the higher temperature as well. [13]

When hazard and vulnerability increase, higher risk is expected. It is necessary to have a more thorough research on the risk assessment model. Future studies might be done in context of climate change and sea level raise. Modeling should be associated with astronomic tide and sea wave; synthesis risk mitigation should be taken based on risk assessment of multiple coastal disasters such as coastal subsidence and urban inundation.

## Conclusions

This paper reviews the existing storm surge risk assessment models after an introduction of recent statement of storm surge risk assessment including basic information of storm surge, storm surge in China and the current statement of the risk assessment of storm surge. Comparison among the typical models concerning model type (data-based model, scenario-based model and statistical model), application scope, analysis process and outcome were carried out accordingly. We analyze the advantage and limitations of the models reviewed. Some methodologies applied in risk assessment models are presented. General steps for storm surge assessment are brought out performing as a guideline on storm surge risk assessment. Last but not least, aiming at improving risk assessment in China, we discuss a probable trend of storm surge risk and give a research direction on future study. This paper is a threshold of our research, further study will be continued.

**Acknowledgments** This research is partially supported by the National Natural Science Foundation (No.41371496) and the National "Twelfth Five-Year" Plan for Science & Technology Support (No. 2013BAK05B04).

## References

[1] Information on http://www.nhc.noaa.gov/surge/surge_intro.pdf
[2] H. Wang, Q. Li Editors. 11-2 Coastline of main coastal countries (regions). China Oceanic Statistical Yearbook. (2012). (In Chinese)
[3] State oceanic Administration People's Republic of China Editor. China oceanic disasters communique, (2012). (In Chinese)
[4] R. Jelínek, E. Krausmann, M. González, et al: Approaches for tsunami risk assessment and application to the city of Cádiz, Spain. Natural hazards. Vol. 60(2012), p. 273
[5] R. Jelínek, E. Krausmann: Approaches to tsunami risk assessment. Joint Research Centre, Institute for the Protection and Security of the Citizen, European Commission: 2008.
[6] J. Davidson, J. Rynn: Contemporary Assessment of Tsunami Risk and Implications for Early Warnings for Australia and its Island Territories. Science of Tsunami hazards. Vol. 17(1999), p. 107
[7] F. Nadim, Glade: On tsunami risk assessment for the west coast of Thailand. ECI conference on geohazards (Lillehammer, Norway. 2006), p.1
[8] S. Tinti, A. Armigliato: The use of scenarios to evaluate the tsunami impact in southern Italy. Marine Geology. Vol. 199(2003), p. 221
[9] P. Apivatanagul, R. Davidson, B. Blanton, et al: Long-term regional hurricane hazard analysis for wind and storm surge. Coastal Engineering. Vol. 58(2011), p. 499
[10] N. Lin, A. Emanuel, A. Smith, et al: Risk assessment of hurricane storm surge for New York City. Journal of Geophysical Research: Atmospheres (1984–2012). Vol. 115(2010)
[11] B. R. Jarvinen, M. B. Lawrence: An evaluation of the SLOSH storm-surge model. Bulletin of the American Meteorological Society. Vol. 66(1985), p. 1408
[12] J. Pickands III: Statistical inference using extreme order statistics. The Annals of Statistics (1975), p.119
[13] G. Yang: Historical change and future trends of storm surge disaster in China's coastal area. Journal of Natural Disaster. Vol. 9(2000), p. 23 (In Chinese)
[14] L. Tan, K. Chen, J. Wang, L. Yu: Assessment on Storm Surge Vulnerability of Coastal Regions During the Past Twenty Years. Scientia Geographical Sinica. Vol. 31(2011), p. 23 (In Chinese)
[15] Q. Liu, Y. Zhang: Modeling for vulnerability zoning of storm surge disaster and its application in Qingdao. Marine Geology Frontiers. Vol. 28(2012), p. 46 (In Chinese)

*Applied Mechanics and Materials Vols. 580-583 (2014) pp 2635-2641*
*© (2014) Trans Tech Publications, Switzerland*
*doi:10.4028/www.scientific.net/AMM.580-583.2635*

# A Forecast and Risk Assessment Model for Storm Surge Impacts

Ling Zhang[1, a], Qiang Liu[1, b], Shuo Yang[1, c]

[1]Engineering College, Ocean University of China, Qingdao, Shandong, 266100, China

[a]zljoan@163.com, [b]liuqiang@ouc.edu.cn, [c]iamsure89@126.com

**Keywords:** Strom Surge; Risk assessment; Numerical Modelling; Extended Kalman Filter (EKF)

**Abstract.** A new approach to risk assessment of storm surge and prediction problems was suggested. The model is based on the Extended Kalman Filter (EKF) equations, which simply linearises all nonlinear models so that the traditional Kalman filter can be applied. Key factors describing storm surge disasters are considered in the model. Numerical simulations were carried out and tested with some actual observations of recent storm surge events and related damages in coastal regions of China. The results show a reasonable fit for storm surge disaster prediction and encourage the possibility of using the method for future studies.

## Introduction:

The recent devastating impact by Typhoon Haiyan (2013) associated with record wind speed (105 m/s), heavy rainfall again showed Southeast Asia, as well as coastal regions in China is among the most vulnerable areas to storm surge and coastal flooding around the globe, in terms of both the probability of being hit by major storm surges and the potential consequences. [1] Although wind speeds were extreme, the major cause of property damage and loss of life appears to have been storm surge. People in Asia coastal regions are recognizing the impacts of tsunami after the events of 2004 in Indian Ocean and 2011 in Japan; however, they have little knowledge of storm surge risk, let alone risk mitigation and climate adaptations measures, such as an early warning system [2, 3].

Fast industrial developments with densely populated coastal areas in China are particularly vulnerable to these hazards. While planning, early warning and mitigation for these hazards is an ongoing and continuous process, significant challenges lie ahead for central and local government in China tasked with planning for the potential impacts of climate change on the magnitude and frequency of coastal hazards [3, 10].

Previous studies dedicated to different storm surge modeling efforts based on general circulation models (GCMs) and hydrodynamic models to predict the maximum winds and rainfall rates. [4, 6, 7] The models are either based on the historical maximum storm surge sea level and time distribution or statistical analysis with presumed scenarios. These models found useful applications in risk assessment for storm surge hazards by hurricanes in the East coast in US. [5]

However, risk assessment efforts have substantial uncertainty in some areas with few historical records. In such cases, it may be more reasonable to use simplified approaches for an operational storm surge real-time forecast systems. Despite the complexity nature of storm surge phenomena, the direct disaster impacts are coastal flooding i.e. the maximum sea surface level and its distribution of time which results inundation near coastal regions. [8, 9]

The main objective of this study is to set up a simple forecast model and to quantitatively examine the risk of sea level rise and related damages duo to storm surge based on the observational data.

## Modelling

The key factors taken into account influencing coastal urban storm surges include: 1) rainfall: **r** (mm); 2) protective object distance off shore: **d** (m); 3) wind speed: **V1** (m/s); 4) wave height: **h** (m); 5) wave propagation speed: **V2** (m/s). Storm surge hazard forecast indicators come from these key influencing factors are as follow:

1) Risk severity of storm surge: **R**, which divided into 4 Categories based on return period: I: 1000 years, II: 100 years, III: 10 years, IV: 1 year.

2) Property losses: **P** (in billion USD)

3) Loss of lives: **L** (in person).

Fig.1 and Fig.2 illustrate the property and population losses caused by storm surge in recent years in China.

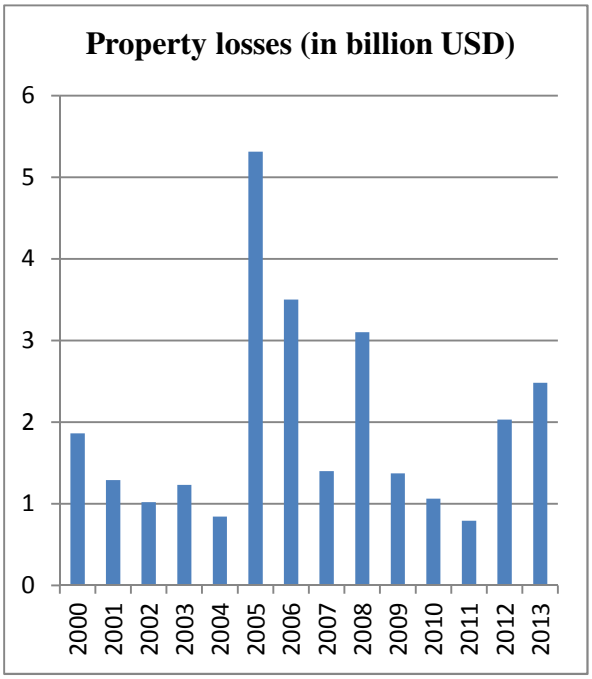


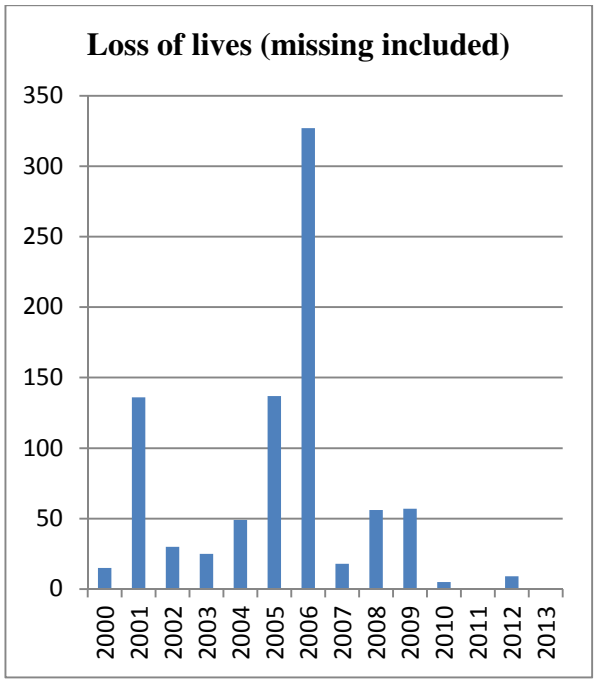


**Fig.1** Property losses caused by storm surge

**Fig.2** Loss of lives caused by storm surge

**Storm surge disaster forecast approaches for coastal cities based on Extended Kalman Filter**

This section analyzes the storm surge disaster influencing factors. We present a simple approache to establish a forecast model. The test the validity of the model is also discussed.

**(1) Methodology**

Recently, Extended Kalman Filter (EKF) approach has been applied widely in disaster forecast and assessment. [10, 11] However, traditional Kalman Filter model only fits on simple linear system models, the real disaster system models tend to be more complicated nonlinear system models. An EKF approach is aimed to establish a real time forecast associated with the basis and modeling advantages on information theory and signal processing.

Based on the key influence factors of urban inundation and storm surge disaster in coastal cities, this approach established a quantitative description on the key influence factors. Because of the fact that EKF is a recursive algorithm and the calculation and storage amount is small, dynamic tracking instantaneity of storm surge inundation and flood could have been realized.

**(2) Model establishment and risk assessment based on EKF**

State vector is shown as:

$$\mathbf{X}(k)=\begin{bmatrix} R(k) \\ P(k) \\ L(k) \end{bmatrix} \tag{1}$$

Observed value:

$$\mathbf{Z}(k)=\begin{bmatrix} r(\mathrm{k}) \\ d(k) \\ V1(k) \\ h(k) \\ V2(k) \end{bmatrix} \tag{2}$$

When system is unstable, state will mutate, and then state equation will be nonlinear. State equation is established as follow:

$$\mathbf{x}(k+1)=\Phi(x(k),k)+\mathbf{w}(k) \tag{3}$$

$$\mathbf{z}(k)=\mathbf{h}(x(k),k)+\mathbf{v}(k) \tag{4}$$

Where, $\Phi(\cdot)$ and $h(\cdot)$ are nonlinear functions respectively, w(k) is dynamic noise, z(k) is observed value, v(k) is measurement noise.

Practical functions are based on data condition. Recursion formula according to the model above is established as follow:

$$\hat{x}(k/k)=\hat{x}(k/k-1)+K(k)\tilde{z}(k/k-1) \tag{5}$$

$$K(k)=P(k/k-1)C^{T}(k)R_{L}^{-1}(k) \tag{6}$$

$$R_{L}(k)=C(k)P(k/k-1)C^{T}(k)+R(k) \tag{7}$$

$$\tilde{z}(k/k-1)=z(k)-h(\hat{x}(k/k-1),k) \tag{8}$$

$$\hat{x}(k/k-1)=\Phi(\hat{x}(k-1/k-1),k-1) \tag{9}$$

$$P(k)=(I-K(k)C(k))P(k/k-1) \tag{10}$$

$$P(k/k-1)=A(k,k-1)P(k-1)A^{T}(k,k-1)+Q(k-1) \tag{11}$$

Where, $C(k)=\dfrac{\partial h(k)}{\partial\hat{x}(k/k-1)}$, $A(k,k-1)=\dfrac{\partial\Phi(k-1)}{\partial\hat{x}(k-1/k-1)}$

After system set up the initial values of $\hat{x}(0)=E\{x(0)\}$ and P(0), recursion will continue until the arithmetic meets the convergence conditions. Then the state estimation will be the storm surge hazard forecast indicators we are looking for.

**(3) Simulation results**

Based on data from available records, [12] simulated observation value of the vectors is presented in Table 1. There are simulated data of 20 years, which can be used to compare the simulated results with the risk level of real storm surges and resulted losses.

Risk of storm surge outputs in 4 levels based on return period: I: 1000 years, II: 100years, III: 10 years, IV: 1 year. In order to be easy to display, R is taken into logarithm, value of 4 levels becomes 3, 2, 1, and 0 respectively.

Based on the observed data, the identification method is established as follow:

$$\dot{x}=\begin{bmatrix} \alpha R(\mathrm{t}) \\ \beta P(\mathrm{t})R^{2}(\mathrm{t}) \\ \gamma R(\mathrm{t})\sqrt{L(\mathrm{t})} \end{bmatrix}+w(\mathrm{t}) \tag{12}$$

$$z(\mathrm{t})=\begin{bmatrix} 3.2\sqrt{R(\mathrm{t})}+0.4\,\mathrm{P(t)}+10L(\mathrm{t}) \\ 54/P(\mathrm{t})+11/L(\mathrm{t}) \\ R(\mathrm{t})/20+4.3\sqrt{P(\mathrm{t})}+6L(\mathrm{t}) \\ \sqrt{R(\mathrm{t})}/5+0.2P(\mathrm{t})+0.3L(\mathrm{t}) \\ 6.4\log_{10}R(\mathrm{t})+2.2P(\mathrm{t})+3L(\mathrm{t}) \end{bmatrix}+v(\mathrm{t}) \tag{13}$$

Simulated values applying EKF and real values are shown in Fig.3, Fig.4 and Fig.5. Fig.3 shows the estimate risk; Fig.4 shows the comparison results between estimate losses and the real one; Fig.5 shows the comparison results between estimate tolls and the real ones.

**Table1** Simulated data of r, d, V1, h and V2

| Year | r | d | V1 | h | V2 |
|---|---|---|---|---|---|
| 1 | 4 | 226 | 8 | 2 | 5 |
| 2 | 3 | 313 | 6 | 2 | 3 |
| 3 | 4 | 227 | 8 | 2 | 5 |
| 4 | 2 | 401 | 4 | 1 | 3 |
| 5 | 0 | 3056 | 0 | 0 | 0 |
| 6 | 15 | 65 | 30 | 10 | 19 |
| 7 | 4 | 244 | 8 | 2 | 5 |
| 8 | 0 | 1635 | 1 | 0 | 0 |
| 9 | 5 | 180 | 11 | 3 | 6 |
| 10 | 6 | 149 | 13 | 4 | 8 |
| 11 | 0 | 6237 | 0 | 0 | 0 |
| 12 | 3 | 252 | 7 | 2 | 4 |
| 13 | 2 | 377 | 5 | 1 | 3 |
| 14 | 2 | 396 | 5 | 1 | 3 |
| 15 | 3 | 320 | 6 | 2 | 3 |
| 16 | 8 | 113 | 17 | 5 | 11 |
| 17 | 3 | 329 | 6 | 2 | 3 |
| 18 | 13 | 76 | 26 | 8 | 16 |
| 19 | 5 | 196 | 10 | 3 | 6 |
| 20 | 4 | 231 | 8 | 2 | 5 |

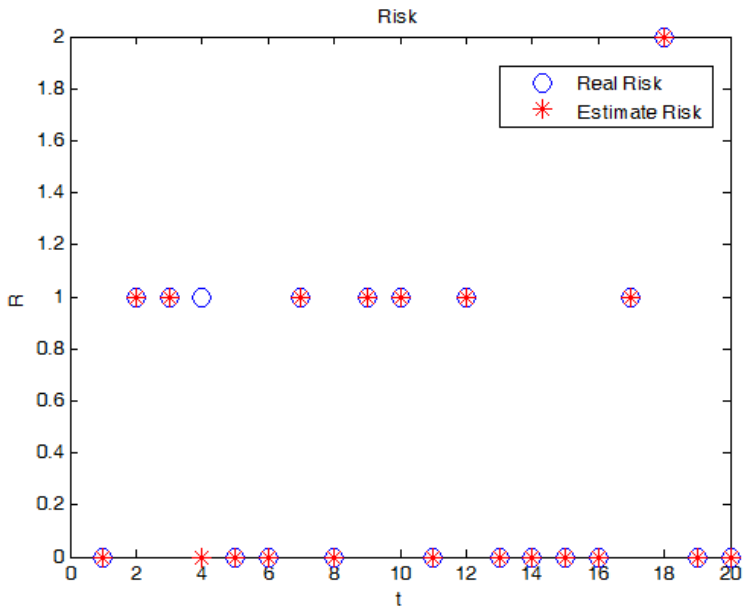


**Fig. 3** Estimate risk estimation level
X axis stands t for year, Y axis stands R for Risk level

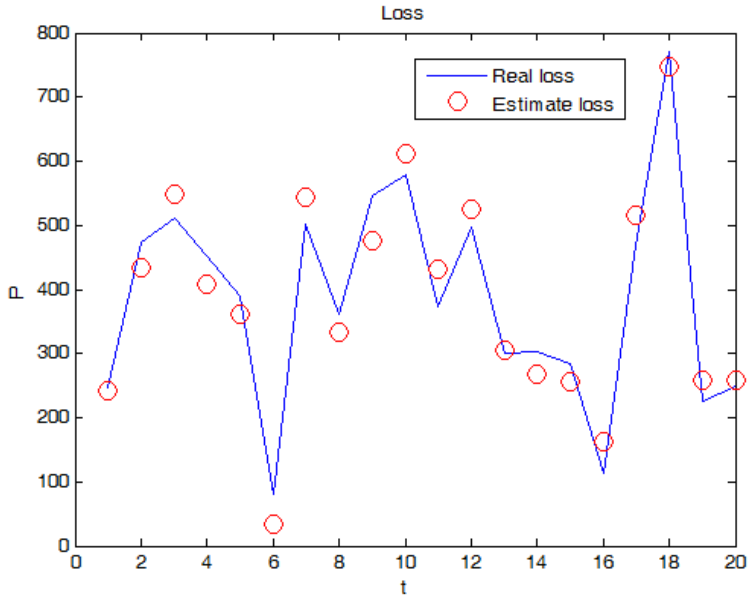


**Fig. 4** Estimate property losses
X axis stands t for year, Y axis stands P for Property loss (in millions RMB)

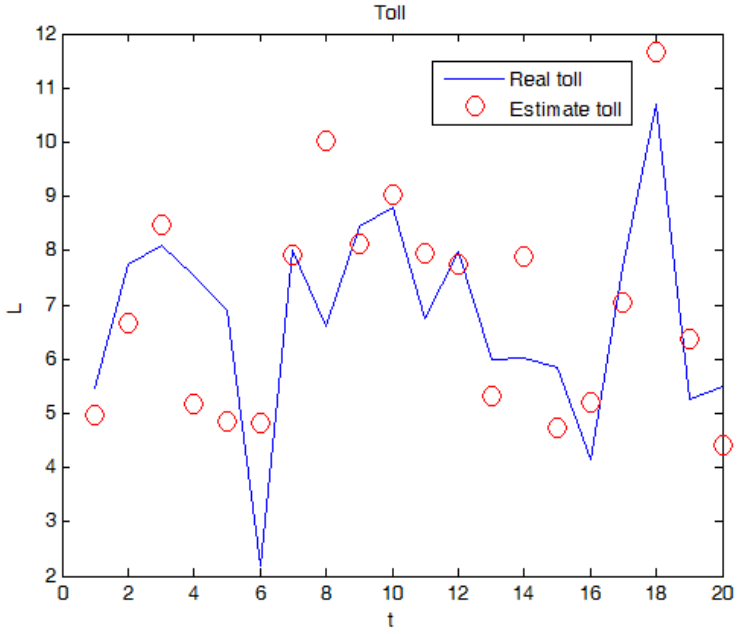


**Fig. 5** Estimate loss of lives
X axis stands t for year, Y axis stands L for loss of lives

The simulated results proved the validity of the EKF based forecast approach for storm surge risk level, property losses and loss of lives. According to the results in Fig.3, only in the 4th year, there is a deviation of ±1 level between the estimate level and the real one. The other estimate values correspond to the real values. A conclusion could be made that the forecast storm surge risk level matches the reality in a reasonable fit. Furthermore, it will be more corresponding to the reality after an adjustment of the parameters when more data would be available. Results from Fig. 4 show a consistency between the estimate loss and the real one, and then show a validity of the EKF when forecasting the property losses. Estimate loss of lives in Fig.5 shows a small deviation to the real value (<=3 persons). Based on the analysis above, it is effective to forecast storm surge risk level, property losses and loss of lives utilizing EKF. Especially, the forecast results are not only within the error range, but also have a high consistency with the reality. It is encouraging to follow the studies and develop more applicable systems in practice of storm surge forecast.

**(4) Arithmetic Advantages**

After looking into the arithmetic model i.e. EKF, the fact EKF reflects most of the real system is found. Through piece-wise linearization, we can solve a major class of problem. So as long as the modeling is reasonable, simulated objects will adapt this arithmetic. Therefore, if we identify the model structure and parameters associated with the system identification method, and apply EKF to dynamic tracking and forecast, we will solve practical issues more conveniently.

From the operation and calculation of the arithmetic, we can conclude that EKF only need to store the estimate values from the earlier year and the observation values of the year, so the calculation and the storage decreases in a large scale, which satisfying the real-time requirement. The urban disaster forecast system consists of a large number of factors and observational data, so it is meaningful to have an arithmetic method with low complexity for a quick response system.

From the arithmetic theory, based on the current observation data, the arithmetic can obtain not only the current estimate value but also the later forecast value of the storm surge and flood disasters. It makes the real-time quantitative forecast possible; thereby disaster forecast will be more convenient using this arithmetic.

## Summary and Conclusions

Disaster preparedness and prevention, prediction measures are the integrated procedures in disaster management. We have developed a simple approach of numerical model to estimate and forecast the key factors of storm surge hazards based on some historical data. The model is based on the Extended Kalman Filter (EKF) equations, which are extensively used to determine the uncertainties in the system. Preliminary results show that it is feasible to estimate and forecast the value of the disaster based on the arithmetic after quantifying the key factors influencing coastal urban storm surges. Thereby a more sophisticated forecast system plan could be set up. Once one of the key influencing factors dominated, there would have been a specific forecast plan and a relevant response. Thus a risk optimizing system associated with simulation and reality could be set up accordingly. This model can extend to other practical field as well, e.g. analysis of the unstable and nonlinear effect from rainstorm and hurricane. In this case, state equation could be improved to quantify the dynamic process. Similar studies are ongoing in our research team.

**Acknowledgments** This research was partially supported by the National Natural Science Foundation (Grant Nos: 41072176; 41371496), and the Ministry of Science and Technology in China (Grant Nos: 2009DFA22420; 2013BAK05B04).

## References:

[1] N. Lin et al: Physically Based Assessment of Hurricane Surge Threat Under Climate Change. Nature Climate Change. Vol. 2 (2012), p.462

[2] C. C. Shepard, V. N. Agostini, B. Gilmer, T. Allen, J. Stone, W. Brooks and M. W. Beck: Assessing future risk: quantifying the effects of sea level rise on storm surge risk for the southern shores of Long Island, New York. Natural Hazards. Vol. 60 (2012), p.727

[3] J. Yin, D. Yu, Z. Yin, J. Wang and S. Xu: Modelling the combined impacts of sea-level rise and land subsidence on storm tides induced flooding of the Huangpu River in Shanghai, China. Climatic Change. Vol. 119 (2013), p.919

[4] P. Orton, N. Georgas, A. Blumberg and J. Pullen: Detailed modeling of recent severe storm tides in estuaries of the New York City region. JOURNAL OF GEOPHYSICAL RESEARCH. Vol. 117 (2012)

[5] E. Scileppi, J. P. Donnelly: Sedimentary evidence of hurricane strikes in western Long Island, New York, Geochem. Geophys. Geosyst. Vol. 8 (2007)

[6] G. Yang: Historical change and future trends of storm surge disaster in China's coastal area. Journal of Natural Disaster. Vol. 9(2000), p. 23 (In Chinese)

[7] B. Poulter and P. N. Halpin: Raster modelling of coastal flooding from sea-level rise. Int J Geogr Inf Sci Vol. 22 (2008), p.167

[8] H. Liu, Takenori Shimozono, Tomohiro Takagawa et al. The 11 March 2011 Tohoku Tsunami Survey in Rikuzentakata and Comparison with Historical Events Pure Appl. Geophys. Vol. 170 (2013), p.1033

[9] H. M. Fritz, D. A. Phillips, Akio Okayasu et al. The 2011 Japan tsunami current velocity measurements from survivor videos at Kesennuma Bay using LiDAR. Geophysical Research Letters. Vol. 39 (2012)

[10] M. Verlaan, A. Zijderveld, H. de Vries, et al. Operational storm surge forecasting in the Netherlands: developments in the last decade. Philosophical Transactions of the Royal Society A: Mathematical, Physical and Engineering Sciences. Vol. 363(2005), p.1441

[11] J. W. Lin, C. W. Chen, C. Y. Peng. Kalman filter decision systems for debris flow hazard assessment. Natural hazards. Vol.60 (2012), p.1255

[12] W. Wang, J. Y. Su, D. H. Ma, et al. Integrated risk assessment of complex disaster system based on a non-linear information dynamics model. Sci. China: Tech Sci. Vol.1 (2012), p.71 (In Chinese)

[13] C. B. Field, editor. Managing the risks of extreme events and disasters to advance climate change adaptation: special report of the intergovernmental panel on climate change. Cambridge University Press. (2012)

*Applied Mechanics and Materials Vols. 580-583 (2014) pp 2642-2645*
*© (2014) Trans Tech Publications, Switzerland*
*doi:10.4028/www.scientific.net/AMM.580-583.2642*

# Survey of Fire load in building furniture store

Jinping Wang

China Academy of Building Research, Beijing 100013, China

wangjinping@126.com

**Keywords:** building furniture store; fire load; survey.

**Abstract.** There are many combustible materials in building furniture stores with complex people traffic and high risk of fire disaster. Fire load as the represent of flammable material, and the building fire risk can be grasped by the data obtained. Through investigation and statistics on the fire load density value of building furniture store, it is convenient for performance fire safety design. According to the survey, fire load density average value is determined of 382.71 $MJ/m^2$ , the standard deviation is of 143.46 $MJ/m^2$ . After fitting the survey data, the data distribution do not refuse to obey the extreme-value Ⅰ distribution, so this distribution can be the basis of fire design in other corresponding building furniture stores.

## Introduction

Along with China's social economic progress, and the improvement of people's living standard, more and more luxury decoration is appeared in domestic, and building furniture materials market has developed rapidly in the country, so far kinds of building furniture materials market has grown to more than 4000. The good and bad building materials market and merchants are intermingled, resulting in the occurrence of high fire rate in the world, and building materials market have many goods, so fire will cause a great loss of property. The fire happened in largest building materials trading center in northern Thailand has to be estimated the loss of nearly 3,000,000,000 baht.

(a)Decoration Condition

The area of large building materials market is mostly more than 50,000 square meters to 80,000 square meters, and the floor height can reach 4 ~ 5 layer, usually with underground, and adjacent to several blocks. The product categories are among with decoration materials, home furnishing supplies and accessories, such a long industrial chain and all of home decoration products.

Large building materials market in general will be installed of spray, alarm system and fire shutter, a plurality of fire safety export, and goods partition layout.

In china building materials market the ceiling is usually not burning gypsum board, and the ground for marble and other non-combustible material, but in the counter area will generally be twice decorated into wood floor. Fire hazard in small building furniture store is more serious, such as electrical wiring production and processing of inconsistent specifications, and market buildings did not take fire department, and illegal structures occupy fire prevention space, and paint shop in the building furniture store without business license of dangerous goods, etc.

(b) Fire characteristics

Fire characteristics of large building materials stores is as follows: there is many flammable goods and large fire load, so the fire is generally larger than other place; space span is large and upper and lower connectivity, so the fire spread quickly and easily lead to large three-dimensional combustion; electrical lighting equipment is always too much to cause more fire, and small fire is more frequently happened in the store.

## Investigation of Fire Load

### Fire load investigation of building furniture stores

There are many commodity types in large building furniture market, and distribution of fire load is very uneven. Stone, sanitary ware area has less combustible material, but the curtain, furniture and other areas have large number of combustibles, so fire load density values will appeared to be very large, and fire danger will be higher. So the furniture area is chose as the building materials market fire load statistics place, mainly because of the more flammable items, and goods is very concentrated and expensive, so the fire load is larger than other area of the market. In the fire design the larger value is used may decline the fire hazard.

In the statistical process floor area method is used to add total calorific value of one brand, and divided by the brand area. In the investigation one brand area has large regional area among 79 square meters to 324 square meters, which made the statistical work great, but such practices decrease the margin of error and make the data more representative. In the total investigation more than 10,000 square meters floor area is done.

Combustible mainly focused of furniture, such as wardrobe, bookcase, bed and mattress, desk, chair, sofa. So wood is the main fuel material. The polymer products are in small amount. For large furniture it is hard to weigh, so it is determined by the method of density multiplied by the volume which is called inventory method in NFPA 557.

(a) One store in Taiyuan with the business area of 60,000 square meters is surveyed, decoration materials, modern furniture, classical furniture, decoration material are all concentrated in the building materials shopping center.

Fig. 1 Taiyuan spring store of Easyhome

Fig. 2 Beijing shilihe store of Easyhome

(b) One store on the Shilihe located in Beijing is surveyed, with the business area of 51,000 square meters.Unexpectedly the store is to provide home furnishing design and decoration materials, furniture and home furnishing accessories for customers, with a total of four venues, including one to three building "decoration materials hall ", 4 as "furniture hall ". The furniture building is a four floor building and one floor is under ground.

(c) Another store in Beijing is surveyed, with the total building area of more than 50,000 square meters, which is divided into hardware, decorative materials, modern furniture, sofa, children's furniture and other regions.

### Results of the survey and statistical

According to the investigation of the three building materials market 72 valid data is obtained, although the number is small but the area is great so the data is also typical. The maximum value is of 708.97 $MJ/m^2$, and the minimum value is of 83 $MJ/m^2$, through the data group it can be seen the mostly data are between 200～300 $MJ/m^2$ and the statistical parameters are obtained, the mean

value is of 382.71 $MJ/m^2$, and the standard deviation is of 143.46 $MJ/m^2$. The fire load density histogram figure is as follows in fig.3.

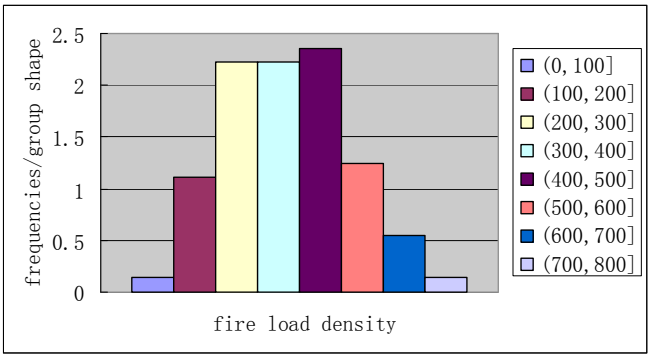


Fig. 3 Fire load histogram

Then analysis of statistics is progressed. To fit the data group, normally distributed, logarithmic normal distribution, the distribution of extreme value type Ⅰ, generalized extreme value, generalized Pareto distribution were processed [4]. After the calculation, the data distribution is not refused to obey the extreme value type I distribution, and its distribution can be expressed by the formula:

$$F(x) = \exp\{-\exp[-0.0089(x-318.15)]\}$$

The maximum value probability distribution during the period of design basis distribution as follows:

$$F_{iT} = \exp\{-\exp[-0.0089(x-493.67)]\}$$

Statistical parameters of $F_T(x)$ for the design basis period of T are as follows:

$\mu_{LT} = 558.23$

$\sigma_{LT} = 143.35$

According to the group preliminary work [3], there carried out calculation of fire load standard value to the exhibition building, the standard value is as follows:

$u_k = 897.96 MJ/m^2$

## Conclusions

The fire load standard value of building furnishing stores values slightly smaller than residential value, this is mainly because of the furniture in home furnishing stores is often vacant, although furniture is placed compactly, but which still decrease the content of fire load.

In the survey it is found that organic gas release rate in home furnishing stores is high, which relates to poor air quality in the store, therefore in the fire toxic gas is extremely easy to cause higher fire hazard, so in the fire design the value of home furniture store should be designed lower for fire load security, so as to decrease the release damage of harmful substances.

## Acknowledgements

This work was supported by the Projects “Typical building fire load survey and statistical analysis” of China Academy of Building Research Institute (N0. 20120111330730062).

**References**

[1]Jinping Wang, Hongtao Liu. Calorific value of commonly used building materials and furniture and fire load density determination [J].Building Science. Vol. 25-5 (2009) :19-21

[2]Yingqing Li, DaoZhen Ma, Jian Xu, Structural fire design calculations and construction processing [M] Beijing: China Building Industry Press, 1991.

[3]Jinping Wang, Jiang Zhu, Beijing residential activity room fire load survey analysis and the standard values determination [J].Building Science. Vol. 26-1 (2010):24-29

[4]Jinping Wang. The theoretical study of active fire load determination in construction[C], proceedings of 2009 international symposium of fire science and fire-protection engineering. 2009(11)

[5] Jinping Wang. The discussion on fire load maximum of building [J].Applied Mechanics and Materials Vols. 166-169 (2012):2709-2712

*Applied Mechanics and Materials Vols. 580-583 (2014) pp 2646-2648*
*© (2014) Trans Tech Publications, Switzerland*
*doi:10.4028/www.scientific.net/AMM.580-583.2646*

# The research on structure fire resistance test of fire retardant rigid polyurethane

Jinping Wang

China Academy of Building Research, Beijing 100013, China

wangjinping@126.com

**Keywords:** rigid polyurethane foam; fire safety; fire resistance test

**Abstract.** The developed rigid polyurethane foam is added several inorganic materials, which made the polyurethane foam release less poisonous gases in fire. The oxygen index value can reach more than 32 percent, and under the standard heating curve the retardant rigid polyurethane foam can present the performance of 1h fire resistance test.

## Introduction

Rigid polyurethane foam with excellent physical and chemical properties, which thermal conductivity is lower than the polystyrene foam and natural insulation materials, and it can be site casting or spray molding, combined with other materials into one constructure, making the insulation, sealing better, all of these advantages make this material widely used in the world. Its fire safety is a huge security risk, because the polyurethane foam containing flammable hydrocarbon chains, low density, large surface area, and the oxygen index value of 17 percent, so polyurethane foam in the air can burn, and decomposition will produce large amounts of toxic fumes. Through the horizontal burning test, it can be found poor thermal stability, and be classified as combustible.

Because of the fire happened in insulation field frequently in china, from March 2011 to December 2012 the Ministry of Public Security issued a document prohibited the use of materials below Class A fire performance. In the inner decoration, number of fire caused by the polyurethane foam is also huge, it shows that the polyurethane foam used widely domestic, but the current dilemma mostly due to the illegal use of the factory and constructionm worker. China has been very concerned about the fire caused by combustible materials, rigid polyurethane foam fire resistant performance has become the important technical indicators of being building materials, there is developed a flame retardant rigid polyurethane foam, and carried on fire resistance test.

## Testing Method

Structural fire resistance test used of flame-retardant polyurethane foam, the choice of several inorganic retardants used in conjunction with best flame-retardant effect, and the oxygen index can reach 39 percent, and the foam's physical and chemical properties are excellent.

Oxygen index, horizontal burning method, vertical burning method, smoke density test, construction fire test are carried on the fire retardant rigid polyurethane foam. It is found that the fire retardant polyurethane foam can reach 32 percent of the oxygen index value, smoke density value of 50-90, the polurethane foam can go through the horizontal and vertical test.

In the structural fire resistance test, the size of the test components reference *GB23864-2009 firestop material*, concrete block size is 800mm*600mm*120mm, rectangular hole size is 510mm*110mm*120mm. In the hole it is filled with flame retardant rigid polyurethane foam prepared, the oxygen index of the polyurethane foam is 35 percent. In the experiment, the concrete block back surface to fire was placed two thermocouples, foam back face and adjacent to concrete block are placed two thermocouples respectively, in the test if the test piece back fire surface or hot gas flow is the loss of integrity, thermocouple temperature rise to 180℃ for the specimen lose heat insulation.Figure 1 shows specimen installed, Figure 2 shows the test is terminated.

Figure 1 Installed foam

Figure 2 Test terminating

In the figure 2 the polyurethane foam reached fire limit and it maintained a fire touched face throughout the experiment, the furnace temperature rise in accordance with the standard temperature curve, the curve of the standard curve and the furnace temperature state as follows in figure 3.

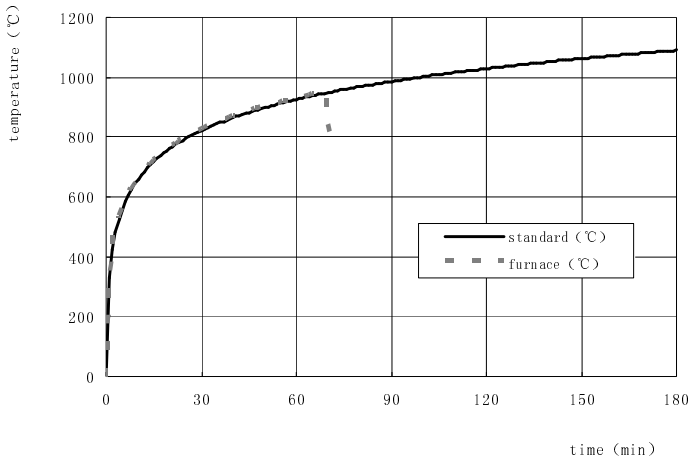


Figure 3 The curve of the standard curve and the furnace temperature

## Results

The following table 1 lists the value of the thermocouple temperature during the experiment.

Table 1 The thermocouple temperature value during the experiment

| Test time | Foam tempera-ture | Foam tempera-ture | Foam tempera-ture | Foam tempera-ture | Construction temperature | Construction temperature |
|---|---|---|---|---|---|---|
| 1 | 0.6 | 0.7 | 0.7 | 0.6 | 0.4 | 0.5 |
| 15 | 0.9 | 0.9 | 0.9 | 0.9 | 0.7 | 0.7 |
| 30 | 2.2 | 2.1 | 0.9 | 0.8 | 6.3 | 4.7 |
| 45 | 11.1 | 11.5 | 1.7 | 1.5 | 28.2 | 21.9 |
| 60 | 42.1 | 32.7 | 2.8 | 3.1 | 49.1 | 47.2 |
| 66 | 59.5 | 48.1 | 4.7 | 6.3 | 54.3 | 54.1 |
| 70 | 137.2 | 64.5 | 4.1 | 6.4 | 148.5 | 60.2 |

Test specimen lost integrity ended, specimen shrinkage, and gas leakage. It can be seen from the above thermocouple data, after lose the integrity, the thermocouple temperature of rigid polyurethane foam remains lowly, which good insulation effect will still be able to prevent temperature rising of side unexposed to fire and good flame-retardant effect of 1h fire resistance.

The polyurethane foam with excellent thermal insulation properties, and in the foam the expanded graphite and porous flame-retardant materials such as aluminum hydroxide, Ammonium polyphosphate, melamine are used, which will be inflated by fire, so polyurethane foam release the gas concentration is smaller than the ordinary foam in the test.

Figure 4 Underside surface in fire

Figure 5 The side opposite fire

Fig. 4 of flame-retardant polyurethane foam claims that although as a thermosetting material there is still a little bubble contraction, and the formation of cracks resulting in leakage of flue gas. The charred solid maintain a good bonding state by observing its combustion products.

The developed polurethane foam demonstrate the excellent characteristics of thermosetting materials, flame retardants added to enhance the fire resistance, the test proved that the foam can promote the use in a large number of building through preventing the spread of fire.

## Conclusions

The inorganic compound flame retardant materials added to the polyurethane rigid foam, which is easy to operate, and more environmentally friendly, reasonable price, the technology is easy to promote, develop low smoke direction of the flame-retardant rigid polyurethane foam, which will greatly reduce the fire hazard of polyurethane foam.

The structural fire resistance test proved that the fire retardant polyurethane foam with excellent thermal insulation properties, maintain a good fire performance to achieve 66min fire resistance under the temperature rise in the standard curve state.

For flame-retardant polyurethane industry we should continue to strengthen the importance of the flame retardant properties, and focus on reducing the toxic fumes, and promote the quality of construction supervision to ensure the material meets the national standard.

## References

[1] GB23864-2009 fire blocking material. In chinese

[2] jinping wang, Jinghui Chen, flame-retardant rigid polyurethane foam in the construction field, fire technology and product information .2011.3 In chinese

*Applied Mechanics and Materials Vols. 580-583 (2014) pp 2649-2653*
*© (2014) Trans Tech Publications, Switzerland*
*doi:10.4028/www.scientific.net/AMM.580-583.2649*

# Tornado hazard loss of nuclear power plant building during design service period

Tuo Song [a], Lingyi Lu [b]

School of Civil Engineering, Southeast University, Nanjing 210096, China

[a] longjun_expert@163.com, [b] lylu@seu.edu.cn

**Keywords:** tornado; hazard; fragility; LCC; Markov model; nuclear power plant

**Abstract.** Based on the concept of Life Cycle Cost, we propose a methodology to evaluate the expected economic loss of building caused by tornado disasters during design service time and this methodology is examined by applying to a simplified nuclear power plant main house model.

## Introduction

Tornado is common natural disaster that can be observed frequently. Nuclear power plant buildings are expected to perform their high level of safety and continuous service of their intended function when encountering extreme tornado disaster during their service life[1]. As these structures aging or deterioration with time, their bearing capacities decrease year by year, but the annual probability of tornado hazard occurance may seem to be relatively stable from probabilistic viewpoint. Thus, the structure deterioration level and total economic loss that caused by nature hazard may increase with time. Nature hazard loss contains cost of damage and repairment, meanwhile, risk and loss due to tornados can be reduced by strengthening existing structures and improving their ductility. To decide an optimized strategy for reducing total cost from existing structures' reinforcement, it is necessary to consider total economic loss of nuclear power plant buildings during their design life. For this purpose, we use the concept of 'Life Cycle Cost (LCC)' to evaluate the expected loss caused by tornado disasters during the planned service time of structures and this methodology is applied to an example of nuclear power plant main house .

## Tornado hazard estimation

Tornado intensity is usually measured by Fujita's F scale, from F1 to F5[1]. In this paper, tornado maximum wind speed (MWS, m/s) is employed to represent tornado intensity. MWS lower bound of a tornado that in scale F$M$ is calculated by Eq.(1):

$$V_{\mathrm{F}M} = 6.30\left(M+2\right)^{1.5} \quad M = 1, 2, \cdots, 5 \tag{1}$$

Tornado observation record is generally indicated as the number of tornadic occurrence within a period of time at specific geographic location. If $N$ is the total number of tornadic occurrence at a certain zone and $n_0$ to $n_5$ represent the number of tornados that observed corresponding to F0 to F5 Fujita scales, the probability relation between tornado intensity distribution and tornado observed data can be illustrated as Eq.(2):

$$P\left(V < V_{\mathrm{F}M}\right) = \sum_{i=0}^{M\text{-}1} n_i / N \qquad M = 1, 2, \cdots, 5 \tag{2}$$

Comparing different types of probability distribution that often used in meteorology, it shows that observed tornado intensities can be much better described by Weibull distributions. The cumulative distribution function (CDF) of Weibull distribution is given by Eq.(3):

$$F(x) = \begin{cases} 1 - \mathrm{e}^{-(x/\alpha)^k} & \mathrm{x} \geq 0 \\ 0 & \mathrm{x} < 0 \end{cases} \tag{3}$$

Taking the logarithm twice from Eq.(3), we obtain Eq.(4):

$$\ln\left[-\ln\left(1-F(x)\right)\right]=k\ln x - k\ln\alpha \tag{4}$$

This has the form $Y$=B$X$+A, where $X=\ln x$ and $Y=\ln[-\ln(1-F(x))]$. Linear regression then yields B=$k$ and A=$-k\ln\alpha$. Then the Weibull parameter $\alpha$ is determined by formulas of B and A.

Eq.(3) represents tornado hazard estimation of $N$ years observing time. To get the annual tornado intensity distribution $F_1$ ($V$), we suppose that the CDF $F_1$ ($V$) obeys the same distribution and the random variable $V$ is independent every year. For a deterministic value $V_C$, the relation between $F_N$ ($V_C$) and $F_1(V_C)$ is shown as Eq.(5):

$$\begin{aligned} F_N(V_C) &= P_N\{V \le V_C\} \\ &= \prod_{i=1}^{N} P_1\{V \le V_C\} = \left[F_1(V_C)\right]^N \end{aligned} \tag{5}$$

The annual occurrence probability of a tornado at nuclear power plant site should be evaluated through tornado risk analysis. However, it's not an easy task and many parameters to conduct this analysis are not known exactly. To evaluate the tornadic occurrence that the MWS ranges from very low (<10m/s) to very high (>100m/s), the meteorological concept of return period is used. If tornadic return period of a region is estimated to be $S$ years, the annual occurrence probability is therefore computed by Eq.(6).

$$P_{\mathrm{OCC}}^{1}=1/S \tag{6}$$

**Deterioration model of structure**

Building's bearing capacities will decrease as the structure deterioration with time. It is important to treat such deterioration as stochastic process and to evaluate the probability of damage to structures taking into account the effect of deterioration.

A Markov chain model that the future condition of structures is depend only on the present state and is independent on the past stat is employed to express the deterioration process. Knowing the present state of structure, the future state can be predicted through the multiplication of present state vector and the transition probability matrix as shown in Eq.(7):

$$\boldsymbol{S}(t+1)=\boldsymbol{S}(t)\cdot\boldsymbol{P} \tag{7}$$

where $\mathbf{S}(t)$ is a state vector which consist of the probability that the condition lies in state $i$ at time $t$, and $\boldsymbol{P}$ is the transition probability matrix. They can be written as Eq.(8) and Eq.(9):

$$\mathbf{S}(t)=\{s(1,t) \quad s(2,t) \quad , \quad \cdots \quad s(k,t)\}, \qquad \sum_{i=1}^{k} s(i,t)=1 \tag{8}$$

where $k$ is the number of deterioration levels.

$$\boldsymbol{P}=\begin{bmatrix} p_{11} & p_{12} & \cdots & p_{1k} \\ 0 & p_{22} & \cdots & p_{2k} \\ \vdots & \vdots & \ddots & \vdots \\ 0 & 0 & \cdots & p_{kk} \end{bmatrix} \qquad \sum_{j=1}^{k} p_{ij}=1 \quad i=1,\cdots,k \tag{9}$$

Considering the deterioration of structure material with time, the relation between time $t$ and bearing capacity $\varphi(t)$ of steel structure can be expressed by Eq.(10) and Table 1 to Table 3[3]:

$$\varphi(t)=1-\left[0.7\times\left(t-t_c\right)^3/10000\right]\times 0.04\times\alpha\times\varepsilon \tag{10}$$

**Table 1 Selection of parameter $t_c$**

| Rot proofing condition | Value of $t_c$ |
|---|---|
| No proofing | 0 |
| Basic proofing (Painting) | 5 |
| Medium proofing (Hot galvanizing) | 10 |
| Advanced proofing (Composite coating) | 15 |

**Table 2 Selection of parameter $\alpha$**

| Ordinary steel | Weathering resistant steel |
|---|---|
| 1 | 0.7 |

**Table 3 Selection of Parameter $\varepsilon$**

| Air condition | Value of $\varepsilon$ |
|---|---|
| Clean and dry air in suburb | 0.6 |
| Urban air | 0.75 |
| Ocean air | 0.8 |
| Polluted air | 0.85 |
| Severely polluted air | 1 |

**Fragility analysis of structure**

Hazard curve and fragility curve are tools that often used in natural disasters research. Tornado hazard curve represents the relation between tornado intensity and the exceeding probability at a concerned area; meanwhile, fragility curve represents the relation between tornado intensity and failure probability of a given structure. It is important to evaluate damage probability to a structure due to tornado strike by the numerical integration in Eq.(11):

$$P_f = \int_0^{\infty} F_{\mathrm{H}}(V) \frac{dF_R(V)}{dV} dV \tag{11}$$

where $F_H(V)$ denotes tornado hazard curve of a concern zone and $F_R(V)$ denotes fragility curve of buildings that locates at the zone. By definition, tornado hazard curve can be obtained conveniently from tornado intensity distribution, however, computing structure fragility curve is not an easy task and often through the way of stochastic finite element analysis.

**Assessment of tornado hazard loss**

To estimate the tornado hazard loss of NPP building during its service time, the loss of structure hazard damage $C_{\mathrm{D}}$, the loss of temporary shutdown of NPP $C_{\mathrm{S}}$ and the cost of build repairment $C_{\mathrm{R}}$ should be determined. $C_{\mathrm{D}}$ is usually defined corresponding to each deterioration level and will increase with annual inflation rate $\gamma$. To define $C_{\mathrm{R}}$, the assumption is needed that the cost of repairment will not exceed the cost of damage and is equal to the damage. Thus, considering the traffic, labor and equipments cost, $C_{\mathrm{R}}$ chooses the value of $1.5C_{\mathrm{D}}$. However, the most difficult to estimate is the loss of temporary shutdown $C_{\mathrm{S}}$, because the huge influence to society and may cause enormous economic loss. For simplification, $C_{\mathrm{S}}$ chooses the value of $10C_{\mathrm{D}}$ which seems to be large enough but may be conservative in truth. Now, the expectation of tornado hazard loss of NPP building during its $N$ year service time can be evaluated by Eq.(12), where $n$ represents the deterioration level of building and $P_f^1$ represents annual damage probability caused by tornado risk.

$$\begin{aligned} HL^N &= \sum_{t=1}^{N} P_{\mathrm{OCC}}^1 \left[ \sum_{i=1}^{n} S(i,t) P_{fi}^1 \left( C_{\mathrm{D}i} + C_{\mathrm{S}i} + C_{\mathrm{R}i} \right) \right] (1+\gamma)^t \\ &= 12.5 P_{\mathrm{OCC}}^1 \sum_{t=1}^{N} \left[ \sum_{i=1}^{n} S(i,t) P_{fi}^1 C_{\mathrm{D}i} \right] (1+\gamma)^t \end{aligned} \tag{12}$$

**Application to nuclear power plant main house**

A simplified steel frame model of nuclear power plant main house is taken for tornado hazard analysis. FEM model of the main house is showed in Fig. 1. The size of the frame is: 72m (length), 50m (width) and 30m (height). Structural material uses Chinese Q235B steel (columns：HA800×400×16×25; beams: HA600×400×16×25) and Chinese C30 concrete (floor thickness: 120mm). Material elastic modules are considered as log-normal random variables for fragility analysis. The design life of the structure is 50 years. Tornado observation record in F-scale from 1949 to 1999 at nuclear power station site is listed in Table 4.

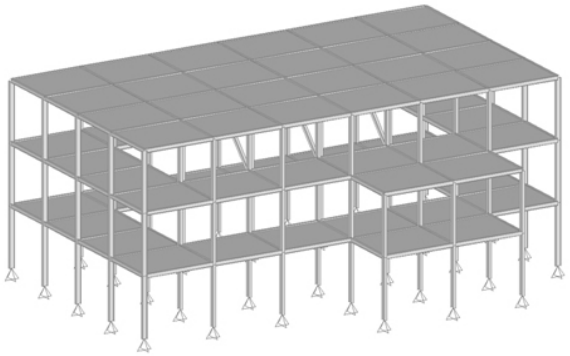

**Fig. 1 FEM model of NPP main house**

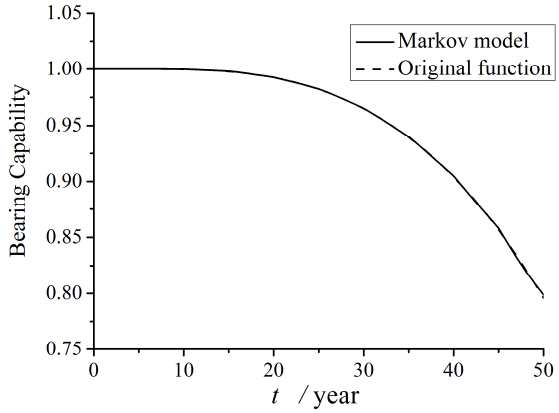


**Fig. 2 Comparison of Markov model expectation and original function**

**Table 4 Observation records of tornado in F scales**

| Event | $V$ /(m/s$^{-1}$) | Number | $P$ ($V$<$V_{FM}$) |
|---|---|---|---|
| F0 | <33 | 111 | 0.464 |
| F1 | 33~49 | 67 | 0.745 |
| F2 | 50-69 | 47 | 0.941 |
| F3 | 70-92 | 13 | 0.996 |
| F4 | 93-116 | 1 | 1.000 |
| F5 | 117-140 | 0 | 1.000 |

Based on the tornado observation records, the tornado intensity distribution of Weibull was derived by linear regression that introduced in previous chapter and the result is shown in Eq.(13), where $V$ is tornado MWS and $F_{50}(V)$ is tornado intensity distribution of 50 years.

$$F_{50}(V)=\begin{cases}1-\mathrm{e}^{-(V/36.964)^{1.834}} & V\geq 0\\ 0 & V<0\end{cases} \tag{13}$$

For Markov model evaluation, we choose $t_c=10$, $\alpha=1$, $\varepsilon=0.8$ and the $\varphi(t)$ curve are plotted in Fig. 2. To determine the transition matrix $\boldsymbol{P}$, we consider a four levels deterioration model for structure and a group of objective functions are established to evaluate elements of $\boldsymbol{P}$ in a short period (5 years):

$$\text{Minimize}\sum_{t=5i-4}^{5i}\left|\varphi(t)-E(t,\boldsymbol{P})\right| \qquad i=1,\cdots,10 \tag{14}$$

Solving these objective functions in Matlab software and computing resistance expectation of the structure in 10 short periods by Eq.(15), the comparison of curves between Markov model and original function that computed from Eq.(10) is shown in Fig.2.

$$E(t,\boldsymbol{P})=\boldsymbol{S}(t)\cdot[1,0.9,0.8,0.7]^{\mathrm{T}} \tag{15}$$

Structure fragility curves corresponding to each deterioration level can be obtained by SSFEM analysis[4] or MonteCarlo simulation. The results of annual tornado hazard curve and fragility curves

corresponding to different levels are shown in Fig. 3. Thus, the annual damage probabilities of different deterioration levels are calculated by Eq.(11) and the results are listed in Table 5. At last, the expectation of tornado hazard loss during service period can be evaluated in Table 6.

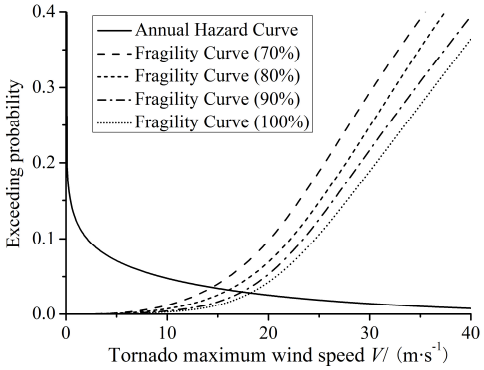


**Fig. 3 Fragility curves of deterioration levels and annual hazard curve**

**Table 5 Annual tornado damage probability of structure**

| Bearing capability level | Level 1 (remain 100%) | Level 2 (remain 90%) | Level 3 (remain 80%) | Level 4 (remain 70%) |
|---|---|---|---|---|
| Annual damage probability $P_{fi}^{1}$ | 0.0856 | 0.0959 | 0.1097 | 0.1291 |

**Table 6 Examples of tornado hazard loss evaluation**

| | Example 1 | Example 2 |
|---|---|---|
| Tornado return period (year) | 50 | 100 |
| $C_{D1}$ (ten thousand yuan) | 800 | 500 |
| $C_{D2}$ ( ten thousand yuan) | 1000 | 700 |
| $C_{D3}$ ( ten thousand yuan) | 1500 | 1000 |
| $C_{D4}$ ( ten thousand yuan) | 2000 | 1200 |
| Annual inflation rate $\gamma$ | 0.02 | 0.03 |
| $HL^{50}$ ( ten thousand yuan) | 2193.3 | 975.1 |

## Conclusions

We propose a methodology to evaluate the expected tornado hazard loss of building during its design service time. This methodology is applied to an example of nuclear power plant main house for examining its applicability. Although there are many assumptions of data used in this paper, result of this analysis is relatively credible after changing assumptions to investigative data.

## References

[1] HAD101-10, *Extreme weather events of the nuclear power plant site selection (excluding tropical cyclone)*. (The National Nuclear Security Administration, Beijing 1991) p.765-771. (in Chinese)

[2] Sato, T, Yoshida, I, etc. Prioritization of Seismic Reinforcement for Road Bridges Based on the Concept of Life Cycle Cost. Life-Cycle Performance of Deteriorating Structures (2003): p. 219-228.

[3] Yang Bo., Dai Guoxing, etc. Journal of Chongqing Jianzhu Univer sity, Vol.30 No.5(2008), p. 95-99. (in Chinese)

[4] Ghanem R G, Spanos P D. *Stochastic finite elements—a spectral approach*. (Dover Publications, New York 2003).

*Applied Mechanics and Materials Vols. 580-583 (2014) pp 2654-2657*
*© (2014) Trans Tech Publications, Switzerland*
*doi:10.4028/www.scientific.net/AMM.580-583.2654*

# Comparative Analysis of Wind Load for Transmission Tower between Chinese and American codes

Zhen Xu[1, a], Yujie Zeng[2, b], Danjing Cao[1, c], Xujun Lang[1, d], Li Tian[2, e]

[1] Shandong Electric Power Engineering Consulting Institute Co. Ltd., Jinan, Shandong, 250013, China

[2]School of Civil and Hydraulic Engineering, Shandong University, Jinan, Shandong, 250061, China

[a]172103458@qq.com, [b]ouraka@sina.com, [c]sdjncdj786@163.com, [d]xjlang @163.com, [e]tianl-007@163.com

**Keywords:** Transmission tower, wind load, computation parameters, comparison.

**Abstract.** Wind load computation formula for transmission tower of 《Technical code for the design of tower and pole structures of overhead transmission line》and《Design of latticed steel transmission structures》 are studied in this paper. The differences of basic wind speed, height variation factor of wind pressure, shape factor and wind load factor are compared in detail, respectively. The results show that the wind load defined in the Chinese code is little different from the American code. However, some parameters are still worthy of further discussion. The analysis results can be a reference for the design of transmission tower.

## Introduction

With the growing development of transmission line projects in the international market, more and more overseas projects require the use of foreign codes for design. In order to make the design companies in a strong position in the competition, it is necessary for designers to comprehend and master the similarities and differences between domestic and foreign standards. In the field of the design for high voltage transmission tower,《Guidelines for electrical transmission line structural loading》[1] (ASCE74—2009) is one of the important transmission line code in the world, which is widely applied and used for reference in 《Technical code for the design of tower and pole structures of overhead transmission line》[2-3].

Wind load is the control load for transmission line. For safe and reliable operation of transmission lines, the differences of specifications on the wind load between these two codes need to be fully understood and the wind load calculation method must be mastered accurately.So, this paper selects the 《Technical code for the design of tower and pole structures of overhead transmission line》（DL/T5154-2012） and the 《Design of latticed steel transmission structures》[4]（ASCE10-97）to compare. The calculated values of relative parameters including basic wind speed, height variation factor of wind pressure, shape factor and wind load factor are compared in detail.

## The Basic Formula

The standard value of the Chinese wind load shall be taken as follows:

$$W_s = W_0 \bullet \mu_z \bullet \mu_s \bullet B_2 \bullet A_s \bullet \beta_z \tag{1}$$

where, $W_s$ is the standard value of wind load. $W_o$ is the standard value of reference wind pressure. $\mu_z$ is the height variation factor of wind pressure. $\mu_s$ is the shape factor; $\beta_z$ is the wind load factor. $B_2$ is the enhancement coefficient of wind load under ice accretion. $A_s$ is the area projected on a plane normal to the wind direction.

The design value of the American wind load shall be taken as follows:

$$F = \gamma_w Q K_z K_{zt} (V_{50})^2 G_t C_f A \tag{2}$$

where, F is the wind force in the direction of wind unless otherwise specified. $\gamma_w$ is the load factor to adjust the force F to the desired return period. Q is numerical constant (0.613 metric units). $K_z$ is the velocity pressure exposure coefficient, which modifies the basic wind speed for various heights above ground and for different exposure categories. $K_{zt}$ is the topographic factor. $V_{50}$ is basic wind speed, 50-year return period, 3-sec gust. $G_t$ is the gust response factor for structures. $C_f$ is the force coefficient values. A is the area projected on a plane normal to the wind direction.

## The Computation Parameters

**Basic wind speed.** Basic wind speed is defined by prescriptive landform and height. The specific comparison is shown in table 1.

Table 1 The comparison of the Chinese and American basic wind speed

| Codes | Standard Height | Standard Landforms | Time Duration | Return Period | Wind Speed Limit | Samples of Maximum Wind Speed | Linear Distribution of Maximum Wind Speed |
|---|---|---|---|---|---|---|---|
| China | 10m | B | 10min | 110～330 kV 30-year<br>500～750 kV 50-year | 23.5 m/s<br>27 m/s | year | The distribution curve of extreme value for type I |
| America | 10m | C | 3s gust | 50-year | 31.3m/s | year | The distribution curve of extreme value for type I |

**Height variation factor of wind pressure.** The Chinese height variation factor of wind pressure is given in the following form:

$$u_z^B = \left(\frac{z}{10}\right)^{0.32} \tag{3}$$

where, z is the height to the center of each tower section.

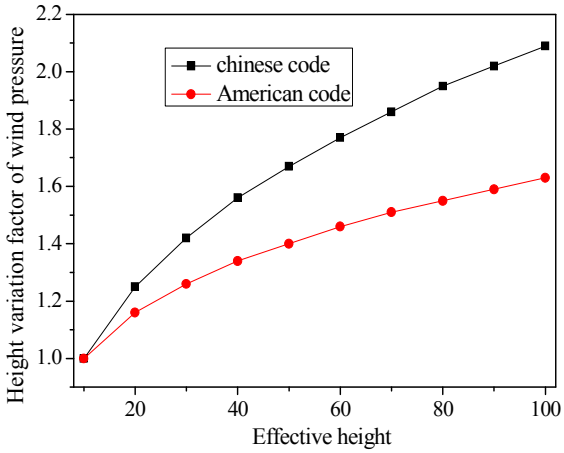


Fig. 1 Contrast curves of the height variation factor of wind pressure

The American height variation factor of wind pressure is given in the following form:

$$K_z = 2.01\left(\frac{z_h}{z_g}\right)^{\frac{2}{\alpha}}, \quad 10\text{m} \le \mathbf{z}_h \le z_g \tag{4}$$

where, $z_h$ is the effective height. $z_g$ is the gradient height. α is the power law exponent.

The height variation factors of wind pressure are calculated in the range of 100m height from Chinese and American codes. Fig. 1 shows the contrast curves of the height variation factor of wind pressure between the Chinese and American codes. It can be seen from the Fig. 1 that the height variation factor of wind pressure in the Chinese code should be less than the American code, and the difference in value is gradually increasing with the increase of height.

**Shape factor.** The Chinese shape factors of towers made up of the steel members is 1.3×(1+η) and the round-section members is (0.7～1.2)×(1+η). η is the lee sid reduction coefficient.

According to the cross-sectional shape of the latticed truss structures which is divided into the square and triangle, the force coefficient can be available from the table in the American code. For towers with round-section member shapes, the force coefficients must multiply the correction factors.

Choose the square-section angle steel towers and steel tube towers as the research object. According to the Chinese and American codes, the shape factors can be calculated easily.The comparison curves of the angle steel towers' shape factors are showed in Fig. 2 and the comparison curves of the steel tube towers' shape factors are showed in Fig. 3. It can be seen from the figures that the American shape factor is always greater than the Chinese code. When solidity ratio is 0.6 or higher, the Chinese shape factors remain the same, but the American shape factors grow as the solidity ratio increases.

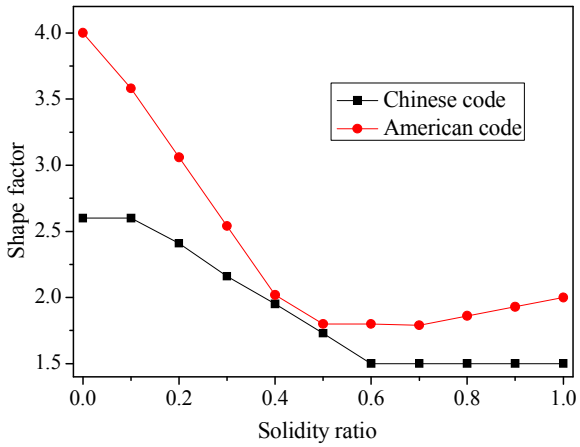


Fig. 2 Comparison curves of the angle steel towers' shape factors

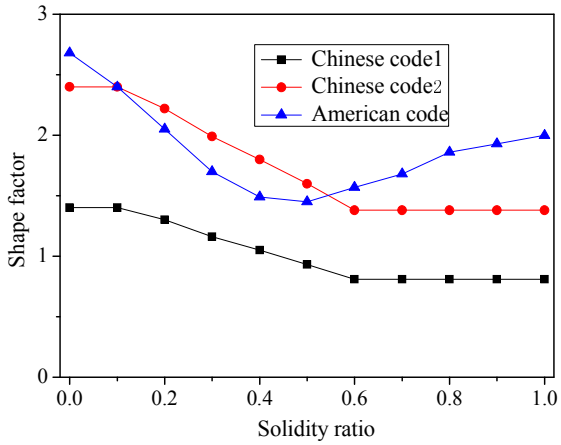


Fig. 3 Comparison curves of the steel tube towers' shape factors

**Wind load factor (Gust response factor).** In the Chinese code, the tower whose height is not more than 60m has only one wind load factor.This factor can be checked from the tables of the Chinese code.

The gust response factor in the American code shall be taken as follows:

$$G_t = \frac{1+2.7E\sqrt{B_t}}{K_v^2} \tag{5}$$

$$E = 4.9\sqrt{\kappa}\left(\frac{33}{z_h}\right)^{\frac{1}{\alpha_{FM}}}, \quad B_t = \frac{1}{1+\frac{0.56z_h}{L_s}} \tag{6}$$

where, $z_h$ is the effective height. $K_v$ whose value is 1.43 is the ratio of the 3-sec gust wind speed to the 10-min average wind speed,. $\alpha_{FM}$ is the power law exponent of the sustained wind. $\kappa$ is the surface drag coefficient. $L_s$ is the turbulence scale.

Fig. 4 shows the contrast curves of the Chinese and American wind load factor. It can be seen in the Fig. 4 that when the height is small, the Chinese wind load factor is less than the American code. With the increase of the height, the wind load factors are gradually approaching.

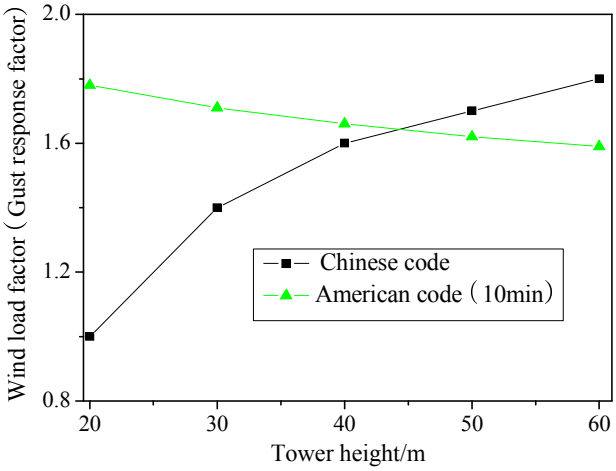


Fig. 4 Contrast curves of the Chinese and American wind load factor

## Conclusions

The comparison between the wind load of transmission tower of the Chinese and American codes are studied in the paper. The differences of basic wind speed, height variation factor of wind pressure, shape factor and wind load factor are researched, respectively. Based on the above results, the following conclusions are drawn:

(1) The differences about the basic wind pressure are on the definition of the wind speed's time duration. The ratio of American 3s gust wind speed to Chinese 10min average wind speed is 1.43:1. It can be seen that the American wind speed is greater than the Chinese code.

(2) If the tower height is less than 60m, the effective height in Chinese code is the height to the center of each tower section, but in American code, it uses too-thirds of the total structure height for the effective height. The height variation factor of wind pressure in Chinese code should be less than the American code, and the difference in value is gradually increasing with the increase of height.

(3) The Chinese and American shape factors are all related with the solidity ratio. While the solidity ratio is greater, the shape factor gets smaller. The American shape factor is always greater than the Chinese code.

(4) With increasing height, the Chinese wind load factor increases. On the contrary, the American gust response factor reduces as the height increases.

## References

[1] Guidelines for electrical transmission line structural loading (ASCE74-2009).

[2] Technical code for the design of tower and pole structures of overhead transmission line (DL/T5154-2012). (In Chinese)

[3] Code for design of 110kV～750kV overhead transmission Line (GB50545-2010). (In Chinese)

[4] Design of latticed steel transmission structures (STD/ASCE10-97).

*Applied Mechanics and Materials Vols. 580-583 (2014) pp 2658-2662*
*© (2014) Trans Tech Publications, Switzerland*
*doi:10.4028/www.scientific.net/AMM.580-583.2658*

# Landslide Susceptibility Zonation Based on the Analytic Hierarchy Process and Information Method

DandanQiu[1,2,a], RuiqingNiu[1,b],YannanZhao[1,c]

[1]Institute of Geophysics and Geomatics,China University of Geosciences,Wuhan,China, 430074;

[2]School of Resource and Civil Engineering,Wuhan Institute of Technology, Wuhan,China,430073

[a]dada_qdd@163.com, [b]rqniu@163.com,[c]yannan-1985@163.com

**Keywords**:analytic hierarchy process; information value; landslide; susceptibility zonation

**Abstract**: Landslide susceptibility zonation is one of the research hotspots in the field of landslide research. It is important in the process of disaster prevention and land planning. Select Wan Zhou as study area;it is one portion of the Three Gorges Reservoir Area.According to existing landslide statistical data, select lithology, slopegradient, slope structure and reservoir gradeas impact factors. Useanalytic hierarchy process andinformation method to calculate weighted value of each factorrespectively, and then combine them.The landslide susceptibility zonation was done by ArcGIS. This method can unite the advantages of the disaster data and expert experience.According to statistics, resultaccuracy rate is 90.3%.The key areaof landslide disaster prevention can be obtained from the landslide susceptibility zonation map.

## Introduction

Landslide susceptibilityzonationis the comprehensive study which involves the occurrence and development of landslide hazard and thelandslide disastersdistribution.The divided result is the sciencebasis, correct and timely forecasting landslide hazards [1]. According to different research objectives and targets,the methods can be divided into two categories: qualitative methods, quantitative methods. Qualitative methods are expert scoring method, AHP methodand so on. The quantitative methods are deterministic method, artificial intelligence method,information methodand so on.Many scholars have done a lot of job on this research [2-4].

Above described methods are widelyusedin practice, but they have significant differences and disadvantages in the weight value. Qualitative method has a direct relationship with the expert experience, and quantitative methods influenced by the training data. In the other hand,complementationcan also be found on the two methods. Therefore, the combination of analytic hierarchy process and information model is applied on the land susceptibilityzonation. The research area is Wan Zhou,which is one portion of the Three Gorges Reservoir Area.

## Basic Principles

### AnalyticHierarchy Process

AHP (analytic hierarchy process)basic principleis: make the various elements relating to the evaluation system are decomposed into three levels, which are goals , guidelines and programs, then make decision by qualitative and quantitative analysis on this basis[3, 5]. This approach analyzes the actual decision-making problems from the expert experience angle, and then use a

littlequantitative information digitalized decision-making process. It is a digital qualitative approach reliedon experience. The methodsteps as follows: First, establishing a hierarchy according to the problem, and then constitute a judgment matrix, use judgment matrix to calculate the weight vector, and do the consistency test.

**Information Model**

The theoretical basis of information model is information theory.It uses entropy decreasein the process of geological disasters to characterize geological disasters occurred. The factors togeological disasters have uncertainty degree. The average reduction of uncertainty degree equal to the entropy changes in the geological disasters system[4], equationisshown in Eq1:

$$I(Y, x_1x_2 \cdots x_n) = ln\frac{P(Y,x_1x_2\cdots x_n)}{P(Y)} \quad (1)$$

$I(Y, x_1x_2 \cdots x_n)$ isthe landslide information value, which provided by factorscombination$x_1x_2 \cdots x_n$, $P(Y, x_1x_2 \cdots x_n)$is the probability of the landslide occurrence under the set of factors $x_1x_2 \cdots x_n$,$P(Y)$is the landslide occurrenceprobability[6].

In the actual calculation, use the area ratio to calculate the information value, and overall information value in a single evaluation unit as this landslides unit comprehensive index.The higher the value, the landslide more likelyoccurrence, unit landslide risk is also higher.

## The example analysis

**Study area overview**

Wan Zhou locateson the eastern margin of the Sichuan Basin, northeastern edge of Chongqing. It locates at longitude 107 ° 55'22" ~ 108 ° 53'25", latitude 30 ° 24'25" ~ 31 ° 14'58". It is the typical geological disaster-prone area in the Yangtze River. The main geological disasters are landslides and collapse.Wan Zhou belongs to warm and humid subtropical climate zone, mild climate, abundant rainfall. Rainfall is mainly accounted from May to September;daily rainfall can up to 100mm or more.The main geomorphic units of Wan Zhou haveerosion and deposition of river floodplain, terraces, tectonic denudation,low mountains and hills.Wan Zhou locates in eastern Sichuan fold belt, Iron Mountain anticline north, Fangdoushan anticline south, eastern Sichuan fold belt towards the north east[7].

**Factor layer**

Landslide is the result of various factors'comprehensive function. According to study arearegularitysummary, select lithology, slope gradient, slope structure and reservoir gradeas impact factors.Use the existing geological map 1:10000, 1:50000 contours, remote sensing data, can get impact factor layers, which aremade by ArcGIS software. In order to unifycalculation, all the layers are converted into raster; the size is 10 m × 10 m.

(1) Lithology

In order to simplify calculation, lithology formations will be divided into three categories: soft rock, hard rock,alternate with soft and hard, is shown in Table 1.

(2)The slope structure

Slope structurecontrols the landslide development intensity. Slope with different structure has different landslide properties, characteristics and developmentextent.Consequent slope is prone to form large or giant rock landslide. Reverse slope is easy to form soil landslide. Transverse slope is not developed or less developed to landslide. According to the space relationships of slope gradient, aspect, underlying rock dip direction and inclination angle, slope structure is divided into the followingtypes: massive rock, nearly horizontal layered slope, consequent slope (including Floating

inclined slope, Stacked slope and Steep Inclined slope), slant slope (including Forward inclined slope, Contrary inclined slope) , Backward slope, Transverse slope [8].

**Table1 Lithology classification**

| Stratigraphic names | Lithology classification |
|---|---|
| Lower Jurassic Pearl Chong group | soft rock |
| Mid Jurassic Shang Sha-xi Temple group | soft rock |
| Mid Jurassic Xin-tian-gougroup | soft rock |
| Middle-Lower Jurassic Zi-liu Well group | soft rock |
| Upper Triassic Xu-jia-he group | alternate with soft and hard |
| Mid Triassic Ba-dong group | alternate with soft and hard |
| Upper Jurassic Peng-lai town group | alternate with soft and hard |
| Upper Jurassic Sui-ninggroup | alternate with soft and hard |
| Lower Triassic Jia-ling rivergroup | hard rock |

(3)The slope gradient

Terrain gradient is closely related to the landslidespatial distribution;it also affects thesoil thickness, hydrological conditions and lithological characteristics.It is an important factor of controlling landslide occurred. Through statistical relationship between the study area and terrain slope landslide, the study area slope gradient is divided into four levels : 0 ° ~ 15 °, 15 ° ~ 30 °, 30 ° ~ 45 °,> 45 °

(4)The reservoir grade

Periodicity change and erosion of reservoir's water level is an important factor to landslide. This paper proposes a method to determine reservoir waterscope, which is combine statistical analysis and engineering geologic analogy. After statistics, if landslide has the front edge's altitude from 60m to 110m, its average elevation D-value is 255.58m from front to rear edge. If altitudevalue over 110m,its average elevation D-value is 143.91m. Based on these data, the reservoir water affected area will be divided into four intervals: 60m-110m, 110m-253.91m, 253.91m-365.58m,> 365.58m. This is the natural state, the water level in the Three Gorges reservoir is 145m-175m after store water, according to the same method and rounding, the reservoir water scope will be divided into four intervals : 145m-175m (fluctuation zone ), 175m-320m ( strongly affected zone ), 320m-430m (medium affected area ),> 430m ( weakly affected zone ).

**Weight calculation by AHP**

Establish landslide hazard zonation hierarchy structure model in study area,isshown in Figure 1.

**Construct the judgment matrix and eigenvectors calculations**

According to the hierarchy structure model of study area, construct Wan Zhou landslide hazard judgment matrix, is shown in Eq2.

$$k = \begin{bmatrix} 1 & 1/5 & 1/7 & 1/7 \\ 5 & 1 & 1/3 & 1/3 \\ 7 & 3 & 1 & 1 \\ 7 & 3 & 1 & 1 \end{bmatrix} \tag{2}$$

According $k$ ,calculating normalized eigenvector $\omega = (0.04829, 0.1645, 0.3936, 0.3936)^T$ , $\lambda_{max} = 4.075$,and calculates$I_C = \frac{\lambda_{max}-n}{n-1} = 0.025$， $R_I = 0.8931$,$R_C = \frac{I_C}{I_R} = \frac{0.025}{0.8931} = 0.028 < 0.1$， so this matrix satisfy consistency. The feature vector ωcan be regard as AHPweight vector.

**Information value calculation by Information model**

According to the statistical landslide of Wan Zhou data, create landslide data layer, which overlay lithology, slope structure, slope gradient and reservoir graderespectively. Then calculate each impact factor layer's information value, is shown in Table2.

**Table2 Information Value and action indexof each impact factor**

| Impact factor | Classification | Information value | Actionindex |
|---|---|---|---|
| Reservoir grade | fluctuation zone | 1.225783 | 0.9 |
| | strongly affected zone | 0.873626 | 0.9 |
| | medium affected zone | 0.201298 | 0.5 |
| | weakly affected zone | -1.31837 | 0.3 |
| Lithology | Soft rock | 0.213647 | 0.5 |
| | hard rock | -10 | 0.1 |
| | alternate with soft and hard | -0.9084 | 0.95 |
| Slope structure | Nearly horizontal layered slope | 0.394681 | 0.5 |
| | Floating inclined slope | -0.78095 | 0.8 |
| | Stacked slope | -10 | 0.1 |
| | Steep inclined slope | -0.28216 | 0.4 |
| | Forward inclined slope | -0.48066 | 0.6 |
| | Transverse slope | 0.387899 | 0.3 |
| | Contrary inclined slope | -0.21696 | 0.3 |
| | Backward slope | -0.10478 | 0.2 |
| Slope gradient | <15° | 0.269371 | 0.4 |
| | 15°~30° | -0.15371 | 0.6 |
| | 30°~45° | -0.59201 | 0.8 |
| | >45° | -0.97889 | 0.9 |

**Combine method**

According to outdoor surveys and data analysis, judge the action index of each impact factor in AHP on the basis ofimpact factor classification in this article. Thenstandardize each data, which normalize between 0 and 1, detailsare shown in Table 2on the right.

Multiply AHP's weight value and action index ofimpactfactor then add information value, this isthe final risk index.Equation is shown in Eq3:

$$B_L = \sum_{i=1}^{n}(\omega_i n_i + I_i)/2 \quad (3)$$

$B_L$isrisk index of each unit , $\omega_i$ is the weight of AHP each factor, $n_i$ is the action index of each factor , $I_i$ is the information value.

According to the calculated risk index, landslide susceptibility study area will be divided into four zones:extremely high risk zone, high risk zone, danger zone andlow risk zone by using natural breakpoint method (Natural Break).

**The results**

Select 20% of past landslidedataas validated sample, the rest participate used as the training data. Thesum of hazard point as validated is 53, accuracy rate is 90.3% (extremely high risk zoneaccounted for66.4%, high-risk zone accounted for 14.9 %, 9.1% in the danger zone), is shown in Figure2.So the key areaof landslide disaster prevention is the extremely high risk zone,high-risk zone and danger zone can have reference selection. Low risk zone is not as focused on prevention.

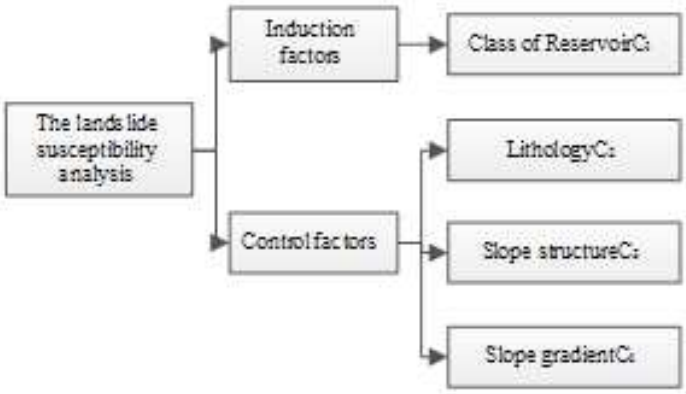


**Fig.1 Hierarchy structure modelof study area**

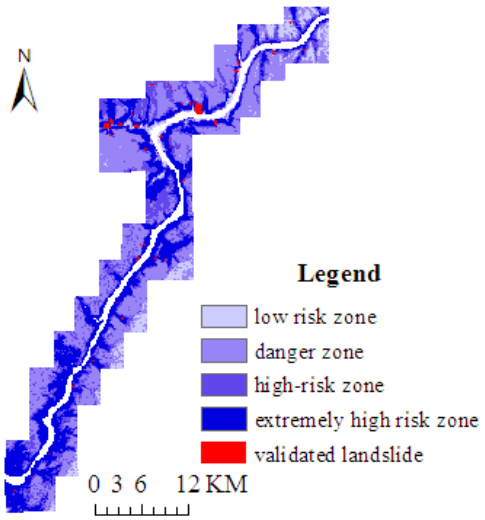


**Fig.2 The landslide susceptibility zonationmap of Wan Zhou**

## Conclusion

Information method evaluates landslide susceptibility uncertainty for each factoris greatly influenced by the existing landslide data.AHPis influenced by experience. So theyare complementary. According to this paper's test, combine information method and AHP could be more reasonable to weights,and get better result. However, this method still used grid evaluation unit, split the landslideintegrity; Secondly , the final risk index is to take a simple average value of the two methods, did not consider further detail, can be improved in the future.

## Acknowledgements

This work is supported bythe national "863" high technology research and development program project (2012AA121303).

## References

[1]MiaoFang,JinlongZhang,ZhenXu:Remote sensing technology and application,2011(06): 845-854(In Chinese)

[2] WenZhang, ShibiaoBai, JianWang: Journal of Geological Hazards and Environment Preservation,2010(04): 20–23+37. (In Chinese)

[3] XiaoyiFan, JianpingQiao, YongboChen:Journal of natural disasters, 2004(01): 72–76. (In Chinese)

[4] LiangfengZhu, XincaiWu, KunlongYin, XiuguoLiu:Journal of Earth Sciences and Environment, 2004(03): 52–56. (In Chinese)

[5] LixinWu, JianguoWang, JizhunYang: Nonferrous Metals (mine area), 2009(04): 66–69. (In Chinese)

[6] KechangGao,PengCui,ChunyongZhao,FangqiangWei:Chinese Journal of Rock Mechanics and Engineering, 2006(05): 991–996. (In Chinese)

[7] ZhijianWang:China University of Geosciences.2008. (In Chinese)

[8] JingfuLi, RuiqingNiu:Yangtze River, 2009(19): 38–40. (In Chinese)

*Applied Mechanics and Materials Vols. 580-583 (2014) pp 2663-2666*
*© (2014) Trans Tech Publications, Switzerland*
*doi:10.4028/www.scientific.net/AMM.580-583.2663*

# Modelling of the Human Behavior in Evacuation

Lan Wei[1, a], Chaoyang Zhao[1, b], Weifeng Yuan[1, c]

[1]Southwest University of Science and Technology, Mianyang, China 621010

[a]weilan@swust.edu.cn, [b]1069225983@qq.com, [c]yuanweifeng@swust.edu.cn

**Keywords:** Evacuation, Cellular automaton, Human behavior

**Abstract.** Emergency evacuation is an important issue in fire safety. In this study, a cellular automaton (CA) model in which the human behaviour termed 'flow with the stream' is considered is proposed to simulate the procedure of emergency evacuation. Based on the CA model, the influence of the number of guiders to the evacuation from a large compartment is analyzed through numerical test. The result shows that the proposed CA model is a promising tool that may be used in fire safety design.

## Introduction

In the light of homeland security, simulation of evacuation from a compartment of fire origin to a safe refuge is attracting more and more attention. In the past decades, quite a number of approaches have been developed for the modelling of evacuation, among which CA is widely used [1]. As a useful class of numerical tools for the simulation of complex system, CA has been successfully applied to simulate various complex systems, such as theoretical biology [2], computability theory [3], fluid dynamics [4], earthquakes and traffic flow, etc. The development of CA can be traced back to 1940s when Neumann [5] studied biological reproduction and crystal growth. Basically, CA is a discrete model, which consists of a regular grid of cells, each cell in one of a finite number of states.

## Cellular automaton model

When CA is used in evacuation simulation, the space is normally discretized into uniform grid, and the time domain can be discretized into a series of finite time steps $t_1$, $t_2$,…, and $t_i$. In a CA model, each cell is vacant or occupied by an evacuee. A specific evacuee makes his/her decision based on the states of his/her neighboring cells at the last time step.

It is well known that a CA model is constructed from basic rules. The research focuses on the simulation of crowd movement after all the occupants start to evacuate from a smoke-filled room. The rules in the proposed model include:

(a) Each evacuee stays within one CA cell at time $t_i$.

(b) Each evacuee selects an exit to move towards.

At the current position, the evacuee has $N$ choices since there are $N$ exits. However, this evacuee can only select one exit at each time step based on the consideration of spatial distance and occupant density [6]. In this study, the movement direction of the evacuee is determined by probability analysis. For instance, the probability of exit $i$ to be selected at $t_k$ is given by:

$$P_i = \frac{\alpha P_{i-S} + \beta P_{i-D}}{\alpha + \beta} \tag{1}$$

where $\alpha$ and $\beta$ are two constants. The terms $P_{i-S}$ and $P_{i-O}$ be calculated by Eq. 2.

$$P_{i-S} = \frac{1}{R_i \cdot \sum_{j=1}^{N} \frac{1}{R_j}}, \quad P_{i-O} = \frac{1}{D_i \cdot \sum_{j=1}^{N} \frac{1}{D_j}} \tag{2}$$

where $R_i$ is the distance from the evacuee to Exit $i$ and $D_i$ is the occupant density at Exit $i$. It can be proved that $\sum_{i=1}^{N} P_{i-S} = 1$ and $\sum_{i=1}^{N} P_{i-O} = 1$. The expressions of $\alpha$ and $\beta$ are given by:

$$\alpha = \frac{\theta}{N} \cdot \sum_{j=1}^{N} \left| 1 - \frac{N}{R_j \cdot \sum_{k=1}^{N} \frac{1}{R_k}} \right|, \quad \beta = \frac{(1-\theta)}{N} \cdot \sum_{j=1}^{N} \left| 1 - \frac{N}{D_j \cdot \sum_{k=1}^{N} \frac{1}{D_k}} \right| \tag{3}$$

Obviously, it can be approved that $\sum_{i=1}^{N} P_i = 1$ since $\sum_{i=1}^{N} P_{i-S} = 1$ and $\sum_{i=1}^{N} P_{i-O} = 1$. In Eq. 3, the term $\theta$ is used to adjust the influence of spatial distance and occupant density. It is a constant which varies in $[0, 1]$.

(c) After the movement direction has been determined, each evacuee will only select one cell among all adjacent cells surrounding the current one as the potential position at time $t_{i+1}$. The evacuee perceives the new selected cell to be safer than the current one.

(d) If a cell is chosen by several evacuees at the same time step, it will be randomly assigned to one of the evacuees. The other evacuees who have no cell to move in have to wait within their current cells until the next time step.

(e) All evacuees update their positions at time $t_{i+1}$, and then based on the new situation, choose new exits and cells for themselves at time $t_{i+2}$.

'Flow with the stream' is regarded as a kind of human behavior. This phrase is usually used to describe the psychological phenomenon that people intend to follow the lead of other people and react to their opinions or actions passively. During emergent evacuation, if it is hard to an individual to make a decision forthwith, for instance, he cannot see the exit in a smoke-filled compartment and he does not know where to move, he may decide to just follow the other people who are near to him. To simulate 'Flow with the stream', the proposed CA model is modified based on Fig. 1.

In Fig. 1, the cells represent cellular automaton grid. The visible domain of an evacuee at cell $O$ is defined as the area surrounded by a circle with a radius denoted by $R_V$. It must be mentioned that $R_V$ may not be constant in the course of time since it may be affected by smoke concentration in a fire compartment. To simulate 'flow with the stream', it is assumed that this evacuee cannot see the exit since it is out of his visible domain. It is also assumed that there are $M$ evacuees within his visible domain, including a typical evacuee denoted by $i$. It is defined that an evacuee at cell $O$ has eight movement directions denoted by $d_1 \sim d_8$ at each time step. Among all the $M$ occupants, the $k^{th} (1 \le k \le M)$ occupant is defined as a guider because he always knows the location of the exit even though he may not able to see the exit due to limited visibility. The evacuee at $O$ determines his movement direction by following the rule:

(1) At time $t_i$, check the status whether the evacuee at cell $O$ can see the exit. If it is true, the evacuee will move towards the exit by comparing the importance of spatial distance and occupant density. Otherwise, proceed to the next step.

(2) Check if there is a guider among the $M$ occupants. If it is true, the evacuee at $O$ just follows the guider to move. Otherwise, proceed to the next step. If there are two or more guiders within the visibility domain, one of them will be chosen randomly to follow.

(3) Based on the state at time $t_{i-1}$, count the number of evacuees who are within the visibility domain and divide them into groups according to their movement directions. Since there are eight possible directions around the cell $O$, the maximum number of groups is also eight. Each group consists of several evacuees who are moving in the same direction.

(4) The group which contains most evacuees is defined as the leading group. The movement direction of the leading group is defined as the principal direction. If there are two or more leading groups (principal directions) around cell $O$, one of them will be chosen randomly to be followed by the evacuee at cell $O$.

The way for the evacuee at $O$ to follow a guider or a group is described below:

(1) Select a target that might be followed, using the way provided in the four steps for 'flow with the stream'. The target can be a guider or a leading group.

(2) Once the target is fixed, the evacuee has two options: a) a probability (value=$\eta$) is set for the evacuee to give up following the target and moves along a direction selected randomly. b) a probability (value=$(1-\eta)$) is set for the evacuee to follow the target.

(3) If the evacuee decides to follow the selected target, a probability with value of $\lambda$ is given to him to make himself closer to the target. When the target is a guider, the evacuee will move towards the guider, but if the target is a leading group, the evacuee will approach the center of this group. As a result, a probability with the value of $(1-\lambda)$ is given to him to just move along the movement direction of the target. In this situation, he will not intend to shorten the distance between him and the target.

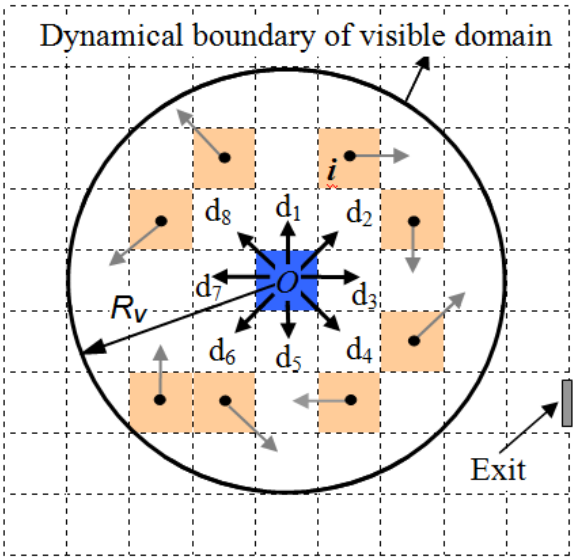


Fig. 1. Illustration of the determination of an evacuee's movement direction

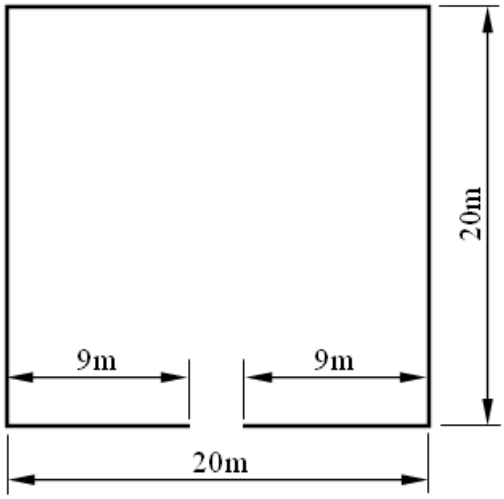


Fig. 2. Dimension of a single square room with an exit

**Numerical example**

As an example, the evacuation from a compartment shown in Fig. 2 is modelled by the proposed CA model. Intuitively, the number of guiders (NOG) will play a key role in the evacuation. To investigate the influence of NOG, it is assumed that 300 evacuees are randomly distributed in the compartment before an evacuation starts. In total, six scenarios are simulated for the case that the visibility range is 2m. Without loss of generality, each scenario has one trial run and the results are depicted in Fig. 3. The NOG in the simulation varies from 0 to 40 (denoted by G0~G40 in Fig. 3).

Fig. 3 shows that NOG does affect the evacuation procedure significantly. The curves indicate that the greater the number of guiders, the more the evacuees evacuated within 300 time steps. However, it can also be seen that the corresponding curves become very similar when NOG varies from 30 to 40.

For further investigation, 10 trial runs are conducted for each case of various scenarios and the average results are depicted in Fig. 4. From this figure, one knows that the gradient of the curve becomes smaller as NOG becomes larger. This reveals that the evacuation procedure is more sensitive to NOG when it is small. Moreover, the curve in Fig. 4 has an obvious platform, which shows that the change of NOG does not affect the evacuation significantly when $30 \le \text{NOG} \le 40$. This finding is very useful to fire safety design.

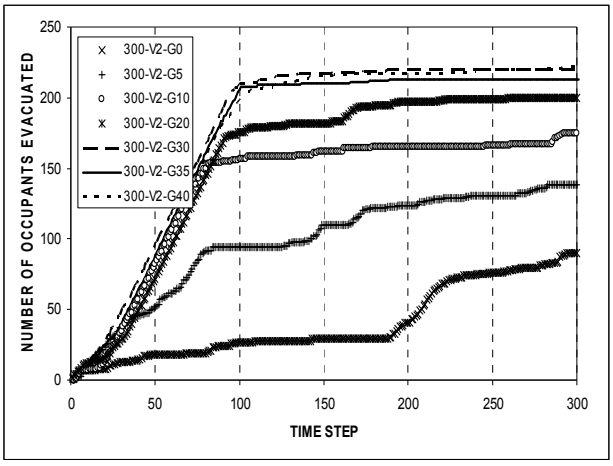


Fig. 3. Evacuation procedures under various NOG and $R_v = 2$m

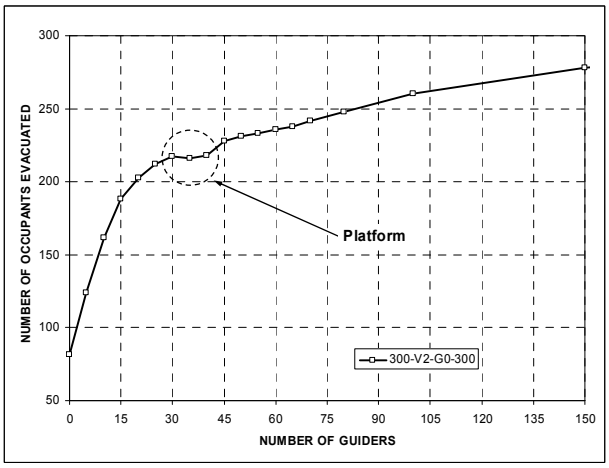


Fig. 4. Effect due to number of guiders

## Conclusions

In this study, a CA model is developed for the simulation of an evacuation from a large compartment where the visibility range is limited. Numerical example proves that the proposed model can be used to model the psychological phenomenon termed 'flow with the stream'. Numerical investigation reveals that the number of guiders can affect the evacuation duration significantly. Meanwhile, the reasonableness of the numerical results indicates that the CA model is a promising tool which may provide quantitative analysis for fire safety design.

## Acknowledgements

This work was financially supported by the SWUST Doctoral Foundation (12zx7105).

## References

[1] X.P. Zheng, T.K. Zhong and M.T. Liu: Building and Environment, Vol. 44 (2009), p. 437

[2] G.B. Ermentrout, L. Edelstein-Keshet: Journal of Theoretical Biology, Vol. 160 (1993), p. 97

[3] Th. Buchholz, M. Kutrib: Acta Inform, Vol. 35 (1998), p. 329

[4] S. Wolfram. Journal of Statistical Physics, Vol. 45 (1986), p. 471

[5] A.W. Burks: *Theory of self-reproduction automata*, *John Von Neumann*, (University of Illinois Press, Urbana, 1966)

[6] W.F. Yuan and K.H. Tan. Physica A: Statistical Mechanics and its Applications, Vol. 384 (2007), p. 549

*Applied Mechanics and Materials Vols. 580-583 (2014) pp 2667-2670*
*© (2014) Trans Tech Publications, Switzerland*
*doi:10.4028/www.scientific.net/AMM.580-583.2667*

# Numerical simulation on ghosting fire in the confined underground space

Peihong Zhang[1, a], Xiaowei Lu[2, b] and Xiaoming Zhang[2, c]

[1]Subway Research Institute, Shenyang Jianzhu University, Shenyang, Liaoning, China

[2]Municipal and Environmental Engineering Department,Shenyang Jianzhu University, Shenyang, Liaoning, China

[a]bczhangph@sina.com, [b]smartmlu@163.com, [c]544524107@qq.com

**Keywords:** underground; confined space; ghosting fire; numerical simulation; FDS

**Abstract.** The phenomenon of ghosting fire development in underground confined space is simulated to analyze the impacts of ghosting fire generation via some conditions -- different air vent sizes and different fire source areas. FDS is used to establish a physical model of underground fire laboratory in Northeastern University, the simulation is conducted by setting two parameters, the air vent size and the fire source area. The fire heat release rate, temperature, concentration of CO, $O_2$ are measured to analyze the case of ghosting fire generation in underground confined space with different air vent sizes and different fire source areas. It's most likely to generate ghosting fire when the simulating parameter is that the air vent size is 0.4m × 0.4m and the fire source area is 0.96$m^2$. The conclusion is that increasing the air vent size is not a simple ascending and descending relationship with the occurrence time and duration time of the ghosting fire. Increasing the fire source area can improve the fire heat release rate effectively, and promote the formation of ghosting fire.

## Introduction

Ghosting fire is a special phenomenon, which can be seen easily in the confined space. Because of poor ventilation, low content of $O_2$ is caused by continuous combustion, and fire smoke contains large amounts of combustible ingredients because of incompletely burning of fuel. Combustible composition and $O_2$ concentration exist in the confined space, which leads to the flame far from the fuel surface and has been appearing in the other areas beyond the flame area[1] . Sugawa etc.[2] used small size of closed cabin compartments to conduct ethanol pool fire experiments, and they pointed out that ghosting fire was a kind of unstable combustion phenomenon which had an influence on the mass burning rate. Pearson[3] increased the height of the fire source to make the vents below the fire and observed similar flame travel in experiments. In their opinion, the result of the ghosting fire was that the speed of premixed flame is faster than the speed of natural convection. Utiskul etc. [4-5] proposed the determination case of appearing ghosting fire, the concept of the global equivalent ratio (GER) was introduced as a determination case judgment of appearing ghosting fire. Changhai Li etc. [6] conducted the heptane pool fire experiments in the enclosed space of 17.55$m^3$ without opening, and they found that forming the ghosting fire was not a monotonous increasing relationship with simply to improve fire source location. In this paper, FDS was used to simulate and analyze flame walk, and the calculation of the smoke and the heat of fire transfer process was studied to analyze the impact of air vent size and fire source area for the ghosting fire.

## The Underground Fire Laboratory Model

1.1 **Establishment of Geometric Model.** The model is established on the basis of the underground fire laboratory of Northeastern University, which is divided into two parts. The ground part sets three air supply outlets(4.8m × 1.6m) with 1.5m/s velocity and two opens(4.0m × 1.6m), and the ground wind field which is affected by the surrounding buildings was simulated to make the simulation more real and reliable. The main building of the underground part is 18 m (L) ×6.9 m (W) ×2.9 m (H), a natural air vent was set 9 m far from the fire source, heptane is used as the fuel, the simulation time is 1000s, the initial temperature was set to 18 ℃. Specific arrangement is shown in figure.1.

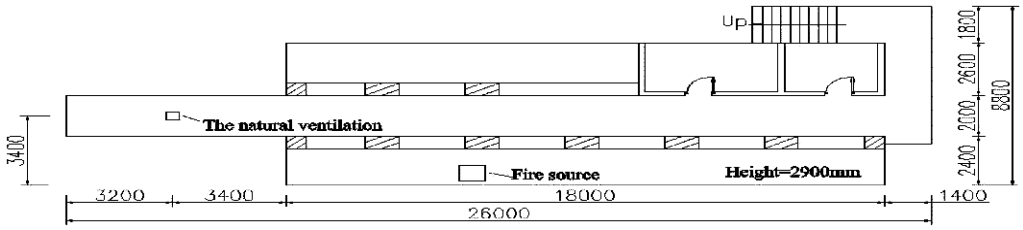


Fig.1.The vertical view of underground fire laboratory

**1.2 Simulation Cases.** The fire behavior in the underground fire laboratory was simulated through changing the size of natural air vent and the fire source area. Nine cases are simulated while the natural air vent size is set to 0.2m×0.2m, 0.4m ×0.4m, 0.6m×0.6m and the fire source area is set to $0.32m^2$, $0.64m^2$, $0.96m^2$. The mechanism of ghosting fire is analyzed and judged through the comparison of the nine cases data with ghosting fire or not. The simulation cases are shown in Table 1. Audouin etc.[7] found that the flame from the fuel surface moved to air vents and became stable near them until the end of the experiment. Around the natural air vent where ghosting fire occurred very easily, a series of measuring points were set to extract data of the temperature and the average value of CO, $O_2$ concentration along with time in each case.

Table.1
Simulation cases

| Cases | Fuel | The natural ventilation | Fire area | Ghosting fire occurs time |
|---|---|---|---|---|
| One | Heptane | 0.2m×0.2m | 0.32 ㎡ | Unhappen |
| Two | | | 0.64 ㎡ | 580s |
| Three | | | 0.96 ㎡ | 236s |
| Four | | 0.4m×0.4m | 0.32 ㎡ | Unhappen |
| Five | | | 0.64 ㎡ | 466s |
| Six | | | 0.96 ㎡ | 206s |
| Seven | | 0.6m×0.6m | 0.32 ㎡ | Unhappen |
| Eight | | | 0.64 ㎡ | Unhappen |
| Nine | | | 0.96 ㎡ | 269s |

**Analysis on the trend of development of fire under different cases**

The numerical simulation in nine cases of fire model in underground fire Laboratory shows that stable suspension of ghosting fire occurred in the natural air vent in case two ,case three, case five ,case six and case nine; while there is no ghosting fire in case one, case four, case seven and case eight during the simulation and fire gathered around the surface of fire source. Specific time that ghosting fire occurred were listed in Table.1. In case two, case five, and case eight, the fire area was the same($0.64m^2$), the natural air vent had three different sizes(0.2m × 0.2m, 0.4m × 0.4m, 0.6m × 0.6m), ghosting fire appears first in the case five. When the fire area is set to the $0.32m^2$, burning intensity of fire was weaker than other cases and no ghosting fire occurred. However, when the fire area was set to the $0.96m^2$, the fire burn more fiercely compared with other cases, and in the underground space there were sporadic ghosting fires, but the ghosting fire in the natural air vent is the most stable, as shown in Fig.2.

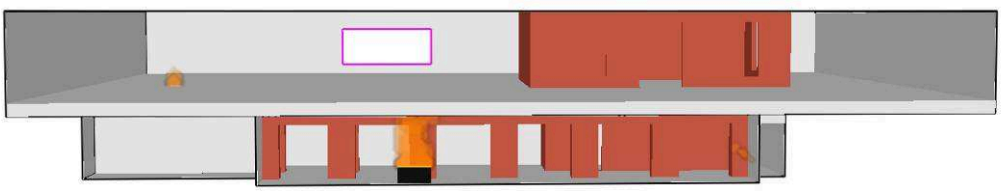

Fig.2.Ghosting fire profiles in underground lab fire

**2.1 Influence of natural ventilation opening size.** The fire area was the same in case two, case five, case eight. The data of these three cases were used to analyze the effects of different air vent size to

the ghosting fire. Figure.3 is the heat release rate curve diagram for case two, case five and case eight. The curve diagram indicates when ghosting fire occurred, the fire power peak was all at 1.1MW in three cases. As the fire developed to a certain time, because of the weak ventilation case, the heat release rate of case two and case five decreased (case two at 525s, case five at 650s), but case eight is not the situation.

Figure.4 is the volume concentration curve of $O_2$ in the underground laboratory natural air vent at case two, case five and case eight. From Figure.4, when ghosting fire occurred, the volume concentration curve of $O_2$ is 13% at case two, 13.7% at case five. The volume concentration curve of $O_2$ reached a minimum value of 12.4% at 525s, then increased, finally tends to be stable at case two and reached a minimum value of 12.4% in 650s, then increased, finally tends to be stable at case five, too. The decreasing speed of $O_2$ concentration in the combustion process is the slowest at 0.6m × 0.6m opening of case eight. Finally, the $O_2$ concentration at three cases is all between 14%~15%, reaching to stuffy quenching concentration of the heptanes in the inner space of underground laboratory. Figure.5 is the volume concentration curve of CO varying with time at case two, five and eight. From the CO content, the changes in content of combustible component in the hot flue gas can be observed. When ghosting fire occurred, the CO volume content at case two was 208ppm, 190ppm at cases five. From Figure.5 it can also be seen that when CO volume concentration reaches for the peak at case two and case five , and the heat release rate curves begin to fall . Figure.6 is temperature curve diagram at three cases affected by the decreasing of heat releasing rate. The temperature at case two and case five also showed a downward trend. When the natural ventilation opening at case eight increased to 0.6m×0.6m, the underground chamber is well ventilated; the combustion process is little affected by ventilation control counter effect, the heat release rate, temperature, $O_2$ and CO concentration at the stage of ventilation control has been in a steady state.

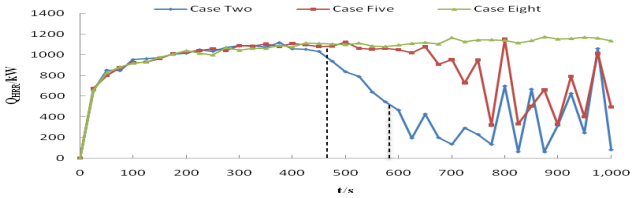


Fig.3.The heat release rate curve of fire source

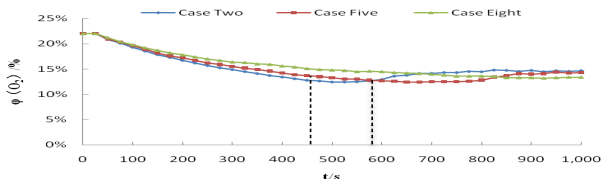


Fig.4.The oxygen concentration

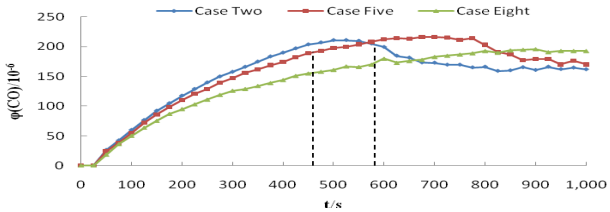


Fig.5.The carbon monoxide concentration curve

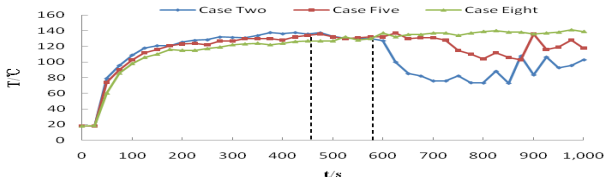


Fig.6.The temperature curve

By comparing these three cases, undersize natural air vent size, such as case two, a weak state of ventilation was caused in underground. In the process of combustion, $O_2$ volume concentration near the fire source rapidly reduces, which leads to the incomplete burning of fuel, and finally the oxygen concentration influenced the combustion intensity, the heat release rate decreased, following by a series of changes of $O_2$, CO, temperature. Because of the 0.6m×0.6m natural air vent at case eight, there was no ghosting fire during simulation. The underground laboratory is well ventilated, so the combustion process is less affected by ventilation control counter effect, the heat release rate and the temperature at the stage of ventilation control has been in a stable growth, $O_2$ concentration tends to a slow decrease until being stable, CO concentration has slow growth. The natural air vent size is not a simple ascending and descending relationship with the occurrence time of the ghosting fire, an undersized natural air vent, resulting in low $O_2$ concentration. While oversized natural air vent led to the more sufficient combustion, the combustion process reduced the generation of CO.

**2.2 The influence of fire source area for the ghosting fire.** Three kinds of parameters were designed in the simulation (0.32m$^2$, 0.64m$^2$, 0.96m$^2$). In these cases, the area of 0.32 m$^2$ fire heat

release rate peaks are 0.4 MW, 0.64 $m^2$ fire heat release rate peaks are 1.1 MW, 0.96 $m^2$ fire heat release rate peaks are 1.9 MW. The cases four, case five, case six have the same natural air vent size, the data of these three cases was used to analyze. The larger of the fire source area, the bigger of the fire heat release rate peak ,the sooner the ghosting fire appeared. The larger of the fire source area, the bigger of the fire heat release rate peak, and at the same time the temperature of the underground laboratory rise sharply, the accumulation of CO content will be accelerated, which accelerate to relight the combustible components in natural vent. Increasing the fire source area has played a significant role in promoting affection for the ghosting fire to occur.

## Conclusions

The change of the natural ventilation is not a simple ascending and descending relationship with the formation of the ghosting fire. An undersized nature air vent restricts the $O_2$ content in the formation. And the oversized natural air vent restricts the CO content, which slows the growth of the temperature of in natural air vent. Therefore, the formation of the ghosting fire is affected by these factors. And increasing fire area improves the fire heat release rate effectively, promoting the formation of ghosting fire in confined underground space. Weak ventilation situation exists in the confined underground space, once a high intensity fire occured, the ghosting fire would occur easily. In the process of the formation of the ghosting fire, the whole underground laboratory fire ceiling temperature reached 200℃, it is easy to cause another fire behavior "flashover" in this situation. Ghosting fire and flashover will be explored whether there is some kind of inevitable connection in the future.

## Acknowledgements

This work was financially supported by the National Natural Science Foundation of China (51174046 and 51374050),

## References

[1] Foote K L.1986 LLNL enclosure fire tests data report: UCID-21236［R］. Livermore, CA: Lawrence Livermore National Laboratory,1987.
[2] Sugawa O, Kawagoe K, Oka Y, et al. Burning Behavior in a Poorly-ventilated Compartment Fire-Ghosting Fire［J］.Fire Science and Technology,1989,9(2):5-14.
[3] Pearson A, Most J M, Drysdale D. Behaviour of a confined fire located in an unventilated zone ［J］. Proceedings of the Combustion Institute, 2007, 31:2529-2536.
[4] Utiskul Y, Quintiere J G, Rangwala A S, et al. Compartment fire phenomena under confined ventilation［J］. Fire Safety Journal, 2005,40: 367-390.
[5] R.J. Ong, J.T. Dawley and P.G. Clem: submitted to Journal of Materials Research (2003).
[6] Changhai Li, Shouxiang Lu, et al.Studies on ghosting fire from pool fire in closed compartments ［J］. Journal of university of science and technology of China,2010(07).
[7] Audouin L, Such J M, Malet J C, et al. A Real Scenario for a Ghosting Flame［C］//Fire Safety Science-Proceedings of the Fifth International Symposium on Fire Safety Science. Melbourne: IAFSS,1977:1261-1272.

*Applied Mechanics and Materials Vols. 580-583 (2014) pp 2671-2674*
*© (2014) Trans Tech Publications, Switzerland*
*doi:10.4028/www.scientific.net/AMM.580-583.2671*

# Research on Concrete Columns Seismic Performance of Super Early-Strength Composite Fibers after High Temperature

Changzheng Sun [1,2,a], Ruixiao Wu [1,b],Hainan Zhao[2,c]

[1] School of Civil Engineering, Shenyang Jianzhu University, Shenyang Liaoning,110168,China

[2] Architectural design and research institute, Shenyang Jianzhu University, Shenyang Liaoning,110168,China

[a]759179142@qq.com, [b]wuruixiaode@126.com, [c]474670207@qq.com

**Keywords:** High Temperature; Quasi-Static; Seismic Performance; Hysteretic Curve; Skeleton Curve

**Abstract.** Super early-strength composite fiber concrete has been widely used. Seismic Performance of super early-strength composite fiber concrete columns needs to be known after high temperature, quasi-static tests under different high temperatures are experimented. The experiment showed that: the downtrend of hysteretic curves and skeleton curves are consistent, but reductions for both hysteretic curves and skeleton curves are diverse after different duration.

## Introduction

China is a many earthquakes nation.The fire often takes place following destructive earthquake. The fire often takes place following the destructive earthquake.Structure safety is the important obje ctive of performance-based seismic design and fire resistant. Column is an important load-bearing element of construction. When the buildings affected by the fire after earthquake, the inner member may be formed of non-uniform distribution of temperature field, material properties will be change, which leads to the structure bearing capacity decreased. Therefore it supplies a basis for the calculation of remainder load bearing capacity and evaluate of damage about the Super early-strength composite fiber concrete structure post fire and earthquake.

## Experiment and Related Parameters

**Experimental Axial Compression Ratio.**In the experiment, axial compression ratio of experiment is 0.4, axial compression ratio [1] is defined below. $N$ is force; $f_{ck}$ is axial compressive strength standard value; $A$ is area.

$$n' = \frac{N'}{f_{ck} \times A} \tag{1}$$

According the impact of the design specifications of concrete structure [2] and the permanent load factors, which can get the design axial compression ratio is 0.672.

**Specimen Design.**Duration of high temperature has significant effect on hysteretic behavior and remainder load bearing capacity. Therefore, duration of high temperature is the most important factor on concrete columns of super early-strength composite fiber seismic performance. In this experiment, the main parameters of columns are shown in figure 1.

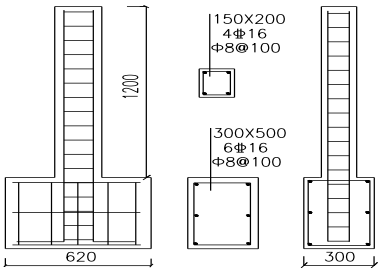


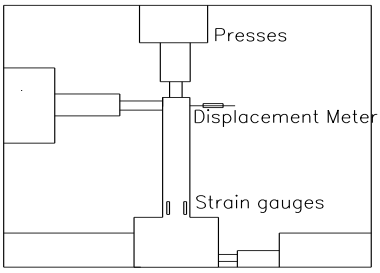


**Fig.1** Main parameters of the specimen **Fig.2** Diagrammatic of experimental device

**Parameters.** The main parameters are shown in table1.

**Tab. 1** Test parameters of specimens

| Specimen | temperature | high temperature duration | axial compression ratio | load |
|---|---|---|---|---|
| Z-1 | 600℃ | 30 | 0.4 | repeated |
| Z-2 | 600℃ | 60 | 0.4 | repeated |

## Specimens Yield Experiments

**Yield Test Apparatus and Loading System**. First, 200t hydraulic jack applies the vertical force, then 60t hydraulic jack applies horizontal force, in the test, force control method is used, Horizontal force is controlled from 10kN to 40kN by 5kN increment[3], it is stop until the turning point appears[4]. Data acquisition is finished by EIC-300 logger type IMP. The experimental apparatus is shown in Figure 2.

**Experimental Phenomena and Hysteretic Curve.** Specific experimental phenomena and the hysteretic curve are shown in the figure 3 and 4.

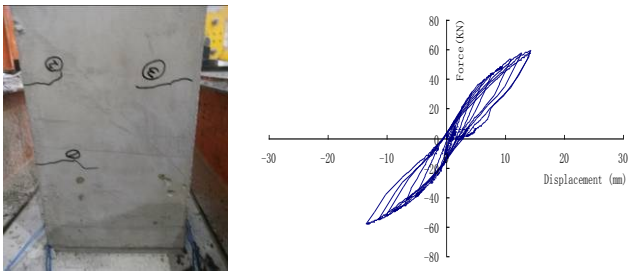


**Fig.3** Z-1 failure pattern and hysteretic curve

**Fig.4** Z-2 failure pattern and hysteretic curve

## Fire Test

**Yield Test Apparatus and Loading System.** In the experiment, fire-resistant cotton wraps the position of top column and column pier. Specimen are put into the heat treatment device which controls temperature to 600℃ for 30min or 60min [5]. Finally, the specimens are cooled to room temperature. The experimental device uses electric heating method.

**Experimental Phenomena.** During the heat treatment, a small amount of visible water vapor spill from the top of the gap. After experiment, the specimen surface are appeared noticeable color, the width and number of surface cracks increased obviously, experimental phenomena is shown in figure 5.

**Fig.5** Z-1, Z-2 The color change of the specimens after high temperature

**After the Multi-hazard Seismic Experiment**

**Experimental Phenomena and Hysteretic Curve.** Specific experimental phenomena and the hysteretic curve are shown in the figure 6 and 7.

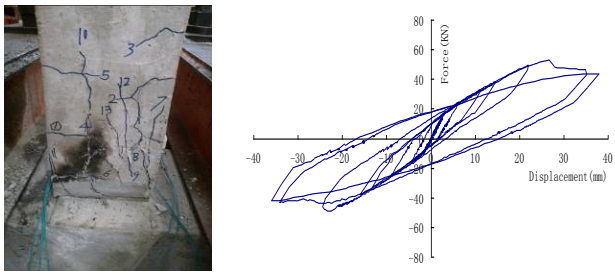


**Fig.6** Z-1 failure pattern and hysteretic curve

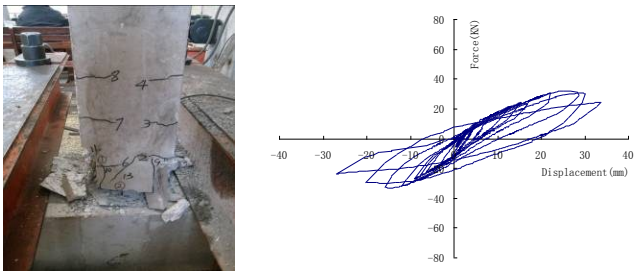


**Fig.7** Z-2 failure pattern and hysteretic curve

Load-Displacement curve can be analyzed about the structure of remainder load bearing capacity, ductility of the columns. Conclusion and suggestion are summarized below.

(1) At the beginning of loading, the columns are in the elastic phase, the latter, load bearing capacity will gradually descend, slope of the curve is reduced, high temperature and cyclic load are the reasons of material strength reduction.

(2) Displacement control is used in experiment at second stage, strength and stiffness of the specimen decline noticeably, load bearing capacity is reduced.

**Skeleton Curve.** As the skeleton curve can be analyzed variation of the bearing capacity and ductility detailed，it can be assessed the seismic performance objectively, skeleton curve is shown below8.9.

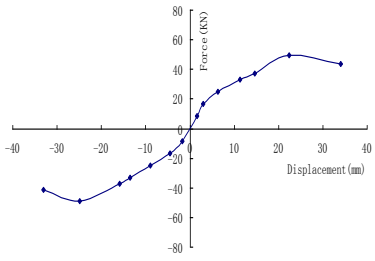


**Fig.8** Z-1 skeleton curves

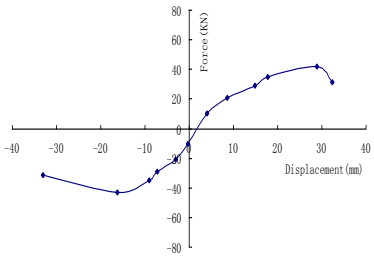


**Fig.9** Z-2 skeleton curves

We can Analysis the skeleton curve above that:

(1) At the beginning of loading, specimen still maintain some elastic state. With load increasing, it appears plastic deformation, cracking phenomenon is very serious.

(2)The longer of the duration high temperature lasts, the more serious material damaged. The damage phenomenon is more obvious

**Ductility Factor.** Specimen damage appearances the ductility deformation [6]. It is often used ductility factor to reflect the ductility index of the specimen, which is defined formula [7].

$$\mu_{\Delta} = \frac{|\Delta_{+u}| + |\Delta_{-u}|}{|\Delta_{+y}| + |\Delta_{-y}|} \quad (2)$$

Use the formula, ductility factor can be got in the table 2.

**Tab.2** Specimen ductility factor

| Specimen | Z-1 | Z-2 |
|---|---|---|
| $\mu_{\Delta}$ | 2.27 | 2.02 |

## Conclusion

(1) Hysteretic curves, skeleton curves, ductility factor can better reflect the specimen seismic performance;

(2) The longer of the duration high temperature lasts, the more serious material damaged. The damage phenomenon is more obvious;

(3) The duration of high temperature is the key indicator effect on seismic performance of the specimen.

## Acknowledgement

The projects of state Twelfth Five-Year science and technology plans( 2012BAJ11B02).

## Reference

[1] Qingwen Yang. Seismic behavior of reinforced concrete short columns after the fire[D]. Huaqiao university master's degree thesis, 2012.

[2] National Standard of China. Design of concrete structures GB50011-2011[S]. Beijing: Building industry press of China, 2011.

[3] Yu Zhang. Experimental Investigation on the seismic behaviors of seriously damaged reinforced concrete columns repaired [D]. Shenyang Jianzhu university master degree thesis,2011.

[4] Guofan Zhao. Reinforced concrete structures of higher School [M]. Press of machinery Industry,2008.

[5] Fengbin Li. Mechanical properties of concrete and frost resistance after fire[D]. Xi'an University of Architecture and Technology master's degree thesis, 2002.

[6] Priestley MJN, Verma R, Xiao Y. Seismic shear strength of reinforced concrete columns [J]. Journal of Structural Engineering, ASCE, 1994,120(8): 2310-2329.

[7] Boquan Liu. High axial compression ratio of high-strength concrete experimental study on seismic behavior of frame columns[J]. Journal of Civil Engineering, 2005.

*Applied Mechanics and Materials Vols. 580-583 (2014) pp 2675-2678*
*© (2014) Trans Tech Publications, Switzerland*
*doi:10.4028/www.scientific.net/AMM.580-583.2675*

# The analysis of hysteretic behavior of Concrete filled Double Skin Steel Tubular after exposure to fire

Xiao Liu[1 a,] Juntao Bao[1, b,] Bing Wang [1, c]

[1]School of Architectural and Civil Engineering, Shenyang University, Shenyang,Liaoning, 110044, China

[a]liuxiao19740701@sina.com,[b]992966224@qq.com, [c]489298344@qq.com

**Keywords:** Post-fire, concrete filled double skin steel tubular, Seismic performance, Hysteretic behavior, Displacement ductility.

**Abstract.** In recent years, frequent fires and earthquake make the buildings damage badly, and it causes huge economic loss. Concrete filled double skin steel tubular(Hereinafter referred to as CFDST)as a new member of structure, its mechanical properties are similar to concrete filled steel tubular, at the same time has better fire performance and seismic capacity. Based on this background, the paper expounds study the mechanical performance of CFDST is very important, the hysteretic behavior is the main mechanical indexes of the seismic performance of CFDST after exposure to fire. The study of it will fill the new component in the blank of seismic performance research.

## The research background of the project

Fire refers to the time or space out of control caused by combustion of the disaster, in our country fire happened frequent, and in recent years showed a rising trend, it happened up to 130000 per year on average, in current, our country building fire problem has also become a social problem, according to incomplete statistics, from 2000 to 2010, fire has happened 3237 times in high-rise building in total, more than 10000 persons lost their lives in fire, direct economic losses as high as 35.83 billion of yuan.In recent years, the frequent fires caused great loss to human society, such as on December 25, 2000, fire happened on dongdu commercial building of Luoyang, it has caused 309 deaths and 7 injured, on February 15, 2004, fire happened on zhongbai commercial building of Jilin province and it caused 54 people died(As shown in Fig.1 a), on December 25,2005, fire happen on Liaoyuan central hospital of Jilin province, which caused 40 people died, on November 15,2010, in Shanghai yuyao road jiaozhou road, there has fire happened on a high-rise building(As shown in Fig.1 b), this accident caused 58 deaths, on February 3, 2011, the dynasty in Shenyang wanxin fire accident caused property losses of 3 billion yuan(As shown in Fig.1 c), on November 28,2013, fire has happened on a "Asia's first covered bridge" which located in qianjiang of Chongqing (As shown in Fig.1 d), on the bridge, all wooden buildings were burned out, and this fire caused great economic losses.

In the same time , our country is a earthquake-prone country, China is in the Circum-Pacific seismic belt and seismic zone of the Himalayas, in our country, the earthquake greater than magnitude six happened four times per year on average, the earthquake greater than magnitude seven happened two times per three years on average, such as on July 28,1976,a magnitude 7.8 earthquake struck Tangshan of Hebei province, this accident caused 242000 people lost their lives and direct economic losses more than 10 billion yuan,( As shown in Fig.1 e), on May 28,2008,a magnitude 8 earthquake happened in Wenchuan county of Sichuan province, it caused 69172 and 374159 injured, and direct economic losses more than 14.08 billion yuan(As shown in Fig.1 f),on April 14,2010, a magnitude 7.1 earthquake happened in Yushu of Qinghai province, it caused 2220 people lost their lives, and direct economic losses more than a few billions of yuan.

With the development of economic and the acceleration of urbanization, the following thing is people to the requirement about functions and forms of architectural are continue to increasing, the structure on the ground towards to tall even super-tall, large span and complicated structure body development, the structure underground from the original layer toward multi-level, three-dimensional

development.In these towering structures, the length of the column will be increased, and become longer and thinner. When these towering structures want to withstand wind loads and relatively large horizontal seismic force, it requires the columns have a large horizontal bearing capacity and a good level of flexural rigidity[1].In the range of the medium long column the main factors that determine the bearing capacity of the column is the stability of the column. Its carrying capacity is mainly controlled by the stiffness. But neither the reinforced concrete nor the concrete filled steel tubular cannot be fully expressed their section bearing capacity of strength, and the CFDST have a very good flexural rigidity and a high bearing capacity, so the CFDST has a great advantage when it used in the filed of resistance to earthquake[2].

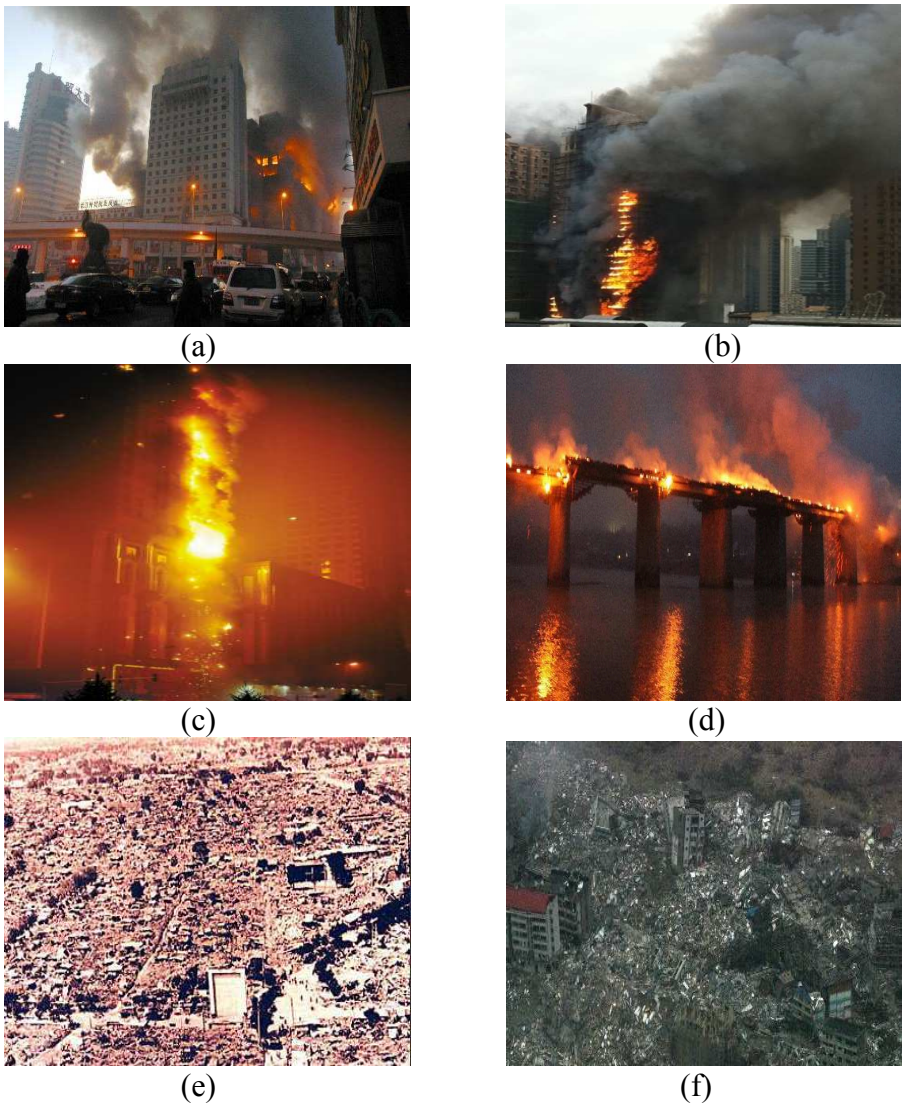

(a) (b) (c) (d) (e) (f)

Fig .1 Architectural disasters occur frequently

A fire in the high-rise building is increasing, it makes the analysis of hysteretic behavior of concrete filled double skin steel tubular after exposure to fire become a very challenging thing. After the fire, the structure also has a bearing capacity. So the research in hysteretic behavior of CFDST after exposure to fire and insure its mechanical properties such as strength, stiffness, ductility and energy dissipation capacity is very important.

**The characteristics of concrete filled double skin steel tubular**

CFDST refers to the two concentric placed between the steel tubes filled concrete composite structures, concrete filled double skin steel tubular is a new type of composite components which is developed on the basis of concrete filled steel tubular. Not only concrete filled double skin steel tubular has the laminate what concrete filled steel tubular has, such as, a high carrying capacity, good ductility, fire resistance, easy construction and good economic results[1]-[6], but also it has the advantage what the concrete filled steel tubular did not have.

**(1)Light weight and good earthquake resistance**

A large number of experiments and theoretical studies have show that under the condition of reasonable in design, CFDST has a greater carrying capacity than concrete filled steel tubular which has a same size and same cross, and concrete filled double skin steel tubular is a special hollow structure, in the case of same size, the weight of CFDST is lighter than the weight of concrete filled steel tubular and reinforced concrete, so in the practical application, we can design the CFDST which has a very high carrying capacity and good earthquake resistance.

**(2) Section unfold, flexural stiffness great**

The same weight of CFDST, because of its hollow structure, the section unfold is better. At the same time due to its section unfold, the flexural stiffness of CFDST become greater, if under the larger bending moment, it can give full play to the mechanical of materials, and it becomes more economic and reasonable.

**Conclusion**

So far research on mechanical properities of CFDST after exposure to fire and after high temperature have:In 2005, Yang Youfu, and Han Linhai [7] under the terms ISO-834 and GB/T9978-1999 standard temperature curve of CFDST columns under warming a study of the mechanical properties. In 2008, Yang and Han[8] study on mechanical properties of CFDST members after exposure to fire. In 2009 experimental research on mechanical properties of six circular CFDST after exposure to fire by Yuxin and Tao zhong[9]. To date on mechanical properties of CFDST was rarely report, and the hysteresis behavior of concrete filled double skin steel tubular after exposure to fire and after high temperature was not report, so it should research on hysteretic behavior of concrete filled double skin steel tubular after exposure to fire. In order to lay the foundation for application of CFDST in engineering practices.

**Acknowledgement**

It is a project supported by National Science Foundation (51308347) .

It is a project supported by colleges and universities in Liaoning Province Outstanding Young Scholar growth plans (21503040399).

**References**

[1] Hong Huang. Behavior of concrete filled double-skin steel tubular beam-column[D]. Fuzhou, Fuzhou univorcity,2006.

[2] Xuejia Chen, Hong Huang, Chen Huang. Study on the model of hysteretic behavior of concrete rete-filled double skin (CHS inner and CHS outer) steel tubular beam-column[J]. Railway Construction,2011,141-144.

[3] Lin-Hai Han, Zhong Tao, Hong Huang, Xiao-Ling Zhao. Concrete-filled double skin (SHS outer and CHS inner) steel tubular beam-columns [J]. Thin-walled Structures, 2004,42(9): 1329 -1355.

[4] Lin-Hai Han. Concrete filled steel tube structure—theory and practice[M].Beijing, Science Press,2006.

[5]Johnson R P. Some research on composite structures in the U. K. 1960-1985. Proc. of an Engineering Foundation Confer. on Steel-Concrete Composite Structures, ASCE. Irsee, 1996. 15-25.

[6]Roik E H K. Review of the development of composite structures in Germany. Proc. of an Engineering Foundation Confer. on Steel-Concrete Composite Structures, ASCE. Irsee, 1996. 55-74.

[7]Youfu Yang, Lin-Hai Han. Fire behavior of concrete-filled double skin (CHS inner and CHS outer) steel tubular columns[J]. Journal of Harbin Institute of Technology,37(S1),2005:400-403.

[8] Yang Y F, Han L H. Concrete-filled double-skin tubular columns under fire [J].Magazine of Concrete Research,2008, 60(2):211-222.

[9]Xin Yu, Zhong Tao. Residual strength of concrete-filled double skin steel tubular stub columns after exposure to fire[J]. Industrial building,39(4),2009:9-13.

*Applied Mechanics and Materials Vols. 580-583 (2014) pp 2679-2685*
*© (2014) Trans Tech Publications, Switzerland*
*doi:10.4028/www.scientific.net/AMM.580-583.2679*

# The Construction of Emergency Logistics System Framework and Information Platform System

Weike Chen[1, a], Cui Hua[2, b]

[1] School of Management, Tianjin University of Technology, Tianjin, 300384, China

[2] School of Management, Tianjin University of Technology, Tianjin, 300384, China

[a]chenweike7@163.com, [b]975509985@qq.com

**Keywords:** Emergency; Emergency logistics; Emergency Logistics System; Information Platform System

**Abstract.** This paper, based on the analysis of the characteristics of emergency logistics and the problems existing in its development, proposes hierarchical structure and the basic framework of the emergency logistics system, and explains the specific content of each subsystem. In addition, this paper constructs intelligent and multilevel collaborative information platform system, which is oriented to the emergency logistics system, and expounds its main functions to provide technical support for the operation of emergency logistics system.

## Introduction

With the rapid development of modern society, all kinds of emergencies happen more and more frequently. In general, emergencies have many characteristics such as suddenness, urgency, uncertainty, severity of consequences [1]. The outbreak of the emergencies tends to produce large amounts of aid needs. In dealing with the emergency, logistics has played a vital role, and if an emergency is mishandled, it will have large negative effects on economic and social life. Whether emergency logistics system can guarantee the need of relief supplies in time will directly affect the efficiency of emergency disposal. The frequent occurrence of emergency makes logistics management become a research focus in the social management, and the research on emergency logistics has become a new field.

When all kinds of public emergencies occur, it is an urgent and critical task, in the first time, to deliver appropriate quantity and quality of emergency supplies to destination in a reasonable way, which has a great significance to guarantee the safety of people's lives and property, quickly return the country to the normal order of social life, reduce all kinds of losses and minimize the negative impact on the social economy and politics as far as possible. In the practice of dealing with all kinds of major emergencies, China has had a certain support capability of emergency material. But in most cases, it is difficult to ensure the supply of emergency materials in the first time as a whole. The reason is mainly due to the construction of emergency logistics system lags behind [2]. The degree of development and improvement of emergency logistics system directly determines the support capability of emergency supplies, and the lag of construction of emergency logistics system is shown as: the relative lag of infrastructure construction, the organizational mechanism is not perfect, serious shortage of emergency logistics companies, emergency materials reserve system is not reasonable, etc.

Responding to emergencies has to enable emergency logistics. Emergency logistics system is an open complex giant system, and provides powerful support for emergency management. Only through the bridge of logistics can emergency supplies provide uninterrupted supply of materials for on-site assistance. Emergency logistics is an important force in national security system. When emergencies occur, they need a lot of emergency supplies within a short time, which largely depends on the capability of emergency logistics. Perfect emergency logistics system can continuously supplement consumption of relief materials, restore the relief strength, and it gradually becomes an important force in the national security system [3]. In order to promote the construction and development of emergency logistics in China, we must strengthen systemization, standardization and informatization in the construction of emergency logistics.

This paper, based on the characteristics of emergency logistics and the problems in its development, puts forward Chinese emergency logistics system framework, in order to realize the optimal allocation of social resources and improve the efficiency of the operation of emergency logistics. At the same time a kind of intelligent information platform system is proposed for the system, providing technical support for the emergency logistics system.

## The concept and basic characteristics of emergency logistics

### (1)The concept of emergency logistics

Emergency logistics is a special logistics activity, which can meet the urgent needs of emergency goods and materials, personnel and funds in response to sudden natural disasters, public health events, public security events and military conflicts and other emergencies, in order to pursue the greatest time benefit and the least loss of disaster[4].

Emergency logistics system is a complex giant system, which is composed of all kinds of subsystems, and every subsystem has mutual contacts and interactions, in order to complete the task of emergency logistics [5].

### (2)The characteristics of emergency logistics

1) Strong timeliness

The most prominent feature of emergency logistics, triggered by unexpected incidents, is the timeliness of the logistics activity. A large number of emergency supplies must be quickly delivered to where needs in a very short period of time. Due to the requirement--strong timeliness of the emergency logistics, the operation mechanism of general logistics is difficult to meet the needs in the state of emergency logistics [6].

2) Unpredictability

Emergency leads to uncertainty of emergency logistics in flow direction (the spatial distribution of the supply and demand places), and quantity of flow (the amount and type of emergency supplies). So it is difficult to predict emergency logistics demand accurately, and the emergency logistics system cannot make plan in advance.

3) Diversity of demand

After the incident, a lot of emergency materials, from special rescue equipment, medical equipment, communications equipment to articles for daily use, are needed in a short period of time. At the same time, the deterioration of logistics environment is often associated with emergencies. In addition to needing to complete the required items in time, the items also need to be delivered timely, which is a very serious test for emergency logistics system.

4) Weak economy

General logistics system emphasizes that effective management can help achieve the best economic benefit, so it makes efforts to reduce costs on the premise of guaranteeing service quality. While the emergency logistics system has the characteristic of weak economy, then it pays more attention to public welfare, and focuses on the social benefit. Therefore, in many cases, emergency logistics obtains the logistics benefit through the realization of the efficiency of logistics.

## The existing problems in the development of emergency logistics

The development of emergency logistics in China is still in its infancy, our country passed 《Emergency Response Law of the People's Republic of China》 in 2007, and in 2009 《Logistics Industry Restructuring and Revitalization Plan》 was issued by the State Council, which lists the construction of emergency logistics as one of the nine key projects[7]. In recent years, the government and the society gradually realize the importance of emergency logistics.

But various emergencies that happened in recent years in our country, such as the South Snow Disaster, Wenchuan Earthquake, Yushu Earthquake, exposed that the emergency logistics system exists many problems in China.

(1) Insufficient predictability. It manifests that the supply of relief materials cannot meet the demand, causing serious imbalance between supply and demand.

(2) Lack of a unified command. No professional and dedicated permanent emergency organs in China, hence there lacks unified management and control in emergency logistics management.

(3) Departing from market. When emergency occurs, the government is responsible for forming a temporary emergency organization, without making full use of existing logistics enterprises in the market.

(4) Informatization level is relatively low. Our country has not yet set up a sound information platform system for publishing and sharing information, causing that the source of information is not detailed and the information is reported not timely, and affecting the efficiency of the operation of emergency logistics.

## The construction of emergency logistics system framework

Systematism is one of the core ideas of emergency logistics, namely global optimization. To make the whole emergency logistics system form a large system that can run efficiently, we should, from an overall point of view, coordinate construction and development of emergency logistics. Emergency logistics system is a new strategy for emergency physical management. There are three kinds of flow--fund flow, material flow and information flow-- in the process of emergency logistics, and the three flows are integrated together in the larger sense. By the optimal allocation of internal resources, the system achieves global and dynamic optimization.

**(1)The principles of the construction of emergency logistics system**

On the basis of summarizing the results of previous studies, we get the corresponding principles in the construction of emergency logistics system. These principles are shown in Table 1.

Table.1 The principles of the construction of emergency logistics system

| | principles | details |
|---|---|---|
| 1 | leading by government, civil-military integration | The system should be led by government, and make full use of the two systems: the military logistics and the local logistics |
| 2 | focus on the emergency, balance at ordinary and urgent times | Not only meet the demand of emergency, but also achieve normalized construction of emergency logistics, then balance urgent time with peacetime. |
| 3 | on the basis of existing , use while building | Integrate the existing resources, improve the ability and level of emergency, and use while building. |
| 4 | improve efficiency, focus on economic costs | Emergency logistics has the characteristic of weak economy, so we should pay attention to the social and economic benefits while improving the emergency capability. |
| 5 | from a global perspective, demand-oriented | From an overall point of view, we take the demand of responding to emergencies as direction, promoting the systematism development of emergency logistics. |

The construction of emergency logistics system takes emergency needs as direction, which is based on advanced information technology, takes modern logistics technology as support, takes administrative system, laws and regulations and public policy as the background, to build integrated, high efficient and fast logistics system. The details of the hierarchical structure are shown in Figure 1.

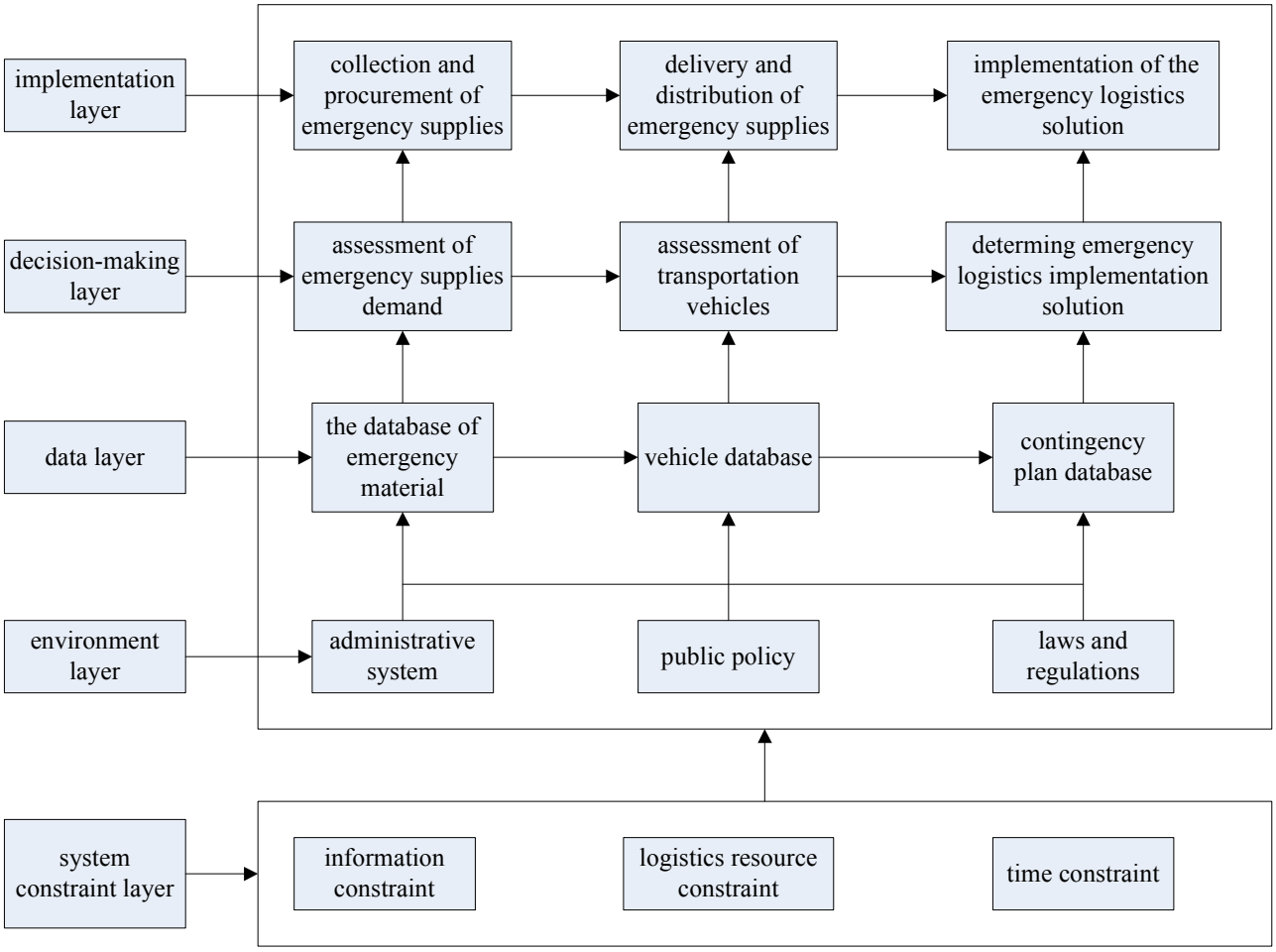


Fig. 1 The hierarchical structure of the emergency logistics system [8]

**(2)The constraints of emergency logistics system**

In the construction and operation of emergency logistics system, many objective conditions limit the realization of the goals of emergency logistics system. The main constraints are as follows: 1) Information constraint. Due to the uncertainty of emergency, it is difficult to get the full grasp of demand information of emergency logistics in a short time, thus possibly resulting in mistakes in prediction and decision-making. 2) Logistics resource constraint. Resource constraints include many aspects, such as material resources, transportation resources, and infrastructure resources. 3) Time constraint. Emergency logistics task should be implemented in a certain time, otherwise it will affects the efficiency of emergency logistics management.

**(3)The composition of the emergency logistics system**

The composition of this system includes emergency supplies subsystem, organizational subsystem, command subsystem, information subsystem, distribution subsystem and support subsystem, which are related to and constrained by each other, as shown in Figure 2. Every subsystem is an important part of the emergency logistics system, and play a key role in distributing emergency supplies accurately and timely and reducing emergency logistics cost.

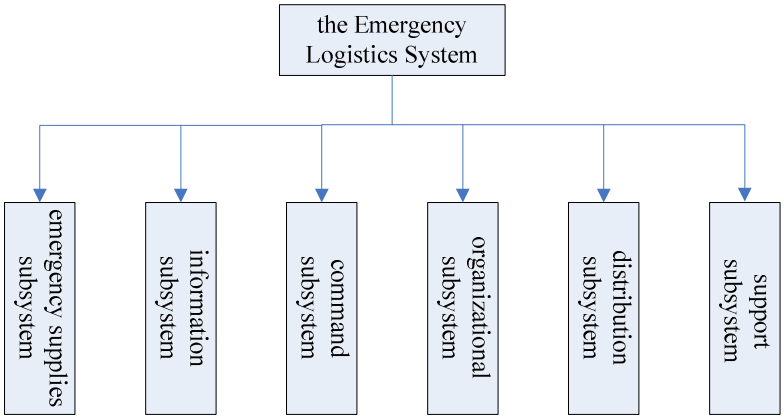


Fig. 2 The composition diagram of emergency logistics system

1) The emergency supplies subsystem. It, as the object of action of the emergency logistics system, is composed of breed structure, quantity and scale, layout form, production capacity, existing state of emergency supplies and other related elements. At present, a reasonable scale of emergency supplies reserves is of great significance for the construction of emergency supplies system. We should follow "the state, the army, the local, market and family" this reserve form to build emergency materials reserve system.

2) The information subsystem of emergency logistics. Information subsystem should be established and keep close contact with command center, even with each subsystem, relevant government departments, and logistics enterprises who takes part in. And in this way it can improve the timeliness and effectiveness of commanding and decision-making of emergency logistics. In addition, the system is an effective channel for the government to publish official news and the masses to provide feedback information.

3) The command subsystem of emergency logistics. Command subsystem refers to a special logistics command center in the government's response to various emergencies, which is established to make good preparations for raising, scheduling, distributing, transporting emergency supplies and other work. Our country should, according to the structure of government and the process of logistics operation, establish a permanent and professional emergency command center, which is dedicated to rescue as an important guarantee for the efficient operation of the emergency logistics.

4) The organizational subsystem of emergency logistics. It should be composed of four elements: decision-making body, emergency response administration, monitoring organization, executing agency.

5) The distribution subsystem of emergency logistics. The ultimate achievement of the goals of emergency logistics system depends on whether the emergency supplies are delivered directly to disaster area timely and accurately. We constantly consider that under both these aspects: the government signs agreements with the domestic professional logistics enterprises in the form of market and gets their help, ultimately integrates social resources effectively; A new emergency logistics mode, namely civil-military logistic integration, should be applied to optimize the allocation of resources.

6) The support subsystem of emergency logistics. It includes infrastructure support and legislative guarantee. We should strengthen the legislation of emergency logistics, to make settlement body, responsibility and power distribution and the source of funds more clear when an emergency occurs. The laws for emergency logistics management can help ensure that emergency logistics moves in the right direction.

**The information platform system of emergency logistics**

**(1)The structure of information platform system**

Building a good information platform system is the key to the construction of emergency logistics system, and the premise of ensuring efficient operation of emergency logistics system. In our country, there is not a good emergency logistics information platform system, and information-based level is

low, causing information transferred irregularity. Based on the emergency needs and the needs of logistics cooperation, this paper proposes the overall framework of information platform system. In this way, we can activate the emergency logistics system through the information technology and then realize the information sharing and collaborative communication among different participants. The structure of the information platform system is shown in Figure. 3.

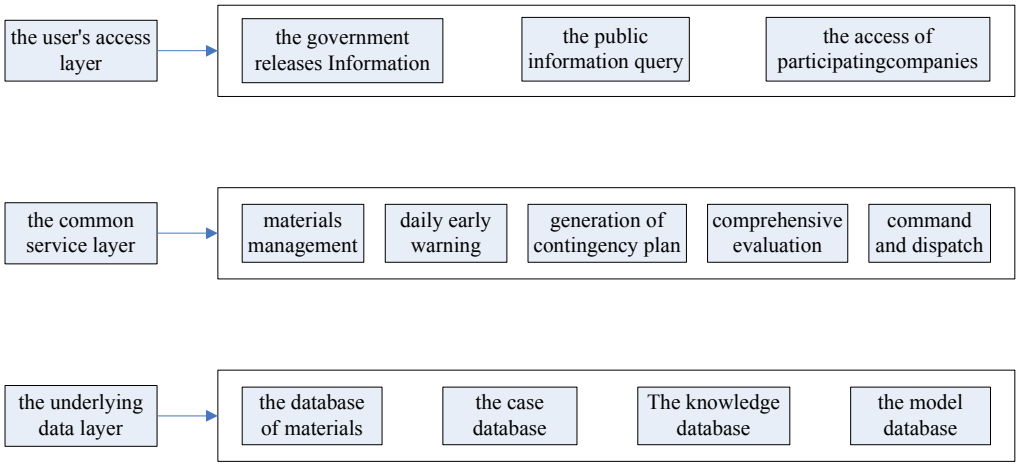


Fig. 3 The structure of information platform system [9]

**(2)Functions of information platform system**

The public information platform system of emergency logistics is divided into underlying data layer, the common service layer, the user's access layer, the three layers are joined together and interact with each other, and they have many functions as the follows:

1) It can collect the supply and demand information of emergency logistics, and achieve accurate perception of emergency logistics demand.

2) The second one is making this information platform system, the existing public logistics information platform and commercial logistics information platform be linked into network, to integrate the emergency logistics resources effectively.

3) It matches emergency logistics participants with relevant information, such as the manufacturer and the demander of emergency supplies, logistics center and logistics enterprise which joins in, in order to avoiding unbalance between supply and demand of emergency supplies and capacity.

4) It can provide useful information of decision-making and supervision for leaders at all levels of emergency logistics, which helps manage the collection, transportation, warehousing, distribution of emergency supplies effectively in the process of the whole operation.

5) It also provides real-time information for relevant departments, such as earthquake, meteorology, health and epidemic prevention and transport departments, which helps to improve the relationship with other subsystems of emergency logistics.

6) The information platform system, as the effective channel for emergency management department to release information to the public timely and the masses to provide real-time feedback information, on the one hand improves the efficiency of the emergency logistics, on the other allows the functions of emergency logistics management system into full play.

## Conclusion

Based on the in-depth analysis of the characteristics of emergency logistics and the existing problems in its development in China, this paper puts forward the hierarchical structure of emergency logistics system, and builds its integrated framework. Then an intelligent and multilevel collaborative information platform system oriented to the emergency logistics system is constructed. This research promotes the systematization and informationization development of emergency logistics management, and provides theoretical references for realizing spatial information service resources share and interoperation. Finally it achieves efficient allocation of social resources in the process of emergency logistics management.

**References**

[1] Li He, Bingyuan Lu: Urban Problems. (2011), p.70-73 (in Chinese)

[2] Jigang Wei, Yuan Zhang: China Business and Market. (2009), p.15-17 (in Chinese)

[3] Zeneng He, Xiong Zuo, Changgui Guan, Yong Mei: Science and Technology Management Research. (2010), p.110-115 (in Chinese)

[4] Kunpeng Jing, Zhijie Song: Science and Technology Management Research. (2009), p.59-62 (in Chinese)

[5] Zongxi Wang: China Business and Market. (2009), p.20-22 (in Chinese)

[6] Chuanping Song: China Business and Market. (2011), p.21-24 (in Chinese)

[7] Information on http://www.gov.cn/zwgk/2009-03/13/content_1259194.htm

[8] Xuping Wang, Kejun Fu, Xiangpei Hu : China Soft Science. (2005),p.127-131(in Chinese)

[9] Jinlou Zhao, Yingzhao Wang: Science and Technology Management Research. (2009), p.357-360 (in Chinese)

*Applied Mechanics and Materials Vols. 580-583 (2014) pp 2686-2693*
*© (2014) Trans Tech Publications, Switzerland*
*doi:10.4028/www.scientific.net/AMM.580-583.2686*

# Vulnerability Assessment of Truss Structure Based on Strain Energy and Damage Scenarios

Yan XU[1, a], Xian-cai YU[1,b] and Wei-bin LI [1,c]

[1] Schoolof Civil Engineering, Southeast University, Nanjing 210096, China

[a]xuyan0909@gmail.com, [b]905324418@qq.com, [c]liwb@seu.edu.cn

**Keywords:** vulnerability assessment; strain energy; damage demand; local damage; damage scenario.

**Abstract.** The method of structural vulnerability assessment presented in this paper is closely in accordance with the definition based on two aspects, strain energy of structure and damage demand of members. The search process of damage scenarios was carried out by an example of truss structure, and the results of analyses included importance factor of members, damage scenarios with the minimum number of killed members, and local damage occurred in advance. The influence of loading on member importance factor and vulnerability index was discussed and it showed that though with the agreement of general trend, the rank of importance factor or *VI* index under a specified scenario varied greatly. The analysis could be utilized as the proof of measures to enhance structural capacity to meet the extreme event.

## Introduction

With the maturity of structural design principals and the development of advanced computational tools, engineers have more and more knowledge about structural performance, while they still face huge challenges in structural design due to some manmade extreme accidents or terrorist attacks.

Generally, the property that disproportionate damage occurs easily in the structure under extreme events is regarded as the vulnerability, which is the opposite of robustness. Currently researchers have proposed several methods to evaluate the vulnerability of a structure which could be roughly divided into two categories [1], 1) based on structural attributes, 2) based on structural performance. Researchers from University of Bristol [2] proposed assessment method based on structural topology among which structures are regarded as the combination of rings and clusters, and the influence of structural formation under different damage scenarios was utilized to identify the weak point. Ye etc. [3] proposed an index, Generalized Stiffness ($K_{stru}$) with loads in consideration to give structural assessment, which was based on both the stiffness matrix and loading condition, and reflected the ability of structural deformation under specified loads. The methods based on structural performance include deterministic and probabilistic method. Among the deterministic methods, bearing capacity of the system[4, 5], the development level of damage[6], structural deformation energy[7] were selected as the assessment index while the probability of structural failure[8] and the risk [9]are more common utilized in probabilistic methods.

Without consideration of loading distribution path, methods proposed from the structural topology or stiffness matrix for structural vulnerability assessment did not reflect accurately the influence of members on stress redistribution. Structural vulnerability has close link to structural attributes and geometric topology while structural damage shows different patterns under different loading conditions. Currently no assessment index or method has reached general consent among the world though a bunch of scholars have conducted researches on the identification of weak point and significant member among the system.

The method proposed in this paper is based on the strain energy of the system as well as the damage demand under different damage scenarios. Member removal is utilized to simulate the member failure while the selection of damaged members is arbitrary combination to consider the random of initial failure under extreme events. The strain energy in critical condition is normalized by

strain energy under normal loading condition which is regarded as structural performance parameter, and the damage demand is defined as the work done to destroy isolated member. Among single member removal scenarios, the normalized strain energy reflects the member significance; among multi-member removal scenarios, significant members and weak part in the system is obtained through comparison of vulnerability index under different damaged scenarios while regression to geometric mechanism is regarded as structural failure.

**Vulnerability Assessment Method**

The method proposed in this paper is based on the assumptions following:

1. The initial failure is replaced by member removal while the subsequent failure development is regarded as the internal force redistribution among different members.

2. The loads are assumed as the normal loading combination under the service period without change after the initial failure. The force caused by member drop or impact is not considered in this paper as well as the dynamic influence of forces.

3. The structure is assumed as the conservative system without energy dissipation.

Among the conservative system, the work done by the external force is transformed totally to the structural strain energy. The external force is denoted by $\{F\}=F_{max}\{v\}$ in which $F_{max}$ is the maximum value in force vector and $\{v\}$ is the force distribution vector. The work done by the external force is,

$$W_{ext}=U_{sys}(F)=\sum U_i=\sum\int U_i^d(F)dV \tag{1}$$

where $U_{sys}(F)$ denotes structural strain energy and $U_i^d(F)$ denotes strain energy of member I under loading $F$.

In this paper, structural strain energy is obtained from finite element analysis realized in the FE software ANSYS. The material attribute is defined as bilinear model to consider both elastic and plastic deformation. The first load step is specific to the intact structure while the damaged members are killed in the second load step. The strain energy is normalized as,

$$E_r=\frac{E_{sys}^d-E_{sys}^0}{E_{sys}^d}=1-\frac{E_{sys}^0}{E_{sys}^d} \tag{2}$$

where $E_{sys}^d$ is for the damaged system and $E_{sys}^0$ is for the intact system.

The normalized strain energy could reflect the structural performance under a specified damage scenario. The structure has better performance and is less vulnerable to this damage scenario if $E_r$ is small. When $E_r$ is less than zero, it shows that the structure is stable enough.

Currently most evaluation methods are designed to identify the sensitivity to initial failure by comparing the performance of a single structure under different scenario while they seldom could be applied to the performance comparison of different structures. England etc. [10] built the risk level map under damaged scenarios, which realized the generalization of vulnerability assessment.

Different structures have different level of redundancy according to structure importance level. If $E_{sys}^0$ for the intact system is defined as the loading condition of normal loads $\{F\}$, the critical point at the boundary in the risk level map will be different for a specified system due to different level of initial redundancy. It is proper to define $E_{sys}^0$ as the strain energy under a limit state which could be applied to any structure.

During the service period, the stress of member in the truss meets the following requirement,

$$\begin{aligned}&\beta_i^+=\sigma_i^+/\sigma_i^0\le 1.0\\&\beta_i^-=\left|\sigma_i^-\right|/\left(\mu_i\sigma_i^0\right)\le 1.0\end{aligned} \tag{3}$$

where $\beta_i$ is the stress factor, $\sigma_i^0$ is the ultimate tension stress and $\mu_i$ is the stability coefficient under the compression. In this paper, $E_{sys}^0$ is specified in the limit state that the maximum $\beta_i$ of all the members in the system reaches 1.0.

The damage demand is a measure of the effort required to create a deteriorating event, where a deteriorating event is the result of actions which would cause damage to the structure. The damage demand is the actual work causing failure of a member under a specific limit condition like buckling,

tension or bending, and the measure from the member level is determined from the area under the force v.s. the displacement curve.

The damage demand is normalized as,

$$D_r = \frac{D^f}{D^{sum}} = \frac{\sum D_i^f}{\sum D_j} \tag{4}$$

where $D^{sum}$ is the sum of actual work required for failure for all members included in the structure, $D^f$ is the sum of actual work required for failure for all damaged members in a specified damage scenario. The value of $D_r$ is among 0 and 1, while $D_r = 0$ represents no failure member and $D_r = 1$ represents that all members are failed initially.

The damage demand of a single member is obtained from finite element analysis in the FE software ANSYS. The process is that 1) build the member model pinned at both ends, and apply compression force, 2) define the critical state as that the deflection at the middle point reaches 1/200 of the whole member length, and 3) calculate the actual work done at the critical state.

From the definition of structure vulnerability, we could predict that the vulnerability index should be higher if the structural performance is greatly sensitive to the local failure. The vulnerability index is in direct proportion to structural strain energy while it is inversely proportional to damage demand. Based on this, the vulnerability index is defined as,

$$VI = \frac{E_r}{D_r} \tag{5}$$

where $VI$ is the vulnerability index, $D_r$ is the normalized damage demand, and $E_r$ is the normalized strain energy. If $VI$<0, it means that the initial failure is under the redundancy rate.

## Searching of Damaged Scenarios

The initial local failure could cause the change in loading distribution and structure performance, and the structure will undertake progressive failure if current loading is out of the bearing capacity of the damaged system. The combination of initial damaged members is regarded as damage scenario and among each scenario sequence of member failure is out of consideration.

For the truss structure, the system failure could be defined as the loss of geometric stability. That means in truss structure the determinant of stiffness matrix for the damaged system is below zero.

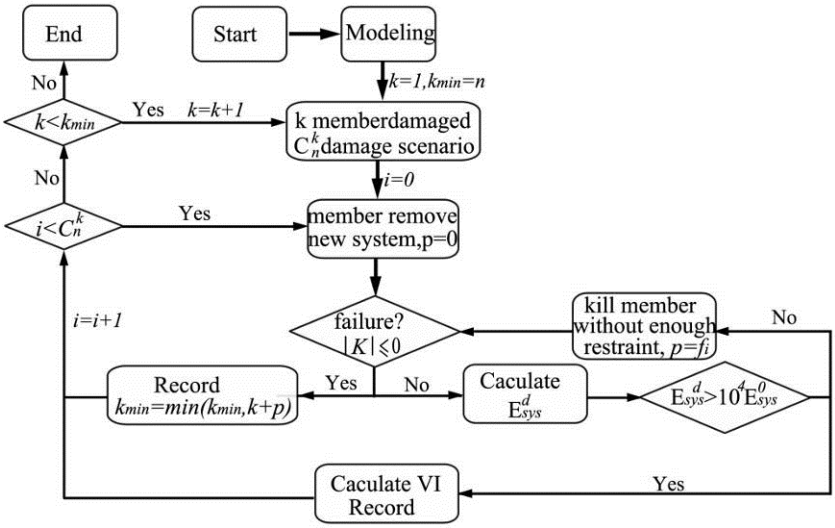


Fig. 1 Searching process of damage scenarios

The searching process is illustrated in Fig. 1, and the main steps are as follows,

1. Build the finite element model in ANSYS, find the specified limit state and calculate $E_{sys}^0$,

2. Define the initial value, $k$=1, $k_{min}$=$n$ (the total number of members included in the truss),

3. Remove the members failed in the damage scenario $i$, and set the number of members without enough constraint $p$=0,

4. Calculate the stiffness matrix of the damaged truss, and judge the geometric stability,

a) if the *det*(K)>0, calculate the strain energy of the damaged truss. Judge whether the value of $E_{sys}^{0}$ is abnormal (extreme large); if $E_{sys}^{d} > 10^{4} E_{sys}^{0}$, kill the member without enough constraints, and re-judge the geometric stability; else calculate the vulnerability index VI, and record the combination of damaged members followed by a new start ($i$+1).

b) if the *det*(K) ≤0, record the combination of damaged members and damaged members in the shortest failure path is $k_{min}$=min($k_{min}$, $k$+$p$).

5. When $i$ reaches $C_n^{k_{\min}}$, the searching reaches the end.

## Example

The structure analyzed in this paper is a 2-storey, 2-bay plane truss in reference [10]. The geometric model and member number are illustrated in Fig. 2, and the member section attributes and damage demand of each member are in Table 1.

The loads are from Reference [11]: DL=3.0 $kN/m^2$, LL=2.0 $kN/m^2$, and for the static analysis, the vertical load set is Load=2(DL+LL), a bit higher than the designed loads. For the beam, the loading width out of the plane is 4 m and the external force is illustrated in Fig. 3.

Table 1 Section of members and damage demand

| Type | No. | Length | Area | $I_{yy}$ | $I_{zz}$ | Stability | $Pu$ | Damage Demand |
|---|---|---|---|---|---|---|---|---|
| Column | 1-6 | 3 | 19.82 | 812 | 89.7 | 0.270 | 181 | 277.8 |
| Beam | 7-10 | 4 | 54.51 | 6490 | 677 | 0.395 | 692 | 1782.6 |
| Brace | 11-18 | 5 | 19.82 | 812 | 89.7 | 0.130 | 64.6 | 114.8 |

Note: the type is just the division from the member position, while each member is pinned at both sides.

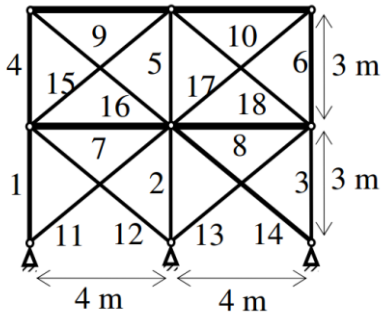


Fig. 2 An example of 2-bay plane truss [10]

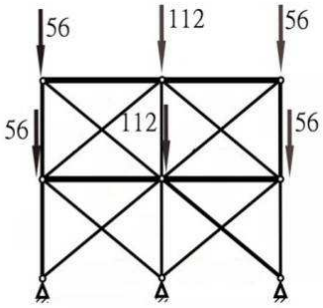


Fig. 3 Loads in the truss (unit: kN)

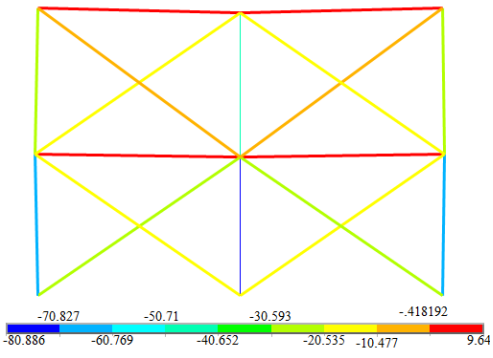


Fig. 4 Stress diagram under critical state (intact)

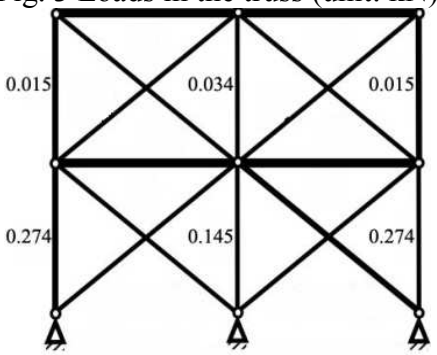


Fig. 5 Member importance factor $E_r$

Note: for uncharted members, $E_r$ is close to 0.

In order to find the specific loading state to calculate $E_{sys}^{0}$, gradually increase the force vector in the truss until the maximum stress index reach 1.0. While reaching the critical state, the principle stress is illustrated in Fig. 4. In the critical state, the compression stress of middle column at the 1st floor reaches 80.9 MPa, ranking 1st among all the members, while the load index is 1.16 and the strain energy is 3.57e-2$J$.

### Importance Factor of Members

The normalized strain energy $E_r$ under single member removal scenario reflects the importance of the member. The member with a higher $E_r$, is more important in the intact system and has a bigger influence on the structural performance; When $E_r$ is close to zero, the removed member is less important to the structure and the damaged system is safe enough. The member importance factor is illustrated in Fig. 5 and it shows that 1) the 1st-floor side column has the largest contribution to structural performance followed by the 1st-floor middle column, 2) the importance of the 2nd-floor column is less than that of the 1st-floor column, 3) after the removal of a single member like a beam or a brace, the influence on the structural performance is not that obvious and the damaged structure is still safe enough. Table 2 shows the change of principal stress in several members after the removal of the 1st-floor side column ( Member No. 1): the largest compression stress is existed in the 1st-floor middle column reaching 100.4MPa; compression stress in another 1st-floor side column ( Member No. 3) decreased from 63.2MPa to 25.7MPa.

Table 2 Principal stress change after the removal of Member No. 1

| Member No. | Principal stress in intact | Principal stress in damaged |
|---|---|---|
| 1 | -63.230 | -- |
| 2 | -80.886 | -100.380 |
| 3 | -63.230 | -25.469 |
| 4 | -30.445 | -16.623 |
| 5 | -45.619 | -62.143 |
| 6 | -30.445 | -14.794 |

Table 3 Analysis result of damage scenario ($k$=2)

| Scenario No. | Member Set | $E_r$ | $D_r$ | $VI$ |
|---|---|---|---|---|
| 2-1 | (1,12)/(3,13 | 0.62 | 0.040 | 15.46 |
| 2-2 | (1,11)/(3,14) | 0.45 | 0.040 | 11.370 |
| 2-3 | (5,15)/(5,18 | 0.45 | 0.040 | 11.197 |
| 2-4 | (2,3)/(1,2) | 0.58 | 0.057 | 10.211 |
| 2-5 | (3,5)/(1,5) | 0.55 | 0.057 | 9.736 |

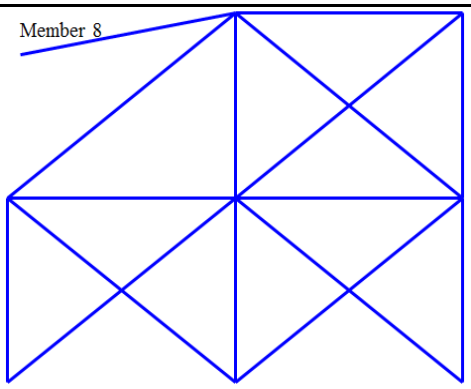


Fig. 6 Local mechanism in damage scenario (4,16)

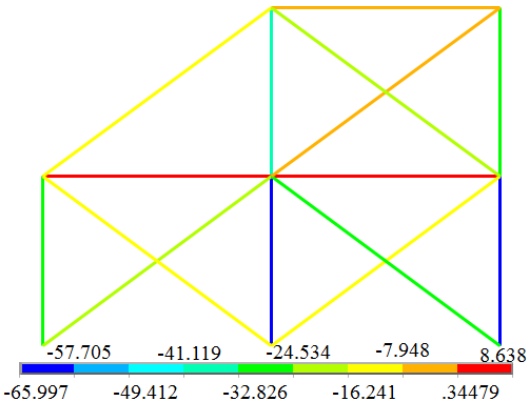


Fig. 7 Principle stress of the residual system after the removal of member 8

### Damage Scenario with the Initial Failure of Two Members

Among damage scenarios with the failure of two members, the local mechanism is existed when removing members linked 2nd floor side node, including removal member set (4,9), (4,16), (9,16) or the symmetric (6,10), (6,17), (10,17). In the damage scenario with removal member set (4,16), member 8 does not have enough restraint showed in Fig. 6. If considering the influence of local mechanism like the dropping of member and additional loads, it is hard to predict the structural safety. If the influence of local mechanism is out of consideration, the residual system works well after the removal of member 8, and the principle stress figure is showed in Fig. 7.

Among other damage scenarios with the failure of two members, when $E_r$ is larger than the maximum member importance factor (0.274), the removed members must include at least one member 1, 2, 3, 5(1st floor column, 2nd floor middle column). Table 3 gives the 5 most vulnerable scenarios among 2-member failed scenario: the first three scenarios are member set of column and brace while the 4th and 5th scenarios is member set of two columns.

### Damage Scenario with the Initial Failure of Three Members

Among damage scenarios with the failure of three members, a new local mechanism is existed in the 2nd floor middle node. As showed in Fig. 8, when removing member set (5,15,18), member 9, 10 lack enough restraint. If the removal of member 9, 10 has no side influence on the residual system, it works well and the principle stress figure is in Fig. 9.

Among other damage scenarios with the failure of three members, the 15th most vulnerable scenarios showed in Table 4, are the member set of (2 columns+1 brace) or (1 columns+2 brace) while the initial failed members do not include any beam member; the 6th most vulnerable scenarios are the member set of (1st floor side column + 2 braces).

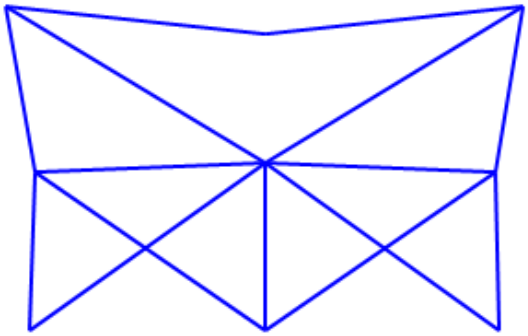

Fig. 8 Local mechanism in damage scenario (5+15+18)

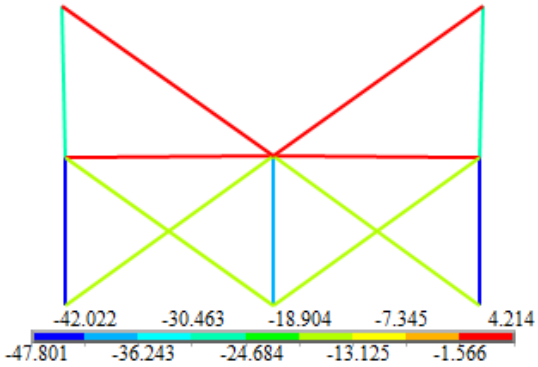


Fig. 9 Principle stress the residual system

Table 4 Analysis result of damage scenario ($k$=3)

| Scenario No. | Member Set | $E_r$ | $D_r$ | $VI$ |
|---|---|---|---|---|
| 3-1 | (3,13,17)/(1,12,16) | 0.704 | 0.052 | 13.476 |
| 3-2 | (1,12,17)/(3,13,16) | 0.703 | 0.052 | 13.459 |
| 3-3 | (3,11,13)/(1,12,14) | 0.683 | 0.052 | 13.087 |
| 3-4 | (1,11,12)/(3,13,14) | 0.678 | 0.052 | 12.981 |
| 3-5 | (3,13,15)/(1,12,18) | 0.654 | 0.052 | 12.514 |
| 3-6 | (3,13,18)/(1,12,15) | 0.653 | 0.052 | 12.511 |
| 3-7 | (2,3,14)/(1,2,11) | 0.858 | 0.069 | 12.438 |
| 3-8 | (5,15,17)/(5,16,18) | 0.636 | 0.052 | 12.179 |
| 3-9 | (1,2,12)/(2,3,13) | 0.836 | 0.069 | 12.117 |
| 3-10 | (3,12,13)/(1,12,13) | 0.625 | 0.052 | 11.972 |
| 3-11 | (3,5,13)/(1,5,12) | 0.815 | 0.069 | 11.805 |
| 3-12 | (3,12,14)/(1,11,13) | 0.583 | 0.052 | 11.166 |
| 3-13 | (4,5,15)/(5,6,18) | 0.721 | 0.069 | 10.446 |
| 3-14 | (5,15,16)/(5,17,18) | 0.533 | 0.052 | 10.215 |
| 3-15 | (2,4,15)/(2,6,18) | 0.696 | 0.069 | 10.083 |

### Damage Scenario with the Initial Failure of Four Members

The truss is 4th statically indeterminate structure, so a bunch of damaged structures after the removal of four members lose the geometric stability and the index $VI$ goes to infinity. Some failure scenarios are listed in Table 5. For member set 4-1 (1,2,11,12), the deformation of new system is showed in Fig. 10, and the system is going to collapse.

### Influence of Load Distribution

A specified member has different contribution to the bearing capacity of the structure under different loading conditions, and the level of loading re-distribution is different as well. So it is necessary to

discuss the difference of vulnerability index under different loading conditions. The load set mentioned in the previous section is defined as LS1, while the load set of LS2 is illustrated in Fig. 11.

Table 5 Damage scenario ($k$=4)

| Scenario | Member Set | Scenario | Member |
|---|---|---|---|
| 4-1 | (1,2,11,12) | 4-6 | (1,5,7,17) |
| 4-2 | (1,2,11,13) | 4-7 | (1,5,15,18) |
| 4-3 | (1,2,12,14) | 4-8 | (1,7,9,12) |
| 4-4 | (1,5,6,7) | 4-9 | (1,7,9,15) |
| 4-5 | (1,5,7,10) | 4-10 | (1,9,12,15) |

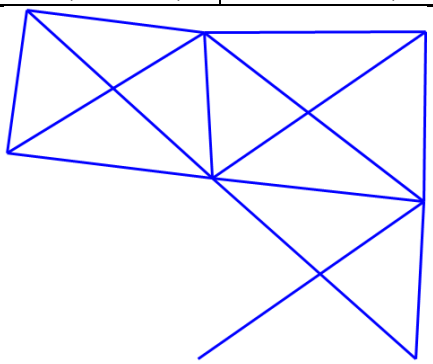

Fig. 10 Deformation of new system under member set 4-1

Table 6 Comparison of importance factor

| LS1 | | LS2 | |
|---|---|---|---|
| Member No. | $E_r$ | Member No. | $E_r$ |
| 1 | 0.274 | 1 | 0.358 |
| 3 | 0.274 | 3 | 0.358 |
| 2 | 0.145 | 4 | 0.115 |
| 5 | 0.034 | 6 | 0.115 |
| 4 | 0.015 | 2 | 0.024 |
| 6 | 0.015 | 5 | 0.000 |

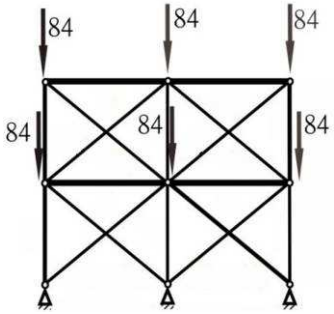


Fig. 11 Load set of LS2(unit: kN)

This section is to discuss the importance factor and VI index under 2-member removal scenario. Table 6 gives the importance factor of member under two loading conditions. The similarity is that the 1st floor side column is the most significant member and makes the largest contribution to structural safety.

The difference includes: 1) In LS1, the rank of most important members is 1st floor side column>1st floor middle column>2nd floor middle column>2nd floor side column>beams & braces, while in LS2, the rank of most important members is 1st floor side column>2nd floor side column >1st floor middle column>2nd floor middle column & beams & braces; 2) The largest importance factor $E_r$ in LS1 is 0.274 while that in LS2 is 0.358, much larger than the former one; 3) The importance factor of 2nd floor middle column in LS1 is 0.034 while that in LS2 is 0, which means the removal of 2nd floor middle column under the load set LS2 is under the structure redundancy and has little influence on structure safety.

The similarity in $VI$ analysis under two member removal scenarios includes that the local mechanism is formed in 2nd floor side point in both load set.

The total number of scenarios with $VI$>0 under two member removal is respectively 43 and 39. Among 29 scenarios, vulnerability index $VI$ in LS1 is less than that in LS2, while among10 scenarios $VI_1$>$VI_2$.

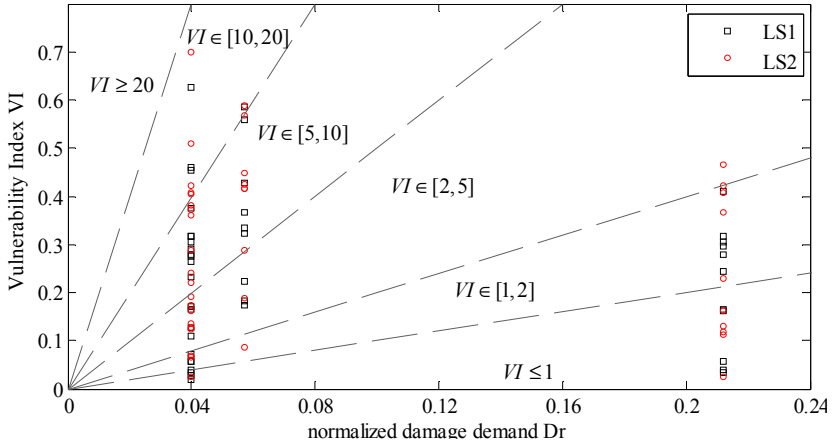


Fig. 12 The risk level map under damaged scenarios of one and two member removal

The risk level map under damaged scenarios is illustrated in Fig. 12, which showed that: 1) when $VI \in [10,20]$, the maximum *VI* in LS1 is larger than that in LS2, 2) the number of damage scenarios in each risk division is similar, 3) with the same normalized damage demand, the scenarios with the maximum and minimum *VI* are both under the load set LS2.

Under two different load set, member importance factor ranks differently. Importance factor of 1st floor middle column in LS1 is 5.1 times of that in LS2, but the general principle is similar that the column is much important than beam and brace. Among two-member removal scenarios, the maximum difference in *VI* under two load sets is 5.7 times; the most vulnerable scenarios is the failure of member (1+15), and the total number of scenarios in each risk division is similar.

According to the previous analysis, the load set in the structure has great influence on the member importance factor and vulnerability index of damage scenarios. So it is essential to consider accurately the load distribution in order to reach correct conclusion about vulnerability assessment.

## Conclusion

The method of structural vulnerability assessment presented in this paper is closely in accordance with the definition based on two aspects, strain energy of structure and damage demand of members.

1. The search process of hazard scenarios was carried out by an example of truss structure, and the results of analyses were including important factor of members, hazard scenarios with the minimum number of killed members, and local damage occurred in advance.

2. The influence of loading on member importance factor and vulnerability index is discussed and it shows that though with the agreement of general trend, the rank of importance factor or VI under a specified scenario varies greatly. So it is essential to consider accurately the load distribution in order to reach correct conclusion about vulnerability assessment.

3. The analyses could be utilized as the proof of measurement to enhance structural capacity of the truss to bear the extreme event. It also could be extended to the frame or more complex system since the assessment process is similar, but some aspects like the selection of parameter to stand for structural performance, the measurement of structural failure, and the simulation of member failure need to re-consider.

## References

[1] U. Starossek, M. Haberland: Measures of structural robustness–requirements and applications. ASCE SEI Structures Congress (2008).

[2] J. Agarwal, D. Blockley, N. Woodman: Struct Saf. Vol. 25 (2003), p.263-286.

[3] L. Ye, X. Lin, Z. Qu, X. Lu, P. Pan: Journal of Architectural and Civil Engineering. Vol. 27 (2010), p.1-6. (In Chinese)

[4] U. Starossek, M. Haberland: Structure and Infrastructure Engineering. Vol. 7 (2010), p.625-631.

[5] M.A. Maes, K.E. Fritzsons, S. Glowienka: Structural Engineering International. Vol. 16 (2006), p.101-107.

[6] D. Wisniewski, J.R. Casas, M. Ghosn: Structural Engineering International. Vol. 16 (2006), p.161-166.

[7] J.W. Smith: Structural Engineering International. Vol. 16 (2006), p.118-123.

[8] N.C. Lind: Reliab Eng Syst Safe. Vol. 48 (1995), p.1-6.

[9] J.W. Baker, M. Schubert, M.H. Faber: Struct Saf. Vol. 30 (2008), p.253-267.

[10] J. England, J. Agarwal, D. Blockley: Comput Struct. Vol. 86 (2008), p.1042-1051.

[11] GSA: Progressive collapse analysis and design guidelines for new federal office buildings and major modernization projects, US (2003), p. 2-9.

*Applied Mechanics and Materials Vols. 580-583 (2014) pp 2694-2701*
*© (2014) Trans Tech Publications, Switzerland*
*doi:10.4028/www.scientific.net/AMM.580-583.2694*

# Deformation Monitoring and Prediction of a Reservoir Landslide in Sichuan Province, China

Bing Han[1, 2, a,*], Shengshan Hou[2, b], Bin Zhu[1, c],
Lichao Wang[2, d], Ang Li [2, e], Hejiong Ye[2, f]

[1] China University of Geosciences (Beijing), Beijing 100083, China

[2] China Institute of Geo-Environment Monitoring, Beijing 100081, China

[a]hanb@mail.cigem.gov.cn, [b]houss@mail.cigem.gov.cn, [c]314869196@qq.com,

[d]wanglc@mail.cigem.gov.cn, [e]lia@mail.cigem.gov.cn, [f]yehj@mail.cigem.gov.cn

**Keywords:** reservoir; Hongyanzi landslide; multi-parameter monitoring; ground water; deformation prediction

**Abstract:** Hydropower reservoirs change the local geo-environment greatly and often induce reservoir bank landslides. Hongyanzi landslide is a large rejuvenated ancient landslide in Pubugou Hydropower Station reservoir area in western China Sichuan Province. To study the deformation of the Hongyanzi landslide, we arranged multi-parameter monitoring using GPS, fixed borehole tilt-meter, osmometer, and crack-meter and collected continuous data of displacement and ground water table. The monitoring data, together with the reservoir water level data, show that the landslide deforms obviously during reservoir water level is falling, while it deforms little in the other period. Comprehensive analysis of the deformation and reservoir water level implies that the seepage force caused by water level difference between the inner and outer slope may be the key factor. Through regression analysis, the authors established a forecast model for landslide deformation based on ground water table and reservoir water level; thus concluded that reducing the falling velocity of reservoir water level may slow the landslide deformation down.

## Introduction

A large amount of hydropower stations were built in recent years in China, and many of them have a large reservoir to preserve water energy. During the running of hydropower plants, reservoir water level will change periodically. The cycling change of reservoir water level induces many reservoir bank landslides. According to the study, more than 90% of reservoir bank landslides are closely related to the fluctuation of reservoir water level[1]. About 40-49 % of reservoir-induced landslides occur in the rising period of reservoir water table, while 30-60 % of them occur in the dropping period. Large reservoir bank landslides often take place when the water level drops rapidly[2-5].

More than 75% of reservoir bank landslides are rejuvenated ancient landslides[6]. The reservoir bank landslides are very harmful, due to release of a large amount of rock and soil into the reservoir, reducing the reservoir capacity, and they can even produce huge water wave when sliding with high speed.

Hongyanzi landslide is a typical reservoir-related landslide in Hanyuan County, Sichuan Province. To investigate the deformation and the main impact factors of the landslide, a multi-parameter monitoring network was installed in the sliding body; detailed data of surface movement, deep movement, and ground water level were measured.

## General settings

Hongyanzi landslide is located in the right bank of Dadu River, a secondary tributary of the Yangtze River. The landslide is about 23km away from the Pubugou Dam (Fig.1).

The slope of Hongyanzi landslide area is 20-30° in average with a steep head scarp about 40-50°. The general shape of Hongyanzi landslide is irregular half-round. The sliding direction is about 340° (Fig.2). The altitude of Hongyanzi landslide ranges from 954 meter above sea level (masl) to 810 masl, the length is 600m, and the width is 580m. The thickness of the landslide is about 20-50m, thicker in the front part and thinner in the rear part. The volume of the landslide is about $7.5\times10^6 m^3$. The sliding surface is relatively flat in the front and steep in the rear (Fig.3). The left and right boundaries can be identified easily in the field because of the distortions up to 1.7m vertically of the Lake Road.

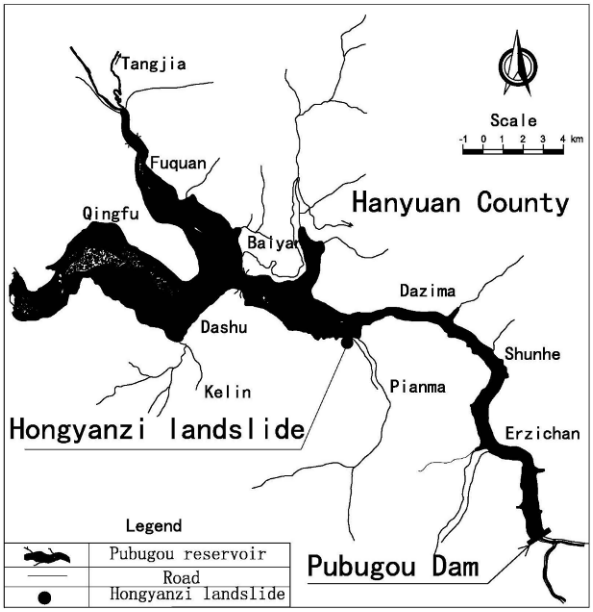


Fig.1 Location of Hongyanzi landslide

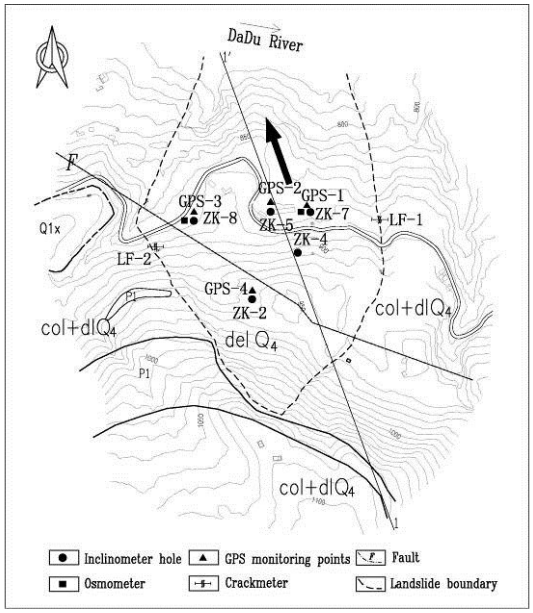


Fig.2 Setting of monitoring apparatus

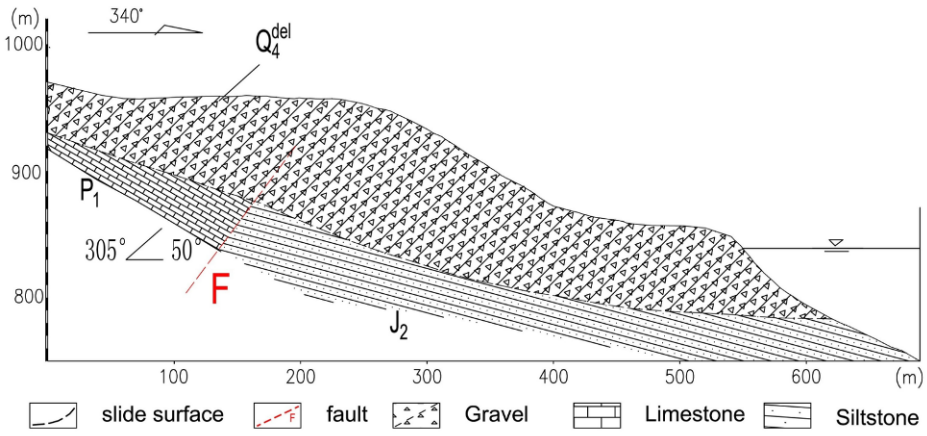


Fig.3 Geologic profile of Hongyanzi landslide

According to the investigation, Hongyanzi landslide is an ancient landslide. The sliding body consists of Quaternary gravel, silty clay, and many boulders with diameter of 1-3m in the body. The gravel and boulders are mostly fractured limestone, with a compact structure. The stratum of sliding bed is Jurassic reddish sandstone in the footwall of Hanyuan-Zhaojue fault, and Permian limestone in hanging wall of the fault[7,8].

The hydrogeological condition of the Hongyanzi landslide area is relatively simple. The ground water is mainly phreatic water, and the main recharge is from precipitation. The topography is very steep, facing the Dadu River in the north, and gullies in the east and west, which is convenient for the ground water to discharge. So the ground water table is very low. The water level of hydropower reservoir varies from 790 to 850masl; the largest landslide submerged height is about 55m. The fluctuations of reservoir water level have a great impact on the groundwater table.

Hongyanzi landslide was in an overall stable state before the Pubugou reservoir was built. When the water filled the reservoir, landslide deformation started. The reservoir began to store water and the power plant started operation in November 2010. Hongyanzi landslide deformed significantly in February 2011; the displacement was up to 1-2m. Significant deformation occurred again in 2012 when the reservoir water level dropped. The maximum displacement exceeded 2m during March-May 2013. But in the rising periods of the reservoir water level, the deformation slowed down, and the landslide came into a relatively stable state again.

## Multi-parameter monitoring

A multi-parameter monitoring system was installed in Hongyanzi landslide at the end of 2012, in order to study the deforming characteristics and influencing factors. The apparatuses include 5 GPS receivers (4 as the measurements and 1 for reference), fixed tiltmeters (three boreholes in the

mid-front: ZK5, ZK7 and ZK8), and osmometers (also in ZK5, ZK7 and ZK8), crack displacement meters (near the left and right boundaries), and a rain gauge. Manual measurement using a tiltmeter at ZK2 and ZK4 is also arranged. The setting map is shown in Fig.2.

The measurement started since the end of 2012. In this paper, datasets of different monitoring apparatuses were chosen, to study the principles of the deformation of the Hongyanzi landslide.

**Rainfall.** The rainfall of the landslide area is up to 250mm from January to June. There is barely effective rain before the middle of March. Two precipitation events over 50mm occurred in March 26 to April 12 and 19-26 June, respectively. The maximum daily rainfall, up to 40.8mm, appeared on June 30. The second largest daily rainfall is 23.1mm, took place on May 24. For both rainfall processes, no significant deformation of the landslide was monitored.

**Ground water table.** An osmometer was installed at ZK5, near GPS-2; it measured the groundwater table. Because of the borehole depth, we got ground water table data above 825 masl (Fig. 4). There is a positive correlation between groundwater table of ZK5 and the reservoir water level. From October 2012 to April 2013, the reservoir water level kept dropping, the ground water table of ZK5 was also descending. The descending speed of groundwater table of ZK5 was almost equal to that of reservoir water level before February 2013. After that, the dropping of reservoir water level accelerated, the difference between groundwater and reservoir water increased. From May 2013, the reservoir began refilling and the groundwater table of ZK5 also rose slowly.

**Surface displacement.** Four sets of GPS were installed on the landslide. GPS data and reservoir water level are shown in Fig.5. The total displacement from January to June is up to 1800mm. The value from GPS-1(right front) is the largest, then GPS-4(middle rear), GPS-2(middle front), the value from GPS-3(middle left) is the smallest. The data from GPS-1, GPS-2, and GPS-3 show the same change pattern, with a moving direction of NNW22-24°. Date from GPS-4 show a vertical-dominate displacement, probably induced by the local relief near the measuring site.

A positive correlation between the surface displacement and reservoir water level is observed here again. Before February 2013, the reservoir water level dropped slowly and steady, the surface displacement was very small. During March to April, with the reservoir water dropping speed rising, surface displacement accelerated, with a daily increase up to 60mm. From May on, with the reservoir began refilling, the surface displacements slowed down.

**Other data.** The data acquired from tiltmeters at ZK2, ZK4 and ZK7 and crack displacement meters near left and right boundaries also show a spontaneous change pattern with the reservoir water level, i.e., relatively stable before February, accelerating during March-April, and slowed down again in May-June (Fig.6 and Fig.7).

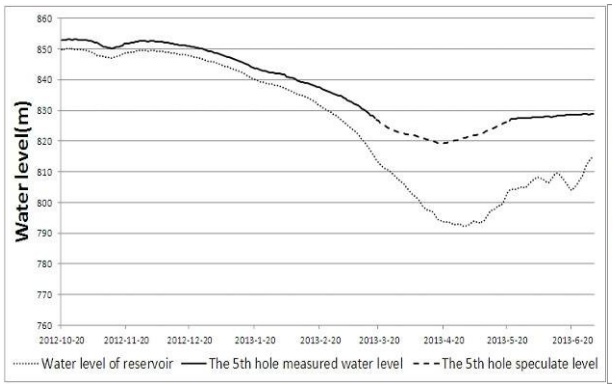


Fig.4 Reservoir water level and ground water table at ZK5

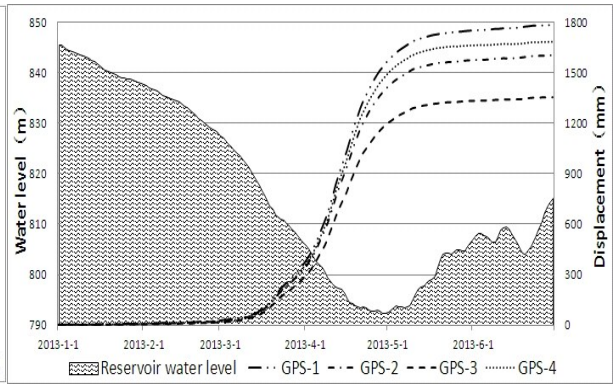


Fig.5 Reservoir water level and GPS Displacement

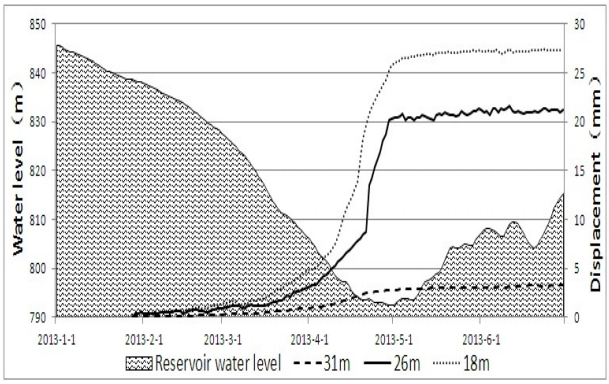


Fig.6 Reservoir water level and deep displacement of ZK7

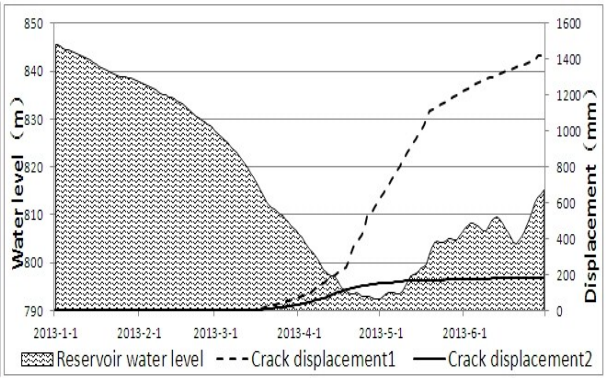


Fig.7 Reservoir water level and crack displacement

The epicenter of the April 20, 2013 Lushan MS7.0 earthquake was about 100km from Hongyanzi landslide. The seismic intensity in the landslide area was about VI degree, the maximum seismic acceleration nearby was about 0.4g[9,10]. GPS and deep tiltmeter measurements did not show significant deformation during the earthquake. The crack displacement meters showed a little bit quicker movement of 50mm in the right boundary and 10mm in the left boundary which may be resulted in the local relief response to the earthquake.

**Deformation forecasting of Hongyanzi landslide**

The monitoring data show that the landslide deformation starts significantly when the reservoir water level dropping speed reaches a certain value. The mechanisms behind this may be as the following. When the reservoir water level drops, the ground water in the landslide drops as well. However, because of the limited permeability of landslide mass, the groundwater table cannot drop as fast as that of the reservoir water level does. So the difference between reservoir water level and ground water table increases and the seepage pressure in the landslide body also increases, it seems

to be this increased seepage pressure that reduces the stability coefficient, and the landslide starts to deform. This phenomenon is distinct especially when the permeability of rock mass is low（11-14).

The surface deformation and the difference between the reservoir water level and the ground water table of ZK5 is plotted in Fig.8. When the difference is less than 7m, the deformation is very small. The deformation accelerates with the difference growth. The changes can be fitted with equation 1 and the fitting coefficient ($R^2$) is 0.91.

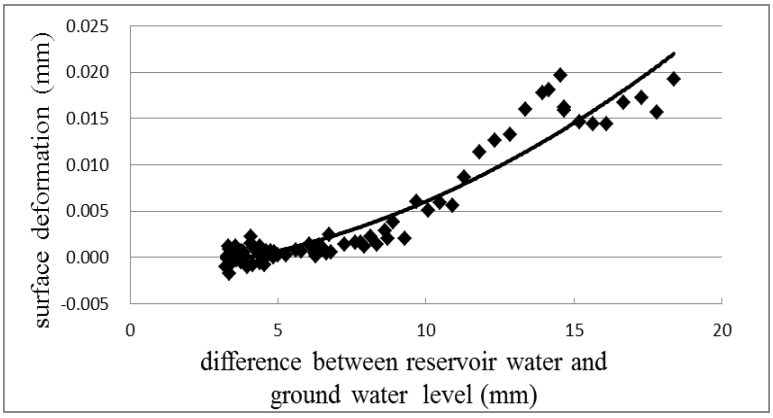


Fig.8 Relationship between surface deformation and the difference between reservoir water level and ground water table of ZK5

The regression equition in Fig.8 is:

$$D_n = 6\times10^{-5}\times(B_n-A_n)^2+0.0001\times(B_n-A_n)-0.0015 \quad (1)$$

where $D_n$ is the deformation value of day n, $B_n$ is the ground water table of ZK5 of day n and $A_n$ is the reservoir water level of day n.

The difference between reservoir water level and ground water table can be derived through the following linear fitting (data are shown in Fig.4):

$$B_n - A_n = 1.019\times(B_{n-1}-A_{n-1}) + 0.448\times (A_{n-1}-A_n) – 0.154 \quad (2)$$

From (1) and (2), we got:

$$D_n = 6\times10^{-5}\times(1.019\times (B_{n-1}-A_{n-1}) + 0.448\times(A_{n-1}-A_n) - 0.154)^2 + 0.0001\times(1.019\times(B_{n-1}-A_{n-1}) + 0.448\times(A_{n-1}-A_n)-0.154) - 0.0015 \quad (3)$$

Thus, we can get the pricipited deformation value in one day ahead.

We can also tell that, in order to lower the expected deformation value, we can reduce the speed of the reservior water level dropping ($A_{n-1}$-$A_n$ in equation 3).

## Conclusions

Through this study, we can draw the following conclusions:

(1) Hongyanzi landslide deforms significantly when the reservoir water level drops fast and the maximum deformation is up to 1800mm. The influences from rainfall and Lushan Earthquake are relatively small.

(2) Seepage pressure due to the difference between reservoir water level and ground water table plays a key role in landslide deformation.

(3) We put forward a formula to predict the landslide deformation on day in advance, using quadratic fitting.

(4) The landslide deformation can be relieved to a certain degree by lowering down the dropping speed of reservoir water level.

## Acknowledgements

This study was supported by China Geological Survey (Project No.1212011140016) and Chinese key science and technology project (No. 2010ZX03006-007).

## References

[1] Wu Yan-qing, Groundwater flow and geological hazards, Underground Space, 1999, 19(4) 303－310.(In Chinese)

[2] Jones F. O., Embody D. R., Peterson W. L., Landslides along the Columbia River Valley, Northeastern Washington, US Geol. Surv. Prof. 367, 98(1961).

[3] Hiroyuki N, Discussion on the reservoir landslide, Bulletin of Soil and Water Conservation, 1990, 10(1): 53－64.

[4] Wang Shitian, Liu Hanchao, Zhang Zhuoyuan, Research on the water-rock interaction and its environmental effects in reservoir areas, Journal of Geological Hazards and Environment Preservation, 1997, 8(1): 69–88. (In Chinese)

[5] Tang Hui-ming, Zhang Guang-cheng, Study on slope stability during reservoir water level falling, Rock and Soil Mechanics, 2005, 26(SUP.2): 11－15. (In Chinese)

[6] Committee on Reservoir Slope Stability, Reservoir Landslides: Investigation and Management, Paris: International Commission on Large Dam (2002).

[7] Chengdu Hydroelectric Investigation & Design Institute, Geological hazard assessment of Pubugou Hydropower Station(2003). (In Chinese)

[8] Sichuan Institute of Geological Engineering Investigation, Drilling and experiment report for Hongyanzi landslide(2013). (In Chinese)

[9] China Earthquake Administration, Seismic intensity map for Lushan Ms7.0 Earthquake(2013).

[10] China Strong Motion Networks Center, Strong motion records for Lushan Ms7.0 Earthquake(2013). (In Chinese)

[11] Zhu Dong-lin, Ren Guang-ming, Nie De-xing, Effecting and forecasting of landslide stability with the change of reservoir water level, Hydrogeology and Engineering Geology, 2002,23(3): 378－381. (In Chinese)

[12] Liao Hong-jian, Sheng Qian, Gao Shi-hang, Influence of drawdown of reservoir water level on landslide stability, Chinese Journal of Rock Mechanics and Engineering, 2005,24(19): 56－60. (In Chinese)

[13] Liu Xin-xi, Xia Yuan-you, Zhang Xian-shu, Effects of drawdown of reservoir water level on landslide stability, Chinese Journal of Rock Mechanics and Engineering, 2005,24(8): 1439－1444. (In Chinese)

[14] Liu Xin-xi, Xia Yuan-you, Lian Cao, Research on method of landslide stability valuation during sudden drawdown of reservoir level, Rock and Soil Mechanics, 2005,26(9): 1427－1432. (In Chinese)

*Applied Mechanics and Materials Vols. 580-583 (2014) pp 2702-2707*
*© (2014) Trans Tech Publications, Switzerland*
*doi:10.4028/www.scientific.net/AMM.580-583.2702*

# Mechanical performance calculation of single-layer cable mesh point-supported glass curtain wall under fire conditions

Gong Lingfeng[1], Bai Yin[1], Li Shiqi[1]

[1]School of Transportation Science and Engineering, Beihang University, Beijing 100191, China

[a]smileglfsmile@163.com, [b]baibowenbai@buaa.edu.cn

**Keywords:** single-layer cable, mechanical performance, glass breakage, critical temperature, fire-resisting design

**Abstract:** High-strength prestressed cables were main bearing parts in single-layer cable mesh point-supported glass curtain wall structures, and it was always unable to take effective fire prevention measures on steel cables due to small sections. That the elastic modulus and yield strength of prestressed cables decreased sharply under fire conditions would threaten safety performance of the whole structure seriously. When glass breakage is considered and not considered, nonlinear finite element complete-process analysis for the single-layer cable mesh point-supported glass curtain wall structure was conducted. Influences of various factors on structure mechanical performance were studied under fire conditions. Through the calculation analysis of different joint constraint models, the ultimate temperature table suitable for different sizes and cable spacing of glass curtain walls was obtained under uniform heating conditions, and proposals for fire-resisting design were given.

## Introduction

The single-layer cable mesh point-supported glass curtain wall structure (Gu, Hao, and Luo, 2011) provides spacious internal space, and it can be constructed easily and conveniently. As a kind of new large space building structure, it represents the developing trend of large-dimensional curtain wall structures.

The single-layer cable mesh point-supported glass curtain wall structure adopts the prestressed cable system to provide the initial stiffness. Not only the performance of steel cables (Perrin, Gaillet, and Tessier, 2010) and glass (Samuel, et al, 2007; Kai, 2009; Popea and Bailey, 2007), but also the synergistic effect (Wang, 2008; Gao, and Hu, 2011) between steel cables and glass under different joint constraint models should be considered when making the design of the structure. The elastic modulus and yield strength of high-strength prestressed cables decreases significantly (Bai, et al, 2010), and glass breaks at a different degree under fire conditions. Both lead to mechanical performance of the whole structures changing distinctly. Mechanical performance of the single-layer cable mesh point-supported glass curtain wall structure under fire conditions was studied when glass breakage is considered and not considered in this paper.

## Finite element analysis of the glass curtain wall structure

### Numerical calculation model

The diameter of steel cables simulated by LINK10 takes 16mm in calculation models. The glass panel is simulated by SHELL181, and the tension-compression spring by COMBIN14. The deadweight of curtain wall connectors and glass take 0.2kN/m2 and 0.26kN/m2 respectively. Horizontal load takes 1.0kN/m2.

Two kinds of temperature rising models are calculated depending on different fire locations. All steel cables are regarded to be uniformly heated up to 600℃ when the fire is far away from the glass curtain wall. When the fire is close to the glass curtain wall, the steel cables close to the fire are considered to be heated to 600℃ quickly, and others to 100℃.

Three kinds of joint constraint models (Wang, et al, 2007; Yin and Zhang, 2004) are calculated in this paper, including cross coupling (CPM1), tension-compression spring (CPM2) and fully coupled model (CPM3). CPM0 is the joint constraint model without considering the effect of glass panels, as

shown in figure 1. According to the development situation of the glass curtain wall in recent years, five kinds of glass curtain walls are chosen in this paper, numbering A, B, C, D, E, as shown in table 1.

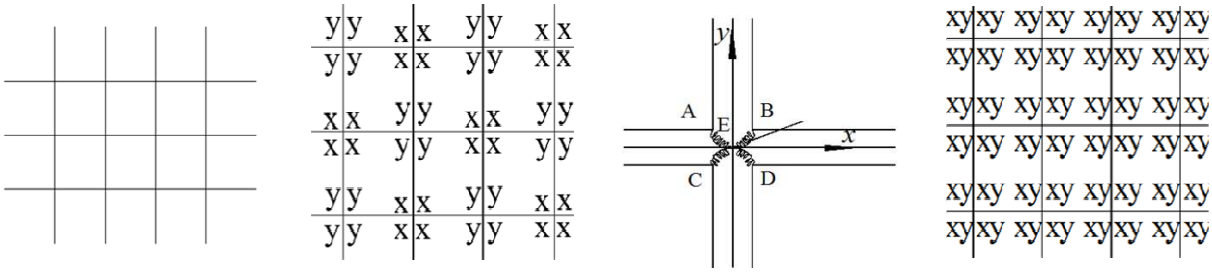


(a) CPM0 (b) CPM1 (c) CPM2 (d) CPM3

Figure1 Joint constraint models between glass and supported system

Table1 Sizes of the curtain wall

| Number | A | B | C | D | E |
|---|---|---|---|---|---|
| Cable space (m) | 1 | 1.5 | 2 | 1 | 2.5 |
| The curtain wall area ($m^2$) | 15×15 | 15×15 | 20×20 | 10×10 | 20×20 |

**Failure criterion**

The single-layer cable mesh point-supported glass curtain wall structure is regarded as destruction under the following cases. 1) Global displacement of the curtain wall is greater than 1/50 of the span (Jussi, 1999; Rice and Hugh, 1995), 2) The temperature of glass is greater than 450℃,3) The cable stress is greater than 844MPa.

**Mechanical performance of the glass curtain wall under fire conditions without considering glass breakage**

**The influence of joint constraint on the glass curtain wall global displacement**

The initial stress of horizontal and vertical cables takes the same value, 90.6kN, in calculation models. The displacement variation of different joint constraint models under fire conditions is shown in figure 2.

According to figure 2, when the overall sizes of glass curtain walls are the same, glass curtain wall displacements decrease with decreasing of cable spacing. And glass curtain wall displacements decrease with the overall sizes decreasing when the cable spacing is kept the same. The steel cable displacements under the non-uniform heating conditions are greater than that under the uniform heating conditions. The reason is that the cable stiffness decreases uniformly under the uniform heating conditions, and the global stiffness is smaller than that under the non-uniform heating conditions.

Under conditions of the same temperature and section area, the stronger the joint constraint is, the smaller the curtain wall displacement is. The case of that glass curtain wall displacements without considering the glass rigid effect are smaller than that with considering the glass rigid effect occurs at the low temperature range. The reason is that concentrated loads are applied at the cable nodes when without considering the glass rigid effect, and uniform loads are applied on the glass panels when considering the glass rigid effect.

**The critical temperature value of the curtain wall without considering the glass breakage effect**

L/50 is used as the ultimate displacement of the single-layer cable mesh point-supporting glass curtain wall structure under fire conditions (L is the span of the curtain wall). The ultimate temperature of glass is 450℃, and the glass curtain wall is considered to have been broken when the glass temperature is greater than 450℃. The critical temperature takes the smaller value between 450℃ and the temperature value corresponding to the displacement of L/50, as shown in table 2.

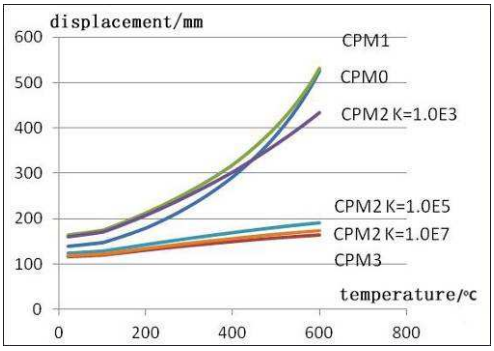


a) The uniform heating of A curtain wall

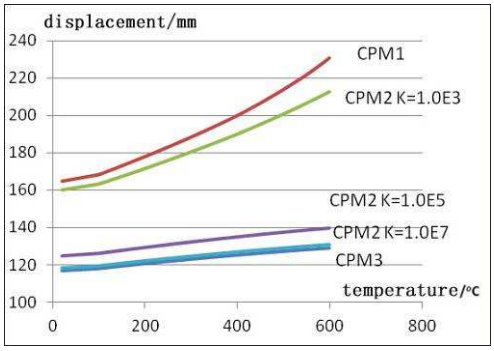


b) The non- uniform heating of A curtain wall

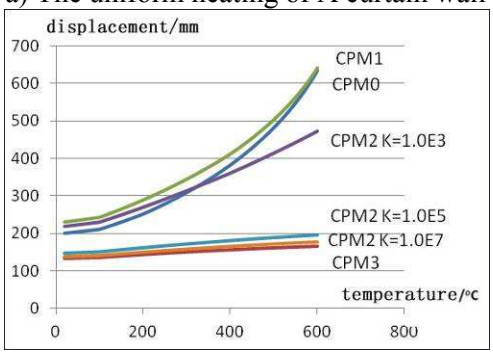


c) The uniform heating of B curtain wall

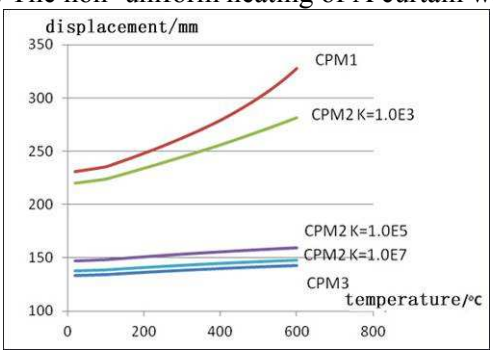


d) The non- uniform heating of B curtain wall

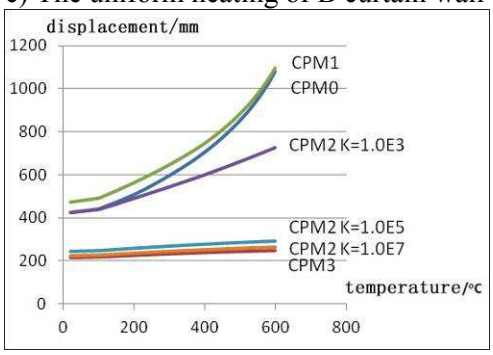


e) The uniform heating of C curtain wall

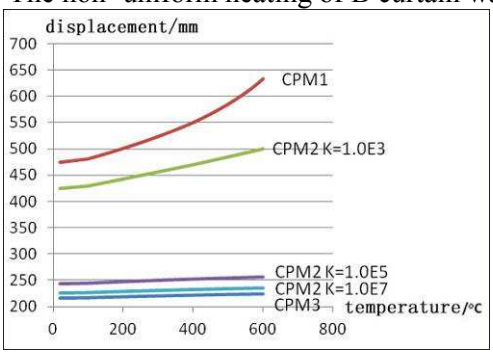


f) The non- uniform heating of C curtain wall

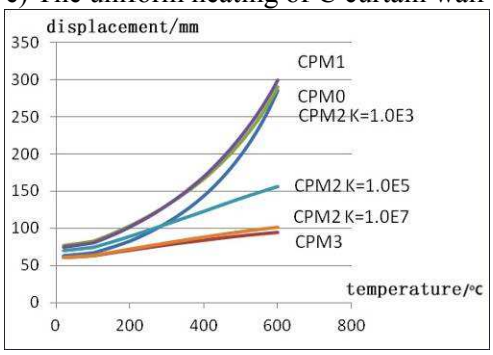


g) The uniform heating of D curtain wall

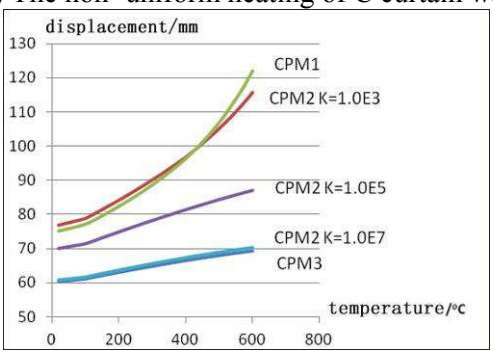


h) The non-uniform heating of D curtain wall

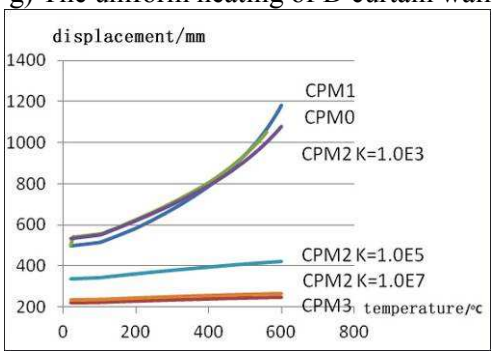


i) The uniform heating of E curtain wall

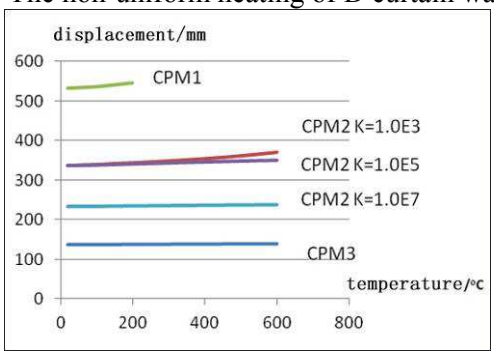


j) The non-uniform heating of E curtain wall

Figure 2 The variation displacement figures of different joint constraint models under fire conditions

Table 2 The critical temperature table of different kinds of glass curtain walls (℃)

| Kinds of curtain wall | CPM0 | CPM1 | CPM2@10E3 | CPM2@10E5 | CPM2@10E7 | CPM3 |
|---|---|---|---|---|---|---|
| A | 409 | 368 | 392 | 450 | 450 | 450 |
| B | 281 | 218 | 264 | 450 | 450 | 450 |
| C | — | — | — | 450 | 450 | 450 |
| D | 450 | 450 | 450 | 450 | 450 | 450 |
| E | — | — | — | 432 | 450 | 450 |

**Mechanical performance of glass curtain wall structures under fire conditions with considering glass breakage**

The glass panels participate in structural bearing, and have a certain influence on the structure rigid. Under fire conditions, that a part of glass in curtain walls breaks will lead to the variation of global and localized rigid of the structure. So the study of mechanical performance on single-layer cable mesh point-supported glass curtain walls after glass breaks still has a great significance. Two kinds of joint constraint models, CPM1and CPM2, are calculated in this paper.

**Cable mesh force analysis after glass breaks**

The largest cable forces when the effect of glass breakage is considered are shown in table 3-6.

The calculation results show that the largest cable force under non-uniform heating conditions is greater than that under uniform heating conditions. But, the cable force variance is smaller than that of the latter after glass breaks. For the CPM1 joint constraint model, the largest cable forces after glass broke increase 33.33% uniformly than that before glass breaks under uniform heating conditions. However, under non-uniform heating conditions, this value is just 4.75%. The reason is that a small rigid area has been existed in the cable mesh before glass breaks under non-uniform heating conditions, so glass breakage can't lead to the largest cable forces changing significantly.

Table 3 CPM1: the largest cable force under uniform heating conditions (kN)

| State of the glass | A | B | C | D | E |
|---|---|---|---|---|---|
| unruptured | 45.001 | 54.545 | 79.365 | 38.635 | 39.196 |
| ruptured | 63.810 | 71.932 | 93.034 | — | — |

Table 4 CPM1: the largest cable force under non-uniform heating conditions (kN)

| State of the glass | A | B | C | D | E |
|---|---|---|---|---|---|
| unruptured | 102.222 | 109.394 | 137.758 | 93.660 | — |
| ruptured | 97.736 | 103.908 | 126.740 | 91.739 | — |

Table 5 CPM2: the largest cable force under uniform heating conditions (kN)

| Spring stiffness | unruptured | | | | | ruptured | | | | |
|---|---|---|---|---|---|---|---|---|---|---|
| | A | B | C | D | E | A | B | C | D | E |
| $10^5$ | 35.621 | 37.163 | 40.994 | 32.338 | 41.247 | 52.948 | 67.564 | 88.551 | 45.687 | 95.079 |
| $10^7$ | 29.967 | 30.372 | 31.796 | 28.616 | 31.833 | 49.690 | 60.132 | 73.675 | 44.740 | 77.673 |

Table 6 CPM2: the largest cable force under non- uniform heating conditions (kN)

| Spring stiffness | unruptured | | | | | ruptured | | | | |
|---|---|---|---|---|---|---|---|---|---|---|
| | A | B | C | D | E | A | B | C | D | E |
| $10^5$ | 97.772 | 97.823 | 107.016 | 94.060 | 108.787 | 111.261 | 112.265 | 123.299 | 102.229 | 114.848 |
| $10^7$ | 90.239 | 91.412 | 126.095 | — | 95.265 | 111.234 | 106.413 | 130.515 | — | 105.164 |

**Displacement analysis of the single-layer cable mesh point-supported glass curtain structure after glass breaks**

The displacements of glass curtain walls are calculated by ANSYS, and the calculation results are shown in table 7-10.

The data in table 7-10 show that glass breakage has little effect on displacements of glass curtain walls under uniform heating conditions. For the CPM1 joint constraint model, the curtain wall displacements will decrease at an instant with glass breaking under non-uniform heating conditions. The largest reduction rate reaches 21.6%, while the displacements keep mostly unchangeable under the condition of the CPM2 joint constraint model. The reason is that mechanical performance of the structure changes because of glass breakage. There are only steel cables participating in structural bearing after glass breaks, and the global displacements tend to increase. At the same time, glass

breakage leads to the external load, especially the wind load, decreasing, and the global displacements tend to decrease.

Table 7 CPM1: curtain wall displacements under uniform heating conditions (mm)

| State of the glass | A | B | C | D | E |
|---|---|---|---|---|---|
| unruptured | 357.547 | 454.721 | 809.642 | 189.236 | 876.590 |
| ruptured | 359.207 | 456.827 | 810.233 | 190.288 | — |

Table 8 CPM1: curtain wall displacements under non- uniform heating conditions (mm)

| State of the glass | A | B | C | D | E |
|---|---|---|---|---|---|
| unruptured | 220.029 | 303.622 | 581.615 | 102.110 | 548.349 |
| ruptured | 175.699 | 247.118 | 497.499 | 83.0450 | —— |

Table9 CPM2: curtain wall displacements under uniform heating conditions (mm)

| Spring stiffness | unruptured | | | | | ruptured | | | | |
|---|---|---|---|---|---|---|---|---|---|---|
| | A | B | C | D | E | A | B | C | D | E |
| $10^5$ | 237.210 | 257.684 | 396.574 | 131.666 | 402.598 | 238.593 | 264.401 | 408.765 | 133.988 | 424.042 |
| $10^7$ | 162.003 | 170.720 | 257.660 | 91.917 | 259.850 | 164.047 | 178.649 | 269.923 | 95.708 | 280.788 |

Table 10 CPM2: curtain wall displacements under non uniform heating conditions (mm)

| Spring stiffness | unruptured | | | | | ruptured | | | | |
|---|---|---|---|---|---|---|---|---|---|---|
| | A | B | C | D | E | A | B | C | D | E |
| $10^5$ | 166.774 | 202.931 | 484.611 | 84.171 | 348.349 | 164.027 | 210.224 | 452.950 | 78.319 | 361.506 |
| $10^7$ | 129.902 | 147.566 | 368.557 | 68.883 | 238.677 | 147.136 | 173.363 | 368.557 | — | 255.014 |

**Influence of factors on curtain wall mechanical performance under fire conditions**

Glass size has a great influence on global rigid of glass curtain wall structures. When the global size of the glass curtain wall is determined, the glass size is larger, the number of steel cables is smaller, and the global displacement of the structure is larger. And the security of the glass curtain wall structure will decrease. Under the non-uniform heating conditions, the global displacement of the B glass curtain wall structure is 38% larger than that of the A glass curtain wall before glass breaks, and this value is 41% after glass broke.

The larger the joint constraint rigid is, the smaller the global displacement of glass curtain wall structure is. Under uniform heating conditions, the uniform global displacements of five kinds of glass curtain walls with CMP2 joint constraint model (k=105 N/m) is 48% greater than that of glass curtain walls with CMP2 joint constraint model (k=107 N/m). And this value is 34% under non-uniform heating conditions. However, when the joint constraint rigidity is too high, the glass panel deformation will be restricted remarkably under fire conditions, and the deformation of glass panels and the cable net will be very different. Glass panels will lead to structural displacement increasing and cause unfavorable effect. Therefore, the joint constraint rigidity should not be designed too stiffed in order to insure fire-resisting performance.

Glass panels have a certain contribution on the structure stiffness. The glass breakage will lead to mechanical performance of the whole structure changing distinctly during fire heating process. Therefore, the finite element analysis when glass breakage is considered can simulate the real situation.

**Conclusion**

1) When the joint constraint rigidity is high, it will always lead to fragmentation of glass panels and large structural displacement with the rise of temperature. The joint constraint rigidity should not be designed too stiffed in order to insure the fire-resisting performance.

2) The largest cable force under non-uniform heating conditions is larger than that under uniform heating conditions, which leads to single-layer cable mesh point-supported glass curtain walls breaking more easily.

3) The structure global displacements continue to decrease with the temperature rise. Through the calculation analysis of different joint constraint models, the ultimate temperature table suitable for

different sizes and cable spacing of glass curtain walls was obtained under uniform heating conditions, as shown in table 2.

**Foundation**

This work was supported by National Natural Science Foundation of China (Grant Nos. 51208019), Research Fund for the Doctoral Program of Higher Education of China (Grant Nos. 20091102120034).

**References**

[1]Gu, J., Hao, W. F., Luo, Y. (2011). "Investigation of damage identification for glass curtain wall based on Hilbert-Huang transform and transmissibility function", Internal Journal of Modeling, Identification and Control, Vol. 13, No. 1-2, pp.38-45.

[2]Perrin, M., Gaillet, L., Tessier, C. (2010) "Hydrogen embrittlement of prestressing cables", Corrosion Science, No.6, pp.1915-1926.

[3]Samuel, L., Richard, G., and Scott, R. (2007) "An experimental determination of a real fire performance of a non-load bearing glass wall assembly", Fire Technology, Vol. 43, No.1, pp. 77-89.

[4]Kai Kang. (2009). "Assessment of a model development for window glass breakage due to fire exposure in a field Model", Fire Safety Journal,Vol. 45, pp. 415-424.

[5]Popea, N.D., Bailey, C.G. (2007) "Development of a Gaussian glass breakage model within a fire field model", Fire Safety Journal,Vol. 42,pp. 366–376.

[6]Wang, D. (2008) "Theory and experimental analysis of interaction between flexible point-supported system and glass plane", Architectural and structural design, No. 4, pp. 23-26.

[7]Gao, Y. T., Hu, X. (2011). "Analysis on Integral Performance of Unit Glazing Curtain Wall Considering the Contribution of Glass Rigidity", Advances in Structures, Vol. 163-167, pp. 2454-2458.

[8]Bai, Y., Cheng, S. F., Shi, Y. J. (2010). Critical temperatures determination for monolayer cable net glass curtain wall under fire conditions, Proceedings of the Eleventh International Symposium on Structural Engineering, science press, Beijing.

[9]Wang, Y. Q., Sun, F., Wu, L. L., (2007). "Influence of glass and joint constraint on loading capacity of monolayer cable net for point supported glass buildings", Journal of Harbin Institute of Technology, vol. 39, No. 8, pp. 1309-1313.

[10]Yin, Y. W., Zhang, Q. L., (2004), "Experimental study on load bearing capacity of point-supported mid-hollow and laminated glasses", Joural o building structures, vol. 25, No. 1

[11]Jussi, K.(1999), "Joint and fastenings in steel-glass facades. [Master's thesis of Helsinki university of technology], Germany: Department of Civil and Environmental Engineering of Helsinki University of Technology

[13]Rice, P., Hugh, D. (1995) Structural glass. E & EN SPON, London, England.

*Applied Mechanics and Materials Vols. 580-583 (2014) pp 2708-2712*
*© (2014) Trans Tech Publications, Switzerland*
*doi:10.4028/www.scientific.net/AMM.580-583.2708*

# Design and Realization of 3S Technology-based Geological Disaster Database System in Liaoning Province

Hua Ding[1,a], Lishuang Sun [1,b] , Jingli Wang [1,c] and Xin Wang[1,d]

[1]Institute of civil engineering, Shenyang Jianzhu University, Liaoning, 110168, China

[a]cehding@sjzu.edu.cn, [b]celssun@ sjzu.edu.cn, [c]cejlwan@ sjzu.edu.cn, [d]cexwang@sjzu.edu.cn

**Keywords:** 3S, geological disaster, 3D model, ArcGIS.

**Abstract:** This paper absorbs much successful experience from geological disasters database system designed and built at home and abroad, based on remote sensing (RS), geographic information systems (GIS) and GPS technology, adopt AHP, fuzzy comprehensive evaluation model and method of establishing three-dimensional model of geological disasters in high-risk areas, the paper constructs geological disasters database system in Liaoning Province, this database system can manage and monitor geological disasters and provide strong support analysing geological disasters for Liaoning province areas.

## Introduction

Geological environment is very complex and natural variation is intense in Liaoning province so it is one of provinces which is easily suffering from geological disasters in China. Geological disaster features have many types, extensive distribution and great harmfulness. Geological disaster types are mainly ground fissure, land subsidence, landslide, debris flow, etc. At present, there are 6448 checked hidden trouble areas of geological disaster in the whole province while there are 1685 land subsidence areas, 535 landslide areas, 1759 debris flow areas, 1497 land collapse areas, 157 ground crack areas and 1742 unstable slopes.

Geological disaster causes harm to people's lives as well as property and influences urban planning layout in Liaoning province, efficient utilization of land and rational exploitation of underground space so it has become a non-negligible factor to restrict economic and social sustainable development in Liaoning province. In order to actively and effectively develop geological disaster prevention work, take feasible prevention measures, avoid and reduce losses which are caused by geological diaster to people's life and property, it is necessary to apply advanced technology to set up a comprehensive functional geological diaster database system and realize science, information, standardization and visualization of geological disaster prevention management.

In recent decades, 3S technologies (geological information system(GIS), global positioning system (GPS), Remote sensing (RS)) are extensively applied in geological diaster investigation and prevention field, which achieves better effect.He Zhengwei [1],etc, apply remote sense and GIS technology to study comprehensive broadcast on landslide stage, landslide region danger evaluation method and establish geological disaster determination supporting geographical information system in Tianshan highway.Tang Chuan[2], etc, applies p5 remote sensing data after Wenchuan earthquake, aerial remote sensing data after earthquake and SPOT5 after Septermber 24th storm to carry out remote sensing investigation and analysis on source area features of Beichuan debris flow and perform dynamic monitoring on three classical areas(Tang jiashan-Beichuan, Jiaba, Leiguzhen) in high seismic intensity area in WenChuan.In Oct,19th 2011, 3S-based technology three gorges reservoir area 1:10000 disaster geological map compilation and database construction program accomplishes acceptance. 1:10000 disaster geological maps are completed and database construction is completed according to technology requirement. All data are put in base and they can complete seamless integration with geological disaster prewarning commanding system.

In this paper, remote sensing image processing platform in American Exelis Visual Information Solutions company is applied to process multi-temporal and high accuracy remote sensing image.

This paper uses GPS R4 receiver which adopts point-to-net to perform accuracy monitoring in geological disaster areas in American Trimble company and utilize commercial GIS software platform Arcgis10.0 in ERSI company to establish multi-source fusion geological disaster database system which takes visual studio 2010 as the developed environment.

## System Design

1.Data Preparation

Geological disaster data in Liaoning province mainly contain 1:500000 geological disaster distribution map (whose format is *.jpg) in Liaoning province in 2008, remote sensing image data and monitoring point data of GPS sampling. Geological disaster distribution map in Liaoning province performs division rendering on geological disaster types and development in Liaoning province and it marks the suffered geological disaster position and types in detail.From this map, Liaoning province belongs to frequent occurrence area including collapse, landslide and debris flow. Remote sensing data are mainly recent 3-year-landsat satellite data in eastern region of Liaoning province and QuickBird satellite data in some high risk regions. Remote sensing data process is divided into two aspects: at one aspect, envi4.8 is applied to interpret remote sensing data. At the other aspect, remote sensing data after explanation is introduced into ArcMap to edit, process and update image data and attribute data in database system. In order to accurately construct 3 dimensional model, GPS receiver is applied to net-arrangement monitor monitoring points which are designed in high risk area .

2. Systematic Overall Framework

According to practical requirements, geological disaster database system in Liaoning province is divided into four layers: users' interface layer, functional module layer, technological supply layer and data layer (refer with: Fig. 1).User interface layer is the layer that system directly faces users. Through various functions which are provided by interface, users can operate in visualization to check geological disaster situation in various regions of Liaoning province, query, analyze and perform statistics on geological disasters.Function module layer is various functions of system realization which contains data management, map operation, query analysis, geological disaster evaluation, 3 dimensional display, etc. Technology support layer is technological means which is used during systematic development (i.e. database access technology), advanced programming language (VS2010) and assistant software. Geological disaster information has features of multi-sources, non-determinacy, random abruptness, etc. It is essential for geological diaster database system to establish a database which can fuse multi-source data and database is the basis for system to develop and operate.

3 .Main Function Modules

This system applies 3S technology, adopts multi-source data fusion method and solves difficulties including huge data quantity of geological disaster and strong timeliness as well as spatiality of data. The system also performs mutual query, spatial analysis and statistical analysis on geological disaster data and studies spatial distribution, change tendency and inducing factors. This is the main function for system realization.On the other hand, attribute data based on database in system utilizes hierarchy method to determine various index weight.it adopts fuzzy comprehensive evaluation model to combine GIS technology to establish geological disaster risk evaluation model and to perform hazard analysis as well as evaluation on geological disaster in Liaoning province. It uses combined generating three dimension image model of DEM which is generated by high-definition two-dimension remote sensing image (QuickBird) and GIS platform. It carries out multi-view angle and multi-scale dynamic monitoring on geological disaster in high risk area. These are assistant functions of system realization.

In order to effectively realize system functions, this system mainly designs data management, query analysis, map operation, risk evaluation and three dimension image for users.

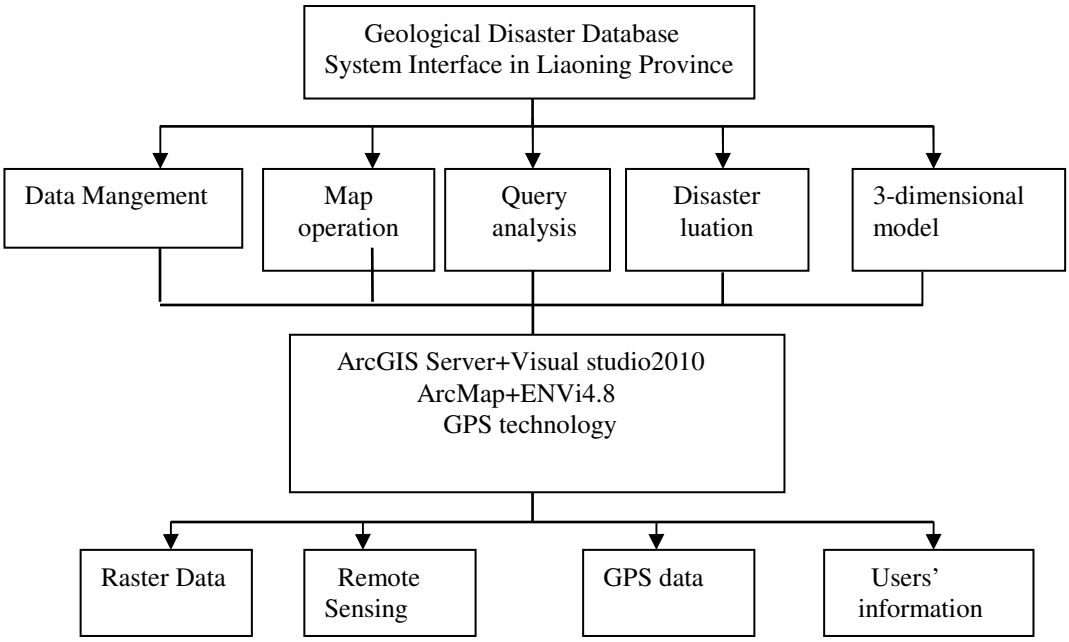


Fig.1 Overall Framework Figure in System

**Systematic Key Technology**

1. 3S-based Technology Integration

3S refers to remote system, global positioning system and geographic information system. 3S integrated technology refers that RS, GPS and GIS are integrated a united organism and it is a very effective space information technology.

Geological disaster information has multi-sources, timeliness, spatiality and random abruptness. In addition, geological disaster needs huge data quantity, these factors become a bottleneck which restricts development and application of geological disaster database system.

In order to solve this problem, this system applies 3S technology to design and research of geological disaster database system in Liaoning province. 3S integration will promote GIS to obtain the ability of accurate acquisition and rapid positioning on current remote sensing information. It can realize rapid updating of database. Under support of analyzing decision model, GIS can rapidly complete multiple dimensions and multiple elements compound analysis .GPS can rapidly and accurately realize precise positioning of disaster area, border characteristic point positioning and observing subsidence observation point. It imports results into space database to provide accurate point-source information for space information analysis of geological diaster. With 3S integration technology, this system can utilize large-area synchronized observation as well as interpretation of remote sensing data, GPS high accuracy and observation and real-time observation and apply functions of GIS platform intelligent analysis, 3 dimension modeling, decision support, etc to construct 3S-based technology geological disaster database system in Liaoning province.

2. ArcEngine Technology

ArcGIS Engine is the new product of ESRI based on ArcGIS9 version. It is a set of complete embedded GIS component library and tool library. It uses GIS application program which is developed by ArcGIS Engine. Meanwhile, it can be operated without ArcGIS Desktop. Using ArcGIS Engine development kit can realize browsing map, query analysis, layer rendering, map layer displaying thematic map, dynamic drawing real-time data, etc.

This system adopts ArcEngine+Vb.net redevelopment method, that is, .net language as programming development language of ArcEngine. At first, through ArcMap to edit, processing multi-source data to generate map, the developed system of ArcEngine+Vb.net is applied to perform query analysis on the generated map data to produce various thematic map and finally constructs model to perform risk evaluation.

## System Realization

1. System Development Environment and Equipment

System adopts object-oriented interface design and uses ArcGIS10.0 series software as development platform. In Vs2010 environment, target-oriented Visual Basic.NET language is applied to develop and system makes use of ArcSDe spatial database engine to store and manage space map data and two dimensions and three dimension map data are made through desk software such as ArcMap and ArcGlobe.

2. Main Interface of System Realization

In order that users can rapidly master geologic disaster database system in Liaoning province, system adopts simple and intuitive interface style. Under condition that interface elements are consistent, according to principle of prominent key-point and clear level, approximate Windows application programming interface is designed.System interface contains 12 forms which are main interface, overlay analysis, SQL query, map layout, etc. Main interface in system is constituted by data display, layers showing and geological disaster introduction, etc.

3. Space Analysis Module

Space analysis is an important part in geographical information system and is also one of important indexes in geographical information system function. The basic purpose of space analysis lies in to obtain new information through deep processing or analyzing space data and applies powerful data management and space analysis function of GIS technology to provide strong technological support for evaluating, predicting and prewarning of geological disaster. Through analyzing geological condition and its relevant environmental background condition, distribution principle of geological disaster is performed comprehensive research and provide direct data support for regional geological disaster easy-occurrence and risk area.

4. Map Operation Module

Map operation in this system contains map element edit and attribute data edit. Besides adding and deleting map element, map element edit also contains space calculation between map elements. Attribute data edit contains attribute table maintenance and attribute value maintenance. In addition, it also has map output function. Map element edit function makes system to perform data maintenance in time and provides powerful support for systematic query analysis, three dimension dynamic display, etc.

## Summary

Geological disaster occurrence has seriously influenced economic and social development in Liaoning province for many years. In particular, recently, with people's lives improvement, social economy rapidly develops, resource exploitation and consumption largely intensifies geological disaster occurrence. Constructing an effective geological disaster database, updating geological disaster data in time and establishing effective geological disaster management as well as analysis model can reduce losses of humans' lives and properties which are caused by geological diaster.

This system applies ArcGis series software as the developed platform. Under Visual Studio program environment, target-oriented Visual basic.net programming language is applied to develop 3S integration technology-based geological disaster database system in Liaoning Province. This system has functions including query analysis, risk evaluation and thematic analysis and three dimension modeling to realize geological disaster management and evaluation in Liaoning Province.

Although system can successfully realize corresponding functions of geological disaster database design, since system development manipulating time is short and it also has some problems which are needing to be improved. Dynamic three dimensional modeling process in high risk area needs to consume a lot of memory and too huge data quantity cause system to slowly operate.

Since Liaoning province area is very large, geological disaster in many areas cannot be updated in time and collecting quantity of GPS data point is still not enough.

**References**

[1] Haifeng Li, Dezheng Gao: *GIS-based Geological Disaster Information Management System Design and Development* (Sichuan Geological University Journal, China 2006).

[2] Xiaodong Wang: *GIS-based Geological Disaster Database Design* (Henan Technology University, China 2007).

[3] Xiaojun Long, Zhengwei He: *Environmental Geological Investigation Management Information System Research Combining AE and Workflow* (Science of Surveying and Mapping, China 2011)

[4] Hao Chen, Zhongliang Cai: *ArcGIS Engine-based Geological Disaster Information Management and Application* (Journal of Geometics, China 2010)

[5] Chonggui Li: *ARCGIS ENGINE GIS Software Development and Application* (Science Press, Peking 2012).

*Applied Mechanics and Materials Vols. 580-583 (2014) pp 2713-2716*
*© (2014) Trans Tech Publications, Switzerland*
*doi:10.4028/www.scientific.net/AMM.580-583.2713*

# Monitoring of flooding water under coal mine based on improved fuzzy clustering

Mengya Nie [1, a], Mengran Zhou [2, b] and Xueqiang Fu [3, c]

[1] Department of Electric Engineering, Anhui University of Science and Technology, Huainan, China

[2] Department of Electric Engineering, Anhui University of Science and Technology, Huainan, China

[3] Department of Electric Engineering, Anhui University of Science and Technology, Huainan, China

[a]709040554@qq.com, [b]mrzhou8521@163.com, [c]1053779421@qq.com

**Keywords:** water quality monitoring, fuzzy clustering, FCM, PSO-FCM.

**Abstract.** Due to the complicated coal mine flooding water quality monitoring data, in order to extract the effective data from vast amounts of data， this article used the fuzzy clustering to analyze the monitoring data processing. This study makes a brief analysis of monitoring data structure， then analyzes the shortcomings of fuzzy C mean clustering algorithm（FCM），which also proposes fuzzy C-means algorithm based on particle swarm optimization (PSO-FCM). Finally samples of the underground water data are used to carry out the instance simulation. The experiment results showed that in dealing with data samples. The algorithm had some advantages and it was worthy of research.

## Introduction

Coal is the main energy sources, coal mine production safety influence the coal industry sustainable development and national energy security which also influence more than 500 million lives and safety and health of miners.

Therefore this paper proposes a clustering analysis will be applied to real-time monitoring of coal mine flooding water system. The system includes a data acquisition, wireless transmission, monitoring and analysis system with integrated real-time display. Because of many kinds of water monitoring data, within a certain period of time the amount of data will be accumulated to a certain extent. It is difficulty to collect early effective warning informations in the vast data. In this paper, a method for using the PSO-FCM to analyze the amount of mine flooding water data can save time and improve efficiency.

## The analysis of coal mine water quality data

Underground water quality monitoring mainly are about the major ion concentration of water, temperature, PH value monitoring. Because of the complexity of coal mine geological environment, water quality data obtained by many, it is unable to determine whether the mine will produce water inrush based on particular ion data. It is necessary to cluster analysis of water quality data. Cluster analysis of water quality data can be available for the qualitative analysis of water quality. Classification algorithms can classify if the ion concentration in the water is within safe value. The clustering algorithm is capable of clustering monitoring data of the underground water quality, the clustering results determine whether the occurrence of future mine water inrush[1].

From the entire real-time monitoring system, including data acquisition modules, wireless communication module and data analysis module, the overall structure is shown in Fig. 1.

Data acquisition device collect the mine flooding water data through sensor, which contains the water temperature, PH value, the ion concentration and the location of measurement data. Wireless transmission will sent the collection data to a remote data monitoring center via GPRS transmission

mode. The data will be received by the monitoring center for data pre-processing and cluster analysis, determine the rationality of data expert systems, and the results is output via graphics and multimedia output.

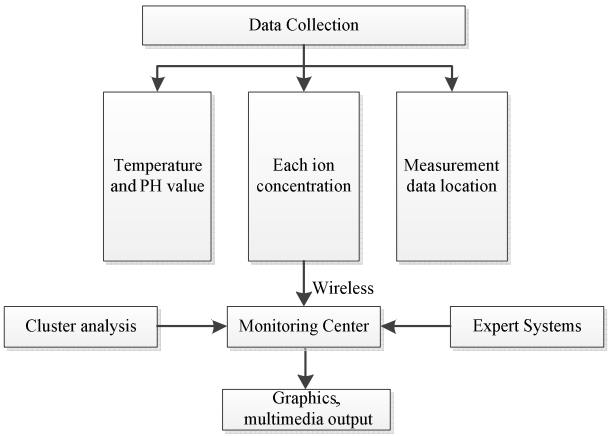


Fig. 1 The structure diagram of underground water quality monitoring data

**FCM algorithm**

Let monitoring samples collection $X=\{x_1, x_{2,\ldots,}x_n\} \in R^s$is a limited sample set in n modes of pattern space, $x_k=\{x_{k1},x_{k2},\ldots,x_{ks}\}^T \in R^s$is a set of data samples,$x_{kj}$ is the monitoring value of the j indicators for the sample $x_k$.

$u_{ik}=u_{xi}(x_{ik})$ ($u_{ik} \in [0,1]$) shows the affiliations about sample $x_k$ and subset $\{x_i\}$. Plurality of subsets of the membership function can be denoted by: $U=[u_{ik}]_{c\times n}$。

Clustering prototype model $P=\{p_1,p_2,\ldots,p_c\}$ ,$p_i$ (i=1,2,…,c) on behalf of the class i for class center .

The calculating process of FCM algorithm is to ensure a minimum objective function $J_m$, then solve the partition matrix U and cluster prototype P.Expression is calculated:

$$J_m(U,P) = \sum_{k=1}^{n}\sum_{i=1}^{c} u_{ik}^m\, d(x_k,p_i). \quad (1)$$

Among $\sum_{i=1}^{c} u_{ik} = 1, u_{ik} \in [0,1], \forall k: d(x_k,p_i) = \|x_k,p_i\|$ ,m is the weighting function, $d(x_k,p_i)$ represent the degree of difference between $x_k$ and $p_i$ , the distance measured between the two vectors.

The formula of iteration rule is as follows:

$$p_i = \frac{\sum_{k=1}^{n} u_{ik}^m x_k}{\sum_{k=1}^{n} u_{ik}^m}, (i = 1,2,\cdots,c). \quad (2)$$

FCM process is as follows:

① Given the number of categories of clustering c, set the iteration stop threshold ε, initialize the cluster prototype model $P^{(0)}$. Set iteration counter b = 0;

② Using formula (2) updates the partition matrix $U^{(b)}$;

③ For $\forall i,k$ ,if $\exists\, d_{ik}^{(b)} > 0$， then： $u_{ik}^{(b)} = \dfrac{1}{\left(\sum_{j=1}^{c} \dfrac{d_{ik}^{(b)}}{d_{jk}^{(b)}}\right)^{\frac{2}{m-1}}}$. (3)

Using equation (3) updates the clustering prototype of pattern matrix $P^{(b+1)}$;

④ If $\left\|p^{(b)} - p^{(b+1)}\right\| < \varepsilon$, then the algorithm stops and divided matrix U and cluster prototype P will be output.Otherwise let b = b +1, go to step two. ‖■‖is a suitable matrix norm[2].

Since the FCM algorithm is find by gradient descent method, so when the number of samples in the larger cluster of cases, algorithm exist locally optimal problems. In addition, initial value impact the convergence speed of FCM. This article uses the advantages of PSO algorithm about global optimization and fast convergence, combining with FCM algorithm presents a new fuzzy clustering algorithm. Using PSO algorithm instead of the iterative process of FCM achieves fuzzy clustering.

## Improved particle swarm optimization algorithm based on FCM

The direction of particle motion not only affected by formerly experience, but also affected by its companion experience. If remember the position of the i particle of the j is $x_i(j)$. The optimal solution search by itself and the whole Particle swarm are $q_i(j)$ and $q_g(j)$.The movement velocity vector for it is $v_i(j)$, then the j +1 generation of the i particle will move:

$$v_i(j+1) = \omega\emptyset_1 v_i(j) + \beta_1\emptyset_2\big(q_i(j) - x_i(j)\big) + \beta_2\emptyset_3\left(q_g(j) - x_i(j)\right). \quad (4)$$

$$x_i(j+1) = x_i(j) + v_i(j+1). \quad (5)$$

$\omega$, $\beta_1$, $\beta_2 \in [0,1]$ are adjustable parameters, $\Phi_1$, $\Phi_2$, $\Phi_3 \in [0,1]$ are random numbers.

For the evaluation of each particle, we define the following fitness function:

$$f(a_i) = \frac{1}{J(\mu,P)+1}. \quad (6)$$

If the clustering effect is better, then J (μ, P) is smaller, individual fitness $f(a_i)$ is higher.

PSO encoded $p_i$. For any particle can be encoded $A_i$ as follows:

$$a_i = \left(p_{i1}, p_{i2}, \cdots, p_{ij}, \cdots, p_{ic}\right). \quad (7)$$

$p_{ij}$ is the i cluster approach in the j cluster center[3].

Each class of n dimensional cluster centers uses real-coded and ultimately P represents the optimal solution. The process of PSO-FCM algorithm can be described as:

① A fuzzy index m was given. The number of categories of clustering c is given. The particle colony scale N is given. Individual cluster centers c samples are randomly selected. In order to compose of an individual we do N times to produce N × c sample points. The random rate of $v_i$ for each individual is update.

② According to the fitness function f(x) and the fitness value of each individual fit calculate $q_i(j)$ and $q_g(j)$. According to the formula (4) the speed of each individual new $v_i$ can be calculated. By formula (5) we a new generation $x_i(j+1)$is obtained.

③ If the abort condition $\left\|p^{(b)} - p^{(b+1)}\right\| < \varepsilon$ is satisfied, the algorithm terminates.

## The simulation

In this paper, the monitoring of a total of nine factors namely are water temperature, PH value, , $C_a^{2+}, M_g^{2+}, K^+, N_a^+, HCO_3^-, Cl^-, SO_4^{2-}$ and other factors. These elements are obtained by sensors, data collected by sensors are passed to the monitoring center via a wireless network. The experimental simulation data are shown in Table 1.

Table1 Monitoring data from underground water quality

| | PH | T/℃ | $\rho(C_a^{2+})$ | $\rho(M_g^{2+})$ | $\rho(K^+)$、$\rho(N_a^+)$ | $\rho(HCO_3^-)$ | $\rho(Cl^-)$ | $\rho(SO_4^{2-})$ |
|---|---|---|---|---|---|---|---|---|
| | 7.36 | 20.98 | 167.46 | 52.38 | 994.27 | 198.29 | 1074.95 | 900.17 |
| | 7.60 | 21.59 | 167.33 | 52.33 | 994.21 | 198.33 | 1074.78 | 900.11 |
| Top | 7.76 | 22.12 | 167.20 | 52.20 | 994.12 | 198.22 | 1075.03 | 900.32 |
| Sand | 7.81 | 22.32 | 166.50 | 51.65 | 994.37 | 198.48 | 1075.22 | 900.61 |
| Layer | 7.42 | 21.23 | 166.97 | 51.97 | 994.23 | 198.39 | 1074.92 | 900.01 |
| | 7.13 | 21.79 | 167.32 | 52.46 | 994.02 | 198.31 | 1074.90 | 799.96 |
| | ... | ... | ... | ... | ... | ... | ... | ... |

To succeed warning before flooding occurs, the data recorded in Table1 are need to use, randomly selected 100 samples from the database as a source of clustering. Software VB6.0 are used to

simulation and use MFC to achieve clustering results, programming and run the program FCM.exe. Enter nine monitoring factors of values in the clustering parameters, set the appropriate parameters, the number of classes c is set to 10, the population size N is 20, weight index m is set to 2, iterative threshold is set to 0.01, and then click on the "clustering" button display the results shown in Fig.2.

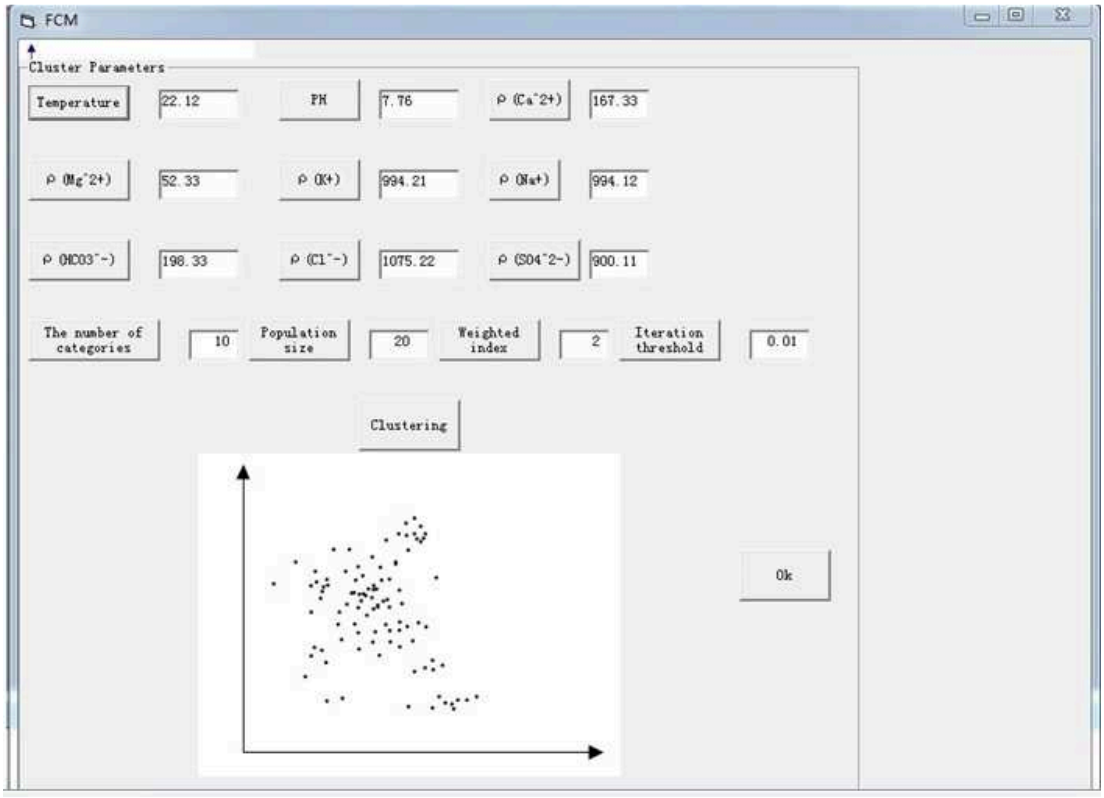


Fig. 2 Simulation results

## Conclusions

From the simulation results In coordinate system the horizontal axis represents the probability of flooding occurs. Cluster analysis is concentrated in a position not far from the origin. Water quality data are in the normal range. In this paper, PSO-FCM algorithm are used to clustering analysis for monitoring data from underground water quality, and achieve early warning case underground flooding disasters occur[4] .First traditional FCM algorithm processes are described, analyzed the shortcomings of the algorithm, so that PSO-FCM algorithm is proposed. Experimental verification, when dealing with incomplete data samples huge cluster, the algorithm has excellent properties, so it is suitable for clustering analysis monitoring data from underground water quality.

## Acknowledgements

This work was financially supported by Key Projects in the National Science & Technology Pillar Program during the Twelfth Five-year Plan Period(2013BAK06B01) and the Anhui academic & technology leaders & back-up candidate research activity funds support projects.

## References

[1] Cunhan Huang, Junjie Huang : Proceedings of AIMSEC /IEEE. IEEE, 982 – 985,(2011)
[2] Weina Wang, Yunjie Zhang, Yi Li and Xiaona Zhang: Proceedings of WCICA /IEEE. IEEE, 3604-3607, (2006)
[3] Dong Y Y, Zhang Y J, Chang C L: Proceedings of MLC/IEEE. IEEE, 2069-2073, (2004)
[4] Chi Zhou, Haibing Gao, Liang Gao: Application Research of Computers, 7-11, (2003).In Chinese.

*Applied Mechanics and Materials Vols. 580-583 (2014) pp 2717-2721*
*© (2014) Trans Tech Publications, Switzerland*
*doi:10.4028/www.scientific.net/AMM.580-583.2717*

# Review on Study of Fire Behavior of Bridges in China

Yongjun Liu[a], Yue Yao[b], Xixin Li[c], Xiaodong Chen[d]

School of Civil Engineering, Shenyang Jianzhu University, Shenyang, Liaoning, 110168, China

[a]liuyongjun1966@163.com, [b]410361971@qq.com, [c]735508469@qq.com, [d]1132298958@qq.com

**Keywords:** Bridge, Fire hazard, Fire scenario, Research needs, Collapse

**Abstract.** In recent years, numerous bridges have been damaged seriously even destroyed by fire hazards in China. Fires in bridges can result in significant losses of life and property, as well as traffic jam. Therefore, fire hazard in bridges is becoming a growing concern in the whole life cycle of design, construction, use and maintenance. There are few literatures on bridge fire incidents and research data in developed countries. In this paper, several typical bridge hazards in China shall be introduced firstly. Some research progress on bridge fire in China is described secondly. Critical research needs and are pointed lastly. The authors hope this paper may be a useful reference for people who hope to learn about the situation and research progress of bridge fires in China.

## Introduction

Recently, numerous bridges have been damaged seriously even destroyed by fires hazards in China (vide Table 1). Although numerous research projects on building fire have been conducted all over the world, much of the data on fire resistance from building elements and cannot directly be used for bridge members. In recent decades, there has been a move toward performance-based design, adoption of which implies a shift away from dependence on empirical and experience-based conventions and toward a rational design and assessment process more firmly rooted in the realistic prediction of structural response under realistic loading, fire, and failure conditions. For predicting realistic performance under performance-based codes, fire hazard in bridges should be an important design consideration.

**Table 1 Major bridge fire incidents in China in recent years**

| No. | Bridge and location | Date | Cause of fire | Damage description |
|---|---|---|---|---|
| 1 | Zhuoshui Covered Bridge cross Qian River, Chongqing | November 28, 2013 | Unknown reasons. | The wooden bridge was destroyed completely. |
| 2 | Guangzhou-Shenzhen Highway bridge near Xiagang | June 29, 2012 | A gasoline tanker was crashed by a heavy truck and ignited the wood beneath the bridge. | Column piers and beam were damaged seriously. 20 people died. |
| 3 | Caogou Bridge of G210 highway in Yulin | August 2, 2011 | Tanker truck exploded. | Eight prestressed box girders were damaged. |
| 4 | Yuqing Bridge, Wuyishan | May 28, 2011 | Children played fire and ignited the wood bridge. | The wooden bridge was destroyed completely. |
| 5 | G15/G324 interchange in Guokeng town | June 26, 2010 | Gasoline tanker truck overturned. | Beam, concrete girders, and underside of the deck were damaged seriously. |
| 6 | Hedong cable-stayed bridge in Guangzhou | December 26, 2008 | Landscape lamps burned. | More than 10 cables were damaged. |

## Typical Bridge Fire Incidents in China

**Historical wood bridges.** China is a country with a long history and large number wood bridges were constructed and some of them are used up to now. Wood can burn in fires, so it is important to

prevent fire initiation and growth in bridges. Otherwise, wood bridges may be destroyed in fires. Yuqing Bridge was a wood bridge erected in 1889, located at Wuyishan, Zhejiang province, China. On May 28, 2011, Yuqing Bridge was destroyed by fire which resulted from playing with fire of two girls (vide Fig.2). Zhuoshui Covered Bridge, crossing Apeng River, Chongqing, was built in 1591 and is recognized as the longest covered bridge in Asia(vide Fig.3). On November 28, 2013, the 303-metre wooden bridge was destroyed after a fire because it was constructed entirely of wood without any nails (vide Fig.4).

Fig.1 Yuqing Bridge

Fig.2 Yuqing Bridge in fire

Fig.3 Zhuoshui Covered Bridge, crossing Apeng River, Chongqing

(a)

(b)

Fig.4 Zhuoshui Covered Bridge during fire

**Concrete girder bridges.** Reinforced concrete is commonly used as a primary material in bridge girders, bridge piers, roadway slabs. The mechanical properties of concrete, such as initial stiffness, are not immune to degradation when subjected to elevated temperatures. On the evening 21:30 of August 2nd 2011, a tanker truck carrying 24 tons of gasoline crashed with a truck carrying coal on the Caogou Bridge of G210 in Yulin, Shanxi Province, China. The tanker truck exploded and total 9 trucks caught fires (vide Fig.5). Eight damaged prestressed box girders of the bridge were changed (vide Fig.6) according to the on-site inspection, and the bridge opened to public after closed 56 days.

Fig.5 Caogou Bridge fire

Fig.6 Install a new box girder

On the morning 4:35 of June 26th 2010, a tanker truck carrying 21 tons of gasoline overturned and burst into flames (vide Fig.7) on the G15/G324 interchange in Guokeng town, Fujian Province, China. The tanker truck fire damaged the bridge seriously because the concrete cover of some main girders spalled (vide Fig.8) and steel reinforcements exposed to fire directly and some fell down to ground, as a result, the bridge was demolished.

Fig.7 Guokeng highway bridge during fire

Fig.8 Guokeng highway bridge after fire

On the morning 4:30 of June 29, 2012, a tank truck carrying 40 tons of solvent oil impacted by a lorry full of concrete poles on the Guangzhou-Shenzhen Highway bridge near Xiagang, and the oil leaked out and ignited the large amount of wood beneath the bridge (vide Fig.9), 20 people lost their life. The column piers and beam were damaged seriously (vide Fig.10).

Fig.9 Bridge in fire

Fig.10 Bridge after fire

**Cable-stayed bridges.** It is necessary to consider the impact of fire on a major cable-stayed bridge because that collapse or closure of the bridge may lead to unacceptable commercial consequences. Hedong cable-stayed bridge (vide Fig.11), in Guangzhou, China, crosses Pearl River with the main span of 360m. On the evening 19:10 of December 26, 2008, fire occurred round more than 10 cables at the level of more than 100m above the bridge. The fire last 4 hours, and total 144 cables were checked after the fire. Xupu Bridge is a cable-stayed bridge span Huangpu River in Shanghai, China. Since its completion, Xupu Bridge has seen occasional fires in 2008 and 2011. On May 3, 2011, the bridge caught fire due to a chemical tank truck carrying xylene burst into flames (vide Fig.12). The bridge was immediately closed to traffic.

Fig.11 Hedong bridge, Guangzhou

Fig.12 Close up of Xupu bridge fire

## Review of Research Progress in China

**Numerical simulation.** The thermal and structural behavior of a steel girder of highway bridge overpass in the East Bay's MacArthur Maze in Oakland collapsed on April 29, 2007 was studied by using general purpose finite element analysis software ABAQUS and ANSYS[1,2](vide Fig.13). It is difficult to conduct full-scale test study of fire effect on overall behavior of cable-stayed bridges. Numerical simulation is a useful way. Potential fire scenarios relevant for a cable-stayed bridge crossing the Yangtze River are analyzed by Liu and Ning[2]. The temperature distribution in key elements and the global structural behavior of the bridge under tanker truck fires is calculated by using general purpose finite element analysis software ANSYS(vide Fig.14).

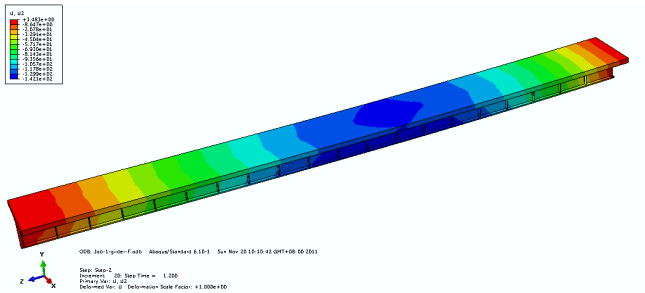

Fig.13 Vertical displacement of girder in fire[1]

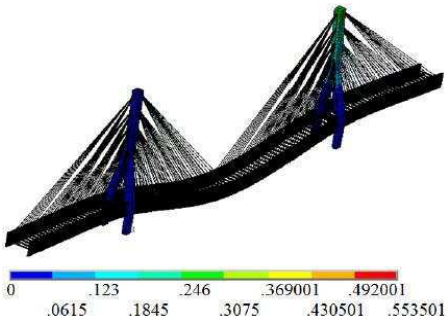


Fig.14 Vertical displacement in fire[2]

**Test study.** Identification of failure modes and validation of advanced numerical models requires well controlled full-scale experiments. Some experimental program was performed to analyze the effects of fire on bridges. Recently, a new facility in Shenyang Jianzhu University (SJZU), Liaoning Province of China, was established for structural fire research (vide Fig.15).

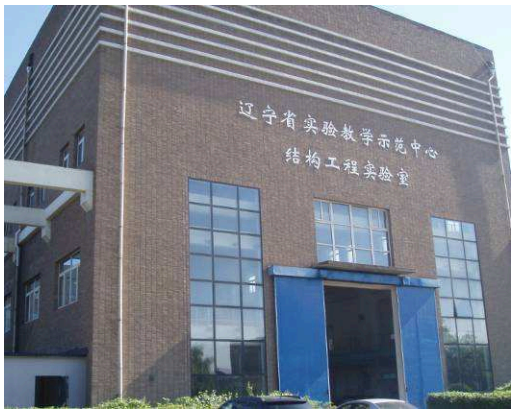


(a) Exterior view

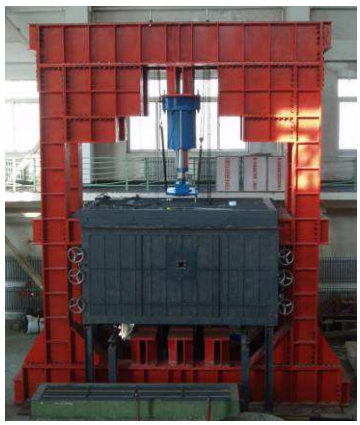

(b) Furnace and loading system

Fig.15 New facility in SJZU for structural fire research

## Research Needs in China

**Test study on fire scenarios.** The selection of suitable fire scenarios for bridge fire resistance design is very important. Therefore, special experimental studies on temperature-time curves of tanker truck fires, which are commonly the cause of bridge fires, are urgent to be conducted.

**Fire prevention and protection technology.** If fire prevention and protection technologies were used in some collapsed wood and steel bridges, the collapse could have been prevented. There is a need to develop performance based design guidelines and standards for fire protection design of steel bridges.

**Rapid girder replacement technology for concrete bridge.** Concrete girder bridges have been widely used in highway bridges, which are critical components of the nation's transportation network. Some research projects are needed to identify strategies and technologies to restore the use of a damaged bridge quickly. In addition, how to estimate the remaining fatigue life of bridges exposed fire is a key issue to study.

**International cooperation.** China is a developing country**,** it is essential to cooperate with experts of developed country for Chinese researchers. The cooperation includes sharing fire test data, co-designing large scale bridges for fire safety such as Tianxingzhou cable-stayed bridge cross Yangtze River in Wuhan[3].

## Conclusions

Conclusions derived from the work include the following:

(1)Fire hazards have occurred in bridges frequently in China, and some fires have led to partial or complete collapse of bridges. Critical bridges, say large span cable-stayed bridges, should be designed to have satisfactory fire resistance and to endure severe fire hazard without major damage or collapse.

(2)Extensive researches including large scale fire test of bridges are urgently needed, which is the base for us to put forward detailed guides, codes, and standards for fire safety design of bridges.

## Acknowledgments

This work is supported by the Scientific Research Foundation for the Returned Overseas Chinese Scholars, State Education Ministry of P.R. China.

## References

[1] Y. Liu, G. Wang, Y. Song, "Finite element analysis of fire behavior of steel girders in bridges". Advanced Materials Research, Vol.594-597(2012), p.2296

[2] Y. Liu, B. Ning, Y. Wang, "Study on thermal and structural behavior of a cable-stayed bridge under potential tanker truck fires". Applied Mechanics and Materials, Vol.238(2012), p.684

[3] S. Montens, H. Lam, P. Moine, J. Vollery, "Tianxingzhou bridge: world record span for railway cable-stayed bridges". Proceedings of 34th International Symposium on Bridge and Structural Engineering, Venice(2010), p.1

*Applied Mechanics and Materials Vols. 580-583 (2014) pp 2722-2726*
*© (2014) Trans Tech Publications, Switzerland*
*doi:10.4028/www.scientific.net/AMM.580-583.2722*

# Risk Assessment of Debris Flow Based on Multi-Objective Fuzzy Pattern Recognition Method in Mountain Highway Construction

Yue Wang

Inner Mongolia Kaitong Construction Co., Ltd, Erdos Street, Huhehaote, 010010, China

ktwy6789@sina.com

**Keywords:** debris flow, multi-objective fuzzy pattern recognition, evaluation index, grade of risk

**Abstract:** It is inevitable that road routes cross the valley landforms in the construction of mountain road, and the debris flow risk assessment is one of the important basis works of engineering geological investigation. This paper presents the evaluation indexes and the classification standards of the danger evaluation based on the surveying data of road and analysis of the developing characteristic, formation conditions and influent factors of the debris flow in mountain highway construction area, Zhangjiakou city. With the multi-objective fuzzy pattern recognition method, the evaluation model is also established. With this model, the 15 debris flow valleys in the construction area are evaluated. The result is consistent with the field surveying result, which proves that the model represented by this paper is feasible and effective, and the results can reflect the actual situation. Thus, the multi-objective fuzzy pattern recognition method can be one of the methods to evaluate the danger grade of the debris flow.

## Introduction

Debris flow is a common unexpected geological disaster in mountainous areas. It happens suddenly, lasts shortly, destroys strongly and endangers greatly. The danger evaluation of debris flow is focus on its possibility of happening, which is mainly in the debris flow research. Danger evaluation is important for the economic development layout in mountainous area, the forecasting of debris flow and the disaster controlling of debris flow. Danger evaluation is an extremely complex job. After the research of many scholars, some evaluation methods have been mastered, such as the empirical formula law, multivariate statistics method and fuzzy evaluation method [1]. Each method has advantages and disadvantages. At present, there isn't a widely accepted method for the evaluation.

Based on the surveying data in mountain highway construction area, Zhangjiakou city, this paper applied the multi-objective fuzzy pattern recognition method to establish a model for calculating the debris flow danger grade. With this model, the 15 debris flow valleys in the construction area are evaluated. The result is consistent with the field surveying result, which proves that this model is feasible and effective.

## Selection and classification of danger evaluation index of debris flow

According to current situation and studying level of the debris flow in Beijing mountain area, the danger is divided to 5 grades, which is no danger (I), low danger (II), medium danger (III), less high danger (IV) and high danger (V). Thus, the danger grades of debris flow are made up of the field V = { I , II , III , IV , V }.

Based on the previous research, we find that whether the debris flow can occur and the possibility of this occurring depend on three basic conditions[2], which are the rich solid masses, precipitous landform and concentrated water replenishment. These conditions are controlled by geology, geomorphic, climate, plant cover and human activities. Based on the research of the development characteristic, formation condition and activity regular of the debris flow in Huairou County, this

paper chose basin area ($F_1$), relative differential height of basin ($F_2$), gradient of valley ($F_3$), degree of slope ($F_4$), percentage of the plant coverage ($F_5$), quantity of the loose fill ($F_6$), frequency of joint fissure ($F_7$), average rain in flood season ($F_8$), the most daily rain in flood season ($F_9$) and the most hour rain in flood season ($F_{10}$) to be the evaluation indexes. The division standards of each index are shown in Table 1. Thus, the evaluation indexes are made up of the field $F = \{F_1, F_2,\ldots, F_{10}\}$.

Table 1. Evaluating index and classification

| index | | Danger grades | | | | |
|---|---|---|---|---|---|---|
| | | Ⅰ | Ⅱ | Ⅲ | Ⅳ | Ⅴ |
| landform | basin area（$km^2$）$F_1$ | >10 | 10~5 | 5~1 | 1~0.5 | <0.5 |
| | relative differential height of basin（m）$F_2$ | <200 | 200~300 | 300~400 | 400~500 | >500 |
| | gradient of valley（‰）$F_3$ | <50 | 50~100 | 100~150 | 150~200 | >200 |
| | degree of slope（°）$F_4$ | <15 | 15~25 | 25~35 | 35~45 | >45 |
| | percentage of the plant coverage（%）$F_5$ | >80 | 60~80 | 40~60 | 40~20 | <20 |
| geology | quantity of the loose fill（$10^4m^3$）$F_6$ | <0.1 | 0.1~1 | 1~3 | 3~5 | >5 |
| | frequency of joint fissure（peice/$m^2$）$F_7$ | <5 | 5~10 | 10~15 | 15~20 | >20 |
| Water source | average rain in flood season（mm）$F_8$ | <350 | 350~400 | 400~450 | 450~500 | >500 |
| | the most daily rain in flood season（mm）$F_9$ | <100 | 100~200 | 200~300 | 300~400 | >400 |
| | the most hour rain in flood season（mm）$F_{10}$ | <30 | 30~60 | 60~90 | 90~120 | >120 |

**Multi-objective fuzzy pattern recognition model for danger evaluation**

According to fuzzy pattern recognition theory, danger evaluation problem is defined as limited region *U*. The n coming valleys are the element in the region. Each element can be described by m factors. The relation of above definition is expressed as:

$$U = \begin{bmatrix} u_{11} & u_{12} & \ldots & u_{1m} \\ u_{21} & u_{22} & \ldots & u_{2m} \\ \ldots & \ldots & u_{ij} & \ldots \\ u_{n1} & u_{n2} & \ldots & u_{nm} \end{bmatrix} \tag{1}$$

$u_{ij}$ is the value of the $j$ th index in $i$ th debris flow valley ( $i$ =1,2…, $n$; $j$ = 1,2,…$m$).

The grading is defined as evaluation field V and divided to $c$ grades, which is represented as:

$$V = \begin{bmatrix} a_{11} & a_{12} & \ldots & a_{1m} \\ a_{21} & a_{22} & \ldots & a_{2m} \\ \ldots & \ldots & a_{ij} & \ldots \\ a_{c1} & a_{c2} & \ldots & a_{cm} \end{bmatrix} \tag{2}$$

$a_{ij}$ is the value of the $j$ th index in $i$ th grade ( $i$ =1,2…, $c$; $j$ = 1,2,…$m$).

**Determination of the membership grade.** The membership grade is divided to increasing type and decreasing type based on the increasing and decreasing of the index value.

The increasing type is that when the index value is bigger, whose membership grade $\gamma_{ij}$ is getting bigger. The relation is represented as

$$\gamma_{ij} = (u_{ij} - a_{i\min}) / (a_{i\max} - a_{i\min}) \tag{3}$$

The decreasing type is that when the index value is bigger, whose membership grade $\gamma_{ij}$ is getting smaller. The relation is represented as

$$\gamma_{ij} = (a_{i\max} - u_{ij}) / (a_{i\max} - a_{i\min}) \tag{4}$$

The value $a_{i\max}$ and $a_{i\min}$ are the maximum and minimum value of the *j* th index in matrix V.

The value $\gamma_{ij}$ is the relative membership grade of the *j* th index in *i* th debris flow valley ( $i$ =1,2…, $n$; $j$ = 1,2,…$m$). Thus, the relative membership grade matrix $R$ can be obtained. In this matrix, there are *n* debris flow valleys with *m* indexes.

$$R = \begin{bmatrix} \gamma_{11} & \gamma_{12} & \cdots & \gamma_{1m} \\ \gamma_{21} & \gamma_{22} & \cdots & \gamma_{2m} \\ \cdots & \cdots & \gamma_{ij} & \cdots \\ \gamma_{n1} & \gamma_{n2} & \cdots & \gamma_{nm} \end{bmatrix} \tag{5}$$

Based on the above analysis, we can find that there is an optimum grade, each of whose relative membership grade value is 1; there is a worst grade, each of whose relative membership grade value is 0.

**Determination of weight.** Value $\omega$ is presented to reflect the weight of each evaluation index to the result. The weight vector is $\omega = (\omega_1, \omega_2, ..., \omega_m)$. The sum of the value $\omega$ is 1.

$$\sum_{i=1}^{m} \omega_i = 1 \tag{6}$$

Debris flow is the synthetically result of various factors. However, their influence and position are different. To reflect this difference objectively, the weight of each index is determined by step analysis method and the expert marking method.

$$\omega = \{0.062, 0.105, 0.098, 0.096, 0.034, 0.207, 0.095, 0.102, 0.100, 0.101\} \tag{7}$$

**Establishing the model.** There are various kinds of multi-objective fuzzy pattern recognition operators. Among these operators, the weighted average operator can not lose the information. Thus, the model with the least sum of the distance based on the generalized weight is chosen [3].

The value $u_i$ expresses the relative excellent membership grade of *i* th sample, and the value $(1-u_i)$ expresses the relative bad membership of *i* th sample. In fuzzy field theory, membership grade can be used as weight [4]. Equation (8) and (9) can used to calculate the distance from the sample to the excellent and bad grades.

The distance from sample to excellent grade can be expressed as

$$D_{ig} = u_i p \sqrt{\sum_{j=1}^{m} [w_j (1-\gamma_{ij})]^p} \tag{8}$$

The distance from sample to bad grade can be expressed as

$$D_{ib} = (1-u_i) p \sqrt{\sum_{j=1}^{m} [w_j (\gamma_{ij}-0)]^p} \tag{9}$$

In equation (8) and (9), $P$ is a distance modulus. When $P$ =1, it is the Haiming distance; when $P$=2, it is the Euclidean distance.

To find the solution of value $u_i$, an optimize criterion is built as follows: Sum of the excellent distance square and the bad distance square is minimal [5], which is expressed as

$$\min F(u_i) = D_{ig}^2 + D_{ib}^2 = u_i^2 \left\{ \sum_{j=1}^{m} [w_j (1-\gamma_{ij})]^p \right\}^{2/p} + (1-u_i)^2 \left\{ \sum_{j=1}^{m} [w_j (\gamma_{ij}-0)]^p \right\}^{2/p} \tag{10}$$

To differentiate the equation (10) and make the value $u_i$ to be zero, the solution is as

$$u_i = \frac{1}{1+\left[\frac{\sum_{j=1}^{m}(w_j \mid \gamma_{ij}-1\mid)^p}{\sum_{j=1}^{m}(w_j * \gamma_{ij})^p}\right]^{2/p}} \tag{11}$$

Equation (11) is the model with the least sum of the distance based on the generalized weight.

According to the current situation and studying level of this area, the danger grade can be decided by the logics method with four values and five grades. The calculated result can be intercepted and formatted as a table of the fuzzy danger grade. With the value $u_i$, the danger grade of the debris flow can be looked up from table 2.

Table 2 Danger grading characteristic of the debris flow

| grades | Danger grades | Fuzzy field | Characteristic description |
|---|---|---|---|
| Ⅴ | High danger | $u$>0.65 | Each index is the most dangerous |
| Ⅳ | Less high danger | 0.5<$u$<0.65 | Each index is dangerous, has great threaten |
| Ⅲ | Medium danger | 0.35<$u$<0.5 | Few indexes are dangerous, can breakout a disaster |
| Ⅱ | Low danger | 0.2<$u$<0.35 | Very few indexes are dangerous, may have a disaster |
| Ⅰ | No danger | $u$<0.2 | No danger |

**Example analysis**

According to the surveying data of the debris flow in mountain highway construction area, Zhangjiakou city, the danger division is made for 15 typical valleys. The measured values of each valley are shown in Table 3.

Table 3 Measured values of the valley debris flow

| No. | Valley name | $F_1$ | $F_2$ | $F_3$ | $F_4$ | $F_5$ | $F_6$ | $F_7$ | $F_8$ | $F_9$ | $F_{10}$ |
|---|---|---|---|---|---|---|---|---|---|---|---|
| 1 | Nanling valley | 5.25 | 225 | 111 | 27.8 | 85 | 2.1 | 5.3 | 412.5 | 115 | 38 |
| 2 | Beidadi valley | 5.14 | 375 | 105 | 37.5 | 80 | 5.04 | 5.4 | 412.5 | 115 | 37 |
| 3 | Xiaodong valley | 5.37 | 367 | 67 | 17.4 | 60 | 4 | 5.4 | 415 | 115 | 38 |
| 4 | Mingzi valley | 5.05 | 301 | 120 | 20 | 80 | 4.14 | 5.4 | 412.5 | 114 | 38 |
| 5 | Dongyu valley | 5.98 | 354 | 115 | 16.5 | 85 | 2.76 | 11 | 412.5 | 105 | 36.5 |
| 6 | Detian valley | 5.77 | 344 | 60 | 28 | 80 | 2.9 | 5.9 | 420 | 102 | 36 |
| 7 | Longquanyu valley | 3.42 | 512 | 121 | 17.5 | 75 | 5.3 | 12.1 | 412.5 | 102 | 36 |
| 8 | Qian'anling valley | 5.07 | 478 | 57 | 16.8 | 80 | 3.87 | 6.5 | 412.5 | 100 | 35 |
| 9 | Xishandong valley | 2.54 | 380 | 137 | 21 | 85 | 2.5 | 12.8 | 413.5 | 102 | 37 |
| 10 | Xinshanxi valley | 5.19 | 450 | 129 | 36 | 80 | 5.1 | 3 | 412.5 | 102 | 36.5 |
| 11 | Sancha valley | 6.04 | 365 | 78 | 20 | 70 | 5.2 | 13.1 | 412.5 | 103 | 37 |
| 12 | Yingbei valley | 5.13 | 324 | 100 | 17.5 | 80 | 4.1 | 2 | 415.5 | 103 | 37 |
| 13 | Dong'anzi valley | 3.12 | 345 | 147 | 17.5 | 85 | 5.13 | 6.3 | 412.5 | 101 | 36 |
| 14 | Yangshu valley | 5.41 | 305 | 109 | 17.5 | 85 | 5.19 | 2 | 412.5 | 81 | 32 |
| 15 | Shuiquanyu valley | 5.04 | 984 | 65.6 | 38.99 | 85 | 5.4 | 11.2 | 412.5 | 119 | 41 |

The danger value of each sample can be calculated by equation (10). In the calculation, the value $n$ is 15, $m$ is 10, $P$ is 2, $c$ is 5. The results are shown in table 4. From the values in table 4, we can find that the calculation results are almost the same as the measured results, which proves that the multi-objective fuzzy pattern recognition method is feasible in the danger evaluation of debris flow.

Table 4 Danger evaluation results of the debris flow valley

| No. | Valley name | Danger value | grade | Measured results |
|---|---|---|---|---|
| 1 | Nanling valley | 0.178 | Ⅰ | Ⅰ |
| 2 | Beidadi valley | 0.595 | Ⅳ | Ⅳ |
| 3 | Xiaodong valley | 0.405 | Ⅲ | Ⅲ |
| 4 | Mingzi valley | 0.432 | Ⅲ | Ⅲ |
| 5 | Dongyu valley | 0.294 | Ⅱ | Ⅱ |
| 6 | Detian valley | 0.283 | Ⅱ | Ⅱ |
| 7 | Longquanyu valley | 0.629 | Ⅳ | Ⅲ |
| 8 | Qian'anling valley | 0.427 | Ⅲ | Ⅲ |
| 9 | Xishandong valley | 0.349 | Ⅲ | Ⅲ |
| 10 | Xinshanxi valley | 0.587 | Ⅳ | Ⅳ |
| 11 | Sancha valley | 0.560 | Ⅳ | Ⅳ |
| 12 | Yingbei valley | 0.410 | Ⅲ | Ⅲ |
| 13 | Dong'anzi valley | 0.548 | Ⅳ | Ⅳ |
| 14 | Yangshu valley | 0.489 | Ⅲ | Ⅲ |
| 15 | Shuiquanyu valley | 0.658 | Ⅴ | Ⅳ |

## Conclusions

The risk Degree of debris flow is closely related with the factors such as topography, geology, rainfall, vegetation, rainfall, etc. During these factors, some is difficult to choose and to decide the number. The multi-objective fuzzy pattern recognition method can obtain all of the influent factors and have advantages in the multi-objective synthesis judgment problem of debris flow. From the risk evaluation of debris flow valleys in mountain highway construction area, Zhangjiakou city, the model represented by this paper is proved to be feasible and effective, and the results can reflect the actual situation. Thus, the multi-objective fuzzy pattern recognition method can be one of the methods to evaluate the danger grade of the debris flow.

The risk evaluation of debris flow is an extensively involved and synthesis problem. The research of multi-objective fuzzy pattern recognition method in this field is not many. In this paper, the application of this method is superficial discussed. Further, the choosing of the evaluation index and membership grade function establishing need more research.

## References

[1] Xuewu1 Wang. Application of Multi-Layer Fuzzy Comprehensive Evaluation Method in Debris Flow Assessment, Journal of Catastrophology, Vol.19 No.2 (2004), p.1-6.

[2] Yongming Wei, Youyu Xie, Yongqiu Wu. Applications of Relativity Analysis Method and Fuzzy Synthetic Assessment Method in Classification of Dangerous Degree of Debris Flow. Journal of Natural Disasters, Vol.7 No.2 (1998), p.109-117.

[3] Kaili XU, Yongjiu Wang, Baozhi Chen. Multi-Objective Fuzzy Assessment Models and Calculate Method of Assessment Grade, Journal of Northeastern University（Natural Science） Vol.22, No.5 (2001), p.568-571.

[4] Keping Zhou, Yong Gao, Hongwei Deng, Feng Gao. Application of Fuzzy Pattern Recognition Model in Re-vegetation Suitability Evaluation in a Mining Site, Journal of Safety and Environment, Vol.12 No.5 (2012), p.142-146.

[5] Peizhuang Wang. Fuzzy Field and the Application. Shanghai: Shanghai Science Press. (1983).

*Applied Mechanics and Materials Vols. 580-583 (2014) pp 2727-2730*
*© (2014) Trans Tech Publications, Switzerland*
*doi:10.4028/www.scientific.net/AMM.580-583.2727*

# Case study of fire risk management of tourist hotels

Ruei-JiunShiu[1,a], Shao-Tsai Cheng [2,b] , I-Tsen Liu [3,c]

[1]Graduate, Department of Construction Management, ChungHuaUniversity, HsinChu, Taiwan

[2]Professor, Department of Construction Management, ChungHuaUniversity, HsinChu, Taiwan

[3] Ph.D.Student, Department of Civil Engineering, ChungHuaUniversity, HsinChu, Taiwan

[a]elvis1008@yahoo.com.tw, [b]shaotsai@chu.edu.tw, [c] a380901@gmail.com

**Key words:** Fire, safety, risk management.

**Abstract**. Tourist hotels are part of service industry, thus fire safety issues are particularly important. Due to the complexity of the hotel's construction, most of the tourists are not familiar with the environment.In case of fire it would be hard for them to evacuate the building. Therefore, this study collects and organizes documents, regulations and cases. By applying risk management this study summarizes the key items of the fire safety risk assessment application are: Whether fire evacuation facilities have been blocked and major risk items must be examined daily.

## Preface

The patterns of area usageintourist hotels are complex, most of the tourists are not familiar with the living environment. Hotels' managers' attitude toward fire safety, maintenance of fire evacuation facilities and adaptation to fire are all important factors of fire safety. It is hard for people to evacuate from a fire, thus fire safety depends on managers'self-reinforcingof fire safety. The study's intentions are to find out hotels' damage caused by fire and provide quantization of fire safety risk identification and analysis methods, as to be standers and operation examples of each tourist hotels' fire safety risk assessment.

Examples of fire safety assessment techniques are ISO/PD 16732[1], BSI 7994-7[2], NFPA 551[3] and etc. In addition, there arefire safety assessment guidesin SFPE [4-6]. On the aspect of regulations, there are many references of fire risk and construction risk in ICC and ICC Performance Code for Buildings and Facilities [7,8]. NFPA 5000[9] and NFPA 101[10] have reveal the importance of reorganization of the smallest risk and reliability factors.

This study has collected domestic tourist hotels-related public places' fire safety assessment documents. Through brain storming, deeply interview with experts, cases analyzing and etc. And then comprehensively summarize factors of fire management's risk assessment.

## Impact factors of tourist hotel's fire safety.

Contents of expert's questionnaire are made of secondary information collection, brainstorming, interview with experts, domestic construction and fire-related regulation, conflagration cases, then sum up the impact factors of tourist hotels' fire risk identification. This study concludes the aspects of fire risk identification, among them there are 108 impact factors. As shownin Table1.

Table1 Tourist's hotel's fire risk factors and terms.

| Factors of fire risk identification | terms | Factors of fire risk identification | terms |
|---|---|---|---|
| **1. Fire preventions** | | 2.2 Prevention of fire spreading methods. (According construction regulations) | 4 |
| 1.1 Electronic fire | 5 | 2.3Evacuation lighting facilities. | 2 |
| 1.2.Smoke | 5 | 2.4 Fire safety signs and instructions. | 2 |
| 1.3 Arson | 3 | 2.5Fire alarm facilities. | 4 |

| | | | |
|---|---|---|---|
| 1.4 Potable heat facilities. | 3 | 2.6Fire extinguishers. | 2 |
| 1.5Cooking | 3 | 2.7Automatic fire extinguish systems. (According firefighting regulations) | 4 |
| 1.6Lighting | 1 | 2.8Fixed systems and facilities. | 1 |
| 1.7Environmental sanitation | 5 | **3.Fire safety management.** | |
| 1.8 Damage caused by Exterior contractor and interior construction. | 3 | 3.1Disaster response procedures, and deployment. | 13 |
| 1.9 hazardous material | 1 | 3.2Training and drill. | 14 |
| 1.10 Other major hazards including normal fire prevention methods. | 1 | 3.3Examination and maintain. | 11 |
| **2. Fire protections.** | | 3.4Records. | 5 |
| 2.1 Fire evacuation facilities. (According to public safety examinations) | 16 | | |

**Questionnaire results and analysis.**

**Questionnaire.**Applying qualitative risk analysis, this study use Likert scale to estimate the three aspects of 108 factors' risk occurring rate and severe degree. 8 tourist hotels, 6 international hotels and 2 normal tourist hotels in Taichung are targets of the questionnaire. International hotels are as followed:Howard Hotel, Windsor Hotel, Hotel National, Splendor Hotel, Evergreen Laurel Hotel and Plaza International Hotel. Normal hotels are Taichung Harbor Hotel and Dragon Valley Hotel. The questionnairesare also finished by firefighting-related people, insurance companies employees total of 31 experts questionnaires were handed out and finished

**Results and discussion.**This study statistic analyzed the results of the questionnaire, calculated the average and by the product of the probability of the risk occurring and severe degree, this study calculated the RPN value and risk order. This study applied Plato 80-20 law to find out top 20% items. There are 22 major impact factors. Major impacts are as shown in table 2, C stands for severe degree, P stands for rate of occurring and R stands for risk priority number (RPN).

Table 2.Top 20% of tourist's hotels fire risk analysis major items.

| Order | Risk impact factors | C | P | R=C*P |
|---|---|---|---|---|
| 1 | 2.1.12 Whether hotels' evacuation passages(corridors, stairs and safety stairs) are blocked or not? | 3.61 | 3.16 | 11.42 |
| 2 | 1.1.1Is there any prevention of electronic fire measure in hotel? | 3.13 | 2.84 | 8.88 |
| 3 | 2.1.14 Whether the evacuation roof top has blocked the way of evacuation? | 3.10 | 2.81 | 8.69 |
| 4 | 1.2.4 Whether it is forbidden to smoke in some special area(such as places stocked with many inflammables)? | 2.71 | 2.55 | 6.91 |

| | | | | |
|---|---|---|---|---|
| 5 | 2.2.4 Whether there is a fire proof Rolling Door to protect the evacuation facilities? Or facilities that can protect evacuation facilities from early stage of fire, smoke and heat? | 2.65 | 2.58 | 6.83 |
| 6 | 3.1.1 Is there a firefighting administrator? | 2.61 | 2.55 | 6.66 |
| 7 | 3.1.3 Whether firefighting management missions have been firmly executed.? | 2.61 | 2.55 | 6.66 |
| 8 | 1.8.1 Whether exterior contractor fully comprehends the fire safety regulations? | 2.61 | 2.52 | 6.57 |
| 9 | 3.1.12 Whether there is a good contact with fire station? | 2.55 | 2.55 | 6.49 |
| 10 | 1.4.1 Is there any management measures for portable heat facilities? | 2.58 | 2.52 | 6.49 |
| 11 | 1.3.1Prevention of arson? | 2.65 | 2.45 | 6.48 |
| 12 | 2.1.4Whether it is easy to open the safety doors? | 2.58 | 2.45 | 6.33 |
| 13 | 3.1.2Designation of experts for assist of fire prevention and protection measures? | 2.58 | 2.45 | 6.33 |
| 14 | 2.1.1Facilities that can help people successfully evacuate in the case of fire? | 2.52 | 2.48 | 6.25 |
| 15 | 2.1.5 Whether exists are open toward to the right evacuation way? | 2.58 | 2.42 | 6.24 |
| 16 | 2.7.3 Installation of CO2 fire extinguishers in power room and boiler room? | 2.55 | 2.42 | 6.17 |
| 17 | 2.1.2Whether evacuation routes conform to regulations? | 2.48 | 2.45 | 6.09 |
| 18 | 1.1.5 Is there a person in charge of management of extension cords and transforms usage? | 2.42 | 2.52 | 6.09 |
| 19 | 2.1.3 Whether there are enough exits? | 2.55 | 2.39 | 6.08 |
| 20 | 1.5.1 Is there any fire safety protection to prevent cooking fire? | 2.48 | 2.42 | 6.01 |
| 21 | 1.1.2 Whether fixed electronic facilities are examined and test regularly? | 2.55 | 2.35 | 6.00 |
| 22 | 1.5.3 Installation of oil fire extinguishers in kitchen? | 2.55 | 2.35 | 6.00 |

The questionnaire separates into tourist hotel managers, insurance companies' employees and firefighting facilities managers, firefighting technician sections. The case that the result has the highest overall score, Such case as firefighting related person believes that electrician would ignore the indoors decoration's regulations in order to save money, and thus buried the risk of electric fire.

From this study's questionnaire analysis, could found out that in the keys of fire prevention measures, fire evacuation facilities to impact factors, whether it is easy to open evacuation door has the highest value of RPN impact factors. This shows that it is the first priority that tourist hotel fire risk analyses have to cope with. It is also the most important factor of fire safety.

**Fire safety managementstrategy.** This study has put 22 major risk items into a daily examination management table and 86 of subordinate risk items into seasonal examination management table, by these two tables we can efficiently lower the risk of fire.

## Conclusion

1. According to questionnaire analysis, whether fire evacuation facilities have been blocked has the highest RPN value, it is also the first implementation priority of tourist's hotel fire risk management assessment. It can effectively prevent the failure of evacuation.
2. Implementation of daily risk items check up can improve the tourist's hotel safety and it can also simplify the examination procedures.
3. From the aspect of fire risk management assessment, major risk items assessment can reduce the risk of fire, simplify examination procedures. It is worth it to promote the rules of fire risk management assessment.

## References

[1] ISO/PD 16732:2005, Fire Safety Engineering－Guidance on fire risk assessment,ISO.

[2] ISO/PD 16733:2006, Fire Safety Engineering－Selection of design fire scenarios and design fires, ISO.

[3] NFPA 551, Evaluation of Fire Assessments, NFPA.

[4] Society of Fire Protection Engineers, 2005, SFPE Engineering Guide to Application of Risk Assessment in Fire Protection Design (Review Draft).

[5] Society of Fire Protection Engineers, 2007, SFPE Engineering Guide to Performance-Based Fire Protection.

[6] Meacham, B.J., 2008, Building Fire Risk Analysis, Sec.5, Chap. 12, SFPE Handbook of Fire Protection Engineering, 4th Ed., NFPA.

[7] Meacham, B.J., 2004, Understanding Risk: Quantification, Perceptions, and Characterization, J. Fire Protection Engineering, Vol. 14, p.199-227.

[8] Meacham, B.J., 2004, Performance-Based Building Design Concepts, International Code Council.

[9] NFPA 5000, Construction and Safety Code, NFPA.

[10] NFPA 101, Life Safety Code, NFPA.

*Applied Mechanics and Materials Vols. 580-583 (2014) pp 2731-2734*
*© (2014) Trans Tech Publications, Switzerland*
*doi:10.4028/www.scientific.net/AMM.580-583.2731*

# Multivariate Geometric Factors Contributing to Crashes and Injuries in Mountainous Freeways: A Case Study from Jiangxi, China

Ming Li[a], Yonggang Wang[b], Xin He[c]

School of Highway, Chang'an University, Xi'an 710064, China

[a]jasonlee199105@163.com, [b]wangyg@chd.edu.cn, [c]406846617@qq.com

**Keywords:** Mountainous freeways; Geometric factor; Crash occurrence; Vertical alignment; Horizontal alignment; Cross section

**Abstract.** Mountainous freeway goes through complex geographic and geological regions and causes safety problem. Making clear of the inner relationship of the crash occurrence and the geometric factors is the most fundamental prerequisite to solve the problem. This paper reveals the contributing geometric factors through analyzing the crash data from Changjin Freeway, a typical mountainous freeway located in Jiangxi Province, China. Based on crash records and designed alignment data, contributing geometric factors are generally classified into three categories: vertical alignment, horizontal alignment, and cross section. And then detailed effects of geometric variables are separately discussed and quantified through the relation with crash rate (CR).

## Introduction

China has a tremendous area of territory, which more than 70% was covered by mountain and hilly terrain, especially in South China. In the past 20 years, China has made great achievements in freeway construction, resulting in reaching 96,200 kilometers up to 2012. And a large portion of it goes through mountainous regions. However, due to the mountainous landscape, the mountainous freeway's safety condition is serious. Over the past years, with the enormous losses to society resulting from crashes and fatalities on mountainous highways, numerous researches have continually sought a variety of quantitative ways to gain a better understanding of factors and causes that affect the occurrence likelihood of crashes so as to provide decision-making support for policies and countermeasures for reducing the crashes and facilities [1-5].

This study focused on exploring the affecting mechanism of variable alignment on crashes using a statistical analysis method. Changjin Freeway is used as a case to conduct this study based on total 1023 crash records and detailed geometric information. For a precise analysis, the count of the number of crashes is viewed as a function of various geometric contributing factors (e.g. radius of curvature and gradient). Several statistical models such as a linear-regression model are used [6].

## Date description

Changjin Freeway (K905+000~K982+600) is a section of Hukun Freeway in Jiangxi. The crash data was provided by the Department of Transport of Jiangxi Province. It collected 1,023 crash records from 2006 to 2012, including 182 common accidents and 841 simple accidents, respectively. It should be pointed out that common accidents mean those which cause serious injuries or casualties or more than 5,000 CHY losses, while the simple accidents representing the opposite cases. In this study, average crash rate (*CR*) of segment *i* can be then considered as the average count of crashes (*ACC*) per 100 million entering vehicles (100MEV), obtained as:

$$CR_i = \frac{ACC_i}{365AADT_i \cdot L_i} \times 10^8 \quad (1)$$

where, $ACC_i$ = crash count of segment $i$; $AADT_i$ = average daily volume of segment $i$, pcu/day; $L_i$ = length of segment $_i$, km.

**Typical geometric factors analysis and comment**

The contributing factors are classified into three components consisting of: vertical alignment includes: (1) grade; (2) radius of curve; horizontal alignment includes (3) maximum curvature; (4) angle of deflection; and cross sections.

**Vertical alignment.** In the past years, many accidents, especially truck involved cases, have frequently occurred at segments with big grades. When a vehicle brakes at down grade, it always takes longer distance than that of up grade at the same speed. Thus, it is difficult for driver to keep safe distance with the front vehicle when a emergency brake occurred. At long-down grade sections, the situation seems much more serious, especially for trucks due to that the brake function will decrease when the brake block get hotter. Generally, locations at down grade witnesses more crash occurrences. Figure 1 presents a comparison of CR values at locations of up and down grades.

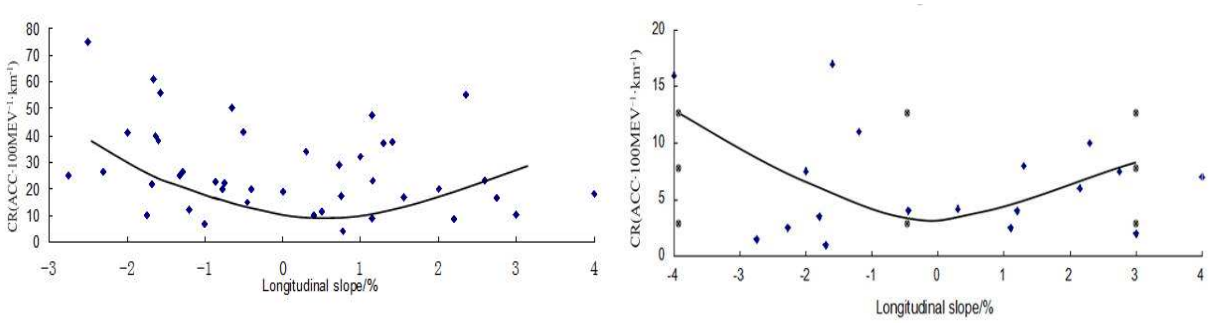


a. simple accidents b. common accidents

Fig.1 Comparison of crash rates at locations of down and up-grades of Changjin Freeway

Reconsidering the above listed Fig. 1, it is clear that both types of *CR* values come to a great increase with an increase grade. That's mainly due to less effective brake system performance and driver's incorrect operation under stress.

The vertical curve can be categorized into crest and concave. It's the necessary part to join two sections with different grades. However, it brings down the driver' sight distance and cause potential risk, particularly over crests. The radius of vertical curve determines the effect of transition between two different segments. The bigger, driver's sight distance gets better; the smaller, the worse. It should be pointed out that at the same vertical radius, crest curve generally witness bigger *CR* values than that of concave curve. By crash records of Changjin Freeway, 88 crashes occurred at crest sections while 53 at concave.

**Horizontal alignment.** Safety performance has a close relation with the maximum value of horizontal curvature in mountainous freeway. Fig. 2 shows the relation between CR with the radius of horizontal curve of Changjin Freeway.

Through the Fig. 2, we could find that CR values decline with the increase of the radius. It should also be pointed out that driving on curves with different radius behaves more dangerous than that with same or similar radius. Particularly, it is much more dangerous when a small radius curve is inserted into long and straight line. That is partly due to the driver's unconsciousness of speed on the latter and may cause overturn or run off road crashes on the curve.

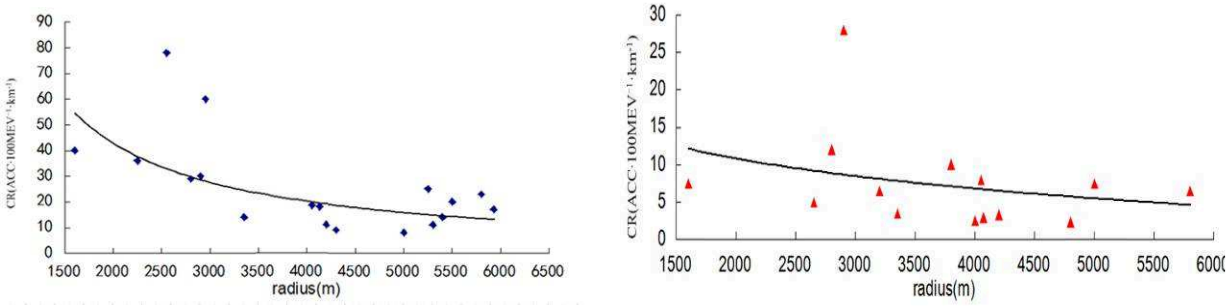


a. simple accidents b. common accidents

Fig.2 Crash rates related to radius of horizontal curve

Angle of deflection has a direct influence on the driving safety. In the geometric database of Changjin Freeway, the maximum and minimum angles of deflection are 41°26′40″ and 12°12′14.4″, respectively. Crash rates vary with the angle of deflection, as shown in Fig. 3.

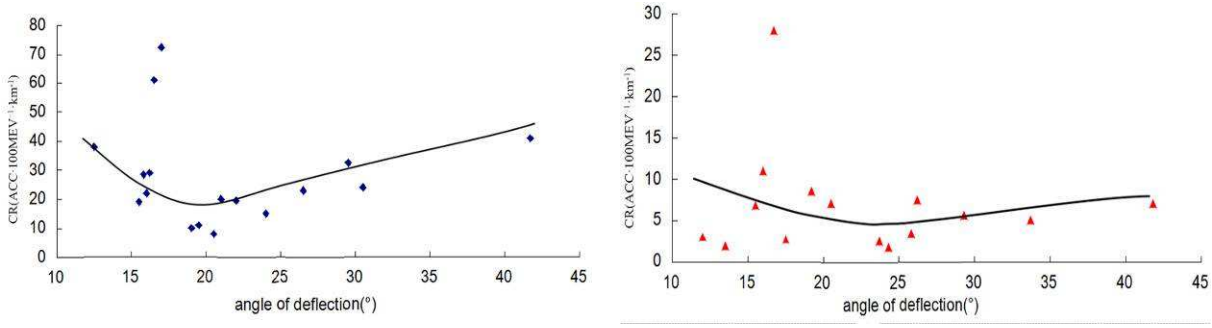


a. simple accidents b. common accidents

Fig.3 Crash rates with angle of deflection of Changjin Freeway

Reconsidering these two figures, we see the lower CR values, when the angle of deflection varies over 17°-25° for Changjin Freeway. This is because drivers could have a better view sight, when the angle of deflection locate within this scope. Otherwise, part of curve are beyond driver's sight and discontinuous pavement view is more prone to crashes, as shown in Fig. 4.

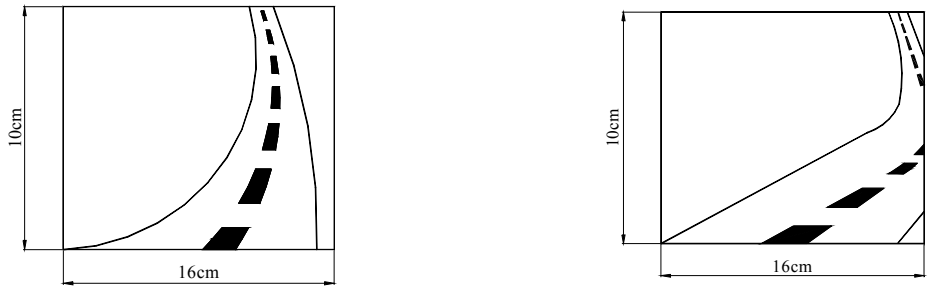


a. when the angle of deflection is 20° b. when the angle of deflection is more than 30°

Fig.4 Schematic design of angle of deflection for roadway safety

**Cross section.** Run off crashes, rear end crashes are the most common type of crash on mountainous freeway. And cross section is closely connected with these crashes. The width of roadway is important to driving safety, which consist of travel line, hardship and grass verge. Generally speaking, driving in wider sections is safer than that in narrow ones. Particularly, the width of hardship is also important, for it can provide a "buffer region" for drivers when emergency cases occur. Additionally, turnover is another common type of crashes with a higher crash rate,

which is mainly caused by high sub-grade design of roadway. Thus, it is better not to use high sub-grade and otherwise, enough traffic claim signs and other kind of safety facilities must be equipped together. Another factor that is worth investigating is the roadway number of lanes.

## Conclusion

Aiming at identifying contributory geometric factors which contributing to higher crash rate and sever injuries or deaths in mountainous area, a series of statistics investigation research has been performed. The considered or discussed geometric factors that affect or relate to safety and operational quality of mountainous freeway include: vertical alignment, horizontal alignment and cross section. By this research, we made a deeper understanding of the mechanism of crash occurrence and its relation with different roadway alignment. Surely, crashes may be affected by many factors (human, environment, vehicle, roadway etc.). Therefore, we should still make more quantitative researches to overcome this difficult issue.

## Acknowledgment

This research is supported by the Key Programs of Department of Transport of Jiangxi, China (No. 2011C0062).

## Reference

[1] Council FM. 1998. Safety benefits of spiral transitions on horizontal curves on two-lane rural roads. Transportation Research Record, 1635, 10-17.

[2] Polus A, Pollatschek MA, Mattar-Habib, C., et al. 2005. An enhanced integrated design-consistency model for both mountainous highways and its relationship to safety. Road and Transport Research, 14 (4): 13-26.

[3] Kopelias P., Papadimitriou F., Papandreou K., et al. 2007. Urban freeway crash analysis geometric, operational, and weather effects on crash number and severity. Transportation Research Record, 2015, 123-131 DOI: 10.3141/2015-14

[4] Fontaine, M. D. 2008. Effect of truck lane restrictions on four-lane freeways in mountainous areas. Transportation Research Record, 2078, 135-142 DOI: 10.3141/2078-18

[5] Gintalas V., Zilioniene D., Dimaitis M., et al. 2008. Analysis of design solutions in the subjects of gravel roads paving programme in terms of traffic safety. The Baltic Journal of Road and Bridge Engineering, 3(2): 93 – 100.

[6] Wang YG, Chen KM, Hu LW, et al. 2010. Voluntary killer: multivariate highway geometric factors contributing to crashes and collisions in China's mountainous regions. Technics Technologies Education Management - TTEM, 5(3): 531-543.

*Applied Mechanics and Materials Vols. 580-583 (2014) pp 2735-2739*
*© (2014) Trans Tech Publications, Switzerland*
*doi:10.4028/www.scientific.net/AMM.580-583.2735*

# The analysis of safety investment behavior of the long-term incentive mechanism in construction enterprise

SHUI Yong-Bo[1, 2a], LI Qian[1b], LI Hua[3c]

[1] School of Energy Engineering, Xi'an University of Science and Technology, Xi'an 710054, China;

[2] Center of Shaanxi provincial production safety publicity and education, Xi'an 710006, China;

[3] College of Materials and Mineral Resources, Xi'an University of Architecture and Technology, Xi'an 710055, China;

[a]88771582@qq.com; [b]928081425@qq.com;[c]lihua@xauat.edu.cn

**Keywords:** construction enterprise; safety Investment; safety economic

**Abstract:** Too many construction accidents have happened, which mainly caused because of the lack of safety investment. Analyzing the inner reason of the lack of investment in the construction of our country, looking for measures on guaranteeing that safety fund can be well applied on, increasing safety investment are preconditions to assure producing safety.

## Introduction

Therefore, how to improve the level of safety management in construction enterprises has becoming the main problems and attract the attention from the government, business and academia. Safety investment should be injected in the production of construction enterprise. It is a kind of economic behavior to improve the system's safety, prevent different kinds of accidents and to ensure production management runs smoothly[1]. It is generally held views that in safety activities need more safety investment, such as professional staff, safety devices, safety education and training costs, individual labor protection and health care costs. However, in a long time, illegal behavior of safety investment is an objective phenomenon[2]. The safety production and debates isn't received adequate attention, especially in stated-owned construction enterprises, small and medium enterprises and individual enterprises[3]. As a result, analyzing the inner reason of non-rational behaviors in safety investment and put forward the useful coal-mining safety solutions.

## The basic utility model

The investment behavior of the safety construction enterprise is not only affected by its internal factor, but also by the external environment, namely, the influence of social environments. There are two constraint conditions about the construction enterprise manager: regulation constrains and quality constrains[4]. Only by these two constrains can be realized the social income maximization. In order to prevent the irregularities on safety investment, the visible hand—the national safety regulations and the invisible hand --- quality of construction enterprise must be observed. From these two ways, we can discuss the irregularities and put forth the long-term and effective inspiriting mechanism.

When the construction enterprise make a decision on safety investment (it can be called '$\tau$'), they must make clear about the expected effectiveness which is come from the cognition and evaluation. On the rational assumption, the effectiveness has totally cognition and evaluation. But on the non-rational assumption, just because of the little knowledge about the effectiveness, the cognition and evaluation are limited. Based on this, we are concluded the safety investment function like this:

$$U(T) = \sigma \int_0^i u(t)dt + \int_i^m u(t)dt + \lambda \int_m^T u(t)dt \quad (1)$$

U(T) is the safety investment that the construction enterprise to continue the effect of T time ,which will bring the timeline effect. Assuming that the utility function U(T) is the continuous distribution function, its density function u(t) is continuously differentiable from the interval t [0， T].

Among them, in the interval （i，m）, the effect of the safety investment is recognized in the reason vision. Safety investment has a big effect for construction enterprise. For the effect in the interval of （0，i）to （m，T）can not be known. Irrational factors- σ, λ are existed separately.

In general state, the value of σ, λ is among (0,1). In this state, the utility function of the construction enterprise is u(T). The Utility function u(T) above the rational state is $\int_0^T u(t)dt$ . When λ, σ equals to one, it states that the safety investment of the construction enterprise is totally rational before $\tau$ or after $\tau$ . At present, the expected utility function is $\int_0^T u(t)dt$ . Therefore, in common state, the construction enterprise is irrational, and its expected utility function does not equal to the totally rational expected utility function.

**External inspiriting of national regulation**

The importance of safety regulations are determined by how to make it comprehensive and how to make the operation mechanism runs smoothly. The regulations laid down by the state will be helpful to prevent the irregularities on safety investment and purse it can make full use of its external inspiriting function to encourage the behavior on the right safety investment[5]. Through the enforcement regulations will be decrease the damage which is caused by irregularities investment behavior, and make effort the damage turn into the internal costs, namely the inside spillover accident[6]. If the illegal safety investment will be caused the risk of construction's business and make it difficult for the further development. The safety regulations, on one hand, it limited the occurrence and expand it's the illegal safety investment. On the other hand, it increases the market invisible value and lays a foundation for a good reputation. If the external constrains go smoothly and it may shaped into a behavior which would be expel the safety investment from passive adaptation to active consciousness. And finally, the concept will lead to active choice in the construction enterprises.

Based on the safety regulation, we will analyse the changes in the investment's security of the cognitive and the expected utility. After introduce the safety rules, the construction enterprise will have a certain understanding on the legal and illegal behavior.

Safety regulation factor is expressed by y, irrational factor δ and λ are functions of regulatory factors of y. $\sigma(y)$ and $\lambda(y)$ are equation which can be continuously differentiable. Among them, $y \in [0,+\infty)$, $d^2\delta / d^2 y < 0$， $d^2\lambda / d^2 y < 0$. Therefore, the expected utility function of the safety investment of the construction enterprise is as follows:

$$U_a(T) = \sigma(y)\int_0^i u(t)dt + \int_i^m u(t)dt + \lambda(y)\int_m^T u(t)dt \tag{2}$$

While considering to the non-perfection of making the safety regulatory rules and the limit of the safety monitoring behavior, which the violations of the construction enterprise under safety rules can not be totally prevented. That is to say, when $d\sigma / dy = 0$, $\bar{y}$ should be existed. Derivative

$$\sigma'(y) = 0， \quad 1 > \sigma\left(\bar{y}\right) \geq \sigma\left(y \neq \bar{y}\right) \tag{3}$$

In the same way , when $d\lambda / dy = 0$, at least a $y^*$ should be existed. That means derivative $\sigma'(y) = 0$, and also $1 > \lambda(y^*) \geq \lambda(y \neq y^*)$,

So, $\max \sigma(y) = \sigma\left(\bar{y}\right) < 1$， $\max \lambda(y) = \lambda(y^*) < 1$， $\sigma(0) \neq 0$， $\lambda(0) \neq 0$， (4)

$$\max U_a(T) = \max[\sigma(y)\int_0^i u(t)dt + \int_i^m u(t)dt + \lambda(y)\int_m^T u(t)dt]$$

$$= \sigma(\bar{y})\int_0^i u(t)dt + \int_i^m u(t)dt + \lambda(\bar{y})\int_m^T u(t)dt < \int_0^T u(t)dt$$

From the analysis above, if regulatory rules are needed to regulate the safety investment of construction enterprise, the value of expected utility of construction enterprise is less than the expected utility under rational condition. Therefore, only to adopt the regulatory rules to normalize the safety investment behavior can not achieve the biggest effect of it. Pareto opitimal goal is unable to achieve.

**The internal excitation mechanism**

In a certain degree, safety regulations can weaken the choices of the unlawful behavior, but it can't eliminate the foundation radically. If we can't take some effective measures to put an end on it, which will be cause more negative effects to society[7]. For the sake of the right investment behavior in construction enterprises, we should combine safety regulations with the internal quality. Both of this can prepare for bigger tasks and increase the control of the investment. All in all, we must obey by the regulations and also should take the quality of our own construction enterprises into deeply consideration.

It is important to introduce the quality factor to change the original model. The quality is a conception. The quality of construction enterprises can be identified as moral quality and septennial quality. It aims at to improve the quality. From safety investment, the moral quality is the rational support of safety investment. It will have two results: development and unbalanced development. The higher moral quality, the weaker costing is. On the contrary, the costing still increases, the internal control will affect moral quality.

At first, intellectual qualities x are added in irregular state. Among them, the higher intellectual and the control of construction enterprises are included.. Here we consider these intellectual qualities as independent variable. When these elements play a key role, the function can be nearly one. Here we give a function form which add the intellectual quality to safety investment function:

$$U_b(t)=\sigma(x,y)\int_0^i u(t)dt+\int_i^m u(t)dt+\lambda(x,y)\int_m^T u(t)dt \tag{5}$$

The formal function λ（y）, σ（y）now turns into intellectual element x and safety regulatory element y, that isλ(x，y)，σ(x，y). Among them, assuming, $x\in[0,+\infty)$， $\partial\lambda/\partial x>0$， $\partial\sigma/\partial x>0$ ， $\sigma(0,y)\neq 0$， $\sigma(0,y)\neq 0$，

$$\partial^2\lambda/\partial^2 x<0,\ \partial^2\sigma/\partial^2 x<0,\ \partial^2\lambda/\partial x\partial y=\partial^2\lambda/\partial y\partial x \tag{6}$$

$$\lim_{\substack{x\to+\infty\\ y\to\bar{y}}}\lambda(x,y)=1,\ \lim_{\substack{x\to+\infty\\ y\to\bar{y}}}\sigma(x,y)=1$$

Therefore, when $x\to+\infty$,

$$\max_{x,y}U_b(T)=\lim_{\substack{x\to+\infty\\ y\to\bar{y}}}[\sigma(x,y)\int_0^i u(t)dt+\int_i^m u(t)dt+\lambda(x,y)\int_m^T u(t)dt]$$

$$=\int_0^i u(t)dt+\int_i^m u(t)dt+\int_m^T u(t)dt \tag{7}$$

$$=\int_0^T u(t)dt$$

From the above we can seen that safety investment's irrational coefficient will be tend to 1 when it shows more rational and understanding attitudes toward the investment behaviors. The quality of sapiential will make better understanding on the safety investment. Only by this way, the rational investment will play an important role and make more profits to eh construction enterprises. The rational investment will promote the understanding, the quality of sapiential and beneficial to the initiative about their safety investment. The factor of initiative is the necessary condition for the rational development of construction enterprise.

The function is different between moral quality and sapiential quality. Moral quality gives expression on the spirit of humanity, impartial, generous and public welfare. It will produce altruism

and bring about more profitable effects. From that point of safety investment, "People First" is the important management philosophy. If we want to realize that we should build scientific development perspective, put people's life and property at first and make safety and prevention first.

Z can be used for intellectual morality, $\varepsilon(z)$ stands that the effect which can be produced in safety investment of construction under the control of intellectual morality. These morality elements can be added to the safety investment expected utility function as follows:

$$U_c(T)=\sigma(x,y)\int_0^i u(t)dt+\int_i^m u(t)dt+\lambda(x,y)\int_m^T u(t)dt+\varepsilon(z) \tag{8}$$

Among them, $\varepsilon(z)>0$ is under the morality of construction enterprise because of paying attention to the outer effect which can be produced from safety investment. In it, $\varepsilon(z)/dz>0$, $\varepsilon^2(z)/d^2z<0$ .Therefore, the constraint of safety investment behavior will be an effect of construction enterprise $\varepsilon(z)$, and $\varepsilon(z)>0$. At this time, if construction enterprise is under outer control of safety ruls and the constraint of their own morality of construction. The utility function of construction enterprise will be :

$$U_c(T)=U_b(T)+\varepsilon(z)>U_b(T) \tag{9}$$

But in fact, the safety investment behavior of the construction enterprise is hard to do all things well, for example, if the construction enterprise lack the intellectual morality, the utility function of the safety investment of construction will be :

$$U_d(T)=\sigma(y)\int_0^i u(t)dt+\int_i^m u(t)dt+\lambda(y)\int_m^T u(t)dt+\varepsilon(z) \tag{10}$$

This utility function will be smaller to rules and the expected utility function of moral qualities;

$$U_d(T)=U_a(T)+\varepsilon(z)<U_b(T) \tag{11}$$

Safety regulations and the internal quality is the necessary condition during the development of rational safety investment, both safety regulations and septennial quality is vital element to the operation for its safety investment, the moral quality is complementary factor and will have affect on the long-term development. In conclusion, the construction enterprises must change their concept thoroughly and the behavior must translate the principle of harm others into the conception of "Double Win".

## Conclusions

All in all, the external control of safety investment and the internal quality of construction enterprises would not decrease the illegal behavior. Draw on advantages and disadvantages are the immanent conception on construction enterprises. This would be give rise to more opportunism. In this background, the construction enterprise emphasize its internal quality and external control may be too weakness that would be cause resistant to the safety investment. Only combine the internal quality with external control, it can build rational atmosphere in safety investment. Finally, the aim to decrease or reduction the illegal behavior for safety investment can be reached.

## References

[1] LI Hua. Wan Xiufeng. Investigation and analysis on construction enterprise employee of occupational hazard perception of influence factor [J]. Journal of Safety Science and Technology, 2012, 44(3):431-434

[2] TIAN Shuicheng. etc. Modern safety economic theory and practice [M].China university of mining press, 2004.3:39-86

[3] LV Jing-gang, LI Shu-quan.Continuous improvement of knowledge management-based construction safety[J]. Quest,2012(2):57-59

[4] Krista M. Perreira,Frank A. Sloan. Living healthy and living long: Valuing the nonpecuniary loss from disability and death[J]. Journal of Risk and Uncertainty. 2002 (1)

[5] Ulf Persson, Anna Norinder, Krister Hjalte, Katarina Gralén. The value of a statistical life in transport: findings from a new contingent valuation study in Sweden[J]. Journal of Risk and Uncertainty . 2001 (2)

[6] K. R. Shanmugam. Valuations of life and injury risks[J]. Environmental and Resource Economics. 2000 (4)

[7] TU Wenjuan, ZHANG Chao, TANG Peirong. Study on technical and economic analysis of safety investment in enterprises based on economic value of life[J]. China Safety Science Journal. 2003,13(10)

*Applied Mechanics and Materials Vols. 580-583 (2014) pp 2740-2742*
*© (2014) Trans Tech Publications, Switzerland*
*doi:10.4028/www.scientific.net/AMM.580-583.2740*

# Research on Functional Adaptation of Sport Venues as a Disaster Prevention Refuge

Lidi Huang [1, a], Tianyu Zhang[1, b]

[1] College of Civil and Architecture Engineering, Northeast Petroleum University, Daqing, Heilongjing, 163318, China

[a]rain_0403@126.com, [b]609970@qq.com

**Keywords:** prevention refuge, sport venues, evacuation, safety, earthquake

**Abstract.** Through the survey of the current situation of sport venues as disaster refuge at home and abroad, the advantages of sport venue were widely dissussed from open space outside the sports venues, characteristic of main stadium and information transceiver system. The distribution structure of the hierarchical network of sport venues was analysised. Finally, some examples of sport venues as disasger refuge were proposed. It will be new development trend of stadium and sport venue in the future.

## Introduction

All previous significant disaster demonstrates that, when disaster takes place, a large number of people will evacuate to the same or multiple directions. At that time people want to know where to escape, where is the safety place and how to arrive at refuges [1]? Therefore, reasonably constructing prevention refuges can greatly minimize life and property losses and lower secondary disasters when disaster approaches, which is an important subject in various fields. Sport veneus has good disaster prevention capability and can become temporary or fixing asylums, disaster prevention control centers and medium-term or long-term shelters, etc, so, studying sport veneu as a disaster prevention refuge has an extremely important practical significance [2].

## The present situation of sport venues as a disaster prevention refuge at abroad and home

**At abroad.** In Japan, earthquake frequently occurs, so Japanese have extensive experiences in asylum evacuation sites and resettlement victims from ancient times. On early the Edo Period，when earthquake or fire disaster took place, local government immediately built "Protection Shelter" to rescue victims and provide relevant assistances [1]. Now, refuges in Japan include parks, green places, schools, sport veneus, and other public halls. Among which, sport veneus are playing a significant role. In modern Japanese Kanto earthquake and Kobe earthquake, sport veneus sheltered more than 200,000 refugees and were equipped with enough supplies for victims [3].

**At home.**In recent years, the Chinese Government attaches great importance to succor, recovery and reconstruction effort from disasters, and has promulgated a series of related regulations. The regulation of / Planning and Management Requirements of Urban Seismic and Disaster Prevention / was officially executed on November 1, 2003. Article 9 of the regulation stipulates planning of urban seismic and disaster prevention should include earthquake prevention passages, evacuation sites (such as green places, squares) in the city and district, setting evacuation centers and measures of refugee evacuation.

Currently, many cities have proposed comments and suggestions about planning and construction of disaster prevention refuges. On October 1, 2003, in Beijing City， Beijing Yuan Dadu City Wall Relics Park was completed and opened, which is the first systematic planning emergency shelter in China. The park has 11 functions with emergency escape.

**Advantage of sport venue as a disaster prevention reduge**

Sport veneu has such a great deal of open and public space that it becomes an indispensable earthquake disaster prevention site. The planning land areas of sport venue are generally in a few hectares or more, easily to meet the areas requirements of temporary refuges and center refuges. The overall layout, facilities configuration, traffic organization of sport veneu are carefully designed, scope of services including peripheral dozens of hundreds of kilometers. Once a great disaster happening, even warning level high, a large number of victims, the duration of disaster long, sport venues can become the ideal places for victims and concentrated zones against disaster.

- There is a large open space outside the sports venues, where can be used as emergency shelters lands and a helicopter parking apron.
- Sport venues have high construction standards and perfect safety performance. First, the main stadium structures designed according to seismic focus class fortification, can withstand the great earthquake. Secondly, sport venues are equipped with emergency generator room, transformer room, EPS power supply equipment, and other facilities, which can guarantee the power supply requirements of refuge in the disaster. Thirdly, the installation of automatic fire alarm smoke control facilities system, sprinkler system and high sensitivity,which can effectively ensure the fire safety evacuation of victims; Fourthly, sports facilities base should have at least one surface or two surfaces of adjacent city road, to provide more favorable conditions for evacuation and rescue
- Part of the Event Management District Housing and security monitoring room are equipped with advanced information transceiver system, which can be used as a disaster emergency command center.

Experience has shown that the investment of construction costs less and the effects is obvious and quick to reform the existing stadium into a disaster prevention refuge, and operational conditions are good and relatively safe. The sport veneu applies to establish command center of disaster rescue, disaster resistance and disaster prevention, the center of information and communication facilities, disaster relief supplies and transit sites, the camps of disaster relief militaries, and ideal offices for various government departments. The proposed stadiums should be designed to have function of disaster prevention at the planning phase to make contributes for urban disaster prevention system.

**The distribution structure of the hierarchical network of sport venues**

Through long-term research, Japanese experts consider that by highly organized and spatial planning, victims will be quickly moved to safey places, and to be stabilized their psychology, which is the significant key to reduce the casualties in disaster prevention planning. Therefore, Japanese disaster prevention system pays special attention to "shelter" plans, whose classification is more detailed, though which, authority institutes could purposefully design refuges and set function allocation.

In our country, the system of stadium in city is generally formed by ‘ small, middle, large scale,’ three dimensions sports venues, which exactly coincided with three levels of refuge,that is, community , district and city sport venues,which was divided by urban administrative divisions[4], shown in Fig.1. Each refuge level has corresponding service radiu standards, and takes on different task in disaster prevention, disaster relief, post disaster reconstruction, and evacuation process, constituting a reasonable and hierarchical network structure. The structure is widely covered and each venue can work independently, but also through the city road connectivity and collaborative operation, which set up urban refuge system in the general. In this system, from the bottom up, the venue size, service radius, the allocation of resources are increasing [5].

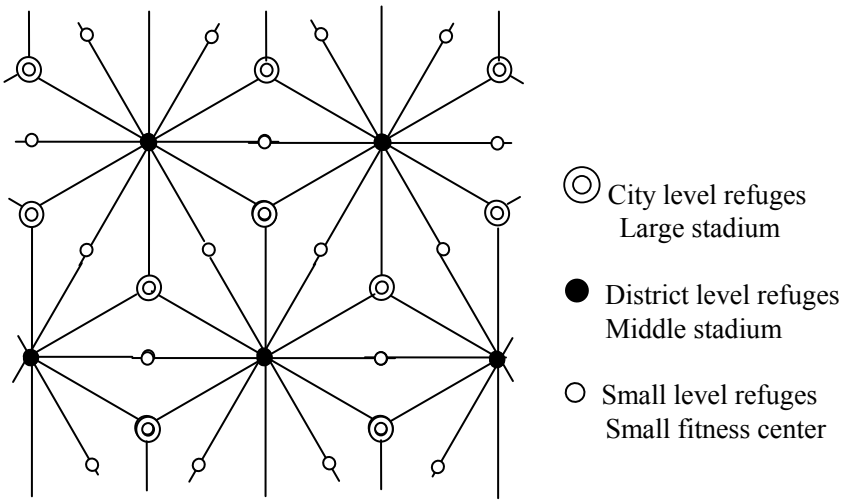


Fig.1 Structure of sport venues [4]

**Examples of sport venues as a disaster prvention reduge**

When "Katrina" hurricane attacked New Orleans City of the United States in 2005, a lot of residents unanimously escaped to the Super Dome Stadium. Mianyang Jiuzhou Stadium which occupied 22 ha. , had accommodated a total of more than 100 thousands people and even maximum capacity of 4.5 million people in a single day in 512 Wenchuan earthquake in 2008. It has been named "the most populous disaster shelter in the world." by overseas media. Not only Jiuzhou Stadium, but also South-River Sports Center in Nanyang city, Deyang Sports Center, even Mianzhu Sports Center not having completed, Dujiangyan Stadium, Beichuan middle school sport veneu all became the best sites for temporary evacuation and disaster reduction shelters for victims. To some extent, this phenomena also reflects that stadiums as a function of disaster prevention is insufficient [5].

**Conclusions**

Sport venue as important urban public construction, its safety and disaster prevention must be concerned about. In addition to meeting essential function, simultaneously the project argumentation and design should be evaluated in urban disaster prevention system. First, Urban Culture Sports Park and Olympic Sport Center, should be incorporate into the urban disaster prevention space system, which will play essential role for urban disaster prevention. Second, the existing sports centers should be transformed with local condition, and combined with demand for urban disaster prevention, to make contributes for the city disaster prevention system planning. Finally, to meet the requirements of urban disaster prevention system, we promote disaster prevention in the overall planning and design phase for future construction of the proposed stadium. Based on these efforts, better requirements of urban disaster prevention and disaster prevention function of stadium can be achieved fundamentally.

**References**

[1] Peng Rui, Liu Jieyi: New Architecture. Vol. 2 (2009), p. 102. (in Chinese)

[2] Huang Lidi: Urbanism and Architecture. Vol. 121 (2013), p. 36. (in Chinese)

[3] Huang Lidi, Liu Deming: Mathematical Problems in Engineering (2013), Article ID 64791, 7 pages. http://dx.doi.org/10.1155/2013/364791

[4] Sun Yimin, J—j Hui: China Civil Engineering Journal. Vol.45 (2012).p 113. (in Chinese)

[5] Huang Lidi, Liu Deming: “Research on structural safety design of sport venue as a disaster prevention refuge”,The 3rd International Disaster and Risk Conference, Switzerland, 30 May to 3 June(2010). Harbin: Harbin Institute of Technology Press,p.255.

# CHAPTER 12:

# Cartography and Geographic Information System

*Applied Mechanics and Materials Vols. 580-583 (2014) pp 2745-2748*
*© (2014) Trans Tech Publications, Switzerland*
*doi:10.4028/www.scientific.net/AMM.580-583.2745*

# A Research on Digital City Three-Dimensional Visualization System Based on Skyline

Hongbao Dai [1, a], Xiangjun Yue [2,b] and Jiying Xu [3,c]

[1] School of Earth Sciences and Engineering, Suzhou University, Anhui,China

[2] School of Earth Sciences and Engineering, Suzhou University, Anhui,China

[3] School of Earth Sciences and Engineering, Suzhou University, Anhui,China

[a]95243529@qq.com, [b]527845261@qq.com, [c]70959017@qq.com

**Keywords:** GIS; Visualization; Digital; City; Model.

**Abstract.** As an important living place for human beings, city is regarded as a main place for the birth, spread and development of human civilization. This paper, based on the principle of system development and combining with the need of building "Digital City", makes an overall design of the "Digital City" 3D visualization system. Firstly, a 3D ground objects model, i.e. .x files, is made through inputting the ground objects of the experimental area into 3DSMAX, then, the .x files are converted to .xpc files in order to achieve a better displaying effect in producing a 3D landscape. Secondly, the author makes corresponding pre-processing to the aerial photos, satellite images, topographic data, digital elevation models and a variety of vector geographic data, and then superimposes and loads these data into Terra Builder module of Skyline software, which generates 3D topography landscape, that is, .MPT files and forms the terrain database required in Terra Explorer Pro software. Next, a 3D landscape is preliminarily established by inputting the 3D terrain model and the 3D ground objects model, i.e. .MPT files and .xpl files, in Terra Explorer Pro, and by editing a real and accurate 3D geographic model and a real Digital City 3D landscape model, that is, FLY files, are respectively formed. Finally, on the basis of the 3D landscape model, the system is developed by using Visual Basic + TerraDeveloper and the basic operation of 3D, spatial analysis, visible analysis and other basic functions are preliminarily achieved.

## Introduction

As a part of Digital Earth, Digital City is regarded as the development direction of city information technology, and 3D GIS is a kind of important foundation spatial information of Digital City. The establishment of 3D city can provide people with a variety of city scenes in omni-directional and intuitive ways and build a real and intuitive virtual city environment, which greatly helps the city administrators implement effective measures in making scientific, cultural, and ecological plans[1].

To realize 3D GIS involves many aspects including geography, mapping, computer technology, database technology and others. Currently, there are four major soft-wares used on this issue, namely, Google Earth, the World Word developed by NASA, Geo Fusion's Geo Matrix kit and Skyline [2]. This study takes the example of an experimental area in Tianjin using Skyline software as a platform and combining with 3D model software, and attempts to build and develop a Digital City 3D landscape，finally achieving its basic functions in Digital City.

## System Design

Taking image data, terrain data and 3D architectural model as its cores, this system makes full use of the features and advantages of images and GIS technology, and integrates technologically GIS, RS and virtual simulation technology to build a 3D geographical information platform. The design of this system involves data processing, 3D landscape model establishment, system development and other series of issues. In order to make sure that all jobs are closely related to a database establishment and its application, the building of the system is operated in the following steps:

Firstly, the relative data collection and collation are made, including two-dimensional (2D) data and 3D landscape data. Since the data processing in the primary stage plays an important role in the system operation, it's very crucial to make precise data collection and pre-treatment data.

Secondly, the 3D landscape model is the core of the system, hence, in order to obtain 3D landscape documents and create 3D model quickly, DEM and image data are very vital in running the system. In this step, the DEM and image data are inputted into TerraBuilder to generate the running foundation of the system—3D topography landscape, i.e., .MPT files, then, .MPT files combining with 3D ground objects model are inputted into Terra Explorer Pro and FLY file are produced at last.

Finally, the establishment and application of the system concerning with 3D GIS are carried out and the required functions of the system are basically achieved.

**The Development of 3D Model**

In the geographical landscape, in accordance with the distribution characteristics, the geographic objects can be divided into two categories: terrain objects and ground objects. The former belongs to field-based objects, such as topography, soil type distribution, and etc.; the latter is featured as discrete entity, such as buildings, trees, telephone booths, street lamps, and so on. In city 3D model, different application situations require different ground objects expressions methods and 3D data quality, likewise, data collection and processing methods are also different [3]. In the following section, the study makes some processing of ground objects model and terrain landscape respectively, and the ground objects processing is divided into independent processing and batch processing in order to highlight some important independent objects. Building Digital City 3D landscape scenes is composed of the following four steps:

**2.1 Processing of Independent Ground Objects Model.**

The spatial single model built in 3DS Max has the features of fine structure and clear texture, so this kind of model can be used for some important or symbolic independent objects, and the whole process includes five steps: texture procession[4], importing CAD drawings, building 3D model, mapping design and data export.

(1) Handling texture. In this experiment, images obtained in the experienced field are required to be rotated, stretched, cut, stitched and other processions in Photo Shop to produce a complete texture image of the certain side. Meanwhile, all the texture images colors in the work area must be in balance; textures of independent objects should be processed respectively.

(2) Modifying the CAD drawings. The original data should be converted into DXF format if they are not, and then, inputting CAD drawings in 3DS Max.

(3) Building 3D model. Several methods are mainly used in this process, including stretching, lofting, spinning, Boolean operations and others. To build the 3D model, researchers should firstly take the shape of the model into serious consideration, then, choose the most appropriate modeling method and try to use the method that produces less edge lines, which can help to reduce the amount of data model and increase the operating speed of 3D system.

(4) Mapped mapping of 3D model. By associating the surface of the buildings with their textures, the mappings are just attached to the appropriate position of the 3D model, making sure that different objects should be chosen different mapping projection mode to ensure the realistic sense of 3D model [5].

(5) Exporting 3D model. Finally, the established model is imported into .X format, and buildings models are added to MPT in Terra Explorer Pro module. During this process, Z-axis is not needed to be rotated, and each model is taken as an object to output respectively. Acquiring center coordinates of the building before it is exported, and then, the model files are exported into. X format.

**2.2 Processing of Batch Ground Objects Model**

In 3D scenes, there are many ordinary buildings, such as, a piece of residential or industrial areas, if all of them are used in 3DS MAX model, the cost will be pretty high and the amount of data will also increase, which will affect the system's 3D roaming effect. Skyline is chosen to be a platform to build batch ground objects model, and the building steps are as follows:

(1) Vectorization on buildings after adding 3D images of the experimental area to Arcmap.

(2) Through the investigation in the experimental area, the researchers mark the attribute information of the buildings as well as the number of floors on images; furthermore, gather the texture information to lay the foundation for building model.

(3) Some attribute information is added to Arcmap, including the buildings' codes, floors, height and others, and then, exporting Shp format files and importing them into Skyline.

(4) Adding texture data. After dealt with in Photo Shop, the texture data of different layers are separately put on their folders of each layer, adding texture data according to the height of the floors.

(5) 2D vector data are overlaid in Terra Explorer Pro by connecting spatial databases, labeling and coloring them, also, connecting vector data to Skyline using SED streaming media technology in order to ensure the convenience of updating data later.

**2.3 Processing of 3D Terrain Scenes**

3D geometry spatial data of the terrain objects are the foundation in building 3D geographic model. It can not only add the capability of 3D analysis, but also strengthen the 3D representation of GIS spatial query and analysis, which is convenient for different users to better understand various spatial distribution relationships [6].

Next, a 3D terrain landscape is built using Terra Builder. Terra Builder, as a component of Skyline, is used for terrain visualization application to create a 3D ground model with an accurate geography registration and real sense of scenes. Then, by using Terra Builder, a new experimental area is built and the coordinate system and the ellipsoid information are identified, after that, adding various types of data, images and DEM to the experimental area to generate 3D scenes of the experimental area, that is, MPT format.

**2.4 The Establishment of 3D Landscape**

Skyline is an interactive environment created by the use of aerial imagery, satellite data, digital elevation models and other 2D or 3D information sources . To build a 3D landscape, firstly, the 3D terrain model of "Digital Earth" is imported in Terra Explorer Pro, according to the corresponding requirement, vector data should be overlaid, tagged and colored. Next, 3D ground objects model data are required to import in Terra Explorer Pro, adjusting their location, size and position, and the FLY format project files are finally produced.

## Realization of System Functions

The 3D landscape system can be developed after being established, and this study, taking Terra Developer as its development platform, uses an integrated secondary development model to do the secondary development to 3D landscape.

**3.1 3D Navigation and Information Retrieval Panel**

In the left bottom of the main interface, the system provides switch tabs of both 3D navigation and information retrieval panel, in which data, navigation and query of sceneries, and searching and viewing thematic information can be found.

(1) 3D navigation

Clicking the 3D navigation tab, many functions can be achieved in the panel, such as, 3D landscape navigation, coordinates positions query, 3D ground objects query, browsing helping information and Hawkeye view navigation.

(2) Information retrieval

All the data contained in the item of "digital city 3D visualization system" can be viewed and asked by clicking the Information Retrieval tab.

**3.2 Toolbar**

Toolbar classified gives some common buttons for browse, inquiry, measurement and analysis, also, it provides many functions of 2D and 3D objects, and the following part shows some widely used functions:

(1) Spatial Analysis

As one of the core functions of Digital City system, spatial analysis can provide supporting decisions for city administrators, improving the modernization of city management. Digital City

system based on Skyline can achieve visible analysis, area measurement, space measurement, terrain profile analysis and other 3D spatial analysis functions.

(2) Measurement

User can make vertical, horizontal and area measurement to 3D terrain through measurement tools.

(3) Visible Analysis

Visible analysis is to judge whether the sight between two points has blocks or not, and it can not be used if the two points are blocks.

(4) Query and Position

User can find the required attribute information conveniently if they provide the query conditions, and they can also use coordinate location to find the place where they want.

## Conclusions

This paper takes Digital City as an example and builds Digital City visualization system based on Skyline by establishing model in 3DSMAX and Terra Builder, using Photoshop processing texture, building a database in Arcgis, and the secondary development through Visual Basic + Terra Developer. The feature of this study is to process 3D model in different levels and layers, emphasizing accuracy on some important ground objects and efficiency on batch ground objects. With the further development and deepening of the construction of digital cities, virtual display technology, spatial information visualization technology, GIS technology has developed rapidly. The 3D visualization platform, as one of the key technologies of digital earth, organically combines the virtual display with 3D GIS by using 3D model and visualization technology. The establishment of city virtual 3D visualization can provide a platform for the application of 3D GIS in every walk of life and build various city scenes in a omni-directional and intuitive way, which greatly improves the sharing and using level of city spatial information.

## Acknowledgements

This work was financially supported by the The National College Students' innovation and entrepreneurship training program (201210379028), the provincial natural science research project of Anhui Province (KJ2013B290) and the scientific research foundation of Suzhou University (2011yss03).

## References

[1] Feng-xia Wang, Chao Zhang. Construction and Study on “the Digital Shanghai”. Areal Research and Development(In Chinese), 2004, vol. 23, no. 12, pp. 38-41.

[2] Feng-xia Yan, Ming-deng Zhang. The Construction technology of Three- Dimentional Digital City(In Chinese). Surveying and Mapping, 2009, vol. 32, no. 2, pp. 93-96.

[3] Jiao Li , Jian-ping Wu, Ying-jie Hu. Development of Three-Dimensional Urban Scanning System Using TerraExplorer Pro(In Chinese). Computer Technology and Development, 2009, vol. 19, no. 6, pp. 240-242.

[4] Yu Wang. Development and Activement of Three-Dimensional Visualization in Digital Oilfield Based on Skyline(In Chinese). Master thesie of Chang’ an University, 2009.

[5] Miao-le Hou, Zhong-zhen Liu, Wei-xian Sun. Three-Dimensional Visibility of Digital Campus Based on Skyline(In Chinese). Journal of Beijing University of Civil Engneering and Architecture, 2008, vol. 24, no. 4, pp. 18-21.

[6] Hong-bao Dai. Research of Digital City 3D Visible System Based on Skyline——For Example of Some Area in Tianjin(In Chinese). Master thesis of Xi’ an University of Science and Technology, 2010.

*Applied Mechanics and Materials Vols. 580-583 (2014) pp 2749-2755*
*© (2014) Trans Tech Publications, Switzerland*
*doi:10.4028/www.scientific.net/AMM.580-583.2749*

# A Study on Informatization Construction of Sharing "One Map" between Land and Planning Departments

Guang Yang[1, a], Tiantian Zhou[2,b]

[1]College of Surveying and Geo-information,Tongji University

[2]Information and Communication Office, Zhenjiang Public Security Bureau

[3]1239Siping Road ,Shanghai,200092,China

[3]9Jiuhuashan Road, Zhenjiang,212000,China

[a]yangguang@tongji.edu.cn, [b] qitianshang128@163.com

**Keywords:** informatization;GIS;sharing "One-Map"; land and planning management

**Abstract.** Based on the full research on the recent information construction of land and resource department and planning department, and the requirement of the related business management, this article has a detailed illustration of the popular construction ideas, "resources sharing" and "One-Map", along with the construction conception of geographic information system with sharing "One-Map" between land and planning departments.

## Introduction

In recent years, with the construction and application of the GIS platform, planning and land management department has a higher requirement for the information platform on the basis of the original information construction. In terms of domain, the platform needs the smooth interface of the information systems and comprehensive information data sharing, in order to focus on the longitudinal business information together instead of internal management and optimization. In terms of object, the needs transfer from traditional simple data processing to a higher level of information management such as integrated data processing, information extraction and the creation, knowledge management and auxiliary decision-making. In terms of function, the platform's development changes from the traditional standardized to across institutions, cross-industry individuation. At the same time, each information systems has the higher requirements of the personalized needs for different management areas.

At the same time, in the past few years, planning and land departments have been vigorously promoting the construction of "one map". Especially, the Ministry of Land and Resources is launching a national "one map" project construction. Although the "one map" projects between the planning and land apartments are different in content, they both focus on gathering various kinds of data on a unified platform, along with business management synergy. After comparing the contents of the two "one picture", it is not difficult to find much duplication of resources on both platforms. In practical management work, planning and land departments have strong demand in sharing data.
Currently, the geographic information system is used in many aspects of land resources management and planning management, and dozens of working system platforms are set up. However, the information system has not become the core part of planning and land resources management by now, and the management behaviors also have not completely been finished in a unified platform. To some extent, problems exist, such as the basis database not cover enough, poor present situation, data repeating and figures and attributes not corresponding. Data standardization and integrity of management class need to be improved. System construction is isolated and diversification, which is still not fully in accordance with the requirements for full life-cycle management to solve the gap between management departments and steps, achievement of the data connectivity to support all planning departments of land and resources management. The effective support ability of informatization on the resource management has larger development space. Systems available now are mostly isolated, at the same time collaborative work platforms which

have collection of various functions and perfect integration of various aspects of land and planning management business can rarely find.

Based on this background, studying how to promote the level of land and planning management relying information technology has important significance. Not only we can impel a informationization and fine daily land and planning management business, promote the cooperation of business departments, but also improve the decision-making efficiency and quality, make sure to manage and use land fine.

**Daily Land and Planning Management**

**2.1 Land management business**

The major functions of land management department include: to formulate the jurisdiction of the land use planning and land reserve resources development planning; review the scope and quantity of land requisitions; charge implementation of land supervision, investigation and punishment of the illegal cases, as well as land disputes' conciliation; management the land use right transfer, lease, sale, exchange, alteration, donation, inheritance, termination in accordance with the law and deal with relevant formalities; protect cultivated land resources according to the relevant laws and regulations combined with the general and special land use plans, etc.

**2.2 Land planning management**

Urban planning management business mainly includes to organize the formulation of urban planning management, and the implementation management. Planning implementation management comprise planning permission management which including "one note and two card" and supervision after approval.

**Present Informationization Situation of Land and Planning Departments**

**3.1 The "one map" Construction of Land Resources**

"One map" project of land and resources is based on the second national land survey results at the moment of implying the "golden soil project". The project is integrating all the business data of land and resources, trying to establish a comprehensive supervision platform, which contains five application systems of approving, supply, use, management and supervision. Through data concurrent, scraping, updated in real time and establishing data sharing mechanism, we can ensure the present situation and authenticity of "one map", which make sure its vitality.

At present, there are successful cases of "a map" project construction. Tianjin City has done a great job which take the lead to achieve the "one map" management mode through the city, and the efficiency is very obvious. The News of Land and Resources carried a special report on their experience and practice .

**3.2 The "one map" construction of land planning**

"One map" project on land planning earliest originated from the building database after the complete coverage of regulatory detailed planning. Because the regulatory detailed plans are isolated, the edges are hard to be match when plans put in the data warehouse. Since then all the planning unit need to do put edge processing according to neighboring relationship , to ensure data integrity, make its combined complete "regulatory map", and make sure its dynamic updating maintenance. The purpose is to cover the entire city of regulatory detailed planning can complete seamlessly into the database.

In recent years, with the need of resource integration, "one map" on land planning gradually extend from "a graphic map" to "a space map". It means now from the perspective of geographical space, it is a construction of composite all regional planning data collection of information resources based on geographic coordinate system in space unity, so as to realize composite show and comparative analysis function in the information system. From the view of time, it need realize dynamic update, at the same time relying on the powerful function of GIS it can manage data versions, which bringing great convenience for examination and approval of planning business.

**3.3 The foundation geography sharing platform construction**

The real time of the construction into the implementation of basic geographic information sharing platform in our country is not long. In the past there were individual cities to promote the construction, but the effect is not ideal. The main reason is that the application level of construction

is not high. Although some cities have lots of sharing departments, but very few really combine with the business, while most departments only achieve simple browse and query function.

**Analysis of Existing Problems**

**4.1 Independent coordinate systems**

With Yangzhou city as an example. Before 2008, the planning and land departments in Yangzhou were using a same coordinate system which called "54 Beijing coordinate system". Since in 2008 the second of land and resources survey adopted "80 Xian coordinate system", the land resources department built new system based on new data, which leads to the current difficult in interface of land construction coordinates of two departments. In many cities, there are similar problems. On 1st. July, 2008, China started to use the "2000 coordinate system" . The conversion of the data in different coordinate systems in actual work is very difficult. Therefore, in the next period of time, the inconsistent of coordinate systems will be a big problem in data resource sharing.

**4.2 Difficult to share information resources**

Even in Shanghai, land resources and planning departments have merged as Shanghai planning and land resources administration, data resource sharing is also facing many problems on both procedure and system. Especially on the aspects of the integration of historical data has great difficulty. In places there are to separate two independent departments, information resource sharing is much harder.

In communication during the survey, there are some obvious reasons. First of all, each department value own information resources very much. There is factor like department interests, but there are other concerns. Such as planning department would like to share the cadastral data, but the department of land management can not make sure all cadastral data is right. Once the sharing data become basis for other departments to make approvals, governors need to be responsible for bad influence. Second, such as the problems mentioned above like inconsistent coordinate systems and disunity data standard, even if sharing data on one platform, the data is also differ in thousands ways and difficult to correspond.

**4.3 Basic geographic data redundant construction**

During the period of "11th five-year plan", the construction of geographic information system is hot. Not only departments need GIS application very much such as planning and land departments are promoting vigorously, but also be popularizing across the country as an application of digital urban management. For GIS application, every department can not across the construction of basic geographic information data, so we can find redundant construction of the geographic information data in almost every department. The repeated collection and building databases consumes a lot of financial capital. This situation not only caused waste of resources, also influence the practical application effect of systems.

In practical work, planning and land departments both need to refer topographic map, cadastral map and planning data. Therefore they can implement supervision and management through contrasting the real data and planning data. In the existing departments settings, even if the two departments belong to same ministry, the actual planning and land departments' work are separate, the exchange of information still exist certain problems. As a result, it is hard to avoid the basic geographic data collection in order to completely master needed data. Both departments do this work, to a certain extent caused the basic geographic data redundant construction. Even if there can be a merger, it is likely to have built a unified database figure inconsistent or attributes related to one figure. Because each of planning and land departments holds a set of surveying and mapping data, not only there exists data redundant construction, but also they update in different ways.

**Conception of Geographic Information System Construction of Land and Planning Based on Sharing**

**5.1 construction thoughts**

5.1.1 Unified coordinate system and data standards

(1) Unified coordinate system

Although in some cities the functions of planning and land have been merged, but the vast majority of urban planning and land departments are in independent offices. Due to belonging to different ministries, for a long time, planning and land departments exist many differences in informatization standards. In practical work, they are the only two government departments which need docking position relationship. Therefore, uniform spatial reference frame is the premise to realize data sharing, which is also inevitable.

So far, based on the different space reference system, three kinds of coordinate systems are used in our country, namely the 54 Beijing coordinate system, 80 Xi 'an coordinate system and the national 2000 geodetic coordinate system. The state bureau of surveying and mapping has clear requirement to supply the 2000 coordinate system on July 1th, 2008. There is a file which specailly to require the exsit geographic information systems to switch the coordinate system to the 2000 coordinate system in 8 to 10 years. At the national level have realised that a series of problems have been caused without a unified coordinate system.

(2) Unified data standards

In the process of the planning and construction of data layer, it is necessary to formulate uniform database building standards and corresponding data exchange standards. In this way, data can smoothly exchange in related organizations, which avoid hindering data sharing between different organizations and applications due to the difference of data definitions. We should also establish a unified data standard, and formulate corresponding mechanism of the process of data collection to ensure the accuracy and effectiveness of the collected data. Meanwhile, updating in real time and strengthening the quality inspection of the data while data warehousing. To adopt centralized database storage method will make management more convenient.

5.1.2 construction of "one map" Based on the co-construction and sharing

(1) Integration of a set of public fundamental geographic database

Based on To land 1:500 scale topographic map, multi-period aerial image and satellite image in the production of the second survey organized by the land and resources department in 2008, we can establish a GIS database including conventional based geographic data layers, which conclude surveying control points, drainage system, landscape, vegetation and soil property, inhabitants and facilities, geographical names, transportation, pipelines, boundaries and administrative divisions, digital ortho image.

(2) Integration of thematic data of land and planning "one map"

In the daily business work, planning department may want to know about land cadastral distribution and properties and so on, while the land and resources department need to master design conditions such as planning of land use and land indicators when go through land transfers or examination and approval procedures. In this case, the two departments need to integrate their respective business data and the examination and approval data to one map.

**5.2 conception of system architecture supporting distribution**

Considering that in most cities, the planning and land management functions are independent and belong to different departments, the system needs to support sharing of distributed deployment, which means basic geographic database, land management database and planning database may be deployed in different office environments. To achieve the goal of multi-sectoral data sharing would require building a support distributed system architecture.

All kinds of data and information based on the "one map" can be organized and put into database by planning and land departments respectively based on the uniform data standards and technical standards. The databases should be deployed within each data center, and meet the technical requirements for data distribution, resource sharing, maintenance on their own and collaborative management. In this way can prompt the relevant departments of information

management making effective management and information update maintain, maintain efficient collaboration and clear department responsibility at the same time, so as to realize distributed system in a common data support.

Because the business is handled by many departments work together, so the system should run in a network environment. Spatial data, attribute data and document data need be stored on multiple physical distribution devices, forming a physically distributed in each node of the network, while logically exist in a database, as is shown in Fig.1.

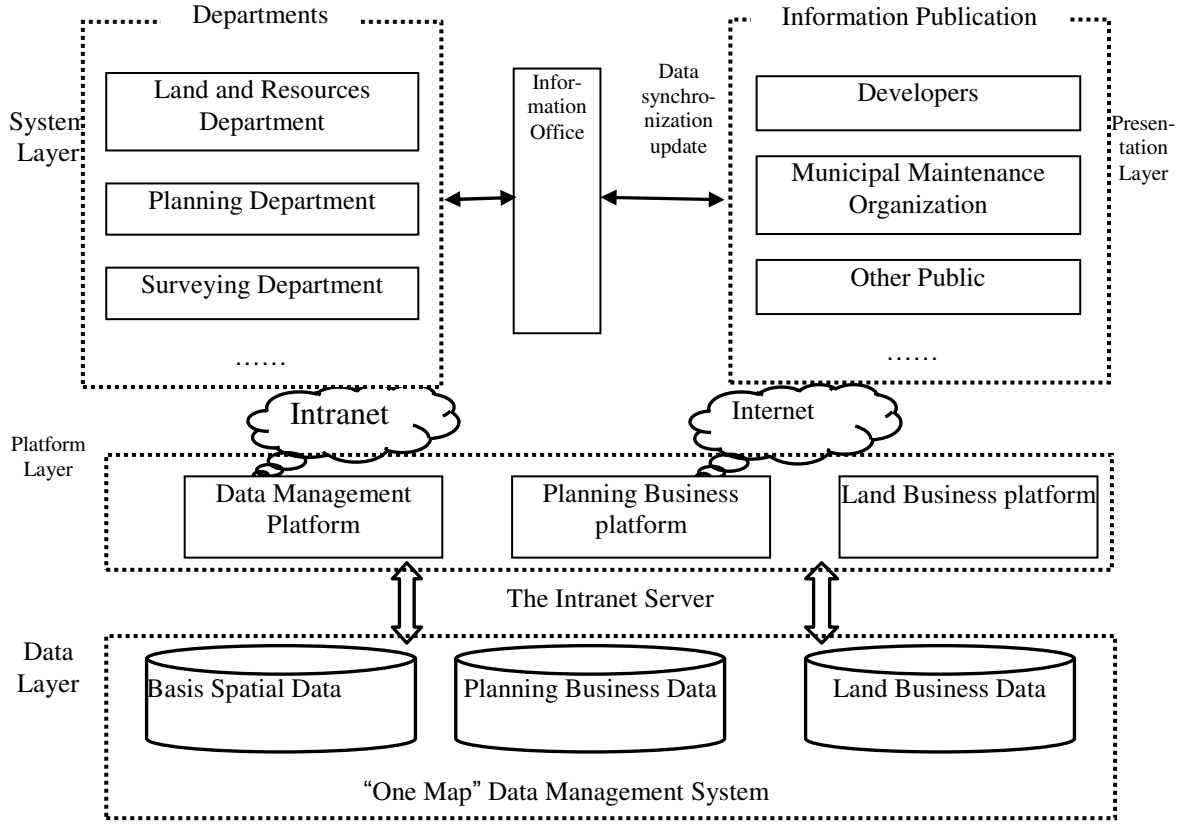


Fig.1. The idea of system structure

Data layer: on the basis of sharing "one map", real-time update the business data. It is responsible for the storage, maintenance and management of the corresponding basic geographic data, planning and land business data and historical archive. All the data should be put in the "one map" management mode in accordance with the unified standards included.

The platform layer: the construction of united application supporting platform, which realize the business system to expand dynamic and sustainable. Unified platform and database will bring great convenience to management. Based on the forward informatization construction and planning, we can modular step by step to achieve full information. Specifically, there are following aspects: unified user management, implement unified identity authentication and single sign-on (SSO); unified workflow to adapt to the changes in the business process; GIS management which provide a unified geographic information services; unified data services to provide the unified basis data services.

System layer: on the basis of the business of real estate resources, set up comprehensive business system and form a multi-level, scalable management technology platform. System function design can be tailored set according to the differences of regions and specific business situation, which realizing step by step. In addition, we need design suitable interface in order to dock the existing OA system.

The presentation layer: with the development of digital and wisdom cities, the concept of mobile office has applied gradually to daily work and life. Information construction in the future will keep pace, fully using the latest scientific and technological achievements, letting the development and construction of information management system to a new level. In addition, there can be related interface make smart phones, tablets and other mobile terminals access to the system conveniently. It will provide quick and convenient access for managers working out to access the system. It also will be easy to access system data and information, which provide statistical analysis on the spot and auxiliary decision-making.

**5.3 establish dynamic updating mechanism of data**

Whether if the "one map" project can be applied normal and sustainable, stable system support and guarantee to update data in time is the key. If the system is not stable, "one map" project cannot run normally. If data condition is poor, the project cannot achieve the desired effect. So there is a strong need to set up a system of data dynamic updating along with effective management mechanism.

In the survey, data update has been a problem in the management. Lots of projects has spend repeated money due to the data can not be updated in time. "One map" project has a great quantity, wide range and huge investment, so we must establish a system including normal operation guarantee mechanism, data update maintenance mechanism and long-term management mechanism.

Update about basic geographic data layer is found going well. Image data update through regular purchase, while terrain data can be synchronous updated due to management function.

Refer to some cities' experience, thematic or management data of land and planning departments can realize dynamic update of figures and attributes through the examination and approval of construction projects and other daily management work, combining with respective administrative functions and meet the business needs at the same time.

## Conclusion

Based on the field research in HongQiao business district management committee in Shanghai and planning and land departments in Yangzhou, and sufficient investigation on the needs of the current government departments, conception of shared "one map" construction is in accordance with the future development direction. For further work, it will help to summarize the needed applications of the land and planning departments more comprehensive and research more deeply about its management system and approval process. the construction of "one map" is more in-depth understanding, make the construction of the "one map" and the system design can combinate business management work better.

As the "Twelfth Five-year" National Informationization Construction Planning has been launching and implementing step by step, the future informationization process of daily work of land and planning is a trend. Continuous development of GIS technology will make better software platform better. Its powerful processing power of figures and attributes is bound to better achieve the construction of information platform. Therefore, it must have a profound impact to the management system of land and planning departments.

## References

[1] Yizhong Sun, Aiqin Li, Lan Zhou, Bin Ye. Urban Planning Management information system(second edition)[M].Bei Jing:The Scientific Publishers. 2011.

[2] Xiaodong Song, Xinyi Niu. The tutorial Practice of geographical information system(ArcGIS 9.x)[M].Bei Jing:The Scientific Publishers2007.

[3] Shiwei Liu. The organizational research of urban planning administration date that be based on the GIS platform ——Take Shanghai as an example.Shang Hai:Tongji University. 2008.

[4] Jingming Feng. The main case and the development of ideas about the Planning of Shanghai and the informatization. [J].Land and Resources Informatization. 2010, 1：3-7.

[5] Lingfei Wang. "A map" seeking the new way of land regulation. [J].Shanghai Informatization .2010, 7: 20-23.

[6] Guang Yang, Jiang Lou. The application of New technology of GIS in land management information system.[J].Dongbei Surveying and Mapping.2002, 25(1)：43-44.

[7] Yang Fu, Guangming Zeng, Chunyan Du, Lin Tang, Jianfei Zhou, Zhongwu Li. Spatial analyzing system for urban land-use management based on GIS and multi-criteria assessment modeling[J]. Progress in Natural Science. 2008, 18(10)：1279-1284.

*Applied Mechanics and Materials Vols. 580-583 (2014) pp 2756-2759*
*© (2014) Trans Tech Publications, Switzerland*
*doi:10.4028/www.scientific.net/AMM.580-583.2756*

# The Visualization of Health Monitoring System for Bridge Using CORS and GIS

Qiaoli Kong[1,2, a], Yuhang Li[1], Litao Han[1,2] and Jinyun Guo[1,2]

[1] College of Geomatics, Shandong University of Science and Technology, Shandong, Qingdao, 266590, China

[2] Key Laboratory of Surveying and Mapping Technology on Island and Reef, State Bureau of Surveying and Mapping, Shandong, Qingdao, 266590,China

[a]kqlabc3334@163.com

**Keywords:** CORS, GIS, Dynamic monitoring, SQL Server.

**Abstract.** CORS is called Continuous Operational Reference System, which comprise a network of Global Positioning System receivers. Traditional sensors were used to determine the working environment parameters and mechanical property parameters of the bridge, and CORS technology was applied to obtain the positions of bridge monitoring points in three axis directions, besides the technology was adapted to combine GIS software with the relational database, in which the function of GIS and SQL Server were to manage the spatial information and the corresponding attribute data. In this paper the technology route was designed in detail to realize the real-time dynamic monitoring and visualization analysis of the deformation of large bridge. This system was developed to evaluate valuable information such as the stability, durability and reliability of the bridge.

## Introduction

Since the emerge of CORS technology in 1990s up to now, many CORS network have been established in big cities, such as Hongkong, Shenzhen, Beijing, Guangdong Province[1]. The main technology of CORS is developed rapidly, and its application is becoming mature. CORS is not only the product of GPS, but also a system combined with internet technology, wireless communication technology, the computer network management and GPS technology.

Health monitoring of large bridges is to determine the features of position change for major feature point in the effect of temperature, wind, load, earthquake and other external factors, and to evaluate the damage, stability and residual life and so on. In the past, due to technical limitations, the major methods of measure the vibration and displacement of structure for huge bridges includes: displacement sensor testing method, accelerometer method, laser interference test and total station measurement [2]. A certain purpose can be achieved although using these methods, some problems still exist, these traditional methods can't meet the needs of continuity, real-time and automatically dynamical observation of bridge monitoring. In recent years, the CORS system are applied in the large-scale cross-sea construction projects, and special CORS have been established for the Hangzhou bay cross-sea bridge, Zhoushan Island mainland Jintang bridge engineering and the Jiaozhou bay bridge [3].

CORS make the continuity, real time and dynamic of monitoring for large bridge become a reality. GIS is a effective tool for collection, storage, management, analysis and display for the data relating to geographic distribution, and it can simultaneous manage the spatial information and attribute data, besides it can establish a dynamic database of monitoring data, and regularly update, backup and recovery the monitoring data. In order to realize the sharing of monitoring data, we used the database management system based on network environment, such as the SQL Server database system. Visualization can clearly reflect the dynamic change situation of the structure. Therefore, the visualization of monitoring data is one of the essential functions of dynamic monitoring system for the bridge health.

## CORS system

CORS is composed of a base station, data processing center, data communication link and the user part. CORS can provide GNSS (Global Navigation Satellite System) data consisting of carrier phase and code range measurements which can provide data for three dimensional position, meteorology, space weather and geophysical applications. Surveyors, GIS users, engineers, scientists can use CORS data to improve the precision of their positions. The data communication between base station and data processing center can use DDN (Digital Data Network) data network or wireless communication method. Bidirectional data communication between station and data processing centers can be realized by GPRS, CDMA [4]. Single reference station system can not solve the problem of the long distance positioning. In order to achieve the goal of the baseline accuracy better than 3 cm for the multi-reference station system, the reference stations should be established densely in a region, and the distance between stations should be less than 30 km. While the CORS technology has a wide precision coverage, and the precision distributes evenly in the covered region. At present, CORS technology have been tested and applied widely both in hardware and software in many countries, such as in Canada, Norway, America, Brazil, South Korea and so on. The CORS system in American has more than 500 reference stations, which is run by NGS (National Geodetic Survey) belonging to Oceanic and Atmospheric Administration. In China, GPS CORS technology has been developed and applied in many projects, according to the actual measurement data, real-time positioning accuracy of CORS can reach ± 3cm in plane and ± 5cm in vertical [4, 5], even up to 1-2cm [6]. The earliest application of the network RTK technology in China is the CORS system in Shenzhen city.

## Method and technology route description

In this paper, we applied the traditional sensors to determine the working environment parameters and the mechanical property parameters, and used CORS techniques to determine the displacements of bridge monitoring point in three axis directions. SQL Server database management system was adopted to manage the bridge monitoring data in the design of the software part, so as to realize the management of the massive data. The monitoring data in some time windows was used to establish the dynamic database, and then to realize the establishment, backup, restore and visit. The visualization technology were applied to describe the key part displacement and the overall displacement of the bridge in real time. The interaction between GIS and other modules was achieved by GIS software, so as to realize the functions of monitoring data input into the database, database backup and restore, database visit through the local area network and visualization of a variety of the access information.

In order to collect on-line information of the bridge, different types of sensors should be mounted on the critical points of the bridge, such as the working environment parameters and mechanical property parameters of the bridge. The displacement of bridge monitoring point in three axis directions should be determined by the CORS technology. GIS and database technology were integrated to transmit the data to the database through the network, the spatial information and the and corresponding relation database were managed by GIS, besides the monitoring data were managed by the relational database. The interfaces were developed, and the reports or charts were also be generated, besides the health condition information of the bridge structure and operational status should be published on online for the user to visit data in real time conveniently.

## Design of database

In order to display the relationship between real-time monitoring data sheets, GPS monitoring point information table and warning information table of the every monitoring point, a primary key between two tables in a database diagram were created. The relationship between real-time monitoring data sheets of the measured point and GPS monitoring point information table was mainly displayed in real time on the displacement of the bridge. During the process of real-time monitoring,

the GPS software could automatically solve the coordinates of GPS monitoring point and these data will be stored in the corresponding MonitorNo table to display the displacement of each point, and the database diagram is established as Fig. 1.

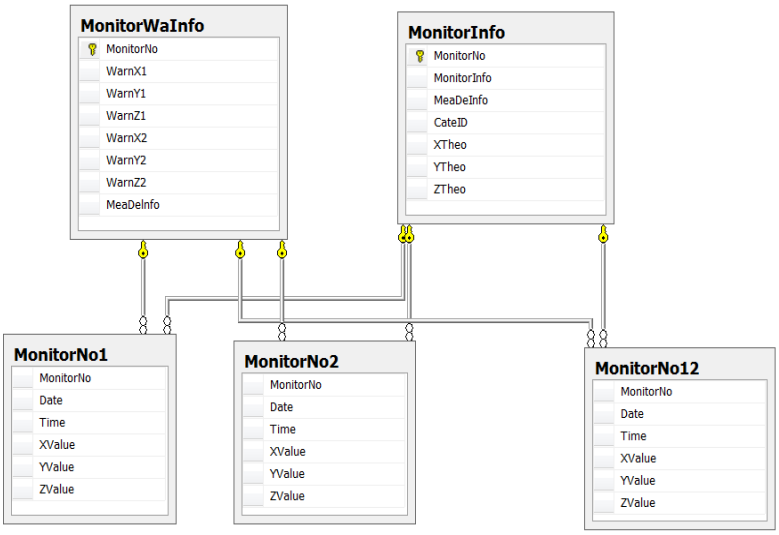


Fig. 1 Database diagram

According to Fig. 1 we were able to make a timely response to the dangerous situations according to the difference between the warning thresholds and displacements of the monitoring point, the number of monitor was set from 1 to 12.

## System function design and realization

Functional design of the system is an important part of system development. This system adopted the modular idea, and the modules were both interactive and independent between each other. The system could be divided into five big modules according to the function: basic operation module, two and three dimensional linkage module, the path planning module, path dynamic demo module and road network extraction module, and the partial functions were listed in Fig. 2, and the interface of realization for these functions was plotted in Fig. 3.

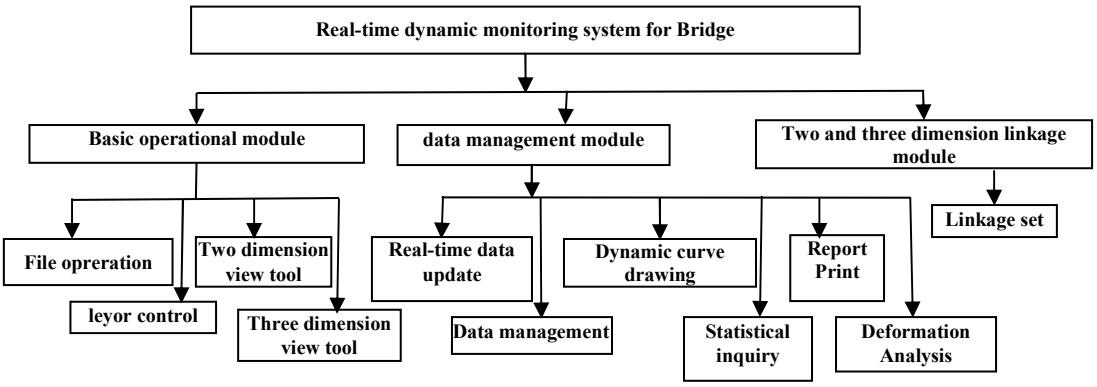


Fig. 2 The function design

In this paper, we developed detail functions for this monitoring system, such as file operation, layer control, two dimension view tool and so on, and Fig. 2 just showed part of functions of this system.

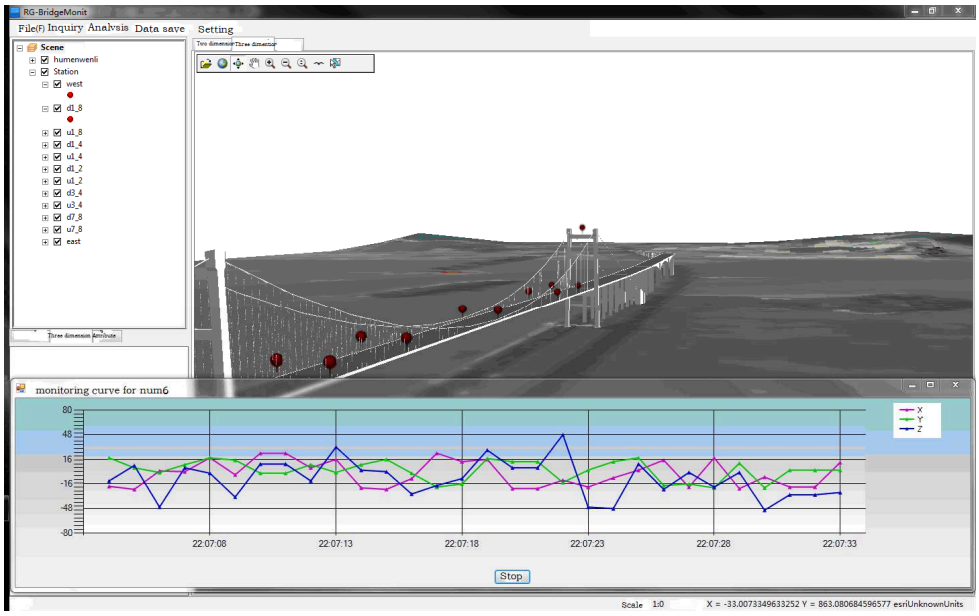


Fig. 3 The interface of visualization of health monitoring system for bridge

Fig.3 showed that according to the displacement of monitoring point this system could draw the curve of displacement of monitoring point 6 as a time series, and the other curves for the other monitoring points can be plotted, at the same time, the three dimension figure of the bridge could be plotted, and the information could be saved according to the table of the interface.

## Conclusions

On the basis of CORS technology and GIS, the health monitoring system for bridge was designed and realized. The application of GIS has enriched the ability of the system, such as storage, management, analysis and visualization for the graphic and attribute data of bridges and sensors. We have applied SQL Server to manage the massive monitoring data, and the developed friendly interface is convenient to inquiry and visit for users. The continuous real-time dynamic monitor and data management for the critical parts of a large bridge could provide valuable messages such as stability, durability and reliability, and the visualization of health monitoring system for bridge was achieved.

## Acknowledgment

This work was supported by the National Natural Science Foundation of China (grant No. 41201381)Key Laboratory of Advanced Engineering Surveying of NASMG (grant No. TJES1203), the Key Laboratory of Surveying and Mapping Technology on Island and Reef of NASMG, China (grant No. 2012B02).

## References

[1] D.J. Wu, W. Xiong, R. X. Zhou, C. J. He: Science surveying and mapping Vol. 38 (2012), p. 62-64 (in Chinese).

[2] J.W. Lovse, W.F. Tesky，G. Lachapelle: Journal of Surveying Engineering Vol. 121 (1995)，p. 35-40.

[3] S.X. Han, Z.X. Zeng, X.W. Wang, S.C. Zheng: Journal of Shandong University of Science and Technology(Natural Science) Vol. 26 (2007), p.1-3(in Chinese).

[4] H. Liu, J.N. Liu, S.J. Yang, X.Y. Shi, H.P. Luo, Z.J. Yang. Bulletin of surveying and mapping Vol. 9 (2003), p.33-36(in Chinese).

[5] X. Zou, W.M. Tang, M.R. Ge, J.N. Liu: Acta geodaetica et cartographica sinica Vol.40 (2011), p. 1-5(in Chinese).

[6] M. Tang: Science & Technology Information Vol. 3 (2011), p.49(in Chinese).

*Applied Mechanics and Materials Vols. 580-583 (2014) pp 2760-2764*
*© (2014) Trans Tech Publications, Switzerland*
*doi:10.4028/www.scientific.net/AMM.580-583.2760*

# Research on the 3-D scene quick build method of virtual city and implementation method of basic GIS function

Yang Chang[1, a], Li Hao[2, b],GaoPeng[3, c], Zhang Rongchun[4, d]

[1-4]School of Earth Sciences and Engineering,

Hohai University, Nanjing, Jiangsu, China

[a]yycc122300@163.com,[b]lihao_64@163.com, [c]gpyc0720@163.com

**Keywords:**virtual city, Virtual GIS, 3D modeling, AutoCAD VBA

**Abstract.**Aiming at the common problems of virtual city modeling,such as low efficiency and large amount of data, this paper proposes a quick method to build a virtual city.The method realizes data read automatically through AutoCAD VBA programming, generated the VRML code automatically, buildthree-dimensional scene by the VRML code integration and realize the Web publishing of virual city via Web.

## Introduction

At present, people mainly use software such as OpenGL, 3D MAX, VRML to realize the construction of virtual city. However, therearestill many shortcomings in current virtual city development project, such as the relatively large workload, overelaborated program, the low system efficiency and so on. Face with the shortcoming above, this paper proposes a simple and rapid method. The method takes AutoCAD VBA, VRML and database technology as the main means, automatically completes data reading, 3D modeling, texture mapping, Integration and rendering in combination with other modeling software, realizes the basic function of GIS and punishes via the WEB. The specific method is as follows:

## Quick build method of Virtual city

### Data preparation and processing

**Datapreparation**.

The virtual city 3D model needs a lot of data. The data mainly includes the building and affiliated facilities thereof, traffic and affiliated facilities(railway, road, traffic signs, bridge, shelters, toll station andso on), public service(power line, line of communication, Street lamp, mailbox, gas station,bin ,flagpole signs), Landscape and recreation facilities（sculpture, miniature landscape, playground）, the vegetation and green belts(grass, trees, flowers), water (rivers, lakes, reservoirs, etc.).Descriptive Information is encoded according to the classification,and essential attribute is marked as unique identification code. Information database is established with SQL as the platform.

**Dataprocessing.** Because only graphic data can be stored in AutoCAD,the method pays attention to separating graphics data and the graphic datain the data collection. The layer can be divided into: baseboard, building, road, water, vegetation, people, car and so on.Baseboard, building and road are line objects, and their main body is closed polyline, their elevation attribute is their physical

altitude. Vegetation is dot features, its kind can be expressed via color. Some ground objects are not on the map, such as people and cars. They must be drawn on the layer by hand. The AutoCAD sketch map is as below:

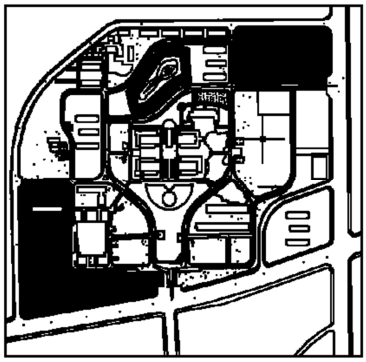

Figure1:Exampleof AutoCAD sketch map.

**Set up texture lab**

**Acquisition and processing of texture data.**There are two main types of texture data acquisition method. The texture with high precision requirements are shot on location, so their volume of data will be large and the texture is hard to disposal.

The texture of the general can be synthesized by computer software (such as 3D MAX) to Reduce the amount of data and increase efficiency. Whereas, for this reason of spatial location, vision angle and meteorological factors, orthogonal projection image cannot be got during the actual acquisition process. So the images should be dealt with. Graphics processing operations mainly includes: distortion correction, removing the mask, image enhancement, and data redundancy reduction.

**Texture encoding and texture information storage.** Processed digital image texture should be code and to realize the automatic modeling. Ground objects can be characterized in the form of geometric shapes in AutoCAD. Because geometry handle is unique in AutoCAD, graphical information, texture information and related graphic data can be linked to each other.

**Automatic 3D modeling**

This paper takes VRML as a modeling tool for the reason of network transmission. However, it will be huge effort to model only depend on VRML.The method links to database via VRML to read the AutoCAD graphic data, automatically complete modeling and automatically generate VRML file. Several kinds of modeling method is introduced as follow:

**Topography modeling method .**The establishment of the real city is based on complex terrain. Topography model is set up in the first place to showcase the virtual city scene. Firstly, write code via VBA, read the corresponding topographic map data and build landscape model. Figure 2 is AutoCAD topographic map, Figure 3 is modeling working sketches.

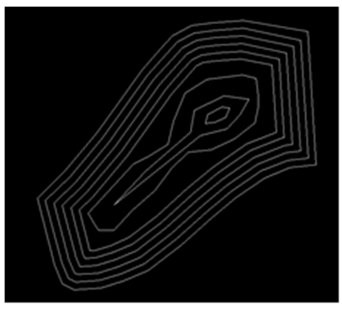

Figure2:Dataof AutoCAD.

Figure3: Sketch map.

**Ground objects modeling method.** Building is the larger proportion in the urban landscape. Most of the building model are more common. They can be modeled in 3D MAX. The model that built

by 3D MAX is distinct, fine and smooth. However, the method's Achilles heel is that data volume is greatly, roaming is difficult, and the workload is huge. A common building group in the city has a standard geometric features. Read data via automatic programming, batch processing of the model and reduce the workload and the amount of data that scene. The following to a specific example. Figure 4 is AutoCAD topographic map of buildings. Define the building outline as AcadLPolyline object, write code via AutoCAD VBA, stretch processing line, and automatically generate 3D models. Generate models as shown in Figure 5. Connect with the texture library via AutoCAD VBA and map the texture. The scenario building is established by VRML, the part of the code is as follows:

```
Sub GetVrmlMdlFromCAD ()
Dim ExTendV as Double, num As Integer, n As Integer, i As Integer,e As AcadEntity, Pl as AcadLWPolyline, xy () As Double
For Each enIn ThisDrawing.ModelSpace
If e. Object Name = "AcDbPolyline" And e.Layer = "house" Then
Set Pl = e
xy = Pl. Coordinates ()
n = UBound (xy)
num = num + 1
Open "house.wrl" For Output As #1
Print #1, "#VRML V2.0 utf8"
Print #1, "Transform {translation 674.33 0 -311.27"
,Print #1, " coord Coordinate {point [-1.2 0 0.0, 1.2 0 0, 1.2 3
0,-1.2 3 0]"
Print #1, "} coordIndex [0, 1, 2, 3]"
Print #1, " Transform {translation 607.18 0 -311.23 children
USE house1}"
……
Print #1, " Transform {translation 710.63 0 -304.08 children
USE house1}"
End if
Close #1
End Sub
```

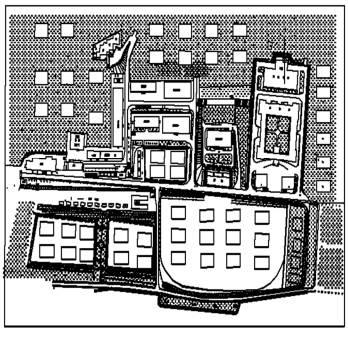

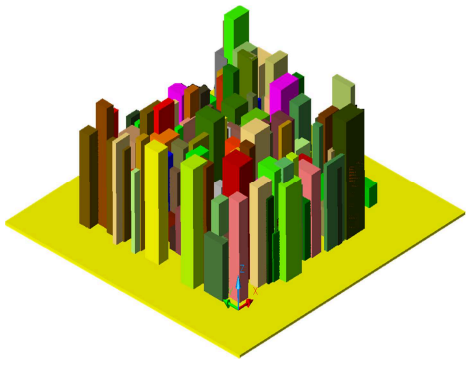

Figure4: Blocks CAD topographic map. Figure5: Diagrammatic figure.

Furthermore, complicated model should be model by 3D MAX.Link models to the corresponding data in the database, and import into 3D MAX to build 3D model. 3 D model will be exported as WRL format, and integrated in VRML.

**Planar feature modeling method.** Models of river network, green belt, grassland in the cityscape can be built via the method of planar feature modeling method. Similar to the geometric entity

modeling method, read the AutoCAD topographic map and conversion to generate planar entities. Due to the reason that precision and texture quality requirement of such a model is not high, map the model by linking to the texture lab.

**The point feature modeling method.** In order to showcase city landscape, improve the fidelity and immersion of the system, trees, pedestrian and vehicle should be added into the model. These features are often occupies little space resources and they can be expressed as dot in the map. Geographic position can be expressed as dot. Due to the shape of the feature is irregular and model data volume is large, transparent texture mapping method is used to build scene. Next, take billboard technology for example to introduce the modeling methods.Data is loaded to determine the object position. Generate planes in the position, and map the planes transparent materials. Models made by the method has small amount of data. Part of the model are as follows:

Figure6: Pedestrian'smodel.

Figure7: Vegetation's model.

Figure8: Vehicle'smodel.

**Automatic 3D modeling.**

The real city scene is very complicated. The paper uses different modeling methods to restore the original landscape realistically.VRML is used as a platform to integrate scene. Models made by AutoCAD can be transformed to VRML code via AutoCAD VBA.Models made by 3D MAX can be generated directly WRL code. Finally the code will be integrated together by link function. The code examples as follows:

Inline {URL "house.wrl"}

The code is adding the file named "house" into the scene. Other integration method of the scene is same to it. The scene after integration is still just structure, cannot be real-time browsing. As the reason of above, the light, sky background, is added into the scene to improve the spectator.

**Basic GIS functions of Virtual city**

**Dynamic interaction function of the 3D scene**

**Manual roaming and automatic roaming function.** Users browse the scene via VRML plug-in to improve immersion and practicability of the system.

According to the different needs, the users can adopt manual roaming and automatic roaming function to browsing scenarios. Users can browse the scene manually via the tools provided by roaming control panel.Following is a manual roaming figure:

Figure9: Virtual roaming.

Besides, users can preset roaming paths, generate show animationtorealize automatic roaming function and roam in the virtual scene along the specified path by setting the speed and height.

**Implementation of viewpoint switching and automatic positioning function.**In the virtual city scene, the method takes hyperlink as main means and combines with the JavaScript program and VRML functions. Part code is as follows:

Function SetVP (cam) {Scene. Engine. Nodes (cam). Fields ("Set bind") = true ;}

<a Href="JavaScript: SetVP ('xiaoqu')">xiaoqu</a>

**The bidirectional query functions**

**Attribute database design.**Only the graphical information of the city can be recorded and displayed in the virtual scene, attribute information of landscape display incomplete. So attribute information database of virtual scene is built to realize the bidirectional query of spatial data and attribute data. One-to-one correspondence is built to provide information services. Users can select query options, such as unit name, corporate, etc., and input the query keywords, like “MA steel Heling”, click on the search.

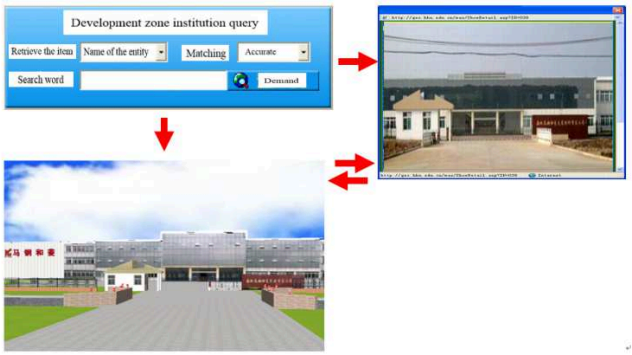


Figure10: Information query.

**Summary**

This scheme takes AutoCAD and AutoCAD VBA as a platform without special software of virtual city, and reduces the operation difficulty. Complete the data read, model and texture map via AutoCAD. In addition, virtual city landscape scene will be released for network by VRML technology. Users complete the data query and browse by VRML plug-in and a WEB browser.

**References**

[1] KIM S, CHOI B． Hi gh dynami c range image textrue mappi ngbased on VRML [J]. Lecture Not es in Comput er Science, 2003, 2669： 488497.

[2] MA Jun, ZHU Heng-jun, GONG Jian-hua. Simulation of Real-time Water Surface Based on Cg and OpenGL [J]. Journal of System Simulation, 2006, 18(2): 395-400.

[3] Nick Foster, Dimitri Metaxas. Realistic Animation of Liquids [J]. Graphical Models and Image Processing (S1077-3169), 1996, 58(5): 471-483.

[4] Kei Nakano. Water Surface Using Particle System [EB/OL]. (2002) [2008].

[5]Terrasolid SoftwareforprocessingLiDA R point cloudsandimages［EB/OL］.

[6] Chen.Filteringairbornelaser streamingdatawithmorphological methods ［J］PE& RS, 2007, 73( 2) : 175－187.

*Applied Mechanics and Materials Vols. 580-583 (2014) pp 2765-2768*
*© (2014) Trans Tech Publications, Switzerland*
*doi:10.4028/www.scientific.net/AMM.580-583.2765*

# Application of Three-dimensional Visualization Technology in Real Estate Management

Jian Cui[1,a], Jiju Ma[2,b] , Dongling Ma[1, c] and Nana Yang[3,d]

[1] School of Civil Engineering, Shandong Jianzhu University, Jinan 250101, China

[2]School of Transportation Engineering, Shandong Jianzhu University, Jinan 250101, China

[3]Jinan Research Institute of Real Estate Surveying and Mapping, Jinan, 250001, China

[a]cuijian1202@126.com,[b]majiju88@gmail.com,

[c]mdling2003@126.com,[d]yang_n19871221@163.com

**Keywords:** Three-dimensional (3D) modeling; Visualization; Real estate management

**Abstract.** Real estates are the material basis of the survival and development of a city, and are important parts of urban development. We use 3ds Max as a tool to create 3D models of buildings and Supermap Deskpro.NET as a platform to make an effective combination of 3d models, real estate graphic data and real estate attribute data. Three-dimensional display of surveying and mapping information and three-dimensional visualization management of house property information are realized.

## Introduction

Based on computer graphics, visualization technology and virtual reality technology (VR) etc., 3D visualization technology has been widely used in geographical informatics, ecology, science of surveying and mapping, architecture, medicine and other fields of science, greatly promoted the development of related disciplines with a series of achievement [1].

As the substantial components of digital city geospatial framework construction, real estate surveying and mapping informatization and 3 d visualization lead to spatialized, elaborate, dynamic, visual and actualized real estate information and services, which cover accurately each building, each period of time and each area, so that the property management implements its evolution from extensive management to precise management, from bull management to unified management. This paper starts from the graphic and attribute data of real estate, using 3ds Max to create 3D models of buildings and Supermap Deskpro.NET as an integration platform to realize 3D display of surveying and mapping information and 3D visualization management of house property information.

## Data Preparation

Real estate surveying and mapping information is the main content of the real estate information, it consists of two parts, i.e., real estate surveying and mapping graphic data and attribute data [2]. The former mainly includes building property map and basal relief map, and the latter mainly refers to the attribute information of each building, of each layer and of each household. In order to conform to reality, we also collected the 2D plan of the building, and carried on the field survey, capturing photographs of campus landscape and landmark buildings in Shandong Jianzhu University for textures.

## Establishment of 3D Models

In terms of 3D models of buildings, they are momentous constituents of 3D real estate information management system, which play the decisive role in the quality of the system [3].

**Modification of the Base Ma**p. Import 2D plans of the research area into the CASS software, and remove unnecessary ground objects and landforms, e.g. parterres, street trees, street lamps, etc.

Then modify the 2D plans of buildings the same way, deleting appendages of buildings, remaining brief plans to construct three dimensional models.

**Production of Textures.** To meet the requirements of modeling, photographs need to be refined in PhotoShop software, including adjustment of the shape, restoration of the shadow, etc. After that, we will import the 2D plans of a building, already modified in the procedure above (format: *.dwg), into 3ds Max, then zoom the base maps in the view of Top, Front, Left, Perspective to a suitable size respectively.

**Production of blank models (semifinished product).** In the next, we will use polygon as a major tool to establish the model of each building one by one [4]. As the outline of a building is available through the 2D base map, we can sketch the contour of the building, and then convert it to an editable polygon, on this basis, we extrude the polygon to appropriate height, and that results in a blank model without bottom, which is the so-called semifinished product. And then, detail structures of the building require to be crafted in order to generate a complete 3D model. Over the course, modifiers and tools (like Extrude, Attach, Chamfer, Connect, Cut, Boolean, etc.) are frequently used.

**Texture Mapping.** So far, we have produced textures as well as blank models, what we should do next is just making a combination of the two, i.e., mapping textures for the models. It's not difficult using UVW Mapping modifier to adjust the right picture suitably to a corresponding model. Up to this point, we have finished the whole process of making a lively 3D model for a building.

**Light Configuration.** Proper light illumination results in the optimal effect of material [5]. We use three Target Spot and one Free Spot in the scene, and they are set in different positions. We can adjust the shadow of each spot respectively, so that the scene will looks more alive.

## The Realization of Three-dimensional Visualization Technology

Three-dimensional visualization is a more intuitionistic technique to display 3 d data [6]. As it can show the spatial data more factually, and simulate geographic-information reality more realistically, three-dimensional visualization technology has brought great new technical innovation for GIS.

**Loading of 3D Models.** Taking campus buildings for example, we've created 3D model for each building, and will load them into the 3D scene in the rest. Before that, it is necessary to install the SuperMap plugin for 3ds Max. Merge all of the models together in 3ds Max, use the script tool of the plugin to return the origin of coordinates of each model to its center then bottom.

Now for the most important part, we will take advantage of SuperMap plugin to generate model cache which can be loaded into SuperMap Deskpro.NET later. Click the function button 'To generate cache', enter the corresponding latitude and longitude values in the dialog box and select the file path for texture files, then press the OK button to finish the process.

Import the digital orthophoto map (DOM) and digital elevation model (DEM) into SuperMap Deskpro.NET respectively as image dataset and grid dataset, both of them with the same projected coordinate system. Then load them as well as the model cache into the same new scene to establish a primary3D scene as shown in Fig.1.

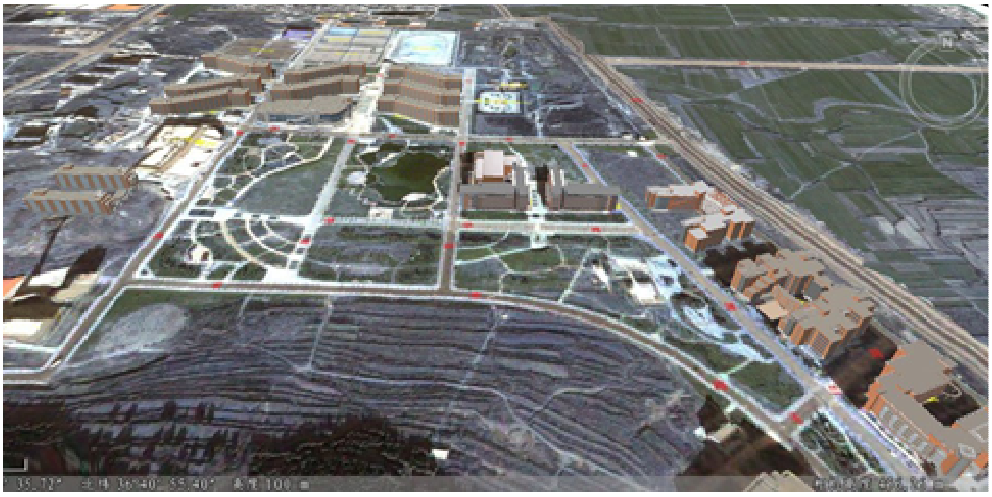

Fig. 1 Display of the primary 3D scene

**Three-dimensional Environment.** In this section we will discuss the embellishment of the 3D environment, including the modeling of vegetation and roads and the setting of flying route.

Modeling of vegetation. The vegetation types in a City are various, and there is no need modeling separately for some kinds of features, e.g., it's feasible to use DOM to express the grassy area of a city or dense forest on a hillside. But in order to keep the sense of reality, it's necessary to model the ornamental plants. It's convenient to realize the visualization of trees in SuperMap Deskpro.NET. Just simply add points that correspond to where the trees lie, then load the point dataset into the existing 3D scene as a layer and change the style of the layer. In more detail, choose a proper 3D tree model in the point database as the layer's style and the points will successfully display as trees in the scene. By the way, you can also produce your own tree model in the editor.

Modeling of roads. In terms of road modeling, it's similar with tree modeling, just create a new line dataset and vectorize along the center of the each road, then put it into the scene and choose a proper 3D line symbol as the layer's style.

Setting of Flying Route. Specifying the route and perform a 3D flying is one of the way to browse the 3D scene [7]. In SuperMap Deskpro.NET , a flying route is specified according to the points on the line. Information of the points stores in a file whose format is *.gml. So pick some points at the desirable places, then set an appropriate height and speed for the route and perform it to check it out. The final result is shown in Fig.2.

Fig. 2 Final result of the 3 d campus

## Conclusions

Three-dimensional visualization of real estate information can effectively implement function as estate information release and display, real estate transaction, real estate planning, residential property management so on and so forth [8]. In our research, 3D models of building were crafted in 3ds Max on the basis of graphic and attribute data of buildings in the campus, and a 3D scene was established realizing the three-dimensional visualization.

Within the scope of super fine little scene production, there is a further dimension we have not delved into: terrain matching. We intend to pursue this line of work in the future to make it perfect.

## Acknowledgements

This work was financially supported by Science and Technology Project of Colleges and Universities of Shandong Province (Grant No.J12LG53), Ministry of Construction P.R.China Science & Technology Planning Project (Grant No.2010-K9-24) and Housing and Urban-rural Development project of Shandong Province (Grant No.2011YK026).

## References

[1] MOC of the P.R.C: Technical Specification for Urban Fundamental Geographic Information System (China Architecture & Building Press, China 2004).

[2] MOHURD of the P.R.C: Technical Code for Three Dimensional City Modeling (China Architecture & Building Press, China 2010).

[3] Q. Zhu, D.R. Li, Y.J. Gong and H.J. Xiong: Geomatics and Information Science of Wuhan University, Vol. 26 (2001) No.1, p.8.

[4] P. Chen, H. Lin, P.C. Zhang, and S.Z. Wu: Geospatial Information, Vol. 9 (2011) No.3, p.65.

[5] L. Cheng, Y.J. Zhang, J.Y. Gong, and X.G. Song: Science of Surveying and Mapping, Vol. 33 (2008) No.1, p.119.

[6] Z.L. Jia and Y.L. Liu: Geospatial Information, Vol. 7 (2009) No.6, p.10.

[7] X.W. Zhao, F.X. Jin, Y.L. Li, J. Wang and W.W. Xiao: Journal of Geomatics, Vol. 34 (2009) No.4, p.11.

[8] M. Trapp, A. Semmo, R. Pokorski, C. D. Herrmann, J. Döllner, M. Eichhorn and M. Heinzelmann: International Journal of Heritage in the Digital Era, Vol.1 (2012) No.1, p.45-74.

*Applied Mechanics and Materials Vols. 580-583 (2014) pp 2769-2773*
*© (2014) Trans Tech Publications, Switzerland*
*doi:10.4028/www.scientific.net/AMM.580-583.2769*

# Calculation of Land Consolidation Potential Based on GIS

Yanhua Liu [1,3, a], Weiqing Chen [2,4,b]

[1] Faculty of Resource and Environmental Sciences,Guangxi Teachers Education University, Nanning, China

[2] College of Civil and Architectural Engineering,Guangxi University,Nanning, China

[3] Key Laboratory of Beibu Gulf Environment Change and Resources Use (Guangxi Teachers Education University), Ministry of Education, China

[4] Guangxi Key Laboratory of Disaster Prevention and Engineering Safety,Guangxi University,

[a] lyh_lucy@sina.com, [b] gxcwq@163.com

**Keywords:** Land consolidation potential, Cultivated land, Rural residential land, Geographic information system (GIS)

**Abstract.** Through the analysis of land use actuality, this paper summarizes the characteristics of land use, in virtue of geographic information system(GIS) platform, the database of land consolidation is constructed, combining with different calculation models of cultivated land and rural residential land consolidation potential, the consolidation potentials of cultivated land and rural residential land are calculated, and the thematic maps about land consolidation potential of each village and town in study area are mapped out. The results show that the land consolidation areas are mainly concentrated in the middle of study area.

## Introduction

Land is the important strategic material base and resources for the sustainable development of human economy and society. It's not only the organic component of natural resources, also an essential nonrenewable resource of human production activities. In recent years, with the rapid development of economy, the scope of non-agricultural construction lands is infinitely expanded. Because of the shortage of reserve cultivated land resources and ecological environment constraints, the contradictions are increasingly prominent between cultivated land and construction land [1]. The objective demand of rapid economic development can't achieve dynamic balance of total cultivated land by strictly controlling land supply. So land consolidation becomes an effective way to resolve land tensions at present [2, 3]. Land consolidation potential analysis is preliminary work for land consolidation. That is, under the current economic and technological conditions, analyzing theoretical effective area of increasable cultivated land or farming land by land consolidation [4]. According to land suitability and less reserves, some types of lands such as unused, abandoned and idle lands will not necessarily become cultivated land after they are consolidated. Therefore, cultivated land consolidation and rural residential land consolidation become the main part of land consolidation [5]. This paper takes Mashan County, Guangxi, China as the study area, discussing the land consolidation potential of cultivated land and rural residential land in this region, expecting to provide reference for regional land management planning.

## Calculation model of land consolidation potential

**Calculation model of cultivated land consolidation potential.** The sources of cultivated land consolidation potential include sporadic land and current land feature which is increasable cultivated areas by consolidating cultivated land and uncultivated land such as country roads, irrigation canals, raised path through fields and sporadic land. The calculation method of cultivated land consolidation potential is:

$$S_C = S_x + \sum_{i=1}^{n} (M_i - Y_i) * S_i \quad (1)$$

where, $S_C$ is the cultivated consolidation potential in district, $S_x$ is the area of sporadic land, $n$ is the slope series of cultivated land, $M_i$ is the covering coefficient of linear feature in $i$ slope cultivated land consolidation region, $Y_i$ is the covering coefficient criterion of linear feature in $i$ slope cultivated land consolidation region, $S_i$ is the area of consolidating land.

**Calculation model of rural residential area land consolidation potential.** Rural residential area land consolidation potential is calculated according to villages and towns through questionnaire and other information to statistics resources of rural collective construction land, including population, households, construction land area, homestead area, idle land area, the natural population growth rate and other relevant information. The calculation method of rural residential area land consolidation potential is:

$$S_R = S_0 - B * (Q_0 * (1+r)^t \pm \Delta Q) \quad (2)$$

where, $S_R$ is the rural residential area consolidation potential in district, $S_0$ is the area of current rural construction land, $B$ is the planning land per capita, $Q_0$ is the current rural population, $r$ is the natural population growth rate, $t$ is the planning period, $\triangle Q$ is the mechanical changes in population.

## Land utilization status of land resources in study area

The study area is Mashan County in Nanning City, Guangxi, China, which Contains seven town and four townships. According to the population census data in 2010,the total population is 542700, the birth rate is 26.81‰,the population mortality is 7.08‰,the natural population growth rate is 19.73‰.According to the second national land survey and survey data of land use change in 2010, the structure of land use is shown in figure 1.

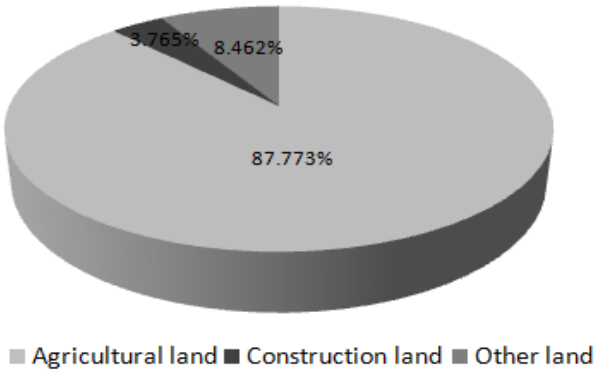


Fig.1 Land use structure

Through the analysis about the present situation of land use, Mashan county land use has some characteristics as follows:① agricultural land is the main land use types of the county, traffic and water conservancy facilities land has small proportion;② agricultural land is mainly farmland and woodland, especially woodland, so the county has high forest coverage rate;③low land reclamation rate and less per-capita cultivated land;④ the quality of cultivated land is not high, and the percentage of paddy fields is low.

**Construction of land consolidation potential database**

Before calculation land consolidation potential, database of land consolidation should be constructed. The databases of land consolidation mainly include databases of cultivated land consolidation and rural residential land which can be constructed by ArcGIS. Taking the cultivated land consolidation as an example, the database structure is shown in table 1.

Table 1 Database structure of cultivated land

| fields | type | width | decimal |
|---|---|---|---|
| township | character | 6 | |
| land class | character | 6 | |
| polygon area | float | 10 | 2 |
| fragmentary land area | float | 10 | 2 |
| consolidation potential | float | 10 | 2 |
| potential absolute coefficient | float | 5 | 2 |
| potential level | integer | 2 | |

**Analysis of cultivated land consolidation potential**

**Present situation investigation of cultivated land consolidation potential.** There are cultivated land areas of 46207.22 hectares in Mashan County. The cultivated land areas, percentages and grades of different gradients are shown in table 2.

Table 2 Classification of cultivated land gradient

| classification | ≤2° | 2～6° | 6～15° | 15～25° | ≥25° |
|---|---|---|---|---|---|
| area[ha] | 14128.98 | 10699.67 | 11870.02 | 2364.78 | 7143.77 |
| percentage[%] | 30.58 | 23.15 | 25.69 | 5.12 | 15.46 |
| level | 1 | 2 | 3 | 4 | 5 |

**Calculation of cultivated land consolidation potential.** In ArcGIS platform, the cultivated land of different gradient, rural roads and ditches are isolated. Combining with specific circumstance of Mashan County, with reference to the cultivated land consolidation standards in Guangxi, the covering coefficient of linear feature in different gradient cultivated land are calculated shown in table 3.

Table 3 The covering coefficient of linear feature in different gradient cultivated land[%]

| gradien level | roads covering coefficient | ditches covering coefficient | ridges covering coefficient | linear feature covering coefficient |
|---|---|---|---|---|
| 1 | 1.8 | 1.2 | 0 | 3.0 |
| 2 | 2.2 | 1.8 | 6.0 | 10.0 |
| 3 | 2.5 | 1.8 | 8 | 12.3 |
| 4 | 2.6 | 1.4 | 15 | 19.0 |
| 5 | 3.1 | 1.6 | 25 | 29.7 |

According to formula (1), the total potential of cultivated land consolidation in Mashan County is 836.00 hectares. The distributions in different township are shown in table 4.

### Analysis of rural residential land consolidation potential

**Present situation investigation of rural residential land consolidation potential.** In Mashan County, there are 5383.46 hectares rural residential area, and 499774 rural populations, land per capita 107.718 square meters. According to the natural population growth rate of Mashan County in recent years, taking 2010 as the base year, there will be 517770 rural population in 2015.

Referring to land use planning and the national economy "twelfth five-year" development planning of Mashan County, the rural residential planning land per capita is determined to be 96 square meters.

**Calculation of rural residential land consolidation potential.** According to formula (2), the total potential of rural residential land consolidation in Mashan County is 512.38 hectares. The distributions in different township are shown in table 4.

Table 4 The distribution table of cultivated land and rural residential land consolidation potential

| administrative district | cultivated land consolidation potential [ha] | cultivated land consolidation potential absolute coefficient[%] | rural residential land consolidation potential[ha] | rural residential land consolidation potential absolute coefficient[%] |
|---|---|---|---|---|
| Baishan | 75.52 | 9.03 | 82.02 | 16.01 |
| Bailongtan | 24.32 | 2.91 | 4.52 | 0.88 |
| Guling | 86.59 | 10.36 | 82.30 | 16.06 |
| Guzai | 38.63 | 4.62 | 73.11 | 14.27 |
| Jiafang | 64.24 | 7.68 | 78.53 | 15.33 |
| Jincha | 42.52 | 5.09 | 34.58 | 6.75 |
| Lidang | 12.85 | 1.54 | 0.00 | 0.00 |
| Linxu | 165.28 | 19.77 | 45.28 | 8.84 |
| Qiaoli | 125.48 | 15.01 | 65.41 | 12.77 |
| Yongzhou | 65.04 | 7.78 | 26.95 | 5.26 |
| Zhoulu | 135.53 | 16.21 | 19.68 | 3.84 |

### Classification of land consolidation potential

According to the absolute coefficient of cultivated land consolidation potential and rural residential land consolidation potential total land consolidation potential in table 3, taking towns as unit, the land consolidation potential and the absolute coefficient of each town is input into database, with the GIS software platform, the cultivated land consolidation potential and rural residential land consolidation potential are separately divided into four levels, shown in figure 2.

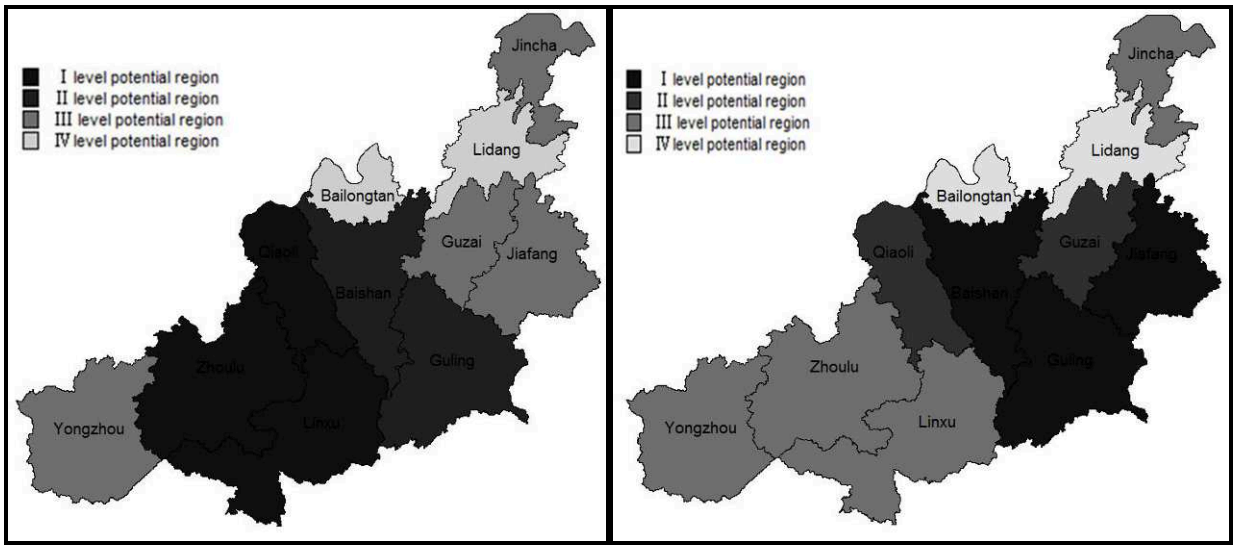


(a) classification of cultivated land consolidation potential

(b) classification of rural residential land consolidation potential

Fig.2 Classification of the land consolidation potential level in Mashan County

## Conclusions

According the absolute coefficient of land consolidation potential, the land consolidation potential of cultivated land and rural residential land in Mashan County can be separately divided into four levels. The results show that the higher land consolidation potential areas are mainly concentrated in the middle of Mashan County, such as Qiaoli village, Guling town, Baishan town; the lowest land consolidation potential areas are Lidang village and Bailongtan town.

## Acknowledgements

This work was financially supported by the Guangxi Natural Science Foundation (2013GXNSFAA019287) and Systematic Project of Guangxi Key Laboratory of Disaster Prevention and Structural Safety (2013ZDX03).This work was also supported by Key Laboratory of Beibu Gulf Environment Change and Resources Use(Guangxi Teachers Education University) and Guangxi Key Laboratory of Disaster Prevention and Engineering Safety(Guangxi University).

## References

[1] G.W. Ji, A.L. Wang and Z.X. Zhu: J. Shandong Agricultural University (Natural Science), Vol.42 (2011), pp.597 (In Chinese)

[2] Q.Q. Liu, L. Qin and Y.N. Song: J. Chinese Agricultural Science. Vol. 28 (2012), pp. 204 (In Chinese)

[3] W. Liu, M.M. Cao and H.J. Qiu: J. Soil and Water Conservation. Vol. 33(2013), pp.196 (In Chinese)

[4] Z.F. Zhang, B.M. Chen: J. Natural Resources. Vol. 17 (2002), pp.664 (In Chinese)

[5] Y.S. Liu, R. Yang and Y.H. Li: J. Geogr. Sci. Vol. 23(2013), pp.503

*Applied Mechanics and Materials Vols. 580-583 (2014) pp 2774-2777*
*© (2014) Trans Tech Publications, Switzerland*
*doi:10.4028/www.scientific.net/AMM.580-583.2774*

# Information Management of Maritime Work based on GIS

LIU Jun-ping[1,a *], DONG Fei-long[1,b] and SHAO Jia-wei[1,c]

[1]College of Civil Engineering and Architecture, Zhejiang University of Technology, Hangzhou 310014, China

[a]LJP23@163.com, [b]dongfeilong86@126.com, [c]rain542380809@live.com

**Keywords:** Geographic information system, Maritime work, Spatial information, Feedback.

**Abstract.** Seawall is an important barrier of Zhejiang coastal strip. To effectively manage the information of maritime work in Zhejiang and convert the traditional management into the modern management, the information management system of maritime work based on GIS is developed. Take Kaomen seawall for example, the overall structure of information management system based on GIS is designed, focusing on the data entry, spatial attribute show, spatial attribute query, spatial information statistics and analysis. This design plays a significant role in the flood control and disaster reduction in the future, making the information management of maritime work convenient and practical.

## Introduction

Zhejiang province is near the seashore. Affected by natural conditions, the tide frequently attacks buildings and has a bad impact on local residents' life, therefore, the seawall comes into being[1]. The seawall originated in the mouth of Qiantang river, which was used to prevent the tide entering living quarters and protecting the cultivated land. Today, seawall is still the barrier of the Yangtze river delta. Besides, seawall plays an important role in Zhejiang province economic development which cannot be replaced.

With the development of economy and science, traditional seawall management has been unable to meet the demand of current social development. Based on geographic information system (GIS), the seawall information management can integrate engineering information into electronic map, which can bring convenient information databases and provide a new method for acquising and analysing the seawall information. Take Kaomen seawall for example, information management system based on GIS was designed.

## Introduction of geographic information system

GIS is a kind of important specific spatial information system with various features of information system. With the help of computer hardware and software, combining with geography, GIS is used to collect, store, analyze, manage and deal with a variety of information related to the project[2]. Meanwhile, it is a widely-used technology system. Through the analysis of model and image, the spatial information database is established, which can handle various thematic maps, engineering information, observations and so on[3].

## Information management of maritime work based on GIS

**The overall structure.** Zhejiang kaomen standard seawall is located in Daishan of Zhoushan. It is 3512 meters long. Kaomen seawall forms the closed area with kaomen dam together. And it protects area of 7, 853, 000 square meters and benefits more than twelve thousands people. At the end of July 2007, the government completed the reinforced maintenance engineering of dam.

On the basis of seawall structure model, geological conditions, the settlement of roof and seawall orientation, five section stations are selected, which are 200, 1100, 1800, 2500, 3200. Figure 1 is interface of information management system of Kaomen seawall based on GIS.

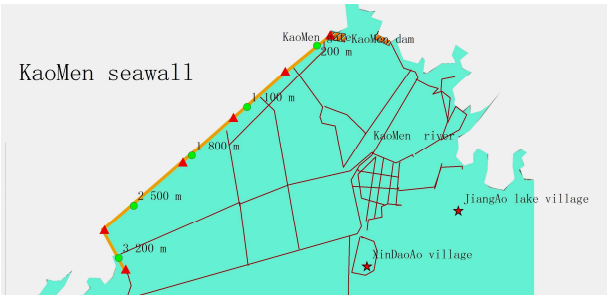


Fig.1 Interface of information management system of Kaomen seawall based on GIS

Information management system of Kaomen seawall sets up a geographical information system by ArcGIS, and then inputs seawall information into the database of geographic information system, making computer graphics and database integrated together. It provides data and mature management mode for seawall management. Afterwards, on the basis of database, data is obtained quickly by attribute query. The information management system achieves high efficiency and practicability. Then the data is processed simply by using the function of the software to realize the visualization of distribution about seawall engineering and data system. It provides technical support for dam safety, and provides theory basis for moistureproof and disaster mitigation. Figure 2 is a simple flowchart of ArcGIS application.

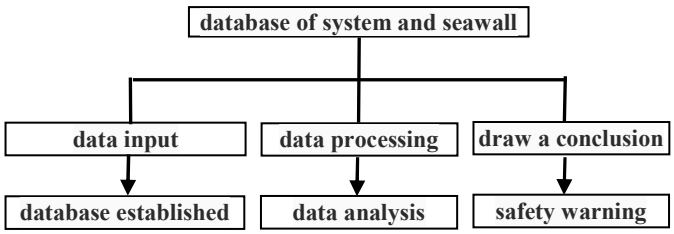


Fig.2 A simple flowchart of ArcGIS application

**Data input.** Engineering data are input into geographic information system of Kaomen seawall. First, information management system establishes seven layers in the same framework, which are "boundaries", "sections", "places", "profile", "inland", "waters" and "buildings". Each layer has a corresponding attribute table. For example, the layer of "sections" has a table of "Attribute of sections". The attribute table adds the required fields and data according to the specific situation. The data of Kaomen seawall is mainly input in sheets of "profile", "table of typical sections" and "table of height and size about cross sections". In addition, the system has many data of five sections, because the comparison is mainly about it. Therefore, two more attribute tables of "Dbase Table" are added, which are "table of typical sections" and "table of height and size about cross sections ".

## The query of attribute

**Attribute table.** In ArcGIS, each spatial data has its corresponding attribute table. The attribute table is one part of the database. It is generally used to check each attribute of geographical elements[4-5]. The attribute table can store much information about elements, and it also can connect with spatial data. The particular elements can be identified in the attribute table. At the same time, the elements of selected on the map are used to update the attributes to reflect changes in the geographical engineering.

Such as geographic information system of kaomen seawall, it adds two attribute tables for each element in the layer of "sections", which are "name" and "profile picture".

**Function of image display.** In ArcGIS, hyperlink is a channel. Users can inquire elements and their attributes in extended table of attribute data. Hyperlink is generally stored in fields. And it can be displayed through clicking on the corresponding elements on the map. Hyperlink is usually used to load images to make the external image showing in ArcMAP. It also provides a great convenience for

query and using. For example, each section has its corresponding images, and they are loaded in the cross section. The image of the cross sections can be displayed by clicking one of them.

**Function of connection and displaying attribute tables.** The function of query is extended by Establishing the connection between two tables. When two attribute tables are checked at the same time, there are two ways to connect two attribute tables, which are "Join" and "Relate". In the first method, a set of data is added to another according to the corresponding field. In the second method, two tables are associated on the logic without changing the appearance. Elements of one attribute table are selected, the corresponding part in another table can be showed at the same time by using the way of "relate". So it is convenient to inquire in different attribute tables. As shown in Figure 3, "Section" and "Table of typical section" are linked through using this function.

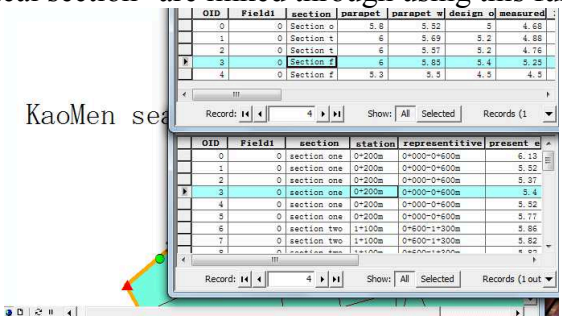


Fig.3 The relationship between two forms

**Information of Kaomen seawall display.** Users can't directly understand some data of the corresponding section through the map document, because the map document only display graphic symbol of sections. To quickly acquire these data, the data can be displayed directly on the diagram. In this way, it is not only easy to see, also to compare, and it can avoid displaying when not needed. It's easy to manage due to the data can be changed along with the change of graphic symbol. So don't worry to zoom in and out of graphic symbol.

Field is one element of a particular attribute, it can be shown on the map, and it will move with geographical elements. It also can zoom in and out with the geographical elements.

### Statistical information of kaomen seawall

The section information mainly deposites in the layer of "profile", "table of typical sections" and "table of height and size about cross section". A rectangular statistical which is used to compare complete elevation with present elevation will be obtained by selecting data related to the elevation into statistical records such as Figure 4.

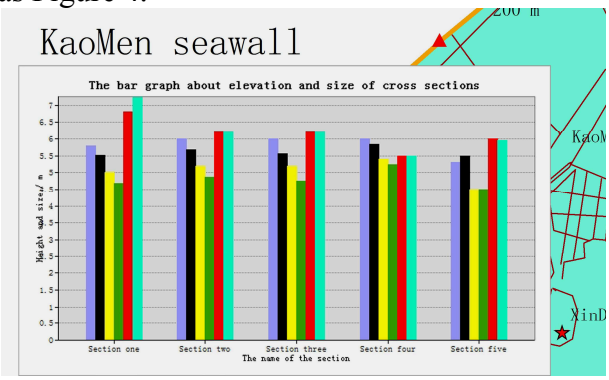


Fig.4 The bar graph about elevation and size of cross sections

Moreover, using ArcGIS, before-after and horizontal comparison of data can proceed at the same time. Various information of each section is recorded in the list of "table of height and size about cross section". Another rectangular statistical diagram of comparison can be gained by the same operation, such as Figure 5. It is apparent that which section has an obvious gap between measured value and designed value from figures. Dangerousness of sections become visual.

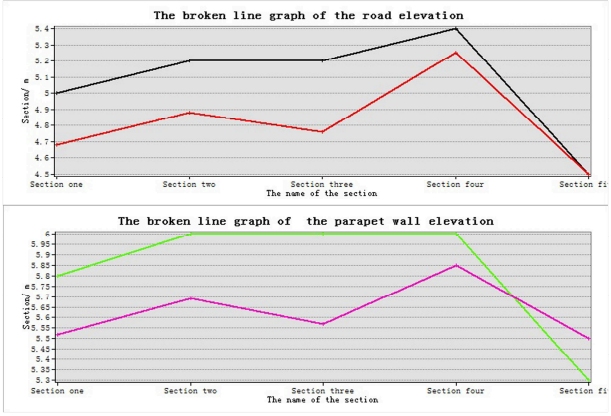


Fig.5 The broken line graph of the section information

## Safety warning of kaomen seawall engineering

Geographic information system is not only used in query and retrieval, but also in comparison and identification of seawall security by processing information. The safety of seawall is a significant item in the seawall management. Five typical cross-sectional elevation of kaomen seawall shows that the size of the constructed road and platform can still meet the designing requirements and the specific requirements. However, every section appears settlement in different degree. After a long time operating, wave facilities are destroyed seriously, and back slope is seriously corroded. But structural integrity is good. There is no phenomenon such as sliding, tilting, and cracking.

## Summary

Information can be inquired and processed conveniently by geographic information system based on ArcGIS. It improves the traditional manual management which was complicated. Attribute tables can be used to complete the query and retrieval quickly by inputting information. Then the safety of the seawall can be monitored through comparing the results in time. And the unknown accident will also be reduced. Geographic information system is used in the seawall engineering to solve some substantive issues. However, more works need to be done to improve the system such as realizing three-dimensional ArcGIS in seawall, which is what we need to study and solve.

## Acknowledgements

This work was financially supported by the Key Scientific and Technological Innovations Teamwork Project(Grant No. 2012R10035-11).

## References

[1] LIU Nan, LIU Ren-yi, GIS-based sea embankment flood prevention information system, Journal of Natural Disaster. 14 (2005) 116-120.

[2] LIU Ying-chun, Design and implementation of geographic information system in Xiaoheshan campus, Journal of Zhejiang University of Technology. 35 (2007) 418-421.

[3] CAO Lei, Geographic Information System and Its Further Appliance, Technology & Economy in Areas of Communication. 3 (2008) 102-103.

[4] LIN Jia-ping, LIU Jun-ping, A Design for Rural Drinking Water Supplying Network Based on GIS, Yellow River. 35 (2013) 58-60.

[5] ZHANG Mei-yu, HU Qi, Research on the key technology and design for mobile GIS-based urban MIS, Journal of Zhejiang University of Technology. 37 (2009) 411-415.

*Applied Mechanics and Materials Vols. 580-583 (2014) pp 2778-2781*
*© (2014) Trans Tech Publications, Switzerland*
*doi:10.4028/www.scientific.net/AMM.580-583.2778*

# Design and Fabrication of Dynamic Thematic Maps Based on Flash

Yixin Xu [1,a], Junwei Yang [2,b]

[1] Department of Materials and Engineering, Zhejiang University, Zheda Road No. 38, Hangzhou, China, 310027

[2]Henan Province geological environment Investigation Company, Zheng Zhou, China, 450018

[a]1xuyixin@163.com, [b]1827628998@qq.com

**Key words:** Dynamic, Thematic Maps, Flash, Element, Source Material

**Abstract:** This paper exemplified by the dynamic thematic map under different data sources has explained scientifically the dynamic data storage in session objects, thematic map making by aid of the development's function of an object-oriented environment, a real-time map displaying. Experience has proved that the measure in flash platform which editing the geographical map, designing the map elements, doing movie clips, constituting them together,importing sound,etc, is very effective and more flexible.

## Introduction

The traditional statistical thematic maps display geographic spatial distribution attributes, trend information in different ages and variable in a static and digital way. Map users cannot interoperate with the map, read not straightforward. As application popularizes of the computer technology in cartography, the pattern of thematic maps has been gradually converted to dynamic from static [1]. The first act of dynamic thematic maps has been widely recognized across industries and gained rapid application development for its intuitive, easy to read, visible and expressive characteristic. The thematic maps concerning the area, population, GDP throughout all the provinces is designed and fabricated based on Flash platform in this paper, and demonstrate clearly the relation between income growth and increasing environment pollutions.

## Overall Design Ideas

Firstly, collecting information about population, economy, atmospheric condition in recent years, and secondly, make cartographic base by aid of SuperMap software, thirdly, drawing elements in Flash environment, reassemble the elements into the animation, finally, after beautifying the interface , Publishing the results. The flowchart shown in Fig.1.

## Material Preparation

### Collection of Data

Collect the China map in the bmp format, longitude and latitude coordinates of provincial capital city, statistics on area, Population, GDP throughout all the provinces in recent years through various means.

### Make a Cartographic Base

By aid of Supermap software , the China map has imported to data source on bmp format. After a projection setup, finishing a map orientation by executing a image registration command, converting the raster to vector and actualizing a map digitizing by hand, revising the attribute table structure by adding one text field for storing variable name of all provinces ,and four double precision field for the area, population, GDP and atmospheric pollution, tabling the attribute data.

**Production of Dynamic Thematic Maps**

**Production of Elements** [2]

**(1)Production of Push-button Elements**

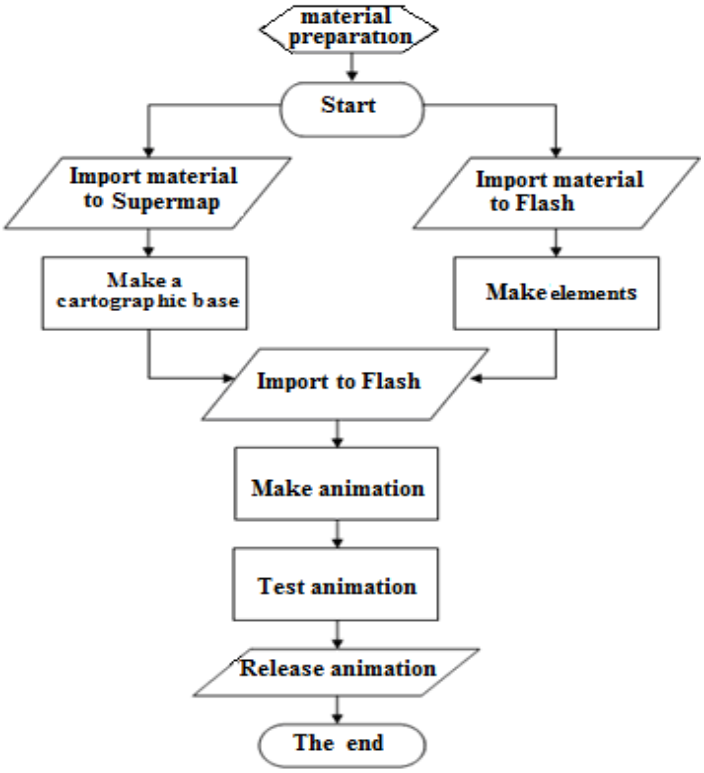


Fig.1 Design Flow

The source materials collected and underlying graph produced has been imported to flash library panel. A new-built element has a timeline containing 4 frames, bouncing, slipping, pressing, clicking respectively, the 3 frames in front displaying three states of the mouse when bouncing, slipping, pressing, the fourth frame defining a living area for the push-button. Three push-buttons for the populations, GDP and air pollution have been made, saved. Returned to the scene 1, the push-button elements have been dragged to the stage, and see the testing effect by clicking self-made push-buttons.

**(2) Production of Movie Clip Elements** [3]

There are two methods of making a movie clip. The one is dragging materials to the stage and right-clicking the material, clicking *Convert to Symbol* on the shortcut menu, selecting *Movie Clip* on the popup windows and naming. The other is making movie clip by inputting command of new-built elements and getting into exclusive scenes.

**(3) Production of Graphic Symbol**

The graphic symbol is the elementary element and the smallest unit, has a timeline. Its playing has highly been affected by the main scene, and therefore the graphics cannot be set up for a ActionScript. The elements have been arranged respectively to the corresponding library folder.

**Scenes Creation and Setup**

First of all, new-building a flash file, setting document attributes, including the speed of frame, stage area, background color, etc. Then creating several layers on the opening scenes, and naming each layer as *Window* for gray background of stage area, *Background* for a copy of the China map, *Contour* for the total outline of animation area, *Push-Button* for the content of push-button, *Headline* for the text of thematic maps, *Playlist* for the listings area, *Areamap* for the movie clip of area graphics.

**Movie Clip Creation of the Thematic Map**

Creating several layers in area graphic 1 of the new-built movie clips, as shown in fig.2. It is worthwhile to note that the element location in movie clip layers must be consistent in the main scene. The playing screen has been placed on the *Background* layer, the china map on the *Base Map* layer, the push-button on the *Push-Button* layer, the playlist button on the *Playlist* layer.

**Animation Production**

In the presentation layer, the key frame has been inserted in certain time interval. The each frame animation has been finished by placing individually each province's area element on the clip stage containing corresponding key frame. The tween animation has been made by clicking the mouse right key, selecting *creating tween animation* on the shortcut menus opened by selecting one of two keys frames in the timeline of the same layer and clicking. As shown Fig.3.

Fig. 2 Movie Clip of the Area Thematic Map

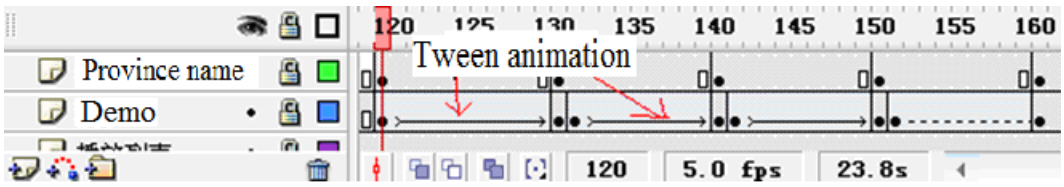


Fig. 3 Tween Animation

**Sound Importing and Editing**

The sound file has been imported to stage by opening dialog box which the needful sound file can be selected, selecting the needful sound file in the pop-up dialog box, clicking *OK* button. After adding the sound file, its attribute has been edited by *Attribute Panel* to a higher degree according with animation demand.

**Controlling Animation Working by ActionScript Language**

Firstly, it need to lock all layers in the main scene and turn on only the *Playlist* layer. Secondly, select the *Area map* button, opening *Action* panel, input script language as below and save.

```
on (release)
{ this.mjt1.play();
  this.tz.play();
  this.zt.play();}
```

Afterwards, turn on the button layer except the other movie clip, select , , , , button one by one, open action panel, respectively input script language as Play, Pause, Stop, Fast Forward, Fast Backward as shown in table 1 and save.

Table 1 Script Code

| Play | Pause | Stop | Fast Forward | Fast Backward |
|---|---|---|---|---|
| on(press) {play();} | On(press) {stop();} | on (press) {gotoAndPlay( );} | on (release) {gotoAndPlay(_currentframe+10);} | on (release) {gotoAndPlay(_currentframe-10);} |

**Releasing of Dynamic Thematic Map** [4]

After the production, the animation can be released in flash format, by clicking File--Releasing Setup to open setting dialogue box in where many items can be set up, for example, the player, loading sequence, ActionScript version, JPEG quality, audio frequency, playback security and the other option [5]. The independent animation software now has finished.

**Questions and Suggestion**

During applying Flash software, there are many problems, for one thing, the similar elements cannot be copied and pasted so that a lot of the repetitive elements production must increase working strength and decrease work efficiency, for another, the animation of flash format can be played only in flash player against the others', the third one is that the bitmap cannot be accurately controlled in locations and sizes when it be imported to the stages [6].

In spite of this, Flash software is still a simple, easy to learn, powerful tool for making animation, the dynamic thematic maps based on flash platform have changed the traditional maps' contents and notation having the characteristics of concise, intuitive, and embodied. Its high qualities not only behave in small memory, but also cannot be changed along with the size's zooming. Its shortcoming will be solved admirably in the near future as updating and improving.

**References**

[1] L.Zhu,Z.A.Zhou,X.P.Han: *New Cartography Course* (Higher Education Press,Beijing,China 2010).

[2] Z.Q.Wang, Z.Z.Chi: *Chinese Version of Flash Standard Tutorial* (China Power Press, Beijing, China 2010).

[3] N.Wu, M.Xu, L.Tong: *200 Cases of Classic Flash Animation Design* (Science Press, Beijing, China 2011).

[4] Z.D.Zhang, H.K.Wu, G.R.Zhong: *SUPERMAP Application and Development of GIS Tutorial* (Wuhan University Press, Wuhan, China 2006)

[5]H.W.Hang, J.T.Mei, J.Li: *Design and Application of Statistical Map Based on Flash Technology*, Editied by Yunnan Science and Technology Information Research Institute, Kunming, China (2012).

[6] Information on http://www.gov.cn

*Applied Mechanics and Materials Vols. 580-583 (2014) pp 2782-2785*
*© (2014) Trans Tech Publications, Switzerland*
*doi:10.4028/www.scientific.net/AMM.580-583.2782*

# Development of Topographic Maps Symbols Library

Caimin Sun [1,a], Yixin Xu [2,b]

[1] North China Institute Of Science And Technology, Yanjiao, Beijing East, China,101601

[2] Department of Materials and Engineering, Zhejiang University, Zheda Road No. 38, Hangzhou, China, 310027

[a] Sun888888@ncist.edu.cn, [b]1xuyixin@163.com

**Key words:** Auto LISP, Topographic Maps, Symbols Library, Development

**Abstracts:** Visual LISP language is favored by many people for its simple and practical. Because of most CAD teaching materials centre on introducing concrete languages' use and single symbol making, lack of a comprehensive description of the whole process of developing professional symbols library, it is very difficult for People having mastery of LISP languages to developing professional symbol library by this language. In this article, the authors develop a symbols library for common Topographic Maps and design an environment to transfer and input the symbols with the aid of Visual LISP language, including defining graphic coordinates systems, coordinates transformations, putting library files in order, calling user-defined file etc. This paper provides great help for people who Devote oneself to map symbol library system development.

## Introduction

Autolisp is an important secondary development tool. Differing from other Languages, it is a best Graphics programming language of being encoded in CAD and invoking all internal commands. Even though having many graphic tool commands in CAD, it can't draw sophisticated curve, such as iron chain bridge etc, being deficiency of professional graphic symbols library. It appears particularly important of developing Maps Symbols Library, customizing professional application system, improving mapping efficiency, by the aid of Auto LISP language programming.

## Typical surveying application based on Autolisp

### Execution and Edition of a simple Autolisp program

Example: Drawing a multipoint house[1].

(1) Edit a Autolisp program in a text editor.

(2) Select [save as] submenu from [files] menu, input 'duodianfangwu.lsp' as file name in following dialogue box, press " ok " button.

(3) Loading the 'duodianfangwu.lsp' file. Select 'Tools'→'Autolisp' →'Loading' command, in subsequent dialogue box, selecting 'duodianfangwu.lsp' is ok. A message appears in prompt line: ' loading duodianfangwu.lsp succeed'.

(4) Input 'duodianfangwu' in command line and run it, then a multipoint house displaying on screen as shown in Figure. 1.

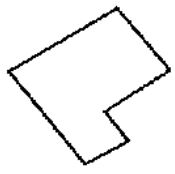

figure.1

## A development process of symbols Library

Here is a detailed Process of developing surveying symbols library by LISP language.

### Defining graphic coordinate system

AutoCAD screen coordinate system differs from surveying coordinate system. Here a surveying coordinate system and proportional scale must be set up. These functions can be achieved by following programs.

1. The program for defining proportional scale and surveying coordinate[2].

```
(DEFUN READ_XYM()
        (setq m (getvar "USERR1")        ;m scale
```

```
                x0 (getvar "USERR2")      ;x0    origin north coordinate
                y0 (getvar "USERR3")      ;y0     origin east coordinate
                hm (getvar "USERR5")      ;hm      elevation scale……
            )
```

This program could share by all graphic programs aimed to get graphic parameters in order to implement coordinate conversion.

2. The program for coordinate conversion[3].

This program is used to change surveying coordinate system (X,Y,Z) into AutoCAD UCS (x,y,z).

```
(defun dtx (hs)    ;Y-x

            (setq hs (- hs y0))
            (setq hs (/ (* hs 1000.0) m))
            (setq hs (+ hs 100))
)
(defun dty(hs)     ;X-y
            (setq hs (- hs x0))
            (setq hs (/ (* hs 1000.0) m))
            (setq hs (+ hs 100))
)
(defun dth(hs)     ;H-z
            (setq hs (/ (* hs 1000.0) hm))
)
```

3. Defining data input mode in surveying coordinate system.

By programming for symbols library, different coordinate data input mode must be considered in order to improve the programs' adaptability, for example, mouse input mode, data files entry mode etc.

(1) The program for input coordinate data from mouse.

```
(defun READS()     ;program name reads.lsp
            (read_xym)     ;
            (setq p (getpoint "\n Input point:"))
)
```

(2) The program for input coordinate data from keyboard.

```
(defun READC()        ;File name;    READC.LSP
          (read_xym)     ;
          (setq p (getpoint "\n Input surveying point(Y,X):"))
        (if p (setq p (list (dtx(car p))))
        (serq p nil)
           )
)
```

(3) The program for read data from files.

```
      (defun PREAD(); File name: READM.lsp
            (read_xym)
            (setq p (getstring    \n point /<point name>:"))
          (if (= strcase p) "P")(setq p (getpoint "\n Mouse position:"))
                (progn
                     (if p (setq p(read p) p (assoc p readh) p (cdr p)))
                     (if p (setq p (list (dtx (car p)) (dty(cadr p))))
                     (setq p nil)
                       )
              (princ)          )
```

**Program for professional symbols library[4].**

There are some tasks must done before programming, such as Analysis each entity symbol features; Define symbol parameters; Encode every graphic element; Design the computing method for coordinate value of positioning base point, in order to improve efficiency of symbol automated drafting. Below is an example for developing a graphic symbols library of an entity similar to iron chain bridge.

1. Example for user-defined file (User.def)

```
1404000                         [symbol code]
1                               [point symbol]
A00                             [layer name:A00]
Land032                         [block name:Land032.dwg]
0                               [no rotate ]
Well symbol                     [symbol name]
3209000                         [symbol code]
2                               [line symbol]
.....          ;END
```

2. Transfer user-defined: rr.lsp

```
(defun C:(/kcode tc code)       ;
                (Chbm)      ;Taking code out
                (user)
 );End
 (defun CHBM()
            (setvar "cmdecho" 0)
            (initget 1 "1")
            (setq code (getreal "\n Input features code (7bites):"))
 )
(defun User(/ f tt name lb kw code1 s n n0 s1)
                    Qq ok code2 lb1 name1 tc1 kw1 code3
 )
  (setq code2(*(fix (/ code 100.0))100.0))
  (setq f (open "user.def" "r"))
  (setq TT (read-line f))
  (while(/ = tt "-End-"))
          (setq code1 (atof tt))
          (setq LB (read-line f) TC(read-line f)
          Name (read-line f) KW(read-line f)
    ) .....
        (princ "\n")
   )
```

3. Build professional symbols library.

Programming graphic subprograms in symbols library such drafting iron chain bridge.

```
;File name:   TSQK.LSP
  (defun H_TSQ(/ pt1 pt ang h width 1 width p1 s1 s2 s3 ang2 ang3 p2 p3 p4 code1 ang1 pt4 pt5
pt6 pt7 pt8 code2 p11 p22 pt2 pt3 os
 )
(setvar "cmdecho" 0)(setq os (getvar "osmode"))
(setq code1 ( + ( * (atof (substr (rtos code 2 0 ) 1 5 ) 100) 3.0)
          code2( - code1 1.0) .....
 )
(command "line" p11 p22 "")
      (setq s3 ( + s3 s0) s2 ( + s2 s1))
 )
```

```
(command "layer" "m" "bound" "s" "bound" "")
(command "elev" "" ( + code1 5.0))
(command "pline" p1 "w" 0 0 p2 p3 p4 "c")
(b_xdata)
(command "layer" "s" "0" "")
(command "elev" "" "0")
(setvar "osmode" os)
(princ "\n symbol finished!")
(princ)
)
```

4. Create folder for symbols library and add search path[5].

Suppose creating folder named Lisp on hard disk. Put created files which including READ_XYM, HXYH.LSP ,READS.LSP ,READC.LSP ,READM.lsp ,User.def ,rr.lsp ,TSQK.LSP into the folder. Select 'tools' → 'option'→ 'file', select 'file search paths' and click 'add' putton, put 'lisp' folder in search path.

5. Transfer symbols library.

```
;Plotting iron chain bridge symbols; File name :TSQ.LSP
 (defun C:TSQ()
            (setq TC "DLSS")          ;Setting layers parameter
            (setq Code 4650000)       ;Setting code parameter
            (setq b_xdata nil)        ;Initializing attribute table
            (SCSFH_JL)                ;Recording  starting point
            (TSQK)                    ;Transferring  symbol library
 )
```

**Realization to symbols library program**

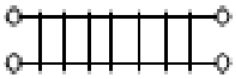

figure. 2

**Load necessary library files.**

First of all, necessary files must be loaded in AutoCAD environment . These files are: *READ_XYM,CHXYH.LSP,READS.LSP,READC.LSP,READM.lsp,User.def,rr.lsp,TSQK.LSP.* Inputting 'load file name' on command line is ok.

**Run program of iron chain bridge named TSQ.**

Input TSQ on command line and 'Enter', then according to prompt message,input proportional scale, coordinate value. After inputting data of three feature points of iron line bridge, finish symbol appears on screen. Shown as Figure. 2.

## Conclusion

Considering experience of developing professional library and purpose by AutoLISP language, this paper introduces detailed producing process and skill of professional library by typical example, help programmers to resolvine difficulties faced.

## References


[1] F.ZH. ZHANG., k. Li and H.jie. *WANG: AutoCAD VBA Development Wonderful Examples Tutorial*(Beijing: Qinghua University Press, China 2004),P.150. (In Chinese)

[2] Y.K. WANG: *The Redevelop Technology and.Project Application of CAD* (Qinghua University Press, China 2008). P.50. (In Chinese)

[3] A.j. XIE, W.W. QIAO: *The Redevelop Technology Case Tutorial of Computer Aided Design* (Beijing University Press, China 2009), P.33. (In Chinese)

[4] J.H. SUN: *Computer Aided Design* (Higher Education Press, China 2010). P.76. (In Chinese)

[5] L.SH. WANG: Publishing House of Surveying and Mapping, Vol.102 (1993) NO.3, P.83. (In Chinese)

# CHAPTER 13:

# Surveying Engineering

*Applied Mechanics and Materials Vols. 580-583 (2014) pp 2789-2792*
*© (2014) Trans Tech Publications, Switzerland*
*doi:10.4028/www.scientific.net/AMM.580-583.2789*

# Application of Total Station in the Measurement of Transmission Line

Fangru Gui

Sichuan College of Architectural Technology, Deyang, Sichuan, 618000,china

116211747@qq.com

**Keywords:** transmission line , measurement, point guiding alignment, coordinate , total station

**Abstract.** Through analyzing the difficulties in the measurements of Wangling hydropower station's transmission line, this paper proposes an idea that total station is applied to complete line measurement on the basis of the point guiding alignment measuring technique, which aims at providing a reference for other similar projects.

## Introduction

With the development of society, the demands for power resources become more and more, and power grid also develops increasingly faster. The measurement of transmission line is a systematic work in the engineering construction of transmission line, and also a specialized measurement conducted for power engineering construction, therefore, it plays a very important role in the engineering construction of transmission line

## Project Overview

This project is the measuring engineering of 35kV transmission line from Yuexi County 110kV substation to Wangling hydropower station. As its exit number from the 110kV substation is 305 # , this transmission line is called the 305 # power line. This line project is spread along Tiantang Town, Lianyun Village , Zhongguan Village, Xiawuhe , Liufan and Xifo Village of Yuexi County, the overall length of transmission line is 17.5km, and the conductor type is LGJ-185/20. The terrain of the whole line is mainly mountain and steep slope, the way from Huilong Mountain to Wangling hydropower station is spread with high mountains, the terra is advantageous, the region is wooded, resulting in the great difficulties in survey . If the project is put into operation, the western grid structure of Yuexi County would be strengthened and the reliability of power supply in hydroelectric power supplying region would be improved, which is conducive to the development and utilization of water resources in the Dabie Mountains and also further promotes the economic development of mountainous areas .

## Difficulties of the Project

In the measurement of 305 # power line, the measuring instrument used is Nikon 352-O type total station which is qualified with high measuring accuracy and is commonly applied by power supply companies in the counties of Anhui Province. In the mountainous area, the terra is advantageous and the region is wooded, resulting in short range of visibility in the measurement. Therefore, the effectiveness of this measuring instrument is not satisfying, and completing the measurement of the three relatively longer linear segment determined by this line is a major problem

## Implementation of Measurement

To solve the problems in measuring the linear segment of transmission line, a number of new measuring technologies of transmission line engineering are applied in the measurement of 305 # transmission line, and the main technologies are" point guiding alignment measuring technology" and "coordinate back calculation to control direction measuring technology ", which can only be realized

through the field measurement of the total station, the computational analysis of computer software and the computer-aided design. Through the comprehensive application of these two new technologies in the 305 # transmission line, the difficulties in the measurement and orientation caused by the overlength linear segment of transmission lines in mountainous areas are solved. And these two new technologies are also applied in the engineering measurement of 35kV voltage class transmission line in Yuexi County for the first time .

"Guiding point alignment method " is a new measuring and orienting method of transmission line summarized from the actual measuring work of transmission line by Yuexi Power Supply Company, and combined with "coordinate back calculation to control direction method", it can fundamentally solve the difficulties in the measurement and orientation of transmission lines in mountainous areas and is suitable for the orientation measuring engineering of transmission lines in large-scale mountainous area.

In the field measurements, the line route and the basic data of line channels and terrain are preliminarily determined according to topographic map, and total station is applied to measure each linear point, feature point and turning point for obtaining the coordinate and elevation of each point. The coordinate orientation of each point and the relationship between the points would be recorded by the total station. When it comes to the measurement of a turning point, instrument is required to determine the turning direction and turning angle. At this time, terrain condition of mountainous area will affect the measurer 's range of visibility. Meanwhile, the application of the general angle measured by protractor in the topographic map that is 1:1000000 in the field measurements often leads to some unexpected effects, resulting in subsequent rerouting of power lines and the increase in engineering investments. To ensure that the basic directions of field investigation and transmission line determined in accordance with the figure are the same, whether the transmission line can accurately pass the selected feature point of line after turning should be determined.

“Point guiding alignment method " is applied at this time, and instrument is used to measure guiding point from the turning points, to guide the measuring point to the more accurate point ahead. The instrument will record the actual coordinates orientation and elevation of feature points. Then "coordinate back calculation to control direction method" is applied to calculate the coordinate azimuth and horizontal distance between the turning point and the feature point, As shown in Fig.1. And then the turning angle is calculated based on the calculated coordinate azimuth, so as to ensure that direction of transmission line after turning is consistent with the basic direction of transmission line determined by the figure and to reduce the repeated tree felling in the measurement channel of transmission line. The application of this method, whether the line passes complex terrain or even forest, as long as it is measured along this angle, the predetermined direction of line can be guaranteed.

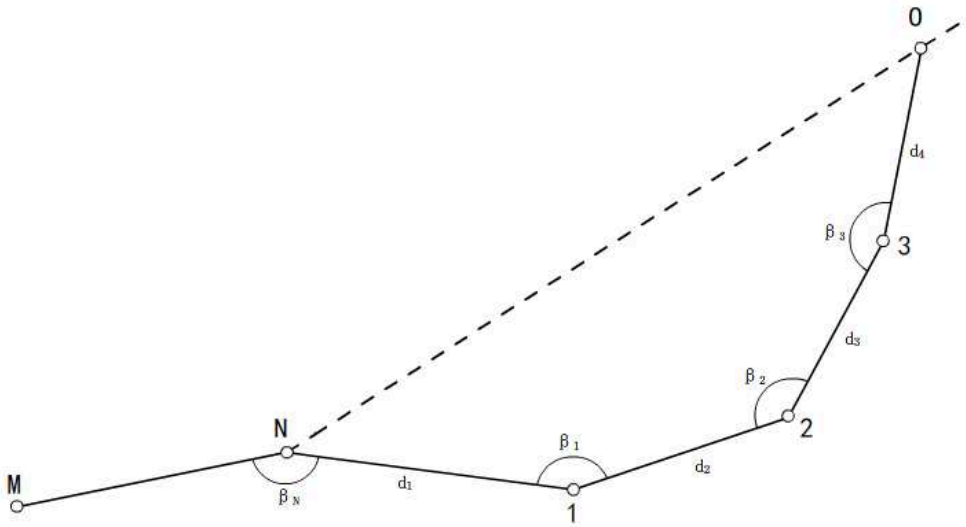


Fig.1 Schematic Diagram of Point Guiding Alignment Method

The specific operational method of "point guiding alignment method " is shown in Figure 1. When measuring transmission line passes through Point M to Point N, the transmission line need to turn left at Point N to Point O according to the design requirements. However, after setting up instrument in the actual place of Point N, it is discovered that the distance between Point N and Point O is long, they are even blocked by mountains, and Point O can not be directly seen from the Point N, so that angle orientation can not be conducted at Point N, and Point O can not continue to be measured.At this moment, the coordinates and azimuth angles of Point M and Point N are determined. If coordinate data of Point O is obtained, the included angle of MN and NO can be calculated according to the coordinates, and then measuring angle can be provided to the instrument installed in Point N for measuring. Therefore , applying "point guiding alignment measuring technique" can measure No.1 Point that is easy to be observed from Point N, and identify the angle βN and horizontal distance d1; measure the No.2 Point, and identify the angle β1 and horizontal distance d2; measure No.3 Point, and identify the angle β2 and horizontal distance d3; and then measure Point O from No.3 Point, and identify the angle β3 and horizontal distance d4. According to the calculation methods of wire measurement, coordinates of Point 1, 2, 3 and O can be determined.

When the coordinates of Point O are determined, the coordinates of Point N and O are calculated according to "coordinate back-calculation to control direction method ". As is shown in Fig.2, the azimuth angle $\alpha_{NO}$ and horizontal distance DNO from Point N to Point O is calculated. Therefore, the ligature of Point N and Point O is determined. The method to calculate the horizontal distance and coordinates azimuth of the two end points of the straight-line NO when the coordinates of Point N and O ($X_N$, $Y_N$) ($X_O$, $Y_O$) are known is called coordinate back-calculation method.

Both methods are used in the extension of the three relatively longer straight lines of 305# transmission line, the surveying effect is perfect, and the accuracy meets the design requirements. The advantages of total station and computer software in the measurements of transmission line are given full play, while the measurement accuracy and efficiency are far superior to the theodolite. In the measurement of transmission line, the actual application of these two measuring technologies of total station is worthy of promotion.

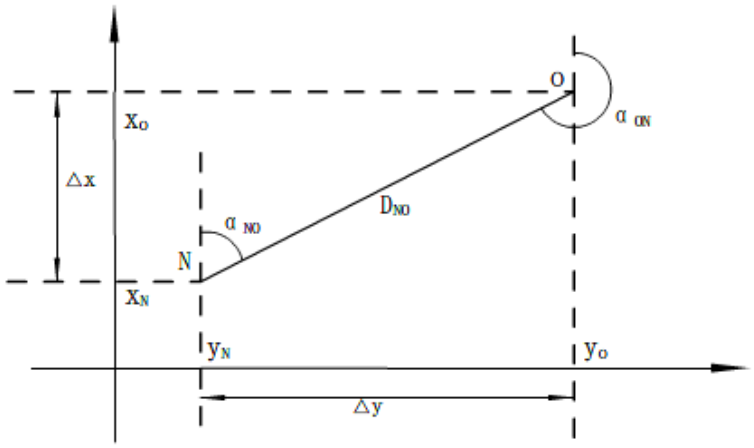


Fig.2 Schematic Diagram of Coordinate back-calculation to Control Direction Method

## Conclusion

In the application of total station, the following problems should be noted. Total Station should not be installed in the place within the range of the electromagnetic field effects, such as in the vicinity of high-voltage object, otherwise it will affect the measurement accuracy. Wireless call should be suspended while measuring; observation station and mirror station should be protected by specially-assigned person after installing the equipment, in case that the equipment would displace or fall. The facing of the lens of total station to the sun and strong light is strongly prohibited, other reflectors located in the measuring line or its extension line ranging should be avoided while measuring, because the total station is very sensitive to light and glare can damage its electronic

measuring system. In the observation, prism surface should be aligned with the ranging lens of total station, and especially when the measuring angle is large, they should be aligned with each other. The instrument has higher measurement accuracy within the range of 30° in elevation to 30° in depression, so the measurement of the elevation and depression that are larger than 30° should be prevented, to avoid the affection of measurement accuracy. The instrument instructions should be strictly observed, the observation should be stopped once abnormal phenomenon arises, and the reasons should be analyzed, to ensure the correctness of measurement results and the safety of instrument.

## References

[1] GeYajian, Sunlei. Several methods of measurement of electronic total station in transmission lines [J]. Journal of information science and technology, 2011, (25).

[2] Zhang Xueli, Wang Qipeng. GoogleEarth application in overhead transmission line measurement [J]. Journal of heilongjiang science and technology information, 2013, (26).

[3] Yang wangfang Song Jiyu. Tianbao space measurement, the application of video technology in overhead transmission lines [J]. Bulletin of surveying and mapping, 2012, (3)

[4] Qi Zhenhai. Measurement the application of CORS in overhead transmission lines [J]. Urban construction theory research, 2012, (25)

*Applied Mechanics and Materials Vols. 580-583 (2014) pp 2793-2796*
*© (2014) Trans Tech Publications, Switzerland*
*doi:10.4028/www.scientific.net/AMM.580-583.2793*

# Chinese Geodetic Coordinate System 2000 and Its Comparison with WGS84

Houpu LI [1, a], Shaofeng BIAN [1,b] and Zhongmei LI [1,c]

[1] Dept. of Navigation Eng., Naval Univ. of Engineering, Wuhan, 430033, China
[a]lihoupu1985@126.com, [b]sfbian@sina.com, [c]15827116839@163.com

**Keywords:** geodetic datum; geocentric coordinate system; CGCS2000; WGS84

**Abstract:** It is a general trend to adopt the geocentric coordinate system as a geodetic datum for the international measurement community. The definition and realization of Chinese geocentric three-dimensional coordinate system (CGCS2000) which has been employed since July 1st, 2008 were introduced in detail. The defining parameters and derived constants of the reference ellipsoid used were given. The comparison between CGCS2000 and WGS84 was carried out. The differences of geodetic coordinates of a point between the two coordinate systems, normal gravity and vertical gradient of normal gravity on the two ellipsoids caused by the change of the flattening of the ellipsoid were analyzed. The results show that these differences could be neglected in view of present measurement accuracies.

## Introduction

The geodetic coordinate system is not only an important basis of the Earth's spatial framework, but also a three-dimensional reference datum which represents the Earth's spatial physical location. Defining and adopting national geodetic coordinate system scientifically will exert an influence on fields such as aeronautics, astronautics, navigation, positioning, earthquake monitoring, geophysical prospecting, etc[1]. The geodetic coordinate system can be divided into reference-ellipsoid-centric coordinate system and geocentric coordinate system according to the position of its origin relative to the Earth's center of mass. The origin of the reference-ellipsoid-centric coordinate system is offset from the Earth's center of mass by about tens to hundreds of meters, while the origin of the geocentric coordinate system is theoretically coincident with the Earth's center of mass, but inevitably there is some deviation in fact[2].

Beijing coordinate system 1954, Xi'an coordinate system 1980 and modified Beijing coordinate system 1954 have been established by our country since the foundation of the New China. These coordinate systems are non-geocentric, and once played a great role in Chinese economy and defense construction, but they could not meet the necessity of science and technology especially the space technology because the precision of their achievements is relatively low due to technical conditions at that time. In view of the development needs of economy, society, science and technology, the geocentric three-dimensional coordinate system, Chinese Geodetic Coordinate System (CGCS2000), has been formally adopted as Chinese new generation of geodetic datum since July 1, 2008[3,4].

## The Definition of CGCS2000

CGCS2000 is a right-handed, Earth-Centered Earth-fixed (ECEF) orthogonal coordinate system, and its origin and axes are defined as follows:

(1) The origin of CGCS2000 coincides with the Earth's center of mass.

(2) Its Z-axis directs from the origin to the IERS Reference Pole (IRP).

(3) Its X-axis directs from the origin to the intersection of the IERS Reference Meridian (IRM) and the plane through the normal to the Z-axis.

(4) Its Y-axis completes a right-handed, Earth-Centered and Earth-Fixed (ECEF) orthogonal coordinate system.

An equipotential ellipsoid of revolution is taken as the form for the CGCS2000 reference ellipsoid. Its geometric center coincides with the origin of CGCS2000, and axis of revolution coincides with the Z-axis of CGCS2000. Its surface is geometrically the datum plane for surveying calculation, and physically equipotential surface of the Earth's normal gravity. The four defining parameters of the CGCS2000 reference ellipsoid are: semi-major axis, $a = 6378137\text{m}$, flattening, $f = 1/298.257222101$,

Earth's gravitational constant, $GM = 3.986004418 \times 10^{14}\,\mathrm{m^3 s^{-2}}$ , angular velocity of the Earth, $\omega = 7.292115 \times 10^{-5}\,\mathrm{rad\,s^{-1}}$.

According to the above four defining parameters, the more commonly used geometric and physical constants associated with the CGCS2000 ellipsoid derived by [5] are listed in Table 1 and Table 2 respectively.

Table 1 Derived geometric constants for the CGCS2000 ellipsoid

| Constant | Notation | Value | Constant | Notation | Value |
|---|---|---|---|---|---|
| Semi-minor Axis | $b$ | 6356752.31 4140356( m) | Axis Ratio | $b/a$ | 0.9966471893 188177 |
| Linear Eccentricity | $E$ | 521854.009 700248 (m) | Meridian Quadrant | $Q$ | 10001965.7 2923047( m) |
| Polar Radius of Curvature | $c$ | 6399593.62 5864023 (m) | Volume of the Ellipsoid | $V$ | 1083207319783.546(km$^3$) |
| First Eccentricity Squared | $e^2$ | 0.006694380022900788 | Area of the Ellipsoid | $S$ | 5100656217184915(m$^2$) |
| First Eccentricity | $e$ | 0.08181919104281579 | Mean Radius of Semi-axes | $R_1$ | 6371008.771380119(m) |
| Second Eccentricity Squared | $e'^2$ | 0.0067394967 75478959 | Radius of Sphere of Equal Area | $R_2$ | 6371007.180883518(m) |
| Second Eccentricity | $e'$ | 0.08209443815191720 | Radius of Sphere of Equal Volume | $R_3$ | 6371000.789974134(m) |

Table 2 Derived physical constants for the CGCS2000 ellipsoid

| Constant | Notation | Value | Constant | Notation | Value |
|---|---|---|---|---|---|
| Normal Potential of the Ellipsoid | $U_0$ | 62636851.71491325(m$^2$s$^{-2}$) | Normal Gravity at the Pole | $\gamma_p$ | 9.83218493 7864707 (ms$^{-2}$) |
| Second Order Zonal Harmonic Coefficient | $J_2$ | $1.082629832202536\times10^{-3}$ | Mean Value of Normal Gravity | $\bar{\gamma}$ | 9.797643222390407(ms$^{-2}$) |
| Fourth Order Zonal Harmonic Coefficient | $J_4$ | $2.37091125582152\times10^{-6}$ | Normal Gravity at 45° N | $\gamma_{45}$ | 9.806197769458409(ms$^{-2}$) |
| Sixth Order Zonal Harmonic Coefficient | $J_6$ | $-6.083465257111045\times10^{-9}$ | Gravity Flattening | $f^*$ | $5.302441382844182\times10^{-3}$ |
| Eighth Order Zonal Harmonic Coefficient | $J_8$ | $1.42681100\ 87861944\times10^{-11}$ | $k = b\gamma_p/(a\gamma_e)-1$ | $k$ | $1.93185261\ 9557306\times10^{-3}$ |
| $m = \omega^2 a^2 b/(GM)$ | $m$ | $3.449786506783957\times10^{-3}$ | Normal Gravity at the Equator | $\gamma_e$ | 9.78032533 6065076(ms$^{-2}$) |

**The Comparison between CGCS2000 and WGS84**

There are many GPS data at present and GPS will still be a main means for obtaining spatial data in future. Since GPS adopts WGS84 coordinate system, it is necessary to compare CGCS2000 with WGS84 in order to guide practical work.

CGCS2000 is consistent with WGS84 in the definitions of the origin, scale, orientation and time evolution of orientation. The reference ellipsoids of the two coordinate systems are also very close to each other. Specifically only the minor difference, $df$, which is equal to $1.64348\times10^{-11}$ exists in the flattening of the four defining parameters.

The geodetic longitude of a point in CGCS2000 is the same as that in WGS84, but the geodetic latitude and height are different. The differences of geodetic latitude and height, designated $dB$ and $dH$ respectively, are shown in Fig. 1 and Fig. 2.

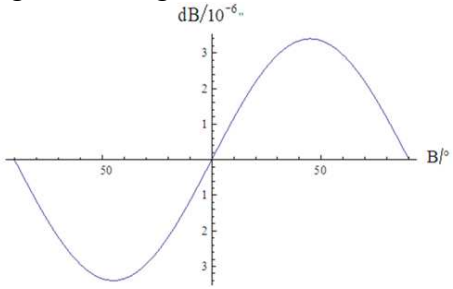


Fig. 1 The difference of geodetic latitude of a point between CGCS2000 and WGS84

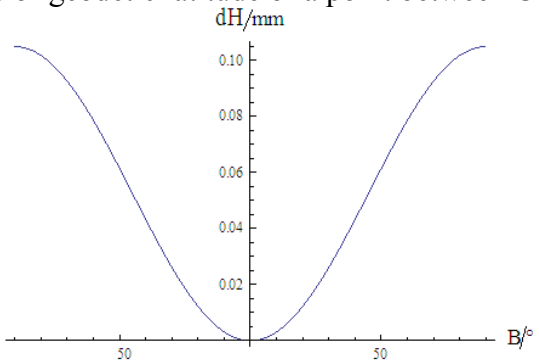


Fig. 2 The difference of geodetic height of a point between CGCS2000 and WGS84

From Fig. 1 and Fig. 2, we could find that the difference of geodetic latitude of a point between CGCS2000 and WGS84 changes by rule of sinusoidal curve with the minimal absolute value being 0 at the equator and poles and the maximal absolute value being about $3.4\times10^{-6}\,''$ which is equal to 0.105 mm after arc second is converted into meter at $45^\circ$N and $45^\circ$S, while the difference of geodetic height changes by rule of inverse cosine cure with the minimal value being 0 at the equator and the maximal value being 0.105 mm at the poles. Generally speaking, the differences of geodetic coordinates between CGCS2000 and WGS84 could be neglected on condition that the present measurement accuracy is at the level of 1 mm. The differences of normal gravity and vertical gradient of normal gravity, designated $d\gamma$ and $dv$, which change with the geodetic latitude on CGCS2000 and WGS84 ellipsoids are shown in Fig. 3 and Fig. 4 respectively.

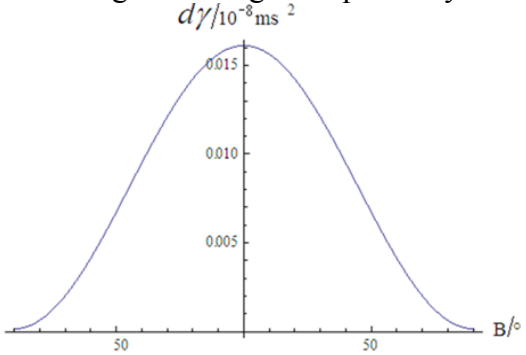


Fig. 3 The difference of normal gravity on CGCS2000 and WGS84 ellipsoids

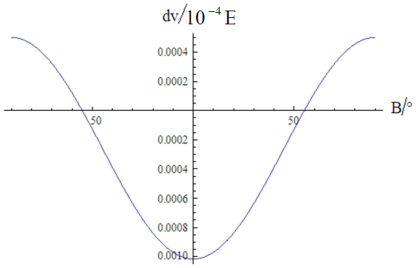


Fig. 4 The difference of vertical gradient of normal gravity on CGCS2000 and WGS84 ellipsoids

From Fig. 3 and Fig. 4, we could find that the normal gravity on CGCS2000 ellipsoid is a little greater than that on WGS84 ellipsoid, with the minimal value of the difference being $0.00016\times10^{-8}\,\mathrm{ms}^{-2}$ at the poles and the maximal value being $0.016\times10^{-8}\,\mathrm{ms}^{-2}$ at the equator, while the maximal absolute value of the difference of vertical gradient of normal gravity is $0.001\times10^{-4}\,\mathrm{E}$ ($1\mathrm{E}=10^{-9}\,\mathrm{s}^{-2}$) at the equator and the minimal absolute value is 0 E at $55^{\circ}\mathrm{N}$ and $55^{\circ}\mathrm{S}$. Generally speaking, these differences could be neglected on condition that the present measurement accuracies of normal gravity and vertical gradient of normal gravity are $10^{-8}\,\mathrm{ms}^{-2}$ and $10^{-4}\,\mathrm{E}$ respectively.

## Conclusions

(1) Geodetic coordinate systems have been established in main developed areas and neighboring countries. The three-dimensional geocentric coordinate system with high precision, CGCS2000, is adopted as Chinese new generation of geodetic datum, which could help us most effectively make use of space technology and derive much benefit from it to great extent.

(2) The maximal differences of geodetic latitude and geodetic height of a point between CGCS2000 and WGS84 are $3.4\times10^{-6}\,''$ and $0.001\times10^{-4}\,\mathrm{E}$ respectively, and the maximal differences of normal gravity and vertical gradient of normal gravity on CGCS2000 and WGS84 ellipsoids are $0.016\times10^{-8}\,\mathrm{ms}^{-2}$ and $0.001\times10^{-4}\,\mathrm{E}$ respectively. The differences of geodetic coordinates of a point between the two coordinate systems, normal gravity and vertical gradient of normal gravity on the two ellipsoids could be neglected in view of present measurement accuracies.

## Acknowledgements

This work was financially supported by National Key Basic Research and Development Program (973 Program) (2012CB719902) and National Natural Science Foundation of China (41201478, 41374018).

## References

[1] Cheng P F, Wen H J and Cheng Y Y. Parameters of the CGCS2000 Ellipsoid and Comparisons with GRS80 and WGS84. Acta Geodaetica et Cartographica Sinica Vol.28(2009), p. 189-194. (in Chinese)

[2] Wei Z Q. National Geodetic Coordinate System: to Next Generation. Geomatics and InformationScience of Wuhan University Vol.28(2003), p.138-143. (in Chinese)

[3] Yang Y X. Chinese Geodetic Coordinate System 2000. Chinese Science Bulletin Vol.54( 2009), p. 2714-2721. (in Chinese)

[4] Cheng P F, Wen H J, Cheng Y Y, et al. China Geodetic Coordinate System 2000. Eighteenth United Nations Regional Cartographic Conference for Asia and the Pacific. Bangkok, Thailand,2009.

[5] Li H P. The Research on the Precise Calculation Theory of Geodetic Coordinate System and Its Application Based on Computer Algebra System. Naval University of Engineering,Wuhan(2010) (in Chinese)

*Applied Mechanics and Materials Vols. 580-583 (2014) pp 2797-2800*
*© (2014) Trans Tech Publications, Switzerland*
*doi:10.4028/www.scientific.net/AMM.580-583.2797*

# Discussion on the Measurements in Cantilever Construction with Guyed Hanging Basket

Fangru Gui

Sichuan College of Architectural Technology, Deyang, Sichuan, 618000,china

116211747@qq.com

**Keywords:** girder, construction, elevation , location , hanging basket

**Abstract.** Guyed hanging basket is qualified with reasonable structure , great carrying ability and clear construction process, and also can provide a good operating space for beam segment construction. Applying cantilever pouring construction with guyed hanging basket should be the development direction of the construction of large-span reinforced concrete cable-stayed bridge. By taking the girder construction of the grand bridge over Beijing-Hangzhou Canal as an example, this paper introduces the measurements in cantilever construction with guyed hanging basket, aiming at providing reference for other similar projects.

## Introduction

Cantilever construction with hanging basket is one of the most commonly used construction methods among large-span prestressed concrete cantilever beam, continuous beam and rigid frame bridge in the industry. Hanging basket generally has the following types: beam hanging basket, cable-stayed hanging basket, guyed hanging basket, steel beam type and supporting frame type. And guyed hanging basket mainly consists of load-bearing system, anchorage elevating and shear reisting system, positioning adjustment system , running system and template system. As guyed hanging basket is qualified with simple structure, lightweight design and convenient utilization, it is commonly applied in the cantilever pouring construction of large-span bridge .

## Project Overview

Grand bridge over Beijing-Hangzhou Canal is controlling node project of Jiangliu expressway, bridge type of its main bridge is a cable-stayed bridge of semi-floating system with double pylons and double cable planes , the length of the main bridge is 464m, and auxiliary piers are installed along the side span. The girder which stretches across the Grand Canal is vertical and horizontal two-way prestressed concrete structure. As the river shipping is busy, the security risk of hanging basket construction on the shipping lane is high, especially the security risk when the hanging basket is being lowered or is moving. The girder applies the construction method of front pivot guyed hanging basket which has high requirements for hanging basket system. Front pivot guyed hanging basket pouring cannot convert easily in different working conditions, linear control is used in the girder, elevation control is difficult, and the difficulty of safety control is high.

## Construction Measurement of 0 # Block

Zero block's construction is a key part of hanging basket assembly, which is directly related to the orderly connection of the standard blocks along the girder and the elevation control of the entire deck ( bottom). Zero block often applies brack construction beside the pier, and zero block's brack assembly beside the pier must be guaranteed sufficient strength and rigidity. Before paving baseboard , ballast is required to eliminate non-elastic deformation, observation and recording should be carried out before and after the ballast, and the measured data of elastic deformation can be used as a reference for installing template. Baseboard should be paved after unloading floor, paving elevation is equal to the sum of design elevation, elastic deformation and camber value, and the control points of

construction plane are applied to carry out plane lofting on the beam line and block line. After the baseboard , web and partition rebar have been strapped , relative elevation relationships with baseboard should be maintained to position internal model elevation. After the roof rebar has been strapped, elevation lofting of concrete's top surface should be conducted according to the relative height difference with the baseboard, point density is required to meet the requirements of the construction site , which could be a powerful guarantee for the lateral and longitudinal gradient of beam plane. Settlement observation should be carried out in the pouring process. Observations of completion and transformation are required after the templates are removed.

## Measurements of Hanging Basket Ballast Test

### 3.1 Purposes of Hanging Basket Ballast Test

The test is to examine whether the overall load-carrying ability of hanging basket can meet the requirements of design documents and specifications, to eliminate the inelastic deformation of hanging basket and measure the elastic deformation of hanging basket under the design load for providing data for the linear control of section construction, and also to examine the safety and reliability of hanging basket.

### 3.2 Measurements of Hanging Basket Ballast Test

After the completion of hanging basket assembly , ballast test should be carried out on the assembled hanging basket for effectively eliminating the plastic deformation during hanging basket construction and actually measuring elastic deformation of hanging basket under loaded state. Applying equivalent load to simulate beam weight and conducting hanging basket are the most unfavorable for conducting safety inspection of hanging basket structure with loading in working condition.

## Construction Measurement of the Girder's Standard Segment

### 4.1 Lofting of Plane's Temporary Control Point

According to the control points on the girder, temporary plane control points of controllable blocks without pouring are set out on the poured block. In order to ensure the plane position's controllability of the block to be poured, 8 controllable points are set out on the poured block, and the longitudinal distance between points and block line should be the length in which instrument can be set up ( the best distance between each segment is a constant 0.5m or 1m ) .

### 4.2 Longitudinal Positioning of Hanging Basket

Longitudinal positioning of hanging basket is mainly to facilitate hanging basket's forward moving along a correct direction, so as to prevent the condition that the front-end plug template cannot be set up on the theoretical block line, which would affect the positioning of box beam's internal components. Based on the front-end temporary control lines of poured block, longitudinal positioning of hanging basket applies hammer ruler and plumb bob to conduct distance measurement, and if the measured value is inconsistent with the design value, it would apply jack to adjust the mileage direction of hanging basket to make the difference between the measured values and design value be less than ± 10mm.

### 4.3 Lateral Positioning of Hanging Basket

Lateral positioning of hanging basket is mainly to prevent the abnormal closure of the bridge caused by segment centerline's deviation from the centerline of the entire bridge after pouring. Immediately after initial setting elevation, the lateral deviation adjustment of hanging basket is conducted, theodolite is placed at the front-end bridge axis points of the poured block during adjustment, which is treated as another point of the bridge axis, and then the deviation value between hanging basket midline mark and centerline direction of the girder is measured with directional line method or reverse mirror method. Due to the existence of errors in point location, mirror positioning and so on, the lateral deviation of hanging basket should be controlled within ± 5mm, the central hang

should be locked after adjustment, and the lateral deviation of hanging basket should be measured again after locking, until the error is controlled within the range of ± 5mm .

**4.4 Lofting of Hanging Basket's Front-end Mileage Line**

Lofting of hanging basket's front mileage line is mainly to prevent the problem like beams of varying width after pouring, and this problem would affect the construction of next beam segment.After the lateral positioning of hanging basket( before the rebar is strapped), the total station is set up in the bridge axis point of the temporary control points along the girder, observation station data and back vision azimuth angle are set to conduct operation on the front-end theoretic block line of hanging basket. The lofting point should control the transverse direction of the girder simultaneously, and the density of points should meet the requirements of construction.

**4.5 Examination before Pouring**

The examination contents before pouring concrete include location of cross wall on the top of beam, location and elevation of internal model , location of embedded part, longitudinal position of beam top block line, retest of cableway pipe, web position of box girder's front section, control of beam sideline and so on.

**4.6 Elevation Discharging of Beam Surface before Pouring and Embedding Elevation Measurement Point**

After passing various examinations, the lofting of concrete top elevation can be carried out before pouring. Lofting method is to maintain the relative height between the baseboards of hanging basket, and the density of lofting elevation point should meet the requirements of the construction site, to powerfully guarantee the lateral and vertical gradient of beam surface. In order to facilitate deflection observation, three elevation observation points are required to be embedded in the fracture surface of front-end hanging basket.

**Construction Measurement of Closure Segment**

Before closure , the relative height difference between the beam bottom sections of closure opening's two sides should be measured to find out whether adjustment is needed. After adjustment, changes like girder elevation and temperature field of closure opening's two sides should be observed for 48 hours, and girder vertical displacement measurement, girder centerline measurement, tower deviation measurement and so on are carried out at the same time. According to the change rule of beam temperature and atmospheric temperature, changes of beam elevation in different time and temperatures, relationship between the beam longitudinal expansion volume and temperature and etc., data is collected to identify the most stable period of girder changes, so as to guide the stiff skeleton locking time and pouring time of closure segment. Before the locking of closure segment, the girder elevation and vertical displacement should be measured again, and the data is used as the initial data. After the closure segment is locked, the observation content before locking should be repeated, and the deformation observation should be conducted every 2 hours within 24 hours to test locking effect . In the concrete pouring process, the main work is to conduct tracking measurement on the girder elevation deflection of closure opening's two sides.

**Full-bridge Adjusting Measurement**

An inevitable problem may arise in the construction process, that is, the top or bottom line of girder is not very smooth, and its difference from the design line is always not the same, so that it is necessary to adjust the actual line. After the stretch-draw of girder closure and prestress, full-bridge cable force should be adjusted, the size of adjustment is based on the whole line of girder, and 24-hour observation of deflection on girder and tower deviation measurements should be conducted before the adjustment. Measuring time should be arranged in the constant temperature period of girder, level gauges, as many as possible, should be applied to observe simultaneously, in order to shorten the observation time. In the process of adjusting, tracking measurement on girder deflection and tower

deviation should be conducted until the full-bridge cable force and line meet the requirement. After the adjustment of cable force is completed, full-bridge girder line should be measured once again.

## Conclusion

Measurement control must be strengthened in the construction measurement of the girder, conditions to conduct re-check should be created as much as possible in the measurement process of cantilever construction, to ensure the accuracy of the measuring results. The control on the construction elevation of hanging basket's each block should be strengthened at the same time, to ensure that the final line of girder is smooth. And the measured deflection, elevation and other parameters of girder under various working conditions should be fed back to the designer in advance, so that designers can adjust and control the elevation of pouring block to ensure the successful completion of the girder's construction measurement .

## References

[1] Wang Shihong. Guy type hanging basket internal force analysis method [J]. Journal of central south road engineering, in September, 2000, 25 (3)

[2] Peng Jian. Continuous rigid frame bridge hanging basket cantilever construction measurement and deformation control study [J]. Transportation standardization, 2013, (16)

[3] Zhou Lixin Li Baodong, Yong jing comes up out of the Yellow River bridge hanging basket a three-tower suspension casting survey control [J]. Highway, 2012, (1)

*Applied Mechanics and Materials Vols. 580-583 (2014) pp 2801-2804*
*© (2014) Trans Tech Publications, Switzerland*
*doi:10.4028/www.scientific.net/AMM.580-583.2801*

# Error Analysis of The Settlement Observation

LiuWang[a *],LinFang[b],BoZhang[c]and ChangchengHuang[d]

Research Institute of Structural Engineering and Disaster Reduction，Tongji University，

Shanghai 200092，China

[a]wangliu201355@163.com, [b]flawsy@163.com, [c] hope.zb@163.com,[d]jggcs@tongji.edu.cn

**Keywords:**settlement observation,leveling rod,surveying errors

**Abstract.**Thisdocumentbases on settlement observation of a residential district which is influenced by the subway construction in Shanghai China.Because of the long-term measurement,therewere some equipment boxes installed on the top of the settlement marks.Thus making the leveling rod in an leaning angle to the right or left direction relative to the sight line.In order to know the error of the measurement,wemake analysis of the error.And it also can be a reference for other surveyings when encounter this similar circumstance.

## Introduction

Settlement observation is a fundamental and important part not only in the site construction but also the building's detection and reinforcement.It is significant to reduce the error of the measurement.

The typical factors influence the measurement are:instrumentalerror, malobservation, externalconditions,observationtime,benchmark,settlement marks and observation route[1].In the actual situation,these factors are integrative that some of them can offset each other.And the error will be tiny and satisfy the precision requirement when the measurement is operated according to the regulation.

But there comes endless situations in engineering.Forexample,in order to make a detection and reinforcement to a residential district which is influenced by the subway construction.Some settlement marks were made aroundthe buildings.With the long-term settlement observation,there were some equipment boxes installed on the top of the settlement marks.Thus making the leveling rod in an leaning angle to the right or left direction relative to the sight line(Fig.1).The surveying errors is what we care about most in such circumstance.

## The Error of The Settlement Observation

There will be four cases in Fig.1 to analyze the error.

**Case One.**The level rod was palcedin the same palce in the two successive surveyings(Fig.2).Assuming that the actual settlement is $y$,sight height is $x$,the leaning angel of the leveling rod to the right is α.

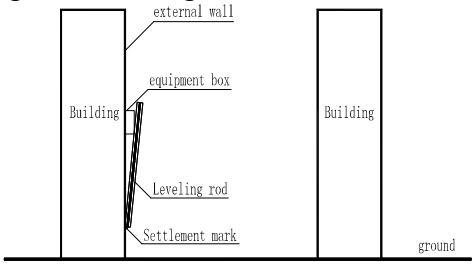


Fig.1 Circumstance of making leveling rod tilt

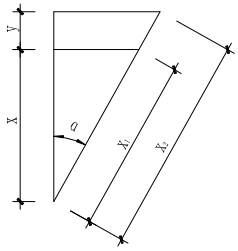


Fig.2 The geometric relationship of the settlement in circumstance 1

The error $\Delta_1$ is(mm):

$$\Delta_1 = x_2 - x_1 - y = \frac{x+y}{\cos\alpha} - \frac{x}{\cos\alpha} - y = \frac{y}{\cos\alpha} - y \tag{1}$$

where,$x_1$ is the first time's reading,$x_2$ is the second time's reading.According to the Eq.1 and in line with the actual,we get some errors in case1 showed in Table 1.

Table.1The measurement error in case 1[mm]

| y (mm) | α | | | |
|---|---|---|---|---|
| | 1° | 3° | 5° | 7° |
| 1 | 0.00 | 0.00 | 0.00 | 0.01 |
| 5 | 0.00 | 0.01 | 0.02 | 0.04 |
| 10 | 0.00 | 0.01 | 0.04 | 0.08 |
| 50 | 0.01 | 0.07 | 0.19 | 0.38 |
| 100 | 0.02 | 0.14 | 0.38 | 0.75 |

Note:The situation we met was that the leaning angle $\alpha$canbe 6°.That is: $\alpha$=tan$^{-1}$(200/1900)= 6°,where 200 is the equipment boxes' thickness is 200 mm,1900 is the vertical length between the benchmark and the equipment box is 1900mm.

We can get the conclution that the error is tiny if the two times' operation are kept on the same.This also verifies the suggestion mentioned in[3].

**Case Two.**The leveling rod was put in the outside and inside in the respective time(Fig.3) and the geometric relationship of the settlement shows in Fig.4.The error $\Delta_2$ is (mm):

$$\Delta_2 = x_2 - x_1 - y = \frac{x+y}{\cos\alpha_2} - \frac{x}{\cos\alpha_1} - y \tag{2}$$

where,$\alpha_1$ is leaning angle of the leveling rod in the first surveying,$\alpha_2$is leaning angle of the leveling rod in the second surveying,the other parameters is the same with the Equ.1.

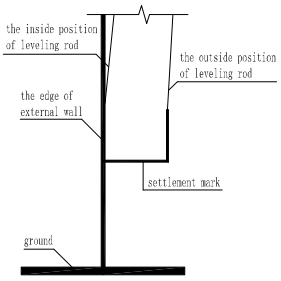


Fig.3 Sketch map of leveling rod's position

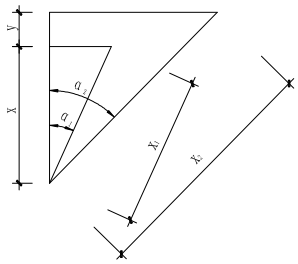


Fig.4 The geometric relationship of the settlement in case 2

According to the Eq.2 and in line with the actual,we get some errors in case 2 showed in Table 2,3.

Table.2 The errors in case 2(1)[mm]

| $x$ (mm) | y (mm) | $\alpha_2$ | $\alpha_1$ | | | |
|---|---|---|---|---|---|---|
| | | | 5.0° | 5.4° | 5.8° | 6° |
| 1500 | 2 | 6° | 2.54 | 1.59 | 0.55 | 0.01 |
| 1540 | | | 2.61 | 1.63 | 0.57 | 0.01 |
| 1580 | | | 2.68 | 1.67 | 0.58 | 0.01 |
| 1500 | 20 | | 2.64 | 1.69 | 0.65 | 0.11 |
| 1540 | | | 2.71 | 1.73 | 0.67 | 0.11 |
| 1580 | | | 2.78 | 1.77 | 0.68 | 0.11 |

Table.3 The errors in case 2(2)[mm]

| $x$ (mm) | $y$ (mm) | $\alpha_2$ | $\alpha_1$ | | | |
|---|---|---|---|---|---|---|
| | | | 1° | 1.4° | 1.8° | 2° |
| 1500 | 2 | 2° | 0.69 | 0.47 | 0.18 | 0.00 |
| 1540 | | | 0.71 | 0.48 | 0.18 | 0.00 |
| 1580 | | | 0.72 | 0.49 | 0.18 | 0.00 |
| 1500 | 20 | | 0.70 | 0.48 | 0.19 | 0.01 |
| 1540 | | | 0.72 | 0.49 | 0.19 | 0.01 |
| 1580 | | | 0.73 | 0.50 | 0.20 | 0.01 |

According to Eq.2 and Table2,3,we can get the conclutions that:

(1)The same D-vlaue in the leaning angle of leveling rod,the more value the benchmark angle the larger the errors.(For example,case A's error is larger than case B's error.where case A is:$x$=1500mm,$y$=2mm,$\alpha_1$=5.4°,$\alpha_2$=6°;case B is :$x$=1500mm,$y$=2mm,$\alpha_1$=1.4°,$\alpha_2$=2° )

(2)The actual settlement $y$'s influence to errors is so tiny that can be ignored.

**Case Three.**Beacause of the bubble on the leveling rod can not reach to the center,the leveling rod may tilt in both right-left and fore-and-aft directions.The geometric relationship of the settlement shows in Fig.5.The error $\Delta_3$ is (mm):

$$\Delta_3 = x_2 - x_1 - y = \frac{x+y}{\cos\alpha_2 \cos\alpha_2'} - \frac{x}{\cos\alpha_1 \cos\alpha_1'} - y \tag{3}$$

where,$\alpha_1$ is the right-left leaning angle of the first time observation, $\alpha_1'$ is the fore-and-aft leaning angle of the first time observation,$\alpha_2$ is the right-left leaning angle of the second time observation, $\alpha_2'$ is the fore-and-aft leaning angle of the second time observation,the other parameters are the same with Eq.2.Thus according to the Eq.3 and in line with the actual,we get some errors in case 3 showed in Table 4.

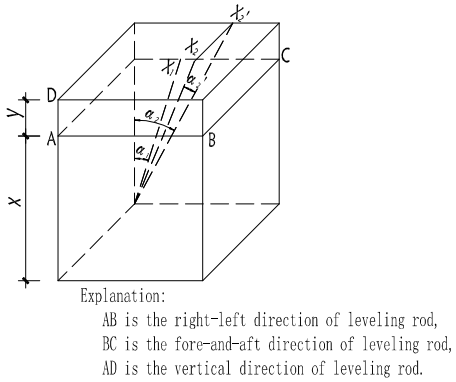


Fig.5 The geometric relationship of the settlement in case 3

Table4The errors in case 3[mm]

| $x$ (mm) | $y$ (mm) | $\alpha_2$ | $\alpha_2'$ | $\alpha_1$ | | | |
|---|---|---|---|---|---|---|---|
| | | | | 5.0° | 5.4° | 5.8° | 6° |
| 1500 | 2 | 6° | 0.0° | 2.54 | 1.59 | 0.55 | 0.01 |
| | | | 0.4° | 2.58 | 1.62 | 0.59 | 0.05 |
| | | | 0.8° | 2.69 | 1.73 | 0.70 | 0.16 |
| | | | 1.2° | 2.87 | 1.92 | 0.89 | 0.34 |
| | | | 1.6° | 3.13 | 2.18 | 1.14 | 0.60 |
| | | | 2° | 3.46 | 2.51 | 1.48 | 0.93 |

(1)We can get the conclution from Eq.3 that leveling rod's right-left leaning and fore-and-aft leaning have the same degree influence on the observation errors.

**Case Four.**The errors caused by reading on the leveling rod(Fig.6).The error $\Delta_4$ is (mm):

$$\Delta_4 = x_2 - x_1 + K\cdot\tan\alpha_2 - y = \frac{x+y}{\cos\alpha_2 \cos\alpha_2'} - \frac{x}{\cos\alpha_1 \cos\alpha_1'} + K\cdot\tan\alpha_2 - y \tag{4}$$

where,$K$ is the length of tick mark on the leveling rod(mm),the other parametes are the same with Eq.3.Thus according to the Eq.4 and in line with the actual,we get some errors in case 4 showed in Table 5.

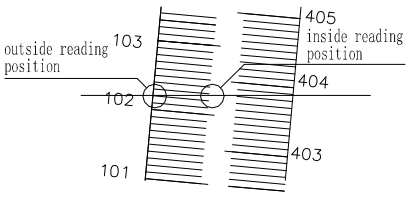


Fig.6 The reading error on the level ruler

Table5 The errors in case 4[mm]

| $x$ (mm) | $y$ (mm) | $K$ (mm) | $\alpha_2$ | $\alpha_2'$ | $\alpha_1$ | | | |
|---|---|---|---|---|---|---|---|---|
| | | | | | 5.0° | 5.4° | 5.8° | 6° |
| 1500 | 2 | 10 | 6° | 0.0° | 3.59 | 2.64 | 1.61 | 1.06 |
| | | | | 0.4° | 3.63 | 2.67 | 1.64 | 1.10 |
| | | | | 0.8° | 3.74 | 2.78 | 1.75 | 1.21 |
| | | | | 1.2° | 3.93 | 2.97 | 1.94 | 1.39 |
| | | | | 1.6° | 4.18 | 3.23 | 2.20 | 1.65 |
| | | | | 2.0° | 4.52 | 3.56 | 2.53 | 1.98 |

**Coarse Judgement of The Observation's Errors**

According to [4],this kind of error belongs to random error(also called accidental error).Its distribution is or approximate normal distribution.And its mathematical expectation is zero.Thus this error Δ's frequency function is :

$$f(\Delta)=\frac{1}{\sqrt{2\pi}\sigma}\exp\left\{-\frac{\Delta^2}{2\sigma^2}\right\} \tag{5}$$

Basing on the above-mentioned result,we can assume that Δ's probability is 95% and 98% respectively in the [-4,4] section.Thus we can get other probability in the different section showed in Table 6.

Table6 The probability distribution ofΔ

| Δ's section | [-4,4] | [-3,3] | [-2,2] | [-1,1] |
|---|---|---|---|---|
| Probability 1 | 95% | 85.8% | 67.3% | 37.6% |
| Probability 2 | 98% | 91.8% | 75.4% | 43.8% |

At the end, we can estimate the error of this settlement observation according to Table 6.

**Conclusions**

According to the analysis mentioned above,we can get the conclutions that:

(1)The error is tiny if the two times' conditions(including instrument, observationmethod,surveying crew ect.) are kept on the same.And we should maintain consistent to reduce the error.

(2) Leveling rod's right-left leaning ang fore-and-aft leaning have the same degree influence on the observation errors.

(3) The actual settlement $y$'s influence to errors is so tiny that can be ignored.

(4) The same D-vlaue in the leaning angle of leveling rod,the more value the benchmark angle the larger the errors.(For example,case A's error is larger than case B's error.where case A is:$x$=1500mm,$y$=2mm,$\alpha_1$=5.4°,$\alpha_2$=6°;case B is :$x$=1500mm,$y$=2mm,$\alpha_1$=1.4°,$\alpha_2$=2° )

**References**

[1] L.Q.Zhang, Y.Q.Niu,Introduction to settlement measurement method of error analysis and control, J.SCIENCE & TECHNOLOGY INFORMATION,Vol.05,102-103,2012

[2] Y.Y.Xu,Y.Luo,Surveying,third ed.,ChinaCommunications Press, 2009

[3] Ministry of Construction of the People's Republic of China,"JGJ8-2007 Code for deformation measurement of building and structure",China Architecture and Building Press, 2007（in Chinese）

[4] S.H. Wang,Error Theory and measurement adjustment, TONGJI UNIVERSITY PRESS,China, 2010

*Applied Mechanics and Materials Vols. 580-583 (2014) pp 2805-2809*
*© (2014) Trans Tech Publications, Switzerland*
*doi:10.4028/www.scientific.net/AMM.580-583.2805*

# Application of stereo vision measurement technology in the detection of round hole

Wang Qiang [1, a], Cui Ximin[1, b], Li Cong[1], Cui Jiajie[1], Li Liangjian[1]

[1]College of Geoscience and Surveying Engineering,

China University of Mining & Technology(Beijing), Beijing, China

[a]wangqiang_study@163.com, [b]cxm@cumtb.edu.cn

**Keywords:** Round hole; stereo vision; edge detection; online measurement

**Abstract.** In precision machining, we often detect the location of some round holes or other geometric parameters. Given the disadvantages of traditional method is contacted, artificial and time-consuming, this paper has proposed a image measurement method based on stereo vision. It uses the method of digital image processing to perform the denoising, binarization, edge detection, and gets centralized location of the orifice image, and analyzes the accuracy of the hole machining and arrangement. Experimental results show that the error of image measurement proposed is less than 0.14mm, which meets the general requirements of the hole measurement in precision and is applicable to online measurement that the accuracy requirement is not high and the task with large amount of object to detect.

## Introduction

The progress of industry proposes higher requirements on the components size measurement accuracy, and also needs to achieve real-time online measurement. The round hole is an important feature in many components, so machining quality of the round hole affects the components normal function. Currently, the method measuring geometric parameters of the round hole is divided into contact measurement and non-contact measurement. The contact measurement tools are caliper, inside micrometer, gauges etc, which are restricted by the size of the hole and the measuring instruments, and sometimes even can not measure the tiny hole and large-size hole. The non-contact measurement methods are universal tool microscope, image measurement, X-rays etc. The disadvantages of universal tool microscope and X-rays are high cost, long cycle and expensive price. Therefore, they are not suitable for the needs of modern industrial development[1-2].

The stereo vision measurement is stable, reliable, non-contact, and rapid speed etc. The extraction algorithm using the accuracy level of pixels and sub-pixel to access the center of the round hole can improve the speed and accuracy of center coordinates detection. The article describes how to use a linear and array type stereo camera and digital image processing technology to detect whether the distance between the hole and the neighboring hole in the industrial components has meet the design standard. Figure 1 is the stereo camera system's sketch map used in this paper.

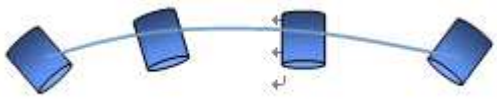

Figure 1 The stereo camera system sketch map

## Multi-camera stereo vision measuring principle

The multi-camera stereo vision measuring principle is getting two or more digital images of the same object in different locations and orientations, after image matching processing by computer and related mathematical calculations, to obtain accurate three-dimensional coordinates of the target point. The schematic diagram is shown in figure 2.

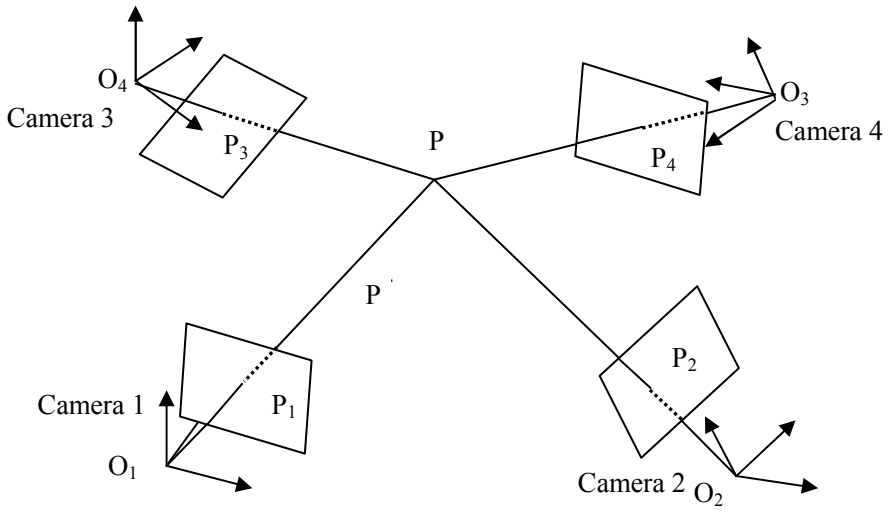


Figure 2 Multi-camera stereo measurement

In photogrammetry, objects imaging model is perspective projection model of a pinhole. Known from Fig.2, for any point P on the surface of the three-dimensional object, if you can see P located $P_1$ in the image from camera 1, but we could not obtain the three-dimensional position of point P. Because for any point P ' in the straight line $P_1O_1$ ($O_1$ is optical center of camera 1 ), the image points are $P_1$. Thus, from the position of point $P_1$, we only know that point in space is located in a position on the straight line P1O1, but do not know the exact location of the point P (namely do not know the deep information). However, if we the observe point P with two cameras: camera 1 and camera 2 simultaneously, the spatial point P is both located on the $P_1O_1$, and on the $P_2O_2$. Point P is the intersection of the straight line $P_1O_1$ and $P_2O_2$. The three-dimensional position of point P is uniquely determined up. These are the basic principles of three-dimensional point reconstruction. Similarly, with camera 3 and camera 4 four camera overall adjustment calculation, we can get a more precise three-dimensional coordinates of point P.

**Corner point extraction edge detection method**

Accurate extraction of corner point position is the premise of high-precision distortion correction. The corner point of image is also known as the turning point, which refers to the points with high curvature in image. It is formed by the larger curvature areas of the target edge, or intersection of two and more edge[3].

Corner point detection method in this paper operates directly on the gray-scale image using sub-pixel corner extraction method of Harris operator. The detection methods can be divided into two steps. The first step is to extract the pixel-level position (x,y) of the corner point based Harris operator. The second step is to do quadratic polynomial interpolation using (x,y) and eight pixels points around. Then we get the sub-pixel position of corner point. The formula of polynomial interpolation is shown as (1)[4].

$$a_0 + a_1x + a_2y + a_3x^2 + a_4xy + a_5y^2 = R(x, y) \quad (1)$$

In the formula, R(x,y) is the reaction function of the corner point. Use 9 pixels to establish overdetermined equation with six coefficients $a_0 \sim a_5$, Then, solve the overdetermined equation using the least squares method.

The sub-pixel position of corner point corresponds maximum of quadratic polynomial, so we calculate the derivation of the quadratic polynomial, as the formula (2), thus, the solution of the binary equations is the sub-pixel position of the corner point[5].

$$\begin{cases} \dfrac{\partial R}{\partial x} = 2a_3 x + a_4 y + a_1 = 0 \\ \dfrac{\partial R}{\partial y} = 2a_5 y + a_4 x + a_2 = 0 \end{cases} \tag{2}$$

**Edge detection**

The detection accuracy of the round edge in the measured hole image directly affects the measurement accuracy. Obtaining the edge of the round hole will be divided into three steps in the paper. The first step is to suppress image noise with the median filtering method. The second step is to extract sub-pixel coordinates of the image edge points based on the principle that least-squares fitting of Gaussian curves. Namely, position the edge roughly with the canny operator. Then, accurately position the edge with fitting a quadratic curve based on least squares fitting method. The third step is to fit the curve equation of the round edges based on least-squares fitting with the edge sub-pixel coordinates. So the radius of the circular edge and exact parameters of the center position can be gained[6-8].

Assuming the center position of the circular edge is $(x_0, y_0, z_0)$, $(x_i, y_i, z_i)$ is the sub-pixel coordinate of edge point, the radius is R. Then, the circle curved equation of edge is the formula (3).

$$(x_i - x_0)^2 + (y_i - y_0)^2 + (z_i - z_0)^2 = R^2 \tag{3}$$

Establish the object equation of the least squares method, as the following formula (4).

$$E = \sum_{i=1}^{n} ((x_i - x_0)^2 + (y_i - y_0)^2 + (z_i - z_0)^2 - R^2)^2 \tag{4}$$

The least squares method here is to find $x_0, y_0, z_0$ and R, and make E is the optimal minimum value. To facilitate solving the equation, order

$$h = x_0^{\,2} + y_0^{\,2} + z_0^{\,2} - R^2 \tag{5}$$

Simplify the formula (5) to equation (6)

$$E = \sum_{i=1}^{n} (x_i^{\,2} - 2x_0 x_i + y_i^{\,2} - 2y_0 y_i + z_i^{\,2} - 2z_0 z_i + h)^2 \tag{6}$$

Using the least squares method, solve the partial derivative of equation (6) and let each partial derivative be 0, as the following equation (7).

$$\begin{cases} \dfrac{\partial E}{\partial x_0} = -4\sum_{i=1}^{n} x_i (x_i^{\,2} + y_i^{\,2} + z_i^{\,2} - 2x_i x_0 - 2y_i y_0 - 2z_i z_0 + h) = 0 \\ \dfrac{\partial E}{\partial y_0} = -4\sum_{i=1}^{n} y_i (x_i^{\,2} + y_i^{\,2} + z_i^{\,2} - 2x_i x_0 - 2y_i y_0 - 2z_i z_0 + h) = 0 \\ \dfrac{\partial E}{\partial z_0} = -4\sum_{i=1}^{n} z_i (x_i^{\,2} + y_i^{\,2} + z_i^{\,2} - 2x_i x_0 - 2y_i y_0 - 2z_i z_0 + h) = 0 \\ \dfrac{\partial E}{\partial h} = 2\sum_{i=1}^{n} (x_i^{\,2} + y_i^{\,2} + z_i^{\,2} - 2x_i x_0 - 2y_i y_0 - 2z_i z_0 + h) = 0 \end{cases} \tag{7}$$

From the formula (7), $x_0$, $y_0, z_0$ can be obtained.

**The identification process of the round hole and the results**

The basic identification process of the round hole image is to obtain the image with multiple orifice firstly, and process the image binarization, then carry on the following operations for the binarization image, corner detection, contour extraction, the geometric center calculation of the hole to obtain the distance between the holes. The processing flow is shown in Figure 3.

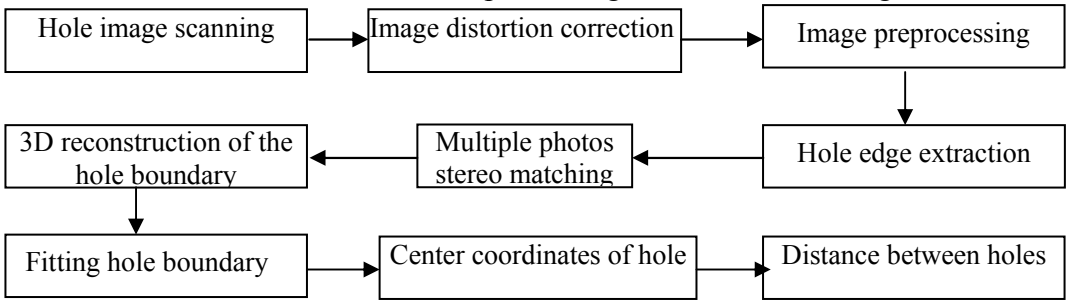


Figure 3 The hole identification processing flow

In order to facilitate inspection and comparison, the experiment used an aluminum-alloy plate. There are uniform distribution of the holes drilling by precision drill. Before the experiment, the measured distance between holes as the standard value by micrometer. The original image and the preprocessing results obtained by software processing are shown in figure 4.Edge detection and circle fitting are shown in figure 5.

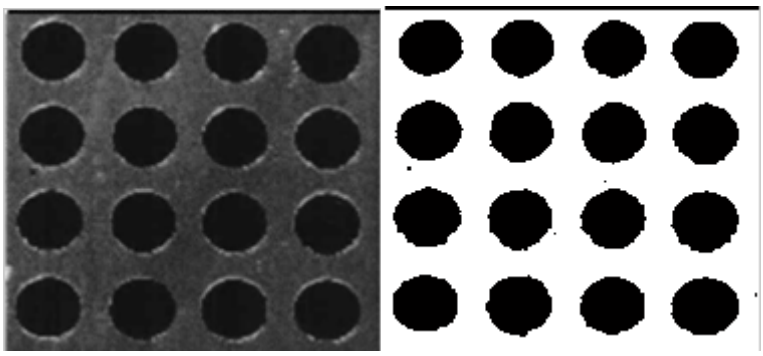

(a) The original image (b) The preprocessing image

Figure 4 The original image and the preprocessing results

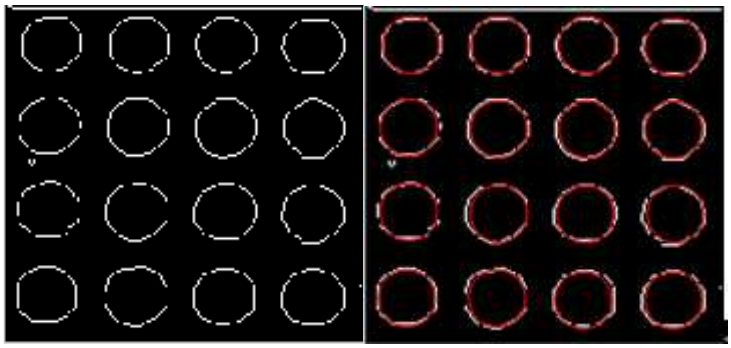

(a) Edge detection results (b) Circle fitting results

Figure 5 Edge detection and circle fitting

By matching multiple images, three-dimensional coordinates of the edge points are obtained. After the hole center location, we can calculate the distance between adjacent holes di (i=1,2,3,4), shown as figure 6. Compared with the standard value of micrometer measurements, we can measure the accuracy of the measurement of stereoscopic images.

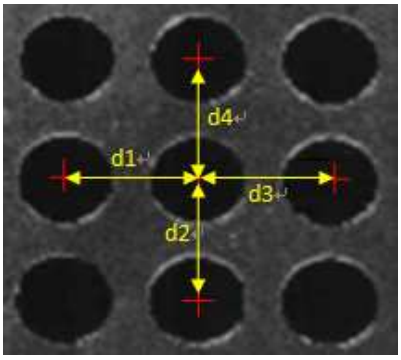


Figure 6 The hole center and center distance

Table 1 Comparison of hole spacing measured results(unit: mm)

| Measurements serial | $d_1$ | $d_2$ | $d_3$ | $d_4$ |
|---|---|---|---|---|
| Hole spacing measured by Micrometer | 13.546 | 13.186 | 13.504 | 13.118 |
| Hole spacing measured in image | 13.463 | 13.287 | 13.644 | 13.053 |
| Differentials | 0.083 | 0.101 | 0.14 | 0.065 |

From Table 1, the measurement error of the hole spacing by stereoscopic measurement is less than 0.14mm, which can be adapted to the measurement tasks of not high precision requirements. Analyzing the reasons, it may be related to the following factors. the internal distortion of camera and the calibration of external parameter exists error; There is noise in the image preprocessing; Edge extraction is inaccurate etc. For high precision measurement tasks, we need further improvement from the above aspects in order to meet the requirements of high-precision measurement.

## Conclusions

Through the introduction of the hole detection theory, the paper processed and analyzed the orifice using noise removal, binarization, edge extraction and other digital processing method, and the the measurement error is less than 0.14mm. This method can be used in rough measurement of the round hole, which is great significance for industrial bulk-production. If we improve it a little, while eliminating the sources of error as far as possible. The high precision measurement of the round hole can be achieved.

## References

[1] P LIU. J WANG. S Q WANG. Journal of Applied Optics 2011, 32 (2), 291-295.

[2] H W LENG. C G XU. Z W FENG. Journal of Image and Graphics 2010,15(7), 1084-1090.

[3] J M LIANG. H M GAO. Transactions of the China Welding Institution 2006, 27 (2), 102-105.

[4] G J ZHANG. Machine Vision.Beijing, Science Press,2005.

[5] T A.Clarke,J G Fryer.The Development of Camera Calibration Methods and Models. Photogramm. Rec 1998,16 (91), 51-66.

[6] L S LIU. Y ZHANG. H Q LU. Journal of Optoelectronics laser 2005, 16 (8), 993-996.

[7] Q B TONG. Z L DING. Y B DONG. Journal of Jilin University(Engineering and Technology Edition) 2009, 39 (1) 154-159.

[8] Jensen K. Anastassiou D.Sub-pixel edge localization and the interpolation of still images. Trans on Images Processing 1995, 4 (3) 285-295.

*Applied Mechanics and Materials Vols. 580-583 (2014) pp 2810-2814*
*© (2014) Trans Tech Publications, Switzerland*
*doi:10.4028/www.scientific.net/AMM.580-583.2810*

# Application of Model GM (1,1) to Settlement Forecast of High-fill Airport

Youping WU [1, a], Jiabang WANG [2,b], Chuntao WANG [1,c]

[1] Nanchang University College of Science and Technology , Nanchang, Jiangxi, 330029, China
[2] Land Resources Planning Institute of Guangxi Zhuang Autonomous Region, Nanning, Guangxi, 530021, China
[a] tjwyp123@126.com, [b]373218966@qq.com, [c] 150572482@qq.com

**Keywords:** GM (1,1) Model; Settlement; Forecast

**Abstract.** GM (1,1) model was created to forecast the development and change of a high-fill settlement by viewing the high-fill settlement process as a grey system, conducting generation treatment and taking the settlement incremental data sequence as the original data sequence. According to example which demonstrated that the measured settlement at the forecasted model analyzing and monitoring point was practical and relatively accurate.

## Introduction

As the data volume obtained from the observation of a high-fill airport construction process was limited, it was difficult to accurately forecast the actual working conditions of the airport. Although the settlement value had been measured, it was difficult to make a precise description due to the complex relations among these factors. A grey model was created to analyze the development and change of the high-fill settlement by using the grey system theory, viewing the high-fill settlement process as a grey system and conducting generation treatment by taking the settlement incremental data sequence as the original data sequence[1~4].

## Creation of Model [4]

Taking the settlement incremental data $x^{(0)}(k)$ within the same time interval as the original data sequence:

$$x^{(0)}(k) = \left\{x^{(0)}(1), x^{(0)}(2), \mathrm{L}, x^{(0)}(n)\right\} \tag{1}$$

The cumulative settlement volume generation sequence $x^{(1)}(k)$ was obtained by conducting a cumulative generation:

$$x^{(1)}(k) = \left\{x^{(1)}(1), x^{(1)}(2), \mathrm{L}, x^{(1)}(n)\right\} \tag{2}$$

A whitening differential equation of $GM(1,1)$ model of $x^{(1)}(k)$ was created according to the grey theory GM (1,1) model:

$$\frac{dx^{(0)}(k)}{dt} + \alpha x^{(1)}(k) = u \tag{3}$$

By recording the grey parameter column as $\hat{a}$, the least square solution was determined: $\hat{a} = (a \quad u)^T = (B^T B)^{-1} B^T y_n$ , Where:

$$B = \begin{bmatrix} -\frac{1}{2}\left[x^{(1)}(1) + x^{(1)}(2)\right] & 1 \\ -\frac{1}{2}\left[x^{(1)}(2) + x^{(1)}(2)\right] & 1 \\ \mathrm{M} & \mathrm{M} \\ -\frac{1}{2}\left[x^{(1)}(n-1) + x^{(1)}(n-1)\right] & 1 \end{bmatrix} , \quad y_n = \left(x^0(2) \quad x^0(3) \quad \mathrm{K} \quad x^0(n)\right)^T$$

Under the initial value condition $x^{(1)}(1) = x^{(0)}(1)$, the solution of $GM(1,1)$ whitening differential equation (or the time response equation) was solved:

$$\hat{x}^{(1)}(k+1) = \left[ x^{(1)}(1) - \frac{u}{\alpha} \right] e^{-\alpha k} + \frac{u}{\alpha} \tag{4}$$

Then, the reducing value of simulation of the mode was obtained by conducting cumulative generation:

$$\hat{x}^{(0)}(k+1) = \hat{x}^{(1)}(k+1) - \hat{x}^{(1)}(k) \tag{5}$$

When the original data was the measured settlement time sequence, $GM(1,1)$ forecast model was created to conduct fitting to $x^{(1)}$ directly by taking the original data as $x^{(1)}$ and the generated sequence from one cumulative deduction as $x^{(0)}$。

**Model Accuracy Test [4]**

After the establishment of $GM(1,1)$ the forecast model and obtaining the model forecast value (the reducing value), the accuracy of the model, that is, the model fitting degree, must be evaluated in order to evaluate the reliability of the forecast. The common evaluation methods include:

(1) Residual error Test, in which the residual error of the model value and the measured value was tested point by point.

The residual error between the measured value $x^{(0)}(k)$ and the model value $\hat{x}^{(0)}(k)$ and the relative residual error at moment $k$ was recorded to be $q(k)$ and $e(k)$, respectively, $q(k)$ and $e(k)$ were tested point by point, in which:

$$\begin{cases} q(k) = x^{(0)}(k) - \hat{x}^{(0)}(k) \\ e(k) = \dfrac{q(k)}{x^{(0)}(k)} \\ k = 1,2,\mathrm{L},n \end{cases} \tag{6}$$

(2) Test of degree of association, in which the similarity between the model value curve and the modeling sequence curve was tested.

(3) Variance test, in which the statistic property of the residual error distribution was tested, which were jointly descried by the two indexes of the variance specific value $C$ and the small probability of error P. See Table 1.

Table 1 Grey Model Accuracy Class

| Accuracy Class | Relative Residual Error | Variance Ratio C | Small probability Error P |
|---|---|---|---|
| Class One (Good) | 0.01 | <0.35 | >0.95 |
| ClassTwo (Qualified) | 0.05 | <0.45 | >0.80 |
| Class Three (Moderate) | 0.10 | <0.50 | >0.70 |
| Class Four (Disqualified) | 0.20 | ≥0.65 | ≤0.70 |

$x_1$ was recorded to be the variance of $x^{(0)}(k)$, and $\overline{q}$ and $x_2$ the average value and variance of nonzero residual error in $q(k)$ , then:

$$C = \frac{x_2}{x_1}, \quad P = P\left\{ \left| q(k) - \overline{q} \right| < 0.6745 x_1 \right\} \tag{7}$$

For forecast with a good extrapolation, $C$ must be small, a small $C$ indicated a large $x_1$ and a small $x_2$, a small $x_1$ indicated that the observation data discretization was large and the regularity was poor; a small $x_2$ indicated that the residual error discretization was small, so the smaller $C$ was,

the better, which indicated that though the original data regularity was poor, the residual error fluctuation amplitude was small.

When the extrapolation was good, $P$ was large, and a large $P$ indicated that there were more points where the difference between the residual error and the residual average value was smaller than the specified value. Therefore, the smaller $C$ was, the large $P$ was, and the higher its forecasted accuracy was.

**Residual Model Revision**

If $GM(1,1)$ model created in accordance with the original data failed to pass the test, or if its accuracy was not high enough, a residual error model could be considered to be created to revise the original model.

The residual error was as follows:

$$q^{(0)}(k) = x^{(1)}(k) - \hat{x}^{(1)}(k) \qquad k = 1,2,\mathrm{L},n \tag{8}$$

Taking $k = i, i+1, \mathrm{L}, n$, we had residual sequence:

$$q^{(0)} = \left\{ q^{(0)}(i), q^{(0)}(i+1), \mathrm{K}, q^{(0)}(n) \right\} \tag{9}$$

For the sake of convenience of calculation and expression, we rewrote it as:

$$q^{(0)} = \left\{ q^{(0)}(1'), q^{(0)}(2'), \mathrm{K}, q^{(0)}(n') \right\} \quad , \quad n' = n - i \tag{10}$$

Creating a residual error $GM(1,1)$ model to $q^{(0)}$, and adding the $GM(1,1)$ model into the original model, we obtained a revised model as:

$$\hat{x}^{(1)}(k) = (x^{(0)}(1) - \frac{u}{a})e^{-a(k-1)} + \frac{u}{a} + \delta(k-i)(-a')(q^{(0)}(1') - \frac{u'}{a'})e^{-a'(k-i)} \tag{11}$$

Where: $\delta(k-i) = \begin{cases} 1 & k \geq i \\ 0 & k < i \end{cases}$

**Project Example**

The original data after adjustment statistics of a high-fill airport is shown in Table 2.

Table 2 Accumulative Settlement Volume of the Taxiway [ mm]

| Date | XD01 | XD02 | XD03 | XD04 | XD05 | XD06 | XD07 | XD08 | XD09 | XD10 | XD11 |
|---|---|---|---|---|---|---|---|---|---|---|---|
| 8.15 | 0.00 | 0.00 | 0.00 | 0.00 | 0.00 | 0.00 | 0.00 | 0.00 | 0.00 | | |
| 8.18 | -0.09 | -2.05 | -2.86 | -2.94 | -2.19 | -2.03 | -1.36 | -1.25 | -0.39 | | |
| 8.21 | -0.23 | -1.97 | -3.07 | -3.50 | -2.47 | -2.66 | -2.16 | -2.15 | -0.42 | | |
| 8.24 | -0.52 | -2.53 | -2.99 | -2.99 | -2.27 | -2.69 | -1.80 | -2.22 | -0.46 | | |
| 8.27 | -0.50 | -2.54 | -4.11 | -3.84 | -2.74 | -3.23 | -2.27 | -2.06 | -0.37 | | |
| 9.2 | -0.65 | -2.72 | -3.76 | -3.32 | -2.54 | -3.36 | -2.28 | -2.30 | -0.51 | | |
| 9.5 | -1.14 | -3.20 | -5.23 | -4.38 | -3.14 | -3.66 | -2.02 | -2.33 | -0.75 | 0.00 | 0.00 |
| 9.8 | -1.04 | -2.90 | -4.52 | -4.32 | -3.02 | -4.08 | -2.49 | -2.60 | -0.82 | -2.20 | -2.01 |
| 9.12 | -1.11 | -3.32 | -4.97 | -4.27 | -2.91 | -4.12 | -2.52 | -2.73 | -0.54 | -1.80 | -1.83 |
| 9.6 | -1.07 | -3.11 | -5.05 | -5.13 | -2.90 | -3.99 | -2.27 | -2.47 | -0.64 | -3.10 | -1.94 |
| 9.13 | -1.21 | -3.12 | -5.08 | -4.53 | -3.17 | -3.68 | -2.55 | -2.21 | -0.70 | -2.90 | -2.01 |
| 9.20 | -1.23 | -3.48 | -6.98 | -6.01 | -3.55 | -4.25 | -2.99 | -2.29 | -0.85 | -3.10 | -2.10 |
| 9.27 | -1.27 | -3.56 | -7.08 | -5.85 | -3.65 | -4.79 | -2.92 | -2.47 | -0.95 | -3.70 | -2.19 |
| 10.4 | -1.21 | -2.98 | -6.42 | -5.52 | -3.69 | -4.46 | -2.93 | -2.55 | -1.02 | -4.30 | -2.08 |
| 10.11 | -1.38 | -3.06 | -6.79 | -6.25 | -4.01 | -4.69 | -2.91 | -2.54 | -0.96 | -3.50 | -0.64 |

Considering incomplete observation data of the airport, the lack of a long term observation data, and the stable data tendency, a grey $GM(1,1)$ model was used for the modeling and forecast of the vertical displacement of the airport settlement monitoring point XD10.

(1) $GM(1,1)$ modeling

Original sequence: $x^{(0)}(k) = (2.2,1.8,3.1,2.9,3.1,3.7,4.3,3.5)$

One accumulated generating sequence $x^{(1)} = (2.2,4.0,7.1,10.0,13.1,16.8,21.1,24.6)$

The solution of the whitening differential equation (or the time response equation) was:

$$\hat{x}^{(1)}(k+1) = \left[x^{(1)}(1) - \frac{u}{\alpha}\right]e^{-\alpha k} + \frac{u}{\alpha} = 27.019e^{0.0864k} - 24.8194 \tag{12}$$

(2) Accuracy test

Based on the computational simulation value of the whitening response equation, the calculation results and residual error are shown in Table 3.

Table 3 Residual Error Test Calculation Value of XD10 Point

| Sequence | $x^{(0)}(k)$ | $\hat{x}^{(0)}(k)$ | Residual Error $q(k)$ | Relative Residual Error $\varepsilon(k)$ |
|---|---|---|---|---|
| k=2 | 1.8 | 2.4384 | -0.6384 | -0.35467 |
| k=3 | 3.1 | 2.6585 | 0.4415 | 0.142419 |
| k=4 | 2.9 | 2.8985 | 0.0015 | 0.000517 |
| k=5 | 3.1 | 3.1601 | -0.0601 | -0.01939 |
| k=6 | 3.7 | 3.4454 | 0.2546 | 0.068811 |
| k=7 | 4.3 | 3.7564 | 0.5436 | 0.126419 |
| k=8 | 3.5 | 4.0954 | -0.5954 | -0.17011 |

From calculation of Table 3, we had: the average residual error: $\overline{q} = \frac{1}{n-1}\sum_{k=2}^{n}\left|q(k)\right| = 0.1205$, the average accuracy: $P = (1-\overline{q}) \times 100\% = 87.95\% > 80\%$, variance error $C = 0.54$, small error probability $P = 100\%$.

Taking the accuracy represented by the optimal data of each test index as the accuracy of $GM(1,1)$, it showed that the accuracy of the above $GM(1,1)$ model was qualified.

(3) Forecast

Based on the whitening response equation (5) and (12), Plugging $k = 8$ into the above two equations, we got $\hat{x}^{(1)}(9) = 29.1143$, the value was $3.2$, then the forecasted relative residual error of $\hat{x}^{(0)}(9) = 4.5143$ was $\varepsilon(9) = \frac{3.2 - 4.5143}{3.2} \times 100\% = -0.4107\%$.

Taking the accuracy represented by the optimal data of each test index as the accuracy of $GM(1,1)$, it showed that the accuracy of the above $GM(1,1)$ model was qualified.

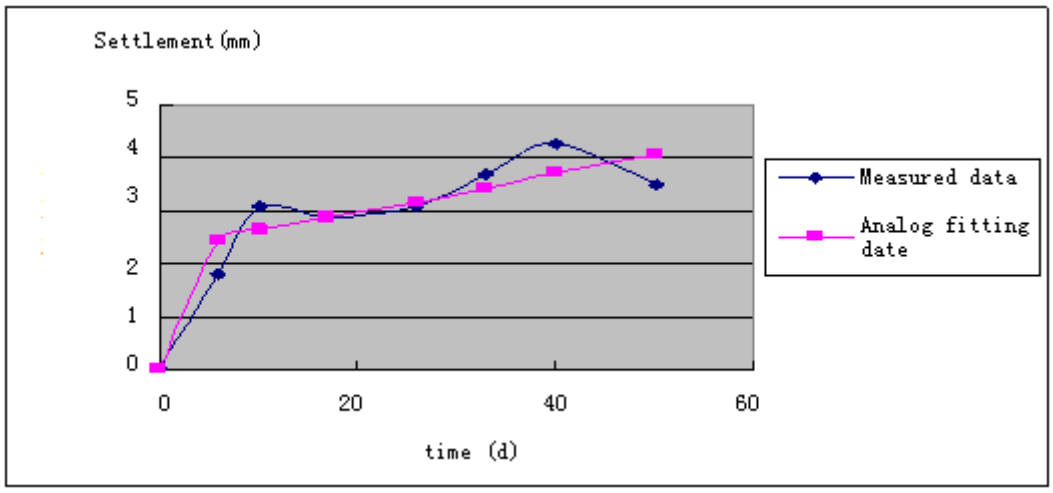


Fig. 1 Comparison Chart of the Fitting Curve of Settlement Monitoring Point XD10 Model and the Measured Curve

From Table 2, Table 3 and Fig. 1, it could be seen that the model accuracy class was good, the accuracy was high, and the model fitting curve agreed very well with the measured settlement curve, indicating that it was practical and accurate to analyze the measured settlement of this observation point by using the grey forecast model.

## Conclusions

The grey model can be used for short term and long term forecasts, which has such merits as less required original information volume, simpler calculation and higher measured accuracy.

(1) Compared with the measured settlement, the accuracy of the high-fill airport settlement forecast by applying the grey forecast model is good.

(2) It is necessary to conduct an accuracy test when carrying out a high-fill airport settlement forecast by using the grey forecast model and the residual error can be revised if the accuracy is not inadequate.

## Acknowledgements

This work was financially supported by the Open Fund Program of Digital Land Key Laboratory, Jiangxi Province (DLLJ201304)

## References

[1] Li Wang,Shuangcheng Zhang, Yahong Li, Journal of XI'an University of Science and Technology, Vol. 3(2005), p. 328-332. In Chinese.

[2] Julong Deng, Basic Approach of Grey System, Huazhong University of Science and Technology Press (1987). In Chinese.

[3] Sifeng Liu, Yaoguo Dang, et al., Grey System Theory and Its Application, Science Press (2004). In Chinese.

[4] Hongyuan Fu, Forecast of Expressway Subgrade Settlement and Construction Control, China Communications Press (2007). In Chinese.

*Applied Mechanics and Materials Vols. 580-583 (2014) pp 2815-2819*
*© (2014) Trans Tech Publications, Switzerland*
*doi:10.4028/www.scientific.net/AMM.580-583.2815*

# Research and Extended of Semi-parametric Model Additional System Parameter

Youping WU [1, a], Chuntao WANG [1,b], Jiabang WANG [2,c]

[1] Nanchang University College of Science and Technology , Nanchang, Jiangxi, 330029, China

[2] Land Resources Planning Institute of Guangxi Zhuang Autonomous Region, Nanning, Guangxi, 530021, China

[a]tjwyp123@163.com, [b]150572482@qq.com, [c]373218966@qq.com

**Keywords:** System parameters. principle of penalized least square, semi-parametric model.

**Abstract.** In this paper, a new solution to the semi-parametric estimation of a mixed model additional system parameters was conducted to derive a calculation method of parameter adjustment at the model regularization matrix, and determine the estimation of parameters and non-parameters as well as the accuracy evaluation formula of the model. The effectiveness of the semi-parametric estimation method was demonstrated through simulation examples, and the semi-parametric model additional system parameters was further extended.

## Introduction

The way to reduce and eliminate the affect of system errors in high accuracy measurement is the main content to improve the adjustment result accuracy. Therefore, it appears to be very important to create a mathematic model that better conforms to the objective reality. The way that is commonly used at present is to regard system errors as model errors of the adjustment model, which are compensated by a function model or random model to reduce and eliminate their impact as a whole so as to ensure a high accuracy of the adjustment result; meanwhile, through estimation of system errors and hypothesis testing, as well as analysis and researches, there have been more understanding to the impact of system errors, followed by adjustment to the model, making it more accurate. This is the superiority of the adjustment processing system error and the intended objective [1]. The concrete methods include the following: parameter adjustment method additional system parameters, additional system power method, additional system parameters and system power method [2], and partial parameter weighting adjustment method [3]. The author puts forward a mixed model semi-parameter method additional the system parameters, and the acquired results are very close to those by the method provided in Reference [3].

## Semi-parameter Model Additional System Parameters

Only a small part of the system parameters in the issue of measurement are random quantities. Some can only be processed as non-random parameters because it is impossible to determine accurately the prior features though they can be regarded as random quantities, and most of the system parameters have random quantities. Additional the prior features of system parameters in the model can eliminate the potential inaccuracy in the model and improve the accuracy of the adjustment results, in fact, this is hard to achieve; therefore, this undoubtedly limits the application scope of the existing model, such as the adjustment model in Reference [1~3]. However, the signal in the semi-parameter model can be random quantities, partial random quantities or non-random quantities, which can be estimated only by the method of parameter estimation, without consideration of the statistical property. Therefore, the author introduced the idea of the semi-parameter model to create a new model, that is, an adjustment model that contains both non-random system parameters and random system parameters, the function model of which is:

$$L = BX + Y + \Delta \tag{1}$$

where $L$ is the observation value, $B$ is coefficient matrix, $X$ is adjustment main parameter vector, $Y$ is a signal, which can be a random quantity, partial random quantity or non-random quantity, $\Delta$ is noise, $\Delta \sim N(0, D_\Delta)$, $D_\Delta = \sigma_0^2 P^{-1}$; as in Reference [3], decomposed as follows: $Y = AS$, $S = \begin{bmatrix} S_1 \\ S_2 \end{bmatrix}$, $S_1$ is a non-random vector additional system parameters, $S_2$ is a random vector additional system parameters, $S_1$ is related to $S_2$ statistics, $Q_{SS} = \begin{pmatrix} Q_{S_1S_1} & Q_{S_1S_2} \\ Q_{S_2S_1} & Q_{S_2S_2} \end{pmatrix}$; $\underset{n\times u}{A} = [A_1 \quad A_2]$, $A_1$ and $A_2$ are the coefficient matrix of $S_1$ and $S_2$, respectively.

Then the formula (1) can be expressed as follows:

$$\underset{n\times 1}{L} = \underset{n\times t}{B}\ \underset{t\times 1}{X} + \underset{n\times u}{A}\ \underset{u\times 1}{S} + \Delta \tag{2}$$

Its corresponding error equation is:

$$V = B\hat{X} + A\hat{S} - L \tag{3}$$

(1) The Estimated Solution of the Semi-parameter Model

We can solve $\underset{n\times u}{A}\ \underset{u\times 1}{S}$ in formula (3) by taking it as a non-parameter component and construct function according to the estimated criterion of penalized least square principle by using the idea of semi-parameter model:

$$\Phi = V^T PV + \alpha \hat{S}^T R\hat{S} + 2K^T (B\hat{X} + A\hat{S} - L - V) \tag{4}$$

Where $R$ is an appropriately given normalized matrix, $\alpha$ is a given smooth factor, and $K$ is Lagrange constant.

Deriving from formula (2), let $\frac{\partial \Phi}{\partial V} = 0, \frac{\partial \Phi}{\partial \hat{S}} = 0, \frac{\partial \Phi}{\partial \hat{X}} = 0$, the following equations are obtained:

$$PV = K \tag{5}$$

$$\alpha R\hat{S} + A^T K = 0 \tag{6}$$

$$B^T K = 0 \tag{7}$$

Uniting formula (3), (5), (6) and (7), the estimated solution of the semi-parameter model is obtained:

$$\begin{cases} \hat{S} = (A^T PA + \alpha R)^{-1} A^T P(L - B\hat{X}) \\ \hat{X} = (B^T P(I - G)B)B^T P(I - G)L \\ G = A(A^T PA + \alpha R)^{-1} A^T P \end{cases} \tag{8}$$

Then the estimated valve of the observation value $L$:

$$\begin{aligned} \hat{L} &= B\hat{X} + A\hat{S} \\ &= B\hat{X} + G(L - B\hat{X}) \\ &= ((I - G)B(B^T P(I - G)B)^{-1} B^T P(I - G) + G)L \\ &\cong U(\alpha)L \end{aligned} \tag{9}$$

Where, $U(\alpha) = (I - G)B(B^T P(I - G)B)^{-1} B^T P(I - G) + G$, $U(\alpha)$ is hat matrix.

The correction value $V$:

$$\begin{aligned} V &= B\hat{X} + A\hat{S} - L \\ &= \hat{L} - L \\ &= (U(\alpha) - I)L \end{aligned} \tag{10}$$

In this way, we can acquire the sole solution of $\hat{X}, \hat{S}$ by selecting appropriate $\alpha, R$ according to the actual condition, and then obtain $\hat{L}, V$ value. When the normalized matrix $R$ is positively defined, we can separate the non-parameter component and parameter component from the observed value to improve the accuracy of the model.

(2) Accuracy Assessment of Semi-parameter Model

Variance matrix of $\hat{X}$:

$$D_{\hat{X}} = G_1 D_{LL} G_1^T = G_1 D_\Delta G_1^T$$
$$G_1 = (B^T P(I-G)B)^{-1} B^T P(I-G) \tag{11}$$

Variance matrix of $\hat{S}$:

$$D_{\hat{S}} = G_2 D_{LL} G_2^T = G_2 D_\Delta G_2^T$$
$$G_2 = (A^T PA + \alpha R)^{-1} A^T P(L - B(B^T P(I-G)B)^{-1} B^T P(I-G)L \tag{12}$$

Variance matrix of $V$:

$$D_V = (U(\alpha)-I)D_{LL}(U(\alpha)-I)^T = (U(\alpha)-I)D_\Delta(U(\alpha)-I)^T \tag{13}$$

Variance matrix of $\hat{\sigma}_0$:

$$\hat{\sigma}_0^2 = \frac{V^T PV}{n - tr(U(\alpha))} \tag{14}$$

Formulas (8) ~ (14) are the adjustment formulas of semi-parameter model additional system parameters.

**Simulation Examples**

Assuming the observation equation is: $\underset{n\times 1}{L} = \underset{n\times t}{B}\ \underset{t\times 1}{X} + \underset{u_1\times 1}{S_1} + \underset{u_2\times 1}{S_2} + \Delta$, in which

$$BX = \begin{pmatrix} 1 & x_1 - \bar{x} & y_1 - \bar{y} \\ 1 & x_2 - \bar{x} & y_2 - \bar{y} \\ \text{L} & \text{L} & \text{L} \\ 1 & x_n - \bar{x} & y_n - \bar{y} \end{pmatrix} \begin{pmatrix} a_0 \\ a_1 \\ a_2 \end{pmatrix} \tag{15}$$

Where $\bar{x}, \bar{y}$ represent the average value of the observation point coordinate, respectively, $\alpha_0$, $\alpha_1$ and $\alpha_2$ are the parameters to be determined in the function, that is, the adjustment main parameter vector $X = \begin{pmatrix} a_0 \\ a_1 \\ a_2 \end{pmatrix}$. $A_1 = A_2 = I$, $P_1^{'}$ and $P_2^{'}$ are non-random system parameters $S_1$, $P_1 \sim P_4$ are random system parameters, the observation value $L$ of the six observation points of $S_2$, $P_1 \sim P_4$, $P_1^{'} \sim P_2^{'}$ and their plane coordinates $x_i, y_i$ are shown in Table 1, and the variance of the observation error (noise) is $D_\Delta = (0.03)^2 I$. Try to calculate the estimated value of $P_1 \sim P_4, P_1^{'} \sim P_2^{'}$.

Table 1: The observation value $L$ of the six observation points $P_1 \sim P_4$, $P_1^{'} \sim P_2^{'}$ and their plane positions.

| Number of the Point | $L[m]$ | $x[m]$ | $y[m]$ |
|---|---|---|---|
| $P_1$ | -0.55 | +6.40 | +4.80 |
| $P_2$ | -0.23 | +4.40 | +4.00 |
| $P_3$ | +0.58 | +1.40 | +1.40 |
| $P_4$ | -1.80 | +6.20 | +1.80 |
| $P_1^{'}$ | | +5.00 | +3.00 |
| $P_2^{'}$ | | +4.60 | +3.00 |

(1) Solution Steps of Semi-parameter Method:

Selection of regular matrix $R$:

$R=(s_{ij})_{n\times n}$, $s_{ij}=\left|t_i-t_j\right|$ is used, where $t$ represents the plane coordinate $(x,y)$, and the distance

$R=\begin{bmatrix}0 & 2.15 & 6.05 & 3.01\\ 2.15 & 0 & 3.97 & 2.84\\ 6.05 & 3.97 & 0 & 4.82\\ 3.01 & 2.84 & 4.82 & 0\end{bmatrix}$ is obtained.

Selection of smooth factor $\alpha$:

By using generalized cross check method $GCV(\alpha)=n^{-1}\sum_{i=1}^{n}(\frac{L_i-\hat{L}_i}{1-n^{-1}tr(U(\alpha))})^2=\min$, $\alpha=0.4$ is found.

Solution of the estimated value:

According to the data given by Table 1, we find from formula (15),

$B=\begin{bmatrix}1 & +1.8 & +1.8\\ 1 & -0.2 & +1.0\\ 1 & -3.2 & -1.6\\ 1 & +1.6 & -1.2\end{bmatrix}$ is found.

From formula (8), we can obtain:

$\hat{X}=(-0.4114,-0.5011,0.3838)^T,\hat{S}_1=(0.0701,0.1346,-0.2923,-0.1219)^T,\hat{S}_2=(-0.1911,-0.2036)^T$

(2) Weighted Adjustment Method of Some Parameters

The idea of solution in Reference [3] is to find the solution by using the weighted adjustment of some parameters, and solve the simulation examples of formula (7) ~ (12) in Reference [3] to obtain the following results (only the calculation results are listed due to space limitation): $\hat{X}=(-0.4109,-0.5013,0.3847)^T,\hat{S}_1=(0.0706,0.1361,-0.2926,-0.1215)^T,\hat{S}_2=(-0.1908,-0.2041)^T$

By comparing the solution results of the two methods, we find that the estimation results of the two methods are very close to each other.

**Semi-parameter Model Extension Additional System Parameters**

Conclusions identical to those in Reference [3] can be drawn by analyzing model (2),

(1) When $S_1=0$, that is, when the model contains only random system parameters, the model becomes a collocation model $\underset{n\times 1}{L}=\underset{n\times t}{B}\underset{t\times 1}{X}+\underset{n\times u_2}{A_2}\underset{u_2\times 1}{S_2}+\Delta$, the solution of which is:

$$\begin{cases}\hat{S}=S_2=(A^TPA+\alpha R)^{-1}A_2P(L-B\hat{X})\\ \hat{X}=(B^TP(I-G)B)B^TP(I-G)L\end{cases}$$

The adjustment principle of collocation model is: $V^TPV+S_2^T\sum_{S_2}^{-1}S_2=\min$. In a semi-parameter model, if the covariance matrix of the signal is known, then a normalized matrix $R=\sum_{S_2}^{-1}$ is selected, at this moment, the adjustment principle of the semi-parameter model is : $V^TPV+\alpha S_2^T\sum_{S_2}^{-1}S_2=\min$, when the smooth factor $\alpha=1$, the semi-parameter model is equivalent to the collocation model, which shows that the semi-parameter model includes the collocation model[6] .

(2) When $S_1 = 0$, $E(S_2) = 0$ and $S_2$ can not be expressed in the function model, the function model becomes: $\underset{n\times 1}{L} = \underset{n\times t}{B}\ \underset{t\times 1}{X} + +\Delta$, and the adjustment principle is $V^T PV = \min$.

(3) When $S_1 \neq 0$, and $S_2$ can not be expressed in the function model, or when $S_2 = 0$, or $A_2 = 0$, the function model becomes: $\underset{n\times 1}{L} = \underset{n\times t}{B}\ \underset{t\times 1}{X} + \underset{n\times u_1}{A_1}\ \underset{u_1\times 1}{S_1} + \Delta$, and the adjustment principle is: $V^T PV + \alpha \hat{S}_1^T R \hat{S}_1 = \min$.

## Conclusions

Semi-parametric estimation of a mixed model additional system parameters is conducted to derive a calculation method of parameter adjustment at the model regularization matrix, and determine the estimation of parameters and non-parameters and the accuracy evaluation formula of the model; the effectiveness of the semi-parametric estimation method is demonstrated through simulation examples; and the semi-parametric model additional system parameters is further extended. It can be explained that the semi-parametric model has the same results in many aspects with the mixed model put forward in reference [3].

## Acknowledgements

This work was financially supported by the Open Fund Program of Digital Land Key Laboratory, Jiangxi Province (DLLJ201304)

## References

[1] Genxiang Chai, Shengyan Hong, Semi-parameter Model, Anhui Education Press, Hefei(1995), In Chinese.

[2] Benzao Tao, et al, Journal of Institute of Surveying and Mapping, Vol. 19 (2002), p. 79-81. In Chinese.

[3] Qingli Liu, et al, Journal of Institute of Surveying and Mapping, Vol. 21(1) (2004), p. 5-7. In Chinese.

[4] Xizang Cui, et al, Generalized Measurement Adjustment (New Edition), Wuhan Technical University of Surveying and Mapping Press, Wuhan(2001). In Chinese.

[5] Xiong Pan, Estimation Theory of Semi-parametric Theory and Its Application Research, Wuhan University Press, Wuhan, (2005), In Chinese.

[6] Zhenjie Wang, et al, Bulletin of Surveying and Mapping, Vol. 9 (2004), p. 4-6. In Chinese.

*Applied Mechanics and Materials Vols. 580-583 (2014) pp 2820-2823*
*© (2014) Trans Tech Publications, Switzerland*
*doi:10.4028/www.scientific.net/AMM.580-583.2820*

# Research on Control Methods of Measuring Super High-rise Buildings

Xuyang Xie

Sichuan College of Architectural Technology, Deyang, Sichuan, 618000,china

10001858@qq.com

**Keywords:** control points, control net, measuring, total station, setting

**Abstract:** This paper took Guangzhou New TV Tower as an example to introduce how to ensure the systematicness and controllability of vertical measurement through the control survey in the process of constructing the high-rise buildings, how to ensure the unity of the each axis system in monomer construction and unity of the whole structure, providing a reference basis for similar projects.

## Project Features

This project is Guangzhou New TV Tower located in the bank of the Pearl River, with a structural height of 610m, and slender tower structures, the structures are prone to shake due to the impact of wind load in the process of construction; The exterior steel frame tube steel column is tilted in three dimensional space, in addition to 3D point positioning, it should still be consider the impact of rotational components; The control requirements of measuring transmission cumulative error is high at the top of the structure and floor structures are irregular, the visibility conditions for measuring are poor.

## Settings of Surveying Control Network

### 2.1 Layout of Plane surveying control network

Combined with the characteristics of the engineering, the three-level control network is set up in the measuring plane control network of the engineering according to the survey grid level and specific application in different parts of this engineering.

#### 2.1.1 First-level GPS Plane Control Network

The first-level control network is set up in the stable and reliable site far away from the construction site, acting as the role of the overall control. The first-level measuring plane control network which is composed of five external locus of control uses the GPS static technology for observation, assisting the high-precision total station for review.

As for the external locus of control, the stable ground or the roof of the building with the age of more than 5 years and height of 50m below is selected for setting observation pillars or stations. Nearby the point location, there is no obstacle above 15° elevation angle, with broad vision; the point location should be far away from the wireless launch station, high-voltage power lines and other interference sources.

As shown in Fig 1, 5 points are laid out in the first-level GPS point. The observation pillar must be built on the control point. The forcible centering device is installed on the top of the pillar, so as to improve the accuracy of plane control, to reduce the error of centration, for the convenience of construction layout. The forcible centering basal disc is laid out on the surface of the pillar, and is connected to the instrument base through a center screw.

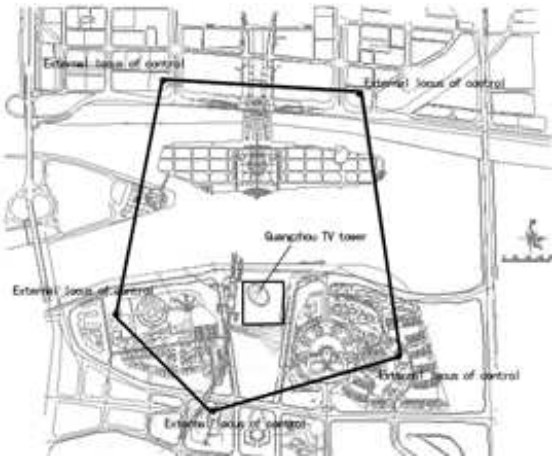


Fig1 Level 1 measuring plane control points arrangement

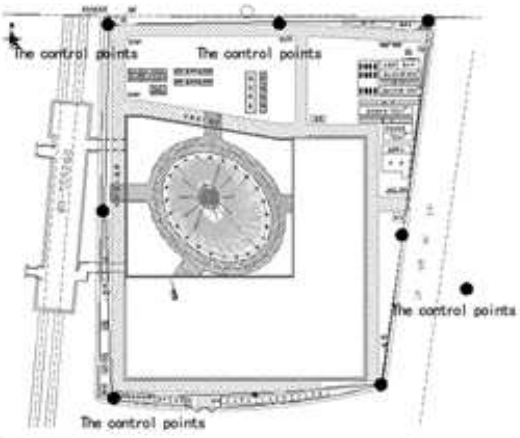


Fig2 Level 2 measuring plane control points arrangement

**2.1.2 Secondary-level Plane Control Network**

The secondary-level control network is used to provide a benchmark for the recovery of the lower-level control network which is likely to be damaged. At the same time, the control point is also directly used in this control network to measure important or critical procedures. Its establishment is based on the first-level control network. The secondary-level control network should be set up around one stable side of the site road of the project, and the convenience of use should be taken in account. The secondary-level network is set as the third-level closed traverse network. The measurement personnel should make an on-the-spot survey before the points are laid out, and data should be rigorously adjusted after field measurement, as shown in Fig.2 Schematic Diagram for Secondary-level Plane Control Network.

**2.1.3 Third-level Control Network**

The third-level control network is laid out on the foundation slab, and is surveyed according to the standard of the first-level square grid. It is primarily used for the measurement of underground structure construction phase, having the nature of short-term use. The use of this control network should be adjusted at any time according to the settlement and deformation in the construction phase. The operating conditions of the engineering are changed greatly, and the third-level control network is laid out within the site and easy to be damaged by the construction. In the process of actual measurement, therefore, besides the real-time adjustment is required in the above cases, the layout position of the network should be adjusted according to the construction situation. The network layout depends on the superior control network. On the ±0.000 floor, the vertical control points of the TV tower and the secondary-level control network are measured simultaneously. As a carrier, the core tube transfers it vertically, with layer-upon-layer closure, As shown in fig 3.

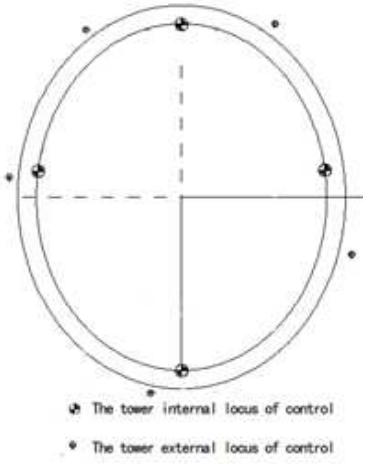


Fig3 Level 3 measuring plane control points arrangement

### 2.2 Layout of Elevation Surveying Control Network

The elevation surveying control network is to provide a stable, unified elevation reference system for long-term construction of the engineering structure. The elevation value is determined by the urban elevation system. In this engineering, the secondary-level elevation control network is set up: the first-level elevation control network is set up in the reliable place outside the construction site. Within the construction site, the secondary-level elevation control network is laid out.

## 3 Construction Measuring Methods

### 3.1 Measuring Methods for Underground Construction Phase

#### 3.1.1 Layout of Plane Control Axis

The down-top construction method is used for basement structure of the TV tower, and the outer control method is used for the plane control. The specific information is as follows:

1) The secondary-level plane control points are used, 2 to 3 temporary transfer stations are set up nearby the foundation pit as a starting point. The temporary transfer stations should be reviewed. If no error, the next step is done;

2) The reviewed temporary transfer stations are used for lofting the construction control axis and for projecting the measurement to the base under-layer.

3) The instrument is moved to Point C on the under-layer for setting a station, and the coordinate method is used for precision review of the interrelationship between control points. Later, the construction control points on the under-layer are used for back vision of each point on the same axis, and a construction chalk line is marked on the under-layer.

#### 3.1.2 Transmission of Elevation Control Points

1) Based on the first-level standard control points, a precise level and the third-class leveling method are adopted, and the elevation is led to the temporary leveling point on the edge of the foundation pit.

2) The elevation for vertical transmission is searched on the edge of the foundation pit. A fixed support is erected, and one end of a steel rule is fixed on the hook of the support, with a heavy hammer for hanging.

3) Two levels are used for the simultaneous measurement up and down. The level above transmits the elevation of the temporary leveling point to the steel rule. The level below transmits the elevation on the steel rule to the construction layer.

### 3.2 Core Tube Control Survey

The core tube of the TV tower is 436.75m in height, and the thickness of its outer wall is changing. The horizontal structure lags behind the construction in the condition of construction. At the same time, controls the vertical deformation of the structure, leading to difficulties in the measurement location.

#### 3.2.1 Measurement of Floor Plane Control Axis

1) A location is calibrated on the internal wall of the core tube (as shown in Fig.3 Internal Locus of Control) to fix the layout of the forced centering platform. The upward projection of integral lifting the steel die is used to fix the layout of the control point receiving platform in place.

2) The total station is set as a station on the monomer control point of the core tube, to measure the center coordinates of the forced platform.

3) The zenith gauge station is set as a station on the force platform, and the plane position of the forced platform center is vertically projected to the control point receiving platform.

4) The above steps are repeated, so that the control points of all forced platform can be vertically projected to the control point receiving platform.

#### 3.2.2 Floor Elevation Control Survey

1) The total station is set as a station on the forced platform, and the sight line of the lens core is adjusted to be vertical.

2) The ranging function is used to lead the ground elevation to the receiving platform.

3) A level is used to transmit the receiving platform elevation to the required position in the construction. It will be put into construction use after reviewed by the supervisor.

### 3.2.3 Floor Control Network Migration

The zenith method used in the measurement of high-rise buildings requires that with the rise of the structure, the benchmark control network on the ±0.000 floor is migrated vertically. The measurement practice of super high-rise buildings, such as Jin Mao Tower and Shimao International Plaza in Shanghai, shows that the building top generates the continuous, slow vertical deformation of the structure in the construction process, and the deformation range increases with the rise of the height. For reasons such as limited instrument resolution capability, the floor control network cannot but be migrated vertically. The migration process will certainly cause the precision losses, thus, the floor control network migration is set up at three times for the engineering. The specific settings are as follows:

1) The total station is set as a station on the monomer control point of the ±0.000 floor, and the control points on the ground are converted to the forced platform, so that each forced platform constitutes the control sub-network of the core tube. The migration mainly refers to the migration of this control network.

2) The layout of the control network migration (conversion) layer is carried out when the core tube is constructed up to 100m, 200m and 300m. Before migration, the control network of the main building should be reviewed to eliminate the displacement of control points caused by structural deformation, etc.

3) The migration of the control network should be carefully operated. After completion of migration, a strict re-survey should be implemented to ensure no error.

## Conclusions

In the construction of this engineering, the role of advanced measuring techniques gives full play in the special-shaped super high-rise buildings construction. In the whole construction process, therefore, the spatial position of the buildings is within a controlled range, to ensure the spatial localization timely, accurate and reasonable, to satisfy the requirements for construction quality and schedule.

## References

[1] Yuan Chunmei. To explore the characteristics of the high-rise building construction and new progress [J]. Journal of building knowledge (academic publication), 2012, (B12)

[2] Xu Guangxia Liu Duo kay, Liu Shaokun. Introduction to high-rise building construction method [J]. Journal of architecture and budget, 2007, (2)

[3] Ye Jingwei. Introduction to construction engineering surveying method and actual application [J]. Journal of urban construction, 2010, (24)

*Applied Mechanics and Materials Vols. 580-583 (2014) pp 2824-2827*
*© (2014) Trans Tech Publications, Switzerland*
*doi:10.4028/www.scientific.net/AMM.580-583.2824*

# Correction of atmospheric effect in EnviSAT ASAR repeat-pass interferometry with MODIS water vapor

Guangtong Sun[1, a], Ping Song[1,b], and Xiaoyang Liu[1,c]

[1]Institute of Disaster Prevention, Sanhe Hebei, China, 065201

[a]sun-0312@163.com, [b]ping_0976@163.com, [c]liuxiaoyang1209@163.com

**Keywords:** InSAR, MODIS, ASAR, atmospheric correction, surface deformation

**Abstract:** The atmospheric phase delay due to tropospheric water vapor has been one of the major limitations for the application of high precision repeat pass InSAR. In this paper, we present the atmospheric correction methods and key technology for ASAR interferograms with MODIS integrated water vapor data, then, conduct the atmospheric corrections using ASAR interferometric pair over the Taiyuan region as examples. The experimental results show that the MODIS\ASAR atmospheric correction method can greatly improve the quality of interferogram, and the deformation inversion accuracy can be significantly improved, verify the necessity and reliability of MODIS and ASAR data fusion for obtaining information of surface deformation.

## Introduction

Synthetic Aperture Radar Interferometry（InSAR）has been a widely used geodetic technique for measuring the Earth's surface, especially for mapping the Earth's topography and deformations due to its all-weather and day-and-night imaging capability, wide spatial coverage, fine resolution, and high measurement accuracy. However, like other astronomical and space geodetic techniques, InSAR also has its shortcomings. One of the most intractable problems is the effect of the atmosphere, especially the atmospheric water vapor. The radar signal through the atmosphere due to the distribution of temporal changes in the atmosphere, the atmospheric phase delay is unavoidable, thereby affecting the measurement accuracy of the topographic measurement and deformation. Therefore, the effect of atmospheric must be considered when high-precision interferometry.

Massonnet first identified such effects, he first noticed the impact of atmospheric interference fringes in InSAR interferogram in the 1992 Landers earthquake research (Massonnet et al. 1994). Zebker research on SIR-C/X-SAR (Zebker et al. 1997), the results showed that spatial and temporal changes of 20% in the relative humidity of the troposphere could lead up to 10 to 14cm errors in the measured ground deformations and 80 to 290m errors in derived topographic maps for baselines ranging from 100 m to 400m. Since then, some intensive research has been carried out aiming to better understand and mitigate the effects and made a series of achievements. Currently, InSAR atmospheric correction methods can be roughly divided into two categories internationally, the first category is the removal of atmospheric effects based on the data itself features, such as linear correction method (Massonnet et al. 1995), stochastic filtering method (Crosetto et al. 2002), stacking method (Emardson et al. 2003) and timing analysis (Ferretti et al. 2000); the second category based on an external independent data, calculated by modeling the atmospheric effects , such as meteorological information modeling method (Delacourt et al. 1998), numerical weather prediction model method (Foster et al. 2006), GPS measurements (Li et al. 2006) and satellite remote sensing measurements of water vapor (Li et al. 2009,) .The distribution of worldwide vapor can be effectively measured using the existing space-based monitoring systems (such as MODIS, MERIS, FY, etc), so the combined of these satellite remote sensing water vapor data and sparse GPS data is a direction in InSAR atmospheric correction.

The NASA Moderate Resolution Imaging Spectroradiometer(MODIS) is a key instrument on the Terra satellites, and through the descending node equator at around 10:30 am local time, so MODIS images acquired within half an hour of ENVISAT satellites, having a good time consistency. It's

feasible to carry out research on InSAR atmospheric correction methods based on MODIS water vapor data. This paper attempts to correct atmospheric effects in Taiyuan ASAR interferogram using MODIS water vapor data, thereby to evaluate the accuracy and reliability of using MODIS water vapor data to correct InSAR atmospheric effects.

## Integration of ASAR interferometry with MODIS water vapour product

### Overview of the approach

This article will use the MODIS water vapor product MOD05_L2 to correct the atmospheric effects of ASAR interferogram. For the purpose of InSAR atmospheric correction, MODIS precipitable water vapor amount(designated hereafter as MODIS-PWV) needs to be converted into zenith wet delay(ZWD) using the formula (1):

$$ZWD = \left[ 10^{-6} \rho_w \cdot (k' + \frac{k}{T_M}) \cdot R_v \right] \cdot PWV = \Pi \cdot PWV \quad (1)$$

Where $k'$ and $k$ is the refraction constant, $\rho_w$ is the density of liquid water, $T_M$ is the mean temperature of the column containing the water vapour, $R_v$ is a specific atmosphere constant. The conversion factor of $\Pi$ usually varies from 6.0 to 6.5, approximately equal to 6.2.

The spatial resolution and coordinate systems are different between MODIS and ASAR, we need to apply co-registration between ZWD and SAR interferogram firstly. Zenith Path Delay Difference (ZPDDM) can be produced by differencing the ZWD values from two different water vapor fields, and then converted into the phase delay amount in the gaze direction. To achieve the purpose of atmospheric correction, the phase delay amount is subtracted from the calculated difference ASAR. The flow chart of MODIS / ASAR atmospheric correction method is shown in Fig.1.

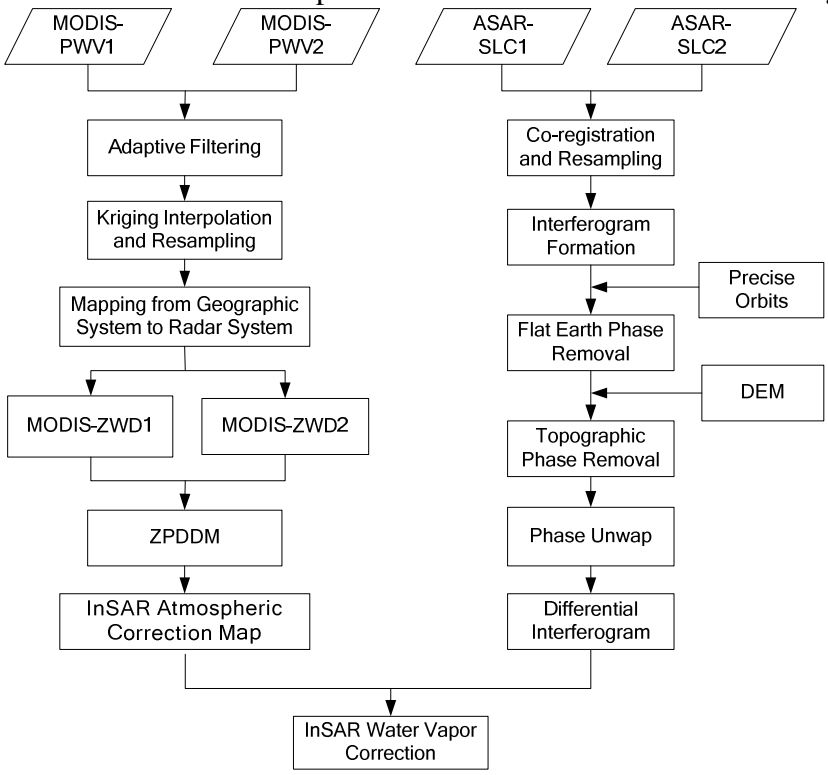


Fig.1 Flowchart of MODIS\ASAR atmospheric correction method

## MODIS water vapor product and process

MODIS water vapor is sensitive to the presence of clouds, when the cloud is present, the calculated value of water vapor is undervalued due to sunlight reflected, so only the water vapor retrievals under cloud-free conditions can be used correct the atmospheric effect, which means the MODIS-PWV

retrieved under cloudy conditions should be corrected first. In order to fill the data vulnerability caused by the presence of cloud, taking into account the large differences between the MODIS water vapor data and ASAR image in resolution, MODIS-PWV need to be interpolated. In this article, we use the Kriging interpolation method.

To properly reduce water vapour effects on interferograms, the step of mapping ZWD from the geographic coordinate system to the radar coordinate system is crucial. Using information from a precise DEM and the satellite orbit, a radar image can be simulated so that its amplitude depends on the local topographic slope and the SAR geometry. As part of this SAR image simulation, a mapping table is generated, mapping each geographic location to the corresponding range-azimuth coordinates. Then the parameters of an affine transformation between the simulated and actual SAR images can be calculated by fitting offsets determined by using a cross-correlation matching algorithm to adjust for any unmodelled geometric parameters. With the simulation mapping table and affine transformation parameters, the ZWD can be mapped from the geographic coordinate system to the SAR coordinate system. This matching method can obtain 1 SAR pixel, 20 m approximately, bearing in mind that the spatial resolution of the ZWD is 1 km, the uncertainty due to matching errors can be neglected.

In order to obtain InSAR atmospheric delay correction phase, ZPDDM need to be converted to phase information, and mapped to the radar line of sight direction(LOS) using the formula (2). The process of InSAR atmospheric correction means removing the calculated atmospheric delay correction phase form ASAR interferometric phase.

$$\Delta\phi_{ifm_atm} = \Delta\phi_{atm1} - \Delta\phi_{atm2} = \frac{4\pi}{\lambda}\frac{ZPDDM}{\cos\theta} \qquad (2)$$

where $\lambda$ is the wavelength of ASAR, and $\theta$ is angle of incidence of radar signal.

## Experimental results

In this paper, ASAR images of July 17, 2005 and August 21, 2005 and the corresponding MODIS water vapor were selected in Taiyuan City. Since the two ASAR image were acquired in 35 days interval, in so short period, there is almost no surface deformation between the two image acquisitions. So the main case of the phase variation may be the tropospheric water vapor. Fig.2 show a comparison between the original interferogram and the interferogram after tropospheric water vapor correction.

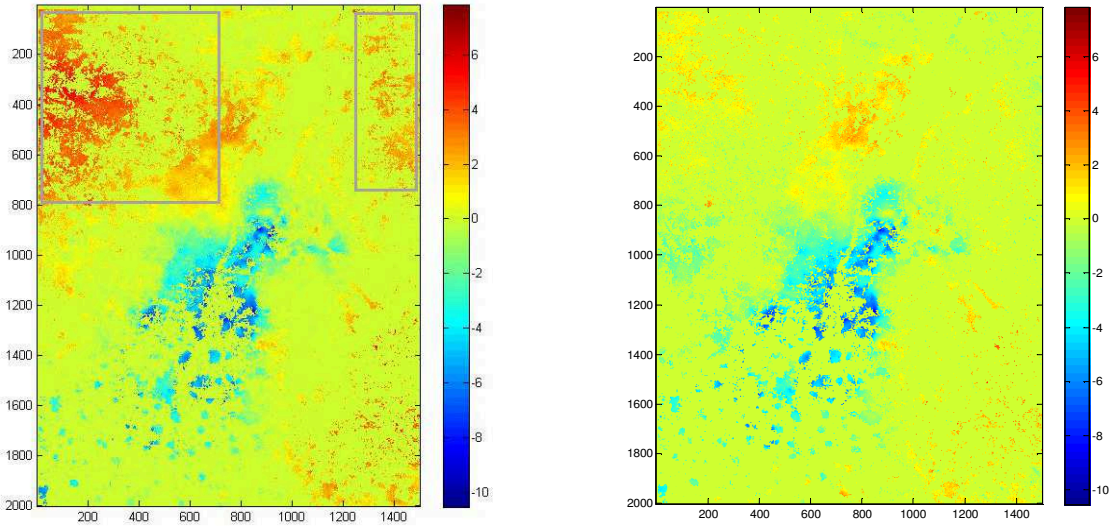


Fig. 2 The interferogram before atmospheric correction (left) and after atmospheric correction (right)

As can be seen from the figure2, the atmospheric effects in original interferogram(block circle) is obvious. After atmospheric correction, the atmospheric effects are significantly reduced. To quantify the effect of correction using a standard deviation of the interference pattern as evaluation criteria, the

standard deviation is 2.88rad before correction, while after correction, the standard deviation reduced to 2.18rad, improving the quality of 24.3% for the interferogram.

Meanwhile, in order to better validate the effect, we made a comparion between the leveling data and InSAR monitoring results before and after atmospheric correction, the result showed that InSAR monitoring results after atmospheric correction were close to the leveling data, and the RMS difference between leveling data and InSAR decreased form 1.40 cm to 1.08 cm, the degree of improvement reached 22.1%, confirming the correction of atmospheric water vapor based on MODIS data validity and reliability.

## Summary

Studying the atmospheric influence on InSAR has become an important field of research. In this paper, MODIS water vapor data was applied to reduce the atmospheric effect on ASAR interferogram. After correction using MODIS water vapor, InSAR deformation measured accuracy has been greatly improved, compared with the same period of leveing data, the RMS differences reduced from 1.40 cm to 1.08 cm, the degree of improvement reached 22.1%. But we should also note that, even after atmospheric correction, InSAR measurements still have a gap comparing with the measured data that may exist many other factors. So in our further study, more operational and accurate technique will be proposed.

## Acknowledgements

This work was financially supported by the Youth Science Fund for Disaster Prevention and Reduction (201202), Teachers' Scientific Research Fund of China Earthquake Administration (20120102) and Technical Services-SAR image precision land cover classification.

## References

[1] Massonnet D, Feigl K, Rossi M and Adragna F. Nature, 1994, 369: 227-230.

[2] Zebker H A, Rosen P A and Hensley S. Journal of Geophysical Research, 1997, 102(B4), 7547-7563.

[3] Massonnet D and Feigl K L. Discrimination of geophysical phenomena in satellite radar interferograms[J]. Geophysical Research Letters, 1995, 22(12):1537-1540.

[4] Crosetto M, Tscherning C C, Crippa B, et al. Geophysical Research Letters, 2002, 29 (9): 26.

[5] Emardson T R, Simons M and Webb H F. Journal of Geophysical Research, 2003, 108 (B5): 2231.

[6] Ferretti A, Prati C and Rocca F. IEEE Transactions on Geoscience and Remote Sensing, 2000, 38(5):2 202-2 212.

[7] Delacourt C, Briole P and Achache J. Geophysical Research Letters, 1998, 25 (15):2849-2852.

[8] Foster J, Brooks B, Cherubini T, et al. Geophysical Research Letters, 2006, 33, L16304.

[9] Li Z H, Fielding E J, Cross P, et al. Journal of Geophysical Research, 2006, 111 (B2):404.

[10] Li Z H, Fielding E J, Cross P, et al. International Journal of Remote Sensing, 2009, 30:3343-3363.

*Applied Mechanics and Materials Vols. 580-583 (2014) pp 2828-2832*
*© (2014) Trans Tech Publications, Switzerland*
*doi:10.4028/www.scientific.net/AMM.580-583.2828*

# Analysis of Underground Space Azimuth Measuring and Data Processing in A Tunnel

Tao Wang[1,2,a], Hurong Duan[3,b] , Liutao Jiang[1,c] ,Shun Liu[1,d]

[1]Department of Surveying and Mapping, Shaanxi Railway Institute, Weinan, PR China

[2]College of Geology Engineering and Geomatics, Chang'an University, Xi'an, PR China

[3] College of Surveying and Mapping, Xi'an University of Science and Technology, Xi'an, PR China

[a]survey-tao@sohu.com, [b]duanhurong@sina.com, [c]53201070@163.com, [d]56048828@qq.com

**Keywords:** GAT magnetic suspension gyro station, Tunnel, Gyro-orientation, Instrumental constant.

**Abstract.** In this paper, we studied high accuracy azimuth measuring on improving the precision of traverse azimuth from the perspective of transfixion measurement error in a tunnel project. On the basis of a feasible scheme using Gyro Total Station measurement is given. Data processing theory and method are also introduced with a successful tunnel transfixion case. The transfixion results show that the instrument constant measurement precision is 3.7", baseline coordinates azimuth measurement accuracy is 4.8" into tunnel, the final orientation coordinate azimuth value and traverse measurement values differ is 11", to guide the construction of the gyro orientation with survey results achieved tunnel through smoothly.

## Introduction

Since the middle of 20th century, underground engineering survey has been rapid development. It has been widely used in underground military facilities, underground buildings, underground mining, sewers, underground highways, underground railway tunnel and cross-river tunnel[1]. Underground engineering survey played any other technique irreplaceable role, especially in the large tunnel through, underground engineering measurement is correct through a key technology. For a long time, precision traverse have been used in underground engineering of conventional measuring method, with extension of the engineering lead, a variety of error accumulation increases, then will affect the smoothly through underground engineering. Therefore, people often used the method of plus gyro azimuth measuring to determine the correct direction of underground traverse in underground engineering. The method of measuring not only reducing errors on initial direction through but also limits the accumulation of systematic errors. The method also can be on the traverse direction conduct checklist, thereby enhancing and improving the accuracy and reliability of underground traverse[2].

Based on the accuracy of better than ±5" high-precision measuring instruments azimuth orientation-GAT maglev Gyro Station, combined with a passenger line length of 10.8km tunnel directional gyro measurement project, carried out inside the cave, on the outside observer and adjustment, realize the precise localization of underground traverse. In azimuth directional data as an important reference data to guide the construction, the construction of other similar underground engineering measure to carry out has certain reference significance.

## A new type of gyro total station azimuth measurement principle

Unlike traditional gyro theodolite: GAT gyro total station is used for gyro north ontology and total station cooperate together to determine gyro orientation of any survey line. As shown in figure 1: the big circle represents maglev gyroscope horizontal circle, small circle represents the total station horizontal circle, O point is the gyroscope with total station public vertical axis. OT is find north direction of gyro, OM is gyro rotor axis, OL is total station zero horizontal circle direction, OC is total station sighting telescopes line direction of the target.

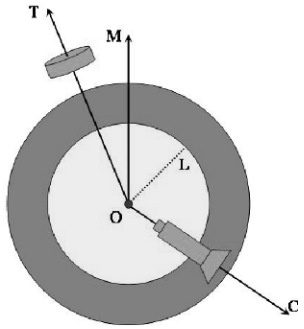


Figure 1 The diagram of GAT gyro total station orientation principle[3, 4]

In azimuth orientation process, the gyro north finder can use at first maglev constitute a pendulum of earth rotation angular velocity gyro sensitive northerly form found north of moment, the moment balance feedback method, the determination of the axis of the gyro angular momentum and astronomical north Angle, and gives the gyro find north direction and the gyro rotor axis Angle (mirror surface normal direction) $\angle TOM$ .

Then, the observer uses the total station observer sighting target direction, according to the direction of the measurement requirements, measure the angle $\angle LOC$ between the goal line and the total station horizontal direction dial zero bits. Thus,

$$\angle TOM + \angle MOL + \angle LOC + \Delta_I = A = \alpha + \gamma \tag{1}$$

In the formula (1), $\Delta_I$ means the instrument constant, $\alpha$ means a known coordinate azimuth survey line, $\gamma$ means convergence of meridian. This can be done by measuring direction of a known survey line and real meridian line direction $\alpha + \gamma$ comparison, to determine

$$\angle MOL + \Delta_I = \alpha + \gamma - \angle TOM - \angle LOC \tag{2}$$

As $\angle MOL + \Delta_I$ be written to $\Delta_I'$. The above measurement process in tunnel hole known online, main purpose is to obtain the instrument constant value. When the hole measurement, also need to measure the gyro find north direction of gyro motor shaft angle $\angle TOM'$; and hole closed line direction and the direction of the total station horizontal dial zero angle $\angle LOC'$ , this hole closed line of gyro directional results can be calculated according to the formula:

$$\alpha' = \angle TOM' + \angle LOC' + \Delta_I' - \gamma \tag{3}$$

## The new gyro total station measurement data processing

The orientation precision of gyro theodolite mainly gyroscopic azimuth error $m_T$ and a directional error $m_\alpha$ in measurement [5]. After the completion of all part of the surveyed area measurement work, first calculated instrument constants $K$ and the accuracy of measurement data according to the hole measurement data. Instrument constants calculated for each observation in the unit to calculate.

Measurements before and after the measurement outside the tunnel measuring the same number of rounds, the rounds are $n$. Let baseline $AB$ measurements outside the tunnel, and known coordinates azimuth is $\alpha_{AB}$ , point $A$ meridian convergence angle is $\gamma_A$ , and each observation angle measurements and gyroscopic measurements respectively are $L_i$ and $T_i$ (i = 1,2, ..., 2 $n$), then

$$K_i = \alpha_{AB} - (L_i + T_i + \gamma_A) \quad (i = 1, 2, \cdots, 2n) \tag{4}$$

Instrument constant $K$ is obtained by calculating the average formula (4). Instrument constant $K$ measuring precision of the calculation method and the azimuth angle and the gyroscope, same as follows

$$\sigma_K = \pm\sqrt{\frac{\sum V_i V_i}{2n-1}} \tag{5}$$

Among them $V_i = K_i - K$ （$i = 1, 2, \cdots, 2n$）。

Instrument constant measurement accuracy checklist meet the conditions, then start all measured baseline coordinates azimuth calculation, calculation formula is as follows:

$$\alpha_i = K + \overline{L_i} + \overline{T_i} + \gamma_i \tag{6}$$

According to the law of error propagation, the coordinate azimuth angle measurement accuracy using the following formula

$$\sigma_{\alpha i} = \pm\sqrt{\sigma_K^2 + \sigma_{\overline{Li}}^2 + \sigma_{\overline{Ti}}^2} \tag{7}$$

Meridian convergence angle according to the meridian convergence angle in geodetic calculation method to calculate, calculated by the geodetic coordinate $(L, B)$ plane meridian convergence angle $\gamma$ formula is:

$$\gamma = \sin B \cdot l + \frac{1}{3}\sin B\cos^2 B \cdot l^3(1 + 3\eta^2 + 2\eta^4) + \frac{1}{15}\sin B\cos^4 B \cdot l^5(2 - t^2) + o(l^5) \tag{8}$$

In Formula (8)： $t = \tan B, \eta = e' \cdot \cos^2 B$ ($e'$ is the second eccentricity)， $B$ is latitude， $l$ is longitude difference。

According to the formula (7), we can also estimate the azimuth angle of each side of the baseline coordinates precision. Assuming total station horizontal angle measured precision is ±2", and precision of gyroscope azimuth measurement is ±5 " in one observation set, all station total station and gyroscope observation three observation set. The constant measurement accuracy of instrument

$$\sigma_K = \pm\sqrt{\frac{5^2 + 2^2}{6}} = \pm 2.2'' \tag{9}$$

Inside the tunnel baseline coordinates azimuth angle measurement accuracy

$$\sigma_{\alpha i} = \pm\sqrt{2.2^2 + \frac{(2^2 + 5^2)}{3}} = \pm 3.8'' \tag{10}$$

## Analysis of azimuth directional and results in underground space

Selection of ground control network Y1→JQ1 two control points make the line of constant instrument calibration, due to limited space, the original observation data is not on this list. According to ground control point coordinate, calculation of line Y1→JQ1 coordinates azimuth and meridian convergence angle measurement site. Can be obtained from the formula $A = \alpha + \gamma$ a ground survey line Y1→JQ1 the true north azimuth

$$A_{Y1 \to JQ1} = 265^\circ 31' 02'' - 0^\circ 03' 47'' = 265^\circ 27' 15''$$

According to $A = T + \Delta$ combination with the ground of the gyro orientation, can be calculated gyro instrument constants, as shown in table 1.

Table 1 Constant of instrument calibration results

| Survey line | Gyro azimuth | True north azimuth | Instrumental constant | V | VV |
|---|---|---|---|---|---|
| Y1→JQ1 | 265°27′22″ | 265°27′15″ | -7″ | -4″ | 16″ |
| | 265°27′19″ | | -4″ | -1″ | 1″ |
| | 265°27′18″ | | -3″ | 0″ | 0″ |
| | 265°27′23″ | | -8″ | -5″ | 25″ |
| | | Average value | -5″ | ∑ | 42″ |
| Error in a measurement instrument constant: $m_\Delta = \pm\sqrt{\frac{[VV]}{n-1}} = \pm\sqrt{\frac{42}{4-1}} = \pm 3.7''$ | | Instrument constant or the most value of error: $M = \frac{m_\Delta}{\sqrt{n}} = \pm 1.8''$ | | | |

Inside traverse side azimuth measurement method and outside constant calibration is same in tunnel, limited space, underground traverse side direction measurement observation data is not in the list. The above calculated instrument constants, cooperate with directional gyro orientation, on the edge of the results, can get underground geographical azimuth, as shown in table 2.

Table 2 The traverse of tunnel hole azimuth measurement results

| Survey line | Gyro calculate azimuth | True north azimuth |
|---|---|---|
| Y11→Y10 | 276°26′55″ | 276°26′51″ |
| Y11→SY14 | 97°33′55″ | 97°33′51″ |
| Y11→Y13 | 96°53′38″ | 96°53′34″ |

According to the traverse point coordinate calculation every directional edge of coordinate azimuth and meridian convergence angle measurement site, as shown in table 3.

Table3 Coordinate azimuth Angle of directional edge

| Instrument station | Convergence of meridians | Sighting point | Gyro calculate azimuth |
|---|---|---|---|
| Y11 | -0°02′54 | Y10 | 276°29′45″ |
| | | SY14 | 97°36′45″ |
| | | Y13 | 96°56′28″ |

## Conclusions

Through the tunnel of underground space azimuth directional can draw the following conclusion:

1) High precision gyro orientation to get the coordinates of the azimuth Angle, compared with the original wire calculate the coordinates of the azimuth is as shown in table 4.

Table 4 Gyro orientation compared with traverse calculated results

| Instrument station | Sighting point | Gyro calculate azimuth | Traverse coordinates azimuth | Difference value |
|---|---|---|---|---|
| Y11 | Y10 | 276°29′45″ | 276°29′37″ | 8″ |
| | SY14 | 97°36′45″ | 97°36′36″ | 9″ |
| | Y13 | 96°56′28″ | 96°56′17″ | 11″ |

2) From the four rounds of the ground constant edge directional gyro measurements assessed in one observation set measurement error is 3.7 ", inside of tunnel the baseline measurement coordinate azimuth measurement accuracy of 4.8", which belongs to high-precision measurement results.

3) For Y11→Y10, Y11→SY14, Y11→Y13 traverse side, it is recommended to make appropriate reference to the outcome of the gyro directional orientation correction.

## Acknowledgements

This work was supported by the National Natural Science Foundation of China under Grant No. 41074006, No.41304013, Shaanxi Provincial Education Department under Grant No.12JK0798 and the Shaanxi Railway Institute Natural Science Foundation. The authors thanks Dr. Zhen SHI of Chang'an University for experimental assistance.

**References**

[1] J.X. ZHAO, K.Y. LV ,Y.J NIE. Development of Underground Project Surveying: Review and Prospect. Bulletin of Surveying and Mapping, 2006(10):51-52

[2] Q.Z HAN, H.S. GENG, Y. LI. The optimum place research of adding to survey the top-shaped azimuth angle in guide line survey of underground project. Journal of Northwest Agriculture and Forestry University of Science and Technology(Natural Science Edition), 2004. 12: 116-120

[3] Z.Q. YANG. System development and application of GAT high accuracy maglev gyro total station.Xi'an:Surveying and Spatial Information Research Institute of Chang'an University.2008

[4] Z. SHI, Z.Q. YANG, S. YANG, D.B. HUANG. The Research of a New Gyro Orientation Method and Some Relevant Issues Based on Circle Configuration. Bulletin of Surveying and Mapping, 2011(2):87-89

[5] W. CHEN, H.G. TANG, T. ZHANG, et al. Application of Total Station Gyroscope in Small Mine Transverse Survey. Zhongzhou Coal, 2009(8).35-37

*Applied Mechanics and Materials Vols. 580-583 (2014) pp 2833-2837*
*© (2014) Trans Tech Publications, Switzerland*
*doi:10.4028/www.scientific.net/AMM.580-583.2833*

# Study on Application of terrestrial 3D laser scanning technology in the calculation of the fine earthwork

Feng Xiao-gang[1,a] ,Li Meng[1,b] ,Liu Jing-xiu[1,c]

[1]Xi'an University of Architecture and Technology, School of Architecture , Building Research Institute survey , Xi'an 710055

[a]Fendao_ren@163.com, [b]Li-Meng@163.com, [c]Liu-Jingxiu@163.com,

**Keywords:** Terrestrial 3D laser scanning; earthwork; fine calculation;GPS RTK

**Abstract:** Supported by terrestrial 3D laser scanning technology, by using the GPS RTK technology as the verification. Explored the application of terrestrial 3D laser scanning technology in the calculation of fine earthwork, including the whole process from program design, pre-organization, field measurements applied to the calculation and submit of indoor operation results. In addition, Lanhaiwan project in xi'an of shannxi province was taken as a case to introduce detailed processes of fine earthwork calculation, The results show that the terrestrial 3D laser scanning technology can be well used for accurate measurement of the earthwork.

## Introduction

With the accelerating pace of urbanization, urban construction has become the core of the whole process of urbanization. Earthwork engineering involved in city construction projects, the size of earthwork not only related to the budget of earthwork excavation engineering, but also will affect the investment budget of the whole project. So, accurate calculation if earthwork has important economic significance and practical value on earthwork and the whole investment project.

Traditional earthwork field survey methods most are level measuring method, total station method or GPS RTK method. And traditional methods are measured by selecting feature points of different height, do measure and record to finish the field measurement. inner calculation usually by related software measured the coordinates of discrete points outside the industry as the foundation, in order to achieve the purpose of calculating the amount of earthwork through the establishment of related earthwork calculation model, usually depending on the actual situation and the multi-use method such as one or several sections , grid method , contour method, the average elevation method, region or irregular earthwork balance method of triangulation method .Since the study area to obtain the original data are characterized by discrete point -based , so the final calculation of earthwork accuracy often depends on obtaining accuracy and density characteristics of the study area the original area of the point of the point .Typically , the stacking surface of earth in the study area shape complexity, and actual measurement characteristics of the limited number of discrete points , resulting in the elevation part can not obtain or omitted to save costs and little change in the characteristics of human point, thus resulting in linear interpolation calculation model based earthwork a difference between the results obtained with the actual earthwork .In general, the larger the absolute amount of earthwork difference between the two is greater.Thus, if more accurate access to earthwork within the study area to provide accurate calculation of earthwork has become a key issue under urbanization earthwork calculations are to be solved.

The emergence of terrestrial 3D laser scanning technology to solve these problems has opened up a new way .3D laser scanning technology known as " Virtual replication technology (High definition Survey, HDS)", is one of today's most advanced measurement techniques .This article aims to 3D laser scanning technology as the basis to build massive point cloud data with high accuracy DEM model for the earthwork calculations, supported by means of GPS RTK to verify explore three-dimensional laser scanning technology in earthwork refined calculation of processes, including program design , pre organizations outside the industry Surveying and achievements within the industry consolidation and other related processes , and be verified by actual cases , with

a view to terrestrial 3D laser scanning technology provides a standard reference in the application process paradigm fine calculation of earthwork.

## 3D laser measuring principle and earthwork calculation mode

### 2.1 3D laser measuring principle

The main structure of the 3D laser scanner include: a high-speed precision laser ranging system, a set of guiding the laser reflection and reflector uniform angular velocity scan azimuth deflection controller, the elevation angle of deflection controller, data output processor , part of the instrument also has a built-in digital camera.The basic process is a three-dimensional laser scanner transmits a laser pulse transmitter signal , after the diffuse reflection surface , almost the same along the reverse path back to the receiver , the target can be calculated from the point P to the scanner S, control encoder Simultaneous measurement of each laser pulse observations horizontal scan angle α and vertical scanning angle observations β.Usually the laser scanning instrument defined coordinate system , X -axis in the transverse scan plane , Y -axis in the transverse direction perpendicular to the scanning plane and the X -axis , Z -axis perpendicular to the transverse scan plane and together form a right-handed coordinate system is shown in Figure 1.The coordinates of point P (X, Y, Z) is shown in Figure 2.

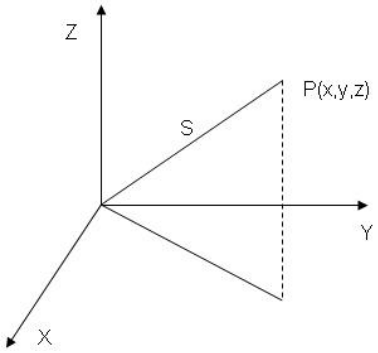


$$\begin{cases} X = S\cos\theta\sin\alpha \\ Y = S\cos\theta\cos\alpha \\ Z = S\sin\theta \end{cases}$$

Figure.1. Positioning principle terrestrial laser scanning system Figure.2. The coordinates of any point is calculated

### 2.2 earthwork calculation model

More model earthwork calculations, including section method, grid method , contour method, the average elevation law , regional earthwork balance method and irregular triangulation method. The different methods have advantages and disadvantages and accuracy of different, which many scholars have done research.High resolution mass point cloud data based on 3D laser scanning to obtain the base, moving fitting based on the point by point interpolation, the idea of constructing triangulated irregular network (Triangular Irregular Network, referred to as TIN) model, considering the spatial resolution of DEM is the exact characterization of the study area of surface morphology.Terrain processing module based on ArcGIS, precise calculation and precision evaluation of regional earthwork using high resolution DEM model.

## Application example analysis

### 3.1 The general situation of research area

Study area for a housing construction site in Xi'an city of shaanxi province named Lanhaiwan project, an area of about 6000m$^2$, undulating terrain with slopes, pits and bulldozers and so on.According to owner required within the project area needs to provide accurate earthwork size, in order to provide accurate data for the later earthwork project implementation .Based on this, we use the Leica C10 laser scanner to obtain a three-dimensional precision earthwork project area data. Meanwhile, we used the GPS RTK technology to verify the results.

**3.2 Field reconnaissance**

With terrestrial 3D laser scanner refined estimates of the amount of earthwork .First, according to the actual site conditions, production planning scanned sketches should include: outside the industry operators, scan area and time, station location, the target location.Secondly, in order to avoid duplication of convenient scanning and post- stitching, etc., need science station and two stops to ensure that the target of sigh.Finally set the target position specification, requiring a solid target, while furnishings, in addition to checking not collinear, the target the best set in the two largest public space station at a distance to ensure the accuracy of different splice sites of point cloud data .

**3.3 Establish control network**

Since the scanner is based on data obtained for the center instrument station coordinates heart, in order to make known control point scan data with the Party providing geo-spatial coordinates coincide, it is necessary to establish Surveying Control Network .Surveying method of establishing control network can draw wire control measure ideas.After completion of the control point layout , with 2 " Leica Total Station to get the geographical coordinates of the control point , the project according to the situation of setting three control points , the control point coordinates to obtain the results shown in Table 1 .

**3.4 Surveying course**

The 3D laser scanner mounted on the 1st test site was on the leveling , will be set up in the special target of known control points near the rear-view A as directed .When the directional precision engineering to meet the needs of targeted directly applied to the results of this scanning process.Next, set the resolution and point intervals were scanned , and the exposure setting texture database collected to obtain the target image and the image of the scanning area .The scanning resolution is set to 5cm × 5cm, set to start after the completion of the scanning station , when the scan is complete start scanning the target ( target position coordinates can get by Leica total station measurements Prism ) , scanning is best to follow the target from far and near , or order from near and far at the same time , be sure that the same target at different scanning stations winning consistency of the target number.Otherwise it will cause splicing errors. After scanning every one station can be checked by looking at the function of the station directly scan data results are in line with the accuracy requirements, if it satisfies the requirements, re- moving station .Outside the industry scan task until completed.

At the same time, by using the GPS RTK technology acquisition 0.5m every finite point coordinates of the study area, data collection is completed, the acquired data into CASS9.0, TIN models constructed on the basis of draw contour map survey area, and contour lines based earthwork calculations.

**3.5 Point cloud data processing**

Due to the interference of external factors in the process of field Surveying, the measured point cloud data so that unnecessary noise data, the noise data will reduce the presence of the calculation accuracy of the model .Therefore , the data must be made to eliminate the noise .Common methods include removing the computer automatically removed and set the threshold manually delete two kinds. This project uses manually delete the actual situation the way noise is removed , and can easily achieve the purpose of removing noise , thus ensuring the accuracy of the point cloud data .

Based on this, the use of known control points and the target coordinate point cloud data based on known data splicing control points and check the accuracy of stitching , stitching the project results shown in Figure 3.As can be seen from the stitching error , the maximum error is spliced 0.002m, the smallest error is 0m, thus indicating the measured data processing industry outside the industry to meet the accuracy requirements .After freezing and other operating data , and exported in text format.

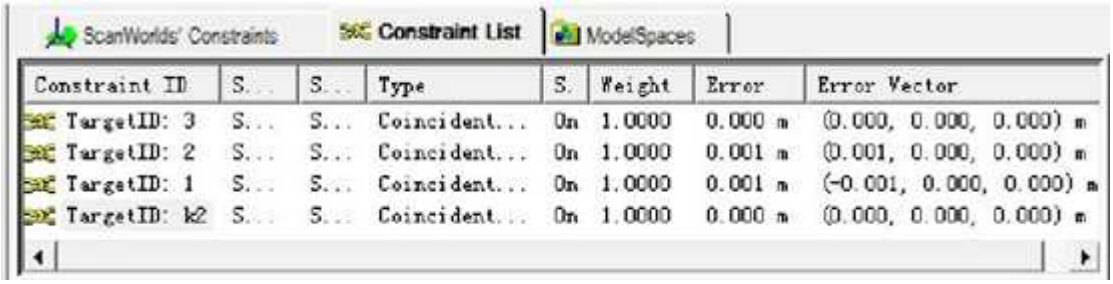


Figure.3. Data based Cyclone splicing error table

### 3.6 Earthwork calculations

The splicing point cloud data. Based on data parsing. Exported to text format. TIN generation model was made in ArcGIS. Open the TIN model in the ArcGIS environment. Analysis of the volume and area of TIN model by the using the 3D surface model. Set the reference elevation of 390.685 meters for the calculation results and output as the text format. The calculation results of the earthwork is the total area is 3224.2m$^2$,the surface soil excavation volume is 9863.6m$^3$,the surface soil fill volume is 12.1m$^3$.

### Result analysis

In this project, the measured point sampling interval is 5cm, and after extracting 20 cm, using the TIN fitting surface three-dimensional model. It can be considered that the model can fully reflect the true sate of surface relief.Therefore,the surface of earthwork calculation based on 3D model can be ignored. At the same time, in order to compare the conventional the GPS technology using by dynamic RTK model to measure the precision of earthwork, outside using zhonghaida V30 GPS RTK method is used to obtain the physiognomy of surveying and mapping. The cumulative gain 1380 detain point data, using CASS 9.0 software calculation function of earthwork, the abnormal point elimination, boundary definition and reference level determination (H=390.685m) and other work, using the same 20cm interval to calculate earthwork grid method based on the calculation results, the total area is 3224.2m$^2$, the surface soil excavation volume is 9880.3m$^3$, the surface soil fill volume is 12.3m$^3$.

Comparative analysis shows that, the latter than the former on the excavation volume more than 16.7m$^3$, fill volume compared with the former more than 0,2m$^3$. Analysis of the causes is that the original morphology fragmentation, 3D laser scanner to complete records this broken form of the landscape, the traditional single point mapping method cannot complete record of the landscape of ups and downs, and only through the measured feature point and feature point encryption method is detailed as the original form of the landscape. Therefore, the traditional single point of surveying and mapping is unable to complete the original form of expression of landforms, the calculation results can only be based on what the measured points and infinite close to the real value, are often short of real value. 3D laser scanning technology, however, it overcomes the defects of this technology, therefore, the used of 3D laser scanning technology to measure the surface condition quantify can reach the point of zero error.

### Conclusions

In this paper, the ground three-dimensional laser scanner LeicaC10 instrument as an example, this paper discusses the three dimensional positioning principle and conditions of pure calculation principle, and mainly discusses the 3D laser scanner is applied to the measuring technology of conditions process and data processing method in the industry, with GPS RTK technique is complementary, compared the results. Analysis found that: (1) through 3D laser scanner to get point cloud data calculated conditions can meet the conditions of high precision calculating the requirements of the project; (2) the traditional single point also has higher measurement precision of surveying and mapping, to meet the demand of the general project, at the same time, in order to

improve the observation accuracy, homework can through the feature points in the process of encryption to improve the calculation precision of the results.

**Acknowledgements**

This work was financially supported by the Foundation for young scientists of Shaanxi Natural Science Foundation (2013JQ5011), Special fund project in Shaanxi province department of education (11KJ0756), talent foundation of Xi'an University of Architecture and Technology (RC1214).

**References**

[1] D.Jiachong, T.Hungchao. 3D laser scanning and GPS technology for landslide earthwork volume estimation. Automation in Construction, Vol.16, 657-663, 2007.

[2] L.Bin, R.Lei, C.Chengqi. Research on the Application of 3D Laser Scanning in Earthwork Volume Calculation .Bulletin of Surveying and Mapping, Vol.10, 62-64,2012.

[3] W.Jingwei, D.Ning, Z.Tonglong. The method of 3D visualization of calculation of earthwork site formation quantity.Surveying and Mapping Engineering,Vol.15, 15-19,2006.

[4] W.Jiexian, H.Dongya, D.Bingbing. Application of 3D laser scanner indisposition volume calculation. Bulletin of Surveying and Mapping, Vol.7,54-56,2013.

[5] H. Kui.Application of 3D laser scanning in the earthwork calculation.Mine Surveying, Vol.1,70 - 72,2013.

[6] Z.Tingting, W.Tieliang. Research on the calculation method of earthwork.Anhui Agricultural Sciences,Vol.22,6047-6050,2006.

[7] L.Bin. Leica 3D laser scanning system applied in the field cultural relics protection. Bulletin of Surveying and Mapping, Vol.6, 72-73,2008.

[8] Z.Zhiqiang. Calculation method of the Comparison and Analysis. The Western Exploration Engineering, Vol.21,167-168,2009.

[9] L.Siyu. Based on the results of the 3 d scanning conditions. Journal of Henan Science and Technology, Vol.8,13-14,2013.

*Applied Mechanics and Materials Vols. 580-583 (2014) pp 2838-2841*
*© (2014) Trans Tech Publications, Switzerland*
*doi:10.4028/www.scientific.net/AMM.580-583.2838*

# Application and Research of 3D Laser Scanning Technology in Steel Structure Installation and Deformation Monitoring

Dongling Ma[1,2, a], Jian Cui[2,b] and Shiyan Wang[1,c]

[1] Institute of Navigation and Aerospace Target Engineering, Information Engineering University, Zhengzhou 450001, China

[2] School of Civil Engineering, Shandong Jianzhu University, Jinan 250101, China

[a]mdling2003@126.com, [b]cuijian1202@126.com, [c]wsyx_80@163.com

**Keywords:** laser radar technology; point cloud data; steel; deformation monitoring; quality control

**Abstract.** The traditional steel structure deformation monitoring generally uses Total Station and GPS to do monitoring quality control, but there are some disadvantages of these methods. Laser radar technology is a new non-contact measurement technology emerged in recent years. It is ideal for installation and slip construction quality monitoring of large-span steel structure. This paper use laser radar technology to monitor large-span steel structure construction, use laser scanner to scan on steel every period of time and collect 3D point cloud data of the feature points after a period of time. Through the comparative analysis of the data and the chart which reflect the amount of deformation of the feature points, it can accurately obtain the result of structural deformation, oblique direction, and the deviation between the actual coordinates and the design coordinates, which provides the most accurate and direct information for the project. Laser radar technology solves the difficult issues such as workload outside the industry and difficulties in visibility of the traditional measurement methods, greatly improves accuracy and efficiency compared to traditional methods, and achieve a high-precision quality control over the construction.

## Introduction

Over the past decade, with the development of China's economic and continuous progress of science and technology, different patterns of large span steel structure has developed rapidly, which has increasing span and scale and more complex structure in the form, and is widely used in sports stadiums, convention centers, theaters, airport stations and other buildings[1,2]. Because of the main truss span, high precision requirements of fabrication and installation and the distortion produced during the construction process, whether the size of the deformation is reasonable will directly affect the project progress and quality of the construction. So it becomes particularly important to do the high-precision quality monitoring over the whole steel structures [3,4].

Traditional means of steel works deformation monitoring are generally based on a single point acquisition method of three-dimensional coordinates. In recent years, a new type of laser radar technology comes to be widely used. It is very suitable for large-span steel structure construction deformation monitoring [5,6].

This paper uses laser radar technology to monitor large-span steel structure construction process and use three-dimensional model of point cloud data model to get a true visual reproduction of the steel structure. Thus we can accurately get the deformation, oblique direction, as well as the deviation between actual coordinates and design coordinates of the structure observed through the measurement and analysis of the main structure of the model. It provides the most accurate and direct information for the project in progress or to be undertaken to solve such issues like workload

outside, visual difficulties in traditional measurement, and it improves the accuracy and efficiency of the traditional methods and achieve high-precision quality control over the construction process.

**Data Collection**

1) Station. Considering the scanning of opera may be covered in the space, we should change the working position of the instrument to resolve the problem, the so-called "shifting station." we set a total of four sites to get the full data of opera building.

2) Setting common point. We use the reference ball as a common point, altogether five reference balls. Considering that there should be the height difference between the reference balls, we set two reference balls on the ground of the opera house, three reference balls on the second floor.

3) Scanning. After scanning each station we must turn off the scanner, unplug the power cord, and then continue the next stop scanning. We totally collect 4 stops' data from scanning the Opera House on the first phase. After sometime, we complete the second phase of data collection of 4 stops placing the scanner on the first set of base stations.

**Processing point cloud data with Faro software**

**Mass stitch the point data.** We get the scan data every time the 3D laser scanner work, and the data is called a site. Because of the limit of the 3D laser scanning principle, we only get the part of the data when we scan the building. Thus we have to splice the data and make them unified in coordinate system we need if we want a complete building surface point cloud data. The specific approach is as follows.

1) Import the point cloud data into the SCENE software, splice two stations by two stations, and find the reference ball (common point) in the plan view of a station and number the reference ball. For convenience, from number 01, click OK to finish one. Follow the same procedure to the other reference balls with 02, 03……in sequence.

2) As one station is finished, do the same in the next station. Find the same ball and compile the same number. Note: The same ball in each station must be compiled with the same number.

3) After the completion of numbering the reference balls in other stations, select "arrangement" in the workspace to complete the mosaic. Load the rest of the stations in sequence, and complete stitching point cloud data of Opera House .The results is shown in Fig.1:

Fig.1 Original 3D point cloud view

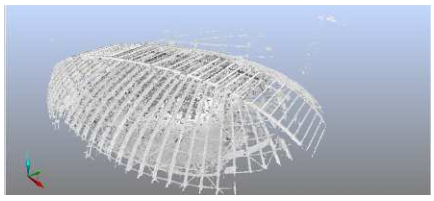

Fig.2 3Dpoint cloud view after denoising

**Denoise the point cloud.** Open 3D view of point cloud data stitched, as indicated in fig.1, we can see many noise points in area of Opera House, which requires denoising. Use polygon selector on the toolbar to select the above noise points and remove them. The effect is shown in Fig.2.

**Export point cloud.** Export point cloud after the above process, and then model and post-process by Cyclone, CAD, 3Dmax. The point cloud data can be changed into XYZ format in the analysis of the data in order to calculate and draw the table.

**Generate 3D model of point cloud data.** There are many ways to reconstruct a 3D model after exporting the point cloud data. The point cloud data derived can be imported into CAD to draw the front view, the left view, the top view, and then put it into 3Dmax to make reconstruction. Here we

use Cyclone software to build the model. Do one scanning of the Opera House and another after sometime. Cut two phases' data of the same part of the Opera House in Faro SCENE software and export it to do 3D modeling analysis.

1) Import coordinates data. Export the required parts of the study point cloud data after finished stitching, and open the Cyclone software to import data coordinates.

2) Fit the model. 3D modeling is to convert the point cloud data to CAD objects. The modeling process in the Cyclone software is using point cloud to do precise calculation and coordinate process. We can choose a clear point cloud to model, for example: select a pipe or point clouds of a sphere surface, then run the command in Cyclone software, and you can automatically fit pipe or a sphere, generate CAD format, and then complete the other operations.

We can find object ball, as well as pipelines in modeling in the third leg of the point cloud.

3) Import to CAD. Draw the building fitted in the CAD and export when finished.

4) Import to 3Dmax to complete modeling. Import the files exported from CAD into 3Dmax to realize 3D modeling of steel structures, as shown inFig.3, Fig.4:

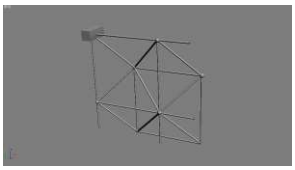

Fig.3 Steel's scan 3D model in first phase

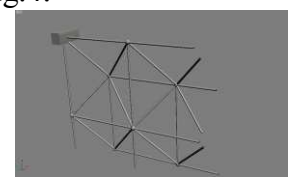

Fig.4 Steel's scan 3D model in second phase

We can see the deformation by two-phase's 3D model, and acquire more intuitive deformation monitoring conditions of the building by comparing the analysis of the two phases' data.

**Analysis of monitoring Data**

1) Select feature points. Before scanning, choose a fixed point in order to compare the characteristics of each of the analysis. The most obvious point in steel is welded ball, so we have a six-point mark on the ball, which can directly reflect changes in the steel structure by comparison.

After making the marks, scan the feature points on the ball in two phases, then do some relevant treatment in Faro software and export the data. In summary, we study monitoring deformation of the steel mainly by analyzing such feature points' data comparatively.

2) Export feature point coordinates. Select 'Export' and 'Export with XYZ format'. So you can see the 3D coordinates of the feature points.

3) Analyze the deformation. The test selects 6 feature points, (X, Y, Z) is the coordinate of the first scan, (X ', Y', Z ') is the coordinate of the second scan. The results are shown in Table 1 and Table 2.

Table 1 X, Y, Z coordinates of six feature points

| coordinate / point number | X | Y | Z | X ' | Y ' | Z ' |
|---|---|---|---|---|---|---|
| 1 | 3.306676 | 22.492647 | 4.077191 | 3.306464 | 22.502067 | 4.065279 |
| 2 | 3.308649 | 22.489273 | 4.068587 | 3.308591 | 22.504867 | 4.074805 |
| 3 | 3.31099 | 22.498175 | 4.086661 | 3.310351 | 22.504558 | 4.071875 |
| 4 | 3.311052 | 22.43841 | 4.071934 | 3.310427 | 22.457629 | 4.080919 |
| 5 | 3.312407 | 22.497925 | 4.089451 | 3.312939 | 22.5041 | 4.095687 |
| 6 | 3.336145 | 22.47812 | 4.123097 | 3.335982 | 22.490137 | 4.138946 |

Table 2 The overall oblique measurement value of feature points

| Point number | Length（mm） | North-South bias（mm） | East-west Bias（mm） | △Z(mm) |
|---|---|---|---|---|
| A-A' | 9.422 | North Bias 9.420 | West Bias 0.212 | -11.912 |
| B-B' | 15.594 | North Bias15.594 | East Bias 0.261 | -6.218 |
| C-C' | 6.415 | North Bias 6.383 | East Bias 0.639 | -14.786 |
| D-D' | 19.229 | North Bias 19.219 | West Bias 0.625 | 8.985 |
| E-E' | 6.198 | North Bias 6.175 | East Bias 0.532 | 6.236 |
| F-F' | 12.018 | North Bias 12.017 | West Bias 0.163 | 15.849 |

By the Table, we can know that: plane displacement, angle offset, and space offset of each point meet the accuracy requirements in the acceptable range in the construction deformation, which also confirms that the application of 3D laser scanning technology in large-span steel structure deformation monitoring is feasible.

## Conclusions

In this paper, laser radar technology is applied to do deformation monitoring of a steel structure. Firstly, we make two scans of the opera (a certain period interval between two scan of before and after). Secondly, model in 3Dmax and extract feature point data in 3D model. Finally, we acquire the amount of deformation through the analysis of comparison with two phases' data. Compared with the construction standards, each offset of steel is within the deformation range of the steel construction requirements.

Practice has proved that using laser radar for steel structure deformation monitoring is feasible and simple, has high precision and fast speed, and greatly reduces the workload of measurements outside the industry. The data observed is more comprehensive, the contrast of 3D model created is very objective, and the analysis of the data by chart is more convincing, which are useful for the Opera steel slip deformation monitoring.

## Acknowledgements

This work was financially supported by Science and Technology Project of Colleges and Universities of Shandong Province (Grant No.J12LG53), Ministry of Construction P.R.China Science & Technology Planning Project (Grant No.2010-K9-24) and Housing and Urban-rural Development project of Shandong Province (Grant No. KY004).

## References

[1] Qun Zhao,Jian Liu and Jinke Chen: Science of Surveying and Mapping, Vol. (03) (2007), p. 110

[2] F.Xi,Y.Liu and H.-Y.Feng: The international Journal of Advanced Manufacturing Technology, Vol. 59(3)(2001) , p.207

[3] Dongfeng Jia and Xiaojun Cheng: Science of Henan, Vol. (09) (2009), p. 114

[4] Yanmin Wang and Guoli Wang. engineering investigation, Vol. (12) (2009), p. 17

[5] Renzhong Li and Jie Liu: Chongqing Architecture, Vol. (10) (2010), p. 42

[6] Aiwu Zhang,Weidong Sun and Fengting Li:Journal of system simulation, Vol. (02) (2005), p. 384

*Applied Mechanics and Materials Vols. 580-583 (2014) pp 2842-2847*
*© (2014) Trans Tech Publications, Switzerland*
*doi:10.4028/www.scientific.net/AMM.580-583.2842*

# Discussion on the application of GPS technology in bridge construction plane control net and in survey of bridge axis lofting

Siyi Jiang

Guangxi Polytechnic of Construction, Nanning, Guangxi, China, 530003
1633496530@qq.com

**Key words**: GPS technology; Construction control net; Length of side conversion; Bridge axis lofting

**Abstract**.The article introduces that the GPS technology in the bridge construction survey turns the bridge axis lofting spots and the construction control net into the overall net after completing the plane control net, to centrally gathering information and simultaneously adjustment processing, so as to satisfy the high accuracy request of the bridge axis lofting.

## Introduction

GPS technology are widely applied to various measurement work,because of its high speed,high precision,all-weather,cost saving,a high degree of automation,and not the terrain constraints,etc [1].And with its continuous advancement and improvement, some of the traditional measurements are gradually being replaced by it.

Traditional goniometric net,triangulateration net and trilateration net,demand a good visibility between adjacent control points for the measurement of edge and angle,which bring about a difficulty to the actual setpoint work.So this can demonstrate GPS's superiority.Construction control net call for a high precision to the interior of various control points and a high requirement to the relative accuracy between points.And the interior of GPS observation data meet high precision which is unmatched by conventional measurement methods.Therefore,the use of GPS for surveying control network has very important significance.

Because the processed GPS,s observed data is the corrected results of Gauss projection,for improving the internal precision of control network and facilitating construction use,measurement process and data processing should adopt appropriate technical measures,combined with the characteristics of construction control net and the specific requirements ,to reach the construction control Network requirements.This paper take the GPS construction plane control net and bridge spool thread lofting project about Nanning Huluding Bridge as an example.After the completion of plane control net and bridge axis stakeout work, the bridge axis stakeout points and the control points,in order to satisfy the requirement of the bridge axis lofting precision, have been linked together into a overall net to centrally gathering information and simultaneously adjustment processing.It fully embodies the advantages of GPS technology.

## Technology design

**Overview of the surveyed area.**The GPS measurements is to provide measurement control point for Huluding bridge construction.Huluding Bridge is the main part of nan-ning rapid ring road, baisha road west, east and Zhuxi Avenue extension line, across the Yongjiang river.

The original G1, G2 etc four-level GPS control point is in good condition.So according to the principle in standard that the GPS net can set the overall net in same level [2],a plane control network can be established based on the above starting two points.The new net lay out four four-level GPS plane control points which distribute on the both sides of Yongjiang river and there is a good visibility between the above points.

**Coordinate system design**.The GPS net that used Beijing coordinate system in 1954 lay ou t by four-level net.It don,t be modified by Gauss projection,but in order to in line with the construction projection plane,observation length should projected to the elevation surface he ight of 81.5 m. The datum plane adopt Yellow Sea elevation height datum.

**Layout idea and flow chart.**Adopting four Southern Lingrui S60 static GPS receiver (5mm+1ppm) and it contains a baseline solution and net adjustment software which is used for calculating construction control network.

Then conducting bridge spool thread lofting measurement by the construction control points and linking the bridge axis stakeout points and the control points together into a overall net.Finally using GPS in centrally gathering information and simultaneously adjustment processing, so as to meet the high accuracy request of the bridge spool thread lofting.Layout flow chart as shown in fig.1.

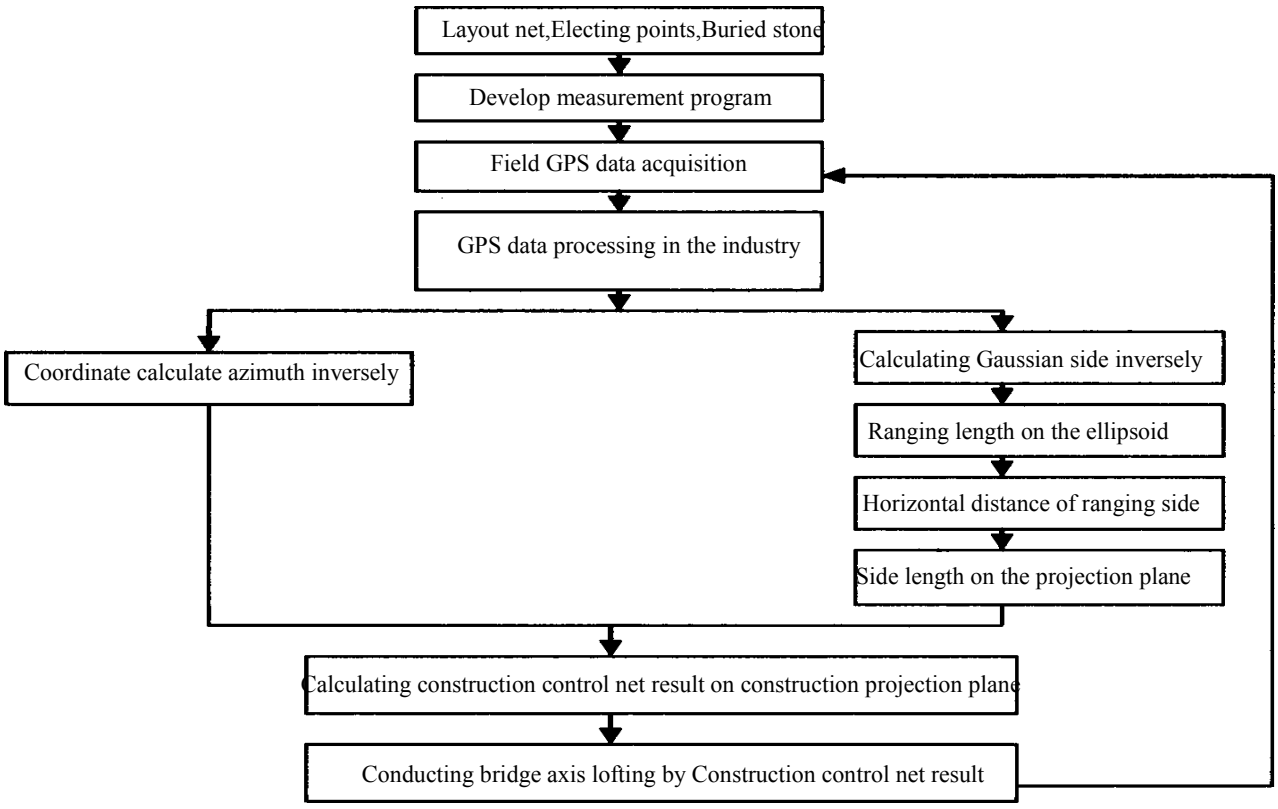


Fig.1 GPS measurement and data processing flow chart

**Math model of side length conversion.**The length that the gauss plane reduction to the ranging side length of reference ellipsoid [3],such as equation 1.

$$D_1 = D_2 / \left[1 + y_m^2 / (2 \times R_m^2) + (\Delta y)^2 / 24 \times R_m^2\right]. \quad (1)$$

where $D_1$ is the reduction ranging side length of reference ellipsoid(unit : m), $D_2$ is the length on the gauss plane(unit : m),$\Delta_y$ is the difference between the two endpoint abscissa of ranging side(unit : m), $y_m$ is the mean between the two endpoint abscissa of ranging side(unit : m),$R_m$ is The average curvature radius of ranging side midpoint on the reference ellipsoid( unit : m).

The ranging side length that reference ellipsoid reduction to the measured horizontal distance,such as equation 2.

$$D = D_1 / \left[1 - (H_m + h_m)/(R_A + H_m + h_m)\right]. \quad (2)$$

Where $h_m$ is The altitude difference that the geoidal surface of measurement area is higher than the reference ellipsoid(unit : m),$H_m$ is the average elevation that the ranging side is higher than the geoidal surface(unit : m),$R_A$ is the bend radius of normal section line to the ranging side(Unit : m),D is the horizontal distance of ranging side length(unit : m).

The ranging side length that the horizontal distance reduction to the average elevation plane of measurement area or any other elevation plane,such as equation 3.

$$D_0 = D\left[1 + (Hp + H_m)/R_A\right]. \quad (3)$$

Where $D_0$ is the ranging side length that reduction to the average elevation plane of measurement area(unit : m),$H_P$ is the average elevation measurement area or any other elevation( unit : m).

**GPS construction control net measurement and precision analysis**

**The construction plane control net figure is shown in Fig.2(a).**

**GPS data processing and precision statistics.Baseline solution.**After completion of field data acquisition, conducting data processing by the baseline solution and net adjustment software that was given by Southern Company. The longest side of the whole net is 1691 meters, the shortest side is 411 meters, with an average side length of 1039 meters.The precision statistics of the synchronized loop Calculated through the net are shown in table 1 and the precision statistics of the asynchronous loop Calculated through the net are shown in table2.The precision statistics of a repeat baseline Calculated through the net are shown in table 3.

Table 1 The precision statistics table of the synchronized loop (Unit: mm)[4]

| NO. | Edge number (n) | Edge length **d** (km) | $W_x$ | $W_{xTolerance}$ $W_{xTolerance} \le d\times 6$ | $W_y$ | $W_{yTolerance}$ $W_{yTolerance} \le d\times 6$ | $W_z$ | $W_{zTolerance}$ $W_{zTolerance} \le d\times 6$ | $W_{Closer}$ | $W_{Closing\ error\ Tolerance}$ $W_{Closing\ error\ Toleranc} \le d\times 10$ |
|---|---|---|---|---|---|---|---|---|---|---|
| 1 | 3 | 4.12 | 3 | 24.72 | -8 | 24.72 | -9 | 24.72 | 3.37 | 41.20 |
| 2 | 3 | 2.24 | 2 | 13.44 | 6 | 13.44 | 3 | 13.44 | 2.42 | 22.40 |
| 3 | 3 | 2.55 | 6 | 15.30 | 4 | 15.30 | 7 | 15.30 | 3.83 | 25.50 |
| 4 | 3 | 3.99 | -3 | 23.94 | 1 | 23.94 | -2 | 23.94 | 1.25 | 39.90 |
| 5 | 3 | 2.23 | 1 | 13.38 | 9 | 13.38 | O | 13.38 | 3.41 | 22.31 |

Table 2 The precision statistics table of the asynchronous loop (Unit: mm)

| NO. | Edges number (n) | Average edge length $d(km)$ | $\sigma$ $\sigma=\sqrt{a^2+(bd)^2}$ | $W_x$ | $W_{xTolerance}$ $W_{xTolerance}\le 2\sqrt{n}\sigma$ | $W_y$ | $W_{yTolerance}$ $W_{yTolerance}\le 2\sqrt{n}\sigma$ | $W_z$ | $W_{zTolerance}$ $W_{zTolerance}\le 2\sqrt{n}\sigma$ | $W_{\text{Closer}}$ $W_{\text{Tolerance}}=\sqrt{W_x^2+W_y^2+W_z^2}$ | $W_{Closing\ error\ Toleranc}$ $W_{Closing\ error\ Toleranc}\le 2\sqrt{3n}\sigma$ |
|---|---|---|---|---|---|---|---|---|---|---|---|
| 1 | 3 | 1.40 | 10.39 | 4 | 35.99 | 9 | 35.99 | 14 | 35.99 | 17.12 | 62.34 |
| 2 | 3 | 0.65 | 10.08 | 5 | 34.92 | 7 | 34.92 | 3 | 34.92 | 9.11 | 60.48 |
| 3 | 3 | 0.71 | 10.11 | -3 | 35.02 | -9 | 35.02 | 4 | 35.02 | 10.30 | 60.66 |
| 4 | 3 | 1.18 | 10.27 | -5 | 35.58 | -4 | 35.58 | -16 | 35.58 | 17.23 | 61.62 |
| 5 | 4 | 1.17 | 10.27 | 10 | 41.08 | 15 | 41.08 | 12 | 41.08 | 21.66 | 71.15 |

Table 3 The precision statistics table of the repeat baseline (Unit: mm)

| NO. | Average edge length $d(km)$ | $\sigma=\sqrt{a^2+(bd)^2}$ | ΔS | $\Delta S_{\text{Tolerance}}\le 2\sqrt{2}\,\sigma$ |
|---|---|---|---|---|
| 1 | 0.51 | 10.08 | 2 | 28.51 |

**Two dimensional constraint adjustment precision statistics.**The GPS net use 2 starting points(G1, G2) to conduct two dimensional constraint adjustment and the precision statistics are shown in table 5. Using four-level point PD that coincided with the GPS control net of Huluding bridge to do the external check and its coordinate Comparison are shown in table 4.To the reliability of checking adjustment results , we use the total station to test four GPS side through field site. Processing side length correction and conversion,and the test results are shown in table 6.

Table 4 The coordinate comparison of the GPS control net coincident point of Huluding bridge (Unit:mm)

| Points NO. | ΔX | ΔY | Comment |
|---|---|---|---|
| $P_D$ | -0.005 | 0.012 | |

Table 5 The precision statistics table of the two dimensional constraint adjustment (Unit: mm)

| Baseline name | Edge length **d**(km) | $\sigma$ $\sigma=\sqrt{a^2+(bd)^2}$ | $V_{\Delta x}$ | $V_{\Delta xTolerance}$ $V_{\Delta xTolerance}\le 3\sigma$ | $V_{\Delta y}$ | $V_{\Delta yTolerance}$ $V_{\Delta yTolerance}\le 3\sigma$ | Relative error |
|---|---|---|---|---|---|---|---|
| $G_2$–$P_D$ | 0.83 | 10.12 | 2 | 30.36 | 1 | 30.36 | 1:396000 |
| $G_2$– $G_1$ | 1.61 | 10.50 | 3 | 31.50 | 2 | 31.50 | 1:525536 |
| $G_2$– $P_C$ | 1.00 | 10.21 | 2 | 30.63 | 2 | 30.63 | 1:422160 |
| $P_D$–$G_1$ | 1.70 | 10.56 | 2 | 31.68 | 3 | 31.68 | 1:585588 |
| $P_D$ – $P_A$ | 1.02 | 10.21 | 2 | 30.63 | 2 | 30.63 | 1:433986 |
| $P_D$ – $P_B$ | 0.76 | 10.11 | 2 | 30.33 | 3 | 30.33 | 1:233062 |
| $P_D$ – $P_C$ | 0.41 | 10.02 | 1 | 30.06 | 1 | 30.06 | 1:237700 |
| $G_1$–$P_A$ | 1.48 | 10.43 | 3 | 31.29 | 2 | 31.29 | 1:507743 |
| $G_1$– $P_C$ | 1.37 | 10.38 | 2 | 31.14 | 2 | 31.14 | 1:452180 |
| $P_A$ – $P_B$ | 0.78 | 10.12 | 2 | 30.36 | 2 | 30.36 | 1:215300 |
| $P_A$ – $P_C$ | 0.68 | 10.09 | 3 | 30.27 | 2 | 30.27 | 1:281036 |
| $P_B$ – $P_C$ | 0.81 | 10.15 | 2 | 30.45 | 2 | 30.45 | 1:243000 |

Table 6 The test table of flied site

| Station | Target | Detection distance | Inverse distance | D-value | The relative D-value |
|---|---|---|---|---|---|
| $P_C$ | $P_D$ | 408.533 | 408.531 | O.002 | 1/204266 |
| | $P_A$ | 678.231 | 678.234 | -0.003 | 1/226077 |
| $P_B$ | $P_D$ | 769.112 | 769.107 | O.005 | 1/153821 |
| | $P_A$ | 783.567 | 783.569 | -O.002 | 1/391784 |

**The bridge axis lofting measurement**

**The bridge axis lofting.**①Get point A and point B on the bridge axis through using total station and utilizing control points in the construction control network.Then build a good mark On-the-spot.

②Use GPS to observe uniformly each control point and A,B points,and then calculating coordinate inspection A',B' of A,B.It should be compare with its theoretical value. If the D-value is greater than the standard requirement, we need to do as follows. With total station at point A, point A ' as station coordinates,and point B ' used fou orientation, rotating equipment and with making the line of sight direction in A' A azimuth, setting point C two meters in that direction.Then calculating distance D between point A and point B. In order to ensure the point A″, measuring the distance D from A' to C through the steel rule and then making a mark in labeled heart. Processing point B in the same way above.

③ Repeat step (2), until the D-value between the Coordinate inspection of point A and point B and its theoretical value meet the standard requirement

**The GPS net diagram of the bridge axis lofting is shown as Fig.2(b)**.

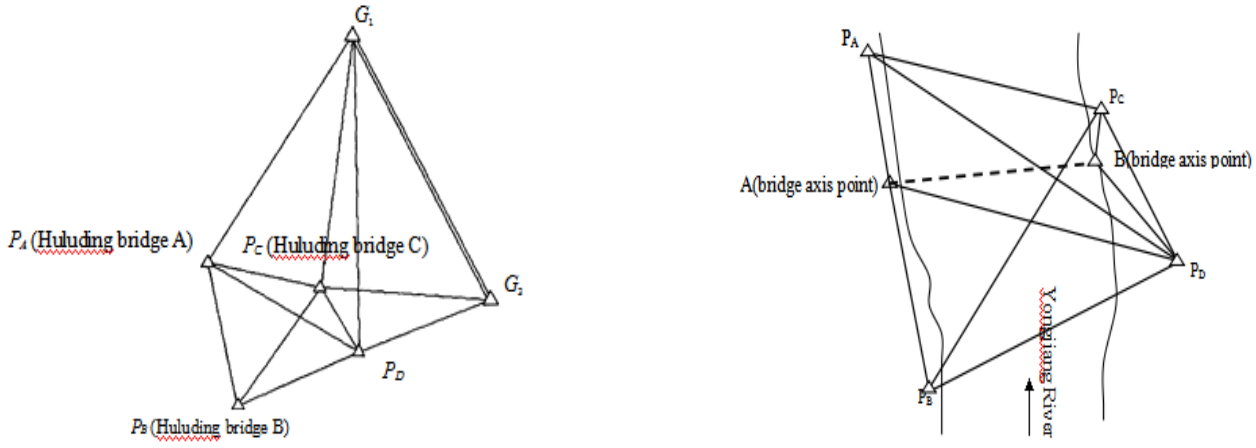


(a) (b)

Fig.2 The construction plane control net diagram(a) and The GPS net diagram of the bridge axis lofting(b)

**The GPS accuracy statistics to detect bridge axis lofting .**Get point A and point B on the bridge axis through construction control points.Then Use GPS for testing,and testing accuracy are shown in table 7

Table 7 Precision statistics table (Units:mm)

| Point name | mean square error of a point | Relative error |
|---|---|---|
| A | 2.236 | 1/203750 |
| B | 2.345 | |

## Conclusions

The control survey conducted with GPS were judged collectively outstanding in quality because of its reasonable net layout and its high accuracy that meet the standard requirements overall.Due to limitations of the terrain, the average side length do not meet the requirements of the four-level GPS net.But after careful measurement, the relative mean square error of each edge side length is very small, only 1/215330 of the largest,fully achieving "urban measurement standard"[5] in the demands of four-level sides.For the requirement of high precision construction control net and the characteristics of shorter edge length,the experience in the practical application is as follows:

① It is reliable for GPS net to replace the classic construction control net.

②The joint measurement method of GPS net and bridge axis lofting point in precision and efficiency are better than the traditional bridge axis lofting method.

③In order to make sure that the observation of long-short baseline edge is not restricted,using dual-frequency GPS receiver to observe.

④On the basis of standard, an appropriate extension of the observation time and an increase of the repeat observations can make the observation results more reliable.

⑤Select a period of satellite observations in good condition to observe, to ensure the reliability of the data.

⑥Observing more than 2 edges length by the high precision Rangefinder for checking.

## Acknowledgements

This work was financially supported by the Shanghai Natural Science Foundation (0666666), Innovation Program of Shanghai Municipal Education Commission (060000) and Shanghai Leading Academic Discipline Project of Shanghai Municipal Education Commission (0555555).

## References

[1] Dajie Liu, Yimin Shi, JingJun Guo.Global Positioning System (GPS) and data processing[M].Tongji University Press,1996(In Chinese).

[2] Xiangyuan Kong, Jimin Guo. Control Surveying (upper and lower volumes). Wuhan University Press,2006(In Chinese).

[3] GB/T18314-2001, Global Positioning System (GPS) surveying standard(In Chinese).

[4] CJJ73-97, Global Positioning System City measurement techniques regulations(In Chinese).

[5] CJJ8-99, Cities measurement standard(In Chinese).

*Applied Mechanics and Materials Vols. 580-583 (2014) pp 2848-2852*
*© (2014) Trans Tech Publications, Switzerland*
*doi:10.4028/www.scientific.net/AMM.580-583.2848*

# Improved BP Neural Network Model Applied in Settlement Analysis

Liangbo Gao[1, a]

[1]University of Science and Technology Liaoning,Anshan,China

[a]gaoliangbo3456@163.com

**Keywords:** the subway; settlement; BP neural network; Analysis and forecasting.

**Abstract.** According to the settlement and deformation of pavement in subway construction, the paper improved on the basis of gray system theory and BP neural network forecasting model. The method is adapted to modified residual prediction model to predict with engineering examples. It provides decision-making basis for construction engineering and monitoring.

## Introduction

The subway construction has a great impact on the road, can also cause a threat to the safety of vehicular traffic. It is particularly important for subsidence monitoring subway along the road, not only can provide useful information for the construction but also for the construction and road transportation to provide security. Therefore, this paper focuses on the analysis of monitoring data and research on settlement prediction model.

## An improved BP network model established

The improved BP neural network modified grey linear regression residual prediction model. The model is the integration of grey linear regression model and improved BP neural network. It uses the residuals of gray linear regression model as the input samples of an improved BP neural network. The network is trained to predict the samples.

The modeling method of the improved BP neural network modified grey linear regression residual prediction model as follows:

1. The original data sequence $\{x^{(0)}(i)\}, i = 1,2,\cdots,n$ , the use of linear regression model was fitted. Simulation and prediction value is obtained, $\hat{x}^{(0)}(i), i = 1,2,\cdots,n$ .It is provided with a residual sequence:

$$e^{(0)}(i) = x^{(0)}(i) - \hat{x}^{(0)}(i), i = 1,2,\cdots,n \tag{1}$$

2. Establish equal dimension and new information model of BP network of a residual sequence $\{e^{(0)}(i)\}$ . Let the number of prediction for K, using the information of $e^{(0)}(i-1), e^{(0)}(i-2),\cdots, e^{(0)}(i-k)$ to predict value of i time. $e^{(0)}(i-1), e^{(0)}(i-2),\cdots, e^{(0)}(i-k)$ as the input of BP network model is trained. The value of $e^{(0)}(i)$ as the target output value for the BP network model. The residuals sequence of BP neural network model by further training, so that different input vectors to obtain a corresponding output value. Then using trained model to simulate and predict the residual sequence.

3. Determine the new prediction values of the residual sequence $\{e^{(0)}(i)\}$ .using BP neural network model to simulate and predict $\{e^{(0)}(i)\}$ and getting new residual sequence $\{\hat{e}^{(0)}(i)\}$ . According to the residual sequence construct a new predictive value $\hat{y}^{(0)}(i)$ :

$$\hat{y}^{(0)}(i) = \hat{x}^{(0)}(i) + \hat{e}^{(0)}(i), i = 1,2,\cdots,n \tag{2}$$

The improved BP network model is an improved model on the basis of BP network model. On the one hand is to improve the standard gradient descent method includes adaptive learning rate, increasing momentum term. On the other hand is the standard of value optimization method includes

the step secant method, quasi Newton method, conjugate gradient method and the Levenberg-Marquardt algorithm.

In view of the small and medium-sized BP neural network is the best use of the Levenberg-Marquardt algorithm, which has faster convergence speed, storage capacity is low.

## Application of improved BP neural network model

This paper chooses a monitoring point for example, the residual sequence: $e^{(0)}$= {0.0127,-0.0114, -0.021,-0.0426, 0.179,-0.1645, 0.044, 0.0064, 0.2779,-0.1949,-0.7554}. Using BP neural network model to simulate and predict $\{e^{(0)}(i)\}$ and getting new residual sequence $\{\hat{e}^{(0)}(i)\}$. According to the residual sequence construct a new predictive value $\hat{y}^{(0)}(i)$.

Residual every 3 value as a cycle, the first three residual values as input samples of improved BP neural network, following period of residual value as the output samples, the formation of 6 training samples and two test samples.

Table 1 Grey neural network sample selection table

| Sample number | | input sample /mm | | | Output sample /mm |
|---|---|---|---|---|---|
| The training sample | 1 | 0.0127 | -0.0114 | -0.0210 | -0.0426 |
| | 2 | -0.0114 | -0.0210 | -0.0426 | 0.1790 |
| | 3 | -0.0210 | -0.0426 | 0.1790 | -0.1645 |
| | 4 | -0.0426 | 0.1790 | -0.1645 | 0.0440 |
| | 5 | 0.1790 | -0.1645 | 0.0440 | 0.0064 |
| | 6 | -0.1645 | 0.0440 | 0.0064 | 0.2779 |
| The test sample | 7 | 0.0440 | 0.0064 | 0.2779 | -0.1949 |
| | 8 | 0.0064 | 0.2779 | -0.1949 | -0.7554 |

Through the test algorithm, Selection of hidden layer neurons as 4 is the best. The formation of the topological structure of BP neural network is 3-4-1. We need to normalize sample data, The transfer function in the input layer is ‘tansig’, The transfer function of hidden layer is ‘logsig’, The transfer function in the output layer is ‘purelin’. The training function of network select Levenberg-Marquardt algorithm—‘trainlm’. Then by using the improved Levenberg-Marquardt algorithm of BP neural network was used to train the neural network. The improved BP network train diagram is shown in fig.1.

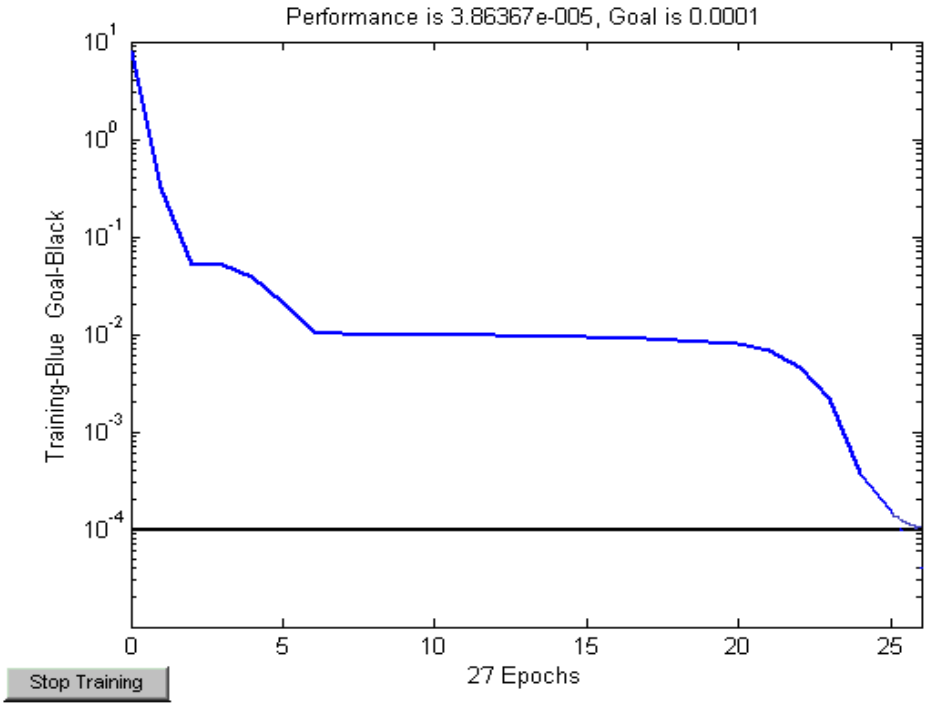


Fig. 1 The improved BP network train diagram

Fig.1 show that in the case of the training function is 'trainlm', to achieve the target error set 0.0001, only need to train 27 iterations. The time compared with BP neural network training is short and less training time.

Table 2 Improved BP neural network modified grey residual prediction results table

| Serial number | original value /mm | Predicted values /mm | Absolute error /mm | Relative error /% |
|---|---|---|---|---|
| 1 | 10.14 | 10.14 | 0 | 0 |
| 2 | 10.44 | 10.44 | 0 | 0 |
| 3 | 10.69 | 10.69 | 0 | 0 |
| 4 | 10.99 | 10.9893 | 0.0007 | 0.006 |
| 5 | 11.61 | 11.6098 | 0.0002 | 0.002 |
| 6 | 11.76 | 11.7607 | -0.0007 | 0.006 |
| 7 | 12.58 | 12.5953 | -0.0153 | 0.121 |
| 8 | 13.3 | 13.299 | 0.001 | 0.008 |
| 9 | 14.51 | 14.5134 | -0.0034 | 0.023 |
| 10 | 15.2 | 15.3724 | -0.1724 | 1.134 |
| 11 | 16.08 | 16.5713 | -0.4913 | 3.055 |

According to table 2 shows the sum of squared residuals of SSE is 0.2713, the average relative error of MRE is 0.5443%, the mean square error of MSE is 0.0339.

The results of simulate and predict models in Table 3.

Table 3 The model prediction and error comparison

| Serial number | actual value | Grey linear regression model | | BP neural network model | | Improved combination model | |
|---|---|---|---|---|---|---|---|
| | | Predicted values/mm | Relative error/% | Predicted values/mm | Relative error/% | Predicted values/mm | Relative error/% |
| 1 | 10.14 | 10.127 | 0.13 | —— | —— | —— | —— |
| 2 | 10.44 | 10.451 | 0.11 | —— | —— | —— | —— |
| 3 | 10.69 | 10.71 | 0.20 | —— | —— | —— | —— |

| | | | | | | | |
|---|---|---|---|---|---|---|---|
| 4 | 10.99 | 11.033 | 0.39 | 10.983 | 0.06 | 10.989 | 0.006 |
| 5 | 11.61 | 11.431 | 1.54 | 11.625 | 0.13 | 11.610 | 0.002 |
| 6 | 11.76 | 11.925 | 1.4 | 11.712 | 0.41 | 11.761 | 0.006 |
| 7 | 12.58 | 12.536 | 0.35 | 12.600 | 0.16 | 12.595 | 0.121 |
| 8 | 13.3 | 13.294 | 0.05 | 13.404 | 0.78 | 13.299 | 0.008 |
| 9 | 14.51 | 14.232 | 1.92 | 14.425 | 0.59 | 14.513 | 0.023 |
| 10 | 15.2 | 15.395 | 1.28 | 15.662 | 3.03 | 15.372 | 1.134 |
| 11 | 16.08 | 16.835 | 4.7 | 15.775 | 1.89 | 16.571 | 3.055 |

According to table 3 shows that modified combined model prediction effect is the best. In order to predict the effect of the above models and level of precision, using three error indexes including sum of squares error SSE, mean square error MSE and the average relative error of MRE is analyzed, by comprehensive evaluation of forecasting results.

Table 4 Model prediction error evaluation

| Model evaluation index | SSE | MRE/% | MSE |
|---|---|---|---|
| Grey linear regression model | 0.750 | 1.097 | 0.068 |
| BP neural network model | 0.328 | 0.881 | 0.041 |
| Improved combination model | 0.271 | 0.544 | 0.034 |

According to table 3 shows that forecast effect and the accuracy of combination model is highest.the precision index are better than other models, thus the engineering examples show that there is the best application effect of the improved model.

## Conclusions

1. The improved BP neural network modified grey linear regression residuals model capable of small sample, poor information based on data sample, a strong self-learning and adaptive model.
2. The model is solved stochastic of BP neural network model, prediction precision than GM (1,1) model, grey linear regression model and BP neural network model has greatly improved, forecast effect is improved obviously.
3. The model is feasible and practical in the actual project application.

## References

[1]Jvlong Deng. Gray theory [M]. Wuhan：Huazhong University of Science and Technology press, 2002.

[2]Sifeng Liu, Yaoguo Fang. Grey system theory and its application [M].Beijing：Science Press, 2004.

[3]Teng Huang, Jingling Sun, Jianyue Tao.Subsidence monitoring and analyzing in subway tunnel construction[J]. JOURNAL OF SOUTHEAST UNIVERSITY, 2006,36(2):262～266.

[4]Yi Fang, Xianghong Hua, Haiying Li. The application of grey neural network model to deformation forecasting of buildings [J]. ENGINEERING OF SURVEYING AND MAPPING, 2008,17(2): 51～57.

[5]Lee-Ing Tong,Yi-Hui Liang.Neural network and grey analysis and forecast the field failure data for repairable system[J].Journal of Gray System,2002,14(4):341～344.
[6]Si-Feng Liu,Jeffrey Forrest.Advances in Grey Systems Theory and Its Application[C].Proceedings of 2007 IEEE International Conference on Grey Systems and Intelligent Services,Nanjing,2007:1～6.
[7]Nai-ming Xie,Si-feng Liu.Discrete grey forecasting model and its optimization[J].Applied Mathematical Modelling,2009,33(2):1173-1186.

*Applied Mechanics and Materials Vols. 580-583 (2014) pp 2853-2859*
*© (2014) Trans Tech Publications, Switzerland*
*doi:10.4028/www.scientific.net/AMM.580-583.2853*

# Multi-scale Classification Based on Remote Sensing

LI Peng-li[1,a] ,TI Wei-ping[1,b], LI Jia-chun[1,c]

[1] Key Laboratory for Special Area Highway Engineering of Ministry of Education, Chang'an University, Xi'an 710064, China

[a]li.pengli@sohu.com , [b]fz03@chd.edu.cn, [c]fz03@chd.edu.cn

**Key words：** multi-scale classification, segmentation, eCognition approache

**Abstract:**Due to the broadly application of remote sensing imagery, there is an eager need for the classification of objects in the images. The multi-scale classification based on object oriented analysis is not a usual approach for image classification because the users of multi-scale classification do not know how to use the information from multiple scales to do multi-scale classification. Many users rely on some easily accessible tools. nearest neighbour classifier, to do multi-scale classification. The multi-scale classification classifies the images from different scales. The feature values of the object vary from different scales and they may have some trends against scales. These trends may help us to understand multi-scale classification better. This is the scale dependency of features. The difference between multi-scale classification and single-scale classification is not only multiple scales, but also the use of information from different scales. In order to explore the connection between different scales, the research of new features is necessary.

## Introduce:

In current researches, the object in OOA has two meanings. One is the segments in segmentation. Another one is the meaningful composition of pixels in the imagery, e.g. one road or one house in the image. OOA begins with segmentation. Segment means subdivide entire/part of images at a pixel level, and the object is a set of pixels segmented in software (Definiens, 2009)[1]. In OOA, the segmentation is the previous procedure of classification. At first, the image will be segmented by any kinds of algorithms or knowledge-driven threshold. There also a lot of segmentation algorithms. The basic algorithms are edge detection and region extraction. One simple algorithm for edge detection is the local variance. The edge of regions in the image has the relatively bigger heterogeneity in the image, which means it has the relatively bigger local variance. Oppositely, the principle of region extraction is that the pixels in a region are relatively homogeneous. One way to find these regions is that: set a threshold for this homogeneity and merge the neighbor pixels by some searching algorithms. Another way is the transform algorithms, e.g. watershed transform in morphology segmentation (Vincent & Dougherty, 1994)[2]. Just as the name, morphology segmentation assumes the boundaries of regions are similar to the ridgeline of the landform of gray level. The gray level of the regions gradually increases from the center of regions to the boundaries and these centers are the major extrema of the whole image. OOA also have obvious backwards, notwithstanding it is better than pixel-based classification. The segments in segmentation are image objects and the real matters in natural are natural objects, e.g. a highway, a house, etc. But the image objects cannot perfectly match the natural objects due to the accuracy of segmentation and classification (Esch, Thiel, Bock, Roth, & Dech, 2008; Ranasinghe, 2008)[3-5] The image is an IKONOS pan-sharpen imagery of Delhi (see the location in Appendix A. The whole imagery is not

available), and the acquisition date is Jun. 3, 2001. The segmentation is drawn by eCognition software. The whole image is segmented into many objects. During the classification, some of the objects will be classified as object of interest (train station)[6-8].

## Segmentation

### Number of scales

The scales of segmentation depend on the scales of the structure of image objects. Before the segmentation, the number of scales needs to be decided roughly. The complicated structure in the object makes multi-scale classification a necessity. The segmentation should reflect the boundaries of objects and the sub-level of segmentation matches the boundaries of their sub-objects. The number of segmentation scales/levels should not be less than the number of structure scales, there are at least two scales: one scale show the boundaries of road, the second scale reflects the boundaries of lanes with asphalt, mid-barrier in the road, and trees in the road. Sometimes, an extra scale will be used to delete the false positive.

The hierarchy of classification in a planar image is actually a nested system. The object is nested in its super-objects, which means the number of scale is the number of nested layer in hierarchy, e.g. in the image of road, the asphalt pavement, mid-barrier, trees are paralleled object and they are nested in each other, but they are nested in their super-object road.

### The texture of objects

The structure of objects decides which multi-scale feature will be used. The using of multi-scale features will be stated in section 3.1.2: classification. The segmentation should coincide with the texture of objects. For example, in the image of the train station, the segmentation of finer scales should represent the distribution of sub-objects: coaches. The segmentation in sub-level should match the boundaries of elements of texture. The elements of the texture .

These objects match the shape of coach. The group of these objects makes the using of some special features—standard deviation of main direction of sub-objects or the mean of main direction of sub-objects possible.

### The optimal scales

In order to reduce the under/over-segmentation, the choosing of optimal scale is necessary. As stated in section 2.3: optimal scale, there are several methods to select the best segmentation scale. Actually, they all try to distinguish the objects in the whole scene. For single scale classification, the user would like to get a best distinction for all the interesting objects in the image so the ESP tool (Dragut et al., 2010) or plateau objective function (Martha et al., 2011) are good methods; however, for multi-scale classification, the segmentation of a certain object and its sub-objects is extremely important because of the multi-scale features. The user needs an improved strategy for the segmentation the multi-scale analysis.

## Classification

The multi-scale classification is majorly manipulated through multi-scale features. The multi-scale features provide the connection between different scales. They are the major difference between the single-scale classification and multi-scale classification. This section will illustrate the using of multi-scale features. There are five kinds of multi-scale features:

### The first kind of features

One is the “existence of sub-objects” and some geometric features, e.g. “center of the super-object”. “Existence of sub-objects” is used to tell whether an object has a sub-object of a

certain class or not. Similarly, "center of the super-object" tell if an object is the center of its super-object. This kind of features usually was not directly used to classify the object. Usually, the super-object or sub-objects of current objects are classified preliminarily, then current object is classified based on these features.

The Figure1 is the images of farmland and it is a part of image from the Geo-eye 1 pan-sharpen image of Delhi. The bright shining part is water in the wet paddy field. In Figure 1 (a), the parcel of farmland was segmented. And, the shining water is identified in the finer scale segmentation. In single scale, the wet paddy field may be classified by the threshold of brightness or NDVI. Actually, some dry paddy field also has the similar brightness value or NDVI value as the wet field, so they cannot be identified by brightness or NDVI in single scales. In multi-scale classification, the wet field can be identified by its sub-objects—the shining water. And, the brightness of the shining objects is above 131. It is much higher than other objects.

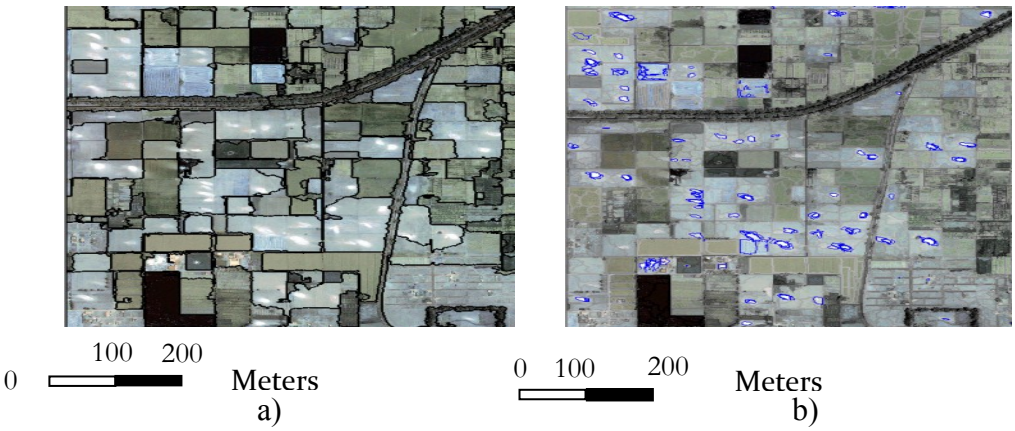


Figure 1: The classification of paddy wet field

When the shinning water is classified, the wet fields can be classified by "existence of sub-objects in shinning water class", i.e. if shining water objects is the sub-objects of one object, then this object will be classified as wet field.

**The second kind of features**

"Existence of super-objects" also describes the hierarchical relation and it is very commonly used in multi-scale classification for large class hierarchy tree. The related strategy of this feature is that: classify the super-objects first, and then classify its sub-objects with this feature to restrict the objects of sub-levels to the region of super-objects.

**The third kind of features**

Another kind of features is the statistical shape features of sub-objects. The shape feature of them are normally used as a replacement of GLCM to describe the texture, e.g. 'mean direction of sub-objects', 'average mean difference to neighbors of sub-objects: asymmetry' etc.

The GLCM is the count of the frequency of neighboring pixel pairs in a moving window. The statistic moment of the GLCM will be recorded in the central pixels of the window. In some OOA software, the GLCM features are not calculated in image objects instead of a moving window. Because the pixels are represented with squares, the direction of 0°, 45°, 90° and 135° is easily calculated.

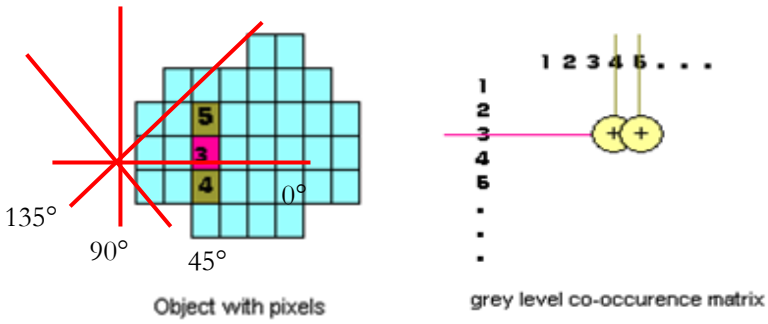


Figure 2: The directionality of GLCM (Definiens, 2009)

The Figure 2 shows the direction of GLCM. The number of the same pair-wise of pixel values will be recorded in the matrix. As a matrix, it has two diagonal: left diagonal and right diagonal. Theoretically, it has 8 directions. Due to calculation method: the pixels with the same value as its left or right neighbour are recorded always in positive value, the number of direction of GLCM is reduced to four. The value relies on the direction of count and the 0°, 45°, 90° and 135° GLCM is very commonly applied) (Definiens, 2009; Roumi, 2009). The usage of the GLCM features depends on their directionality. The GLCM mean and GLCM dissimilarity are the first-order GLCM moment. There are three commonly used second-order GLCM features: GLCM entropy, GLCM contrast. Strictly speaking, the GLCM features do not measure the texture or pattern. They measure the distribution of different sets of neighbouring pixels, the distribution of pair-wise pixels with distance 0 in one object.

Compared to GLCM, the multi-scale features have these advantages:

The GLCM features are only good at measuring the texture in eight directions, but the multi-scale features are not dependent on the direction.

The multi-scale features can identify the type of features more accurately. If an object has linear texture, the mean and standard deviation of main direction of sub-objects or the mean and standard deviation of asymmetry can detect the type of texture. But for GLCM, only the GLCM homogeneous/dissimilarity/contrast can find: in which direction, the object is homogeneous/heterogeneity, which can indirectly indicate the directionality of pattern.

Some multi-scale features can measure the heterogeneity of objects.

**The fourth kind of features**

The fourth kind of features is the statistical spectral features of sub-objects. The statistical spectral features are usually calculated to measure the heterogeneity of objects, e.g. two kinds of vegetation have similar NDVI but the texture is different.

Two examples are below. There are two kind of vegetation in Figure 3. The green object is the vegetation mixed with buildings and the red object is a sparse wood along a highway.

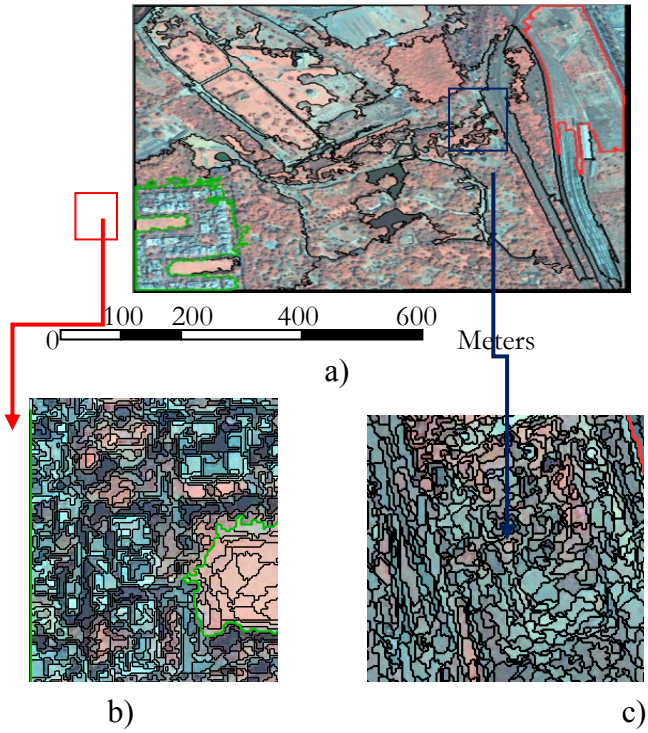


Figure3: Two places (within the red box and the blue box) has nearly same NDVI but the different mean difference of NDVI:

The NDVI of these two objects (within the red box and the blue box in Figure 3 (a)) are 0.098 and 0.091. They are very close. But, when the image is segmented into smaller objects, the mean absolute difference of NDVI has bigger difference between two kinds of vegetation than NDVI. They are 0.079 and 0.064 and the sparse woods have the smaller value. The structure of the two kinds of vegetation is different. In Figure 3 (b), the objects of trees and objects of buildings has big contrast; whereas in the Figure 3 (c), the NDVI of sub-objects of sparse woods change almost gradually.

Actually, NDVI of the red object and the green object are both 0.28. The values of the standard deviation of NDVI of them are 0.62 and 0.39 respectively. The standard deviation is different in these two objects because the red object is not absolutely homogeneous and there are some darker parts in this object.

If possible, the geo-statistic spectral features can be used to detect the texture more precisely.

## The Approaches in eCognition

The features and algorithms in eCognition show some backwards of GUIof eCogntion. Some of the features and algorithms in the software are apparently designed on the basis of feasibility and difficulty of programming instead of the habit of image processing/OOA analyst. There are a great many of featuresin the software. Obviously, not all of them are useful. the class color in the “class hierarchy tree” is a kind of feature, but it is very difficult to think when the user can use it.

The features can be used in multi-scale classification

**Create Customized Features-> Relational Customized Features**

All the multi-scale features can be created in the relational customized features. Some basic statistic parameters of the sub-objects can be calculated. The pattern of image can be measured by these customized features.

**Object Features: Layer Values->To Superobject**

Calculate the basic statistic parameters with the reference of the super-object or compare the statistic parameters with super-object.

**Object Features: Geometry->To Superobject**

Calculate the geometric position of the current objects in the extent of their super-object.

**Object Features: Texture -> Layer Value: Texture Based on Sub-objects**

Measure the texture based on the statistic parameters of spectral values of the sub-objects. It can be customized in relational customized features.-> Shape Texture: Based on Sub-objects

Measure the texture based on the statistic parameters of geometric values of the sub-objects. It can be customized in relational customized features.

The algorithm can be used in multi-scale classification

Multi-resolution Segmentation: this is common segmentation algorithm for multi-scale classification. The FNEA is embedded in it.

Multi-resolution segmentation region growing: just as its name, it can be used after the segmentation of the first scale. The principle is also FNEA.

Convert to Sub-objects: There is no real optimal scale. In some cases, when facing the under segmentation in a small part of the image, we can use it to convert the current object to its smaller sub-objects.

Hierarchical Classification: It is an algorithm similar to decision tree, but it is not real multi-scale classification we want.

## Summery

The major difference between the real multi-scale classification and the single-scale classification is the using of information from multiple scales. This information can be many kinds and they are sorted into five kinds of multi-scale features. They have great potentials to detect the texture. Before the operation of multi-scale classification, the structure of image will be analyzed first, and then the segmentation and classification can be manipulated with multi-scale features. The segmentation also need to match the boundaries of natural objects or texture elements so the multi-scale features can be calculated precisely. These features in eCognition are listed after the conceptualization to help the researcher use eCognition to do multi-scale classification. The algorithm available for multi-scale classification is no more than multi-resolution segmentation. The choosing of parameters is also discussed.

**References：**

[1] Atkinson, P. M., & Aplin, P. Spatial variation in land cover and choice of spatial resolution for remote sensing[J]. International Journal of Remote Sensing, 2004,25(18), 3687-3702.

[2] Benz, U. C., Hofmann, P., Willhauck, G., Lingenfelder, I., & Heynen, M. (2004). Multi-resolution, object-oriented fuzzy analysis of remote sensing data for GIS-ready information[J]. ISPRS Journal of Photogrammetry and Remote Sensing, 2004,58(3-4), 239-258.

[3] Blaschke, T., & Hay, G. J. Object-oriented image analysis and scale-space theory and methods for modeling and evaluating multiscale landscape structure[J]. International Archives of Photogrammetry and Remote Sensing,2001 34, 22-29.

[4] Burnett, C.. A multi-scale segmentation/object relationship modelling methodology for landscape analysis[J]. Ecological Modelling, 2003168(3), 233-249.

[5] Dragut, L., Tiedec, D., & Levickd, S. R. ESP: a tool to estimate scale parameter for multiresolution image segmentation of remotely sensed data[J]. International Journal of Geographical Information Science,2010 ,(6), 1-13.

[6] Esch, T., Thiel, M., Bock, M., Roth, A., & Dech, S.. Improvement of Image Segmentation Accuracy Based on Multiscale Optimization Procedure[J]. IEEE GEOSCIENCE AND REMOTE SENSING LETTERS, 2008,5(3), 463-467.

[7] Liu, D. S., Song, K., Townshend, J. R. G., & Gong, P. Using local transition probability models in Markov random fields for forest change detection[J]. Remote Sensing of Environment, 2008,112(5), 2222-2231.

[8] Hall, O., & Hay, G. J. (2003). A multiscale object-specific approach to digital change detection[J]. International Journal of Applied Earth Observation and Geoinformation, 2003,4(4), 311-327.

*Applied Mechanics and Materials Vols. 580-583 (2014) pp 2860-2864*
*© (2014) Trans Tech Publications, Switzerland*
*doi:10.4028/www.scientific.net/AMM.580-583.2860*

# Research on GPS height partition fitting method

Chang Wang[1, a]

[1] University of Science and Technology Liao Ning School of Civil Engineering, AnShan LiaoNing

[a]wangchang324@163.com

**Keywords**: Partition Fitting;The Quadric Surface Fitting; Mobile Triangle Method

**Abstract.** In Diaobingshan area, Use 76 data points (geodetic height and normal height are known) as experimental data, the quadric surface fitting mean square error as GPS height partition fitting basis in the area. In 76 data points, some data points which GPS height fitting residual value is less than the quadric surface fitting mean square error in a region, other points which GPS height fitting residual value is more than the quadric surface fitting mean square error in a region, in the same time, individual regions(data points is less) use mobile triangle method to establish GPS height the fitting model. The experiment prove that the effect of this kind partition fitting method is better than that of no partition fitting method, has a certain reference value.

## Introduction

With the development of GPS technology, more and more construction units use GPS technology, GPS technology get elevation data belongs to the geodetic height, but use the normal height system as elevation system in China, so geodetic height converting normal height is a urgent problem in the aspect of application of GPS Technology. At present, GPS height fitting method is an effective method. But this method is also influenced by modeling point distribution and areas high low fluctuation, sometimes the effect of the GPS height fitting is not very ideal. This paper mainly studies the GPS height partition fitting method in Diaobingshan area ,uses 76 data points, the quadric surface fitting mean square error as partition basis to establish the fitting model，individual regions use mobile triangle method[1][2].

## GPS Height Fitting Method

1.The Quadric Surface Fitting

the quadric surface polynomial theory formula[3][5]：

$$F(x,y) = a_0 + a_1 x + a_2 y + a_3 xy + a_4 x^2 + a_5 y^2 \tag{1}$$

Among them, $a_i$ as the coefficients which was obtained by least square method.

2.Mobile Triangle Method

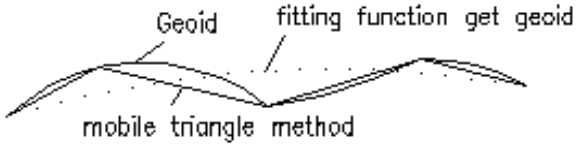


Fig. 1 Different fitting level surface schematic diagram

The basic idea: point A landed in a triangle, elevation abnormal and plane coordinate of the three vertices of the triangle are $(x_1, y_1, \xi_1)$, $(x_2, y_2, \xi_2)$ and $(x_3, y_3, \xi_3)$, determining the plane equation by three points is:

$$\begin{vmatrix} x & y & \xi & 1 \\ x_1 & y_1 & \xi_1 & 1 \\ x_2 & y_2 & \xi_2 & 1 \\ x_3 & y_3 & \xi_3 & 1 \end{vmatrix} = 0 \tag{2}$$

Height anomaly of point A:

$$\xi = \xi_1 - \frac{(x-x_1)(y_{21}\xi_{31} - y_{31}\xi_{21}) + (y-y_1)(\xi_{21}x_{31} - \xi_{31}x_{21})}{x_{21}y_{31} - x_{31}y_{21}} \quad (3)$$

Height of point A:

$$h_p = H_p + \xi_p \quad (4)$$

**Experiment and GPS height fitting model precision analysis**

1.GPS height Fitting model precision analysis in no partition situation

In 76 points, select 42 points as modeling points,34 points as check points, the quadric surface Fitting as GPS height fitting method, we can see modeling points graph and the quadric surface fitting accuracy from figure2 and table1[4],

Table 1 The quadric surface fitting accuracy unit mm

| name | the quadric surface fitting |
|---|---|
| internal accord precision | 12.9 |
| external accord accuracy | 18.2 |

Fig.2 Model points graph (● as modeling points)

From fig.2, table 1, we can see that modeling points should cover the entire region, the quadric surface fitting internal accord accuracy and external accord accuracy are less than 2 cm.

2.GPS height Fitting model precision analysis in partition situation

1）GPS height Fitting Partition method

76 data points as modeling points, get mean square error and the residual value of each point by the quadric surface fitting. in 76 data points, some points which GPS height fitting residual value is less than the quadric surface fitting mean square error in a region, other points which GPS height fitting residual value is more than the quadric surface fitting mean square error in a region. Due to the number of points is less, individual regions use mobile triangle method to establish the fitting model, Fig. 3

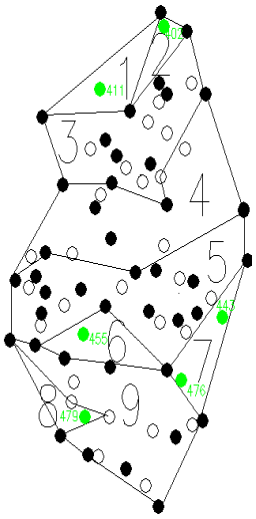


Fig.3 Zoning map

●as modeling point; ○as check points ; ● as mobile triangle method fitting point

From fig.3 ,we can know that the residual value of all points in 3 area, 5 area and 9 area is less than the quadric surface fitting mean square error; the residual value of all points in 4 area is more than the quadric surface fitting mean square error; using mobile triangle method to establish the fitting model in 1 area, 2area , 6area, 7area and 8 area.

2）Partition fitting precision analysis

（1）Use the quadric surface fitting to establish fitting method in 3 area, 4 area, 5 area and 9 area. There are 20 point in 3 area, 12 points as modeling points, 8 points as check points; There are 26 point in 5 area, 18 points as modeling points, 8 points as check points; There are 18 point in 9 area, 10 points as modeling points, 8 points as check points; There are 15 point in 4 area, 10 points as model building points, 5 points as check points.

（2）Use mobile triangle method to establish GPS height fitting method in 1 area, 2area , 6area, 7area and 8 area, from table2, 3 and fig.4～7 can see GPS height fitting result,

Table 2 The quadric surface fitting accuracy in four regions unit :mm

| name | 3region | 5region | 9region | 4region |
|---|---|---|---|---|
| internal accord precision | 11.7 | 8.4 | 8.8 | 17.3 |
| external accord accuracy | 8.6 | 9.3 | 11.0 | 29.8 |

Table 3 Mobile triangle method fitting accuracy unit :mm

| 1 region | check point residual value | 2 region | check point residual value | 6 region | check point residual value |
|---|---|---|---|---|---|
| | δ=46.29 | | δ=1.96 | | δ=31.73 |
| 411 | 46.29 | 402 | 1.96 | 455 | 31.73 |
| 7 region | check point residual value | 8 region | check point residual value | | |
| | δ=17.9 | | δ=33.82 | | |
| 443 | 17 | 479 | 33.82 | | |
| 476 | 18.78 | | | | |

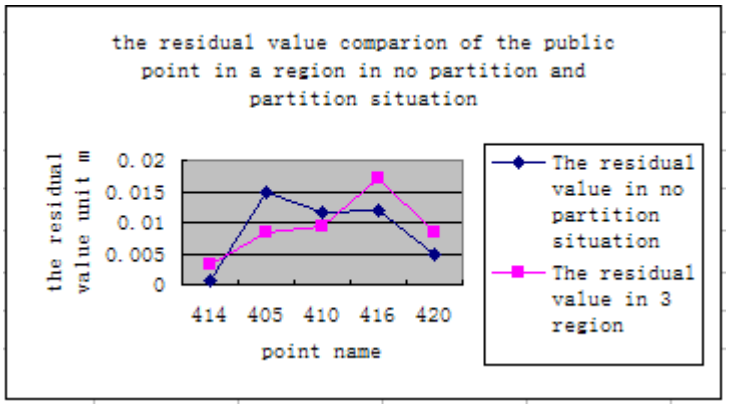


Fig.4 The residual value comparison of the public point in 3 region in no partition and partition situation

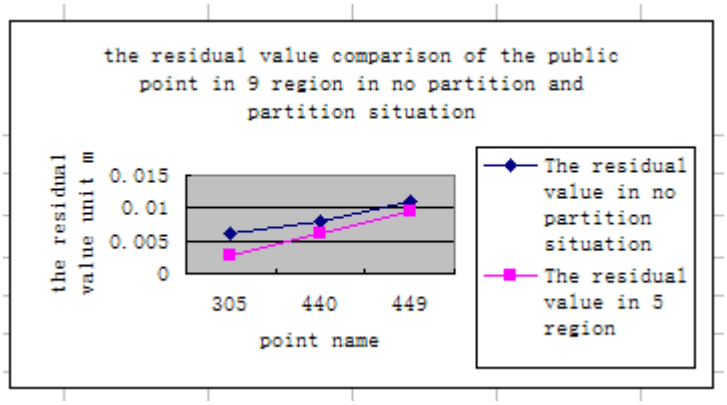


Fig.5 The residual value comparison of the public points in 5 region in no partition and partition situation

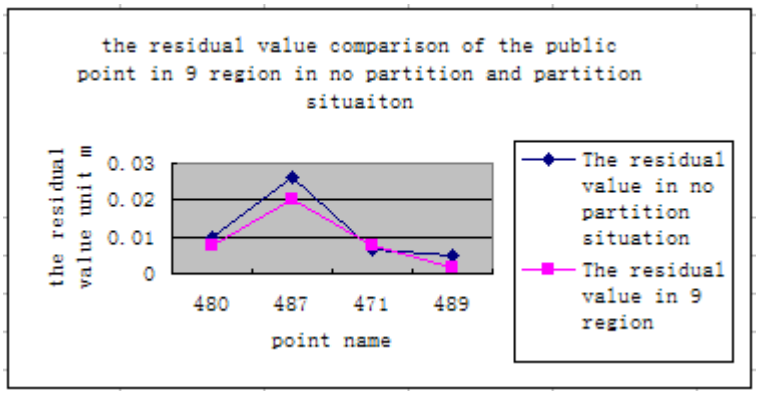


Fig.6 The residual value comparison of the public point in 9 region in no partition and partition situation

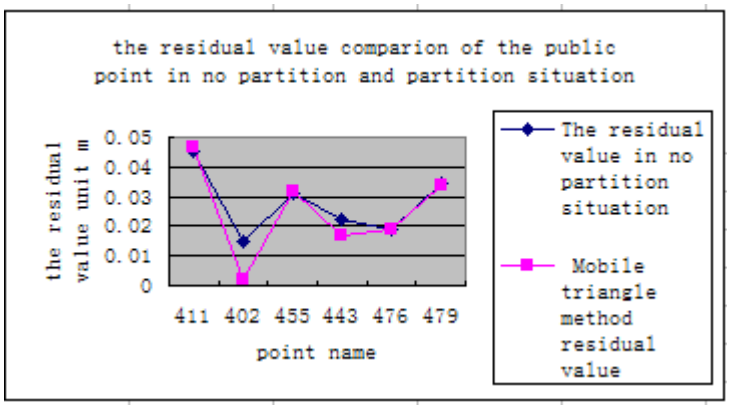


Fig.7 The residual value comparison of the public point in no partition and partition situation

From table 2 ,we can see that internal accord precision and external accord accuracy are higher than that in no partition situation in 3 region, 5 region, 9 region; internal accord precision and external accord accuracy are less than that in no partition situation in 4 region, so 4 region is not suitable for partition fitting.

From fig.5, fig.6 ,we can see that the residual value of public points in partition situation is less than that in no partition situation in 5 region, 9 region.

From fig.7,we can see that the residual value of three points(402, 443, 479) is less than that in no partition situation by mobile triangle method in 2 region, 7 region and 8 region.

**Summary**

1.If the effect of GPS height fitting is better in whole region, use partition fitting to establish fitting model in this region can effectively improves the fitting precision.
2. In Diaobingshan area, use quadric surface fitting mean square error as partition basis, points which fitting residual value is less than the quadric surface fitting mean square error in a region, the effect of GPS height fitting in partition situation in this region is better than that in no partition situation, points which fitting residual value is more than the quadric surface fitting mean square error in a region, the effect of GPS height fitting in no partition situation in this region is better than that in partition situation.
3.there are less data points in some regions, use mobile triangle method to establish GPS height fitting model in these region, can effectively improve the fitting accuracy, and the program design is relatively simple.

**Reference**

[1]Gongyusheng. Research on GPS level model and its application[D].Fuxin: Liaoning Technical University

[2]Wanghuinan. the principle and application of GPS navigation[M].Beijing: Science Press,2003

[3]Yaojili,Chulili,Yuzhilu. Research on GPS geoid fitting method[J].Surveying and Mapping Engineering2005(4):23-26

[4]Lichangchun.Study on some problems of GPS height partition fitting[J].Mine Survying.2004(9): 19-21

[5] Zhaochangsheng.Survey adjustment[M]. Education Science Press:2000

*Applied Mechanics and Materials Vols. 580-583 (2014) pp 2865-2871*
*© (2014) Trans Tech Publications, Switzerland*
*doi:10.4028/www.scientific.net/AMM.580-583.2865*

# GPS RTK Techniques for Construction Monitoring of Super Deep-water Open-caisson

Hao Yanguang [1, a], Liu Xiangliang [2,b] ,Liu Jianbo [3,c]

（Cccc WuHan Harbour Engineering Design And Research Co.Ltd,wuhan，china,430040）

[a]haoyg1314@163.com, [b]67821205@qq.com

**Keywords:** GPS RTK Techniques, super deep-water open-caisson, Taizhou Yangtze River Bridge, positioning system of anchor piers, real-time monitoring.

**Abstract.** The super open-caisson foundation of Taizhou Yangtze River Bridge was used by positioning system of anchor piers. GPS RTK Techniques was used to real-time monitor the open-caisson and by software compute current geometric posture of open-caisson timely. This could provide guarantee for sinking of caisson, and shorten construction period and save cost.

## Introduction

Taizhou Yangtze River Bridge is located in the middle of the Yangtze River in Jiangsu Province, between Jiangyin Yangtze River Bridge and Runyang Yangtze River Bridge. It connects Taizhou city in the north and Zhenjiang city and Changzhou city in the south. The three-tower suspension bridge consists of 390＋1080＋1080＋390m spans in the main body. The width of main bridge is 33m with designed vehicle speed of 100km/h. The middle tower falls into the gate-type steel structure and the towers in the north and south belong to concrete structure. The distribution of main bridge structures is shown in Fig. 1.

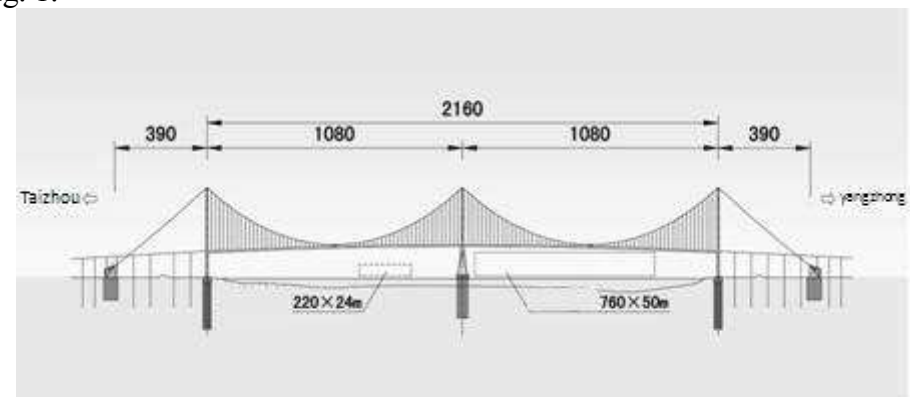


**Fig.1 Distribution of Main Bridge Structures**

The middle tower adopts super deep-water open-caisson foundation and the dimensions of standard caisson section are 44*58m, the radius of transition arc is 8m. The design elevation of caisson cutting-edge is -70m and the bearing layer is fine sand. The total height of caisson is 76m, wherein 38m on the lower part is steel-shell structure, filled with concrete, and 38m on the upper part is concrete structure. The concrete caisson height is completed in three times. The caisson structures and compartment distributions are shown in Fig. 2.

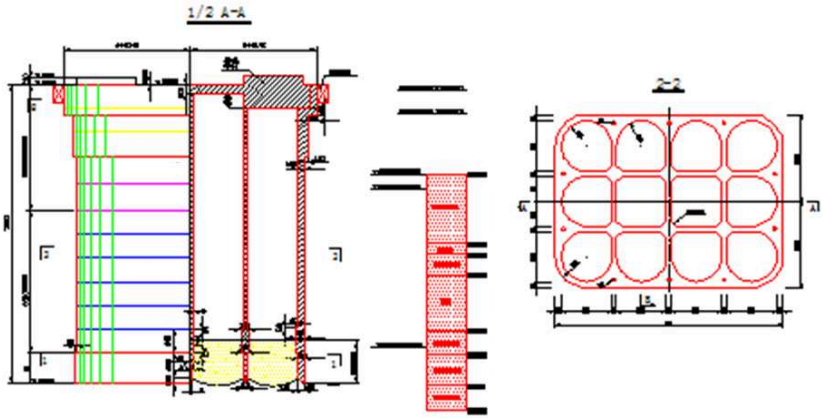

**Fig. 2 Caisson Structures**

## Foundation Construction

The middle tower of Taizhou Yangtze River Bridge is located in deep and rapid current. The riverbed will be greatly affected by rapid current during the process of sinking, which brings big risks to the construction. According to the characteristics of the construction as well as comparison of domestic and foreign data research and scheme selection, the construction of steel caisson will adopt the positioning system of anchor piers in the upstream and downstream.

### 2.1 Positioning System

**1) Design of Positioning System**

The positioning system consists of such equipment as anchor pier, anchor, chain, wire rope and hoist. The plan size of upstream anchor pier is 28*21m, with 20 pieces of φ1200*14mm steel pipe piles as the foundation. The plan size of downstream anchor pier is 25*21m, with 16 pieces of φ1200*14mm steel pipe piles as the foundation. On the platform of every anchor pier distributed with 12 hoists and the wire rope will connect anchor and caisson to the hoist by means of connecting devices. The positioning of steel caisson will be realized by controlling hoist to change the pulling forces, as shown in Fig. 3.

**Fig. 3 Positioning System of Steel Caisson**

**2) Calculation and Analysis of Caisson Resistance**

Positioning of caisson will be affect by external factors such as wind load, current force and wave forces, which will influence the accuracy. According to the hydro geological data and field observation, the external load data will be set as follows:

① wave force: Wave height is 0.5m and period is 3.15s, wave length is 15.5m;

② current force: Current velocity is 1.2m/s, with 10°of southern intersection angle to the upstream and downstream axis at caisson;

③ wind load: Wind speed is 20.8m/s when caisson is positioning and wind speed is 13.8m/s when caisson is implanted; and

④ Other basic data: The high-tide level in construction is +2.50m, riverbed elevation at piers is -15.0m, and the standard section size of caisson is 44.0m*58.0m, with total height 38m.

The unfavorable combination of water resistance, wind resistance and wave forces when caisson is sinking to be implanted will be regarded as the designed load of positioning system in calculation. The caisson assistance will be calculated as in following Table 1:

**Table 1 Calculation of Caisson Resistance Conditions**

| Conditions | | Draft (m) | height above water (m) |
|---|---|---|---|
| Condition 1 | Caisson floated in place | 12.15 | 25.85 |
| Condition 2 | No erosion | 17.5 | 20.5 |
| Condition 3 | 10m of erosion | 27.5 | 10.5 |

Calculations of front and side resistance on caisson in various conditions are shown in Table 2 and Table 3:

**Table 2 Calculation of caisson front resistance (parallel to river)**

| condition | Max Velocity m/s | Draft (m) | Current Force (kN) | Wind Force (kN) | Wave Force (kN) | Joint Force (kN) |
|---|---|---|---|---|---|---|
| Condition 1 | 1.2 | 12.15 | 655.5 | 307.1 | 723.8 | 1686.4 |
| Condition 2 | 1.2 | 17.5 | 944.1 | 243.5 | 906 | 2093.6 |
| Condition 3 | 1.2 | 22.5 | 1483.6 | 55 | 1119.7 | 2658.3 |

**Table 3 Calculation of caisson side resistance (vertical to river)**

| Condition | Max Velocity m/s | Draft (m) | Current Force (kN) | Wind Force (kN) | Wave Force (kN) | Joint Force (kN) |
|---|---|---|---|---|---|---|
| Condition 1 | 1.2 | 12.15 | 335.2 | 451.8 | 582.4 | 1369.4 |
| Condition 2 | 1.2 | 17.5 | 511.6 | 321 | 687.2 | 1519.8 |
| Condition 3 | 1.2 | 27.5 | 803.9 | 72.5 | 849.4 | 1725.8 |

3) Positioning Construction of Caisson

Positioning of steel caisson parallel to river: Steel caisson positioning shall be controlled by 12 sets of hoists and tackles installed on upstream and downstream anchor piers.

Positioning of steel caisson in north-south direction: To lift side anchors at northern and southern side of caisson, and connect the cables on side anchors to the hoist on anchor pier platform through guide device on caisson. Adjust the tensions of each anchor cable to control the plane position.

Positioning of steel caisson consists of preliminary positioning, tilt adjusting and accurate positioning, and the procedures in various construction periods are as follows:

① Preliminary positioning The procedures of preliminary positioning of caisson: Steel caisson floated to pier position; adjust each pull cable in position through anchorage system; adjust the main pull cable on upstream and downstream through hoist system on anchor pier platform and make adjustment to the position parallel to river currency; adjust caisson positions through side anchor cables at northern and southern sides.

② Tilt adjusting The procedures of caisson tilt adjusting: strictly control the pull force of each pull cable when caisson is in position and supervise on drop cables and main cables at upstream, adjust the force on each cable at all time to ensure even stresses on cables. During the process of water

filling, strictly control every compartment and the surveyors conduct overall observations on top elevation differences of caisson. If the differences are too large, adjust drop cable and main cable; when adjust to be horizontal, tighten side anchor cable, drop cable and main cable.

③ Accurate positioning When caisson is filled with water and dropped to the place where there are two meters between cutting edge and riverbed, the accurate positioning of caisson will be conducted. The adjustment method is the same with the preliminary positioning of steel caisson.

### 2.2 Excavation Sinking of Caisson

The caisson sinking at middle tower of Taizhou Bridge will adopt the method of excavation without water drainage, and the overall construction technological process is shown in Fig. 4 as follows:

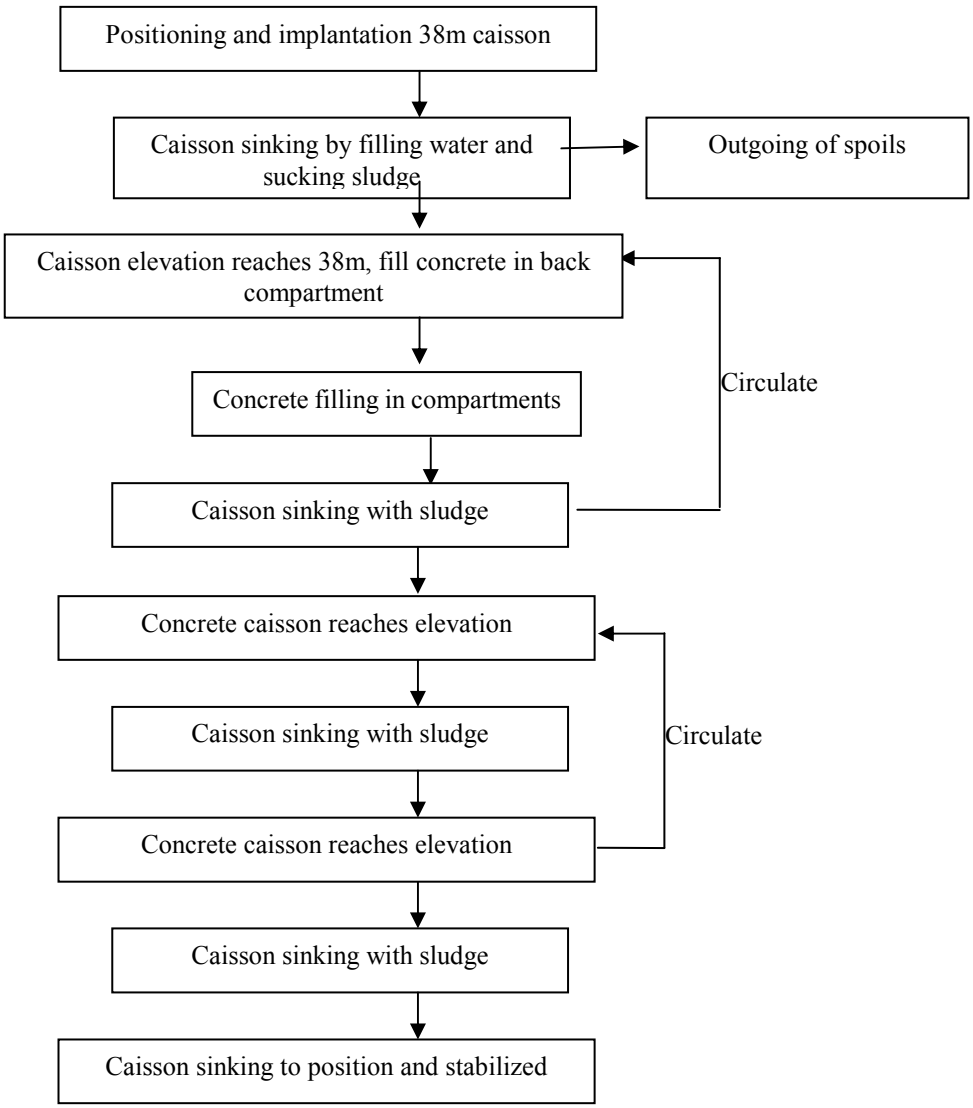


**Fig. 4 Construction Process of Caisson Sinking**

According to on-site geological and environmental conditions, caisson sinking shall adopt the suction method, with diving drill methods as a supplement. On September 2, 2008, the 76m caisson successfully sank to designed elevation.

## Construction Monitoring System of Caisson Positioning

### 3.1 Monitoring System

By means of GPS RTK technology and self-developed software, the monitoring system successfully helped to realize caisson positioning and implantation as well as real-time monitoring

during sinking construction. The monitoring system consists of data acquisition, data processing and data management, and the operating procedures are as follows: GPS device automatically collects data and transmit the real-time data to receiving station through Wireless communication technology. The self-developed software packages will process such data and display the real-time geometric attitudes of caisson such as plane deviation, tilt, subsidence and torsion. GPS measuring instruments and monitoring software interface are shown in Fig. 5 as follows:

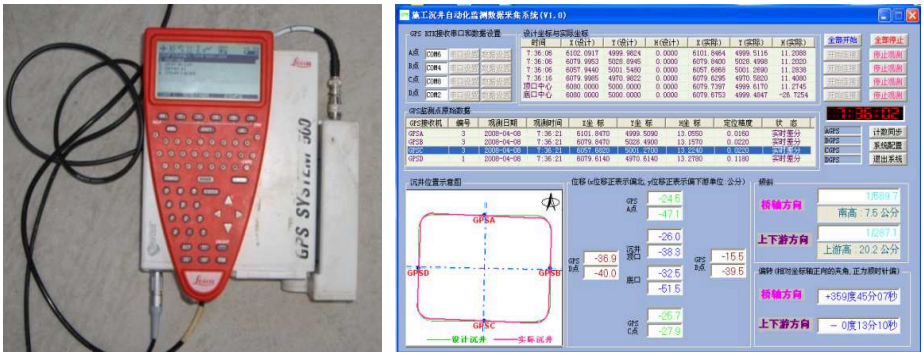

**Fig. 5 Measuring Instrument and Screenshot of Monitoring Software**

### 3.2 Distribution of Measuring Points

In order to accurately display the geometric attitudes of caisson during the process of positioning, implantation and sinking with sludge, measuring points are arranged at the center of all axis on caisson top, which are shown in Fig. 5 as follows.

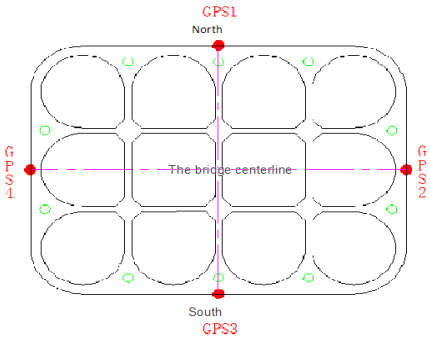


**Fig. 5 Distribution of GPS Measuring Points**

### 3.3 Data Analysis

The foundation construction of middle tower caisson consists of following procedures, such as positioning, implantation, concrete filling in compartment, sinking with sludge and elevation joint of concrete caisson, etc. Wherein, the elevation joint process of concrete caisson is not real-time monitored. In Fig. 6 to Fig. 10, the curve of caisson sinking, the curve of center deflection, the curve of torsion angle and curve of elevation difference in two axis directions.

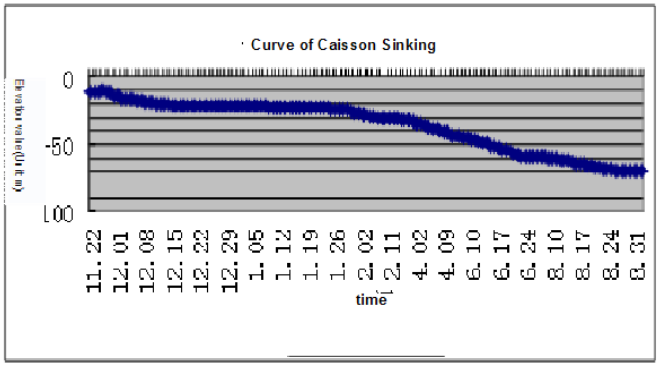


**Fig. 6 Curve of Caisson Sinking (Unit: m)**

According to Fig. 6, in initial period of caisson positioning and implantation, there are elevation fluctuations on cutting edge bottom of caisson, which is due to rise and fall of the river tides. When cutting edge elevation of caisson reaches -21.00m, concrete begins to fill in compartment walls, but sinking with sludge is not started. The curve during such period is nearly horizontal and decreasing a little, that's because the concrete in compartment walls added the self-weight of the whole structure. Meanwhile, we can find that there are several decreasing period in the curve, which means caisson is in the process of sinking with sludge. When caisson cutting edge is approaching design elevation, the sinking speed will be controlled for sake of sinking accuracy, therefore the sinking curve is decreasing quite mildly.

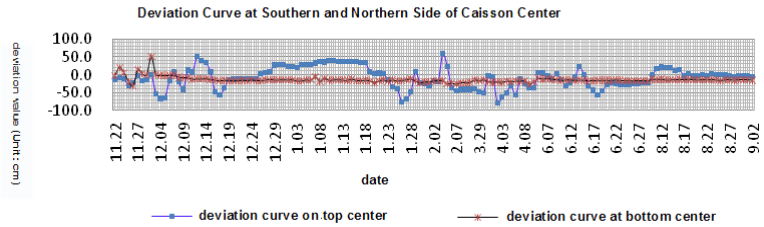


**Fig. 7 Deviation Curve at Southern and Northern Side of Caisson Center (Unit: cm)**

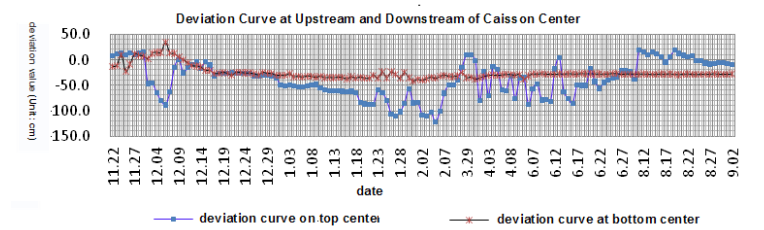


**Fig. 8 Deviation Curve at Upstream and Downstream of Caisson Center (Unit: cm)**

In Fig. 7 and Fig. 8, there are curves of two axis-direction deviations at caisson center, and the north-south deviation will take north as positive, upstream-downstream deviation will take south as positive. The curve with ■ means deviation curve on top center point, which shows big swing amplitude during the process of sinking. But when caisson is sinking to the designed elevation, the swing amplitude is small and deviation value is within 12cm (designed value is 50cm). The curve with ※ means deviation curve at bottom center point. After caisson implantation, especially the compartment concrete has been cast, the deviation is always in a stable condition. We can see that there are certain amounts of reserved deviations at the downstream site of bottom center point of caisson during the initial period of implantation. During the process of sinking, the bottom center point deviated toward upstream gradually, which is due to different side pressures aroused by riverbed elevation difference at upstream and downstream.

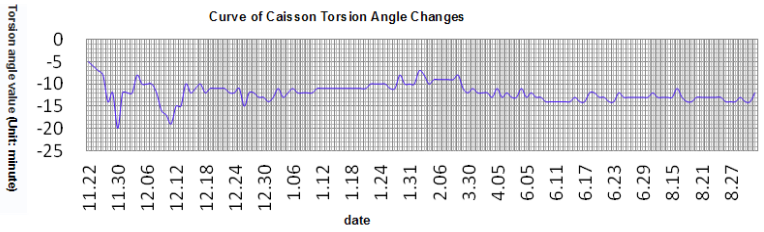


**Fig. 9 Curve of Caisson Torsion Angle Changes (Unit: minute)**

Fig. 9 shows the curve of caisson torsion angle changes, which takes clockwise direction as positive. The caisson torque is always controlled within 20 minutes, which means caisson is under the state of symmetric stress during the process of sinking and elevation joint. When sinking to position, the torque angle of caisson is 12 minutes, which is also in the allowable ranges.

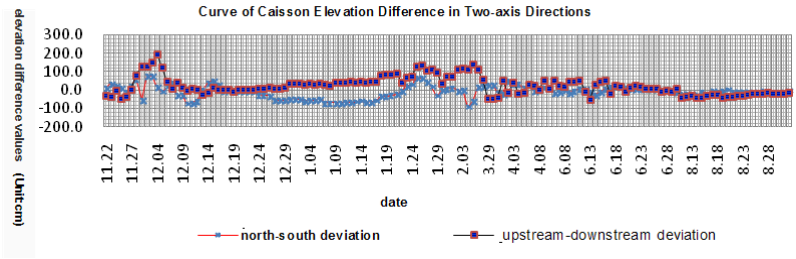


**Fig. 10 Curve of Caisson Elevation Difference in Two-axis Directions (unit: cm)**

Fig. 10 shows the relative elevation difference of caisson in two-axis direction, the north-south deviation will take north as positive and upstream-downstream deviation will take south as positive. In initial period of sinking, the elevation difference in two-axis direction may be large, but the elevation difference values will gradually change mildly after prompt adjustment. According to the Fig, when caisson is sinking to position, the top surface will in the horizontal condition.

In short, when caisson is sinking to position, the maximum deviation of top plane will be 11.4cm, tilt angle will be 1/363 and the torsion angle will be 10.8′, which are all less than the permissible values.

## Conclusion

Monitoring system of GPS positioning successfully completed the whole-process monitoring on middle-tower caisson construction of Taizhou Bridge. During construction, it really realized the automation, information monitoring technology, real-time display of caisson geometric postures, so as to provide technical support to caisson positioning, implantation and sinking with sludge. Meanwhile, because this technology is not influenced by the external environmental factors, it will greatly ensure the construction progress and shorten the construction period, then provide valuable references to similar projects, especially those under harsh environmental conditions.

## Reference

[1]. Xie Rong'an Application of GPS RTK Technology in Marine Charting [J] *Geographic Spatial Information*, 2007, (04).

[2]. Lai Jiwen GPS Technology and Application in Engineering Survey [J] *Geological Mineral Charting,* 2006, 22(3):11-13.

[3]. Zhou Ruixiang Application of GPS-RTK Technology in Pile Foundation Construction of Donghai Bridge [J] *Railway Survey*, 2004, (01): 59-61.

[4]. Wang Hong, Feng Changsheng GPS-RTK Technology in Bridge Monitoring [J] *World Bridge,* 2003, (03): 74-76.

*Applied Mechanics and Materials Vols. 580-583 (2014) pp 2872-2875*
*© (2014) Trans Tech Publications, Switzerland*
*doi:10.4028/www.scientific.net/AMM.580-583.2872*

# Triangle Interpolation on Discrete Point Set

Hongfei Jiang

School of Civil Engineering, Central South University, Changsha China 410075

jhf1967@163.com

**Keywords:** Cone; Interpolation; Discrete points; Mesh; Triangle

**Abstract.** An algorithm for triangle interpolation on discrete points is presented in the paper. It creates a square mesh which covers all the discrete points, then puts the points into the mesh and records the relationship between grids and points. When interpolating elevation of an interpolation point, it can fast find the discrete points which are near the interpolation point and these discrete points can be used to create a special triangle which contains the interpolation point. The elevation of the interpolation point can be obtained from the triangle. The method has the advantage of fast speed, high precision and needing less memory.

## Introduction

Interpolation based on discrete points has a wide variety of applications in GIS and CAD .It not only can create 3D terrain, to calculate ground slope and earthwork, but also is the foundation of realizing 3D visual design in civil engineering.

The key of the algorithm for interpolation is generation of a curved surface which can be used to calculate the value of the interpolation point, in general, the curved surface should not be created based on all discrete points for the number of discrete points is huge, in order to improve the interpolation speed and accuracy it only consists of several points which are near the interpolation point. There are two methods to create curved surface for interpolation. The first method uses a square mesh to administrate discrete points, discrete points can be easily positioned through square mesh; it uses the discrete points which are near the interpolation point to create a curved surface for interpolation, quadric surface or cubic surface is the most popular one for interpolation and it can be created by surfaces fitting method; the principle of this algorithm is simple and the method is easy to realize. The second method must create a triangular mesh based on the discrete points and every triangle can be used for interpolation, it uses the triangle which contains the interpolation point to calculate the value of the interpolation point; the method has higher precision, the shortcomings of the algorithm are that creating triangular mesh need much calculation and saving the triangles need much memory and the speed of searching the triangle which contains the interpolate point is slower.

In reference[4], a method for interpolation based on discrete points is presented, the method can fast find out the discrete points which is correlative to the given point by data blocking technology and block search technology, then interpolating the value of given point by distance weighted interpolating method, the method has a fast speed, but the precision of interpolation is not high because the method can not assure the distribution of discrete points selected by the method to interpolate the value of a given point is even and in some regions there are sudden changes which cannot be well described by discrete points.

In this paper a method for interpolation based on discrete points is presented, the method indexes the discrete points by a square mesh so we can fast find out the discrete points to take part in interpolation as long as we know the grid which the given point locates in when interpolating the

value of the given point, then a interpolating triangle which includes the given point can be created using the discrete points and the value of the given point can be obtained from the triangle.

**Principle of the Algorithm**

When interpolating the value of a given point, we know the value of the given point is mainly decided by the discrete point near the given point, so we hope to create an interpolation triangle to calculate the value of the given point and the triangle contains the given point and the vertices of the triangle are nearest to the given point.

Based on the idea, the algorithm of interpolation in this paper is based on discrete point digital terrain model, so we must build discrete point digital terrain model by general method before interpolation. Through the discrete point digital terrain model we can fast find out the discrete points which are correlative to the given point based on discrete point digital terrain model. To create the triangle, we first select two points which are nearest to the given point; then we select the third point to form a triangle which includes the given point and use the triangle to interpolate the value of the given point.

In order to introduce the algorithm in detail, the definition of cone is given as follows:

if C is a set in $R^n$ and C is not null, $x \in C, \forall p \in R^n \forall$ ,if $x + p \in C$, then $x + tp \in C(t \geq 0)$, set C is called a cone of vertex x. If cone C is convex, set C is called convex cone [5].

A set combined with several vectors $V_0, V_1, ..., V_m$, e.g. $c = \left\{ x \middle| x = x_0 + \sum_{i=0}^{m} r_i V_i, r_i \geq 0 \right\}$ is a convex cone of vertex $x_0$.

Especially, in 2D space, a convex cone making up of vector BA and vector BC is the ∠ABC (the angle is less than π).

In figure 1, the value of O is unknown, in order to calculate the value of O, At first, we can find out point A and point B in discrete points digital terrain model which are the nearest to point O, secondly, find out point P which is near point O and ΔPAB contains O and the shape of ΔPAB is good, finally, we can use ΔPAB to interpolate the value of point O.

In order to get point P, find out the points which is in the convex cone R making up of vector OC(namely -OB) and vector OD(namely -OA) . In following we prove that O is in ΔABP only when P is in convex cone R.

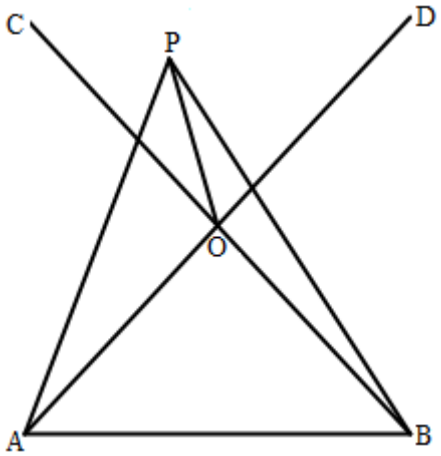

Fig.1 Interpolation triangle formation

Proof:

See figure 1, we can get:

$$OP = r_1 AO + r_2 BO, PB = -OP - BO, PA = -OP - AO \quad (1)$$

Then

$$PO = (r_1 PA + r_2 PB)/(1 + r_1 + r_2) \quad (2)$$

$$PA = PO + OA = (1 + r_1)OA + r_2 OB \quad (3)$$

$$AB = OB - OA \quad (4)$$

Now it is easy to get that:

$$AO = (AP + r_2 AB)/(1 + r_1 + r_2) \tag{5}$$

The following conclusion is available:

(1)When point P is in convex cone R, this means $r_1 \geq 0$ and $r_2 \geq 0$.

$r_1/(1+r_1+r_2) \geq 0$ and $r_2/(1+r_1+r_2) \geq 0$ is true. According to (2) and (5), we know O is not only in the convex cone making up of vector PA and vector PB but also in the convex cone making up of vector AP and vector AB, that means ∆PAB contains point O.

(2)When point P is not in convex cone R, then at least one of r1 and r2 must be less than 0.

$r_1/(1+r_1+r_2)$, $r_2/(1+r_1+r_2)$, $1/(1+r_1+r_2)$ must not be greater than 0 at same time. According to (2) and (5), we know that O is not only in the convex cone making up of vector PA and vector PB but also in the convex cone making up of vector AP and vector AB is impossible, so ∆PAB can not contain point O.

The following theorem can be gotten:

THEOREM: Given three points A,B,O, the sufficient condition of O is in ∆PAB is that P is in the convex cone making up of vector AO and vector BO.

The interpolating triangle can be built according to the following steps:

1.Search for point A and point B which are the nearest to point O to form the first side of interpolating triangle; then create a convex cone R by vector AO and vector BO, the vertex of the convex cone is O;

2.Find point P which is in convex cone R near point O, and ∆PAB is an interpolating triangle, if there are two or more points in convex cone R, several interpolating triangles can be created, the triangle which minimum angle is the greatest is the best for this method can avoid creating long and narrow interpolating triangle, and we certainly can use other law to select the third vertex of interpolating triangle.

It is possible that there are not any discrete points in convex cone R, if this happens, we cannot form an interpolating triangle but it is probable to create an interpolating triangle if we use other two points to form the first side of interpolating triangle, but the new two points should near O as far as possible, so we must consider this circumstances.

**Processing of Terrain Feature Lines**

According to the method presented in this paper, an interpolation triangle must be created for interpolating the height of given point, the shape of the interpolation triangle will greatly influence the precision of interpolation. Because the max-min angle law is used to create interpolation triangle, narrow and long interpolation triangle is effectively restricted. For general terrain, interpolation triangle is close to ground; when interpolation triangle crosses any terrain feature line, it is not close to ground, the precision of interpolation will be reduced. How to deal with this problem? An effective method is to keep interpolation triangle on one side of any terrain feature line; this measure can be taken on a special DTM with terrain feature lines; In this special DTM every grid in square mesh, which administrates discrete points, adds a message to record terrain feature lines which pass through it.

Now we can fast find out the disordered points and terrain feature lines which are near to interpolation point; these disordered points and vertexes of the terrain feature lines can be used to

create a triangle which contains the interpolation point by the method described above; if any side of the triangle do not cross any terrain feature line, the triangle is a interpolation triangle; otherwise, the triangle vertex should not take part in interpolation when the vertex and interpolation point are not on the same side of any terrain feature line and interpolation triangle must be created again until the triangle do not cross any terrain feature line.

## Conclusions

In order to test speed and accuracy of the interpolation method presented in this paper. Firstly, we build a discrete digital terrain model and a triangular grid digital model with the same discrete points, then creating a data elevation model (DEM) with three different interpolation methods. The first method is moving triangle interpolating method; the second method is triangular grid digital terrain model interpolating method; the third method is distance weighted interpolating method. There are 250000 discrete points and 50000 interpolating points, triangular grid digital terrain model interpolating method used 6 min, distance weighted interpolating method used 65s, moving triangle interpolating method used 90s, so moving triangle interpolating method has a fast interpolating speed.

After comparing the value of 1000 points which interpolated by three methods, we find the error of value of 10% points interpolated by distance weighted interpolating method is greater than 1.0 meter, and the max error of value is 5.1 meters; the corresponding values of moving triangle interpolating method are 1.8% and 1.72 meters; the corresponding values of triangular grid digital terrain model interpolating method are 2.3% and 1.80 meters. The contrast between the value of interpolation and practical terrain value is remarkable, the reason is in some areas density of the discrete points is too sparse so sometimes the shape of terrain can not be described with discrete points. Moreover, the test result shows that the precision of moving triangle interpolating method is higher than the precision of triangular grid digital terrain model interpolating method, the reason is the vertices of interpolating triangle creating with moving triangle interpolating method is selected based on interpolating point, the influence of three vertices upon the interpolating point is maximal; but the shape of triangles in triangular grid is considered based on whole triangular grid, so some triangles are not optimal to some interpolating points and the precision of moving triangle interpolating method is higher than the precision of triangular grid digital terrain model interpolating method at some time.

It can be seen that the moving triangle interpolation method based on normal discrete point digital terrain model presented in this paper can replace the interpolation method based on triangular grid digital terrain model. The algorithm can also increase the efficiency.

## References

[1] Janos Kalmar. DEM-Based Surface and Volume Approximation—Geographical Applications. Computer&Geosciences, Vol. 21(1995),p.147-163

[2] Tsai V.J.D. Delaunay Triangulations in TIN Creation: An Overview and a Linear-time Algorithm. Int. J. of GIS, Vol. 7(1993),p.501-524

[3] George Nagy, Sharad Wagle. Geographic Data Processing, Computing Surveys. Vol. 11(1979),p.139-181

[4] Wang Yongming, Lin Xinggan. A Fast Algorithm for Generating DEM. Computer Application and Software. Vol.15(1998),p.28-33

[5] Xue Jiaqing. The Principle and Algorithm of Optimization. Beijing: Metallurgy Industry Publishing Company. 1983

# CHAPTER 14:

# Applied and Computational Mechanics

*Applied Mechanics and Materials Vols. 580-583 (2014) pp 2879-2882*
*© (2014) Trans Tech Publications, Switzerland*
*doi:10.4028/www.scientific.net/AMM.580-583.2879*

# Effect of ring support position and geometrical dimension on the free vibration of ring-stiffened cylindrical shells

Xiaowan Liu, Bin Liang

Civil Engineering School, Henan University of Science and Technology, Luoyang, 471023, China

**Key Words:** Ring-stiffened cylindrical shell; Free vibration; Rayleigh-Ritz method.

**Abstract:** Effect of ring support position and geometrical dimension on the free vibration of ring-stiffened cylindrical shells is studied in this paper. The study is carried out by using Sander's shell theory. Based on the Rayleigh-Ritz method, the shell eigenvalue governing equation is derived. The present analysis is validated by comparing results with those in the literature. The vibration characteristics are obtained investigating two different boundary conditions with simply supported-simply supported and clamped-free as the examples.

## Introduction

Ring-stiffened cylindrical shells，relying on its excellent strength , stiffness and buckling behaviors, have received considerable attention in many engineering applications. Studies on the cylindrical shells with intermediate ring support are rare. Among those who has studied vibrational behavior of the isotropic shells include Loy[1], Li gan[2], and composite shells contain Najafizadeh[3]. There are also some good reviews on the coupled vibration of shells with consideration of hydrostatic pressure[4]. Due to the complexity of the ring-stiffened factor and the limitations of analytic method, work on the vibrations of ring-stiffened cylindrical shells has some deficiencies so far.

Based on the Sander's shell theory and Rayleigh-Ritz method, the natural frequency of the cylindrical shell with Clamped-Free and Simply supported ends boundary conditions is obtained. Results are presented on the influence of ring support position and the influence of geometrical dimension.

## Theoretical formulation

Consider a cylindrical shell with internal ring support is shown in Figure 1. $R$ is the radius, $L$ is the length, $h$ donates the thickness and $a$ is the position of the ring support along the axial direction of

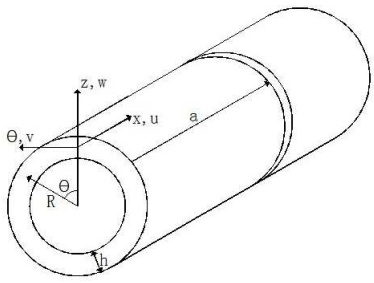


Fig.1 Geometry of ring-stiffened cylindrical shell

the cylindrical shell. The reference surface is taken to be the middle surface of the cylindrical shell where an orthogonal coordinate system $(x,\theta,z)$ is fixed. The $x,\theta$ and z are the axial coordinate, circumferential coordinate and radial coordinate, respectively.

The energy functional $\prod$ is given by the following Lagrangian function.

$$\prod = T_{\max} - U_{\max} \tag{1}$$

where $U_{\max}, T_{\max}$ are the maximum strain energy and kinetic energy.

$$\begin{aligned} U = \frac{1}{2}\int_0^L \int_0^{2\pi} \{ & \frac{E}{1-\mu^2} h[(u_x{}^2 + \frac{1}{R^2}(v_\theta + w)^2 + \frac{h^2}{12} w_{xx}{}^2 + \frac{h^2}{12R^4}(w_{\theta\theta} - v_\theta)^2 + \frac{2\mu}{R} u_x (v_\theta + w) + \\ & \frac{\mu h^2}{6R^2} w_{xx}(w_{\theta\theta} - v_\theta)] + \frac{Eh}{2(1+\mu)}(v_x + \frac{1}{R}u_\theta)^2 + \frac{Eh^3}{6(1+\mu)R^2}(w_{x\theta} + \frac{1}{4R}u_\theta - \frac{3}{4}v_x)^2 \} R dx d\theta \end{aligned} \tag{2}$$

$$T = \frac{1}{2}\int_0^L \int_0^{2\pi} \rho h \left[ u_t{}^2 + v_t{}^2 + w_t{}^2 \right] R dx d\theta \tag{3}$$

Where $E$ is the Young's modulus, $\rho$ is the mass density, $\mu$ is Poisson's ratio, and $u, v, w$ is the deformations in the $x, \theta, z$ directions.

The displacement field can be written in the following form.

$$\begin{cases} u(x,\theta,t) = A\dfrac{\partial \phi(x)}{\partial x}\cos(n\theta)\cos(\omega t) \\ v(x,\theta,t) = B\phi(x)\sin(n\theta)\cos(\omega t) \\ w(x,\theta,t) = C\phi(x)\prod_{i=1}^{N}(x-a_i)^{\xi_i}\cos(n\theta)\cos(\omega t) \end{cases} \tag{4}$$

where $A, B$ and $C$ denote the amplitudes of the vibrations in the $x, \theta$ and z directions, $n$ stands for the number of circumferential waves, $\omega$ is the natural angular frequency of the vibration, $\phi(x)$ is the axial function that satisfies the geometric boundary conditions [1], $a_i$ is the position of the $i$ th ring support and $N$ denotes the number of ring supports, $\xi_i$ is a parameter having a value of 1 when a ring support exists and 0 if there is no ring support.

Minimizing the energy functional with respect to the unknowns $A, B$ and $C$, a set of equations can be expressed as follows.

$$\begin{pmatrix} C_{11} & C_{12} & C_{13} \\ C_{12} & C_{22} & C_{23} \\ C_{13} & C_{23} & C_{33} \end{pmatrix} \begin{bmatrix} A \\ B \\ C \end{bmatrix} = \begin{bmatrix} 0 \\ 0 \\ 0 \end{bmatrix} \tag{5}$$

For a non-trivial solution of Eq.(5), equating the characteristic determinant to zero, a polynomial is obtained as follows.

$$\alpha_0\omega^6 + \alpha_1\omega^4 + \alpha_2\omega^2 + \alpha_3 = 0 \tag{6}$$

The three natural frequencies can be obtained by solving Eq.(6), and the smallest of the three ones is the frequency studied in the present study.

**Results and discussion**

To validate the present analysis, results for simply supported-simply supported and clamped-free cylindrical shells without ring supports are compared with Loy [1], see table 1, 2. The comparison show that the present results agree well with those in the literature.

Tab.1 Comparison of natural frequencies (HZ) for a simply supported cylindrical shell

| n | m | Loy[1] | present | different/% |
|---|---|---|---|---|
| 2 | 1 | 2043.8 | 2043.8 | 0 |
| | 2 | 5635.4 | 5635.4 | 0 |
| | 3 | 8932.5 | 8932.5 | 0 |
| | 4 | 11407.5 | 11407.5 | 0 |
| | 5 | 13253.2 | 13253.2 | 0 |

Tab.2 Comparison of natural frequencies (HZ) for a clamped-free cylindrical shell

| m | n | Loy[1] | present | different/% |
|---|---|---|---|---|
| 1 | 2 | 319.5 | 319.4 | 0.03 |
| | 3 | 769.9 | 769.8 | 0.04 |
| | 4 | 1465.7 | 1465.7 | 0 |
| | 5 | 2366.9 | 2366.9 | 0 |
| | 6 | 3479 | 3479 | 0 |

In this paper, studies are presented the influence of ring support position and geometrical dimension on a ring-stiffened cylindrical shell for simply supported-simply supported (S-S) and clamped-free (C-F) boundary conditions. Frequency parameter $w_f = \omega R\sqrt{(1-\mu^2)\rho/E}$, and Poisson ratio $\mu = 0.3$.

Figure 2 shows the vibration of the frequency parameter $w_f$ with the position of the ring support $a/L$ for S-S, C-F boundary conditions. For the same end conditions, such as S-S, the frequency cure is symmetrical about the center of the shell. Taking account of the frequency increasing with the ring support moving from the end to the center of the shell, the maximum frequency can be achieved with the ring support at the middle of the shell, and there is a significant difference between the maximum and minimum. But, for asymmetric end conditions, such as C-F, the frequency cure is not symmetrical about the center of the shell, and the maximum frequency lies in the range $a/L = 0.7 - 0.9$. Similarly, huge difference appears with the variation about the position of the ring support.

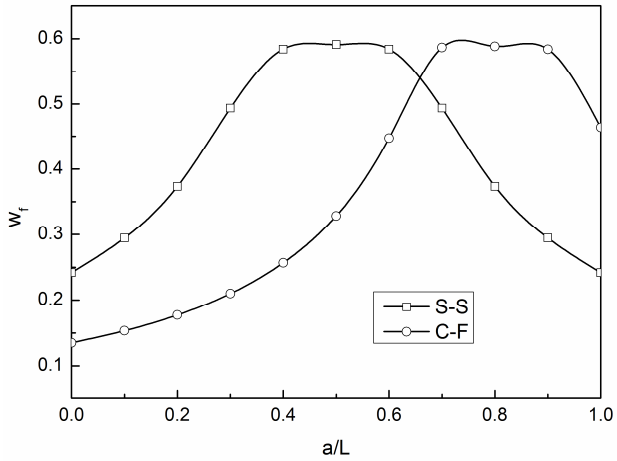


Fig.2 Variation of frequency parameter of cylindrical shells with the position of the ring support a/L

$$(L/R = 20, h/R = 0.01, m = 1, n = 1)$$

Figure 3 and 4 presented the influence of geometrical dimension on the vibration of the shell. Figure 3 shows the vibration of the frequency parameter with the position of the ring support $a/L$ at different $L/R$ ratios for the two boundary conditions. It is apparent that the frequencies are higher at small $L/R$, and the influence of the ring support position on the fundamental frequencies is significant at large $L/R$. Figure 4 shows the vibration of the frequency with the position of the

ring support $a/L$ at different $h/R$ ratios. As can be observed, the frequencies increase with the increasing $h/R$ ratio, and the influence on the fundamental frequencies is significant at small $h/R$ ratios.

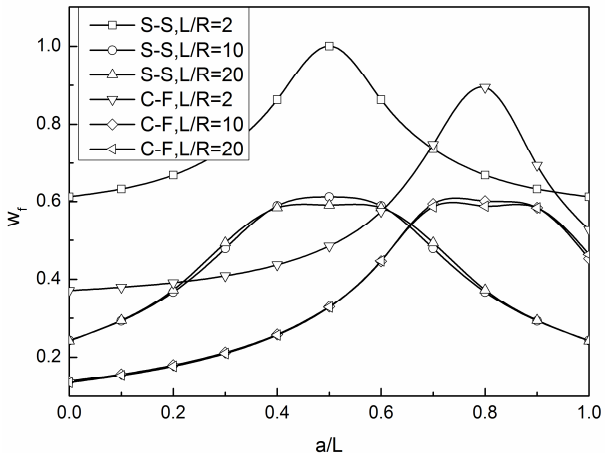


Fig.3 Variation of frequency parameter of cylindrical shells with different $L/R$ ratios ($h/R=0.01, m=1, n=1$)

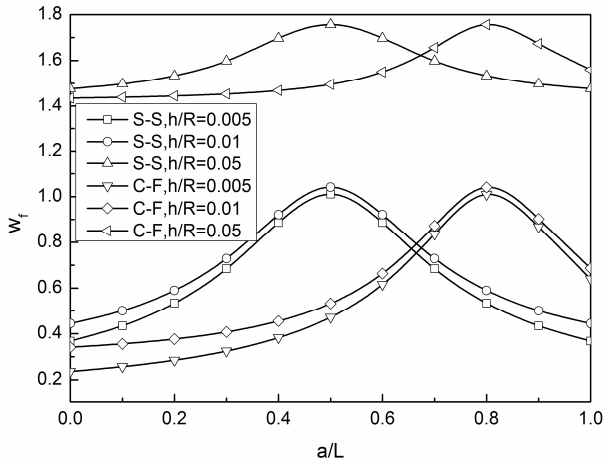


Fig.4 Variation of frequency parameter of cylindrical shells with different $h/R$ ratios ($L/R=20, m=1, n=10$)

## Conclusions

Based on the analysis of the frequency cures with the control factors, the study showed that the position of the ring support has a significant influence on the natural frequency, thus, appropriate ring support position should be taken into consideration in the structure design. The influence of geometric dimensioning on the vibrational behavior mainly presented at small $L/R$ ratio and large $h/R$ ratio.

## References

[1] Loy C T, Lam K Y. Vibration of cylindrical shells with ring support[J]. International Journal of Mechanical Sciences, 1996, 35(4): 455-471.

[2] Lin G, Li X B, Zhang Z. Free vibration analysis of ring-stiffened cylindrical shells using wave propagation approach[J]. Journal of Sound and Vibration, 2009, 326(3-5): 633–646.

[3] Najafizadeh M M, Isvandzibaei, Mohammad Reza. Vibration of functionally graded cylindrical shells based on different shear deformation shell theories with ring support under various boundary conditions[J]. Journal of Mechanical Science and Technology. 2009, 23(8): 2072-2084.

[4] Liu Z Z, Li T Y, Zhu X, Zhang J J. Effect of Hydrostatic Pressure on Input Power Flow in Submerged Ring-stiffened Cylindrical Shells[J]. Journal of Ship Mechanics. 2011,15 (3):301-312.

*Applied Mechanics and Materials Vols. 580-583 (2014) pp 2883-2889*
*© (2014) Trans Tech Publications, Switzerland*
*doi:10.4028/www.scientific.net/AMM.580-583.2883*

# Increment-dimensional Precise Integration Method of Oil-water Coupling Flows in a Low Permeability Reservoir with Capillary Pressure

Fuliang Mei[1, a] and Guiling Li [1,b]

[1] Institute of Civil & Engineering, Jiaxing College, Jiaxing ,Zhejiang ,314001,China

[a]Flmei2005@126.com , [b]Lgljx@126.com

**Key words**: low permeability reservoir, startup pressure gradient, capillary force, two-phase flow, increment-dimensional precise integration method (IDPIM), state equation

**Abstract.** The simulation of two-phase oil-water coupling flows in a low permeability reservoir with capillary pressure and start-up pressure gradient was carried out. First of all, the state equations with all the oil pressures at grid nodes were established based on lump-centre finite difference method. Secondly, the recurrence formulae of all the oil pressures and water saturations at grid nodes were built up according to IDPIM and an explicit difference method, respectively. Finally, the simulation of two-phase oil-water coupling flows for a typical five point area water injection as an example was carried out. Simulating results show that capillary pressure has a little effect on moisture rate and oil production, but startup pressure gradients have an outstanding effect on them. Therefore the existence of startup pressure gradients will enhance the difficulty of oil development.

## Introduction

In the procedure of water-injected oil recovery for a low permeability reservoir, the governing equations of two-phase oil-water coupling seepages were always solved by IMPES [1-5], namely, implicitly find oil/water pressures and explicitly find water saturation. Although the implicit method is unconditionally steady, it can inevitably result in numerical instability and decline of accuracy when time step length or grid size is up to a degree. For satisfying requirements of numerical stability and accuracy the time step length or grid size has to be got small enough, but it takes much more CPU to simulate. In more than ten years IDPIM numerical stability and accuracy can be satisfied when time step length is got big enough in the simulation of structural dynamic response and fluid-solid coupling seepages in geotechnical mechanics, but IMPES's numerical stability can not be satisfied at the same time step length as IDPIM [7-8]. In this treatise IDPIM was first introduced into two-phase oil-water coupling flows in a low permeability reservoir with capillary pressure and startup pressure gradients in order to relieve or resolve the numerical instability due to bigger time step length or bigger grid size with IMPES.

## Mathematical Model

It is well-known that water/oil movement does not abide by Darcy flow law in a low permeability reservoir. Here a non-linear flow model with startup pressure gradients is used. Assuming oil, water and rock skeleton are tiny compressible. According to multi-phase fluid flow theory in a pore media, two-phase oil-water coupling seepage equations can be expressed as follows:

$$\nabla\cdot\left(\frac{KK_{rl}}{\mu_l}\nabla P_l\right)+\nabla\left(\frac{KK_{rl}}{\mu_l}G_l\right)+q_{lv}=\phi_i S_l C_{lt}\frac{\partial P_l}{\partial t}+\phi_i\frac{\partial S_l}{\partial t}\qquad (l=o,w) \tag{1}$$

Where $K$ is natural permeability, $K_{rl}$ relative permeability, $G_l$ startup pressure gradient, $\mu_l$ dynamic viscosity, $\phi_i$ initial porosity, $S_l$ saturation, $P_l$ pore pressure, $C_{lt}$ comprehensively compressive coefficient, $t$ time.

Subservience equation can be written as follows:

$$S_{\mathrm{o}}+S_{\mathrm{w}}=1 \tag{2}$$

Capillary force equation may be written as follows:

$$P_c(S_w)=P_o-P_w \tag{3}$$

Where $P_c$ is capillary pressure and it is a function of water saturation ( $S_W$ ).

Choosing oil pressure as unknown function and removing water pressure, a governing seepage equation can be written as follows:

$$\nabla\cdot(\alpha\nabla P_o)+\nabla\beta-\nabla\cdot(\gamma\nabla P_c)+q_{ov}+q_{wv}=\phi_i c_t\frac{\partial P_o}{\partial t} \tag{4}$$

Where $C_{\mathrm{t}}=S_{\mathrm{o}}C_{\mathrm{o}}+S_{\mathrm{w}}C_{\mathrm{w}}+C_{\varphi}$, $\alpha=K\left(\frac{K_{\mathrm{ro}}}{\mu_{\mathrm{o}}}+\frac{K_{\mathrm{rw}}}{\mu_{\mathrm{w}}}\right)$ , $\beta=K\left(\frac{K_{\mathrm{ro}}G_{\mathrm{o}}}{\mu_{\mathrm{o}}}+\frac{K_{\mathrm{rw}}G_{\mathrm{w}}}{\mu_{\mathrm{w}}}\right)$, $\gamma=\frac{KK_{ro}}{\mu_o}$, $C_{\mathrm{t}}$ is the comprehensively compressive coefficient .

**Formulations**

In this section all the formulae were deduced for two-dimension oil water coupling seepages in a low permeability reservoir. Supposing $\Delta x$ and $\Delta y$ be a uniform spacing along x and y–direction respectively, and $\Delta x=\Delta y$ . According to lump-centre finite difference principle and Eq.(4), a finite difference equation at ay grid node $(i,j)$ can be expressed as follows:

$$\begin{aligned}
&\phi_i C_t\Delta x^2\frac{\partial P_{oi,j}}{\partial t}=\alpha_{i,j+\frac{1}{2}}P_{oi,j+1}+\alpha_{i+\frac{1}{2},j}P_{oi+1,j}-(\alpha_{i,j+\frac{1}{2}}+\alpha_{i+\frac{1}{2},j}+\alpha_{i,j-\frac{1}{2}}+\alpha_{i-\frac{1}{2},j})P_{oi,j}\\
&+\alpha_{i,j-\frac{1}{2}}P_{oi,j-1}+\alpha_{i-\frac{1}{2},j}P_{oi-1,j}-\gamma_{i,j+\frac{1}{2}}P_{ci,j+1}-\gamma_{i+\frac{1}{2},j}P_{ci+1,j}+(\gamma_{i,j+\frac{1}{2}}+\gamma_{i+\frac{1}{2},j}+\gamma_{i,j-\frac{1}{2}}+\gamma_{i-\frac{1}{2},j})P_{ci,j}\\
&-\gamma_{i,j-\frac{1}{2}}P_{ci,j-1}-\gamma_{i-\frac{1}{2},j}P_{ci-1,j}+\Delta x\left(\beta_{i+\frac{1}{2},j}-\beta_{i-\frac{1}{2},j}\right)+\Delta x\left(\beta_{i,j+\frac{1}{2}}-\beta_{i,j-\frac{1}{2}}\right)+Q_{OVi,j}+Q_{WVi,j}
\end{aligned} \tag{5}$$

Volumetric water flux per thickness locating at a water-injected well is calculated as follows:

$$Q_{WV1}=\frac{2\pi KK_{\mathrm{rw}}(1-S_{\mathrm{or}})(P_{\mathrm{w}i}-P_{wi,j}-r_{\mathrm{e}}G_{\mathrm{w}})}{\mu_{\mathrm{w}}\ln\frac{r_{\mathrm{e}}}{r_{\mathrm{w}}}} \tag{6}$$

Where $P_{wi}$ is water fluid pressure at a water-injected well, $r_w$ radius of the water-injected well, $r_e = 0.208\sqrt{\Delta x \Delta y}$ equivalent supply radius .

Volumetric water/oil fluxes per thickness locating at a liquid-recovered well are computerized respectively as follows:

$$Q_{\mathrm{WV}\,2} = \frac{2\pi KK_{\mathrm{rw}}\left(P_{wi,j} - P_{\mathrm{wp}} - r_{\mathrm{e}}G_{\mathrm{w}}\right)}{\mu_{\mathrm{w}}\ln\dfrac{r_{\mathrm{e}}}{r_{\mathrm{w}}}} \qquad Q_{\mathrm{OV}\,2} = \frac{2\pi KK_{\mathrm{ro}}\left(P_{oi,j} - P_{\mathrm{op}} - r_{\mathrm{e}}G_{\mathrm{o}}\right)}{\mu_{\mathrm{o}}\ln\dfrac{r_{\mathrm{e}}}{r_{\mathrm{w}}}} \tag{7}$$

Where $P_{wp}$ and $P_{op}$ stand for water and oil pressure at the liquid-recovered well, respectively.

Assembling Eqs.(4-7) together, a group of state equations with all the unknown oil pressures can be expressed as follows:

$$\frac{\partial \mathbf{x}}{\partial t} = \mathbf{H}\mathbf{x} + \mathbf{y} \tag{8}$$

Where $\mathbf{x}$ is a column vector of all the unknown oil pressures, $\mathbf{H}$ coefficient matrix of $\mathbf{x}$, $\mathbf{y}$ column vector of all the non-homogeneous items . Assuming all the unknown oil pressures is N. For sake of avoiding calculating the inverse matrix of $\mathbf{H}$, IDPIM is used. Introducing a new variable $x_{N+1}$ and supposing $x_{N+1}$ is a constant of 1, Eq.(8) can be transformed as follows:

$$\dot{X} = \begin{bmatrix} \dot{\mathbf{x}} \\ \dot{x}_{N+1} \end{bmatrix} = \begin{bmatrix} \mathbf{H} & \mathbf{y} \\ \mathbf{0} & 0 \end{bmatrix} \begin{bmatrix} \mathbf{x} \\ x_{N+1} \end{bmatrix} = \mathbf{W}\mathbf{X} \tag{9}$$

Where $\dot{\mathbf{X}} = \partial \mathbf{X}/\partial t$, $\dot{\mathbf{x}} = \partial \mathbf{x}/\partial t$, $\mathbf{W} = \begin{bmatrix} \mathbf{H} & \mathbf{y} \\ \mathbf{0} & 0 \end{bmatrix}$.

It should be noted that Eq.(9) is a group of nonlinear homogenous state equations in form. Uniformly averaging time domain, say, $t_k = k\Delta t\ (k = 0,1,2,\cdots)$. Where $\Delta t$ is time step length. In interval $[t_k, t_{k+1}]$, Eq.(9) may be rewritten as follows:

$$\dot{\mathbf{X}}(t) = \mathbf{W}(t)\mathbf{X}(t) \tag{10}$$

Where $\mathbf{W}(t)$ may be viewed as a constant matrix in the interval $[t_k, t_{k+1}]$ when the time step length $\Delta t$ is small enough, say, $\mathbf{W}(t)$ can be equal to $\mathbf{W}(k\Delta t)$. Based on matrix theory the solution of Eq.(11) can be written as follows:

$$\mathbf{X}((k+1)\Delta t) = \exp(\Delta t \mathbf{W}(k\Delta t))\mathbf{X}(k\Delta t) = \left[\exp\left(\mathbf{W}(k\Delta t)\cdot \Delta t / m\right)\right]^m \mathbf{X}(k\Delta t) \tag{11}$$

Where the exponent matrix in Eq.(11) can be calculated using a time-precise integration method in literature[9] .

Using Eq.(11) and all the known oil pressures at $t_k$, all the unknown oil pressures can be found at $t_{k+1}$. And then all the unknown water pressures can be computed at $t_{k+1}$ utilizing Eq.(3) and all the known water saturations at $t_k$. Above the calculating procedure is called as IDPIM.

For Eq.(1) using a lump-centre finite difference method in spatial domain and a backward difference method in time domain, respectively, a finite difference equation at a grid node $(i, j)$ can be got as follows:

$$S_{wi,j}^{k+1} = S_{wi,j}^{k} + \frac{\Delta t}{\phi_i \Delta x^2}\left[\alpha^k_{wi,j-\frac{1}{2}} P^{k+1}_{wi,j-1} + \alpha^k_{wi-\frac{1}{2},j} P^{k+1}_{wi-1,j} - \left(\alpha^k_{wi,j-\frac{1}{2}} + \alpha^k_{wi-\frac{1}{2},j} + \alpha^k_{wi,j+\frac{1}{2}} + \alpha^k_{wi+\frac{1}{2},j}\right) P^{k+1}_{wi,j}\right.$$

$$\left. + \alpha^k_{wi,j+\frac{1}{2}} P^{k+1}_{wi,j+1} + \alpha^k_{wi+\frac{1}{2},j} P^{k+1}_{wi+1,j} - \Delta x\left(\beta^k_{wi+\frac{1}{2},j} - \beta^k_{wi-\frac{1}{2},j}\right) - \Delta x\left(\beta^k_{wi,j+\frac{1}{2}} - \beta^k_{wi,j-\frac{1}{2}}\right) + Q_{WVi,j}\right]$$

$$- \phi_i C_{wt}\left(P^{k+1}_{wi,j} - P^{k}_{wi,j}\right) \tag{12}$$

**Results and Analysis**

There is a typical five-point injection water reservoir as an example. Its distance is 150m from the water-injected well to the oil-recovered well, and its thickness is 10m. Other parameters are: natural permeability $K$ is $0.01\,\mu m^2$, initial fluid pressure is 12Mpa, $P_{wp}$ is 18Mpa, $P_{wi}$ is 6Mpa, $\mu_o = 1$mPa.s, $\mu_w = 5$mPa.s, $G_o$=0.01Mpa and $G_w$=0.1$G_o$. Relations between capillary pressure and water saturation $(S_w)$ and relative permeability curves with relation to oil/water-phase from literature [10]. For sake of investigating the effects of capillary pressure, start-up pressure gradients on the accumulated oil production quantity, oil production rate and moisture content at the oil-recovered well, the start-up pressure gradient $G_o$ is from 0.0Mpa to 0.04Mpa while $G_w$ is 0.1 times of $G_o$, two case with relation to capillary pressure are utilized as follows: capillary pressure and no capillary pressure , and other parameters are the same as those in previous section. Computational results are shown in Figs.(1-3).

Fig.(1) gives the accumulated oil production with time. The accumulated oil production is proportional to time within initial stage of oil recovery, but it nonlinearly increases with time within later stage of oil recovery. The increase of the accumulated oil production within initial stage of oil recovery is much bigger than that within later stage of oil recovery. The accumulated oil production decreases with the increase of start-up pressure gradients.

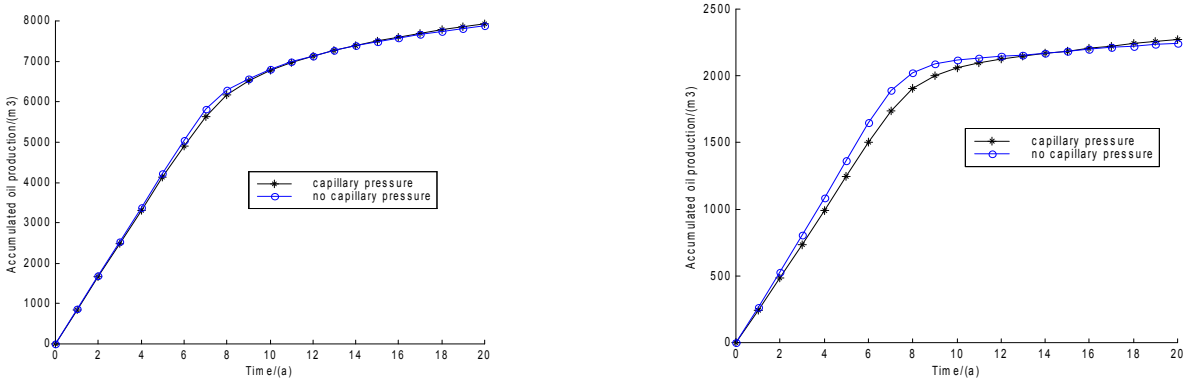


(a) $G_o = 0.0MPa, G_w = 0.1G_oMPa$ (b) $G_o = 0.04MPa, G_w = 0.1G_oMPa$

Fig.1 Accumulated oil production versus time

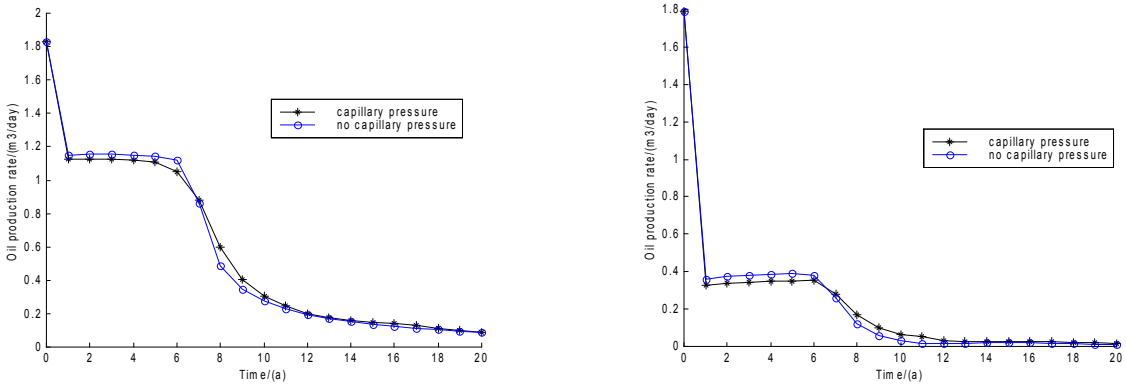


(a) $G_o = 0.0MPa, G_w = 0.1G_oMPa$ (b) $G_o = 0.04MPa, G_w = 0.1G_oMPa$

Fig.2 Oil production rate versus time

Fig.(2) describes the oil production rate varying with time. It can be seen from Fig.(2) that oil production rate changing with time can be divided four stages: first fast decline ( 0-1 year), constant(1-6 years), second fast decline(6-10 years), smooth-steady ( after 10 years). The start-up pressure gradients have an important influence on the oil production rate. The oil production rate decreases with increase of the start-up pressure gradients. The capillary pressure has a little influence on the oil production rate, too. The oil production rate with capillary pressure is smaller than that without capillary pressure within the constant stage of the oil production rate. And then the decline of the oil production rate with capillary pressure is slower than that without capillary pressure within the second fast decline stage of the oil production rate. But the oil production rate with capillary pressure is basically the same as that without capillary pressure within the first fast decline and smooth-steady stages.

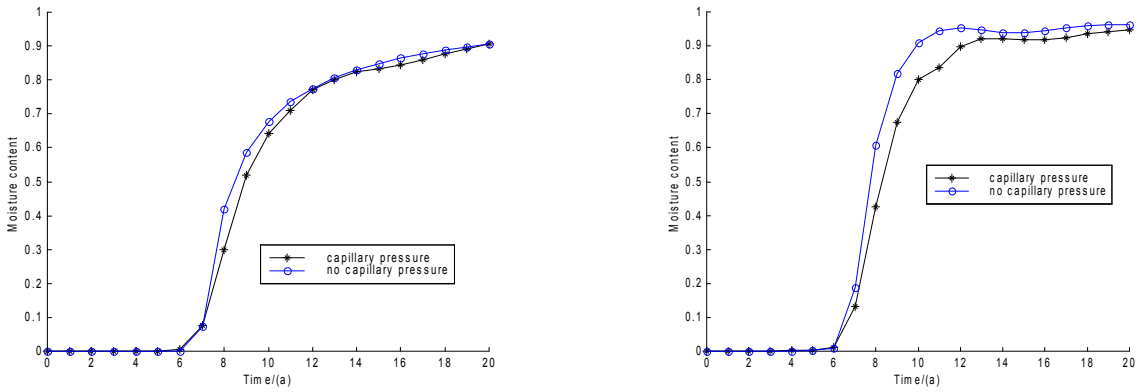


(a) $G_o = 0.0MPa, G_w = 0.1G_oMPa$ (b) $G_o = 0.04MPa, G_w = 0.1G_oMPa$

Fig.3 Water saturation at an oil-recovered well versus time

Fig.(3) describes the water saturation at the oil-recovered well varying with time. It goes through three stages: no water-production, fast water-production, slow water-production. The start-up pressure gradients have an important influence on the water saturation after water begins to come out at the oil-recovered well, and the water saturation increases with increase of the start-up pressure gradients. The appearance of water at the oil-recovered well with capillary pressure is earlier than that without capillary pressure.

## Conclusions

There are a few conclusions:(1) IDPIM is a higher property numerical method;(2) In a word, the start-up pressure gradients have a more important influence on oil-recovered parameters such as oil production rate than the capillary pressure;(3) The decline of oil production with capillary pressure is slower than that without capillary pressure around the appearance of water at the oil-recovered well. The anhydrous harvest period with capillary pressure is shorter than that without capillary pressure, and the rise of water production with capillary pressure is slower than that without capillary pressure;(4) The smaller is oil production the bigger are start-up pressure gradients. The rise of water saturation with start-up pressure gradients is faster than that without start-up pressure gradients. Therefore the existence of start-up pressure gradients enhances the difficulty of oil development.

## Aknowledgements

This work was financially supported by the Science & Technology Project of Zhejiang Province No.2009C31124).

## References

[1] F.H.Li ,Liu Ci-qun:Well Testing (in Chinese) (1997)

[2]Y.C.Guo,D.T.Lu,L.X.Ma:Journal of Hydrodynamics,Ser.A (in Chinese) (2004)

[3]Y.C.Guo,Q.H.Zeng,Z.X.Wang:Engineering Mechanics(in Chinese) (2006)

[4]S.Q.Cheng, M.Z.Chen: Shiyou Kantan Yu Kaifa(in Chinese)(1998)

[5] F.Q.Song,C.Q.Liu:Journal of the University of Petroluim(in Chinese)(1999)

[6]H.M.Shu, Z.Q.Zhang,C.W.Cui:ACTA PETROLEI SINICA(in Chinese((2007)

[7]S.Y.Zhang, Z.C.Deng: Chinese Journal of Computational Mechanics(in Chinese)(2003)

[8]F.L.Mei Industrial Construction (in Chinese) (2006)

[9]W.X.Zhong:Chinese Journal of Computational Mechanics(in Chinese)(1994)

[10]S.W.Rao,C.C.He,F.Zhao: Computer Application of Petroleum(in Chinese) (2008)

*Applied Mechanics and Materials Vols. 580-583 (2014) pp 2890-2893*
*© (2014) Trans Tech Publications, Switzerland*
*doi:10.4028/www.scientific.net/AMM.580-583.2890*

# Influence of vertical vibration on surface velocity of a liquid bridge

Ruquan Liang[1], Zhihui Zhang[1], Taiyin Gao[2], Fusheng Yan[3]

[1]Key Laboratory of National Education Ministry for Electromagnetic Processes of Materials, Northeastern University, No.3-11, Wenhua Road, Shenyang 110819,China

[2]School of Materials and Metallurgys, Northeastern University, No.3-11, Wenhua Road, Shenyang 110819, China

[3]Research Academy, Northeastern University, No.3-11, Wenhua Road, Shenyang 110819, China

liang@epm.neu.edu.cn, (86)24-83685996, (86)24-83681758

**Keyword:** Vertical vibration; Surface velocity; Liquid bridge, Level set method

**Abstract.** In this paper, the vertical vibration influence on the surface velocity of a 5cSt silicone oil liquid bridge has been investigated numerically. The Navier-Stokes equations coupled with the energy conservation equation are solved on a staggered grid, and the two-phase surface is captured by using the mass conserving level set method. The present results indicate that the axial and radial surface velocities of the liquid bridge are suppressed by the external vertical vibration.

## Introduction

Buoyancy convection becomes relatively weak in the microgravity environment and the convection driven by surface tension rises to dominance. The thermocapillary convection is a typical convection induced by the gradient of surface tension on the gas-liquid surface, which has a strong application background of space material processing. So many researches about this convection have been carried out in recent years. The influence of vibration on the surface flow field of half-floating zone liquid bridge has also been greatly concerned, and this kind of researches may help understand the mechanism of thermocapillary convection.

Kanashima et al.[1] studied the influence of G-jitter on the liquid bridge surface deformation in the thermocapillary convection experiment at the International space station. They discovered that the surface deformation of natural thermocapillary convection can distinguish with surface deformation generated on resonance and non-resonant frequency. Tang and Hu[2] studied influence of high frequency vibration on the critical Ma number and they pointed out that when the frequency of the applied vibration is large enough, the extent of temperature fluctuation disappears. Moreover, the surface of the liquid bridge does not exhibit fluctuation due to the inertia effect. Anilkumar[3] studied the relationship between amplitude, temperature on the liquid bridge surface and additional vertical vibration under normal gravity. They concluded that the velocity of the surface flow increases along as the increasing of the vibration frequency, amplitude and length of floating zone, while the velocity of the surface flow decreases as a decreasing in the viscosity of the liquid bridge. Moreover, they also discussed influence of the vertical vibration on the internal temperature distribution in the liquid bridge.

The present paper studies the vertical vibration influence on the surface velocity of a 5cSt silicone oil liquid bridge. The free surface deformation is captured by introducing the mass conserving level set method[4].

## Physical and Mathematic models

**Physical Model.** The simplified model of the floating-zone method is adopted in the present paper as shown in Fig.1.

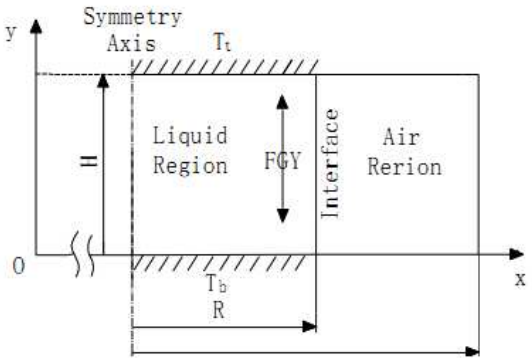


Fig. 1 Schematic of a half-zone liquid bridge model

The height of the liquid bridge is H. $T_t$ is the temperature at the upper disk, and $T_b$ is temperature at the bottom disk. The difference of the upper and the bottom disks is $\Delta T = T_t - T_b$. The radius and height of the liquid bridge are R and H, respectively.

**Controlling Equations.** The basic governing equations of half-floating zone thermocapillary convection include the mass, momentum, and energy conservation equations. Basic non-dimensional governing equations are given as following:

$$\mathbf{u}_t + (\mathbf{u}\cdot\nabla)\mathbf{u} = \mathbf{g}_u + \frac{1}{\rho}\left(-\nabla p + \frac{1}{\mathrm{Re}}\nabla\cdot(2\mu\mathbf{D}) + \left(\frac{1}{\mathrm{We}} - \frac{\mathrm{Ca}}{\mathrm{We}}\Theta\right)\kappa\delta(d)\mathbf{n}\right) + FGY \tag{1}$$

$$\nabla\cdot\mathbf{u} = 0 \tag{2}$$

$$\frac{\partial\Theta}{\partial t} + \nabla\cdot(\mathbf{u}\Theta) = \frac{1}{Ma}\nabla^2\Theta \tag{3}$$

$$\frac{\partial\phi}{\partial t} + \overline{V}\cdot\nabla\phi = 0 \tag{4}$$

where $\mathbf{u} = (u,v)$ is the fluid velocity, $\rho = \rho(\mathbf{x},t)$ is the fluid density, $\mu = \mu(\mathbf{x},t)$ is the fluid viscosity, $\mathbf{D}$ is the viscous stress tensor, $\kappa$ is the curvature of the interface, $d$ is the normal distance to the interface, $\delta$ is the Dirac delta function, $\mathbf{n}$ is the unit normal vector at the interface, $t$ is the dimensionless time, $p$ is the pressure. The surface tension coefficient is considered to be a linearly function of temperature and defined as $\sigma = \sigma_c - \sigma_T(T - T_b)$, where $\sigma_c$ is a reference value of surface tension and $\sigma_T$ is the temperature coefficient of surface tension and we denote $\sigma_T = \partial\sigma/\partial T$, and $T$ is the temperature. $FGY$ is a body force induced by a external acceleration, which is used when a external acceleration is applied, $FGY = g_y\overline{L}/U_\infty^2$, $g_y$ is the external acceleration in Y direction, $g_y = A\omega^2\sin\omega\bar{t}$, $A$ is the vibration amplitude, and $\omega$ is the angular frequency, $\omega = 2\pi f$, and $f$ is the vibration frequency. $\overline{L}$ is characteristic length and we take $\overline{L} = D$, where $D$ is the initial diameter of the droplet. $U_\infty$ is the characteristic velocity and we take $U_\infty = \sqrt{Dg}$ under normal gravity, while $U_\infty = \sigma_T\Delta T/\mu_l$ under microgravity, where $g$ is the gravitational acceleration, $\bar{t}$ is dimensional time, $\bar{t} = t/\overline{L}/U_\infty$.

The key parameters are $\rho_g/\rho_l$ and $\mu_g/\mu_l$, the dimensionless density and viscosity ratio inside the ambient air region, respectively. $\rho_l$ and $\mu_l$ are the dimensional density and viscosity of the liquid bridge, respectively, while $\rho_g$ and $\mu_g$ are the dimensional density and viscosity of the ambient air, respectively. The dimensionless density ($\rho_l/\rho_l$) and viscosity ($\mu_l/\mu_l$) inside the liquid bridge are both equal to 1. $\mathrm{Re} = \rho_l U_\infty\overline{L}/\mu_l$, Reynolds number, $\mathrm{We} = \rho_l U_\infty^2\overline{L}/\sigma$, Weber number, $\mathrm{Pr} = \mu_l/\rho_l a$, Prandtl number, $\mathrm{Ca} = \mu_l U_\infty/\sigma$, Capillary number, $a$ is the thermal diffusivity and $\mathbf{g}_u$ represents a unit gravitational force, $\overline{V} = (u,v)$ is fluid velocity, $\phi$ is the level set function.

### Boundary and Initial conditions

All walls of the computational region are assumed to be adiabatic，and the temperatures at the hot and cold disks of the liquid bridge are maintained at constant temperature $T_t$ and $T_b$, respectively, with a temperature difference of $\Delta T$. Consequently, the following boundaries conditions should be satisfied.

$$\Theta = 0 \quad (z = 0), \Theta = 1.0 \quad (z = 1.0)$$

No-slip boundary condition is adopted on the wall, $\mathbf{u}(t=0) = 0$

Initial conditions is used as follow, $\mathbf{u}(t=0) = 0$

### Results and Discussion

In this paper, we study the vertical vibration influence on the surface velocity of a 5cSt silicone oil liquid bridge under external vertical vibration. The diameter of upper and bottom disks is D=10 mm. The aspect ratio (H/R) is 0.5. We add a 20mg vertical vibration (FGY) to the liquid bridge. The main parameters involved in the calculation include Reynolds number Re=320, Weber number We=3.5, Prandtl number Pr=69, Capillary number Ca=5. The temperature difference between the top and bottom of the disc is $25°C$, density ratio is $\rho_g / \rho_l = 1.350\times10^{-3}$, and viscosity ratio is $\mu_g / \mu_l = 5.528\times10^{-3}$.

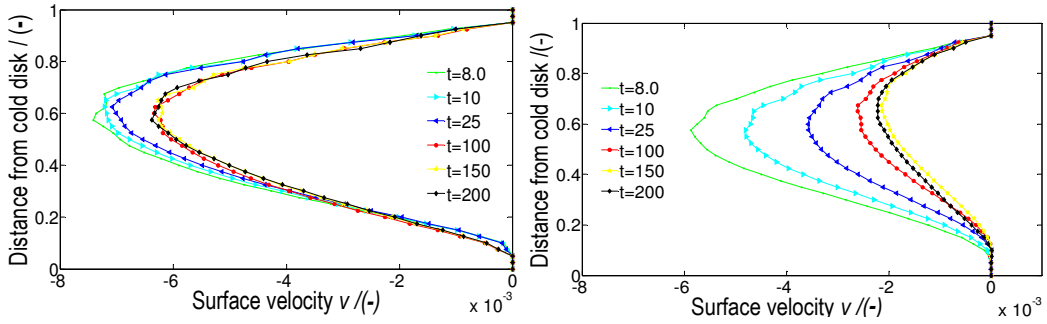


(a) 0Hz (b) 5Hz

Fig. 2 Surface axial velocity at different times（Pr=69, Re=320, Ma=22037, FGY=20mg） (a) 0Hz, (b) 5Hz

Figure 2 shows the surface axial velocity distribution of the liquid bridge without or with an external vertical vibration of 5Hz. It can be found that the surface axial velocities are all below zero in Fig.2 (a)-(b), indicating that the surface liquid flows from the upper disk to the cold disk, and the maximum of axial surface velocity is obtained at the distance of 0.6H from the cold disk. In Fig. 2(a), the axial surface velocity decreases from t=8.0 to t=100, and then it becomes stable from t=100 to t=200, which illustrates that the axial surface velocity becomes gradually small and then reaches a steady state. In Fig. 2(b), the axial surface velocity decreases from t=8.0 to t=150, and then it becomes stable from t=150 to t=200, which illustrates that the axial surface velocity becomes gradually small. In addition, the difference between the surface axial velocity at t=8.0 and t=200 in Fig. 2(b) (with external vibration) is greatly larger than that in Fig. 2(a) (without external vibration), indicating that the external vibration suppresses the surface axial velocity.

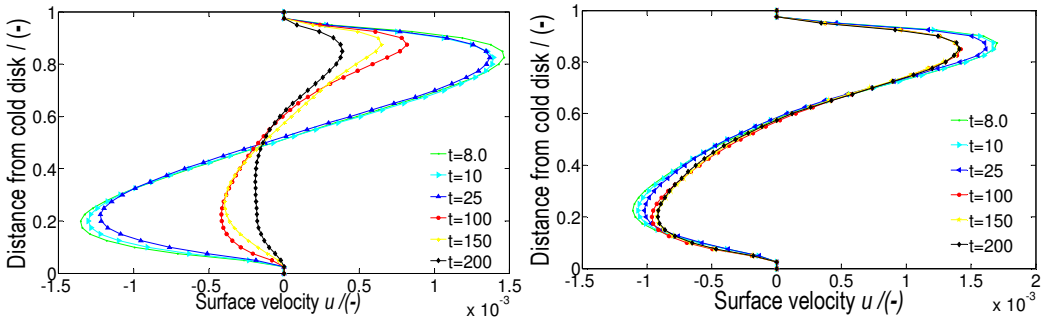


(a) 0Hz (b) 5Hz

Fig. 3 Surface radial velocity at different times（Pr= 69, Re=320, Ma=22037, FGY=20mg） (a) 0Hz, (b) 5Hz

Figure 3 shows the surface radial velocity distribution of the liquid bridge without or with an external vertical vibration of 5Hz. In Fig. 3(a), the radial surface velocity changes slightly from t=8.0 to t=25, while it decreases greatly from t=25 to t=200, which illustrates that the radial surface velocity becomes gradually small and then reaches a steady state. The positive and negative values of velocities indicate that the direction of the fluid motion. Its value is positive at the positions above 0.5H distance from the cold disk and negative at the positions below 0.5H from the cold disk, which means that the radial velocity of the liquid bridge surface is positive near the upper disk and is negative near the cold disk. The radial velocity of the liquid bridge surface is zero in the middle region. It reflects that the radial velocity distribution of thermocapillary convection in the liquid bridge as well as the trend of the liquid bridge surface deformation. The maximum of the negative velocity appears at 0.2H from the cold disk and the maximum of the positive velocity appears at 0.8H from the cold disk in Fig. 3(a)-(b). As shown in Fig. 3(b), the radial velocity of the liquid bridge changes little from t=8.0 to t=200 under the external vertical vibration of 5Hz. Therefore, the external vibration makes the difference of the radial velocities at different times becoming small.

## Conclusions

In this paper, we studied the 5cSt silicone oil liquid bridge under the vertical direction to study the vertical vibration influence on the surface velocity of the liquid bridge, and the following conclusions are drawn,

1. The axial and radial velocities on the surface of the liquid bridge change a lot at the initial period with the external vertical vibration, while it changes little at the stable period. Moreover, the radial and axial velocities are suppressed by the the external vertical vibration.
2. The maximum of the axial surface velocity of the liquid bridge appears at 0.6H from the cold disk, while the maximum of the radial surface velocity appears at 0.2H and 0.8H from the cold disk, respectively, with and without the external vertical vibration.
3. The external vibration suppresses the surface axial velocity, while the external vibration makes the difference of the radial velocities at different times becoming small.

## Acknowledgements

The present work is supported financially by the National Natural Science Foundation of China under the grants of 11072057 and 51376040.

## References

[1] Y. Kanashima, K. Nishino,S. Yoda:Effect of g-jitter on the thermocapillary convection experiment in ISS [J], Microgravity Sci. Technol, 16(1):285-289(2005)
[2] H. Tang, W.R. Hu:Effects of high frequency vibration on critical marangoni number [J], Adv. Space Res, 16(7):71-74.71-74(1995)
[3] A. V. Anilkumar , R. N. Grugel, et al. : Control of thermocapillary convection in a liquid bridge by vibration [J],Journal of Applied Physics, 73(9): 4165 (1993)
[4] S. Osher, J. Sethian,: Fronts propagating with curvature-dependent speed: algorithms based on Hamilton-Jacobi formulations[J]. Comput.Phys.79,12-49 (1988)

*Applied Mechanics and Materials Vols. 580-583 (2014) pp 2894-2897*
*© (2014) Trans Tech Publications, Switzerland*
*doi:10.4028/www.scientific.net/AMM.580-583.2894*

# Linear Analysis of the Constitutive Relation of Concrete Elastoplastic Disturbance

Jiemin Liu [1, a], Weinan Wang [2, b] and Shuang Liu [1, c]

[1]School of Science, Shenyang Jianzhu University, 110168 Shengyang, China

[2]School of Civil engineering, Shenyang Jianzhu University, 110168 Shengyang, China

[a]liujiemin1954@163.com, [b]wangwn1988@126.com, [c]liush0229@163.com

**Keywords:** constitutive equation of concrete, linear equation, disturbance variable, finite element analysis.

**Abstract.** A linearization method of the uniaxial non-fitting nonlinear stress-strain curve given by the author of the paper is presented. The evolution equation between disturbances variable $D$ and plastic strain $\varepsilon_p$ is derived based on Theory of Duality Disturbance. A simple method for concrete structures preforming elastoplastic analysis is presented (including softening analysis).

## Introduction

Concrete is a kind of multiphase material composed of sand and cement. The mechanical behavior is very complicated due to influences of the water-cement ratio, curing conditions, loading path, ect. Display nonlinear damage, strain softening, the hydrostatic pressure effect [1].

Scholars presented different damage models in accordance with specific constitutive relation of concrete[2-5]. However, most of them are difficult to be used in engineering because of the particularity of its application conditions and the model complexly. It is important to establish the constitutive relation that is of succinct mechanical concepts,can be used to simulate complex mechanical behaviors of concrete structures.

A reduced method of uniaxial non-fitting nonlinear stress-strain curve is given in this paper. The linearization method for concrete structure preforming elastoplastic disturbance simulation is set up based on Theory of Duality Disturbance[6].

## Non-fitting stress - strain equation

Stress-strain relation is the essential constitutive relation of describing concrete mechanical properties. Numerous scholars established the concrete stress-strain equation [7-9]. The first author of the paper established a non-fitting nonlinear stress-strain curve by means of the experimental data of concrete under uniaxial tension-compression, using the informations about the initial elastic modulus $E_0$, peak stress $\sigma_{cb}$, peak strain $\varepsilon_{cb}$, stress inflexion $\sigma_{inf}$ and strain inflexion $\varepsilon_{inf}$, the continuity of curve and the softening inflexion information such as the second derivative is zero, after that established the non-fitting of the nonlinear stress-strain relationship [10]. Uniaxial compression stress-strain curve, Fig.1.

$$\sigma = a\varepsilon(1+b\varepsilon^m) \tag{1}$$

Where, $a = E_0$, $m = \dfrac{E_0 - E_0\varepsilon_{cb} + \sigma_{cb}}{E_0\varepsilon_{cb} - \sigma_{cb}}$, $b = \dfrac{\sigma_{cb} - E_0\varepsilon_{cb}}{E_0\varepsilon_{cb}^{(E_0 - E_0\varepsilon_{cb} + \sigma_{cb})/(E_0\varepsilon_{cb} - \sigma_{cb})}}$. The stress-strain relationship in the stage of softening of uniaxial compression is expressed as

$$\sigma = C/(1 - Ae^{-B\varepsilon}) \tag{2}$$

Where, $C = 3\sigma_{inf}/2$, $B = \ln(3\sigma_{inf}/\sigma_{cb} - 2)/\xi_{inf}$, $A = 1 - 3\sigma_{inf}/2\sigma_{cb}$, $\xi_{inf} = \varepsilon_{inf} - \varepsilon_{cb}$,

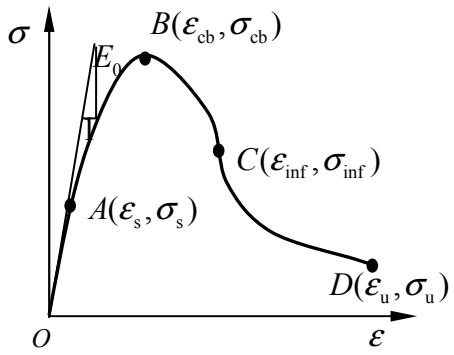


Fig.1 Uniaxial compression

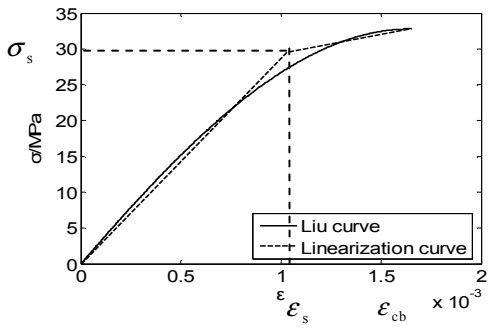


Fig.2 Linearized nonlinear stress-strain equation

**Linearization of the non-fitting stress-strain equation**

The first author of the paper presents a linearization method of nonlinear equation which based on the assumption of strain energy equivalent [11].

According to the assumption of strain energy equivalent, have

$$U_{\text{Non-linear}} = U_{\text{linear}} \tag{3}$$

Where, $U_{\text{Non-linear}}$ is the area of nonlinear reinforcement under the strain of changeover portion; $U_{\text{linear}}$ is the area of the linear under the stress and strain. Using the above condition, the linearize relation is expressed as

$$\begin{cases} \sigma = E_L \varepsilon & (0 \le \varepsilon \le \varepsilon_s) \\ \sigma = \sigma_s + E_1(\varepsilon - \varepsilon_s) & (\varepsilon_s < \varepsilon \le \varepsilon_{cb}) \end{cases} \tag{4}$$

Where, $\varepsilon_s = (a+1)\varepsilon_{cb} - 2W/\sigma_{cb}$, $W = a\left[\varepsilon_{cb}^2/2 + b\varepsilon_{cb}^{m+2}/(m+2)\right]$, $\alpha = (2W/\sigma_{cb} - \varepsilon_{cb})E_0/(\varepsilon_{cb}E_0 - \sigma_{cb})$, $E_L = \alpha\sigma_{cb}/[(a+1)\varepsilon_{cb} - 2W/\sigma_{cb}]$, $E_1 = (\sigma_{cb} - \sigma_s)/(\varepsilon_{cb} - \varepsilon_s)$ .The linearization stress-strain curve in strengthen potion of Kupper test is shown as dotted line in Fig.2.

**The basic equations of the Theory of Duality Disturbance**

The first author of this paper put forword the Theory of Duality Disturbance [6]. The constitutive equation of Theory of Duality Disturbance is expressed as

$$\sigma_{ij}^{o} = (1-D)\sigma_{ij}^{n} + D\sigma_{ij}^{c} \tag{5}$$

Where, $\sigma_{ij}^{o}$ is observed stress; $\sigma_{ij}^{n}$ is the stress at Relatively Non-Disturbed (RND) state; $\sigma_{ij}^{c}$ is the stress at Relatively Complete Disturbed (RCD) state. $D$ is disturbance variable. It is assumed that $D$ is the function of plastic strain trajectory $\xi^{p}$ . i.e.

$$D = D(\xi^{p}) \tag{6}$$

$$\xi^{p} = c\int \mathrm{d}\xi^{p} = c\int \sqrt{\mathrm{d}\varepsilon_{ij}^{p}\mathrm{d}\varepsilon_{ij}^{p}} \tag{7}$$

Where, $\xi^{p}$ shows the accumulation of plastic strain in whole process of deformation(including loading and unloading processes), which is a increasing function. Equation (5) is applied to three-dimensional stress state. In order to make $\xi^{p}$ veduced as uniaxial plastic strain $\varepsilon^{p}$ for uniaxial stress state, the parameter $c = c(\mu)$ is introduced. Where $\mu$ is Poisson's ratio.

For uniaxial observed stress state as shown in Fig. 3 , RND stress-strain curve $\sigma^{n} - \varepsilon^{n}$ and RCD stress-strain curve $\sigma^{c} - \varepsilon^{c}$ are taken as

$$\sigma^{n} = E_0\varepsilon^{n}, \sigma^{c} = 0 \tag{8}$$

From Fig.3, we can see that observed strain $\boldsymbol{\varepsilon}^{o}$, RND strain $\boldsymbol{\varepsilon}^{n}$ and RCD strain $\boldsymbol{\varepsilon}^{c}$ are equal. i.e. $\boldsymbol{\varepsilon}^{o}=\boldsymbol{\varepsilon}^{n}=\boldsymbol{\varepsilon}^{c}=\boldsymbol{\varepsilon}$.This is so called total strain equivalent assumption .

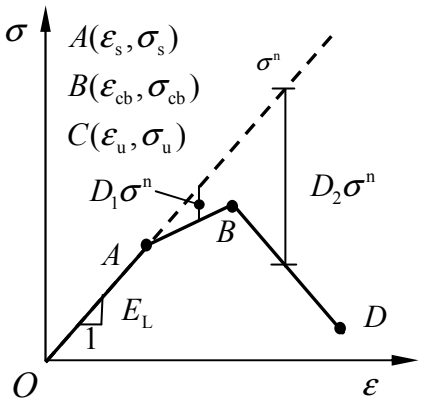


Fig.3 $\sigma^{n}-\varepsilon$ curve and $\sigma^{o}-\varepsilon$

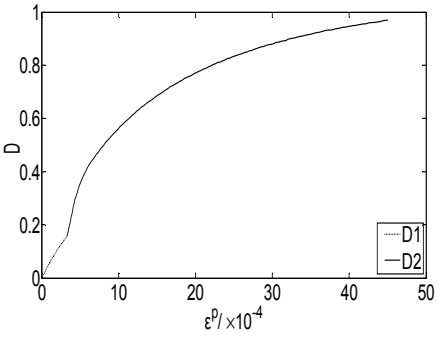


Fig.4 Disturbance *D*-plastic strain $\varepsilon_{p}$ curve of *ABD*

$D=D(\varepsilon_{p})$ curve can be derived by $D=1-\sigma^{o}/\sigma^{n}$. For the linear hardening stage (*OAB*), the observed stress $\sigma^{o}$ is expressed as

$$\sigma^{o}=\sigma_{s}+E_{1}\varepsilon_{p}/(1\text{-}E_{1}/E_{L}) \tag{9}$$

Where, $\varepsilon_{s}\le\varepsilon\le\varepsilon_{cb}$, $\varepsilon_{p}=\varepsilon-\varepsilon_{e}=\varepsilon-\sigma^{o}/E_{L}$.

The relation between disturbance variable $D_{1}$ and plastic strain $\varepsilon_{p}$ can be expressed as

$$D_{1}=1-\frac{\sigma_{s}+E_{1}(\sigma^{o}/E_{L}+\varepsilon_{p}\text{-}\varepsilon_{s})}{\sigma_{s}+E_{1}\varepsilon_{p}} \tag{10}$$

For the softening damage stage (*BD*), the observed stress $\sigma^{o}$ is expressed as

$$\sigma^{o}=k\varepsilon+b=k(\varepsilon_{e}+\varepsilon_{p})+b=k(\sigma^{o}/E+\varepsilon_{p})+b\quad(\varepsilon_{cb}\le\varepsilon\le\varepsilon_{u}) \tag{11}$$

Where, $E=E_{0}[1-\alpha(\varepsilon/\varepsilon_{u})^{n}]$, n=1.5, $\alpha=1-E_{u}/E_{0}$, $\varepsilon_{p}=\varepsilon-\varepsilon_{e}=\varepsilon-\sigma^{o}/E$, $k=(\sigma_{u}-\sigma_{cb})/(\varepsilon_{u}-\varepsilon_{cb})$, $b=\sigma_{cb}-k\varepsilon_{cb}$, $\sigma_{u}$-Ultimate stress, $\varepsilon_{u}$-Ultimate strain.

The relationship between disturbance variable $D_{2}$ and plastic strain $\varepsilon_{p}$ can be expressed as

$$D_{2}=1-[k(\varepsilon_{p}+\sigma^{o}/E)+b]/[E_{L}(\varepsilon_{p}+\sigma^{o}/E)] \tag{12}$$

The relation between disturbance variable $D$ and plastic strain $\varepsilon_{p}$ based on Kupfer text is showed as in Fig. 4. $D_{1}$ and $D_{2}$ correspond to strengthening stage (*AB*) and softening damage stage (*BD*), respectively.

**Verification of the constitutive equation**

Applying the linearization method set up in this paper to predict the compression behavior of the concrete used in Kupfer text. The finite element model is taken as a concrete block of 50mm×150mm×50mm, $E_{0}=26.7$GPa, $\mu=0.2$. The lower end (*xOy* surface) is restrained, i.e, $u_{x}=u_{y}=u_{z}=0$. Uniform lode $q$ is exerted at the upper surface, as showed in Fig.5. In this paper, in order to certify the result of the analysis model, ANSYS code is used to perform linear elastic finite element analysis. Select a RND model $\sigma^{n}=E_{0}\varepsilon$. $q$ is exerted from 10MPa to 150MPa with load step =10MPa.

The stress-strain relation of the node, which is at the *AB* axle and 10mm from *B*, is analyzed. The stress-strain relation in a RND model is shown with solid dots, and the observed stress-strain relation in concrete $\sigma^{o}-\varepsilon$ predicted by the linearization method present in this paper is shown with asterisks, as showed in Fig.6.

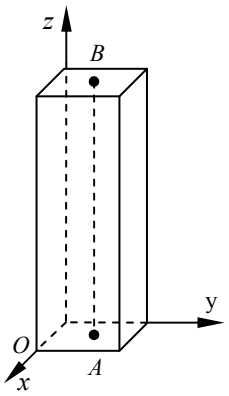


Fig.5 The finite element model

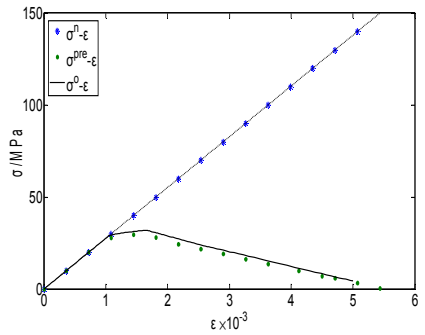


Fig.6 The stress analysis corresponding to $\sigma^{n}-\varepsilon$ curve in pressure

Experimental results show that the simulation results are in agreement with experimental results, which prove the correctness of the linearization model.

## Conclusions

The linearization method of non-fitting nonlinear equation is given based on the assumption of strain energy equivalent. Taking RND model as linear elastic, the evolution equation of disturbance with plastic strainis derived based on Theory of Duality Disturbance. A simple method simulating complex mechanical behavior of concrete structures is presented.

## References

[1] W.F.Chen. Constitutive equation of Civil Engineering Materials. Wuhan: Huazhong University of Scie-nce and Technology Press (2001) (in Chinese)

[2] Brannon R M, Leelavanichkul S. International Journal of Fracture, Vol.163 (2010), p.133.

[3] L. Contrafatto , M. Cuomo. International Journal of Plasticity . Vol.22 (2006), p.2272

[4] Hua Xiong, Mingfu Fu, Luo Qifeng. Chinese Quarterly of Mechanics, Vol.25 (2004), p.342(in Chinese)

[5] Jason L, Huerta A, Pijaudier-Cabot G, Ghavamian S. Computer Methods in Applied Mechanics and Engineering. Vol.195 (2006), p.7077

[6] Jiemin Liu. Finite element analysis of mechanical of disturbed materials. Beijing: China Power Press (2010) (in Chinese)

[7] Yan Zhang, Linhua1 Jiang, Da Chen. Chinese Journal of Computational Mechanics. Vol. 27 (2010), p. 1096 (in Chinese)

[8] Grassl P，Lundgren K，Gylltoft K. International Journal of Solids and Structures, Vol.39 (2002), p.5205

[9] Xinpu Shen , Lu Yang , Fusheng Zhu, A Plasticity-based Damage Model for Concrete [J]. Advances in Structural Engineering.Vol.7 (2009), p.461 (in Chinese)

[10] Jiemin Liu, Yuxia Yang, Weinan Wang. Journal of Shenyang Jianzhu University (Natural Science), Vol.30 (2014), p.104 (in Chinese)

[11] Jiemin Liu, Toshiyuki Sawa. Journal of Adhesion Science and Technology. Vol. 14 (2000), p. 67

*Applied Mechanics and Materials Vols. 580-583 (2014) pp 2898-2902*
*© (2014) Trans Tech Publications, Switzerland*
*doi:10.4028/www.scientific.net/AMM.580-583.2898*

# Method of Extended Domain and General Principles of Mesh Approximation for Boundary Problems of Structural Analysis

Pavel A. AKIMOV[1, a], Marina L. MOZGALEVA[2,b]

[1,2] 26, Yaroslavskoe Sh., Moscow, 129337, Russia, Moscow State University of Civil Engineering

[a] pavel.akimov@gmail.com, [b] marina.mozgaleva@gmail.com

**Keywords:** method of extended domain, numerical methods, boundary problem, structural analysis, mesh functions, approximation of operators, averaging

**Abstract.** The distinctive paper is devoted to general principles of mesh approximation for boundary problems of structural analysis with the use of so-called method of extended domain, proposed by Prof. Alexander B. Zolotov [1-4]. In particular we studied questions dealing with approximation of domain, approximation of functions and approximations of operators. Mesh functions are introduced as well as corresponding mesh operations and various types of implementation. The results are rather efficient algorithms in respect to number of operations, computing time and required memory.

## Approximation of domain.

Let Ω be the domain occupied by considering structure. The given domain Ω is embordered by extended one $\omega$ of arbitrary shape, particularly elementary (for instance, parallelepiped, cylinder and others) [4]. Cross-section of extended domain perpendicular to basic direction is optimally approximated by mesh, topologically equivalent to rectangular (Fig. 1).

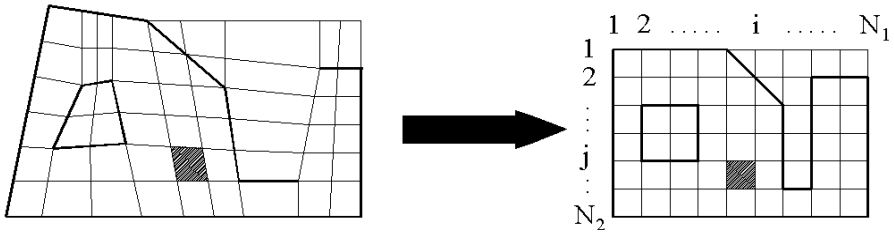


Fig. 1. Sample of approximating mesh.

Concept of topological equivalence in the distinctive case implies that this mesh can be constructed from rectangular one by nondegenerate deformation of its cells without twisting. This type of meshes enables approximations of various structures and buildings on the one hand and allows application of simple regular numeration of nodes on the other hand. This leads to convenient mathematical formulas, effective computational schemes and algorithms, simple data processing and so on. Switch to rectangular mesh can be performed by introduction of corresponding local coordinate system within each cell. General form of equations stays invariable after mesh lining in distinction from matrix elements of original equation set. Direct application of rectangular meshes is especially effective in many instances due to considerable simplification and speed-up of all algorithms. In this connection researcher can use high-density meshes with number of nodes more than ever before and consequently obtain solution with extra accuracy. We should stress the point that inconformity of mesh and contour of structure is allowed [4].

## Approximation of functions.

**2.1. Mesh functions and corresponding operations.** All functions and parameters of boundary problem can be represented with the use of mesh functions. Mesh functions yields dimensions with the same bounds $\varphi(i_1,...,i_N)=\varphi(i)=\overline{\varphi},\ \ i_k=1,...,m_k,\ \ k=1,...,N.$

We will turn down symbol "-" for short in some formulas. Notation $\varphi(i_k \pm 1)$ symbolize increase (decrease) by one of index number $k$: $\varphi(i_k \pm 1) = \varphi(i_1, ..., i_{k-1}, i_k \pm 1, ..., i_{k+1}, ..., i_N)$.
We should also introduce mesh operations in each index line $k = 1, ..., N$:

– "shift": $(C_k^{\pm}\varphi)(i) = \varphi(i_k \pm 1)$; (1)

– "averaging" $(T_k^{\pm}\varphi)(i) = \varphi(i) + \varphi(i_k \pm 1)$; (2)

– "forward difference" $(D_k^{+}\varphi)(i) = \varphi(i_k \pm 1) - \varphi(i)$; (3)

– "backward difference" $(D_k^{-}\varphi)(i) = \varphi(i) - \varphi(i_k - 1)$; (4)

– "identity operator" $(E\varphi)(i) = \varphi(i)$; (5)

– scalar product $(\varphi, \psi) = \sum_{i_1=1}^{m_1} \dots \sum_{i_N=1}^{m_N} \varphi(i_1, ..., i_N)\psi(i_1, ..., i_N)$. (6)

$$T^{\pm} = E + C^{\pm}; \quad D^{+} = C^{+} - E; \quad D^{-} = E - C^{-}; \quad C^{\pm}C^{\mp} = E; \quad C^{\pm}\varphi C^{\mp}u = [C^{\pm}\varphi]u. \tag{7}$$

Let us note that $k$ is arbitrary in (7) and therefore it is turned down. Operations (1)-(5) take into account that $\varphi(i) = 0$ if $i_k < 1$ or $i_k > m_k$, $k = 1, ..., N$. Square brackets in (7) are used for restriction of range of operation. Symbol "+" in the notations of forward operations will be turned down as well. Conjugate operations relative to scalar product are used instead of backward ones. We can also use the following notation: $C = C^{+}$, $T = T^{+}$, $D = D^{+}$. It can be shown in the usual way that $(C^{+}u, v) = (u, C^{-}v)$ and $C^{*} = C^{-}$. In a similar manner $(C^{-})^{*} = C^{+} = C$. Since $E^{*} = E$, it follows that $C^{*} = C^{-}$, $T^{*} = T^{-} = C^{*} + E$, $D^{*} = -D^{-} = C^{*} - E$. Finally note that this operators are commutative in each index line(s) $k$. Let us also remark that mesh operations are vector-mode to the effect that they operate on data bulk. We believe that low-level programming language (for instance Assembler) is especially useful for PC realization. In any case formulation of discrete analogues in mesh terms leads to fastest computing circuits [4].

**2.2. Implementation of mesh functions.** Mesh functions are defined by their nodal values, however original continual boundary problem is defined at all points of the considering domain. Thus we have to implement mesh functions in additional points. This implementation is performed locally at each cell. In most cases we use piece-wise linear (multilinear) approximation within cells and local coordinate systems are introduced in this connection: $x = (x_1, ..., x_N) \Rightarrow (i_1, ..., i_N; t_1, ..., t_N) = (i, t)$. Rectangular meshes with unit array pitch in all directions are considered: $u(x) \Rightarrow u(i, t)$, where $t_k \in [0, 1]$ are local coordinates within mesh elements; $u(i, t)$ is implemented mesh function. For instance, in *N*-dimensional case mesh function is implemented by formulas

$$u(i, t) = \prod_{k=1}^{N} (1 + t_k \Delta_k) u(i), \quad x_k \in [x_k(i), x_k(i_k + 1)], \quad k = 1, ..., N; \tag{8}$$

$$\bar{u}(t) = \Lambda \bar{u}, \quad 0 \le t_k \le 1, \quad \Lambda = \prod_{k=1}^{N} \Lambda_k, \quad \Lambda_k = E + t_k D_k; \quad \partial_k \bar{u}(t) = D_k \tilde{\Lambda}_k \bar{u}, \quad \tilde{\Lambda}_k = \prod_{s \ne k} \Lambda_s, \tag{9}$$

where $\bar{u} = u(i)$ is mesh function; $\bar{u}(t)$ is implemented function, defined in each point of the considering domain; $t = (t_1, ..., t_N)$.
Piece-wise constant implementation of mesh function $\varphi(i)$ within cell elements is wide-spread as well in problems of structural analysis. In particular it can be used for functions corresponding to physical parameters of structures. Here we have $\varphi(i) = 0$ if there is some $i_k = m_k$.

**2.3. Scalar product of implemented functions.** Let us use the following notations for short

$$\sum_{i}^{m-1} = \sum_{i_1=1}^{m_1-1} \dots \sum_{i_N=1}^{m_N-1} \; ; \quad \int_0^1 (\;) dt = \int_0^1 \dots \int_0^1 (\;) dt_1 \dots dt_N \; . \tag{10}$$

Thus, we have

$$(u,v)_x = \sum_{i_1=1}^{m_1-1} \dots \sum_{i_N=1}^{m_N-1} \int_0^1 \dots \int_0^1 u(i,t)v(i,t)dt_1 \dots dt_N = \sum_{i}^{m-1} \theta_\omega(i) \int_0^1 u(i,t)v(i,t)dt = \int_0^1 (\theta_\omega \bar{u}(t), \bar{v}(t))_i dt \; ; \tag{11}$$

$$\theta_\omega(i) = \begin{cases} 1, & i_k < m_k \quad \text{for all} \quad k = 1, ..., N \\ 0, & \text{otherwise i.e. } \exists k : \; i_k = m_k . \end{cases} \tag{12}$$

$\theta_\omega$ is piece-wise constant characteristic function of the mesh, which indicates belonging of the considering mesh element to interior of the extended domain. Symbol $(\;,\;)_i$ denotes scalar product which is taken over $i$ i.e. we have mesh scalar product; $t$ is parameter. The application of formula of implementation yields to the following expressions:

$$(u,v)_x = \int_0^1 (\theta_\omega \Lambda \bar{u}, \Lambda \bar{v})_i dt = \int_0^1 (\Lambda^* \theta_\omega \Lambda \bar{u}, \bar{v})_i dt = (\int_0^1 \Lambda^* \theta_\omega \Lambda dt \cdot \bar{u}, \bar{v})_i \; ; \tag{13}$$

$$(Lu,v)_x = \int_0^1 (L\Lambda \bar{u}, \Lambda \bar{v})_i dt = \int_0^1 (\Lambda^* L \Lambda \bar{u}, \bar{v})_i dt = (\int_0^1 \Lambda^* L \Lambda dt \cdot \bar{u}, \bar{v})_i \; . \tag{14}$$

Let's note, that we normally have situation when functions $u$ or $v$ represent expression $L\varphi$ including characteristic function $\theta$ of the original domain. Support of $\theta_\omega$ contain support of $\theta$ and we can turn down first function. Thus we can get final discrete relations depending on (14), form of $L$ and method of integration with respect to $t$. Hereinafter we will turn down for short indexes $x$ and $i$ indicating space for scalar product.

**2.3. Approximation of operators.** Discrete approximation of original boundary problem presupposes its consideration in the space of implemented mesh functions. Solution of the problem $\boldsymbol{L}u = \boldsymbol{F}$ is considered as a generalized i.e. $(\boldsymbol{L}u, v) = (\boldsymbol{F}, v)$, where $v$ is arbitrary exploratory function. We have to take $u$ and $v$ from mesh functions class in order to obtain approximation of the problem. Elliptic second order differential operator $L$ is the main part of $\boldsymbol{L}$,

$$L = \{L_{pq}\}_{p,q=1,...,M} \; ; \quad L = \{L_{pq}^{st}\}^{s,t=1,...,N} \; ; \quad L_{pq}^{st} = \partial_p^* a_{p,q}^{s,t} \partial_q \; . \tag{15}$$

Hence consideration of $L = \partial_p^* a \partial_q$ or expression $(\partial_p^* a \partial_q u, v) = (a \partial_q u, \partial_p v)$ is of paramount importance. Here $a = \theta a$. Subtracting implemented mesh functions for $u$ and $v$ after taking into account commutativity of $D$ and $\Lambda$ we get

$$(Lu,v) = ((\int_0^1 (D_p^* \tilde{\Lambda}_p^* a D_q \tilde{\Lambda}_q dt)\bar{u}, \bar{v}) \; . \tag{16}$$

We can perform analytical integration with respect to $t$ here. However restriction of the problem to the class of implemented functions in itself leads to errors and therefore analytical integration is

beside the purpose. Approximate integration is recommended here but for all that method of integration should have the order of error equal to corresponding order in mesh approximation. This leads to more simple formulations, fast and effective algorithms. We particularly mentioned method of trapezoids here. Functions $a_{pq}^{st}$ in their turn for many real-world problems can be approximated by functions with constant values in the cell. The results are most compact formulas. They can be obtained in the usual way with the use of (8) and commutativity of all $\Lambda_k$ with each other and other operators. Moreover we take into consideration their sole depending on $t_k$, (10) and commutativity of integrals. Using method of trapezoids we get the auxiliary formulas:

$$\int_0^1 \Lambda_k dt_k \approx 0.5 \cdot T_k; \quad \int_0^1 \Lambda_k^* a \Lambda_k dt_k \approx 0.5 \cdot [T_k^* \alpha]; \quad \int_0^1 \Lambda_k^* dt_k \approx \frac{1}{2} T_k^*; \quad \int_0^1 a dt_k \approx \alpha, \tag{17}$$

where $\alpha$ is the piecewise constant mesh function. The final formulas of discrete approximation of operators can be obtained on the basis of (17) and after numerous transformations have the form:

$$(\partial_p^* a \partial_q u, v) \approx \frac{1}{2^N} (D_p^* T_q^* \left[ \prod_{\substack{k \neq p \\ k \neq q}} T_k^* \alpha \right] T_p D_q \bar{u}, \bar{v}), \quad p \neq q; \quad (\partial_p^* a \partial_p u, v) \approx \frac{1}{2^{N-1}} (D_p^* \left[ \prod_{k \neq p} T_k^* \alpha \right] D_p \bar{u}, \bar{v}). \tag{18}$$

Formulas of approximation of zero order and first order operators are the following

$$(\partial_p^* a u, v) \approx \frac{1}{2^N} (D_p^* \left[ \prod_{k \neq p} T_k^* \alpha \right] T_p \bar{u}, \bar{v}); \quad (a \partial_p u, v) \approx \frac{1}{2^N} (T_q^* \left[ \prod_{k \neq p} T_k^* \alpha \right] D_q \bar{u}, \bar{v}); \tag{19}$$

$$(au, v) \approx \frac{1}{2^N} (\left[ \prod_{k=1}^N T_k^* \alpha \right] \bar{u}, \bar{v}). \tag{20}$$

Consider a general case of elliptic second order self-adjoint differential operator

$$L\bar{u} = \sum_{i=1}^N \sum_{j=1}^N \partial_i^* A_{i,j} \partial_j \bar{u}; \quad A_{i,j} = \begin{bmatrix} a_{i,j}^{1,1} & a_{i,j}^{1,2} & \dots & a_{i,j}^{1,M} \\ a_{i,j}^{2,1} & a_{i,j}^{2,2} & \dots & a_{i,j}^{2,M} \\ \dots & \dots & \dots & \dots \\ a_{i,j}^{M,1} & a_{i,j}^{M,2} & \dots & a_{i,j}^{M,M} \end{bmatrix} = \{a_{ij}^{pq}\}_{p,q=1,\dots,M}; \quad \bar{u} = \begin{bmatrix} u_1 \\ u_2 \\ \dots \\ u_N \end{bmatrix}; \quad A_{i,j} = A_{j,i}^*. \tag{21}$$

Using (18)-(20) we get explicit formula of its discrete approximation:

$$L\bar{u} = \sum_{p=1}^N \left( D_p^* \tilde{A}_{p,p} D_p + \sum_{q \neq p} D_p^* T_q^* \tilde{A}_{p,q} T_p D_q \right) \bar{u}; \quad \tilde{A}_{p,p} = \frac{1}{2^{N-1}} \prod_{k \neq p} T_k^* \bar{A}_{p,p}; \quad \tilde{A}_{p,q} = \frac{1}{2^N} \prod_{k \neq p,q} T_k^* \bar{A}_{p,q}, \tag{22}$$

where $N$ is the number of coordinates; $M$ is function space dimension; $\bar{u}$ is piecewise linear mesh function approximating original function; $\bar{A}_{p,q}$ – piecewise constant mesh approximation of operator coefficients. In arbitrary coordinate system we have

$$\mathsf{A}_{p,q} = J \alpha_{Ep}^* A_{p,q} \alpha_{Eq}; \quad \alpha_E = \alpha \otimes E_M; \quad \alpha_E^* = \alpha^* \otimes E_M; \tag{23}$$

$$\bar{A}_{pq} = \int_0^1 \mathsf{A}_{pq} dt = \int_0^1 \dots \int_0^1 J \alpha_{Ep}^* A_{pq} \alpha_{Eq} dt_1 \dots dt_N. \tag{24}$$

where $\alpha_{Ei}$ is block column of matrix $\alpha_E$ with Jacobian $J$ and Jacobi matrix corresponding to local element transformation of original coordinate system into system where approximating mesh become rectangular with unit array pitch; $E_M$ is identity matrix of the $N$ th order; $\otimes$ is the symbol of direct product. If we choose piecewise constant mesh approximation for $\alpha_{pq}$, $J$ and $\alpha_{pq}$ taking corresponding values in centers of cells, we will have the most simple formula

$$\overline{A}_{p,q} = J\alpha^*_{Ep} A_{p,q} \alpha_{Eq}, \quad t_1 = \ldots = t_N = 0.5. \tag{25}$$

In a special case with rectangular mesh

$$\overline{A}_{p,q}(i) = \frac{1}{h_p(i)h_q(i)} \int_{x_1(i_1)}^{x_1(i_1+1)} \ldots \int_{x_N(i_N)}^{x_N(i_N+1)} A_{p,q} dx_1 \ldots dx_N; \quad \alpha_{p,q} = \begin{cases} 1/h_p, & p = q \\ 0, & p \neq q; \end{cases} \quad J = h_1 \ldots h_N; \tag{26}$$

$$h_p(i) = x_p(i_p + 1) - x_p(i), \quad p = 1, ..., N. \tag{27}$$

Generally $J$ and $\alpha$ depends solely on mesh geometry and normally computed once at the beginning of data processing. In problems with constant $a^{s,t}_{p,q}$ (linear problems with standard parameters) matrices $\widetilde{A}_{p,q}$ computed once too. Piecewise linear approximation leads to effective final formulas of discrete operators. However rapid varying of coefficients within one cell due to heterogeneity of materials, their physical parameters or curvature of cell cause considerable errors. Therefore correct mesh allows strong reducing of errors. The above formulas of discrete approximation for elliptic second order differential operator represent algorithm for computing $Lu$. In other words they may be included into arbitrary step-by-step method. We should stress that operator matrix forming is not required. Upon the whole this is rather efficient method in respect to number of operations, computing time and required memory [4].

**Acknowledgements**

This work was financially supported by the Grants of Russian Academy of Architecture and Construction Sciences (3.1.7, 3.1.8).

**References**

[1] Akimov P.A.: *Correct Discrete-Continual Finite Element Method of Structural Analysis Based on Precise Analytical Solutions of Resulting Multipoint Boundary Problems for Systems of Ordinary Differential Equations*. // Applied Mechanics and Materials Vols. 204-208 (2012), pp. 4502-4505.

[2] Akimov P.A., Mozgaleva M.L.: *Correct Wavelet-based Multilevel Numerical Method of Local Solution of Boundary Problems of Structural Analysis*. // Applied Mechanics and Materials Vols. 166-169 (2012), pp. 3155-3158.

[3] Akimov P.A., Sidorov V.N. Correct Method of Analytical Solution of Multipoint Boundary Problems of Structural Analysis for Systems of Ordinary Differential Equations with Piecewise Constant Coefficients. // Advanced Materials Research Vols. 250-253, 2011, pp. 3652-3655.

[4] Zolotov A.B., Larionov A.V., Mozgaleva M.L., Mskhalaya J.I. *Formulation and approximation of boundary problems with the use of method of ex-tended domain*. MGSU, Moscow, 1992, 86 pages (in Russian).

*Applied Mechanics and Materials Vols. 580-583 (2014) pp 2903-2906*
*© (2014) Trans Tech Publications, Switzerland*
*doi:10.4028/www.scientific.net/AMM.580-583.2903*

# Numerical simulations of the internal fluid field for porous scaffold used in tissue engineering

Liu Qinggang[1,a], Jiang Jingzhi[1,b], Cui Haiting[1,c], Yu Xinqi[1,d], Peng Peiying[1,e]

(Hebei university of science and technology, Shijiazhuang, Heibei, China, 05001s8)

[a]qgliu81@163.com, [b]jjzhi2000@126.com, [c]cuiht@126.com, [d]yxqyxq0016@163.com, [e]pengpeiy@163.com

**Key words**: Tissue engineering, Porous scaffold, Velocity distribution, Pressure distribution

**Abstract:** Models with main-branch channel, crossing channel and net type channel are established and nutrient liquid with a velocity of 0.01m/s is adopted in the study to investigate the fluid field in the channel by using FEA software FLUENT. The velocity and pressure distribution have been obtained in the investigation. By comparing the results in the three models, pressure and velocity distribution in the second and the third models are relatively uniform and are appropriate for the bionics principles. Studies in this paper will be of benefits for the development of tissue engineering.

## Introduction

Tissue engineering is a kind of new technology which is also called regenerative medical science, and in this technology bioactive tissues are manufactured outside organisms, and can be used for repairing or replacing organ or tissue for organism [1]. This technology was first declared by the US national science fund committee in 1987, and was developed quickly in the following years. Today, this technology has spread into many science and technology fields such as biology science, material science [2]. This technology has been used in many organs such as bone [3-5].

In this paper, fluid fields in models of porous scaffolds with different internal channels have been studied by using FEA software FLUENT, and the studies in this paper may of a certain sense for the development in tissue engineering.

## Models and the corresponding parameters

As shown in Fig.1, three models are adopted in this study.

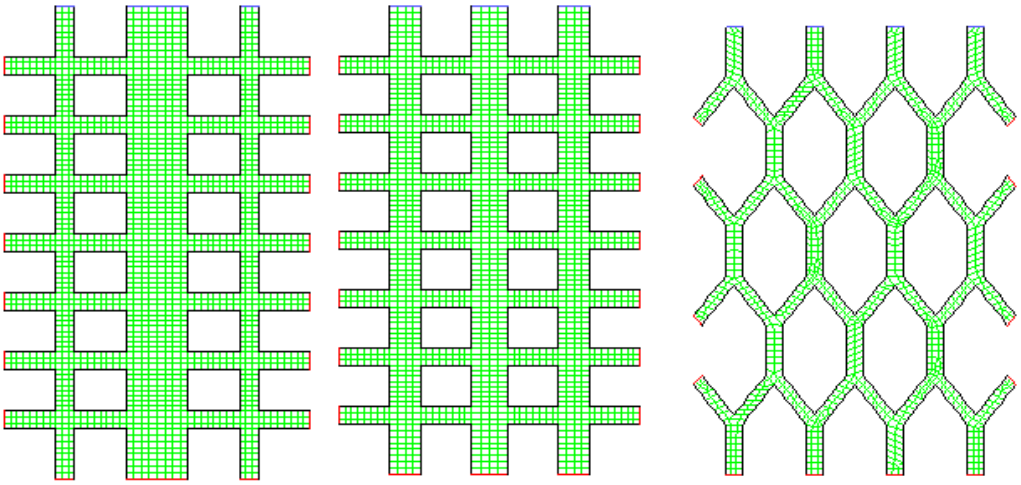

Model 1 Model 2 Model 3

Fig.1 Models

In Fig.1, Model 1 is consist of one main channel and several branch channels and is call a main-branch channel model. Model 2 is consist of several horizontal and vertical channels and is called a crossing channel model. In model 3, channels are arranged in net type and model 3 is called a net type channel model. Nutrient liquid used in this simulation is considered to be of a velocity of

0.01m/s, a density of 1000kg/m$^3$, and a viscosity of 0.0018 Pa·s. The power device in the simulation is set as peristaltic pump. By using FEA software FLUENT, velocity and pressure distribution of the nutrient liquid in the channels have been obtained.

**Simulation results and analysis**

Velocity and pressure distributions for the three models are shown in Fig.2 to Fig. 4. In these figures, the unit of pressure is Pa and the unit of the velocity is m/s.

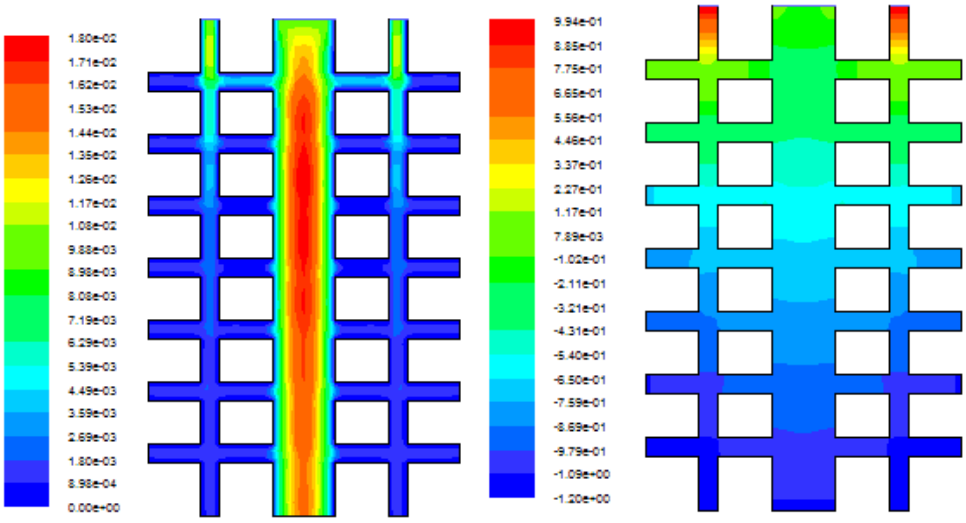


(a) Velocity distribution (b) Pressure distribution

Fig. 2 Velocity and pressure distribution for model 1

As in Fig.2, the velocity does not distribute uniformly and has an obviously difference from the inlet to the outlet. The velocity at the bottom is low. On the same vertical level, the velocity of the main channel varies in great degree and is no uniform. From the inlet to the outlet, the average velocity in the main channel increases first and then decreases while the nutrient liquid processes the main channel. In the branch channels, the velocities distribute uniformly, but the values are generally small i.e. local resistance of a relatively great value exists in these positions. In the flowing process, flow separation appears and a back flows are generated in some areas.

As seen in Fig. 2(b), at the same horizontal line of the inlet, pressures at the left and right sides are higher than that at the center, and it is because they are of the different distance to the inlet point. But at the other horizontal line which is far away from the inlet, pressures in both the main channel and the branch channels are of nearly the same value. A relatively great resistance exists in this model.

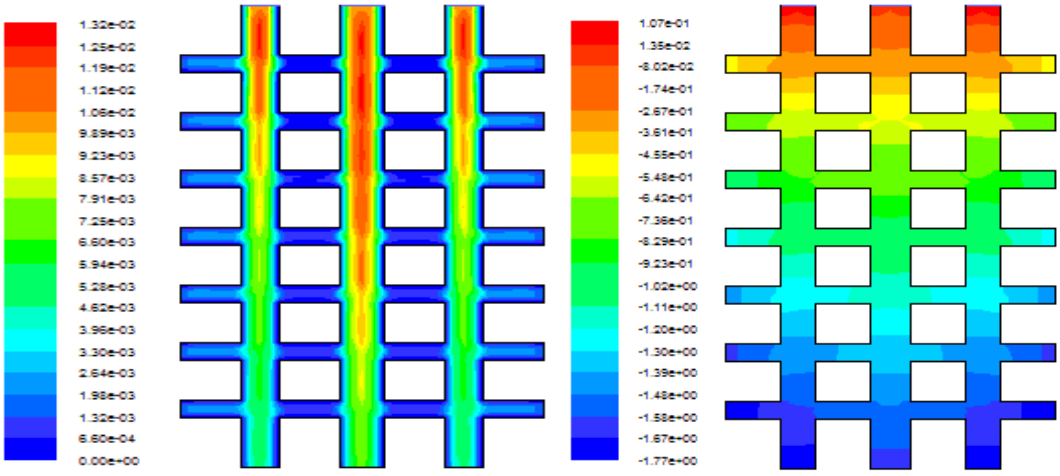


(a)Velocity distribution (b) Pressure distribution

Fig. 3 Velocity and pressure distribution in model 2

In Fig. 3(a), the average velocity values are not obviously different from the model 1, but the distribution of the velocity is a bit more uniform than that in model 1. In the vertical channel on the center, the velocity is great on the inlet, then decreases gradually with the process of the travel, and gets the minimum on the outlet. Other two vertical channels on the left and the right sides are of the same velocity distribution style as the one in the center, and it is suitable for the growth of the cells. In the horizontal channels, velocity does not distributes so uniform, but at the bottom, it gets a bit uniform that other places. On the top and middle parts of the model, velocities in the vertical channels are great, but small in the horizontal channels, and it is not fit for the growth of the cells. In this model, flowing separation and back flow also exist and it is more obvious in the horizontal channels.

Just as the velocity in this model, the pressure is at the top value on the inlet, then gradually decreases in the middle and gets the minimum in the outlet at the bottom of the model. At the same horizontal line, the pressures are almost the same in the middle channel to the channels at the left and the right sides.

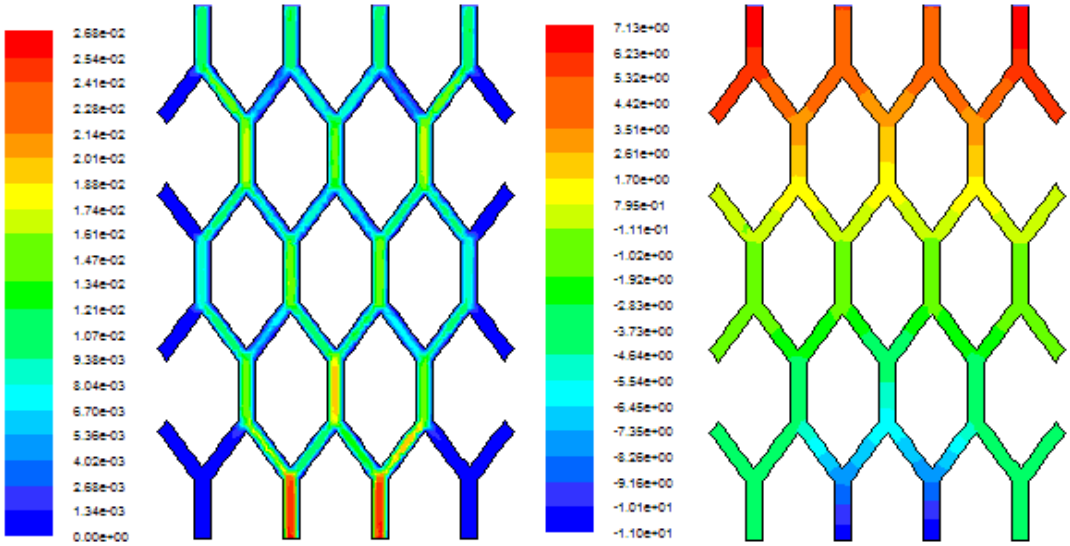


(a) Velocity distribution (b) Pressure distribution

Fig. 4 Velocity and pressure distributions in the model 3

In model 3, velocity distributes uniformly in the entire model. From the inlet on the top to the outlet on the bottom, the velocities in the oblique channels are lower than in the vertical channels, and this distribution style is suitable for the flow of the nutrient liquid and the growth of the cells. But at the outlet on the bottom, the velocities distribute not as uniform as others, and velocities in the two outlets in the middle are obviously greater the two on the two sides. Also, velocities in the two oblique channels on the bottom are also small, and this situation is not suitable for the nutrient liquids flowing in the tissues.

In Fig. 4(b), the pressure decreases slowly form the inlet to the outlet, and the pressure gradient on the vertical direction is not as great as the model 1 and model 2. On the horizontal line of the inlet, pressure in the middle channel is almost the same as that in the channel on the two sides. But on the outlet, the pressure in the middle channel is smaller that in the two side.

Generally, velocity in model 3 is uniform and the flow is gentle. The local resistance is small, and the model 3 is fit for the principles of the bionics. Model 3 can provide a fitful environment for the supplies of the nutrient liquids for the tissue and is beneficial for the cell growth. Model 3 is the most suitable model among the three models mentioned in this paper.

## Conclusions

By conducting the numerical simulation for the three models, the internal velocity and the pressure distributions have been obtained, and the main conclusions are as follows.

(1)In model 1, the velocity is greatly different in the main channel from the branch channel, and the velocity does not distribute uniformly. Local resistance is great and flow separation and back flow exist in the bottom of the model.

(2)In model 2, velocity has not changed greatly, and local resistance and flow separation also exist.

(3)In model 3, velocity distributes uniformly and the local flowing resistance is small. So model 3 is a kind of excellent model.

(4)By comparing the three models, fluids flow gently in model 2 and model 3, and the velocity and the pressure distribute uniformly. That is, model 2 and model 3 are more suitable for the tissue engineering.

**Acknowledgement**

The study is financially supported by the Project of Natural Science Foundation of Hebei Province (Grant number: E2012208049) and the Key Technology R&D Program of Hebei Province (Grant number: 13211222).

**Referance**

[1 ] Ren Jie, Zhu Jing, Ren Tianbin. Recent development of fabrication technology of biodegradable porous scaffold for tissue engineering, Journal of Tongji university (Natural science), 2005,33(12):1164-1167+1176

[2] Wang Han, Zhang Hua. Present situation of development of porous scaffolds for tissue engineering, Journal of Tianjin polytechnic university, 2006,25(6):20-24

[3] Wu Jingmei, Wu Ruofeng. Fabrication and characterization of the porous scaffolds for bone tissue engineering, New chemical materials, 2004,32(9): 17-20

[4] Zhao Jin, Yuan Xiaoyan, Yao Kangde, Progress in the fabrication technology of tissue engineered porous scaffolds, Chemical industry and engineering progress, 2002,21(9): 644-647

[5] An Xiao, Shi Yanchun, Chen Meihua, et al. Experimental study on tissue engineering scaffolds in treatment for spinal cord injury. Space medicine & medical engineering, 2013,26(1):56-59

*Applied Mechanics and Materials Vols. 580-583 (2014) pp 2907-2911*
*© (2014) Trans Tech Publications, Switzerland*
*doi:10.4028/www.scientific.net/AMM.580-583.2907*

# Preliminary Application of Software Package GPPS to Spare Linear Systems from Meso Scale Simulation of Concrete Specimen

Jianping Wu[1, a], Huaifa Ma[2, b], Jun Zhao[1, c], Shuchang Wang[1, d]

[1] School of Computer Science, National University of Defense Technology, Changsha, Hunan, 410073, China

[2] Earthquake Engineering Research Center, China Institute of Water Resources and Hydropower Research, Beijing, 100048, China

[a]wjp@nudt.edu.cn, [b]mahf@iwhr.com, [c]zhaojun@nudt.edu.cn, [d]wangshuchang@126.com

**Keywords:** Parallel algorithm, preconditioner, subspace iteration, sparse linear system, meso-scale simulation of concrete.

**Abstract.** The general parallel preconditioning subspace iteration software GPPS is developed based on the integration of various preconditioning methods, parallelization techniques, and subspace iterations, to solve general sparse linear systems. The software has several characteristics, including high computational performance, good readability, simple interface, and excellent scalability. In this paper, the functions of the software are outlined, and then it is used to solve the sparse linear systems from meso-scale simulation of concrete specimens. The numerical experiments show that GPPS is clearly superior to the software package AZTEC, which is used in the simulation up to now, and in addition, ICT and the parallelization technique based on factors combination outperform other preconditioning techniques integrated in the software.

## Introduction

Solution of linear systems is one of the core problems in scientific and engineering computing. The so-called Krylov subspace method is the most popular iteration, but the convergence rate depends on the distribution of the spectra of the coefficient matrix. The more concentrated the eigenvalues, the faster convergence it will have. The construction of preconditioners is to make the eigenvalues of the preconditioned matrix more concentrated, so it is very important[1].

The efficiency of preconditioners depends not only on the ability to reduce the distribution area of the eigenvalues, but also on its construction cost and the cost to apply it to vectors. Incomplete factorization preconditioning is very cheap in construction, the application is very economic, and the effectiveness can also be controlled by the number and the position of nonzero fill-ins in the incomplete factors, which makes it to be one of the most effective preconditioning techniques[1]. There are many variants of incomplete factorizations, among which ILU(0)[1], ILUT[1], MRILUT[2], and ICT[3] are the most efficient ones.

Incomplete factorization is very efficient, but it is very difficult to be parallelized. Therefore, many techniques are provided, including multi-coloring[1], non-overlapped domain decomposition[4], pseudo-overlapped incomplete factorization[5], and overlapped domain decomposition[6]. Multi-coloring can increase the degree of parallelization, but will degrade the effectiveness. In pseudo overlapped incomplete factorization, the overall domain is decomposed into multiple non-overlapped sub-domains, but the incomplete factors are corrected with the pseudo overlapped nodes.

In non-overlapped domain decomposition, the off-diagonal fill-ins related to the links between different sub-domains are discarded, and each diagonal block can be incompletely factorized further. This method can be improved by Schur complement, and multicolor resorting can be used to the quotient graph to control the number of fill-ins. Overlapped domain-decomposition is one of the most efficient parallelization method. In this method, the solution related to each sub-domain is approximated directly, and then these local approximations are simply averaged, with certain damping factors during the summation, to derive the global solution, which is in general called

additive Schwarz. To improve the convergence, the local solution corresponding to overlapped nodes can be averaged with weights. Cai and Sarkis provide a simple improvement[7], the restricted additive Schwarz. In this method, the frequency and volume of communication are both halved, and the convergence rate is also often much faster than the additive Schwarz. However, the additive Schwarz and the restricted version are both not tend to the corresponding serial incomplete factorization with the increase of the degree of overlapping. To overcome this shortcoming, there provided a new parallelization method called factors combination[8].

The general parallel preconditioning subspace iteration software GPPS is developed with the currently most efficient incomplete factorizations, incorporated with the widely used non-overlapped and overlapped domain decomposition based parallelization, and several preconditioned Krylov subspace iterations. It can be used to solve not only symmetric positive definite linear systems, but also un-symmetric ones. In this paper, there provide some preliminary results from simulating concrete specimens with meso-scale scheme, to verify the actual performance of the software.

## Outline of GPPS

GPPS is a software package, abbreviated from the first character of four words, i.e. general, parallel, preconditioning, and subspace. It is a general purpose parallel preconditioning subspace package, used to solve general sparse linear systems in parallel. The options that can be selected as preconditioners include none, Jacobi, SSOR, ILU(0), ILU(k), ILUT, MRILUT, ICT and etc. Except none and Jacobi, each preconditioning technique can be parallelized with one of the five methods, i.e., additive Schwarz(AS), restricted additive Schwarz(RAS), additive Schwarz with harmonic extension(ASH), factors combinations (FC), and the block Jacobi analog(BJ). The incorporated subspace iterations include CG, GMRES, BiCGSTAB, CGS, and TFQMR. GPPS is written in Fortran90 and the MPI message passing interface. In parallel computation, the user can specify the partition for the matrix rows and the vectors.

The framework of GPPS can be described as in figure 1, where the linear solver is implemented by invoking the interface to initialize the environment, the interface to invoke preconditioning construction and application, and the interface to invoke subspace iterations. The environment initialization interface is used to input all kinds of parameters for the solver from name-list files, and initialize the distribution of data related to distributed memory parallel computation, then perform some settings and vector structure constructions which will be used during the process of matrix-vector multiplications. The preconditioner interface provides a unified interface to invoke preconditioners, including Jacobi and all other parallelized versions. This interface contains some parameter configurations, memory allocation for both integer and float type data, and actual construction of parallel preconditioners. The subspace iteration interface provides a unified interface to invoke Krylov subspace iterations. Each subspace method needs to set the related initial solution vector, applying matrix vector multiplication and preconditioning process, and invoking basic linear algebraic subroutines and abnormity processing subroutine.

There are two ways to use GPPS. The first is to use the compiled executable program to solve sparse linear systems directly, which requires that the order of the system, the matrix information in CSR format, the right hand side, the number of processed to perform in parallel, and the identification number of each vector component are stored in a input file. The second is to invoke three interfaces provided in the package, that is, the environment initialization interface, the preconditioner construction interface and the subspace iteration unified interface, to solve sparse linear systems. In this situation, the GPPS_mod module should be used in the user program, the sparse matrix should be given in distributed CSR format, and consecutive rows should be distributed to each process. The right hand vector and the solution vector are distributed in the same manner. Before these interfaces are invoked, the parameters locLenN and locBegN in the module GPPS_mod should be given, where locLenN is the number of rows on this process, and locBegN is the global label of the first row on this process. When packages to partition graphs are used, the rows distributed to each process are not

consecutive. At this time, we can reorder the nodes of the graph, to turn it into the consecutive form and invoke the GPPS interfaces.

The function of GPPS is determined by two namelists, preconParameter and solverParameter. The namelist preconParameter contains five parameters, omega, droptol, nr, lfil and idprec, which are used to set various parameters of preconditioners. Different serial preconditioners can be incorporated with each of the provided parallelization schemes, to derive different preconditioning processes. While the namelist solverParameter contains 4 parameters, rstep, maxit, maxeps and imthd, which are used to set the restarted step, the maximum allowed number of iterations, the precision requirement of the current residual vector to the initial residual vector, and the specific type of iterations selected.

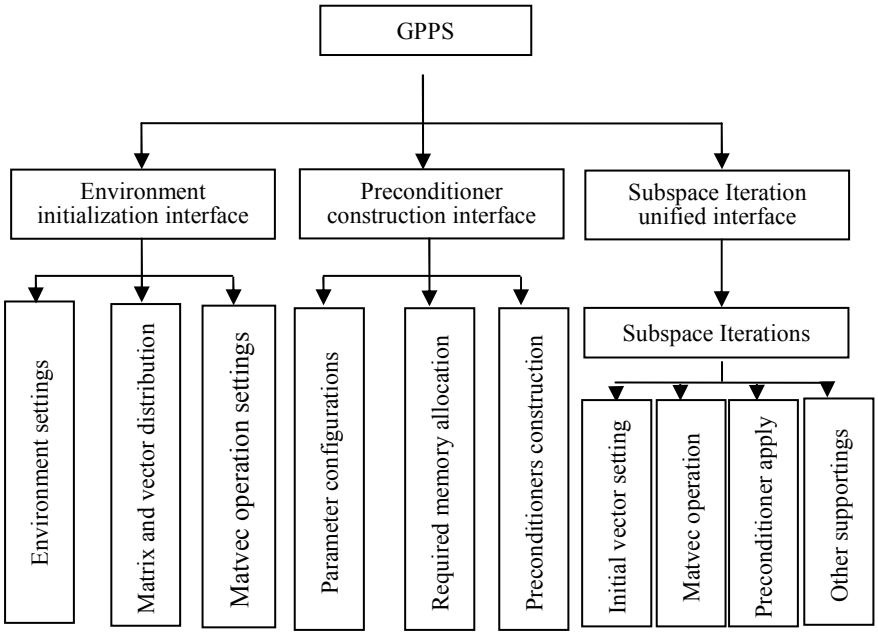


Fig. 1 Framework of GPPS

**Numerical simulation for meso-scale simulation of concrete specimen**

In this section, we will give some of the numerical results with the package GPPS to compute the linear systems from meso-scale simulation of concrete specimen. All the given results are derived on a cluster of Intel(R) Xeon(R) CPU 5150@2.66GHz(cache 4096KB), which are interconnected by infiniband. The operating system is Linux of Red Hat 4.1.2-52. The message passing interface used is mvapich2 and the compiler used is Intel Fortran 11.1.059. For all the linear systems are symmetric positive definite here, only the conjugate gradient(CG) and symmetric preconditioners are tested. The stop criterion is selected as the Euclid norm of the residual vector is reduced by 1E-4. The domain decomposition is based on the software package METIS, and the graph partitioning interface based on bisection is invoked. To use GPPS, all the nodes from partitioning is reordered, such that the nodes belonging to the same partition is labeled consecutively, and the related rows of the coefficient matrix and vector components are distributed to the same process. All the time results are in seconds.

In meso-scale simulation, the specimen can be regarded as a three-phase composite material consisting of aggregate, mortar and interface between them, and it is approximated by the finite element method. We experiment on a cubic concrete specimen of wet-sieved, with size of 550mm x 150mm x 150mm, which is described in [8]. There are 71013 discrete nodes and the number of finite elements is 78800 in all. The two supporting columns lay at $x = -0.15$m and $z = 0$m, and at $x = 0.3$m and $z = 0$m, that is, lay at the bottom and with distances 0.05m from left and right boundaries, respectively. While two loading columns are located at $x = 0$m and $z = 0.15$m, and at $x = 0.15$m and $z = 0.15$m, that is, at the top and with distances 0.2m from left and right boundaries, respectively.

As in [8], we will test GPPS for the linear systems both in static and dynamic loading. In static loading, the loads are increased step by step. The load step is 0.25kN during the numerical simulation. There occur damaged elements at the 59th step, and the specimen is completely cracked at the 94th step. If there are damaged elements at a certain step, several linear systems need to be solved to update the displacements. There are 178 linear systems in all.

In table 1, there list the results of preconditioned conjugate gradient with software package AZTEC and GPPS. For AZTEC, the optimal preconditioning, namely the non-overlapped parallel ILU(0), is used. For GPPS, several symmetric parallel preconditioners is tested, where the relaxation parameter for SSOR is selected as 1.0, the number of non-zeros allowed in each row of ICT factors is 25 and the dropping threshold is selected as 1E-3. In the table, NP denotes the number of processors used. It is clear that the number of iterations from factors combination(FC) parallelization is often less than that from additive Schwarz(AS) or block diagonal approximation(BJ). When factors combination is used, the time required to solve the linear system is also often less than additive Schwarz and block Jacobi. Meanwhile, when parallelization ILU(0) is selected, the number of iteration used with GPPS is often less than AZTEC. But the time elapsed is less than AZTEC only when the number of processors is 64. When parallelized ICT is used as preconditioning process, and the optimal preconditioning is used in AZTEC, GPPS is uniformly better than AZTEC.

Table 1. Average iterations and time[seconds] to solve each linear system during static loading

| | | AZTEC | Parallelized ILU(0) | | | Parallelized ICT(25,1E-3) | | |
|---|---|---|---|---|---|---|---|---|
| | | | AS | FC | BJ | AS | FC | BJ |
| Averag. Iter. | NP=08 | 254.65 | 195.86 | 188.73 | 227.96 | 202.08 | 193.41 | 229.93 |
| | NP=16 | 267.44 | 202.08 | 192.79 | 239.41 | 205.26 | 194.14 | 244.44 |
| | NP=32 | 274.09 | 203.17 | 192.40 | 243.22 | 195.28 | 187.16 | 251.92 |
| | NP=64 | 290.60 | 211.48 | 197.42 | 255.65 | 206.61 | 194.33 | 272.44 |
| Averag. time | NP=08 | 2.5967 | 2.8101 | 2.6475 | 3.0432 | 1.9415 | 1.8019 | 2.0486 |
| | NP=16 | 1.8372 | 2.3411 | 2.1995 | 2.5088 | 1.5961 | 1.4758 | 1.7341 |
| | NP=32 | 1.1718 | 1.5638 | 1.4771 | 1.6256 | 1.0780 | 0.9975 | 1.2117 |
| | NP=64 | 1.1080 | 1.0302 | 0.9669 | 1.0250 | 0.7478 | 0.6990 | 0.8686 |

In dynamic loading, the time step is selected as 0.001 seconds, and the loads is increased linearly with increment of 0.8kN. The sample is completely damaged at the 38th step. Prior to actual test for loading, some eigenvalues should be computed to determine related parameters used in the simulation, which involves the solution of linear systems. Therefore, there are 220 linear systems to be solved in all for the whole simulation process. The average iterations and time elapsed for the solution of each linear system is listed in table 2. From the table, it is clear that though for ILU(0), the time used with factor combination based parallelization is shorter than that with AZTEC when 64 processors used, when preconditioning process other than ICT is used, the time with GPPS used is longer than that with AZTEC. When ICT preconditioning is used, the efficiency of GPPS is better than that of AZTEC in general, especially when factor combination based parallelization technique is incorporated in the iterations, where the iteration time is significantly reduced. Meanwhile, we can see that for GPPS itself, factor combination based parallelization is better than additive Schwarz and block diagonal approximation.

**Summary**

In this paper, the general parallel preconditioning subspace iteration software GPPS is simply described and tested through the solution of linear systems encountered in the meso-scale simulation of concrete sample. The simulation results show that, when the option of ICT preconditioning is used, the performance of GPPS is better than AZTEC incorporated with the best preconditioning option.

Meanwhile, among the preconditioning schemes provided in GPPS, ICT have significant privileges, and the factors combination method outperforms additive Schwarz and block diagonal approximations. At the same time, when ILU(0) used both in AZTEC and GPPS, the time used to solve a linear system in average with GPPS is longer in general than that with AZTEC, which implies that the software package GPPS can be improved further. In future, the parallel implementation of matrix-vector multiplication and the data structures used will be investigated carefully to make it more efficient.

Table 2. Average iterations and time[seconds] to solve each linear system during dynamic loading

| | | AZTEC | Parallelized ILU(0) | | | Parallelized ICT(25,1E-3) | | |
|---|---|---|---|---|---|---|---|---|
| | | | AS | FC | BJ | AS | FC | BJ |
| Averag. Iter. | NP=08 | 248.89 | 189.30 | 182.03 | 217.10 | 195.85 | 188.90 | 222.35 |
| | NP=16 | 261.70 | 192.22 | 184.72 | 227.96 | 202.68 | 193.39 | 239.11 |
| | NP=32 | 266.66 | 192.66 | 183.09 | 229.61 | 193.89 | 185.04 | 249.30 |
| | NP=64 | 283.48 | 200.53 | 187.22 | 244.07 | 203.75 | 192.04 | 267.57 |
| Averag. time | NP=08 | 2.5353 | 2.7048 | 2.5508 | 2.9011 | 1.8848 | 1.7549 | 1.9815 |
| | NP=16 | 1.8011 | 2.2478 | 2.1068 | 2.5175 | 1.7254 | 1.5004 | 1.7831 |
| | NP=32 | 1.1400 | 1.4803 | 1.4056 | 1.5392 | 1.0703 | 0.9835 | 1.1991 |
| | NP=64 | 0.9295 | 0.9802 | 0.9135 | 0.9854 | 0.7423 | 0.6938 | 0.8567 |

**Acknowledgements**

This work was financially supported by NSFC(61379022 and 51079164), and special fund for water resources research in the public interest(201201053).

**References**

[1] Y. Saad. Iterative Methods for Sparse Linear Systems. PWS, Boston, 1996

[2] J. P. Wu, X. P. Liu, Z. H. Wang, Z. H. Dai, and X. M. Li, Two new preprocessing methods to 2-dimension energy equations with three temperatures, Chinese J. Comput. Phys., 2005, 22(4): 283–291.

[3] Wu Jianping, Wang Zhenghua, Li Xiaomei. Problems and improvements to the incomplete Cholesky decomposition with thresholds. Journal on Numerical Methods and Computer Applications, 2003, 24(3):207-214

[4] K. Nakajima, H. Okuda. Parallel Iterative Solvers with Localized ILU Preconditioning for Unstructured Grids on Workstation Clusters. International Journal of Computational Fluid Dynamics, 1999, 12(3): 315-322

[5] M. M. monga Made, H. A. van der Vorst. Parallel incomplete factorizations with pseudo-overlapped subdomains. Parallel Computing, 2001, 27:989-1008

[6] R. Bru, F. Pedroche, D. B. Szyld. Overlapping Additive and Multiplicative Schwarz Iterations for H-matrices. Linear Algebra and its Applications, 2004, 393:91–105

[7] X.-C. Cai, M. Sarkis. A restricted additive Schwarz preconditioner for general sparse linear systems. SIAM J. Sci. Comput., 1999, 21:792-797

[8] Jianping Wu, Jun Zhao, Junqiang Song, and Xiaomei Li. A parallelization technique based on factor combination and graph partitioning for general incomplete LU factorization. SIAM J. Sci. Comput., 2012, 34(4): A2247–A2266

*Applied Mechanics and Materials Vols. 580-583 (2014) pp 2912-2915*
*© (2014) Trans Tech Publications, Switzerland*
*doi:10.4028/www.scientific.net/AMM.580-583.2912*

# Mechanical Behavior Analysis of Concrete Short Columns Pushed Out from Over-thick Steel Tube

Jiemin Liu [1, a], Jialiang Yang[2,b] and Shuang Liu[1,c]

[1] School of Science, Shenyang Jianzhu University, Shenyang China, 110168, China

[2] School of Civil Engineering, Shenyang Jianzhu University, Shenyang China, 110168, China

[a]liujiemin1954@163.com, [b]yangjl0912@163.com, [c]liush0229@163.com

**Keywords:** over-thick steel tube, mechanical model, adhesive thin-layer of steel tube/concrete, adhesive shearing stress.

**Abstract.** An axial symmetry elasticity model of the concrete short column which is pushed out from over-thick steel tube is set up, and the equations of displacement method are derived. The experiment of push-out test of the short column was carried out. On the base of the test, the adhesive thin-layer between the concrete and the over-thick steel tube is introduced. The experimental results show that the shearing stress in the adhesive thin-layer is uniform along the height, which is coincide with the results obtained by the axial symmetry elasticity model of the concrete short column set up in this paper. Therefore, the adhesive shearing stress between steel tube and concrete can be precisely measured by the push-out test of the concrete short column and the relation of shearing stress-shearing strain of the adhesive thin-layer can be determined.

## Introduction

Composite structures of concrete-filled steel tube have a number of advantages over conventional steel-reinforced concrete members [1]. It can provide excellent earthquake-resistance properties such as high strength, high ductility and good energy absorption capacity.

The adhesive stresses created between the concrete core and the steel tube is premise guaranteeing the interaction between the concrete core and the outer steel tube. Because of properties difference between steel and concrete, slip on the interface of steel tube/concrete will take place, especially in the case of high-stress level. Unfortunately, the slip is difficult to be effectively measured. How to establish a mechanical model to simulate the slip is noticed [2-6]. Spring-contact model of simulating the slip is studied widely. The fault of the model is that modeling process is complex, and a lot of calculation has to be carried out.

The authors of this paper consider that the interface between concrete and steel tube is essentially adhesive thin-layer. A theoretical elasticity model of the concrete short column which is pushed out from the over-thick steel tube is presented. The test of measuring the adhesive thin-layer is carried out.

## Mechanical model of concrete short column pushed out from over-thick steel tube

**Equations of displacement method.** Considering **t**hat a circular concrete short column constrained with over-thick steel tube is pushed out from over-thick steel tube due to slipping of the interface between the concrete and the over-thick steel tube. The interface is essentially an adhesive thin-layer and subjected mainly to shearing. Under the condition of critical state of the concrete column being pushed out, the ultimate shearing stress in the adhesive thin-layer is far lower than those in the concrete and in the steel tube. The radial constrain normal stress in the steel tube is small. Thus suppose that:(1)Radial stiffness of steel tube is infinite; (2)only axial strain in the concrete column takes place, radial strain is vanish, that is, $\varepsilon_r = 0$ .Mechanical model of the concrete constrained with circular steel tube subjected to axial compression load is shown in Fig.1.

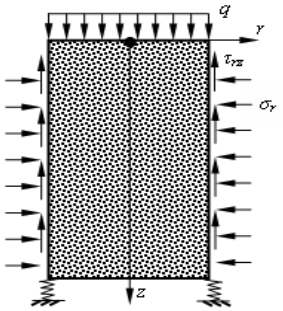


Fig.1 The stress state of the concrete short column

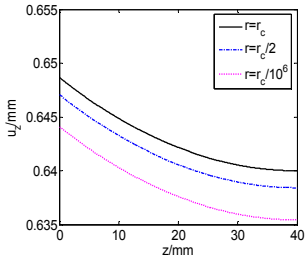


Fig.2 The displacement curves of $u_z$

Basic equations of displacement method for axial-symmetry problems of are expressed as

$$\theta_{,r}/(1-2\mu)+\nabla^2 u_r - u_r/r^2 = 0\ ,\quad \theta_{,z}/(1-2\mu)+\nabla^2 u_z = 0 \tag{1}$$

Whrer, $\theta=\varepsilon_r+\varepsilon_\theta+\varepsilon_z=u_{r,r}+u_r/r+u_{z,z}$ $\varepsilon_r$ , $\varepsilon_\theta$ and $\varepsilon_z$ are radial, loop and axial strain, respectively. $u_r$, $u_\theta$, and $u_z$ are radial, loop and axial displacement, respectively. Right lower subscript "$,x$" expresses derivation to the variable $x$.

For the mechanical model shown in Fig.1, $\varepsilon_\theta = 0$ , $\varepsilon_r = 0$ , and corresponding displacements $u_r$, $u_\theta$ are zeros and volume strain $\theta = u_{z,z}$ . Eq. 1 is reduced as,respectively

$$u_{z,rz}=0 \tag{2}$$

$$\frac{2(1-\mu)}{1-2\mu}u_{z,zz}+u_{z,rr}+\frac{1}{r}u_{z,r}=0 \tag{3}$$

The solution of equations(2)and(3)can be obtained as

$$u_z=\frac{cz^3}{6}+\frac{az^2}{2}+bz+c_1+c_2r^{t_2}+c_3r^{t_3}+\frac{cr^3}{3} \tag{4}$$

$$t_2=\frac{-1+\sqrt{5}}{2}=0.618\ ,t_3=\frac{-1-\sqrt{5}}{2}=-1.618 \tag{5}$$

**Solution of the basic equations**

The stress components $\sigma_r$ , $\sigma_\theta$ and $\sigma_z$ can be expressed as

$$\sigma_r=\sigma_\theta=\frac{\mu_c E_c\varepsilon_z}{(1+\mu_c)(1-2\mu_c)},\quad \sigma_z=\frac{(1-\mu_c)E_c\varepsilon_z}{(1+\mu_c)(1-2\mu_c)},\quad \tau_{zr}=G_c\gamma_{zr}=\frac{E_c u_{z,r}}{2(1-2\mu_c)} \tag{6}$$

Thus, $\varepsilon_z$ and $u_{r,z}$ can be expressed as

$$\varepsilon_z=u_{z,z}=\frac{cz^2}{2}+az+b \tag{7}$$

$$u_{z,r}=c_2t_2r^{t_2-1}+c_3t_3r^{t_3-1}+cr^2 \tag{8}$$

Because $\varepsilon_z$ is independent to hoop coordinate $r$, $\sigma_r$ , $\sigma_\theta$ and $\sigma_z$ are also only related to coordinate $z$. From Eq.7, it can be seen that the shearing stress $\tau_{zr}$ is not relate to $z$ only to $r$. According to equilibrium of the whole concrete column, have

$$\overline{\tau}_{rz}\pi d_c l_c = F=\int_{A_c} q\mathrm{d}A \tag{9}$$

Where $\overline{\tau}_{zr}$ is shearing stress on the column surface of $r$=$r_c$, and $F$ is the resultant of the distributive loads $q$ exerted to the upper surface ($z$=0).

The boundary conditions used to determine the constants in Eq. 4 are Eq.10.

$$\int_{A_c}\sigma_z(0)\mathrm{d}A=-F,\quad \overline{\tau}_{zr}\pi d_c\left(l_c-z\right)=\int_{A_c}\sigma_z(z)\mathrm{d}A\quad(0\le z\le l_c),\quad \int_{A_c}\sigma_z(l_c)\mathrm{d}A=0$$
$$(\tau_{rz})_{r=r_c}=\overline{\tau}_{rz},\quad (u_z)_{z=l_c}=\overline{u}_z,\quad (u_{z,r})_{r=0}=0 \tag{10}$$

Where $\overline{u}_z$ is the vertical displacement $w_3$ of the lower surface of the concrete column measured according to the test (see section 3). The constants $c$ , $a$ , $b$ , $c_1$ , $c_2$ and $c_3$ are determined from boundary conditions (10) as

$$a=\frac{(1+\mu_c)(1-2\mu_c)F}{(1-\mu_c)E_cA_cl_c},\quad b=\frac{-(1+\mu_c)(1-2\mu_c)F}{(1-\mu_c)E_cA_c},\quad c=0, \tag{11}$$
$$c_1=\overline{u}_z+\frac{2(1+\mu_c)(1-2\mu_c)F}{2(1-\mu_c)E_cl_c}\left[\frac{l_c^2}{A_c}-\frac{2(1-\mu_c)}{0.618\pi(1-2\mu_c)}\right],c_2=\frac{Fr_c^{0.382}}{0.618\pi d_cl_cG},\quad c_3=0$$

The average vertical displacement $u_{z,\mathrm{av}}$ at cross-section $z$ is expressed as

$$u_{z,\mathrm{av}}(z)=\frac{1}{A_c}\int_{A_c}u_z\mathrm{d}A=(\frac{az^2}{2}+bz+c_1)+\frac{c_2\pi r_c^{2.618}}{2.618A_c} \tag{12}$$

The displacement curves of $u_z$ is shown in Fig.2.

## Experimental study

**Prepare of specimens and test.** Three series of specimens were designed. The first series has 3 circular concrete columns used to measure the mechanical properties of the concrete. The diameter and length of the specimens were 40mm and 100mm, respectively, so named as c-40-100. The concrete columns were made up plane concrete, course sand (diameter 0.2-1mm) and reduced stone (diameter 3-5mm) through top pouring. The second series has 3 circular steel tubes with diameter of 40mm, thickness of 2mm and length of 300mm, used to measure the mechanical properties of the steel tube, named as s-40-2-300. The third series has 3 thick-walled concrete filled steel tubes. The steel tubes were with diameter of $d_s$=40mm, thickness of $t_s$=6mm and length of $l_s$=100mm, and the concrete column were with diameter of $d_c$=28mm and length of $l_c$=40mm. The series was named as c-s40-6-100-c40. The specimens were made up through pouring the concrete into the steel tubes. Before pouring, the in-surfaces of the steel tubes were degreased with acetone.

The put-out test is shown in Fig.3. The thickness $t_a$ of the adhesive thin thin-layer was approximately determined as 1mm through observation for the debonded interface between concrete and steel tube. Displacement meters Dis.M1, Dis.M2, and Dis.M3 were used to measure the vertical displacement of the upper surface of the concrete, the vertical displacement of the upper surface of the steel tube, and the vertical displacement of the lower surface of the concrete, respectively.

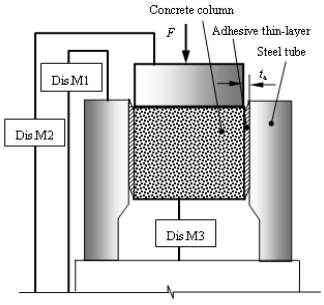


Fig. 3 Test set-up

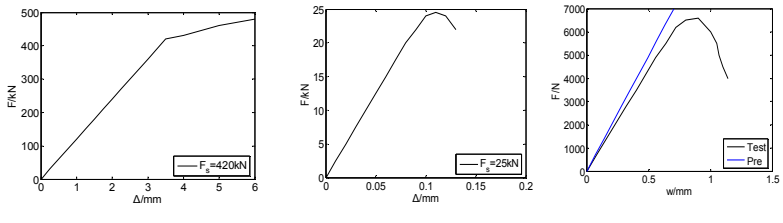


Fig.4 Test curves[(a) steel tube; (b) concrete column; (c) push-out test

## Results

The test results of s-40-6-300 and c-40-10 are shown in Table 1 and Fig.4(a) and (b). The test results of c-s40-6-100-c40 are shown in Table 2 and Fig.4(c). The $w_1$, $w_2$ and $w_3$ in Table 2 are the vertical displacements measured from displacement meter 1, 2 and 3, respectively.

Table 1 Specimens and material properties

| Types of tests | $F_s$ /kN | $F_u$ /kN | $\Delta_s$ /mm | $\sigma_s$ /MPa | $\varepsilon_s$ /$10^{-3}$ | $E$ /GPa |
|---|---|---|---|---|---|---|
| c-40-100 | 22 | 29 | 0.08 | 17.5 | 80.3 | 22 |
| s-40-6-300 | 420 | 560 | 3.3 | 742.7 | 5.3 | 193.1 |

Table 2 Results of c-s40-6-100-c40

| Typical loads/kN | $w_1$/mm | $w_2$/mm | $w_3$/mm |
|---|---|---|---|
| $F_s$= 4 | 0.001 | 0.50 | 0.48 |
| $F_u$= 6.5 | 0.002 | 0.68 | 0.64 |

The comparison between the test result and the predicted result (straight line) from Eq.25 is shown in Fig.4(c). It is shown that predicted result is good agreement with test one. The slip between the concrete short column and over-thick steel tube is expressed by $s$. The curve of $s-z$ is shown in Fig.5. It can be seen from Fig.5 that the slip at the upper surface is almost equal to that at the lower surface, which means that the slip $s$ is almost uniform with $z$.

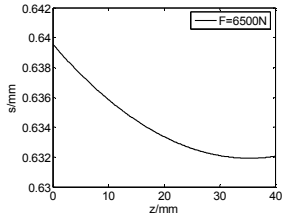


Fig.5 Variation of slip with height

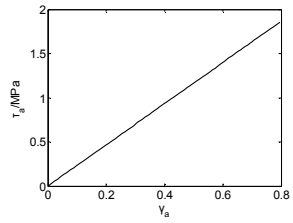


Fig.6 Relation of adhesive shearing stress and shearing strain in adhesive thin layer

The curve of $\tau_a - \gamma_a$ is shown in Fig.6. From Fig.6, it can be seen that the relation between shearing stressing $\tau_a$ and shearing strain $\gamma_a$ in the adhesive thin-layer is linear, i.e., $\tau_a = G_a \gamma_a$. Shearing modulus $G_a$ is 2.3321MPa.

## Conclusions

(1) The shearing stress between the steel tube and concrete is uniform along height for the concrete short column which is pushed out from over-thick steel tube, and the slip between the steel tube and concrete is also approximately uniform along height.

(2) The push-out test shows that the average vertical displacement at the upper surface of the steel tube is proportional to push-force. The average vertical displacement at the upper surface of the concrete column is also proportional to push-force, but very greater than that at the upper surface of the over-thick steel tub. The slip between the steel tube and concrete is approximately uniform along height. The adhesive stress in the adhesive thin-layer can be well determined and shearing modulus of the adhesive thin-layer can be valuated by the push-out test.

## References

[1] L. Han: Structures of concrete-filled steel tube: theories and practice, Beijing: Science Press, (2004).

[2] Kang Xiliang, Zhao Hongtie, Xie Jianyang: Journal of Xian University of Architecture and Technology(2006), Vol. 38(3), p. 321(in Chinese)

[3] Kang Xiliang, Zhao Hongtie, Xue Jianyang: Eng. Mech.(2007), Vol. 24(1), p. 101

[4] G. Monti, E. Spacone: Struc. Eng.(2000), Vol. 126(6), p. 654

[5] E. Spacone, S. Limkatanyu: Structural Journal(2000), Vol. 97(6), p. 831

[6] G. Chen, G. Baker: Journal of Structural Engineering(2003), Vol. 129(11), p. 1515

*Applied Mechanics and Materials Vols. 580-583 (2014) pp 2916-2919*
*© (2014) Trans Tech Publications, Switzerland*
*doi:10.4028/www.scientific.net/AMM.580-583.2916*

# Study on numerical simulation of explosion in soil based on fluid-solid coupling arithmetic

Juan Song[1,a], Shucai Li[1,b]

[1] School of Civil Engineering, Shandong University, Jinan, China

[a]songjuan@sdu.edu.cn, [b] lishucai@sdu.edu.cn

**Keywords:** explosion, soil, shared-node, contact, ALE

**Abstract.** Numerical simulations play a significant role in explosion in a mass of soil due to an underground explosive. Common methods available in hydrocode for fluid-solid coupling process are contact algorithm, Lagrange algorithm, and Arbitrary Lagrange-Euler(ALE) algorithm. A numerical simulation of explosion process with concentrated charge in a mass of soil was carried out by using three methods in this paper. The dynamic response of soil medium, the formation and development law of explosion cavity and the explosion wave propagation law in soil were simulated. Merits and drawbacks of three different methods are analyzed in the aspect of modeling, simulation results and computing cost.

## Introduction

As a matter of fact, the response of surrounding soil media to nearby explosions is complicated by the drastic spatial and time variation of the blast loads. This buried blast usually produces a cavity or a crater and result in the interaction of surrounding soil media and detonation product gas. Furthermore, the propagation of blast-induced stress wave will induce the acceleration of soil particle and soil pressure in the surrounding soil media. It is meaningful to study the interaction between the explosion and soil response because different structures are affected differently, causing deformation due to detonations, which have been widely reported in the literature over the past five decades. Effects of explosions on a soil medium and underground structures can be studied through full-scale model tests, reduced scale/ enhanced acceleration physical tests (as in centrifuge tests), empirical method and numerical modeling. In the recent decades, several experimental and numerical investigations have been carried out to determine the overpressure and crater depth of explosive materials into/on different soil types [1-4]. Accurate prediction of explosion in soil by numerical simulation is needed, due to the fact that the numerical simulations can minimize the number of experimental cases, saving considerable amounts of cost and time. Different types of solvers available in a hydrocode, such as LS-DYNA and AUTODYN, are Lagrange, Euler, Smoothing Particle Hydrodynamics (SPH) and Arbitrary Eulerian-Lagrangian (ALE) [5]. The paper is concentrated on the validation of the methodology that has been implemented in LS-DYNA, to be able to simulate explosive and soil structure interaction problems. Structures with more details and complex geometry will be analyzed next.

## The description of simulation model

**The initial condition.** Only a quarter of the problem domain was simulated, which has the size of 75 cm×75cm×150cm, as shown in Fig 1. There are three materials: explosive, soil, air. Point A was marked in Fig.2 for the convenient reference when presenting the simulation results. The charge with weight 10kg explosive is buried at a depth of 65cm from ground surface along the central axis. The corresponding FEM mesh was illustrated in Fig.2 with a total of 72000 hexahedron elements inclusive of 8 elements for the explosive.

This numerical model has following boundary conditions: Vertical displacements at the bottom are fixed to restrain rigid body movement. Symmetrical boundary is applied to all horizontal displacements along the symmetry plane. The top surface is free surface which can reflect the stress waves. The non-reflecting boundaries are applied to minimize the stress wave reflection at the sides.

**Description of various formulations model.** In this method, there have identical density and the number of nodes in the interface between explosive meshes and structure meshes, which make them shared in nodes. A contact type algorithm is used to handle the coupling between soil and explosive[6]. The difference between shared-node formulation and contact formulation is separate interface for explosive and structure, which can be divided by different mesh size. Namely two kinds of mesh are independent and irrelevant. In this paper, three modes of contact were applied: SURFACE_TO_SURFACE, SLIDING_ONLY, ERODING_SURFACE_TO_SURFACE, respectively[7]. In preprocess phase, the ALE algorithm enable to conduct two spaces which can be intersected and overlapped, one for the explosive and ALE space, and another for structure. An ALE zone is defined for the area around the charge as shown in Fig 3.

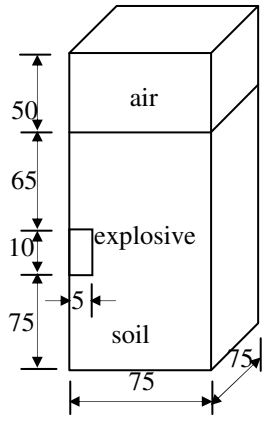


Fig.1 Sketch of model

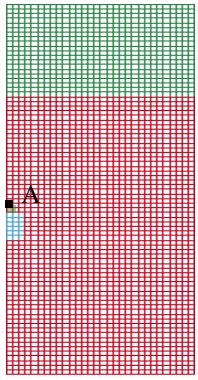


Fig.2 Sketch of mesh

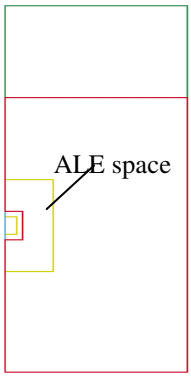


Fig.3 Sketch of ALE formulation

**Constitutive models in computation.** The empirical Jones-Wilkins-Lee (JWL) equation of state is widely used in mine blast calculations (see Table 1), where $A, B, R_1, R_2$ and $\omega$ are material constants, $V$ is the relative volume of detonation product and $E_0$ is the internal energy per initial volume. The model parameters used in simulation are listed in Table 2 for soil, where $\alpha_0$, $\alpha_1$ and $\alpha_2$ are material constants.

Table 1 Explosive Parameters of TNT Dynamite

| Density[ $g \cdot cm^{-3}$ ] | D[ $m \cdot s^{-1}$ ] | $P_{cj}$[GPa] | $A$[GPa] | $B$[GPa] | $R_1$ | $R_2$ | $\omega$ | $E_0$[ $J \cdot m^{-3}$ ] |
|---|---|---|---|---|---|---|---|---|
| 1.6 | 6930 | 18.5 | 371.2 | 3.231 | 4.15 | 0.95 | 0.3 | 7.0e+9 |

Table 2 Soil Parameters for Soil Model

| Density[ $g \cdot cm^{-3}$ ] | Poisson's ratio | $G$[MPa] | $E$[MPa] | $K$[MPa] | $\alpha_0$ [$MPa^2$] | $\alpha_1$ [MPa] | $\alpha_2$ |
|---|---|---|---|---|---|---|---|
| 1.80 | 0.48 | 16.01 | 47.36 | 394.8 | 2.4e-6 | 0.0136 | 0.1232 |

Material Type 9 of LS-DYNA(*MAT_NULL) is used for the air. The standard material constants of air $\gamma = 1.4$, $\rho = 1.2 \times 10^{-3} g \cdot m^{-3}$, $e = 2.5 \times 10^4$ Pa are used, Where $e$ is the internal energy per volume, $\rho$ is the current density of the material, and $\gamma$ is the ratio of specific heat, respectively.

## Comparison and discussion of simulation results

**Computation cost.** A comparative analysis for computational efficiency of various explosion simulation methods has been done when simulation time was set 1500μs as shown in Table.3. It can be seen that the contact algorithm for computing efficiency is the lowest, which can be illustrated by mesh distortion mainly due to the explosive mesh of expansion and caused by calculating step gradually becoming smaller, which resulted in calculation of termination. And sometimes because of the contact calculation does not converge in the calculation process, usually the grid computation

process suddenly was terminated without warning information. The shared-node and ALE algorithm have higher computational efficiency because of the relatively stable step, especially the explosives and the air flowing in the ALE space. So there is no distortion problem of grid and rarely computing termination phenomenon. But the ALE algorithm with higher requirements on memory, is 7-8 times than other algorithms.

Table 3 Comparative result between various methods

| | Shared-node | Eroding | Sliding-only | Surface-to-surface | ALE |
|---|---|---|---|---|---|
| CPU time | 2238 | 6850 | 6372 | 8226 | 2805 |
| memory | 6203180 | 6249329 | 6249473 | 6249329 | 55026614 |
| minimal step | 4.13E-02 | 9.93E-03 | 1.01E-02 | 4.92E-03 | 4.13E-02 |

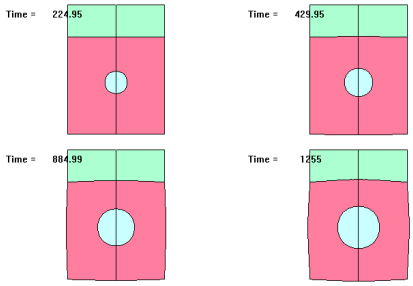

Fig.4 Cavity formed in shared-node method

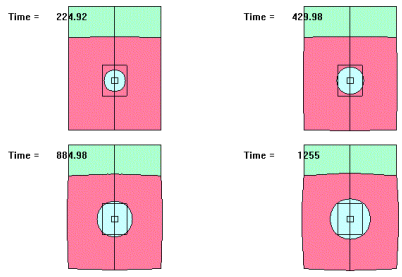

Fig.5 Cavity formed in ALE

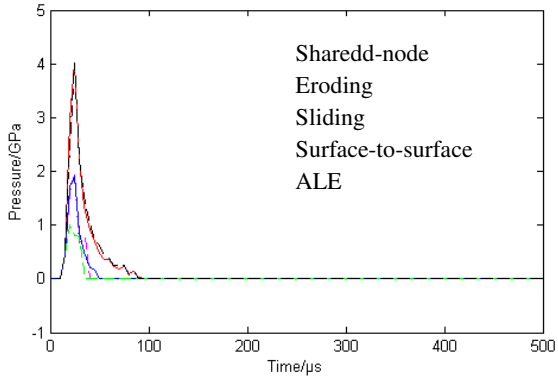


Fig.6 Comparison of blast overpressure

**Simulation process of explosion in soil.** Detonation of explosives generates compressive stress waves in a mass of soil. After detonation, the blast stress waves propagate outwards from the blast hole in all directions. Simultaneously a high velocity shock front departs from the explosive source to the surrounding soil and the particle of soil gain the radial velocity to broaden the blast cavity. With the rapid attenuation of blast energy, over pressures is under the strength limitation of soil. This moment the expand process of cavity reach to the status of termination and the bulge, not the evident crater, is observed in the air. Fig. 4 and Fig.5 shows the shape of the spherical cavity in a mass of soil by using shared-node and ALE at different simulation time, respectively. A very good agreement is observed between the cavity diameter obtained with shared-node method and ALE method. Furthermore, the radius of cavity obtained in two cases is about six times the size of charge, which is in a good agreement with the experimental result of 5~7 times[8]. In the formation of cavity, the contact formulation can be performed up to 600μs in time, after this time, the problem was prevented to run up to physical time. So the simulation result of contact algorithm is not perfect.

**Pressure-time history at reference point.** Fig. 6 shows the comparison of the five pressure time history at point A. It can be seen that all of curves presented a brutal increase of the pressure at

shock arrival time, $t = 24\mu s$, and rapid increment as well as the peak value were captured very well by the numerical simulation. Generally, the numerical simulation of the post-peak dissipation of the stress shows similar trend of the measured curve although with faster dissipation rate. As can be seen, the results of curve shape, magnitude of overpressure and duration time were very similar between the shared-node and ALE, which shows good correlation between the two results. Marked difference is observed in the peak overpressure, where the contact algorithm results exhibit much smaller peak pressure than from other results, as a result of configuration of contact parameters. In practical application, parameters should be adjusted lightly based on experimental result to make identical between simulation and experiment.

## Conclusions

This paper discusses the prediction of blast cavity in a mass of soil due to underground explosion by using different numerical simulation methods. Some meaningful conclusions have been drawn through the following aspects: computational cost and simulation results.

1) As mentioned in the introduction, the Lagrangian formulation is simple in modeling and accurate for material boundary where the mesh is deformed but not highly distorted. Good agreement for the pressure transient in the explosion was obtained using the Lagrangian and ALE method.

2) Unlike the Lagrangian method, the ALE coupling method has no limitation concerning high mesh distortion since the problem is performed using ALE remeshing techniques. This technique can be used for more complex problems where the structure can be defined with all its details. But the limitations of ALE formulation were complicated modeling process and high computational cost.

3) The simulation by using the contact algorithm was terminated due to the configuration of contact parameter or mesh density of slave and master boundary.

## References

[1] Laine L, and Sandvik A. 2001. Derivation of mechanical properties for sand. In 4thAsia-Pacific Conference on Shock and Impact Loads on Structures, Singapore : 361–368.

[2] Niekerk B. 2001. Land mine protection – Dealing with the uncertainties. In 10th European AFV Attack and Survivability Symposium, Shrivenham, UK.

[3] Gupta AD. 2002. Modeling and analysis of transient response in a multilayered composite panel due to explosive blast. In 20th International Symposium on Ballistics, Orlando, USA.

[4] Niroumand H, & Kassim KA. 2009. Analytical and Numerical Study on Explosion into/on Cohesion less Soils. Eur. J. Sci. Res., 46(4): 554-562.

[5] T.J.R. Hughes, & W.K. Liu, & T.K. Zimmerman. 1981. Lagrangian Eulerian finite elements formulation for viscous flows, J. Comput.Methods Appl. Mech. Engrg. 21: 329-349.

[6] Belytschko T, & Neal MO. 1989. Contact-impact by the pinball algorithm with penalty, projection, and Lagrangian methods. In: Proceedings of the sympo- sium on computational techniques for impact, penetration, and performation of solids AMD, vol. 103, New York, NY: ASME; 97–140.

[7] Livermore Software Technology Corporation (LSTC). 2003. LS-DYNA keyword user’s manual, Version 960. Livermore, CA.

[8] Xu lianpo, & Jin huei, & Zhang peide. 1982. Development of explosion cavity in soil. J. Mech. in Chinese (5)：500-504.

*Applied Mechanics and Materials Vols. 580-583 (2014) pp 2920-2923*
*© (2014) Trans Tech Publications, Switzerland*
*doi:10.4028/www.scientific.net/AMM.580-583.2920*

# Study on stability of functionally graded cylindrical shells subjected to hydrostatic pressure

Xiaowan Liu, Bin Liang, Rong Li

Civil Engineering School, Henan University of Science and Technology, Luoyang, 471023, China

**Key Words:** critical pressure; functionally graded material; cylindrical shell; hydrostatic pressure

**Abstract:** The stability of submerged functionally graded (FG) cylindrical shell under hydrostatic pressure is examined in this paper. Based on the Flügge's shell theory, the coupled frequency of submerged FG cylindrical shell is obtained, using wave propagation method and Newton method. Then the critical pressure of FG cylindrical shells is given by applying linear fitting method. Results are compared to known solutions, where these solutions exist. The effects of constituent materials, volume fraction, boundary condition and dimensions on the critical pressures of submerged FG cylindrical shell are illustrated by examples.

## Introduction

Studies on coupled vibration of submerged cylindrical shells have received considerable attention, which can be seen in the literature [1-2]. The liquid medium has significant impact on the vibration characteristics of cylindrical shell, especially for the effect of hydrostatic pressure. Because the structure will create instability when the hydrostatic pressure is larger than critical pressure, at this point, it no longer makes sense to do calculate the natural frequency. So the structural analyses need to be carried out in the presence of critical pressure. However, since FG cylindrical shell is a group of innovative material structure, the research on the mechanical behavior of submerged FG cylindrical shell is very limited.

Based on the Flügge shell theory, the coupled frequency of submerged FG cylindrical shell is derived. Then the critical pressure of FG cylindrical shells is given by applying linear fitting method. Results are presented the effect of constituent materials, volume fraction, boundary condition and dimensions on critical pressures of submerged FG cylindrical shell.

## Theoretical formulation

A FG cylindrical shell is considered with radius $R$, length $L$ and thickness $h$, as shown in Fig.1. The reference surface is taken to be the middle surface of the cylindrical shell where an orthogonal coor-

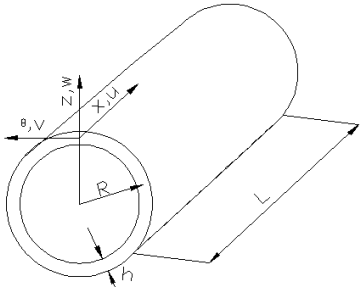


**Fig.1. Geometry of a FG cylindrical shell**

dinate system $(x,\theta,z)$ is fixed. The $x,\theta$ and z are the axial coordinate, circumferential coordinate and radial coordinate, respectively.

When a shell composed with two materials, the material parameters are defined as the Young's modulus $E_1, E_2$, Poisson ratio $\mu_1, \mu_2$ and the mass density $\rho_1, \rho_2$, respectively. So along the thickness of the shell, the Young's modulus $E$, Poisson ratio $\mu$ and the mass density $\rho$ can be expressed as

$$\begin{cases} E = E(z) = (E_1 - E_2)(z/h + 1/2)^N + E_2 \\ \rho = \rho(z) = (\rho_1 - \rho_2)(z/h + 1/2)^N + \rho_2 \\ \mu = \mu(z) = (\mu_1 - \mu_2)(z/h + 1/2)^N + \mu_2 \end{cases} \tag{1}$$

Where $N$ is the power-law exponent $(0 \le N \le \infty)$.

By using Flügge's theory, the equations of motion for a cylindrical shell subjected to hydrostatic pressure are obtained.

$$\begin{cases} \dfrac{2+T}{2}u_{xx} + \dfrac{1-\mu}{2}u_{\theta\theta} + \dfrac{1+\mu}{2}v_{x\theta} + \mu w_x + K\left(\dfrac{1-\mu}{2}u_{\theta\theta} - w_{xxx} + \dfrac{1-\mu}{2}w_{x\theta\theta}\right) + T(u_{\theta\theta} - w_x) = Hu_{tt} \\ \dfrac{1-\mu}{2}v_{xx} + \dfrac{1+\mu}{2}u_{x\theta} + v_{\theta\theta} + w_\theta + K\left(\dfrac{3(1-\mu)}{2}v_{xx} - \dfrac{3-\mu}{2}w_{xx\theta}\right) + \dfrac{T}{2}v_{xx} + T(v_{\theta\theta} - w_\theta) = Hv_{tt} \\ \mu u_x + K\left(\dfrac{1-\mu}{2}u_{x\theta\theta} - u_{xxx} - \dfrac{3-\mu}{2}v_{xx\theta} + w + w_{xxxx} + 2w_{xx\theta\theta} + w_{\theta\theta\theta\theta} + 2w_{\theta\theta}\right) + v_\theta + w - \dfrac{T}{2}w_{xx} \\ \qquad - T(u_x - v_\theta + w_{\theta\theta}) + \dfrac{\rho R^2(1-\mu^2)}{E}w_{tt} = -\dfrac{H}{\rho h}\psi \end{cases} \tag{2}$$

where $T = \dfrac{R}{Eh}(1-\mu^2)P_0$, $K = \dfrac{h^2}{12R^2}$, H= $\dfrac{\rho R^2(1-\mu^2)}{E}$, $P_0$ is the hydrostatic pressure, $\psi$ is the acoustic pressure.

$$\psi = [\omega^2 \rho_f / k_r H_n^{'}(k_r R)] W_m \cos(n\theta) H_n(k_r r) e^{i\omega t - ik_m x} \tag{3}$$

where $H_n()$ is the Hankel function of the second kind, $H_n^{'}()$ denotes differentiation with respect to the argument $k_r R$, $\rho_f$ is the density of the contained fluid in the shell, $k_r$ is radial wave number.

The displacements of the cylindrical shell can be expressed in the form of wave propagation.

$$\begin{cases} u(x,\theta,t) = U_m \cos(n\theta) e^{(i\omega t - ik_m x)} \\ v(x,\theta,t) = V_m \sin(n\theta) e^{(i\omega t - ik_m x)} \\ w(x,\theta,t) = W_m \cos(n\theta) e^{(i\omega t - ik_m x)} \end{cases} \tag{4}$$

where $U_m, V_m, W_m$ are the wave amplitudes in the $x, \theta, z$ directions, $\omega$ is the natural angular frequency.

Substituting Eq.(4) into Eq.(2), which consideration of acoustic pressure on the shell Eq.(3), the equations of motion of coupled system can be obtained. The Newton method is used to acquire the natural frequency of the shell. Because of linear relation between the natural frequency squared and hydrostatic pressure [3], the critical pressure can be derived using linear fitting method.

**Results and discussion**

To validate the present analysis, results for critical pressures for submerged isotropic cylindrical shell are compared with the theoretical formula [4], see table 1. The comparison show that the present results agree well with the traditional method.

**Tab.1 Comparison of critical pressures** ( MPa ) **for a submerged isotropic cylindrical shell**

| h/R | L/R | | | | | |
|---|---|---|---|---|---|---|
| | 2 | | 5 | | 10 | |
| | Present | theoretical values | Present | theoretical values | Present | theoretical values |
| 0.005 | 36.448 | 36.115 | 2.6929 | 2.6586 | 0.2079 | 0.2072 |
| 0.01 | 73.049 | 72.333 | 5.4377 | 5.3692 | 0.461 | 0.4599 |
| 0.02 | 147.1 | 145.48 | 11.287 | 11.154 | 1.2832 | 1.2831 |

As examples, critical pressures with different $h/R$ , $L/R$ , boundary conditions, constituent materials and volume fractions are studied. The functionally graded material has ceramic on its inner surface and metal on its outer surface. The material properties are given in Tab.2.

**Tab.2 Properties of functionally graded materials**

| Properties | outer materials | | inner materials | |
|---|---|---|---|---|
| | Stainless steel | Ti-6Al-4V | $Si_3N_4$ | Zirconia |
| $E$ (N/m²) | $2.07788 \times 10^{11}$ | $1.0570 \times 10^{11}$ | $3.2227 \times 10^{11}$ | $1.68 \times 10^{11}$ |
| $\mu$ | 0.317756 | 0.2981 | 0.24 | 0.3 |
| $\rho$ (kg/m³) | 8166 | 4429 | 2370 | 5700 |

The variations of critical pressures of FG cylindrical shells with various boundary conditions are presented in Fig.1. It is shown that both boundary condition and constituent material have evident influence on critical pressure. The critical pressures for clamped-clamped boundary condition are higher than those for other boundary conditions. There is a significant difference about the pressure values among the selected composite materials, and the combination of stainless steel and $Si_3N_4$ has an advantage over the others.

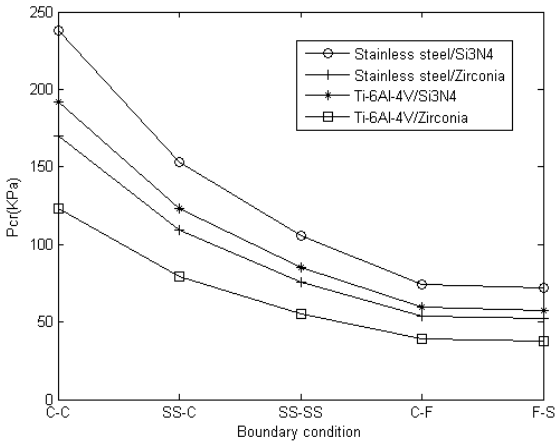


**Fig.1 Variation of critical pressure for a submerged cylindrical shell with various boundary conditions.**

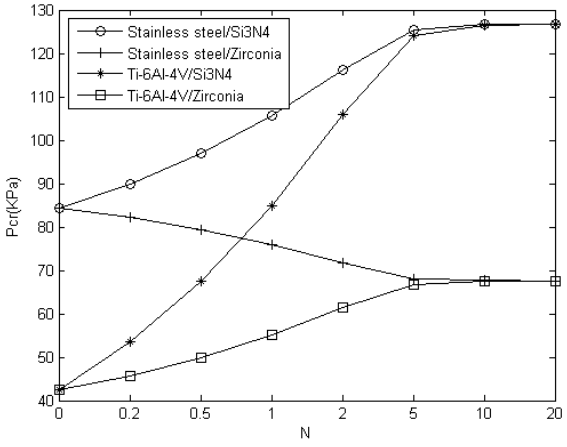


**Fig 2. Variation of critical pressures for a submerged cylindrical shell for some different values of power-law exponent.**

Fig.2 shows the curves of critical pressures of FG cylindrical shells for various values of power-law exponent. It is shown that the effects of power-law exponent on critical pressure are evident. The influences of power-law exponent on critical pressures are mainly reflected in the cases of small power-law exponent. With the increasing of power-law exponent, the functionally graded material is from a pure metal material to a pure ceramic material. This is due to the FG cylindrical shell is reduced to an isotropic cylindrical shell. Since critical pressure is material property dependent, use the FG cylindrical shell which composed of Stain steel and Zirconia as an

example. Because of the critical pressure of pure Stain steel cylindrical shell is larger than pure Zirconia cylindrical shell, the critical pressure decreases with the increasing of power-law exponent.

The critical pressures of simply supported FG cylindrical shells for different $h/R$ are shown in Fig. 3. It is shown that with the increasing of $h/R$, the critical pressure increases rapidly. The influences of constituent material on critical pressure are mainly reflected in the cases of large $h/R$.

For $m=1$ and $n=2$, the curves of critical pressures of simply supported FG cylindrical shells for different $L/R$ are shown in Fig. 4. The critical pressures first increased and then decreased with $L/R$. And the critical pressures for lower $L/R$ ratios are higher than those for higher $L/R$ ratios. The influences of constituent material on critical pressure are mainly reflected in the cases of small $L/R$ ratio. When $L/R$ comes to a certain degree, the effect of dimension on the critical pressure is not significant.

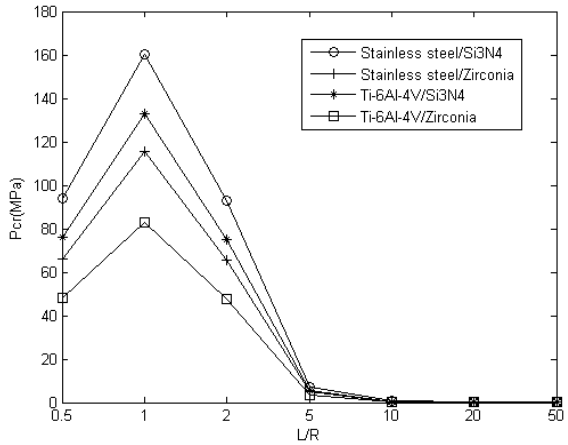


**Fig.3 Variation of critical pressures of submerged cylindrical shell with different $h/R$ ratios.**

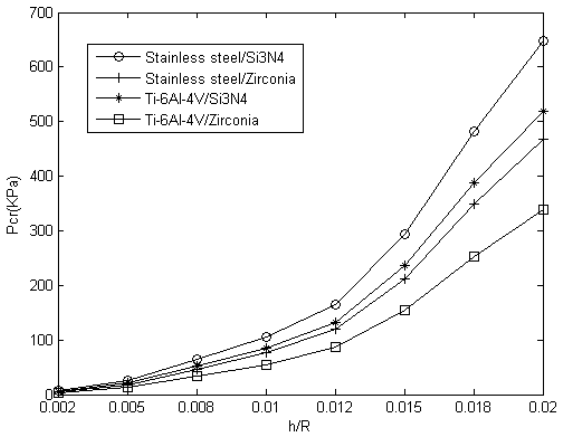


**Fig.4 Variation of critical pressures for a submerged cylindrical shell with different $L/R$ ratios.**

## Conclusions

Based on the analysis of the critical pressures with the control factors, the study showed that the constituent material and boundary conditions have a significant influence on the critical pressure. Critical pressure values of the composite cylindrical shell lie between those of the two kinds of homogenous material structure. The influences of constituent material on critical pressure are mainly reflected in the cases of large $h/R$ and small $L/R$ ratio. The characteristics of critical pressure will certainly provide guidance to the practical use and risk averse.

## References

[1] Zhang, X.M, 2002. Frequency analysis of submerged cylindrical shells with the wave propagation approach. J. International Journal of Mechanical Sciences. 44 (7), 1259-1273.

[2] Sheng,G.G, Wang,X., 2008. Thermomechanical vibration analysis of a functionally graded shell with flowing fluid. J. European Journal of Mechanics -A /Solids. 27(6), 1075-1087.

[3] Abramovich H, Singer J, Weller T. Repeated buckling and its influence on the geometrical imperfections of stiffened cylindrical shells under combined loading. International Journal of Non-Linear Mechanics. 2002, 37(4-5): 577–588.

[4] WU Lian-yuan. Theory of plates and shells[M]. Shanghai: Shanghai Jiaotong University Press, 1989.330. (in Chinese)

*Applied Mechanics and Materials Vols. 580-583 (2014) pp 2924-2927*
*© (2014) Trans Tech Publications, Switzerland*
*doi:10.4028/www.scientific.net/AMM.580-583.2924*

# Theoretical Foundations of Correct Wavelet-Based Approach to Local Static Analysis of Bernoulli Beam

Pavel A. AKIMOV[1, a], Mojtaba ASLAMI[2,b]

[1,2] 26, Yaroslavskoe Sh., Moscow, 129337, Russia, Moscow State University of Civil Engineering

[a] pavel.akimov@gmail.com, [b] aslami.mojtaba@gmail.com

**Keywords:** wavelet-based methods, boundary problem, local structural analysis, static analysis, Bernoulli beam, discrete wavelet, Haar basis, averaging, reduced wavelet coefficients

**Abstract.** This paper is devoted to correct and efficient method of local static analysis of Bernoulli beam on elastic foundation. First of all, problem discretized by finite difference method, and then transformed to a localized one by using the Haar wavelets. Finally, imposing an optimal reduction in wavelet coefficients, the localized, reduced results can be obtained. It becomes clear after comparison with analytical solutions, that the localization of the problem by multiresolution wavelet approach gives exact solution in desired regions of beam even in high level of reduction in wavelet coefficients. This localization can be applied to any arbitrary region of the beam by choosing optimum reduction matrix and obtaining exact solutions with an acceptable reduced size of the problem.

## Introduction.

Need for providing an accurate and efficient method for the local structural analysis can be determined with the considering of large-scale or complex structures and with the using of personal computers with limited performance. On the other hand, it is practically impossible or very time consuming to obtain the exact (high-accuracy) solution for the entire structure. For instance, we can obtain high-accuracy results with the use of finite-element method (FEM) by choosing smaller element size, leading in its turn to increasing the numbers of finite elements and therefor time of analysis [5]. This is possible as long as the solution is achievable in common personal or even professional computers and in a reasonable time. However, exact solution normally is not required in all regions, and due to structural or loading conditions, the location and approximate dimensions of critical regions of the structure can be determined. The stress-strain state in these regions are important from the standpoint of analysis and design, and may lead to structural failure or cause impairment in structural performance. Thus, using an appropriate method we can achieve sufficient accuracy in these selected regions with a smaller number of unknowns. For covering this goal we can use multilevel analysis of the stress-strain state of the structures. The proposing method allows qualitative and quantitative assessments of the degree of localization of various kinds of phenomena. Wavelet analysis has become one of the most effective and popular contemporary sources for this kind of research in the recent years [1, 2, 3, 4].

## Initial Formulation of the Problem and Transition to Haar Wavelet Basis.

It is commonly known that after discretization of the problem of static beam analysis with the use of finite difference method (FDM) we can obtain the following resultant system of linear algebraic equations

$$A\bar{y} = \bar{f}\,, \tag{1}$$

where $A$ is the coefficient matrix; $\bar{y}$ is the vector of nodal unknowns (displacements); $\bar{f}$ is the right-side vector.

Decomposition of corresponding discrete function with the use of wavelet multiresolution analysis allows obtaining more information about it. We used discrete Haar wavelet (which is one of the simplest and best suited to this purpose) and corresponding direct and inverse algorithms of transformations, proposed by Prof. A.B. Zolotov [5]. We have ($Q_h$ is the transformation matrix; $\bar{v}$ is the vector of Haar wavelet coefficients)

$$\bar{y} = Q_h \bar{v} . \tag{2}$$

Thus, by substitution the equation (2) in equation (1) and then multiplying both sides by $Q_h^T$ (transponsed matrix $Q_h$), the transformation process has been completed:

$$A_v \bar{v} = \bar{f}_v , \quad \text{where} \quad A_v = Q_h^T A Q_h , \quad \bar{f}_v = Q_h^T \bar{f} . \tag{3}$$

**Imposing reduction in wavelet coefficients.**

Localized high-accuracy solution in selected regions and reduced size of the problem

$$A_v^r \bar{v}^r = \bar{f}_v^r \tag{4}$$

can be obtained with the use of appropriate algorithm for the reduction of wavelet coefficients,

$$\bar{v} = R \bar{v}^r , \tag{5}$$

where $R$ is rectangular matrix with a size $n \times n^r$ (so-called reduction matrix, $n^r < n$); $A_v^r$ is the reduced coefficient matrix; $\bar{f}_v^r$ is the reduced right-side vector; $\bar{v}^r$ is the reduced wavelet coefficients after imposing reduction defined by vector $\bar{\chi}$,

$$\bar{v} = [\,(\bar{v}^0)^T \;\; (\bar{v}^1)^T \;\; \ldots \;\; (\bar{v}^M)^T\,]^T , \text{ where } \bar{v}^p = \{v_j^p\}_{j=\overline{1,N_p}}, \; p = \overline{0,M} ; \; N_p = \begin{cases} n/2^{p+1}, & 0 \le p < M \\ 1, & p = M; \end{cases} \tag{6}$$

$$\bar{v}^r = [\,(\bar{v}^{r,0})^T \;\; (\bar{v}^{r,1})^T \;\; \ldots \;\; (\bar{v}^{r,M})^T\,]^T , \quad \text{where} \quad n^r = \sum_{p=0}^{M} \sum_{j=1}^{N_p} \chi_j^p ; \tag{7}$$

$$\bar{\chi} = [(\bar{\chi}^0)^T \;\; (\bar{\chi}^1)^T \;\; \ldots \;\; (\bar{\chi}^M)^T\,]^T , \text{ where } \bar{\chi}^p = \{\chi_j^p\}_{j=\overline{1,N_p}}, \; p = \overline{0,M} ; \; \chi_j^p = \begin{cases} 1, \text{if } v_j^p \text{ is reduced} \\ 0, \text{if } v_j^p \text{ isn't reduced.} \end{cases} \tag{8}$$

$M$ is the maximum order of Haar basis function; $N_p$ is the number of Haar basis of the order $p$; $n = 2^M$; $\bar{v}^{r,p}$ is $n^r$-dimensional vector, obtained by eliminating elements of $v_j^p$ for which $\chi_j^p = 0$.

Let's introduce global indexing system for elements of vector (6) in accordance with formula

$$k \;\Leftrightarrow\; (j,p) , \quad \text{where} \quad k = j + \sum_{q=0}^{p-1} N_q ; \tag{9}$$

$k$ is global index; $j, p$ are initial indexes (multiindex).

We will use the following notations:

$$N_{tot}^{-1} = 0; \quad N_{tot}^{s} = \sum_{q=0}^{s} N_q, \quad s = 1, 2, ..., M. \tag{10}$$

Special algorithm of computing indexes $p$ and $j$ on the base of index $k$ is presented below.
1) Let's assign $s = M$. 2) Compute $N_{tot}^{s}$.
3) Compute $\tau_s$ in accordance with formula (notation $[a]$ means integer part of $a$)

$$\tau_s = [(k-1)/N_{tot}^{s}]. \tag{11}$$

4) If $\tau_s = 1$ then indexes $p$ and $j$ are computed by formulas

$$p = s+1; \quad j = k - N_{tot}^{s}. \tag{12}$$

If $s > 0$ and $\tau_s = 0$ then $s$ must be decremented by one and we shoud go to the second step of the distinctive algorithm. If $s = 0$ and $\tau_s = 0$ then

$$p = 0; \quad j = k. \tag{13}$$

Let's introduce global indexing system for elements of vector (7) in accordance with formula

$$k \;\Leftrightarrow\; (j, p), \quad \text{where} \quad k = \sum_{q=1}^{j} \chi_j^p + \sum_{q=0}^{p-1} N_q^r; \quad N_p^r = \sum_{j=1}^{N_p} \chi_j^p; \tag{14}$$

$k$ is global index; $j, p$ are initial indexes (multiindex).
We will use the following notations:

$$N_{tot,red}^{-1} = 0; \quad N_{tot,red}^{s} = \sum_{q=0}^{s} N_q^r, \quad s = 1, 2, ..., M. \tag{15}$$

Special algorithm of computing indexes $p$ and $j$ on the base of index $k$ is presented below.
1) Let's assign $s = M$. 2) Compute $N_{tot,red}^{s}$. 3) Compute $\tau_s$ in accordance with formula

$$\tau_s = [(k-1)/N_{tot,red}^{s}]. \tag{16}$$

4) If $\tau_s = 1$ then index $p$ and ancillary quantity $t$ are computed by formulas

$$p = s+1; \quad t = k - N_{tot,red}^{s}. \tag{17}$$

Procedure of computing of index $j$ is presented below.
a) Let's assign $m = 1$. b) Compute $r_m$ in accordance with formula

$$r_m = \sum_{i=1}^{m} \chi_i^p. \tag{18}$$

c) If $t = r_m$ then $j = m$. Otherwise $m$ must be incremented by one and we shoud go to step „b“ of the distinctive procedure. If $s > 0$ and $\tau_s = 0$ then $s$ must be decremented by one and we shoud go to the second step of the distinctive algorithm. If $s = 0$ and $\tau_s = 0$ then $p = 0$ and index $j$ can be defined by steps „a“, „b“ and „c“ of the procedure.

Algorithm of computing of reduction matrix is presented below.

1) Let‘s assign initially $R = 0$. 2) Let’s assign $i_1 = n$.

3) In accordance with above-described alogithm we compute indexes $p$ and $j$ of the corresponding element of the vector (6) on the base of index $i_1$.

4) We should consider two possible cases.

4.1) If $\chi_j^p = 1$ then in accordance with above-described alogithm we compute index $i_2$ of the corresponding element of the vector (7) on the base of indexes $p$ and $j$ and then compute element of reduction matrix $R_{i_1,i_2} = 1$, where $i_1$ and $i_2$ are numbers of row and column of reduction matrix.

4.2) If $\chi_j^p = 0$ then we compute the following parameters:

$$m = 1; \quad q = p + 1; \quad t = j; \quad s = [(t+1)/2]. \tag{19}$$

4.2.1) If $\chi_s^q = 1$ then in accordance with above-described alogithm we compute index $i_2$ of the corresponding element of the vector (6) on the base of indexes $q$ and $s$ and then compute element of reduction matrix ($\beta$ is averaging coefficient)

$$R_{i_1,i_2} = \beta^m; \quad \beta = 1/(2\sqrt{2}). \tag{20}$$

4.2.2) If $\chi_s^q = 0$ then $m$ must be incremented by one, $q$ must be incremented by one, we shoud assign $t = s$ and go to formula (19).

**Acknowledgements**

This work was financially supported by the Grants of Russian Academy of Architecture and Construction Sciences (3.1.7, 3.1.8).

**References**

[1]. Akimov P.A., Mozgaleva M.L. Correct Wavelet-based Multilevel Discrete-Continual Methods for Local Solution of Boundary Problems of Structural Analysis. // Applied Mechanics and Materials Vols. 353-356 (2013), pp. 3224-3227.

[2]. Akimov P.A., Mozgaleva M.L. Wavelet-based Multilevel Discrete-Continual Finite Element Method for Local Plate Analysis. // Applied Mechanics and Materials Vols. 351-352 (2013), pp. 13-16.

[3]. Akimov P.A., Mozgaleva M.L. Wavelet-based Multilevel Discrete-Continual Finite Element Method for Local Deep Beam Analysis. // Applied Mechanics and Materials Vols. 405-408 (2013), pp. 3165-3168.

[4] Akimov P.A., Mozgaleva M.L.: Correct Wavelet-based Multilevel Numerical Method of Local Solution of Boundary Problems of Structural Analysis. // Applied Mechanics and Materials Vols. 166-169 (2012), pp. 3155-3158.

[5] Zolotov A.B., Akimov P.A., Sidorov V.N., Mozgaleva M.L. Mathematical Methods in Structural Mechanics. Moscow, ASV Publishing House, 2008, 336 pages (in Russian).

*Applied Mechanics and Materials Vols. 580-583 (2014) pp 2928-2931*
*© (2014) Trans Tech Publications, Switzerland*
*doi:10.4028/www.scientific.net/AMM.580-583.2928*

# Theory Analysis of Functionally Graded Materials Cylindrical Shell Buckling under Pure Bending

Wei Cheng[1, a], Zhigang Wang[1,b] and Shuchang Long [1,c]

[1] School of Civil Engineering and Transportation, South China University of Technology, Guangzhou, Guangdong, 510640, China

[a]503204886@qq.com, [b]wzgscut@126.com, [c]249412226@qq.com

**Keywords:** Functionally graded materials, Cylindrical shell, Buckling of bending

**Abstract.** Buckling behavior of functionally graded materials cylindrical shell under pure bending is studied in this paper. The stability equations of functionally graded materials cylindrical shell are derived using the classical plate and shell theory with Kirchhoff hypothesis, importing the bending boundary condition to obtain the critical buckling load. The result shows that the critical moment is linear with the radius, quadratic with the thickness and irrelevant with the length of the cylindrical shell. In addition, the critical moment is decreased by increasing the power law index of the material bulk, trending to a constant finally.

## Introduction

In 1984, the Japanese scientists synthesised the heterogeneous materials-functionally gradient materials(FGMs)which was made of ceramic and metal. FGMs is a new type of micro heterogeneous material whose most remarkable characteristic is that its mechanical properties is very smooth and its physical properties is stable without mutations, thus it is a good way to avoid stress concentration problem. Also, this kind of materials has the outstanding designability characteristic so we can change each component material's volume of space distribution to achieve the goal of optimizing the structure's inner stress distribution. As a kind of high performance refractory materials, FGMs has been applied in various industries, such as the nuclear industry, aerospace, chemical industry, civil, etc.

At present, buckling behavior of functionally graded materials cylindrical shell under pure bending has been studied by many schlars. Feldman and Aboudi have studied the buckling of functionally graded materials plate subjected to uniaxial loading [1]. They used the micro mechanics and structure mechanics method to obtained the critical buckling load. Cheng and Batra used the higher order shear plate theory to study the bucking and vibration of the simply supported functionally graded material plate subjected to axial loading in temperature field [2]. Na and Kim used the finite element model to study thermal buckling of functionally graded material plate in three dimensional temperature field [3]. Shariat and Javaheri discussed the buckling of defective functionally graded material plate under in-plane loading based on the classical plate theory [4]. Woo and Meguid used the higher order shear theory to study the post-buckling of medium thickness shell under thermal-mechanica interaction based on von karman nonlinear theory [5], and they obtained the Fourier series results. Ma Liansheng [6] analysed the buckling of functionally graded materials circular (ring) plate.

This article uses the classical plate and shell theory with Kirchhoff hypothesis to derive the basic equations of functionally graded material cylindrical shell, then obtains the critical moment under pure bending.

## Theory Analysis of Functionally Graded Materials Cylindrical Shell Buckling under Pure Bending

We consider the functionally graded materials cylindrical shell whose radius ,length,thickness are respectively *R, L, h* as is shown in Fig.1. As we use the thin shell theory, the $h/R \leq 0.02$.We suppose that its young's modulus changes as follows:

$$E(z)=E_m+\left(\frac{2z+h}{2h}\right)^N(E_c-E_m) \quad (1)$$

The subscript "m" and "c" represent the metal materials and ceramic materials respectively, and the letter "N" is the power law index of the material bulk.

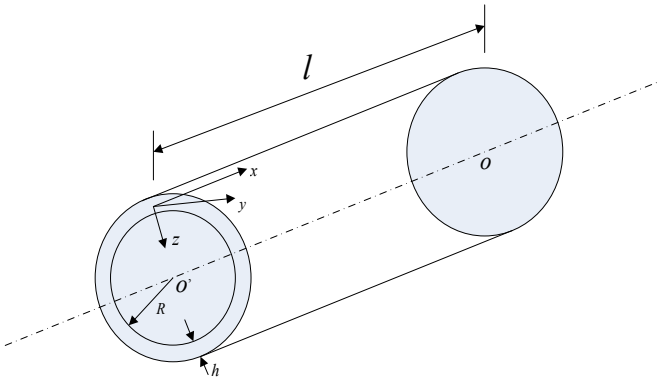


Fig.1 Physical dimension of functionally graded cylindrical shell

Here we set E = E (z), v is a constant.Then the physical equations of functionally graded materials cylindrical shell as follow:

$$\begin{aligned}
N_x &= \int_{-h/2}^{h/2}\sigma_x dz = D_1(\varepsilon_x+\nu\varepsilon_y)+D_2(\chi_x+\nu\chi_y)\\
N_y &= \int_{-h/2}^{h/2}\sigma_y dz = D_1(\varepsilon_y+\nu\varepsilon_x)+D_2(\chi_y+\nu\chi_x)\\
N_{xy} &= N_{yx} = \int_{-h/2}^{h/2}\tau_{xy} dz = \frac{1-\nu}{2}(D_1\gamma_{xy}+2D_2\chi_{xy})\\
M_x &= \int_{-h/2}^{h/2}\sigma_x z dz = D_2(\varepsilon_x+\nu\varepsilon_y)+D_3(\chi_x+\nu\chi_y)\\
M_y &= \int_{-h/2}^{h/2}\sigma_y z dz = D_2(\varepsilon_y+\nu\varepsilon_x)+D_3(\chi_y+\nu\chi_x)\\
M_{xy} &= M_{yx} = \int_{-h/2}^{h/2}\tau_{xy} z dz = \frac{1-\nu}{2}(D_2\gamma_{xy}+2D_3\chi_{xy})
\end{aligned} \quad (2)$$

Among them，

$$D_1=\int_{-h/2}^{h/2}\frac{E(z)}{1-\nu^2}dz, D_2=\int_{-h/2}^{h/2}\frac{E(z)z}{1-\nu^2}dz, D_3=\int_{-h/2}^{h/2}\frac{E(z)z^2}{1-\nu^2}dz \quad (3)$$

Using the classical plate and shell theory, we can obtain the linear buckling equation:

$$D\nabla^8 w+\frac{D_1(1-\nu^2)}{R^2}\frac{\partial^4 w}{\partial x^4}-\left[N_x\nabla^4\left(\frac{\partial^2 w}{\partial x^2}\right)+2N_{xy}\nabla^4\left(\frac{\partial^2 w}{\partial x\partial y}\right)+N_y\nabla^4\left(\frac{\partial^2 w}{\partial y^2}\right)\right]=0 \quad (4)$$

Among them，

$$D=D_3-D_2^2/D_1 \quad (5)$$

Under pure bending M,the compression zone occurs bucking first .At this time,the membrane force as follows:

$$N_x = N_1\cos\frac{y}{R} \quad (6)$$

Among them,

$$N_1=\frac{M}{\pi R^2} \quad (7)$$

For the homogeneous isotropic cylindrical shell, the critical stress under axial compression and the critical stress under pure bending almost have the same value.So here we think that the functionally graded materials cylindrical shell is also in accordance with the law, namely

$$N_{cr-bending} = N_{cr-comp} \tag{8}$$

Now transform the problem into obtaining the critical bucking stress under axial compression of functionally graded materials.So we assume , the axial compression membrane as follows:

$$N_x = N_1, N_y = N_{xy} = 0 \tag{9}$$

Here,the bucking deflection function as follows:

$$w = \sum_{m=1}^{\infty}\sum_{n=1}^{\infty} f_{mn} \sin \alpha x \sin \beta y \tag{10}$$

Among them,

$$\alpha = \frac{m\pi}{L}, \beta = \frac{n}{R} \tag{11}$$

Put formula (9) and (10) into the linear buckling control formula(4).

Since $f_{mn} \neq 0$ , $\sin \alpha x \sin \beta y \neq 0$ ,we obtain

$$N_1 = \frac{D}{\alpha^2}\left(\alpha^2 + \beta^2\right)^2 + \frac{D_1\left(1-\nu^2\right)\alpha^2}{R^2\left(\alpha^2+\beta^2\right)^2} \tag{12}$$

So the critical stress of pure bending is

$$M = \pi R^2\left[\frac{D}{\alpha^2}\left(\alpha^2 + \beta^2\right)^2 + \frac{D_1\left(1-\nu^2\right)\alpha^2}{R^2\left(\alpha^2+\beta^2\right)^2}\right] \tag{13}$$

Using the mean inequality,we have

$$M_{cr} = 2\pi R\sqrt{DD_1\left(1-\nu^2\right)} \tag{14}$$

According to formula (1), when the power law index of the material bulk $N = 0$,the FGMs tube degenerates into the pure ceramic isotropic material cylindrical tube. At this time the result of formula (14)has the same value with the isotropic ceramic material pipe.

## The Calculation Results and Analysis

Here we use the functional gradient materials which is made of aluminium and zirconia. Aluminum: *Em=70* GPa, *v=0.3*; Zirconia:*Ec=151*GPa, *v =0.3*.

**Critical Moment Versus Radius**.Now considering the power law index of the material bulk $N = 1$,the thickness *h=0.004 m,* the critical moment along with the change of the radius is shown in Fig.2.The Fig.2 shows that the critical moment is linear with the radius.

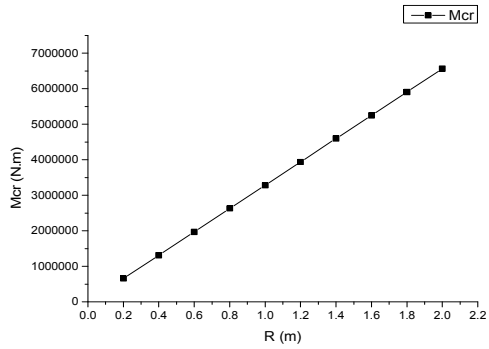


Fig.2 Critical moment versus radius

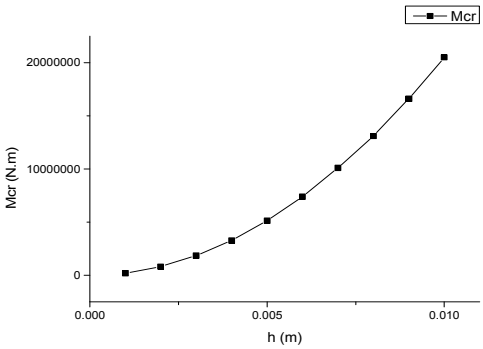


Fig.3 Critical moment versus thickness

**Critical Moment Versus Thickness.**Now we consider the thickness's impact on the critical moment.Here we assume that the power law index of the material bulk *N=1*and other parameters are under certain conditions. In this paper the shell belongs to thick shell, so we assure that R/h>50. From

formula(14) $M_{cr} = 2\pi R\sqrt{DD_1(1-\nu^2)}$ ,and according to formula (3) and (5) ,we have $D_1 \propto h, D \propto h^3$ , namely $M_{cr} \propto h^2$ .As is shown in Fig.3, the critical moment is quadratic with the thickness *h*.

**Critical Moment Versus The Power Law Index of The Material Bulk *N*.** Now we consider the the power law index of the material bulk *N*'s impact on the critical moment.Here we assume *R = 0.2 m, R = 0.6 m, R = 1 m*,and the FGMs tube thickness *h = 0.004 m*.As is shown in Fig.4,the critical moment decreases with the increase of the power law index of the material bulk *N*.When $0 \le N \le 2$,the critical moment decreases quickly with the increase of *N*; When *N>2*, the change become significantly reduced; when *N>5*,the change is no longer apparent. In addition, with the increase of *N*, metal composition is dominant, the critical moment will eventually tend to a constant finally.

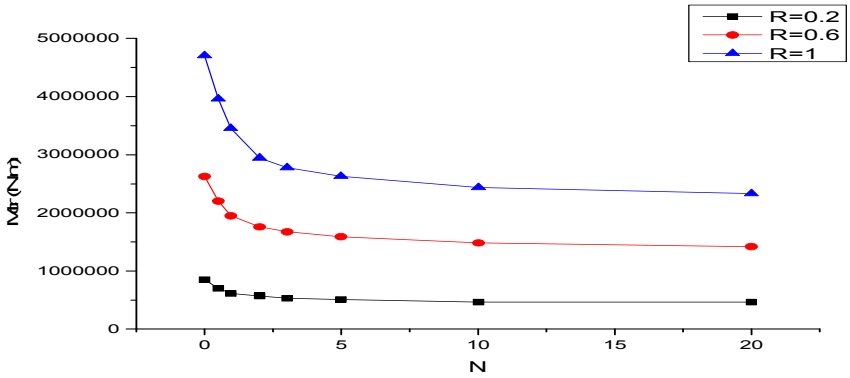


Fig.4 Critical moment versus the power law index of the material bulk *N*

## Summary

This article derives the critical moment expressions of functionally graded materials shell buckling under the pure bending based on the classical plate and shell theory. The result shows that the critical moment is linear with the radius,quadratic with the thickness and irrelevant with the length of the cylindrical shell.In addition,the critical moment is decreased by increasing the power law index of the material bulk *N*. And if *N > 5*, the critical moment changes no longer obvious.At this time,the metal composition is dominant, and the critical moment tends to be the critical moment of the pure metal cylindrical shell along with the increase of *N*.

## References:

[1] Esther Feldman , Jacob Aboudi. Buckling analysis of functionally graded plates subjected to uniaxial loading . Composite Structures , 1997,38:29-36

[2] Z.-Q.CHENG ,R.C.BATRA .Exact correspondence between eigenvalues of membranes and functionally graded simply supported polygonal plates .Journal of Sound and Vibration , 2000,229, 879-895

[3] Kyung-Su Na , Ji-Hwan Kim .Three-dimensional thermal buckling analysis of functionally graded materials . Composites Part B: Engineering.2004,35,429-437

[4] B.A.Samsam Shariat, R.Javaheri ,M.R. Eslami . Buckling of imperfect functionally graded plates under in-plane compressive loading . Thin-Walled Structures.2005,43,1020-1036

[5].J.Woo,S.A.Meguid,J.C.Stranart,K.M.Liew.Thermome-Chanical postbuckling analysis of moderately thick functionally graded plates and shallow shells .International Journal of Mechanical Sciences. 2005, 47,1147-1171

[6] Liansheng Ma,Yonggang Zhao, Buckling analysis of functionally gradient materials circular (ring) plate.Journal of gansu university of technology,2003,29(4):140-143

*Applied Mechanics and Materials Vols. 580-583 (2014) pp 2932-2935*
*© (2014) Trans Tech Publications, Switzerland*
*doi:10.4028/www.scientific.net/AMM.580-583.2932*

# Numerical decision of problems of structural mechanics with nonideal unilateral constraints

Anatoly Lukashevich[1,a], Leonid Rozin[1,b]

[1]Polytechnical Street, 29, ICE SPbSTU, St.-Petersburg, 195251, Russia

[a]a.luk@bk.ru, [b]ezlarh@mail.ru

**Keywords:** contact problem, unilateral constraints, friction, step-by-step analysis, working scheme, discrete model, contact element

**Abstract.** Here computational models of contact of elastic systems with the contact finite elements (CFE) in a 2D or 3D frame-rod systems are reviewed. The solution is based on the method of the step-by-step analysis taking into account the character of loading, the complicated conditions of the contact and other factors consideration of which approaches the calculation circuit of the task to the real operating conditions of any structures or construction

Constructionally nonlinear problems with unilateral constraints and friction with unknown before contact area are frequent while calculation of any structures or construction. For instance, construction and functional joints in the structure can open and close both with frictional sliding and cohesion of conjugated surfaces with different combinations of external loading. The same process can occur at the place of contact of foot construction and its bottom, or in different supporting blocks assuming either detachment or frictional sliding of a construction resting on them. At the same time it is the state of contact area that determine the evaluation of stress strain behavior of structures or construction and their resistibility and working efficiency [1].

Tasks with complicated conditions of contact, the consideration of which is meant to approach the design scheme to the real operating conditions of a construction, are of special interest. It is, for example, solid friction with normal forces of interaction depending on the solution, accounting strain and initial strength of unilateral constraints, sequence of erection and loading, dynamic action of loading and etc. In such cases contact problem becomes more complicated in terms of mathematics and its computational solution becomes more complicated as well. As the consideration of listed factors makes the solution of such tasks depending on character and history of the loading facilities, modeling of contact interaction, and the solution based on the method of the step-by-step analysis respectively, appear appropriate.

While making a solution of unilateral contact problems models of finite elements and algorithm of their numerical implementation are used in this work. So, for unilateral constraints modeling the contact finite elements (CFE), are applied that are be introduced in zones of possible contact of interacting bodies thus discretizing a thin layer (fake or real) between the contacting surfaces. This contact layer combines interacting bodies into a unified system and, due to special properties having given to it and taken into account by numerical computation, can meet the necessary requirements for contact. That sort of approach allows structural nonlinearity of the given system, that is a problem of structural mechanics with unilateral constraints and friction between contacting bodies and brings directly to consideration of the nonlinear discrete contact layer. In our situation contact finite elements in a 2D or 3D frame-rod are suggested for using [2]. The data of CFE interact with common finite elements in a 2D or 3D frame-rod and provide a contact between grid nodes, situated on the boundary surfaces of contacting bodies.

While using the mentioned contact elements there is no necessity for matching of coordinates of conjugated surfaces nodes, i.e. uncorrelated grids can be applied. CFE can be introduced both immediately and consequently, while contacting function between boundary surfaces of bodies, thus performing a registration of contact area state, as well as modeling various contact relations (detachment, bonding, sliding etc.). Moreover, having applied CFE one can consider various characteristics of unilateral connections, such as elastic flexibility, physical nonlinearity, initial strength and etc. Modeling of contact relations is conducted through changing of contact layer physical properties, which are, in their turn, manifested through stiffening characteristics of frame CFE cores.

Let's consider horizontal contact problem for linear elastic body $V^+$ and $V^-$, between boundary surfaces of which ($S_c^+$, $S_c^-$) unilateral constraints and Culon's friction are presented. For modeling of contact in discrete analytical model the suggested core framed contact elements are used (fig. 1).

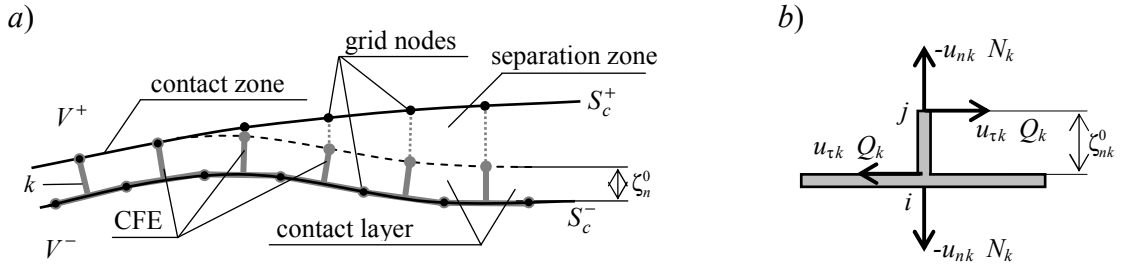


Fig. 1. Contact interaction using by frame CFE

Boundary condition in contact can be manifested through strain and deformation in individual CFE:

$$u_{nk} \le 0;\ \ N_k \le 0;\ \ u_{nk} N_k = 0;\ \ |Q_k| \le |Q_{pk}| = -f_k N_k;\ \ Q_k u_{\tau k} \ge 0;\ \ (Q_k - Q_{pk}) u_{\tau k} = 0,\quad k \in S_c. \quad (1)$$

Where $N_k$, $Q_k$ are contact force in *k*- CFE; $u_{nk}$, $u_{\tau k}$ are mutual displacement of opposed node points on $S_c^+$ and $S_c^-$ ($S_c = S_c^+ \cup S_c^-$) normally and tangentially, $f$ is constant of friction.

For making a solution of unilateral contact problems both methods of nonlinear programming, leading to iterative procedure as the final result, and incremental methods are applied. In the latter case, numerical implementation of boundary conditions (1) is conducted by step-by-step analysis of loading process and conversion of contact in the mentioned core framed model. The moment of state conversion is respectively disconnection, unilateral connection, frictional sliding or locking mating engagement. The step-by-step analysis is the most effective method for contact problems keeping under review, besides, there is a possibility of managing of discrete contact layer in accordance with loading condition, current state of contact area, stress strain behavior level etc.

Static loading is modeling by step-by-step application of the given loading. We assume that between two consecutive events the system deforms in linear fashion - in this case the solution of linearly elastic problem is formed within each step according to the arrangement of common loading. As a result the solution of linearly elastic problem will present a solution of series of linear problems, under the conditions of operating configuration of a construction modification. The procedure of settlements consists of testing and base pitches of loading. Analysis of testing pitches determines the moment of approaching of a recurrent event in contact. The base pitch results in new condition of contact and, in its turn, analysis of operating configuration modification results in designating of a new testing pitch. This allows to refine not only intensity of the current load step but forecast further steps as well, thus building the loading process, optimal in terms of length and complexity [3].

The moments of approaching of a frictional sliding event, detachment or contact for *k*-connection, which before this has been in bonding condition ($k \in S_{1c}$), one-side contact ($k \in S_{2c}$) or detachment, are determined ($k \in S_{3c}$) by the following formulations:

$$\Delta\lambda_k^{s+1} = \Delta\tilde{\lambda}^{s+1}\left(\frac{Q_{pk}^s - Q_k^s}{\Delta\tilde{Q}_k^{s+1} - \Delta\tilde{Q}_{pk}^{s+1}}\right),\ k \in S_{1c};\ \ \Delta\lambda_k^{s+1} = \Delta\tilde{\lambda}^{s+1}\left(\frac{-N_k^s}{\Delta\tilde{N}_k^{s+1}}\right),\ k \in S_{2c};\ \ \Delta\lambda_k^{s+1} = \Delta\tilde{\lambda}^{s+1}\left(\frac{-u_{nk}^s}{\Delta\tilde{u}_{nk}^{s+1}}\right),\ k \in S_{3c}. \quad (2)$$

Conversion from sliding state to bonding state during step (*s*+1) is determined by the conditions: $\left(\Delta\tilde{u}_{\tau k}^{s+1} / \Delta u_{\tau k}^s\right) < 0$, $\Delta u_{\tau k}^s \ne 0$, $k \in S_{2c}$. Where $\Delta\tilde{Q}_k^{s+1}$, $\Delta\tilde{Q}_{pk}^{s+1}$, $\Delta\tilde{N}_k^{s+1}$, $\Delta\tilde{u}_{\tau k}^{s+1}$, $\Delta\tilde{u}_{nk}^{s+1}$ are incrementations of contact forces and reciprocal deflections for *k*-CFE during testing step $\Delta\tilde{\lambda}^{s+1}$.

During dynamic action of loading structural nonlinearity is manifested in operating configuration of a construction modification through time. The moment of contact event modification, i.e. the ap-

proaching of succeeding event, in such case is determined by step-by-step (in time) analysis of core framed contact models with the use of corresponding approximate formulations for transferring, velocities in step $\Delta t$. Furthermore the duration of time step is corrected and subjected to re-computation. As a result the new contact state at this time is settled and, thus the current operating configuration of a construction is modified [4].

Matrix equation of motion is presented here in the form, allowing to lead the solution of constructive nonlinear dynamic contact problems to the solution of succession of linear dynamic problems on the basis of step time analysis of contact condition of the discrete FEM model under consideration:

$$\mathbf{M}\ddot{\mathbf{U}}^{t+\Delta t} + \mathbf{C}\dot{\mathbf{U}}^{t+\Delta t} + \mathbf{K}\Delta\mathbf{U}^{t+\Delta t} = \mathbf{P}^{t+\Delta t} - \mathbf{K}\mathbf{U}^{t}. \tag{3}$$

Besides, the availability of unilateral connection, boundary contact condition, recorded for time $t$, must be performed:

$$u_{nk}^{t} \le 0; \quad N_k^t \le 0; \quad u_{nk}^{t} N_k^t = 0; \quad \left|Q_k^t\right| \le \left|Q_{pk}^t\right|; \quad Q_k^t \dot{u}_{\tau k}^t \ge 0; \quad (Q_k^t - Q_{pk}^t)\dot{u}_{\tau k}^t = 0, \quad k \in S_c. \tag{4}$$

Where $\dot{u}_{\tau k}^t$ is the speed of reciprocal tangent deflections of opposite node points of $k$-CFE in time $t$. Contact states will be determined by the following constraint: when bonding $u_{nk}^t = 0$, $N_k < 0$, $\dot{u}_{\tau k}^t = 0$, $\left|Q_k^t\right| < \left|Q_{pk}^t\right|$; when sliding $u_{nk}^t = 0$, $N_k^t < 0$, $\dot{u}_{\tau k}^t \ne 0$, $\left|Q_k^t\right| = \left|Q_{pk}^t\right|$; when detachment $u_{nk}^t < 0$, $N_k^t = 0$.

Computational solution of dynamic contact problems will present the performing of step-by-step integration in time equation (3) under the conditions in contact in the form of (4). Formulations for the definite time $\widehat{t}_k$ of approaching event – sliding, bonding, detachment or contact correspondingly for $k$-connection will be the following:

$$\begin{aligned}
&\widehat{t}_k = t + \Delta t\left(\frac{Q_{pk}^t - Q_k^t}{(Q_k^{t+\Delta t} - Q_k^t) - (Q_{pk}^{t+\Delta t} - Q_{pk}^t)}\right), \ k \in S_{1c}; \qquad \widehat{t}_k = t + \Delta t\left(\frac{-\dot{u}_{\tau k}^t}{\dot{u}_{\tau k}^{t+\Delta t} - \dot{u}_{\tau k}^t}\right), \ k \in S_{2c}; \\
&\widehat{t}_k = t + \Delta t\left(\frac{-N_k^t}{N_k^{t+\Delta t} - N_k^t}\right), \ k \in S_{1c}, S_{2c}; \qquad\qquad \widehat{t}_k = t + \Delta t\left(\frac{-u_{nk}^t}{u_{nk}^{t+\Delta t} - u_{nk}^t}\right), \ k \in S_{3c}.
\end{aligned} \tag{5}$$

The mentioned CFE models and methods of their calculation can be easily extended to the solution of unilateral constraint problems by taking physical characteristics of contact layer and other complementary factors into account. So, while taking elastic flexibility in unilateral connections into account boundary condition (1) will take the form:

$$\left.\begin{aligned}
&u_{nk} + u_{nk}^{c} \le 0; \ \ N_k \le 0; \ \ (u_{nk} + u_{nk}^{c})N_k = 0; \ \ u_{nk}^{c} = N_k / C_{nk}; \ \ u_{\tau k}^{c} = -Q_k / C_{\tau k} \\
&\left|Q_k\right| \le \left|Q_{pk}\right| = -f_k N_k; \ \ Q_k(u_{\tau k} + u_{\tau k}^{c}) \ge 0; \ \ (Q_k - Q_{pk})(u_{\tau k} + u_{\tau k}^{c}) = 0
\end{aligned}\right\} \ k \in S_c. \tag{6}$$

Where $u_{nk}^{c}$, $u_{\tau k}^{c}$ is longitudinal and transverse strain of $k$-CFE, corresponding to squeezing and shift of contact layer with initial thickness $\zeta_n^0$; $C_{nk} = A_k / \rho_{nk}$, $C_{\tau k} = A_k / \rho_{\tau k}$, $\rho_n = (1 - \mu_c^2)\zeta_n^0 / E_c$, $\rho_\tau = 2(1 + \mu_c)\zeta_n^0 / E_c$ are characteristics of toughness and mechanical compliance of the layer normally and tangentially correspondingly; $A_k$ is a contact area, referring to contact element. Physical nonlinearity of a contact layer can be reduced to internal nonlinearity of frame contact elements, whereas nonlinear properties of as layer will be prescribed with the help of nonlinear properties of CFE.

When taking into account the initial strength of the contact seam disruption and cross section contact conditions will take the following form:

$$\left.\begin{aligned}
&u_{nk} + u_{nk}^{c} \le 0; \quad N_k + \left|Q_k\right| / \alpha_R \le N_{Rk}; \quad (u_{nk} + u_{nk}^{c})(N_k + \left|Q_k\right| / \alpha_R - N_{Rk}) = 0 \\
&\left|Q_k\right| \le Q_{Rk} - \alpha_R N_k; \quad Q_k(u_{\tau k} + u_{\tau k}^{c}) \ge 0; \quad (Q_k - Q_{Rk} + \alpha_R N_k)(u_{\tau k} + u_{\tau k}^{c}) = 0
\end{aligned}\right\} \ k \in S_c. \tag{7}$$

Where $N_{Rk}$, $Q_{Rk}$ are maximum permissible contact tensile and shift forces for *k*-discrete unilateral connection (i.e. *k*- CFE). It should be emphasized that conditions (7) are valid only before until failure of the connections in the contact point, after that conditions (6), describing unilateral connection with friction, will be valid. Thereby, one step-by-step process provide both simultaneous consideration of strength of the contact seam, and exposing or friction of its surfaces in areas where bounding is collapsed.

The mentioned computational models and methods are represented in complex of computational procedures, intended for solving static and dynamic problems of contact interaction. With their assistance computation of a number of structures or construction are performed, taking into account corresponding contact conditions and mode of external actions. Based on the analysis of the obtained results, some proposals concerning structural concepts of structures and loads acting on them have been made [5, 6].

**References**

[1] G.S. Kolosova, V.V. Lalin, A.V. Kolosova, The effect of construction joints and cracks on the stress-strain state of the arch-gravity dam, Magazine of Civil Engineering, No. 5, 76–85 (2013)

[2] A.A. Lukashevich, Construction and realization of schemes of the direct finite element method for the decision of contact problems, Izvestiya VUZ Construction, No. 12, 18–23 (2007)

[3] A.A. Lukashevich, L.A. Rozin, On the decision of contact problems of structural mechanics with unilateral constraints and friction by step-by-step analysis, Magazine of Civil Engineering, No. 1, 75–81 (2013)

[4] L.A. Rozin, A.A. Lukashevich, The numerical decision of contact problems with friction at dynamic loads, Scientific and technical sheets S-PtSPU, No. 4, 288–294 (2010)

[5] V. N. Bukhartsev, A.A. Lukashevich, The solution of problem on interaction of water-fight plate at a pressure pulsation in dumped stream, Hydraulic engineering construction, No. 4, 52–55 (2010)

[6] V. N. Bukhartsev, A.A. Lukashevich, Stability assessment of a structure subject to asymmetric load application on a rock -free bed Power Technology and Engineering, Springer New York Consultants Bureau, Vol. 45, No. 5, 346–350 (2012)

*Applied Mechanics and Materials Vols. 580-583 (2014) pp 2936-2942*
*© (2014) Trans Tech Publications, Switzerland*
*doi:10.4028/www.scientific.net/AMM.580-583.2936*

# Some Recent Developments in Coupling of Finite Element and Boundary Element Methods - Part I: An Overview

Wael Elleithy[a] and Lau Teck Leong[b]

Department of Civil Engineering, University of Nottingham Malaysia Campus

Selangor 43500, Malaysia

[a]wael.elleithy@nottingham.edu.my, [b]teckleong.lau@nottingham.edu.my

Department of Civil Engineering, University of Nottingham Malaysia Campus

Selangor 43500, Malaysia

**Keywords:** FEM; BEM; coupling; domain decomposition.

**Abstract.** Conventional and a class of domain decomposition finite element–boundary element coupling (FEM–BEM) methods are reviewed. This is Part I of two papers. In Part II, a review of the mixed Dirichlet-Neumann domain decomposition FEM-BEM coupling method is presented and optimal dynamic values of the relaxation parameters for the mixed Dirichlet-Neumann FEM-BEM coupling method are, furthermore, derived.

## Introduction

Coupling of the finite element method (FEM) and the boundary element method (BEM) has a rich tradition, see e.g. [1-20] and the references cited therein. This is justified as researchers were motivated to develop coupled methods in order to utilize "appropriate" discretization techniques in different sub-domains of the original problem, a need that arises from the different physics of sub-domains and/or for a better computational efficiency and accuracy.

In the conventional finite element-boundary element coupling (FEM-BEM) formulation, the discretized equations from the BEM and FEM sub-domains are coupled into a unique system of algebraic equations. However, the conventional coupling methods suffer some disadvantages. As an alternative to the conventional coupling of FEM and BEM, a "class" of domain decomposition methods has been developed by many researchers. In these coupling methods there is no need to combine the coefficient matrices of the FEM and the BEM sub-domains, as required in the conventional coupling methods. The domain decomposition coupling methods preserve the nature of both the finite element and boundary element methods. This class of coupling methods can be classified as overlapping and non-overlapping. Overlapping, known also as Schwarz, domain decomposition FEM-BEM coupling methods have been proposed in [1,2]. The domain of the original problem is subdivided into a FEM sub-domain, a BEM sub-domain, such that the two sub-domains partially overlap over a common region. The common region is modelled by both methods. Recently, more elaborate non-overlapping domain decomposition FEM-BEM coupling methods have been developed for a wide range of problems, see e.g. [3-20] and the references cited therein. The non-overlapping coupling methods exhibit advantages compared to the overlapping ones. The systems of equations of the sub-domains are solved independently of each other. The interaction effects are taken into account as boundary conditions, which are imposed on the coupling interfaces. Iterations are performed in order to enforce satisfaction of the coupling conditions. Within the iteration procedure, a relaxation operator is applied to the interface boundary conditions in order to enable and speed up convergence. The non-overlapping domain decomposition coupling methods are easier to implement. However, there are challenging questions concerning the practical applications of such methods and their convergence and optimal convergence conditions.

The main objective of this paper is to present an overview of the FEM-BEM coupling methods. An outline of the paper is as follows. Section 2 briefly reviews the conventional coupling methods. An

overview of several overlapping and non-overlapping domain decomposition FEM-BEM coupling methods is presented in Sections 3 and 4, respectively.

**Conventional FEM-BEM Coupling Methods**

For simplicity, consider the 2-D non-transient, either linear (e.g., potential, elasticity) or nonlinear (e.g., elasto-plasticity), problem of Fig. 1. The original problem is modelled using the BEM and FEM. The corresponding boundary integral equation for the BEM subdomain (linear potential or elasticity problems) can be written in sub-structured form as

$$\begin{bmatrix} \mathbf{H}_{11} & \mathbf{H}_{12} \\ \mathbf{H}_{21} & \mathbf{H}_{22} \end{bmatrix} \begin{bmatrix} \mathbf{u}_B^B \\ \mathbf{u}_B^I \end{bmatrix} = \begin{bmatrix} \mathbf{G}_{11} & \mathbf{G}_{12} \\ \mathbf{G}_{21} & \mathbf{G}_{22} \end{bmatrix} \begin{bmatrix} \mathbf{q}_B^B \\ \mathbf{q}_B^I \end{bmatrix} \text{ on } \Gamma_B, \tag{1}$$

where, $\mathbf{H}$ and $\mathbf{G}$ are influence coefficient matrices. $\mathbf{u}_B^I$ and $\mathbf{u}_B^B$ are the interface and non-interface potentials (displacements) in the BEM sub-domain, respectively. $\mathbf{q}_B^I$ and $\mathbf{q}_B^B$ are the nodal values for interface and non-interface fluxes (tractions), respectively. After solving for the unknowns in Eq. (1), the potentials (displacements) inside the domain can be obtained as

$$\mathbf{u} = \begin{bmatrix} \mathbf{H}_{11}^* & \mathbf{H}_{12}^* \\ \mathbf{H}_{12}^* & \mathbf{H}_{22}^* \end{bmatrix} \begin{bmatrix} \mathbf{u}_B^B \\ \mathbf{u}_B^I \end{bmatrix} + \begin{bmatrix} \mathbf{G}_{11}^* & \mathbf{G}_{12}^* \\ \mathbf{G}_{21}^* & \mathbf{G}_{22}^* \end{bmatrix} \begin{bmatrix} \mathbf{q}_B^B \\ \mathbf{q}_B^I \end{bmatrix}. \tag{2}$$

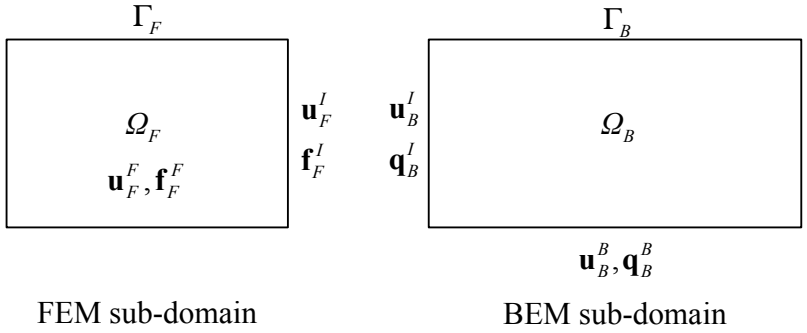


Fig. 1: Domain decomposed into FEM and BEM sub-domains.

For the FEM sub-domain (linear potential or elasticity problems), the assembled element equations in sub-structured form can be written as

$$\begin{bmatrix} \mathbf{K}_{11} & \mathbf{K}_{12} \\ \mathbf{K}_{21} & \mathbf{K}_{22} \end{bmatrix} \begin{bmatrix} \mathbf{u}_F^F \\ \mathbf{u}_F^I \end{bmatrix} = \begin{bmatrix} \mathbf{f}_F^F \\ \mathbf{f}_F^I \end{bmatrix} \text{ in } \Omega_F, \tag{3}$$

where, $\mathbf{K}$ is the stiffness matrix for the system. $\mathbf{u}_F^I$ and $\mathbf{u}_F^F$ are the interface and non-interface potentials (displacements) in the FEM sub-domain, respectively. In the same way, the integrated flux (force) vectors $\mathbf{f}_F^I$ and $\mathbf{f}_F^F$ are defined.

At the interface $\Gamma^I$, the compatibility and equilibrium conditions are $\mathbf{u}_B^I = \mathbf{u}_F^I$ and $\mathbf{f}_F^I + \mathbf{M}\,\mathbf{q}_B^I = 0$, where $\mathbf{M}$ is the converting matrix due to the weighing of the boundary fluxes (tractions) by the interpolation function on the interface.

The standard conventional FEM-BEM coupling methods treat the BEM sub-domain as a large finite element. The potentials (displacements) - fluxes (tractions) equations governing the BEM sub-domain are transformed into FEM-like potentials (displacements) - integrated flux (force)

stiffness equations. In order to combine the FEM and BEM, both sides of Eq. (1) is multiplied by $\mathbf{MG}^{-1}$ which yields

$$\mathbf{M}\begin{bmatrix}\mathbf{G}_{11} & \mathbf{G}_{12}\\ \mathbf{G}_{21} & \mathbf{G}_{22}\end{bmatrix}^{-1}\begin{bmatrix}\mathbf{H}_{11} & \mathbf{H}_{12}\\ \mathbf{H}_{21} & \mathbf{H}_{22}\end{bmatrix}\begin{bmatrix}\mathbf{u}_B^B\\ \mathbf{u}_B^I\end{bmatrix}=\mathbf{M}\begin{bmatrix}\mathbf{q}_B^B\\ \mathbf{q}_B^I\end{bmatrix}. \tag{4}$$

Eq. (4) can be written as

$$\begin{bmatrix}\overline{\mathbf{K}}_{11} & \overline{\mathbf{K}}_{12}\\ \overline{\mathbf{K}}_{21} & \overline{\mathbf{K}}_{22}\end{bmatrix}\begin{bmatrix}\mathbf{u}_B^B\\ \mathbf{u}_B^I\end{bmatrix}=\begin{bmatrix}\mathbf{f}_B^B\\ \mathbf{f}_B^I\end{bmatrix}, \tag{5}$$

which has the same form as that in the finite element method and therefore can be assembled with the FEM matrices to form a global stiffness matrix. The coupled FEM-BEM equations is then formulated as

$$\begin{bmatrix}\mathbf{K}_{11} & \mathbf{K}_{12} & \\ \mathbf{K}_{21} & \mathbf{K}_{22}+\overline{\mathbf{K}}_{22} & \overline{\mathbf{K}}_{21}\\ & \overline{\mathbf{K}}_{12} & \overline{\mathbf{K}}_{11}\end{bmatrix}\begin{bmatrix}\mathbf{u}_F^F\\ \mathbf{u}^I\\ \mathbf{u}_B^B\end{bmatrix}=\begin{bmatrix}\mathbf{f}_F^F\\ \mathbf{f}^I\\ \mathbf{f}_B^B\end{bmatrix}. \tag{6}$$

Some force terms in (2) may be a function of displacement, $u$, or stress may be a nonlinear function of strain, $\varepsilon$, as a result of material non-linearity such as plasticity. In all of these cases, a nonlinear solution procedure is required. Eq. (2) will not be generally satisfied at any stage of computation, and thus the equilibrium equation can be restated in the form of a residual (or out-of-balance) force vector. The FEM equations, in incremental form, are solved at each iteration using a tangent FEM stiffness matrix $\mathbf{K}_T$. The coupled FEM-BEM equations for a typical iteration is then formulated as

$$\begin{bmatrix}\mathbf{K}_{T,11} & \mathbf{K}_{T,12} & \\ \mathbf{K}_{T,21} & \mathbf{K}_{T,22}+\overline{\mathbf{K}}_{22} & \overline{\mathbf{K}}_{21}\\ & \overline{\mathbf{K}}_{12} & \overline{\mathbf{K}}_{11}\end{bmatrix}\begin{bmatrix}\Delta\mathbf{u}_F^F\\ \Delta\mathbf{u}^I\\ \Delta\mathbf{u}_B^B\end{bmatrix}=-\begin{bmatrix}\Delta\boldsymbol{\psi}_F^F\\ \Delta\boldsymbol{\psi}^I\\ \Delta\boldsymbol{\psi}_B^B\end{bmatrix}, \tag{7}$$

where $\boldsymbol{\psi}$ is the residual (or out-of-balance) force vector.

The conventional coupling methods suffer some disadvantages such as:

1- the conventional coupling methods may destroy the desirable features originally existing in the FEM matrices, namely, symmetry, sparsity and bandedness,

2- in dynamic analysis, the conventional coupling methods necessitate an assignment of the same time discretization in both the FEM and BEM sub-domains. In general, based on energy considerations, we are led to incompatible time steps in both FEM and BEM sub-domains,

3- in nonlinear analysis (e.g. elasto-plasticity), with the direct FEM-BEM coupling and at each load increment, solution procedure requires iterations over computation with a combined system of equations,

4- implementation of the direct coupling method needs an integrated FEM-BEM computational environment and results in a highly undesirable requirement of accessing their source codes.

**Overlapping Domain Decomposition Coupling Methods**

The domain of the original problem is subdivided into FEM and BEM sub-domains, such that the two sub-domains partially overlap over a common region that is modeled by both methods (Fig. 2).

References [1,2] treated the coupling of FEM and BEM by a multiplicative Schwarz method, which leads to solving a symmetric positive definite system arising from the FEM discretization and a nonsymmetric system from collocation BEM or a symmetric system from Galerkin BEM. Fast solvers for the FEM and BEM sub-models can be used. The overlapping, however, may create serious complications in the Schwarz method even when the problem is of a simple geometry.

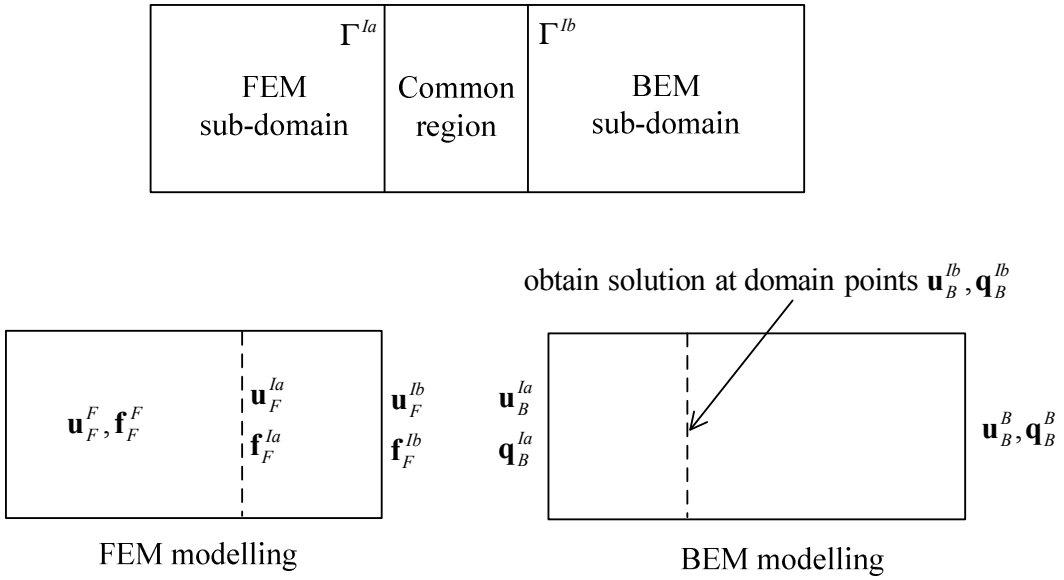


Fig. 2: Overlapping domain decomposition FEM-BEM coupling.

To describe the coupling method [2], let us define $\mathbf{u}_B^{Ia}$, $\mathbf{u}_B^B$ and $\mathbf{u}_B^{Ib}$ as the potentials (displacements) on $\Gamma^{Ia}$ approached from the BEM sub-domain, potentials (displacements) in the BEM sub-domain except at $\mathbf{u}_B^{Ia}$ and potentials (displacements) on $\Gamma^{Ib}$ computed as internal points for the BEM sub-domain, respectively. $\mathbf{u}_F^{Ia}$, $\mathbf{u}_F^F$ and $\mathbf{u}_F^{Ib}$ are the potentials (displacements) on $\Gamma^{Ia}$ approached from the FEM sub-domain, potentials (displacements) except at $\mathbf{u}_F^{Ia}$ and $\mathbf{u}_F^{Ib}$ and potentials (displacements) on $\Gamma^{Ib}$, respectively. Similarly, one can define the BEM fluxes (tractions) by $\mathbf{q}_B^{Ia}$ and $\mathbf{q}_B^B$ and the integrated flux (force) vectors by $\mathbf{f}_F^{Ia}$, $\mathbf{f}_F^F$ and $\mathbf{f}_F^{Ib}$ for the FEM sub-domain. The overlapping domain decomposition method is described as [2]

Set the initial guess $\mathbf{u}_{B,0}^{Ia}$.

Do for $n = 0, 1, 2, ...$

for the BEM sub-domain: solve Eq. (1) for $\mathbf{q}_{B,n}^{Ia}$ and boundary unknowns

for the BEM sub-domain: solve Eq. (2) for $\mathbf{u}_{B,n}^{Ib}$

for the FEM sub-domain: set $\mathbf{u}_{F,n}^{Ib} = \mathbf{u}_{B,n}^{Ib}$

for the FEM sub-domain: solve Eq. (3) for $\mathbf{u}_{F,n}^{Ia}$

apply $\mathbf{u}_{B,n+1}^{Ia} = \mathbf{u}_{F,n}^{Ia}$

**Domain Decomposition (Interface Relaxation) FEM-BEM Coupling Methods**

References [3-8] report a number of FEM-BEM domain decomposition (interface relaxation) FEM-BEM coupling applications in potential flow as well as elastostatics. It did not take long until some researchers started to extend the interface relaxation FEM-BEM coupling algorithms for applications in elasto-plasticity, three-dimensional transient elastodynamics, nonlinear dynamic

analysis, and acoustic-acoustic, elastodynamic-elastodynamic, acoustic-elastonynamic and nonlinear solid-fluid interaction, see e.g. [9-16] and the references cited therein.

Several existing domain decomposition coupling methods (Dirichlet-Neumann, Neumann-Neumann, and geometric construction based) are reviewed in Table 1. For simplicity, the 2-D non-transient (e.g., potential, elasticity) problem of Fig. 1 is considered.

Table 1: Review of several existing domain decomposition FEM-BEM coupling methods.

| Dirichlet-Neumann FEM-BEM Coupling [3-7] | |
|---|---|
| Set the initial guess $\mathbf{u}^I_{B,0}$.<br>Do for $n = 0, 1, 2,...$<br>for the BEM sub-domain:<br>solve Eq. (1) for $\mathbf{q}^I_{B,n}$<br>for the FEM sub-domain:<br>solve $\mathbf{f}^I_F + \mathbf{M}\,\mathbf{q}^I_B = 0$ for $\mathbf{f}^I_{F,n}$<br>solve Eq. (3) for $\mathbf{u}^I_{F,n}$<br>apply $\mathbf{u}^I_{B,n+1} = (1-\theta)\,\mathbf{u}^I_{B,n} + \theta\,\mathbf{u}^I_{F,n}$,<br>where $\theta$ is a relaxation parameter. | The convergence and optimal convergence conditions are established in [6,7].<br>Procedures for dynamic calculation of the relaxation parameter $\theta$ are presented in [17].<br>The method is not suitable for problems when the Neumann boundary conditions are specified on the entire real boundary of the FEM sub-domain. |
| Neumann-Neumann FEM-BEM Coupling [3] | |
| Set the initial guess $\mathbf{q}^I_{B,0}$ and $\mathbf{q}^I_{F,\mathbf{0}}$.<br>Do for $n = 0, 1, 2,...$ until convergence<br>for the BEM sub-domain:<br>solve Eq. (1) for $\mathbf{u}^I_{B,n}$<br>for the FEM sub-domain:<br>solve $\mathbf{f}^I_{F,n} = \mathbf{M}\,\mathbf{q}^I_{F,n}$ for $\mathbf{f}^I_{F,n}$ and Eq. (3) for $\mathbf{u}^I_{F,n}$<br>apply $\mathbf{q}^I_{B,n+1} = \mathbf{q}^I_{B,n} + \gamma\,(\mathbf{u}^I_{F,n} - \mathbf{u}^I_{B,n})$,<br>where $\gamma$ is a relaxation parameter.<br>apply $\mathbf{q}^I_{F,n+1} = -\mathbf{q}^I_{B,n+1}$. | The convergence and optimal convergence conditions are established in [7].<br>Procedures for dynamic calculation of the relaxation parameter $\gamma$ are presented in [17].<br>The method is not suitable for problems when the Neumann boundary conditions are specified on the entire real boundary of either the FEM or BEM sub-domain. |
| Geometric Construction Based FEM-BEM Coupling [8] | |
| Set initial guess $\mathbf{u}^I_{F,0}$ and $\mathbf{u}^I_{B,0}$.<br>For $n = 0, 1, 2,...$, do until convergence<br>for the BEM sub-domain:<br>solve Eq. (1) for $\mathbf{q}^I_{B,n}$<br>for the FEM sub-domain:<br>solve Eq. (3) and $\mathbf{f}^I_{F,n} = \mathbf{M}\,\mathbf{q}^I_{F,n}$ for $\mathbf{q}^I_{F,n}$<br>apply $\mathbf{u}^I_{B,n+1} = \mathbf{u}^I_{B,n} - \varphi\,(\mathbf{q}^I_{B,n} + \mathbf{q}^I_{F,n})$ and<br>$\mathbf{u}^I_{F,n+1} = \mathbf{u}^I_{B,n+1}$,<br>where $\varphi$ is a relaxation parameter. | The method includes scaling of $\mathbf{q}$ while selecting $\varphi$.<br>The convergence conditions are not available in the literature and to be established.<br>Procedures for dynamic calculation of the relaxation parameter $\varphi$ are presented in [17]. |

**Summary**

In this paper, conventional and a class of domain decomposition finite element–boundary element coupling (FEM–BEM) are reviewed. Procedures for dynamic calculation of relaxation parameters for the mixed Dirichlet-Neumann domain decomposition FEM-BEM coupling method and an example application are given in Part II of this paper.

**Acknowledgements**

The author acknowledges the support of the University of Nottingham Malaysia Campus.

**References**

[1] E. Stein, M. Kreienmeyer, Coupling of BEM and FEM by a Multiplicative Schwarz Method and its Parallel Implementation, Engineering Computations, 15 (1998), pp. 173-198.

[2] W.M. Elleithy, H. J. Al-Gahtani, An Overlapping Domain Decomposition Approach for Coupling the Finite and Boundary Element Methods, Engineering Analysis with Boundary Elements, 24 (2000), pp. 391-398.

[3] N. Kamiya, H. Iwase, E. Kita, Parallel Computing for the Combination Method of BEM and FEM, Engineering Analysis with Boundary Elements, 18 (1996), pp. 221-229.

[4] C.C. Lin, E.C. Lawton, J.A. Caliendo, L.R. Anderson, An Iterative Finite Element-Boundary Element Algorithm, Computers & Structures, 39 (1996), pp. 899-909.

[5] Y.T. Feng, D.R.J. Owen, Iterative Solution of Coupled FE/BE Discretization for Plate-Foundation Interaction Problems, International Journal for Numerical Methods in Engineering, 39 (1996), pp. 1889-1901.

[6] W.M. Elleithy, H.J. Al-Gahtani, M. El-Gebeily, Iterative Coupling of BE and FE Methods in Elastostatics, Engineering Analysis with Boundary Elements, 25 (2001), pp. 685-695.

[7] M. El-Gebeily, W.M. Elleithy, H.J. Al-Gahtani, Convergence of the Domain Decomposition Finite Element-Boundary Element Coupling Methods, Computer Methods in Applied Mechanics and Engineering, 191 (2002), pp. 4851-4867.

[8] W.M. Elleithy, M. Tanaka, Interface Relaxation Algorithms for BEM-BEM Coupling and FEM-BEM Coupling, Computer Methods in Applied Mechanics and Engineering, 192 (2003), pp. 2977-2992.

[9] W. M. Elleithy, M. Tanaka, A. Guzik, Interface Relaxation FEM-BEM Coupling Method for Elasto-Plastic Analysis, Engineering Analysis with Boundary Elements, 28 (2004), pp. 849-857.

[10] D. Soares Jr, O. von Estorff, W. J. Mansur, Iterative coupling of BEM and FEM for nonlinear dynamic analyses, Computational Mechanics, 34 (2004), pp. 67-73.

[11] O. von Estorff, C. Hagen, C., Iterative coupling of FEM and BEM in 3D transient elastodynamics, Engineering Analysis with Boundary Elements, 29 (2005), pp. 775-787.

[12] D. Soares Jr, W. J.Mansur, An Efficient Time-Domain BEM/FEM Coupling for Acoustic-Elastodynamic Interaction Problems, Computer Methods in Engineering and Sciences, 8 (2005), pp. 153-164.

[13] D. Soares Jr, O. von Estorff, W. J. Mansur, Efficient Nonlinear Solid-Fluid Interaction Analysis by an Iterative BEM/FEM Coupling, International Journal for Numerical Methods in Engineering, 64 (2005), pp. 1416-1431.

[14] D. Soares Jr, Coupled numerical methods to analyze interacting acoustic-dynamic models by multidomain decomposition techniques, Mathematical Problems in Engineering, 2011 (2011), Article ID 245170, 28 pages.

[15] D. Soares Jr, FEM-BEM iterative coupling procedures to analyze interacting wave propagation models: fluid-fluid, solid-solid and fluid-solid analyses, Coupled Systems Mechanics, 1 (2012), pp. 19-37.

[16] D. Soares Jr, and L. Godinho, An overview of recent advances in the iterative analysis of coupled models for wave propagation, Journal of Applied Mathematics, 2014 (2014), Article ID 426283, 21 pages.

[17] W. Elleithy, Interface Relaxation FEM-BEM Coupling: Dynamic Procedures of Determining the Relaxation Parameters, Sixth Alexandria International Conference on Structural and Geotechnical Engineering (AICSGE6), Alexandria, Egypt, (2007), pp. ST1-ST15.

[18] A. Eslami Haghighat, S. M. Binesh. Domain Decomposition Algorithm for Coupling of Finite Element and Boundary Element Methods, Arabian Journal for Science and Engineering, in press.

[19] W. Elleithy, Multi-Domain Analysis by FEM-BEM Coupling and BEM-DD. Part I: Formulation and Implementation, Applied Mechanics and Materials, (353-356) 2013, pp. 3263-3268.

[20] W. Elleithy, Multi-Domain Analysis by FEM-BEM Coupling and BEM-DD. Part II: Convergence, Applied Mechanics and Materials, 353-356 (2013), pp. 3269-3275.

*Applied Mechanics and Materials Vols. 580-583 (2014) pp 2943-2947*
*© (2014) Trans Tech Publications, Switzerland*
*doi:10.4028/www.scientific.net/AMM.580-583.2943*

# Some Recent Developments in Coupling of Finite Element and Boundary Element Methods - Part II: Dynamic Procedures for Determining the Relaxation Parameters for the Mixed Dirichlet-Neumann Domain Decomposition FEM-BEM Coupling Method

Wael Elleithy[a] and Lau Teck Leong[b]

Department of Civil Engineering, University of Nottingham Malaysia Campus

Selangor 43500, Malaysia

[a]wael.elleithy@nottingham.edu.my, [b]teckleong.lau@nottingham.edu.my

Department of Civil Engineering, University of Nottingham Malaysia Campus

Selangor 43500, Malaysia

**Keywords:** FEM; BEM; coupling; domain decomposition.

**Abstract.** Part I of this paper presents an overview of the conventional and a class of domain decomposition finite element-boundary element coupling methods. In this part, a review of the mixed Dirichlet-Neumann domain decomposition coupling method, procedures for dynamic calculation of relaxation parameters for the mixed Dirichlet-Neumann FEM-BEM coupling method and an example application are presented.

## Introduction

The main purpose of coupling the finite element method (FEM) and the boundary element method (BEM) is to use the advantages of both methods for solving various problems in applied science and engineering. Each method has areas of applications in which it is superior to the other. The FEM is most suitable for problems where the material is non-homogeneous and/or behaves nonlinearly. The BEM on the other hand, is most suitable when the domain is unbounded and in applications involving a high accuracy of boundary stresses. The theory and algorithms of coupling FEM and BEM (FEM-BEM) reached, by now, a fairly matured state.

In Part I of this paper, an overview of the conventional and a class of domain decomposition finite element-boundary element coupling methods are presented. The main objective of this paper is to derive procedures for dynamic calculation of relaxation parameters for the mixed Dirichlet-Neumann FEM-BEM coupling method. An outline of the paper is as follows. Section 2 reviews the mixed Dirichlet-Neumann FEM-BEM coupling method. Optimal dynamic values of the relaxation parameters are derived in Section 3. Example application is given in Section 4.

## Mixed Dirichlet-Neumann FEM-BEM Coupling [1,2]

In this coupling method, both the Dirichlet and Neumann boundary conditions are assumed on the interface between the sub-domains. For simplicity, consider the 2-D non-transient linear (e.g., potential, elasticity) problem. The original problem is modelled using the BEM and FEM. The corresponding boundary integral equation for the BEM subdomain (linear potential or elasticity problems) can be written in sub-structured form as

$$\begin{bmatrix} \mathbf{H}_{11} & \mathbf{H}_{12} & \mathbf{H}_{13} \\ \mathbf{H}_{21} & \mathbf{H}_{22} & \mathbf{H}_{23} \\ \mathbf{H}_{31} & \mathbf{H}_{32} & \mathbf{H}_{33} \end{bmatrix} \begin{bmatrix} \mathbf{u}_B^B \\ \mathbf{u}_B^{I1} \\ \mathbf{u}_B^{I2} \end{bmatrix} = \begin{bmatrix} \mathbf{G}_{11} & \mathbf{G}_{12} & \mathbf{G}_{13} \\ \mathbf{G}_{21} & \mathbf{G}_{22} & \mathbf{G}_{23} \\ \mathbf{G}_{31} & \mathbf{G}_{32} & \mathbf{G}_{33} \end{bmatrix} \begin{bmatrix} \mathbf{q}_B^B \\ \mathbf{q}_B^{I1} \\ \mathbf{q}_B^{I2} \end{bmatrix} \text{ on } \Gamma_B, \tag{1}$$

where, $\mathbf{u}_B^B$ are the non-interface potentials (displacements) in the BEM sub-domain. $\mathbf{u}_B^{I1}$ and $\mathbf{u}_B^{I2}$ are the interface potentials (displacements), approached from the BEM sub-domain, on $\Gamma^{I1}$ and $\Gamma^{I2}$, respectively. Similarly, one can denote the BEM nodal values for the fluxes (tractions) by $\mathbf{q}_B^B$, $\mathbf{q}_B^{I1}$, and $\mathbf{q}_B^{I2}$.

For the FEM sub-domain (linear potential or elasticity problems), the assembled element equations in sub-structured form can be written as

$$\begin{bmatrix} \mathbf{K}_{11} & \mathbf{K}_{12} & \mathbf{K}_{13} \\ \mathbf{K}_{21} & \mathbf{K}_{22} & \mathbf{K}_{23} \\ \mathbf{K}_{31} & \mathbf{K}_{32} & \mathbf{K}_{33} \end{bmatrix} \begin{bmatrix} \mathbf{u}_F^F \\ \mathbf{u}_{F,n}^{I1} \\ \mathbf{u}_{B,n}^{I2} \end{bmatrix} = \begin{bmatrix} \mathbf{f}_F^F \\ \mathbf{f}_F^{I1} \\ \mathbf{f}_F^{I2} \end{bmatrix} \text{ in } \Omega_F, \tag{2}$$

where, $\mathbf{u}_F^F$, $\mathbf{u}_F^{I1}$ and $\mathbf{u}_F^{I2}$ are non-interface potentials (displacements) in the FEM sub-domain, interface potentials (displacements) on $\Gamma^{I1}$ and $\Gamma^{I2}$ (approached from the FEM sub-domain), respectively. Similarly, one can denote the integrated flux (force) vectors by $\mathbf{f}_F^F$, $\mathbf{f}_F^{I1}$ and $\mathbf{f}_F^{I2}$.

At the interface $\Gamma^I$, the compatibility and equilibrium conditions are $\mathbf{u}_B^{I1} = \mathbf{u}_F^{I1}$, $\mathbf{u}_B^{I2} = \mathbf{u}_F^{I2}$, $\mathbf{f}_F^{I1} + \mathbf{M}_1 \mathbf{q}_B^{I1} = 0$ and $\mathbf{f}_F^{I2} + \mathbf{M}_2 \mathbf{q}_B^{I2} = 0$.

The mixed Dirichlet-Neumann FEM-BEM coupling method may be described as [1,2]

Set initial guess $\mathbf{u}_{B,0}^{I1} = \overline{\mathbf{u}}$ and $\mathbf{q}_{B,0}^{I2} = \overline{\mathbf{q}}$.

For $n = 0, 1, 2, \ldots$, do

for the BEM sub-domain: solve Eq. (1) for $\mathbf{q}_{B,n}^{I1}$ and $\mathbf{u}_{B,n}^{I2}$

set $\mathbf{f}_{F,n}^{I1} + \mathbf{M}_1 \mathbf{q}_{B,n}^{I1} = 0$ and $\mathbf{u}_{F,n}^{I2} = \mathbf{u}_{B,n}^{I2}$

for the FEM sub-domain: solve $\mathbf{f}_{F,n}^{I2} = \mathbf{M}_2 \mathbf{q}_{F,n}^{I2}$ and Eq. (2) for $\mathbf{u}_{F,n}^{I1}$ and $\mathbf{q}_{F,n}^{I2}$

apply $\mathbf{u}_{B,n+1}^{I1} = (1-\alpha)\mathbf{u}_{B,n}^{I1} + \alpha \mathbf{u}_{F,n}^{I1}$ and $\mathbf{q}_{B,n+1}^{I2} = (1-\beta)\mathbf{q}_{B,n}^{I2} - \beta \mathbf{q}_{F,n}^{I2}$

where, $\alpha$ and $\beta$ are relaxation parameters to ensure and/or accelerate convergence.

The mixed Dirichlet-Neumann domain decomposition FEM-BEM coupling method is capable of handling problems with any type of boundary conditions imposed on the entire real boundary of the FEM and BEM sub-domains. The convergence conditions for the mixed Dirichlet-Neumann domain decomposition FEM-BEM coupling method are established in [3]. The convergence depends on the mesh density of the FEM and BEM sub-domains, the specified types of boundary conditions, and the geometrical as well as material properties.

## Dynamic Selection of Relaxation Parameters for the Mixed Dirichlet-Neumann FEM-BEM Coupling Method

The convergence/optimal convergence of the mixed Dirichlet-Neumann FEM-BEM domain decomposition coupling method is ensured by properly set relaxation parameters that can be assigned constant values for all iterations. The optimal and applicable ranges of static relaxation parameters may be obtained by experimenting with different values. Alternatively, prior to coupled FEM-BEM calculations, static values of the relaxation parameters may be obtained [3]. It requires, however, some sort of intricate matrix manipulations. In this Section, we derive optimal dynamic relaxation parameters for the mixed Dirichlet-Neumann FEM-BEM coupling method.

The optimal value of $\alpha$, at successive iterations, can be determined by minimizing the square error functional of the next and current iterations. Substituting

$$\left(\mathbf{u}_B^{I1}\right)_{n+1} = (1-\alpha)\left(\mathbf{u}_B^{I1}\right)_n + \alpha\left(\mathbf{u}_F^{I1}\right)_n \tag{3}$$

into functional

$$g(\alpha) = \left\| \left(\mathbf{u}_B^{I1}\right)_{n+1} - \left(\mathbf{u}_B^{I1}\right)_n \right\|_2^2 \tag{4}$$

results in

$$\begin{aligned} g(\alpha) = \alpha^2 \left\| \left(\mathbf{u}_F^{I1}\right)_n - \left(\mathbf{u}_F^{I1}\right)_{n-1} \right\|_2^2 + (1-\alpha)^2 \left\| \left(\mathbf{u}_B^{I1}\right)_n - \left(\mathbf{u}_B^{I1}\right)_{n-1} \right\|_2^2 , \\ + 2\alpha(1-\alpha)\left(\left(\mathbf{u}_F^{I1}\right)_n - \left(\mathbf{u}_F^{I1}\right)_{n-1}\right).\left(\left(\mathbf{u}_B^{I1}\right)_n - \left(\mathbf{u}_B^{I1}\right)_{n-1}\right) \end{aligned} \tag{5}$$

where $\|\cdot\|_2$ is Euclidean ($l_2$) norm.
Differentiation of (5) with respect to $\alpha$ yields:

$$\begin{aligned} g'(\alpha) = 2\alpha \left\| \left(\left(\mathbf{u}_F^{I1}\right)_n - \left(\mathbf{u}_F^{I1}\right)_{n-1}\right) - \left(\left(\mathbf{u}_B^{I1}\right)_n - \left(\mathbf{u}_B^{I1}\right)_{n-1}\right) \right\|_2^2 - 2 \left\| \left(\left(\mathbf{u}_B^{I1}\right)_n - \left(\mathbf{u}_B^{I1}\right)_{n-1}\right) \right\|_2^2 , \\ + 2\left(\left(\mathbf{u}_B^{I1}\right)_n - \left(\mathbf{u}_B^{I1}\right)_{n-1}\right).\left(\left(\mathbf{u}_F^{I1}\right)_n - \left(\mathbf{u}_F^{I1}\right)_{n-1}\right) \end{aligned} \tag{6}$$

and $g''(\alpha) = 2\left\| \left(\left(\mathbf{u}_F^{I1}\right)_n - \left(\mathbf{u}_F^{I1}\right)_{n-1}\right) - \left(\left(\mathbf{u}_B^{I1}\right)_n - \left(\mathbf{u}_B^{I1}\right)_{n-1}\right) \right\|_2^2 > 0$, i.e., Eq (6) corresponds to a minimum. Setting $g'(\alpha) = 0$, we get

$$\alpha_{n+1}\,(\text{optimal}) = \frac{\left\| \left(\left(\mathbf{u}_B^{I1}\right)_n - \left(\mathbf{u}_B^{I1}\right)_{n-1}\right) \right\|_2^2 - \left(\left(\mathbf{u}_B^{I1}\right)_n - \left(\mathbf{u}_B^{I1}\right)_{n-1}\right).\left(\left(\mathbf{u}_F^{I1}\right)_n - \left(\mathbf{u}_F^{I1}\right)_{n-1}\right)}{\left\| \left(\left(\mathbf{u}_F^{I1}\right)_n - \left(\mathbf{u}_F^{I1}\right)_{n-1}\right) - \left(\left(\mathbf{u}_B^{I1}\right)_n - \left(\mathbf{u}_B^{I1}\right)_{n-1}\right) \right\|_2^2} . \tag{7}$$

Similarly, optimal value of $\beta$, at successive iterations, can be determined by minimizing the square error functional of the next and current iterations. Substituting

$$\mathbf{q}_{B,\,n+1}^{I2} = (1-\beta)\,\mathbf{q}_{B,\,n}^{I2} - \beta\,\mathbf{q}_{F,\,n}^{I2} \tag{8}$$

into functional

$$g(\beta) = \left\| \left(\mathbf{q}_B^{I2}\right)_{n+1} - \left(\mathbf{q}_B^{I2}\right)_n \right\|_2^2 \tag{9}$$

results in

$$\begin{aligned} g(\beta) = \beta^2 \left\| \left(\mathbf{q}_F^{I2}\right)_n - \left(\mathbf{q}_F^{I2}\right)_{n-1} \right\|_2^2 + (1-\beta)^2 \left\| \left(\mathbf{q}_B^{I2}\right)_n - \left(\mathbf{q}_B^{I2}\right)_{n-1} \right\|_2^2 . \\ - 2\beta(1-\beta)\left(\left(\mathbf{q}_F^{I2}\right)_n - \left(\mathbf{q}_F^{I2}\right)_{n-1}\right).\left(\left(\mathbf{q}_B^{I2}\right)_n - \left(\mathbf{q}_B^{I2}\right)_{n-1}\right) \end{aligned} \tag{10}$$

Differentiation of (10) with respect to $\beta$ yields

$$\begin{aligned} g'(\beta) = 2\beta \left\| \left(\left(\mathbf{q}_F^{I2}\right)_n - \left(\mathbf{q}_F^{I2}\right)_{n-1}\right) + \left(\left(\mathbf{q}_B^{I2}\right)_n - \left(\mathbf{q}_B^{I2}\right)_{n-1}\right) \right\|_2^2 - 2 \left\| \left(\left(\mathbf{q}_B^{I2}\right)_n - \left(\mathbf{q}_B^{I2}\right)_{n-1}\right) \right\|_2^2 , \\ - 2\left(\left(\mathbf{q}_B^{I2}\right)_n - \left(\mathbf{q}_B^{I2}\right)_{n-1}\right).\left(\left(\mathbf{q}_F^{I2}\right)_n - \left(\mathbf{q}_F^{I2}\right)_{n-1}\right) \end{aligned} \tag{11}$$

and $g''(\beta)=2\left\|\left(\left(\mathbf{q}_F^{I2}\right)_n-\left(\mathbf{q}_F^{I2}\right)_{n-1}\right)+\left(\left(\mathbf{q}_B^{I2}\right)_n-\left(\mathbf{q}_B^{I2}\right)_{n-1}\right)\right\|_2^2>0$, i.e., Eq. (11) corresponds to a minimum. Setting $g'(\beta)=0$, we get

$$\beta_{n+1}\,(\text{optimal})=\frac{\left\|\left(\left(\mathbf{q}_B^{I2}\right)_n-\left(\mathbf{q}_B^{I2}\right)_{n-1}\right)\right\|_2^2+\left(\left(\mathbf{q}_B^{I2}\right)_n-\left(\mathbf{q}_B^{I2}\right)_{n-1}\right)\cdot\left(\left(\mathbf{q}_F^{I2}\right)_n-\left(\mathbf{q}_F^{I2}\right)_{n-1}\right)}{\left\|\left(\left(\mathbf{q}_F^{I2}\right)_n-\left(\mathbf{q}_F^{I2}\right)_{n-1}\right)+\left(\left(\mathbf{q}_B^{I2}\right)_n-\left(\mathbf{q}_B^{I2}\right)_{n-1}\right)\right\|_2^2}. \tag{12}$$

Using values of $\alpha$ and $\beta$ obtained by (7) and (12), respectively, with calculations involving simple vector algebra, significantly reduces the required number of iterations.

**Example Application**

Procedures for dynamic calculation of relaxation parameters for the mixed Dirichlet-Neumann domain decomposition FEM-BEM coupling method are presented in Section 3. In this section, example application is given for elaboration.

Consider the potential flow problem shown in Fig. 1. The two sub-domains $\Omega_B$ and $\Omega_F$ are governed by Laplace equation, i.e., $k_i\nabla^2 u=0$ in $\Omega_i$, $i=1,2$, where $k_i$ is the material property in the sub-domain $\Omega_i$. The domain is decomposed to FEM and BEM sub-domains with $0\le x\le a$. The boundary conditions are $u(0,y)=0$, $u(a,y)=200$, and zero flux ($k_i\nabla u$) elsewhere.

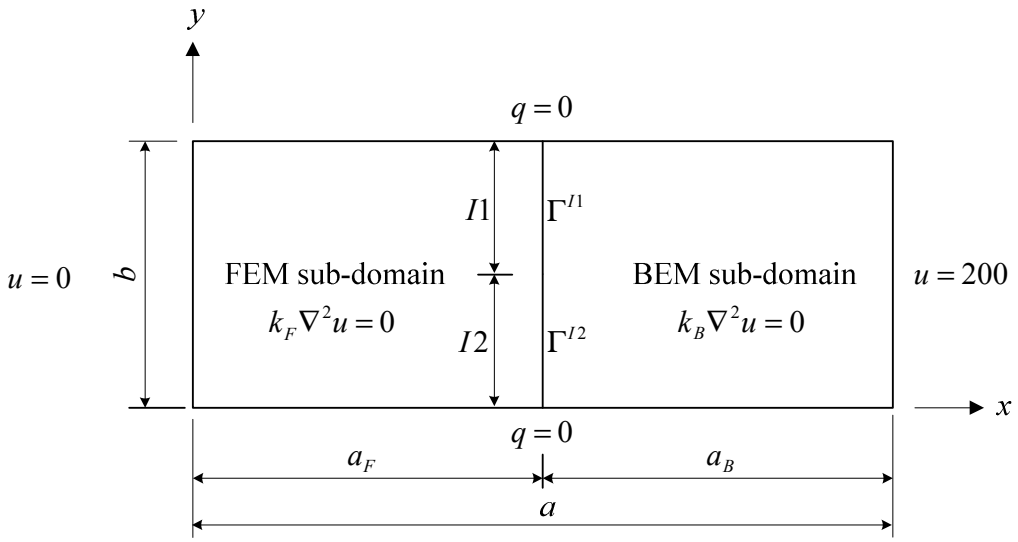


Fig. 1: Potential flow problem.

The problem is solved numerically using the mixed Dirichlet-Neumann domain decomposition FEM-BEM coupling method for different values of $a_B/a_F$ and $k_B/k_F$. The results are in good agreement with the analytic solutions. Table 1 shows the applicable ranges of the relaxation parameters $\alpha$ and $\beta$ for different combinations of $a_B/a_F$ and $k_B/k_F$. Beyond the values shown in Table 1, the method will not converge. The limit values of the relaxation parameters are in close agreement with the theoretical analysis given in [3]. Table 1 clearly shows that the proper choice of the relaxation parameter is problem dependent. Here comes the contribution of this paper. The dynamic procedures presented in Section 3, significantly reduce the required number of iterations. It is worth emphasizing that the interface update using the dynamically calculated relaxation parameters reduces the required iterations for all values of $a_B/a_F$ and $k_B/k_F$ to less than 3. Furthermore, the dynamic procedures for determining the relaxation parameters eliminate the disadvantage of a user prior definition of the relaxation values.

Table 1: Applicable range of the relaxation parameters [3].

| $a_B/a_F$ | relaxation parameter | $k_B/k_F$ | | | |
|---|---|---|---|---|---|
| | | 0.25 | 0.50 | 1.0 | 2.5 |
| 0.25 | $\beta$ | 0.01-0.99 | 0.01-1.42 | 0.01-1.59 | 0.01-1.81 |
| | $\alpha$ | 0.01-0.99 | 0.01-0.66 | 0.01-0.39 | 0.01-0.18 |
| 1.0 | $\beta$ | 0.01-0.39 | 0.01-0.66 | 0.01-0.99 | 0.01-1.42 |
| | $\alpha$ | 0.01-1.59 | 0.01-1.33 | 0.01-0.99 | 0.01-0.57 |
| 5.0 | $\beta$ | 0.01-0.09 | 0.01-0.18 | 0.01-0.33 | 0.01-0.66 |
| | $\alpha$ | 0.01-1.90 | 0.01-1.81 | 0.01-1.66 | 0.01-1.33 |

**Summary**

In this paper, the mixed Dirichlet-Neumann domain decomposition FEM-BEM coupling method is reviewed. The method is capable of handling problems with any type of boundary conditions imposed on the entire real boundary of the FEM and BEM sub-domains. Procedures are derived for dynamic calculation of relaxation parameters for the mixed Dirichlet-Neumann coupling method. With the dynamic selection of relaxation parameters, the required number of FEM-BEM coupling iterations is significantly reduced. Furthermore, the dynamic procedures presented eliminate the disadvantage of a user prior definition of the relaxation parameters.

**Acknowledgements**

The author acknowledges the support of the University of Nottingham Malaysia Campus.

**References**

[1] A. Eslami Haghighat, S. M. Binesh. Domain Decomposition Algorithm for Coupling of Finite Element and Boundary Element Methods, Arabian Journal for Science and Engineering, in press.

[2] W. Elleithy, Multi-Domain Analysis by FEM-BEM Coupling and BEM-DD. Part I: Formulation and Implementation, Applied Mechanics and Materials, (353-356) 2013, pp. 3263-3268.

[3] W. Elleithy, Multi-Domain Analysis by FEM-BEM Coupling and BEM-DD. Part II: Convergence, Applied Mechanics and Materials, 353-356 (2013), pp. 3269-3275.

*Applied Mechanics and Materials Vols. 580-583 (2014) pp 2948-2953*
*© (2014) Trans Tech Publications, Switzerland*
*doi:10.4028/www.scientific.net/AMM.580-583.2948*

# State Space Solution of Response for Piles Subjected to Lateral Loads

Fuliang Mei[1,a], Guiling Li[1,b]

[1] Institute of Civil & Engineering, Jiaxing College, Jiaxing ,Zhejiang ,314001,China

[a]Flmei2005@126.com , [b]Lgljx@126.com

**Keywords**: soil-structure interaction, pile, state space method, foundation reaction method, tri-parameter method

**Abstract:** A state space method has been put forward for finding the deformations and internal forces of piles subjected to lateral loads. First of all, a pile was divided into a number of pile segments, on which the foundation reaction coefficients were viewed as a constant based on the three parameter method. Secondly, state space equations of all the pile segments were established according to Euler-Bernoulli's beam theory and the equilibrium conditions of a pile segment. At last, a state space solution of a pile subjected to lateral loads was obtained using the boundary conditions at the top and bottom end of the pile and the continuous conditions at the interfaces between two adjacent segments. Numerical results show that the state space solution agrees well with the semi-analytical one, and all the computational formula, procedure and programming are very simple.

## Introduction

Not only are upright piles subjected to axial loads such as the gravity of upper structures and piles themselves, but also are they subjected to lateral loads such that waves, wind, earthquake, soil pressures and impact forces between vessels and piles. Now domestic and overseas research institutions and scholars usually study the mechanical characteristics of piles subjected to lateral loads by means of theoretical analysis, numerical simulation and in-situ test methods. Then the theoretical analysis method includes limit foundation reaction force, foundation reaction force and elastic theory methods, of which a linearly elastic foundation reaction force method is one of more popular methods for a several tens of years at home and abroad. The linearly elastic foundation force method can be classified into one, dual and tri-parameter methods according to the foundation reaction parameter amount.

At present there are a few of theoretical methods such that analysis and power series (M.H.Zhao, 1987; Z.Wang, *et al.*, 2005; W.Z.Li, *et al.,*2005),variation (W.D.Guo, *et al.*, 2001;W.Y.Shen, *et al.*, 2004; K.Yang , *et al.* 2006;J.Han , *et al.,*2000) , dimension (H.Matlock, *et al.*,1960), varied stiffness (H.L.Wu,2000) and finite difference method (Z.H.Dai *et al.*,2004). Former three kinds of which were put forward for one parameter method and later three kinds were suggested for a dual parameter method. H.L.Wu [1] has pointed out that both of one and dual parameter methods can not accurately reckon the upper soil reaction force, and thus he has further developed a tri-parameter method which can more precisely reflect the upper soil reaction force. But there is only a semi-analytical method for solving the static response of piles subjected to lateral loads based on the tri-parameter method (L.Zhang , *et al.,*2011).

In this treatise the foundation reaction force coefficients are evaluated according to the mentioned tri-parameter method. First of all, the state space equations for a pile subjected to lateral loads are deduced based on the Euler-Bernoulli's beam theory on Winkler's elastic foundation.

Secondly, for avoiding the difficulty of finding directly above the state space equations, the foundation reaction force coefficient on a tiny segment can be viewed as a constant after a pile can be divided into a number of tiny segments, and the state space equations expressed with the horizontal displacement, rotational angle, shear force and bending moment of all the segments are obtained. Thirdly, the space state equations for all the segments are first solved by matrix theory ,and then the state space solution is obtained by means of prescribed horizontal force, bending moment or horizontal displacement and rotational angle at the top and bottom end of the pile, force equilibrium and continuous and smooth conditions at the interface between two adjacent subsections. At last numerical solution is given and compares with the semi-analytical solution [8].

**Basic equations**

A uniform section pile and a system of coordinate are shown in Fig.1. The length and flexural stiffness are $L$ and $EI$, respectively. A prescribed bending moment and a horizontal force are applied on the top end of the pile by $M_0$ and $Q_0$ respectively. In general the action of surrounding soil on the pile can be simulated by a series of discrete and continuous springs according to the linearly elastic Winkler's foundation beams, and foundation reaction force $p(z,u)$ is

$$p(z,u) = kbu \tag{1}$$

Where b defines the width or diameter of the pile, $u$ the horizontal displacement, $k$ the foundation reaction force coefficient, and z the distance down from the top end of the pile.

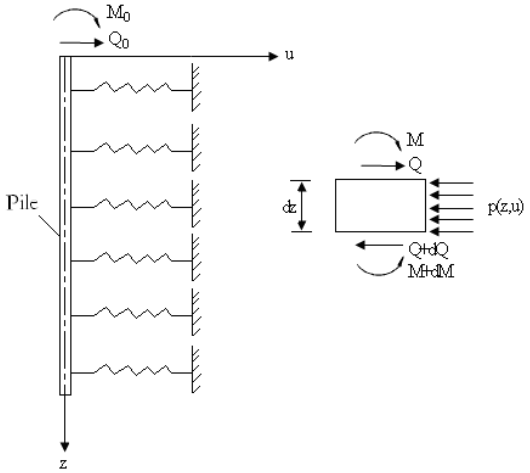


Fig.1 Diagram of a pile and force analysis of a segment

According to the tri-parameter method [1], the foundation reaction force coefficient $k$ is

$$k = m(z_0 + z)^n \tag{2}$$

Where $z_0$ defines an equivalent depth ,namely, deformation resistance capacity of soil body in the vicinity of ground, $m$ and $n$ denote the proportional factor and index of the foundation reaction force size, respectively. The linearly elastic foundation reaction force method can be classified into one ($z_0 = 0$, $n$=constant, $m \neq$ constant), dual ($z_0 = 0$ ,both of $n$ and $m$ are not constant) and tri parameter methods (all of $z_0$ , $n$ and $m$ are not constant) according to the different evaluation

of $z_0$, $m$ and $n$. The one parameter method can further be classified into constant $(n=0)$, $m$ $(n=1)$ and C value methods $(n=0.5)$.

Using the equilibrium conditions for a tiny segment, we can obtain

$$\frac{dQ(z)}{dz} = -p(z) \tag{3}$$

$$\frac{dM(z)}{dz} = Q(z) \tag{4}$$

Where $Q(z)$ and $M(z)$ denote the shear force and bending moment of the pile at z coordinate.

And utilizing Euler-Bernoulli's beam theory, we can acquire

$$\frac{du(z)}{dz} = \varphi(z) \tag{5}$$

$$\frac{d\varphi(z)}{dz} = \frac{M(z)}{EI} \tag{6}$$

Where $\varphi(z)$ denotes the rotational angle of the pile at z coordinate.

Assemble Eqs.(3-6), we can acquire following state space equations in the matrix form

$$\frac{d}{dz}\begin{Bmatrix} u(z) \\ M(z) \\ Q(z) \\ \phi(z) \end{Bmatrix} = \begin{bmatrix} 0 & 0 & 0 & 1 \\ 0 & 0 & 1 & 0 \\ -k(z)b & 0 & 0 & 0 \\ 0 & 1/EI & 0 & 0 \end{bmatrix} \begin{Bmatrix} u(z) \\ M(z) \\ Q(z) \\ \phi(z) \end{Bmatrix} \tag{7}$$

Eq.(7) is a system of homogeneous state equations with variable coefficients. Its analysis solution is difficult to determine.

**State space solution**

For avoiding the difficulty of finding directly Eq.(7), we evenly divide the pile into $N$ segments where the length of every segment equals to $H/N$ and establish a local coordinate system for a segment $i$ as shown in Fig.2 (b).

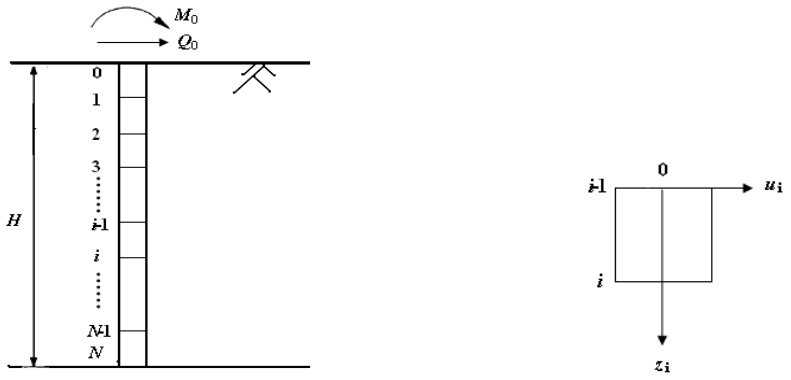


Fig.2 Partition of the pile, number of segment and the local coordinate system of a segment

The foundation reaction force coefficient within the segment can be viewed as a constant when the length of a segment is much smaller. For segment i, $k_i$ can be evaluated by means of Eq.(8)

$$k_i = \frac{m\int_{\frac{(i-1)H}{N}}^{\frac{iH}{N}} (z_0+z)^n\,dz}{H/N} = \frac{Nm\left[\left(z_0+\frac{iH}{N}\right)^{n+1}-\left(z_0+\frac{(i-1)H}{N}\right)^{n+1}\right]}{(n+1)H} \quad (i=1,2,3,\cdots,N) \tag{8}$$

Following Eq.(7), a system of state space equations for segment i is

$$\frac{d}{dz_i}\mathbf{U}_i(z) = \mathbf{G}_i\mathbf{U}_i(z_i) \qquad (i=1,2,3,\cdots,N) \tag{9}$$

Eq.(9) is a system of homogeneous state space equations with constant coefficients, and is very easy to determine. Where $\mathbf{U}_i(z_i)=[u_i(z_i) \quad M_i(z_i) \quad Q_i(z_i) \quad \varphi_i(z_i)]^T$ stands for a state space vector of segment i, $u_i(z_i), \varphi_i(z_i), \quad M_i(z_i)$ and $Q_i(z_i)$ denote the horizontal displacement, rotational angle, bending moment and shear force of segment i, respectively. The transfer matrix $\mathbf{G}_i$ of segment i is

$$\mathbf{G}_i = \begin{bmatrix} 0 & 0 & 0 & 1 \\ 0 & 0 & 1 & 0 \\ -k_i b & 0 & 0 & 0 \\ 0 & 1/EI & 0 & 0 \end{bmatrix} \tag{10}$$

Based on matrix theory, the solution of Eq.(9) can be expressed as follows

$$\mathbf{U}_i(z_i) = e^{\mathbf{G}_i z_i}\mathbf{U}_i(0) \tag{11}$$

Where $\mathbf{U}_i(0)$ stands for the state space vector at the top end of segment i. When $z_i = H/N$ (at the lower end of segment i), Eq.(11) can be written as follows

$$\mathbf{U}_i(H/N) = \mathbf{\Omega}_i\mathbf{U}_i(0) \tag{12}$$

Where $\mathbf{\Omega}_i = e^{\mathbf{G}_i H/N}$, and $\mathbf{U}_i(H/N)$ denotes the state space vector at the lower end of segment i. Eq.(12) establishes the relation between two state space vectors at the upper and lower ends of segment i.

Smooth and continuous conditions of state space vectors at the interface between two adjacent segments is

$$\mathbf{U}_i(0) = \mathbf{U}_{i-1}(H/N) \qquad (i=2,3,\cdots,N) \tag{13}$$

The state space vector can be written when the top end of the pile is free of constraint.

$$\mathbf{U}_1(0) = [u_1(0) \quad M_0 \quad Q_0 \quad \varphi_1(0)]^T \tag{14}$$

Where $u_1(0)$ and $\varphi_1(0)$ denote the undetermined horizontal displacement and rotational angle at the top end of the pile.

The state space vector can be written when the bottom end of the pile is free of constraint

$$\mathbf{U}_N(H/N) = [u_N(H/N) \quad 0 \quad 0 \quad \varphi_N(H/N)]^T \tag{15}$$

Where $u_N(H/N)$ and $\varphi_N(H/N)$ denote the undetermined horizontal displacement and rotational angle at the top end of the pile.

The state space vector can be written when the bottom end of the pile is fixed

$$\mathbf{U}_N(H/N) = [0 \quad M_N(H/N) \quad Q_N(H/N) \quad 0]^T \tag{16}$$

Where $M_N(H/N)$ and $Q_N(H/N)$ denote the undetermined bending moment and shear force at the bottom end of the pile.

Using Eqs.(12-13), the relation between the two state space vectors at the top and bottom end of the pile can be set up as follows

$$\mathbf{U}_N(H/N) = \mathbf{\Omega}_N \mathbf{\Omega}_{N-1} \cdots \mathbf{\Omega}_1 \mathbf{U}_1(0) \tag{17}$$

The undetermined variables $u_1(0)$ and $\varphi_1(0)$ at the top end of the pile by means of Eq.(17) and the given state space vectors at the top and bottom ends of the pile. And then the state space vectors $\mathbf{U}_i(H/N)(i = 1,2,\cdots N)$ at the bottom end of segment i can be found step by step using Eq.(12). The above solution is called as a state space method.

**Example and analysis**

There is a reinforced concrete pile whose length, width and flexural rigidity are 12m, 1.8m and $8.85\times10^5\, kN.m^4$ respectively. The top and bottom end of the pile are free and fixed, respectively. The horizontal force and bending moment are $30\, kN$ and $135\, kN.m$ at the top end of the pile. Foundation reaction coefficients are that $m = 1.5\times10^4 kN/m^4$, $z_0 = 0m$, $n = 1$.Tab.1 reflects the effect of uniform segments $N$ on the maximum horizontal displacement, maximum bending moment by means of the state space method (SSM). It can be seen from Tab.1 that both of the maximum horizontal displacement and the maximum bending moment do not change after $N$ is equal to or bigger than 30. Thus $N$ equals 30 for following numerical results. Fig.3 describes the curves of the horizontal displacement, rotational angle, bending moment and shear force with the depth of the pile by SSM and semi-analytical method (SAM) [8]. We find that the SSM solution is in line with the SAM one.

Table 1 Relationships among $N$, maximum horizontal displacement $U_{\max}$ and maximum bending moment $M_{\max}$

| $N$ | 10 | 15 | 20 | 25 | 30 | 35 | 40 |
|---|---|---|---|---|---|---|---|
| $U_{\max}(mm)$ | 1.5540 | 1.6143 | 1.6364 | 1.6469 | 1.6526 | 1.6561 | 1.6581 |
| $M_{\max}(kN.m)$ | 156.00 | 159.30 | 159.90 | 161.40 | 161.50 | 161.70 | 162.10 |

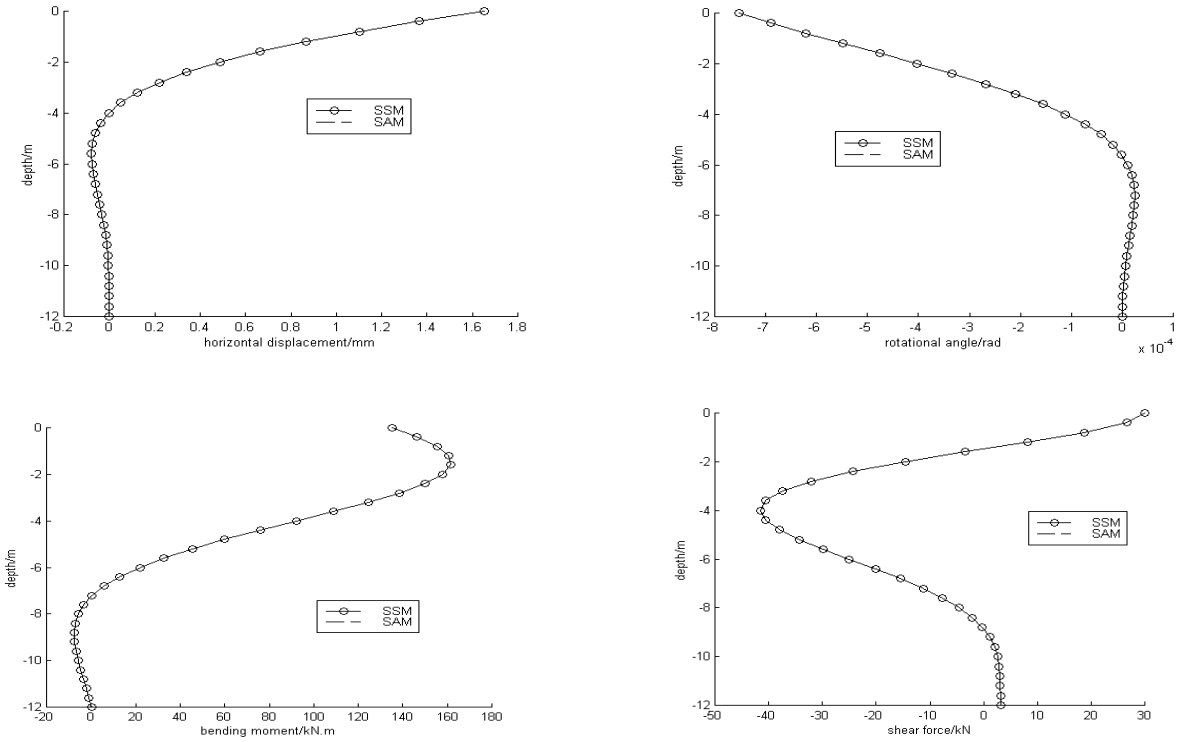


Fig.3 Comparison of SSM solution and SAM one for pile responses

**Conclusions**

In this paper the state space method is developed for the deformations and internal forces of piles subjected to lateral loads. Comparing with SAM solution that method is of faster convergence, easier programming, simpler formula and convenient use.

**Acknowledgements**

This work was financially supported by the Science & Technology Project of Zhejiang Province No.2009C31124) and the Science & Technology Project of Jiaxing City(No.2013AY11018).

**References**

[1] H.L.Wu: *Composite Stiffness Principle for Thrust Calculation of Piles & Dual-parameter Method*: Bejing, China Communications Press, 2000 (in Chinese)

[2] K.Yang, R.Liang Journal of Geotechnical and Geo-environmental Engineering, ASCE (2006)

[3] M.H.Zhao: Journal of Hunan University (in Chinese)( 1987)

[4] Z.Wang, X.N.Gong: Journal of University of Science and Technology of Suzhou (Engineering and Technology) (in Chinese)(2005)

[5] W.Z.Li, M.H.Zhao,Y.M.Shen, *et al*: Central South Highway Engineering,(in Chinese) (2005)

[6] J.,Han J.D.Frost: International Journal fro Numerical and Analytical Methods in Geo-mechanics(2000)

[7] H.Matlock, L.C.Reese: Journal of the Soil Mechanics and Foundation division ASCE (1960)

[8] Z.H.Dai, P.S.Shen,J.W.Zhang: Chinese Journal of Rock Mechanics and Engineering(in Chinese)( 2004)

[9] 9.W.D.Guo ,F.H.Lee: International Journal of Numerical and Analytical Methods in Geo-mechanics( 2001)

[10] 10.W.Y.Shen,C.I.Teh:Journal of Geotechnical and Geo-environmental Engineering ASCE(2004)

[11] 11.L.Zhang, X.N.Gong,J.L.Yu:Journal of Sichun University(Engineering Science Edition)(in Chinese) (2011)

*Applied Mechanics and Materials Vols. 580-583 (2014) pp 2954-2957*
*© (2014) Trans Tech Publications, Switzerland*
*doi:10.4028/www.scientific.net/AMM.580-583.2954*

# Study on downburst wind field characteristics under mountainous terrain

Haitao Shi[1, a], Yuanze Wu[1],Sun Yi[1], Baifeng Ji[2]

[1] School of Civil Engineering and Architecture, Wuhan University of Technology Wuhan, China, 430070

[2] Hubei Key Laboratory of Roadway Bridge &Structure Engineering, Wuhan University of Technology Wuhan, China, 430070

[a]1559913750@qq.com

**Keywords:**downburst; dimensional hillside;computational fluid dynamics;velocity pressure contours;

**Abstract.** Downburst is a strong downdraft thunderstorm in the ground formed after the violent impact and spread along the ground very sudden and destructive winds near the ground short. From an engineering point of view for the structure of wind-resistant design, researching downburst wind field characteristics and ultimately determining a reasonable downburst wind profile is one of the core objectives of the study. Terrain conditions are the major factors of downburst wind field characteristics based on the typical mountain terrain on the wind storm flow condition, this paper established typical 2D slope mountain terrain model, using the method of computational fluid dynamics to calculate the velocity contours and pressure cloud in different locations of the mountain. Finally we get the two-dimensional slope typical mountain terrain wind field distribution.

## Introduction

The effect of Downburst ranges from 2 km to 40 km [1] levelly. Downbursts in small-scale micro downburst occur frequently, and the probability of occurrence of a small-scale micro downburst in thunderstorm reaches up to 60% -70% [2]. Australia's recent analysis of strong wind velocity shows that Downburst belongs strong wind type [3] at a height of 10m. Downburst in the world caused a lot of damage to engineering structures .Melbourne [5] proposed in1972 that downburst should be incorporated into the consideration of the structural design wind load. Terrain condition is a major factor which influences the wind field characteristics of downburst. Under the action of downburst studying the air flow of surrounding two-dimensional slopes and real Mountain is the main purpose for us to seek the wind pressure distribution of the downburst near the ground in two-dimensional slope and real mountain and seek the change rule of the field characteristic before or after the downburst going by the slope. All we have stated above is to establish a theoretical foundation which reflects the wind load of downburst in the characteristics of the mountain terrain. In this paper, we get the features of wind field of special topography by studying a two-dimensional model of a typical hillside, and using CFD numerical simulation.

## Standard Model

In the standard $k-\varepsilon$ model, the turbulent kinetic energy and turbulent energy dissipation rate equations are:

$$\frac{\partial(\rho k)}{\partial t}+\frac{\partial(\rho k u_i)}{\partial x_i}=\frac{\partial}{\partial x_j}\left[\left(\mu+\frac{u_t}{\sigma_k}\right)\frac{\partial k}{\partial x_j}\right]+G_k+G_b-\rho\varepsilon-Y_M+S_k \quad (1)$$

$$\frac{\partial(\rho\varepsilon)}{\partial t}+\frac{\partial(\rho\varepsilon u_i)}{\partial x_i}=\frac{\partial}{\partial x_j}\left[\left(\mu+\frac{u_t}{\sigma_\varepsilon}\right)\frac{\partial\varepsilon}{\partial x_j}\right]+G_{1\varepsilon}\frac{\varepsilon}{k}(G_k+G_{3_\varepsilon}G_b)-G_{2\varepsilon}\rho\frac{\varepsilon^2}{k}+S_\varepsilon \quad (2)$$

**Dimensional geometric model and parameter settings hillside**

This article gives the initial conditions as blow: jet muzzle velocity Vjet = 29m / s, jet initial diameter Djet = 600m. Geometry reduced scale is 1: 2000, using a reduced scale velocity 1:3 which have been recommended by Mason [7]. Reynolds number is defined as blow, Vjet is the initial velocity jet, Djet is the jet initial diameter, υ is the kinematic viscosity of air, then the corresponding Reynolds number Re = 195000. In this paper, we use 2D as the impact of the jet model. Considering the full development of the turbulence and the impact of the size of the wind field simulation, we use 20 × 10Djet computational domain, the initial injection inlet position is defined as the distance to the ground H / D = 4, the computational domain of geometric proportions with Hangan [6] The computational domain is consistent . Figure 1 is the schematic diagram of the computational domain for anterior hill at 15 °,after we change 15 ° into the 30 °, 45 °, 60 ° respectively , there will be another three computing models. Figure 2 is the schematic diagram of the computational domain for posterior hill at 15 °, after we change 15 °into the 30 °, 45 °, 60 °respectively, there will be another three computing models. Select all axes model as shown in Fig.1 and Fig.2.

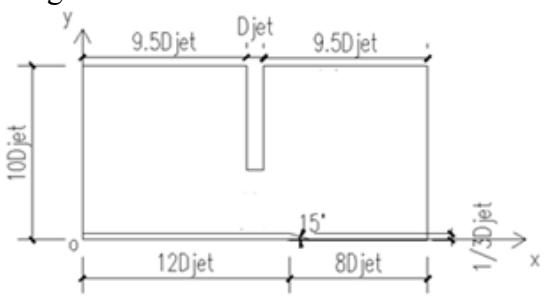


Fig. 1 The schematic diagram of anterior hill

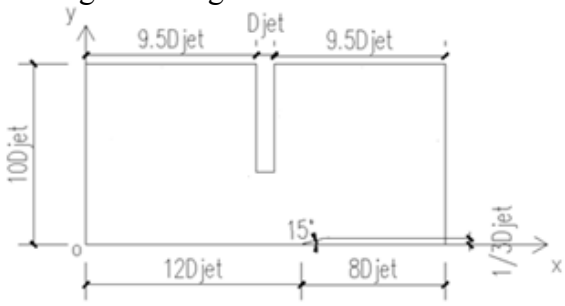


Fig.2 The schematic diagram of posterior hill

**Comparison and analysis of simulation results**

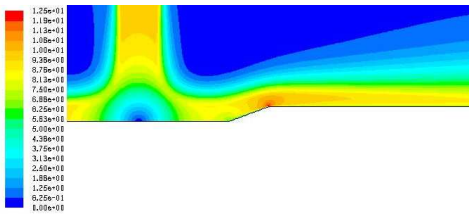

(a) anterior hill at 15 ° local speed cloud

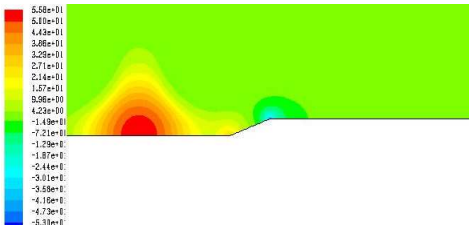

(b) anterior hill at 15 °local pressure cloud

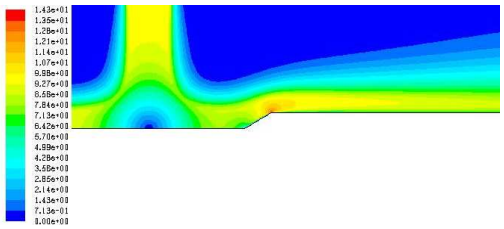

(c) anterior hill at 30 °local speed cloud

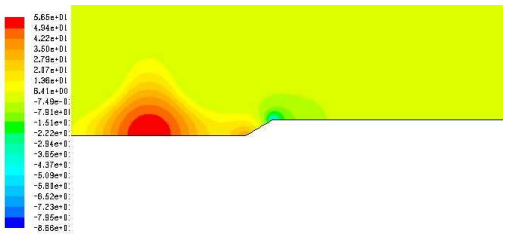

(d) anterior hill at 30 °local pressure cloud

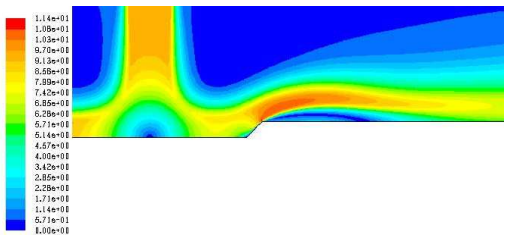

(e) anterior hill at 45 °local speed cloud

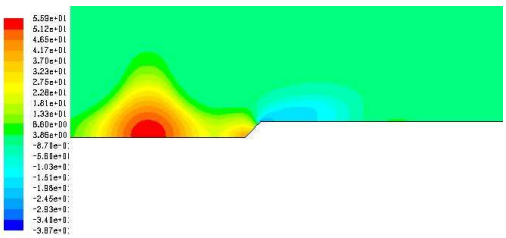

(f) anterior hill at 45°local pressure cloud

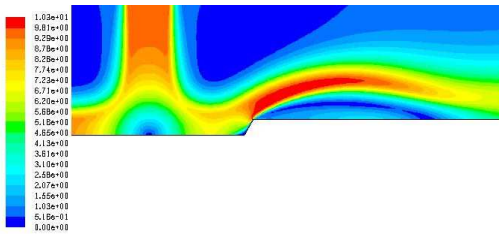

(g) anterior hill at 60°local speed cloud

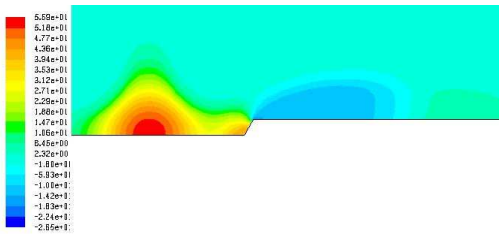

(h) anterior hill at 60°local pressure cloud

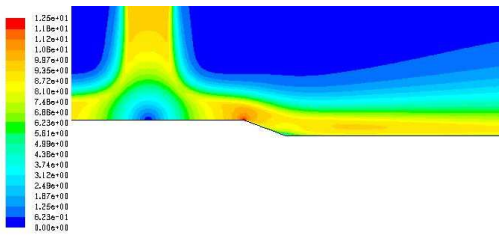

(i)posterior hill partial cloud speed at 15 °

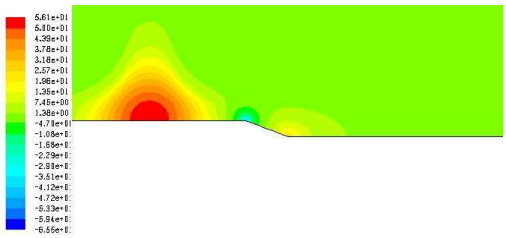

(j)posterior hill partial cloud speed at 15 °

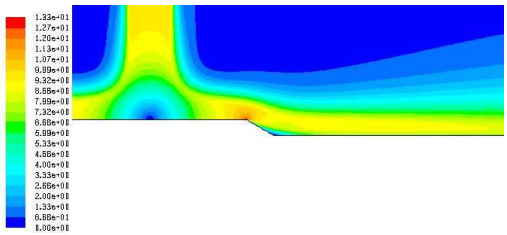

(k)posterior hill partial cloud speed at 30 °

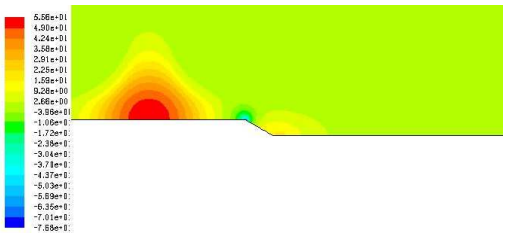

(l)posterior hill partial cloud speed at 30 °

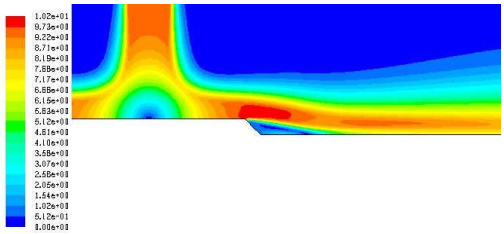

(m) posterior hill partial cloud speed at 45°

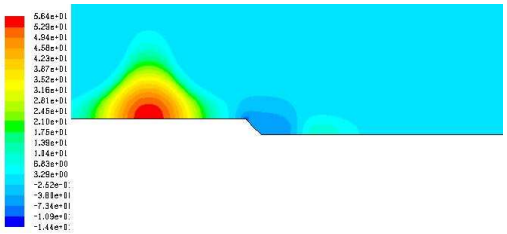

(n) posterior hill partial cloud speed at 45

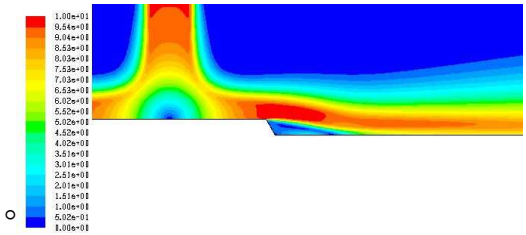

(o)posterior hill partial cloud speed at 60°

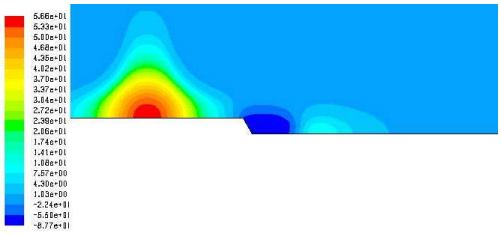

(p)posterior hill partial cloud speed at 60 °

Fig.3 Partial cloud of speed and pressure for each model

From the Fig.3. In the anterior hill ,the maximum speed usually appears near the highest point of slope,.Slope is from 15 degrees to 45 degrees, maximum speed is at the peak of the slope and vertical to the first layer of grid height, Maximum speed is at slope peak for a little right when slope is 60 degrees . When the slope becomes larger, the right side of the slope peak velocity with height changes

more significantly. On the other hand, in the first order type slopes, slope peak nearby appears the negative pressure within a certain range, the slope is greater, the negative pressure range is larger .

From the figure we also know as flow. In the posterior hill , the maximum velocity generally appear in near the highest point slope.Slope is from 15 degrees to 45 degrees, maximum speed is at the peak of the slope and vertical to the first layer of grid height . Maximum speed is at slope peak for a little right when slope is 60 degrees .When the slope becomes large, the speed in the bottom of the slope on the right side changes at smaller range On the other hand, slope peak appears the negative pressure within a certain range, the slope is larger, negative pressure range is bigger, and the negative pressure tends to spread to the slope bottom.

**Acknowledgment**

This work is supported by National students' innovation and entrepreneurship training program(20131049706005), National Natural Science Foundation of China (51308430),the Specialized Research Fund for the Doctoral Program of Higher Education of China (No.20110143120003) and the Fundamental Research Funds for the Central Universities (WUT:2013-IV-019).

**References**

[1] Fujita T.T.The downburst report of Projects NIMROD and JAWS[R].Chicago:University of Chicago,1985.
[2] Proctor Fred H.Numerical Simulations of an Isolated Microburst.Part I:Dynamics and Structure[J].Journal of the Atmospheric Sciences.1988,45(21):3137-3160.
[3] Holmes J.D.A Re-analysis of Record Extreme Wind Speed in Region A[J].Australian Journal of Structure Eng,2002,4(1):29-40.
[4] Melbourne W.H.Modeling of structures to measure wind effects[C].Proceedings Structural models Conference,School of Architectural Science,University of Sydney,1972.
[5] Jongdae Kim,Horia Hangan.Numerical simulations of impinging jets with application to downdrafts[J].Journal of Wind Engineering and Industrial Aerodynamics,2007,95(4):279- 298.
[6] Mason M.Physical simulation of thunderstorm downbursts[D].Masters thesis,Lubbock(TX, USA):Texas Tech University,2003.

*Applied Mechanics and Materials Vols. 580-583 (2014) pp 2958-2961*
*© (2014) Trans Tech Publications, Switzerland*
*doi:10.4028/www.scientific.net/AMM.580-583.2958*

# Study on Downburst Wind Load under Characteristic Topography

Yuanze Wu[1, a], Yi Sun[1], Haitao Shi[1] and Baifeng Ji [2]

[1] School of Civil Engineering and Architecture, Wuhan University of Technology Wuhan, China, 430070

[2] Hubei Key Laboratory of Roadway Bridge &Structure Engineering, Wuhan University of Technology Wuhan, China, 430070

[a]353968180@qq.com

**Key Words:** downburst; CFD; Landform types; roughness; numerical simulation; wind field characteristics.

**Abstract.** Gemorphological type is the important factor influencing the downburst wind profile. In this thesis, firstly we determine four categories of landform types under the criteria of roughness. The CFD pre-processing software GAMBIT was used to build considering the landscape type's downburst CFD computational model. Then, the established CFD computational model was imported to the calculated hydrodynamics software FLUENT to take the numerical simulation of the downburst under different landforms. Finally, in allusion to the numerical simulation result, make the research of the wind characteristics.

## Introduction

Downburst is a strong downdraft thunderstorm in the ground formed after the violent impact and spread along the ground very sudden and destructive winds near the ground a short time, the level of influence in the range of 2 to 40 km [1]. In the world, including Australia, the United States, Japan and other countries and regions, it has been causing extensive damage to engineering structures [2]. Due to the strong destructive they cause, it has become a hot topic in the international architecture and cutting-edge field of wind engineering. The topography is characterized by an important factor downburst wind load impact in the atmospheric boundary layer. The surface roughness of the vertical distribution of wind conditions will have a greater impact near the ground [3]. Surface roughness is an important indicator for the study of landforms characterized downburst impact, it's also an important parameter distribution vertical profiles of wind farm research. The current domestic and international use of CFD simulations considered the influence of surface roughness, but didn't make fine-grained roughness, when doing the wind field experiments, Fine attainment roughness has a greater impact on CFD simulation results, its simulation and study to wind field have an important significance. Therefore, it is necessary to set the fine roughness conditions when simulating the complex terrain wind farm CFD numerical in progress.

## Downburst wind field characteristics

Fujita's definition of downburst is a strong downdraft caused by strong damaging winds near-surface[1]. Chay et al [4] make a further discussion of the general characteristics that downburst of air convection updraft generated, will head a strong buoyancy of warm air to the high altitude location, with highly increasing air cooling and liquefaction, rise process stops. At this point, the air density increases after cold start fast sinking to the ground. When such a strong downdraft impact to spread around the ground, it produced a downburst wind. This wind farm, especially in the impact location near the ground, with the atmospheric boundary layer near the wind has a fundamental difference.

## Turbulence model

Numerical simulation equations in this article is based on continuity equation and Navier - Stokes equations (NS equation), does not consider heat exchange, which shielded the energy equation. Turbulence model uses a standard k-ε turbulence model, which was proposed by the Lauder and Spalding in 1972, k and ε corresponding transport equation is:

$$\frac{\partial(\rho k)}{\partial t}+\frac{\partial(\rho k u_i)}{\partial x_i}=\frac{\partial}{\partial x_j}\left[\left(v+\frac{v_T}{\sigma_k}\right)\frac{\partial k}{\partial x_j}\right]+G_k+G_b-\rho\varepsilon-Y_M+S_k \quad (1)$$

$$\frac{\partial(\rho\varepsilon)}{\partial t}+\frac{\partial(\rho\varepsilon u_i)}{\partial x_i}=\frac{\partial}{\partial x_j}\left[\left(v+\frac{v_T}{\sigma_g}\right)\frac{\partial\varepsilon}{\partial x_j}\right]+C_{1g}\frac{\varepsilon}{k}\left(G_k+C_{3g}G_b\right)-C_{2g}\rho\frac{\varepsilon^2}{k}+S_g \quad (2)$$

## Numerical simulation and calculation parameters

Since the surface roughness of the main effects of the near-surface winds blow flow field under storm flow, close to the ground using a grid in the form of encryption, mesh size increases up by the next, both rectangular grid rules. Bert Blocken [5] et al concluded that in order to ensure a high degree of accuracy of grid computing, the first floor of the grid should be a minimum height of not less than twice the rough ground. considering the translation of this article has reached the maximum roughness height 0.2m,and reducing the height of the first floor of the grid as possible to improve the quality of the grid, so the height of the first floor of the grid choose 0.4m.Mesh area is shown in Fig. 1 and Fig. 2.

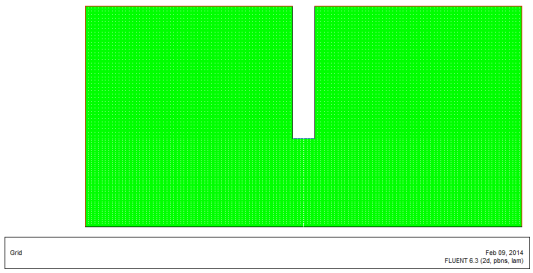

Fig. 1 Overall two-dimensional mesh

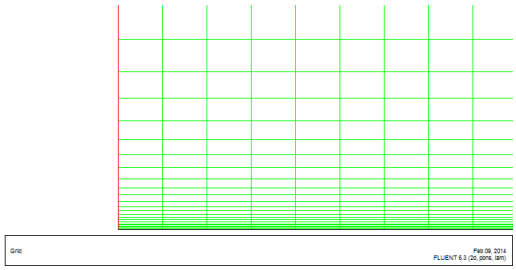

Fig. 2 Mesh encrypted area near the ground

This article is incompressible flow, which can use velocity-inlet boundary. Wherein Velocity Magnitude of 27m / s, Turbulence Specification Method Select Intensity and Hydraulic Diameter, Turbulence Intensity of 1%, Hydraulic Diameter of 900m. Export uses pressure outlet boundary condition. Using Pressure Outlet flow outlet boundary conditions to define the static pressure, when there is a reflux, the boundary conditions used to replace the pressure outlet of the flow boundary conditions often have better convergence results [6]. Gauge Pressure is 0, Backflow Direction Specification Method Select Normal to Boundary. The remaining set is consistent with the speed of the export settings.

## Numerical analysis

Selected as the vertical wind profile from the center line downburst width of 0.5D, 1D, 1.5D, 2D, 2.5D Department, a total of five wind profile, horizontal wind profiles from the ground height of 10m, 50m, 100m, 450m Department, a total of four wind profile. Each vertical wind velocity profile as shown in Fig. 3:

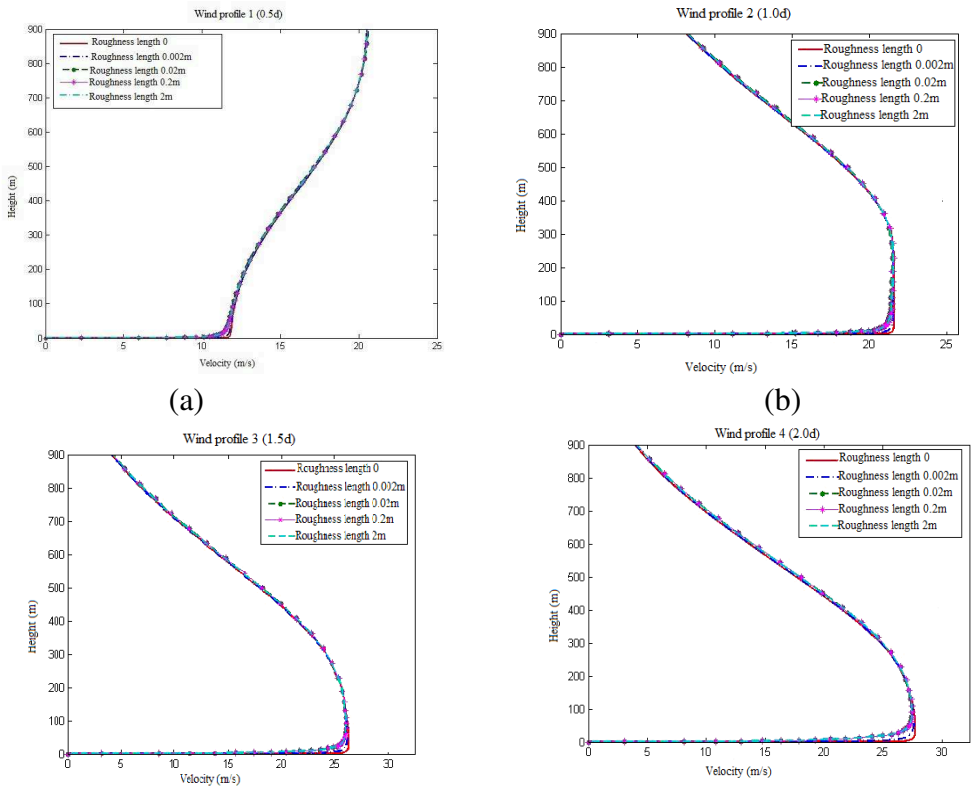


Fig. 3 Each vertical wind velocity profile

Each horizontal wind velocity profile is shown in Fig. 4.

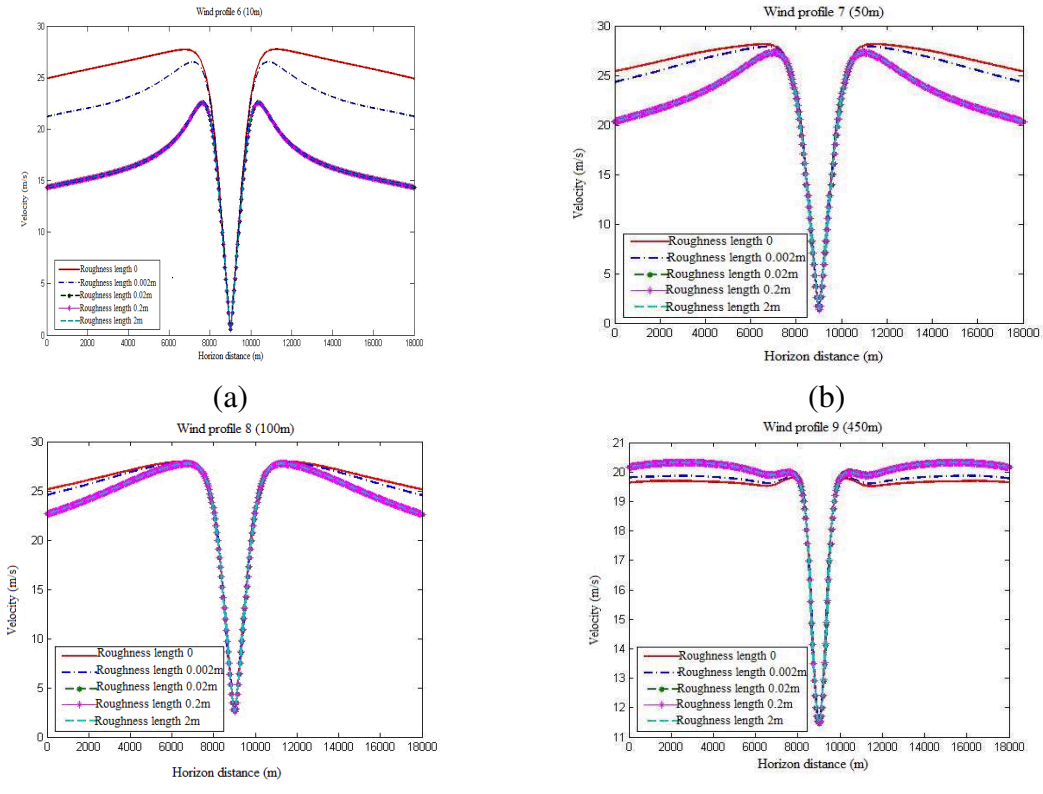


Fig. 4 Each horizontal wind velocity profile

## Conclusions

Based on impinging jet theory, numerical simulation of two-dimensional downburst wind farm built on FLUENT software, by setting different surface roughness conditions, the influence of the roughness conditions downburst wind profile. The study results the following conclusions:

(1) From the vertical wind profile, the effects of roughness on the downburst wind loads are mainly in the area near the ground below 100m , with the increase in the height of the surface roughness of the gradual reduction , when the height of more than 100m altitude , rough a small degree of influence on the wind speed .

(2) From the horizontal wind profile view, away from the center line downburst approximately 1000m ( approximately 1D) within the range of roughness less impact on the wind, when the outside this range, the roughness on the wind speed was become more apparent.

(3) Wind conditions on the effects of surface roughness downburst wind loads , not completely change with changes in the length of the rough , the local table type of class Ⅰ topography ( ie roughness length 0.002m) , the roughness on the wind small, local table type Ⅱ, Ⅲ, Ⅳ class topography ( ie roughness length of 0.02m, 0.2m, 2m), the effects of roughness on the wind speed is no longer with the roughness changes.

## Acknowledgements

This work is supported by National students' innovation and entrepreneurship training program(20131049706005), National Natural Science Foundation of China (51308430),the Specialized Research Fund for the Doctoral Program of Higher Education of China (No.20110143120003) and the Fundamental Research Funds for the Central Universities (WUT:2013-IV-019).

## References

[1] Fujita T.T. The downburst report of Projects NIMROD and JAWS[R]. Chicago :University of Chicago, 1985.

[2] Holmes J.D. Modeling of extreme thunderstorm winds for wind loading of structures and risk assessment[C]//Wind Engineering into 21st Century, Proceedings, 10th International Conference on Wind Engineering,Copenhagen,Denmark.1999:1409-1415.

[3] Yuanchang Deng, Sha Liu, Zhi Yu, Xuelan Zeng , CFD simulation of the actual impact of the wind farm terrain roughness analysis [J] Solar Technology, 2010,31 (12) 1645-1648.

[4] Chay M.T. Letchford C.W. Pressure distributions on a cube in a simulated thunderstorm downburst -Part A: Stationary downburst observations[J]. Journal of Wind Engineering and Industrial Aerodynamics, 2002, 90(7):711-732.

[5] Blocken B, Stathopoulos T, Carmeliet J. CFD simulation of the atmospheric boundary layer: Wall function problems [J]. Atmospheric Environment,2007, 41(2):238-252.

[6] Zhanzhong Han, Jing Wang, Xiaoping Lan .FLUENT fluid engineering simulation examples and application (first edition) [M] Beijing: Beijing Institute of Technology Press, 2004:1-22.

*Applied Mechanics and Materials Vols. 580-583 (2014) pp 2962-2965*
*© (2014) Trans Tech Publications, Switzerland*
*doi:10.4028/www.scientific.net/AMM.580-583.2962*

# The Study on Differential Equations Method for Solving Column-Pile Structural System Internal Forces

Decheng Fu [1,2, a], Yuhui Wen[2, b], Lei Wang[1, c]

[1]College of Construction Engineering, Jilin University, Changchun 130021, China;

[2]The Department of Architectural and Engineering, Jilin Province Economic Management Cadre College, Changchun 130012, China

[a]fudecheng@126.com, [b]yuhui_wen@126.com, [c]wlei@jlu.edu.cn

**Keywords:** differential equations; column-pile; boundary conditions.

**Abstract.** Based on material mechanics theory that loads-internal force-deformation relationship of rod, this paper establish elastic foundation beam model, and establish loads-internal force-deformation differential equation of piles and columns, and identified boundary conditions according to mechanical analysis of piles and columns, Based on the boundary conditions, deformation coordination and internal force equilibrium conditions, solving differential equations, then obtain column - pile components' internal forces. This method has good mechanical model support, and using mathematical computing software can derive the analytical expressions.

## Introduction

Generally, bridge column - pile foundation shared lateral load[1], Column - pile structure, Elastic foundation beam method usually be used to calculate internal force of pile foundation, in this method ,the soil computing unit between piles structure be treated as a beam on elastic foundation, Displacement of components make the soil compression, soil resistance for components. There are many method to solve elastic foundation beam model, such as semi-analytical methods, finite element method and finite difference method. Internal forces of columns can be solved by cross-sectional method, and using the formula method for solving the deformation. This method is not easy for practice, and the formula derivation process is complex. Many researchers study the solving method of piles with horizontal loads, Guo etc.[2]and Basu etc.[3]use variation method to calculate the internal forces and displacements of piles with horizontal loads. Zhou etc[4]. get elastic modulus of soil with different stress states through analyzing p-y curve. Zhao writ an improved layer- finite calculation program for solve piles with horizontal loads. Poulos assuming soil is elastic continuous medium, considering the pile-pile, pile-soil interaction, using the interaction coefficients method to analysis group pile.

Differential relationship of load-internal force-deformation already established in mechanics of materials, but it only applies to solve the internal forces and deformation of a member. This paper establish differential equations to solve internal force and deformation of column-pile structure.

## Establish differential equation

### 1.1 Differential equation of column

The vertical rod differential equations has been established in material mechanics, the column differential equations is same as it.as follows:

$$\frac{dx_z}{dz} = \theta \tag{1}$$

$$EI\frac{d\theta}{dz} = M \tag{2}$$

$$\frac{dM}{dz} = Q \tag{3}$$

$$\frac{dQ}{dz} = q \tag{4}$$

Where $x_z$ is horizontal displacement perpendicular column axis, $z$ is column length, $\theta$ $\theta$ is rotation angle of axis, $M$ is moment, $Q$ is shear force. Combining Eq.1, Eq.2 Eq.3, Eq.4, to obtain the column differential equations as follows:

$$E \cdot I \cdot \frac{d^4 x_z}{dx^4} = -q(x) \tag{5}$$

### 1.2 Differential equations of pile

According to the above principle, We can draw differential equations of pile, as follows:

$$E \cdot I \cdot \frac{d^4 x_z}{dz^4} + m \cdot z \cdot x_z \cdot b_1 = 0 \tag{6}$$

Where $m$ is coefficient,$b_1$ is width of pile.

Differential equation of column is different with pile's, With the change in the soil, M value also vary, When the size of the column section change, I value changed. E value varies with the material change. Q values vary if there have a force applied to the column, M values vary if there have a moment applied to the column. Therefore, establishing differential equations must based on the actual situation.

## Boundary conditions

### 2.1 Pile bottom boundary conditions

When the external force applied on the structural system, pile bottom line displacements and rotations occur. Using the relationship between the soil resistance and rotation angle of the pile to create a boundary condition, as follows:

$$EI\frac{d^2 x_z}{dz^2} = -\frac{dx_z}{dz} \cdot C_0 \cdot I_0 \tag{7}$$

Where z=h, h is length of pile, $C_0$ is soil factor, $I_0$ moment of inertia.

Shear force of the friction piles bottom is 0, the boundary condition is shown as follows:

$$EI\frac{d^3 x_z}{dz^3} = 0 \tag{8}$$

### 2.2 Column top boundary conditions

When the top of column is free, upper structure applied bending moment C1 and shear force C2 to the top of the column, the boundary condition is shown as follows:

$$\begin{cases} EI\dfrac{d^2x_z}{dz} = C_1 \\ EI\dfrac{d^3x_z}{dz^3} = C_2 \end{cases} \tag{9}$$

When the top of column is elastic embedding, upper structure applied shear force C2 to the top of the column, and rotation angle of column top is 0, the boundary condition is shown as follows:

$$\begin{cases} \dfrac{dx_z}{dz} = 0 \\ EI\dfrac{d^3x_z}{dz^3} = C_2 \end{cases} \tag{10}$$

### Caps border coordination condition

Based on the assumption of rigid cap, the cap only occur rigid translational and rotation, Caps is rigid, so horizontal displacement and rotation angle of each pile is equal, the border coordination condition is shown as follows:

$$\begin{cases} x_{zA} = x_{zB} \\ \dfrac{dx_{zA}}{dz} = \dfrac{dx_{zB}}{dz} \end{cases} \tag{11}$$

Axial displacement of the pile caused by cap rotation and vertical deformation, vertical displacement of the pile which caused by vertical deformation of cap is equal, the vertical displacement causes by rotation angle is equal to product of cap rotation angle and the distance between pile and cap center. Establishing the border coordination condition as follows:

$$u_{zA} - l \cdot \frac{dx_{zA}}{dz} = u_{zB} + l \cdot \frac{dx_{zB}}{dz} \tag{12}$$

### Internal forces balance relationship

Caps and columns - pile internal force analysis diagram shown in Fig. 1, Establishing level, vertical, rotating balance equation as follows:

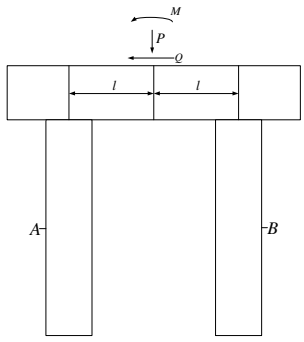


Fig.1 Caps and columns-pile internal force analysis diagram

$$E \cdot I_A \frac{d^3 x_{zA}}{dz} + E \cdot I_B \cdot \frac{d^3 x_{zB}}{dz} = Q \tag{13}$$

$$E \cdot A_A \cdot \frac{du_A}{dz} + E \cdot A_B \cdot \frac{du_B}{dz} = P \tag{14}$$

$$E \cdot A_A \cdot \frac{du_A}{dz} \cdot l + E \cdot A_B \cdot \frac{du_B}{dz} \cdot l + E \cdot I_A \cdot \frac{d^2 x_{zA}}{dz^2} + E \cdot I_B \cdot \frac{d^2 x_{zB}}{dz^2} = M \tag{15}$$

## Conclusion

In this paper, the column-pile components are divided according to the differential equation, establishing a differential equation for each unit, Based on the boundary conditions, deformation coordination and internal force equilibrium conditions, solving differential equations, then obtain column - pile components' internal forces.

Compared with traditional methods, this method has good mechanical model support, and using mathematical computing software can derive the analytical expressions. This method can be used to calculate internal forces of column-pile structure, it's able to simplify the calculation process and improve calculation accuracy.

## References

[1] Huaming Zhao etc.: Foundation Engineering [M]. Higher Education Press.(2010)

[2] Guo W D，Lee F H:Load Transfer Approach for Laterally Loaded Piles[J]. International Journal for Numerical and Analytical Methods in Geomechanics.(2001)

[3] Basu D，Salgado R: Analysis of Laterally Loaded Piles with Rectangular Cross Sections Embedded it Layered Soil [J]. International Journal for Numerical and Analytical Methods in Geomechanics.(2008)

[4] Qionghua Lai: P-S Curve Calculation Method of Pile[J].Chinese Journal of Geotechnical Engineering.(2003)

*Applied Mechanics and Materials Vols. 580-583 (2014) pp 2966-2969*
*© (2014) Trans Tech Publications, Switzerland*
*doi:10.4028/www.scientific.net/AMM.580-583.2966*

# Theory of Duality Disturbance of Elastoplasticity

Jiemin Liu[1,a], Shuang Liu[1,b], Jialiang Yang[2,c], Yazhen Sun[1,d]

[1]School of Science, Shenyang Jianzhu University, Shenyang, 110168, China

[2]School of Civil Engineering, Shenyang Jianzhu University, Shenyang, 110168, China

[a]liujiemin1954@163.com, [b]liush0229@163.com, [c]yangjl0912@163.com, [d]syz16888@126.com

**Keywords:** duality disturbance, elastoplasticity, relatively non-disturbed material, relatively complete disturbed material.

**Abstract.** The basic thinking, basic assumptions and basic formula system of duality disturbance theory are given in this paper. The theoretical and practical implications of duality disturbance theory are analyzed. The principles of the method of selecting the Stress-Strain relationships of relative non-disturbance material and relative complete disturbance material are given.

## Introduction

Theory of Duality Disturbance (TDD) is a theoretical model of simulating deformable solid bodies mechanical behavior proposed by the author of the paper [1-4]. The basic thinking, basic assumptions and formula system are completely described in this paper. The purpose by doing this is offering help for researchers are interested in TDD in terms of understanding, application developing the TDD.

The traditional deformable solid bodies had elastic, mechanical models of elastoplastic, viscoelasticity and damage models [5-7]. Those models can simulate the mechanical behavior of deformable solid bodies under different research levels, and solve a lot of engineering problems. However, the above models can not predict effectively complexed mechanical behavior material such as strain softening and after-softening-re-hardening materials. TDD can predict and simulate the mechanical behavior of the materials of complexed stress-strain relationship.

## Basic assumptions

Basic assumptions used in TDD are that the mechanical properties of engineering material in service will be changed in comparison to the initial state. The change may be degradation, or hardening. The material changed in properties is called disturbed material. The Ultimate degradation State of the disturbed material is called complete disturbed state. Ideal initial state is considered as complete elastic static, called as ideal non-disturbed state. However, both the ideal non-disturbed state and the complete disturbed state are not exist in nature. Thus the concepts of relative non-disturbed state and relative complete disturbed state are introduced. TDD assumes that the mechanical behavior of disturbed material can be described by relative non-disturbed (RND) material and relative complete disturbed (RCD) material. Disturbed tensor $\boldsymbol{D}$ is considered as a bridge connected RND material and RCD material. Disturbance D expresses a diverge from relative non-disturbed stress $\boldsymbol{\sigma}^{\mathrm{n}}$ to obverse stress $\boldsymbol{\sigma}^{\mathrm{o}}$. The relationship among $\boldsymbol{D}$, $\boldsymbol{\sigma}^{\mathrm{n}}$, $\boldsymbol{\sigma}^{\mathrm{o}}$ and $\boldsymbol{\sigma}^{\mathrm{c}}$ can be expressed as

$$\boldsymbol{\sigma}^{\mathrm{o}}=\left(\boldsymbol{I}-\boldsymbol{D}\right)\cdot\boldsymbol{\sigma}^{\mathrm{n}}+\boldsymbol{D}\cdot\boldsymbol{\sigma}^{\mathrm{c}} \tag{1}$$

The disturbance tension $\boldsymbol{D}$ can be degenerated as a scalar $D$. For uniaxial state, the relation among observed stress $\sigma^{\mathrm{o}}$, RND stress $\sigma^{\mathrm{n}}$, RCD stress $\sigma^{\mathrm{c}}$ and $D$ is expressed as Eq.2 and shown as in Fig.1.

$$D=\frac{\sigma^{\mathrm{n}}-\sigma^{\mathrm{o}}}{\sigma^{\mathrm{n}}-\sigma^{\mathrm{c}}} \tag{2}$$

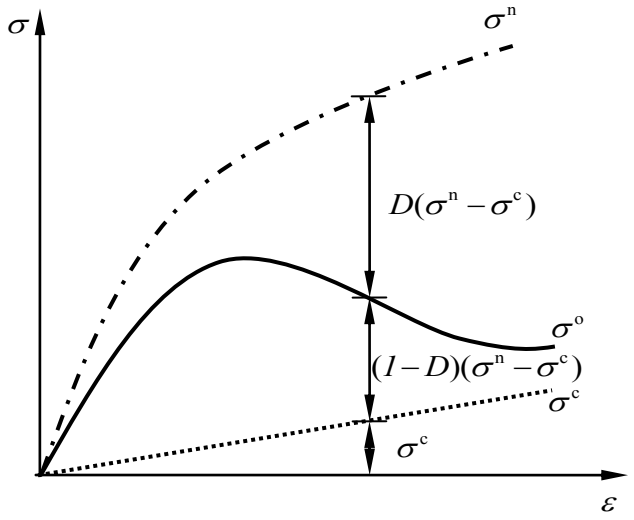


Fig.1 The relation among $D$, $\sigma^{o}$, $\sigma^{n}$ and $\sigma^{c}$

Although $D$ can be defined by Eq.2, Eq.1 is not of general significance due to $\sigma^{o}$ not being a monotropic function in the case of un-loading. Therefore, the key of determing $D$ is finding a monotropic vector $\boldsymbol{\alpha}$ which is related to $\boldsymbol{\sigma}^{o}$, $\boldsymbol{\sigma}^{n}$ and $\boldsymbol{\sigma}^{c}$. The relation between $\boldsymbol{D}$ and $\boldsymbol{\alpha}$ can be expressed as

$$\boldsymbol{D} = \boldsymbol{D}(\boldsymbol{\alpha}) \tag{3}$$

From Fig.1, we can see that the condition of verification of Eq.2 is

$$\boldsymbol{\varepsilon}^{o} = \boldsymbol{\varepsilon}^{n} = \boldsymbol{\varepsilon}^{c} = \boldsymbol{\varepsilon} \tag{4}$$

Eq.4 is called as assumption of total strain equivation. Eq.4 expresses that strain tensions $\boldsymbol{\varepsilon}^{o}$, $\boldsymbol{\varepsilon}^{n}$ and $\boldsymbol{\varepsilon}^{c}$ taken placed in disturbed material, RND material and RCD material, respectively, are equal. Further assume that un-loading elastic strain $\boldsymbol{\varepsilon}^{o}$, $\boldsymbol{\varepsilon}^{n}$ under action of $\boldsymbol{\sigma}^{o}$, $\boldsymbol{\sigma}^{n}$ are also equal, that is

$$\boldsymbol{\varepsilon}_{e}^{o} = \boldsymbol{\varepsilon}_{e}^{n} = \boldsymbol{\varepsilon}_{e}^{c} \tag{5}$$

have,

$$\boldsymbol{\sigma}^{o} = \boldsymbol{C}_{e}^{o}\boldsymbol{\varepsilon}_{e}, \quad \boldsymbol{\sigma}^{n} = \boldsymbol{C}_{e}^{n}\boldsymbol{\varepsilon}_{e}^{n}, \quad \boldsymbol{\sigma}^{c} = \boldsymbol{C}_{o}^{c}\boldsymbol{\varepsilon}_{e}^{c} \tag{6}$$

For the uniaxial stress state, Eq.6 is reduced as

$$\sigma^{o} = E_{e}^{o}\varepsilon_{e}, \ \sigma^{n} = E_{o}^{n}\varepsilon_{e}, \quad \sigma^{c} = E_{o}^{c}\varepsilon \tag{7}$$

**Reduced form of disturbance tension $D$**

For anisotropy disturbance, disturbed variable $\boldsymbol{D}$ should be expressed by two-power tensor, as show in Eq.1 and Eq.3. However, it is very difficult to determine $\boldsymbol{D}$ .For isotropy disturbance, disturbed variable $D$ should be a scalar. If scalar $D$ is used to descript the anisotropy disturbance, then the scalar $D$ reflects an average disturbed level of the anisotropy material. Thus, scalar $D$ is of important engineering significance.

Internal variable $\boldsymbol{\alpha}$ in Eq.3 is key of determining disturbed scalar $D$ . Considering the micromechanisms of disturbance caused in engineering material are commonly fracture of atomic bonds (including molecular bond ) and initiation and development of micro-crack, which gives rise to increasing of plastic strain, taking plastic strain tensor $\boldsymbol{\varepsilon}_{p}^{o}$ as the argument of $D$ is reasonable. Thus, Eq.3 is reduced to

$$D = D(\boldsymbol{\varepsilon}_{p}^{o}) \tag{8}$$

The plastic strain $\boldsymbol{\varepsilon}_{p}^{o}$ of disturbed material is difficult to be determined, since unloading information of the disturbed material is difficult to be known. However, under condition of Eq.4, the

plastic strain $\boldsymbol{\varepsilon}_{\mathrm{p}}^{\mathrm{o}}$ of disturbed material will be equal to that $\boldsymbol{\varepsilon}_{\mathrm{p}}^{\mathrm{n}}$ of RCD material, Eq.8 can be further reduced as

$$D = D(\xi^{\mathrm{p}}) \tag{9}$$

$$\xi^{\mathrm{p}} = c\int \mathrm{d}\xi^{\mathrm{p}} = c\int \sqrt{\mathrm{d}\boldsymbol{\varepsilon}^{\mathrm{p}} : \mathrm{d}\boldsymbol{\varepsilon}^{\mathrm{p}}} \tag{10}$$

Where, $\xi^{\mathrm{p}}$ is called as plastic strain trajectory. $\xi^{\mathrm{p}}$ shows the accumulation of plastic strain in whole process of deformation (including loading and unloading processes), which is a increasing function. Eq.10 is applied to three-dimensional stress state. In order to make $\xi^{\mathrm{p}}$ veduced as uniaxial plastic strain $\varepsilon^{\mathrm{p}}$ for uniaxial stress state, the parameter $c = c(\mu)$ is introduced. Where $\mu$ is Poisson's ratio. The condition of determining disturbed variable $D$ increasing is

$$G = \xi^{\mathrm{p}} - \xi_{\max}^{\mathrm{p}} \geq 0 \tag{11}$$

$\xi_{\max}^{\mathrm{p}}$ in Eq.11 is the maximum plastic strain had taken placed in the deflection history.

The concrete form of Eq.9 can be determined according to the observed stress-strain curve (including unloading information), the stress-strain curve of RND material and the stress-strain curve of RCD material [11-12]. $D$ can be expressed commonly as Webull curve shown as

$$D = D_{\mathrm{u}}(1 - \mathrm{e}^{A(\xi_{\mathrm{p}})^{B}}) \tag{12}$$

Where, $D_{\mathrm{u}}$ is ultimate disturbance value, and $A$, $B$ in Eq.12 are disturbed material constant.

Due to both ideal non-disturbed state and ideal complete disturbed state are untouchable ideal models. Selecting reasonable RND & RCD material models are important. Some possible RND material models are shown in Fig.2.

The RND material model of $\sigma_1^{\mathrm{n}}$, $\sigma_2^{\mathrm{n}}$ and $\sigma_3^{\mathrm{n}}$ is linear, bilinear and elastoplastic strengthen model, respectively. The RCD material model express by $\sigma_1^{\mathrm{c}}$, $\sigma_2^{\mathrm{c}}$ and $\sigma_3^{\mathrm{c}}$ is linear, hydrotatic and void model.

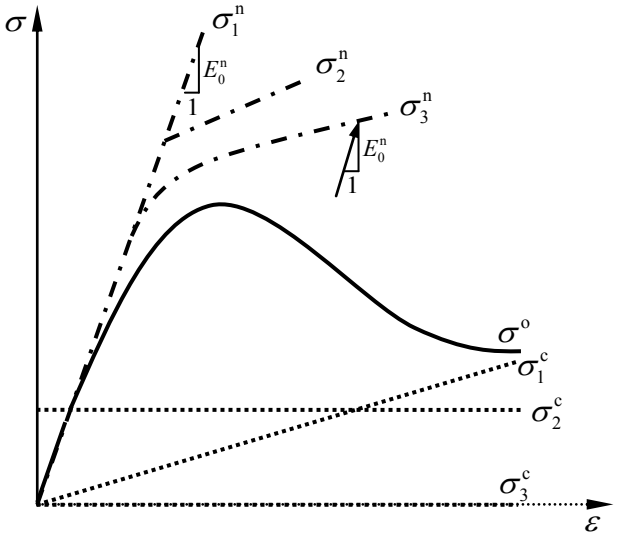


Fig.2 Types of $\sigma - \varepsilon$ curves of RND and RCD material

Although disturbed variable $D$ varies with RND and RCD material models, the varieties of $D$ have little influence for the results of simulating mechanical behavior of disturbed material. This is because that the theory of duality disturbance is self-consistent.

**Applications of TDD**

An important application of TDD is that performing mechanical analysis for softening engineering material based adult elastoplastic finite element method. It was well known that elastoplastic theory is only suitable for strengthen material. It can be used to simulate the mechanical behavior of RND

material model in TDD, such as $\boldsymbol{\sigma}^{n}$, $\boldsymbol{\varepsilon}^{n}$, $\boldsymbol{\varepsilon}_{p}^{n}$ and $\boldsymbol{u}^{n}$. From Eq.2 and Eq.9, stress $\boldsymbol{\sigma}^{o}$ and strain $\boldsymbol{\varepsilon}^{o}$ of disturbed material in uniaxial stress state can be obtained. The solution steps of mechanical behaviors of engineering material based TDD is shown as follows.

1. Set up uniaxial $\sigma^{o}$-$\varepsilon^{o}$ relation (including unloading information);
2. Select RND and RCD material models, set up unit-axial $\sigma^{n}$-$\varepsilon^{n}$, $\sigma^{c}$-$\varepsilon^{c}$ relations;
3. Set up disturbed evolution Eq.9, based Eq.2, Eq.4, Eq.5;
4. Set up the geometry, loading and restrain models of disturbed material;
5. Set up the geometry, loading and restrain models of RND material, which is the same as that of disturbed material;
6. Perform elastoplastic FEA for RND model, obtain $\boldsymbol{\sigma}^{n}$, $\boldsymbol{\varepsilon}^{n}$, $\boldsymbol{u}^{n}$, equivalent stress $\boldsymbol{\sigma}_{eff}^{n}$, equivalent strain $\boldsymbol{\varepsilon}_{eff}^{n}$;
7. Find $\boldsymbol{\sigma}^{o}$, $\boldsymbol{\varepsilon}^{o}$, $\boldsymbol{\varepsilon}_{p}^{o}$, $\boldsymbol{u}^{o}$ from Eq.1, Eq.4 and Eq.5. Find observed external loads exerted on the disturbed material from equivalent cross-section method [8];
8. Further performing strength, stiffness analysis for the disturbed material (member).

## Conclusions

(1) The basic thinking, basic assumptions and basic formula system of TDD are introduced.
(2) The principles of the method of selecting the Stress-Strain relationships of relative non-disturbance material and relative complete disturbance material are given.
(3) The steps performing mechanical analysis for disturbed materials by TDD is given.

## Acknowledgements

This work was financially supported by the fund of subject promotion of Shenyang Jianzhu University.

## References

[1] Jiemin Liu and Yazhen Sun: *Prediction of mechanical behavior of equivalent adhesive-layer using theory of duality of damage* [C]. New York: IMECE(2006)

[2] Jiemin Liu, Zhiyong Zhang and Yazhen Sun: Journal of Shenyang Jianzhu University: Natural Science. Vol. 24 (2008), p. 424 (in Chinese)

[3] Jiemin Liu, Zhongkui Guo and Yazhen Sun. Journal of Shenyang Jianzhu University: Natural Science. Vol. 25 (2009), p. 1084 (in Chinese)

[4] Jiemin Liu. Journal of Harbin Institute of Technology. Vol. 43 (2011), p. 213 (in Chinese)

[5] Zhuping Huang: Foundation of continuum mechanics [M]. Beijing: Publisher of Higher Education (2004) (in Chinese)

[6] Yazhen Sun and Jiemin Liu: *Coupling analysis of fracture mechanics and damage mechanics for fiber-reinforced asphalt concrete pavements* [C]. New York: IMECE (2006)

[7] Grassl P, Jirasek M. International Journal Solids and Structures. Vol. 43 (2006), p. 7166

[8] Jiemin Liu: Mechanical of Materials [M]. Beijing: China Power Press (2011) (in Chinese)

*Applied Mechanics and Materials Vols. 580-583 (2014) pp 2970-2973*
*© (2014) Trans Tech Publications, Switzerland*
*doi:10.4028/www.scientific.net/AMM.580-583.2970*

# Thermocapillary Convection of Low Prandtl Number Fluids Under Uniform Magnetic Fields

Ruquan Liang[1,a], Di Bei[1], Fusheng Yan[2], Dianqiao Geng[1]

[1]Key Laboratory of National Education Ministry for Electromagnetic Processes of Materials, Northeastern University, No.3-11, Wenhua Road, Shenyang 110819, China

[2]Research Academy, Northeastern University, No.3-11, Wenhua Road, Shenyang 110819, China

[a]liang@epm.neu.edu.cn

**Keywords:** Thermocapillary convection, Low Pr number fluid, Liquid bridge, Uniform magnetic field

**Abstract.** Numerical simulations on thermocapillary convection of low Pr number molten tin under uniform magnetic field have been conducted under microgravity. The Navier-Stokes equations coupled with the energy conservation equation are solved on a staggered grid, and the free surface is captured by using the level set method. The present results show that the transverse uniform magnetic field can restrain the thermocapillary convection, and the fluid velocity at the hot corner fluctuates with a constant frequency at the steady state.

## Introduction

The floating zone method is widely used in the preparation of crystalline material, which avoids contamination of the crucible wall to materials and greatly enhances the purity of the material products. Because natural convection tend to disappear under microgravity, the cross-sectional area and height of the floating zone increase significantly, and the floating zone method can be widely used in growing large single crystals in microgravity. An important topic in the floating zone method is the thermocapillary convection induced by the temperature gradient on the free surface, which may result in the striation on the crystal surface and degrade the quality of the crystals. Therefore, it is important to understand the flow mechanism and control thermocapillary convection. The static magnetic field can suppress effectively thermocapillary convection and decrease the generation of crystal surface streaks, which can improve the quality of the crystal.

In 1996, Chedzey and Hurle investigated the effect of magnetic field on the crystal growth firstly [1]. The main effect of the static magnetic field is to inhibit the melt convection and lower convection velocity of the melt, so the quality of the generating crystal is improved to some extent. Kimura et al. [2] studied the effects of transverse magnetic field on the growth of doped silicon single crystal. The shape of growth interface of crystals tends to be flat in 0.18T magnetic field strength. However, when the magnetic field strength was increased to 0.55T, the growing interface tends to be flat and the layer of interfacial diffusion to be thicker, but there is no inhibition on the growth of impurities stripes. Dold et al. [3] studied the growth of silicon crystals in the axial static magnetic field, and they can get elemental silicon crystal of almost no streaks when the magnetic field strength is higher than 240mT. Pablo and Rivas [4] studied numerically the floating zone melt convection that was in uniform axial magnetic field of moderate-intensity under micro-gravity and analyzed the influence of magnetic field strength and temperature difference on the approximate static area of the center of the floating zone. They got the conclusions that with the increase of the magnetic field strength, the central region was extended and the shape of the central region was more similar to the cylindroid in smaller temperature difference. Although many experiments and numerical calculations have been conducted to study the mechanism of the thermocapillary convection in liquid bridges and verified the effects of static magnetic fields, the most existing studies ignored the effects of free surface deformation of liquid bridges. In this paper, the free surface deformation of liquid bridges and the ambient air will be considered to investigate thermocapillary convection in liquid bridges of low Pr molten metal under the static magnetic fields.

**Physical and Mathematic Models**

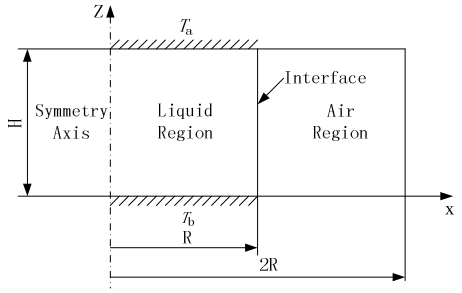


Fig. 1. Schematic of a half-zone liquid bridge model

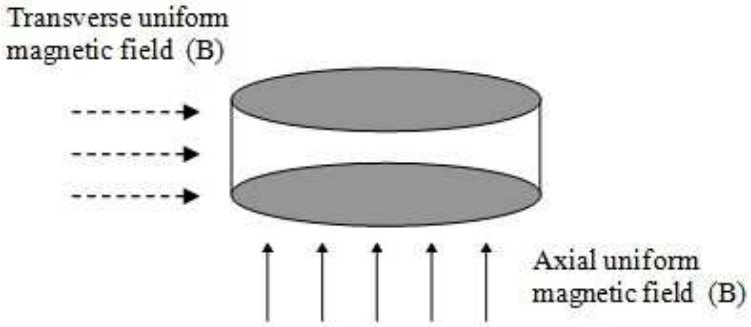


Fig. 2. Schematic of a uniform magnetic field

In our investigation, a liquid bridge with radius R and height H is suspended between two coaxial disks and surrounded by the air in a rectangular container with height H and diameter 4R as shown in Fig.1. The temperature difference between the two disks is $\Delta T=T_t-T_b$, where $T_t$ and $T_b$ are the temperature of the upper and lower rods, respectively.

Figure 2 shows an axial and a transverse uniform magnetic fields. This paper mainly studies the effects of the uniform magnetic field on the thermocapillary convection of the liquid bridge.

Based on the above physical model, we can get the dimensionless equations of the liquid bridge under uniform magnetic fields, which are outlined below.

$$\rho[\vec{u}_t+(\vec{u}\cdot\nabla)\vec{u}]=-\nabla p+\frac{1}{\mathrm{Re}}\nabla\cdot(2\mu D)+\left(\frac{1}{\mathrm{We}}-\frac{\mathrm{Ca}}{\mathrm{We}}\Theta\right)\kappa\delta(d)\vec{n}+\frac{\mathrm{Ha}^2}{\mathrm{Re}}(\vec{U}\times\vec{B}\times\vec{B}) \tag{1}$$

$$\nabla\cdot\vec{u}=0 \tag{2}$$

$$\frac{\partial\Theta}{\partial t}+\nabla\cdot(\vec{u}\cdot\Theta)=\frac{1}{\mathrm{Re}\,\mathrm{Pr}}\nabla^2\Theta \tag{3}$$

$$\frac{\partial\phi}{\partial t}+\vec{u}\cdot\nabla\phi=0 \tag{4}$$

(4)

where $\vec{u}=(u,v)$ is the fluid velocity, $\rho=\rho(\vec{x},t)$ is the fluid density, $\mu=\mu(\vec{x},t)$ is the fluid viscosity, D is the viscous stress tensor, $\kappa$ is the curvature of the interface, $d$ is the normal distance to the interface, $\delta$ is the Dirac delta function, $\vec{n}$ is the unit normal vector at the interface, $p$ is the pressure. The surface tension coefficient is considered to be a linearly function of temperature and defined as $\sigma=\sigma_c-\sigma_T(T-T_b)$, where $\sigma_c$ is a reference value of surface tension and $\sigma_T$ is the temperature coefficient of surface tension and we denote $\sigma_T=\partial\sigma/\partial T$, and $T$ is the temperature. $\mathrm{Re}=\rho_l U_\infty \bar{L}/\mu_l$, Reynolds number, $\mathrm{We}=\rho_l U_\infty^2 \bar{L}/\sigma$, Weber number, $\mathrm{Pr}=\mu_l/\rho_l a$, Prandtl number, $Ca=\sigma_T(T_{high}-T_{low})/\sigma_c$, Capillary number, $\mathrm{Ma}=\sigma_T\Delta T\bar{L}/\mu_l a=\mathrm{Re}\,\mathrm{Pr}$, Marangoni number, $\Theta=(T-T_{low})/(T_{high}-T_{low})$, excess temperature, $\mathrm{Ha}=\mathrm{B}_0\bar{L}\sqrt{\beta/\mu_l}$, Hartman number, $a$ is the thermal diffusivity. $U_\infty$ is the characteristic velocity and we take $U_\infty=\sigma_T\Delta T/\mu_l$ under microgravity. $\bar{L}$ is the characteristic length and we take $\bar{L}=2R$. $\phi$ is the level set function.

The Lorentz force generated by the magnetic field is **F** = **J** × **B**, where **J** is the current density vector defined by **J** =$\beta$ ($-\nabla\varphi+$ **U** × **B**), where $\beta$ is the electric conductivity of the liquid, $\varphi$ is the induced electric potential, **U** is the velocity vector. For axial magnetic fields and axisymmetric flows in 2 dimensional cases, no electric potential is induced, hence the Lorentz force reduces to **F** = $\beta$ (**U** × **B**) × **B** [5].

The present mesh adopted is a staggered grid, and the equations of motion are solved by the SIMPLE algorithm. At the same time, the CSF (Continuum Surface Force) model is adopted to calculate the surface tension on the free surface.

## Results and Discussion

The present mathematical and physical models can be applied to numerically simulate the thermocapillary convection in a static magnetic field. The diameter and aspect ratio of the liquid bridge considered are D=5.0mm and H/R=1, respectively. The temperatures of the upper and bottom disks are $T_a$=730K and $T_b$=705K, respectively. The density and viscosity of molten tin are $\rho_g = 6793kg/m^3$ and μ=$1.318\times10^{-3} Pa\cdot S$, respectively, and the density ratio and viscosity ratio of gas phase and liquid phase are $\rho_g / \rho_l = 1.795\times10^{-3}$ and $\mu_g / \mu_l = 1.37\times10^{-2}$, respectively; and Pr=0.09, Re=2000, Ma=20, We=118, Ca=0.005, B=0.01, Ha=3.

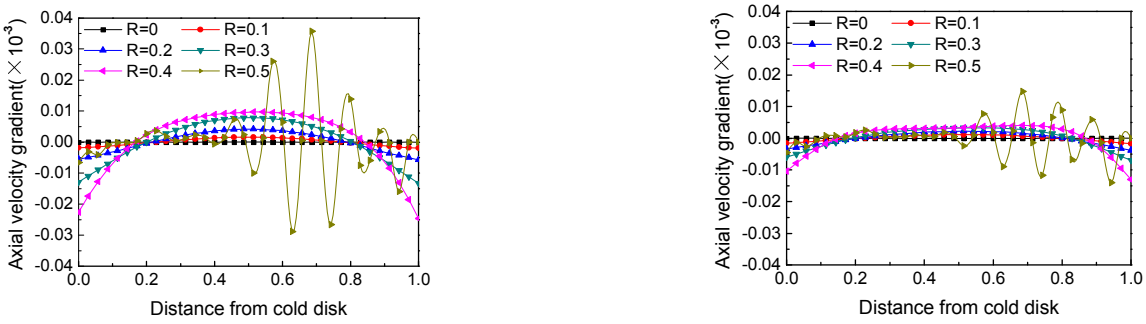


(a) B=0.01T (b) B=0.1T

Fig.3. Axial velocity gradient at different radius positions

Figure 3 Shows the distribution of the axial velocity gradient at different radius under transverse uniform magnetic field, where R = 0 represents the center axis of the liquid bridge, R = 0.5 means the free surface of liquid bridge. From the Fig. 3(a) we can see that the distribution of the axial velocity gradient at different radius is different. The velocity gradient at the center area of the liquid bridge (R=0 and R=0.1) is constant almost. The velocity gradient at the interlayer (R=0.2, R=0.3 and R=0.4) increases first and then decreases with the increasing of the distance from the cold disk. At the free surface(R=0.5) the velocity gradient fluctuates slightly at the distance from the cold disk less than 0.4, however, as the distance increases to 0.4 or more, the velocity gradient fluctuates greatly. Comparing Fig. 3(a) (B=0.01T) with Fig. 3(b) (B=0.1T), it also can be found that as the increasing of the transverse uniform magnetic field strength, all the velocity gradients at various radius decrease, indicating that the transverse uniform magnetic field suppresses the thermocapillary convection inside the liquid bridge.

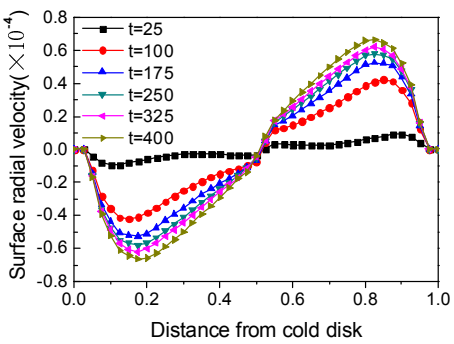


Fig.4 Surface velocity distribution in radial direction

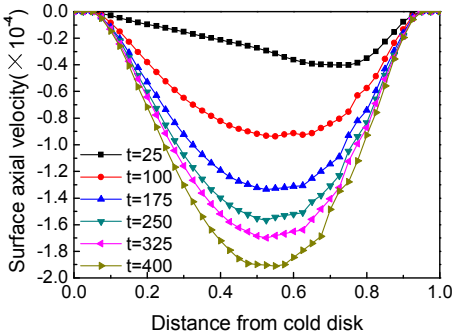


Fig.5 Surface velocity distribution in axial direction

Figure 4 characterizes the surface velocity distribution in radial direction of the liquid bridge at different times under an axial uniform magnetic field. We find that the surface velocity in radial

direction is negative in the positions below the mid-height, and it is positive in the positions above the mid-height. The maximum value of the radial velocity can be obtained at the distances away from the cold disk H=0.2 and H=0.8, respectively. As the development of thermocapillary convection, the value of radial velocity increases, and it reaches steady state until t=400.

Figure 5 characterizes the surface velocity distribution in axial direction of the liquid bridge at different times under an axial uniform magnetic field. We can see that the axial velocity is negative at all times, indicating that the surface flow of liquid bridge flows from the hot disk to the cold disk. Over the time, the maximum value of the axial velocity moves gradually from the hot disk to the midheight of the liquid bridge, and the value also increases. At the distance from cold disk being around 0.7, there are some floating-points, which is due to the effect of hot corner.

The hot corner is a launching point of thermocapillary convection and an important affecting factor to the thermocapillary convection. However, the thermocapillary convection in the hot corners is complex. Figure 6 shows the axial velocity distribution at the hot corner of the liquid bridge in a steady state. It can be observed that the value of the axial velocity at the hot corner is not constant, and the value fluctuates with an amplitude and the frequency is constant approximately. From Fig. 7 we can find that the radial velocity distribution has the same characteristics with that in the axial direction.

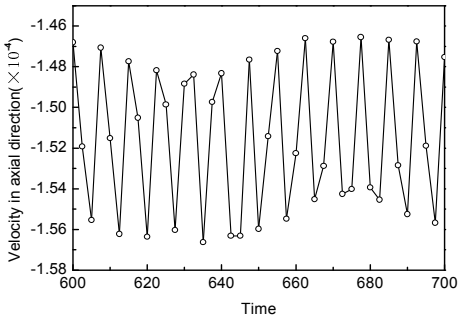


Fig. 6 Axial velocity distribution at hot corner

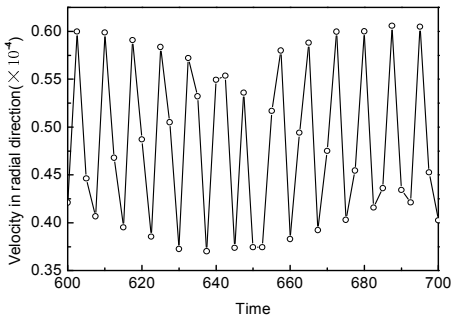


Fig. 7 Radial velocity distribution at hot corner

## Conclusions

This paper takes the molten tin as the object to study thermocapillary convection in the liquid bridge under the uniform magnetic field. It is found that the transverse uniform magnetic field can restrain the thermocapillary convection. Over the time, thermocapillary convection in the liquid bridge becomes gradually a stable state, and the center of thermocapillary convection moves from the hot disk to the mid-height of the liquid bridge. Thermocapillary convection mainly concentrates near the surface of the liquid bridge due to the effect of the axial uniform magnetic field. The velocity at the hot corner fluctuates with a constant frequency at the steady state.

## Acknowledgements

The present work is supported financially by the National Natural Science Foundation of China under the grants of 11072057, 51376040, and 51304038.

## References

[1] H.Chedzey, D.Hurle: Nature Vol.210(1996), p. 933-934.
[2] S.Nakamura, T.Hibiya, K.Kakimoto, N.Imaishi, S.Nishizawa, A.Hirata, K.Mukai, S.Yoda and T.S.Morita: Journal of Crystal Growth, Vol.186(1998), p. 85-94.
[3] P.Dold, A.Croll, K. Benz: Journal of Crystal Growth, Vol.183(1998), p.545-553.
[4] D.P. Valentín, R. Damián : Advances in Space Research, Vol.36( 2005),p.48-56.
[5] M.Prange, M.Wanschura, H.C.Kuhlmann, H.J.Rath: Journal of Fluid Mechanics, Vol.394(1999), p. 281–302

*Applied Mechanics and Materials Vols. 580-583 (2014) pp 2974-2977*
*© (2014) Trans Tech Publications, Switzerland*
*doi:10.4028/www.scientific.net/AMM.580-583.2974*

# Two-dimensional problem moisture elasticity for inhomogeneous flat annular area

Anatoly S. Avershyev[a],Vladimir I. Andreev[b],

Russia, 129337 Moscow, Jaroslavskoje Sh., 26, MGSU

[a]fullbuss-@mail.ru,[b] asv@mgsu.ru

**Keywords:** plane problem, moisture transfer, moisture elasticity, inhomogeneity, forced deformation, thick-walled shell, numerical-analytical calculation method, clay

**Abstract.**The numerical-analytical solution of the non-axisymmetric problem of moisture-elasticity for hollow cylindrical soil massive is provided. We consider the steady-state water transfer. Inhomogeneity of the array due to the dependence of the deformation modulus on the soil moisture. Stress state of the array caused by forced deformations and uneven pressure rebuff of the soil. The method for solving non-axisymmetric problems with radial inhomogeneity in polar coordinates is described. Diagrams on the stress fields in homogeneous and inhomogeneous formulations of the problem are provided. In the paper made a comparative assessment of the impact on the stress state of the power factors and inhomogeneity of the soil

## Introduction

This paper considers the problem of determining the stresses within the soil mass resulting from the process of swelling from moisture penetrating from the ruptured pipe deep into the array.If there is clearancebetween ground and the tube the liquid at first is distributed along the tube and then begins to penetrate into the soil.Thus the problem of moisture conductivity is axisymmetric. At the same time the problem of determining the stress field caused by the swelling of the soil as well as by rebuff of ground will be two-dimensional.Feature of the work is the account of own weight of soil, as well as depending its deformation characteristics on the humidity.

## Problemsetting

Spread of moisture in stationary one-dimensional mode is described byequality:

$$w(\rho) = \frac{w_0 \cdot \ln(\rho/\rho_a) - w_s \cdot \ln(\rho/\rho_b)}{\ln(\rho_b/\rho_a)}. \qquad (1)$$

Here $\rho = r/a$ - the dimensionless radius, $a$ and $b >> a$ - the inner and outer radii of the array (Fig. 1).

For clays relationship between forced deformities of swelling and humidity is practically linear [2] – $\varepsilon_f = \beta(w - w_s)$ and is determined by the swelling coefficient β. The dependence of the modulus of elasticity of moisture $E$ ($w$) described in [1, 2]:

$$E(w) = E_0 \cdot (w/w_s)^{-\gamma}, \qquad (2)$$

where$E_0$ = 19.88 MPa – deformation's modulus of unsaturated clay,$w_s$ = 0.363 – humidity of unsaturated clay,γ = 2.4.

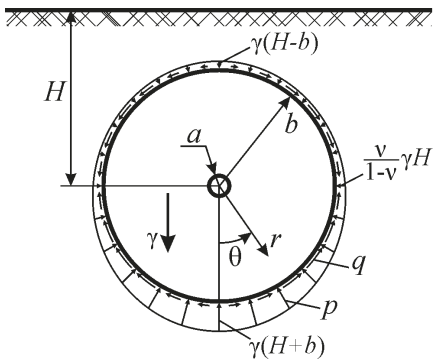


Fig 1. Loading system for solving the problem of stress distribution near an underground cylindrical cavity.

In calculating the stresses we consider a cylindrical hole, located at an average depth (Fig. 1) when $H \cong b$. In this case the normal ($p$) and shear loads ($q$) attached to the outer surface of the cut of the array will not be axisymmetric.The resultant of external pressure balances the weight of the cut volume, i.e. problem should be solved taking into account the volume forces which equal to the specific gravity of the

breed γ [3].Below is the solution for the following geometrical characteristics: $a$ = 0.25 m, $b$ = 2.5 m, $H$ = 5 m. As soil we selected clay which is characterized by the following parameters [1, 4]: $w_s$ = 0.363; $w_0$= 0.2; $\gamma_s$ = 26.95 kN/m3; β = 0.6 - coefficient of linear expansion of moisture; ν = 0.4, the function $E$ ($w$) is described by equation (2).

Boundary conditions on the inner and outer surfaces of the array are of the form:

$$r = a: \quad \sigma_r = 0; \quad \tau_{r\theta} = 0, \tag{3}$$

$$r = b: \quad \begin{cases} \sigma_r = -\dfrac{\gamma \cdot H}{2(1-\nu)} - \dfrac{3-2\nu}{4(1-\nu)} \cdot \gamma \cdot b \cdot \cos\theta - \dfrac{1-2\nu}{2(1-\nu)} \cdot \gamma \cdot H \cdot \cos 2\theta - \dfrac{1-2\nu}{4(1-\nu)} \cdot \gamma \cdot b \cdot \cos 3\theta; \\ \tau_{r\theta} = \dfrac{1-2\nu}{4(1-\nu)} \cdot \gamma \cdot (b \cdot \sin\theta + 2H \cdot \sin 2\theta + b \cdot \sin 3\theta). \end{cases} \tag{4}$$

Bulk forces due to own weight, equal

$$R = \gamma \cdot \cos\theta; \quad \Theta = -\gamma \cdot \sin\theta. \tag{5}$$

We seek a solution of the problem in terms of displacements. Expressions for the stresses in terms of displacements

$$\sigma_r = \lambda \cdot \left( \frac{\partial u}{\partial r} + \frac{u}{r} + \frac{1}{r} \cdot \frac{\partial v}{\partial \theta} \right) + 2\mu \cdot \frac{\partial u}{\partial r} - 3K \cdot \varepsilon_f; \tag{6}$$

$$\sigma_\theta = \lambda \cdot \left( \frac{\partial u}{\partial r} + \frac{u}{r} + \frac{1}{r} \cdot \frac{\partial v}{\partial \theta} \right) + 2\mu \cdot \left( \frac{u}{r} + \frac{1}{r} \cdot \frac{\partial v}{\partial \theta} \right) - 3K \cdot \varepsilon_f; \tag{7}$$

$$\tau_{r\theta} = \mu \cdot \left[ r \cdot \frac{\partial}{\partial r} \left( \frac{v}{r} \right) + \frac{1}{r} \cdot \frac{\partial u}{\partial \theta} \right], \tag{8}$$

where $\lambda = \dfrac{E \cdot \nu}{(1+\nu) \cdot (1-2\nu)}$, $\mu = \dfrac{E}{2(1+\nu)}$, $K = \dfrac{E}{3(1-2\nu)}$ – Lame parameters depending on $r$.

Substituting (6) – (8) in equilibrium equations we get

$$\begin{aligned} &(\lambda + 2\mu) \cdot \left( \frac{\partial^2 u}{\partial r^2} + \frac{1}{r} \cdot \frac{u}{r} - \frac{u}{r^2} \right) + \frac{\mu}{r^2} \cdot \frac{\partial^2 u}{\partial \theta^2} + \frac{\lambda + \mu}{r} \cdot \frac{\partial^2 v}{\partial r \partial \theta} - \frac{\lambda + 3\mu}{r^2} \cdot \frac{\partial v}{\partial \theta} + \frac{\partial(\lambda + 2\mu)}{\partial r} \cdot \frac{\partial u}{\partial r} + \\ &+ \frac{1}{r^2} \cdot \frac{\partial \mu}{\partial \theta} \cdot \left( \frac{\partial u}{\partial \theta} + r \cdot \frac{\partial v}{\partial r} - v \right) + \frac{1}{r} \cdot \frac{\partial \lambda}{\partial r} \cdot \left( u + \frac{\partial v}{\partial \theta} \right) - 3 \frac{\partial}{\partial r} (K \cdot \varepsilon_в) + R = 0; \end{aligned} \tag{9}$$

$$\begin{aligned} &\mu \cdot \left( \frac{\partial^2 v}{\partial r^2} + \frac{1}{r} \cdot \frac{v}{r} - \frac{v}{r^2} \right) + \frac{\lambda + \mu}{r} \cdot \frac{\partial^2 u}{\partial r \partial \theta} + \frac{\lambda + 3\mu}{r^2} \cdot \frac{\partial u}{\partial \theta} + \frac{\lambda + 2\mu}{r^2} \cdot \frac{\partial^2 v}{\partial \theta^2} + \frac{1}{r} \cdot \frac{\partial \mu}{\partial r} \cdot \left( \frac{\partial u}{\partial \theta} + r \cdot \frac{\partial v}{\partial r} - v \right) + \\ &+ \frac{1}{r} \cdot \frac{\partial \lambda}{\partial \theta} \cdot \frac{\partial u}{\partial r} + \frac{1}{r^2} \cdot \frac{\partial(\lambda + 2\mu)}{\partial \theta} \cdot \left( u + \frac{\partial v}{\partial \theta} \right) - 3 \frac{\partial}{\partial \theta} (K \cdot \varepsilon_в) + \Theta = 0. \end{aligned} \tag{10}$$

Solution of equations (9) - (10) will be sought in the form of the following series [5]:

$$\begin{aligned} \begin{pmatrix} u \\ v \end{pmatrix} = &\begin{pmatrix} \varphi_0 \\ \psi_0 \end{pmatrix} + \begin{pmatrix} \varphi_1 \\ \psi_1 \end{pmatrix} \cdot \theta + \begin{pmatrix} \varphi_2 \\ \psi_2 \end{pmatrix} \cdot \theta \cdot \sin\theta + \begin{pmatrix} \varphi_3 \\ \psi_3 \end{pmatrix} \cdot \theta \cdot \cos\theta + \begin{pmatrix} \varphi_4 \\ \psi_4 \end{pmatrix} \cdot \sin\theta + \begin{pmatrix} \varphi_5 \\ \psi_5 \end{pmatrix} \cdot \cos\theta + \\ &+ \sum_{n=2}^{\infty} \left[ \begin{pmatrix} \varphi_{sn} \\ \psi_{sn} \end{pmatrix} \cdot \sin n\theta + \begin{pmatrix} \varphi_{cn} \\ \psi_{cn} \end{pmatrix} \cdot \cos n\theta \right], \end{aligned} \tag{1}$$

were $\varphi_0,...\psi_{cn}$ – functions depending on $r$. Functions $\varepsilon_f(r)$, $R(r)$ and $\Theta(r)$ have a form: $\varepsilon_f = \varepsilon_{f,0}$, $R = R_5 \cdot \cos\theta$, $\Theta = \Theta_4 \cdot \sin\theta$. Given the form of the boundary conditions (3), (4), in (11) we can restrict the terms:

$$u = \varphi_0 + \varphi_5 \cdot \cos\theta + \varphi_{c2} \cdot \cos 2\theta + \varphi_{c3} \cdot \cos 3\theta; \quad v = \psi_4 \cdot \sin\theta + \psi_{s2} \cdot \sin 2\theta + \psi_{s3} \cdot \sin 3\theta \tag{12}$$

Substituting (12) in (9) and (10) we get a system of ordinary differential equations for $\varphi_i$ and $\psi_i$:

$$(\lambda + 2\mu) \cdot \left( \varphi_0'' + \frac{\varphi_0'}{r} - \frac{\varphi_0}{r^2} \right) + (\lambda' + 2\mu') \cdot \varphi_0' + \frac{\lambda'}{r} \cdot \varphi_0 - 3\left(K \cdot \varepsilon_{в,0}\right)' = 0; \tag{2}$$

$$-\frac{\lambda+\mu}{r} \cdot \varphi_5' - \frac{\lambda+3\mu}{r^2} \cdot \varphi_5 + \mu \cdot \left( \psi_4'' + \frac{\psi_4'}{r} - \frac{\psi_4}{r^2} \right) - \frac{\lambda+2\mu}{r^2} \cdot \psi_4 - \frac{\mu'}{r} \cdot (\varphi_5 - r \cdot \psi_4' + \psi_4) + \Theta_4 = 0; \tag{3}$$

$$\begin{gathered} (\lambda + 2\mu) \cdot \left( \varphi_5'' + \frac{\varphi_5'}{r} - \frac{\varphi_5}{r^2} \right) - \frac{\mu}{r^2} \cdot \varphi_5 + \frac{\lambda+\mu}{r} \cdot \psi_4' - \frac{\lambda+3\mu}{r^2} \cdot \psi_4 + \\ + (\lambda' + 2\mu') \cdot \varphi_5' + \frac{\lambda'}{r} \cdot (\varphi_5 + \psi_4) + R_5 = 0; \end{gathered} \tag{4}$$

$$\begin{gathered} -\frac{\lambda+\mu}{r} \cdot 2\varphi_{c2}' - \frac{\lambda+3\mu}{r^2} \cdot 2\varphi_{c2} + \mu \cdot \left( \psi_{s2}'' + \frac{\psi_{s2}'}{r} - \frac{\psi_{s2}}{r^2} \right) - \\ - \frac{\lambda+2\mu}{r^2} \cdot 2^2 \cdot \psi_{s2} - \frac{\mu'}{r} \cdot (2\varphi_{c2} - r \cdot \psi_{s2}' + \psi_{s2}) = 0; \end{gathered} \tag{5}$$

$$\begin{gathered} (\lambda + 2\mu) \cdot \left( \varphi_{c2}'' + \frac{\varphi_{c2}'}{r} - \frac{\varphi_{c2}}{r^2} \right) - \frac{\mu}{r^2} \cdot 2^2 \cdot \varphi_{c2} + \frac{\lambda+\mu}{r} \cdot 2\psi_{s2}' - \\ - \frac{\lambda+3\mu}{r^2} \cdot 2\psi_{s2} + (\lambda' + 2\mu') \cdot \varphi_{c2}' + \frac{\lambda'}{r} \cdot (\varphi_{c2} + 2\psi_{s2}) = 0; \end{gathered} \tag{6}$$

$$\begin{gathered} -\frac{\lambda+\mu}{r} \cdot 3\varphi_{c3}' - \frac{\lambda+3\mu}{r^2} \cdot 3\varphi_{c3} + \mu \cdot \left( \psi_{s3}'' + \frac{\psi_{s3}'}{r} - \frac{\psi_{s3}}{r^2} \right) - \\ - \frac{\lambda+2\mu}{r^2} \cdot 3^2 \cdot \psi_{s3} - \frac{\mu'}{r} \cdot (3\varphi_{c3} - r \cdot \psi_{s3}' + \psi_{s3}) = 0; \end{gathered} \tag{7}$$

$$\begin{gathered} (\lambda + 2\mu) \cdot \left( \varphi_{c3}'' + \frac{\varphi_{c3}'}{r} - \frac{\varphi_{c3}}{r^2} \right) - \frac{\mu}{r^2} \cdot 3^2 \cdot \varphi_{c3} + \frac{\lambda+\mu}{r} \cdot 3\psi_{s3}' - \\ - \frac{\lambda+3\mu}{r^2} \cdot 3\psi_{s3} + (\lambda' + 2\mu') \cdot \varphi_{c3}' + \frac{\lambda'}{r} \cdot (\varphi_{c3} + 2\psi_{s3}) = 0. \end{gathered} \tag{8}$$

Substituting (12) in (6) – (8) we get boundary conditions for $\varphi_i$ and $\psi_i$ included in (13) – (19), that completely determines the boundary value problem.

**Results**

Numerical solution of the system (13) - (19) with boundary conditions has been implemented in the software package Matlab. Fig. 2 and 3 show the distribution of normal stresses along the radius for the typical values of the angle θ. For comparison the results of analytical solutions for the homogeneous material when $E$ = const = $E_{av}$. As averaged modulus $E_{av}$ is selected:

$$E_{av} = \frac{\int_a^b E(w(r))dr}{b-a} = 52{,}27\text{MPa}.$$

To avoid overloading graphs for comparison in Fig. 2, 3, the solution for the homogeneous material is given for only one value of the angle $\theta = \pi / 4$ (dotted lines).

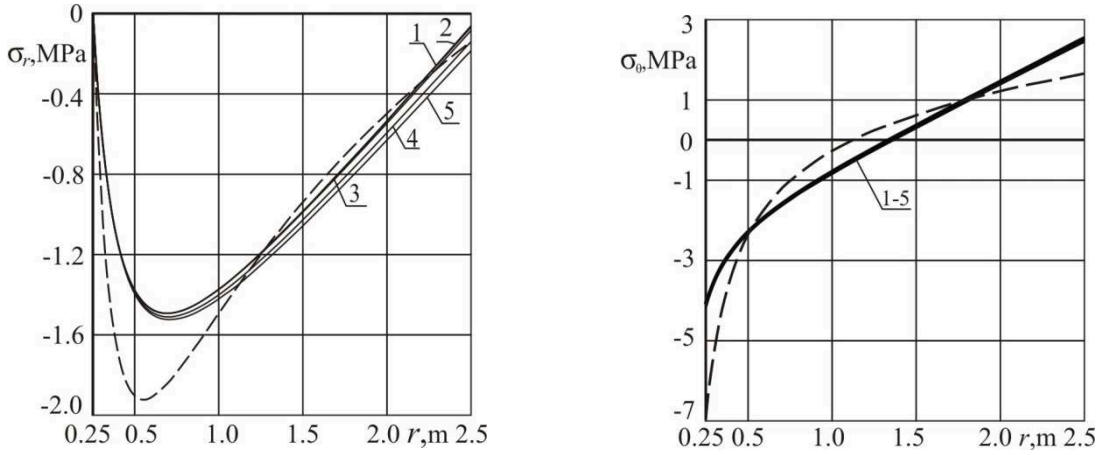


Fig. 2. Diagrams of normal stresses for different values of θ:
1 – θ = π; 2 – θ = 3π/4; 3 – θ = π/2; 4 – θ = π/4; 5 – θ = 0.
—— inhomogeneous material; - - - homogeneousmaterial (θ = π/4).

## Conclusions

Accounting deformation inhomogeneity makes substantial adjustments in the stress state of a cylindrical array with a hole. The most circumferential stressesin the most dangerous stretch zone are 1.5 times higher than the same stresses without regard inhomogeneity.

As can be seen from Fig. 2, the difference between stresses $\sigma_r$ for different values of θ is small, and the curves $\sigma_\theta(r)$ practically coincide.The difference between diagrams 1 - 5 in the figure for $\sigma_r$ is due just to the asymmetry of external pressure.Stresses of its own weight of the array are around 10% of the stresses caused by the swelling soil.Thus it can be concluded that the calculation of the stress state in this problem can be carried out in an axisymmetric formulation [1].

With regard to stresses $\tau_{r\theta}$ (Fig. 3), their values one order less than the values of normal stresses.

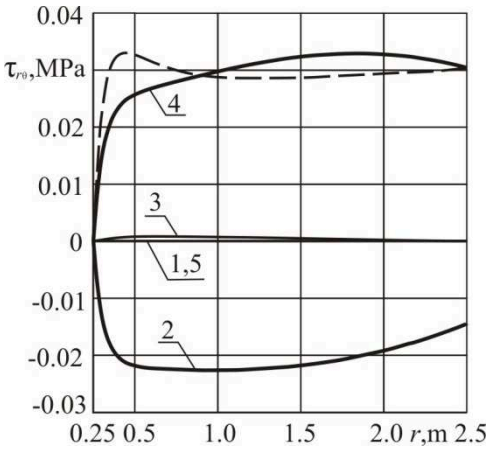


Fig. 3. Diagrams of shear stresses for different values of θ:
1 – θ = π; 2 – θ = 3π/4; 3 – θ = π/2;
4 – θ = π/4; 5 – θ = 0.
—— inhomogeneous material; - - - homogeneousmaterial (θ = π/4).

## References

[1]Andreev V.I., Avershyev A.S.. Stationary Problem of Moisture-elasticity for Inhomogeneous thick-walled Shells. Advanced Materials Research, Vols. 671-674 (2013) pp. 571-575. Trans Tech Publications, Switzerland, 2013.

[2]GolliO.R. Ispolzovanie zakonomernostey nabukhaniya glinistykh gruntov v stroitelstve // Rekonstruktsiya gorodov I geotekhnicheskoe stroitelstvo, №8/2004. S. 131-141.

[3]Andreev V.I. Nekotoryyezadachiimetodymekhanikineodnorodnykh tel. M.: Izd-vo ASV, 2002. 286 s.

[4]Ter-Martirosyan Z.G. Mekhanikagruntov. M. :Izd-vo ASV, 2005. - 488 s.

[5]Andreev V.I. Ob odnommetoderesheniya v peremeshc heniyakhploskoyzadachiteoriiuprugostidlyaradialnoneodnorodnogotela //Prikl. mekh. 1987. T. 23. №4. S 16-23.

*Applied Mechanics and Materials Vols. 580-583 (2014) pp 2978-2982*
*© (2014) Trans Tech Publications, Switzerland*
*doi:10.4028/www.scientific.net/AMM.580-583.2978*

# Application of energy method for determining loss factor in dynamic systems with hysteretic damping

Vladimir Smirnov[1,a], Vladimir Mondrus[2,b]

[1]Postgraduate student, Department of Structural Mechanics, Moscow State University of Civil Engineering (MGSU), 26 Yaroslavskoechaussee, Moscow, 129337, Russian Federation

[2]Doctor of Technical Sciences, Professor, Head of department, Department of Structural Mechanics, Moscow State University of Civil Engineering (MGSU), 26 Yaroslavskoechaussee, Moscow, 129337, Russian Federation

[a]belohvost@list.ru, [b]mondrus@mail.ru

**Keywords:**hysteretic damping, vibration isolation, micro seismic activity, low-frequency vibration isolation, precision equipment, numerical modelling.

**Abstract.**The article studies the energy method for determining loss factor due to hysteretic damping in systems of vibration and seismic isolation. Typical measure of damping is $\tan\varphi$, where φ is the phase angle between stress and strain sinusoids [1], or damping constant δ ($\delta = \pi \tan\varphi$ [2, 3]). Both of these parameters are acquired through experimental investigations for each type of boundary conditions or element's cross section. Proposed energy method is capable of loss factor ψ determination for different types of beams based on only one experimental investigation. This method is used in the paper to determine the damping ratio of elastic element in vibration isolation system of precision equipment.

## Introduction

Currently, a lot of work is devoted to the protection of high – precision equipment from both ambient vibration, micro seismic and seismic activity [4, 5, 6]. Experiments shows, that damping of structural metals is very low (according to [1]: steel 0,0001; brass $9\times10^{-5}$ and aluminum alloy $<10^{-5}$). Therefore, structural damping is obtained through additional materials with high damping (e.g., rubber pads) or specially designed structures (e.g. viscous dampers). Because vibration isolators of precision equipment have to be effective in the range of 1 – 100 Hz [4, 5], their damping characteristics should possess high values at resonance and low values beyond one. This factor defines the use of dampers with high internal friction, which may in particular be achieved by using compressed beams [1, 2, 8]. One of the vibration isolator types is an isolator, consisting of compressed steel beam that supports the isolated equipment [7, 8]. At the moment, the problem of computing the elastic curve of such isolators is well-studied. However, less attention is given to the problem of calculating the damping characteristics of such isolators. Some authors [1, 7] investigate the influence of internal friction on oscillations of compressed bars, but they measure damping with $\tan\varphi$ parameter. Therefore, they need to perform independent experimental investigations for each type of boundary conditions and cross section type. This paper focuses on the energy model of internal friction, developed in works of Panovko [2]. We investigate the influence of internal damping at low vibrations of compressed beam with variable cross section with initial curvature.

## Proposed energy method

To create a well-posed theory it is important to mention the following experimental fact: energy $\Psi_0$, dissipated per cycle per unit volume of the material depends only on the amplitude value $\varepsilon_0$of deformation. Besides this basic qualitative result, experiments have established for a number of materials particular relationships for uniaxial stress state:

$$\Psi_0 = \Psi_0(\varepsilon_0). \tag{1}$$

Usually, the results of experimental investigations are non-dimensionalized and instead of energy dissipation $\Psi_0$, its ratio to the maximum potential energy of the cycle is used:

$$\psi_0 = \frac{2\Psi_0(\varepsilon_0)}{E\varepsilon_0^2} \tag{2}$$

This ratio, also called the absorption coefficient [2] or loss factor [3], usually depends on the amplitude value of deformation $\varepsilon_0$.

Consider that the vibration mode has the form:

$$X = X(x). \tag{3}$$

We shall normalize it so that the value of X equals unity in a typical section, which deflections are taken as a generalized coordinate. Then the deflection of any section of the beam in the process of oscillations are determined by formula:

$$v(x,t) = X(x)T(t). \tag{4}$$

In Eq. (4)T(t) – is the generalized coordinate, that defines the deflection of the mentioned typical section of the beam. Let the A be the amplitude value of T(t). When the dynamic system is exposed to external excitations, the value of A is constant, but when the system undergo free oscillations, the value of A changes from cycle to cycle. The greatest deviation from the equilibrium position of the system correspond to the deflections:

$$v_{\max} = AX(x). \tag{5}$$

The curvature of the beam in a state of maximum deviation is determined by the approximate expression:

$$\chi = A\frac{d^2X}{dx^2}. \tag{6}$$

Therefore, the amplitude of maximum stress in any point on the beam is determined by:

$$\sigma_0(x,y) = E|\chi y| = EA\left|\frac{d^2X}{dx^2}\right|. \tag{7}$$

As described in [2], further calculations should be based on a specific form of the material dependence – Eq. (1)/ There are various ways of representing these functions, widely discussed in [2, 3]. In our analysis, we will use following simple relation:

$$\Psi_0 = \beta\sigma_0^{n+1}. \tag{8}$$

In Eq. (8)β and n – are the material constants.

Relation (8)can be constructed from the test results, for example from envelope analysis of the beam's free oscillations due to simple constraints, with further approximation of the experimental curve in Curve Fitting Toolbox from MatLab software. According to Eq. (8), Eq. (2) has the form:

$$\psi_0(\sigma_0) = \frac{\Psi_0}{\Pi_0} = 2\beta E\sigma_0^{n+1}. \tag{9}$$

In Eq. (9) $\Pi_0 = \frac{\sigma_0^2}{2E}$ - is specific potential energy in the state of maximum deformation. In order to find all the energy dissipated per cycle, substitute in Eq. (8) the expression σ0, given by Eq. (7) and integrate the result over the entire volume:

$$\Psi = \int_V \Psi_0 dV = \beta(EA)^{n+1} J^* \int_0^l \left|\frac{d^2X}{dx^2}\right|^{n+1} dx. \tag{10}$$

In Eq. (10) $J^* = J(n) = \int_0^l \iint_F |y|^{n+1} dF dx.$ - is a kind of physical – geometric characteristic that depends not only on the shape and cross section size, but also on the beam material.It is important, that the RHS of the equation depends not only on the properties of the material (β and n coefficients), but also on the structure en bloc, besides on the form of the excited vibrations (the latter determines the mode function). In order to get the reduced absorption coefficient, we have to

divide Eq. (10) by potential energy of the beam related to the state of the greatest deviation from the equilibrium position, which has the form:

$$\Pi = \int_V \Pi_0 dV = \frac{EJA^2}{2} \int_0^l \left( \frac{d^2X}{dx^2} \right)^2 dx. \tag{11}$$

After dividing (10) by(11) we will get the reduced absorption coefficient for the whole beam:

$$\psi = 2\beta \frac{J^*}{J} E^n A^{n-1} \frac{\int_0^l \left| \frac{d^2X}{dx^2} \right|^{n+1} dx}{\int_0^l \left( \frac{d^2X}{dx^2} \right)^2 dx}. \tag{12}$$

The absorption coefficient usually depends not only on the material properties, but also on the considered waveform, which defines the form of the derivative $\frac{dX}{dx}$. In addition, it should be noticed, that when n = 1, we obtain a value of the absorption coefficient of the material $\psi = 2\beta E$ .Moreover, Eq. (12) states the fact that the absorption coefficient depends on the amplitude of oscillations.

**Application**

Consider the problem of mass *m* free oscillations on the fixed – fixed compressed beam of variable cross section with initial curvature, which is schematically plotted in Fig. 1.

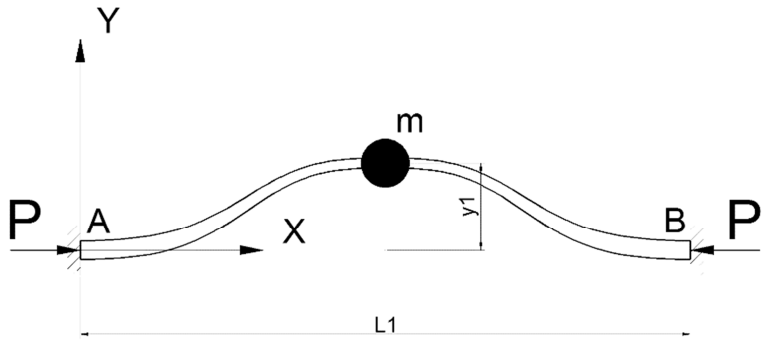


Fig. 1. Scheme of the problem.

Variable beam cross section is described by:

$$EJ(x) = EJ_0 f(x). \tag{13}$$

Consider that the beam's waveform coincides with the curve of static bending subjected to a point force acting in mid span. Since the bending curve in this problem is obtained numerically, it is necessary to represent the Eq. (6) in the finite difference form:

$$A \frac{d^2X}{dx^2} = A \frac{X_{i+1} - 2X_i + X_{i-1}}{h^2}. \tag{14}$$

Then to compute Eq. (12) taking into account Eq. (13) and Eq. (14) we will use formulas for numerical integration like trapezoidal rule or Simpson's rule. Moreover, if the problem involves massive computations, for example,if we need to investigate damping properties for a large number of different beams, parallel integration methods can be applied [9]. In the paper, we consider the following types of variable cross-section, presented in Table 1.

Table 1. Types of variable cross – section.

| №№ | Description | Scheme |
|---|---|---|
| 1 | Linearly varying cross-section | 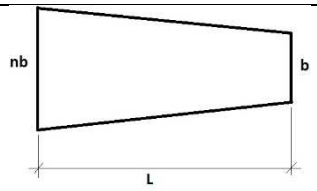  |
| 2 | Parabolically varying cross - section | 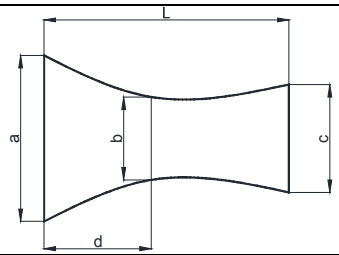  |

The results of calculations are presented on Fig. 2 – 3 for different type of cross section from Table 1. The β and n coefficient were obtained experimentally from beam envelope analysis as stated in [2]. For steel alloy we gathered β = 0,0013, n = 1,3.

a) n = 1 b) n = 1.5

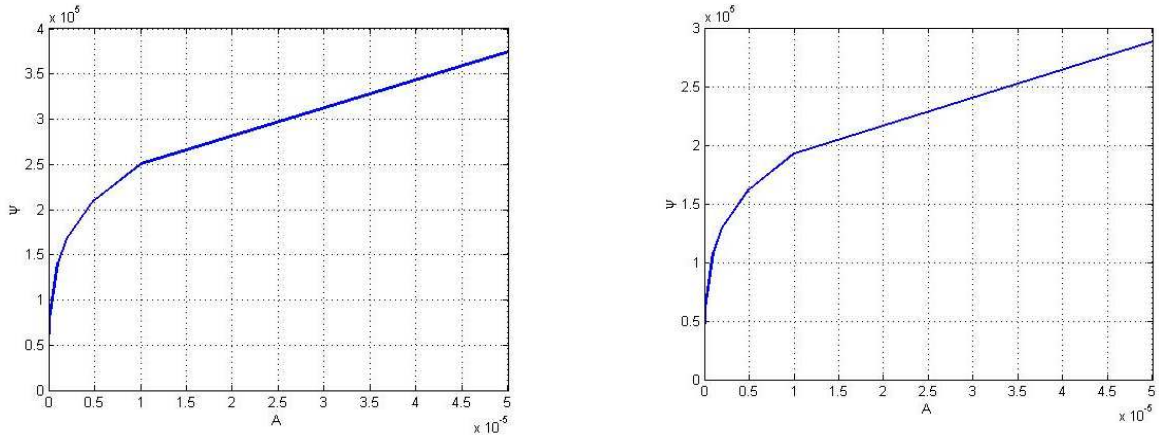


Fig. 2. Curves $\psi - A$ forcrosssectiontype №1.

Cross section type №2 from Table 1 can be made symmetrical or asymmetrical. Cross section type influences both the bending curve and absorption coefficient. Curves $\psi - A$ for symmetrical and asymmetrical cross section of type №2are shown in Fig. 3 in dimensionless form.

a) b)

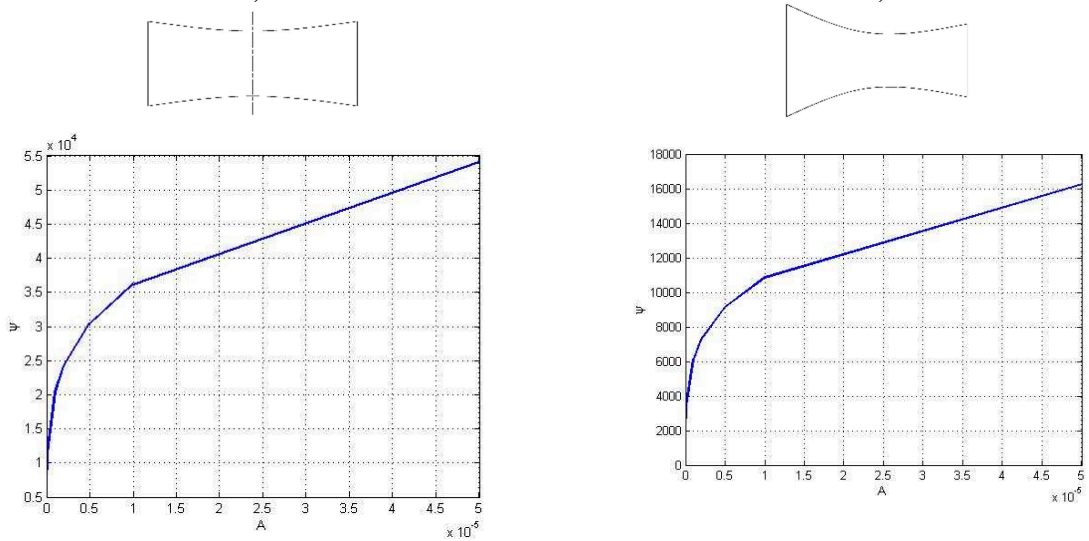


Fig. 3. Curves $\psi - A$ forcrosssectiontype№2.

## Results and discussion

The analysis of calculation results shows that the maximum loss factor has a symmetrical beam with variable cross section of type №2 from Table 1. The lowest loss factor has the beam with asymmetrical cross section of type №2. It can also be noted, that the loss factor is greater in those beams, where the compression zone area is larger. Due to the fact, that asymmetrical cross section beams has smaller compression zone area, compression stresses there are lower, which results in lower potential energy of that part of the beam and lower overall loss factor. That is why it is recommended to use symmetrical cross section beams in applications that require higher internal damping. Although beams with variable asymmetric cross section has lower loss factor, their stiffness characteristics can more convenient in some applications, for example they can possess "soft stiffness", which is favorable for low-frequency vibration isolation purposes. In this case, the process of developing the best isolation system is an optimization problem in which the damping coefficients can be obtainedfrom the calculations presented.

## Conclusion

Energy model for determining the internal friction in the beams takes into account not only the properties of the beam material, but also its boundary conditions and cross section parameters. For this calculation,we do not require numerous experimental studies, which is an advantage of the approach. Thus, the results show that the compressed beam with a variable cross-section have a considerable internal friction, which allows to reduce the amplitude of the resonant oscillation, thereby improving the performance of vibration isolation systems.

## References

[1] Liang Dong, Roderic Lakes. Advanced damper with high stiffness and nigh hysteresis damping based on negative structural stiffness. International Journal of Solids and Structures. Vol. 50, pp. 2416 – 2423 (2013).

[2] PanovkoJa. G. Oscillations of elastic systems with internal friction. FizMatLit (1960).

[3] Postnikov V.S. Internal friction in metals. Metallurgical Engineering. (1974).

[4] HalAmick, Michael Gendreau, Todd Busch.Evolving Criteria for Research Facilities: Vibration. Proceedings of SPIE Conference 5933: Buildings for Nanoscale Research and Beyond, Vol. 5933, pp. 16 – 28 (2005).

[5] Eugene I. Rivin. Vibration isolation of precision objects. Precision engineering, Vol. 1, pp. 12 – 20 (1995).

[6] K. Hasselmann, A statistical analysis of the generation of micro-seisms. Review of Geophysics, Vol. 1, issue 2, pp 177–210 (1963).

[7] B. Ravindra and A.K. Mallik. Hard duffing-type vibration isolators with combined coulomb and viscous damping. Journal of Nonlinear Mechanics. Vol. 28, issue 4, pp. 427–440 (1993).

[8] Smirnov V.A. Nonlinear vibration isolator for kinematic vibration isolation of vibration-sensitive equipment. Sci-tech journal of Moscow State University of Civil Engineering. Issue 3, Vol. 1,pp. 107 – 112 (2011).

[9] Smirnov V.A. Parallel integration using OpenMP and GPU to solve engineering problems. Applied Mechanics and Materials. Vols. 475-476, pp. 1190-1194(2014).

*Applied Mechanics and Materials Vols. 580-583 (2014) pp 2983-2989*
*© (2014) Trans Tech Publications, Switzerland*
*doi:10.4028/www.scientific.net/AMM.580-583.2983*

# Hexahedron-dominant Mesh Generation for Blocks with Constrained Triangulated Boundary Surfaces

Xuebin Pei[1, a], Nengxiong Xu[2,b]

[1]Mining Company, Anshan Iron and Steel Group Corporation, Anshan, Liaoning, China

[2]School of Engineering & Technology, China University of Geosciences, Beijing, China

[a]agkyjs@163.com, [b]xunengxiong@cugb.edu.cn

**Keywords:** Geological modeling; Hexahedron-dominant mesh generation; Wire frame; Mesh mapping; Block.

**Abstract.** In the field of geotechnical engineering, a numerical simulation model is established by meshing a three-dimensional geological model, which is composed of many seamlessly connected blocks. Each block is enclosed with constrained, triangulated boundary surfaces and called as a constrained block. Due to the complexity of geological structures, a three-dimensional geological model is very complicated in most cases, and will be very difficult to decompose this kind of model into hexahedral mesh by those commonly-used methodologies. Thus, we propose a new mesh generation method which is special for blocks with constrained, triangulated boundary surfaces: hexahedron-dominant mesh generation based on templates (HMGT). In this method, several regular blocks including cuboids, prism, pyramid, tetrahedron, cylinder and their combinations, are decomposed into hexahedron-dominant meshes that serve as mesh templates. Then, a constrained block is abstracted into a simple block, and the simple block is divided into two parts by shrinking: the crust and core. Next, a mesh template of regular blocks or their combinations is selected and mapped to the core of the simple block, and the crust of which is filled with pyramids and tetrahedra in order to obtain the subdivision of the simple block. Finally, the mesh of a simple block is directly mapped to the original constrained block to generate target hexahedron-dominant mesh.

## Introduction

In geotechnical engineering, numerical simulation methods such as finite element methods (FEM) have become indispensable tools. A prerequisite for numerical simulation in geotechnical engineering is the establishment of a computational model representing the geological phenomenon of interest with high mesh quality. Before generating a mesh, it is necessary to establish a realistic geological model using 3D modeling tools. Such geological models consist of a number of closed and connected blocks, and each block is composed of several geological interfaces represented by triangular surfaces. We have proposed a sealed engineering geological modeling method, SEGM [1], to generate the above mentioned geological models. The mesh generation method proposed in this paper is specially designed for this kind of geological model.

At present, the common hexahedral subdivision algorithms include the following: the mapping method, the grid method, tetrahedral decomposition, and the axial surface decomposition method. Cook and Oakes [2] proposed the mapping method. In this method, a mapping function is accepted to transfer a regular mesh unit onto a Euclidean space, and then generate an actual mesh. Price and Armstrong [3,4] divided a meshing area into simple convex areas using central axis planes, and then they decomposed the sub-region into a hexahedral mesh by the mapping method. Chiba, et al. [5,6] developed a semi-automatic all-hexahedral meshing system based on physical recognition and boundary adaptation. Min [7] proposed a hexahedron-dominant mesh method. This method firstly divides a three-dimensional object into a series of convex polyhedrons. For each polyhedron, borders are contracted inward, forming cavities between the old and new borders that are then filled with the four units described above, resulting in the formation of a mesh network.

Building on these advancements, this paper presents a hexahedron-dominant mesh generation method called hexahedron-dominant mesh generation based on templates (HMGT). This method is suitable and valid for generating subdivisions of seamlessly connected blocks with fixed boundaries. The term "hexahedron-dominant" here means that the total space occupied by all hexahedral elements is larger than that by non-hexahedral ones.

## Geometrical Features of Constrained Blocks

In this study, a geological model used in numerical simulation is composed of many blocks, and it is represented using Boundary Representation (B-Rep). Each block is closed by a number of triangular surfaces. The adjacent blocks must meet the conditions of geometrical continuity and topological consistency [1]. A constrained block has the following geometrical features: (1) It is a closed, bounded polyhedron (Fig. 1a); (2) All the boundary surfaces of a constrained block are triangulated (Fig. 1a); (3) Each of its boundary surfaces is continuous and has a closed border loop with no cavity inside the boundary surface. Such a boundary surface is called a simple surface. In Fig. 1b, S1 and S2 are two simple surfaces of Block 2; (4) All interfaces between two connected surfaces of a constrained block are seamless, which means that the two connected surfaces share the same boundary. For example, in Fig. 1b, L is a boundary line shared by S1 and S2; and (5) It is simply connected, with no internal cavity.

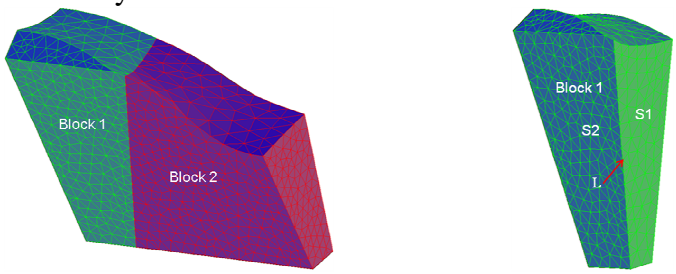


**a** **b**

**Fig. 1** (a) Block 1 and Block 2 are two seamlessly connected blocks, and S1 is a boundary surface shared by Block 1 and Block 2; (b) S1 and S2 are two simple surfaces of Block 1, and L is a boundary line shared by S1 and S2

## Methodology

The key procedures of HMGT are as follows. Firstly, some regular blocks, including cuboids, prism, pyramid, tetrahedron, cylinder and their combinations, are divided into hexahedron-dominant meshes that serve as mesh templates. Secondly, a constrained block is abstracted to be a simple block, which is obtained by replacing the simple surfaces of the constrained block with planes. Thirdly, the simple block is divided into two parts: the crust and core. Fourthly, the hexahedral mesh template of a regular block is mapped to the core to obtain mesh of the core. Fifthly, the crust is filled with pyramids and tetrahedrons without any change to the outer surfaces of the block and the core. Lastly, the mesh of a simple block is mapped to the original constrained block to generate subdivision of the constrained block.

## The Hexahedral Mesh Template for Regular Blocks

Although a constrained block can theoretically be any shape, we find that the geological model can be abstracted into several typical regular blocks or their combinations after analyzing a large number of examples. In this paper, cuboid, prism, pyramid, tetrahedron, and cylinder are selected as the typical regular blocks. Since the subdivision method for each regular block is fixed, the mesh quality and the speed of subdivision could be effectively improved. Mesh templates for the cuboid (Fig. 2a), cylinder (Fig. 2b), tetrahedron (Fig. 2c), pyramid (Fig. 2d) and prism (Fig. 2e) are created in this paper.

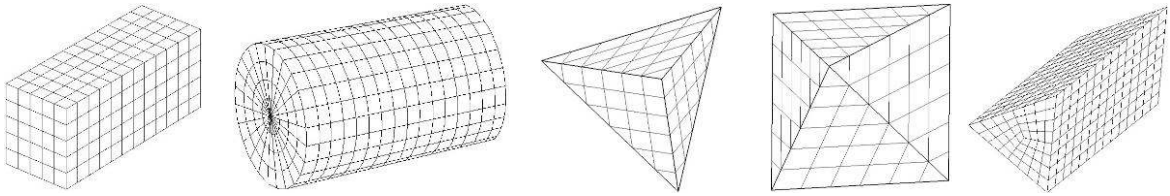

a b c d e

**Fig. 2** (a) Mesh template of cuboids; (b) Mesh template of cylinder; (c) Mesh template of tetrahedron; (d) Mesh template of pyramid; (e) Mesh template of prism;

## Identification and Abstraction of Constrained Blocks

**Shape identification for constrained blocks.** This study presents a method based on geometrical characteristic vertices for shape identification of a constrained block. The method consists of five main steps as follows:

(1) Calculating the average normal for each simple surface of a constrained block

The simple surface of a constrained block is composed of a number of triangles. We can firstly calculate the surface normal of each triangle and then calculate the average normal for a simple surface. The average normal is presented as the direction cosine. In addition, the positive direction of the average normal goes from the inside of a constrained block to the outside. However, if the geometry of a simple surface is very complex, it should be broken down into two or more simple surfaces.

(2) Generating the wire frame for a constrained block

The constrained block in a geological model is enclosed by a number of simple surfaces. Each simple surface is a continuous and connective surface, which is triangulated, and has a closed border loop. The border loops of all simple surfaces form the unedited wire frame for the constrained block.

(3) Editing the wire frame

The wire frame of a constrained block is actually the outline of the block, which is able to demonstrate the block geometry in a simplified way. The wire frame consists of two kinds of simple arcs. One kind of simple arcs includes the geometrical characteristic curves of a block. In the absence of such a simple arc, which is called the geometrical characteristic simple arc, the shape of the block will not be completely. The presence or absence of another kind of simple arc does not affect the shape of the block. This kind of simple arc is called non-characteristic simple arc. The purpose of editing the wire frame is to remove the non-characteristic simple arcs. Because a simple arc is the intersection line of two simple surfaces, removing a simple arc actually merges two connecting simple surfaces together. Obviously, if the average positive normal vectors of two connecting simple surfaces are close, they can be combined into one single simple surface. The process of editing the wire frame is as follows: ① Select each simple arc of the wire frame one by one, and if the angle of the average positive normal between the two simple surfaces sharing this simple arc is less than 30°, remove the arc. ② Remove all simple arcs for which the endpoints belong to only one simple arc.

(4) Determining the geometrical characteristics vertices

There are two types of vertices in the wire frame of a constrained block: characteristic vertices and non-characteristic vertices. Characteristic vertices determine the geometry of a constrained block. If a characteristic vertex is deleted from the wire frame, the geometry of the constrained block will change significantly; if a non-characteristic vertex is deleted from the wire frame, the geometry of the constrained block will not change significantly. Characteristic vertices have the following properties: ① Each characteristic vertex must be an intersection of three or more simple surfaces, meaning that the vertex is shared by three or more simple surfaces; and ② If a node is a characteristic vertex, the angle of the average positive normals between any two connecting simple surfaces sharing the node must be greater than or equal to 30°. After editing the wire frame by removing the non-characteristic simply arcs, the simple surfaces with an angle of average positive

normals less than 30° are merged. We only need to evaluate whether the number of simple surfaces sharing a certain node is greater than or equal to three. Whether or not the node is a characteristic vertex can be determined accordingly.

(5) Determining the geometrical type of a constrained block

Determining the geometrical type of a constrained block involves determining which regular block or block combination is similar to the constrained block. We can determine the geometrical type of a constrained block based on the geometrical characteristic parameters of its wire frame including, the number of characteristic vertices, the number characteristic vertices shared by 3 or 4 simple surfaces, the number of closed loops and the number of simple surfaces. Obviously, the five regular blocks and their combinations can serve as the special constrained blocks. The geometrical characteristic parameters of each type of regular block are listed in Table 1.

**Table 1** The geometrical characteristic parameters of five regular blocks

| Type of regular block | Number of characteristic vertices | Number of characteristic vertices shared by 3 surfaces | Number of characteristic vertices shared by 4 surfaces | Number of closed loops | Number of simple surfaces |
|---|---|---|---|---|---|
| Cuboid | 8 | 8 | 0 | 6 | 6 |
| Prism | 6 | 6 | 0 | 5 | 5 |
| Pyramid | 5 | 4 | 1 | 5 | 5 |
| Petrahedron | 4 | 4 | 0 | 4 | 4 |
| Pylinder | 0 | 0 | 0 | 2 | 3 |

**Abstracting a constrained block.** Abstracting a constrained block involves replacing the triangulated surfaces of the constrained block with planes such that a polyhedron with planar boundaries is formed. Such polyhedron is defined and known as a simple block. When creating a simple block, the geometrical characteristic parameters of the simple block and the constrained block must be the same. The size and shape of the simple block and the constrained block should also match as closely as possible. The specific method for abstracting a constrained block is as follows:

(1) Creating a simple block. ① Select each simple surface on the wire frame of the constrained block one by one, and use the nodes in its closed border loop to fit a plane. ② Compute the intersection of these planes and search a closed loop consisting of the intersecting lines in each plane to form a new wire frame. ③ Calculate the geometrical characteristic parameters for the new wire frame. If the geometrical characteristic parameters for the new wire frame are the same as those for the wire frame of the constrained block, the block surrounded by the new wire frame is a simple block. If not, move and rotate the fitting plane appropriately until a simple block similar to the constrained block is obtained.

(2) Determining the type of simple surface in the constrained block. Each simple surface of the constrained block has a closed boundary loop corresponding to a closed loop in the wire frame of the constrained block. The type of simple surface can be determined according to the number of the characteristic vertices on this closed loop. The types of simple surfaces corresponding to the regular blocks and combination blocks described above include triangle, quadrilateral, pentagon and circle.

(3) Determining the correspondence between the simple surfaces of the constrained block and the boundary planes of the simple block or the corresponding regular block. According to the type of the simple surfaces of the constrained block, its correspondence with the boundary planes of the simple block or regular block can be determined in advance.

(4) Determining the correspondence between the characteristic vertices of the constrained block and those of the simple block or the corresponding regular block. After the preliminary identification of the correspondence between the simple surfaces of the constrained block and the boundary planes of the simple block or regular block, the correspondence between the characteristic

vertices of the constrained block and the vertices of the simple block or corresponding regular block can be established.

### Mesh Mapping Based on the Direct Method

In brief, mesh mapping is the conversion of a surface or block with a certain shape and effective mesh to another surface or block while maintaining the same mesh topology and mesh effectiveness. When the same mesh topology is used for two meshes, it means they have the same number of elements and nodes and the same relationship between the elements and the nodes. They also have the same adjacent relationships among nodes. The spatial coordinates of nodes, however, can be different. In short, everything between two surfaces or blocks is the same only except the coordinates of some of their nodes.

This study applies the direct method to process of mesh mapping for a surface or a block. Proposed by Balendran [15], the direct method is a mesh optimization method for triangular or quadrilateral surfaces. The main idea of this method is to treat the mesh as a deformable object. Maintaining the topological consistency of the mesh, nodes are moved such that each triangle on the mesh remains as close to an equilateral triangle as possible. Similarly, each quadrilateral is kept close to a square, and in this way, mesh optimization is achieved. Because the common types of block mesh elements are hexahedron, pyramid, prism and tetrahedron, these common elements are all surrounded with triangles and/or quadrangles. Therefore, the direct method can also be used for optimization of a block mesh [16]. Because the direct method has been discussed in detail in the literatures [15,16], we will not provide a description here.

### Mesh Generation for a Constrained Block

In this study, the mesh of a constrained block is obtained from mesh mapping with the corresponding simple block. The mesh generation for a constrained block involves two main processes: mesh generation of a simple block and mesh mapping from the simple block to the constrained block.

**Mesh generation of a simple block.** A simple block is formed by the abstraction of a constrained block, which is a transition status in between a constrained block and a regular block. The mesh generation for a simple block is the key step in our proposed algorithm. To show how it is carried out clearly, the mesh generation process of a simple block is introduced with an example. Let B be a constrained block. Using the methods described in Section 5, the corresponding simple block β and regular block b can be obtained.

(1) Division of crust and core in a simple block

If the outer surfaces of a simple block β shrinks inward in parallel, a block with the same shape as β and a smaller block size is obtained, which is called the core. This process divides β into two parts: the crust and the core. The distance between the surfaces of a core and the outer surfaces of β depends on the given mesh size, which is generally the same as that of the element.

(2) Mesh mapping for the core

Core subdivision is to divide the core into a mesh with the same structure as a regular block b, which has the same geometrical characteristic parameters. Using the block mapping method described in Section 6, the mesh of regular block b can be mapped onto the core of a simple block β to get the mesh of the core of β.

(3) Mesh mapping for the surfaces of the simple block

The subdivision of a constrained block is to generate a hexahedron-dominant mesh while the boundary meshes are immutable. Therefore, we must ensure that each mesh on the boundaries of the simple block and its correspondence on the boundaries of the constrained block have an identical structure. The boundary surfaces as well as the characteristic vertices have a one-to-one correspondence between β and B, because the simple block β is the abstraction of the constrained block B. Using the surface mapping subdivision method introduced in the foregoing section, each

boundary surface of B can be mapped onto the corresponding boundary surface of β. In this way, the mesh mapping for the surfaces of a simple block is achieved.

(4) Subdivision for the crust of a simple block

The crust of a simple block is the cavity between the outer surface of the simple block and the outer surface of its core. Because the meshes of the outer surfaces of a simple block are often different from those of the outer surfaces of the core, it is difficult to divide the crust into a hexahedral mesh. Using the filling method, the crust can be divided into a collection of pyramids and tetrahedrons. To introduce easily, the outer surfaces of a simple block and the outer surfaces of its core are respectively called the outer boundary and inner boundary of the crust in the following description.

The filling method is performed as follows: ① Each quadrilateral is selected orderly from the mesh of the inner boundary and treated as the bottom of a pyramid. The coordinates of the centroid of this quadrilateral are calculated. Then, the centroid of the quadrilateral is shifted outward a certain distance along the border of its normal direction to form a vertex. A pyramid is created by connecting the vertex and four vertices of the quadrilateral. After this treatment, the inner boundary is changed from a quadrilateral mesh into a triangular mesh. ② By accepting the algorithm of Constrained Delaunay Triangulation (CDT), the rest part of the crust is subdivided into tetrahedrons.

**Mesh mapping of a simple block onto a constrained block.** After mesh generation of a simple block, the nodes on the outer boundary surfaces of a constrained block are used to replace the corresponding nodes on the boundary surfaces of the simple block. Then, using the direct method, the coordinates of nodes in the simple block are moved to the appropriate positions such that subdivision of the constrained block is achieved.

## An Example of Mesh Generation for a Constrained Block

A constrained block B, of which the simple block is similar to a combination of a cuboid and a prism, is also selected and then meshed (Fig. 3).

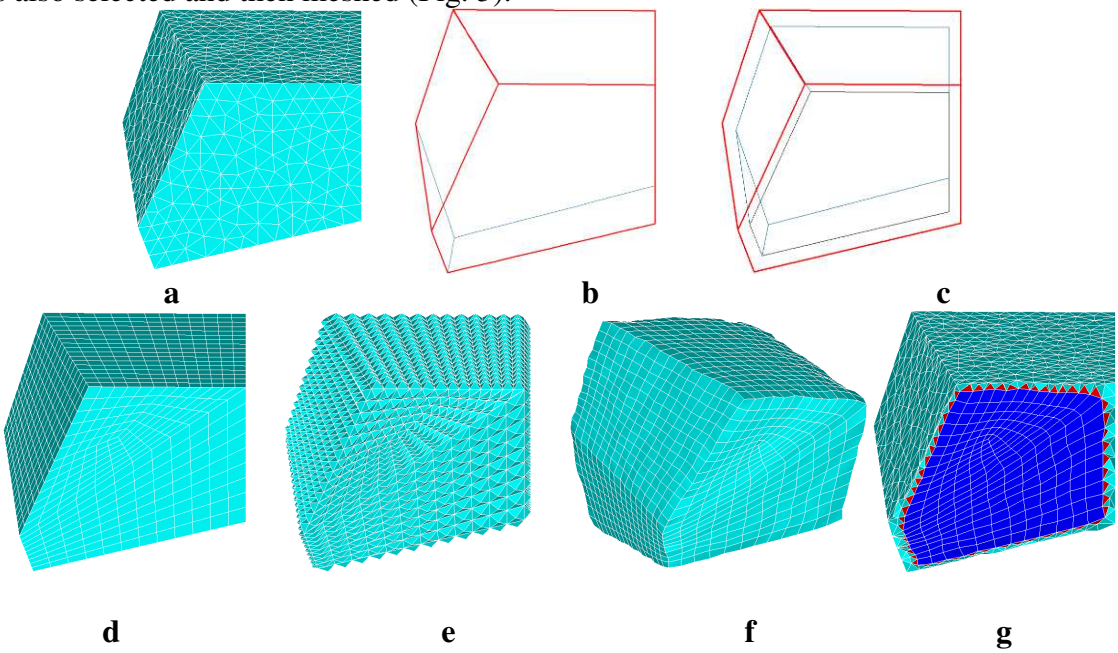


**Fig. 3** (a) A constrained block B; (b) The wire frame of the constrained block; (c) The core and crust of the simple block of B; (d) Hexahedrons of the core of the simple block; (e) Pyramids grown from the boundary surfaces of the core; (f) Hexahedrons in the core of B

## Conclusions

Aiming at the individual constrained block from the three-dimensional geological model, we propose a hexahedron-dominant subdivision method, hexahedron-dominant mesh generation based on templates (HMGT), to decompose the block with constrained triangulated boundary surfaces into hexahedron-dominant meshes. To hold the conditions of geometrical continuity and topological consistency between blocks, the triangular meshes on the border surface of the block are kept in the process of subdivision. The main procedures of HMGT are follows: firstly, a constrained block is abstracted to be a simple block, and the simple block is divided into crust and core by shrinking; secondly, the hexahedral mesh template of a regular block is mapped to the core to obtain its mesh, and the crust is filled with pyramids and tetrahedrons without any change to the outer surfaces of both the block and the core; finally, the mesh of a simple block is mapped to the original constrained block to generate the required subdivision of the constrained block.

## References

[1] N.X. Xu, H. Tian: Comput Geosci Vol. 35(2009), p.1582-1591

[2] W.A. Cook, W.R. Oakes: Comput Mech Eng Vol. 8(1982), p. 67-72

[3] M.A. Price, C.G. Armstrong: Int J Numer Methods Eng Vol. 38(1995) , p.3335-3359

[4] M.A. Price, C.G. Armstrong:Int J Numer Methods Eng Vol. 40(1997) , p. 111-136

[5]N. Chiba, I. Nishigaki and Y. Yamashita: Proceedings of 5th International Meshing Roundtable(1996), p. 281-290

[6] N. Chiba, I. Nishigaki and Y. Yamashita:Comput Methods Appl Mech Engrg Vol. 161(1998), p.145-154

[7] W.D. Min (1997) Generating hexahedron-dominant mesh based on shrinking-mapping method. In: Proceedings of 6th International Meshing Roundtable

*Applied Mechanics and Materials Vols. 580-583 (2014) pp 2990-2995*
*© (2014) Trans Tech Publications, Switzerland*
*doi:10.4028/www.scientific.net/AMM.580-583.2990*

# High-Precision Structured Finite Volume Model for Numerical Simulation of Dam- and Dyke-Breach Flow

Yuntao Ye[1, a], Lili Liang[1,b] ,Shuanghu Zhang[1,c],Yunzhong Jiang[1,d]

[1]State Key Laboratory of Simulation and Regulation of Water Cycle in River Basin, China Institute of Water Resources and Hydropower Research, Beijing,100038,China

[a]yyt2001@126.com, [b]liangli0921@163.com, [c]zhangshh@iwhr.com,[d]lark@iwhr.com

**Keywords:** Hydraulics; dam breach; shallow water equations; structured grid; finite volume method

**Abstract.** A high precision structured-based finite volume model for numerical simulation of dam-and dyke-breach flow was proposed. The model regarded the fully two-dimensional shallow water equations as the governing equations, and used the Godunov-type finite volume shock-capturing schemes HLLC to calculate flow flux. Its spatial and temporal accuracy were improved to two order accuracy using the slop limiter and predict-correct method, and the slope source terms and friction source terms were treated with central difference scheme and fully implicit method respectively. And then a robust procedure was adapted in the model to efficiently and accurately simulate the movement of wet and dry boundary and a method of high calculation efficiency was applied in the treatment of complex boundary. A popular example was used to validate the capability of the model. The result shows that the model can capture flow processes over irregular boundary accurately and shows good stability and accuracy.

## Introduction

Frequency of the flood disaster in China have caused tremendous damage to people's lives and property, a combination measures of engineering and non- engineering is used to avoid the risk of flooding and reduce flood losses. As a part of non-engineering, the flow mathematical model is widely applied in the aspects of flood forecasting, dam-and dyke-breach, flood control plan, and river training, etc. [1], which provides a solid foundation for the study on spatial and temporal evolution laws, disaster preparedness and mitigation and risk regulation.

The conventional flow numerical model is suitable for the gradually varied flow, but the good results cannot be achieved when applied in the rapidly varied flow simulation, such as dam- and dyke-breach flood, the mountain flood caused by the strong rainfall, the tidal estuary flow. However, the high performance finite volume computational scheme capturing the shock wave and contact break, along with the two-dimensional shallow water equation, provides the research idea to solve the problem. When using the above method to simulate flow process under the condition of complex topography and boundary, the four aspects as follows merit attention: firstly, the failure to effectively balance the bottom slope and flux will cause false flow velocity [2] ;secondly, it is difficult in the wet-and dry-boundary treatment when rapidly varied flow on the complex terrain[3]; thirdly, complex irregular boundaries treatment will directly affect the numerical reliability, accuracy and computational time[4]; fourthly, complex computational mesh generation is not propitious for the further application in the productive practice.

Some studies or explorations in these aspects are conducted by the scholarships at home and aboard, and good results are acquired [2, 3, 4, 5, 6, 7, 8]. On the basis of relevant research results from scholarship at home and aboard, A high precision structured-based finite volume model for numerical simulation of dam-and dyke-breach flow is proposed, which is built upon the fully two-dimensional shallow water equations and handling efficiently the problems appeared in modeling unsteady and steady flow over topography with wetting and drying and complex boundary.

**Governing Equations**

Under the assumption of the horizontal scale of water in the rivers, lakes, or flood plain being much larger than the vertical scale, hydrostatic pressure distribution, the smaller vertical acceleration, and the neglecting the surface stress term, Coriolis effects term and viscous term, the two-dimensional shallow water equations derived by depth-integrating the three-dimensional Reynolds-averaged Navier-Stokes equations can be expressed as given below.

$$\frac{\partial \zeta}{\partial t}+\frac{\partial (uh)}{\partial x}+\frac{\partial (vh)}{\partial y}=0 \tag{1}$$

$$\frac{\partial (uh)}{\partial t}+\frac{\partial (u^2h)}{\partial x}+\frac{\partial (uvh)}{\partial y}=-\frac{\tau_{bx}}{\rho}-gh\frac{\partial \zeta}{\partial x} \tag{2}$$

$$\frac{\partial (vh)}{\partial t}+\frac{\partial (uvh)}{\partial x}+\frac{\partial (v^2h)}{\partial y}=-\frac{\tau_{by}}{\rho}-gh\frac{\partial \zeta}{\partial y} \tag{3}$$

where, $t$ denotes time, $x$ and $y$ are Cartesian coordinates, $\zeta$ is the free surface elevation above still water depth ($h_s$), $h(=\zeta+h_s)$ is total water depth, $h_s$ is still water depth, $u$ and $v$ are depth-averaged velocity components in the two Cartesian directions; $g$ is the gravitational acceleration, $\rho$ is the density of water, $\tau_{bx}$ and $\tau_b$ are bed friction stresses. To overcome the drawback when water flows over initially dry land, while retaining the mathematical balance the flux gradient and source terms, the free surface gradient term $gh\partial\zeta/\partial x$ and $gh\partial\zeta/\partial y$ in the $x$-and $y$-direction momentum equation can be written as given below[9].

$$gh\frac{\partial \zeta}{\partial x}=\frac{g}{2}\frac{\partial (\eta^2-2z_b\eta)}{\partial x}+g\eta\frac{\partial z_b}{\partial x},\quad gh\frac{\partial \zeta}{\partial y}=\frac{g}{2}\frac{\partial (\eta^2-2z_b\eta)}{\partial y}+g\eta\frac{\partial z_b}{\partial y} \tag{4}$$

where, $\eta$ is surface water level above the datum, $z_b$ is terrain elevation above datum, and water depth is obtained by $h=\eta-z_b$.

Substituting the free surface gradient terms in equation (2) and equation (3) with equation (4), the equation (1), (2), (3) may be written as in the matrix form as given below.

$$\frac{\partial \mathbf{U}}{\partial t}+\frac{\partial \mathbf{F}}{\partial x}+\frac{\partial \mathbf{G}}{\partial y}=\frac{\partial \mathbf{U}}{\partial t}+\nabla\cdot\mathbf{E}=\mathbf{S} \tag{5}$$

where,**U** and **E** are vectors representing conserved variable and the flux of convective flux respectively, **F** and **G** are vectors representing fluxes in $x$- and $y$- direction respectively, **S** is the vector representing source term including bed slope term and friction term.

These vectors are given below.

$$\mathbf{U}=\begin{bmatrix}\eta\\ uh\\ vh\end{bmatrix},\mathbf{F}=\begin{bmatrix}uh\\ u^2h+\frac{1}{2}g\left(\eta^2-2\eta z_b\right)\\ uvh\end{bmatrix},\mathbf{G}=\begin{bmatrix}vh\\ uvh\\ v^2h+\frac{1}{2}g\left(\eta^2-2\eta z_b\right)\end{bmatrix},\mathbf{S}=\begin{bmatrix}0\\ -\frac{\tau_{bx}}{\rho}-g\eta\frac{\partial z}{\partial}\\ -\frac{\tau_{by}}{\rho}-g\eta\frac{\partial z}{\partial}\end{bmatrix} \tag{6}$$

where, $\tau_{bx}$ and $\tau_{by}$ are bed stress terms representing the energy dissipation influence of bed roughness on flow and are calculated empirically from the equations as given below.

$$\tau_{bx}=\rho g n^2 u\sqrt{u^2+v^2}\,/\,h^{1/3},\quad \tau_{by}=\rho g n^2 v\sqrt{u^2+v^2}\,/\,h^{1/3}.$$

The physical significance of other variables is the same as the above relevant content.

**Finite Volume Model**

Governing equations are discretized on the rectangular grid cells, and Fig.1 shows the schematic diagram of a discrete control cell. The adjacent cells of a controlling cell $(i, j)$ is $(i, j\text{-}1)$, $(i\text{+}1, j)$ $(i, j\text{+}1)$, $(i\text{-}1, j)$, and the public boundaries are $(i, j\text{-}1/2)$ $(i\text{+}1/2, j)$ $(i, j\text{+}1/2)$ $(i\text{-}1/2, j)$ respectively. The length of the cells at horizontal axis $x$ is $\Delta x$, while $\Delta y$ at the vertical axis $y$. The model basic variables of $h$ or $z$, $u$, $v$ are stored in the cell center and the terrain elevation is stored in the node of the cell when controlling equations are distributed, so the center elevation is calculated directly from the node elevation interpolation when the model calculates them.

Choosing any of the controlling cell $V_{(i,j)}$, the integral of formula (5) in the controlling cell is:

$$\int_{V_{(i,j)}} \frac{\partial \mathbf{U}}{\partial t} dV + \int_{V_{(i,j)}} \nabla \cdot \mathbf{E} dV = \int_{V_{(i,j)}} \mathbf{S} dV \qquad (7)$$

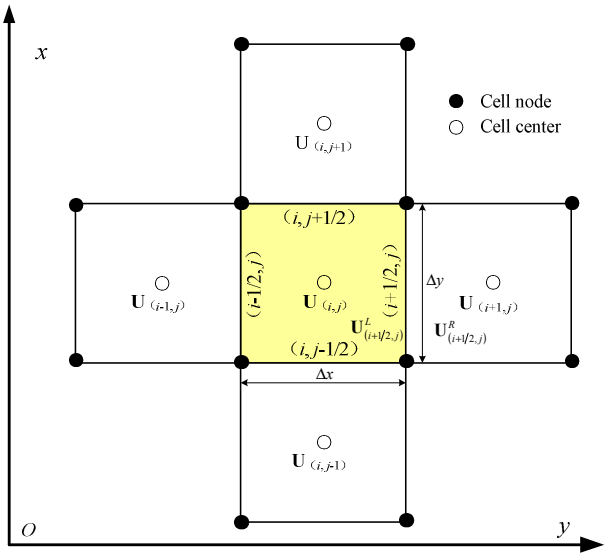


**Fig.1 Schematic diagram of a controlling cell**

Assuming that the average value **U** of the cell is stored in the cell center, converting the second term of area integral in the left of the formula (7) to line integral along the boundary of the controlling cell using the Gauss-Green, then formula (7) can be transformed into the integral equations as given below.

$$\int_{V_{(i,j)}} \frac{\partial \mathbf{U}}{\partial t} dV + \oint_{L_{(i,j)}} \mathbf{E} \cdot \mathbf{n} dL = \int_{V_{(i,j)}} \mathbf{S} dV \qquad (8)$$

where, $L(i,j)$ is the boundary of the grid cell$(i,j)$ , and the formula (8) can be written as follows:

$$\frac{\partial \mathbf{U}}{\partial t} \Delta A_{(i,j)} = -\sum_{k=1}^{4} \mathbf{E}^{k}_{(i,j)} \cdot \mathbf{n}^{k}_{(i,j)} \Delta L^{k}_{(i,j)} + \mathbf{S}_{(i,j)} \Delta A_{(i,j)} \qquad (9)$$

where,$\Delta A(i,j)$ represents the area of the cell$(i,j)$, and $\Delta A(i,j)= \Delta x \Delta y$; $\mathbf{E}^{k}_{(i,j)}$ is the flux of the boundary $k$, $k$=1,2,3,4, corresponding to the lower, right, upper and left boundary; $\mathbf{n}^{k}_{(i,j)}$ is the unit normal vector of boundary $k$; $\Delta L^{k}_{(i,j)}$ is the length of the boundary $k$, and the length of the left and right boundaries is$\Delta y$, while the upper and lower boundary is $\Delta x$. So you can get:

$$\mathbf{U}^{n+1}_{(i,j)} = \mathbf{U}^{n}_{(i,j)} - \frac{\Delta t}{\Delta x}\left(\mathbf{E}_{(i+1/2,j)} - \mathbf{E}_{(i-1/2,j)}\right) - \frac{\Delta t}{\Delta y}\left(\mathbf{E}_{(i,j+1/2)} - \mathbf{E}_{(i,j-1/2)}\right) + \Delta t \mathbf{S}_{i,j} \qquad (10)$$

where, $n$ represents the time, $(i,j)$is the cell index, and $\mathbf{E}_{(i\text{-}1/2,j)}$, $\mathbf{E}_{(i\text{+}1/2,j)}$, $\mathbf{E}_{(i,j\text{+}1/2)}$ and $\mathbf{E}_{(i,j\text{-}1/2)}$ represent the fluxes of the left and right boundaries, and that of the upper and lower boundaries of the cell$(i,j)$ respectively.

**Numerical Flux Calculation**

A Godunov-type scheme solves local Riemann problems at each cell interface to evaluate interface fluxes. The HLLC approximate Riemann solver is chosen to solve these local Riemann problems due to its advantages in offering automatic entropy fix and easy treatment of wetting and drying. Compared with the original HLL approach, the HLLC approximate Riemann solver also presents major benefits in modeling two-dimensional flows, especially when the solute transport is include. Ignoring the middle wave, the two-wave assumption of the HLL Riemann solver is only correct for purely one-dimensional problems an may result in excessive smearing of contact discontinuities for multidimensional simulations. Here, the two-dimensional shallow water equations are considered and hence the HLLC solver should be used [10].

**Time Integral**

MUSCL-Hancock method, where MUSCL stands for Monotone Upwind Schemes for Conservation Laws, is employed to achieve the second-order accuracy in time for the governing equations. It updates flow variables over a time interval via predictor and corrector steps in an explicit scheme.

In the predictor step, the time-marching formula for updating the cell-centered flow variables from formula (10) is：

$$\mathbf{U}_{(i,j)}^{n+1/2}=\mathbf{U}_{(i,j)}^{n}-\frac{\Delta t}{2}\left[\frac{\left(\mathbf{E}_{(i+1/2,j)}^{*}-\mathbf{E}_{(i-1/2,j)}^{*}\right)}{\Delta x}+\frac{\left(\mathbf{E}_{(i,j+1/2)}^{*}-\mathbf{E}_{(i,j-1/2)}^{*}\right)}{\Delta y}-\mathbf{S}_{(i,j)}\right] \tag{11}$$

where, the subscript $(i, j)$ represents cell index, the superscript $n$ denotes the time level，$\Delta t$ represents the time step, $\Delta x$ and $\Delta y$ are the cell sizes in the $x$- and $y$-direction. The bed slope terms are approximated with central differences and interface fluxes are determined at the midpoint of each cell face with linear interpolation.

In the corrector step, the flow variables are calculated over a full time step based on flow data from the predictor step. The explicit updating formula is given below.

$$\mathbf{U}_{(i,j)}^{n+1}=\mathbf{U}_{(i,j)}^{n}-\Delta t\left[\frac{\left(\mathbf{E}_{(i+1/2,j)}^{*n+1/2}-\mathbf{E}_{(i-1/2,j)}^{*n+1/2}\right)}{\Delta x}+\frac{\left(\mathbf{E}_{(i,j+1/2)}^{*n+1/2}-\mathbf{E}_{(i,j-1/2)}^{*n+1/2}\right)}{\Delta y}-\mathbf{S}_{(i,j)}^{n+1/2}\right] \tag{12}$$

Numerical fluxes are calculated using the HLLC approximate Riemann solver, where the face values of the flow variables are again obtained using slope-limited interpolation formula.

**Discretization of Source Terms**

The discretization of the bed slope term and friction term are treated respectively.

The bed slope terms are calculated with the central difference scheme, compatible with the Godunov- type finite volume model, in the $x$- and $y$-direction. And the discretized equations are given below.

$$-g\eta\frac{\partial z_b}{\partial x}=-g\overline{\eta}\left(\frac{z_{bi+1/2,j}-z_{bi-1/2,j}}{\Delta x}\right),\quad -g\eta\frac{\partial z_b}{\partial y}=-g\overline{\eta}\left(\frac{z_{bi,j+1/2}-z_{bi,j-1/2}}{\Delta y}\right) \tag{13}$$

Where $\overline{\eta}=\left(\eta_{i-1/2,j}^{R}+\eta_{i+1/2,j}^{L}\right)/2$， $\overline{\eta}=\left(\eta_{i,j-1/2}^{R}+\eta_{i,j+1/2}^{L}\right)/2$。

The friction source terms are solved by a splitting point-implicit scheme for better stability [11] and it is equivalent to solve the following ordinary differential equations as given below.

$$\frac{d\mathbf{U}}{dt}=\mathbf{S}_f \tag{14}$$

where，$\mathbf{S}_f=[0\ S_{fx}\ S_{fy}]^{\mathrm{T}}$，$S_{fx}=-\tau_{bx}/\rho, S_{fy}=-\tau_{by}/\rho$. The formula (14) is expanded in the Taylor series to obtain the implicit expression as given below.

$$\mathbf{S}_f^{n+1} = \mathbf{S}_f^n + \left(\frac{\partial \mathbf{S}_f}{\partial \mathbf{U}}\right)^n \Delta \mathbf{U} + o\left(\Delta \mathbf{U}^2\right) \quad (15)$$

where, $n$ represents the time level,$\Delta\mathbf{U}=\mathbf{U}^{n+1}-\mathbf{U}^n$, $(\partial\mathbf{S}_f/\partial\mathbf{U})$ is the Jacobian matrix of $\mathbf{S}_f$. The formula (15) can be transformed into the equation as given below.

$$\left[\mathbf{I} - \Delta t\left(\frac{\partial \mathbf{S}_f}{\partial \mathbf{U}}\right)^n\right]\Delta \mathbf{U} = \Delta t \mathbf{S}_f^n \quad (16)$$

where, $\mathbf{I}$ is identity matrix.

## Treatment of Complex Boundary Conditions

Wet and dry boundary treatment is a hot and difficult question in the calculation of extreme flow. The processes of wet and dry on the complex terrain are treated through amending the governing equations, and it can use a method to amend the local bed [9] to avoid the generation of the false flow on the dry bed.

Incorrect treatment of wall boundary will bring a false viscosity in the numerical solution when applied to the curve or irregular boundary and result in numerical oscillations. A simple and practical boundary treatment method proposed in the paper [12] is used to handling this problem.

## Validation Using a Popular Example

The purpose of this example is to test the ability of the model to deal with discontinuity and the ability to adapt to the complex boundary. The calculation area is a flat rectangle channel of 40m long, the width of the entrance on the upper reach of the channel is 30m, while it has a inward contraction of 8.95 degrees on the right bank of the river 10 meters away from the entrance. Hydraulic jumps of a certain angle are formed when the water flows to the contraction of the channel. A boundary of rapid flow is given at the entrance, that is, $u$=8.57m/s, $v$=0m/s, the initial water depth $h$=1m, and then a boundary of a free outflow is given at the outlet. The frictional resistance is not taken into account when calculating.

Analytical solution for the given boundary conditions is that: it generates a steady-state supercritical flow, and the study area is divided into two parts by the hydraulic jump; also there is an angle of 30 degrees between the flow direction and the hydraulic jump, and the water depth of the hydraulic jump is 1.5m.

The model ability of adapt to the complex boundary is shown in Fig.2 without treatment of the boundary when the sharp and steep peaks appear on the water surface near the boundary, causing numerical oscillations, and the flow direction is inconsistent with the boundary direction, incompatible with the real physical phenomena. The model ability of adapt to the complex boundary is shown in Fig.3 after treatment of the boundary. An angle of 30 degrees exists between the flow direction and the hydraulic jump, and the water depth of the hydraulic jump is 1.5m, well capturing the shock wave in 2-3 grid cells, which shows that the model adopted can well adapt to the complex boundary and deal with discontinuous solutions with high accuracy.

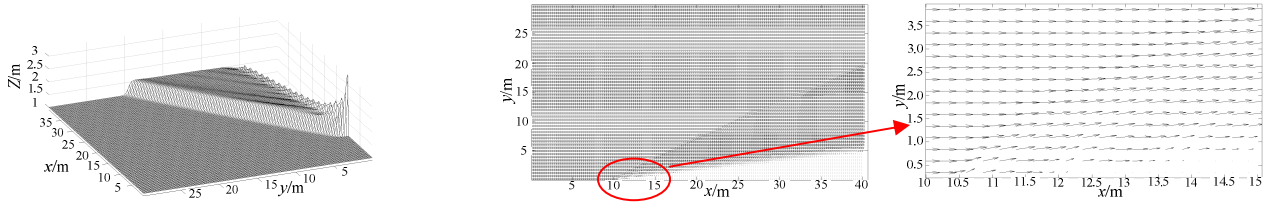


（a）Three-dimensional water level （b）Velocity distribution

**Fig.2 Computational results without boundary treatment**

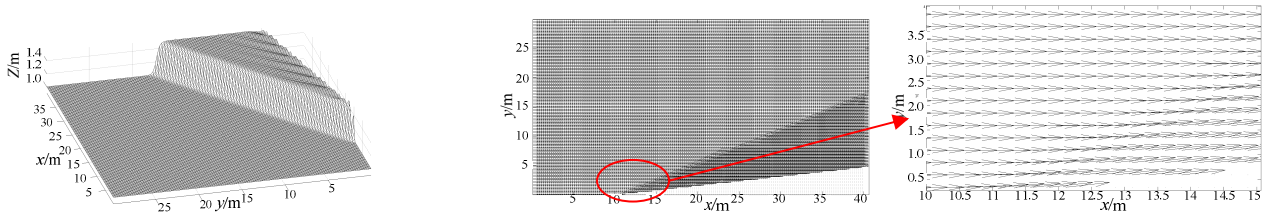


（a）Three-dimensional water level （b）Velocity distribution

**Fig.3 Computational results after boundary treatment**

## Conclusions

A high precision structured-based finite volume model for numerical simulation of dam-and dyke-breach flow was proposed. The model regarded the fully two-dimensional shallow water equations as the governing equations, and used the Godunov-type finite volume shock- capturing schemes HLLC to calculate flow flux. Its spatial and temporal accuracy were improved to two order accuracy using the slop limiter and predict-correct method, and the slope source terms and friction source terms were treated with central difference scheme and fully implicit method respectively. And then a robust procedure was adapted in the model to efficiently and accurately simulate the movement of wet and dry boundary and a method of high calculation efficiency was applied in the treatment of complex boundary. A popular example was used to validate the capability of the model. The result shows that the model can capture flow processes over irregular boundary accurately and shows good stability and accuracy.

## Acknowledgement

This work was financially supported by the National Natural Science Foundation of China (No. 51309254), the National Key Technologies R&D Program of China during the 12th Five-year Plan Period (No. 2013BAB05B01), the Special Scientific Research Fund of China Institute of Water Resources and Hydropower Research (No.1401), the National Natural Science Foundation of China (No.51209223) and the National Key Basic Research Program of China (No.2013CB036406).

## References

[1] P.F. Hei, H.W. Fang, Z.C. Chen, J.X. Xia: Journal of Hydraulic Engineering No.2, Vol.44 (2013), p.173.(in Chinese)

[2] Z.Y. Yue,Z.X Cao,Y.W. Li,Z.M. Fu,J. Yan: Chinese Journal of Hydrodynamics, Ser.A, No.3, Vol.26(2011), p.359.(in Chinese)

[3] J.M. Zokagoa, A Soulaimani: Computer Methods in Applied Mechanics and Engineering, Vol. 199(2010), p.2281.

[4] B.B Huang, H.W. Fang,B. Liu: Chinese Journal of Hydrodynamics, Ser. A, No.6, Vol. 18 (2003), p.679.(in Chinese)

[5] L.Begnudelli,B.F.Sanders: Journal of Hydraulic Engineering, No.4, Vol.132 (2006), p.371.

[6] A. Valiani, L Begnudelli: Journal of Hydraulic Engineering, No.7, Vol.132 (2006), p.652.

[7] P.A. Sleigh, P.H Gaskell:Computers & Fluids,No.4,Vol.27(1998),p.479.

[8] P. Brufau, M.E. Vazquez-Cendon, P Garcia-Navarro: International Journal of Numerical Methods in Fluids, No.3, Vol.39 (2002), p.247.

[9] Q. H. Liang, A. G. L Borthwick: Computers & Fluids, Vol.38(2009),p.221.

[10] L. Fraccarollo, E.F. Toro: J. Hydraul. Res., No.6, Vol.33 (1995), p.843.

[11] F.R. Fiedler, J.A Ramirez: International Journal for Numerical Methods in Fluids, No.2, Vol.32 (2000), p.219.

[12] Q.H. Liang, A.G.L. Borthwick: International Journal for Numerical Methods in Fluids, No.11, Vol.56 (2008), p.2091.

*Applied Mechanics and Materials Vols. 580-583 (2014) pp 2996-3002*
*© (2014) Trans Tech Publications, Switzerland*
*doi:10.4028/www.scientific.net/AMM.580-583.2996*

# Novel partitioned integration method based on Newmark's scheme for structural dynamic problems

JIA Chuanguo[1,a*], LI Yingmin[2, b], XIA Hongliu[3,c], LIU Liping[4,d]

[1] Key Laboratory of New Technology for Construction of Cities in Mountain Area, College of Civil Engineering, Chongqing University, Chongqing 400045, P. R. China

[2] Key Laboratory of New Technology for Construction of Cities in Mountain Area, College of Civil Engineering, Chongqing University, Chongqing 400045, P. R. China

[3] Key Laboratory of New Technology for Construction of Cities in Mountain Area, College of Civil Engineering, Chongqing University, Chongqing 400045, P. R. China

[4] Key Laboratory of New Technology for Construction of Cities in Mountain Area, College of Civil Engineering, Chongqing University, Chongqing 400045, P. R. China

[a]jiachuanguo@cqu.edu.cn, [a]liyingmin@cqu.edu.cn, [c]xhlpjy@163.com, [d]zhhllp@163.com

**Keywords:**differential-algebraic equations, Newmark methods, subcycling, partitioned methods

**Abstract:** Systems of ODEs arising from transient structural dynamics generally exhibit high-frequency/low-frequency and linear/nonlinear behaviours of subsets of state variables. This paper resorts to the use of different time integrators with different time steps for subsystems, to tailor each method and its time step to the solution behaviour of the corresponding subsystem. Anovel partitioned integration method with the acceleration continuity is proposed whose velocity continuity is also ensured by means of the mass projection strategy. Both its stability and accuracy properties are examined through numerical analysis on Single-DoF split mass system.

## Introduction

Systems of Ordinary Differential Equations (ODEs) arising from transient structural dynamics, like structure-soil interaction problems or structural control problems, very often exhibit high-frequency/low-frequency and linear/nonlinear behaviours of subsets of state variables. In view of those systems, researchers have devoted significant effort to implement partitioned time integration methods to achieve greater computational efficiency. Those with different time steps are also called subcycling[1] or multi-time-step methods[2]. Arnold et al.[3] restricted the communication between subsystems to discrete synchronization points and required interpolation/extrapolation owing to the use of different time steps. They stated that subcycling techniques could suffer from numerical instability that might be further exacerbated by discretization errors introduced by interpolation/extrapolation. To improve stability and/or accuracy, many partitioned integration methods were conceived, including stabilization techniques [4-6].

In transient structural dynamics, partitioned methods mainly relied on Linear Multi-Step methods that were applied to the Euler-Lagrange form of equations of motion[7]. A distinct feature of these algorithms was the use of dual unknowns, i.e. the Lagrange multipliers, in order to enforce the continuity between subsystems. Gravouil and Combescure solved the DAE system of equations with a structural integrator, i.e. the Newmark-$\beta$ scheme[8], thus obtaining a multi-time-step explicit-implicit method [2], hereafter referred to the GC method. In a greater detail, they conceived a method that was endowed with a conservation law and therefore was spectrally stable. However, the accuracy reduced to first order when subcycling was employed.

It was found that the GC method reduced to be first order accuracy due to its velocity continuity and if the acceleration continuity was considered within the framework of the GC method the second order accuracy could be retained. Moreover, the implementation of the acceleration continuity may cause instability and inneglectable displacement drift at the interface. In this respect, a stabilization technique, i.e. the mass projection, is required at the end of each system time step. To

overcome the order reduction without increasing drift and computational cost, a novel method is conceived considering the acceleration continuity and the mass projection. Successively, numerical analyses on single DoF split-mass systems are carried out to investigate its stability and accuracy. Lastly, the insight gained from the analyses of those analyses and the consequent conclusions are confirmed by means of numerical experiments on Single- and Two-DoF split-mass systems.

## Novel partitioned time integration method

For simplicity, consider a system divided into two subdomains *A* and*B*. The basic principles of the novel method can also be illustrated in Fig. 1. Its solution procedure can be detailed as:

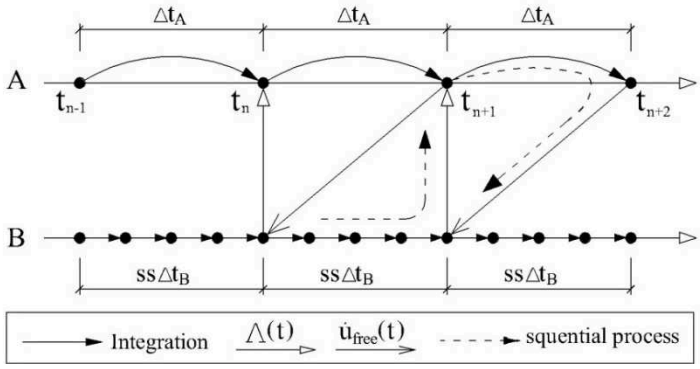


Fig. 1 The solution procedure of the proposed method

1. Solve the free problem in subdomain*A*.

$$\begin{aligned} \tilde{\mathbf{M}}_A \ddot{\mathbf{u}}^A_{n+1,free} &= \mathbf{F}^A_{ext,n+1} - \mathbf{K}_A \tilde{\mathbf{u}}^A_n - \mathbf{C}_A \tilde{\dot{\mathbf{u}}}^A_n \\ \mathbf{u}^A_{n+1,free} &= \tilde{\mathbf{u}}^A_n + \alpha^A_1 \ddot{\mathbf{u}}^A_{n+1,free} \\ \dot{\mathbf{u}}^A_{n+1,free} &= \tilde{\dot{\mathbf{u}}}^A_n + \alpha^A_2 \ddot{\mathbf{u}}^A_{n+1,free} \end{aligned} \tag{1}$$

where

$$\begin{aligned} \tilde{\mathbf{u}}^A_n &= \mathbf{u}^A_n + \Delta t \dot{\mathbf{u}}^A_n + \Delta t^2 \left( \frac{1}{2} - \beta_A \right) \ddot{\mathbf{u}}^A_n \\ \tilde{\dot{\mathbf{u}}}^A_n &= \dot{\mathbf{u}}^A_n + \Delta t \left( 1 - \gamma_A \right) \ddot{\mathbf{u}}^A_n \\ \alpha^A_1 &= \beta_A \Delta t^2 \quad \text{and} \quad \alpha^A_2 = \gamma_A \Delta t. \end{aligned} \tag{2}$$

2. Interpolate the free velocity in subdomain*A*.

$$\dot{\mathbf{u}}^A_{n+j/ss,free} = \left( 1 - \frac{j}{ss} \right) \dot{\mathbf{u}}^A_{n,free} + \frac{j}{ss} \dot{\mathbf{u}}^A_{n+1,free}. \tag{3}$$

3. Solve the free problem in subdomain B.

$$\begin{aligned} \tilde{\mathbf{M}}_B \ddot{\mathbf{u}}^B_{n+j/ss,free} &= \mathbf{F}^B_{ext,n+j/ss} - \mathbf{K}_B \tilde{\mathbf{u}}^B_{n+(j-1)/ss} - \mathbf{C}_B \tilde{\dot{\mathbf{u}}}^B_{n+(j-1)/ss} \\ \mathbf{u}^B_{n+j/ss,free} &= \tilde{\mathbf{u}}^B_{n+(j-1)/ss} + \alpha^B_1 \ddot{\mathbf{u}}^B_{n+j/ss,free} \\ \dot{\mathbf{u}}^B_{n+j/ss,free} &= \tilde{\dot{\mathbf{u}}}^B_{n+(j-1)/ss} + \alpha^B_2 \ddot{\mathbf{u}}^B_{n+j/ss,free} \end{aligned} \tag{4}$$

where

$$\begin{aligned}
\tilde{\mathbf{M}}_B &= \mathbf{M}_B + \alpha_1^B \mathbf{K}_B + \alpha_2^B \mathbf{C}_B \\
\tilde{\mathbf{u}}^B_{n+(j-1)/ss} &= \mathbf{u}^B_{n+(j-1)/ss} + \frac{\Delta t}{ss}\dot{\mathbf{u}}^B_{n+(j-1)/ss} + \left(\frac{\Delta t}{ss}\right)^2\left(\frac{1}{2}-\beta_B\right)\ddot{\mathbf{u}}^B_{n+(j-1)/ss} \\
\tilde{\dot{\mathbf{u}}}^B_{n+(j-1)/ss} &= \dot{\mathbf{u}}^B_{n+(j-1)/ss} + \frac{\Delta t}{ss}(1-\gamma_B)\ddot{\mathbf{u}}^B_{n+(j-1)/ss} \\
\alpha_1^B &= \beta_B\left(\frac{\Delta t}{ss}\right)^2 \quad \text{and} \quad \alpha_2^B = \gamma_B\frac{\Delta t}{ss}.
\end{aligned} \tag{5}$$

4. Calculate the Lagrange multiplier at end of the substep and solve the link problem in Subdomain $B$. The Lagrange multiplier can be obtained with the following equations

$$\Lambda_{n+j/ss} = -\left(\mathbf{H}^*\right)^{-1}\left(\mathbf{G}_A\ddot{\mathbf{u}}^A_{n+j/ss,free} + \mathbf{G}_B\ddot{\mathbf{u}}^B_{n+j/ss,free}\right) \tag{6}$$

where $\mathbf{H}^* = G_A\tilde{\mathbf{M}}_A^{-1}G_A^T + G_B\tilde{\mathbf{M}}_B^{-1}G_B^T$. With the Lagrange multiplier at the end of the substep, we can calculate the link solution.

$$\begin{aligned}
\tilde{\mathbf{M}}^B\ddot{\mathbf{u}}^B_{n+j/ss_{link}} &= \left(\mathbf{G}^B\right)^T\Lambda_{n+j/ss} \\
\mathbf{u}^B_{n+j/ss_{link}} &= \alpha_1^B\ddot{\mathbf{u}}^B_{n+j/ss_{link}} \\
\dot{\mathbf{u}}^B_{n+j/ss_{link}} &= \alpha_2^B\ddot{\mathbf{u}}^B_{n+j/ss_{link}}.
\end{aligned} \tag{7}$$

Finally, the kinematic quantities in subdomain $B$ can be obtained with summing the free solutions and link solutions.

$$\begin{aligned}
\mathbf{u}^B_{n+j/ss} &= \mathbf{u}^B_{n+j/ss,free} + \mathbf{u}^B_{n+j/ss_{link}} \\
\dot{\mathbf{u}}^B_{n+j/ss} &= \dot{\mathbf{u}}^B_{n+j/ss,free} + \dot{\mathbf{u}}^B_{n+j/ss_{link}} \\
\ddot{\mathbf{u}}^B_{n+j/ss} &= \ddot{\mathbf{u}}^B_{n+j/ss,free} + \ddot{\mathbf{u}}^B_{n+j/ss_{link}}.
\end{aligned} \tag{8}$$

5. Solve the link problem in subdomain $A$.

$$\begin{aligned}
\tilde{\mathbf{M}}^A\ddot{\mathbf{u}}^A_{n+1_{link}} &= \left(\mathbf{G}^A\right)^T\Lambda_{n+1} \\
\mathbf{u}^A_{n+1_{link}} &= \alpha_1^A\ddot{\mathbf{u}}^A_{n+1_{link}} \\
\dot{\mathbf{u}}^A_{n+1_{link}} &= \alpha_2^A\ddot{\mathbf{u}}^A_{n+1_{link}}.
\end{aligned} \tag{9}$$

Similarly, the kinematic quantities in subdomain A can be obtained as follows,

$$\begin{aligned}
\mathbf{u}^A_{n+1} &= \mathbf{u}^A_{n+1,free} + \mathbf{u}^A_{n+1_{link}} \\
\dot{\mathbf{u}}^A_{n+1} &= \dot{\mathbf{u}}^A_{n+1,free} + \dot{\mathbf{u}}^A_{n+1_{link}} \\
\ddot{\mathbf{u}}^A_{n+1} &= \ddot{\mathbf{u}}^A_{n+1,free} + \ddot{\mathbf{u}}^A_{n+1_{link}}
\end{aligned} \tag{10}$$

6. Perform the mass projection. The additional Lagrange multiplier can be calculated as

$$\Gamma = -\left(H^*\right)^{-1}\left(G_A\dot{u}^A_{n+1} + G_B\dot{u}^B_{n+1}\right). \tag{11}$$

And then the updated solution of velocity can be obtained as

$$\tilde{\dot{u}}_{n+1}^{A} = \dot{u}_{n+1}^{A} + \left(\tilde{M}_{A}\right)^{-1} G_{A}^{T}\Gamma \quad \text{and} \quad \tilde{\dot{u}}_{n+1}^{B} = \dot{u}_{n+1}^{B} + \left(\tilde{M}_{B}\right)^{-1} G_{B}^{T}\Gamma \tag{12}$$

To continue the computation in the next time step, the following formulations are needed:

$$\dot{u}_{n+1}^{A} = \tilde{\dot{u}}_{n+1}^{A} \text{ and } \dot{u}_{n+1}^{B} = \tilde{\dot{u}}_{n+1}^{B}. \tag{13}$$

This solution procedure does not increase computation cost remarkably, with respect to the original GC method. In the procedure, only the mass projection increases the computation cost and this increment of computation cost is limited for the reason that both Lagrange multipliers requires the same inverse matrix $\mathbf{H}^{*-1}$.

**Numerical performance evaluations of the novel method**

A test problem is considered where a Single-DoF system is split into two subsystems *A*and *B* linked by an interface reaction force $\Lambda$indicated in Figure 2. This test problem were widely used to assess partitioned methods[9, 10]. For simplicity, we choose the following system variables $m=1$ and $k=1$, and $b_1$ defined as

$$b_1 = \frac{m_A}{m_B} = \frac{k_B}{k_A} \tag{14}$$

**Stability analysis**

As mentioned before, the acceleration continuity suffers from stability problem and the mass projection is benefit for its stability. In the sense, the stability of the proposed partitioned method is unknown. In this subsection, the stability analysis is performed by the spectral approach on a Single-DoF split-mass system. In order to highlight the numerical dissipation property of the partitioned method, we consider no physical damping. Moreover, no external force is involved. The application of the methods to this model problem leads to recursive formula of this type, $\mathbf{y}_{n+1} = \mathbf{R}\mathbf{y}_n$. $\mathbf{R}$ defines the amplification matrix. Let $|\lambda_i|$ denote the modulus of an eigenvalues of $\mathbf{R}$. The stability condition requires that $|\lambda_i| \le 1$ and $|\lambda_i| = 1$ with multiplicity 1.

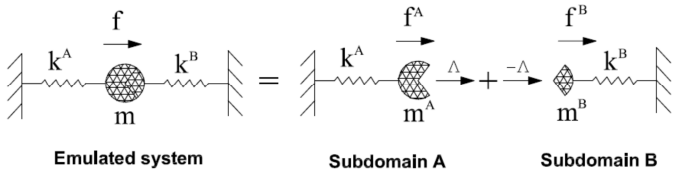


Fig. 2 A Single-DoF emulated system with the relevant split mass

It is noted that the method is not self-starting which requires initialization step. And therefore choosing sufficient state variables for the state vector $\mathbf{y}_n$ is required. It is founded in the solution procedure that the interpolation equation (3) requires the free solution of previous step. Therefore, the state vector $\mathbf{y}_n$ must include the state variables at time $t_{n-1}$. Moreover, the method imposes not only acceleration constraint and velocity constraint at the interface. As a consequence, the state vectors involved in the spectral stability analysis is considered as follows:

$$y_n = \left\{u_{n-1}^{A}, \dot{u}_{n-1}^{A}, \ddot{u}_{n-1}^{A}, u_n^{A}, \dot{u}_n^{A}, \ddot{u}_n^{A}, u_n^{B}\right\} \tag{15}$$

Differently from a direct integration method, $\mathbf{R}$ of a partitioned method does not only depend on system characteristics but also on *ss* and $b_1$ For this reason, two scenarios are intentionally investigated: *ss*=10, $b_1$=1 and *ss*=5, $b_1$=2.

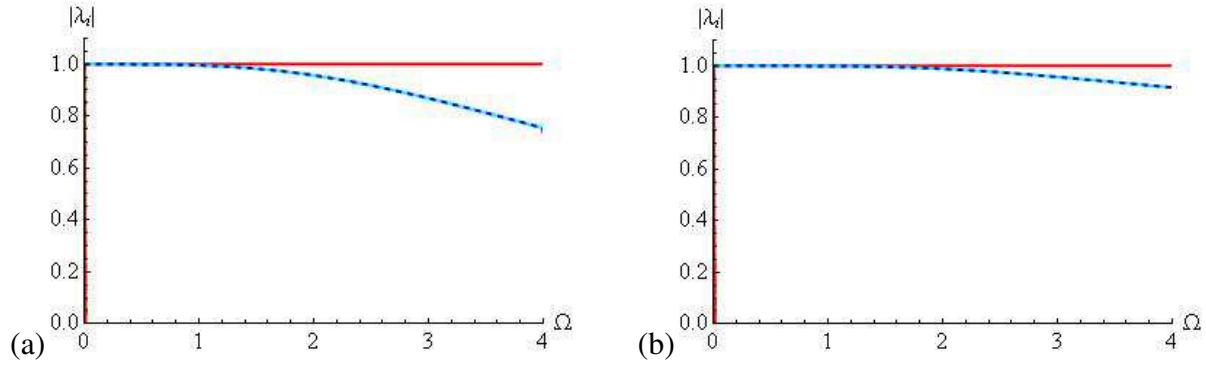


Fig. 3 $|\lambda_i|$ for the partitioned method: (a) $b_1 = 1, ss = 10$ and (b) $b_1 = 2, ss = 5$.

The influences of the acceleration constraint and the mass projection on the stability of the underlying method is analysed in Fig. 3. The number of eigenvalues involved in the recursive formula is 7, which coincides with the size of the state vector $\mathbf{y}_n$. Only two of them are principal eigenvalues which are complex conjugate, whereas the others are spurious which are unitary or zero. This is because both acceleration constraint and velocity constraint at the interface are imposed. Moreover, it can be concluded from the spectral radius plots that the proposed method appears to be stable within all cases considered and slight numerical dissipation is introduced.

**Accuracy analysis**

Numerical study on the single-DoF split mass system is considered. Again, the single-DoF split mass system is assumed be linear and undamped. Its external force is only considered on Subdomain $A$, i.e., $F^A = \sin(2t)$ and its initial displacement and velocity are set to be 0 and 1, respectively. Two cases are considered here: $b_1 = 2, ss = 10$ and $b_1 = 4, ss = 5$. The global errors at $t = 5s$ versus the system time steps $\Delta t_A$ are depicted in Fig 4. The results of the accuracy analysis are in agreement with the fact that the acceleration constraint endows with second order accuracy in displacement, velocity and acceleration responses.

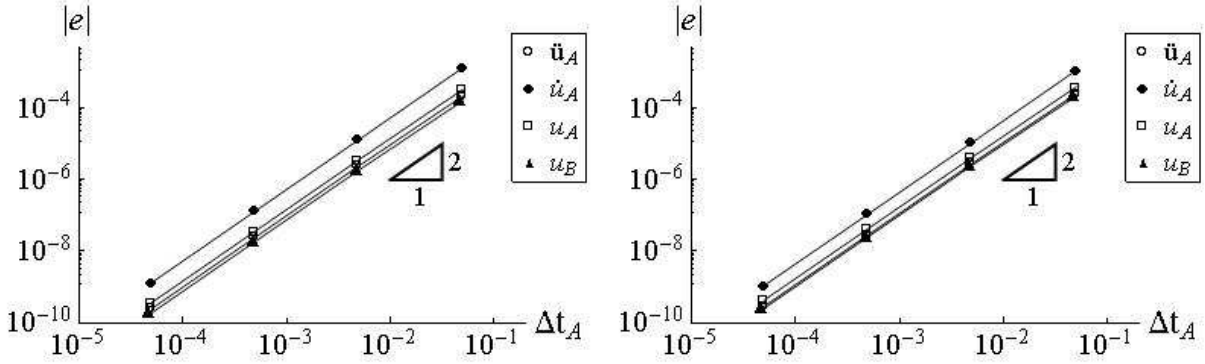


Fig. 4 Global error of the Single-DoF split mass system integrated by the proposed method: (a) $b_1 = 2, ss = 10$ and (b) $b_1 = 4, ss = 5$.

**Representative numerical simulations**

To investigate the merits of the novel method, a series of simulations are conducted on a Single- and Two-DoF system by means of the GC method, and the acceleration-constrained methods without and with the mass projection. The additional mass and spring in the Two-DoF system as shown in Fig 5 are set to be $m_2 = 2$, $k_2 = 3$. In order to examine numerial discrepancies of those methods, a relatively large time step is used, i.e., $\Delta t_A = 0.5s$.

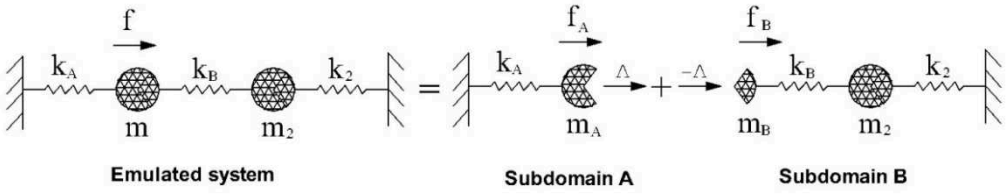


Fig. 5 An emulated Two-DoF system

The numerical solutions in terms of displacement are plotted in Fig 6. It is observed that the original GC method exhibits noticeable oscillation decay and slight period delay. For the method based on the acceleration continuity, less oscillation decay is perceived but slight drift appears at the interface. Obviously, the method with the mass projection entails favourable results: moderate oscillation decay and negligible drift at the interface. Moreover, it is observed in the simulations that the computation time of the novel method only slight overpasses the GC method.

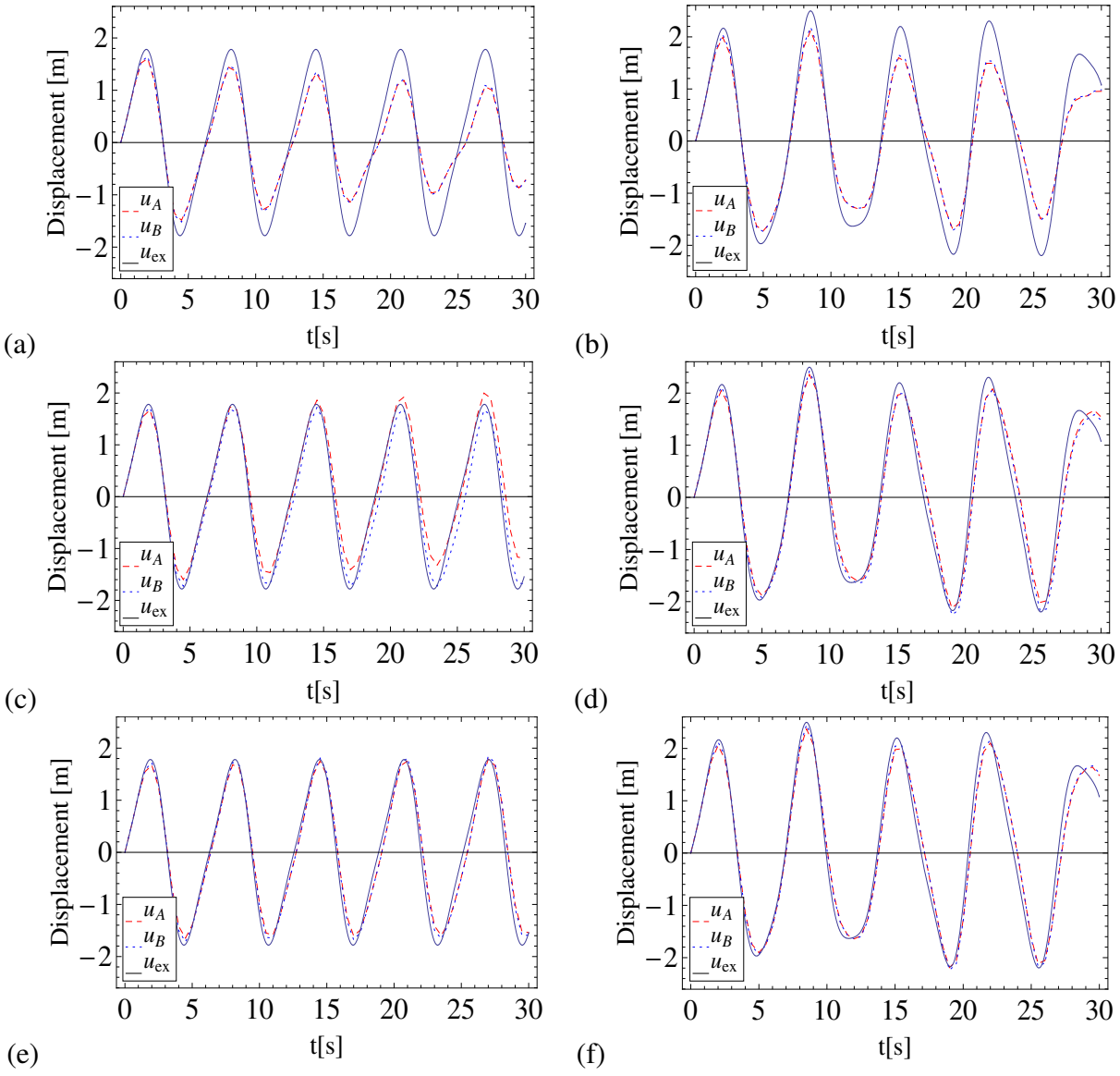


Fig. 6 Numerical simulations of the Single-DoF split mass system with $b_1$=2 (the left figures) and the Two-DoF system with $b_1$=1 (the right figures) integrated by the partitiioned methods with$ss$=10: (a) and (b) the original GC method; (c) and (d) the modified method without projection; (e) and (f) the modified method with projection.

## Conclusions

In this parper, we extend a partitioned integration method with subcycling from the velocity continuity to the acceleration continuity in order to improve its order of accuracy.This extension renders second-order accuracy but induces drift-off effect at the interface. In this respect, the mass projection technique is conceived at the end of each system time step to stabilize the method and to diminish drift-off effect.Furthermore, numerical analyses of the novel method are performed in terms of its stability and accuracy. It is observed that the method allows all the kinematic quantities to be second order accurate without losing stability. Finally, numerical simulations are carried out on Single- and Two-DoF systems with split mass. The simulation results are consistent with the numerical analysis.

## Acknowledgements:

The authors gratefully acknowledge the financial support from the Foundation for Sci & Tech Research Project of Chongqing (No. CSTC2 011BB6077).

## Reference

[1] Daniel WJT. A study of the stability of subcycling algorithms in structural dynamics [J]. Computer Methods in Applied Mechanics and Engineering[ISSN 0045-7825], 1998, 156(1):1-13.

[2] Gravouil A, and Combescure A. Multi-time-step Explicit-Implicit Method for Non-linear Structural Dynamics [J].International Journal for Numerical Methods in Engineering[ISSN 1097-0207], 2001, 50(1): 199-225.

[3] Arnold M,Carrarini A,Heckmann A, Hippmann, G. Simulation techniques for multidisciplinary problems in vehicle system dynamics [J].Vehicle System Dynamics[ISSN 0042-3114], 2003, 40(1): 17-36.

[4] Baumgarte J. Stabilization of constraints and integrals of motion in dynamical systems [J]. Computer Methods in Applied Mechanics and Engineering[ISSN 0045-7825], 1972, 1: 1-16.

[5] Blajer W. Augmented Lagrangian formulation: geometrical interpretation and application to systems with singularities and redundancy [J]. Multibody System Dynamics[ISSN 1384-5640], 2002, 8(2): 141-159.

[6] Bayo E, Ledesma R. Augmented Lagrangian and mass-orthogonal projection methods for constrained multibody dynamics [J]. Journal of Nonlinear Dynamics[ISSN 0924-090x], 1996, 9(1): 113-130.

[7] Farhat C, Crivelli L,Gèradin.M. Implicit time integration of a class of constrained hybrid formulations - Part I: Spectral stability theory [J]. Computer Methods in Applied Mechanics and Engineering[ISSN 0045-7825], 1995, 125(1): 71-107.

[8] Hughes TJR. The Finite Element Method, Linear Static and Dynamic Finite Element Analysis [M]. Englewood Cliffs:Prentice-Hall,1998: 490-569.

[9] Bonelli A, Bursi O S, He L, Pegon P,Magonette G. Convergence analysis of a parallel interfield method for heterogeneous simulations with dynamic substructuring [J]. International Journal for Numerical Methods in Engineering[ISSN 1097-0207], 2008, 75(7): 800—825.

[10] Prakash A. A. Multi-time-step Domain Decomposition and Coupling Methods for Non-Linear Structural Dynamics[D]. Ph. D. dissertation, Urbana-Champaign:University of Illinois, 2007.

*Applied Mechanics and Materials Vols. 580-583 (2014) pp 3003-3006*
*© (2014) Trans Tech Publications, Switzerland*
*doi:10.4028/www.scientific.net/AMM.580-583.3003*

# Subgrade limit bearing capacity calculation using slip line method

Qianqian Sun[1, a], Taiquan *Zhou [1, b], Xiaojie Gu[1, c]

[1]School of Environmental and Civil Engineering, Jiangnan University, Wuxi Jiangsu 214122, China;

[a]sunqq_2@126. [b]zhoutaiquan@163.com [c]xgyx2007@126.com

**Keywords:** slip line method; bearing capacity of foundation soil; Terzaghi bearing capacity of foundation soil

**Abstract:** Limit bearing capacity of foundation soil was studied in the paper using slip line method. Slip line results are found to be consistent with the results calculated by Terzaghi theoretical formula and Hansen theoretical formula. Then the influence of factors such as cohesion and friction angle is studied under complete smooth or complete tough conditions. The results show that in a certain range, limit bearing capacity of foundation increases with the increase of $C_0$, Φ. Limit bearing capacity of foundation under complete smooth condition is lower than the complete tough one.

## Introduction

The purpose of studying limit bearing capacity is that the pressure on the underside of the building foundation must be limited. The subgrade limit bearing capacity is not allowed to reach the limit bearing capacity. Besides, the subgrade limit bearing capacity has a certain degree of safety to ensure that the foundation will not occur sliding failure. At the same time, to ensure that the structure will not be due to excessive deformation of foundation affects their normal use. Therefore, determining the limit bearing capacity of foundation is an urgent problem to engineering practice to solve.

There are two main methods to determine the limit bearing capacity, the first one is field test methods, such as standard penetration test, static cone penetration test and pressure meter text. After the establishment of a regional relationship, limit bearing capacity of foundation value can be obtained. The other one is theoretical calculation. In 1920, according to the limit equilibrium theory Prandtl derived the formula of limit capacity of strip foundation. When Prandtl derived the formula, he assumed the underside between the foundation and the soil smooth and the soil under foundation without the weight. So the sliding surface obtained is in form of two flat and intermediate transition logarithmic spiral surface. Duo to the assumption made by Prandtl inconsistent with the actual conditions, the result is rough. In 1940s according to the basic theory of Prandtl, Terzaghi proposed limit bearing capacity formula considering the weight of the soil under foundation. In 1950s Meyerhoff proposed limit bearing capacity formula applicable to deep foundation. To be more accurate researching limit bearing capacity of foundation, we use the analysis software Analysis of Bearing Capacity to study it.

## Slip line theory

In calculating the limit bearing capacity of foundation with slip line method, assuming the soil is the ideal rigid-plastic material, obey Mohr-Coulomb criterion or Terzaghi theory. Under load, in certain direction the soil in the plastic zone flowing freely, the deformation of soil large and elastic deformation ignored, the rigid-plastic assumption can deduce more reliable approximate solution. Otherwise, it may lead to large errors. In geotechnical stability problems—the problem of foundation bearing capacity, stress problems of retaining walls and stability problems of slope, the slip line theory has been widely applied.

## Software

ABC (Analysis of Bearing Capacity)is a computer program that uses the method of stress characteristics (also known as the slip line method) to solve the classical geotechnical bearing

capacity problem of a rigid foundation, resting on a cohesive-frictional soil mass, loaded to failure under a central vertical force. Fig.1 shows the terminology used.

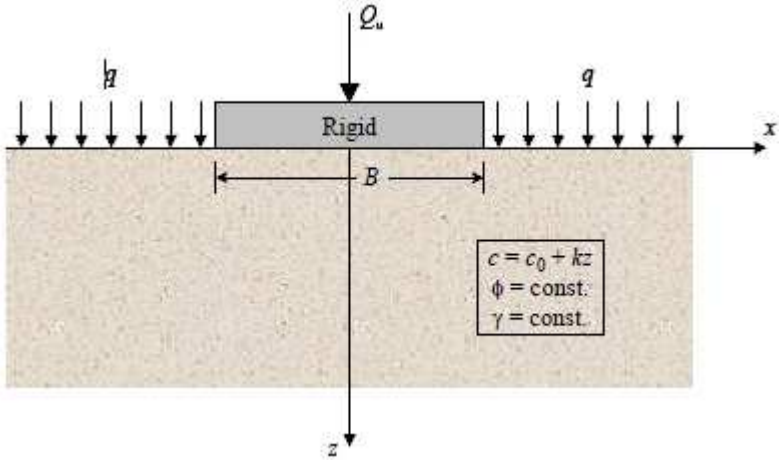


Fig.1 Problem definition

**Basic example**

Foundation soil gravity $\gamma$=17KN/m$^3$, friction angle $\Phi$=18°, cohesion $C_0$=10KPa, foundation width B=2.8m (circular foundation R=2.8m), the foundation depth=2m.At this point the depth is not considered directly. Instead it is replaced by a surcharge pressure of q=$\gamma$ D to simplify the equilibrium. According to the basic example, four foundations with different material strength parameter under smooth or tough conditions are considered in the analysis. The basic information for the model is shown in Table.1 The values and the modes of soil failure are obtained using the ABC softare,shown in Fig.2. Slip line results using the software—ABC are found to be consistent with the results calculated by Terzaghi theoretical formula and Hansen theoretical formula, shown in Fig.3.

Table.1Denote for four computational models

| The type of foundation | Strip and smooth | Strip and tough | Circular and smooth | Circular and tough |
|---|---|---|---|---|
| Number | F1 | F2 | F3 | F4 |

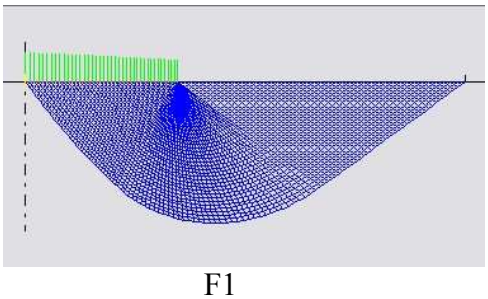

F1

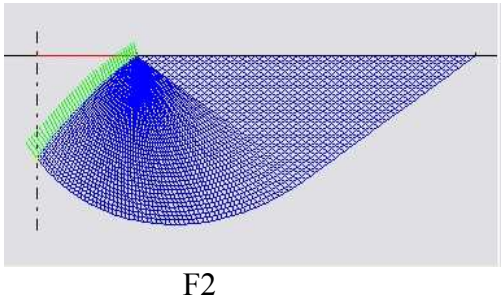

F2

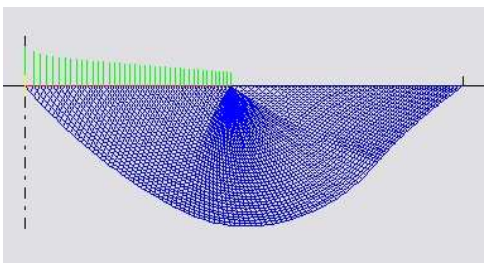

F3

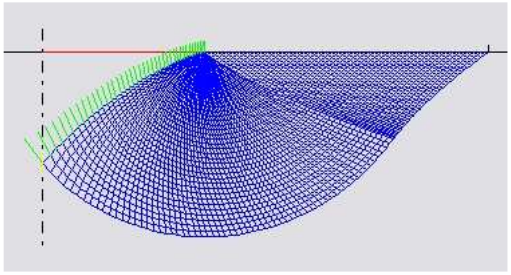

F4

Fig.2 Computational model for 4 subgrade limit bearing capacity groups

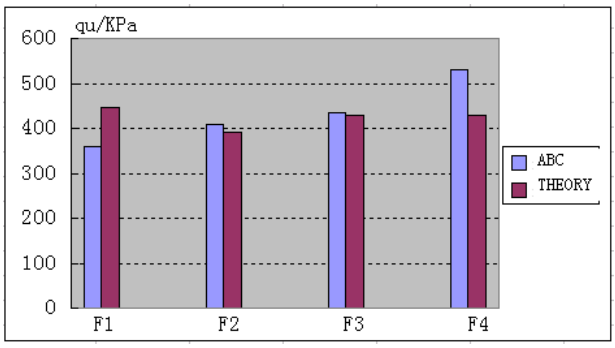


Fig.3Comparison results between ABC and theoretical solution

**Analysis of influence parameter**

In order to analysis the substrate roughness, friction angle and cohesion on the influence of the limit bearing capacity of foundation, three group models are considered as shown in Table.2.

1)F1-1:Strip and Smooth, F2-1:Strip and Tough:$\gamma$=17KN/m$^3$, $C_0$=10KPa, B=2.8m

2)F1-2:Strip and Smooth, F2-2:Strip and Tough:$\gamma$=17KN/m$^3$, $\Phi$=18°,B=2.8m

3)F3-1:Circular and Smooth,F4-1:Circular and Tough:$\gamma$=17KN/m$^3$, $C_0$=10KPa,R=2.8m

Table.2Material strength parameters for the model

| F1-1 | F2-1 | F1-2 | F2-2 | F3-1 | F4-1 |
|---|---|---|---|---|---|
| Φ/° | Φ/° | Co/KPa | Co/KPa | Φ/° | Φ/° |
| 0 | 0 | 0 | 0 | 0 | 0 |
| 6 | 6 | 5 | 5 | 6 | 6 |
| 12 | 12 | 10 | 10 | 12 | 12 |
| 18 | 18 | 15 | 15 | 18 | 18 |
| 24 | 24 | 25 | 25 | 24 | 24 |

The bearing capacity for the three group models is performed using ABC software, as shown in Fig. 4. It can be found in a certain range and the other parameters in the same situation, in a certain range, limit bearing capacity of foundation linear increases with the increase of $C_0$.

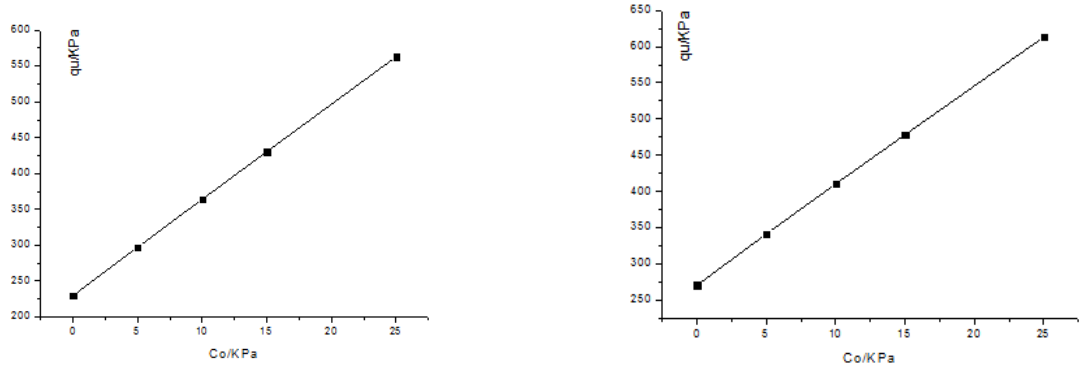


F1-2 F2-2

Fig.4 Relationship between the limit bearing capacity and cohesion.

It can also be found in a certain range and the other parameters in the same situation, limit bearing capacity of foundation nonlinear increases with the increase of Φ as shown in Fig.5 (a) (b), Fig.6 (a) (b).

At the same time, we can find, limit bearing capacity of foundation under complete smooth condition is lower than the complete tough one in the same parameters shown in Fig.5(c), Fig.6(c).

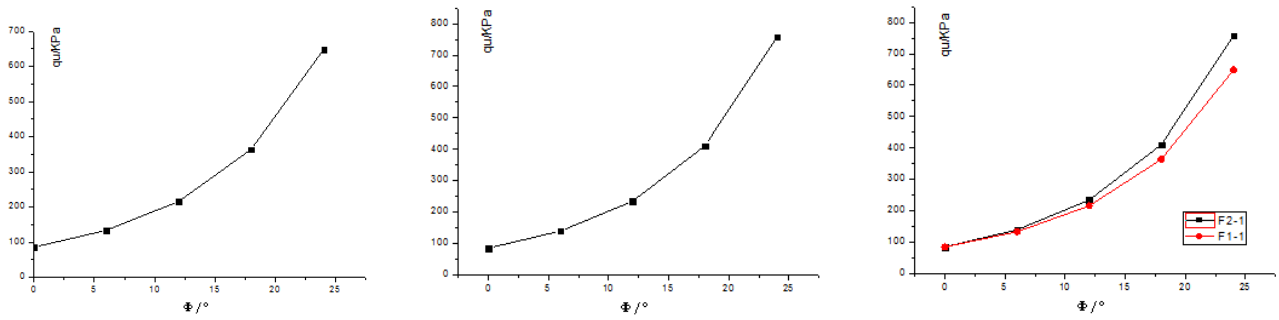


(a) F1-1 (b) F2-1 (c) Comparsion between F1-1 and F2-1

Fig.5 Relationship between the limit bearing capacity and friction angle.

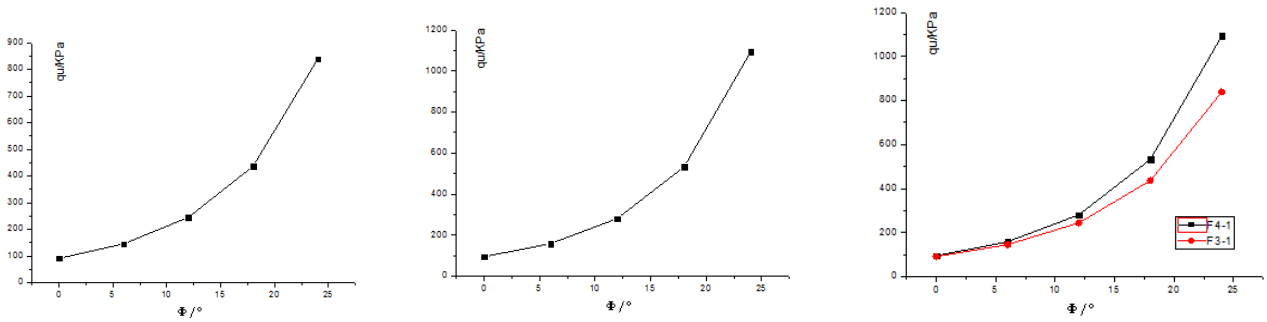


(a) F3-1 (b) F4-1 (c) Comparsion between F3-1 and F4-1

Fig.6 Relationship between the limit bearing capacity and friction angle.

## Conclusions

In the paper , the limit bearing capacity of foundation analysis software ABC was used, the main conclusions are as follows:

1)In an ideal situation, using software Analysis of Bearing Capacity to analysis the limit capacity, the calculation results is high reliable.

2)In a certain range, limit bearing capacity of foundation increases with the increase of $C_0$, Φ.Limit bearing capacity of foundation under complete smooth condition is lower than the complete tough one.

## References

[1]Datong Zheng.Foundation limit bearing capacity calculation[M]. Beijing: China Building Industry Publishing House, 1979.

[2]Kegong Zhang, Songyu Liu. Soil Mechanic [M]. Beijing: China Building Industry Publishing House, 2010.8

[3]Changfeng Lu. Higher precision solution for soil limit bearing capacity under complex boundary condition[D]. Jiangsu University of Science and Technology, 2008.

[4]C.M. Martin.User Guide for ABC – Analysis of Bearing Capacity Version 1.0. Department of Engineering Science University of Oxford.

*Applied Mechanics and Materials Vols. 580-583 (2014) pp 3007-3012*
*© (2014) Trans Tech Publications, Switzerland*
*doi:10.4028/www.scientific.net/AMM.580-583.3007*

# 3-D Numerical Simulation of Flow Structures in a Sharp Bend of the Lower Yangtze River

Dongdong Jia[1,a], Yinjun Lu[2], Xingnong Zhang[1] , Xibao Zhang[3]

[1] State Key Laboratory of Hydrology-Water Resources and Hydraulic Engineering, Nanjing Hydraulic Research Institute, Nanjing 210029, China

[2] Jiangsu Surveying and Design Institute of Water Resources Co., Ltd, Yangzhou 225127, China

[3] CCCC Second Harbor Consultants Co.,Ltd, Wuhan 430071, China

[a]ddjia@nhri.cn

**Keywords:** flow structures; channel bends; the Yangtze River; 3-D numerical simulation.

**Abstract.** The three-dimensional (3-D) flow structures in the Taiziji Waterway of the Lower Yangtze River were simulated by a 3-D numerical model, where the river plan form is a sharp bend and island-braided. The verification results of the 3-D model indicated that the simulated results agree with the measured data. The patterns of 3-D flow structures in this sharp bend with different discharge were analyzed based on the calculated results.The simulated results demostrated that strong 3-D features of flow structures can be found in the sharp bend of Taiziji Waterway, the bottom velocity vectors point to the convex bank while the surface vectors point to the concave bank. The velocity distribution alone the lateral direction in the sharp bend depends mostly on the flow discharge. The discharge ratio of the left branch increases as flow discharge increases.

## Introduction

Meandering river is a common plan form of alluvial channels. This channel pattern is generally composed of straight reaches and river bends. Flow structures in river bends are more complicated than those in straight channels, especially for the sharp bends. Helical flow in river bends is composed of the main flow velocity and the secondary currents, which resulting in bed degradation at concave banks and deposition at convex banks. Thus, the investigation of three-dimensional (3-D) flow structures in natural channel bends is of critical important for the understanding of meander evolution mechanisms.

In the previous studies, flow structures in experimental channel bends with idealized cross-sectional profile were measured. Turbulence intensity distributions in a 90º bend and a 60º bend were studied by Liu (2005) [1]. Flow velocities in a U-shaped bend were measured by H J de Vriend (1979) [2]. Transport and lateral mixing of neutral substance by turbulent flow in a two-connected 90º bend were investigated by Chang (1971) [3]. With the advances of computational technology, flow structures in channel bends were simulated by 2-D numerical models [4, 5]. However, strong 3-D features of flow structures can be found in the sharp bend. More reliable results could be obtained if 3-D model were applied [6]. In this study, the 3-D flow structures in the Taiziji Waterway of the Lower Yangtze River were simulated by a 3-D numerical model, where the river plan form is a sharp bend and island-braided, as shown in Fig.1. The characteristics of flow structures in this sharp bend were analyzed based on the calculated results with different discharge.

## Mathematical Model

The fully 3-D mathematical model used in the present study for the simulation of turbulent flow in a natural river bend was developed by Jia[7,8]. Due to the complexity of the river bends boundary, the Reynolds averaged Navier Stokes equations are solved numerically in a non-orthogonal coordinate system. Turbulence closure is provided by the standard $k-\varepsilon$ turbulence model, which apply a Boussinesq eddy viscosity. The governing equations are solved in a collocated grid system, and the

wall-function is employed to simulate the bed resistance. The finite volume method was applied to discrete the governing equations.

The governing equations for 3-D water flow are described as following:

$$\frac{\partial u_i}{\partial x_i} = 0 \tag{1}$$

$$\frac{\partial u_i}{\partial t} + \frac{\partial (u_i u_j)}{\partial x_j} = -\frac{1}{\rho}\frac{\partial p}{\partial x_i} + \frac{1}{\rho}\frac{\partial \tau_{ij}}{\partial x_j} + F_i \tag{2}$$

where $u_i$ (i=1,2,3) are velocity components; $F_i$ is the gravitational force per unit volume; $\rho$ is the fluid density; and $p$ is the pressure; $\tau_{ij}$ are turbulence stresses ,which can be calculated with the standard $k-\varepsilon$ turbulence model as following:

$$\frac{\partial k}{\partial t} + u\frac{\partial k}{\partial x} + v\frac{\partial k}{\partial y} + w\frac{\partial k}{\partial z} = \frac{\partial}{\partial x}\left[\left(\nu + \frac{\nu_t}{\sigma_k}\right)\frac{\partial k}{\partial x}\right] + \frac{\partial}{\partial y}\left[\left(\nu + \frac{\nu_t}{\sigma_k}\right)\frac{\partial k}{\partial y}\right] + \frac{\partial}{\partial z}\left[\left(\nu + \frac{\nu_t}{\sigma_k}\right)\frac{\partial k}{\partial z}\right] + G - \varepsilon \tag{3}$$

$$\frac{\partial \varepsilon}{\partial t} + u\frac{\partial \varepsilon}{\partial x} + v\frac{\partial \varepsilon}{\partial y} + w\frac{\partial \varepsilon}{\partial z} = \frac{\partial}{\partial x}\left[\left(\nu + \frac{\nu_t}{\sigma_\varepsilon}\right)\frac{\partial \varepsilon}{\partial x}\right] + \frac{\partial}{\partial y}\left[\left(\nu + \frac{\nu_t}{\sigma_\varepsilon}\right)\frac{\partial \varepsilon}{\partial y}\right] + \frac{\partial}{\partial z}\left[\left(\nu + \frac{\nu_t}{\sigma_\varepsilon}\right)\frac{\partial \varepsilon}{\partial z}\right] + \frac{C_1\varepsilon}{k}G - C_2\frac{\varepsilon^2}{k} \tag{4}$$

The generation rate of turbulent kinetic energy $G$ is calculated as following:

$$G = \upsilon_t\left\{2\left[\left(\frac{\partial u}{\partial x}\right)^2 + \left(\frac{\partial v}{\partial y}\right)^2 + \left(\frac{\partial w}{\partial z}\right)^2\right] + \left(\frac{\partial u}{\partial y} + \frac{\partial v}{\partial x}\right)^2 + \left(\frac{\partial v}{\partial z} + \frac{\partial w}{\partial y}\right)^2 + \left(\frac{\partial w}{\partial x} + \frac{\partial u}{\partial z}\right)^2\right\} \tag{5}$$

The turbulent eddy viscosity can be calculated by the turbulent kinetic energy $k$ and its dissipation rate $\varepsilon$ used the expression of $\nu_t = c_\mu k^2/\varepsilon$.

**Verification of the numerical model**

The Taiziji Waterway is a part of the lower Yangtze River, where the river plan form is a sharp bend and island-braided, as shown in Fig.1. The computatial domain has a total length about 21 km from inlet to outlet. The computational grids are 40~60 meters in length alone the river length direction and 5~10 meters in length alone the river width direction.

Hydrological data measured in November 2011 in this river section are used for model verification, and the corresponding discharge is 29200 $m^3/s$ (close to the annual mean discharge 28700 $m^3/s$). Comparision of water level profiles alone the left and right banks between the calculated results and the measured data are shown in Fig. 2. The difference between the measured data and the simulated results is less than 0.1 m, indicating that the roughness values for this sharp bend applied in the present study are accurate. The Manning's roughness of the study reach changes within the range of 0.018~0.032.

Fig. 3 shows comparisons of depth-averaged velocity distributions at typical cross-sections between the simulated results and the measured data with the discharge of 29200 $m^3/s$ on November

2011. The locations of the cross-sections can be found in Fig.1. It can be seen that the simulated results agree well with the observrd data, and the numerical model can be applied to predict flow patterns in this sharp bend with complex boundary.

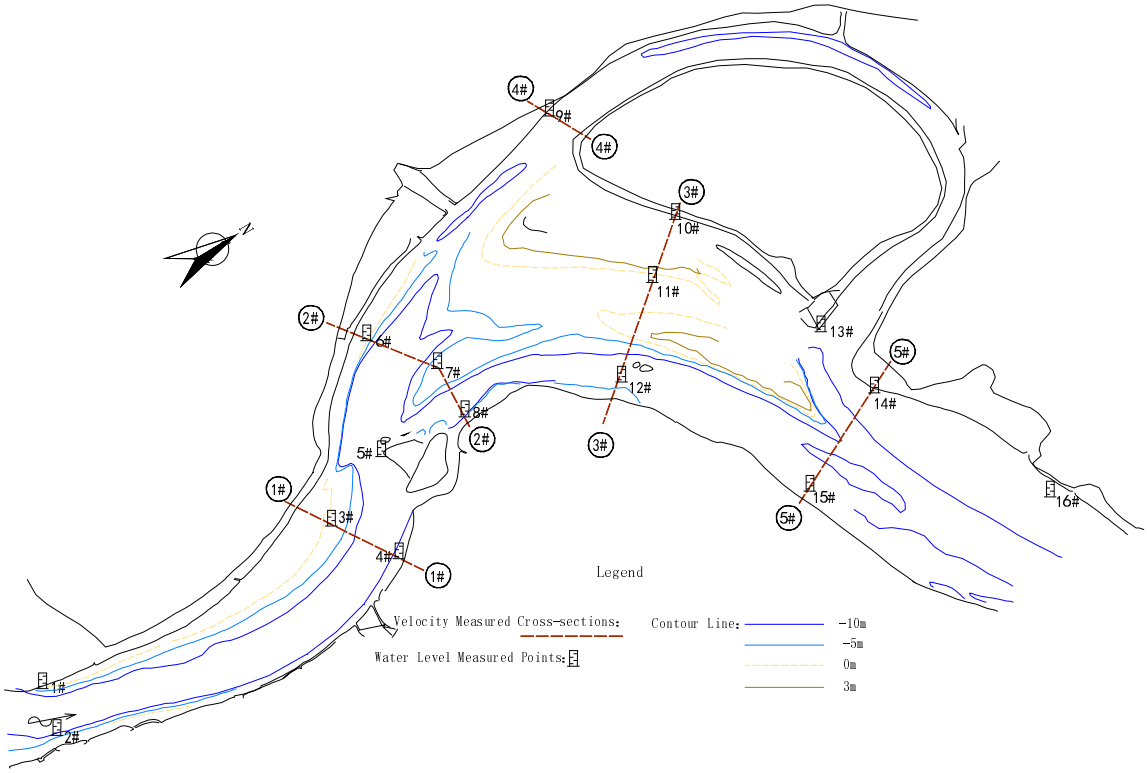


Figure 1. Sketch of the Taiziji Waterway in the Lower Yangtze River

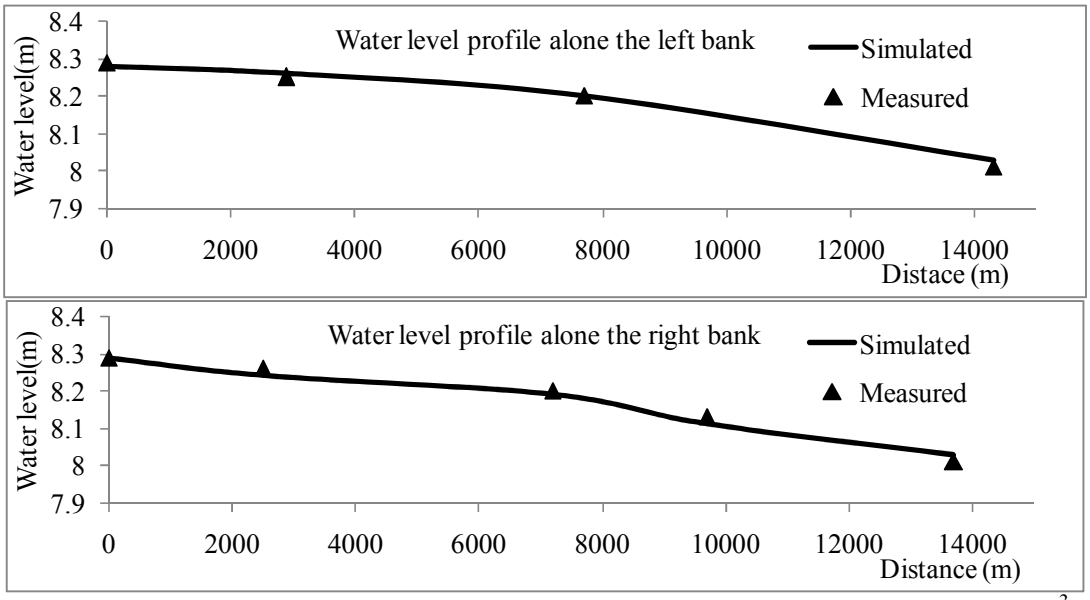


Figure 2. Comparisons of simulated and measured water level profiles (Q=29200 $m^3/s$)

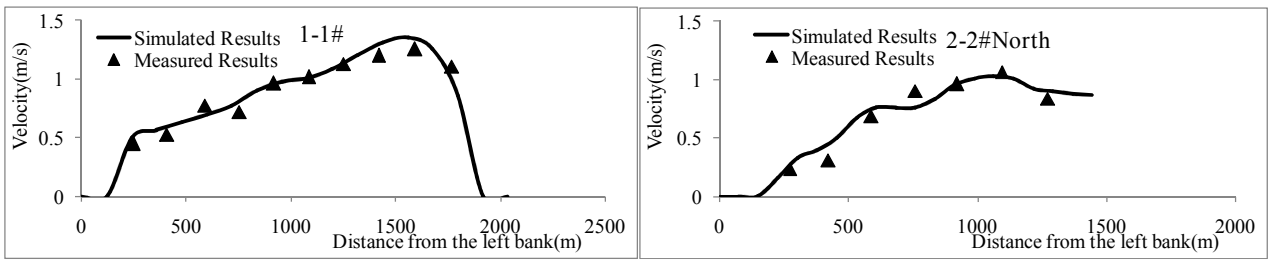

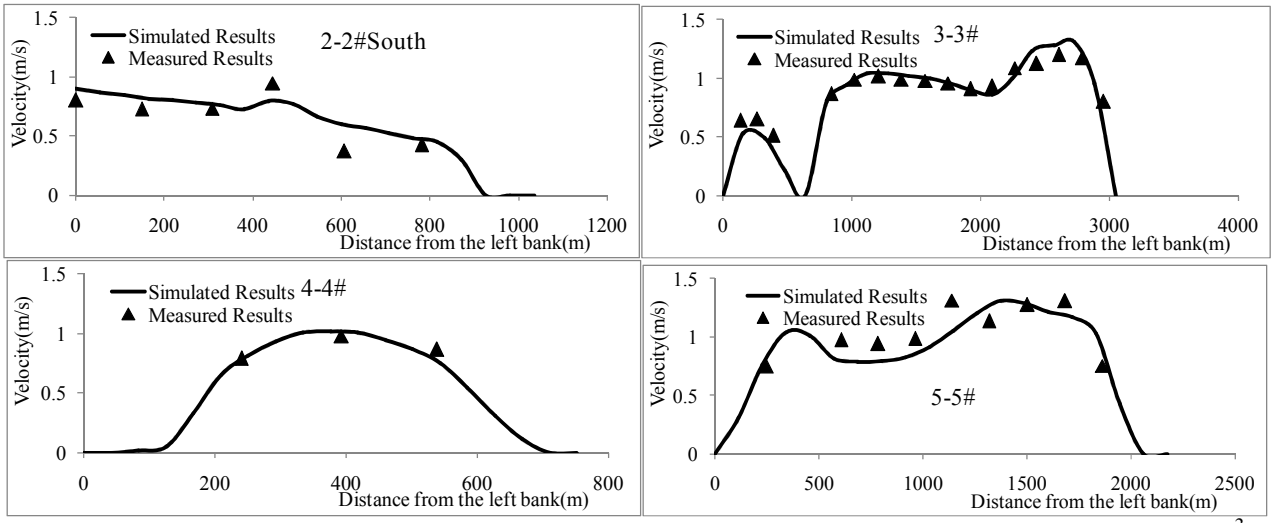


Figure 3. Comparisons of simulated and measured velocity at typical cross-sections (Q=29200 $m^3/s$)

**Three-dimensional Flow Structures**

After the calibration of the 3-D model, the flow patterns in the sharp bend with different discharge are predicted. Figures 4~6 show calculated flow velocities at both the free surface and bottom in the Taiziji Waterway with flow discharge of 11000 $m^3/s$, 29200 $m^3/s$ and 46700 $m^3/s$, respectively. Strong 3-D features can be seen in the bend flows of the Taiziji Waterway, the secondary currents are significant. The bottom velocity vectors point to the convex bank while the surface vectors point to the concave bank (as shown in Figures 4~6, black lines are vectors close to water surface, and red lines are vectors close to bed bottom). In addition, the discharge ratio of the left branch (cross-section No 4-4, the cross-section location is given in Fig.1.) as well as the right branch (cross-section No 3-3, the cross-section location is given in Fig.1.) is calculated based on the simulated values of velocity and water depth. As shown in Table 1, the discharge ratio of the left branch (cross-section No 4-4) increases from 11.80% to 14.10% as flow discharge increases from 11000 to 46700$m^3/s$. Conversely, the discharge ratio of the right branch (cross-section No 3-3) decreases from 88.20% to 85.90% as flow discharge increases. These results imply that the velocity distribution alone the lateral direction in the sharp bend depends mostly on the flow discharge.

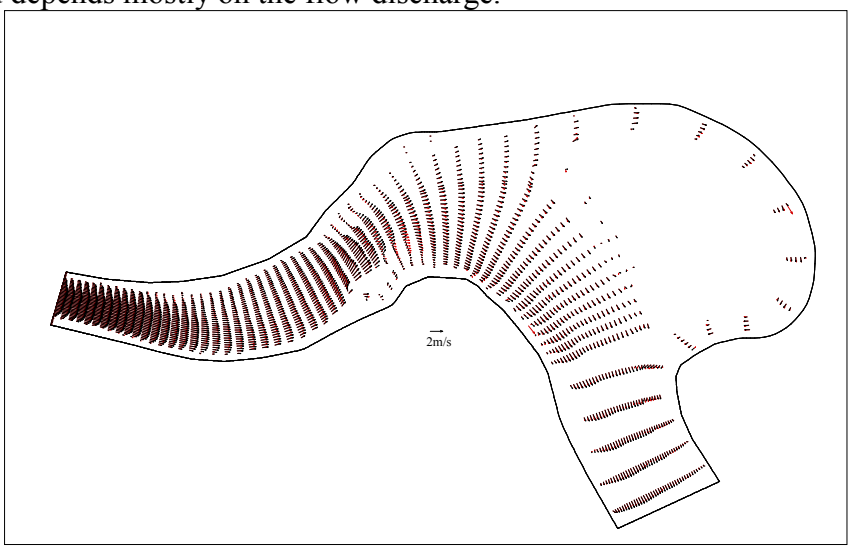


Figure 4. Calculated velocity fields close to bottom and water surface (Q=11000 $m^3/s$)

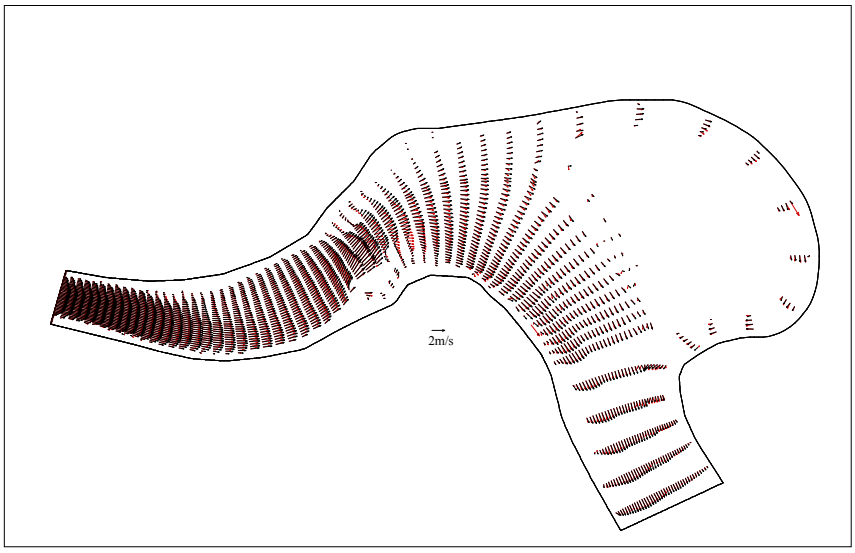


Figure 5. Calculated velocity fields close to bottom and water surface (Q=29200 $m^3/s$)

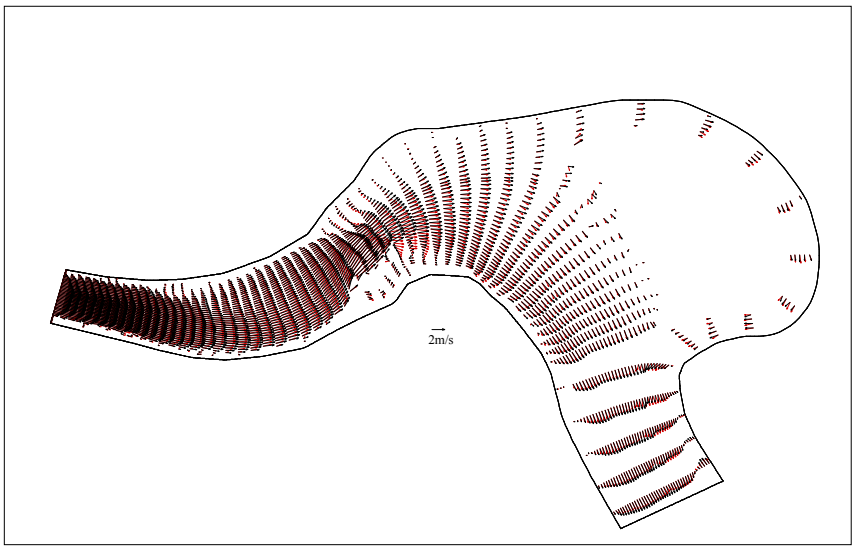


Figure 6. Calculated velocity fields close to bottom and water surface (Q=46700 $m^3/s$)

Table 1. Variation of discharge ratio at Cross-sections No 3-3 and 4-4

| Discharge | 11000$m^{3/}s$ | 29200$m^3/s$ | 46700$m^3/s$ |
|---|---|---|---|
| Left branch Cross-section No 4-4 | 11.80% | 13.00% | 14.10% |
| Right branch Cross-section No 3-3 | 88.20% | 87.00% | 85.90% |

## Conclusions

In the present study, the three-dimensional flow structures in the Taiziji Waterway of the Lower Yangtze River were simulated by a 3-D numerical model, where the river plan form is a sharp bend and island-braided. The characteristics of flow structures in this river bend were analyzed based on the calculated results with different discharge.

The calculated results demostrated that strong 3-D features of flow structures can be found in the sharp bend of Taiziji Waterway, the secondary currents are significant. The bottom velocity vectors point to the convex bank while the surface vectors point to the concave bank. The velocity distribution alone the lateral direction in the sharp bend depends mostly on the flow discharge. The discharge ratio of the left branch (cross-section No 4-4) increases from 11.80% to 14.10% as flow discharge increases from 11000 to 46700$m^3$/s. Conversely, the discharge ratio of the right branch (cross-section No 3-3) decreases from 88.20% to 85.90% as flow discharge increases. It demonstrates that the 3-D model is an effective prediction tool for the investigations of 3-D flow patterns in natural rivers with complex boundary, especially for the channel bends.

**Acknowledgements**

The work presented in this paper is financed by the National Key Project of Scientific and Technical Supporting Programs funded by Ministry of Science & Technology of China (No. 2012BAB04B03), the National Basic Research 973 Program of China (Grant No. 2012CB417002), the Nanjing Hydraulic Research Institute Foundation (No.Y213009), and the National Natural Science Foundation of China (Nos. 51109140, 51109112).

**References**

[1] Liu Yue-qin, Zheng Shao-Wen, Wu Qiang. *Experimental study of 3-D turbulent bend flows in open channel*, Journal of Hydrodynamics, Ser. B, 17(6):704-712(2005).

[2] J de vriend. *Flow measurments in cured rectangular channel*, Internal report 9-79.University of Delft, The Netherlands. (1979)

[3]Chang Y C. *Lateral mixing in meandering channels*, Ph. D. thesis, University of Iowa, USA.(197 1 )

[4] HC Lien, TY Hsieh, JC Yang, et al. *Bend-flow Simulation Using 2D Depth-Averaged Model*. J. Hydr. Engrg., ASCE, 123(10): 1097-1108. (1999)

[5] Fang chunming. *Simutation of bend secondary flow effect in a planar 2D depth-averaged model*.Journal fo China Institute of Water Resourses and Hydropower Research, 1(3): 190-193.(2003)

[6] Wu W., Rodi W., Wenka T. *3D numerical modeling of flow sediment and transport in open channels*. Journal of Hydraulic Engineering ASCE. 126(1):4-15(2000).

[7] Jia DD, Shao XJ, Wang H, et al. *Three-dimensional modeling of bank erosion and morphological changes in the Shishou bend of the middle Yangtze River*, Advances in Water Resources, 33(3):348-360(2010).

[8] Jia Dong-dong, Shao Xue-jun, Zhang Xing-nong, et al. *Sedimentation Patterns of Fine-Grained Particles in the Dam Area of the Three Gorges Project 3D Numerical Simulation*. Journal of Hydraulic Engineering ASCE. 139(6):669-674(2013).

*Applied Mechanics and Materials Vols. 580-583 (2014) pp 3013-3016*
*© (2014) Trans Tech Publications, Switzerland*
*doi:10.4028/www.scientific.net/AMM.580-583.3013*

# About Verification of Correct Wavelet-Based Approach to Local Static Analysis of Bernoulli Beam

Pavel A. AKIMOV[1, a], Mojtaba ASLAMI[2,b]

[1,2] 26, Yaroslavskoe Sh., Moscow, 129337, Russia, Moscow State University of Civil Engineering

[a] pavel.akimov@gmail.com, [b] aslami.mojtaba@gmail.com

**Keywords:** wavelet-based methods, boundary problem, local structural analysis, static analysis, Bernoulli beam, discrete wavelets, Haar basis, verificarion, analytical solution

**Abstract.** This paper is devoted to verification of correct and efficient wavelet-based method of local static analysis of Bernoulli beam on elastic foundation, proposed by authors [1]. Corresponding results for sample problem have been compared with analytical solutions. Comparison shows that the localization of the problem with reducing its size by proposed method provide high-accuracy results for desired regions of the structure even in high level of reduction in wavelet coefficients. It should be noted that, the wavelet analysis [1, 2, 3, 4, 5] can exactly decompose problem and the sources of the observed error between the analytical solution and numerical result, is based mainly on applied method for solving (in this case, finite difference method), and can be improved.

## Formulation of the Sample Problem.

For the purpose of the paper and comparison with analytical solution [6], the Bernoulli beam on the elastic foundation which is loaded at mid-span with a concentrated force has been considered (Fig. 1).

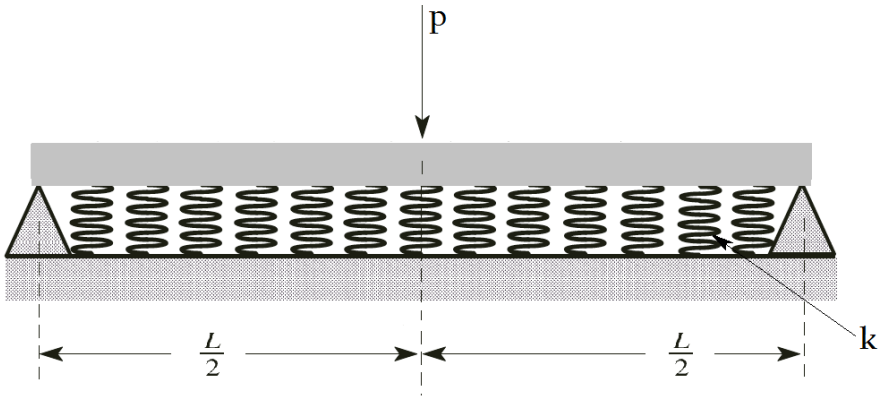


Figure 1. Bernoulli beam on the elastic foundation with concentrated force.

The elastic modelling of the soil bed is considered as one-parameter Winkler model which assumes that the vertical displacement of a point of the elastic foundation is proportional to the pressure at that point. This model can be interpreted as a system of mutually independent vertical springs with stiffness $k$. The General governing equations and boundary conditions for transverse displacement of the beam ( $y$ ) as follows:

$$\begin{cases} y^{(4)}(x) + y(x) = F(x), \quad 0 < x < L \\ y(0) = y(L) = 0 \\ y^{(2)}(0) = y^{(2)}(L) = 0; \end{cases} \qquad 4\alpha^4 = \frac{kb}{EJ}; \quad F(x) = \frac{P}{EJ}\delta\left(x - \frac{L}{2}\right); \tag{1}$$

where $L$ is the length of beam; $b$ is the width of sole of beam; $EJ$ is the bending stiffness of beam; $\delta(x)$ is the Dirac delta function.

**Numerical example and comparison of the solutions.**

Theoretical Foundations of Correct Wavelet-Based Approach to Local Static Analysis of Bernoulli Beam have been presented in [1]. The simple numerical example is under consideration in the distinctive paper (for illustrating the efficiency of this method). We have a Bernoulli beam on the elastic foundation (k=6700 kN/m3) which is loaded at mid-span with a concentrated force of F=1000 kN/m. The beam is 20m long, 0.5m wide and has bending stiffness of EJ = 1125000 kNm2. Solutions of the problem are obtained by using the authoring software software (Fortran programming language). The various input parameters (different numbers of nodes and different order of reduction), corresponding solution and comparison with analytical results are shown at Table 1.

Table 1

| No. case | No. $\bar{v}$ | No. $\bar{v}^r$ | Interval for local analysis (m) | Bending moment (KN.m) | Analyt. solution (Bending moment) | Error 1 % | Error 2 % | Shear force (KN) | Analyt. solution (shear force) | Error 1 % | Error 2 % |
|---|---|---|---|---|---|---|---|---|---|---|---|
| 1 | 64 | 64 | 10.0 | -763 | -804 | -5.4 | 0.0 | 227 | 250 | -10.0 | 0.0 |
| | | 47 | | -768 | | -4.7 | +0.7 | 227 | | -10.0 | 0.0 |
| | | 39 | | -768 | | -4.7 | +0.7 | 227 | | -10.0 | 0.0 |
| | | 35 | | -768 | | -4.7 | +0.7 | 227 | | -10.0 | 0.0 |
| 2 | 128 | 128 | | -784 | | -2.6 | 0.0 | 238 | | -5.0 | 0.0 |
| | | 93 | | -790 | | -1.8 | +0.8 | 238 | | -5.0 | 0.0 |
| | | 76 | | -794 | | -1.3 | +1.3 | 238 | | -5.0 | 0.0 |
| | | 64 | | -794 | | -1.3 | +1.3 | 238 | | -5.0 | 0.0 |
| 3 | 256 | 256 | | -794 | | -1.3 | 0.0 | 245 | | -2.0 | 0.0 |
| | | 186 | | -799 | | -0.6 | +0.6 | 244 | | -2.5 | -0.4 |
| | | 151 | | -804 | | 0.0 | +1.3 | 244 | | -2.5 | -0.4 |
| | | 134 | | -806 | | +0.2 | +1.5 | 244 | | -2.5 | -0.4 |
| | | 126 | | -807 | | +0.4 | +1.6 | 244 | | -2.5 | -0.4 |
| | | 122 | | -807 | | +0.4 | +1.6 | 243 | | -2.9 | -0.8 |
| | | 110 | | -831 | | +3.6 | +4.7 | 241 | | -3.7 | -1.7 |

Remark: *Error 1* has been obtained by comparison between analytical and numerical results and *Error 2* by comparison between numerical results with, and without reduction in wavelet coefficients.

According to the applied force, the middle point of the beam has been considered as a local zone for verifying of the proposed method. Then the problem was solved in three cases with various types of reduction in wavelet coefficients. The diagrams of the bending moment and shear force, by comparison with analytical solutions [6] are shown in Figures 2, 3. We can maintain accuracy in the desired region and reduced size of the problem to half. The results converge to analytical solution after increasing numbers of nodes. We can keep this accuracy in the desired region by using the proposed algorithm and also reduce number of unknowns as much as the obtained results are accurate enough. Therefore, reduction performed in the beginning and ending of the beam. Observations showed, that index has been increased by nearing the reduction to the point of loading errors. Results after reduction may be unacceptable in the other zones. The effect of reduction on results, out of the desired region, is proportional to the order of the derivative of transverse deflection ( $y$ ) in the beam.

**Conclusions**

The obtained results show an efficiency of the method and also reducing the size of the problem. By comparing with analytical solution, it is clear that the localization of the problem by multiresolution wavelet, give good results for desired zone even in high level of reduction in wavelet coefficients.

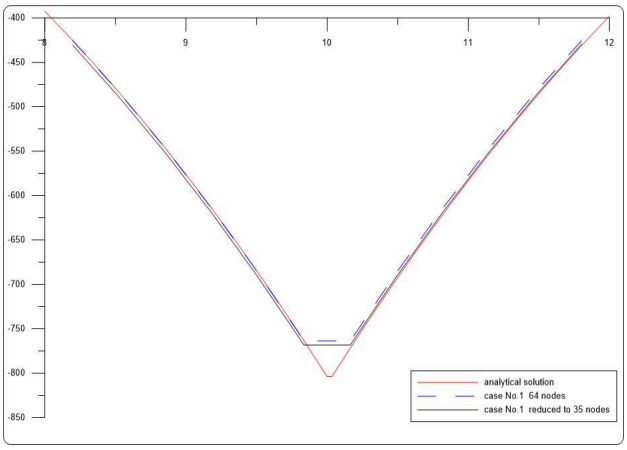


Figure 2a. Bending moment for case No.1 in interval 8-12m.

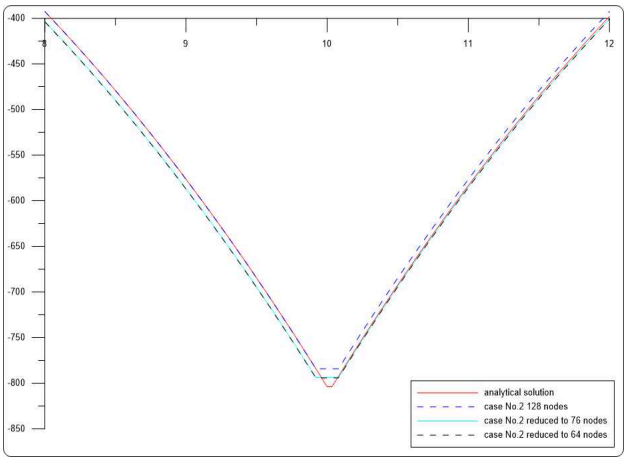


Figure 2b. Bending moment for case No.2 in interval 8-12m.

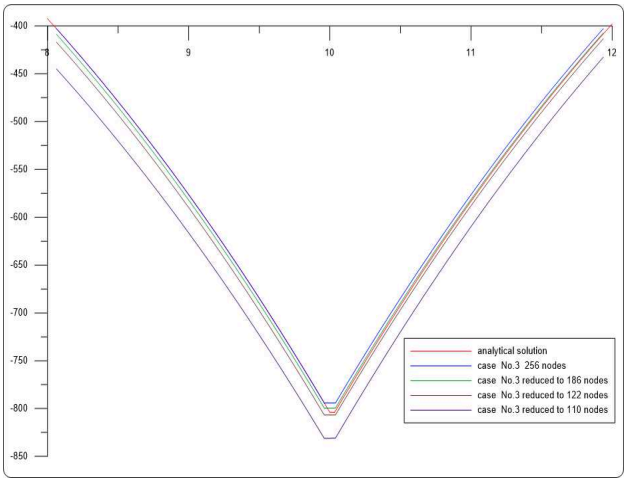


Figure 2c. Bending moment for case No.3 in interval 8-12m.

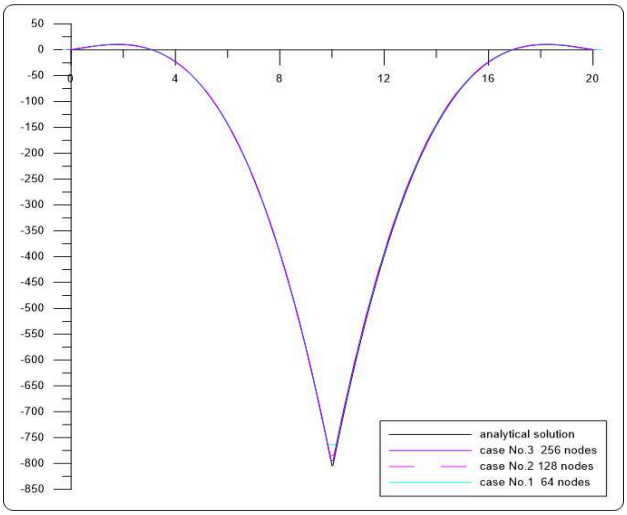


Figure 2d. Bending moment for all cases.

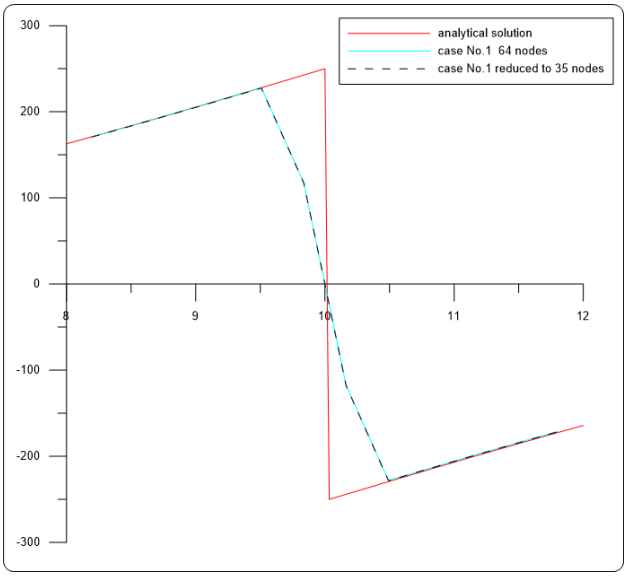


Figure 3a. Shear force for case No.1 in interval 8-12m.

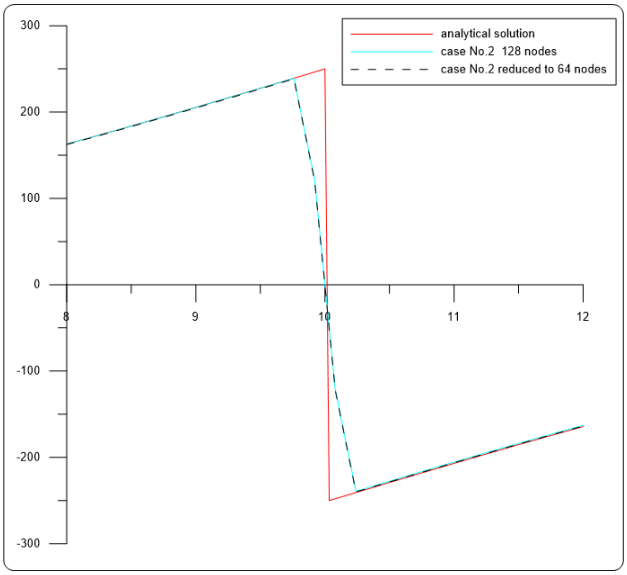


Figure 3b. Shear force for case No.2 in interval 8-12m.

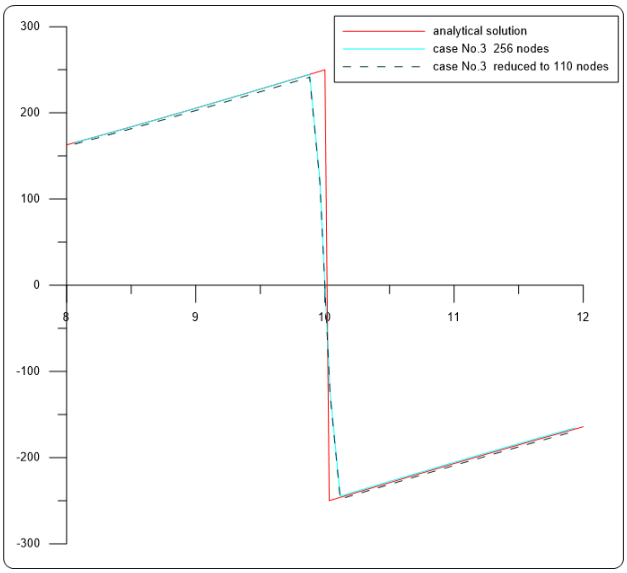


Figure 3c. Shear force for case No.3 in interval 8-12m.

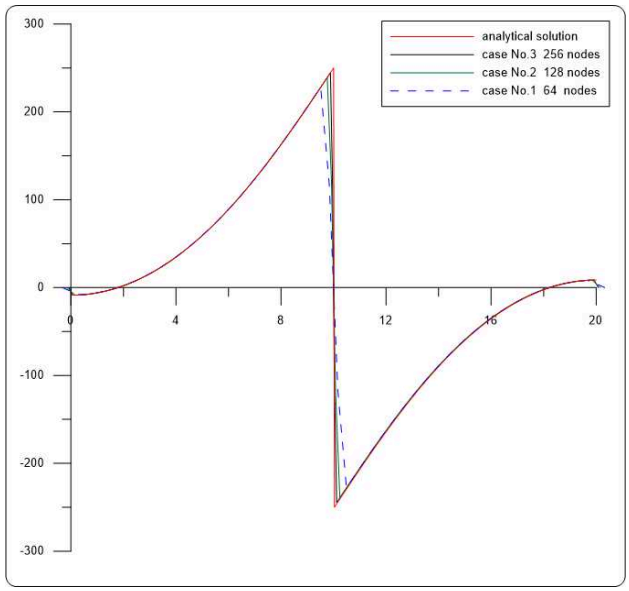


Figure 3d. Shear force for all cases.

This localization can be imposed to any arbitrary point in the beam and, by choosing an optimum reduction matrix, obtain exact solutions with an acceptable reduced size of the problem. Note that, the wavelet analysis can exactly decompose problem and the sources of the observed error between the analytical solution and numerical result, is based on applied method for solving the problem (in this case, finite difference method), and can be improved.

**Acknowledgements**

This work was financially supported by the Grants of Russian Academy of Architecture and Construction Sciences (3.1.7, 3.1.8).

**References**

[1] Akimov P.A., Mojtaba Aslami. *Theoretical Foundations of Correct Wavelet-Based Approach to Local Static Analysis of Bernoulli Beam*. // Accepted by the Scientific Committee of CEABM 2014 and will be published in journal "Applied Mechanics and Materials".

[2] Akimov P.A., Mozgaleva M.L. *Correct Wavelet-based Multilevel Discrete-Continual Methods for Local Solution of Boundary Problems of Structural Analysis*. // Applied Mechanics and Materials Vols. 353-356 (2013), pp. 3224-3227.

[3] Akimov P.A., Mozgaleva M.L. *Wavelet-based Multilevel Discrete-Continual Finite Element Method for Local Plate Analysis*. // Applied Mechanics and Materials Vols. 351-352 (2013), pp. 13-16.

[4] Akimov P.A., Mozgaleva M.L. *Wavelet-based Multilevel Discrete-Continual Finite Element Method for Local Deep Beam Analysis*. // Applied Mechanics and Materials Vols. 405-408 (2013), pp. 3165-3168.

[5] Akimov P.A., Mozgaleva M.L.: *Correct Wavelet-based Multilevel Numerical Method of Local Solution of Boundary Problems of Structural Analysis*. // Applied Mechanics and Materials Vols. 166-169 (2012), pp. 3155-3158.

[6] Zolotov A.B., Akimov P.A., Sidorov V.N., Mozgaleva M.L. *Mathematical Methods in Structural Mechanics*. Moscow, ASV Publishing House, 2008, 336 pages (in Russian).

*Applied Mechanics and Materials Vols. 580-583 (2014) pp 3017-3020*
*© (2014) Trans Tech Publications, Switzerland*
*doi:10.4028/www.scientific.net/AMM.580-583.3017*

# Determining the frequency of free oscillations geometrically nonlinear shell using the mixed finite element method

Leonid U. Stupishin[1, a], Konstantin E. Nikitin[2, b]

[1]Urban, road construction and structural mechanic department, South-West State University (SWSU), 305040, Kursk, Russia

[2] Urban, road construction and structural mechanic department, South-West State University (SWSU), 305040, Kursk, Russia

[a]lusgsh@yandex.ru, [b]niksbox@yandex.ru

**Keywords:** Mixed Finite Element Method (FEM); geometrical nonlinearity; free oscillations; shells

**Abstract.** Considered small oscillations geometrically nonlinear shallow shell of revolution relative to the initial deformed state. Isotropic material model is considered. Problem is solved by mixed finite element method. Results of solution of test task are represented.

## Introduction

The methodic of determining the frequencies and axisymmetric modes of free oscillation of a shallow shell of revolution freeform with a median surface formed by smooth monotonic curve.

Considered small oscillations geometrically nonlinear shell relative to the initial deformed state. The initial deformed state of shell can be caused by action of static load, for example, dead weight, snow load, etc.

Oscillation equations is linearized in a small deviations of the system relation to the initial equilibrium state. The initial deformed state of shell determined by the solution geometrically nonlinear problem of the deformation of shell under the action initial loads.

Problem is solved by mixed finite element method.

## Solution of the problem

Equations of state of the shell obtained on the basis of the quadratic nonlinear theory of shallow shells [1]. Neglecting the influence of inertial forces in the radial direction and rotation inertia, we have:

$$\frac{1}{Eh}\frac{1}{r}\frac{\partial}{\partial r}\left(r\frac{\partial}{\partial r}\left(\frac{1}{r}\frac{\partial}{\partial r}\left(r\frac{\partial\varphi(r,t)}{\partial r}\right)\right)\right)-\frac{1}{r}\frac{\partial}{\partial r}\left(\frac{\partial w(r,t)}{\partial r}\frac{\partial f(r)}{\partial r}\right)+\frac{1}{2r}\frac{\partial}{\partial r}\left(\frac{\partial w(r,t)}{\partial r}\right)^2=0, \tag{1}$$

$$\begin{aligned}&D\frac{1}{r}\frac{\partial}{\partial r}\left(r\frac{\partial}{\partial r}\left(\frac{1}{r}\frac{\partial}{\partial r}\left(r\frac{\partial w(r,t)}{\partial r}\right)\right)\right)+\frac{1}{r}\frac{\partial}{\partial r}\left(\frac{\partial\varphi(r,t)}{\partial r}\frac{\partial f(r)}{\partial r}\right)-\\&-\frac{1}{r}\frac{\partial}{\partial r}\left(\frac{\partial\varphi(r,t)}{\partial r}\frac{\partial w(r,t)}{\partial r}\right)=q-\frac{\gamma h}{g}\frac{\partial^2 w(r,t)}{\partial t^2},\end{aligned} \tag{2}$$

where $\varphi$ - stress function, $w$ – deflection function; $q$ – projection of the distributed loading on the z-axis coordinate; $df(r)$ - generatrix function for shell of revolution, $r$ – radial coordinate, $h$ – thickness of the shell; $E$ - elastic modulus, $D$ - modulus of rigidity of shell, $\nu$ - Poisson ratio; $\gamma$ - volume weight of the material; $g$ - acceleration of gravity; $t$ – time coordinate.

We introduce the dimensionless quantities:

$$r=\frac{h}{\sqrt[4]{\mu}}\rho,\ t=\bar{t}\Big/\sqrt{\frac{gE}{\gamma h^2}},\ \frac{\partial\varphi}{\partial r}=-\frac{Eh^2}{\sqrt[4]{\mu^3}}\overline{\Phi},\ \frac{\partial w}{\partial r}=\frac{1}{\sqrt[4]{\mu}}\overline{\theta},\ \frac{\partial f(\rho)}{\partial\rho}=\frac{h}{\sqrt{\mu}}K,\ \mu=12\left(1-\nu^2\right), \tag{3}$$

and write the function the influence of inertial forces in form:

$$\alpha=\alpha(\rho,t)=\frac{\sqrt{\mu}}{h\rho}\int_{\rho_0}^{\rho}\rho\frac{\partial^2 w(\rho,\bar{t})}{\partial\bar{t}^2}d\rho. \tag{4}$$

where $\bar{t},\rho$ - dimensionless coordinates, $\overline{\Phi}$, $\overline{\theta}$ – dimensionless stress function and the function of the angles of rotation of shell's generating curve.

Integrating over r system of equations (1), (2) once considering (3), (4) we obtain equations:

$$\begin{aligned}
&\rho\frac{\partial}{\partial\rho}\left[\frac{1}{\rho}\frac{\partial}{\partial\rho}(\rho\overline{\Phi})\right]-\frac{\overline{\theta}^2}{2}+\overline{\theta}K=A_1,\\
&\rho\frac{\partial}{\partial\rho}\left[\frac{1}{\rho}\frac{\partial}{\partial\rho}(\rho\overline{\theta})\right]+\overline{\Phi}\overline{\theta}-\overline{\Phi}K+\alpha\rho=\frac{\sqrt{\mu}}{E}\int_{\rho_0}^{\rho}q\rho d\rho+A_2,\\
&\frac{\partial}{\partial\rho}\left(\frac{1}{\rho}\frac{\partial}{\partial\rho}(\alpha\rho)\right)=\frac{\partial^2\overline{\theta}}{\partial\bar{t}^2}.
\end{aligned} \tag{5}$$

Here, $A_1$ and $A_2$ - the constant of integration. It can be shown that $A_1$=0. If the shell is closed at the top, then $A_2$=0.

The last of the equations (5) is obtained by double differentiation on ρ equation (4) and replacement $\frac{\partial^3 w(\rho,\bar{t})}{\partial\bar{t}^2\partial\rho}=\frac{\partial^2\overline{\theta}}{\partial\bar{t}^2}$ according to (3).

We represent the functions $\overline{\Phi}$ and $\overline{\theta}$ as a sum of components defining the initial state of the shell ($\Phi_0$, $\theta_0$) and components describing deviation of the system in the process of oscillation ($\Phi$, $\theta$):

$$\overline{\Phi}=\Phi_0+\Phi;\ \overline{\theta}=\theta_0+\theta. \tag{6}$$

Equations (5) linearize the small deviations of the system relation to the initial equilibrium state. The system of equations is separated into system, which defines the initial deformed state the shell and the system describing the oscillations of a shell. The first system of equations is similar to the one in [2]. Second, after linearization (including the smallness of $\Phi$ and $\theta$), written as:

$$\begin{aligned}
&\rho\frac{\partial}{\partial\rho}\left[\frac{1}{\rho}\frac{\partial}{\partial\rho}(\rho\Phi)\right]+\theta K-\theta_0\theta=0,\\
&\rho\frac{\partial}{\partial\rho}\left[\frac{1}{\rho}\frac{\partial}{\partial\rho}(\rho\theta)\right]-\Phi K+\Phi_0\theta+\Phi\theta_0+\alpha\rho=0,\\
&\frac{\partial}{\partial\rho}\left(\frac{1}{\rho}\frac{\partial}{\partial\rho}(\alpha\rho)\right)=\frac{\partial^2\theta}{\partial\bar{t}^2}.
\end{aligned} \tag{7}$$

Boundary conditions on the support contour for elastic-supple fastening are given as:

$$n\Phi-\rho_1\frac{\partial\Phi}{\partial\rho}=0,\ m\theta-\rho_1\frac{\partial\theta}{\partial\rho}=0,\ \alpha=0, \tag{8}$$

where $n$ and $m$ - the elasticity of fastening [2].

Boundary conditions at the top closed shell taken as:

$$\theta=0,\Phi=0,\alpha=0 \tag{9}$$

Creation of a finite element carried by the Galerkin method [3] in the weak form [2].

A finite element equation for the determination of the initial deformed state of the shell is similar, that considered in [2].

Finite element equations for determining the frequency of small free oscillations of shell have the form of a generalized eigenvalue problem:

$$\left[S^*\right]\left\{q^*\right\}=\omega^2[\mathrm{M}]\left\{\mathrm{q}^*\right\}, \tag{10}$$

where $[S^*]=[S_1]+[S_0]$ - state matrix element (stiffness matrix), $[M]$ - mass matrix element, $\left\{q^*\right\}=[\Phi_1,\theta_1,\alpha_1,\Phi_2,\theta_2,\alpha_2]$ - vector of nodal parameters,

$$[M]=\begin{bmatrix} 0 & 0 & 0 & 0 & 0 & 0 \\ 0 & 0 & 0 & 0 & 0 & 0 \\ 0 & e_{11} & 0 & 0 & e_{12} & 0 \\ 0 & 0 & 0 & 0 & 0 & 0 \\ 0 & 0 & 0 & 0 & 0 & 0 \\ 0 & e_{12} & 0 & 0 & e_{13} & 0 \end{bmatrix}, \tag{11}$$

$$[S_0]=\begin{bmatrix} 0 & \frac{e_5}{20}\theta_1^0+\frac{e_8}{60}\theta_2^0 & 0 & 0 & \frac{e_8}{60}\theta_1^0+\frac{e_7}{60}\theta_2^0 & 0 \\ \frac{-e_5}{20}\theta_1^0+\frac{-e_8}{60}\theta_2^0 & \frac{-e_5}{20}\Phi_1^0+\frac{-e_8}{60}\Phi_2^0 & 0 & \frac{-e_8}{60}\theta_1^0+\frac{-e_7}{60}\theta_2^0 & \frac{-e_8}{60}\Phi_1^0+\frac{-e_7}{60}\Phi_2^0 & 0 \\ 0 & 0 & 0 & 0 & 0 & 0 \\ 0 & \frac{e_8}{60}\theta_1^0+\frac{e_7}{60}\theta_2^0 & 0 & 0 & \frac{e_7}{60}\theta_1^0+\frac{e_6}{20}\theta_2^0 & 0 \\ \frac{-e_8}{60}\theta_1^0+\frac{-e_7}{60}\theta_2^0 & \frac{-e_8}{60}\Phi_1^0+\frac{-e_7}{60}\Phi_2^0 & 0 & \frac{-e_7}{60}\theta_1^0+\frac{-e_6}{20}\theta_2^0 & \frac{-e_7}{60}\Phi_1^0+\frac{-e_6}{20}\Phi_2^0 & 0 \\ 0 & 0 & 0 & 0 & 0 & 0 \end{bmatrix}, \tag{12}$$

$$[S_1]=\begin{bmatrix} \frac{e_3}{2(\chi-\eta)} & \frac{K}{12}e_1 & 0 & \frac{\chi(\eta+\chi)}{2(\eta-\chi)} & \frac{K}{12}\left(\eta^2-\chi^2\right) & 0 \\ -\frac{K}{12}e_1 & \frac{e_3}{2(\chi-\eta)} & e_9 & \frac{K}{12}\left(\chi^2-\eta^2\right) & \frac{\chi(\eta+\chi)}{2(\eta-\chi)} & e_{10} \\ 0 & 0 & \frac{e_3}{2(\chi-\eta)} & 0 & 0 & \frac{\chi(\eta+\chi)}{2(\eta-\chi)} \\ \frac{\eta(\eta+\chi)}{2(\eta-\chi)} & \frac{K}{12}\left(\eta^2-\chi^2\right) & 0 & \frac{e_4}{2(\chi-\eta)} & -\frac{K}{12}e_2 & 0 \\ \frac{K}{12}\left(\chi^2-\eta^2\right) & \frac{\eta(\eta+\chi)}{2(\eta-\chi)} & e_{10} & \frac{K}{12}e_2 & \frac{e_4}{2(\chi-\eta)} & e_{11} \\ 0 & 0 & \frac{\eta(\eta+\chi)}{2(\eta-\chi)} & 0 & 0 & \frac{e_4}{2(\chi-\eta)} \end{bmatrix}, \tag{13}$$

$$e_9=\frac{\eta^3+2\eta^2\chi+3\eta\chi^2-6\chi^3}{30}, e_{10}=\frac{3\eta^3+\eta^2\chi-\eta\chi^2-3\chi^3}{60}, e_{11}=\frac{6\eta^3-3\eta^2\chi-2\eta\chi^2-\chi^3}{30}, \tag{14}$$

$\eta,\chi$ - dimensionless coordinates of the first and second element nodes, respectively,

Assembling generalized matrices and vectors of the problem is usually carried out for the finite element method.

Account the boundary conditions for the functions $\Phi$ and $\theta$ on the support contour is performed by adding the corresponding diagonal elements of the generalized matrix with values $\eta(1-n)$ (for $\Phi$ function) and $\eta(1-m)$ (for $\theta$ function).

Determining the frequency of free oscillation of a shell is carried out in two stages. First, solve the problem of determining the initial deformed state of the shell [2]. The resulting values are substituted into (10), and then solve the problem of determining the frequency of free oscillation of a shell. Generalized eigenvalue problem (10) has been solved Z-decomposition method.

**Checking the results of calculations**

Table 1 shows the calculation results of minimum frequency value of free oscillations for build-in contour base ( $m=\infty$, $n=-\nu=-0{,}3$ ) shallow spherical shell of revolution under a=0.06 [m]; h=0.001 [m]; $E=1\cdot10^{11}$ [Pa]; $\nu=1/3$; $\rho=10160\,[\text{kg/m}^3]$; q=0. Table 1 also shows the difference in % between the values $\omega_{min}$ obtained by this methodic and the values $\omega_{min}$ obtained by the developed methodic.

Table 1

| Calculation methodic | $\omega_{min}$, [rad/sec] | Value $\omega_{min}$ obtained by the developed methodic [rad/sec] | $\varepsilon$, % |
|---|---|---|---|
| [4] | 11034 | 11680 | 5,7 |
| [5] | 9085 | | 29 |
| COSMOS/M | 10950 | | 6,2 |

As you can see, the frequencies close to those obtained by finite difference method in [4], and the results of calculation using FEM in displacements (COSMOS/M). The difference with the results of [5] explained by the use simplified approach that takes into account only two boundary conditions on a support contour of the three.

**Conclusions**

The developed methodic of determining the free oscillations frequency for shell of revolution, based on the mixed finite element method shows good accuracy and convergence results. The methodic allows to taking into account the effect of the initial deformed state the shell that determined considering the geometric nonlinearity, to evaluate small frequencies of shell's free oscillations.

**References**

[1] Kh.M. Mushtary Nonlinear theory of shells (Nauka Publ. Moscow (in Russian), 1990)

[2] L.U. Stupishin, K.E. Nikitin Mixed finite element of geometrically nonlinear shallow shells of revolution (Applied Mechanics and Materials Vols. 501-504 (2014) pp 514-517. Trans Tech Publications, Switzerland)

[3] C.A.J. Fletcher Computational Galerkin methods (Springer-Verlag New York Inc., 1984)

[4] N.V. Valishvili Methods for calculating the shells of revolution on a computer (Mashinostroenie Publ. Moscow (in Russian), 1976)

[5] Strength, stability, oscillation. Handbook in 3 volumes. Vol. 3. Ed. by I.A. Birger, Y.G. Panovko (Mashinostroenie Publ. Moscow (in Russian), 1988)

[6] V.I. Andreev, I.A. Dubrovskiy Stress state of the hemispherical shell at front movement radiating field (Applied Mechanics and Materials Vols. 405-408 (2013) pp 1073-1076. Trans Tech Publications, Switzerland)

[7] L.U. Stupishin, A.G. Kolesnikov Geometric Nonlinear Orthotropic Shallow Shells Investigation (Applied Mechanics and Materials Vols. 501-504 (2014) pp 766-769. Trans Tech Publications, Switzerland)

*Applied Mechanics and Materials Vols. 580-583 (2014) pp 3021-3025*
*© (2014) Trans Tech Publications, Switzerland*
*doi:10.4028/www.scientific.net/AMM.580-583.3021*

# Dynamical Analysis on Underground Powerhouse of Yixing Pumped-Storage Power Station

Fang Han [1,2,a],Dongwang Zhong [1,2,b],Jiyun Mo[1,2,c],Guijuan Chen[1,2,d]

[1]School of Science, Wuhan University of Science and Technology, Wuhan,430065, China,

[2]Hubei Province Key Laboratory of Systems Science in Metallurgical Process, Wuhan University of Science and Technology, Wuhan,430081, China

[a]hanfang522@163.com, [b]zhongdw123@263.net, [c]mojiyun@hotmail.com, [d]chenguijuan@wust.edu.cn

**Keywords:** underground powerhouse, pumped-storage power station, dynamical analysis, vibration response

**Abstract.** The vibration characteristics and vibration response under different load cases in the underground powerhouse structure of Yixing pumped-storage power station were studied by establishing three-dimensional finite element model. The harmonic and transient analysis methods were proposed to study the vibration response of the powerhouse structure under various generating unit dynamic loads and in transient process. The numerical results were evaluated according to the related rules and regulations. The result shows that the vibration response of the power house structure is in the limit of the rules and regulations and there was little chance of resonance.

## Introduction

Hydropower plant is the supporting structure of the unit. The partial or integral vibration of the hydropower plant may be caused by mechanical force, electromagnetic force or hydraulic exciting force, especially for pumped-storage power station [1-3]. Compared with normal power station, the pumped-storage power station have higher water head, higher speed, bidirectional work and transition process, its vibration problem is more prominent[4-5]. The harmful vibration of supporting structure such as unit foundation may be induced by vibrational excitation [6-7]. In order to analyze the dynamic characteristics of the pumped-storage power station, the three-dimensional numerical simulation for Yixing power station is analyzed as an example and the theoretical basis for structural design and operation is summarized.

## Finite element model

The total installed capacity of Yixing pumped-storage power station in Jiangsu Province is 4× 250MW. The normal rotate speed is 375r/min and the runaway speed is 562r/min. The underground powerhouse cavern group is located to the middle of the water conveyance system and is composed of main and assistant powerhouse, main transformer hole and draft tube. The excavation size of the main and assistant powerhouse is 155.3m×22m×52.4m(length×width×height). The erection bay lies to the left of the cavern group with the length 15m. The main powerhouse is composed of dynamo-layer floor, middle-layer floor, turbine-layer floor and volute-layer floor. The structural joints are set for each unit. The dynamic responses of the underground powerhouse is simulated with the software ANSYS. Solid 45 element is used to simulate the floors, columns and surrounding rock, shell 63 element is used to simulate the turbine. Basic material parameters are shown in Table1. The whole and the profiles of the finite element model are shown in Fig.1 and Fig.2.

Table 1 Basic material parameters

| Material | Elastic modulus/GPa | Poisson ratio | Bulk density/kg.m$^{-3}$ |
|---|---|---|---|
| steel | 210 | 0.300 | 7 850 |
| concrete | 28.0 | 0.167 | 2 500 |
| rock | 3.0 | 0.300 | 2 400 |

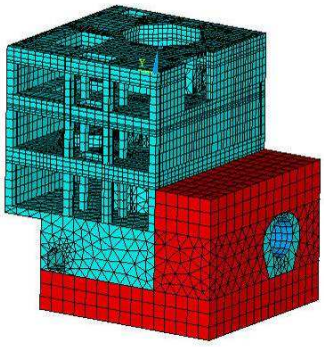

Fig.1 Finite element model of powerhouse

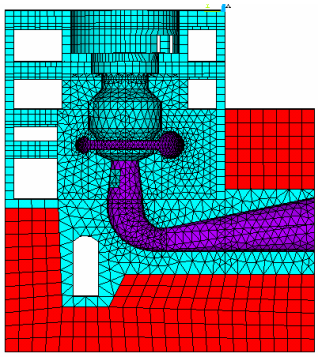

Fig.2 Profiles of the finite element model

**Analysis of vibration characteristics**

The boundary conditions of the side wall upstream and downstream are simplified as the four models below in order to analyze the rock influence on the vibration frequency.

Model 1: The fixed constrains for the boundary nodes.

Model 2: The elastic horizontal constrains for the boundary nodes, the elastic modulus of the surrounding rocks increases to 4GPa.

Model 3: The elastic horizontal constrains for the boundary nodes, the elastic modulus of the surrounding rocks increases to 6GPa.

Model 4: The elastic horizontal constrains for the boundary nodes, the elastic modulus of the surrounding rocks increases to 4GPa, considering the elastic modulus of the cohesive force upstream and downstream as 4GPa.

The natural vibration frequencies calculated for each model are shown in Table 2.

Table 2 Natural vibration frequency of Yixing powerhouse/Hz

| Order | Model 1 | Model 2 | Model 3 | Model 4 |
|---|---|---|---|---|
| 1 | 27.374 | 16.230 | 16.252 | 18.027 |
| 2 | 31.688 | 19.328 | 20.811 | 19.551 |
| 3 | 40.106 | 21.502 | 22.368 | 23.127 |
| 4 | 40.502 | 25.262 | 25.295 | 25.285 |
| 5 | 42.307 | 30.475 | 31.260 | 30.543 |

The result form Table 2 indicates that natural vibration frequencies increases with the enhancement of the boundary conditions. Absolutely model 1 has the highest vibration frequency for its strongest constraints, then the frequency decrease from model 4 to model 3, at last to model 2. In addition, the frequencies of model 2 and model 3 are approximately the same. The frequencies of model 1 and mode 2 are the upper and lower bound of the underground powerhouse structure of Yixing pumped-storage power station. Model 4 is the most close to the real model.

Table 3 Vibration source frequencies of Yixing powerhouse/Hz

| Vibration source | Frequency | Vibration source | Frequency |
|---|---|---|---|
| Normal speed | 6.25 | Low-frequency eddy band | 1.25~2.08 |
| Runaway speed | 9.37 | Number of hydro turbine blade | 56.25 |
| Electromagnetic force | 50.00 | Pressure pulsation after the guide vane | 162.50 |

There are much vibration sources for the water-turbine generator unit such as mechanical force, electromagnetic force and hydraulic force. The frequencies of primary vibration sources are shown in Table 3.According to the design code for hydropower house (SL266-2001), the natural vibration frequency should keep certain distance from the load frequency in order to avoid the resonance effect [8-9]. The results form Table 2 and Table 3 indicate that the above four models are accordance with the criterion, the design scheme is reasonable.

## Analysis of vibration response

Harmonic response analysis is calculated on the assumption that all the load frequency is harmonic. Under normal operation condition the corresponding frequency is normal speed frequency 6.25Hz and under runaway operating status the corresponding frequency is runaway speed frequency 9.37Hz. Both of the two load cases have the same phase position which should be calculated as the worst checking condition.

The load frequency in the transient process is changing with time from 6.25Hz to 9.37Hz. The load amplitude also changes from normal speed to runaway speed. The assumptions are as follows in order to simplify the load curve:

(1) The load frequency is changing linearly from 6.25Hz to 9.37Hz.

$$W(t) = W_{normal} + \frac{W_{runaway} - W_{normal}}{t_{transient}} \tag{1}$$

Where $W$ is the load frequency and $t_{transient}$ is the time needed in transient process. In this project $t_{transient} = 7s$ . Subscript *normal* denotes the load frequency for normal speed and subscript *runaway* denotes the runaway speed, respectively.

(2) The load amplitude is basically in direct proportion to square of rotor speed.

$$P(t) = P_{normal} + (P_{runaway} - P_{normal})(\frac{r - r_{normal}}{r_{runaway} - r_{normal}})^2 \tag{2}$$

Where $P$ is the load amplitude and $r$ is the rotor speed. The subscript *normal* and *runaway* have the same meaning above.

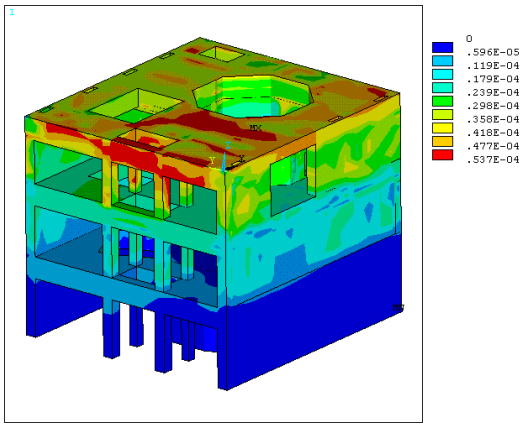


Fig.3(a) Displace envelope diagram-normal

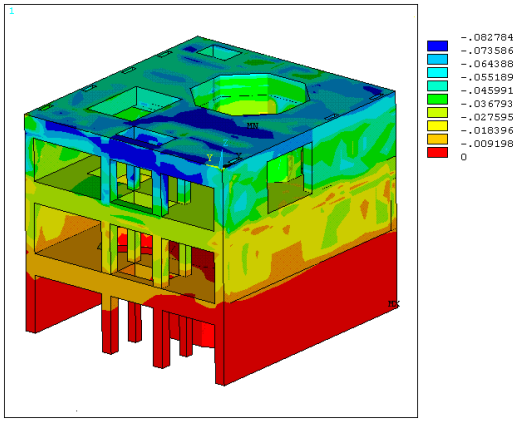


Fig.3(b) Acceleration envelope diagram-normal

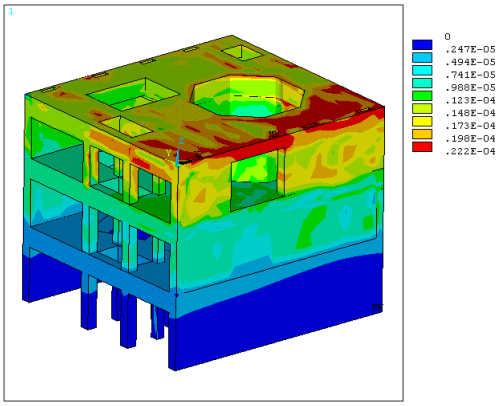


Fig.4(a) Displace envelope diagram-runaway

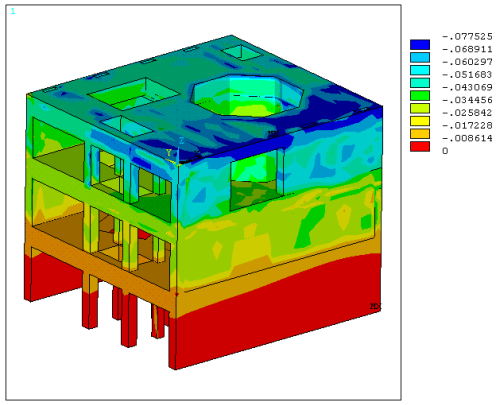


Fig.4(b) Acceleration envelope diagram-runaway

The vibration responses such as displacement and acceleration under different load cases are calculated. Take the horizontal displacement and acceleration as example. Fig.3(a) and Fig.4(a) show the displace envelope diagram under normal load case and runaway load case, respectively.Fig.3(b) and Fig.4(b) show the acceleration envelope diagram under normal load case and runaway load case, respectively.

The results in Fig.3(a) and Fig.4(a) indicate that both the max displacement under two different load cases are less than 0.15mm which satisfy the design requirements. The diagrams also show that the displacement from large to small in turn is dynamo-layer floor, middle-layer floor and turbine-layer floor. The max displacement concentrates around the floor hole. The results in Fig.3(b) and Fig.4(b) indicate that both the max acceleration under two different load cases are less than 85mm/s$^2$ which also satisfy the design requirements. The diagrams also show that the acceleration from large to small in turn is dynamo-layer floor, middle-layer floor and turbine-layer floor. The max acceleration also concentrates around the floor hole. So the floors, beams and columns are the weak parts of the underground powerhouse of pumped-storage power station. The weak parts need more attention at the initial design stage.

## Conclusions

In this paper, dynamical analysis on underground powerhouse of pumped-storage power station is presented. The conclusions are shown as follows:

(1)The vibration problem is more prominent for pumped-storage power station compared with other normal power station, so it is important to control and predict the vibration level at the initial design stage in order to realize the optimization design of vibration resistance.

(2)The vibration characteristic and response of the whole underground powerhouse verify the reasonability of the structural design. The underground powerhouse of Yixing pumped-storage power station satisfies the building vibration control and the human body health standard.

(3)For the lack of special criterion for the underground powerhouse of pumped-storage power station, the corresponding results can be meaningful to the similar project.

## Acknowledgement

This work was financially supported by the Natural Science Foundation of China (51108358 and 51174147) and Hubei Province Key Laboratory of Systems Science in Metallurgical Process (Y201304).

**References**

[1]Wenwu Li. Research on optimizing operation of the single reservoir of hybrid pumped storage power station. DRPT 2011-2011 4th International Conference on electric Utility Deregulation and Restructuring and Power Technologies,Yi Chang:(2011),p.1389.
[2]Eykhoff P. System Identification-parameter and state estimation. New York: Wiley (2010).
[3] Goodwin G C, Payna R L. Dynamic system identification. New York: Academic, (2009).
[4]Chunyi Wang. Automation of Electric Power Systems.Vol.31 (2007),p.32.(in Chinese).
[5]Gyeong-Ho Kim, Youn-Sik Park. Mechanical Systems and Signal Processing,Vol.18(2010),p.59.
[6]Hogberg,Kjell-Erik. Allmaenna Svenska Elektriska Aktiebolaget, Vol. 49(2000),p.51.
[7]Taniguchi, Haruhito. Electrical Engineering in Japan(English translation of Denki Gakkai Ronbunshi).Vol.112(1995),p.197.
[8]Vajnberg,A.I.Fiziko-Tekhnicheskie Problemy Razrabotki Poleznykh Iskopaemykh. Vol.10 (1998), p.33.
[9]S.Kanev, F.Weber, and M.Verhaegen. Journal of sound and vibration, Vol.300(2009),p.394.

*Applied Mechanics and Materials Vols. 580-583 (2014) pp 3026-3029*
*© (2014) Trans Tech Publications, Switzerland*
*doi:10.4028/www.scientific.net/AMM.580-583.3026*

# Experimental and finite element study on the fatigue growth of a semi-elliptical surface crack in aX80 pipeline steelspecimen

Qiao Jin[1,a], Zeyu Sun[1,b]Wannan Guo[1,c]

[1]School of Civil Engineering, Shenyang Jianzhu University, Shenyang, China

[a]goldenfss@163.com, [b]sunzeyu900429@163.com，[c]guownlove@126.com

**Keywords:**fatigue crack growth test; semi-elliptical surface crack; Stress intensity factor; X80 pipeline steel specimen; relative crack depth; crack aspect ratio

**Abstract.**In this paper, a fatigue test of a X80 pipeline steel specimen with a semi-elliptical defect was performed to study the fatigue propagation stages of the Surface cracks.Based on the obtained test data, a three dimentional finite element procedure was developed for the crack growth estimation of the surface crack in the specimen. In the numerical analysis ofcrack growth, both the crack depth direction and the surface direction were investigated by using two different evolution equations. The stress intensity factors along the crack front were determined by applying the virtual crack closure technique. The predictions of crack growth were compared with the test data.

## Introduction

The emerging carbon capture and storage(CCS) technology has been recognized worldwidely as a promising solution for green-house gas(GHG) emission reduction. Up to now, several demonstration projects have been established in China. Experimentation with enhanced oil recovery(EOR) has been conducted in the Jilin fields and the Shengli fields[1]. The rapid deployment and implementation of CCS in China makes new demands on pipelines, which have been expected to play a significant role in the required transportation infrastructure that links anthropogenic $CO_2$ sources and storage sites[2].For $CO_2$ -transporting pipelines, the traditional crack-arrest design of oil&gas pipelines characterized by Charpy V-notch impact energy of pipeline steels can not be directly introduced herein, i.e.,not only fracture propagation control but fracture initiation control should be considered in the design of $CO_2$ pipelines[3].Therefore, it is significant that the propagation behavior of a very small surface defect in $CO_2$ pipelines are studied before a through-wall defect are formed in the pipe wall.

Given that the assumption that an actual part-through flaw can be replaced by an equivalent elliptical-arc crack has been experimentally verified[4], an experimental and finite element (FE) study was developed in this paper to examine the fatigue crack growth of a X-80 pipeline steel specimen with a semi-elliptical surface crack. In the crack growth analysis, both the crack depth direction and the surface direction were investigated.

## Tension-tension fatigue tests

The fatigue specimen was made of a steel plate which was cut from a segment of a X80 pipeline, as shown in Fig.1. In Fig.1(a), the initial semi-elliptical defect, made by wire electric cutting, was arranged at the central part of the lateral surface of the specimen body, the geometry parameters of which are as follows: $a_0$=0.28mm, $b_0$=0.8mm.The specimen was subjected to axial loading with a constant amplitude, $P_{max}$=170KN and a stress ratio of $R$=0.1.It can be seen from Fig.1(b) that the crack propagation path of the specimen under cyclic axial tention-tention loading remains an elliptical arc plane on the whole. Therefore, the defect configuration can be described by the relative crack depth $\xi = a/t$ in correspondence to the deepest point $A$ on the crack front, and the crack aspect ratio $\alpha = a/b$(seeing Fig.1(d) ). Meanwhile, in order to examine the fatigue propagation stages in the process of crack growth and make a comparison with those by the subsequent numerical simulation, three marks were made through adding different loadings in intervals.Correspondently, three sets of major and minor axis of the semi-elliptical crack were obtained and measured: (1) $a_1$=6.40mm,

$b_1$=7.70mm;(2) $a_2$=7.73mm, $b_2$=10.3mm;(3) $a_3$=9.37mm, $b_3$=12.6mm. The material characteristics of X80 pipeline steel are: $\sigma_y$=560MPa, $E$=206Gpa, $\nu$=0.3.

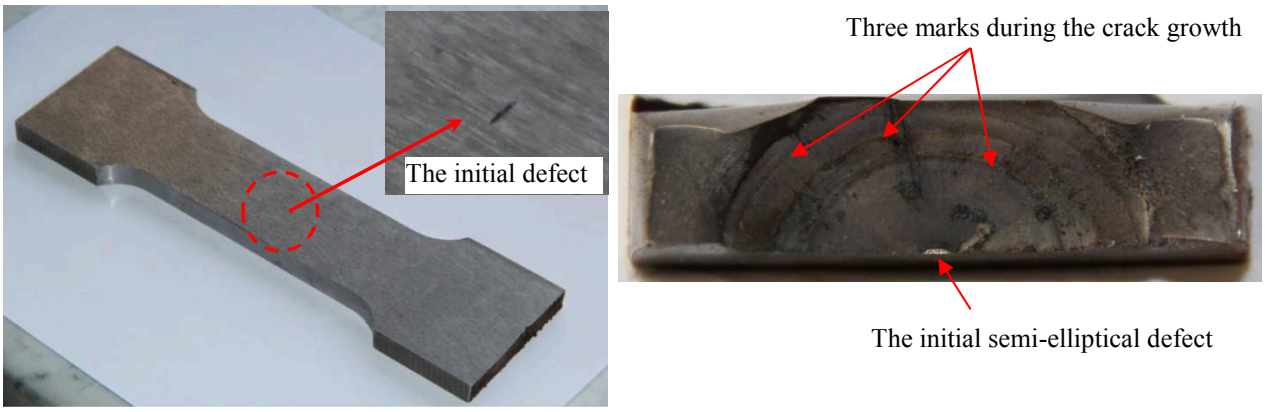


(a) View of the actual specimen with the initial defect(b) The failure surface of the specimen

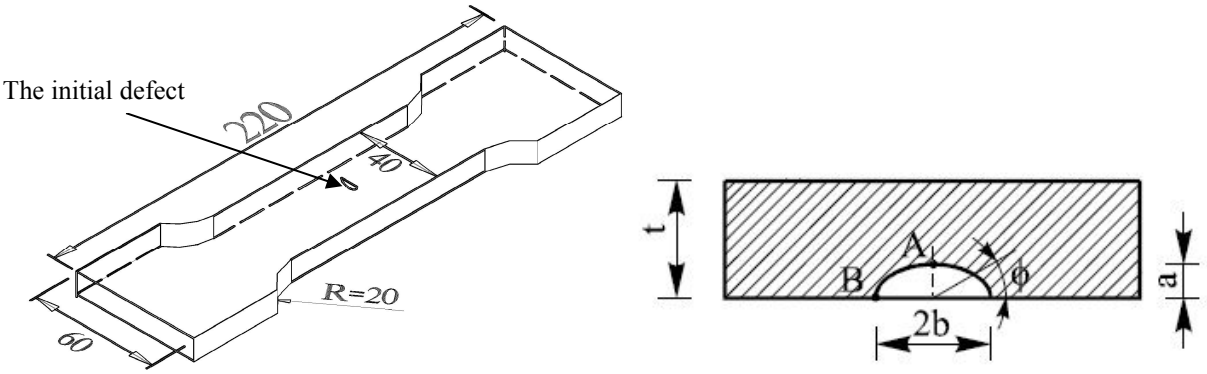


(c) The specimen shape and dimension(units:mm) (d) The geometry parameters of the defect

Fig.1 Geometry of the X80 pipeline steel specimen with a semi-elliptical surface crack

## FE modeling of the specimen with an semi-elliptical crack

Since the objective of this paper is to investigate the fatigue behavior of the embeded semi-elliptical surface crack in the specimen, the important aspect is to obtain accurate distributions of stress intensity factor along the crack front. We applied the virtual crack closure technique[5-7] to the FE model of the specimen for calculation of the stress intensity factors. Based on the ABAQUS software platform, we completed the modelling work of a three dimensional (3D) finite plate with a semi-elliptical surface crack, as shown in Fig. 2. For comparison's sake, the initial geometric sizes , material constants , mechanical parameters and loading ways of the FE model were made identical with those of the actual fatigue specimen, including the specimen itself and the crack in it.

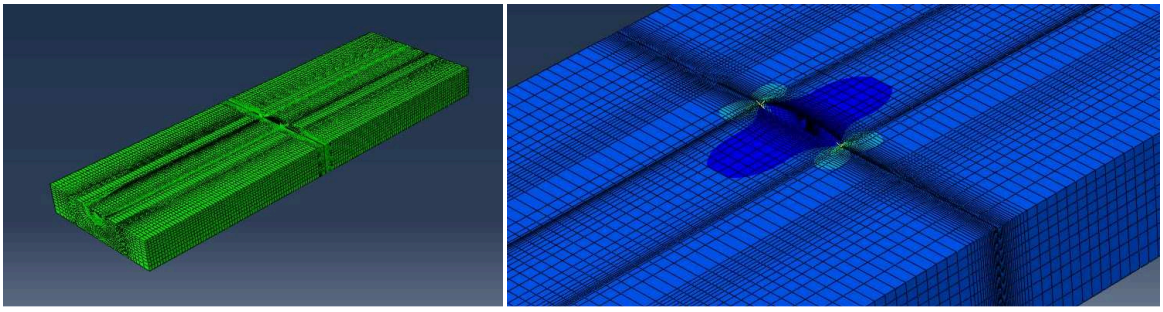

(a)View of the FE model (b) Close-up of the semi-elliptical surface crack

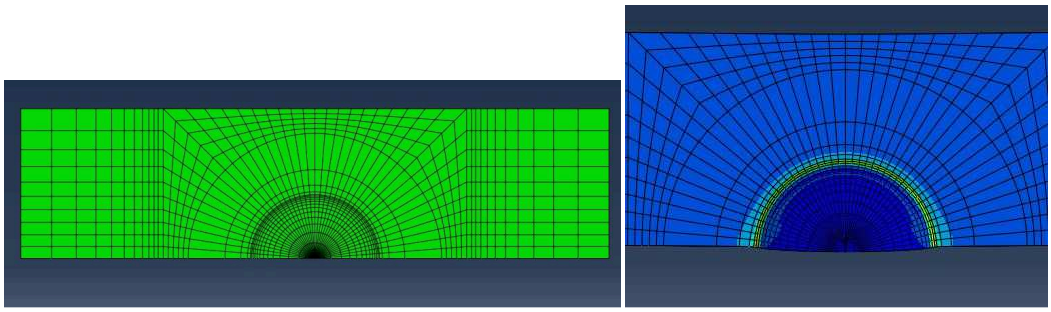

(c) Meshing of the crack surface (d) Stress contour of the crack surface

Fig.2 FE model of the plate with a semi-elliptical crack

## Calculation of the fatigue crack growth

The fatigue propagation analysis of a semi-elliptical surface crack problem requires considering two crack growth directions. Actually, Newman and Raju[8]introduced that the aspect ratio change of surface cracks should be calculated by assuming that a semi-elliptical profile is always maintained and it is adequate to use two coupled Paris fatigue laws known as "two-point plus semi-ellipse" method:

$$\frac{da}{dN} = C_A(\Delta K_A)^{m_A} \tag{1}$$

$$\frac{db}{dN} = C_B(\Delta K_B)^{m_B} \tag{2}$$

Where $\Delta K_A$ and $\Delta K_B$ are the ranges of the stress intensity factor at the depth and the surface points of the surface crack; $C_A$, $C_B$, $m_A$ and $m_B$ are material constants.

In this paper, two different cases were considered :(1) Case1: $C_A = C_B, m_A = m_B$; (2) Case2: $C_B = (0.9)^m C_A, m_A = m_B$.

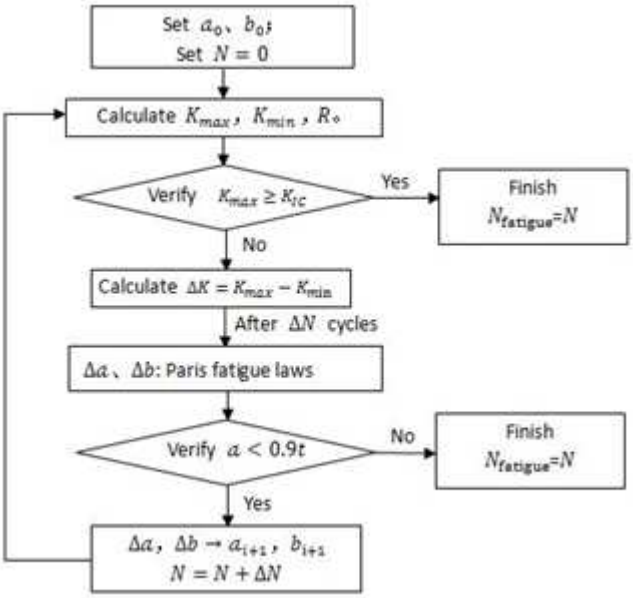


Fig.3 Histogram of crack growth calculating algorithm

## Numerical results

By using the two different evolution equations of the fatigue crack growth along the depth and surface directions, i.e., Case1 and Case2, we calculated two fatigue propagation paths of the semi-elliptical

surface crack through the numerical method, as shown in Fig.3. Although only three marks were made in the fatigue test(Fig.1(b)), which yet could not cover the whole process of crack growth, we still can make a conclusion that the simulated crack growth path by using the "Case1" evolution equation is more in accordance with the actual results of the fatigue test(Fig.4).

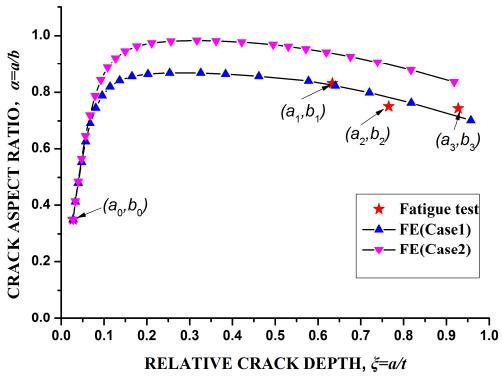


Fig.4 Fatigue propagation paths of the surface crack

## Conclusions

In this paper, we developed an ABAQUS-based three dimensional finite element method to study the fatigue propagation calculation of a semi-elliptical defect in a X80 pipeline steel specimen. the following conclusions could be drawn:

(1) Based on two different evolution equations , a 3D FE procedure is used to analyze the crack growth path of the surface crack. The numerical results show that one of the two simulated paths have a good agreement with the data from the specimen test .
(2) In the process of fatigue crack growth, a large part of crack propagation life is due to the propagation of a very small crack.
(3) The crack aspect ratio of the surface crack tends towards stability when the relative paths of the surface crack reaches around 0.15.

## Acknowledgements

This work was financially supported by the Natural Science Foundation for the Youth (51008049).

## References

[1]. Sun, L. and W. Chen, *The improved ChinaCCS decision support system: A case study for Beijing–Tianjin–Hebei Region of China.* Applied Energy, 2013. **112**: p. 793-799.
[2]. IPCC, *Carbon dioxide capture and storage.* Special report prepared by Working Group III of the intergovernmental panel on climate change, 2005.
[3]. Yong, Z., et al., *Study of relationship between fatigue crack growth rate and fatigue life for pipeline steels.* Acta metallurgica sinica, 2005. **41(5)**: p. 523-528.
[4]. Carpinteri, A. and R. Brighenti, *Circumferential surface flaws in pipes under cyclic axial loading.* Engineering Fracture Mechanics, 1998. **60**(4): p. 383-396.
[5]. Rybicki, E.F. and M.F. Kanninen, *A finite element calculation of stress intensity factors by a modified crack closure integral.* Engineering Fracture Mechanics, 1977. **9**(4): p. 931-938.
[6]. Xie, D. and S.B. Biggers Jr, *Strain energy release rate calculation for a moving delamination front of arbitrary shape based on the virtual crack closure technique. Part I: Formulation and validation.* Engineering Fracture Mechanics, 2006. **73**(6): p. 771-785.
[7]. Xie, D. and S.B. Biggers Jr, *Strain energy release rate calculation for a moving delamination front of arbitrary shape based on the virtual crack closure technique. Part II: Sensitivity study on modeling details.* Engineering Fracture Mechanics, 2006. **73**(6): p. 786-801.
[8]. Newman, Jr., Raju, I.S.. Analysis of surface cracks in finite plates under tension and bending loads. NASA TP-1578, 1979.

*Applied Mechanics and Materials Vols. 580-583 (2014) pp 3030-3033*
*© (2014) Trans Tech Publications, Switzerland*
*doi:10.4028/www.scientific.net/AMM.580-583.3030*

# Finite Element Analysis on Negative Wind Pressure Stress of External Wall Insulation Layer

Youhui Zhang[1,a], Liping He [2,b], Yingjun Zhang[3,c] and Chen Li* [4,d]

[1,2,3,4]Taiyuan University of Science and Technology，Taiyuan 030024, China

[a,c]1444706361@qq.com, [b]18636180650@163.com, [d]tydz_lc@126.com

**Keywords:** external wall insulation, phase change material, negative wind pressure, finite element analysis

**Abstract.** With excellent flame retardation and thermal insulation properties, SY self-temperature regulation and phase change energy-saving wall insulation material (the material) is composed of concrete and volcano perlite. At present, applied research of this material is not very thorough，especially under the condition of temperature variation, seasonal wind change in North China. In this paper, finite element analysis of external wall insulation layer of the Experimental Teaching Building in Taiyuan University of Science and Technology under negative wind pressure effect is performed. The negative wind load calculated is applied to the surface of the thermal insulation layer as uniform load, and the results show that the material used in the building which shorter than 80 meters in the Taiyuan area has no shedding or destruction under the negative air pressure. This material is safe and available.

## Introduction

The main composition the material is cement, volcano perlite and fly ash. These elements accounted for 17%, 60% and 7%, respectively. In addition, the material also contains 2% powder, 4-5% fibrous tissue, 8-9% ceramic sintered material, and some cement retarder. Its density is 370~400 kg/m$^2$, close to the lightweight cement's. Some properties of the material are shown in table 1.

Table 1 Properties of SY self-temperature regulation and phase change energy-saving material

| Test items | dry density | Latent heat matter | anti - press strength | Compression shear bond strength | Linear shrinkage | Combustion performance | Wet flow density of steam | Equivalent thermal conductivity |
|---|---|---|---|---|---|---|---|---|
| Units | kg/m$^3$ | kJ | MPa | kPa | % | | g/(m$^2$·h) | W/(m·h) |
| Test results | 360 | 6420 | 0.52 | 116 | 0.29 | Level A | 1.51 | 0.027 |

The weathering test for SY self-temperature regulation and phase change energy-saving material has be done in laboratory. After 80 heat raining cycles and 5 thermal cold cycles in the test, this material does not appear fading, discoloration, cracking, chalking and other damage. The experimental results show that this material has sufficient weatherability. Further, the maximum tensile stress of the material is measured out by drawing experiment. The value of the maximum tensile stress is 0.19MPa.

## Finite element analysis of negative wind stress of SY self-temperature regulation and phase change energy-saving material

The above test can not verify the destruction of the material under temperature stress and negative wind pressure. With the change of day and night or the seasons, the temperature will be significantly different. This phenomenon will cause great temperature stress which may cause the insulating layer falling. Taiyuan city is located in the North Central China. In spring and autumn, this place will have a lot of wind which can produce huge negative wind pressure. The negative wind pressure will produce great suction on the insulating layer and cause the insulating layer shedding or separation.

Therefore, it is necessary to perform a finite element analysis of the insulating material under the negative wind pressure.

**The problem to analysis.** Taking the Experimental Teaching Building in Taiyuan University of Science and Technology (TYUST) as an example, a finite element analysis by ANSYS software on the resistance of SY self-temperature regulation and phase change energy-saving material under negative wind pressure has been performed in this paper.

1. According to "the load code for the design of building structures" (the Code) released in January 10, 2002, the once-in-50-years wind pressure should be taken. The wind pressure changes with height, so two cross sections (at the height of 10 meters and 50 meters) which perpendicular to the direction of building height has be taken in the calculation. Take the wind pressure at same height as uniform load.

2. The construction principle of the material is that mixing the material with water directly, and brushed the mixture to the exterior wall. Then the grid cloth or wire mesh is added into the exterior wall. Finally a layer of anti-crack mortar is brushed outside the insulating layer. When the negative wind pressure occurs, the wind load affects on the anti-crack mortar, and then transferred to the insulating layer. The anti-crack mortar, grid cloth or wire mesh will not affect the value of the wind load. So, the effect of anti-crack mortar, grid cloth and wire mesh can be ignored when the analysis model is constructed. The combination of wall and insulation layer is built directly, in which the thickness of wall and insulation layer is 0.24 meters and 0.04 meters, respectively.

**The basic assumption.** Assuming the stress-strain curve of the material is linear, ultimate strength is 0.52MPa, and its density is 400kg/m$^3$.The properties of and rubber concrete are very similar. In the simulation, the stress-strain curve of rubber concrete can be taken as the material's.

In the analysis, the material is assumed as isotropic elastic body, its elastic modulus is assumed to be 360MPa.

In the research of phase change material, the Poisson ratio is assumed to be 0.3.

**Calculation of Negative Wind Pressure**. According to the Code, the wind pressure calculation must meet certain standards.

The general direction of wind in Taiyuan is northwest according to some data and the long-term living in Taiyuan, and the wind direction is perpendicular to the face of building. According to the Code, when the wind is perpendicular to the surface of a building, the nominal values of wind load should be in accordance with Eq. 1:

$$w_k = \beta_z \mu_s \mu_z w_0 \tag{1}$$

Where, $w_k$ is the nominal value of the wind load. $w_0$ is the reference wind pressure (kN/m$^2$). $\mu_z$ is the exposure factor of wind pressure. $\mu_s$ is the shape factor of wind load. $\beta_z$ is the dynamic response factor of wind load at height z.

Experimental Teaching Building in TYUST is sixteen stories high, which is a high-rise building. Two cross sections (at the height of 10 meters and 50 meters) which perpendicular to the direction of building height has been taken in the analysis. The value of reference wind pressure is 0.3kN/m$^2$ (at the height of 10 meters) and 0.4kN/m$^2$ (at the height of 50 meters) in Taiyuan. Considering the experimental teaching building is a towering structure, the above values of reference wind pressure should be increased to 0.35kN/m$^2$ (at the height of 10 meters) and 0.45kN/m$^2$ (at the height of 50 meters) appropriately.

For the flat or slightly undulating terrain, the exposure factor of wind pressure should be determined by the given table based on the terrain roughness categories. There are a lot of buildings in the place where TYUST is located, so the region should be classified as Class C. The exposure factor of wind pressure is selected as 0.74 (at the height of 10 meters) and 1.25(at the height of 50 meters).

According to the Code, the local shape factor of wind load can be used in the calculation of retaining structure and its connection strength. The structure studied in this paper belongs to building

envelope. Therefore, the calculated shape factor of wind load is -1.0(at the negative pressure zone) and -1.8(at the corner).

For the general cantilever structure, such as high structure frame, tower, chimney, and high-rise buildings whose height is greater than 30m, or whose height to width ratio is greater than 1.5, and the reverse effect could be ignored, only the effect of the first mode is considered. The wind load of the structure could be calculated according to the above formula. Dynamic Response Coefficient of Wind Load at Height z can be calculated as Eq. 2:

$$\beta_z = 1 + \frac{\xi \nu \varphi_z}{\mu_z} \tag{2}$$

Where, $\xi$ is the Fluctuating Amplifying Coefficient. $\nu$ is the Fluctuation Influence Coefficient. $\varphi_z$ is the Coefficient of Vibration Mode. $\mu_z$ is the Exposure Factor of Wind Pressure.

Fluctuation Influence Coefficient can be found in the tables, whose value is 1.39 $kNs^2/m^2$. The Fluctuation Influence Coefficient at the class C region (based on the terrain roughness categories) is 0.64 (at the height of 10 meters) and 0.85(at the height of 50 meters). The Coefficient of Vibration Mode can be determined as 0.17 (at the height of 10 meters) and 0.86(at the height of 50 meters) according to special tables.

Two special interfaces at each height (the height of 10 meters and 50 meters) were calculated. One interface is close to the window, as the window is a symmetric structure, so just 1/4 of the interface has been taken in the calculation. The calculated values of negative wind pressure that close to window are 311Pa (at the height of 10 meters) and 1020Pa (at the height of 50 meters). The other interface is at the corner of wall, its negative wind pressure values are 560Pa (at the height of 10 meters) and 1840Pa (at the height of 50 meters).

**Analysis results**. A comparison has been made between the calculated maximum stress and the limit stress of the material. If the calculated maximum stress is smaller than the limit stress of the material, it means that the insulating layer can resistance the negative wind stress, which also proofed that the material is safe and available.

At the height of 10 meters, the stress of insulating layer close to window as shown in table 2.

Table 2 The value of stress

| principal stress | Maximum[Pa] | Minimum[Pa] | direction of shear stress | Maximum[Pa] | Minimum[Pa] |
|---|---|---|---|---|---|
| X | 352.297 | 0 | XY | 37.4 | -62 |
| Y | 294.702 | -103.434 | YZ | 126.761 | -5.949 |
| Z | 224.341 | -95.5 | XZ | 67.37 | -44 |

From table 2, the maximum principal stress along X direction, its absolute value is 352.297Pa; the maximum shearing stress along YZ direction, its absolute value is 126.761Pa. X direction and XZ direction stress cloud chart as shown in Fig.1.

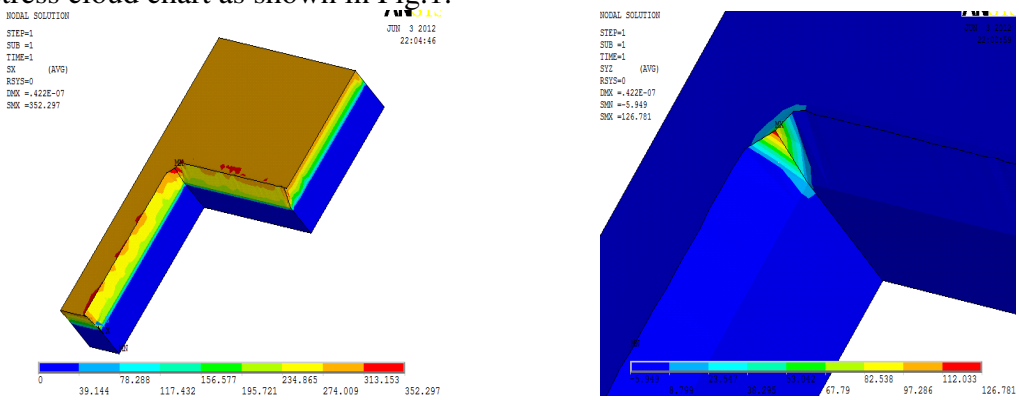


Fig. 1 Stress cloud chart of insulating layer at the height of 10 meters close to window

At the height of 50 meters, the stress of insulating layer close to window as shown in table 3.

Table 3 The value of stress

| principal stress | Maximum[Pa] | Minimum[Pa] | direction of shear stress | Maximum[Pa] | Minimum[Pa] |
|---|---|---|---|---|---|
| X | 1155 | 0 | XY | 122.773 | -205.465 |
| Y | 966.548 | -340.388 | YZ | 415.81 | -19.511 |
| Z | 735.38 | -314.308 | XZ | 220.984 | -146.041 |

From table 3, the maximum principal stress along X direction, its absolute value is 1155Pa; the maximum shearing stress along YZ direction, its absolute value is 415.81Pa.

At the height of 10 meters, the stress of insulating layer at the corner of wall as shown in table 4.

Table 4 The value of stress

| principal stress | Maximum[Pa] | Minimum[Pa] | direction of shear stress | Maximum[Pa] | Minimum[Pa] |
|---|---|---|---|---|---|
| X | 838.439 | -78.569 | XY | 46.169 | -40.26 |
| Y | 417.546 | -121.999 | YZ | 48.195 | -47.818 |
| Z | 735.751 | -157.35 | XZ | 294.866 | -470.164 |

From table 4, the maximum principal stress along X direction, its absolute value is 838.439Pa; the maximum shearing stress along XZ direction, its absolute value is 470.164Pa.

At the height of 50 meters, the stress of insulating layer at the corner of wall as shown in table 5.

Table 5 The value of stress

| principal stress | Maximum[Pa] | Minimum[Pa] | direction of shear stress | Maximum[Pa] | Minimum[Pa] |
|---|---|---|---|---|---|
| X | 2735 | -258.154 | XY | 151.699 | -132.282 |
| Y | 1372 | -400.854 | YZ | 158.354 | -157.116 |
| Z | 2417 | -517.007 | XZ | 968.847 | -1545 |

From table 5, the maximum principal stress along X direction, its absolute value is 2735Pa; the maximum shearing stress along XZ direction, its absolute value is 1545Pa.

## Conclusion

It confirmed that the material is completely suitable for the environmental conditions in Taiyuan. With excellent flame retardation and simple construction techniques, the material is easy to be got, and its performance is too good to its price, which is the development trend of insulating material.

## Acknowledgements

This work was financially supported by the Shanxi Natural Science Foundation (20091035, 2013011005-4), National Natural Science Foundation (11372207).

## References

[1] Yuanfeng Wang , Yaping Liang. Study on Modulus of Elasticity and Poisson Ratio of High Performance Concrete[J].Journal of Beijing Jiaotong university,2004,28(1),5-7,in Chinese.

[2] Anzhong Deng, Shengbo Li, Chunlong Zhuang etc. Study on light phase change thermal storage wall material[J]. Journal of Tongji University, 2008, 11(5) 5-8, in Chinese.

[3] Ying Chou, Qisheng Wu, Shuiping Li, Xuejun Liu, Hesheng Xun. Research on phase change energy storage wall materials[J]. Journal of Jiangsu University, 2011, 12 (3) 39-42, in Chinese.

[4] Qiusheng Li, Yonggui Li, Lunhai Zhi. Experimental study on characteristics of wind pressure distribution on typical high-rise building[J]. Journal of Hunan University, 2011, 38 (4), 11-16, in Chinese.

[5] Lili Chen, Zhenhua Wang. Numerical simulation of wind pressure distribution on high-rise buildings[J]. Shanxi Architecture, 2008, 34 (11), 4-6 (2003), in Chinese.

[6] Jigui Liu, Gang Luo, Yanchen Tian, Gang Su. Study on field test method of negative pressure performance of exterior wall insulation system[J]. New Building Materials, 2011，87（2），87-92, in Chinese.

*Applied Mechanics and Materials Vols. 580-583 (2014) pp 3034-3037*
*© (2014) Trans Tech Publications, Switzerland*
*doi:10.4028/www.scientific.net/AMM.580-583.3034*

# Mechanics Analysis of Tower Crane

Zhijun Yang[1,a] , Zhidan Ai [2,b] and Hongwei An[3,c]

[1]Architecture and Civil Engineering School, Inner Mongolia University of Science and technology, Baotou, 014010, China

[2]Architecture and Civil Engineering School, Inner Mongolia University of Science and technology, Baotou, 014010, China

[3]Architecture and Civil Engineering School, Inner Mongolia University of Science and technology, Baotou, 014010, China

[a] Yzj4569@sina.com, [b]yang2003060@163.com,[c] yangzhijun200360@163.com

**Keyword:** Tower crane, Finite element model, Working condition, Stability, Strength

**Abstract.** With accelerating urbanization construction, especially with the scale enlargement of high-rise buildings, the crane's hoist boom length and height is increasing.The hoist boom will produce strength and buckling failure easily on the working condition of complex combination, such as gravity, wind load and inertia force.The TC6010 crane was analyzed the mechanics by finite element method. This thesis got its stability and strength data in four kinds of working conditions. It can provide certain reference value for other crane's design and calculation.

## Introduction

With accelerating urbanization construction, especially with the scale enlargement of high-rise buildings, the crane's hoist boom length and height is increasing[1,2]. The hoist boom will produce strength and buckling failure easily on the working condition of complex combination, such as gravity, wind load and inertia force. So not only static analysis was carried out on the tower crane, the dynamic analysis is also very important. This thesis uses the ANSYS finite element method, analyzes its strength and stability and check calculation[3,4]. The calculation results are obtained. In this thesis, the research conclusion can provide a certain reference value for other crane's design and optimization.

## Establish the calculation model

Tower crane structure is complex. There are different forms of the pole in the tower cranes as shown in Fig.1[5,6]. Besides mainly bear axial stress $\sigma_x$ , all kinds of pole also bear the bending stress $\sigma_y$ and $\sigma_z$ along the y direction and z direction, when the tower crane stress under different working conditions. So beam188 were adopted to simulate and the total of more than 3000 nodes.

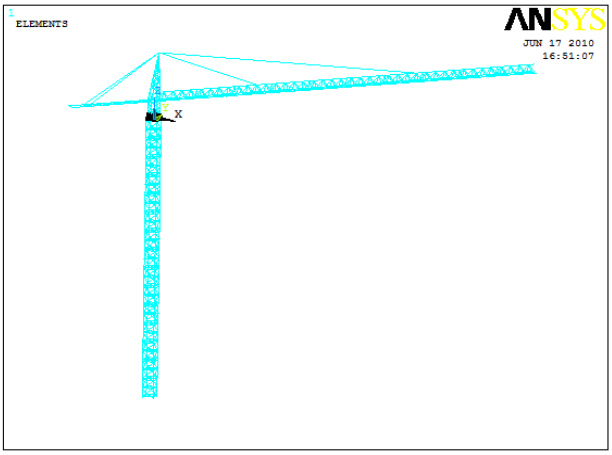


Fig.1 The diagram of tower crane model

The intersection points of web member and chord member are rigid joint. The junction of knuckle arm and knuckle arm, the junction of tie rod and the tower top and the junction of various parts are also processed as rigid joint. The main technical performance parameters: rated load moment for 97t.m, maximum load moment for116t.m, maximum lifting load for 6t, lift height for stationary type 45m , attached type 200m, working range for max=60mand min=2.5m.

Elasticity modulus E=210GPa, Poisson's ratio $\mu$ =0.3, wind load w=620KN/m$^2$, and the density $\rho$ =7800kg/m$^3$, gravitational acceleration is 9.8m/s$^2$.

## Calculation and analysis of stress and deformation under the various working conditions

**Load.**The load that effects on the tower crane include dead weight load $F_g = 43750\times 4\mathrm{N}$, hoisting load $F_g = 627430\mathrm{N}$, inertial load (impact load) $F_c = 2\times F_q$ and wind load $F_w = 4794.03\mathrm{N}$.

**Analysis and calculation of Working condition.** Resistance to overturning stability of tower crane should be checked in accordance with the wording conditions listed as shown in Tab.1[7].

Tab.1 Checking wording conditions

| wording conditions | instructions |
|---|---|
| basic stability | working condition，static state，breezeless |
| dynamic stability | working condition，dynamic state，windiness |
| the storm hitting | off working state |
| sudden unloading | working condition，hopper uninstall |

The design of the concrete foundation used by fixed tower crane should satisfy the resistance to overturning stability condition and strength condition. According to the following formula, the resistance to overturning stability of the concrete foundation can be calculated.

$$e = \frac{M + F_h \times h}{F_v + F_g} \le \frac{b}{3}$$

In the formula, e for eccentric distance; $M$ for bending moment effecting on the foundation; $F_v$ for vertical load effecting on the foundation; $F_h$ for horizontal load effecting on the foundation; $F_g$ for the gravity of the concrete foundation.

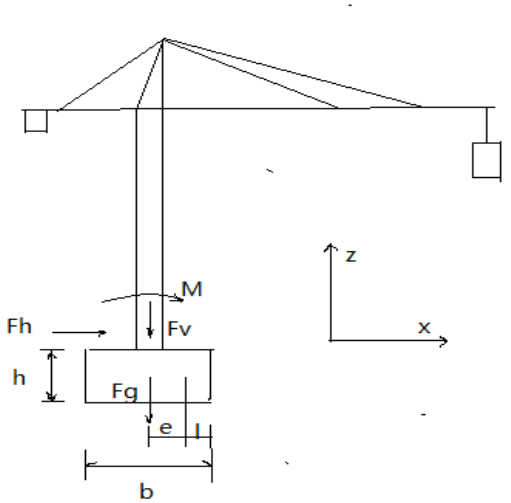


Fig.2 Calculation diagram of resistance to overturning stability

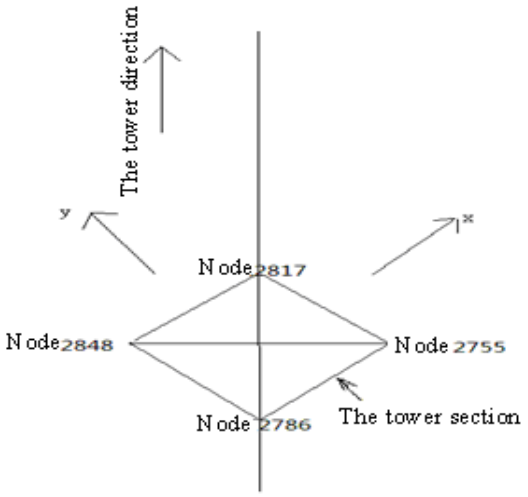


Fig.3 Calculation and introductions

**Calculation the various working conditions.**Considering the length, here will introduce working condition two: including wind load, hoisting load, impact load and dead weight load,as shown in Fig.4,Fig.5 and Tab.2.

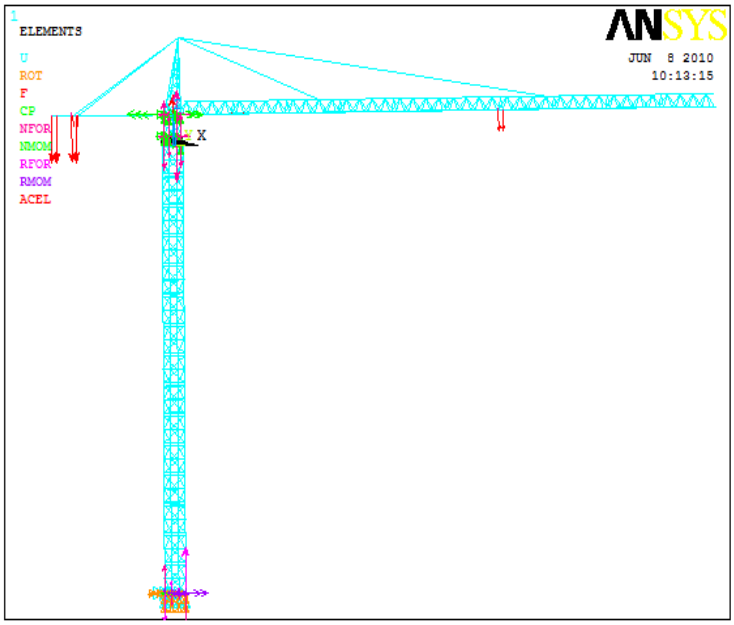


Fig.4 The forced diagram of tower crane

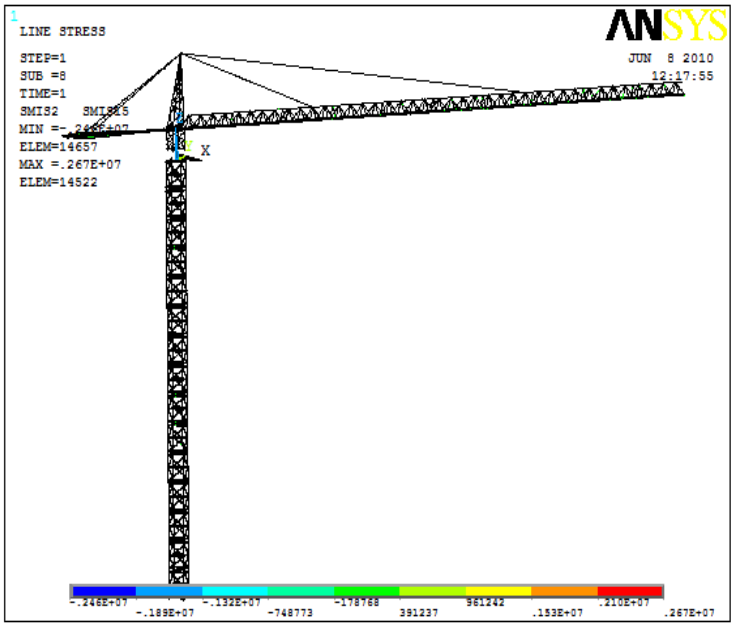


Fig.5 The bending moment diagram of tower crane

Tab.2 The support reaction

| node number | FX | FY | FZ | MX | MY | MZ |
|---|---|---|---|---|---|---|
| 2848 | 6844.8 | -4725.8 | 0.69080E+06 | 1646.4 | 4772.6 | -136.92 |
| the value of resultant force | 23313. | -22685 | 0.66832E+06 | 11792 | 13863 | -903.19 |

Calculate the resistance to overturning stability according to standard

$$M_{x(z)} = (F_{2786} + F_{2848} - F_{2755} - F_{2817}) \times \frac{1.665}{2} = 1.735 \times 10^6 \,\mathrm{N \cdot m}$$

$$e_y = \frac{M_{x(z)} + M_x - F_y \times h}{F_z + F_g} = 0.8 < 2.3$$

Therefore, the whole tower crane is stable. We can known that the maximum Misses stress appears on the root of the tower and is $\sigma = 117.07\mathrm{MPa} \le [\sigma] = 170\mathrm{MPa}$ by looking up information. The whole crane is satisfied in the strength conditions.

## Conclusion

Looking from the static analysis: the whole tower crane is lower stress levels on the four working conditions concluding basic stability, dynamic stability, the storm hitting and sudden unloading. Only at the bottom of the tower, the Mises equivalent stress of some poles is larger on the various kinds of working conditions. This position is the most dangerous and yields easily. The Mises stress of this position's poles reach to 166.58MPa on the working condition three that is the storm striking working condition and almost reach the allowable stress, so The whole crane is satisfied in the strength conditions.

Looking from the stability: this tower crane is satisfied in whole resistance to overturning stability condition. On the most dangerous working condition three that is the working condition three, the biggest eccentric distance is only 1.08 m which is produced by the tower crane. So the tower crane is stable enough.

After doing finite element analysis to the tower crane TC6010, we can find out the most dangerous section and the most dangerous working condition. It is of great significance in checking poles intensity and check the stability. According to this analysis, it is also easy to find the parts of smaller stress. So we can optimize the design to tower crane and save the cost of tower crane, according to strengthen the poles section of dangerous parts and weaken the poles section of smaller stress. It is helpful to improve the stability and strength.

## References

[1] Peiheng Liu.Instruction Manual of Tower Crane [M]. China Machine Press,January, 2005, 1-80.

[2] Standard in Germany.DIN15018. August, 1974.

[3] Xi'an University of Architecture and Technology. Steel Structure Foundation，China Building Industry Press. 83-137.

[4] Chuanbo Ren,Wangming Yu,Dazhen Yun.Timoshenko A New Method for Bending Beam Analysis,Dalian University of Technology.

[5] The Design Instruction of Tower Crane TC6010 in Baotou Capgemini Construction Machinery Company.

[6] Lixin Gu,Haibin Zhen. The Finite Element Analysis to Tower Crane Jib Structure and Stability, Mechanical and Electrical Engineering Technology, 2005.

[7] Xiaohua Chang,Chunhua Wang.The determination of Tower Crane Jib Danger Point, Construction Mechanization.

*Applied Mechanics and Materials Vols. 580-583 (2014) pp 3038-3041*
*© (2014) Trans Tech Publications, Switzerland*
*doi:10.4028/www.scientific.net/AMM.580-583.3038*

# Mixed Time Integration Parallel Algorithm for Nonlinear Dynamic Analysis

Chaojiang Fu

College of Civil Engineering, Fujian University of Technology, Fuzhou, 350108, China

email: cjfu@163.com

**Keywords:** Parallel Computing; Mixed Time Integration; Domain Decomposition; Dynamic Analysis

**Abstract.** The mixed time integration parallel algorithm for nonlinear dynamic analysis was presented by synthesising the implicit and explicit time integration techniques. The parallel algorithm employing mixed time integration technique was devised with domain decomposition. Concurrency was introduced into this algorithm by integrating interface nodes with explicit time integration technique and solving local subdomains with implicit algorithm. Numerical example was implemented to validate the performance of the parallel algorithm. Numerical studies indicate that the proposed algorithm is superior in performance to the implicit algorithm.

## Introduction

For large-scale structural dynamic analysis with nonlinearities, the implicit time integration algorithms become highly compute intensive. The equation-solving phase is the most dominating computational phase in these algorithms. With emergence of parallel processing, it provides an effect way for solving this kind of problem[1].

The explicit time integration algorithms like central difference method can easily be moved onto parallel processing machines, as the resulting dynamic equilibrium equations are uncoupled when mass and damping matrices are diagonal. However, explicit algorithms are conditionally stable and cannot be applied efficiently for structural dynamic analysis[2]. On the other hand implicit algorithms are unconditionally stable, but parallel implementation is not so straightforward.

Parallel algorithm research on structure dynamic analysis has been very active. Noor have completed parallel the explicit integration algorithm in the pipeline vector computer[3]. Chiang and Fulton investigated implicit Newmark type methods in shared memory MIMD environment[4]. Noor and Peter derived the finite element discretisation based on a mixed formulation on multiprocessor computers[5]. These studies mainly developed in the vector machine and shared storage MIMD parallel computer. In recent years, parallel computing system based on distributed MIMD network cluster has become one of the mainstream for parallel computer development[6].

In this paper the mixed time integration parallel algorithm for nonlinear dynamic analysis is studied by synthesising the implicit and explicit time integration techniques on workstation cluster. Numerical studies indicate that the proposed algorithm is correct and effective.

## Newmark's Time Stepping Algorithm

The governing equilibrium equation of structural dynamics can be expressed as[7]

$$\boldsymbol{Ma}+\boldsymbol{Cv}+\boldsymbol{Kd}=\boldsymbol{f}(t) \tag{1}$$

where $\boldsymbol{M}$ is the mass matrix, $\boldsymbol{C}$ is the damping matrix and $\boldsymbol{K}$ is the stiffness matrix. $\boldsymbol{a}$, $\boldsymbol{v}$ and $\boldsymbol{d}$ are the acceleration, velocity and displacement vectors, respectively, $\boldsymbol{f}(t)$ is load vector. Solution of this initial value problem requires integration through time. This is achieved numerically by discretising in time the continuous temporal derivatives. The most widely used family of direct time integration methods for solving Eq. (1) is the Newmark family of methods[2]. These methods are based on equilibrium at the ($n$+1)th time step, i.e. at time ($t_{n+1} = t_n + \triangle t$), and is given by

$$\boldsymbol{Ma}_{n+1}+\boldsymbol{Cv}_{n+1}+\boldsymbol{Kd}_{n+1}=\boldsymbol{f}(t)_{n+1} \tag{2}$$

The velocity and displacement vectors are expressed by finite difference approximations

$$\boldsymbol{d}_{n+1} = \boldsymbol{d}_n + \Delta t \boldsymbol{v}_n + 0.5\Delta t^2\{(1-2\beta)\boldsymbol{a}_n + 2\beta \boldsymbol{a}_{n+1}\} \quad (3)$$

$$\boldsymbol{v}_{n+1} = \boldsymbol{v}_n + \Delta t\{(1-\gamma)\boldsymbol{a}_n + \gamma \boldsymbol{a}_{n+1}\} \quad (4)$$

The parameters $\beta$ and $\gamma$ define the Newmark family of algorithms. Solving $\boldsymbol{a}_{n+1}$ and $\boldsymbol{v}_{n+1}$ from Eqs. (3) and (4) and substituting them in Eq. (2), the following system of equations can be obtained, which can be solved for $d_{n+1}$

$$\left(\boldsymbol{K} + \frac{1}{\beta\Delta t^2}\boldsymbol{M} + \frac{\gamma}{\beta\Delta t}\boldsymbol{C}\right)\boldsymbol{d}_{n+1} = \boldsymbol{f}_{n+1} + \boldsymbol{M}\left[\frac{1}{\beta\Delta t^2}\boldsymbol{d}_n + \frac{1}{\beta\Delta t}\boldsymbol{v}_n + (\frac{1}{2\beta}-1)\boldsymbol{a}_n\right] + \boldsymbol{C}\left[\frac{\gamma}{\beta\Delta t}\boldsymbol{d}_n + (\frac{\gamma}{\beta}-1)\boldsymbol{v}_n + \Delta t(\frac{\gamma}{2\beta}-1)\boldsymbol{a}_n\right] \quad (5)$$

**Central Difference Algorithm**

For explicit time integration, central difference algorithm is popularly being used. The difference expressions for $\boldsymbol{v}_n$ and $\boldsymbol{a}_n$ can be written as

$$\boldsymbol{v}_n = (\boldsymbol{d}_{n+1} - \boldsymbol{d}_{n-1})/(2\Delta t) \quad (6)$$

$$\boldsymbol{a}_n = (\boldsymbol{d}_{n+1} - 2\boldsymbol{d}_n + \boldsymbol{d}_{n-1})/(\Delta t^2) \quad (7)$$

Substituting these expressions in the dynamic equilibrium equation, and rearranging terms it can be written as

$$\boldsymbol{d}_{n+1} = (\boldsymbol{M} + \boldsymbol{C}\Delta t/2)^{-1}[\Delta t^2(\boldsymbol{p}_{n-1} - \boldsymbol{f}_{n-1})] + 2\boldsymbol{M}\boldsymbol{d}_n - (\boldsymbol{M} - \boldsymbol{C}\Delta t/2)\boldsymbol{d}_{n-1} \quad (8)$$

where $\boldsymbol{p}$ is the internal force vector. If both $\boldsymbol{M}$ and $\boldsymbol{C}$ are diagonal matrices, the solution for $\boldsymbol{d}_{n+1}$ does not require factorisation. Since the central difference algorithm does not require assembly of global matrices and can be handled at degrees of freedom level, the parallel implementation is pretty straightforward. The interprocessor communication requirement per time step is very small when compared to the implicit algorithms[2].

**Mixed Time Integration Algorithm**

In the mixed time integration algorithms, both implicit and explicit algorithms are employed on implicit and explicit mesh partitions, respectively. In the explicit and implicit mesh partitions, the flexible part of the mesh is integrated explicitly and the stiff part of the mesh is integrated implicitly. In the domain decomposition techniques, the finite element mesh is partitioned into as many numbers of submeshes as the number of processors configured. Each submesh is assigned to an individual processor to solve independently with some cooperation with the neighbouring processors. With this, the global system of equations to be solved in the implicit time integration algorithm are partitioned into smaller subsets and can be solved independently in their assigned processor. The interfaces of all the submeshes are solved employing parallel explicit algorithm.

The nodes in each of the submesh are formed into two distinct groups as interface nodes and interior nodes. Employing the implicit–explicit algorithm, the interface nodes can be integrated explicitly (using parallel explicit algorithm) where the interprocessor requirements are trivial. Once the interface values are known, the interior nodes can be integrated implicitly by constraining interface nodal degrees of freedom with the known values already obtained by using parallel explicit algorithm. It can be observed that submeshes to be integrated with implicit time integration algorithm are totally detached due to the introduction of the explicit integration at the interfaces. With this, the implicit algorithm can be executed on the local submeshes.

**Parallel Implementation of Mixed Time Integration Algorithm**

In the parallel domain decomposition based mixed time integration algorithm, nodes lying along the interface are divided into primary boundary nodes and secondary boundary nodes, with each interface node being a primary boundary node in a submesh and secondary boundary node in all other submeshes sharing that particular node. The nodes which are not interface nodes are called internal nodes. Internal elements are those, which do not have any boundary nodes. The elements, which consist of boundary nodes, are border elements[8].

Once the given finite element mesh is partitioned into required number of submeshes, the primary and secondary boundary nodes of each submesh are identified, the parallel mixed time integration commences first by integrating the identified boundary nodes with explicit time integration technique. This explicit time integration is performed in each processor on their respective primary boundary nodes and the displacements thus computed at these nodes will be communicated to the neighbouring processors. The internal force vector for the elements connected to primary boundary nodes are computed in their respective processors and these partial values are transmitted to their neighbouring counter parts and at the same time receive the corresponding partial internal force vector computed in their neighbouring processors. With this, the time integration of the boundary nodes of the finite element mesh can be accomplished without any load imbalances. The time integration of these interface nodes is continued up to N explicit time steps.

The next step is to compute the dynamic responses in the local submeshes assigned to each processor. This can be accomplished by performing the time integration with Newmark's implicit algorithm on these local submeshes by constraining the boundary nodes with the values obtained from explicit integration. With the proposed implementation, the global solution of equations is no longer needed. The solution of equations is confined only to their assigned submeshes. This results in significant savings in communication time and also computational time, as the bandwidth of the local submesh matrix is considerably smaller than the global matrix.

**Numerical Example**

The numerical example is performed on DELL workstation cluster. It is a cluster with 8 processors arranged in 4 dual-processor nodes with 2.4GHz Intel Xeon chips (512KB cache) and 1.0GB of memory per node. These nodes are connected with a 100.0Mbps Ethernet interconnect. The MPI communication libraries have used to manage the message passing[9].

One quarter of the cylindrical shell is shown in Fig.1. Geometric nonlinearity is considered. The stability and accuracy are examined by the time step size $0.2\times10^{-3}$s. The A nodal displacement time history response computed by the Newmark method and the proposed algorithm are shown in Fig.2. It can be observed that the proposed algorithm yields acceptable results and the solution is in good agreement with the conventional Newmark's solution. This illustrates that the proposed algorithm possess highly the stability and accuracy.

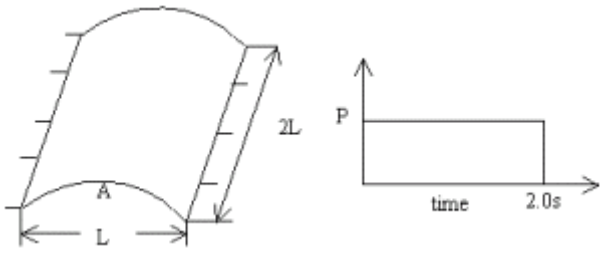


Fig.1 Description of the example

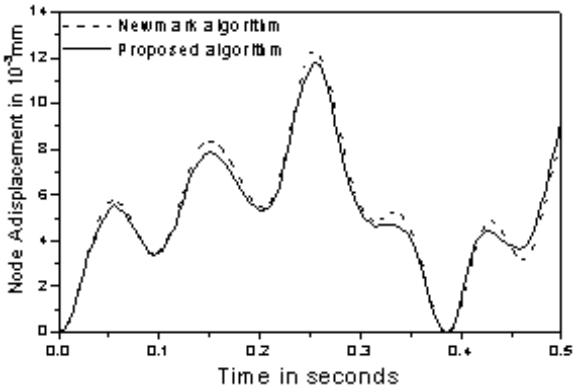


Fig.2 Displacement response of node A

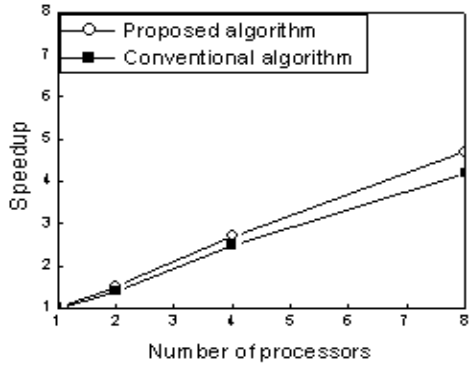


Fig.3 Speedup of algorithm with 4710 dof

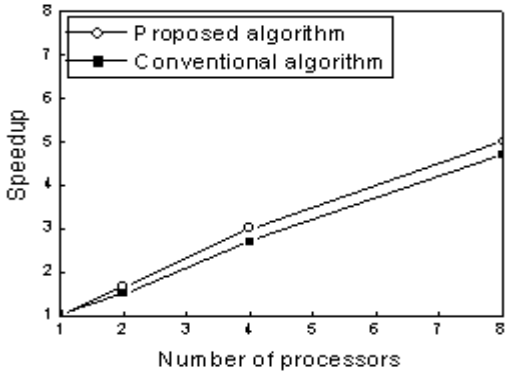


Fig.4 Speedup of algorithm with 17322 dof

To evaluate the performance of the proposed parallel algorithm, the problem size(i.e., degree of freedom) is increased by refining the finite element mesh. The speedups are shown in Fig.3 and Fig.4. It can be observed that the performance of the parallel algorithms improves with increase in the problem size and also the proposed parallel algorithm exhibits superior performance. The proposed parallel algorithm is better than implicit algorithm.

## Conclusions

The parallel mixed time integration algorithm is studied by using synthesis of implicit and explicit time integration technology. The domain decomposition technique is employed in this algorithm. Concurrency is introduced into this algorithm by integrating interface nodes with explicit time integration technique and solving local subdomains with implicit algorithm. Without the need for a parallel solver, the solving equations is significantly reduced. The solving equations is carried out in the local subdomains. Thus half bandwidth of global matrix is significantly reduced. Numerical studies indicate that the proposed algorithm is superior in performance to the implicit algorithm.

## Acknowledgements

In this paper, the research was sponsored by the National Natural Science Foundation of China((Project No.51378124) and Natural Science Foundation of Fujian Province ((Project No. 2012J01187) and Fujian Excellent Talents in University(FETU).

## References

[1] J. F. Hajjar, J. F. Abel: Comput & Struct. Vol.30(1988),p.1237
[2] J. Sziveri, BHV. Topping: J. Comput. Civil Engng. Vol. 14(2000),p.79
[3] A. K. Noor: Comput. & Struct. Vol.10(1979),p.7
[4] K. N. Chiang, R. E. Fulton: Comput. & Struct. Vol.36(1990),p.1031
[5] A. K. Noor, J. A. Peter: Comput. & Struct. Vol. 31(1989),p.795
[6] K. T. Danielson, R. R. Namburu: Adv Engng Software. Vol. 29(1998),p.179
[7] Chaojiang Fu, Wu Zhang: Chinese Journal of computational Mechanics. Vol. 23(2006),p. 783(in Chinese).
[8] D. M. Day, M. K. Bhardwaj: Comput. Methods Appl. Mech. Engrg. Vol. 192(2007),p. 763
[9] Chaojiang Fu: The research on parallel computation of finite element structural analysis based on MPI cluster (Shanghai University press, 2006) (in Chinese).

*Applied Mechanics and Materials Vols. 580-583 (2014) pp 3042-3045*
*© (2014) Trans Tech Publications, Switzerland*
*doi:10.4028/www.scientific.net/AMM.580-583.3042*

# A Comparison Between the Matrix Displacement Method and the Finite Element Method in Solving Frame Structure with SM Solver Software

Lijuan Cheng [a *], Xinchi Yan[b*]

School of Environment & Civil Engineering, Jiangnan University, Wuxi 214122, China

[a]523075436@qq.com, [b]skywalker@jiangnan.edu.cn

**Keywords:** Matrix displacement method, Finite element method, SM Solver.

**Abstract:** Using matrix displacement method and the finite element method to calculate the internal force of the same frame, and then comparing the results. Meanwhile, due to the theory that SM Solver can calculate the exact solution of rigid frame structure forces, we use it to support our experiment. Finally, we succeed in calculating and proving that Matrix displacement method and the finite element method have the same result in solving the rigid frame structure forces.

## Introduction

As we all known, Matrix displacement method is mainly used in the analysis of truss structure and frame structure. Comparing to it, the finite element method has a broader scope. Not only can it be applied to rigid frame and truss, it can also apply to plates, shells, shear walls, bridges and prestressed concrete structures. In addition, you can also analyze the natural frequencies, modal, structural stability and slope stability of structures, etc.

When Matrix displacement method is used for the analysis of the structure of the rod, it can also be called FEM of rod structure which will draw exact conclusions. Well, when the finite element method is used in analyzing the two-dimensional or three-dimensional structure of the physical structure, it will draw approximate conclusions. [1]

Matrix displacement method is the prototype of the finite element method, so structure matrix analysis is sometimes called the finite element method of rod structure.

## Characteristics of matrix displacement method

In the matrix displacement method, the task of element analysis is to establish the element stiffness equation and form element stiffness matrix. The main task of the overall analysis is to turn units into entirety, to form an overall stiffness matrix by the element stiffness matrix according to the stiffness integration rules and to establish the basic equations of the overall structure with displacement method, so we can find answers.

Matrix displacement method in Structural mechanic is expressed by matrix and solved by computers, so it can be used to analyze the complex frame structures. At the same time, these structures are composed by rods whose feature may be analyzed by classical displacement method. [2]

## Characteristics of the finite element method

The key of the finite element method is to split overall structure into several units firstly (Each rod is generally taken to be a unit), which is called discretion, and then turn these units into entirety

according to certain conditions. We transform the calculation of complex structures into simple elements analysis and collection issues in this process. [3]

As we can see, FEM has the similar analysis steps with the matrix displacement method. Its analysis scope is expanded from truss structures to non-stick continuous structures.

**Four distinctive features of plane frame.**

(1) The entire structure consists of several elongate rods and each rod is rigidly connected
(2) The axis of each rod is not on an axis generally.
(3) Each unit of a plane frame is flexural member, which has axial deformation and bending deformation. So not only can it transmits force, but also it can transmit torque.

(4) In terms of each node of frame, we should consider the angular displacement $\theta_i$ of section as well as linear displacement called $u_i$, $v_i$ in both directions. Therefore, each node has three displacement components $u_i$, $v_i$, $\theta_i$, which correspond to three nodal force components $U_i$, $V_i$, $M_i$ differently. [4]

Comparison **between** matrix displacement method and finite element method

According to above-mentioned frame features, analysis in matrix displacement method of such structure can be handled as follows:
(1) Collate raw data and code unit and the frame locally and generally;

(2) Form element stiffness matrix $\bar{k}^e$ in the local coordinate system;
(3) Form element stiffness matrix $k^e$ in the global coordinate system;
(4) Form the overall stiffness matrix *K* with element integration method;

(5) Find unit equivalent nodal loads $\bar{P}^e$ in local coordinate system and convert them into unit equivalent nodal loads $P^e$ in global coordinate system; form equivalent nodal loads $P$ of overall structure by element integration method;
(6) Solve equations $K\Delta = P$ and obtain node displacement $\Delta$;

(7) Find rod end internal forces $\bar{F}^e$ of each rod.[3]

Finite element analysis of such structures can be handled as follows:
(1) Establish mechanical model and make unit number and node number;

(2) Find the element stiffness matrix $\left[\bar{k}\right]^e$ in local coordinate system;

(3) Find the element stiffness matrix $[k]^e$ in whole coordinate system;

(4) Seek overall stiffness matrix $[K]$;

(5) Form load vector;
(6) Introduce support conditions;

(7) Solve equations to seek node displacement;
(8) Seek the rod end internal forces of each unit. [4]

Generally speaking, we should Superimpose on a "Fixed end forces" item when we compute rod end force with Matrix Displacement Method. However, we seek nodal forces by displacement derivation in FEM, which result in a significant decline in the accuracy of stress.

Now we are going to compare the matrix displacement method and the finite element method through a simple frame structure.

**Examples**

Frame as shown in figure 1, assuming these two rods have same rod length and cross-sectional dimension, its section is shown in figure 2,1m length, 0.5m wide, 5m length of rod, $E = 3\times10^7\ KN/m^2$, $I = \frac{1}{24} m^4$. Seeking rod end internal forces of frame.

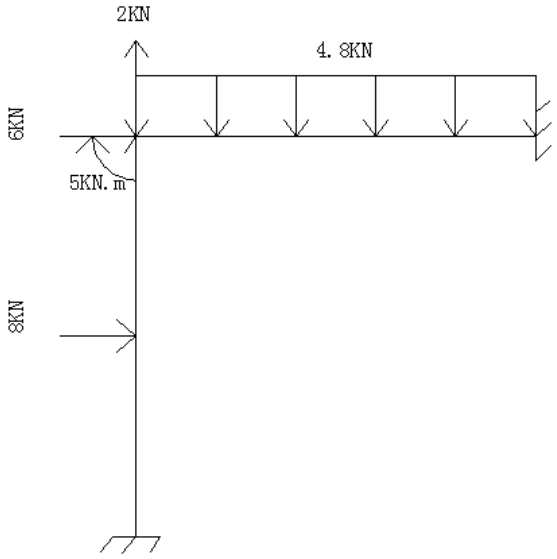


Fig. 1 Frame

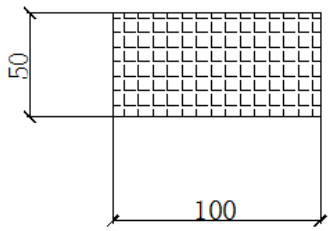


Fig. 2 Rod cross-section

Split the frame structure into the following units ①, ②:

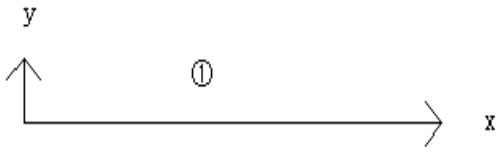


Fig. 3 Unit ①

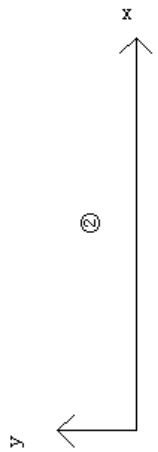


Fig. 4 Unit ②

The results of calculating the internal forces with matrix displacement method and the finite element method as well as auxiliary calculations of SM Solver are shown in Table 1.

Table 1 Comparison of the results

| | | | Matrix Displacement Method | Finite Element Method | SM Solver |
|---|---|---|---|---|---|
| Unit 1 | Rod end 1 | Axial force[N] | 11100.53 | 11100.54 | 11100.5331 |
| | | Shear[N] | 10130.24 | 10130.24 | 10130.2361 |
| | | Moment[N*m] | -4038.46 | 4038.47 | 4038.46153 |
| | Rod end 2 | Axial force[N] | -11100.53 | -11100.54 | -11100.5331 |
| | | Shear[N] | -13869.76 | 13869.78 | 13869.7638 |
| | | Moment[N*m] | -13387.28 | 13387.28 | 13387.2810 |
| Unit 2 | Rod end 1 | Axial force(N) | -13387.28 | 8130.24 | -8130.23610 |
| | | Shear(N) | 2899.47 | 2899.47 | 2899.46686 |
| | | Moment(N*m) | 3535.80 | 3535.80 | 3535.79588 |
| | Rod end 2 | Axial force(N) | -8130.24 | -8130.24 | -8130.23610 |
| | | Shear(N) | 5100.53 | 5100.53 | 5100.53313 |
| | | Moment(N*m) | -9038.46 | -9038.46 | -9038.46153 |

## Conclusion

According to above analysis, solving simple frame is completely equivalent no matter it is Matrix Displacement Method or FEM. The reason is that the rod structural problem, as a kind of simple elasticity problem, can be solved easily. Matrix Displacement Method establishes algebraic equations expressing structural problem characteristic of rod directly by using analytic solutions. FEM, starting from the differential equation, solve the original problem by assuming the demand function. The problem is simple so we assume the unknown displacement function is a linear function, which meets the analytic solutions of the problem. As a result, we will get the same answer. [5]

When we need to solve the exact internal force of plane frame, we can get accurate solutions conveniently with SM Solver software.

## References

[1] Guozhi Wen, Zhengliang Li. Structural analysis of the finite element method, Wuhan: Wuhan University of Technology Press, 2010.4

[2]Yanqing Zhang. finite element method structural analysis, Beijing, Science Press, 2012

[3]Yuqiu Long, Shihua Bao. Structural Mechanics, Beijing, Higher Education Press, 2006.12

[4]Shenghong Wang, Jiaqi Wu, Huiming Xie. Basic and applied finite element method, National Defense University Press, 1990.5

[5]Ridong Liao. Concise Guide tothe principles ofthe finite element method, Beijing: Beijing Institute of Technology Press, 2009.9

*Applied Mechanics and Materials Vols. 580-583 (2014) pp 3046-3050*
*© (2014) Trans Tech Publications, Switzerland*
*doi:10.4028/www.scientific.net/AMM.580-583.3046*

# Crack ExtensionCalculation UnderTensile and ShearLoad by XFEM

MiaoYu[1,a], Zhihong Dai[1,b] andGuijuan Hu[2,c]

[1]College of Management Science & Engineering, Guangxi University of Finance & Economics, Nanning 530003, China

[2]Guangxi Polytechnic of Construction, Nanning 530004, China

[a]yumiao-211@163.com, [b]snowgx@qq.com, [c]hgj1973@sina.com

**Keywords:**XFEM; Crack Propagation; Tensile and Shear Load

**Abstract:** The extended finite element method (XFEM) is a numerical method for modeling discontinuity such as cracks, holes, inclusions etc within a standard finite element framework. In the XFEM, special functions which can reflect the problem's solution characteristics are added to the finite element approximation using the framework of partition of unity. Compared with the standard finite element method, it obtained more accuracy without remeshing. In this paper, we studied crack propagation behavior under different proportions of tension and shear loads by XFEM.

## Introduction

Northwestern University in the United States in 1999 for the finite element method Belytschko[1] proposed amendments to the finite element method (material weak intermittent problem and geometric strong intermittent problem) intermittent problems - a method for processing extended finite element method (XFEM ). Important improvements in the conventional finite element method based on discontinuous finite element method handle crack interface drawbacks [2].

XFEM is in the framework of the standard finite element method, continuous area using standard finite element method, finite element method displacement approximation functions within a narrow area contains discontinuous boundary correction, and the description of the continuous boundary method. By means of the research questions already known , the increase in displacement approximation functions satisfy the partition of unity under the premise to better reflect the actual discontinuous function of the characteristics of items ( called enrichment function ) , to improve the calculation accuracy .

Since the XFEM retain conventional finite element (CFEM),to solve the conventional finite element required in the difficulties brought about by the stress concentration high density divided unit on the basis of all the advantages. Modeling crack growth without re-meshing, and has been a rapid development[3]. XFEM uses level set method described intermittent interface that allows uninterrupted description is independent of the finite element mesh, avoid remeshing the calculation process. Extended finite element method has been considerable development in just a decade. It has been applied in dynamic fracture, dynamic extension of the shear zone, cohesive fracture polycrystalline interfaces and grain boundaries and dislocations of research fields [4].

## The extendedfinite element based on the partition of unity

The Extended Finite element based of decomposition. The basic idea of unity method is arbitrary function in the solution domain can be expressed as:

$$\psi(x)=\sum_{I} N_I(x)\, q_1 \Phi(x) \tag{1}$$

Where $N_I(x)$ is the standard finite element shape functionsatisfy the partition of unity. $u_I$ is the standard nodal degrees of freedom . The Extenders $\psi(x)$ is used to improve the knowledge field characteristics. $\Phi(x)$ is the expansion of the function .

XFEM add the extender on the basis of the standard field approximation to a more precise description of complex unknown field. Finite element approximation of the unknown field $u^h$ consists of two parts:

$$u^h = \sum_I N_I(x) u_I + \sum_J \psi_J(x) q_J \tag{2}$$

In type 2, solving problems specific need to use a different expansion function. The constructed expansion function, you need to make it having certain characteristics of the unknown field true solution in order to increase the convergence speed. In actual use, often based on the solution space of real solutions to select.

**Level set method**

Level set method is a numerical method for tracking mobile interface proposed by Osher and Sethian. Extended finite element method , using the level set method or the method described in geometric position discontinuities rapid advance its expansion process , so that no continuous surface description is independent of the finite element mesh , which in discontinuous surface extensions can't the complex grid reconstruction [4 ] .

A common level set function constructor signed distance function

$$f(x,t) = \pm \min_{x_\gamma \in \gamma(t)} \left\| x - x_\gamma \right\| \tag{3}$$

It has the physical meaning of the computational domain signed distance function of the arbitrary point is equal to the shortest distance from this point to the discontinuity , and intermittently on both sides of a point having a different symbol .This function can be described through the crack from solving domain interruption. But when a crack in the solution domain is terminated, only one function can't reflect the position of the crack tip , so it needs to define a level set function.

$$g_i = (x - x_i) \cdot \frac{v_i}{\left\| v_i \right\|} \tag{4}$$

Therefore the location of the crack surface can be expressed as the level set function

$$\Gamma_c^0 = \{ x \in \Omega_0 \mid f(x) = 0, g(x,t) > 0 \} \tag{5}$$

**The expansion shape function of discontinuous**

There are two types of typical discontinuous problems in solid mechanics [5]. The first class is weak because the material properties caused by mutations discontinuity problems,The other is inside the object geometry caused by mutations in the strong discontinuous crack problem is that the representatives of such problems.

Those cracks completely through the unit, on both sides of the crack surface displacement the field occurred jump, the expansion of the shape function can take the following forms :

$$\psi_J(x) = N_J(x) H(f(x)) \tag{6}$$

Where $H(x)$ is the Heaviside step function given by

$$H(x)=\begin{cases}1, & x\geq 0\\ -1, & x<0\end{cases} \tag{7}$$

$f(x)$ is a function of the level set.

$$\psi_J(x)=N_J(x)\Phi(x) \tag{8}$$

Where $n^+$ is the discontinuity of the unit normal vector on $\Gamma_0^c$ . For any point $x$ not on the interface r $\Gamma_0^c$ . $f(x)$ is the shortest distance from $x$ to $\Gamma_0^c$.

Nodes around the crack tip, the expansion of the shape function can use the following form:

$$\psi_J(x)=N_J(x)\Phi(x) \tag{9}$$

Where $\Phi(x)$ can be a combination of the following function groups.

$$\Phi(x)=\left[\sqrt{r}\sin\frac{\theta}{2},\sqrt{r}\sin\frac{\theta}{2}\sin\theta,\sqrt{r}\cos\frac{\theta}{2},\sqrt{r}\cos\frac{\theta}{2}\sin\theta\right] \tag{10}$$

Using the two expansion -shaped function, with the displacement of the crack two - dimensional flat field can be expressed as:

$$u^h(x)=\sum_{I\in S}N_I(x)u_I+\sum_{J\in S_h}N_J(x)H(f(x))a_J(t)+\sum_{K\in S_c}N_K(x)\Phi(x)b_K(t) \tag{11}$$

Where $S_h$ is the crack completely cut off unit node, $S_c$ are nodes around the crack tip unit, $a_J$ and $b_k$ is the node additional degree of freedom.

For weak discontinuity can use the following form:

$$u^h(x,t)=\sum_{I\in S}N_I(x)u_I(t)+\sum_{J\in S_{\text{interface}}}N_J(x)\Phi(x)q_J \tag{12}$$

In which the absolute value function

$$\Phi(x)=\sum_I|f(x_I)|N_I(x)-\left|\sum_I f(x_I)N_I(x)\right| \tag{13}$$

**Numerical examples**

Specimen forms shown in the picture, 60cm*30cm*5cm, and specimens left central with a length of 5cm edge crack. At the bottom of the specimen is fixed, the topfaceloading with displacement.There are 6 kinds of loading, a pure tensile loading, pure shear loading, then keeps the tensile displacement and changing the shear displacement, the tensile displacement and sheardisplacement ratio is 1:1, 1:2.5, 1:5, 1:10. These six kinds of combination of load test of crack propagation is shown in figure 1.

As can be seen, with the increase in tensile and shear displacement ratio, the greater the angle of crack propagation. Crack is not propagation along a straight line extended, but along the arc

extension. The crack angle becomes smaller with the expansion. This is because at the beginning of the crack starts is dominated by shear. With the crack growth, gradually stretching effect is enhanced and then dominated by stretch.

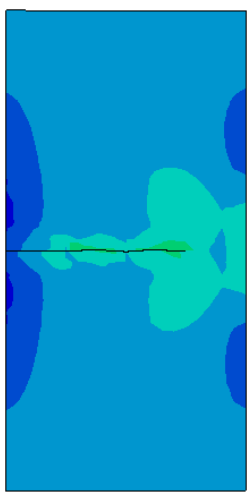

(a) Pure tensile

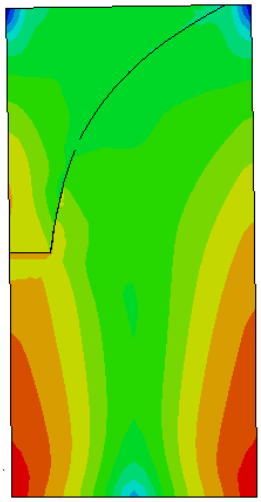

(b) Pure shear

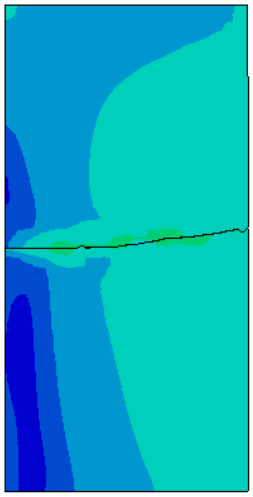

(c) Tensile shear ratio is 1:1

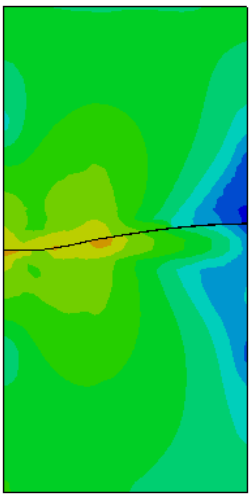

(d) Tensile shear ratio is 1:2.5

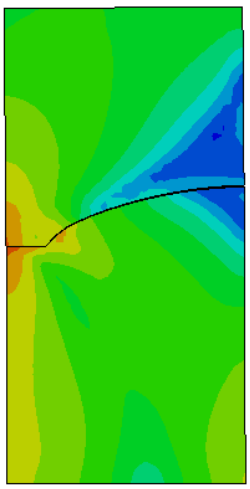

(e) Tensile shear ratio is 1:2.5

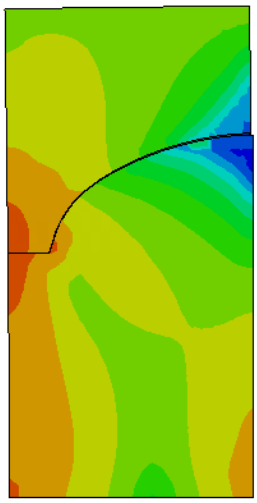

(f) Tensile shear ratio is 1:2.5

Fig1. The path of crack under different load

## Conclusions

This paper introduces the basic theory of XFEM, and simulatedcrack extension on the different load ratio under tension shear, results show; XFEM can simulate any crack propagation behavior well.Crack propagation path does not depend on the mesh,The crack can be expansion through the mesh. With the increase of the ratio of tension and shear displacement, the angle of crack propagation became smaller. The crack is not a straight line extension, but with the crack growth, the crack angle becomes smaller gradually.

## Acknowledgements

Support of GuangxiEducation Department Science Research Subject (Grant No: 2013LX137), and Guangxi University of Finance & EconomicsSubject (Grant No: 2012C04) for this work are gratefully acknowledged.

**Reference**

[1] T. Belytschko, T. Black. Elastic crack growth in finite element with minimal meshing.J.International Journal For Numerical Methods in Engineering. Int. J. Numer. Meth.Engng. 45. 601-620(1999).

[2] Z. Zhuang. The Extended Finite Element Method.Tsinghua University press. Beijing.2012.In Chinese

[3] H. Xie. Research of the Extended Finite Element Method.Shanghai Jiao Tong University. 2009.In Chinese

[4] L.L. Guo, Z.F. Chen, J.R. Luo. and G. Chen. A Review of the Extended Finite Element Method and its Applications.J.Chinese Quarterly of Mechanics. 2011(4): 612-625. In Chinese

[5] L.X. Li, T.J. Wang. The Extended Finite Element Method and Its Applications —— A Review. J. Advance in Mechanics. 2005(1): 5-20.In Chinese

*Applied Mechanics and Materials Vols. 580-583 (2014) pp 3051-3056*
*© (2014) Trans Tech Publications, Switzerland*
*doi:10.4028/www.scientific.net/AMM.580-583.3051*

# Finite Element Solution in Fluid Mechanics using exponential function based interpolation

Shaowen Fang[1,a], Xingfei Yuan[1,b] ,Ruojun Qian[2,c], Shuhui Jiang[1,d]

[1] Space Structures Research Center, Zhejiang University, Hangzhou, P.R.China, 310058.

[2]College of civil Engineering, Tongji University, Shanghai, P.R.China, 200092

[a]fang_shaowen@163.com, [b]yuanxf@zju.edu.cn, [c]prjqtj@163.com, [d]11312051@zju.edu.cn

**Keywords**: convection diffusion equation; finite element in fluid mechanics; numerical wave; exponential function based interpolation (EFBI); morphological analysis

**Abstract:** The wave problem of finite element solution of one dimensional stationary convection diffusion equation is analyzed. The reason for wave is the poor continuity of linear Lagrange shape function. By using exponential function based interpolation (EFBI), the results of finite element solution are compared with that of the analytical solution. The results indicate that EFBI is effective to deal with the problem of numerical wave. The shape function of three dimensional EFBI is derived and analyzed. Morphological analysis shows that EFBI has good differentiability and adaptability.

## Introduction

The weak form of Standard Galerkin (SG) finite element format is usually adopted to solve partial differential equations, which relaxes the requirements for the continuity of solution. The finite element method has been proved mathematically to converge to exact solutions when the elements become infinitesimal. However, as it is applied to fluid mechanics analysis, the traditional finite element solution can't satisfy continuity requirements, and can't satisfy the flux conservation conditions[1-2], neither. So there is some error in finite element solution. Since there is no analytical solution to Navier-Stokes equation of fluid mechanics, a lot of research is put on numerical solution. Many researchers study one dimensional stationary convection diffusion equation by simplifying it to constant coefficient differential equation. They compare the solution of finite element method with analytical solution and find finite element numerical wave[3-4]. The famous American mechanics professor Ted Belytschko analyzes the reasons for wave and proposes solutions to improve finite element method. On the basis of the study, Professor Huge puts forward SUPG method. British research team led by professor Zienkiewicz introduces the CBS algorithm , which has been widely used[5-7].

In the paper, the wave problem of finite element solution of one dimensional stationary convection diffusion equation is analyzed. The reason for wave is the poor continuity of linear Lagrange shape function. By using EFBI, the results of finite element solution are compared with that of the analytical solution. The results indicate that EFBI is effective to deal with the problem of numerical wave. EFBI is applied to three-dimensional fluid mechanics. The shape function is derived and analyzed. Morphological analysis shows that it has good differentiability, which can prevent numerical wave in the element, and good adaptability in the process of approximation.

**Finite element solution of one dimensional stationary convection diffusion equation using EFBI**

1.1 Traditional finite element solution

The domain considered is $0 \le x \le L$, with variable $\phi$， the one dimensional stationary convection diffusion equation is

$$u \cdot \frac{\partial \phi}{\partial x} - v \frac{\partial^2 \phi}{\partial x^2} = 0 \tag{1}$$

where $v$ is kinematic viscosity; $u$ is velocity; $\phi$ is independent variable; $x$ is coordinate value, $0 \le x \le L$。

As approximation problem of the initial problem, for the case of constant $u$, the equation above is simplified to constant coefficient differential equation. By introducing boundary conditions ($\phi|_{x=0}=0$, $\phi|_{x=L}$), we can get the analytical solution

$$\phi = \frac{1 - e^{ux/v}}{1 - e^{uL/v}} \tag{2}$$

Eq. (1) can be written as weighted residual form. When Standard Galerkin finite element method is adopted, we can obtain

$$\int_{\Delta x} \boldsymbol{N}^{\mathrm{T}} u \frac{\mathrm{d}\boldsymbol{N}}{\mathrm{d}x} \mathrm{d}x \phi_e - \int_{\Delta x} \boldsymbol{N}^{\mathrm{T}} v \frac{\mathrm{d}^2 \boldsymbol{N}}{\mathrm{d}x^2} \mathrm{d}x \phi_e = 0 \tag{3}$$

Integrating the second term by parts gives the weak form

$$\int_{\Delta x} \boldsymbol{N}^{\mathrm{T}} u \frac{\mathrm{d}\boldsymbol{N}}{\mathrm{d}x} \mathrm{d}x \phi_e + \int_{\Delta x} v \frac{\mathrm{d}\boldsymbol{N}^{\mathrm{T}}}{\mathrm{d}x} \frac{\mathrm{d}\boldsymbol{N}}{\mathrm{d}x} \mathrm{d}x \phi_e = 0 \tag{4}$$

where $N$ is shape function, $\phi = N\phi_e$, $\phi_e$ is the nodal values of $\phi$. For linear shape function

$$N = \left[ 1 - \frac{x}{\Delta x} \quad \frac{x}{\Delta x} \right] \tag{5}$$

Insertion of Eq. (5) into Eq. (4) gives the finite element solution, in which error is existed. For the case of L=1, J=10, $v$=0.1, $u$ is 8 and 16, the solution shown in Fig. 1 gives the wave situation of finite element solution. The reasons for wave are non-differentiability of linear Lagrange shape function and the discontinuity of first derivative between elements. So choosing the interpolation function with better continuity is effective to deal with the problem of numerical wave[8].

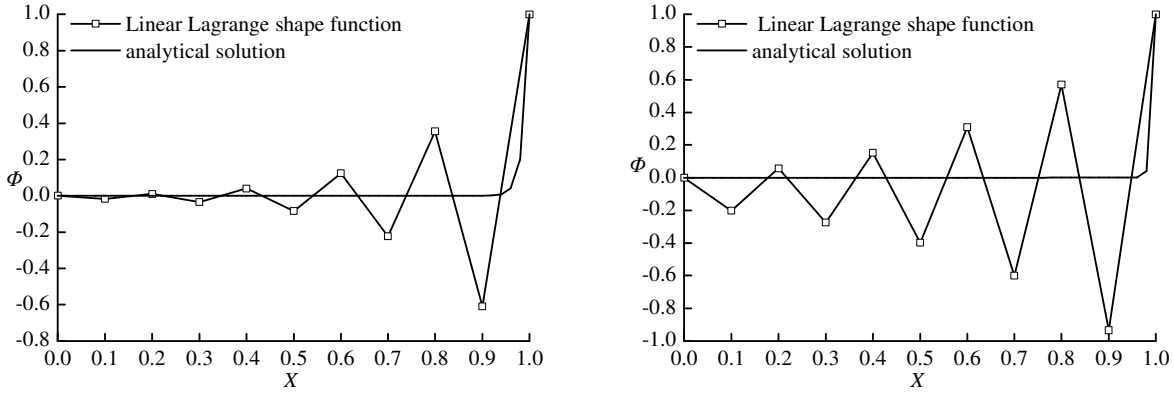


(a) $u$=8 (b) $u$=16

Fig. 1 Traditional finite element solution and analytical solution

1.2 Finite element solution using EFBI

Considering Two-node element, assume that finite element solution is $\phi=c_1+ c_2e^{ax}$, shape function is $N=\left[1-\frac{1-e^{ax}}{1-e^{a\Delta x}} \quad \frac{1-e^{ax}}{1-e^{a\Delta x}}\right]$.The value of $a$ is related to the properties of flow field, with a=$\phi$/$v$ referring to analytical solution.

For the case of L=1, J=10, $v$=0.1, $u$ is 8 and 16, the solution shown in Fig. 2 gives the finite element solution of EFBI and analytical solution.

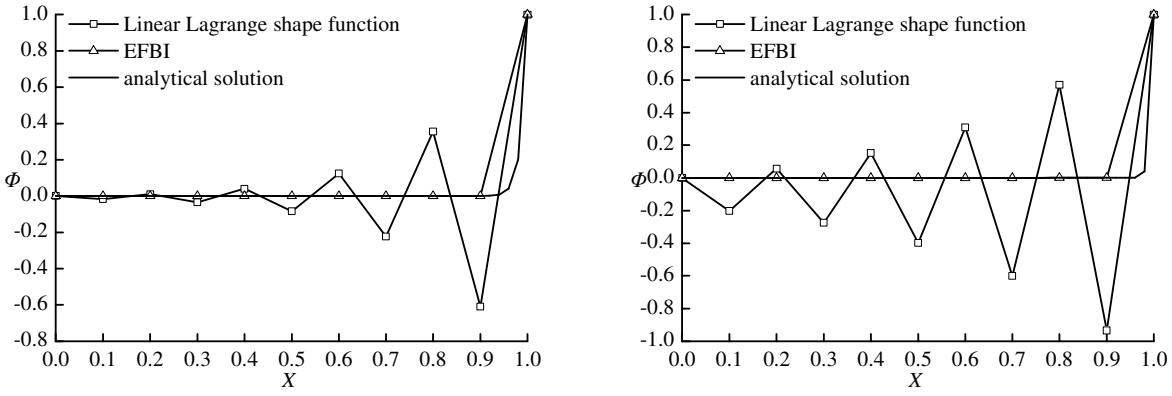


(a) $u$=8 (b) $u$=16

Fig. 2 Finite element solution using EFBI

As is shown in Fig. 2, compared with traditional finite element solution, EFBI is effective to deal with the problem of numerical wave. Because of its good continuity, which can simulate the distribution of variables within the element accurately, EFBI achieves better numerical solution.

**Three-dimensional fluid mechanics using EFBI**

Compared with that obtained by traditional standard Galerkin (SG) finite element method, the results obtained by EFBI show better accuracy. For the purpose of applying EFBI to three-dimensional fluid mechanics, velocity shape function of tetrahedron element using EFBI is derived. Velocity in the element can be written as[1]

$$U = C_1e^{a_1L_i} + C_2e^{a_2L_j} + C_3e^{a_3L_k} + C_4 \tag{6}$$

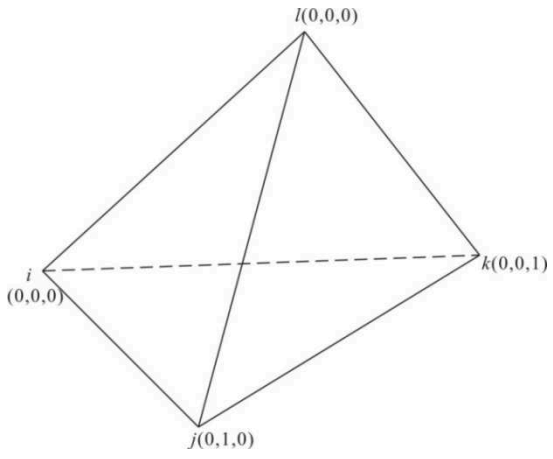


Fig. 3 Tetrahedron element

where

$a_1 = \frac{|v_x|}{v}; a_2 = \frac{|v_y|}{v}; a_3 = \frac{|v_z|}{v}$. $L_i$, $L_j$, $L_k$ are volume coordinates.

For matrix form, the equation above becomes

$$U = LC \tag{7}$$

where

$$L = \begin{bmatrix} e^{a_1 L_i} & e^{a_2 L_j} & e^{a_3 L_k} & 1 \end{bmatrix}, C = \begin{bmatrix} C_1 & C_2 & C_3 & C_4 \end{bmatrix}^T.$$

As is known, the coordinate value of each point is, $i(1,0,0)$, $j(0,1,0)$, $k(0,0,1)$, $l(0,0,0)$.Put them into Eq. (7), we obtain

$$u_e = L_e C \tag{8}$$

where

$$L_e = \begin{bmatrix} e^{a_1} & 1 & 1 & 1 \\ 1 & e^{a_2} & 1 & 1 \\ 1 & 1 & e^{a_3} & 1 \\ 1 & 1 & 1 & 1 \end{bmatrix}$$

From Eq. (8) we have

$$C = L_e^{-1} u_e \tag{9}$$

substituting Eq. (9) into Eq. (7) to obtain

$$U = LC = L \cdot L_e^{-1} u_e = N_u u_i \tag{10}$$

$$\therefore \boldsymbol{N}_u = L \cdot L_e^{-1} = \begin{bmatrix} e^{a_1 L_i} & e^{a_2 L_j} & e^{a_3 L_k} & 1 \end{bmatrix} \begin{bmatrix} e^{a_1} & 1 & 1 & 1 \\ 1 & e^{a_2} & 1 & 1 \\ 1 & 1 & e^{a_3} & 1 \\ 1 & 1 & 1 & 1 \end{bmatrix}^{-1} \tag{11}$$

Thus the shape function

$$\boldsymbol{N}_u = \begin{bmatrix} N_i & N_j & N_k & N_l \end{bmatrix} \tag{12}$$

where

$$N_i = \frac{e^{a_1 L_i} - 1}{e^{a_1} - 1}; \quad N_j = \frac{e^{a_2 L_j} - 1}{e^{a_2} - 1}; \quad N_k = \frac{e^{a_3 L_k} - 1}{e^{a_3} - 1};$$

$$N_l = \left( L_i - \frac{e^{a_1 L_i} - 1}{e^{a_1} - 1} \right) + \left( L_j - \frac{e^{a_2 L_j} - 1}{e^{a_2} - 1} \right) + \left( L_k - \frac{e^{a_3 L_k} - 1}{e^{a_3} - 1} \right) + L_l.$$

Verification shows that the shape function above satisfies the conditions of Kronecker delta and normalization.

**Morphological analysis of EFBI**

The effectiveness and applicability of EFBI has been researched and confirmed in one dimensional convection diffusion equation. The morphology of EFBI will also be analyzed for the purpose of applying it to three dimensional fluid mechanics.

We can find that the shape function of EFBI and linear Lagrange interpolation are rotational symmetry. To be simple, the first terms are taken to analyze.

assuming

$$y_1 = \frac{e^{a_1 L_i} - 1}{e^{a_1} - 1};\ y_2 = L_i;\ y = y_1 - y_2 = \frac{e^{a_1 L_i} - 1}{e^{a_1} - 1} - L_i \tag{13}$$

When $a_1$ approach to infinite decimal $\delta$, $e^{a_1}$ and $e^{a_1 L_i}$ can be Taylor expanded.

$$e^{a_1} = 1 + \delta + \frac{\delta^2}{2!} + \frac{\delta^3}{3!} + \frac{\delta^4}{4!} + \frac{\delta^5}{5!} + \cdots$$

$$e^{a_1 L_i} = 1 + \delta L_i + \frac{(\delta L_i)^2}{2!} + \frac{(\delta L_i)^3}{3!} + \frac{(\delta L_i)^4}{4!} + \frac{(\delta L_i)^5}{5!} + \cdots$$

Take the first six items into Eq. (13) to obtain

$$y = \frac{e^{a_1 L_i} - 1}{e^{a_1} - 1} - L_i = \frac{\delta L_i + \frac{(\delta L_i)^2}{2!} + \frac{(\delta L_i)^3}{3!} + \frac{(\delta L_i)^4}{4!} + \frac{(\delta L_i)^5}{5!}}{\delta + \frac{\delta^2}{2!} + \frac{\delta^3}{3!} + \frac{\delta^4}{4!} + \frac{\delta^5}{5!}} - L_i < \frac{\left(\delta + \frac{\delta^2}{2!} + \frac{\delta^3}{3!} + \frac{\delta^4}{4!} + \frac{\delta^5}{5!}\right) L_i}{\delta + \frac{\delta^2}{2!} + \frac{\delta^3}{3!} + \frac{\delta^4}{4!} + \frac{\delta^5}{5!}} - L_i = 0$$

So the shape function of EFBI is equivalent to linear Lagrange interpolation if $a_1$ is small enough.

For example, in Fig. 4, when the precision $\sigma$= 0.0126($\sigma = \sqrt{\sum_{i=1}^{j} \left( \frac{y_i - y_i'}{y_i} \right)^2}$, where $y_i$ and y' are nodal values of Lagrange interpolation and EFBI), $a$=0.015. In this situation the functions can be seen as equal.

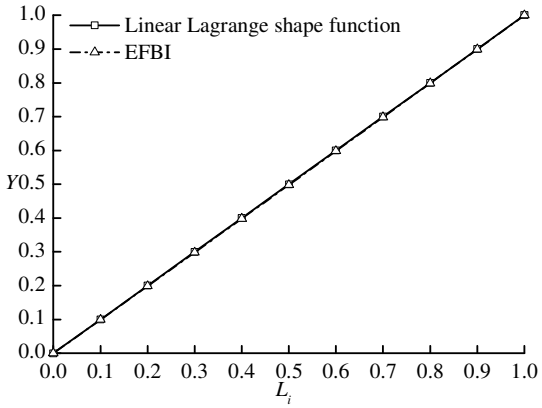


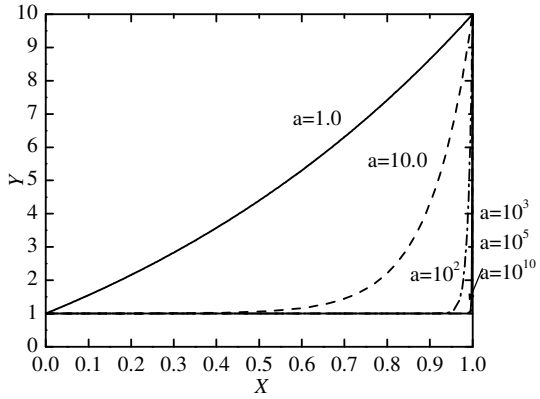


Fig. 4 Linear Lagrange shape function and EFBI when $a$=0.015 Fig. 5 Curve with different $a$

The above analysis clearly demonstrates that EFBI is equivalent to linear Lagrange interpolation if $a_1$, $a_2$ and $a_3$ are less than 0.015.

The value of $a$ in EFBI determines curvature of the curve.when $a$=1.0, $10^2$, $10^3$, $10^5$, $10^{10}$, the curves are shown in Fig. 5.

The solution shown in Fig. 5 tells us that the curve converges when $a$ increases ($a$>1000). The value of $a$ changes with $\phi$, making it adaptable.

The above solution shows that EFBI can approach to linear Lagrange interpolation. They are equivalent when a≤0.015. EFBI has good differentiability, which can prevent numerical wave in the elements. The value of $a$ in EFBI determines curvature of the curve. Choosing a suitable $a$ can improve the accuracy of solution, and it is adaptable in the approaching process. However, the amount of calculation may be increased.

## Conclusions

(1)Finite element method can be used in fluid mechanics. Though there is numerical wave in standard Galerkin (SG) finite element method for one dimensional stationary convection diffusion equation, improving the continuity of the shape function is effective to deal with the problem.

(2)Compared with linear Lagrange interpolation, EFBI has better continuity, which can simulate the distribution of variables within the element accurately. So it can get good solution and is effective to deal with the problem of numerical wave.

(3) The shape function of three dimensional EFBI is derived, but its accuracy needs to be verified by the sample application.

(4) Morphological analysis shows that EFBI has good differentiability, which can prevent numerical wave in the elements. The value of $a$ in EFBI determines curvature of the curve. Choosing a suitable $a$ can improve the accuracy of solution, and it is adaptable in the approaching process.

## Acknowledgements

The work is supported by National Natural Science Foundation of China (51278461) and Zhejiang Provincial Natural Science Foundation of China (LZ14E080001).

## References

[1] Qian Ruojun, Yuan Xingfei, Lin Zhibin, The analysis theory and finite element method for solid and structure, Southeast University Press, 2013(In Chinese).

[2] Wang Xucheng, Finite element method, Tsinghua University Press, 2003(In Chinese).

[3] Zienkiewicz O.C. & Taylor R. L., The Finite Element Method for Fluid Dynamics (5th edn)[M], Elsevier: Amsterdam, 2000:79-105.

[4] Ted Belytschko, Wing Kam Liu & Brian Moran. Nonlinear Finite Elements for Continua and Structures[M]. NY, John Wiley & Sons Ltd., 2000

[5]Hughes, T.J. and A. Brooks, A multidimensional upwind scheme with no crosswind diffusion. Finite element methods for convection dominated flows, AMD, 1979. 34: p. 19-35.

[6] Hughes T. J. R. & Brooks A. N., A theoretical framework for Petrov-Galerkin methods with discontinuous weighting function, in Finite Elements in Fluids (eds R.H. Gallagher et al.)[J], Wiley, Chichester, 1982, Vol. 4: 47-65

[7]Nithiarasu P., Codina R. & Zienkiewicz O. C., The Characteristic-Based Split (CBS) scheme—a unified approach to fluid dynamics[J]. Numerical Methods in Engineering, 2006, Vol.66: 1514-1546.

[8]Fang Shaowen, Yuan Xingfei, Qian Ruojun, Numerical Wave of Finite Element Solution in Fluid Mechanics Using Different Interpolation Function, Engineering mechanics[J], 2013,30(11): 266-272(In Chinese).

*Applied Mechanics and Materials Vols. 580-583 (2014) pp 3057-3061*
*© (2014) Trans Tech Publications, Switzerland*
*doi:10.4028/www.scientific.net/AMM.580-583.3057*

# Numerical Simulation of Flow around High-rise Buildings Based on Reynolds Stress Model

Zupeng Zhang[1,a], Wei Zhang[1,b] and Guoping Chen[1,c]

[1]School of Civil Engineering and Architecture, Southwest University of Science and Technology, Mianyang, Sichuan, China, 621010

[a]swusthot00106@163.com, [b]zwell@swust.edu.cn, [c]guopingchen2002@163.com

**Keywords:** Numerical simulation, Reynolds Stress Model(RSM), Atmosphere boundary layer(ABL), Flow around high-rise buildings.

**Abstract.** In this paper, a modified inlet atmosphere boundary layer (ABL) which satisfies the turbulence model equations is applied to computational wind engineering. The new inflow turbulence boundary condition applied to simulating the flow in the cavity is verified that it is more in line with the actual flows, and then it is used to establish the numerical wind tunnel model to simulate the flow around high-rise buildings. The results are in good agreement with the wind tunnel experimental data, which show the modified ABL combined with Reynolds Stress Model (RSM) is able to better simulate the flow around high-rise buildings.

## Introduction

In the numerical simulation of flow around the bluff body in the building wind engineering, the selection of the turbulence model and the boundary conditions of ABL have a significant effect on the computed result. The frequently-used turbulence model have k-ε model, RSM, k-ω model and Large Eddy Simulation (LES) model, etc. Where k-ε model is widely used to calculate the shear flow, interior flow and many other flow phenomena, Richard and Hoxey[1] based on the k-ε model proposes that wind speed and turbulence of the inflow boundary be in accordance with the transport equation for k and ε, but Hargreaves and Wright[2] pointed out there are certain errors in it. Then Yi Yang and Ming Gu[3] proposed a new inflow boundary condition and acquired the mathematical expression of k and ε through the transport equation of k and ε based on the turbulent flow balance and the standard k-ε model, but Ya Zhang and Shuyan Liu[4] pointed out that k-ε model is a simple mode which based on the Boussinesq eddy viscosity hypothesis, which is hard to reflect the anisotropic features on many kinds of flow conditions, and the better method is to directly resolve the transport equations varied on Reynolds Stress, in a word, to adopt the RSM model. Feng Xu and Jinping Ou[5] researched the unsteady flow of the square cylinder using the RSM model and the k-ε model and resulted that the RSM model is better performed in anticipating the boundary layer and the shear flow around the square cylinder. K-ω model can be applied to the wall constraints flow and the free shear flow, but this model mainly focus on low Reynolds number, compressibility and shear flow, and major error will occur for the flow around the bluff body with high Reynolds number. Wei Yang and Yong Quan[6] carried out the numerical simulation and experimental research on the wind load of low-rise buildings based on the k-ω model and found that this model have a huge influence on the results through comparison. The longest calculation time among several turbulence flow models needs higher computers' properties when Large Eddy Simulation

(LES) model is used. Richards and Younis[7] pointed out that different boundary conditions will lead to sizable deviation of the calculation results, especially in the areas of near the wall boundary. On the basis of extensive research, the turbulent kinetic energy 'K', turbulent dissipation rate 'ε' and the inlet velocity 'u' as user defined function (UDF) are added into the inlet boundary, which constitute a new type of ABL to simulate the flow around the three-dimensional high-rise buildings.

**Numerical method and physical models**

The Reynolds stress model is adopted in this paper, which abandoned the Boussinesq eddy viscosity hypothesis, thus directly establishes the differential equation of Reynolds stress and simultaneously solves the Reynolds average equation. The complete Reynolds stress model consists of 12 partial differential equations: three momentum equation, a continuity equation of the mean motion, six Reynolds stress equations, a ε equation and a k equation. The continuity equation and the momentum equation for average motions of turbulent flows are as followed:

$$\frac{\partial u_i}{\partial x_i} = 0 \tag{1}$$

$$\frac{\partial(\rho u_i)}{\partial t} + \frac{\partial}{\partial x_j}(\rho u_i u_j) = -\frac{\partial p}{\partial x_i} + \frac{\partial}{\partial x_i}\left(\mu \frac{\partial u_i}{\partial x_j} - \rho \overline{u_i' u_j'}\right) + S_i \tag{2}$$

where $u_i$ is the component of the fluid infinitesimal body in the velocity vector field towards the $i$ direction ($i = 1,2,3$. 1 indicates the flow direction, 2 and 3 indicate direction of perpendicular to the flow direction), $\rho$ is the air density, p is the wind pressure, $S_i$ is the source term of $u_i$, The Reynolds stress transport equation after dimensional analysis is as following:

$$\frac{\partial\left(\rho \overline{u_i' u_j'}\right)}{\partial t} + \frac{\partial\left(\rho u_i \overline{u_i' u_j'}\right)}{\partial x_k} = \frac{\partial}{\partial x_k}\left(\frac{\mu_i}{\sigma_k}\frac{\partial \overline{u_i' u_j'}}{\partial x_k} + \mu \frac{\partial \overline{u_i' u_j'}}{\partial x_k}\right) - \rho\left(\overline{u_i' u_k'}\frac{\partial u_j}{\partial x_k} + \overline{u_j' u_k'}\frac{\partial u_i}{\partial x_k}\right)$$
$$-C_1\rho\frac{\varepsilon}{k}\left(\overline{u_i' u_j'} - \frac{2}{3}k\delta_{ij}\right) - C_2\left(P_{ij} - \frac{1}{3}P_{kk}\delta_{ij}\right) - \frac{2}{3}\rho\varepsilon\delta_{ij} \tag{3}$$

where $C_1 = 1.8$, $C_2 = 0.60$, $P_{ij}$ is the item generated by shear stress, $\delta_{ij}$ is the tensor notation of " Kronecker delta ", under the condition that $i = j$ and $\delta_{ij} = 1$, otherwise $i \neq j$, $\delta_{ij} = 0$. As for RSM, the equation of turbulence kinetic energy k and the dissipation rate $\varepsilon$, satisfy their respective conservation equations, which produces :

$$\frac{\partial(\rho k)}{\partial t} + \frac{\partial(\rho k u_i)}{\partial x_i} = \frac{\partial}{\partial x_j}\left[\left(\mu + \frac{\mu_i}{\sigma_k}\right)\frac{\partial k}{\partial x_j}\right] + \frac{1}{2}\left(P_{ij} + G_{ij}\right) - \rho\varepsilon \tag{4}$$

$$\frac{\partial(\rho\varepsilon)}{\partial t} + \frac{\partial(\rho\varepsilon u_i)}{\partial x_i} = \frac{\partial}{\partial x_j}\left[\left(\mu + \frac{\mu_i}{\sigma_\varepsilon}\right)\frac{\partial \varepsilon}{\partial x_j}\right] + C_{1\varepsilon}\frac{1}{2}\left(P_{ij} + C_{3\varepsilon}G_{ij}\right) - C_{2\varepsilon}\rho\frac{\varepsilon^2}{k} \tag{5}$$

where $G_{ij}$ is buoyancy-produced term, $G_{ij} = 0$; $C_{1\varepsilon}$, $C_{2\varepsilon}$, $C_\mu$, $\sigma_k$ and $\sigma_\varepsilon$ are model constants for incompressible fluid, which are usually assigned the values 1.44, 1.92, 0.09, 0.82 and 1.0. The inlet boundary is connected with the UDF compiled in the equations (6) (7) and (8) to form a new type of boundary, which the inlet velocity, turbulent kinetic energy and turbulent dissipation rate are as follows:

Eq. (6) (7) and (8) are quoted from the paper by Wei Yang, Yong Quan [6]. $u_1$ is a function related with the height above ground z, $z_o$ is the roughness length, the related parameters Ks and Cs

$$u_1 = \frac{u_*}{\kappa}\ln\left(\frac{z+z_0}{z_0}\right), u_2 = 0, u_3 = 0 \tag{6}$$

$$K = \frac{u_*^2}{\sqrt{C_\mu}}\sqrt{C_1 \ln\left(\frac{z+z_0}{z_0}\right) + C_2} \tag{7}$$

$$\varepsilon = \frac{u_*^3}{\kappa(z+z_0)}\sqrt{C_1 \ln\left(\frac{z+z_0}{z_0}\right) + C_2} \tag{8}$$

are derived from the paper of Blocken B, Stathopoulos[8]. $u_*$ is the friction velocity; κ is the von Karman constant of 0.42; C1, C2, Cμ are model constant usually assigned with the values -0.17,1.62 and 0.028. Model 1 as follows is to verify the accuracy of the atmospheric boundary layer conditions. In addition, as for the velocity, the turbulent kinetic energy and the turbulent dissipation rate is validated. Model 2 research on the flow around the high-rise buildings based on the conclusions of model 1.

## Numerical examples and analysis

**Model 1.Cavity model** There is no obstacle inside of the model, which primarily verifies the correctness of the UDF compiled above. The size of calculation domain is L×B×H=12m× 1.8m×1.8m, meanwhile, the L, B and H are respectively corresponds to the x, y and z axis. Structured grid is adopted in this model. The height of first mesh layer above the ground is set as 0.01m, and the vertical growing factor of mesh point is 1.06. The mesh size in horizontal and lateral direction is uniform, which is 0.1m. The total grid number is 181440. The RSM model and constant algorithm are adopted calculation. The computational set the SIMPLEC algorithm for pressure-velocity coupling, and the Second Order Upwind are adopted for the turbulent kinetic energy, turbulence dissipation rate, momentum and pressure. The convergence criteria of the scaled residuals for all components and the continuity equation are set as $10^{-6}$. The side faces and upper face of computational domain are set as freeslip. The ground surface is set as Wall. Inlet boundary is set as inlet velocity, which compile with the UDF. Outlet boundary is set as pressure-outlet. The reference mean wind speed $U_H$ is 10m/s at the height of one meter.

The calculation results are shown in Fig.1 and Fig.2, which compared with the SKE2 conclusion in quotation[3], the results of the inlet velocity, the outlet velocity and turbulent dissipation rate are good agreement. It verifies the rationality of the boundary settings and the accuracy of the UDF.

**Model 2.Models for flow around buildings** This model computational domain is the same as that of the model1.But the model 2 has a building inside, which size is L×B×H=0.2m×0.2m×0.8m, and the distance between the building's windward side and the inlet boundary is 1.5m, the distance between the leeside and the outlet boundary is 10.3m, meanwhile, the size from the building sides to the flow field sides is 0.8m respectively, the pttern is shown in Fig.3. Partitioned structured grid is adopted in the model 2 and the grid number is 455600. The computational set the SIMPLEC algorithm for pressure-velocity coupling, and the Second Order Upwind are adopted for the turbulent kinetic energy, turbulent dissipation rate, momentum and pressure. Unsteady algorithm is adopted calculation. The convergence criteria of the scaled residuals for all components and the continuity equation are set as $10^{-6}$. The boundary conditions are the same as that of the model1. In

addition, the wall of the building is regarded as non-sliding wall, among which the $K_s$=0 and $C_s$=0.5.

The across wind force power spectral curve obtained by fast fourier transform is shown in Fig.4, from which we can observe the spectral peak frequency when frequency conversion nB/U is about 0.1. The dimensionless converting frequency nB/U is used as the horizontal axis, n is the frequency (Hz as the unit), U is the gradient wind, and dimensionless power spectrum $nS(n)/\sigma^2$ is set as vertical axis and $\sigma^2$ is the square value of a cross-wind fluctuating wind speed. According to the Fig.4, which compared with the experimental data of the wind tunnel in quotation[9], when $\sqrt{H/BL}=4$, $L/B=1$, the result well matches the data. Hence, the accuracy of the numerical simulation is verified. Besides, acquired from the across wind force power spectral curve, it is equal to the predominant frequency of the vortex shedding, in a word, the Strouhal number. Therefore, the instantaneous development of the vortex can be obtained in one period T, is shown in Fig.5 (a), (b), (c) and (d).

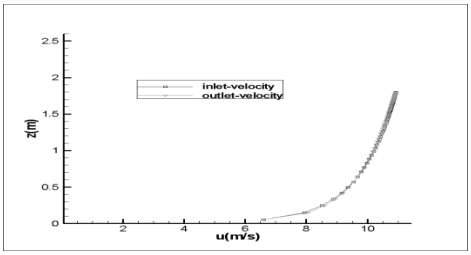


Fig.1 Velocities of inlet and outlet

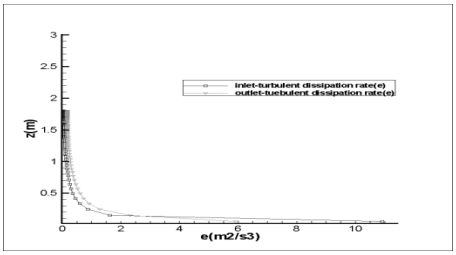


Fig.2 Turbulent dissipation rate of inlet and outlet

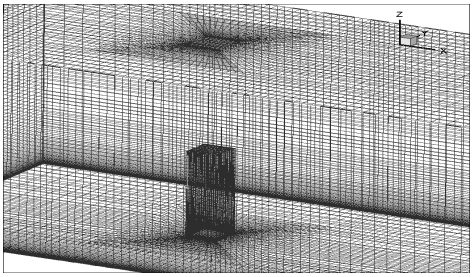

Fig.3 Partial enlarged drawing of building model

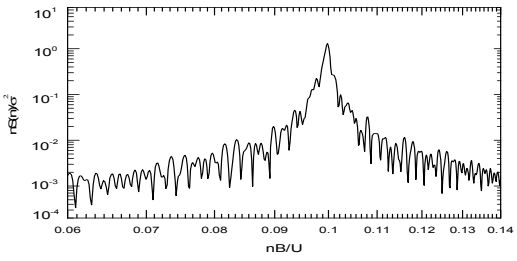


Fig.4 Across-wind force power spectra

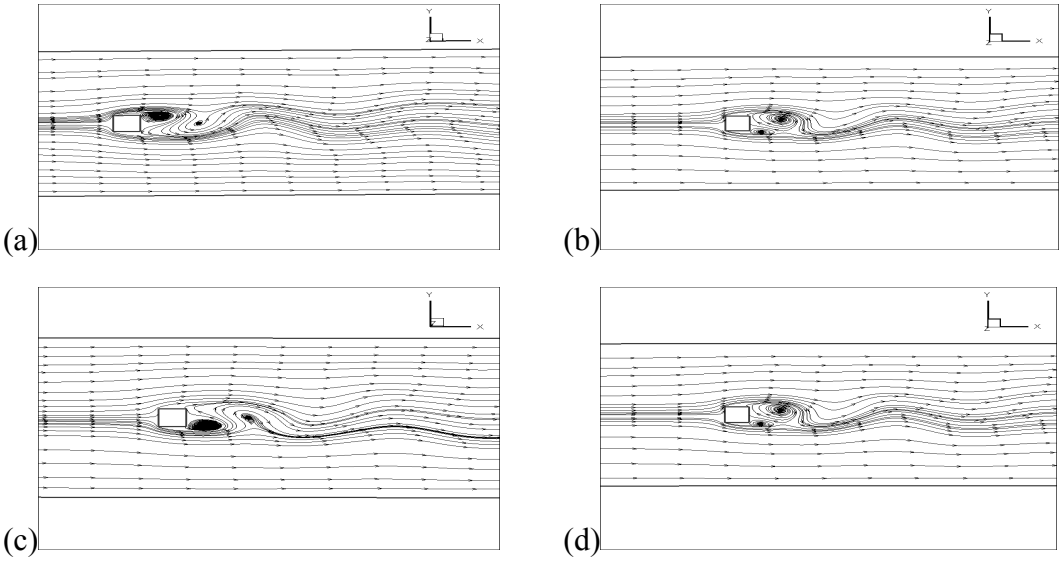


Fig.5 Instantaneous streamlines at z=0.2m (a) t=1/4T, (b) t=2/4T, (c) t=3/4T, (d) t=4/4T.

As can be seen from the Fig.6 (a) (b) and (c), along with the flow of the wind, close to the windward side of the building, the wind began to weaken and bypass the building's sides and superstructure, at the moment, the negative wind velocity of the wind speed at the top corners of the building and the formation of large eddy in the leeward side of the building occurs, which generates vortex and results in the occurrence of the negative pressure zone on the back of the building. With the further flow of the wind, the regular off-vortex phenomenon appears in the leeward sides of the building, which verifies that turbulence is relatively active in this region.

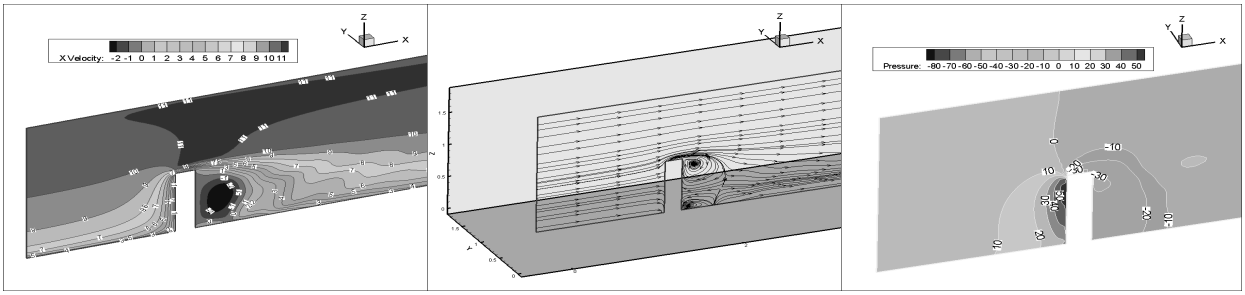


(a) (b) (c)

Fig.6 Instantaneous flow pattern at y=0.9m (a) X-velocity (b) Streamline (c) Pressure

## Conclusions

(1) Through the calculation for the cavity model, the validity of the boundary conditions established by the Eq. (6) (7) (8) is verified. Meanwhile, the inlet and outlet boundary speed and the turbulent kinetic energy dissipation rate graph verify the rationality of the Reynolds stress model (RSM) combined with the boundary conditions.

(2) Peak spectral frequency of wind power spectral curve well matches the converting frequency obtained by the wind tunnel experimental of the quotation [9], which is about 0.1, thus verifies the feasibility of the new boundary conditions combined with RSM for flow around the three-dimensional high-rise buildings.

## References

[1] Richards PJ, Hoxey RP. J. Wind Eng. Ind. Aerodyn. 46&47(1993): 145–153.
[2] Hargreaves DM, Wright NG. J. Wind Eng. Ind. Aerodyn. 95(2007): 355–369.
[3] Yang Y, Gu M, Chen S, Jin X. J. Wind Eng. Ind. Aerodyn. 97(2009): 88–95.
[4] Ya Zhang, Shuyan Liu, Baoguo Wang. Journal of Aerospace Power, Vol.20(4), (2005): 572 – 576(In Chinese )
[5] Feng Xu, Jingping Ou. Journal of Southeast University (Natural Science Edition), Vol.35 Sup (I)(2005): 35-39 (In Chinese )
[6] Wei Yang, Yong Quan. J. Wind Eng. Ind. Aerodyn. 96(2008): 2080 – 2092.
[7] Richards PJ, Younis BA. J. Wind Eng. Ind. Aerodyn. 34(1990): 107–110.
[8] Blocken B, Stathopoulos, T,Carmeliet. Atmospheric Environment. 41(2007): 238–252.
[9] Shuguo Liang, Shengchun Liu, Liangliang Zhang. Acta Aerodynamica Sinica, Vol.20(1) (2002): 32-39 (In Chinese)

*Applied Mechanics and Materials Vols. 580-583 (2014) pp 3062-3065*
*© (2014) Trans Tech Publications, Switzerland*
*doi:10.4028/www.scientific.net/AMM.580-583.3062*

# Reconstruction of Shallow Shells for increase Bearing Capacities and Operating Characteristics

Leonid U.Stupishin[1, a], Alexander G.Kolesnikov[2,b]

[1]Chair of Urban and road construction and structural mechanic department, South-West State University (SWSU), 305040, Kursk, Russia

[2] Urban and road construction and structural mechanic department, South-West State University (SWSU), 305040, Kursk, Russia

[a]lusgsh@yandex.ru, [b]ag-kolesnikov@mail.ru

**Keywords:** shallow shells, bearing capacities, nonlinearity, critical force, stress.

**Abstract.** Bearing capacities and operating characteristics cover of a building deteriorate since time. Reconstruction of shallow shells cover by increase of their thickness in the center or at the edge. Critical force and stress of shell are considered with the geometric nonlinearity consideration. Vertical static loading and various types of a fixing are investigated. The method allows to describe various forms of shells with defects/

## Introduction

When operating shells coatings possible defects by corrosion, unplanned influences and other's reason. It leads to emergence of inadmissible deflections of a cover, reduction of bearing capacity, change of its form. Recovery of characteristics possibly by changing of the cross-sectional area of a construction along it generating line.

The description of a new form of a middle surface of shallow shells acquired owing to accumulation of defects, it is possible to present by function with the set parameter of a form $\xi_0$ and the set size of raises $f_0^1$ [1] different from initial value at a size of vertical movements received in use (Fig. 1).

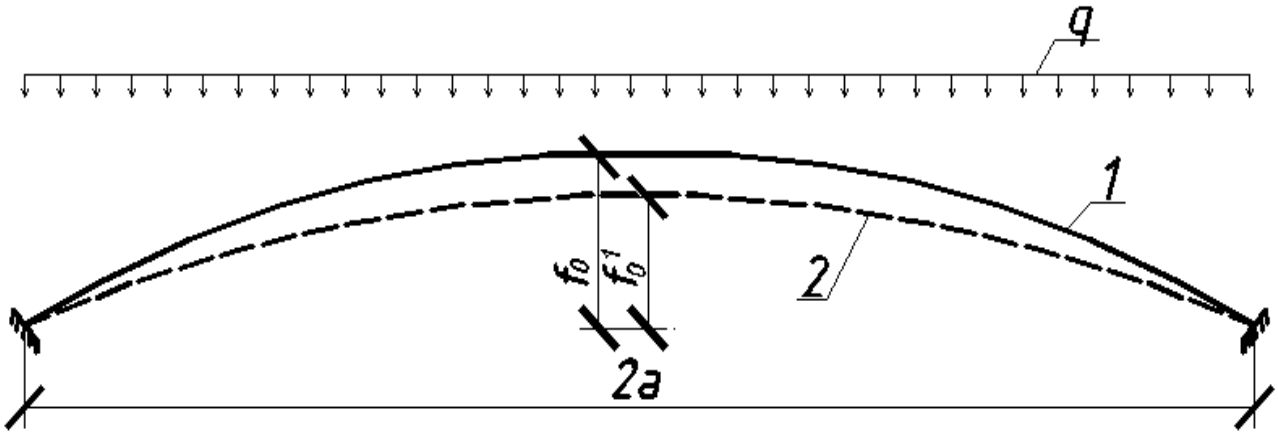


Fig. 1 - Possible changes of a form of a middle surface of shallow shell (a section along an axis x): 1-initial form of shallow shell, 2 – a form of shallow shell owing action uniform the distributed loading and accumulation of defects

## Problem statement

If it is required to restore bearing capacity of shell, it is possible to execute search of a new form of shell, having accepted its thickness of a variable along generating line, but a form of a median surface fixed. Changes for thickness of shells from the center to edge is defined as [2,3]

$$h(x,y) = t\left(1+\kappa\left(\frac{x}{a}\right)^{2\eta}\right)\left(1+\kappa\left(\frac{y}{b}\right)^{2\eta}\right). \quad (1)$$

Where

$t = \frac{h_0}{f}$ - the relative thickness of the shell,

$f$ - rise of arch in the center of the shell,

$a, b$ - dimensions in plan,

$\eta$ - changes in the shape parameter of the shell thickness,

$k$ - parameter responsible for the ratio of the shell thickness at the edge and center (when $k < 0$ the thickness of the shell in the center more than at the edge; when $k > 0$ - shell thickness in the center is smaller than at the edge; when $k = 0$ - shell thickness is constant along middle surface),

$h_0$ - thickness of the shell in the center (Fig. 2).

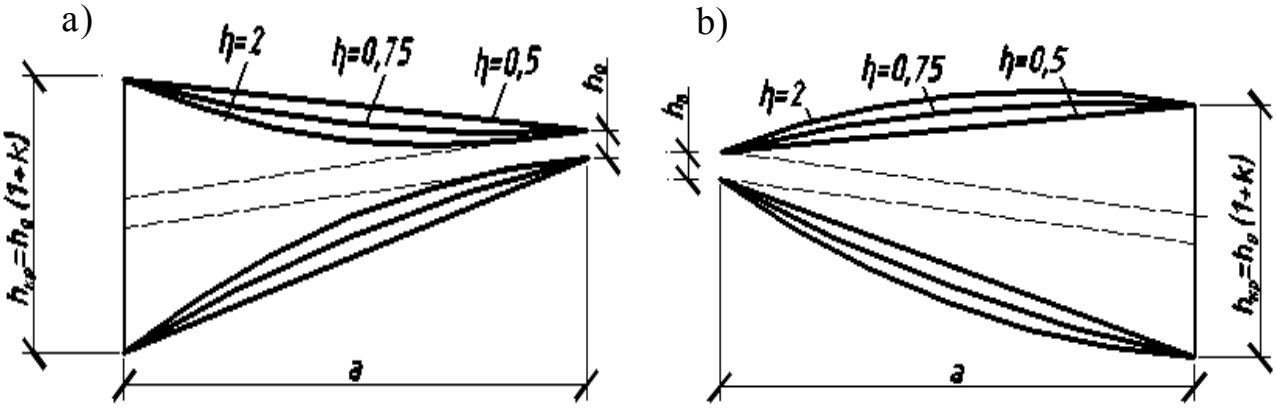


Fig. 2 – Distribution of the shell thickness: a) when k>0; b) when k<0.

The problem of restoration of bearing capacity can be formulated as:

$$\begin{cases} V(k,t,\eta) \to V_{min}, \\ p(k,t,\eta) \geq p_0, \\ \sigma(k,t,\eta) \leq \sigma_0, k \in G, t \in G, \xi \in G, \eta \in G. \end{cases} \quad (2)$$

$$G = \left\{ \begin{array}{l} \eta : 0{,}5 < \eta_y < 2, y = \overline{1,l}; \\ t : 0{,}001 < t_j < 0{,}1, j = \overline{1,m}, k : -1 < k_u < \left(\frac{1}{10}\sqrt{\frac{2a}{h}-1}\right), u = \overline{1,r} \end{array} \right\} \quad (3)$$

It is required to find such distribution of thickness of fixed form shell that the volume of an added material was minimum, when stability and durability conditions performed. Provided mechanical characteristics of a material consider decrease in bearing capacity owing to accumulation of defects.

At change of thickness of shell it is possible to achieve effect of change a form of a median surface of shell (Fig. 3), at the fixed rise of arch.

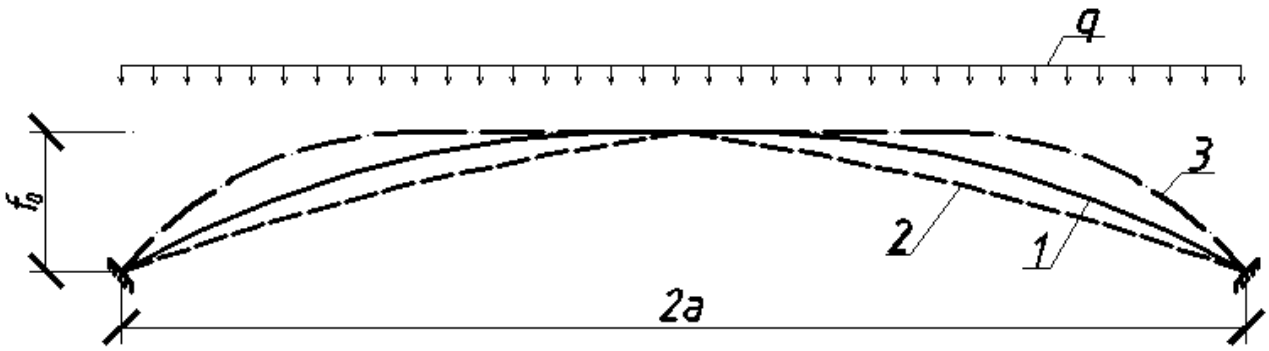


Fig. 3 – Possible changes of a form of shell median surface caused to change of its thickness: 1-initial form of shell, 2 – form of shell median surface (form parameter $\xi < 1{,}0$ ), 3 - form of shell median surface (form parameter $\xi > 1{,}0$ ).

**Solution of a task**

At restoration of bearing capacity it can be increased by increase in cross section (Fig.4).

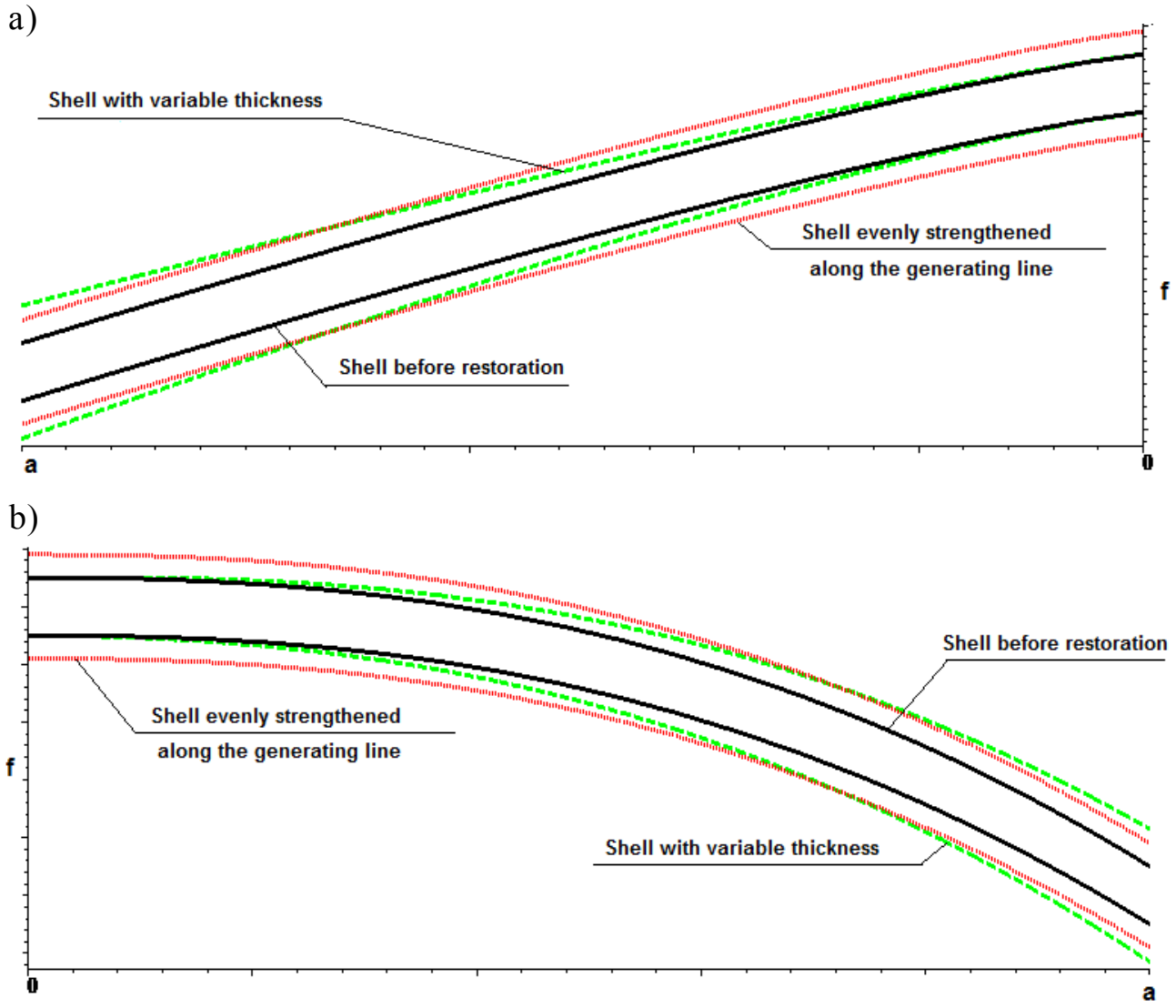


Fig. 4 – Forms of possible distribution of thickness of shell at reconstruction: a) for parameter of a shell's form $\xi < 1{,}0$ , b) for parameter of a shell's form $\xi > 1{,}0$ .

In this case restoration of shell's bearing capacity can be formulated as follows:

$$\begin{cases} V(k,t,\xi,\eta) \to V_{min}, \\ p(k,t,\xi,\eta) \ge p_0, \\ \sigma(k,t,\xi,\eta) \le \sigma_0, k \in G, t \in G, \xi \in G, \eta \in G. \end{cases} \quad (4)$$

$$G = \left\{ \begin{array}{l} \xi : 0{,}75 < \xi_i < 2, i = \overline{1,n}; \eta : 0{,}5 < \eta_y < 2, y = \overline{1,l}; \\ t : 0{,}001 < t_j < 0{,}1, j = \overline{1,m}, k : -1 < k_u < \left( \frac{1}{10} \sqrt{\frac{2a}{h} - 1} \right), u = \overline{1,r} \end{array} \right\}. \quad (5)$$

Algorithms of the solution of tasks are realized in the "Maple" environment. In both options of statement of tasks the decisions, allowing projecting rational strengthening of shells by change of their thickness are received [4,5]. Comparing spherical shells with constant thickness with projects of strengthening, in some cases due to rational distribution of thickness of a cover with defects it is possible to receive economy of a material to 35% at considerable reduction of weight of a design.

The offered technique, allows to put and solve problems of restoration of bearing capacity of shallow geometrically nonlinear shells due to optimum distribution of thickness at:

- restoration of demanded value of stress in a median surface of shell at restriction on value of used material volume;
- restoration of demanded value of critical loading at restriction on value of construction's material volume for any kinds of fixing;
- restoration of demanded value of stress in a median surface of shell at the set size of critical force and restriction on value of volume of used material;
- restoration of demanded value of critical loading at restriction on value of stress in cross sections of shell and construction's material volume for any kinds of fixing.

## Conclusion

The developed optimization algorithm of thickness distribution for restoration of bearing ability of geometrically nonlinear shallow shells can be used at restoration of bearing capacity and operational characteristics of shallow shells of coverings of buildings and constructions.

## References

[1] L.U. Stupishin, A.G. Kolesnikov: Nonlinear Geometrically Variable Form For Rectangular Plan Shallow Shells Examination// Promyshlennoe I Grazhdanskoe Stroitelstvo Vol. 1 (2009), p.24.

[2] L.U. Stupishin. Mixed finite element of geometrically nonlinear shallow shells of revolution: K.E.Nikitin, L.U. Stupishin// Applied Mechanics and Materials Vols. 501-504 (2014) pp 514-517© (2014) Trans Tech Publications, Switzerlanddoi: 10.4028/ www.scientific.net/ AMM.501-504.514

[3] L.U. Stupishin, A.G. Kolesnikov: Geometric Nonlinear Shallow Shells for Variable Thickness Investigation//Advanced Materials Research Vols. 919-921 (2014) pp 144-147© (2014) Trans Tech Publications, Switzerlanddoi:10.4028/www.scientific.net/AMR.919-921.144

[4] V.I. Andreev. About one way of optimization of the thick-walled shells. Applied Mechanics and Materials. Vols. 166-169, pp. 354-358, Trans Tech Publications, Switzerland, 2012.

[5] V.I. Andreev. Optimization of thick-walled shells based on solutions of inverse problems of the elastic theory for inhomogeneous bodies. Computer Aided Optimum Design in Engineering XII (OPTI XII). WIT Press. 2012, p.189-201

*Applied Mechanics and Materials Vols. 580-583 (2014) pp 3066-3070*
*© (2014) Trans Tech Publications, Switzerland*
*doi:10.4028/www.scientific.net/AMM.580-583.3066*

# Study on reduced order model in large-span roof vibration under wind actions

Fangjin Sun[1, a], Daming Zhang[2, b]

[1]College of Civil Engineering & Architecturure, Liaoning Technical University, Fuxin, 123000, P.R.China

[2] Technical and Economic Institute, Liaoning Technical University, Fuxin, 123000, P.R.China

[a]email,e_dm@163.com, [b]email, zhang_daming@21cn.com

**Keywords:** Large-span roofs. Vibration under wind actions. Reduced order model

**Abstract.** Reduced order model was for the first time employed for the large-span structure by system identification approach. The structure's modal amplitudes are utilized to construct strain energy function of the system. A high fidelity finite element model is adopted to calculate modes and strain energy information to determine the unknown coefficients in the strain energy function. Wind-induced responses of a large-span structure were computed by the proposed method. The results were compared well with those obtained from the high fidelity finite element model and experiments. It proves that reduced order model is an effective way to compute large-span structure responses under wind actions when taking aero-elastic effects into account.

## Introduction

Wind-induced vibration of large-span structure shows a characteristic of fluid-structure interaction, i.e. aero-elastic effects. The aero-elasticity has a very significant effect on wind-induced vibration of large-span structure, and it is necessary to attach great importance. One of the key problems in numerical simulation is to establish the structural model of large-span structures, which decides complicity of the process and accuracy of the final results. Reduced model is very effective in establishing structural model and in recent years it is widely used in aeroelasticity. Various reduced models have been developed and the most commonly used is normal mode reduced modal methods[1], which have been used in the field of structural dynamics for many years. A lot of work has been done in linear system identification and great progress have been achieved. As far as nonlinear system identification is concerned, though research is being done and some progress has been made, many problems are still need to be solved. In recent work by Epureanu and Dowell, a multivariate, third order polynomial was used as the functional form for a nonlinear structural model [2]. Gabbay and Mehner et al. used polynomial functions whose coefficients were identified using strain energy data to model a microelectromechanical system[3]. Silverder et al. have used a Volterra series approach to identify linear and nonlinear aerodynamic systems[4].

The reduced model for nonlinear large-span structure is constructed by system identification of a high fidelity structural model. The strain energy of the system is written as a polynomial function of the structure's modal amplitudes. And the unknown coefficients of the polynomials are determined by modes and strain energy information calculated from a high fidelity finite element model. Wind-induced responses of a large-span structure are calculated using the proposed method.

## Reduced order aero-elastic equations

The general form of the aero-elastic system can be written in the following manner in terms of modal coordinates [5]

$$\vec{\Phi}^{\mathrm{T}}\vec{\mathrm{M}}\vec{\Phi}_{\ddot{\mathrm{q}}} + \vec{\Phi}^{\mathrm{T}}\vec{\mathrm{C}}\vec{\Phi}_{\dot{\mathrm{q}}} + \vec{\mathrm{F}}^{\mathrm{SE}}(\mathrm{q}) = \vec{\Phi}^{\mathrm{T}}\mathrm{F}^{\mathrm{P}} \tag{1}$$

Where the vector $\bar{\mathrm{u}}$ contains the structural nodal degrees of freedom, the matrix, $\vec{\mathrm{M}}$ is the mass matrix, $\vec{\mathrm{C}}$ is the damping matrix and $\vec{\mathrm{F}}^{\mathrm{P}}$ is the load vector due to the aerodynamic pressure.

The nodal degrees of freedom are expressed as a linear combination of the modes,

$$\vec{u} = \sum_{i=1}^{N_F} q_i(t)\vec{\varphi}_i \tag{2}$$

And the matrix $\vec{\Phi}$ contains the mode shape vectors $\vec{\varphi}_i$. Also, in Eq.(2) $q_i$ is the ith modal degree of freedom and $N_F$ is the total number of structural degrees of freedom. Note that now the force vector due to strain energy, $\widetilde{F}^{SE}$, is a function of the modal amplitudes $q_i$. In practice the summation in Eq.(2)is truncated at N modal degrees of freedom where N is a number much less than $N_F$.

Likewise the aerodynamic equations of motion can now be expressed as

$$\vec{A}_b\vec{\Gamma}_b^{n+1} = \vec{E}\vec{\Phi}\dot{\vec{q}}^{n+1/2} + \vec{E}\vec{d}\vec{\Phi}\vec{q}^{n+1/2} + \vec{\alpha} - \vec{A}_w\vec{I}_w^n \tag{3}$$

Where the matrix $\vec{d}\vec{\Phi}$ is the matrix of x derivations of the modal functions, $\vec{\Gamma}_b$ and $\vec{\Gamma}_w$ are vectors of large-span structure and airflow circulations respectively. The matrices $\vec{A}_b$ and $\vec{A}_w$ are the large-span structure and airflow influence coefficient matrices and the matrix E is the matrix of interpolation coefficients needed to transfer quantities from the finite element mesh to the aerodynamic mesh.

Now a functional form for the strain energy U in terms of the modal coordinates will be defined. Here a multivariate Lagrange polynomial is used. The form of this polynomial can be written as:

$$U = \sum_{i=0}^{M_1}\sum_{j=0}^{M_2}\sum_{k=0}^{M_3}\sum_{l=0}^{M_4}\cdots\sum_{o=0}^{M_N} A_{ijkl\ldots o}q_1^i q_2^j q_3^k \cdots q_N^o = \sum_{i=1}^{N_t} A_i\psi_i(q_1, q_2 \cdots q_N) \tag{4}$$

Where U is the strain energy functional for the system, the coefficients $A_i$ are found using a least squares fit of strain energy data generated using a finite element package and the $\psi_i$ are the Lagrange basis functions. The number of basis functions used, Nt is the product of the values M1,M2,…,MN.

**System identification process**

In order to compute coefficients in Eq.(4), the strain energy U must be computed for various out-of plane spatial distributions $u_Z(x,y)$. The structure is displaced to a static configuration $u_Z^i(x,y)$ determined by the prescribed modal amplitudes $q_j^i$:

$$\vec{u}_Z^i = \sum_{j=1}^{N} q_j^i\varphi_j \tag{5}$$

The strain energy for this ith configuration, Ui, is then computed by solving a nonlinear statics problem. In this paper, this was accomplished by using ANSYS.

Once all of the strain energy values have been calculated using the finite element model, the coefficients in Eq.(4) can be computed using a least square solution of the following set of linear equations:

$$\vec{A}\vec{x} = \vec{b} \tag{6}$$

Where the vector $\vec{b}$ contains the strain energy values for each individual configuration and the vector $\vec{x}$ contains the Nt polynomial coefficients. The marix $\vec{A}$ consists of the basis functions used in the polynomial expansion evaluated for each individual configuration.

**Numerical results**

Using the method developed above, results of wind-induced responses of a flat large-span roof in literature [6]are presented. Its geometry are depicted in Fig.1. Its thickness is 1mm, elastic modulus E=7.1×1010N/m2, its density ρ＝2420kg/ m3, Poisson's ratio γ＝0.31. Wind velocity are range from 8m/s to 12m/s and wind direction angle are from 0°～45° , increasing 15° at a time. The experimental results are also from the literature [6].

The high-fidelity structural finite element model constructed using ANSYS contained 869 thin shell bending elements, with 967 nodes and a total of 5802 degrees of freedom. The structural nonlinearities modeled include large rotation and stress-stiffening. In the reduced model, the values used for the Mi in Eq. (7) are:

$$M_i = 4, i \le 4$$
$$M_i = 2, i \rangle 4 \quad (7)$$

The number of individual values for each mode used for generating strain energy was (from mode 1 to mode 6): 9, 7, 7, 7, 5, 5. In the following results, if it is said four modes have been used to generate the strain energy, then there would be 9×7×7×7×5＝15435 configurations used.

Table1 gives comparison of acceleration mean square deviation for prescribed points on the roof using the first 6 modes, experimental results and ANSYS respectively at a flow velocity of 10m/s.

Tab.1 Comparison of acceleration mean square deviation for prescribed points using different methods（$m/s^2$）

| Wind direction angles \ Prescribed points | | 1 | 2 | 3 | 4 | 5 |
|---|---|---|---|---|---|---|
| 0° | Experimental | 0.80 | 0.60 | 0.30 | 0.90 | 0.60 |
| | ANSYS | 0.71 | 0.64 | 1.17 | 0.69 | 0.51 |
| | Reduced model | 0.59 | 0.57 | 0.97 | 0.60 | 0.59 |
| 15° | Experimental | 0.80 | 0.60 | 0.30 | 0.90 | 0.60 |
| | ANSYS | 0.94 | 0.65 | 0.97 | 0.76 | 0.76 |
| | Reduced order model | 0.79 | 0.54 | 0.81 | 0.62 | 0.90 |
| 30° | Experimental | 0.80 | 0.70 | 0.30 | 1.10 | 0.60 |
| | ANSYS | 0.65 | 0.51 | 0.87 | 0.83 | 0.66 |
| | Reduced order model | 0.47 | 0.42 | 0.63 | 0.62 | 0.82 |
| 45° | Experimental | 0.80 | 0.70 | 0.30 | 1.10 | 0.60 |
| | ANSYS | 0.74 | 0.57 | 1.24 | 0.85 | 0.54 |
| | Reduced order model | 0.56 | 0.46 | 0.92 | 0.60 | 0.74 |

From the table above, it can be seen that the results obtained using the reduced order model developed in this work tallied well with the results from the experiments and ANSYS. And the results from the reduced order model were more close to those using ANSYS. It illustrates that using reduced order model to construct structural model in simulating its wind-induced vibration of large-span structure is feasible and accurate.

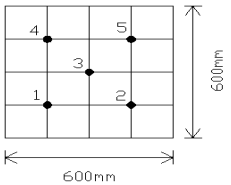


Fig.1Geometry of the flat large-span structure

Fig.2 shows plots of acceleration mean square of prescribed points 1 and 4 using various number of modes at wind azimuth of 0° at various flow velocities. Fig.3shows acceleration mean square of prescribed points 2 and 5 using various number of modes at wind azimuth of 30° at various flow velocities. Fig.4 gives acceleration mean square of prescribed point 3 at wind azimuth of 15° and 45° at various flow velocities.

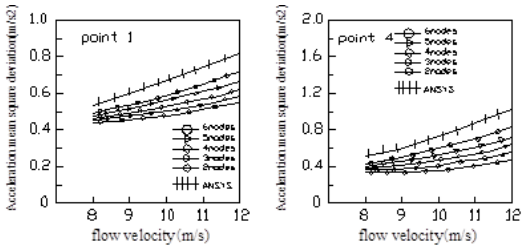


Fig.2 Acceleration mean square deviation of points 1 and 4 at wind azimuth of 0°

As seen from Fig.2 and Fig.3, for wind azimuth of 0° and 30° with various wind velocities, acceleration mean square obtained from reduced order models are compared well with those from ANSYS. With the increase of modes used, the system identification results are approximating to the results from ANSYS. As seen from figure 4, the simulation results are closer to those from ANSYS at wind azimuth 15° than 45°. Thus, more modes are required for more accurate results. In the example, 7 equations are required at most for the structure, 3 order less than using nonlinear finite element models, reducing 2 order the total computer hours, improving the computing efficiency as a result.

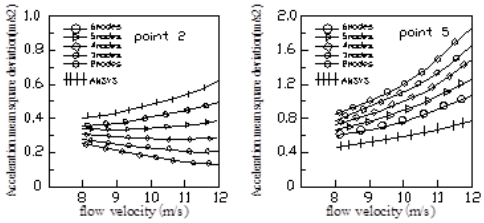


Fig.3 Acceleration mean square deviation of points 2 and 5 at wind azimuth of 30°

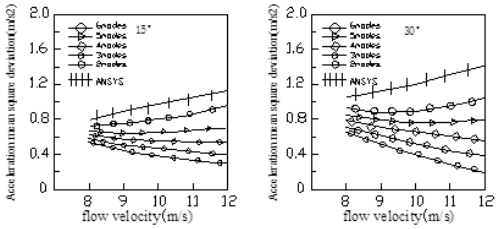


Fig.4 Acceleration mean square deviation of point 3 at wind azimuth of 15° and 45°

## Conclusions

For the first time, the reduced order model was introduced to construct nonlinear structural model in wind-induced vibration of large-span structure. The results of wind-induced vibration of large-span structure obtained using the reduced order model were compared with those from experiments and from ANSYS model. We can reach the following conclusions:

(1)As the numbers of modes used in reduced order model increase, the system identification results would be increasingly accurate. As the wind direction angle increases, numbers of modes need increase to obtain increasingly accurate results.

(2) (1) Structural reduced order model and its system identification is feasible and accurate in wind-induced vibration of large-span structure considering aero-elasticity, with higher efficiency.

## Acknowledgments

The research described in this paper was financially supported by National Natural Science Foundation of China (Contract No. 51108345) , opening foundation of State Key Laboratory for Disaster Reduction in Civil Engineering of China (Contract No. SLDRCE-MB-04), and Foundation of Liaoning province education administration (Contract No.L2013134).

**References**

[1] Jérôme Breil, Stéphane Galera, Pierre-Henri Maire. Computers & Fluids, Vol46, (2011), p. 161

[2] Menicovich, D., Gallardo, D., Bevilacqua, R., Vollen, J.O., Generation and integration of an aerodynamic performance data-base within the concept design phase of tall buildings. In: Proceedings of the 2012 ACADIA Conference, San Francisco, (2012).

[3] Gabby, L.D., Mehner, J.E., Senturia, S.D., Journal of Microedectro mechanical System. Vol 9 (2000), p.262

[4] Silva, W.,Reveh, D.E., Development of unsteady aerodynamic state-space models from CFD based unsteady loads. AIAA Paper, (2001).

[5] Lucia, D., Beran, P., Silva, W., Aerospace Science. Vol40, (2004), p.51

[6] Feng Lu, Study on wind-induced responses and wind-induced vibration coefficient of flat large-span roof structures. Doctoral thesis of Zhejiang University, 2001 (in Chinese)

*Applied Mechanics and Materials Vols. 580-583 (2014) pp 3071-3074*
*© (2014) Trans Tech Publications, Switzerland*
*doi:10.4028/www.scientific.net/AMM.580-583.3071*

# The coupling of Pseudo-spectral Method and Domain Decomposition Method for the Elastostatic Problem

Ding Rui[1, a], Chen Fujun[1,b*], Shen Quan[2,c] and Liu Ling[1,d]

[1] School of Mathematical Sciences, Soochow University, Jiangsu Province, China

[2] School of Urban Rail Transportation, Soochow University, Jiangsu Province, China

[a]dingrui@suda.edu.cn, [b]rapidray@sina.com, [c]shenquan@suda.edu.cn, [d]20104207026@suda.edu.cn

**Keywords:** Pseudo-spectral method, domain decomposition method, elastostatic problem, unit decomposition principle

**Abstract.** It presents the coupling of Pseudo-spectral method (PS) and domain decomposition method (DDM) for the elastostatic problem. First, the original problem is decomposed into several sub-problems by DDM. Next combining the advantage of easy programming and high accuracy of Pseudo-spectral method, we can solve these sub-problems in parallel by PS. Finally the global numerical solution is obtained by the partition of unity approximation. Some numerical experiments illustrate the effectiveness and accuracy of our method.

## Introduction

Domain decomposition method (DDM) [1] is one of most effective methods used in large-scale numerical computation. DDM has the advantage that, through decomposition of the area, it can reduce the scale of the problem, and researcher can also use different numerical method according to the characteristics of corresponding problems in different regions, so to achieve a parallel computation of the engineering problems and improve the computation speed.

The pseudo-spectral method is an innovative meshless method with the advantages of simple implementation and high precision, it gradually gains much attention. Based on the research of B.Fornberg and D.Gottlieb et al, Trefethen firstly gave a comprehensive overview of the pseudo-spectral method in the literature [2]. Then, Fasshauer proposed pseudo spectral method based on radial basis function[3], which enhances the applicability of the pseudo-spectral method, and breaks the bottleneck that the method can only applied to solve the problem in regular region.

We propose the coupling of pseudo-spectral method and domain decomposition method, due to the characteristics of each method. This paper is divided into two sections. Section 1 gives the mechanical description of the elastostatic problem, with detailed description of the main coupling idea of the pseudo-spectral method and domain decomposition method (PS-DDM); In Section 2, it presents the numerical examples of the classic cantilever beam, the experimental results show that the coupling method has the advantages of high accuracy and computing speed.

## The coupling of PS and DDM for the Elastostatic Problems

We consider an linear elastostatic problem[4] defined on the region $\Omega \in R^n$ with boundary $\Gamma$, assume that $\Gamma$ is composited by the displacement boundary $\Gamma_D$ and force boundary $\Gamma_t$, $\hat{\mathbf{u}}$ represents a prescribe displacement boundary conditions, $\hat{\mathbf{t}}$ indicates a prescribe traction on the force boundary, $\mathbf{f}$ expresses the density of body force . The elastic body is in the equilibrium state. Three classic equations are: Equilibrium equation $div\ \boldsymbol{\sigma} + \mathbf{f} = \mathbf{0}$, in $\Omega$. Constitutive equation $\boldsymbol{\sigma} = \mathbf{C}\boldsymbol{\varepsilon}$, in $\Omega$. Relationship of strain tensor and displacement tensor: $\boldsymbol{\varepsilon}(\mathbf{u}) = \left(\nabla\mathbf{u} + (\nabla\mathbf{u})^T\right)/2$. Here $\boldsymbol{\sigma} = (\sigma_{ij})_{d\times d}$ is stress tensor, $\boldsymbol{\varepsilon} = (\varepsilon_{ij}(\mathbf{u}))_{d\times d}$ is strain tensor, $\mathbf{C}$ is elasticity tensor. Boundary conditions on displacement boundary $\Gamma_D$ and force boundary $\Gamma_t$ are given as below:

$$\mathbf{u} = \hat{\mathbf{u}}, \quad on\ \Gamma_D, \qquad \boldsymbol{\sigma}\mathbf{v} = \hat{\mathbf{t}}, \quad on\ \Gamma_t.$$

Here $\mathbf{v}$ stands for the unit outward norm vector. We can reorganize the above problem as follows:

$$\begin{cases} \mathbf{Lu}+\mathbf{f}=\mathbf{0} & in\ \Omega, \\ \mathbf{u}=\hat{\mathbf{u}} & on\ \Gamma_D, \\ \mathbf{Tu}=\hat{\mathbf{t}} & on\ \Gamma_t. \end{cases} \tag{1}$$

Where $\mathbf{L},\mathbf{T}$ denote differential operators.

PS method is an efficient method for solving partial differential equations, it has the advantage of easy programming and high accuracy, but is rarely involved in large-scale computation. DDM is one of the most effective methods of large-scale scientific computing. Therefore we hope that the coupling of PS method and DDM can be used to solve the problem (1), that is, region $\Omega$ is divided into several sub-regions $\{\Omega_i\}$, and then PS method is used in parallel to solve the corresponding PDEs defined on these sub-regions. In the following we give the introduction of PS method and the process of the coupling of PS-DDM in detail.

We consider the following PDE problem,

$$\begin{cases} Lu=f & in\ \Omega, \\ Bu=g & on\ \partial\Omega\setminus\Gamma, \\ u=\overline{u} & on\ \Gamma. \end{cases} \tag{2}$$

here $L,B$ denote differential and boundary operators respectively. We use approximate function:

$$u^h(\mathbf{x})=\sum_{j=1}^{N} c_j\Phi_j(\mathbf{x}),\ \mathbf{x}\in\Omega, \tag{3}$$

where $c_j, j=1,\cdots,N$ are unknown coefficients, $\Phi_j, j=1,\cdots,N$, are certain basis functions.

By inserting (3) into the PDE and boundary conditions and forcing these equations to be satisfied at the collocation points $\mathbf{x}_i, i=1,\ldots,N$, we have

$$\mathbf{A}_L\mathbf{c}=\mathbf{f},\ \mathbf{A}_B\mathbf{c}=\mathbf{g},\ \mathbf{A}_D\mathbf{c}=\overline{\mathbf{u}}. \tag{4}$$

Where $\mathbf{A}_L=\left(L\Phi_j(\mathbf{x}_i)\right)_{N_I\times N}, \mathbf{A}_B=\left(B\Phi_j(\mathbf{x}_i)\right)_{N_B\times N}, \mathbf{A}_D=\left(\Phi_j(\mathbf{x}_i)\right)_{N_D\times N}$, $\mathbf{c}=(c_1,\cdots,c_N)^T$ is unknown coefficient vector, $N_I$ denotes the number of nodes in the interior of $\Omega$, $N_B$, $N_D$ respectively denotes the number of nodes on the boundary $\Gamma$ and $\partial\Omega\setminus\Gamma$, here $N=N_I+N_B+N_D$. $\mathbf{f},\mathbf{g}$ and $\overline{\mathbf{u}}$ respectively stands for the vector composed by the values of $f$, $g$ and $\overline{u}$ at the collocation points.

Here $\mathbf{u}=(u_1,\cdots,u_N)^T$ is discrete function vector, from (3) we can obtain $\mathbf{u}=\mathbf{Ac}$, where $\mathbf{A}=\left(\Phi_j(x_i)\right)_{N\times N}$. Assuming that $\mathbf{A}$ is invertible, we can obtain $\mathbf{c}=\mathbf{A}^{-1}\mathbf{u}$. Then the discretized linear systems (4) becomes

$$\begin{pmatrix} \mathbf{A}_L \\ \mathbf{A}_B \\ \mathbf{A}_D \end{pmatrix}\mathbf{A}^{-1}\begin{pmatrix} \mathbf{u}_I \\ \mathbf{u}_B \\ \mathbf{u}_D \end{pmatrix}=\begin{pmatrix} \mathbf{f} \\ \mathbf{g} \\ \overline{\mathbf{u}} \end{pmatrix}. \tag{5}$$

Where $\mathbf{u}_I$ collects the values in the interior of $\Omega$, $\mathbf{u}_B$ and $\mathbf{u}_D$ collect the values on the boundary $\Gamma$ and $\partial\Omega\setminus\Gamma$. Therefore, $\mathbf{u}$ is obtained by solving linear system (5).The Process of the coupling of PS-DDM method is as below:

Step 1: Domain Decomposition and set the initial value

Assuming that $\Omega\subset R^n, n=1,2,3$, we construct two artificial boundarys $\Gamma_1,\Gamma_2$, decomposed $\Omega$ into two sub-regions $\Omega_1,\Omega_2$, and $\Omega_1\cap\Omega_2\neq\phi$. Then we arbitrarily select the initial values $\mathbf{u}_1^0,\mathbf{u}_2^0$ on the artificial boundary, let $k:=0$, $\varepsilon>0$.

Step 2: Obtain $\mathbf{u}_1^n,\mathbf{u}_2^n$ via parallel computing the following systems using PS method in the sub-regions $\Omega_1,\Omega_2$

$$\begin{cases} \mathbf{L}\mathbf{u}_1^n + \mathbf{f} = \mathbf{0} & in\ \ \Omega_1, \\ \mathbf{u}_1^n = \hat{\mathbf{u}} & on\ (\partial\Omega_1 \cap \Gamma_D)\backslash\Gamma_1, \\ \mathbf{T}\mathbf{u}_1^n = \hat{\mathbf{t}} & on\ (\partial\Omega_1 \cap \Gamma_t)\backslash\Gamma_1, \\ \mathbf{u}_1^n = \mathbf{u}_2^{n-1} & on\ \ \Gamma_1. \end{cases} \quad \begin{cases} \mathbf{L}\mathbf{u}_2^n + \mathbf{f} = 0 & in\ \ \Omega_2, \\ \mathbf{u}_2^n = \hat{\mathbf{u}} & on\ (\partial\Omega_2 \cap \Gamma_D)\backslash\Gamma_2, \\ \mathbf{T}\mathbf{u}_2^n = \hat{\mathbf{t}} & on\ (\partial\Omega_2 \cap \Gamma_t)\backslash\Gamma_2, \\ \mathbf{u}_2^n = \mathbf{u}_1^{n-1} & on\ \ \Gamma_2. \end{cases} \tag{6}$$

Step 3: If $\max\left(\left\|\mathbf{u}_1^n - \mathbf{u}_1^{n-1}\right\|, \left\|\mathbf{u}_2^n - \mathbf{u}_2^{n-1}\right\|\right) < \varepsilon$ ,stop iteration, otherwise $k = k+1$, return to Step 2.

Step 4: Using partition of unity approximation to obtain global approximation function [7]

At the end of iteration, two local approximate functions $\mathbf{u}_1^h(\mathbf{x}), \mathbf{u}_2^h(\mathbf{x})$ are finally obtained in the sub-regions $\Omega_1, \Omega_2$. In order to get the global approximate function in the entire region, partition of unity approximation approach is used here. we define compactly supported functions $\omega_i(\mathbf{x})$ in each sub-region, which should satisfy the partition of unity condition, namely $\sum_{i=1}^{2} \omega_i(\mathbf{x}), \mathbf{x} \in \Omega$. Then the global approximation function can be represented as $\mathbf{u}^h(\mathbf{x}) = \sum_{i=1}^{2} \omega_i(\mathbf{x})\mathbf{u}_i(\mathbf{x})$. There are many kinds of compactly supported functions, such as MLS shape functions, finite element shape functions, Shepard function, etc. In this paper, we use $\omega_i(\mathbf{x})$ as below:

$$\omega_i(\mathbf{x}) = \begin{cases} \kappa_i(\mathbf{x}) & \mathbf{x} \in \Omega_1 \cap \Omega_2\ , \\ 1 & \mathbf{x} \in \Omega_i \setminus (\Omega_1 \cap \Omega_2)\ , \\ 0 & \mathbf{x} \in \Omega \setminus \Omega_i\ . \end{cases}$$

where $\kappa_i(\mathbf{x})$ satisfies： $\sum_{i=1}^{2} \kappa_i(\mathbf{x}), \mathbf{x} \in \Omega_1 \cap \Omega_2$.

**Numerical experiments**

We consider the problem of cantilever beam, the left end is fixed, and an external force $P$ is applied at the right end, this will cause beam bent downward and deformed. Here, the beam length $L = 12m$ , The beam width $D = 2m$ , pressure at the end $P = 6N$ , Young's modulus $E = 10^4 Pa$ , Poisson's ratio $\mu = 1/3$ , rotational inertia $I = D^3/12$ . This problem has an analytical solution [4, 5].

(1) Standard RBF-PS method. $11 \times 25$ uniform collocation points are chosen as Fig.1, (including the inner and boundary points). And the basis function is the Gaussian shape function $\Phi(r) = e^{-(\varepsilon r)^2}$ , where $\varepsilon$ is 0.15. Fig.2 shows the curved figures obtained by RBF-PS and analytical solution, it reveals that the solution via RBF-PS method completely coincides with the analytical solution.

The results are sensitive to the choose of parameter, Fig3 ,Fig 4 respectively show parameter - error figure based on Gaussian shape function and MQ shape function( $\Phi(r) = \sqrt{r^2 + c^2}$ ), which intuitively illustrate the impact of the parameter on the result.

(2) RBF-PS and DDM method. Fix a mesh step $h$ , then two sub-regions are $\Omega_1 = [0, L/2 + 2h] \times [-D/2, D/2]$, $\Omega_2 = [L/2 - 2h, L] \times [-D/2, D/2]$. Here we take $h = L/16$, Fig.5 shows the nodes distribution in two sub-regions, as we can see, the middle part is overlapping region.

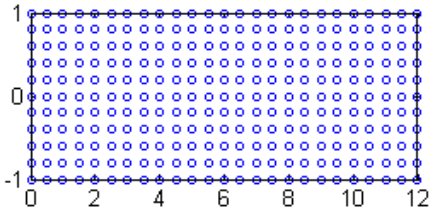


Fig. 1 Node distribution

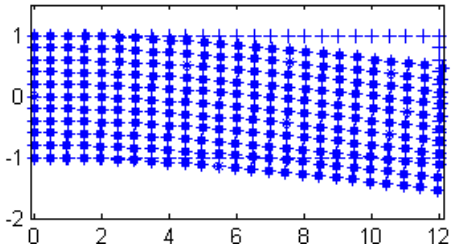


Fig. 2 Curved figures by RBF-PS and analytical solution (' o 'denotes RBF-PS solution, '* ' denotes analytical solution)

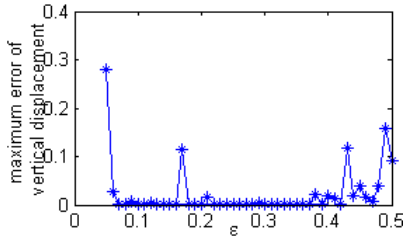


Fig.3 Parameter-maximum error using Gaussian-based PS approach

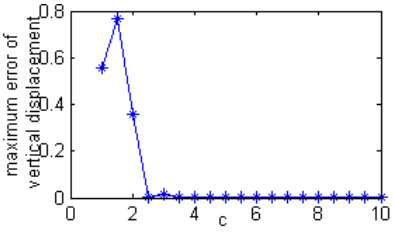


Fig.4 Parameter-maximum error using MQ-based PS approach

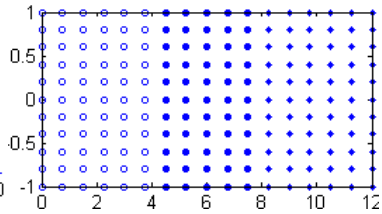

Fig. 5 Nodes distribution

MQ shape function ($c=3.1$) is selected in the two sub-regions, and set $\kappa_i(x)=0.5,\ i=1,2$. When the number of iterations is 129, displacement error has reached $10^{-4}$. As shown in Table1, we can find out that PS-DDM method ($c=3.1$) obtains more precise result than Standard RBF-PS method ($c=3.1$), while it has almost the same accuracy as Standard RBF-PS method under the optimal parameter.

Table 1 Results via coupling method of PS-DDM and Standard RBF-PS method

| | Max displacement error in $\Omega_1$ | Max displacement error in $\Omega_2$ | Max displacement error in $\Omega$ | RMS displacement error in $\Omega$ | Time(s) |
|---|---|---|---|---|---|
| Coupling method | 8.541 (-5) | 2.403 (-3) | 2.403 (-3) | 5.359(-4) | 1.175 |
| Standard RBF-PS (c=3.1) | | | 1.874 (-2) | 8.220 (-3) | 0.338 |
| Standard RBF-PS (c=5 optimal | | | 5.835 (-4) | 3.564 (-4) | 0.515 |

Fig. 6-8 show the results of displacement, normal stress and shear stress. Little difference can be seen from the results via PS-DDM method ($c=3.1$) and RBF-PS method ($c=5.0$). And as the boundary condition in $\Omega_1$ is a Dirichlet-type, while it is a mixed type in $\Omega_2$ (artificial boundary condition is the Dirichlet, the rest boundary condition is Riemann), the graphs reveal that $\Omega_1$ performs a better approximation effect than $\Omega_2$.

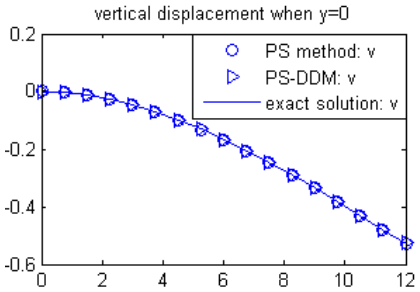


Fig. 6 Vertical displacement on the x-axis

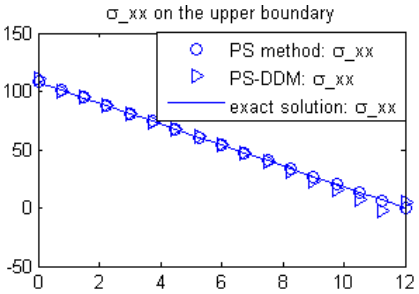


Fig. 7 Normal stress on upper boundary

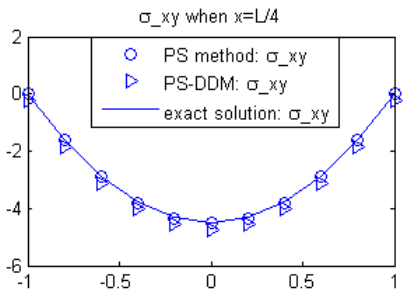


Fig. 8 Shear stress when x=L/4

**References**

[1]. B. F.Smith, Domain decomposition methods for partial differential equations, Parallel Numerical Algorithms, 4 (1997)225-243.
[2]. L.N. Trefethen, Spectral Methods in MATLAB, SIAM , Philadelphia, 2000.
[3]. G.E. Fasshauer, Meshfree Approximation Methods with MATLAB,World Scientific Publishing, Singapore,2007.
[4]. X. Zhang, Y. Liu, Meshfree Method,Tsinghua University Press,Peking, 2005.
[5]. X. Zhang, W. Hu, X.F. Fan and N.W. Lu, Meshless weighted least-square method. Acta Mechanica Sinica, 35(2003):425-431.

*Applied Mechanics and Materials Vols. 580-583 (2014) pp 3075-3078*
*© (2014) Trans Tech Publications, Switzerland*
*doi:10.4028/www.scientific.net/AMM.580-583.3075*

# The foundation of Nonlinear finite element model

Bing Wang [1, a], Xiao Liu[1, b], Baidong Zhao [1,c]

[1]School of Architectural and Civil Engineering, Shenyang University, Shenyang, 110044, China

[a]liuxiao19740701@sina.com, [b]489298344@qq.com , [c]283292935@qq.com

**Keywords:** Finite element mode, Constitutive relation, Steel tube filled with steel reinforced concrete column.

**Abstract.** This paper introduces the process of the nonlinear finite element model which is established by using ABAQUS software, and introduces the characteristics of ABAQUS software, meanwhile, lists the constitutive relation of steel pipe, steel and concrete, finally introduces some experimental model.

## The characteristics of ABAQUS

ABAQUS is applicable to all sectors of the large general-purpose finite element analysis software on the most advanced international, can effectively solve the technical problems associated with the calculation, powerful computing performance and extensive analog performance, has the rich of unit base, material model and the analysis process capacity . Both linear elastic analysis of simple problems, or include a variety of different materials, to complex mechanical and thermal loading process, nonlinear combinatorial problem and the change of contact conditions; whether the analysis of static and quasi-static problems, or stable and dynamic problem; whether explicit or implicit solution, ABAQUS is used to calculate the analysis and obtain satisfactory results[1].

## The constitutive relation of steel pipe

For steel commonly used Q235, Q345 and Q390 in the architectural engineering, the relationship of stress-strain is divided into the five stage model :elastic, elastic-plastic, plastic, plastic flow, strengthening and two plastic flow[2] , (see figure 1).

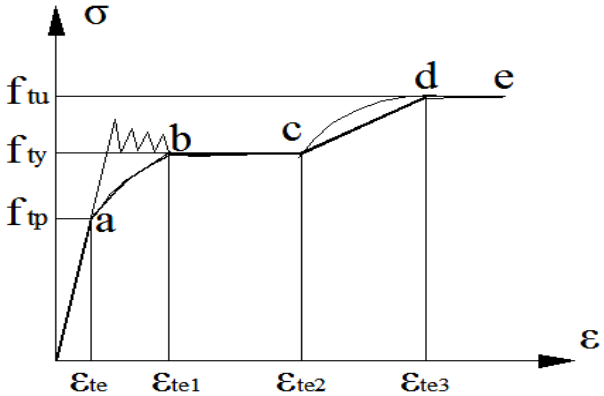


Fig.1 The constitutive relation of steel tube

At the same time, take the following three assumption:

(1)Strengthen stage as a straight line;

(2)Strength reaches the point of D, the steel into the two plastic flow;

(3)Neglecting the radial relative small stress.

According to figure 1 steel stress-strain constitutive relationship can be in accordance with the five stage simplified, the mathematical expressions is:

$$\sigma=\begin{cases} E_t\varepsilon_t & (\varepsilon_t\le\varepsilon_{te}) \\ -A\varepsilon_t^2+B\varepsilon_t+C & (\varepsilon_{te}\le\varepsilon_t\le\varepsilon_{te1}) \\ f_{ty} & (\varepsilon_{te1}\le\varepsilon_t\le\varepsilon_{te2}) \\ f_{ty}\left[1+0.6\dfrac{\varepsilon_t-\varepsilon_{e2}}{\varepsilon_{e3}-\varepsilon_{e2}}\right] & (\varepsilon_{te2}\le\varepsilon_t\le\varepsilon_{te3}) \\ 1.6f_{ty} & (\varepsilon_t>\varepsilon_{te3}) \end{cases}$$

In the formula:

$A=\dfrac{0.2f_{ty}}{(\varepsilon_{te1}-\varepsilon_t)^2}$； $B=2A\varepsilon_{te1}$； $C=0.8f_{ty}+A\varepsilon_{te}^2-B\varepsilon_{te}$； $\varepsilon_{te}=0.8f_{ty}/E_t$； $\varepsilon_{te1}=1.5\varepsilon_{te}$； $\varepsilon_{te2}=10\varepsilon_{te}$ ； $\varepsilon_{te3}=100\varepsilon_{te}$； $E_t$ −The elastic modulus of steel pipe； $f_{ty}$ −The yield strength of pipe； $f_{tu}$ −The ultimate strength of steel pipe.

**The constitutive relation of the core concrete**

The core concrete in steel tube has a lot of core concrete stress - strain relationship model , the Tsinghua University professor Han Linhai proposed the stress - strain model [4]is very widely used, it presents the curve equation of uniform rising section and the descending section of the equation, and use less parameters, many researchers use it.

The test results of axial compression short column of the research group of Wang Lianguang[5], in the steel pipe concrete basis for the stress - strain model[6], considering the influence of steel on the ductility of composite columns, was modified, the specific expression:

$$\sigma_c=f_{cc}(2x-x^2) \qquad (x\le1)$$

$$\sigma_c=\begin{cases} f_{cc}\left[1+q(x^a-1)\right] & (\theta\ge1.12) \\ f_{cc}\left(\dfrac{x}{\beta(x-1)^2+x}\right) & (\theta<1.12) \end{cases} \qquad (x>1)$$

In the formula:

$\sigma_c$ −Concrete compressive strain corresponded by the stress of $\varepsilon_c$; $\varepsilon_c$ −Concrete axial compressive strain; $f_{cc}$ −The compressive strength of concrete confined ;

$x=\dfrac{\varepsilon}{\varepsilon_0}$ ， $\varepsilon_0=\varepsilon_{cc}+[1400+800\left(\dfrac{f_c^{'}}{24}-1\right)](\theta+0.37\rho)^{0.2}$ $(\mu\varepsilon)$ $\varepsilon_{cc}$ −corresponding concrete compressive strain by $f_{cc}$ ； $\varepsilon_{cc}=1300+12.5f_c^{'}$ $(\mu\varepsilon)$ ； $\theta=\dfrac{A_tf_{ty}}{A_cf_{ck}}$ −Confinement index; $\rho=\dfrac{A_sf_{sy}}{A_cf_{ck}}$ −Steel index; $A_t, A_s, A_c$ −the area of Steel pipe, steel and concrete ; $f_{ty}, f_{sy}, f_{ck}$ −the yield strength of pipe, axial compressive strength standard value of concrete;

$\alpha=0.1\theta-0.3\rho$； $\beta=(2.36\times10^{-5})^{[0.25+(\theta-0.5)^7+(\rho-0.2)^5]}f_c^{'2}\times3.51\times10^{-4}$； $q=\dfrac{\theta^{0.545}+\rho^{0.3}}{1+\theta+2\rho}$

**The finite element modeling of steel tube filled with steel reinforced concrete column**

According to the requirement of stress components, steel pipe, steel and core concrete, end plate and the establishment of the corresponding model and assembled in the ABAUQS finite element analysis software.

In the component module, the steel tube is defined as the 3D variability shell, define the core concrete and the built-in steel for 3D deformable solid, definition of end plate for the three-dimensional analytical rigid body, created using the ABAQUS drawing function to finish each part. Because of the specimen is small,select the whole component to calculate.

In the feature modules, based on the determination of each material constitutive relation, respectively, to steel, concrete and beam core material to give the corresponding cross-section and assign sections, of which the core concrete section type end plate and beam for uniform entity , uniform steel casing, casing pipe default reference plane for the neutral surface thickness direction, and in order to meet the accuracy requirements in the thickness direction of the shell using 9 points Simpson integration points.

In the assembly module, create the various components of the entity, types are non independent entities, and the positioning tool to complete the assembly of the whole model of mobile. All member entities and their effect by the completion of the assembly as shown in figure 3.

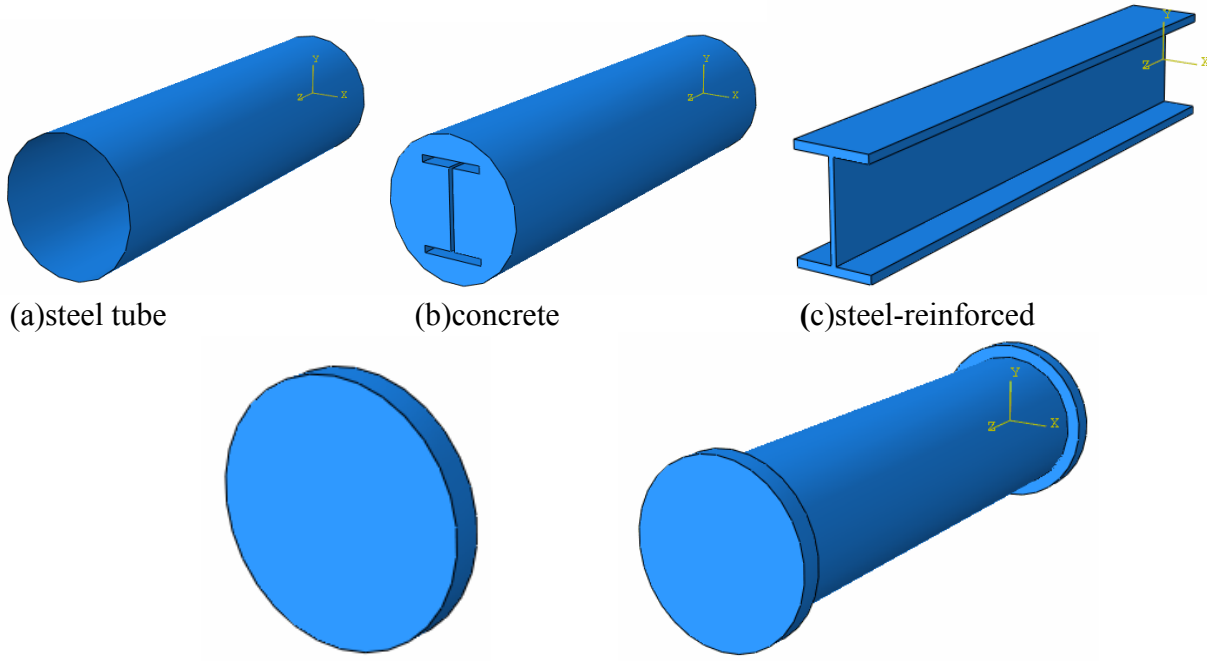

(a)steel tube (b)concrete (c)steel-reinforced

(d) end plate (e)Model of the whole model

Fig.3 Model component diagram

**Acknowledgement**

It is a project supported by National Science Foundation (51308347) .

It is a project supported by colleges and universities in Liaoning Province Outstanding Young Scholar growth plans (21503040399).

**References**

[1] Yiping Shi,Yurong Zhou.ABAQUS finite element analysis examples [M]. Beijing Machinery Industry Press, 2006.

[2] Zhong Tao,Qing Yu.The new combined structure column [M]. Beijing: Science Press, 2006: 40 - 45.

[3] Meichun Zhu. Steel reinforced self compacting high-strength mechanics of concrete filled square steel tube column properties of [D]. Dalian: Dalian University of Technology School of civil engineering, 2003.

[4] Dazhou Zhao.Steel fiber reinforced properties, mechanical composite column of high strength concrete [D] Dalian, Dalian University of Technology, 2003.

[5] Linhai Han,Youfu Yang.Technology of modern steel pipe concrete structure [M]. Beijing: Chinese Architecture Industry Press, 2004

[6] Bing Wang,Lianguang Wang,Xiao Liu. Steel tube filled with steel reinforced concrete short columns under axial compression stress analysis of the whole process[J]. Journal of Shenyang Construction University (Natural science edition), 2009

*Applied Mechanics and Materials Vols. 580-583 (2014) pp 3079-3082*
*© (2014) Trans Tech Publications, Switzerland*
*doi:10.4028/www.scientific.net/AMM.580-583.3079*

# Properties and moving time average for Lévy walks with power-law waiting-time distributions

Kaiying Deng[1,2,a], Jingwei Deng[1,b*]

[1]College of Mathematics and Computer Science Northwest University for Nationalities

Lanzhou 730124, China

[2] School of Computer Science and Information Technology &School of Geographical Science,

Northeast Normal University, Changchun 130024, China

[a]dengky0420@163.com, [b*]djw_1205@163.com

**Keywords:** Lévy walks; aging phenomena; moving time average; power-law waiting-time distribution

**Abstract.** Lévy walks are a natural model for the description of sub-ballistic, superdiffusive motion. The waiting times and jump lengths of Lévy walks are coupled in the form $\psi(x,t) \propto \frac{1}{2}\delta(|x|-vt)\psi(t)$. The $\delta$-coupling introduces a time cost for each jump in the form of the generalized velocity $v$, such that long jumps get penalized by a higher time cost. In this paper, we firstly investigate the properties of Lévy walks with power-law waiting-time distributions; then discuss its moving time average.

## Introduction

Lévy walks were originally introduced by Klafter and Shlesinger within the framework of the continuous time random walk model[1]. One advantage of Lévy walks is that they allow for a continuous transition from diffusive (Brownian) random walks, through superdiffusion, to ballistic (straight-line) motion. Lévy walk thus provides an important conceptual link between these modes of movement. Another important feature of Lévy walks is that they are scale-free, meaning that they do not have any characteristic spatial scale, and exhibit the same patterns regardless of the range over which they are viewed. In particular, Magziarz et al.[2] showed how to phrase Lévy walks in terms of a dual subordination method based on the Langevin equation. The studies of Viswanathan et al.[3-4] sparked an explosion of interest in Lévy walk and the twin streams of empirical and theoretical research continued in subsequent years.

Aging behavior is found in complex dynamical systems like spin glasses, glasses, and polymers[5]. Aging in diffusion processes yields an interesting insightful perspective on dynamics in disordered medium, and more generally is used as a tool to probe complex systems such as blinking quantum dots, spin glasses, Anderson insulators, and colloidal suspensions.

In this paper, we further analyze the various properties of Lévy walk with power-law waiting-time distribution; and discuss their moving time averages.

## Properties

We are interested in processes evolving in continuous physical time. In Lévy walk, a random walker jumps from one site to another, the waiting times probability density function follows asymptotically a power law $\psi(t) \propto t^{-1-\alpha}$, with $0<\alpha<2$. It takes a flight time proportional to the flight length. Lévy walk is a natural model for the description of super-diffusive motion, in which the waiting times and jump lengths are coupled in the form[6],

$$\psi(x,t) \propto \frac{1}{2}\delta(|x|-vt)\psi(t) \quad (1)$$

The temporal and spatial variables of Lévy walks are strongly correlated, where $\psi(t) \propto t^{-1-\alpha}$ is the so-called waiting time distribution. The spatiotemporal coupling $\delta(|x|-vt)$ ensures the existence of a finite velocity of propagation and existence of the second moment $<x^2(t)>$.

The aging Lévy walk describes the following process: a particle is trapped on the origin for time $t_1$; it then jumps to $r_1$; the particle is then trapped on $r_1$ for time $t_2$; and then it jumps to a new location; the process is then renewed. Thus the aging Lévy walk process is characterized by a set of waiting time $\{r_1,\cdots,r_n,\cdots\}$. The time elapsing between start of observation at $t=0$, and the first jump event is denoted by $t_1$. Here we denote the probability density function of the first waiting time $t_1$ with $\psi(t_1,t_a)$. In aging Lévy walk the random walker during the time interval $\Delta t$ starting not at $t=0$ but at $t=t_a>0$, there $\psi(t_1,t_a)$ depends on age of the process $t_a$. The waiting times $\{t_n\}$ with $n>1$ are independent and identically distributed with a common probability density $\psi(t)$.

In order to address the dependence on the aging time, we have to know how long the walker has to wait from its initiation time until making its first step after the observation started. When the aging time was assumed to be zero, and for this case $\psi(t_1,t_a)=\psi(t)$.

We can get two types of behaviors for $\psi(t_1,t_a)$ .The first is the average waiting time $<t>=\int_0^\infty t\psi(t)dt$ is finite; and then in the long aging time limit one obtains $\lim_{t_a\to\infty}\psi(t_1,t_a)=\dfrac{\int_0^{t_1}\psi(t)dt}{<t>}$. The second case corresponding to a power law waiting time probability density function $\psi(t)\propto t^{-1-\alpha}$, with $0<\alpha<1$. When $t$ is long, the Laplace transform of such a distribution is given by $\psi(s)\sim 1-\beta s^{\alpha}$, where $s$ is small, and $\beta$ is a positive parameter. According to

$$\psi(t_1,t_a)=\int_0^{t_a}k(t')\psi(t_a-t'+t)dt' \quad , \tag{2}$$

where $k(t')=\sum_{n=0}^{\infty}\psi_n(t)$. The Laplace transform of the shifted waiting-time probability density function $\psi(y+t)$ in $y$ reads[7]:

$$\int_0^\infty\psi(y+t)e^{-uy}dy=e^{ut}[\psi(u)-\int_0^t\psi(y)e^{-uy}dy] \tag{3}$$

therefore,

$$\begin{aligned}\psi(t_1,u)&=L\{\psi(t_1,t_a);u\}\\&=\frac{1}{1-\psi}e^{ut}[\psi(u)-\int_0^t\psi(y)e^{-uy}dy]\,.\end{aligned} \tag{4}$$

Then performing the inverse Laplace transform to obtain $\psi(t_1,t_a)$, we rewrite Eq. (4) as

$$\begin{aligned}\psi(t_1,s)&=\frac{1}{1-\psi(s)}e^{st}\int_t^\infty e^{-sy}\psi(y)dy\\&=\frac{\alpha e^{st}}{\Gamma(1-\alpha)}\Gamma(-\alpha,st)\,.\end{aligned} \tag{5}$$

Now, according to the properties of Gamma function, we can take an inverse Laplace transform of Eq. (5) with respect to $s$,

$$\psi(t_1,t_a)=\frac{\sin(\pi\alpha)}{\pi}\cdot\frac{t_a^{\alpha}}{t_1^{\alpha}(t_1+t_a)} \tag{6}$$

For large $t_a$ the forward waiting-time probability density function $\psi(t_1,t_a)$ shows two distinct types of behavior: For $t>t_a$ its decay follows $\psi(t)\propto t^{-1-\alpha}$, which is a pattern of the decay of $\psi(t)$; while for $t<t_a$ the decays as $t^{-\alpha}$, which is quite a slow delay.

**Moving time average**

In order to distinguish between systems with normal and anomalous diffusion, one typically looks at the mean squared displacement (MSD) of particles. Concentrating on the one-dimensional case, the MSD for regular diffusion is given by $< x^2(t) >= 2Kt$, where $K$ is the diffusion coefficient. For anomalous diffusion, the MSD is $< x^2(t) >= \frac{2K_\alpha}{\Gamma(1+\alpha)} t^\alpha$, where $\alpha \neq 1$ and $K_\alpha$ being the anomalous diffusion coefficient. System with $0 < \alpha < 1$ displays subdiffusion, which values of $\alpha > 1$ correspond to superdiffusion[8-9].

We use the Lévy walk to describe the motion of particles. In this model, the MSD at time $t$ defined as the ensemble average over many realizations of the process behaves as $< x^2(t) >_{ens} \propto t^\alpha$, follows a superdiffusive pattern[8-9].

We can analyze the time series $x(t)$ of the particle trajectory and determine the time averaged MSD:

$$< \Delta x^2(t) >_T = \frac{1}{T-t} \int_0^{T-t} (x(t+\tau) - x(\tau))^2 \, d\tau . \tag{7}$$

For normal diffusion, $< \Delta x^2(t) >_{ens} = < \Delta x^2(t) >_T$ provide that $T$ is large enough, which can be referred to as an ergodic property. The behavior of the double (temporal and ensemble) average of the data as given by $<< x^2(t)_T >>_{ens}$.

Note that if the variance (MSD $\sigma^2 = < l^2 >$) of a step displacement in a symmetric random walk exist, the MSD after $n$ steps behave as

$$< x^2(t) >= < l^2 >< n(t) > . \tag{8}$$

For the symmetric aging Lévy walk, we get

$$< x^2(\Delta t) >= < l^2 >< n(\Delta t, t_a) > , \tag{9}$$

where $n(\Delta t, t_a)$ is the number of steps done between $t_a$ and $t_a + \Delta t$.

$$<< \Delta x^2(t) >_T >_{ens} = << \Delta x^2(t) >_{ens} >_T = \frac{1}{T-t} \int_0^{T-t} < (x(t+\tau) - x(\tau))^2 >_{ens} \, d\tau$$

$$= K_\alpha \frac{t}{T^{1-\alpha}} . \tag{10}$$

where $K_\alpha = < l^2 > / \beta$ is the generalized diffusion coefficient. We see that the effective diffusion coefficient depends explicitly on the averaging time $T$. Lévy walks have a mean squared displacement $< x^2(n) > \propto n^r$ with $1 < r < 2$, where $r = 1$ corresponds to normal Brownian diffusion and $r = 2$ is ballistic motion. To calculate the double average

$$< x^2(n) > \propto << (n(t+\Delta t) - n(t))^r >_{ens} >_T . \tag{11}$$

We proceed as follows. For given $t$ the ensemble average corresponds to the average of $< n^r(\Delta t; t_a) >$ of the corresponding power of the number of steps of Lévy walk aged up to the time $t_a$. Let us denote by $t_f$ the forward waiting time for the first step of a Lévy walk aged up to the time $t_a$. The number of steps $n$ entering the average $< n^r(\Delta t; t_a) >_{ens}$ is the number of steps done by Lévy walk during the time $t' = \Delta t - t_f$ between the first step in the interval between $t_a$ and $t_a + \Delta t$.

$$< n^r(\Delta t; t_a) >_{ens} = \int_0^{\Delta t} < n^r(\Delta t - t_f) > \psi_1(t_f; t_a) dt_f . \tag{12}$$

where $\psi_1(t_f; t_a)$ corresponds to $\psi(t_1; t_a)$ is given by Eq.(6), and then

$$< n^r(t) > \approx n^{-\frac{1}{\alpha}-1+r} L_\alpha \left( \frac{t}{\tau n^{\frac{1}{\alpha}}} \right) dn = \left( \frac{t}{\tau} \right)^{\alpha r} \frac{\Gamma(1-r)}{\Gamma(1-\alpha r)} . \tag{13}$$

Since the behavior for $\Delta t << t_a$ will be relevant for what follows, we can use the approximation $\psi_1(t_f;t_a)=\frac{\sin(\pi\alpha)}{\pi}\cdot\frac{t_a^{\alpha-1}}{t_f^{\alpha}}$. Thus

$$< n^r(\Delta t;t_a) >_{ens} \approx const\cdot\frac{t_a^{\alpha-1}}{\tau^{\alpha r}}\Delta t^{1-\alpha(1-r)}, \quad (14)$$

Aging Lévy walk describes a Lévy walk process which begun at time $t_a$. When $t_a$ becomes long we show that a type of an equilibrium process emerges which still depends on time scale $t_a$. Thus generally Lévy walk and aging Lévy walk exhibit different behaviors.

## Summary

As expected from the above theoretical studies of Lévy walks, we further notice that Lévy walks are random processes with an underlying spatiotemporal coupling. This coupling penalizes long jumps, and therefore Lévy walks give a proper stochastic description for a particle's motion with broad jump length distribution. In this work, we study the properties of Lévy walks with the power-law waiting-time distribution; then discuss the moving time average for aging Lévy walks. Lévy walks have a mean squared displacement $< x^2(t) >\sim t^{\alpha}$ with $1<\alpha<2$, where $\alpha=1$ corresponds to normal Brownian diffusion and $\alpha=2$ is ballistic motion.

## Acknowledgements

This work was financially supported by the Fundamental Research Funds for the Central Universities (Northwest University for Nationalities) under Grant No. 31920130007, the Humanities and Social Sciences Youth Projects of the Ministry of Education of P R China under Grant No. 12YJCZH027 and No. 13YJCZH029, and the Humanities and Social Sciences Planning Projects of the Ministry of Education of P R China under Grant No. 11YJAZH053.

## References

[1] M F Shlesinger, J Klafter, Y M Wong. Random walks with infinite spatial and temporal moments [J]. Journal of Statistical Physics, 1982, 27(3): 499-512.

[2] M Magdziarz, R Metzler, W Szczotka, et al. Correlated continuous-time random walks—scaling limits and Langevin picture[J]. Journal of Statistical Mechanics: Theory and Experiment, 2012, 2012(04): P04010.

[3] G M Viswanathan, V Afanasyev, S V Buldyrev, E J Murphy, P A Prince, H E Stanley, Lévy flight search patterns of wandering albatrosses [J]. Nature, 1996, 381: 413-415.

[4] G M Viswanathan, S V Buldyrev, S Havlin, M G E da Luz , E P Raposo, H E Stanley, Optimizing the success of random searches [J]. Nature, 1999, 401: 911-914.

[5] L C E Struik. Physical aging in amorphous polymers and other materials [M]. Amsterdam: Elsevier, 1978.

[6] J Klafter, I M Sokolov. First steps in random walks: from tools to applications [M]. OUP Oxford, 2011, P114.

[7] J Klafter, I M Sokolov. First steps in random walks: from tools to applications [M]. OUP Oxford, 2011, P58.

[8] A Lubelski, I M Sokolov, J Klafter. Nonergodicity mimics inhomogeneity in single particle tracking [J]. Physical review letters, 2008, 100(25): 250602.

[9] I M Sokolov, J Klafter, A Blumen. Fractional kinetics [J]. Physics Today, 2002, 55(11): 48.

*Applied Mechanics and Materials Vols. 580-583 (2014) pp 3083-3088*
*© (2014) Trans Tech Publications, Switzerland*
*doi:10.4028/www.scientific.net/AMM.580-583.3083*

# The Scattering of Circular Cylindrical Cavity with Time-Harmonic SH Waves in Infinite Strip Region

Liming CAI[1,a], Hui QI[1,b], Xiangnan PAN[1,c]

[1]College of Aerospace and Civil Engineering, Harbin Engineering University, Harbin 150001, China

[a]cailiming@hrbeu.edu.cn, [b]qihui205@sina.com, [c]panxiangnan@hrbeu.edu.cn

**Keywords:** SH waves; scattering; circular cylindrical cavity; strip region; dynamic stress concentrations

**Abstract.** The scattering of time harmonic SH waves by arbitrary positions of circular cylindrical cavity is studied in continuous, homogeneous, isotropic, elastic strip region. In this paper, the completely analytical expression of total wave field is explicitly presented and the dynamic stress distribution is symbolically visualized in the strip region. The total wave field is divided into four sub wave fields, incident wave field and scattering wave field by the upper bound, the lower bound and the cylindrical bound, on big arc supposition. Specific wave functions are employed for each wave field expansion in series, such as circular cylindrical functions, respectively. Corresponding infinite linear algebraic equations are constructed by means of solving coefficients of Fourier series expansion on each sub wave field. Coefficients of cylindrical function expansion of each sub wave field are determined by truncated equations, which are reduced number of coefficients on pre-given computational accuracy. Numerical results graphically describe the dynamic stress concentration factor around the circumference of the cavity and the normalized dynamic stress along the cross section directly above the cavity.

## Introduction

The determination of dynamic stress distribution is interesting and exciting problem in the strip region with circular cylindrical cavity, which is disturbed by incident elastic waves. In this paper, the completely analytical expression of this problem has been presented under steady state time harmonic SH waves incident. The dynamic stress distribution is symbolically displayed as the dynamic stress concentration factor around the cylindrical bound of the cavity and the normalized dynamic stress along the cross section directly above the cavity.

Since the theory of elastic waves was constructed by Lamb and Love, the scattering by inclusion or cavity have been widely researched in infinite medium [1]. Y.H. Pao and C.C Mow systematically expounded the diffraction of elastic waves by circular, elliptical, parabolic cylinder and spherical inclusion in infinite medium [2]. D.K. Liu et al originally invented the method of complex functions to dynamic stress analysis [3]. Anti-plane shear motion is the simplest model of elastic waves, SH waves scattering problem has relative mature theories. However, there are many unsolved boundary value problems, only fewer papers were given to the scattering problem by cylindrical cavity in strip region. S. Itou and U. Zakout, N. Akkas obtained some valuable results about transient response of cavity in infinite strip [4, 5]. Recently, Hui Qi et al calculated the scattering of circular inclusion with SH waveguides in infinite strip [6]. Hui Qi and Jie Yang et al researched scattering of SH waves by circular cylindrical inclusion near interface in bi-material half space and some near interfacial problems in half space [7, 8].

In this paper, we divide total wave field into four sub wave fields, incident wave field, scattering wave field by the upper bound, the lower bound and the cylindrical bound on a big arc supposition in the strip region. Four sub wave fields are expressed as specific wave function series expansion, respectively. The boundary value problems have been solved with converted infinite linear algebraic equations by using the effective truncation. Meanwhile we obtained coefficients of wave function expansion on four sub wave fields, separately. The completely analytical expression of total wave field has been presented in the strip region, simultaneously.

## Theoretical background

The simplest model of the scattering problems of elastic waves is SH wave incident, and it only has anti-plane displacement along axis *z* and the displacement is barely a function of *x* and *y*, when the medium impacted by SH waves. The simplest model of the scattering problems of SH waves is time-harmonic steady state SH wave incident, and it has separable variables about time and space.

In this paper, the scattering problem of circular cylindrical cavity in infinite strip region has been investigated with time-harmonic steady state SH wave incident. As Fig.1 shows, one circular cylindrical cavity is located in the homogeneous, isotropic infinite strip region, in which is propagating time-harmonic steady state SH waves.

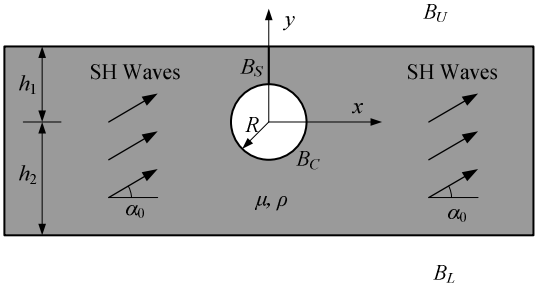


**Fig.1.** The scattering of cylindrical cavity with SH waves in strip region.

The displacement wave function of the total wave field is presented as expression (1) in the strip region. It can be divided into a product of a spatial variable (displacement function) and a time variable (harmonic function which angular frequency is notated as $\omega$). Displacement function $w(x, y)$ is satisfied governing equation (2) in the rectangular coordinate system; $w(r, \theta)$ is satisfied governing equation (3) in the polar coordinate system. Wherein, $k=\omega/c_s$, $c_s^2=\mu/\rho$, $k$ notates the wave number of steady state SH waves, $c_s$ notates phase velocity of shear waves in the strip region.

$$w = w(x, y, t) = w(x, y)e^{-i\omega t} = w(r, \theta, t) = w(r, \theta)e^{-i\omega t} \tag{1}$$

$$\frac{\partial^2 w}{\partial x^2} + \frac{\partial^2 w}{\partial y^2} + k^2 w = 0 \tag{2}$$

$$\frac{\partial^2 w}{\partial r^2} + \frac{1}{r}\frac{\partial w}{\partial r} + \frac{1}{r^2}\frac{\partial^2 w}{\partial \theta^2} + k^2 w = 0 \tag{3}$$

## Wave fields analytical expressions

In this paper, the total wave field is divided as incident wave field and scattering wave field on principle of superposition. We introduce big arc supposition for decomposition of the scattering wave field.

As Fig.2 shows, a straight line is seen as infinite radius arc. In the coordinate (*x, y*), the upper bound of the strip region is treated as infinite radius arc, which convex to the negative direction *y*. In a similar way, the lower bound of the strip region is treated as infinite radius arc, which convex

to the positive direction *y*. Where upon, two bound of the infinite strip region are idealize as a pair of symmetrical infinite radius arcs, so the infinite plane strip is converted to infinite concave strip. This supposition is accurate enough to theoretical researches and engineering applications, if only the radius of the big arc is greater than the length of the infinite strip region by an order of magnitude. Therefore, the total wave field consists of four sub wave fields, incident wave field which is directly disturbed by incident time-harmonic steady state SH waves, and scattering wave fields by the upper bound $B_U$, the lower bound $B_L$, and the circular cylindrical cavity bound $B_C$, respectively. In this paper, $w$ notate the total wave field, $w^{(i)}$ notate the incident wave field, and $w^{(S)}$ notate the resultant scattering wave field, $w^{(U)}$, $w^{(L)}$, $w^{(C)}$ notate scattering wave by $B_U$, $B_L$, and $B_C$, respectively, as expression (4).

$$\begin{aligned} w &= w^{(i)} + w^{(s)} \\ w^{(s)} &= w^{(U)} + w^{(L)} + w^{(C)} \end{aligned} \tag{4}$$

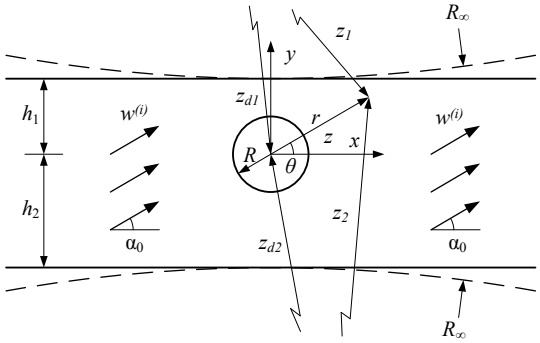


**Fig.2.** The big arc supposition.

On complex function description, the incident wave field $w^{(i)}$ is presented as expression (5), Wherein $w_0$ notate the amplitude of the incident SH waves, and $\alpha_0$ notate the angle of incidence, from direction *x* to incident direction.

$$w^{(i)}(\vec{r},t) = w^{(i)}\left(z,\bar{z}\right)e^{-i\omega t} = w_0 \exp\left[\frac{ik_1}{2}\left(z\cdot e^{-i\alpha_0} + \bar{z}\cdot e^{i\alpha_0}\right)\right]e^{-i\omega t} \tag{5}$$

The scattering wave field consists of three sub wave fields, by the upper bound $B_U$, the lower bound $B_L$, and the circular cylindrical cavity bound $B_C$, which is notated as $w^{(S)}$, $w^{(U)}$, $w^{(L)}$, $w^{(C)}$ in the strip region. On complex function description, $w^{(C)}$ is presented as expression (6), where $A_n$ is undetermined coefficient, which is the coefficient of scattering wave on Fourier-Hankel cylindrical function series expansion by the circular cavity bound $B_C$, $H_n^{(1)}(\cdot)$ is the first kind Hankel function of *n* order. $H_n^{(1)}(\cdot)$ *exp*(-*iωt*), the product of $H_n^{(1)}(\cdot)$ and time harmonic function *exp*(-*iωt*), is represented as circular cylindrical wave which is propagating from origin to infinity, mathematically, it is satisfied Sommerfeld radiation condition.

$$w^{(C)}(\vec{r},t) = w^{(C)}\left(z,\bar{z}\right)e^{-i\omega t} = w_0\sum_{n=-\infty}^{+\infty} A_n H_n^{(1)}\left(k|z|\right)\left(\frac{z}{|z|}\right)^n e^{-i\omega t} \tag{6}$$

On the big arc supposition, we construct two moved right handed circular cylindrical coordinate systems, whose polar point is placed in the center of the upper bound $B_U$ and the lower bound $B_L$, and polar axis is paralleled with positive axis *x*, respectively. Meanwhile, two corresponding complex plane are produced by established polar coordinate systems as expression (7).

$$z_1 = z_{d1} + z = r_1 e^{i\theta_1}, z_2 = z_{d2} + z = r_2 e^{i\theta_2} \tag{7}$$

On complex function description, $w^{(U)}$ is presented as expression (8), where $B_n$ is undetermined coefficient, which is the coefficient of scattering wave on Fourier-Hankel circular cylindrical function series expansion by the upper bound $B_U$. Correspondingly, $w^{(L)}$ is presented as expression (9), where $C_n$ is undetermined coefficient, which is the coefficient of scattering wave on Fourier-Hankel circular cylindrical function series expansion by the lower bound $B_L$.

$$w^{(U)}(\vec{r_1},t)=w^{(U)}\left(z_1,\overline{z_1}\right)e^{-i\omega t}=w_0\sum_{n=-\infty}^{+\infty}B_nH_n^{(1)}\left(k\left|z_1\right|\right)\left(\frac{z_1}{\left|z_1\right|}\right)^n e^{-i\omega t} \tag{8}$$

$$w^{(L)}(\vec{r_2},t)=w^{(L)}\left(z_2,\overline{z_2}\right)e^{-i\omega t}=w_0\sum_{n=-\infty}^{+\infty}C_nH_n^{(1)}\left(k\left|z_2\right|\right)\left(\frac{z_2}{\left|z_2\right|}\right)^n e^{-i\omega t} \tag{9}$$

## Calculations and discussions

In this paper, three boundary conditions have been considered, which comprise three stress free surfaces on the upper bound $B_U$, the lower bound $B_L$, and the circular cylindrical cavity bound $B_C$. It is presented as Eqs. (10).

$$\begin{aligned}&\tau_{yz}=\tau_{yz}^{(i)}+\tau_{yz}^{(C)}+\tau_{yz}^{(U)}+\tau_{yz}^{(L)}=0;\quad y=h_1,-h_2\\&\tau_{rz}=\tau_{rz}^{(i)}+\tau_{rz}^{(C)}+\tau_{rz}^{(U)}+\tau_{rz}^{(L)}=0;\quad r=R\end{aligned} \tag{10}$$

We substitute related stress expressions of Eq. (5),(6),(8),(9) into Eq. (10) in uniform coordinate system on stress transformative relations. Then, we take three infinite dimensions linear algebraic equations about $A_n$, $B_n$ and $C_n$.

We solve boundary value equations (10) with Fourier series expansion method, which transform three infinite dimensional linear algebraic equations about $A_n$, $B_n$ and $C_n$, into three groups of infinite number of infinite dimensional linear algebraic equations, respectively.

Numerical results are explicitly displayed in this section as symbol of the dynamic stress distribution in the strip region.

As Fig.3 shows, the value of the DSCF (Dynamic Stress Concentrations Factor) around the circular cylindrical cavity bound $B_C$ is given with relatively low frequency incident waves ($kR$=0.1), where the center of the circular cylindrical cavity at the different positions in the strip region.

As Fig.4 shows, the value of the DSCF around the circular cylindrical cavity bound $B_C$ is given with relatively high frequency incident waves ($kR$=1), where the center of the circular cylindrical cavity at the different positions in the strip region.

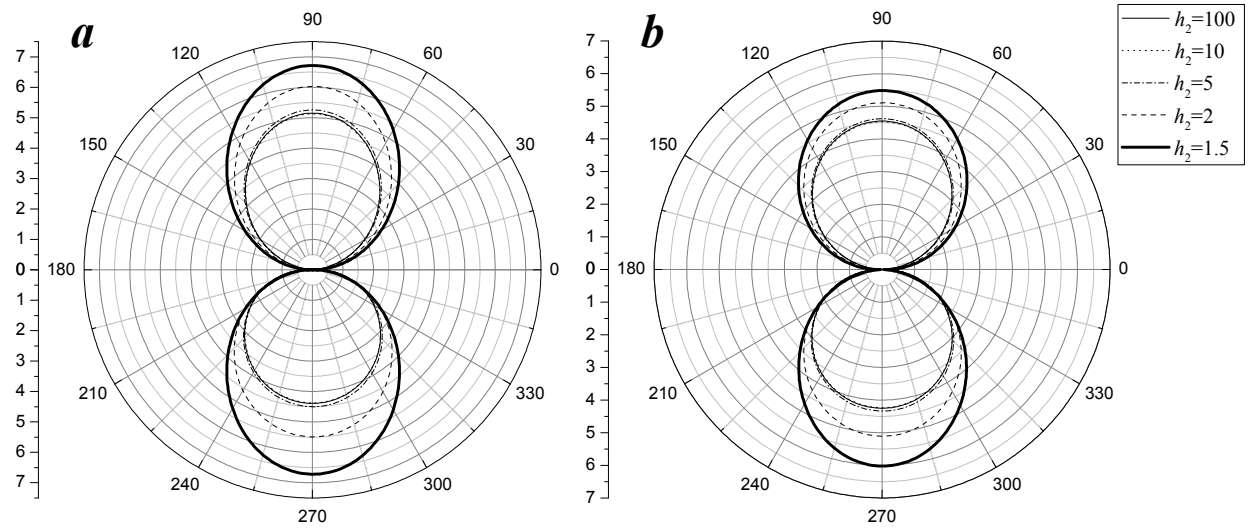


**Fig.3.** Distribution of the DSCF around the cavity with $kR$=0.1, ***a.*** $h_1$=1.5, ***b.*** $h_1$=2.

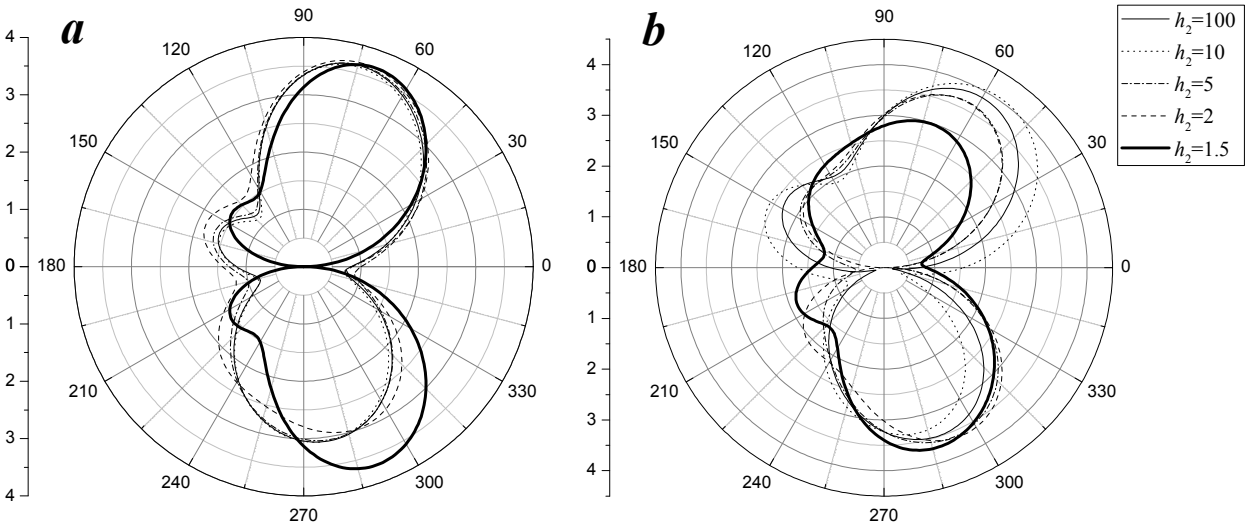


**Fig.4.** Distribution of the DSCF around the cavity with $kR$=1, ***a.*** $h_1$=1.5, ***b.*** $h_1$=2.

## Conclusions

The numerical results definitely depicted the effect of distance between the circular cylindrical cavity and the upper bound and the lower bound, and the effect of different incident angles, with different frequencies. The upper bound and the lower bound have a great influence on the dynamic stress distribution around the circular cylindrical cavity with the relatively high frequency incident waves. Contrarily, the upper bound and the lower bound have a little influence on the dynamic stress distribution around the circular cylindrical cavity with the relative low frequency incident waves, except the cylindrical bound is very close to the bounds of the strip region. However, the maximum dynamic stress around cylindrical cavity with the relatively low frequency incident waves is significantly greater than the relatively high frequency incident waves. Likewise, the dynamic stress distribution with the relatively low frequency incident waves is significantly greater than the relatively high frequency incident waves along the cross section directly above or below the circular cylindrical cavity, especially, in near cylindrical bound, as the distance increased from the cylindrical bound, this effect is decreased rapidly.

**References**

[1] J.D. Achenbach, Wave propagation in elastic solids, North-Holland, Amsterdam (1973).
[2] Y.H. Pao, C.C. Mow, Diffraction of elastic waves and dynamic stress concentrations, Crane and Russak, New York (1973).
[3] D.K. Liu, B.Z. Gai, G.Y. Tao, Applications of the method of complex functions to dynamic stress concentrations, Wave Motion 4 (1982) 293-304.
[4] S. Itou, Diffraction of a stress wave by two circular cylindrical cavities in an infinite elastic strip, Computers & Structures 31.2 (1989) 131-137.
[5] U. Zakout, N. Akkas, Transient response of a cylindrical cavity with and without a bonded shell in an infinite elastic medium, Int. J. Eng. Sci. 35.12/13 (1997) 1203-1220.
[6] Hui Qi, Yong Shi, J. X. Zhao, Scattering of SH waves from a circular inclusion in an infinite strip region, Journal of Vibration and Shock (in Chinese) 28.5 (2009) 142-145.
[7] Hui Qi, Jie Yang, Yong Shi, Scattering of SH-waves by cylindrical inclusion near interface in bi-material half-space, Journal of Mechanics 27.1 (2011) 37-45.
[8] Hui Qi, Jie Yang, Dynamic analysis for circular inclusions of arbitrary positions near interfacial crack impacted by SH-wave in half-space, Euro. J. Mech. A-Solid 36 (2012) 18-24.

*Applied Mechanics and Materials Vols. 580-583 (2014) pp 3089-3092*
*© (2014) Trans Tech Publications, Switzerland*
*doi:10.4028/www.scientific.net/AMM.580-583.3089*

# Numerical simulation of the wind load on the mast at different wind angles

Rongsheng Cao [1,a], Yuanyuan Fang [2,b] , Wang Ling[3,c]

[1]Automation and Electronic Engineering,

Qingdao University of Science and Technology, 53 Zhengzhou Road, Sifang District, China, 266042

[2]Mechanical and Electrical Engineering,

Qingdao University of Science and Technology, 99 Songling Road, Laoshan District, China, 266061

[3]Guangzhou Shipbuilding and Marine Engineering Design and Research Institute,

126Gexin Road, Haizhu District, China, 510250

[a]caorongsheng@sina.com, [b]3584121@126.com, [c]wangling0211@163.com

**Keywords:** Mast, Wind load, Wind angle, Numerical simulation

**Abstract.** The wind load acted on ship mast at different wind angles of large Reynolds number is numerically simulated in this paper. CFX software was used to analyze the trend of constant and fluctuating forces that the mast surface suffered at different Reynolds numbers.The vortex shedding strength of the wind load around the mast was also analyzed according to the trend of Strouhal number varing with the simulated Reynolds numbers. The results show that the wind angle has an important impact on the lift, drag, and vertical forceof the mast. The vertical force of the inclined side wall on the mast can not be ignored,and the angle of direction wind has great impact on the Strouhal number at different Reynolds numbers.

## Introduction

The load which the mast suffers not only coming from the propeller, host and other sorts of excitation source, but also from the wind when ship navigates in the storm. When the horizontal vortex shedding frequency caused by the air flow through the mast is close to the mast structure frequency, it will lead to the mast's transverse vortex-induced vibration, which sometimes gives rise to the damage of the radar, the weather instrument and communications antenna on the mast. Therefore, CFX software is used in this paper, and the numerical simulation of wind load on ship mast at different wind angles in uniform flow field at high Reynolds number (Re) has a strong engineering practicality.

## Calculated condition

The wind load of the mast of this numerical simulation is shown in Table 1.

Table 1 Numerical simulation condition of wind load on the mast

| condition | wind velocity (m/s) | Re ($\times 10^5$) | wind angle α (°) | | | |
|---|---|---|---|---|---|---|
| 1 | 5 | 1.41 | 0 | 15 | 30 | 45 |
| 2 | 10 | 2.82 | 0 | 15 | 30 | 45 |
| 3 | 18 | 5.08 | 0 | 15 | 30 | 45 |
| 4 | 26 | 7.34 | 0 | 15 | 30 | 45 |

The mast model is a cone of columnar structure that is quadrilateral and its surface has inclination. Specific dimensions and the defination of the wind angle are shown in Fig.1.

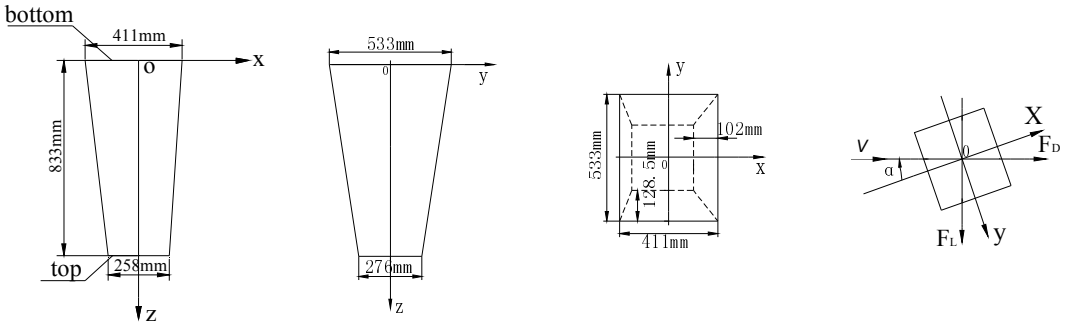


(a)Front view (b)Side view (c)Top view wind angle

Fig.1 Schematic diagram of mast model and wind angle

The CFX software used in this numerical simulation is to utilize hexahedral grid to discretize the computational domain.The flow field near the mast requires denser grids, while other regions require relatively rare grids.The curvature change of the jointed part of every regional grids should not be too large, otherwise it cannot accurately describe the vortex shedding form when the air flow through the mast[1]. After repeated numerical simulation ,the division of grids that can clearly describe the form of the vortex shedding form is determined as illustrated in Fig. 2.

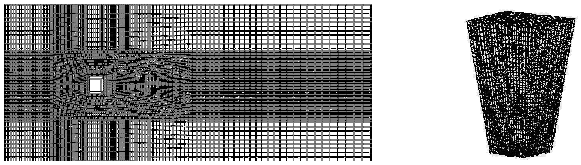

Fig. 2 Division of the grids of the munerical simulation model

The air is selected for the flow field, the surface of inlet is the entrance of wind load, medium turbulence intensity, the the velocity of the flow field of the surface of outlet resumes to the initial wind velocity. The mast is rigid and no-slip and the walls of the flow field is free-slip.

**Lift, drag and vertical force on the mast**

The average lift coefficient $C_l$ and the fluctuating lift coefficient $C_l'$ can be defined as follows.

$$C_l = \frac{\overline{F_l}}{1/2 \cdot \rho V^2 A} \tag{1}$$

$$C_l' = \frac{\sqrt{\sum (F_l - \overline{F_l})^2 / N}}{1/2 \cdot \rho V^2 A} \tag{2}$$

Where, $\overline{F_l}$ and $F_l$ are the average and instantaneous value of the fluid lift that the mast suffers;A is the max projected area where the model is perpendicular to the flow direction when the attack angle is 0º. $V$ , $\rho$ are fluid velocity and density.

The definitions of the average drag coefficient $C_d$ ,the fluctuating drag coefficient $C_d'$, the average vertical force coefficient $C_v$ and the fluctuating vertical force coefficient $C_v'$ are similar to Eq. 1 and Eq. 2.The trend of these coefficients changing with Re are showed in Fig. 3, Fig. 4 and Fig. 5.

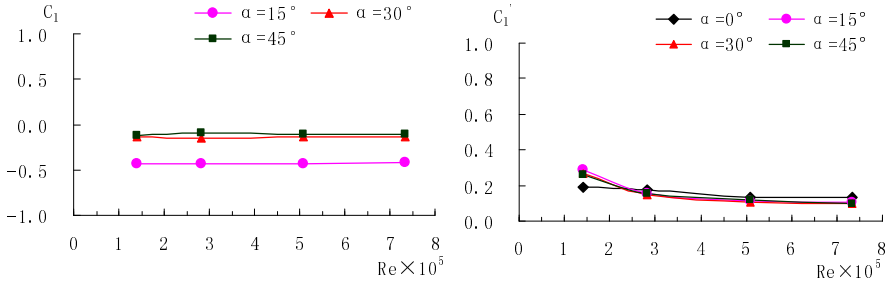


Fig. 3 The trend of $C_l$ and $C_l'$ changing with Re

As is shown in Fig. 3, $C_l$ varies little with Re and is similar to the changes of $C_d$ with Re which can be regarded as constant. The change of $C_l^{'}$ with Re is small when α is 0 and is almost the horizontal line. $C_l^{'}$ decreases with the increasing of Re, and the simulation results when α is 0 are greater than the other wind angles.

We can see in Fig. 4 and Fig. 5, $C_d^{'}$ and $C_v^{'}$ at stable period is about 0.03 while $C_l^{'}$ varies more apparently at different α and is 2 to 3 times bigger than both $C_d^{'}$ and $C_v^{'}$.

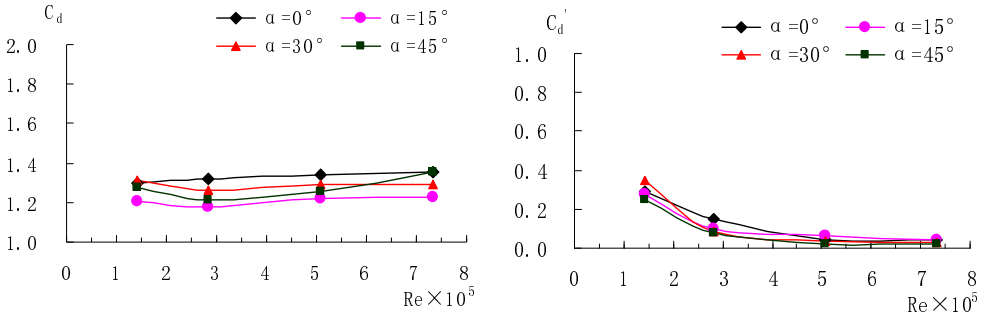


Fig. 4 The trend of $C_d$ and $C_d^{'}$ changing with Re

The mast model is symmetry to the entrance when α is 0, since $C_l$ will be 0[2]. In Fig. 4, $C_d$ varies little with Re and can be regarded as constant. Under the simulation condition, the value of $C_d^{'}$ is relatively small and varies little in the range of wind angle α, and it has smaller influence on $C_d^{'}$ than on $C_d$ .Then wind angle α's influence can thus be ignored in the research of $C_d^{'}$.

The force of superstructure at the bottom of mast will be changed when the vertical force is caused by fluid influence due to the inclination of mast surface.

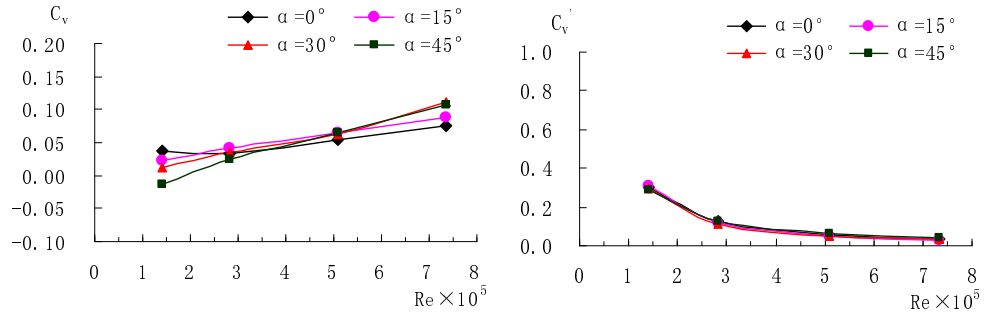


Fig. 5 The trend of $C_v$ and $C_v^{'}$ changing with Re

Fig. 5 shows that $C_v$ increases with Re while $C_v^{'}$ deceases with Re , but both of them share the mild changes. The vertical component will be vertically upward when the force of mast surface is positive while it will be vertically downward when the force is negative. The boundary layer zone will be larger when Re is smaller and the zone of positive pressure will be larger than that of negative pressure, since $C_v$ is smaller or negative. The separation point of boundary layer on mast surface will move forward when Re is higher, since $C_v$ becomes larger and positive .The value of vertical force is related with mast surface gradient and the value will becomes larger if inclination does[3].The vertical force will be very little due to the mast model surface gradient being small.

The natural frequency of mast vibration in flow field will decease or increase due to the changes of vertical force direction when the wind angle α changes , which enlarges bandwidth of natural frequency in the flow field[4]. The mast undertakes lots of electronic equipments on the ship, while the normal operation of electronic equipments entails rigid requirements on virbration, since that enlarging the bandwidth of the natural frequency of mast in flow field is detrimental to the normal operation of electronic equipments.

**Strouhal number**

The definition of Strouhal number is defined as follow:

$$S_{tr} = f_s \times l / V \tag{3}$$

where, $f_s$ is the vortex shedding frequency which is the maximum frequency of amplitude in the fluctuating lift spectral density function $S(f)$, $V$ is the velocity of incoming flow, $l$ is the lenth of the mast.

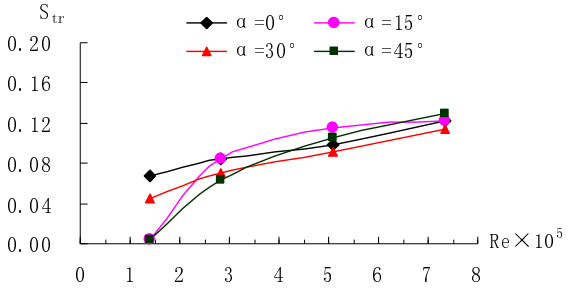


Fig. 6 The trend of $S_{tr}$ changing with Re

As is shown in Fig 6, $S_{tr}$ increases with Re and α. Re has a more sensitive influence on $S_{tr}$ changes when α is 0 and 30 than that of 15 and 45. $S_{tr}$ changes little with α and is around 0.12 when Re is above $5.0\times10^5$.We can see that there is still obvious vortex shedding frequency when air flows around mast model .To circular sectioned cylinder structure $S_{tr}$ is around 0.2 when Re is between $1.0\times10^2$ and $2.0\times10^5$, while the vortex shedding frequency vanishes when Re is not below$1.0\times10^5$[5].Vortex strength of mast model will be bigger than that of cylinder at large Re.

**Conclusions**

(1) $C_d$ and $C_l$ of mast model changes mildly with Re while changes obviously with α, $C_v$ changes obviously with both Re and α.

(2) $C_d^{'}$ and $C_v^{'}$ are both around 0.03 at the stable period while $C_l^{'}$ varies widely at various α and is 2 to 3 times than $C_d^{'}$ and $C_v^{'}$.

(3) $S_{tr}$ is about 0.12 at this numerical simulation Re range. The wind angle α exposes obvious influence on the vortex shedding form ,especially on the region of vortex shedding concentration.

**References**

[1] Xiongliang Yao, Yuanyuan Fang, Zhuang Kang: Journal of Hydrodynamics, Vol. 21(2006), p.354
[2] Yu hai, Ashan Kareem: Journal of Wind, Engineering and Industrial Aerodynamics, Vol. (1997)67-68, p.195
[3] Xiongliang Yao, Aman Zhang, Ling Wang,etc: Journal of Naval University of Engineering, Vol. 20(2008), p.32 (In Chinese)
[4] Xianding Jin, Deyou Zhao: The hull vibration(Shanghai Jiaotong University Publishers,China 2000 ,In Chinese)
[5] Zonghu Lin: The vortex shedding characteristics of gas-liquid two-phase flow and its engineering application(Chemical Industry Press, China 2001, In Chinese)

*Applied Mechanics and Materials Vols. 580-583 (2014) pp 3093-3097*
*© (2014) Trans Tech Publications, Switzerland*
*doi:10.4028/www.scientific.net/AMM.580-583.3093*

# MIDAS-based Finite Element Analysis of The Short Line Method of The Precast Segmental Bridge Construction

Linkun Guan[1, a], Xiedong Zhang[1,b] and Hui Lei [1,c]

[1] School of Transportation, Wuhan University of Technology, Wuhan, Hubei, 430063, China

[a]Guanlk936@163.com, [b]Zhangxd@189.cn, [c]leihui8905@163.com

**Keywords:** Short Line Method, Segmental Precast Construction, Construction Control.

**Abstract.** This paper studies the precast and cantilever erection process of pre-stressed concrete continuous beam bridge alignment control in short line method, basis on the construction of a light rail. Various stages of bridge construction performed on simulation analysis and calculated by the finite element software MIDAS, concluded the ultimate internal force and deformation values, and the maximum deformation are within the scope of design elevation deviation 20 mm allowed, as to achieve the target of bridge assembly.

## Introduction

With the continuous development of urban transport, increasing demand for road and bridge construction, bridge construction requires the city to seek a new technique, fast, economical and convenient method of construction. In the city bridge construction, precast segmental box girder construction gradually being adopted. This construction process has little effect on the daily traffic, high level of construction technology, as opposed to the traditional method of bridge construction, which reduces the impact of construction on the surrounding environment.

Long line method is the traditional way of concrete bridge construction, linear control is relatively simple, but the bottom mold to pre-linear aspect cannot be changed, so each must be consistent across the linear, limited to non-horizontal line of the straight bridge, and lower utilization of the bottom die after increasing the number of templates, steel banding spent 45% the total time of segmental precast cycle. The production cycle of short line method is shorter, suitable for straight bridges and all kinds of bridge models, regarding the number of segments more long-span bridges and bridge of a horizontal curve is more suitable. It can be easy to move inside and outside the template, commonly used on the steel mold precast segmental reinforced steel skeleton and then lifted into the pedestal. Short line method will assembling reinforcement the process from order to parallel construction, greatly shorten the segmental precast cycle, production efficiency compared to more than double that of long line method. Short line method of precast precision is higher, computer and professional programs require auxiliary work. In addition, compared with the traditional way of concrete bridge construction, precast segmental construction with short line method, covers an area of less, construction speed is quick, construction control accurate precision, impact of under bridge traffic is small and other advantages, the work can be completed prefabricated in the factory, production molds and production equipment can be reused, therefore, not only to reduce supplies, saving resources and costs, and reduce the impact on the surrounding environment, is advantageous to the concrete quality assurance, thus increasing the service life of the bridge structure, with a significant economic and social benefits.

## Linear control prefabrication and assembly phase

**Technology of prefabricated construction.** Short line method refers to a method of prefabricated sections divided into several sections, within prefabricated pedestal factory fixed template system is presented the matching, segmental precast concrete box girders of flowing water of a kind of construction technology. Prefabricated start from # 1 segment, the first # 1 segment pour between the

fixed end and a movable end die casting mold, this segment is called the initial segment, then the segmental moved forward as the matching section (acts as the activity mode) and second section prefabricated, and so forth, reach the section I segment as the first match of the section I + 1 segment until all segments of precast completed. Before pouring, by adjusting the relative position to match the planar segment and elevation error correction to eliminate the accumulated error, control the geometry of the segment to be cast, so as to achieve the required prefabricated linear.

**The assemble phase linear control process.** If precast segments have sufficient accuracy in the process, at the time of assembly, a section of the segments assembled together to meet the design requirements of linear. Assembly phase linear control theory is assembled by linear analysis, the target coordinates of the beam segment control point coordinates of the user to follow these installation, then these control points were measured to obtain the measured value. Structural analysis based on these measured values to obtain a pre-fight linear displacement values, input linear control program, you can get generated by the pre-fight six linear control point coordinates, then the coordinate values of the coordinate values and comparing the resulting linear design and error analysis, get the beam section adjustment suggestions.

## Engineering project

**The project profile.** This construction began united span arrangement of 13 different concrete link rigid frame composed with span of 20.2m ~ 45.0m, and average of 31.9m. Main beam using a single box single room concrete box girder, beam width is ranging from 9.68 m ~ 11.39 m, standard high beam is 1.8m, in line with a long-span, depth of beam associated to the 11th highest 2.2m. Main beam precast segment method using short line method, lifting the cantilever construction method, the box girder segment is generally 2.5m, weight 31t.

**Finite element simulation of bridge.** Using Midas Civil software to analyze the viaduct construction of the spatial structure with computational analysis as shown in Fig. 1, the model for the x-axis to the bridge longitudinal and transverse axis y, z axis is vertical, the bridge girder using beam element simulation, when moving vehicle loads applied bridge deck surface is set to two-lane, one-way traffic; beam bottom support is divided into two constraints: both ends of the sliding constraints (constraints DX, DZ, RX) and intermediate cross-fixed constraint (constraint DX, DY, DZ, RX).

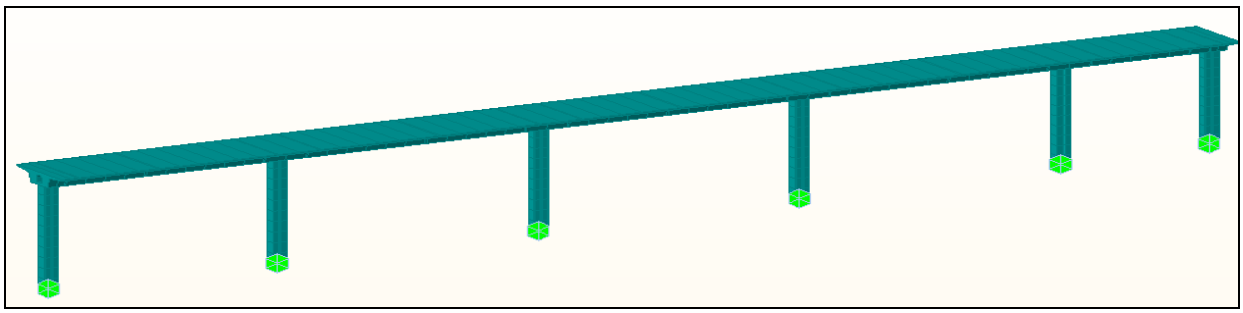

Fig. 1 Calculation model of bridge longitudinal

**Service stage of rebar maximum tensile stress calculation.**

According to specification: service stage of pre-stressed concrete flexural member normal section of pressure stress and the tensile stress of pre-stressed steel, shall meet the following requirements

To steel strand and steel wire of no cracking component $\sigma_{pe} + \sigma_{p} \leq 0.65 f_{pk}$

$\sigma_{pe}$ -Fully prestressed concrete and A kind of prestressed concrete flexural member, effective prestress of prestressed tension zone after deducting all the loss of prestress.

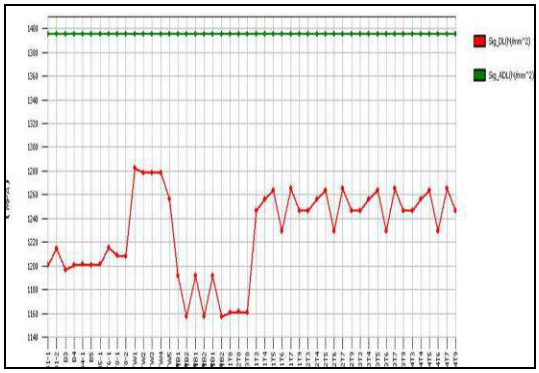

Fig. 2 Calculation of rebar tensile stress (1)

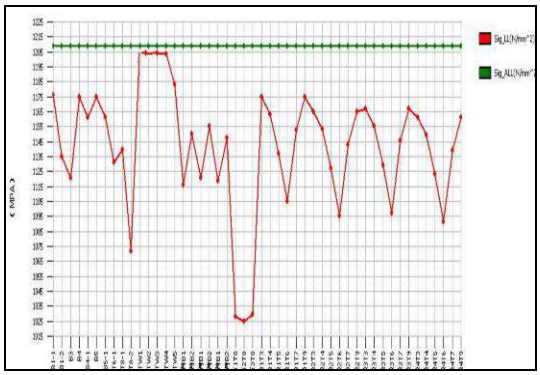

Fig. 3 Calculation of rebar tensile stress (2)

From the above, according to the results of the calculation procedure as shown in Fig. 2 and Fig.3, lasting condition tendons maximum tensile stress 1205MPa <0.65fpk (1209MPa), the construction phase of the largest pre-stressed tension control stress is 1283MPa <0.75fpk (1395MPa) to meet regulatory requirements.

**Transient situation of pre-stressed concrete member normal compressive stress check**

Pre-stressed concrete flexural members, pre-stressed and components under the weight of other construction loads cross section of the edge of the normal stress should meet the following requirements:

Tensile stress

l) When $\sigma_{ct}^{t} \leq 0.70\, f_{tk}^{'}$, pre-stretched areas should configure its reinforcement ratio of not less than 0.2% of the longitudinal reinforcement ;

2) When $\sigma_{ct}^{t}$ =1.15 $f_{tk}^{'}$, the pre-tension areas should configure its reinforcement ratio of not less than 0.4% of the longitudinal reinforcement;

3) When0.70 $f_{tk}^{'} < \sigma_{ct}^{t} <$1.15 $f_{tk}^{'}$, the longitudinal reinforcement ratio pre-tensioners area should be configured according to the straight line drawn above two interpolation. Tensile stress $\sigma_{ct}^{t}$ should not be more than 1.15 $f_{tk}^{'}$ .

pressure stress $\sigma_{cc}^{t} \leq 0.70\, f_{ck}^{'}$

In the formula, $\sigma_{cc}^{t}$, $\sigma_{ct}^{t}$ - when calculated according to a transient situation of preloading conditions , edge of the concrete in pretension area, pressure stress and the tensile stress ;

$f_{ck}^{'}$, $f_{tk}^{'}$ - With the production, transportation, installation of concrete cube in each construction stage compressive of the curvature $f_{tu}^{'}$ of the corresponding axial compressive strength and standard value of tensile strength.

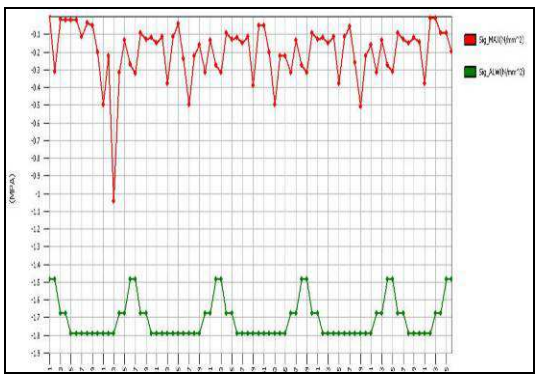

Fig. 4 Calculation of tension stress

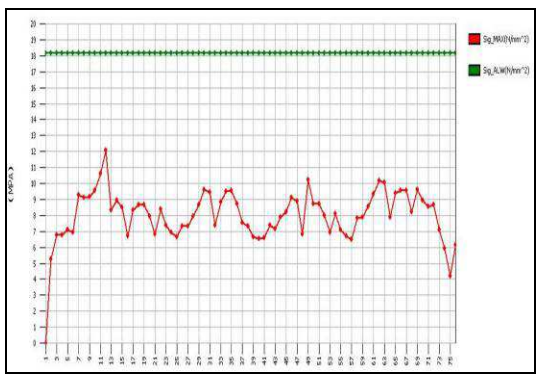

Fig. 5 Calculation of compression stress

As shown in Fig.4 and Fig.5, transient situation pre-stressed concrete members normal direction tensile stress max 1.01MPa <0.70 $f_{tk}^{'}$ (1.28 MPa), the maximum compressive stress 12.1MPa

<0.70 $f_{ck}^{'}$ (15.68 MPa), transient situation pre-stressed concrete members normal direction tensile stress meet the specification requirements.

**Computation of Shear Strength.** Accordance to specification, calculate of carrying capacity ultimate limit state of bridge member, should adopt the following expression: $\gamma_0 S \leq R$

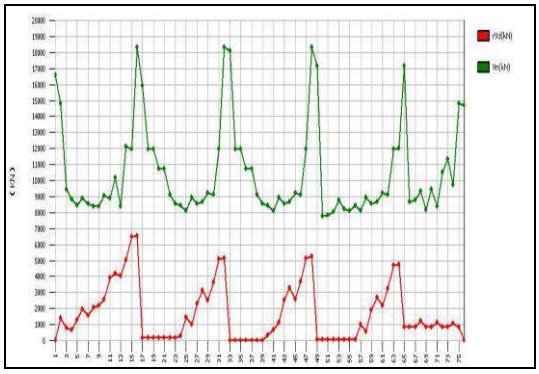

Fig. 6 Computation of Shear Strength

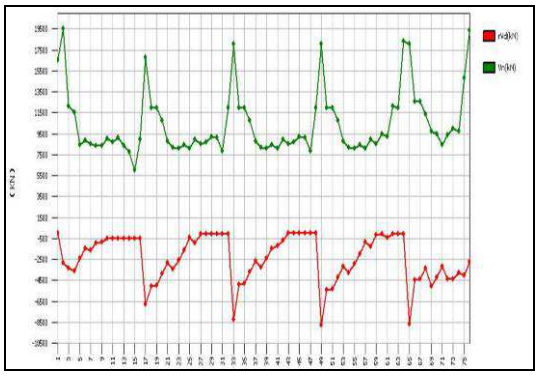

Fig. 7 Computation of Shear Strength

As shown in Fig. 6 and Fig. 7, the safety factor greater than 1, shear strength meet the specification requirements.

**Check and calculation of anti-crack and anti-bending in oblique section.** Pre-stressed concrete flexural member should crack resistance of inclined section calculation according to following provisions. Oblique oblique section of concrete cracking section of the main tensile stress $\sigma_{tp}$ member checking, and shall meet the following requirements: Class A and Class B pre-stressed concrete members, in the role (or load) Short-term effects of group.

Cast in place (including prefabricated assembly) components

$\sigma_{tp} \leq 0.5 f_{tk}$

$\sigma_{tp}$ - principal tensile stress by the action (or load) and short-term effects of a combination

$f_{tk}$ - Standard value of tensile strength of concrete.

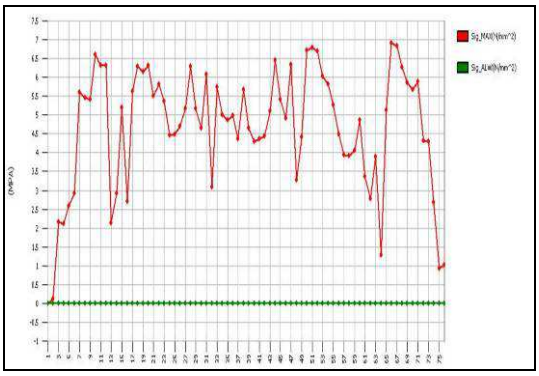

Fig. 8 Calculation of anti-crack

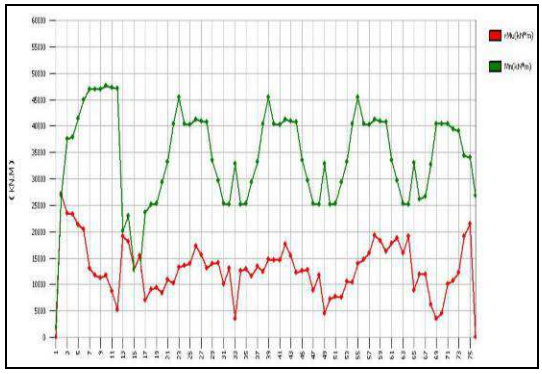

Fig. 9 Calculation of anti-bending

Accordance to specification, calculate of carrying capacity ultimate limit state of bridge member, should adopt the following expression:

$$\gamma_0 S \leq R$$

As shown in Fig. 8 and Fig. 9, there was no tensile stress, oblique section crack is checked and counted meet specifications. Flexural strength of component greater than the factor of safety components, meet regulatory requirements.

**Summary**

Through the modeling analysis and calculation, in view of the bridge process simulation analysis, then get internal force and deformation values of bridges in dead load, settlement of the base, temperature difference, dynamic loads and combined loads. The results show that, The biggest deformation caused by load are in the design elevation level within the scope of allowable deviation of 20 mm. This conclusion also provide a theoretical basis for construction control, Assembly of bridge linear can achieve expected goals, the whole construction process control method and the error processing method has certain feasibility. Precast segmental of short line method is in short construction period, can be large-scale production, standardized production, high quality and efficiency, the continuation of the traffic speed, good stability, less expansion joints in pre-stressed concrete continuous girder bridge, and will be preferred alternative of highway bridge and urban viaduct.

**References**

[1] People's Republic of China industry standard. Precast segmental of prestressed concrete assembled bridge across by Technical Specification for Construction (CJJ / T 111-2006). Beijing: China Architecture & Building Press, 2006.

[2] Ge Yaojun. Analysis and control of section construction [M].Beijing: People's Communications Press .2003.

[3] Zhang Hong, Zhang Xigang, Ding Feng, Tian Wei. New research of segmental precast assembling bridge in short line matching method[J], Road. 2011（2）, 76-82

[4] Ai Zongliang, Guo Zhengxing. Short-line matching prefabrication and cantilever construction technology research of box girder[D] Nan Jing: southeast university, 2006.

[5] SEGMENTAL BRIDGECASTING Machines [C], 29th Nova Award Nomination, 2001.

[6] Prestressed Concrete Bridge Construction with Stepping Formwork Equipment, Detroit: ACI Publication, 1969.

[7] C.Romaro, G.Romaro, Italy Erection of Arch and Arch-Frame Bridges， Structural Engineering International，2000，Vol．10，No．4.

*Applied Mechanics and Materials Vols. 580-583 (2014) pp 3098-3105*
*© (2014) Trans Tech Publications, Switzerland*
*doi:10.4028/www.scientific.net/AMM.580-583.3098*

# Simulation of Acoustic Cavitation Bubble Motion by Lattice Boltzmann Method

Xi Zhou[1, a], Minglei Shan[1, b], Changping Zhu[1, c]

Bingyan Chen[1], Cheng Yin[1], Qinggong Ren[2], Qingbang Han[1], Yibin Tang[1]

[1]Changzhou Key Laboratory of Sensor Networks and Environmental Sensing, Jiangsu Key Laboratory of Power Transmission and Distribution Equipment Technology, Hohai University, Changzhou 213022, Jiangsu, China;

[2]School of Petrochemical Engineering, Changzhou University 213022, Jiangsu, China

[a]shuangyu226@126.com, [b]shangming2003@126.com, [c]zhucp5126082@126.com

**Keywords:** acoustic cavitation; lattice Boltzmann method; single-component multiphase flow; Keller equation.

**Abstract.** The motion characteristic of cavitation bubble is one of the major factors affecting acoustic cavitation. In this paper, a cavitation model coupled with acoustic pressure is established using lattice Boltzmann pseudopotential model. Aimed at demonstrating the feasibility of applying LB method in acoustic cavitation, the acoustic cavitation simulations are compared with the predictions of Keller equation. The comparison of theoretical prediction and numerical simulation shows that LB method is suitable for acoustic cavitation simulation.

## Introduction

Acoustic cavitation is a series of the kinetic processes of shocking, growing, shrinking and collapsing of tiny gas nucleus in the liquid due to the vibrations of sound waves when pressure level of the sound exceeds the cavitation threshold of the liquid [1]. When the bubble collapses rapidly, the cavitation effect would release huge energy and create special environment that strengthens certain physical and chemical processes. This makes acoustic cavitation widely applied in medical, ultrasonic cleaning, ultrasonic water treatment and many other areas [2-3].

Numerous studies have found that, the motion characteristic of cavitation bubbles is one of the major factors affecting acoustic cavitation [4]. In terms of theory researches, Rayleigh first put forward the dynamic model of single spherical cavitation bubble in infinite incompressible liquid in 1917. Then Plesset et al. modified the Rayleigh equation by considering different factors [5]. By introducing acoustic radiation to Rayleigh-Plesset equation, the earliest acoustic cavitation motion equation was deduced [6]. Since the oversimplified theoretical model (often single and spherical) was incapable of obtaining the analytical solution to the motion rule of cavitation bubbles, numerical methods on cavitation bubble's motion were widely considered. Existing numerical simulation methods of non-spherical cavitation bubble mainly include the volume of fluid (VOF) [7], the finite volume method (FVM) [8], the boundary element method (BEM) [9] and the lattice Boltzmann method (LBM).

The burgeoning lattice Boltzmann method in the recent two decades is a numerical method based on microscopic model and mesoscopic particle dynamics equation [10-11]. In LBM multiphase flows area, the pseudopotential LB model proposed by Shan and Chen (also called Shan-Chen model), which introduced inter-particle potential to describe the interactions among different phases or components, is widely used for its conceptual simplicity and easy implementation [12-13]. Sukop and Or verified the feasibility of LBM on cavitation by simulating the cavitation phenomenon using Shan-Chen model [14]. Zhang et al. studied on the relationship between initial bubble radius and cavitation phenomenon by simulating 3D cavitation phenomenon using Shan-Chen model [15].

Xiao-Peng Chen simulated the cavitating bubble growth with the LBM in both quiescent and shear flows, where the results are compared with the Rayleigh-Plesset equation [16]. Then, Xiao-Peng Chen et al. simulated cavitation bubble of large density ratio by coupling exact difference method (EDM) and Carnahan-Starling real-gas equation of state (EOS) in the Shan-Chen LB model [17]. The known researches have investigated the dynamic characteristics of cavitation bubble and its relationship with several thermodynamic parameters. Some of them have compared experimental results with theoretical ones, and verified the feasibility of the LBM numerical simulation on cavitation. When introducing the influence of acoustic perturbation, the cavitation bubble's motion grows much more complex. Whereas, as far as we are aware that reports about the LBM numerical simulation of cavitation bubble with influence of acoustic pressure have not been published.

In this paper, the acoustic pressure is coupled in the LB Shan-Chen multiphase flow model to set up an acoustic cavitation model. With this model, the expansion, contraction and collapse processes of the cavitation bubble with the acoustic perturbation is simulated. The purpose of this paper is to validate the model by comparing the results with Keller equation to demonstrate the feasibility of using the LBM in simulating acoustic cavitation.

## LBM Model

LBM is a mesoscopic numerical simulation method based on statistical physics and developed from lattice Gas Automata (LGA). The evolution equation with Bhatnagar-Gross-Krook (BGK) collision term can be written as [18]

$$f_a\left(\boldsymbol{x}+\boldsymbol{e}_a\cdot\delta t,\mathrm{t}+\delta t\right)-f_a\left(\boldsymbol{x},\mathrm{t}\right)=-\frac{1}{\tau}\left[f_a\left(\boldsymbol{x},t\right)-f_a^{eq}\left(\boldsymbol{x},t\right)\right],a=0,1,\ldots\ldots\mathrm{b}, \tag{1}$$

where $f_a$ denotes the distribution function along each velocity direction $a$, $f_a^{eq}$ denotes the equilibrium distribution function, $b$ is the number of the neighbors, $\boldsymbol{x}$ is the lattice site coordinates and $\boldsymbol{e}_a$ velocity towards each direction. The function is of single relation time, which is decided by viscosity $\upsilon=(\tau-1/2)c_s^2\delta t$. The motion of particles in LBM is divided into the process of streaming and collision, representing moving from one node to a nearest neighbor node and a relaxation toward a local equilibrium respectively, as the left hand side and the right hand side of equation (1) shows. The discrete velocity in the two-dimensional D2Q9 model is defined as

$$\boldsymbol{e}_a=\begin{cases}(0,0),a=0\\ c\left(\cos\left[(a-1)\frac{\pi}{2}\right],\sin\left[(a-1)\frac{\pi}{2}\right]\right),a=1,2,3,4\\ \sqrt{2}c\left(\cos\left[(2a-1)\frac{\pi}{4}\right],\sin\left[(2a-1)\frac{\pi}{4}\right]\right),a=5,6,7,8\end{cases}, \tag{2}$$

where the lattice speed $\mathrm{c}=\delta x/\delta t$, $\delta x$, $\delta t$ is the lattice unit and time step, respectively.

The equilibrium distribution function satisfying the Maxwell distribution is depicted in D2Q9 model as

$$f_a^{eq}\left(\boldsymbol{x},t\right)=\rho\omega_a[1+3\frac{\boldsymbol{e}_a\cdot\boldsymbol{u}}{c^2}+\frac{9(\boldsymbol{e}_a\cdot\boldsymbol{u})^2}{2c^4}-\frac{3\boldsymbol{u}^2}{2c^2}], \tag{3}$$

where $\boldsymbol{u}$ is the macro-velocity, and the weights $\omega_a$ are set $\omega=4/9$ when $a=0$, $\omega=1/9$ when $a=1,2,3,4$, and $\omega=1/36$ when $a=5,6,7,8$.

In this paper, the widely used Shan-Chen model in LBM multiphase area is applied, which introduced the inter-particle interaction force to simulate the single component multiphase flows.

When the force is large enough, it will lead to phase transition. Consider the nearest-neighbor interactions as

$$\mathrm{F}(\boldsymbol{x},t) = -G\psi(\boldsymbol{x},t)\sum_a \omega_a \psi(\boldsymbol{x}+\boldsymbol{e}_a\delta t,t)\boldsymbol{e}_a, \tag{4}$$

where G denotes the interaction strength whose magnitude controls the interaction potential and sign determines whether it is attractive or repulsive. $\psi$ is the interaction potential with the form $\psi = \psi_0 e^{-\rho_0/\rho}$ , $\psi_0$ and $\rho_0$ are arbitrary constants.

In Shan-Chen model, the interaction force is incorporated into the model by shifting the velocity in the equilibrium distribution function [19], namely,

$$u^{eq} = u(x,t) + \Delta u, \tag{5}$$

$$\Delta u = \frac{\tau \cdot \delta t \cdot F(\boldsymbol{x},\mathrm{t})}{\rho(x,t)}, \tag{6}$$

where the macro-density $\rho$ and macro-velocity $u$ of the fluid are defined as

$$\rho(\boldsymbol{x},t) = \sum_0^8 f_a(\boldsymbol{x},t), \tag{7}$$

$$u(\boldsymbol{x},t) = \frac{\sum_0^8 \boldsymbol{e}_a f_a(\boldsymbol{x},t)}{\rho(\boldsymbol{x},t)}, \tag{8}$$

The Shan-Chen single-component multiphase LBM EOS is of the form

$$p = \rho RT + \frac{GRT}{2}\psi(\rho)^2, \tag{9}$$

where $RT = 1/3$ . For the chosen form $\psi = \psi_0 e^{-\rho_0/\rho}$ , the equation is a nonmonotonic increasing function at certain T, and has the essential feature of the Van der Waals equation that allows liquid-vapor phase coexistence. When the value of G is less than the subcritical interaction strength $G_C$ , phase separation is possible to take place.

## Numerical Simulation

**Determination of thermodynamic parameters.** Cavitation is a transient, multiphase and complex phenomenon with vapor and various gas components inside the cavitation bubble. In this paper, Shan-Chen single-component multiphase (SCMP) model is applied, implying that only saturated vapor inside bubble taken into consideration. To determine the density value of liquid and vapor, the coexisting density of phase segregation result is first presented as the basis of the simulation. Throughout the paper, the lattice unit is adopted for all data if not specially announced, e.g. the unit of length is lattice unit (lu), the unit of time is time step (ts), and the unit of mass is mass unit (mu). The computational domain is set in a 200×200 square gird with periodic boundary conditions applied at four boundaries. The initial density is evenly distributed with slight random perturbations $\delta\rho = \rho_0 \times 1.0(1 - 2\times \mathrm{rand})$ , where rand denotes the random numbers in [0,1]. The equilibrium phase densities are obtained as $\rho_v = 82.0971$ , $\rho_l = 520.4809$ in the equilibrium liquid-vapor system with the parameters $\psi_0 = 4$ , $\rho_0 = 200$ , $G = -120$ and $\tau = 0.8$ , thus the vapor pressure $P_v = 24.9158$ and liquid pressure $P_l = 25.11$ are computed through EOS.

The surface tension can be estimated by simulating a series of drops or bubbles of various initial radii and measuring the pressure difference $\Delta P$ inside and outside the bubble. According to the

Young-Laplace law, pressure difference of stable bubble/droplet is inversely proportional to the radius. As a result, the slope of the plot of curvature $1/\mathrm{R}$ and pressure difference $\Delta\mathrm{P}$ represents the surface tension, the value which is $\sigma = 11.427$ lu mu ts$^{-2}$ as Fig. 1 shows for the parameters used here.

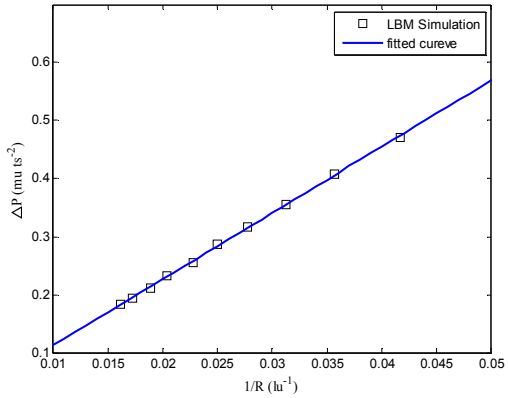


Fig. 1 Pressure difference inside and outside bubble with different curvature

**Establishment of acoustic model.** As a pressure wave [20], acoustic pressure can be introduced into the model by setting the values of distribution function $f_a$ at the inlet boundary to the values of $f_a = f_a^{eq}(\rho_S^A(\mathrm{t}), u_S^A(\mathrm{t}))$. $\rho_S^A(\mathrm{t})$ and $u_S^A(\mathrm{t})$ are the sinusoidal density and velocity perturbations at the inlet, as the equation (10) and (11) shows

$$\rho_S^A(\mathrm{t}) = \rho_S^{(0)} + \delta\rho_s \sin(\omega_s t_s), \tag{10}$$

$$u_S^A(\mathrm{t}) = \delta u_s \sin(\omega_s t_s), \tag{11}$$

where $\rho_S^{(0)}$ is the ambient density, $\omega_s$ is the angular frequency of the sound wave, $\delta\rho_s$ and $\delta u_s$ are the amplitudes of the density and velocity variations respectively with the relationship of $\delta u_s = (\delta\rho_s \cdot c_s / \rho_S^{(0)}, 0)$.

Consider a plane sound wave propagating in an unbound fluid channel along x direction. The domain is set 200 in x-direction and 20 in y-direction, with periodic boundaries on upper-side and down-side boundaries. The sound wave is initialized at the inlet boundary as mentioned above. Full developed boundary is applied on the outlet boundary using the scheme $f_{3,6,7}(N_x, j) = f_{3,6,7}(N_x - 1, j)$, since quantities such as density and velocity can be approximately seen unchanged in mainstream direction in this way, making the instantaneous velocity distribution curve in the centerline of channel maintain relatively stable when the acoustic wave propagates to the boundary. In simulation, the viscosity of fluid is $\upsilon = 0.1$, the density of fluid is set as $\rho_S^{(0)} = 500$ according to the phase segregation result, and amplitudes of density variations is $0.01\rho_S^{(0)}$. As seen, the Mach number here is $\mathrm{Ma} = \dfrac{\delta u_s}{c_s} = \dfrac{\delta\rho_s}{\rho_S^{(0)}} = 0.01 << 1$.

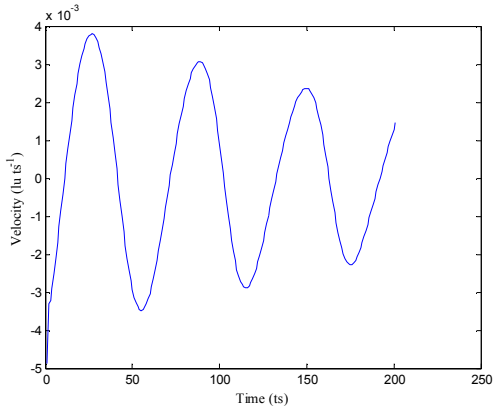


Fig. 2 Instantaneous velocity distribution curve in the centerline of channel(t=10000)

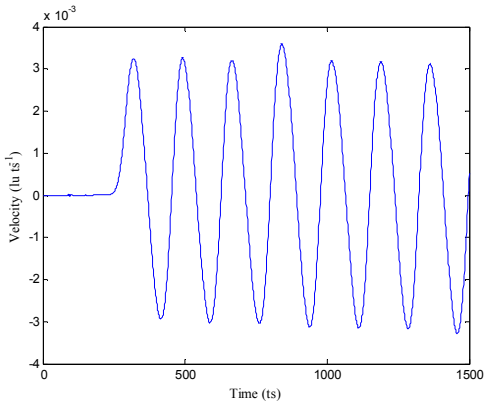


Fig. 3 Velocity evolving curve in (100, 10), t=1500

With the parameters adopted above and wave length $\lambda = 100$, the instantaneous velocity distribution curve in the centerline of channel of stable acoustic field (t=10000) is presented in Fig. 2. The velocity evolving curve in the middle of the domain (100, 10) after propagating in channel for a while (t=1500) is presented in Fig. 3.

**Validation of acoustic cavitation model with Keller equation**. The behavior of a spherical cavitation bubble can be precisely described by Rayleigh-Plesset equation. Taking the acoustic radiation effect caused by the changing bubble into account, Keller deduced the bubble vibration equation of acoustic cavitation on the basis of Rayleigh-Plesset equation, which is called Keller equation [21]. The equation makes following assumptions about the described model: the bubble keeps spherical shape and fixed center in movement; the bubble wall only has radial motion; the influence of gravity is ignored; the gas inside bubble is approximately regarded as ideal. The equation is described as

$$R\ddot{R}+\frac{3}{2}\dot{R}^2=\frac{1}{\rho_L}\left[\left(P_0+\frac{2\sigma}{R_0}-P_v\right)\frac{R_0^{3\kappa}}{\left(R^3-a^3\right)^{\kappa}}-\frac{2\sigma}{R}-\frac{4\mu_L\dot{R}}{R}-P_0+P_v\text{-}P_A\sin wt\right]+$$
$$\frac{R}{\rho_L c}\frac{d}{dt}\left[\left(P_0+\frac{2\sigma}{R_0}-P_v\right)\frac{R_0^{3\kappa}}{\left(R^3-a^3\right)^{\kappa}}\text{-}P_A\sin wt\right], \quad (12)$$

where $R_0$ denotes the initial bubble radii, $R$ the bubble radii at any moment, $\dot{R}$ the change rate of bubble radii, $\ddot{R}$ the rate of bubble's fluctuation speed. In equation (12), $\sigma$ is the surface tension, $\mu_L$ is dynamic viscosity, $P_0$ is ambient pressure, $P_v$ is saturated vapor pressure, $P_A$ is amplitude of acoustic pressure, $\rho_L$ is density of liquid, $c$ is speed of sound in water, $w$ is angular frequency of acoustic wave, $a$ is Van der Waals radius, $\kappa$ is polytropic index.

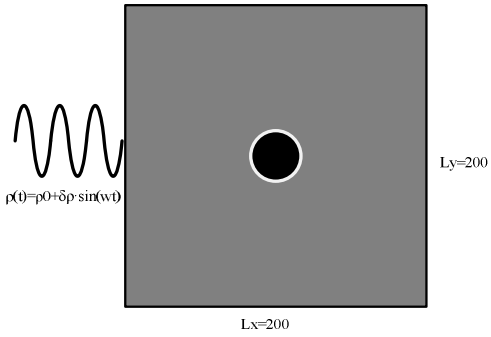


Fig. 4 Physical model of acoustic cavitation (Gray represents liquid phase, black represents vapor phase)

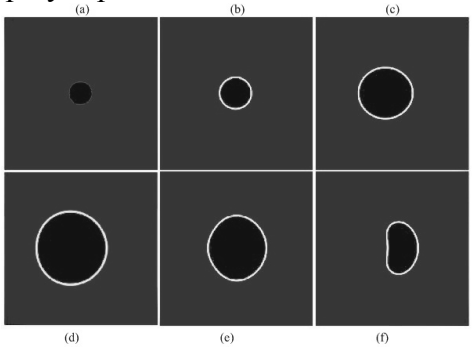


Fig. 5 Growth of acoustic cavitation bubble ((a)~(f) t=0,t=300,t=600,t=900,t=1200,t=1500)

The computational domain of acoustic cavitation simulation is set 200×200. As the physical model show in Fig. 4, the acoustic source is located in x=1, and the cavitation bubble is located in the middle of the flow field (100,100). The initial condition is set as follows, the density inside bubble $\rho_V = 80$, the density outside bubble $\rho_L = 500$, initial radii of bubble $R_{\text{ini}} = 15$. The acoustic pressure is introduced by imposed density and velocity as mentioned above, giving the speed of sound $c_s = 1/\sqrt{3}$ and amplitude of the density variation $\delta\rho_s = 5\%\rho_L = 15$. Nonequilibrium extrapolation scheme is applied on the outlet boundary, and periodic boundaries are applied on the top and bottom. With the acoustic effect, the evolution process of bubble's shape over time within a period is shown in Fig. 5, where the interval of picture (a)~(f) is set t=300. As the figure shows, in the expansion phase, the bubble radius increases gradually remaining spherical; while in the compression phase, the bubble gradually deformed to take on a non-spherical look due to the fact that the side closer to sound source suffers from greater pressure than the other side with the action of acoustic wave.

For the Keller equation, the four step Runge-Kutta algorithm is adopted to solve this second order nonlinear differential equation [22]. Before that, equation (12) should be converted into first order differential equations which substituted by certain initial conditions of lattice unit. Parameters like $\rho_L$, $\sigma$, $\mu_L = \rho_L \upsilon$ is measured from previous simulations, and other parameters in the equation are set as follows. The initial bubble radius $R_0 = 15$, Van der Waals radius $a = R_0 / 8.54$, polytropic index $\kappa = 1.33$. According to the principle that acoustic Reynolds number Re is consistent in lattice unit and physical unit, it is inferred that the sound wave produces approximately 222 times atmosphere pressure if the density perturbation remains 1%. Accordingly, pressure parameters are set $P_0 = 0.0075$, $P_v = 1.74\text{e-}4$, $P_A = 3.5$ respectively.

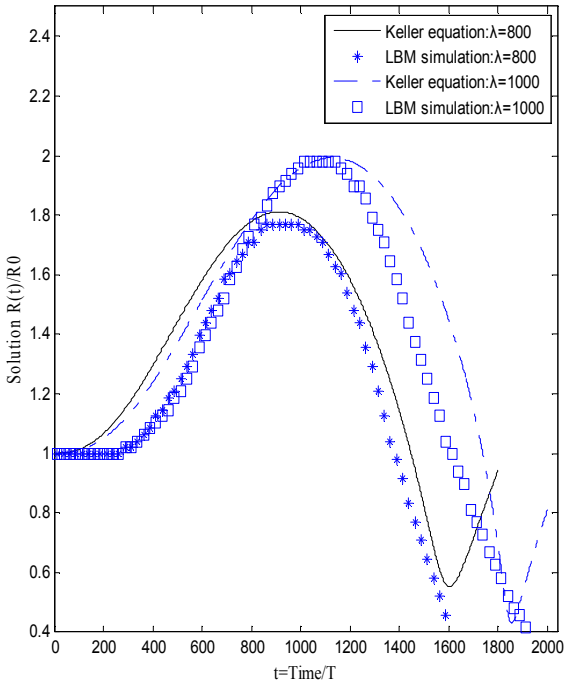


Fig.6 Comparison of simulation of LBM and prediction of Keller equation

Considering two wavelengths of $\lambda = 800$ and $\lambda = 1000$, the bubble radius comparison of numerical simulation results using LB method and prediction results of Keller equation is shown in Fig. 6. Keller equation is based on the assumption of fixed center and spherical shape, while in simulation (as Fig. 5 shows), the cavitation bubble performs certain deformation in acoustic wave and the center moves slightly as well. Therefore, as seen in Fig. 6, there exist slight deviation between

prediction curve and theoretical curve. Meanwhile, the density ratio used in simulation is relatively small against the large density ratio assumption of Keller equation, which is one of the reasons for deviation in the results.

## Conclusion

On the basis of the establishment of acoustic field, the acoustic pressure is coupled in the LB Shan-Chen single-component multiphase pseudo-potential model to build an acoustic cavitation model in this paper. According to the lattice unit conversion results, two wave lengths of $\lambda = 800$, $\lambda = 1000$ are chosen in the model to simulate the acoustic cavitation phenomenon. The comparison of LB simulation with the model and the prediction of Keller equation initially validates the feasibility of applying LB method in acoustic cavitation simulation.

Compared with other numerical simulation methods, LB method takes distinct advantages over simplicity and efficiency. The simulation and validation of acoustic cavitation achieved by LB method in this paper lays a foundation for exploiting the inherent parallelism of LB method to realize the simulation of multi-bubble cavitation in future.

## Acknowledgements

This work was financially supported by the Natural Science Foundation of China Grant (No.11274092, No.11274091, No.11304026), Fundamental Research Funds for the Central Universities of Hohai University (No. 2013B08814), Natural Science Foundation of Jiangsu Province (NO.BK20130238), Changzhou Science and Technology Support Projects (No.CJ20130008, CE20120080).

## References

[1] R. Feng and H.M. Li: Sonochemistry and its application(Anhui Press, China 1992).(In Chinese)

[2] Didenko Y T, McNamara W B, Suslick K S. Nature (London), 2000, 407: 877~879.

[3] Ying C F, An N. Sci China, Ser. A, 2002, 32(4): 305-313.

[4] Li Z C, Lin S Y. Journal of Shanxi Normal University ( Natural Science Edition), 2008, 36(1): 38-42.(In Chinese)

[5] Qi D M, Lu C J, He Y S, et al. Shanghai Journal of Mechanics. 1999,20(1)：1-9.(In Chinese)

[6] Prosperetti A., Lezzi A.. Journal of Fluid Mechanics, 1986, 168, 457-478.

[7] C. Vortmann, G. Schnerr, S. Seelecke. Int. J. Heat Fluid Flow, 2003,24: 774–783.

[8] Chau S W, Hsu K L, Kouh J S, et al. Journal of marine science and technology, 2004, 8(4): 147-158.

[9] Yao X L, Ye X, Zhang A M. Acta Physica Sinica, 2013,62(24): 244701-1-11.(In Chinese)

[10] S. Succi: The lattice Boltzmann equation: for fluid dynamics and beyond(Oxford university press, UK 2001).

[11] M.C. Sukop and D.T. Thorne: Lattice Boltzmann modeling: an introduction for geoscientists and engineers ( Springer, USA 2007).

[12] Shan X, Chen H. Physical Review E, 1993, 47(3): 1815.

[13] Shan X, Chen H. Physical Review E, 1994, 49(4): 2941.

[14] Sukop M C, Or D. Physical Review E, 2005, 71(4): 46703.

[15] Zhang X M, Zhou C Y, Shams, et al. Acta Physica Sinica, 2009,58(12): 8406-8414.(In Chinese)

[16] Chen X. Communications in Computational Physics, 2010, 7(1): 212.

[17] Chen X P, Zhong C W, Yuan X L. Computers & Mathematics with Applications, 2011, 61(12): 3577-3584.

[18] Y.L. He, Y. Wang and Q. Li: Theory and Applications of Lattice Boltzmann Method (Scientific Press, China 2011). (In Chinese)

[19] Z.L. Guo and C.G. Zheng: Theory and applications of Lattice Boltzmann Method(Scientific Press, China 2008). (In Chinese)

[20] Cosgrove J A, Buick J M, Campbell D M, et al. Ultrasonics, 2004, 43(1): 21-25.

[21] Keller J B, Miksis M. The Journal of the Acoustical Society of America, 1980, 68(2): 628-633.

[22] Shen Z Z, Lin S Y. Acta Physica Sinica, 2011, 60(10): 418-425.(In Chinese)

*Applied Mechanics and Materials Vols. 580-583 (2014) pp 3106-3110*
*© (2014) Trans Tech Publications, Switzerland*
*doi:10.4028/www.scientific.net/AMM.580-583.3106*

# Research and Development on Similarity Principle of Model Pile

WANG Xinquan[1, a], ZHANG Shimin[1,b], LIAO Juan[1,c], HUANG Yingsheng[1,d]

[1]Department of Civil Engineering, Zhejiang University City College, Hangzhou 310015, China

[2]School of civil engineering, Henan Polytechnic University, Jiaozuo 454000, China

[a]wangxq@zucc.edu.cn, [b]zhangsm@zucc.edu.cn, [c]liaoj@zucc.edu.cn , [d]huangys@zucc.edu.cn

**Keywords:** Similarity Principle. model test. model pile. Static load test.

**Abstract**. Similarity Principle, applied to model test, is an important theoretical basis for simulation of the prototype test. By simulating the prototype test. On the base of model test to make research on this field indirectly. Saving time and energy, the article is based on the similarity principle, and combine with the model pile static pressure test, discuss the application of similarity principle.

## The origin of similarity principle

The similarity theory research is the crystallization of human wisdom. Since ancient times, man has been to explore nature, and through experimental method, people got a lot of important results and conclusions. But many experiments can't be done directly, so it needs to simulate similar conditions to take the model experiments. And people in the exploration of nature gradually formed a special theory: the similarity theory. Similarity theory involves almost all human subjects, it is of great contribution to the research in science.

## The basic theory of similarity

Similar in which each element of the component model must be similar to the prototype of the corresponding elements[1], and it includes geometric and physical elements. The specific performance is: a series of physical elements are similar in a particular field. If there are two physical phenomena of the physical element on the corresponding points and the corresponding moment is proportional to the size and the corresponding vectors are in the same direction, the two physical phenomena are similar. In general, pile of static compressive model test shall meet the following conditions:

## The geometric similarity

In the model test, the structure should satisfy the geometrical similarity between model and prototype, which is between the model and the prototype structure size should be proportional to the corresponding, they have the same similar constant. Now with the subscript m and p respectively stands for model and prototype[2].

Length, Width and Height ratio:

$$\frac{l_m}{l_p}=\frac{b_m}{b_p}=\frac{h_m}{h_p}=C_l \tag{1}$$

Area ratio:

$$\frac{A_m}{A_p}=\frac{b_m h_m}{b_p h_p}=C^2{}_l \tag{2}$$

Modulus of section:

$$\frac{W_m}{W_p}=\frac{\frac{1}{6}b_m h_m^2}{\frac{1}{6}b_p h_p^2}=C_l^3 \tag{3}$$

Moment of inertia:

$$\frac{I_m}{I_p}=\frac{\frac{1}{12}b_m h_m^3}{\frac{1}{12}b_p h_p^3}=C_l^4 \tag{4}$$

The relationship between displacement of pile and the pile top strain:

$$\frac{x_m}{x_p}=\frac{\varepsilon_m l_m}{\varepsilon_p l_p}=C_\varepsilon C_l \tag{5}$$

**The load similarity**

In the vertical bearing capacity of pile model test, the pile top load should in the same direction, probability proportional to size. The pile top load belongs to a concentrated load, the similarity coefficient of concentrated loading: $C_f=\frac{F_m}{F_p}=\frac{A_m\sigma_m}{A_p\sigma_p}=C_l^2 C_\sigma$ (6)

When under horizontal load of pile top , pile bending moment of the similarity coefficient is

$$\frac{\sigma_m W_p}{\sigma_m W_p}=C_\sigma C_l^3 \tag{7}$$

**Physical similarity**

Physical similarity refers to the model and prototype is similar to the relationship between stress and strain, etc. In the static load test of pile includes the following elements:

The vertical stress similarity: $\frac{\sigma_m}{\sigma_p}=\frac{E_{\mathrm{m}}\varepsilon_m}{E_p\varepsilon_p}=C_E C_\varepsilon$ (8)

Shear stress: $\frac{\tau_m}{\tau_p}=\frac{G_m\gamma_m}{G_p\gamma_p}=C_G C_{\mathrm{m}}$ (9)

Poisson's ratio similarity: $\frac{\nu_m}{\nu_p}=C_\nu$ (10)

Constant stiffness similarity: $C_k=\frac{C_p}{C_x}=\frac{C_\sigma C_l^2}{C_l}=C_\sigma C_l$ (11)

$C_\sigma, C_E, C_\varepsilon, C_\tau, C_G, C_\gamma, C$ respectively stand for the similarity constant of the vertical stress, elastic modulus, normal strain and shear stress, shear modulus, shear strain, Poisson's ratio.

**Similarity criterion[3]**

In theory, the vertical and horizontal displacement of the pile and the stress and strain under static load are decided by related differential equations and related theory. When simulate pile static loading, it need to make sure that the model test and prototype test have the same mechanical characteristics and differential equations. Only by doing this can it guarantee model test in the same conditions. In addition, the model test also requires some single-valued condition. The single valued condition must also be similar. The single valued conditions include:

1 The initial conditions: magnitude of force the frequency of force exerting.

2 Geometrical conditions: the size of the Model groove and pile should meet the similarity conditions.

3 maximum conditions: The prototype pile's ultimate bearing capacity and the ultimate displacement.

4 physical conditions: cohesive forces and inner friction angles of soil specific weight of the soil.etc

Therefore, the load-test of the pile must satisfy the vertical load of the pile, the end resistance of the pile, the friction resistance of the pile and the top-displacement of the pile agree with the similarity t heory. When the pile under horizontal load, the top-horizontal displacement of the pile, the bending moment of the pile and the soil pressure besides the pile which changes with the depth also agree wi th the similarity conditions corresponding.

**similarity theorem[4]**

**The first similarity theorem**

For a similar phenomenon, the similarity index is 1. Here said the similarity index refers to the similar phenomenon meet the basic differential equation, and after the convert the number of the coefficient equation is one. Similar to the first theorem is proposed by Baer Tran, put forward the theory to determine the relevant similarity criteria.

For example, in the case of the vertical bearing capacity of pile, the pile reach equilibrium states under the load F, the bearing capacity of pile tip is[5] $F = Q_{\mathrm{uk}} = Q_{\mathrm{sk}} + Q_{pk} = 2\pi r l q_{sk} + \pi r^2 q_{pk}$ (12)

For model pile: $F_m = C_F F_p, r_m = C_r r_p, l_m = C_l l_p, q_{sk_m} = C_{q_{sk}} q_{sk_p}, q_{pk_m} = C_{p_{sk}} q_{pk_p},$ (13)

Take (13) into (12), and according to the first similarity theorem.

$$\frac{C_r C_l C_{q_{sk}}}{C_F} = 1, \frac{C_r^{\,2} C_{q_{pk}}}{C_F} = 1 . \tag{14}$$

$\frac{C_r C_l C_{q_{sk}}}{C_F}, \frac{C_r^{\,2} C_{q_{pk}}}{C_F}$ are the similarity index. The above formula indicates that Similarity coefficient between prototype and the model is not arbitrary, but connect with each other. And in accordance with the relevant conditions, the related parameters can be determined in the model pile.

**The second similarity theorem**

Second Similarity theorem was firstly put forward in 1914 by the British scholar buckingham, when a phenomenon represented by a function of n physical quantities, and the quantities which contains m basic dimension , it can get (n, m) similarity number, the n physical quantities can be expressed as the function relationship on similarity theorem between

$\pi_1\pi_2\pi_3\cdots\cdots\pi_{\text{n-k}}$, according to the second theorem, $f(\pi_1\pi_2\pi_3\cdots\cdots\pi_{n-k})=0$, (15)

When the prototype and the model is similar, if the corresponding points and corresponding time of similarity criterion would remain the same, then the relation of them should be the same, that is

$f(\pi_1\pi_2\pi_3\cdots\cdots\pi_{n-k})_m=0, f(\pi_1\pi_2\pi_3\cdots\cdots\pi_{n-k})_p=0$ (16)

which $\pi_{1m}=\pi_{1p},\pi_{2m}=\pi_{2p},\pi_{3m}=\pi_{3p}.....\pi_{(n-k)m}=\pi_{(n-k)p}$ (17)

For example, the pile foundation in a certain stage of stress can be based on second similarity theory, need not every data of similarity transformation, greatly reducing the amount of calculation.

The second similarity theorem shows that in each other similar phenomena, the similarity criterion can't be derived by the similarity index, the equation describing the relationship between various physical quantities are converted into dimensionless equation form, all the equations are similar criteria.

**Summary:**

The similarity theory is a bridge between model and prototype, combined with the first similarity theory and third similarity theory, according to the known similar conditions, identify other similar parameters. And through the second similarity between model and prototype theory can make the similarity calculation become simplified.

**Acknowledgements**

This material is based upon work funded by Zhejiang Provincial Natural Science Foundation of China under Grant No. LQ12E09002; Project (51308497) supported by National Natural Science Foundation of China.

**Reference**

[1] Xu Ting.Similarity Principle and Model Test, [M] first edition. Beijing: Chinese agricultural machinery press, 1982

[2]Yao Zhenggang, Liu Zuhua. Design of Building Structure [M]. first edition. Shanghai: Tongji University press, 1996.

[3]Zhang Lianyang.The Experimental Method of Pile Foundation Model[J]. Survey of science and technology.1991.1:6-11.

[4]Yi Gang, Gong Daiyu. Discussion On the Design of Structure Model Similarity Theory [J]. Science and Technology of Overseas Building Materials, 2004, 25(5):38-39

[5]Yuan Juyun. Foundation Engineering Design Theory[M]. first edition. Shanghai:Tongji University press, 2001.

*Applied Mechanics and Materials Vols. 580-583 (2014) pp 3111-3114*
*© (2014) Trans Tech Publications, Switzerland*
*doi:10.4028/www.scientific.net/AMM.580-583.3111*

# Study on the downburst field characteristics under the influence of two-dimensional continuous mountains at different distance

Yi Sun[1, a], Yuanze Wu[1], Haitao Shi[1], Baifeng Ji[2]

[1] School of Civil Engineering and Architecture, Wuhan University of Technology Wuhan, China, 430070

[2] Hubei Key Laboratory of Roadway Bridge &Structure Engineering, Wuhan University of Technology Wuhan, China, 430070

[a]274118038@qq.com

**Keywords:** downburst; wind field characteristics; continuous mountains; CFD numerical simulation;

**Abstract.** Downburst is an outburst strong wind on or near the ground, and its wind field characteristics are significantly different from boundary layer winds. Continuous mountains at different distance are one of the main factors for the influence of downburst wind field characteristic. In this thesis, the changes of the wind field characteristics under the influence of continuous mountains at different distance after the downburst happened are studied by CFD numerical simulation. The impact of downburst is analysed and summarized through the charts.

## Introduction

Downburst is an outburst strong wind on or near the ground, and its wind field characteristics are significantly different from boundary layer winds [1]. Microbursts are common phenomenon during thunderstorm weathers, which have been detected on 60% to 70% of the days during thunderstorms[2]. Downburst shave great destructiveness for engineering structures in many countries, including Australia, America, South Africa, Japan and any other countries around the world[3]. In the beginning, the study of downburst was mainly focused on Meteorology and aeronautics. Whitingham [4] found the importance of downburst in the extreme wind in Australia in 1960s,and Melbourne [5] proposed that we should take downburst into wind engineering and structural design consideration. Because of the exchange of heat, terrain-induced and any other reasons, it is common for mountain to have effects on acceleration and changes of direction which are produced by wind flow. So downburst as a strong downdraft which induces an outburst of damaging winds on or near the ground can even do big damage to construction.

## Numerical computational model

*Wind field model.* At present, there are essentially two forms of simplified models for the wind field associated with downburst, namely the "ring vortex" model and the "impinging jet" model [6]. The impinging jet model schematic diagram shows in Fig.1.

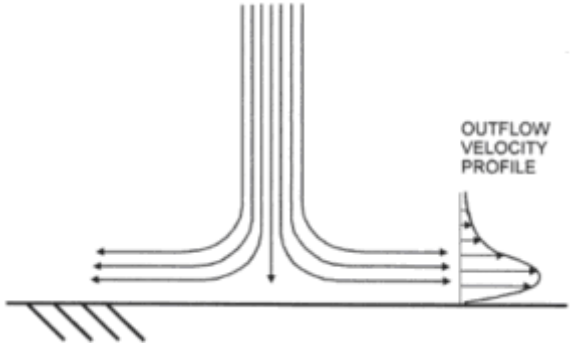


Impinging jet model

Fig.1 Impinging jet model models for the wind field

*Governing equations.* Any motions are based on Law of conservation of mass and Law of conservation of energy, and due to the continuous mountains, the two-dimensional wind field of downburst is conducted using the standard k-ε, model. Governing equations of computational simulation studying on two-dimensional continuous mountains at different distance are given by:

$$\frac{\partial p}{\partial t}+\sum_{i=1}^{3}\frac{\partial(\rho u_i)}{\partial x_i}=0 \tag{1}$$

$$\frac{Du_i}{Dt}=f_i-\frac{1}{\rho}\cdot\frac{\partial p}{\partial x_i}-\frac{1}{\rho}\cdot\frac{\partial}{\partial x_i}\left(\frac{2}{3}\mu\frac{\partial u_j}{\partial x_j}\right)+\frac{1}{\rho}\cdot\frac{\partial}{\partial x_i}\left[\mu\left(\frac{\partial u_i}{\partial x_j}+\frac{\partial u_j}{\partial x_i}\right)\right] \tag{2}$$

$$\varepsilon=\frac{\mu}{\rho}\overline{\left(\frac{\partial u_i}{\partial x_k}\right)\left(\frac{\partial u_i}{\partial x_k}\right)} \tag{3}$$

Eq.1 is Law of conservation of mass.Eq.2 is Law of conservation of energy.Eq.3 is standard k-ε model.

**Numerical computational model**

Continuous mountains at different distance adopt cosine equation y=1+ [1+cos (∏r/2$L_1$)] ($L_1$ is the length of half slope showed in Fig.2.).The distance between the mountain which is closed to the center of downburst is 2$D_{jet}$.The initial conditions in this paper are assumed that initial jet diameter $D_{jet}$=1800,Geometric scale 1:3000,initial jet velocity $V_{jet}$=27m/s,Velocity scale based on Mason's [7]study is 1:3. Schematic diagram of computational domain shows in Fig.3.

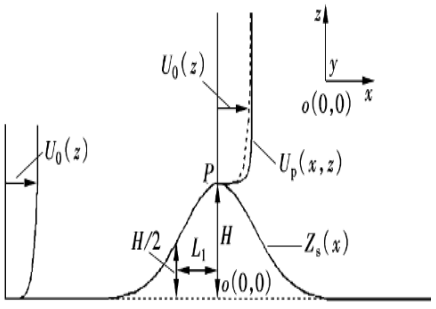


Fig.2 The length of half slope

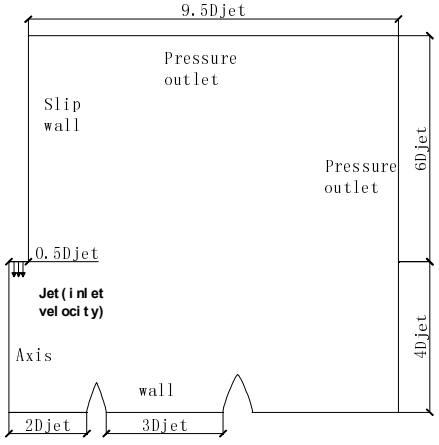


Fig.3 Schematic diagram of computational domain

**Results and discussion**

Wind velocity represents the most basic wind field characteristics.Fig.4 depicts wind distribution of wind velocity at different distance between continuous mountains.Fig.5 depicts the wind speed profile.

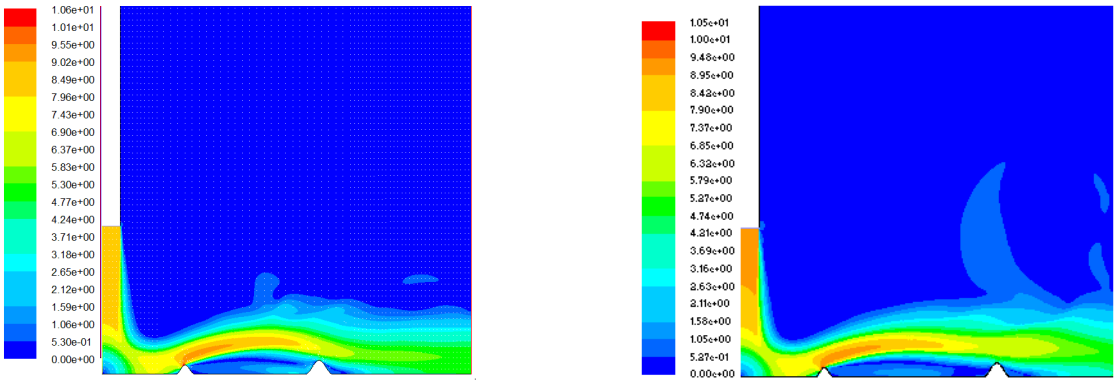


(a)D=3$D_{jet}$ (b)D=4$D_{jet}$

Fig.4 Wind velocity contours at different distance between continuous mountains

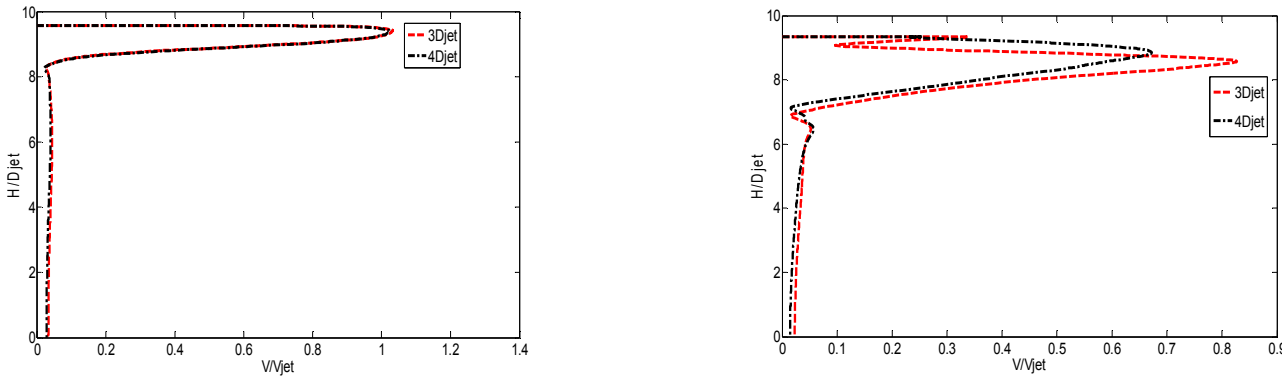


(a) Mountains on the left (b) Mountains on the right

Fig.5 Wind speed profile

As shown in the Fig.4 and Fig.5.There is a velocity distribution of different distance (respectively D=3$D_{jet}$ and D=4$D_{jet}$) between the mountains. We can find the velocity of the top of the first mountain is larger than second's, and the velocity of second mountain of 3$D_{jet}$ is larger than 4$D_{jet}$.Besides,the longer distance between the mountains is, the gentler decrease of velocity is, and the velocity of the district which is between the mountain is essentially the same as the other one.

## Conclusions

The numerical computational simulation method is employed to investigate downburst field characteristics under the influence of two-dimensional continuous mountains at different distance. The two-dimensional wind field of downburst is conducted using the standard k-ε model.The corresponding boundary conditions and boundary treatments make the model more realistic. And CFD method using commercial software FLUENT can effectively simulates the whole process of the downburst field characteristics under the influence of two-dimensional continuous mountains at different distance.

## Acknowledgment

This work is supported by National students' innovation and entrepreneurship training program(20131049706005), National Natural Science Foundation of China (51308430),the Specialized Research Fund for the Doctoral Program of Higher Education of China (No.20110143120003) and the Fundamental Research Funds for the Central Universities (WUT:2013-IV-019).

**References**

[1] Fujita T.T. The downburst. Report of Projects NIMROD and JAWS[R].Chicago: University of Chicago, 1985.
[2] Proctor Fred H. Numerical Simulations of an Isolated Microburst. Part I: Dynamics and Structure [J].Journal of the Atmospheric Sciences.1988, 45(21): 3137-3160.
[3] Holmes J.D. Modeling of extreme thunderstorm winds for wind loading of structures and risk assessment[C].Proceedings, 10th International Conference on Wind Engineering, Copenhagen, Denmark, 1999:1409-1415.
[4] Whittingham H.E. Extreme wind gusts in Australia[R] 1Bulletin No. 46, Bureau of Meteorology, Melbourne, Australia, 1964.
[5] Melbourne W.H. Modelling of structures to measure wind effects [C].Proceedings of Meteorology, Melbourne, Australia, 1972.
[6] Hangan H, RobertsD, Xu Z, et al. Downburst simulations experimental and numerical challenges[C].Proceedings of the 2004 Structures Congress 2Building on the Past: Securing the Future, 2004: 1657 – 1664
[7] Mason M. physical simulation of thunderstorm downbursts [D].Masters thesis, Lubbock (TX, USA): Texas Tech Unversiity, 2003.

*Applied Mechanics and Materials Vols. 580-583 (2014) pp 3115-3118*
*© (2014) Trans Tech Publications, Switzerland*
*doi:10.4028/www.scientific.net/AMM.580-583.3115*

# Investigation on the Wind Pressure Asymmetric Coefficient of Transmission Line

Wei Hao [1,2, a], Bo Li [1,2,b],Jing-boYang[3,c],Fengli Yang[3,d]

[1] School of Civil Engineering, Beijing Jiao tong University, Beijing, 100044, China

[2] Beijing's Key Laboratory of Structural Wind Engineering and Urban Wind Environment, Beijing Jiao tong University, Beijing, 100044, China

[3] China Electric Power Research Institute, Beijing, 100055, China

[a]13121025@bjtu.edu.cn, [b] libo_77@163.com, [c]yjb@epri.sgcc.com.cn, [d]17870644@qq.com

**Keywords:**wind pressure, asymmetric coefficient, transmission line, wind speed, code

**Abstract.** The wind pressure asymmetric coefficient is used to express the variation of wind distribution along the transmission line. In this paper, the value of the wind pressure asymmetric coefficient in some international codes is discussed and compared. It's shown that the coefficient has no relationship with the span length of transmission only in Chinese code.When the span of the checked transmission line is small, the wind pressure calculated based on Chinese code will be smaller than that based on others.

## Introduction

The wind pressure is a random dynamic load, which is not only variable in time but also in space. In usual, the dimension of structure, especially in horizontal direction, is small compared with the turbulence integral length of wind which is used to express the mean dimension of vortex in wind. So, we usually ignore the variation of wind in horizontal direction, which means wind is full-correlation and change synchronously. But, when the structure system is larger than the turbulence integral length of wind, the previous assumption is not suitable. For the transmission line, the distance between two transmission towers is much large than the turbulence integral length of wind, so we must consider the variation of wind along the transmission line [1][2][3].

The wind pressure asymmetric coefficient $\alpha$ is used to express the variation of wind distribution along the transmission line. When we design the transmission line, wind pressure is firstly calculated according to the design wind speed. Then, the wind pressure asymmetriccoefficient is used to discount the wind pressure. But, the value of the coefficient $\alpha$ is related to characteristic of wind flow in nature. At present, we depend on the field measurement to pursue the parameters of wind, which is a big task and many works are carrying out [4][5][6].

In china, the wind pressure asymmetric coefficient $\alpha$ has been provided in codes for twenty years and used to check the stress and wind deflection of wire. But, many accidents occur due to wind deflection of wire beyond the limitation. For example, there are at lest 21 accidents of 500kV transmission line belong to State Grid in summer, 2004, which results a huge damage to power system in China[7][8].

In this paper, the value of the wind pressure asymmetric coefficient $\alpha$ in international codes is discussed and compared in order to provide modifications for the coefficient.

## Specification in Codes

### *China*

Specification of the wind pressure asymmetric coefficient in the Electric Power Industry Standard of China "Code for Design of 110 ~ 500 kV Overhead Transmission Line" (DI/T5092) is shown in Tab. 1.When checking the electrical clearance of tower, if wind speed V ≥120 m/s, $\alpha$ is equal to 0.61[9][10].

**Table 1The wind pressure asymmetric coefficient**

| Span length of transmission line /m | Coefficient |
|---|---|
| ⩽150 | 1.0 |
| 300 | 0.8 |
| 450 | 0.7 |

Notes:

1. Intermediate values can be calculated by the insertion method
2. The coefficient ignores the influence of the wind fluctuation.

### *Japan*

According to the Electrical Association Standardof Japan"Overhead Power Transmission Codes" (JEAC6001), it should multiply by a reduction factor involving the structure scale when calculating the wire wind pressure.The reduction factor $\beta$ can be calculated by the following equation:

$$\beta=0.5+40/S \quad (1)$$

Where,S is the span length and the unit is m.

This provision also states that when the wire windage yaw is calculated using simplified algorithm, if the span length is more than 200 m, $\beta$ will be taken as 0.7. Japanese wire windage yaw was calculated based on the statistically mean wind speed —10 m high above the ground, 10 min and 50 years return period—deriving from the meteorological conditions.

### *Germany*

In the light of Europe Standard "The first part of the high-lifted alternating-current system over 45 kVgeneral conditions and codes" (EN 50341),Germany provides the terms in"The German standard interpretation"(NNA).When designing a new high-lifted alternating-current system,the wind pressure and windage yaw can be calculated according to the following formulation:

$$Q_{WC}=q_c C_{XC} G_{XC} DL \quad (2)$$

Where,$G_{XC}$ is the wire response coefficient, which can be determined by:

$$G_{XC}=\begin{cases}0.75 & L<200m\\ 0.45+60/L & L\geq 200m\end{cases} \quad (3)$$

### *Russia*

According to the provisionof Russian "Electrical installation regulation", thewind pressure can be calculated by the following formulation:

$$P=\alpha K_1 C_X q F \sin^2\psi \quad (4)$$

Where, $\alpha$ is the wind pressure asymmetric coefficient and shown in Table 2; $K_1$ is the span length coefficient:

$$K_1 = \begin{cases} 1.2 & L = 50m \\ 1.0 & L = 100m \\ 1.05 & L = 150m \\ 1.0 & L \geq 200m \end{cases} \quad (5)$$

**Table 2The wind pressure asymmetric coefficient**

| **Wind pressure/（kg·m$^{-2}$）** | 27 | 40 | 55 | 76 |
|---|---|---|---|---|
| **Wind speed /(m·s$^{-1}$)** | 20.8 | 25.3 | 29.7 | 34.9 |
| $\alpha$ | 1.0 | 0.85 | 0.75 | 0.7 |

Considering the cases of wind speed at 29.7 m/s and 25.3 m/s and the provisions of the span length coefficient $K_1$,Table 3 shows the wind pressure asymmetric coefficients changing with the variation of span lengths, and intermediate values are calculated by the insertion method.

**Table 3Thereduction of the wind pressure**

| **Wind speed (m·s$^{-1}$)** | **Span length/m** | | | | |
|---|---|---|---|---|---|
| | 50 | 100 | 150 | 200 | ≥250 |
| 29.7 | 0.81 | 0.743 | 0.709 | 0.692 | 0.675 |
| 25.3 | 1.02 | 0.935 | 0.893 | 0.871 | 0.85 |

**Comparison and analysis**

The values of $\alpha$ based on different international code are compared in Table 4.

**Table 4The comparison of values of $\alpha$**

| **Span length/m** | | | | | | | | | | | | **Codes** |
|---|---|---|---|---|---|---|---|---|---|---|---|---|
| 50 | 100 | 150 | 200 | 250 | 300 | 400 | 450 | 500 | 600 | 800 | 900 | |
| 0.61 | | | | | | | | | | | | Chinese code |
| 0.90 | | 0.77 | 0.70 | 0.66 | 0.63 | 0.60 | 0.59 | 0.58 | 0.57 | | 0.55 | Japanese code |
| | 0.75 | | | 0.69 | 0.65 | 0.60 | 0.58 | 0.57 | 0.55 | 0.53 | 0.52 | German code |
| 0.81 | 0.74 | 0.71 | 0.69 | | 0.675 | | | | | | | Russian code |

It can be seen that compared with other accessory methods, in the design regulation of China, $\alpha$ is equal to 0.61, which covers a wide range of wind speeds and is suitable to all the span lengths.In the range of small span lengths, $\alpha$ is still 0.61, which is significantly lower than the values of the regulations of other countries. For example, in the case that the span length is less than 363 m, $\alpha$ calculated based on Japanese codes is greater than 0.61 . When the span length is 250 m, $\alpha$ of Japanese, German, and Russian codes is respectively 0.66, 0.69 and 0.675,which are all greater than the value of 0.61. Because the $\alpha$ in Chinese codes has no relationship with the span length, the smaller the span length is, and the greater the wind pressure difference between the windage yaw calculation and load calculation is.It runs contrary to the rules shown in the regulations of all countries' design codes.

## Conclusions

In the paper, specifications in code about wind pressure asymmetric coefficient are investigated. It's shown that the coefficient is 0.61 in Chinese code, and has no relationship with the span length of transmission. But, in other codes, the coefficient depends on the span length, which is more reasonable. When the span is small, the wind pressure based on Chinese code is small, which is dangerous in practice.So, it's necessary to revise the specification in Chinese code.

## Acknowledgements

This study is supported by the Fundamental Research Funds for the CentralUniversities (2014JBM088) and the Science and Technology Project of the China State Grid Group (GC17201200078).

## References

[1]Von Karman. Progress in the statistical theory of turbulence [C]. Proceedings of the NationalAcademy of Sciences of the United States of America, 1948, 34(11): 530-539.
[2] Harris R I.The nature of the wind [C].Proceedings of the Seminar on the Modern Design of Wind SensitiveStructures.London, England: Institution of Civil Engineers, 1970: 29-55.
[3] Holmes JD. Wind Load of Structures[M], New York: Spon Press, 2001.
[4]Caracoglia L, Jones N P. Analysis of full-scale wind and pressure measurements on a low-rise building [J]. Journal of Wind Engineering and Industrial Aerodynamics, 2009, 97: 157-173.
[5]Liu Z, Prevatt D O, Aponte-Bermudez L D. Field measurement and wind tunnel simulation of hurricane wind loads on a single family dwelling [J]. Engineering Structures, 2009, 31(10): 2265-2274.
[6]Giammanco, I.M., Schroeder, J.L., Powell, M.D. GPS dropwindsonda and WSR-88D observations oftropical cyclone vertical wind profiles and their characteristics [J]. Weather Forecasting,http://dx.doi.org/10.1175/WAF- D-11-00155.1
[7]Engelhardt J S and Basu S P. Design Installation, and Field Experience with an Overhead Transmission Dynamic Line Rating System [J]. IEEE paper 0-7803-3522-8/96, 1996.
[8] H. D. Chiang, A. J. Flueck, and K. S. Shah, "A practical tool for tracing power system steady-state stationary behavior due to load and generation variations," IEEE Trans. Power Syst., vol. 10, no. 4, pp. 623–632,Nov. 1995.
[9]GB 50009—2012. Load code for the design of building structures [S]. Beijing: China Architecture & Building Press, 2012.
[10]GB 50545—2010.Code for design of 110~750kV overhead transmission line[S].Beijing: China Architecture & Building Press, 2010.

*Applied Mechanics and Materials Vols. 580-583 (2014) pp 3119-3124*
*© (2014) Trans Tech Publications, Switzerland*
*doi:10.4028/www.scientific.net/AMM.580-583.3119*

# Three-Parameter Damage Evolution for Quasi-Brittle Solids

ZHANG Ji

School of Civil Engineering, Tongji University, Shanghai, China

zhang_ji@tongji.edu.cn

**Keywords:** brittle solid; damage evolution; triaxial compression; hydrostatic stress; deviatoric stress

**Abstract.** This paper aims to investigate the performance of a new three-parameter damage mechanics model which describes three basic damage mechanisms of quasi-brittle solids: tension, shear, and hydrostatic compression. The stress is first decomposed into its positive part and negative part, and then the latter is further decomposed into its deviatoric part and hydrostatic part, whereby a three-parameter damage description is formulated. Through matrix representation of the tensor formulation, specific forms of the three-parameter damage theory are illustrated in various stress states. It is found that the proposed framework of three-parameter damage theory can inherit the existing two-parameter models and extend them to a broader scope of application.

## Introduction

One of the complexities of the mechanical behavior of quasi-brittle materials lies in the diversity of damage and failure modes in various stress states. A positive-negative split of the stress advocated by Ladevèze [1] is efficient for the description of different damage mechanisms in tension and compression and has been widely used in subsequent damage models (e.g. that by Voyiadjis et al. [2]). A traditional volumetric-deviatoric split of the strain is featured in many kinds of constitutive models for quasi-brittle materials and has been playing an important role in microplane models since Bažant and Prat [3].

It is the purpose of the present study to combine the benefits from both positive-negative and hydrostatic-deviatoric splits of the stress in a new three-parameter damage model and analyze the qualitative characteristics of its damage evolution in various loading scenarios. It is intended that the successful performance of the existing two-parameter damage models in plane stress problems can be inherited and the inability of them in triaxial compression overcome.

## Tensor Formulation

**Two-Parameter Damage.** In a positive-negative split, the effective stress $\bar{\boldsymbol{\sigma}}$ is decomposed into its positive part $\bar{\boldsymbol{\sigma}}^+$ and negative part $\bar{\boldsymbol{\sigma}}^-$ as

$$\bar{\boldsymbol{\sigma}} = \bar{\boldsymbol{\sigma}}^+ + \bar{\boldsymbol{\sigma}}^-, \tag{1}$$

whose meaning can be clearly expressed with the dyadic forms in the pincipal coordinate system

$$\bar{\boldsymbol{\sigma}} = \sum_i \bar{\sigma}_i \boldsymbol{n}_i \otimes \boldsymbol{n}_i, \quad \bar{\boldsymbol{\sigma}}^+ = \sum_i \langle \bar{\sigma}_i \rangle \boldsymbol{n}_i \otimes \boldsymbol{n}_i, \quad \bar{\boldsymbol{\sigma}}^- = -\sum_i \langle -\bar{\sigma}_i \rangle \boldsymbol{n}_i \otimes \boldsymbol{n}_i, \tag{2}$$

where $\bar{\sigma}_i$ are the principal effective stresses, $\boldsymbol{n}_i$ the corresponding principal direction unit vectors, and the Macaulay brackets $< >$ defined as $< x > = ( | x | + x ) / 2$.

With Eq.(1), a two-parameter damage description can be formulated intuitively as [4]

$$\boldsymbol{\sigma} = (\mathbf{I} - \boldsymbol{D}) : \bar{\boldsymbol{\sigma}} = (1 - d^+)\bar{\boldsymbol{\sigma}}^+ + (1 - d^-)\bar{\boldsymbol{\sigma}}^-, \tag{3}$$

where $\mathbf{I}$ is the fourth-order symmetric identity tensor, $\boldsymbol{D}$ the fourth-order damage tensor, $d^+$ the tensile damage variable, and $d^-$ the compressive damage variable.

**Three-Parameter Damage.** On the basis of Eq.(1), $\bar{\boldsymbol{\sigma}}^-$ is further decomposed into its deviatoric part $\bar{\boldsymbol{\sigma}}_{\mathrm{v}}^-$ and hydrostatic part $\bar{\boldsymbol{\sigma}}_{\mathrm{h}}^-$, forming an overall split of $\bar{\boldsymbol{\sigma}}$

$$\bar{\boldsymbol{\sigma}} = \bar{\boldsymbol{\sigma}}^+ + \bar{\boldsymbol{\sigma}}_{\mathrm{v}}^- + \bar{\boldsymbol{\sigma}}_{\mathrm{h}}^-, \tag{4}$$

where

$$\bar{\boldsymbol{\sigma}}_{\mathrm{v}}^- = \bar{\boldsymbol{\sigma}}^- - \frac{1}{3}\mathrm{tr}\left(\bar{\boldsymbol{\sigma}}^-\right)\mathbf{I}, \quad \bar{\boldsymbol{\sigma}}_{\mathrm{h}}^- = \frac{1}{3}\mathrm{tr}\left(\bar{\boldsymbol{\sigma}}^-\right)\mathbf{I}, \tag{5}$$

in which tr( ) is the trace, and $\mathbf{I}$ the second-order identity tensor (also known as the Euclidean metric).

With Eq.(4), a three-parameter damage description can be formulated intuitively as

$$\boldsymbol{\sigma} = (\mathbf{I} - \boldsymbol{D}) : \bar{\boldsymbol{\sigma}} = \left(1 - d^+\right)\bar{\boldsymbol{\sigma}}^+ + \left(1 - d_{\mathrm{v}}^-\right)\bar{\boldsymbol{\sigma}}_{\mathrm{v}}^- + \left(1 - d_{\mathrm{h}}^-\right)\bar{\boldsymbol{\sigma}}_{\mathrm{h}}^-, \tag{6}$$

where $d_{\mathrm{v}}^-$ is the shear damage variable, and $d_{\mathrm{h}}^-$ the hydrostatic compressive damage variable.

**Matrix Representation**

In order to illustrate the specific forms of the three-parameter damage formulation, in this section the respective stress tensors are represented by their corresponding matrices in the principal coordinate system, from which the evolution modes of the three damage variables can be revealed.

Transposing $\bar{\boldsymbol{\sigma}}$ in Eq.(6) leads to a more straightforward damage expression

$$\bar{\boldsymbol{\sigma}} - \boldsymbol{\sigma} = \boldsymbol{D} : \bar{\boldsymbol{\sigma}} = d^+\bar{\boldsymbol{\sigma}}^+ + d_{\mathrm{v}}^-\bar{\boldsymbol{\sigma}}_{\mathrm{v}}^- + d_{\mathrm{h}}^-\bar{\boldsymbol{\sigma}}_{\mathrm{h}}^-. \tag{7}$$

Matrix representation of Eq.(7) in various typical stress states is listed as follows, where $T_i\left(\bar{T}_i\right)$ and $C_i\left(\bar{C}_i\right)$ are the absolute values of the principal tensile and compressive (effective) stresses $\sigma_i\left(\bar{\sigma}_i\right)$, respectively.

**Uniaxial / Biaxial / Triaxial Tension.**

$$\begin{bmatrix} \bar{T}_1 - T_1 & & \\ & \bar{T}_2 - T_2 & \\ & & \bar{T}_3 - T_3 \end{bmatrix} = \boldsymbol{D} : \begin{bmatrix} \bar{T}_1 & & \\ & \bar{T}_2 & \\ & & \bar{T}_3 \end{bmatrix} = d^+ \begin{bmatrix} \bar{T}_1 & & \\ & \bar{T}_2 & \\ & & \bar{T}_3 \end{bmatrix} \tag{8}$$

**Uniaxial Compression.**

$$\begin{bmatrix} 0 & & \\ & 0 & \\ & & -\left(\bar{C}_3 - C_3\right) \end{bmatrix} = \boldsymbol{D} : \begin{bmatrix} 0 & & \\ & 0 & \\ & & -\bar{C}_3 \end{bmatrix}$$
$$= d_{\mathrm{v}}^{-} \begin{bmatrix} \frac{1}{3}\bar{C}_3 & & \\ & \frac{1}{3}\bar{C}_3 & \\ & & -\frac{2}{3}\bar{C}_3 \end{bmatrix} + d_{\mathrm{h}}^{-} \begin{bmatrix} -\frac{1}{3}\bar{C}_3 & & \\ & -\frac{1}{3}\bar{C}_3 & \\ & & -\frac{1}{3}\bar{C}_3 \end{bmatrix} \tag{9}$$

It can be seen from Eq.(9) that $d_{\mathrm{v}}^{-}=d_{\mathrm{h}}^{-}$ since $\bar{\sigma}_1 = \bar{\sigma}_2 = 0$.

**Biaxial Compression.**

$$\begin{bmatrix} 0 & & \\ & -\left(\bar{C}_2 - C_2\right) & \\ & & -\left(\bar{C}_3 - C_3\right) \end{bmatrix} = \boldsymbol{D} : \begin{bmatrix} 0 & & \\ & -\bar{C}_2 & \\ & & -\bar{C}_3 \end{bmatrix}$$
$$= d_{\mathrm{v}}^{-} \begin{bmatrix} \frac{\bar{C}_2 + \bar{C}_3}{3} & & \\ & \frac{-2\bar{C}_2 + \bar{C}_3}{3} & \\ & & \frac{\bar{C}_2 - 2\bar{C}_3}{3} \end{bmatrix} + d_{\mathrm{h}}^{-} \begin{bmatrix} -\frac{\bar{C}_2 + \bar{C}_3}{3} & & \\ & -\frac{\bar{C}_2 + \bar{C}_3}{3} & \\ & & -\frac{\bar{C}_2 + \bar{C}_3}{3} \end{bmatrix} \tag{10}$$

It can be seen from Eq.(10) that $d_{\mathrm{v}}^{-}=d_{\mathrm{h}}^{-}$ since $\bar{\sigma}_1 = 0$.

**Biaxial Tension-Compression.**

$$\begin{bmatrix} \bar{T}_1 - T_1 & & \\ & 0 & \\ & & -\left(\bar{C}_3 - C_3\right) \end{bmatrix} = \boldsymbol{D} : \begin{bmatrix} \bar{T}_1 & & \\ & 0 & \\ & & -\bar{C}_3 \end{bmatrix}$$
$$= d^{+} \begin{bmatrix} \bar{T}_1 & & \\ & 0 & \\ & & 0 \end{bmatrix} + d_{\mathrm{v}}^{-} \begin{bmatrix} \frac{1}{3}\bar{C}_3 & & \\ & \frac{1}{3}\bar{C}_3 & \\ & & -\frac{2}{3}\bar{C}_3 \end{bmatrix} + d_{\mathrm{h}}^{-} \begin{bmatrix} -\frac{1}{3}\bar{C}_3 & & \\ & -\frac{1}{3}\bar{C}_3 & \\ & & -\frac{1}{3}\bar{C}_3 \end{bmatrix} \tag{11}$$

It can be seen from Eq.(11) that $d_{\mathrm{v}}^{-}=d_{\mathrm{h}}^{-}$ since $\bar{\sigma}_2 = 0$.

**Triaxial Tension-Tension-Compression.**

$$\begin{bmatrix} \bar{T}_1 - T_1 & & \\ & \bar{T}_2 - T_2 & \\ & & -\left(\bar{C}_3 - C_3\right) \end{bmatrix} = \boldsymbol{D} : \begin{bmatrix} \bar{T}_1 & & \\ & \bar{T}_2 & \\ & & -\bar{C}_3 \end{bmatrix}$$

$$= d^+ \begin{bmatrix} \bar{T}_1 & & \\ & \bar{T}_2 & \\ & & 0 \end{bmatrix} + d_{\mathrm{v}}^- \begin{bmatrix} \frac{1}{3}\bar{C}_3 & & \\ & \frac{1}{3}\bar{C}_3 & \\ & & -\frac{2}{3}\bar{C}_3 \end{bmatrix} + d_{\mathrm{h}}^- \begin{bmatrix} -\frac{1}{3}\bar{C}_3 & & \\ & -\frac{1}{3}\bar{C}_3 & \\ & & -\frac{1}{3}\bar{C}_3 \end{bmatrix} \tag{12}$$

It can be concluded from Eq.(12) that $d_{\mathrm{v}}^- = d_{\mathrm{h}}^-$ because the damage evolution of principal tensile stresses $(\bar{T}_1, \bar{T}_2)$ should not be subject to that of principal compressive stresses $(-\bar{C}_3)$.

**Triaxial Tension-Compression-Compression.**

$$\begin{bmatrix} \bar{T}_1 - T_1 & & \\ & -\left(\bar{C}_2 - C_2\right) & \\ & & -\left(\bar{C}_3 - C_3\right) \end{bmatrix} = \boldsymbol{D} : \begin{bmatrix} \bar{T}_1 & & \\ & -\bar{C}_2 & \\ & & -\bar{C}_3 \end{bmatrix}$$

$$= d^+ \begin{bmatrix} \bar{T}_1 & & \\ & 0 & \\ & & 0 \end{bmatrix} + d_{\mathrm{v}}^- \begin{bmatrix} \frac{\bar{C}_2 + \bar{C}_3}{3} & & \\ & \frac{-2\bar{C}_2 + \bar{C}_3}{3} & \\ & & \frac{\bar{C}_2 - 2\bar{C}_3}{3} \end{bmatrix} + d_{\mathrm{h}}^- \begin{bmatrix} -\frac{\bar{C}_2 + \bar{C}_3}{3} & & \\ & -\frac{\bar{C}_2 + \bar{C}_3}{3} & \\ & & -\frac{\bar{C}_2 + \bar{C}_3}{3} \end{bmatrix} \tag{13}$$

It can be concluded from Eq.(13) that $d_{\mathrm{v}}^- = d_{\mathrm{h}}^-$ because the damage evolution of principal tensile stresses $(\bar{T}_1)$ should not be subject to that of principal compressive stresses $(-\bar{C}_2, -\bar{C}_3)$.

**Pseudo-Triaxial Compression—Compressive Meridian.** In this case, the lateral compression $C_1 = C_2$ is less than the longitudinal comression $C_3$.

$$\begin{bmatrix} -\left(\bar{C}_1 - C_1\right) & & \\ & -\left(\bar{C}_1 - C_1\right) & \\ & & -\left(\bar{C}_3 - C_3\right) \end{bmatrix} = \boldsymbol{D} : \begin{bmatrix} -\bar{C}_1 & & \\ & -\bar{C}_1 & \\ & & -\bar{C}_3 \end{bmatrix}$$

$$= d_{\mathrm{v}}^- \begin{bmatrix} \frac{-\bar{C}_1 + \bar{C}_3}{3} & & \\ & \frac{-\bar{C}_1 + \bar{C}_3}{3} & \\ & & \frac{2\bar{C}_1 - 2\bar{C}_3}{3} \end{bmatrix} + d_{\mathrm{h}}^- \begin{bmatrix} -\frac{2\bar{C}_1 + \bar{C}_3}{3} & & \\ & -\frac{2\bar{C}_1 + \bar{C}_3}{3} & \\ & & -\frac{2\bar{C}_1 + \bar{C}_3}{3} \end{bmatrix} \tag{14}$$

It can be seen from Eq.(14) that $d_{\mathrm{v}}^{-}$ and $d_{\mathrm{h}}^{-}$ evolve independently of each other.

**Pseudo-Triaxial Compression—Tensile Meridian.** In this case, the lateral compression $C_2 = C_3$ is greater than the longitudinal comression $C_1$.

$$\begin{bmatrix} -\left(\bar{C}_1 - C_1\right) & & \\ & -\left(\bar{C}_3 - C_3\right) & \\ & & -\left(\bar{C}_3 - C_3\right) \end{bmatrix} = \boldsymbol{D} : \begin{bmatrix} -\bar{C}_1 & & \\ & -\bar{C}_3 & \\ & & -\bar{C}_3 \end{bmatrix}$$

$$= d_{\mathrm{v}}^{-} \begin{bmatrix} \dfrac{\bar{C}_1 - \bar{C}_3}{3} & & \\ & \dfrac{\bar{C}_1 - \bar{C}_3}{3} & \\ & & \dfrac{2\bar{C}_3 - 2\bar{C}_1}{3} \end{bmatrix} + d_{\mathrm{h}}^{-} \begin{bmatrix} -\dfrac{\bar{C}_1 + 2\bar{C}_3}{3} & & \\ & -\dfrac{\bar{C}_1 + 2\bar{C}_3}{3} & \\ & & -\dfrac{\bar{C}_1 + 2\bar{C}_3}{3} \end{bmatrix} \tag{15}$$

It can be seen from Eq.(15) that $d_{\mathrm{v}}^{-}$ and $d_{\mathrm{h}}^{-}$ evolve independently of each other.

**True Triaxial Compression.**

$$\begin{bmatrix} -\left(\bar{C}_1 - C_1\right) & & \\ & -\left(\bar{C}_2 - C_2\right) & \\ & & -\left(\bar{C}_3 - C_3\right) \end{bmatrix} = \boldsymbol{D} : \begin{bmatrix} -\bar{C}_1 & & \\ & -\bar{C}_2 & \\ & & -\bar{C}_3 \end{bmatrix}$$

$$= d_{\mathrm{v}}^{-} \begin{bmatrix} \dfrac{-2\bar{C}_1 + \bar{C}_2 + \bar{C}_3}{3} & & \\ & \dfrac{\bar{C}_1 - 2\bar{C}_2 + \bar{C}_3}{3} & \\ & & \dfrac{\bar{C}_1 + \bar{C}_2 - 2\bar{C}_3}{3} \end{bmatrix} + d_{\mathrm{h}}^{-} \begin{bmatrix} -\dfrac{\bar{C}_1 + \bar{C}_2 + \bar{C}_3}{3} & & \\ & -\dfrac{\bar{C}_1 + \bar{C}_2 + \bar{C}_3}{3} & \\ & & -\dfrac{\bar{C}_1 + \bar{C}_2 + \bar{C}_3}{3} \end{bmatrix} \tag{16}$$

It can be seen from Eq.(16) that $d_{\mathrm{v}}^{-}$ and $d_{\mathrm{h}}^{-}$ evolve independently of each other.

**Summary**

Several damage evolution properties can be summarized from the above matrix representation:

1) $d^{+}$ evolves independently of $d_{\mathrm{v}}^{-}$ and $d_{\mathrm{h}}^{-}$.
2) In stress states other than triaxial compression, $d_{\mathrm{v}}^{-} = d_{\mathrm{h}}^{-}$, evolving in synchronization.
3) In triaxial compression, $d_{\mathrm{v}}^{-}$ and $d_{\mathrm{h}}^{-}$ evolve independently of each other.

In the present three-parameter damage model, the positive-negative split of $\bar{\boldsymbol{\sigma}}$ is in the first level, and the volumetric-deviatoric split of $\bar{\boldsymbol{\sigma}}^{-}$ second. The positive-negative split is superordinate to the volumetric-deviatoric split, which leads to property 1. When zero or positive principal stresses are present, the volumetric-deviatoric split is limited to part of the stress components, which leads to property 2. When no zero or positive principal stresses are present, the volumetric-deviatoric split is implemented on all the stress components, which leads to property 3.

It is seen that in stress states other than triaxial compression, the three-parameter damage model reduces to the existing two-parameter one, i.e. $d^- = d_v^- = d_h^-$. So the proposed framework of three-parameter damage description can inherit the successful two-parameter models and extend them to a broader scope of application.

**Acknowledgements**

Financial supports from the National Natural Science Foundation of China (Grant Nos. 51108336, 51378377) are greatly appreciated.

**References**

[1] P. Ladevèze: *Sur une théorie de l'endommagement anisotrope* (Laboratoire de Mécanique et Technologie, France 1983).

[2] G.Z. Voyiadjis, Z.N. Taqieddin, P.I. Kattan, "Anisotropic damage-plasticity model for concrete", International Journal of Plasticity, vol. 24, 2008, p.1946–1965.

[3] Z.P. Bažant, P.C. Prat, "Microplane model for brittle-plastic material. I: Theory", Journal of Engineering Mechanics, ASCE, vol. 114, 1988 p.1672–1688.

[4] R. Faria, J. Oliver, M. Cervera, "A strain-based plastic viscous-damage model for massive concrete structures", International Journal of Solids and Structures, vol. 35, 1998, p.1533–1558.

# CHAPTER 15:

# CAD/CAE/Computer Technology

*Applied Mechanics and Materials Vols. 580-583 (2014) pp 3127-3133*
*© (2014) Trans Tech Publications, Switzerland*
*doi:10.4028/www.scientific.net/AMM.580-583.3127*

# An Integrated Simulation System for Building Structures

Duan Jin[1,a], Chen Xiao-ming[1], Qi Hu[1], Li Yun-gui[1]

[1]China State Construction Technical Center, Beijing, 101300, PR China

[a] duanjin78@126.com

**Key words**: structural simulation, system integration, FEA, BIM

**Abstract:** In this paper, an integrated simulation system for building structures is presented to satisfy the engineering requirements for high performance simulation.It is a coalition of the traditional design softwares and general finite element analysis (FEA)softwares. This system is developed in the platform ofIntel Fortran, using theprogramming language of Fortran2003/2008.For simplicity, it would be introduced and discussedbriefly in the following article.Andcombining with YJK and ABAQUS,this system is implemented to perform dynamic analysis for a high-rise building.Its capacity and validity would be demonstrated by the numerical results.

## 1. Introduction

With the rapid development of high-rise buildings and long-span structures in the recent years, high performance simulation (HPS) is becoming more and more important, sometimes even crucial, for the structure design and building construction. The traditional design softwares, such as PKPM, ETABS, MIDAS, YJK, and so on, can't match the advanced requirements of HPS. On the other hand, the large scale general finite element analysis (FEA) softwares, such as ABAQUS, ANSYS, ADINA, etc., although have the powerful computational abilities, but can't be applied directly to the architecturalstructure analysis and design, due to the fact that their preprocessors are inconvenient for building modeling and their postprocessors can't present computational results according to the building structure specifications, say, the civil codes and the custom of engineering.

To satisfy the above engineering requirements for HPS, the authors and their co-workers havebeen developingan integrated simulation system for building structures, which is a coalition of some secondary software developments together with the traditional design softwares and general FEA softwares. This simulation system will serve as a sub-system of building information model (BIM) and provide high performance computation, simulation and technical supports for the design and construction of large and complex buildings.

According to the simulation system, there are many important technical indicators needing to be emphasized and enforced, typically the following aspects: (1) data input from the building design softwares, such as PKPM, MIDAS, YJK, etc.; (2) data transformation from the structural model or geometrical model to FEA model; (3) data input to the general FEA softwares, such as ABAQUS, ANSYS, ADINA, etc.; (4) data calculation and sorting-out in statistics according to the building structure specification; (5) a parallel FEA computing kernel developed specially for the building structures, serving as the supplements to the general FEA softwares. All of the above technical indicatorsdeserve seriousand vast consideration,but for simplicity of expression, they are introduced and discussed briefly, say, some details will be omitted in this paper.And finally, to demonstrate the validity of the integrated simulation system, some computational results for the complex building will be presented and discussed.

## 2. Description of the simulation system

The integrated simulation system of building structures would be introduced from two points of view, one the objective of this system and the other its program architecture according to the software development.

### *2.1 Objective of the simulation system*

The ultimateobjective of the simulation system is to provide high performance computation, such as elastic-plastic dynamic analysis, wind-resistant dynamic analysis, etc., for complex building structures, by a simple and even fool mode.That is to say the complicated and redundant computing theories and options are isolated from the user interface. The building structure can be modeled with any popular design software, such as PKPM, MIDAS, YJK, ETABS, etc. And then it can be imported into the simulation system and transformed into FE models automatically, including FE meshing and boundary conditions setting. The general FE software, such as ABAQUS, ANSYS, etc., can be called as a computing kernel to solve the above FE model. And in addition, an independent parallel FEA kernel has been developing, not finished yet, by the authors to act as the supplement of the general business softwares. The calculated results of FEA would be transferred automatically to the postprocessor, which would assessment the structural damage and estimate its security and comfort level according to the theory of mechanics and building structure specifications. And finally, the post-processor would present the calculation reports with WORD and PDF files.The main capabilities and basic flowsof the integrated simulation system are shown in Fig.1.

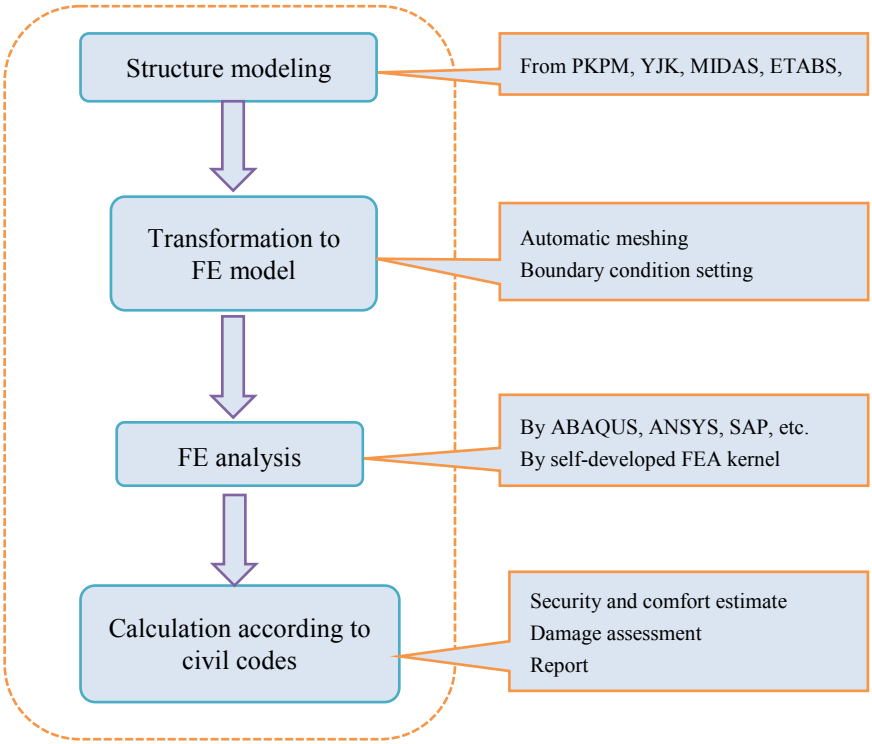


Fig.1 Illustration of the simulation system

### *2.2 Program architecture of the simulation system*

The present simulation system is not a simple binding and piling up of the design softwares and general FE softwares, but a software development with a massive amount of coding, using the

Fortran 2008 language[1,2]. The design softwares, such as PKPM, MIDAS, etc., and general FEA softwares, such as ABAQUS, ANSYS, etc., are integrated into the present software, or system,in the same way as libraries calls in programming. The program architecture of the simulation systemis shown in Fig.2, from which it can be seen that the hard-core of this system is the data processingcenter. This center containsmost of the system codes, including the structural models import, the FE models transformation, i.e., automatic mesh generation[3~5], the programming interface to the general FEA software, and so on. The other codes mainly consist of the auxiliary FEA kernel and the post-processor, which would sort-out in statistics the calculated data results according tostructural engineering and present reports for the engineers. The simulation system presented in this paper istheoretically designed to be strong and open, in other words, any structuraldesign software or FEA software can be added to this system, as long as their data interfaces arenot classified. That's the primary reason why this simulation system can be regarded as a sub-system of building information model (BIM).

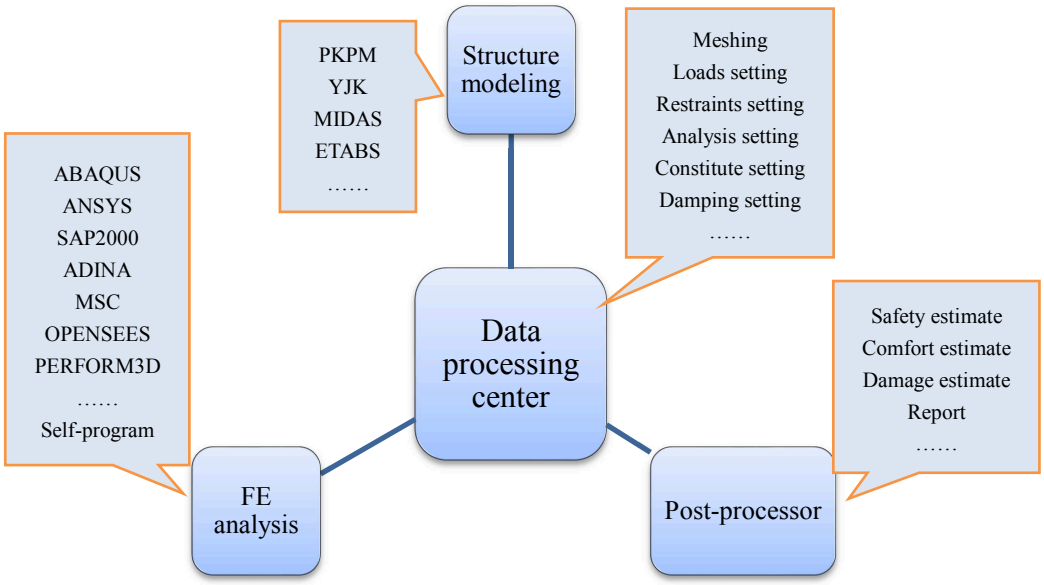


Fig.2 Program architecture of the simulation system

### *2.3 Interface of the simulation system*

The interface of the simulation system is developed by Intel Visual Fortran, shown in Fig.3. It consists of five major parts: (1) data input from the building design softwares, such as YJK, MIDAS, etc.; (2) data transformation from the structural model to FEA model, including transformation options setting and mesh generation, see Ref.[6]; (3) FEA analysis, including constitutive models setting anddata input to the general FEA softwares, such as ABAQUS, and the self-developed computing kernel, seeRef.[7]; (4) data calculation and sorting-out according to the building structure specification; (5) results output and display.

Obviously, the design softwares and FEA softwares have been integrated into a whole. The structure models could be input from the traditional design softwares. The miscellaneous work of mesh generation for the complex buildings has been auto-completed by the system itself. The obscure parameters-setting for nonlinear mechanics analysis has been isolated from the users. The FEA softwares just serve as one of the computing kernels. And finally, the computational results would be recalculated and sorted-out according to the engineering requirements.So using this integrated system, HPS for the complex building are not so profound and complicated as before.

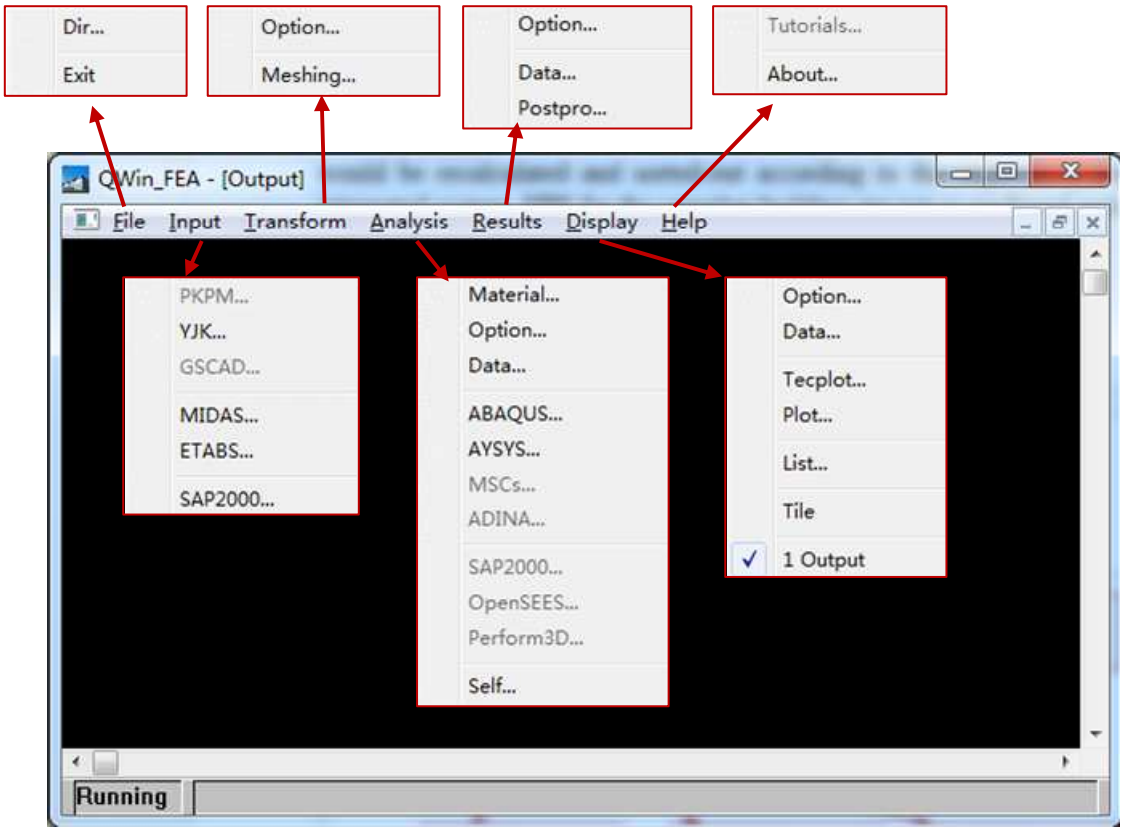


Fig.3 Interface of the simulation system

## 3. Numerical examples

To demonstrate the capacity of the simulation system,a tall-building numerical example would be provided in the following. This building structure is modeled in YJK, meshed by the present system and analyzed by ABAQUS.

### *3.1 Description of the model*

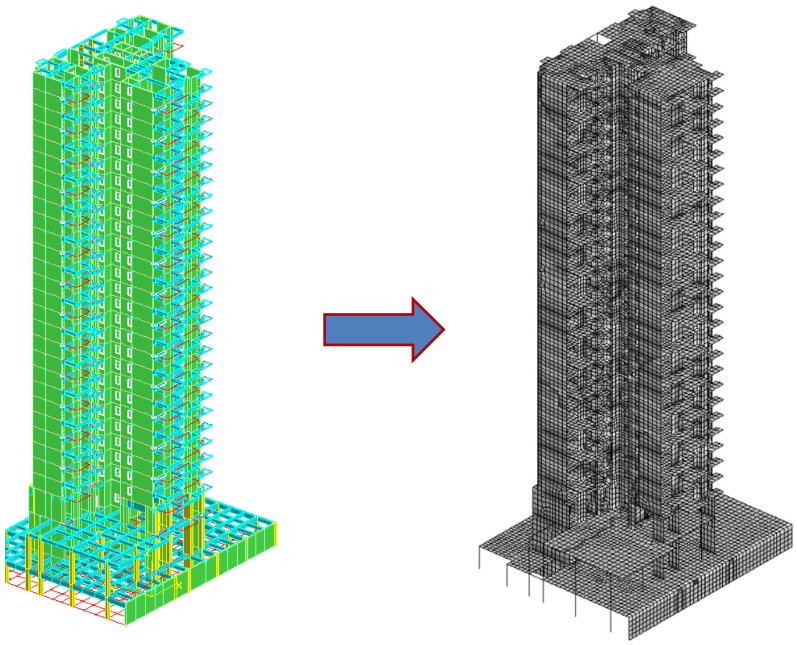

Fig.4 Structural model (YJK) and FE model

The structural model was imported from YJK and transformed into FE model automatically in the system, shown in Fig.4. The most noteworthy feature of this structure is the plane irregularity. Intuitively, the connective bands at the central zone of the floor may be the weak zone of this structure.

In the dynamic analysis, the one-dimensional constitutive model for beams, columns and braces uses that of the code for design of concrete structures (GB-50010-2010) [8], while the two-dimensional constitutive model for walls and slabs adopts the concrete damaged plasticity model of ABAQUS, seeing Abaqus theory manual [9]. The dynamic loads take the seismic wave of America EI Centro (1940.5.18, magnitude is 7, depth is 10 km), whose acceleration history of the first 20 seconds is shown in Fig.5.

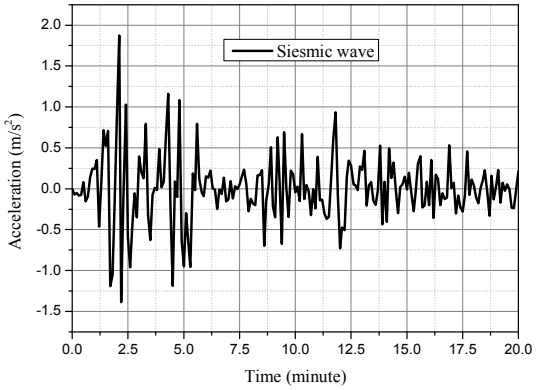


Fig.5Seismic acceleration (America EI Centro)

### *3.2Calculated results*

For simplicity, this paper would only present the response history of the top displacement and base shear, plus the damage assessments of the structure. The other results, especially the statistical results according to the building codes, would be omitted.

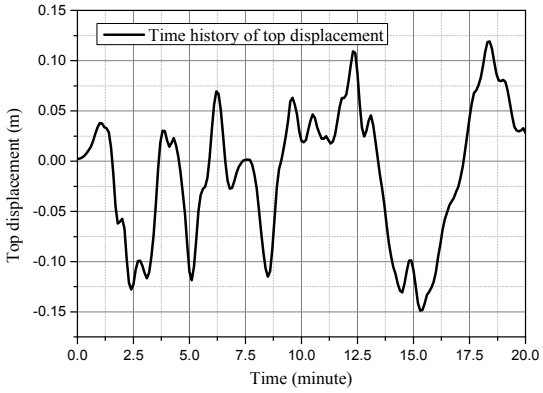


Fig.6 Time history of top displacement

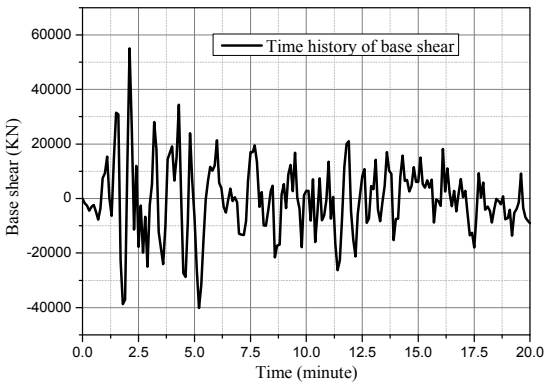


Fig.7 Time history of base shear

The time history of top displacement is shown in Fig.6 and the base shear is shown in Fig.7, from which it can be seen that the history shape of the base shear is very similar to that of seismic acceleration, shown in Fig.5. While if they are normalized and plot in the same graph, seeing Fig.8, the differences become conspicuous. The reasons leading to the differences include the transmission of elastic wave and the others, which are beyond the scope of this paper.

The damage of the structure can be described by the factor of stiffness degradation, which is assumed to be functions of plastic strains and the other field variables. This factor indicates the

degradation of elastic stiffness. Its value belongs to 0~1 interval, in which "0" means no damage has occurred while "1" means the components have been completely damaged. The stiffness degradation of walls, slabs and frames are shown in Fig.9, Fig.10 and Fig.11 respectively, from which it can be observed easily that the damage concentrates at the connective bands at the central zone of the floor, which is identical with the prediction of section 3.1.

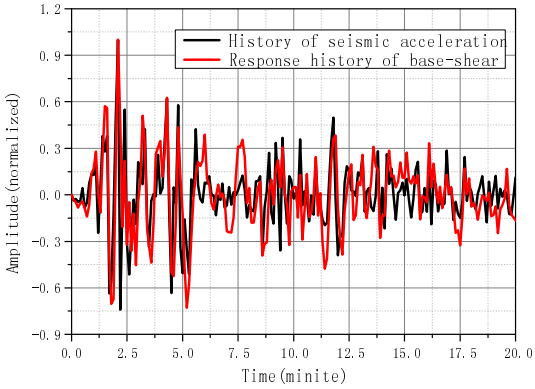


Fig.8Normalization of the seismic input and response

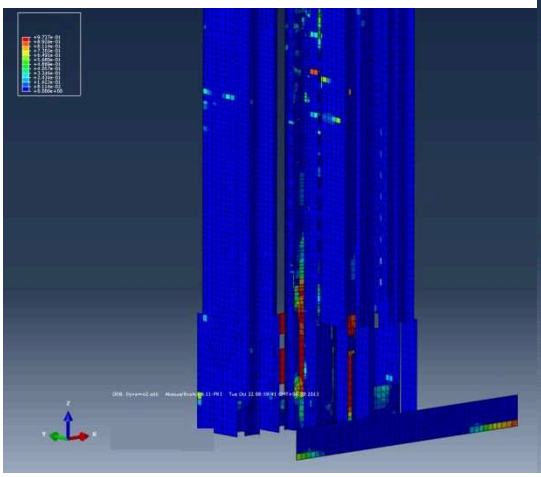

Fig.9The stiffness degradation of walls

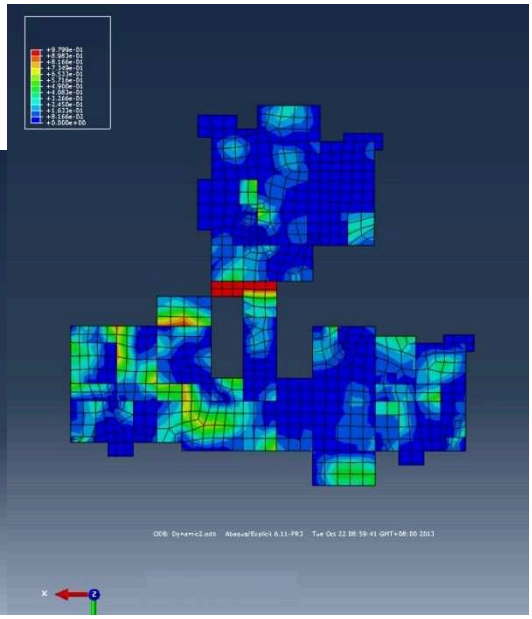

Fig.10 The stiffness degradation of slabs

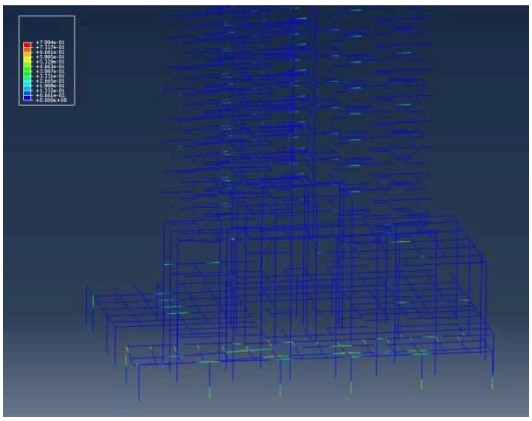

Fig.11The stiffness degradation of frames

## 4. Conclusions

The integrated simulation system of this paper is developed for the high performance computation of building structures, including security assessment and optimization design. And above all, the first purpose is to provide elasto-plastic dynamic analysis for the seismic resistance design of high-rise buildings. To achieve this aim effectively, the popular structural design softwares and the general FEA softwares have been integrated into a whole system by secondary development. Certainly this system has not been completely finished yet, whileitsvalidity for complex building simulation has been demonstrated by the numerical example of sect.3.

## Reference

[1] WD 1539-1. F2008 working document. J3/10-007r1(2010).

[2] N.S.Clerman, and W. Speckor. *Modern Fortran Style and Usage*. New York, USA: Cambridge University Press(2012).

[3] T.D.Blacker, and M.B. Stephenson. Paving: A New Approach to Automated Quadrilateral Mesh Generation,*International Journal for Numerical Methods in Engineering*, Vol. 32(1991), p.811-847.

[4] T.D. Blacker, M.B. Stephenson,and S.A. Canann. Analysis automation with paving: a new quadrilateralmeshing technique, *Proceedings of Design Productivity Institute and International Conference*, University ofMissouri-Rolla, Honolulu(1991).

[5] Park, C., Noh, J.S, Jang, I.S., and Kang, J.M.A new automated scheme of quadrilateral mesh generation for randomly distributed line constraints. *Computer-Aided Design*,Vol.39(2007), p.258-267.

[6] Duan Jin, Chen Xiao-ming, Li Yun-gui.Automatic Mesh Generation for Building Structures. *Journal of Building Structures*.(in Chinese, submitted 2014)

[7] Duan Jin, Chen Xiao-ming, LiYun-gui.A Parallel FEA Solver for Building Structures.*Journal of Building Structures*. (in Chinese, submitted 2014)

[8] GB-50010-2010.*Code for Design of Concrete Structures*. Beijing: China Building Industry Press(2011). (in Chinese)

[9] *Abaqus 6.11Theory Manual*.Providence, RI, USA: Dassault Systèmes Simulia Corp(2011).

*Applied Mechanics and Materials Vols. 580-583 (2014) pp 3134-3137*
*© (2014) Trans Tech Publications, Switzerland*
*doi:10.4028/www.scientific.net/AMM.580-583.3134*

# Simulation Analysis of Built Environment Based on Design Builder Software

Lin Zhang

Sichuan College of Architectural Technology, Deyang, Sichuan, 618000,china

7854278 @qq.com

**Keywords:** built environment , building simulation , Design Builder (DB)

**Abstract.** This paper introduces Design Builder (DB) software and analyzes the computational simulation capacity of Design Builder that is used to deal with built environmental issues, in order to help readers to have a more comprehensive understanding of Design Builder's simulation capacity in processing built environment.

## Introduction

Built environment is determined by the outdoor weather conditions, the heating condition of various indoor heat sources, and indoor and outdoor ventilation . As the variation of built environment is a complex process determined by numerous factors, using computer to simulate computing method is required to predict the conditions of built environment, such as indoor temperature and humidity changes over time, HVAV's realtime energy consumption and the energy required by the environment control of building throughout the year. With people's increasingly higher demands for the quality of built environment and increasing emphasis on building energy efficiency , building simulation is increasingly becoming one of the indispensable tools for design , evaluation and analysis.

In the field of building and environmental control, the study on built environment and dynamic simulation of control system had already begun in the mid-1960s. The main research contents in the initial period are the basic theory of heat transfer and calculation method of load. Due to the development of computer technology, in the 1990s , research emphasis of simulation technology was transferred from simulation modeling to simulation software, so that simulation technology could be more widely applied. Today, building simulation technology has been widely applied in built environment related fields , including design , construction, operation, maintenance and management.

## Target of Built Environment Simulation

The built environment can be divided into built light environment , built acoustic environment , built thermal environment and built wind environment .

Built light environment mainly includes sunlight sheltering , indoor lighting and solar radiation. Built acoustic environment mainly includes outdoor noise and indoor sound. Built thermal environment mainly includes indoor temperature condition without air-conditioning and air-conditioning energy consumption in air-conditioned room. And built wind environment mainly includes outdoor wind environment and indoor natural wind .

## Design Builder (DB) Software of Built Environment Simulation

Design Builder is an integrated graphical user interface simulation software developed for dynamic simulation program (Energy Plus) of building energy consumption. It can be applied at any stage of the design process, to optimize the design and evaluation by providing the performance data , and even can be carried out in the initial design stage before the entire design is determined .

Design Builder is applicable to architects, HVAC engineers, energy consultant companies, universities and some research institutions..

### 3.1 Main Purposes

Evaluating the relevant setting items of building envelope from the aspects of overheating, energy consumption and visual effects; optimizing the use of natural light , conducting simulation on lighting control system and calculating the amount of lighting energy savings ; calculating speed, temperature and pressure distribution in the internal and external field of building with CFD module ; visualizing and shading of venue layout ; simulating the natural ventilation of buildings ; HVAC(Heating, Ventilating and Air Conditioning) designing, including the calculation of heating and cooling equipment's capacity.

Design Builder can be easily utilized, so that even a non-professional user can quickly conduct modeling for a complex building . Using data templates , by selecting from the drop-down list, general building structure, activities inside building, HVAC, lighting systems and model can be loaded. The buildings of the same type can be used repeatedly, and also can be added to the template. This function is linked to the database, which can make changes to the building and surrounding area. And in the design and evaluation phase, each building model can be detailedly set.

### 3.2 Main Functions of Design Builder

Design Builder uses OpenGL solid modeler which is easy to operate. Thus , when " block " is configurated in 3D space , by stretching and shearing, building model production can be intuitively carried out . The thickness of building component and the area and volume of room can be controlled visually.

CFD function is combined with simulation model, and CFD boundary conditions can be defined based on the data output by Energyplus.

British EPCS ( Level 3 and 4 ) standard applies the computing method of SBEM.

Natural ventilation simulating.

Natural lighting module：simulation is carried out for lighting control system and the amount of energy savings of lighting is calculated.

Shading can be achieved through blinds, hanging visor , side sun visor, internal shading and curtains' setting.

All the simulation data can be displayed according to one year, one month , one day, one hour , and even more smaller time intervals: building energy consumption , expressed as the consumption of fuel or energy ; indoor temperature ; meteorological data ; heat transfer that gets through walls, roofs , ventilation and other building envelope; heating and cooling loads ; CO2 output .

To determine the capacity of heating or cooling equipment by referring to local meteorological data.

Compact HVAC provides a simple method for detailedly analyzing commonly used heating and cooling systems.

CAD data or scans can be imported, and 3D CAD model can be imported by gbXMl formats.

Parameters analysis panel can be used to adjust the design parameters within its action range, so as to analyze its impact effect.

Rendering image and animation of architectural design can be output, including shading effect.

Design Builder has the latest ASHRAE ( American Society of Heating Refrigerating and Airconditioning Engineer ) world meteorological data and observation location data ( 4429 sets of data) , and can use hourly meteorological files of Energy Plus for free.

## Application of Design Builder (DB) Software in the Built Environment Simulation

### 4.1 Visualization of Design Builder

Through the visualization of Design Builder , vivid images of real texture can be obtained with the least amount of effort . At any stage of model making, the rendering image can be obtained by clicking on the label of visualization. Besides, the appearance of the building can be confirmed through amplification and movement, and the interior of the building can be confirmed through browsing function. After the processing of visualization on Design Builder model, 3D model can be output to other softwares and can play a role during the presentation .

### 4.2 HVAC Analysis

Design Builder v3 provides a more powerful and flexible way to access Energy Plus HVAC model, and uses the complete ASHRAE 90.1 baseline HVAC system type to analyze gas load and water route.

### 4.3 Daylighting Analysis

Internationally accepted American Radiance lighting analysis core is applied to map isophotes and calculate the average lighting factor. Through Energyplus daylighting analysis, artificial lighting time can be shortened, to reduce energy consumption and carbon emissions. Radiance rendering is applied to generate realistic lighting analysis chart, and detailed reports can be issued according to LEED EQ8.1 , BREEAM HW1 and Green Star IEQ4 standard .

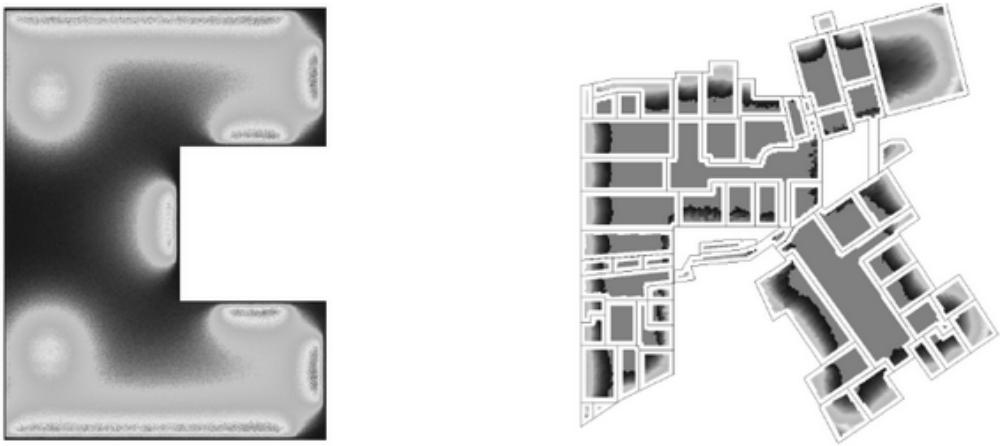

Contour plot showing daylight availability across a floorplan Daylight distribution within a zone

Fig 1 Daylighting analysis diagram

### 4.4 Design Builder CFD

Integrating the concept of CFD( Computational Fluid Dynamics ) into building model can simulate the air flow and temperature environments inside and outside the building. Specifically, the installation position of air conditioner , the configuration of the shape, window , ventilation, and intake port of building, indoor temperature environment, outdoor air flows and so on can be analyzed .

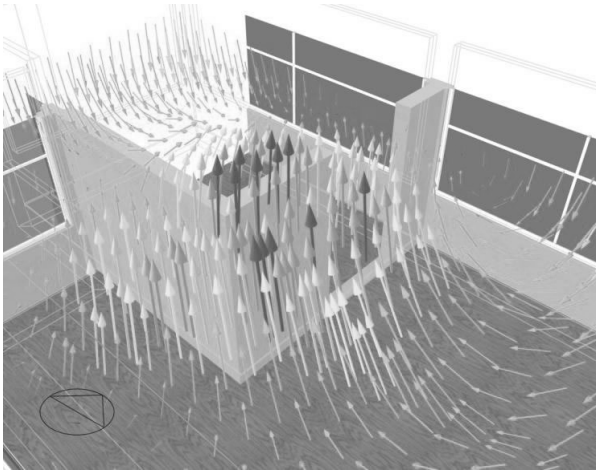

Fig 2 The air flow simulation

## Conclusion

Design Builder building software, through analyzing the basic information of project and the difference of building types , develops different technical route strategies and project location; through providing a rich selection library of products, helps designers effectively analyze the built environment; and through establishing a unified data model, completes the computational analysis of

energy conservation, simulation of building energy conservation, integrated design of solar energy water heater and architecture, and some relevant simulation work, which greatly improves the design efficiency.

**References**

[1] Wu Yizhang, Li Yang ,qi Chang Sheng, building wind environment simulation and its comfort judgment [J], journal of zhengzhou university (natural science edition), 2001 (1)

[2] Zhang tao, Chen Baoming, building wind environment simulation and its comfort analysis [meeting] , 2006

[3] Xu Yinchun, urban high-rise building near the residential area between indoor and outdoor wind environment simulation research [dissertation], 2008

*Applied Mechanics and Materials Vols. 580-583 (2014) pp 3138-3143*
*© (2014) Trans Tech Publications, Switzerland*
*doi:10.4028/www.scientific.net/AMM.580-583.3138*

# Simulation on SHTB Apparatus Design Based on ANSYS/LS-DYNA

Xiao Gui-feng [1, a], Jiang Xi-quan[1,b], Zhou Ying-chun[1,c], and Yan jun[1,d]

[1]Nova Institute of Technology 091 mailbox, Hefei, Anhui 230031, China

[a]xgf2009@aliyun.com, [b]xiobai2012@sina.com, [c]zyc@sina.com,[d]yanjun@126.com

**Keywords:** finite element method; SHTB; stress wave problem

**Abstract.** Split Hopkinson Tensile Bar (SHTB) apparatus is widely used in experimentally investigating the mechanical properties of materials. The experimental results are significantly depended on the amplitude, the shape and the wave length of incident wave. However, there's no research on the effect of incident wave especially the influence of parts of the SHTB equipment has been put forward. The mechanism of the overlying and the amplitude of incident wave by FEM has been analyzed, which can give much help for the theory basis of SHTB apparatus design.

## Introduction

Split Hopkinson Tensile Bar (SHTB) apparatus is widely used in experimentally investigating the mechanical properties of materials. Typical experimental device is as Fig.1[1-9] shows.

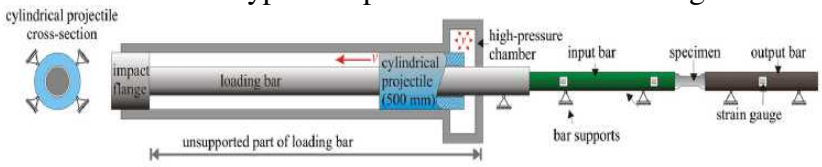


Fig.1 SHTB experimental device

The basic principle is to use a tubular bullet to impact the flange of the incident bar to generate compression waves, which being directly converted to tensile wave by the flange.

currently at home and abroad, the experimental apparatus is used to study the dynamic tensile properties of the material. For tensile wave generation, in particular the size of the components of the experimental apparatus did not see systematic research, and such problems are the key to success SHTB device.

In this paper, dynamic finite element analysis software ANSYS/LS-DYNA is applied to simulate the effects of the size of the components of SHTB experimental apparatus to provide a reference for experimental apparatus improvement.

## Theoretical analysis problem of one-dimensional elastic stress wave overlay

Stress wave propagated in the absence of external force truss is bound to meet the following two conditions at the interface of the variable cross-section rod:

1, Equal internal forces on both sides of the interface, namely Eq.1

$$A_1(\sigma_I + \sigma_R) = A_2\sigma_T \quad (1)$$

2, Particle velocity must be continuous on both sides of the interface, namely

$$v_I - v_R = v_T \quad (2)$$

In which $A_1$ is the cross sectional area of the incident bar, $A_2$ is the cross sectional area of the transmit bar, $\sigma_I$ is incident stress wave, $\sigma_R$ is reflected stress wave, $\sigma_T$ is transmitted stress wave, $v_I$ is incident particle velocity, $v_R$ is reflective particle velocity, $v_T$ is transmission particle velocity.

From Newton's second law formula $Fdt = mdv$ and $m = \rho Adl$, $F = \sigma A$, $C = \frac{dl}{dt}$, we can obtain Eq.3:

$$\sigma = \rho C v \tag{3}$$

In which C is elastic wave velocity of bar, $dl$ is disturbed bar length. Substitute Eq.3 into Eq.2, we can obtain Eq.4:

$$\frac{\sigma_I}{\rho C} - \frac{\sigma_R}{\rho C} = \frac{\sigma_T}{\rho C} \tag{4}$$

For one-dimensional elastic stress wave problem, assuming the bar density and wave velocity are constant, then we can obtain Eq.5:

$$\sigma_I - \sigma_R = \sigma_T \tag{5}$$

Substitute Eq.5 into Eq.1, we can obtain Eq.6 and Eq.7:

$$\sigma_T = \frac{2A_1\sigma_I}{A_1 + A_2} \tag{6}$$

$$\sigma_R = \frac{A_2 - A_1}{A_2 + A_1}\sigma_I \tag{7}$$

When the bullet impact the flange, it generates a reverse tensile wave $\sigma_t^1$ as well as a compress wave $\sigma_c^1$ propagated in the same direction. $\sigma_c^1$ will form reverse tensile wave $\sigma_t^2$ after reflected at the free end of the flange. As Eq.6, Eq.7 shows that the reverse tensile wave $\sigma_t^2$ propagates to the impact surface, part of the wave transmits into the incident bar to form tensile wave $\sigma_t^3$, part is reflected back to flange to form another compress wave $\sigma_c^2$. If the length of the flange is smaller than the length of the stress wave, the transmitted tensile wave $\sigma_t^3$ will overlay with the tensile wave $\sigma_t^1$ at moment of impact, the reflected compress wave $\sigma_c^2$ can be transmitted and reflected again and overlay with previous wave, ultimately form the incident tensile wave for the experiment.

Fourier series by the general cycle shows that any incident wave can be decomposed into a finite number of sine wave form. Assuming the incident wave is expressed as: $A\sin(a\pi t + b)$, cycle is $\frac{2}{a}$, the fourth cycle at the same expression in the form of the incident wave is expressed as: $A\sin[a\pi(t + \frac{1}{2a}) + b]$. Applying the trigonometric function we can transform above formula into $A\cos(a\pi t + b)$. Two incident wave overlay, transform into formula: $A\sin(a\pi t + b) + A\cos(a\pi t + b) = A\sin(a\pi t + c)$, in which $c = \arccos\frac{\cos b - \sin b}{\sqrt{2}}$. Namely two incident waves can be superimposed as one incident and superimposed upon the same cycle, only the different phases. Therefore, the bullet impact the flange while simultaneously generating a compression wave 1 and tensile wave 2, if the head of the tensile wave 3 reflected by compression wave 1 reaches the cross-section, the tensile wave 2 goes through fourth cycle, then they can become a tensile wave. Therefore the length of the impact end of flange is the eighth of the length of stress wave, it will be a similar tensile wave with no overlaid wave.

## Numerical simulation of one-dimensional elastic stress wave overlay

A. Building finite element model

ANSYS/LS-DYNA is universal explicit dynamic finite element analysis software for solving various speed collision problems of nonlinear structures, explosion and other impact dynamic problems. This paper simulates stress pulse propagation process in elastic bar. We use solid 164 solid element to establish a complete finite element model of solid elastic bar. Specific parameters are shown in Table 1. We build the LS-DYNA data model of bar without two-dimensional simplification

and axisymmetric process to ensure accuracy of numerical simulation results. Material is defined as ideal elastic model, material properties are shown in Table 2.

Table 1. Simulate parameter of solid bar (unit mm)

| | Flange length | Bar length | Flange diameter | Diameter of solid bar |
|---|---|---|---|---|
| Solid bar | 500 | 6000 | 100 | 75 |
| | 250 | 6000 | 100 | 75 |
| | 125 | 6000 | 100 | 75 |

Table 2. Material properties

| Material | Modulus of elasticity | Density | Poisson's ratio |
|---|---|---|---|
| Steel | 2.1E11Pa | 7800kg/m3 | 0.3 |

Given the truss shape is regular, we use mapped meshing. Finite element model of the bar system is created in LS-DYNA in fig.4.

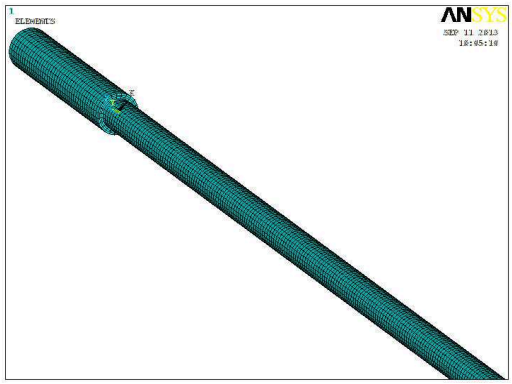


Fig.4 Finite element model of 500mm end of solid bar

Certain pressure load is defined as Table 3. shows on the annular tapered stem unit.

Table 3. Time-press value

| NO | Time/s | Press/MPa |
|---|---|---|
| 1 | 0 | 0 |
| 2 | 2.4E-5 | 55.87 |
| 3 | 1.34E-4 | 55.87 |
| 4 | 1.56E-4 | 0 |
| 5 | 1.7E-4 | 0 |

B. Research on wave overlay problems of different flange length of incident bar

Select a surface measurement point of incident bar to get its Y direction stress time curve, as fig.5 shows.

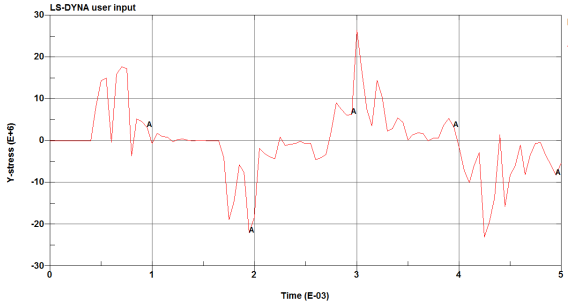


Fig.5 Stress-time curve in solid bar of 500mm end

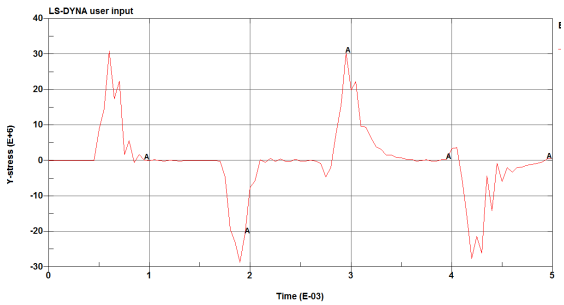


Fig.6 Stress-time curve in solid bar of 250mm end

As the flange length is 250mm, the y direction stress-time curve of the same measurement point is shown in fig.6. As we can see from the figure, a plurality of waves coming sequentially, reflected and transmitted stress wave can't catch up with the front of the wave and the wave hasn't overlay. stress amplitude is relatively small.

As the flange length reducing to 125mm, the y direction stress-time curve is shown in fig.7.

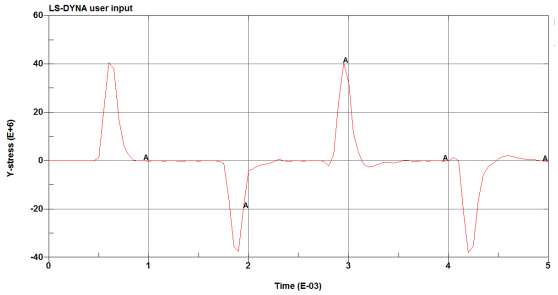


Fig.7 Stress-time curve in solid bar of 125mm end

By simulation we found that when the length of the flange is 125mm, the stress wave superposition is idealized waveform, consistent with the above theoretical derivation. That is, at the measuring point of the incident bar after impacting, when the length of the stress wave propagation in a pulse time is 1000mm, twice the length of the end 500mm, the tensile wave generated by impacting doesn't really overlay with the tensile wave generated by the compression wave reflected at the free surface. When the impact end is 125mm, as it is one-eighth of the stress wave length, they overlay to be a perfect wave.

## Theoretical and numerical simulation of one-dimensional elastic stress wave amplitude value

A. Theoretical analysis of one-dimensional elastic stress wave amplitude value

When the bullet impacts the flange, the compression wave generated at the impact end spreads to the impact end after being reflected at free surface and be reflected and transmitted again, resulting in reflect stress wave and transmit stress wave. This process ends inside repeatedly, if transmit wave reciprocated is too much, it is not conducive to the transmission overlay.

From the Eq.6, Eq.7, we know that stress wave generated by multiple reflection is Eq.8,

$$\sigma_{nR} = \left( \frac{A_2 - A_1}{A_1 + A_2} \right)^n \cdot \sigma_0 \tag{8}$$

The stress wave repeated transmitted is as Eq.9 shows

$$\sigma_{nT} = \frac{2A_1 (A_2 - A_1)^{(n-1)}}{(A_1 + A_2)^n} \sigma_0 \tag{9}$$

Where $\sigma_0$ is the compression stress generated by the bullet impacting the flange, A1, A2 is respectively the flange and the incident bar. Clearly, in order to improve the tensile wave superposition effect, by reducing the number of reflections flange stress waves, reducing the amplitude of the reflected wave to reach.

Form Eq.8, we can know when the cross-sectional area of the flange is close to the incident bar, the generated reflected wave amplitude is smaller and the header wave number of the transmitted wave is also reduced.

B. Numerical simulation of one-dimensional elastic stress amplitude value

192KN impact force is applied to the annular surface of the solid bar. Specific parameters are shown in Table 4, material properties and pressure value are like with above.

Table 4. Different dimension of 500mm end of solid bar

| | Flange length | Bar length | Flange diameter | Diameter of solid bar |
|---|---|---|---|---|
| Solid bar | 500 | 6000 | 100 | 80 |
| | 500 | 6000 | 100 | 50 |
| | 500 | 6000 | 100 | 20 |

Stress-time curve were obtained of the solid bar having different diameters at a measuring point, as fig.8 shown.

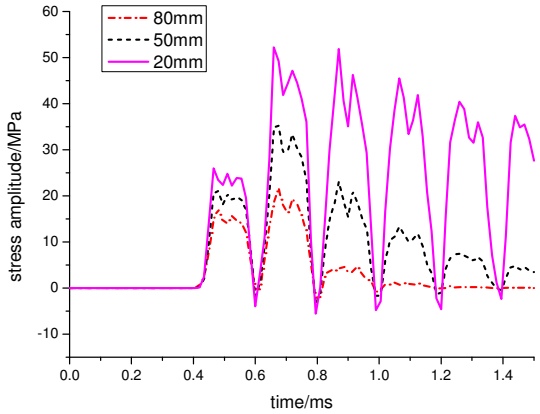


Fig.8 Stress amplitude time curve of 500mm end solid bar with different diameter

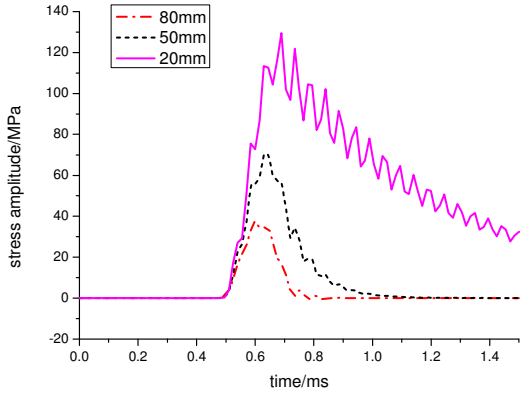


Fig.9 Stress amplitude time curve of 125mm end solid bar with different diameter

When the flange length is 125mm, change the diameter of the incident bar from 80mm, 50mm to 20mm, we get the stress amplitude curve of the same measuring point of the solid bar, as fig.9 shows.

It can be easily seen that, with the decrease of the diameter of the incident bar, although the amplitude of the stress is gradually increased, the number of the transmission waveform is more and is unfavorable for the superposition of the incident wave.

Consistent with the previous derivation, in comparison, the thick solid bar is better than thin solid bar.

## Conclusion

In this paper, we use solid modeling techniques and cell meshing of ANSYS/LS-DYNA to study the effects of the size of the components of SHTB experimental apparatus and find the size and quality of the experimental device is related to the incident wave form.

These results concluded that:

(1) When the flange is one-eighth of the stress wave length, two tensile wave generated around the opposite tensile bar can interfere with each other to become a perfect tensile superimposed wave.

(2) Tensile waveform generated by the superposition of the incident bar that the stress wave of thick bar superimposed effect is the best and the amplitude get the maximum, the thin solid bar superimposed worst.

Through theoretical and modeling studies of the different sizes of the incident bar, the device is expected to optimize SHTB equipment.

## References

[1] Chen W, Lu F and Cheng M: Polymer Testing, Vol. 21(2) (2002), p.113-121.

[2] Taniguchi N, Nishiwaki T and Kawada H: Advanced Composite Materials,Vol.16(2) (2007), p167-180.

[3] Huh H, Kang WJ and Han SS: Experimental Mechanics, Vol. 42(1) (2002), p8-17.

[4] Smerd R, Winkler S, Salibury C, Worswick M, Lloyd D and Finn M: International Journal of Impact Engineering, Vol. 32(1-4)(2005), p.541-560.
[5] Yokoyama T: Strain, Vol. 39(4)(2003), p.167-175.
[6] Nie X, Song B, Ge Y, Chen WW and Wearasooriya T: Experimental Mechanics. Vol.49(4)(2009), p.451-458
[7] Noble JP, Harding J. : Measurement Science & Technology. Vol.5(1) (1994), p.1161-1171.
[8] Gerlach R, Siviour CR, Wiegand J and Petrinic N: Composites Science and Technology, Vol. 72(3)(2012), p.397-411.
[9] Arthington MR, Siviour CR and Petrinic N: International Journal of Impact Engineering, Vol. 46(0)(2012), p.86-96.

*Applied Mechanics and Materials Vols. 580-583 (2014) pp 3144-3148*
*© (2014) Trans Tech Publications, Switzerland*
*doi:10.4028/www.scientific.net/AMM.580-583.3144*

# Numerical simulation of SHPB test for concrete under confining pressure

Hua Zhang[1,a] , Aoyu XIE[1,b] , Yuwei Gao[2,c]

[1] College of Civil and Transportation Engineering, Hohai University, Nanjing 210098, China

[2] No.277, Shihua Village 2, Jinshan district, Shanghai, China

[a] zhanghuacd@hotmail.com, [b] xayevan@163com, [c] yuwei-gao@163.com

**Key words:** SHPB, confining pressure, HJC constitutive model, strain-stress curve, strain rate.

**Abstract**: Using the HJC dynamic constitutive model, the Split Hopkinson Pressure Bar (SHPB) impact test with confining pressure for concrete was simulated in the software ANSYS/LS-DYNA. The confining pressure was simulated by applying constant pressure around the specimen. The triangle velocity wave, which has less diffusion, is used as loader in the simulation. The confining pressures used were 0MPa, 2MPa, 4MPa, 8MPa and 16MPa and the stress-strain curves were presented. The influence of confining pressure on the dynamic properties was analyzed by comparing the stress-strain curves of concrete under different stress states. The strain rate decreases sensitively as long as the confining pressure increases. By debugging the impact velocity, the stress-strain curves under the similar strain rate were obtained, which indicate the toughening and reinforcing effect with the increase of confining pressure.

## Introduction

In real-life engineering, many constructions have already been in triaxial stress state before they withstand the dynamic load. A number of studies show that concrete has special mechanical behaviors under confining pressure. But currently, in case of confining pressure, the research about the dynamic mechanical properties of concrete is still not enough, especially under high strain rates. Under high strain rates, the coupling effect of confining pressure and strain rate results in the increase of the peak stress for concrete and its failure mode will change from brittle failure to ductile failure with the increase of confining pressure [1,2].

The Split Hopkinson Pressure Bar (SHPB) experiment with confining pressure is a commonly useful method to investigate the dynamic mechanical behaviors for concrete in triaxial stress state. In the recent decades, the technology of SHPB with confining pressure is developing constantly. In 1972, R. J. Christenson et al. did firstly the SHPB test for the rock under confining pressure [3] and after that, Yu et al. carried on a further research [4]. Candappa et al. made an intensive experiment in order to determine the effect of lateral confinement on the ductility of high strength concrete [5,6]. In 2000, an improved 3-Axis SHPB device was designed by S.Nemat-Nasser and they carried out a research on mortar.

However, the current experimental method has quite a few drawbacks. The numerical simulation can put aside the insufficient such as electromagnetic interference, effects of interfacial friction in the experiment. In this paper, the SHPB test with confining pressure device is simulated by LS-DYNA finite element software using the HJC dynamic constitutive model. The data obtained by numerical simulation are applied in the analysis of dynamic properties for concrete influenced by confining pressure.

## SHPB techniques and data processing

### 2.1. SHPB with active confinement device

The Ø74mm SHPB device with variable cross-section core bars is shown in Fig.1. The length of striker bar, input bar and output bar are, respectively, 400mm, 3200mm, 1600mm and the diameter of the striker bar is 37mm. The input bar is variable cross-section, with the diameter increasing from 37mm to 74mm.

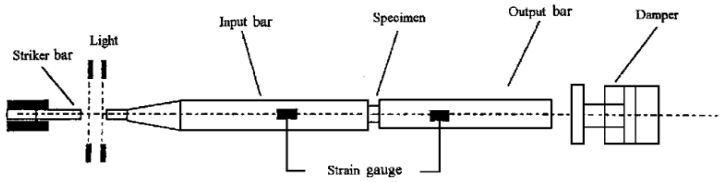


**Fig.1** Schematic illustration of SHPB with variable cross-section

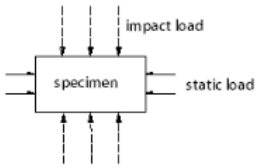


**Fig.2** Schema of SHPB test with confining pressure

Currently, in the commonly used SHPB device, the confinement is obtained by pumping hydraulic oil in the closed oil room as soon as the pressure of the oil room reaches the needed value. The pressure is putted on the specimen by rubber interlayer. The confining pressure value can be adjusted freely in the experiment.

SHPB test with confining pressure is used to investigate dynamic mechanical properties of materials in the triaxial stress state. However, it's hard to get the triaxial stress state because the cylindrical specimen is commonly subjected to impact load in the axial direction and pressure in the radial direction in the test, i.e. two-dimensional load, shown as Fig.2. The load simulates just approximately the triaxial stress state in the real-life engineering project.

### 2.2. Method of data processing

For large diameter SHPB device, the dispersion of waves is wide. We used two waves, the incident wave $\varepsilon_i(t)$ and the transmitted wave $\varepsilon_t(t)$ in the data processing [7]:

$$\varepsilon(t) = \frac{2c_0}{L_0}\int_0^t(\varepsilon_i(t) - \varepsilon_t(t))dt \tag{1}$$

$$\sigma(t) = \frac{A}{A_s} E\ \varepsilon_t(t) \tag{2}$$

where E, $C_0$, A are, respectively, elastic modulus, the propagation velocity of the impact wave in the bars, the cross-sectional area of the bar; $A_s$, $L_0$ the original cross-sectional area, the original length of the concrete specimen, respectively. $\varepsilon_i(t), \varepsilon_t(t)$ the strain signals of incidence, transmitted waves, respectively. Because the numerical simulation experiments can put aside the interference of electrical noise during the experiment, the start location of the incident wave can take the intersection of the incident wave and the baseline [8]. The delay time τ of transmitted wave, relative to the incident wave, is:

$$\tau = \frac{l_1 + l_2}{c_0} + \frac{L_0}{c_1} \tag{3}$$

Where $l_1$, $l_2$ are, respectively, the distance from data collection points of incident wave and transmitted wave to the specimen interface. $c_1$ is the propagation velocity of elastic wave in the concrete specimen.

**Discussion of SHPB numerical simulation methods**

The numerical simulation is carried out by the finite element software ANSYS/LS-DYNA and on the basis of HJC constitutive model. The parameters of HJC model is provided by reference [9], shown as table1.

**Table1.** Parameters of HJC dynamic constitutive model

| $\rho_o$/kg/m$^3$ | $f_c$/Pa | A | B | C | $S_{MAX}$ | G/Pa |
|---|---|---|---|---|---|---|
| 2.4E$^3$ | 48E$^6$ | 0.79 | 1.60 | 0.007 | 7.0 | 14.86E$^9$ |
| $D_1$ | $D_2$ | N | EFMIN | T/Pa | $p_c$/Pa | $\mu_c$ |
| 0.04 | 1.0 | 0.61 | 0.01 | 4E$^6$ | 16.0E$^6$ | 0.001 |
| $P_l$/Pa | $\mu_l$ | $k_1$/Pa | $k_2$/Pa | $k_3$/Pa | E/Pa | |
| 0.8E$^9$ | 0.1 | 85E$^9$ | -171E$^9$ | 208E$^9$ | 35.7E$^9$ | |

The solid 164 unit is used to simulate the pressure bars and the specimen. The linear elastic materials chosen for the input and output bar have the following properties: $\rho_0$=7850 kg/m$^3$, $E_0$=210GPa, $\mu$=0.25. The stress wave is gathered at 1.2m and 0.4m over the end of the strike place. In order to reduce the quantity of calculation，1/4 compressive bar model is constructed, and the constraint is applied on the symmetric boundary.

For the meshing, the input and output bar are divided into 12 parts along the radial direction; the length of axial grid is 10 mm. The concrete specimen is treated with compaction and it is divided into 24 parts radially and 8 parts axially. The total number of units is 56940. The SHPB model with mesh partition is shown in Fig.3.

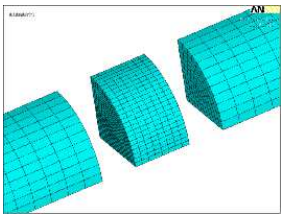

**Fig.3** The SHPB bar model with meshing partition

Considering the wave dispersion of variable cross-section bar and overshoot in the head of stress wave, the triangle velocity wave, which has less dispersion, is used as a loader here. The principles of loading by triangle velocity wave are: the length of the velocity wave is twice the length of the striker bar; the velocity wave that loads directly in the pressure bars interface, whose value is half of the impact velocity [10].

Considering the unit failure of specimen during the course of loading, we will use the corrosion contact ERODING-SURFACE-TO-SURFACE to define the interfaces, which is a kind of interaction between surfaces. The SHPB test with confining pressure can be simulated by applying the constant pressure peripherally the specimen, which will not be influenced by the deformation of

specimen. It is found that the data are stable when rigidity scale factor f takes the default value 0.1. To ensure sufficient damage evolution of materials, the impact velocity is taken as 20m/s and the confining pressure used were 0MPa, 2MPa, 4MPa, 8MPa and 16MPa.

**Material properties analysis of concrete under different confining pressure**

By the numerical simulation, the concrete stress-strain curves under different confining pressure are shown in Fig.4. From Fig.4, it can be seen that the general shapes of the curves are similar. The concrete strength increases as the confining pressure increases and so increase the peak strain, the ultimate strain. That is to say, the ductility and the toughness increase with the increase of confining pressure. The concrete elastic modulus decreases as the confining pressure increases and the triaxial stress makes the concrete deformation become slow. When the confining pressure reaches 16MPa, due to the insufficiency of material damage evolution, it reflects a certain degree of viscoelastic hysteresis.

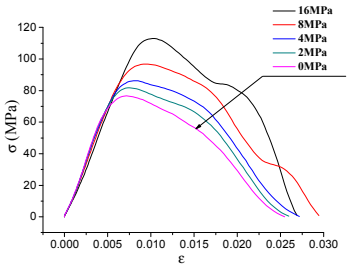


**Fig.4** The concrete stress-strain curves under different confining pressure in the impact velocity of 20m/s

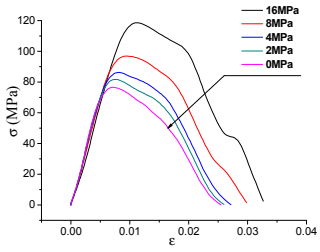


**Fig.5** The concrete stress-strain curves at similar strain rate

The confining pressure restricts the concrete deformation velocity and at the same impact velocity, the average strain rate decreases as the confining pressure increases. To study the confining pressure strengthening effect at the similar strain rate, it is needed to increase the striker bar impact velocity. Here, we debugged only the situation of 8MPa and 16MPa because the strain rates at the confining pressure of 0MPa, 2MPa, 4MPa are very similar. By debugging the impact velocity, it is found that in the event that the confining pressure increases every 4MPa, the impact velocity should be increased about 1m/s. After the debugging, the concrete stress-strain curves at similar strain rate are shown in Fig.5. Fig.5 indicates that at the similar strain rate, the confining pressure improve the strength and the toughness of the concrete. As the confining pressure increases, the damage form changes from the brittle failure in the uniaxial stressed state to the ductile failure in the triaxial stress state.

**Conclusions**

(1) Based on the results of numerical simulations, the finite element software ANSYS/LS-DYNA is an efficient method to analyze the SHPB test with confining pressure. HJC dynamic constitutive model of concrete can be well used to simulate the SHPB test.

(2) According to the obtained concrete stress-strain curves, as the confining pressure increases, so increase the strength, ductility and toughness. The damage form in the material changes with the increase of confining pressure.

(3) The method of numerical simulation of SHPB confining test is given. However, it is also two-dimensional load because in the triaxial stress state, the pressures of bar unit fluctuate and transmitted and reflected waves oscillate. Further experimental and simulation-based researches are necessary to ascertain the response of concrete in triaxial stress state.

**References**

[1] HE Man-chao, XIE He-ping, PENG Su-ping, JIANG Yao-dong. Study on rock mechanics in deep mining engineering [J]. Chinese Journal of Rock Mechanics and Engineering, 2005, 24(16): 2803-2813.

[2] GUO Wen-bing, LI Xiao-shuang. Research status of deep coal and rock mass mechanic properties under high temperature and high confining pressure [J]. Journal of HENAN polytechnic university (nature science), 2007, 26(1): 16-20.

[3] Christensen R J, Swanson S R, Brown W S. Split-Hopkinson-bar tests on rock under confining pressure[J]. Experimental Mechanics, 1972, 12(11): 508-513.

[4] Yu Yalun. The study of impact test on the rock using three axis SHPB device[J].Nonferrous Metals (Mining Section), 1983(06):32-36.

[5] Candappa D P, Setunge S, Sanjayan J G. Stress versus strain relationship of high strength concrete under high lateral confinement [J]. Cement and Concrete Research, 1999, 29(12): 1977-1982.

[6] Candappa D C, Sanjayan J G, Setunge S. Complete triaxial stress-strain curves of high-strength concrete[J]. Journal of Materials in Civil Engineering, 2001, 13(3): 209-215.

[7] Wu Xutao, Yang Boyuan, Li Heping, Dong Gang. Numerical simulation and error analysis of large diameter SHPB[J]. Chinese Journal of Applied Mechanics, 2006, 23(3): 431-434.

[8] Li Yinglei, Hu Changming, Wang Wu. A discussion on the data processing of SHPB experiment [J]. Explosion and Shock Waves, 2006, 25(6): 553-558.

[9] Holomquist T J, Johnson G R, Cook W H. A computational constitutive model for concrete subjective to large strains, high strain rates, and high pressures[A]. Jackson N, Dickert S. The 14th International Symposium on Ballistics. USA: American Defense Prepareness Association, 1993:591－600.

[10] Dong Gang. The numerical simulation of split Hopkinson pressure bar experiment technique[D]. HeFei University of Technology, 2005.

*Applied Mechanics and Materials Vols. 580-583 (2014) pp 3149-3153*
*© (2014) Trans Tech Publications, Switzerland*
*doi:10.4028/www.scientific.net/AMM.580-583.3149*

# Engineering Practice of Elasto-plastic Time-history Analysis on Super High-rise Using ABAQUS

Yu Zhou[1,a], Songran Hong[1,b],Yong Chen[1,c]

[1] China Northeast Architectural Design & Research Institute Co., Ltd., Shenyang 110006, China

[a]zhouy.0407@163.com, [b]hongsongran@163.com ,[c] dr_cy@126.com

**Keywords:** Elasto-plastic time-history analysis, ABAQUS, Super high-rise, Seismic response

**Abstract.** As a general-purpose finite element program, ABAQUS's strong non-linear calculation capacity make it especially suitable for elasto-plastic time-history analysis, in this paper, with a super high-rise project, the experience of elasto-plastic time-history analysis using ABAQUS is described, include the modeling process, material constitutive model, numerical integral method and evaluation of analysis results, some reference will be provided to the other engineering practices.

## Introduction

Compare with the elasto-plastic static analysis method, elasto-plastic time-history analysis method is considered to be a more accurate seismic analysis method, by using the method, engineers can get a more clear understanding of the response of super high-rise buildings under rare earthquake. In recent years, the rapid development of high-rise buildings in China put pressing needs on elasto-plastic time-history analysis method, it has became the key technique in structure seismic reascrh and design.

Currently, ABAQUS is recognized to be the most authoritative software in elasto-plastic time-history analysis, as a general-purpose finite element program, ABAQUS has strong non-linear calculation capacity, which make it suitable for analyze the response of super high-rise buildings under rare earthquake. By sevreal years development, ABAQUS has accumulated much successful experiences in the field of seismic analysis.

In this paper, with a case of engineering practice, the procedures of elasto-plastic time-history analysis using ABAQUS is described to provide reference to the other projects.

## Engineering practice

The engineering practice is a super high-rise office building in Shenyang(shown in Fig.1), the structure is in the form of reinforced concrete frame core tube, the total height of the building is 151.2m, exceeding the limit height (130m) as prescriptive in Technical specification for concrete structures of tall building(JGJ 3-2010) to frame core tube structure in 7 degree seismic intensity. The area of structure is 59,000m$^2$, the shape and dimensions of standard layer are shown in Fig.2 .

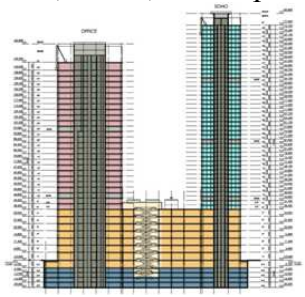

Fig. 1 The office building.

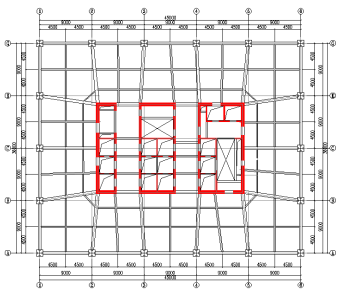

Fig. 2 Standard layer of the building.

## Modeling process

An accurate elastic-plastic model is the foundation of elasto-plastic time-history analysis, since the elasto-plastic model is particularly complex, modeling by ABAQUS/CAE is not feasible. The

modeling process in this paper is establish the elastic analysis model by structural design software YJK, and then transform the elastic model into the ABAQUS elasto-plastic model by using a self-developed interface program, the ABAQUS elasto-plastic model is shown in Fig.3.

In this model, shear walls, coupling beams and slabs are simulated by shell element S4R or S3R, layers of reinforcement in these components are defined by using the Rebar Layer option in ABAQUS. Beams and columns are simulated by beam element B31, layers of reinforcement in Beams and columns are simulated by B31 element with box-section.

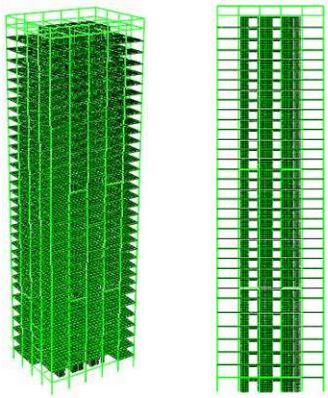

Fig. 3 ABAQUS elasto-plastic model.

**Material constitutive models**

Two kinds of material constitutive model were used in this ABAQUS model, kinematic hardening model was used to simulate the steel constitutive, plastic-damage model was used to simulate the concrete constitutive[1,2], since the plastic-damage model could not be used for B31 element, an ABAQUS user material subroutine of damage constitutive model for concrete under uniaxial stress was developed[3,4], which can be used for B31 element.

**Numerical integration method**

In elasto-plastic time-history analysis, the direct integration method was used to solve the dynamic equations, implicit and explicit are the two main direct integration method. Compare with the implicit method, explicit method neither requires matrix inversion nor the formation of stiffness matrix, thus much shorter time is enough to solve the dynamic equations, moreover explicit method can also avoid divergence problem caused by serious non-linearity in structure as the implicit method encountered, for these two reasons, explicit method is more suitable to solve large-scale computing.

**Model validation**

In order to verify the accuracy of the ABAQUS model, modal analysis was conducted respectively by ABAQUS and SATWE, the comparison of results was given in tab.1, as seen in table, the structural total mass, each order periods and modals calculated by the two softwares are basically the same, thus the ABAQUS model was proved to be correct.

Tab. 1 Comparison of modal analysis

| | | SATWE | ABAQUS | Modal |
|---|---|---|---|---|
| Total mass /ton | | 100363 | 98912 | |
| Period | T1/s | 3.78 | 3.85 | 1st-order translation in X |
| | T2/s | 3.63 | 3.81 | 1st-order translation in Y |
| | T3/s | 2.82 | 2.73 | 1st-order torsion |
| | T4/s | 1.17 | 1.16 | 2nd-order translation in X |
| | T5/s | 0.97 | 0.96 | 2nd-order translation in Y |
| | T6/s | 0.92 | 0.93 | 2nd-order torsion |

**Analysis results**

In order to analyze the seismic response of the structure under rare earthquake, one artificial seismic wave and two natural seismic waves were chosen to input for analysis, according to the analysis results, the maximum vertex displacement and inter-story drift angle of structure under each waves are shown in tab.2, the inter-story drift angle curve are shown in Fig.4, the x direction maximum inter-story drift angle is 1/120, the y direction maximum inter-story drift angle is 1/125, both occurred under the seismic wave of US397, and do not exceed the limit as prescriptive in Code for seismic design of buildings(GB 50011-2010).

Tab. 2 The maximum vertex displacement and inter-story drift angle

| Waves | X direction | | Y direction | |
|---|---|---|---|---|
| | Maximum vertex displacement /m | Maximum inter story drift angle (Floor) | Maximum vertex displacement /m | Maximum inter story drift angle (Floor) |
| art | 0.75 | 1/149 (18F) | 0.539 | 1/200 (10F) |
| US397 | 0.879 | 1/120 (23F) | 0.903 | 1/125 (19F) |
| DSL11 | 0.482 | 1/213 (22F) | 0.716 | 1/135 (25F) |

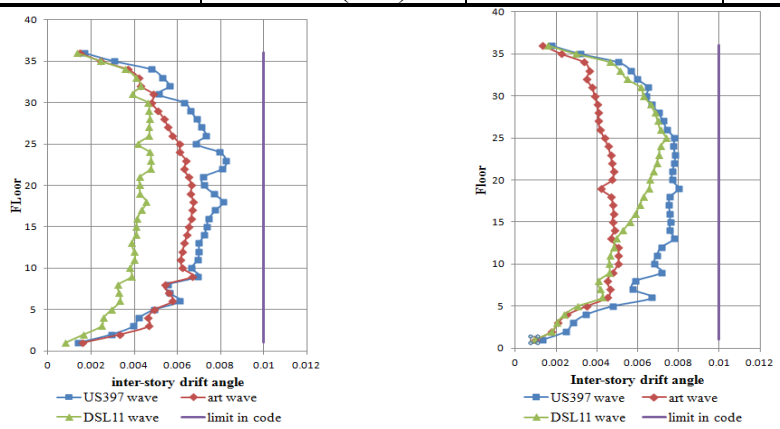


a) X-direction b) Y-direction

Fig. 4 Inter-story drift angle curve.

The inter-story shear curve are shown in Fig.5, the shear weight ratio of structure under each waves ranging from 3.8%~5.22%, meeting the requirements of Code for seismic design of buildings(GB 50011-2010).

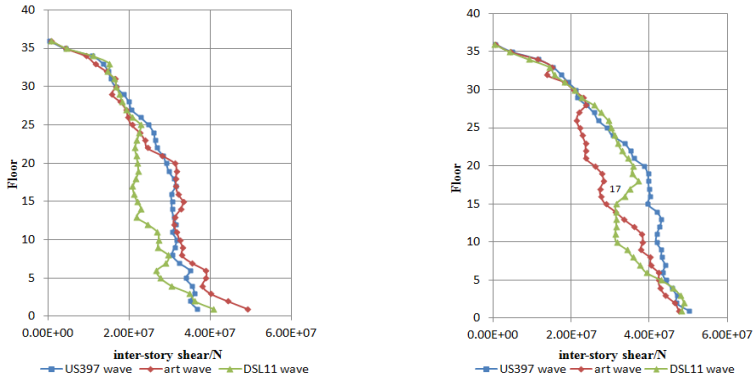


a) X-direction b) Y-direction

Fig. 5 Inter-story shear curve.

According to the analysis results, The structure was damaged most severely under the seismic wave of US397. The plastic damage nephogram of shear walls under the seismic wave of US397 is shown in Fig.6, except for a few areas, no severe plastic damage appeared in shear walls, the concrete of shear walls was still in elastic state. During the analysis, most of the coupling beams have a serious destruction, and the destruction is acceptable, which can dissipate seismic energy and reduce damage to other members.

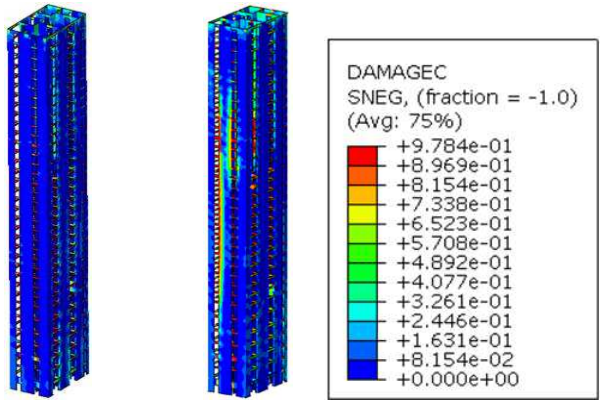


a) X-direction b) Y-direction

Fig. 6 Plastic damage nephogram of shear walls.

The plastic damage nephograms of columns and beams under the seismic wave of US397 are shown in Fig.7, the maximum plastic damage factor of concrete in columns was about 0.283, the concrete in these sections was just in the peak stress state, and most of the concrete in other sections was still in elastic state. Some beams in core tube suffered serious damage under the seismic wave, the maximum plastic damage factor of concrete in these beams was about 0.839, the plastic hinges were formed in these areas.

The stresses nephograms of reinforcement in columns and beams are shown in Fig.8, the maximum stress of reinforcement in columns was 230.7MPa, the reinforcement was still in elastic state. The maximum stress of reinforcement in beams was 386.3MPa, the reinforcement has already yield.

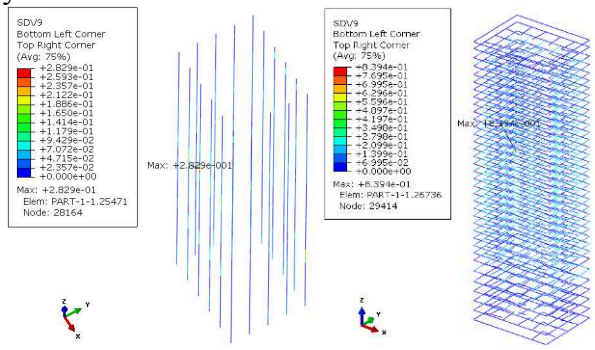

a) damage in columns b) damage in beams

Fig.7 Plastic damage in columns and beams.

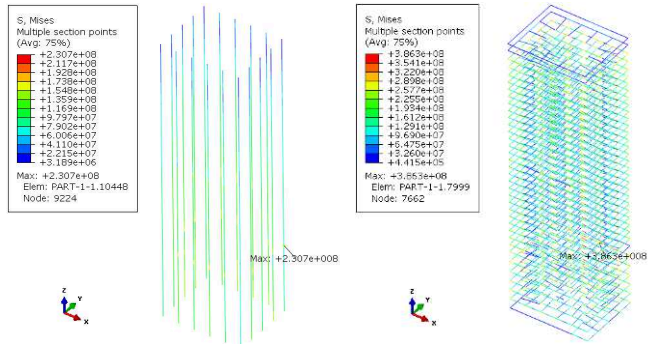

a) reinforcement in columns b) reinforcement in beams

Fig. 8 Stresses of reinforcement in columns and beams.

## Summary

With the progress of computer technology, the elasto-plastic time-history analysis has a rapid development in recent years, as a general-purpose finite element program, ABAQUS has accumulated much successful experiences in this field, its strong non-linear calculation capacity make it especially suitable for analyze the response of super high-rise buildings under rare earthquake, it can help engineers to improve the performance of building in seismic design.

## Acknowledgement

This work was financially supported by China State Construction Engineering Corporation (Grant No: CSCEC-2013-Z-23).

**References**

[1] J. LEE, G. L. FENVES: Journal of Engineering Mechanics, Vol.124(8)(1998), p. 892

[2] J.LUBLINER, J. OLIVER: International Journal of Solids and Structures, Vol.25(3)(1989), p.229

[3] J.B. Mander, M.J.N. Priestley, R. Park: Journal of Structural Engineering, Vol.114(8)(1988), p.1804

[4] ABAQUS, Inc: *ABAQUS Analysis User's Manual*(Rhode Island USA 2010)

*Applied Mechanics and Materials Vols. 580-583 (2014) pp 3154-3157*
*© (2014) Trans Tech Publications, Switzerland*
*doi:10.4028/www.scientific.net/AMM.580-583.3154*

# Calculation on internal force effect of a high-speed highwayprestressed concrete Extra-dosed cable-stayed bridge

XingzhouChen[1, a]

[1]School of Civil Engineering, Southwest Jiaotong University, Chengdu, Sichuan 610031, China
[a]chenxingzhou@live.com

**Keywords:**Prestressed concrete,Extra-dosed cable-stayed bridge,Internal force effect,Dead load, Live load.

**Abstract.**The Extra-dosed cable-stayed bridge is considered as a new popular type of bridge structure in recent 20 years, whose mechanical properties and economic span both lie between continuous beam (or rigid frame ) bridges and cable-stayed bridges.This design is a double-cable-plane (85+150+85)m prestressed concrete Extra-dosed cable-stayed bridge, whose maximum Design speed is 100km/h and its width is 25.50m. The form of the highway is sextuple line which is 10.75m far away,and the cross-sectional slope is 2%.The girder body adopts three cell and single box,the height of beam takes quadratic parabola relation, which is 5m high at the middle support, while at the side support and the midspan is 3m.Vehicle standard load was applied on the bridge.The design uses Midas/Civil to establish the finite element model that is reasonable and simple, analyzing the structure behavior of the girder body under loading, especially the internal forces of bridge structure under dead load, live load and additional force.

## Introduction

Prestressed concrete Extra-dosed cable-stayed bridge's constant load force calculation has a direct relationship with construction methods used. Main girder internal force of dead load consists of the weight internal forces of main girder caused by dead weight and the late girder internal force of dead load caused by secondary dead load (such as pavement, railings, etc.).This design uses midas program to calculate internal force.

## Dead load internal force calculations

**Material Properties.**

(1) C50 grade concrete

Modulus of elasticity: $Ec$＝34500MPa

Axial compressive strength standard limit: $f$ck＝32.4MPa;

Axial tensile strength standard limit: $f$tk＝2.65MPa;

Bulk density:24.1kN/m.

(2)Strand

Modulus of elasticity:$Ep$＝195000MPa;

Axial tensile strength limit:$f$pk＝1860MPa;

Tension control stress: $\sigma con$＝0.6$fpk$＝1116MPa.

(3)Ordinary reinforced

HRB335 steel as main reinforcement($\varphi$12～28)，$f$pk＝335MPa.

**Sectionfeatures.**The whole bridge is divided into three section type, cantilever construction stage unit length beams were 3.5 m, 4.0 m, 5.0 m and 6.0m, middle fold 2.0m long.

**Construction loads.**Construction loads are considered in the process of construction with all kinds of load acting on each beam segment,and they are simplified as a pair of concentrated force acting on anchor point of hanging basket.Concentrated force is calculated from the various stages of hanging basket weight,weight steel mesh,concrete weight and with due consideration on load center of gravity position caused by different beam lengths.The value of the design's construction loads is 750kN.

**Secondary dead load.**The value of the design's secondary dead load is 90.4kN/m.

**Calculation model.**The calculation model for the operational phase is shown Fig.1.

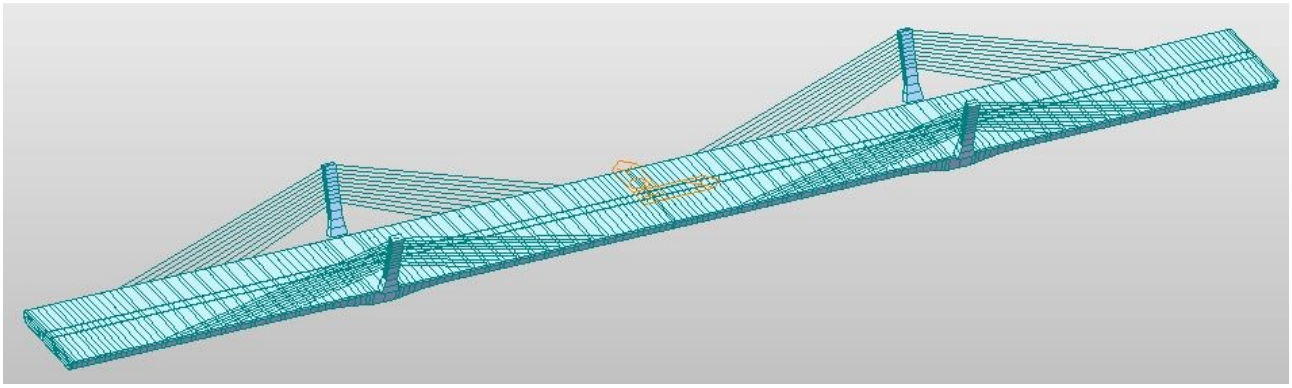

Fig. 1Calculation mode

Dead load calculations.Structure moment is shown in Fig.2, Fig.3 and Fig.4. Structural internal force under dead load is shown in Table 2.

Fig. 2 Moment in maximum cantilever (kN.m)

Fig. 3Moment in middle cross close (kN.m)

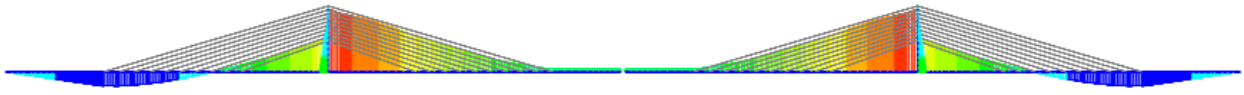

Fig. 4Moment in creep and shrinkage (kN.m)

Table 1 Dead load calculations

| Stage | Maximum cantilever | | Middle cross close | | Creep and shrinkage | |
|---|---|---|---|---|---|---|
| Unit | M（kN•m） | N（kN） | M（kN•m） | N（kN） | M（kN•m） | N（kN） |
| 1 | 0 | 0 | 0 | -1112.62 | 0 | 282.67 |
| 2 | 0 | 0 | 0 | -22094.3 | 0 | 4805.41 |
| 3 | 0 | -726.73 | 0 | -38038.4 | 0 | 11589.52 |
| 4 | 0 | -2664.67 | 0 | -24835.1 | 0 | 18373.62 |
| 5 | 0 | -5167.84 | 0 | -7780.87 | 0 | 27136.43 |

| | | | | | | |
|---|---|---|---|---|---|---|
| 6 | 512.84 | -11689 | 2007.87 | 901.3 | 2020.46 | 27771.7 |
| 7 | 268.6 | -22426.8 | 3085.7 | 3628.73 | 2997.63 | 22245.61 |
| 8 | -554.1 | -35807 | 3370.14 | 1177.48 | 3108.97 | 12041.83 |
| 9 | -1734.27 | -50879.5 | 3050.27 | -4966.92 | 2581.65 | -1264.22 |
| 10 | -3013.45 | -67246.5 | 2360.84 | -13817.2 | 1686.05 | -16674.4 |
| 11 | -3183.07 | -85887.6 | 2248.97 | -25887.2 | 1512.66 | -35484.3 |
| 12 | -3323.46 | -99989.7 | 2132.58 | -37590.5 | 1343.06 | -52533.9 |
| 13 | -3013.45 | -108371 | -7084.88 | -121905 | -6903.1 | -122585 |
| 14 | -3296.9 | -97204.2 | -7420.47 | -109655 | -7226.14 | -110816 |
| 15 | -3137.87 | -81708.7 | -7240.12 | -92098.9 | -7052.72 | -93935.3 |
| 16 | -2378.54 | -63490.4 | -6630.67 | -68617.4 | -6429.68 | -71344.7 |
| 17 | -1114.88 | -47413.6 | -5791.52 | -47594.6 | -5538.05 | -51177.7 |
| 18 | -83.27 | -32569.5 | -5273.68 | -29021.7 | -4946.35 | -33386.2 |
| 19 | 475.18 | -19515.1 | -5320.23 | -13647.3 | -4894.5 | -18680.7 |
| 20 | 360.62 | -9342.49 | -6128.2 | -2754.52 | -5575.7 | -8296.29 |
| 21 | 0 | -4521.86 | -6866.9 | 637.2 | -6239.13 | -5080.89 |
| 22 | 0 | -2180.18 | -6866.9 | 637.2 | -6239.13 | -5080.89 |
| 23 | 0 | -242.24 | -6866.9 | 637.2 | -6239.13 | -5080.89 |

**Live load internal force calculations**

**Calculation Method.**The main beam is statically indeterminate structure, live load internal force still impacts line load method for calculating.We generally use the force influence line of the main beam,then load at the most unfavorable position in the direction of the force influence line in order to seek the maximum live load force of the main beam.For highway bridge,we use concentrated load and equivalent uniform load.

$$S = (1+\mu)(q_k\Omega + P_k y_k) \quad (1)$$

$S$——The unknown section's moment or shear;
$1+\mu$——Impact factor of vehicle standard load;
$q_k$——Uniform load;
$\Omega$——Influence line area of moment or shear;
$P_k$——Concentrated load;
$y_k$——Influence line value of force.

**Live load factor calculations.**The role of live load factor:Program first applied concentrated loadand uniform loadon the main beam,then the obtained result is multiplied by the live load's factor to obtain the final result of loading.

Impact factor calculations:According to general code for design of highway bridges and culverts,we use vehicle vertical static live load multiplied by the power ($1+\mu$) to obtain vehicle vertical load considering the vertical force of vehicle live load.

Under vehicle standard load, $\mu = 0.05$, when $f < 1.5\,Hz$; $\mu = 0.1767\ln f - 0.0157$, when $1.5\text{Hz} \le f \le 14\text{Hz}$; $\mu = 0.45$, when $f > 14$ Hz, $f$ means the structural fundamental frequency, Therefore,$1+\mu$=1.45

**Live load calculation.** Structural internal force under live load is shown in Table 3.Structure moment is shown in Fig.5

. Table 2 Live load calculations

| Unit | $N_{max}$（kN） | $M_{max}$（kN•m） | $N_{min}$（kN） | $M_{min}$（kN•m） |
|---|---|---|---|---|
| 1 | 0 | 617.52 | 0 | -189.52 |
| 2 | 0 | 9811.34 | 0 | -3221.86 |
| 3 | 0 | 21191.79 | 0 | -7770.38 |

| | | | | |
|---|---|---|---|---|
| 4 | 0 | 29730.74 | 0 | -12318.89 |
| 5 | 0 | 36718.66 | 0 | -18194.06 |
| 6 | 238.88 | 38963.23 | -954.73 | -21495.45 |
| 7 | 337.9 | 37290.82 | -1778.79 | -23364.16 |
| 8 | 352.63 | 32096.13 | -2496.01 | -23766.95 |
| 9 | 334.21 | 24041.37 | -3116.2 | -23052.11 |
| 10 | 344.03 | 14260.99 | -3628.43 | -22119.86 |
| 11 | 331.99 | 6463.24 | -3693.5 | -25635.86 |
| 12 | 310.06 | 2393.15 | -3764.51 | -35975.99 |
| 13 | 1055.37 | 5886.79 | -5167.06 | -59955.62 |
| 14 | 1057.64 | 6353.36 | -5418.69 | -48432.23 |
| 15 | 1058.69 | 10241.08 | -5266.91 | -36621.17 |
| 16 | 1030.52 | 15687.69 | -4839.94 | -25939.34 |
| 17 | 959.63 | 21508.78 | -4085.24 | -18803.7 |
| 18 | 866.44 | 27553.8 | -3248.12 | -15105.55 |
| 19 | 782.31 | 33333.14 | -2408.71 | -12370.24 |
| 20 | 792.09 | 38510.36 | -1694.75 | -10171.56 |
| 21 | 805.52 | 43135.53 | -1370.47 | -8415.43 |
| 22 | 805.52 | 46991.28 | -1370.47 | -7671.22 |
| 23 | 805.52 | 48251.9 | -1370.47 | -7063.8 |

Fig. 5Moment under live load (kN.m)

## Conclusions

The design uses Midas software to establish the finite element model,which is widely used in various bridge design.With this design study,we analy the structure behavior of the girder body under loading, especially the internal forces of bridge structure under dead load and live load in order to provide some basis for the later similar bridge design.

## References

[1]Gu Anbang:Bridge project (part ii) ,China Communications Press. (2000)
[2]FanLichu:Bridge project (part i), China Communications Press. (2001)
[3] Liu Shilin, Meng Fanchao: Cable stayed bridges, China Communications Press. (2002)
[4] Xiang Haifan: Advanced Theory of Bridge Structures, China Communications Press. (2001)
[5] Zou Yisong, Wang Yinhui:Continuous beam bridge, China Communications Press. (2009)
[6] Yongming Zhao, Study on internal force effect of a high-speed rail (40+56+40) m prestressed concrete continuous beam bridge.

*Applied Mechanics and Materials Vols. 580-583 (2014) pp 3158-3162*
*© (2014) Trans Tech Publications, Switzerland*
*doi:10.4028/www.scientific.net/AMM.580-583.3158*

# Establishing the digital model of hydraulic system in simulation vibration table

Rui Li[1, a], Xuesen Li[1], Hong Xu[1]

[1] School of Civil Engineering, Xi'an University of Architecture and Technology, Xi'an, Shaanxi,China

[a] liruijsj@xauat.edu.cn

**Key words:** simulation vibration table; hydraulic servo system; actuators; simulation model

**Abstract:** Based on the analysis of the development, defects and motion of present hydraulic system vibrating table, it is divided into several single disciplinary system modes which are organic related in this paper. Establishing unified digital model in integrated simulation environment through analyzing the function of these models, which will guide the design of digital vibration table system.

## Introduction

Simulation vibration table is a kind of test instrument which can reappear and simulate the earthquake effect on specimen, and is one of the most widely used experimental apparatus in structure seismic test [1]. Because of it is a means of simulation which can effectively avoid many defects of using vibration table and maximize the advantages of vibrating table, digital simulation shaking table has been trend in the research of shaking table [2]. What's more, it also can provide incentives for various simulation test [3] - [6], and has significance guidance for the simulation of different dynamic test.

In this paper, hydraulic system of vibration table will be divided into single disciplinary system models which are organic related at first; then, establishing the mathematical model for each of them; finally, estimate the correctness of the simulation model of whole system on account of the system sensitivity analysis of main parameters.

## Modeling

The analysis of the entire hydraulic system is expressed by form of transfer function by mathematical means, which transform the relationship of the demand and actual output of vibrating table into the input and output signal. The whole model is modularized for the convenience of modeling.

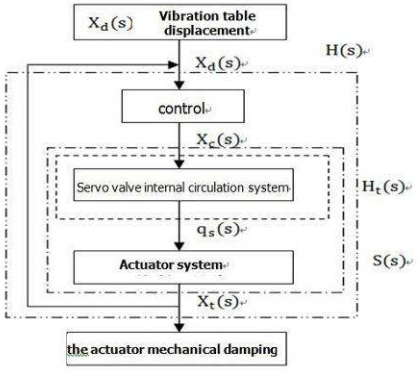


Fig.1 The signal change and the functional scope of Hydraulic system

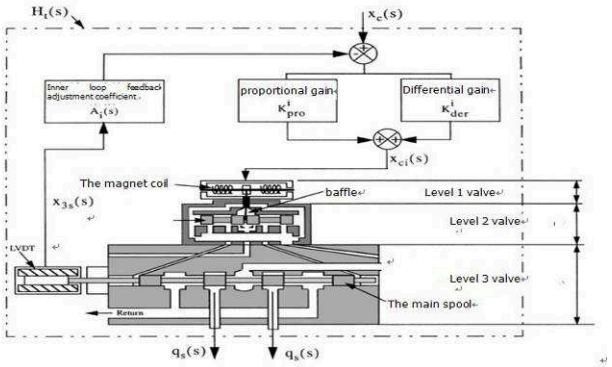


Fig. 2 The third order sketch servo valve's structure and function

Fig.1 shows the shaking table system can be broken down into three transfer function. According to the inclusion relation between them, they are expanded from small to big as following: (1) the servo transfer function $H_t(s)$; (2) the mathematical model of servo - actuator $S(s)$; (3) the servo hydraulic system mathematical model $H(s)$. The establishment of them will be introduced below.

**The third order mathematical model for servo valve**

Because of shaking table always use redundant drive [7] and for large shock tests, and require great actuator and precision, so it often adopt three-stage electro-hydraulic servo valve control system and use symmetrical valve control symmetrical cylinder structure. The three-stage electro-hydraulic servo control system is the first step of the vibration control, known as the inner feedback control loop.

Internal feedback control system is the basic control of the third order servo control system, and is corresponding to the external control, which will also affect the vibration table control system. It is shown in figure 2 that the signal of servo valve command $X_C(s)$ is converted to electrical signals of inner loop $X_c(s)$ by the proportional and differential control, and then join in the work of the third order for servo valve.

According to the working principle of the three-stage electro-hydraulic servo valve aforementioned [8] [9] the linear hypothesis, the three working stages of the whole servo valve is controlled by PID circulation, which suppose that the oil flow velocity from servo valve to the actuator pressure chamber $q_s(s)$ is the output signal, the servo valve command signal $X_C(s)$ is the input signal, and then the transfer function of the servo valve is expressed as the following:

$$H_t(s) = \frac{q_s(s)}{X_C(s)} \tag{2-1}$$

$$= k_{xq} \frac{k_1 k_2 (k_{pro}^i + s k_{der}^i)}{1 + A_i(s) k_1 k_2 (k_{pro}^i + s k_{der}^i)} \tau \tag{2-2}$$

Where $k_{pro}^i$ is the inner loop proportional gain coefficient; $sk_{der}^i$ is the inner loop integral gain coefficient; $A_i(s)$ is the inner loop feedback transfer coefficient.

In addition, in order to reflect the delay phenomenon initiated by the process of signal transmission, such as from external signals to the servo valve and servo valve inside, the delay time $\tau$ is introduced in this paper. It can be understood as that the time which is taken by actuator to overcome the mechanical and hydraulic inertia of the servo valve. Here it is defined as the difference value of time that the time of electrical signal arrive in the first level of servo valve and the time of triple valve response accordingly.

So the original function is turned into the following:

$$X_{3S}(t) = k_1 k_2 X_{ci}(t - \tau) \tag{2-3}$$

And then it is transformed by Laplace:

$$X_{3S}(t) = k_1 k_2 X_{ci}(s) e^{-\tau s} \tag{2-4}$$

It can be cleared up that the transfer function of the servo valve is:

$$\begin{aligned} H_t(s) &= \frac{q_s(s)}{X_C(s)} \\ &= k_{xq} \frac{k_1 k_2 (k_{pro}^i + s k_{der}^i)}{1 + A_i(s) k_1 k_2 (k_{pro}^i + s k_{der}^i) e^{-\tau s}} e^{-\tau s} \end{aligned} \tag{2-5}$$

**The mathematical model of the servo actuator**

Servo and actuator is connected by the oil, the oil in them will keep balance in all time and the amount is a constant. The servo - actuator transfer function S (s) is according to these conditions.

According to the continuity of the oil flow, the flow equation of actuator is obtained:

$$q_s(s) = q_{pm}(s) + q_{le}(s) + q_{comp}(s) \tag{2-6}$$

Where $q_{pm}(s)$ is the variation of volume; $q_{le}(s)$ is the velocity of seepage flow; $q_{comp}(s)$ is the oil amount of compression; and

$$q_{pm}(s) = A \dot{X}_t(t) \tag{2-7}$$

Where $\dot{X}(t)$ is the speed of drive ratio; A is the effective sectional area of actuator piston.

Suppose the relation between the seepage of actuator in seal chamber and the fluid stress in pressure chamber is linear, then:

$$q_{le}(s) = k_{le}^{'} \frac{F_a(t)}{A} = k_{le} F_a(t) \tag{2-8}$$

Where $k_{le}^{'}$ is percolation flow coefficient.

On the basic of the oil amount of compression definition, it can be concluded that compression rate can be defined as a variation of oil volume in pressure chamber:

$$\begin{aligned} q_{comp}(s) &= \frac{d}{dt}[\Delta V(t)] \\ &= \frac{V}{4\beta A} \dot{F_a}(t) \end{aligned} \tag{2-9}$$

Take the above three parts of the oil flow into fluid continuity equation, the oil flow per second in the actuator pressure can be expressed:

$$q_s(s) = q_{pm}(s) + q_{le}(s) + q_{comp}(s) \quad = SA\dot{X_t}(s) + k_{le}F_a(s) + \frac{V}{4\beta A}\dot{F_a}(s) \tag{2-10}$$

Combining with the previous transfer function

$$H_t(s) = \frac{q_s(s)}{X_C(s)} \quad \text{and} \quad S(s) = \frac{X_t(s)}{X_C(s)}$$

It is acquired that the transfer function of servo valve and actuator is:

$$S(s) = \frac{X_t(s)}{X_C(s)} = \frac{H_t(s)}{SAX_t(s) + k_{le}F_a(s) + \frac{V}{4\beta A}F_a(s)} \tag{2-11}$$

**The mathematical model of servo hydraulic system**

To the electrical signals which entrance the servo valve $X_C(s)$, it could be seen as the displacement signals of the actual need movement of actuator. is calculated through the external loop control system of earthquake simulation shaking table of. The $X_C(s)$ is consist of multiple control command in the system, mainly divided into the following several parts:

$$X_C(s) = \varepsilon(t) + X_{ff}(t) + X_{dp}(t) \tag{2-12}$$

For $\varepsilon(t)$ is ratio error value of the flat (that is the ratio error value of the displacement flat needs $X_d(t)$ and the actual output displacement of actuating arm). Due to the external loop control system is feedback control, which is monitored by the error value, so the ratio error value can be a better reflection of the effects of control system for actuators. PID control is used to describe the table error here:

$$\varepsilon(t) = \left[k_{pro} + \frac{1}{s}k_{\text{int}} + sk_{der}\right]\left[x_d(s) - x_t(s)\right] \tag{2-13}$$

$k_{pro}$ is the proportional control gain; $k_{\text{int}}$ is the integral control gain; $k_{der}$ is the differential control gain.

In order to prevent the difference between actual and feedback signal is great in the process of control, giving the value of command a change according to the system performance is frequently. For example: a displacement increment will be given in advance to reflect the feed forward control system's influence on the actuator.

$X_{ff}(t)$ is the proportion of feed forward signal ( the ratio of differential displacement required) :

$$X_{ff}(s) = Sk_{ff}xX_d(s) \tag{2-14}$$

Among them, $k_{ff}$ is the feed forward control gain; $X_{dp}(t)$ is the piston displacement of actuator obtained by different pressure.

$$X_{dp}(s) = k_{dp}\Delta P(s) \tag{2-15}$$

$k_{dp}$ is defined as the pressure change control gain; $\Delta P(s)$ is defined as the change of stress in the pressure cavity.

The driving force of the actuator also can be expressed as following:

$$\Delta P(s) = \frac{F_a(s)}{A} \tag{2 -16}$$

Through mathematical deduction, making the displacement of actuator's actuating arm as output object and the actual displacement of flat needed as the input object, the whole servo hydraulic system transfer function is:

$$H(s) = \frac{x_t(s)}{x_d(s)} = \frac{S(s)\left[(\frac{1}{s})k_{\text{int}} + k_{pro} + S(k_{ff} + k_{der})\right]}{1 + S(s)\left[(\frac{1}{s})k_{\text{int}} + k_{pro}) + Sk_{der}) - \left(\frac{k_{dp}}{A}\right)\left(\frac{F_a(s)}{x_t(s)}\right)\right]} \tag{2-17}$$

**The dynamic model of actuator**

The simulation model of seismic shaking table is often a single-rigid dynamics model, which always ignore the analysis of the stress state of pull rod and hydraulic cylinder under actual working condition. In the process of vibration table movement, as the final output link, the actuator plays an important role on the final results, and the mechanical performances of pull rod and hydraulic cylinder themselves should not be neglected, too. So in this section mathematical model will be established by aiming at actuator, and the process of force in actuator will be simulated.

For the physical model of actuator as figure 3 shows, the quality of is so small compared with the machine body and specimen that its inertia force can be neglected [10]. But the tie rod I slender and long, it is very easy to out of shape in the process of outputting force. So the stiffness and damping of it should not be overlooked. For the hydraulic cylinder, the mass, stiffness and damping of it cannot be ignored because its internal stress is larger, and the walls of the hydraulic cylinder is thicker. Because of the travel of the actuator is shorter and the geometrical non-linearity of the actuator is small, the linear approximation model is used as the mechanical model [11].

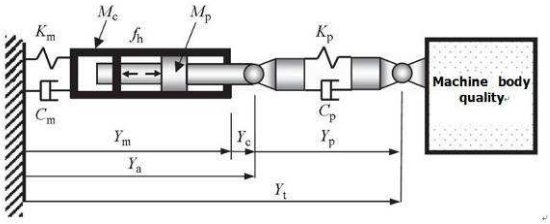


Fig. 3 The schematic structure and symbol of actuator

As shown in figure 3, the actuator drive displacement is written by $Y_t$, and the deformation of the rod length is written by $Y_p$, the actual deformation length of hydraulic cylinder is written by $Y_c$; $Y_a$, $Y_c$, $Y_m$, $Y_p$, $Y_t$, as actual displacement of hydraulic actuator's different parts in the equilibrium states, which is that no force and no displacement output from actuator, the elongation length of them is expressed as $y_a$, $y_c$, $y_m$, $y_p$, $y_t$.

The following hydraulic cylinder and pull rod function is established according to the composition of the final displacement:

$$y_m = -\frac{1}{M_C S^2 + C_m S + k_m} f_h \tag{2-18}$$

$$y_a = \frac{f_h - k_p y_t - C_p \dot{y}_t}{M_p S^2 - C_p S - k_p} \tag{2-19}$$

According to figure 3, and equation (2-18) (2-19) ， the final expression is obtained:

$$y_c = y_a - y_m$$

$$= \frac{f_h - k_p y_t - C_p \dot{y}_t}{M_p S^2 - C_p S - k_p} - \frac{1}{M_C S^2 + C_m S + k_m} f_h \tag{2-20}$$

When $y_c$ is used as actuator actual output values, its physical meaning can be understood as the actual output values that after the actuator drive arm overcomes its own dynamic characteristics.

## Conclusions

As a new method in the research and development of shaking table, the establishing and realizing of the digital model of hydraulic system in simulation vibration table will offer one way for the design of shaking table., The hydraulic system model of multiple subsystems is integrated into a unified digital model in this paper. Set up its system structure and the preliminary simulation of it is established, structure and some key parameters in the system is analyzed and optimized in this paper, which can provide reference for the digital simulation of the vibration table design process, the distribution of precision and error analysis of it.

## Acknowledgements

This work was financially supported by the NSFC(41172237).

## References

[1] Wang Xiangying. Study on structural hybrid testing method with shaking table.[D].Harbin Institute of Technology,2010.1(in Chinese)

[2] Qiu Fawei,Qian Jiaru,Chen Zhipeng, Structural seismic test method[M].Bei Jing: Science press，1999. (in Chinese)

[3] Shimizu N, ShinoharaY, YabukiH and Sato E. Control simulation of shaking table with non-linear structure. Proceedings of ACMD2004, 478–485.

[4] J. P. Conte1 and T. L. Trombet. Linear dynamic modeling of a uni-axial servo-hydraulic shaking table system [J]. Journal of Earthquake Engineering and Structural Dynamics, 2000, 29:1375-1404.

[5] Bradford K Thoen, Patrick N. Laplace. Offline Tuning of Shaking Tables [J]. 13th World Conference on Earthquake Engineering, 2004, No. 960.

[6] Shao Xiaoyun, A.M.ASCE, Andrei M. Reinhorn, F.ASCE, and MettupalayamV. Sivaselvan. Real-Time Hybrid Simulation Using Shake Tables and Dynamic Actuators [J]. Journal of Structural Engineering , July 2011:748-760.

[7] Andrew Plummer. A general co-ordinate transformation framework for multi-axis motion control with applications in the testing industry [J]. Journal of Control Engineering Practice, 2010(18):598-607.

[8] Li Hongren, Guan Guangfeng, Guo Hongbo, Cong Dacheng, ZhangHui, Ye Zhengmao. Modeling, simulation and experiment on valve controlled asymmetry piston considering valve port error[J].Chinese journal of mechanical engineering,2007.43（9）：33-38. (in Chinese)

[9] Li Chang. Research of force loading control based on 6-dof motion platform[D]. Harbin Institute of Technology，2011，6. (in Chinese)

[10] He Jingfeng, Li Baoping, Tong Hongbin, Han Junwei, DOF control and inner force balancing of hydraulically redundant actuated shaking table[J]. Journal of vibration and shock，2011，30（3）：74-78. (in Chinese)

[11] A. R. Plummer. A Detailed Dynamic Model of a Six-Axis Shaking Table [J]. Journal of Earthquake Engineering, 2008,No.12: 631–6

*Applied Mechanics and Materials Vols. 580-583 (2014) pp 3163-3166*
*© (2014) Trans Tech Publications, Switzerland*
*doi:10.4028/www.scientific.net/AMM.580-583.3163*

# Research on SketchUp Application in Graphing of Civil Engineering

Qiang Dong[1, a] Yongshou Yang[1, b]

[1]Shandong Jiaotong University 5001 Haitang Road, Changqing District, Jinan City, Shandong Province, P.R.China, 250357

[a]email:1733834941@qq.com

[b]email:yangyongs616@163.com

**Keywords:** Graphing of Civil Engineering, SketchUp, Modeling, Model Base

**Abstract.** This paper introduces to the application of the software---SketchUp in teaching process, which will make the abstract graph visualize, inspire students' interest and help them to have a better grasp of civil engineering structure. We use SketchUp to create models, assist the teaching of civil engineering Graphing and recognition, improve students' space imagination and cultivate their creativity.

Applied undergraduate education is also called employment education. In order to cultivate advanced applied talents who have sufficient theoretical knowledge and proficient skill, it's necessary to use the personnel evaluation criterion in company to build the evaluation criterion in class teaching, so it's necessary to have the teaching revolution. This article discusses how to use SketchUp (three-dimensional architectural sketch master) of Google company for civil engineering modeling, and the teaching method revolution and methods of projection knowledge in Civil Engineering Graphing and recognition.

## Course Highlights

Civil engineering Graphing and image recognition is the professional basic course for civil engineering major and can cultivate students' ability to map recognition and Graphing. This course is mainly edited by Yong Liu and Qiang Dong, and adopted < Descriptive Geometry and Civil Engineering Graphings> (the second edition) published by National Defence Industry Press. And this book contains three parts: basic knowledge for projection, civil engineering cartography and image recognition. Projection is an abstract part, it demands space imagination ability and operation ability. What's more, this project can overcome some defects in teaching which uses handmade models [1].

## Software Overview

SketchUp is one of the few design tools with design process orientation directly. It helps designers with visual conception in computer. Along with the clearer conception, more and more details, the final model can be passed to other rendering software to do the final render. In this way, designers can decrease mechanical rehandling and control the accuracy of design outcomes.

SketchUp is so simple and easy to learn that college teachers and students can grasp it through short time study. SketchUp is not only limited to sketch design, it also can do accurate Graphing and has convenient push-pull function. Using this software, designers can generate 3D geometry by a graph, instead of complex three-dimensional modeling. It combines the grace of penciling and the natural of Graphing, and it can form, show and edit three-dimensional modeling swiftly. At the same time, it can guide into CAD and image file, guide out two-dimensional image and three-dimensional model, combine AutoCAD, Revit,3DMAX, PIRANESI and some other software, swiftly guide in and out DWG, DXF, JPG, 3DS format file, achieve perfect combination between scheme design and effect picture and construction picture Graphing, provide plug-in with AutoCAD, ARCHICAD and other design tools. In addition, it can smoothly link up with other LightScape, guide the models in

SketchUp into 3ds Max, correct material and model and anew lighting. So it can make construction picture with high quality easily.

## Application in Engineering Graphing

### 3.1 Application in Projection

Line includes projective plane parallel line ( parallels to only one plane and inclines to other two planes, includes horizontal line, flat line and side flat line), projective plane perpendicular line ( perpendicular to one plane, includes plumb line,horizontal--profile line and W-perpendicular line) and normal position line (inclines to three projective planes). Plane includes projective plane parallel surface (parallels to one plane, includes horizontal plane, flat plane and side flat plane), projective plane perpendicular surface (perpendicular to one plane, while inclines to other two planes, includes plumb plane, V-perpendicular plane and W-perpendicular plane) and normal position surface (inclines to three planes). We can build projective line and plane easily and quickly by SketchUp, like Fig.1. It can be showed in the class to increase sensory awareness and cultivate space imagination [2].

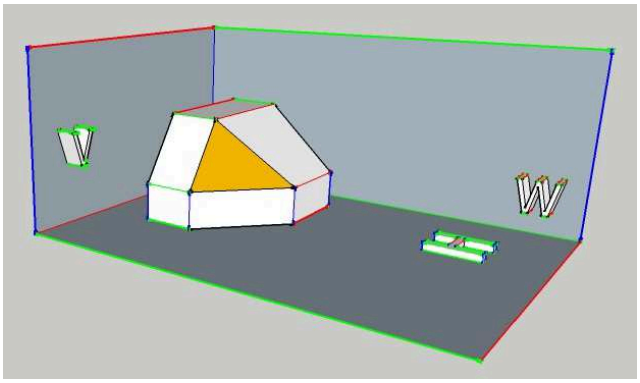


Fig.1 Display of Projective Lines and Planes

### 3.2 Application in Building Configuration

Building three-dimensional model is like Graphing on paper by pencil, SketchUp can automatically recognize these lines and seize them. Its modeling process is forming pictures by lines, then do extrusion forming, which is easy and clear, and this is the most popular method for staircase modeling.

Staircase is the main facility linking the upper and lower space, mainly contains flight, platform and guard rail. Staircase plan mainly shows its location, thickness of wall, flight for each floor, platform, handrail, length and width of staircase, width of each step. When teaching staircase construction, we can guide in CAD graph (Fig.2), then change the plane to three-dimensional shape (Fig.3&Fig.4) by push and pull tool. It is easy to correct and edit, easy to convey the detail of stair construction and makes the class rich and lively.

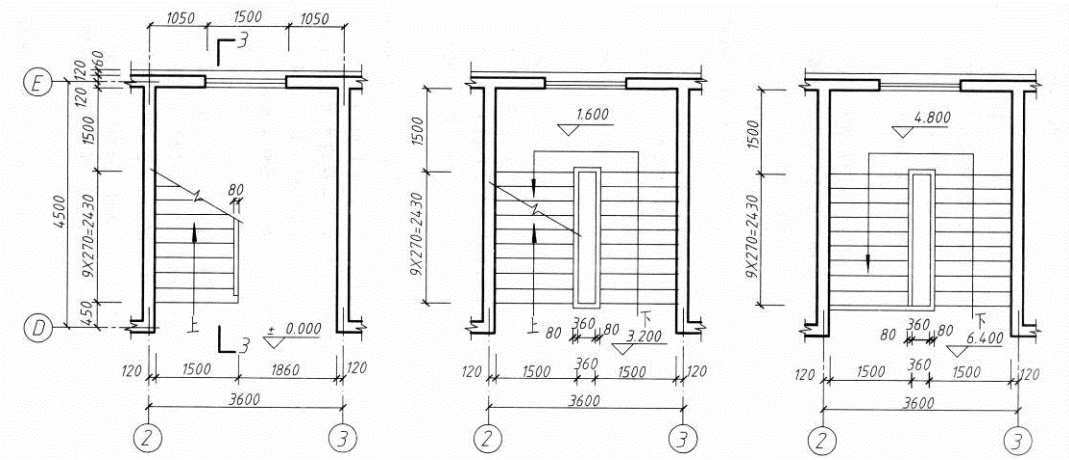


Fig.2 Detail of Staircase

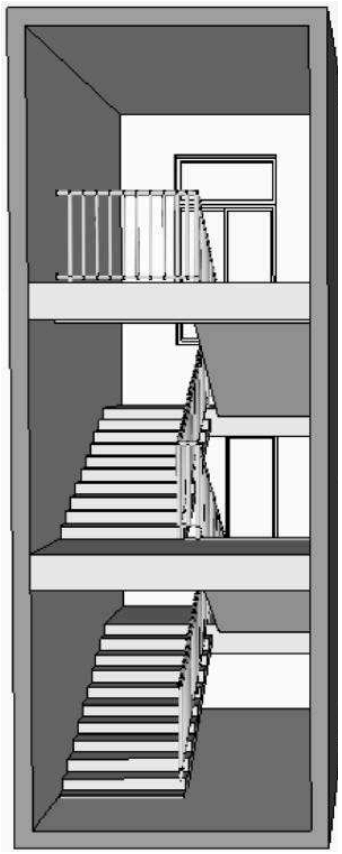

Fig.3 Scenograph of Double Run Stair

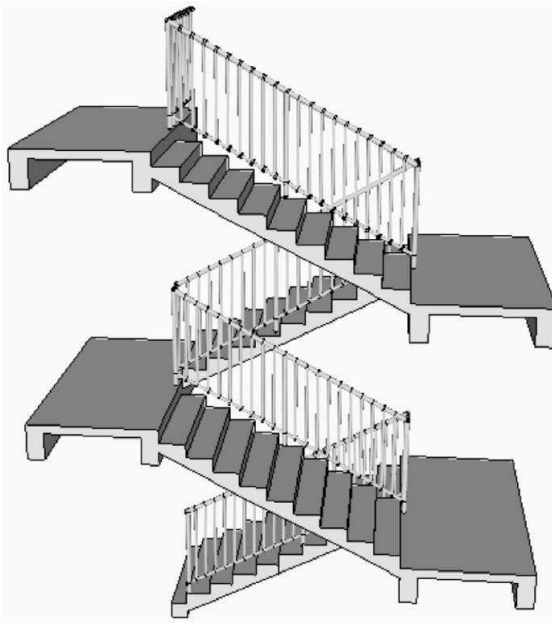

Fig.4 3d Model of Stair Flight and Platform

Application of SketchUp in teaching staircase will not only help students to grasp detail of stair, but also cultivate their space imagination, which lays the foundation for the recognition of the complex modern construction Graphing.

3.3 Structuring Model Base

By the powerful function of SketchUp, we can build various engineering models and form model base, like bridge and culvert model base, like showed in Fig.5-Fig.8. This is helpful to improve recognition ability and cultivate professional skills. With model base, we can calculate construction amount, do feasibility research and three-dimensional simulation.

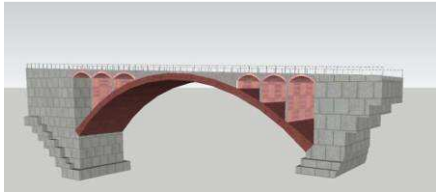

Fig.5 Model Lbase ---Arch bridge

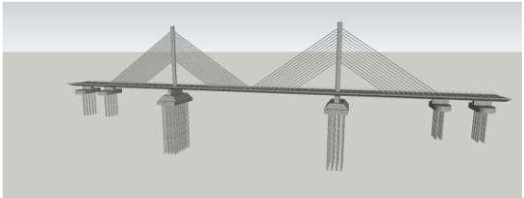

Fig.6 Model Base ---Cable-Stayed Bridge

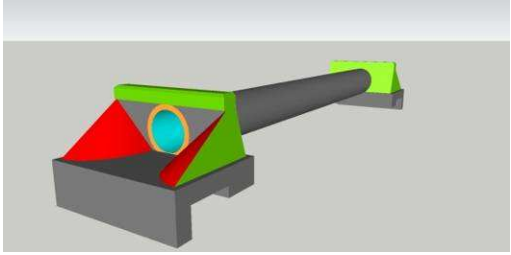

Fig.7 Model Base ---Circular Culvert

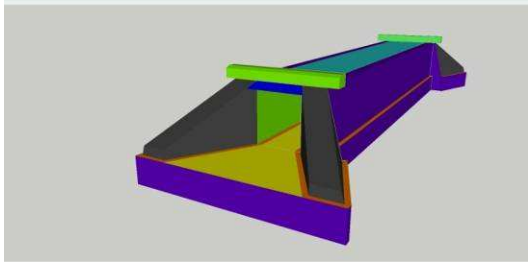

Fig.8 Model Base ---Slab Culvert

3.4 Cultivate Students' Space Imagination

Application of SketchUp cartoon function in class can cultivate students' outsight. As we all known, mental activity of imagination is based on objective things. No observation, no imagination, no creation. In this display teaching, we should attach great importance to students' spatial perception ability. And this needs long-term systematical training.

3.5 Fast Identification for Construction Picture

Modern structure publicizing individuality has unique appearance and complex plane layout. If they only depend on the orthography projective law of point, line, surface and body, it is difficult for students to imagine the space form of structure and grasp the detail. Through the application of SketchUp, students can have a better understanding of design intention and read construction Graphing quickly by simple modeling study and building the complex engineering body.

## Conclusion

SketchUp is an epochal invention, which shows the intuitive design concept "what you see is what you get". Through one term's teaching practice, the author deeply feels that SketchUp has great advantage in engineering cartography, which helps students to grasp basic knowledge and cultivates students' space imagination ability. This lays the root for further study. How to combine projective body with actual complex engineering body together, how to use this software to make reinforcement model for base, beam, board, column and shear wall, and how to do mechanics analysis on models by structure analyze software, remain to be further discussed.

All manuscripts must be in English, also the table and figure texts, otherwise we cannot publish your paper.

Please keep a second copy of your manuscript in your office. When receiving the paper, we assume that the corresponding authors grant us the copyright to use the paper for the book or journal in question. Should authors use tables or figures from other Publications, they must ask the corresponding publishers to grant them the right to publish this material in their paper.

Use italic for emphasizing a word or phrase. Do not use boldface typing or capital letters except for section headings (cf. remarks on section headings, below).

## References

[1] Yong Liu, Qiang Dong: Descriptive Geometry and Graphing of Civil Engineering (National Defence Industry Press, Beijing 2013).

[2] Xiaofei Zhang, Mingming Lv, Zhe Ma, etc: The Helping Role of SketchUp in Grade 2 Architecture Design Teaching: Higher Building Educatio Vol. 18(2009), p. 70

*Applied Mechanics and Materials Vols. 580-583 (2014) pp 3167-3170*
*© (2014) Trans Tech Publications, Switzerland*
*doi:10.4028/www.scientific.net/AMM.580-583.3167*

# Analysis of the flow characteristics of multiphase flow fields in the mixing agitator

Xiaobing Wang[1 a]

[1] School Petroleum Engineering of Changzhou University, Changzhou, 213016, China

[a]czdxwxb@163.com

**Keywords:** mixture and agitation; large eddy simulation; Multiphase flow; flow characteristic; numerical analysis

**Abstract.** The numerical simulation for the flow characteristics of multiphase flow fields in the multiple-blade mixing agitator is carried out by means of combining of the large eddy simulation (LES) and multiphase flow model. Then the flow pattern changes and material mixing rule at different speed conditions are analyzed. The result shows that complicated circular flows form among the four groups of blades in the axial cross section. In the mixing process, the upper solid-liquid mixture is transported to the bottom of the agitator under the action of gravity and fluid shear. Finally it mainly distributes at the agitator walls and the inverted cone manifold in the center of the agitating shaft. With the gradually increasing in the agitation rate, there are a large amount of vortex structures near the blade. Then spiral vortex distribution areas are formed.

## Introduction

The agitator is widely used in the architecture, chemical, food and other industries. There is a big difference between geometric shape and impeller type based on different operational goals. Because of the complexity and diversity of the agitator, there are defects of the complex design process, long period and structure without optimization in the semi-empirical design methods used at present. With the development of CFD technology, numerical simulation methods are taken to study the flow characteristics in the mixing process [1-3], which not only save research funding but also get some dates that can't be gotten from the experiment. According to the structural property of the mixing agitator, numerical calculation model is established to calculate the flow structure of multiphase flow fields in different operating conditions and to analyze the inner flow characteristics combined with hydrodynamic mechanism, which provides theoretical basis for further improvement of the mixing agitator.

## The turbulence model

Large eddy simulation control equation is the averaged equation after filtering the N-S equation.

$$\frac{\partial \overline{u_i}}{\partial t}+\frac{\partial}{\partial x_j}\left(\overline{u_i u_j}\right)=-\frac{1}{\rho}\frac{\partial \overline{p}}{\partial x_i}+\nu\frac{\partial^2 \overline{u_i}}{\partial x_j^2}+f_i \tag{1}$$

The micro compressible flow field model is used in the continuity equation.

$$\frac{\partial P}{\partial t}+K\frac{\partial \overline{u_i}}{\partial x_i}=0 \tag{2}$$

In the above equation, horizontal line presents the quantity after filtering. Relation between the filtration rate $\overline{u_i}$ and actual speed $u_i$ in the large eddy model is $u=\overline{u_i}+u_i'$. K is the square of fluid elastic wave velocity. Nonlinear term exits in the momentum equation. $\overline{u_i u_j}=\overline{\overline{u_i}\,\overline{u_j}}+\overline{u_i'\overline{u_j}}+\overline{\overline{u_i}u_i'}+\overline{u_i'u_j'}$. The first item is large scale component and the other three items are small scale components, that is sub-grid reynolds stress. Then it can be expressed as $\overline{u_i u_j}=\overline{\overline{u_i}\,\overline{u_j}}+R_{ij}$.

$R_{ij}$ is the new unknown after filtering, so sub-grid reynolds stress model is established. Then box-filter function is used and the equation (1) can be expressed as follows.

$$\frac{\partial \overline{u}_i}{\partial t}+\frac{\partial}{\partial x_j}\left(\overline{u_i u_j}\right)=-\frac{1}{\rho}\frac{\partial \overline{p}}{\partial x_i}+\nu_t\frac{\partial^2 \overline{u}_i}{\partial x_j^2}-\frac{\partial \tau_{ij}}{\partial x_j}+f_i \tag{3}$$

According to the average concept of the turbulence energy generated and dissipation, Smagorinsky assumes $\nu_t=(C_s\Delta)^2\left(2\overline{S}_{ij}\overline{S}_{ij}\right)^{1/2}$ and $\overline{S}_{ij}=\frac{1}{2}\left[\frac{\partial \overline{u}_i}{\partial x_j}+\frac{\partial \overline{u}_i}{\partial x_i}\right]$. $\Delta$ is filter width, generally it is grid spacing and $\Delta=\left(\Delta_x\Delta_y\Delta_z\right)^{1/3}$. $C_s$ is not only the model coefficient but also empirical constant. When it is taken as 0.1 the result consistent with the experiment can be obtained. So in this paper $C_s$ is 0.1.

Considering the material movement and the effectiveness of evolution law in the agitator, mixture model is taken to calculate the multiphase flow. Mixture model mainly applies to two-phase flow or multi-phase flow. The phases are regarded as unified continuum structures. At the same time the concept of slip velocity is used to allow the phases move at different speeds.

## The calculation model and boundary condition

The middle of the mixing agitator is cylindrical shell, the top is elliptical head, the bottom is conical head and impeller is installed in the center. The above three stage impeller is three-blade rectangular skewed propeller and the lower impeller is two-blade straight propeller. The overall three-dimensional modeling of the agitator flow is established and the calculation model is shown in Figure 1. The flow fluid is discretized by the unstructured meshes. To improve the calculation accuracy, the blades, the interface griddings, as well as the near-wall region are refined. Computing grid is 1,167,268 and mesh of the agitator is shown in Figure 2.

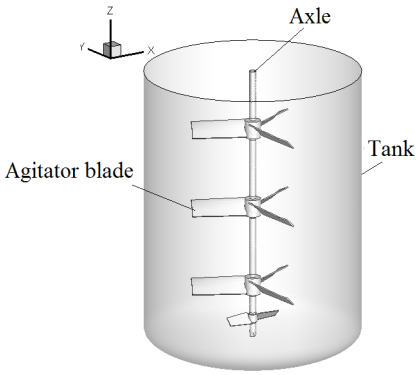


Fig 1 Calculation model and mesh

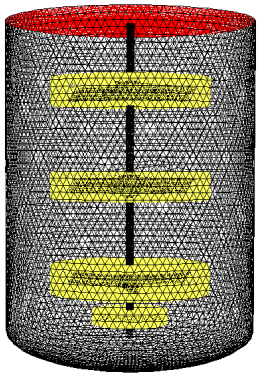

Fig 2 Meshing diagram

A finite volume method is taken to solve the discrete equations, the SIMPLE algorithm is used to couple the pressure and velocity, and Mixture model is applied to simulate the phase separation. The cylinder wall and the blade are set as wall, the type of wall motion is set as moving wall and the starting point of the rotation axis is located in the origin. Moving Reference Frame is taken to simulate fluid motion and the direction of rotation is around the axis direction. In this paper the calculated mediums are water and solid liquid mixtures. For easy figures, the medium is taken as a single component liquid with the higher density and viscosity than water. Rated speeds are 50 r/min, 100 r/min and 200 r/min.

## The calculation results and analysis

Unsteady numerical simulation is used to analyze the distribution law and flow characteristics of the two materials in the mixing agitator. Figure 3 is the volume fraction distribution of the mixture in the

shaft section and the overall barrel at different moments with the rated speed 100 r/min. From Figure 3(b), it can be seen that at the beginning of the mixing, volume fraction of the solid liquid mixtures is small at the bottom center of the agitator and the areas around the agitator bottom, while it is large at the top and the areas near the upper wall. In the mixing process, the force is mainly a combination of gravity and fluid shear owing to the higher density of the solid liquid mixtures. Flow rate near the blade is high and the solid liquid mixtures are gradually transported to the bottom of the agitator under the action of gravity and fluid shear. From Figure 3(d), it can also be obtained that because of the inverted cone manifold near the mixing shaft and the action of the centrifugal force on the mixtures, volume fraction of the solid liquid mixtures is large in the shaft and the area near the cylinder wall.

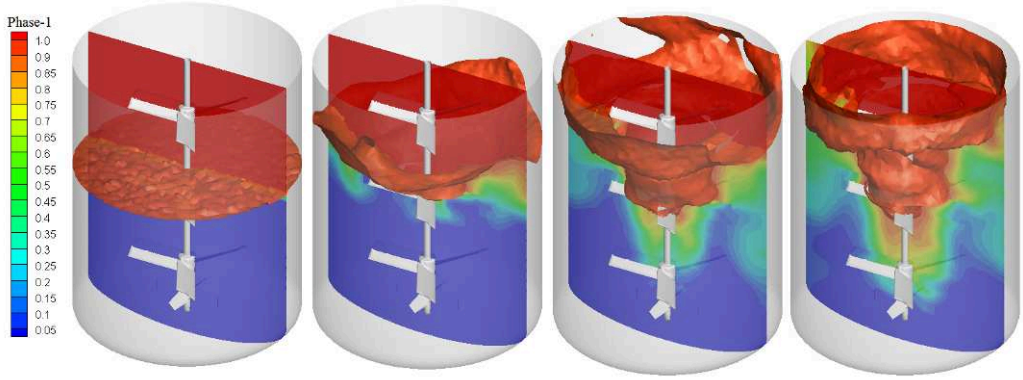


Fig 3 The volume fraction distribution of the mixture at different moments with the rated speed 100 r/min

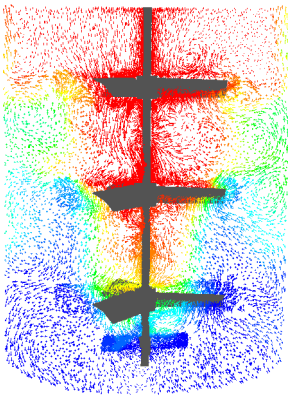

Fig 4 The velocity vector distribution of the axial cross section at X=0m

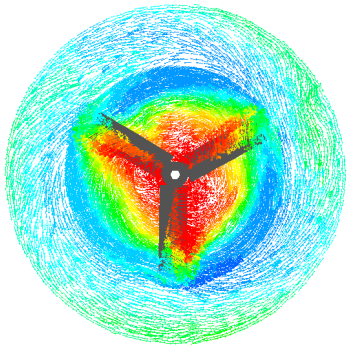

Fig 5 The velocity vector distribution of the radial cross section at Z=2.3m

Figure 4 is the velocity vector distribution of the axial cross section at X=0m. The main loop area is clearly existed among the four blades. At the same time there are two groups of vortex near the third layer of blade tip, which are respectively clockwise vortex and anti-clockwise vortex. Then the mixture is entrained to the second layer of blade rotation area. After analysis of the radial direction vector distribution of the third layer of the blade, it can be seen from Figure 5 that mixture is transported to other area of the agitator by significant speed and high-intensity turbulence near the blade tips.

Coloring the constant vorticity according to Q criterion, the vorticity contours in the agitator flow at different speed conditions are analyzed. The vorticity contour is shown in Figure 6 when Q is 100. A large number of the vortex structures generate near the blade with the increasing agitation rate, and finally they are mainly distributed along the leaf blades. From Figure 6(c), it can be seen that when the speed is 200 r/min, spiral vortex distribution areas are formed near the blade. The radial velocity distributions are shown in Figure 7 at three different speeds. The peak velocity near the hub is in the opposite direction to that near the blade tip. And with the increasing speed, the radial velocity peak difference has become more and more large. Therefore the main loop area is clearly generated between the hub and the blade tip.

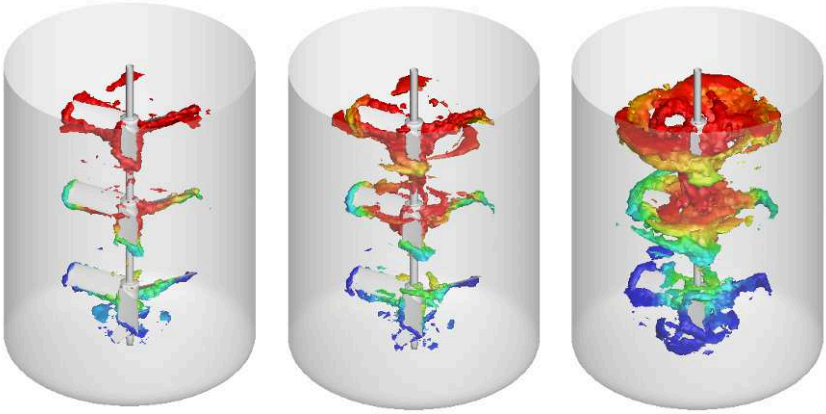

Fig 6 The vorticity contour when Q is 100 and $t$=100s

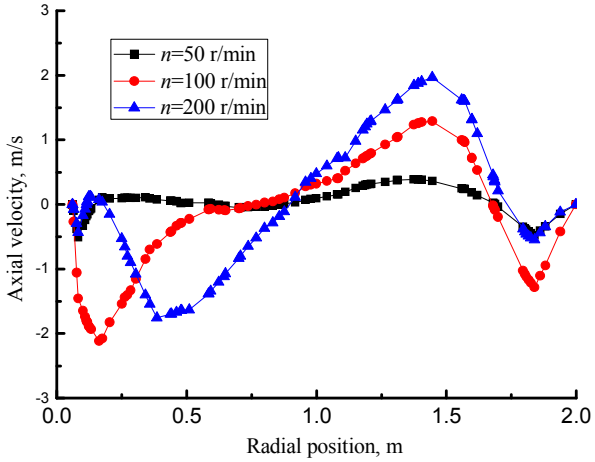


Fig 7 The radial velocity distributions at different speeds

## Conclusions

The flow pattern changes and material mixing rule in the mixing agitator at different speed conditions are analyzed by means of combining of the large eddy simulation (LES) and multiphase flow model. The result shows that complicated circular flows form among the four groups of blades in the axial cross section. In the mixing process, the upper solid-liquid mixture is transported to the bottom of the agitator under the action of gravity and fluid shear. Finally it mainly distributes at the agitator walls and the inverted cone manifold in the center of the agitating shaft. With the gradually increasing in the agitation rate, there are a large amount of vortex structures near the blade. Then spiral vortex distribution areas are formed.

## References

[1] T Hiroshi, N Kuni, K Hideki, et al. Numerical simulation of mixing flows in agitated vessel with impellers and baffles [J].Computers Fluids,1993, 22(4):223-228.

[2] R K Avinash, A T Philippe. CFD simulation of gas-liquid flows in stirred vessel equipped with rushton turbine: influence of parallel, merging and diverging flow configurations [J]. Chemical Engineering Science, 2008, 63: 3810-3820

[3] A Delafosse, A Line, J Morcjain, et al. LES and URANS simulation of hydrodynamics in mixing tank: Comparison to PIV experiments [J]. Chemical Engineering Research and Design, 2008, 86: 1322-1330

*Applied Mechanics and Materials Vols. 580-583 (2014) pp 3171-3174*
*© (2014) Trans Tech Publications, Switzerland*
*doi:10.4028/www.scientific.net/AMM.580-583.3171*

# Building Information Modeling (BIM) and Analysis of More Traditional CAD

Li Jian

Architecture and Civil Engineering School Inner Mongolia University of Science and Technology, Baotou, China

nkdlj@163.com

**Keywords:** BIM, Building Information Modeling, modeling software, traditional CAD

**Abstract.** Building Information Modeling (Building Information Modeling) is the relevant information and data as the basis for building projects model, building model be established to simulate the real information through the building of digital information. It has five characteristics of visualization, coordination, simulation, optimize and can plot and so on. As the construction industry in a brand-new concepts and technologies, BIM has been increasingly used in various construction projects in the country. Building Information Modeling (BIM) provides a platform to complete the continuity and consistency of all information within the whole life cycle of buildings.

## about Building Information Modeling (BIM)

### 1.1 BIM concept and its core modeling software

Building Information Modeling (BIM) is a simulation of a building, which covers the real information about the actual building. BIM is not just software, but an idea - from planning construction projects, design, construction, operation until the removal of the entire life cycle of production and management process to achieve full digitization. Achieve full digitization request, building applications are no longer just using CAD software to complete construction projects or projects so simple, but to use a range of software. BIM software types as shown below as follows:

Core BIM modeling software systems is the carrier for the realization of BIM application platform. The general civil construction using Autodesk Revit, plant design and construction using Bentley series, single professional architectural firms using both can be used. The related software is shown in Fig.1

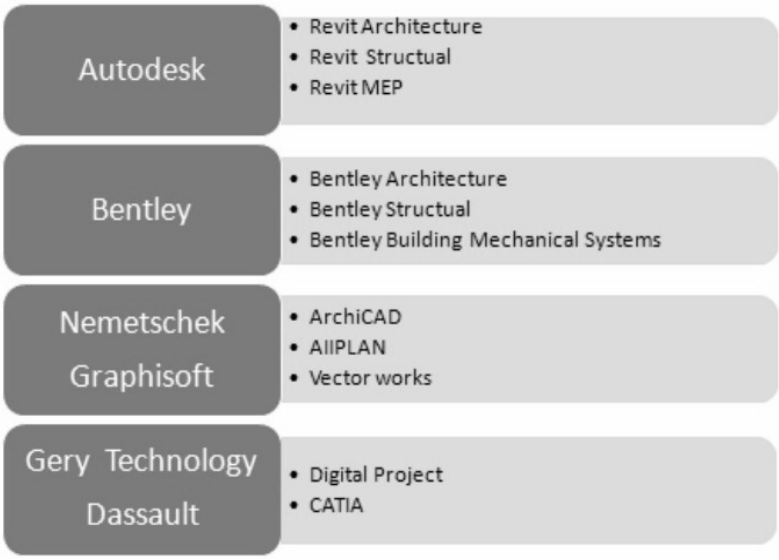


Fig.1. The related software

### 1.2 Application of BIM home and abroad

BIM technology began in the United States. 2009 , Wisconsin requires new intrastate first large-scale public construction projects using BIM technology , while Texas Public Utilities Commission also calls for the design and construction of the project proposes the application of state

government investment BIM technology. In 2010, the government enacted Ohio BIM Protocol. Japan's transport ministry announced the implementation of BIM technology in 2010, has been the rise in the country by the government to vigorously promote. In addition, a number of European government agencies are developing appropriate standards for BIM applications. China's construction industry from the 2003 introduction of BIM technology, and industry associations by the government attaches great importance to the emergence of a variety of domestic and BIM training contest. Shanghai Modern Architectural Design Group, China Construction Design International Ltd. (CCDI) and the U.S. Aedis Architecture and Planning Chinese companies and other companies are beginning to gradually increase the use of BIM technology. However, due to the country's software and hardware environment, BIM technology is still the main stay in the architectural design phase of the major design institutes.

## BIM technology comparisons with conventional CAD

### 2.1 3D/4D (3D+ time) parametric design

Traditional software such as AutoCAD is generally based on two-dimensional graphic design. Build three-dimensional models (AutoCAD comes with three-dimensional modeling software, there are many defects) by Sketch up modeling software, such as when doing renderings, but the two are independent. In the BIM system can be Sketch up, Rhino and From information input into the BIM modeling software core, the core can also be used directly BIM modeling software to build the model (massing studies and architectural design complexity encountered in the early stages When modeling, using Sketch up software is more convenient). This will not affect the use of independent software flexibility while more conducive to the consistency and integrity of project information. Three-dimensional model analysis automation, intelligent provides a platform for the energy building design. BIM's 3D parametric design with specialized three-dimensional design tools, real-time three-dimensional visualization, and more advanced model of collaborative design, create construction details and schedules base map automatically by the model, supporting the analysis and simulation design tools. BIM technology to improve the building design stage information, three-dimensional space also allows designers richer design inspiration. BIM improve the system and shorten the design period, designers no longer have to blindly bury more time for drawing and design innovation. Traditional two-dimensional CAD design construction plans cannot express some complex modeling; BIM through 3D parametric design can be the perfect expression of the designer's creativity. BIM can efficiently solve complex problems spatial arrangement pipeline. All in all, BIM has brought great convenience in the design, construction aspects.

### 2.2 collaborative design and operation

Compared with the traditional CAD technology, BIM ensures the construction operation in various stages of each link in the whole life cycle. It does not only emphasize building projects in planning, design, construction, operation in one aspect, but more emphasis on the process (and the various aspects). Therefore, BIM enables independent operations in each stage while more sophisticated, more prominent BIM technology synergies.

#### 2.2.1 Collaborative Design

(1) With in the same professional collaborative design. Under the conditions of a clear division of labor, with different members of the project design of the project, design and timely content synchronized to the file server, available to other members of the design is used by reference or used a crossover design.

(2) The collaborative design between professionals. BIM platform proposed by various professional requirements, identify problems and timely communication to solve problems.

(3) Coordination between the various systems with each other to avoid the system is affected in space, functionality, usability, ease of management.

(4) Synergies with other software. As described herein, BIM is not software but a series of software. The BIM platform with the core modeling software for the foundation, choice of every aspect of the utility maximum of several software, absorb anything and everything to meet the building life cycle each stage requirements.

By BIM platform, building projects at the design stage to avoid misunderstanding and lack of communication have all kinds of unnecessary error. So the BIM technology can shorten the design cycle, improve the design efficiency and facilitate the design process management.

### 2.2.2 Collaboration

In the design phase, BIM technology to help deal with a variety of design files and office document management, design and planning of any proofreaders flow services, project status query statistics aided design work, and even interactive and collaborative document communication designers, owners, supervision side, the construction side and suppliers between. So, to save a lot of manpower and resources, reduce costs and enhance all aspects of efficiency, thereby increasing business efficiency.

### 2.3 simulation, optimization and plot

BIM in simulation, optimization is the traditional AutoCAD technology not available. AutoCAD technology to do traditional items head only when requested by the owners of green buildings alone will do for a project simulation and optimization. This will extend the operational cycle of the construction project, and the individual is difficult to ensure the accuracy of the simulation. But for 3D visualization model and various boundary conditions of the BIM technology in the simulation and optimization of this block is to make it more simple and. The traditional AutoCAD do projects because of their technical limitations, generally only in accordance with the requirements of relevant standards roughly consider the request parameters such as structure and energy consumption.

In the BIM system, we construct the project is basically the same with the real simulation program solver for buildings with architectural performance analysis, energy analysis , day lighting analysis , sunshine Dan analysis, evacuation analysis, the surrounding buildings and internal flow field analysis , etc. These data will be more accurate to traditional CAD technology, practical. Aspects of the plot, 3D model to ensure the accuracy of the figure drawings. In addition, BIM also offers the possibility for the paperless office.

### 2.4 BIM shortcomings

BIM application has many advantages, but it has not in the domestic promotion, showing it has its own drawbacks. The whole BIM application environment requires high. Throughout the entire project using BIM technology, Aft need to use a variety of software to nearly include all aspects of planning, design, construction, operation four stages. The use of BIM technology for building the project participants is an inherent requirement: the ability to accept, operate and understand this new system. Because of these two points, now the country's BIM mainly stay in the design phase.

In addition, BIM technology is not able to completely fit the actual situation in China now, the lack of comprehensive statistics for the domestic variety of building materials and analysis of the database, the lack of demand for the domestic market and the cost feasible technology system.

## Conclusion

In summary, BIM CAD technology continues the tradition although the specific processes and systems, but in many ways it is more sound and feasible. One day, it will replace the now popular CAD technology.

(1) Visualization model of 3D/4D to ensure the integrity and consistency of project information, help the innovative designer of space design, design and construction problems to solve complex space, complex pipeline. At the same time, 3D technology can shorten the design period, the liberation of the drawing hard on traditional CAD designer. Make BIM truly aided design tools.

(2) In various forms, all kinds of digital content collaboration capabilities to avoid misunderstanding and lack of communication have all kinds of unnecessary errors in the design phase, reducing the consumption of human and material resources. In addition, BIM technology to shorten the design cycle and improve design efficiency and facilitate the management of the entire design process.

(3) The actual digital building model, and a series of precise analysis of the virtual buildings, quantify relevant indicators. According to the simulation to optimize the design reasonable, the actual building is almost perfect in theory.

(4) BIM, there are some drawbacks. Their entire life cycle to achieve architectural hardware requirements are relatively high running BIM is now mainly used for the main reason Institute. BIM in the country as a novelty, the need for a run-in period to allow the construction industry to accept, use it. For the domestic market, BIM lack the necessary database and viable technological system.

## Prospects

Since 2003 the country since the introduction of BIM technology, continue to have the company from a strategic point of view or from starting the actual requirements BIM is applied to actual construction projects. BIM concepts, technologies and related software in the country have been recognized by the building industry. BIM technology because now the Chinese market demand combined with problems in their own small part of the defect, so that by the arrest in China of promotion. However, with respect to BIM used in the construction industry is now mainstream - CAD technology, with more advanced concepts, more intuitive results, better management. In this article, the obvious superiority of BIM technology in the near future, it will replace the current mainstream and become the next generation of mainstream construction industry software architecture.

From CAD to the rapid development of BIM, IT architects create for the complete liberation of the shackles of thinking and expression conditions, new techniques may provide endless architectural creation, a door opened another space in the architect's mind fan windows. Whether you're in the developed or developing city coins, always feel the new building brings an unprecedented strong visual impact, At the same time, from two-dimensional to three-dimensional design, from extensive accurate expression to describe various features of digital simulation models and programs through deduction, control and achieve sustainability while building design products, but also for the design itself sustainability foreshadowed. And all this from a new design concept, design methodologies, design tools and design tools, and a new design pattern thus formed.

The ultimate goal of this new model is BIM. Background as an architect IT managers, when I wrote the above paragraph and character when the mood is excited and spirited, But faced with the reality of the current design , when they had to mind flat, lowered expectations , from CAD to BIM, the future is bound to be bright, but the road is bound to be tortuous.

## References

[1] Yun Zhang. From the building information model (BIM) and energy consumption management life cycle thinking in terms of building [J], Green building, 2012, (04):29 -30. In Chinese

[2] Ho Kwan Pui. BIM and BIM related software [J], Civil Engineering and Architecture Information Technology, 2010, 2 (04):110 -117.

[3] Qinghua He, Qian Lili, Duan Yun Feng, Li Yongkui. BIM study [J] status and barriers in domestic applications. Engineering Management, Newspaper, 2012, 26 (01):12 -16. In Chinese

[4] Qin. The application of BIM architectural design phase of [J], Architectural feat, 2011, Z1:160-163

[5] Application Mode Li Heng, Guo Hong Ling, Huang Ting, Chen Jingyuan, Chen Jin. BIM in construction projects [J]. Engineering Management, 2010, 24 (05):525 -529.

*Applied Mechanics and Materials Vols. 580-583 (2014) pp 3175-3178*
*© (2014) Trans Tech Publications, Switzerland*
*doi:10.4028/www.scientific.net/AMM.580-583.3175*

# From CAD to the rapid development of BIM

Li Jian

Architecture and Civil Engineering School Inner Mongolia University of Science and Technology, Baotou, China

nkdlj@163.com

**Keywords:** BIM, Building Information Modeling, Architectural design, construction industry, informationization

**Abstract.** While architectural design went into the time of BIM, it meant not only the update of tools and methods, but also the update of design procedures and thinking model. In the meantime, while engineering construction went into the time of BIM, it meant not only the update of design delivery methods, but also the update of interactive mode and consequence among the links of entire industry. Therefore, there are so many obstacles to overcome and it depends on the rapid upgrade of information technology application and management standards of the related enterprises as well as the entire industry.

## Introduction

From CAD to the rapid development of BIM, IT architects create for the complete liberation of the shackles of thinking and expression conditions, new techniques may provide endless architectural creation, a door opened another space in the architect's mind fan windows. Whether you're in the developed or developing city coins, always feel the new building brings an unprecedented strong visual impact, At the same time, from two-dimensional to three-dimensional design, from extensive accurate expression to describe various features of digital simulation models and programs through deduction, control and achieve sustainability while building design products, but also for the design itself sustainability foreshadowed. And all this from a new design concept, design methodologies, design tools and design tools, and a new design pattern thus formed.

The ultimate goal of this new model is BIM. Background as an architect IT managers, when I wrote the above paragraph and character when the mood is excited and spirited, But faced with the reality of the current design , when they had to mind flat, lowered expectations , from CAD to BIM, the future is bound to be bright, but the road is bound to be tortuous.

## What BIM applications

The English called BIM Building Information Modeling, Chinese multi translated building information model. But everyone one will find that M is rather Modeling Model; it is referred to, and play a role in the formation process of the model rather than the model itself. So BIM should be accompanied by a building from scratch from birth to death the whole process of digital models of life processes. Discussion of these seemingly little hypocritical, but only make it clear that, in order to truly understand the significance of BIM.

Since it is accompanied by the whole life of the building, then the whole lifetime of BIM which applied?

BIM application project pre- planning stage for the economic, social and environmental benefits of projects to contribute; BIM application design phase for the construction of features, performance, safety, quality and cost control to contribute; construction phase BIM application for the construction of process efficiency, quality and contribute; BIM application for the operation and management of the operational phase of the monitoring architecture to contribute. Contribution BIM application for building the above stage is full of life in terms of revenue they get, not at all stages of their expression.

Very obvious contribution to the design phase of BIM application date, the value will eventually be reflected in the construction and operational phases.

Only from the perspective of the economy and the quality of the contribution the design stage of the building of the whole life is enormous. Although the design of the building itself occupies only 5% of the whole life of the total cost, but decided 70% of its total cost. According to the U.S. BSA (buildings MART alliance) data, the cost of building construction process only 25% of the total cost of the whole life cycle, while the cost of using the operational phase has to account for 75%. According to the U.S. construction-related agency data show that the construction industry practice waste (75%) than manufacturing practices (26%) more than doubled. China's relevant statistics I did not find, but I believe will not be good at this level. This data shows that in the construction industry performance potential is enormous, and the contribution which the design phases will occupy a huge share.

This shows that, aside social and environmental benefits of this concept is not that big, square or building owner will get the most economical in BIM applications, the construction side will reap huge gains in efficiency in BIM applications, and design side before the application of BIM provides benefits both premise and its benefits are designed to enhance the quality of the earnings is not reflected in the economy, at least not therefore significantly improve the design fees in the short term. Meanwhile BIM is unlikely to improve the efficiency of the design phase, but also cannot ignore the design side in which the design itself is more sustainable, such as accumulation and continuous optimization of the basic building blocks of information, data accumulation and analysis of the complete design statistics, these undoubtedly a huge role for the rapid design and submit the results to the design of the control confidence.

**BIM's contributions as well as contributions to the design of BIM**

As discussed previously BIM application in each stage of the whole building life cycle contribution. If we want to compare, there is no doubt in the design phase of the application greatest contribution. BIM application design phase of construction features, improved performance, improved design quality and degree of completion, and for the cost of control, the role of extraordinary.

On the architectural features, BIM capabilities to analyze and optimize the design phase of the program can be integrated urban transport coordination function contradictory impact, environmental impact, such as seeking the most reasonable flow lines, sight and other internal use features allow the design to get rid of dependence on experience get relatively perfect building program through rational analysis and calculation; on building performance, BIM preliminary design stage performance analysis and optimization, you can get a variety of adverse conditions after the safest reasonable tradeoff structure of the program, you can get different internal thermal Under the overall energy, sunshine and lighting features analysis of environmental conditions, in order to identify the most reasonable performance programs; quality in design and finish degrees, professional integrated coordination and conflict checking construction design stage, you can solve almost impossible under the CAD method avoid collisions and other professional errors and omissions touch contradiction pipeline missing issues can help avoid normative specification validation errors, improve the quality of legitimacy; while improving the overall process design stage BIM models, continue to refine engineering report that the project cost has remained under control.

Design from scratch for the construction of full life cycle BIM contribution, from basic to perfect. Thanks to the above contribution BIM design, the design is complete BIM delivery model has almost completed the construction of a virtual equivalent to the state. This is designed to pay for work which of course cannot be mentioned in the same way with the CAD language.

**What BIM tools**

Often hear people ask, BIM is what software? Or, BIM Revit is it? In fact, look at the table in front of BIM applications can know, BIM impossible just software. In the design phase it should at least

include modeling and simulation analysis (including cost management) two categories of software, of course, since it is called Building Information Modeling, BIM modeling is certainly its most important aspects. BIM modeling software also varied, as varied as CAD software. Civil design commonly used modeling software have our very familiar in the era of CAD company Autodesk and Bentley companies , Autodesk 's Revit family of products and Bentley 's GC (General Consultant) series products are still the most widely used . Another GT (Gerry Technology) French Dassoult use Catia software development company DP (Digital Project) series. Different modeling software for different construction projects, GC Series DP Series software and physical modeling of complex building more suitable, of course, capital and technology into applications DP is relatively much higher. In addition, some modeling software such as Sketch up and Rhino is more commonly used design stage modeling software.

Analysis of the model will use a series of simulation analysis simulation software , as usual for the pipeline comprehensive conflict checking software Autodesk Navisworks, Bentley Project wise Navigator and Solibri Model Checker , commonly used in a variety of performance analysis ETABS, Ecotech, IES , etc., is frequently used in the design phase .

**BIM is still a long way road**

As a designer, just to see these tools mentioned earlier, you can learn how different future design and traditionally. Those described earlier application also tells us that we can know in advance exactly how we designed the building will run. All of these, of course we need to do more work in advance. When BIM show a perfect prospect, exciting and inspiring, but when faced with a tight schedule and heavy tasks of the project design fees were not high, if not required or forced, it seems that we have been unable to pursue the beauty of BIM. From the entire construction industry, manufacturing information compared with the relatively low level of applications, this is a special complex industry brings. Although the construction industry is not cutting-edge technology, but it does not need to put so many cutting-edge technology to integrate and industrial chain length, number of participants, BIM to walk every step in this long chain, has experienced numerous participants, their difficult to imagine.

Domestic experts in this transformation from CAD to BIM, the construction side is the biggest beneficiary of the macro, but the technology can be put in enough power is relatively low; designer is the largest contributor to its technical strength and most strong, but the actual benefit the smallest, power can only be living in the middle; while living in the middle of construction technology side, the largest of its actual income, its power is also the largest. Therefore considers the construction side BIM revolution will be the primary ground.

During the construction phase is the construction phase after more biased, the power of BIM applications, is bound to affect its first upstream design stage, therefore, the greatest contribution BIM design side will be dragged into the BIM applications. If you did not become a tool and means BIM design side, the design side facing passive situation. In fact, the domestic situation is not entirely true, arguably those sighted design, and strong technical force and have the industry has taken the lead in the unit responsible BIM way off.

BIAD (Beijing Architectural Design and Research Institute) of BIM road, started in those complex spatial shape description and manipulation needs. Looking at the domestic civil design industry, which is likely to be a general rule. This shows that complex shapes cannot be described by two-dimensional tool design creativity needs, and with the three-dimensional parametric design of interactive, BIM enthusiasm led the design phase, and this power is in front of experts did not notice. Thus embarked on the road to perhaps BIM is Chinese characteristics, but there is that is reasonable, but do not let the minutiae obscures the trunk, a tributary of the collateral as the mainstream.

Although the intersection of BIM has come, but we still have a long road to BIM, we are still far from the ideal of BIM goals. Which requires the popularity and mastery of technology and operations has been very complicated, and change the designer’s thinking and work habits but not an easy task?

From the technical point of view it is especially outside, even completely solve the problem of the design phase; it is only a small part of the completion of the road BIM. First, our CAD foundation is not solid. While we work to complete the design using CAD tools from the beginning has been more than 20 years, but also to a large extent and mode of thinking with print manual era. CAD and document data does not smoothly flow in the various stages of the construction process; the last stage of delivery to the next stage is still mostly hard-copy documents. Leaving aside the electronic document accuracy, reliability and legal validity of the certificate is not to say, even if some of the documents in electronic form, in which the file data standards will also bring trouble confusing the little convenience canceled out. Britain and other countries, if read carefully CAD standards, difficult to find, BIM many of the basic concepts and ideas, has long been lurking in CAD, just waiting for technology to enhance, stimulate and extend it and make it more perfect realization. Secondly into BIM era, the scope and content of the work is more widespread, extending from the enterprise to participate in the entire construction process between the relevant authorities and enterprises, including government, the construction side, the design side, the construction side and suppliers and so on. Collaborative front longer, more complex data flow lines, more unified standards, and these are precisely the construction industry in our short board.

But anyway, BIM is the development direction of the construction industry; this conclusion is the consensus of all parties. And as technology advances and to strengthen the management of this goal will be achieved in the not too distant future. Looking at the domestic construction industry for nearly 30 years history of information technology, it can be said in the 1980s mainly to solve the problem of structural design calculations calculated as the main content of the 1990s basically solved the problem of computer-aided drawing, the early 21st Century Computer and network-assisted solve management problems, then the next 5-10 years, will be based on the industry's BIM-based information integration applications.

**References**

[1] Pengdong Yu, Jianguo Chen, Dan-heng Yang, construction Information Sharing Technology Research and Application Analysis [J] Construction Economics, 2010 (10) :18-22. In Chinese

[2] R. Sacks R. Barak. Teaching Building Information Modeling as an Integral Part of Freshman Year Civil Engineering Education [J]. Journal of Professional Issues in Engineering Education and Practice 2010 1 :30-38. In Chinese

[3] Adil Sharag-Eldin Nawari. O. Nawari. BIM in AEC Education[C]. 2010 Structure Congress 1676-1688.

[4] J Zhang building information modeling in engineering design industry in the application of Disability Research [J] Project Management Journal, 2010 (4) :387-392. In Chinese

[5] Xudong Have, Ang Zhao. Based BIM technology building energy design applications [J]. Chongqing Architecture University, 2006, 28 (02):33 -35. In Chinese

[6] Jianguo Chen, Xing Zhou based BIM is an integrated multi-dimensional realization of the construction -based management [J]. Scientific and technological progress and to Policy, 2008, 25 (10):150 -153. In Chinese

*Applied Mechanics and Materials Vols. 580-583 (2014) pp 3179-3182*
*© (2014) Trans Tech Publications, Switzerland*
*doi:10.4028/www.scientific.net/AMM.580-583.3179*

# Model reuse technology in building electrical parameters design

Hongke Pu[1, a*], Qingchao Wei[1,b]

[1] School of Civil Engineering, Beijing Jiaotong University, Beijing 100044, China

[a]peakhill@163.com, [b]qcwei@bjtu.edu.cn

**Keywords:** Building electrical design, parameterization, reuse technology, CAD, secondary development.

**Abstract.** Electrical design in a variety of electrical equipment needs to search, copy and modify constantly, so it is inefficient. Parametric design technology is the most common way to achieve rapid design, but less in the electrical design of the specific application. With the electrical equipment model parameterization and the reuse technology model, develop electrical equipment design software based on CAD secondary development. Use of software, design by three levels of reuse technology on the equipment for quick drawing, editing, statistics, to avoid duplication of work more efficiently, to improve design efficiency and reduce human waste.

## Introduction

In electrical design, engineers copy the corresponding equipment drawings from other CAD drawings to the current project, and then layout equipment according to the needs. Each type of equipment having as many as hundreds of equipment is a painful thing for the designers to create the base one. In addition, each device in different places may need to set different parameter information, such as size, power and so on, in order to display the corresponding information of statistics. If according to the traditional way for processing, equipment layout, editing and statistics will spend a lot of time, waste of manpower, and still can't get clear and accurate statistics.

Parametric design technology can realize the rapid drawing design[1]. Using design of mass customization mode, set up the equipment in a large amount of information, including size information. Configuration design as the main means of design, complete product customized design, rapid response to the needs of users. The comprehensive utilization of modular design technology, the configuration design technology and database management technology is used for parameterized system development research. The aim of modular design is to improve the efficiency of product design, shorten product design cycle and reduce production cost. Classify the electrical equipment by the function of different or the same function but different performance module, input the equipment type to the database management according to category, help users quickly find equipment needed.

Design reuse through the reuse of the existing design elements to improve speed and quality of design[2,3], it is widely used in mechanical engineering and software engineering, and other fields, its application in construction engineering fields there are urgent needs and great potential applications. In the electrical design, the basic equipment units in accordance with the requirements of choice, assembled to form a collection of reusable equipment unit can also be designed to be assembled into a standard room in the form of reusable equipment. Based on this theory, this article is to determine the reuse unit, name reuse, and provide a basis for the deployment in order to realize the automatic operation process and achieve rapid equipment drawing[4,5,6].

## Process

Equipment to reuse the basic three levels: reuse unit, reuse collection, reuse of floor (Fig. 1).

- Reuse unit is the most basic equipment parts, separately to editor
- Reuse is set according to a certain region (such as a room), chooses corresponding combination unit assembled, forming regional library equipment
- Reuse is assembled the reuse of composite applications to the whole floor

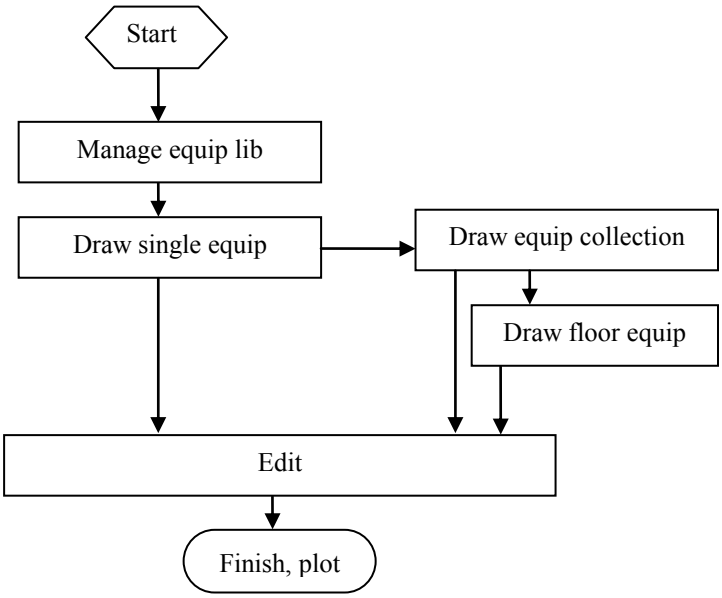


Fig. 1 Design process

The original library needs to input common unit devices by classification. Settings interface, convenient for the user at any time to add new equipment, forming the basic unit library, which is the most basic unit of reuse.

- Analysis of product structure, divided into modules
- According to finalize the design product design units
- Establish parametric model
- Forming block and add to library

The basic unit can be used for electrical equipment layout, fast editing and other functions, but not to play to maximum effect. Multiple devices to select by area layout, are stored in the current database in order to draw quick and batch edit. If the floor number is more, the same or a similar device collection of the region can be used and you can quickly achieve layout floor equipment.

After the device drawing is complete, the device can be unified treatment. According to the device name, device properties, equipment size for device information filtering, select needed device for rapid batch editing process. The select equipment set can also be edited directly in accordance with the device's region, floor.

**Process Model**

Based on AutoCAD secondary development platform and using Visual C++ and ObjectARX SDK development tools to develop functional electrical equipment layout software. Equipment classification and definition of information are stored in the equipment database. Design appropriate tools of device library management (Fig. 2): Equipment classification, equipment input, equipment editor, equipment parameter processing. Each device uses block as the basic unit placed in storage in a single dwg type file, each block having the appropriate device information stored in the block properties in the block mode. When the device is arranged according to the user's choice, export the appropriate equipment from lib to draw the corresponding block and block references to the current drawing, each device has only one block. If there is difference between the current drawing device and the device in the library, you can modify current device before adding to storage, used as a new device. In the drawing, you can set the parameter information for device and describe the device features.

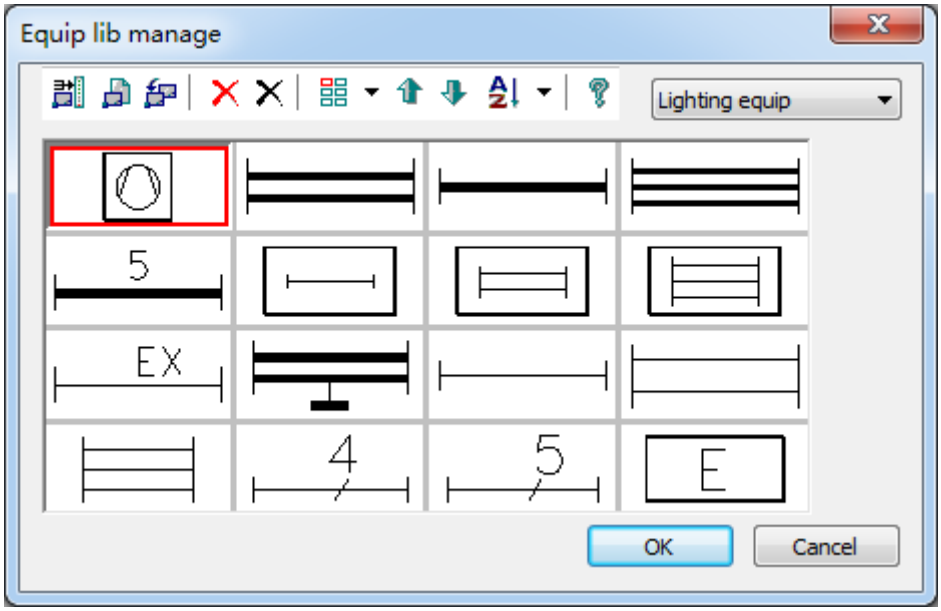


Fig. 2 Lib manage section

Reuse region collection and reuse floor collection are created by the user with the appropriate class name and managed by the user: edit, modify and delete operations. Reuse collection requires the user to select from a collection of drawings to extract information stored in the database, and to get the appropriate base point used for user to insert collection into the drawing. Reuse floors need to select multiple reuse collections from collection lib, and set the location of each set of equipment. Every time draw a lot of equipment rapidly.

With the current tool to draw electrical equipment, you can quickly get statistical information on all devices (Fig. 3): including the number of devices, size, room equipment information, certain floors of the device information, it is convenient for user to quickly understand the final arrangement and construction unit ready to purchase material.

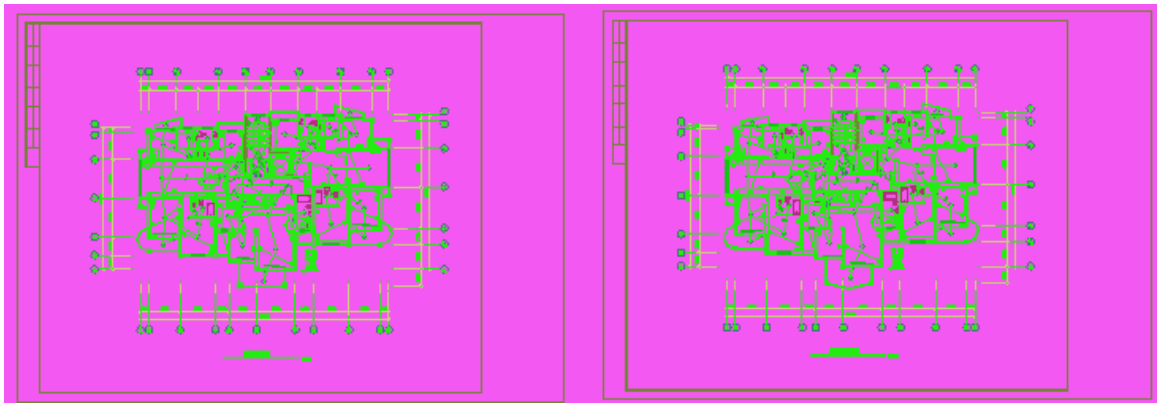

Fig. 3 Equip synchronization draw

## Summary

This article is based on AutoCAD secondary development technique, with the help of a database, develop automated processing software. Fully use parametric model reuse technology in the design, effectively control the reuse scope and the method. Use parameterized module processing electric equipment, realize the different level of reuse of equipment model. The design engineer can carry on the equipment layout, fast and efficient batch edit, thus reducing repetitive work. Allowing designers release from tedious drawing work, apply time to more professional study.

**References**

[1] CHEN Bo, LU Xin-juan, GU Ju. On a Model's Dynamic Displaying System Dependent on Design-Parameters Using the ObjectARX Technolog[J]. Journal of Jiangnan University(Natural Science Edition), 2013, 12(3)：p.283-287(in Chinese)

[2] Chen Li, Shao Zengzhen. Research on supporting reuse in an architecture design pattern system [J]. Mini-Micro Systems, 2004, 25(2)：p.291—294 (in Chinese)

[3] Altmeyer J, Ohnsorge S, Scharmann B. Reuse of design objects in CAD frameworks [C] Proceedings of IEEE/ACM International Conference on Com puter-Aided Design, Digest of Teehnical Papers, San Jose, 1994：p.754—761

[4] Cat Wenqin, Peng Peilin, Jiang Shoushan. Knowledge representation and reuse in aircraft design[J]. Computer Integrated Manufacturing Systems, 2004, 10(1)：p.55—58 (in Chinese)

[5] Dong Y, Tan J R, Xu J. Design reuse method for assemblies in concept design[J]. Chinese Journal of Mechanical Engineering：English Edition, 2005, l8(1)：p.132-138

[6] Demian P, Fruchter R. Measuring relevance in support of design reuse from archives of building product models[J]. Journal of Computing in Civil Engineering, 2005, 19(2)：p.119-136

*Applied Mechanics and Materials Vols. 580-583 (2014) pp 3183-3186*
*© (2014) Trans Tech Publications, Switzerland*
*doi:10.4028/www.scientific.net/AMM.580-583.3183*

# Normally consolidated Subgrade limit bearing capacity calculation using slip line method

Chen Ming[1, a], *Zhou Taiquan[1,b]

[1]College of Environmental and Civil Engineering, Jiangnan University, Wuxi, Jiangsu 214122, China

[a]my.cm1993@gmail.com,[b]zhoutaiquan@163.com

**Keywords:** slip line method; ultimate bearing capacity of foundation; Terzaghi ultimate bearing capacity of foundation.

**Abstract.** Normally consolidated subgrade limit bearing capacity of foundation soil was studied in the paper using slip line method. Slip line results are found to be consistent with the results calculated by Terzaghi theoretical formula and Hansen theoretical formula. Then the influence of cohesion, friction angle for normally consolidated subgrade is studied under complete smooth or complete tough conditions. The results show that the normally consolidated subgrade limit bearing capacity increases linearly with the increase of k, γ, while it increases nonlinear with the increase of Φ and the increasing growth rate improves with increasing value of Φ.

## Introduction

The purpose of studying limit bearing capacity is that the pressure on the underside of the building foundation must be limited. The subgrade limit bearing capacity is not allowed to reach the limit bearing capacity. Besides, the subgrade limit bearing capacity has a certain degree of safety to ensure that the foundation will not occur sliding failure. At the same time, to ensure that the structure will not be due to excessive deformation of foundation affects their normal use. Therefore, determining the limit bearing capacity of foundation is an urgent problem to engineering practice to solve.

There are two main methods to determine the limit bearing capacity, the first one is field test methods, such as standard penetration test, static cone penetration test and pressure meter text. After the establishment of a regional relationship, limit bearing capacity of foundation value can be obtained. The other one is theoretical calculation. In 1940s according to the basic theory of Prandtl, Terzaghi proposed limit bearing capacity formula considering the weight of the soil under foundation. In 1950s Meyerhoff proposed limit bearing capacity formula applicable to deep foundation. To be more accurate researching limit bearing capacity of foundation, we use the analysis software Analysis of Bearing Capacity to study it.

## Slip line theory

In calculating the limit bearing capacity of foundation with slip line method, assuming the soil is the ideal rigid-plastic material, obey Mohr-Coulomb criterion or Terzaghi theory. Under load, in certain direction the soil in the plastic zone flowing freely, the deformation of soil large and elastic deformation ignored, the rigid-plastic assumption can deduce more reliable approximate solution. Otherwise, it may lead to large errors. In geotechnical stability problems—the problem of foundation bearing capacity, stress problems of retaining walls and stability problems of slope, the slip line theory has been widely applied.

## Software

ABC (Analysis of Bearing Capacity)is a computer program that uses the method of stress characteristics (also known as the slip line method) to solve the classical geotechnical bearing capacity problem of a rigid foundation, resting on a cohesive-frictional soil mass, loaded to failure under a central vertical force. Fig.1 shows the terminology used.

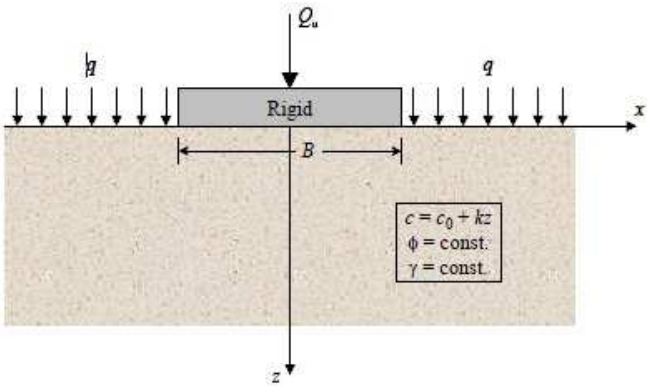


Fig.1 Problem definition

**The Basic Examples**

Severe soil γ =18kN/ $m^3$, friction angle Φ=18°, cohesion coefficient $c_o$ = 10kPa, base width B = 3.0m (round base R = 3.0m), the depth D = 2m. At this depth above the soil as side load to deal with. According to the study, the design of the four foundations, obtained by numerical simulation software, and has been the foundation failure mode, as shown in Fig.2, and the resulting calculation of ultimate bearing capacity $q_u$ calculated values as obtained with Terzaghi, Hansen theoretical formula contrast, the feasibility of the software simulation, as shown in Fig.3.

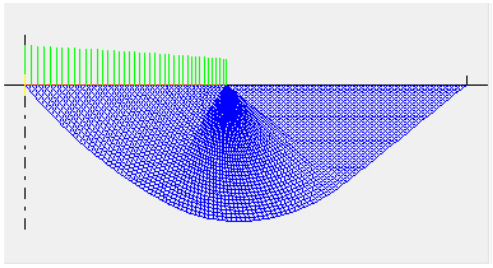

Fig.2.1 Strip and smooth

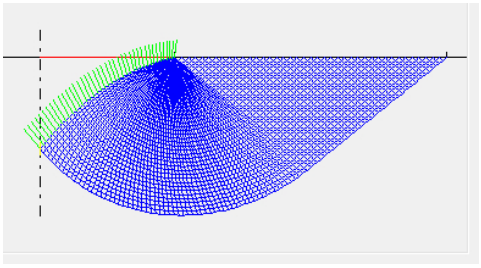

Fig.2.2 Strip and rough

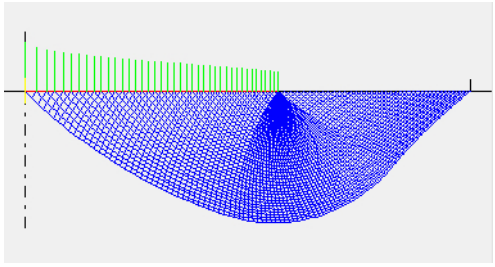

Fig.2.3 Circular and smooth

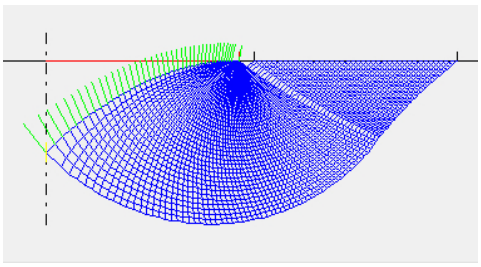

Fig.2.4 Circular and rough

Fig.2 Computational model for 4 subgrade limit bearing capacity groups

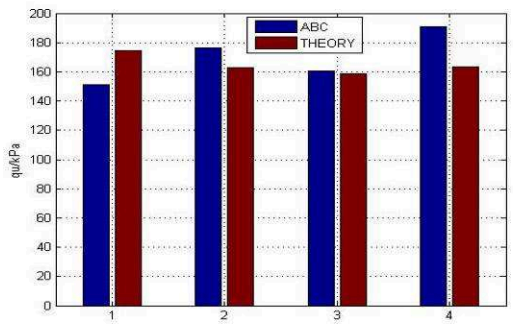


Fig.3 Comparison results between ABC and theoretical solution

**Analysis of influence parameter**

In order to analysis k, γ, Φ parameters on the influence of the limit the bearing capacity of the foundation. Design when $c_0$ = 1.2kPa, Φ = 18°, B = 3.0m, base completely friction strip foundation, depth d = 2m, k = 1,2,3,4 kPa / m, when γ = 18, 19,20 kN/m$^3$. The bearing capacity for the total of 12 sets of models is performed using ABC software, as shown in Fig. 4.

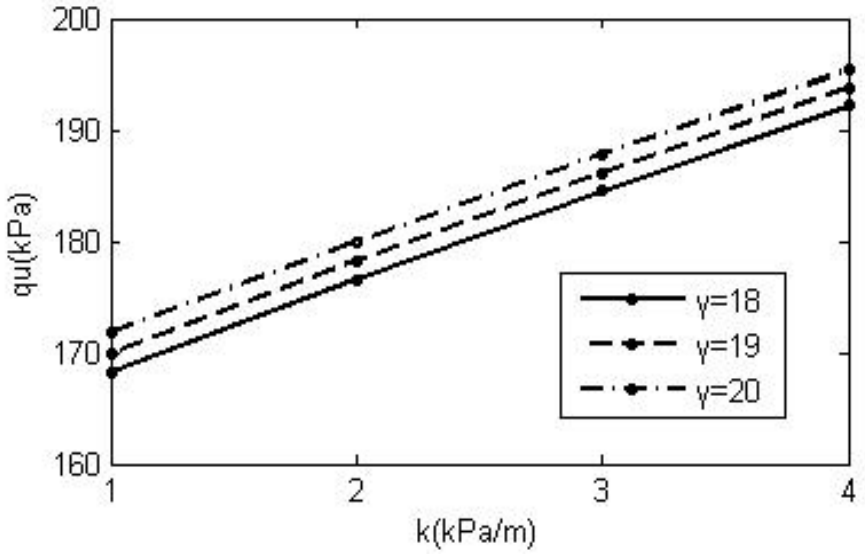


Fig.4 Relationship between the limit bearing capacity and k，γ.

Within a certain range, the other parameters in the same situation, with the increase of γ, the ultimate bearing capacity increase, can be found to improve the bearing capacity of the foundation is approximately linear. Similarly, other parameters in the same situation, with increasing k, the foundation bearing capacity also increased, which also showed a linear rise.

Design When $c_0$ = 1.2kPa, γ = 18kN/m$^3$, B = 2.0m, base completely friction strip foundation, depth d = 2m, respectively, when k is equal to 0,1,2,3,4 kPa / m, Φ = 10,13,16,20 °, the foundation bearing capacity of a total of 20 group model. Solving the size of the foundation bearing capacity, suchTab.1:

Tab.1 Limit bearing capacity of foundation under different k and Φ.

| k\Φ | 10 | 13 | 16 | 20 |
|---|---|---|---|---|
| 0 | 119.725 | 163.741 | 224.992 | 347.561 |
| 1 | 125.121 | 170.702 | 234.041 | 360.599 |
| 2 | 130.218 | 177.381 | 242.807 | 373.336 |
| 3 | 135.073 | 183.824 | 251.334 | 385.811 |
| 4 | 139.728 | 190.068 | 259.653 | 398.056 |

And when k = 1,2,3,4 kPa / m, respectively, and k = 0 comparative analysis made into a line Fig.5:

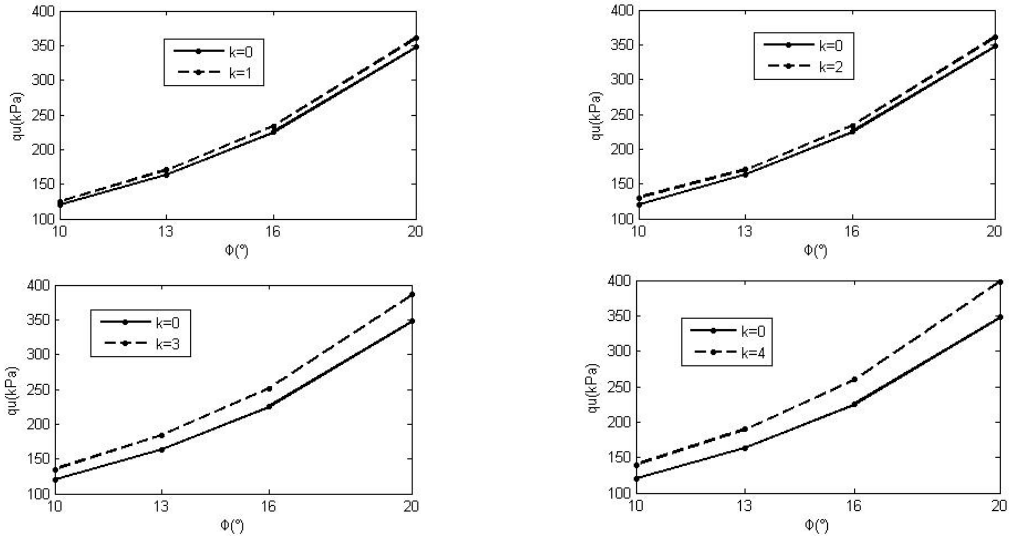


Fig. 5 Relationship between the limit bearing capacity and k and Φ.

Analysis obtained within a certain range, under the same conditions of the other parameters, with increasing k, the limit bearing capacity increases linearly, change contrast foundation bearing capacity Φ = 10,13,16,20 °, the greater the value of Φ , linear foundation bearing capacity increasing faster; while under consistent conditions as other parameters, the foundation bearing capacity values with Φ non-linear increase, and increase more and more, that is, $q_u$-Φ curve slope increases, contrast curve slope k = 0,1,2,3,4 kPa / m when, when Φ is the same, the slope of the curve with a positive correlation between the value of k.

## Conclusion

In the paper, the limit bearing capacity of foundation analysis software ABC was used, the main conclusions are as follows:

1 within a certain range, Analysis of Bearing Capacity Analysis of bearing capacity, the results of the calculation results obtained with Terzaghi, Hansen there are no significant difference between the theoretical formula.

2 Since the limit bearing capacity of the foundation formula Terzaghi theory applies only to the condition k=0, and the actual situation should be considered in the consolidation of the soil, so the method described in this article has some practical significance and innovative;

3 Under certain conditions, limit bearing capacity increases linearly with the increase of k, γ, increases nonlinear with the increase of Φ and increasing growth rate improves with that of Φ.

## References

[1] Zheng Datong .Foundation limit bearing capacity calculation[M]. Beijing: China Building Industry Publishing House, 1979.

[2] Zhang Kegong,Liu Songyu. Soil Mechanic [M]. Beijing: China Building Industry Publishing House, 2010.8

[3] User Guide for ABC – Analysis of Bearing Capacity Version 1.0. C.M. Martin Department of Engineering Science University of Oxford.

*Applied Mechanics and Materials Vols. 580-583 (2014) pp 3187-3191*
*© (2014) Trans Tech Publications, Switzerland*
*doi:10.4028/www.scientific.net/AMM.580-583.3187*

# Numerical simulation and testing of 45 Architecture steel Welded based on Gaussian heat source

Jianbo Ji[1,a],Jinzhou Zhang[2,b],Lei Zhang[1,c]

[1]Chemical Engineering Institute, Xuzhou College of Industrial Technology, Xuzhou 221140, China

[2]College of Mechanical Engineering, Yangtze University, Jingzhou, Hubei,434023

[a]jijb@mail.xzcit.cn,[b]87221914@qq.com,[c]89202974@qq.com

**Key words:** numerical simulation; weld; stress; strain

**Abstract:** Using sysweld software based on the Gauss heat source, simulated welding process of 45 steel plate, analysed welding temperature field, stress and strain. The maximum stress value appeared at the initial welding position of junction of base metal and weld. As the most dangerous section, the maximum strain value appeared at the end welding position of the junction of base metal and weld. Compressive strain appeared at the central part of weld and the tensile strain appeared at the junction of base material and weld. The deformation was of upward warping, which is helpful to explore the numerical simulation of welding structure.

## Introduction

45 Steel is a type of high-quality carbon structural steel and widely used as building materials. Because of uneven distribution of the heat cycle during welding, it is easy to form larger welding residual stress and lead to adverse effects for the performance of the welded components, such as static load strength, fatigue strength, fracture toughness and so on. Much more high demands is needed to analyze the stress and strain of the welding structure[1][2].

## 1 Numerical simulation of 45 steel welded joints

The materials exit nonlinearity and geometric nonlinearity in the welding stress field. So, taking the complexity of the welding thermal stress and accurate calculation and the function of FEA software into consideration, we took the welding thermal stress field as a problem about material nonlinear transient analysis. Meanwhile, we selected elastic-plastic mechanical model and incremental theory to analyze the problem.

### 1.1 Establishing heat source model

Because the hot spread quickly in metal, highly concentrated heat source was used to transfer much more heat to workpiece in an instant and causes time-variation and unsteady characteristics during welding. we selected realistic model of normal heat considering materials' physical properties changes with temperature[3].

Gauss heat source: Practice has proved that takes heat density as surface heat [4] distribution, positive attitude is more effective during welding. Assuming the distribution of heat is Gaussian normal distribution function, then integrates the equation is:

$$q^* = q^*_{\max} \exp(-kr^2) \tag{1}$$

$$q = \int_F q(r)dF = \int_0^\infty q_{\max} e^{-kr^2} 2\pi r dr \tag{2}$$

$$q = \frac{\pi}{k} q_{\max}, \therefore q^*_{\max} = \frac{k}{\pi} q \tag{3}$$

Where:
q—effective heat power, J/s；
k—heat concentration factor,1/mm2；
r—the distance between a point within the circle heat source and the center.

According to a Gaussian distribution curve, the Heat source in infinite distance was close to zero. Therefore, the role of regional heat source must have a limit. We determined the size of the heating spot and the heat spots takes over more than 95% of heat, namely:

$$q^*_{\min} = 0.05 q^*_{\max} \quad (4)$$

The outer diameter of the heating spot is:

$$d_n = 2\sqrt{3}/\sqrt{k} \quad (5)$$

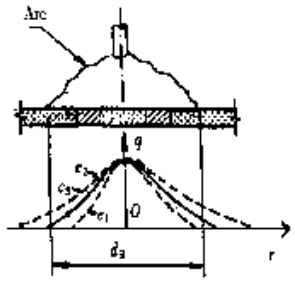


Fig.1 Gauss heat source

**1.2 Establishment of the finite element model**

We use the finite element method to analyze the situation of 45 steel. For the simple shape of the plate member, we can build the model by visual-mesh, and then imported the meshing into the sysweld before meshing it. The Three-dimensional model is shown in Figure 2[5].

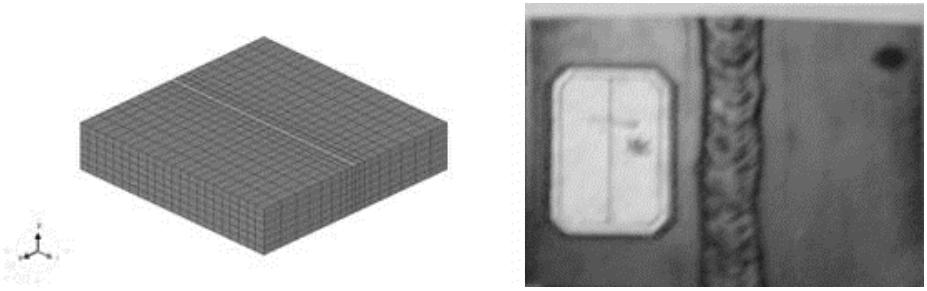

Fig.2 Three-dimensional model and welding sample

**1.3 Mechanical constraints set**

We impose symmetric rigid constraints on both sides of plate.

**1.4 Welding parameters**

The heat efficiency of TMAW is $\eta = 0.8$, the welding voltage, welding speed and Welding current are U=40v, V=0.8mm/s and I=70A, then starts the welding simulation.

**Numerical simulation results analysis**

**2.1 Welding temperature field analysis**

Arc welding processes require heating from beginning to end, so temperature field has an important influence on welding quality and improving welding productivity.[6]

It can be seen from Figure 3 that the temperature field is symmetric and closer to the heat, the temperature gets higher. It becomes Normal atmospheric temperature at some distance. When welding start 0.3s, the highest temperature only rise to 1394.82 ℃, and at the second of 6.2, the heat has come to the edge of the plate and the maximum temperature is 1430.49 ℃. That is to say, at the beginning and the end of weld, the temperature does not reach the melting point of steel and varies a lot. So we should Increase welding time and slow welding speed here.

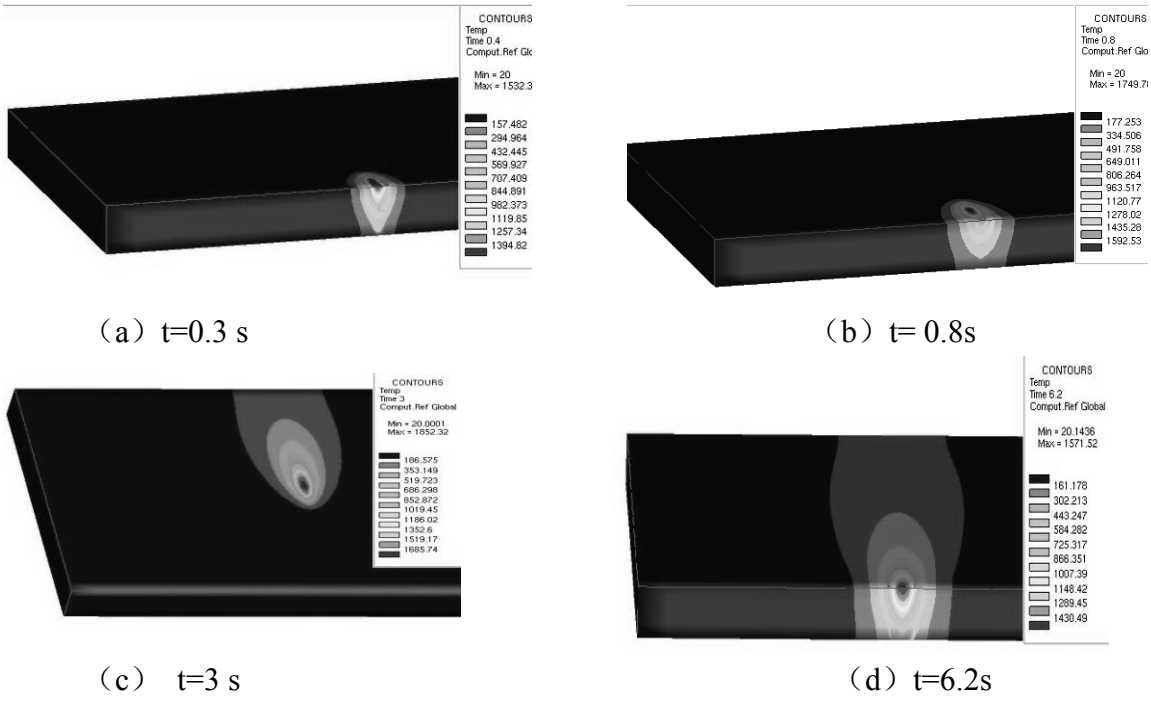


（a）t=0.3 s （b）t= 0.8s

（c） t=3 s （d）t=6.2s

Fig.3 Welding temperature field

**2.2 Welding stress analysis**

Because we heat part of the weldment while welding, the weld area is heated to a high temperature and so are both sides of the base metal because of welding heat. The farther away from the weld, the temperature gets lower. Therefore, judging from thermal expansion and contraction properties of the metal, different parts of the weldment will get different temperatures, and will lead to different thermal expansion.

It can be seen from Figure 4(a) that at the second of 0.3, the weld area reaches to the highest temperature, and the temperature decreases with distance increases. For the sake of plate is not free to elongate as a whole, all parts of elongation contain each other. Welding heat source heat metal to melt and the weld center gets the highest temperature, so the welding-line area gets the maximum heat expansion. And the welding-line area expansion is limited because of contain around the base metal, so it brings compressive plastic deformation. However, the materials thermal expansion close to molten pool affected by mental around gets deeper than that away from weld seam, which will result in the materials In the weld and around subject to relatively large compressive stress. On the contrary, that away from weld seam gets small compressive stress.

The Figure 4(d) shows transverse magnetic memory testing data in weld central at 1000 seconds. And the points below zero stand a large stress concentration. The bigger slope over zero, the larger is the stress concentration, namely, larger residual stress.

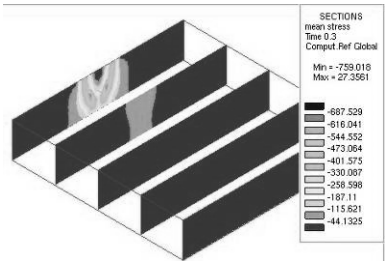


(a) Simulation diagram (t= 0.3s)

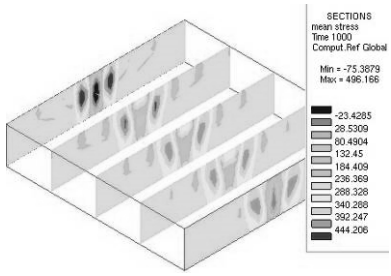


(b) Transverse simulation diagram (t= 1000s)

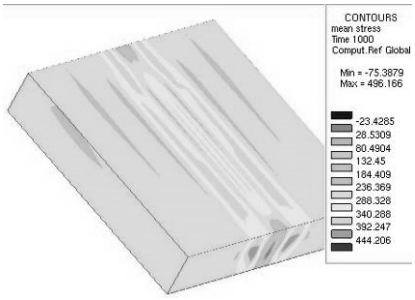


（c）Longitudinal simulation diagram (t=1000s)

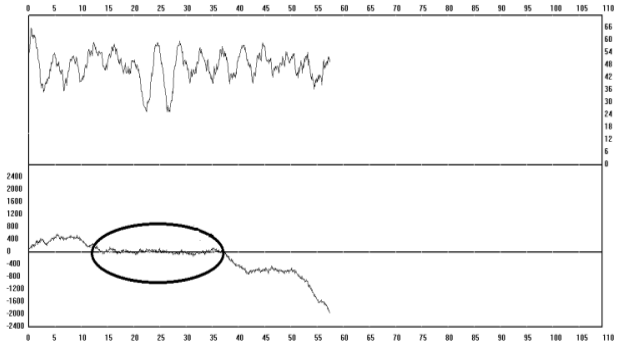

(d) Transverse magnetic memory testing value on Central weld (t= 1000s)

Fig.4 Welding stress

It can be seen from Figure 4(b), (c) and (d)that as the weld-metal zone has generated a compression of plastic deformation after cooling, so the length will shorten. However, both sides of the metal sheet hinder the central weld zone shortened. At the same time, the weld zone support tensile stress and both sides of the metal bear compressive stress and reach equilibrium. Weld and its annex area appears mainly tensile stress and the beginning welding parts bear compressive stress. The maximum tensile stress (about 440MPa) appears at the junction of the base metal and weld, where the dangerous section lies. And so does the welding stress at central longitudinal seam, stabilized. The sheet stress of the upper parts is Significant greater than the half bottom. In cooling process, the weld metal cools and shrinks. Meanwhile, the weld metal shrinkage limited by the surrounding material is greater than that away from it. Therefore, the tensile stress near the weld is bigger than that away from the weld.

**2.3 Welding strain analysis**

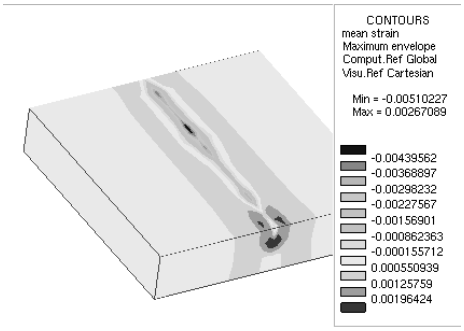


(a) Strain simulation diagram

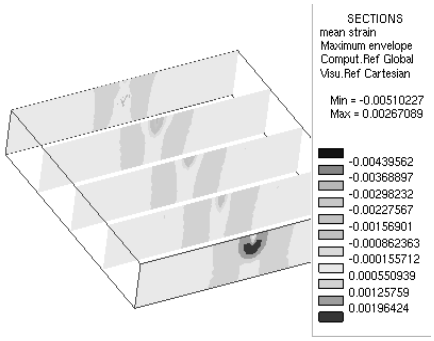


(b)Strain simulation diagram on Weld cross section

Fig.5 Welding strain (t=1000s)

The Figure 5 shows that the welding symmetrically distributed strain after 100 seconds of welding. The seam center appears compressive strain and tensile strain appears at the junction of the base metal and weld. The sheet strain of upper parts is much larger than the half bottom. The strain rises from small to stable with welding, and at the end of welding it increases suddenly. The maximum strain appears at the final position of the base metal and the weld seam junction.

## Conclusions

(1)The result of temperature field simulation indicates that the temperature from positions of welding at the beginning and end varies a lot. We should increase welding time to avoid the lack of penetration and lack of fusion.

(2) The result of stress field modeling indicates that the welding stress main is tensile stress after welding, and maximum stress occurs at the beginning of the welding position. Weld stress between Parent metal and weld remains relatively large, and the sheet stress of the upper parts is larger than the half bottom. What is more, Stress distributes uniform.

(3) The analysis of strain field shows that the seam center bears compressive strain and tensile strain appears at the junction of the base metal and weld. As a result, the plate deformations upwards and the maximum strain appear at the end of welding.

## Acknowledgements

This work was financially supported by the "the 12th Five-Year" National Technology Support( Program issues 2011BAB05B02). The corresponding author is jinzhou zhang.

## Reference

[1] Jinzhou zhang.Welding Stress Analysis Of Manhole Of Liquid Ammonia Storage Tank Based On Gauss Heat Source[J],Applied Mechanics and Materials,2011,04:1942~1946.

[2] Lei Zhang.Numerical Analysis Of Liquid Ammonia Storage Tank Welding Stress [J], 2nd International Conference on Advanced Design and Manufacturing Engineering,2012,vol.206: 1532-1537.

[3] Jiuhuan chen,Li chen,Yousheng yu. The Research Progress of Welding Heat Source Model[J],Welding Technology,2004,33(1):13~15.

[4] Anli lu,Qinyu shi,Haiyan,zhao,Aipin wu. Temperature Field of Thick Welding Process, Three-dimensional Finite Element Numerical Simulation of the Stress Field[J],Chinese Mechanical Engineering,2001,12(2):183~186.

[5] Jinzhou zhang,Hegen xiong,Xiong yang. Welding Stress and Deformation Numerical Analysis of X70 Pipeline Based on Combined Welding Heat Source. Thermal Processing 2012,41(11):196~198.

[6] Xuemei liu,Liancai gao,Yanhua zhang. Weld Analysis on X70 Pipeline Steel [J]. Welder,2004，34(7):14~15,23.

*Applied Mechanics and Materials Vols. 580-583 (2014) pp 3192-3195*
*© (2014) Trans Tech Publications, Switzerland*
*doi:10.4028/www.scientific.net/AMM.580-583.3192*

# Research on Tunnel Construction Quality Based on Visualization Management

Qian Li

College of Civil Engineering and Mechanics, Central South University of Forestry and Technology, Changsha 410004, China

semese_li@163.com

**Keywords:** Visualization Management, Tunnel Construction Management, 4D Model

**Abstract.** Through the comprehensive application of modern information technology, network technology and modern construction management 4D theory has carried out the systematic study on the implementation method of the tunnel construction quality information rapid collection, visual management, centralized control and highly sharing. Based on the development of tunnel construction quality information management system, by logging data of design, construction, monitoring, supervision and test during the construction period, digital network management would be achieved in the tunnel construction process. mainly to complete: 1) combined with 3D models and tunnel construction schedule, build a tunnel 4D model; 2) Take additional tunnel construction quality management information for 4D theory to achieve dynamic visualization of construction quality management and query; 3) through practical engineering applications, the system is proved innovation in the tunnel construction quality management.

## Introduction

At the present, tunnel construction management is based on 2D form such as the text, tables and network diagrams. Which is not enough visual image and increases the frequency of communication in the participate parties of construction projects, it is difficult to achieve effective information exchange and share, and reduces the efficiency of construction management [1]. Also, the used software in the project management generally lack tunnel 3D models and cannot achieve a three-dimensional visualization of the building construction management. With the development of computer and network technology, tunnel construction process can be simulated on a computer, using three-dimensional modeling to real-time reflect tunnel construction and completed picture. Meanwhile 4D theory has made considerable progress and applied to the construction in the projects [2, 3]. This article will introduce theory of 4D in construction process and three-dimensional model of the tunnel as the carrier, integrate the tunnel construction progress and management information, achieve efficient management of engineering information and real-time control of the progress of the project, and provide adequate and effective information support for engineering management decisions.

## Development Infrastructure and Major Structure

**Develop infrastructure and hierarchy.** The system developed with *ActionScript* and *Java*-based [4] can be applied on multiple platforms, using *Eclipse* integrated development environment and *B / S* multi-network application for the solution. That makes the system easy to

use and simplify the management and maintenance [5]. Build three-dimensional model of the tunnel use *Flash 3D* modeling techniques. Taking into account the amount of network applications and data is large, so using *SQLServer* 2005 database to process data. System has a certain independence, but also consider and compatible with other management systems [5]. The system runs in the user's browser *Flash Player* plug-in and handles the interaction with the user.

**Design database.** Establish the quality database of construction as shown in Figure 1.

On the basis of the interaction *JDBC* with the database, this system uses *Hibernate* for *JDBC* a lightweight object package [5]. The designer can easily use object-oriented program thinking to manipulate the database.

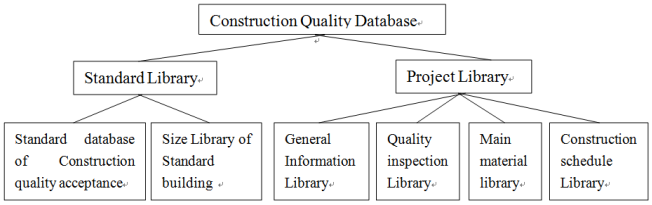


Fig.1 Structure of quality information database

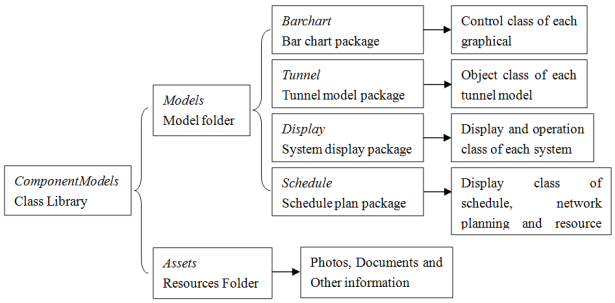


Fig.2 Structure of class library

**Design the system's main class.** *ComponentModels* class Library: Based on object-oriented, this system build a *ComponentModels* class Library as shown in Figure 2.

*QualityManagement* Radical Database: Based on object-oriented, this system builds a *QualityManagement* Radical Database as shown in Table.1.

Table.1 List of member variables and functions of the base class QualityManagement

| *member variables and functions of the base class* | *The main function* |
|---|---|
| isFlowChart | Boolean variables, used to determine whether the flow chart |
| getmapname | Character class variable, used to name for the map |
| pileNo | Integer variables, used to Stake |
| init() | Initialization function |
| InitProjectInfoResult(event:ResultEvent) | Return to the organizational structure of the project xml data, used to treeProject controls |
| OnTunnelComponentClick(event:MouseEvent3D) | Click event handling model components |
| searchComponent(name:String) | Query component, used to Tree node manipulation functions |
| queryFileResult(event:ResultEvent) | For quality check（Including inspection lot, Scene photos, Acceptance forms, etc.） |
| onQuaTextChange(event:ListEvent) | Flowchart and information inquiry |
| GetComponentProperties(event:ResultEvent) | Overloaded in a derived class, used to draw specific model |

Corresponding operation class was established to upload and retrieve flow chart, scene photos and inspection lot in this system. Through local loads and remote upload to collect into the server, simply call these classes can display pictures, documents, etc. on the screen.

### Build a Tunnel 3D Model

To use *Alternativa3D* engine (i.e. *Flash* scripting language *ActionScript*) and *Flash* three-dimensional model draw framework for joint programming and achieve drawing and display of three-dimensional model of tunnel component rendering. And follow the steps to build a three-dimensional model of the tunnel:

**Background mosaic.** In order to the true and image on tunnel model, the first, establishing the corresponding background pattern. Background image mosaic using *Flex* technology embeds a background image into the framework, which generate 3D model on full sense of the scene. This technology allows designers to change the background according to project different images.

**Build model.** To use *Alternativa3D* engine midpoint, line and polygon drawing functions build complex tunnel space model. That means the tunnel model is decomposed into unit structure, then using the appropriate functions draw three-dimensional model of each unit components, and finally combining the parts into a whole three-dimensional model of the tunnel. To enhance the realism of the model are required to model the use of light and texture mapping in the drawing process of the model. On the one hand the use of light functions defined in the view class achieve illumination mapping of suitable project. On the other hand the use of processing three-dimensional model of the surface texture *alternativa.engine3d.materials.SurfaceMaterial* class of each component color fill, or after setting the texture coordinates; define *alternativa.types.Texture* classes on the various components mosaic texture material pictures.

**Show three-dimensional model.** Finally, a series of coordinate transformation complete the transformation from model space to paper space, and display graphics on the screen window. Setting response functions of the mouse actions achieve to using the mouse to drag to change the viewing angle of the model, so that the model were observed from different orientations.

### Implementation of Tunnel Construction and Quality Information Management

**Establish a tunnel construction management 4D model.** Using object-oriented thinking, the system will integrate schedule information, quality information, material information and other information to established dimensional model to form 4D model of the tunnel, to process dynamic simulation of tunnel construction. The tunnel model based on 4D can be inquired by tunnel construction schedule and manage construction information which achieve a three-dimensional visualization of tunnel construction management [5].

**Draw construction schedule.** Construction schedule chart is drawn by the form of dual-period comparison. In accordance with construction organization design determines a reasonable plan-time [5]. With construction total time limit as the timeline length of the construction process and working day as the step, the planned time of each component on the timeline is highlighted. In addition, according to the actual schedule, the actual time of each component is determined. The actual duration compared with the planned duration, is able to directly reflect the relationship of the actual schedule and planned schedule to facilitate the project all parties participating in the construction grasp the actual progress of the project.

**Collect construction quality of the information.** The system includes the information collection module of the construction quality, which includes some multi-source and multi-format data such as

text, data, voice, image and vector files etc. that need to classify and sort and manage. In addition to the above these, but also includes data provided by the supervision unit and the testing units, etc. it need to classify and sort. To respectively demonstrate among the system, that make structured and clear categorized of information management. Tunnel construction management information is entered by three ways: general information input; real-time information input; existing system data input.

**Classify the quality information.** In the 3D state, construction design schedule and quality acceptance criteria of separated parts of a project as the two axes, query and export inspection items and engineering information and quality standards information and raw information and material testing information etc of separated parts of a project.

**Establish a quality evaluation system.** This system will classify examination indexes of the separated parts of the tunnel project; get the weight of each unit's indicator by consulting specialists of the design and construction units; score for each index by the construction process of the quality test results and expert evaluation; finally obtain overall weight of the index and evaluation results. Those ease management personnel to overall grasp the construction quality.

## Conclusions

Above a comprehensive study of the tunnel construction and the development of key technologies of the quality of management information systems based on theory 4D, mainly to complete: 1) combined with 3D models and tunnel construction schedule, build a tunnel 4D model; 2) In the 4D theory, based on the additional tunnel construction quality management information, to achieve dynamic visualization of construction quality management and query; 3) through practical engineering applications, the system is proved innovation in the tunnel construction quality management. On this basis, future research should focus on the perfect of many types and complex tunneling model library, and optimization of construction schedule, resource and cost management library and optimization of construction schedule, resource and cost management of the tunnel.

## Acknowledgements

This work was financially supported by Hunan Provincial Education Department Science Foundation (12C0460).

## References

[1] Chenghan Zhou, Weidong Wang: GeoHunan2009 International Conference, (2009), p.138-145. (In Chinese)

[2] Jianping Zhang, Hongjun Wang. : submitted to china civil engineering journal (2003). (In Chinese)

[3] Yang Zhang, Jianping Zhang: 8th National Information Technology on Construction Field and Multimedia-aided Engineering Forum, (2005), p.378-384. (In Chinese)

[4] Xiaopeng Lv, in: *master Flex3.0-based on ActionScript3.0*, edited by People's Post Publisher, Beijing, (2008). (In Chinese)

[5] Chenghan Zhou, in: *Research and Implementation on Bridge Construction Dynamic Simulation System Based on 4D*, edited by Central South University, Changsha, (2009). (In Chinese)

*Applied Mechanics and Materials Vols. 580-583 (2014) pp 3196-3203*
*© (2014) Trans Tech Publications, Switzerland*
*doi:10.4028/www.scientific.net/AMM.580-583.3196*

# Analysis on Application Prospect of BIM Technology in Granary Designing

CHEN Gui-xiang[1, a], HAO Bing-hui[1, b], ZHAO Yi-qing[1, c]

([1]College of Civil Engineering and Architecture, Henan University of Technology, Zhengzhou 450001, China)

[a]cgx@haut.edu.cn，[b]haobinghui88@163.com,[c]hbh88328@163.com

**Keywords:** basic concept of BIM, granary, characteristics of BIM Technology, analysis on BIM application

**Abstract:** BIM is a kind of multidimensional model information technology based on CAD which has been applied in some large projects at home and abroad. The technology of BIM has the characteristics of 3D visualization, virtual design and collaborative design and so on. In this paper, ideas about applying BIM Technology in granary projects have been put forward from the design stage, project implementation stage and the stage of cost control by taking a big diameter underground silo of reinforced concrete for example, simulating the architecture, structure, process of construction and process of grain flowing of underground silos, then creating the model of architecture, dynamic construction model of 4D. The article provides a new approach of applying BIM technology to granary facilities.

**CLC:** TU9 **WM:** A

## Introduction

With the development of information technology and globalization of internet, digital technology as an important tool, has been developed at very fast speed. Information technology has already brought manufacturing and electronics industry huge and innovative changes, the application of which in construction industry is still at very low level. BIM brings brand-new inspiration for the whole building industry, and it is an information-based technical revolution. BIM shall be promoted in the building industry in China as soon as possible [1].

Grain safety is always the major global strategic issue related to national economic development, social harmony and stability, national security and self-reliance. China's various markets become fully in line with international standards. The grain industry is also faced with severe challenges and good opportunities for development from the production, processing, circulation to consumption. The safety of national grain is mainly measured by the safety coefficient for grain storage. As the key equipment of access in the grain circulation link, granary plays an important role in grain safety, which is related to national security and calls for intensive construction.

This paper proposes to apply BIM to the construction of granary. The roles of BIM in the design stage, project implementation stage and the cost control stage of granary construction are analyzed based on the main technical characteristics of BIM, promoting the construction of grain industry standardization.

**Development of BIM at home and abroad**

BIM, namely Building Information Modeling, is based on all the related information of the construction project to establish the building model. The core of BIM is a database of computer three-dimensional model, including various stages throughout the whole project life cycle, design, construction, operations management and so on. All the information is built in the same database from beginning to end.

The idea of BIM dates back to the 1970s. Auto desk company proposed the word Building Information Modeling（BIM）in 2002, and indicated that BIM is the innovation of architectural design.

The United States National BIM Standard gives the following four levels of interpretation for the meaning of BIM:

a. the digital expression for physical and functional properties of a facility (project).

b. a shared knowledge resource.

c. a process of sharing information about the facility and providing reliable basis for the facility from concept beginning for all decisions in the full lifecycle.

d. At different stages of the project, different stakeholders reflect the collaboration between them through inserting in, extracting, updating and modifying information in BIM [2].

The thought of BIM developed rapidly throughout the world after proposed. In 2009, Wisconsin in the United States became the first state requiring large new public works projects in the state using BIM, and Texas Infrastructure Committee also announced that design and construction projects invested by the state should apply the BIM technology. Ministry of Land, Japan announced the implementation of BIM Technology in 2010. Several government agencies in Europe and South Korea have been dedicated to BIM application standards [3].

Many domestic projects have used the BIM technology after the 2008 Olympic Games under the influence abroad [4]. For example, the Hong Kong subway project, Olympic Sports Center Stadium in Hangzhou and Expo Culture Center in Shanghai all adopted BIM in the design, construction and operation phases. Fig. 1 is the working sketch of Expo Culture Center in Shanghai. BIM was listed as state science and technology support program in the 11th Five-Year Plan in 2011. In the information age, the development and application of BIM have become a trend [5].

Fig. 1 The working sketch of Expo Culture Center in Shanghai

**Main technical characteristics of BIM**

BIM mainly has the following characteristics:

**2.1 Three-dimensional visualization**

For designers, large amount of design work is still based on CAD, using flat, vertical and section 2D drawings to express and show the design results. But the information traditional 2D drawings

conveyed is not intuitive, which is hard for people with little knowledge of architecture and structure to understand. The design software based on BIM popularizes the professional and abstract description of two-dimensional buildings and visualizes three-dimensional buildings. So professional designers, owners and other non-professional technicians can judge whether requirements of the project have been met more clearly and efficiently, thus making decisions more accurately [6]. Fig. 2 is the whole building model of the granary. And Fig. 3 is the whole architectural section of the granary.

Fig. 2 The whole building model of the granary

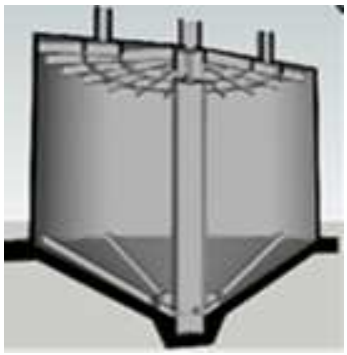

Fig. 3 The whole architectural section of the granary

**2.2 Parametric design**

Parametric design is one of the important ideas of BIM. All the drawings, including 2D and 3D views, reflect the information of the whole project model in design software based on BIM. The component information in BIM is also parameterized, and the designer can modify the components in the model. Parameter changes caused by the moving, deleting and size modifying of the components will be automatically linked to other related components. With the help of these parameterized information, software based on BIM can automatically recognize different components in the model, and get statistics on the number of different components in the model, forming a database to facilitate later modifications. Take the steel as an example, the name, number and size of the required steel can all be generated directly in the BIM model and all the information will always keep consistent with the design [7].

### 2.3 Collaborative design

Current collaborative design is mainly based on CAD, and can not fully achieve the exchange of information between professions. BIM uniformly puts previous scattered and isolated design data and information into the model through a complete 3D model. Various information that different professions need can all be obtained from this model, and data sharing between various professional designs is realized [8].（As shown in Fig. 4）

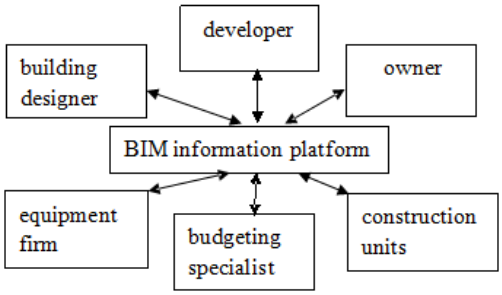


Fig. 4 Various professions sharing BIM information platform

In addition, BIM can not only realize the data connection of different professions, but also check the modified information on project of different professions at any time. This facilitates designers to increase and change the project relevant to their professions timely [9]. Therefore, the concept of using BIM for project collaborative design is realizing different professions draw all dynamic linkage data information for a project model completely utilizing BIM simulation platform.

## The idea of applying BIM in granary projects

### 3.1 Preliminary planning

In the early days of granary construction projects, an argument of stepwise refinement is needed. Collect relevant information and systematically study the overall planning of granary projects according to the rationality of granary medium-term and long-term plans and grain logistics, and make site selection in the preliminary planning stage, preliminarily proposing the development scheme [10].

The main method for preliminary planning based on BIM is: First, create the terrain surface based on exploratory data of the project. Then lead in mass building information of granary projects and geographic data of surrounding environment, intuitively simulating all the information related to the whole granary project. Thereby conveniently design the road, greening, landscape structures and other fields and determine the most reasonable scheme of logistics and transport [11].

### 3.2 The design phase

Designing by BIM is the maturest phase for applying the concept of BIM. Fig.5 lists the application frame in the design phase of BIM. At present the application of BIM is also the most at this stage. The main application value of BIM concept in the design phase is visualization, collaborative design, simulation, optimization and drawing. In traditional design, the designer draws 2D drawings using architectural software like CAD, and it is also the 2D drawings that are finally delivered for audit. However, the traditional 2D drawings are not intuitive, and the information transmission is not clear [12].

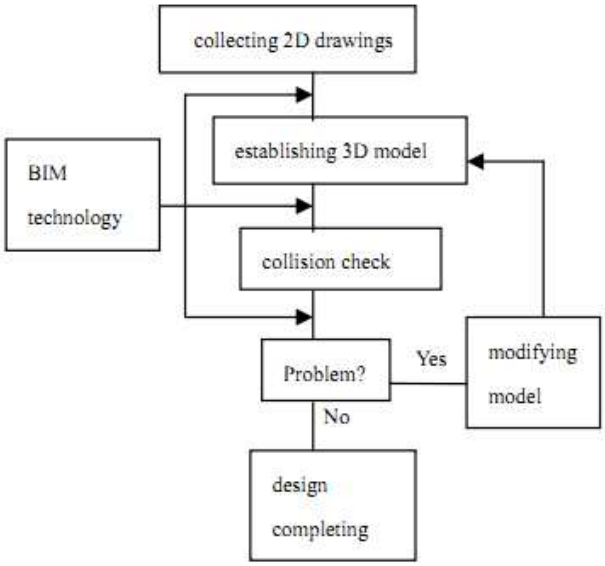


Fig. 5 Application idea in the design phase

Fig.6 and Fig.7 are respectively reinforcement figure of the bottom of an underground granary drawn through CAD and Revit software based on BIM. Comparing Fig.6 and Fig.7, it can be seen obviously that the information conveyed by the software design based on BIM is quite intuitive. And even people with little knowledge of building structure can understand the information contained.

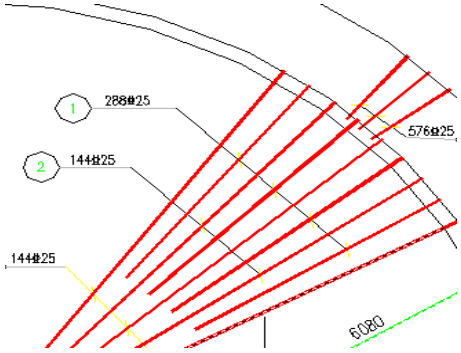


Fig. 6 2D reinforcement figure of the bottom of an underground granary in CAD

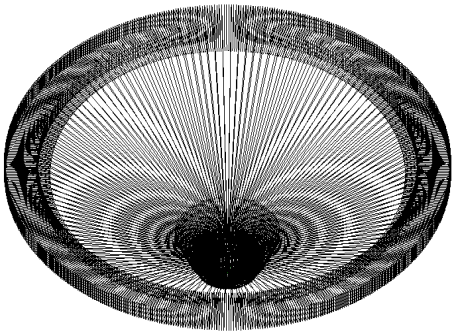

Fig. 7 3D reinforcement figure of the bottom of an underground granary in Revit

In the design phase, a 3D model is created utilizing the modeling software based on the idea of BIM (such as the Revit series software). The 3D model contains all the information of preliminary planning, design, granary construction and structure [13]. The 3D model also provides necessary information for different professions. Different professions can all perform collaborative work on

the 3D model through uniform data format. For example, professions responsible for design and technique can coordinate with each other in the design phase, reducing the possible collision and design changes later.

**3.3 Project implementation stage**

For the construction process, the BIM model established in the design stage and construction planning information, coupled with the construction schedule are simulated through a visualizing process. The feasibility of construction process, schedule and resource allocation is analyzed to constantly improve the construction scheme [14]. Project personnel import construction progress into a 3D model of granary using the software based on BIM technology to simulate the 4D construction process of granary [15]. Fig.8 is the simulation for the construction of granary wall. Fig.9 shows the construction site of granary wall. In this process, the construction personnel can intuitively see the intraday engineering work and schedule from the model through vivid and intuitive process simulation and analyze whether the construction process and the pouring of concrete is reasonable. Once construction problem is found, timely coordination between different professions and modification of construction scheme are required, and simulate again until the optimal construction scheme before construction is obtained so as to ensure the smooth progress of construction and the project quality [16].

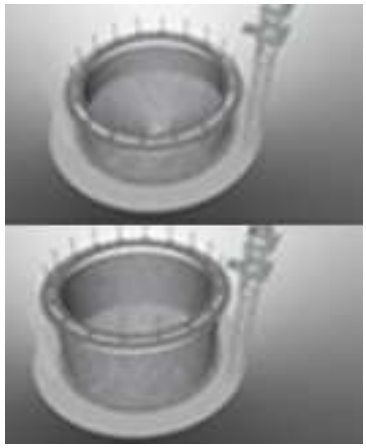

Fig. 8 The simulation for the construction of granary wall

Fig. 9 The construction site of granary wall

### 3.4 The stage of cost control

The 3D building model of granary project is generated using the software based on BIM, and granary schedule is made to form the granary construction schedule. First decompose the granary project objectives with the decomposition model of WBS. Judge and input the expected value of project duration. Create timelines and organize them. Allocate resources to each subproject and specify the relationship and date between these tasks. Then check whether the whole granary bar chart meets the requirements [17]. Finally associate the components of 3D model with schedule table and investment control table, forming the 5D model to intuitively show construction progress.

The "3D + time + cost" multidimensional system is formed after the establishment of relational database on 5D construction resource information model based on BIM, as shown in Fig.10. Let the actual cost data enter into the 5D relational database in time, forming a cost summary statistical table. Build BIM model of the actual cost, adjust and maintain the model on time periodically (month, season) to meet the demands of various cost analysis of the project [18].

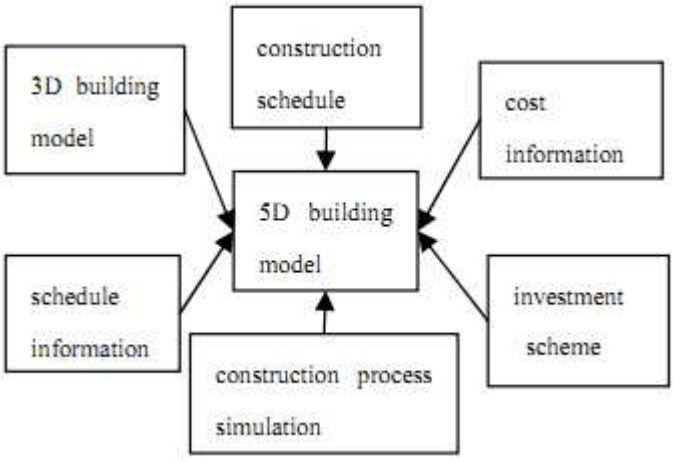


Fig. 10 Multidimensional system flow chart of BIM information

## Conclusion

This paper presents the preliminary idea of applying BIM concept to the granary construction based on the illustration of BIM concept and the developing status of granary. In the preliminary planning stage, prepare feasibility study and make site selection. In the design phase, use the software based on BIM for 3D modeling and conduct detection analysis. In project implementation stage, import construction progress into a 3D model of granary to simulate the 4D construction process of granary. At the stage of cost control, establish the relational database on 5D construction resource information model based on BIM. The application of BIM in granary construction is a long-term process. There are still some problems in unified standard and the software. But BIM has a strong vitality and broad prospect. As BIM is becoming maturer, it will definitely be widely used in granary projects or even the whole construction engineering.

**Funded projects:** Key Projects in the National Science & Technology Pillar Program during the Twelfth Five-year Plan Period (2011BAD03B01); National High Technology Research and Development Program of China (2012AA101608); Henan Higher Education Core of the Youth Instructor Support Program (2010GGJS-083)

**Author abstract:** CHEN Gui-xiang (1976- ), female, Ph.D., Associate professor, Master tutor, coming from Henan Zhengzhou, engaged in research and teaching on reliability assessment of structural optimization design and security management.

**References：**

[1] Wang Jun. Study on the Application of BIM Principle and BIM Software in Construction Projects [D]. Southwest Jiaotong University Master Degree Thesis, May, 2011.
[2] United States National Building Information Modeling Standard, Version1-Part 1[R]. National Institute of Building Sciences.
[3] He Qinghua, Qian Lili, Duan Yunfeng, Li Yongkui. Current Situation and Barriers of BIM Implementation [J]. Journal of Engineering Management. 2012,26(1):12-16.
[4] Wang Aijuan. Modeling of Schedule Risk Analysis for BIM [D]. Harbin Institute of Technology. 2011.
[5] Long Wenzhi. BIM Technology Shall Be Promoted in Building Industry As Soon As Possible [J]. Architecture Technology. 2011,42(1):9-14.
[6] Yao Yuan. The Current Situation of Collaborative Design Based on BIM [J]. Sichuan Building Materials. 2011,37(1):153-154.
[7] Li Yanni. Research of the Structure Model of Architecture Based on BIM [D]. Xi'an University of Architecture and Technology Master Degree Thesis, May, 2012.
[8] Zhao Ang. Exploration of BIM Technology Application in Computer Aided Architectural Design [D]. Master Dissertation of Chongqing University, June, 2006.
[9] Li Li. The Preliminary Research on Building Collaborative Platform Based on BIM Technology [D]. Dissertation Submitted to Shanghai Jiao Tong University for the Degree of Master, Feb, 2012.
[10] Wang Youqun. Application of BIM in Three Main Objectives of Project Management [D]. A Thesis Submitted to Chongqing University in Partial Fulfillment of the Requirement for the Master's Degree of Engineering, April, 2012.
[11] Lu Zhuqing. Application Analysis of BIM in Railway Construction Projects [J]. Railway Standard Design. 2011(10):4-7.
[12] Niu Bosheng. Application Study on Project Schedule Management Base on BIM [D]. A Thesis Submitted to Chongqing University in Partial Fulfillment of the Requirement for the Professional Degree, April, 2012.
[13] Zheng Cong. BIM-based Construction Integrated Design [D]. The Thesis for Master's Degree of Central South University, May, 2012.
[14] Li Hongxue, Guo Hongling, Gao Yan, Liu Wenping, Wei Xiaomei. BIM-based Optimization of Design and Construction for Bridge Projects [J]. Journal of Engineering Management. 2012,26(6):48-52.
[15] Liu Juanhua. The Research of Virtual Construction Technology Based-on BIM [D]. Xi'an University of Architecture and Technology Master Degree Thesis, May, 2012.
[16] Zhang Jianping, Li Ding, Lin Jiarui, Yan Gangwen. Application of BIM in Engineering Construction [J]. Construction Technology. 2012,371(41): 10-17.
[17] Wang Qingwei，Zhang Jianping. Control of the Project Investment Based on BIM [J]. Industrial Construction. 2011(41):1016-1019.
[18] Fang Houchun. Full Process Management of Project Cost Based on BIM [D]. A Thesis Submitted to Dalian University of Technology in Partial Fulfillment of the Requirement for the Professional Degree, May, 2012.

*Applied Mechanics and Materials Vols. 580-583 (2014) pp 3204-3207*
*© (2014) Trans Tech Publications, Switzerland*
*doi:10.4028/www.scientific.net/AMM.580-583.3204*

# Intelligent and complex monitoring in intelligent buildings

Volkov Andrey, prof., DSc.[1,a], Latyshev Konstantin [2,b],

[1,2] Moscow state university of civil engineering, 129337, Russia, Moscow, Yaroslavskoye shosse, 26

[a]volkov@mgsu.ru, [b] konstantin73@inbox.ru

**Keywords:** complex technics, intelligent building, intelligent monitoring, complex monitoring, building automation systems.

**Abstract.** Conversion of intelligent buildings (IB) is based on a data search, data pattern recognition, data processing and storage of data of projects of intelligent buildings (IB), automated systems (AS) and theirs elements. Author developed a model of a system for data monitoring, allowing for analysis and synthesis of intelligent buildings conversion projects. An intelligent monitoring allows to analyze data both of projects and elements of IB and AS. Complex monitoring allows to synthesize the data used in elements of IB and AS. It is possible to create CAD system and monitoring system for IB and AS conversion using principles described in this article. Vendors of elements for intelligent buildings, vendors of software used in controllers, adapter, etc., can find opportunity to found open community and establish rules for "internet specification" for intelligent elements for AS. Modern state of technology in intelligent search encourages me to say about full-automatic search, assembling and installing of software updates for AS elements of IB. I see that we can use industrial MDM and hypersearch software widely used in big internet vitrines.

Increasing number of buildings obtain automating systems for sustaining proper consumer-valued characteristics. Such buildings become "Intelligent Buildings" (IB). During exploitation, a consequent change of requirements leads to changes in automating systems already created and leads to consequent conversion of IB. At the current state of improvement of internet data searching systems a possibility to delegate functions of technical monitoring and inventory of IB to the IB itself does exist. We suggest that an IB can perform periodic searches in internet for software updates and design changes needed for coming possible IB conversion of it as well. Therefore, it is time to introduce notion "IB Conversion project". An "IB Conversion project" transfers a "conventional IB" to "Converted IB".

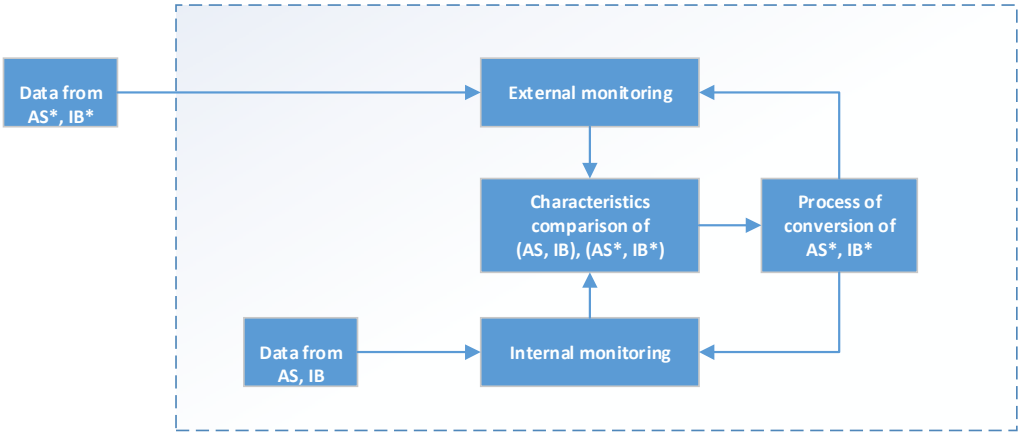


Diagram 1. "Selfconversion of IB"

"Internal monitoring", while providing estimation of running of IB, can be called as "traditional" (conventional). The result of "Internal monitoring" is repair of some out-of-order elements and replacement of some expired elements of (AS, IB).

"External monitoring", while providing estimation of (AS*, IB*), results in "short list" of improvement-promising (AS*, IB*).

Transition from "conventional monitoring" to "Intelligent monitoring" (IM) is necessary in case we need to monitor changes in both internal and external processes. Thus, intelligent monitoring must be multi-criteria and multi-targeted. IM is system union of external monitoring and external one and therefore it provides sufficiently detailed statuses of external environment and inner part of IB to get reliable presentation of IB functioning. In construction industry field (human activity domain) we can define IM as a technology for detecting of system changes of the constructed object to support decision: does an IB meet customer's requirements or does not.

We can regard a system for monitoring of "technology-and-organization safety level of IB functioning" (TOS level of IBF) as example of such IM. The IM functions as follows:

Based on "Consuming resources delivering plan for IB" an average estimation of TOS level can be obtained. This estimation characterizes an organization of IB functioning as whole. Data treatment have be done iteratively to obtain average result of fixed accuracy. This value is input parameter for "IM organization project testing module". TOS level estimation and IM output data are essential for an IB conversion project.

All data obtained in calculations must be stored in a statistics module (statistics warehouse). Data of statistics warehouse (SWH) are used in projects of IB conversion. Gain and treatment of termed data of operative monitoring allows making comparison of measurable indicators, which characterizes functioning of some AS of similar IB in comparable conditions. In frame of schema described we can calculate optimal values of TOS level.

Relations of high-level modules composing Converted IB project creation are drew in the diagram below. Interaction of the modules is transfer of both raw IB monitoring data and accumulated results. To get results that are more accurate we must increase number of data sources for monitoring.

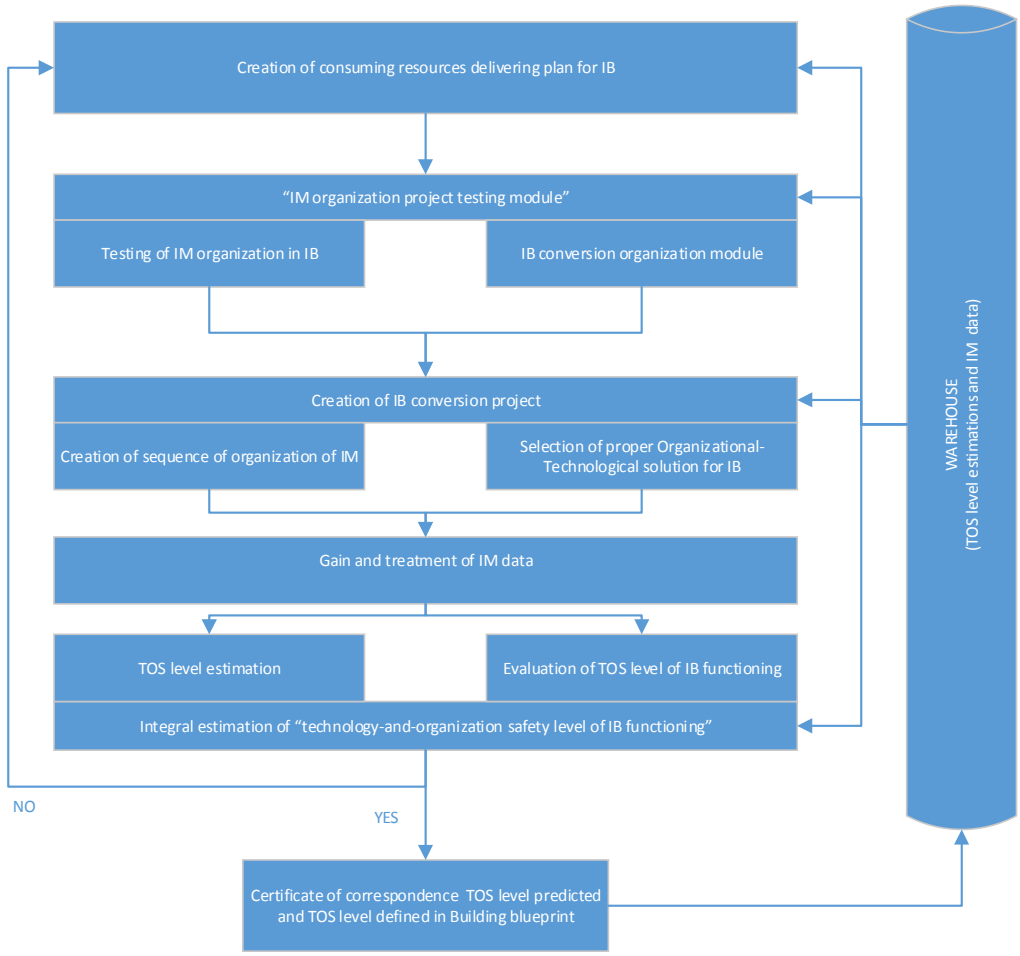


Diagram 2: Monitoring of TOS level of an IB

Multi-criteria data analysis is used to analyze data flow from IM. AS operator can change control parameters of IB. Control parameters of IB can affect control parameters of IM.

Transition from IM to Complex Monitoring (CM), is necessary in case we have “power user-consumer” who exploits and control an upgraded IB. It is clear that modernization of any technical appliance is related to learning of user to use new properties added by modernization. In case of IB which was essentially changed (improved), a consumer not aware of this change, can seriously decrease TOS level of IB functioning. Then an IB and consumer inside it will be in danger. According these reasons, IM must be accomplished by consumer education for he could effectively participate particularly in IM of IB and be engaged in IB modernization in general. “Intellectualization” of Intelligent Building must be complemented by “intellectualization” of a consumer.

According to defined in notion of CM in Constructing, CM is technology of detecting of system changes in process of building improvement towards increasing consumer demands.

According to definition described in this article, CM is complex union of two kinds of monitoring: internal monitoring and external one. CM runs to catch states of both BI and consumer inside it in order to get reliable facts about theirs mutual functioning and select possible IB conversion project.

Conversion of intelligent buildings (IB) is based on a data search, data pattern recognition, data processing and storage of data of projects of intelligent buildings (IB), automated systems (AS) and theirs elements. Specifications of fulfilled projects of IB, statuses of IB and AS before and after successful conversion must constitute a DataBase “IB conversions reference DB”. Another Database “IB conversion elements DB” must contain information about controllers, detectors, etc.

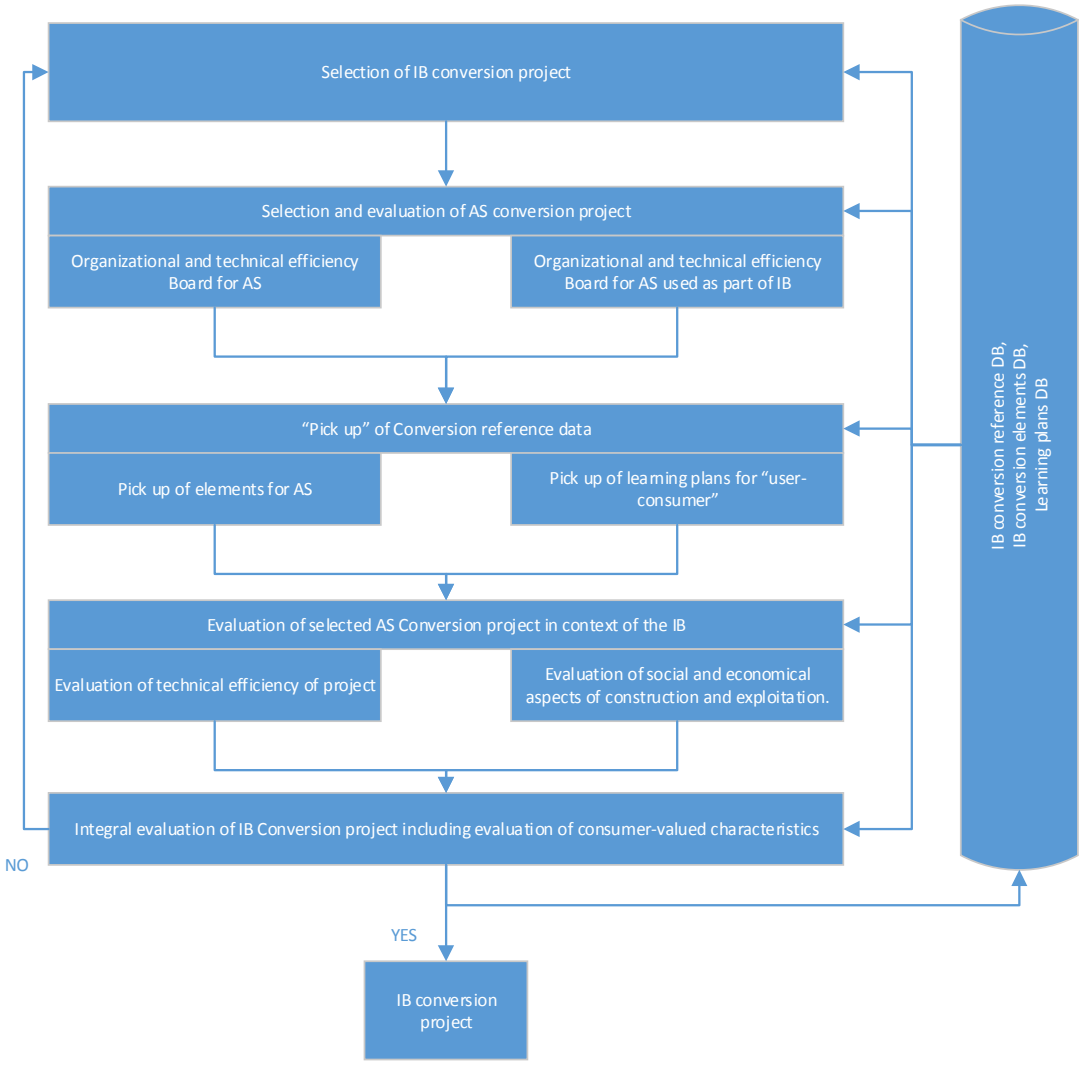


Diagram 3: General IB conversion process.

Next step in general IB conversion process is “pick up” of elements. The main criteria of successful combination is “organizational and technical efficiency”.

Final integral evaluation of IB conversion project must include evaluation of consumer-valued characteristics.

It is possible to create CAD system and monitoring system for IB and AS conversion using principles described in this article. Vendors of elements for intelligent buildings, vendors of software used in controllers, adapter, etc., can find opportunity to found open community and establish rules for “internet specification” for intelligent elements for AS. Modern state of technology in intelligent search encourages me to say about full-automatic search, assembling and installing of software updates for AS elements of IB. We can use industrial MDM and hypersearch software widely used in big internet vitrines.

## References

[1] *Volkov A.* Building Intelligence Quotient mathematical description // Applied Mechanics and Materials (Trans Tech Publications, Switzerland). – Vols. 409–410 (2013). – pp. 392–395.

[2] *Sedov A., Volkov A., Chelyshkov P.* Usage of building information modeling for evaluation of energy efficiency // Applied Mechanics and Materials (Trans Tech Publications, Switzerland). – Vols. 409–410 (2013). – pp. 630–633.

[3] *Volkov A., Vodnev N.* System engineering numerical representation of the quality parameters living and working environment. Recursive procedure dive into levels detailization of objects: basic mathematics and logic // Promishlennoye i grazhdanskoye stroitelstvo. – 2013. – №9. – pp. 6–8.

[4] *Volkov A.* General Information Models of Intelligent Building Control Systems: Basic concepts, determination and the reasoning.// Advanced Materials Research (Trans Tech Publications,Switzerland).–Vols.838-841(2014).–pp.2969-2972.

[5] *Volkov A.,* General Information Models of Intelligent Building Control Systems: Basic concepts, determination and the reasoning // Advanced Materials Research (Trans Tech Publications, Switzerland). –Vols. 838-841 (2014) pp. 2973-2976

[6] *Chelyshkov P., Volkov A., Sedov A.* Application of computer simulation to ensure comprehensive security of buildings // Applied Mechanics and Materials (Trans Tech Publications, Switzerland). – Vols. 409–410 (2013). – pp. 1620–1623.

[7] *Volkov A.A.* Homeostatic control of buildings // Housing construction. 2003. № 4. pp.9-10.

[8] *Vikulin D, Mokhov A* Complex Monitoring of Buildings and Structures for Ensuring Their Power Efficiency // Promishlennoye i grazhdanskoye stroitelstvo – 2010, – №11. – pp. 78–79.

*Applied Mechanics and Materials Vols. 580-583 (2014) pp 3208-3214*
*© (2014) Trans Tech Publications, Switzerland*
*doi:10.4028/www.scientific.net/AMM.580-583.3208*

# Numerical Analysis of Bridge Expansion-Induced Rail Deformation of Ballast Truck

Zhenwei Xiong [1, a], Xinling Liang [1, b], Xianxing Dai [1, c] and Ping Wang [1, d]

[1] Southwest Jiaotong University, Chengdu 610031, China

111 North Second Ring Road, chengdu, china

[a]544470791@qq.com, [b] 993954621@qq.com, [c] 995305844@qq.com, [d]wping@home.swjtu.edu.cn

**Key words:** Ballast truck; Rail deformation; Granular flow; Numerical analysis

**Abstract:** when the ballast track stretch with the bridge, ballast which is near expansion joint will move confusedly. As a result, rail produced vertical deformation. The deformation will affect the running safety and comfortability of train. At present, there are two kinds of treatments which are cover board structure and baffle structure to deal ballast's movement. Aiming at the different modes of stretching when the two kinds of structures and different arrangement condition of bridge plate are applied, the rail-sleeper-ballast discrete element model is developed by the method of two-dimensional granular flow. The relationship between rail deformation and bridge expansion is analyzed on the foundation of the model. Results show as flows: when bridge extends or shortens, rail always produced upwarp deformation. Bridge plate should arrange asymmetrically. Like this, the rail deformation decrease by 40%. And adopting the baffle structure can effectively reduce the influence of bridge expansion in ballast truck.

When ballast track is paved on long-span bridges, in order to prevent the bridge expansion leading ballast to fall from beam end, the measure that beam end are equipped with cover plates is generally made at present. After cover plates are installed, whether the beam ends of long-span bridges are equipped with expansion joint or not, the motion of ballast easily leads to rail deformation. The reasons for this phenomenon are that the changes of temperature lead to the bridge expansion, at that time, the ballast is affected by friction, which makes it moved in the direction of the beam deformation. No matter how the temperature changes, it makes ballast distributed uneven, which will cause all kinds of diseases such as rail vertical irregularity. In order to solve these problems mentioned above, the ballast bed at bridge expansion joint is separated by using the ballast boards on the part of bridges, but the specific effect of this solution lacks theoretical research. Therefore, studying the relation between the bridge expansion and the rail deformation has theoretical and practical value.This paper used PFC2D discrete element software to build particles flow numerical analysis model to study the relation between the bridge expansion and the rail deformation. [1~4]

## The calculation model and basic parameters

### 1.1 Building the model

Building the model of vertical section of the ballast bed under rail, it was divided into four parts. Firstly, Useing wall simulated bridge plate, plate and baffle. Secondly, The disc was used to

simulate ballast articles. Thirdly, that twenty two disk particles with the same size were spliced to simulate the sleepers. The last a series of disk particles were used to simulate the rails. The schematic diagram of model is as follows:

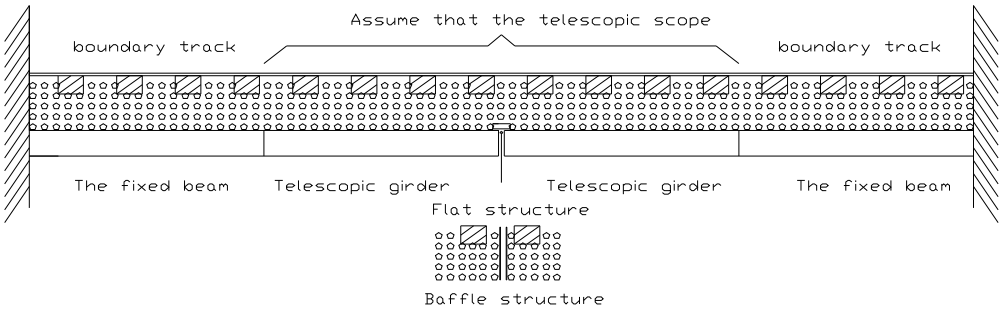


Figure 1.1 Schematic diagram of model

The model was only considered the expansion deformation of the telescopic beam that was 8m from the end of two beams. In conclusion, this paper calculated eight kinds of working conditions in total. For detailed working conditions, see the table below.

Table1.1 Calculation conditions

| Working condition No. | Details |
|---|---|
| 1 | Cover plate structure and beam-slab extend symmetrically |
| 2 | Cover plate structure and beam-slab shrink symmetrically |
| 3 | Cover plate structure and beam-slab extend asymmetrically |
| 4 | Cover plate structure and beam-slab shrink asymmetrically |
| 5 | Baffle structure and beam-slab extend symmetrically |
| 6 | Baffle structure and beam-slab shrink symmetrically |
| 7 | Baffle structure and beam-slab extend asymmetrically |
| 8 | Baffle structure and beam-slab shrink asymmetrically |

**1.2 Parameter selection**

In numerical simulation experiment, the method that the weight of the ballast under the half sleeper and the weight of the half sleeper were integrated into the vertical section under rails was adopted. The thickness of the disk particles is 0.03m in the model. The length of the sleepers is 2.5m. The macroscopic parameters of the rails are showed as follows. The weight of the rails is 60kg/m. The length of the rails is 32.04m, and its sectional area is 77.45cm$^2$. The elasticity modulus of the rails is 2.1e11 Pa, and its shear modulus is 8.1e11Pa. Converting the above parameters to the microscopic parameters of particles is as follows:

（1）The parameter of ballast

The macroscopic density of the particles is 2920kg/m3. Because the ballast under the half sleeper was integrated into the vertical section under rails in the model, the density of the particles needs to be multiplied by an amplification factor. And its value is as below.

$$u = \frac{2.5}{2} \div 0.03 = 41.67 \quad (1)$$

The other parameters can be found by referring to the relevant literature, so the parameter of the ballast particles are as the following table: [7~9]

Table 1.2 Parameters of ballast particles

| Normal stiffness | Shear stiffness | Friction coefficient | Density | Non-stick |
|---|---|---|---|---|
| 1e9N/m | 1e9N/m | 1.0 | 121676.4kg/m$^3$ | / |

（2）The parameter of sleeper

The sleepers are simulated by 22 disk particles whose radii are 0.03m. The density of the concrete is 2500kg/m$^3$. To calculate its integrated density, the density of the sleepers also needs to be multiplied by an amplification factor. The concrete particles are bonded by adopting the method of parallel connection, and for its strength and stiffness, see the table below:

Table 1.3 Parameter of sleeper particle

| Normal stiffness | Shear stiffness | Friction coefficient | Density |
|---|---|---|---|
| 2e9N/m | 2e9N/m | 1.0 | 104175kg/m3 |
| Bonding normal stiffness | Bonding shear stiffness | Bonding normal strength | Bonding shear strength |
| 2e11Pa/m | 2e11Pa/m | 1e20Pa | 1e20Pa |

（3）The parameter of rail

The rails are simulated by 535 disk particles whose radii are 0.03m in the PFC2D model, and the adjacent particles are bonded by adopting the method of parallel connection to bear the effect of shearing force and bending moment. The bonding radii between the particles are 0.03m. When the rails are under stress, in order to ensure that the parallel connection between the particles aren't damaged, the bonding normal strength and the bonding shear strength can be set to a higher value that is 1e20Pa in this paper. There are 16.67 balls within one meter, so the weight of the rails is 3.6kg within the length of the diameter of each ball. The density of the rails can be calculated by the formula below.

$$\rho_g = 3.6 \div (\pi 0.03^2 \times 0.03) = 42454 kg / m^3 \quad (2)$$

When the macroscopic parameters of the model are known, according to the strength equivalent principle, the microcosmic parameters of the particle flow can be confirmed in the PFC2D model. [10] For the final parameters of the rails in the paper, see the table below:

Table 1.4 Parameter of rail particle

| Normal stiffness | Shear stiffness | Friction coefficient | Density |
|---|---|---|---|
| 4.04e11N/m | 4.04e11N/m | 0.15 | 42454kg/m3 |
| Bonding normal stiffness | Bonding shear stiffness | Bonding normal strength | Bonding shear strength |
| 3.5e12Pa/m | 1.35e13Pa/m | 1e20Pa | 1e20Pa |

**The results of the calculation**

According to the above eight kinds of working conditions, the model was calculated in turn to acquire the relation between the movement of the beam-slab and the rail deformation at the center of the beam joint, the relation between the friction force of the beam-slab and its displacement, the relation between the integral rail deformation and the movement of the beam-slab and so on. And then the results were analyzed contrastively.

（1）Using the cover board structure

Working condition 1:

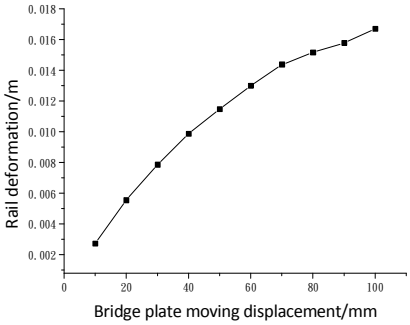


Figure 2.1 The rail deformation1 in the center of beam joints

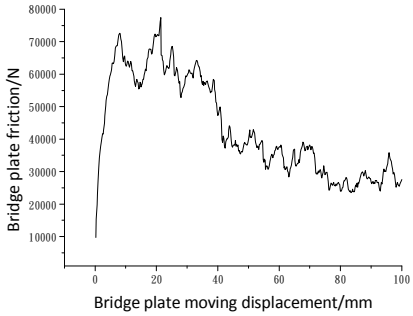


Figure 2.2 The relation 1 between displacement and bridge plate friction

Working condition 2:

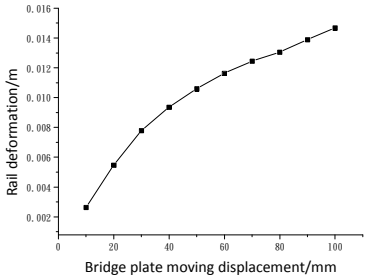


Figure 2.3 The rail deformation 2 in the center of the beam joints

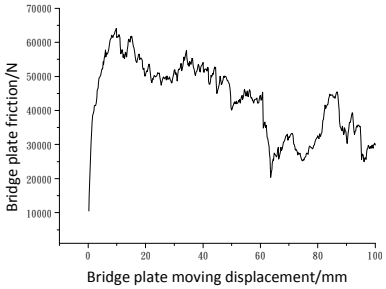


Figure 2.4 The relation 2 between displacement and bridge plate friction

It can be seen that the rail deformation in the center of the beam joints increased gradually with the displacement of the beam-slab by the figure 2.1 and figure 2.3, but the increment decreased gradually, and their corresponding relation was nonlinear relation. The reasons of the rail deformation consisted of two parts. Firstly, the expansion of the bridge plate caused the movement of the ballast, and the ballast rolled to generate dilatancy effect, which caused the rising deformation of the rails within the scope of the whole bridge. The figure 2.2 showed that with the displacement of the beam-slab increasing, the ballast and the beam-slab generated large relative sliding, and the static friction was transformed into the sliding friction or the rolling friction, as generating the shear failure surface, which made the friction decreased gradually. After the movement of the beam-slab reached to 60mm, the friction was stable at 30~40kN, so the increment of the rail deformation decreased. Secondly, when the beam-slab moved because of warming, the ballast at the beam joints was blocked by the ballast on the another beam, and when the beam-slab moved because of cooling, the ballast was blocked by the ballast at the boundary, which leaded the ballast to move up, and increased the deformation of the rails. At the same time, the rail deformation that warming leaded to was slightly greater than the deformation that cooling leaded to by contrasting the figure 2.1 and the figure 2.3.

Working condition 3:

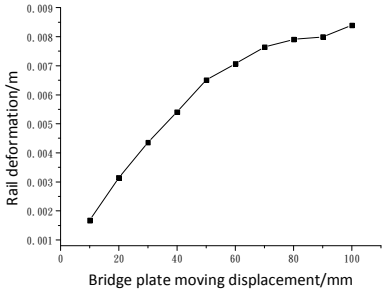


Figure 2.5 The rail deformation 3 in the center of the beam joints

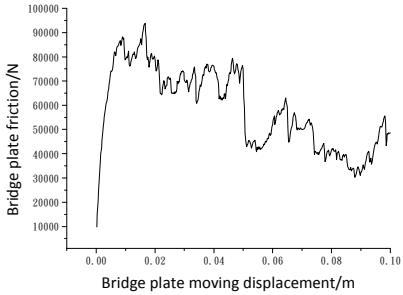


Figure 2.6 The relationship 3 between displacement and bridge plate friction

Working condition 4:

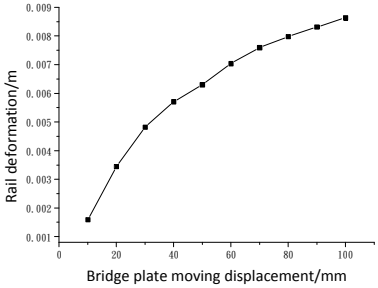


Figure 2.7 The rail deformation 4 in the center of the beam joints

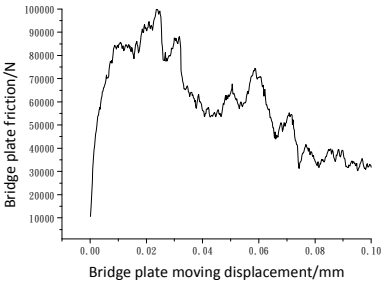


Figure 2.8 The relation 4 between the displacement and bridge plate friction

Analyzing the above four figures knew that the calculation results of the working condition 3 and the working condition 4 were almost the same, and their methods of causing the rail deformation were all due to the movement of the single beam with the fixed ballast blocking. Comparing with the working condition 1 and the working condition 2 knows that the relation between the friction of the beam-slab and the displacement of the beam-slab remained unchanged basically at this moment, and that meant the increasing laws of the rail deformation and the displacement of the beam-slab were the same, but the deformation was about 40% less than theirs. So it should be avoided that two free ends were adjacent, when the bridge was arranged.

（2）Using the baffle structure

The above analysis showed that when the cover board was used, no matter which method of the bridge expansion was used, the rail deformation was great. In order to reduce the influence, the baffle structure was proposed. When the baffle structure was adopted, the calculation results of all kinds of working conditions were as follows.

Working condition 5 and working condition 6:

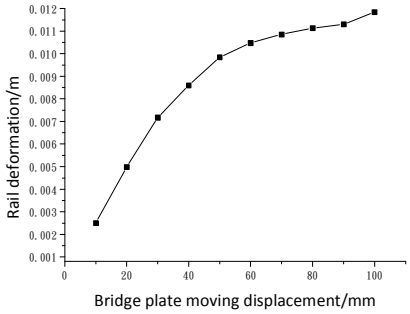


Figure 2.9 The rail deformation 5 in the center of the beam joints

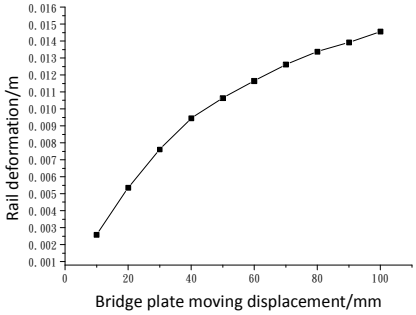


Figure 2.10 The rail deformation 6 in the center of the beam joints

Working condition 7 and working condition 8:

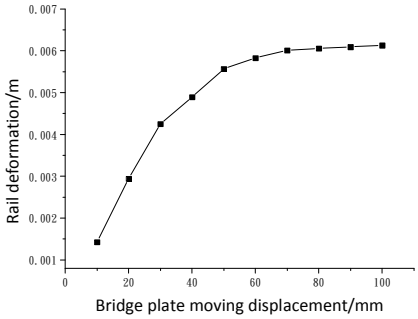


Figure 2.11 The rail deformation 7 in the center of the beam joints

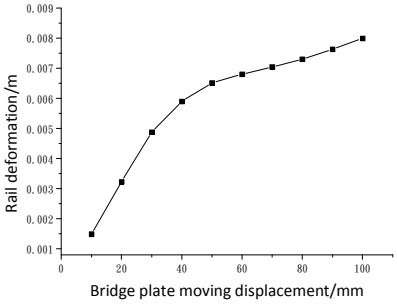


Figure 2.12 The rail deformation 8 in the center of the beam joints

Contrasting the above eight figures knew that when the baffle structure was used at the beam joints, the rail deformation that warming leaded to can be reduced effectively, and the increment of the rail deformation decreased rapidly. When the bridge was extended symmetrically, the increment was stable at 11mm roughly in the end, and when the bridge was extended asymmetrically, the increment was stable at 11mm roughly in the end. However there was little influence on the rail deformation that cooling leaded to. That was because that after the baffle structure was used, as the bridge extended, the front of the ballast at the beam end had little blocking effect, which reduced the rail deformation, and as the bridge shrank, the boundary of the ballast bed still blocked the movement of the ballast, so the rail deformation didn't be decreased.

## Conclusions

（1）No matter whether the bridge extend because of warming or shrank because of cooling, as long as the beam-slab moved, the ballast bed moved under the effect of the friction. The shear dilatancy of the ballast bed occurred at this moment because of the characteristics of the granular mixtures, which made the rails generate the vertical deformation. Because the shear failure surface was generated gradually, the increment of the rail deformation would be smaller and smaller, and if there was no other influence, the value would be stable at 6mm finally.

（2）The bridge should avoid that two adjacent free ends were installed as far as possible, and when the beam joints and beam ends extended and shrank at the same time, the rail deformation would be almost doubled.

（3）When the ballast bed at the expansion joint of the bridge used baffle structure, the effect of blocking in the extension direction of the ballast bed was removed, which made the rail deformation that the extension of the bridge caused decreased greatly, but there was little influence on the rail deformation, as the bridge shrank.

**References**

[1] Fu Long-long, Gong Quanmei. Relationships between ballasted track settlement and differential subgrade settlement under train load [J]. Vibration and shock, 2013, 32(14):23~28.

[2] Particle flow code in 2 dimensions online manual table of contents.PFC2D Version3.1,Itasca Consulting Group,Inc.

[3] Sun Jicheng, Wang Guangqian. Introduction to granular material mechanic [M]. Beijing: Science Press, 2009:63

[4] Xiao Hong, Gao Liang, Hou bowen. Analysis of ballast dynamic behavior with three-dimensional discrete element method [J]. Journal of Railway Engineering Society, 2009,132(9):14-17

[5] Wang Ping Wan Fuguang. The fabric of the ballast bed description [J]. Journal of Social Sciences of Southwest Jiaotong university, 2009,132(9):14-17

[6] Luo Yong. Simulation of soil mechanical behaviors using discrete element method based on particle flow code and it application [D]. Zhejiang University, 2007.

[7] Yin Xiaotao. Study on the engineering characteristics of rock and soil material based on numerical test [D]. The Chinese Academy of Sciences, 2008.

[8] Yan Dongxiao. Research of laboratory tests and $PFC^{3D}$ numerical simulation for the steady state of sand [D]. Tongji University, 2007.

[9] Zhou Guoqing, Zhou Jie. Selection of damping parameters used in a particle flow code($PFC^{2D}$) [J]. Journal of China University of Mining & Technology, 2011(5):667~672.

[10] Chang Zai. Theoretical and numerical research on granular mechanics of soils [D]. Tsinghua University, 2008

*Applied Mechanics and Materials Vols. 580-583 (2014) pp 3215-3218*
*© (2014) Trans Tech Publications, Switzerland*
*doi:10.4028/www.scientific.net/AMM.580-583.3215*

# Real-Time Dynamic Simulation System for Tunnel Construction Based on OpenGL

Qian Li

College of Civil Engineering and Mechanics, Central South University of Forestry and Technology, Changsha 410004, China

semese_li@163.com

**Keywords:** tunnel construction, simulation, real-time system, OpenGL

**Abstract.** Comprehensively using the theories and techniques in connection with the tunnel engineering, geometric modeling, computer graphics, object-oriented method and software engineering, the authors in this paper have made research on the techniques for the three-dimensional solid modeling, tunnel realistic scene graphics rendering and tunnel construction real-time dynamic simulation and on the basis of the research, the authors developed an *openGL*-based real-time dynamic simulation system for tunnel construction. The application of the developed system to a practical tunnel shows that the system has very good vista of application in aspect of the progress control, organization and management of the tunnel construction.

## Introduction

With the development of modern tunnel technology, the complexity of the technical content and construction management of tunnel construction are increasing, tunnel construction project has become a comprehensive, complex production activities. How to make a reasonable construction plans, accurately grasp the construction process, scientific arrange the construction yard, shorten the construction period, reduce costs, improve quality, these have become hot research of tunnel construction management. Meanwhile, *CAD* technology and simulation technology have also been widely used in tunnel engineering.

The currently, simulation of the domestic and international project mainly has focused on two areas: Firstly, the engineering structural design simulation has mainly studied the structure under the load occur deformation, displacement and destruction, which are the main research on abroad. Secondly, in the field of construction engineering, simulating the whole process of the actual construction of the project provide decision making for the construction organization design and project management, which is still in its infancy stage. Systematic studied and applied only in water conservancy and hydropower sector [1, 2, 3], while such study is very rare in the field of railways, highways, municipal, and other high-rise buildings.

## Development tools selection and system Architecture

### System Architecture

Using *Visual C + +* as a language tool and *OpenGL* graphics library to create graphics platform [4,5,6] establish simulation system of real-time dynamic of tunnel construction. The system is mainly to achieve three functions: 1) Building three-dimensional model of the tunnel; 2) Achieving realistic graphics display; 3) Simulating Tunnel construction process.

### Systematic class library structure

On the basis of object-oriented approach design the structure of simulation system of real-time dynamic of the tunnel construction and give definition and implementation of corresponding *Visual C+ +* class. The tunnel as a whole is composed by other simple objects among the tunnel itself， the various components of tunnel hole body, tunnel portal, tunnel subsidiary building and other parts of these components (i.e. lining). These are respectively comprehended as an each object and established

specific object class. Using the inherited and derived idea among object-oriented methods establish a unified base class *CTunnelBase*, in which defined some basic, necessary variables and functions. Some of these functions overloaded in a derived class result in new implementations, such as *OnDraw ( )* function; others will only be used in the implementation of the base class, the derived class because the inheritance relationship with the same implementation, such as *Display ( )* function. Meanwhile, among the base class *CTunnelBase* has defined some related variables of the model such as texture mapping, visibility and time parameters , and are given their settings functions. Member variables and functions of the base class are shown in Table 1.

Table.1 List of member variables and functions of the base class *CTunnelBase*

| *member variables and functions of the base class* | *The main function* |
|---|---|
| BOOL m_bVisible | Boolean variables, used to control the visibility of model |
| CTexture2D* m_pTex | Texture class variables, used to texture mapping of the model |
| CTunnelBase() | The default constructor |
| virtual~CTunnelBase() | The Default destructor |
| BOOL IsVisible() conset | Back visibility model |
| void Set Visible (BOOL bVisible=TRUE) | set visibility model |
| void SetTime(int time=0) | Set the data of the duration |
| int GetTime() const | Back the data of the duration |
| virtual void Display() | Virtual function, used to display the model |
| Virtual void Draw() | Pure virtual function, overloads in a derived class , used to draw the specific model |

Other specific classes of implementation of various components of the tunnel are derived by *CTunnelBase*, these hierarchies of specific class shown in Figure 1.

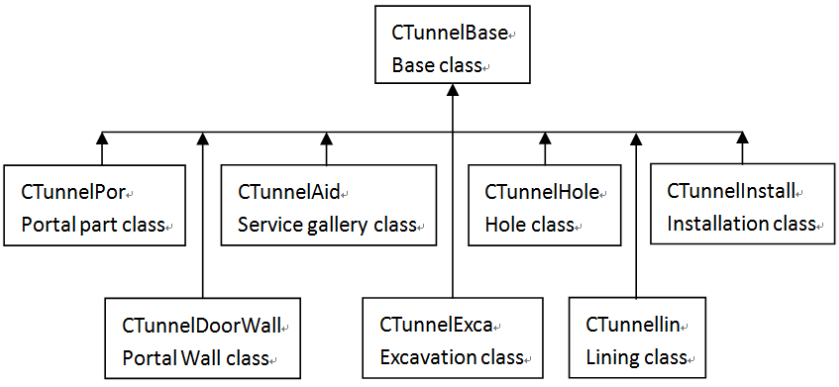


Fig.1 Class hierarchy

**Build three-dimensional model of the tunnel**

*OpenGL* as graphics hardware interface achieve the establishment of three-dimensional model of the tunnel. *OpenGL* is drawing in windows, firstly, it must be rendering graphics scene of *OpenGL*, this system use *wglCreateContext* function to create the rendering scene of *OpenGL* associated with a display device, which is drawing the scene of the model. After the scene is rendered, to use *OpenGL* point, line and polygon draw functions, create complex spatial model. Using the drawing function to generate three-dimensional graphics of each member of the tunnel, then combined into a three-dimensional model of the tunnel overall. In order to achieve realistic graphics rendering must also use lighting and texture mapping in the drawing process of the model. Use of light functions and

texture class *CTexture2D* defined in the view class are realized scene lighting and texture mapping model respectively. Finally, a series of coordinate transformation of the model complete the transformation from model space to paper space, and achieve graphics displayed on the screen window.

## Implementation of Construction Simulation

### Determined Construction period

The system is based on the construction period of all components and considered the construction schedule and flow construction requirements, according to the calculation method of construction organizations to the relevant construction period determine a reasonable period, using irregular flow construction organization get construction period of the whole tunnel. To use the total construction period is obtained by the above steps as the time axis of the simulation process of the system, with 1 day as a simulation step, by time step method to achieve simulation of tunnel construction process. Thus, this system will provide the simulation results of progress status, resource requirements and project completion in any time.

### The realization of animation process

The animation of this system adopts time function of *MFC* to achieve the double buffering technology of *OpenGL*, which can achieve frame memory mapping and exchange both before and after [4,5]. Use *MFC* clock cycle, each cycle add up 1 step to the time axis, and according to the new get time axis length calculated the completed amount of the project, re-instantiated tunnel model object, realized the redrawing of the tunnel model, thus the time axis length can realize smooth animation display of tunnel construction process.

### Interactive and dynamic real-time view

This system gives the model observed the three ways: browsing static and local model, browsing construction status at any time, showing animation throughout the construction process. Through the mouse action response function, the system can use the mouse to drag to achieve angle transformation of the model to observe from different azimuth. Combined with the static browse mode, can achieve all-round browsing tunnel model and each tunnel component.

## Case study

In this paper, to Yangheyan No. 1 tunnel in Jihuai Highway as an example is simulating. Dimension data of the tunnel and construction schedule data input in the system, can be obtained the simulation effect model in each observation mode.

The system is under static observation mode, the project management staff can observe simulation model of various construction process, components and the entire tunnel，which form intuitive understanding to size, location and materials of holes and component of the tunnel and enhance the project management staff to awareness and understanding of the design results on the plane.

Use browsing of construction conditions of simulation system any time, the project management staff can understand in advance project progress at any time, compare with actual project schedule, judge the gap between the actual progress and the plan progress, that is the application of the simulation results, the project management staff achieve the visualization prediction and control of construction process.

Animation can simulate the whole process of project construction, and the production of three-dimensional model of the tunnel changes with time. The animation has different roles in the different stages of the tunnel construction. In the bidding stage, the animation can be used as construction organization design results displayed the owners, which is visual image, and increase the chance of winning. In the construction stage, Demonstration to the related construction personnel deepens their understanding throughout the construction process of the project. In the completion acceptance stage, the animation can clear expression to construction process of the tunnel to

inspection personnel. Through animation, to different people use digital way clear expression of the construction process of the tunnel, overcomes the shortcomings of traditional graphic expression, such as network diagram and Gantt chart, which is not intuitive, difficult to understand.

Compared with the traditional method of network diagram and Gantt chart, three-dimensional model presents project schedule has the characteristics of clear, simple, intuitive and easy to understand. And the application of three-dimensional model, the project management staff can directly obtain the gap between the actual progress and the plan progress, without having to spend a lot of time to study the network chart or bar chart, which is beneficial to improve the efficiency of management of the tunnel construction.

## Summary

This paper comprehensively has studied the key technologies of real-time dynamic simulation of tunnel construction process, established a tunnel model library, developed tunnel modeling and real-time dynamic simulation system, and proved the practicality of the system in tunnel construction management through the practical application. On this basis, future research should focus on the field of building three-dimensional model of the complex tunnel, and simulation optimization of construction schedule, resources and costs.

## Acknowledgements

This work was financially supported by the Hunan Provincial Education Department Science Foundation (12C0460), the Guizhong Provincial Communications Department Science Foundation (2011-321-022).

## References

[1] Denghua Zhong, Jingru Li, Guijian Liu: submitted to Journal of Tianjin University (2003) (in chinese)

[2] Denghua Zhong, Huiru Zhu, Donghai Liu: submitted to advances in science and technology of water resources (2003) (in chinese)

[3] Yonghong Wong, Hongzhong Xie, Zhongping Xia, in: Concrete Dam Construction Simulation, edtied by Beijing Electric Power Press, beijing, (2003) (in chinese)

[4] Yanping Zhu, Jianjun Bai, Xiaodong Bian, in: OpenGL programming examples, edited by People's Posts and Telecommunications Press, beijing, (1999) (in chinese).

[5] Qinghui Wang, Biao Wang, in: Visual C++ CAD Application development technology, edited by Machinery Industry Press, beijing, (2003) (in chinese).

[6] Youliang Jiang: submitted to Central South University, Changsha, (2004). (In Chinese)

*Applied Mechanics and Materials Vols. 580-583 (2014) pp 3219-3222*
*© (2014) Trans Tech Publications, Switzerland*
*doi:10.4028/www.scientific.net/AMM.580-583.3219*

# Study on multiple points matching in different images of intelligent building

Zhiling Lin[1, 2,a], Enzeng Dong[1,b] and Peng Ju[3,c]

[1]School of Electrical Engineering, Tianjin University of Technology, China

[2]Tianjin Key Laboratory for Control Theory & Applications in Complicated Systems, China

[3]Orich Medical Equipment(Tianjin) Co.LTD, China

[a]linzl2002@163.com, [b]dongenzeng@163.com, [c]jp@orch.com.cn

**Keywords:** three-dimensional reconstruction; epipolar lines constrains; linear searching

**Abstract.** It is important for identifying the correspondences of points in different images. A double epipolar lines approach based on linear searching was proposed to identify the corresponding points in three images. First the component expressions of a given point epipolar equation were derived from the known epipolar model. Then the linear searching method was utilized to solve the problem of no analysis solutions since the numbers of state variables in these expressions were more than those of independent equations. Finally the target was found in looking for the corresponding points. The simulation shows it is effective.

## Introduction

The visual information of intelligent building comes from an abundance of images which are collected by kinds of cameras. Up to now the scenes by these images are all in form of planes. The loss of information cannot be avoided since the real world is three-dimensional. If these planes can be made up to a three-dimensional objection it will approach the real world.

A problem of a three-dimensional objection reconstructing from planes is how to find the corresponding point in different images. Hu presented a matching algorithm for obtaining feature point correspondences across images containing rigid objects undergoing different motions[1]. Papadaki focused on combining photogrammetric and machine vision measurement techniques, through an automated model generation tool based upon dynamic Delaunay triangulation[2]. Jiang put forward a kind of 3D reconstruction method based on affine transformation[3]. Chua attempted to identify (and thereby reject) such mismatched correspondences, within the framework of an affine projection model and the use of three images[4]. The others are in references [5-10]. In this paper an approach of double epipolar lines with linear searching is proposed to meet multiple points matching in different images and has a good result.

## The epipolar lines constraint

**The component expression for a given point.** Suppose the calibration matrix of two cameras is $M_1$ and $M_2$ respective which is in form of

$$M_1 = \begin{bmatrix} m_{111} & m_{112} & m_{113} & m_{114} \\ m_{121} & m_{122} & m_{123} & m_{124} \\ m_{131} & m_{132} & m_{133} & m_{134} \end{bmatrix} = [M_{11} \quad M_{12}] \tag{1}$$

$$M_2 = \begin{bmatrix} m_{211} & m_{212} & m_{213} & m_{214} \\ m_{221} & m_{222} & m_{223} & m_{224} \\ m_{231} & m_{232} & m_{233} & m_{234} \end{bmatrix} = [M_{21} \quad M_{22}] \tag{2}$$

where

$$M_{11}=\begin{bmatrix} m_{111} & m_{112} & m_{113} \\ m_{121} & m_{122} & m_{123} \\ m_{131} & m_{132} & m_{133} \end{bmatrix}, M_{12}=\begin{bmatrix} m_{114} \\ m_{124} \\ m_{134} \end{bmatrix}, M_{21}=\begin{bmatrix} m_{211} & m_{212} & m_{213} \\ m_{221} & m_{222} & m_{223} \\ m_{231} & m_{232} & m_{233} \end{bmatrix}, M_{12}=\begin{bmatrix} m_{214} \\ m_{224} \\ m_{234} \end{bmatrix}$$

So the projection equation of cameras expresses

$$Z_{c1}u_1 = M_1 x_p = (M_{11} \quad M_{12})x_p \tag{3}$$

$$Z_{c2}u_2 = M_2 x_p = (M_{21} \quad M_{22})x_p \tag{4}$$

Where $x_p$ is the homogeneous coordinates of a space point P in the world coordinate system and $x_p = (x_{wp} \quad y_{wp} \quad z_{wp} \quad 1)^T$, in which $x_{wp}, y_{wp}$ and $z_{wp}$ is the x-component, y-component and z-component of $x_p$. $u_1, u_2$ is the homogeneous coordinates of $P_1$ in plane α and $P_2$ in plane β respective. $Z_{c1}$,$Z_{c2}$ is the coordinates of space point P in α-camera coordinate system and in β-camera coordinate system respective.

Definition: An antisymmetric matrix of a three dimensional vector t is defined as in form of

$$[t]_x = \begin{bmatrix} 0 & -t_z & t_y \\ t_x & 0 & -t_x \\ -t_y & t_x & 0 \end{bmatrix} \tag{5}$$

Where $t = (t_x \quad t_y \quad t_z)^T$ and $t_x \quad t_y \quad t_z$ is the x-component, y-component and z-component of t respective.

Let $x_p = (x^T \quad 1)^T$ and $m = M_{22} - M_{21}M_{11}^{-1}M_{12} = [mx1\ mx2\ mx3]^T$, where $x = (x_{wp} \quad y_{wp} \quad z_{wp})^T$, mx1, mx2 and mx3 is the x-component, y-component and z-component of m respective. The epipolar equation (3) and (4) are transformed to equation (6) by eliminating the $Z_{c1}$ and $Z_{c2}$.

$$u_2^T [m]_x M_{21}M_{11}^{-1}u_1 = 0 \tag{6}$$

For a determined $u_1$ let $e = M_{21}M_{11}^{-1}u_1 = [e1 \quad e2 \quad e3]^T$ where e1, e2 and e3 is the x-component, y-component and z-component of e respective. According to the property of antisymmetric matrix there is a component equation for a given point in formula (7) .

$$(mx2 \cdot e3 - mx3 \cdot e2)x + (mx3 \cdot e1 - mx1 \cdot e3)y + (mx1 \cdot e2 - mx2 \cdot e1) \tag{7}$$

**The double epipolar lines approach.** Suppose there are three images denoted as α, β and γ and their calibration matrix is $M_1$, $M_2$ and $M_3$ respective.

Let $m1 = [mx11\ mx12\ mx13]^T = M_{22} - M_{21}M_{11}^{-1}M_{12}, m2 = [mx21\ mx22\ mx23]^T = M_{32} - M_{31}M_{11}^{-1}M_{12}, m3 = [mx31\ mx32\ mx33]^T = M_{32} - M_{31}M_{21}^{-1}M_{22}$.

So the epipolar equations become

$$u_2^T [m1]_x M_{21}M_{11}^{-1}u_1 = 0 \tag{8}$$

$$u_3^T [m2]_x M_{31}M_{11}^{-1}u_1 = 0 \tag{9}$$

$$u_3^T [m3]_x M_{31}M_{21}^{-1}u_2 = 0 \tag{10}$$

Where $u_1$, $u_2$ and $u_3$ is the homogeneous coordinates of $P_1$ in plane α, of $P_2$ in plane β and $P_3$ in plane γ respective and $u_1 = [x_1 \quad y_1 \quad 1]^T, u_2 = [x_2 \quad y_2 \quad 1]^T, u_3 = [x_3 \quad y_3 \quad 1]^T$.

There are six unknown variables in the epipolar equations set (formula (8)-(10)) which has three explicit relations. It is impossible to solve this equation set by analysis. But it is a case in reality that how to find the responding points in the other images while a curtain point in a plane is given. So without lose generality a random point $P_1$ is given in plane α and its responding point $P_2$ in plane β and $P_3$ in plane γ must lie in their epipolar lines.

Let $e1 = M_{21}M_{11}^{-1}u_1 = [e11 \quad e12 \quad e13]^T, e2 = M_{31}M_{11}^{-1}u_1 = [e21 \quad e22 \quad e23]^T, e3 = M_{31}M_{21}^{-1}u_2 = [e31 \quad e32 \quad e33]^T$, so $P_2$ satisfies the epipolar lines of plane β which is in formula (11)

$$(mx12 \cdot e12 - mx13 \cdot e12)x_2 + (mx13 \cdot e11 - mx11 \cdot e13)y_2 + (mx11 \cdot e12 - mx12 \cdot e11) = 0 \quad (11)$$

$P_3$ satisfies the epipolar lines of plane γ which is in formula (12)

$$(mx22 \cdot e22 - mx23 \cdot e22)x_3 + (mx23 \cdot e21 - mx21 \cdot e23)y_3 + (mx21 \cdot e22 - mx22 \cdot e21) = 0 \quad (12)$$

On the other hand both $P_2$ and $P_3$ satisfy formula (10).

The formula (10), (11) and (12) make up the epipolar equations set of a given point which has four variables and three explicit relations. So it also has no analytical solutions. Consider $x_2$ and $y_2$ expresses the same point and has an implicit relation. So do $x_3$ and $y_3$. A searching method is used to find the numerical solution. The problem is transformed to: how to find a point P' in plane γ which satisfies

(1)P" is the crossing point between the epipolar line of P' in plane β and the line determined by formula (11).

(2)The given point $P_1$ is just in the epipolar line of P" in plane α.

So the point P' is the responding point $P_3$ of $P_1$ in plane γ and point P" is the responding point $P_2$ of $P_1$ in plane β.

The epipolar line constraint can reduce the potential responding points of a given point in the other image from two dimensions to one dimension. The searching range of P' in plane γ is narrowed to the epipolar line which is in formula (12).

Object: find P' in the epipolar line of plane γ in order to satisfy $P_1 \epsilon l_1'$, where $P_1$ is the given point in plane α and $l_1'$ is the epipolar line of P" in plane α.

s.t. (1) Epipolar lines constrains. e.g. formula (8), (9) and (10)

(2)Visional windows constrains: e.g. $P'\epsilon\alpha$ in $(x_{\gamma min}, x_{\gamma max})$ and $(y_{\gamma min}, y_{\gamma max})$ and $P''\epsilon\beta$ in $(x_{\beta min}, x_{\beta max})$ and $(y_{\beta min}, y_{\beta max})$ where $x_{\gamma min}, x_{\gamma max}$ is the minimum and the maximum of x coordinate in the visional window of plane γ and $y_{\gamma min}, y_{\gamma max}$ is of y coordinate. $x_{\beta min}, x_{\beta max}$ is the minimum and the maximum of x coordinate in the visional window of plane β and $y_{\beta min}, y_{\beta max}$ is of y coordinate.

**Simulation**

Three cameras are used to take photos for interior scenes from different angles. A point $P_1$ in image α is selected and its responding point $P_2$ in image β and $P_3$ in image γ are determined by the proposed approach and the result is in figure 1 in which the selected point $P_1$ is remarked as notation '*' and the responding points $P_2$ and $P_3$ are remarked as notation 'o'.

Fig.1. The result of a given point $P_1$

The results of $P_1$ at different positions are in table 1 in which the manual data are obtained by data cursor of MATLAB after the responding point is determined by visual method and the automotive

data are obtained by the proposed approach. The absolute errors use Eula distances, e.g. $Err_A = |P_{iA} - P_{iM}|$,(i=1,2,3) and the relative errors use the ratios between the absolute errors and the manual data, e.g. $Err_r = \frac{|P_{iA}-P_{iM}|}{P_{iM}} \times 100\%$.

i

Table 1 The results in different $P_1$

| times | | 1 | 2 | 3 |
|---|---|---|---|---|
| $P_1$ | | 98,148 | 151,308 | 248,206 |
| $P_2$ | Manual data($P_{2M}$) | 100,133.6 | 158,278.1 | 208,353.6 |
| | Automative data($P_{2A}$) | 106,127.78 | 158,282.84 | 215,340.27 |
| | Absolute errors （Err_a） | 0.8568 | 4.129 | 7.7371 |
| | Relative errors（Err_r） | 0.51% | 1.29% | 1.89% |
| $P_3$ | Manual data($P_{2M}$) | 109,137 | 158,282.8 | 219,352.4 |
| | Automation data($P_{2A}$) | 106,121.84 | 158,278.1 | 215,339.53 |
| | Absolute errors （Err_a） | 13.5753 | 4.0948 | 13.0281 |
| | Relative errors（Err_r） | 7.75% | 1.26% | 3.14% |

It is seen from table 1 that the maximum of absolute errors and relative errors happens on $P_3$ and its numbers are 13.5753 and 7.75% while the relative errors of other points are below 5%. It means the proposed approach has high accuracy.

**Acknowledgements**
This work is supported by State Key Laboratory of Synthetical Automation for Process Industries.

**References**

[1] Hu Xiaoping, Ahuja, Narendra. *Matching point features with ordered geometric, rigidity, and disparity constraints*. IEEE Transactions on Pattern Analysis and Machine Intelligence, Vol. 16, (1994), p 1041-1049.

[2] Papadaki. H, Robson. S, Chapman. D, Woodhouse. N. *Towards the automated extraction of accurate 3D models from close range photogrammetric networks*. Proceedings of SPIE-The International Society for Optical Engineering, Vol. 4309 (2001), p 267-277.

[3] Jiang Zetao, Chen Zhongxiang, Zheng Bina, Wu Min. *A kind of 3D reconstruction method based on affine transformation*. 3rd International Conference on Genetic and Evolutionary Computing, (2009), p 358-361.

[4] Chua Chin-Seng, Ho Yeong Khing, Liang Y. *Rejection of mismatched correspondences along the affine epipolar line*. Image and Vision Computing, Vol. 18 (2000), p 445-462.

[5] Sagüés. C, Murillo. A.C, Escudero. F, Guerrero. J.J. *From lines to epipoles through planes in two views*. Pattern Recognition, Vol. 39 (2006), p 384-393.

[6] Shahid Shafiq. M, Turgut Tümer. S, Cenk Güler. H. *Marker detection and trajectory generation algorithms for a multicamera based gait analysis system*. Mechatronics, Vol. 11 (2001), p 409-437.

[7] Zeng Jie-Xian, Yu Sheng, Fu Xiang, Li Chao-Xia. *A line segments matching method based on epipolar-line constraint and line segment features*. Journal of Software, Vol. 6 (2011), p 1746-1754.

[8] Yuan Jianying, Liu Xianyong, Qiu Zhi Qiang. *A robust feature points matching algorithm in 3D optical measuring system*. Advanced Materials Research, Vol. 383-390 (2012), p 5193-5199.

[9] Yen Jou-Yu, Chen Liang-Chien. *Line matching from multiple aerial images for building reconstruction*. ACRS 2012, Vol. 2 (2012), p 1279-1285.

[10] Sha Yuejin, Cheng Disheng, Zhang Xiaoqin. *Determination of homonymy points' local interval in image matching based on epipolar line constraint*. Journal of Southeast University (Natural Science Edition), Vol. 43 (2013), p 283-285.

*Applied Mechanics and Materials Vols. 580-583 (2014) pp 3223-3226*
*© (2014) Trans Tech Publications, Switzerland*
*doi:10.4028/www.scientific.net/AMM.580-583.3223*

# The soft soil foundation consolidation numerical Simulation based on the model of modified cam-clay

Xiaojie Gu[1, a], Taiquan Zhou[1,b] and Song Cheng[1,c]

[1] School of Environment and Civil Engineering, Jiangnan University, Wuxi, China, 214122

[a]xgyx2007@126.com, [b] 846158321@qq.com, [c] 1005733514@qq.com

**Keywords:** abaqus embankment, the soft soil foundation, consolidation and settlement

**Abstract** The clay layer finite element analysis model , which is established by using finite element program to simulate the embankment filling , takes the intercoupling between water and clay in drainage consolidation process into full account. The use of the effective stress principle consider the characteristics of clay such as nonlinerity , large deformation and so on ,carry out the plane strain finite element analysis on the clay and solve a series of engineering problems.

## Introduction

The subgrade filling for expressway is a preloading process. Studying and analyzing the development regularity and mechanism of settlement after preloading is of great significance to ensure the expressway security and improve the economic benefit of the expressway.

Some bad engineering geological condition soft clay often occurs in expressway subgrade construction. Because the soft clay has large void ratio, high natural moisture content, low strength, high compressibility, low permeability, long duration of consolidation deformation, etc.. The soft clay roadbed settlement often be calculated by using the method which recommended by the present code of highway soft foundation. The finite element method develops more and more quickly in recent years.

Finite element method can consider the complex boundary conditions, the nonlinear stress-strain relationship of soil, the soil stress history and stress on water and the skeleton of the coupling effect, can consider the interaction of soil and structure, soil anisotropy, also can simulate the scene of loading step by step, can consider the influence which exerted by lateral deformation and the three dimensional seepage on settlement, and can calculate the changes of settlement, horizontal displacement and pore water pressure and effective stress at any time.

This topic research the two kinds of elastic-plastic constitutive model (Mohr - Coulomb model, Cam Clay model), using large-scale finite element software ABAQUS to carry out the numerical simulation of pilot projects, through the contrastive analysis between the measured results and the results of the calculation of two kinds of constitutive model, studies the applicability of the finite element method for soft soil foundation settlement, so as to further guide the practice and guide the construction.

**1.1 Introduction of ABAQUS.** ABAQUS is one of the strongest large general finite element software in the world which contains a wealth of unit model, material model and the analysis process. It can control the very complex problem and simulate highly nonlinear problem. .It has good applicability for the highly nonlinear character of the rock and clay .The excellent analysis and simulation of complex systems reliability of ABAQUS makes the ABAQUS play an important role in a large number of high-tech product research .

**1.2 Cam-clay model.** Cam—Clay model is set up by the British Roscoe and his colleagues at the university of Cambridge .It is a typical clay elastoplastic model, the model adopts the elliptic yield surface and the adaptive flow criterion, and uses the plastomer strain as the hardening parameter .This model is widely accepted and applied in the world.

(1)Yield surface: such as Fig.1 the yield surface function in ABAQUS is slightly different from the expression of soil mechanics by contrast, but the essence is the same. The M in formula is critical state line (CSL), a is an ellipse with CSL line size of the intersection of p.β is the parameters to control the shape of yield surface , in the side of the $t > M_p$ β = 1;In $t < M_p$ side, β cannot equal to 1, affect the yield surface shape.

$$\frac{1}{\beta^2}\left(\frac{p}{a}-1\right)^2+\left(\frac{t}{Ma}\right)^2-1=0$$

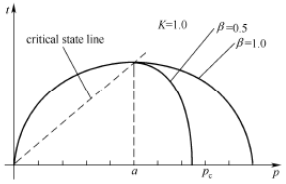


Fig.1 Yield surface

2) The plastic potential surface.Cam Clay model USES the associated flow rule, namely the plastic potential surface is the same as the yield surface

(3) Hardening rule.In ABAQUS, when the β is not equal to 1, $a = p_c / (1 + beta)$, when the β = 1, $a = p_0/2$.

## ABAQUS model

**2.1 Model overview.** Finite element calculation area as shown in figure, along the embankment centerline take 1/2 model as the calculated area, as shown in **Fig. 2**.A 1.8-m-high embankment found on a 4.57-m-thick clay layer, underground water and clay surface are in one place.Below the clay layer bottom is impervious layers, top surface is free to drain.The embankment is constructed in three equal layers, each 0.6 m thick.

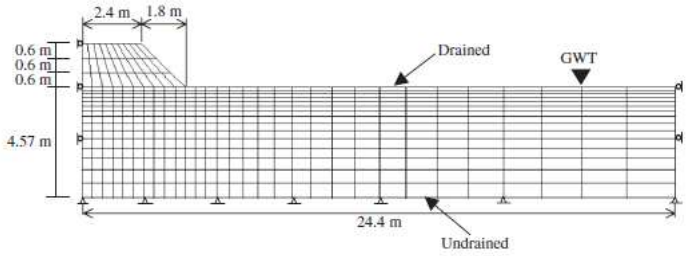


Fig.2 Finite element Discretization of an embankment on a soft foundation

Each embankment layer is constructed in a two-day period, during which consolidation of the clay layer takes place. The total construction time is six days. Assume that the embankment material is linear elastic with ρ = 1923 kg/m3, E = 478 kPa, ν = 0.3, k = 0.1 m/s, and e0 = 1.5. Assume that the clay layer is elastoplastic, obeying the extended Cam clay model (Chapter 2). The Cam clay model parameters for the clay layer are given in Table 1.

Table 1 The Cam clay model parameters for the clay layer

| General | | Plasticity | |
|---|---|---|---|
| ρ (kg/m³) | 1923 | λ | 0.174 |
| $k$ (m/s) | $2.5 \times 10^{-8}$ | Stress ratio, $M$ | 1.5 |
| $\gamma_w$ (kN/m³) | 9.81 | Initial yield surface size = $p_0'/2$ (kPa) | 103 |
| $e_0$ | 0.889 | Wet yield surface size | 1 |
| Elasticity | | Flow stress rate | 1 |
| κ | 0.026 | | |
| $\nu$ | 0.28 | | |

**2.2 The establishment of calculated model.**

1) Definite the model size according to the general situation, establishes the components and use partition function divide the embankment into three layers with the same height. 2) Set up the material and sectional characteristic, set up a Cam - Clay model for clay layer, set up a Mohr - Coulomb model for the embankment layer. 3) Build up member. 4) Define analysis step. Define the type of Geostatic analysis of gravity, this analysis step is used to exert gravity on clay layer .Define three types of soiled analysis step layer1, layer2, layer3, each step time is 2 days, these are used respectively to simulate the load in the process of three layer embankment filling.Define the consolidation step in order to simulate the process of consolidation settlement of clay layer. 5) Define boundary conditions. a. According to survey data, regulate the model with vertical and horizontal seepage , the surface of the foundation is specified for drainage boundary conditions, the bottom of the foundation is specified as undrained boundary. b. Considering the symmetry plane of symmetry subgrade fixed displacement in horizontal direction, it is set to undrained boundary. c. Calculation of right boundary, because the section is far enough away from the roadbed center, it can be set to undrained boundary, and be the fixed horizontal displacement. 6) Define load. 7) Mesh 8) Result

**The analysis of the model calculation results**

**3.1 The analysis of settlement** Figure 3 is the carve of the settlement value in the finite element calculation in the embankment bottom center line changing with time , obviously with the increase of time, settlement increases gradually, and accord well with those of the actual value, the deviation is small.

From the calculated value, the early filling subgrade settlement quantity is big, this because the shape deformation of the saturated soil foundation causes initial sedimentation, and then the settlement stability increases, which reflects the process of the consolidation settlement of foundation. After the stop filling load, along with the soil consolidation gradually completed, the settlement curve changes slow and tends to be stable, this indicates that sedimentation rate became smaller and the subgrade develop in the direction of the stability.

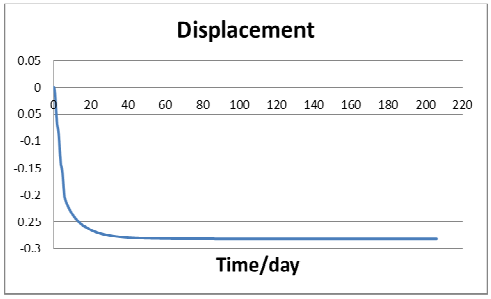


Fig.3 The settlement of embankment

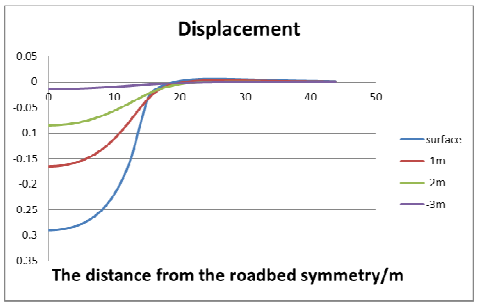


Fig.4 Settlement of different depth

Figure 4 is the different depths of surface settlement curve after the roadbed consolidation settlement. Firstly, the downward settlement of subgrade surface can be seen from the Fig.4 is the largest, but sedimentation increasingly decreases with depth. Secondly, away from the plane of symmetry, the soil has a slightly upward uplift, namely soft soil roadbed settlement within the embankment slope toe is very big, the slope foot outside slightly uplift because of compaction effect.

In the gravity analysis steps , simulate the self-respect through exert physical load on foundation , in analysis steps of layer1 , layer2 and layer3 respectively fill vertical physical load on one, two and three layer , simulate filling process step by step.

**3.2 Analysis of pore pressure.** Fig.5 is the pore pressure of subgrade change over time in 15 days. It can be seen gradually filling 3 layers, pore pressure increasing, after the third layer completed , namely 6 days later, the pore pressure is the maximum in the foundation, especially within the embankment slope toe. But then under the action of vertical force on the load of soil consolidation settlement speeds up, pore water pressure dissipated and the clay tends to be stable.

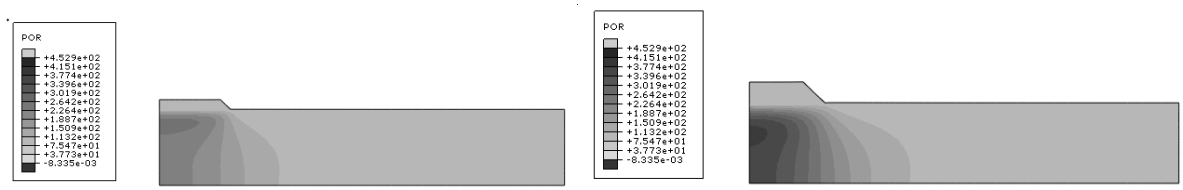


(A) End of constructionof layer 1 elapsed time, 2 days (B)End of construction of layer 2: elapsed time

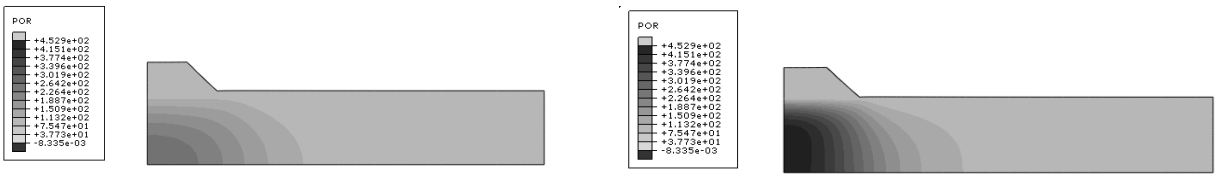


(C) End of construction of layer 3: elapsed time, 6 days (D) Elapsed time, 15 days

Fig.5 The change of pore pressure over time

As shown in figure 6, the change carve of super static pore water pressure in the construction of foundation soil reflects the changes of the super static pore water pressure of soil. We can find that pore water pressure increases quickly as a whole is a first and then gradually evaporate, but there are small fluctuations, this is due to the in the interval of two fill time, the pore water pressure drop because of soil consolidation, but the speed of construction is quick, immediately began the next filling, pore pressure rise again. After the full fill construction, subgrade soil under overlying load to consolidation, the pressure drop with the increase of time, until the consolidation becomes stable.

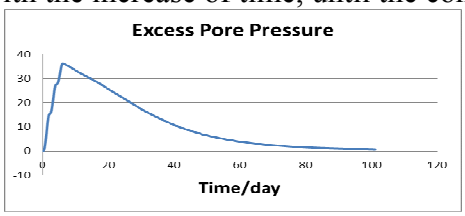


Fig.6 Excess pore water pressure change over time

## Conclusion

(1)Use the finite element program ABAQUS in a successful way, the Mohr - Coulomb model and Cam Clay model are constructed successfully, a numerical simulation is performed for construction of the soft roadbed embankment .Simulate the dynamic subsidence regularity in the process of embankment filling and the settlement size and curve shape, it can guide the construction through calculating feedback.

(2) In the project of embankment fill, there is a great relationship between the super static pore water pressure in soil and the filling rate of construction , the change of pore water pressure in the process of construction is wavy and its change law reflects the process of soft foundation consolidation.

Construction should not be too fast or too quickly in order to prevent the accumulation of excessive pore water pressure which may cause damage in the process of filling subgrade soil.

(3) Clay is a highly nonlinear anisotropic material; we need to carefully and earnestly carry out on-the-spot investigation and measurement, not be superstitious in numerical value and software, reducing the loss of personal property as much as possible

## References

[1] Zhang FeiKang.: *ABAQUS application in the geotechnical engineering*. (Beijing: China water conservancy and hydropower press, 2009) (in Chinese)

[2] Yang YanGuang: Using ABAQUS to calculate the consolidation settlement of soft soil embankment filling process, the modern enterprise culture, 2009 (05) (in Chinese)

*Applied Mechanics and Materials Vols. 580-583 (2014) pp 3227-3230*
*© (2014) Trans Tech Publications, Switzerland*
*doi:10.4028/www.scientific.net/AMM.580-583.3227*

# 3D models as Vista information management governance in the field of development of underground space in cities

V. Belyaev

Moscow State building University RussiaVbelyaev2011@mail.ru

**Keywords:**underground space city, information management, 3D models, 3(D) inventory.

**Abstract.**Consideredespecially the "underground city" in Russia on the example of the three largest cities in approaches to information management governance improvement of spatial development by building 3-d geological and geotechnical models and 3(D) the real estate cadastre.

Due to the fact that underground buildings and facilities (hereinafter CCD) are the objects of capital construction, according to the Russian legislation is regulated within the framework of urban development. The range of these relationships is, in our view, even overly broad to include schema-level interval from the spatial planning of the Russian Federation to the exploitation of a building site. This defines an integrated (sintetičnyj) nature of Russian town-planning and presupposes the existence of effective structures of governance in this area, which for two decades, a return to a market economy has not yet emerged.

"Subterranean town planning" is even more tricky section, because technologically connected not only with traditional land use, but also with the use of underground space (hereinafter-pp). To ensure the effectiveness of the management of this case requires the coordination of a number of federal departments that for Russian conditions it is extremely difficult. For example, for urban planning and design (this is the primary management function) are two different ministries, for land management and cadastre, land use, respectively, two of the Ministry.

Requires the creation of an adequate system of legal, scientific, informational and other types of public administration in this area, which also has not yet been established, for example, legislation in the fields of urban planning and mineral resources requires urgent harmonization, as the most focused solely on mining. However, the special role ofis the information because, as we know, can be thought of as special processing of the information. In urban planning for the information management system of urban development (ISOGD) at municipal level, and it was followed by the Federal spatial planning information system. ISOGD is recreated at the regional level. State Cadastre of real estate is developing in the direction of the technological link to the registry of real property rights. It is planned that all of these systems will be integrated with a single Russian spatial data infrastructure (SDI). However, these systems were essentially a two-dimensional character. At the same time, the PM is, by definition, three-dimensional and the challenges of urban development and protection require the format 3(D). in this connection, in Moscow and some other major cities where the development of PP is the most important issue in pilot mode started work in this direction.

It is essential that in the city of Moscow is tasked to develop integrated automated information system "A geo information space and the works are carried out in the framework of the medium-term public urban programmes" information city "and" town-planning policy. This system within the ideology of SDI is intended, through a common framework to integrate and coordinate the granting of the spatial data contained in information resources of State bodies and organizations of the city of Moscow. Open access to official data already created web application "electronic Atlas. It is also important that the system included data on the territory of the city, presented in three dimensions, covering, including the PM. Tasked with creating a three-dimensional simulation of urban PM and creating three-dimensional digital models of CCD. The main emphasis is on underground engineering communications, and it is only on the territory of the city within the boundaries of the 2011 year.

Meanwhile, in 2012, to Moscow annexed the new territory of almost 1.5 times larger than the old area of the city. In 2014, it should be updated, and as a matter of fact, a new general plan of Moscow. The area of the city was in the engineering-geological terms is well understood, in particular the possibility to build in 2009 year twelve large-scale thematic geological maps. The new territory requires further study, therefore, materials on the master plan for the city to complement the modern 3D modelling estimates. Similar operations recently carried out on European funds, for example, in the Chinese city of Suzhou with the development of a special GIS [1].

Such modelling is proposed as part of the development of GIS "Geology of Moscow», which is to support a specific feature of a 3D model, with level-by-level geological maps in a three-dimensional model rendering fragments of PM [2]. The simulation based on the concept of geological mapping object, which is the subject of a description in the content of the digital model of the geological structure of the territory. With regard to the construction of a 3-d geological model of the PM made the following basic requirements: 1) a description of the geological model elements must correspond to a single stratigraphic scheme; 2) geological boundaries cannot cross, and simulated space must be continuous; 3) build models based on a single, an adapted map database and based on the classification of objects within the model (classifiers, with a list of properties that define the minimal description of objects developed).

Proposed incremental build of several models, based on the fact that specialists in Geotechnics eventually interested in building base of CCD, and watering the soil properties, the presence of dangerous geological processes and phenomena. The geological correlation in the 3D model is solved by applying the method of layer-by-layer geological mapping to a depth of 100 m. in the modeling of geological structure of Stratigraphic sequence and is used in modeling the structure of geological layer sequence indexing locations lithologic strata. Hydrogeological model PP is based on geological 3D model and reflects the spatial location pairs "aquifer SYN.semi-". Engineering geological model PP based on lithological structure that contains data about the properties of rocks and drilling geological processes and phenomena. It is the basis for the creation and implementation of analytical materials and multiple projections (see below).

Digital 3-d geological model of the city and the appropriate software (in this article it is not) allow you to simply and clearly obtain geological information at any point or aspect, by specifying the coordinates. Effective GIS, built on the basis of volume of engineering geological model, should make it possible to assess the risks of interference of the geological environment, built environment, the PLC and the favourableness of the PP for urban design. Methods of evaluating the quality of the test has already been tested in some of the planning works in the central zone of the city of Moscow [2].

At the same time, both for Moscow and other major cities of the country is faced with the task of creating such 3(D)models of both standing and for the entire territory of cities. in tandem with the formation and maintenance of the State Fund for engineering materials and data (GFMiDII) [3] it will give you the opportunity to optimize the many managerial and technical solutions for the development of the territory. that is the direction in the city of St. Petersburg, for example, is devoted to the report of the author of this article, together with e. Lomakin and Alpatov at the international forum «Great Rivers» in May 2014 [4].

Unlike the Moscow program implemented by the Institute of territorial development of three-dimensional models of St. Petersburg until approved. At the same time, in consultation with the Committee for the development of underground space of the National Association of builders has prepared a draft program of work on the creation of different scale models-information base the development of underground space of the BIM technologies. It is extremely important the system approach to the problems of PP on legal, organizational, and information technology (its main provisions discussed below). Emphasis on complexity (both underground and surface objects), as well as on the management aspect of the problem.

The original principle is that planning for the integrated development of PM is only possible after detection of the Geotechnical structure. With detection through the collaboration of full (taking

into account the amount of engineering geological information), multidimensional (3D, 4 d, 5D), multi-scaled (for level of PL for the level region of the city, to the level of a particular object) ongoing integrated geotechnical models (PDGM). BIM models contain descriptions of underground and surface objects (PNS) at all stages of their design, construction and operation.

All construction and calculations are carried out within the framework of specialized technologies. Construction of 3D-PDGM-the under the direction of e. Lomakina information technology maintenance research, design and construction (IT-RPB). Construction of 4 d-PDGM-the software "FEM models» («Georekonstrukcia»), numerically and graphically visualize describing working with geological and PNs. Construction of 5 d-PDGM-in the system and the full multi-dimensional managerial, sociological, and techno-economic models ("system and group projects), vividly describing the interaction of various development projects PP based on subject 4 d-PDGM Description is in terms of operational feasibility assessment of the implications of alternative management and social decision-making.

Using a multidimensional model allows decision-makers to fully document the information and be accompanied by implementation of urban development (GR), planning (PL) and design (ETC). By continually bringing new data that gives the opportunity to create an evolving information environment that enables you to solve problems related to the development and protection of the PP. So on the basis of 3D-PDGM can be the unification of engineering-geological surveys, spatial "coupling" unified information, integration of different scale spatial models. The model 4 d format give Visual spatial images that describe the conditions of alternative design and planning decisions, assessing the completeness and accuracy of the engineering-geological information. This is important not only for the prospector and designer, but for example and for expert. The alkaloids models provide a comprehensive subject, social and technical-economic assessment of the conditions of implementation of specific planning and management decisions on the basis of an analysis of the effectiveness of the terms of use.

Investment attractiveness of the models is the possibility of multiple, multidimensional use. Models are created on the basis of a unified and coherent in the stock information and the results of ongoing surveys (in this respect is crucial, as already indicated, integration with GFMiDII). For unification as well as a system of classifiers in Moscow Engineering-geological conditions of Saint Petersburg. In order to implement the project in the framework of public private partnership filed an application for registration of the specialized private organization as a centre of interaction with the Government of St.-Petersburg, exploration, design, and building community.

One promising application of models would be to create 3(D)the real estate cadastre. Despite this region belongs to the land and property relations, it is closely related to urban development specifically in the context of a single investment and management of the construction cycle and the whole life cycle of the CCD in particular.

When urban development: it's not just about education "flat land", but also on the formation of large immovable objects: hidden underground subsoil areas of EI and State registered in the cadastre and registration of rights deals with the CCD. Meanwhile in Russia, as in other countries the cadastre and registration system is two-dimensional. The problem is the lack of an adequate display underground facilities. For the purposes of the cadastral unit CCD on the land is defined as the set of edges of parts on the surface of the Earth. There are difficulties with the mapping and description of the CCD, in particular non-linear objects. They are often held under several land plots cross each other at different depths. Legal and physical link CCD with an appropriate plot of land is not always obvious, so the principle of accounting and registration of real estate accounting and registration of rights to the land doesn't always work. In market terms, it does not give sufficient guarantees to owners, is less secure, is controversial and the courts (usually the PLC are the most complex, expensive and often dangerous objects with significant service life).

Respond to this call, the national cadastre and registration rights. Where there are intermediate, tradeoffs 2, 5 d inventory (Netherlands, Spain, Canada, Australia, Belarus). However, the main trend is to build three-dimensional inventories that maximally meet the specifics of Government underground construction, allowing the record rights and limitations on CCD [5]. The difficulty is

that the main source of information about the 3D objects are land registration documents, and only through the cadastral map you can view and check vertical borders and giving juridical force 3D parcellam has not yet been achieved. However, in some countries, conducted research in this area, improved legislation and standards.

Objective prerequisites for the transition to the model of the three-dimensional cadastre formed and in the cities of Russia in 2010-2012, the inventory Agency and Rosregister registration of land and cartography of the Netherlands took place on the territory of the city of Nizhny Novgorod, a joint pilot project for the establishment of model 3(D)real estate cadastre, including with respect to several types of CCDS. The Russian Government has set the task of creating, legislative and organizational-technological fix to 2018, the possibility of amending the State real estate cadastre of real estate object information to the description in the 3D space [6].

## Summary

The experience of the three largest Russian cities shows that the use of 3D models is a key area for improving information management governance in the field of development of underground space.

## References

[1] http://infoscience.epfl.ch/record/188099.

[2] A. Antipov, v. Belyaev, m.n. Buchkin, B.v. Potapov to create a 3-d model of the underground space of the city of Moscow.Magazine "town planning", Russia (2014).No. 1.pp. 70-78.

[3] http://www.iziskately.ru/download/office_(d)8bb62(c)75faae1aade683(f)6459aed475.pdf.

[4] http://www.yarmarka.ru/content//2014velikie_reki/program.html?exhib= 114.

[5] V. Belyaev, v. Romanov *experience and prospects of application of 3D cadastre in the management of urban underground space development.*Journal of property relations in the Russian Federation, Russia(2014).No. 1.pp. 53-76.

[6] http://government.ru/media/files/41(d)4(d)1071886(c)943ddd4.pdf.

*Applied Mechanics and Materials Vols. 580-583 (2014) pp 3231-3233*
*© (2014) Trans Tech Publications, Switzerland*
*doi:10.4028/www.scientific.net/AMM.580-583.3231*

# Using CAD for selecting different ACS engineering systems of buildings and structures in the presence of interference and restrictions

Volkov Andrey, DSc, prof., Rector of MSUCE [1],

Sedov Artem, Ph.D., Head of the Intelligent Systems Laboratory[2],

ChelyshkovPavel, Ph.D., Head of the Information Systems in Construction Laboratry[3], Doroshenko Anna, Ph.D.[4]

Russia, Moscow, Moscow state university of civil engineering, Yaroslavskoeshosse 26

[1]volkov@mgsu.ru, [2]sedovav@mgsu.ru, [3]chelyshkovpd@mgsu.ru, [4]pochta.avd@gmail.com

**Keywords***:* CAD, Automations, Building Management Systems, ACS.

**Abstract.**The complexity of modern design objects, especially automatic control systems (ACS), the constant tightening of requirements for projects, the very high price of erroneous design decisions are inconsistent with the traditional tools of technology and design. A way out is to develop and implement a new set of tools - tools of the designer - computer-aided design.

In developing the ACS engineering systems of buildings and structures we should take into account the real (non-idealized) physical characteristics and the nature of its elements, their sources of energy, forms of energy conversion methods and signals inclusions control actions. In the design and manufacturing techniques become essential assembly operation and harmonization of various design and technological forms of individual devices. Designing control systems associated with the development, both the hardware and algorithmic and software that greatly expands the range of issues addressed by designers compared with the recent past. ACS trials are becoming a major design stage as never succeed in developing concepts to take into account all the special design, technological and physical properties of individual devices in ACS.

Complex dynamics control processes ACS associated with number of reasons:

- heterogeneity of devices and components included in the ACS;
- continuous dynamic process of their functioning;
- multicriteriality conditions of use and performance , with many contradictory criteria (accuracy and stability, reliability and weight and size);
- uncertainty of set parameters and disturbing, might be determined by the presence of not only external but also internal "noise" , the time parameters of devices ACS;
- availability of multidimensional control systems.

Unlike engineering systems themselves, which consist of individual devices, ACS is a system of devices working in the mode of control of these systems engineering. At the same time become very important such project procedures as stability analysis, quality and accuracy of the ACS, the synthesis of regulators, the construction of mathematical models of objects and control of individual devices regulators, mathematical modeling, assembly and docking of individual structural units.

ACS design process engineering systems of buildings and structures can be represented as a system design that unites designers, designers tools, measuring instruments, mathematical models, computer, communications with organizations subcontractors, chief designer and experience aimed at issue satisfies the various requirements of technical documentation for production engineering of ACS systems of buildings and structures under given constraints.

The quality of any project ACS engineering systems of buildings and structures can be expressed as:

$$W = F\left[f_1(z), f_2(z), ..., f_n(z)\right],\ z = \{z_i\}, i = \overline{1,n}. \qquad (1)$$

where $z$ - multitude of design decisions taken in the implementation of project procedures $\Pi = \{\Pi_i\}, i = \overline{1,N}$ ; $F$ - functional quality of the project; $f_1, f_2, ..., f_n$ - functions representing the pro-

ject's quality criteria, which take specific numerical values depending on the values of the argument $z$.

Functions $f_1, f_2, ..., f_n$ and functional $F$ will be specific numerical values after substituting for variable specific design solutions $z^*$ (structures by ACS-tion scheme and the composition of its devices, making the electrical and wiring diagrams and constructive process). The physical meaning of the functions $f_1, f_2, ..., f_n$ can be read $f_1$ - labor contribution on the project, $f_2$ - the project time, $f_3$ - difference between the results from the requirements of the terms of reference of the project and so on.

Total cost of project procedures for creating ACS engineering systems of buildings and structures can be represented as:

$$W = F\left(\sum_{i=1}^{n} a_i f_i\right) \tag{2}$$

where $a_1$ - the price of standard-hour of project procedure $\Pi_i$; $f_i$ - planned complexity $\Pi_i$.

When designing the ACS engineering systems of buildings and structures, we should also take into account the various constraints which can be given as:

$$G(g_1, g_2, ..., g_m) \le G_O \tag{3}$$

where $g_1$ - allowable cost of the project, $g_2$ - the resources of project department, $g_3$ - allowed time of the design, quantity and composition of components and so on. Also, in addition to controlled, controllable factors, which include active agents, we should consider uncontrollable factors. To uncontrollable factors may be included various life situations as short supply of components and materials to the object, absenteeism and tardiness of the project staff, fundamentally unexpected results when tested beforehand unknown tactics of customers and designers in coordination of the terms of reference and more. These uncontrollable factors can be expressed in the following set:

$$\delta = \{\delta_k\}, k = \overline{1, M} \tag{4}$$

Accordingly o this, the ACS system design of engineering systems of buildings and structures can be represented by a model:

$$\begin{cases} W = F[f_1(z), f_2(z), ..., f_n(z)], \\ G[g_1(z), g_2(z), ..., g_m(z)] \le G_O, \\ L\{\Pi_i[t, z_{i-1}(t-\tau_1), \delta(t-\tau_2)]\}, i = \overline{1, N}, \end{cases} \tag{5}$$

where $L$ - the choice operator of both the design procedures $\Pi_i$ and their execution sequence (linear sequence, parallel execution, joint implementation, and so on); $\tau_1, \tau_2$ - the inevitable time-lag necessary to obtain information on the previous design decision $z_{i-1}$ and uncertain factors $\delta$ on the processing of information in the design procedure $\Pi_i$ and making design decisions $z_i$.

System of expressions (5) shows mathematically aspiration designed system to increase its performance criterion in the presence of interference and restrictions.

This article was carried out as part of scholarship of the President of the Russian Federation.

**References**

[1] Volkov A.A., General Information Models of Intelligent Building Control Systems Scientific problem and Hypothesis // Advanced Materials Research (Trans Tech Publications, Switzerland). –Vols. 838-841 (2014) pp. 2969-2972

[2] Volkov A., General Information Models of Intelligent Building Control Systems: Basic concepts, determination and the reasoning // Advanced Materials Research (Trans Tech Publications, Switzerland). –Vols. 838-841 (2014) pp. 2973-2976

[3] Volkov A.A., Chelyshkov P.D., Sedov A.V. Abstraktnaya kharakteristika nadezhnosti (dolgovechnosti)pri vybore optimalnoy struktury sistemy avtomaticheskogo upravleniya v SAPR [Abstract Characteristic of Reliability (Durability) in Selection of the Optimal Structure of an Automatic Control System in CAD]. Vestnik MGSU [Proceedings of Moscow State University of Civil Engineering]. 2013, no. 1, pp. 218—224.

[4] Volkov A.A., Chelyshkov P.V., Sedov A.V. Metodika otsenki effektivnosti raspredelennykh intellektual'nykh sistem upravleniya energopotrebleniem kompleksov ob"ektov v usloviyakh proizvol'nykh ogranicheniy resursov [Methodology for Construction of Distributed Intelligent Power Management Systems Applicable to a Network of Building Facilities in the Context of Arbitrary Limitation of Resources]. Vestnik MGSU [Proceedings of Moscow State University of Civil Engineering]. 2013, no. 5, pp. 220—225.

[5] Chelyshkov P., Volkov A., Sedov A. Application of computer simulation to ensure comprehensive security of buildings // Applied Mechanics and Materials (Trans Tech Publications, Switzerland). – Vols. 409–410 (2013). – pp. 1620–1623.

[6] Volkov A.A. Intellekt zdanij: formula [Intelligence of buildings: formula]. // *Promishlennoye i grazhdanskoye stroitelstvo* [Civil Engineering]. – 2012. – no 3. – p. 54–57.

[7] Volkov A.A, Lebedev V.M. *Proektirovanie sistemokvantov rabochih operacij i trudovyh stroitel'nyh processov v srede informacionnyh tehnologij.* [ Designing sistemokvantov working operations and labor of building processes in the IT environment ] // Vestnik MGSU [Proceedings of Moscow State University of Civil Engineering]. – 2010. – no 2. – P. 293-296.

[8] Volkov A.A., Yarulin R.N. *Avtomatizatsiya proektirovaniya proizvodstva remontnykh rabot zdaniy i inzhenernoy infrastruktury* [Computer–Aided Design of Repairs of Buildings and the Engineering Infrastructure]. // Vestnik MGSU [Proceedings of Moscow State University of Civil Engineering]. 2012. – no. 9. – P. 234-240.

*Applied Mechanics and Materials Vols. 580-583 (2014) pp 3234-3238*
*© (2014) Trans Tech Publications, Switzerland*
*doi:10.4028/www.scientific.net/AMM.580-583.3234*

# The integration of BIM and the reinforcement information expressions

Chao Shen [1, a], Dahua Li [2,b]

[1] ShuShan district, HeFei, ZiYun road 292.

[2] ShuShan district, HeFei, ZiYun road 292.

[a]email:shenchaode369@foxmail.com, [b]email:ldh2006a@163.com

**Keywords:** Building Information Modeling; the reinforcement information expressions; three-dimensional design

**Abstract.** BIM (Building Information Modeling) as a new idea and technology, has been attached more and more attention in architecture and BIM is gradually changing the model of traditional 2D products images and decentralized design of construction process. This paper expounds the method of the integration of BIM and the reinforcement information expressions and its obstacles in the process of realization through the introduction of BIT technology.

## Introduction

As the pillar industry of national economy, construction industry has always faced with problems such as low efficiency, severe resource waste, how to conduct energy conservation and emissions reduction. The improvement of the utilization rate of resources has always been a problem urgently to be solved in the construction industry. Research shows that BIM technology can effectively speed up the progress of project schedule by 10% and reduce rework by around 60%.Therefore, the application of BIM technology is the development trend in the field of construction. With the rapid development of our country's economy, all kinds of complex planar structure of the high-rise buildings sprang up, mand the use of the shop drawing has been beyond the traditional reinforcement information expressions, the development of BIM technology in domestic is in full swing.

## Whate is BIM

What is BIM? The American standard (2006) defined it as follows: "A Building Information Model(BIM) is a digital representation of physical and function characteristics of a facility. As such it serves as a characteristics of a facility. As such it serves as a shared knowledge resource for information about a facility forming a reliable basis for decisions during its life-cycle from inception onward. "that is to say, the Building Information Modeling (BIM), is a physical and functional characteristics of the construction of digital expression, for construction in the full life cycle to provide reliable decision and the reliable information resource sharing platform. It is a data model that based on 3D technology and integrated with various kinds of relevant information in construction project, which is a comprehensive expression of the relevant information about the project. The idea was first proposed by the Autodesk company, whose core is the construction entity of virtual simulation and building highly integrated information. So as to realize the industry of information sharing and collaborative work, which greatly improve the work efficiency and work quality, save resources and reduce energy consumption. BIM modeling is based on construction engineering, which can be used for the whole life cycle of construction projects, including design, construction, completion acceptance, sales, fire safety and so on(as shown in figure 1). The use of BIM technology in the whole life cycle of construction projects, its advantage is mainly embodied in the following several parts:

① The architect can use BIM related software such as Revit 3D modeling to express their design ideas, visualize the preliminary design, and benefit to the parties to communicate and work together.

② In deepening the design stage, the use of visualization can detect collisions, find design errors and omissions conveniencely, so that solve problems before construction.

③ In the construction stage, through integratting mass data of the construction, make use of the basis using of BIM technology to realizing calculation, manage, and sharing information.Such as calculation of quantities, steel sample, tall shuttering lookup, material usage analysis, and other functions. It can quickly find and solve the technical problem may arise, so as to shorten the construction period, save material, reduce the project cost.

④ After completion, by using the as-built BIM model, the project owner can make engineering reform, operation and maintenance effectively.It can avoid defects that the traditional paper-based as-built drawings is not easy to save and unviewable.

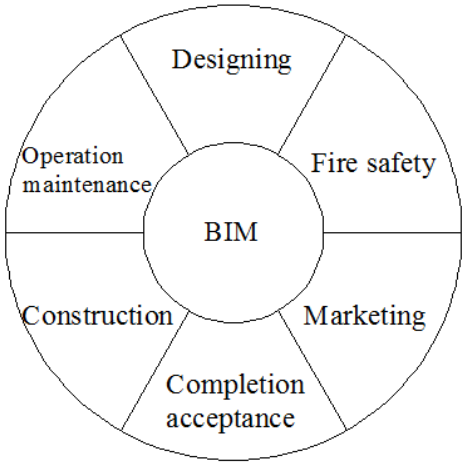


**Fig.1 The application of BIM**.

**The three-dimensional structure design based on BIM**

The three-dimensional model of BIM information not only the geometry information describing building components and status information and its properties, but also includes non-component object state information. All information is closely linked by a certain logic relationship. At various stages of design and even the whole process of project life cycle is around the three-dimensional model of BIM, what's more, it also can constantly modify and join the present stage of information, so that the BIM model can be constantly enriched and perfected.

There is a bidirectional data exchange in BIM model. BIM provides an information sharing and exchanging platform, improving the working efficiency for project participants. For example, when BIM was used to modify the error for three-dimensional design, any operation, together with other relevant information in the process of change can be synchronously processed, which greatly improves the work efficiency, and this is the advantage of three-dimensional BIM design compared with the traditional 2D reinforcement information expressions mapping.

BIM can also be used for simulating the project, making it visualizated. projects will be visualized in the three-dimensional form, such as beam, slab, column and other component connection form of the space. Each structure of the components (reinforcement, space, shape, etc.) can be found in the BIM model by real time, which make it easier for project participants to understand the design intent of the drawings. Construction units can also visually predict construction schedule, safety, and construction plan of the deficiencies, so as to adjust in time. The owner can quickly grasp the latest situations and project information of various project participants through the use of BIM projects.

**The integration of the reinforcement information expressions and BIM**

" the reinforcement information expressions " is the method that make building structure construction drawing expression into a complete set of drawings in the form of graphic design of whole specification, also known as the planar mapping rules of integral representation. It makes the structural working drawing have the standarded plane whole design expression, implementing the national unity of structural working drawing, ensuring the quality of the design and construction.

At present, the reinforcement information expressions still is a common way of construction drawing in building industry of China. Its uniformity and standardization are irreplaceable by other two-dimensional graphics mode. the reinforcement information expressions, with the 2D form, separates graphic symbols of building information with its data, expressing the properties of components succinctly to constitute the structure construction drawing in the form of structure plane as a whole at last. All the information of components are fixed in the whole drawing, making it very difficult to change and update. Lots and lots of work need to be modified one by one by hand, and easily lead to information leakage, error and deviation between the structural drawings. In the design process, the collision check of various professional drawings examination is hard to proceed, thus reducing the efficiency of work. Secondly, the reinforcement information expressions is 2D drawings, which can only presents the surface concrete form of structure layers. When face of complicated structure form, it is not easy to understand and grasp by the parties because its expressing ability is limited,. The Germany pavilion of Shanghai world expo, for example, have complex architectural modeling and spatial relationships, enormous dimension and tight construction schedule. The traditional reinforcement information expressions is obviously unable to meet the requirements. Therefore, the three-dimensional structure drawing of BIM technology is the development trend of current construction drawing.

The traditional reinforcement information expressions goes against the development requirements of BIM, but it is undesirable to completely abandon it accordingly. Thought the reinforcement information expressions is unable to keep up with the development of construction industry era tide, it can not be fully replaced as for all because it is widely recognized by industry as well as unified use according to the development situation of domestic construction industry.

Now many foreign series of BIM software development companies are focusing on "information processing" of the reinforcement information expressions, such as Autodesk Revit software company of American, Bentley MicroStation software company in the United States, Graphsoft ArchiCAD series, etc.

“Autodesk Revit Constructure” is widely used in structure design software of BIM. It is the structural design software based on the three-dimensional model, which can achieve the real time linkage model to modify, provide judge structures connected relations tool, and significantly improve the efficiency of design work. The company of Autodesk has taken the lead in developping the program integrated the reinforcement information expressions and BIM effectively, and includes reinforced symbol of "Chinese localization pack" word stock. The reinforcement information expressions with the fusion of BIM also obtained the further solution. Figure 2 shows the software of Revit Constructure interface after the reinforcement information expressions of flat structure plan (as shown in figure 2) and perspective three-dimensional bar graph (as shown in figure 3).

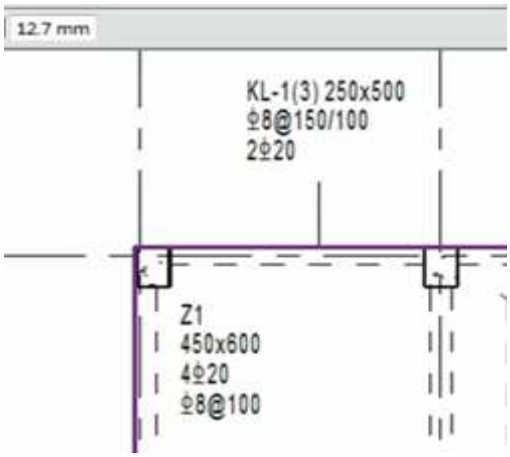


**Fig.2 The reinforcement information reinforced .**

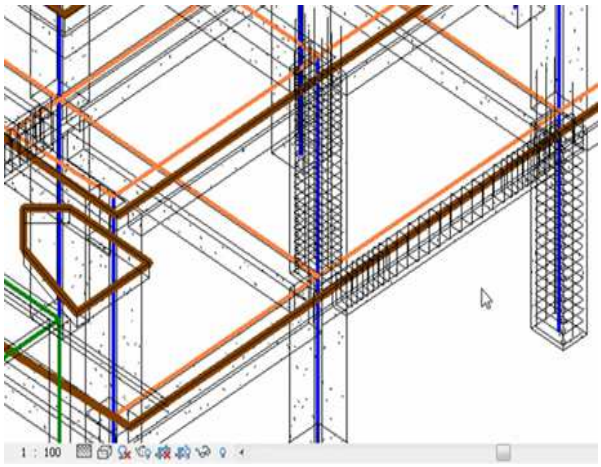

**Fig.3 The three-dimensional viewgraph of expressions expressed by Revit Constructure.**

**Problems of the integration of the reinforcement information expressions and BIM**

At present BIM standard in China is still in the stage of formulation. Compared with foreign architectural industry, China's existing system is not unified and lack of complete BIM standards (CBIMS).To make the reinforcement information expressions perfectly integrate into BIM, improved BIM standards should be developed, making contribute to the traditional reinforcement information expressions to the trend of development to realize the sustainable design.

In the future BIM application practice, more normative regulations should be put forward to divide the responsibility of various project participants. The issues such as design responsibility of each stage, the model information which need to be improved and how much information should have improved are clearly represented. Which kinds of form and the model of the maturity of the interactive data between the parties also need to be clearly defined.

**Conclusion**

The emergence of BIM can be referred to as the second revolution of the construction industry. Because of the unified BIM model, visualization, informatization, collaborative design and construction will be possible. In this new mode, the transition of the traditional reinforcement information expressions to the BIM model is inevitable trend. Therefore, absorbing advantages of the reinforcement information expressions and its information and using computer to digital processing method of standard components will adapt the graphic symbols and data correlation to meet the requirement of BIM viable path. Engineering software developers at home and abroad have tried this method and achieved great effect. But the promotion and application of BIM can not be achieved overnight. The constant improvement of BIM standards in China need to be promoted. At the same time, the joint efforts of the construction industry is also necessary.

**Acknowledgements：**

In 2012, AnHui provincial Natural Science Research Project in colleges and universities (KJ2012Z048)

**References**

[1]Jian-ping Zhang. Building whole lifetime oriented integrated BIM modeling research. Information technology in civil engineering and construction, 2012. “In Chinese”.
[2]Hui-yuan Long. Structure construction drawing method and BIM. Information technology in civil engineering and construction, 2011. “In Chinese”.
[3]Qing-qing Zhao. Flat method based on BIM construction drawing expression. Information technology in civil engineering and construction, 2012. “In Chinese”.
[4] <The Reinforcement Information Expressions Atlas 11G101—l>, China building standard design and research institute, 2011. “In Chinese”.
[5]< PKPM user manual>, 2010. “In Chinese”.
[6]Hai-peng Yin. Based on BIM longyan financial center B3 building structure design in the morning. Chinese architectural design and research institute, 2012. “In Chinese”.
[7]Wen Chen. Based on the design idea of BIM Revit Structure application. Architectural design management, 2012. “In Chinese”.

# Keywords Index


In Situ Test 264, 296
1956-2007 2029
3D Finite Element Numerical Analysis 532
3D Geomat 782
3D Inventory 3227
3D Model 2708
3D Modeling 2760
3D Models 3227
3D Numerical Simulation 3007
3rd Mining Area of Jinchuan 870
3S 2708
4D Model 3192
Contact Problem 2932


## A


ABAQUS 733, 1767, 2228, 3149
ABAQUS Embankment 3223
ABAQUS Finite Element Method 711
Accumulated Rainfall 391
Accumulative 544
Accurate Algorithm 1692
Acid Fracturing 2495
Acid Wastewater 750
Acoustic Cavitation 3098
Acoustic Emission (AE) 623
Acoustic Emission Signal 606
ACS 3231
Activation 851
Actual Distribution of Expenses 2403
Actuators 3158
Additional Bending Moment 474
Adhesion Performance 674
Adhesive Shearing Stress 2912
Adhesive Thin-Layer of Steel Tube/Concrete 2912
Advanced Detection 1649
Aeolian Sand 191, 278
Aging Phenomena 3079
Air Column Interval Charging Structure 2550
Air Conditioning System Energy-Saving Design 2461
Air Cooling 1932
Airport Apron 1197
ALE 2916
Allocation of the Erosion and Deposition Area 1893
Allowable Stress 2000
Ambient Currents 2166
Ambient Temperature 1238
Amplification Effect 1604
Analogue Simulation 1112
Analysis 152, 1218
Analysis and Forecasting 2848
Analysis on BIM Application 3196
Analytic Calculation 579
Analytic Hierarchy Process (AHP) 2658
Analytical Hierarchy Process (AHP) 991
Analytical Solution 560, 3013
Anchor 596, 1223
Anchoring Trench 143
Ancient Timber Structure 1595
ANFIS 566
Anisotropic 243
Anisotropic Bounding Surface 977
Annual Cost 2421
ANSYS 1742, 2224
ANSYS Finite Element Analysis 302
Anti-Arch Dam Segment 2063
Anti-Seepage Measure 552
Anti-Seismic 1511
Anti-Slide Pile 711
Anti-Sliding Stability 2096
Approximate Solution 1803
Approximation Algorithm 1692
Approximation of Operators 2898
Aquifer 1946
ArcGIS 2708
Arch Dam 1812, 1961, 2088
Arch Effect 2074
Architectural Design 3175
ARIMA Model 2082
Arrangement Location 2232
Artificial Boundary Condition 1680
Artificial Seismic Wave 1687
Artificially Frozen Soil 962
ASAR 2824
ASCE No.79 2000

Asphalt Pavement 105, 632
Assembled Composite Wallboard 2299
Assembled Precast Concrete Residence 1755
Assembly Integral Shear Wall Structure 2257
Assignment and Documenting of Models 2281
Asymmetric Coefficient 3115
Atmosphere Boundary Layer (ABL) 3057
Atmospheric Correction 2824
Attenuation 1662
Attenuations of PGAs 1528
Auto LISP 2782
AutoCAD VBA 2760
Automated Analyzer 903
Automated Ventilation System 2480
Automations 3231
Available Water Resources 1906
Average Damage Ratio 1667
Averaging 2898, 2924
Axial Compression Ratio 1759
Axial Load 524

## B

Back Analysis 1072
Back-Analysis from Measured Displacement 395
Baihetan Hydropowerstation 1042
Bailong River 701
Balanced Point Position 78
Ballast Truck 3208
Bank Stability 2071
Bare Frame Structure 1458
Basalt Residual Soil 460
Base Isolation 1776
Base-Isolation Building 1700
Baseline Correction 1528, 1533
Basic Concept of BIM 3196
Basic Law 1888
Beach Evolution 2194
Beach Restoration 2194
Bearing Capacity 113, 165, 415, 655, 746, 3062
Bearing Capacity of Foundation Soil 3003
Bearing Character 572
Bearing Characteristic 302, 432
Bearing Properties 371
Bed Slope Source Term 1793
Bedding Rock Slope 445
BEM 2936, 2943
Bench Method with Reserved Core Soil 1051
Benching with a Small Pilot Tunnel Tunneling Method 1100
Bend Reach 1918
Bending Resistance 2332
Bending Test 2213
Bentonite-Sand Mixtures 359
Bernoulli Beam 2924, 3013
Bichromatic Bi-Directional Waves 2166
Bifurcation Tunnel 983
BIM 3127, 3171, 3175
BIM Technology 1174
Biofilter 2354
Biological Treatment 2354
BiWei Highway 460
Blanking Length 2277
Blasting Construction 1051
Blasting Face 2550
Blasting Parameters 2550
Block 2983
Bolt Support 1335
Bolt Technology 445
Bored Pile 589
Borehole 2558
Borehole Arrays 1604
Borehole Camera 641
Bottom-Business Multi-Story Masonry Structure 1463
Bottom Frame Structure 1676
Bottomland Change 1807
Boundary Conditions 2962
Boundary Problem 2898, 2924, 3013
BP Artificial Network 823
BP Neural Network (BPNN) 1382, 2848
Braced Excavation 524
Braided Reach 1842
Bridge 1555, 2015, 2717
Bridge Area 1883
Bridge Axis Lofting 2842
Bridge Engineering 432
Bridging 2228, 2232
Brittle Rock 260
Brittle Solid 3119
Broken Rock Zone 1321

Bubble Curtain 73
Buckling of Bending 2928
Building 1439, 2253
Building Automation Systems 3204
Building Electrical Design 3179
Building Energy-Saving Design 2461
Building Furniture Store 2642
Building Information Modeling (BIM) 3171, 3175, 3234
Building Management Systems 3231
Building Simulation 3134
Built Environment 3134
Bumps 2572
Buried Pipeline 156, 791
Buried Tube Heat Exchanger 2488
Buttressed Quay 2185

## C

C# Language 291
Cable Anchor Support 1347
Cable Force 2124, 2129
CAD 3179, 3231
Calcareous Sand 268
Calcareous Sandrock 847
Calculation Method 224, 2074
Calculation Model of Value Range 334
Calculation of (Soil) Settlement 98
Capacity Spectrum Method 1600
Capillary Force 2883
CAS Theory 2528
Cascade Hydropower Stations 1864
Cascaded Reservoirs 1953
Cataclastic Rock 971
Catamaran Raft 2170
Caving Goaf 897
Cavity Expansion 405
Cd Method 1051
Cellular Automaton 2663
Cement Fly-Ash Gravel Pile Composite Foundation 518
Cement Mixing Pile 2244
Cement Soil 256
Cemented Sand and Gravel 1846
Central Difference Method 1574
Centrifuge Model 38
CFD 1254, 2415, 2447, 2958
CFD Numerical Simulation 3111
CFS Column 2612
CGCS2000 2793
Chair-Shaped Cataclinal Bank Slopes 2589
Change Rate of Curvature 1382
Channel Bends 3007
Channel Improvement 1966
Channel Regulation Parameters 1870
Character 701
Characteristic Period 1729, 1750
Characteristics of BIM Technology 3196
Checking Parameters 1515
Checking Point 135
Chemo-Mechanical Coupling 386
Chenghe-Second Coal Mine 862
Chinese Ancient Buildings 1759
Chinese Water Resource Management 1856
Choice of Transfer Manner 1402
Circular Cylindrical Cavity 3083
Classification Index 1352
Classification Method 1352
Clay 812, 2974
Clay Minerals 912
Clay Shale 879
Cleanroom 2428
Clearance Convergence 1342
Cluster 2528
$CO_2$ Flooding 2502
Coal 201
Coal Failure 623
Coal Gangue Hill 935
Coalmine Fire 831
Coarse-Grained Soil 93
Coarse Particles Saline Soil 329
Coarse Sands 231
Coastal Levee Construction 2120
Code 3115
Coherency 1570
Cohesion 165
Cold Attic 2308
Collapse 1412, 2717
Collapse Margin Ratio 1763
Collapse Model 1676
Collapse-Resistance Measure 1676
Collapse-Resistant Design 1708
Column-Pile 2962
Combination of Milestones 2294
Combined Load 371
Combustible Ice 376
Combustibles 1238

Comfortable Quality of Vibration 1178
Compacted Loess 185
Compactness 278
Comparison 903, 2654
Compatibility 278
Compatibility Times 278
Complete Quadratic Combination (CQC) 1786
Complex Adaptive 2528
Complex Materials 17
Complex Monitoring 3204
Complex Rocks and Soils 243
Complex Technics 3204
Composite Foundation 38, 302, 2328
Composite Foundation Settlement 669
Composite Foundation with Cement-Fly Ash-Gravel Piles 715
Composite Foundation with Rigid Long and Short Piles 723
Composite Inorganic Fibers 2239
Composite Soil Nailing 83
Composite Soil Nailing Technology 503
Composite Supporting 596
Composite Wallboard 2285
Compound Micro-Polluted Groundwater 2370
Comprehensive Evaluation 1985
Comprehensive Heat Transfer Coefficient 2415
Computation Parameters 2654
Computational Fluid Dynamic (CFD) 2954
Computer Program 2398
Computerization and Intellectualization of Activity and Control over it 2281
Concealed Bracing 1696
Concrete 606, 1092, 1134
Concrete Aggregate 1932
Concrete Cogging 2096
Concrete Constitutive Relation 1564
Concrete Filled Double Skin Steel Tubular 2675
Concrete-Filled Steel Tube (CFST) 2320
Concrete Pouring Sequence 2235
Concrete Temperature 2303
Concrete with Low Longitudinal Reinforcement Ratio 1515
Cone 2872
Cone Tip Resistance 585
Configuration 1458
Confined Compression 185
Confined Space 2667
Confining Pressure 191, 3144
Conglomerate Reservoir 2518
Conglomerate Rock 847
Connecting Passage 2266
Connections 2262
Conservation 2408
Consolidation 123, 160
Consolidation and Settlement 3223
Consolidation Ratio 191
Consolidation Settlement 213, 518
Constitutive Equation of Concrete 2894
Constitutive Model 386, 2134
Constitutive Relation 17, 312, 3075
Construction 539, 935, 2007, 2277, 2797
Construction Applications 1301
Construction Checking 2285
Construction Control 971, 3093
Construction Control Net 2842
Construction Craft 2249
Construction Enterprise 2735
Construction Industry 3175
Construction Mechanics 1192
Construction Method 983, 997, 1100
Construction Monitoring 797
Construction of Buildings 2253
Construction Parameter 2495
Construction Quality 1134
Construction Site 2294
Construction Technology 209, 2266, 2316
Construction Waste 2336
Contact 2916
Contact Element 2932
Contact Oxidation Filtration 2370
Contact Time 2354
Contaminant Extraction 560
Contingency Plan 2346
Continuous Mountains 3111
Continuous Wall 697
Contracted Depth 1803
Contrast Test 48
Control Net 2820
Control Points 2820
Control Standards 1127, 1273

Convection Diffusion Equation 3051
Cooperative Design 1174
Coordinate 2789
Coordinate Transformation 966
Coral Reef 641
Core Rockfill Dam 1852
Correlation 1734
Corrosion 847
CORS 2756
Cost 1174
Countermeasure 2324
Coupling 2936, 2943
Crack 1369, 1377
Crack Aspect Ratio 3026
Crack Propagation 767, 3046
Cracking 1134
Cracking Temperature 2303
Crash Occurrence 2731
Creep Coefficient 355
Cretaceous Formation 962
Crisis Situation 2346
Critical Force 3062
Critical Line 391
Critical Pressure 2920
Critical Sliding Field 755
Critical Slip Surface 291
Critical Temperature 2583, 2702
Cross Section 2731
Cross Section Parameter 464
Crown Settlement 1342
CSFRC 2213
Cubic Spline Interpolation 205
Cultivated Land 2769
Curing Age 450
Curve Fitting 509
Curved Girder Bridges 1723
Cut-Off Wall 1816
Cutterhead 1232
Cyclic Loading 191
Cyclic Loads 2177
Cyclic Pushover 1430
Cyclic Triaxial Test 455
Cylindrical Shell 2920, 2928

## D

D-P Criterion 312
Dam Breach 2990
Damage 606
Damage Demand 2686
Damage Evaluation 2092
Damage Evolution 3119
Damage Identification 1382
Damage Mechanism 1426
Damage of Mortise-Tenon Joint 1595
Damage Ratio 1667
Damage Scenario 2686
Damping 73, 1477, 1564
Damping Effect 1776
Damping Ratio 455, 1776
Dangerous Point 1486
Data Analysis 797
Data Assimilation 1923
Data Processing 509, 1528
DCS 2466
Dead Load 3154
Deamplification 1570
Debris Flow 701, 2722
Deep Biological Wastewater Treatment 2367
Deep Excavation 395
Deep Foundation Pit 28, 440, 636, 787, 1061, 1112, 1249
Deep Horizontal Displacement 636
Deep Soft Ground 296
Deep Splitting Grouting 1197
Defects 1279
Deficiency 1559
Deformation 83, 338, 415, 556, 787, 805, 971, 997, 1143, 1249, 1430, 1511, 2063, 2228
Deformation and Failure of Slope 364
Deformation Characteristic 224, 1297
Deformation Control 636
Deformation Coordination 1092
Deformation Monitoring 2838
Deformation Prediction 2694
Deformation Process 175
Degree of Compaction 68
Degree of Consolidation 774
Degree of Membership 316
Denitrification 2367
Density 93
Depth of the Active Zone 98
Design Builder (DB) 3134
Design Optimization Analysis 715
Design Parameter 118

Design Supply and Return Water Temperature 2432
Design Technique 544
Detector 1223
Development 2007, 2782
Development Factor 919
Development Survey 2363
Deviatoric Stress 3119
Dewatering Design 440
DIALux 1024
Diaphragm Wall 380, 797
Diatomaceous Earth 2380
Different Configurations 2572
Different Sections 1408
Differential-Algebraic Equations 2996
Differential Equations 2962
Diffusion Path 1254
Digital 2745
Dimensional Hillside 2954
Direct Burial Cooling Pipe 2466
Direct Method 1901
Directivity Effect 1499
Discharge 1828
Discrete Element Method 897
Discrete Fracture Network Model 857
Discrete Model 2932
Discrete Points 2872
Discrete Wavelet 2924, 3013
Disintegrating Test 68
Dispersion 1639
Displacement 987
Displacement Ductility 2675
Displacement Field 494, 1327
Displacement Prediction 1264
Displacement Rate 778
Displacement Time Series 436
Dissipation Function 308
Distance 524
Distributed Optical Fiber 572
Distribution Rules 1042
Disturbance Variable 2894
Dl/T 5141-2001 2000
Domain Decomposition 2936, 2943, 3038
Domain Decomposition Method 3071
Dopant Amount 61
Double-Row Piles 596
Double Skin Facades 2415
Downburst 2954, 2958, 3111
Downstream Sinking 1910
Drainage Cushion 2023
Drainage Rate 2558
Drilling Field 2558
Drinking Water 2358
Drinking Water Treatment 2380
Drive Speed 2550
Droplet Size 2508
Duality Disturbance 2966
Dump Landslide 2600
Duncan E-B Model 1940
Dynamic 2778
Dynamic Analysis 1419, 1680, 1704, 3038
Dynamic Characteristic 169, 1467
Dynamic Constitutive Relationship 1435
Dynamic Interaction 1481
Dynamic Mechanism 851
Dynamic Mesh 1494
Dynamic Modulus 455
Dynamic Monitoring 2756
Dynamic Numerical Simulation 1971
Dynamic Prediction 395
Dynamic Propertry 977
Dynamic Response 169, 273, 1122
Dynamic Retention 2518
Dynamic Stress Concentrations 3083
Dynamic Tensile Test 1435
Dynamic Time-History Analysis 1975
Dynamical Analysis 3021

## E

Early Warning Criterion 481
Early Warning System 919, 2120
Earth Dam 954, 2041
Earth Pressure 2074
Earthquake 1676, 1742, 1771, 1975, 2092, 2740
Earthquake Action 1746, 1750
Earthquake Collapse 1708
Earthquake Damage Matrix 1667
Earthquake Ground Motion 1439
Earthquake-Reduction and Seismic-Isolation 1506
Earthquake Simulation Shaking Table Test 1463
Earthwork 2833
Eco-Compensation 1864
Eco-Hydrology 1953

Ecognition Approache 2853
Ecological Revetment 2181
Ecology 2007, 2367
Economic Analysis 2421, 2441
Edge Detection 2805
Effect Analysis of Parameters 760
Effect Coefficient Method 1412
Effective Anchorage Length 129
Effective Range 2508
Efficiency of Vibratory Pile Driving 2272
Egg-Shaped Section 1901
Elastic Modulus 632, 962
Elastic-Plastic 1564
Elastic-Plastic Analysis 1321
Elastic Wave Velocity 847
Elasto-Plastic Time-History Analysis 3149
Elastoplasticity 2966
Elastostatic Problem 3071
Element 2778
Elevation 2797
Embankment 38
Emerge 2528
Emergency 2346, 2679
Emergency Evacuation 1033
Emergency Logistics 2679
Emergency Logistics System 2679
Emergency Preparedness Plan 2346
Emergency Situation 2346
Emergency Water Supply 2346
Empirical Calculation Method 2277
Emulsifier 2524
Emulsifying Machine 2539
End Bearing Pile 1481
Energy 260
Energy Absorption Characteristics 2572
Energy-Dissipation 1545, 1595, 1624
Energy Efficiency 2308, 2403, 2466
Energy Principle 420
Energy Slope 1828
Engineering Application 243
Engineering Behavior 296
Engineering Characteristics 256, 460
Engineering Effects 1842
Engineering Field Test 420
Engineering Mechanics 1192
Engineering Property 409
Enthalpy Method 2452
Entropy Principle 9
Entropy Weight Method 2350
Environment Temperature 2045
Environment Vibration 1153
Environmental Impact 1864
Environmental Impact Appraisal Model 24
Environmental Vibration 1088
Epipolar Lines Constrains 3219
EPS Silt Mixed Lightweight Soil 499
Equivalent Circle Zone 1072
Erosion-Deposition 2189
Error Analysis 589
Estimation on Stability 697
Estuary 2202
Estuary with Sluice 2037
Eurocode 3 2332
Eutrophication 2350
Evacuation 2663, 2740
Evaluating Methods 2441
Evaluation 2350
Evaluation Index 2722
Evolution Characteristics 893
Exact Solution 1559
Example Analysis 1402
Excavated Channels 2023
Excavation Procedure 2011
Exertion of Bearing Capacity 723
Existing Buildings 1782
Existing Pipeline 344
Existing Railway 1218
Expansive Soil 469, 544, 552, 1369
Expected Annual Loss 1763
Experiment and Research 2129
Experiment Research 2124
Experimental Investigation 2103
Experimental Research 2272
Experimental Study 129, 1490
Expert Scoring 2600
Explosion 2916
Explosion Energy 268
Exponential Function Based Interpolation (EFBI) 3051
Exposed Penstock 1975
Exposed Penstock Laid on Ground 2000
Extended Kalman Flter (EKF) 1923, 2635
Exterior Walls 2257
External Wall Insulation 3030

Extra-Dosed Cable-Stayed Bridge 3154
Extreme Disaster 2092
Extreme Earthquakes 1555

## F

Factor of Safety 291, 424
Failure 260
Failure Characteristic 767
Failure Condition 243
Failure Mechanism 415
Failure Mode 544, 601
Failure Process 689
Fatigue Crack Growth Test 3026
Fault Growth 883
Fault Structure 862
Fault System 883
Fault Zone 1184
FCM 2713
FDS 2667
Features 2262
Feed 2354
Feedback 2774
FEM Model 320
FEM Numerical Simulation 1105
FEM Strength Reduction 1419
Fender Pile 787
Fibre Distribution 2213
Fibre Orientation 2213
Field Experiment 579
Field Observations 320
Field Research 1658
Field Test 329
Filling Method 897
Fine Calculation 2833
Finite Element 1358
Finite Element (FE) 56, 395, 697, 782, 1581, 1755, 1852
Finite Element (FE) Simulation 619, 1293
Finite Element Analysis (FEA) 83, 1471, 1645, 2235, 2894, 3030, 3127
Finite Element in Fluid Mechanics 3051
Finite Element Method (FEM) 405, 746, 1001, 1184, 1369, 1961, 1975, 2055, 2108, 2185, 2936, 2943, 3042, 3138
Finite Element Mode 3075
Finite Element Model (FEM) 1723, 3034
Finite Element Modeling (FEM) 2266
Finite Element Numerical Calculation 579
Finite-Infinite Element 1481
Finite Reliability Analysis 1581
Finite-Volume Formulation 1793
Finite Volume Method 1494, 2146, 2990
Finite Water Depth 2166
Fire 2727
Fire Accidents 1029, 1033
Fire Disaster 2583
Fire Fighting System 2374
Fire Hazard 2717
Fire Load 2642
Fire Resistance 2612
Fire Resistance Test 2646
Fire-Resisting Design 2702
Fire Risk Evaluation Tree 2616
Fire Safety 2646
Fire Scenario 2717
Fire Severity 831
Fire Severity Coefficient 831
Fire Smoke 1037
Fishing Port Project 2198
Fissured Stope Hangingwall 283
FLAC$^{3D}$ 24
FLAC$^{3D}$ 238, 2011
FLAC3D 2513
Flammable Gas 831
Flash 2778
Flexibility Matrix 579
Flexible Base 632
Flexible Mattress 1910
Floatation Response 791
Floating Breakwater 2170
Flood Controlling 2015
Floor 2185
Flow around High-Rise Buildings 3057
Flow Characteristic 3167
Flow Filed 2115
Flow Resistance 1932
Flow Structures 3007
Flow Velocity 2015, 2457
Fluent 2150
Fluid Flow 841
Fluid-Structural Interaction 1494
Fluid Structure Interaction (FSI) 1704
Force Analysis 1188

Forced Deformation 2974
Forecast 2810
Forecasting 823
Formation Equipment 805
Formation Mechanism 175
Forming Method 450
Formwork Support 2224
Foundation Bearing Capacity 135
Foundation Design 619
Foundation Engineering 287
Foundation Pit 401, 494, 697, 2289
Foundation Pit Excavation 1001, 1258
Foundation Pit in Soft Soil 474
Foundation Pit Support 539
Foundation Pitdewatering 24
Foundation Reaction Method 2948
Foundation Reinforcement 2328
Foundation Settlement 113, 320
Foundation Treatment 742
Four Bench Cut Method 1096
Fractal 966
Fractal Theory 862
Fractional Dimension 61
Fracture 1168
Fracture Failure 1081
Fracture Mechanics 1377
Fracture Parameter 2495
Fracture Spacing 907
Fracture Storage Layer 349
Fractured Rock 857
Fractured Rock Mass 679, 907
Fractured Surrounding Rock 1364
Fragility 2649
Frame and Shear Wall Structure 1551
Frame Structure 1718, 2579
Free Oscillations 3017
Free Vibration 2879
Freeze Pipe Spacing 738
Freeze under Pressure 48
Freeze without Pressure 48
Freezing Damage 2579
Frequency-Dependent Stiffness 1153
Frequency-Domain Method 1153
Friction 2932
Friction Pile 1096
Full State Function 17
Fully-Grouted Cable Bolts 283
Fully Mechanized Caving Face 1331
Functionally Graded Material (FGM) 2920, 2928
Fuzziness 89
Fuzzy Clustering 2713
Fuzzy Comprehensive Mathematics 1288
Fuzzy Logic 566
Fuzzy Matter-Element Method 1985
Fuzzy Point Evaluation 89

## G

Galvanized Iron Wire 1435
Gas Prsssure 2558
Gasbag 1860
GAT Magnetic Suspension Gyro Station 2828
Gauge Disc Cutter 1232
Generalized Hoek-Brown Criterion 334
Genesis Mechanism 875
Geo-Grid 1419
Geo-Modeling 866
Geocentric Coordinate System 2793
Geodetic Datum 2793
Geographic Information System (GIS) 2769, 2774
Geohazard 923
Geologic Factor 919
Geological Disaster 2708
Geological Engineering 893
Geological Environment 1008
Geological Evaluation 870
Geological Modeling 2983
Geological Structure 971
Geological Survey 641
Geomechanics 98
Geometric Factor 2731
Geometric Form 755
Geometrical Discrete-Equivalent Model 841
Geometrical Nonlinearity 3017
Geometry Characters 883
Geotechnical Parameter 9
Geotechnical Seismic Isolation (GSI) System 1490
Geotextile 338
Geotextile-Reinforced Soil 415
GFRP Bars 420
Ghosting Fire 2667
Girder 2797

GIS 2078, 2350, 2389, 2745, 2749, 2756
Glass Breakage 2702
Glass Curtain Wall 2583
GM(1,1) 1143
GM(1,1) Model 2810
Gob 887
Golf 324
Governing by Nature 1856
GPS RTK 2833
GPS RTK Techniques 2865
GPS Technology 2842
Grade of Risk 2722
Grain Size Distribution 450, 2103
Granary 3196
Granular Flow 3208
Graphic Method 148
Graphing of Civil Engineering 3163
Gravelly Gobi 180
Gravity Dam 1799, 2063, 2092
Gravity Dam-Foundation System 1680
Gravity Head Coefficient 2432
Gravity Similarity 1878
Grey System 1143
Griding Aids 2545
Griding Efficiency 2545
GRNN 264
Groudwater 1906
Ground Explosion 1122
Ground Motion 1499, 1662
Ground Settlement 1072, 1342
Ground Source Heat Pump 2421, 2457
Ground Water 1981, 2694
Groundwater Control 2289
Groundwater Monitoring Technology 1946
Groundwater Pressure 2589
Grouting 1347
Grouting Anchor 129
Grouting Sleeve Connection Technology 2257
GSI 250
GUI 148
Gunary Model 185
Gypsum Mine 324, 897
Gyro-Orientation 2828

## H

Haar Basis 2924, 3013
Hanging Basket 2797
Hanging Wall Effect 1499
Harbor Resonance 2154
Hardening Soil Model 320
Hazard 2649
Hazards Assessment 701
HDPE Membrane 143
Health Diagnosis 991
Healthy Housing 2484
Heat Balance Equation 2308
Heat Exchange Performance 2488
Heat Preservation Benzene Board 2045
Heat Pump 2475
Heat Recovery 2421
Heating 349
Hedonic Pricing 1306
Hematite 2545
Hermit Interpolation 1533
Heterogeneity 767
Hexahedron-Dominant Mesh Generation 2983
High-Density Slurry 231
High Fill Slope 935
High-Formwork 2228, 2232, 2235
High Geostress 260
High-Permeability 2533, 2539
High Permeability Permeate Layer Emulsification Asphalt 2524
High-Pile Wharf 2202
High Pressure Grouting 52
High-Rise Building 1511, 2316
High-Rise Civil Buildings 2616
High-Speed Railway Continuous Girder Bridge 1618
High Steep Rock Slope 532
High-Strength Interfacial Agent 2239
High Strength Piles 38
High-Temperature 2612, 2671
High Temperature Resistant 2320
Highway Slope 729
Highway Tunnel 1377
Hilbert Transform 1734
Hilly Terrain 2567
HJC Constitutive Model 3144
Hoek-Brown 250
Hongyanzi Landslide 2694

Horizontal Alignment 2731
Horizontal Displacement 420
Horizontal Ground Stress 334
Horizontal Load 287
Horizontal Velocity Distribution 1893
Horizontal Vibration 109
Hot and Rainy 940
Hot Dry Rock 349
Hsiao-Ching River Basin 2029
Huangmaohai Bay 1989
Hub Downstream 1883
Human Behavior 2663
Human Comfort 2055
Human Spine 1511
Humidity 674
Hybrid Nozzle 2239
Hybrid Structure 1633
Hydraulic Engineering 1928, 2041
Hydraulic Model 2394
Hydraulic Resistance 2403
Hydraulic Servo System 3158
Hydraulic Structure 1680, 2055
Hydraulics 1901, 2990
Hydro-Junction 1883
Hydrodynamic Impact 2146
Hydrodynamic Load 1812
Hydrologic Cycle 1823
Hydrologic Response 1823
Hydropower Station 2000
Hydrostatic Pressure 2920
Hydrostatic Stress 3119
Hyperbolic Model 651
Hysteresis Curve 1696
Hysteretic Behavior 2675
Hysteretic Characteristic 1506
Hysteretic Curve 1629, 2671
Hysteretic Damping 2978
Hysteretic Energy 1430
Hysteretic Loop 1767
HZM Bridge 2146

## I

Ice-Dam 2308
Ice Pressure 2579
Ice Storage Air-Conditioning System 2441
Ice Storage System 2452
Icicle 2308
Identification 1227
Image Segmentation 316
Immersed Tunnel 1293
Impact Load 623
Impervious Wall 1860
Impingement Component 2572
*In Situ* Shear Test 180
Incidence-Angle of Soil-Nails 83
Increment-Dimensional Precise Integration Method (IDPIM) 2883
Incremental Dynamic Analysis 1763
Indoor Air Quality 2471
Induced Deformations 812
Inductive Test 2213
Industrialized Production 2299
Inelastic Spectra 1600
Inertial Coefficient 1692
Infilled Wall 1545
Infilled Wall Frame Structure 1458
Influence 1807
Influencing Factor 746
Information Management 3227
Information Platform System 2679
Information Value 2658
Informationization 3175
Informatization 2749
Inhomogeneity 812, 2974
Initial Damage of Lining Structure 1311
Initial Geostress Field 334
Initial Static Deviator Stress 191
Initial Tension 1388
Inland Waterway 2181
InSAR 2824
Instability 38
Instability Mechanism 750, 805
Installation Forms 1081
Instrumental Constant 2828
Intake Tower 1742
Integrated Documenting 2281
Integrated Waste Water Treatment 2354
Intelligent Building 3204
Intelligent Monitoring 3204
Intensity 2253
Intensity of Work 2294
Interbedded Drift Angle 1755
Interface's Mechanical Behavior 1481
Interfacial Interaction 684
Internal Force 2185
Internal Force Effect 3154
Internal Friction Angle 165
Internal-Melt Ice-On-Tube 2452

Interpolation 2872
Inversion 1799
Investigation 1218
Iron 2370
Irradiation Room 2607
Irrgation Amount 2343
Irrigated Area 2045
Irrigation Channels 1803
Isochronous Curve Method 205
Isual (Infographic) Modeling 2281

## J

Jacked Pipe Pile 801
Jackup 2206
Jerk 1521
Jinping I Hydropower Station 2108
Jinsha River Area 875
Joint 1013
Joint Filler 674
Joint Inclination Angle 610
Joint Regulation and Storage 1981

## K

K-Means Clustering 2082
K<sub>0</sub> Consolidation 355
Karst Area 1008
Karst Tunnel 1288
Keller Equation 3098
Knowledge Innovation 2528

## L

Laboratory Test 499
Labour Force 2253
Land and Planning Management 2749
Land Consolidation Potential 2769
Landform Types 2958
Landslide 391, 544, 819, 923, 2658
Landslide Cycle 927
Landslide Dam 2103
Lao Tzu's Philosophy 1856
Large Building 2289
Large Caisson 2129
Large-Cantilever 1786
Large Cylinders 2074
Large Eddy Simulation 3167
Large-Section 997
Large-Span 1786
Large-Span Roofs 3066
Large-Tonnage Pile 78
Laser Radar Technology 2838
Lateral Displacement 524
Lateral Migration 2232
Lattice Boltzmann Method 3098
Lay-Down Thickness 278
Layer-Penetration Oil 2533, 2539
Layered Settlement 1993
Layout Mode 1024
LCC 2649
Leakage of Reservoir Area 2071
Least Square 1799
Least Squares Support Vector Machine (Ls-SVM) 947
Length of Side Conversion 2842
Leveling Rod 2801
Lévy Walks 3079
Life-Cycle Environmental Load Evaluation Techniques 2244
Life Safety 1029
Lifting 2262
Lighting System Energy-Saving Design 2461
Limestone Cave 52
Limit Analysis 1148
Limit Equilibrium Theory 143
Limit Tensile Strain 2108
Linear Density 219
Linear Density Correction 219
Linear Equation 2894
Linear Searching 3219
Lining 1398
Lining of Tunnel 1358
Lining Split 1019
Linxia Basin 912
Liquid Bridge 2970
Liquid Bridge, Level Set Method 2890
Lithofacies Model 866
Lithosphere 851
Live Load 3154
Load Combination 2000
Load Transfer 118
Local Cubic Law 841
Local Damage 2686
Local Structural Analysis 2924, 3013
Location 2797
Loess Cavity 1358
Loess Landslide 927

Loess Plateau 927
Loess Region 78
Loess Tunnel 997
Logistic Curve Function 486
Logistic Curve Model 651
LOI 903
Long Distance and High Lift Water Delivery 1874
Long-Span Tunnel 983
Long Spiral 1301
Long Wave 2154
Long-Wave Irregularity 1273
Looping 2403
Loose Rockmass 1096
Lop Nor 180
Love Wave 1639
Low-Cycle Fatigue 1426
Low Cyclic Load 1624
Low-Frequency Vibration Isolation 2978
Low Mix Additions 256
Low Permeability Reservoir 2883
Low Pr Number Fluid 2970
Low Strain Method 589
LS-SVM 1264
LSSRLI-1 1559
Lumped Mass Method 1910
Lushan Earthquake 1499
Lushan Ms7.0 Earthquake 1528

## M

Macroscopic Property 767
Magnification Factor 1729
Main Drive Sealing 1081
Main Form of Structure 503
Main Powerhouse 2055
Main Principle 503
Maintenance 2389
Manganese 2370
Mantle Convection 851
Marine Environment 2115
Marine Geotechnical Medium 268
Marine Sediments 376
Maritime Work 2774
Markov Chain 436, 1264
Markov Model 2649
Masonry Infilled Wall 1746
Masonry Structure 1486, 1629
Mass Concrete 2324
Mast 3089
Material and Technical Resources 2253
Material Parameter 1799
Mathematical Expectation 2432
Mathematical Model 1989
MATLAB 148
MATLAB Technology 1116
Matric Suction 514, 705
Matrix Displacement Method 3042
Maximum Deviation Point 205
Maximum Dry Density 278
Maximum Length 2466
Mean Spacing 219
Measure 2249
Measurement 2789
Measurement Area 1024
Measuring 2820
Mechanical Characteristic 1910
Mechanical Mechanism 556
Mechanical Model 628, 2589, 2912
Mechanical Parameters 250
Mechanical Performance 2702
Mechanical Property 376, 1188, 2583
Mechanical Strength 879
Mechanical Test 958
Mechanics 883
Mechanics Analysis 1279
Mechanism 283
Mechanism of Action 2545
Mechanism of Cumulative Damage 1311
Mesh 1564, 2872
Mesh Functions 2898
Mesh Mapping 2983
Meso-Scale Simulation of Concrete 2907
Mesoscopic Model 1168
Method of Extended Domain 2898
Method of Limit Equilibrium 364
Metro 1088, 1297, 1301, 1412
Metro Station 1013, 1061
MGM (1, n) Model 669
Micro Pile 544
Micro-Pressure Inner Loop Reactor 2050
Micro Seismic Activity 2978
Micro-Seismic Monitoring 156
Micropile 887

Microstructure 213
Mid-Span Deflection 464
MIDAS GTS 1112
Midas/Gen Procedure 1786
Middle Reaches of the Yangtze River 1807
Middle Route Project of SNWT 2023
Middle Wall 1188
Middle Water Tank 2374
MIKESHE 1823
Mild-Slope Model 2154
Mild Steel Dampers 1767
Mining Engineering 324
Mining Roadway 1331
Minor Earthquake 1515
Mitigation of the Tributaries Confluence 1953
Mixed Finite Element Method (FEM) 3017
Mixed Time Integration 3038
Mixture and Agitation 3167
Mixture Model 2050
Mobile Triangle Method 2860
Mobility 2253
Model 1203, 2745
Model Base 3163
Model Experiment 693
Model Pile 3106
Model Test 109, 113, 371, 655, 3106
Modeling 123, 2628, 3163
Modeling Software 3171
MODIS 2824
Modulus of Elasticity 105
Mohr- Coulomb Yield Condition 195
Moisture Balance Method 359
Moisture Content 68, 409
Moisture-Elasticity 812, 2974
Moisture Transfer 812, 2974
Mold-Unloading-Lifting 2285
Monitoring 320, 787, 954, 1249, 1993, 2194
Monitoring Analysis 636
Monitoring and Measuring 1297
Monitoring and Prediction 623
Monitoring Measurement 1056
Monitoring System 2120
Monolayer Cable Net 2583
Monte Carlo Finite Element 1398
Monte Carlo Method 907
Monthitoring and Measurement 1127
Monthly Average Decline Range 919
Monthly Rainfall 2019
Mooring 2150
Mooring Manner 2124
Morison Equation 1494, 1692
Morphological Analysis 3051
Motion Equation 1232
Mountainous Freeways 2731
Movable-Bed Model 1878
Moved 2253
Movement 2129
Moving Time Average 3079
MSVR 1227
Mudding Weak Permeability Media 893
Multi-Arch Tunnel 1188
Multi-Modal 1430
Multi-Objective Fuzzy Pattern Recognition 2722
Multi-Parameter Monitoring 2694
Multi-Point Displacement Meter 1321
Multi-Scale Classification 2853
Multi-Variable Control 1521
Multilevel Monitoring Technology 1946
Multiphase Flow 3167
Multiple Mixed Nozzle 2239
Multiple Trains 1178
Multivariate Empirical Mode Decomposition 1734
Mw9.0 Tohoku Earthquake 1533

## N

Narrow Velley 1852
Natural Density 135
Natural Hazard 2628
Natural Ventilation 2447
Natural Vibration Period 1776
Navigation Conditions 1842
Navigation Obstruction 1918
Navigation Security 1883
Near-Fault Pulse-Like Ground Motion 1700
Necessary Width 1918
Negative Skin Friction 693
Negative Wind Pressure 3030
Neighborhood Tunnel 1327
Network Simulation 679
New Air System 2484

New Construction Equipment 1065
New Norm 2277
New Technology 503, 1065
Newmark Methods 2996
Nitrification 2367
No Sand Cushion 585
No.5 Coal Seam 862
Node Connection 2224
Non-Destruction 2220
Non-Embedded Pile-Board Structure (NEPBS) 296
Non-Engineered Building 1667
Non-Equal Time-Interval 1143
Non-Homogeneous Saturated Soil 273
Non-Linear 243
Non-Linear Free Vibration 1388
Non-Pressure Pipes 2384, 2398
Non-Stationary Ground Motions 1734
Non-Structural Components 1609
Non-Unidirectional Airflow 2428
Nondestructive Testing 1223
Nonlinear Analysis 1581
Nonlinear Dispersion Relation 2166
Nonlinear Flow 893
Nonlinear Seismic Response Analysis 1712
Nonlinear Static Method 1782
Nonlinear Time History Analysis 1700
Nonlinearity 3062
Normal Depth 1901
Normal Distribution Analysis 2019
Northern Shaanxi 1906
Nuclear Power Plant (NPP) 2649
Numbering Analysis 1072
Numerical Analysis 287, 552, 1408, 1928, 2134, 2572, 3167, 3208
Numerical-Analytical Calculation Method 2974
Numerical Methods 2898
Numerical Model 2037, 2146
Numerical Modelling 2635, 2978
Numerical Simulation 118, 238, 432, 596, 665, 689, 827, 983, 1019, 1037, 1056, 1061, 1076, 1100, 1258, 1268, 1273, 1297, 1315, 1327, 1335, 1816, 2011, 2023, 2050, 2115, 2150, 2154, 2189, 2447, 2452, 2554, 2667, 2958, 3057, 3089, 3187
Numerical Simulation Method 1392
Numerical Wave 3051

## O

Ocean Tide Model 2141
Offshore Engineering 264
Offshore Oilfield 2206
Offshore Structure 2177
Oil-Water Ratio 2539
Old Bridges 1771
One Dimension 123
Online Measurement 2805
Open-Pit Copper Mine 750
OpenGL 3215
Opening 1443
Opensees 1653
Operation Regulation 2432
Operation Tunnel 1279
Optical Fiber Cable 2266
Optical Fiber Sensor 338
Optimization Design 1961
Optimum Design 755
Optimum Moisture Content 278
Organic Matter 2358
Organisation 2253, 2281
Origin Software 509
Original Rock Stress 1335
Orthogonal States 34
Orthogonal Test Method 1940
Outburst 2558
Over-Shallow-Embedded Metro 296
Over-Thick Steel Tube 2912
Overall Structure Calculation 1551
Overlapping Area 1883
Overload 655

Overload Analysis 2088

## P

P-Velocity 250
P-Wave Attenuation 268
P-Y Curve 287
$P_1$ Wave 1570
Paleoclimate 912
Palygorksite 912
Panel 2202
Paoziling Tunnel 1392
Parallel Algorithm 2907
Parallel Computing 3038
Parameter Tuning 1538
Parameterization 3179
Parameters 2508
Partial Connection Number 1283
Particle Breakage 268
Particle Segregation 2103
Particle Size Scale 1878
Particle Swarm Optimization (PSO) 436, 486
Particle Swarm Optimization Neural Network 1940
Particles Removal 2428
Partition Fitting 2860
Partitioned Methods 2996
Passive Control 1545
Passive Earth Pressure 405
PC Strand 420
Peak Story Drift 1439
Pearl River Estuary 2141
Penchala River 2078
Penetrating Agent 2524
Penetration Depth 2533
Percolation 93
Performance-Based Engineering 1581
Performance-Based Seismic Design 1609
Performance Levels 1609
Performance Requirements 1618
Permanent Constructions 2253
Permanent Displacement 1533
Permeability 201, 659, 893, 2502
Permeability Condition 2524
Permeation Resistance 2524
pH 386
Phase Change Material 3030
Phase of Deformation 940
Phase Velocity 1639
Phenomenological Characteristics 614
Philosophical Reflections 1856
Photocatalysis 2358
Physical and Mechanical Characteristics 1364
Physical Model Test 2198
Pile 693, 1301, 2948
Pile-Anchor System 238
Pile Foundation 113
Pile Inserting and Pulling 2206
Pile Side Displacement 733
Pile-Soil Dynamic Interaction 109
Pile-Soil-Foundation 628
Pile-Soil Interaction 715
Pile Stiffness 524
Pile Ultimate Bearing Capacity 2206
Piled Raft 3
Pillar 897
Pipe Roof Protection 1096
Pipeline Manufacturing 2363
Pipelines Network 2384
Plane Problem 2974
Planning 1174
Plant 34
Plastic Concrete 1816
Plastic Flow 851
Plastic Zone 195, 997
Platen Method 1081
Platform on Piles 344
Plaxis 320
Plaxis 3D Foundation 3
Plunge Pool Slab 1897
Point Cloud Data 2838
Point Guiding Alignment 2789
Point Load 958, 1116
Poisson Random Distribution 312
Pollutant Concentration 2471
Polymer 2518
Pore-Air 160
Porosity 893, 1932
Porous Media 1570
Porous Scaffold 2903
Positioning 2129
Positioning System of Anchor Piers 2865
Post-Earthquake 991
Post-Fire 2675
Post-Grouting Filling Pile 572

Post-Peak 610
Power Consumption 2457
Power-Law Waiting-Time Distribution 3079
Power Spectral Density (PSD) Analysis 1742
Pre-Anchoring 283
Pre-Stress FRP Sheet 2220
Pre-Stressed Reinforcement 1019
Precast Concrete Frame 1645
Precast Fabricated Structure 2285
Precast Shear Wall Structure 1696
Precipitation 2029
Precise Integration Method 1574
Precision Equipment 2978
Precoat Filtration 2380
Preconditioner 2907
Predict-Correct Method 1574
Prediction 669
Prediction Method 264
Prediction Model 61
Predictive Control 947
Predominant Period 1604
Prefabricated 1013, 1443, 2262
Prefabricated Components 2257
Prefabricated Composite Wall 2257
Prefabricated Construction 2299
Prefabricated Frame Joints 1471
Pregnant and Sliding Mechanism 2589
Pressure Appearance Law 1331
Pressure Distribution 2903
Pressure Fluctuation 2055
Pressure Gas and Water 2508
Pressure Gradient 2502
Pressure Grouting 52
Pressure Loss 2403
Pressure Observation 1331
Pressure Pipes 2384
Pressurized Conduit 1828
Prestressed Concrete 3154
Prestressed Concrete Cylinder Pipe 2363
Prevention Measures 2589
Prevention Refuge 2740
Principle of Penalized Least Square 2815
Probabilistic Model 679
Probability Distribution 9
Probability of Collapse 1763
Process Control 395
Processing Status 2336
Production and Transportation 2262
Project Design 1207
Projection Pursuit 486
Protection Range 1258
Pseudo-Dynamic Test of Structures 1574
Pseudo-Spectral Method 3071
PSHA 1662
PSO 1227
PSO-FCM 2713
Pullout Test 684
Pumped-Storage Power Station 3021
Punch-Through Analysis 2206
Punching Pile Construction 156
Pure Electric Vehicles 2475
Pushover 1653
Pushover Analysis 1449, 1591, 1613

## Q

Qinglong Landslide 875
Quadratic Parabola 1803
Quadric Surface Fitting 2860
Quality 2343
Quality Accident 2120
Quality Control 2249, 2838
Quality Defects 1207
Quality Inspections 2120
Quantify Tension 2220
Quasi-Static 2671

## R

Radial Heat Exchange Wells 2488
Radioactive Sources 2607
Radon Transformation 1649
Rail Deformation 3208
Rail Pad 1153
Rail Transit 1065
Railroad Tunnel Engineering 1392
Railway Tunnel 1096, 1207
Rain-Flood Resources 1985
Rain Infiltration 729
Rainfall 391
Rainfall Distribution 2019
Rainfall Intensity 391
Rainstorm Condition 923
Random Sampling 2394
Random Vibration Theory 1439

Range of Light Effects 1024
Rankine Approach 2612
Rankine's Earth Pressure Theory 380
Rapid Characteristic Analysis 1966
Raw Water 2350
Rayleigh-Ritz Method 2879
RC Frame 1712
RC Frame Building 1613
RC Frame-Wall 1467
RCC 2088
Real Estate Management 2765
Real-Time Monitoring 2865
Real-Time System 3215
Reasonable Thickness 105, 632
Rebound 1116
Reclaimed Soil 213
Reclamation 344
Reconstruction 2354
Recovery Ventilation 2480
Recuperation 2480
Recycled Concrete 2320
Red Clay 409
Reduced Order Model 3066
Reduced Wavelet Coefficients 2924
Reflection and Transmission 273
Regional Stress 1042
Regression Analysis 1042
Regular Bridge 1723
Regularization 1799
Regulating Reservoir (Diversion and Storage Reservoir) 1874
Regulation Classification 1207
Regulation Scheme 1883
Regulation Water Level 1870
Regulation Width 1870
Reinforce 2096
Reinforced Band 684
Reinforced Concrete Bridge Pier 1430
Reinforced Earth-Retaining Wall 1419
Reinforced Ground 655
Reinforced Retaining Wall 338
Reinforced Soil Foundation 746
Reinforcement 52, 445
Reinforcement Information Expressions 3234
Reinforcement Measure 1076
Relative Crack Depth 3026
Relative Density 659
Relatively Complete Disturbed Material 2966
Relatively Non-Disturbed Material 2966
Relaxation 2108
Reliability 135
Reliability Analysis 89
Removal Efficiency 2358
Renormalization Group 93
Renovation 2398
Renovation and Expansion Project 827
Replacement 2346
Research Needs 2717
Research Progress 1223
Research Status 1352
Reservoir 2694
Reset 1511
Residential District 2447
Residential Industrialization 2257
Residential Property Value 1306
Residue Pile 302
Resilience-Recompression 518
Resistance Coefficient 2150
Resistance Similarity 1878
Resource Utilization 2336
Response Measures 1138
Response Modification Factor 1449
Response Spectra 1729
Response Spectrum 1687, 1750
Response Spectrum Analysis 1786
Retaining Structure 1112
Retention Capacity 705
Reuse Technology 3179
Reynolds Stress Model (RSM) 3057
RFPA 689
RFPA-Centrifuge 665
Rheological Experiment 509
Rheological Long-Term Strength 205
Rheological Model 320
Rheological Properties 231
Rift 851
Rigid Equilibrium Limit Method 2096
Rigid Polyurethane Foam 2646
Ring-Stiffened Cylindrical Shell 2879
Risk 1412
Risk Assessment 1243, 1782, 2628, 2635
Risk Evaluation Index 2622
Risk Management 1243, 2727
Risk Measurement 1288
Risk Mitigation 2622
Risk Source 1065
Risk Trend Assessment 1283

River and Reservoir Networking 1874
River Network 1923
River Terrace 927
Riverbed Erosion and Deposition 1888
RMR 870
RMS Misfits 2141
Roadbed 469
Roadway 1335
Roadway Surrounding Rock 1352
Rock Anchor Foundation 601
Rock Bolt Foundation 619
Rock Classification 1116
Rock Deformation 1100
Rock-Fill Dam 1940
Rock Fracture 219, 841
Rock Landslides 2589
Rock Mass Hydraulics 857
Rock Mass Integrity 641
Rock Mass Quality Classification 847
Rock Masses Classification 870
Rock Mechanics 879
Rock-Mechanics Model 1398
Rock Parameter 1227
Rock Rheological Mechanics 205
Rock-Socket Pile 432
Rock Specimen 958
Rock Stress 1192
Rock Tunnel 1315
Rocking Isolation 1555
Romanian Seismic Design Code 1600
Roof Covering 2308
Room-and-Pillar Mining 1268
Rotary Drilling Cast-In-Place Pile 2249
Rotational Motion 1639
Rough Model Method 1828
Rough Set 2600
Roughness 2958
Round Hole 2805
RPS2000 1581
Rubber Beam 1629
Rubber-Sand Mixture (RSM) 1490
Ruins 705
Rural Residential Land 2769
Rushan River 1985

## S

Safety 2727, 2740
Safety Economic 2735
Safety Factor 83, 729, 782, 935
Safety Investment 2735
Safety Management 2316
Sag 1388
Saline 2071
Salt Content 329
Salt Expansion Rate 329
Sand 693
Sandstone 386
Sandstone Ground 601
Sandy Pebble Reach 1888
Sandy Soil 113
Sanitary Landfill 143
Saturated Sands 308
Saturation Degree 1570
Saturation Line 1928, 2041
Scattering 3083
Scattering-Filling Rubble Stone Layer 760
Scheme 1203
Seawall 1993, 2134
Secondary Development 3179
Secondary Lining 1105
Section07 866
Sector Coverage 2239
Security 1486
Security Analysis 1019
Security Coal Pillar 2554
Sediment 1989
Sediment Numerical Model 1893
Sediment Transport 2037, 2189
Sedimentation Control 1197
Seepage 729
Seepage Field 1816
Seepage Field Regulations 2023
Seepage Force 614
Seepage-Proofing 2033
Seepage Stability 1928
Segmental Precast Construction 3093
Segmentation 2853
Seismic Analysis 1559
Seismic Bearing 1506
Seismic Behavior 1471, 1696
Seismic Coefficient 1729
Seismic Damage Assessment 1667
Seismic Damage Investigation 1613
Seismic Damage of Bridges 1771
Seismic Design 1551, 1581, 1613, 1759

Seismic Ductility 1696
Seismic Dynamic Response 1494
Seismic Effect 1618
Seismic Fortification Measures 1746
Seismic Issues 1658
Seismic Liquefaction 2071
Seismic Performance 1443, 1458, 1477, 1595, 1629, 1645, 1712, 2671, 2675
Seismic Reduction 1633
Seismic Reinforcement of Bridges 1771
Seismic Resistant Capacity 1463
Seismic Response 1467, 1687, 1700, 1704, 1718, 1723, 3149
Seismic Response Analysis 1755
Seismic Time History Analysis 1486
Seismic Wave 1680, 1718
Self-Anchored Suspension Bridge 1687
Self-Balanced Load Test 78
Self-Centering 1471, 1645
Self-Drilling Type Hollow Bolt 935
Semi-Elliptical Surface Crack 3026
Semi-Parametric Model 2815
Semi-Rigid Foundation 105
Semi-Rigid Joint 2224
Semi-Transverse Ventilation 1037
Sensitivity Analysis 238, 1940
Separated Tunnel 1105
Sequential Quadratic Programming Method 1961
Set-Pair Analysis (SPA) 1283
Setting 2820
Settlement 3, 28, 655, 693, 2810, 2848
Settlement Analysis 518
Settlement and Deformation 61
Settlement Observation 2801
Settlement of Foundation 344
Settlement Prediction 651, 1993
Settlement Trough 1273
Sewer Network 2398
SFRSCC 2213
SH Wave 273, 3083
Shaft Station 1347
Shaking Table 1467, 1521, 1538
Shaking Table Test 1435, 1490, 1776
Shall Large Span Tunnel 1100
Shallow Buried Structure 1122
Shallow Mining Method 1065
Shallow Shells 3062
Shallow Tunnel 1148
Shallow-Underground Cut Method 1051
Shallow Water Equations 2990
Shallow Water Flows 1793
Shandong Province 2082
Shape Memory Alloys 1591
Shared-Node 2916
Sharing "One-Map 2749
Shear Band 175
Shear Bond 2612
Shear Strength 165, 180, 209, 409, 514, 659, 742, 774
Shear Wall 1443
Shear Wave Velocity 264
Shells 3017
Shield 73
Shield Construction 1138
Shield Launching 738
Shield Machine 1081
Shield Machine in Shallow Soil 1197
Shield Method 1013
Shield Tunnel 1001, 1072, 1273
Shield Tunnel Method 987
Shift Line 2513
Ship Model 1918
Shock Absorption 1545
Short Line Method 3093
Shortest Seepage Path 857
SHPB 3144
Shrinkage 705
Shrinkage and Creep Effect 987
Shrinkage Crack 2324
SHTB 3138
Side Detection 1649
Side Friction 432
Side Resistance 801
Sight Instrument 1335, 1347
Siltation Characteristics 2037
Silty Clay 355
Similarity Principle 3106
Simplified Bishop Method 291
Simplified Dispersion Curve 1639
Simulation 2475, 3215
Simulation Analysis 2045

Simulation Model 3158
Simulation Validation 1538
Simulation Vibration Table 3158
Single-Component Multiphase Flow 3098
Single-Layer Cable 2702
Single Pile 287
Site Coefficient 1750
Site Test 742
Skeleton Curve 2671
SketchUp 3163
Sleeve Valve Tube 887
Slender Plate Girder 2332
Slide Surge 2092
Sliding Damping 1629
Sliding Support 1975
Slip Line Method 3003, 3183
Slippage Effects 201
Slope 152, 486, 940, 971, 1718
Slope early Warning System 481
Slope Excavation 827
Slope Monitoring 819
Slope Stability 195, 291, 424, 481, 755, 2289
Slope Stability Prediction 566
Slope Strengthening 129
Slope Treatment 778
Slotting 1860
Slurry-Trench 805
SM Solver 3042
Small Hydropower 2007
Small Samples 9
Small Spacing Tunnel 1254
Smear Effect 560
SMW 1249
SOC Determination 903
Socketed Pile Length 424
Soft Clay 395, 733, 774, 977
Soft Foundation 209
Soft Rock 1347
Soft Rock Roadway 556
Soft Sites 1559
Soft Soil 320, 344, 2328
Soft Soil Foundation 3223
Soft Sub-Grade 651
Software Design 819
Soil 34, 812, 2916
Soil Anchor 401
Soil Clod Analysis 614
Soil-Like Slope 750
Soil Liquefaction 791
Soil Mechanics 98
Soil Models 320
Soil Nailing 596
Soil Nailing Wall 539
Soil Particle Analysis 614
Soil Pressure 401
Soil Pressure Control 1197
Soil Sample 2272
Soil Slope 665, 711
Soil-Structure Interaction 1718, 2948
Soil-Water Characteristic Curve 359
Solid Pier 1515
Soundless Crack 689
Source Material 2778
Sparse Linear System 2907
Spatial Information 2774
Spatial Structure 2408
Specially Shaped Column 1712
Specific Heat 962
Spiral Conveyor Spewing 1138
Spiral Pump Pressure CFG Pile 2244
Spontaneous Combustion 1238
Sport Venues 2740
Spray 2508
Spread Foundation 1555
Spread Regularity 1966
Spring Village 2408
SQL Server 2756
Squeezed Branch Pile 109, 371
Squeezing and Consolidation Composited Technology 2244
SRC Frame-Rc Core Wall 1708
Stability 152, 324, 486, 711, 782, 827, 2235, 3034
Stability Analysis 148, 490, 532, 923, 1419
Stability Classification 1352
Stability Monitoring 778
Stability of Slope 445
Stability of Surrounding Rock 2554
Stages 2253
Stand Column Bulge 474
Standardize 1013
Startup Pressure Gradient 2883
State Equation 2883

State Space Method 2948
Static Adsorption 2518
Static Analysis 2924, 3013
Static-Dynamic Property 1846
Static Load Test 619, 3106
Static Strength 191
Statistical 1398
Statistical Analysis 679
Steam Curing 2299
Steel 2838
Steel Frame 1477, 1624, 1767
Steel Line 2124
Steel Reinforced Concrete Piers 1430
Steel Structure 2583
Steel Tube Filled with Steel Reinforced Concrete Column 3075
Step by Step Analysis 2932
Stereo Vision 2805
Stiffener Rigidity 2332
Stiffness Matrix 1639
Stilling Basin 1971
Stirrup 2277
Stochastic Fracture Network 907
Stochastic Modeling 866
Stochastic Weighted 9
Stope Stability 1268
Stopping Line 2554
Storm Surge 2622, 2628
Story Isolation 1776
Strain 1168, 3187
Strain Energy 175, 2686
Strain on-Site Monitoring 1105
Strain Rate 1435, 1467, 3144
Strain-Stress Curve 3144
Strength 3034
Strength Check 1092
Strength Deduction Method 697
Strength Degradation 1315
Strength Influencing Factors 450
Strength Reduction Factors 1600
Strength Reduction FEM 195
Strength Reduction Method 424
Strength Reserve Coefficient Method 2096
Strength Theory 17
Strengthening 34
Stress 2063, 3062, 3187
Stress and Strain 499
Stress Deformation 1852
Stress Field 1327
Stress Intensity Factor (SIF) 1377, 3026
Stress Release 1056
Stress-Strain Relationship 185
Stress Treatment Measures 2303
Stress Wave Problem 3138
Stretching Fractured Zone 887
Strip Region 3083
Strom Surge 2635
Strong Earthquake 1633
Strong Seismic Records 1604
Structural Analysis 2898
Structural Design 1293
Structural Displacement 1061
Structural Materials 17
Structural Parameter 185
Structural Parameter Optimization 1268
Structural Simulation 3127
Structural Style 2181
Structural Vulnerability 1782
Structure Design 2033, 2579
Structure Monitoring 28
Structure of Soft Soil 774
Structure Reliability 1398
Structured Grid 2990
Stuck Radioactive Sources 2607
Subcycling 2996
Subgrade Engineering 552
Submarine Flexible Pipeline 1704
Submerged Floating Tunnel 1388
Subspace Iteration 2907
Substitutive Fuel 2007
Subway 1033, 1134, 1178, 1203, 2848
Subway Construction 1243
Subway Station 1029, 1249
Subway Tunnel 1153
Subway Vibration 1212
Suction 359
Super Deep-Water Open-Caisson 2865
Super High-Rise 3149
Super-Long Pile 733
Supertanker 2124
Supplementary Pile 52
Support Measure 665
Support of Foundation Pit 697
Support Technology 556
Support Type 1184

Support Vector Machine (SVM) 436
Supporting 539
Supporting of Roadway 1364
Supporting Piles 420
Supporting Structure 401
Surcharge Load 733
Surface Deformation 2513, 2824
Surface-Layer Improvement 585
Surface Mine 89
Surface Morphology 966
Surface Soil 180
Surface Subsidence 24
Surface Velocity 2890
Surface Water 1906, 1981
Surrounding 1100
Surrounding Rock 1321
Surrounding Rock Deformation 1364
Surrounding Rock Pressure 1148
Surrounding Rock Stability 1127
Survey 2642
Surveying Errors 2801
Survival Probability 1763
Susceptibility Zonation 2658
Swell Shrink Mechanism 469
Swing Structure System 1653
Symbols Library 2782
System 2253
System Development 2389
System Identification 1538
System Integration 3127
System Operation 2457
System Parameters 2815
System Simulation 1521
System with Ring Beam and Structural Concrete Column 1486

## T

T-Shaped Soil-Cement Deep Mixing Column 118
Tailing Dam 1928
Tailings 455
Taizhou Yangtze River Bridge 2865
Tall Buildings 2567
TangDao Bay 2115
Tanjiaba Mountain Tunnel 1288
Target Decomposition 2082
Technique Feature 2181
Technologization 2281
Tectonic Movement 927
Tectonic-Stress-Type Mining 2513
Temperature Crack 2324
Temperature Distribution 1932
Temperature Field 738
Temperature Rebound 2045
Tenon-Mortise Joints 1759
Tensile and Shear Load 3046
Tensile Strength 674
Tension Fixture 2220
Terrestrial 3D Laser Scanning 2833
Terzaghi Bearing Capacity of Foundation Soil 3003
Terzaghi Ultimate Bearing Capacity of Foundation 3183
Tether 1388
The Analytic Method 628
Thematic Map 2778
Theoretical Analysis 760
Theory of Linear Elastic Damage 1311
Theory of Saturated Porous Media 169
Thermal Channel 2415
Thermal Conductivity 2045
Thermal Performance 2415
Thermocapillary Convection 2970
Thermodynamics with Internal Variables 308
Thick Transferring Plate 1551
Thick-Walled Shell 812, 2974
Thickness 98
Thickness-Diameter Ratio 715, 723
Thickness of Cushion 723
Third-Order Theory 2166
Three Dimensional 2198
Three-Dimensional (3D) Modeling 2765
Three-Dimensional Design 3234
Three-Dimensional Reconstruction 3219
Threshold 316
Tianjin Subway 1112
Tidal Current 1989
Tidal Prediction 2141
Timber Structures 1759
Time-Dependent Deformation 1315
Time Effect 2041
Time-Frequency Analysis 1734
Time-History Analysis 1458, 1564, 1591, 1624
Time-History Method 1687
Time Sequence 823
Time to Ignition 2607
Time-Varying Effect 987

Tip Resistance 801
Tissue Engineering 2903
Tomato 2343
Topographic Effect 1499
Topographic Map 2782
Tornado 2649
Total Station 2789, 2820
Tower Crane 3034
Tower Foundation 490
Traditional CAD 3171
Traditional Dwellings 1658
Traffic Engineering 1402
Transfer Station of Subway 1402
Transfinite Structure 1786
Transfixion Joint 610
Transformation of Open-Pit to Underground Mining 364
Transmission Line 490, 601, 2789, 3115
Transmission Tower 2654
Trapezoidal Shaped Conduit 1828
Treating Techniques 1207
Treatment 469
Treatment Plants 2354
Treatment Plants Reconstruction 2367
Treatment Program 1254
Trenchless Renovation 2384
Trenchless Technologies 2398
Trend Analysis 2029
Tri- Parameter Method 2948
Triangle 2872
Triaxial Apparatus 514
Triaxial Compression 3119
Triaxial Drained Creep Test 355
Triaxial Test 376, 409, 879
True Triaxial Stress State 312
TSC Pile 464
TSP203 1412
Tugging 2150
Tunnel 1008, 1168, 1184, 1342, 1408, 2828
Tunnel Collapse Treatment Technique 1161
Tunnel Construction 1127, 3215
Tunnel Construction Management 3192
Tunnel Deformation Analysis 1264
Tunnel Disease 1218
Tunnel Displacement 1258
Tunnel Engineering 983, 1105, 2011
Tunnel Fire 1238
Tunnel in South China 991
Tunnel Intersection 1076
Tunnel Lighting Experiment 1024
Tunnel Lining 1019
Tunnel of High Railway 1311
Tunnel Portal 1096, 1279
Tunnel Surrounding Rock 1116
Tunneling 1192
Tunneling Machine 1232
Turbidity 2380
Turbulent Flow 1828
Two-Dimensional Beam 169
Two-Dimensional Finite Element 2134
Two-Dimensional Landslide Model 947
Two-Parameter Liner Reciprocal Function 185
Two-Phase Flow 2883
Type 2408
Typical Masonry Building 1486

## U

U-Type Canal 2033
Ultimate Bearing Capacity of Foundation 3183
Ultimate Displacement 1759
Ultimate Flexural Capability 464
Ultimate State 1555
Ultimate Uplift Bearing Capacity 601
Ultra-High-Rise-Building 2374
Ultra-Low Temperature 2475
Ultra-Soft Ground 56
Ultra Soft Soil 585
Ultrasonic Test 1335
UMAT Subroutine 977
Unascertained Evaluation System Design 2616
Uncertainty Analysis 954, 2177, 2394
Uncertainty Correction 1662
Underground 2667
Underground Building 494
Underground Continuous Wall 224
Underground Engineering 1061
Underground Engineering Structure 1382
Underground Garage 1369
Underground Mining 324
Underground Pipeline 1283
Underground Powerhouse 3021

Underground Space City 3227
Underground Station 1174
Underground Water 1369
Underpass 1056
Underwater Blasting 73
Underwater Vibrating Compaction 760
Uniaxial Compression 610
Uniaxial Compressive Strength 958
Uniform Magnetic Field 2970
Unilateral Constraints 2932
Unit Decomposition Principle 3071
Unlayerd Soil 123
Unloading Loose 940
Unsaturated Loess 68
Unsaturated Soil 160, 514
Unsteady Flow 1966
Uplift 1001
Uplift Force. Power Spectrum 1897
Urban Rail Transit 1306
Urban Traffic Link Tunnel 1037
Urban Tunnel 1051
Utilization Efficiency 1985

## V

Vacuum Preloading 56, 209, 585, 742
Vane Shear Strength 1993
Vane Strength 135
Variable Frequency Drive 2480
Variable Permeability Coefficient 56
Vault Settlement 1076
Velocity Distribution 2903
Velocity Pressure Contours 2954
Ventilation 1238, 2471
Ventilation in Public Catering 2480
Verificarion 3013
Vertical 1860
Vertical Action 1750
Vertical Alignment 2731
Vertical Frozen Soil Wall 738
Vertical Vibration 2890
Vibration 1812, 2055
Vibration Control 156
Vibration Displacement 1212
Vibration Isolation 2978
Vibration Measurement 1088
Vibration Mitigation Measuremen 1088
Vibration Mode 1618
Vibration Response 3021
Vibration under Wind Actions 3066
Vibration Velocity 1212
Vibratory Pile Driving 2272
Virtual City 2760
Virtual GIS 2760
Viscous Damper 1633
Visual Basic 819
Visual Basic(VB) Technology 2616
Visualization 2745, 2765
Visualization Management 3192
VOF Method 1971
Volumetric Joint Count 907
Vulnerability Assessment 2686

## W

Wall Rock 1342
Wall Structure 1092
Warning 778
Warning Thresholds 481
Wastewater 2354, 2367
Water-Bursting Accident 1392
Water Content 148, 201, 552, 684
Water Distribution System 2394
Water Environmental Management 1823
Water Gushing Yield Forecast 1392
Water Inrush 1288
Water Inrush ( Gushing) 1008
Water Level 2015
Water Pressure Head 2023
Water Pumping Station 1874
Water Quality Modelling 2078
Water Quality Monitoring 2713
Water Resources 1906
Water Resources Shortage 1874
Water Supply 2363
Water Supply and Drainage System 2374
Water Supply Network 2389
Water Temperature Change 349
Water Usage 2408
Water Utilization Efficiency 2082
Waterway Conditions 1807
Wave 2198
Wave Absorbing 73
Wave-Attenuating and Oscillation-Inhibiting Device 2170
Wave Force 2202
Wave Kinematics and Pressure Fields 2166

Wavelet-Based Methods 2924, 3013
Weak Form Quadrature Element 380
Wedge Devices 1624
Weight Calculation 2600
Weld 3187
Well-Balanced Roe-Type Scheme 1793
Well Injection Depth Extraction (WIDE) 560
Well-Points Dewatering 440
Wellsite 2206
WGS84 2793
Whole Life Cycle 2421
Wind Angle 3089
Wind Field Characteristics 2958, 3111
Wind-Induce Vibration 2567
Wind Load 2654, 3089
Wind Pressure 3115
Wind Speed 2567, 3115
Wind Tunnel Test 2567
Winged Column 1463
Wire Frame 2983
Working Condition 3034
Working Performance 2063
Working Scheme 2932

## X

X Shaped Flaring Gate Pier 1971
X80 Pipeline Steel Specimen 3026
XFEM 3046
XiangJiaba Hydropower Station 2096

## Y

Y-Eccentric Braced Steel Frames 1449
Yangma Island 2189
Yellow River Water Diversion and Irrigation 2071
Yield 2343
Yield Function 308
Yield Stress Model 231
Yield Surface Rotation 308
Yiliang Earthquake 1426

## Z

Zhengyangmen Gate Tower 1212
Zhuangke 1658

# Authors Index


## A

Abdalhi, M.A.M. 2343
Achour, B. 1828
Aguado, A. 2213
Ai, Z.D. 3034
Akimov, P.A. 2898, 2924, 3013
An, H.W. 3034
An, J. 2616
An, Y.N. 2206
An, Z.T. 689
Andreev, V.I. 812, 2974
Andrianov, A. 2398
Arai, K. 338
Aslami, M. 2924, 3013
Averkeev, I. 2384
Avershyev, A.S. 812, 2974

## B

Ba, D.H. 870
Bai, C.X. 655
Bai, C.Z. 450
Bai, D.C. 665
Bai, H. 296
Bai, L. 2457
Bai, R.Q. 729
Bai, Y. 1112, 1352, 2583, 2702
Bakri, M. 424
Bao, J.T. 2675
Bao, L.S. 2220
Bao, X.K. 539, 1223
Bedjaoui, A. 1828
Bei, D. 2970
Belyaev, V. 3227
Berrah, M. 1570
Bian, S.F. 2793
Bian, Y. 1704
Brodsky, V.I. 2253, 2294

## C

Cai, B. 1311
Cai, G.T. 1264
Cai, L.L. 1327
Cai, L.M. 3083
Cai, P.L. 213, 1412
Cai, S.B. 494
Cai, Z.Y. 355
Cao, D.J. 2654
Cao, H.Q. 2266
Cao, L.J. 1134, 1408
Cao, P.Z. 1449
Cao, R.S. 3089
Cao, X.F. 1928
Cao, Y. 1755
Cao, Z.W. 2299
Cavalaro, S. 2213
Chelyshkov, P. 3231
Chen, B.Y. 3098
Chen, C. 835
Chen, C.L. 923
Chen, C.X. 324, 334, 897, 2513
Chen, D.B. 1426
Chen, F.J. 3071
Chen, G.F. 1138
Chen, G.J. 3021
Chen, G.P. 2154, 3057
Chen, G.R. 250
Chen, G.X. 1382, 3196
Chen, G.Y. 316
Chen, H. 767
Chen, H.D. 113
Chen, H.M. 409
Chen, H.W. 2082
Chen, J. 1029, 1033, 1342, 2134, 2181, 2475, 2554
Chen, J.F. 987
Chen, J.P. 875
Chen, J.W. 1443
Chen, J.X. 572
Chen, J.Y. 308, 2092
Chen, K.L. 1001
Chen, K.M. 1402
Chen, K.S. 1127
Chen, L. 1232, 2272
Chen, M. 3183
Chen, Q. 977
Chen, Q.C. 1953
Chen, S.G. 1072

Chen, S.J. 879
Chen, S.L. 787
Chen, S.M. 2037
Chen, S.Z. 1377
Chen, T. 28, 2475
Chen, T.L. 935, 2071
Chen, W. 113, 1024, 1458
Chen, W.H. 1212
Chen, W.K. 2679
Chen, W.Q. 2769
Chen, X. 679, 2363
Chen, X.C. 1515, 2589
Chen, X.D. 2717
Chen, X.F. 2316
Chen, X.H. 2045
Chen, X.M. 1564, 3127
Chen, X.Q. 1946, 2029
Chen, X.Z. 3154
Chen, Y. 705, 1591, 3149
Chen, Y.F. 1923
Chen, Y.N. 738
Chen, Y.X. 148
Chen, Z. 490, 991, 2343
Chen, Z.J. 760
Chen, Z.K. 180
Cheng, J. 2370
Cheng, L.J. 3042
Cheng, M.L. 1910
Cheng, P. 2316
Cheng, S. 3223
Cheng, S.T. 2727
Cheng, W. 2928
Cheng, W.Q. 268, 883
Cheng, X.B. 1918
Cheng, X.F. 2170
Cheng, Z.L. 684
Chu, F.Y. 1852
Chulkov, V. 2281
Chung, K.J. 1555
Craifaleanu, I.G. 1600
Cui, H.d. 2023
Cui, H.T. 2903
Cui, J. 2765, 2838
Cui, J.B. 1358
Cui, J.J. 2805
Cui, K. 460
Cui, N. 2447
Cui, P.B. 1112
Cui, Q.H. 755
Cui, W.J. 2266
Cui, X.M. 2805
Cui, X.X. 2277
Cui, Z.K. 1708

## D

Dai, H.B. 2745
Dai, H.D. 962
Dai, H.S. 697
Dai, J.W. 1676
Dai, X.X. 3208
Dai, Y.J. 1293
Dai, Z.H. 3046
Dang, X.Y. 1024
de Freitas Neto, O. 659
de la Fuente, A. 2213
Deng, J.D. 1430
Deng, J.W. 3079
Deng, K.Y. 3079
Deng, L. 2374
Deng, N. 2567
Deng, S.C. 1633
Deng, S.N. 791
Deng, Y.E. 893
Deng, Y.L. 1704
Di, S.J. 264, 268, 883
Dimane, F. 123
Ding, H. 2708
Ding, H.X. 1812
Ding, K.W. 24
Ding, R. 3071
Ding, Z.W. 1759
Dong, E.Z. 3219
Dong, F.L. 2350, 2774
Dong, G.H. 524
Dong, M. 2150
Dong, Q. 3163
Dong, T.X. 2484
Dong, X. 1347
Dong, X.M. 2115
Dong, X.Y. 556
Dong, Y. 746
Dong, Y.B. 324
Doroshenko, A. 3231
Dou, L.J. 2579
Dou, X.P. 2015
Du, H.B. 1458

Du, J. 376
Du, W.B. 268
Du, W.H. 614
Du, X.L. 175
Du, Z.H. 2461
Duan, H.R. 2828
Duan, J. 1564, 3127
Duan, X.S. 1746
Duan, Y. 1961

## E

Ekaterina, A. 320
El Alami, Z. 1581
El Ghoulbzouri, A. 1581
El Hannoudi, S. 1581
Elleithy, W. 2936, 2943

## F

Fachratov, M. 2281
Fan, B.B. 1506, 1771
Fang, G.K. 596
Fang, L. 2801
Fang, R. 767
Fang, S.W. 3051
Fang, X.W. 359
Fang, Y. 2524
Fang, Y.Y. 3089
Feng, B.B. 371
Feng, H. 338
Feng, H.L. 364
Feng, J.G. 1846
Feng, M.Y. 1288
Feng, T.G. 195
Feng, W.X. 2421
Feng, X. 1799
Feng, X.G. 2833
Feng, Y. 499, 2488
Feng, Y.J. 2589
Feng, Y.Q. 209, 401, 742
Feng, Z. 469
Feng, Z.H. 947
Fu, C.J. 3038
Fu, D. 2055
Fu, D.C. 2962
Fu, H. 334, 1846
Fu, J.B. 760
Fu, S.D. 2082
Fu, X.C. 1092
Fu, X.Q. 2713
Fu, X.Y. 705
Fu, Y.Z. 2432

## G

Gan, D.Q. 835
Gan, P.L. 560, 1076
Gao, B. 983, 1061
Gao, C.Y. 509, 1203
Gao, G.Q. 750
Gao, J.Y. 148
Gao, L.B. 2848
Gao, P. 2063, 2760
Gao, Q. 870, 2457
Gao, Q.C. 509
Gao, R. 954, 2177
Gao, S. 1591
Gao, T. 2502
Gao, T.Y. 2890
Gao, X.J. 109
Gao, X.L. 469
Gao, Y.W. 3144
Gao, Y.Y. 420
Gao, Z.H. 1940, 2457
Gao, Z.M. 1364
Gazaryan, R. 2281
Ge, H. 1893
Geng, B.L. 2198
Geng, D.Q. 2970
Geng, D.Y. 1134, 1203, 1408
Geng, P.F. 1143
Gogina, E. 2367
Gogina, E.S. 2354
Gong, C.Z. 432
Gong, H.L. 1823
Gong, L.F. 2583, 2702
Gong, L.Y. 1443
Gong, Q.Q. 1708
Gong, W.M. 693
Gong, Z.G. 2063
Grigoryeva, L.S. 2253, 2294
Gu, J.B. 34
Gu, Q. 1449
Gu, X.J. 711, 3003, 3223
Guan, C.M. 2007
Guan, L.K. 3093
Guan, M.S. 1458
Guan, Q. 2539

Guan, Q.H. 1946, 2029
Guan, W. 1932
Gui, F.R. 2789, 2797
Gui, Y.X. 1081
Gulshin, I. 2367
Guo, B.L. 440
Guo, C. 38, 2220
Guo, C.H. 1932
Guo, F.H. 409
Guo, G.J. 287
Guo, H. 1184
Guo, J.H. 1618
Guo, J.L. 958
Guo, J.Q. 1212
Guo, J.Y. 2756
Guo, N. 1327
Guo, P. 1212
Guo, W.D. 1143
Guo, W.N. 1696, 3026
Guo, X. 1463
Guo, Y. 2518
Guo, Y.C. 572
Gutiu, S.I. 2332

## H

Hadid, M. 1570
Hai, Y. 308
Han, B. 2694
Han, C.X. 679
Han, F. 3021
Han, H. 89
Han, H.Q. 1846
Han, J.Q. 1842
Han, J.Y. 532
Han, L.T. 2756
Han, M.M. 2545
Han, Q.B. 3098
Han, S.Y. 2120
Han, W.F. 371
Han, Y. 250
Han, Z.Q. 641
Hanafi, I. 123
Hao, B.H. 3196
Hao, L. 445
Hao, W. 3115
Hao, X.H. 1874, 2115
Hao, X.Y. 1335
Hao, Y.G. 2865
Hao, Z.J. 2554
He, C.L. 432
He, F.D. 1928
He, H. 544
He, J. 907, 1138, 1807, 1989, 2146
He, J.L. 2074
He, K. 923
He, L.P. 3030
He, P. 1273
He, Q.M. 1700
He, S.Y. 1024
He, T.Y. 962
He, X. 1042, 2731
He, X.R. 2495
He, Y. 3, 296
He, Y.Q. 701
He, Z.M. 827
Hezza Azahar, S.A. 2078
Hong, H.L. 912
Hong, M. 1138
Hong, S.R. 3149
Hong, X.F. 113
Hou, J.F. 1342
Hou, S.S. 2694
Hou, S.W. 175
Hou, X.K. 927
Hu, C.J. 1477
Hu, C.Q. 420
Hu, G. 2533
Hu, G.J. 3046
Hu, H. 180
Hu, H.H. 2466
Hu, H.Y. 73, 879
Hu, J. 738
Hu, J.C. 148
Hu, L. 2000
Hu, L.W. 1001
Hu, Q.G. 827
Hu, S.J. 1264
Hu, W. 1481
Hu, X.X. 524, 2612
Hu, Y.B. 1649
Hu, Y.X. 1358
Hua, C. 2679
Hua, X. 610, 1742
Huang, C. 2328
Huang, C.C. 2801
Huang, C.L. 1742
Huang, G.Q. 1734

Huang, H. 991, 2166
Huang, H.X. 1207
Huang, J.S. 1398
Huang, J.W. 1823, 2029, 2082
Huang, L.D. 2740
Huang, M.Y. 1555
Huang, P.L. 324, 897
Huang, S.Q. 1249
Huang, T. 693
Huang, X. 405
Huang, X.F. 185
Huang, X.J. 2124, 2129
Huang, Y.D. 93
Huang, Y.S. 464, 3106
Huang, Y.Y. 2045
Huang, Z.M. 73
Huang, Z.Q. 2071
Huang, Z.Z. 544
Hui, C. 2415

## J

Ji, B.F. 2954, 2958, 3111
Ji, H.G. 606
Ji, J.B. 1521, 1538, 3187
Ji, W. 2050
Ji, Y.C. 455
Jia, C.G. 2996
Jia, D.D. 3007
Jia, L.G. 1786
Jia, L.L. 1218
Jia, N. 723
Jiang, B. 1096, 2124, 2129
Jiang, B.S. 738
Jiang, H.F. 2872
Jiang, J.L. 1624
Jiang, J.Z. 1463, 2903
Jiang, L. 219, 2141
Jiang, L.M. 445
Jiang, L.T. 2828
Jiang, P. 1238
Jiang, S.H. 3051
Jiang, S.K. 2285
Jiang, S.P. 1008
Jiang, S.Y. 2842
Jiang, W. 1662
Jiang, W.X. 1528
Jiang, X.Q. 3138
Jiang, Y. 746
Jiang, Y.D. 841
Jiang, Y.J. 238
Jiang, Y.Z. 958, 2990
Jiao, Z.X. 2015
Jie, L. 1419
Jin, C.Y. 2011
Jin, J.Y. 2019
Jin, L. 755, 1595
Jin, Q. 1696, 1786, 3026
Jing, X.H. 1092
Ju, H.Y. 750
Ju, J.W. 243
Ju, P. 3219

## K

Kang, B. 1629
Kang, G.C. 1511
Kang, Z.M. 1932
Kasa, A. 566
Kazaryan, R. 2281
Kolesnikov, A.G. 3062
Kong, D.H. 819
Kong, J. 1364, 2554
Kong, K. 1985
Kong, Q.L. 2756
Kong, X.S. 1352
Kong, Y. 185
Kong, Y.F. 1293
Kong, Y.W. 2408
Kou, X.T. 1551
Kuda, F. 2346
Kung, G.T.C. 391
Kyzina, O. 2281

## L

Lai, X.J. 2461
Lang, S.F. 2441
Lang, X.J. 2654
Latyshev, K. 3204
Lee, T.Y. 1555
Lei, F. 1704
Lei, H. 3093
Lei, J.S. 1624
Leng, X.L. 1042
Leong, L.T. 2936, 2943
Li, A. 2694

Li, A.G. 2475
Li, A.L. 1718
Li, B. 238, 1283, 1467, 2082, 3115
Li, C. 797, 1105, 1953, 2299, 2805, 3030
Li, C.F. 1426
Li, C.H. 359
Li, C.J. 469
Li, C.L. 1545
Li, D. 349, 450, 455
Li, D.H. 224, 3234
Li, F.F. 1521
Li, F.L. 1803, 1946
Li, G.F. 376
Li, G.L. 2166, 2883, 2948
Li, G.P. 1723
Li, H. 935, 1486, 2120, 2735, 2760
Li, H.F. 966, 2063
Li, H.J. 2475
Li, H.L. 2277
Li, H.N. 1639
Li, H.P. 940, 971, 2793
Li, H.W. 585
Li, H.X. 89, 596
Li, J. 518, 1188, 1192, 2092, 2206, 3171, 3175
Li, J.C. 2853
Li, J.F. 1352
Li, J.H. 750
Li, J.J. 1100
Li, J.L. 1398
Li, J.W. 1088
Li, J.Y. 2518
Li, K. 1184
Li, K.G. 1268
Li, L. 524, 1506, 1771, 2185
Li, L.C. 1315
Li, L.J. 2805
Li, L.Q. 679, 1842
Li, M. 819, 1729, 2731, 2833
Li, M.C. 2189
Li, M.Y. 56
Li, N. 1521
Li, P. 78, 143, 927
Li, P.B. 1138
Li, P.F. 2324
Li, P.L. 2853
Li, Q. 733, 2735, 3192, 3215
Li, R. 2920, 3158
Li, R.B. 912
Li, R.J. 1065, 1081, 1197
Li, R.S. 1197, 1559
Li, S. 774
Li, S.C. 1297, 2916
Li, S.L. 701
Li, S.Q. 2583, 2702
Li, S.X. 1793
Li, T. 589, 962
Li, T.L. 927
Li, T.Q. 1645
Li, T.T. 2550
Li, W. 268
Li, W.B. 395, 2686
Li, W.J. 180
Li, W.Q. 1382
Li, X. 1435, 1467
Li, X.G. 2475
Li, X.H. 386, 420
Li, X.J. 875, 1499, 1521
Li, X.L. 1227
Li, X.R. 606
Li, X.S. 3158
Li, X.W. 674, 887
Li, X.X. 1268, 2717
Li, Y. 380, 1860, 2041
Li, Y.G. 1564, 3127
Li, Y.H. 2756
Li, Y.J. 767
Li, Y.L. 1402
Li, Y.M. 1629, 2996
Li, Y.N. 1105, 2441
Li, Y.Q. 1700
Li, Y.S. 851
Li, Y.Z. 1463, 1490
Li, Z. 544, 1051
Li, Z.H. 912
Li, Z.L. 2567
Li, Z.M. 2793

Li, Z.Q. 1051
Lian, J.Y. 1511
Liang, A.H. 56
Liang, B. 1024, 2545, 2879, 2920
Liang, D.Q. 316
Liang, G.Q. 1993
Liang, H.A. 879
Liang, L.J. 1223, 2328
Liang, L.L. 2990
Liang, R.Q. 2890, 2970
Liang, S. 1168
Liang, S.S. 2600
Liang, X.L. 3208
Liang, Y. 1321
Liang, Y.D. 1463
Liao, J. 464, 3106
Liao, L. 2213
Liao, Q.L. 1065
Liao, W.Y. 679
Liao, Y. 797
Lin, G.R. 2508
Lin, H. 1471, 1645
Lin, J.H. 1439
Lin, J.J. 1430
Lin, J.Q. 791
Lin, L. 2029
Lin, M.J. 2289, 2471
Lin, S.S. 623
Lin, Z. 1426
Lin, Z.L. 3219
Ling, H. 1846
Liu, A.M. 256
Liu, A.R. 1430
Liu, B. 118, 2554
Liu, C. 1692
Liu, C.L. 1971
Liu, C.R. 514, 2447
Liu, C.X. 401, 623
Liu, D. 1653
Liu, D.D. 2045
Liu, D.P. 191
Liu, F.C. 1013
Liu, F.J. 987, 2336
Liu, G.B. 135
Liu, G.M. 1680
Liu, H. 395, 1105
Liu, H.B. 440, 619, 1961
Liu, H.H. 1223
Liu, H.M. 1750
Liu, H.T. 395
Liu, H.Y. 919
Liu, I.T. 2727
Liu, J. 524, 1081, 1347, 1352, 2029
Liu, J.B. 2865
Liu, J.C. 2050
Liu, J.H. 1148
Liu, J.J. 1718
Liu, J.M. 2894, 2912, 2966
Liu, J.P. 2350, 2774
Liu, J.Q. 851
Liu, J.X. 2833
Liu, J.Y. 474, 494
Liu, K. 962
Liu, L. 2224, 2228, 2232, 2235, 3071
Liu, L.P. 1718, 2996
Liu, L.S. 1056
Liu, L.X. 1658
Liu, M. 1105
Liu, P. 705
Liu, Q. 2622, 2628, 2635
Liu, Q.G. 2903
Liu, Q.Q. 2471
Liu, R. 1574
Liu, R.C. 238
Liu, S. 2828, 2894, 2912, 2966
Liu, S.L. 750, 2528
Liu, S.Y. 778
Liu, T. 474
Liu, W. 556
Liu, W.D. 2518
Liu, W.L. 1870, 1878
Liu, W.N. 1013
Liu, X. 28, 450, 455, 1883, 1966, 2320, 2675, 3075
Liu, X.D. 1293, 1347
Liu, X.F. 1878, 1888
Liu, X.H. 623
Liu, X.L. 68, 2865
Liu, X.M. 324, 897, 2513
Liu, X.W. 2879, 2920

Liu, X.Y. 2824
Liu, Y. 474, 494, 774, 1975, 2452, 2457
Liu, Y.F. 329, 1856
Liu, Y.H. 2374, 2769
Liu, Y.J. 1331, 2389, 2717
Liu, Y.L. 532
Liu, Y.N. 2224, 2228, 2232, 2235
Liu, Y.R. 2103
Liu, Y.S. 556
Liu, Y.W. 1639
Liu, Z. 1273
Liu, Z.J. 1249
Liu, Z.Q. 1358
Liu, Z.R. 302
Liu, Z.T. 947
Liu, Z.W. 1515
Liu, Z.X. 1649
Long, S.C. 2928
Lou, N. 2266
Lou, Q.X. 2518
Lu, C.Y. 371
Lu, F. 1932
Lu, G.R. 129
Lu, G.S. 2092
Lu, H.J. 835
Lu, L. 338, 415
Lu, L.Y. 2649
Lu, M. 1499, 1667
Lu, M.Q. 1618
Lu, Q.R. 879
Lu, S.J. 113
Lu, S.L. 711
Lu, S.Q. 847
Lu, X.L. 733
Lu, X.W. 2667
Lu, Y.J. 3007
Lu, Z.R. 38
Luan, T.T. 2600
Lukashevich, A. 2932
Luo, C.T. 750
Luo, F.Z. 2528
Luo, G.C. 827
Luo, J.H. 1279
Luo, M.L. 243
Luo, P.F. 715, 723
Luo, W.T. 2103
Luo, W.X. 1624
Luo, X. 827
Lv, B. 109, 1793
Lv, H. 1812
Lv, J.Y. 1197, 1335
Lv, N. 919
Lv, T.Z. 2441
Lv, Y.X. 2124, 2129

## M

Ma, D.F. 287
Ma, D.L. 2765, 2838
Ma, F.H. 1243
Ma, F.J. 1692
Ma, H.F. 2907
Ma, H.W. 1232
Ma, J.J. 2765
Ma, Q. 169
Ma, S.Y. 2550
Ma, W.Q. 1471
Ma, X.C. 2589
Ma, X.Y. 2350
Ma, Y. 1786
Ma, Y.D. 1168
Ma, Z.F. 2508
Maksotovna, N.L. 98
Man, K. 966
Mao, W.F. 819
Mao, Z.J. 191
Mata Cabrera, F. 123
Mehiaoui Hadjebar, M.Y. 1570
Mei, F.L. 2883, 2948
Meng, F.B. 1545
Meng, X.H. 1782
Meng, Z.B. 1755
Mi, H.J. 2421
Mi, H.Z. 329
Miao, Q.Q. 1008
Min, Z.H. 2108
Mo, J.Y. 3021
Moga, C. 2332
Mohamed Elamin, A.E. 2078
Mohamed, T. 566
Mondrus, V. 2978
Mouse, G.J. 2103
Mozgaleva, M.L. 2898
Muhammad, S.A. 2078

## N

Nemova, D.V. 2308
Nguyen, T. 3
Nie, M.Y. 2713
Nie, X.B. 2518
Nikitin, K.E. 3017
Nikolaevich, B.A. 98
Ning, C. 1096, 1613
Ning, Q.C. 2185, 2202
Niu, J.G. 509, 1203
Niu, J.L. 651
Niu, J.T. 1860
Niu, M.H. 1981
Niu, R.Q. 2658
Niu, Y.F. 1767
Niu, Z.L. 1398

## O

Oleinik, P.P. 2253, 2294
Orlov, V. 2384, 2398
Othman, F. 2078
Ou, X.Y. 1763
Ou, Z. 334

## P

Pan, B. 857
Pan, G.B. 1024
Pan, X.N. 3083
Pan, Y.S. 2572
Pan, Z.Z. 2466
Pang, C.R. 1258
Pang, L.Y. 866
Pei, L. 1515
Pei, X.B. 2983
Pei, Y.B. 499
Peng, C.X. 73
Peng, H. 2363
Peng, J.H. 1369
Peng, L.L. 1734
Peng, L.Q. 2272
Peng, P.Y. 2903
Peng, Q.D. 1953
Peng, W.T. 791
Peng, X. 893
Peng, Y. 1148
Peng, Z.M. 2471
Petrichenko, M. 2308
Pham, D. 3
Proske, Z. 2346
Pu, H.K. 1174, 3179

## Q

Qi, H. 1564, 3083, 3127
Qi, Y.B. 1398
Qi, Z.S. 2457
Qian, J.L. 1923
Qian, R.J. 3051
Qian, Y.M. 152
Qiao, D.P. 231
Qiao, G.D. 1755
Qiao, W. 1680
Qin, L. 2019
Qin, W. 1321
Qin, Y.Z. 977
Qiu, C. 1971
Qiu, D.D. 2658
Qiu, D.H. 1297
Qiu, Q.C. 589
Qiu, S. 180, 1633
Qiu, Z.Z. 2150
Qu, J.H. 175
Qu, S.Y. 1545
Que, M.H. 539

## R

Ran, A. 445
Ren, Q.G. 3098
Ren, Y.H. 1331
Rozin, L. 2932
Ruan, B.Q. 1856
Ruan, H.N. 243
Ruan, J.L. 2394
Ruan, L.F. 1306
Ruan, Y.K. 819
Ruzhitskaya, O.A. 2354

## S

Santos Jr, O. 659
Sedov, A. 3231
Severo, R. 659
Sha, C. 674
Shan, M.L. 3098
Shan, R.C. 1676

Shan, R.L. 1065, 1081, 1197, 1335, 1352, 1729
Shan, R.X. 940
Shan, Z.G. 264
Shang, F. 1347
Shang, Q. 344
Shao, A.L. 364
Shao, J.W. 2350, 2774
Shao, J.Y. 2239, 2244
Shao, X.X. 705
Shao, X.Y. 655
Shao, Y. 552
She, Y.H. 156
Shen, C. 3234
Shen, C.N. 359
Shen, F.M. 1238
Shen, H.R. 1249
Shen, Q. 3071
Shen, W.M. 1076
Shen, Y. 614, 1723
Shen, Y.H. 1148
Shi, C.G. 260
Shi, C.Z. 1975, 2000
Shi, H.T. 2954, 2958, 3111
Shi, L.P. 1989
Shi, M.Y. 805
Shi, R.J. 1449
Shi, Y. 2185, 2202
Shi, Y.N. 1658
Shilkina, S. 2480
Shiu, R.J. 2727
Shu, B. 1369
Shu, S.H. 2394
Shui, Y.B. 2735
Si, Y.N. 2374
Smirnov, V. 2978
Song, A.D. 835
Song, C.L. 606
Song, F.G. 805
Song, G. 883
Song, H.D. 349
Song, J. 2916
Song, L.L. 1538
Song, L.Y. 2495, 2502
Song, P. 2824
Song, Q. 1212
Song, Q.F. 2206
Song, R.X. 273
Song, T. 2649
Song, T.J. 875
Song, T.S. 1533
Song, T.Y. 1723
Song, Y.C. 1153
Song, Y.R. 1138
Song, Y.W. 1197, 1352
Song, Y.Y. 2015, 2037
Song, Z.C. 1940
Staritcyna, A.A. 2308
Stupishin, L.U. 3017, 3062
Su, H.F. 1013
Su, J.K. 1105
Su, J.S. 1494
Su, L.Y. 105, 632
Su, Q. 296
Su, Y. 1604
Su, Y.P. 1443
Su, Y.W. 1734
Su, Z.B. 1388
Sun, C. 774
Sun, C.M. 2782
Sun, C.Z. 2671
Sun, F.J. 3066
Sun, G.S. 1692
Sun, G.T. 2824
Sun, H.X. 787
Sun, J.L. 2033
Sun, L.H. 887, 2518
Sun, L.J. 1538
Sun, L.S. 2708
Sun, M.S. 1545
Sun, Q.J. 302
Sun, Q.Q. 3003
Sun, S.G. 755
Sun, S.N. 1388
Sun, S.Z. 2324
Sun, W. 2041
Sun, W.B. 746
Sun, X.H. 715, 723
Sun, Y. 1746, 2567, 2958, 3111
Sun, Y.B. 1288
Sun, Y.J. 1989, 2146
Sun, Y.S. 782
Sun, Y.Z. 2966
Sun, Z.H. 1910
Sun, Z.J. 997
Sun, Z.Y. 1786, 3026
Suo, F.F. 2336

## T

Tan, C.Y. 2466
Tan, L.J. 1127
Tan, M.X. 619
Tan, M.Z. 1718
Tan, P.Y. 1528
Tan, X.R. 1218
Tang, A.J. 260
Tang, D.W. 1932
Tang, J. 1712
Tang, L.X. 665, 689
Tang, S.L. 887
Tang, T.C. 958
Tang, X.S. 1419
Tang, X.W. 560, 1076
Tang, Y. 2029
Tang, Y.B. 3098
Tang, Y.G. 391
Tang, Z. 2572
Tao, W. 1729, 2415
Tao, X.X. 1662, 1750
Tao, X.Y. 2041
Tarasova, D.S. 2308
Teichmann, M. 2346
Tejero Manzanares, J. 123
Ti, W.P. 2853
Tian, C.J. 1946
Tian, G.F. 1232
Tian, L. 1335, 1347, 2654
Tian, M. 1426
Tian, S.W. 1412
Tian, Z.C. 1331
Tian, Z.Y. 386
Tong, J.X. 715, 723
Trusov, A. 2480
Tuo, L. 1100

## V

Volkov, A. 2281, 3204, 3231
Vu, A. 3

## W

Wang, A.M. 935, 2071
Wang, B. 1729, 2224, 2228, 2232, 2235, 2320, 2415, 2675, 3075
Wang, C. 636, 1398, 1687, 2860
Wang, C.F. 1662
Wang, C.H. 1918
Wang, C.T. 1812, 1897, 2810, 2815
Wang, C.Y. 641
Wang, D. 243, 2239, 2370
Wang, D.B. 1435, 1467
Wang, D.K. 2019
Wang, D.Z. 1676
Wang, E.H. 445
Wang, E.Y. 1358
Wang, F. 1613, 2103
Wang, F.M. 1227
Wang, G. 1932, 2558
Wang, G.H. 1874
Wang, G.L. 2194
Wang, G.S. 78
Wang, G.Y. 782
Wang, H. 143
Wang, H.B. 129, 424, 1574
Wang, H.Q. 2466
Wang, H.Y. 560, 1076
Wang, J. 93, 191, 213, 589, 862, 1412
Wang, J.B. 2810, 2815
Wang, J.C. 641, 2224, 2228, 2232, 2235
Wang, J.H. 260
Wang, J.J. 1494
Wang, J.K. 1538
Wang, J.L. 2023, 2708
Wang, J.P. 2642, 2646
Wang, J.T. 801
Wang, J.Y. 1750
Wang, K. 436, 481, 486
Wang, K.Y. 579
Wang, L. 359, 610, 623, 1604, 2801, 2962, 3089
Wang, L.C. 2694
Wang, L.L. 83
Wang, L.Q. 250

Wang, M.M. 2466
Wang, M.S. 17
Wang, N.Q. 68
Wang, P. 1143, 3208
Wang, Q. 1645, 1786, 2805
Wang, Q.H. 2488
Wang, Q.J. 38
Wang, Q.P. 655
Wang, Q.T. 68
Wang, R. 1321
Wang, R.F. 579
Wang, R.H. 958, 2488
Wang, R.L. 1342
Wang, R.X. 1116
Wang, S. 835, 1207, 1511
Wang, S.C. 2907
Wang, S.F. 2441
Wang, S.Y. 2838
Wang, T. 2828
Wang, W. 386, 2272, 2579
Wang, W.C. 1331
Wang, W.J. 160
Wang, W.N. 2894
Wang, W.S. 585
Wang, X. 1981, 2708
Wang, X.B. 3167
Wang, X.G. 61
Wang, X.H. 2389
Wang, X.J. 2096
Wang, X.L. 376, 1595
Wang, X.M. 746, 2134, 2181
Wang, X.Q. 464, 1311, 2120, 3106
Wang, X.W. 1477
Wang, X.Y. 1746
Wang, Y. 260, 669, 684, 954, 1649, 2177, 2189, 2257, 2428, 2722
Wang, Y.F. 355, 636
Wang, Y.G. 2731
Wang, Y.H. 1092
Wang, Y.L. 165, 278, 684
Wang, Y.M. 919
Wang, Y.Q. 1729, 2415
Wang, Y.W. 596
Wang, Y.X. 1687
Wang, Z. 2380, 2389
Wang, Z.D. 445
Wang, Z.G. 2928
Wang, Z.J. 338, 415, 778
Wang, Z.L. 1188, 1192
Wang, Z.Y. 2447
Wei, G. 1001
Wei, H.B. 291, 1122
Wei, H.Y. 1993
Wei, J.C. 2502
Wei, K. 1153
Wei, L. 2663
Wei, L.F. 1335
Wei, Q.C. 1174, 3179
Wei, X.B. 2045
Wei, Y. 552
Wei, Z.H. 17
Wen, H. 1901
Wen, R.Z. 1533
Wen, X. 1258
Wen, Y.H. 2962
Wu, D.X. 2023
Wu, F.M. 1065
Wu, F.W. 28
Wu, H.G. 1975, 2000, 2055
Wu, J. 1238
Wu, J.B. 1112
Wu, J.L. 907
Wu, J.P. 2907
Wu, L. 1112, 1712, 2316
Wu, L.L. 1729
Wu, L.M. 778
Wu, M. 651
Wu, Q.X. 1232
Wu, R.X. 2671
Wu, S. 1105, 2550
Wu, S.S. 1511
Wu, W. 1816
Wu, W.Z. 831
Wu, X.G. 870
Wu, X.J. 1906
Wu, Y. 701, 1301
Wu, Y.H. 1458
Wu, Y.P. 2810, 2815
Wu, Y.Q. 1649
Wu, Y.Y. 1708
Wu, Y.Z. 2954, 2958, 3111

Wu, Z.W. 1024

## X

Xi, J.Y. 1347
Xi, P.S. 118
Xia, G.X. 2202
Xia, H.L. 2996
Xia, J.T. 1249
Xia, K.Z. 324, 897, 2513
Xia, X.X. 2257
Xia, Y. 2088
Xia, Y.Y. 424
Xian, L.N. 1763
Xiang, D. 2041
Xiang, T. 113
Xiao, B. 344, 2108
Xiao, G.F. 3138
Xiao, Y.H. 1335
Xiao, Z.R. 9
Xie, A.Y. 3144
Xie, B.H. 1897
Xie, C.C. 1856
Xie, F.D. 1297
Xie, H. 1029, 1033
Xie, H.L. 2508
Xie, H.P. 841
Xie, H.T. 1283
Xie, H.Y. 316
Xie, J. 1692
Xie, L.L. 1533
Xie, Q.C. 1528
Xie, W.W. 2432
Xie, X.F. 532
Xie, X.M. 312
Xie, X.Y. 2820
Xie, Y.H. 2000
Xie, Z.H. 2600
Xin, C.L. 983, 1061
Xin, Y. 78, 143
Xing, J.H. 1667
Xing, L. 532
Xing, M. 1315
Xing, W.Z. 552
Xing, X.L. 927
Xing, Y.Y. 1254
Xiong, W. 1490
Xiong, Z.W. 3208
Xiu, Y. 1985
Xu, B.B. 56
Xu, B.L. 2045
Xu, B.S. 238
Xu, C. 1767, 1786
Xu, C.L. 2285
Xu, C.Y. 2285, 2299
Xu, F. 436, 481, 486
Xu, G.H. 152
Xu, H. 3158
Xu, H.F. 160
Xu, H.L. 1776
Xu, J. 52
Xu, J.Y. 2745
Xu, M. 1392
Xu, M.G. 1759
Xu, M.Y. 2579
Xu, N.X. 2983
Xu, Q. 2092
Xu, S.C. 2011
Xu, S.M. 1528
Xu, W.X. 436, 481
Xu, W.Y. 386
Xu, X. 2550
Xu, X.M. 2502
Xu, X.P. 201
Xu, X.T. 729
Xu, X.Y. 264, 268, 883
Xu, Y. 450, 518, 544, 2686
Xu, Y.H. 2115
Xu, Y.X. 2778, 2782
Xu, Y.Y. 1029, 1033
Xu, Z. 2654
Xu, Z.H. 1981, 1985
Xu, Z.J. 9
Xue, H.J. 1364, 2554
Xue, J.L. 1364
Xue, Q. 68
Xue, X.C. 862
Xue, Y. 2421
Xue, Y.G. 1297
Xun, J.S. 729

## Y

Yan, F.S. 2890, 2970
Yan, G.X. 1816
Yan, J. 3138
Yan, J.Y. 875
Yan, L. 2285, 2299

Yan, M.L. 715, 723
Yan, M.R. 1490
Yan, Q. 1940
Yan, S.W. 760
Yan, X. 2370
Yan, X.C. 3042
Yan, Z.B. 2550
Yan, Z.F. 302
Yan, Z.Y. 2484
Yang, B.S. 185
Yang, C. 195, 1528, 2760
Yang, C.M. 1143
Yang, F. 1153, 2257
Yang, F.L. 3115
Yang, G. 669, 2749
Yang, G.S. 312
Yang, G.Z. 1782
Yang, J. 2154
Yang, J.B. 3115
Yang, J.L. 2912, 2966
Yang, J.S. 1148
Yang, J.W. 2778
Yang, J.Z. 1081
Yang, K. 89
Yang, L. 887
Yang, L.F. 991
Yang, L.Q. 954, 2177
Yang, N.N. 2765
Yang, P. 329
Yang, Q. 1024
Yang, R. 1096
Yang, S. 2628, 2635
Yang, S.F. 2447
Yang, S.S. 1985
Yang, T. 697
Yang, W. 971
Yang, W.X. 1449
Yang, X. 287, 1928, 2185, 2202
Yang, X.H. 28, 191, 715, 723, 1161
Yang, X.Y. 1327
Yang, Y. 460, 1700
Yang, Y.N. 1392
Yang, Y.S. 3163
Yang, Z. 2380
Yang, Z.J. 3034
Yang, Z.Q. 870
Yantsen, O.V. 2354
Yao, K.C. 679
Yao, L.K. 93
Yao, X.L. 1037, 2607
Yao, Y. 2612, 2717
Ye, H. 2380
Ye, H.J. 2694
Ye, J.N. 135
Ye, P. 283
Ye, W. 2189
Ye, Y.T. 2990
Ye, Z.W. 1888
Yi, C. 841
Yi, H.W. 1463
Yi, S. 2954
Yi, Y.N. 755
Yin, C. 3098
Yin, J. 518
Yin, J.P. 1306
Yin, L. 180
Yin, M.L. 962, 1364
Yin, X.L. 2141
Yin, Y.J. 152
Yin, Y.Z. 165, 278
Yin, Z.G. 2050
Yin, Z.J. 1953
Yu, C.Q. 835, 1742
Yu, H.Y. 1528, 1860
Yu, J. 610, 893
Yu, J.Q. 585
Yu, L.J. 1402
Yu, M. 3046
Yu, N. 912
Yu, Q.C. 1430
Yu, Q.X. 1729
Yu, T. 1499
Yu, X. 2320
Yu, X.C. 2686
Yu, X.M. 1134, 1408
Yu, X.Q. 2903
Yu, Y. 1667
Yu, Y.Y. 2088
Yu, Z.L. 684
Yuan, K. 1629
Yuan, T.K. 224
Yuan, W. 1961
Yuan, W.F. 2663
Yuan, X.F. 3051
Yuan, X.M. 1559
Yuan, Z.C. 1116

Yuan, Z.Z. 2622
Yue, C.X. 420
Yue, F. 78
Yue, P.J. 1878
Yue, X.J. 2745

## Z

Z, A. 1662
Zeng, H. 738
Zeng, L. 1708
Zeng, M. 1932
Zeng, W.H. 1897
Zeng, Y. 503
Zeng, Y.J. 2654
Zha, Z.X. 160
Zhai, J.F. 2134, 2181
Zhan, F.L. 283
Zhan, J.H. 797
Zhan, P.Y. 1538
Zhang, B. 1227, 1696, 2033, 2801
Zhang, B.Q. 1178
Zhang, C.H. 201, 2198
Zhang, C.J. 1993
Zhang, C.L. 2380
Zhang, C.M. 2328
Zhang, C.Y. 2249
Zhang, D. 689, 2380
Zhang, D.D. 1799
Zhang, D.L. 17
Zhang, D.M. 3066
Zhang, D.P. 1696
Zhang, F.C. 767
Zhang, G. 2303
Zhang, G.J. 1100
Zhang, H. 1435, 1467, 3144
Zhang, H.M. 312
Zhang, H.W. 2103
Zhang, H.Y. 705, 2363
Zhang, J. 715, 1823, 2134, 2181, 3119
Zhang, J.C. 2495
zhang, J.F. 2023
Zhang, J.H. 1435
Zhang, J.J. 1227
Zhang, J.P. 782
Zhang, J.R. 2545
Zhang, J.W. 1019, 1207
Zhang, J.Y. 689, 2272
Zhang, J.Z. 3187
Zhang, K. 787
Zhang, K.X. 912
Zhang, L. 209, 742, 1506, 1771, 2635, 3134, 3187
Zhang, L.H. 1874
Zhang, L.N. 2616
Zhang, L.W. 129
Zhang, L.X. 1860
Zhang, M. 2103
Zhang, M.J. 1658
Zhang, M.L. 1888
Zhang, P.H. 2667
Zhang, Q. 291, 1122, 1392, 2019, 2616
Zhang, Q.Y. 205, 636
Zhang, R.C. 2760
Zhang, S.F. 1249
Zhang, S.H. 2990
Zhang, S.J. 9, 38, 628, 2033
Zhang, S.M. 224, 464, 3106
Zhang, S.Y. 48
Zhang, T.Y. 2447, 2740
Zhang, W. 684, 991, 1624, 2023, 2389, 3057
Zhang, W.H. 835, 903
Zhang, W.M. 405
Zhang, W.Z. 2129
Zhang, X. 1029, 1033, 2082, 2244
Zhang, X.B. 1893, 2124, 3007
Zhang, X.D. 3093
Zhang, X.M. 2667
Zhang, X.N. 3007
Zhang, X.T. 118, 636
Zhang, X.X. 231
Zhang, X.Z. 24, 2015, 2037
Zhang, Y. 316, 601, 1481
Zhang, Y.C. 73
Zhang, Y.F. 175, 450, 1946
Zhang, Y.H. 1481, 3030
Zhang, Y.J. 1746, 3030

Zhang, Y.L. 1515
Zhang, Y.N. 2257
Zhang, Y.S. 219, 857
Zhang, Y.W. 665
Zhang, Y.Y. 903
Zhang, Z. 349, 1860, 2508
Zhang, Z.G. 819, 1037, 1293
Zhang, Z.H. 2890
Zhang, Z.L. 1105
Zhang, Z.P. 3057
Zhang, Z.Q. 2088, 2461
Zhao, B.D. 3075
Zhao, C.H. 1506, 1771
Zhao, C.Y. 2663
Zhao, D.P. 1218
Zhao, D.X. 1494
Zhao, F. 24
Zhao, G. 1609
Zhao, G.T. 1551
Zhao, H.J. 2154
Zhao, H.N. 2671
Zhao, J. 83, 1056, 2907
Zhao, J.B. 349, 455
Zhao, J.H. 291, 1122, 2358
Zhao, K. 1662, 1742
Zhao, L. 1953
Zhao, L.B. 2545
Zhao, M. 1864
Zhao, M.L. 205
Zhao, N. 823
Zhao, Q. 1042
Zhao, W.F. 1335
Zhao, W.H. 296
Zhao, W.J. 1696
Zhao, X.F. 1528
Zhao, X.L. 2088
Zhao, X.S. 2146
Zhao, X.X. 2096
Zhao, Y. 250, 966
Zhao, Y.H. 2262, 2277, 2370
Zhao, Y.M. 1667, 1700
Zhao, Y.N. 2658
Zhao, Y.Q. 3196
Zhao, Y.S. 1283, 1755
Zhao, Y.X. 1767
Zhao, Z.C. 2421
Zhao, Z.M. 2558
Zhen, P.F. 185
Zheng, B. 415
Zheng, C.B. 52
Zheng, G.C. 1776
Zheng, H.P. 2272
Zheng, J.H. 693
Zheng, S.L. 2415
Zheng, T.Q. 962
Zheng, W.F. 601
Zheng, X. 1243
Zheng, X.C. 2324
Zheng, X.M. 2394
Zheng, Y.R. 1419
Zheng, Z. 1823
Zhong, D.W. 3021
Zhong, H.Z. 380
Zhong, J.F. 1192
Zhong, L. 9
Zhou, B.F. 1528, 1533
Zhou, C.B. 296
Zhou, C.L. 1746
Zhou, D.H. 679
Zhou, D.N. 344, 2108
Zhou, F.X. 169, 273
Zhou, G.H. 2475
Zhou, H.P. 1358
Zhou, H.Q. 1127
Zhou, J. 371, 935, 1799
Zhou, M. 2374
Zhou, M.J. 1293
Zhou, M.R. 2713
Zhou, P. 250, 665
Zhou, Q.J. 2063
Zhou, S.F. 1985
Zhou, T.H. 572
Zhou, T.Q. 711, 3003, 3183, 3223
Zhou, T.T. 2749
Zhou, W.Q. 2380
Zhou, X. 3098
Zhou, X.J. 1096
Zhou, X.M. 1864
Zhou, X.Q. 409
Zhou, Y. 3149
Zhou, Y.C. 334, 2513, 3138
Zhou, Y.K. 224
Zhou, Z.D. 287, 1928

Zhou, Z.G. 355
Zhou, Z.L. 1072
Zhou, Z.Y. 2249
Zhu, B. 2694
Zhu, C.P. 3098
Zhu, C.S. 1161
zhu, G.S. 2023, 2220
Zhu, H.G. 841
Zhu, H.H. 1609
Zhu, J.F. 135
Zhu, K.Z. 1279
Zhu, L. 2141
Zhu, L.L. 1893
Zhu, M.X. 432
Zhu, N.L. 1591
Zhu, P. 847
Zhu, Q.Q. 1008
Zhu, W.H. 1742
Zhu, X.J. 2572
Zhu, Y.D. 1807
Zhu, Y.P. 329
Zhu, Y.Y. 738
Zhu, Z.Q. 1633
Zhuang, S. 623
Zhuo, K.H. 224
Zolotova, J. 2403
Zou, Y. 1471
Zuo, X. 1382
Zuo, Y.Z. 684